



VOLUME 1

Edited by Billy L. Edge

Coastal  
Engineering  
1992

Proceedings of the  
twenty-third international conference

*Jane M'Kee Smith*

VOLUME 1

# Coastal Engineering 1992

## Proceedings of the twenty-third international conference

October 4-9, 1992  
Venice, Italy

Conference held under the auspices of the  
Coastal Engineering Research Council of the  
American Society of Civil Engineers

Organized by the Ministry of Public Works and by  
Consiglio Nazionale delle Ricerche (CNR) with support of  
Veneto Region and of Venice local Government and  
co-sponsored by the International Association for  
Hydraulic Research (IAHR), by the Permanent International  
Association of Navigation Congresses (PIANC) and by the  
Associazione di Ingegneria Offshore e Marina (AIOM).

Edited by Billy L. Edge



Published by the  
American Society of Civil Engineers  
345 East 47th Street  
New York, New York 10017-2398



## ABSTRACT

This proceedings contains over 260 papers presented at the 23rd International Conference on Coastal Engineering which was held in Venice, Italy, October 4-9, 1992. The book is divided into seven parts: 1) Characteristics of waves and currents; 2) long waves and storm surges; 3) coastal structures; 4) the Italian coast; 5) coastal processes and sediment transport; 6) coastal, estuarine and environmental problems; and 7) case studies. The individual papers include such topics as the effects of wind, waves, storms and currents as well as the study of sedimentation and beach nourishment. Special emphasis is given to case studies of completed engineering projects. With the inclusion of both theoretical and practical information, these papers provide the civil engineer and related fields with a broad range of information on coastal engineering.

### Library of Congress Cataloging-in-Publication Data

Coastal engineering, 1992 : proceedings of the twenty-third international conference, October 4-9, 1992, Venice, Italy / edited by Billy L. Edge.  
p.cm.

Conference held under the auspices of the Coastal Engineering Research Council of the American Society of Civil Engineers; organized by the Ministry of Public Works and by Consiglio nazionale delle ricerche (CNR) with support of Veneto Region and of Venice local government and co-sponsored by the International Association for Hydraulic Research (IAHR), by the Permanent International Association of Navigation Congresses (PIANC), and by the Associazione di ingegneria offshore e marina (AIOM).

"Twenty-third International Conference on Coastal Engineering"  
— Foreword.

Includes index.

ISBN 0-87262-933-3

1. Coastal engineering—Congresses. 2. Ocean waves—Congresses. I. Edge, Billy L. II. Coastal Engineering Research Council (U.S.) III. International Association of Navigation Congresses. IV. Permanent International Association of Navigation Congresses. V. Associazione di ingegneria offshore e marina.

TC203.5.C618 1993

627'.58—dc20

93-7616

CIP

The Society is not responsible for any statements made or opinions expressed in its publications.

Authorization to photocopy material for internal or personal use under circumstances not falling within the fair use provisions of the Copyright Act is granted by ASCE to libraries and other users registered with the Copyright Clearance Center (CCC) Transactional Reporting Service, provided that the base fee of \$1.00 per article plus \$.15 per page is paid directly to CCC, 27 Congress Street, Salem, MA 01970. The identification for ASCE Books is 0-87262/93.\$1+.15. Requests for special permission or bulk copying should be addressed to Reprinting/Permissions Department.

Copyright © 1993 by the American Society of Civil Engineers,  
All Rights Reserved.

Library of Congress Catalog Card No: 93-7616

ISBN 0-87262-933-3

ISSN 0893-8717

Manufactured in the United States of America.

## FOREWORD

The Twenty-third International Conference on Coastal Engineering was a truly successful Conference. Its success was marked by the culmination of extensive planning and coordination. More than 678 abstracts were submitted for consideration, but only 321 could be accepted for presentation at the Conference. Moreover, owing to mechanical requirements of the printing process to keep the *Proceedings* in three volumes, papers were limited in pages and some contributions which should have been included could not be accepted for the final publication.

The Twenty-third Conference also marked a major milestone in the continuous contribution of Professor Robert L. Wiegel to the organization and conduct of these conferences; at this Conference he announced his retirement from the leadership of the Council. For forty-two years he has been directly involved with every conference since the first conference was held in Long Beach, California. He served as Vice-Chairman of the Council on Wave Research of the Engineering Foundation in the early years of the Conference and later as Chairman of the Coastal Engineering Research Council of the American Society of Civil Engineers. Because of his long and dedicated service and leadership of the coastal engineering community, the Council voted to dedicate the *Proceedings* of the Twenty-third Conference to Professor Robert L. Wiegel.

### *Robert L. Wiegel*

Professor Wiegel is Professor Emeritus of the Department of Civil Engineering of the University of California at Berkeley. He graduated from the University of California at Berkeley in 1943 with a degree in Mechanical Engineering. After serving in the Second World War, he returned to Berkeley where he obtained a Master of Science degree. He stayed on at Berkeley as a Research Engineer and later a Lecturer in Mechanical Engineering until he became a Professor in the Department of Civil Engineering. He subsequently served as Director of the State's Technical Services Program and also as Acting Dean of the College of Engineering. Most of the readers of this volume know many of the 26 Doctoral students he supervised who have gone on to become leaders in this area or one of the many Masters students he prepared to work in the area of coastal engineering. His teaching, research and professional contributions at Berkeley are well known and respected by his peers around the world.

Professor Wiegel has been bestowed many honors and awards in recognition of his outstanding accomplishments. He received the Research Prize from the American Society of Civil Engineers in 1962 and in 1969 he was invited to give the General Lecture at the Symposium to Dedicate the Delft Hydraulics Laboratory Facilities. In 1975, he was elected Member of the National Academy of Engineering. He is currently an Honorary Member and Fellow of the American Society of Civil Engineers and holds an extensive record of service to the Society. In 1977 he was elected to Senior Queens Fellow in Marine Science, Aus-



tralia. He received the Moffatt-Nichol Harbor and Coastal Engineering Award and International Coastal Engineering Award in 1978 and 1985, respectively, from the American Society of Civil Engineers.

During his active professional career, he has served on many boards, panels and commissions of the State of California, the United States, the United Nations, NATO and many individual nations. He has lectured in most countries with coastal resources and problems and many countries without these resources. Professor Wiegel has also been a Visiting Professor to The Polish Academy of Sciences and the University of Cairo. He received the Outstanding Civilian Service Medal from the U.S. Army Corps of Engineers in 1985. Professor Wiegel was the General Chairman and organizer of the *Symposium to Honor Morrrough P. O'Brien: Working Solutions*, which was sponsored by the American Shore and Beach Preservation Association and the Coastal Engineering Research Council, the ASCE Waterway, Port, Coastal and Ocean Engineering Division and the University of California's College of Engineering.

Professor Wiegel has authored more than 125 publications and 100 technical reports on various phases of coastal and ocean engineering, including the famous text *Oceanographical Engineering* which was published in 1964. He is currently the editor for *Shore & Beach*, the Journal of the American Shore and Beach Preservation Association.

Needless to say, it is with pleasure that the writer is able to dedicate the *Proceedings* of the Twenty-third International Conference on Coastal Engineering to Professor Robert L. Wiegel.

Billy L. Edge, Secretary  
Coastal Engineering Research Council  
American Society of Civil Engineers

# ACKNOWLEDGMENTS

## COMMITTEE OF HONOR

The Patriarch of Venice  
The president of Regione Veneto  
The Mayor of Venice  
The Chief of Staff of the Italian Navy  
The President of Magistrato alle Acque  
The Alderman for Culture of Venice  
The Superintendent to the Harbor of Venice  
The President of Cini Foundation  
The President of CNR  
The Minister of Public Works

## LOCAL ORGANIZING COMMITTEE

### Chairman:

Ugo Tomasicchio, Ministry of Public Works

### Organizing Committee:

Giuseppe Matteotti, University of Padua  
Attilio Adami, University of Padua  
Edoardo Benassai, University of Naples  
Fabio Capocaccia, Genoa Port Authority  
Leonardo Sarti, National Assoc. of Civil Engineering Contractors  
Alberto Tomasin, CNR, University of Venice  
Alberto Lamberti, Secretary, University of Bologna

### Scientific Committee:

Enrico Marchi, University of Genoa  
Eco W. Bijker, Delft University of Technology  
Giampaolo Di Silvio, University of Padua  
Hans F. Burcharth, Aalborg University  
Alberto Noli, University of Rome

## COASTAL ENGINEERING RESEARCH COUNCIL (ASCE)

### Chairman:

Robert L. Wiegel

**Vice-Chairman**

Orville T. Magoon

**Secretary:**

Billy L. Edge

**Members:**

Eco W. Bijker

Robert A. Dalrymple

Robert G. Dean

Kyoshi Horikawa

Stephen A. Hughes

J. William Kamphuis

Ronald M. Noble

Thorndike Saville, Jr.

D. Harry Swart

**FINANCIAL SUPPORT**

Almagia S.p.A.

CIR S.p.A.

CogefarImpresit S.p.A.

Consorzio Venezia Nuova

Cooperativa Muratori & Cementisti - C.M.C. - di Ravenna

Estramed S.p.A.

ENEL

Fondedile S.p.A.

Furlanis S.p.A.

Girola S.p.A.

Grassetto S.p.A.

Gruppo Mazzi S.p.A.

ITABO S.p.A.

Lodigiani S.p.A.

Recchi S.p.A.

S.A.I.L.E.M. S.p.A.

S.A.P.I.R. S.p.A.

Ing. Giuseppe Sarti & C.S.p.A.

Societa Italiana Condotte D'acqua S.p.A.

Impresa ing. Sparaco Spartaco S.p.A.

Todini Costruzioni S.p.A.

Torno S.p.A.



# CONTENTS

WELCOME ADDRESS.....	1
<i>Ugo Tomasicchio</i>	
COASTAL ENGINEERING IN VENICE.....	4
<i>Enrico Marchi</i>	
A DESCRIPTION OF THE “ACQUA ALTA” EVENT ON 5TH OCTOBER.....	3496
<i>Organizing Committee</i>	

## PART I

### CHARACTERISTICS OF COASTAL WAVES AND CURRENTS

Chapter 1	
BREAKING WAVES PROPAGATING OVER A SHOAL.....	42
<i>J. A. Battjes, S. Beji</i>	
Chapter 2	
TRANSFORMATION OF NONBREAKING WAVES OVER A BAR.....	51
<i>S. Beji, T. Ohyama, J. A. Battjes, K. Nadaoka</i>	
Chapter 3	
PRACTICAL COMPARATIVE PERFORMANCE SURVEY OF METHODS USED FOR ESTIMATING DIRECTIONAL WAVE SPECTRA FROM HEAVE-PITCH-ROLL DATA .....	62
<i>Michel Benoit</i>	
Chapter 4	
THE MODELLING OF SHORT WAVES IN SHALLOW WATERS: COMPARISON OF NUMERICAL MODELS BASED ON BOUSSINESQ AND SERRE EQUATIONS .....	76
<i>M. Brocchini, M. Drago, L. Iovenitti</i>	
Chapter 5	
COMPUTATION OF BREAKING WAVES WITH A PANEL METHOD.....	89
<i>Jan Broeze</i>	
Chapter 6	
BAR/TROUGH EFFECTS ON WAVE HEIGHT PROBABILITY DISTRIBUTIONS AND ENERGY LOSSES IN SURF ZONES .....	103
<i>Maolong Cai, David R. Basco, Joe Baumer</i>	

Chapter 7	
THE MEDITERRANEAN SEA WAVE FORECASTING SYSTEM.....	116
<i>Luigi Cavaleri, Luciana Bertotti</i>	
Chapter 8	
CURRENT-DEPTH REFRACTION AND DIFFRACTION MODEL FOR IRREGULAR WATER WAVES.....	129
<i>Jang W. Chae, Shin Taek Jeong</i>	
Chapter 9	
TRANSIENT PROPAGATION OF WAVES IN A FLUME.....	142
<i>Kwok F. Cheung, Michael Isaacson, Etienne Mansard</i>	
Chapter 10	
IRREGULAR WAVE TRANSFORMATION PROCESSES IN SURF AND SWASH ZONES .....	156
<i>Daniel T. Cox, Nobuhisa Kobayashi, Andojo Wurjanto</i>	
Chapter 11	
NUMERICAL MODELLING OF WAVES AND CURRENTS WITH REGARD TO COASTAL STRUCTURES.....	170
<i>M. Fischer, J. Juhl, E. B. Rasmussen</i>	
Chapter 12	
ON THE TESTING OF MODELS IN MULTIDIRECTIONAL SEAS.....	3454
<i>E.R. Funke, E.P.D. Mansard</i>	
Chapter 13	
THE INTERACTION OF DEEP-WATER GRAVITY WAVES AND A CURVED SHEARING CURRENT.....	184
<i>Marius Gerber</i>	
Chapter 14	
TRANSFORMATION OF WAVE CREST PATTERN IN SHOALING WATER .....	199
<i>Yoshimi Goda</i>	
Chapter 15	
PARTICLE IMAGE VELOCIMETRY (PIV) IN THE COASTAL ENGINEERING LABORATORY.....	212
<i>C.A. Greated, D. J. Skyner, T. Bruce</i>	
Chapter 16	
DIRECTIONAL NEARSHORE WAVE PROPAGATION OVER A RIP CHANNEL: AN EXPERIMENT.....	226
<i>Luc Hamm</i>	

Chapter 17	
WAVE SETUP ON BEACHES AND IN RIVER ENTRANCES .....	240
<i>David J. Hanslow, Peter Nielsen</i>	
Chapter 18	
CHARACTERISTICS OF A SOLITARY WAVE BREAKING CAUSED BY A SUBMERGED OBSTACLE .....	253
<i>Masanori Hara, Takashi Yasuda, Yukio Sakakibara</i>	
Chapter 19	
EIGHT YEARS WAVE HINDCAST AND ANALYSIS OF WAVE CLIMATE .....	267
<i>Yoshio Hatada, Masataka Yamaguchi</i>	
Chapter 20	
CHARACTERISTICS OF ABSORBING DIRECTIONAL WAVEMAKER.....	281
<i>H. Hirakuchi, R. Kajima, T. Shimizu, M. Ikeno</i>	
Chapter 21	
A NEW NEARSHORE DIRECTIONAL WAVE GAGE .....	295
<i>Gary L. Howell</i>	
Chapter 22	
ENERGY DISSIPATION AND AIR BUBBLES MIXING INSIDE SURF ZONE .....	308
<i>H.H. Hwung, J.M. Chyan, Y.C. Chung</i>	
Chapter 23	
INSTRUMENTAL EVALUATION OF THE DEEP WATER DIRECTIONAL WAVE CLIMATE ALONG THE MEDITERRANEAN COAST OF ISRAEL .....	322
<i>Ya. A. Iosilevskii, D.S. Rosen, A. Golik, D.L. Inman</i>	
Chapter 24	
VARIATION OF POTENTIAL AND KINETIC WAVE ENERGY IN THE SURF ZONE .....	336
<i>Koichiro Iwata, Takashi Tomita</i>	
Chapter 25	
MODELLING OF WAVE-CURRENT BOUNDARY LAYER IN THE COASTAL ZONE .....	350
<i>Leszek M. Kaczmarek, Rafal Ostrowski</i>	
Chapter 26	
SPECTRAL EVOLUTION OF DIRECTIONAL FINITE AMPLITUDE DISPERSIVE WAVES IN SHALLOW WATER .....	364
<i>James M. Kaihatu, James T. Kirby</i>	

Chapter 27	
AN ADDITIONAL PARAMETER FOR THE ZERO CROSSING WAVE DEFINITION AND ITS PROBABILITY DISTRIBUTION .....	378
<i>A. Kimura, T. Ohta</i>	
Chapter 28	
TIME-DEPENDENT SOLUTIONS OF THE MILD-SLOPE WAVE EQUATION .....	391
<i>James T. Kirby, Changhoon Lee, Chris Rasmussen</i>	
Chapter 29	
NON-LINEAR WAVE-CURRENT INTERACTIONS IN THE SWADE RESEARCH PROGRAM .....	405
<i>S. P. Kjeldsen, H. C. Graber</i>	
Chapter 30	
TIME-DEPENDENT MILD SLOPE EQUATION FOR RANDOM WAVES .....	419
<i>Yasuhiro Kubo, Yasuo Kotake, Masahiko Isobe, Akira Watanabe</i>	
Chapter 31	
EVALUATION OF NUMERICAL MODELS ON WAVE-CURRENT INTERACTIONS .....	432
<i>Jung L. Lee, Hsiang Wang</i>	
Chapter 32	
WAVE TRANSFORMATIONS OVER A SUBMERGED BAR: EXPERIMENTS AND THEORETICAL INTERPRETATIONS .....	447
<i>Gianfranco Liberatore, Marco Petti</i>	
Chapter 33	
NONLINEAR TRANSFORMATION OF IRREGULAR WAVES IN SHALLOW WATER .....	460
<i>Per A. Madsen, Ole R. Sorensen, Hemming A. Schaffer</i>	
Chapter 34	
NUMERICAL VALIDATION OF DIRECTIONAL WAVEMAKER THEORY WITH SIDEWALL REFLECTIONS .....	3468
<i>E.P.D. Mansard, M.D. Miles, R.A. Dalrymple</i>	
Chapter 35	
HYBRID FREQUENCY-DOMAIN KDV EQUATION FOR RANDOM WAVE TRANSFORMATION .....	474
<i>Hajime Mase, James T. Kirby</i>	
Chapter 36	
BREAKING OF IRREGULAR WAVES ON A SLOPE .....	488
<i>Masaru Mizuguchi</i>	

Chapter 37	
OSCILLATING WATER COLUMN MODELLING .....	502
<i>Iain G. Morrison, Clive A. Greated</i>	
Chapter 38	
NEW APPROACH FOR ESTIMATING THE SEVEREST SEA STATE FROM STATISTICAL DATA .....	512
<i>Michel K. Ochi</i>	
Chapter 39	
MODELING THE TRANSFORMATION OF NONLINEAR WAVES PASSING OVER A SUBMERGED DIKE .....	526
<i>Takumi Ohyama, Kazuo Nadaoka</i>	
Chapter 40	
PROBABILISTIC CALCULATION MODEL OF DIRECTIONAL RANDOM WAVES .....	540
<i>Wi-Gwang Pae, Hajime Mase, Tetsuo Sakai</i>	
Chapter 41	
DIRECTIONAL WAVE MEASUREMENTS IN RIO DE JANEIRO COAST .....	551
<i>C.E. Parente, C.P. Hanse, R.M. Sampaio, J.M. Lima, J.L.B. Carvalho</i>	
Chapter 42	
ON THE ATTENUATION OF WAVES PROPAGATING WITH A CURRENT.....	563
<i>Michio Sato</i>	
Chapter 43	
A TWO-DIMENSIONAL SURF ZONE MODEL BASED ON THE BOUSSINESQ EQUATIONS.....	576
<i>H.A. Schaffer, R. Deigaard, P. Madsen</i>	
Chapter 44	
FIELD VERIFICATION OF NUMERICAL MODELS FOR CALCULATION OF NEARSHORE WAVE FIELD .....	590
<i>Takuzo Shimizu, Akiyuki Ukai, Masahiko Isobe</i>	
Chapter 45	
BOTTOM SHEAR STRESSES IN THE BOUNDARY LAYES UNDER WAVES AND CURRENTS CROSSING AT RIGHT ANGLES .....	604
<i>Richard R. Simons, Tony J. Grass, Mehrdad Mansour-Tehrani</i>	



Chapter 46	
THE EFFECT OF SHEARED CURRENTS ON WAVE KINEMATICS AND SURFACE PARAMETERS .....	618
<i>D.J. Skyner, W.J. Easson</i>	
Chapter 47	
LABORATORY STUDY ON WAVE TRANSFORMATION ON BARRED BEACH PROFILES .....	630
<i>Ernest R. Smith, Nicholas C. Kraus</i>	
Chapter 48	
ESTIMATION OF IRREGULAR WAVE KINEMATICS FROM A MEASURED RECORD .....	644
<i>Rodney J. Sobey</i>	
Chapter 49	
ON SPECTRAL INSTABILITIES AND DEVELOPMENT OF NON-LINEARITIES IN PROPAGATING DEEP-WATER WAVE TRAINS .....	658
<i>C.T. Stansberg</i>	
Chapter 50	
INTERACTION OF NONLINEAR WAVE AND CURRENT .....	672
<i>S. Supharatid, H. Tanaka, N. Shuto</i>	
Chapter 51	
A STREAM FUNCTION SOLUTION FOR WAVES ON A STRONGLY SHEARED CURRENT .....	684
<i>Christopher Swan</i>	
Chapter 52	
WAVE, TURBULENT AND MEAN MOMENTUM FLUXES ACROSS THE BREAKING WAVE TRANSITION REGION IN THE SURF ZONE .....	698
<i>R. J. Thieke</i>	
Chapter 53	
EFFECTS OF THE GULF STREAM ON WIND WAVES IN SWADE.....	712
<i>Hendrik L. Tolman</i>	
Chapter 54	
AN IMPROVED ARRANGEMENT FOR THE PROGRESSIVE WAVE ABSORBER .....	726
<i>S.W. Twu, C.C. Liu</i>	
Chapter 55	
INTERRELATION OF CNOIDAL WAVE THEORIES .....	737
<i>Masataka Yamaguchi</i>	

Chapter 56  
**FREAK WAVES IN UNIDIRECTIONAL WAVE TRAINS AND  
THEIR PROPERTIES** .....751  
*Takashi Yasuda, Nobuhito Mori, Kazunori Ito*

Chapter 57  
**A METHOD FOR ESTIMATING REFLECTION COEFFICIENT IN  
SHORT-CRESTED RANDOM SEAS** .....765  
*Hiromune Yokoki, Masahiko Isobe, Akira Watanabe*

Chapter 58  
**ESTIMATING INCIDENT AND REFLECTED WAVE FIELDS  
USING AN ARBITRARY NUMBER OF WAVE GAUGES**.....777  
*J.A. Zelt, James E. Skjelbreia*

**PART II**

**LONG PERIOD WAVES, STORM SURGES AND WAVE GROUPS**

Chapter 59  
**LABORATORY TESTS ON THE INTERACTION BETWEEN  
NONLINEAR LONG WAVES & SUBMERGED BREAKWATERS**.....792  
*Marco Petti, Piero Ruol*

Chapter 60  
**FIELD OBSERVATION OF SURF BEATS OUTSIDE THE  
SURF ZONE** .....804  
*Tsunehiro Sekimoto, Takuzo Shimizu, Kosuke Kondo, Yasuhiro Kubo*

Chapter 61  
**LOW FREQUENCY WAVES IN THE SURF ZONE** .....818  
*Gary Watson, D. Howell Peregrine*

Chapter 62  
**LOW FREQUENCY WAVES IN INTERMEDIATE WATER DEPTHS** .....832  
*E.C. Bowers*

Chapter 63  
**INFRAGRAVITY-FREQUENCY (0.005–0.05 HZ) MOTIONS  
ON THE SHELF** .....846  
*T.H.C. Herbers, Steve Elgar, R.T. Guza, W.C. O'Reilly*

Chapter 64  
**BREAKPOINT-FORCED AND BOUND LONG WAVES IN THE  
NEARSHORE: A MODEL COMPARISON**.....860  
*Jeffrey H. List*

Chapter 65	
THE EFFECT OF WAVES ON SURGES IN THE NORTH SEA .....	874
<i>C. Mastenbroek</i>	
Chapter 66	
DISTRIBUTION OF UNDERTOW AND LONG-WAVE COMPONENT VELOCITY DUE TO RANDOM WAVES.....	883
<i>Akio Okayasu, Hiroyuki Katayama</i>	
Chapter 67	
OCCURRENCE DISTRIBUTION OF MAXIMUM WAVE HEIGHT INCLUDING WAVE GROUPING EFFECT.....	894
<i>Kosuke Kondo, Tsunehiro Sekimoto, Takuzo Shimizu, Sumio Imai</i>	
Chapter 68	
AN EXPERIMENT AT SEA ON MECHANICS OF THE WAVE GROUPS .....	907
<i>Paolo Boccotti, Giuseppe Barbaro, Lucio Mannino</i>	
Chapter 69	
WAVE GROUP MODULATIONS IN CROSS-SHORE BREAKING PATTERNS.....	918
<i>T.C. Lippmann, R.A. Holman</i>	
Chapter 70	
PROBABILISTIC STRUCTURE OF RANDOM WAVE GROUPS .....	932
<i>Ke Yu</i>	
Chapter 71	
STATISTICS OF WAVE GROUP PARAMETERS.....	946
<i>Gerbrant Ph van Vledder</i>	
Chapter 72	
VERIFICATION OF A ONE-DIMENSIONAL SURFBEAT MODEL AGAINST LABORATORY DATA .....	960
<i>J.A. Roelvink, H.A.H. Petit, J.K. Kostense</i>	
Chapter 73	
INCIDENT WAVE GROUPS AND LONG WAVES IN THE NEARSHORE ZONE .....	974
<i>Y. Foote, D. Huntley, M. Davidson, P. Russell, J. Hardisty, A. Cramp</i>	
Chapter 74	
GENERATION OF INFRAGRAVITY WAVES IN BREAKING PROCESS OF WAVE GROUPS.....	990
<i>Satoshi Nakamura, Kazumasa Katoh</i>	

**PART III**  
**COASTAL STRUCTURES**

Chapter 75	
MONITORING MOUND BREAKWATERS: THE CASE OF SINES .....	1006
<i>F. Abecasis, C. Pita</i>	
Chapter 76	
REAR SIDE STABILITY OF BERM BREAKWATERS .....	1020
<i>O.H. Andersen, J. Juhl, P. Sloth</i>	
Chapter 77	
OBLIQUE WAVE ATTACK ON BLOCK REVETMENTS.....	1030
<i>Adam Bezuijen, Mark Klein Breteler</i>	
Chapter 78	
THE PENETRATION OF SHORT-CRESTED WAVES THROUGH A GAP .....	1044
<i>N. Booij, L.H. Holthuijsen, P.H.M. de Lange</i>	
Chapter 79	
DESIGN OF DOLOS ARMOUR UNITS.....	1053
<i>Hans F. Burcharth, Zhou Liu</i>	
Chapter 80	
RESULTS OF MEASUREMENTS ON LARGE MODEL TETRAPODS AND TRANSFER TO PROTOTYPE UNITS.....	1067
<i>W.W. Burger, H.-J. Smidt, H.W. Partenscky</i>	
Chapter 81	
THE MOVEMENT OF SUBMERGED BODIES BY BREAKING WAVES .....	1078
<i>M.J. Cooker, D. H. Peregrine</i>	
Chapter 82	
PLEA FOR THE PLACEMENT OF ARMOUR BLOCKS IN ORDERLY PATTERNS .....	1091
<i>Fernando V. Costa</i>	
Chapter 83	
NONLINEAR WAVE TRANSFORMATION OVER A SUBMERGED PERMEABLE BREAKWATER.....	1101
<i>Eric C. Cruz, Masahiko Isobe, Akira Watanabe</i>	
Chapter 84	
MODEL TESTING OF WAVE TRANSMISSION PAST LOW-CRESTED BREAKWATERS .....	1115
<i>B.L. Davies, D.L. Kriebel</i>	

Chapter 85  
GRAVITY DRAINAGE: A NEW METHOD OF BEACH  
STABILISATION THROUGH DRAINAGE OF THE WATERTABLE.....1129  
*Greg A. Davis, David J. Hanslow, Kevin Hibbert, Peter Nielsen*

Chapter 86  
HARMONIC GENERATION AND TRANSMISSION PAST A  
SUBMERGED RECTANGULAR OBSTACLE .....1142  
*Andrew M. Driscoll, Robert A. Dalrymple, Stephan T. Grilli*

Chapter 87  
THE SUBMERGED PLATE AS A WAVE FILTER:  
THE STABILITY OF THE PULSATING FLOW PHENOMENON .....1153  
*Kai-Uwe Graw*

Chapter 88  
WAVE IMPACT FORCES ON MIXED BREAKWATERS .....1161  
*Stephan T. Grilli, Miguel A. Losada, Francisco Martin*

Chapter 89  
LOADS ON SLOPING SEADYKES AND REVETMENTS FROM  
WAVE-INDUCED SHOCK PRESSURES .....1175  
*Joachim Grune*

Chapter 90  
NUMERICAL MODELING FOR WAVE ENERGY DISSIPATION  
WITHIN POROUS SUBMERGED BREAKWATERS OF IRREGULAR  
CROSS SECTION.....1189  
*George Z. Gu, Hsiang Wang*

Chapter 91  
TWO DIMENSIONAL EFFECTS IN MODELLING BERM OR  
RESHAPING BREAKWATERS.....1203  
*Kevin R. Hall*

Chapter 92  
PRELIMINARY ANALYSIS OF THE STABILITY OF  
RUBBLEMOUND BREAKWATER CROWN WALLS.....1217  
*David G. Hamilton, Kevn R. Hall*

Chapter 93  
NEW STABILITY FORMULA FOR DOLOSSE .....1231  
*A.H. Holtzhausen, J.A. Zwamborn*

Chapter 94  
EFFECT ON WIND SPEED TO WAVE RUN-UP.....1245  
*Jea-Tzyy Juang*



Chapter 95	
SCATTERING OF WATER WAVES BY VERTICAL CYLINDERS WITH A BACKWALL .....	1258
<i>Shohachi Kakuno, Kazuki Oda, Philip L.-F. Liu</i>	
Chapter 96	
HYDRAULIC MODEL EXPERIMENTS ON SEAWALLS.....	1272
<i>J.W. Kamphuis, K.A. Rakha, J. Jui</i>	
Chapter 97	
MOVEMENT AND STATIC STRESS IN DOLOSSE: SIX YEARS OF FIELD MONITORING AT CRESCENT CITY .....	1285
<i>Thomas R. Kendall, Jeffrey A. Melby</i>	
Chapter 98	
IRREGULAR WAVE INTERACTION WITH PERMEABLE SLOPES.....	1299
<i>Nobuhisa Kobayashi, Andojo Wurjanto</i>	
Chapter 99	
3-D ANALYSIS OF FLOW AROUND A VERTICAL CYLINDER ON A SCOUR BED .....	3482
<i>Tomonao Kobayashi</i>	
Chapter 100	
VERTICAL WAVE BARRIERS: WAVE TRANSMISSION AND WAVE FORCES .....	1313
<i>David L. Kriebel</i>	
Chapter 101	
INTERACTION OF NONLINEAR WAVES WITH COASTAL STRUCTURES.....	1327
<i>J.J. Lee, C. Chang, F. Zhuang</i>	
Chapter 102	
PONTA DELGADA BREAKWATER REHABILITATION RISK ASSESSMENT WITH RESPECT TO BREAKAGE OF ARMOUR UNITS .....	1341
<i>H. Ligteringen, J.C. van der Lem, F. Silveira Ramos</i>	
Chapter 103	
DURABILITY AND TESTING OF STONE FOR USE IN RUBBLEMOUND STRUCTURES.....	1354
<i>O.T. Magoon, W.F. Baird, J.P. Aherns, B.L. Edge, H.D. Converse, D.D. Davidson, S.A. Hughes, J.F. Burcharth, D.D. Treadwell, C.I. Rauw, A.W. Sam Smith</i>	

Chapter 104	
DYNAMIC RESPONSE OF VERTICAL STRUCTURES TO BREAKING WAVE FORCES—REVIEW OF THE CIS DESIGN EXPERIENCE .....	1357
<i>J.G. Marinski, H. Oumeraci</i>	
Chapter 105	
A ROBUST ARMOR DESIGN TO FACE UNCERTAINTIES .....	1371
<i>Josep R. Medina</i>	
Chapter 106	
DOLOS DESIGN USING RELIABILITY METHODS.....	1385
<i>Jeffrey A. Melby, George F. Turk</i>	
Chapter 107	
LABORATORY INVESTIGATION ON THE STABILITY OF A SPHERICAL ARMOR UNIT OF A SUBMERGED BREAKWATER.....	1400
<i>N. Mizutani, K. Iwata, T.M. Ruffin, Jr., K. Kurata</i>	
Chapter 108	
NEW TYPES OF SHORE PROTECTION, POSSIBILITIES OF APPLICATION ALONG THE COAST OF FRANCE.....	1414
<i>P. Monadier, F. Ropert, B. Bellessort, J. Viguier</i>	
Chapter 109	
FIELD ANALYSIS OF WAVE ACTION ON BREAKWATER .....	1420
<i>Alessandro Muraca, Vito Rossi</i>	
Chapter 110	
WAVE ENERGY DISSIPATION ON AND IN RUBBLE MOUND STRUCTURES.....	1434
<i>M. Muttray, H. Oumeraci, C. Zimmermann, H.W. Partenscky</i>	
Chapter 111	
ARMOUR DISPLACEMENTS ON RESHAPING BREAKWATERS.....	1448
<i>P.A. Norton, P. Holmes</i>	
Chapter 112	
THE BREAKING AND RUN-UP OF SOLITARY WAVES ON BEACHES .....	1461
<i>Ashwini Otta, Ib A. Svendsen, S.T. Grilli</i>	
Chapter 113	
IMPACT LOADING AND DYNAMIC RESPONSE OF CAISSON BREAKWATERS—RESULTS OF LARGE-SCALE MODEL TESTS .....	1475
<i>H. Oumeraci, H.W. Partenscky, S. Kohlhase, P. Klammer</i>	

Chapter 114	
WAVE FORCES ON CROWN WALLS.....	1489
<i>Jan Pedersen, Hans F. Burcharth</i>	
Chapter 115	
OPTIMAL DESIGN OF RUBBLE MOUND STRUCTURES UNDER THE IRREGULAR WAVE .....	1503
<i>Cheong-Ro Ryu, Yoon-Koo Kang, Jong-Wook Kim</i>	
Chapter 116	
NUMERICAL SIMULATION OF NONLINEAR WAVE INTERACTING WITH PERMEABLE BREAKWATERS .....	1517
<i>T. Sakakiyama, R. Kajima</i>	
Chapter 117	
WAVES ON PERMEABLE LAYERS .....	1531
<i>Toru Sawaragi, Ichiro Deguchi</i>	
Chapter 118	
IMPACT LOADS INDUCED BY PLUNGING BREAKERS ON VERTICAL STRUCTURES.....	1545
<i>R. Schmidt, H. Oumeraci, H.-W. Partenscky</i>	
Chapter 119	
PROFILE CHANGES OF ROCK SLOPES BY IRREGULAR WAVES.....	1559
<i>W. G. Smith, Nobuhisa Kobayashi, Shuji Kaku</i>	
Chapter 120	
WAVE-INDUCED UPLIFT CHARACTERISTICS ON CONCRETE BLOCK SLOPE REVETMENTS .....	1573
<i>Uwe Sparboom, Wolf Debus</i>	
Chapter 121	
FIELD MEASUREMENTS ON PLACED BLOCK REVETMENTS.....	1587
<i>Theo Stoutjesdijk, Ben Rieger, Adam Bezuijen</i>	
Chapter 122	
NUMERICAL DETERMINATION OF WAVE INDUCED FLOW IN RUBBLE MOUND BREAKWATERS .....	1599
<i>Z. C. Sun, A. F. Williams, N.W.H. Allsop</i>	
Chapter 123	
CHARACTERISTICS OF WAVE DISSIPATION BY FLEXIBLE SUBMERGED BREAKWATER AND UTILITY OF THE DEVICE.....	1613
<i>Masahiro Tanaka, Takumi Ohyama, Tetsushi Kiyokawa, Takaaki Uda, Atsushi Omata</i>	

Chapter 124	
FIELD EXPERIMENTS ON A DUAL CYLINDRICAL CAISSON BREAKWATER .....	1625
<i>Katsutoshi Tanimoto, Hiroshi Endoh, Shigeo Takahashi</i>	
Chapter 125	
PRESSURE OSCILLATIONS DURING WAVE IMPACT ON VERTICAL WALLS.....	1639
<i>M.E. Topliss, M.J. Cooker, D.H. Peregrine</i>	
Chapter 126	
WATER PARTICLE VELOCITIES ON A BERM BREAKWATER.....	1651
<i>Alf Torum, Marcel van Gent</i>	
Chapter 127	
RUBBLE-MOUND BREAKWATER STABILITY: RESULTS OF IN-SITU MEASUREMENTS.....	1666
<i>L. Van Damme, J. De Rouck, D. Vermeir</i>	
Chapter 128	
A UNIVERSAL ANALYSIS FOR THE STABILITY OF BOTH LOW-CRESTED AND SUBMERGED BREAKWATERS.....	1679
<i>C. Vidal, M.A. Losada, R. Medina, E.P.D. Mansard, G. Gomez-Pina</i>	
Chapter 129	
THE MAINTENANCE OF HYDRAULIC STRUCTURES.....	1693
<i>J.K. Vrijling, H. Kuiper, R.E. Jorissen, H.E. Klatter</i>	
Chapter 130	
FINITE ELEMENT SIMULATION OF WAVE-INDUCED INTERNAL FLOW IN RUBBLE MOUND STRUCTURES .....	1706
<i>H. Wibbeler, H. Oumeraci</i>	
Chapter 131	
THE PERMEABILITY OF RUBBLE MOUND BREAKWATERS. NEW MEASUREMENTS AND NEW IDEAS.....	1720
<i>A.F. Williams, H.F. Burcharth, H. den Adel</i>	
Chapter 132	
NEW METHODS TO EVALUATE WAVE RUN-UP HEIGHT AND WAVE OVERTOPPING RATE .....	1734
<i>Yoshimichi Yamamoto, Kiyoshi Horikawa</i>	
Chapter 133	
USE AND BEHAVIOR OF GABIONS IN COASTAL PROTECTION.....	1748
<i>Kees d'Angremond, Egbert J.F. van den Berg, Jan H. de Jager</i>	

Chapter 134  
 WAVE RUNUP AND OVERTOPPING ON COASTAL STRUCTURES ...1758  
*J.P. de Waal,, J.W. van der Meer*

Chapter 135  
 NUMERICAL SIMULATION OF WAVE MOTION ON AND IN  
 COASTAL STRUCTURES .....1772  
*J.W. van der Meer, H.A.H. Petit, P. van den Bosch, G. Klopman,  
 R.D. Broekens*

Chapter 136  
 IMPACT BREAKING WAVE PRESSURES ON VERTICAL WALLS .....1785  
*Masataro Hattori, Atsusu Arami*

Chapter 137  
 NUMERICAL MODELLING OF THE STABILITY OF  
 RUBBLE BASES .....1799  
*Wojciech Sulisz*

**PART IV**  
**THE VENETIAN COAST**

Chapter 138  
 DEVELOPMENT OF THE VENICE MORPHOLOGICAL SYSTEM.....1812  
*P. Silva, A. Mol*

Chapter 139  
 ON THE CHAOTIC STRUCTURE OF TIDE ELEVATION IN  
 THE LAGOON OF VENICE.....1826  
*Giovanna Vittori*

Chapter 140  
 THE ITALIAN WAVES MEASUREMENT NETWORK .....1840  
*M. DeBoni, L. Cavaleri, A. Rusconi*

Chapter 141  
 EVALUATION OF DESIGN WAVES ALONG THE COAST AND  
 AT THE INLETS OF THE VENICE LAGOON.....1851  
*Paolo De Girolamo, Giancarlo Passacantando, David Hurdle,  
 Alberto Noli*

Chapter 142  
 EFFECTS OF NON-UNIFORM SEDIMENT GRAINSIZE IN THE  
 LONG-TERM EVOLUTION OF TIDAL LAGOONS .....1865  
*G. Di Silvio, P. Teatini*



Chapter 143  
MIXING PROCESSES IN A SHALLOW LAGOON.....1867  
*Jorg Imberger, G. Di Silvio*

Chapter 144  
WATER FLOW MODELLING OF THE VENICE LAGOON .....1869  
*Enrico Marchi, Attilio Adami, Alfredo Caielli, Giovanni Cecconi*

Chapter 145  
HYDRAULIC AND MATHEMATICAL MODELLING OF HISTORICAL  
AND MODERN SEAWALLS FOR THE DEFENCE OF  
VENICE LAGOON.....1879  
*Leopoldo Franco, Giuseppe R. Tomasicchio*

## **PART V**

### **COASTAL PROCESSES AND SEDIMENT TRANSPORT**

Chapter 146  
OBSERVATIONS OF GRANULAR-FLUID MIXTURE UNDER AN  
OSCILLATORY SHEET FLOW.....1896  
*Toshiyuki Asano*

Chapter 147  
FINE-SCALE MEASUREMENT OF SEDIMENT SUSPENSION BY  
BREAKING WAVES AT SUPERTANK .....1910  
*Stephen F. Barkaszi, Jr., William R. Dally*

Chapter 148  
STATISTICALLY SIGNIFICANT BEACH PROFILE CHANGE WITH  
AND WITHOUT THE PRESENCE OF SEAWALLS.....1924  
*David R. Basco, Douglas A. Bellomo, Cheryl Pollock*

Chapter 149  
PREDICTION OF TURBIDITY CURRENTS WITH BOUSSINESQ  
VISCOSITY AND SECOND-MOMENT CLOSURE MODELS.....1938  
*Bard Brors, Karl J. Eidsvik*

Chapter 150  
CROSS-SHORE TRANSPORT MODELLING IN TERMS OF  
SEDIMENT CONCENTRATIONS AND VELOCITIES.....1947  
*Zhiwen Chen*

Chapter 151  
EVOLUTION OF A BEACH WITH AND WITHOUT A SUBMERGED  
BREAKWATER: EXPERIMENTAL INVESTIGATION.....1959  
*G. Chiaia, L. Damiani, A. Petrillo*

Chapter 152  
EQUILIBRIUM BEACH PROFILES WITH RANDOM SEAS.....1973  
*Christopher G. Creed, Robert A. Dalrymple, David L. Kriebel,  
James M. Kaihatu*

Chapter 153  
AN OVERVIEW OF THE BRITISH BEACH AND NEARSHORE  
DYNAMICS (B-BAND) PROGRAMME.....1987  
*M.A. Davidson, P.E. Russell, D.A. Huntley, J. Hardisty, A. Cramp*

Chapter 154  
LONGSHORE BAR GENERATION MECHANISMS .....2001  
*Robert G. Dean, Rajesh Srinivas, Trimbak M. Parchure*

Chapter 155  
SHEET FLOW UNDER NONLINEAR WAVES AND CURRENTS .....2015  
*Mohammad Dibajnia, Akira Watanabe*

Chapter 156  
ASSESSMENT OF COASTAL PROCESSES FOR THE DESIGN  
AND THE CONSTRUCTION OF THE ZEEPIPE LANDFALL  
IN ZEEBRUGGE .....2029  
*A. Eide, B. Malherbe, M. Mercanti, B. Lahousse*

Chapter 157  
A FIELD EXPERIMENT ON A NOURISHED BEACH .....2043  
*A.J. Fernandez, G. Gomez-Pina, G. Cuenca, J.L. Ramirez*

Chapter 158  
THIRTY YEAR EROSION PROJECTIONS IN FLORIDA:  
PROJECT OVERVIEW AND STATUS .....2057  
*Emmett R. Foster*

Chapter 159  
GRAIN-SORTING OVER RIPPLES INDUCED BY SEA WAVES .....2071  
*Enrico Foti, Paolo Blondeaux*

Chapter 160  
OSCILLATORY BEDLOAD TRANSPORT STUDIES BY IMAGING  
OF TRACERS .....2084  
*E.L. Gallagher, R.J. Seymour*

Chapter 161  
WAVE-INDUCED POREWATER PRESSURE AND SEABED  
STABILITY .....2095  
*A. Hattori, T. Sakai, K. Hatanaka*

Chapter 162	
INTERCOMPARISON OF COASTAL PROFILE MODELS .....	2108
<i>Ida B. Hedegaard, J.A. Roelvink, H. Southgate, P. Pechon, J. Nicholson, L. Hamm</i>	
Chapter 163	
OSCILLATORY FLOW BEHAVIOR IN THE VICINITY OF RIPPLE MODELS .....	2122
<i>Kiyoshi Horikawa, Suguru Mizutani</i>	
Chapter 164	
BERM FORMATION AND BERM EROSION .....	2136
<i>Kazumasa Katoh, Shin-ichi Yanagishima</i>	
Chapter 165	
COUPLING OF A QUASI-3D MODEL FOR THE TRANSPORT WITH A QUASI-3D MODEL FOR THE WAVE INDUCED FLOW .....	2150
<i>Irene Katopodi, Nukos Kitou, Huib J. de Vriend</i>	
Chapter 166	
FIELD OBSERVATION ON SAND RIPPLES UNDER ROUGH SEA STATE .....	2164
<i>Yoshiaki Kawata, Toru Shirai, Yoshito Tsuchiya</i>	
Chapter 167	
ABOUT CONDITIONS FOR THE WAVE RIPPLE EXISTENCE .....	2176
<i>Ruben K. Kos'yan, Alexander d. Kochergin</i>	
Chapter 168	
SUPERTANK LABORATORY DATA COLLECTION PROJECT .....	2191
<i>Nicholas C. Kraus, Jane McKee Smith, Charles K. Sollitt</i>	
Chapter 169	
A FIELD EXPERIMENT ON THE FORMATION OF BEACH CUSPS .....	2205
<i>Michio Sato, Keiji Kuroki, Tomoaki Shinohara</i>	
Chapter 170	
DYNAMICS OF LONGSHORE BARS .....	2219
<i>Magnus Larson, Nicholas C. Kraus</i>	
Chapter 171	
THE PUNTA UMBRIA (HUELVA) SPIT .....	2233
<i>Antonio Lechuga, Jose Maria Medina-Villaverde</i>	
Chapter 172	
COMPLEX PRINCIPAL COMPONENT ANALYSIS OF SEASONAL VARIATION IN NEARSHORE BATHYMETRY .....	2242
<i>Guoxiong Liang, Thomas E. White, Richard J. Seymour</i>	

Chapter 173	
TEMPORAL AND SPATIAL CROSS-SHORE DISTRIBUTIONS OF SEDIMENT AT “EL PUNTAL” SPIT, SANTANDER, SPAIN .....	2251
<i>M.A. Losada, R. Medina, C. Vidal, I.J. Losada</i>	
Chapter 174	
THREE-MODE PRINCIPAL COMPONENT ANALYSIS OF BATHYMETRIC DATA, APPLIED TO “PLAYA DE CASTILLA” (HUELVA, SPAIN) .....	2265
<i>Raul Medina, Cesar Vidal, Miguel A. Losada, Antonio J. Roldan</i>	
Chapter 175	
WAVE BREAKER TURBULENCE AS A MECHANISM FOR SEDIMENT SUSPENSION.....	2279
<i>G.P. Mocke, G.G. Smith</i>	
Chapter 176	
GRAIN-SIZE DISTRIBUTION OF SUSPENDED SEDIMENTS .....	2293
<i>Ryuichiro Nishi, Michio Sato, Kazuo Nakamura</i>	
Chapter 177	
BED BOUNDARY LAYERS.....	2307
<i>B.A. O'Connor, J.M. Harris, H. Kim, Y.K. Wong, H.U. Oebius, J.J. Williams</i>	
Chapter 178	
TIMESCALES OF BED RESPONSE IN A LOW ENERGY SURF ZONE .....	2321
<i>Philip D. Osborne, Christopher E. Vincent</i>	
Chapter 179	
SHORELINE CHANGE AT OREGON INLET TERMINAL GROIN .....	2332
<i>M.F. Overton, J.S. Fisher, W.A. Dennis, H.C. Miller</i>	
Chapter 180	
NUMERICAL SIMULATION OF SAND IN PLUNGING BREAKERS .....	2344
<i>C. Pedersen, R. Deigaard, J. Fredsoe, E.A. Hansen</i>	
Chapter 181	
SHINGLE BEACH PROFILES AND WAVE KINEMATICS.....	2358
<i>Keith A. Powell, Paul A. Quinn, Clive A. Greated</i>	
Chapter 182	
BEACH CHANGES AND SEDIMENT MOVEMENT IN THE SURF ZONE .....	2370
<i>Zbigniew Pruszk, Ryszard B. Zeidler</i>	

Chapter 183	
VELOCITY MEASUREMENTS CLOSE TO RIPPLED BEDS .....	2383
<i>K.I. Mahesha Ranasoma, J.F.A. Sleath</i>	
Chapter 184	
FIELD OBSERVATION OF WAVE-INDUCED POREWATER	
PRESSURES .....	2397
<i>T. Sakai, H. Mase, D.T. Cox, Y. Ueda</i>	
Chapter 185	
SAND TRANSPORT UNDER GROUPING WAVES .....	2411
<i>Shinji Sato</i>	
Chapter 186	
QUASI-TURBULENT BOUNDARY LAYER OF OSCILLATING	
FLOW OVER RIPPLES .....	2424
<i>Yukio Sato, Ken-ichiro Hamanaka</i>	
Chapter 187	
LONG PERIOD WAVE AND SUSPENDED SAND TRANSPORT IN	
THE SURF ZONE.....	2438
<i>Tomoya Shibayama, Akio Okayasu, Mikio Kashiwagi</i>	
Chapter 188	
OBSERVATION OF FORESHORE VARIATION IN IWO-JIMA .....	2450
<i>Toshiyuki Shigemura, Kenjiro Hayashi, Kojima Fujima</i>	
Chapter 189	
SHORE NOURISHMENT AND THE ACTIVE ZONE:	
A TIME SCALE DEPENDENT VIEW.....	2464
<i>Marcel J.F. Stive, Huib J. De Vriend, Robert J. Nicholls,</i>	
<i>Michele Capobianco</i>	
Chapter 190	
METHOD FOR ARTIFICIAL BEACH NOURISHMENT .....	2474
<i>Henk J. Verhagen</i>	
Chapter 191	
FIELD INVESTIGATION AT A MOUTH OF SMALL RIVER .....	2486
<i>Hitoshi Tanaka, Hobuo Shuto</i>	
Chapter 192	
ENTRAINMENT AND TRANSPORT OF FINE SAND BY COMBINED	
WAVES AND CURRENT:AN EXPERIMENTAL STUDY.....	2500
<i>C. Villaret, B. Latteux</i>	

Chapter 193	
A TIME-DEPENDENT NEARSHORE MORPHOLOGICAL RESPONSE MODEL.....	2513
<i>Hsiang Wang, Gang Miao, Li-Hwa Lin</i>	
Chapter 194	
TOTAL RATE AND DISTRIBUTION OF LONGSHORE SAND TRANSPORT.....	2528
<i>Akira Watanabe</i>	
Chapter 195	
COMBINED FLOW SAND TRANSPORT: FIELD MEASUREMENTS .....	2542
<i>Richard J.S. Whitehouse</i>	
Chapter 196	
NUMERICAL SIMULATION OF POCKET BEACH FORMATION .....	2556
<i>Takao Yamashita, Yoshito Tsuchiya</i>	
Chapter 197	
A CRITICAL REVIEW OF AVAILABLE DATA FOR CALIBRATION AND/OR VERIFICATION OF SEDIMENT TRANSPORT MODELS.....	2567
<i>Julio A. Zyserman</i>	
Chapter 198	
A FEASIBILITY STUDY OF A PERCHED BEACH CONCEPT IN THE NETHERLANDS .....	2581
<i>Joost H.M. de Ruig, Piet Roelse</i>	
Chapter 199	
ARTIFICIAL SAND FILLS IN WATER.....	2599
<i>J. van't Hoff, M.B. de Groot, J.C. Winterwerp, H. Verwoert, W.T. Bakker</i>	
Chapter 200	
SEDIMENT TRANSPORT BY CURRENTS AND WAVES .....	2613
<i>Leo C. van Rijn, Aart Kroon</i>	
Chapter 201	
A WAVE-CURRENT SEDIMENT BOUNDARY LAYER .....	2629
<i>Keith Bedford, Jongkook Lee</i>	
Chapter 202	
LONGSHORE CURRENT AND LATERAL MIXING IN THE SURF ZONE .....	2642
<i>Ichiro Deguchi, Toru Sawaragi, Masanobu Ono</i>	

Chapter 203  
LONGSHORE CURRENT INSTABILITIES: GROWTH TO FINITE  
AMPLITUDE .....2655  
*Nicholas Dodd, Edward B. Thornton*

Chapter 204  
PROFILE DEVELOPMENT OF DUNES DUE TO OVERFLOW .....2669  
*Henk J. Steetzel, Paul J. Visser*

Chapter 205  
THE CONTRIBUTION OF SUSPENSION EVENTS TO SEDIMENT  
TRANSPORT IN THE SURF ZONE .....2680  
*Bruce Jaffe, Asbury Sallenger, Jr.*

Chapter 206  
THE SHORT TERM PROFILE RESPONSE OF SHINGLE SPITS  
TO STORM WAVE ACTION .....2694  
*A.P. Bradbury, K.A. Powell*

**PART VI**

**COASTAL, ESTUARINE AND ENVIRONMENTAL PROBLEMS**

Chapter 207  
INTERACTION BETWEEN WATER WAVES AND VEGETATION .....2710  
*Toshiyuki Asano, Hirosh Deguchi, Nobuhisa Kobayashi*

Chapter 208  
PREDICTION OF CURRENT AND SEDIMENT DEPOSITION  
PATTERNS IN PUERTO MIRANDO OIL TERMINAL USING  
2-D MATHEMATICAL MODELS .....2724  
*Carlos Villoria, Reinaldo Garcia, Eduardo Valera*

Chapter 209  
DISPERSION PROCESS AND THE SETTLEMENT PATTERN OF  
MUD DUMPED IN OCEANS .....2735  
*Eiji Yauchi, Ken Katoh*

Chapter 210  
PORT OF LISBON-IMPROVEMENT OF THE ACCESS CONDITIONS  
THROUGH THE TAGUS ESTUARY ENTRANCE .....2745  
*I.B.M. Oliveira*

Chapter 211  
A MIXING MECHANISM IN THE NEARSHORE REGION .....2758  
*Uday Putrevu, Ib A. Svendsen*

Chapter 212	
FORMATION AND REDUCTION PROCESSES OF RIVER DELTAS: THEORY AND EXPERIMENTS.....	2772
<i>Hossam El-din A. Refaat, Yoshito Tsuchiya</i>	
Chapter 213	
THEORETICAL STUDY OF THE WAVE ATTENUATION IN A CHANNEL WITH ROUGHENED SIDES.....	2786
<i>A.J. Roldan, M.A. Losada, I.J. Losada</i>	
Chapter 214	
LOCAL SCOUR AROUND A LARGE CIRCULAR CYLINDER ON THE UNIFORM BOTTOM SLOPE DUE TO WAVES AND CURRENTS .....	2799
<i>Eiichi Saito, Tomoya Shibayama</i>	
Chapter 215	
VERTICALLY VARYING VELOCITY FIELD IN Q-3D NEARSHORE CIRCULATION.....	2811
<i>A. Sanchez-Archilla, F. Collado, A. Rodriguez</i>	
Chapter 216	
VERTICAL STRUCTURE OF THE NEARSHORE CURRENT AT DELILAH: MEASURED AND MODELED .....	2825
<i>Jane McKee Smith, Ib A. Svendsen, Uday Putrevu</i>	
Chapter 217	
A REVIEW OF WAVE/CURRENT-INDUCED SCOUR AROUND PIPELINES.....	2839
<i>B. M. Sumer, J. Fredsoe</i>	
Chapter 218	
TURBULENCE AND MUD SEDIMENTATION: A REYNOLDS STRESS MODEL AND A TWO-PHASE FLOW MODEL .....	2853
<i>C. Teisson, O. Simonin, J.C. Galland, D. Laurence</i>	
Chapter 219	
MECHANISM OF SEDIMENT TRANSPORT AROUND A LARGE CIRCULAR CYLINDER.....	2867
<i>Takao Toue, Hidehiro Katsui, Kazuo Nadaoka</i>	
Chapter 220	
SILTATION STUDY IN A LONG APPROACH CHANNEL ON LARGE SCALE MUDDY TIDAL FLAT .....	2879
<i>Hiroichi Tsuruya, Kazuo Murakami, Isao Irie, Kazumasa Katoh</i>	



Chapter 221	
MODELLING OCEAN WAVES IN THE COLUMBIA RIVER	
ENTRANCE.....	2893
<i>L.A. Verhagen, L.H. Holthuijsen, Y.S. Won</i>	
Chapter 222	
SEDIMENT TRANSPORT IN DREDGED TRENCHES.....	2902
<i>S.O. Vithana</i>	
Chapter 223	
MOTION OF MOBILE BEDS AT HIGH SHEAR STRESS.....	2917
<i>Kenneth C. Wilson, Fidelia N. Nnadi</i>	
Chapter 224	
PORT SITE SELECTION ON COAST WITH RADIAL SANDBANKS.....	2926
<i>Yixin Yan, Yen Kai</i>	
Chapter 225	
LIQUEFACTION AND EROSION OF CHINA CLAY DUE TO	
WAVES AND CURRENTS .....	2937
<i>P.J. de Wit, C. Kranenburg</i>	
Chapter 226	
CONSOLIDATION OF SOFT MARINE SOILS: UNIFYING	
THEORIES, NUMERICAL MODELLING AND IN SITU	
EXPERIMENTS.....	2949
<i>Alain Alexis, Philippe Bassoullet, Pierre Le Hir, Charles Teisson</i>	
Chapter 227	
EFFECTIVE STRESSES AND PERMEABILITY IN	
CONSOLIDATING MUD .....	2962
<i>Jean Berlamont, Lut Van de Bosch, Erik Toorman</i>	
Chapter 228	
COHESIVE PROFILE EROSION BY WAVES .....	2976
<i>Craig Bishop, Michael Skafel, Rob Nairn</i>	
Chapter 229	
THE KINEMATICS OF WAVE INDUCED FLOWS AROUND	
NEAR-BED PIPELINES .....	2990
<i>T. Bruce, W.J. Easson</i>	
Chapter 230	
MIXING BY SHEAR INSTABILITIES OF THE LONGSHORE	
CURRENT .....	2999
<i>J.C. Church, E.B. Thornton, J. Oltman-Shay</i>	

Chapter 231	
BOTTOM STRESS MODIFICATION BY BREAKING WAVES WITHIN A LONGSHORE CURRENT MODEL .....	3012
<i>J.C. Church, E.B. Thornton</i>	
Chapter 232	
HYDRODYNAMICS AND SEDIMENT CONCENTRATIONS AT WALKER BAY.....	3026
<i>R.C. Coppoolse, J.S. Schoonees, G.G. Smith, G.P. Mocke</i>	
Chapter 233	
WATER WAVE PROPAGATION IN JETTIED CHANNELS.....	3040
<i>Robert A. Dalrymple</i>	
Chapter 234	
DISPERSION MODEL OF DREDGE SPOIL DUMPED IN COASTAL WATERS .....	3054
<i>G. Drapeau, D. Lavallée, J.F. Dumais, G. Walsh</i>	
Chapter 235	
A MODIFIED METHOD OF CHARACTERISTIC TECHNIQUE COMBINED WITH GALERKIN FINITE ELEMENT METHOD TO SOLVE SHALLOW WATER MASS TRANSPORT PROBLEMS.....	3068
<i>A. Garzon, L. D'Alpaos</i>	
Chapter 236	
SEDIMENTATION AND EROSION PROBLEMS OF YAKAKENT FISHERY HARBOR.....	3081
<i>A.R. Gunbak, K. Tunc Gokce, Isikhan Guler</i>	
Chapter 237	
A STUDY ON MUD MASS TRANSPORT UNDER WAVES BASED ON AN EMPIRICAL RHEOLOGY MODEL.....	3093
<i>Masahiko Isobe, Trien N. Huynh, Akira Watanabe</i>	
Chapter 238	
SETTLING PROPERTIES OF COHESIVE SEDIMENTS IN A COOLING WATER INTAKE BASIN .....	3107
<i>Susumu Kanayama, Takuzo Shimizu, Kazuhiro Ueki</i>	
Chapter 239	
SEDIMENT TRANSPORT MODELLING IN A MACROTIDAL ESTUARY: DO WE NEED TO ACCOUNT FOR CONSOLIDATION PROCESSES? .....	3121
<i>Pierre Le Hir, Nancy Karlikow</i>	

Chapter 240	
WAVE-INDUCED PORE PRESSURE ACTING ON A BURIED SUBMARINE PIPELINE .....	3135
<i>Waldemar Magda</i>	
Chapter 241	
HYDRAULIC APPROACH TO DETERMINING OPTIMUM INTERVAL OF DISCHARGE SITES OF BARGE IN CONSTRUCTING RUBBLE FOUNDATION OF DEEP WATER BREAKWATER .....	3149
<i>Yoshiharu Matsumi, Akira Kimura</i>	
Chapter 242	
VORTEX TRAIN IN AN OFFSHORE ZONE.....	3163
<i>Nobuhiro Matsunaga, Kosei Takehara</i>	
Chapter 243	
THE VARIATION OF FLOC SIZES WITHIN A TURBIDITY MAXIMUM AT SPRING AND NEAP TIDES .....	3178
<i>J.C. McCabe, K.R. Dyer, D.A. Huntley, A.J. Bale</i>	
Chapter 244	
DISPERSION OF HEAVY SUSPENSIONS IN WAVE BOUNDARY LAYERS .....	3189
<i>Chiang C. Mei, Chimin Chian</i>	
Chapter 245	
COMBINED CONVECTION-DIFFUSION MODELLING OF SEDIMENT ENTRAINMENT .....	3202
<i>Peter Nielsen</i>	
Chapter 246	
MOVEMENTS OF MOORED SHIPS IN HARBOURS .....	3216
<i>Th. Elzinga, J.R. Iribarren, O.J. Jensen</i>	
Chapter 247	
WAVE AGITATION CRITERIA FOR FISHING HARBOURS IN ATLANTIC CANADA.....	3230
<i>Charles P. Fournier, Michael W. Mulcahy, K. Ander Chow, Otavio J. Sayao</i>	

## PART VII

### CASE STUDIES

Chapter 248	
EROSION OF THE DAMIETTA PROMONTORY, THE NILE DELTA .....	3246
<i>A.M. Fanos, A.A. Khafagy, P.D. Komar</i>	

Chapter 249	
NEARSHORE COASTAL CHANGES ALONG THE NILE DELTA SHORES.....	3260
<i>A.A. Khafagy, M.G. Naffaa, A.M. Fanos, R.G. Dean</i>	
Chapter 250	
NILE DELTA PROFILES AND MIGRATING SAND BLANKETS .....	3273
<i>Douglas L. Inman, M. Hany S. Elwany, Ahmed A. Khafaagy, Abraham Golik</i>	
Chapter 251	
DESIGN AND CONSTRUCTION OF THE BOSTON OUTFALL.....	3285
<i>Y. Eisenberg, P. Brooks</i>	
Chapter 252	
MODELLING AND MONITORING OF A PERCHED BEACH AT LIDO DI OSTIA (ROME).....	3305
<i>Andrea Ferrante, Leopoldo Franco, Sander Boer</i>	
Chapter 253	
THE RESTORATION OF BATE BAY, AUSTRALIA– PLUGGING THE SINK.....	3319
<i>Angus D. Gordon</i>	
Chapter 254	
PRESENT SITUATION OF SEA-SAND MINING IN KYUSHU ISLAND, JAPAN AND ITS INFLUENCE ON COASTAL ENVIRONMENT .....	3331
<i>M. Hashida, N. Matsunaga, T. Komatsu</i>	
Chapter 255	
PATRAS BREAKWATER FAILURE DUE TO SEISMIC LOADING.....	3343
<i>Constantine D. Memos, John N. Protonotarios</i>	
Chapter 256	
FUNCTIONING OF GROINS AT WESTHAMPTON BEACH, LONG ISLAND, NEW YORK .....	3357
<i>Gilbert K. Nersesian, Nicholas C. Kraus, Fulton C. Carson</i>	
Chapter 257	
SEA LEVEL TRENDS IN THE HUMBER ESTUARY: A CASE STUDY.....	3371
<i>Patrick Parle</i>	
Chapter 258	
PROJECTS, WORKS AND MONITORING AT BARCELONA COAST.....	3385
<i>Carlos Pena, V. Carrion, A. Castaneda</i>	

Chapter 259	
STUDY OF 50 YEARS COASTAL CHANGES AT HADERA, ISRAEL .....	3399
<i>Dov S. Rosen</i>	
Chapter 260	
INTERVENTIONS ON THE COAST SOUTH OF BRINDISI.....	3413
<i>Giuseppe R. Tomasicchio, Fiore Uliana</i>	
Chapter 261	
SANDY BEACH STABILIZATION: PRESERVATION OF SHIRARAHAMA BEACH, WAKAYAMA .....	3426
<i>Yoshito Tsuchiya, Yoshiaki Kawata, Takao Yamashita, Teruo Shibano, Masahiko Kawasaki, Shin Habara</i>	
Chapter 262	
WAVE POWER CONVERSION BY A PROTOTYPE WAVE POWER EXTRACTING CAISSON IN SAKATA PORT.....	3440
<i>Shigeo Takahashi, Hiroaki Nakada, Hideaki Ohneda, Masazumi Shikamori</i>	
SUBJECT INDEX.....	3505
AUTHOR INDEX.....	3511

# WELCOME ADDRESS

**Prof. Ing. Ugo Tomasicchio**  
**Chairman of the Conference**

On On. Sottosegretario ai Lavori Pubblici, signora Vice Presidente della Regione Veneto, signor Sindaco, signor Presidente del Magistrato alle Acque, signor Capo di Stato Maggiore della Marina, signor Assessore alla Cultura, signor Provveditore al Porto, signor Presidente del Consiglio Nazionale delle Ricerche, signor Presidente del Coastal Engineering Council, grazie della vostra presenza.

All'on. Francesco Merloni oggi sono dovuti anche gli auguri onomastici, che tutti gli rivolgiamo con vivo sentimento.

Un benvenuto a tutti gli amici e collaboratori.

**Welcome**, welcome to you all, welcome to Italia and to Venezia!

It's with great pleasure that, in the name of the Organizing Committee of the 23rd International Conference on Coastal Engineering, I have the honour to give you, distinguished guests and colleagues, a warm welcome.

I thank very much all of the National District and City Authorities for their presence and especially the honourable Minister of Public Works, the Vice President of the Regione Veneto, the Mayor of Venezia, the President of National Council of Research, and the Superintendent of the Port, who have all in many ways supported us in organizing and funding this Conference.

I also thank the Coastal Engineering Research Council and its Chairman Prof. Robert L. Wiggel, eminent man of science, for choosing Italia and Venezia for this 23rd ICCE.

Also I give many thanks to the many private sponsors and especially to the Italian Contractors, without whose financial support we would not have been able to resolve the many organizational problems.

The tradition of the ICCE is to reduce as much as possible the time spent on the opening ceremony to give more prominence to the scientific sessions. Excellent tradition! So, as Master of Ceremony, according to the definition of Prof. Bijker, Chairman of the last Conference in Delft, I don't want to break the tradition. But, please, first let me express some brief considerations.

**Genesis** (5.1) talks about God who put Man in the garden of Eden "to cultivate and care for it". Giving the creation to the care of Man, God gave him special gifts: the word, intelligence and freedom, sparks of divine nature of the Creator. So, Man was named: mirror of God (B. Pascal) and *homo Dei*; the Italian Philosopher G. B. Vico uses the expression "*Simia Dei*".

Aristotle defined Man "*ζῷον λογος εχον*" as literally the animal who has the word. The word, the logos, the verbum, this exclusive feature of Man, is the first vehicle of communication of knowledge, of science. The word, the dialogue was the teaching method of philosophic and scientific truth as in Aristotle, Plato, Socrates, Pascal and innumerable other thinkers, but also it was that of Christian Revelation; the Evangelist John begins with the admirable words: "in principio erat Verbum et Verbum erat apud Deum et Deus erat Verbum".

Then came intelligence and freedom: two indivisible gifts to choose the best, that is making the best use of intelligence. In fact, it is intelligence which permits Man the knowledge of the things, starting from his own experience, according to Galilei and Bacon; the knowledge transforms itself in Science when it becomes common property of humanity. Human science, and particularly knowledge of physical phenomena, developed with incredible speed in the past and the fruit of Man's experience, always asks for more work, with the consequent necessity of repetitive and frequent exchanges of information among the scientists, researchers and technicians. That explains the usefulness, the necessity of the meetings of groups of specialists, meetings either to evaluate the state of art or to coordinate and to press for new research.

And history, nevertheless its cycles and recycles often contradictory, demonstrates that Man travels along the path of civilization, caring for and improving the natural environment in which he lives. It is possible to see, for example, many examples of hydraulic engineering in flood control, land reclamation, coastal defense.

To the **Hydraulic Engineer** we can certainly give the credit for taking care of the environment with which he was entrusted. Coastal Engineering has recently reached the level of a science; you can consider that it was only a few decades ago that Man was able to make a real model of the sea, an object of observation from the beginning of civilization. We can take 1950, the year of the first International Conference on Coastal Engineering, as the year of the official birth of the new hydraulic maritime science. Not without reason, we are finding, among the promoters of ICCE, the most famous names in coastal engineering.

From 1950 until today, the Proceedings of the 22 conferences already held illustrate the big development of this new science; consequently it seems that we could consider the ICCE the midwife of the new maritime hydraulics, according to the Socratic teaching. ICCE is today, without any doubt, the most important scientific international conference of civil maritime engineering; the high number of participants coming from over 50 countries, the number and the level of printed papers. Its growing reputation in the scientific world confirms this.

In this 23rd Conference 682 papers have been submitted (not including those arriving too late). The CERC has chosen about 330, which will take all the available time in the five sessions.

This is the first time in the history of ICCE that the Conference has been held in Italia. We believe that the choice was not casual, in that it is taking place in the fifth centenary of the discovery of America by the great Genoese Navigator Cristoforo Colombo.

Also the venue has a clear motivation connected with this anniversary. It is in fact in Venezia, the Serenissima Repubblica Marinara, that, at the beginning of the modern era, shone in all its brilliant light the Italian Renaissance, which has radiated throughout Europe and the whole world. In Venezia was designed the "Planimondo" which was used by Colombo and other intrepid Navigators of his time (as Amerigo Vespucci), to chart the route to the new world.

It was also in Venezia that you could admire, and you can still admire, the wonderful City, the masterpiece of Man's creation, built in a very poor physical environment. **The history of Venezia is**

also the history of man "homo faber", i.e. of the Engineer in constant confrontation with natural forces: sea-storms, flooding, subsidence, etc.

Venezia is the demonstration of how much Man, using intelligently his inventive ability, can achieve, caring for cultivating the garden which was entrusted to him. This attentive caring does not permit any respite. Furthermore, you know well the present problems of the defense of Venezia, for those hard working engineers. The problems of the defense of Venezia against the sea will be discussed in many of the papers in this Conference.

Meanwhile, admire and enjoy Venezia: a precious pearl of human engineering and art; Venezia: the most beautiful City in the water, admirable lighthouse of civilization.

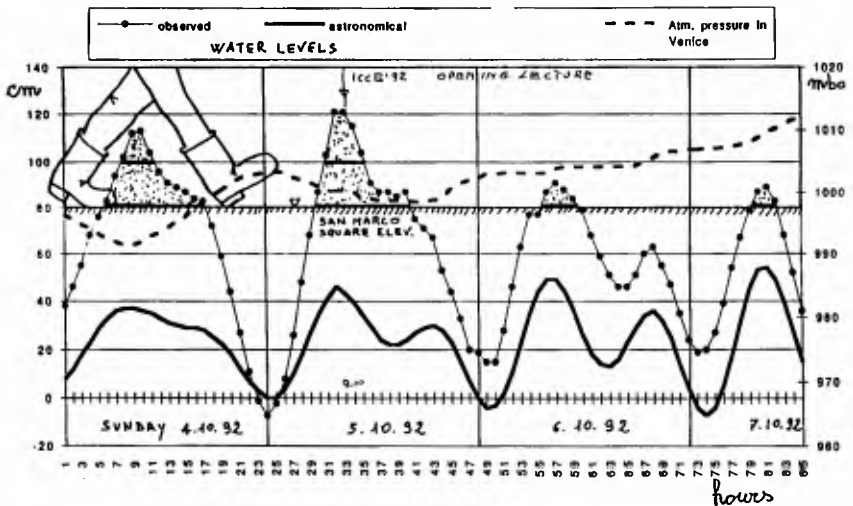
And let me finish at this point with many good wishes for a successful Conference. The Organizing Committee apologizes if everything is not perfect, but we hope our hospitality will be acceptable.

Grazie e benvenuti a Venezia. Thank you again.

( Prof. Ing. Ugo Tomasicchio  
Chairman of the Conference )



ICCE'92 4-9 October 1992 VENICE  
THE FIRST 'ACQUA ALTA' OF THE YEAR





# Coastal Engineering in Venice

Enrico Marchi<sup>1</sup>

## 1 Introduction

Venice is well known in the world as a fantastic city, full of interest for visitors to its palaces, churches, art galleries and fascinating corners. However, there is more than this: the history of Venice (see, for example, Zorzi, 1980), its development as a refuge from invaders to an imperial marine city offers extraordinary examples of applications of coastal engineering.

Venice has always taken immense care of its Lagoon which completely surrounds it and has for centuries afforded protection for the city, a haven for its fleet and the gateway to the open sea. In order to defend this Lagoon the Venetians have had to face and overcome numerous risks: the aggradation of the basin, the erosion of the littoral barrier, the reduction in depth at the inlets due to the action of the sea waves, through to the recent risks caused by industrial and agricultural pollution and to the increasingly frequent submersion of vast areas and living quarters as a result of high tides combined with land subsidence and eustasy. A brief look at each of these problems and the ways in which they have been tackled could be an effective subject for thought on the part of the participants of this Congress.

## 2 Origin of the Lagoon

More than 10.000 years ago, in the era of the last great glaciation of the Quaternary, Italy had an emerged territory much larger than its present one especially in the Adriatic zone. At the end of the glaciation, the rise in sea level submerged a great part of the alluvial plains formed by the river Po and its affluents. The line of separation of *terraferma* from the North Adriatic Sea - as a result of the gentle declivity of the plane towards the sea, and probably

---

<sup>1</sup>Professor of Hydraulics, Head, Institute of Hydraulics, University of Genoa, Via Montallegro, 1 - 16145 Genoa, Italy

due to the combined effect of more moderate sea level variations as well as to the breaking of the waves - assumed an indented and irregular form. Long series of dunes parallel to the coast separated the open sea from the internal basins - the lagoons - that had a more or less narrow rectangular form with the greater side parallel to the sea. They received fresh water from the west and north-west estuaries and communicated with the sea towards the east by means of large inlets. Could we consider that the transverse dimensions of the adriatic lagoons have a connection with the length of the tidal waves which give them "life"? It is difficult to find proofs since many independent factors, sometimes of anthropic type, have successively conspired to modify the lagoon basin's size. However, a hypothesis proposed by Luigi De Marchi as far back as 1904 was taken up again by Di Silvio (1991) correlating the propagation time of the tide with the period of resonance of the lagoon basin.

The maximum flow through a lagoon inlet takes place when the length of the lagoon itself is such that the effective crossing time for the tidal wave becomes equal to the resonance time. The latter is about a quarter of the tidal period and turns out to be largely independent of the value of the flow resistance. The flow rates, and thus the tidal amplitudes, do not always increase with the dimension of the basin; when the crossing time of the tide is greater than the resonance one - meaning that the basin length is great enough to be larger than a quarter of the length of the effective tidal wave in the lagoon - the level oscillation can increase if the basin dimensions become reduced. In fact this is the case, for example, of the Zuiderzee (Ijsselmeer) when, after the damming reduced the notable original length of the basin, the tidal amplitudes have been clearly increased.

The Venice Lagoon originally consisted of shallower basins than the present ones and it is possible that its surface dimensions were commensurate with the resonance conditions. Now, the tidal propagation through each of the three basins in which the lagoon can be divided takes noticeably less time than that of resonance, if we exclude the extreme ramifications of the north-east zone where the tidal flow is controlled for the fishing areas. The Venice Lagoon behaves today substantially as a "short" basin. In fact, the tides - whose mean component has a period of 12 hours - have in most of the lagoon delays of less than 2 hours and slight amplitude attenuations that in general do not exceed 20% of the sea amplitudes.

### 3 Historical evolution

In Roman times the Lagoon had more or less the same form that it has today but with a larger open surface and at least eight inlets. The settlement of the "Veneti" in the small islands spread through the Lagoon happened after the fall of the Roman Empire, especially after the migration due to the invasion of the Lombards in Italy. The Torcello cathedral was built in the first part of the 7th century. The communities, settled in various small centers and in particular in Malamocco, made up the "Lagoon Province", formally linked to the

Byzantine Empire but really autonomous. Thus it was able to hold out against the pressure of the Franks in the IXth century and to establish at Venice-Rialto, the new capital, a community that was definitely detached from the land. One can say that Venice was born with the vocation to be, since that time, a bridge of communication and commerce between the East and the West. Gradually its independence became affirmed and so that power which brought it to its greatest splendour between the XIIIth and XVIth centuries. It was during the period of the mature Republic that the greatest problems of hydraulic and coastal engineering were faced, entrusting the responsibility for works to a single organization: the "Magistrato alle acque", an absolute water authority.

In that period the inlets of the Lagoon, called "mouths", were already the three present ones: Lido, Malamocco and Chioggia (Fig. 1) The mouths, however, do not have now the form shown in the figure; a point to be discussed later. Fig. 2 shows the present state of the Venice Lagoon. Note the characteristic network of submerged channels that ramify from each mouth and become progressively narrower and shallower; they represent the fastest ways for the tide to enter the Lagoon. The basin is moon-shaped and has a length of more than 50 km, a width that varies from 8 to 14 km and a mean depth of about 0.65 m (Rusconi, 1987).



Figure 1: The Lagoon in XVIth century with the three mouths.

In the Lagoon there are several inhabited islands, other than those on which Venice was built, such as the famous isles of Murano and Burano. Furthermore there exist - or existed - many low-lying lands, called "barene", which are regularly submerged during high tide since they have a level higher than the mean level of the sea but less than about +30 cm. These predominant green areas are typical of the lagoon scenery. They have undergone, especially during



the second half of the XXth century, a heavy surface reduction and they are also at present subject to border erosion.

The evolution of the Lagoon areas occupied by land and water is not easy to evaluate because the most precise surveys, carried out in 1950 and 1970, necessarily had different points of reference (Cavazzoni, 1977). According to the evaluation of the Hydrographic Office of the "Magistrato alle Acque" (Rusconi, 1987) the measurements are as follows (Tab. 1):

Tab. 1

Lagoon surfaces (km <sup>2</sup> )		
Years	1930	1970
Lagoon area not affected by tides	125.8	136.7
Barene	72.5	47.5
Water surface at 0 level	353.0	367.0

Today a project is underway for the morphological reconstruction of some of the "barene" and for the protection of existing ones in the context of the reclamation plan of the Lagoon on behalf of Consorzio Venezia Nuova (1992).

#### 4 Protection from aggradation

Aware of the importance of the lagoon basin for military use and of the convenience that its great size could have for the renewal of the inner water, the Venetians put the preservation of the lagoon before any other undertaking.

The first, and perhaps the most serious threat they had to face, was that of the basin silting up due to the sediment transport of the water courses entering the Lagoon. Even if the water discharges through the lagoon mouths have a maximum value in the range of 5,000 to 10,000 m<sup>3</sup>/s, as great as the highest flows of the river Po, the sediment movement within the lagoon - as well as in the internal network of submerged channels - is very slight. A slow but progressive lengthening of the river mouths took place, however, within the lagoon and the free surface of the basin was being reduced.

The first work dates from the XIVth century and consisted in the deviation of the mouth of the Brenta, which was in front of Venice, to a more southerly position. Many other works were carried out during the XVth and, above all, the XVIth century. The Brenta was finally excluded from the Lagoon in 1613 through the so-called "taglio nuovissimo" (the newest cut). The Bacchiglione was deviated to the sea in the middle of the XVIth century. The Piave was completely excluded from the Lagoon in 1639 and the Sile in 1683, using as well a stretch of the old bed of the Piave. Fig. 3 gives an idea of these enormous works carried out in more than two centuries.

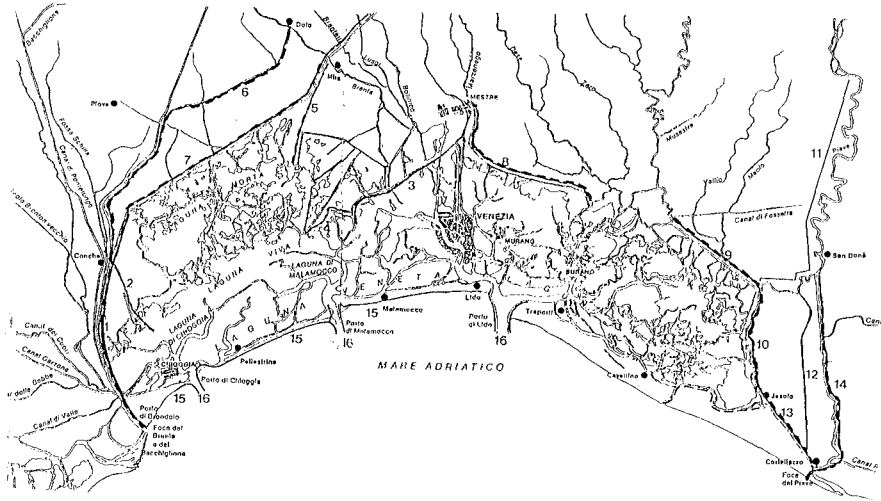


Figure 3. Deviation of the water courses entering the Lagoon (from Zorzi, 1980).

Particular mention should be made of a most important alteration that, although outside the Lagoon, was undertaken in 1598-1604 in order to remove the risks of sediment transport into the Lagoon caused by the mouths of the Po delta. This was the so-called "Taglio di Porto Viro" (the Porto Viro cut) by means of which the main mouth of the Po, which had the tendency to move northward, was deviated towards the East thus assuming its present form.

## 5 Protection of the Venetian littoral

From the earliest times of the Venetians' definitive settlement on the Lagoon islands many conservation works were carried out on the lagoon banks and sea shores. Typical embankments were built since the 11th century with willow branches and stones (Tomasicchio, 1983). This is an elastic and unsinkable protection also largely used to defend the banks of the river Po from erosion.

Timber was extensively used by the Venetians above all in the form of piers that, fixed into the muddy and sandy ground, compacted it so as to make it able to support the weight of massive structures, such as jetties and moles or even buildings.

In the XVII century the state of the littoral barrier which divides the lagoon from the sea was already particularly delicate. The sediment transport of the river Piave to the sea was lessened, probably because of the improvement to

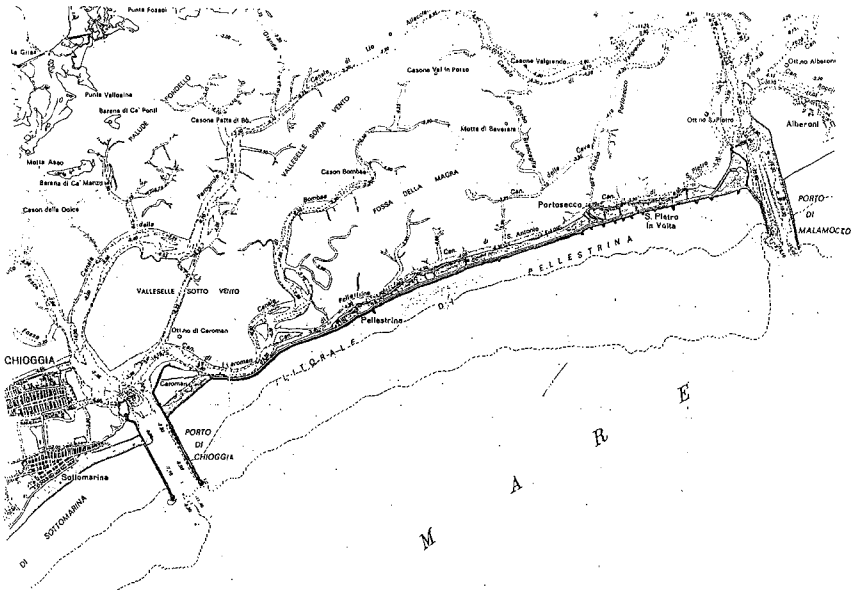


Figure 4. The narrow stretch of land between Malamocco and Chioggia.

the middle and lower river bed. This fact rendered insufficient the renewal of sediments brought by the littoral currents that develop along the Venetian coast. The erosive action of the breaking sea waves therefore made the state of the narrow stretch of land and its littoral, especially that between the inlets of Malamocco and Chioggia (Fig. 4), particularly dangerous.

Until the end of the XVIIth and the beginning of the XVIIIth centuries attempts to protect the littoral using flexible systems of piers, branches and stones were repeated. At last, the Republic engaged Bernardino Zendrini, State Mathematician, and the experts Giovanni Filippini, Overseer to the Lidos, Matteo Lucchese, Overseer to the Lagoon, and Tommaso Ternanza, Overseer to the Rivers, in order to work on a project for stable defence. The Report ("Relazione" of June 1st, Zendrini, 1743) contained the design for the "murazzi" (Venetian massive walls). The primary idea is mainly traced back to Abbot Coronelli in about 1706 and the name was already current in Venice for protective works using pozzuolanic cement (Benigni, 1983). The original design of the "murazzi" attached to Zendrini's report is reproduced in Fig. 5. The "reinforcement plan" was carried out during a period of about 40 years and this protection has lasted up to the present time (Gottardo, 1976). However, some repairs have been necessary, particularly after the exceptional storm of 1825 and the recent one of 1966. We must bear in mind, though, that the construction of the long breakwaters defending the mouths, which took place between the end

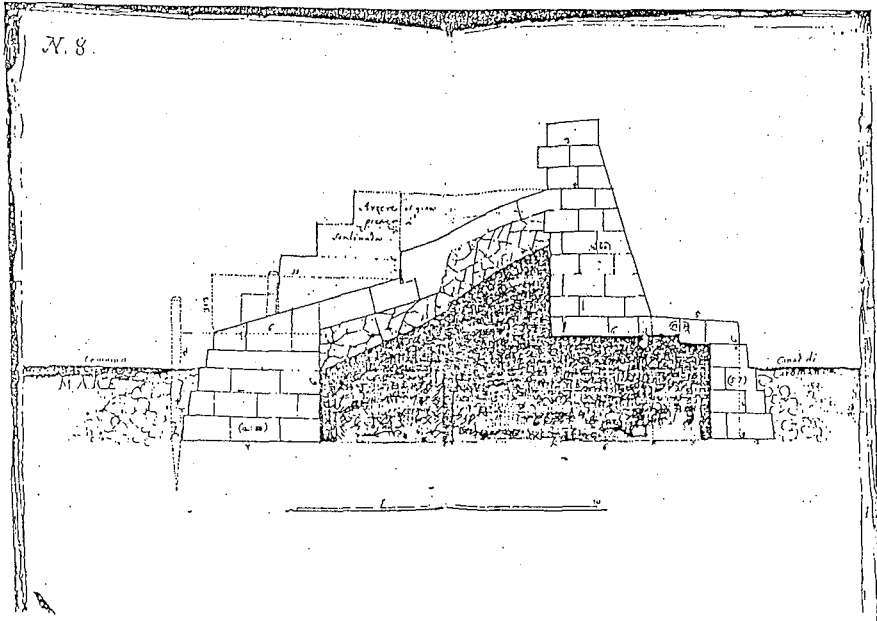


Figure 5. Original design for the "murazzi" (Zendrini, 1743)

of the XIXth and the beginning of the XXth centuries cut down both northern and southern sediment transport to the physiographic unity confined by the Lido and Chioggia moles, including the narrow Caroman littoral.

The state of the "murazzi" deteriorated as a result of the erosion made by waves at the toe of the wall. The reinforcement was not limited to reconstructing and strengthening the rubble mound at the toe of the "murazzi", as shown in Fig. 6. It was necessary to consider the foreseeable possibility of isolating the lagoon from the sea, on different levels, in the case of exceptional tide. Therefore measures were taken to protect the foundation of the "murazzi" from the risk of siphoning using an impermeable diaphragm of reinforced concrete, sunk as far down as a layer of clay situated at about 20 m below sea level. Since this main diaphragm had to be constructed on the lagoon side, a second and shorter diaphragm was sunk at the toe of the "murazzi" in order to lessen the effects of underpressure waves reflected by the first diaphragm. Such an effect was experimentally observed *in situ* under the breakwater of Genoa harbour (Marchi e Stura, 1976). The cause, in that case, was attributed to the natural silting up of the internal porosity of the breakwater rubble mound.



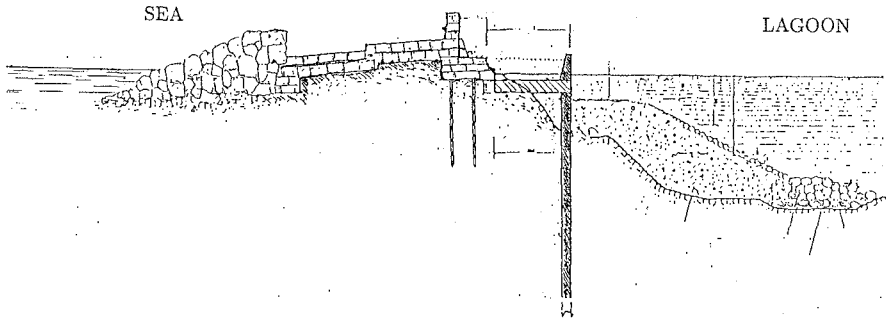


Figure 6. Reinforcement of the "murazzi" after 1966.

## 6 Conservation of the Water Depth at the Mouths

The Venice Lagoon behaves, as already noted, like a "short" basin. Under this condition the tidal "prism", that is the volume entering the basin in one tidal cycle, is correlated with the basin surface. A relationship between the same tidal prism and the section area of the inlet was suggested by O'Brien (1969) and supported by others, in particular by Jarrett (1976), who based the result on a series of field measurements. The correlation form is analytically justifiable and the theoretical study (Marchi, 1990) has confirmed the experimental relationship between the area  $\Omega$  of the inlet section and the power 6/7 of the volume  $P$  of the tidal prism:  $\Omega = kP^{6/7}$  (Fig. 7). Furthermore, it has shown the factors on which the correlative coefficient  $k$  depends, in particular its functional dependence on the value of the shear stress at which the bed erosion begins and on the roughness of the bed itself.

Given the proportionality of the tidal prism  $P$  to the surface  $S$  of the basin, we could think that a simple relationship of the former type is valid also for  $S$ . However, it must be noted that the tidal prism is not only a linear function of the basin surface but also of the inside tidal amplitude which is still a function of the area  $\Omega$ . From this derives a more complex relationship between  $S$  and  $\Omega$ . Fig. 8 shows the curves relative to the three present mouths of the Lagoon. Note that if the opening has a value lower than a given limit (the asymptotic value of the left branch of the curve  $S = f(\Omega)$ ) the mouth cannot resist. Above such value the area  $\Omega$  increases by erosion until it arrives at the stability which depends on the balance between the maximum shear stress imposed at the bottom by the tidal current and the resistance to erosion of the bed surface. As  $\Omega$  increases, its influence on the tidal amplitude has the tendency to vanish and the relationship becomes of the previous type ( $\Omega = K_1 S^{6/7}$ ), as shown by the right branch of the curves in Fig. 8.

The conservation of the basin surface thus assures the conservation of the

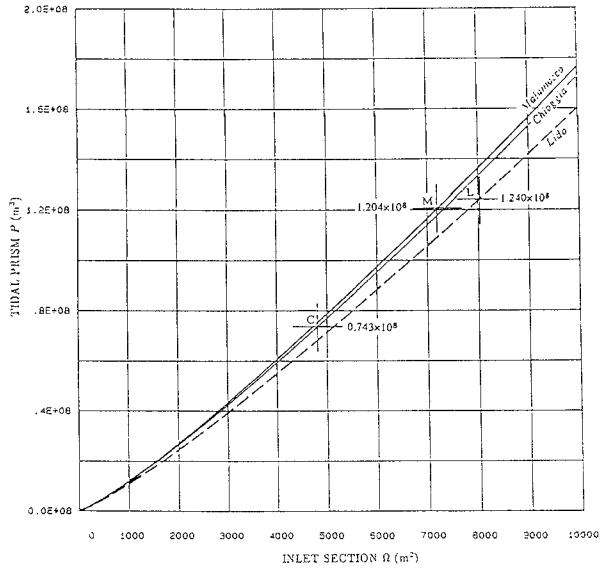


Figure 7. Relationship between the tidal prism  $P$  and the inlet section  $\Omega$  (from Marchi, 1990).

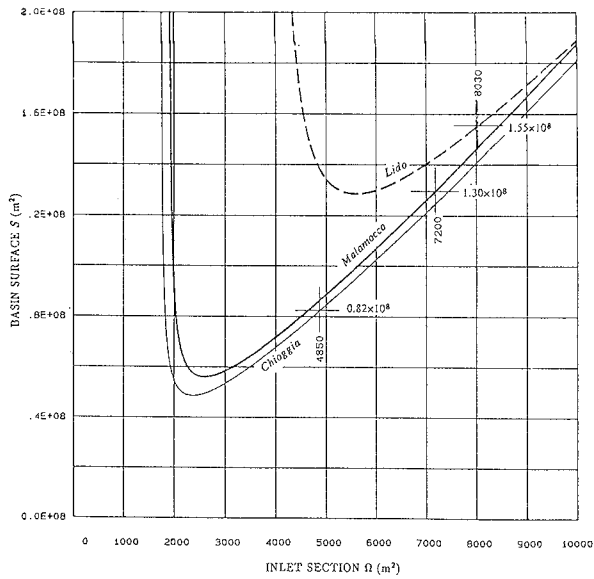


Figure 8. Relationship between the basin surface  $S$  and the inlet section  $\Omega$  (from Marchi, 1990).

section area of the mouth if stable conditions have been reached (Bruun, 1978). However, the section area, by and large, can be maintained even if, as a result of the action of the sea waves, the water depth tends to diminish; for this it is enough for the width to increase accordingly. This can happen by the erosive action of the tidal currents. An example is represented in Fig. 9 by the evolution of the Lido mouth during the period 1552-1968 (Baroncini et al., 1983).

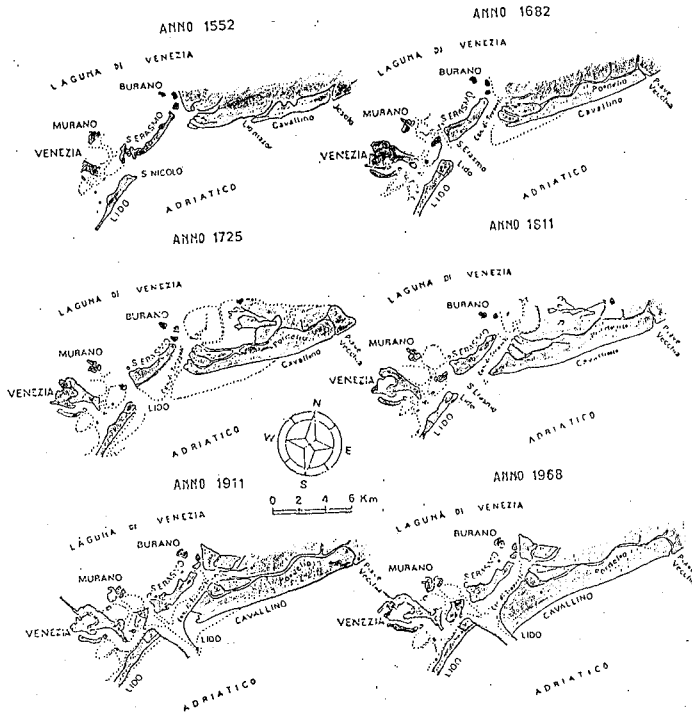


Figure 9. Evolution of the Lido mouth during the period 1552-1968 (from Baroncini et al., 1983).

In the XVIIth century shipping, especially through the Lido mouth, had already become difficult. Access to the Lagoon for loaded ships - although they were sailing ships with a small draught - was possible only during the hours of high tide and, in some cases, required a lightening of the load at sea. The situation rapidly became worse with the coming of steam ships which had a considerably larger draught.

In the first half of the XIXth century the Malamocco mouth was the only navigable inlet, since those of Lido and Chioggia had depths of only two meters. In order to conserve and increase the navigability of the Malamocco mouth, at the

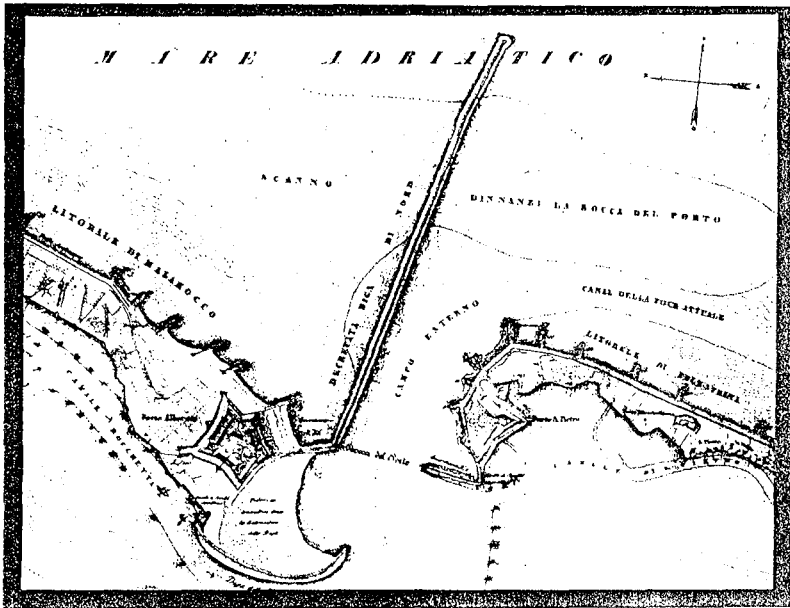


Figure 10. Protective jetty to the North of the Malamocco mouth (from Tomasicchio, 1983).

beginning of the XIXth century a technical commission nominated by Napoleon proposed the construction of a protective jetty to the North of the mouth (Fig. 10). After many ups and downs, the work was carried out toward the middle of the century, as a result of the authoritative influence of Pietro Paleocapa (Noli, 1990). It was completed with the construction of the south jetty in 1872. With the width of the mouth limited in this way to about 500 m, the tidal currents began to erode the bottom and its deepening took place with different speeds according to the different resistance of the ground layers (Fig. 11) (Cavazzoni et al., 1983). This process continued until the middle of the present century and increased the depths to mean values of about 15 m, with an area of the minimal section of about 7300 m<sup>2</sup> that can now be considered stable (Consorzio Venezia Nuova, 1980).

The result obtained at Malamocco stimulated similar works at the mouths of Lido (1882-1910) and Chioggia (1911-13), which assumed the configurations visible in Fig. 2. Probably an overvaluation of the efficiency of the Lido mouth suggested a width of 900 m for this canal. In effect, the Lido water flow is hardly different from that of Malamocco and so the depth of the former mouth is established at 10 m for a large part of the section and is smaller near the north jetty.

If, on one hand, the construction of the mouth embankments has assured

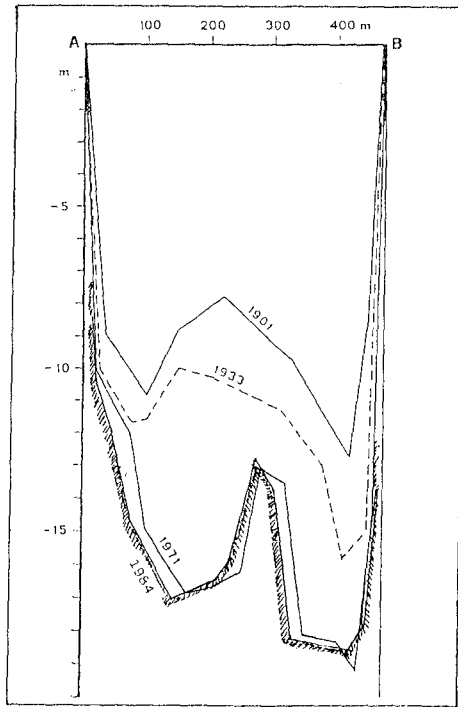


Figure 11. Changes to the section of the Malamocco mouth following the construction of the jetties (Cons. Venezia Nuova, 1989).

the presence of great depths and thus continued navigability, on the other hand the seaward protrusion of the jetties has stopped the sediment transport by the littoral current. The present increase to the shores north of Lido and, partially, south of Chioggia is the evident result. On the contrary, the intermediate shores have become unstable and now require an artificial nourishment between Lido and Malamocco (Wallingford H.R. as consultant) and protection work to the "murazzi" between Malamocco and Chioggia, as earlier mentioned (Tomasicchio, 1983; Baroncini et al., 1983).

## 7 Protection against tidal effects

### 7.1 Tides

Venice arose on the group of islands around Rialto and so is in a central position with regard to the Lagoon but very close to the largest of its openings,

the Lido mouth. Therefore it has always been subject to floods, known by the name of "acque alte" (high waters), caused by the spreading out into the Lagoon of unusually high tides.

The ordinary Adriatic tides (Tenani, 1935; Polli, 1959; Defont, 1961) are of an astronomic nature and have a fairly small amplitude, around 0.60 m with a maximum of 0.90 m at the northern end of the Adriatic during the syzigial period. To the astronomic tide, characterized by a mean period of 12 hours and a secondary period of 24 hours, can be added the effect of atmospheric phenomena such as winds and low pressure. We can maintain that the action of the "sirocco", a southern wind, alone can cause a rise in the sea-level of as much as 0.90 m in exceptional conditions. A further factor in the increase of the maximum levels is represented by the seiche of the Adriatic around a transversal axis. These factors, when they act together, create tides of exceptional height and a non-periodic form, such as that illustrated in Fig. 12 which relates to the 1966 disaster.

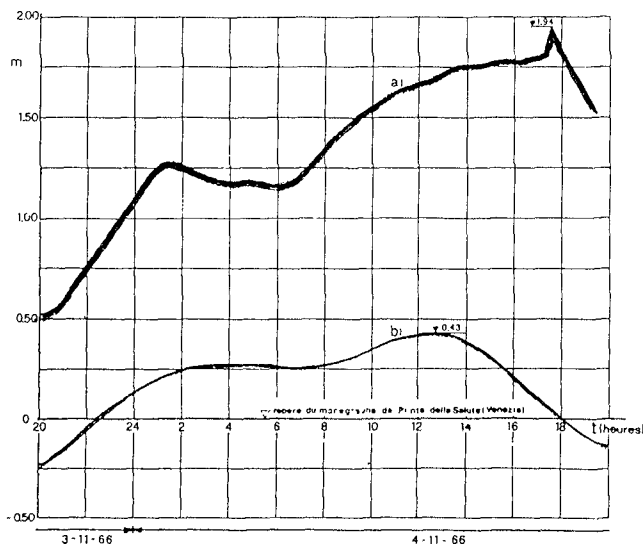


Figure 12. Exceptionally high tide of 1966: a) measured level, b) astronomic forecast.

The tides enter the Lagoon through the three mouths and mainly propagate through a ramified system of submerged channels. The tidal elevations in Venice are usually referred to the tide gauge at Punta della Salute, on which the zero mark is still anchored to the mean level of the sea in 1897 (Comune di Venezia, Ufficio Idrografico del Magistrato alle Acque, CNR). The "acque alte" start at the 0.70 m mark, when water appears in St. Mark's Square, and so far have reached a maximum of 1.94 m in November 1966.

Table 2 shows the percentages of the flooded city which correspond to the various levels:

Tab. 2

Tide elevation at Punta della Salute	Flooding of the city
1.0 m	5%
1.1 m	15%
1.2 m	33%
1.3 m	62%
1.4 m	almost complete

A review of the highest tidal levels at Punta della Salute in Venice reveals a notable increase both in value and, above all, in the frequency of each level during this century.

Fig. 13 shows a tidal frequency curve at Venice in the decade 1975-1984 (Consorzio Venezia Nuova, 1989). Note that the 1.20 m mark, which until the last century was rarely reached (once every two or three years), has now been attained or surpassed twice every year. This worsening situation culminated in November 1966 when the highest tide in living memory covered St. Mark's Square with more than a meter of dirty water (Dorigo, 1969).

The causes of these changing phenomena, that seriously threaten the very survival of Venice, are to be found in three different factors (Ghetti et al., 1983):

- i) the eustasy, that is the rise in the mean sea-level;
- ii) the subsidence of the Lagoon territory and, particularly, the sinking of Venice;
- iii) the increase of the tidal amplitude in the Lagoon.

The aforesaid factors have various origins and different weights in the context of the phenomena being considered.

## 7.2 Eustasy

After the last glaciation the Adriatic sea level notably rose, to about 90 meters, and this obviously modified the coastal and lagoon morphology, as already said. During the last centuries, however, the sea level appears to be rather stable, at least so as not to reveal evident changes with regard to the level of the buildings. The traditional mark for the building level in Venice was that of the mean high tide. In fact, the oldest buildings (XIIIth-XVth centuries, see for example Fig. 14) seem nowadays to have thresholds and ground floors lower, in comparison to the sea level, than the buildings of the XVIth-XVIIth centuries (see for example Fig. 15). From these illustrations we cannot say if this is due

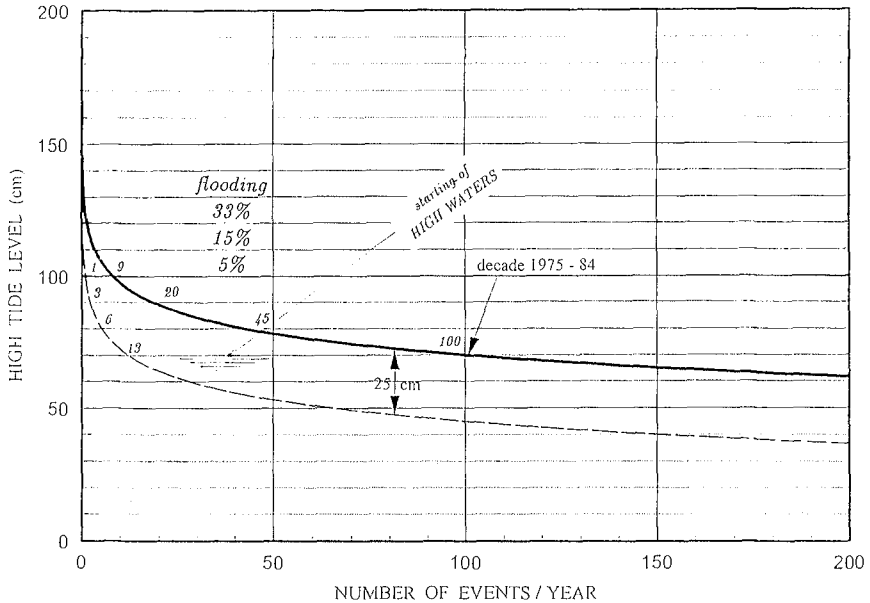


Figure 13. Frequency curve of "high water" in Venice in the decade 1975-84. The dotted line represents the same curve translated downstream by 25 cm.

only to a rise in the sea level or to a land subsidence as well. What is certain is that from the beginning of this century the rate of the rise in the sea level has increased and it has been possible to measure an average rise of 1.27 mm per year. Altogether we can consider, during the present century, a sea level increase of about 10 cm (Consorzio Venezia Nuova, 1989).

The forecast is not optimistic even for the immediate future. The change of the world climate due to the greenhouse effect shows a tendency to the increase of the mean temperature and so to a regression of the glaciers and to a sea level rise. Despite uncertainties that still exist about the interpretation and, above all, on the forecast of climate phenomena, there is a substantial agreement about a scenario which foresees a sea level rise of several centimeters already in the year 2000 and in the order of tens of centimeters up to more than 1 meter in the next century (Thomas, 1986).

In the project for safeguarding the lagoon environmental system eustasy values variable between 0 and 60 cm have been considered.

### 7.3 Subsidence

The Venice subsidence is a phenomenon determined first of all by a natural component of a geological type. The alluvial nature of the layers that make up the superficial area of the lagoon land and the tectonic deformations of



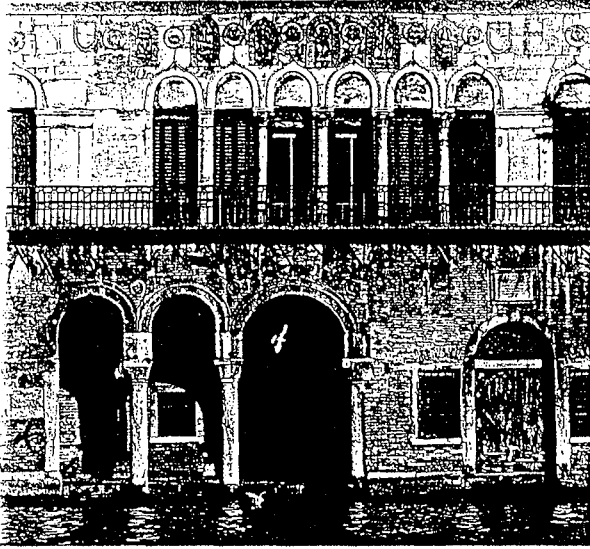


Figure 14. A XIIIth century palace (Ca' da Mosto).

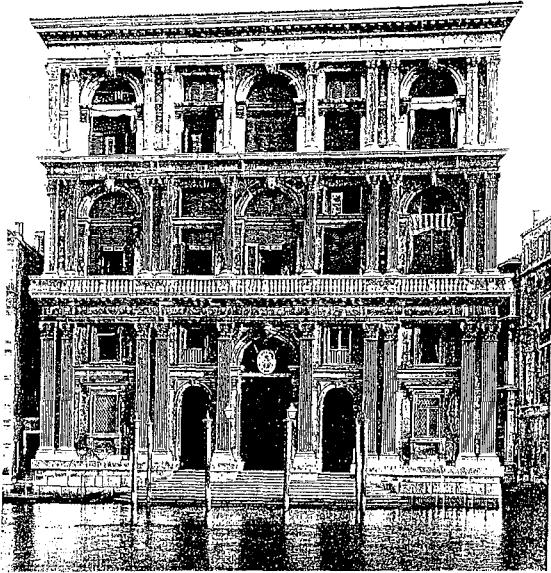


Figure 15. A XVIth century palace (Grimani palace).

the substratum provoke a slow consolidation of deposits and a lowering of the Adriatic coast which can be a source of worry after several centuries. At present the mean rate of natural subsidence is estimated at 0.4 mm per year.

On the other hand, in the first half of the XXth century, and in particular from 1930 onwards, the subsidence was rapidly worsened by an anthropic component and the ground became lowered to values first of 2 mm/year and then, after 1950, up to 7 mm/year. The cause of this extraordinary increase in subsidence lies in the effect of overall heavy groundwater withdrawals in the Venice's surrounding region for the needs of Marghera's industry and also for civil and agricultural use. Between 1950 and 1970 this process of impoverishment of the groundwater layers and the consequent soil lowering continued indiscriminately. The alarm sounded late in conjunction with the increasing frequency of the "acque alte" (Carbognin et al., 1981). Accurate level surveys recorded the gravity of the risk (CNR, 1970; Consorzio Venezia Nuova, 1988) and the process was also mathematically simulated (Gambolati et al., 1973, 1974). Thus, between 1970 and 1975 pumping was gradually stopped. The artesian layers rapidly recovered the piezometric levels of 1950, but the soil lowering, at least up till now, appears to be irreversible. The mean level of the Venice land was lowered by 9 cm between 1952 and 1969 (Caputo et al., 1971) and during the entire century we can now estimate a total subsidence of 15 cm for the city.

If the two effects of eustasy and subsidence are added up one obtains a variation of the land level relative to the mean level of the sea at Venice of around 25 cm (Supino, 1978). Applying such a variation to the frequency curve plotted in Fig. 13 (see the dotted curve) it can be seen that the frequency increase of the "acque alte" caused by this change is truly impressive and corresponds to that observed over the last hundred years. The 80 cm mark, which without eustasy and subsidence would have had a frequency of 6 times per years, has been reached at present more than 45 times; the level of 1 m has passed from a frequency of 1 time to the present 9 times per year.

## 7.4 Amplitude of the lagoon tide

### 7.4.1 General remarks

The amplitude of the tides at Punta della Salute is roughly the same as that of the tides recorded at sea on the outer mole of the Lido mouth. The amplitude of the tide waves is scarcely reduced by their propagation through the inlets because of the slight resistance that is offered by the mouth canals. On the other hand, the speeds remain contained because they are correlated to the limit erosion values and, consequently, they model the form and area of the section. Obviously, this process depends on the nature of the bottom and on the distribution of sediment in the chanal. Thus, the probable silting up of the Lido mouth during the period of the last war (1940-45) resulted in a resistance increase and so in a small reduction of the tide amplitude between Lido and Punta della

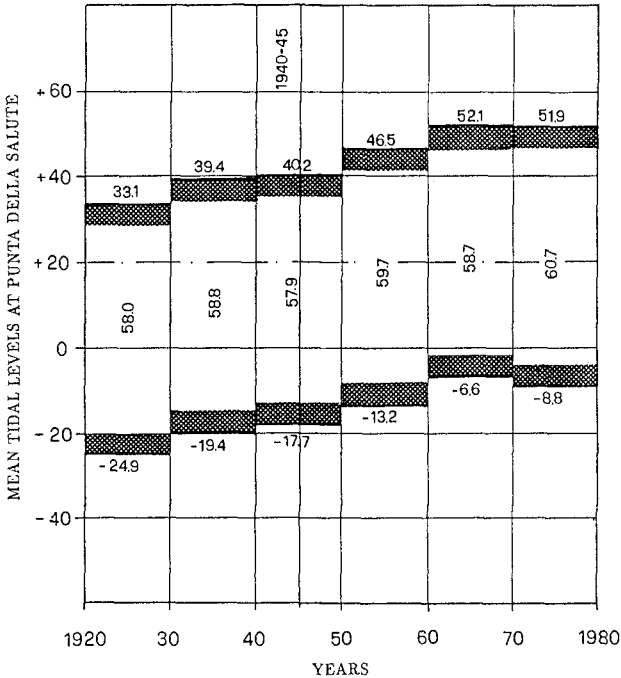


Figure 16. Variations in tide amplitude during the century.

Salute (Adami, 1974); this reduction was of about 5% as seen in Fig. 16. On the contrary, the general lowering of the land during the '70s, increasing the depths of the inlets and of all the lagoon channels, slightly reduced the resistance and so increased a little the amplitude so as to make the Punta della Salute tide equal or even 1-2% superior to that of Lido (Gottardo, 1975).

These observations show the marginal influence of the considered factor - the variation of the tidal amplitude between the sea and Venice - on the phenomenon of the "acque alte" increase. Further confirmation has been provided with studies carried out using mathematical and physical models.

#### 7.4.2 Mathematical models

The tidal oscillations in the Lagoon have been studied with various types of mathematical models, which can be substantially reduced to three types: static model, one-dimensional propagation model and two-dimensional propagation model.

The *static models* study the relationship between marine oscillations and those in the Lagoon assuming the surface of the lagoon basin to be always

horizontal and considering effective only the flow resistance of the inlet. Numerous solutions have been reached after the original proposal by Poleni in 1717. A detailed review will be found in Ghetti's report of 1979 at the XVIII IAHR Congress in Cagliari (1979), and in his recent paper (1991) on Italian contributions to the lagoon hydraulics. A. Ghetti also promoted an eleven volume rich collection of studies on the Lagoon environment published by the Istituto Veneto di Scienze, Lettere ed Arti.

The results obtained using the static method are clearly confirmed by the tidal records at the Lido mouth (Adriatic Sea) and at Punta della Salute (centre of Venice). This type of model has been used to examine the effects on the Venice tidal levels caused by the artificial narrowing of the lagoon mouths. It has been observed that also very strong reductions, to the limits of the mouths' navigability, such as to lessen the section area to about one third of the present one, can reduce the maximum level of a periodic syzygial tide at Punta della Salute by about 20% (Ghetti et al., 1972). But such narrowings cease to be effective with regard to the long aperiodic tides, being able, for example, to lower by only 5% the maximum level of an exceptionally high tide like that of November 1966 (Fig. 17).

The propagation of tidal waves inside a lagoon was deeply studied by Supino (1955) and Pezzoli (1958) in the 1950's; contributions to knowledge of the process have been subsequently carried out by the same authors (1970) and also by the present writer (1986).

After the great flooding of 1966, the numerical mathematical models have become widely diffused.

The *one-dimensional propagation model* allows the study of the tidal flow into the Lagoon following the existing submerged channels, applying the de Saint-Venant equations to all stretches and satisfying the condition of volume and level conservation in the nodes. This type of model, originally proposed by Dronkers (1969, 1972) received substantial contributions from the research of Datei (1972), Di Silvio and D'Alpaos (1972) and Di Silvio (1978). Further improvements, both as regard the speed of computation and the more detailed description of the Lagoon, have been introduced in the recent model which has been developed by "Technital", with D'Alpaos as consultant, on behalf of "Consorzio Venezia Nuova" (1985). The consequences of certain modifications of the Lagoon basin have been examined with this model. The situations that have been compared are those before and after the digging of the "oil canal" and the filling up of some areas for industrial use. These two modifications, which bring opposite effects, have shown to have a slight influence on the volumes exchanged between Lagoon and sea: they have increased by some per cent at Malamocco and Chioggia and decreased by the same amount at Lido. Thus, the simulated opening of the fishing areas to the tides appeared to have very slight influence on the levels of "acque alte" at Venice. Despite a surface increase of about 80 km<sup>2</sup> (from 370 to 450 km<sup>2</sup>) the lowering of the maximum level in the central Lagoon and particularly at Punta della Salute turned out to be no more than a

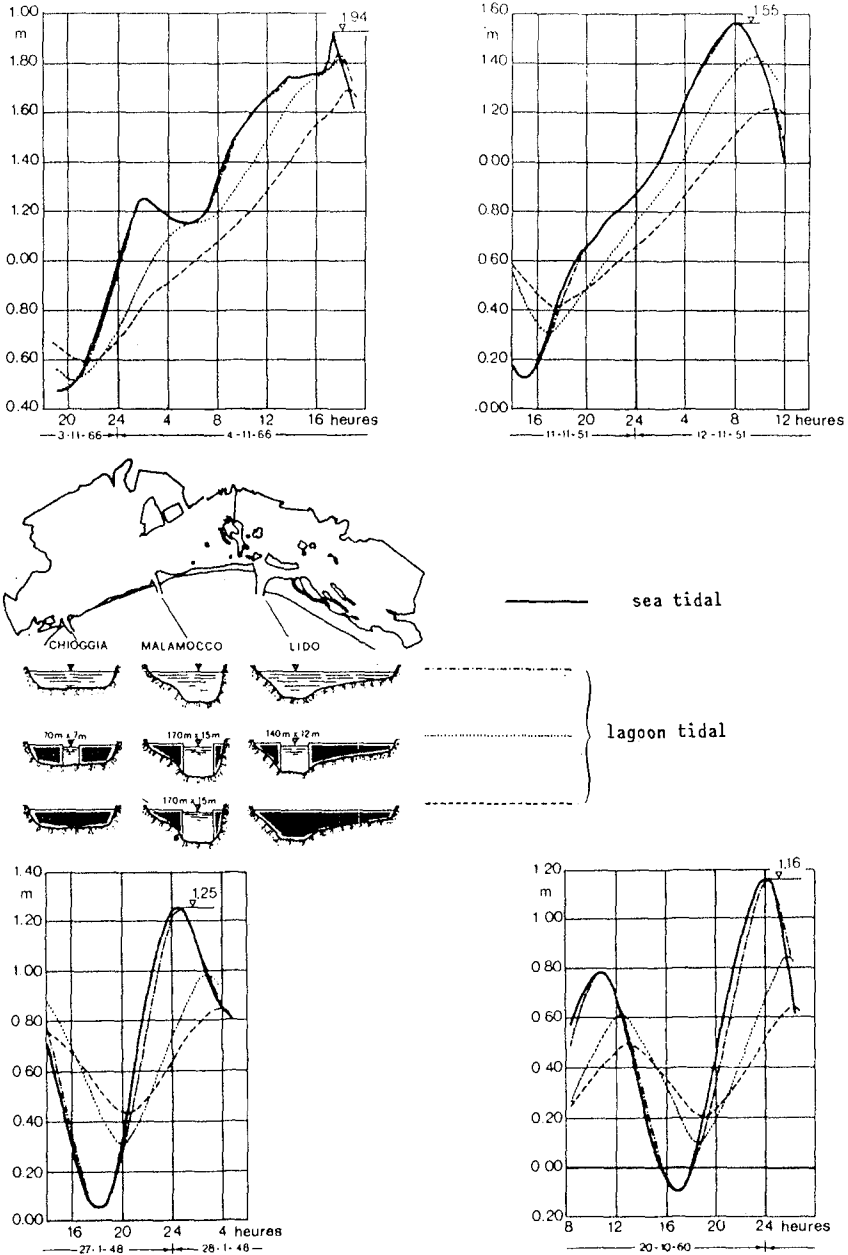


Figure 17. Tide reduction due to mouth narrowings (from Ghetti et al., 1972).

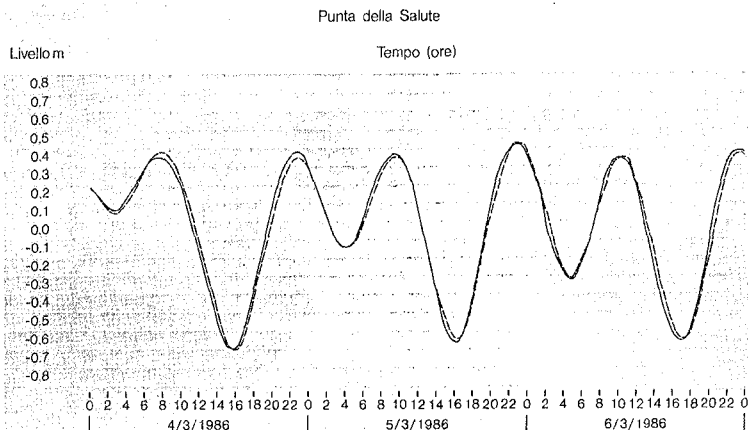


Figure 18. Calibration of the D.H.I. two-dimensional model (from Cons. Venezia Nuova, REA 1989).

few centimeters in the case of high tides with a level above 1 meter.

These observations have been confirmed by a more recent and sophisticated type of model, the *two-dimensional propagation model* based on the finite difference method and developed by the Danish Hydraulic Institute.

The mathematical procedure is the one originally proposed by Leendertse (1967) on the basis of the theory of low-water waves (Stoker, 1957) and it uses the continuity and momentum equations of the two-dimensional flow with quadratic resistance. The first application of such a model to the Venice Lagoon was carried out by the Venice IBM Center (Chignoli and Rabagliati, 1976) with a rather large grid. Further more refined developments have been undertaken by the same IBM Center. A grid size of 225 m has been used in the model prepared by the Rijkswaterstaat Laboratory collaborating with the Institute of Hydraulics of Padua University (D'Alpaos and Di Silvio, 1979) in order to study the behaviour of the central Lagoon.

The aforementioned DHI model (Consorzio Venezia Nuova, 1987-88) uses grid of 300 m size, reduced to 100 m in the areas surrounding the mouths. An example of calibration of the model by comparison with the March 1985 tide, recorded in various points of the Lagoon, is shown in Fig. 18.

Compared to the one-dimensional model, the two-dimensional one gives a better general picture of the deep water flow. A further improvement in the representation of such areas and also of the ramifications of the channel network can be obtained by the passage from the finite difference to the *finite elements model*. One gains in descriptive detail without an increase of, indeed with a reduction of, the total number of nodes.

The equations used and the resolution methods adopted for the finite elements model are those proposed by Backhaus (1976), Gray and Linch (1977), Duwe

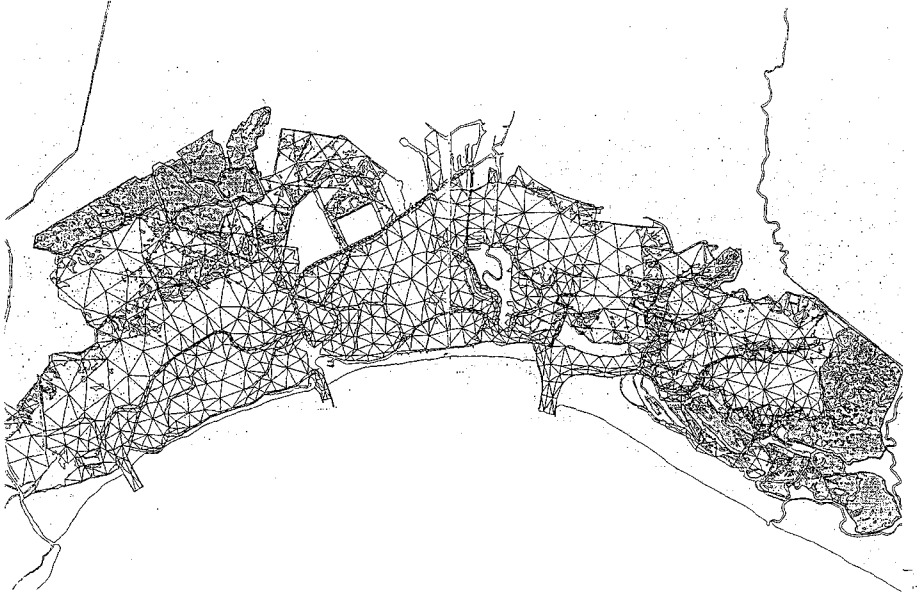


Figure 19. The planimetric mesh of the finite elements model (from Cons. Venezia Nuova, REA 1989).

Andamento del campo di moto alle ore 19



Figure 20. Flow field simulated by the finite element model (4th Feb. 1985 tide; from Cons. Venezia Nuova, REA 1989).

and Hewer (1982). Fig. 19 shows the planimetric mesh and Fig. 20 gives an instantaneous representation of the flow field corresponding to the simulation of the 4th February 1985 tide (Consorzio Venezia Nuova, REA 1989).

Models of the same type were used to investigate the hydrodynamic behaviour of the mouths (Consorzio Venezia Nuova, REA 1989) and an example of the ebb current at the Lido mouth is represented by Fig. 21.

*Lagrangian models* were used to examine the so-called "residual" circulation in the lagoon (Datei, 1978; Cheng et al., 1982; Rinaldo et al., 1987) and to describe processes dominated by convective transport (D'Alpaos and Degan, 1977), while *dispersion models* have been developed on the basis of the diffusion equation (Fiorillo, 1978; Di Silvio et al., 1977, 1980, 1988; Dejak et al., 1984).

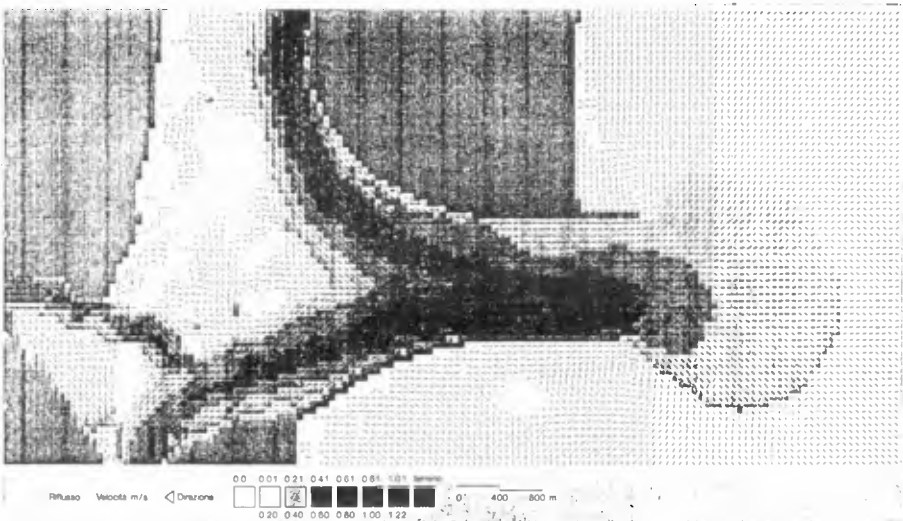


Figure 21. Example of the ebb current at the Lido mouth (from Cons. Venezia Nuova, REA 1989).

### 7.4.3 Physical models

The phenomenon of the hydrodynamics of the mouths has also been analysed by means of *physical models*, both aerodynamic and hydraulic. The *aerodynamic models* have been built to the planimetric scale 1:3,000 and the altimetric scale 1:1,000. Given the great reduction in size, the evaluation of the velocities and of the head losses was effective more for the comparison of the reactions in different possible projects than in absolute terms (Adami et al., 1981; Da Deppo et al., 1987; Consorzio Venezia Nuova, 1988).

The *hydraulic models* have been constructed at the Voltabarozzo Experimental Center run by the Ministero dei Lavori Pubblici (Italian Ministry



of Public Works). A general model of the Lagoon with a horizontal scale 1:250 and a vertical scale of 1:20 has been built with a stable bed covering an area of about 16,000 m<sup>2</sup> (Baroncini, 1983). Difficulties arising from its use, above all regarding the space and time distribution of tide among the three mouths and the adjusted reproduction of wall friction because of the very high distortion of the model, have slowed down its effective use. Nevertheless, some results enable us to understand the behaviour of the inner area of the Lagoon, where the three dimensional features of the flow become important. Greater use has been made of separate models of the three mouths, each built to the geometric scale of 1:60 (both horizontal and vertical). Such models, which are applied under steady conditions, have provided useful information about the flow field and the losses distribution of the tidal currents (Consorzio Venezia Nuova, 1986). They still have the task of selecting the best conditions for the projected solutions.

## 7.5 Surface waves

The Venetian Gulf is not subject to particularly heavy sea waves because it has an "effective" maximum fetch of 300 km in the "sirocco" direction 130°-140° N and of 80 km in the "bora" direction 70°-80° N. Furthermore, the depths remain fairly uniform; they do not go beyond 25 m in the bora direction and increase in the sirocco direction being under 40 m at 100 km from Venice.

The wind regime shows two directional modes that can be seen also in the waves. Information about significant heights and directions of the waves (Fig. 22) has been provided by the Hydrological Service of ENEL (the Italian general Electric Company) at a depth of about 25 m in front of the Po-Delta, and by CNR-IDGM (Dynamic Mass Institute of the National Research Council) and Consorzio Venezia Nuova on a platform placed at about 15 km in front of Malamocco at a depth of 16 m (Consorzio Venezia Nuova, 1987, 1988). In effect the two prevalent directions, around 70° N and 130° N, have been confirmed. Significant waves with a height  $H_s \geq 3$  m have a frequency of less than 1%, while the height  $H_s \geq 1$  m appears with a frequency of 10%.

Regarding wave propagation in the inlets, both direct measurements and evaluations using physical and mathematical models have been carried out. Various mathematical models have been commissioned by the Consorzio Venezia Nuova from the Wallingford Hydraulic Research Laboratory and the Delft Hydraulics (Consorzio Venezia Nuova, 1987), each model having a specific field of application: from the open sea to the mouths, and from the areas surrounding the jetties as far as the interior of the mouth canals.

## 7.6 The planned defense works

Protection from the "acque alte" must be carried out with the assurance of an exchange of the basin water that is sufficient to avoid worsening the ecological state in the lagoon. Even if the effects of new purification plants can be counted

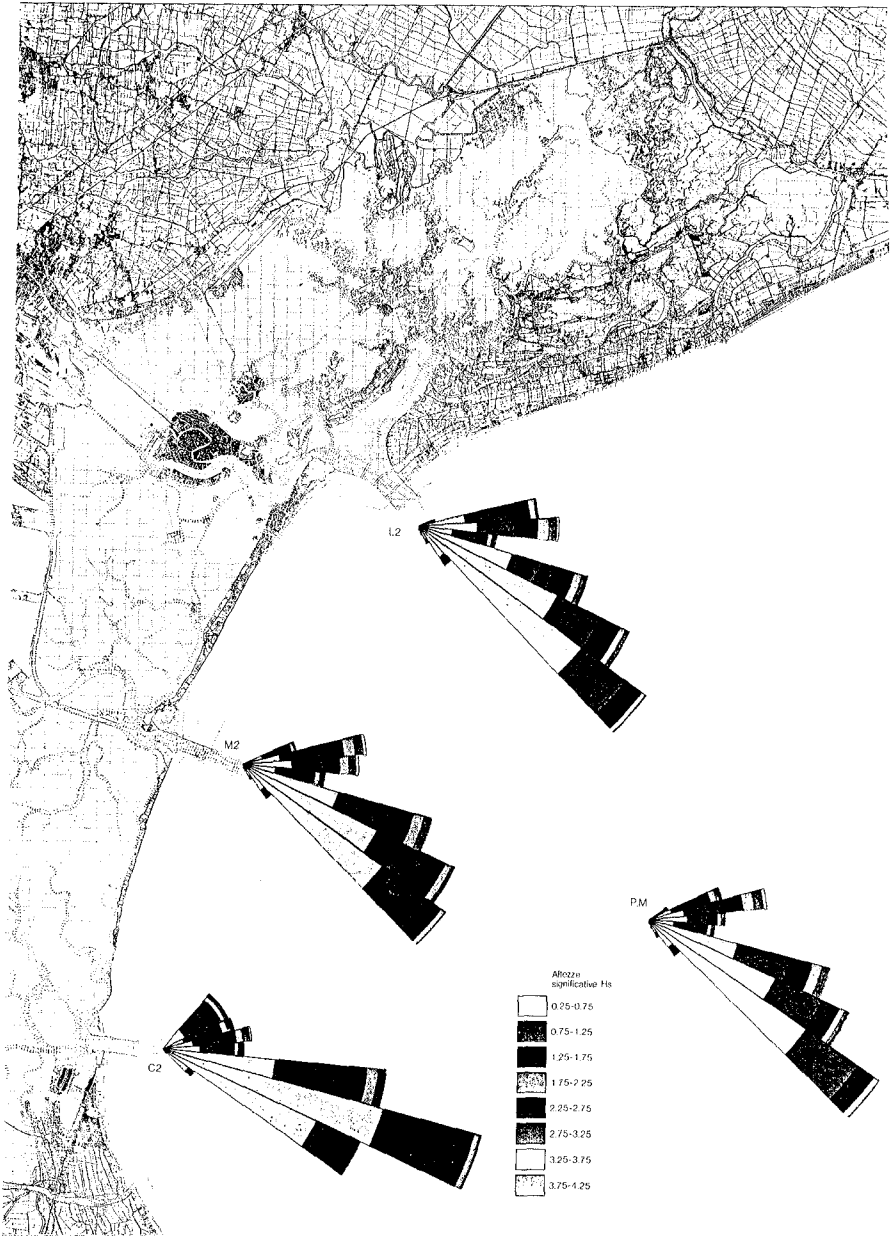


Figure 22. Sea wave directions and amplitudes (from Cons. Venezia Nuova, REA, 1989).

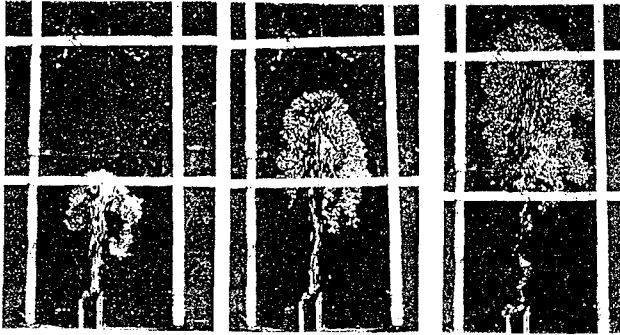


Figure 23. Experiments on the dispersion of pollutants in the sea caused by the ebb current (from Arato et al., 1983).

on as far as regards the reduction of industrial pollution, the agricultural and, partially, anthropic contribution is still high. Therefore, the ebb and flow of the tide into and out of the lagoon is still a factor essential for its vitality.

The process concerning the tidal currents around the openings of the inlets was studied by Blondeaux, De Bernardinis and Seminara (1982). The flow has been considered irrotational in the flood phase, while the shedding of vorticity in the ebb phase has been simulated by a discrete vortex technique. The resulting asymmetry of the flowfields during the different tidal phases justifies the dispersion of pollutants in the sea, also experimentally verified (Arato et al., 1983) (Fig. 23).

A second binding condition for the defence works is evidently to conserve the navigability of the mouths, with regard to the manoeuvrability of ships and the depth of the waterways and also to the duration of their possible use. Accordingly, current velocities must not exceed 2.00-2.50 m/s.

Furthermore, such works should not provoke erosion and, in general, not modify the morphological condition. Finally, they must not stand out in the lagoon landscape.

The planning studies, carried out by TECHNITAL on behalf of CONSORZIO VENEZIA NUOVA, have shown up the interconnections among the "acque alte" defence works and those of morphological re-equilibrium of the lagoon system and for the protection of littorals and the lagoon contours. The morphological evolution of the lagoon can be predicted on the basis of a long-term balance of sediment suspension and transport (Di Silvio and Gambolati, 1990). Thus, before carrying out the safeguarding works against high tides, some morphological modifications are being undertaken. These are the necessary works for the littoral protection, mentioned above, and the experimental ones (such as the reconstruction of the "barene") to halt the environmental deterioration of the Lagoon in danger of becoming a bay.

On the other hand, as regards the real safeguarding against the "acque alte", we had a choice between two ways (Agema et al., 1983).

- A) to have recourse to *permanent narrowings* of the mouths or, anyway, to concentrate resistances so as to provoke a considerable reduction of the tidal amplitude in the Lagoon, particularly in Venice;
- B) to install *mobile floodgates* at the mouths, able to interrupt completely the tidal flow when they are in use and which are not visible and do not interfere with the flow when they are open.

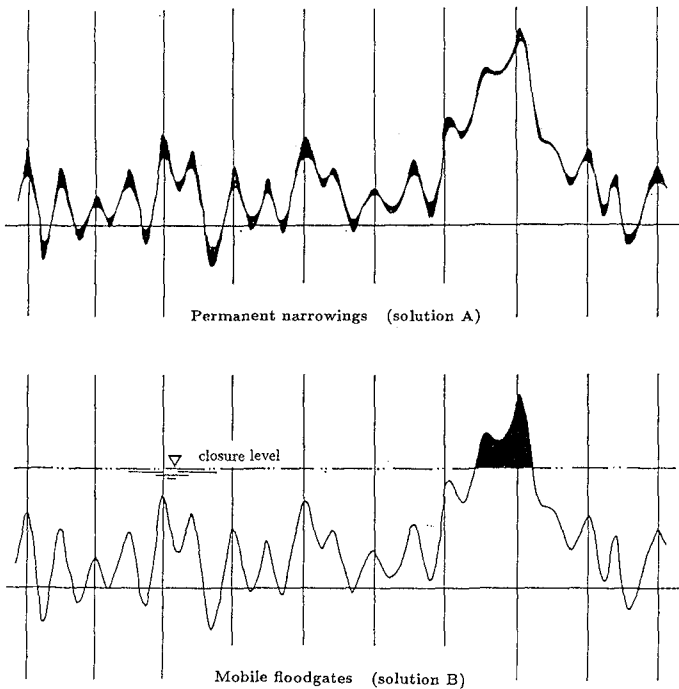


Figure 24. Comparison between the solutions A and B.

The differences between the two criteria are pointed out by Fig. 24. The first solution has the advantage of being simpler to construct and that of reducing the middle-high tides that are the most frequent. On the contrary the disadvantages are: the high tides of aperiodic kind are not sufficiently reduced, as already said, the currents become very fast in the narrowings and would therefore be dangerous for navigation and bottom erosion and, above all, the volume of sea-lagoon exchange would be permanently reduced. Such a reduction, in relative terms, would be greater or at least equal to the relative reduction of the tidal amplitude,

thus resulting in an equivalent relative increase of pollutant concentration in the Lagoon.

The *permanent narrowings* solution appears as a *defence system* against high tide whose efficiency is conditioned by the dynamics themselves of the tides.

The other solution, using *mobile floodgates*, behaves as a *control system* of the lagoon tides, able to limit the maximum levels to a given threshold, completely independent of the kind of tide. The influence on the water exchange is evidently limited to the periods when the gates are closed, periods that should now be relatively short in the course of a year.

The current project is based on this second criterion, having also rejected the possible use of partial permanent narrowings to support the mobile floodgates. This last choice is a result of the consideration that the benefit in the cost reduction seems lower than the disadvantages of the presence of obstructions, as sources of vorticity and as reducers of the mouth efficiency in the exchange of water. It is always possible, though, to reduce partially the openings even with the mobile gates.

## 7.7 The floodgates

The criterion of being able to close with moveable barriers wide passages at the mouths had already been adopted in 1981 by the group of Experts commissioned by the Ministero dei Lavori Pubblici (1981) to study the feasibility of the tidal protection of the Venice Lagoon. Since that time the chosen barriers were of the type with a hinge at the base, normally at rest on the bottom of the passage. The closure is obtained through the gate floating up due to the expulsion of water from its compartments by compressed air.

Such a choice is connected with the ability of the system to work in very wide canals without intermediate piers, with no superstructure and with an apparatus which can be hidden completely within the bottom. This type of mobile barrier exercises only a limited reflection of the open sea waves in so far as it oscillates with them.

Many variations of the modular barrier units have been proposed in recent years, both as to form, structure and foundations and, above all, as to the operative pneumatic system and position control.

Without going into further detail, Fig. 25 suffices to illustrate the transversal section of a component. An experimental prototype, called MOSE, was installed for a few years at the interior of the Lido mouth, towards Treporti. It provided useful information about the opening and closing operation and about the assembly and dismantling of the component, necessary for its maintenance and repair.

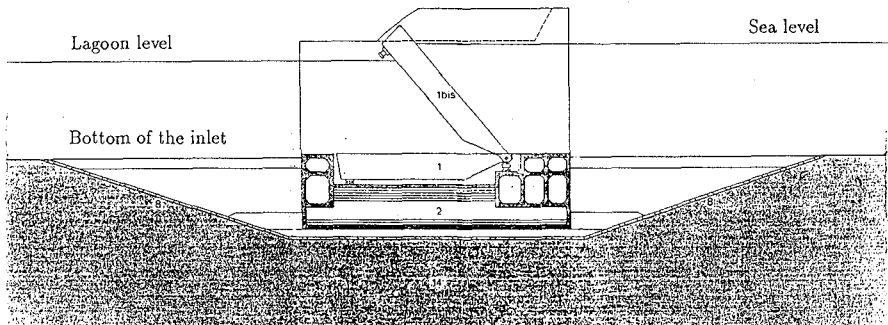


Figure 25. Section of a mobile floodgate.

## 7.8 The works at the mouths

The planimetric design of the floodgates at the mouths is almost complete today. It notably differs from the 1981 feasibility study above all because the present gates take up the entire opening of each inlet, without need of the fixed side barriers and without the breakwaters foreseen in the earlier design.

The above decision was the result of two principal motives. The first is the necessity of not reducing the flow through the openings in order to maintain the steady renewal of water, with the advantage of a flow without obstacles which cause dangerous vorticity. The second arises from the positive experiments carried out by Estramed (Roma) and in progress in Delft and in Voltabarozzo using physical models that prove the safe behaviour of the floodgates under attack from the sea waves.

Fig. 26 shows the design of the works planned for the Lido mouth, where an isle of support is foreseen in the center of the canal; Fig. 27 shows the works designed for Malamocco and Fig. 28 those for Chioggia. A refuge harbour is located on a side of each mouth.

I end my report with these images. They illustrate works of a new technology which must be absorbed into one of the richest areas in the world for nature and art. At the same time, however, they point out a way - perhaps the only way - of defending Venice against the assault of that very sea which is also its vocation and its life.

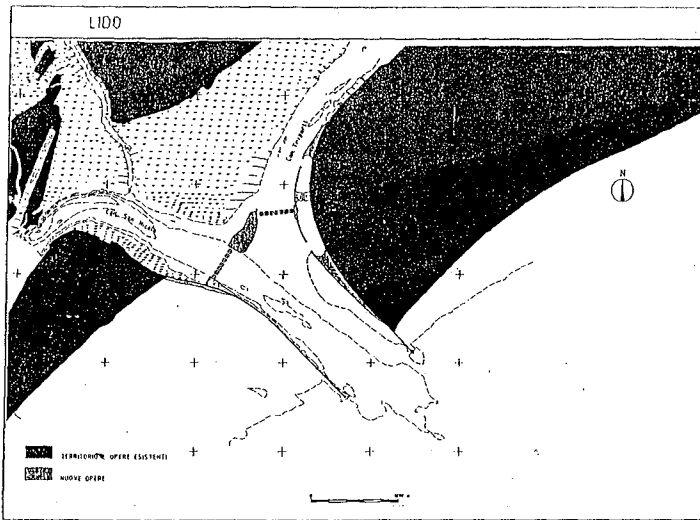


Figure 26. Design for the Lido mouth project.

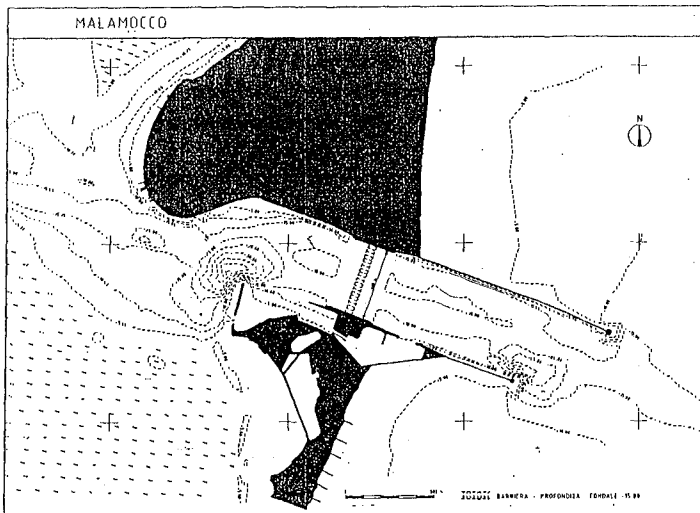


Figure 27. Design for the Malamocco mouth project.

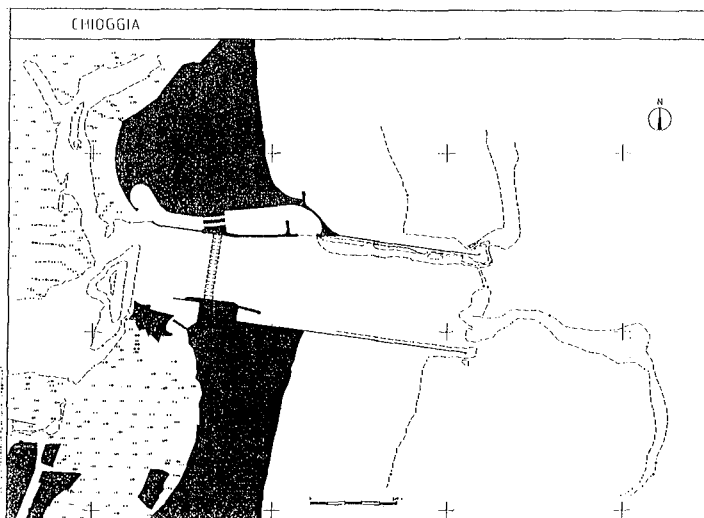


Figure 28. Design for the Chioggia mouth project.

## References

- Adami A., *Analisi statistica di un lungo periodo di maree sizigiali contemporanee all'interno e all'esterno della Laguna di Venezia*, Riv. Ital. di Geofisica, vol. XXIII, n. 5/6, 1974.
- Adami A., Alfonsi A., Da Deppo L., *Su un'applicazione di un modello aerodinamico in scala molto piccola*, "L'Energia Elettrica", vol. LVIII, n. 11, 1981.
- Agema I., Frassetto R., Ghetti A., Marchi E., Matildi P., Passino R., Pezzoli G., *Il criterio di progettazione delle opere per la difesa della Laguna di Venezia*, Conv. "Laguna, fiumi, lidi...", Magistrato alle Acque, Venezia, 1983.
- Arato E., Blondeaux P., De Bernardinis B., Seminara G., Stagi L., *Sul meccanismo del ricambio lagunare: modello teorico e primi rilievi sperimentali*, Conv. "Laguna, fiumi, lidi...", Magistrato alle Acque, Venezia, 1983.
- Backhans J., *Zur hydrodynamik im flachwassergebiet. Ein numerisches modell*, Deutsche Hydrographische Zeitschrift, a. XXIX, n.6, 1976.
- Baroncini E., *Il modello generale della Laguna di Venezia*, Convegno "Laguna, fiumi, lidi...", Magistrato alle Acque, Venezia, 1983.
- Baroncini E., Carretta A., Muraca A., *Sull'evoluzione dei litorali antistanti la Laguna di Venezia*, Convegno "Laguna, fiumi, lidi...", Magistrato alle Acque, Venezia 1983.
- Benigni N.A., *Gli interventi veneziani sui litorali veneti nel XVIII secolo. I murazzi*, Convegno "Laguna, fiumi, lidi...", Magistrato alle Acque, Venezia, 1983.
- Blondeaux P., De Bernardinis B., Seminara G., *Correnti di marea in prossimità di imboccature e loro influenza sul ricambio lagunare*, Atti XVIII Conv. Idraulica e Costr. Idr., Bologna, 1982.
- Bruun P., *Stability of Tidal Inlets*, Elsevier Scientific Publishing Co., New York 1978.



- Caputo M., Folloni G., Gubellini A., Pieri L., Unghendoli M., *Survey and geometric analysis of subsidence in the region of Venice and its hinterland*, Tech. Rep. 9, CNR-ISDGM, Venezia 1971.
- Carbognin L., Gatto P., Mozzi G., *La riduzione altimetrica del territorio veneziano e le sue cause*, Ist. Veneto di Sci., Lett. Arti, Comm. Studio per la Difesa di Venezia, vol. VIII, 1981.
- Cavazzoni S., *Variazioni batimetriche ed idrografiche nella Laguna di Venezia intercorse tra il 1933 e il 1971*, Ist. Veneto Sci., Lett. Arti, Rapporti e studi, vol. VII, Venezia 1977.
- Cavazzoni S., Gottardo D., *Processi evolutivi batimetrici e morfologici della Laguna di Venezia*, Convegno "Laguna, fiumi, lidi:.....". Magistrato alle Acque, Venezia 1983.
- Cheng R.T., Casulli V., *On Lagrangian residual currents with application in South San Francisco Bay*, "Water Resources Research", 18, 6, 1982.
- Chignoli C., Rabagliati R., *Un modello matematico per la Laguna di Venezia*, "Sistemi e Automazione", vol. 22, 1976.
- CNR-ISDGM (Istituto per lo Studio della Dinamica delle Grandi Masse), *Livellazione geometrica di precisione della città di Venezia (1970)*, CNR, Venezia 1971.
- Comune di Venezia, Ufficio Idrografico del Magistrato alle Acque, Istituto del CNR per lo Studio della Dinamica delle Grandi Masse, *Previsioni delle altezze di marea per il bacino di San Marco*, Roma, Ist. Poligrafico dello Stato, pubblicazione annuale.
- Consorzio Venezia Nuova, *Modello matematico idrodinamico unidimensionale della Laguna di Venezia*, Res. performed by Technital with prof. L. D'Alpaos as consultant, Convenz. n. 6393, Venezia, 1985.
- Consorzio Venezia Nuova, *Gestione del modello fisico in scala 1:60 della bocca di Lido a Voltabarozzo, gestione del modello fisico in scala 1:60 della bocca di Malamocco, gestione del modello fisico in scala 1:60 della bocca di Chioggia*, Res. performed by Ist. di Idraulica Univ. Padova, Convenz. n. 6393, Venezia, 1986.
- Consorzio Venezia Nuova, *Valutazione del moto ondoso davanti al litorale veneziano*, Res. A.1.2 performed by TEI, Venezia, 1987.
- Consorzio Venezia Nuova, *Studio con modello matematico della propagazione del moto ondoso entro le bocche di Malamocco e Chioggia fino alle opere*, Res. B.5.4/5 performed by Delft Hydraulics Lab., Venezia, 1987.
- Consorzio Venezia Nuova, *Modello matematico idrodinamico bidimensionale alle differenze finite della Laguna Veneta*, Res. performed by Danish Hydraulic Institute, Convenz. n. 5479, Venezia, 1987-88.
- Consorzio Venezia Nuova, *Valutazione dei valori estremi del moto ondoso davanti al litorale veneziano*, Res. A.1.4. performed by TEI, Venezia, 1988.
- Consorzio Venezia Nuova, *Modello aerodinamico della bocca di Lido, modello aerodinamico della bocca di Malamocco, modello aerodinamico della bocca di Chioggia*, Res. performed by Protecno and Istituto di Idraulica Univ. Padova, Convenz. n. 6479, Venezia, 1988.
- Consorzio Venezia Nuova, *Rilievi batimetrici e correntometrici alle bocche*, Res. A.2.7. Ecomar, Venezia, 1988.
- Consorzio Venezia Nuova, *Studio sullo stato delle conoscenze in materia di subsidenza ed eustatismo e per la realizzazione di un caposaldo profondo*, Ist. di Costr. Marittime e di Geotecnica, Univ. Padova, Venezia, 1988.

- Consorzio Venezia Nuova, *Misure di moto ondoso e meteorologiche all'interno e all'esterno delle bocche di porto*, Res. A.5.2. performed by ECOMAR, Venezia, 1988.
- Consorzio Venezia Nuova, in "Interventi alle bocche lagunari per la regolazione dei flussi di marea", cap. 11, *Evoluzione delle bocche di porto*, Min. LL.PP., 1989.
- Consorzio Venezia Nuova, *Modello idrodinamico bidimensionale di dettaglio della bocca di Lido, modello idrodinamico della bocca di Malamocco, modello idrodinamico della bocca di Chioggia*, Danish Hydraulic Institute, Convenz. n. 6479, Venezia, 1989.
- Consorzio Venezia Nuova, *Progetto R.E.A. Vol. 2. Descrizione dell'ecosistema*, Parti I e II, Venezia, 1989.
- Consorzio Venezia Nuova, *Progetto di massima degli "Interventi per il recupero morfologico della Laguna"*, Rapporto finale - Vol.1. Sintesi, Gennaio 1992.
- Da Deppo L., Rinaldo A., *Aerodynamic modelling of the inlet tidal embayments*, Proc. XXII, Congresso IAHR, Hydraulic Modelling, p. 246-251, 1987.
- D'Alpaos L., Degan F., *Un modello matematico lagrangiano per lo studio del movimento dell'acqua nella Laguna di Venezia*, Ist. Veneto Sci. Lett. Arti, Comm. Studio per la difesa di Venezia, Rapporti e Studi, vol. VII, 1977.
- D'Alpaos L., Di Silvio G., *Utilizzazione dei risultati per la taratura dei modelli matematici*, in "Le correnti di marea nella Laguna di Venezia", Min. LL. PP., Padova, 1979.
- Datei C., *Sulla propagazione della marea in una laguna schematica secondo l'impostazione bidimensionale*, Ist. Veneto Sci. Lett. Arti, Com. Studio per la Difesa di Venezia, Rapporti e Studi, vol. V, 1972.
- Datei C., *Contributo allo studio delle portate residue in una laguna schematica*, Atti XVI Conv. Idraulica e Costr. Idraul., Torino, 1978.
- Defont, A., *Physical Oceanography*, Pergamon Press, vol.2, 1961.
- Dejak C., Mazzei La latta I., Acanfora D., Pecenic G., *Predisposizione di modelli bi-tridimensionali e loro estensioni a 8 variabili chimico, fisiche e tropiche nella Laguna di Venezia*, Ist. Veneto Sci., Lett., Arti, Comm. Studio per la difesa di Venezia, Rapporti e Studi, vol. IX, 1984.
- De Marchi L., *La morfologia lagunare e il regime stazionario di marea*, Atti R. Ist. Veneto Sci. Lett. Arti, a.a. 1904-1905, Tomo LXIV, Parte II.
- Di Silvio G., D'Alpaos L., *Il comportamento della Laguna di Venezia esaminato col metodo propagativo unidimensionale*, Ist. Veneto Sci. Lett. Arti, Comm. Studio per la difesa di Venezia, Rapporti e Studi, vol. V, 1972.
- Di Silvio G., Fiorillo G., Degan F. *A dispersion model for the Lagoon of Venice*, Proc. XVII Congress IAHR, Baden Baden, 1977.
- Di Silvio G., *Physical and mathematical models of the Lagoon of Venice*, XX I.G.E.S. Users Group Worldwide Conference, Padova, 1978.
- Di Silvio G., Fiorillo G. *Modelling of lagoons: the experience of Venice*, Symposium on "Predictive Activities of Surface Water Flow and Transport Models", Berkeley, California, 1980.
- Di Silvio G., Fiorillo G., *Verification of a Dispersion Model for the Lagoon of Venice by Temperature Measurements*, Advances in Environmental Modelling, Ed. by Marani, Amsterdam, Elsevier, 1988.
- Di Silvio G., Gambolati G., *Two-dimensional model of long-term morphological evolution of tidal lagoons*, in 'Computational Methods in Surface Hydrology', Springer-Verlag, 1990.

- Di Silvio G., *Delimitazione topografica di una laguna a marea: implicazioni idrodinamiche e morfologiche*, Convegno promosso da Ist. Veneto Sci. Lett. Arti, Venezia, 14-16 marzo, 1991.
- Dorigo L., *Livelli marini eccezionali a Venezia*, in: Ministero dei LL.PP. "L'evento alluvionale del Novembre 1966", Roma, 1969.
- Dronkers J.J., *Tidal computation for rivers, coastal areas and seas*, Proc. ASCE, Jou. Hyd. Div., vol. 95, No. HY1, paper 6341, 1969.
- Dronkers, J.J. *Des considerations sur la marée de la Lagune de Venise*, Ist. Veneto di Sci. Lett. Arti, Comm. Studio per la difesa di Venezia, Rapporti e Studi, vol. V, 1972.
- Duwe K.C., Hower R.R., *Ein semi-implizites Gezeinmodell fur Wattgebiete*, "Deutsche Hydrographische Zeitschrift", a. XXXV, n. 6, 1982.
- Fiorillo G., *Modello unidimensionale per lo studio della dispersione di inquinanti nella Laguna di Venezia*, Convegno "Metodologie numeriche per la soluzione di equazioni differenziali dell'idrologia e dell'idraulica". Bressanone, 1978.
- Gambolati G., Freeze R.A., *Mathematical simulation of the subsidence of Venice*, 1. *Theory*, Water Resources Res., vol. IX, n. 3, 1973.
- Gambolati G., Gatto P., Freeze R.A., *Mathematical simulation of the subsidence of Venice*, 2. *Results*, Water Resources Res., vol. X, n. 3, 1974.
- Gambolati G., Gatto P., Freeze R.A., *Predictive simulation of the subsidence of Venice*, Science, vol. CLXXXIII, 1974.
- Ghetti A., D'Alpaos L., Dazzi R., *La regolazione delle bocche della Laguna di Venezia per l'attenuazione delle acque alte indagata col metodo statico*, Ist. Veneto Sci. Lett. Arti, Comm. Studio per la difesa di Venezia, Rapporti e Studi, vol. V, 1972.
- Ghetti A., *Hydraulic problems of the Lagoon of Venice*, Giornale Economico, Venezia, 1974.
- Ghetti A., *Etudes concernant les problèmes hydrodynamiques de la Lagune de Venise*, invited lecture, Proc. XVIII, Congress IAHR, Comp. Rend., vol. 5, Cagliari 1979.
- Ghetti A., Batisse M., *The overall protection of Venice and its Lagoon*, Nature and Resources, vol. XIX n. 4, 1983.
- Ghetti A., *Italian contributions to hydraulics of lagoons*, "Excerpta", vol. 5, 1990.
- Gottardo D., *Propagazione della marea nella Laguna di Venezia*, Giornale Economico, No. speciale, Luglio-Agosto 1975.
- Gottardo D., *Interventi per il rafforzamento dei murazzi*, Giornale Economico, n. 5-6, C.C.I.A.A. Venezia, 1976.
- Gray W.C., Lynch D.R., *Time-stepping schemes for finite element tidal model computations*, "Advances in Water Resources", vol. I, n. 2, 1977.
- Jarrett J.T., *Tidal Prism - Inlet Area Relationships*, G.I.T.I. Report 3, U.S. Army Corps of Engineers, Coastal Eng. Res. Center, Fort Belvoir, Virginia 1976.
- Leendertse J.J., *Aspects of a computational model for long-period water-waves propagation*, Memo. no. RM-5294, P.R., The Rand Corporation, Santa Monica (California), 1967.
- Marchi E., Stura S., *Sottopressioni dinamiche alla base di una diga marittima*, XV Conv. Idraulica e Costr. Idr., Roma, 1976.
- Marchi E., *Valutazione della velocità nelle bocche lagunari*, Atti XX, Conv. Idraulica e Costr. Idr., Padova 1986.

- Marchi E., *Sulla stabilità delle bocche lagunari a marea*, Rend. Fis. Acc. Lincei, Serie IX, vol. 1, Fasc. 2, 1990.
- Ministero dei LL.PP., *Difesa della Laguna di Venezia dalle acque alte*, Studio di fattibilità e progetto di massima, Venezia, 1981.
- Noli A., *L'attività del Paleocapa nel campo delle costruzioni marittime e la sistemazione del porto di Malamocco*, Conv. su "Ingegneria e politica nell'Italia dell'Ottocento: Pietro Paleocapa", Ist. Veneto di Sci. Lett. Arti, Venezia, 1990.
- O'Brien M.P., *Equilibrium Flow Areas of Inlets of Sandy Coasts*, J. of the Waterways and Harbour Division, ASCE, vol. 95, no. WW1, Proc. Paper 6405, 1969.
- Pezzoli G., *Contributo allo studio dei bacini a marea*, Atti Acc. Sci. Istituto di Bologna, Cl. di Sci. Fis., S. XI, Tomo V, 1958.
- Pezzoli G., *Alcuni problemi sulla propagazione delle maree*, "Giornale del Genio Civile", vol. 108, no. 9-10, 1970; Atti Acc. Lincei, Rend. Cl. Sci. Fis., vol. XLVIII, no. 5, 1970.
- Poleni G., *De Motu Aquae Mixto Libri Duo*, Patavii, Typis J. Coniini, 1717.
- Polli S., *La propagazione delle maree nell'Adriatico*, Atti Convegno Ass. Geog. 71, Roma, 1959.
- Rusconi A., *Variazione delle superfici componenti il bacino lagunare*, Pubbl. n. 160, Ufficio Idrografico del Magistrato alle Acque, Venezia, 1987.
- Stoker J.J., *Water Waves*, Interscience Publisher Inc., N.Y., 1957.
- Supino G., *Le Regime des basins à marée et le calcul hydraulique des embouchures*, VI Congress IAHR, Comptes Rend., vol. I, La Haye, 1955.
- Supino G., *The propagation of the tide inside a lagoon*, "Meccanica" vol. 5, n. 1, 1970.
- Supino G., *Fenomeni idraulici e subsidenza nella Laguna di Venezia. Rimedi possibili*, Atti Acc. Sci. Bologna, Serie XIII, Tomo V, 1978.
- Tenani M., *Maree e correnti di marea*, Ist. Idrografico della Marina, 1935.
- Thomas R., *Future sea-level rise and its early detection by satellite remote sensing*, Environmental Protection Agency, vol. IV, Washington, 1986.
- Tomasicchio U., *La conservazione dei lidi a protezione della Laguna Veneta*, Convegno "Laguna, Fiumi, Lidi...", Magistrato alle Acque, Venezia 1983.
- Zendrini B. et al., *Relazione agli Ill.mi ed Ecc.mi Signori Savi*, 1 Giugno 1743, Archivio di Stato di Venezia.
- Zorzi A., *Una Città, una Repubblica, un Impero. Venezia 697-1797*, A. Mondadori Ed. 1980.



# **PART I**

## **Characteristics of Coastal Waves and Currents**



*San Maria di Leuca*

# CHAPTER 1

## BREAKING WAVES PROPAGATING OVER A SHOAL

J.A. Battjes<sup>a</sup> and S. Beji<sup>b</sup>

### Abstract

Spectral evolution of breaking and nearly breaking waves propagating over a submerged trapezoidal bar has been investigated in laboratory experiments. It is found that wave breaking itself does not play a crucial role in the evolution of the spectral shape, but contributes simply by extracting energy roughly in proportion to the local spectral density. For nonbreaking waves, a Boussinesq model with improved dispersion characteristics is found to simulate the wave evolution very well. On the basis of these findings, it is suggested to combine a semi-empirical model for the overall energy dissipation with a nondissipative Boussinesq model so as to obtain a model for simulation of spectral evolution of breaking waves.

### 1. Introduction

Harmonic generation in waves passing over submerged obstacles has long been known experimentally (Johnson et al., 1951; Jolas, 1960; Byrne, 1969; Young, 1989). On the theoretical side, Phillips (1960), Bretherton (1964), Mei and Unlüatta (1972) and Bryant (1973), among others, clarified the basic mechanisms of harmonic generation.

---

<sup>a</sup>Professor, Dept. of Civil Eng., Delft University of Technology, P.O. Box 5048, 2600 GA, Delft, The Netherlands.

<sup>b</sup>Former post-doctorate fellow at Delft University of Technology. Present employment: Naval Architecture and Ocean Engineering Faculty, Istanbul Technical University, Turkey.

While for nonbreaking waves the generation of high-frequency energy may entirely be attributed to conservative nonlinear effects, the role of wave breaking in this process has not been clarified. The aim of the work reported here is to help resolve this question and to contribute to the development of capabilities for numerical modelling of the dominant processes involved.

A full account of the work reported here can be found in Beji and Battjes (1992a, 1992b) for the experimental and the numerical aspects, respectively.

## 2. Experiments

The experiments were carried out in a wave flume of the Department of Civil Engineering, Delft University of Technology. The flume is 37.7 m long and 0.8 m wide. In its midsection, a trapezoidal bar was built. See Figure 1. At the downwave end a gently sloping spending beach was present from previous experiments. The still-water depth was 0.4 m over the original, horizontal flume bottom and had a minimum of 0.10 m above the bar crest. Periodic and irregular input waves were used, the latter with a JONSWAP-type spectrum and a very narrow band spectrum. Peak frequencies were  $f_p=0.4$  Hz,  $f_p=0.5$  Hz and  $f_p=1.0$  Hz. Measurements of the free surface elevations were made with parallel-wire resistance gages at eight different locations as sketched in Figure 1.

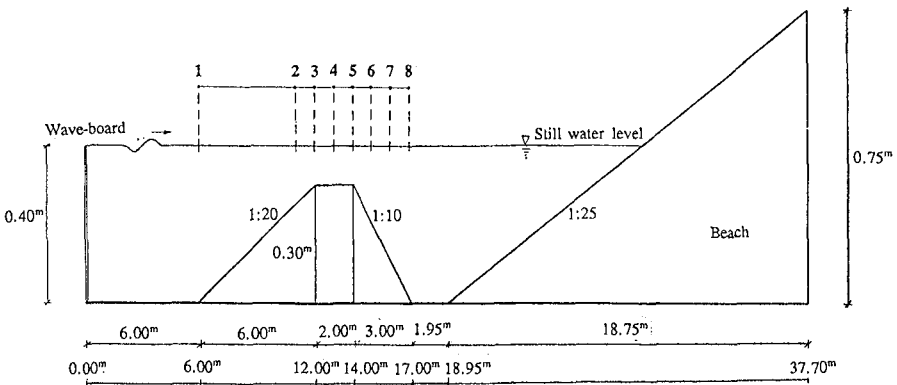


Figure 1. Longitudinal sections of wave flume



### 3. Experimental Results

Experiments with three different wave conditions were done: steep but non-breaking waves, spilling breakers and plunging breakers.

In order to make direct comparisons of spectral evolutions for different wave conditions, spectral estimates obtained at stations 2, 4, 6, and 8 for JONSWAP type incident waves ( $f_p=0.4$  Hz), for non-breaking and plunging breakers, are normalized and plotted together. The normalization is such that the total area under the spectrum for every case is unity. Figure 2 shows these comparisons. Obviously, the spatial evolution of the spectral shape follows almost identically the same trend regardless of the occurrence of wave breaking. The same was observed in the case of narrow-banded incident waves with the same peak frequency (not shown here).

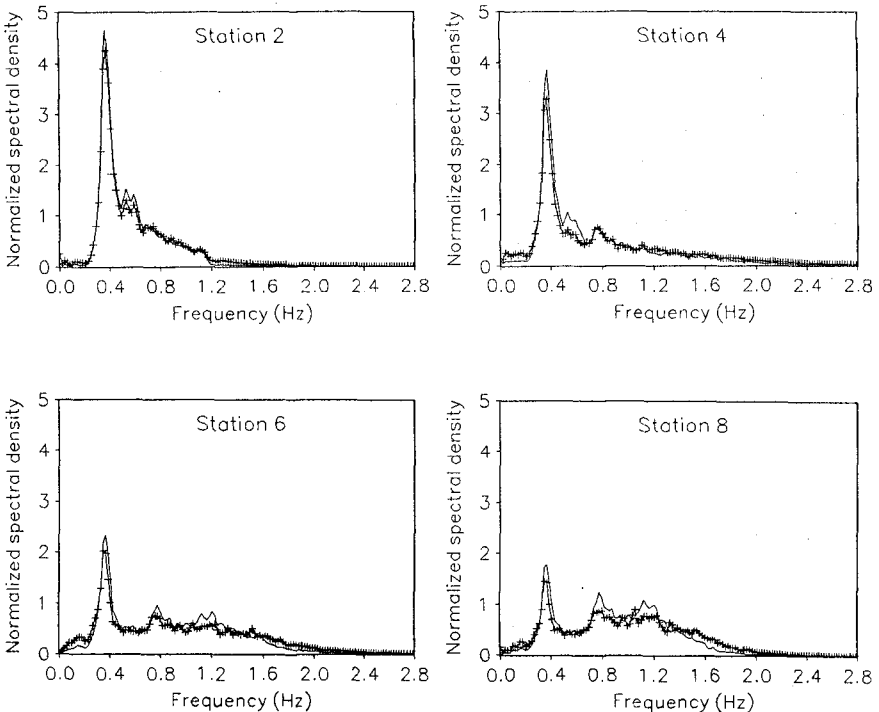


Figure 2. Normalized spectra at different stations; —: Non-breaking waves; +++: Plunging breakers. Incident waves: Jonswap-spectrum with  $f_p=0.4$  Hz.

The measurements with the short waves ( $f_p=1.0$  Hz) revealed little spectral shape evolution over the obstacle. See Figure 3. The shape of the input spectrum in every case remained nearly intact over the entire region and only a relatively small amount of high frequency energy was generated. For this reason we shall not pursue this case any further.

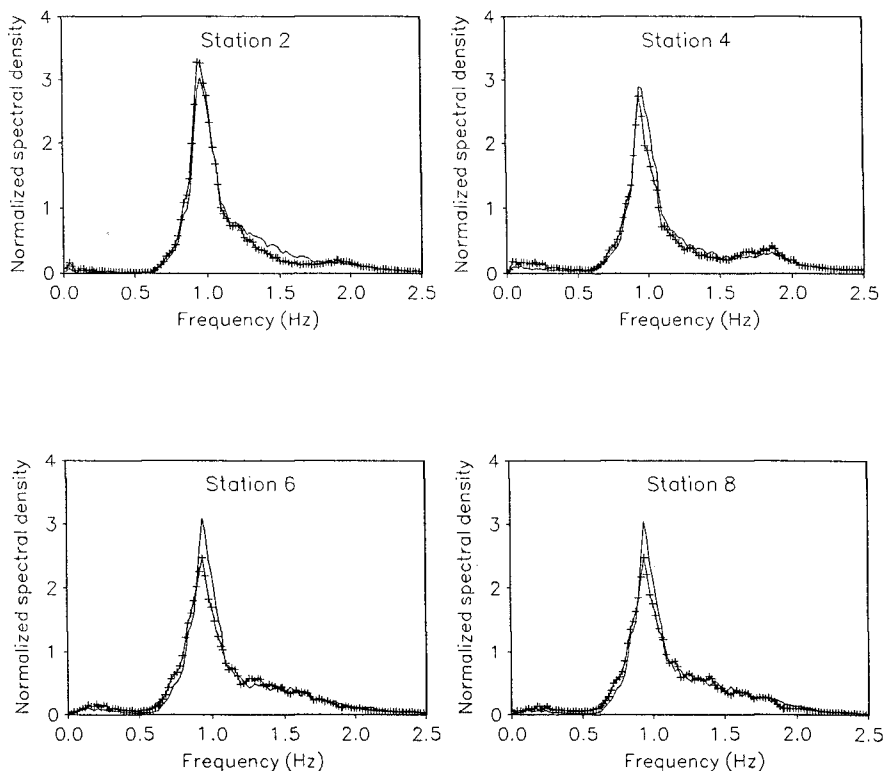


Figure 3. Normalized spectra at different stations; —: Non-breaking waves; +++: Plunging breakers. Incident waves: Jonswap-spectrum with  $f_p=1.0$  Hz.

#### 4. Numerical modeling

##### 4.1 Nonbreaking waves

A Boussinesq type model with improved dispersion characteristics was chosen as the wave propagation model. We used it in the following form:

$$u_t + uu_x + g\zeta_x = \frac{1}{3}h^2 u_{xxt} + hh_x u_{xt} + bh^2 (u_t + g\zeta_x)_{xx}$$

$$\zeta_t + [(h+\zeta)u]_x = 0$$

where  $\zeta$  denotes the surface displacement and  $u$  the vertically averaged horizontal velocity. For  $b=0$  the momentum equation reduces to its standard form as it was derived by Peregrine (1967) for mildly sloping bottoms. For  $b=1/15$  a major improvement for the dispersion characteristics is achieved. This extension to the original Boussinesq equations was first suggested by Witting (1984) and further elaborated by Madsen et al. (1991). A model with good dispersion characteristics is essential in this study because of the decomposition of the wavefield behind the submerged obstacle into free high frequency components which may be regarded as relatively deep water waves.

In the numerical treatment of the governing equations, we basically followed the guidelines given in Peregrine (1967), except for some minor but crucial adjustments.

In Figure 4, the left column gives measured and computed free surface elevations for nonbreaking but significantly nonlinear random waves at selected stations. The right column shows the comparisons for the measured and computed spectra at the same stations. The agreement is remarkable and justifies our choice of the governing equations.

#### 4.2 Breaking waves

The observation that in our experiments the evolution of the spectral shape is not significantly affected by wave breaking suggests the possibility of using a (non-spectral) model for the dissipation of total wave energy by breaking (e.g., Battjes and Janssen, 1978), in conjunction with a conservative (potential-flow) model incorporating nonlinear wave-wave interactions.

Results of a fully integrated model of the kind indicated here are not yet available. Nevertheless, to indicate the potential feasibility of this approach we show results for the plunging breaker case (JONSWAP spectrum,  $f_p = 0.4$  Hz) for which the initial surface elevations are reduced (in the calculations) with a factor 1.5 so as to ensure

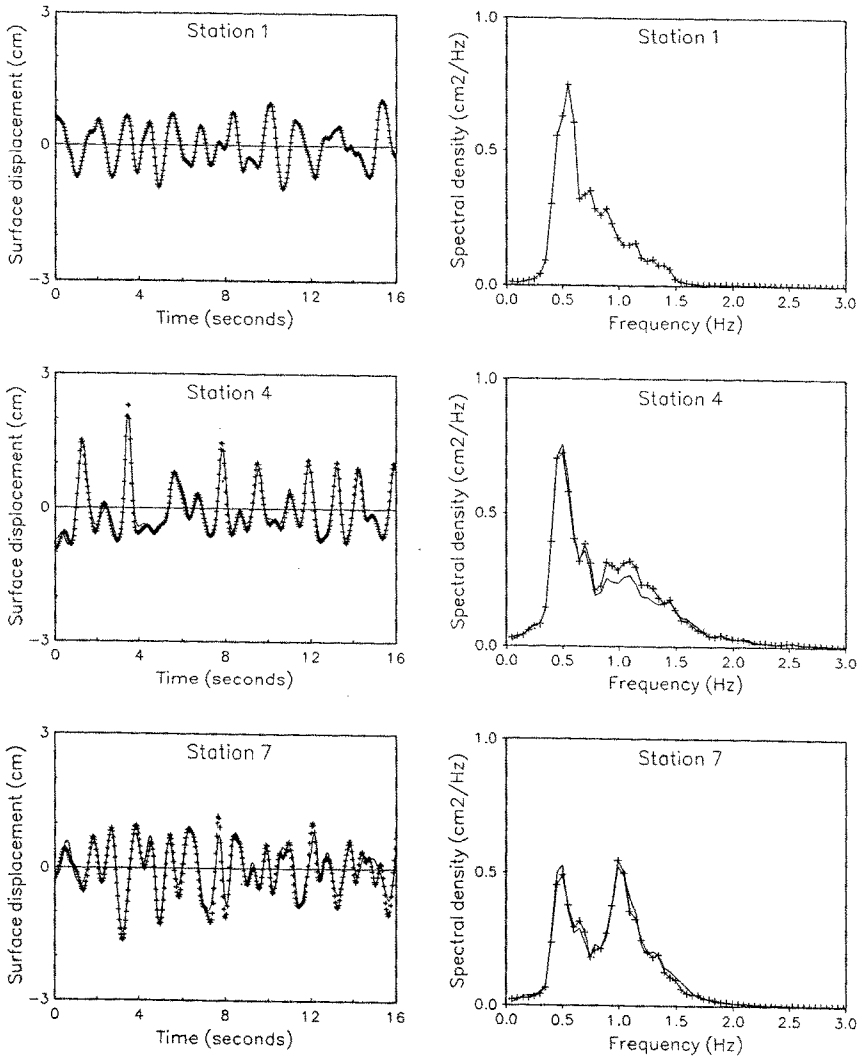


Figure 4. Comparisons of measured (—) and computed (+++) surface elevations (Left) and spectra (Right) at different stations. Incident waves: Jonswap-spectrum with  $f_p=0.5$  Hz; No breaking.

non-diverging calculations, as in the case of the steep but non-breaking waves simulated at full strength. The idea behind this is that the strength of the nonlinearities in post-breaking waves is expected to be comparable to that in non-breaking waves of similar height.

Figure 5 compares the evolutions of the measured spectral shape for plunging breakers with those of the computations carried out with the down-scaled amplitudes. All the spectra shown have been normalized, as in Figure 2, so that their integral is unity. (Minor differences between the measured spectra in the two figures are due to the fact that the spectra in Figure 5 were calculated from a partly different set of time series, and with a coarser frequency resolution, than those shown in Figure 2.) It can be seen in Figure 5 that the spectrum, computed on the basis of an artificially reduced initial wave height, evolves in a similar manner as the observed spectrum does for the breaking waves.

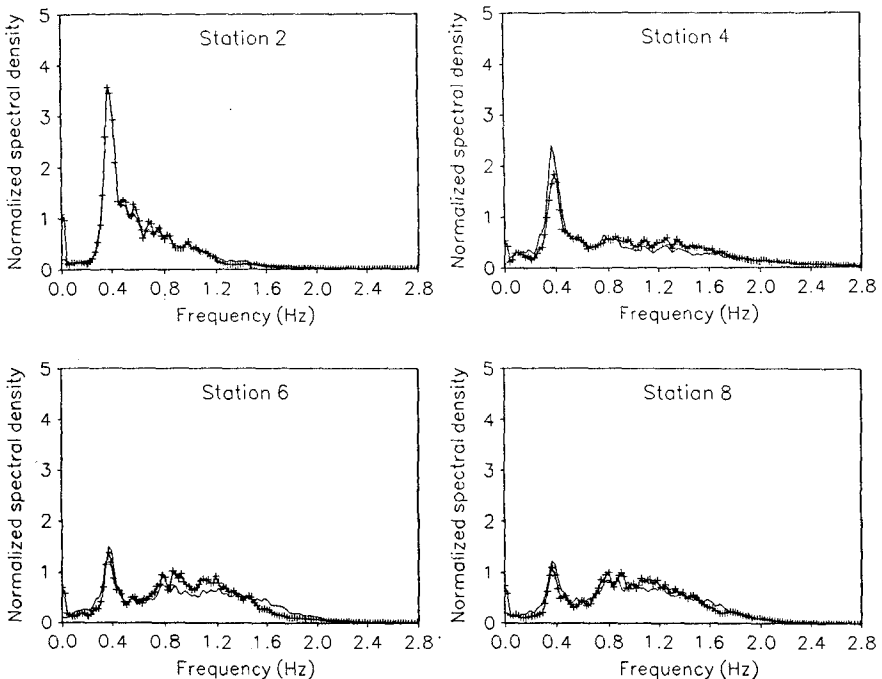


Figure 5. Comparison of measured (—) normalized spectra for plunging waves and normalized spectra computed with reduced initial values of surface elevations (+++). Incident waves: Jonswap-spectrum with  $f_p=0.4$  Hz.

This is taken as an indication that it is worthwhile to develop the combined modeling approach sketched above.

## 5. Conclusions

Energy spectra obtained from laboratory measurements are analyzed to clarify the effects of wave breaking on the inherently nonlinear phenomenon of high frequency energy generation and transfer in the spectra of waves traveling over submerged profiles. For the conditions in these experiments, it is found that wave breaking merely dissipates energy in averaged manner and does not introduce drastic alterations to the spectral shape.

A practical application of this finding is the possibility of combining a weakly nonlinear non-dissipative model with a semi-empirical dissipation formulation for the total energy.

## Acknowledgements

Financial support for this project was provided in part by the EC-MAST program within the framework of the WASP-project under contract number MAST-0026-C(MB).

## References

- Battjes, J.A. and J.P.F.M. Janssen, 1978, Energy loss and set-up due to breaking in random waves, Proc. 16th ICCE, pp. 569-587.**
- Beji, S. and J.A. Battjes, 1992a. An experimental investigation of breaking and nearly breaking waves traveling over a bar. To be published in Coastal Engineering.**
- Beji, S. and J.A. Battjes, 1992b. Numerical simulation of nonlinear wave propagation over a bar. Submitted for publication.**
- Bretherton, F.P., 1964. Resonant interactions between waves. The case of discrete oscillations. J. Fluid Mech., 20-3, pp. 457-479.**
- Bryant, P.J., 1973. Periodic waves in shallow water, J. Fluid Mech., 59, pp. 625-644.**

- Byrne, R.J.**, 1969. Field occurrences of induced multiple gravity waves. *J. Geophys. Res.* **74-10**, pp. 2590-2596.
- Johnson, J.W., R.A. Fuchs and J.R. Morison**, 1951. The damping action of submerged breakwaters. *Trans Amer. Geophys. Union*, **32-5**, pp. 704-718.
- Jolas, P.**, 1960. Passage de la houle sur un seuil. *La Houille Blanche.*, **2**, pp. 148-152.
- Madsen, P.A., R. Murray and O.R. Sørensen**, 1991. A new form of the Boussinesq equations with improved linear dispersion characteristics, *Coastal Eng.*, **15-4**, pp. 371-388.
- Mei, C.C. and Ü. Ünlüata**, 1972. Harmonic generation in shallow water waves. Waves on beaches, ed. R.E. Meyer, Academic, New York, pp. 181-202.
- Peregrine, D.H.**, 1967. Long waves on a beach, *J. Fluid Mech.*, **27**, pp. 815-827.
- Phillips, O.M.**, 1960. On the dynamics of unsteady gravity waves of finite amplitude. Part 1: The elementary interactions. *J. Fluid Mech.*, **9**, pp. 193-217.
- Witting, J.M.**, 1984. A unified model for the evolution of nonlinear water waves, *J. Comp. Phys.*, **56**, pp. 203-236.
- Young, I.R.**, 1989. Wave transformation over coral reefs. *J. Geophys. Res.*, **94**, pp. 9779-9789.

## CHAPTER 2

### Transformation of nonbreaking waves over a bar

S. Beji<sup>1</sup>, T. Ohyama<sup>2</sup>, J.A. Battjes<sup>3</sup> and K. Nadaoka<sup>4</sup>

#### Abstract

Data collected from measurements performed in waves propagating over a trapezoidal bar on a horizontal bottom are used to test a fully nonlinear numerical model. The experiments include both regular and random waves. Wave form evolutions in the shoaling region, the near resonant wave-wave interactions over the bar, and finally the decomposition behind the bar are well predicted. The results provide assurance for the reliability of the numerical model.

#### 1. Introduction

Numerical modeling of evolving surface gravity waves based on the full nonlinear equations for irrotational motion was initiated by Longuet-Higgins and Cokelet (1976). Numerous alternative models have been presented since (Vinjé and Brevig, 1981; Dold and Peregrine, 1984). Surface profiles predicted by these models are in general quite realistic, even in the phases of profile steepening and turnover as in plunging breakers

---

<sup>1</sup>Former post-doctorate fellow at Delft University of Technology. Present employment: Naval Architecture and Ocean Engineering Faculty, Istanbul Technical University, Turkey.

<sup>2</sup>Research scientist, Env. Eng. Div., Shimizu Corp., Etchujima 3-4-17, Koto-ku, Tokyo 135, Japan.

<sup>3</sup>Professor, Dept. of Civil Eng., Delft University of Technology, P.O. Box 5048, 2600 GA Delft, The Netherlands.

<sup>4</sup>Assoc. Prof., Dept. of Civil Eng., Tokyo Institute of Tech., O-okayama, Meguro-ku, Tokyo 152, Japan.



(prior to impact). However, quantitative comparisons between predictions and observations are rarely given. The purpose of the present paper is to give such comparisons, for the demanding case of deformation and decomposition of near-breaking waves passing over a shallow bar.

It is known that relatively long waves passing over a bar or another submerged obstacle decompose into shorter components. In the shoaling region the amplitudes of the bound harmonics are initially relatively small. If the wave field continues to propagate into a shallower region, such that the medium becomes non-dispersive for this particular wave field, then the near resonance conditions for triplet-interactions are satisfied (Phillips, 1960). At this stage, a rapid energy flow from the primary wave components to the higher harmonics is observed and the amplitudes of higher harmonic components become appreciable.

The passage into deeper water results in the release of the bound harmonics followed by interactions taking place among these released wave components, which introduces drastic and rapid changes in wave forms. During this final stage, the amplitude of higher harmonics become comparable with, in some cases larger than, the primary wave amplitudes (Kojima, H. et al., 1990; Ohyama and Nadaoka, 1991; Beji and Battjes, 1992). Obviously, predicting the evolutions of a given incident wave field in such regions poses a real challenge; this suggests a good test case for a nonlinear numerical wave propagation model.

The paper presents a brief account of a comparison of results of simulations with a numerical nonlinear model with experimental data for conditions as described above. For details, reference is made to Ohyama et al. (1992).

## 2. Experiments

The measurements reported here were carried out as a subset of a larger program, an account of which can be found in Beji and Battjes (1992).

The experiments were performed in a wave flume of the Department of Civil Engineering, Delft University of Technology. The flume is 37.7 m long, 0.8 m wide, and 0.75 m high. It is equipped with a hydraulically driven, piston-type random-wave generator. The bottom profile is sketched in Figure 1.

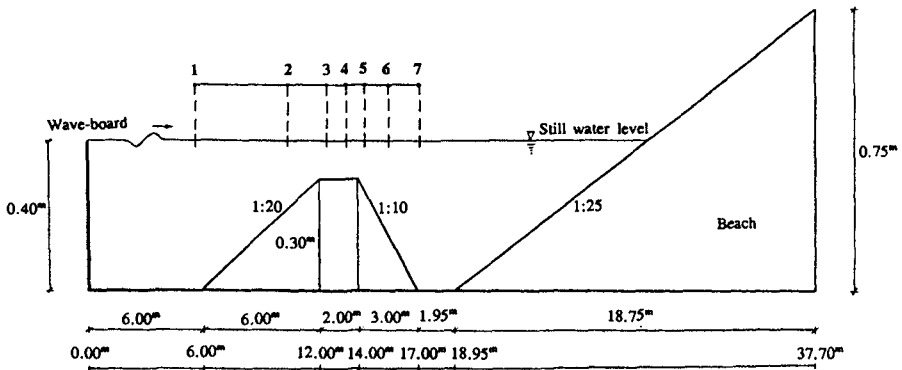


Figure 1. Definition sketch of wave flume and locations of wave gages.

A submerged trapezoidal bar with an upslope of 1:20 and a 2 m horizontal crest followed by a 1:10 downslope was constructed. The still water depth was 0.4 m in the deeper region and 0.1 m in the shallowest part above the horizontal section. At the end of the flume opposite to the wave generator, a roughened plane beach with a 1:25 slope served as a wave absorber.

Measurements of the free surface displacements were made with parallel-wire resistance gages at 7 different locations as shown in Figure 1. The time history of the wave-board displacement was recorded also. In each run, data were recorded simultaneously from 8 separate channels at a sampling frequency of approximately 25 Hz.

Four different measurements were realized: two different spectral shapes (periodic waves with a spike spectrum and random waves with a JONSWAP target spectrum), and two different peak frequencies (0.5 Hz and 0.8 Hz, referred to as the "long" waves and the "short" waves, respectively). All the measurements reported here were for non-breaking waves. The following incident wave heights were selected for regular waves: 2.0 cm for 0.5 Hz, and 2.5 cm for 0.8 Hz. Irregular waves required somewhat smaller incident significant wave heights to prevent occasional breaking. Thus, for irregular waves the following incident significant waves heights ( $H_{1/3}$ ) were used: 1.8 cm for 0.5 Hz, and 2.3 cm for 0.8 Hz.

### 3. Numerical model

Computations have been carried out with a numerical model developed by Ohya and Nadaoka (1991). It is based on the time-dependent boundary element method for potential flow. The field equations outside the sponge layer at the downwave side (Bernoulli and Laplace) and the boundary conditions at the bottom and the free surface are standard and are not reproduced here.

Figure 2 is an illustration of the numerical "wave tank", specifying the geometry and the labelling of the contour around the computational domain.

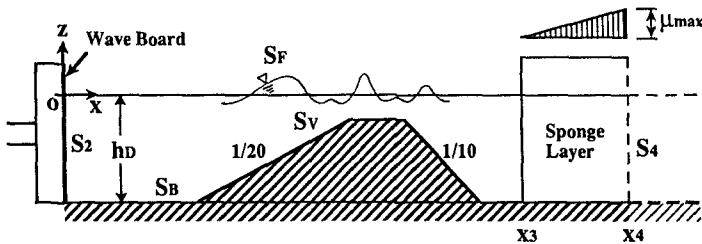


Figure 2. Computational domain.

The original version of the model contains a non-reflective wave generator, which combines a vertically distributed wave-making source with a numerical filter. However, in the present calculations the same wave generating method (piston-type) is used as in the model experiments, as expressed by the following equation:

$$\frac{\partial \phi}{\partial x} = U(t) \quad (\text{on } S_2), \quad (1)$$

in which  $\phi$  is the velocity potential and  $U$  is the horizontal velocity of the wave board.

A numerical wave-absorption filter is located at the trailing end of the domain for the open boundary treatment. The filter is composed of a sponge layer, which absorbs the incoming wave energy by frictional damping according to the following equation:

$$\frac{\partial \phi}{\partial x} = -\frac{1}{\sqrt{gh_D}} \left( \frac{\partial \phi}{\partial t} + \mu \phi - \int_{x_3}^{x_4} \frac{\partial \mu}{\partial x} \phi \Big|_{on S_F} dx \right) \quad (on S_4), \quad (3)$$

in which  $\mu$  is the damping factor of the sponge layer, of which the magnitude is distributed linearly in the layer, as shown in Figure 2, in order to reduce the wave reflection at the leading side of the layer. In view of the results of a previous study (Ohyama and Nadaoka, 1991), the width of the sponge layer is set nearly equal to the incident wave length (corresponding to the peak frequency in case of random waves), and the maximum value of the damping factor in the sponge layers,  $\mu_{max}$ , is given as  $\mu_{max}(h_D/g)^{1/2}=0.25$ . At the leeside of the sponge layer, a Sommerfeld type radiation condition was applied to absorb whatever wave energy would be left after passing through the sponge layer.

Applying Green's theorem and the weighted residual method to the governing equations, integral equations can be derived; these are discretized spatially by using linear elements. In the discretized equations,  $\phi$  (on  $S_F$ ,  $S_V$ ,  $S_2$  and  $S_4$ ), and  $\partial \phi / \partial t$ ,  $\eta$  and  $\partial \eta / \partial t$  (on  $S_F$ ) are invoked as unknown variables. These variables are rewritten by using  $\Delta \phi$  and  $\Delta \eta$  which are the increments of  $\phi$  and  $\eta$ , respectively, during the time increment  $\Delta t$ . Linear algebraic equations to be solved for  $\Delta \phi$  (on  $S_F$ ,  $S_V$ ,  $S_2$ , and  $S_4$ ) and  $\Delta \eta$  (on  $S_F$ ) are consequently obtained.

In all the computations examined, the time increment,  $\Delta t$ , was set to 1/32 of the incident wave period (spectral peak period for random waves). The horizontal projection of the distance between the surface nodes,  $\Delta x$ , on the other hand, was varied in space. The values relative to the incident wave lengths,  $\Delta x/L$ , were 1/15 for the interval  $0 \leq x \leq 7.6m$  and 1/40 for  $x > 7.6m$  for the 0.5-Hz waves, and were 1/15 for  $0 \leq x \leq 10.0m$  and 1/20 for  $x > 10m$  for the 0.8 Hz-waves.

The only experimental data used as input to the numerical model are the bottom profile, the still-water level, and the time history of the wave-board displacement (used to calculate the wave-board velocity  $U(t)$  in eq. 1); on the downwave side, full absorption has been assumed. The initial condition for each case was the still-water condition, i.e.,  $\phi=\eta=0$ . Numerical results after 10 periods from the cold start are used for the subsequent discussion.

#### 4. Comparisons of measurements and computations

For the case of the long ( $f = 0.5$  Hz), monochromatic waves, Figures 3a-3d show the comparisons of measured and computed wave profiles at the stations 1, 3, 5, 7, and Figure 4 shows the spatial evolutions of the lowest three harmonics amplitudes of the surface displacement. The elevations have been normalized with  $H_0$ , the target value of the incident wave height.

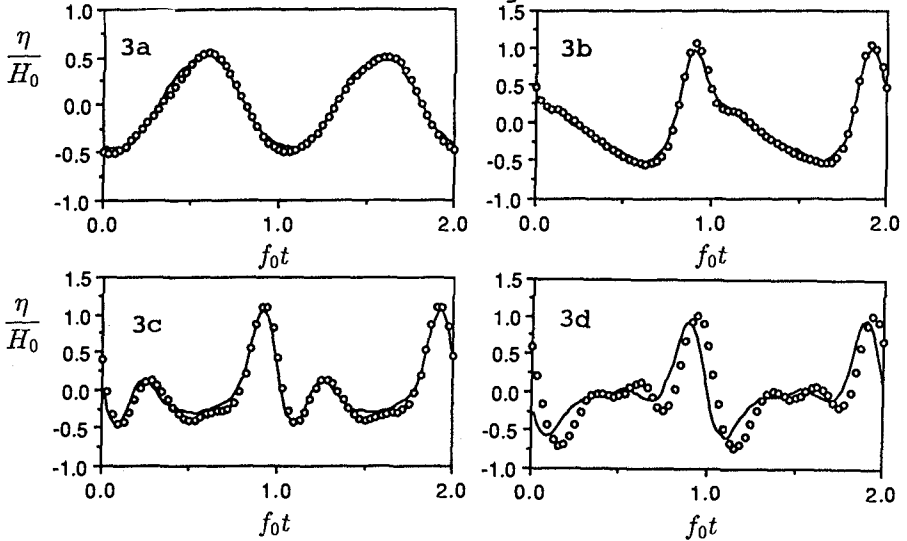


Figure 3. Measured (—) and computed (ooo) wave profiles for monochromatic waves,  $f=0.5$  Hz, at stations 1, 3, 5 and 7 (a, b, c and d).

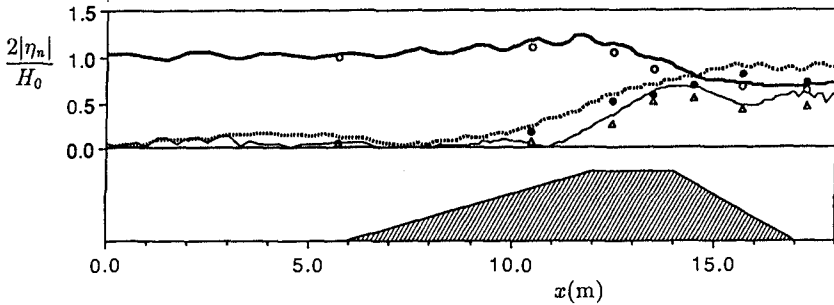


Figure 4. Measured (o:  $n=1$ )( $\cdot$ :  $n=2$ )( $\Delta$ :  $n=3$ ) and computed (—:  $n=1$ )(.....:  $n=2$ )(- - -:  $n=3$ ) spatial evolution of harmonic amplitudes for monochromatic waves,  $f=0.5$  Hz.

The overall agreement is excellent, especially in the upslope region and over the horizontal part. In the downslope region, some minor differences between measurements and computations are observed. These discrepancies are attributed mainly to the fact that the spatial resolution may not have been sufficient in the downslope region because in this region waves with smaller wavelengths become dominant (see Figure 4) and consequently the initially adopted resolution becomes relatively coarse.

Figures 5a-5d and Figure 6 show similar comparisons for the short monochromatic waves. The wave form in this case (short waves) does not evolve appreciably. The wave is closer to being a higher order Stokes type wave and does not behave as a shallow-water wave. Consequently, even in the shallowest region, the near resonant conditions for three-wave interactions are not satisfied and the growth rate of higher harmonics remains low.

The agreement between computations and observations for the short-wave case is not as good as that for the long waves. The reasons for this are believed to be as follows. First, the effect of wave energy dissipation is not taken into account in the numerical model. The error due to this is expected to increase with frequency, therefore should be more significant for the 0.8-Hz waves than it is for the 0.5-Hz waves. A second reason is related to the spatial resolution of the computation. The adopted relative resolution for the 0.8-Hz waves is less than for the 0.5-Hz waves, and may not have been sufficient, especially for the higher harmonics.

For the random incident waves, comparisons are given only for the "long" waves ( $f = 0.5$  Hz) at the odd-numbered stations. The results are shown in Figure 7 (time records) and Figure 8 (spectra). (The surface elevations in Figure 7 have been normalized with  $H_p$ , the target value of  $H_{1/3}$ .) The spectral evolution is substantial and so is the amount of high frequency energy generation.

For the shorter waves (results not shown here), a negligible amount of high frequency energy generation was observed. The spectral shape was found to remain nearly intact at all stations.

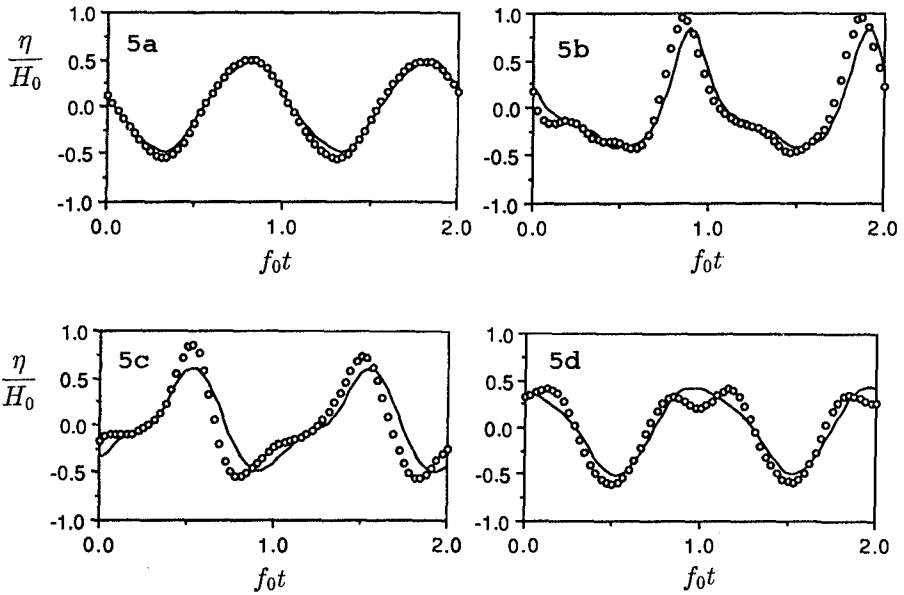


Figure 5. Measured (—) and computed (ooo) wave profiles for monochromatic waves,  $f=0.8$  Hz, at stations 1,3,5,7 (a,b,c,d)

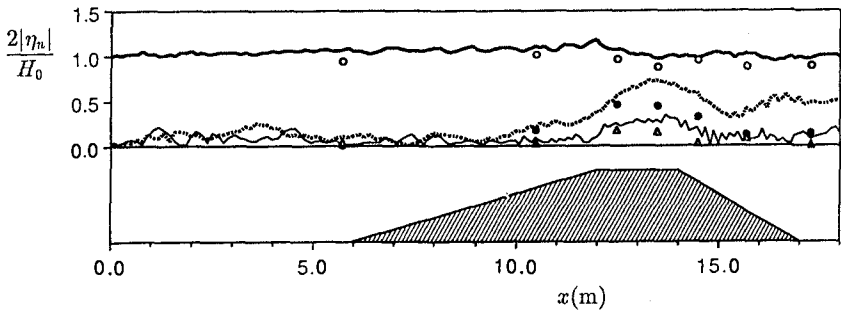


Figure 6. Measured ( $\circ$ :  $n=1$ )( $\cdot$ :  $n=2$ )( $\Delta$ :  $n=3$ ) and computed ( $\text{---}$ :  $n=1$ )( $\text{.....}$ :  $n=2$ )( $\text{---}$ :  $n=3$ ) spatial evolution of harmonic amplitudes for monochromatic waves,  $f=0.8$  Hz.

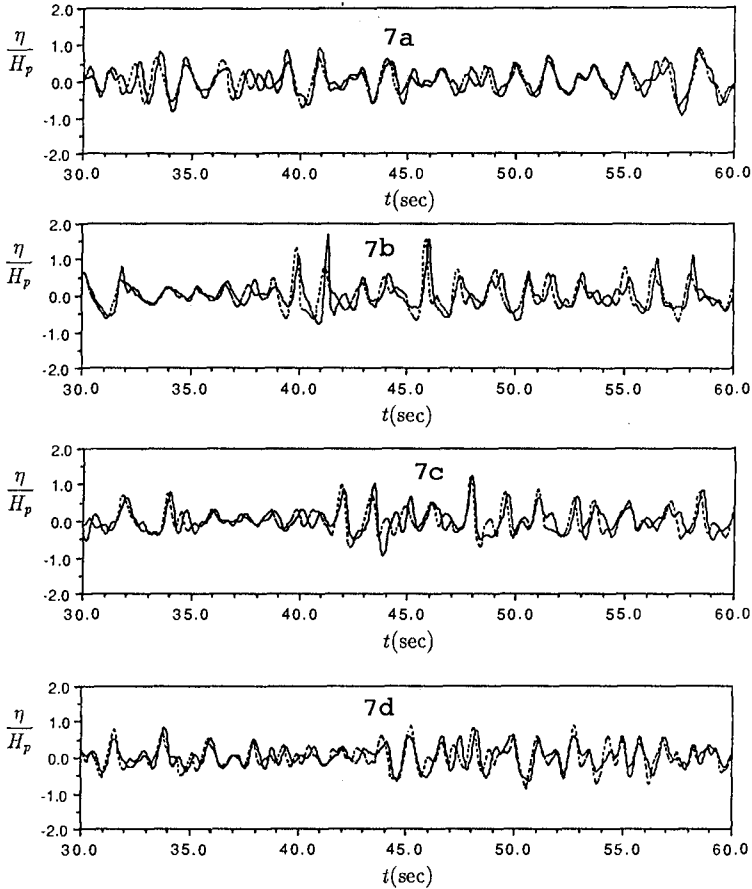


Figure 7. Measured (—) and computed (---) surface elevations for random waves,  $f=0.5$  Hz, at stations 1,3,5,7 (a,b,c,d,)

Although the overall evolution of the random wave forms and energy spectra are well predicted by the numerical model, detailed inspection of the time domain records shows significant differences in amplitude and phases, even in the constant-depth region between wave generator and slope. These are ascribed to insufficient resolution; the normalized mesh size  $\Delta x/L$  was set to  $1/15$  in the initial propagation domain. This may not have been sufficient to reproduce the propagation of the higher-frequency components in the (incident) waves.



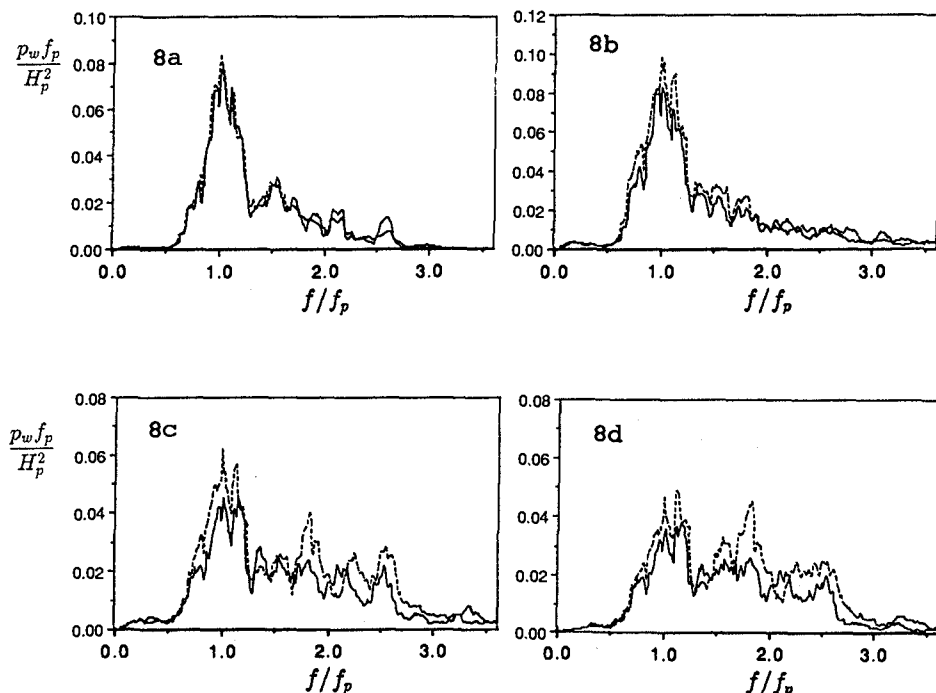


Figure 8. Measured (—) and computed (---) energy density spectra of random waves,  $f=0.5$  Hz, at stations 1, 3, 5, 7 (a, b, c, d)

It may further be noticed that the observed energy levels are overestimated in the computations (see e.g. the spectra at station 5 and 7 in Figure 8); the differences increase with propagation distance. This is ascribed to viscous dissipation, which is absent in the computations.

## 5. Conclusions

General agreement between the measurements and the computations is quite satisfactory, provided the computations are done with sufficient resolution. For the long waves the numerical model performs very well, the discrepancies are usually small. The performance of the model is less for the short waves, but still acceptable.

The comparisons presented here show some discrepancies due the absence of dissipation in the

computational model, but that is not considered a serious shortcoming for the intended applications, i.e. near-field computation of strongly non-uniform and steep wave fields near localised topographical features. In such cases, the dissipation plays a minor role, particularly at full-scale (high Reynolds number) instead of the small-scale laboratory situation of the observations discussed here.

Summarising, the results presented here confirm the reliability of the numerical model. As the cost of computing becomes lower, numerical models such as the one tested here will find wider use in engineering applications.

## References

- Beji, S. and J.A. Battjes**, 1992. An experimental investigation of breaking and nearly breaking waves traveling over a bar. To be published in Coastal Engineering.
- Dold, J.W. and D.H. Peregrine**, 1984. Steep unsteady waves: an efficient computational scheme. Proc. 19th Internat. Conf. Coastal Eng. A.S.C.E. Houston 1, 955-967.
- Kojima, H., T. Ijima, and A. Yoshida**, 1990. Decomposition and interception of long waves by a submerged horizontal plate. Proc. 22th Coastal Eng. Con., Delft, The Netherlands, 2:1228-1241.
- Longuet-Higgins, M.S. and E.D. Cokelet**, 1976. The deformation of steep surface waves on water; 1. A numerical method of computation. Proc. Roy. Soc. Lond. A 350, 1-26.
- Ohyama, T and K. Nadaoka**, 1991. Development of numerical wave tank for analyses of nonlinear and irregular wave field. Fluid Dynamics Res., 8:231-251.
- Ohyama, T., S. Beji, K. Nadaoka and J.A. Battjes**, 1992. Experimental verification of a numerical model for nonlinear waves. Submitted for publication.
- Phillips, O.M.**, 1960. On the dynamics of unsteady gravity waves of finite amplitude, Part 1. The elementary interactions, J. Fluid Mech., 9:193-217.
- Vinjé, T, and P. Brevig**, 1981. Numerical simulation of breaking waves. Adv. Water Resources 4, 77-82.

## CHAPTER 3

### PRACTICAL COMPARATIVE PERFORMANCE SURVEY OF METHODS USED FOR ESTIMATING DIRECTIONAL WAVE SPECTRA FROM HEAVE-PITCH-ROLL DATA

Michel BENOIT <sup>1</sup>

#### Abstract

Twelve methods used for estimating the directional wave spectrum from heave-pitch-roll data are compared on realistic numerical simulations. These methods are based on different modelling approaches including simple and sophisticated ones : Fourier Series decomposition, Fit to unimodal or bimodal parametric models, Variational fitting technique, Maximum Likelihood Methods, Eigenvector Methods, Maximum Entropy Methods and Bayesian approach. The comparison is performed in terms of practical aspects such as estimation error, computation time, implementation difficulty... This study must be regarded as a preliminary step devoted to the choice of optimal methods for operational in situ measurements.

#### **1. Introduction :**

The knowledge of directional properties of waves is of greatest interest in ocean and coastal engineering and the directionality of waves has appeared to have a great influence for offshore situations : moored vessels, oil-platforms,... as for nearshore problems : stability of coastal structures, harbour agitation, coastline morphodynamic evolution... A great effort has been devoted in the recent years to the determination of the directional wave spectrum. Several measurement techniques have been proposed for in situ or laboratory applications. They can be divided into several groups depending on the way they proceed :

- the single-point systems that measure at the same location several properties of waves. From this type of sensors one can mention the heave-pitch-roll buoy (Kobune *et al.*, 1985 ; Lygre and Krogstad, 1986 ; Mardsen and Juszko, 1987), the two-component current meter associated with a pressure sensor (Briggs, 1984) and the cloverleaf buoy (Mitsuyasu *et al.*, 1975).
- the gauge arrays that are composed of several sensors set up at various locations. The sensors may be either identical or of various types including for instance current meters and pressure sensors (Hashimoto *et al.*, 1987)
- the remote-sensing systems including active microwave radars (Jackson *et al.*, 1985), aerial stereo-photography techniques...

---

<sup>1</sup> Research Engineer

EDF - Laboratoire National d'Hydraulique, 6, quai Watier 78400 CHATOU, FRANCE

Among these systems the heave-pitch-roll buoy is probably the most widely employed for operational use because it is a compact single-point measurement system of moderate cost and easy keeping. In the meantime the sampling of wave statistics is limited to three properties : the sea-surface elevation (heave) and two orthogonal slopes of sea-surface (pitch and roll). Starting with only three measured quantities the estimation of the directional wave spectrum is a difficult inverse problem for which no unique method can be exhibited. To take maximum advantage of these rather limited information, several methods based on various modelling approaches have then be proposed.

The aim of this study is to compare a large number of these methods on numerical representative sea-state simulations. In this study we are interested in evaluating the ability of the methods to estimate the simulated directional spectra (estimation error) and studying practical aspects of their use (implementation problems, computing time). This preliminary work aims to exhibit practical recommendations for the choice of optimal methods that could then be applied in laboratory or in the field.

## 2. Problem formulation

The directional wave spectrum  $S(f,\theta)$  is a function of wave frequency  $f$  and direction of propagation  $\theta$ . The following classical decomposition is used :

$$S(f,\theta) = E(f).D(f,\theta) \quad (1)$$

in which  $E(f)$  is the one-sided frequency spectrum that may be estimated by a single record of sea-surface elevation. It is related to the directional spectrum by :

$$E(f) = \int_0^{2\pi} S(f,\theta) d\theta \quad (2)$$

$D(f,\theta)$  is the directional spreading function satisfying two important properties :

$$D(f,\theta) \geq 0 \text{ over } [0, 2\pi] \quad \text{and} \quad \int_0^{2\pi} D(f,\theta) d\theta = 1 \quad (3)$$

The following pseudo-integral relation may be written between the directional spectrum and the sea-surface elevation  $\eta$  :

$$\eta(x,y,t) = \int_0^{\infty} \int_0^{2\pi} \sqrt{2.S(f,\theta).df.d\theta} \cdot \cos[2\pi ft - k.(x.\cos\theta+y.\sin\theta) + \varphi] \quad (4)$$

In the present study we assume that the buoy is able to measure the sea-surface elevation and two orthogonal slopes on the sea-surface :

$$\begin{aligned} \eta(t) &= X_1(t) \\ \frac{\partial \eta}{\partial x}(t) &= \eta_x(t) = X_2(t) \\ \frac{\partial \eta}{\partial y}(t) &= \eta_y(t) = X_3(t) \end{aligned} \quad (5)$$

By applying spectral analysis procedures it is possible to compute the cross-spectra  $G_{ij}(f)$  between each couple  $(X_i, X_j)$  of the three measured properties :

$$G_{ij}(f) = 2 \cdot \int_{-\infty}^{+\infty} R_{ij}(\tau) e^{-i2\pi f\tau} d\tau \quad \text{with } R_{ij}(\tau) = \lim_{T \rightarrow \infty} \frac{1}{T} \int_0^T X_i(t) \cdot X_j(t+\tau) dt \quad (6)$$

The cross-spectra or spectral cross-correlation coefficients are in the general case complex quantities which are often written in the following form :

$$G_{ij}(f) = C_{ij}(f) - i \cdot Q_{ij}(f) \quad (7)$$

$C_{ij}(f)$  is called "coincident spectral density function" or "co-spectrum" and  $Q_{ij}(f)$  is called "quadrature spectral density function" or "quad-spectrum".

By using (4) and the linear relationship between the elevation and the slopes of sea-surface it may be shown that the cross-correlation coefficients for the heave-pitch-roll buoy take the following expressions :

$$\left. \begin{aligned} C_{11}(f) &= \int_0^{2\pi} S(f, \theta) d\theta = E(f) & Q_{11}(f) &= 0 \\ C_{22}(f) &= E(f) \cdot k^2 \int_0^{2\pi} D(f, \theta) \cdot \cos^2(\theta) d\theta & Q_{22}(f) &= 0 \\ C_{33}(f) &= E(f) \cdot k^2 \int_0^{2\pi} D(f, \theta) \cdot \sin^2(\theta) d\theta & Q_{33}(f) &= 0 \\ C_{12}(f) &= 0 & Q_{12}(f) &= E(f) \cdot k \int_0^{2\pi} D(f, \theta) \cdot \cos(\theta) d\theta \\ C_{13}(f) &= 0 & Q_{13}(f) &= E(f) \cdot k \int_0^{2\pi} D(f, \theta) \cdot \sin(\theta) d\theta \\ C_{23}(f) &= E(f) \cdot k^2 \int_0^{2\pi} D(f, \theta) \cdot \cos(\theta) \cdot \sin(\theta) d\theta & Q_{23}(f) &= 0 \end{aligned} \right\} \quad (8)$$

From the twelve real cross-correlation coefficients only six are non equal to zero. Furthermore  $C_{11}(f)$  does not carry any information about the directional distribution and  $C_{11}(f)$ ,  $C_{22}(f)$ ,  $C_{33}(f)$  are tied by the following relation :

$$C_{22}(f) + C_{33}(f) = k^2 \cdot C_{11}(f) \quad (9)$$

that we can use for the calculation of the wave number expression :

$$k = \sqrt{\frac{C_{22}(f) + C_{33}(f)}{C_{11}(f)}} \quad (10)$$

As established so far it is possible to compute by spectral analysis only five independent coefficients at each frequency from which one is devoted to the estimation of the frequency spectrum  $E(f)$  and the four others may be used for the computation of the directional spreading function  $D(f, \theta)$  at this frequency. The problem of directional spectrum estimation is then to determine a continuous function over  $[0, 2\pi]$  satisfying (3) with only four independent integral properties from (8). It is clear that finding a solution to this difficult inverse problem can not be proceeded in an unique way because of the too feeble number of constraints.

### 3. Review of methods used for estimating the spreading function

Among the theoretical modelling approaches proposed in the literature to solve the above exposed problem, twelve operational methods have been selected and implemented in the software **PRD-WAS 1.0** (Pitch and Roll Data - Wave Analysis Software) developed at LNH (Benoit, 1991). Only a short description of the theoretical background of each method is reported below. Further information may be found in the mentioned references.

1. Truncated Fourier Series (TFS): the directional spreading function is expressed as a truncated series whose first four coefficients are easily computed from the spectral cross-correlation coefficients :

$$D(f, \theta) = \frac{1}{\pi} \left( \frac{1}{2} + a_1(f) \cdot \cos \theta + b_1(f) \cdot \sin \theta + a_2(f) \cdot \cos 2\theta + b_2(f) \cdot \sin 2\theta \right) \quad (11)$$

2. Weighted truncated Fourier Series (WFS): Following Longuet-Higgins *et al.* (1963) a weighting function is used to avoid negative values of the former method :

$$D(f, \theta) = \frac{1}{\pi} \left( \frac{1}{2} + \frac{2}{3}(a_1(f) \cdot \cos \theta + b_1(f) \cdot \sin \theta) + \frac{1}{6}(a_2(f) \cdot \cos 2\theta + b_2(f) \cdot \sin 2\theta) \right) \quad (12)$$

3. Fit to Unimodal Gaussian Model (1MF): A unimodal parametric model of gaussian type (Borgman, 1969) is used whose two unknown parameters  $\alpha$  et  $\sigma$  are computed from the first two Fourier coefficients of the spreading function :

$$D(f, \theta) = \frac{1}{\sqrt{2\pi} \sigma} \exp\left(-\frac{(\theta - \alpha)^2}{2\sigma^2}\right) \quad (13)$$

4. Fit to Bimodal Mitsuyasu Model (2MF): A bimodal parametric model obtained from linear combination of two unimodal Mitsuyasu-type models is used:

$$D(f, \theta) = \frac{\lambda}{\Delta(s_1)} \cos^{2s_1}\left(\frac{\theta - \theta_1}{2}\right) + \frac{1 - \lambda}{\Delta(s_2)} \cos^{2s_2}\left(\frac{\theta - \theta_2}{2}\right) \quad (14)$$

Its five unknown parameters are calculated from the spectral cross-correlation coefficients by using a method based on the least-square method (Benoit, 1991).

5. Variational Fitting Technique: Long-Hasselmann Method (LHM): Long and Hasselmann (1979) developed this method by which an initial simple estimate is iteratively modified to minimize a "nastiness" function that takes into account the various conditions on the spreading function.

6. Maximum Likelihood Method (MLM): By this method the spreading function is regarded as a linear combination of the cross-spectra :

$$D(f, \theta) = \sum_{i=1}^3 \sum_{j=1}^3 w_n^*(\theta) \cdot w_m(\theta) \cdot G_{ij}(f) \quad (15)$$

The weighting coefficients  $w_n$  are calculated with the condition of unity gain of the estimator in the absence of noise (Oltman-Shay and Guza, 1984).

7. Iterative Maximum Likelihood Method (IMLM): The estimator obtained by the former method is not consistent with the data cross-spectra. It is also iteratively modified to let its spectral cross-correlation coefficients become closer to the ones obtained from the data (Oltman-Shay and Guza, 1984).

8. EigenVector Method (EVM): Mardsen and Juszko (1987) proposed a refinement of the MLM in which the data are partitioned into signal and noise through the calculation of the eigenvalues of the spectral cross-correlation matrix.

9. Iterative EigenVector Method (IEVM): the same iterative improvement as proposed for the MLM is applied to the Eigenvector Method.

10. Maximum Entropy Method - Version 1 (MEM1): Lygre and Krogstad (1986) proposed to find an estimate of the spreading function by maximizing :

$$\chi = - \int_0^{2\pi} \ln (D(f,\theta)) d\theta \quad (16)$$

under the constraints given by the spectral cross-correlation coefficients.

11. Maximum Entropy Method - Version 2 (MEM2): The same approach may be considered by using Shannon's definition for entropy (Nwogu *et al.*, 1987) :

$$\chi = - \int_0^{2\pi} D(f,\theta) \ln (D(f,\theta)) d\theta \quad (17)$$

With the former version the expression of the directional estimate is easily obtained, but with the latter a non-linear system of equations has to be solved.

12. Bayesian Directional Method (BDM): With this statistical technique used for regression analysis (Hashimoto *et al.*, 1987), no *a priori* assumption is made about the spreading function which is considered as a piecewise-constant function over  $[0, 2\pi]$ . The unknown values of  $D(f,\theta)$  on each of the  $K$  segments dividing  $[0, 2\pi]$  are obtained by considering the constraints of the spectral cross-correlation coefficients and an additional condition on the smoothness of  $D(f,\theta)$ .

#### 4. Description of the performed tests

Numerical sea-state simulations are performed by following the single direction per frequency method (Miles, 1989) based on a discretization of (4) :

$$\eta (x,y,t) = \sum_{n=1}^N A_n \cos (2\pi.f_n.t - k_n(x.\cos \theta_n + y.\sin \theta_n) + \varphi_n) \quad (18)$$

$$\left. \begin{aligned} \text{with : } A_n &= \sqrt{2 S (f_n, \theta_n) \Delta f_n \Delta \theta_n} \\ \varphi_n &= 2 \pi U [0,1] \quad (\text{random phase}) \\ f_n &= (n - 1) \Delta f \quad \text{with } \Delta f = \frac{f_c}{N} = \frac{1}{T} \\ \theta_n &\text{ are of the form } k.\Delta\theta, \text{ but randomly distributed over } [0, 2\pi] \end{aligned} \right\} \quad (19)$$

The frequency spectrum  $E(f)$  is a classical JONSWAP spectrum with a significant wave height of 4 m, a peak frequency of 0.1 Hz and a peak-factor  $\gamma = 3.3$ .

The directional spreading function is of the form :

$$\Pi_{p1,\alpha1,p2,\alpha2,\lambda}(\theta) = \lambda.\Pi_{p1,\alpha1}(\theta) + (1-\lambda).\Pi_{p2,\alpha2}(\theta) \quad \text{with } 0 \leq \lambda \leq 1 \quad (20)$$

$$\left. \begin{aligned} \text{with : } \Pi_{p,\alpha}(\theta) &= \frac{1}{\Lambda(p)} \cos^2 p(\theta-\alpha) \quad \text{if } \theta \in \left[ \alpha - \frac{\pi}{2}; \alpha + \frac{\pi}{2} \right] \\ \Pi_{p,\alpha}(\theta) &= 0 \quad \text{if } \theta \in \left[ \alpha - \pi; \alpha - \frac{\pi}{2} \right] \cup \left[ \alpha + \frac{\pi}{2}; \alpha + \pi \right] \end{aligned} \right\} \quad (21)$$

$\Lambda(p)$  is a normalizing constant to ensure the properties (3).

A Gaussian real white noise is added to the simulated time series. Its spectral density is constant from zero to the Nyquist frequency  $f_c$ . The noise level is expressed in terms of a percentage of the RMS (root mean square) amplitude of sea-surface elevation as proposed by Nwogu *et al.* (1987).

The simulated time series have a time step of 0.5 s and a duration of 4096 s (8192 points per signal). This represents a record of around 410 waves with 20 points per wave (at peak frequency).

The spectral estimator is based on the technique of the averaged periodogram on the whole simulated sequence partitioned in segments of 1024 points. An overlapping of 25% between adjacent segments is used and a parabolic data window is applied to the common part of two adjacent segments. The resulting frequency resolution is 0.002 Hz.

Three test cases are performed with the following characteristics for the directional spreading function :

- case 1 : Unimodal Broad Spreading Function ( $\lambda=1 \mid p_1=1 \mid \alpha_1=120^\circ$ )
- case 2 : Unimodal Thin Spreading Function ( $\lambda=1 \mid p_1=10 \mid \alpha_1=70^\circ$ )
- case 3 : Bimodal Spreading Function ( $\lambda=0.5 \mid p_1=2 \mid \alpha_1=130^\circ \mid p_2=6 \mid \alpha_2=240^\circ$ )

The first case rather represents a wind-sea with a large spread around a main direction of propagation. In the second case the spread around the main direction of propagation is much lower indicating a rather "old" swell. In the third case we have a crossed-sea with two main directions of propagation. The three directional spreading functions are presented on figure 1.

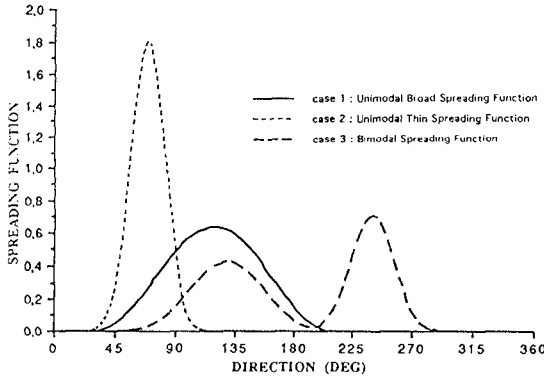


Figure 1: The three Directional Spreading Functions

To perform the comparison of the methods five criterion are taken into account :

a) **the error of the estimate**  $\hat{D}(\theta)$  produced by the method versus the simulated spreading function  $D(\theta)$ . This error is measured by the Weighted Average Percent Error (WAPE) as proposed by Olman-Shay and Guza (1984) :

$$\text{WAPE} = \frac{\sum_{\theta} |\hat{D}(\theta) - D(\theta)|}{\sum_{\theta} D(\theta)} \times 100 \quad (22)$$

- b) **the sensitivity to the shape of the spreading function**
- c) **the computation time** measured on an IBM 3090 Computer
- d) **the noise sensitivity**
- e) **the difficulty of implementation**



## 5. Presentation and discussion of the results

The spreading functions estimated at peak frequency by the various methods on the three cases with a noise level of 20% are reported on figures 2, 3 and 4 respectively. On these figures the target function is represented by a dashed line and the spreading functions estimated at both the frequency surrounding the theoretical peak frequency are represented by continuous lines with different marker symbols. The WAPE and CPU Time are also reported on the same figures. An overview for the comparison of the various methods on the three cases is presented on figure 5 where performance is visualized by points representing WAPE versus CPU Time.

Because on the great volume of results to be presented in such a comparative study only nine methods appear on these figures. Both the Fourier Series methods (TFS and WFS) are not reported because it is now well known that they do not give good results although they are fast and easy to implement. The former often produces negative values which are not acceptable for a spreading function. For the latter the suppression of negative values by a weighting function results in an important smoothing of the curve and strongly under-estimates the peaks of the spreading function. The Iterative Eigenvector Method IEVM is not reported because it has sometimes failed to converge during these tests (in particular on case 2) and produced spurious peaks.

The IMF method (Fit to Unimodal Gaussian Model) is the fastest one and produces good results on the two first cases where the target spreading function is unimodal, but as expected do not give a reliable estimate on case 3.

The extension of this approach to Bimodal Model Fitting (2MF) is very satisfactory on the three cases, more especially as one has to keep in mind that it is tried to determine five model parameters from only four data coefficients. Even if more validation cases are needed for this method currently developed at LNH, the results on these three cases are very promising. Furthermore the computing time may be considered as very short.

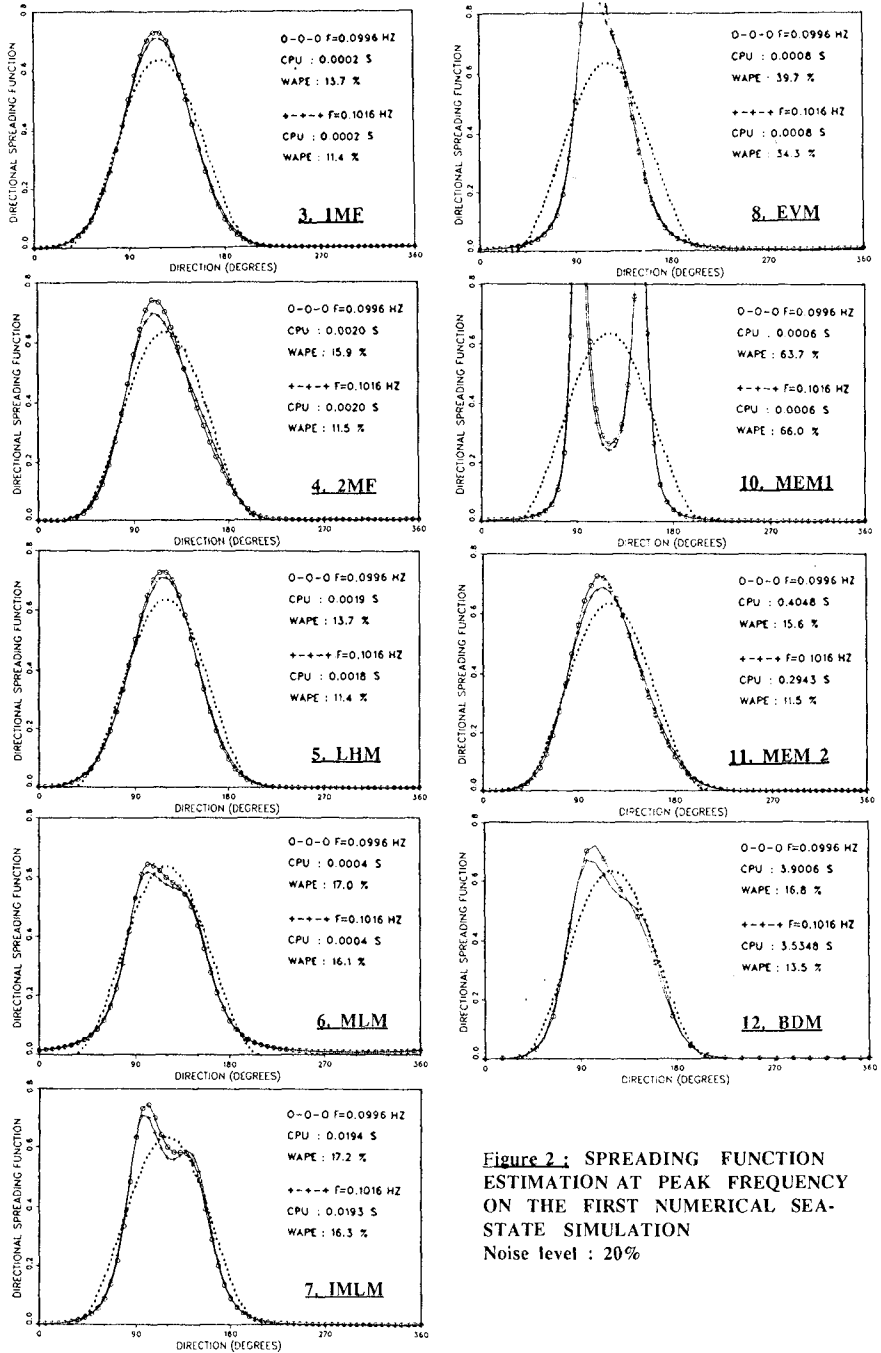
The Variational Fitting Technique of Long and Hasselmann gives good results on the unimodal cases because the initial model (based on IMF method) is already close to the target model, but in the third case when the iterative algorithm has to be activated, the computing time increases rapidly for an estimate that still produces 50% WAPE. At this point of validation this method has not shown definite advantages compared to its rather long and difficult implementation.

The Maximum Likelihood Method produces rather good estimates on all the cases with a very short CPU Time. As it is furthermore rather easy to implement we understand why it is so widely used for operational measurement. Its iterative refinement IMLM improves the estimation on case 3, but also shows a trend to split the peak on unimodal cases. Nevertheless it appears better than the MLM on figure 5 even if the CPU Time is clearly higher. During these tests 10 iterations were performed but further tests are required to optimize this value.

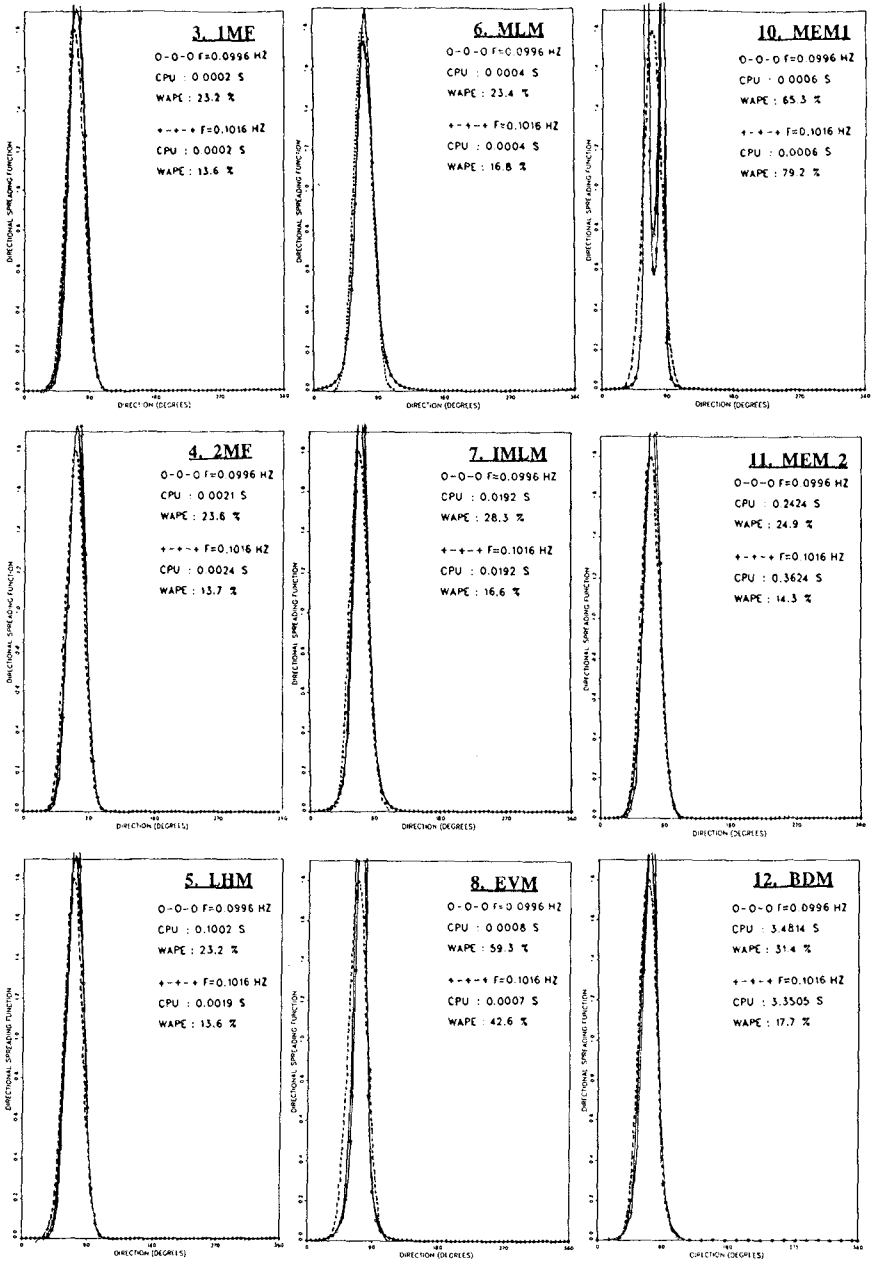
The Eigenvector Method does not reveal here a particular interest : the method is fast but on these cases the estimates are not very accurate. This method should be probably more interesting on cases where the noise level is much higher.

The first version of the Maximum Entropy Method (MEM1) is easy to implement and needs very little CPU time, but the estimate is not reliable and split the peak on unimodal cases. On case 3 the directional spreads are under-estimated.

The MEM version 2 (MEM2) is clearly superior and gives very good estimates on the three cases. On the other hand the CPU time is high and the implementation of this method is not simple.



**Figure 2: SPREADING FUNCTION ESTIMATION AT PEAK FREQUENCY ON THE FIRST NUMERICAL SEA-STATE SIMULATION**  
Noise level : 20%



**Figure 3: SPREADING FUNCTION ESTIMATION AT PEAK FREQUENCY ON THE SECOND NUMERICAL SEA-STATE SIMULATION**  
Noise level : 20%

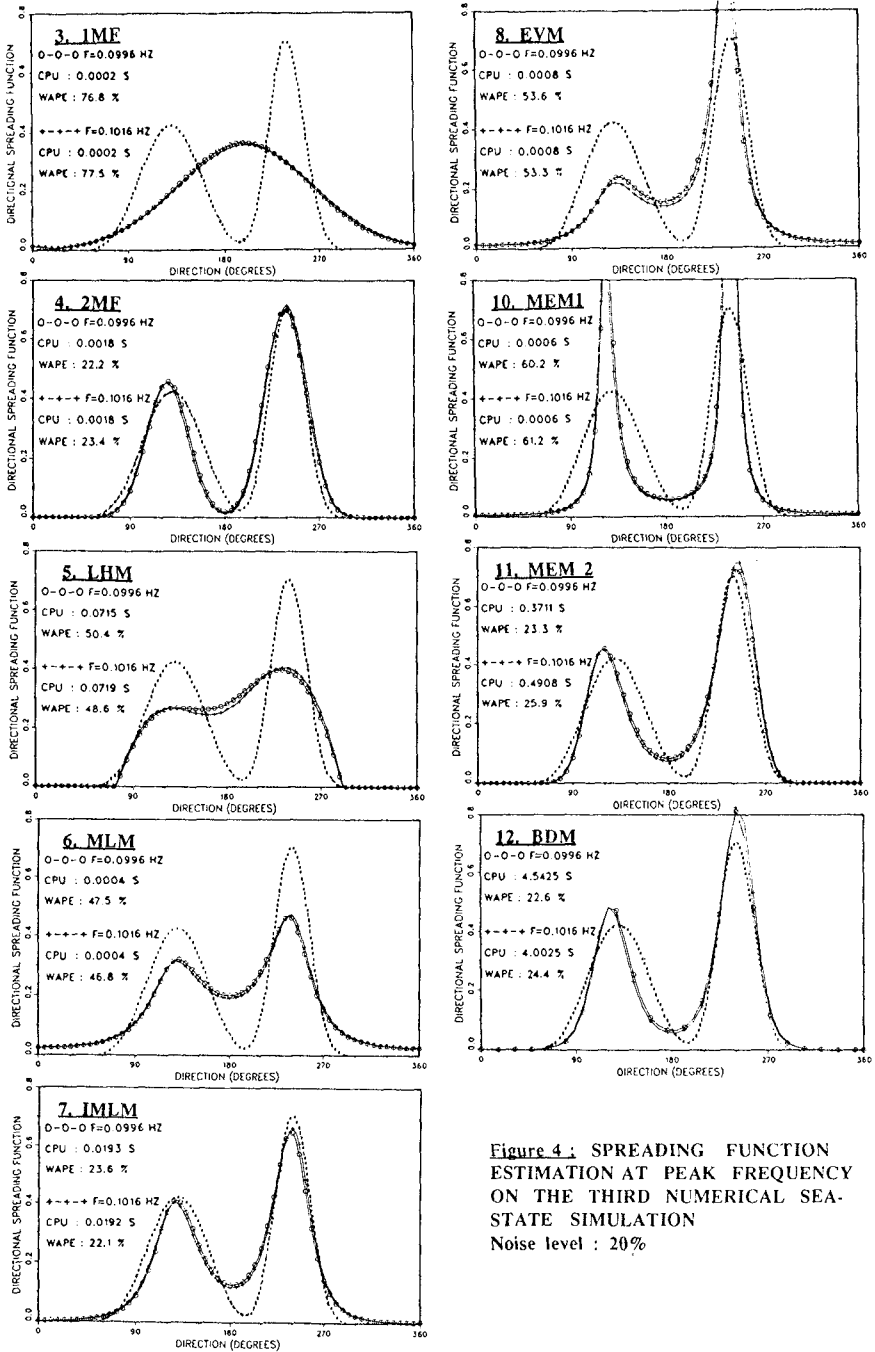
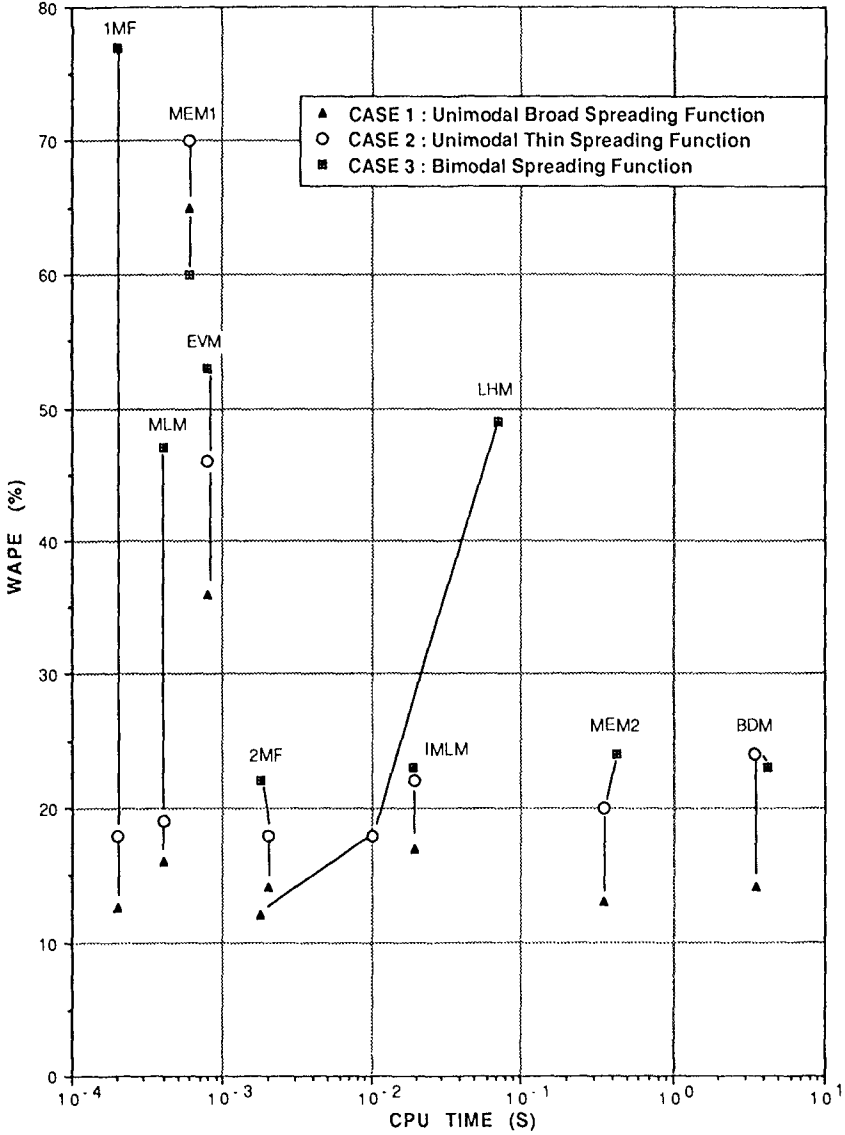
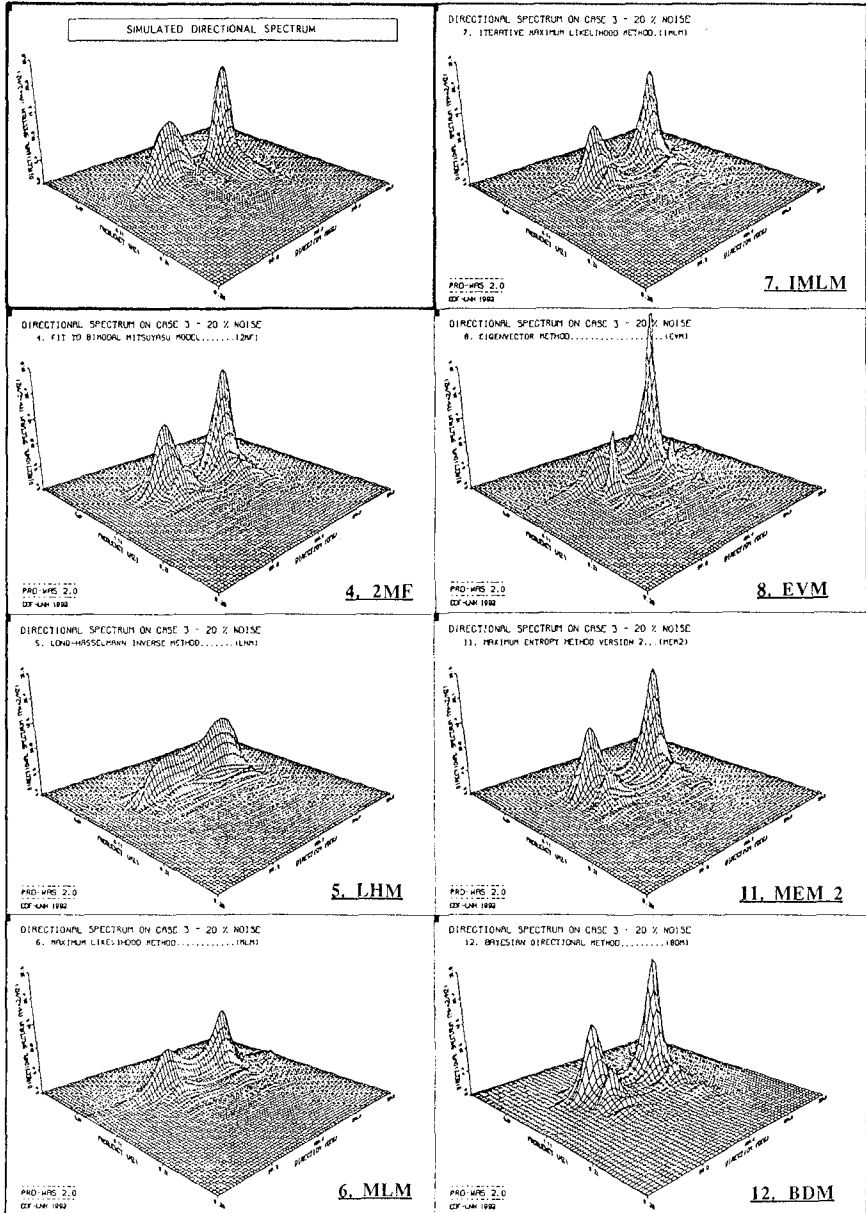


Figure 4 : SPREADING FUNCTION ESTIMATION AT PEAK FREQUENCY ON THE THIRD NUMERICAL SEA-STATE SIMULATION  
Noise level : 20%



**Figure 5 :** PERFORMANCE COMPARISON OF THE VARIOUS METHODS ON THE THREE NUMERICAL SEA-STATE SIMULATIONS

Spreading Function estimated at Peak Frequency - Noise level : 20%



**Figure 7 :** COMPARISON OF DIRECTIONAL SPECTRUM SHAPES ON THE THIRD NUMERICAL SEA-STATE SIMULATION (Bimodal Spreading Function) - Noise level : 20%

The Bayesian Direction Method also produces good estimates on these cases although there are very few information on input. This is also an extreme application of this sophisticated method and the resulting CPU Time is very high. Following its authors we can not affirm this method will always produce reliable estimates for so little amount of data.

From the analysis of figure 5 four methods giving less than 25% WAPE on the three cases may be identified : 2MF, IMLM, MEM2 and BDM (ordered following increasing CPU Time). These methods are rather stable in the sense that the CPU Time is rather constant and the WAPE do not vary in a great manner from a case to an other. Meanwhile the CPU Time is changing in a ratio of around 10 from a method to the following one.

The effect of noise is sensitive as soon as we try to compute the spreading function too far from the peak frequency. As example the variation of directional spread with noise level is reported on figure 6. Following Nwogu *et al.* (1987) who obtained the same conclusions about noise effect study, we would advise not to compute the spreading function out of the range  $[0.75 f_p, 1.5 f_p]$ .

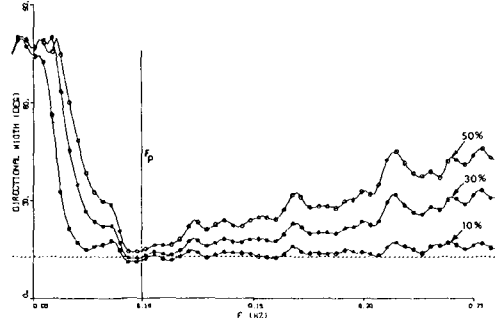


Figure 5 : Effect of Noise Level on Directional Width  
(Case 2 : Unimodal Thin Spreading Function)

Figure 7 shows 3D-plots of the directional spectra estimated by seven of these methods on case 3. The most accurate estimates are clearly given by the above identified four methods : 2MF, IMLM, MEM2 and BDM. The MLM spectrum may be regarded as acceptable. The LHM and EVM spectra are of relative poor quality.

## 6. Conclusion

As major conclusions the following points have to be highlighted :

- the determination of the spreading function from heave-pitch-roll data is a critical problem that should be undertaken only around peak frequencies while on the other hand representative parameters such as main direction, directional spread, etc... may be computed over a much larger frequency range.
- Simple methods as Fourier Series Decomposition (TFS, WFS) or Unimodal Fitting (1MF) are not recommended because their estimates are of poor quality.
- the Maximum Likelihood Method (MLM) may be advised because it is fast and rather easy to implement. Its iterative refinement (IMLM) clearly improves the method and appears as an acceptable compromise between error and CPU Time.
- the Maximum Entropy Version version 2 (MEM2) seems to give the most reliable estimate but its computing time is rather high.
- the Bimodal Fitting (2MF) in its form developed at LNH seems very promising but has to be validated on more simulations.
- Sophisticated refinements as Variational Model Fitting (LHM) or Bayesian Directional Method (BDM) are not interesting for the case of the buoy where only few information are available.

Of course these preliminary conclusions have then to be confirmed or altered by applying the methods to laboratory or field data. Nevertheless guidelines for the choice of *a priori* optimal methods may be extracted from this study.

## 7. Acknowledgements

This study is a joint research program between EDF-LNH and the French "Secrétariat d'Etat chargé de la Mer (STNMTE)".

## 8. References

- BENOIT M. (1991) : Comparison of methods for estimating directional wave-spectrum. Part 1 : Ability of the methods to build theoretical spectra with heave-pitch-roll data by assuming a perfect spectral analysis. *Report. EDF-LNH, HE42/91.32. (in french)*
- BORGMAN L.E. (1969) : Directional spectra models for design use. *Offshore Technology Conference, Houston, Texas*
- BRIGGS M.J. (1984) : Calculation of directional wave spectra by the Maximum Entropy Method of spectral analysis. *Proc. XIX Int. Conf. on Coastal Eng., Paper 33, pp 484-500, ASCE, New York*
- HASHIMOTO N., KOBUNE K., KAMEYAMA Y. (1987) : Estimation of directional spectrum using the Bayesian approach and its application to field data analysis. *Report of the Port and Harbour Research Institute., vol 26, pp 57-100.*
- JACKSON F.C., WALTON W.T., BAKER P.L. (1985) : Aircraft and Satellite Measurement of Ocean Wave Directional Spectra Using Scanning Beam Microwave Radar. *J. Geophys. Res., vol 90, N° C1, pp 987-1004.*
- KOBUNE K., SASAKI H., HASHIMOTO N. (1985) : Characteristics of Ocean Waves off Cape Nokima in the Northwestern Pacific, Measured with a Discuss Buoy. *Report of the Port and Harbour Research Institute., vol 24, N° 3, pp 3-30.*
- LONG R.B., HASSELMANN K. (1979) : A variational technique for extracting directional spectra from multicomponent wave data. *J. Phys. Oceanogr., vol 9, pp 373-381.*
- LONGUET-HIGGINS M.S., CARTWRIGHT D.E., SMITH N.D. (1963) : Observations of the directional spectrum of sea waves using the motions of a floating buoy. *Ocean Wave Spectra, Prentice-Hall, pp 111-136.*
- LYGRE A., KROGSTAD H.E. (1986) : Maximum entropy estimation of the directional distribution in ocean wave spectra. *J. Phys. Oceanogr., vol 16, pp 2052-2060.*
- MARDSEN R.F., JUSZKO B.A. (1987) : An eigenvector method for the calculation of directional spectra from heave, pitch and roll buoy data. *J. Phys. Oceanogr., vol 17, pp 2157-2167.*
- MILES M.D. (1989) : A note on directional random wave synthesis by the Single Summation Method. *Proc. 23rd IAHR Congress, Ottawa, Canada, Vol C, pp243-250*
- MITSUYASU H., TASAI F., SUHARA T., MIZUNO S., OHKUSU M., HONDA T., RIKIISHI K. (1975) : Observations of the directional spectrum of ocean waves using a cloverleaf buoy. *J. Phys. Oceanogr., vol 5, pp 750-760*
- NWOGU O.U., MANSARD E.P.D., MILES M.D., ISAACSON M. (1987) : Estimation of directional wave spectra by the maximum entropy method. *Proc. 17th IAHR Seminar - Lausanne.*
- OLTMAN-SHAY J., GUZA R.T. (1984) : A data-adaptative ocean wave directional-spectrum estimator for pitch-roll type measurements. *J. Phys. Oceanogr., vol 14, pp 1800-1810.*



## CHAPTER 4

The modelling of short waves in shallow waters.  
Comparison of numerical models based  
on Boussinesq and Serre equations.

M. Brocchini<sup>†</sup>, M. Drago<sup>†</sup> and L. Iovenitti<sup>†</sup>

### Abstract

Two different flow models of the surf zone wave-current dynamics based on Boussinesq and Serre equations have been implemented and tested. Good results were obtained while testing the models against many different wave and current data sets. A preliminary calibration was tried but further activities are required to define the proper parameters.

### Introduction

The research in coastal hydrodynamics recently focused its attention on the mathematical and numerical modelling of the water flows in that region where wave breaking takes place.

This was to fill the gap that shallow water wave theories suffered up to now: they could no longer predict wave-current characteristics while approaching the surf zone. This was a very serious limit to the application of predictive models to coastal engineering and to environmental problems.

The latest trend in the modelling of such phenomena is to develop flow models that work at space-time scales much smaller than the wave length and period. Those models are based on the solution of the equations derived from the continuity and approximated Navier-Stokes equations. Of particular interest are the Boussinesq equations, the Su-Gardner equations and a particular approximation called the Serre equations. The presence of turbulence and energy dissipation in the breaking region is introduced by the concept of the 'surface roller'.

---

<sup>†</sup> Snamprogetti S.p.A. - Offshore Division

The roller is the upper turbulent region of the wave. The main hypothesis is that the water mass of the roller does not take part in the wave motion, but only contributes to the internal pressure field. Its main action is, then, to extract energy from the wave motion acting on it, as a first approximation, through an hydrostatic pressure contribution in the momentum equations.

### The Boussinesq equations

In the following an irrotational (the velocity is the derivative of a potential  $\phi$ ), inviscid fluid with constant density  $\rho$  is considered. The water depth is  $h$  and the surface waves are characterized by an amplitude  $A$  and a wave number  $k$ . For shallow waters (the depth to wavelength ratio is smaller than one), considering weakly non linear and moderate long waves the Boussinesq approximation is valid:

$$O(\epsilon) = O(\mu^2) < 1,$$

where  $\mu = kh$  and  $\epsilon = A/h$ . In the following the unidimensional equation including terms in the order of  $O(\epsilon)$  and  $O(\mu^2)$  is considered:

$$\eta_t + [(h + \eta)\bar{u}]_x = 0, \quad (1)$$

$$\bar{u}_t + \bar{u}\bar{u}_x + g\eta_x = \frac{h}{2}[(h\bar{u})_{xxt}] - \frac{h^2}{6}(\bar{u}_{xxt}), \quad (2)$$

where

$$\bar{u} = \frac{1}{h + \eta} \int_{-h}^{\eta} \nabla \phi dz \quad (3)$$

is the horizontal depth-averaged velocity and where the subscripts represent partial derivatives. The velocity vertical profile is related to the mean velocity through a parabolic equation depending on the vertical coordinate  $z$ :

$$u(z) = \bar{u} - \frac{h}{2}(h\bar{u})_{xx} + \frac{h^2}{6}\bar{u}_{xxx} - z(h\bar{u})_{xx} - \frac{z^2}{2}\bar{u}_{xxx}. \quad (4)$$

These equations have a dispersive behaviour as the phase velocity depends on the wave number  $k$ :

$$C = (gh)^{1/2} \left( 2 - \frac{k^2 h^2}{3} \right)^{1/2} \quad (5)$$

This depedance has been introduced by the  $O(\mu^2)$  term. It may be noticed that the same term causes the pressure field not to be hydrostatic:

$$P = \rho g (\eta - z) + \frac{\rho}{2} (z^2 + 2zh) \nabla \cdot \bar{u}_t. \tag{6}$$

The Serre equations

Using the same procedure of Su and Gardner (1969), expanding the Navier-Stokes equations up to the order  $O(\epsilon\mu^2)$  and considering a slowly varying water depth (the horizontal derivatives of the water depth are neglected at the higher order) the Serre approximation is obtained for  $O(\epsilon) = 1$ , and  $O(\mu^2) < 1$ :

$$\eta_t + [(h + \eta)\bar{u}]_x = 0, \tag{7}$$

$$\begin{aligned} \bar{u}_t + g\eta_x + \bar{u}\bar{u}_x = & hh_x\bar{u}_{xt} + \frac{h^2}{3}\bar{u}_{xxt} + \\ & + h\eta_x\bar{u}_{xt} + \frac{2}{3}h\eta\bar{u}_{xxt} + \frac{h^2}{3} [\bar{u}\bar{u}_{xx} - (\bar{u}_x)^2]_x. \end{aligned} \tag{8}$$

The presence of higher order approximation makes the solution (solitary or cnoidal solutions for example) to be less peaked with respect to the Boussinesq's one (see fig.1)

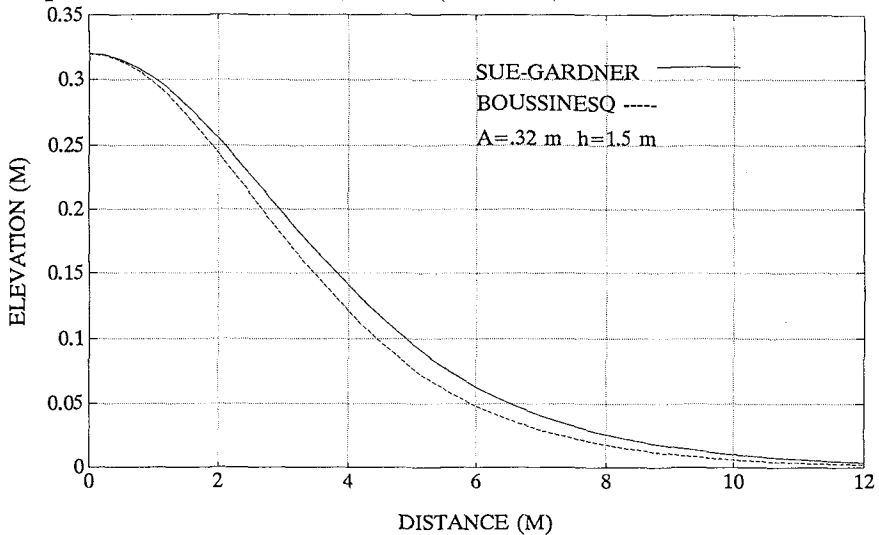


Fig.1 - Solitary solution for Boussinesq and Su-Gardner equations.

The 'Surface Roller'

The description of the breaking process based on the concept of the 'surface roller' was developed by Deigaard (1989). The roller is considered to be that portion of water mixed with air that is formed on the front region of the wave after breaking. The main assumption is that both vertical and horizontal acceleration within the roller are negligible as compared to its other effects on the water beneath. This also means that the pressure field within the roller may be considered hydrostatic. The roller follows the wave crest at a celerity  $C = \sqrt{gh}$ . On these bases the roller may be considered as a solid body that does not take part in the water motion within the wave but only extracts energy from it. This sort of description fits well the spilling breaking process as the overturning of the wave crest and the air-entrainment play a minor role. On the other hand the roller doesn't provide a good representation of a plunging breaker: the overturning of the wave crest generates a too strong jetting within the whole wave to be neglected. Being  $\delta$  the roller elevation above the wave crest and  $\eta$  the wave elevation, the shear stress  $\tau_s$  present at the wave crest-roller interface (Deigaard and Fredsoe (1989)) is:

$$\tau_s dx = -\rho g \delta (\delta_x + \eta_x) dx. \tag{9}$$

It may be deduced that the energy dissipated through a shear stress term in the wave-roller interface is provided by the whole water columns. Considering the spatial derivative  $P_x$  of the Boussinesq pressure vertical profile and neglecting terms in the order of  $O(\epsilon\mu^2)$ :

$$P_x = \epsilon(\eta_x + \delta_x) + \epsilon\mu^2 \left( z h_{xx} \bar{u}_t + 2z h_x \bar{u}_{xt} + \frac{z^2}{2} \bar{u} - xxt \right). \tag{10}$$

This gradient is averaged over the depth giving:

$$\bar{P}_x = \epsilon(\eta_x + \delta_x) + \frac{\epsilon\delta}{h + \epsilon\eta} (\eta_x + \delta_x) - \epsilon\mu^2 \frac{h}{2} (hu)_{xxt} + \epsilon\mu^2 \frac{h^2}{6} \bar{u}_{xxt}. \tag{11}$$

It may be noticed that the Boussinesq equations are obtained neglecting the terms proportional to  $\delta$  and  $\delta_x$ . The dimensional terms due to the roller alone are:

$$\bar{P}_x = -\rho g \left[ \delta_x + \frac{\delta}{h + \eta} (\delta_x + \eta_x) \right]. \tag{12}$$

In the following numerical application this quantity will be multiplied by a factor  $K$  that globally accounts for other energy dissipating phenomena and is calibrated as one of the three 'driving parameters' used in the models. Finally, including the presence of the roller in the mass balance the continuity equation becomes

$$(\eta_x + \delta_x) + [(h + \eta)\bar{u} + \delta C_x]_x = 0, \quad (13)$$

where  $C_x$  is the x-component of the wave celerity.

#### The Roller detection and growth

More consideration is given to correctly represent the surface roller growth from the breaking point toward the shore. Raichlen and Papanicolau (1988) pointed out that the bubble mass on the front face of the wave grows from zero, reaches a maximum and then decreases. Moreover the maximum size of the roller is reached at different distances  $X/h_{br}$  after breaking in dependence on the seabed slope and the breaker type (spilling or plunging). This relative distance ranges between one and ten. In the present model the growth of the roller is governed by the empirical relationship:

$$\delta'(x) = \delta(x) \left[ \frac{\tanh(X/h_{br}) + \tanh(\beta)}{1 + \tanh(\beta)} \right], \quad (14)$$

where  $X$  = distance from the breaking point,  $h_{br}$  = breaking point water depth,  $\beta$  = calibration parameter.

#### The numerical model

Generally speaking, along the curve  $C$  bounding a certain domain  $D$  both open and closed boundary conditions may be encountered. The latter covers all those situations ranging from total reflection to complete absorption. At the open boundaries radiation conditions are applied. They are schematized according to the following relationship:

$$f_{n1} - C\eta = -2C\eta_I f(\alpha), \quad (15)$$

$$u(h + \eta) = f_{n1}, \quad (16)$$

where

$$\begin{aligned} f_{n1} &= \text{outgoing normal flux} \\ \eta &= \text{actual sea surface elevation} \\ \eta_I &= \text{elevation of the incident wave} \end{aligned}$$

$C$  = wave celerity  
 $\alpha$  = the angle between the incident  
 wave and the boundaries

The wave celerity  $C$  is calculated by the appropriate theory: second order cnoidal wave theory. On the other hand the linear theory for shallow waters is applied to determine the celerity for irregular waves. The function  $f(\alpha)$  was firstly evaluated as  $f(\alpha) = 1 + \sin \alpha$ . A numerical analysis carried out with unidimensional and bidimensional models showed that the validity of the above relationship is limited to angles  $\alpha$  close to  $90^\circ$ . The function  $f(\alpha)$  is now considered a calibration parameter of the model, and is empirically evaluated depending on the value of  $\alpha$ . For closed boundaries two different schematizations are used. Total or partial reflection is schematized by the relationship

$$f_{n2} - C(1 - \gamma)\eta = 0, \quad (17)$$

$$u(h + \eta) = f_{n2},$$

where

$f_{n2}$  = incident normal flux  
 $\gamma$  = reflection coefficient ( $\leq 1$ ; 1 for total reflection).

In this case, too, the wave celerity  $C$  is calculated by the appropriate theory: cnoidal for monochromatic waves and linear for irregular waves. Complete absorption is schematized according to a 'sponge layer' approach (Larsen and Dancy, 1983). The 'sponge layer' is simulated by an extension of the model behind the absorbing boundary. In this extension, after each integration time step, the surface elevations and the fluxes are divided by a dumping factor  $\mu(x)$  which is a function of the distance  $x$  from the boundary:

$$\mu(x) = \exp \left[ \left( 2^{-(x_s - x)/\Delta s} - 2^{-x_s/\Delta s} \right) \ln(a) \right], \quad (18)$$

where  $\Delta s$  is the size of the grid mesh and  $a$  is a constant that depends on the number of the grid lines in the 'sponge layer'. As for the behaviour of the roller at the boundaries, it is assumed that there are no incoming rollers from the open boundaries and that they are completely absorbed at the closed boundaries. The basic equations are numerically integrated by a semi-implicit multistep finite difference technique (Brocchini, Cherubini and Iovenitti, (1991)).

The variables are defined on a space-staggered square or rectangular grid. The integration too is staggered in time as the elevations and fluxes are evaluated at half time steps  $(2n + 1)\Delta t/2$ . From the continuity equation (explicit scheme) the water elevation  $\eta$  is calculated, then from the water surface profile a test on the local slope defines the location and thickness of the surface roller. The fluxes are evaluated through the momentum equation (roller contribution included) by a semi-implicit technique made of three different calculation steps.

### Test cases and preliminary calibration

The model has been widely applied to many data sets made available from different European Institutes (Brocchini, Drago and Iovenitti (1992), Drago (1992)). The data sets are relative to wave elevation (Liberatore and Petti (1988), Schaffer (1991), Dette and Oelerich (1991)) and velocity (Quinn et al. (1991)) flume measurements. The waves used in the tests are both monochromatic and irregular; wave breaking occurs over different bottom profiles (sloping or barred). In table 1 a scheme on the analyzed data sets within the validation activities is reported:

Institute	Profile	Type/(Number of tests)	$\frac{H_0}{L_0}$
Padua Un.	Slope 1/30	Irregular (4)	0.0310 ÷ 0.0380
D.H.I.	Barred	Regular (3)	0.0212 ÷ 0.0522
Hannover Un.	Slope 1/20	Irregular (4)	0.0316
Edinburgh Un.	Slope 1/30	Regular (2)	0.0220 ÷ 0.0330

Tab. 1 - Validation data sets.

Table 2 summarizes the percent error  $(H_{exp} - H_{comp})/H_{exp}$  from outside the breaking region to the shore for both Boussinesq and Serre equations.

$\frac{D}{D_b}$	Bouss.	Serre
1.5	+5	+8
1.0	+7	+11
0.6	-15	-8

Tab. 2 - Average percent (%) error on wave height.

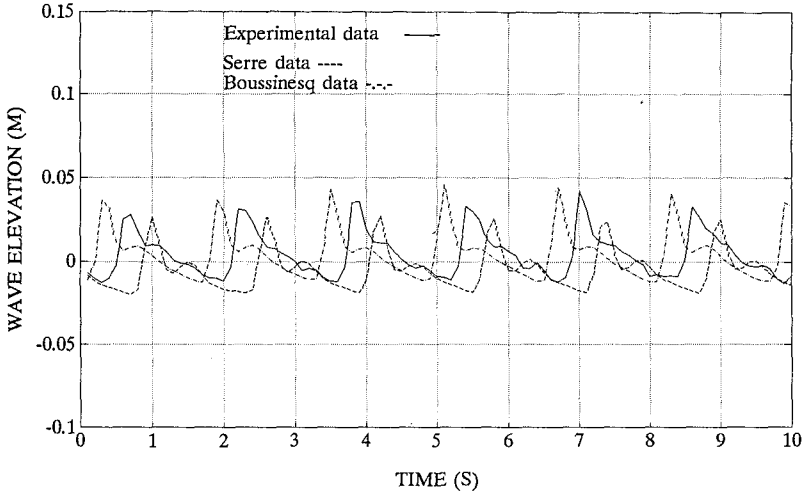


Fig.2 - Wave elevations comparison.  
(Data shifted for better comprehension).

Figure 2 shows an example of computed and measured wave elevation comparison (inside the surf zone) while figures 3 and 4 represent, respectively, a typical comparison of the wave spectra and of the decay pattern for the wave height over a barred profile.

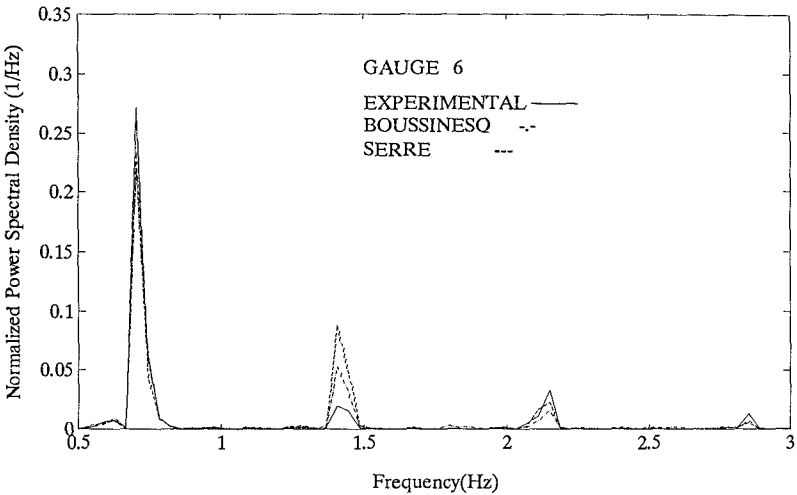


Fig.3 - Wave spectra comparison.



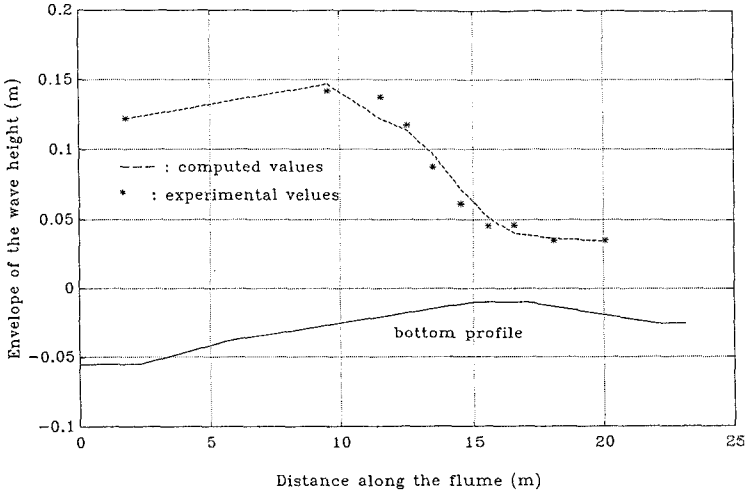


Fig.4 - Wave height decay pattern.

Comparison on velocity data has been worked out both on mean velocity spatial series and on vertical profiles. In fig.5 a typical pattern for mean velocity is shown.

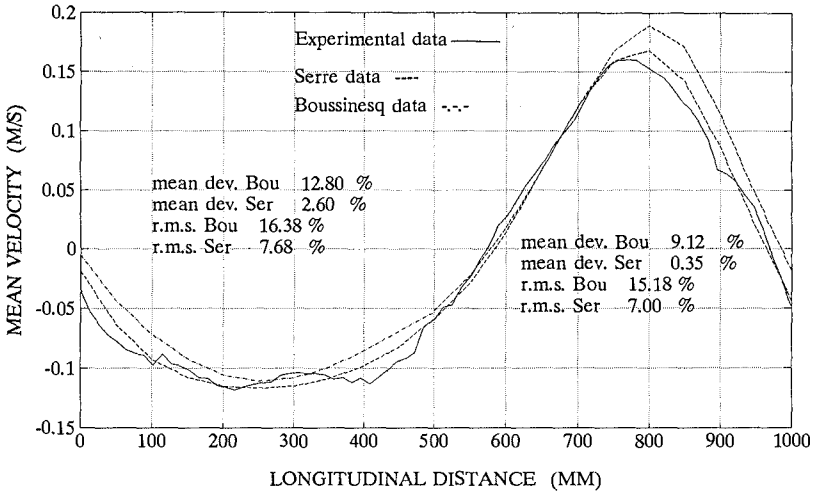


Fig.5 - Mean velocity comparison.

Table 3 sums up the percent error  $(V_{exp} - V_{comp})/V_{exp}$  between experimental and computed velocity profile for two different wave phases and for both Boussinesq and Serre model.

Dist. from bottom(cm)	Crest		Trough	
	Bouss.	Serre	Bouss.	Serre
4.0	-15	-2	-20	-13
6.0	-14	-1	-10	-3
8.0	-9	+3	-5	-5
10.0	-13	-2	+40	+50
12.0	-8	+3		
14.0	-5	+6		

Tab. 3 - Percent error on velocity profiles.

It may be seen that for the maximum phase the Serre model oscillates around the experimental pattern with errors of about 5% while the Boussinesq model gives an almost constant overestimation of the velocity of about 10%. Within the calibration activity typical relationships between wave-seabed characteristics and model breaking parameters ( $\alpha_{br}, K, \beta$ ) were looked for. Thirteen monochromatic wave decay patterns were modelled and compared against the experimental data (Liberatore and Petti (1991)). The experimental waves were characterized by a deep water wave steepness ranging from 0.03 to 0.07 and broke over a submerged bar while eight wave gauges recorded the free water surface from the breaking point to the shoreline. Moreover video camera recordings all along the flume were taken to better evaluate the roller area and the breaking point location.

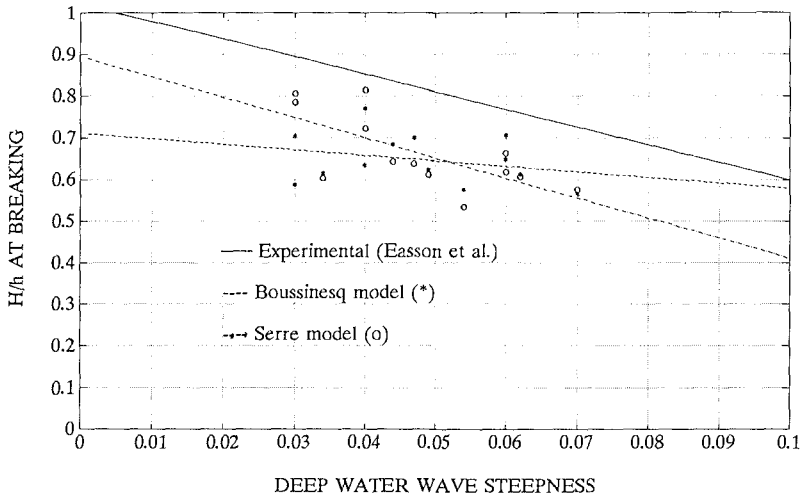


Fig.6 - Adimensional wave height at breaking.

The adopted methodology was to minimize both the differences between the experimental and the computed wave shape and to reproduce the wave height decay pattern all along the flume within a percent error of about 15%. Once the best representation of the wave decay pattern obtained, a first comparison of the results against those coming from wide data sets (Easson et al.(1988)) was tried (see fig.6).

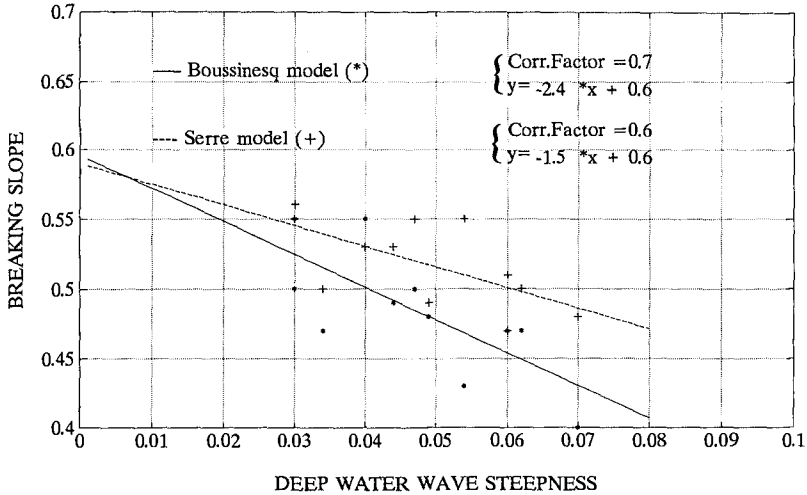


Fig.7 - Preliminary calibration curve for  $\alpha_{br}$ .

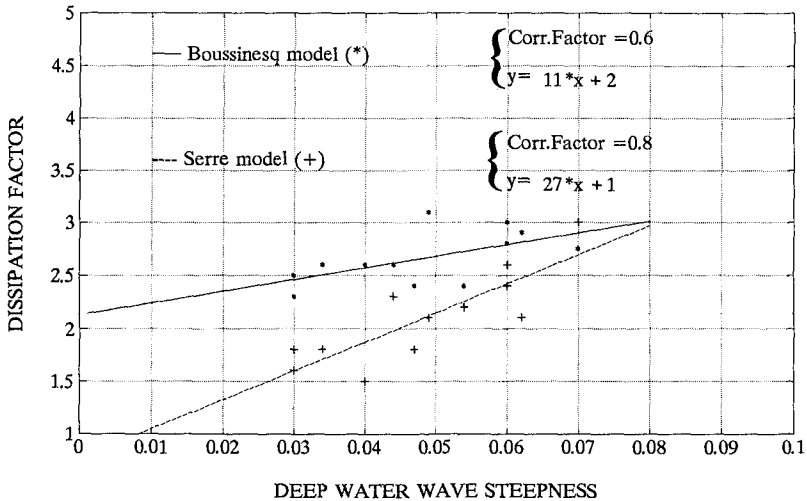


Fig.8 - Preliminary calibration curve for  $K$ .

The underestimation of the  $H/h$  ratio (mainly for the Boussinesq

model) is related to the adopted experimental set-up where the gauges were spaced too far apart to exactly determine the breaking point location. The preliminary calibration curves for the breaking slope  $\alpha_{br}$  and the dissipation factor  $K$  are shown in figures 7 and 8. The correlation factors are not so high as to suggest that the performed calibration is sufficiently reliable. Anyway it is clear that the Boussinesq model needs much higher values for the dissipation parameter with respect to the Serre model to obtain the same energy decay. This is due to the presence of terms proportional to  $O(\epsilon\mu^2)$  which act as a smoothing factor within the surf zone.

### Conclusions

A quite good fit of the experimental wave elevation and spectra has been obtained through the model based on both Boussinesq and Serre equations. A satisfactory description of the wave height decay process in the surf zone was reached (errors of about 15%). The Serre equations give a much better representation of the velocity field than the Boussinesq's. A preliminar calibration of the main parameters was tried but some uncertainties in the determination of the experimental breaking point force a more accurate evaluation on the basis of the camera recordings.

### Acknowledgements

This work was undertaken as part of the MAST-G6 Coastal Morphodynamics Research Programme. It was funded by the Commission of the European Communities, Directorate General for Science, Research and Development, under MAST contract N° 0035-C. The authors wish to thank Mr.Liberatore, Mr.Petti, Mr.Schaffer, Mr.Oelerich, Mr.Dette, Mr.Greated, Mr.Quinn for having provided the data used for models testing and calibration.

### References

- Brocchini, M.,P. Cherubini and L. Iovenitti (1991). An extension of Boussinesq type model to the surf zone. *Proc. 2nd Conf. on Computer Modelling in Ocean Engineering*.
- Brocchini, M.,M. Drago and L. Iovenitti (1992). Modelling of water waves in shallow waters and in the surf zone. *MAST G-6 Final Workshop*, Pisa.
- Deigaard, R., and J. Fredsoe (1989). Shear stress distribution in dissipative water waves. *Coastal Eng.*, Vol.13.
- Deigaard, R., (1989). Mathematical modelling of waves in the surf zone. *Prog. Rep. 69, ISVA, Tech. Univ. Denmark*.

Detle, H. H. and J. Oelerich (1991). Measurements in the Big Wave Flume in Hannover - Individual breaking waves, breaker distribution. *Report N° 1*.

Drago, M. (1992). *Thesis for the degree in mathematical physics - University of Bologna*.

Easson W.J. et al.(1988). Kinematics of breaking waves in coastal regions. *Coastal Eng.*

Larsen, J. and H. Dancy (1983) Open boundaries in short wave simulation: a new approach. *Coastal Engineering*, Vol. 7.

Liberatore, G. and M. Petti (1988) Modifications of random wave characteristics in shoaling waters. *Excerpta*, Vol. 3.

Liberatore, G. and M. Petti (1991) Random wave transformations over a submerged bar. *MAST G-6 Midterm Workshop*, Edinburgh.

Quinn, P.A. et al.(1991) A critical analysis of the particle image velocimetry technique applied to water waves. *Proc. Euro-mech 279 Colloquium*, Delft.

Raichlen, F. and P. Papanicolau (1988) Some characteristics of breaking waves. *Proc. 21st Coastal Eng.*

Schaffer, H.A.(1991) *Private Communication*.

Su, C.H. and C.S.Gardner (1968) Derivation of the Korteweg-de Vries equations and Burgers equations *Journal of Mathematical Physics*, Vol.10, 3.

## CHAPTER 5

# COMPUTATION OF BREAKING WAVES WITH A PANEL METHOD

Jan Broeze<sup>1</sup>

### Abstract

Some basic properties and computational results are presented of a solution method for potential flow problems, with nonlinear waves at the free surface. The results show that stable and accurate results can be obtained for nonlinear wave propagation problems, up to the stage of breaking waves, though no numerical smoothing is applied. Also the interaction with constructions on the bottom can be computed well.

For efficient usage of the available CPU-time, a suitable condition for the time increments in nonlinear computations is given.

### 1. Introduction

In this paper we will consider the description of propagating and breaking waves with a potential model for the fluid flow.

For the description of potential flow problems in two-dimensional and three-dimensional domains, we have developed an accurate panel method. One of the boundaries of the domain is the free surface, on which nonlinear boundary conditions are imposed for the description of the solution in time.

For accurate descriptions of highly nonlinear wave evolution in complex three-dimensional regions, a model should be used that includes the behaviour of

---

<sup>1</sup>Delft Hydraulics, P.O. Box 152, 8300 AD Emmeloord, The Netherlands.

the solution in vertical direction. This can be achieved by discretizing the whole fluid domain. Such an approach makes computations on extreme problems like the development of breaking waves possible.

For incompressible potential flow problems, the field equation reduces to Laplace's equation for the potential. This is an elliptic equation, so that solving the problem on the boundaries of the domain is sufficient. Green's third identity provides a boundary integral relation for the solution on the boundary.

Boundary element methods and panel methods are based on a discretization of Green's third identity in the physical domain. That is why they can be used for modelling the fluid flow in domains with arbitrary boundary shapes.

Time dependence comes into the problem by the time-dependent boundary conditions. These give expressions for the evolution of the free surface position and the velocity potential in time.

Many computations on breaking waves have been discussed in literature (see Peregrine, 1990). However, due to restrictions of the numerical methods, in most cases the chosen initial solution is not physical. For example, an exact solution of a periodic high wave is imposed on a geometry with a smaller depth. In such situations, the numerical results are useful for studying the local solution near the tip of the wave. However, the global solution is not valid in physical situations.

Computations on highly nonlinear wave problems in three-dimensional domains are still very rare. One example can be found in the work by Xü & Yue (1992). They computed the evolution of a breaking wave with a three-dimensional method. A breaking wave was generated by prescribing a non-physical pressure distribution at the surface. However, for practical applications, a method for computing wave evolution due to interactions with a bottom profile is more useful.

Romate has developed a higher order panel method for the computation of three-dimensional potential flow problems with a free surface. As far as the results were presented in his thesis (see Romate, 1989), the method was very well capable of computing the evolution of linear wave solutions and weakly nonlinear waves. However, stable computations of highly nonlinear waves were not possible yet.

On the basis of Romate's work, we have further developed the method for the evolution of highly nonlinear waves. By the improvements, stable results can be obtained for highly nonlinear wave problems up to the stage of the development of breaking waves. For an extensive analysis of algorithms used in the method, the reader is referred to Romate (1989) and Broeze (1993a, 1993b).

In this paper we will briefly describe the method of computation. Furthermore we will show some numerical results on three-dimensional wave propagation problems, including the development of a breaking wave.

## 2. Numerical solution method

The fluid motion is modelled with a higher order panel method. This method is based on the assumption of a potential flow, i.e. the velocity can be derived from a potential  $\phi$ :

$$\underline{v} = \nabla \phi \quad (1)$$

Due to incompressibility, the velocity potential satisfies Laplace's equation:

$$\nabla^2 \phi = 0 \quad (2)$$

In our panel method, the field equation problem is solved by using a boundary integral equation formulation, where Green's third identity is applied:

$$\frac{1}{2} \phi(\underline{x}) = \int_{\partial\Omega} [\phi(\underline{\xi}) G_n(\underline{x}, \underline{\xi}) - \phi_n(\underline{\xi}) G(\underline{x}, \underline{\xi})] dS \quad (\underline{x} \text{ on } \partial\Omega) \quad (3)$$

For the discretization of this equation, the boundary of the domain is divided into a number of smooth panels, with one collocation point near the centre of each panel. Values in the collocation points of a number of adjacent panels are used to determine tangential derivatives.

Green's identity is solved in the physical domain. Up to quadratic variations of the velocity potential and linear variations of its normal derivative are assumed in the discretization of the boundary integral equation. Also contributions due to curvature of the panels are included in the expressions for the influence coefficients. This provides very accurate solutions of the field equation.

Time dependence comes into the problem by the time-dependent boundary conditions.

In our Lagrangian method, at the free surface  $S_f$  we have the kinematic condition, expressing that a fluid particle remains at the free surface:

$$\frac{Dx_f}{Dt} \equiv \underline{v} = \nabla \phi \quad \text{at } S_f \quad (4)$$

and the dynamic boundary condition, expressing zero pressure:

$$\frac{D\phi}{Dt} = -gz + \frac{1}{2}(\nabla \phi)^2 \quad \text{at } S_f \quad (5)$$

where  $g$  is the gravitational acceleration, and  $z$  is the vertical coordinate.

On the bottom  $S_b$ , on fixed constructions and on symmetry boundaries, the no-flux condition should be satisfied:



$$\phi_n = 0 \quad \text{at } S_b \quad (6)$$

where  $\underline{n}$  is the outward directed normal with respect to the fluid domain.

On a moving structure  $S_s$ , or a wave maker, the normal velocity is prescribed according to the motion velocity  $\underline{V}$  of the structure:

$$\phi_n = \underline{V} \cdot \underline{n} \quad \text{at } S_s \quad (7)$$

In order to represent large physical domains with a small computational domain, we can truncate the domain with artificial boundaries  $S_a$ . Radiation boundary conditions, that only allow waves travelling out of the domain with minimal reflections, are needed on these boundaries. A simple example is Higdon's (1987) first order condition:

$$\frac{\partial \phi}{\partial t} = - \frac{c}{\cos \alpha} \frac{\partial \phi}{\partial n} \quad \text{on } S_a \quad (8)$$

where  $\underline{n}$  is the normal with respect to the vertical boundary, positive in outward direction. This condition perfectly radiates waves that travel at phase speed  $c$  and at an angle  $\alpha$  with the normal  $\underline{n}$ . For second order conditions (that can perfectly radiate waves from different directions) the reader is referred to Romate (1992) and Broeze & Romate (1992).

The above described boundary conditions provide values for the time derivatives of the potential and the positions of the collocation points as a function of spatial derivatives of the potential and the vertical coordinate.

Various methods can be used for integrating the problem in time. We have considered the classical fourth order Runge-Kutta method, a third order Taylor method and a 2-stage 2-derivative Runge-Kutta method (that uses first and second order time derivatives on the original and one intermediate time level). We have concluded that the latter method is most favourable for our problem, because it provides accurate results in relatively short CPU times.

An adaptive grid evolution technique was used to obtain desirable grid distributions in time. This is especially important in 3-D computations, where a strongly deformed grid on the lateral boundaries may have negative influences on the accuracy of the solution.

Our method is very suitable for computations of the interaction of highly nonlinear waves with constructions, because there are no restrictions on the shape of the boundaries of the domain. Another favourable property is the stability of the

method, so that no artificial dissipation or smoothing terms need to be added (which may have a large influence on the solution during breaking).

### *Time-step restrictions*

One important aspect that we want to discuss here is the chosen time increment in the numerical computations.

We found that stability restriction based on linear theory (see e.g. Dommermuth et al., 1988) are not suitable in computations on highly nonlinear wave propagation problems.

Another frequently applied condition is that the highest order terms in the Taylor time integration method should be below a given value (see e.g. Nakayama, 1990). Such condition is rather arbitrary, and lacks a theoretical basis.

We have derived a more appropriate condition for the full nonlinear problem.

From a perturbation analysis of the solution around the nonlinear solution, the following evolution equations for small disturbances  $(\varepsilon, \zeta)$  in the potential  $\phi$  and elevation  $\eta$  can be derived:

$$\frac{d}{dt} \begin{bmatrix} \varepsilon \\ \zeta \end{bmatrix} = \begin{bmatrix} -i\phi_s k & -g \\ |k| \cos\gamma & 0 \end{bmatrix} \begin{bmatrix} \varepsilon \\ \zeta \end{bmatrix} \quad (9)$$

where  $s$  represents a tangential coordinate to the surface,  $k$  is the wave number of the disturbance and  $\gamma$  is the local angle of inclination of the free surface.

For stability of the numerical method for nonlinear problems, the eigenvalues of the matrix in eq.(9) should be in the stability region of the domain:

$$\frac{i}{2} \left( -\phi_s k \pm \sqrt{(\phi_s k)^2 + 4g|k|\cos\gamma} \right) \Delta t \in R_{\text{stab.}} \quad \forall k \in [0, \pi/\Delta x] \quad (10)$$

This is a straightforward condition for the time increment. From numerical test computations we found that it is very appropriate: satisfying this condition provides a stable evolution of the solution, whereas instabilities occur if it is violated. For an extensive description of the derivation of condition (10), the reader is referred to Broeze (1993a, 1993b).

Eq. (10) can reduce the required amount of CPU time in highly nonlinear computations with large velocities and fine grids. A maximal time increment can be chosen then.

### 3. Computational results on periodic wave propagation problems

The panel method provides stable and very accurate results for linear (see e.g. Broeze and Romate, 1992), mildly nonlinear and highly nonlinear wave problems (see Broeze, 1993a, 1993b and Broeze et al., 1993). Computations can be performed on highly nonlinear steady propagating waves near the maximum wave height without instabilities, with errors in the elevation of only a few percents after a large number of wave periods.

Fig. 1 shows results of computations on a typical highly nonlinear propagating plane wave problem. The wave height is 5m on 10m water (over 80% of the maximum), with wave length 60m and Eulerian period 6.5s. This figure shows the results of the computations after 0, 1, 2 and 4 Lagrangian periods. The errors in the elevation are within 2% of the wave height.

The results illustrate that the method is well-capable of accurately describing highly nonlinear propagation.

In order to analyze the accuracy of the method for three-dimensional problems, we have computed the same wave solution, where the propagation direction of the wave is at an angle  $\pi/6$  with one of the grid lines.

Fig. 2 shows the numerical boundary shape from 0 to 6s at intervals 2s. Again the results illustrate that no large growing errors occur in the solution.

### 4. The interaction of a solitary wave with a mild slope

A solitary wave is generated on a numerical wave flume with depth 5m. A weak slope (1:10) truncates the domain in horizontal direction. The solitary wave has a height 3.5m (84% of the maximum) and a phase velocity of 9.0m/s. Initially the fluid is at rest. We computed the interaction of the solitary wave and the slope with a two-dimensional variant of our panel method.

The shape of the domain boundaries after 2s, 4s and 6s is given in Fig.3. This figure shows how the wave starts deforming on the slope. When the wave approaches the end of the slope, it starts to break, and a plunging breaker develops. The shape of the jet from  $t=6.6s$  to  $7.3s$  is given in Fig.4. A finer grid would be needed to further continue the computations.

It is noted that in our method, no collocation points occur at the intersection. Also no special condition is applied at the intersection of the slope with the free surface.

In order to analyze the quality of the numerical results of these computations, we have considered a number of theoretical models for the description of breaking waves.

A few theoretical models exist for the evolution of the tip of a breaking wave and the surface region below the jet (see e.g. Longuet-Higgins (1980) and New (1983)). These models were developed for breaking waves on deep water. They cannot be applied to our situation, because of the influence of the slope on the solution.

Peregrine (1990) suggested to check the motion of the tip of the wave (it should be in free fall).

Fig.5 shows the evolution of the coordinates of the tip of the wave during the final stage of computation. Obviously, the free-fall model holds very well from  $t=6.95s$  (when the jet has developed) to  $7.3s$ .

## **5. Results on breaking wave computations with the three-dimensional method**

We have used the three-dimensional panel method to compute the interaction of the highly nonlinear solitary wave with a smooth construction the bottom. Fig.6 shows the bottom profile in these computation.

Fig.7 shows the grid on surface and on the lateral boundaries of the domain when the wave front has started to overturn. Obviously, the method is capable very well to compute the evolution of the solution so far. The well-arranged grid on the lateral boundaries illustrates the suitability of our adaptive grid motion algorithm. The forming of the jet is more clearly illustrated in Fig. 9.

In order to show the height of the construction in comparison with the domain dept, in Fig. 8 the bottom profile and the surface are depicted.

The computations on this wave cannot be further continued due to the small number of panels near the tip of the wave. A large number of extra panels would be needed to increase the grid density near the jet. However, this cannot be achieved due to memory restrictions on our supercomputer.

## **6. Conclusions**

In this paper we have seen that highly nonlinear waves can be very well described with an accurate panel method. Also real three-dimensional effects can be computed. Efficient solution methods for the spatial problem, for the time integration and for the grid motion are of crucial importance for the success of the method.

The results show that even extreme problems like the development of breaking waves due to a construction on the bottom can be modelled. We think that such models offer new possibilities for studies on nonlinear wave propagation problems in complex three-dimensional domains.

## Acknowledgements

The investigations were supported by the Netherlands Technology Foundations (STW). Supercomputer usage was financed by the Dutch National Computing Facilities Foundation (NCF). Professor P.J. Zandbergen is greatly acknowledged for his support and advise.

## References

- Broeze, J. (1993a): *A panel method for 3-D flow computations with a free surface: adaptations for nonlinear water waves*, Ph.D. thesis, Enschede, The Netherlands (to appear).
- Broeze, J (1993b): On the numerical computation of nonlinear free surface waves for potential flow problems in three-dimensional domains, in preparation.
- Broeze, J. and Romate, J.E. (1992): Absorbing boundary conditions for free surface wave simulations with a panel method. *J. Comp. Phys.*, Vol. 99, pp. 146-158.
- Broeze, J., van Daalen, E.F.G. & Zandbergen P.J. (1993): A three-dimensional panel method for nonlinear free surface waves on a vector computer, submitted for publication in the *Int. J. for Num. Methods in Engineering*.
- Dommermuth, D.G., Yue, D.K., Lin, W.M., Rapp, R.J., Chan, E.S. & Melville, W.K. (1988): Deep-water plunging breakers: a comparison between potential theory and experiments, *J. Fluid Mech.*, Vol. 189, pp. 423-442.
- Higdon, R.L. (1987): Numerical absorbing boundary conditions for the wave equation, *Math. Comp.*, Vol. 49, pp. 65-90.
- Longuet-Higgins, M.S. (1980): On the forming of sharp corners at a free surface. *Proc. R. Soc. Lond. A*, Vol. 371, pp. 453-478.
- Nakayama, T. (1990): A computational method for simulating transient motions of an incompressible inviscid fluid with a free surface, *Int. J. for Num. Meth. in Fluids*, Vol. 10, No. 6, pp. 683-695.
- New, A. (1983): A class of elliptic free-surface flows, *J. Fluid. Mech.*, Vol. 130, pp. 219-239.
- Xü, H. & Yue, D.K.P. (1992): Numerical study of three-dimensional overturning water waves, In: *Proceedings of the seventh Int. Workshop on Water Waves and Floating bodies* (ed. R. Cointe), Val de Reuil, (France), pp. 303-307.

- Peregrine, D.H. (1990): Computations of breaking waves. In *A. Torum and O.T. Gudmestad Ed., Waterwave kinematics*, pp. 475-490.
- Romate, J.E. (1989): *The numerical simulation of nonlinear gravity waves in three dimensions using a higher order panel method*, Ph.D. thesis, Enschede, The Netherlands.
- Romate, J.E. (1992): Absorbing boundary conditions for free surface waves, *J. Comp. Phys.*, Vol. 99, No. 1, pp. 135-145.

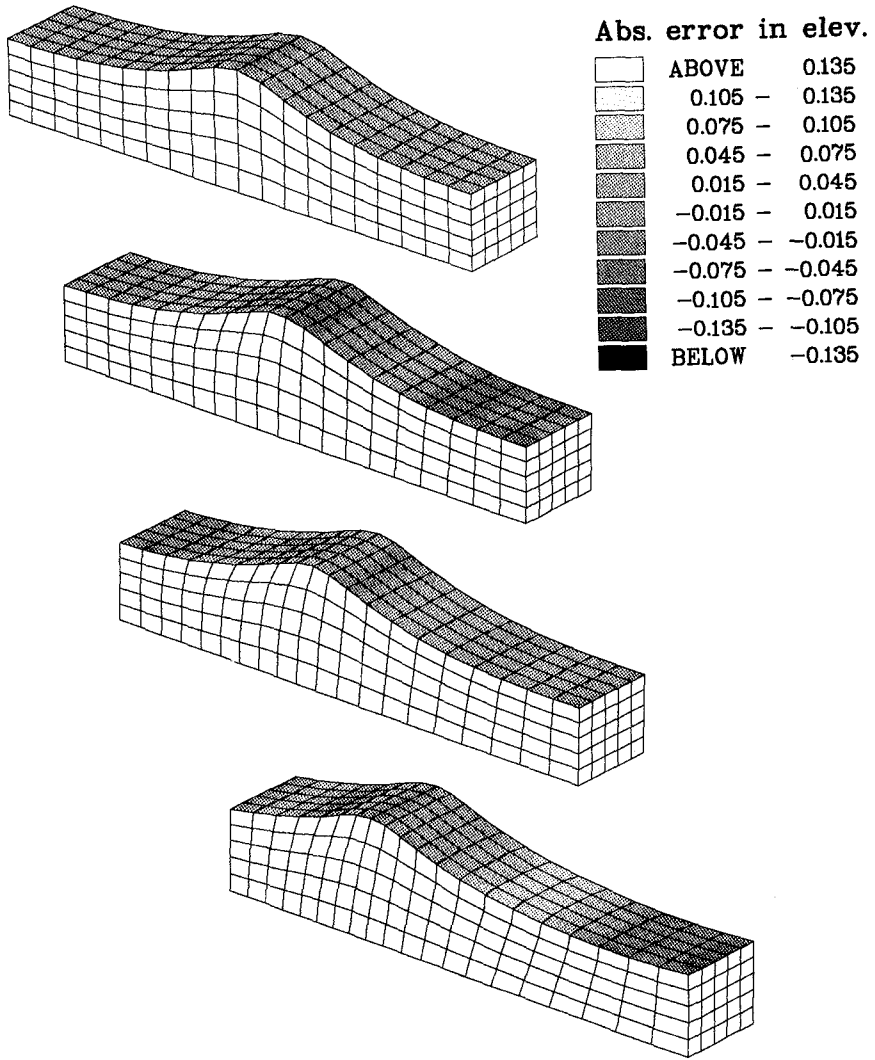


Fig. 1. Numerical results from computations on highly nonlinear wave problem.  
Shape of boundary and errors in elevation after 0s, 7s, 14s and 28s.

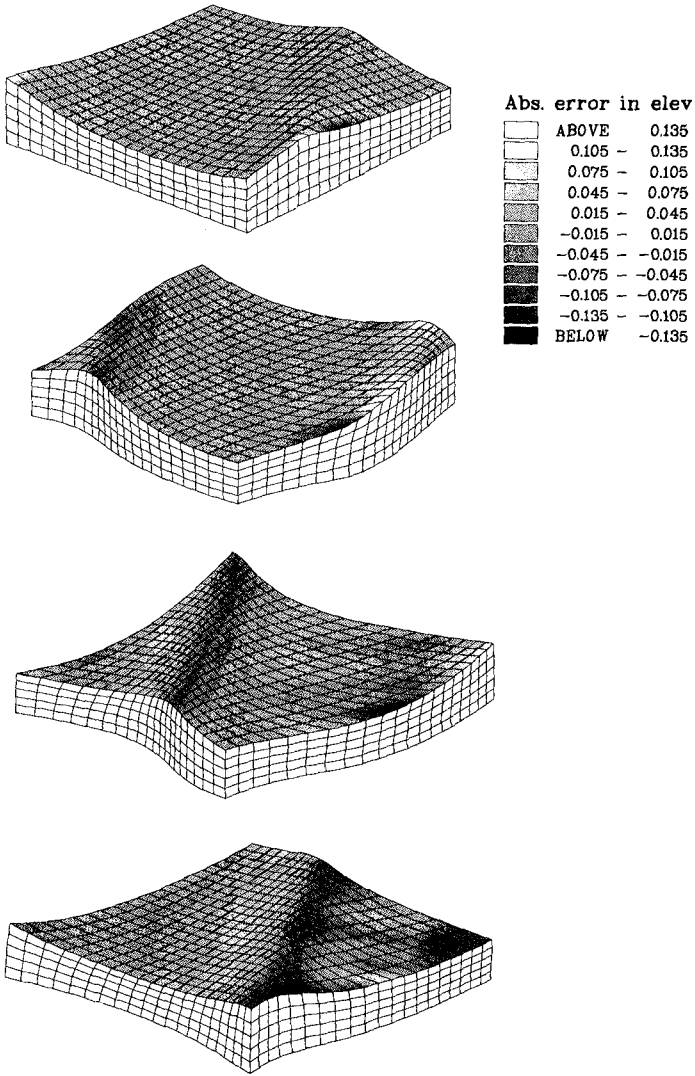


Fig. 2. Numerical results from computations on highly nonlinear wave, propagating at angle  $\pi/6$  with one grid direction. Shape of boundary and errors in elevation after 0s, 2s, 4s and 6s.



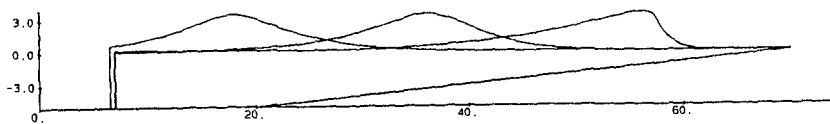


Fig. 3. Shape of the domain boundaries in the 2-D computation of the interaction of a solitary wave with a slope at  $t=2s$ ,  $4s$  and  $6s$ .

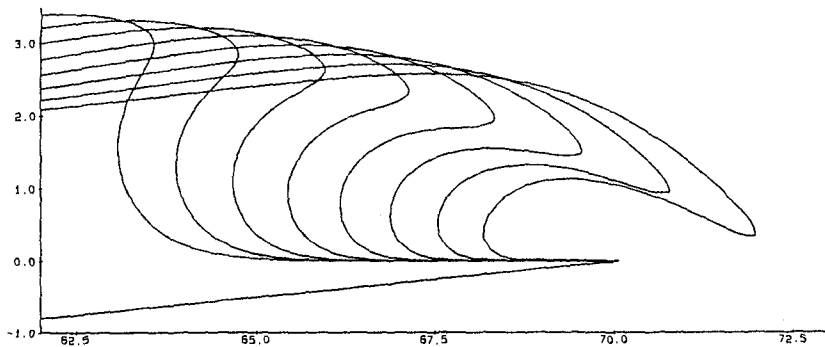


Fig. 4. Jet of the breaking wave in two dimensions from  $t=6.6s$  to  $7.3s$  (every  $0.1s$ ).

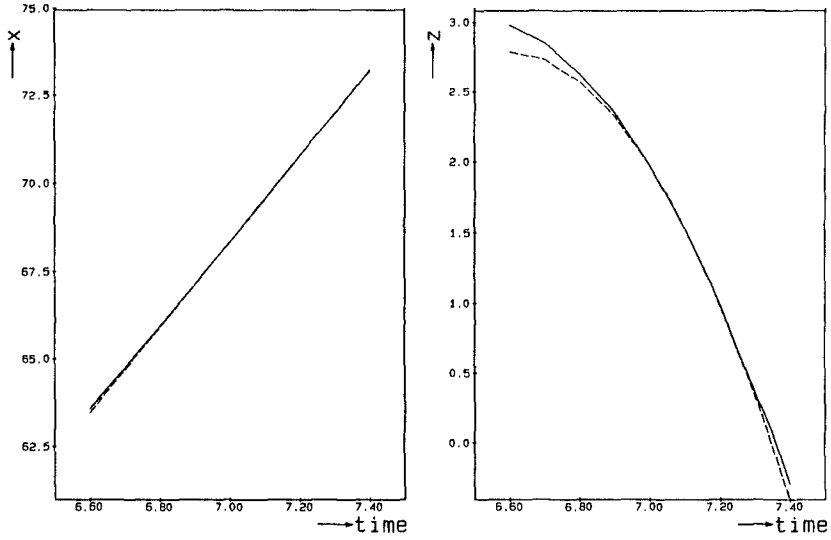


Fig. 5. Evolution of the position of the tip of the wave jet from 6.6s to 7.4s (exact data for particle in free-fall are dotted).

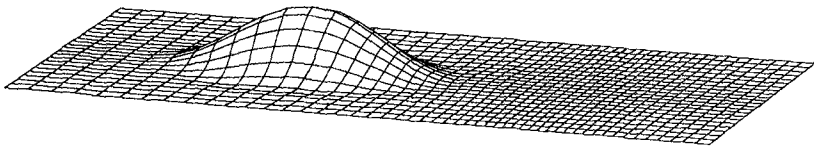


Fig. 6. Shape of bottom profile in 3-D computation on interaction of solitary wave with construction.

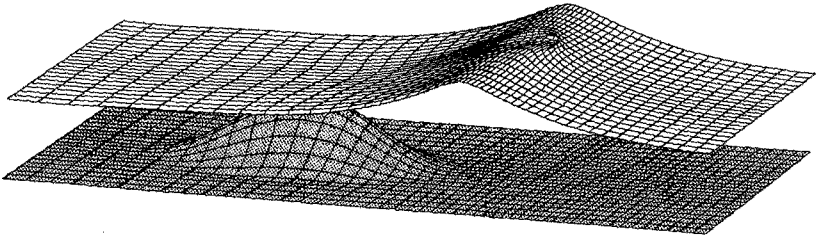


Fig. 7. Shape of the grid on surface and lateral boundaries in computation of a breaking wave in three dimensional configuration.

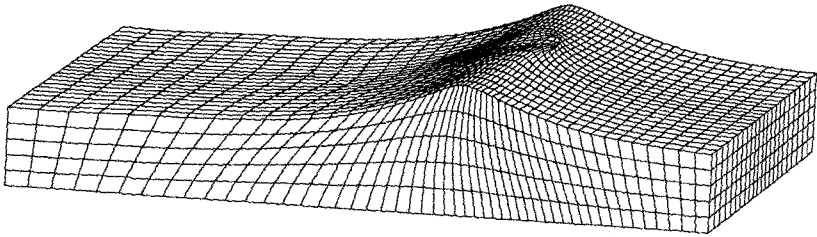


Fig. 8. Surface and bottom profile in computation of breaking wave.

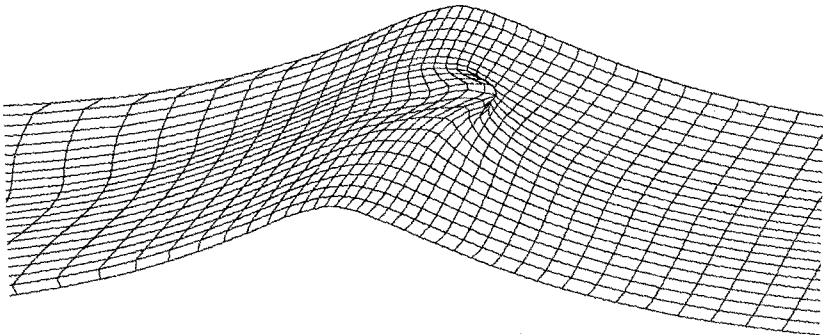


Fig. 9. Surface profile near jet of wave.

## CHAPTER 6

### BAR/TROUGH EFFECTS ON WAVE HEIGHT PROBABILITY DISTRIBUTIONS AND ENERGY LOSSES IN SURF ZONES

Maolong Cai<sup>1</sup>, David R. Basco<sup>2</sup> (Member, ASCE)  
and Joe Baumer<sup>3</sup>

#### Abstract

Laboratory measurements of irregular wave heights across a bar/trough beach profile are being studied to develop improved probability distributions including the subset of breaking waves. The energy dissipation in breaking waves modeled as a periodic bore is inversely proportional to the wave period and this may explain why the bore model appears to underestimate measured average energy dissipation rates. The study is ongoing and preliminary results for one wave period are presented in this paper.

#### 1. Introduction

The transformation of irregular waves across surf zones is dominated by wave breaking. In contrast to regular (single frequency) waves, irregular (multiple frequency) waves can break almost anywhere depending upon the wave characteristics (heights, periods) and the water depth. Thus some waves break because of their steepness, i.e., they behave as if in "deep" water while others break due to a depth limiting criteria for "shallow" water. The nearshore bathymetry, especially the presence of bars dominates the wave transformation process.

The traditional, wave transformation method assumes a slowly-varying, quasi-uniform wave field as represented by the time averaged and depth-integrated wave energy flux per unit surface area and the wave energy balance equation including rate of energy dissipation per unit area. For irregular waves, two different approaches are possible for solving the multiple frequency, wave

---

<sup>1</sup> Graduate Student, <sup>2</sup> Professor, Coastal Engineering Program, Old Dominion University, Norfolk, VA (USA), 23529-0241, and

<sup>3</sup> Coastal Engineer, Shoreline Programs Bureau, Commonwealth of Virginia, Gloucester Point, Virginia (USA)

energy balance equation.

One approach randomly selects offshore waves from a known joint (height, period) distribution, transforms individual waves with the energy balance equation and then reassembles the wave heights into probability distributions across the surf zone. This approach is called the wave-by-wave or Monte-Carlo method and requires computation for hundreds of waves. Dally (1990,1992) presents an excellent review paper and application to field data of this approach.

A second approach, herein called the probability density function (pdf) approach, assumes *a priori*, the wave height distribution functions for all the waves and the subsets of breaking waves. The energy balance equation is then solved only once for the transformation of a single, statistical descriptor wave through the surf zone.

This paper focus on the pdf approach. For coastal engineering applications, especially for two-dimensional wave transformations, it is felt that this approach is more practical. Section 2 briefly reviews the literature and summarizes the objectives of an ongoing study to learn more about the pdf's for bar/trough beach profiles and methods to estimate the breaking wave energy dissipation rates. The laboratory facilities and experimental design is presented in Section 3. Early test results are presented in Section 4. Section 5 gives some conclusions and future directions for the research.

## 2. The Probability Density Function(pdf) Approach

### 2.1. Literature Review

Battjes and Janssen(1978) were the first to integrate the energy flux balance equation using the pdf approach and calculate wave heights over non-monotonic bottom profiles. Previous random wave transformation models (see Thornton and Guza, 1983 for review) used a cut-off model for the pdf when waves broke so that calculated wave heights depended only on the local water depth. On bar/trough beaches this produced physically unrealistic lower energy levels over the bar and energy gains in the adjacent trough.

Thornton and Guza(1983) extended the work of Battjes and Janssen(1978) by including a semi-empirical expression for the breaking wave distribution,  $p_b(H)$  that was a *subset* of the theoretical, Rayleigh distribution,  $p(H)$  for all the waves. The average rate of energy dissipation  $\bar{e}_b$ , in each breaking wave is modeled after a periodic bore (Stoker, 1956) in both these models. However, Thornton and Guza (1983) derived an analytical expression for the ensemble average,  $\langle \bar{e}_b \rangle$  for an irregular wave train by integrating the product  $\bar{e}_b * p_b(H)$  for all the waves. The final expression for  $\langle \bar{e}_b \rangle$  includes two coefficients ( $\gamma$ , B) that require field verification as discussed later in this paper. The ensemble

average,  $\langle \bar{e}_b \rangle$  is also inversely proportional to the wave period and the implications of this result are also reviewed at the end of this paper.

These modelers use the root-mean-square wave height,  $H_{rms}$  as the statistical, descriptor wave and both models give good predictions for the  $H_{rms}$  transformations occurring over real (field) beach profiles (see Battjes and Stive, 1985 for laboratory and field calibrations with Northsea waves,  $T_{max} < 8.7$  sec; and Thornton and Guza, 1983 for West Coast swell waves,  $T = 13-17$  sec). However, this agreement between calculated and observed  $H_{rms}$  required the use of physically unrealistic coefficients as discussed below and also does not mean that the underlying pdf's are correct as noted by these researchers.

## 2.2. Research Objectives

A laboratory study is underway that focuses on the wave height probability distributions for all the waves,  $p(H)$  and the breaking waves as a subset,  $p_b(H)$  as they pass over a synthetic, bar/trough beach profile. One objective is to compare the measured pdf's with those predicted by the Thornton and Guza (1983) theory and to make improvements in the theory, if warranted.

The second objective is to investigate the apparent *underestimation* of the average rate of wave breaking energy dissipation when using the periodic bore model as claimed by some researchers (Svendsen et al., 1978; Stive, 1984).

## 3. Laboratory Facility and Experiments

Experiments are being conducted in the new 18m long by 0.9m deep by 0.9m wide wave tank in the Coastal Engineering Laboratory at Old Dominion University. This facility is equipped with a random wave generator as designed by the Danish Hydraulic Institute (DHI) that includes an automatic wave absorption system at the wave board to remove reflected wave energy in the tank. Wave generation, recording, and analysis is accomplished through a special software package also developed by DHI. Wave heights up to 30cm and a period range between 0.7-3.5sec is possible in this facility.

Fig. 1 schematically shows the 1:20 beach slope with 1:10 artificial bar and dimensions such that the bar crest lies 22cm below the SWL in 60cm water depth. Seven wave gauges are positioned as shown across this synthetic bar/trough beach profile with all dimensions in meters. Four additional locations for wave gauges are shown in the trough region (vertical dashed lines) to provide details in this location.

A JONSWAP spectrum with standard shape parameters is generated at the wave board. The irregular wave train is constructed by a random number generator that always begins with the same seed to permit repetition of the time history of sea surface variation. For the results reported in this paper, the

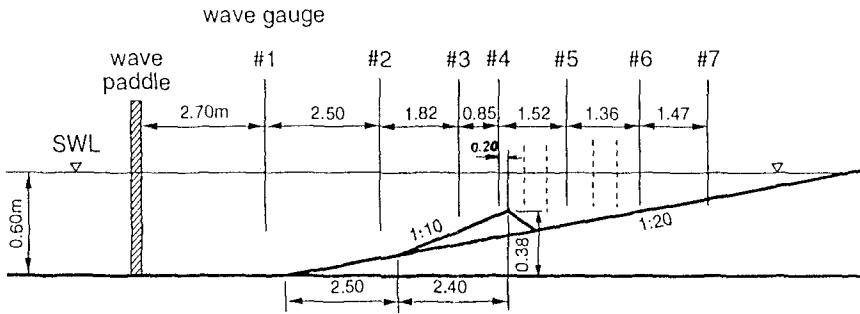


FIG 1. SCHEMATIC OF BEACH PROFILE AND TEST ARRANGEMENT

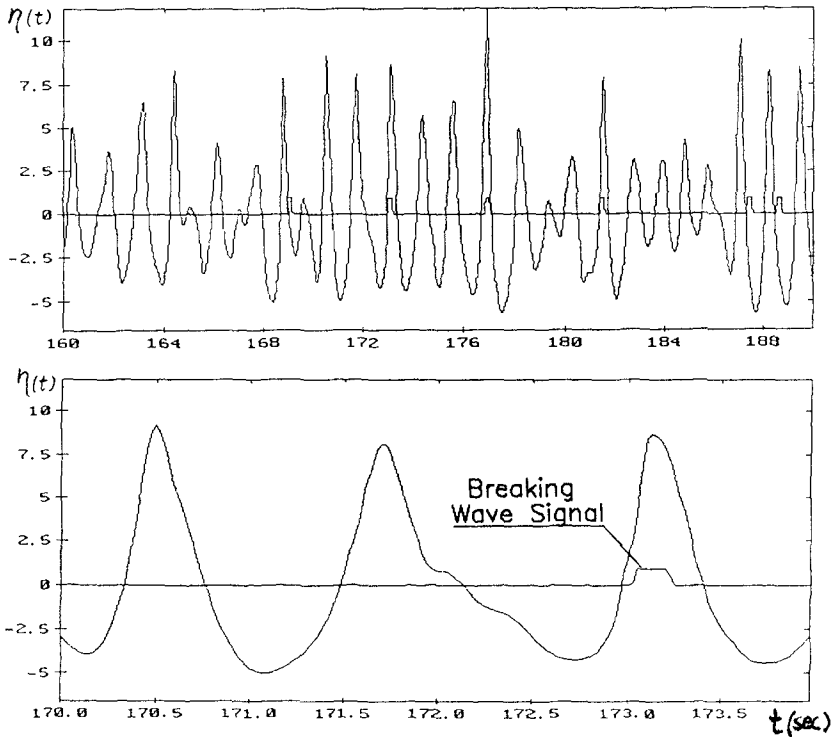


FIG 2. MEASURED WAVE PROFILES & BREAKING WAVE SIGNALS

spectral significant wave height,  $H_{m0}$  was 15.0cm with peak period,  $T_p = 1.30$ sec. These input conditions were verified at wave gauge no. 1 and convert to a relative water depth ( $d/L$ ) ratio of 0.249 and wave steepness of 0.0569 at this position as given from linear wave theory.

Waves were generated for six minutes and approximately 300 were distinguished by the zero-down-crossing method. The number of waves passing each wave gauge was relatively constant. A spectral analysis of the sea surface at each wave gauge location produced similarly-shaped spectrums with reduced energy content. Therefore, the bar/trough shape, position, water depth and wave spectrum chosen did *not* generate higher frequency wave energy after the bar.

Fig. 2 shows an example of the wave train measured over a 30 second interval with an enlargement below it for a 4 second span. Also shown is the impulse voltage signal generated manually into the record by an observer whenever a breaking or broken wave event passed the gauge. This somewhat subjective observation of which waves were classified as "breaking waves" was confirmed by running replicate sets and using different observers. A special, software program has been developed to automatically distinguish the broken waves as a subset of all the waves identified in the record. Note that the largest waves are not always the breaking/broken waves identified in the record.

#### 4. Test Results

##### 4.1. Probability Distributions - All Waves

Wave height histograms were calculated using the DHI software package and checked with specially developed software that also computed histograms for the breaking waves identified as a subset of all the waves. Fig. 3 shows the measured histograms for *all the waves* at four, representative gauge locations, namely: Gauge 2 on the horizontal bottom before the beach slope; Gauge 4 near the bar crest; Gauge 5 in the trough; and Gauge 7 on the plane beach slope.

Also shown are the theoretical, probability distribution functions for all the waves,  $p(H)$  as given by the Rayleigh distribution (dotted line) and the Beta-Rayleigh distribution (solid line). Thornton and Guza (1983) showed that the Rayleigh distribution produced an reasonable description of all surf zone waves (mean period about 14 seconds) transforming over a monotonically decreasing profile (Torry Pines, CA). These authors also reviewed the works of others attempting to explain why the Rayleigh distribution *overpredicts* the number of large waves in the tail when compared with observations.

The Beta-Rayleigh distribution has been offered by Hughes and Borgman, 1989 to ". . . better characterize the wave height distributions for shallow water waves." It is semi-empirical and requires that the  $p(H)$  be bounded by  $H_{max}$ ; be



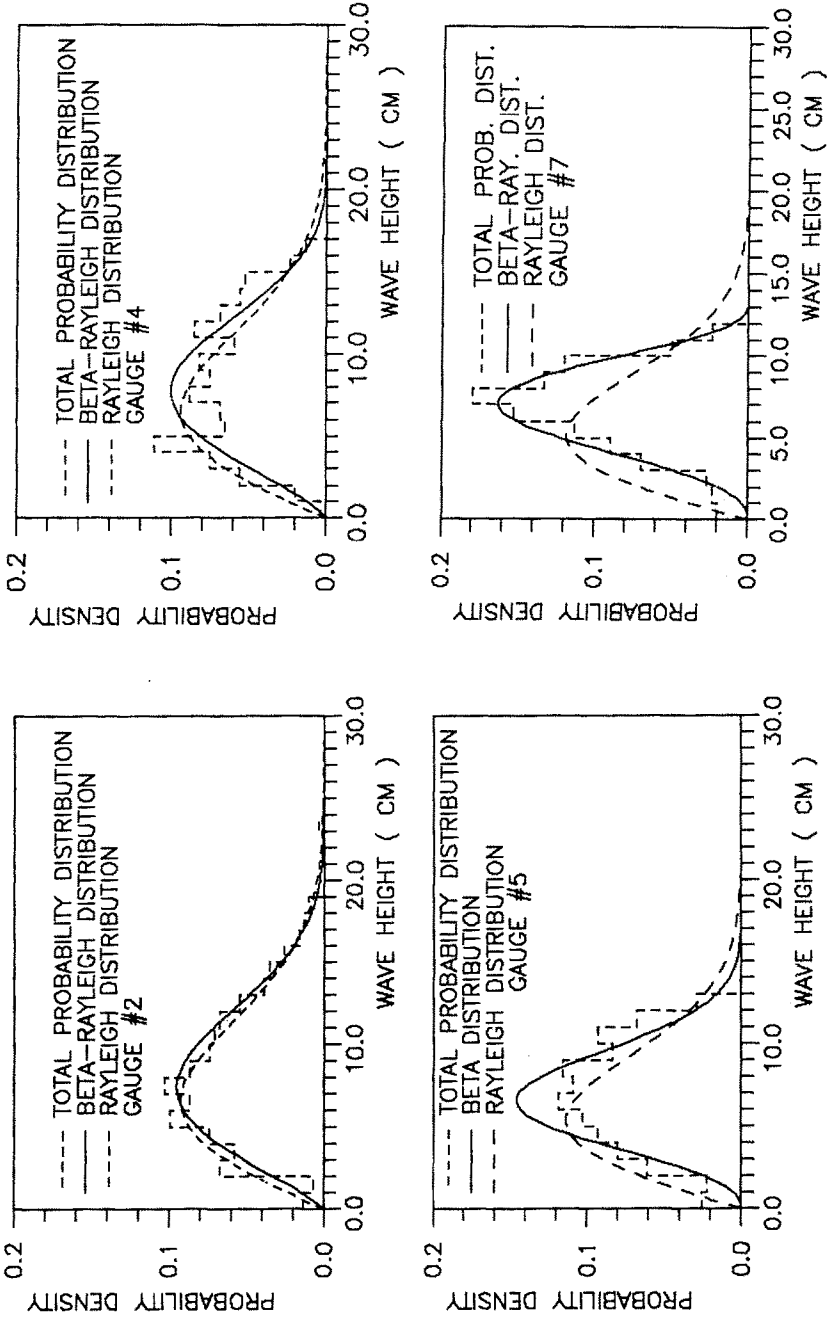


FIG 3. WAVE HEIGHT PROBABILITY DENSITY DISTRIBUTION OF ALL WAVES

skewed toward the larger waves; become the Rayleigh distribution in deep water and; be physically justified. Using the calibration parameters identified by Hughes and Borgman, 1989, we have also presented the Beta-Rayleigh,  $p(H)$  distributions in Fig. 3.

At Gauge 2 in "deep" water, the Rayleigh distribution is found to give a good fit to the measured data. Near the bar crest (Gauge 4) the measured distribution flattens out (or becomes double peaked) and both theoretical curves give a reasonably good fit. In the trough (Gauge 5) both theories give a relatively inaccurate shape compared with the measured distribution, but in different ways. Finally, on the plane beach slope, the Beta-Rayleigh distribution is found to give an excellent fit to the measured histogram, especially for the peak value and in the tail where the Rayleigh distribution *overpredicts* the number of larger waves as discussed above.

#### 4.2. Probability Distributions - Breaking Waves

The measured, breaking wave histograms are plotted in Fig. 4 for the same four gauge location (2, 4, 5, and 7) as discussed above. The scales are constant for each location and reveal that most waves break near the bar and on the plane beach, as expected. Many waves breaking on the bar *continue* through the trough region as broken waves to account for the totals displayed at Gauge 5.

The theoretical, breaking wave distributions,  $p_b(H)$  shown have been computed from the theory of Thornton and Guza (1983). Here,  $p_b(H) = W(H) \cdot p(H)$  where  $p(H)$  is the Rayleigh distribution and  $W(H)$  is a semi-empirical, weighting distribution (model M2) that includes two coefficients ( $\gamma$ ,  $n$ ). Field calibration values of these coefficients ( $\gamma = 0.42$ ,  $n = 2$ ) are used to determine the theoretical curves shown in Fig. 4. Except for Gauge 7 on the plane beach where the shape of  $p_b(H)$  is satisfactory but too large, the theoretical  $p_b(H)$  appears to *under predict* the large wave heights that are measured to be breaking. However, ensemble average, breaking wave energy dissipation,  $\langle \bar{e}_b \rangle$  is determined from the integration of the  $p_b(H)$  distribution so that, at least qualitatively, the areas under the distributions are modeled correctly, except for Gauge 7 on the plane beach.

The length of the test run was doubled to 12 minutes giving approximately 600 waves but no significant difference in the measured histograms for all the waves and the breaking wave subsets were noted.

#### 4.3. Energy Dissipation and $H_{rms}$ Distribution

The measured variation of the root-mean-square wave height,  $H_{rms}(x)$  for eleven positions across the bar/trough profile is shown in Fig. 5(a). The  $H_{rms}(x)$  variation is relatively flat up to the bar crest (near Gauge 4), drops rapidly in the trough region, then recovers again and afterwards drops again as all the wave

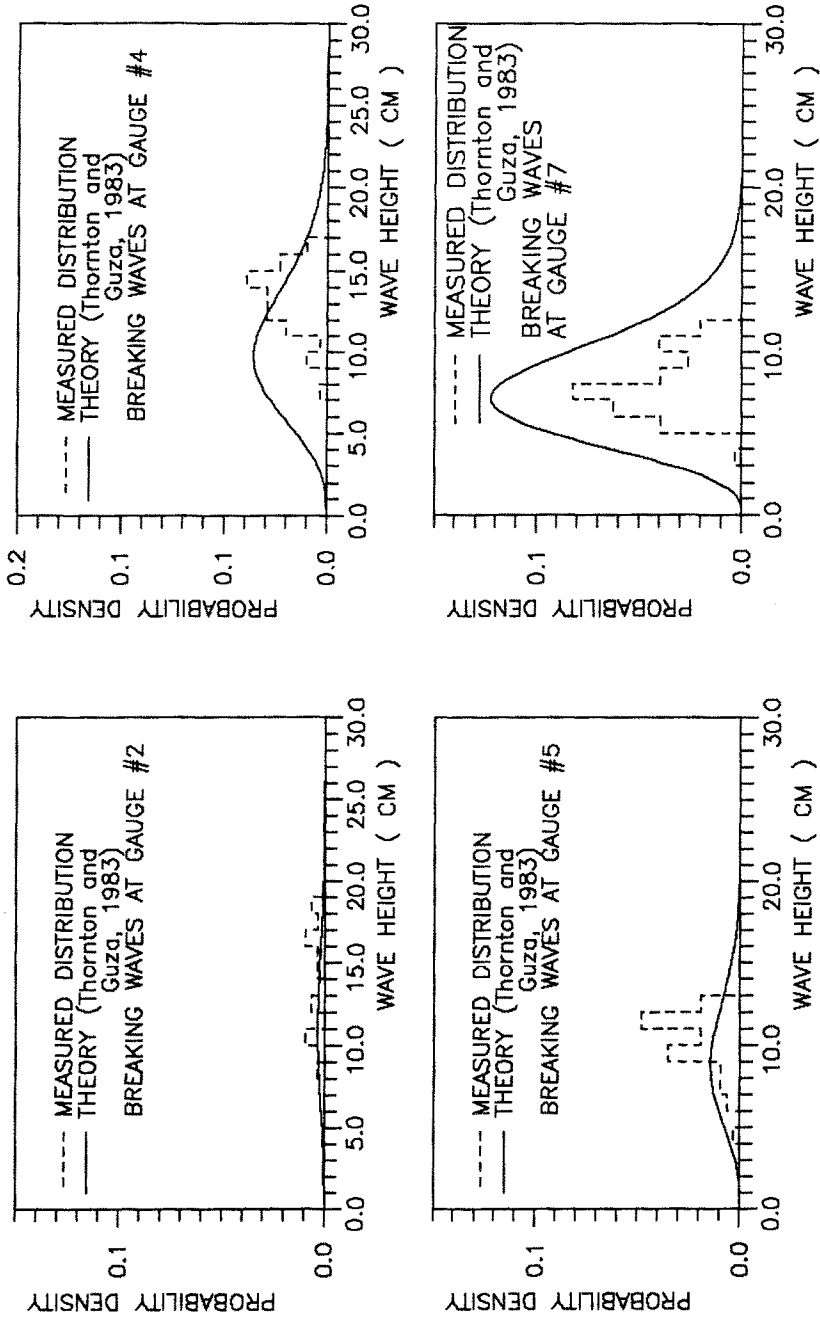


FIG 4. WAVE HEIGHT PROBABILITY DENSITY DISTRIBUTION OF BREAKING WAVES

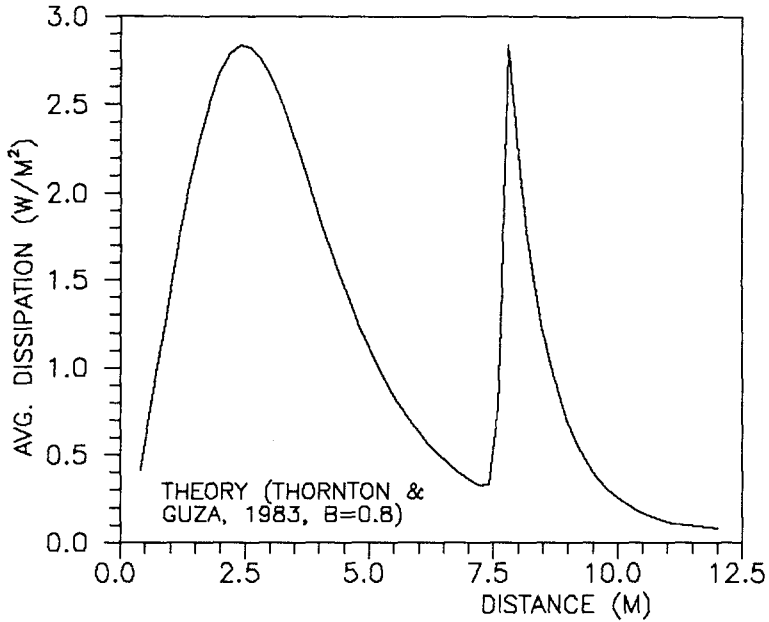


FIG 5b. WAVE ENERGY DISSIPATION ACROSS BEACH

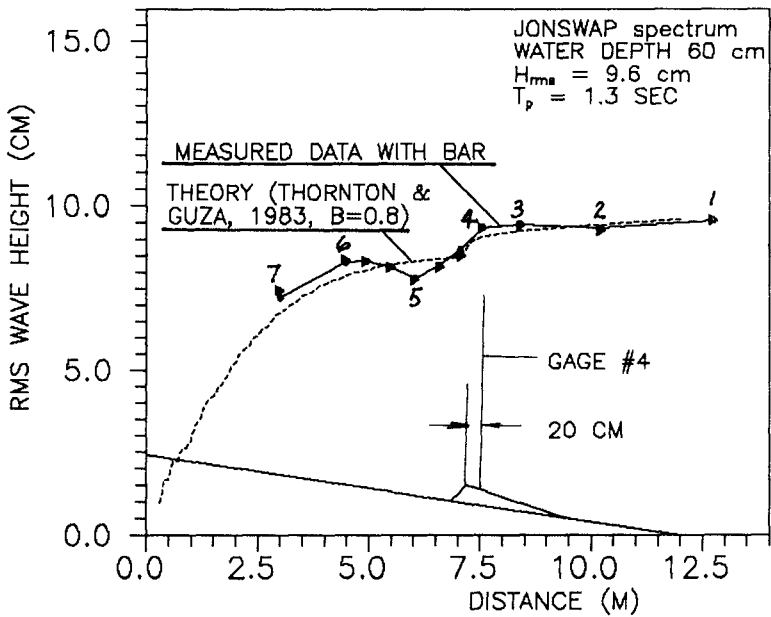


FIG 5a. WAVE HEIGHT DISTRIBUTION ACROSS BEACH

energy is dissipated on the plane beach. Shoaling of individual waves on the slope approaching the bar takes place but so does wave breaking for some of the waves so that the  $H_{rms}(x)$  variation actually decreases slightly as the waves approach the bar crest.

Numerical integration of the energy flux balance equation by a simple, finite-difference approximation using the ensemble average, breaking wave energy dissipation,  $\langle \bar{e}_b \rangle$  from Thornton and Guza (1983) gives the theoretical curve (dotted line) also shown in Fig. 5(a) for the laboratory bar/trough beach profile. The coefficient chosen to give the fit shown for this laboratory data is  $B = 0.8$  where  $B$  is the ratio of the broken wave height to the height of turbulence on the front of the broken wave. Thus  $B \leq 1$  is physically realistic for this laboratory-scale model. Local wave energy flux is computed from linear wave theory for both the average wave energy,  $E$  per unit surface area (i.e.  $\frac{1}{8}\rho g H_{rms}^2$ ) and the group celerity,  $C_g$  for the local water depth. The theory with  $B = 0.8$  and all other approximations ( $\gamma = 0.42$ ,  $n = 2$ ) gives a "smoothed" fit to the data for  $H_{rms}(x)$  but misses the more rapid changes occurring in the trough and wave recovery region on the plane beach. Therefore, even though the theories for the probability distributions  $p(H)$  and  $p_b(H)$  were somewhat inadequate, the results translated into the  $H_{rms}(x)$  distribution are fairly representative of the measured data.

Fig. 5(b) shows the calculated distribution of  $\langle \bar{e}_b \rangle$  across the bar region. The large spike in energy loss at the bar is apparent. The modeled energy loss term then drops way off again in the trough region, as physically expected. However, the theory as presently formulated does not appear to permit the  $H_{rms}(x)$  variation to *increase* again in the trough region as wave shoaling takes place on the plane beach. The  $\langle \bar{e}_b \rangle$  theory extracts too much wave energy in the inner surf zone region on the plane beach and this is postulated to be due to the excessively large area beneath the  $p_b(H)$  theory (see Fig. 4, Gauge 7) as compared to that actually measured.

## 5. Future Directions

### 5.1. Bores and Breaking Waves

Following LeMehauté (1962) many researchers use the theory for the energy dissipation across a moving hydraulic jump (bore) to approximate the rate of energy dissipation in a single breaking wave,  $e_b$  per unit width. Thornton and Guza (1983) took

$$e_b = \frac{1}{4} \rho g C_b \frac{(BH)^3}{d} \quad (1)$$

where  $C_b$  is the wave celerity,  $B$  is the breaker coefficient as discussed above and  $d$  is the local water depth. The average rate of energy dissipation per unit surface area of each wave of length  $L$  is then determined as

$$\bar{e}_b \equiv \frac{e_b}{L} = \frac{1}{4} \rho g \frac{C_b}{L} \frac{(BH)^3}{d} \quad (2)$$

or since  $c \equiv L/T$

$$\bar{e}_b = \frac{1}{4} \rho g \frac{1}{T} \frac{(BH)^3}{d} \quad (3)$$

so that  $\bar{e}_b$  is inversely proportional to wave period,  $T$ .

Consider three waves all of equal height but with periods,  $T$  of 5, 10, and 15 seconds. After breaking in shallow water due to depth-limiting effects, Equation (3) says average wave energy is dissipated but only at one-third the rate for the 15 second wave compared with the 5 second wave. This seems physically unrealistic because the energy dissipation is concentrated between the trough and crest regions and for trough Froude numbers relative to a moving observer, the lengths of hydraulic jumps,  $L_j$  are far less than the wave length,  $L$ .

Fig. 6 is taken from the field calibration efforts of Thornton and Guza (1983) for their theory discussed above. Long period swell waves ( $T = 13 - 18.2$  seconds) were present and each required a different calibration coefficient,  $B$  ranging between 1.3 - 1.7 to get the best fit between measured  $H_{rms}(x)$  in the field and their model computation. In essence, the longer period waves reduced  $\bar{e}_b$  in (3) and consequently require a larger  $B$  coefficient to extract enough energy to get a proper fit for  $H_{rms}(x)$ . Note also that  $B$  values greater than unity are physically unrealistic by definition and that  $B^3$  values needed for "calibration" ranged from 2.2 to 4.9 for these field results. Thornton and Guza (1983) also report setting  $B = 0.8$  to calibrate the laboratory measurements of Battjes and Janssen (1972). For laboratory wave periods,  $L_j$  is closer to  $L$ .

Svendsen, et al. (1978), Stive (1984) and others have argued that the bore model *underestimates* the actual rate of energy dissipation in breaking waves because pressure, momentum and energy distribution coefficients are neglected along with the flux of turbulent energy into and out of the control volume. These factors may account for some of the discrepancy in the use of the bore theory, but using  $L$  to define  $\bar{e}_b$  may be the most important reason.

## 5.2. Current Research

Tests are being conducted with a peak wave period of 2.3 seconds to study longer period effects on  $\bar{e}_b$  and hence  $B$  in the theory. The ratio ( $L/L_j$ ) used as

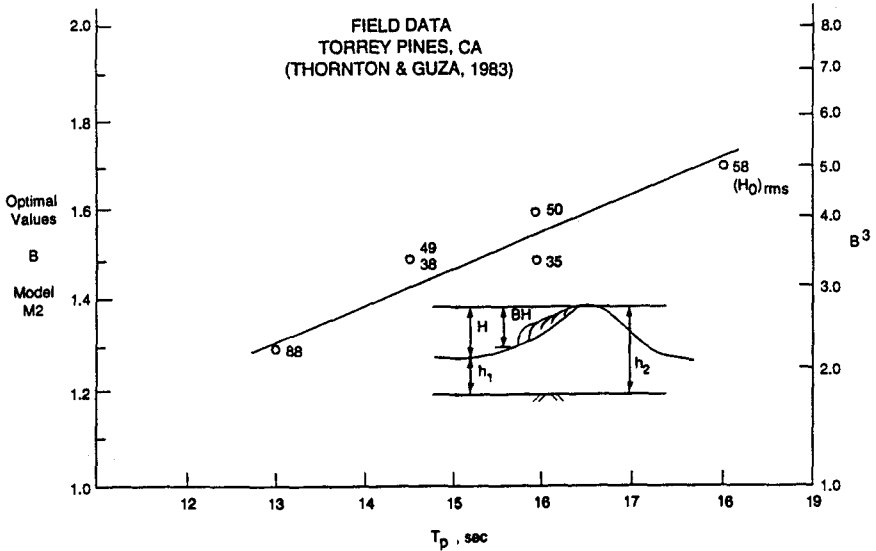


FIG 6. Variation of Calibration Coefficient,  $B$ , with Wave Period (from Thornton & Guza, 1983)

a coefficient (keeping  $B \approx 1$ ) will remove the strong dependency of  $\bar{e}_b$  on the wave period. Various ways to estimate  $L_j$  are being investigated.

Modifications to the probability density functions for all the waves and the breaking waves are also being made to more closely represent shallow water effects on  $p(H)$  and deep water effects (wave steepness) on  $p_b(H)$ .

Field data sets from Duck, NC at the Corps', Field Research Facility (Ebersole and Hughes, 1987) are also being used in this effort.

**6. Summary and Conclusions**

The transformation of an irregular wave train across a bar/trough beach profile by using the (1) energy flux balance equation including the bore model for breaking waves and (2) a single, statistical wave height,  $H_{rms}$ , together with probability functions for all the waves and those breaking as a subset, is a powerful tool for coastal engineers. Laboratory measurements reveal that refinements in the underlying theories are necessary to improve the  $H_{rms}(x)$  prediction especially in the wave height recovery region in the trough. These improvements include incorporating physically realistic coefficients for both laboratory and field data sets that are used to modify and verify the theory.

The completed results will be reported in the Proceedings of the next Conference on Coastal Engineering.

## 7.0 References

- Battjes, J.A. and J.P.F.M. Janssen (1978), "Energy Loss and Set-Up Due to Breaking in Random Waves," Proceedings, 16<sup>th</sup> International Conference Coastal Engineering, pp.569-87.
- Battjes, J.A. and M.J.F. Stive (1985), "Calibration and Verification of a Dissipation Model For Random Breaking Waves," Journal Geophys. Res., Vol. 90, pp.9159-67.
- Dally, W.R. (1990), "Random Breaking Waves: A Closed-Form Solution for Planar Beaches," Coastal Engineering, Vol. 14, No. 3, pp.233-263.
- Dally, W.R. (1992), "Random Breaking Waves: Field Verification of A Wave-By-Wave Algorithm for Engineering Application," Coastal Engineering, Vol. 16, No. 4, pp.369-397.
- Ebersole, B.A. and S.A. Hughes (1987), "DUCK 85 Photopole Experiment," Misc Paper CERC-87-8, USAE, WES, CERC, Vicksburg, MS.
- Hughes, S.A. and L.E. Borgman (1989), "Beta-Rayleigh Distribution for Shallow Water Wave Heights," Proceedings, COASTAL HYDRODYNAMICS 89, University of Delaware, Newark, DE, pp.17-31.
- LeMehauté, B. (1962), " On Non-Saturated Breakers and the Wave Run-Up," Proceedings, 8<sup>th</sup> International Conference Coastal Engineering, pp.77-92.
- Stive, M.J.F. (1984) "Energy Dissipation in Waves Breaking on Gentle Slopes," Coastal Engineering, Vol. 8, No. 2, pp.99-127.
- Stoker, J.J. (1957), Water Waves, Wiley Interscience, New York
- Svendsen, I.A., P.A. Madsen, and J.B. Hansen (1978), "Wave Characteristics in the Surf Zone," Proceedings, 16<sup>th</sup> International Conference Coastal Engineering, pp.520-539.
- Thornton, E.B. and R.T. Guza (1983), "Transformation of Wave Height Distribution," Journal Geophys. Res., Vol. 88, No. C10, pps.5925-5938.



## CHAPTER 7

### THE MEDITERRANEAN SEA WAVE FORECASTING SYSTEM

Luigi Cavaleri, Luciana Bertotti

#### Abstract

We describe the sea wave forecasting system presently operational at ECMWF. After a short description of the meteorological and wave models, we address specifically the problems connected to their application to the Mediterranean Sea. We consider in particular two storms, a Mistral and an African storm, whose results provide clear indication of the present forecasting capability in this area.

#### Background

Following the opening to Optional Projects by the Council of the European Centre for Medium Range Weather Forecasts, Reading, U.K. (henceforth referred to as ECMWF), a project for real time forecast of the sea wave conditions has been proposed and approved by the Centre in May 1991. The aim is to make use of the daily meteorological forecast to produce a corresponding wave forecast on a global basis by means of an advanced wave model. Due to the lack of sufficient resolution the Mediterranean Sea cannot be properly represented on a global grid. Consequently a separate version of the model, with a sufficiently high spacial resolution but otherwise the same physics and numerics of the global version, has been implemented in this basin.

-----  
Istituto Studio Dinamica Grandi Masse, S.Polo 1364, 30125 Venice, Italy

In this paper we briefly describe the meteorological and wave models used for the forecast. Then we point out the problems specifically connected to the Mediterranean area. These are well illustrated by the analysis and forecast of two storms of different characteristics, a Mistral and an African storm. We conclude with an outlook on the expected future developments of the models and their effect on the actual forecast.

### The meteorological and wave models

A 213 components spectral meteorological model is daily run at ECMWF on a global basis for analysis and up to days forecast (Tiedtke et al, 1988). The results are provided at 6 hour interval. Among a wide variety of products the model provides U10, the 10 m height wind, with an effective resolution of approximately 80 km. This wind is used as input to the wave model.

The third generation WAM wave model is used for wave evaluation. The model (amply described in the literature, see e.g. The WAMDI Group, 1988 and Cavaleri et al, 1991) is based on the energy balance equation, and on the physical description of the processes that affect the growth and decay of wind waves. In the present version 300 components, 12 directions and 25 frequency bins, are considered. For each component and at each integration step the balance equation is solved at the knots of a spherical grid with 3 degree resolution, both in latitude and longitude, providing information on the two-dimensional spectrum at each grid point. For application to the Mediterranean Sea a limited area geographical grid, with 0.5 degree resolution, is used. The grid includes 930 sea points. With  $0.3 \times 10^3$  CPU second for each point and each integration step, a 5 day forecast in the Mediterranean Sea requires about 100 second of CPU on a CRAY C90.

### Application to the Mediterranean Sea

The main problem for a correct evaluation of wind wave conditions is the correctness of the input wind field. This is particularly true in basins with complicated geographical shape, as it is the case for the Mediterranean Sea. Limited shift of location or direction of an intense wind distribution can lead to substantial change of fetch in a certain area, and consequently to drastically

different wave conditions. The practical difficulties are also increased by the presence of a complicated orography. Cavaleri et al (1991) and Dell'Osso et al (1992) have discussed the problem of an accurate description of the wind field in the Mediterranean Sea, and they have clearly shown the fundamental role of the surrounding orography in shaping the meteorological situation, in particular the wind field, inside the basin. The present resolution of the ECMWF meteorological model has been shown to be the minimum required for a proper description of the surface wind fields in the Mediterranean basin.

In the following we show different applications of the WAM model, both with analysis and forecast wind. We call attention to the fact that for a wave model there is no difference if operating in hindcast (analysis) or forecast mode. An input wind, however produced, is just an "input wind", and the wave model reacts accordingly, independently of where the wind information comes from. Given the basic characteristics and the intrinsic accuracy of a wave model, its results plainly reflect the accuracy of the input wind fields.

The wave measurements used to verify the results discussed in this paper have been obtained with the Italian network of directional buoys. The network is described in a companion paper in this conference (De Boni et al, 1992).

#### Mistral case

On 17 November 1991 (see figure 1) a strong Mistral wind was blowing across the Western Mediterranean Sea. The Mistral wind is a cold north-westerly wind that, associated to energetic flows from the Atlantic Ocean, enters the Mediterranean Sea across the Carcassone Passage, north of the Pyrenees between Spain and France. The analysis at 12 UTC 17 November 1991 is shown in figure 1a. Figure 2a shows the corresponding wave field. The peak conditions are reached on the west coast of Sardinia, with significant wave height  $H_s$  larger than 6 metre. Figure 3a compares the WAM output at Alghero, indicated with a dot (A) in figure 2a, with the data obtained from the WAVEC wave measuring buoy. The closest grid point to the measurement location was chosen for comparison. Given this approximation and the time variability of the  $H_s$  record, the comparison is quite satisfactory.

Figure 1b,c,d shows the corresponding wind fields evaluated as forecast at day N-1, N-2, N-3 respectively. Remarkably we see that the storm was well described

till 3 days in advance. The associated wave forecasts stress further this point. They are shown in figure 2b,c,d. We note only a limited (a few hours) anticipation of the storm in figure 2d, with wave energy already protruding into the Tyrrhenian Sea.

Note that the actual ECMWF forecast would be much better than this. In routine operations a wave forecast uses as input the analysis wind until time 0 (beginning of the forecast), and then the wind forecast at +1d (day), +2d, etc. We have used a different technique. Considering p.e. the +1d wave forecast (one map of which is shown in figure 2b), for each day N of the run the input wind has been

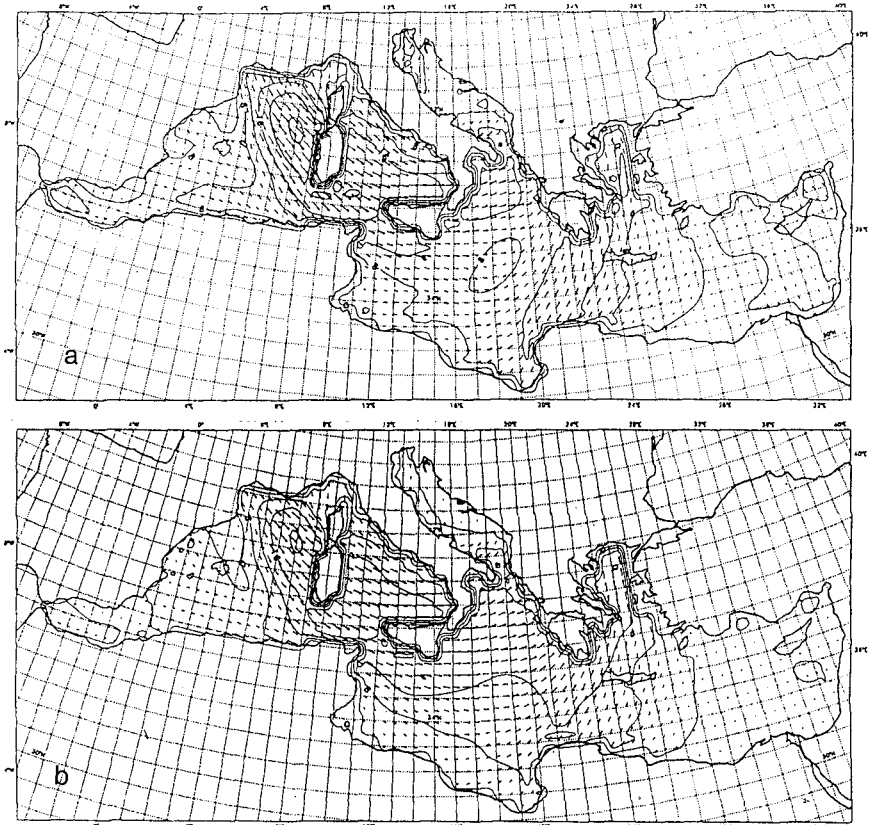


Figure 1 - Wind field on the Mediterranean Sea at 12 UTC 17 November 1991. 10 m height wind; speed is given as m/s. a) analysis, b) 1 day forecast.

given by the wind forecast produced at day N-1. So doing, the wave forecast becomes very sensitive to even small but permanent error in the wind forecast, certainly much more than in the standard routine operation. This leads to a better appreciation of the wave forecast shown in figure 2 and figure 3.

#### African storm

A week after the Mistral case a different condition arose, characterised by an intense African storm. The main feature of African storms is a small minimum that, born over the Sahara desert, moves then northward. When entering the Mediterranean Sea the minimum rapidly intensifies, producing a very localised but deep low. The dominant characteristics of the African storms, at least for what

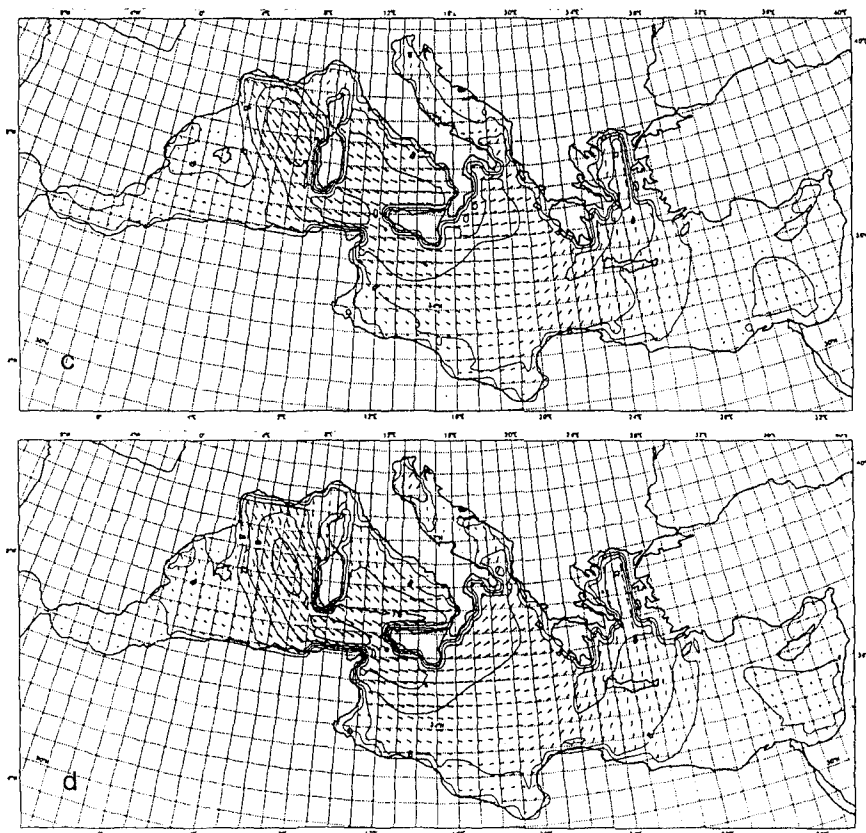


Figure 1 - (cntd) c) as b), but for 2 day forecast, d) 3 day forecast.

concerns the evaluation of wind waves, are the extremely strong winds and the large spacial and temporal gradients. Mutatis mutandis, they resemble small hurricanes.

The meteorological situation at 00 UTC 24 November 1991 is shown in figure 4a. The minimum is located on the western end of Sicily, producing a strong southerly wind on the whole Ionian Sea, south of Italy. The associated wave conditions are represented in figure 5a. Large waves, with  $H_s$  larger than 5 metre, affect the south-eastern coast of Italy.

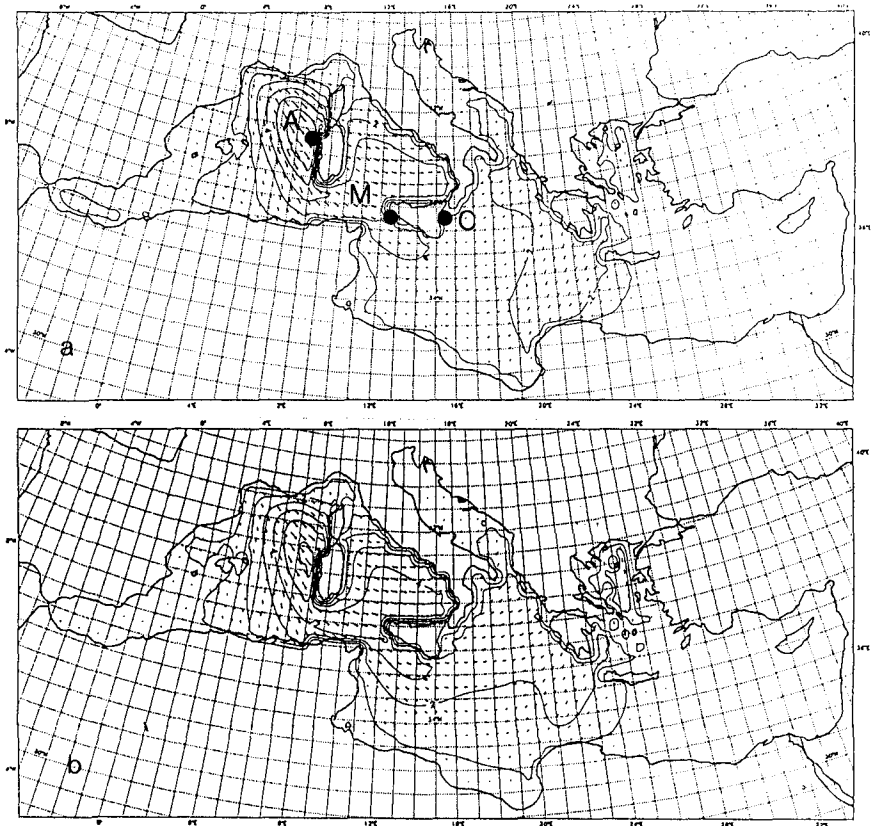


Figure 2 - Wave field on the Mediterranean Sea at 12 UTC 17 November 1991. Significant wave height, in m. a) analysis, b) 1 day forecast. The dots in a) show the position of the wave measuring stations at Alghero (A), Mazara (M), Catania

The comparison of the WAM model output with the measured  $H_s$  at Mazara and Catania (points M and C in figure 2a, respectively) reveals several interesting aspects. The underestimate of  $H_s$  at Mazara and the overestimate at Catania suggest that the analysis has misplaced the actual track of the low to the East. Also, as discussed by Dell'Osso et al (1992), the strength of these storms is often underestimated. The main reason for this is the limited resolution of the meteorological models, consequently unable to resolve the details of the storm and to correctly represent its physics. The limited dimensions of the African storms, and the substantial lack of information on the African territory where they come from, make their prediction a very difficult task. This is apparent in the 1d, 2d, 3d wind forecast in figure 4b,c,d. The storm is present, but weaker and misplaced

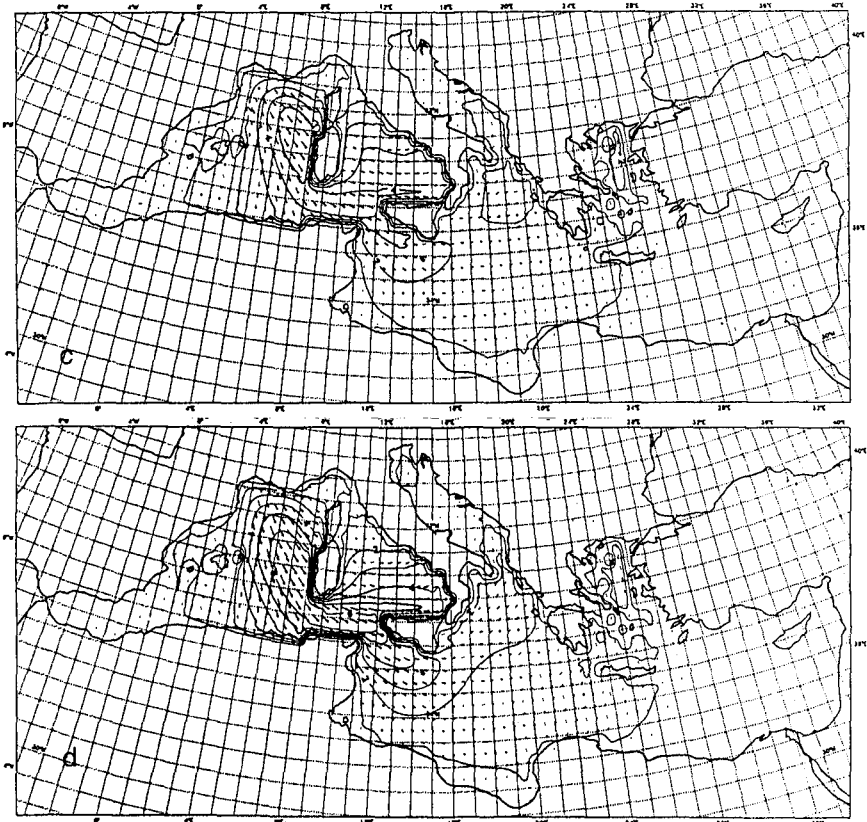


Figure 2 - (cntd) c) as b), but for 2 day forecast, d) 3 day forecast.

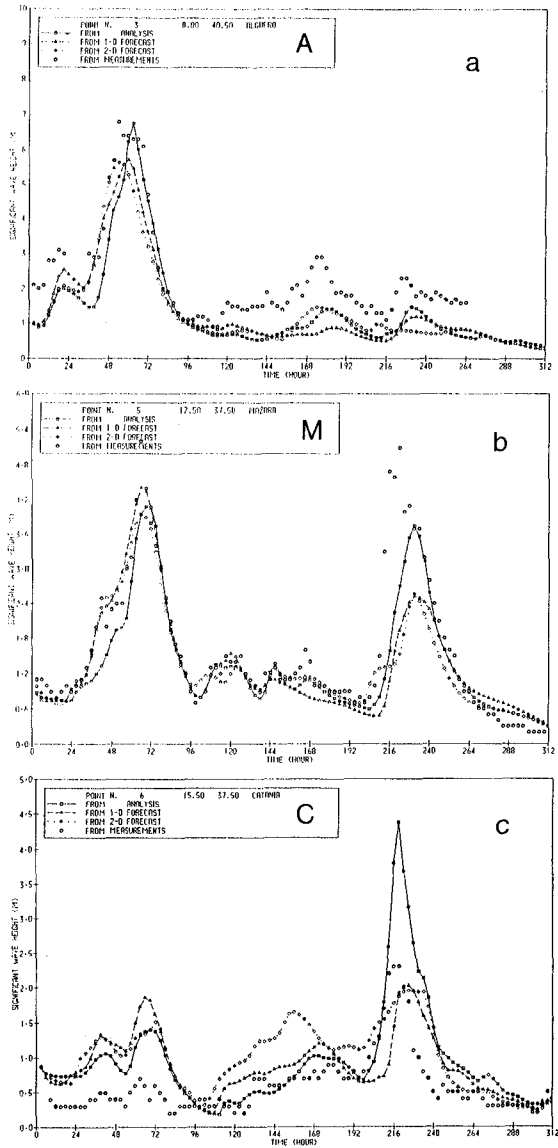


Figure 3 - Timeseries of the significant wave height (m) at the three locations shown in figure 2a. Measured data, and wave model output for analysis wind and 1 and 2 day forecast are shown.



in b, barely discernible in c, absent in d where the minimum over Sardinia has a different genesis. As previously said, the consequences of these poor forecasts are stressed by the corresponding wave forecast (shown in figure 5b,c,d). There is virtually no resemblance with the analysis field in figure 5a. This conclusion is backed by the  $H_s$  comparison in figure 3b,c. Note that the 3d forecast has not been drawn to avoid an unnecessarily large number of diagrams in the figure.

### Conclusions and outlook

The tests carried out until now suggest that in most of the cases the T213 spectral

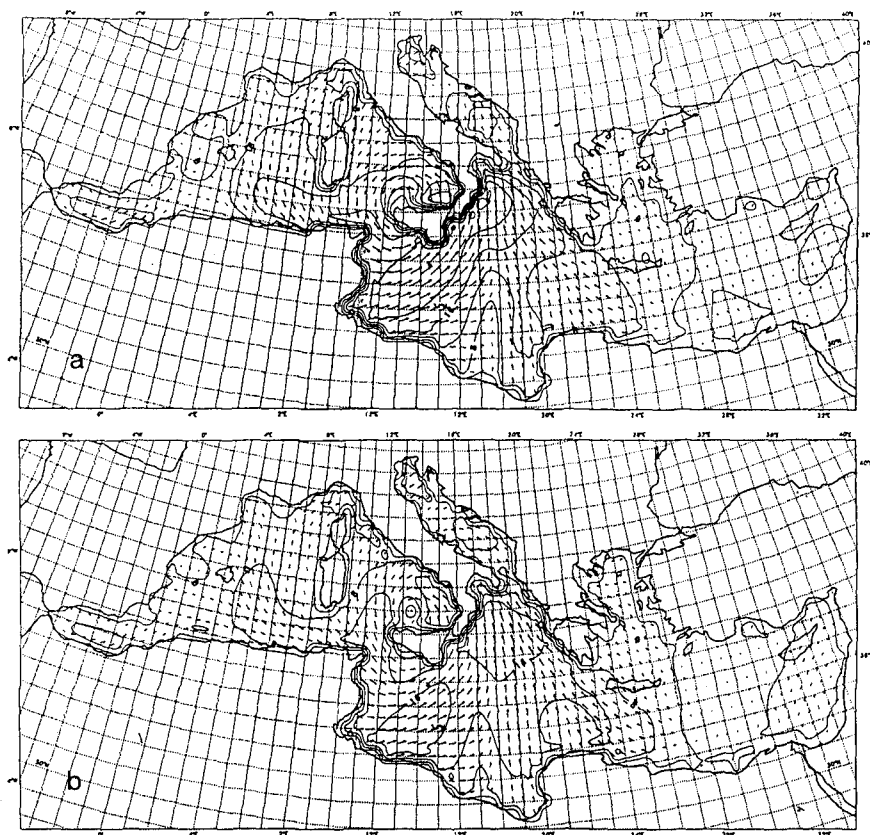


Figure 4 - As figure 1, but at 00 UTC 24 November 1991.

meteorological model presently used at ECMWF provides acceptable surface winds on the Mediterranean Sea. This is true for extended storms with a well defined shape and distribution. It is not the case for small storms, e.g. the African storms, whose structure cannot be resolved in the present resolution of the meteorological model. A similar argument holds for the predictability of the storms, with the further point that the western storms are well documented from several days in advance, while in practice the African storms are not detected by the scarce and scattered meteorological network present on the North-African continent.

In general terms the meteorological and wave predictability is expected to improve in the future, both for the increase of resolution of the models, and for the large

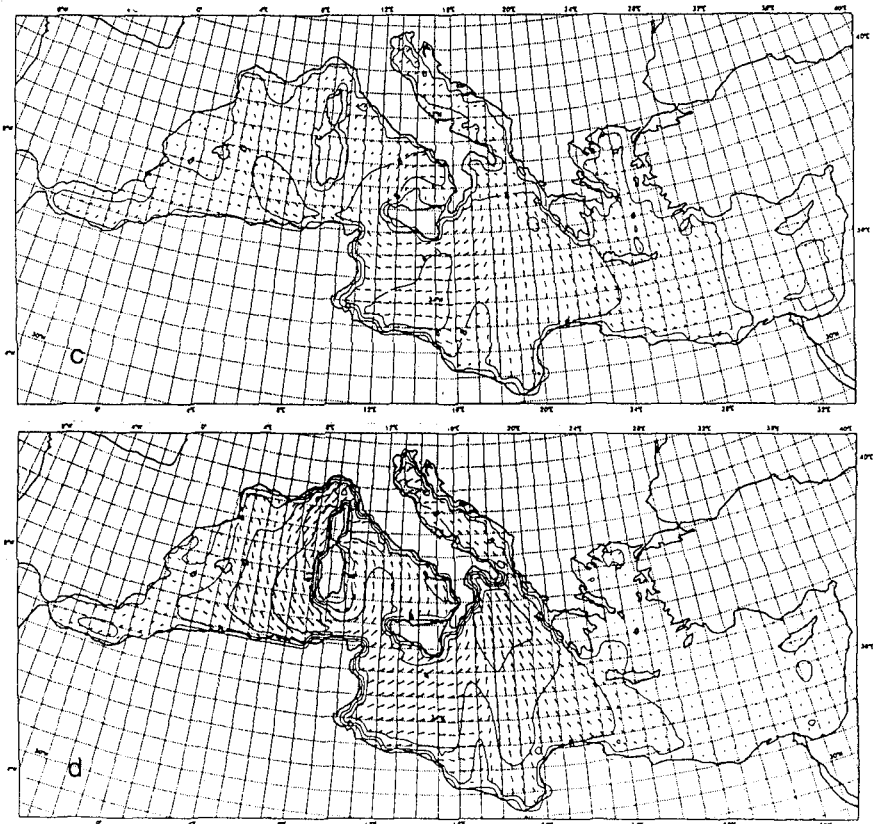


Figure 4 - (cntd).

amount of information provided by the satellite like ERS-1. However, once more the argument is much weaker for the African storms, because of the lack of sufficient information (the ERS-1 scatterometer and altimeter provide estimates of the wind distribution only on the sea). It is true that a better definition of the global meteorological situation will help in detecting the conditions that are at the origin of the African storms. However, the surface observations, providing the truth for the short term accurate forecasts, will still be missing. Similar conditions are found in many parts of the world (Bengtsson, 1991). If the general forecast, and the one on the Mediterranean Sea in particular, is to be substantially improved in the near future, this problem will have to be addressed with will and decision.

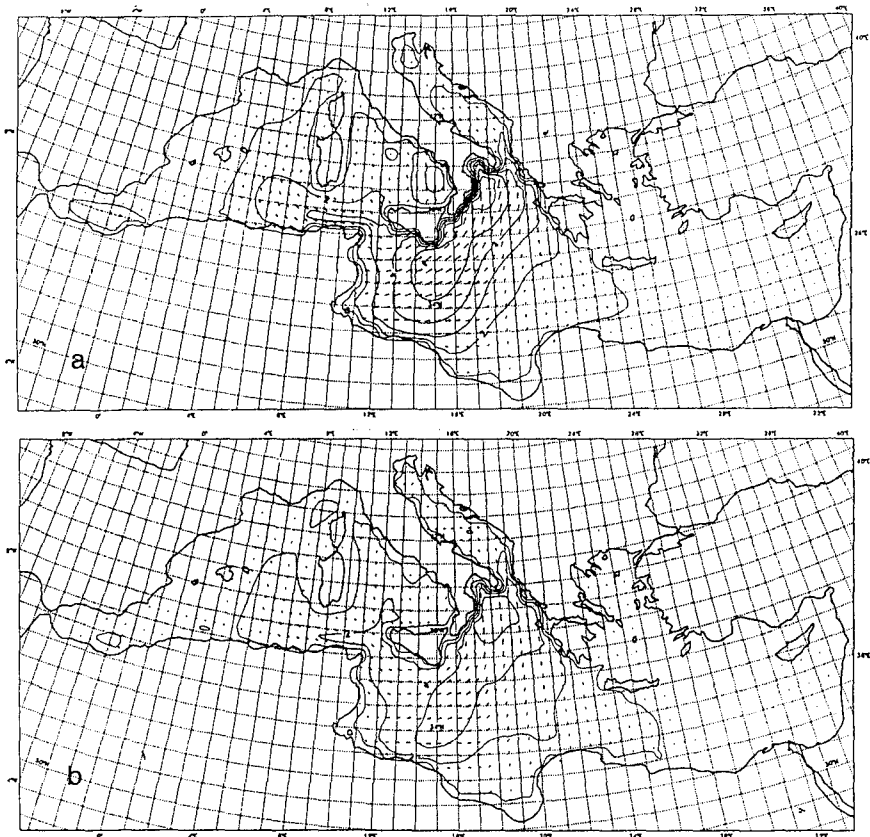


Figure 5 - As figure 2, but at 00 UTC 24 November 1991.

### Acknowledgements

The present work has been executed under MAST contract OO42 of EEC. The calculations have been carried out at the European Centre for Medium Range Weather Forecasts. The help and the suggestions of the local staff, both in technical and physical matters, are warmly acknowledged.

### References

Bengtsson,L., 1991, "Advances and prospects in numerical weather prediction", Q.J.R.Meteorol.Soc., 117, pp.855-902.

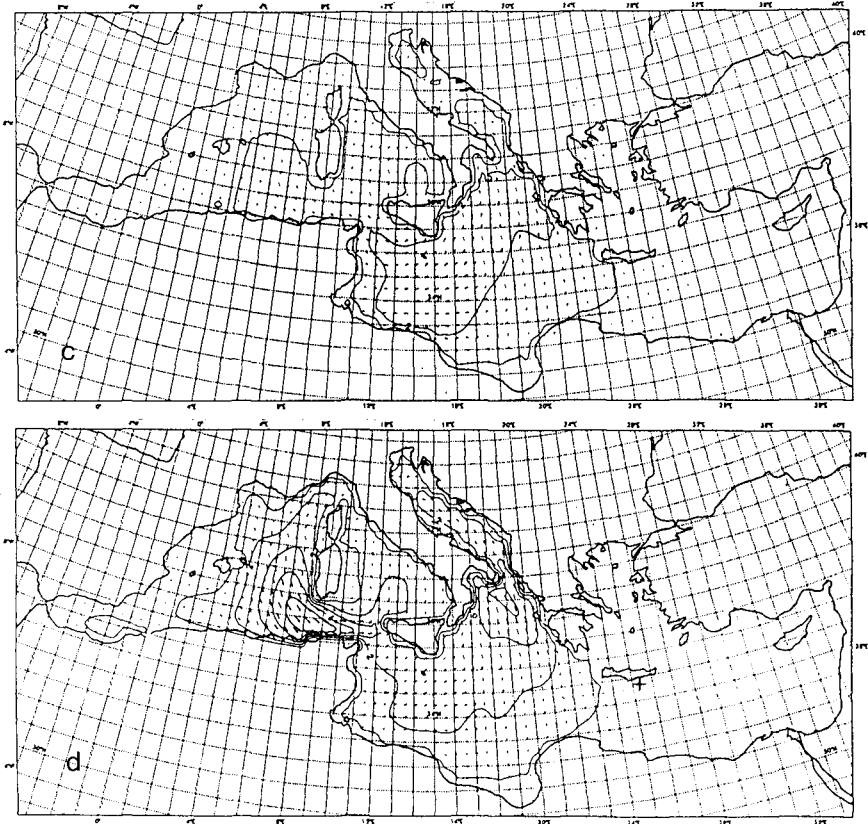


Figure 5 - (cntd).

Cavaleri,L., L.Bertotti, and P.Lionello, 1991, "Wind wave-cast in the Mediterranean Sea", *J.Geophys.Res.*, 96, pp.10739-10764.

De Boni,M., L.Cavaleri, and A.Rusconi, 1992, "The Italian waves measurement network", 23rd ICCE, Venice, October 1992 - In these proceedings -

Dell'Osso,L., L.Bertotti, and L.Cavaleri, 1992, "The Gorbush storm in the Mediterranean Sea: atmospheric and wave simulation", *Monthly Weather Review*, vol.120, 1, pp.77-90.

Tiedtke,M., W.A.Heckley, and J.Slingo, 1988, "Tropical forecasting at ECMWF: the influence of physical parametrisation on the mean structure of forecast and analysis", *Q.J.R.Meteorol.Soc.*, 114, pp.639-664.

The WAMDI Group, 1988, "The WAM model - a third generation ocean wave prediction model", *J.Physic.Ocean.*, 18, pp.1775-1810.

## CHAPTER 8

### Current-Depth Refraction and Diffraction Model for Irregular Water Waves

Jang Won Chae<sup>1</sup> and Shin Taek Jeong<sup>2</sup>

#### Abstract

A numerical model is presented for the prediction of combined refraction-diffraction of waves propagating in the region of slowly varying current and topography. For steady waves, two elliptic-type model equations are derived from the mild-slope equation which can be solved in a similar way to an initial value problem without stability restriction. Therefore, the present model appears to be an efficient tool for irregular wave propagation problem in a large coastal area. Some examples of numerical computations are given for the cases concerning wave-current interaction on a sloping beach and over a mound.

#### Introduction

Waves propagating near a tidal inlet will be transformed due to currents and irregular water depths. The wave-current interaction is one of the most interesting and important phenomena for the prediction of wave climate and resultant sediment transport in coastal areas. The approximation of irregular waves by a monochromatic wave in modeling of wave transformation in coastal areas often introduces large errors in wave heights. There is a definite need for an efficient method for the calculation of irregular wave transformation over large coastal area(Panchang et al., 1990).

---

<sup>1</sup> Principal Res. Engr., Head of Coast. Engrg. Lab., Korea Ocean Res. & Dev. Inst., Ansan P.O. Box 29, Seoul 425-600, Korea.

<sup>2</sup> Senior Res. Engr., Coast. Engrg. Lab., Korea Ocean Res. & Dev. Inst. Ansan P.O. Box 29, Seoul 425-600, Korea.

Recently, a number of studies have been made for the analysis of wave-current system. Booij(1981), Liu(1983), and Kirby(1984) proposed hyperbolic wave equations governing the propagation of waves in water of varying depth and currents in the mild-slope approximation. They used parabolic approximation in order to circumvent the difficulty in calculation of elliptic equations for regular waves. Ohnaka et al.(1988) provided a set of mild-slope equations based on Kirby's equation, which consists of two first-order equations describing the water surface elevation and flow rate. This model includes partially reflective boundary condition.

The models mentioned above employ parabolic- or hyperbolic-type differential equations which are in general not so efficient to use in large area (order of hundreds of wave length). In shallow water they need fine grid resolution to meet sufficient accuracy of numerical results, which is more crucial condition for the high frequency components of wave spectrum.

In the present study, a new set of mild-slope equations describing the deformation of regular waves by a large-scale current field in water of irregular depth is derived, and an efficient numerical method is also presented. The elliptic type governing equations are solved in a similar way to an initial value problem. The accuracy of the numerical method does not greatly depend on grid size and computation time is comparatively short. Therefore, this method is extensively applied to several spectral components in order to simulate irregular wave transformation due to combined refraction-diffraction. Linear superposition of monochromatic-wave calculation is made to obtain spectral estimates. Some results of the computation are compared with analytical solutions, and numerical examples concerning the interactions between waves and currents over a mildly sloping beach and also over a mound are presented.

### Derivation of Governing Equations

The mild-slope equation has been used successfully as a model equation for describing surface water waves propagating over a seabed of mild slope(eg. Berkhoff, 1972). For a wave-current interaction Kirby(1984) derived a general equation. Recently Chae et al.(1990) and Jeong(1990) have rederived the mild-slope equation using variational principle and Green's theorem for linear water waves following Booij's method(1981). The equation can be written as

$$\frac{D^2\Phi}{Dt^2} + (\nabla \cdot \underline{U}) \frac{D\Phi}{Dt} - \nabla \cdot (CC_g \nabla \Phi) + (\sigma^2 - k^2 CC_g)\Phi + W \frac{\partial \Phi}{\partial t} = 0 \quad (1)$$

where  $D/Dt = \partial/\partial t + \underline{U} \cdot \nabla$ ,  $\nabla = [(\partial/\partial x) \mathbf{i}, (\partial/\partial y) \mathbf{j}]$ , and  $\underline{U} = (u, v)$ ,  $\Phi$  the complex velocity potential at the mean surface level,  $\sigma$  the intrinsic

angular frequency,  $k$  wave number,  $C$  and  $C_g$  are the phase and group velocity respectively, which are defined according to  $C = \sigma/k$ ,  $C_g = \partial\sigma/\partial k$ ,  $\sigma^2 = gk \tanh kh$ , and  $W$  dissipation coefficient,

$$\omega = \sigma + \mathbf{k} \cdot \mathbf{U} \quad (2)$$

where  $\omega$  is absolute angular frequency. The velocity potential at an elevation  $z$  is given by

$$\Phi(\mathbf{x}, z, t) = f(z) \phi(\mathbf{x}, t) \quad (3)$$

where  $f(z) = (\cosh k(z+h))/(\cosh kh)$ . Since the bottom is mildly sloping, the derivative of  $f$  with respect to  $\mathbf{x}$  will be small.

For purely periodic waves the velocity potential is given by

$$\phi(\mathbf{x}, t) = \text{Re} \left[ \hat{\phi}(\mathbf{x}) e^{-i\omega t} \right] \quad (4)$$

Substitutions of eq.(4) into eq.(3), and further them into eq.(1) produce an elliptic equation as follows:

$$\begin{aligned} & -i\omega \left[ 2\mathbf{U} \cdot \nabla \hat{\phi} + \hat{\phi} (\nabla \cdot \mathbf{U}) \right] + (\mathbf{U} \cdot \nabla) (\mathbf{U} \cdot \nabla \hat{\phi}) + (\nabla \cdot \mathbf{U}) (\mathbf{U} \cdot \nabla \hat{\phi}) \\ & - \nabla \cdot (CC_g \nabla \hat{\phi}) + (\sigma^2 - \omega^2 - k^2 CC_g) - i\omega W \hat{\phi} = 0 \end{aligned} \quad (5)$$

If  $\mathbf{U} = (0, 0)$ , eq.(5) reduces to Berkhoff's(1972) mild-slope equation.

Here the complex velocity potential  $\hat{\phi}$  can be written in terms of the amplitude  $a$  and the phase  $S$  as

$$\hat{\phi} = -ig \frac{a}{\sigma} e^{iS} \quad (6)$$

where  $g$  is acceleration due to gravity, and  $S(\mathbf{x})$  phase function given by

$$S(\mathbf{x}) = \mathbf{k} \cdot \mathbf{x} - \omega t \quad (7)$$

Then eq.(5) with the substitution of eq.(6) reduces to a set of elliptic equations by separating the resulting equation into real and imaginary parts as follows

$$\nabla \cdot \left[ \mathbf{U} \frac{a^2}{\sigma^2} (\omega - \mathbf{U} \cdot \nabla S) + CC_g \frac{a^2}{\sigma^2} \nabla S \right] + W \frac{a^2}{\sigma} = 0 \quad (8)$$

$$\begin{aligned} & CC_g \frac{a}{\sigma} (\nabla S)^2 - (\mathbf{U} \cdot \nabla S - \omega)^2 \frac{a}{\sigma} + (\sigma^2 - k^2 CC_g) \frac{a}{\sigma} \\ & - \nabla \cdot (CC_g \frac{a}{\sigma}) + (\nabla \cdot \mathbf{U}) (\mathbf{U} \cdot \nabla \frac{a}{\sigma}) + \mathbf{U} \cdot \nabla (\mathbf{U} \cdot \nabla \frac{a}{\sigma}) = 0 \end{aligned} \quad (9)$$

These are the final forms of the wave equation for this numerical model study. In the present paper, we are concerned with the problems where  $W$



is assumed zero for simplicity and the mean current is in the following condition

$$|\underline{U}|^2 \ll CCg \quad (10)$$

Eq.(9) then can be simplified as follows:

$$CCg \frac{a}{\sigma} (\nabla S)^2 - (\underline{U} \cdot \nabla S - \omega)^2 \frac{a}{\sigma} + (\sigma^2 - k^2 CCg) \frac{a}{\sigma} - \nabla \cdot (CCg \nabla \frac{a}{\sigma}) = 0 \quad (11)$$

If we set  $\underline{U} = (0, 0)$ , eqs.(8) and (11) reduce to the Ebersole's(1985) model equations for depth refraction-diffraction. Further, the equation of wave action conservation for steady waves can be simply obtained from eq.(8).

The main wave direction  $\theta$  can be given from eq.(12) with the combination of eqs.(8) and (11). The irrotationality condition of wave number vector is

$$\frac{\partial(|\nabla S| \sin \theta)}{\partial x} = \frac{\partial(|\nabla S| \cos \theta)}{\partial y} \quad (12)$$

### Numerical Computation

Both eqs.(8) and (11) are of the elliptic type and can generally be solved as a boundary value problem using finite element method. If we neglect wave reflections from boundaries, and also if approximate intermediate values of wave properties can be provided at all grid points using a refraction model, the problem can be converted into an initial value problem for the wave diffraction (eg. Ebersole, 1985).

Finite difference method is adopted to solve the governing equations (8), (11) and (12). The coordinate and grid systems as shown in Figure 1 are employed. Forward difference scheme is used in x-direction and centered scheme in y-direction to approximate the eq(8), which yields the following difference equations.

$$(a_j^i)^2 b_j^i = (a_j^{i+1})^2 b_j^{i+1} + \frac{\Delta x}{2\Delta y} [(a_{j+1}^i)^2 b_{j+1}^i - (a_{j-1}^i)^2 b_{j-1}^i] \quad (13)$$

where

$$b_j^i = \left\{ \frac{1}{\sigma^2} \right\}_j^i \left[ U(\omega - \underline{U} \cdot \nabla S) + CCg |\nabla S| \cos \theta + V(\omega - \underline{U} \cdot \nabla S) + CCg |\nabla S| \sin \theta \right]_j^i$$

$$(a_j^{i+1})^2 b_j^{i+1} = \tau (a_{j-1}^{i+1})^2 b_{j-1}^{i+1} + (1 - 2\tau) (a_j^{i+1})^2 b_j^{i+1} + \tau (a_{j+1}^{i+1})^2 b_{j+1}^{i+1}$$

where  $\tau$  is Abbott's dissipative interface factor ( $0 \leq \tau \leq 0.5$ ).

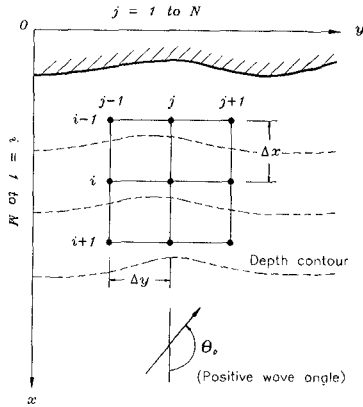


Figure 1. Definition of coordinate system, grid cell and wave angle conventions.

Eq(11) can be rearranged in the standard form of quadratic equation

$$P(|\nabla S|)^2 + Q(|\nabla S|) + R = 0 \tag{14}$$

The solution at a point (i , j) is given as follows

$$|\nabla S|_j^i = \left[ \frac{-Q + (Q^2 - 4PR)^{\frac{1}{2}}}{2P} \right]_j^i \tag{15}$$

where details of P, Q, R are given in Jeong(1990).

Differentiation eq(12) for wave direction  $\theta$  can be written as

$$\theta_j^i = \sin^{-1} \left\{ \frac{1}{|\nabla S|_j^i} \left[ \tau(|\nabla S| \sin \theta)_{j-1}^{i+1} + (1 - 2\tau) (|\nabla S| \sin \theta)_j^{i+1} + \tau(|\nabla S| \sin \theta)_{j+1}^{i+1} - \frac{\Delta x}{2\Delta y} \left\{ (|\nabla S| \cos \theta)_{j+1}^i - (|\nabla S| \cos \theta)_{j-1}^i \right\} \right] \right\} \tag{16}$$

Boundary conditions are now discussed to solve the governing equations. Input wave conditions are to be given along the offshore boundary, which are wave height, period and direction. At the side boundaries waves will be transmitted without reflection. Near the land boundary wave will break and be fully absorbed. Wave breaking criteria  $H_b = 0.78h_b$  is used for simplicity, where  $H_b$  is breaker height and  $h_b$  breaker depth.

Initial wave field is defined at all grid points using the Snell's law. For the calculation of wave diffraction we need intermediate values of wave heights and directions over the modelled area. These can be provided from a refraction model based on energy balance equation for the waves propagating on currents (eg. Chae and Song, 1986).

The computation is made row by row and proceeds toward the shoreward direction as in the method for an initial value problem.

As we use steady-wave iteration approach, the simple iterative method for the solution of the equations may have no stability restrictions (Roach, 1982). From the sensitivity analysis for the waves propagating over a circular shoal, variation of computed wave heights is less than 10% for relative grid sizes ( $L_o/\Delta x$ ) from 4 to 32 and  $L_o/\Delta x = 4$  gives the best fit to the experimental data. It can be said that the grid size of the present model does not significantly depend on wave length. However the restriction is strictly applied to parabolic models. This is one of the major advantages of the present model.

Iterative solution procedure is carried out until the solutions converge to the criterion given as follows

$$\max_{i,j} \left| \frac{(X_j^i)_{\text{new}} - (X_j^i)_{\text{old}}}{(X_j^i)_{\text{old}}} \right| < 0.005 \quad (17)$$

where  $X_j^i$  is the computed value at a grid point (i, j). Then the solutions become coupled ones with three governing equations.

The validity and accuracy of the above mentioned numerical scheme have been proved in Chae et al. (1990) through the comparison with experimental data for depth refraction-diffraction problem of monochromatic waves.

### Calculation of Wave Spectral Changes

As the present monochromatic wave model is computationally fast and stable especially for short period waves, it may be valuable to simulate spectral transformation of irregular waves propagating in water of complex bathymetry and with ambient currents. Input spectrum  $S_o(f, \theta)$  is given as below

$$S_o(f, \theta) = S_o(f) G(f, \theta) \quad (18)$$

where

$$S_o(f) = 0.25 H_{1/3}^2 T_{1/3} (T_{1/3} f)^{-5} \exp[-1.03 (T_{1/3} f)^{-4}] \quad (19)$$

is the Bretschneider-Mitsuyasu(B-M hereafter) frequency spectrum, and the directional spreading function  $G(f, \theta)$  is given by

$$G(f, \theta) = \left\{ \frac{1}{\pi} 2^{2s-1} \frac{\Gamma^2(s+1)}{\Gamma(2s+1)} \right\} \cos^{2s} \left\{ \frac{\theta}{2} \right\} \quad (20)$$

$\Gamma$  : gamma function

$$s = \begin{cases} S_{\max} \cdot (f/f_p)^5 & : f \leq f_p \\ S_{\max} \cdot (f/f_p)^{-2.5} & : f \geq f_p \end{cases} \quad (21)$$

$f_p$  : Peak frequency of  $S(f)$ , ( $f_p = 1/1.05 T_{1/3}$  used)

The frequency spectrum and directional spreading function are divided into equal segments. The lower and upper frequency limits of the spectrum are 0.07Hz and 0.37Hz.  $\Delta f = 0.02$ Hz(15 frequency bins) and  $\Delta \theta = 10^\circ$ (17 directional bins) are used.

The input wave amplitude for a particular frequency-directional component is  $a_o = [2S_o(f, \theta) \Delta f \Delta \theta]^{1/2}$ . The resulting wave amplitude at any location can be computed using the model, and then the transformed spectrum  $S(f, \theta)$  can be obtained as

$$S(f, \theta) = [a/a_o]^2 S_o(f, \theta) \quad (22)$$

### Computation Results and Analysis

To demonstrate the applicability of the model numerical computations are made for two cases. The first case is for the refraction-diffraction due to rip-current in a mildly sloping beach as shown in Figure 2(studied by Arthur, 1950).

The computational domain is divided into square grids ( $\Delta x = \Delta y = 10$  m) and numerical calculations are performed. Normal incident waves of  $H_o = 1$  m,  $T = 8$  s are used as an incident wave condition at the offshore boundary. The background(of initial and intermediate) wave field are specified using the Snell's law and the refraction routine in the program, respectively. The dimensionless wave heights  $H/H_o$  for two transections are plotted in Figure 3. For the purpose of comparison, parabolic model results(Kirby, 1984) are also shown in the same figure. A comparison of the figures shows that they are in good agreement.

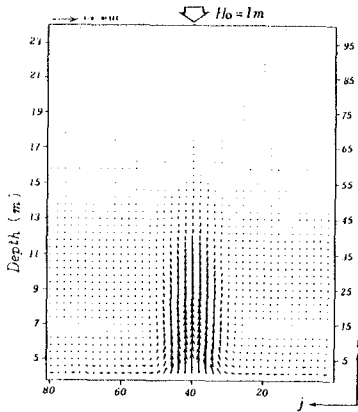


Figure 2. Rip-current field.

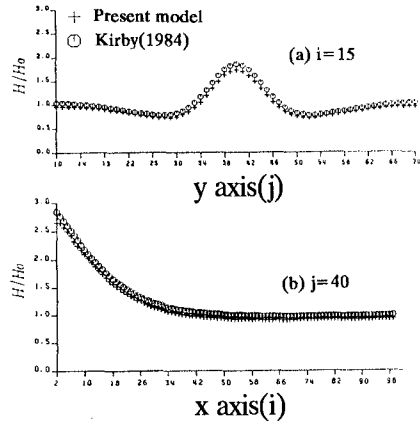


Figure 3. Wave height relative to incident wave for waves interacting with rip current.

The second case is for irregular wave propagation over a shoal as shown in Figure 4, which was recently simulated in a hydraulic laboratory equipped with multi-directional random wave generators (Hiraishi, 1991). The shoal is similar to that used in the experiments of Ito and Tanimoto (1972) with a minimum water depth of 0.05 m at the center of the shoal and constant depth (0.15 m) in the region outside the shoal. B-M spectrum is used for the input spectrum for which  $H_{1/3} = 0.1$  m,  $T_{1/3} = 1.5$  s, and  $S_{\max} = 75$  (narrow directional spectrum) are used. The grid sizes used are  $\Delta x = \Delta y = 0.1$  m. The results are presented in Figure 5, in the form of normalized wave height against the input wave height. The computations agree very well with experimental data which are for the case of non-breaking waves. As the frequency and directional spectra are not available, the comparison for those spectra between computation and experiment can not be made. However, the spectrum can be simulated by linear superposition of monochromatic wave components (eg. Panchang et al, 1990). From those comparisons, the present model appears to be used effectively for the calculation of irregular wave propagation with respects to computation accuracy and time (26 min. with IBM 386 PC).

The present model is used for the analysis of irregular wave transformation due to combined refraction-diffraction while the waves propagate over a circular shoal (Ito and Tanimoto, 1972). The input spectrum is discretized into segments of  $\Delta f$  and  $\Delta \theta$ .  $H_{1/3} = 1.0$  m and  $T_{1/3} = 5.0$  s are used for the frequency spectrum (Figure 6) and angular spreading parameter  $S_{\max} = 25$  and 75 for the broad and narrow directional spectra, respectively. Current velocity fields are generated using

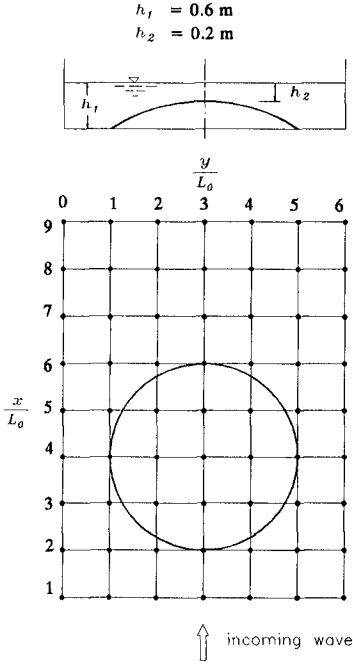


Figure 4. Experimental configuration(Hiraishi, 1991).

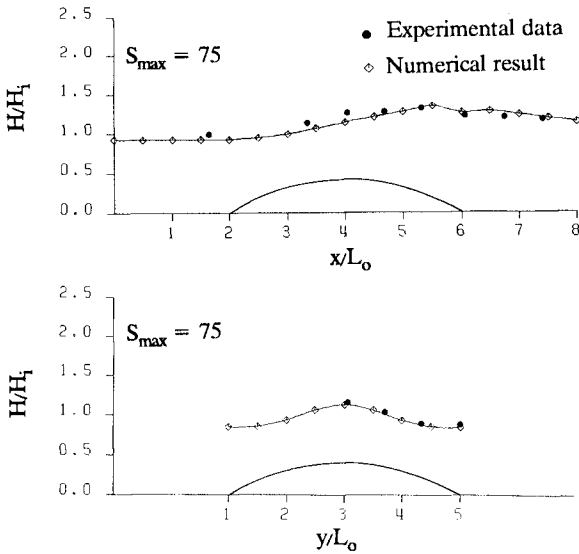


Figure 5. Comparisons between present model results and observed data.

a standard depth-averaged flow model, and assumed frozen during the wave propagation over the field. A uniform current field is assumed at the incoming boundary where the maximum velocity is 0.5 m/s.

The results are shown in Figures 6 and 7. The frequency and frequency-directional spectra are for opposing and following current conditions, and also for broad and narrow directional spreading conditions at a specified point ( $x/L_0 = 7, y/L_0 = 3$ ) behind the circular shoal.

As shown in Figure 7, we can clearly see the differences in spectral shapes of input  $S_0(f, \theta)$  depending on the value of  $S_{max}$ . The smaller value of  $S_{max}$  yields less peaky spectral shape and broader band of energy distribution than those with larger  $S_{max}$ . When the waves propagate on a current field, the wave height and direction are strongly dependent on the magnitude and direction of the current.

In the following current field the velocities over the shoal are generally larger than those in other region. This will increase the celerity and decrease focusing effect of wave rays propagating over that region, but in the opposing current the effect will be adverse. Such a wave-current interaction causes a large peak around centered direction in the opposing current field and a small peak with side humps in the following current. The waves with directionally narrow banded spectrum will produce very sharp peak, which is contributed mainly from the peak region.

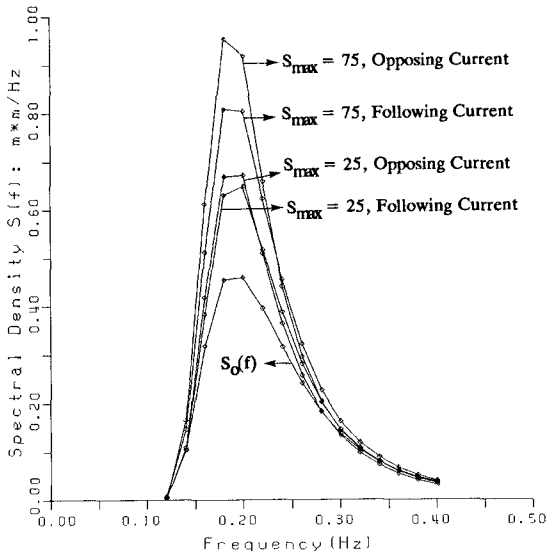


Figure 6. Input frequency spectra( $S_0(f)$ ) and output frequency spectra( $S(f)$ ) at  $x/L_0 = 7, y/L_0 = 3$ .

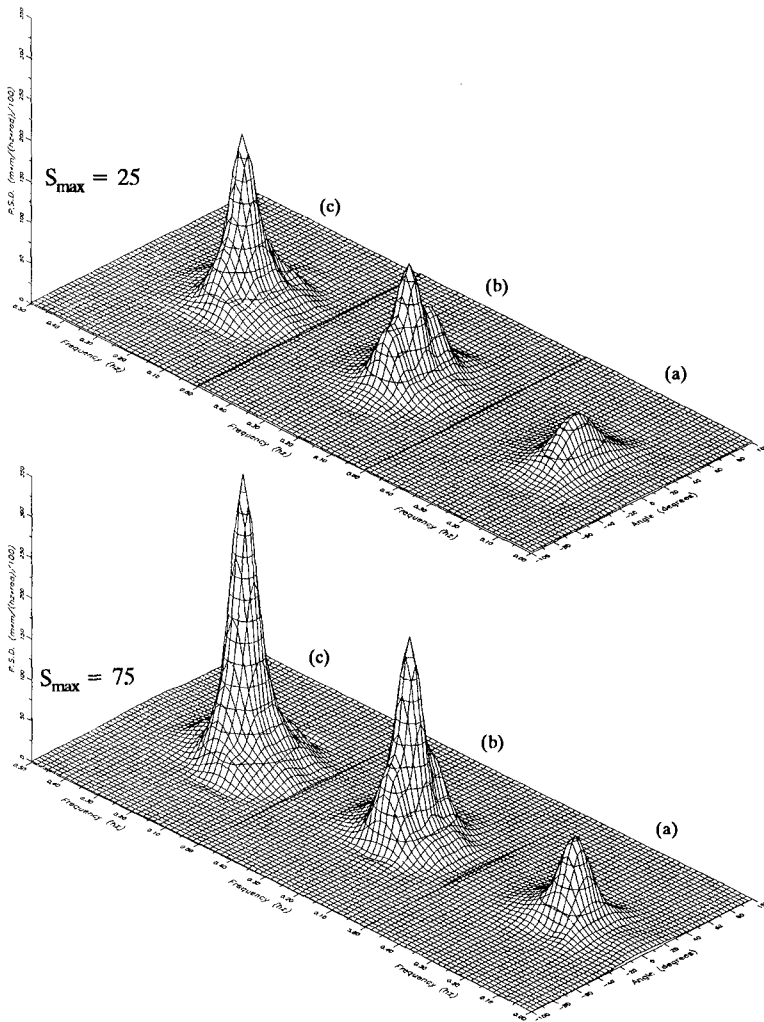


Figure 7. Input directional spectra( $S_o(f, \theta)$ ) and output directional spectra( $S(f, \theta)$ ) at  $x/L_o = 7, y/L_o = 3$  for different  $S_{\max}$  and current conditions. (a)  $S_o(f, \theta)$ , (b)  $S(f, \theta)$  with following current, (c)  $S(f, \theta)$  with opposing current.



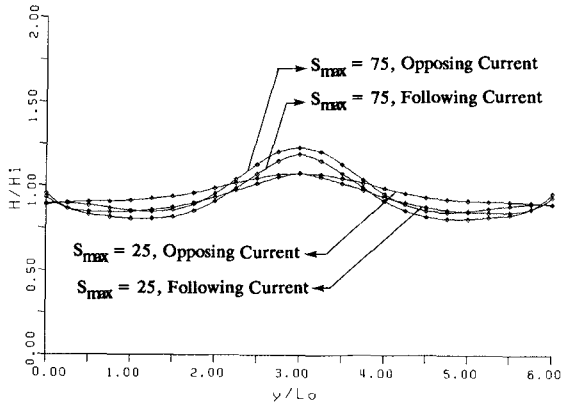


Figure 8. Wave height comparisons, for narrow and broad directional spectra.

The computed frequency spectra are shown in Figure 6. The spectral peaks are almost at the same frequency, the amplification is prominent in the peak frequency region, where the current effects are also dominant.

The propagation of wave spectra with narrow or broad directional spread shows a little difference between the wave heights in the following and opposing current conditions. The wave heights in the opposing current field are generally larger than those in the following current field (Figure 8).

### Conclusions

A set of elliptic type mild-slope equations has been derived for wave-current interactions over a slowly varying topography. Numerical computation method to solve the equations has been presented. The model solves the elliptic equations in a way similar to an initial value problems. Accuracy of numerical computation does not greatly depend on grid size. It can be said that the present model is efficient for wave propagation problems in a large coastal area. Numerical results are shown for transformation of the waves propagating on a rip-current in a mildly sloping beach. They are in good agreement with published ones (Kirby, 1984).

It is also shown that spectral transformation of irregular waves can be satisfactorily simulated by summing up the results from a monochromatic refraction-diffraction model for component waves of a spectrum. From the analysis of frequency-directional spectrum for waves propagating on currents flowing over a mound we can see large differences in spectra

depending on current directions, but there is a little difference in wave heights. When the waves propagate on strong currents in shallow water, non-linearity of the waves and wave breaking will be significant, and therefore this model should not be applied.

### References

- Arthur, R.S.(1950). "Refraction of shallow water waves: the combined effect of currents and underwater topography." *Trans. Amer. Geophys. Union*, 31(4), 549-552.
- Berkhoff, J.C.W.(1972). "Computation of combined refraction-diffraction." *Proc. 13th Int. Coast. Engrg. Conf., ASCE, Vancouver, Canada*, 471-490.
- Booij, N.(1981). "Gravity waves on water with non-uniform depth and current." Report 81-1, Dept. of Civ. Eng. Delft Univ. of Technol., Delft.
- Chae, J.W., Jeong, S.T., Yum, K.D., and Song, W.O.(1990). "Current-depth refraction and diffraction model for regular water waves." 7th Congress APD of IAHR, Beijing, China, 357-362.
- Chae, J.W., and Song, W.O.(1986). "Current-depth refraction of directional wave spectra." 5th Congress APD of IAHR, Seoul, Korea, 3, 15-34.
- Ebersole, B.A.(1985). "Refraction-diffraction model for linear water waves." *J. Wtrway. Port, Coast. Oc. Engrg., ASCE*, 111(6), 939-953.
- Hiraishi, T(1991). "Generation of multi-directional irregular waves and its application." (in personal communication).
- Ito, Y., and Tanimoto, K.(1972). "A method of numerical analysis of wave propagation - application to wave diffraction and refraction." *Proc. 13th Int. Coast. Engrg. Conf., ASCE, Vancouver, Canada*, 503-522.
- Jeong, S.T.(1990). "Wave transformations in regions of slowly varying depths with currents." PhD thesis, Dept. of Civil Eng., Seoul National Univ.
- Kirby, J.T.(1984). "A note on linear surface wave-current interaction over slowly varying topography." *J. Geophys. Res.*, 89(C1), 745-747.
- Liu, P.L.-F.(1983). "Wave-current interactions on a slowly varying topography." *J. Geophys. Res.*, 88(C7), 4421-4426.
- Ohnaka, S., Watanabe, A., and Isobe, M.(1988). "Numerical modelling of wave deformation with a current." *Proc. 21th Int. Coast. Engrg. Conf., ASCE*, 393-407.
- Panchang, V.G., Wei, G., Pearce, B.R., and Briggs, M.J.(1990). "Numerical simulation of irregular wave propagation over shoal." *J. Wtway., Port, Coast. and Oc. Engrg.*, 116(3), 324-340.
- Roache, P.J.(1982). "Computational fluid dynamics." Hermosa publishers.

## CHAPTER 9

### TRANSIENT PROPAGATION OF WAVES IN A FLUME

Kwok Fai Cheung<sup>1</sup>, Michael Isaacson<sup>2</sup>, Member ASCE, and Etienne Mansard<sup>3</sup>

#### ABSTRACT

A recently developed numerical method is applied to the study of transient, nonlinear wave propagation in a flume. The nonlinear free surface boundary conditions and the wave generator boundary condition are expanded about the corresponding equilibrium positions by perturbation expansions. The boundary conditions are then satisfied to second order by a numerical integration in time, and the field solution at each time step is obtained by an integral equation method based on Green's theorem. The propagation characteristics of regular, bichromatic and irregular waves are studied numerically, and the significance of nonlinear effects is highlighted.

#### 1. INTRODUCTION

The numerical prediction of transient wave propagation in a flume has been the subject of investigation for a number of years. To a first approximation, linear wave theory may be used to describe the transient wave field. However, there are a number of shortcomings associated with this approach, which are mainly due to the neglect of higher order forced and free wave components. Although the amplitudes of these higher order components are generally small, these may become important for wave flume and basin tests involving wave interactions with harbours, floating breakwaters or moored vessels.

To account for nonlinear effects, the transient wave problem may be treated numerically by a time-stepping procedure, in which the full nonlinear free surface boundary conditions are applied on the instantaneous free surface and a new system of simultaneous equations is generated and solved at each time step as the free surface

---

<sup>1</sup> Design Engineer, Ports and Marine Department, Sandwell Inc., 1190 Hornby Street, Vancouver, B.C., Canada V6Z 2H6.

<sup>2</sup> Professor, Department of Civil Engineering, University of British Columbia, Vancouver, B.C., Canada V6T 1Z4.

<sup>3</sup> Senior Research Officer, Hydraulics Laboratory, National Research Council of Canada, Ottawa, Canada K1A 0R8.

moves to a new position (e.g. Longuet-Higgins and Cokelet, 1976; Kim et al., 1983; and Brorsen and Larsen, 1987). On the other hand, a second-order model defined on fixed boundaries can be obtained by the application of a perturbation expansion so that a solution to the system of simultaneous equations is required only once rather than at each time step. The boundary conditions to second order are then satisfied on the corresponding equilibrium positions by a numerical integration in time. Based on this approach, Isaacson and Cheung (1991, 1992) have treated the second-order diffraction problems in two and three dimensions respectively.

The theoretical treatment for the extension of the second-order diffraction method in two dimensions to include the effects of a moving wave generator has been described by Isaacson et al. (1993). The computed free surface elevations have been validated through comparisons with experimental results. The present paper summarizes the theoretical and numerical formulations of the method, and places emphasis on numerical results for the propagation of various transient wave trains and wave packets.

## 2. THEORETICAL FORMULATION

A description of the theoretical and numerical formulations has been given in detail by Isaacson et al. (1993) and only a brief outline of the method is given here. With reference to Fig. 1, the two-dimensional problem is defined with respect to a right-handed Cartesian coordinate system  $(x,z)$ . The wave generator is located above a fixed vertical plate and extends from a distance  $h$  above the floor of the flume to the water surface. The generator may produce a combined piston/paddle motion defined by the generator's horizontal displacement  $\delta$  at the still water level together with a rotation  $\theta$  measured clockwise from the  $z$  axis. With the fluid assumed incompressible and inviscid, and the flow irrotational, the fluid motion is described by a velocity potential  $\phi$  which satisfies the Laplace equation within the fluid domain and which is subject to boundary conditions on the generator surface  $S_w$ , the instantaneous free surface  $S_f$  at  $z = \eta$ , the flume floor  $z = -d$ , and a radiation surface  $S_c$ .

When the amplitude of the wave generator displacement is small compared to the height of the generator, and the water depth is not small compared with a typical wavelength, it is possible to apply Taylor series expansions to reduce the wave generator and free surface boundary conditions, originally derived on the instantaneous surfaces, to conditions evaluated at the corresponding equilibrium positions. The problem may then be defined with respect to a time-independent domain  $D$  which is bounded by the equilibrium generator surface  $S_g$ , the still water surface  $S_0$ , the flume floor and the control surface  $S_c$ . The first-order and second-order quantities in the formulation are further separated by introducing perturbation expansions for  $\phi$  and  $\eta$  and taking the specified generator motion variables  $\delta$  and  $\theta$  to be first-order quantities:

$$\phi = \varepsilon \phi_1 + \varepsilon^2 \phi_2 + \dots \quad (1)$$

$$\eta = \varepsilon \eta_1 + \varepsilon^2 \eta_2 + \dots \quad (2)$$

$$\delta = \varepsilon \delta_1 \quad (3)$$

$$\theta = \varepsilon \theta_1 \quad (4)$$

where  $\varepsilon$  is a perturbation parameter related to the amplitude of the horizontal displacement of the wave generator which is small.

Substituting the power series representations for  $\phi$ ,  $\eta$ ,  $\delta$  and  $\theta$  into the Laplace equation and the boundary conditions, including the expanded generator and free surface boundary conditions, separate boundary value problems may be developed for each of the  $\varepsilon$  and  $\varepsilon^2$  terms in the power series. In the  $k$ -th order problem ( $k = 1, 2$ ), the potential  $\phi_k$  satisfies the Laplace equation

$$\nabla^2 \phi_k = 0 \quad \text{in } D \quad (5)$$

and is subject to the boundary conditions applied on the flume floor, the equilibrium generator surface and the still water surface. These are given respectively as

$$\frac{\partial \phi_k}{\partial z} = 0 \quad \text{at } z = -d \quad (6)$$

$$\frac{\partial \phi_k}{\partial n} = f_k \quad \text{on } S_g \quad (7)$$

$$\frac{\partial \phi_k}{\partial z} - \frac{\partial \eta_k}{\partial t} = f'_k \quad \text{on } S_o \quad (8)$$

$$\frac{\partial \phi_k}{\partial t} + g \eta_k = f''_k \quad \text{on } S_o \quad (9)$$

Here  $t$  denotes time,  $g$  is the acceleration due to gravity and  $n$  is distance in the direction of the unit normal vector  $\mathbf{n}$  directed outward from the fluid region. Each of the terms  $f_k$ ,  $f'_k$  and  $f''_k$  represents known expressions which can be evaluated from the specified motion of the wave generator and the solution at first order. In addition, the potential has to satisfy a radiation condition

$$\frac{\partial \phi_k}{\partial t} + c \frac{\partial \phi_k}{\partial n} = 0 \quad \text{on } S_c \quad (10)$$

where  $c$  is the time-dependent celerity of the radiated waves on the control surface (see Orlanski, 1976; and Isaacson and Cheung, 1991). With the boundary conditions on each of the boundaries properly defined, the solution to the boundary-value problem is obtained by the application of a boundary integral equation involving a Green's function.

Initial conditions correspond to a stationary generator and still water in the computational domain. A wave train is subsequently generated by applying a prescribed time series for the generator motion. The generator boundary condition, the free surface boundary conditions and the radiation condition, which together govern the development of the flow, are satisfied by a numerical integration in time. Since the boundaries are invariant in time, the matrix equation obtained through a discretization

of the integral equation need be inverted only once rather than at each time step, with variations in time only affecting the input vector of the matrix equation. The maximum time-step size for a given discretization and excitation wave frequency can be determined by the Courant criterion,  $c\Delta t/\Delta S \leq 1$ , where  $\Delta t$  and  $\Delta S$  denote respectively the time-step and facet sizes. This criterion has been tested numerically in the context of the second-order diffraction problem, and has been found to provide reasonable estimates (Isaacson and Cheung, 1991).

### 3. EXPERIMENTAL SET-UP AND PROCEDURE

In order to verify the present numerical model, a series of physical experiments were performed at the Hydraulics Laboratory of the National Research Council of Canada. The experiments were carried out in a flume of dimensions  $1.2 \times 1.2 \times 67$  m. A beach of uniform slope 1:25 was located at one end of the flume, and consisted of a sub-layer of coarse sand covered by a 10-cm layer of sharp stones (2-3 cm). Earlier measurements of wave reflection by the beach indicated that the reflection coefficient was below 5% over the wave frequency range 0.3 to 1.3 Hz. However, long waves with a frequency range 0.04 to 0.05 Hz encounter a relatively high degree of reflection, corresponding to reflection coefficients of the order of 40 to 50%.

The flume is equipped with a hydraulically driven wave generator which was operated in piston mode only. In the experiments described here, waves were generated in a water depth of 0.7 m and the free surface elevations at 12 different locations along the flume were monitored using twin wire capacitance wave probes. Data acquisition and analysis were performed using the Generalized Experiment control and Data Analysis Package (GEDAP; Miles and Funke, 1989) and the Real-Time Control (RTC) software packages (Crookshank, 1989). These allow all required probes to be sampled simultaneously. The sampling rate was chosen to be 0.05 sec, while the total sampling time for a typical test was chosen to be 100 sec.

### 4. RESULTS AND DISCUSSION

In the numerical and experimental results presented, a generator surface extending from the flume floor to the water surface has been adopted (i.e.  $h = 0$  in Fig. 1) and the piston mode of the generator motion has been applied (i.e.  $\theta = 0$ ). The computation was performed on an IBM 3090/150S computer at the University of British Columbia and double precision was used throughout. The variations of the free surface profiles in time and space are presented and the propagation characteristics of various transient wave trains are described. For the case of an irregular wave packet, simulated nonlinear free surface elevations at twelve different locations along the flume are compared with experimental results.

In the development of a regular or bichromatic wave train, there is a continuous influx of energy from the generator. In order to avoid an abrupt initial condition and allow a gradual development of the wave field, the periodic generator displacement is multiplied by a modulation function  $F_m$  such that the generator develops its motion gradually from zero to the prescribed amplitude over a specified modulation time  $T_m$ . For the case of regular wave diffraction to second order, testing by Isaacson and Cheung (1991) has indicated that, as a suitable choice,  $T_m$  may be taken to be equal to a typical wave period.

#### 4.1 Regular Wave Train

Prior to an examination of results for irregular waves, the development and propagation of a regular wave train in time and space are first examined. For the case considered, the wave generator undergoes a sinusoidal displacement defined by  $\delta(t) = \Delta \sin(\omega t) F_m$ , where  $\omega = 2\pi/T$  is the angular frequency,  $T$  is the wave period and  $\Delta$  is the amplitude of the generator displacement. For a given wave frequency and water depth, the value of  $\Delta$  can be related to the wave height by linear wave generation theory. Figs. 2 and 3 show the variations of the linear and nonlinear free surface profiles in space and time respectively. The incident wave conditions correspond to  $kd = 2$  and  $H/L = 0.08$ , where  $k$ ,  $H$  and  $L$  are respectively the wave number, the wave height and the wavelength of the resulting regular wave train. In the figures,  $A = H/2$  is the wave amplitude. To ensure stability of the simulation, the facet and time-step sizes were taken respectively as  $\Delta S = L/30$  and  $\Delta t = T/60$ , which correspond to a Courant number,  $c\Delta t/\Delta S = 0.5$ .

Fig. 2 shows linear and nonlinear free surface profiles along the flume at selected instants. At  $t = 0$ , the initial condition corresponds to still water everywhere in the computational domain. With the imposition of the generator motion over the first cycle, incident waves are gradually generated and propagate away from the generator at the corresponding group velocity. A steady state solution is developed near the generator after the first cycle, while the flow further from the generator takes somewhat longer to reach a steady state. It is noted that the initial waves of the wave train are unsteady with elongated lengths and smaller amplitudes, and appear to propagate at faster speeds. Without a radiation condition applied at the control surface, the reflection of these elongated initial waves would affect the flow near the test section well before a steady state solution has been developed.

Fig. 3 shows the time histories of the linear and nonlinear free surface elevations at four different locations along the length of the flume. For the location nearest to the wave generator, a stable steady-state solution for the free surface elevation is obtained for the entire period of simulation after a short duration of transient effects. Further down the flume, the duration of transient effects increases, and the initial waves are found to have longer periods as indicated above. It is also observed that a modulation is induced to the initial portion of the wave height envelope for the records at locations far away from the wave generator. At the last record, corresponding to a location 7 wavelengths away from the generator, a slight fluctuation of the free surface elevation is observed immediately after the modulation. These phenomena of wave front modulation and fluctuation have been examined analytically and similar results have been discussed by Mei (1983).

The numerical data also indicates that a system of second-order free waves at twice the incident frequency is also generated at the wave generator and propagates into the computational domain at the corresponding group velocity. These high frequency free waves are due to nonlinear interactions between the second-order free surface and the wave generator, and have also been observed in laboratory tests. Generally, the amplitude of these second-order free waves is small and does not have a significant effect on the overall wave profile. Since the numerical model is based on a second-order approach, the most obvious nonlinear effect in a regular wave train is to give rise to wave profiles with steeper crests and flatter troughs, whereas nonlinear effects on the celerity and group velocity are of higher order and cannot be reproduced here.

## 4.2 Bichromatic Wave Train

A bichromatic wave train at first order is composed of two primary harmonics propagating independently of each other, and each with a behaviour identical to a regular wave train. At second order, cross-interactions between the two harmonics give rise to a wave field which is modified to a greater extent.

Figs. 4 and 5 show the development of a bichromatic wave train in space and time respectively. The driving signal of the bichromatic wave train is obtained by adding a side-span harmonic signal to the excitation described in Section 4.1, such that the resulting signal is given by  $\delta(t) = \Delta [\sin(\omega t) + \sin(0.8\omega t)] F_m$ . Similar to the regular wave train, the bichromatic wave train develops its steady state solution rapidly. In Fig. 4, after a steady state solution has been developed, the same free surface profile repeats itself at an interval of  $5T$  near the generator, which corresponds to the beat frequency of the signal. The free surface profile is also shown to repeat itself along the flume at a fixed interval. In Fig. 5, the time histories of the free surface elevation at selected locations along the flume are found to be virtually identical after an initial duration of a transient signal, which is greater for locations further along the flume.

Nonlinear effects associated with the super-harmonic interactions are indicated in Figs. 4 and 5 at locations where the amplitude of the free surface elevation is high, giving rise to steeper crests and flatter troughs than the linear theory predictions. However, a more careful inspection of the numerical results also indicates the presence of a second-order sub-harmonic component, which is phase-locked to the wave group structure, with troughs beneath the high waves and crests in between the wave groups. In addition, low-frequency spurious free waves which are generated nonlinearly through the second-order boundary conditions are also present in the numerical solution. Although the amplitudes of these second-order components are generally small, the correct reproduction of the second-order wave field is critical in the testing of systems with relatively low natural frequencies. Such considerations have given rise to research into the development of suitable second-order control signals (e.g. Barthel et al., 1983).

## 4.3 Regular Wave Packet

The examples studied so far represent a steady-state influx of energy at the wave generator. Despite a short duration of transient effects associated with the propagation of the initial waves, a steady-state solution near the wave generator can be developed rapidly in time and space. To further illustrate transient effects in wave propagation, the development a regular wave packet is considered here.

The modulation function applied to the regular and bichromatic wave trains is modified to incorporate a gradual decline from unity to zero during the fourth cycle. The regular wave packet is then generated by applying this modulation function to the regular wave signal described in section 4.1. Figs. 6 and 7 show the development of the regular wave packet in space and time respectively. In Fig. 7, immediate adjacent to the generator at  $x/L = 1$ , the amplitude of the wave packet is quite uniform and corresponds to that of a regular wave train. Further away from the generator, the amplitude of the packet increases slightly and then decreases gradually with time and distance away from the generator. The decrease in wave amplitude is associated with an increase in the length of the wave packet as the energy is dispersed to a greater extent.



Despite the changing wave amplitude, the period and wavelength in the core of the wave packet remain relatively constant. In addition to the elongated initial waves, a trail of short waves is also observed to lag behind the packet. Nonlinear effects associated with the superharmonics are more obviously observed, especially at locations of high waves. Due to the decrease in wave amplitude, nonlinear effects also decrease with distance away from the wave generator. On the other hand, the forced and free sub-harmonic components associated with the wave packet is not clearly observed here.

#### 4.4 Irregular Wave Packet

To verify the present numerical procedure, the model has been applied to the simulation of a wave flume experiment performed at the Hydraulics Laboratory of the National Research Council of Canada. The experiment was carried out with a still water depth of 0.7 m. The generator was operated in piston mode and was used to generate an irregular wave packet by applying the generator displacement time history shown in Fig. 8. A spectral analysis of the displacement time history indicated two dominant peaks at 0.48 and 0.64 Hz. For the specified water depth of 0.7 m, these two frequency groups correspond to relative water depths  $kd = 0.92$  and  $1.32$  respectively, and to celerities  $c = 2.30$  and  $2.12$  m/s respectively. In the numerical model, the time-step and facet sizes were selected as 0.025 sec and 0.1 m respectively. On the basis of the Courant criterion, these values correspond to the capability of simulating celerities of up to about 4 m/s.

The measured and simulated nonlinear free surface elevations at twelve different locations along the flume are plotted as functions of time in Fig. 9. In general, comparisons between the numerical and experimental results indicate good agreement with respect to both the amplitude and phase, except for the portions of the records after the occurrence of the maximum amplitude. This may possibly be due to wave breaking that occurred near the generator in the experiment after the highest wave was generated. The discrepancies are first observed in the record corresponding to a location 4.11 m from the generator, with the simulated free surface elevation found to be higher than the measured elevation near time  $t = 25$  sec. These differences appear to spread to a greater extent in the records for locations further down the flume. The discrepancies between the simulated and measured free surface elevations appear to be in the form of high frequency waves which travel at slower speeds, and appear to affect the later part of the records more significantly.

Even though the high and low frequency components in the applied displacement function are generated simultaneously, in the results presented the lower frequency components with higher amplitudes and celerities propagate ahead of the higher frequency components, so that the randomness of the wave profiles as shown in Fig. 9 appears to decrease with time. Although the frequency content of the entire record (100 seconds long) measured at various locations along the flume remains basically the same, the time-histories of the free surface elevations at different locations as shown in Fig. 9 are modified more significantly. Since components of similar frequencies propagate at approximately the same speed, after a long duration of simulation the free surface profile and elevation are characterized by a series of beat phenomena with successive frequencies and amplitudes. The overall decline in wave amplitude with distance from the generator is partly attributed to the segregation of the different frequency components and partly to the amplitude dispersion of a wave packet as discussed in section 4.3.

In addition to predicting the linear and nonlinear wave fields, the present numerical model provides a useful alternative approach in the study and analysis of the various transient, nonlinear wave phenomena. A potential application of the method is to the calculation of suitable first and second-order generator control signals which may be required prior to carrying out particular flume tests.

## 5. CONCLUSIONS

A time-domain second-order method for the simulation of transient, nonlinear wave propagation in a flume is summarized. The boundary conditions are satisfied to second order by a time-stepping procedure, and the field solution at each time step is obtained by an integral equation method based on Green's theorem. Since the boundaries are invariant in time, the solution to the matrix equation obtained through a discretization of the integral equation is required only once and can be applied to different time histories of generator motion. The method is applied to a study of the transient propagation of various wave trains and wave packets.

Free surface profiles along the flume and time histories of the free surface elevation are obtained for a regular wave train, a bichromatic wave train, and regular and irregular wave packets. For the case of a regular wave train, the numerical model is shown to be stable and robust, and is capable of maintaining a steady state condition for a sufficiently long duration of simulation. The propagation of a bichromatic wave train is similar to that of a regular wave train, but includes an additional second-order sub-harmonic component. The propagation of the regular and irregular wave packets is found to be unsteady and transient, given its varying wave profile along the length of the flume. For the case of an irregular wave packet, time histories of the water surface elevation along a wave flume are compared with those predicted by the numerical model and these indicate favourable agreement. Second-order effects in transient wave propagation have been highlighted and potential applications of the second-order wave model are indicated.

## REFERENCES

- Barthel, V., Mansard, E.P.D, Sand, S.E. and Vis, F.C. 1983. Group bounded long waves in physical models. *Ocean Engrg.*, 10(4), 261-294.
- Brorsen, M. and Larsen, J. 1987. Source generation of nonlinear gravity waves with the boundary integral equation method. *Coastal Engrg.*, 11, 93-113.
- Crookshank, N.L. 1989. Experimental control and data acquisition systems at the Hydraulics Laboratory of the National Research Council of Canada. *Proc. Workshop on Instrumentation for Hydraulic Laboratories*, Burlington, Ontario, pp. 92-110.
- Isaacson, M., and Cheung, K.F. 1991. Second-order wave diffraction around two-dimensional bodies by time-domain method. *Appl. Ocean Res.*, 13(4), 175-186.
- Isaacson, M. and Cheung, K.F. 1992. Second-order wave diffraction in three dimensions. *J. Waterway, Port, Coastal and Ocean Engrg.*, ASCE, 118(5), 496-516.
- Isaacson, M., Cheung, K.F., Mansard, E. and Miles, M.D. 1993. Transient wave propagation in a laboratory flume. *J. Hydraulic Res.*, in press.
- Kim, S.K., Liu, P.L.-F. and Liggett, J.A. 1983. Boundary integral equation solutions for solitary wave generation, propagation and runup. *Coastal Engrg.*, 7, 299-317.

- Longuet-Higgins, M. and Cokelet, E.D. 1976. The deformation of steep surface waves on water. I. A numerical method of computation. *Proc. Royal Society London, Ser. A*, 350, 1-25.
- Mei, C.C. 1983. *The Applied Dynamics of Ocean Surface Waves*. John Wiley and Sons, N.Y., 740 pp.
- Miles, M.D. and Funke, E.R. 1989. The GEDAP software package for Hydraulics Laboratory data analysis. *Proc. Workshop on Instrumentation for Hydraulic Laboratories*, Burlington, Ontario, pp. 45-66.
- Orlanski, I. 1976. A simple boundary condition for unbounded hyperbolic flows. *J. Comp. Physics*, 21, 251-269.

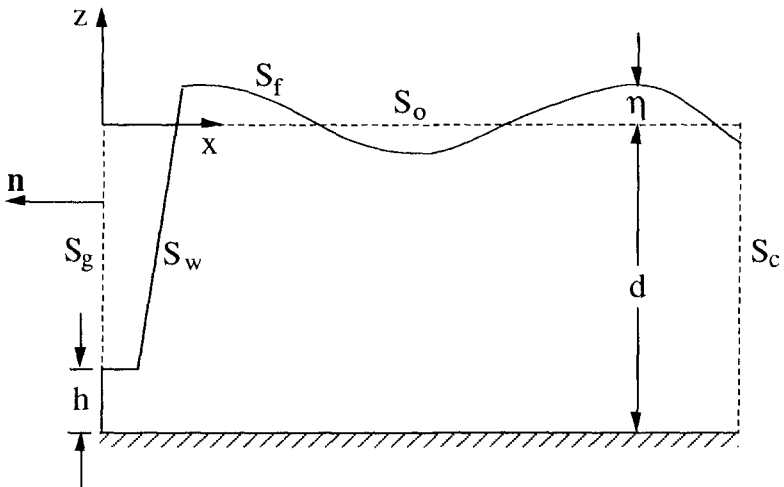


Fig. 1. Definition sketch of mathematical model.

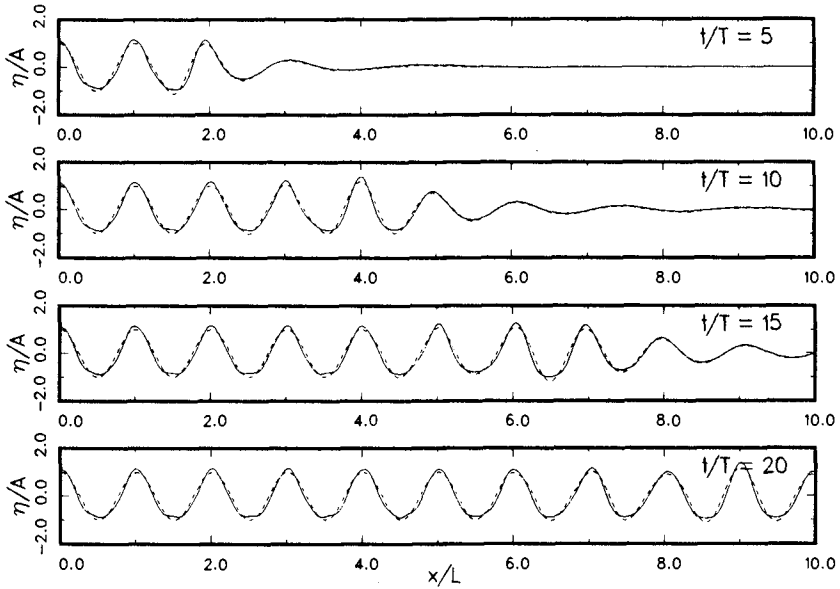


Fig. 2. Free surface profiles along the wave flume at various instants for a regular wave train. - - -, linear solution; —, nonlinear solution.

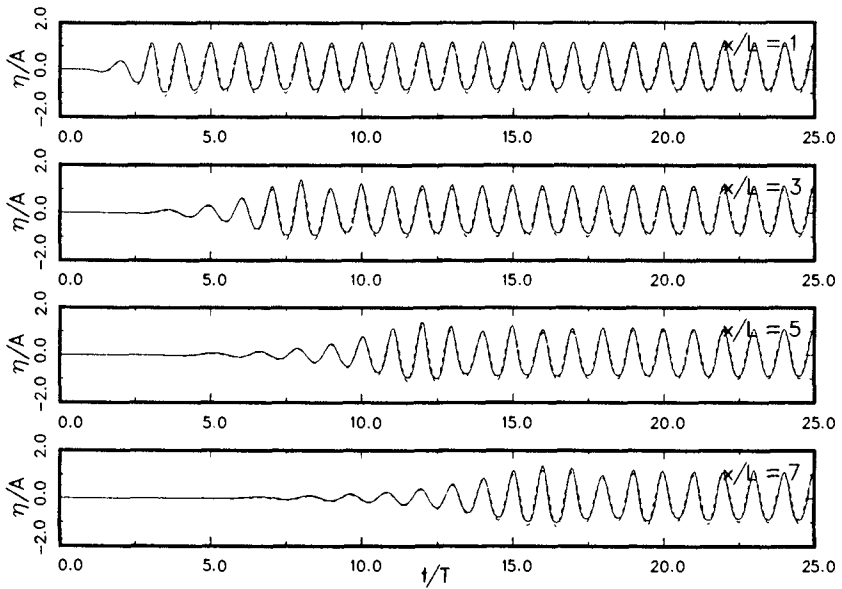


Fig. 3. Time histories of free surface elevation at various locations along the flume for a regular wave train. - - -, linear solution; —, nonlinear solution.

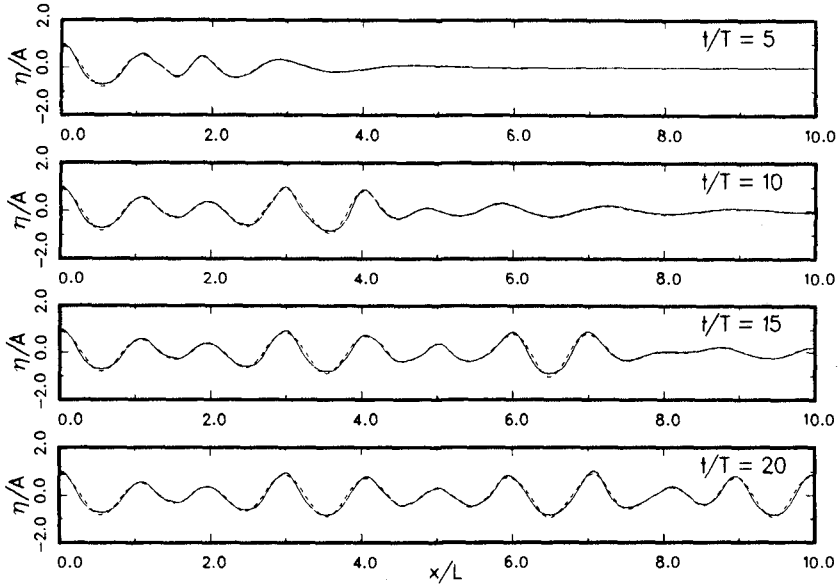


Fig. 4. Free surface profiles along the wave flume at various instants for a bichromatic wave train. - - -, linear solution; —, nonlinear solution.

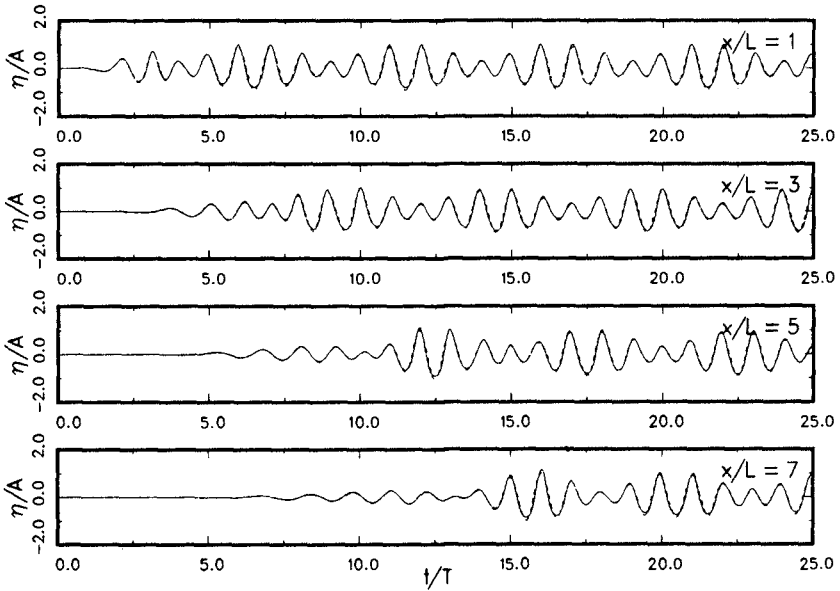


Fig. 5. Time histories of free surface elevation at various locations along the flume for a bichromatic wave train. - - -, linear solution; —, nonlinear solution.

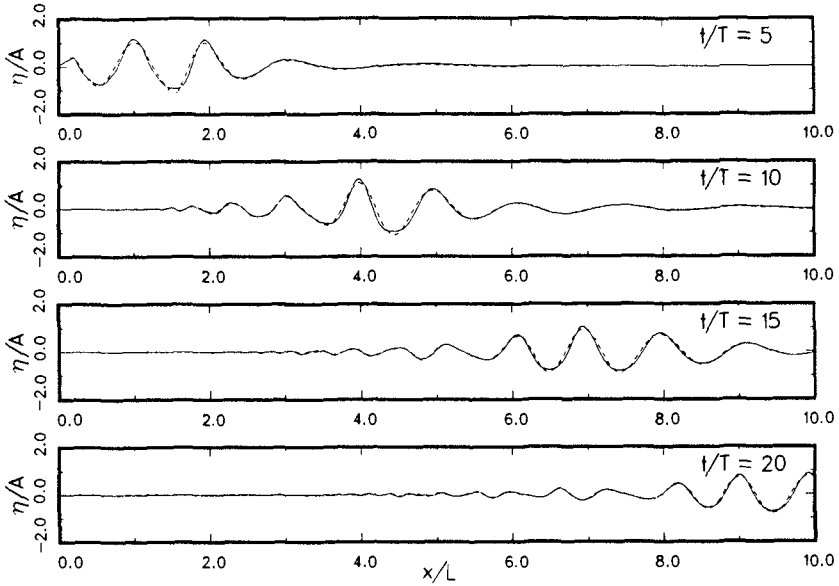


Fig. 6. Free surface profiles along the wave flume at various instants for a regular wave packet. - - -, linear solution; —, nonlinear solution.

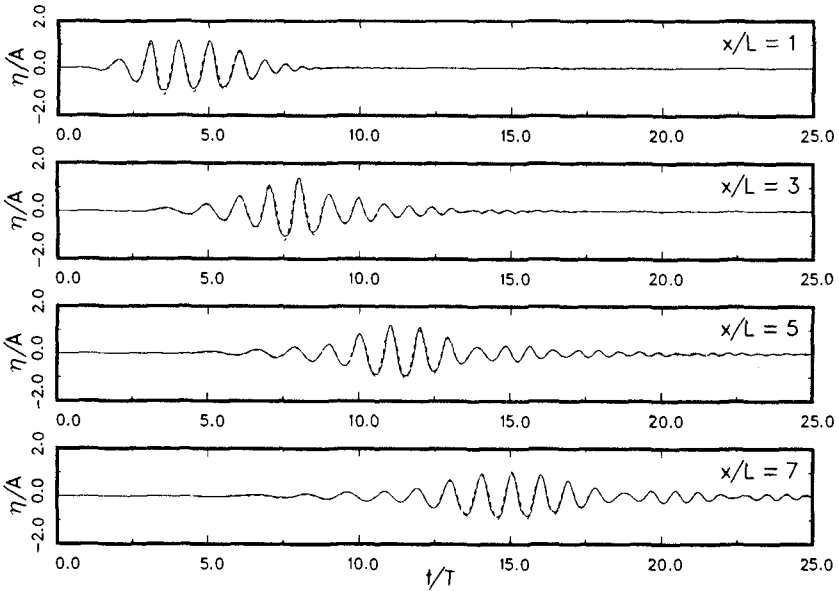


Fig. 7. Time histories of free surface elevation at various locations along the flume for a regular wave packet. - - -, linear solution; —, nonlinear solution.

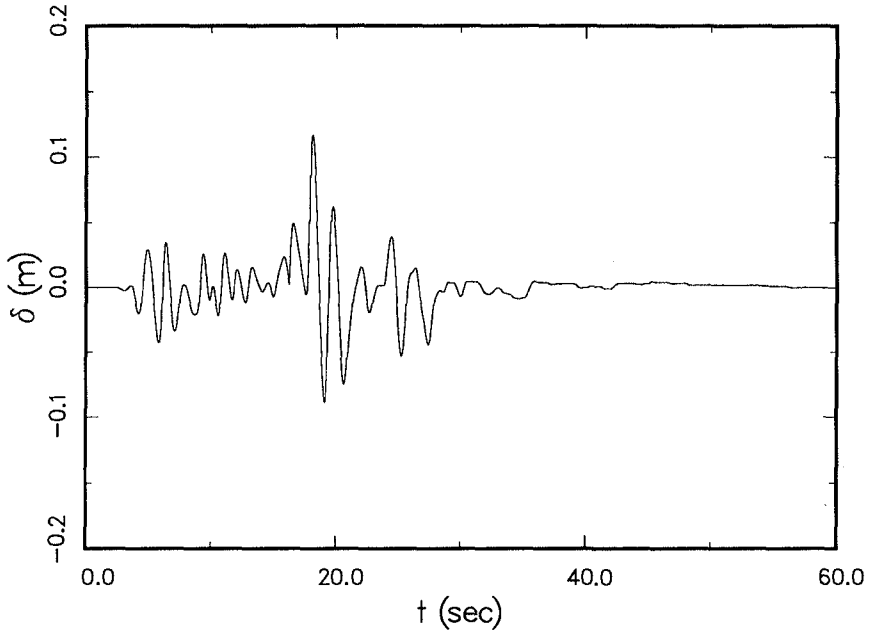


Fig. 8. Time history of wave generator displacement (piston mode) for an irregular wave packet.

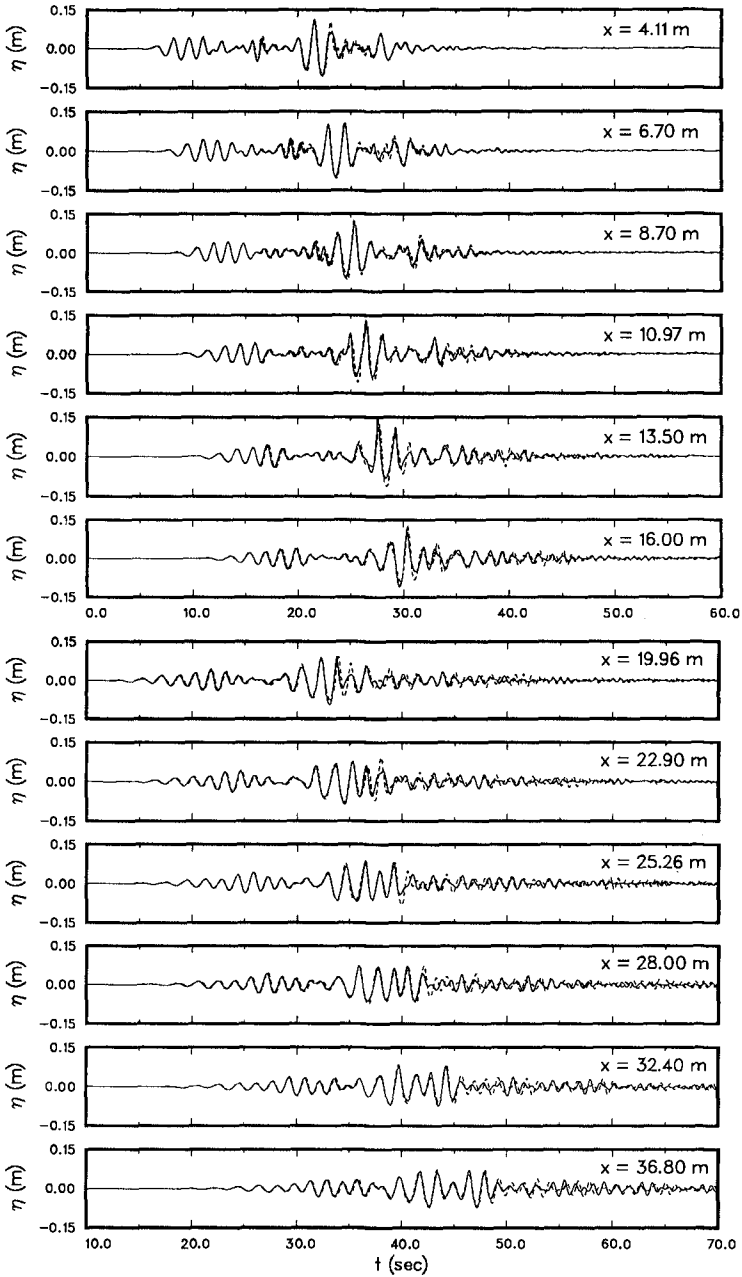


Fig. 9. Time histories of free surface elevation at various locations along the flume for an irregular wave packet. - - -, simulated; —, measured.



## CHAPTER 10

### Irregular Wave Transformation Processes in Surf and Swash Zones

Daniel T. Cox<sup>1</sup>, Nobuhisa Kobayashi<sup>1</sup> and Andojo Wurjanto<sup>2</sup>

**ABSTRACT:** A frequency-domain model is developed for elucidating the nonlinear transformation processes of the Fourier amplitudes and phases of normally incident random waves in surf and swash zones. The vertically-integrated continuity and momentum equations which have been used to describe a turbulent bore on a beach are rearranged to derive the equations expressing the cross-shore variations of the Fourier components of normally incident random waves. The derived equations are solved numerically using forcing terms computed from a previously developed time-domain model. The frequency-domain model attempts to quantify the importance of the nonlinear forcing due to the cross-shore variations of instantaneous radiation stress and bottom shear stress as well as the seaward boundary condition related to incoming low frequency waves for generating two-dimensional surf beat in the surf and swash zones.

#### Introduction

The quantitative understanding of the transformation processes of breaking or broken irregular waves is essential for predicting wave-induced currents and sediment transport in the surf and swash zones. A number of researchers (*e.g.*, Guza and Thornton, 1985) have observed that the low-frequency wave components are dominant near the shoreline of gently sloping beaches. The mechanisms by which these oscillations are generated is not fully understood. Guza and Thornton (1985) explained their observations with a standing wave model on the basis of correlations of the incident wave to measured free surface elevations and velocities in the nearshore region. Their analysis was inconclusive, however, regarding the detail mechanisms by which the incident wind waves are modulated to produce the low frequency motions. Symonds *et al.* (1982) explained the generation of low frequency waves with a time-varying breakpoint model; that is, fluctuations in surf zone width and wave setup lead to the surf beat motions. This model results in a standing wave shoreward of the breakpoint and a progressive wave radiated seaward. More recently, List (1992) proposed a model for two-dimensional surf beat to separate the contributions to the low frequency band by the bound long wave of the wave group envelope and the breakpoint-forced long wave.

In the work presented herein, a frequency-domain model is developed to quantify the importance of the nonlinear forcing due to the cross-shore variations of

---

<sup>1</sup> Center for Applied Coastal Research, Department of Civil Engineering, University of Delaware, Newark, DE 19716

<sup>2</sup> Department of Civil Engineering, Bandung Institute of Technology, Jalan, Ganesha 10, Bandung 40132, Indonesia

instantaneous radiation stress and bottom shear stress as well as the seaward boundary condition related to incoming low frequency waves.

First, the time-domain model (TDM) is briefly introduced, including the specification of the incident wave train at the seaward boundary. Next, the computed results are compared with the measured data of Cox *et al.* (1991) to show that the TDM reasonably predicts the cross-shore variation of the free surface oscillation in the shoaling and surf zones, including the generation of the low-frequency components as well as the shoreline oscillation on a mild slope for irregular waves. The formulation of the frequency-domain model (FDM) is presented in detail, including the model domain, governing equations and boundary conditions. The continuity and momentum equations used in the TDM are rearranged to obtain a linear ordinary differential equation for each Fourier component with nonlinear forcing terms resulting from the interaction of Fourier components. The linear boundary value problem for each harmonic is solved using the nonlinear forcing terms computed by the TDM to avoid solving nonlinear simultaneous equations for Fourier amplitudes and phases. The computed cross-shore variations of low-frequency Fourier amplitudes and phases of the FDM are shown to match those of the TDM. The FDM is then used to examine the effects of each of the nonlinear terms as well as the seaward boundary condition related to incoming low-frequency waves.

### Time-Domain Model

A numerical model based on the nonlinear shallow water equations including the effect of bottom friction (Kobayashi *et al.*, 1989) is probably the simplest one-dimensional, time-dependent model for predicting the nonlinear time-dependent irregular wave characteristics in the surf and swash zones. Kobayashi and Wurjanto (1992) showed that the TDM could predict available field data on shoreline oscillations fairly well. Moreover, Wise *et al.* (1991) compared the numerical model with the laboratory data of Roelvink and Stive (1989) and obtained reasonable agreement except for undertow and odd velocity moments probably because the model does not account for the vertical velocity variation and is not accurate enough to predict small values of the odd moments.

Cox *et al.* (1991) conducted a hydraulic model test in a wave flume to obtain detailed data on the cross-shore variations of the free surface oscillations and shoreline oscillation on a 1:20 smooth impermeable slope. Six wave gages were positioned in the shoaling and swash zones at  $d' = 15.0, 12.5, 10.0, 7.5, 5.0$  and  $3.0$  cm, where  $d'$  is the depth below the still water level (SWL). Additionally, a runup meter provided the time series of the shoreline oscillations. The target spectrum was based on the Pierson-Moskowitz spectrum, and the waves were generated without regard to nonlinear effects or wave reflection. The data were collected at a sampling interval of 0.04 s with a duration sufficient to include roughly 600 waves.

The seaward boundary of the time-domain model was taken at the location of the most seaward gage at  $d' = 15.0$  cm, immediately outside the breaker zone. The TDM requires that the incident wave time series and not the total time series be specified, where reflection can be significant even for mild slopes, particularly at the lower harmonics. The standard spectral technique of separating incident and reflected waves using an array of gages was not employed since the experiment was originally intended for other purposes (Cox *et al.*, 1991). Instead, the incident wave train to be specified was determined by an iterative technique based on a modification of the measured time series at  $d' = 15.0$  cm as follows. From previous work on this data set, it was estimated that the reflection coefficient was near unity for harmonics less than

half of the peak frequency and near zero for harmonics greater than half of the peak frequency. As a first approximation, the Fourier coefficients of the measured time series were modified as follows:

$$(a_n)_{\text{mod}} = \begin{cases} \frac{1}{\sqrt{2}} a_n; & n=1, 2, \dots, N_{p/2} \\ a_n; & n=N_{p/2}+1, \dots, N_{nyq} \end{cases} \quad \text{and} \quad (b_n)_{\text{mod}} = \begin{cases} \frac{1}{\sqrt{2}} b_n; & n=1, 2, \dots, N_{p/2} \\ b_n; & n=N_{p/2}+1, \dots, N_{nyq} \end{cases}$$

where  $a_n$  and  $b_n$  are the real and imaginary parts, respectively,  $N_{p/2}$  indicates the harmonic corresponding to half of the peak frequency, and  $N_{nyq}$  indicates the harmonic corresponding to the Nyquist frequency. The modified time series,  $\eta'_{\text{mod}}$ , was recovered by an inverse Fourier transform. To begin the iterative procedure, the modified time series  $\eta'_{\text{mod}}$  was specified as the incident wave time series,  $\eta'_i$ . For subsequent iterations, the computed reflected wave time series was subtracted from the assumed (modified) wave time series to obtain the new incident wave time series. After the second iteration, an incident wave time series was obtained that when added to the computed reflected wave time series nearly equaled the total measured time series at  $d' = 15.0$  cm. This incident wave time series after the second iteration is used in the following.

The reference wave height,  $H'$ , and period,  $T'$ , for normalization of the TDM computations (Kobayashi and Wurjanto, 1992) were chosen as  $H' = 6.094$  cm and  $T' = 1.72$  s, respectively, based on the spectral estimate of the significant wave height and spectral peak period of the incident wave train,  $\eta_i = \eta'_i/H'$ , at the seaward boundary. The prime denotes a dimensional quantity unless otherwise stated. The duration of the time series specified to the TDM was  $-20 \leq t \leq 520$ , where  $t$  is the time normalized by  $t = t'/T'$  and  $t = -20$  is the start of the computation. To eliminate transitional effects in evaluating the TDM and FDM, the initial part of all the time series was truncated for  $-20 \leq t < 0$ . All spectral calculations in this paper are based on the truncated time series for  $0 \leq t \leq 520$ . The corresponding band width of the normalized frequency,  $f^*$ , is  $\Delta f^* = .00192$ , where  $f^* = 1$  corresponds to the spectral peak of the incident wave spectrum. The spectra presented herein are smoothed using ensemble averaging to give 40 degrees of freedom and corresponding band width of  $\Delta f_{\text{sm}}^* = .0384$ .

The friction factor,  $f'$ , is the only empirical parameter specified to the TDM. The value  $f' = 0.01$  was used in the computed results presented herein. The model was not sensitive to  $f'$  for the range  $0.01 \leq f' \leq 0.05$  for most of the shoaling and surf zones, although it did have some effect in the swash zone where frictional effects are noticeable (Kobayashi and Wurjanto, 1992).

Figs. 1a to 1f compare the normalized spectral densities,  $S_\eta$ , of the measured and computed free surface elevation,  $\eta$ , plotted for the frequency range  $\Delta f_{\text{sm}}^* \leq f^* \leq 3.5$  at the six locations in the shoaling and surf zones. The normalized horizontal coordinate,  $x$ , is defined as  $x = x'/(T'\sqrt{gH'})$ , and the still water shoreline is at  $x = 2.26$ . The agreement in Fig. 1a, located at the seaward boundary, indicates the necessity and partial justification of the iterative technique to specify the incident wave train. It is noted that the computed results using the measured time series as the incident wave train showed an overprediction of the lower harmonics by a factor of roughly two in a figure similar to Fig. 1a. Figs. 1b to 1f show that the TDM can be used to predict the free surface oscillations of irregular waves over a mild slope, including the low frequency components. The disagreement in Figs. 1e and 1f in the low frequency components may be partly due to the measurement difficulties at small

water depths. Fig. 2 shows the measured and computed cross-shore variation of setback or setup,  $\bar{\eta}$ , as well as the node locations where the TDM output was stored. The storage of the TDM output is discussed in further detail in the next section.

Fig. 3 shows the normalized spectral densities,  $S_z$ , of the measured and computed shoreline elevation above SWL for the range  $\Delta f_{\text{min}}^* \leq f^* \leq 3.5$ . The shoreline oscillations are well predicted by the TDM over the entire frequency range of interest, and Fig. 3 shows the dominance of the low-frequency motion. The friction factor  $f' = 0.01$  is used for Fig. 3, and the computed shoreline oscillations for  $f' = 0.02$  and 0.05 were somewhat smaller than that shown in Fig. 3.

### Frequency-Domain Model

A frequency-domain model for normally incident irregular waves on a beach of arbitrary geometry but alongshore uniformity is developed herein to examine the nonlinear wave interactions and elucidate the generation mechanisms of low-frequency waves in the surf and swash zones. The FDM is based on the same continuity and momentum equations as the TDM of Kobayashi and Wurjanto (1992). These equations, where the primes indicating the dimensional variables are omitted for brevity, are rearranged as

$$\frac{\partial(\eta - \bar{\eta})}{\partial t} + \frac{\partial q}{\partial x} = 0 \quad (1)$$

$$\frac{\partial q}{\partial t} + g \bar{h} \frac{\partial(\eta - \bar{\eta})}{\partial x} + g(\eta - \bar{\eta}) \frac{\partial \bar{\eta}}{\partial x} = -g \bar{h} \frac{\partial \bar{\eta}}{\partial x} - \frac{\partial S}{\partial x} - \frac{\tau_b}{\rho} \quad (2)$$

with

$$S = qu + \frac{1}{2} g (\eta - \bar{\eta})^2 \quad (3)$$

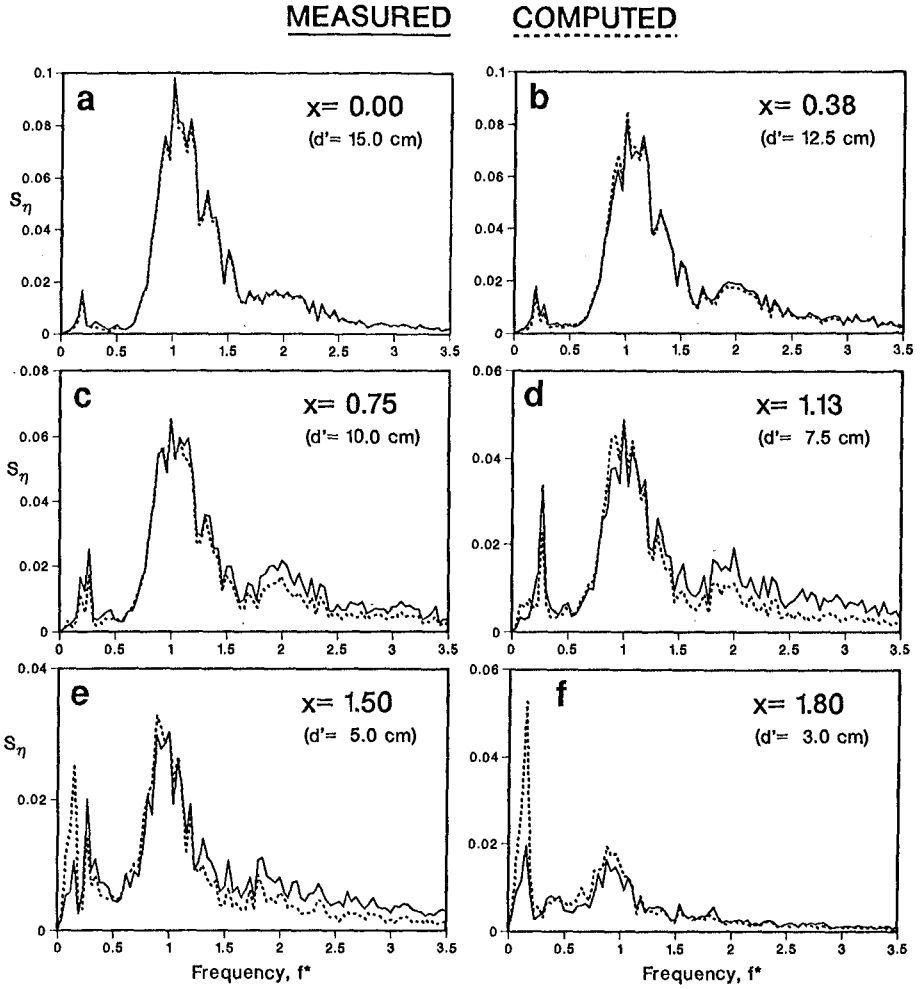
and

$$\tau_b = \frac{1}{2} \rho f' |u| u \quad (4)$$

where  $t$  = time;  $x$  = horizontal coordinate taken to be positive in the landward direction;  $\eta$  = free surface elevation above the SWL;  $q$  = volume flux per unit width;  $g$  = gravitational acceleration;  $h$  = total water depth given by  $h = (\eta + d)$  with  $d$  = water depth below the SWL;  $u$  = depth-averaged horizontal velocity defined as  $u = q/h$ ;  $\tau_b$  = bottom shear stress;  $\rho$  = fluid density; and  $f'$  = empirical bottom friction factor. The overbar in Eqs. 1–3 denotes time averaging.  $S$  defined by Eq. 3 may be termed the instantaneous cross-shore radiation stress since  $\bar{S}$  is the usual radiation stress for the adopted momentum equation (Kobayashi *et al.*, 1989). The time-averaged continuity equation obtained from Eq. 1 yields  $\bar{q} = 0$ . The time-averaged momentum equation obtained from Eq. 2 is the standard equation used to predict the wave setup  $\bar{\eta}$  where  $\bar{\tau}_b$  is normally neglected.  $\bar{\tau}_b$  is retained herein since the computed low-frequency wave motions in the swash zone may be sensitive to the bottom friction. Subtraction of the time-averaged momentum equation from Eq. 2 yields

$$\frac{\partial q}{\partial t} + g \bar{h} \frac{\partial(\eta - \bar{\eta})}{\partial x} + g(\eta - \bar{\eta}) \frac{\partial \bar{\eta}}{\partial x} = -\frac{\partial(S - \bar{S})}{\partial x} - \frac{\tau_b - \bar{\tau}_b}{\rho} \quad (5)$$

If the water depth  $\bar{h}$  below the mean water level is known, Eqs. 1 and 5 are linear in terms of the oscillatory components  $(\eta - \bar{\eta})$  and  $q$  with zero mean except for the nonlinear terms on the right hand side of Eq. 5, which account for the wave-wave interaction effects.



**Figure 1:** Smoothed spectral densities of normalized free surface elevation,  $\eta$ , as a function of normalized frequency,  $f^*$ , at six locations.

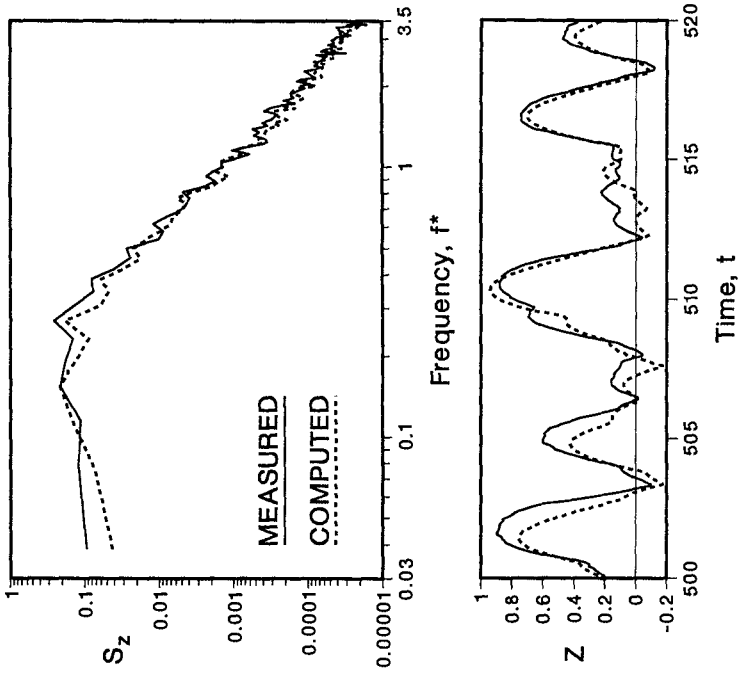


Figure 3: Smoothed spectral density  $S_z$  of normalized shoreline elevation above SWL,  $Z$ , as well as corresponding time series.

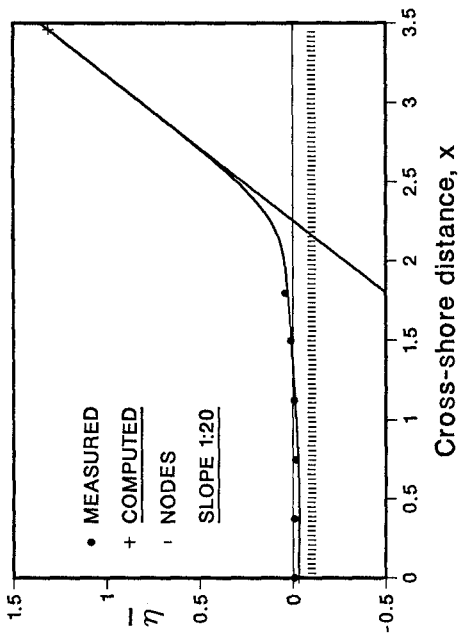


Figure 2: Cross-shore variation of normalized mean free surface elevation,  $\bar{\eta}$ , and location of nodes for storage of TDM output.

The time series  $q$ ,  $\eta$ ,  $S$  and  $\tau_b$  represented by  $v(t,x)$  in the following equation are expressed as Fourier series, viz.,

$$v(t,x) = \bar{v} + \sum_{n=1}^N \left\{ \text{Re}[v_n(x)] \cos(\omega_n t) + \text{Im}[v_n(x)] \sin(\omega_n t) \right\} \quad (6)$$

in which  $v_n(x)$  = complex Fourier coefficient with Re and Im indicating the real and imaginary parts of  $v_n$ ;  $\omega_n$  = angular frequency where  $\omega_n = 2\pi n \Delta f^*$ , for  $n = 1, 2, \dots, N$  and  $\Delta f^*$  is the frequency band width without any smoothing; and  $N$  is the number of harmonics. For the FDM proposed herein, Eqs. 1 and 5 are rewritten in terms of the complex Fourier coefficients as follows:

$$-i \omega_n \eta_n + \frac{dq_n}{dx} = 0 \quad (7)$$

$$-i \omega_n q_n + g \bar{h} \frac{d\eta_n}{dx} + g \eta_n \frac{d\bar{h}}{dx} = -\frac{dS_n}{dx} - \frac{\tau_n}{\rho} \quad (8)$$

Eliminating  $q_n$  from Eqs. 7 and 8 gives

$$g \bar{h} \frac{d^2 \eta_n}{dx^2} + g \frac{d(\bar{h} + \bar{\eta})}{dx} \frac{d\eta_n}{dx} + (\omega_n^2 + g \frac{d^2 \bar{\eta}}{dx^2}) \eta_n = -\frac{d}{dx} \left( \frac{dS_n}{dx} + \frac{\tau_n}{\rho} \right) \quad (9)$$

The resulting ordinary differential equation for each harmonic is solved using  $\bar{h}(x)$  and the complex Fourier coefficients of  $(S - \bar{S})$  and  $(\tau_b - \bar{\tau}_b)$  obtained from  $q(t,x)$  and  $h(t,x) = [d(x) + \eta(t,x)]$  computed by the TDM. As a result, the FDM in this paper is not an independent model but supplements the TDM in interpreting the computed results. For the boundary conditions,  $(\eta - \bar{\eta})$  is assumed to be given at the seaward boundary  $x = 0$ , while  $(\eta - \bar{\eta})$  is taken to be zero at the location of  $\bar{h} = 0$ . Since  $\bar{h} \geq 0$  in the region wetted by water,  $\bar{h}$  approaches zero asymptotically such that  $\bar{h} = 0$  at the maximum runup location during the specified computation duration. This formulation allows the FDM to be evaluated throughout the swash zone, past the still water shoreline (SWSL) to the point of maximum runup, *i.e.* from  $x = 2.26$  to  $x = 3.46$  in the subsequent figures. Further, Eq. 9 can be solved efficiently using a finite difference method of constant grid spacing and a tridiagonal matrix solver (*e.g.*, Press *et al.*, 1989).

The TDM was run twice. First, the model was run to locate the furthest node wetted by water and to determine the locations of the nodes where the output of  $q(t)$  and  $h(t)$  should be stored with the same sampling rate as the data collection. For the work presented here, there were 461 computational nodes in  $x$  with a spatial resolution of  $\Delta x = 0.00752$ . The model was run a second time storing  $q(t)$  and  $h(t)$  at every four nodes or 116 locations as shown in Fig. 2. Cubic splines were used to interpolate the numerical output from 116 to 461 nodes, and a standard IMSL subroutine was employed to compute the derivatives in Eq. 9.

To evaluate the FDM, a large number of harmonics were chosen from the low-frequency band. The computed results for  $f^* = 0.198$  and  $f^* = 0.258$  are shown as examples in the following. The frequency  $f^* = 0.198$  represents a harmonic for which  $x = 0$  appears to be an antinode of the cross-shore variation of  $|\eta_n|$ ; and the frequency  $f^* = 0.258$  represents a harmonic for which  $x = 0$  is nearly a node. It is noted that the FDM did not agree with the TDM for frequencies higher than about  $f^* = 0.3$ , probably due to difficulties in computing the cross-shore derivatives of the instantaneous radiation stress at higher frequencies. In the figures to follow, comparisons are made of the magnitude  $|\eta_n|$  and phase,  $\theta_n$ , where Eq. 6 for  $\eta(t,x)$  is rewritten

$$\eta(t,x) = \bar{\eta}(x) + \sum_{n=1}^N |\eta_n(x)| \cos[\omega_n t + \theta_n(x)] \quad (10)$$

with

$$|\eta_n| = \left\{ \text{Re}[\eta_n(x)]^2 + \text{Im}[\eta_n(x)]^2 \right\}^{\frac{1}{2}} \quad (11)$$

and

$$\theta_n = \tan^{-1} \left\{ \frac{-\text{Im}[\eta_n(x)]}{\text{Re}[\eta_n(x)]} \right\} \quad (12)$$

where Eq.12 is computed such that  $-\pi \leq \theta_n \leq \pi$ .

Fig. 4 shows the cross-shore variation of  $|\eta_n|$  and  $\theta_n$  from the TDM and FDM solutions with the measured data for (a)  $f^* = 0.198$  and (b)  $f^* = 0.258$ . The ability of the TDM to simulate the free surface elevations of irregular wave in the surf and swash zones is further exemplified by the agreement between the TDM solutions and measured data. It is emphasized that the TDM and FDM yield continuous solutions landward of the SWSL located at  $x = 2.26$ . The agreement between the TDM and FDM solutions shows the ability of the FDM to compute the free surface variation of lower harmonics from the nonlinear forcing of the radiation stress and bottom shear stress terms calculated by the TDM. In Fig.4a, the seaward boundary,  $x = 0$ , appears to correspond to an antinode of the free surface for a standing wave in the nearshore, with a phase shift of  $\pi$  at the nodal location near  $x = 1.3$ . Similarly, Fig. 4b shows that the TDM, FDM and measured data are in good agreement. Further, the seaward boundary nearly corresponds to a node of the free surface but the non-zero value of  $|\eta_n|$  and gradual phase shift near  $x = 1.8$  indicates that the low frequency motions are not purely standing in the inner surf zone. The FDM was reformulated to solve for the volume flux,  $q_n$ , instead of the free surface displacement,  $\eta_n$ , from Eqs.7 and 8. The reformulation was also intended to examine the sensitivity of the solutions to the number of differentiations of  $S_n$  and  $\tau_n$  with respect to  $x$ . Solutions for the cross-shore variation of the magnitude  $|\eta_n|$  and its phase  $\theta_n$  from the TDM and FDM for  $f^* = 0.258$  are shown in Fig. 5. Figs.4b and 5 further exemplify the apparent standing wave pattern with nodes of the volume flux corresponding to antinodes of the free surface displacement.

To assess the importance of the nonlinear forcing terms on the right hand side of Eq. 9, the magnitudes of the instantaneous radiation stress and bottom shear stress are examined. Fig. 6 shows the cross-shore variations of  $|S_n|$  and  $|\tau_n|$  for input to FDM for (a)  $f^* = 0.198$  and (b)  $f^* = 0.258$ . The maximum value of instantaneous radiation stress occurs in the breaker zone while the bottom shear stress may become as large as the radiation stress in the swash zone. The oscillations in Fig. 6 are probably caused by the spurious numerical oscillations in the TDM.

A primary purpose of the FDM is to assess the relative importance of the seaward boundary condition and the nonlinear forcing terms. Fig.7 shows the cross-shore variations of  $|\eta_n|$  and  $\theta_n$  from the FDM for the solutions without and with modifications to the seaward boundary condition and to the nonlinear forcing for (a)  $f^* = 0.198$  and (b)  $f^* = 0.258$ . In Fig. 7a, the FDM solution modified by specifying  $\eta_n = 0$  at  $x = 0$ , is greatly affected since  $x = 0$  corresponds to the antinode. Interpretation is somewhat limited, however, because both incident and reflected waves are affected by this boundary condition. It is interesting to note that this solution in the swash zone for  $x \geq 2.5$  is not affected by the boundary condition at  $x = 0$ , suggesting the dominance of the nonlinear forcing terms in the swash zone.



This result is consistent with all other lower harmonics examined. The FDM solution modified by zeroing both of the nonlinear forcing terms is basically unaffected except in the swash zone. This implies that the wave motion at  $f^* = 0.198$  is essentially a standing wave except in the swash zone. In Fig. 7b, the FDM is modified similarly for  $f^* = 0.258$ . Because  $x = 0$  roughly corresponds to a node of the free surface, the solution is affected only slightly by imposing the condition  $\eta_n = 0$  at  $x = 0$ . It is noted that the solution in the swash zone for  $x \geq 2.5$  is unaffected by the seaward boundary condition. By zeroing the nonlinear forcing terms,  $|\eta_n|$  is reduced, but the basic standing wave pattern is apparent with only a slight shifting of the nodal location near  $x = 1.8$ . As a whole, Fig. 7 suggests that the wave motion in the swash zone is dominated by the nonlinear forcing rather than the seaward boundary condition and that the relative importance of these two throughout the surf zone depends on the frequency.

In a further attempt to quantify the relative importance of the radiation stress and bottom shear stress, the FDM is evaluated with modifications to these two terms separately. Fig. 8 shows the cross-shore variations of  $|\eta_n|$  and  $\theta_n$  from the FDM for the three solutions without and with modification to the  $S_n$  and  $\tau_n$  terms. Fig. 8a for  $f^* = 0.198$  shows that the forcing terms do not affect the solution much, consistent with Fig. 7a. Hence, the solutions for  $S_n = 0$  or  $\tau_n = 0$  are similar except that  $S_n$  seems to be the more important of the two in the swash zone. Fig. 8b for  $f^* = 0.258$  shows that the forcing terms individually increase the magnitude  $|\eta_n|$  over most of the surf zone, whereas in Fig. 7b their combined effect is to reduce the magnitude  $|\eta_n|$  by roughly a factor of two. Additionally, Fig. 8b shows that  $\tau_n$  affects the magnitude  $|\eta_n|$  but not the phase  $\theta_n$ . For this frequency,  $S_n$  affects the phase  $\theta_n$  somewhat more.

## Conclusions

Accurate prediction of the low-frequency motions in the surf and swash zones requires specification of incident low frequency waves immediately outside the breaker zone. At present, no reliable theory is available to predict incident bound long waves immediately outside the surf zone except for the simplified model by List (1992). The TDM was shown herein to predict the temporal and cross-shore variations of the free surface elevation in the surf and swash zones fairly well; however, it does not reveal how and where low-frequency waves are generated or transformed in the surf and swash zones. Additional analyses are hence needed to interpret the computed results. The FDM was proposed to elucidate the nonlinear transformation and generation processes of the low-frequency waves in the surf and swash zones. Important to the formulation of this model was the use of  $\bar{h}$ , eliminating the singularity problem of the free surface elevation in the swash zone. The limited computation for one test run suggests that the low-frequency wave motions in the surf and swash zones appear to be standing waves, qualitatively consistent with the field data and analysis of Guza and Thornton (1985), but modified by the forcing terms associated with the instantaneous radiation stress and bottom shear stress. The degree of modifications depends on specific frequencies.

## Acknowledgment

This work is a result of research sponsored by the NOAA Office of Sea Grant, Department of Commerce under grant NA85AA-D-SG033 (SG 92 R/OE-10).

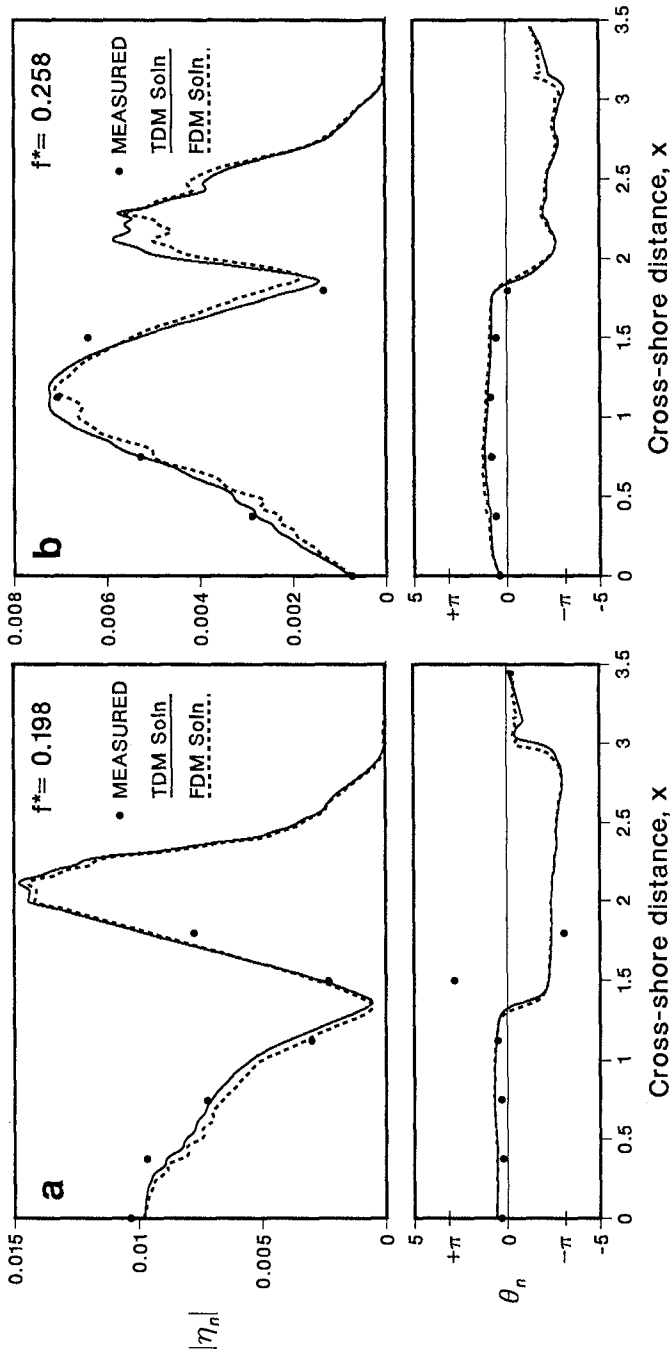


Figure 4: Cross-shore variations of magnitude  $|\eta_n|$  and phase  $\theta_n$  from TDM and FDM solutions with measured data for (a)  $f^* = 0.198$  and (b)  $f^* = 0.258$ .

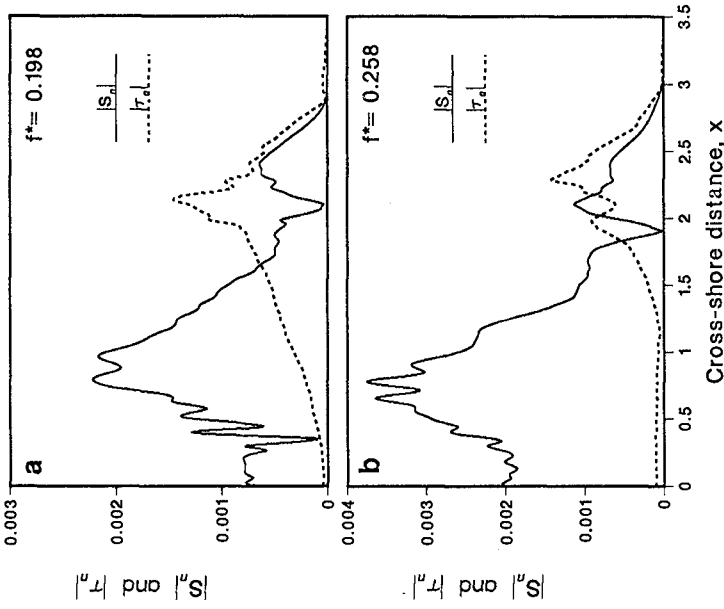


Figure 6: Cross-shore variations of magnitude  $|S_n|$  and  $|\tau_n|$  for input to FDM for (a)  $f^* = 0.198$  and (b)  $f^* = 0.258$ .

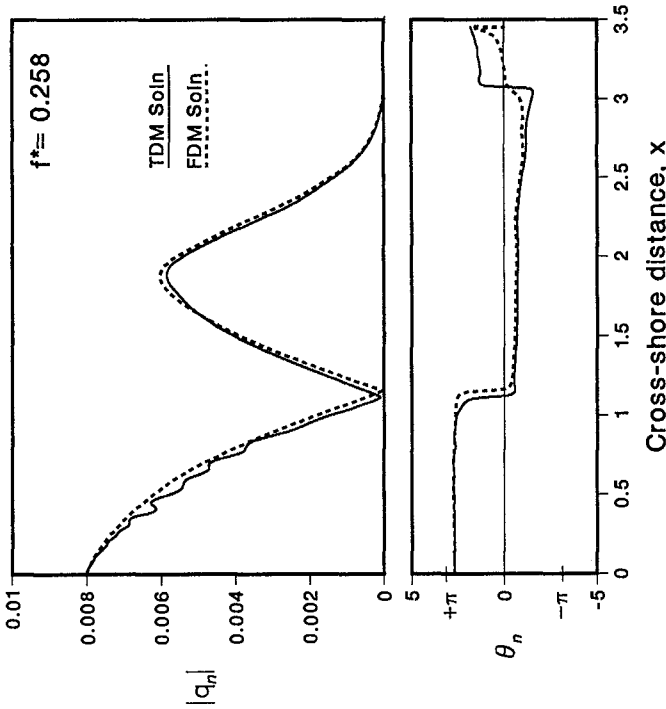


Figure 5: Cross-shore variations of magnitude  $|q_n|$  and phase  $\theta_n$  of volume flux per unit width from TDM and FDM solutions for  $f^* = 0.258$ .

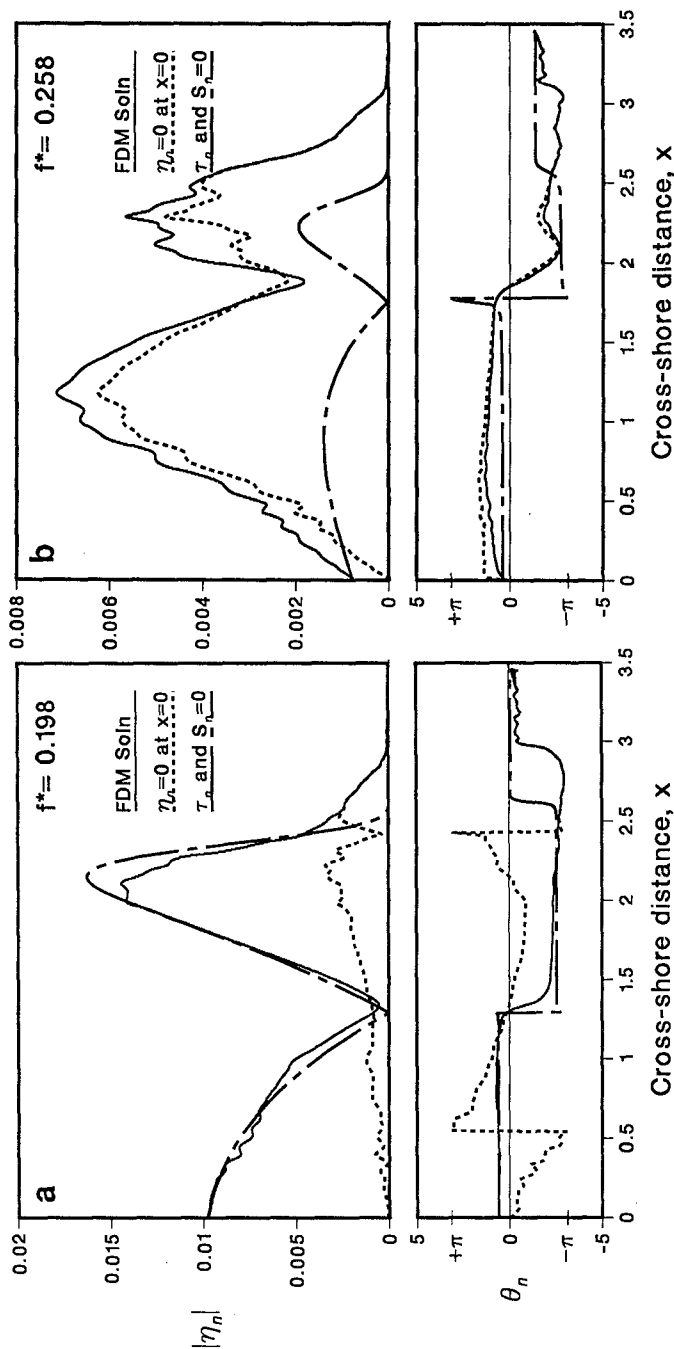


Figure 7: Cross-shore variations of  $|\eta_n|$  and  $\theta_n$  from FDM for three solutions without and with modifications to seaward boundary condition or nonlinear forcing terms for (a)  $f^* = 0.198$  and (b)  $f^* = 0.258$ .

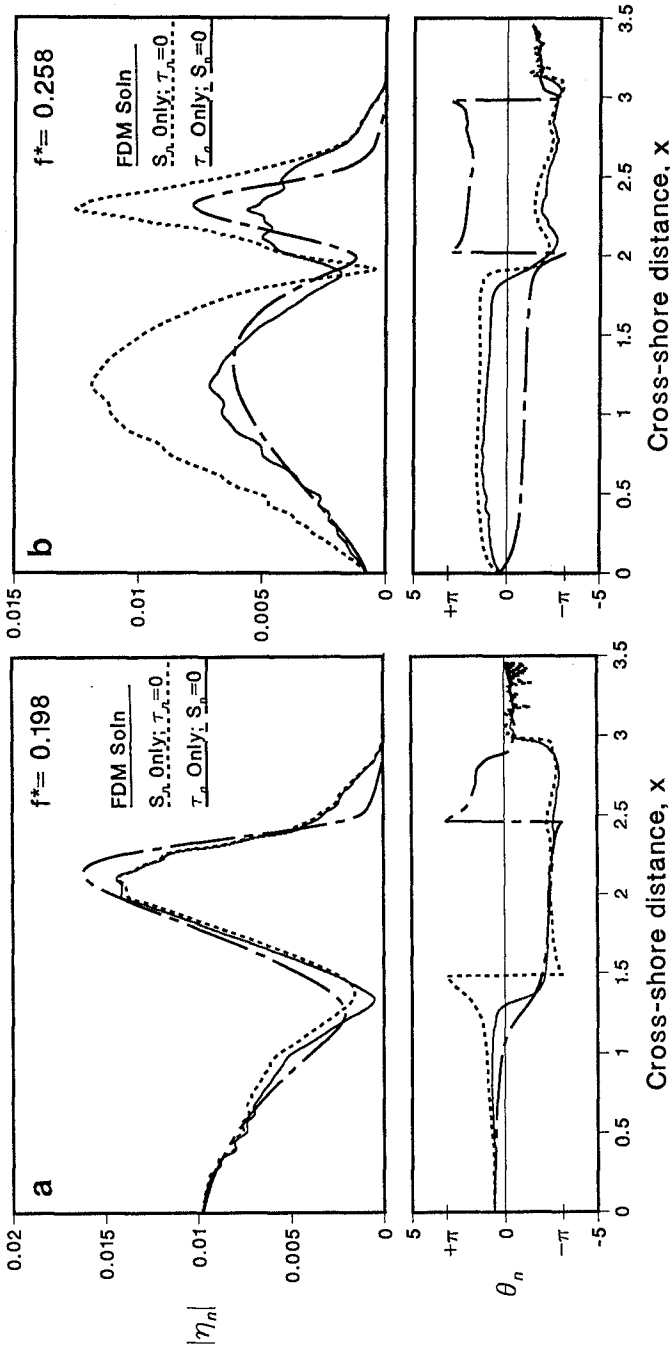


Figure 8: Cross-shore variations of  $|\eta_n|$  and  $\theta_n$  from FDM for three solutions without and with modification to radiation stress or bottom shear stress for (a)  $f^* = 0.198$  and (b)  $f^* = 0.258$ .

## References

- Cox, D.T., Kobayashi, N. and Mase, H. (1991) "Effects of fluid accelerations on sediment transport in surf zones," *Proc. Coastal Sediments '91*, ASCE, 447-461.
- Guza, R.T. and Thornton, E.B. (1985) "Observations of surf beat," *J. Geophys. Res.*, 90(C2), 3161-3172.
- Kobayashi, N., DeSilva, G.S. and Watson, K.D. (1989) "Wave transformation and swash oscillation on gentle and steep slopes," *J. Geophys. Res.*, 94(C1), 951-966.
- Kobayashi, N. and Wurjanto, A. (1992) "Irregular wave setup and run-up on beaches," *J. Waterway. Port Coast. Oc. Engrg.*, ASCE, 118(4), 368-386.
- List, J.H. (1992) "A model for the generation of two-dimensional surf beat," *J. Geophys. Res.*, 97(C4), 5623-5635.
- Press, W.H., Flannery, B.P., Teukolsky, S.A. and Vetterling, W.T. (1989) *Numerical Recipes*, Cambridge University Press, Cambridge, U.K.
- Roelvink, J.A. and Stive, M.J.F. (1989) "Bar-generating cross-shore flow mechanisms on a beach," *J. Geophys. Res.*, 94(C4), 4785-4800.
- Symonds, G., Huntley, D.A. and Bowen, A.J. (1982) "Two-dimensional surf beat: Long wave generation by a time-varying breakpoint," *J. Geophys. Res.*, 87(C1), 492-498.
- Wise, R.A., Kobayashi, N. and Wurjanto, A. (1991) "Cross-shore sediment transport under irregular waves in surf zones," *Proc. Coastal Sediments '91*, ASCE, 658-673.

## CHAPTER 11

### Numerical Modelling of Waves and Currents with regard to Coastal Structures

M. Fischer  
J. Juhl  
E.B. Rasmussen<sup>1</sup>

#### Abstract

This paper describes a two-dimensional numerical model capable of simulating non-stationary flows. Special emphasis has been put on wave motion on and in porous structures, e.g. a rubble mound breakwater. Comparisons of numerical simulations with analytical solutions and model test results have confirmed the applicability of this model for studies of waves and currents with regard to coastal structures.

#### Introduction

In the past coastal structures such as breakwaters mainly have been studied by means of physical modelling and simplified numerical calculations. Recent developments in numerical techniques and methods, however, have implied that advanced numerical tools may be adopted in such studies. These numerical models dedicated to coastal structures are still in their infancy but likewise other branches of the hydraulics it is envisaged that numerical models will play an increasing role in future studies.

In the present paper, a special 2D (x-z) version of Danish Hydraulic Institute's three-dimensional model is described. Details on the three dimensional model

---

<sup>1</sup> Danish Hydraulic Institute, Agern Allé 5,  
DK-2970 Hørsholm, Denmark

adapted here are given in Rasmussen et al. The x-z version is designed especially for flow with regard to coastal structures and porous media. The numerical model is based on the Reynolds-averaged Navier-Stokes equations and the equation for conservation of mass. The equations are discretized into a finite difference scheme imposed on a rectangular, space-staggered grid. The finite difference equations are solved through a non-iterative ADI (Alternating Directions Implicit) technique using the artificial compressibility method.

The energy loss due to both laminar and turbulent effects in porous media is included through the Forchheimer equation. Furthermore, an inertia term has been included in the Forchheimer equation for the case of non-stationary flow.

The free surface boundary in the model has been described applying a subgrid modelling in which the instantaneous position is calculated for each time step by use of linearized momentum equations and kinematic boundary conditions. This implies that the computational domain varies from time step to time step.

The numerical model is applicable to a large range of both dynamic and stationary flow problems with regards to coastal structures such as flows in breakwaters consisting of layers with different porosity, flows through and/or beneath dams and stability of slopes etc. protected by impermeable surface layers likewise.

Model simulations have been compared with both analytical solutions and physical model tests.

### Description of Flows in Porous Media

It is common to apply a macroscopic point-of-view of a porosity layer by describing the porous matrix through characteristic constants. These properties are related both to the fluid and to the granular material in order to describe the penetration of the fluid. This implies that the basic problem is reduced to establish a relation between the pressure gradient and the bulk velocity.

It can be argued as to whether this description is suitable or a microscopic point-of-view is needed. However, such an approach would imply the necessity of a description of each stone with connected geometry and roughness factors. Furthermore, highly sophisticated



turbulence descriptions would be required. This leads to unrealistic demands to both model set-up for a simulation of flow in porous media and to the performance of the model itself, since the computational grid should be very fine in order to produce the required resolution of the geometry.

A breakwater normally consists of three porous layers, i.e. core, filter, and armour layer. This implies the necessity of a porosity description, in which multiple layers with different properties can be specified. Physical model tests have shown the necessity of a description of the energy dissipation including both laminar and turbulent flow as well as energy dissipation due to dynamic effects.

The relation between the bulk velocity,  $u$ , and the pore velocity,  $V$ , is given by

$$u = V \cdot n$$

where  $n$  is the porosity.

#### Forchheimer equation

The Forchheimer equation consists of two terms expressing the hydraulic gradient due to both laminar and turbulent flow, respectively

$$i = a \cdot u + b \cdot u^2$$

where,

- $i$  is the hydraulic gradient
- $a$  is the laminar dissipation factor
- $b$  is the turbulent dissipation factor

Since the linear term,  $a$ , accounts for the laminar effects, it depends on the viscosity. The non-linear term,  $b$ , represents the fully turbulent flow and is only dependent on the granular matrix material.

Several relationships of  $a$  and  $b$  have been proposed in the literature, of which many have been based on a dimensional analysis. In the presented model the relationship proposed by Engelund has been adopted. The laminar and turbulent dissipation terms are described by the constants  $a$  and  $b$ :

$$a = \alpha \cdot \frac{(1-n)^3 \cdot \nu}{n^2 g d^2}$$

$$b = \beta \cdot \frac{(1-n)}{n^3 g d}$$

where

$\nu$  is the viscosity of the fluid  
 $g$  is the gravity  
 $d$  is the stone diameter  
 $\alpha$  is an empiric constant  
 $\beta$  is an empiric constant

The formulation of the hydraulic gradient presented above is only valid for a steady state flow. A model for unsteady flow would be to add a time dependent term to the Forchheimer expression

$$i = a \cdot u + b \cdot u^2 + c \cdot \frac{\partial u}{\partial t}$$

The factor  $c$  can be expressed in the following way:

$$c = \frac{\left(1 + \gamma \cdot \frac{(1-n)}{n}\right)}{g}$$

where  $\gamma$  is the inertia coefficient.

### Implementation of porosity description

The model presented solves the Reynolds-averaged Navier-Stokes equations and the continuity equation in a staggered finite difference grid. The prognostic variables are the three velocity components together with the fluid pressure. The adopted porosity description is based on macro parameters of porosity, stone size and dissipation factors. The implementation of this macro scale porosity description involves two changes to the original balance equations

- 1) Redefinition of terms including velocity with respect to the influence of the porosity.

- 2) Adding of dissipation terms due to the microscopic flow resistance, i. e. flow between stones. The expression given by Forchheimer together with an additional term for the dynamic effect is applied.

The continuity equation reads

$$\frac{1}{\rho \cdot c_s^2} \cdot \frac{\partial p}{\partial t} + \nabla \cdot V_i = 0$$

where,

$\rho$  is the density  
 $c_s$  is the speed of sound  
 $p$  is the excess pressure  
 $V$  is the pore velocity

The momentum equation reads after introduction of the bulk velocity:

$$c \cdot \frac{\partial u_i}{\partial t} + \frac{1}{n^2} \cdot u_j \cdot \frac{\partial u_i}{\partial x_j} =$$

$$-\frac{1}{\rho} \cdot \frac{\partial p}{\partial x_i} - g_i - g \cdot a \cdot u_i - g \cdot b \cdot |u_i| \cdot u_i + \frac{1}{n} \cdot \frac{\partial}{\partial x_j} \left( E \cdot \frac{\partial u_i}{\partial x_j} \right)$$

where E is the eddy viscosity

### Free Surface Description

The applied free surface description of waves is presented in the following. The method is inspired by the VOF method proposed by Nichols and Hirt but splits the volume fraction into space increment fractions in the three coordinate directions, and can as such be considered as a surface tracking method rather than a volume tracking method.

The presented description includes three dependent variables in addition to the velocity components and the fluid pressure. The variables noted  $\alpha$ ,  $\beta$  and  $\gamma$  represent fractions of space increments in the x-, y- and z-direction, respectively, and thus describe the location of the free surface within the current grid cell, see Fig. 1. In the present model the instantaneous position of the water is directly calculated, which is the main difference to the VOF method. The fraction of volume in each cell can be found as

$$V = \alpha \cdot \beta \cdot \gamma$$

A free surface cell is identified as a cell containing a non-zero value of  $V$  and having at least one neighbouring cell that contains a zero value of  $V$ . Cells with zero  $V$  values are empty cells whereas cells with non-zero  $V$  values are treated as full or interior fluid cells.

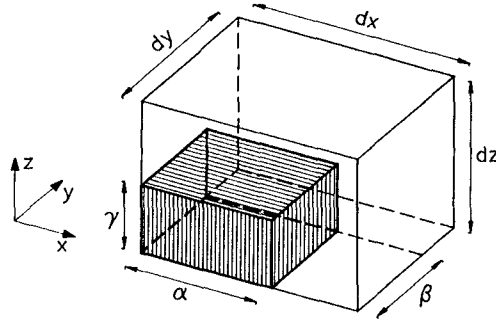


Fig. 1 Description of the free surface by a fraction of volume of fluid technique. The corners represent pressure nodes. For the two-dimensional description  $\beta = dy$ .

Briefly, the basic procedure for advancing a solution in time consists of three steps:

- 1) From the previous time step the dependent variables form the basis for a new discretisation of the conservation of mass and the conservation of momentum equations. The system is solved implicitly taking into account closed boundaries, open boundaries and free surface boundaries.
- 2) By use of the fractions calculated in the previous time step and on the basis of the newly found dependent variables the fractions  $\alpha$ ,  $\beta$  and  $\gamma$  are computed.
- 3) Finally, the fractions defining fluid regions must be used to update the fluid taking into account the fluid in the adjacent cells and the boundaries of the computational domain.

The theory presented in the following is developed in three dimensions. For reasons of simplicity the implementation of the free surface into the three-dimen-

sional model has been done in two dimensions only - one horizontal and one vertical direction.

### The Continuity Equation

In general the continuity equation reads

$$\frac{\partial \rho}{\partial t} + \frac{\partial}{\partial x} (u\rho) + \frac{\partial}{\partial y} (v\rho) + \frac{\partial}{\partial z} (w\rho) = 0$$

where  $\rho$  is the density and  $u$ ,  $v$  and  $w$  are the velocity components.

In order to obtain a hyperbolicly dominated system the pressure is introduced into the continuity equation through an equation of state.

$$\frac{1}{\rho c_s^2} \cdot \frac{\partial p}{\partial t} + \frac{\partial u}{\partial x} + \frac{\partial v}{\partial y} + \frac{\partial w}{\partial z} = 0$$

where  $c_s$  is the speed of sound and  $p$  the excess pressure. In the top layer of the computational domain a cell may not be full of fluid. To obtain the continuity equation for the computational cell at the surface an integration over the fraction of fluid volume is done:

$$\frac{1}{\alpha \beta \gamma} \int_0^\gamma \int_0^\beta \int_0^\alpha \left( \frac{1}{\rho c_s^2} \cdot \frac{\partial p}{\partial t} + \frac{\partial u}{\partial x} + \frac{\partial v}{\partial y} + \frac{\partial w}{\partial z} \right) dx dy dz = 0$$

The result of this integration is the continuity equation described in terms of the fractions of volume

$$\frac{1}{\rho c_s^2} \cdot \frac{\partial p}{\partial t} + \frac{\partial u}{\partial \alpha} + \frac{\partial v}{\partial \beta} + \frac{\partial w}{\partial \gamma} = 0$$

The compressibility of the fluid is expressed by the speed of sound  $c_s$ . In order to make the coefficient matrix of the system diagonally dominated, an artificial value of  $c_s$  should be used.

### The Momentum Equations

The conservation of momentum reads:

$$\frac{\partial u_i}{\partial t} + \frac{\partial(u_i \cdot u_j)}{\partial x_j} = -\frac{1}{\rho} \cdot \frac{\partial P}{\partial x_i} + g_i + \frac{\partial}{\partial x_j} \left( E \cdot \frac{\partial u_i}{\partial x_j} \right)$$

where  $u$  is the velocity,  $P$  the total pressure,  $\rho$  the density,  $g$  the gravity and  $E$  the eddy viscosity of the fluid.

For reasons of simplicity regarding the space and time discretisation only the linear momentum equations are modelled in the surface cells.

The applied momentum equation for a cell containing a free surface in the  $x$ -direction reads

$$\frac{\partial u}{\partial t} = -\frac{1}{\rho} \cdot \frac{\partial}{\partial x} (p + \rho gh)$$

where  $h$  is the local, vertical distance to the surface.

#### Wave Boundary Condition

In order to make simulations of wave impacts on coastal structures an open boundary condition forming propagating waves in the simulation area has been developed. The wave boundary is a mixture of the general Dirichlet type boundary conditions of velocity and level boundaries in the sense that both the level and the velocity are specified. This is presently done by applying a first order wave theory.

#### Verifications and Simulations

A number of simulations have been performed in order to verify and study the applicability of the model. A few examples are shown in the following:

##### Simulation of Steady State Flow in Porous Media

Verification of the porosity description in the case of steady state flow is carried out by a comparison to experimentals made by Burcharth. The characteristic flow properties, such as the hydraulic gradient and the discharge velocity, have been measured in the case of penetration of water through three different gravel materials. For all three cases the principle model set-up both for the experimentals and for the numerical simulations is shown in Fig. 2.

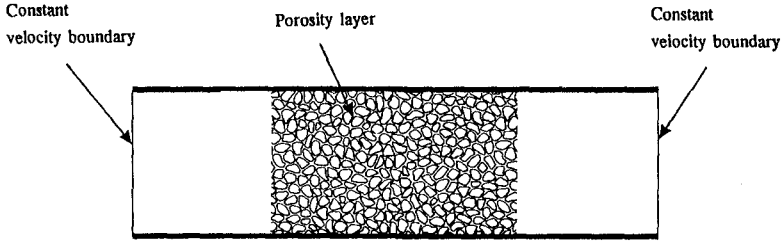


Fig. 2 Model set-up for steady state flow through a porous layer.

The comparison is done in accordance with the following description:

- 1) Since the hydraulic gradient is given as

$$i = a \cdot u + b \cdot |u| \cdot u$$

where,

- $i$  is the hydraulic gradient
- $a$  is the laminar dissipation factor
- $b$  is the turbulent dissipation factor
- $u$  is the bulk velocity

a straight line is expected when  $(i/u)$  is plotted against  $u$ . The slope of the line equals  $b$  and the intersection with the  $(i/u)$ -axis equals  $a$ .

- 2) For the experimentals  $a$  and  $b$  are deduced as described above. In accordance with the Forchheimer expression and by use of the properties of the gravel material measured by Burcharth the dissipation factors  $\alpha$  and  $\beta$  are deduced. For the case of steady state flow the dynamic dissipation term equals zero.
- 3) With the properties of the gravel material and the fluid, simulations of the flow through a porous layer is carried out. Velocity boundaries with a constant value are imposed at both ends of the model area. For each of the three gravel materials the boundary velocity is varied in order to obtain a suitable number of points. The simulations are made with "full slip" closed boundaries, which implies that the pressure gradient is zero outside the porous layer. For all the simulations the kinematic viscosity of the fluid equals  $1.34 \cdot 10^{-6}$

$m^2/s$ , which is in accordance with the viscosity of the water used by Burcharth.

- 4) The comparisons of the experimentals and the numerical simulations for two of the gravel materials are shown in Fig. 3.

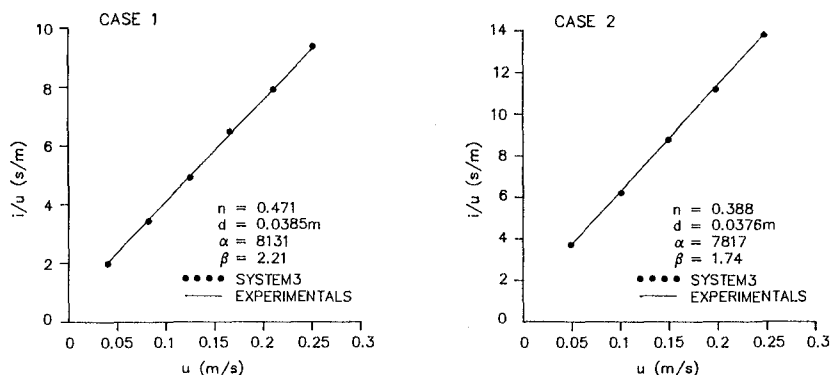


Fig. 3 Comparisons of experimentals and numerical simulations for two cases of steady state flow.

The comparisons show that the model, including a bulk description of the porosity layer, is able to reproduce the measurements for the case of steady state flow.

Simulation of a dam break

Testing of the free surface description is done by simulation of a dam break. Initially a column of water is confined between two vertical walls. When the calculation starts the right wall is removed, and gravity forces the fluid to propagate along the dry floor.

At the beginning of the simulation the fluid is described by  $20 \times 20$  cells with a size of 0.1 m in both the vertical and horizontal direction. The applied time step is 0.01 sec. Examples of results showing the fluid position and the velocity is presented in Fig. 4.

Experimental results for a dam break test case have been reported by Martin and Moyce and form a basis for a comparison to the model generated results.



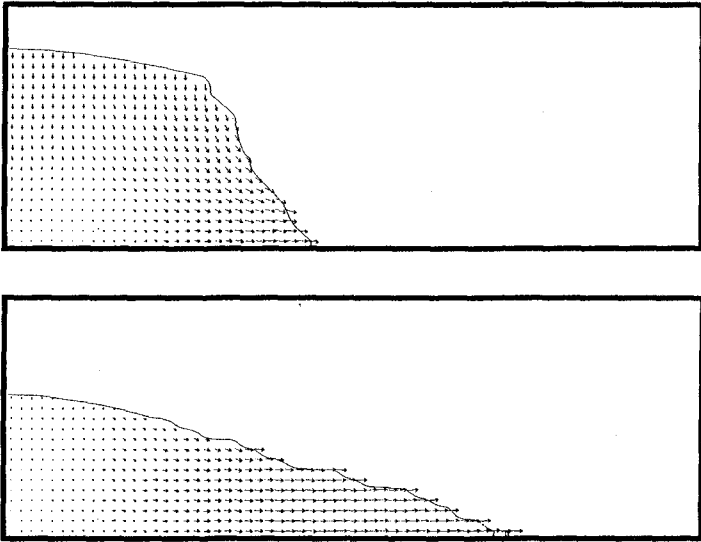


Fig. 4. Example of results for the dam break test. The plots represent the surface location and the velocity for each grid node at time 0.3 sec. and 0.7 sec.

A comparison between model generated results and the experimental results of the toe position vs time is shown in Fig. 5. The largest deviation from the experimental results is everywhere less than one grid spacing.

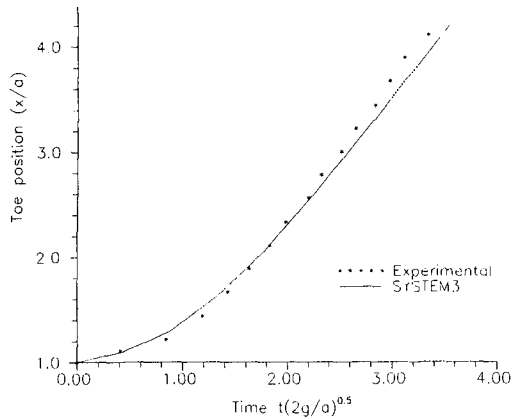


Fig. 5 Comparison of a numerical simulation with experimental data for a dam break.

Wave Run-Up on a Permeable Structure

The combination of porosity layers and a free surface is tested by simulation of wave run-up on a rubble mound breakwater. The breakwater has a sea side slope of 1:2.0 and consists of three porosity layers with the following characteristics:

- a = 14.4, 4.9, 2.0 s/m
- b = 1820.0, 109.0, 50.0 (s<sup>2</sup>/m<sup>2</sup>)
- c = 0.0, 0.0, 0.0
- n = 0.35, 0.37, 0.39

The model grid consists of 100 x 3 x 50 nodes and the general parameters of the simulation are:

$$\Delta x = \Delta y = \Delta z = 0.015 \text{ m}$$

$$\Delta t = 0.002 \text{ sec}$$

At the right end of the model area a wave boundary is applied with the following parameters:

$$H = 0.06\text{m}, T = 1.0\text{s}$$

The still water depth for the simulation is 0.3 m.

An example from a model simulation is shown in Fig. 6. Time series plots of horizontal velocities in three points (as defined in Fig. 6) are shown in Fig. 7.

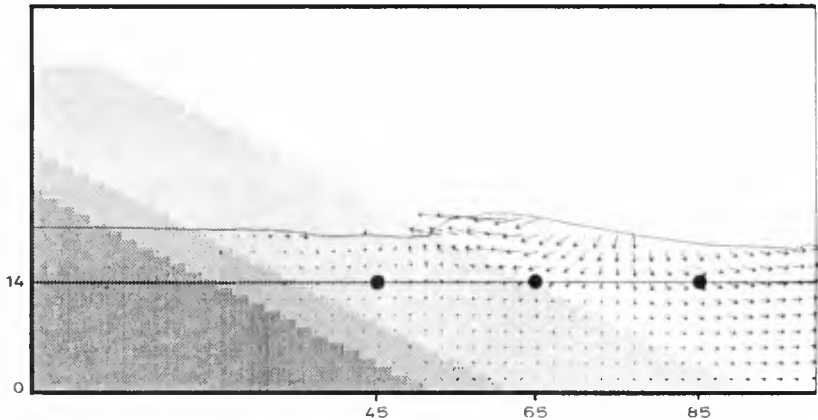


Fig. 6 Example of surface position and velocities during wave run-up on a permeable breakwater. After t = 1.8 s.

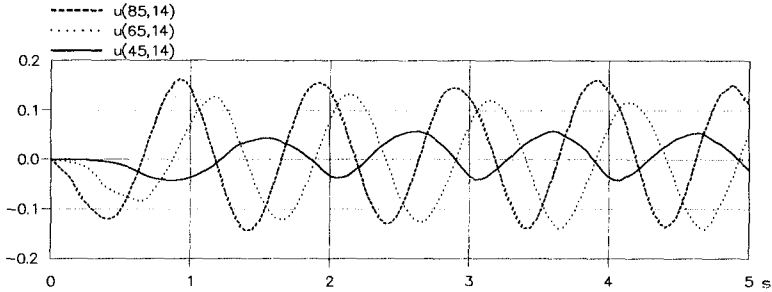


Fig. 7 Time series of horizontal velocities (m/s) at three locations, one outside the breakwater, one at the edge of the breakwater and one in the coarsest porosity layer as shown in Fig. 6.

### Conclusions

A 2D (x-z) numerical model has been developed for description of flows on and in coastal structures. The model includes a description of the energy loss in porous media taking into account both laminar and turbulent effects as well as the inertia effect. Comparisons with analytical solutions and measurements from physical model tests with waves and currents have shown promising results.

In order to correctly simulate the flow on and in porous coastal structures, it will be necessary to establish a better knowledge of the coefficients involved in the energy loss equation and to describe the energy loss due to wave breaking on a slope which implies a formulation of the hereby induced air entrainment.

### Acknowledgement

The research project which started in 1988 has been funded by the Danish Council of Technology through grant no. 880440. The verification of the porosity description has partly been co-sponsored by the Commission of the European Communities under the MAST-programme, contract 0032.

**References**

- Burcharth, H.F. & Christensen, C.  
"On stationary and non-stationary porous flow in coarse granular materials", University of Aalborg, Denmark (1991).
- Engelund, F.  
"On the laminar and turbulent flows of ground water through homogenous sand", Trans. Danish Academy Tech. Science, Vol. 3 (1953).
- Martin, J.C. & Moyce, W.J.  
"An experimental study of the collapse of liquid columns of a rigid horizontal plane", Phil. Trans. Roy. Soc. London A244, 312 (1952).
- Nichols, B.D., Hirt, C.W., Hotchkiss, R.S.  
"SOLA-VOF: A solution algorithm for transient fluid flow with multiple free boundaries", Los Alamos Scientific Laboratory Report LA-8355 (1980).
- Rasmussen, E.B., Vested, H.J., Justesen, P. & Ekebjærg, L.C. "System 3 - A Three-dimensional Hydrodynamic Model", Danish Hydraulic Institute, Denmark (1990).

## CHAPTER 13

### THE INTERACTION OF DEEP-WATER GRAVITY WAVES AND A CURVED SHEARING CURRENT

MARIUS GERBER<sup>1</sup>

#### 1. ABSTRACT:

The interaction of steady deep-water gravity waves with a pre-existing large-scale curved current has been investigated. In order to investigate the influence of the curvature of the current on the wave field, the current field was represented by a section of an annular current with a particular non-dimensional radius  $R$ .

As a first approximation the interaction of a family of linear axi-symmetrical waves and the current was investigated. Exact linear ray solutions were obtained which, in the limit when  $R \rightarrow \infty$ , reduce to the analytical straight current solutions of Longuet-Higgins and Stewart (1961).

#### 2. INTRODUCTION:

The emphasis of this paper is on the linear theory of the interaction of deep-water waves, generated on still water, and pre-existing large scale currents. Longuet-Higgins and Stewart (1960, 1961) were the first to give an accurate description of linear wave-current interactions and introduced the concept of radiation stress. Further contributions in our understanding of the interaction of linear waves and large scale currents came from, among others, Whitham(1962), Bretherton and Garrett(1968) and Peregrine (1976), who examined a number of different situations.

In almost all of the above studies the analysis was confined to two special situations of steady currents, namely (i) straight currents, varying with distance along the stream or (ii) straight

---

<sup>1</sup>Department of Applied Mathematics  
Stellenbosch University  
STELLENBOSCH, SOUTH AFRICA

currents varying across the stream. Exact linear solutions for these situations were derived by Longuet-Higgins and Stewart (1960, 1961).

The purpose of this paper is to extend the linear theory of the interactions of waves with a large scale current to more general current situations. Here we extend the range of known linear solutions by considering the simplest formulation of interaction with a curved current, namely steady axi-symmetrical waves on an axi-symmetrical annular current. This restriction simplifies the mathematics, but even so, solutions have been found for a wide range of cases.

### 3. MATHEMATICAL FORMULATION

Consider, in polar co-ordinates, an annular current of the form

$$\underline{U} = U_{\theta}(r) \underline{e}_{\theta} , \quad (3.1)$$

where  $r$  and  $\theta$  are the polar coordinates and  $\underline{e}_{\theta}$  is a unit vector in the  $\theta$  direction. Equation (3.1) describes an axi-symmetric current with arbitrary velocity profile which is only a function of the radial distance.

For the annular current (3.1) the basic equations of wave kinematics are given by:

DISPERSION:

$$\sigma^2 = gk \text{ or } c^2 = g/k, \quad k = |\underline{k}| \quad (3.2)$$

where  $\sigma$  is the intrinsic frequency of the waves and  $k$  is the corresponding wavenumber. The celerity of the waves is denoted by  $c$ .

DOPPLER SHIFT:

The apparent frequency, i e the frequency of waves passing a fixed point, is

$$\begin{aligned}\omega &= \sigma(\underline{k}) + \underline{k} \cdot \underline{U} \\ &= \sigma + k \sin \alpha U_\theta \\ &= k[c + U_\theta \sin \alpha],\end{aligned}\quad (3.3)$$

where  $\alpha$  is the angle between the wavenumber  $\underline{k}$  and the unit vector  $\underline{e}_r$  in the radial direction (see figure 1).

ANGULAR WAVENUMBER:

$$m = rk \sin \alpha, \quad (3.4)$$

with  $m$  a constant.

Non-dimensional variables may now be introduced to simplify the solutions. Consider a wave ray initially outside the influence of the current and denote, when  $U_\theta = 0$ , the wavenumber  $k$  by  $k_0$  and the wave celerity  $c$  by  $c_0$ . A scaled wavenumber  $K = k/k_0$ , as well as a scaled celerity  $C = c/c_0$ , may then be introduced. Also let  $V = U_\theta/c_0$  denote the scaled current velocity.

In order to depict the outside (or inside) radius of the annulus at the point of entry of the ray, let the radius of the current at this point be  $r_0$ . Assume further that  $U_\theta = 0$  just outside (or inside) the annulus, i e where  $r \rightarrow r_0$ . This suggests a logical choice for the non-dimensional radius is  $R = r/r_0$ .

From the symmetry of the current it is clear that, without loss of generality, a polar angle  $\theta_0 = 0$  can be selected for the point of entry  $r_0$ . Since  $\alpha = \phi - \theta$ , where  $\phi$  is the angle between  $\underline{k}$  and  $\underline{e}_1$ ,  $\alpha_0 = (\phi - \theta)_0$ , and the angle between  $\underline{k}$  and the x-axis at  $r_0$  is then  $\phi_0$  (see figure 1).

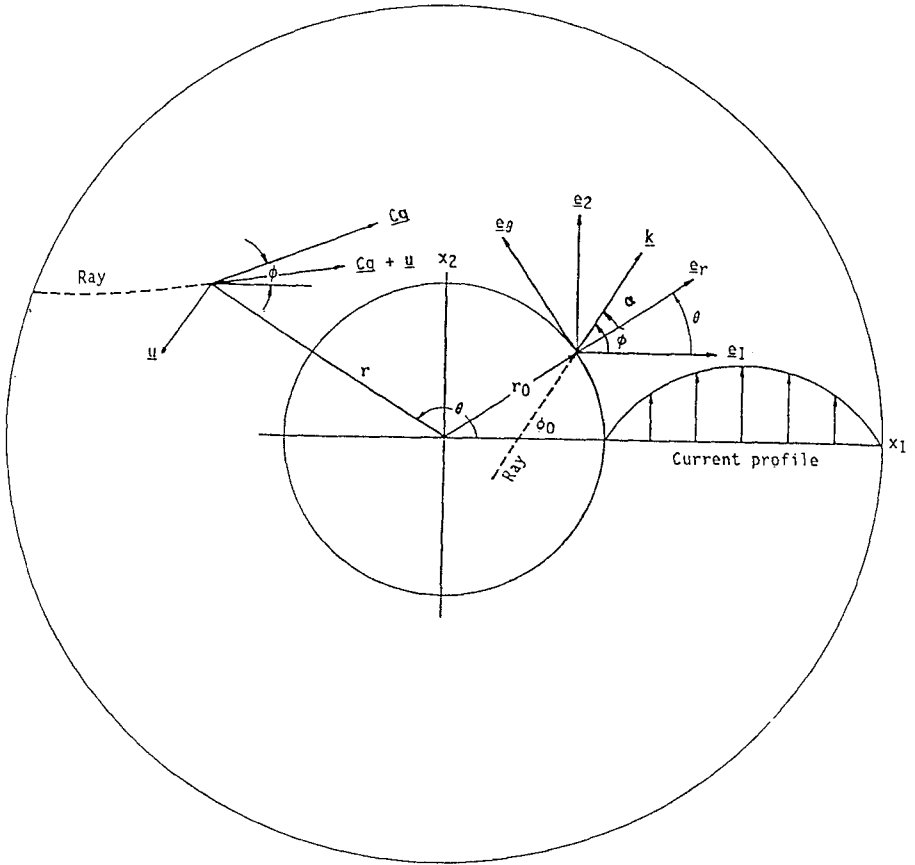


figure 1 : Definition diagram of rays interacting with an annular current.



Equations (3.3) and (3.4), by using (3.2), then become:

$$C = \frac{R \operatorname{cosec} \phi_0}{R \operatorname{cosec} \phi_0 - V} \quad (3.5)$$

$$K = \left[ \frac{R \operatorname{cosec} \phi_0 - V}{R \operatorname{cosec} \phi_0} \right]^2 \quad (3.6)$$

$$\sin \alpha = \frac{R \operatorname{cosec} \phi_0}{[R \operatorname{cosec} \phi_0 - V]^2} \quad (3.7)$$

so that, for a current field given by  $V(R)$ , the wave properties may be found from (3.5), (3.6) and (3.7).

We now also introduce the description that for rays initially outside the annulus, which then penetrate the circular current at  $R = 1$ , so that  $R < 1$  within the annulus where  $V \neq 0$ , the term convex current (to the direction of wave approach) will be used. Conversely, concave currents have waves that originate inside the annulus before they penetrate the annulus at  $R = 1$ .  $R$  will then become greater than unity within the annulus where  $V \neq 0$ . Figure 2 is a schematic representation of convex and concave currents as defined above.

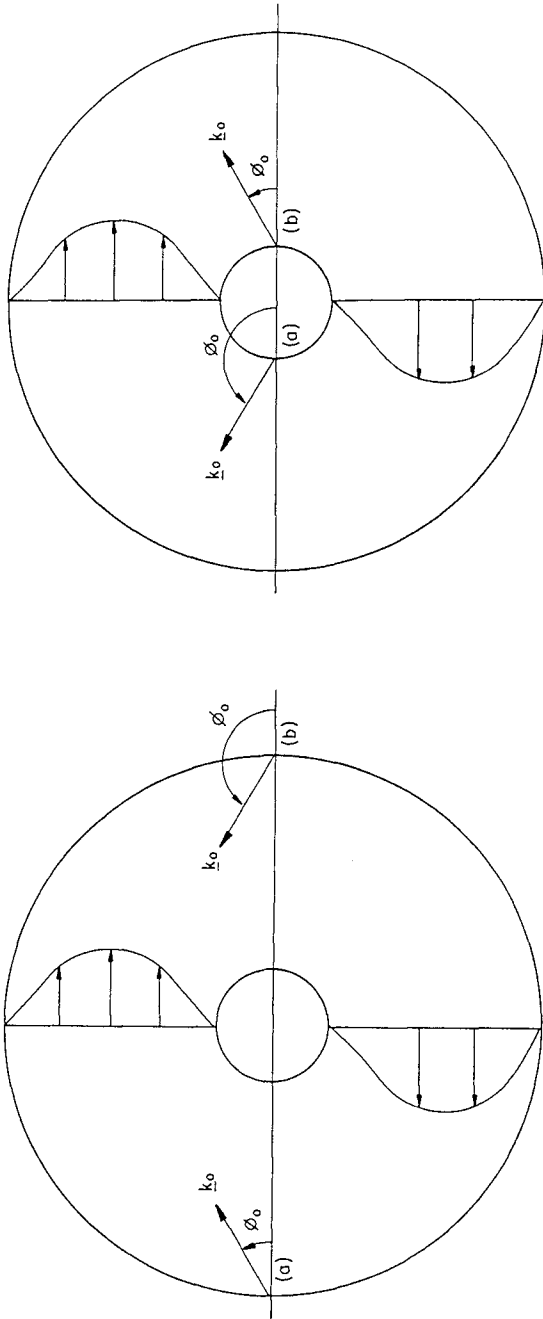
#### 4. SPECIAL SOLUTIONS

It is clear that the right hand side of equation (3.7) can have a magnitude greater than one for a range of  $V$  values. This defines upper and lower limits to  $V$  for which solutions exist.

The critical velocities bounding the region without waves are:

$$V = R \operatorname{cosec} \phi_0 \pm (R \operatorname{cosec} \phi_0)^{\frac{1}{2}} \quad (4.1)$$

At these critical velocities  $\alpha = 90^\circ$  so that the waves travel parallel to the current. In practise the rays are tangent to a caustic curve, concentric with the eddy, and reflection of the rays result. It is important to note that with this model the wave motion along rays is entirely reversible. Note also that "reflection" in this paper imply  $\alpha = 90^\circ$  and  $V \neq 0$ . The



Convex currents

(a)  $R = 1$  ;  $\phi_0 < 90^\circ$

(b)  $R = 1$  ;  $\phi_0 > 90^\circ$

Inside annulus :  $R < 1$ .

Concave currents

(a)  $R = 1$  ;  $\phi_0 > 90^\circ$

(b)  $R = 1$  ;  $\phi_0 < 90^\circ$

Inside annulus :  $R > 1$ .

Figure 2 : Definition diagram for concave and convex currents.

corresponding circular caustic curve is thus at a fixed radius from the origin within the current. For axi-symmetrical wave fields caustics can, however, also occur in the absence of "reflection". This is when the wave rays cross within the core of the annulus and although  $\alpha = 90^\circ$ ,  $V = 0$ .

For currents opposing the direction of wave approach two other refraction configurations, at other  $\alpha$  angles, may also be identified. "Blocking" is when the component of the group velocity in the direction of  $\underline{e}_\theta$ ,  $C_g \sin \alpha$ , becomes equal to  $|U_\theta|$

$$C_g \sin \alpha + U_\theta = 0 \quad (4.2)$$

and the waves are blocked in the  $\underline{e}_\theta$  direction. As in the case of "reflection" a fixed "blocking" radius from the origin may also be identified.

The second, or "stopping", configuration results when the local group velocity of the waves becomes equal and opposite to the convection velocity of the current:

$$C_g + U_\theta \sin \alpha = 0 \quad (4.3)$$

The crests of the waves are refracted to be parallel to the ray direction and the waves are stopped in the  $\underline{k}$  direction. As before, a fixed "stopping" radius from the origin may be identified.

By using equation (3.7) the resultant  $\alpha$  values may be contoured in the  $(R \operatorname{cosec} \phi_0, V)$  plane. Superposition of the current profile, as a function of the radius and the initial angle,  $V(R \operatorname{cosec} \phi_0)$ , then provides an easy mechanism to study the variation of the waves. For equation (3.7) the contours of figure 3 are obtained. The intersection of the various contours with the  $R \operatorname{cosec} \phi_0$  axis then indicate the cosec  $\phi_0$  values of the initial  $\phi_0$  entry angles, that is where  $R = 1$  and  $V = 0$ . As before, since for concave (convex) currents  $R > 1$  ( $R < 1$ ), the abscissa values in figure 3 will be increasing (decreasing) from the initial cosec  $\phi_0$  value when rays penetrate the annulus from the concave (convex) side.

The  $\alpha = 90^\circ$  contour in figure 3 is of particular interest since it represents the linear caustic curve where reflection of the wave rays take place. Other important contours in figure 3 are those

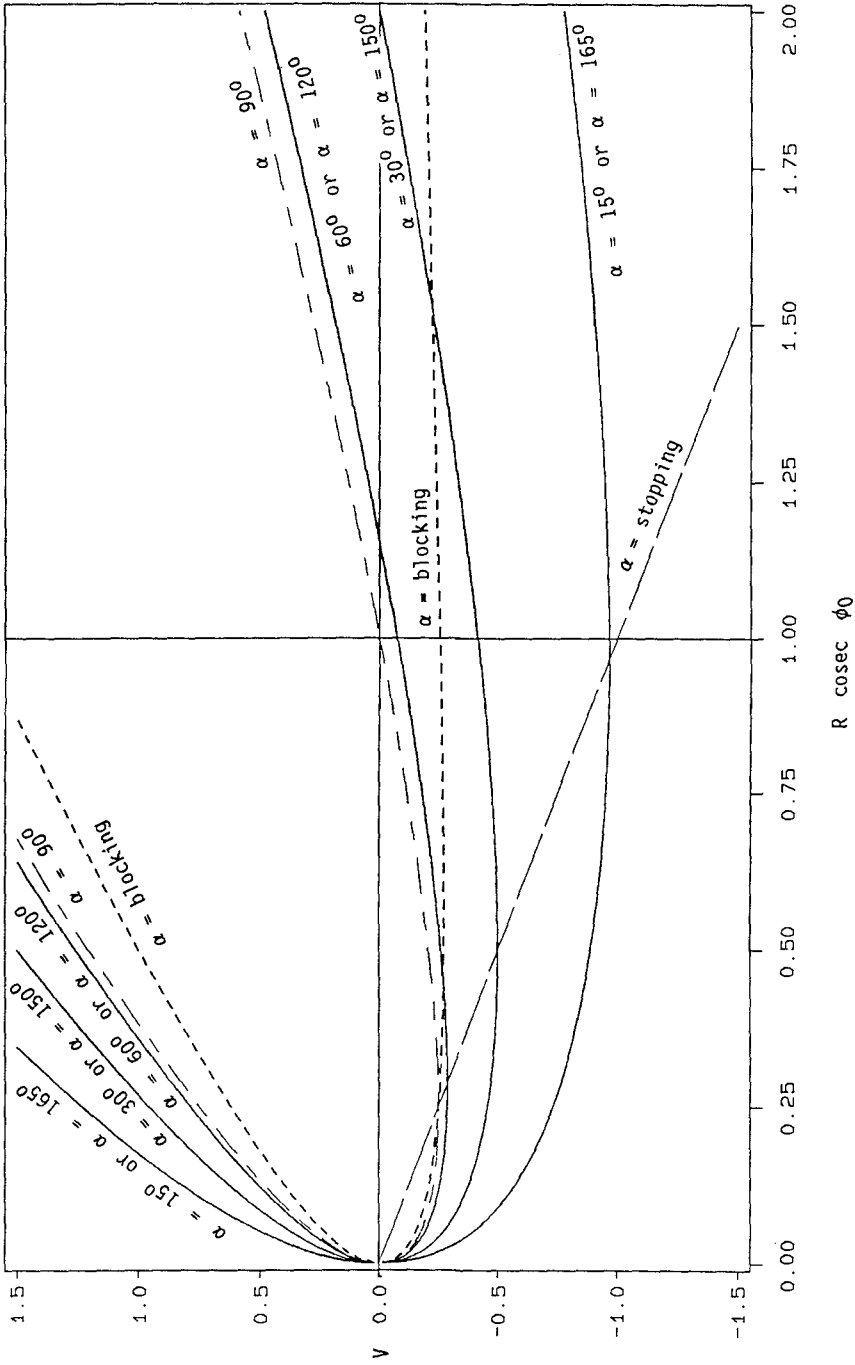


Figure 3 : Contours of  $\alpha$  on the  $(R \operatorname{cosec} \phi_0, V)$  plane.

which indicate where the rays are blocked or stopped by the current. These contours were obtained from equations (4.2) and (4.3). It is clear that only the lower branch of the blocking contour in figure 3 is relevant. Figure 3 also shows that for waves initially on still water, for both concave and convex currents, the blocking condition will always occur before the stopping condition can be satisfied. Furthermore, in practical application the linear stopping velocity condition will only be satisfied for waves of relatively short period. This is due to the relatively large opposing current values needed for (4.3) to apply.

## 5. NUMERICAL RAY SOLUTIONS

Waves interacting with a shearing current can, in general, exhibit four different types of behaviour. That is, the waves can (i) penetrate the current, (ii) be reflected by the current, (iii) become blocked by the current or (iv) are stopped by the current. Whereas all four these types of behaviour can be expected from waves opposed to the flow direction of the current, waves that propagate in the same direction as the current can not be blocked or stopped by the current.

The information contained in figure 3 is very useful since it allows us to illuminate the different features of straight, concave and convex shearing currents. For example, for given initial angle of incidence,  $\phi_0$ , different annular current distributions of the form (3.1) may be superimposed on the  $(R \operatorname{cosec} \phi_0, V)$  plane and the variation of the waves followed graphically. Various numerical ray simulations of an axis-symmetrical wave field interacting with an annular current of the form (3.1) are shown in figures 5 - 11. The point of entry of the rays in each of these figures is marked by "E" while the maximum current velocity within the annulus is indicated by a dashed line. The wave crests are also shown in some of these figures. For each of these figures the corresponding parabolic current profile is shown in figure 4. In particular instances where the waves are reflected by the current the relevant part of the current profile is indicated by a bold line. Also, the position on the ray where the waves are blocked, reflected and stopped by the current are shown by the filled circles marked "B", "F" and "S" in figures 5 - 11.

Figure 5 shows a family of rays penetrating the following concave annular current marked (a) in figure 4. The initial angle between the ray and the x-axis,  $\phi_0$ , was taken as  $45^\circ$ , corresponding to  $R \operatorname{cosec} \phi_0 = 1.41$ . The maximum value of the parameter  $V$  occurs at the dashed centerline-radius of the annulus and for this example  $V_{\max} = 0.28$ .

Figure 6 is an example of two rays interacting with the opposing convex current marked (b) in figure 4. The initial angle  $\phi_0 = 120^\circ$

so that  $R \operatorname{cosec} \phi_0 = 1.15$ . Only the bold part of the profile is relevant since the waves are reflected by the current. The filled circles in figure 6 correspond to the positions where the waves are blocked before being reflected by the current. Since the wave motion along the rays are reversible, the blocking contour is crossed twice (figure 4) before the waves exit the annulus.

It is interesting to note that on a straight opposing current, such as the current marked (c) in figure 4, reflection of the waves is not possible. This is also shown in figure 7. As before, the filled circles indicate the positions where the waves are blocked and stopped by the current. The waves are only stopped at relatively large values of  $V$ ; in this example  $V_{\max} = -0.96$ .

Figure 8 is another example of waves interacting with an opposing convex current. Here the dimensionless current velocity,  $V$ , is such that the waves are both blocked and stopped before they reflect. The initial angle of incidence is, similar to that of figure 6, taken as  $\phi_0 = 120^\circ$  and the relevant current profile is marked (d) in figure 4. The value of  $V_{\max} = -0.96$ .

The current profile marked (e) in figure 4 was used to generate the rays in figure 9. This profile is similar to that used in figure 8, except that here the waves approach the opposing current from the concave side.

Waves may also be trapped by an annular current. Waves generated on still water, before interacting with a concave current, may undergo multiple reflections within a certain radius and thus become trapped inside the annulus. Figure 10 is a trapped ray solution corresponding to the current profile marked (f) in figure 4. The angle of initial incidence  $\phi_0 = 45^\circ$  while  $V_{\max} = 0.64$ .

For this annular configuration, and for waves initially inside the annulus, while propagating in the same direction as the current, it can also be seen from figure 4 that profiles that reach up to the upper branch of the caustic line  $\alpha = 90^\circ$  may have trapped waves on them for chosen initial conditions. Figure 11 is an example of such a single trapped ray. The bold part of the current profile marked (g) in figure 4 corresponds to the ray solution shown in figure 11. It is clear that relatively large  $V$  values are needed to trap the waves. In this example  $V_{\max} = 1.4$ .

## 6. CONCLUSIONS

Exact linear solutions for the interaction of steady, axis-symmetric deep-water gravity waves and an axis-symmetric annular current have been derived. Two important non-dimensional parameters, namely a current velocity parameter,  $V = U_0/c_0$ , and a radius-angle parameter,  $R \operatorname{cosec} \phi_0$ , where  $R = r/r_0$ , were

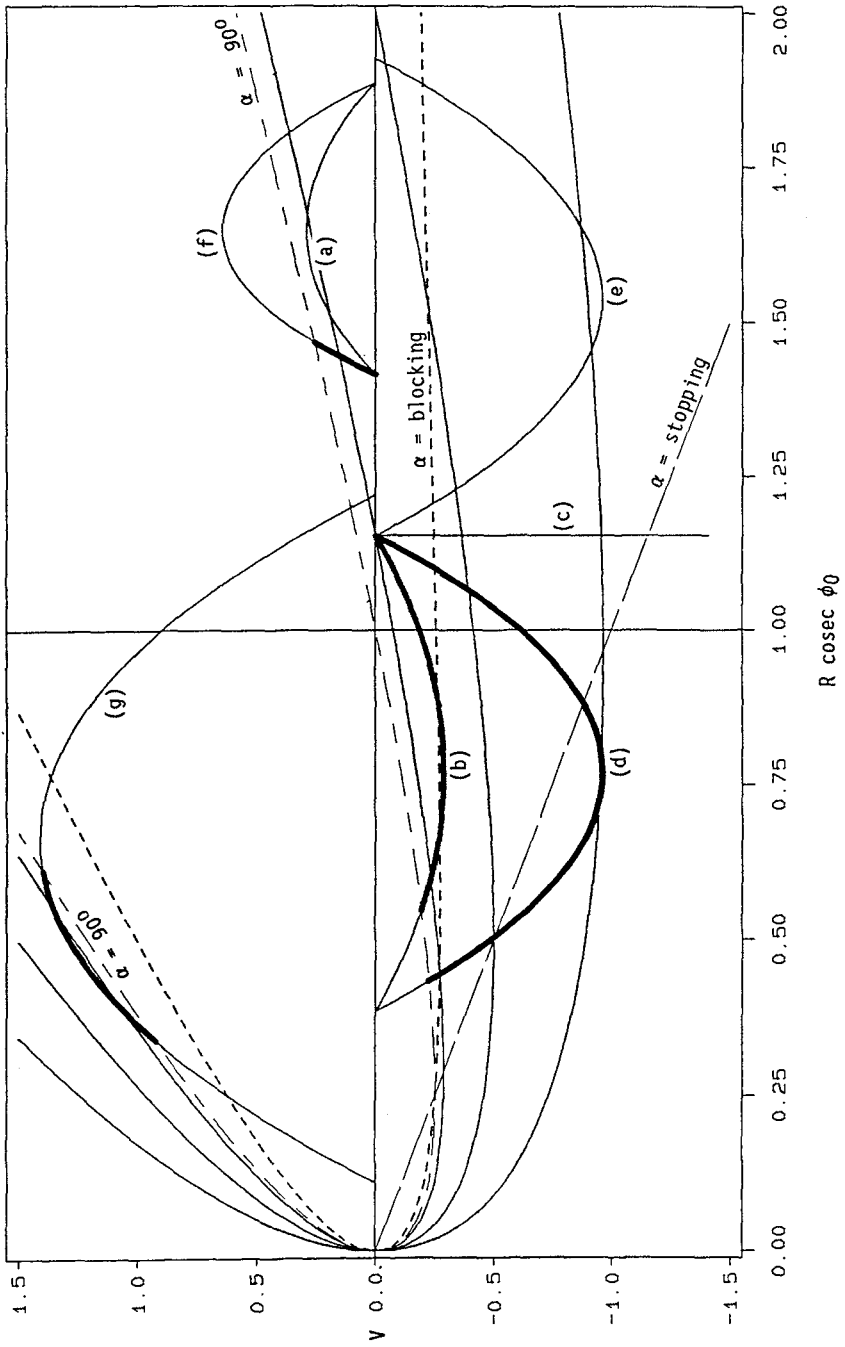


Figure 4 : The annular current configurations used to generate the wave ray examples of figures 5 - 11.

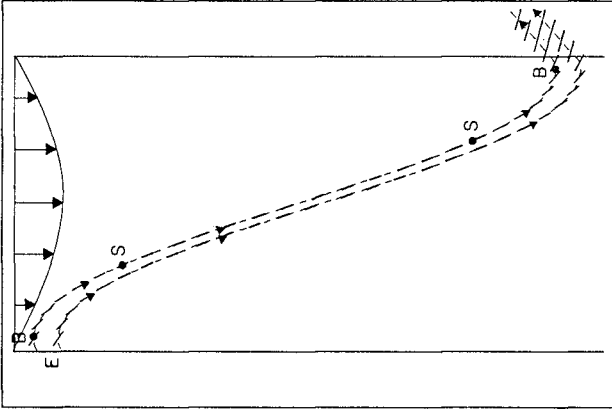


Figure 7 :

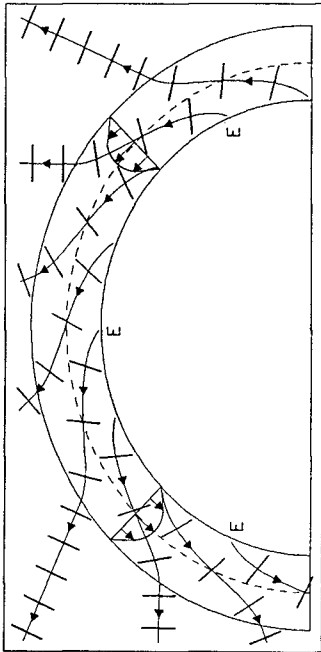


Figure 5 :

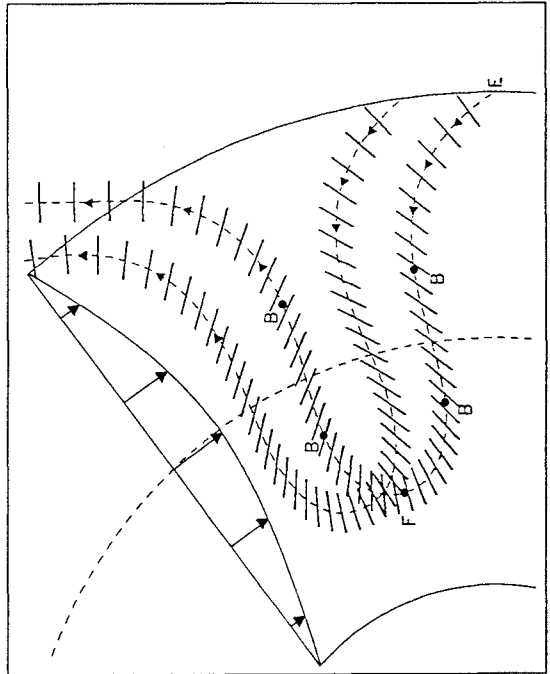


Figure 6 :



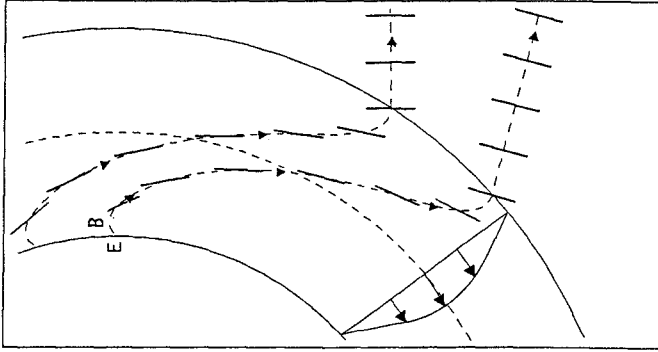


Figure 9 :

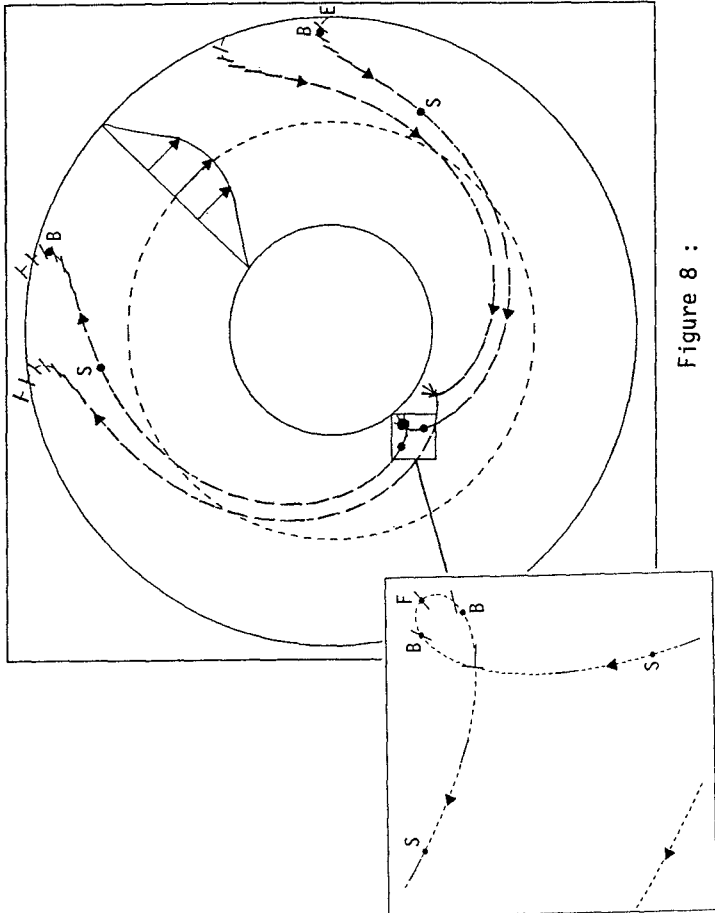


Figure 8 :

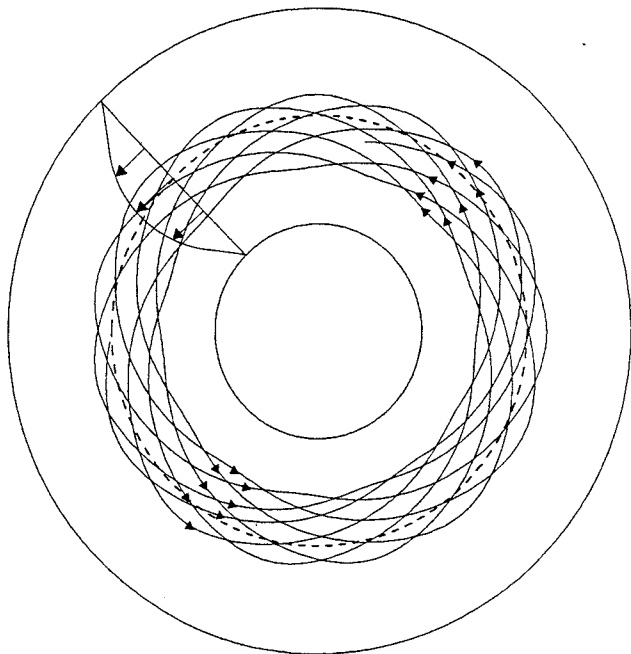


Figure 11 :

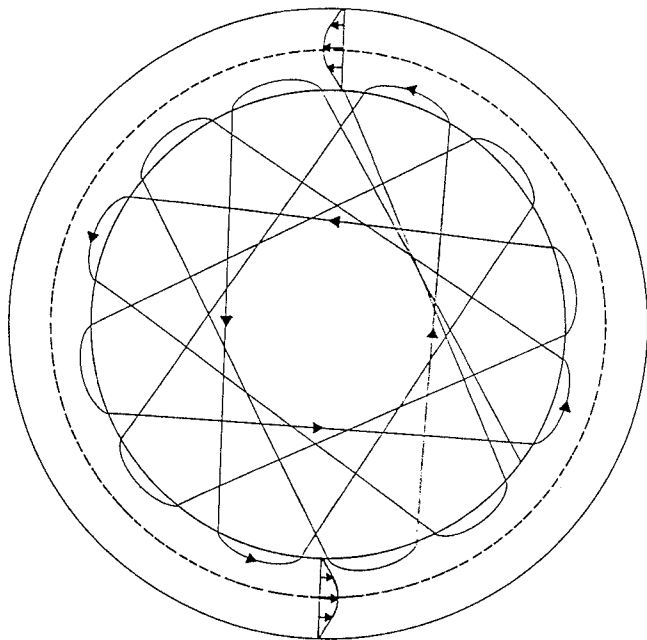


Figure 10 :

identified. For  $R > 1$  concave currents were considered while convex currents have  $R < 1$ .

Wave reflections, as well as blocking and stopping of the waves by the current, were investigated. Both positive convex currents and positive concave currents admit reflections, but reflections are only possible for negative convex currents. Reflections may also occur on opposing convex currents before the waves are blocked. On negative concave currents the linear waves may also be stopped by the current. However, very large opposing current velocities are required to do so. Furthermore, reflections on an adverse convex current will occur more frequently than the "stopping" velocity criterion can be satisfied. This is so since large negative values of  $V$  are needed to stop the waves.

Wave rays may also be trapped within the boundaries of the current. Waves that are generated on still water inside the annulus, and which penetrate the annulus, while travelling in the same direction as the concave current, may undergo multiple reflections and remain trapped within a certain reflection radius of the current. Only waves generated within the boundaries of the annulus can be trapped so as to remain within the annulus. The theory presented in this paper limits the waves, and therefore also the current distributions, to cases where  $R \csc \phi_0 > 1$ . Figure 4 then shows that it is not possible to construct an adverse current configuration which can trap waves.

## 7. REFERENCES

- Bretherton, F P and Garrett, C J R (1968). Wavetrains in inhomogeneous moving media. Proc. Roy. Soc., Lond. A302, 529 - 554.
- Longuet-Higgins, M S and Stewart, R W (1960). Changes in the form of short gravity waves on long waves and tidal currents. J. Fluid Mech. 8, 565 - 583.
- Longuet-Higgins, M S and Stewart, R W (1961). The changes in amplitude of short gravity waves on steady non-uniform currents. J. Fluid Mech. 10, 529 - 549.
- Peregrine, D H (1976). Interactions of water waves and currents. Adv. Appl. Mech. 16, 9 - 117.
- Whitham, G B (1962). Mass, momentum and energy flux in water waves. J Fluid Mech. 12, 135 - 147.

## CHAPTER 14

# TRANSFORMATION OF WAVE CREST PATTERN IN SHOALING WATER

Yoshimi Goda<sup>1</sup>

### Abstract

Spatial distributions of wave crests are examined through numerical simulations of directional random sea surface. As the directional spreading of wave energy becomes narrow, the wave crests become long and the spread of individual crest directions become narrow. Simulations are extended to waves propagating into a planar beach. The areas of wave breaking are identified as the zone of surface elevation higher than the breaking threshold. The lateral spreading speed of breakers is analyzed from consecutive scenes of breaker crest patterns. It is about 30% of the forward advance speed of breakers.

### Introduction

Directional random sea waves are generally described with the directional wave spectrum. The wave field is represented as the superposition of an infinite number of infinitesimal component waves, as illustrated by Pierson, Neumann, and James (1955). The theoretical expression for the root-mean-square wave number in an arbitrary direction has been given by Longuet-Higgins (1957), who introduced the long-crestedness parameter as the ratio of the smallest to the largest wave numbers in the directions 90° degree apart. Isobe (1988) introduced a theory of the joint distribution for the direction, height, and period of individual waves, based on the orbital velocities of water particles on the surface. Such statistics on individual wave directions are the subject to be examined in more details in the present paper.

A direct approach to the statistics of individual wave directions is to analyze the spatial distributions of sea surface elevations. The data of real sea surface elevations are hard to obtain, but the simulation technique can provide as many data as necessary. The contours of simulated wave surface make it possible to identify the areas of wave crests, on which the lengths, heights, and directions of wave crests are examined. The information on the statistics of wave crests will be utilized for the analysis of surfing climate, the necessity of which has been pointed out by Dally (1990).

---

<sup>1</sup> Prof., Yokohama National Univ., Dept. Civil Eng., Hodogaya-Ku, Yokohama 240, Japan, M. ASCE

Analysis of wave crest statistics has been undertaken by Goda and Tokiwa (1991) and by Goda and Mizusawa (1992), but the results are reported in Japanese. The present paper introduces the directional characteristics of wave crests in both uniform and shoaling waters. The aspect of crest length statistics will be reported elsewhere (Goda 1993).

### Directional Wave Spectrum Employed for Simulation

A combination of the modified JONSWAP frequency spectrum and the Mitsuyasu-type directional spreading function was employed as the directional spectrum for numerical simulations. For a given wave height  $H_{1/3}$  and spectral peak period  $T_p$ , the modified JONSWAP spectrum is expressed by Goda (1988) as

$$S(f) = \beta_J H_{1/3}^2 T_p^{-4} f^{-5} \exp[-1.25(T_p f)^{-4}] \gamma^{\exp[-(T_p f - 1)^2 / \sigma^2]} \quad (1)$$

where

$$\beta_J = \frac{0.0624[1.094 - 0.01915 \ln \gamma]}{0.230 + 0.0336\gamma - 0.185(1 + \gamma)^{-1}} \quad (2)$$

$$\sigma = \begin{cases} 0.07 & : f \leq f_p \\ 0.09 & : f > f_p \end{cases} \quad (3)$$

Throughout the simulations, the following height, period, and peak enhancement factor were employed:

$$(H_{1/3})_0 = 2.0 \text{ m}, \quad (T_p)_0 = 8.01 \text{ s}, \quad \gamma = 3.3 \quad (4)$$

where the subscript 0 indicates the values of deepwater waves. The spectral peak period of 8.01 s corresponds to the deepwater wave length of  $(L_p)_0 = 100.0$  m. The significant wave period is estimated as  $T_{1/3} = 7.59$  s. Because the wave linearity is assumed and the results are all presented in dimensionless forms, the above values of height and period merely indicate the input conditions for simulations.

The Mitsuyasu-type directional spreading function is expressed as

$$G(f; \theta) = G_0 \cos^{2S}(\theta/2) \quad (5)$$

where

$$G_0 = \left[ \int_{\theta_{\min}}^{\theta_{\max}} \cos^{2S}(\theta/2) d\theta \right]^{-1} \quad (6)$$

$$S = \begin{cases} (f/f_p)^5 S_{\max} & : f \leq f_p \\ (f/f_p)^{-2.5} S_{\max} & : f > f_p \end{cases} \quad (7)$$

The directional spreading parameter  $S_{\max}$  was given the values of 10, 25, and 75 to represent wind waves, medium-distance swell, and long-distance swell.

### Simulations of Directional Random Wave Profiles in Water of Uniform Depth

The surface elevation of directional random waves  $\eta(x, y)$  is computed by means of double series of the following form:

$$\eta(x, y) = \sum_{m=1}^M \sum_{n=1}^N a_{m,n} \cos(k_m x \cos \alpha_n + k_m y \sin \alpha_n + \epsilon_{m,n}) \quad (8)$$

where  $a_{m,n}$  denotes the amplitude of component wave,  $k_m$  the wave number,  $\alpha_n$  the directional angle,  $x$  and  $y$  the cartesian coordinates, and  $\epsilon_{m,n}$  the random phase angle which is uniformly distributed between 0 and  $2\pi$ . The time  $t$  is dropped in Eq. 8, because the wave profiles in steady state condition is examined in the water of uniform depth.

The number of frequency components was set at  $M = 50$ , while that of directional components was  $N = 30$ . The wave number  $k_m$  was computed by the small amplitude wave theory for the following frequency  $f_m$  :

$$f_m = 1.007 T_1^{-1/3} \{\ln[2M/(2m-1)]\}^{-1/4} \quad (9)$$

The directional angle  $\alpha_n$  was set by equally dividing the directional range between  $[(\alpha_p)_0 - 90^\circ]$  and  $+90^\circ$  in deepwater, where  $(\alpha_p)_0$  denotes the incident wave angle to the depth contour in deepwater. In shallow water, the directional range was reduced by considering the wave refraction effect.

Wave simulations were carried out in deepwater and also in shallow water with the depth  $h = 20, 10,$  and  $5$  m, which corresponded to the relative water depth  $h/L_0 = 0.2, 0.1,$  and  $0.05$ , respectively. The shoaling and refraction effects were taken into account in wave simulations in shallow water, by assuming the depth contours being parallel and straight lines. The bottom slope was assumed nearly horizontal so that the area of computation could be considered of the uniform depth.

The computation area was a square with the side length equal to  $20(L_p)_0$ , and the grid spacing of  $\Delta x = \Delta y = 0.1(L_p)_0$  was employed. For a given condition of wave simulation, 25 surface wave profiles were created by changing the initial phase angle by means of a pseudo random number generating program.

### Detection and Definition of Wave Crests

Wave crests can be defined in many ways. In this paper a wave crest is defined as an enclosed area above a certain threshold elevation. The outermost boundary of this wave crest area defines the length, width, direction of the wave crest. The procedure to detect and define the outermost boundary is as follows.

First, the surface elevation at every grid point in the computed space is checked if it is above the threshold level, and the grid point is marked accordingly. The closed circles in Fig. 1 indicate the point being below the threshold level, while the open circles being equal to or above the threshold level.

Second, a search is made for a change from the open to closed circles or vice versa between the adjoining grid points. The search is made from the left to the right and from the top to the bottom along every grid line. When the change from a closed circle to an open circle takes place, the numeral 1 is assigned to the section of grid line there. The change from an open circle to a closed circle is marked with the numeral 2. No change is marked with N.

Third, a line is drawn by connecting the sections of grid lines marked either with 1 or 2. When such lines are drawn, they are numbered as ①, ②, ③, and so on. These lines are examined if they encounter the peripheries of the computation area. When a line does not form a closed loop by ending up at the peripheries, it is not considered as a complete boundary of wave crest and discarded in the following analysis.

Fourth, the exact location of the wave crest line is determined at each grid line section by a linear interpolation between the surface elevations at the adjoining grid points. The information of the locations of grid-line-crossings is stored for each wave crest line for further analysis.

The threshold elevation for defining wave crests was selected as  $\eta_{\text{thres.}} = 0.1(H_{1/3})_0$  after several examinations. This threshold level is employed throughout this paper except for the case when the breaker area is defined.

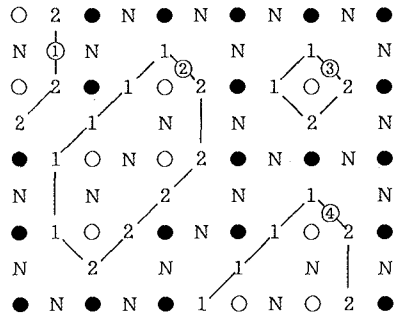


Fig. 1 Explanatory Sketch for Detection of Wave Crest Boundary Line

**Wave Crest Patterns and Crest Lengths in Water of Uniform Depth**

Figure 2 exhibits examples of wave crest areas defined by the above procedure. The four diagrams shown here represent directional random waves with the spreading parameter  $(S_{\text{max}})_0 = 25$  in water of uniform depth. The upper left diagram is for deepwater waves, and the other three diagrams are for waves with the relative depth  $h/L_0 = 0.2, 0.1,$  and  $0.05$ . The incident wave angle is  $(\alpha_p)_0 = 30^\circ$ . As the relative depth decreases, wave crest patterns approach toward the pattern of monochromatic waves, because of the wave refraction and shoaling effects. The apparent long-crestedness of wave patterns in shallow water regions is caused by the shortening in wave length: the absolute lengths of wave crests remain unchanged from deep to shallow water for the same value of directional spreading parameter.

The directional spreading affects the wave crest length. As the range of directional spreading becomes narrow, the crest length increases. Figure 3 shows the relation between the relative crest length  $\lambda/L_p$  and the directional spreading parameter  $S_{\text{max}}^*$ . The crest lengths are measured for crests with the top elevation  $\eta_c$  higher than  $0.75(H_{1/3})_0$ , and the mean length and the upper quartile length have been calculated from the data of 25 wave crest patterns for each condition. The crest lengths are normalized with the local wave length  $L_p$  corresponding to the spectral peak frequency. For waves in the intermediate to shallow water, the directional spreading becomes narrow owing to the wave refraction effect. This causes an apparent increase in the value of  $S_{\text{max}}$  as shown in Fig. 4 (Goda and Suzuki 1975), which is called the equivalent spreading parameter in this paper. The closed symbols in Fig. 3 refer to waves with  $(S_{\text{max}})_0 = 25$  in the intermediate to shallow water. As shown in Fig. 3, the relative crest length is well described as the function of equivalent spreading parameter  $S_{\text{max}}^*$  regardless of water depth.

**Spreading of Individual Crest Directions**

The crest direction is defined as the direction normal to the straight line connecting the two outermost points of a wave crest area. Figure 5 shows the joint distribution of the crest direction  $\theta$  and the relative crest length  $\lambda/(L_p)_0$  of the random waves with  $S_{\text{max}} = 10$  in deep water, while Fig. 6 is for waves with  $(S_{\text{max}})_0 = 25$  in shallow water with  $h/L_0 = 0.05$ . The numerals in Figs. 5 and

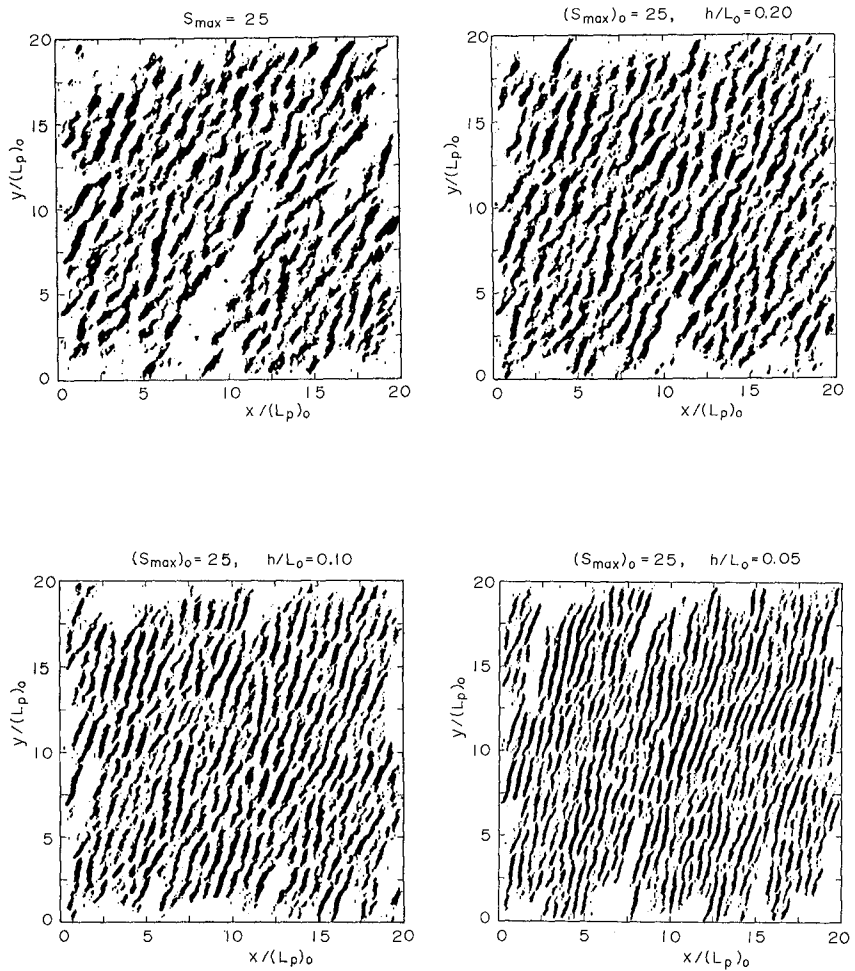


Fig. 2 Wave Crest Patterns in Water of Uniform Depth



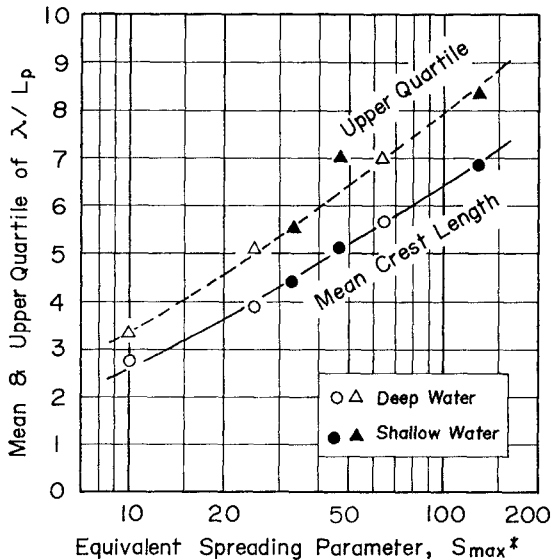


Fig. 3 Mean and Quartile Crest Lengths of Wave Crests Higher than  $0.75(H_{1/3})_0$

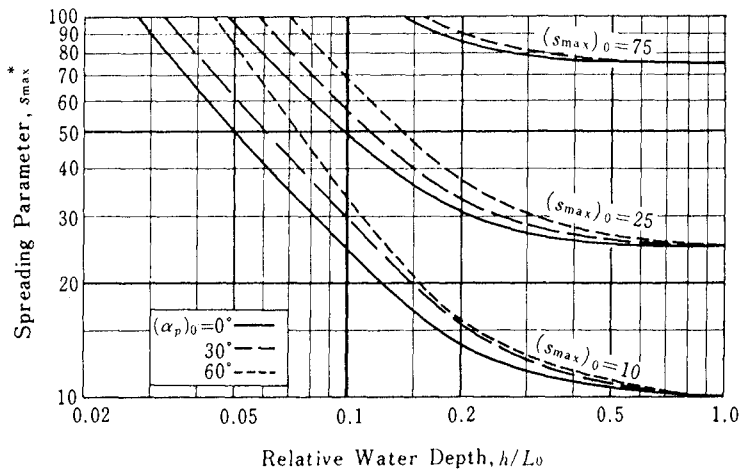


Fig. 4 Equivalent Spreading Parameter  $S_{max}^*$  in Shallow Water Area (after Goda and Suzuki 1975)

6 are the numbers of wave crests within respective blocks of relative crest length and crest direction. The data with crest lengths less than  $(L_p)_0$  are omitted because of inherent errors in assessing the crest direction (the positions of wave crest lines are determined on the  $x$  and  $y$  grid lines only).

The incident wave angle in deep water is  $(\alpha_p)_0 = 30^\circ$ . The mean angle of crest direction in Fig. 5 is  $27.8^\circ$ , and a small difference is probably due to the method of defining crest direction. The mean angle of crest direction in Fig. 6 is  $13.0^\circ$ , which is slightly smaller than the mean direction  $15.0^\circ$  estimated by the calculation of wave refraction with the directional spectrum.

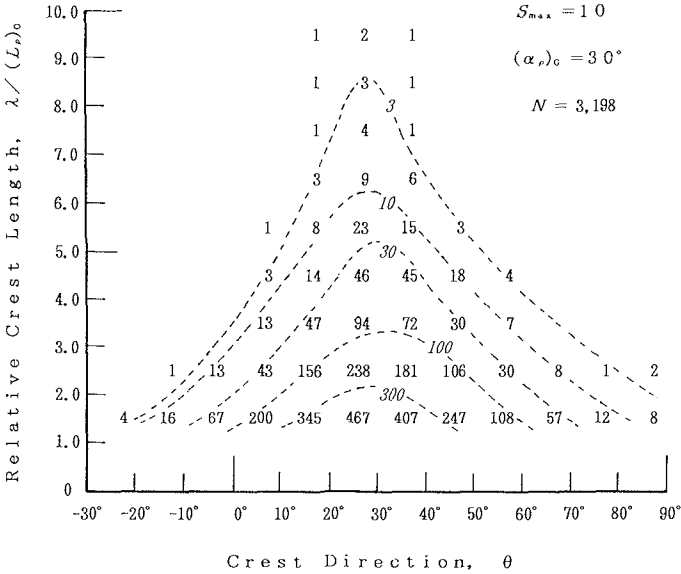


Fig. 5 Joint Distribution of Individual Crest Direction and Relative Crest Length in Deepwater with  $S_{max} = 10$

The spread of individual crest directions is represented with their standard deviations. They are plotted against the equivalent spreading parameter  $S_{max}^*$  in Fig. 7, where the standard deviation of crest direction for the wave crests longer than  $(L_p)_0$  and that of crests higher than  $0.75(H_{1/3})_0$  are shown.

### Simulation of Directional Random Wave Patterns in Shoaling Water

Waves propagating in shoaling water can be simulated by paying due account to the change in phase angle. For the case of one-dimensional waves, the phase angle advances by the amount  $k dx$  over a distance  $dx$ . When waves propagate from  $x_0$  to  $x_I$  and reach to the  $I$ -th grid section, the wave profiles there can be computed by using the following equation:

$$\eta(x_I, t) = a(x_I) \cos[2\pi ft + \epsilon + \sum_{i=0}^{I-1} k(x_i) dx] \quad (10)$$

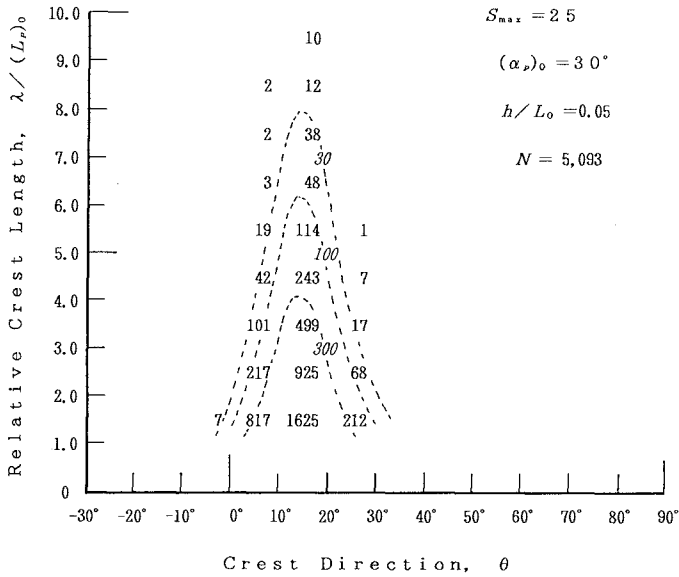


Fig. 6 Joint Distribution of Individual Crest Direction and Relative Crest Length in Shallow Water at  $h/L_0 = 0.05$  with  $(S_{max})_0 = 25$

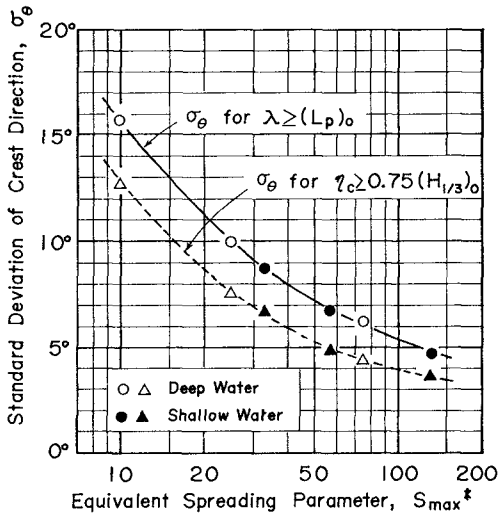


Fig. 7 Standard Deviation of Individual Crest Directions of Wave Crests Longer than  $(L_p)_0$  and Those of Crest Lengths Higher than  $0.75(H_{1/3})_0$

in which  $i$  denotes the order number of the grid section and  $\epsilon$  is the initial phase angle. The amplitude  $a$  is a function of the location  $x_I$  due to the shoaling effect.

Waves propagating toward the shore of coast with parallel straight contours are depicted in Fig. 8. The coordinate  $x$  is set parallel to the shoreline and thus the water depth is constant in the  $y$  direction. The lines with arrows indicate the direction of wave propagation and the dashed lines normal to the arrow lines represent the wave crest lines. The phase angle at each grid point is determined as follows. First, the phase angle at  $(x_0, y_1)$  is greater by the amount  $k(x_0)dy \sin \alpha(x_0)$  than that at the origin  $(x_0, y_0)$ . The advance of phase angle at  $(x_0, y_J)$  is  $J$  times that amount. Along the line  $y = y_J$  the phase angle increases by the amount  $k(x_i) \cos \alpha(x_i)$  when waves propagate from the  $i$ -th section to  $(i + 1)$ -th section. This increase of phase angle is common for all the  $y$ -lines. Thus, the wave profile at the grid section  $(x_I, y_J)$  can be calculated by the following equation:

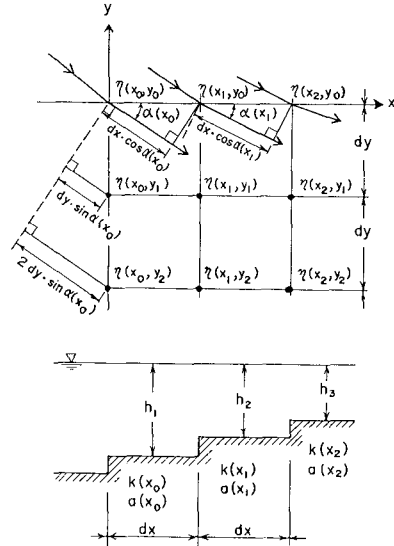


Fig. 8 Explanatory Sketch for Grid System of Planar Beach

$$\eta(x_I, y_J) = a(x_I) \cos[-2\pi ft + \epsilon + k(x_0)Jdy \sin \alpha(x_0) + \sum_{i=0}^{I-1} k(x_i)dx \cos \alpha(x_i)] \quad (11)$$

Wave simulation in shoaling water has been carried out by using Eq. 11, and wave crest areas have been marked out as exemplified in Fig. 9. The bottom slope is assumed as 1/100, and the wave crest pattern in the water depth from 20 m to 0.1 m are shown there. The incident wave conditions are the same as those in Fig.2.

**Spatial Behavior of Breaking Waves in the Surf Zone**

The area in which waves are breaking can be detected through examination of the spatial surface elevations of random waves. It is done by setting the threshold level of wave crest definition at some breaking crest elevation instead of a fixed value such as  $\eta_{thres.} = 0.1(H_{1/3})_0$ . The threshold level of breaking crest area is set in this paper as one-half the breaker height formulated by Goda (1975), i.e.:

$$\eta_b = \frac{1}{2}H_b = 0.085L_0 \left\{ 1 - \exp \left[ -1.5 \frac{\pi h}{L_0} (1 + 15 \tan^{4/3} \theta) \right] \right\} \quad (12)$$

where  $\tan \theta$  denotes the bottom slope. The threshold level varies with the  $x$  coordinate, but the technique of defining the breaking crest area is the same as before. However, the crest lines crossing the peripheries of the simulation area have been kept as the boundary of breaking area.

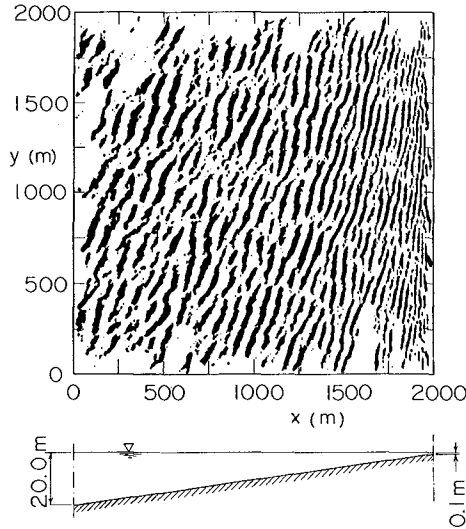


Fig. 9 Wave Crest Pattern in Shoaling Water of Planar Beach with  $(S_{max})_0 = 25$  and  $(\alpha_p)_0 = 30^\circ$

A check on the reliability of simulating random surface elevations has been made by comparing the ratio of breaking wave crest areas to the total water area in a given water depth. From the simulated surface elevations, the total length of breaking wave crests along a given grid line at a constant  $x$ -value (constant water depth) was tabulated and this process was repeated at each grid line. The total length of breaking crest areas when divided by the length  $20(L_p)_0$  provides the breaker ratio at a given water depth. The raw data of breaker ratio has been averaged over 25 diagrams of random wave profiles in order to reduce the effect of statistical variability. The dashed line in Fig. 10 is a result of such analysis.

The theoretical prediction of breaker ratio has been made through the computation of shoaling and refraction of directional random waves. The root-mean-square value of deepwater waves has been transformed to that of shallow water waves by being multiplied with the shoaling and refraction coefficients of directional spectral waves. Because the wave simulation is based on the linear superposition of component waves, the simulated wave elevations should follow the normal distribution. Then the probability of surface elevation exceeding the breaker threshold level by Eq. 12 is simply estimated from the probability table of the normal distribution. The predicted value is shown with the solid line in Fig. 10, and it fits with the result of simulation analysis as expected.

The effect of incident angle upon the breaker ratio is demonstrated in Fig. 11. As the incident angle increases, the breaker ratio at a given depth decreases slightly; the start of wave breaking becomes closer to the shoreline and the surf zone becomes a little narrow. This is due to the more conspicuous decrease in the local wave height by the wave refraction effect in the case of oblique wave incidence than that of the normal wave incidence. The difference between the breaker ratios of different incident angles have also been predicted by theoretical

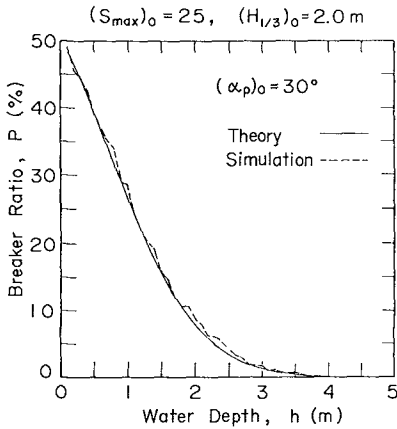


Fig. 10 Comparison of Theoretical and Simulated Ratios of Breaker Areas

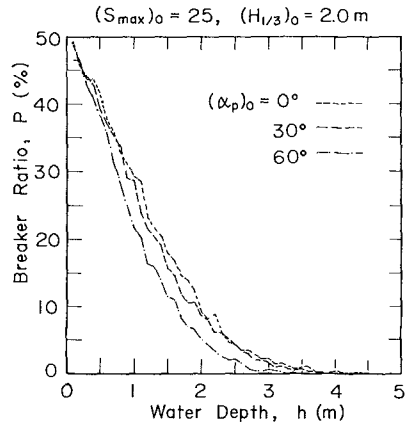


Fig. 11 Effect of Incident Wave Angle on Breaker Ratio

calculation, though not shown in Fig. 11.

**Growth of Wave Breaking Areas in Shoaling Water**

Wave simulations can also reveal the change of individual breaking crest areas. Figure 12 exhibits an example of such analysis. A simulation of wave profiles in the nearshore is made with a certain set of initial phase angles. Then the transformation of that wave profiles is followed from  $t = 0$  to  $t = 9T_p$  with the time step  $\Delta t = T_p$  by using the same set of initial phase angles and by changing the time  $t$  in Eq. 11. Among these consecutive scenes of wave profiles, visual search is made for conspicuous breaking areas which appear in the locations far from the shoreline. Once they are picked up, further search is carried out on the locations of the same breaking areas in the preceding and following scenes. The breaking crest area marked with ② in Fig. 12, for example, has been noted in all of ten simulated wave profiles and its growth has been well observed, whereas the rest of breaking crest areas have appeared at later scenes. In the analysis of the time-sequence change of breaking crest areas, the grid distance  $\Delta x = 5$  m was adopted for finer resolution. The number of grid lines and the bottom slope were the same as before so that the offshoreward water depth was 10.0 m.

The shoreward advances of conspicuous breaking crest areas have been plotted on tracing papers, and the lateral spread lengths of these crest area have been measured on the tracing papers. The lateral spreading speed  $V_s$  of the breaking crest area has been calculated from these data. Figure 13 shows the results of the analysis of the lateral spreading speed of breaking crest area. The abscissa is the forward advance speed  $C_b$  of breaker, which has been approximated as  $\sqrt{gh}$  with the water depth  $h$  at the corresponding locations. The analysis has been carried out for the deepwater directional spreading parameter of  $(S_{max})_0 = 10, 25,$  and  $75$ , but the effect of directional spreading parameter on the lateral spreading speed is insignificant. As seen in Fig. 13, the lateral spreading speed shows a large scatter, but it remains in the range between 0 and  $C_b$ . The regression line

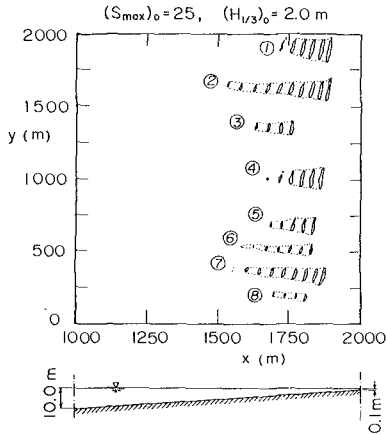


Fig. 12 Time Sequence Change of Breaker Areas with Time Step  $\Delta t = T_p$

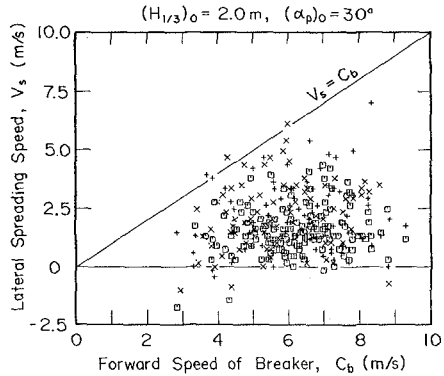


Fig. 13 Lateral Spreading Speed versus Forward Speed of Breaking Crests  
 $\square$ :  $(S_{max})_0 = 10$ ,  $+$ :  $(S_{max})_0 = 25$ ,  $\times$ :  $(S_{max})_0 = 75$

between  $V_s$  and  $C_b$  under the condition that the line should pass through the origin yields the relation  $V_s = 0.30C_b$ .

**Conclusions**

Numerical simulation of directional random sea surface has succeeded in visualizing the wave crest patterns and clarifying the statistics of wave crest lengths and directions. Major conclusions of the present paper can be summarized as follows:

1. The mean crest lengths and the standard deviation of crest directions are governed by the directional spreading parameter  $S_{max}$  of the Mitsuyasu-type directional function.
2. In shoaling water, the effect of relative water depth on the crest statistics can be incorporated by using the equivalent spreading parameter  $S_{max}^*$  shown in Fig. 4.
3. The portion of breaking area within wave crests in shoaling water can be identified by setting the threshold surface level at the breaking crest elevation at respective water depth.
4. The lateral spreading speed of breaking crest area shows a wide scatter, but the average speed is assessed as 0.3 times the forward advance speed of breaker.

The numerical simulations reported hereinabove have been carried out by Messrs. Yasuhiro Tokiwa and Tatsuya Mizusawa as their thesis works at the Department of Civil Engineering, Yokohama National University. The author wishes to express his deep appreciation for their cooperations.

## References

- Dally, W. R. (1990): Stochastic modeling of surfing climate, *Proc. 22nd Int. Conf. Coastal Eng.*, pp.516-529.
- Goda, Y. (1975): Irregular wave deformation in the surf zone, *Coastal Engineering in Japan*, Vol.18, pp.13-26.
- Goda, Y. (1988): Statistical variability of sea state parameters as a function of wave spectrum, *Coastal Engineering in Japan*, Vol.31, No.1, pp.39-52.
- Goda, Y. (1993): Statistics of wave crest lengths based on directional wave simulations, OMAE '93 (to be presented).
- Goda, Y. and Mizusawa, T. (1992): Wave crest statistics based on numerical simulations: Longitudinal profiles and breaking characteristics, *Proc. Coastal Eng., JSCE*, Vol.39, pp.106-110 (*in Japanese*).
- Goda, Y. and Suzuki, Y. (1975): Computation of refraction and diffraction of sea waves with Mitsuyasu's directional spectrum, *Tech. Note of Port and Harbour Res. Inst.*, No.230, 45p. (*in Japanese*).
- Goda, Y. and Tokiwa, Y. (1991): Wave crest statistics based on numerical simulations, *Proc. Coastal Eng., JSCE*, Vol.38, pp.141-145 (*in Japanese*).
- Isobe, M. (1988): On joint distribution of wave heights and directions, *Proc. Int. Conf. Coastal Eng.*, pp.524-538.
- Longuet-Higgins, M.S. (1957): The statistical analysis of a random, moving surface, *Phil. Trans. Roy. Soc., Ser.A*(966), Vol.249, pp.321-387.
- Pierson, W. J., Jr., Neumann, G., and James, R. W. (1955): *Practical Methods for Observing and Forecasting Ocean Waves by Means of Wave Spectra and Statistics*, U. S. Navy Hydrogr. Office Pub. No. 603.



## CHAPTER 15

### Particle Image Velocimetry (PIV) in the Coastal Engineering Laboratory

C.A.Greated<sup>1</sup>, D.J.Skyner<sup>2</sup> & T.Bruce<sup>3</sup>

#### ABSTRACT

The Particle Image Velocimetry (PIV) technique is reviewed, with special reference to its application to coastal engineering problems. The basic principles are described, and strengths and weaknesses of different implementations considered. Examples of some applications of PIV at Edinburgh are described to illustrate the practicalities of its implementation in a hydrodynamics laboratory. Finally, the limitations to the accuracy of PIV in these applications are reviewed and an outline of some new developments in this area is given.

#### INTRODUCTION

Non-intrusive flow measurement techniques are becoming an increasingly familiar part of laboratory experiments in applied hydrodynamics and coastal engineering. Since its inception in 1966, Laser Doppler Anemometry (LDA) has progressed, and aided by developments in other technologies, notably in lasers, fibre-optics and computing, it is now a most useful tool under a wide range of conditions. LDA is, however, fundamentally a point measurement technique; the time evolution of flow velocity can be measured with great accuracy at a point, but if a map of an area of the flow is to be obtained, it must be built up point by point. Thus the flow must be steady or accurately repeatable. PIV gives a quantitative map of instantaneous flow velocities over a large field. An attractive feature of PIV analysis is that the velocity measurements come out on a regular grid and thus post-processing is relatively straightforward.

PIV is sometimes compared to streak photography where the path lengths of individual marker particles in the fluid are measured. Streak photography suffers two major disadvantages. Firstly, only a very few marker particles can be

---

<sup>1</sup>Director of Fluid Dynamics Unit, Dept Physics, the University of Edinburgh, Edinburgh EH9 3JZ, Scotland

<sup>2</sup>Research Associate, Dept Physics (D.Skyner@ed.ac.uk)

<sup>3</sup>Research Associate, Dept Mech Eng (T.Bruce@ed.ac.uk)

used, otherwise their paths overlap too often and the individual particle motions cannot be separated. Secondly, when used with sheet illumination, the particles may move out of the measurement plane, artificially shortening the streak lengths and causing errors in the velocity measurement.

## PARTICLE IMAGE VELOCIMETRY

The basis of PIV is to stroboscopically illuminate a two-dimensional plane of a flow containing small *seeding* particles. A double (or multiple) exposure photograph of this plane is taken. The spacing between the images of each particle on the film gives the local velocity. This photograph is then analysed to obtain the local flow velocities over a grid of points covering the whole field. PIV is normally considered as a two stage process: the acquisition and the analysis of the image.

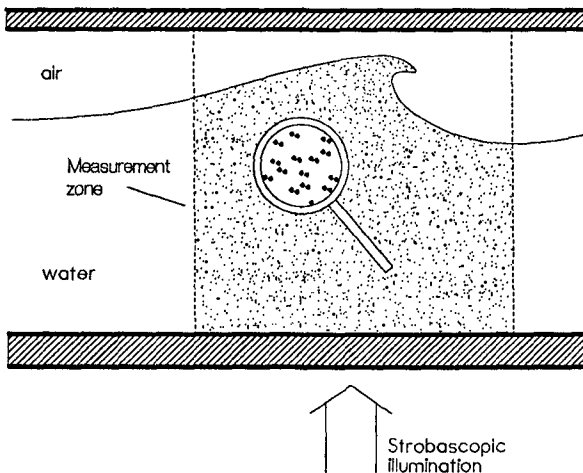


Figure 1: Schematic diagram of PIV acquisition

Figure 1 shows schematically the acquisition stage in a typical application of PIV. The enlarged area shows a portion of the film containing multiple particle images: the optimum form of this area is dictated by the requirements of the subsequent analysis. The acquisition and analysis phases are therefore inextricably linked. The following sections consider the stages of the PIV process: acquisition, ie. illumination and photography, and the automated analysis of the image.

## PIV ILLUMINATION

In general, the two-dimensional plane within the flow is defined by a thin sheet of pulsed laser light. Two different techniques are available for producing this light sheet. In the first of these, a continuous wave (CW) laser is deflected off a

rotating multi-facet mirror so that the beam is scanned through the measurement area, as illustrated in figure 2. In the illustration, the parabolic mirror collimates the beam to give a more even intensity distribution. The shutter opening time on the camera is normally set to be four to six times the period of the beam scan, in order that this number of exposures are recorded on each negative. In the second technique, a pulsed laser, typically a Nd Yag, is used to produce double pulses, the beam being spread out into a sheet using a cylindrical lens as shown in figure 3.

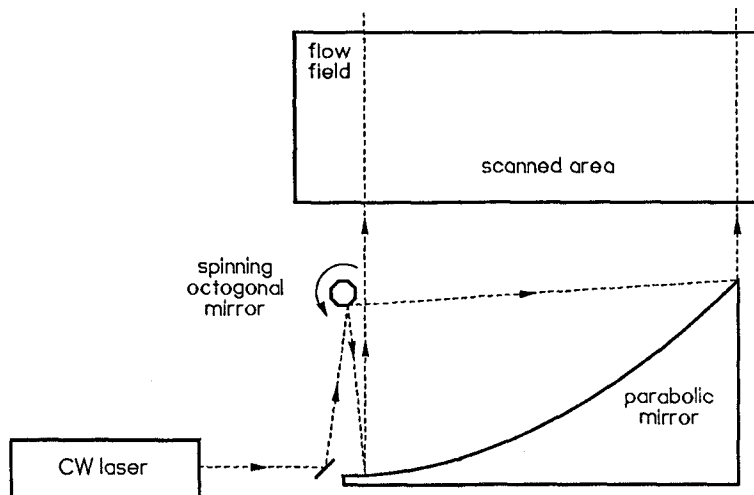


Figure 2: Scanning beam illumination system

A comparison of the illumination techniques shows that the scanning beam method [Gray et al, 1991] is usually the best for use within the velocity ranges normally encountered in the coastal engineering laboratory, i.e. up to a few metres per second. It gives a sufficiently even illumination over a large area and has the advantage that more than two images per particle can easily be obtained, which improves the signal strength in subsequent analysis. For measurement regions of about  $1\text{m}^2$  and flow velocities up to  $2\text{ms}^{-1}$  a  $10\text{W}$  Argon Ion laser is suitable. The upper limit on velocities which can be measured with the scanning beam system can be proportionally increased by, for example, reducing the width of the scanned area. Above about  $10\text{ms}^{-1}$  it is necessary to use a pulsed laser; in this case the energy per pulse is almost constant, so that measuring higher velocities does not require a proportional increase in laser power. However, the use of pulsed lasers has certain drawbacks: such systems are inherently more dangerous; it is harder to obtain an even illumination over the measurement zone; the optical alignment is more difficult. Additionally, with a single laser only two pulses per negative

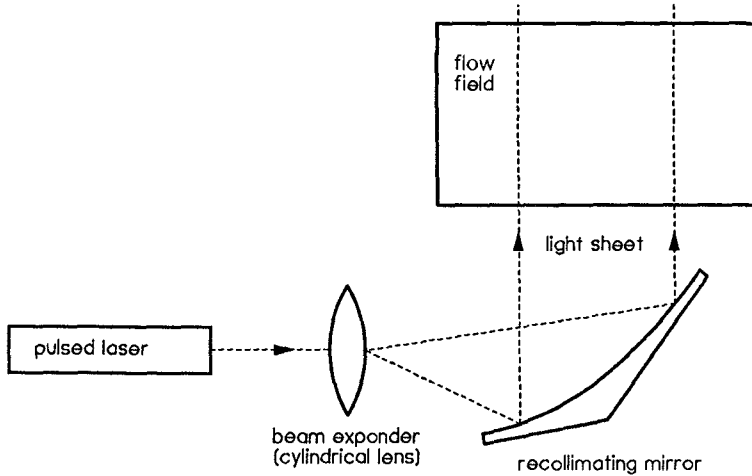


Figure 3: Pulsed sheet illumination

can be obtained easily. It is possible to obtain a four pulse sequence by coupling two lasers, but this is a costly option.

If the surface flow of a fluid is to be measured, then illuminating the measurement zone can be accomplished without the use of lasers. The surface defines the two dimensional plane for measurement and the stroboscopic illumination may be achieved by means of standard flash units. Thus PIV may often be simply and inexpensively applied to such flows.

### Practical Implementation of Illumination

In the fluid dynamics laboratories at Edinburgh the wave flumes and water channels have been designed with the application of PIV in mind. All the tanks are made of glass, giving optical access from the sides and below. The beam from a single laser serves three experimental rigs, considerably saving on the cost. Most of the time involved in carrying out PIV experiments is in setting up the apparatus. When the laser is in use for one experiment, another can be in the preparation stage.

For water channel experiments a 15W argon ion laser is used with scanning beam illumination. The beam from such a high powered laser is potentially very hazardous. For safety reasons, the laser is mounted rigidly in an enclosed area and its beam is directed through pipes to the appropriate experiment by a series of mirrors. With this arrangement the beam is totally enclosed up until the point where it enters the water tank and no longer represents a safety hazard. The scanning beam illumination system is mounted on rails beneath each of the water

channels so that the position of the measurement area can be easily moved.

## PIV PHOTOGRAPHY

The process of acquiring good PIV photographs involves two major stages. The first is selecting appropriate hardware for the application (eg, illumination, seeding, camera and film), and the second is using this hardware to best effect. This section addresses both of the above stages.

### Hardware

The hardware considerations may be divided into four broad and interdependent areas: illumination (already discussed), flow seeding, camera and film. Here the practices adopted in the study of water waves in the Fluid Dynamics Unit (FDU) at Edinburgh are detailed. However, most of the issues covered are also relevant to the application of PIV to other flows.

#### *Seeding*

The selection of a suitable flow seeding is crucial. The seeding used is conifer pollen which meets the most important criteria: it is almost exactly neutrally buoyant, quite reflective at the wavelength of the Argon Ion laser and small enough to follow the flow patterns (typical particle diameters are  $\sim 60\mu\text{m}$ ). It is also quite inexpensive — the cost of seeding a flume containing three tonnes of water is about the same as the cost of the film in the camera.

#### *Camera & Lens*

The choice of the camera and lens is also important. A flat-field lens should be used to minimise distortions of the image plane. Choosing a lens of longer focal length will reduce the apparent effect of any out-of-plane motions of particles in the field, but will increase the difficulty of achieving a sharp focus and make the process more susceptible to vibrations. A Hasselblad 500 *EL/M* camera with 80mm lens has proved suitable for many PIV applications at the FDU.

#### *Film*

The choice of film is generally straightforward, since there are a number of good, high resolution black and white films available at reasonable cost. Kodak TMax is one such film and is well suited to the green light of the Argon Ion laser.

### Taking the Photographs

The important issues remaining are the choice of camera position, achieving the correct seeding density, optimising the focus and optimising the exposure parameters to give good, high contrast photographs. Resolving all these issues involves

making compromises, and the aim of the following paragraphs is to outline the most important considerations. Figure 4 shows a well optimised image.

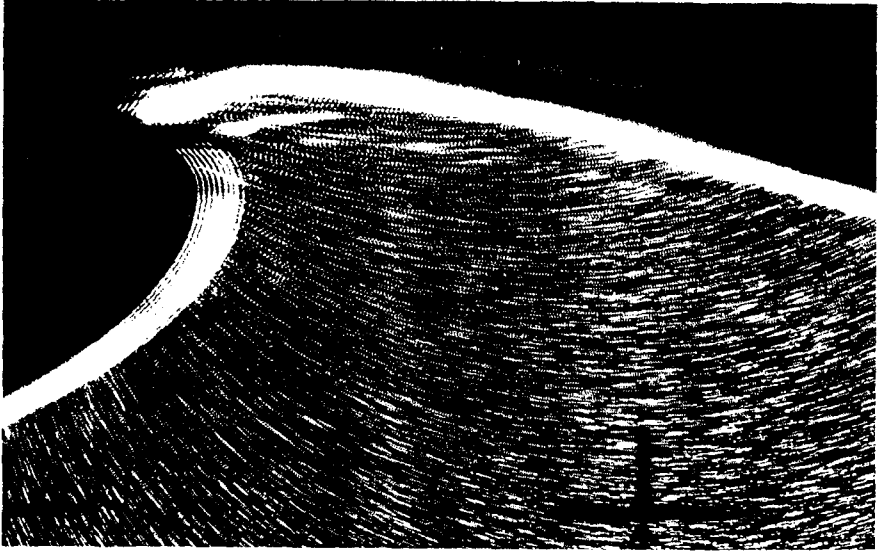


Figure 4: A photographically obtained PIV image

### *Seeding Density*

The optimum seeding density is determined by considering the subsequent analysis of the photograph. In the Edinburgh system, the local flow velocity at a point on the photograph is averaged over a 1mm diameter interrogation region. The seeding density should be high enough that there will always be several particle image pairs in each interrogation area, as shown in figure 1. Experience also plays a large part in getting an optimum level of seeding, and once good results have been obtained, the successful level of seeding can be repeated.

### *Illumination Interval*

As with optimising seeding density, the choice of illumination interval is dictated by consideration of the subsequent analysis. The interval should be set such that the largest velocity in the flow gives particle image separation on the photograph which is the largest resolvable by the analysis system,  $200\mu\text{m}$  for the FDU system. Normally an estimate of the largest velocity can be made, but its often necessary to take a test film trying different intervals in order to optimise the choice.

### *Shutter Speed*

Once the illumination interval has been chosen, the shutter speed is selected to give the required number of exposures. Typically, four to six exposures are used, but it is important to consider whether the flow changes over the exposure time.

### *Focus*

Achieving a sharp focus is vital if good PIV photographs are to be obtained, and can be quite difficult, especially when a large lens aperture or long focal length lens are being used. Again, a test film in which the focus is varied is the usual route to its optimisation.

### *Photographic Magnification*

The magnification from the measurement zone to the film depends upon the focal length of the lens and the distance from the camera to the measurement zone. Its selection is another compromise. It is often desirable to measure as large a region as possible, but the analysis phase must be considered. The implicit assumption is that particle image displacement over the interrogation region is uniform: if there is a strong displacement gradient present, errors are introduced and the resulting data point may be at best inaccurate and at worst, spurious. Therefore the size of the area imaged onto the photograph is typically limited to that which will result in displacement gradients of less than 3% over any 1mm diameter interrogation area.

### *Exposure*

Once the illumination interval and magnification have been established, the only factors left governing the exposure of the film are the lens aperture, the laser power and the film speed (ie, ASA rating). In general, a test film covering various settings of aperture and laser power is required for a new application. The quality of the resulting photographs may then be assessed on the analysis system and the best settings finalised.

If there is scope for choosing an aperture setting, it should be remembered that the largest apertures (smallest  $f$  numbers) give the poorest depth of field, so focussing is more difficult. However, if the particle image size is diffraction limited, the smaller apertures (larger  $f$  numbers) will result in larger particle images. Using  $f/4$  or  $f/5.6$  is usually a good compromise.

In general, the lower the ASA rating of the film, the finer the grain, so it is preferable to work with 100 ASA film. However, if the maximum available laser power and the largest aperture still give insufficient film exposure, then faster film may be used — 400 ASA TMax is widely used in the FDU, and has, on occasion, been *push processed* to as much as 3200 ASA, though this does result in a reduction in resolution.

## PIV ANALYSIS

There are a number of different approaches to extracting the velocity information from the flow photograph. The objective in this phase of the PIV process is to extract the local velocity at an array of positions on the negative from the most correlated separation of the particle images near that point. For high seeding densities, this is most commonly achieved by obtaining the autocorrelation of the intensity distribution within each interrogation area and locating the strongest correlation peak, which yields the average displacement and hence the velocity.

The autocorrelation function can be conveniently calculated using Fourier transforms (Wiener-Khintchine theorem)

$$A(x, y) = FT^{-1}\{[FT\{a(x, y)\}]^2\} \quad (1)$$

where  $a(x, y)$  is the image intensity distribution of the chosen portion of film,  $FT$  is a forward Fourier transform and  $A(x, y)$  is the autocorrelation function of the area.

Fast Fourier transform (FFT) routines are computationally very efficient. Nevertheless, with a fine grid the amount of computation is still considerable and an alternative approach is to produce optical transforms. Three types of analysis system are therefore possible. Both transforms can be performed digitally, both optically, or one of the transforms can be optical and the other digital. The last approach is the one which has been adopted in the FDU [Gray,1989], and is commonly known as the Young's fringe method, since the result of the optical transform is diffraction fringes. This gives adequate processing speed, whilst keeping the optical system relatively simple.

If the transformations are to be carried out purely digitally, white light illumination is used and the image of the particles is captured directly on a CCD array. This approach requires two digital transforms it is more computationally intensive than the fringe method. There are certain advantages, one of the most important being that boundaries can be indentified directly during the analysis phase without the need for additional optics.

A complete optical analysis of the PIV records is the most rapid of all, although the techniques for implementing this have not yet been fully developed. The best approach is probably to use an optically addressed spatial light modulator (SLM) as described by Jakobsen et al [1992].

### Practical Implementation of Analysis

Figure 5 shows the layout of the Edinburgh analysis rig. The negative is mounted onto a two-axis translation stage in the path of the beam from a low power laser. The illuminated area defines the point where the velocity is to be measured. Behind the negative is the "Fourier transforming" lens which images the fringe pattern onto a CCD array in its back focal plane. For a perfect transform the object should be in the front focal plane of the lens, but in practice it is placed



much closer to the lens than this in order to avoid vignetting caused by the finite aperture of the lens.

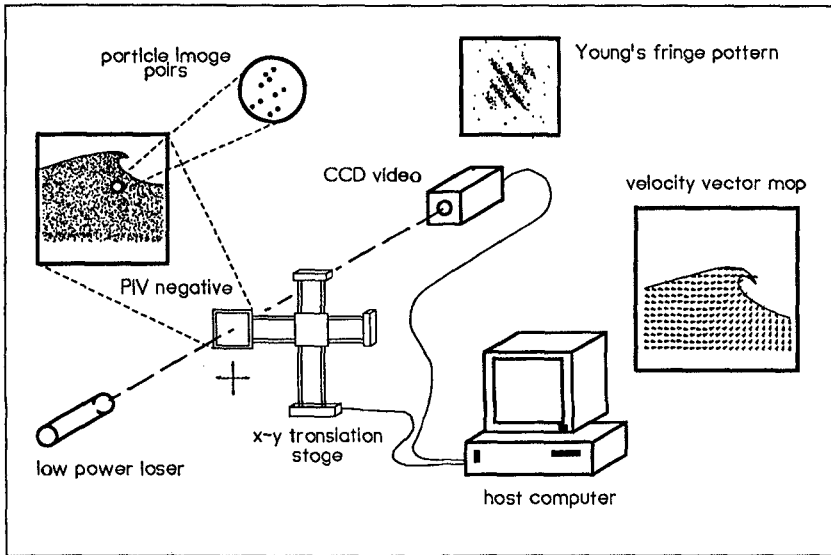


Figure 5: The Edinburgh PIV analysis system

For a typical PIV negative the fringe pattern is shown figure 6. The spacing between the fringes is inversely proportional to the particle spacing, and hence velocity, and their orientation gives the direction of the flow at that point. This fringe pattern is digitised and transferred to the PC. The inverse Fourier transform is then performed using an FFT algorithm.

Figure 6 also shows the computed autocorrelation function, containing two symmetrically placed peaks. The analysis program uses a peak detection routine to locate the position of the correlation peaks; the coordinates of the peaks define the magnitude and direction of the velocity vector at that point. An advantage of the fringe method is that the user can see immediately whether clear fringes are formed at any particular point in the flow. If they are, then the analysis procedure will almost certainly give a reliable velocity reading.

To obtain velocity values on a grid of points in the flow, the translation stage moves the negative relative to the interrogating laser beam. At each point, the analysis takes about 4 seconds, so that a 35mm format negative is analysed on a 1mm grid in under an hour.

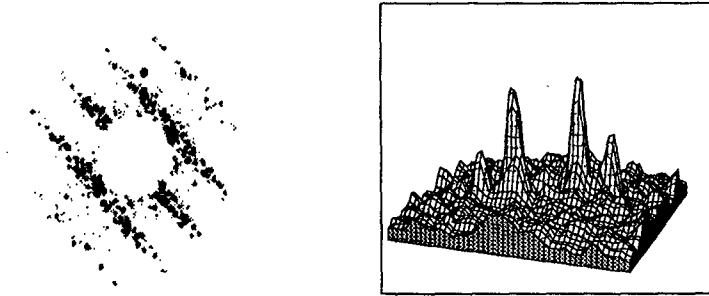


Figure 6: Fringe pattern and autocorrelation function

### Data Validation

In the Edinburgh system, each velocity measurement is accompanied by a value which gives a measure of its reliability. This is determined by strength of the correlation peak compared to the background noise level. Velocity vectors whose “quality” factor lies below a specified threshold can either be discarded or checked individually.

### PIV ERRORS

As with LDA, PIV gives an absolute measurement of velocity, provided that the system is calibrated correctly for known particle displacements. Distortions can also occur in the photographic process, for example by refraction at side walls. The extent of these can easily be checked by inserting a grid into the measurement area and photographing this in place of the illuminated sheet.

The accuracy of PIV data is determined by the uncertainties introduced in the two distinct phases of the process; the photographic recording of the flow, and the analysis of this photograph. The specific problems in the case of PIV applied to wave motion have been considered in detail. For the most reliable results, the flow must be well seeded, and the photographic acquisition parameters selected to ensure that the velocity range present corresponds to the full range measurable in the analysis and that the velocity gradients on the film are not too great. If these conditions are satisfied, then the final error bound on measurements can be less than  $\sim 2\%$  of the maximum velocity measured.

### EXAMPLES OF PIV MEASUREMENTS

In this section the results from applications of PIV at the FDU are presented. Other recent studies using the technique are described in [Powell et Al,1992,

Morrison & Greated,1992, Bruce & Easson,1992, Skyner & Easson,1992(b)].

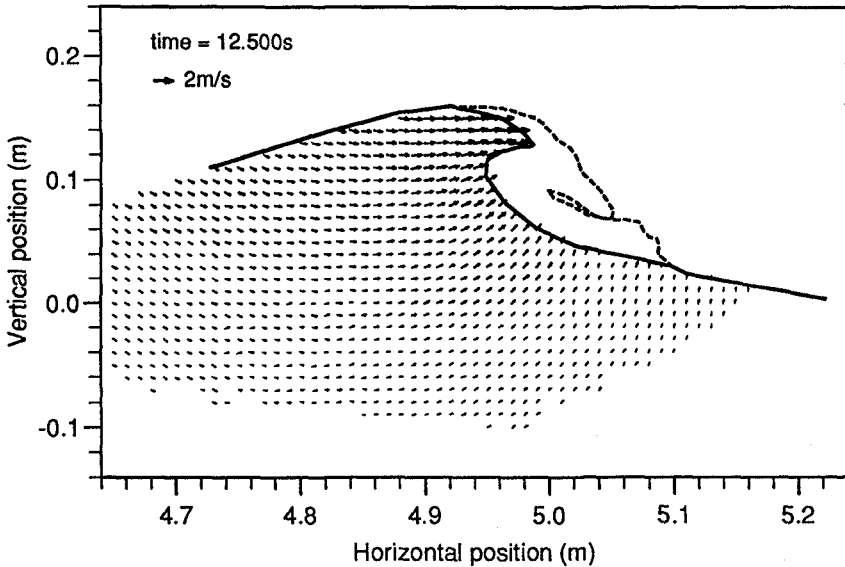


Figure 7: Vector field within a breaking wave

The results of the analysis of a PIV photograph can be displayed as a set of velocity vectors or, alternatively, iso-velocity contours may be plotted. Figures 7 and 8 show matching plots of velocity vectors and iso-velocities for a breaking wave; this type of plot is particularly useful for illustrating wave motions. Further details of this work are given in [Skyner,1992(a)].

For studies of vortex shedding or turbulence, vorticity contours may be the best method of display. Vorticities can be computed at each point by taking central differences in the two coordinate directions. Figure 9 shows a typical vorticity map recorded in the wake of an oscillating cylinder using PIV.

### Other Applications

PIV is potentially applicable to the measurement of two-phase flows and has been used successfully to study particle transport in air streams [McCluskey et al,1989]. It is anticipated that it will give good results in the study of sediment movement in water channels when the sediment density is low.

### FUTURE DEVELOPMENTS

Two new areas of development in PIV are particularly relevant to the coastal engineering laboratory. One is the use of stereoscopic photography to measure

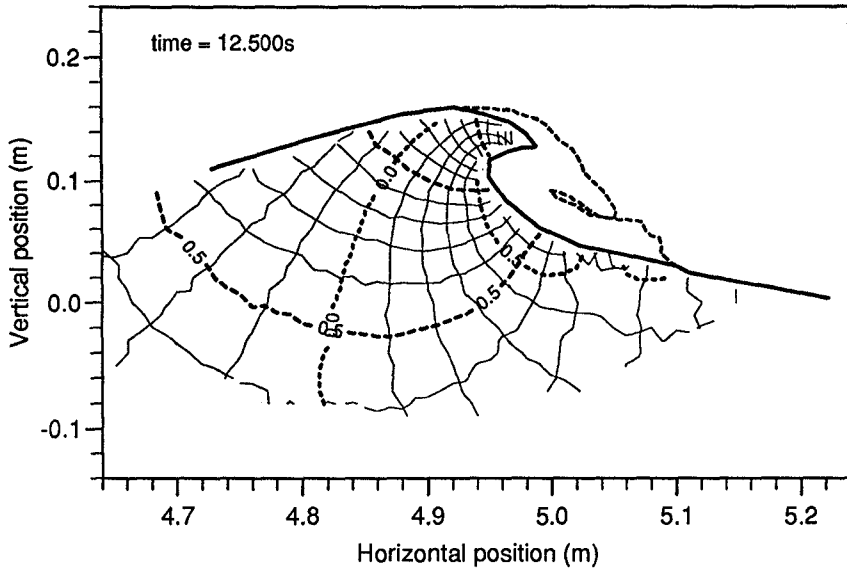


Figure 8: Iso-velocity contours of a breaking wave. Contour interval  $0.1\text{ms}^{-1}$

all three velocity components and the other is the development of on-line PIV using acquisition systems based on a CCD camera.

### Stereoscopic Measurements

In stereoscopic photography the normal methods of illumination are used but the illuminated sheet in the flow is photographed from two different positions at the same time. There are two fundamental optical arrangements. In one of these, two cameras are angled to image the same field. The problem here is that different parts of the sheet are at different distances from the lens so it is difficult to achieve a sharp focus. Secondly, there is a distortion of the image. The other approach is to have both cameras aligned normal to the measurement plane. The problem in this case is that only part of the two images overlap and are usable for measurement. Most researchers have chosen the second method.

Two separate photographs may be taken and analysed and the resulting velocity vector plots combined by triangulation to produce the three components of velocity in a plane. For practical purposes the use of two cameras presents alignment difficulties because the resulting negatives need to be matched very precisely. To overcome this difficulty a number of systems have been developed which use just a single lens and produce the two images on a single piece of film. One such system has been devised by Arroyo and Greated [1991]. Instead of having two separate lenses in front of a single piece of film the two images are formed through the same lens. This is achieved by removing the lens from a

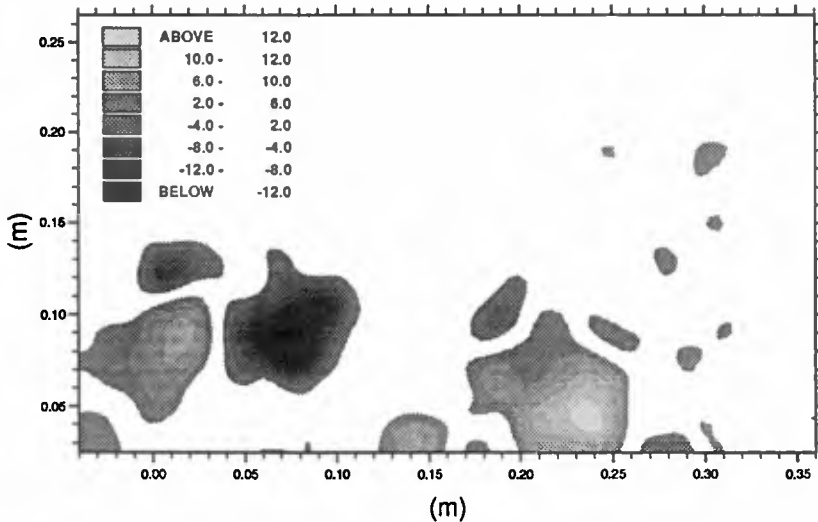


Figure 9: Vorticity in the wake of an oscillating cylinder

conventional camera and placing two parallel mirrors between the lens and the film. Two further parallel mirrors are also placed on the other side of the lens. After alignment, this system can be operated as a conventional camera.

### On-line PIV

It would be attractive if the photographic process could be eliminated completely. This can in fact be done by replacing the film camera with a CCD camera which simply captures an image electronically. Again, with multiple exposures on the same frame, the matrix of pixels needs to be subdivided and correlations carried out digitally. If different frames are used for consecutive exposures or two separate cameras are used, then the autocorrelation can be replaced by crosscorrelation, in which case directional ambiguity is resolved. Systems of this type have been implemented but in the present state of the art they are limited to extremely low velocities and the resolution is extremely poor compared to film.

### Fibre Optic Delivery

Considerable developments have been made in fibre optics in recent years and it is now possible to channel powers of up to 4W through monomode fibres. The use of monomode fibres allows the light to be recollimated back into a narrow beam of light at the other end; with the multimode fibres this is difficult to do. Powers of greater than about 4W can in theory be transmitted by splitting the

beam. Fibre optic linkage makes the PIV system very much more flexible and may be essential where access to the working area is severely constricted. Fibre transmission of pulsed laser beams is much more difficult due to the very high peak power densities.

### ACKNOWLEDGEMENT

The authors wish to acknowledge financial support from the SERC and the EC MAST programme (contract MAST 0035C).

### References

- [1] Arroyo, M.P. and Greated, C.A. . *Stereoscopic Particle Image Velocimetry*. 1991. Measurement Science Technology, 2, pp 1181-1186.
- [2] Bruce T. and Easson, W.J. *The Kinematics of Wave Induced Flows Around Near-Bed Pipelines*. 1992. Proc. 23rd Int. Conf. on Coastal Eng., ASCE.
- [3] Gray, C. *The Development of Particle Image Velocimetry for Water Wave Studies*. 1989. PhD thesis, the University of Edinburgh.
- [4] Gray, C., Greated, C.A., McCluskey, D.R. and Easson, W.J. *An Analysis of the Scanning Beam PIV Illumination System*. 1991. J. Phys. Measurement Science and Technology 2, 717-24.
- [5] Jakobsen, M.L., Hossack, W.J., Greated, C.A. and Easson, W.J. *PIV Analysis Using an Optically Addressed Spatial Light Modulator*. 1992. Applied Optics and Opto-Electronics, Leeds.
- [6] McCluskey, D.R., Easson, W.J., Greated, C.A. and Glass, D.H. *The Use of Particle Image Velocimetry to Study Roping in Pneumatic Conveying*. 1989. 4th European Symposium on Particle Characterization, Nuremburg, Germany.
- [7] Morrison, I.G and Greated, C.A. *Oscillating Water Column Modelling*. 1992. Proc. 23rd Int. Conf. on Coastal Eng., ASCE.
- [8] Powell, K.A., Quinn, P.A. and Greated, C.A. *The Formation of Shingle Beach Profiles due to Wave Impact, and the Measurement of the Wave Velocities using Particle Image Velocimetry* . 1992. Proc. 23rd Int. Conf. on Coastal Eng., ASCE.
- [9] Skyner, D.J. and Easson, W.J. *The Effect of Sheared Currents on Wave Kinematics and Surface Parameters*. 1992. Proc. 23rd Int. Conf. on Coastal Eng., ASCE.
- [10] Skyner, D.J. and Greated, C.A. *The Evolution of a Long-crested Deep-water Breaking Wave*. 1992. Proc. 2nd Conf. Int. Offshore & Polar Eng., 3, ISBN 1-880653-03-6, 132-8.

## CHAPTER 16

### Directional nearshore wave propagation over a rip channel: an experiment

Luc HAMM\*

#### ABSTRACT

The aim of these tests was to study wave propagation on a beach, including the surf zone, and nearshore circulation produced by breakers in the presence of a rip channel. The tests were carried out in a multidirectional wave tank. The initial series of tests concerned the case of a plane beach sloping at 1 in 30. The second series was performed with a rip channel excavated in the beach. Conventional wave measurements were taken at 50 different points. Measurements of the multidirectional waves and rip current were taken at 7 points along the channel centre line. During the tests, various types of wave (monochromatic, random monodirectional and multidirectional) were tested and the results obtained were compared with identical starting conditions.

#### 1. INTRODUCTION

Wave tanks capable of simulating real multidirectional (short-crested) waves are a relatively common means of studying offshore structures, but they are less frequently used in the field of coastal engineering. Nevertheless, this field is rapidly developing at the present time and many shallow-water, multidirectional wave tanks have been built in recent years in Europe and North America. Mention should be made of three recent studies conducted in tanks of this type, which have been devoted to the study of wave propagation in the nearshore area, including the surf zone. Dingemans et al. (1986) studied the propagation of breaking waves on a submerged bar creating a rip current. In this case, where the energy slope is very localised, directional effects do not appear to affect the results to any great extent. Vincent and Briggs (1989) studied the effect of directional spectrum width on the concentration of wave

---

\* Senior engineer, SOGREAH Ingénierie, 6 rue de Lorraine, 38130 ECHIROLLES, France

disturbance behind a shoal. They showed that the results were highly sensitive to this parameter in the case of non-breaking waves. Lastly, Briggs and Smith (1990) and Elgar et al. (1992) have presented results for propagation on a plane beach with a slope of 1 in 30, including a wide range of unimodal and bimodal frequency spectra.

The main interest of these tests was to provide data sets that can be used to validate numerical models of real wave propagation (Dingemans, 1986; Grassa, 1990; Panchang et al., 1990). The tests described here were carried out in line with this philosophy. The bed configuration adopted aims at combining a moderately sloping beach with the creation of a water circulation cell produced by breaking waves.

## 2. EXPERIMENTAL SET-UP

The model was built in a wave tank at the Laboratoire d'Hydraulique de France in Grenoble. The tank measures 30 m by 30 m and is fitted with a multidirectional wave generator consisting of 60 paddles, each 0.5 m wide and 1.40 m high. The sea bed consists of a plane beach sloping at 1 in 30, with a rip channel excavated in the centre (fig. 1).

Direct OXYZ co-ordinates are defined as follows. The OX axis is perpendicular to the generator and forms the axis of symmetry of the wave tank. OY is parallel to the generator and marks the foot of the beach. OZ is vertical, running from the bottom to the top, with its origin at 0.50 m above the flat bed of the wave tank.

The bathymetry may be represented by the following analytical expression (Noda, 1974):

$$Z_f(x,y) = 0.1 - \frac{X}{30} \left[ 1 + 3 \exp\left(-\frac{X}{3}\right) \cos\left(\frac{\pi y}{30}\right) \right] \quad (1)$$

with  $X = 18 - x$

$x$  varies between 0 and 18 m and  $y$  between -15 and +15 m. The longitudinal profile along the centre line of the channel is shown on fig. 2d.

During construction of the sea bed, the channel was temporarily filled in order to carry out prior tests on the plane beach. It should also be noted that the beach only starts at a distance of about 5 m from the generator. This makes for better wave generation and for clear access to the tank.



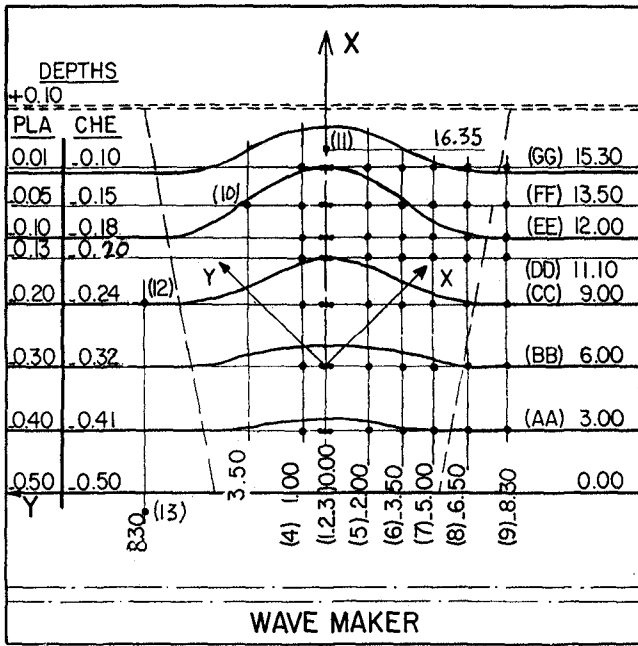


Fig. 1 Experimental set-up

### 3. INSTRUMENTATION

Ten standard wave gauges and a wave direction gauge were installed in the tank. Visual observations (comprising photographs and video films) were also made under rather poor lighting conditions, which it was impossible to improve during the study.

The wave gauges are accurate to within 2%, with 1-5% linearity and very little drift. They were calibrated once a week. The direction gauge consists of a classic resistive wave gauge coupled to an electromagnetic current meter capable of making two-directional horizontal measurements. The main drawbacks encountered with resistive gauges, namely lack of stability, drift and linearity of measurement, were largely offset by using a small platinum electrode that compensates for deviations. In this way, linearity was 0.5% and calibration only had to be performed during maintenance operations.

The electromagnetic current meter is a disk 40 mm in diameter and 18 mm thick, accurate to within about 1%, and covering a measurement range of 0 to 1 m/s. It is calibrated during maintenance operations.

#### 4. MEASUREMENT POSITIONS

The ten wave gauges and wave direction gauge were installed in two groups in the wave tank.

The first group (comprising the direction gauge and six wave gauges) was fixed on a mobile beam running along the axis of the wave tank. These gauges scan an area between  $y = 8.3$  m to  $y = +1$  m and  $x = 1.0$  m to  $x = 15.30$  m. This last position ( $x = 15.30$  m) was only reached by certain gauges when the depth of water was sufficient for the measurement to be taken.

The other four gauges were arranged in a fixed pattern over the tank. They were used to check the repeatability of the measurements and replace any gauges on the beam that might prove to be defective during the tests.

In practice, the beam was moved along 7 axes during each test. This meant that wave disturbance was measured at 53 points in the case of the plane beach and 50 with the channel. The positions of the measuring points are shown on fig. 1 for the tests carried out with a channel.

The electromagnetic current meter was placed at 0.05 m above the bed, except at the last point near the coast, where the distance was reduced to 0.03 m.

#### 5. INCIDENT WAVE CONDITIONS

The wave generator is of the piston type and each paddle is controlled independently by a hydraulic system. The paddle control signal is generated by a program that uses the white noise filtering technique described by Gilbert and Huntington (1991). This method can only be used for waves that are perpendicular to the generator. With oblique waves, the superimposed sinusoidal wave method must be used. During this study, only frontal waves were generated with the white noise filtering technique. 17 wave conditions were selected in order to cover a wide range of steepness values and frequency and direction spectrum widths.

The spectra generated were of the form:

$$S(f, \Theta) = S_{\gamma}(f) \cos^n \Theta \quad (2)$$

$S_{\gamma}(f)$  corresponds to the Jonswap spectrum dependent on the parameter  $\gamma$ , with a value of 3.3 or 7. The angular distribution function depends on the exponent  $n$ , which has the value 2 or 6 in this case. Table no. 1

lists the theoretical incident wave conditions. Wave measurements in front of the generator gave values between 0.95 and 1.15 times the set height. No adjustment was made to correct these deviations.

Each wave condition was generated by identical repetitive cycles. A cycle had a period equal to 260 times the peak period, corresponding to about 320 waves. Repeatability of the waves was found to be very good at the fixed offshore gauges (variance less than 1% in most cases).

	Hs (mm)	Tp (s)		n		Hs (mm)	Tp (s)		n
Monochromatic	40	1.25			Unidirectional	80	1.25	7	
Unidirectional	40	1.25	3.3		Multidirectional	80	1.25	7	6
Multidirectional	40	1.25	3.3	2	Monochromatic	100	1.25		
Unidirectional	40	1.976	3.3		Unidirectional	100	1.25	3.3	
Multidirectional	40	1.976	3.3	6	Unidirectional	100	1.25	7	
Monochromatic	70	1.25			Multidirectional	100	1.25	3.3	2
Unidirectional	70	1.25	3.3		Unidirectional	100	1.976	3.3	
Multidirectional	70	1.25	3.3	6	Unidirectional	130	1.60	3.3	
					Multidirectional	130	1.60	3.3	2

Table 1 Incident wave conditions

## 6. TEST PROCEDURE

This comprised three main phases, as described below:

Preparation of the test: The water surface at rest was measured at each measurement point in order to determine the reference level for subsequent calculation of the set-up and mean rip current. This procedure was essential as the gauges were submerged at different depths from one measurement line to another so as to be adapted to decreasing water depths. The generator was then started up and allowed to run for about 15 minutes in order to achieve a stable rip current pattern.

Measurements: Measurements were made simultaneously on the 13 channels over a period equal to one generation cycle (i.e. about 320 waves) with a frequency of between 20 and 25 Hz depending on the peak period. The trolley was then moved to the following measurement line and the gauges submerged at a suitable level for the water depth in this new position. These operations were repeated seven times during each test, without stopping the generator. They lasted about three hours.

End of test: At the end of the test, all the measurements were checked and any incidents during acquisition noted. Certain tests were repeated when serious incidents had occurred. An initial statistical analysis of measurements from the fixed gauges was also made to check the reproducibility of the wave conditions during the test. The recorded data were then stored on magnetic tape, translated into ASCII and stored on PC-compatible floppy disks.

## 7. STANDARD DATA PROCESSING

The mean values from each measurement point were first of all calculated by comparison with the measurements at rest. The set-up and mean current values were estimated in this way.

Standard processing then involved performing a statistical analysis of all the recordings. The main characteristics ( $H_{1/3}$ ,  $H_{1/10}$ ,  $H_{\max}$  and associated periods and  $H_{\sigma}$ ) were then gathered in the summary tables shown in the complete report (Hamm, 1992).

Graphic representation of these values revealed acquisition anomalies on certain channels. Generally speaking, the checks carried out showed that 90% of the measurements were reliable. Figures 2 to 4 show examples of the results obtained for three series of tests. These figures show a comparison between the significant wave height values ( $H_{1/3d}$ ) and an estimate made on the basis of the variance of the free-surface elevation ( $H_{\sigma}$ ) for unidirectional and multidirectional waves.

These figures are divided into four parts, designated a) to d). Figures a) present the results obtained on the plane beach and b) those obtained in the centre line of the rip channel. Figures c) give the mean rip current measured near the bed in the centre line of the channel. Lastly, figures d) recall the bed contour profiles. It can be seen that there is little difference between  $H_{1/3}$  and  $H_{\sigma}$  except in the case of waves with low steepness (fig. 2) in the surf area. Similarly, there is little difference between unidirectional and multidirectional wave cases. This result appears a little surprising at first, in the presence of the channel, as the rip current tends to generate wave concentrations which should be more attenuated in the case of a multidirectional wave (Vincent and Briggs, 1989). Indeed, the opposite trend may be observed on figure 3b). This may be due to the breaking process.

Figures 5a) and b) give an overall view of the wave heights measured in the case of waves of low steepness. Figure 5a) shows an abnormal value along the channel centre line (line D), which had already been observed on figure 2a). These abnormal results are currently being analysed.

## 8. SPECTRUM ANALYSIS

Measurements with the wave direction gauge were subjected to a conventional spectrum analysis and directional spectrum analysis using the maximum entropy method (MEM) published by Sand and Mynett (1987). This method is one of the most accurate currently available (Benoit, 1992). However, it is not always easy to interpret the results (Van de Meer, 1990) and detailed analysis is currently in progress.

By way of example, figure 6 shows the frequency spectra obtained with unidirectional waves of low steepness in front of the generator and in the surf zone on the plane beach and in the channel centre line. The results are comparable and show a classic type of evolution with the development of sub- and super-harmonics during propagation towards the coast.

Figures 7 and 8 show the change in directional spectrum for these same waves between offshore and the coast, on the plane beach. There is similarity with the change in frequency spectrum observed previously and a marked narrowing of the directional distribution.

## 9. GENERAL COMMENTS AND CONCLUSIONS

The tests presented here represent a valuable data set for validating numerical models of wave transformation and rip current generation. The huge amount of data is still under analysis and the first results presented here tend to show that the directional spreading does not seriously affect the magnitude of the return current and the significant wave heights.

On the other hand, in spite of the large number of recording points (53), the impression given is one of a fairly loose measuring network, particularly in the channel. Indeed, the instability of the rip current could be observed visually in most of the tests. This is clearly demonstrated by the dissymmetry of the wave crests on either side of the channel centre line, and in particular a shift in the breaking point, which varied with time. A denser measuring network would have been needed to quantify this instability. A possible alternative, which is currently being tested, would be to use a video technique of the type used in the field by Holman and Lippmann (1991) in addition to the conventional isolated measurements.

10 ACKNOWLEDGEMENTS

This work was undertaken as part of the MAST G6 Coastal Morphodynamics research programme. It was funded jointly by the Service Technique Central des Ports Maritimes et des Voies Navigables and by the Commission of the European Communities Directorate General for Science, Research and Development, under contract no. MAST 0035C.

11. REFERENCES

- Benoit M. (1992): Practical comparative performance survey of methods used for estimating directional wave spectra from heave-pitch-roll data. Proc. 23rd Int. Conf. on Coastal Eng., ASCE, to appear.
- Briggs M.J. and Smith J.M. (1990): The effect of wave directionality on nearshore waves. Proc. Int. Conf. on Coastal Eng., ASCE, 267-280.
- Dingemans M.W., Stive M.J.F., Bosma J., de Vriend H.J. and Vogel J.A. (1986): Directional nearshore wave propagation and induced currents. Proc. Int. Conf. on Coastal Eng., ASCE, 1092, 1106.
- Elgar S., Guza R.T., Freilich M.H. and Briggs M.J. (1992): Laboratory simulations of directionally spread shoaling waves. J. of Waterways, Port, Coastal and Ocean Eng., Vol. 118, no. 1, ASCE, 87-103.
- Gilbert G. and Huntington S.W. (1991): A technique for the generation of short-crested waves in wave basins. J. of Hyd. Res., Vol. 29, no. 6, 789-799.
- Grassa J.M. (1990): Directional random wave propagation on beaches. Proc. Int. Conf. on Coastal Eng., ASCE, 798-811.
- Hamm L. (1992): Random wave propagation in the nearshore zone. Experiments in a directional wave basin. Internal report, MAST-G6M, to appear.
- Lippmann T.C. and Holman R.A. (1991): Phase speed and angle of breaking waves measured with video techniques. Proc. Coastal Sediments '91, ASCE, 542-556.
- Noda E.K. (1972): Rip currents. Proc. 13th Int. Conf. on Coastal Eng., ASCE, 653-668.
- Panchang V.G., Pearce B.R. and Briggs M.J. (1990): Numerical simulation of irregular wave propagation over shoals. J. of Waterway, Port, Coastal and Ocean Eng., ASCE, Vol. 116, no. 3, 324-340.
- Sand S.E. and Mynett A.E. (1987): Directional wave generation and analysis. Proc. IAHR seminar on wave analysis and generation in laboratory basins. Lausanne, 209-235.
- Van der Meer J.W. (1989): Measurement and analysis of directional seas in a basin. Proc. IAHR Congress, Ottawa, C-267 - C275.
- Vincent C.L. and Briggs M.J. (1989): Refraction-diffraction of irregular waves over a mound. J. of Waterway, Port, Coastal and Ocean Eng., ASCE, Vol. 115, no. 269-284.

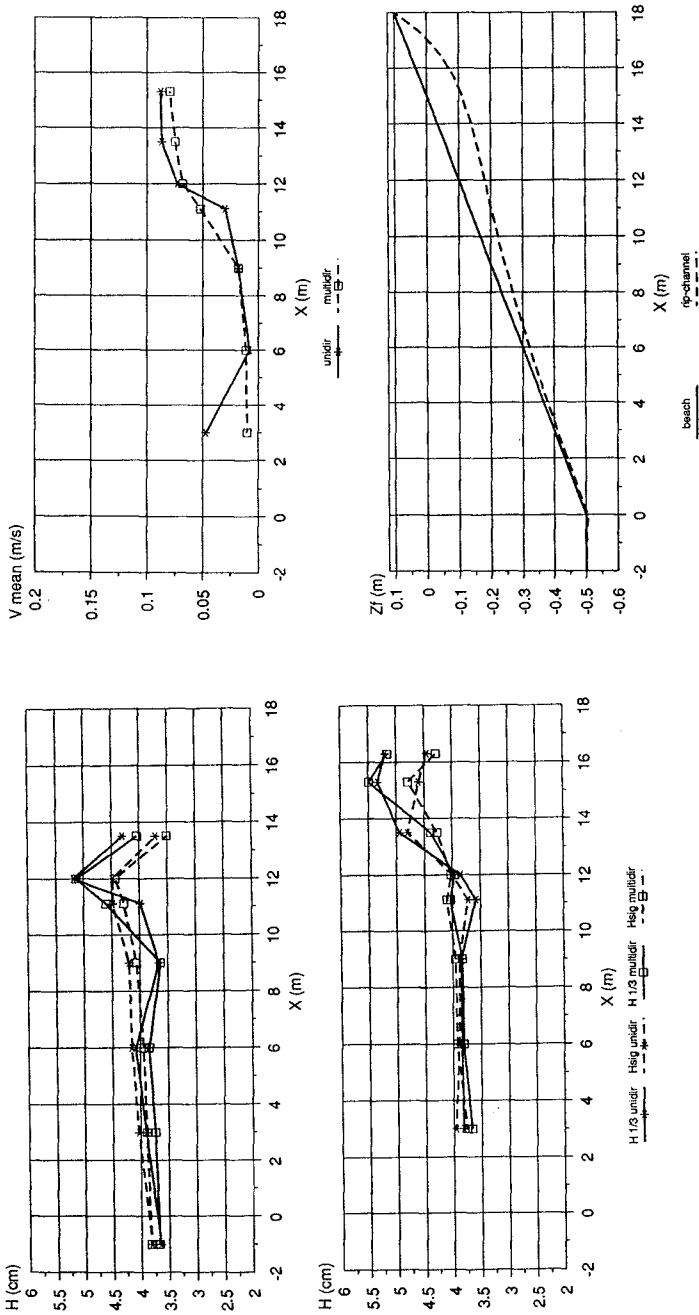


Fig. 2 Experimental results.  $H_s = 0.04$  m -  $T_p = 1.976$  s  
 a. Wave heights along the plane beach profile  
 b. Wave heights along the rip channel axis  
 c. Mean return current near the bottom in the channel axis  
 d. Beach and rip channel profiles

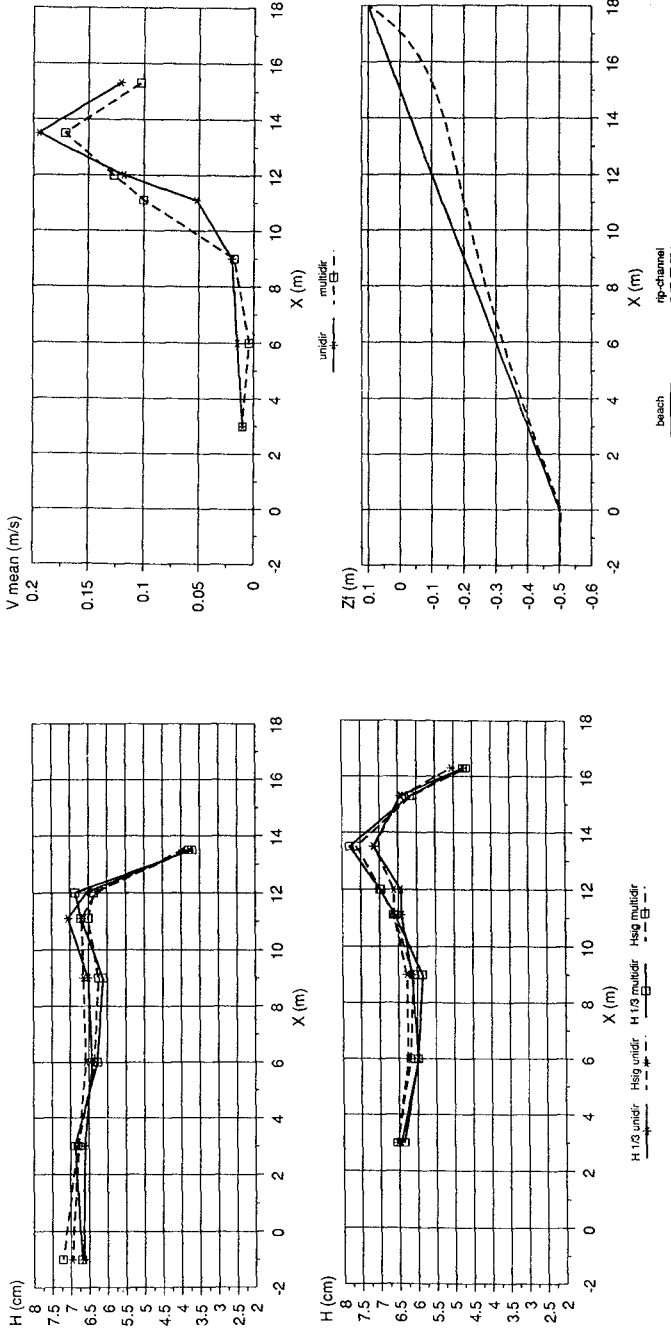


Fig. 3 Experimental results.  $H_s = 0.07$  m -  $T_p = 1.25$  s  
 a. Wave heights along the plane beach profile  
 b. Wave heights along the rip channel axis  
 c. Mean return current near the bottom in the channel axis  
 d. Beach and rip channel profiles



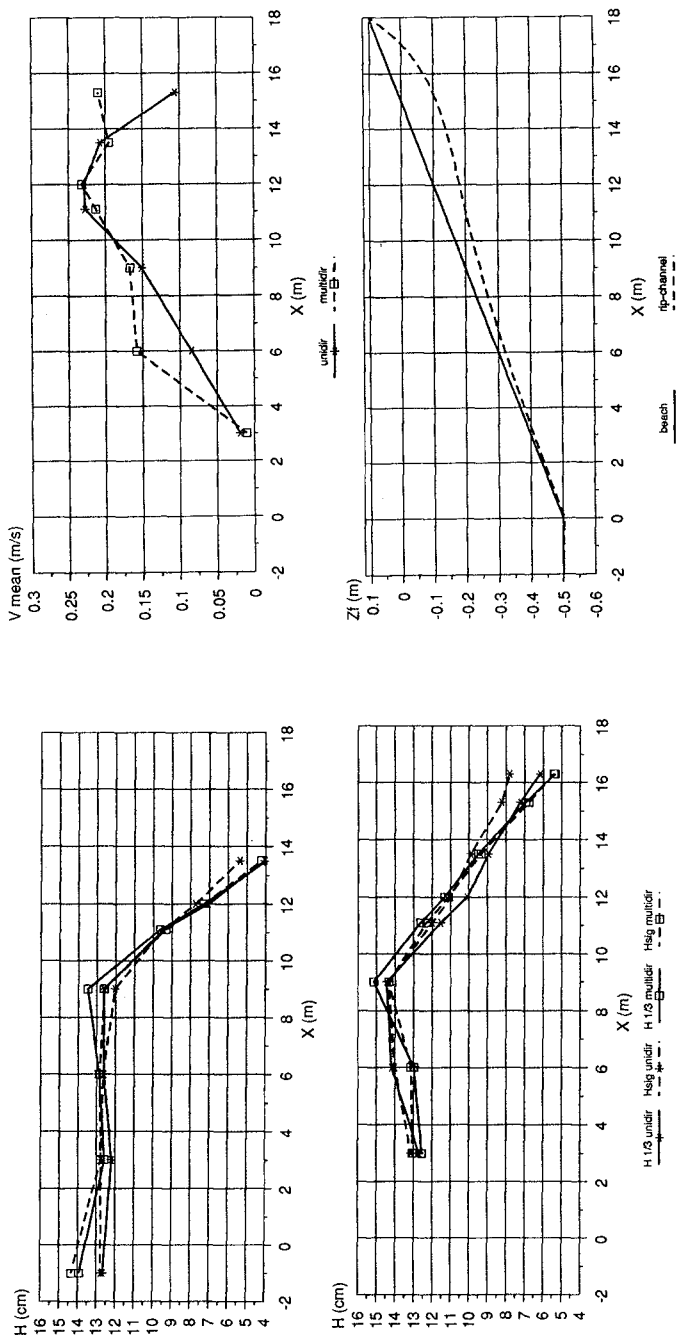


Fig. 4 Experimental results.  $H_s = 0.13$  m -  $T_p = 1.60$  s  
 a. Wave heights along the plane beach profile  
 b. Wave heights along the rip channel axis  
 c. Mean return current near the bottom in the channel axis  
 d. Beach and rip channel profiles

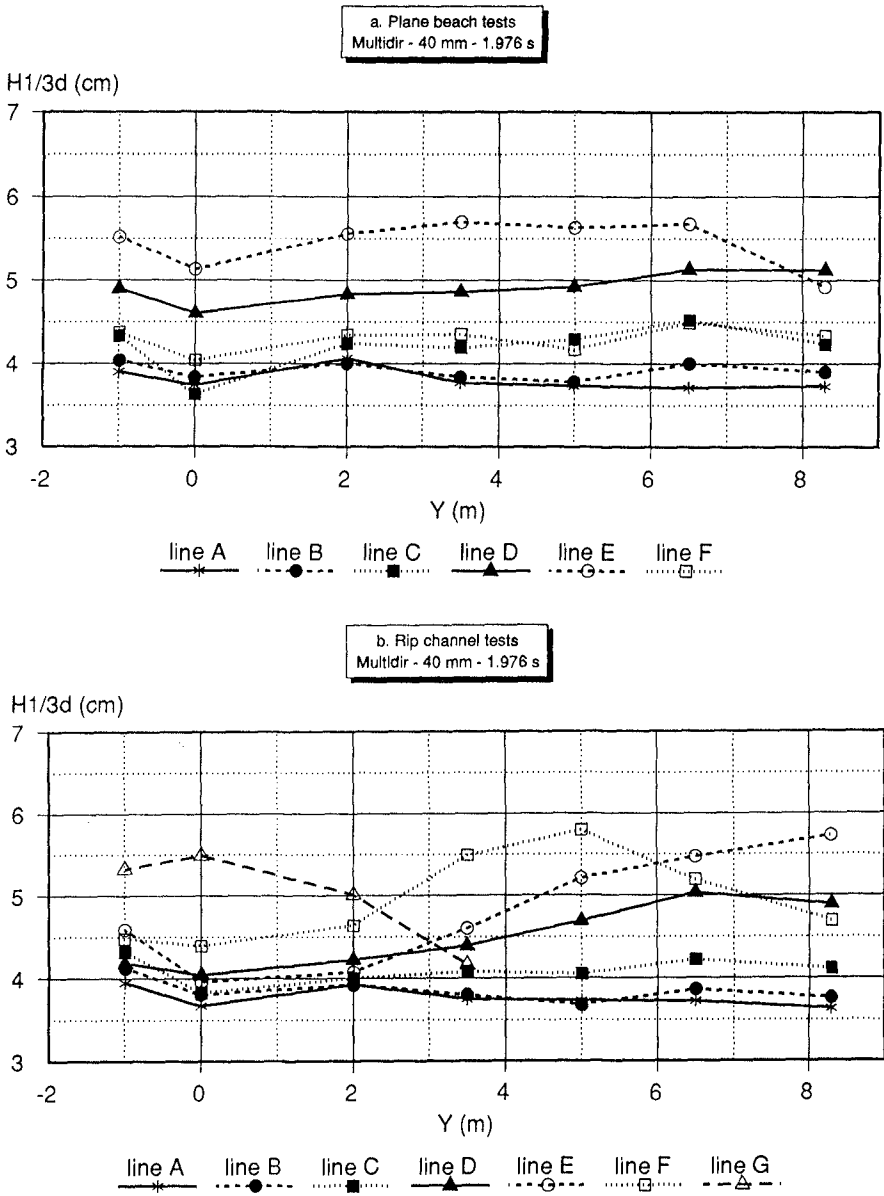


Fig. 5 Wave heights along transversal sections.  $H_s = 0.04$  m -  $T_p = 1.976$  s  
Multidirectional incident spectrum  
a. Plane beach test    b. Rip channel test

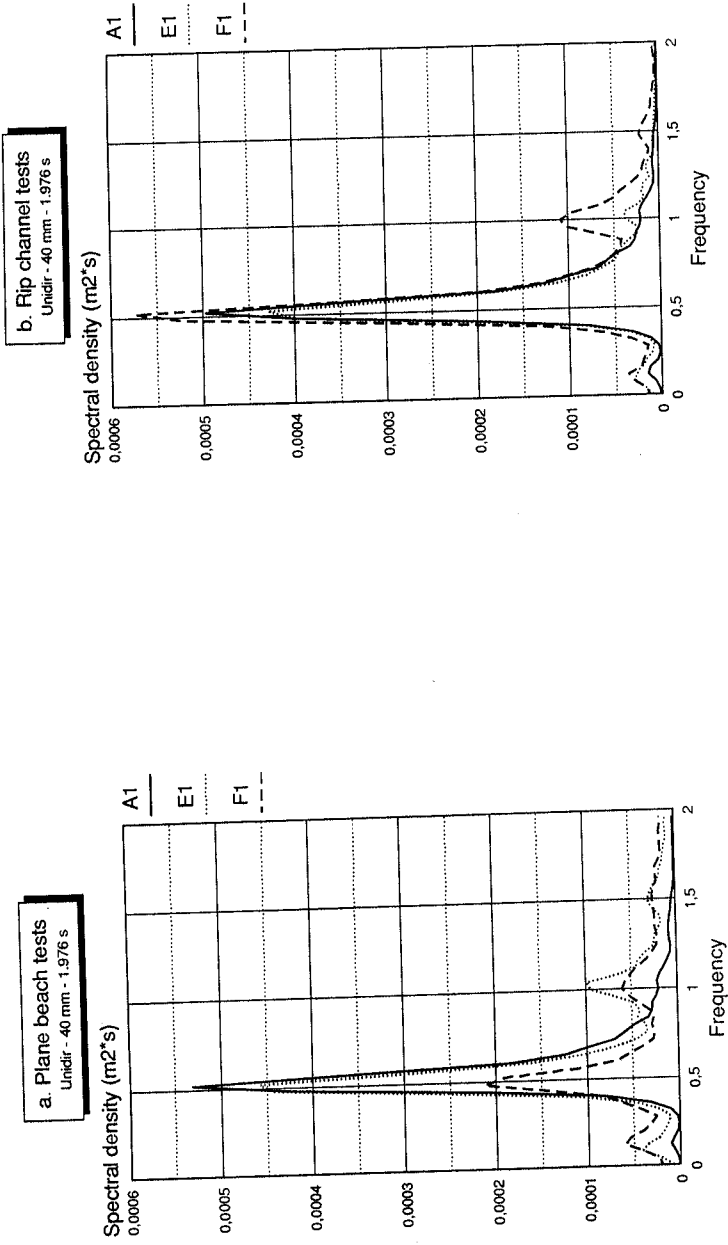


Fig. 6 Frequency spectra at three points along the channel axis  
 $H_s = 0.04 - T_p = 1.976$  s. Unidirectional incident spectrum.  
a. Plane beach test    b. Rip channel test

Fig. 8 Directional spectra on the plane beach. Surf zone condition (point G1).  $H_s = 0.04$  m -  $T_p = 1.976$  s.  
 a. Equidensity curves (10 - 30 - 50 - 70 - 90%) of the spectral density  
 b. Equidensity curves of the spreading function

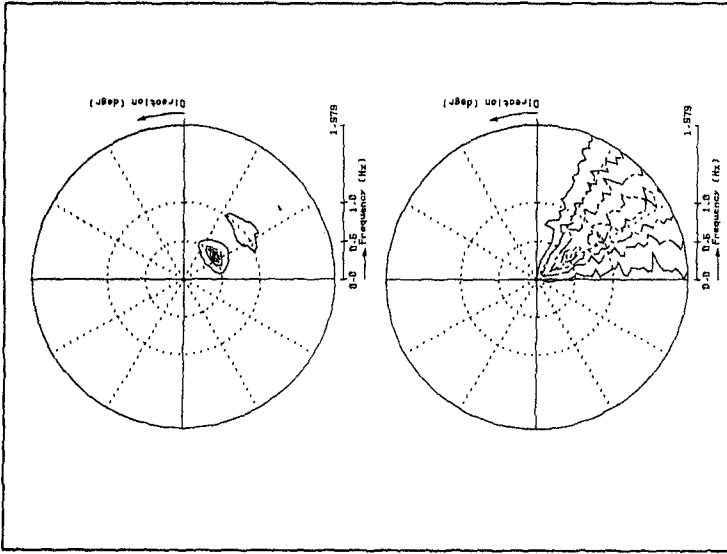
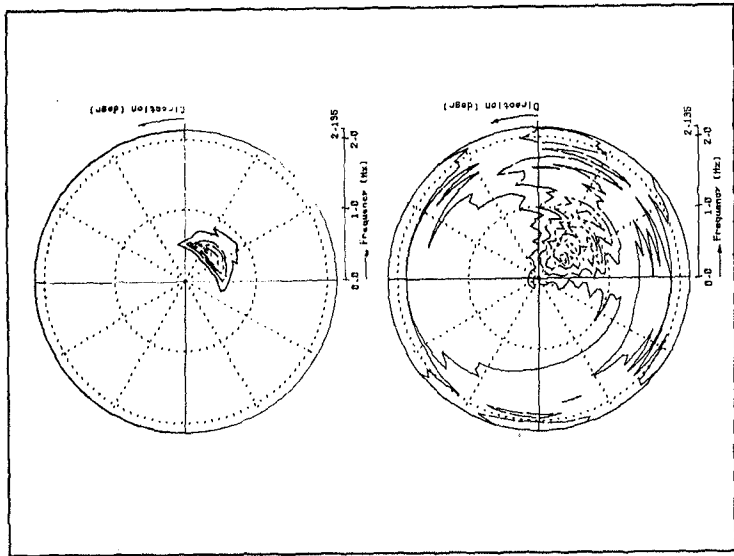


Fig. 7 Directional spectra on the plane beach. Offshore condition (point A1).  $H_s = 0.04$  m -  $T_p = 1.976$  s.  
 a. Equidensity curves (10 - 30 - 50 - 70 - 90%) of the spectral density  
 b. Equidensity curves of the spreading function

## CHAPTER 17

### WAVE SETUP ON BEACHES AND IN RIVER ENTRANCES

David J. Hanslow<sup>1</sup> & Peter Nielsen<sup>2</sup>

#### Abstract

This paper investigates the phenomenon of wave setup both on beaches and within river entrances. Field measurements of the mean water surface through the Brunswick River Entrance on the North Coast of NSW, Australia and on the beach immediately south of the entrance are presented for a variety of incident wave conditions. These include wave heights up to 4m (Deepwater RMS). Data collected show very little setup in the river entrance even though wave breaking occurs across the entrance under relatively small wave conditions. At the same time significant wave setup was measured on the adjacent beach. This resulted in the super-elevation of the beach shoreline level above the mean water level of the adjacent river. This super-elevation has been observed to result in large scour holes as the water finds its way through the entrance training walls.

#### Introduction

The super-elevation or setup of river entrance water levels by wave breaking is a subject of great importance for the modelling of flood inundation levels in coastal rivers and for floodplain management in general. However, very little is known about wave setup within river entrances. Current practice in estimating river entrance setup has been to use either beach shoreline setup or to calculate the likely setup at the point of minimum depth using simple models like that of Bowen et al. (1968).

---

1. Coastal Geomorphologist, Coast and Rivers Branch, NSW Public Works Department, McKell Building, Rawson Place, Sydney 2000, Australia.

2. Senior Lecturer, Department of Civil Engineering, University of Queensland, Queensland 4072, Australia.

Bowen's model gives the setup as a linear function of depth and is based on an assumption of constant wave height to water depth ratio and linear wave theory. Recent field studies have shown, however, that setup versus depth profiles tend to be upward concave steepening considerably near the shoreline (eg. Nielsen, 1988, 1990). This means that while the model of Bowen et al. (1968) tends to under-estimate the shoreline setup it over-estimates the setup across much of the surf zone. These results suggest that both of the above mentioned approaches to the estimation of river entrance setup are likely to be inappropriate. In any case, the application of 'beach results' to river entrances must be subject to considerable uncertainty because of the difference in breaking processes as a result of the current.

The aim of the present project is to investigate wave setup within a river entrance and to compare this with wave setup observed on beaches under similar conditions.

### Concepts & Definitions

Beach and river entrance water levels fluctuate over various time scales. When the local water surface elevation  $\eta(x, t)$  is averaged over a time span longer than the incident wave and surf beat periods but shorter than the tidal period, the result is the local, mean water level  $\bar{\eta}(x)$  which traces the mean water surface (MWS).

Far offshore the mean water level (MWL) approximates the still water level (SWL) which is the level of the still water surface (ie, the sea surface in the hypothetical situation of no waves). The still water level for practical purposes is taken as the mean water level offshore from the surfzone.

The local setup  $B(x)$  is the super-elevation of the mean water level above the still water level.

$$B(x) = \bar{\eta}(x) - SWL$$

Set-down corresponds to the situation where  $B(x) < 0$ .

Beach shoreline setup has in the past been used to approximate likely river entrance setup. The shoreline elevation and the shoreline setup  $B_s$  are defined by the intersection of the mean water surface and the beach sand surface.

### Field Sites

Data for the present study have been obtained from several sites along the New South Wales coast. These include Brunswick Heads, Dee Why Beach, Palm Beach and Seven Mile Beach (figure 1).

The NSW coast is exposed to a moderate to high energy east coast swell environment. Dominant swell direction is from the south-east and deep water significant wave heights at Sydney exceed 1.5m at least 50% of the time and 4m, 1% of the time. The tidal regime is micro-tidal, diurnal with a semi diurnal inequality. Tidal range varies from about 2m at springs to less than 1m at neaps. The tidal regime is uniform along the whole NSW coast.

The main field site used in the present study was Brunswick Heads on the north coast of NSW (figure 2). This site was used to collect river entrance as well as beach setup data. The coastline at Brunswick Heads is oriented north-south and fully exposed to the regional wave climate. The Brunswick River enters the ocean at Brunswick Heads. This river entrance is regulated by rubble mound training walls. The channel width near the end of the training walls is approximately 40m and the mid tide depth is normally 4-5m but can be as shallow as 1-2m on the offshore bar which experiences wave breaking even under relatively small wave conditions (figure 3).

The tidal prism of the Brunswick River is approximately  $4.8m \times 10^6 m^3$  corresponding to spring tidal peak velocities of about 1.8m/s at the entrance.

The setup monitoring installation at Brunswick Heads comprised two lines of manometer tubes, one through the river entrance extending from 300m upstream of the entrance to 150m offshore of the entrance; and the other spanning the surfzone on the beach 150m to the south. This line was 500m long and extends from the beachface to a depth of approximately 10m. The beachface here is relatively flat and the surfzone is characterised by a well developed bar/trough system. Mean swash zone grain size is 0.22mm.

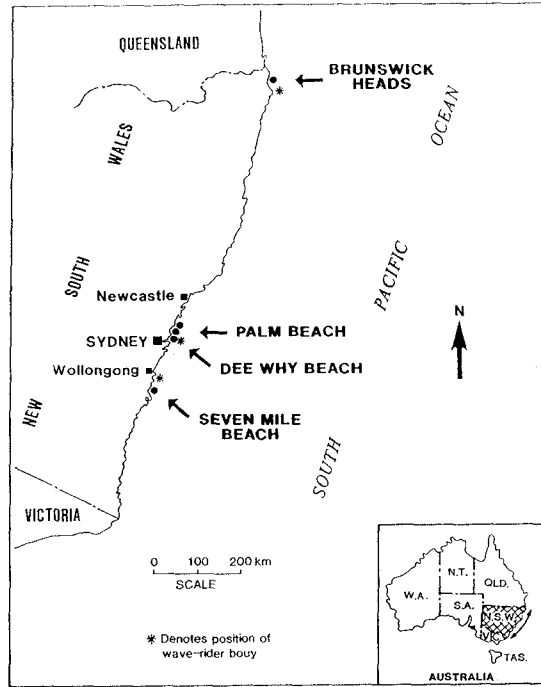


Figure 1: Location of field sites

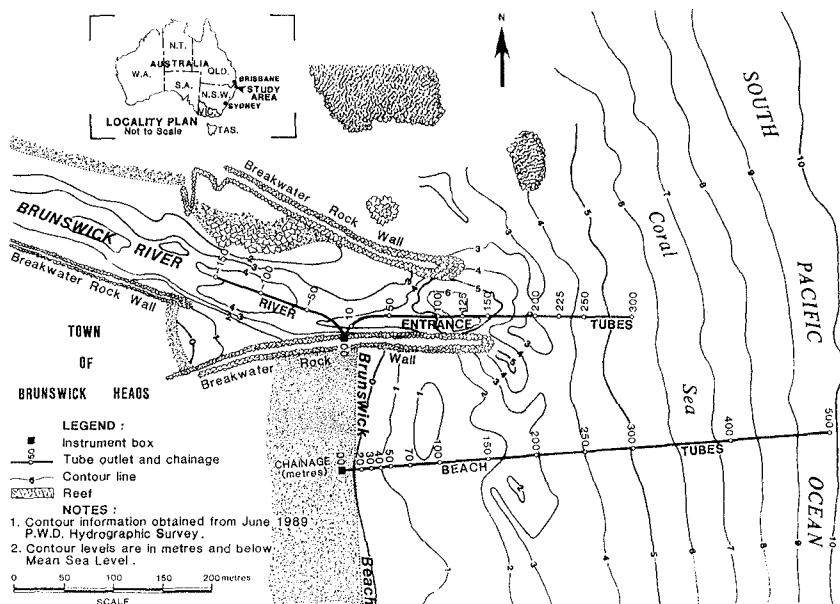


Figure 2: Setup monitoring installation at Brunswick Heads

Subsidiary field sites include Dee Why Beach, Palm Beach and Seven Mile Beach. These locations were used to obtain beach setup measurements from various beach types. Characteristics of these beaches are shown in table 1. A more detailed description of these sites is given in Nielsen & Hanslow (1991).

### Equipment

The equipment and techniques used at the Brunswick Heads field site are in part similar to those described by Davis & Nielsen (1988) and Nielsen (1988).

TABLE 1.

Field Site	Beach Type During Experiments	Swash Zone Grain Size (MEAN)	Range of Beachface Slope During Experiments
Seven Mile Beach	Dissipative	0.18mm	$0.03 < \tan \beta_f < 0.05$
Dee Why Beach	Intermediate/ Reflective	0.5mm	$0.06 < \tan \beta_f < 0.16$
Palm Beach	Intermediate	0.4mm	$0.08 < \tan \beta_f < 0.12$
Brunswick Beach	Dissipative	0.22mm	$0.04 < \tan \beta_f < 0.08$





**Figure 3:** Wave breaking occurs at the Brunswick River entrance even during small to moderate wave conditions

Measurements of the mean water surface elevation were obtained at various points through the river entrance and on the adjacent beach via a system of manometer tubes which are permanently deployed. These tubes are made of hard but flexible nylon material and open to water pressure at their seaward ends. They are attached to a steel chain and became buried shortly after deployment.

At the landward end of each line, each tube is connected to a glass riser tube. The glass riser tubes are closed to the atmosphere but interconnected, so that the air pressures inside are at all times identical. Partial evacuation of the system enables relative water levels at the tube outlets to be monitored. Absolute levels can be obtained by connecting one of the riser tubes to a known (surveyed) water level.

The system facilitated measurements of the mean water surface at fixed locations through the river entrance and across the surfzone on the adjacent beach. Measurements of the mean water surface closer to the beachface at Brunswick Heads as well as the other field sites were obtained using an array of stilling wells. During individual experiments, wells were placed with 2-5m spacing along shore normal transects. The wells were made of clear polycarbonate tubing of 25-35mm internal diameter. The bottom end of each well was covered with geotextile filter cloth to prevent the entry of sand, and were damped with foam to eliminate fluctuation by individual waves and infragravity oscillations. The wells were sunk to at least 20-30cm below the lowest level of the local watertable.

Well top levels were surveyed and measurements taken from the well top to the water surface and to the beach sand surface. This enabled fairly accurate definition of the intersection point between the mean water surface and the beachface otherwise known as the shoreline.

Wave Setup on Beaches

Data collected for the present study confirmed earlier results by Nielsen (1988), (1990) regarding the nature of the mean water surface on natural beaches. That is, as seen in Figure 4, the mean water surface displays an upward concave profile, steepening considerably near the shoreline. Here relative setup is plotted versus still water depth for several data collection exercises at Brunswick Heads. Nielsen's data suggest that Bowen's model

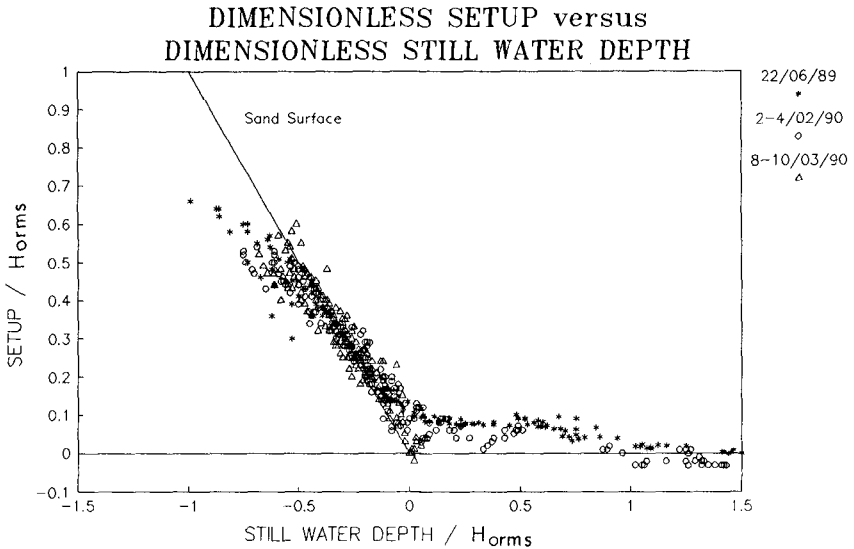


Figure 4: Relative setup plotted versus still water depth for 3 different experiments at Brunswick Heads

may over-estimate setup across much of the surfzone while under-estimating setup at the shoreline.

The elevation of the shoreline above the still water line is plotted as a function of wave height in Figure 5. As seen in this plot a relationship of the form

$$B_s \approx 0.38 H_{orms}$$

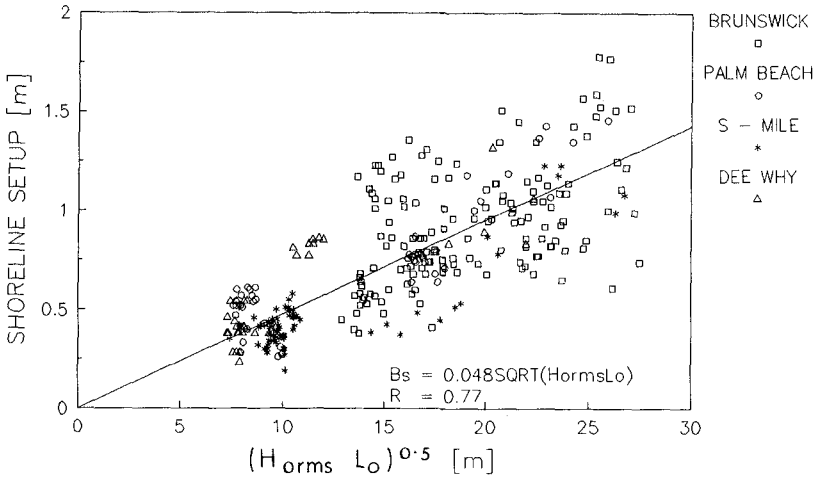


Figure 5: Shoreline setup plotted as a function of wave height ( $H_{orms}$ ) for all data

fits the data fairly well with scatter between  $0.2 H_{orms}$  and  $0.65 H_{orms}$ .

A slightly better relationship is obtained by including wave length as seen in Figure 6. Here the line of best fit is given by

$$B_s = 0.048 (H_{orms} L_0)^{0.5}$$

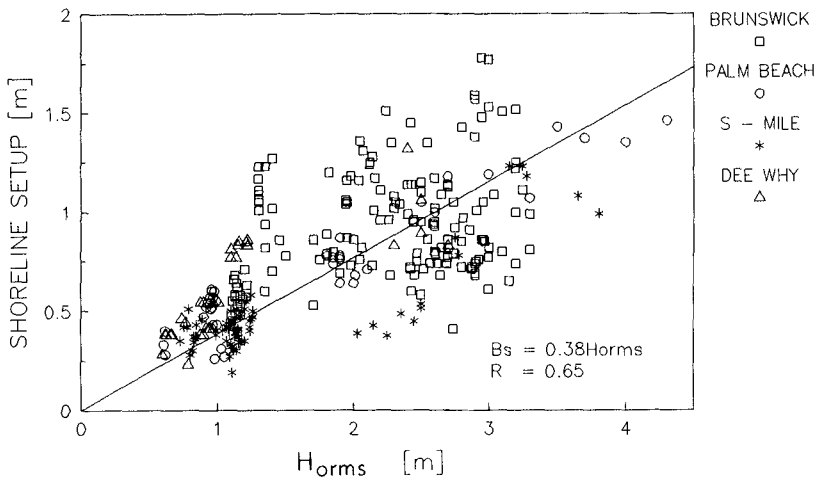


Figure 6: Shoreline setup plotted as a function of  $(H_{orms} L_0)^{0.5}$  for all data

River Entrance Setup

Mean water surface data collected during the present investigation were obtained under widely varying conditions. These included wave heights up to 4m (deepwater RMS), all stages of the tide and two minor flood events.

An example of the mean water surface data collected is given in Figure 7. Here mean water surface profiles through the Brunswick River entrance during an ebbing tide on 17 March, 1992 are presented. The river flow during these observations was assisted by considerable fresh water input. Drogue velocities in the entrance recorded at 11.30 were between 2.0 and 2.5ms<sup>-1</sup> offshore RMS wave height varied between 2.0 and 2.4m while wave period was approximately 8 seconds. Most wave breaking occurred 50–100m seawards of the end of the breakwaters, a distance of 200–250m from the instrument box. The furthest offshore data point in this graph (chainage 500) is the ocean tide level calculated by averaging the recorded tide levels at Coffs Harbour and Sydney Harbour, both corrected for barometric effects. These tide gauges are well removed from the study site but have been included as a check on the level of the offshore manometer tube.

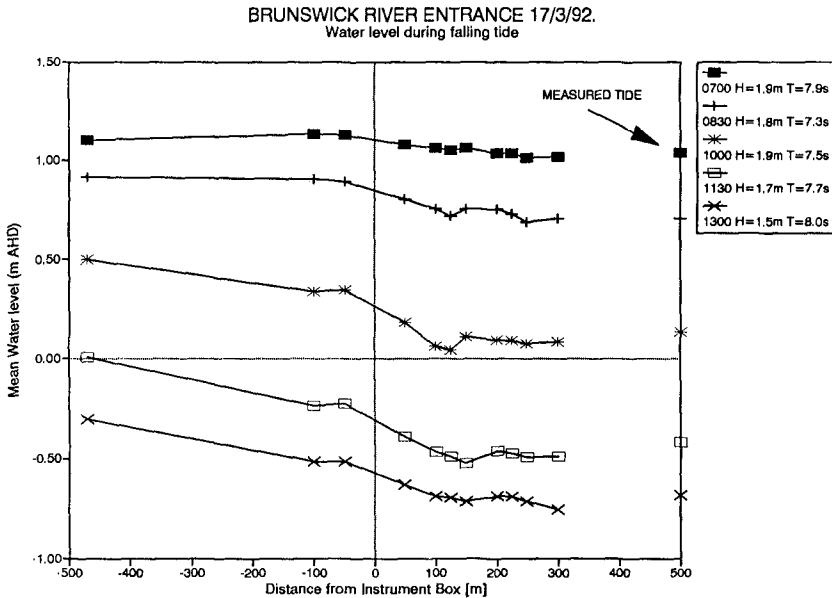


Figure 7: Mean water surface profiles through the Brunswick River entrance during an ebbing tide on 17-3-92

The elevation of the mean water surface increases by an average of 0.05m from the breakpoint (250m) to the 150m or 200m point. There is a small decrease in the mean water surface elevation at (150m) or just landwards of (125m) the end of the breakwaters. Landwards of this region the mean water surface slopes upstream with a maximum gradient of 0.0024.

This data suggests there is very little setup occurring (less than  $0.03 H_{orms}$ ) in the river entrance.

All measurements of the river entrance setup obtained at Brunswick Heads are presented in Figure 8. Here super-elevation of the mean water surface at the river entrance ( $\bar{\eta}_{150m}$  tube —  $\bar{\eta}_{300m}$  tube) is plotted as a function of wave height.

The data presented in this figure show very little wave setup in the Brunswick River entrance under any conditions.

#### All Data

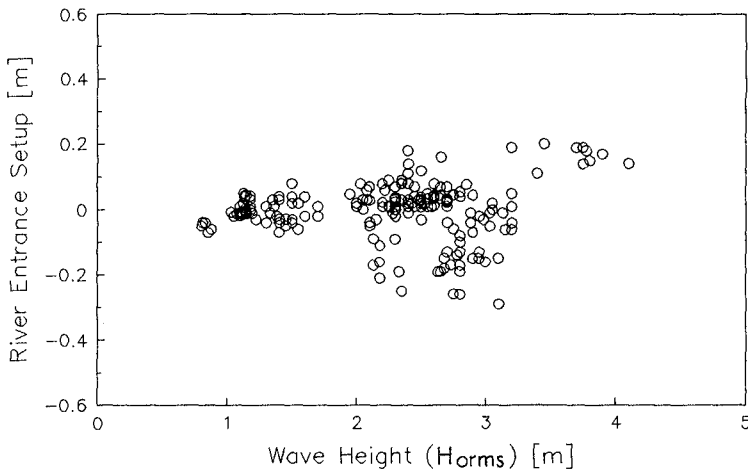
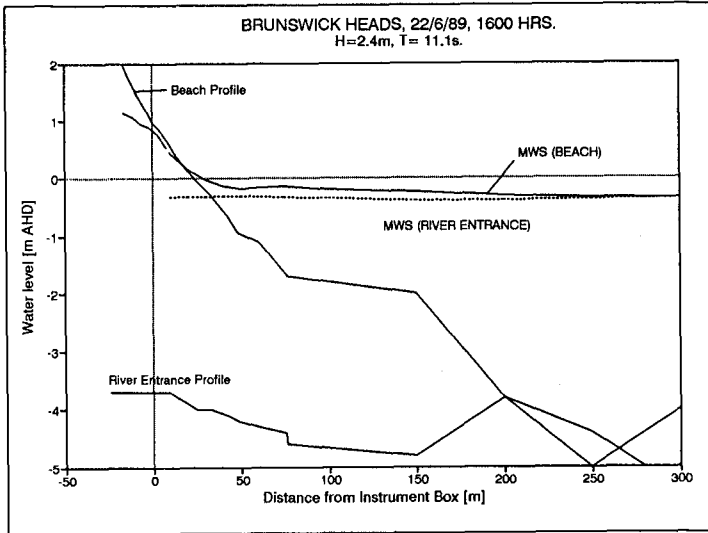


Figure 8: River entrance setup versus wave height for all data

#### Combined Data

The collection of simultaneous river entrance and beach water level data was made difficult during severe weather conditions, thus measurements of this type were limited. However, one data set was collected on 22 June, 1989. Figure 9 presents a mean water surface profile and bed profile through the river entrance and across the surfzone on the adjacent beach, both taken at 1600 hrs on this day. Offshore RMS wave height at this time

was around 2.4m with a period of 11.1/s. This figure illustrates the absence of setup in the river entrance during conditions which produce significant setup on the adjacent beach.



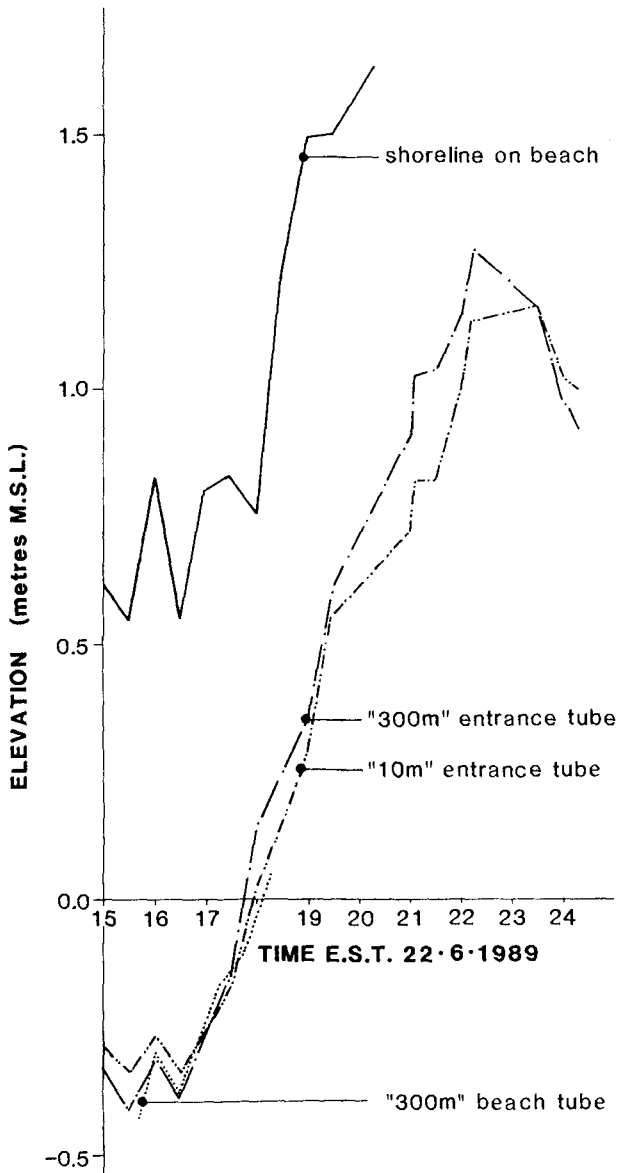
**Figure 9:** Mean water surface through the Brunswick River entrance and across the adjacent beach at 1600hrs on 22-6-89

Comparison between the beach shoreline setup and the water level in the river entrance on 22 June, 1989 is presented in figure 10. On this occasion the offshore RMS wave height increased from 2m at 1500hrs to 3.2m at 2400hrs, while the period averaged 12 seconds. Elevation of the mean water surface at the 10m and 300m stations in the river entrance are plotted together with the shoreline elevation on the adjacent beach over part of a tidal cycle.

The 10m and 300m tubes in the entrance are on opposite sides of the breaker zone in (and offshore from) the entrance. The difference in elevation between the 10m tube and 300m tube suggest there is very little wave setup through the river entrance, in fact their relative elevation changes with the tide suggesting tidal gradients may be more important than any wave induced slopes. At the same time the shoreline on the adjacent beach was consistently about 1m above the offshore water levels.

The setup of the shoreline on the beach above the levels in the river, has been observed to result in large scour holes where water from the beach found its way through the entrance training walls (fig. 11).

## BRUNSWICK HEADS 22·6·1989



**Figure 10:** Time series of water levels in the Brunswick River Entrance (22-6-89) (10m tube and 300m tube) and on the southern beach (shoreline). Offshore RMS wave height increased from 2.4m at 1500hrs to 3.2m at 2400hrs, while wave period averaged 12 seconds.

### Conclusions

Measurements of the mean water surface through the Brunswick River entrance show very little wave setup. This is in spite of the fact that wave breaking occurs across the entrance even under relatively small wave conditions. At the same time measurements of the mean water surface on the adjacent beach show significant setup. This setup occurs mostly close to the beach, and results in the super-elevation of the shoreline above the level of the river. This super-elevation has been observed to result in large scour holes as the water finds its way through the entrance training walls.



Figure 11: Scour hole formed on the beach next to the southern breakwater on 22-6-89

### Acknowledgements

The present study was funded by the Public Works Department of NSW. The authors wish to thank Greg Davis and the other members of the Public Works Department who have helped to collect the data presented in this paper. Thanks are also due to Rolyn Sario and Tim Ruge for their help with the data reduction and analysis, Krystyna Starmach for the drafting and Caroline Harrington for her desktop publishing services.

### References

- Bowen, A. J., Inman, D. L., and Simmons, V. P., (1968). Wave Setdown and Setup. *Journal of Geophysical Research*, Vol. 73, No.8, pp.2569-2577.



- Davis, G.A., and Nielsen, P., (1988). Field Measurement of Wave Setup. Proc. 21st International Conference on Coastal Engineering, pp539-552.
- Nielsen, P., (1988). Wave Setup: A Field Study. Journal of Geophysical Research, Vol.93, No.C12, pp.15,643-15,652.
- Nielsen, P., (1991). Runup, Setup and the Coastal Watertable. 22nd International Conference on Coastal Engineering, pp867-880.
- Nielsen, P. and Hanslow, D. J. (1991). Wave Runup Distributions on Natural Beaches. Journal of Coastal Research, Vol.7, No.4, pp1,139-1,152.

## CHAPTER 18

### CHARACTERISTICS OF A SOLITARY WAVE BREAKING CAUSED BY A SUBMERGED OBSTACLE

Masanori HARA<sup>1</sup>, Takashi YASUDA<sup>2</sup> and Yukio SAKAKIBARA<sup>3</sup>

#### ABSTRACT

This study aims to make quantitatively clear the breaking wave characteristics of a solitary wave incident to a submerged obstacle by performing intensive numerical simulations using a boundary integral method. The incident critical wave height, the break point and the breaker height are formulated through regression analyses based on the simulated results and are shown to be determined uniquely by using the regression equations.

#### INTRODUCTION

A sound knowledge on breaking wave characteristics of coastal waves over a submerged obstacle is clearly important for designing coastal structures. Although many investigations have been made on the characteristics, most of them are concerned with waves on uniformly sloping bottoms. Smith and Kraus(1991) performed laboratory experiments to measure macro-scale properties of breaking waves on barred beaches but simply showed that wave-breaking properties differed on a barred profile. Very little quantitative knowledge is hence available on the breaking wave caused by a submerged obstacle.

It is widely recognized that steep waves on beaches resemble solitary waves. They are in fact representable as a train of solitary waves[Tuchiya & Yasuda, 1984]. It may be hence better to consider each individual wave of coastal waves over a submerged obstacle as an independent solitary wave and to investigate its breaking characteristics, rather than to examine directly those of the waves. Further, considering a submerged step and dike as submerged obstacles, we could reduce the breaking wave problem of the steep coastal waves over a submerged obstacle to that of a solitary wave incident to the step or dike.

---

<sup>1</sup>Civil Engineer, Idemitsu Eng. Co.,Ltd.,37-24 Shinden-Cho Chuo-Ku Chiba 260, Japan

<sup>2</sup>Prof., Dept.of Civil Eng., Gifu Univ., 1-1 Yanagido, Gifu 501-11, Japan

<sup>3</sup>Research Asso., Dept.of Civil Eng., Toyota Col. of Tech., 2-1 Eisei-Cho Toyota 471, Japan

In this study, we focus our attention on the relation of the geometric quantities of the incident wave and obstacle to the breaking wave characteristics and investigate the following three items and their governing law; i)Critical incident wave height  $H_c$  which gives the limiting wave height of the incident wave passing through a obstacle without breaking, ii)Break point and iii)Breaker height. For this purpose, we perform the intensive numerical simulation using a computational model[Yasuda et al.,1990] to describe the time evolution of a solitary wave propagating on a step or dike and formulate three items mentioned above based on the simulated results. The model used here can solve numerically but almost exactly the hydrodynamic equations for fully nonlinear two-dimensional irrotational flows over uneven bottoms and can describe accurately the deformation up to overturning of a solitary wave incident to a step or dike. Its validity has been already verified by comparing the computed results with the experimental measurements[Yasuda et al., 1992]. It could therefore be stated that the results obtained here through the numerical simulation have sufficient accuracy.

### MODIFIED SURF-SIMILARITY PARAMETERS

It is well-known that the breaker height and type of periodic waves on a plane slope with the gradient of  $\tan\theta$  are described by the surf-similarity parameter  $\xi = \tan\theta/(H_0/L_0)^{0.5}$ , where  $H_0$  and  $L_0$  are respectively the wave height and wave length of incident waves in deep water. This parameter can be derived as the ratio of the perturbation term due to depth change to the nonlinear term of incident periodic waves from the variable coefficient KdV equation.

We now regard periodic waves with the incident wave height  $H_1$  on a plane bottom with the still water depth  $h_1$  as a train of solitary waves with the same wave height  $H_1$  and rewrite the nonlinear term by using the lowest order solution of the solitary wave on the plane bottom,  $\eta = H_1 \text{sech}^2[\sqrt{(3/4)(H_1/h_1)}x/h_1]$ , instead of that of the sinusoidal wave,  $\eta = (H_0)/2 \cos(2\pi x/L_0)$ . As a result, we can obtain the following parameter for the solitary wave on a plane slope with the same gradient  $\tan\theta$ ,

$$\xi_s = \tan\theta/(H_1/h_1)^{0.4}. \quad (1)$$

If we then consider the depth change perturbation due to a submerged solid step with the crown height  $R$  (Fig.1) instead of that due to the plane slope and rewrite the perturbation term, we obtain, through some trial and error, the following modified surf-similarity parameter for the solitary wave which has the initial wave height  $H_1$  and is incident to the submerged step.

$$\xi_s^* = (R/h_1)^{0.1}/(H_1/h_1)^{0.4}. \quad (2)$$

The slope gradient  $\tan\theta$  is omitted in eq.(2) because its influence on the breaking characteristics is almost negligible as explained afterwards.

Further, considering the depth change due to a submerged symmetric trapezoidal dike with the crown height of  $R$ , the crown width of  $B$  and the slope gradient of  $\tan \theta$  schematically shown in Fig.2, we can obtain another modified surf-similarity parameter,

$$\xi_s'' = [B/h_1 + (R/h_1)/3.5 \tan \theta]^{0.2} (R/h_1) / (H_1/h_1)^{0.4}, \quad (3)$$

for the solitary wave with the initial wave height  $H_1$  incident to the rectangular trapezoidal dike. This parameter can be rewritten into the parameter  $\xi_s' = (B/h_1)^{0.2} (R/h_1) / (H_1/h_1)^{0.4}$  for the solitary wave incident to a rectangular dike by putting the value of the slope gradient  $\tan \theta$  in eq.(3) as infinity. The parameter  $\xi_s''$  can thus be regarded as a unified parameter applicable to both the dikes.

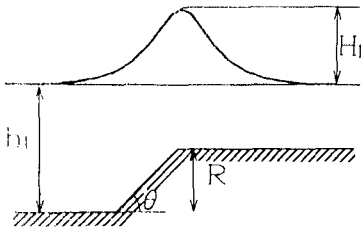


Fig.1 Schematic illustration of solitary wave over a submerged step

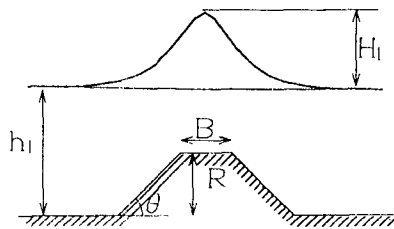
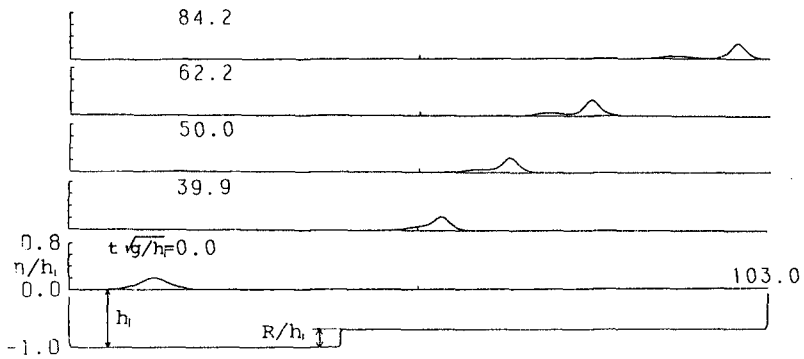


Fig.2 Schematic illustration of solitary wave over a submerged dike

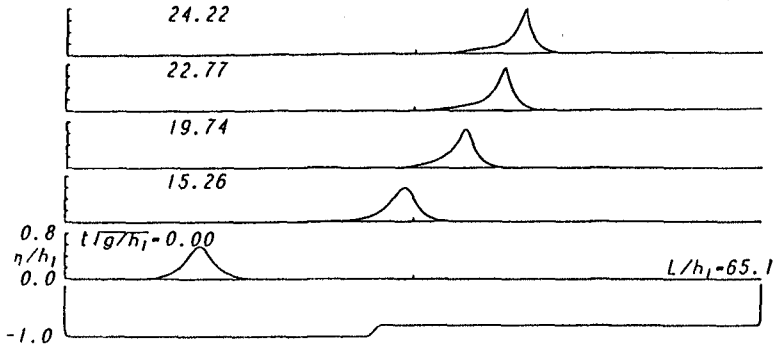
## BREAKING CHARACTERISTICS OF A SOLITARY WAVE INCIDENT TO A STEP

### Wave profiles

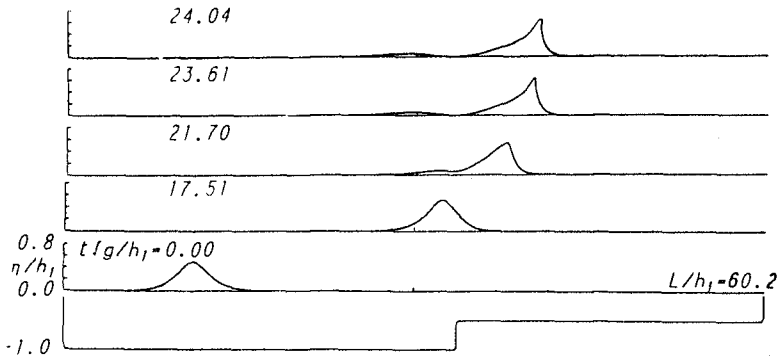
Figure 3 describes representative examples of the propagation process of a solitary wave propagating on a bottom containing a solid step. It is easily found that the stage of the deformation caused by the step clearly depends on the value of  $\xi_s^*$ . Run 1 shows the propagation process of a solitary wave passing over a step without breaking. Not only a reflected wave but also a shelf is generated by the depth change due to the step. The shelf is not indefinitely carried behind the transmitted wave, but separates from it and finally turns to a secondary solitary wave. This means that when an incident solitary wave is perturbed by a step, it tries to be stable by generating a reflected wave and a shelf turning to a secondary solitary wave and distributing the excess energy to them. Both of Run 2 and 3 show the propagating process leading to wave breaking. The onset of wave breaking is defined here as the instant when the front face at the top of the solitary wave becomes just vertical. The validity of this definition is experimentally confirmed by the fact that the onset almost agrees with the time when the



(a) Run1 [ $H_1/h_1 = 0.2, R/h_1 = 0.3, \xi_s^* = 0.57$ ]



(b) Run2 [ $H_1/h_1 = 0.58, R/h_1 = 0.2, \tan \theta = 1/5, \xi_s^* = 1.06$ ]



(c) Run3 [ $H_1/h_1 = 0.5, R/h_1 = 0.6, \xi_s^* = 1.25$ ]

**Fig.3** Time evolution of water surface profile of a solitary wave incident to a submerged step

formation of a jet at the crest is initiated in the real fluid[Yasuda et al.,1992]. While the breaker profile of Run 2( $\xi_s^* = 1.06$ ) seems to be a spilling breaker, that of Run 3( $\xi_s^* = 1.25$ ) could be regarded clearly as a plunging breaker because of its remarkably vertical asymmetry. Although the shelf is generated in both the cases, it runs just behind the transmitted main wave until the transmitted wave begins to break. This means that these depth change perturbations caused by the step are too strong for the excess energy distribution by exciting the reflected wave and shelf to prevent the breaking.

Figure 4 shows the comparison with the wave profile at the onset of the wave breaking among a solitary wave incident to a rectangular step and those incident to trapezoidal steps with a face slope of gradient  $\tan\theta = 1/5$  and  $1/10$ . The breaker profiles almost agree with one another except for the reflected waves and shelves. We could hence say that the gradient of the face slope very little affects the breaking characteristics and its influence is negligible, although it affects on the height of the reflected wave and shelf.

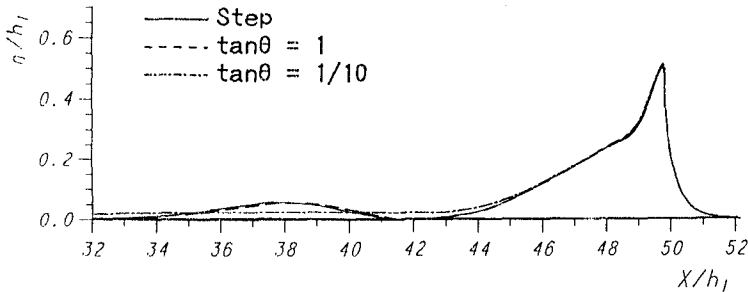


Fig.4 Comparison of water surface profiles of breaking wave between solitary waves over steps with a vertical face and a slope

### Critical incident wave height

When some investigations are made on the characteristics of breaking of a solitary wave caused by a step, it is required at first to answer the question whether the solitary incident to the step breaks or not and make clear the presence of wave breaking. If the value of the critical incident wave height  $H_c$  is available for each dike, the answer to the question can be easily obtained because the value of  $H_c$  gives the limiting wave height of the incident solitary wave which can pass through the step without breaking, that is, the solitary wave of which incident wave height  $H_1$  exceeds  $H_c$  necessarily breaks on the step.

Figure 5 shows the relation of the presence of wave breaking due to a rectangular step to the relative wave height  $H_1/h_1$  and the relative step height  $R/h_1$ .

The circles  $\circ$  indicate the solitary waves that break on the step and the crosses  $+$  indicate other solitary waves that progress on the step without breaking. The solid line is given by the regression equation,

$$H_c/h_1 = 1.012 - 1.063(R/h_1)^{0.46}, \quad 0.2 \leq R/h_1 \leq 0.6, \quad (4)$$

and indicates the relation of the relative critical wave height  $H_c/h_1$  to the relative step height  $R/h_1$ . Although eq.(4) are based on the computed results concerning a solitary wave incident to a rectangular step, it can directly be applied to that incident to a step with the slope gradient over 1/10. Hence, we can now easily answer the aforementioned question almost independently of the slope gradient, only if we substitute the values of the still water depth  $h_1$ , the incident wave height  $H_1$  and the crown height  $R$  of the step into eq.(4) and examine whether the value of  $H_1/h_1$  exceeds that of  $H_c/h_1$  or not.

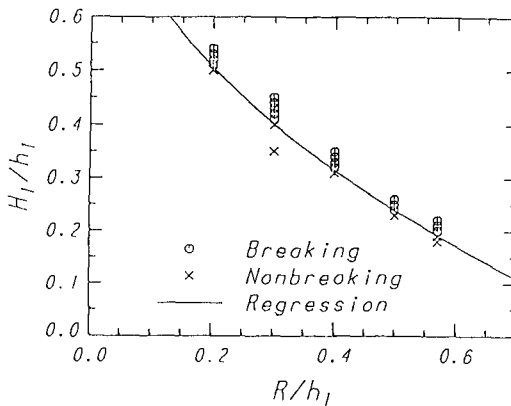


Fig.5 Relation of the presence of breaking caused by a step to the relative wave height  $H_1/h_1$  of an incident solitary wave and the relative step height  $R/h_1$

### Break point

We here aim to establish the method to predict the break point of the solitary wave incident to the step and reply to the question, 'Where the incident wave breaks?'. The break point is defined as the location just under the main crest at the onset of wave breaking and indicated by the break distance  $X_b$  from the top corner of the step to the location.

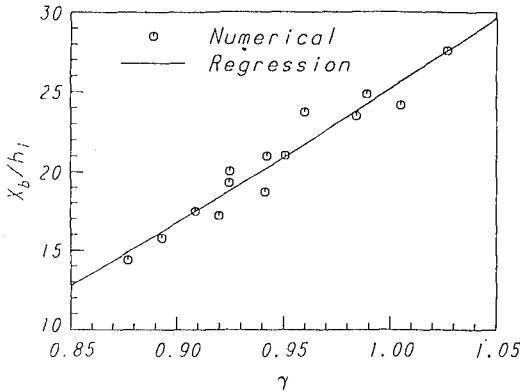
Figure 6 shows the relation between the ratio  $X_b/h_1$  of the break distance to the still water depth and the following parameter  $\gamma$  derived as a function of  $H_1/h_1$  and  $R/h_1$  by a regression analysis,

$$\gamma = (0.78 - H_1/h_1)/(R/h_1)^{-0.83}. \quad (5)$$

The solid line is given by the regression equation,

$$X_b/h_1 = -27.292 + 52.495\gamma^{1.664}, \quad 0.87 \leq \gamma \leq 1.03. \quad (6)$$

The circles  $\circ$  denote the results computed for the solitary wave incident to the rectangular dike. The computed results scatter along the regression curve and hence could be regarded to agree considerably well with it. It is found that the break distance  $X_b$  naturally becomes short and the break point tends to approach the top corner of the step as the values of  $H_1/h_1$  and  $R/h_1$  approach 0.78 and 1, respectively. However, the break distance  $X_b$  is still greater than ten times of the still water depth  $h_1$  under the present condition ( $0.87 \leq \gamma \leq 1.03$ ). This states that the incident waves never break at once after the perturbation due to depth change has affected them but require propagation distances up to breaking. The results shown in Fig.6 demonstrate that the location of the break point approximately obeys eq.(6) and is determined by the value of  $\gamma$  alone. We can thus easily predict the break point of a solitary wave incident to a step by using eqs.(5) and (6) although not exactly.



**Fig.6** Relation between the break distance  $X_b$  from the top corner of a step to the break point and the parameter  $\gamma$

**Breaker height**

Breaker height  $H_b$  is the wave height at the onset of wave breaking and is given here as the wave height at the instant when the top front face of the main crest becomes just vertical. The breaker height usually indicates the maximum value during the propagation process. On the other hand, the breaker depth  $h_b$  is equal to the submerged crown depth of the step and is given as  $h_1 - R$ .

Figure 7 shows the relation between the relative breaker height  $H_b/h_1$  of the solitary wave incident to a step with the slope gradient of  $\tan \theta = 1/5, 1/10$  and  $\infty$ (vertical) and the modified surf-similarity parameter  $\xi_s^*$  defined in eq.(2). The circles  $\circ$ , triangles  $\Delta$ , asterisks  $*$  and squares  $\square$  in Fig.7 denote the computed results for the step with vertical slope and the slope gradient of  $\tan \theta = 1, 1/5$



and 1/10, respectively. The solid line is given by the regression equation,

$$H_b/h_1 = 5.885 - 5.090\xi_s^{*0.133}, \quad 0.2 \leq \xi_s^* \leq 1.1. \quad (7)$$

It is found that all the relative breaker heights  $H_b/h_1$  agree well with the regression curve independently of the slope gradient ( $\tan \theta = 1/10 \sim \infty$ ) and that the values of them are uniquely determined by the parameter  $\xi_s^*$  alone. We can hence easily estimate the breaker height of a solitary wave incident to a step with arbitrary slope gradient by substituting the value of  $\xi_s^*$  into eq.(7). Further, the so-called breaker depth index  $H_b/h_b$  is derived by multiplying the relative breaker height  $H_b/h_1$  into  $h_1/(h_1 - R)$ .

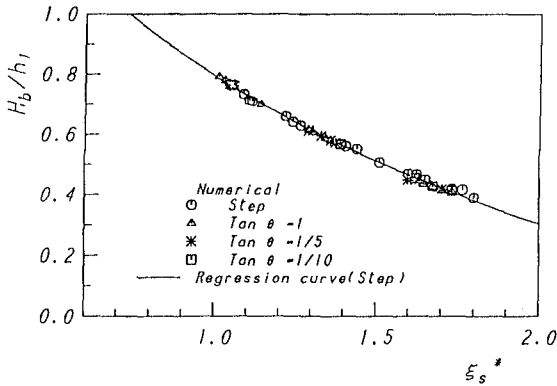
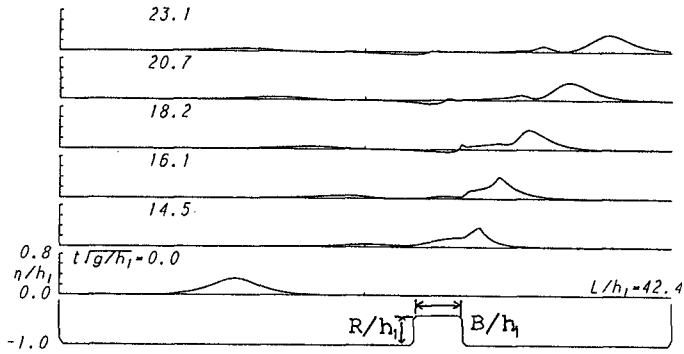


Fig.7 Relation of the breaker height of a solitary wave incident to the submerged step having the slope gradient of  $\tan \theta = 1, 1/5, 1/10$  and  $\infty$ (vertical) to the parameter  $\xi_s^*$

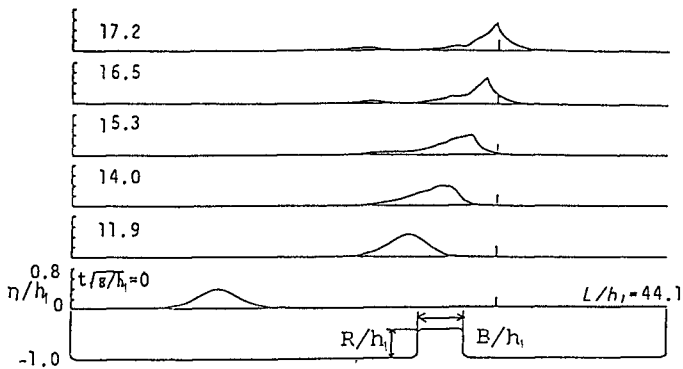
## BREAKING CHARACTERISTICS OF A SOLITARY WAVE INCIDENT TO A DIKE

### Wave profiles

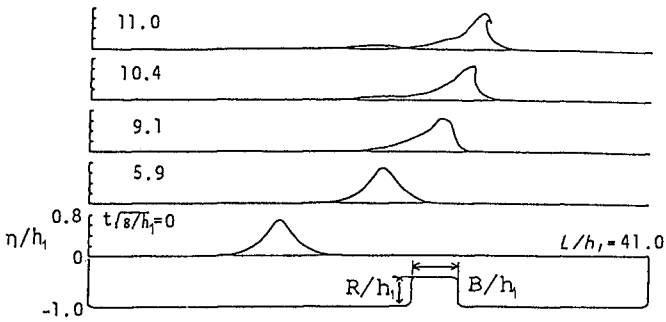
Figure 8 describes the time evolution of a solitary wave propagating on a bottom containing a solid submerged dike. Run 4 shows the propagation process of a solitary wave passing through the rectangular dike without breaking as well as Run 1 shown in Fig.3. Reflected waves of two types are generated in this case; one is a positive reflected wave due to the depth decreasing and another is a negative one due to the depth increasing. However, it is similar with Run 1 that the shelf is generated and finally turns to a secondary solitary wave. This could be said to be a common feature of the solitary wave perturbed by depth change. The breaker profile of Run 2 seems to be a typical spilling breaker, while those of Run 3 and Run 4 could be regarded clearly as plunging breakers because of their vertically asymmetric profiles. However, all of them are in common forward



(a) Run 1

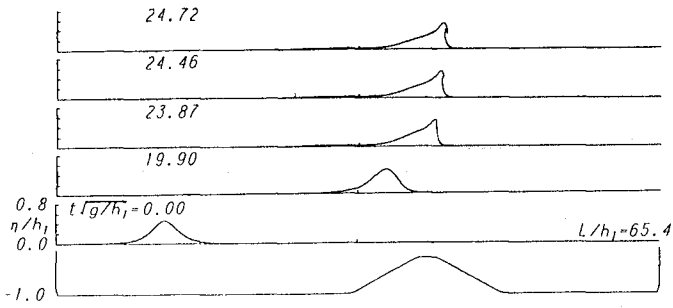


(b) Run 2

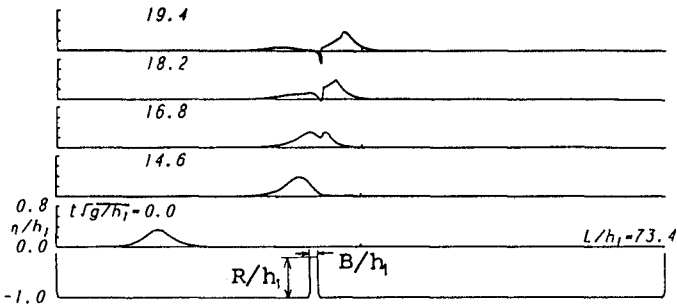


(c) Run 3

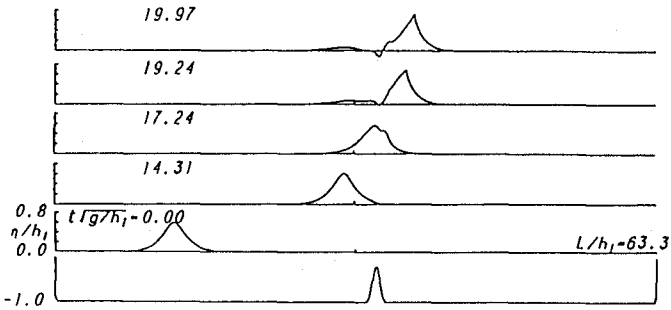
Fig.8 Temporal changes of water surface profiles of a solitary wave passing over a submerged dike



(d) Run 4



(e) Run 5



(f) Run 6

Fig.8 (Continued)

breakers in which the main crests break forward after they have passed through the dike. Whereas the case of Run 5 is remarkably different from them at the point that the surface of the wave on the shelf breaks backward onto the dike. This breaking was firstly found by Cooker et al.(1990) and was called a backward breaker. It is characterized by the backward breaking that occurs before any other breaking event. However, its influence is conjectured to be small and negligible because the height of shelf itself is considerably small in comparison with that of the main crest. Run 6 seems to be the composite type of the backward breaker and the spilling breaker, but this should be strictly classified as a spilling breaker because the forward breaker of the transmitted wave occurs a little faster than the backward breaker of the shelf.

### Critical incident wave height

In order to answer the question whether a solitary wave to a submerged dike breaks or pass through without breaking, we investigate its critical incident wave height  $H_c$  to the trapezoidal dike with the relative crown height  $R/h_1$ , the relative crown width  $B/h_1$  and the slop gradient  $\tan \theta$ . Here, rectangular dikes are included in the trapezoidal ones, because they are regarded as trapezoidal dikes with the vertical slope as mentioned above.

Figure 9 shows the relation between the critical incident wave height  $H_c/h_1$  to each dike and the following parameter  $\gamma$  derived as a function of its geometric quantities,  $R/h_1, B/h_1$  and  $\tan \theta$ , by a regression analysis.

$$\gamma = [(B/h_1) + (R/h_1)/2 \tan \theta]^{0.4} (R/h_1), \quad (8)$$

The symbols of triangle  $\Delta$ , asterisk  $*$  and square  $\square$  respectively denote the values of  $H_c/h_1$  to the trapezoidal dikes with the slop gradient of  $\tan \theta=1, 1/5$  and  $1/10$  and the circles  $\circ$  denote those to the rectangular dikes. These values are obtained by examining the limiting incident wave height of the solitary wave that comes onto each dike and can pass through without breaking. The solid line is given by the regression equation,

$$H_c/h_1 = 0.952 - 0.591\gamma^{0.76}, \quad 10.2 \leq \gamma \leq 1.4. \quad (9)$$

The computed results agree well with the regression curve and could be said to obey almost eq.(10). This states that the critical incident wave height  $H_c/h_1$  to a dike uniquely relates to a single parameter  $\gamma$  and its value is uniquely determined by  $\gamma$  alone. We can hence easily answer the aforementioned question, only if we calculate the value of  $H_c/h_1$  by substituting the geometric quantities of the dike,  $R/h_1, B/h_1$  and  $\tan \theta$ , into eqs.(9) and (10) and examine whether the value of the incident wave height  $H_1/h_1$  exceeds the value of  $H_c/h_1$  or not.

### Break point

All of the forward breakers simulated here occur behind dikes. If a incident wave breaks on a dike before passing through it, the breaking should hence be

treated as the breaker due to the step and is thereby excluded here. As well as the case of the rectangular step, we investigate here the relation between the relative break distance  $X_b/h_1$  from the top corner of the rectangular dike to the break point and the following parameter  $\mu$  derived as a function of  $H_1/h_1$ ,  $R/h_1$  and  $B/h_1$  by regression analysis,

$$\mu = (0.78 - H_1/h_1)^{0.5} (R/h_1)^{-1.2} (B/h_1)^{-0.13} \tag{10}$$

Figure 10 shows the relation of the break distance  $X_b/h_1$  to the parameter  $\mu$ . The circles  $\circ$  denote the results computed in this study and the solid bent line is given by the regression equations,

$$\left. \begin{aligned} X_b/h_1 &= 10.78\mu - 4.14, & 0.6 \leq \mu \leq 1.03 \\ X_b/h_1 &= 1.94\mu + 5.01, & 1.03 \leq \mu \leq 2.2 \end{aligned} \right\} \tag{11}$$

It is noticed that the break point of the solitary wave incident to a dike is shorter compared with that of the step(see Fig.4). This cause is conjectured to be the influence of the twice depth change due to the dike on the incident wave. Since the computed results agree well with the regression curve, the relation governed by eq.(11) seems to hold approximately between the incident wave height and the geometric quantities of the dike. We can hence predict the location of the break point of a solitary wave incident to a rectangular dike by using eqs.(10)and (11).

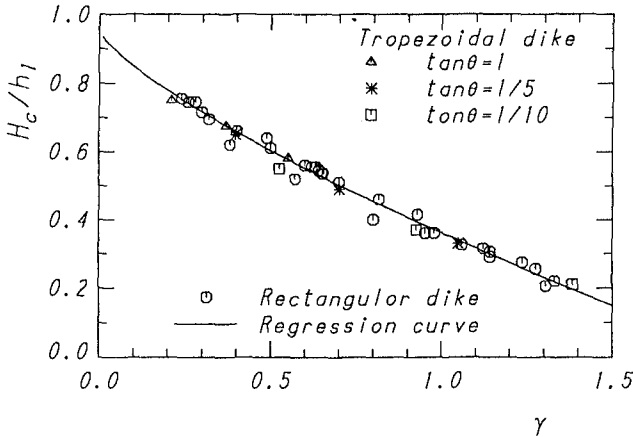


Fig.9 Relation of the critical wave height  $H_c/h_1$  of a solitary wave incident to a submerged rectangular and trapezoidal dike to a parameter  $\gamma$

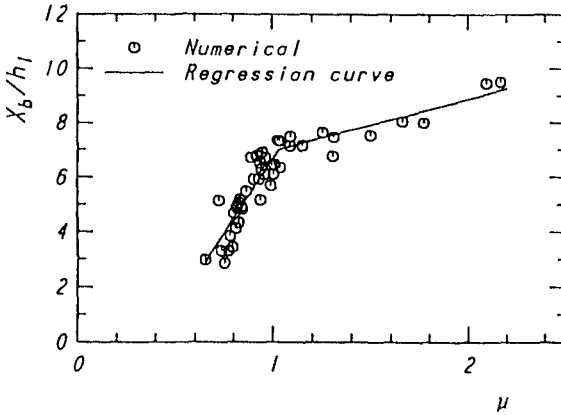


Fig.10 Location of the onset of breaking of a solitary wave caused by a submerged rectangular dike

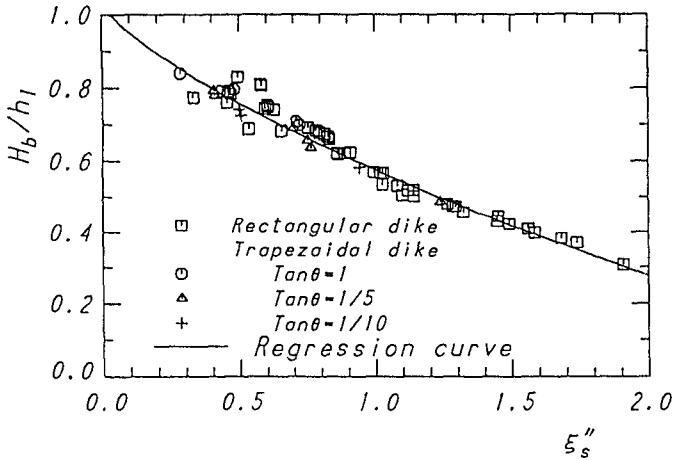


Fig.11 Relation of the parameter  $\xi_s''$  to the breaker height of a solitary wave passing over a rectangular submerged dike or trapezoidal one with face slopes of  $\tan \theta=1, 1/5$  and  $1/10$ .

**Breaking wave height**

Figure 11 shows the relation between the relative breaker height  $H_b/h_1$  of the solitary wave incident to a submerged dike and the modified surf-similarity parameter for the dike  $\xi_s''$  defined in eq.(3). The symbols of circle  $\circ$ , triangle  $\triangle$  and cross  $+$  denote respectively the values of solitary waves incident to the trapezoidal dikes with the slope gradient of  $\tan \theta=1, 1/5$  and  $1/10$  and squares  $\square$  indicate the values of solitary waves incident to the rectangular dike with vertical slope. The solid line is given by the regression equation,

$$H_b/h_1 = -0.463\xi_s''^{0.133} + 1.039, \quad 0.2 \leq \xi_s'' \leq 2.0. \quad (12)$$

All the breaker heights are obtained from the computed surface profiles at the break point and they agree very well with the regression curve. This states that the relative breaker height  $H_b/h_1$  of the solitary wave incident to the dike uniquely relates to the modified surf-similarity parameter  $\xi_s''$  and its value is determined by the parameter  $\xi_s''$  alone. We can hence easily know the breaker height  $H_b/h_1$  only if calculating the value of the parameter  $\xi_s''$  to the given incident wave and dike. Further, the breaker depth  $h_b$  is equal to the still water depth  $h_1$  because the transitted main crest breaks after passing through the dike. The relative breaker height  $H_b/h_1$  is thereby equal to the breaker depth index  $H_b/h_b$ .

## CONCLUSIONS

Intensive numerical simulations using a boundary intergral method were performed to make quantitatively clear the breaking wave characteristics of a solitary wave incident to a submerged step or dike. As a result, the critical incident wave height, the location of the break point and the breaker height were formulated as functions of the incident wave height and the geometric quantities of the step or dike through regression analyses based on the simulated results. Further, their values were shown to be determined almost uniquely by the regression equations. It is thus now possible to determine accurately the persence of the wave breaking, the break point and the breaker height by using the regression equations, as far as concerned with a solitary wave incident to a step or dike. Further study is recommended to establish a unified governing law of the breaking wave characteristics of not only a solitary wave but also periodic waves incident to submerged obstacles having arbitrary shapes.

The present research work was supported by the Grant-in-Aid for Scientific Research(No.04452233), The Ministry of Education, Science, Culture.

## REFERENCES

- Cooker, M.J., D.H. Peregrine, C. Vidal and J.W. Dold (1990), The interaction between a solitary wave and a submerged semi circular cylinder, *J. Fluid Mech.*, Vol.215, pp.1-22.
- Smith, E.R. and N.C. Kraus (1991), Laboratory study of wave-breaking over bars and artificial reefs, *Jour. WPCO, ASCE*, Vol.117, No.4, pp.307-325.
- Tsuchiya, Y. and T. Yasuda (1986), A dynamical expression of waves in shallow water, 19th ICCE, pp.435-451.
- Yasuda, T., M. Hara and M. Tanaka (1990), A computational methods of the deformation including overturning of a solitary wave over a submerged obstacles, *Numerical methods in fluid dynamics II* (Eds. M. Yasuhara, H. Daiguji & K. Oshima, JSCFD), pp919-924.
- Yasuda, T., Y. Sakakibara and M. Hara (1992), BIM simulation on deformation up to breaking of solitary waves over uneven bottoms, *Fluid Flow Modelling* (Eds. W.R. Blain & E. Cabrera, Comp. Mech. Pub.), Hydraul. Eng. Software IV, pp.523-535.

## CHAPTER 19

### Eight Years Wave Hindcast and Analysis of Wave Climate

Yoshio Hatada<sup>1</sup> and Masataka Yamaguchi<sup>2</sup>

#### Abstract

This paper deals with 8 years of wave hindcast at 11 wave observation points along the coast of the Japan Sea using a long-term shallow water wave hindcast system, and investigation of its applicability to the estimation of wave climate. Comparison with observations for not only time variations of significant waves but also long-term sea state indices such as yearly-averaged wave height and period. The availability of the present system and the advantages over the deep water wave hindcast system previously developed by the authors are verified by close and more reasonable agreement with the observed data including mean wave direction.

#### 1. Introduction

Quantitative estimation of long term wave conditions over several years, so-called wave climate is a subject of great importance for the mitigation of wave-caused disaster and efficient utilization of wave energy. Up to now, the analysis of wave climate has relied on the observed wave data or wave data hindcasted with a simple wave prediction model such as the SMB method. In the former case, data of wave direction which are crucial to analysis of shore processes have seldom been observed and wave gauges have often broken down during severe wave conditions. In the latter case, conventional methods do not always give a satisfactory accuracy for hindcasted

---

1 Research Assistant, Dept. of Civil and Ocean Eng.,  
Ehime Univ., Bunkyocho 3, Matsuyama 790, Ehime Pref.,  
Japan

2 Prof., Dept. of Civil and Ocean Eng., Ehime Univ.,  
Bunkyocho 3, Matsuyama 790, Ehime Pref., Japan



waves and tremendous efforts are needed for hindcasting long term wave conditions.

Yamaguchi et al.(1990) developed a long term wave hindcast system which makes it possible to consecutively follow wave conditions over several years with reasonable accuracy. The system was applied to compute wave characteristics over 2 years every hour at 14 selected points along the coast of the Japan Sea. Close agreement between computation and observation for time variations of significant waves and wave direction as well as long term wave statistics verified the validity of the system. But the hindcast period of 2 years is too short to properly evaluate the wave climate when variability of the sea states is taken into account, and the wave model used is a deep water model with an approximate correction for shallow water effect.

The aim of this paper is to re-examine the applicability of a newly-revised system based on the comparison between computation and observation over 8 years at 11 wave observation points along the coast of the Japan Sea.

## 2. Outline of Long-Term Wave Hindcast System

### (1) Wind hindcast model

The system consists of a wind estimation model and a wave estimation model. The wind model produces time variations of wind distribution over sea by spatial interpolation onto a regular grid of atmospheric pressure observed at irregularly-distributed points surrounding the sea area and the application of the wind model proposed by Bijvoet(1957). Either of  $-1^{\circ}\text{C}$  or  $0^{\circ}\text{C}$  or  $1^{\circ}\text{C}$  every year on the entire region was given for data of air-water temperature difference which determines coefficients in the Bijvoet wind model, so that hindcasted results agree with observed results to the best possible degree, because it is hard to acquire long-term data of air and water temperatures.

Fig. 1 is a grid system divided into 28 by 41 with a grid distance of 80 km for the computation of atmospheric pressure and wind distributions over the Japan Sea, which includes 43 pressure observation points with the WMO location number. Surface atmospheric pressure data at the observation points and central positions of lows or highs over 8 years ranging from 1982 to 1989 every 3 hours are acquired from the magnetic tapes of meteorological data prepared by the Japan Meteorological Agency and direct inspection of the weather charts. Extraordinary values of observed pressure data are corrected by checking time series of the data and inspecting the corresponding

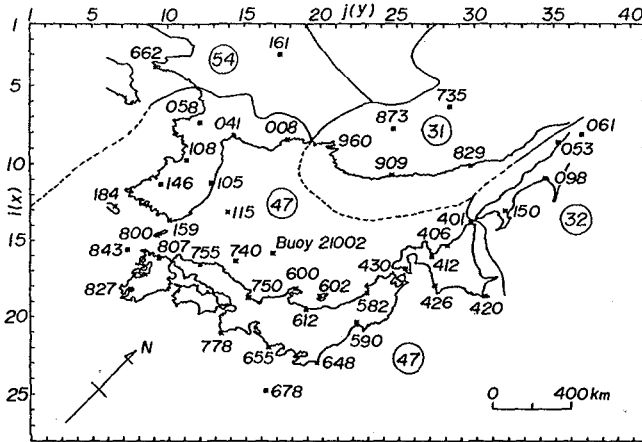


Fig. 1 Grid for computing wind distribution, and input points of observed atmospheric pressure.

weather charts. Before the wind computation, the pressure data interpolated on grids are smoothed three times, making use of a weighted smoothing formula with data of the surrounding 9 grid points in order to avoid overestimation of wind speed.

## (2) Wave hindcast model

Wave estimation is due to a shallow water wave model (Yamaguchi et al., 1987) which belongs to a decoupled propagation model, tracing the change of directional spectrum along a refracted ray of each component focused on a hindcast point. The basic equation in the model is the radiative transfer equation in shallow water and is given by

$$\frac{\partial F}{\partial t} + c_g \cos \theta \frac{\partial F}{\partial x} + c_g \sin \theta \frac{\partial F}{\partial y} + \frac{c_g}{c} \left( \sin \theta \frac{\partial c}{\partial x} - \cos \theta \frac{\partial c}{\partial y} \right) \frac{\partial F}{\partial \theta} = c c_g S(f, \theta) \quad (1)$$

where  $F = c c_g E(f, \theta)$ ,  $c$  is the celerity of a wave component,  $c_g$  the group velocity of a wave component,  $E(f, \theta)$  the directional spectrum,  $f$  the frequency,  $\theta$  the direction and  $S(f, \theta)$  the source function. Source function consists of linear growth term by the Phillips mechanism, exponential growth term by the Miles mechanism and energy dissipation terms by pseudo-viscosity, bottom friction and opposing winds. Energy dissipation due to wave breaking is evaluated by imposing the condition that directional spectrum at growth stage can not exceed beyond an equilibrium directional spectrum in shallow water. This equilibrium spectrum is given by the product of the Pierson-Moskowitz spectrum with the correction term proposed by Thornton (1977) for shallow water effect and  $\cos^4 \theta$

angular spreading function.

Eq. (1) is solved by a fractional time step method which computes propagation equation, and growth or decay equation alternately in each time step. At the first step, the propagation equation setting the right hand side of Eq. (1) to zero is solved by a full ray method or a piecewise ray method, which is a kind of the characteristic method. Full ray method is used for the computation of low frequency components satisfying the condition of  $kh < 4$  at a hindcast point which can be regarded as shallow water waves, where  $h$  is the water depth at a hindcast point and  $k$  the wave number of the corresponding component, and piecewise ray method is used for the computation of high frequency components with  $kh > 4$  which can be regarded as deep water waves. At the second step, the computation of growth or decay equation, which sets the propagation term in Eq. (1) to zero is conducted with the analytical solution using the results of propagation step as an initial value. When the directional spectrum computed at growth stage exceeds the shallow water equilibrium spectrum, it is reduced so as to get equal to the equilibrium spectrum.

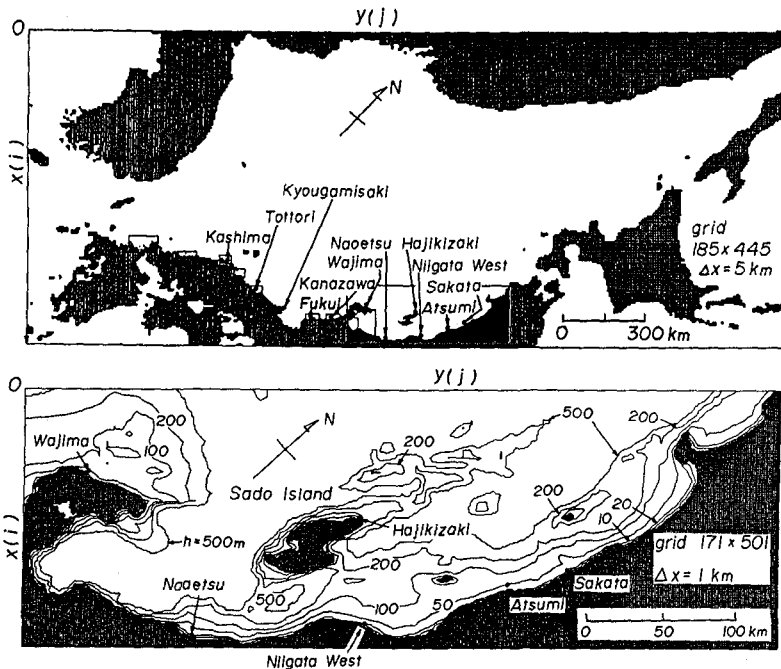


Fig.2 Medium and fine grid systems used in wave hindcast and location of hindcast points.

Wave ray is traced on the nesting grid system composed of the Japan Sea area divided into 185 by 445 with a medium grid size of 5 km and a small sea area surrounding the hindcast point with a fine grid size of 1 km. Fig. 2 shows the medium grid system covering the Japan sea and an example of the fine grid system covering the coastal area off the Hokuriku District, which are used in wave ray computation. The figures also include the locations of 11 wave hindcast points and contour plot of water depth. The numbers of frequency and direction data are 25 and 20 to 25 respectively, and the time step in wave hindcasting is 1 hour. Wind speeds and directions at wave computation points along a wave ray are estimated by applying a bilinear interpolation formula to wind data at 4 wind grid points surrounding the wave computation point. Boundary around the computational sea area is assumed to be land, where the directional spectrum is zero.

Since it is assumed to be three days after the start of computation that the influence of initial condition of calm sea vanishes, the wave hindcasting is carried out every hour for about 8 years from 4 a.m., December 29th, 1981 until 12 p.m., December 31st, 1989.

Fig. 3 is an example of refraction diagram. Directional range of wave rays reaching a hindcast point rather changes every hindcast point due to geographical situation in the vicinity of the hindcast point.

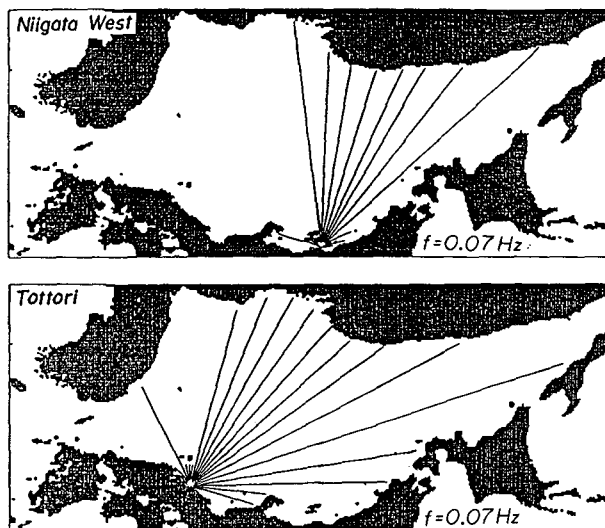


Fig. 3 Examples of refraction diagram at wave hindcast point.

### 3. Applicability of Long-Term Wave Hindcast System

#### (1) Comparison for time variations of significant waves

Spiky noises are often found in the time series of significant wave period data observed during the calm sea state. In general, data observed during the low wave condition are less reliable compared to those during the high wave condition, because of measuring and statistical errors. Thus, wave observation data to be used for comparison with hindcasted results are limited to those which satisfy the condition such as  $H_{1/3\text{obs}}/1.56T_{1/3\text{obs}}^2 > 0.003$ , where  $H_{1/3}$  is the significant wave height,  $T_{1/3}$  the significant wave period, and subscripts 'obs' and 'cal' indicate the observed and hindcasted results respectively. The threshold value of 0.003 is conveniently adopted only for excluding unfavorable observation data and does not have any physical meaning.

Fig. 4 is two examples of the 3 month comparison between hindcast and observation for the time variations of wave height, period and wave direction at Wajima and Tottori indicated in Fig. 2. Wave hindcast was carried out with both the shallow water wave model and the deep water wave model. Both models follow the time variations of

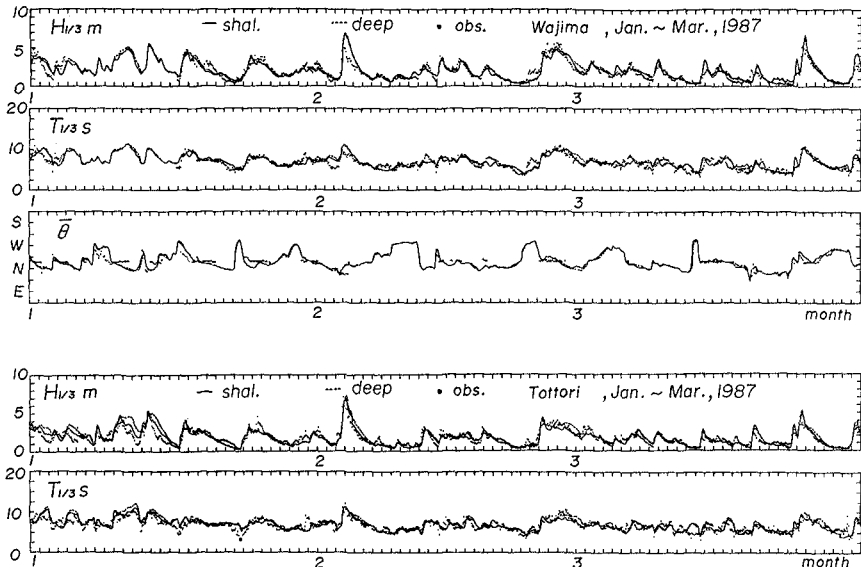


Fig. 4 Comparison between hindcast and observation for time variations of significant waves over 3 months at Wajima and Tottori.

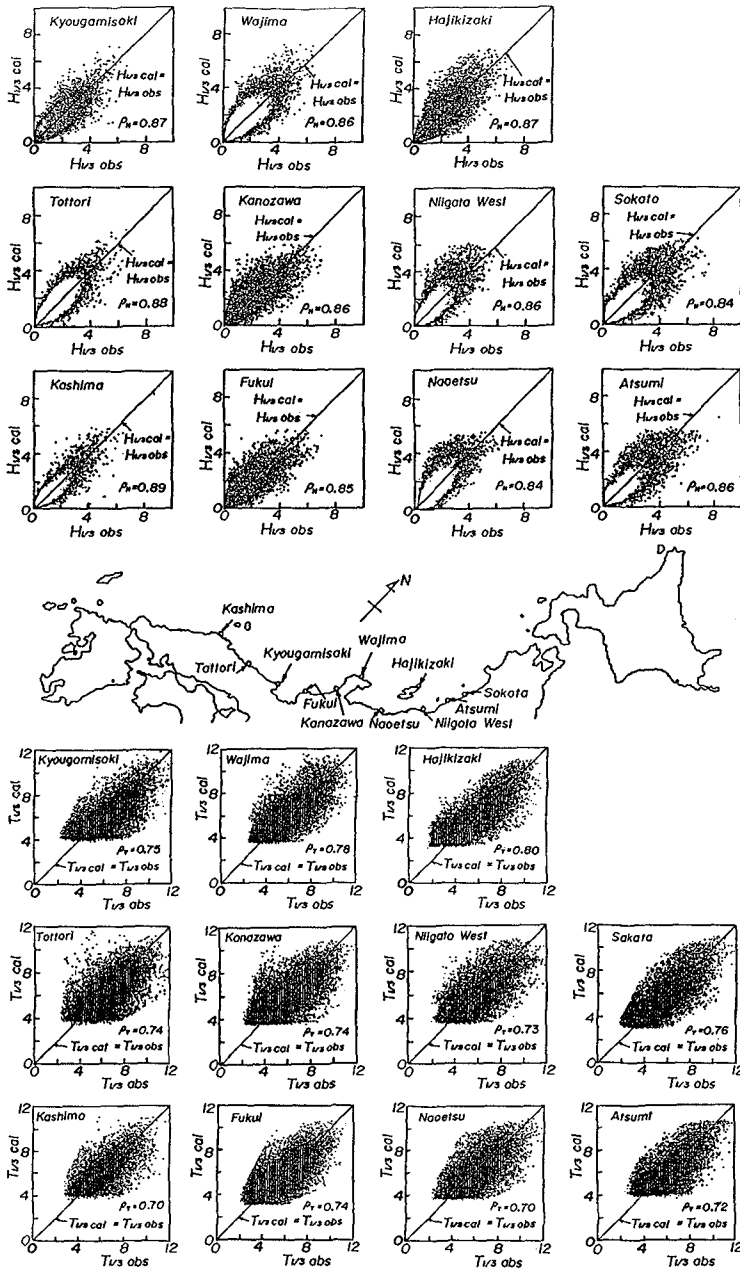


Fig. 5 Scatter diagrams between hindcast and observation for significant waves.

observed waves with acceptable accuracy, and the shallow water wave model gives better estimation than the deep water model during the high wave condition. Hereafter wave hindcast with the shallow water wave model is used for the comparison with wave observation, where no reference is made.

High reliability of the present system is also confirmed in Fig. 5 indicating the scatter diagrams of individual significant wave height and period observed every 2 or 3 hours over 8 years at 11 points along the coast of the Japan Sea. Plotted points almost symmetrically distribute around the line which means the perfect correlation between hindcast and observation, but plotted data for wave period show wider scatter than those for wave height. Accordingly, the correlation coefficient for wave height  $\rho_H$  ranges from 0.84 to 0.89, while the correlation coefficient for wave period  $\rho_T$  shows smaller value of 0.70 to 0.80 than those for wave height.

(2) Comparison for wave climate

Fig. 6 shows the error statistics on yearly-averaged wave height and period at 11 wave observation points along the coast of the Japan Sea, in which  $\bar{H}_{1/3}$  and

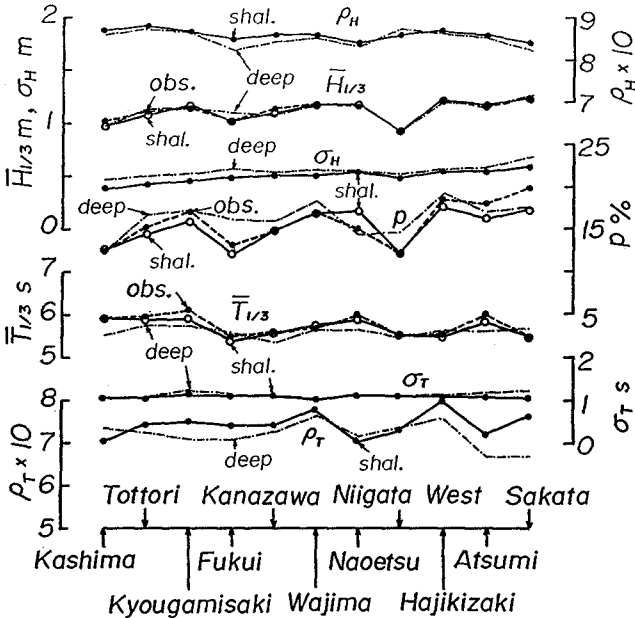


Fig. 6 Error statistics on significant waves hindcasted consecutively over 8 years at 11 points along the coast of the Japan Sea.

$\overline{T_{1/3}}$  are the yearly-averaged significant wave height and period,  $\sigma_H$  and  $\sigma_T$  the root-mean square errors of wave height and period and  $p$  is the occurrence rate of high waves exceeding wave height of 2 m. Overall agreement between hindcast and observation is found in the figure, although wave period is nearly consistently underestimated by about 0.3 s, and the shallow water wave model gives higher correlation coefficient and smaller root-mean square error for both wave height and wave period than the deep water wave model. As for the occurrence rate of high waves, the shallow water wave model has a tendency of underestimation, whereas the deep water wave model has a tendency of overestimation.

Fig. 7 is the monthly variations of mean significant wave height and period and occurrence rate of the high

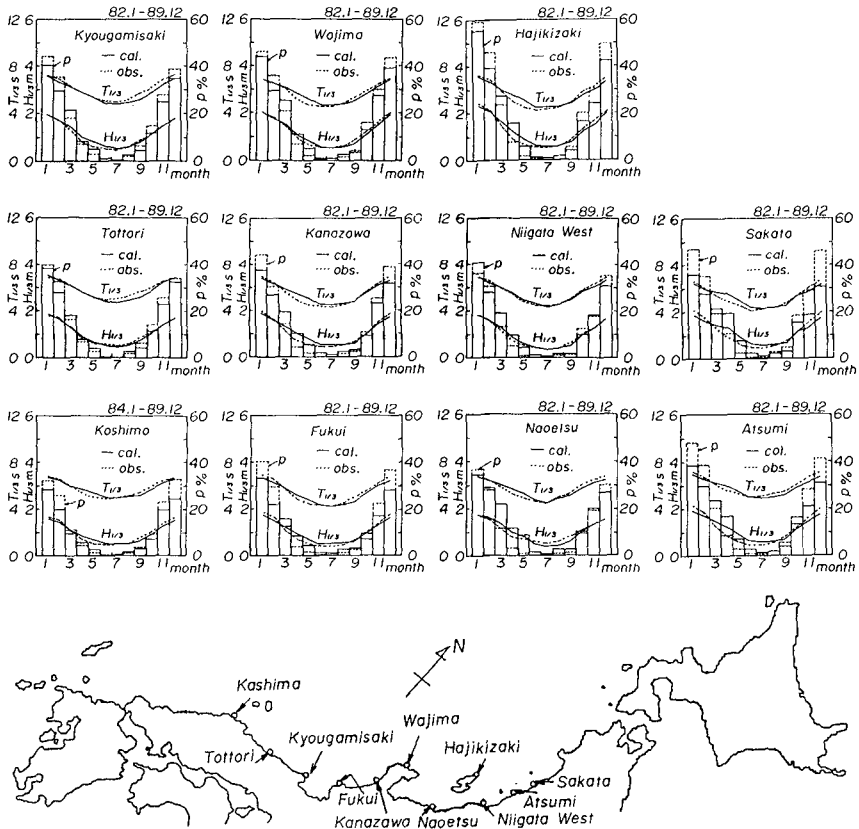


Fig. 7 Comparison of hindcast and observation for monthly variations of mean significant waves and occurrence rate of high waves.



waves at 11 points which are indices representing wave climate. The model reproduces fairly well the seasonal change of wave climate in the Japan Sea where high wave conditions occur in winter and autumn, and calm sea states continue in summer and spring. More precisely, the model tends to overestimate the wave conditions during April to September and to underestimate the one during September to December.

Fig. 8 shows the comparison between computation and observation for histograms of wave height grouped every 0.5 m and wave period grouped every 1 s. The model reproduces well overall distribution of the histograms again. But, underestimation for the occurrence rate of wave height with 0 to 0.5 m and overestimation for the occurrence rate of wave height with 0.5 to 1 m or the contrary tendency are found in the hindcast points located in the northern part of the coast of the Japan Sea such as Naoetsu and Sakata. The model also tends to overestimate the occurrence rates of wave period with 4 to 6 s and to underestimate those of the other ranges.

The above-mentioned applicability of the model is also confirmed in Fig. 9 which shows the comparison for contour plot of correlation between significant wave height and period. As the Japan Sea is almost closed, being surrounded by land boundaries, wind waves are predominant, which have high correlation between wave height and wave period. The model reproduces fairly well the feature of observed data which is described by contour lines extending in the right-upward direction.

Fig. 10 illustrates the comparison of hindcast and observation for the directionally-grouped occurrence rates of high wind speed exceeding 10 m/s and those of wave height exceeding 2 m at 5 observation points. The number of observation data of mean wave direction is much smaller than that of hindcast data used in the analysis, because of the reasons such as undeployment of wave direction measurement device and its break-down by severe sea states. The period of wind observation data used in the analysis is 8 years from 1982 to 1989 at Wajima, 2 years from 1986 to 1987 at Sakata, Hajikizaki and Fukui, and 1 year of 1986 at Niigata West.

At Hajikizaki facing open sea directly, high correlation for the directionally-grouped occurrence rates of both high winds and high waves is found and the distributions of hindcasted data agree well with those of observed data. Difference between the distributions by both shallow water wave model and deep water wave model is small, because water depth of 50 m at Hajikizaki gives almost deep water wave condition even for high waves with

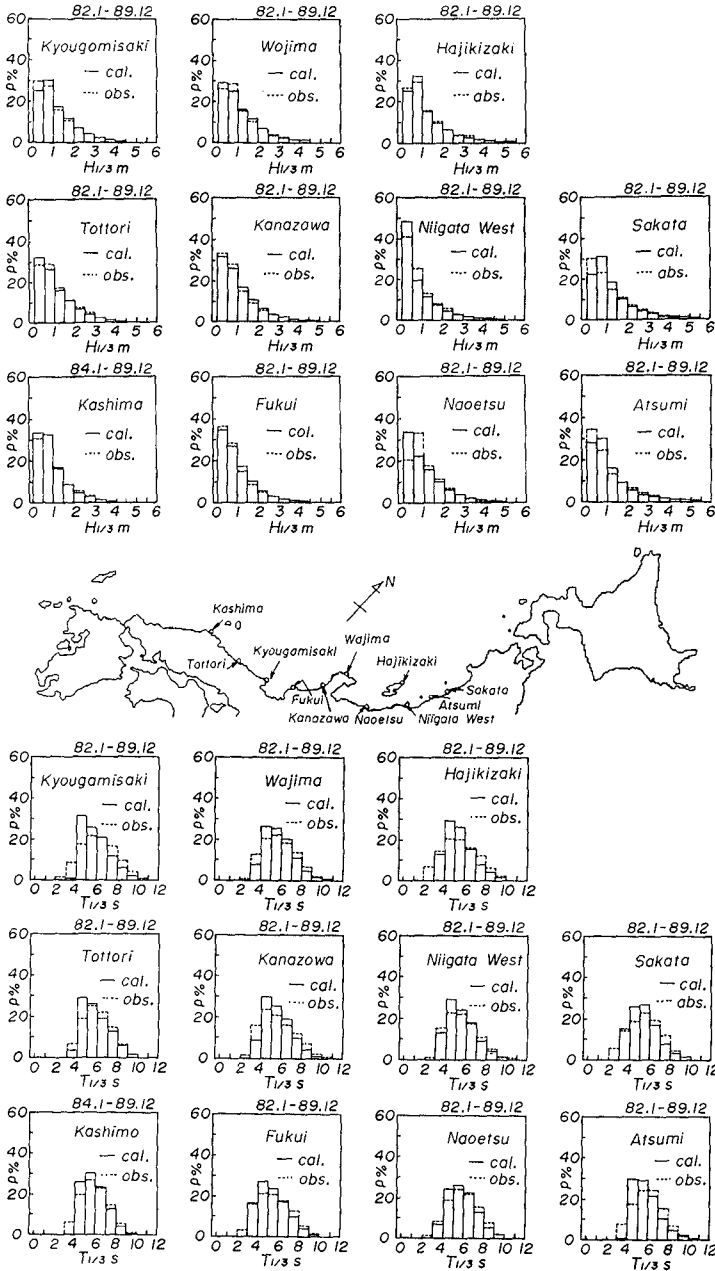


Fig. 8 Comparison of hindcast and observation for histograms of significant wave height and period.

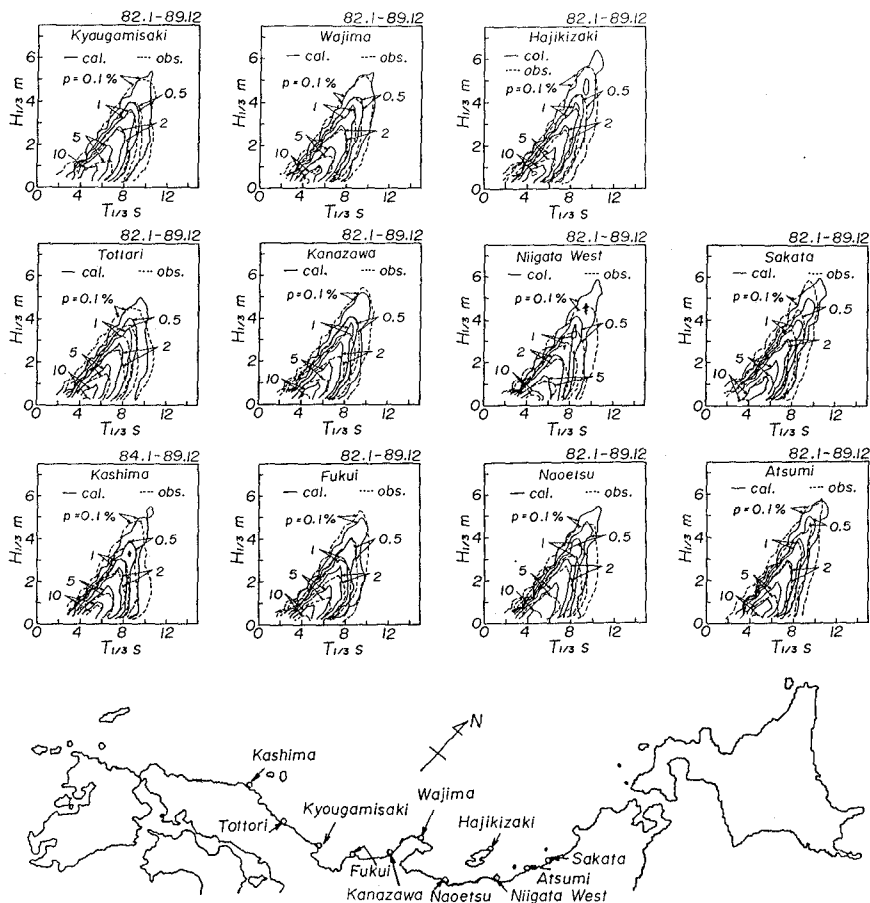


Fig. 9 Comparison of hindcast and observation for correlation diagram between wave height and wave period.

wave period shorter than about 10 s. On the other hand, predominant wave directions estimated by both shallow and deep water wave models at Wajima, where is in observation conditions similar to Hajikizaki are biased against observed wave direction clockwise by about 10 degrees, as estimated predominant wind direction is biased against observed wind direction to similar extent. Observation points at Sakata, Niigata West and Fukui are located in shallow water where water depths are less than 30 m. At Niigata West, predominant wave directions hindcasted with both models are close to the observed direction in

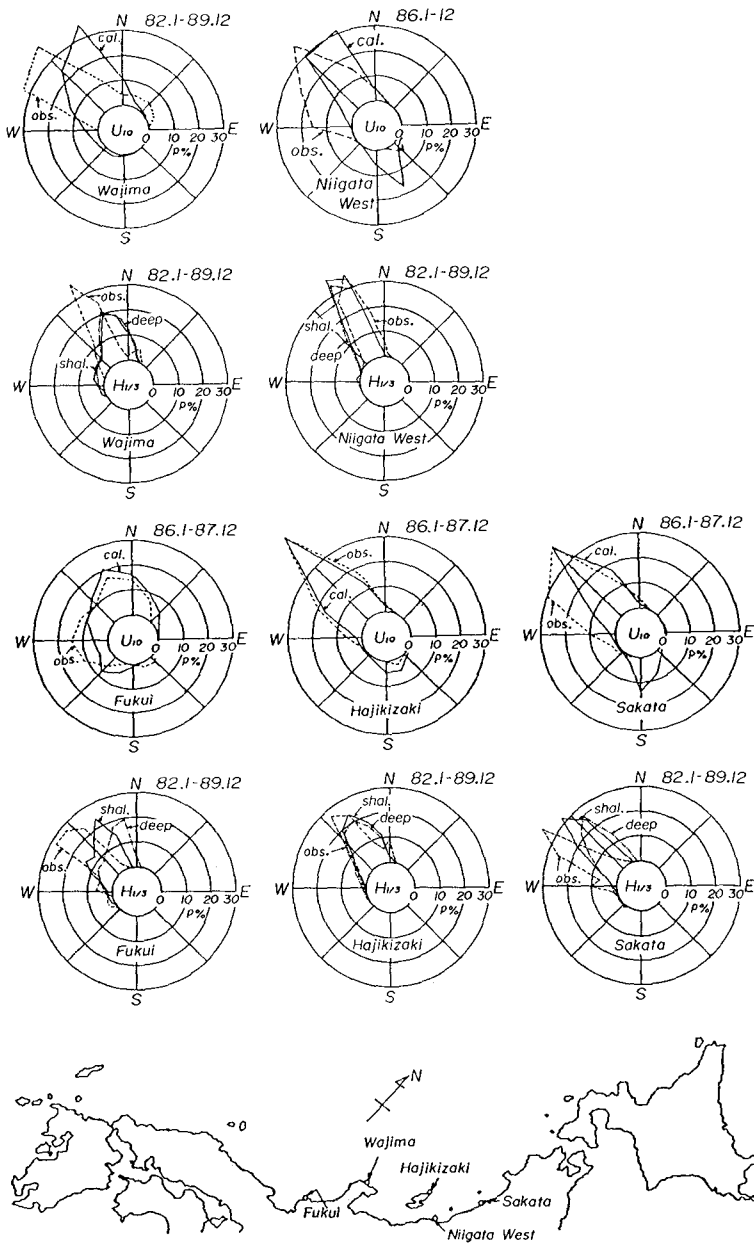


Fig. 10 Comparison of hindcast and observation for directionally-grouped occurrence rates of high winds and high waves.

spite of the difference of predominant wind direction. This suggests that sheltering effect of Sado Island is greater than refraction effect at Niigata West. At Fukui and Sakata, the shallow water wave model gives better estimation to observed predominant wave direction than the deep water wave model, but discrepancy of about 20 degrees still exists.

#### 4. Conclusions

Applicability of the long term wave hindcast system was verified by reasonable agreement between computation and observation over 8 years at 11 wave observation points along the coast of the Japan Sea. Although the shallow water wave model requires more than three times computer processing time compared to the deep water wave model, higher reliability over the deep water wave model leads us to use the shallow water wave model for the estimation of wave climate including wave direction.

#### 5. Acknowledgements

The authors thank the Bureaus of Harbor Construction, Ministry of Transportation and the Prefectural Offices for kindly offering the valuable wind and wave data. Thanks are also due to Mr. M. Ohfuku, Technical Officer of Civil and Ocean Engineering, Ehime University and Mr. T. Hioki, graduate student of Ocean Engineering, Ehime University for their sincere assistance during the study.

#### References

- Bijvoet, H.C.(1957): A new overlay for the determination of the surface wind over sea from surface weather charts, KNMI, Mededelingen en Verhandelingen, Vol. 71, pp. 1-35.
- Thornton, E.B.(1977): Rederivation of the saturation range in the frequency spectrum of wind-generated gravity waves, J. Phys. Oceanogr., Vol. 7, No. 1, pp. 137-140.
- Yamaguchi, M. et al.(1987): A shallow water wave prediction model at a single location and its applicability, Proc. JSCE, No. 381/II-7, pp. 151-160(in Japanese).
- Yamaguchi, M. et al.(1990): Estimation of wave climate along the coast of the Japan Sea based on wave hindcasting, Natural Disaster Science, 9-3, pp. 18-42(in Japanese).

## CHAPTER 20

# Characteristics of absorbing directional wavemaker

H. Hirakuchi <sup>1</sup>, R.kajima, T.Shimizu, M.Ikeno

### ABSTRACT

In order to maintain realistic and expected incident waves, an absorbing directional wavemaker has been developed and its performance is examined experimentally. The directional spectrum of the generated waves in the progressive wave field is analysed by the Bayesian Model (BDM), and the directional spectrum of the incident waves in the combined wave field is separated by the Modified Bayesian Model (MBM). Good agreement is shown between the BDM result and the MBM result. In order to make a further check on the angular spreadings of the directional waves in the progressive and combined wave fields, coherence function of the cross spectrum is measured and compared with the target one derived theoretically.

## 1 Introduction

Hydraulic model tests have often been conducted to solve the various problems associated with the planning and the design of coastal structures. It is very important to reproduce realistic ocean surface waves in a laboratory basin. Major hydraulic laboratories in the world have built the directional wavemakers during the last decade.

To generate short-crested waves by the directional wavemaker, several different random wave synthesis methods have been developed. All of these synthesis methods are based on the simulation of the irregular waves which have the specific directional spectrum. For evaluating the performance of the directional wavemaker, the directional spectrum analysis becomes of importance. Several analysis models are proposed and used for this purpose.

---

<sup>1</sup>Abiko Research Laboratory, Central Research Institute of Electric Power Industry, 1646 Abiko, Abiko-shi, Chiba, JAPAN 277-11

However, it is well known that each model gives the different result, although the same data are used. Therefore, it is very important to use another analysis method except for the directional spectrum analysis method as well as to select the best directional analysis model.

When a model structure is highly reflective and occupies a large part of a width of a basin, re-reflected waves at a paddle affect the incident waves. In the case of the 2-D experiment, an absorbing wavemaker has been developed and used in a wave channel (Hirakuchi et al., 1990b). In order to maintain better controlled wave conditions in a incident and reflected combined wave field, an absorbing directional wavemaker has been developed. To evaluate the absorption performance of the developed wavemaker, it is important to separate the directional spectrum of the incident waves from the combined wave field. For this purpose, Isobe and Kondo(1986) modified the MLM technique, and Hashimoto et al.(1987a) proposed the Modified and the Extended Bayesian Model (MBM and EBM). The separated result would be also affected by the resolution power of each model.

The purpose of this study is to examine the performance of the absorbing directional wavemaker experimentally. We first consider some aspects of the usefulness of the coherence function of the cross spectrum, for evaluation of the wave angular spreadings. Next, we carry out the several experiments in the progressive wave field and the combined wave field with regular and irregular waves, and make comparison of the wave height and the directional spectrum. A further check on the wave spreadings of the generated waves are obtained by comparing the coherence distribution in space and frequency domain.

## 2 Coherence function of directional wave field

Directional wave field used in a wave modelling is usually represented by the following form:

$$S(f, \theta) = P(f) \cdot G(\theta; f) \quad (1)$$

where  $S$ ,  $P$  and  $G$  are the directional spectrum, the frequency spectrum and the angular spreading function, respectively. In the case of Mitsuyasu-type spreading function,  $G$  is:

$$G_M(\theta) = \frac{(2s)!!}{2\pi (2s-1)!!} \left( \cos \frac{\theta - \theta_0}{2} \right)^{2s} \quad (2)$$

where  $\theta_0$  is the mean wave angle, and  $s$  is the angular spreading parameter. In this paper,  $s$  is defined as:

$$s = \begin{cases} s_{max} (f/f_p)^5 & ; f \leq f_p \\ s_{max} (f/f_p)^{-2.5} & ; f \geq f_p \end{cases} \quad (3)$$

where  $f_p$  is a peak frequency of the power spectrum and  $s_{max}$  is a maximum value of the spreading parameter at  $f_p$ .

The general relationship between the directional spectrum and the cross spectrum can be expressed as:

$$\phi_{mn}(\sigma) = \int_{\mathbf{k}} H_m(\mathbf{k}, \sigma) H_n^*(\mathbf{k}, \sigma) S(\mathbf{k}, \sigma) \exp(-i\mathbf{k} \cdot \mathbf{r}_{mn}) d\mathbf{k} \quad (4)$$

where  $\phi_{mn}$  is the cross-spectrum between the point  $\mathbf{x}_m$  and  $\mathbf{x}_n$ ,  $\mathbf{r}_{mn}$  is a space vector ( $\mathbf{r}_{mn} = \mathbf{x}_n - \mathbf{x}_m = (R \cos \alpha, R \sin \alpha)$ ),  $H$  is the complex transfer function relating the water surface elevation to any wave quantity, and  $*$  represents the complex conjugate value.

When the wave quantities measured are wave surface elevations,  $H$  is  $H_m = H_n^* = 1.0$ . In this case, the cross spectrum can be expressed as:

$$\phi_{mn}(\sigma)/P(\sigma) = C_1 - i Q_1 \quad (5)$$

$$C_1 = J_0(kR) + 2 \sum_{j=1}^{[s/2]} \frac{s! s! (-1)^j J_{2j}(kR)}{(s-2j)! (s+2j)!} \cos(2j\delta) \quad (6)$$

$$Q_1 = -2 \sum_{j=0}^{[(s-1)/2]} \frac{s! s! (-1)^j J_{2j+1}(kR)}{(s-2j-1)! (s+2j+1)!} \cos(2j+1)\delta \quad (7)$$

where  $C_1$  and  $Q_1$  are co-spectrum and quadrature spectrum, respectively,  $J$  is a Bessel function and  $\delta$  is:

$$\delta = \alpha - \pi - \theta_0 \quad (8)$$

The cross spectrum is often expressed by the coherence and the phase:

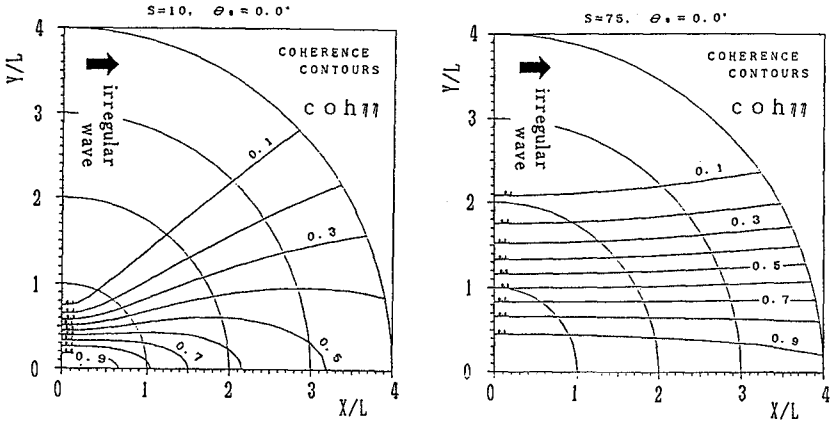
$$coh = \frac{|\phi_{mn}|^2}{\phi_{mm} \phi_{nn}} \quad (9)$$

$$phs = \tan^{-1} \left( \frac{\text{Imag}(\phi_{mn})}{\text{Real}(\phi_{mn})} \right) \quad (10)$$

Fig.1 is an example of the spacial distribution of the coherence function between the origin and any other position in the directional wave field with the spreading parameter of  $s=10$  and  $75$ . It is shown that the coherence value along the main wave direction from the origin keeps very high value, although the coherence value along the wave crest line from the origin decreases very rapidly. In the case of uni-directional waves, the coherence value should be 1.0 all over the field. Therefore, it can be said that the decreasing rate of the coherence value in space domain reflects the angular spreadings of the directional wave field.

In Fig.1, the coherence value along the crest line from the origin becomes less than 0.1 over the range of  $R/L > 2$ , where  $L$  is a wave length. It means

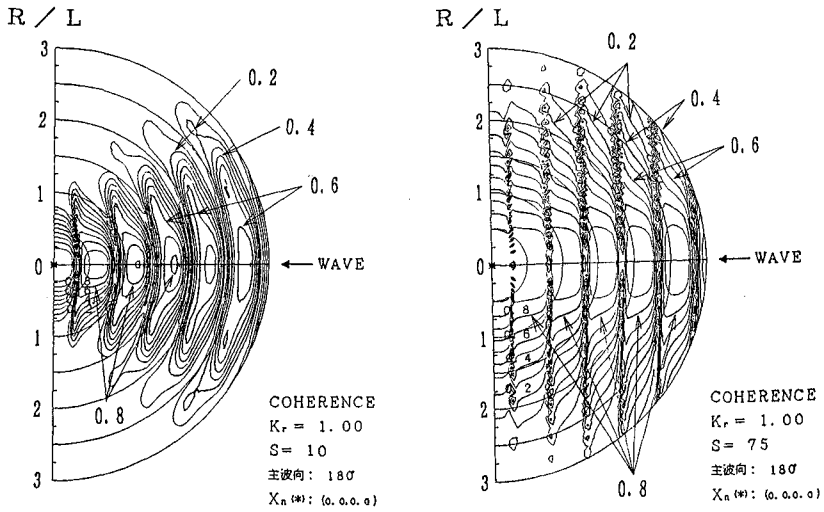




(a)  $s = 10$

(b)  $s = 75$

**Fig.1** Coherence distribution in the progressive wave field.



(a)  $s = 10$

(b)  $s = 75$

**Fig.2** Coherence distribution in the combined wave field.

that the data measured at two points with the distance of  $R/L > 2$  along the wave crest line are statistically independent. It also means that it is possible to get the ststistically independent cross spectra by arranging the several wave arrays, each of which is located with the distance of  $R/L > 2$  along the wave crest line.

The relationship between the crosss and directional spectrum in the incident and reflected combined wave field is derived by Isobe and Kondo(1986):

$$\begin{aligned} \phi_{mn}(\sigma) = & \int_{\mathbf{k}} H_m(\mathbf{k}, \sigma) H_n(\mathbf{k}, \sigma) S(\mathbf{k}, \sigma) \times \\ & [ \exp\{-\mathbf{k} \cdot (\mathbf{x}_n - \mathbf{x}_m)\} + r^2 \exp\{-\mathbf{k} \cdot (\mathbf{x}_{nr} - \mathbf{x}_{mr})\} + \\ & r \exp\{-\mathbf{k} \cdot (\mathbf{x}_{nr} - \mathbf{x}_m)\} + r \exp\{-\mathbf{k} \cdot (\mathbf{x}_n - \mathbf{x}_{mr})\} ] d\mathbf{k} \quad (11) \end{aligned}$$

where  $r$  is the reflection coefficient,  $\mathbf{x}_{nr}$  and  $\mathbf{x}_{mr}$  are symmetrical space vectors of  $\mathbf{x}_n$  and  $\mathbf{x}_m$  against the reflecting boundary, and  $\mathbf{k}$  is a wave number vector of the incident waves defined in a half domain.

The coherence function in the combined wave field can be calculated by the above equation. Fig.2 is an example of the coherence distribution in space domain between the origin and any other position in the half domain under the condition of  $r = 1.0$  and  $\theta_0 = \pi$ . In Fig.2, the coherence value along the wave direction changes very rapidly at the nodal position and gives the maximum value at the anti-nodal position. This figure shows that the coherence distribution in space domain would be useful to evaluate the wave spreadings in the combined wave field.

### 3 Experimental set-up

The dimension of the wave basin is 45m wide, 35m long and 1.1m deep (Fig.3). The absorbing directional wavemaker consists of 48 wave paddles, each of which is controlled independently and is 40cm wide and 120cm high (Hirakuchi et al., 1990a). To detect the reflected waves, a capacitance wave gauge is mounted on the front side of each paddle. It is possible to switch the absorption loop in or out of the control circuit, so this wavemaker also work as a conventional wavemaker. The absorbing principle and its performance for the uni-directional irregular waves in a wave channel have been described and examined by Hirakuchi et al.(1990b).

To examine the performance of wave generation and reflected wave absorption, all four combinations of the following alternatives are considered in the experiments: 1) either with or without the absorption loop, and 2) either with or without the remarkable reflected waves in the basin (with the vertical wall in Fig.4, with absorbing beach in Fig.3).

Regular and irregular wave experiments are carried out at the water



depth of 50cm. The wave height and period used for regular wave experiments are  $H=4\sim 5$ cm and  $T=1.0\sim 1.5$ s. For the directional wave experiments, the Mitsuyasu-type angular spreading function and the Bretschneider-type power spectrum are used as a target spectrum. The significant wave height and period for  $s_{max}=10$  and 75 are  $H_{1/3}=5.0, 4.0$ cm and  $T_{1/3}=1.0, 1.25$ s, respectively. The double-summation model are used for the wave synthesis.

The star arrays in Fig.3 and the linear array in Fig.3 and 4 are used for the directional spectrum analysis. The linear array in Fig.3 and 4 are also used to evaluate the coherence distribution in space and frequency domain.

## 4 Results for progressive wave fields

### 4.1 Regular waves

Firstly, experiments on oblique regular waves were carried out (see Fig.3), and the generated waves were compared with the numerical and analytical results. Fig.5 is an example of the wave height distribution at  $y=9$ m in Fig.3. The black circle is the experimental result, and the break line and the solid line are analytical result proposed by Takayama(1982) and the numerical result calculated by the mild slope equation, respectively. The mild slope equation used in this study is:

$$\left. \begin{aligned} \frac{\partial \mathbf{Q}}{\partial t} + C^2 \nabla \zeta &= 0 \\ \frac{\partial \zeta}{\partial t} + \frac{1}{n} \nabla \cdot (n \mathbf{Q}) + \frac{f_d}{n} \zeta &= 0 \end{aligned} \right\} \quad (12)$$

where  $C$  is the wave velocity,  $\zeta$  is the surface elevation,  $f_d$  is a coefficient for energy dissipation, and  $n$  and  $\mathbf{Q}$  are defined as:

$$n = C_g / C = \frac{1}{2} \left( 1 + \frac{2kh}{\sinh 2kh} \right) \quad (13)$$

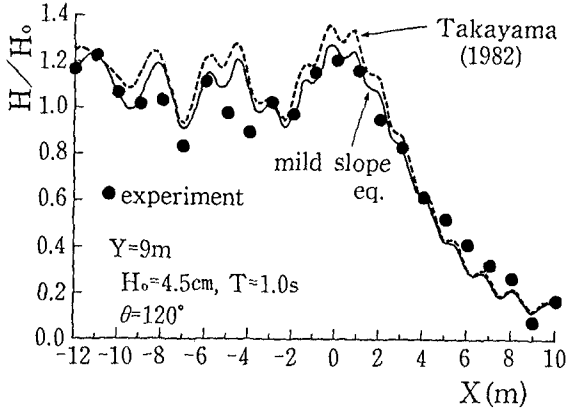
$$\mathbf{Q} = \int_{-h}^0 \mathbf{U} dz \quad (14)$$

in which  $\mathbf{U}$  is the water particle velocity.

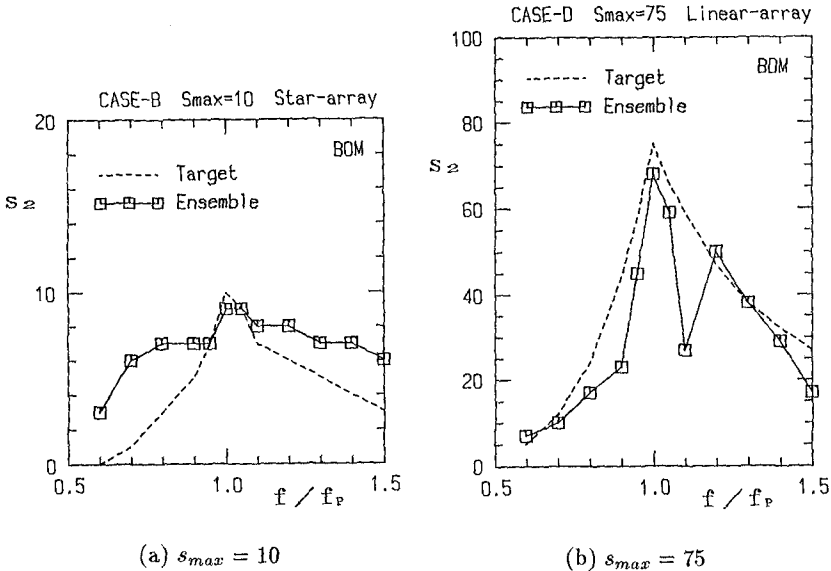
Eq.(12) is equivalent to the mild slope equation with the dissipation term  $f_d$  (Dalrymple, Kirby et al., 1984):

$$\nabla \cdot (nC^2 \nabla \zeta) + n\sigma^2 \zeta + i\sigma f_d \zeta = 0 \quad (15)$$

Fig.5 shows good agreement between the measured wave heights and the numerical results calculated by Eq.(12). It is notified that the analytical result proposed by Takayama is not satisfied with the experimental boundary condition illustrated in Fig.3.



**Fig.5** Wave height distribution of oblique waves in the progressive wave field. ● represents the measured value at  $Y=9m$ , the dotted line is the analytical value by Takayama and the solid line is the numerical value calculated by the mild slope equation.



**Fig.6** Comparison between estimated angular spreading parameter and target one. □ is estimated by Eq.(16) using the directional spectrum analysed by BDM. For the BDM analysis, the averaged cross spectrum for 6 experiments are used.

### 4.2 Directional waves

Directional wave experiments with  $s_{max}=10$  and  $75$  are carried out. In order to reduce the statistical variation, six experiments are carried out, each of which has the same wave parameters but has different random phases. Using the averaged cross spectrum for the six experiments, the directional spectrum is analysed by the Bayesian Model (BDM) proposed by Hashimoto and Kobune(1987b). The spreading parameter of the analysed directional spectrum is calculated by the following form:

$$s = \left( \frac{1}{\gamma^2} - \frac{1}{2} \right) + \left( \frac{1}{\gamma^4} - \frac{3}{4} \right)^{1/2} \tag{16}$$

where  $\gamma$  is a long-crested parameter at a frequency  $f$

$$\gamma(f) = \left[ \frac{(M_{20} + M_{02}) - \sqrt{(M_{20} - M_{02})^2 + 4M_{11}^2}}{(M_{20} + M_{02}) + \sqrt{(M_{20} - M_{02})^2 + 4M_{11}^2}} \right]^{1/2} \tag{17}$$

$$M_{pq}(f) = P(f) \int_0^{2\pi} (k \cos \theta)^p (k \sin \theta)^q G(f, \theta) d\theta \quad ; p, q = 0, 1, 2 \tag{18}$$

Fig.6 is the estimated results of  $s$ , where the dotted line is the target one defined in Eq.(3) and  $\square$  is the measured one calculated by Eq.(16). The estimated values of  $s$  show good agreement with the target ones, although the some results for  $s_{max}=75$  show the small values.

The coherence distribution between P1 and P2~P11 (in Fig.3) are measured. Fig.7(a) gives the result along the crest line ( $\alpha = 0^\circ$ ) at the peak frequency of the long-crested waves: the target value of  $s$  at the peak frequency is  $s=75$ . The solid line is the coherence function of the target waves,  $\square$  is the coherence value of the averaged cross spectrum, and the other six marks represent the coherence values of the six experiments. The agreement between the averaged value and the target value is very good, although the measured value for each experiment varies from  $s = 30 \sim 150$ .

The coherence distribution in frequency domain are also calculated. Fig.7(b) gives the coherence between P1 and P3 along the crest line with the distance of 60cm. The solid line is the coherence value of the averaged cross spectrum, and the dotted line with  $\bullet$  is the coherence value of the target wave with the Mitsuyasu-type spreading function. The averaged coherence value shows good agreement with the expected one.

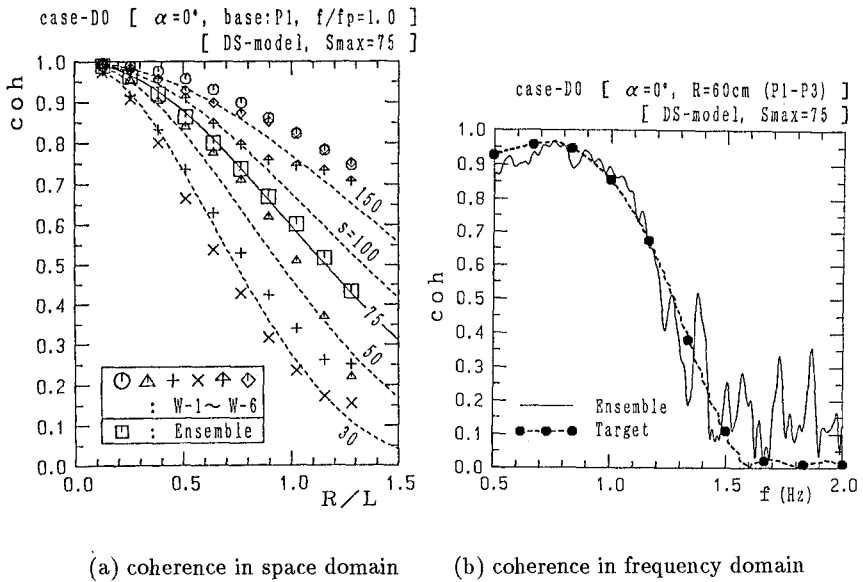


Fig.7 Coherence value measured in progressive wave field ( $s_{max} = 75$ ).

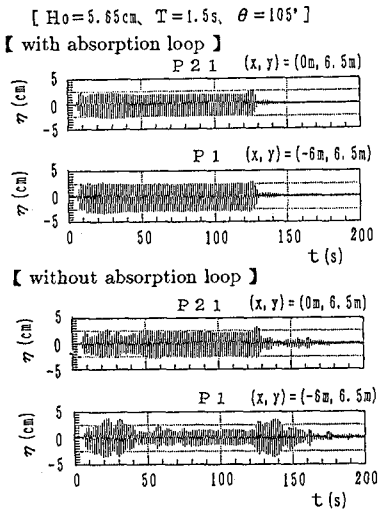


Fig.8 Time histories of generated oblique waves ( $\theta = 105^\circ$ ) with and without the absorption loop in the combined wave field. P1 and P21 are shown in Fig.4

## 5 Results for combined wave fields

### 5.1 Regular waves

To reproduce the incident and reflected combined wave field, a vertical wall with the reflection coefficient of 1.0 are settled as shown in Fig.4. 21 wave gauges (P1~P21) are arranged parallel to the wall and 6 wave gauges are arranged perpendicular to the wall.

Experiments on oblique regular waves were carried out with and without the absorption loop. The time history measured at P1 and P21 are shown in Fig.8. The upper and lower two graphs represent the result with and without the absorption loop, respectively. The waves generated without the absorption loop are unstable, and the multi-reflected waves between the wall and the wavemaker are apparently remained over the range of  $t > 125s$ .

Fig.9 is the result of the wave height distribution along the parallel and perpendicular line to the wall, generated with the absorption loop.  $\square$ ,  $\circ$  and  $\triangle$  are the mean wave heights during several wave periods (T).  $\square$  is the early result of the combined wave field, which may not be affected by the multi-reflected waves. The break line and the solid line are the numerical results of the expected combined wave field calculated by Eq.(12). Fig.9 shows that the wave heights along the both lines are rather stable in time and agree to the expected results.

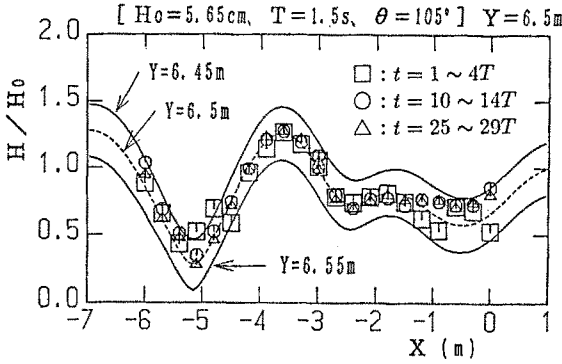
### 5.2 Directional waves

Directional wave experiments with  $s_{max}=10, 75$  and  $\infty$  are carried out with and without the absorption loop, and the combined wave fields are reproduced. The significant wave height along the perpendicular line to the wall are shown in Fig.10. This figure shows that the results with the absorption loop are not affected by the reflected waves. Since the reflection coefficient at the vertical wall is 1.0, the ratio of the significant wave height ( $H/H_0$ ) may be equal to 2.0 at the wall and to  $\sqrt{2}$  at large distances from the wall, and the minimum value may be occurred at  $Y \approx 8m$  ( $L/4$  away from the wall). The agreement with the measured results with the absorption loop and the theoretical values mentioned above is also excellent.

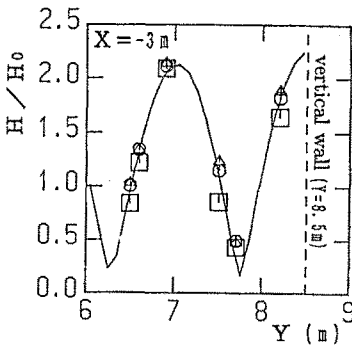
Fig.11 gives the comparison of the directional spectrum with and without the remarkable reflected waves in the basin: Fig.11(a) and (b) are the power spectrum and the directional spreading function, respectively. These results show that the directional spectrum of the incident waves in the combined wave field is not affected by the re-reflected waves at the paddles.

Fig.12 is an example of the coherence distribution along the parallel line (P1~P21) in Fig.4.  $\circ$  represents the coherence value between P11 and





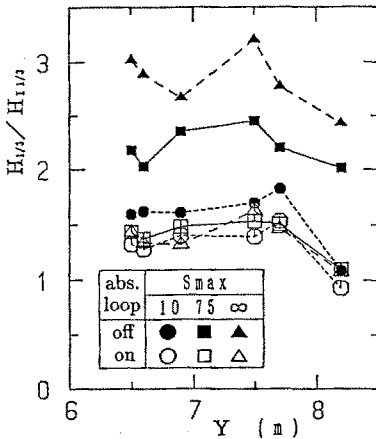
(a)  $Y = 6.5 \text{ m}$   
 (parallel to the wall)



(b)  $X = -3 \text{ m}$   
 (perpendicular to the wall)

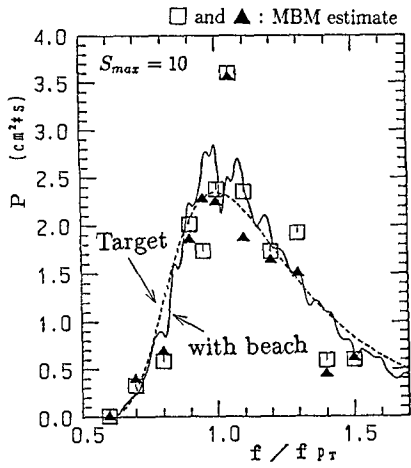
**Fig.9** Comparison between wave height in the combined wave field generated with the absorption loop and numerical results of the mild slope equation (solid and dotted lines).

□, ○ and △ are measured values.

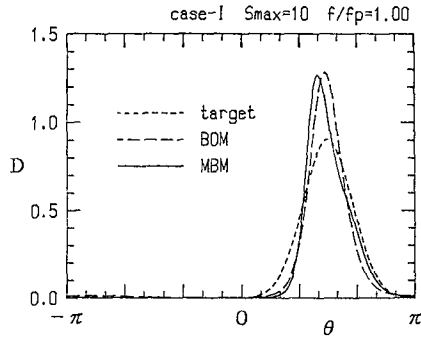


**Fig.10** Comparison of the significant wave height in the combined wave field ( $s_{max} = 10, 75, \infty$ ).

The white and black marks represent experimental results with and without the absorption loop, respectively.

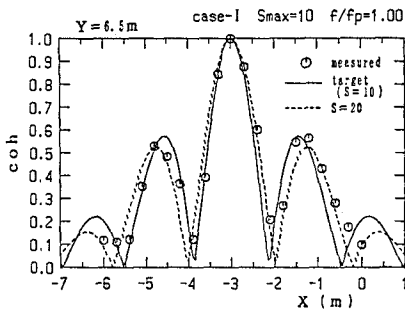


(a) power spectrum

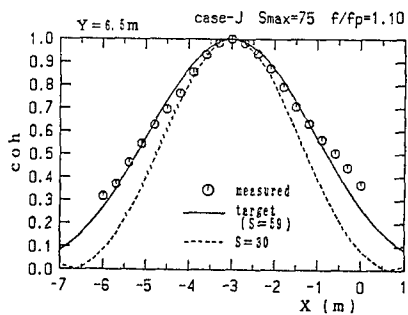


(b) angular spreading function

**Fig.11** Comparison of directional spectrum with and without the remarkable reflected waves in the basin.  $\square$  and  $\blacktriangle$  represent the power spectrum of the incident waves in the combined wave field. These two results are estimated by MBM using the data measured at the different position.



(a)  $s_{max} = 10, f/f_p = 1.0$



(b)  $s_{max} = 75, f/f_p = 1.1$

**Fig.12** Comparison of coherence distribution in space domain in the combined wave field.  $\circ$  represents the observed coherence value between P11 ( $x=-3m$ ) and P1~P21( $x=-6\sim 0m$ ), and solid line represents the theoretical value of the target combined wave field.

P1~P21, so the coherence at P11 ( $x = -3\text{m}$ ) is equal to 1.0. Fig.12(a) is the result for  $s_{max}=10$  at  $f/f_p=1.0$ , and Fig.12(b) is the result for  $s_{max}=75$  at  $f/f_p=1.1$ . The measured coherence value agrees very well to the expected value.

## 6 Conclusion

The absorbing directional wavemaker has been developed, and its performance is examined experimentally. Several experiments were carried out either with or without the absorption loop in the progressive wave field and in the combined wave field. From the comparison of the wave height, the directional spectrum and the coherence function of the cross spectrum, it is shown that the absorbing directional wavemaker has excellent performance to absorb the reflected waves. The wavemaker can reproduce the short- and long-crested waves with the specific directional spectrum, and can maintain the better controlled incident wave field.

## REFERENCES

- Dalrymple, R.A., J.T. Kirby and P.A. Hwang (1984)** : Wave diffraction due to area of energy dissipation, *Proc. ASCE*, Vol.110, No.WW1, pp.67-79.
- Hashimoto, N. et al.(1987a)** : Estimational spectra from a Bayesian approach in incident and reflected wave field, *Report of Port and Harbour Research Inst.*, Vol.26, No.4, pp.3-33 (in Japanese).
- Hashimoto, N. and K. Kobune (1987b)** : Estimation of directional spectrum using the Bayesian approach, and its application to field data analysis, *Report of Port and Harbour Research Inst.*, Vol.26, No.5, pp.57-100.
- Hirakuchi, H. et al. (1990a)** : Laboratory measurement and generation of directional water waves, *Proc. 37th Japanese Conf. Coastal Eng.*, pp.150-154 (in Japanese).
- Hirakuchi, H. et al. (1990b)** : Application of a piston-type absorbing wavemaker to irregular wave experiments, *Coastal Eng. Japan*, Vol.33, No.1, pp.11-24.
- Isobe, M. and K. Kondo (1986)** : Method for estimating directional wave spectrum in incident and reflected wave field, *Proc. 19th ICCE*, pp.467-483.
- Takayama, T. (1982)** : Theoretical properties of oblique waves generated by serpent-type wave-maker, *Report of Port and Harbour Research Inst.*, Vol.21, No.2, pp.3-48.

## CHAPTER 21

# A New Nearshore Directional Wave Gage

Gary L. Howell<sup>1</sup>

## 1 Introduction

A field directional wave gage has been developed for requirements in coastal, port, and harbor engineering. Uses include planning and design studies, long term wave climatology, and post construction monitoring. The gage provides high quality directional wave spectra measurements from a compact, easily installed instrument. Stand alone installation with long term internal data recording is provided. Real time data access may be simultaneously provided by connecting a cable.

The gage is completely bottom mounted with no surface components. Optimized for shallow and intermediate water depths required by coastal engineers, the gage may be reliably deployed in water depths too shallow for buoys or acoustic instruments. The sensors are three high resolution pressure transducers that permit the mounting frame to be resistant to fishing activities.

Reliable data storage and long term deployment are achieved by performing preliminary data analysis within the instrument. Intermediate analysis results are recorded on reliable non-volatile solid state memory. The recorded data may be post processed to obtain simple estimates of mean water level, wave height, period, and direction. If desired, the Fourier series coefficients of the directional spectrum may be computed from the intermediate data. Optionally, modern high resolution methods may be used.

## 2 Background

### 2.1 Motivation

*Deep ocean directional wave measurement has progressed rapidly during the last*

---

<sup>1</sup>U S Army Corps of Engineers, Coastal Engineering Research Center, Waterways Experiment Station Vicksburg, Mississippi 39180-6199 USA

twenty years. In-situ buoy measurements are routinely collected by the industrialized nations. Commercial directional buoys are available for site specific studies. The development of satellite technology has provided deep water measurements assumed to be homogeneous over the large range cells of satellite sensors.

Unfortunately for coastal engineers, progress in nearshore measurements has lagged. The typical coastal regime, characterized by shoaling, refraction, diffraction, and reflection, makes the use of large spatial averaging remote sensors, inappropriate. Data are often required in areas subject to large breaking waves and strong currents. These conditions capsize directional buoys, and aerate the water column, blinding acoustic sensors.

## 2.2 Requirements

Modern coastal engineering practice requires use of increasingly sophisticated models. Properly calibrated and verified, models can yield accurate information on waves at a project site. Frequently data are not available, and models must be employed with only deep water data, or shallow water data from a distant or unrepresentative site. In undeveloped areas, models may be applied without any calibration or verification. The goal of this development is to make high quality, site specific wave data commonplace.

A requirements based design approach was employed to guide development efforts. First, engineering data requirements were identified:

- Wave height
- Wave period
- Wave direction
- Wave spectrum
- Radiation stress
- Water level

While many other statistics could be added, routine availability of these parameters constitutes a useful parameter set. This paper will focus on the key parameter of wave direction, in particular mean wave direction.

## 2.3 Measuring wave direction with arrays

In-situ directional wave gages can be generalized as arrays of sensors that spatially and temporally sample the *true* directional wave spectrum over a section of the sea surface. The estimated directional spectrum is the convolution of the *true* directional spectrum with the transfer function of the sensor array. Isobe et al. (1984) expressed this using the cross power spectra,  $\Phi_{mn}$ , between arbitrary

measured wave parameters and the directional wave spectrum  $S(\vec{k}, \sigma)$ , where  $\vec{k}$  is the wave number vector, and  $\sigma$  is angular frequency.

$$\Phi_{mn} = \int_{\vec{k}} H_m(\vec{k}, \sigma) H_n^*(\vec{k}, \sigma) e^{-i\vec{k}(x_n - x_m)} S(\vec{k}, \sigma) d\vec{k} \tag{1}$$

The  $H_m$  is the hydrodynamic transfer function between the water surface and the  $m$ th sensor and  $x_m$  is the sensor's location vector.

Common practice for engineering applications assumes linear wave theory for the transfer functions  $H_m$ , and a linear dispersion relationship between wave length and frequency expressed as

$$\sigma^2 = (2\pi f)^2 = gk \tanh kd \tag{2}$$

where  $d$  is the water depth.

Equation 1 can then be expressed in the frequency domain as

$$\begin{aligned} \Phi_{mn}(f) = & \int_0^{2\pi} H_m(f, \theta) H_n^*(f, \theta) \{ \cos(k[x_{mn} \cos \theta + y_{mn} \sin \theta]) \\ & - i \sin(k[x_{mn} \cos \theta + y_{mn} \sin \theta]) \} S(f, \theta) d\theta \end{aligned} \tag{3}$$

where  $\theta$  is the wave direction,  $f$  is wave frequency,  $S(f, \theta)$  is the wave frequency directional spectrum, and

$$x_{mn} = x_n - x_m \tag{4}$$

$$y_{mn} = y_n - y_m \tag{5}$$

Directional wave analysis is the method of estimating solutions to the integral equation 3. Horikawa (1988) provides a summary of current methods. For many engineering applications, mean wave direction is sufficient. Note that  $\Phi_{mn}(f)$ , the cross-spectral matrix, is sufficient information to employ any directional analysis technique.

## 2.4 Existing instrumentation

Existing instrumentation and field procedures were reviewed to identify required improvements. The following types of in-situ, nearshore directional measurement instrumentation systems are being used, or have been evaluated in the past.

**PUV** Co-located EM current meter and absolute pressure gage. Both real-time, cable connected, and self recording versions are used routinely.

**Borgman array** Shore parallel array of absolute pressure transducers with spacing comparable to wave lengths (Panicker and Borgman, 1970). This array is capable of high resolution and is routinely used at research facilities.

**$S_{xy}$  array** A 6m right triangle, absolute pressure transducer array, analyzed as a slope array (Higgins, et al., 1981).

**DPG** Differential Pressure Gage. Two orthogonal short base line differential pressure gages, and one absolute gage. Developed and successfully tested by Bodge and Dean (1984).

**ADCP** Acoustic Doppler Current Meter. Measures three components of current velocity at several range cells in the middle part of the water column. The data analysis is similar to a *PUV*.

**Short base-line slope array** A real time, cable connected, 1.6 m equilateral triangle, absolute pressure transducer array, analyzed as a slope array. This gage was developed as a precursor to the gage reported here and has been in routine use by CERC since 1989.

Economy and reliability are the most needed improvements. Measurement and analysis techniques were less so. When the total costs of obtaining an analyzed data report are considered, instrument cost was less important than costs associated with field operations, maintenance, and data analysis.

An integrated approach addressed the entire function from sensor to analyzed data report. Instrument requirements were part of the overall systems analysis. Existing instruments require improvement in one or more of the following areas:

**Directional resolution** Most important for sediment transport formulae, but benefits all applications.

**Gage orientation accuracy** Errors or suspected errors in the orientation of directional gages can render data useless.

**Site selection flexibility** Often sites must be selected based on survivability or operational requirements, rather than engineering data needs.

**Deployment period** Frequent service requirements are a principal cause of high costs. At many sites, weather permits servicing only during the summer.

**Measurement interval** Shallow water wave conditions can change rapidly. Instrument limitations force sub-sampling.

**Reduce total cost of analyzed data** Site specific data costs must be within the budget of a typical engineering project.

## 3 New Developments

### 3.1 Principles of operation

The enabling development is the very short baseline absolute pressure transducer array (Figure 1). Traditional directional wave gages using pressure transducers have relied on arrays with dimensions on the order of water wave lengths (Panicker and Borgman, 1970).



Figure 1: DWG-1 ready for deployment. Base version uses 3 transducers in a 1.6 m equilateral triangle array.

Scripps Institute of Oceanography developed slope gages using absolute pressure transducers in a 6 m right triangle array. Higgins, et al. (1981) analyzed the errors due to length of the baseline. Error was reduced by making the baseline as short as possible, limited only by the noise of the absolute pressure transducers.

Bodge and Dean (1984) demonstrated that differential pressure transducer arrays could employ very short base lines. The differential transducer array requires a fluid filled tubing system to transmit the pressure to the transducer. Construction and maintenance of the tubing system requires care.

The new gage has the advantages of the short baseline array, yet still uses absolute pressure sensors. An absolute pressure sensor using a quartz crystal transducer and a specially designed digitization circuit was developed. The combination provides pressure samples with an order of magnitude less noise than previous strain gage based transducers. The sampling period for this resolution is less than 180msec.

Numerical simulation of various directional wave spectra measurements using the noise characteristics of the new transducer examined the effect of baseline dimension on error in mean wave direction. Results were very encouraging. To verify these results a field experiment was conducted. Figure 2 shows the layout of a seven transducer array of transducers arranged to provide multiple baseline lengths. The array was placed in 8m of water at the CERC Field Research



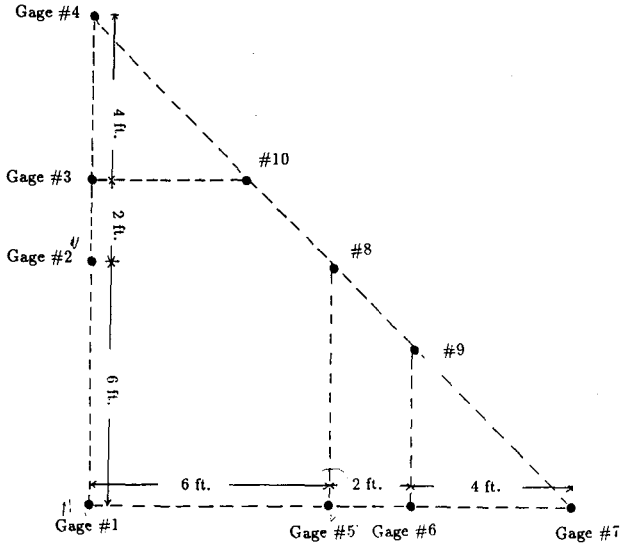


Figure 2: Array layout used at the DUCK 85 field test to evaluate the effect of the baseline length of slope arrays on mean wave direction measurement error.

Facility, Duck, N.C.

A total of 1567 wave records from October to December 1986 were analyzed. Significant wave height ranged to 4 m, and spectral peak periods ranged from 4 to 20 sec. Data from sensor number 1 was discarded due to excessive noise. Virtual sensors 8, 9, and 10 were created by linear interpolation of data from sensors 1 and 4. Figure 3 is an example of a scatter plot of mean direction from a slope analysis of effective 1.2 m and 1.8 m arrays. As predicted by the simulation, the reduction in base line length has little effect on the mean direction estimate.

The new gage has a base configuration of a 1.6 m equilateral triangle, absolute transducer array. This array will give accurate mean direction estimates at low cost. Figure 1 shows the geometry of the standard installation pod. The hexagonal shape allows the minimum configuration triangular array to be augmented with additional transducers. Numerical simulations using the Bayesian analysis method (Hashimoto and Kobune, 1988) have been performed using 4 and 6 transducers. Directional resolution is improved over the minimum three transducers. Directional resolution performance of the new gage will be reported when planned field tests of the four and six transducer versions have been completed.

The short base line reduces construction costs and simplifies installation and recovery. Problems of spatial homogeneity in the complex bathymetry of coastal projects are eliminated. The hexagonal array facilitates design of a high strength, trawler resistant pod.

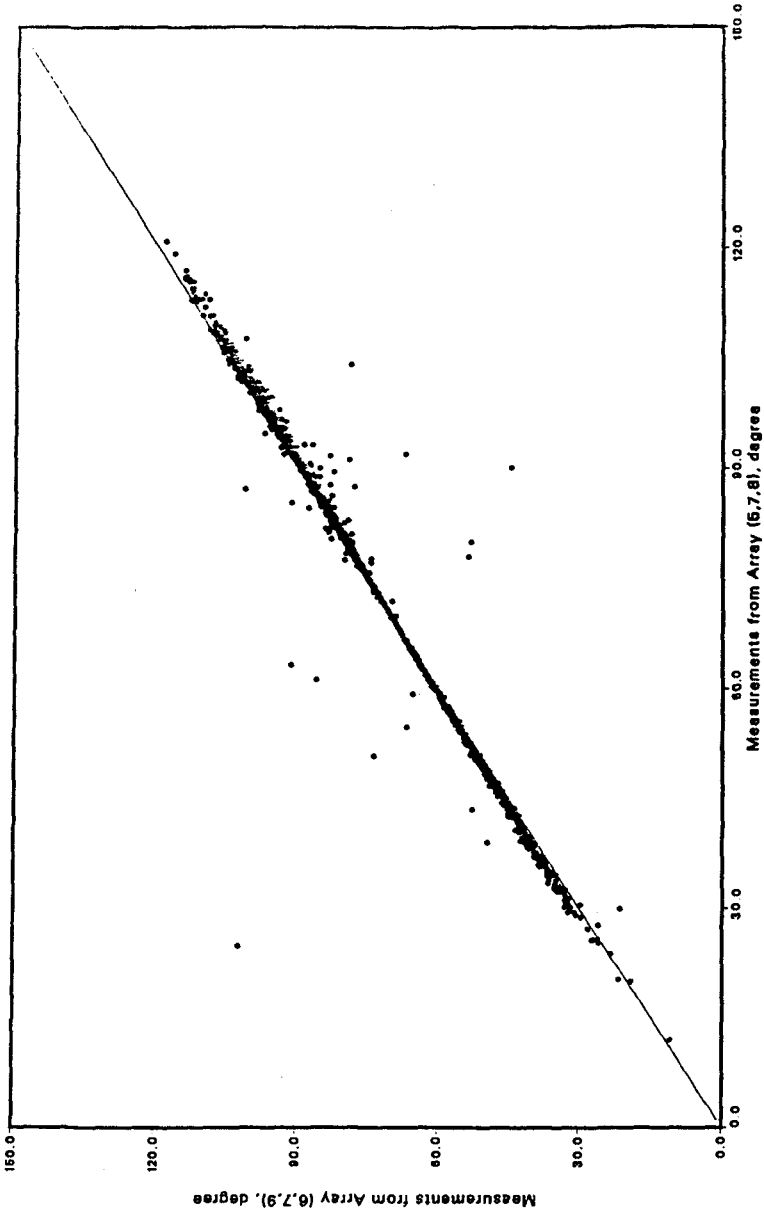


Figure 3: Correlation of mean wave direction estimates from Array (5,7,8) and Array (6,7,9).

### 3.2 Gage design

The performance requirements were translated into the following design specifications.

#### Specifications.

**Internally recorded data:** Mean water level, cross-spectral matrix, and calendar date and time.

**Post-processed data:** Water level, significant wave height, spectral peak period, mean wave direction, and directional spectrum.

**Internal data storage:** Removable EPROM modules.

**Real time option:** Simultaneous with internal recording and analysis, calibrated pressure time series data are available in real time. Adds a standard 7-conductor well logging cable up to 1.7 km length and a shore located PC or modem.

**Principle:** 3-transducer pressure array. 1.6 m equilateral triangle.

**Sampling interval:** Acquires and analyzes 30 min data record every hour.

**Deployment period:** Records hourly data for 13 months.

**Operational depth:** Bottom mounted in water depths from 2 to 20 m.

**Accuracy:** Water level, wave height, and spectral energy error - 1 cm rms. Mean wave direction error - 2 degrees rms.

Implementation of the gage is achieved through very low power microcomputer design and custom firmware. Firmware controls data acquisition, quality control, calibration, analysis, and storage functions. The most difficult specification is simultaneous 13 month deployment, 1 hour continuous record interval, and 30 min record length. Existing instrumentation requires compromise of one or more of these requirements.

Achieving 13 month deployment requires internal data analysis. The cross spectral matrix is computed internally and stored. These data provide the maximum data compacting while still permitting various analysis techniques for post processing. For the base level gage is treated as a space array. To reduce the amount of information saved, redundant information in the cross spectral array is eliminated.

Expressing the cross spectral matrix as real and imaginary parts, the usual definitions of Co (real) and Quad (imaginary) spectra are defined as

$$\Phi_{mn}(f) = C_{mn}(f) - iQ_{mn}(f) \quad (6)$$

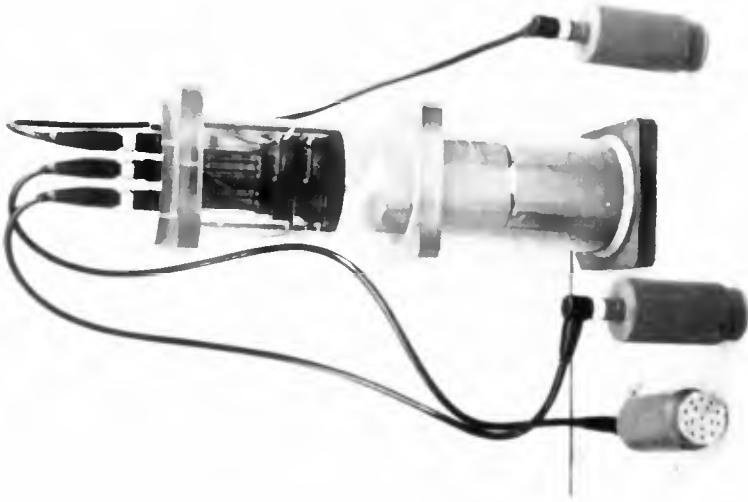


Figure 4: DWG-1 cylinder containing the electronics and batteries. The three pressure transducers connect to the main cylinder.

and for 3 sensors

$$\Phi_{mn} = \begin{bmatrix} C_{11} & C_{12} & C_{13} \\ C_{21} & C_{22} & C_{23} \\ C_{31} & C_{32} & C_{33} \end{bmatrix} - i \begin{bmatrix} Q_{11} & Q_{12} & Q_{13} \\ Q_{21} & Q_{22} & Q_{23} \\ Q_{31} & Q_{32} & Q_{33} \end{bmatrix} \quad (7)$$

Observing that each  $nm$  term is the complex conjugate of the corresponding  $mn$  term, three each Co and Quad spectra are eliminated from storage. By definition  $Q_{11} = Q_{22} = Q_{33} = 0$ , and for the case of a space array,  $C_{11} = C_{22} = C_{33}$  except for statistical variability. Substituting

$$\hat{C} = \frac{C_{11} + C_{22} + C_{33}}{3} \quad (8)$$

and

$$\hat{C}_{nm} \approx \sqrt{\hat{C}^2 - Q_{nm}^2} \quad (9)$$

allows the saved parameters to be reduced to  $\hat{C}$ ,  $Q_{12}$ ,  $Q_{13}$ , and  $Q_{23}$ . These assumptions are sufficient for accurate mean direction estimates. High resolution directional estimates require that Co-spectra terms also be saved, resulting in a small cost increase.

The mean water level computed during the first and last six minutes of each measurement interval are also saved. All data are calibrated in engineering units and tagged with UCT time. Each gage permanently stores its sensor calibrations, identification, location, quality control, and status information in the removable EPROM modules.

A prototype diverless deployment and recovery system has been developed to reduce operation cost and improve the gage directional orientation measurement. The unit is operated from a boat using a PC interface. The fixture contains a remotely operated air jetting controls and release, depth and attitude read outs, and a gyrocompass for orientation measurement.

## 4 Field test results

The completed gage has been field tested at two sites. Both gages functioned successfully, obtaining better than 99% data return. A comparison of the gage results with a 15-element linear array at the Coastal Engineering Research Center (CERC), Field Research Facility (FRF) in Duck, North Carolina was independently conducted by William Birkemeier of the FRF. The linear array is composed of 9 shore parallel and 6 shore normal sensors. Figures 5 and 6, prepared by Mr. Birkemeier, summarize the results. The comparison data represent 1090 records during the period February 1 - March 31, 1992. Records with  $H_s < 0.4 m$  or  $T_p < 4 sec$  were not included. An unexplained time difference of 1 hour between the two data sets was compensated. No manual editing or quality control was applied to data from the new gage.

Both gages rely on the autospectrum of a pressure transducer to estimate significant wave height and peak period. The agreement shown in Figure 5 is expected for properly calibrated and analyzed gages. Fig. 6 compares mean direction estimates. For these data the new gage's mean direction was obtained from a space array analysis. Agreement is quite good. Outliers result from bimodal spectra where approximately equal peaks can cause a different  $T_p$  to be picked by the analysis codes. Agreement is best near shore normal angle of 70 degrees. Waves at oblique angles to the beach are underestimated by the linear array compared to the new gage. Similar differences were observed with comparisons of the linear array to a *PUV* gage.

## 5 Conclusions

The new gage is a high quality, directional wave gage, capable of simple installation, and year long deployment. The low cost availability of nearshore directional wave data will impact the planning, engineering, and maintenance of coastal projects. Wave measurements will be possible in most locations. Stand-alone internally recording gages will be more economical than real-time, cable connected gages. Low cost and site selection flexibility will permit multiple gages

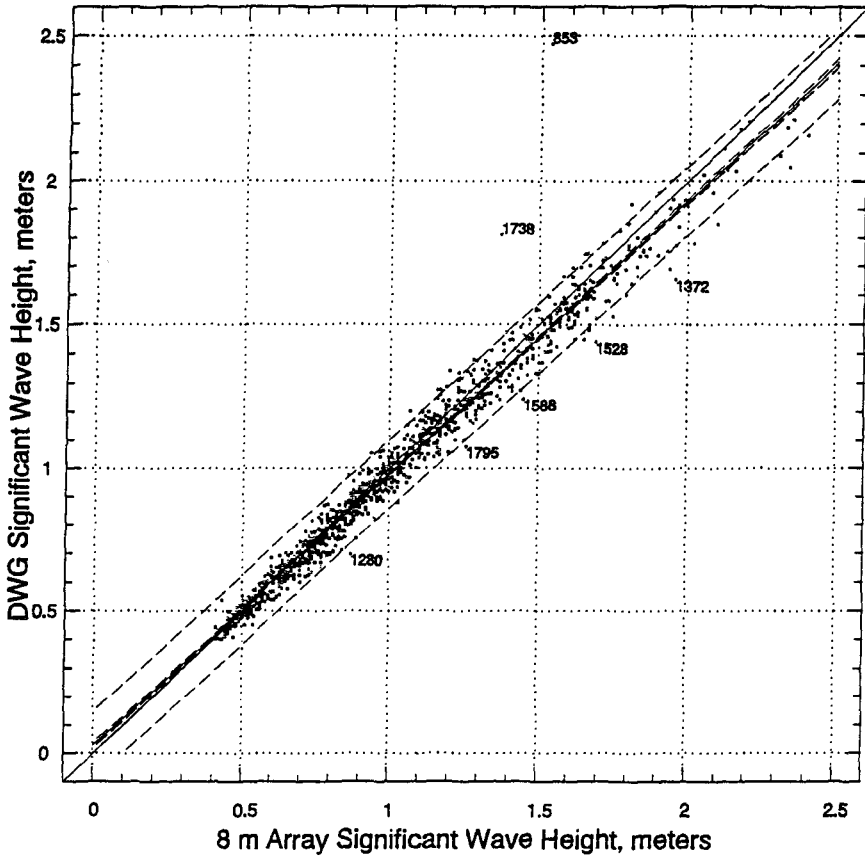


Figure 5: Linear regression of  $H_s$  of DWG-1 and the FRF Linear Array. Outer dashed lines are 95% prediction limits. The correlation coefficient is 0.987.

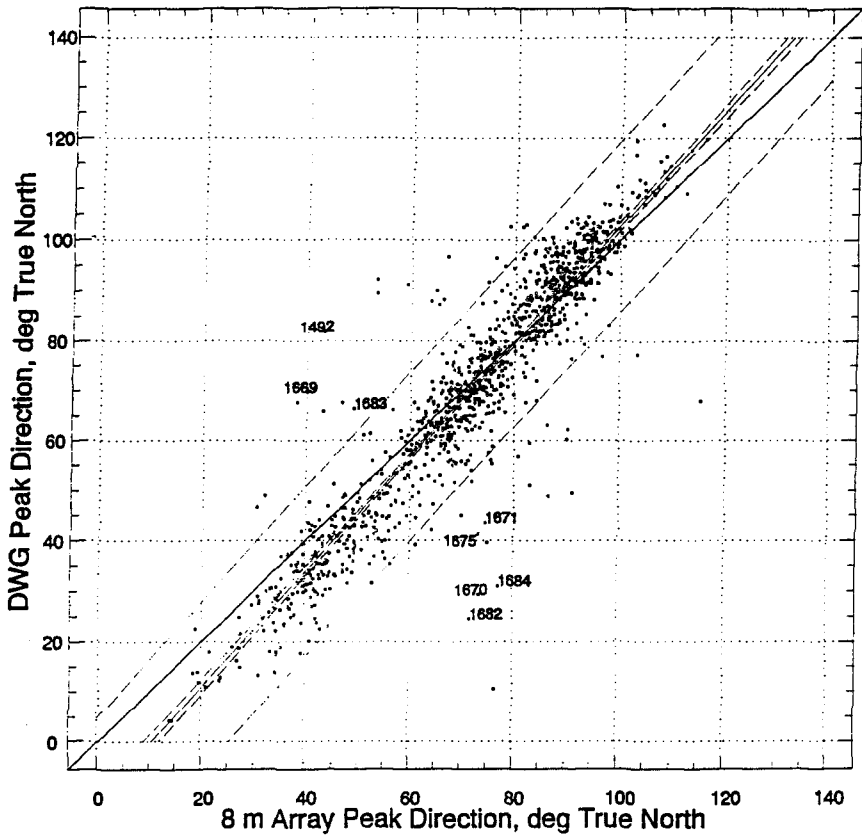


Figure 6: Linear regression of mean wave direction at the spectral peak period of DWG-1 and the FRF Linear Array. Outer dashed lines are 95% prediction limits. The correlation coefficient is 0.931

at a project site. Routine monitoring for engineering requirements will increase. New monitoring objectives of environmental assurance and litigation prevention will emerge.

## Acknowledgments

The author gratefully acknowledges the contributions, discussions, and review of many colleagues. In particular William E. Grogg, Joon P. Rhee, William M. Kucharski, and Michael D. Carpenter of CERC made major contributions. Noriaki Hashimoto of the Japan Port and Harbor Research Institute provided valuable suggestions and comments. Data from the FRF linear array was provided by Charles E. Long. The work described here was performed under the Nearshore Directional Wave Measurement Technology work unit, of the U.S. Army Corps of Engineers, Coastal Research Program. Permission to publish this paper was granted by the Chief of Engineers, U.S. Army Corps of Engineers.

## References

- Bodge, K.R. and Dean, R.G.** "Wave Measurement with Differential Pressure Gages," *Proc. of the 19th International Conference on Coastal Engineering*, 1984.
- Hashimoto, N. and Kobune, K.** "Estimation of Directional Spectra from a Bayesian Approach," *Proc. of the 21st International Conference on Coastal Engineering*, 1988.
- Higgins, A.L., Seymour, R.J., and Pawka, S.S.** "A compact representation of ocean wave directionality," *Applied Ocean Research* vol. 3, no. 3, July 1981, pp 105-112.
- Horikawa, K., ed.** *Nearshore Dynamics and Coastal Processes*, University of Tokyo Press, Tokyo, Japan, 1988.
- Isobe, M., Kondo, K., and Horikawa, K.** "Extension of the MLM for estimating directional wave spectrum," *Proc. Symposium on Description and Modelling of Directional Seas*, Paper No. A-6.
- Paniker, N.N. and Borgman, L.E.** "Directional Spectra From Wave-Gage Arrays," *Proc. of the 12th International Conference on Coastal Engineering*, 1970.



## CHAPTER 22

# ENERGY DISSIPATION AND AIR BUBBLES MIXING INSIDE SURF ZONE

Hwung Hweng Hwung<sup>1</sup> Jih Ming Chyan<sup>2</sup> Yeong Chyang Chung<sup>3</sup>

### Abstract

In order to understand the relationship between entrained air bubbles and energy transfer inside surf zone, a special technique of He-Ne laser and 2D LDV were employed to investigate the characteristics of air bubbles concentration and velocity fields, respectively. The experimental results shows that the concentration profiles of air bubbles decay hyperbolically in the vertical direction and exponentially in the horizontal direction. With appropriate parameter groups, the distributions of air bubbles show a characteristics of similarity. The potential energy, kinematic energy and total energy decrease with the horizontal distance except that the kinematic energy slightly increases between the impinging point and the maximum penetration. Within this region, the energy loss of potential energy and kinematic energy is almost transferred to the air bubbles to merge into the water body.

### Introduction

The wave breaking in the nearshore area is a very important and fascinating phenomenon of wave hydrodynamics. In the instant of wave

---

<sup>1</sup> Professor of Hydraulic and Ocean Engineering Department, Director of Tainan Hydraulics Laboratory, National Cheng Kung University, Tainan, Taiwan, ROC

<sup>2</sup> Assistant Researcher of Tainan Hydraulics Laboratory, National Cheng Kung University, Tainan, Taiwan, ROC

<sup>3</sup> Graduated Student of Hydraulic and Ocean Engineering Department, National Cheng Kung University, Tainan, Taiwan, ROC

breaking, air entrainment destroys the original flow structure, resulting in dissipation of wave energy. With the admixing of air bubbles, the flow fields of broken wave are turbulent and complicated. Although the energy dissipation and air bubbles mixing after wave breaking have been extensively studied in the past thirty years, its mechanism is not fully understood, due to the complex flow fields are essentially beyond the capacity of measuring equipments during that period. From theoretical and experimental studies, Horikawa and Kuo (1966) obtained an exponential decay function of wave height inside surf zone. Führböter (1970) assumed that the wave breaking provided the total dissipation energy to the air bubbles entraining into the water body, and derived the decay functions of wave height for spilling and plunging breakers respectively. Jansen (1986) employed the flow visualization technique and photochromism method to observe the turbulent flow fields of aerated layer in the outer region of surf zone. Recently, Nadaoka (1986) detected the turbulent intensity distributions in the nearshore zone by LDV. In the previous efforts, the connections of air bubbles entrainment with the turbulent energy dissipation had not been fully investigated. In order to understand this relationship, a special technique of He-Ne laser was employed to detect the entrainment process of air bubbles, and a LDV system was used to examine the spatial distributions of two dimensional velocity in wave flume respectively.

### Experiments

It is very difficult to observe the kinematic phenomenon of air bubbles merged in water body. A special installation of He-Ne laser was developed, as depicted in Fig. 1. According to our experience, the transformed voltage signal from the He-Ne laser appears a drop-out when the laser beam is deflected by air bubbles. Such a phenomenon can be used to represent the variations of air bubbles. However, an appropriate threshold of background air concentration obtained in still water has to be determined before the data analysis process. A typical example is shown in Fig. 2 in which both the dash and solid line respectively denote the threshold value and drop-out signal. Furthermore, Lin & Hwung (1992) found out that the broken wave was a three dimensional flow field. Under this circumstance, air bubbles across the test section at the same phase of wave motion can't be identified by the laser beam. It is because that only the first bubble deflects the beam and the rest are hidden in the drop-out signal. Based on this conclusion, to determine a proper test width is very important in this experiment. From the results of total air concentration ( $C_t$ ) with different test widths, as shown in Fig. 3a, it is obvious that a wider one possesses a higher concentration

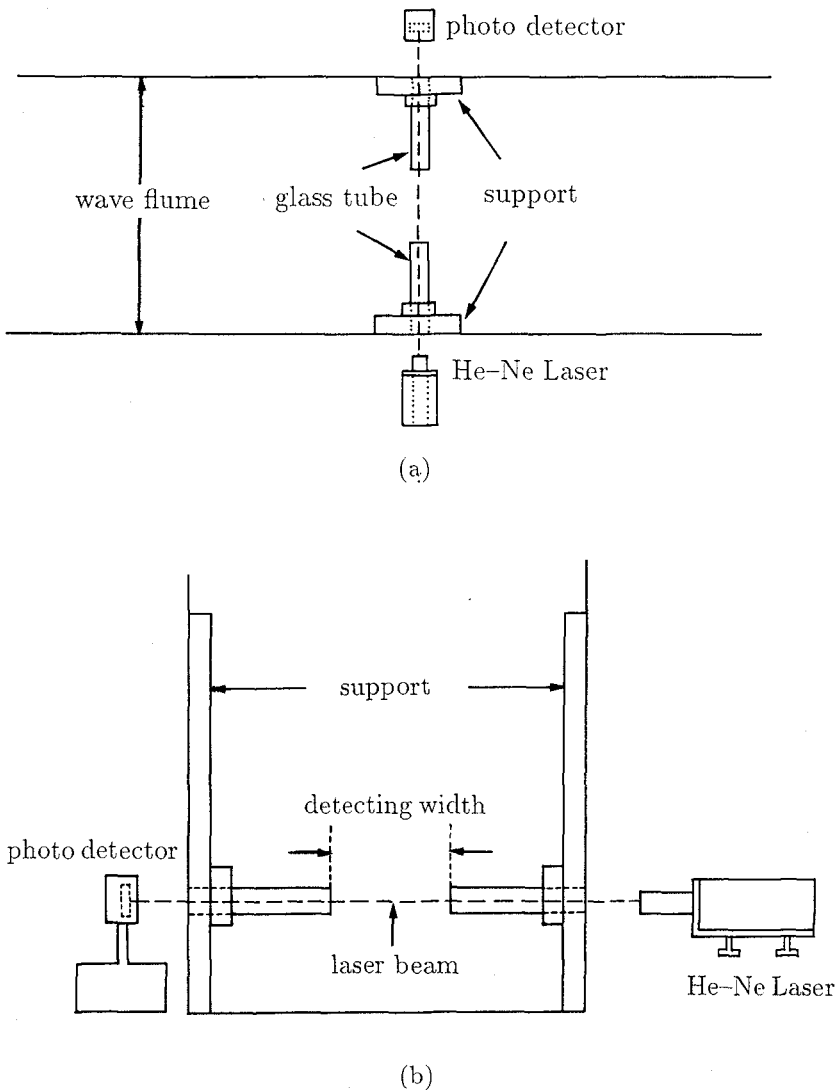


Figure 1. Experimental installation of air bubbles measurements; (a) top view, (b) front view

which doesn't linearly increase with the test width. When they are expressed in air concentration per unit width ( $C_u$ ), as seen in Fig. 3b, the results of both of 3 and 4 cm test width are almost consistent, so that we adopt these two test widths for all of the experiments. In addition to the measurements

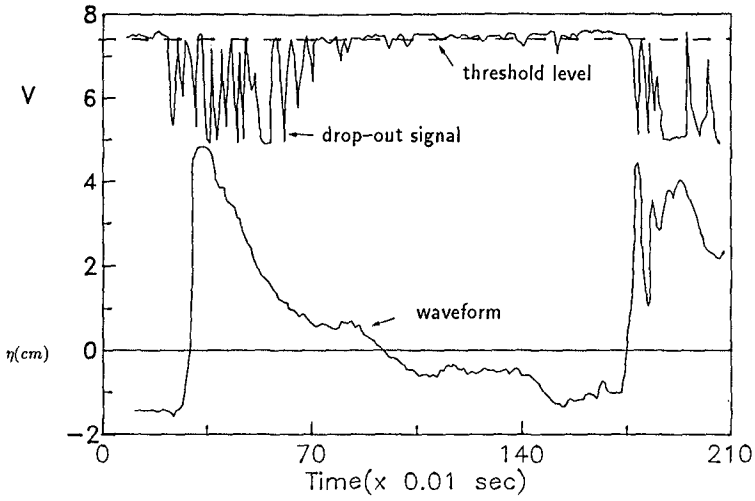


Figure 2. Drop-out signal induced by entrained air bubbles

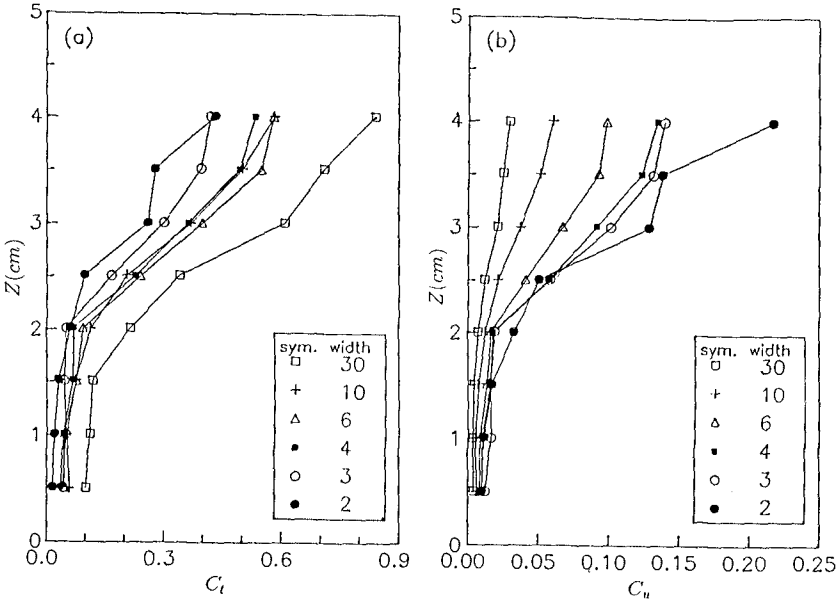


Figure 3. Concentration profiles of various test width; (a) total air bubbles concentration ( $C_t$ ), (b) air bubbles concentration per unit width ( $C_u$ )

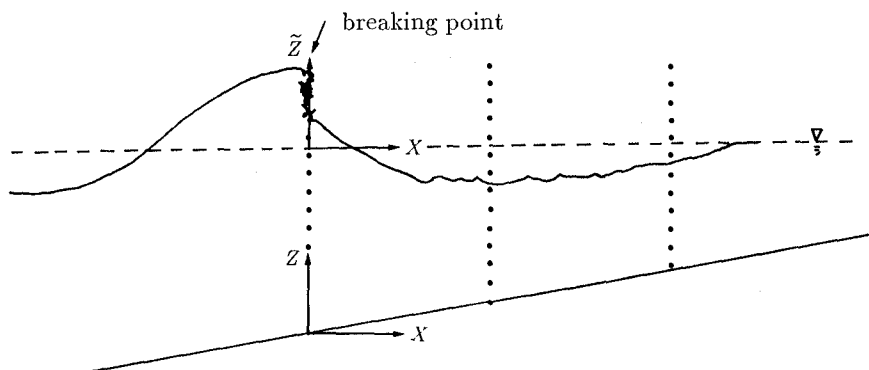


Figure 4. Schematic description of coordinate system and measuring points

Table 1. Experimental conditions

Case	$T$ (sec)	$h_i$ (cm)	$H_i$ (cm)	Breaking type	$H_b$ (cm)	$H_o/L_o$	$h_b$ (cm)	$H_b/h_b$
1	1.29	33.0	6.11	plunging	8.08	0.0259	8.10	0.998
2	0.90	33.0	5.72	spilling	6.57	0.0483	7.00	0.925

of bubbles concentration, the turbulent flow fields in the surf zone was also detected by LDV (TSI—9100-8) of being capable to determine the variations of two dimensional velocity.

Two typical wave breaking were generated in the wave flume and the experimental conditions are tabulated in Table 1; in which  $T$  is the wave period in seconds,  $h_i$  the water depth at the horizontal portion of the flume,  $H_i$  the wave height produced by the wave generator,  $H_b$  the breaking wave height,  $H_o/L_o$  the converted wave steepness at deep water,  $h_b$  the water depth at breaking point, and finally  $H_b/h_b$  the relative water depth at the point of wave breaking. The bed slope of wave flume is 1/15. Fig. 4 shows the coordinate system and the distribution of measuring points. The first test section was positioned at the wave breaking point and the distances between measuring points in  $X$  and  $Z$  directions were 7.5 cm and 0.5 cm respectively.

## Results and discussion

From the elaborate measurements, the vertical distributions of the concentration of entrained air bubbles for the plunging and spilling breakers are plotted in Fig. 5 and Fig. 6, respectively, in which  $L_o$  denotes the wave length in deep water. The concentration of air bubbles hyperbolically decreases with the water depth for both of the plunging and spilling breakers. As shown by Lin & Hwung (1992), the formation of water tongue by the plunging breaker, which violently impinges the water body, enhances the entrainment process of air bubbles. The maximum concentration of it, 18%, is larger than that of a spilling breaker, 12%. The plunging breaker also induces a deeper penetration of air bubbles and a higher concentration within the aerated layer. When normalized by appropriate parameter groups, there exists a similarity function for different profiles and cases, which is shown in Fig. 7 and can be written as;

$$\frac{C}{C_o} = 0.56 \left[ \tanh \left( 5.36 \frac{Z_a}{\eta^+ + h_a} - 1.56 \right) + 1 \right] \quad (1)$$

where  $C$  is the air bubble concentration per unit width,  $C_o$  the air bubble concentration at still water level,  $\eta^+$  the water surface elevation above the still water level.  $h_a$  denotes the penetration depth of air bubble based on the location where the duration of drop-out signal is 10% of total sampling period.  $Z_a$  is the distance from the origin located at the penetration depth of  $h_a$ , and it is positive upward.

The longitudinal distributions of air concentration averaged on the aerated layer for cases of plunging and spilling breakers decrease with the dimensionless distance ( $X/L_o$ ), as shown in Fig. 8. By the comparison with Kuo (1972), it shows that the theoretical prediction coincides with the experimental results of spilling breaker. However, it has much differences between the theoretical and experimental results due to the nonlinearity and strong impingement of plunging breaker. From a non-dimensionalized process, the cross-sectional average of air concentration shows a characteristic of similarity in Fig. 9. The similarity function can be expressed as;

$$\frac{\bar{C} - \bar{C}_{ha.max}}{\bar{C}_{imp} - \bar{C}_{ha.max}} = 2.85 \exp(-1.72X/L_o) - 0.72 \quad (2)$$

where  $\bar{C}$  represents the averaged concentration within the aerated layer,  $\bar{C}_{imp}$  the averaged concentration at the impinging point of breaking wave,

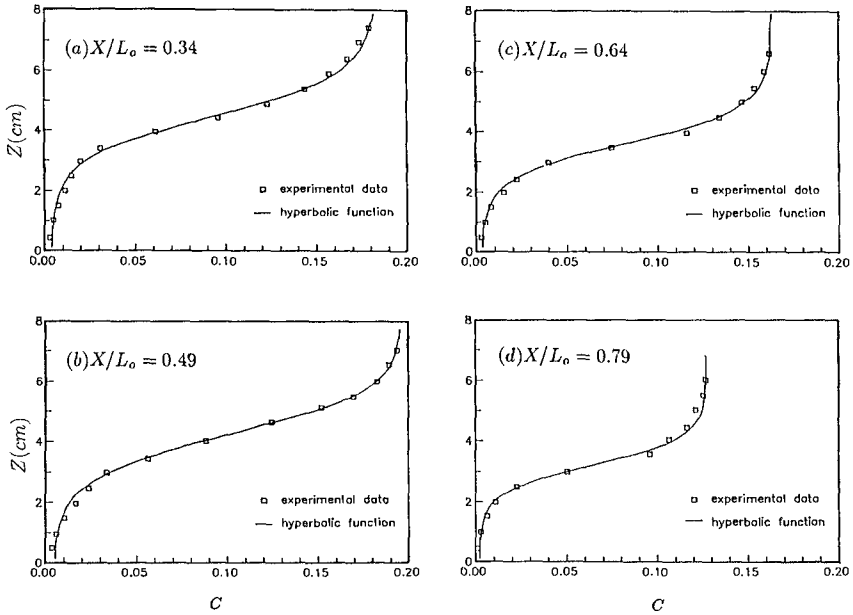


Figure 5. Vertical distribution of air bubble concentration (plunging breaker)

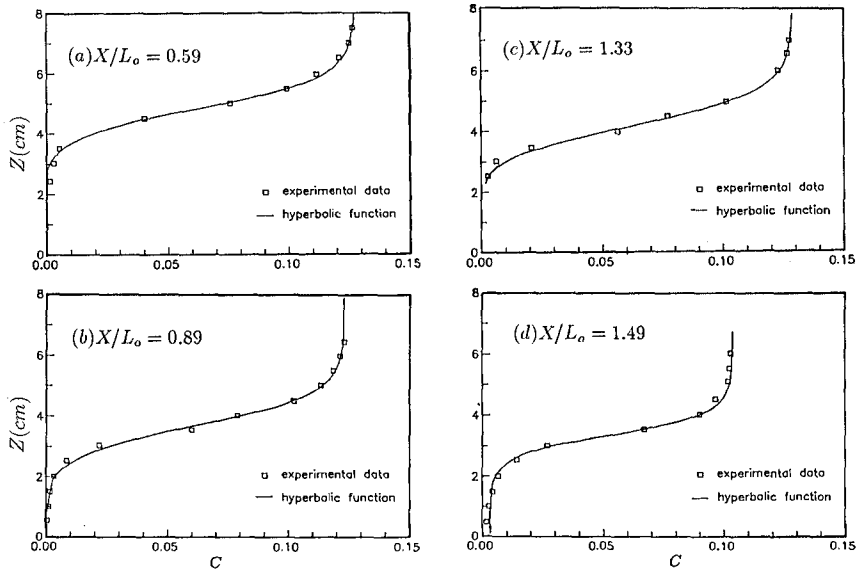


Figure 6. Vertical distribution of air bubble concentration (spilling breaker)

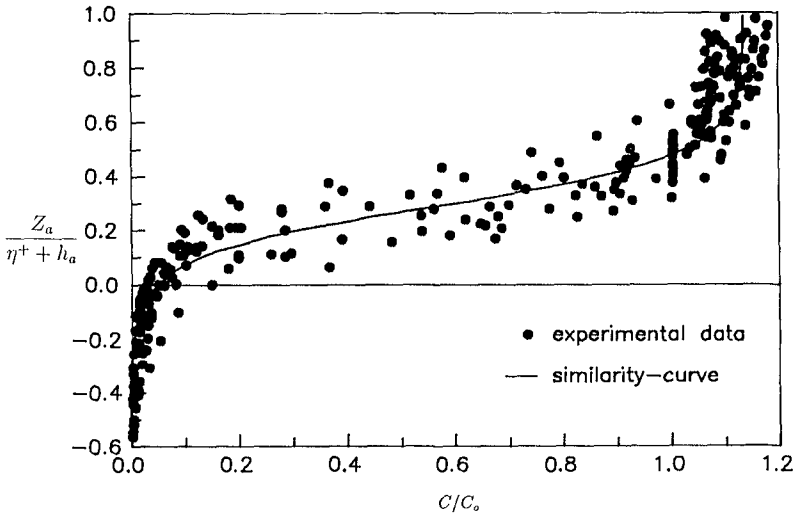


Figure 7. Similarity of vertical distribution of air bubble concentration

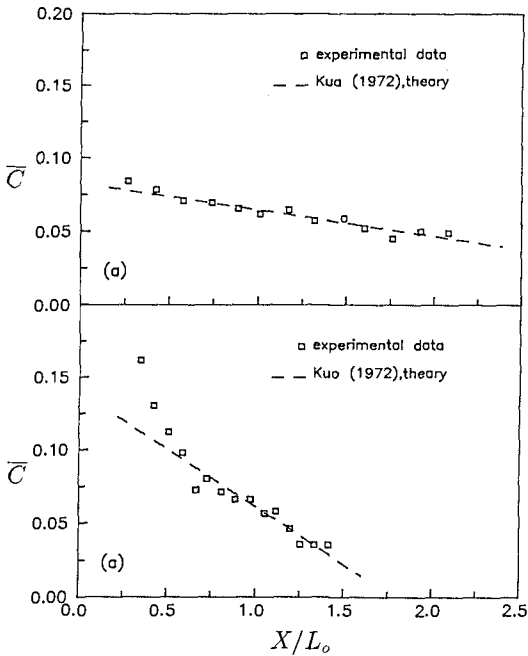


Figure 8. Average concentration along the longitudinal direction; (a) spilling breaker, (b) plunging breaker



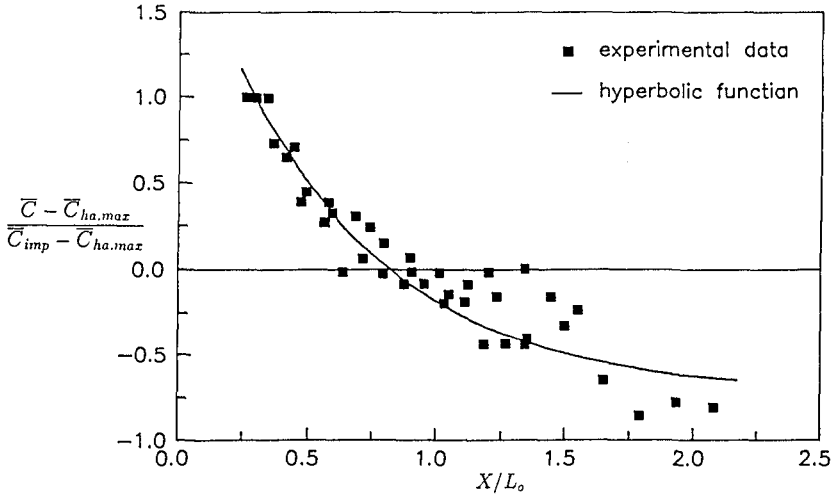


Figure 9. Similarity of cross-sectional averaged concentration of air bubbles

$\bar{C}_{ha,max}$  the averaged concentration at the maximum penetration section of air bubbles.

In order to understand the effect of air entrainment process on the turbulent flow fields after wave breaking, LDV was also employed to measure both of the horizontal velocity ( $u$ ) and vertical velocity ( $w$ ). According to IFFT (inverse fast Fourier transformation) method proposed by Hwung et al.(1989), the spatial distributions of air concentration, turbulent velocity intensities ( $\sqrt{u'^2}$ ,  $\sqrt{w'^2}$ ) and Reynolds stress ( $-\overline{u'w'}$ ) are shown in Fig. 10 and Fig. 11 for cases of plunging and spilling breakers. It is obvious that the maximum of turbulent velocity intensities locate at the maximum penetration of air bubbles and so does the Reynolds stress. However, the positions of the maxima of velocity and its turbulent intensity don't coincide with each other. The former reaches the peak value in the impinging point. It is because that, when the wave breaking, there forms a water jet mixed with air bubbles impinging and penetrating into a deeper water depth. In the maximum of penetration section, the air bubbles begin to ascend due to the buoyancy effects and generate well-correlated velocity fluctuations. It enhances the energy transfer between different dimensions and results in the maximum of turbulent velocity intensities and Reynolds stress.



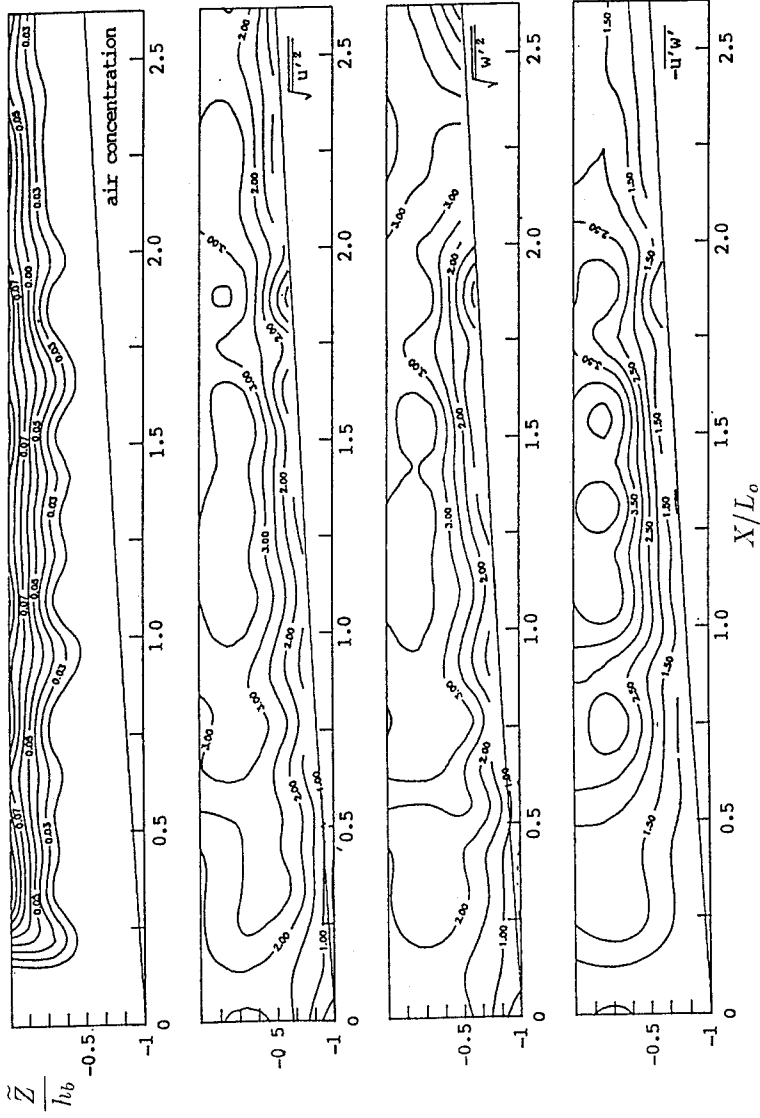


Figure 11. Spatial distribution of air concentration, turbulent velocity intensities and Reynolds stress (spilling breaker)

According to Führböter (1970), the potential energy of air bubbles inside surf zone can be expressed by;

$$E_{air} = \gamma \frac{h_a^2(x)}{2} \frac{\bar{C}}{1 - \bar{C}} \quad (3)$$

where  $\gamma$  is the specific weight of water. In addition to the energy of air bubbles, the potential and kinematic energy ( $E_p$ ,  $E_k$ ) of the broken wave can be written as;

$$E_p = \frac{\gamma}{2} \frac{1}{T} \int_0^T \eta^2 dt \quad (4)$$

$$E_k = \frac{\rho}{2} \int_0^{h+\eta} \left[ \frac{1}{T} \int_0^T (u^2 + w^2) dt \right] dz \quad (5)$$

where  $T$  and  $\eta$  are the sampling duration and the variations of water surface, respectively, while  $\rho$  denotes the water density. From Eq. (3) ~ Eq. (5), the relationships between the energy of air bubbles and that of the turbulent flow fields for both of plunging and spilling breakers are plotted in Fig. 12 where the experimental results are non-dimensionalized by the total energy ( $E_b$ ) at the breaking point of wave motion and  $E$  represents the summation of  $E_p$  and  $E_k$ . By the comparisons of experimental results, it shows that the variations of energy transfer can be divided into three stages in characteristics. The energy rapidly decreases before the impinging point of broken waves. Between the impinging point and the maximum penetration, the energy loss of the flow fields has been almost transferred into the potential energy of air bubbles since the summation of  $E_{air}$  and  $E$  nearly conserves. The kinematic energy slightly increases in the same region. Due to the buoyancy, the air bubbles ascend and induce the turbulence. The total energy of  $E + E_{air}$  gradually decays in the rest region. The decaying tendency for the plunging breaker is faster than that of the spilling breaker since the entrainment of air bubbles is weaker for the spilling breaker.

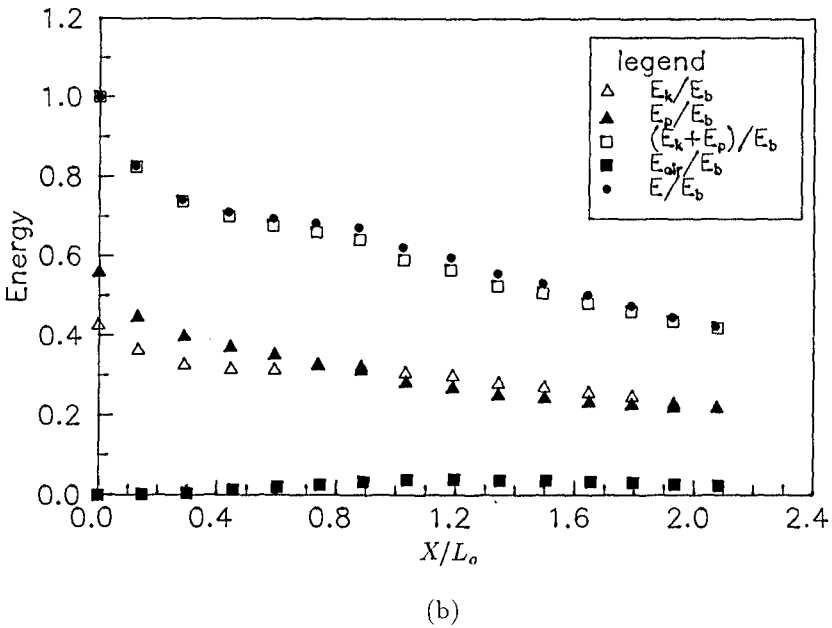
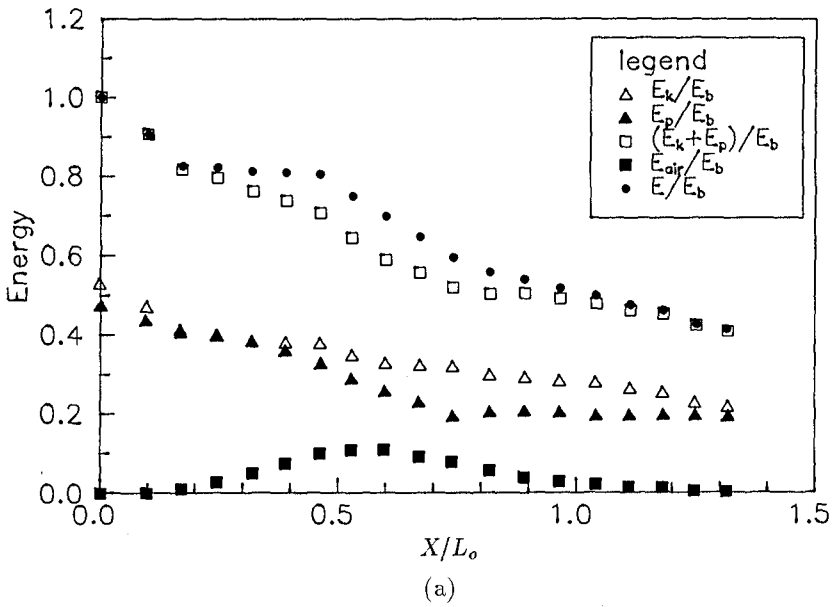


Figure 12. Variations of air bubbles energy, potential energy and kinematic energy ; (a) plunging breaker,(b) spilling breaker

## Conclusion

According to the present study, the most important step in measuring air bubbles is to determine the significant width of detecting section which is 3~4 cm in our experiments. From the experimental results, the profiles of averaged air bubbles concentration decay hyperbolically and exponentially in the vertical and the horizontal directions. There exist similarity functions of air bubbles profiles if the experimental results are non-dimensionalized by appropriate parameter groups. For both of the plunging and spilling breakers, the turbulent velocity intensities and the Reynolds stress reach their maximum at the maximum penetration. The total energy shows multi-stages variations of rapid decrease, conservation and gradual decay in the region divided by the impinging point and the maximum penetration. The energy required for the air bubbles to merge into the water body is almost provided by the potential and kinematic energy.

## Reference

1. Führböter, A.(1970), Air entrainment and energy dissipation in breakers, Proc. 12th Conf. on Coastal Eng., pp.391-398.
2. Jansen, P. C. M.(1986), Laboratory observations of the kinematics in the aerated region of breaking waves, Coastal Eng., Vol. 9, pp.453-477.
3. Horikawa, K. & Kuo, C. T.(1966),A study on wave transformation inside surf zone, Proc. 14th Conf. on Coastal Eng., pp.217-233.
4. Hwung, H. H., Lin, C. & Chyan, J. M.(1989), The characteristics of spectrum and velocity decomposition of the bottom flow in the surf zone, 13th Conf. on Theor. & Appl. Mech., Taichung, Taiwan, ROC, pp.1309-1320 (in chinese).
5. Kuo, S. T.(1972),The wave characteristics inside surf zone, Master these, National Cheng Kung University, ROC (in chinese).
6. Lin, C. & Hwung, H. H.(1992), External and internal flow fields of plunging breakers, Experiments in Fluids, Vol. 12, pp.229-237.
7. Nadaoka, K.(1986), A fundamental study on shoaling and velocity field structure of water waves in the nearshore zone, Technique Report, No. 36, Department of Civil Eng., Tokyo Institute of Technology, pp.33-125.

## CHAPTER 23

Instrumental evaluation of the deep water directional wave climate along the Mediterranean coast of Israel

Ya. A. Iosilevskii<sup>1</sup>, D. S. Rosen<sup>1</sup>, A. Golik<sup>1</sup>, and D. L. Inman<sup>2</sup>

### Abstract

The frequency-directional deep water wave climate along the Mediterranean coast of Israel was evaluated for the first time by computer numerical analysis using *instrumental shallow water measurements*. The shallow water data underlying the study were gathered within the period from 1984 through 1991 by two CAS (Cassette Acquisition System) wave measuring stations located off Haifa (North) and Ashkelon (South) along the Mediterranean coast of Israel. The paper includes a brief description of the data gathering, analysis, and processing methods, and it also includes main results of the study.

### 1. Introduction

It is both expensive and technically complicated to acquire accurate instrumental deep water data needed for computing the respective height, frequency, and direction of water waves. A quite cheap and commonly available practical way to evaluate frequency-directional spectra of water waves in deep water is to reconstruct those spectra from appropriate shallow water measurements. This approach is adopted in this study.

---

<sup>1</sup>National Institute of Oceanography: Israel Oceanographic and Limnological Research, Tel Shikmona P. O. Box 8030, Haifa 31080, Israel

<sup>2</sup>CCS, Scripps Institution of Oceanography, University of California, San Diego, La Jolla, Ca. 92093, U.S.A

In studying or simulating the wave climate in the offshore region, the coastal engineer typically employs the method which may be called '*the representative monochromatic wave method*'. In the framework of this method, the coastal engineer approximates the offshore irregular sea state by the corresponding *representative* (e.g., characteristic) *monochromatic wave*; and he investigates the refraction transformation of this monochromatic wave as it propagates shoreward. Although the representative monochromatic wave method is widely used in coastal engineering practice, the coastal engineer is usually unaware of the degree of accuracy of that method.

In contrast to the representative monochromatic wave method, the method of refraction transformation, which is used in this study, may be called '*the spectral decomposition method*'. It consists of three steps: (i) decomposition of the measured shallow water sea surface displacement from equilibrium into monochromatic wave components (say, by the FFT method); (ii) refraction transformation of each component; (iii) computation of the linear superposition of the component results. The spectral decomposition method is more consistent than the representative monochromatic wave method. Also, from the standpoint of both physical and numerical analysis, the latter method is a particular case of the former method. The two methods are compared in this study.

As contrasted to the evaluations of the present study, none of the previous wave climate evaluations at the Mediterranean coast of Israel, which were reported by Rosen & Kit (1981), Goldsmith & Sofer (1982), Rosen (1982), Carmel *et al* (1985b), had the property to be directional, deep water, and instrumental all together.

The term '*wave weather*', as contrasted to '*wave climate*', is used in this paper interchangeably with the presently common term '*sea state*'. The term '*shallow water*' is used as a class synonym of the term '*not deep water*'.

## 2. Data gathering

The raw data used in this study were collected by two similar CAS (Cassette Acquisition System - see Boyd & Lowe (1985)) wave measuring stations located off Haifa (North) and Ashkelon (South) along the Mediterranean coast of Israel. Each station is composed of a linear array of three pressure gauges with spacings of 12 m and 24 m between two successive gauges. Both arrays are installed at a mean depth of 8.5 m, 0.95 m above the sea bottom. Consequently, the wind water waves of typical periods, say, from 4 sec. to 14 sec., i. e. of wavelengths from approximately 24 m to approximately 124 m



at the station location, undergo refraction due to bathymetry effects before they reach the station.

The wave measuring station located at Ashkelon was intermittently operational from March 1984 through May 1987 and from August 1989 through February 1990. The wave measuring station located at Dado Beach, Haifa, was intermittently operational from March 1984 through April 1987 and from April 1989 through May 1991. Wave measurements have been carried out by each station for 34 min. 8 sec. every 6 hours, at a sampling rate of 2 Hz. A single whole phenomenon of the above duration when a CAS station samples with the rate of 2 Hz is said to be a *fast mode event* (briefly, an FME).

### 3. Physical and mathematical prerequisites

A description of the physical and mathematical concepts underlying the results reported in this paper is beyond its scope. Still, in order to discuss those results conveniently, we will make explicit some elementary physical and mathematical notions, - largely, by introducing the appropriate notation.

#### 3.1. A coordinate system

A local working right-handed rectangular rectilinear coordinate system is chosen in such a way that its XY-plane coincides with the equilibrium sea surface, and its Z-axis is directed vertically upward. The origin of the coordinate system is located somewhere in deep water area, the X-axis is directed shoreward, and the Y-axis is, in a crude sense, parallel to the local shoreline.

#### 3.2. General notation

's' and 'd' are subscript acronyms for 'shallow water' and 'deep water', respectively; '\*' is a subscript ellipsis for 's' or 'd';  $P_*$  is a point on the equilibrium sea surface;  $P_s$  is the shallow water point on the equilibrium sea surface under which the water wave measuring station is located;  $\rho$  is the mass density of sea water, ( $1028.8 \text{ kg/m}^3$ );  $g$  is the acceleration of gravity ( $9.81 \text{ m/sec}^2$ ).

#### 3.3. Parameters characterizing continuous spatiotemporal Fourier transform of the sea surface displacement equilibrium at the point $P_*$

$\nu$  = a monochromatic water wave frequency (Hz);  
 $\tau(\nu) = 1/\nu$  = the period of a monochromatic water wave of frequency  $\nu$  (sec);

- $\vec{n}_*(\nu)$  = the propagation vector of a plane monochromatic water wave of frequency  $\nu$  at  $P_*$  ( $\text{cm}^{-1}$ );  
 $\vartheta$  = the direction of  $\vec{n}_*(\nu)$  relative to the positive direction of the axis  $X$ , positive in the counterclockwise direction (degree or radian);  
 $C_{g*}(\nu)$  = the group celerity of a quasi-monochromatic wave packet of frequency  $\nu$  at  $P_*$  ( $\text{m}/\text{sec}$ );  
 $\mathcal{E}_*(\nu, \vartheta)$  = the continuous frequency-directional energy density per unit area, per unit frequency, and per unit angle at  $P_*$  [ $\text{joule}/\text{cm}^2 \cdot \text{Hz} \cdot \text{deg}$ ];  
 $\mathcal{E}_{*0}(\nu) = \int_{-\pi}^{\pi} \mathcal{E}_*(\nu, \vartheta) d\vartheta$   
 = the continuous frequency-directional energy density per unit area and per unit frequency at  $P_*$  [ $\text{joule}/\text{cm}^2 \cdot \text{Hz}$ ];  
 $\mathcal{F}_*(\nu, \vartheta) = \mathcal{E}_*(\nu, \vartheta) C_{g*}(\nu)$   
 = the continuous frequency-directional energy flux density across unit length, per unit time, per unit frequency, and per unit angle at  $P_*$  [ $\text{joule}/(\text{cm} \cdot \text{sec} \cdot \text{Hz} \cdot \text{deg}) = \text{newton}/\text{deg}$ ];  
 $\mathcal{F}_{*0}(\nu) = \int_{-\pi}^{\pi} \mathcal{F}_*(\nu, \vartheta) d\vartheta$   
 = the continuous frequency-directional energy flux density across unit length, per unit time, and per unit frequency at  $P_*$  [ $\text{joule}/(\text{cm} \cdot \text{sec} \cdot \text{Hz}) = \text{newton}$ ];  
 $\mathcal{R}(\nu, \vartheta)$  = the wave ray of frequency  $\nu$ , which passes through the point  $P_\vartheta$  at the angle  $\vartheta$  relative to the positive direction of the axis  $X$ ;  
 $P_d = \mathcal{P}_d(\nu, \vartheta)$  = the first deep water point on the backward path of  $\mathcal{R}(\nu, \vartheta)$ ;  
 $A_d(\nu, \vartheta)$  = the deep water direction angle of  $\mathcal{R}(\nu, \vartheta)$ ;  
 $K(\nu, \vartheta)$  = the refraction-and-shoaling coefficient (the product of refraction and shoaling coefficients) of  $\mathcal{R}(\nu, \vartheta)$  at  $P_\vartheta$  relative to  $\mathcal{P}_d(\nu, \vartheta)$ ;

3.4. Integral sea weather parameters computed via  $\mathcal{E}_*$   
 versus integral sea weather parameters computed via  $\mathcal{F}_*$

$$m_{E*n}(\nu_1, \nu_2) = \int_{\nu_1}^{\nu_2} \nu^n \mathcal{E}_{*0}(\nu) d\nu$$

= the  $n$ th moment of  $\mathcal{E}_{*0}$  between  $\nu_1$  and  $\nu_2$ ;

$$\nu_{E^*}(\nu_1, \nu_2) = m_{E^*1}(\nu_1, \nu_2) / m_{E^*0}(\nu_1, \nu_2)$$

= the mean wave frequency between  $\nu_1$  and  $\nu_2$   
via  $\xi_{O^*}$  (Hz);

$$\tau_{E^*}(\nu_1, \nu_2) = 1 / \nu_{E^*}(\nu_1, \nu_2)$$

= the mean wave period between  $\nu_1$  and  $\nu_2$   
via  $\xi_{O^*}$  (sec);

$$m_{E^* \rho g}(\nu_1, \nu_2) = \int_{\nu_1}^{\nu_2} \int_{-\pi}^{\pi} \xi_{O^*}(\nu, \theta) |z_{O^*}(\nu)|^{p+q} \cos^p \theta \sin^q \theta d\theta d\nu :$$

$$\vartheta_{E^*}(\nu_1, \nu_2) = \arctan (m_{E^*01}(\nu_1, \nu_2) / m_{E^*10}(\nu_1, \nu_2))$$

= the mean wave direction between  $\nu_1$  and  $\nu_2$   
via  $\xi_{O^*}$  (radian).

The overall mean wave frequency  $\bar{\nu}_{E^*}$ , period  $\bar{\tau}_{E^*}$ , and direction  $\bar{\vartheta}_{E^*}$ , and also the characteristic wave height  $\bar{H}_{E^*}$ , at the point  $P_*$  are defined via  $\xi_{O^*}$  by

$$\bar{\nu}_{E^*} = \nu_{E^*}(0, \infty), \quad \bar{\tau}_{E^*} = \tau_{E^*}(0, \infty), \quad \bar{\vartheta}_{E^*} = \vartheta_{E^*}(0, \infty),$$

$$\bar{H}_{E^*} = H_{*mo} = 4 \sqrt{2 m_{E^*}(0, \infty) / (\rho g)},$$

respectively, in accordance with IAHR (1989).

Let  $\gamma \in (0, 1)$  be a given real number, and  $\nu_{E^*M}$  be the frequency at which  $\xi_{O^*}(\nu)$  reaches its absolute maximum. Let  $\nu_{E^*L}(\gamma)$  be the lowest, and  $\nu_{E^*G}(\gamma)$  be the greatest frequency with the property that

$$\xi_{O^*}(\nu_{E^*L}(\gamma)) / \xi_{O^*}(\nu_{E^*M}) = \xi_{O^*}(\nu_{E^*G}(\gamma)) / \xi_{O^*}(\nu_{E^*M}) = \gamma.$$

Then the overall centroidal  $\gamma$ -peak wave frequency  $\hat{\nu}_{E^*}$ , period  $\hat{\tau}_{E^*}$ , and direction  $\hat{\vartheta}_{E^*}$  at the point  $P_*$  are defined via  $\xi_{O^*}$  by

$$\hat{\nu}_{E^*} = \nu_{E^*}(\nu_{E^*L}(\gamma), \nu_{E^*G}(\gamma)), \quad \hat{\tau}_{E^*} = \tau_{E^*}(\nu_{E^*L}(\gamma), \nu_{E^*G}(\gamma)),$$

$$\hat{\vartheta}_{E^*} = \vartheta_{E^*}(\nu_{E^*L}(\gamma), \nu_{E^*G}(\gamma)),$$

respectively. In this study, we have set  $\gamma = 0.8$ , in accordance with IAHR (1989).

All the above definitions of this subsection, except for the definition of ' $\bar{H}_{E^*}$ ', apply with 'F' and ' $\mathcal{F}$ ' in place 'E' and ' $\xi$ ', respectively.

3.5. Parameters characterizing discrete spatiotemporal Fourier transform of the sea surface displacement from equilibrium at the point  $P_*$

- $\nu_m$  = the low cutoff wave frequency (Hz);  
 $\nu_M$  = the high cutoff wave frequency (Hz);  
 $I$  = the total number of discrete frequencies in the interval  $[\nu_m, \nu_M]$ ;  
 $\Delta\nu$  = the wave frequency increment (Hz);  
 $f(i) = \nu_m + (i - 1)\Delta\nu$   
 = the discrete wave frequency of index  $i \in \{1, 2, \dots, I\}$ ;  
 $\vartheta_{*m}$  = the least (low cutoff) wave ray direction angle at the point  $P_*$  (radian or degree);  
 $\vartheta_{*M}$  = the greatest (high cutoff) wave ray direction angle at the point  $P_*$  (radian or degree);  
 $J_*$  = the total number of discrete wave ray direction angles in the interval  $[\alpha_{*m}, \alpha_{*M}]$ ;  
 $\Delta\vartheta_*$  = the shallow water wave ray direction angle increment (radian or degree);  
 $\vartheta_{*}(j) = \vartheta_{*m} + (j - 1)\Delta\vartheta_*$   
 = the wave ray direction angle of index  $j$  at the point  $P_*$  relative to the positive direction of the X-axis (radian or degree);  
 $E_{*}(i, j) = \mathcal{E}_{*}(f(i), \vartheta_{*}(j))\Delta\nu\Delta\vartheta$   
 = the discrete energy density of indices  $i$  and  $j$  per unit area at  $P_*$  (joule/m<sup>2</sup>).  
 $F_{*}(i, j) = F_{*}(f(i), \vartheta_{*}(j))\Delta\nu\Delta\vartheta$   
 = the discrete energy flux density of indices  $i$  and  $j$  across unit length and per unit time at  $P_*$  [joule/(m·sec) = newton/sec].

4. Expressions for the frequency-directional energy density and energy flux density in deep water in terms of those in shallow water

The general idea of how to express  $E_d$  or  $F_d$  in terms of the respective  $E_s$  or  $F_s$ , is based on this hypothesis:

**Hypothesis 1:** [During a storm caused by a distant source,] the wave pattern in deep water is statistically

(ergodically) uniform over an area of the sea surface whose linear dimensions are small as compared to the distance from the storm source.

The most important specific factors which influence the character of most frequency-directional spectra of sea waves during the winter storms off the Mediterranean coast of Israel are (i) a single narrow window for deep water wave approach and (ii) a fetch of approximately 2200-2300 km in length (see Goldsmith & Golik (1978, p. 22), Carmel et al (1985a, 1985b)). We therefore adopt the following hypothesis:

**Hypothesis 2:** [During a storm caused by a distant source,] for each point  $P_*$  along the Mediterranean coast of Israel, the spatiotemporal discrete Fourier decomposition of the sea surface displacement during an FME contains exactly one plane monochromatic wave whose direction is uniquely determined by its frequency.

To be able to analyze all available data uniformly, we have, in accordance with common practice, extended Hypotheses 1 and 2 by omission of the phrase enclosed between square brackets. Thus, by Hypothesis 2, for each for FME, each  $i \in \{1, 2, \dots, I\}$ , there is exactly one  $j \in \{1, 2, \dots, J\}$  such that  $\theta_*(i) = \vartheta_*(k_*(i))$ , i.e.  $\theta_* = \vartheta_* \cdot k_*$ , where  $k_*$  is a certain integer-valued function of an integer argument, and  $\theta_*$  is a composite real-valued function defined herewith. Hence,

$$E_*(i, j) = E_{o*}(i) \delta_{j, k_*(i)}, \quad E_{o*}(i) = \sum_{j=0}^{J_*} E_*(i, j), \quad (1)$$

where  $\delta$  is the unit diagonal matrix. By Hypothesis 1, we then have

$$E_{od}(i) = E_{os}(i) [K(f(i), \theta_s(i))]^{-2}, \quad (2)$$

$$\theta_d(i) = A_d(f(i), \theta_s(i)). \quad (3)$$

By the respective definitions of Sections 3.3, and 3.5, the variant of (1) with 'F' in place of 'E' is semantically sound. Under Hypothesis 2, equations (2) and (3) solve the problem of expressing  $E_d$  in terms of  $E_s$ , whereas  $F_d = E_d C_{gd}$  and  $F_{do} = E_{do} C_{gd}$ .

### 5. Data processing

Broadly speaking, the data processing underlying this study comprises four steps.

1). The first step of data processing was accomplished with the aid of a package of original FORTRAN programs recently developed by Iosilevskii & Iosilevskii (1991). At this step, each time series of raw shallow water pressure data, gathered by each wave measuring station during the corresponding FME was tested on reliability in accordance with certain criteria, and, if reliable, it was Fourier transformed with the purpose to obtain the respective table  $\langle f, E_{os}, F_{os}, \theta_s \rangle$ . Among some other results, the programs also compute the cumulative longshore energy density flux across unit length over any given span of time; such a flux is commonly associated with the respective longshore sediment transport.

2). The second step of the data processing was accomplished with the aid of *Multi-frequency and multi-ray FORTRAN program for backward and forward refraction of water waves* (briefly, BFRFP) recently written by Iosilevskii (1992). Using the bottom topography data for the neighborhood of the wave measuring station, the program computes, among some other wave ray parameters, the matrix  $A_d$  of deep water wave propagation angles and the matrix  $K$  of products of refraction and shoaling coefficients. The size  $I \times J_s$  of each matrix is specified by the user of the program. Once computed, the matrices  $A_d$  and  $K$  become universal attributes of the neighborhood of the wave measuring station independent of any specific wave weather or wave climate.

In this study, we have used the following values:

$$\begin{aligned} \nu_m &= 6.0 \times 2^{-10} \text{ Hz}, \quad \nu_s^M = 0.25 \text{ Hz}, \quad \Delta\nu = 1024^{-1} \text{ Hz}, \\ \vartheta_{sm} &= -45^\circ, \quad \vartheta_{sM} = 45^\circ, \quad \Delta\vartheta_s = (90/89)^\circ, \\ I &= 251, \quad J_s = 90. \end{aligned}$$

3). The third step of the data processing was accomplished with the aid of *Deep water spectrum FORTRAN program* (briefly, DWSFP) which was recently written by Ya. A. Iosilevskii (to be published). At the first place, the program transforms a sequence of tables  $\langle f, E_{os}, F_{os}, \theta_s \rangle$ , obtained at the first step, into the respective sequence of tables  $\langle f, E_{od}, F_{od}, \theta_d \rangle$ . This is done with the aid of the matrices  $A_d$  and  $K$  obtained at the second step. Then using  $E_{so}, F_{so}, E_{do}$ , and  $F_{do}$  as statistical

weights, the program computes, for each individual FME, the following mean and peak sea state parameters:

$$E_{so} \Rightarrow \bar{H}_s, \bar{\tau}_{Es}, \bar{\vartheta}_{Es}, \hat{\tau}_{Es}, \hat{\vartheta}_{Es}; \quad (4)$$

$$F_{so} \Rightarrow \bar{\tau}_{Fs}, \bar{\vartheta}_{Fs}, \hat{\tau}_{Fs}, \hat{\vartheta}_{Fs}; \quad (5)$$

$$E_{do} \Rightarrow \bar{H}'_d, \bar{\tau}'_{Ed}, \bar{\vartheta}'_{Ed}, \hat{\tau}'_{Ed}, \hat{\vartheta}'_{Ed}; \quad (6)$$

$$F_{do} \Rightarrow \bar{\tau}'_{Fd}, \bar{\vartheta}'_{Fd}, \hat{\tau}'_{Fd}, \hat{\vartheta}'_{Fd}. \quad (7)$$

Most of the parameters listed in (4) and (5) are also computed by the programs used at step 1. The parameters listed (6) and (7) are the desired deep water sea state parameters computed by the *spectral decomposition method*.

$\bar{H}_s$ ,  $\bar{\tau}_{Es}$ , and  $\bar{\vartheta}_{Es}$  can be regarded as the wave height, period, and propagation vector direction of an imaginary monochromatic wave at the point  $P_s$ , and  $\bar{H}'_d$ ,  $\bar{\tau}'_{Ed}$ , and  $\bar{\vartheta}'_{Ed}$  as the similar characteristics of another imaginary monochromatic wave. With the aid of the appropriate matrix elements of the matrices  $A_d$  and  $K$ , the program computes the deep water wave height  $\bar{H}'_{Ed}$  and direction  $\bar{\vartheta}'_{Ed}$  corresponding to the triple  $\langle \bar{H}_s, \bar{\tau}_{Es}, \bar{\vartheta}_{Es} \rangle$ , and it also computes the similar characteristics  $\bar{H}'_{Fd}$  and  $\bar{\vartheta}'_{Fd}$  corresponding to the triple  $\langle \bar{H}_s, \bar{\tau}_{Fs}, \bar{\vartheta}_{Fs} \rangle$ .

$\bar{H}'_{Ed}$ ,  $\bar{\tau}'_{Ed}$ , and  $\bar{\vartheta}'_{Ed}$  are conventional deep water characteristics of sea state computed in the framework of the presently common *representative monochromatic wave method*.  $\bar{H}'_{Fd}$ ,  $\bar{\tau}'_{Fd}$ , and  $\bar{\vartheta}'_{Fd}$  form a similar set of deep water sea state parameters, but this set is not in common usage - it is suggested here for the first time.

4). The fourth step of the data processing comprises statistical analysis and graphic and table presentation of the results obtained. The statistical analysis was done with the aid of programs prepared by the second author. The graphic and table presentation was done with the aid of Quattro Pro Software of Borland Intl.

## 6. Results

The results of this study can be summarized as follows.

1). There is both deterministic and statistical correlation between the deep water sea weather parameters at Haifa and of the respective parameters at Ashkelon, with the exception of the directional parameters. The latter parameters are correlated statistically and,

to a lesser extent, mainly during storms, they are also correlated deterministically.

2). The prevailing wave direction is from West-North-West at Haifa, and it is from West at Ashkelon.

3). For the same place (Haifa or Ashkelon), there is deterministic and statistical correlation between the deep water sea weather parameters computed via  $E_{do}$  and the respective parameters computed via  $F_{do}$ . In this case, the values of ' $\bar{\tau}_{Ed}$ ' and ' $\hat{\tau}_{Ed}$ ' sometimes differ from the respective (simultaneous) values of ' $\bar{\tau}_{Fd}$ ' and ' $\hat{\tau}_{Fd}$ ', whereas  $\bar{\phi}_{Ed}$  and  $\hat{\phi}_{Ed}$  are, as a rule, close to  $\bar{\phi}_{Fd}$  and  $\hat{\phi}_{Fd}$ , respectively.

4). There is both deterministic and statistical correlation between values of the deep water sea weather parameters computed by the spectral decomposition method and the respective parameters computed by the representative monochromatic wave method, although during a storm the former values seem to be more stable (more smooth) in time than the latter.

5). Comparison of the present estimates of the prevailing wave direction at Ashkelon, based on *instrumental measurements*, with the previous estimates of the prevailing wave direction at Ashdod (Rosen (1982)), 15 km North of Ashkelon, based on *visual observations*, shows that the two estimates are grossly different.

Some of the results of this study are illustrated in Figures 1 - 6.

#### Acknowledgements

The research underlying this paper was partly sponsored by the Agency for International Development, U.S.A. BFRFP was written by Ya.A.Iosilevskii under the sponsorship of Israeli Ministry of Energy and Infrastructure. The authors thankfully acknowledge the sponsorship of the above two bodies.

The bathymetry survey to collect the raw data for preparing the two depth grids covering wide regions off Haifa and off Ashkelon along the Mediterranean coast of Israel, where our CAS wave measuring stations are located, was made by Mr. G.Amit and by Mr. A.Golan who also prepared the grids. Mr. P.Artsztein and Mr. A.Cohen digitalized the continuous bathymetric records. Mr. G.Amit and Mr. D.Ramot maintained the wave measuring equipment. The authors are deeply indebted to all the above persons for their cooperation.



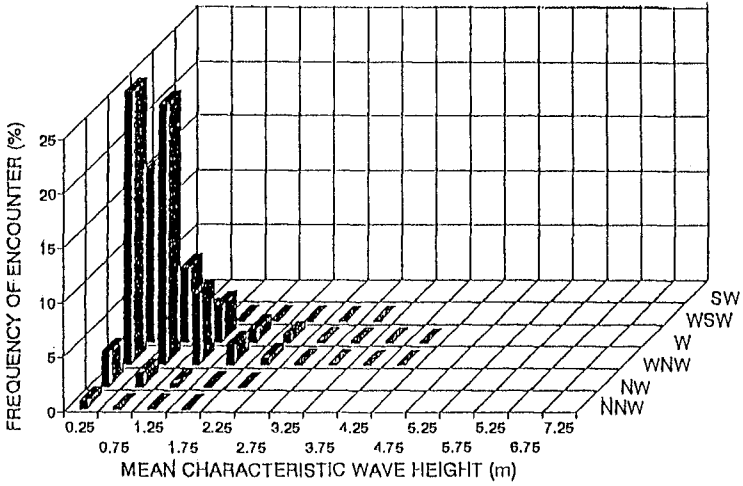


Fig. 1. The yearly deep water wave direction distribution off Haifa (Dado Beach) in 1984 - 1991

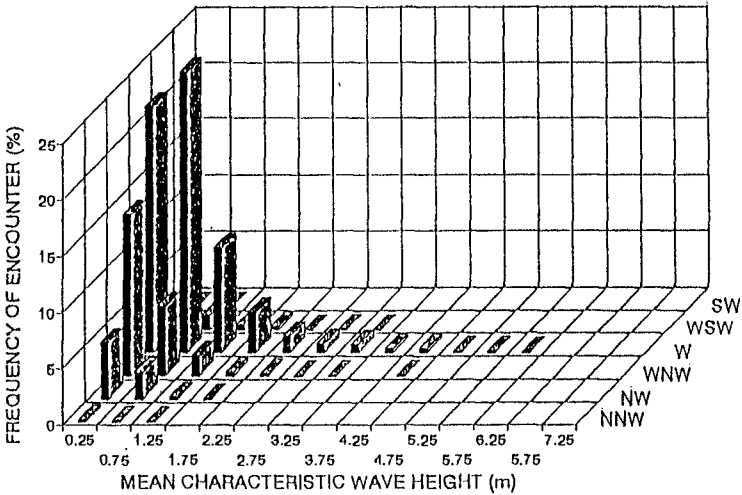


Fig. 2. The yearly deep water wave direction distribution off Ashkelon in 1984 - 1990

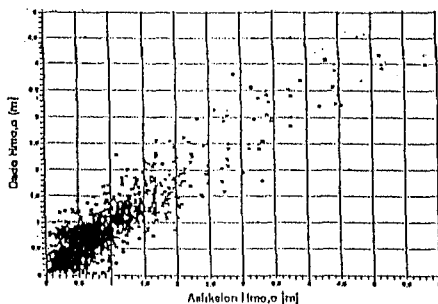


Fig. 3. Comparison of the deep water wave heights ( $\bar{H}_d$ ) off Haifa (Dado Beach) and that off Ashkelon in 1984 - 1990

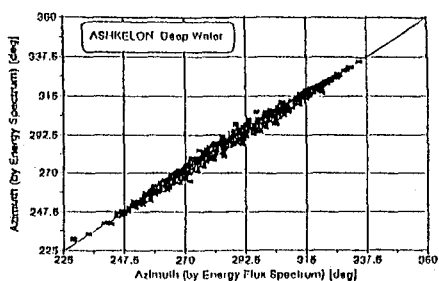


Fig. 4. Comparison of the mean deep water wave directions computed via energy density and those computed via energy density flux; Ashkelon; 1984 - 1990

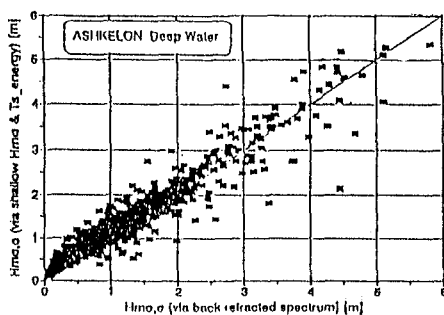


Fig. 5. Comparison of the mean deep water wave heights computed by the spectral decomposition method ( $\bar{H}_d$ , the abscissa axis) and those computed by the representative monochromatic wave method ( $\bar{H}'_{Ed}$ , the ordinate axis); Ashkelon, 1984 - 1990

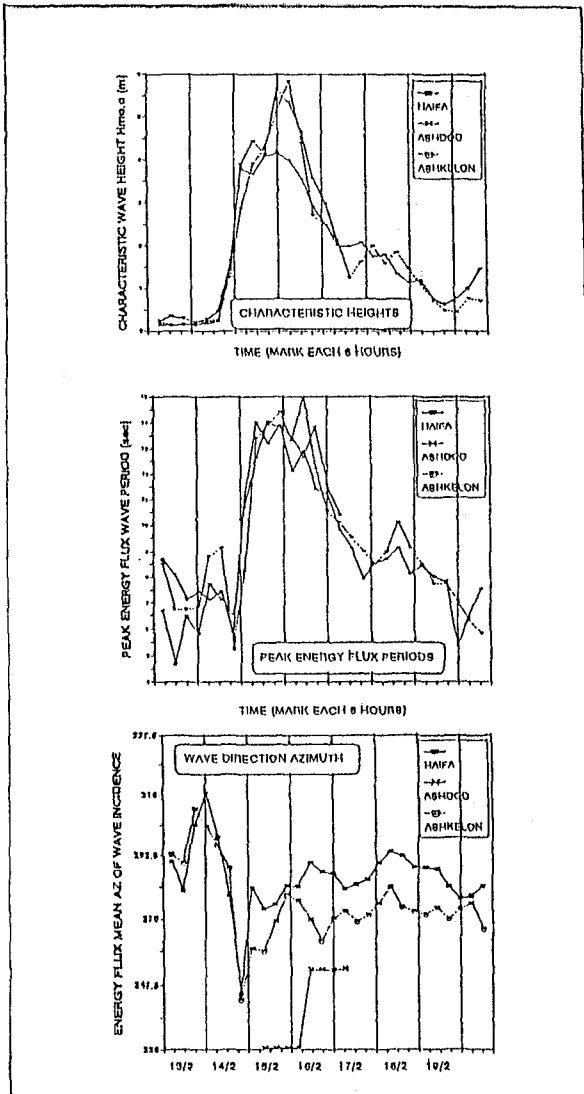


Fig. 6. Comparison of the deep water storm patterns off Haifa (this study), Ashkelon (this study), and Ashdod (visual observations), 13-19 February 1985

Appendix I. References

- Boyd, W., and Lowe R. L. (1985). "A high density cassette data acquisition system." *Ocean*, 85, v.1, 808-809.
- Carmel L. Z., Inman, D. L., and Golik A., (1985a). "Characteristics of storm waves off the Mediterranean coast of Israel." *Coastal Eng.*, 9, 1-19.
- Carmel L. Z., Inman, D. L., and Golik A., (1985b). "Directional wave measurements at Haifa, Israel, and sediment transport along the Nile Littoral Cell." *Coastal Eng.*, 9, 21-36.
- Goldsmith V., and Golik A. (1978). *The Israeli wave climate and logshore sediment transport model*. IOLR Geological Department Report No 78/1, Haifa, Israel. 58 pp. + Appendices A-C.
- Goldsmith V., and Sofer S. (1983). "Wave climatology of the Southeastern Mediterranean." *Israel Journal of Earth-Sciences*, 32, 1-81.
- IAHR (1989). "List of sea-state parameters." *J. Watrwy., Port, Coast, and Oc. Engrg.*, ASCE, 115(6), 293-808.
- Iosilevskii Ya. A., and Iosilevskii G. (1991). *FORTRAN programs for directional spectral analysis of water wave data from a CAS station*. IOLR Report H23/91, Haifa, Israel, 36 pp. + Appendices A-E.
- Iosilevskii Ya. A. (1992). *Multi-frequency and multi-ray FORTRAN program for backward and forward refraction of water waves*. IOLR Report H15/92, Haifa, Israel. 212 pp. 212.
- Rosen, D. S. (1982). *A new deep water wave climate evaluation for Ashdod*. Technical Report P. N. 100/82. Technion, Haifa, Israel, 99 pp.
- Rosen, D. S., and Kit, E. (1981). "Evaluation of the wave characteristics at the Mediterranean coast of Israel." *Israel Journal of Earth-Sciences*, 30, 120-134.

## CHAPTER 24

### VARIATION OF POTENTIAL AND KINETIC WAVE ENERGY IN THE SURF ZONE

Koichiro IWATA\* and Takashi TOMITA\*\*

#### ABSTRACT

This paper is to investigate experimentally variation of the potential and kinetic wave energy in the surf zone. First, a cantilever-type velocimeter is newly devised to measure water particle velocities in an air-entrained water body above as well as below the wave trough. Laboratory experiments are carried out, and it is revealed that the kinetic wave energy is larger than the potential one and that some of the potential wave energy can be transferred to the kinetic one at the early stage of wave breaking.

#### 1. INTRODUCTION

Prediction of variation of the wave energy such as potential, kinetic and total wave energy and elucidation of wave dissipation mechanism in the surf zone is one of very important problems for coastal hydraulics as well as coastal engineering. A lot of knowledge about wave breaking and wave deformation after breaking have been accumulated, but it is still unknown how the potential and kinetic wave energy change and how we estimate them well in the surf zone. In particular, an accurate evaluation of the kinetic wave energy is very useful for prediction of the nearshore current system.

---

\* M. ASCE, D. Eng., Professor, Dept. of Civil Eng., Nagoya Univ., Nagoya 464-01, Japan

\*\* D. Eng., Research Associate, ditto

With this background, this paper discusses experimentally the variation of potential and kinetic wave energy in the surf zone. First of all, a cantilever-type velocimeter is newly devised in order to measure the kinetic wave energy as well as particle velocities in the air-entrained wave body above and below the wave trough. Secondly, laboratory experiments are conducted on the uniform slopes of 1/10 and 1/30, using an indoor wave tank which can generate regular and irregular waves. Based on the laboratory experiments, characteristics of variation of the potential and kinetic wave energy, the wave energy dissipation and the propagation velocity of the total wave energy in the surf zone are discussed in relation to breaker types and breaker-caused turbulence.

## 2. CANTILEVER-TYPE VELOCIMETER

A cantilever-type velocimeter based on the "dynamic pressure principle" is newly devised in order to measure accurately the water particle velocity, especially above the wave trough in the surf zone, since we have no reliable velocimeter which enables us to measure wave kinematics above wave trough including air-bubble and turbulence.

The cantilever-type velocimeter is comprized of two cantilevers, as shown schematically in Fig.1, one of which only responds to a vertical component of the dynamic force and another responds only to a horizontal component of the dynamic force. Each cantilever is constructed with a small-sized sensing rod and a plastic plate which is rigidly fixed to a supporting rod. Two semi-conductor strain gauges are pasted on the plastic plate to convert the wave force acting normally to the cantilever into an electrical signal. The plastic plate and end part of the sensing rod is protectively shielded so as not to be affected by direct attack of waves. The diameter of the sensing rod was carefully designed to 0.9mm in order to respond to the fluid drag force and to be almost insensitive to the fluid acceleration force.

Figure 2 shows that the wave force acting on the sensing element is proportional to square of the velocity. Therefore, the water particle velocities,  $u$  and  $w$  are calculated with

$$u|u| = \left(\frac{X_o}{K_x}\right) \left|\left(\frac{X_o}{K_x}\right)\right| / \sqrt{\left(\frac{X_o}{K_x}\right)^2 + \left(\frac{Z_o}{K_z}\right)^2}$$

$$w|w| = \left(\frac{Z_o}{K_z}\right) \left|\left(\frac{Z_o}{K_z}\right)\right| / \sqrt{\left(\frac{X_o}{K_x}\right)^2 + \left(\frac{Z_o}{K_z}\right)^2}$$
(1)

where,  $u$  and  $w$  are the horizontal and vertical velocities of water particle, respectively,  $X_o$  and  $Z_o$  are the output voltages of horizontally and vertically sensing cantilevers, respectively, and  $K_x$  and  $K_z$  are the correction factors to  $X_o$  and  $Z_o$  which are determined by calibration tests, respectively. High accuracy of this cantilever-type velocimeter has

been confirmed by comparing with data obtained with electromagnetic-type velocimeter, as shown in Fig.3 (Iwata et al., 1983 and Koyama and Iwata, 1986).

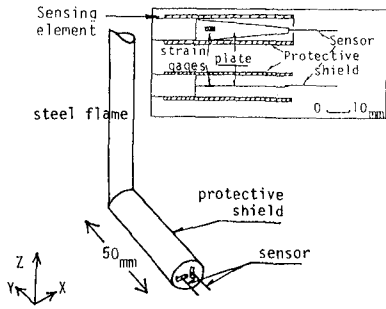


Fig.1 Schematic illustration of cantilever-type velocimeter

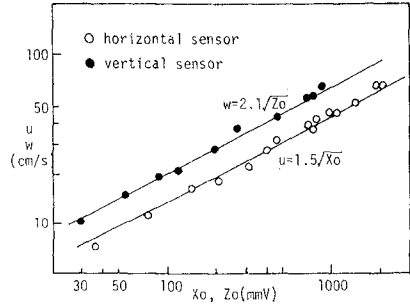
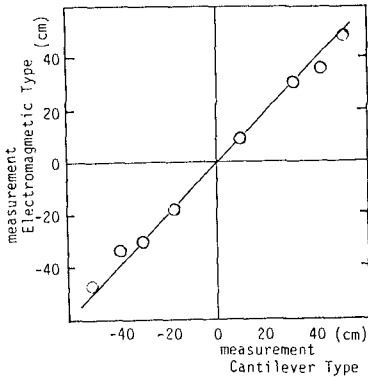
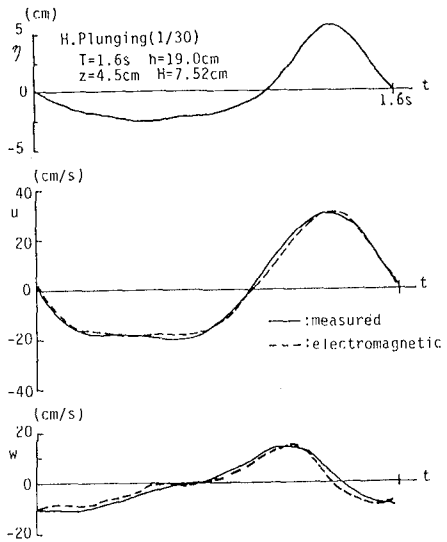


Fig.2 Calibration test curves



(a) amplitude of velocity



(b) time histories of water particle velocities,  $u$  and  $w$ , and water surface profile,  $\eta$

Fig.3 Comparison of velocities of water particle measured with cantilever-type and electromagnetic-type velocimeters

## 3. LABORATORY EXPERIMENT

Laboratory experiments were carried out using an indoor wave tank at Nagoya University, the dimension of which is 25m in length, 0.7m in width and 0.95m in height. At one end of the wave tank we installed a flap-type wave generator controlled by an oil-pressure servo system. The water was perfectly shut out from the area behind the wave board; therefore, the input electrical signal can be converted smoothly to wave board motion. At the other end of the wave tank was constructed a wave-absorbing beach to keep wave reflection to a minimum. The uniform slopes of 1/10 and 1/30 were adopted and three kinds of breakers such as spilling, plunging and heavy plunging were produced on each slope (see Table 1).

Water surface profiles and particle velocities were, respectively, measured with capacitance-type wave gauges and cantilever-type velocimeters. The measuring locations of water particle velocities were more than 126, as listed in Table 1. The measuring region was from near bottom up to near free surface in vertical direction and from before the wave breaking point to near shoreline in horizontal direction. In the experiments, the same wave was generated repeatedly in order to measure particle velocities at so many locations. One example of the measuring locations is shown in Fig.4. For each experimental run, using a 16mm high speed cine camera (50 frames/s), breaking region was filmed through a grid on glass wall of the channel. Analyzing the films, the breaking point, domain of horizontal roller, and region of air-entrainment were determined. Time profiles of water surface and particle velocities were all recorded on a magnetic tape over 2 minutes.

Table 1 Experimental conditions

CASE	BREAKER	SLOPE	T(s)	Ho(cm)	Ho/Lo	Hb(cm)	$h_b$ (cm)	M
1-1	Spilling	1/10	0.95	17.0	0.120	14.0	26.0	126
1-2	Plunging	1/10	1.35	16.9	0.060	14.4	18.8	130
1-3	H.Plunging	1/10	1.35	15.7	0.055	13.4	14.8	146
2-1	Spilling	1/30	1.00	10.5	0.067	10.1	16.0	186
2-2	Plunging	1/30	1.45	7.0	0.021	9.1	13.3	169
2-3	H.Plunging	1/30	1.60	7.1	0.018	9.0	13.7	188

T: wave period, Ho:deep water wave height, Ho/Lo:wave steepness in deep water, Hb:breaking wave height,  $h_b$ :breaking water depth  
M: measuring locations of water particle velocity

## 4. DATA PROCESSING AND ANALYSIS

Time profiles of the water surface profile and particle velocities were divided into 20 discrete values for one wave



cycle to evaluate the potential and kinetic wave energy.

The mean water level  $\bar{\eta}$  is estimated with

$$\bar{\eta} = \frac{1}{T} \int_0^T \eta dt \quad (2)$$

in which, T is the wave period and  $\eta$  is the water surface profile.

The potential wave energy per unit time averaged over one wave period,  $E_p$  and kinetic wave energy per unit time averaged over one wave period,  $E_k$  are, respectively, defined with

$$E_p = \frac{\rho g}{2T} \int_0^T \eta^2 dt \quad (3)$$

$$E_k = \frac{\rho}{2T} \int_0^{h+\eta} ds \int_0^T (u^2 + w^2) dt \quad (4)$$

in which,  $\rho$  is the density of water,  $g$  is the gravitational acceleration,  $h$  is the still water depth,  $s$  is the vertical distance taken upward positive with its origin being on the bottom,  $u$  and  $w$  are the horizontal and the vertical of water particle, respectively. The total wave energy per unit time averaged over one wave period,  $E_T$  is given by

$$E_T = E_k + E_p \quad (5)$$

The energy flux,  $F$  and the energy dissipation rate,  $\Phi$  are evaluated with the following equations;

$$\frac{\partial}{\partial x} (F) = -\Phi \quad (6)$$

$$F = \frac{1}{T} \int_0^T dt \int_0^{h+\eta} u \left( \frac{\rho}{2} (u^2 - w^2) + \rho g \eta \right) ds \quad (7)$$

where,  $x$  is the horizontal distance, and Eq.(7) is derived for the second-order approximation of wave pressure,  $P$ . The calculations of  $E_p$ ,  $E_k$  and  $F$  were performed by applying the trapezoidal formula to Eqs.(3),(4) and (7), respectively, using measured values of  $\eta$ ,  $u$  and  $w$ .

Analysing 16mm motion films by means of a film motion analyzer, the breaking point, air-entrained region, plunging point, domain of horizontal roller, splash zone were determined. The breaking point is defined just as the inception of curling of wave crest. Therefore, the breaking point corresponds to the maximum wave height.

### 3. EXPERIMENTAL RESULTS AND DISCUSSION

#### 3.1 Water particle velocity

Figures 5 and 6 show two examples of water particle velocities before and after wave breaking. It is seen that measured velocities are well predicted with Dean's stream

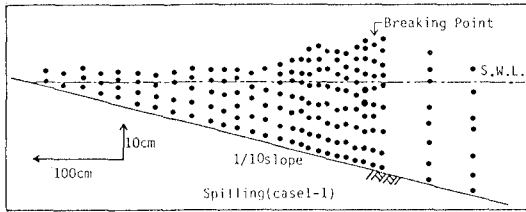


Fig.4 Measuring locations of water particle velocity for case 1-1

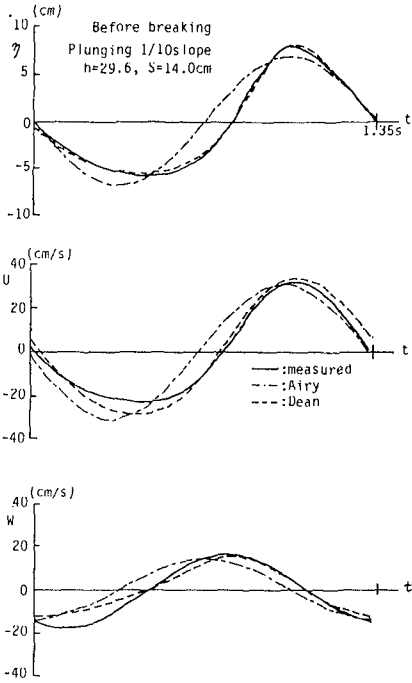


Fig.5 Time histories of water particle velocities (before breaking)

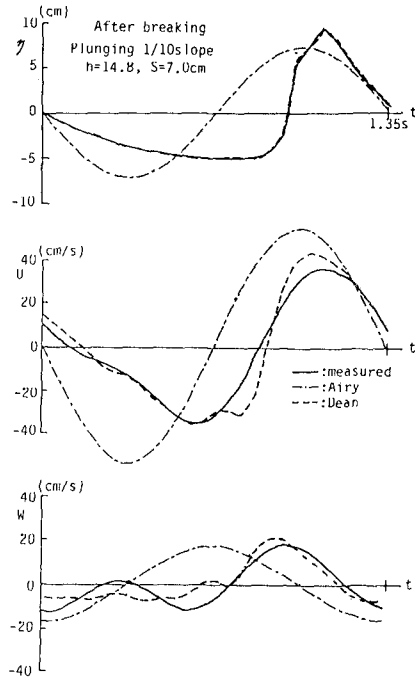


Fig 6 Time histories of water particle velocities (after breaking)

function method (Dean,1965). However, Airy's linear wave theory cannot well evaluate the water particle velocities. Figure 7 shows the time profile of water particle velocities measured at 5cm above the still water level. The particle velocity profiles are quite similar to those of the solitary wave above wave trough (Lee et al.,1982). Figure 8 shows examples of the vertical distribution of the horizontal steady-velocity component,  $\bar{u}$  at three different locations such as before breaking, breaking point and after breaking. The steady-velocity component  $\bar{u}$  is the velocity which is averaged over one wave period both above and below the wave trough. From the figures, it is seen that the on-shore mass transport takes place above the wave trough and offshore mass transport occurs below the wave trough and that conservation of mean mass flux is established. The magnitude of the steady-velocity component (mass transport velocity) corresponds well to foregoing researches (Nadaoka et al.,1982). Thus, as described above, the cantilever type velocimeter devised in this study can safely be said to be highly reliable to measure water particle velocities.

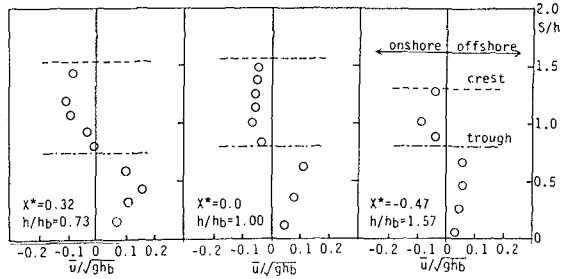
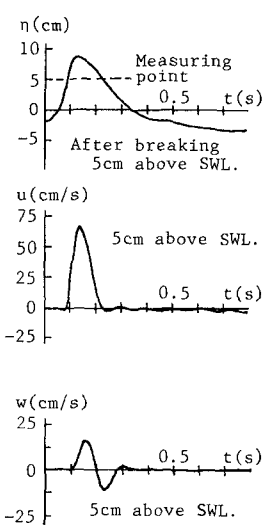


Fig. 7 Time histories of water particle velocities measured at 5cm above the still water level

Fig. 8 Some examples of vertical distribution of horizontal steady-velocity component,  $\bar{u}/\sqrt{gh_b}$  ( $h/h_b=1.57$ ; before breaking,  $h/h_b=1$ ; breaking point,  $h/h_b=0.73$ ; after breaking)

3.2 Variation of potential and kinetic wave energy

Figures 9 shows the variation of the wave height after breaking. Both figures show that the wave height decreases almost monotonously toward the shoreline, as have been pointed out by foregoing researches (Horikawa and Kuo, 1966; Sawaragi and Iwata, 1974).

Figures 10, 11 and 12 show the variation of the potential and kinetic wave energy after breaking in cases of the spilling, plunging and heavy plunging breaker, respectively. In the figures,  $X^*=(x-x_b)/\sqrt{g(h+\bar{\eta})T}$ ,  $x_b$  is the breaking location of  $x$  ( $X^*=0$ ; breaking point),  $E_{tb}$  is the total wave energy at breaking point,  $X_a$  is the location of deepest air entrainment,  $X_o$  is the location of air bubble's disappearance below wave trough,  $X_p$  is the plunging point,  $X_s$  is the location of horizontal roller's disappearance and  $X_v$  is the location at which air bubble covers the front face from crest

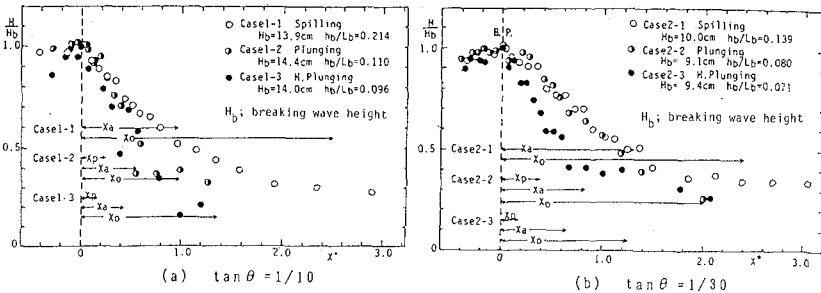


Fig.9 Variation of the wave height after breaking

to trough. The symbols,  $\circ$ ,  $\blacksquare$  and  $\Delta$  are experimental values of  $E_T/E_{Tb}$ ,  $E_k/E_{Tb}$  and  $E_p/E_{Tb}$ , respectively.

(a) Spilling breaker:

The potential wave energy  $E_p$  decreases monotonously from  $X^*=0$  to  $X=X_a$  at which the entrained air depth is maximal for both slopes of 1/10 and 1/30. The potential wave energy  $E_p$  at  $X^*=X_a$  is almost  $0.3E_{pb}$  ( $E_{pb}; E_p$  at  $X^*=0$ ). This indicates that almost 70% of the potential wave energy at breaking point is dissipated from  $X^*=0$  to  $X^*=X_a$ . On the other hand, decay of  $E_p$  in the range of  $X^*>X_o$  is seen to be very small.

The kinetic wave energy  $E_k$  is clearly seen to be larger than the potential one, and  $E_k$  increases at an early stage of wave breaking and then decreases toward the shoreline. This is quite different from the change of  $E_p$  with  $X^*$ . The kinetic wave energy  $E_k$  around  $X^*=0.2$  becomes larger than that at  $X^*=0$ . This fact would indicate that some of the potential wave energy is transferred to the kinetic one, since the potential wave energy continuously decays around  $X^*=0.2$ . The attenuation of  $E_k$  in the range of  $X^*>X_o$  is very small and  $E_k$  is almost equal to  $E_p$ . The magnitude of difference between  $E_k$  and  $E_p$  increases with  $X^*$  in the range of  $X^*<X_a$  and  $E_k/E_p$  becomes maximal around  $X^*=X_a$ ;  $E_k/E_p=2.7$  for case 1-1 and  $E_k/E_p=2.4$  for case 2-1. The value of  $E_k/E_p$  at breaking point is 1.15 for case 1-1 and 1.08 for case 2-1. These values are smaller than those measured on gentler slope of 1/150 by Tsuchiya and Tsutsui (1982).

The total wave energy  $E_T$  decays monotonously from  $X^*=0$  to  $X^*=X_o$ , although  $E_k$  increases around  $X^*=0.2$ . Figure 10 shows that 70% ~ 80% of  $E_{Tb}$  (total wave energy at breaking point) are dissipated between  $X^*=0$  and  $X_o$ .

(b) Plunging breaker:

Rapid decay of the potential wave energy  $E_p$  takes place from  $X^*=X_p$  to  $X^*=X_a$ , and  $E_p$  at  $X^*=X_a$  attenuates to  $0.6E_{pb}$  for case 1-2 and  $0.3E_{pb}$  for case 2-2. The magnitude of attenuation of  $E_p$  on  $S=1/10$  is larger than that on  $S=1/30$ , where  $S$  is the bottom slope.

The kinetic wave energy  $E_k$  after breaking is seen to be smaller than that at breaking point  $E_{kb}$ . In case of 2-2 ( $S=1/30$ ),  $E_k$  attenuates monotonously and the magnitude of decay of  $E_k$  between  $X^*=0$  and  $X_a$  is much larger than that in the range of  $X^*>X_a$ . On the other hand, in case of 1-2 ( $S=1/10$ ),  $E_k$  once increases around  $X^*=X_a$ . The reason of this is thought to be that the energy of splash and horizontal roller is transferred to the kinetic energy. Then, the total wave energy  $E_T$  becomes also larger around  $X=X_a$  in case of run 1-2.

(c) Heavy plunging breaker:

The potential wave energy  $E_p$  decreases rapidly after breaking and  $E_p$  around  $X^*=X_s$  becomes  $0.25E_{pb}$ . The potential wave energy once increases around  $X^*=X_a$ . This is thought to be caused by the combination of splash with main

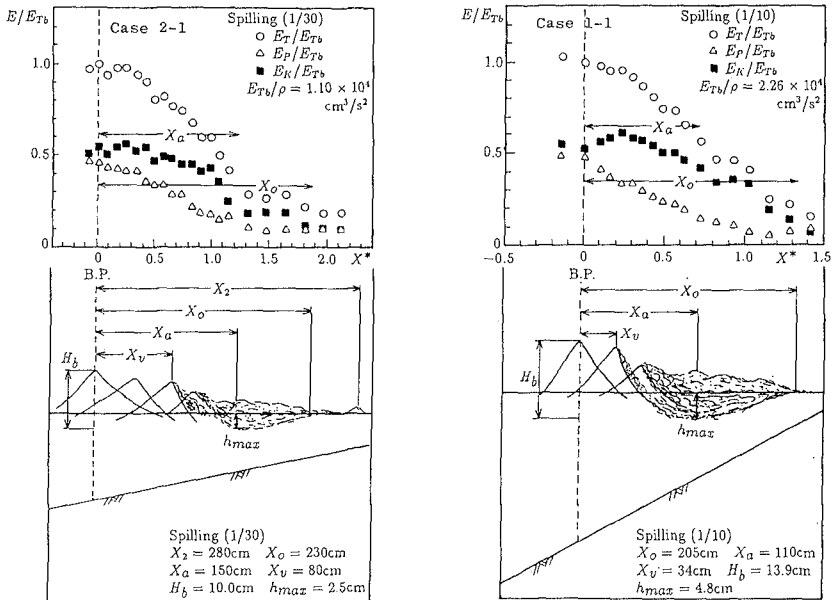


Fig.10 Variation of potential and kinetic wave energy after breaking (Spilling breaker)

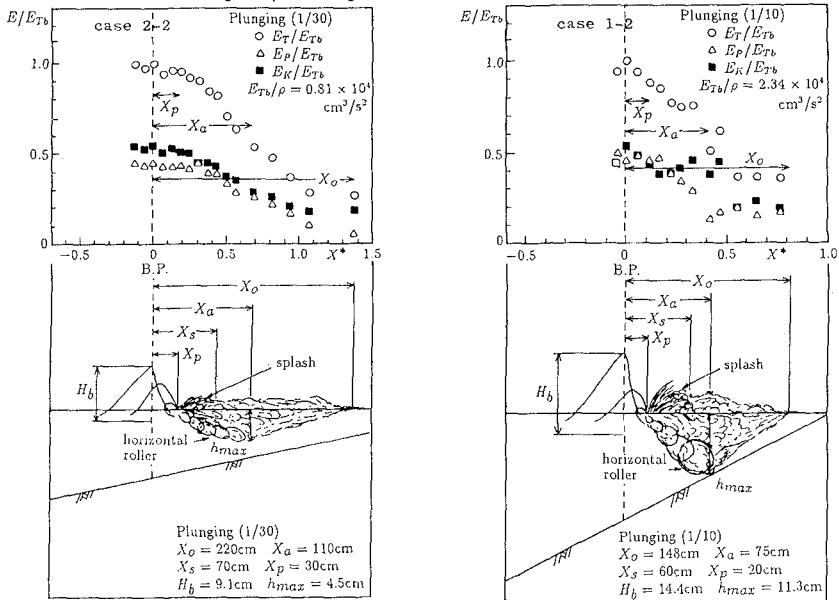


Fig.11 Variation of potential and kinetic wave energy after breaking (Plunging breaker)

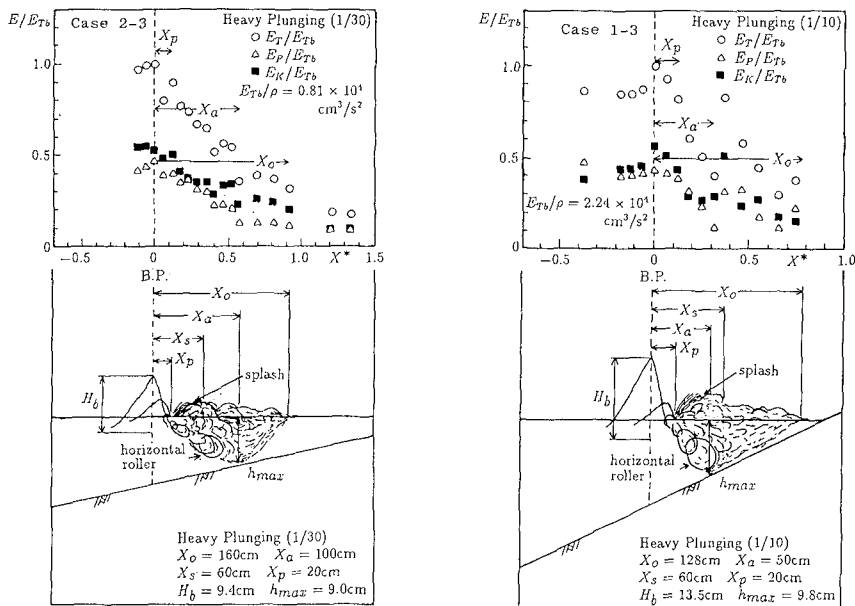


Fig.12 Variation of Potential and kinetic wave energy after breaking (Heavy plunging breaker)

wave body.

The kinetic wave energy  $E_k$  decays rapidly within the short distance between  $X^*=0$  and  $X^*=X_p$ , and 50% and 25% of  $E_{kp}$  are dissipated, respectively, in the cases of 1-3 and 2-3 in this range. The kinetic wave energy  $E_k$  once increases between  $X^*=X_a$  and  $X^*=X_s$  where the splash and horizontal roller's energy seem to be combined with the main wave body. The attenuation of  $E_k$  in the range of  $X^*>X_o$  is very small, like the spilling and plunging breakers.

The total wave energy  $E_T$  decreases rapidly after breaking and once increases between  $X^*=X_a$  and  $X^*=X_s$ , like the plunging breaker. Attenuation of  $E_T$  from  $X^*=X_a$  is small, like the spilling and plunging breakers. The kinetic wave energy  $E_k$  is generally larger than the potential wave energy  $E_p$  and the ratio of  $E_k/E_p$  becomes larger with  $X^*$  and takes a maximum value between  $X^*=X_s$  and  $X^*=X_a$  and then decreases to 1, like other types of breakers. The maximum value of  $E_k/E_p$  in case of 1-3 is 1.62.

As stated above, regardless of breaker types, most of the potential and kinetic wave energy are dissipated from breaking point ( $X^*=0$ ) to  $X^*=X_o$ , especially rapid energy dissipation takes place between  $X^*=0$  and  $X^*=X_a$  at which the depth of entrained air bubble becomes maximum. Thus, it seen that quantity of air bubble is an index of wave energy dissipation.

3.3 Variation of energy flux

Figures 13 and 14 show changes of the nondimensional energy flux  $F/F_b$  with  $X^*$ , where  $F_b$  is the energy flux at breaking point. The magnitude of changes of  $F/F_b$  with  $X^*$  depends on breaker types and bottom slopes. The figures show that  $F/F_b$  attenuates in the order of spilling, plunging and heavy plunging breakers and that the decay of  $F/F_b$  in the range of  $0 \leq X^* \leq X_a$  is much larger than that in the range of  $X^* \geq X_a$ . The splash and horizontal roller are only formed in cases of plunging and heavy plunging breakers and their scale of the heavy plunging breakers are larger than those of the plunging breakers. This causes the most rapid decay of  $F/F_b$  of the heavy plunging breaker among the three breakers. Figure 15 shows the relationship between  $F/\rho$  and  $d (=h+\bar{n})$ , in which the solid and dotted lines indicate, respectively, Eq.(8) and Eq.(9).  $\gamma$  in Eq.(8) and  $\gamma$  and  $\beta$  in Eq.(9) were determined by a least square method, and they

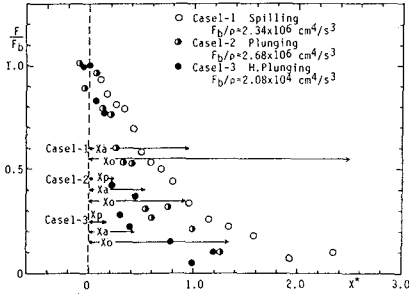


Fig.13 Variation of  $F/F_b$  with  $X^*$  ( $S=1/10$ )

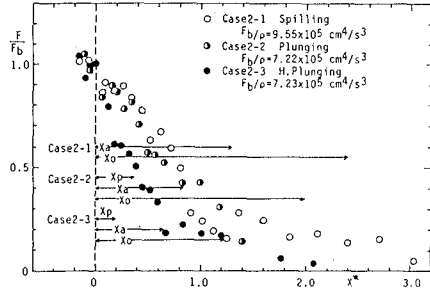


Fig.14 Variation of  $F/F_b$  with  $X^*$  ( $S=1/30$ )

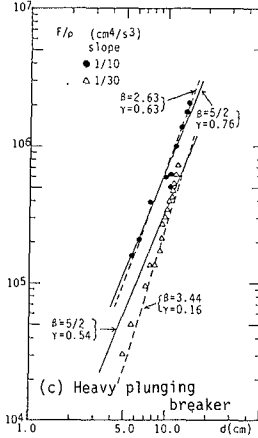
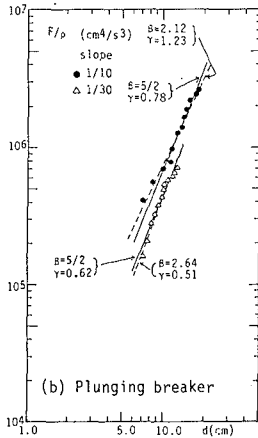
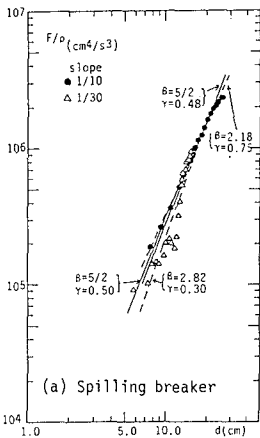


Fig.15 Relationship between  $E/\rho$  and  $d (=h+\bar{n})$

are given in Table 2.

Table 2 Values of  $\beta$  and  $\gamma$

$$\frac{F}{\rho} = \frac{1}{8} g^{\frac{3}{2}} \left(\frac{H}{d}\right) \gamma (d)^{\frac{5}{2}} \quad (9)$$

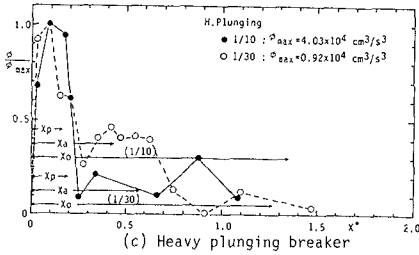
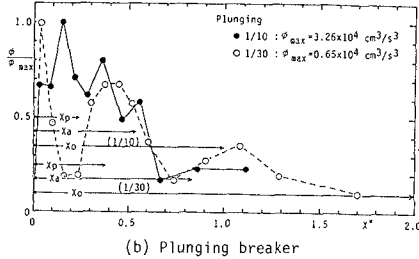
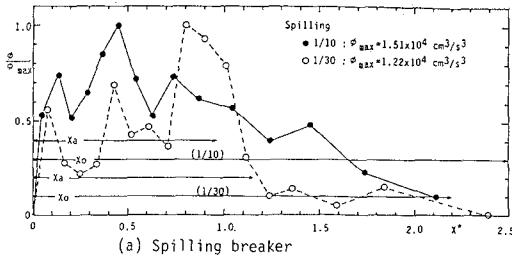
$$\frac{F}{\rho} = \frac{1}{8} g^{\frac{3}{2}} \left(\frac{H}{d}\right) \gamma (d) \beta \quad (10)$$

	$\beta$	$\gamma$	$\beta$	$\gamma$
Spilling(1/10)	5/2	0.48	2.18	0.75
Plunging(1/10)	5/2	0.78	2.12	1.23
H. Plunging(1/10)	5/2	0.76	2.63	0.63
Spilling(1/30)	5/2	0.50	2.82	0.30
Plunging(1/30)	5/2	0.62	2.64	0.51
H. Plunging(1/30)	5/2	0.54	3.44	0.16

$\gamma=2$  and  $\beta=5/2$  are derived for the linear long wave theory (Ishii,1990). Table 2 shows that  $\gamma$  is much smaller than 2, therefore the linear wave theory cannot be applied to evaluate the wave energy flux in the surf zone. However,  $\beta$  is between 2 and 3.5, and then it can be said that  $\beta=2.5$  is well approximated value. The value of  $\gamma$  changes according to breaker types and bottom slopes, and larger values of  $\gamma$  on steeper slope agree well with the foregoing studies.

3.4 Wave energy dissipation rate

Figure 16 shows variations of the nondimensional wave energy dissipation rate,  $\Phi/\Phi_{max}$  with  $X^*$ , where  $\Phi_{max}$  is the maximum value of wave energy dissipation rate. The wave energy dissipation rate  $\Phi$  is not constant, but it changes with  $X^*$ , depending on breaker types and the bottom slope.



In case of spilling breakers,  $\Phi$  is small at the inception of wave breaking, but it gradually increases and becomes maximum around  $X^*=0.8Xa$  ( $X^*=0.45$  for case 1-1 and  $X^*=0.8$  for case 2-1).

In the cases of plunging and heavy plunging breakers, different from spilling breakers, the wave energy dissipation rate  $\Phi$  becomes larger at the inception of wave breaking, and takes a maximum value around  $X^*=Xp$ . The wave energy dissipation rate  $\Phi$  becomes small in the range of  $X^*>Xa$ . As shown in Fig.16, rapid energy dissipation takes place in the order of spilling, plunging and heavy plunging breakers.

Fig.16 Variation of wave energy dissipation rate



3.5 Velocity of wave energy transport

Figure 17 shows two examples of variation of the non-dimensional velocity of wave energy transport  $C_e/C_{eb}$  with  $X^*$ , in which  $C_{eb}$  is the value of  $C_e$  at  $X^*=0$ , and  $C_e$  is defined with

$$C_e = F/E_T \quad (11).$$

The group velocity  $C_g$  and the wave celerity  $C$  given by Airy wave theory are also drawn as solid and dotted lines, respectively, for comparison.

$$C_g = \frac{1}{2} \left( 1 + \frac{2kh}{\sinh 2kh} \right) C \quad (12) \quad C = \frac{gL}{2\pi} \tanh \frac{2\pi h}{L} \quad (13)$$

The velocity of wave energy transport  $C_e$  is, in general, in good agreement with the group velocity  $C_g$  before wave breaking takes place, as shown in Fig.17. On the other hand, the velocity of energy transport  $C_e$  after breaking becomes smaller than the group velocity  $C_g$  and the difference between  $C_e$  and  $C_g$  becomes maximum around  $X^*=0.8X_a \sim X_a$ , in which the kinetic wave energy is much larger than the potential one, as already shown in Figs.10,11 and 12. This discrepancy of  $C_e$  from  $C_g$  is possibly caused by increasing of the offshore steady-velocity below the wave trough as in Fig.8.

The velocity of wave energy transport  $C_e$  is seen to close to the group velocity  $C_g$  in  $X^* > X_o$ , especially in the case of spilling breaker. Since the kinetic energy is almost equal to the potential one in  $X^* > X_o$ . It seems that wave energy is transported with the group velocity under the condition that the kinetic is almost equal to the potential one. The same facts are seen in other experimental cases such as case 1-1,1-2,1-3 and 2-2.

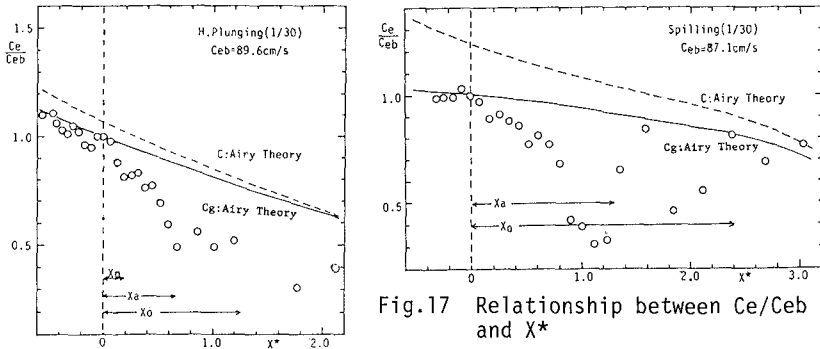


Fig.17 Relationship between  $C_e/C_{eb}$  and  $X^*$

4. CONCLUSION

The variation of the potential, kinetic and total wave energy after breaking has been discussed experimentally in relation to breaker types and bottom slopes. The main results obtained in this study are summarized as follows:

- (1) The kinetic wave energy is larger than the potential

one in the surf zone. The ratio of the kinetic wave energy to the potential one is changed according to breaker types and bottom slopes. The location of the deepest air-entrained depth  $X_a$ , plunging point  $X_p$ , and location of air bubble's disappearance from wave body  $X_o$  can be indexes to the ratio of the kinetic wave energy to the potential one, from macroscopic viewpoint.

(2) Some of the potential wave energy can be transferred to the kinetic one at an early stage of wave breaking in the spilling breaker. The splash and the horizontal roller play an important role to the transfer mechanism between the kinetic and potential wave energy in plunging and heavy plunging breakers.

(3) The attenuation of the kinetic, potential and total wave energy becomes larger in the order of spilling, plunging, heavy plunging breakers. The magnitude of the attenuation increases with steepening of the bottom slope.

(4) The most of wave energy are dissipated in the region between the breaking point and the location of air bubble's disappearance from wave body ( $X^*=X_o$ ).

(5) The wave energy dissipation rate increases in the order of spilling, plunging and heavy plunging breakers. The location at which the maximum wave energy dissipation rate takes place approaches the breaking point in the order of spilling, plunging and heavy plunging breakers.

#### REFERENCES

- Dean, R.G. (1965): Stream function representation of nonlinear ocean waves, *Jour. of Geophy. Res.*, Vol. 70, pp. 4561 - 4572.
- Horikawa, K. and C.T. Kuo (1966): A study on wave transformation in the surf zone, *Proc. 10th ICCE*, pp. 217 - 233.
- Ishii, H. (1990): Variation of wave energy after breaking on slopes, Master thesis to Nagoya Univ., 21p.
- Iwata, K., Koyama, H. and S. Futo (1983): Experimental study on change of wave energy after breaking, *Proc. 30th Japanese Conf. on Coastal Eng.*, pp. 10 - 14 (in Japanese).
- Koyama, H. and K. Iwata (1986): Estimation of water particle velocities of shallow water waves by a modified transfer function method, *Proc. 20th ICCE*, pp. 425 - 436.
- Lee, J.J., Skjelbreia, J.E. and F. Raichlen (1982): Measurement of velocities in solitary waves, *Jour. of waterway, port, coast and ocean Div.*, Vol. 108, No. WW2, ASCE, pp. 200 - 218.
- Nadaoka, K., Kondoh, T. and N. Tanaka (1982): The structure of velocity field within the surf zone revealed by means of Laser-Doppler Anemometry, *Rept. of the Port and Harbour Res. Inst.*, Vol. 21, pp. 49 - 106.
- Sawaragi, T. and K. Iwata (1974): On wave deformation after breaking, *Proc. 14th ICCE*, pp. 481 - 499.
- Tsuchiya, Y. and S. Tsutsui (1982): Wave energy distribution and wave breaking process, *Proc. 29th Japanese Conf. on Coastal Eng.*, pp. 125 - 129 (in Japanese).

## CHAPTER 25

### Modelling of Wave-Current Boundary Layer in the Coastal Zone

Leszek M. Kaczmarek & Rafał Ostrowski <sup>1</sup>

#### Abstract

A 2-D numerical model of bottom turbulent boundary layer is described. The nonlinear effects associated with wave asymmetry and the nonlinear interaction of waves and currents are taken into account. The model provides a relatively simple procedure for determination of both instantaneous and time-averaged quantities of velocity and friction inside the boundary layer.

#### 1 Introduction

The interaction of current and nonlinear waves is characteristic for a coastal zone behind and ahead of surf line because of the balance of wave asymmetry and effects bound with time-averaged current, called a return flow. Inter alia, it is possible that a time-averaged flow is offshore in the entire outer region while in the boundary layer, due to wave asymmetry, onshore flow occurs.

The problem of interaction of waves and currents will be dealt with in two regions: in a potential oscillatory flow with superimposed current and in a boundary layer, with the continuity laws satisfied at the interface of the two regions. The solution in the boundary layer is conditioned by the knowledge of the flow in the outer region.

The model takes into account nonlinear effects (i.e. wave asymmetry and those due to  $\overline{Uw_\infty}$ ). Two steps have been proposed:

- Step *I* — an iterative scheme providing the slip velocity, with  $\overline{Uw_\infty}$  term due to energy dissipation in the boundary layer
- Step *II* — a procedure yielding instantaneous and time-averaged velocity distributions in the boundary layer due to wave asymmetry.

---

<sup>1</sup>Ph. D. & M. Sc. Polish Academy of Sciences' Institute of Hydro-Engineering, IBW PAN, 7 Kościarska, 80-953 Gdańsk, Poland

## 2 Wave nonlinearity

### 2.1 Wave input asymmetry

Within nonlinear approximation the equation of motion in boundary layer has the form:

$$\frac{\partial u}{\partial t} + u \frac{\partial u}{\partial x} = \frac{\partial U}{\partial t} + U \frac{\partial U}{\partial x} + \frac{\partial}{\partial z} \left( \nu_t \frac{\partial u}{\partial z} \right) \quad (1)$$

where  $u(z, t)$  i  $U(t)$  are the velocities inside and at the upper limit of boundary layer, respectively.

Assuming that the velocity  $u$  does not depend on a variable  $x$ , one may neglect the convective terms and simultaneously take the nonlinearity into account by expressing the velocities of bottom oscillations  $U(t)$  in potential motion by nonlinear Stokes approximation. In this way the *asymmetry* of wave with respect to still water level, defined according to the order of nonlinear approximation, is considered.

The linearized equation of motion (Eq. 1) in boundary layer reads:

$$\frac{\partial}{\partial t}(u - U) = \frac{1}{\rho} \frac{\partial \tau}{\partial z} \quad (2)$$

where  $\tau(z, t)$  is the shear stress and  $\rho$  is water density.

To define time distribution of bottom friction velocity  $u_f(t)$ , the assumptions of Fredsoe's model (1981) formulated for sinusoidal wave and the suggestion of Fredsoe, Andersen & Silberg (1985) concerning the possibility of adaptation of the model for nonlinear wave case have been employed.

Integrating Eq. 2 over the thickness of boundary layer  $\delta$  and assuming the logarithmic distribution of velocity one obtains the following differential equation:

$$\frac{dz_1}{d(\omega t)} = \frac{30\kappa^2 U(\omega t)}{k_s \omega e^{z_1}(z_1 - 1) + 1} - \frac{z_1(e^{z_1} - z_1 - 1)}{e^{z_1}(z_1 - 1) + 1} \frac{1}{U} \frac{dU}{d(\omega t)} \quad (3)$$

in which:

$$z_1 = \frac{U\kappa}{u_f} \quad (4)$$

and:

$$\delta = \frac{k_s}{30}(e^{z_1} - 1) \quad (5)$$

where  $k_s$  is Nikuradse roughness parameter and  $k_s/30$  is the theoretical bed level above  $z = 0$ .

It is necessary to point out that the solution of Eq. 3 bases on an assumption that the boundary layer develops anew every time the flow reverses. This implies the neglect of memory effects.

As a result of numerical solution of Eq. 3, the function  $z_1(t)$  is obtained and the temporal distributions of friction velocity  $u_f(t)$  and boundary layer thickness  $\delta(t)$  can be calculated thereafter on the basis of Equations 4 and 5.

The asymmetry of bottom velocity oscillations  $U(t)$  brings about non-uniform growth of boundary layer thickness in crest and trough phases, thus non-uniform friction.

The presented computational procedure permits the determination of the characteristics of bottom friction ( $\delta$  and  $u_f$ ) practically for any input  $U(t)$ .

Making use of the definition of friction velocity:

$$u_f = \sqrt{\frac{\tau}{\rho}} \quad (6)$$

one may determine the mean shear stress within wave period  $T$ :

$$\tau_c = \frac{1}{T} \int_0^T \rho |u_f(t)| u_f(t) dt \quad (7)$$

and the corresponding mean friction velocity:

$$u_{fc} = \sqrt{\frac{\tau_c}{\rho}} \quad (8)$$

On the basis of computations one finds out that the mean friction velocity for an arbitrary nonlinear input is a positive value although the resultant water velocity at the top of the boundary layer is zero. In the computations carried out for a typical nonlinear wave in small scale laboratory tests, represented by 2nd or 3rd Stokes approximation, the quantity  $u_{fc}^2$  has represented about 5% of the maximum shear stress  $u_{fmax}^2$ , where  $u_{fmax} = \max[u_f(t)]$ .

The non-zero mean shear stress reflects the existence of a certain resultant current inside boundary layer, directed accordingly to wave propagation.

All earlier attempts of *theoretical* description of the resultant current induced inside a boundary layer have led to the identification of wave-induced mass flux caused by the displacement in a boundary layer. The flux arises because a phase shift exists between the horizontal and vertical flow velocities at the top of the boundary layer in non-uniform water waves. This effect will be discussed in the next section.

## 2.2 Discussion of vertical momentum transfer induced by the energy dissipated in a wave boundary layer

The non-zero vertical velocity  $w$  in the boundary layer results from continuity equation in the solution of Longuet-Higgins (1953) for the laminar boundary layer. The existence of this velocity indicates that an additional mean (over wave period) shear stress  $\overline{uw}$  is generated inside the boundary layer. This stress attains the maximum value at the upper limit of the layer. It causes the disturbances in the region of potential flow, because there is no vertical momentum exchange represented by the term  $\overline{uw}$  in linear wave motion. The approach of Longuet-Higgins implies that the form of vertical velocity  $w$  induced by the vorticity depends on the linear solution of the equation of motion. Moreover, it can be easily shown that the shear stress induced outside the boundary layer is oriented in the direction of wave propagation and the velocity is smaller by one order of magnitude than its linear counterpart.

In the case of turbulent motion, the determination of the additional shear stress generated inside the boundary layer requires, as in laminar motion, the knowledge of the linear solution of Eq. 2. This solution depends on the distribution of eddy viscosity  $\nu_t$ .

Using the continuity equation and assuming:

$$\frac{\partial}{\partial x} = -\frac{1}{c} \frac{\partial}{\partial t} \tag{9}$$

where  $c$  is a phase velocity of wave, one may determine the additional vertical velocity  $w_\infty$  outside the boundary layer:

$$w_\infty = -\frac{\partial}{\partial x} \int_{\frac{k_s}{30}}^{\frac{k_s}{30} + \delta} (u - U) dz = \frac{1}{c} \int_{\frac{k_s}{30}}^{\frac{k_s}{30} + \delta} \frac{\partial}{\partial t} (u - U) dz \tag{10}$$

After taking into account Eq. 2 integrated over the boundary layer thickness, Eq. 10 transforms into the form:

$$w_\infty = -\frac{\tau_0}{c\rho} = -\frac{u_f |u_f|}{c} \tag{11}$$

The considerations of Deigaard & Fredsoe (1989) reveal that the nonlinearities bound with the generation of an additional vertical velocity  $w_\infty$  at the top of boundary layer i.e. the nonlinearities linked with the terms  $\overline{UW}$  are closely associated with the dissipation of wave energy. If the energy dissipation is neglected one may skip the additional stresses generated at the top of the boundary layer (the current induced by these stresses does not exist).

Finally it is worthwhile pointing out that the stress  $\overline{uw_\infty}$  equals zero at the bottom and reaches the maximum value at the top of boundary layer while the effects of wave asymmetry play the key role very close to the bottom.

The above conclusions will be helpful for formulation of a model in Section 3.

### 3 Wave and current interaction

Integrating Eq. 2 over the thickness of boundary layer in the similar manner as in Section 2.1 and assuming  $\tau(\delta) = -\rho u_{f0}^2$  and  $\tau_0 = \rho |u_f| u_f$ , cf. Fredsoe (1984), one obtains the following differential equation:

$$\frac{dz_1}{d(\omega t)} = \frac{30z_1^2 \left[ \left| \frac{\kappa U}{z_1} - u_{f0} \right| \left( \frac{\kappa U}{z_1} - u_{f0} \right) + u_{f0}^2 \right]}{\omega k_s U [e^{z_1}(z_1 - 1) + 1]} - \frac{z_1(e^{z_1} - z_1 - 1)}{e^{z_1}(z_1 - 1) + 1} \frac{1}{U} \frac{dU}{d(\omega t)} \tag{12}$$

in which:

$$z_1 = \frac{\kappa U}{u_f + u_{f0}} \tag{13}$$

and:

$$\delta = \frac{k_s}{30} (e^{z_1} - 1) \tag{14}$$

In Equation 12 the *nonlinear wave input*  $U(t)$  can be involved, given by any Stokes approximation (for instance of 2nd or 3rd order). Both the current friction velocity  $u_{f0}$  and the variable  $z_1$  are unknown. Therefore the use of iteration method in the first stage of solution is proposed.

Introducing the defect velocity  $u_d(z, t) = u(z, t) - U(t)$  one has the equation of motion (Eq. 2) in the form:

$$\frac{\partial u_d}{\partial t} = \frac{\partial}{\partial z} \left( \nu_t \frac{\partial u_d}{\partial z} \right) \quad (15)$$

The following approximate initial condition is assumed:

$$u_d(z, t_0) = 0 \quad (16)$$

and the boundary conditions are:

$$u_d\left(\frac{k_s}{30}, \omega t\right) = -U(\omega t) \quad (17)$$

$$u_d\left(2\delta_m + \frac{k_s}{30}, \omega t\right) = 0 \quad (18)$$

Eq. 15 is solved numerically by an implicit method involving the Crank – Nicholson scheme. Because the approximate initial condition (Eq. 16) has been assumed, the computations have had to cover the time corresponding to a few wave periods until the compatibility between  $u_d(z, t_0 + N \cdot T)$  and  $u_d[z, t_0 + (N + 1) \cdot T]$  is reached. The number of required runs  $N$  depends on wave parameters and is three to five.

Within the first stage of the solution, an interaction of a *sinusoidal* wave and the steady current is considered. A simple iterative procedure presented by Kaczmarek & Ostrowski (1991) ensures the determination of the current friction velocity  $u_{f0}$  by matching the mean shear stress at the top of boundary layer. Mean velocities are also matched at the upper limit of boundary layer: the slip velocity calculated from equations governing in the outer region and the mean velocity at the top of boundary layer (see Appendix).

Within the second stage of the solution, the temporal distribution of total friction velocity  $u_f$  is determined on the basis of Eq. 12 for the quantity  $u_{f0}$  computed previously and for nonlinear oscillatory input  $U(t)$ .

As a result of numerical solution of Eq. 12, the function  $z_1(\omega t)$  is obtained and the temporal distributions of friction velocity  $u_f(\omega t)$  and boundary layer thickness  $\delta(\omega t)$  are determined from Eqs. 13 and 14, respectively. Then one can easily calculate the root mean square friction velocity  $u_{fc}$  from Eqs. 7 and 8.

The following distribution of eddy viscosity  $\nu_t$  is assumed:

$$\begin{aligned} \nu_t(z) &= \kappa \hat{u}_f z & \text{for } \frac{k_s}{30} \leq z \leq \frac{\delta_m}{4} + \frac{k_s}{30} \\ \nu_t(z) &= \kappa \hat{u}_f \left( \frac{\delta_m}{4} + \frac{k_s}{30} \right) & \text{for } z > \frac{\delta_m}{4} + \frac{k_s}{30} \end{aligned} \quad (19)$$

Let us notice that the above distribution is based on the friction velocity  $\hat{u}_f$ , which couples the effects of a current and wave asymmetry (determined within the two-stage approach). The equivalent friction velocity  $\hat{u}_f$  has been assumed as:

$$\hat{u}_f = \max(|u_f(\omega t)|) \quad (20)$$

while the mean boundary layer thickness the authors propose to determine as:

$$\delta_m = \max(\delta_1, \delta_2) \tag{21}$$

where  $\delta_1$  and  $\delta_2$  are the boundary layer thicknesses at the moments corresponding to maximum and minimum total (oscillatory and current) input  $U(t) + V$ , respectively.

The equation of motion for the case of linear wave and current may be solved separately with separate boundary conditions. As it was pointed out by Kaczmarek & Ostrowski (1991), the assumption of time-independence of eddy viscosity  $\nu_t$  in the boundary layer allows one to treat the combined wave and current motion by separate equations. The effect of nonlinear interaction between waves and a current is incorporated in the eddy viscosity, thus modelling of the turbulent viscosity  $\nu_t$ .

Hence the determination of instantaneous velocities  $u(z, t)$  may be the sum of the solution of equation of motion for wave only with the oscillatory velocity at the top of boundary layer as a boundary condition and the current described by equations:

$$\kappa \hat{u}_f z \frac{\partial u_c}{\partial z} = u_{fc} |u_{fc}| \tag{22}$$

in the range  $< k_s/30; \delta_m/4 + k_s/30 >$  and

$$\kappa \hat{u}_f \left( \frac{\delta_m}{4} + \frac{k_s}{30} \right) \frac{\partial u_c}{\partial z} = u_{fc} |u_{fc}| \tag{23}$$

in the range  $(\delta_m/4 + k_s/30; \delta_m/2 + k_s/30 >$ .

The friction velocity  $u_f(\omega t)$ , the boundary layer thickness  $\delta(\omega t)$  and the root time-mean square friction velocity  $u_{fc}$  are determined from the solution of Equation 12.

Integrating Eqs. 22, 23 and taking advantage of the condition  $u_c(z = k_s/30) = 0$  and the condition of continuity of  $u_c$  at  $z = \delta_m/4 + k_s/30$  one comes up with the formulas:

$$u_c(z) = \frac{u_{fc} |u_{fc}|}{\kappa \hat{u}_f} \ln \frac{z}{\frac{k_s}{30}} \tag{24}$$

in the range  $< k_s/30; \delta_m/4 + k_s/30 >$  and

$$u_c(z) = \frac{u_{fc} |u_{fc}|}{\kappa \hat{u}_f \left( \frac{\delta_m}{4} + \frac{k_s}{30} \right)} \left( z - \frac{\delta_m}{4} - \frac{k_s}{30} \right) + \frac{u_{fc} |u_{fc}|}{\kappa \hat{u}_f} \ln \frac{\frac{\delta_m}{4} + \frac{k_s}{30}}{\frac{k_s}{30}} \tag{25}$$

in the range  $(\delta_m/4 + k_s/30; \delta_m/2 + k_s/30 >$ .

The nonlinear wave on a steady current is the most interesting case from a practical point of view, as the resultant shear stress direction controls the direction of the resultant flow in the combined boundary layer. Therefore the quantity  $u_{fc}$  is of a great importance: if it is positive, the effects of wave asymmetry will prevail and the mean flow in the wave-current boundary layer will be directed shorewards; if  $u_{fc}$  is negative, the steady current will prevail, and the resultant flow in the boundary layer will be directed seawards. For both situations the mean velocity profile can be calculated from of Eq. 24 in the range  $< k_s/30; \delta_m/4 + k_s/30 >$



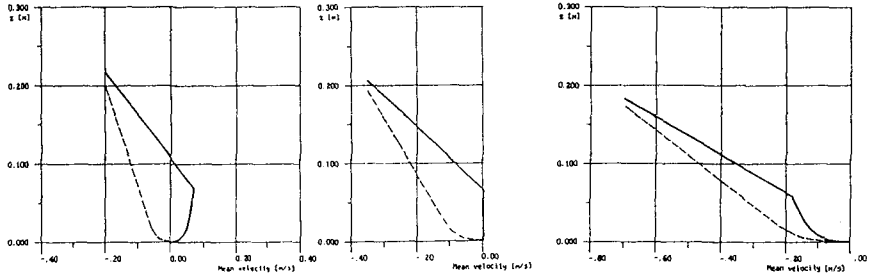


Fig. 1. Mean current velocity distributions in boundary layer as a result of interaction between nonlinear (solid line) or sinusoidal (dashed line) waves and a current

and Eq. 25 in the range  $(\delta_m/4 + k_s/30; \delta_m/2 + k_s/30 >$  as in the case of nonlinear wave and current interaction the shear stress is assumed as constant in the range  $< k_s/30; \delta_m/2 + k_s/30 >$ . The choice of the upper limit where the shear stress is constant is rather arbitrary but it follows an assumption made with respect to wave boundary layer. The authors have proposed the upper limit of this region as the ordinate corresponding to the level at which the maximum (or minimum) velocity profile reaches the free stream velocity. In accordance with Jonsson & Carlsen (1976)  $\delta_m/2 + k_s/30$  is the most consistent measure. In the range  $(\delta_m/2 + k_s/30; 2\delta_m + k_s/30 >$  the mean velocity profile is assumed to change linearly upwards and to attain the value of slip velocity at the top of boundary layer. To analyse and distinguish the two major types of waves propagating against a current, sample computations have been carried out for the wave parameters corresponding to the laboratory experiment by Jonsson & Carlsen (1976):  $h = 10$  m,  $H = 5.3$  m,  $T = 8.39$  s. The wave has been approximated by Stokes theory of 2nd order. Additionally three currents of different slip velocities have been assumed:  $V = 0.20$  m/s,  $V = 0.35$  m/s and  $V = 0.70$  m/s. The resultant mean velocity distributions (solid line) in comparison with the profiles obtained for sinusoidal wave and current interaction (dashed line) are depicted in Fig. 1.

Having solved the equation of motion in boundary layer (Eq. 15) one may superimpose the instantaneous velocity profiles on the mean current distribution given by Eqs. 24 and 25 in the range  $< k_s/30; \delta_m/2 + k_s/30 >$ . In the range  $(\delta_m/2 + k_s/30; 2\delta_m + k_s/30 >$  the mean velocity profile changes linearly upwards and attains the value of slip velocity at the top of boundary layer. This mean current velocity is also superimposed on the instantaneous velocity distributions.

#### 4 Comparison between theory and measurements

##### 4.1 Velocity in wave-current bottom boundary layer

Results of computations have been compared with the laboratory measurements by Hwang & Lin (1990). The experiments were carried out in a  $9.5 \times 0.7 \times 0.3$  m wave tank in which the bottom was adjusted on one-fifteenth slope. The velocities

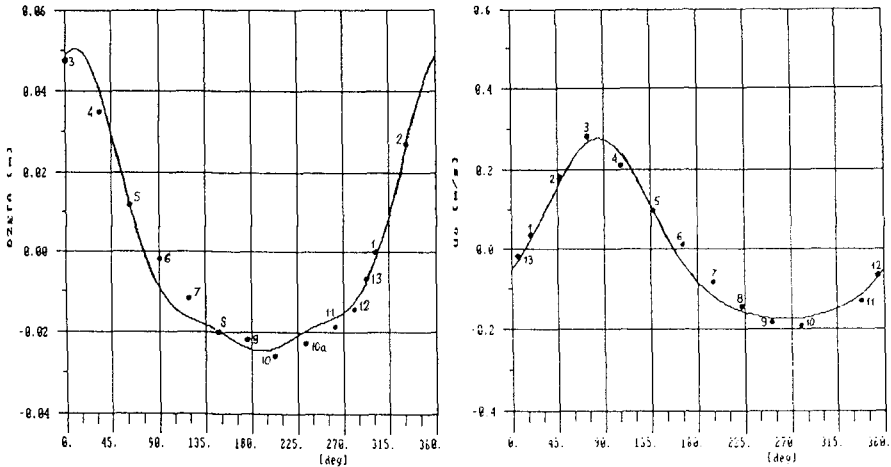


Fig. 2. Measured (●) and calculated (—) water surface elevation (left) and wave input (right)

of water were measured in 13 testing sections (including the boundary layer) situated along the flume. The comparison of computed data and measurements concern *Case 2* of experimental wave parameters: initial depth  $h = 0.33$  m, initial wave height  $H = 6.6$  cm, wave period  $T = 1.23$  s.

Although it is possible to provide a complex solution in the outer region using one of the models dealing with return flow and in the boundary layer using the present approach, it is well worth focusing attention on the precision of solution in the boundary layer, being a major topic of the paper. Therefore the value of the slip velocity  $V$  has been taken from the measurements of Hwung & Lin (1990) to obtain the best fit of the boundary condition at the upper limit of boundary layer.

The computed and measured instantaneous velocity profiles have been compared for the testing section *P4*. The water surface elevation  $\zeta(\omega t)$  and the wave input  $U(\omega t)$  have been determined by the theory of Borgman and Chappelair (Stokes approximation of 3rd order), Fig. 2. The assumed time distributions of  $\zeta(\omega t)$  and  $U(\omega t)$  have been a little bit shifted to obtain the best fit with respect to the recorded ones.

The instantaneous and mean velocity profiles have been computed using the procedure presented in the previous section. The parameter of equivalent roughness  $k_s$  has been estimated as 2 mm. The instantaneous velocities are given in Fig. 3. The agreement of computed and measured instantaneous velocity profiles is satisfactory, especially at the moments corresponding to the best fit between recorded and assumed wave inputs  $U(\omega t)$ .

The calculated mean velocity profiles for the testing sections *P1*, *P3*, *P4* and *P6* are given in Fig. 4. In general, they all correspond to the measured ones very

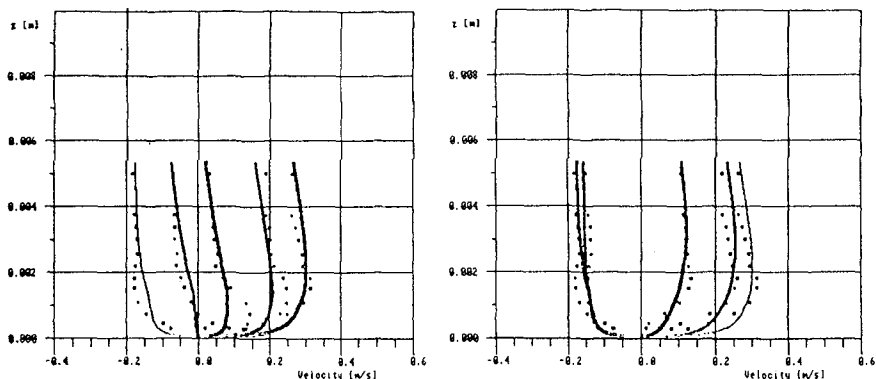


Fig. 3. Measured (●) and computed (—) instantaneous velocity distributions

well. As the testing section *P1* lies in the range of application of Stokes 2nd order theory, the velocity has also been determined with this approximation (dashed line).

#### 4.2 Undertow combined with a bottom boundary layer

The case of the wave propagating perpendicularly to the shoreline is considered. The oscillatory motion is accompanied by the undertow which compensates the mass flux carried shoreward by the breaking waves. The eddy viscosity model (Eqs. 19) in the bottom boundary layer is assumed. The eddy viscosity  $\nu_{tc}$  in outer region is assumed vertically constant. As shown by Svendsen (1984) the inclusion of a conceptually realistic depth-variation of  $\nu_{tc}$  has the effects of secondary importance when compared to the effects of incorporating alternative boundary conditions at the bottom.

The vertical distribution of the mean current velocity in the outer region  $U_c(z)$  may be estimated by the following formula, cf. Svendsen (1984):

$$U_c(z) = \frac{1}{2} \alpha (z+h)^2 + \left( 2 \frac{U_m - V}{d_{tr}} - \frac{1}{3} \alpha d_{tr} \right) (z+h) + V \quad (26)$$

in which

$$\alpha = \frac{\alpha_1(x)}{\nu_{tc}} \quad (27)$$

$$\alpha_1(x) = \frac{\partial}{\partial x} \left( \overline{u_w^2} + g\bar{\eta} \right) \quad (28)$$

where  $U_m$  is the total mean mass flux below the wave trough,  $d_{tr}$  is the distance between sea bottom and wave trough,  $\overline{u_w^2}$  is mean square oscillatory horizontal velocity,  $\bar{\eta}$  is the set-up and  $g$  is the acceleration of gravity. The coordinate system begins at mean water level in this case and  $z$  axis is directed upwards.

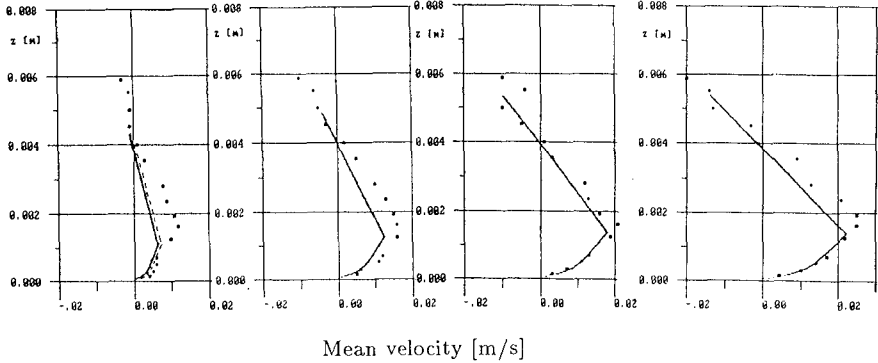


Fig. 4. Measured (●) and computed (-) mean velocity profiles at testing sections P1, P3, P4, P6

The derivative of Eq. 26 reads:

$$\frac{\partial U_c(z)}{\partial z} = \alpha (z + h) + \left( 2 \frac{U_m - V}{d_{tr}} - \frac{1}{3} \alpha d_{tr} \right) \tag{29}$$

The shear stress at the lower limit of the undertow region is given by the formula:

$$\tau_e = \rho \nu_{tc} \left. \frac{\partial U_c(z)}{\partial z} \right|_{z=-h} \tag{30}$$

Basically, the slip velocity  $V$  which corresponds to the one at the top of the boundary layer is unknown and that is the reason of iteration in our solution of the problem. The quantity  $V$  must match the mean velocity at the top of boundary layer as well as  $\tau_e$  must be equal to the mean shear stress at the top of boundary layer calculated on the basis of instantaneous velocity profiles from Eq. 15.

The comparisons between the measurements of Stive & Wind and Hansen & Svendsen experiments (Stive & Wind 1986) and the results obtained with the use of proposed method are shown in Figs. 5 and 6.

As it is seen the slip velocity obtained with the use of presented procedure does not differ much from that which would exist if an assumption was made of  $\tau_e(z = -h)$  equal zero. This confirms experimental observations of Stive & Wind (1986). The above conclusion is of great importance for calculating the undertow velocity distribution in practical use. Thus assuming  $\partial U_c(z)/\partial z|_{z=-h} = 0$  in Eq. 29 one obtains the simplified formula for slip velocity:

$$V = U_m - \frac{1}{6} \alpha d_{tr}^2 \tag{31}$$

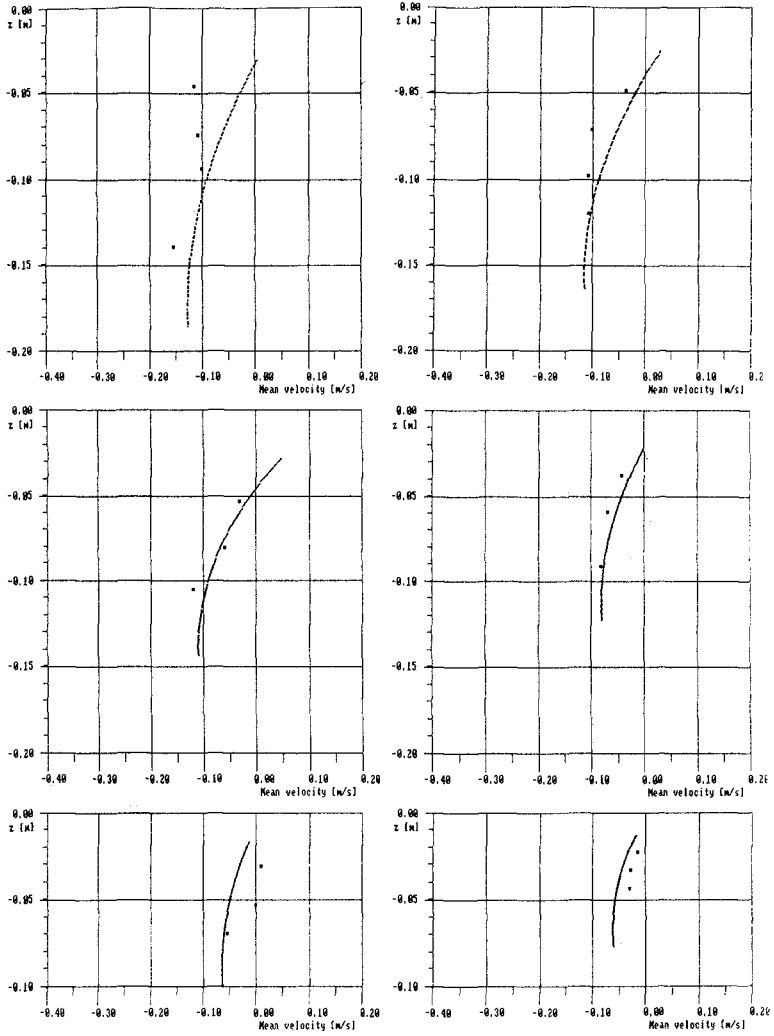


Fig. 5. Measured and calculated undertow; tests by Stive & Wind (1986)

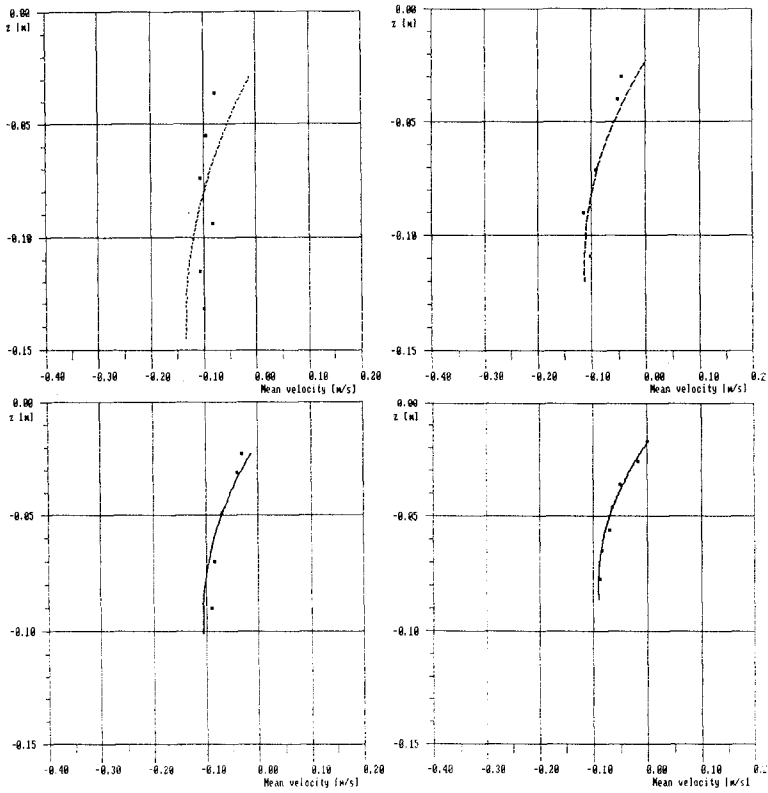


Fig. 6. Measured and calculated undertow; tests by Hansen & Svendsen (Svendsen 1984)

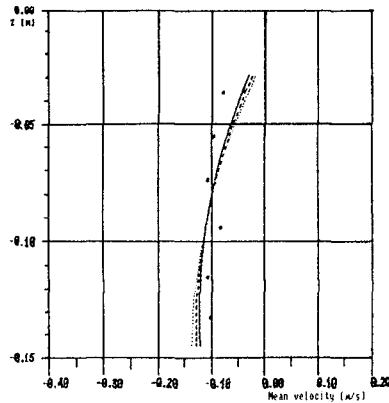


Fig. 7. The  $\overline{Uw_\infty}$  contribution to undertow profile

In the computations  $k_s$  was assumed as 1 mm for all sets of data after Svendsen & Hansen (1988).

It is worthwhile remembering that the  $\overline{UW}$  term originating from the organized orbital motion vanishes at the top of boundary layer, while the  $\overline{Uw_\infty}$  associated with the energy dissipated in a wave boundary layer possesses a certain value, cf. the discussion in section 2.2. It is interesting to evaluate the contribution of this term to the undertow distribution near the bottom. To this end the  $\overline{Uw_\infty}$  term has been estimated from Eq. 11 and incorporated in the iterative scheme by superposition with the undertow shear stress at the top of boundary layer. The effect of  $\overline{Uw_\infty}$  on the undertow distribution has been evaluated for one of the cases of Hansen & Svendsen's (1984) experiment and is depicted in Fig. 7 (solid line) in comparison with the undertow profile without this effect (dashed line). Additionally, the undertow distribution computed with the assumption of zero undertow shear stress at the top of boundary layer is given (dotted line). As one could have expected, the contribution of  $\overline{Uw_\infty}$  is very small and the proposed formula for slip velocity (Eq. 31) obtained with the assumption of zero undertow shear stress at the bottom is sufficient for practical engineering purposes.

## 5 Conclusions

The theoretical model describing both instantaneous and time-averaged quantities of velocity and friction inside the turbulent boundary layer generated by the interaction of nonlinear wave and current has been presented. The treatment of the paper is restricted to the two-dimensional flow, in which the intersection angle between the direction of wave propagation and that of the steady current is either  $0^\circ$  or  $180^\circ$ . The model takes into account nonlinear effects, i.e. wave asymmetry and the effects associated with  $\overline{Uw_\infty}$ .

The results of computations of velocities inside the boundary layer under nonlinear wave and current have been compared with the laboratory data of Hwung

& Lin's (1990) experiment. The agreement of computed and measured, both instantaneous and mean, velocity profiles is satisfactory.

The effect of  $\overline{U}w_\infty$  (associated with energy dissipation in the wave boundary layer) on the undertow distribution has been evaluated for one of the cases of Hansen & Svendsen's (1984) experiment. The contribution of this term has been found out to be very small. This implies that the proposed formula for slip velocity obtained with the assumption of zero undertow shear stress at the bottom is sufficient for practical engineering purposes.

*Appendix:* Iterative scheme for undertow and bottom boundary layer

1. Assumption of  $V$
2. Assumption of  $u_{f0}$
3. Computation of  $u_{fc}$  (Eqs. 12, 13, 7, 8) and  $\tau_e$  (Eq. 30)
4. Verification whether  $\tau_e = \rho u_{fc}^2$
- 5a. IF NOT: correction of  $u_{f0}$  and GO TO item 3
- 5b. IF YES: computation of  $u_c(z)$
6. Verification whether  $V = u_c(2\delta_m + k_s/30)$
- 7a. IF NOT: correction of  $V$  and GO TO item 2
- 7b. IF YES: END

#### *Acknowledgements*

The study has been sponsored by KBN and PAN, Poland, under programme 2 IBW PAN, which is hereby gratefully acknowledged. The Authors wish to thank Prof. R. Zeidler for the discussions and helpful suggestions throughout the study.

#### *References*

- Deigaard R., Fredsøe J. (1989), Shear stress distribution in dissipative water waves, *Coastal Engng.* 13, 357–378
- Fredsøe J. (1981), A simple model for the wave boundary layer, *Prog. Rep.* 54, Inst. Hydrodyn. and Hydraulic Engng. Tech. Univ. Denmark
- Fredsøe J. (1984), Turbulent boundary layer in wave-current motion, *J. Hydraulic Engng.*, ASCE, Vol. 110, No 8
- Fredsøe J., Andersen O.H., Silberg S. (1985), Distribution of suspended sediment in large waves, *J. Waterway, Port, Coast. and Oc. Engng.*, ASCE, Vol. 111, No 6
- Hansen J. Buhr, Svendsen I.A. (1984), A theoretical description and experimental study of undertow, *Proc. 19th Int. Conf. on Coastal Engng.*, Houston
- Hwung H.H., Lin C. (1990), The mass transport of waves propagating on a sloping bottom, *Proc. 22nd Coast. Engng. Conf.*, Delft
- Jonsson I.G., Carlsen N.A. (1976), Experimental and theoretical investigations in an oscillatory turbulent boundary layer, *J. Hydr. Res.*, Vol. 14, No 1
- Kaczmarek L.M., Ostrowski R. (1991), Modelling of wave-current boundary layers with application to surf zone, *Hydrotechnical Archives*, Vol. XXXIX, No 1–2
- Longuet-Higgins M.S. (1953), Mass transport in water waves, *Philos. Trans. R. Soc. London*, Ser. A, 245: 535–581
- Stive M.J.F., Wind H.G. (1986), Cross-shore mean flow in the surf zone, *Coastal Engng.* 10, 325–340
- Svendsen I.A. (1984), Mass flux and undertow in a surf zone, *Coastal Engng.* 8, 347–365
- Svendsen I. A., Hansen J. Buhr (1988), Cross-shore currents in surf-zone modelling, *Coast. Engng.*, Vol. 12, No 1



## CHAPTER 26

### Spectral Evolution of Directional Finite Amplitude Dispersive Waves in Shallow Water

James M. Kaihatu and James T. Kirby <sup>1</sup>

#### Abstract

Two different aspects of nearshore wave modelling are discussed. The first section details a model valid in deeper water than the usual shallow water wave models. We derive a mild-slope equation in which nonlinearity is retained to second order in  $\epsilon$  and dispersion is retained to all orders. The resulting parabolic model is then simplified for expedient calculation. This simplified model is compared to the data of Whalin (1971) with favorable results. The second section concerns the role of vector-sum interactions as compared to colinear, near-resonant interactions. We use the angular spectrum model of Kirby (1990) to determine which sort of interaction is dominant in the nearshore wavefield. A steady wave solution of the model and a case of unsteady wave evolution were investigated. Two simplified data sets with different amounts of directional spread were then run through the model. All three tests indicate that vector-sum interactions contribute significantly to wave field evolution.

#### Introduction

A number of frequency-domain models of nearshore wave evolution have appeared in the literature. Many of these models are based on the Boussinesq equations of Peregrine (1967) or closely-related variants; examples include Freilich and Guza (1984) and Liu, et.al. (1985). All these models calculate the wavefield in the frequency domain by factoring out the time periodicity of each frequency component, and treat the nonlinear terms in the governing equations by three-wave resonant interaction theory, making explicit the energy exchange between frequencies. Directional characteristics of the wavefield, if considered at all, are usually treated by the parabolic approximation (see Liu, et.al. (1985) for an example of this).

This paper is divided into two parts. The first part contains the development of a finite-depth spectral evolution model which can be used in deeper water than the Boussinesq-type models. A slightly simplified version of this model is compared to data, and the

---

<sup>1</sup>Center for Applied Coastal Research, Department of Civil Engineering, University of Delaware, Newark, DE 19716

effect of the simplification discussed. The second part of the paper details an investigation of directional spectral interaction. Specifically, we use the angular spectrum model of Kirby (1990) to determine whether detuned vector-sum interactions are as important in the wavefield as resonant (or near-resonant) colinear interactions.

## Finite Depth Evolution Model

Spectral models based on the Boussinesq equations (Peregrine (1967)) have existed for some time (Friedrich and Guza (1984); Liu, et.al. (1985)). They work well within their range of validity ( $kh \ll 1$ , where  $k$  is the wavenumber and  $h$  the water depth). However, the shoaling mechanism for these models in their lowest-order variants is Green's Law:

$$\frac{A}{A_0} = \left(\frac{h}{h_0}\right)^{\frac{1}{2}} \quad (1)$$

which overpredicts the shoaling of higher-frequency spectral components. Some dispersiveness has been added to the shoaling terms of Boussinesq-type models (e.g., the "dispersive shoaling model" of Friedrich and Guza (1984); Madsen, et.al. (1992)). This added dispersiveness is of at most  $O(kh)^2$ , and is thus only a small correction to the shoaling term.

## Theoretical Formulation

In this paper we seek a model which is valid for all orders of  $kh$ , and retain terms to  $O(\epsilon^2)$ , where  $\epsilon$  is the ratio of wave amplitude to water depth. The derivation follows the method of Bryant (1973, 1974). A similar model, but truncated to two components, was detailed by Keller (1988).

We begin from the boundary value problem:

Governing equation ( $-h < z < 0$ ):

$$\nabla^2 \phi = 0 \quad (2)$$

Combined free surface boundary condition (to  $O(\epsilon^2)$ ) at  $z = 0$ :

$$\phi_z = -\frac{1}{g} \left( \phi_{tt} + \frac{1}{2} (\nabla_h \phi)_t^2 + \frac{1}{2} (\phi_z)_t^2 - \frac{1}{2g} (\phi_t)_{zt}^2 + \nabla_h \cdot (\phi_t \nabla_h \phi) \right) \quad (3)$$

Bottom boundary condition at  $z = -h$ :

$$\phi_z = -\nabla_h h \cdot \nabla_h \phi \quad (4)$$

We then assume the solution for  $\phi$  in terms of a superposition of components:

$$\phi = \sum_{n=1} f_n(k_n, h, z) \bar{\phi}_n(x, y, k_n, \omega_n, t) \quad (5)$$

where the  $f_n$  are the depth dependencies for each mode:

$$f_n = \frac{\cosh k_n(h+z)}{\cosh k_n h} \tag{6}$$

and the  $k_n$  are found using the linear dispersion relation:

$$\omega_n^2 = g k_n \tanh k_n h \tag{7}$$

Following the method of Smith and Sprinks (1975), we obtain the following mild-slope equation modified by nonlinearity:

$$\begin{aligned} \ddot{\phi}_{tt} - \nabla_h \cdot ((CC_g)_n \nabla_h \ddot{\phi}_n) + \omega_n^2 \left(1 - \frac{C_{gn}}{C_n}\right) \ddot{\phi}_n = \\ \frac{1}{2} \left( \sum_l \sum_m \left[ \frac{\omega_l^2 + \omega_m^2}{g^2} (\ddot{\phi}_l \ddot{\phi}_{m,t})_t - \frac{\omega_l^2 \omega_m^2}{g^2} (\ddot{\phi}_l \ddot{\phi}_m)_t \right] \right. \\ \left. - \sum_l \sum_m \left[ (\nabla_h \ddot{\phi}_l \cdot \nabla_h \ddot{\phi}_m)_t + \nabla_h \cdot (\ddot{\phi}_l \nabla_h \ddot{\phi}_m) + \nabla_h \cdot (\ddot{\phi}_{m,t} \nabla_h \ddot{\phi}_l) \right] \right)_n \end{aligned} \tag{8}$$

where the  $l$ ,  $m$  and  $n$  are related according to three-wave interaction conditions. Introducing time periodicity and slow  $x$ -variation in amplitude:

$$\ddot{\phi} = \frac{-ig}{2\omega_n} A_n e^{i(\int k_n dx - n\omega t)} + \frac{ig}{2\omega_n} A_n^* e^{-i(\int k_n dx - n\omega t)} \tag{9}$$

yields an elliptic equation for the evolution of the complex amplitude  $A_n$ . Using the parabolic approximation:

$$((CC_g)_n A_{n,x})_x \ll 2i(kCC_g)_n A_{n,x} \tag{10}$$

and making use of a reference phase function (Kirby and Dalrymple (1983)) to redress the lack of phase dependence on  $y$ ,

$$A_n = a_n e^{(\int k_{n_o}(x) dx - \int k_n(x) dx)} \tag{11}$$

where  $k_{n_o}(x)$  is a  $y$ -averaged wavenumber, gives us:

$$\begin{aligned} 2i(kCC_g)_n a_{n,x} - 2(kCC_g)_n (k_{n_o} - k_n) a_n + i(kCC_g)_{n,x} a_n + ((CC_g)_n (a_n)_y)_y = \\ \frac{1}{4} \left( \sum_{l=1}^{n-1} R(\omega_n, \omega_{n-l}, -\omega_l, k_{n-l}, k_l) a_l a_{n-l} e^{i(\int k_{l_o}(x) + k_{n-l_o}(x) - k_{n_o}(x) dx)} + \right. \\ \left. 2 \sum_{l=1}^{N-n} R(\omega_n, \omega_{n+l}, \omega_l, k_l, k_{n+l}) a_l^* a_{n+l} e^{i(\int k_{n+l_o}(x) - k_{l_o}(x) - k_{n_o}(x) dx)} \right)_n \end{aligned} \tag{12}$$

where:

$$R(\omega_n, \omega_{n+l}, \omega_l, k_l, k_{n+l}) = \frac{g}{\omega_l \omega_{n+l}} (\omega_n^2 k_l k_{n+l} + (k_{n+l} - k_l)(\omega_{n+l} k_l + \omega_l k_{n+l}) \omega_n) - \frac{\omega_n^2}{g} (\omega_l^2 - \omega_l \omega_{n+l} + \omega_{n+l}^2) \quad (13)$$

and all wavenumbers are calculated from full linear theory. Preliminary testing of (12) has demonstrated that the interaction coefficients  $R$  require a large amount of computer time to calculate. Thus we simplified the model somewhat by taking the coefficients to the shallow-water limit (Ukai, et.al. (1990); Abreau, et.al. (1992); Mase and Kirby (1992)), and using the shallow water wavenumber as the reference phase function in (11). Thus we obtain:

$$2i(kCC_g)_n a_{nx} - 2(kCC_g)_n (k'_{no} - k_n) a_n + i(kCC_g)_{nx} a_n + ((CC_g)_n (a_n)_y)_y = \frac{3gn^2 k_1'^2}{4} \left( \sum_{l=1}^{n-1} a_l a_{n-l} + 2 \sum_{l=1}^{N-n} a_l^* a_{n+l} \right)_n \quad (14)$$

where  $k'_n = \frac{n\omega}{(gh)^{\frac{1}{2}}}$ .

### Comparison to Data

To see whether this simplification causes any loss of accuracy, one-dimensional versions of (12) and (14) were compared to flume data from Mase and Kirby (1992); the reader is referred to their paper for details on the experiment. Experimental results for Case 1 are compared to the two one-dimensional models at a depth  $h = 15cm$  (Figure 1), and it is apparent that, save for some slight deviation at the tail of the spectrum, both models compare equally well to the data. However, (14) required roughly 12 percent of the computing time of (12). This indicates that retaining full dispersion in the shoaling terms is the dominant improvement of these models over the Boussinesq equations, and that little is lost in simplifying the nonlinear coefficients as we have done here. The one-dimensional version of (14) is equivalent to that of Mase and Kirby (1992), except for a different dispersion term. Kaihatu and Kirby (1991) have shown that (12) fits experimental shoaling data better than the "consistent model" of Freilich and Guza (1984), particularly in the higher frequency ranges.

We use the data of Whalin (1971) to verify the two-dimensional model equation (14). This particular data set has been used on numerous occasions to evaluate numerical models (e.g. Liu, et.al. (1985); Rygg (1988); Madsen, et.al. (1992)). The experiment consisted of a long channel with bathymetry resembling a cylinder tilted along its longitudinal axis; the experimental layout is shown in Figure 2. Sinusoidal waves of one, two and three second periods were generated at three different amplitudes for each period; higher harmonics were allowed to grow from zero amplitude. The amplitudes of the first

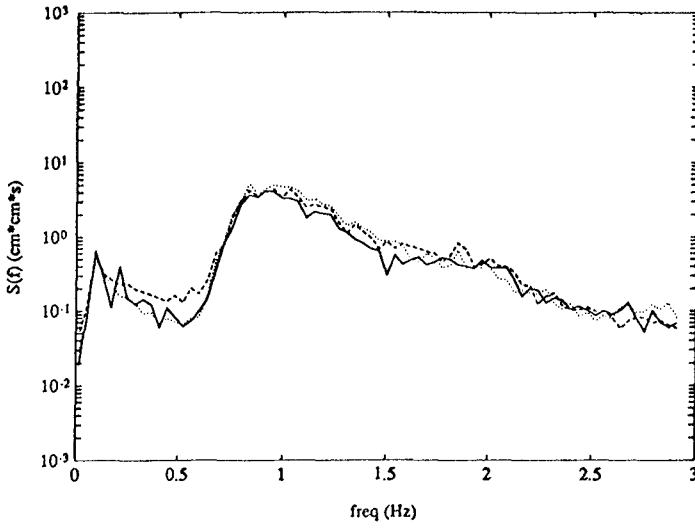


Figure 1: Comparison of Case 1 shoaling data of Mase and Kirby to equations (12) and (14) at  $h = 15\text{cm}$ . Data is solid line, equation (12) is dashed line and equation (14) is dotted line.

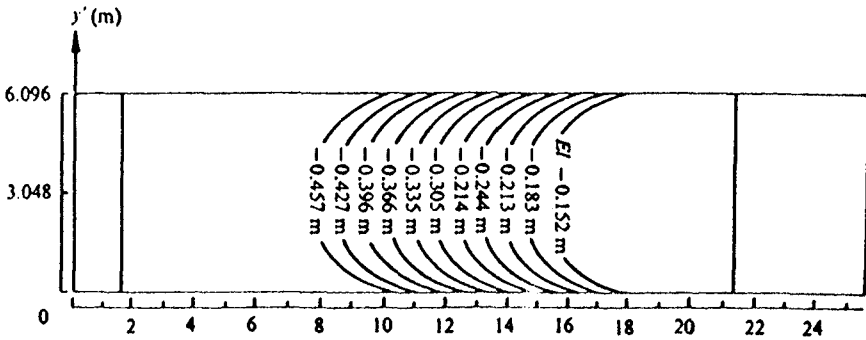


Figure 2: Topography of Whalin's (1971) experiment. From Liu, et.al. (1985)

three Fourier components were recorded along the centerline of the channel.

In this study we used the 3 second case for model-data comparison. This was done to facilitate a fair comparison between (14) and the Kadomstev-Petviashvili (KP) model of Liu, et.al. (1985). The KP model is essentially a lowest-order parabolic Boussinesq model, with a non-dispersive shoaling term and frequency dispersion retained up to  $O(kh)^2$ . Figures 3(a,b,c) show the Fourier amplitudes of the models compared to data along the centerline of the tank. For the most part the present model performs better than the KP model, especially in reproducing the higher harmonics. This is possibly due to the improved dispersion characteristic of the present model, where each mode is shoaled using full linear theory.

## Discussion

To conclude this section, it appears that the simplified fully-dispersive model (14) performs well in both combined refraction-diffraction and in pure shoaling. One drawback of the model is the lowest-order parabolic formulation. This not only restricts the model to small angle of incidence, also gives equal weight to all interactions no matter the direction of approach. This can be remedied by using the angular spectrum approach (Kirby (1990)), as explained in greater detail in the next section.

## Directional Spectra

This section of the paper discusses the role of directional spectral interaction in an evolving wave field. Specifically, we wish to address two recently-published viewpoints concerning whether detuned, vector-sum interactions play as large a role in the evolution of nearshore waves as near-resonant, colinear interactions. Vector-sum interactions place the energy exchanged between two spectral components approaching at different directions at the sum frequency and the vector-sum-wavenumber direction, while the colinear interactions only take place between components travelling in the same direction. This sort of interaction is seemingly stronger, since the two interacting components are very nearly in resonance. However, Freilich, Guza and Elgar (1990, hereafter referred to as FGE) maintain that vector-sum interactions may be as important as colinear interactions, especially when the interactions come from very energetic spectral peaks approaching at different directions. They used field data taken at Torrey Pines Beach, California, where directional arrays were placed at 10m and 4m water depth. Figure 4 is taken from their paper, and shows a contoured frequency-direction plot of waves at the 4m depth. Freilich, et.al. contended that the spectral peak located at  $(0.06Hz, -4^\circ$  from beach normal, marked "A"), interacted with the peak at  $(0.10Hz, +10^\circ$  from beach normal, marked "B"), to produce a peak at  $0.16Hz$  approaching at a direction that was within one degree of the vector-sum wavenumber direction (marked "C").

In direct opposition to this, Abreau, et.al. (1992) argue that only resonant colinear interactions are important. They formulated a collision integral to obtain a wave Boltzmann equation where only colinear interactions were allowed. They compared their results to the data of Freilich, et. al. (1990), and demonstrated qualitatively good agreement. Abreau, et.al. stated that the peak at  $f = 0.16Hz$  in the field data was not due to noncolinear interaction between highly energetic peaks as stated by FGE, but rather to near-resonant, colinear interactions between significantly less energetic

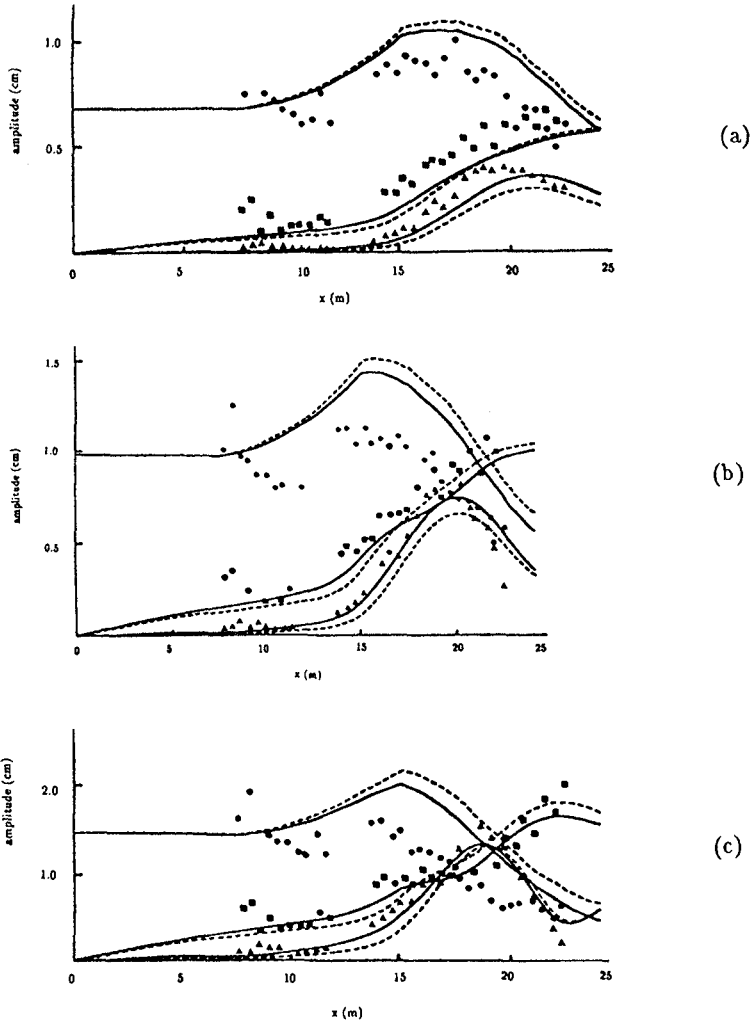


Figure 3: Comparison of equation (14) and KP model of Liu, et. al. (1985) to data of Whalin (1971) along centerline of tank. Solid line is equation (14), dashed line is KP model, and discrete points are data: dots are first harmonic Fourier amplitudes, squares are second harmonic amplitudes and triangles are third harmonic amplitudes. (a):  $a_0 = 0.68\text{cm}$ , (b):  $a_0 = 0.98\text{cm}$ , and (c):  $a_0 = 1.46\text{cm}$

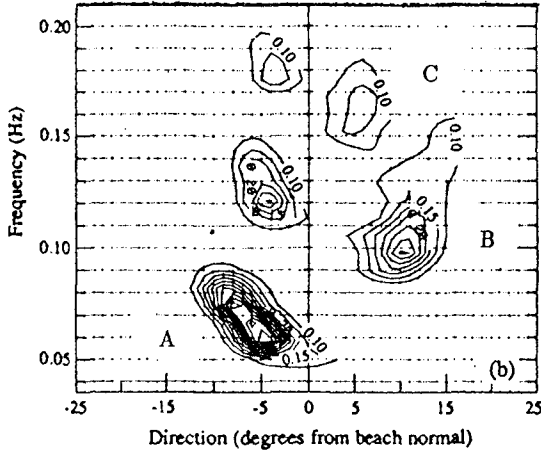


Figure 4: Data of Freilich, et.al. (1990) at 4m water depth, plotted as contours of  $S(f, \theta)$ . From Freilich, et.al. (1990).

components of the two directional spectra. They stated that this interaction occurred because of the directional overlap between the two spectra in deep water.

### Angular Spectrum Boussinesq Model

We wish to ascertain whether the vector-sum interactions are as important as the colinear interactions in wavefield evolution. The Boussinesq equation is used to serve as the diagnostic tool. We have three options concerning the form of the Boussinesq model used: a time-dependent model, a parabolic model and an angular spectrum model. The time-dependent formulation (e.g., Wu and Wu (1982)) treats both the resonant and non-resonant interactions in a non-explicit manner, making it difficult to discern between them. Parabolic models (e.g., Liu, et.al. (1985)) are not helpful in this situation since they treat nonlinear interactions with equal weight regardless of direction. Thus we use the angular spectrum model of Kirby (1990).

The angular spectrum approach consists of decomposing the governing equation into  $2M + 1$  components of the longshore wavenumber  $\lambda (= k \sin \theta)$  as well as  $N$  components of the frequency  $\omega$ . Thus the free surface elevation, for instance, can be written as:

$$\eta_n(x, y, t) = \sum_{n=1}^N \sum_{m=-M}^M A_n^m(x) e^{i(n \int k \tilde{\gamma}_n^m dx + m \lambda_0 y - n \omega t)} + c.c. \quad (15)$$

where :

$$\tilde{\gamma}_n^m = \left(1 - \left(\frac{m}{n}\right)^2 \left(\frac{\lambda_0}{k}\right)^2\right)^{1/2} \quad (16)$$

In contrast to the parabolic approach, where  $N$  coupled partial differential equations



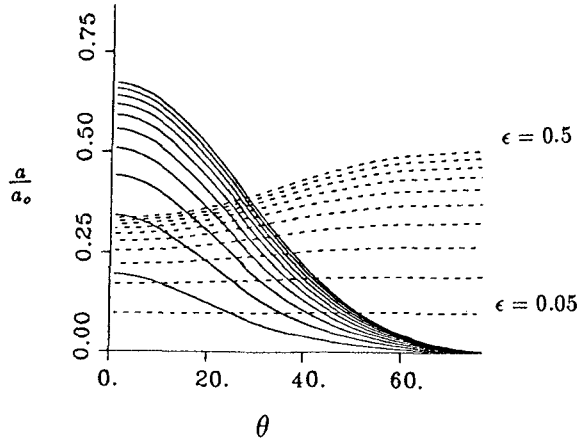


Figure 5: Steady-wave solution of angular spectrum Boussinesq model. Solid lines are amplitudes of vector-sum components, dashed lines are amplitudes of colinear second harmonics.

were solved, the angular spectrum approach computes  $N \times (2M + 1)$  ordinary differential equations. Further details of the derivation of the angular spectrum Boussinesq model can be found in Kirby (1990), along with the governing equations.

We have used the model in two preliminary investigations to determine the relative strength of the vector-sum interaction. For the case of a steady wave field, we generated permanent form solutions using five amplitudes: two primary harmonics of equal amplitude separated by an angle  $2\theta$ , two second harmonics travelling in the same direction as their respective primary harmonics, and one component at the sum frequency and moving at the vector-sum direction. Figure 5 shows a comparison of vector-sum amplitudes to those of the in-line second harmonic for permanent-form solutions and for several values of  $\theta$  and  $\epsilon$ . It is apparent that the vector-sum harmonic amplitude is larger than that of the in-line second harmonic for  $\theta$  up to  $25^\circ$ . This corresponds to a separation angle of  $50^\circ$  between primary components, much larger than the  $14^\circ$  separation between the spectral peaks in the field data of FGE. We also used the model to investigate unsteady wave evolution. We created an initial condition for the model using the same five components as the steady wave example, but the higher harmonics were given zero amplitude. This condition was then run through the model. Figure 6 shows a comparison of the primary amplitude to the vector-sum harmonic and the in-line second harmonic amplitudes. We see that the vector-sum amplitude dominates the in-line second harmonic for much of the domain. We also see evidence of recurrence, whereby the system evolves back into its original state. Recurrence has been shown to be unstable to broad-banded noise (Elgar, et.al. (1990)), so results of this analysis is only moderately applicable to events in the ocean. However, these two investigations do show that vector-sum interactions make non-negligible contributions to wave field evolution.

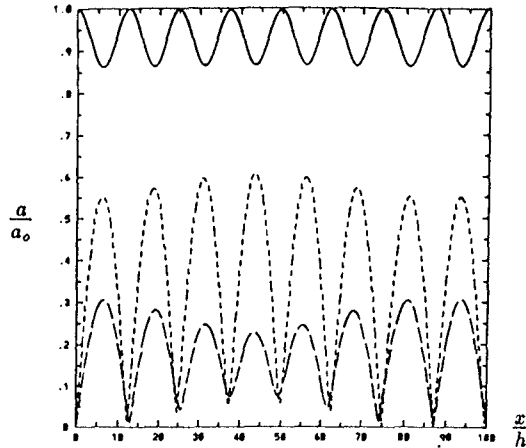


Figure 6: Recurrence test of angular spectrum Boussinesq model for  $\epsilon = 0.1$ ,  $(kh)^2 = 0.36$ ,  $\theta = 10^\circ$ . Solid line is amplitude of primary harmonic, short dashed line is amplitude of vector-sum component, and long-dashed line is amplitude of colinear second harmonic.

## Results

We at first considered using the model directly on the field data, after the appropriate re-mapping into  $(f, \lambda)$  space. We encountered some difficulty in doing so, primarily due to the random-phase assignments to the components of the field data. This attempt is continuing; however, its successful completion would not demonstrate how vector-sum interactions contribute to wave field evolution. This is because the two directional spectra of FGE overlap in direction, making it difficult to determine whether energy at the sum frequency originated from vector-sum interaction at the two peaks or from colinear interaction by directionally overlapped components.

We then decided to create an artificial wave field, one which would demonstrate the importance of vector-sum interactions for both non-overlapping and overlapping spectra but with fewer components. Two cases, both with the same total variance, were considered: one with two non-overlapping spectra, and one where two spectra overlap in direction. Figure 7a shows two spectra in  $(f, \lambda)$  space, each consisting of one frequency component and six longshore wavenumber components. The frequencies and peak  $\lambda$  chosen correspond to the frequencies and directions of the spectral peaks in FGE. This condition was run through (17) using the same bathymetry as FGE. The result at 4m water depth is shown in Figure 7b. The in-line second harmonic for the  $0.06Hz$  peak (marked "A"), the in-line third harmonic for the same peak (marked "B"), the in-line second harmonic for the  $0.10Hz$  peak (marked "C"), and the vector-sum peak (marked "D") and vector-difference peak (marked "E") have all been generated by nonlinear interaction. It is clear that the vector-sum peak is of the same order of magnitude as the in-line second harmonic of the  $0.06Hz$  spectral peak.

The second case is shown in Figure 8a. Two directional spectra with only one frequency component each are positioned at the same frequencies as the first case, but the number of  $\lambda$  components was increased to 20 to allow directional overlap. The result of the

calculation is shown in Figure 8b. Here we see very little energy at the vector-sum peak (marked "D"). Energy in this location was generated by detuned interactions between the spectral peaks, and by colinear interactions between the overlapping components. It is apparent that the colinear interactions between the less-energetic directionally overlapping components did not transfer as much energy to peak "D" as noncolinear detuned interactions between two more energetic spectral peaks did in the non-overlapping case. This shows that, for these cases, the vector-sum detuned interactions are responsible for a significant part of nonlinear energy transfer.

## Discussion

In this section we used the angular-spectrum Boussinesq model of Kirby (1990) to show that vector-sum detuned interactions play an important role in nonlinear energy transfer. This is shown in the two preliminary investigations of steady and unsteady wave evolution discussed herein. Actual input of the field data to the model has proved to be problematic, so we used two simplified wave fields. These simplified wave fields retain much of the character of the actual field data with fewer components. The results show that the vector-sum interactions can be as prominent in wavefield evolution as the colinear interactions. Model investigations using field data, however, are continuing.

It can be argued that the field data of FGE was actually in deeper water than is valid for lowest-order Boussinesq theory. Therefore, future work will focus on the use of a more dispersive Boussinesq-type model than that of Kirby (1990). This model will be similarly cast in the angular-spectrum format. Additional work will also include the use of a directional bispectrum, which is derivable from the model equation. This will allow us to investigate the strength of the different interactions.

## Acknowledgements

This work was supported by a National Defense Science and Engineering Graduate fellowship from the Office of Naval Research (JMK) and by University Research Initiative Grant No. DAAL-03-92-G0116 from the Army Research Office (JTK).

## References

- Abreau, M., Larraza, A., and Thornton, E., Nonlinear transformation of directional wave spectra in shallow water, *Journal of Geophysical Research*, vol. 97, No. C10, 15579-15589, 1992.
- Bryant, P.J., Periodic waves in shallow water, *Journal of Fluid Mechanics*, 59, 625-644, 1973.
- Bryant, P.J., Stability of periodic waves in shallow water, *Journal of Fluid Mechanics*, 66, 81-96, 1974.
- Elgar, S.L., Freilich, M.H., and Guza, R.T., Recurrence in truncated Boussinesq models for nonlinear waves in shallow water, *Journal of Geophysical Research*, vol. 95, No. C7, 11547-11556, 1990.
- Freilich, M.H., and Guza, R.T., Resonance effects on shoaling surface gravity waves, *Philosophical Transactions of the Royal Society of London*, A311, 1-41, 1984.

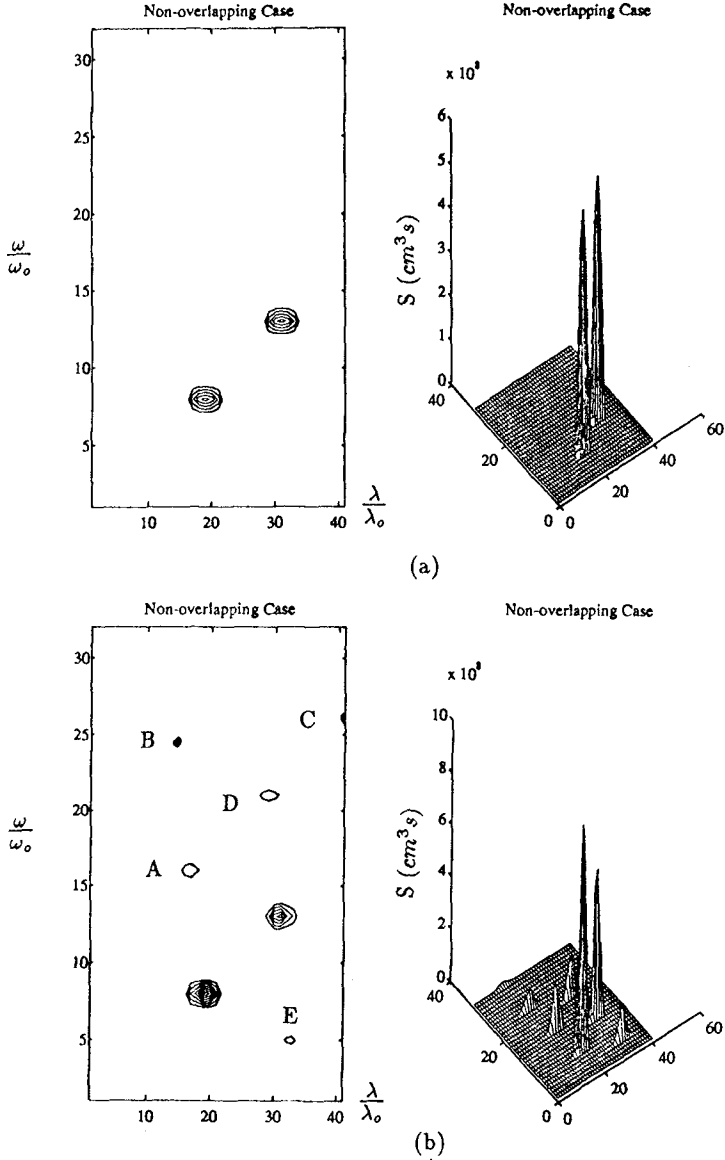


Figure 7: Simplified wave field - narrow directional spread. (a): Contour and surface plots of input condition in  $(f, \lambda)$  space at 10m water depth; (b): Contour and surface plots of result at 4m water depth.

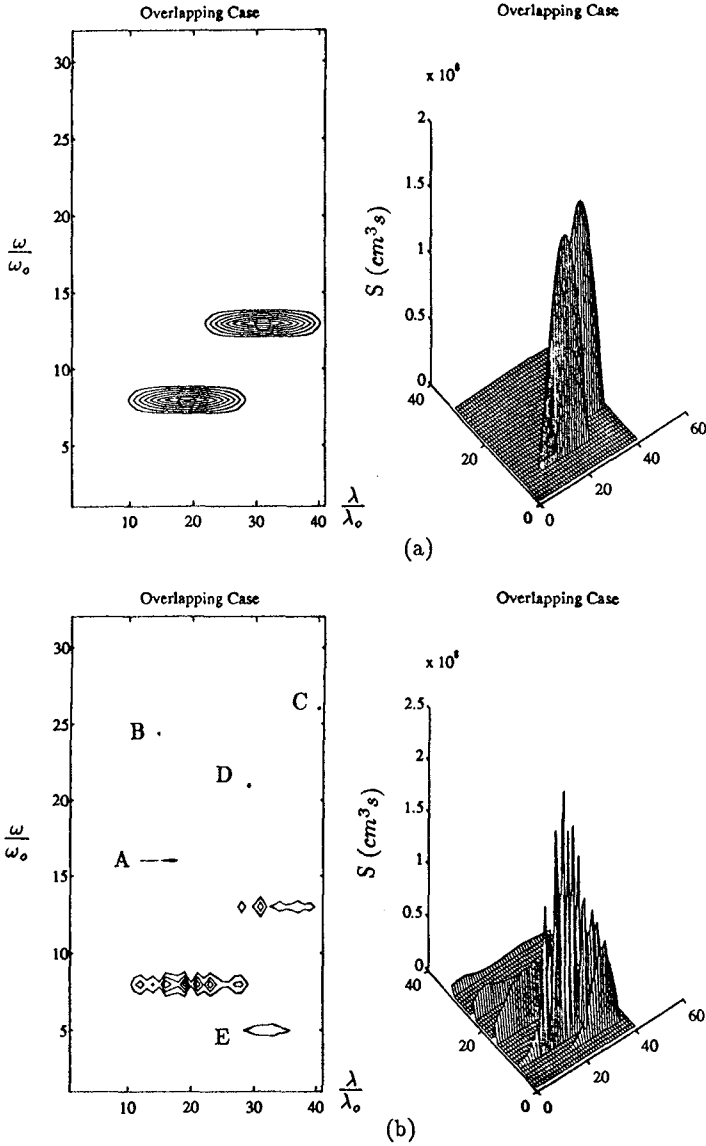


Figure 8: Simplified wave field - broad directional spread. (a): Contour and surface plots of input condition in  $(f, \lambda)$  space at 10m water depth; (b): Contour and surface plots of result at 4m water depth.

- Freilich, M.H., Guza, R.T., and Elgar, S.L., Observations of nonlinear effects in directional spectra of shoaling gravity waves, *Journal of Geophysical Research*, vol. 95, No. C6, 9645-9656, 1990.
- Keller, J.B., Resonantly interacting water waves, *Journal of Fluid Mechanics*, 191, 529-534, 1988.
- Kirby, J.T., Modelling shoaling directional wave spectra in shallow water, *Proc. 22nd International Conference on Coastal Engineering*, 109-121, 1990.
- Kirby, J.T. and Dalrymple, R.A., A parabolic equation method for the combined refraction-diffraction of Stokes waves by mildly-varying topography, *Journal of Fluid Mechanics*, 136, 453-466, 1983.
- Kaihatu, J.M., and Kirby, J.T., Frequency domain water wave evolution in finite depth, *EOS Transactions, American Geophysical Union*, Suppl. p. 253, 1991.
- Liu, P.L.-F., Yoon, S.B. and Kirby, J.T., Nonlinear refraction-diffraction of waves in shallow water, *Journal of Fluid Mechanics*, 153, 185-201, 1985.
- Madsen, P.A., Sorenson, O.R., and Schaeffer, H.A., Nonlinear transformation of irregular waves in shallow water, *Proc. 23rd International Conference on Coastal Engineering*, to appear, 1992.
- Mase, H., and Kirby, J.T., Hybrid frequency-domain KdV equation for random wave transformation, *Proc. 23rd International Conference on Coastal Engineering*, to appear, 1992.
- Peregrine, D.H., Long waves on a beach, *Journal of Fluid Mechanics*, 27, 815-827, 1967.
- Rygg, O.B., Nonlinear refraction-diffraction of surface waves in intermediate and shallow water, *Coastal Engineering*, 12, 191-121, 1988.
- Smith, R. and Sprinks, T., Scattering of surface waves by a conical island, *Journal of Fluid Mechanics*, 72, 373-384, 1975.
- Ukai, A., Yasuda, T., Ito, K., Spatial variation of wave group statistics and representative wave heights of swell, *Proc. 22nd International Conference on Coastal Engineering*, 812-825, 1990.
- Whalin, R.W., The limit of application of linear wave refraction theory in a convergence zone, *Research Report H-71-3*, U.S. Army Engineer Waterways Experiment Station, Vicksburg, MS, 1971.
- Wu, D.M., and Wu, T.Y., Three-dimensional nonlinear long waves due to moving surface pressure, *Proc. 14th Symposium on Naval Hydrodynamics*, 103-125, 1983.

## CHAPTER 27

### AN ADDITIONAL PARAMETER FOR THE ZERO CROSSING WAVE DEFINITION AND ITS PROBABILITY DISTRIBUTION

by A. Kimura<sup>1</sup> and T. Ohta<sup>2</sup>

#### ABSTRACT

In this paper, the distance from the mid point between a wave trough and a consecutive wave crest of a zero-crossing wave (a position of wave height bisection) to the still water level is proposed to be an important zero-crossing wave property. Its roles on certain physical properties of the zero-crossing waves are shown through experimental data in the first part of the paper. Its probability distribution is introduced, in the second part, from the combined probability distribution of the amplitudes of consecutive wave trough and crest of irregular waves. In the last part, the theoretical probability distribution for this property is verified with numerically simulated data for many types of wave spectra.

#### 1. INTRODUCTION

The zero-crossing method has been used to split the irregular wave profile into zero-crossing waves. The overall physical property of irregular waves is evaluated by connecting the relevant physical properties of individual waves and the probability of wave heights and periods. For example, the probability distribution of random wave forces (Kimura et al., 1983) is given as

$$p(f) df = \int_S p(H, T) dHdT \quad (1)$$

$p(H, T)$  is the combined distribution of wave height  $H$  and period  $T$ .  $S$  is the region in which

$$f \leq g(H, T) \leq f + df \quad (2)$$

where  $g(H, T)$  gives the wave force  $f$  of a periodic wave for the wave with  $H$  and  $T$ .

---

1 Prof., Dept. of Social Systems Eng., Faculty of Eng., Tottori Univ., 4-101 Koyama Minami, Tottori, Japan

2 Research Associate, Dept. of Social Systems Eng., Faculty of Eng., Tottori Univ., 4-101 Koyama Minami, Tottori, Japan

The physical properties of the zero-crossing wave are approximated usually by those of a periodic wave with the same wave height and period. The draw back of this method, some times, is that the two properties H and T are not sufficient to express the overall physical wave properties, since the measured and calculated probabilities have shown apparent differences in some physical properties. Therefore some studies have tried to apply supplemental wave properties such as slope of the fore-side face of waves in the examination of wave breaking (Holthuijsen and Herbers, 1986, for example). Among these, important parameters which may affect the physical properties of the zero-crossing wave are listed by the PIANC working group (list of sea state parameters; 1987). The parameter proposed in this study is not involved in the list but may exert an important effect on the waves in a shallow water region. That is a position of wave height bisection (mean position between the wave crest and trough of a zero-crossing wave).

Two waves in Fig.1 have the same wave height and period but different crest heights. In the ordinary definition, these two waves are recognized as having the same property. Figure 2(a) shows the wave height at the breaking point on 1/20 slope (Scyama et al., 1988). H,  $L_0$  and h are the wave height, deep water wave length and still water depth. Subscript b shows the value measured at the breaking points. The same data ( $H/H_b$ ) are plotted against  $h^*$  in Fig.2(b) instead of h, in which  $h^*$  is the distance from the bottom to the center between wave crest and trough (Fig.1). The scattering of data in Fig.2(a) reduces very much in this figure, therefore,  $h^*$  works more effectively as a water depth than h. This  $h^*$  is given by the sum of the still water depth h and the distance d from the still water level to the position of wave height bisection (PWHB; Fig.1). In the next section, the probability distribution for d is introduced theoretically and the result is verified through numerically simulated irregular waves.

2. The definition of d and its characteristics

2.1 Definition

The distance d from the mean water level to PWHB is given by

$$d = (\eta_1 - \eta_2) / 2 \tag{3}$$

in which  $\eta_1$  and  $\eta_2$  are the amplitudes of the wave trough and the consecutive wave crest, respectively. From a definition of the zero-crossing wave, we got  $-H/2 < d < H/2$ .

2.2 Characteristics of d

The numerically simulated values of d are shown first. The FFT method is used to calculate irregular wave profiles for the Wallops type wave spectrum which is given by

$$S(f) = (f/f_p)^{-m} \exp \left[ m/4 \left\{ 1 - (f/f_p)^{-4} \right\} \right] \tag{4}$$

where  $f_p$  is 1.0Hz and the interval of the calculated wave profile,  $\Delta t$  is 0.05s. in the numerical simulations. The 7 different values for the shape parameter m (4, 5, 6, 8, 10, 15, 20) in eq.(4) are used in the calculations. The zero-down-cross method is applied in the irregular wave definition. d is calculated applying eq.(3) for each wave. Figures 3 (a), (b) and (c) show the calculated relations between d/H and  $H/H_m$  ( $H_m$  is the mean wave height) for three values of m (5, 10, 20) in this order. While the spectrum is wide (m=5) d/H distributes up to its limit (-H/2, H/2) where  $H/H_m$



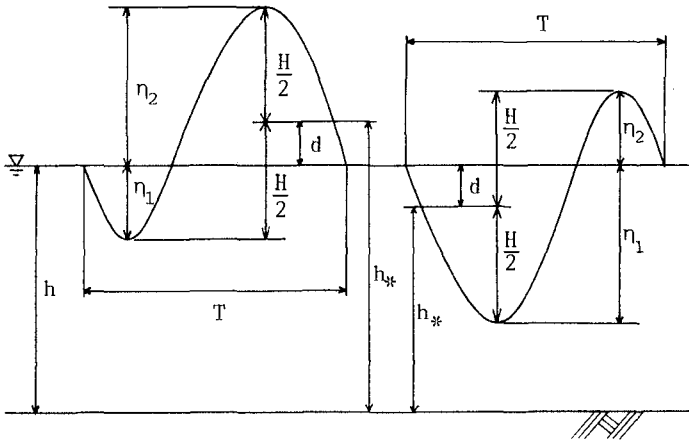


Fig. 1 Zero down cross waves with common H and T

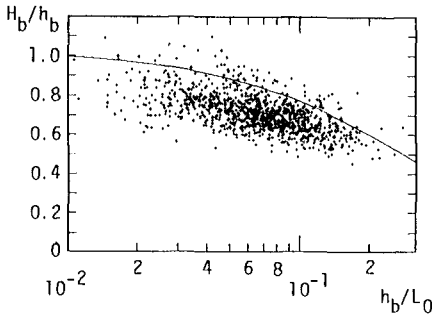


Fig. 2(a) Breaking limit

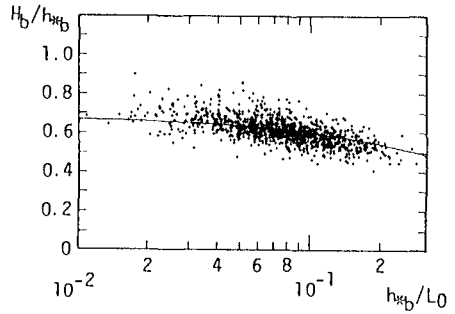


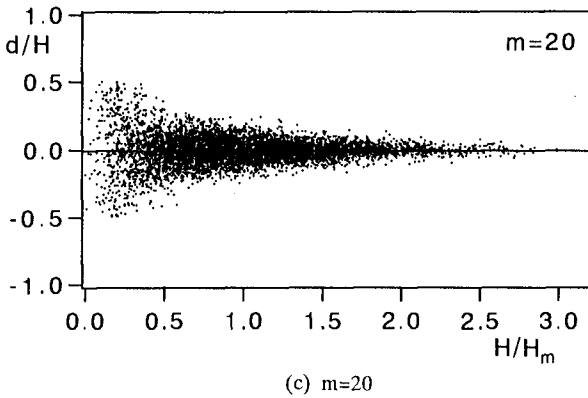
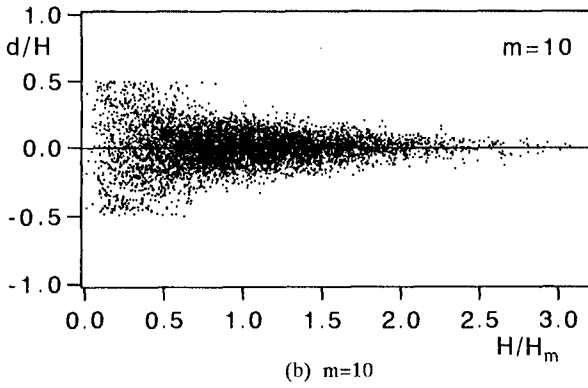
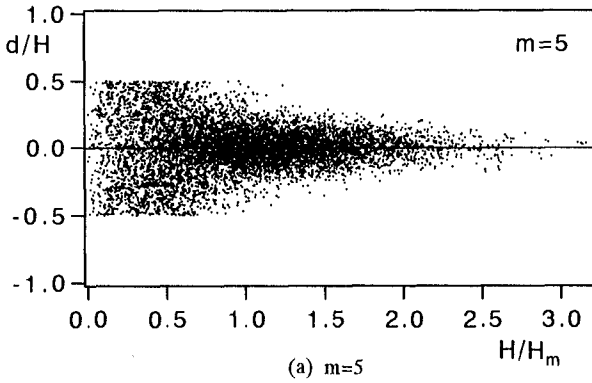
Fig. 2(b) Breaking limit (modified water depth)

<1.0. However the fluctuation decreases at the larger values of  $H/H_m$ . When  $m$  is large ((b),(c)) the fluctuation decreases except for the very small wave height region. From these, the larger the wave height or the narrower the wave spectrum, the more zero-down-cross waves tend to have symmetric profiles.

3. The probability distribution of  $d$

3.1 Two-dimensional Rayleigh distribution

As shown in eq.(3),  $d$  is half the difference between  $\eta_1$  and  $\eta_2$ . If these two values are independent (no correlation), the probability distribution for  $d$  is easily given as

Fig. 3 Distribution of  $d/H$

$$p(d) = \int p\left(\frac{h_1}{2} + d\right) p\left(\frac{h_1}{2}\right) dh_1 \quad (5)$$

where  $p(\cdot)$  is the probability distribution. The time interval between consecutive wave trough and crest is about half the mean wave period on the average. Two values on the wave profile with such a distance inevitably have a correlation. Therefore, this correlation property has to be taken into account when the probability distribution for  $d$  is considered. However the theoretical probability distribution of  $\eta_i$  ( $i=1,2$ ) has not yet been determined. The amplitude of the envelope for the wave profile at the same position of  $\eta_i$  has been used instead (Tayfun et al., 1989) with an error of order  $\nu$  in the noise theory, where  $\nu$  is given by

$$\nu = (m_0 m_2 / m_1^2 - 1)^2 \quad (6)$$

and

$$m_n = \int_0^\infty f^n S(f) df \quad (7)$$

in which  $S(f)$  is the power spectrum of waves.

The present study also used the above approximation. Since the theoretical probability distribution for envelopes is the Rayleigh distribution (Rice, 1945), the combined distribution for  $\eta_1$  and  $\eta_2$  is given by the 2-dimensional Rayleigh distribution (no non-linearity of the wave is considered in the present study). Expressing the amplitudes of wave envelopes at the position of  $\eta_1$  and  $\eta_2$  as  $A_1$  and  $A_2$  respectively, Eq.(3) is approximately expressed as,

$$d = (A_1 - A_2) / 2 \quad (8)$$

The probability distribution for the normalized amplitude  $\xi_i = A_i / A_m$  ( $i=1,2$ ), where  $A_m$  is a mean amplitude, is the Rayleigh distribution.

$$p(\xi_i) = \frac{\pi}{2} \xi_i \exp\left[-\frac{\pi \xi_i^2}{4}\right] \quad (9)$$

The combined probability distribution of the numerically simulated  $\xi_1$  and  $\xi_2$  agrees well with the 2-dimensional Rayleigh distribution,

$$p(\xi_1, \xi_2) = \frac{\pi^2 \xi_1 \xi_2}{4(1-\kappa^2)} \exp\left[-\frac{\pi^2(\xi_1^2 + \xi_2^2)}{4(1-\kappa^2)}\right] I_0\left[\frac{\pi \kappa \xi_1 \xi_2}{2(1-\kappa^2)}\right] \quad (10)$$

in which  $I_0$  is the 0-th order modified Bessel function of the first kind, and  $\kappa$  is the correlation parameter which is calculated as follows,

$$\kappa = \sqrt{(\rho^2 + \lambda^2)} / m_0 \quad (11)$$

where

$$\rho = \int_0^\infty S(f) \cos 2\pi(f - \bar{f}) \frac{1}{2} df$$

$$\lambda = \int_0^\infty S(f) \sin 2\pi(f - \bar{f}) \frac{1}{2} df$$

$$\bar{f} = m_1 / m_0 \tag{12}$$

$t/2$  is the time interval between  $A_1$  and  $A_2$ .  $T_m/2$  is used for this interval in this study where  $T_m$  is the mean wave period. This parameter is explained briefly in 3.3.

Figure 4 shows the comparison between numerically simulated combined frequency distributions of  $\xi_1$  and  $\xi_2$  and eq.(10) (solid line). The values for  $m$  in eq.(4) is (a) 5, (b) 10, and (c) 20 respectively. When  $m=5$  the spectrum is that for a fully developed sea condition. Excellent agreements are obtained for all cases.

3.2 The probability distribution of  $d$

Since  $A_1$  and  $A_2$  are amplitudes of the envelope at the consecutive wave trough  $\xi_1$  and crest  $\xi_2$ , the wave height is given approximately as,

$$H = A_1 + A_2 \tag{13}$$

Both sides of eq.(13) are divided by  $H_m (=2A_m, A_m$ ; mean amplitude of the envelope) to normalize,

$$\zeta = (\xi_1 + \xi_2) / 2 \tag{14}$$

in which  $\xi_i / 2 = A_i / H_m (i=1,2)$  and  $\zeta = H / H_m$

From eq.(14),

$$\xi_2 = 2\zeta - \xi_1 \tag{15}$$

Substituting eq.(15) into eq.(10), the combined distribution of  $\xi_1$  and  $\zeta$  is obtained.

$$p(\xi_1, \zeta) = \frac{\pi^2 \xi_1 (2\zeta - \xi_1)}{2(1 - \kappa^2)} \exp \left[ -\frac{\pi^2 \left\{ \xi_1^2 + (2\zeta - \xi_1)^2 \right\}}{4(1 - \kappa^2)} \right] I_0 \left[ \frac{\pi \kappa \xi_1 (2\zeta - \xi_1)}{2(1 - \kappa^2)} \right] \tag{16}$$

Integration of eq.(16) brings the probability distribution for  $\zeta$

$$p(\zeta) = \int_0^{2\zeta} p(\xi_1, \zeta) d\xi_1 \tag{17}$$

Since the analytical expression of this integration is difficult, a numerical calculation is used. The region of the integration is given from the definition of  $\xi_1, \xi_2 > 0$ . To normalize the region,

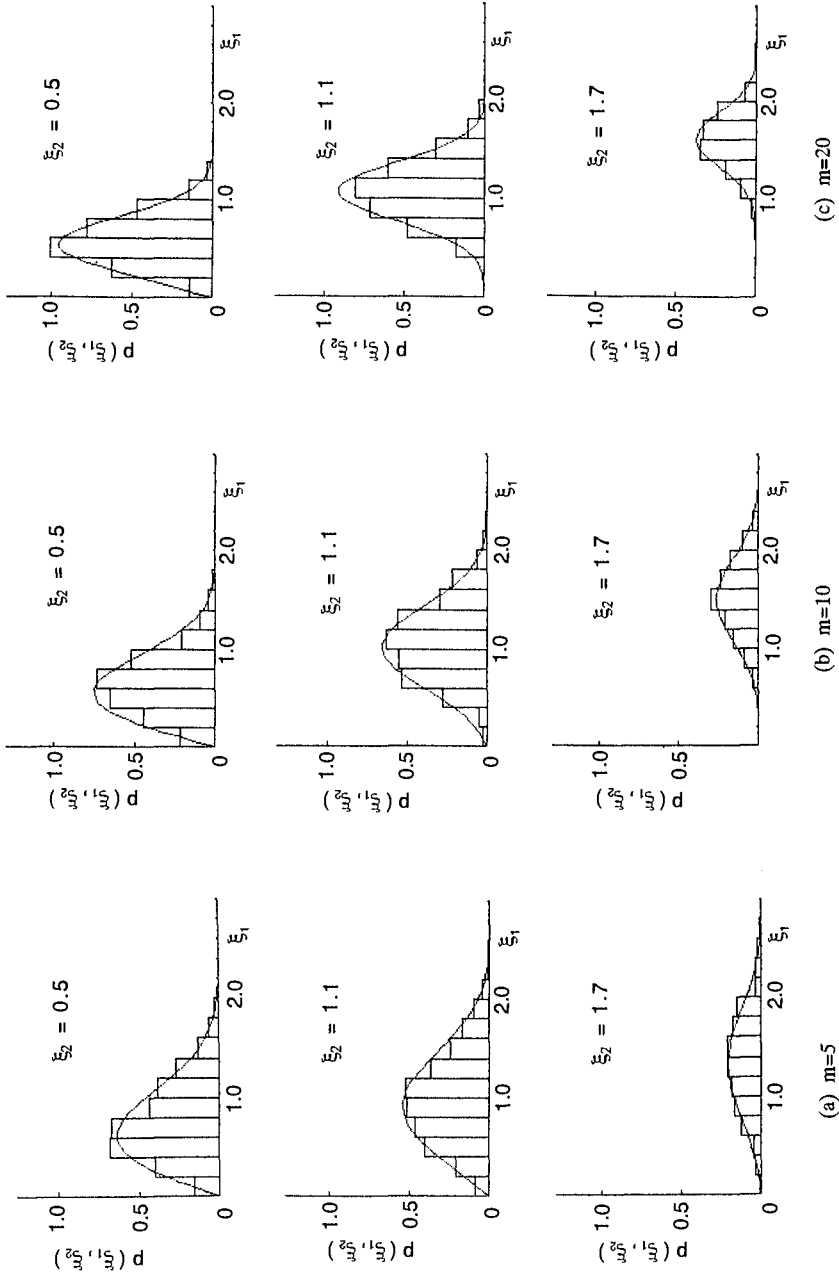


Fig. 4 Combined probability distribution of  $\xi_1$  and  $\xi_2$

eq.(8) is divided by  $H_m$ .

$$\delta = (\xi_1 - \xi_2) / 4 \tag{18}$$

Substitution of eq.(15) into eq.(18) brings

$$\delta = (\xi_1 - \zeta) / 2 \tag{19}$$

then

$$\xi_1 = 2\delta + \zeta \tag{20}$$

Substituting this relation in eq.(16), the combined distribution of  $\delta$  and  $\zeta$  is obtained.

$$p(\delta, \zeta) = \frac{\pi^2 (\zeta^2 - 4\delta^2)}{1 - \kappa^2} \exp\left[-\frac{\pi (\zeta^2 + 4\delta^2)}{2(1 - \kappa^2)}\right] I_0\left[\frac{\pi \kappa (\zeta^2 - 4\delta^2)}{2(1 - \kappa^2)}\right] \tag{21}$$

From the definition,

$$-H/2 < d < H/2 \tag{22}$$

we obtain

$$-\zeta/2 < d < \zeta/2 \tag{23}$$

Since  $\delta$  in eq.(21) changes the range following the change of  $\zeta$ , the new parameter which is given in the next equation is introduced.

$$\epsilon = \delta / \zeta \quad (=d/H) \tag{24}$$

$\epsilon$  takes the value only from -1/2 to 1/2 regardless of  $\zeta$ . Substitution of this parameter in eq.(21) we obtain,

$$p(\epsilon, \zeta) = \frac{\pi^2 \zeta^3 (1 - 4\epsilon^2)}{1 - \kappa^2} \exp\left[-\frac{\pi \zeta^2 (\zeta + 4\epsilon^2)}{2(1 - \kappa^2)}\right] I_0\left[\frac{\pi \kappa \zeta^2 (1 - 4\epsilon^2)}{2(1 - \kappa^2)}\right] \tag{25}$$

The conditional distribution of  $\epsilon$  for given  $\zeta$ , is calculated as

$$p(\epsilon | \zeta) = p(\epsilon, \zeta) / p(\zeta) \tag{26}$$

### 3.3 Time interval between $A_1$ and $A_2$

$\kappa$  which is calculated by eq.(11) plays a very important role in this theory. The representative frequency  $\bar{f}$  is usually given by eq.(12) and the time interval  $t/2$  between  $A_1$  and  $A_2$  is approximately given by the mean wave period. Two definitions for the mean wave period have been used. They are

$$\begin{aligned} T_{01} &= m_0 / m_1 \\ T_{02} &= \sqrt{m_0} / m_2 \end{aligned} \tag{27}$$

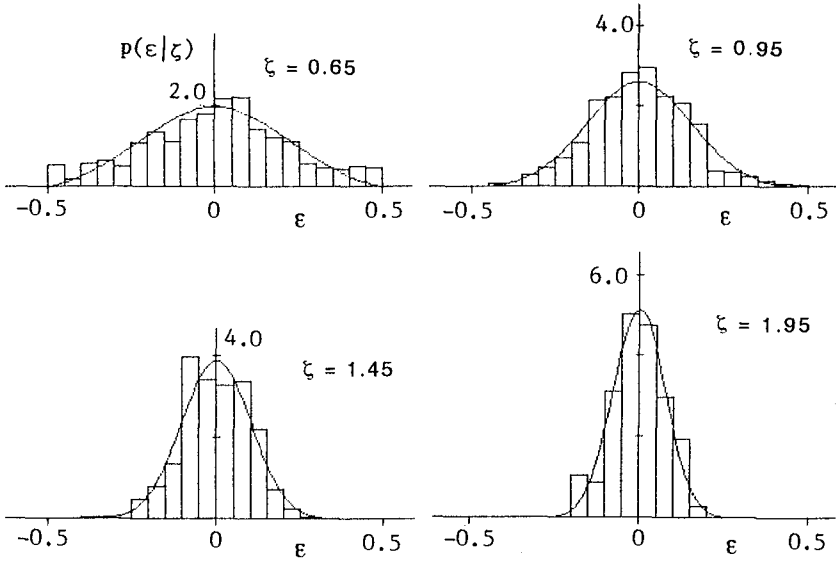


Fig. 5(a) Conditional probability distribution for  $\epsilon$  ( $m=5$ )

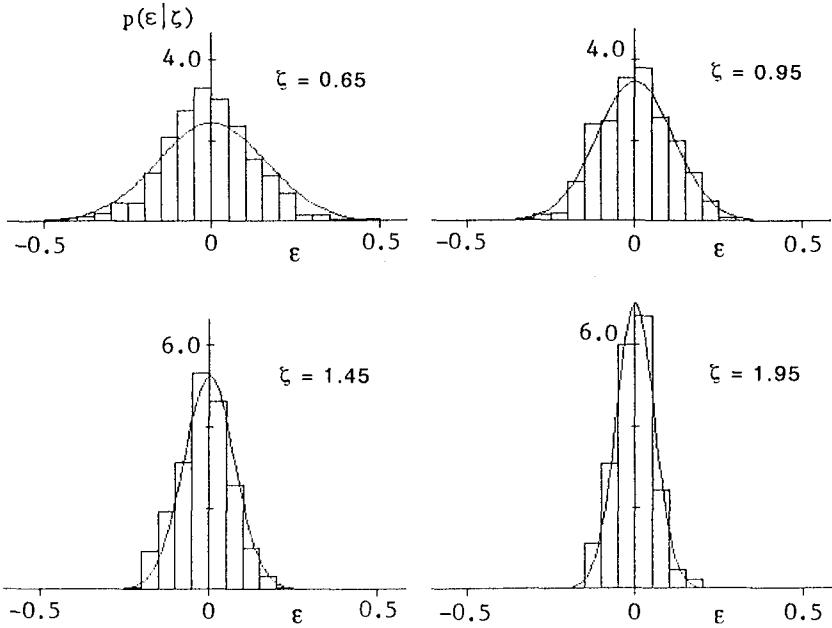


Fig. 5(b) Conditional probability distribution for  $\epsilon$  ( $m=10$ )

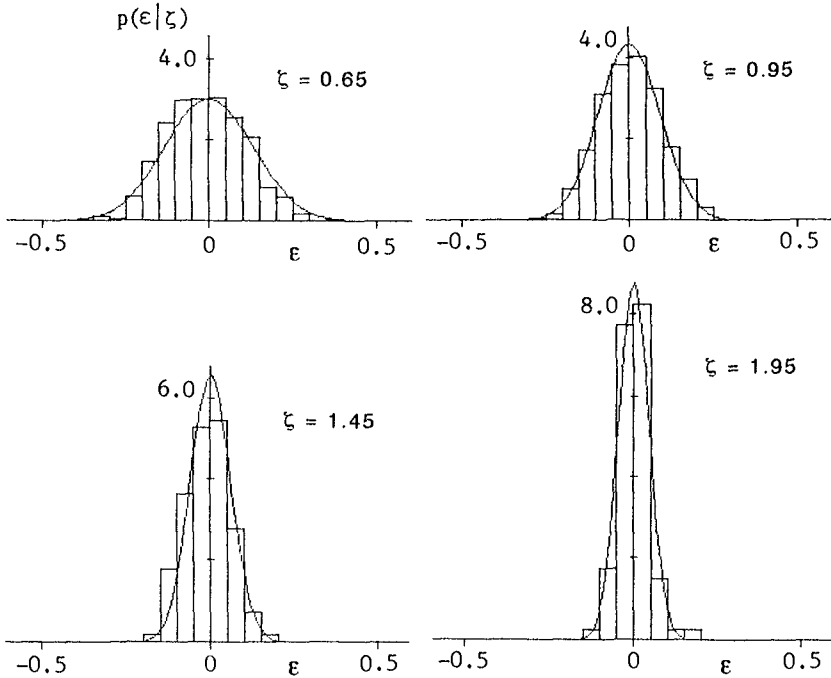


Fig. 5(c) Conditional probability distribution for  $\epsilon$  ( $m=20$ )

The numerical calculations with different values of  $m$  in eq.(4) show that  $T_{02}$  is always closer to the calculated mean zero-crossing wave period than  $T_{01}$ . Therefore  $T_{02}$  is used for  $T_m$  in this study.

4. Verification of the theoretical distribution

Figure 5 shows the comparison between  $p(\epsilon | \zeta)$  and the numerically simulated values of  $\epsilon$  for the several different wave spectra (a)  $m=5$ , (b)  $m=10$ , (c)  $m=20$ . The solid curves shows the theoretical distributions and the columns are the frequency distributions of the numerically simulated data of  $\epsilon$ . Calculated values of  $\epsilon$  which fall in the shown intervals of  $\zeta$  are sorted into ranks of width  $\Delta\epsilon=0.05$  from  $\epsilon=-0.5$  to  $0.5$ . The agreement between the theory and the simulated data are good in all cases except for the very small part of  $\zeta$ . This discrepancy in the region of small  $\zeta$  may be induced by the value of  $\kappa$  used in the calculation of eq.(12), since the time interval between the consecutive wave trough and crest for a small wave is smaller than the average value. However when  $\zeta$  is larger than  $0.6\sim 0.7$ , the theoretical distributions always show good agreements with the data. Fig. 6 shows the comparison between the theoretical standard deviation (solid line) for  $\epsilon$  which is given by

$$\sigma = \left\{ \overline{\epsilon^2} - (\overline{\epsilon})^2 \right\}^{1/2} \tag{28}$$



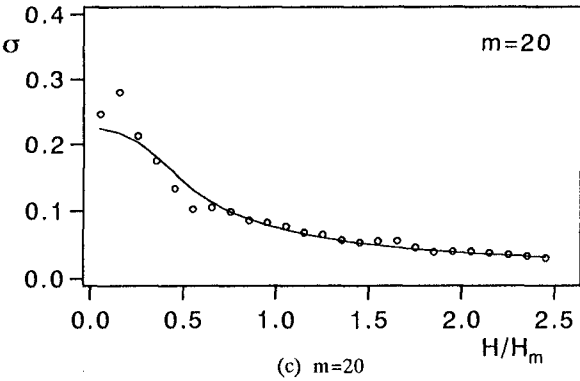
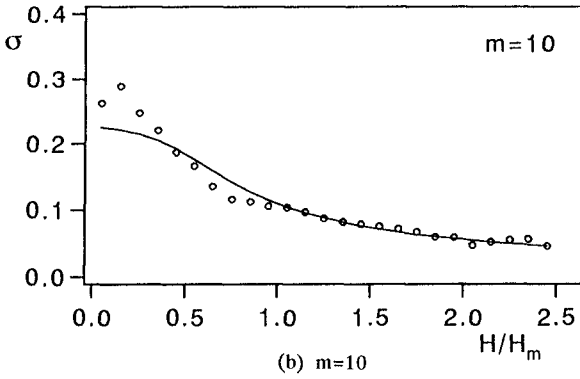
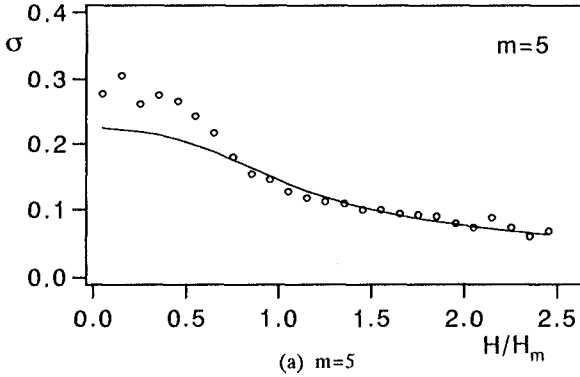


Fig. 6 Standard deviations of  $\epsilon$

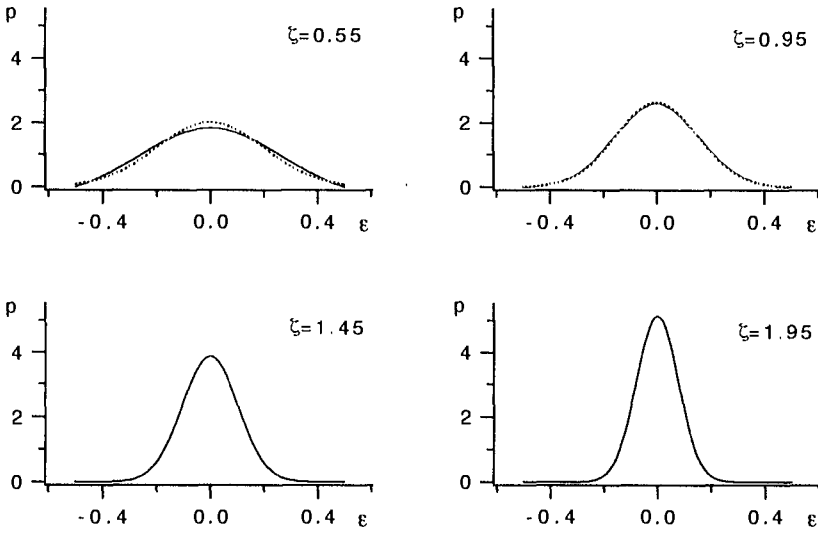


Fig. 7 Comparison between  $p(\epsilon|\zeta)$  and the normal distribution ( $m=5$ ) (solid line;  $p(\epsilon|\zeta)$ , dotted line; the normal distribution)

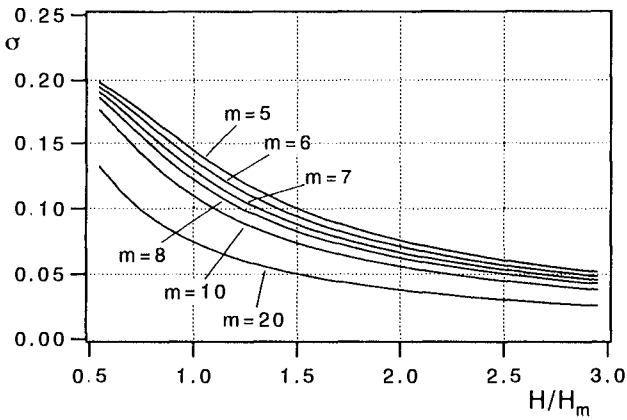


Fig. 8 Theoretical standard deviation for  $p(\epsilon|\zeta)$

where

$$\overline{\epsilon^2} = \int_{-1/2}^{1/2} \epsilon^2 p(\epsilon | \zeta) d\epsilon \quad (29)$$

$$\overline{\epsilon} = \int_{-1/2}^{1/2} \epsilon p(\epsilon | \zeta) d\epsilon$$

and the standard deviations of the numerically simulated data (white circle). Except for the smaller part than  $\zeta = 0.6 \sim 0.7$  their agreements are good. As can be observed in fig. 5, the theoretical distribution  $p(\epsilon | \zeta)$  has a very close form to the normal distribution. Fig.7 shows the comparisons between  $p(\epsilon | \zeta)$  (solid line) and the normal distribution (dotted line) of the zero mean and the standard deviation calculated from eq.(28). The probability distribution  $p(\epsilon | \zeta)$  used in the calculation is that for  $m=5$  (eq.12) in this case. The agreements between  $p(\epsilon | \zeta)$  and the normal distribution always agree well regardless of the spectrum width when the calculated value of the standard deviation by eq.(28) is used beside zero mean. Fig.8 shows the theoretical standard deviation for  $p(\epsilon | \zeta)$  for the several different spectra (eq.4).

## 5. Conclusion

Additional property for the zero crossing wave is proposed newly in this study. That is the distance from the mean water level to the mean position between the consecutive wave trough and crest. Its theoretical distribution is introduced and compared with the numerically simulated data. The theoretical distribution shows excellent agreement with the numerically simulated data regardless of the spectrum width. The theoretical distribution has a very close form to the normal distribution and can be approximated with that distribution, if the standard deviation shown in Fig.8 and the zero mean is applied.

## References

- Holthuijsen, L.H. and T.H.C. Herbers: Statistics of breaking waves observed as white caps in the open sea, *Journal of Physical Oceanography*, Vol.16, No.2, pp.290-297, 1986.
- Kimura, A. and A. Seyama: Statistical properties of displacements of fixed-type offshore structures, *Coastal Engineering in Japan*, Vol.26, pp.193-207, 1983.
- PIANC: List of sea state parameters, Proc. IAHR seminar, Maritime Hydraulics Section, pp.17-44, 1986.
- Rice, S. O. : Mathematical analysis of random noise, Selected papers on noise and stochastic process, N. Wax, ed., Dover, New York, N. Y. , pp.133-294, 1954)
- Seyama, A. and A. Kimura: The measured properties of irregular wave breaking and wave height change after breaking on the slope, Proc. 21st ICCE, pp.419-432, 1988.
- Tayfun, M. A. and J. M. Lo: Envelope, phase, and narrow-band models of sea waves, *Journal of Water way, Port, Coastal and Ocean Engineering*, ASCE, Vol.115, No. 5, pp.594-613, 1989.

## CHAPTER 28

### Time-Dependent Solutions of the Mild-Slope Wave Equation

James T. Kirby, Changhoon Lee <sup>1</sup> and Chris Rasmussen <sup>2</sup>

#### Abstract

Time dependent forms of the mild-slope wave equation are applied to the propagation of regular and irregular wave trains over variable bathymetry. The model equation of Smith and Sprinks is found to be a robust predictor of irregular waves, if the frequency spread for a single component calculation is not made too large. The model is extended to include forced, low-frequency components, and some preliminary results for bound and free long wave computation are shown.

#### Introduction

Based on the work of Smith and Sprinks (1975), the mild-slope wave equation for linear waves with a dominant carrier frequency  $\omega$  and small frequency spread may be written as

$$\tilde{\phi}_{tt} - \nabla_h \cdot (CC_g \nabla_h \tilde{\phi}) + (\omega^2 - k^2 CC_g) \tilde{\phi} = 0 \quad (1)$$

where  $\tilde{\phi}$  is the value of the velocity potential at the mean surface  $z = 0$ . This equation reduces to Berkhoff's (1972) elliptic equation when the time dependence of purely periodic waves is extracted.

In the past, many solutions of the elliptic problem for open coastal zones have been obtained using a parabolic approximation, which treats the forward-propagating portion of the wave field only. This step has often been taken because of its computational efficiency. The applicability of parabolic approximations is limited, however, to regions without complicated structural boundaries. In particular, complex entrance channels and interiors of harbors are not good candidates for this modelling technique, since the wave field is built up by a number of reflections and re-reflections of waves within the enclosed domains. For these applications, full solutions to the complete boundary-value problem must be found. Progress in obtaining efficient solutions using sophisticated pre-conditioning schemes has been made by Panchang et al (1991).

As an alternative to the elliptic equation approach, several authors (Ito and Tanimoto, 1972; Copeland, 1985; Madsen and Larsen, 1987) have obtained solutions to time-dependent, three-equation models using time-stepping techniques based on equations which are first-order in time. These models are essentially numerical analogs to the more familiar shallow water equations. The model solutions are computed until

<sup>1</sup>Center for Applied Coastal Research, Department of Civil Engineering, University of Delaware, Newark, DE 19716

<sup>2</sup>New York District, U.S. Army Corps of Engineers, New York, NY

the amplitude envelopes reach a steady state. The final solutions are only valid for purely periodic wave trains, since the three-equation models used are, for the most part, equivalent to the second order model

$$\tilde{\phi}_{tt} - \frac{C}{C_g} \nabla_h \cdot (CC_g \nabla_h \tilde{\phi}) = 0. \quad (2)$$

This model differs from the correct form (1), and is non-dispersive in the sense that modulations of the carrier wave train propagate at the wave phase speed, rather than at the group velocity, as would be required in a correct time-dependent model.

Since the application of time-stepping solutions to the mild-slope equation is a reasonably efficient line of approach, and since it is desirable to provide a model which is valid for unsteady wave trains, it would be advantageous to use a set of model equations which preserves the proper wave group behavior for non-periodic, narrow-banded wave trains. Such a model would be useful in computing effects such as second-order oscillations forced by wave groups.

In section 2, we derive the time-dependent mild-slope equations. In section 3, the dispersiveness of the resulting model is verified by studying wave group propagation over a flat bottom. In section 4 we consider the propagation of linear and weakly nonlinear waves over an elliptic shoal. Section 5 considers two-dimensional propagation of waves over an elliptic shoal using monochromatic and random waves. Finally, in section 6, we discuss the forcing of long wave components at difference frequencies due to non-resonant wave-wave interactions.

## Derivation of the time-dependent model equations

The model equations are derived here using Hamilton's variational principle. The Lagrangian for irrotational motion is given by

$$L = -\rho \int_{-h}^{\eta} [\phi_t + \frac{1}{2}(\nabla_h \phi)^2 + \frac{1}{2}(\phi_z)^2 + gz] dz \quad (3)$$

The  $z$  dependence is extracted from  $\phi(x, y, z, t)$  according to

$$\phi(x, y, z, t) = \tilde{\phi}(x, y, t) f(z) \quad (4)$$

where

$$f(z) = \frac{\cosh k(h+z)}{\cosh kh} \quad (5)$$

From the variational principle the change of the integral of the Lagrangian,  $L$ , over all time and space must be equal to zero:

$$\delta \int_t \int_y \int_x L(x, y, t, \phi, \nabla_h \phi, \phi_t, \eta) dx dy dt = 0 \quad (6)$$

Substituting (3) into (6) and retaining the terms to the second order in  $\phi$  and  $\eta$  gives

$$-\rho L = \eta \tilde{\phi}_t + \frac{1}{2} g \eta^2 + \frac{1}{2} \frac{CC_g}{g} (\nabla_h \tilde{\phi})^2 + \frac{1}{2} \frac{(\omega^2 - k^2 CC_g)}{g} (\tilde{\phi})^2 \quad (7)$$

Varying the Lagrangian  $L$  with respect to  $\tilde{\phi}$  and  $\eta$  gives

$$\eta_t = -\nabla_h \cdot \left( \frac{CC_g}{g} \nabla_h \tilde{\phi} \right) + \frac{(\omega^2 - k^2 CC_g)}{g} \tilde{\phi} \quad (8)$$

$$\tilde{\phi}_t = -g\eta \quad (9)$$

which are the time-dependent mild-slope equations. The surface displacement may be eliminated from (8) and (9) in order to obtain the model equation (1). In this study, we have employed a number of numerical methods fairly interchangeably, including a second-order, centered-time centered-space finite difference approximation for (1), and a fourth-order accurate Adams-Bashforth-Moulton method for (8) and (9). (Use of this latter method was motivated by a parallel effort for the Boussinesq equations, which will be reported separately.)

As in Madsen and Larsen (1987), it is convenient to remove the fast time behavior from the dependent variables by means of the transformation

$$\eta, \tilde{\phi} = (\hat{\eta}, \hat{\phi})e^{-i\omega t} \quad (10)$$

where  $\omega$  is the frequency used to evaluate the model coefficients. The resulting model equations are

$$\hat{\eta}_t = i\omega\hat{\eta} - \nabla_h \cdot \left( \frac{CC_g}{g} \nabla_h \hat{\phi} \right) + \frac{(\omega^2 - k^2 CC_g)}{g} \hat{\phi} \quad (11)$$

$$\hat{\phi}_t = i\omega\hat{\phi} - g\hat{\eta} \quad (12)$$

instead of (8) and (9), and

$$\hat{\phi}_{tt} - 2i\omega\hat{\phi}_t - \nabla_h \cdot (CC_g \nabla_h \hat{\phi}) - k^2 CC_g \hat{\phi} = 0 \quad (13)$$

instead of (1). The same set of numerical schemes are also used for the revised model.

## Wave group propagation

The basic ability of the model to propagate dispersive linear waves is tested by examining wave group propagation over constant depth. Two numerical experiments were performed. An initial wavelength of  $10m$  was specified, with shallow and deep water depths of  $0.25m$  and  $9m$ , respectively. The initial conditions are  $\eta$  and  $\tilde{\phi} = 0$ . A narrow-banded groupy wavetrain is generated at the boundary according to

$$\tilde{\phi}_x = u_0 \sin(\omega t) \sin\left(\frac{\omega}{20}t\right); \quad t \geq 0 \quad (14)$$

The results shown in figure 1 are water surface elevations plotted at a sequence of twenty time levels spaced one wave period apart. These results were obtained using the Euler Predictor-Corrector method with second-order accurate finite differences (Kirby and Rasmussen, 1991). Two lines are shown on each graph; one following the maximum amplitude of a specific wave group, and the other following a zero crossing of a specific wave. Visually, it appears that in shallow water  $C_g \approx C$ , and in deep water  $C_g \approx C/2$ , which shows the validity of the models to predict wave group velocity. Examination of the wave records and computed envelopes using cross-correlation techniques shows that the phase and group velocities are accurately predicted to within 1% for the differencing resolutions used here.

## Berkhoff, Booij and Radder shoal experiment

As an example of the application of the models in two-dimensions, we study the focussing of waves by a shoal, using the geometry and experimental parameters given in Berkhoff et al. (1982). It is known from parabolic model computations (Kirby and Dalrymple,

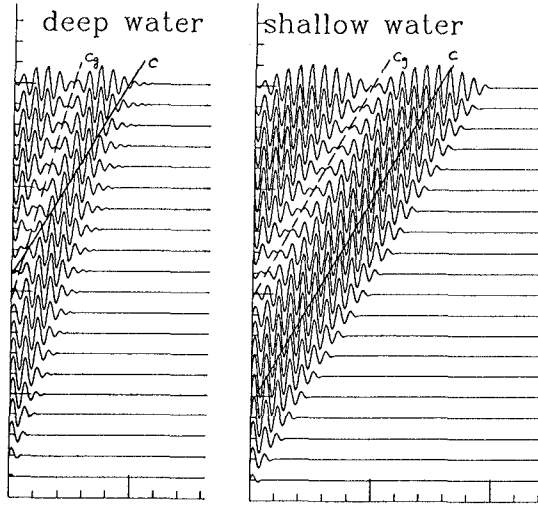


Figure 1: Propagation of wave groups in deep and shallow water.

1984) that the waves in this example are significantly affected by wave nonlinearity. Following the appendix in Kirby and Dalrymple (1984), we provide a heuristic extension to the mild-slope equation that is appropriate only for progressive Stokes waves. The resulting modification to (8) is given by

$$\eta_t = -\nabla_h \cdot \left( \frac{CC_g}{g} \nabla_h \tilde{\phi} \right) + \frac{(\omega^2 - k^2 CC_g + \omega C_g K' |\eta|^2)}{g} \tilde{\phi} \tag{15}$$

where

$$K' = \frac{k^3 C \cosh 4kh + 8 - 2 \tanh^2 kh}{8 \sinh^4 kh} \tag{16}$$

We apply both the linear and nonlinear model equations to the shoal described by Berkhoff et al. (1982). The data on wave amplitude was obtained over the entire vicinity of a refractive focus. The Ursell parameter remains of a reasonably small size over the entire domain of interest, thus indicating that Stokes theory should be a valid representation of the experiment.

In the model test, normally incident waves are generated at a period of 1.0s at the deep end of the wave tank, and are dissipated by a breaking process on a gravel beach at the shallow end. At sections 1 through 8 (see Berkhoff et al) there are arrays of resistance type wave gages spaced 0.5m apart which record time series of water surface elevations.

In order to dissipate wave energy at downwave boundaries, we presently use a wave damping layer at the downwave boundary. Equation (9) is modified to

$$\tilde{\phi}_t = -g\eta - w\tilde{\phi} \tag{17}$$

where

$$w = \begin{cases} 0, & x \leq x_{sponge} \\ \omega \left( \frac{e^{F^n} - 1}{e - 1} \right), & x \geq x_{sponge} \end{cases} \tag{18}$$

$$F = \frac{x - x_{sponge}}{x_{max} - x_{sponge}}, \quad (19)$$

and the sponge length  $x_{sponge}$  is specified as 2.5 times the initial wave length.

Following a method of line approach, the model equations (8) and (17) (linear), or (15) and (17) (nonlinear) are solved using the A-B-M predictor-corrector method. The grid sizes are  $\Delta x = \Delta y = 0.25m$  and  $\Delta t = 1/40s$ . Input wave period is 1s. We run the models until  $t = 80s$  and compute average wave heights between  $t = 70s$  and  $t = 80s$ , after the waves reach steady state.

Referring to figure 2, where model results are compared to measured data along transects 1 through 8, we see that the linear model tends to overpredict maximum amplitudes in the vicinity of focused waves, where wave steepness may become large and nonlinear effects become important. In these regions the nonlinear models give better results. The nonlinear model results appear to contain some spurious amplitude modulations. These are not a manifestation of instability, and the effect may be suppressed by a suitable lagging of the nonlinear term in the numerical scheme.

## Vincent and Briggs shoal experiment

A further study of monochromatic and random wave propagation over a shoal has been performed by Vincent and Briggs (1989). These tests are used here as a validation of the present numerical scheme as a model for irregular wave propagation.

For a random wave train, the water surface elevation may be written as

$$\eta(x, y, t) = \sum_{l=1}^L \sum_{m=1}^M A_{lm} \cos\{k_l \cos \theta_m x + k_l \sin \theta_m y - 2\pi f_l t + \psi_{lm}\} \quad (20)$$

where  $A_{lm}$  is wave amplitude;  $f_l$  is wave frequency;  $\theta_m$  is wave direction; and  $\psi_{lm}$  is random phase independent of frequency and direction. Instead of using a discrete set of wave angles, we use here a discretization of the longshore wavenumber spectrum. The longshore wavenumber  $\lambda_m$  is defined as

$$\lambda_m = k_l \sin \theta_m \quad (21)$$

which determines the wave direction  $\theta_m$  at each frequency. At the upwave boundary ( $x = 0$ ), the water surface elevation is given by

$$\eta(y, t) = \sum_{l=1}^L \sum_{m=1}^M A_{lm} \cos\{\lambda_m y - 2\pi f_l t + \psi_{lm}\} \quad (22)$$

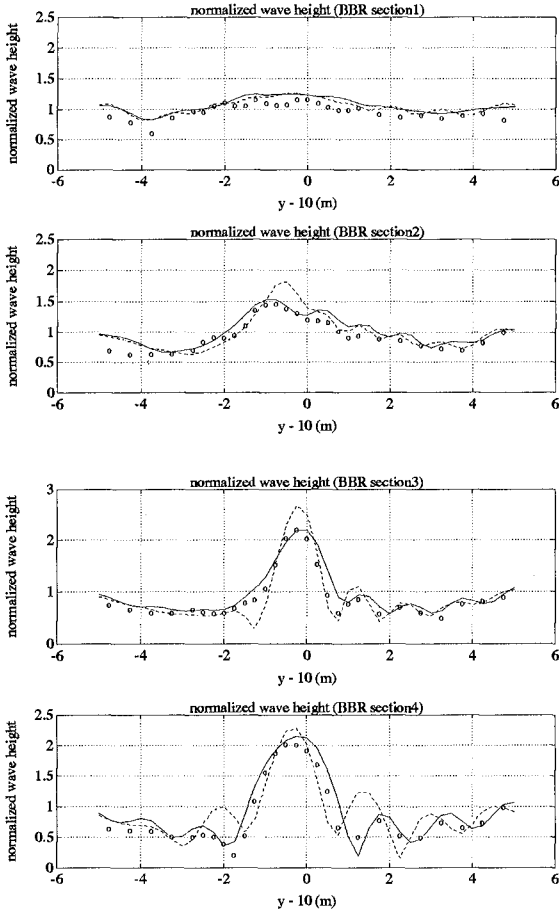
For given frequency  $f_l$  and longshore wavenumber  $\lambda_m$ , we get the amplitude of the water surface elevation

$$A_{lm} = \sqrt{2S_l(f)\Delta f \frac{S_m(\lambda)}{2\pi} \Delta \lambda} \quad (23)$$

where  $S_l(f)$  is the spectral density dependent on the frequency  $f$  and  $S_m(\lambda)$  is the directional spreading function dependent on the longshore wavenumber  $\lambda$ . We can get  $S_m(\lambda)$  from  $D_m(\theta)$  (which is the spreading function dependent on the direction  $\theta$ ) by the condition

$$\int_{-\frac{\pi}{2}}^{\frac{\pi}{2}} D(\theta) d\theta = \int_{-k}^k \frac{S(\lambda)}{2\pi} d\lambda = 1, \quad (24)$$





caption on following page

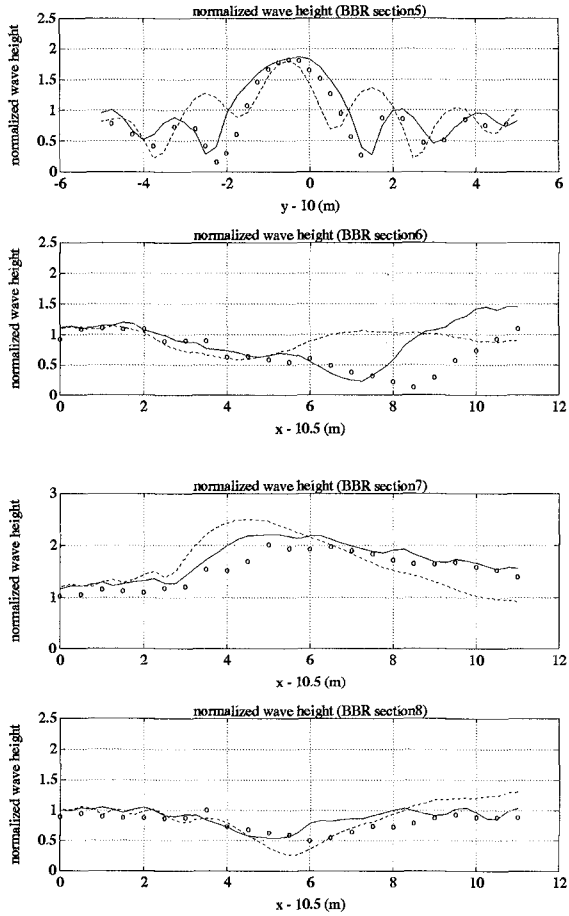


Figure 2: Comparison among linear model (dashed lines), nonlinear model (solid lines), and experimental data of Berkhoff et al. (1982)

and so,

$$\frac{S(\lambda)}{2\pi} = D(\theta) \frac{d\theta}{d\lambda} = \frac{D(\theta)}{k \cos \theta} \quad (25)$$

The  $x$ -component of fluid velocity at  $x, z = 0$  can be obtained from the velocity potential and is given by

$$\tilde{\phi}_x = \sum_{l=1}^L \sum_{m=1}^M B_{lm} \cos\{\lambda_m y - 2\pi f_l t + \psi_{lm}\} \quad (26)$$

where the amplitude  $B_{lm}$  is given by

$$B_{lm} = A_{lm} \frac{g \sqrt{k_l^2 - \lambda_m^2}}{2\pi f_l} \quad (27)$$

When the spectral density  $S(f)$  and the directional spreading function  $D(\theta)$  are given, we can get the amplitude of the wave velocity  $B_{lm}$ . Using a 2-dimensional inverse FFT from the frequency and longshore wavenumber domain to time and  $y$  space domain, we can generate the velocity  $\tilde{\phi}_x$ .

Since the model equation (1) is not valid for an arbitrarily large range of frequencies, we proceed by separating the whole spectrum into several bands. In each frequency band, we then construct a wavemaker or offshore boundary condition using the spectral information falling within that band. The time-dependent mild slope equation is then solved for the narrow-banded irregular sea lying within each frequency band. The final solution is obtained by adding the different bands.

Following Vincent and Briggs (1989), we use the TMA spectrum as the target frequency spectrum and a wrapped normal function as the directional spreading function. The TMA spectrum is given by

$$S(f) = \alpha g^2 (2\pi)^{-4} f^{-5} \exp\{-1.25(\frac{f_p}{f})^4 + (\ln \gamma) \exp[-\frac{(f - f_p)^2}{2\sigma^2 f_p^2}]\} \phi(f, h) \quad (28)$$

$S(f)$  depends on the parameters  $\alpha$  (Phillip's constant),  $f_p$  (peak frequency)  $\gamma$  (peak enhancement factor) and  $\sigma$  (shape parameter). The factor  $\phi(f, h)$  incorporates the effect of the depth  $h$  and may be approximated by

$$\phi = \begin{cases} 0.5\omega_h^2, & \omega_h < 1 \\ 1 - 0.5(2 - \omega_h)^2, & 1 \leq \omega_h \leq 2 \\ 1, & \omega_h > 2 \end{cases} \quad (29)$$

where  $\omega_h = 2\pi f(h/g)^{1/2}$ . The parameter  $\gamma$  is assigned values of 2 (broad frequency) and 20 (narrow frequency). For the cases studied here,  $\gamma$  was assigned a value of 20. The directional spreading function  $D(\theta)$  is obtained by assigning the values of either  $10^\circ$  (narrow spreading) or  $30^\circ$  (broad spreading) to the spreading parameter  $\sigma_0$ :

$$D(\theta) = \frac{1}{2\pi} + \frac{1}{\pi} \sum_{n=1}^N \exp[-\frac{(n\sigma_0)^2}{2}] \cos n(\theta - \theta_0) \quad (30)$$

where  $\theta_0$  = mean wave direction ( $= 0^\circ$ ) and  $N$  = number of terms in the series ( $= 20$ ).

Vincent and Briggs (1989) present a number of cases with a combination of monochromatic, narrow-banded or broad-banded frequency spectra and unidirectional, narrow-banded or broad-banded directional spreads. Here, we show results for three typical

cases: a monochromatic unidirectional sea (M2), a sea with narrow frequency and narrow directional spreading (N4), and a sea with narrow frequency and broad directional spreading (B4). All three cases involve non-breaking waves. Wave period (M2) and peak period (N4, B4) are 1.30s. Wave height (M2) and rms wave height (N4, B4) are 2.54cm. Phillip's  $\alpha$  is taken to be 0.00047.

We separate the whole frequency spectrum into five components with equal band widths. The five components of the frequency spectra cover 95 percent of the total spectral density, and, using the grid spacings chosen below, the ratio of minimum wavelength to spatial grid size is 4.54. We use a weighted average of the frequencies in each frequency band to determine the representative frequency used to compute the model coefficients for each band. The band width is 0.267 Hz (see figure 3). The grid size is  $\Delta x = \Delta y = 0.1905m$  and time step is  $\Delta t = 1.3/80s$ . We compute until  $t = 260s$ . Variances of water surface elevation,  $m_0$  are computed between  $t = 65s$  and  $t = 260s$  and, by the assumption of the Rayleigh distribution of the wave height, significant wave heights are computed according to

$$H_s = 4\sqrt{m_0} \quad (31)$$

In figures 4-6, the water surface elevations in the whole spatial domain at  $t = 260s$  are shown for cases M2, N4, and B4. The figure for Case M2 shows that the waves are long-crested and symmetric along the line crossing the center of the shoal parallel to  $x$  axis. After the waves pass the shoal they become short-crested because of refractive focusing. When we compare the cases with directional spreading (N4 and B4) we clearly see that the wave field with broad directional spreading (B4) is more short-crested than the wave field with narrow directional spreading (N4).

In figure 7, the computed normalized wave heights along the section 4 are compared with measured data for cases M2, N4, and B4. For case M2, the normalized wave height near the centerline is greater than 2, which shows the considerable effects of refractive focusing over the shoal. For case N4, the computed results show underestimation near the centerline and overestimation away from the centerline. For case B4, the computed results show overestimation all along the section. The model results and data indicate that increasing directional spreading leads to much less spatial wave height variation induced by localized topographic irregularities. This result is seen in all spectral wave studies, and is a manifestation of the fact that the local minimums and maximums in the diffraction pattern for each spectral component overlap and experience mostly destructive interference.

Roughly, all three cases show that the model yields reasonably accurate results compared with the measured data. It is found that for directionally broad spreading case (B4) the refractive focussing effects are not noticeable behind the shoal.

## Forced long waves

The forcing of long waves at difference frequencies is of particular interest in coastal design due to the influence of long waves in low frequency harbor seicheing and forces on moored ships. Kirby (1983) extended the linear mild-slope equation to include forced low-frequency components, using the Stokes expansion to second order in the Lagrangian. The model for the additional low-frequency components is given by forced long wave equations, which for variable depth are given by

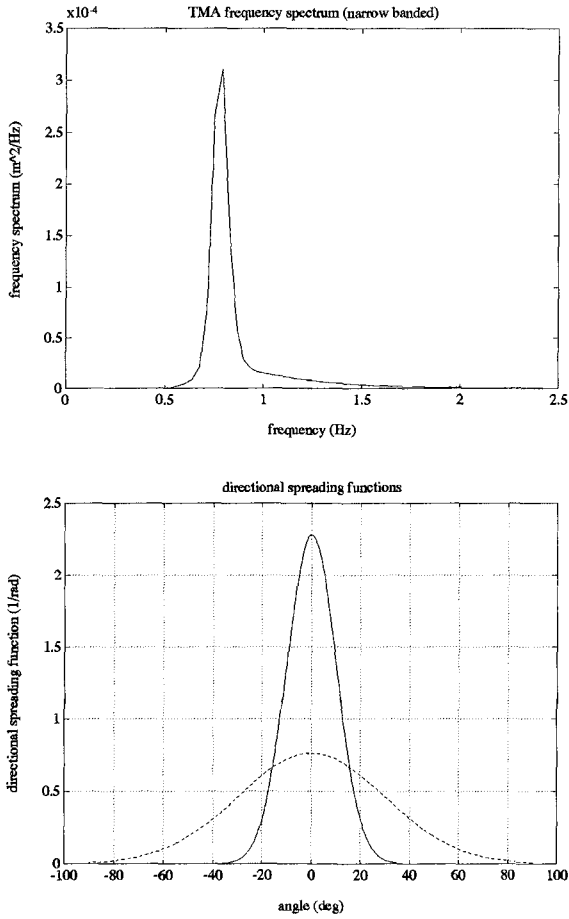


Figure 3: TMA frequency spectra (narrow frequency band) and directional spreading functions (solid lines :  $\sigma_0 = 10^\circ$ , dashed lines :  $\sigma_0 = 30^\circ$ )

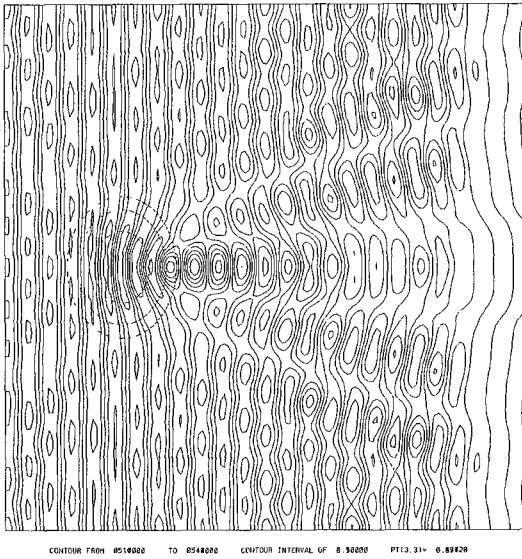


Figure 4: Water surface elevations at  $t = 260$  seconds (case M2)

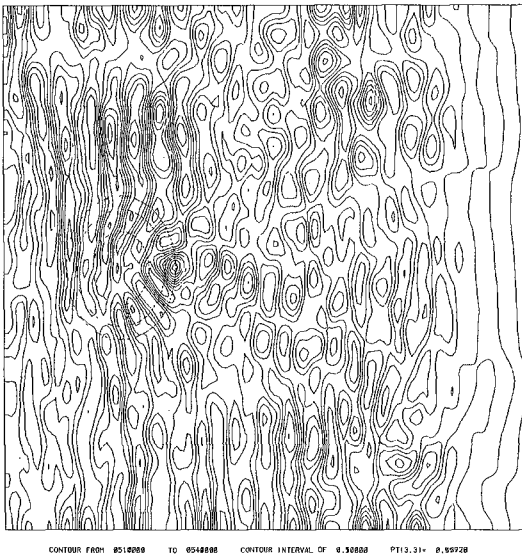


Figure 5: Water surface elevations at  $t = 260$  seconds (case N4)

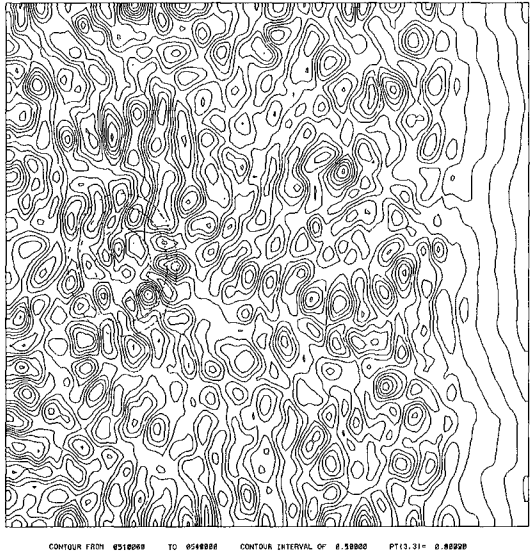


Figure 6: Water surface elevations at  $t = 260$  seconds (case B4)

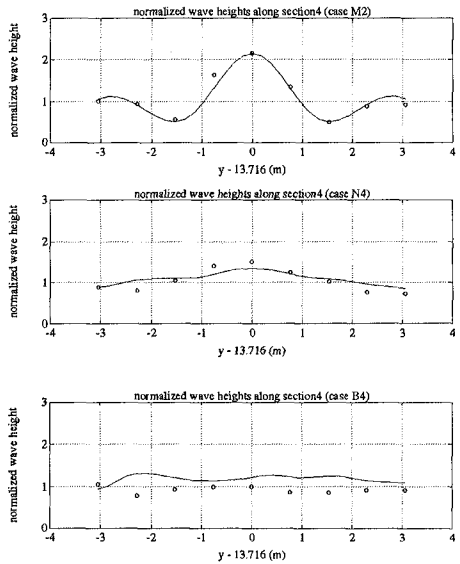


Figure 7: Measured and predicted normalized wave heights on section 4

$$\eta_{2,t} + \nabla_h \cdot \{h \nabla_h \phi_2\} = -\nabla_h \cdot \{\overline{\eta \nabla_h \phi}\} \quad (32)$$

$$\phi_{2,t} + g \eta_2 = \frac{\omega^2}{g^2} \overline{\phi_t^2} - \frac{1}{2} \overline{(\nabla_h \phi)^2} - \frac{\omega^4}{2g^2} \overline{\phi^2} \quad (33)$$

where  $\overline{(\quad)}$  denotes a time average. The correct method for computing time averages in an unsteady wave train is unclear. If the wave train is narrow-banded, we may use the extraction of the dominant frequency in section 2 as the basis for isolating the slowly-varying amplitudes. Following this strategy, (32) and (33) may be further reduced to

$$\eta_{2,t} + \nabla_h \cdot \{h \nabla_h \phi_2\} = -\frac{1}{2} \text{Re} \left( \nabla_h \cdot [\hat{\eta}^* \nabla_h \hat{\phi}] \right) \quad (34)$$

$$\phi_{2,t} + g \eta_2 = \frac{\omega^2}{2} \hat{\eta} \hat{\eta}^* - \frac{1}{4} \left( \nabla_h \hat{\phi} \cdot \nabla_h \hat{\phi}^* \right) - \frac{\omega^4}{4g^2} \hat{\phi} \hat{\phi}^* \quad (35)$$

These equations may also be written as a single second-order equation, analogous to (13), after elimination of  $\eta_2$ . The numerical schemes are again identical to those used for the basic linear equations.

Figure 8 shows a plot illustrating the generation of a single wave group and the associated bound and free long waves in a one-dimensional wave flume. The wavemaker motion used does not compensate for the decrease in total volume (at second order) associated with the entrance of the wave group into the wave channel. There is thus a free long wave generated whose net positive volume compensates for the negative volume associated with the setdown under the wave group. This positive wave propagates away from the wavemaker as a free wave, and thus leads the short wave group in the tank.

Additional results for long wave generation and harbor resonance in 2-D will be reported separately.

## Conclusions

We have developed models for the numerical solution of time-dependent mild-slope equations, and applied the models to the study of irregular and regular wave propagation in the coastal environment. Linear and nonlinear versions of the model were applied to Berkhoff shoal, and, as expected, we found that the nonlinear model showed better results than the linear model. We also applied the linear version of the model to study irregular wave refraction and diffraction by a submerged shoal, and compared model results to experimental data given by Vincent and Briggs (1989). Finally, the models were extended to include additional low frequency components which are forced by the primary wave envelopes, and some preliminary results on long wave generation were shown.

## References

- Berkhoff, J. C. W., 1972, "Computation of combined refraction-diffraction", *Proc. 13th Intl. Conf. Coast. Engineering*, Vancouver, 471-490.
- Berkhoff, J. C. W., Booij, N., and Radder, A. C., 1982, "Verification of numerical wave propagation models for simple harmonic linear waves", *Coastal Engineering*, 6, 255-279.
- Copeland, G. J. M., 1985, "A practical alternative to the 'mild-slope' wave equation", *Coastal Engineering*, 9, 125-149.



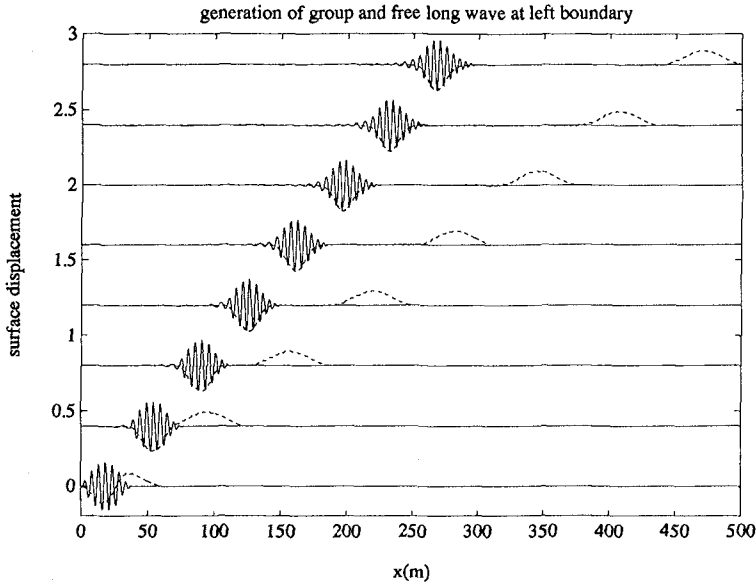


Figure 8: Generation of bound and free long waves during wave group generation.

- Ito, Y. and Tanimoto, K., 1972, "A method of numerical analysis of wave propagation - application to wave diffraction and refraction", *Proc. 13th Intl. Conf. Coast. Engineering*, Vancouver, Chapt. 26.
- Kirby, J. T., 1983, "Propagation of weakly-nonlinear surface water waves in regions with varying depth and current", Ph.D. thesis, University of Delaware.
- Kirby, J. T. and Dalrymple, R. A., 1984, "Verification of a parabolic equation for propagation of weakly-nonlinear waves", *Coastal Engineering*, 8, 219-232.
- Kirby, J. T. and Rasmussen, C., 1991, "Numerical solutions for transient and nearly periodic waves in shallow water", *Proc. ASCE Engineering Mechanics Specialty Conference: Mechanics Computing in the 1990's and Beyond*, Columbus, 328-332, May.
- Madsen, P. A. and Larsen, J., 1987, "An efficient finite-difference approach to the mild-slope equation", *Coastal Engineering*, 11, 329-351.
- Panchang, V. G., Pearce, B. R., Wei, G. and Cushman-Roisin, B., 1991, "Solution of the mild-slope wave problem by iteration", *Applied Ocean Res.*, 13, 187-199.
- Smith, R. and Sprinks, T., 1975, "Scattering of surface waves by a conical island", *J. Fluid Mech.*, 72, 373-384.
- Vincent, C. L. and Briggs, M. J., 1989, "Refraction and diffraction of irregular waves over a mound", *J. of Waterway, Port, Coastal, and Ocean Engineering*, 115, 269-284.

## CHAPTER 29

### NON-LINEAR WAVE-CURRENT INTERACTIONS IN THE SWADE RESEARCH PROGRAM.

S. P. Kjeldsen. \*

H. C. Graber. \*\*

#### Abstract.

This publication gives an introduction to the SWADE experimental programme. It presents examples of results of directional ocean wave spectra in polar format obtained by the third generation met/ocean buoy WAVESCAN. Then focus is made on a new algorithm "CUWA" that simulates non-linear Stokes waves propagating through regions of strong surface current.

#### Introduction.

The surface wave dynamics experiment SWADE was initiated by the Office of Naval Research in U.S.A. as an accelerated research initiative. A large field experimental program was carried out in the fall of 1990 through the spring of 1991 offshore the coast of Virginia. The measurement systems and a team of investigators are funded by the U.S. Office of Naval Research and the National Aeronautics and Space Administration (NASA).

SWADE is concerned primarily with the evolution of the directional wave spectrum in both time and space, and the goal is to provide improved understanding of wind forcing and wave dissipation, and the effects of breaking waves on the air-sea coupling mechanisms. It is well known that this energy transport is strongly coupled to dissipation in breaking waves. Actually 33 % of momentum transferred from the wind to the large scale ocean current systems is due to wave breaking, LONGUET-HIGGINS (1969). Further a particular goal was to

---

\* Assoc. Professor, The Maritime Academy.

Ladehammerveien 6. 7004 Trondheim, Norway.

\*\* Assoc. Professor Rosenstiel School of Marine and Atmospheric Science, Miami. Florida. U.S.A.

investigate the effects of waves on various airborne radar systems such as the surface contour radar (SCR), the remote ocean wave spectrometer (ROWS), and the synthetic aperture radar (SAR). Therefore it became very important in this experiment to have the best available directional wave buoys to provide the sea surface truth, and make it possible to calibrate air-borne radar instruments. The company SEATEX from Trondheim in Norway funded the deployment of such a buoy.

### Field Experiment.

The experiment was performed 100 nautical miles east of the coast of Virginia between Cape Hatteras and Cape Cod. This was an area where the Gulf Stream developed large eddies or rings, and thus interacted strongly with the waves. Fig 1 shows the location of some of the instruments that were deployed in SWADE. Five directional wave buoys were selected for this task, among them the third generation WAVESCAN Met/ocean buoy from SEATEX in Norway. Also a large spar buoy was brought into the experiment but unfortunately the spar buoy was lost in a severe storm that occurred at the site in late October 1990. Therefore a SWATH-ship "FREDERICK G. CREED" from Canada was brought into the experiment. A SWATH is a small waterplane area twin hull catamaran. This ship was equipped with an array of wave gauges that permitted the ship to move to several positions on the site and measure the directional spectra there, see DONELAN et al. 1992. The comparison between directional spectra measured at sea and directional spectra measured with air-borne SAR-radars had a high priority. 5 airplanes from NASA, NADC, CRPE, CCRS and NRL participated, and during the most intensive measuring period, these aircrafts flew over the sea area with a SCR (Surface Contour radar), a ROWS (Radar Ocean Wave Spectrometer), a SAR (X- and C-band Side Looking Real Aperture Radar) and finally a 3-frequency SAR radar. During two intensive weeks not less than 41 flying missions were taken.

Fig 2 shows the site where the experiment took place, and Fig 3 and Fig 4 show examples of directional spectra obtained with the WAVESCAN buoy. The spectra are shown in polar format. Such a format was also used extensively in the Labrador Sea Extreme Waves Experiment LEWEX program, see BEAL (1990). After termination of the LEWEX-experimental program it was recommended by the 8 participating countries to use the polar format as an international standard for directional spectra in order to make practical applications more easy, in particular for ships navigating with access to forecasted directional wave spectra, see KJELSDSEN (1990 c). Also comparisons with satellite and airborne directional wave spectra becomes

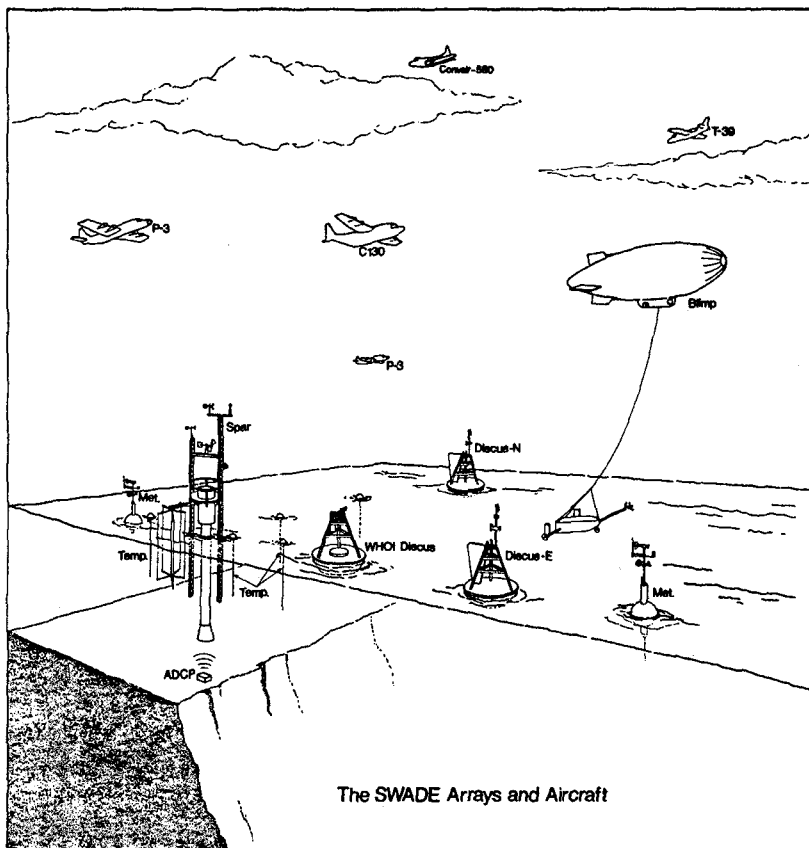


Fig. 1. The SWADE arrays and aircraft.  
 ( From WELLER, DONELAN, BRISCOE, HUANG 1990.)

more convenient when all spectra are referenced to true North.

Fig 5 shows the increase in mean temperature on earth and in carbon dioxide in the period from 1860 to 1985. It is in particular in the two last decades that the carbon dioxide content in the atmosphere has a steep increase. Interaction between oceans and atmosphere are very important in this exchange of carbon dioxide and here the breaking waves plays an important role.

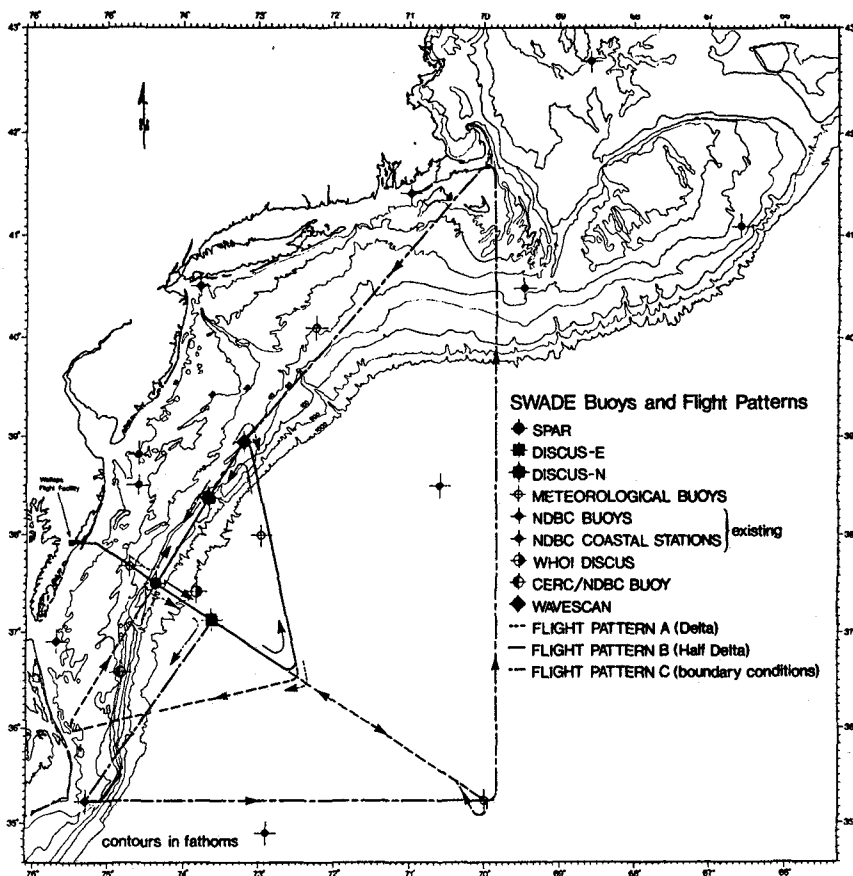


Fig. 2. SWADE buoys and flight patterns.  
( From WELLER, DONELAN, BRISCOE, HUANG 1990.)

Fig 6 shows the third generation met/ocean WAVESCAN buoy. The WAVESCAN system consist of :

1. The met/ocean data buoy which automatically collects the raw data which is then processed onboard before transmission to the end user. A particular feature is the onboard wave directional analysis.
2. A telemetry system which can be used with satellite links and/or UHF radio links.
3. A data presentation system with RTscan software for communication, control and data presentation.

The data is available to the end user in realtime from anywhere in the world's oceans. The system can make use of satellite systems, such as Service Argos, Inmarsat C, Meteosat or GOES, to provide the telemetry link. Locally, UHF radio may be used to provide a two way link to the shore based RTscan receiver/controller station. The data is organised and presented by the RTscan software which also provides the means to control and manage a network of buoys.

For further details see BARSTOW et al. (1991).

The buoy can be configured with sensors for :

- Wave characteristics, (heights, frequencies, directions).
- Wind speed and direction.
- Air temperature, pressure and humidity.
- Solar radiation.
- Current profile, velocity and direction.
- Water temperature.
- Dissolved oxygen.
- Ph-value.
- Salinity.
- Conductivity.
- Redox.

Fig 7 shows the WAVESCAN with an acoustic doppler current profiler, (ADCP) installed below. However this current meter is an additional option and it was not used in the SWADE experiment.

WAVESCAN was found to be the ideal buoy to use in connection with weather routing applications for ships.

#### Comparisons between results obtained with WAVESCAN and results obtained with SAR-radars.

It has been observed that directional ocean wave spectra obtained from wave buoys in some cases were wider than directional wave spectra obtained for the same situation with SAR-radars. A possible explanation is that the buoys are moving in the sea in yaw motion during data acquisition. However the WAVESCAN buoy was calibrated in a large wave calibration project WADIC performed at the EKOFISK field in Norway. Here an array with lasers were used to measure the directional wave spectrum. WAVESCAN calibration equations were then obtained in which yaw motion was eliminated, see ALLENDER et. al. (1989). The WAVESCAN buoy has therefore been used extensively as a key sensor, and used for comparisons both with airborne and with satellite-borne SAR-radars. This was in particular the case during the LEWEX experiment.

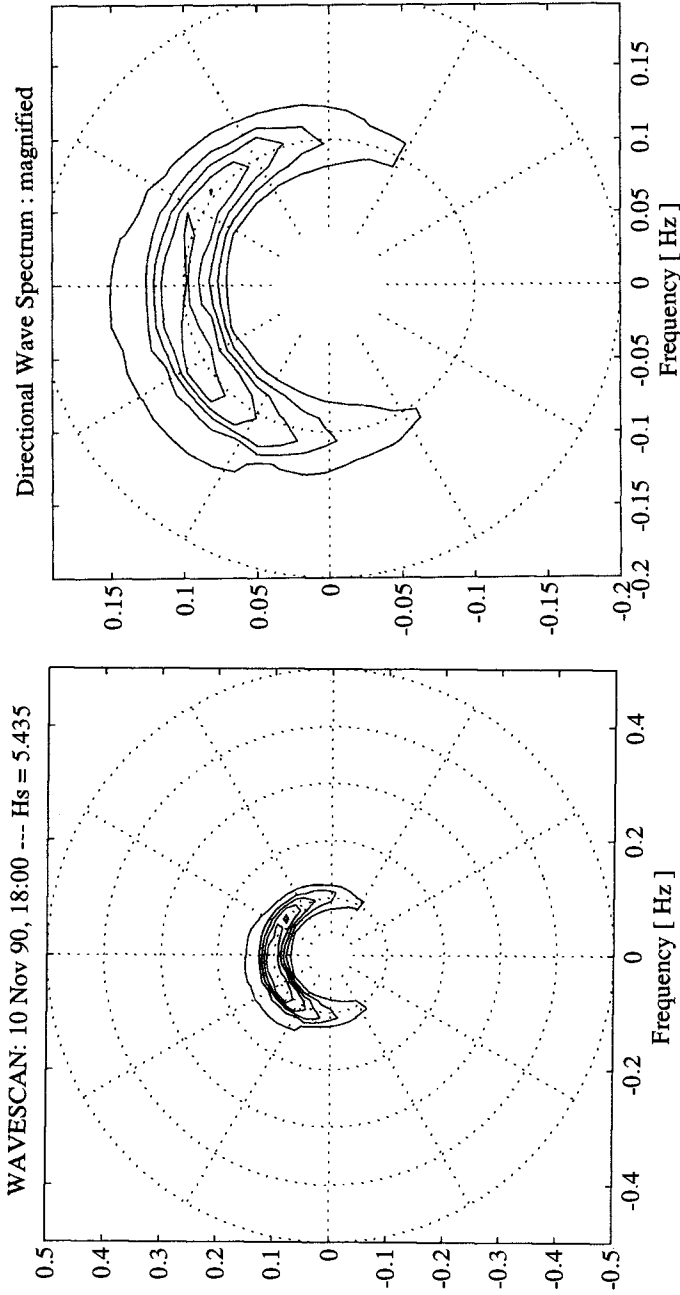


Fig. 3. Directional spectra in polar format obtained from the WAVESCAN Met/ocean buoy during the storm the 10th november 1990 at 1800.

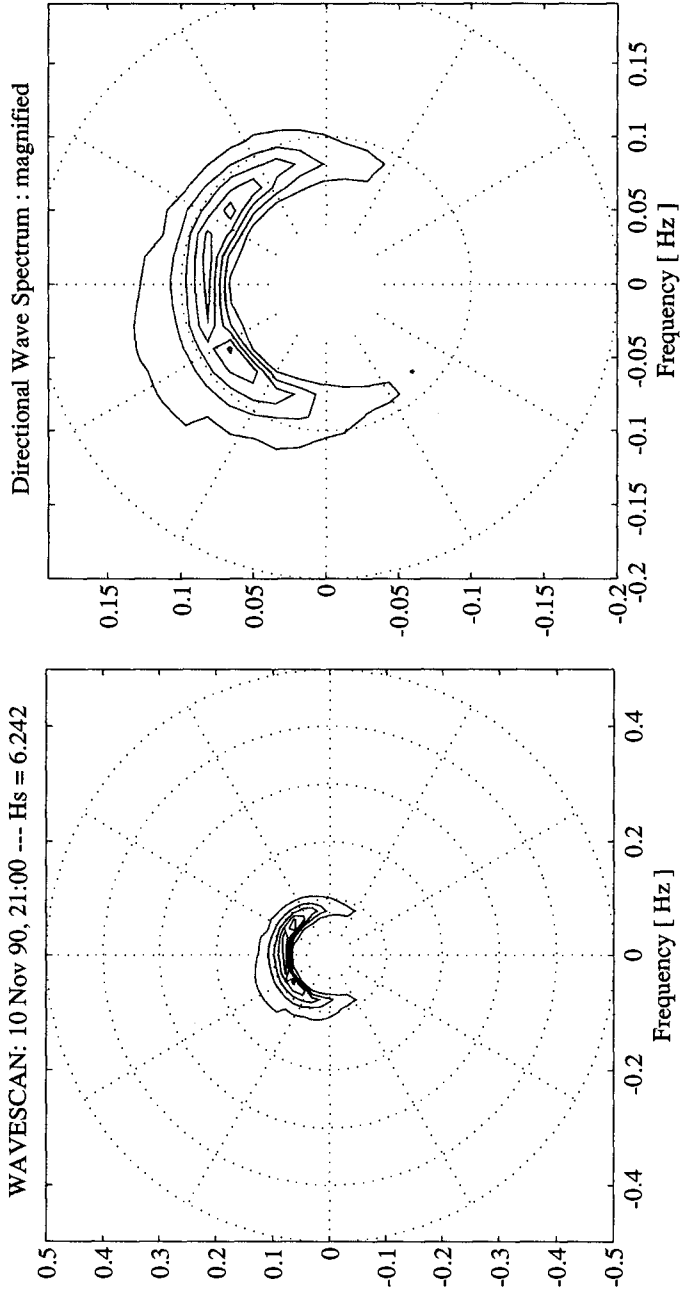


Fig. 4. Directional spectra in polar format obtained from the WAVESCAN Met/ocean buoy during the storm the 10th november 1990 at 2100.



There are various methods that can be used to derive the 3-dimensional spectra such as :

- The Fourier Series Expansion Method.
- The Maximum Likelihood Method.
- The Maximum Entropy Method.
- The Variational Method.
- The Direct Integral Method.

An example of an algorithm used to derive directional spectra from the WAVESCAN buoy is given by KJELDEN, KROGSTAD, OLSEN 1988.

The idea to use data from several directional buoys installed at the same position simultaneously in order to establish a statistical weighted directional spectrum to represent the best estimate to sea surface truth was used both in the WADIC and in the Labrador Sea Extreme Waves Experiment LEWEX, see KJELDEN (1990 b).

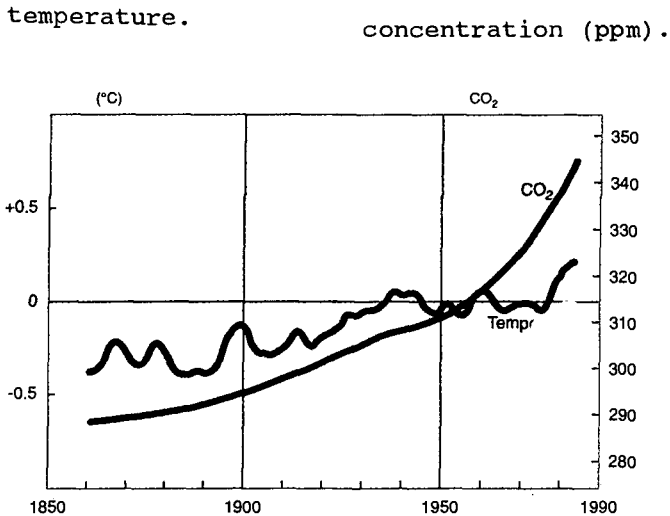


Fig. 5. Increase in mean temperature on earth and in content of carbon dioxide in the atmosphere (ppm) in the period from 1860 to 1985. ( From WORLD RESOURCES INSTITUTE.)

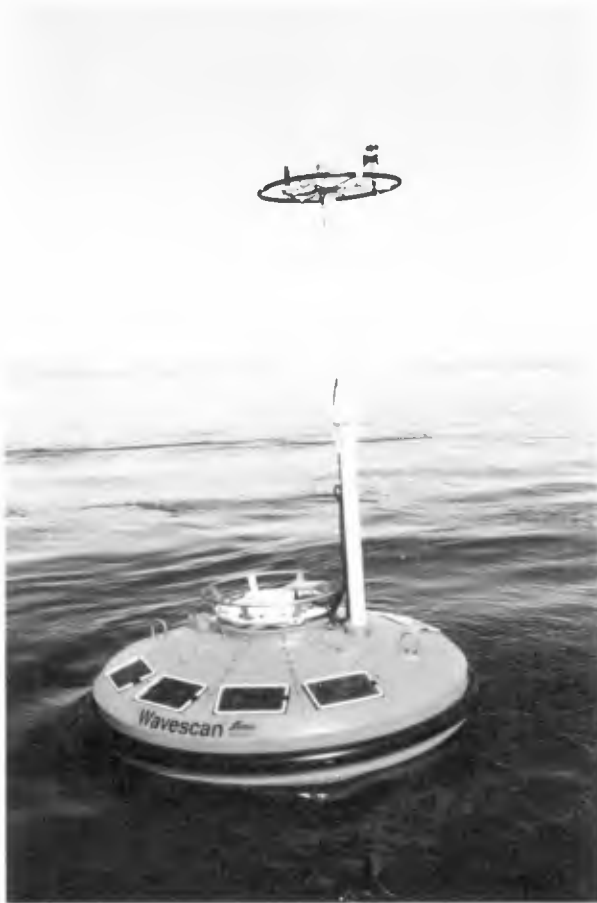


Fig. 6. The Third Generation Met/ocean WAVESCAN buoy.



Fig. 7. An ADCP current meter installed below the WAVESCAN buoy.

**Mathematical Algorithm.**

Interaction between non-linear waves and strong surface currents such as the Gulf Stream is an important problem to consider with many practical applications. The Gulf Stream varies slowly in time and space and large vortex rings develop. In a study of waves on slowly varying currents it is natural to start with specifying the current field in space and time. However, in general, this is not possible. There is an ambiguity in the definition of still water when finite amplitude water waves propagate into the current. This is important because finite amplitude water waves often develop into breaking waves and thus the energy dissipation is governed by this non-linear wave-current interaction. The ambiguity is caused by the Stokes drift velocity. Thus superposition of waves upon a current changes the current and its determination becomes part of the problem.

Let us consider the two equations that governs the problem. First we have the equation for the wave action flux B:

$$B = \frac{\rho g A^2 (U + C_g)}{2\sigma}$$

Here B is the wave action flux,  
 A the wave amplitude  
 U the surface current velocity  
 $C_g$  the group velocity relative to the water  
 $\sigma$  the intrinsic wave frequency  
 $\rho$  the sea water density  
 g the gravity acceleration.

The cyclic wave frequency  $\omega$  is given by the equation :

$$\omega = k(C + U) = \frac{g(C + U)}{C^2}$$

Here k is the wave number and  
 C is the phase velocity relative to the water.

Both the wave action flux and the cyclic wave frequency must be conserved. The problem can then be solved as two equations with two unknowns, namely the wave action and the surface current. When the equations are solved the following conditions must be taken into consideration. The non-linear dispersion relation for the waves is given by :

$$C^2 = \frac{g}{k} (1 + f(A^2 k^2))$$

and the Stokes drift  $S$  is given by :

$$S = 0.5 * k A^2 C$$

A new algorithm "CUWA"-(current-wave-interaction) is developed. Here a test simulation with non-linear Stokes waves propagating against a strong opposing current is considered.

Also a case with linear waves is simulated for comparison. However the linear theory is not valid in this case as the amplitude of the linear waves tends towards infinity.

The performed analysis showed that non-linear wave-current interactions are very important and deserves further attention. The research has many practical applications, such as forecasting of breaking waves, prediction of wave kinematics, pollution control and management of coastal areas and in particular navigation in coastal waters.

#### Further work.

There is a need not only to consider directional ocean wave spectra but also to analyse single waves. In particular measured extreme wave heights and wave groupiness should be analysed from the storm data obtained in november 1990.

Further results obtained from the algorithm "CUWA" should be compared with measurements obtained at positions where strong wave-current interactions have taken place.

An analysis of wave groups and single extreme waves has been initiated in other sea areas, see KJELDEN (1989), KJELDEN (1990 a) and KJELDEN (1991).

**Conclusions.**

1. The final conclusions that are derived from the SWADE experimental programme will not be published by single scientists but will appear as a joint publication from all participants.

2. In nature it is often observed, that a current opposing the waves leads to a significant amount of whitecapping. The energy dissipation is then increased. It is necessary to consider non-linear wave-current interaction computed by an algorithm such as "CUWA" in order to compute dissipation in breaking waves under such circumstances.

3. Directional ocean wave spectra obtained with the WAVESCAN buoy is calibrated against a laser array installed on a fixed platform. Thus movements of this particular buoy during data acquisition is eliminated. The WAVESCAN buoy has therefore been used extensively, in order to establish sea surface truth used in assesment of results with airborne SAR-radars.

**Acknowledgement.**

A special acknowledgement is given to the company SEATEX A/S in Trondheim, Norway for support to the SWADE experimental programme.

**References.**

- ALLENDER J., AUDUNSON T., BARSTOW S.F., BJERKEN S., KROGSTAD H.E., STEINBAKKE P., VARTDAL L., BORGMAN L.E., GRAHAM C., (1989), -  
The WADIC Project: A Comprehensive Field Evaluation of Directional Wave Instrumentation. - Ocean Eng. Vol 16. No 5/6. pp 505-536.
- BARSTOW S.F., UELAND G., KROGSTAD H.E., FOSSUM B.A. (1991): "The Wavescan Second Generation Directional Wave Buoy." IEEE Journal of Oceanic Engineering. Vol 16 No. 3. 1991.
- BEAL R.C., Editor, (1991), - Directional Ocean Wave Spectra - The Johns Hopkins University Press. Baltimore and London.
- DONELAN M.A., DRENNAN W.M., MADSEN N., KATSAROS K.B., TERRAY E.A., FLAGG C.N. (1992) - Directional Spectra from the SWATH Ship in SWADE.- Submitted to Journal Atmos. Ocean Tech.
- LONGUET-HIGGINS, M.S., (1969) - A Nonlinear Mechanism for the Generation of Sea Waves - Proc. Roy. Soc. London, Vol A 311 pp 371-389.
- KJELDSSEN, S.P., (1990 a) - Breaking Waves - in " Water Wave Kinematics " published in cooperation with NATO Scientific Affairs Division by Kluwer Academic Publishers Group. The Netherlands. pp 453-474.

- KJELDSSEN, S.P., (1990 b) - Current-wave interactions observed in the Labrador Sea Extreme Waves Experiment - in " Water Wave Kinematics " published in cooperation with NATO Scientific Affairs Division by Kluwer Academic Publishers Group. The Netherlands. pp 613-619.
- KJELDSSEN, S.P., (1990 c) - The Practical Value of Directional Ocean Wave Spectra - Johns Hopkins APL Technical Digest. July - December 1990. Vol 11 Nos 3 and 4. pp 381-387. Johns Hopkins University. U.S.A.
- KJELDSSEN, S.P., (1989) - Freak Wave Kinematics - in Proc. from Workshop on "Wave and Current Kinematics and Loading" IFP, Paris 25-26th october 1989. Published by The Oil Industry Exploration & Production Forum. 25 Old Burlington Street. London W1X 1LB. England.
- KJELDSSEN, S.P., (1991) - Ocean Currents & Wave Breaking - in Report from Expert Committee I.1. Proc. from 11th ISSC Ships and Offshore Structures Congress Wuxi, China 15-22 sept. 1991.
- KJELDSSEN, S.P., KROGSTAD H., OLSEN R. (1988) - Some Results from the Labrador Sea Extreme Waves Experiment - in Proc. 21st International Conference on Coastal Engineering. Malaga. Spain. June 1988.
- WELLER R.A., DONELAN M.A., BRISCOE M.G., HUANG N.E., (1990) - Riding the Crest - A Tale of two Wave Experiments - National Water Research Institute, Canada.
- WORLD RESOURCES INSTITUTE, (1990), - World Resources 1990-91. - Oxford University Press. ISBN 0-19-506229-9.

## CHAPTER 30

# Time-Dependent Mild Slope Equation for Random Waves

Yasuhiro Kubo,<sup>1</sup> Yasuo Kotake<sup>2</sup>, Masahiko Isobe<sup>2</sup>  
and Akira Watanabe<sup>2</sup>

A time-dependent mild slope equation is derived to simulate the deformation of irregular waves due to refraction, diffraction and breaking. It is based on Berkhoff's mild slope equation, but the resulting model is capable of simulating the time evolution of irregular wave profiles. The validity of the model is verified through comparisons with experimental data in a wave flume. Application examples for two-dimensional problems are given.

### 1 Introduction

The mild slope equation derived by Berkhoff (1972) has widely been used in the numerical calculation of refraction and diffraction of regular waves. However, it is well known that the randomness of sea waves has a significant effect on the wave height distribution due to refraction and diffraction.

In this paper a governing equation for calculating the time evolution of random waves due to refraction and diffraction is derived on the basis of the mild slope equation. An energy dissipation term is added to model the wave breaking. To examine the validity of the equation, the results of calculation are compared with measurements in a wave flume. Examples of model application to two-dimensional random wave computation are also given.

---

<sup>1</sup>Tokyo Electric Power Co. Ltd.

<sup>2</sup>Dept. of Civil Eng. , Univ. of Tokyo ,Bunkyo-ku , Tokyo , 113 , Japan



## 2 Derivation of Governing Equation

The mild slope equation derived by Berkhoff (1972) is written as

$$\nabla(cc_g \nabla \hat{\eta}) + k^2 cc_g \hat{\eta} = 0 \quad (1)$$

where  $c$  is the wave celerity,  $c_g$  the group velocity,  $k$  the wave number, and  $\nabla$  the horizontal gradient operator. The quantity  $\hat{\eta}$  denotes the complex amplitude of the water surface elevation, by which the water surface elevation  $\eta$  is expressed as  $\eta = \text{Re}[\hat{\eta}e^{-i\omega t}]$  ( $\omega$ : the angular frequency). In the above equation, the quantities  $cc_g$  and  $k^2 cc_g$  depend on the frequency, which restricts the applicability of the mild slope equation to waves with a single frequency.

For random waves, the water surface elevation is expressed as the superposition of component waves :

$$\eta = \text{Re}\left[\sum_{m=1}^{\infty} \hat{\eta}_m e^{-i\omega_m t}\right] \quad (2)$$

where  $\omega_m$  is the angular frequency and  $\hat{\eta}_m$  the complex amplitude of the  $m$ -th component waves.

To apply the mild slope equation to the analysis of random wave transformation, we define a variable  $\tilde{\eta}$  such that

$$\eta = \text{Re}[\tilde{\eta}e^{-i\bar{\omega}t}] \quad (3)$$

where  $\bar{\omega}$  is a representative angular frequency such as the peak frequency. Comparing this with Eq. (2), we have

$$\eta = \text{Re}\left[\sum_{m=1}^{\infty} \tilde{\eta}_m e^{-i\bar{\omega}t}\right] \quad (4)$$

and

$$\tilde{\eta}_m = \hat{\eta}_m e^{-i\Delta\omega_m t} \quad (5)$$

where  $\Delta\omega_m = \omega_m - \bar{\omega}$ . The variable  $\tilde{\eta}_m$  is a function of time  $t$ , for which

$$\frac{\partial \tilde{\eta}_m}{\partial t} = -i\Delta\omega_m \tilde{\eta}_m \quad (6)$$

The quantity  $\tilde{\eta}_m$  is a function of time  $t$ , it is a solution of Eq. (1) as well as  $\hat{\eta}_m$ . Therefore, we can rewrite Eq. (1) as

$$\nabla[(cc_g)_m \nabla \tilde{\eta}_m] + (k^2 cc_g)_m \tilde{\eta}_m = 0 \quad (7)$$

Since the quantities  $(cc_g)_m$  and  $(k^2 cc_g)_m$  depend on the angular frequency  $\omega_m$ , it is not possible to superimpose Eq. (7) for all component waves and calculate  $\tilde{\eta}$

directly. Therefore, we modify Eq. (7) and change the quantities  $cc_g$  and  $k^2cc_g$  into constants independent of component angular frequencies.

If we expand the quantities  $(cc_g)_m$  and  $(k^2cc_g)_m$  into Taylor series of  $\Delta\omega_m$  and eliminate powers of  $\Delta\omega_m$  using relations such as  $-i\Delta\omega_m\tilde{\eta}_m = \partial\tilde{\eta}_m/\partial t$  and  $(-i\Delta\omega_m)^2\tilde{\eta}_m = \partial^2\tilde{\eta}_m/\partial^2t$ , we can obtain an equation in which all the quantities can be determined from the representative frequency only.

For example, by truncating the Taylor series at the first order, the first and second terms in Eq. (7) are expressed as

$$(cc_g)_m \nabla \tilde{\eta}_m = [\overline{cc_g} + \frac{d(\overline{cc_g})}{d\omega} \Delta\omega_m] \nabla \tilde{\eta}_m = \overline{cc_g} \nabla \tilde{\eta}_m + i \frac{d(\overline{cc_g})}{d\omega} \nabla \left( \frac{\partial \tilde{\eta}_m}{\partial t} \right) \quad (8)$$

$$(k^2cc_g)_m \tilde{\eta}_m = [\overline{k^2cc_g} + \frac{d(\overline{k^2cc_g})}{d\omega} \Delta\omega_m] \tilde{\eta}_m = \overline{k^2cc_g} \tilde{\eta}_m + i \frac{d(\overline{cc_g})}{d\omega} \frac{\partial \tilde{\eta}_m}{\partial t} \quad (9)$$

where all the quantities  $\overline{cc_g}$ ,  $\overline{d(\overline{cc_g})/d\omega}$ ,  $\overline{k^2cc_g}$  and  $\overline{d(\overline{k^2cc_g})/d\omega}$  are constants. Substitution of Equations (8) and (9) into Eq. (7) yields

$$\nabla(\bar{\alpha} \nabla \tilde{\eta}_m) + i \nabla[\bar{\beta} \nabla(\frac{\partial \tilde{\eta}_m}{\partial t})] + \bar{k}^2 \bar{\alpha} \tilde{\eta}_m + i \bar{\gamma} \frac{\partial \tilde{\eta}_m}{\partial t} = 0 \quad (10)$$

$$\bar{\alpha} = \overline{cc_g} \quad (11)$$

$$\bar{\beta} = \frac{\bar{c}}{\bar{k}} [-2(1 - \bar{n}) + \frac{1}{2\bar{n}}(2\bar{n} - 1)\{1 - (2\bar{n} - 1) \cosh 2\bar{k}d\}] \quad (12)$$

$$\bar{\gamma} = \bar{k}\bar{c}[2\bar{n} + \frac{1}{2\bar{n}}(2\bar{n} - 1)\{1 - (2\bar{n} - 1) \cosh 2\bar{k}d\}] \quad (13)$$

$$\bar{n} = 1/2(1 + 2\bar{k}d/\sinh 2\bar{k}d) \quad (14)$$

Then, superposition of Eq. (10) for an infinite number of component waves yields

$$\nabla(\bar{\alpha} \nabla \tilde{\eta}) + i \nabla[\bar{\beta} \nabla(\frac{\partial \tilde{\eta}}{\partial t})] + \bar{k}^2 \bar{\alpha} \tilde{\eta} + i \bar{\gamma} \frac{\partial \tilde{\eta}}{\partial t} = 0 \quad (15)$$

which is termed as a time-dependent mild slope equation for random waves. For random incident waves,  $\tilde{\eta}$  along the boundary is determined by Eq. (4), and then  $\tilde{\eta}$  in the calculation domain can directly be calculated by Eq. (15).

The above expansion of the quantities  $cc_g$  and  $k^2cc_g$  into the first-order Taylor series of  $\Delta\omega_m$  is equivalent to approximating them as linear functions of  $\omega$ . Fig. 1 illustrates the accuracy of the approximation. As seen in Fig. 1, the error is insignificant when the deviation of the frequency from the representative value is small.

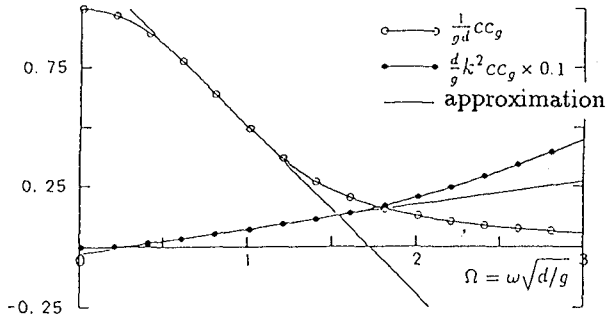


Fig. 1: Accuracy of the approximated quantities

### 3 Modeling of Wave Breaking

To incorporate energy dissipation due to wave breaking, an empirical energy dissipation term based on the model presented by Isobe(1986) is added to Eq. (15):

$$\nabla(\bar{\alpha}\nabla\bar{\eta}) + i\nabla[\bar{\beta}\nabla(\frac{\partial\bar{\eta}}{\partial t})] + \bar{k}^2\bar{\alpha}(1 + if_D)\bar{\eta} + i\bar{\gamma}(1 + if_D)\frac{\partial\bar{\eta}}{\partial t} = 0 \quad (16)$$

where  $f_D$  is the energy dissipation coefficient.

It is convenient to evaluate  $f_D$  by using spatial wave profiles because time series of the spatial profile are obtained as a solution of Eq. (16). In the procedure, we first divide the spatial wave profiles into individual waves by the zero-up crossing method from offshore to onshore as shown in Fig. 2.

To judge the breaking of individual waves, the amplitude to water depth ratio,

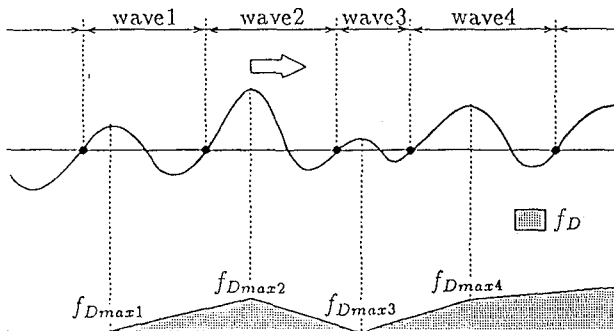


Fig. 2: Evaluation of energy dissipation function due to wave breaking

$\gamma$ , is introduced as follows:

$$\gamma = |\tilde{\eta}|/d \quad (17)$$

where  $|\tilde{\eta}|$  is the amplitude at the wave crest and  $d$  the water depth. If  $\gamma$  is greater than  $\gamma_b$  which is a critical value of wave breaking and determined by Eq. (18), the individual wave is judged to be breaking.

$$\gamma_b = 0.8\gamma'_b \quad (18)$$

$$\gamma'_b = 0.53 - 0.3 \exp(-3\sqrt{d/L_0}) + 5 \tan^{\frac{3}{2}} \beta \exp\{-45(\sqrt{d/L_0} - 0.1)^2\} \quad (19)$$

where  $L_0$  is the representative wavelength in deep water and  $\tan \beta$  the bottom slope. The value 0.8 in Eq. (18) is introduced to consider that random waves are easier to break than regular waves. After breaking, if  $\gamma$  becomes smaller than  $\gamma_r$  which is a critical value of wave recovery determined by Eq. (20), the individual wave is judged to have recovered.

$$\gamma_r = 0.135 \quad (20)$$

To evaluate the spatial distribution of the energy dissipation coefficient, we first determine  $f_{D\max}$  at each crest of breaking waves by Eq. (21), then obtain the energy dissipation coefficient  $f_D$  by interpolating  $f_{D\max}$  linearly as shown in Fig. 2, and finally calculate the water surface profile at the next time step.

$$f_{D\max} = \frac{5}{2} \tan \beta \sqrt{\frac{1}{k_0 d}} \sqrt{\frac{\gamma - \gamma_r}{\gamma_s - \gamma_r}} \quad (21)$$

$$\gamma_s = 0.4 \times (0.57 + 5.3 \tan \beta) \quad (22)$$

where  $k_0$  is the representative wave number. The same procedure is repeated for arbitrary time steps.

## 4 Boundary conditions

The open boundary condition, which allows outgoing waves to propagate freely, is not easy to implement. In addition, along the offshore boundary, the incident waves should be introduced.

We apply a method presented by Ohya *et al.* (1990) to the open boundaries. In the method, the energy of outgoing waves is absorbed in the energy dissipation layer which is added outside of the boundary. To introduce the incident waves from the offshore boundary, terms due to an exciting force are added on the right hand side:

$$\begin{aligned} & \nabla(\bar{\alpha} \nabla \tilde{\eta}) + i \nabla[\bar{\beta} \nabla(\frac{\partial \tilde{\eta}}{\partial t})] + \bar{k}^2 \bar{\alpha} (1 + i f_D) \tilde{\eta} + i \bar{\gamma} (1 + i f_D) \frac{\partial \tilde{\eta}}{\partial t} \\ & = \nabla(\bar{\alpha} \nabla \tilde{\eta}_{in}) + i \nabla[\bar{\beta} \nabla(\frac{\partial \tilde{\eta}_{in}}{\partial t})] + \bar{k}^2 \bar{\alpha} (1 + i f_D) \tilde{\eta}_{in} + i \bar{\gamma} (1 + i f_D) \frac{\partial \tilde{\eta}_{in}}{\partial t} \quad (23) \end{aligned}$$

where  $\tilde{\eta}_{in}$  is the complex amplitude due to the incident waves. The above equation is obtained by substituting component,  $\tilde{\eta}_{out} = \tilde{\eta} - \tilde{\eta}_{in}$ , due to outgoing waves for  $\tilde{\eta}$  in Eq. (16).

## 5 Application and Results

Time-evolutional solutions can be obtained from Eq. (16) by using a finite difference method.

Numerical calculations for the present equation are carried out for one-dimensional cases by using Crank-Nicholson method. Figures 3 and 4 show the result for two component waves with slightly different frequencies,  $0.9\bar{\omega}$  and  $1.1\bar{\omega}$  ( $\bar{\omega}$ : the mean angular frequency). Fig. 3 is for deep water and Fig. 4 for shallow water. Spatial wave profiles are shown at four time steps from the top to the

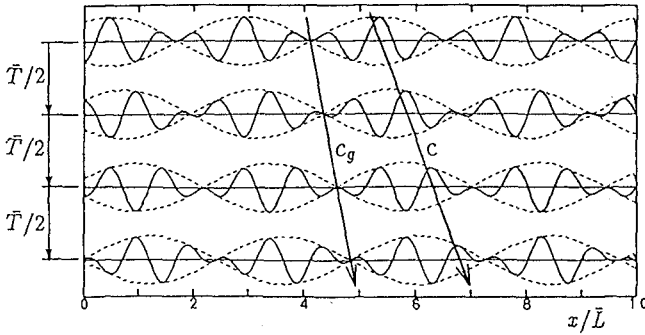


Fig. 3: Propagation of two-component waves (deep water)

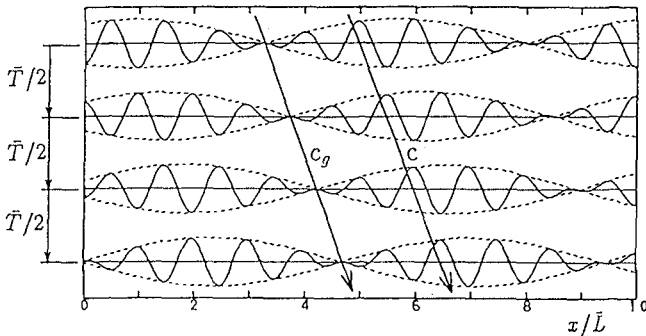


Fig. 4: Propagation of two-component waves (shallow water)

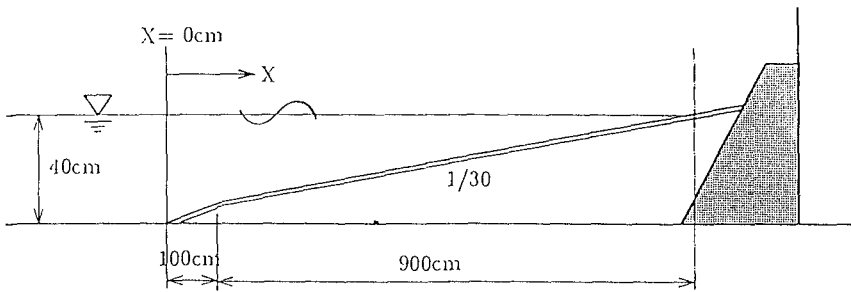


Fig. 5: Wave flume and bottom configuration

bottom with an interval of a half of the mean period. It seems in Fig. 3 that waves propagate with the wave celerity  $c$ , while wave groups propagate with the group velocity  $c_g$ . This can not be reproduced by the previous time-dependent mild slope equation.

Results of numerical calculations are compared with experiments for the wave transformations on a slope to confirm the validity of the present equation. The data were obtained by Watanabe *et al.*(1988) in a wave flume shown in Fig. 5. Figures 6 and 7 compare the measured and calculated wave height variations of random waves on a beach with a slope of  $1/30$ . The offshore boundary condition is given at  $x = -40\text{cm}$  and the shoreline is located at  $x = 1000\text{cm}$ . Fig. 6 is for the plunging-breaker (case 1), while Fig. 7 for the spilling-breaker (case 2).

The peak frequency  $f_p$  and the significant wave height  $H_{1/3}$  of the incident waves are  $0.5\text{Hz}$  and  $5.4\text{cm}$  for case 1, and  $0.75\text{Hz}$  and  $9.2\text{cm}$  for case 2. In the numerical calculations, the incident waves are given by synthesizing component waves with frequency  $0.25f_p \sim 2.5f_p$ , which were extracted from the measured water surface elevation at the offshore boundary by using FFT. The grid size  $\Delta x$  is  $10\text{cm}$  and the time interval  $\Delta t$  is  $0.02\text{s}$ .

In Fig. 6, the calculated significant wave height variations does not agree well with the measured one near the breaking point since the present equation is linear. However, the root mean square of the water surface variation is predicted well due to the empirical formulation of the dissipation term.

Fig. 8 compares the measured and calculated water surface fluctuations for the case 2. Fig. 8 (a) is for the offshore boundary, Fig. 8 (b) for the offshore zone, Fig. 8 (c) for the average breaking point and Fig. 8 (d) for the surf zone. As seen in Fig. 8 (b), a good agreement is obtained in the offshore zone, but in Fig. 8 (d) the difference is large. Owing to the linearity of the equation, the

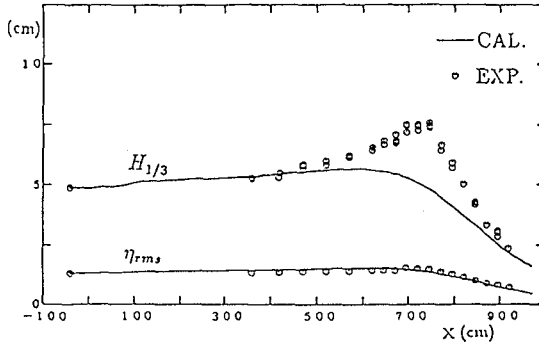


Fig. 6: Comparison of the measured and calculated wave height variations (case 1:  $H_{1/3} = 5.4\text{cm}$ ,  $f_p = 0.5\text{Hz}$ )

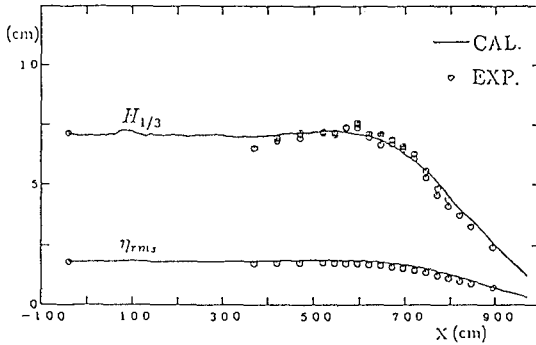


Fig. 7: Comparison of the measured and calculated wave height variations (case 2:  $H_{1/3} = 9.2\text{cm}$ ,  $f_p = 0.75\text{Hz}$ )

present equation can not reproduce the non-linear properties such as skewness of the wave profile. However, the transformation of wave groups is well reproduced.

As examples of application to two-dimensional problems, wave fields on a uniform slope and around a detached breakwater are calculated by the present equation. For two-dimensional problems, the ADI method is used because it reduces the memory size and computation time.

Fig. 9 shows the calculation domain. The contour lines are shown for the energy dissipation coefficient  $f_D$  in the energy dissipation layer. The layer is taken thicker along the offshore boundary than along the onshore boundary because of the difference in wavelengths. The grid size  $\Delta l$  is 2m and the time interval  $\Delta t$  is 0.02s.

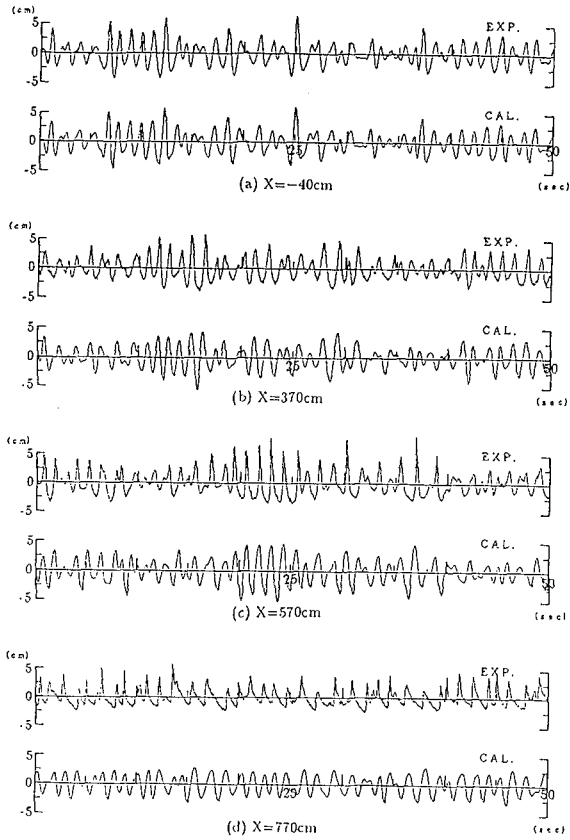


Fig. 8: Comparison of the measured and calculated wave surface fluctuations (case2)

Numerical calculations are carried out for two cases: for regular waves and multidirectional irregular waves. The wave period or significant wave period is 6s, and the wave height or significant wave height is 1m in deep water.

The frequency spectrum of the incident irregular waves is of the Bretshneider-



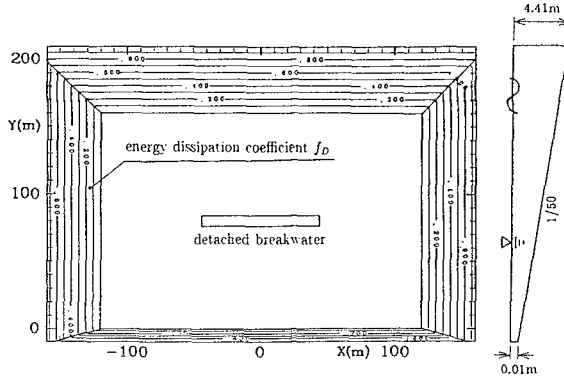


Fig. 9: Calculation domain

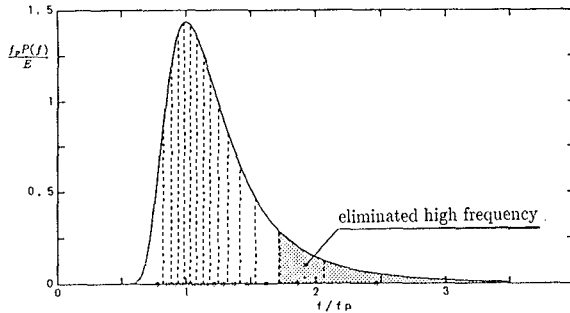
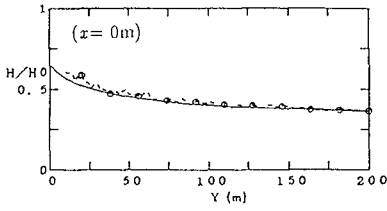


Fig. 10: The frequency spectrum of incident waves

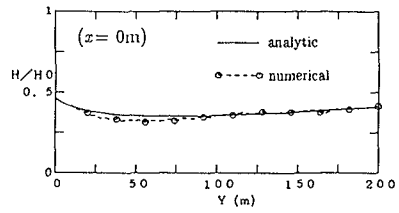
Mitsuyasu spectrum and the Mitsuyasu-type directional distribution function is used with  $S_{max} = 10$ . The incident irregular waves are given by the double summation method in which 13 frequency components and 15 directional components are used. High frequency components are cut as shown in Fig. 10, because the applicability range of the present equation is restricted within a narrow band.

Figures 11 (a) and 11 (b) compare the analytical and numerical solution of wave height variations of component waves due to refraction. Fig. 11 (a) is for the longest wave period 8.09 s and Fig. 11 (b) for the shortest wave period 3.89s. In these figures, the calculated solutions agree well with the analytical ones.

Figures 12 (a) and 12 (b) show the results of the numerical calculation of the wave field around a detached breakwater for regular and irregular waves, respectively. Figures 13 and 14 show the wave height variations along the X- and Y-axis. As seen in these figures, the distribution of wave height is smoother

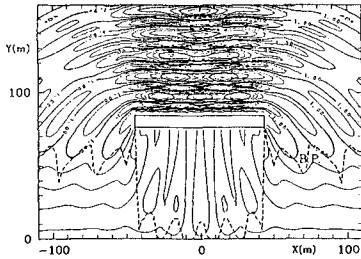


(a) the longest wave period 8.09s

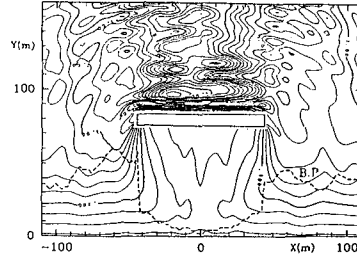


(b) the shortest wave period 3.89s

Fig. 11: Comparison of the analytical and calculated wave height variations of component wave



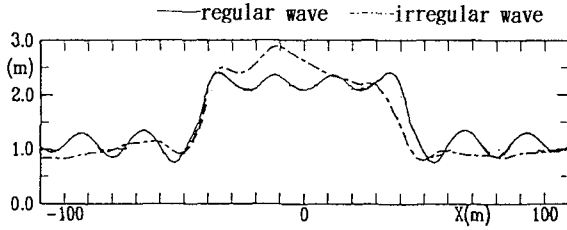
(a) regular wave field



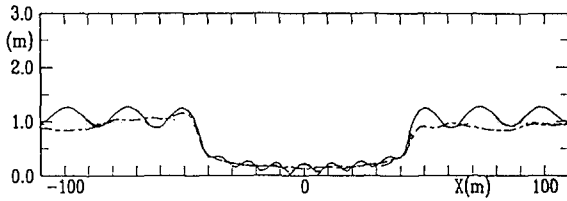
(b) irregular wave field

Fig. 12: Comparison of the regular wave field and irregular wave field around a detached breakwater

for the irregular waves because of the frequency and directional distribution. For the regular waves, nodes and anti-nodes are clearly seen. The asymmetrical distribution of wave height for irregular waves is due to a statistical variation because the significant wave height is obtained by using  $H_{1/3} = 4.004\eta_{rms}$ , where  $\eta_{rms}$  is the root mean square of the water surface elevation.

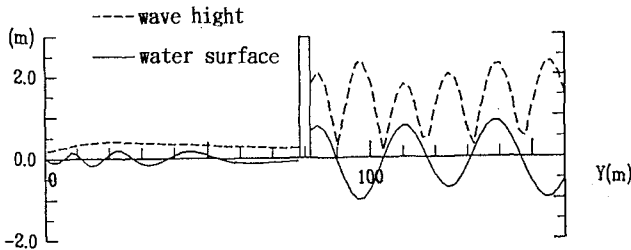


(a) front of detached breakwater

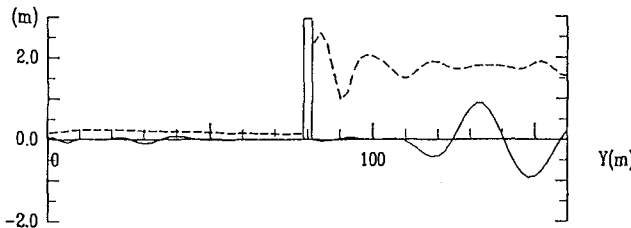


(b) rear of detached breakwater

Fig. 13: Comparison of wave height variations of regular and irregular waves along the  $x$ -axis



(a) regular wave



(b) irregular wave

Fig. 14: Comparison of wave height variations of regular and irregular waves along the  $y$ -axis.

## 6 Conclusion

A time-dependent mild slope equation for random waves was derived from Berkhoff's mild slope equation. An advantage of the present equation is that it allows to calculate the time evolution of the random wave transformation due to refraction and diffraction and can easily incorporate a breaking wave model. The results of numerical calculations were compared with theoretical predictions and laboratory data, which confirmed the validity of the present equation.

## References

- Berkhoff, J. C. W.(1972) : Computation of combined refraction-diffraction, Proc. 13th Int. Conf. on Coastal Eng., pp. 191-203.
- Isobe, M.(1987) : A parabolic equation model for transformation of irregular waves due to refraction, diffraction and breaking, Coastal Eng. in Japan, Vol. 30, No. 1, pp. 38-48.
- Ohyama, T. and N. Nadaoka (1990) : Modeling the transformation of nonlinear waves passing over a submerged step, Proc. Japanese Conf. on Coastal Eng., JSCE, Vol. 37, pp. 16-20 (in Japanese).
- Watanabe, A. , M. Isobe , T. Izumiya and H. Nakano (1988) : Analysis for shoaling and breaking of random waves with time-dependent mild-slope equations, Proc. 35th Japanese Conf. on Coastal Eng., pp. 173-177 (in Japanese).

## CHAPTER 31

### EVALUATION OF NUMERICAL MODELS ON WAVE-CURRENT INTERACTIONS

Jung L. Lee<sup>1</sup> and Hsiang Wang<sup>2</sup>

#### Abstract

Five contemporary numerical models on wave-current interactions are evaluated in this paper. The bases of evaluation are mathematical exactness, degree of computational difficulty and practical applicability in terms of the abilities of handling shoaling, refraction, diffraction, reflection and wave-current interaction. Recommendations are given in matrix form on the relative merit of each model.

#### 1 Introduction

In the past two decades, we have witnessed remarkable progress in modeling nearshore hydrodynamics by numerical techniques. Prediction of nearshore waves took a new dimension with the introduction of the mild slope equation by Berkhoff (1972) which is capable of handling the combined effects of refraction and diffraction. Since then significant progress has been made in computational techniques as well as model capabilities, notably by Radder (1979), Copeland (1985), Ebersole (1986), Yoo and O'Connor (1986a), and Dalrymple et al. (1989).

Prediction of nearshore, wave-induced currents has also advanced considerably since some of the earlier development by Noda et al. (1974) and Ebersole and Dalrymple (1979). Both of these earlier models were driven by a wave refraction model but with no current feed back. More recently, Yoo and O'Connor (1986b) developed a wave-induced circulation model based upon what could be classified as a hyperbolic-type wave equation; Yan (1987) and Winer (1988) developed their interaction models based upon parabolic approximation of the wave equation.

Five wave and current coupled models were selected for evaluation. Of the five wave models, four were selected from existing literature and one was developed by the authors. The main differences among the 5 models are their governing wave equations and the as-

---

<sup>1</sup>Graduate Assistant, Coastal and Oceanographic Engineering Department, Univ. of Florida

<sup>2</sup>Professor, Coastal and Oceanographic Engineering Department, 336 Weil Hall, University of Florida, Gainesville, FL 32611, USA

sociated numerical methods; they include two hyperbolic types, two elliptic types, and one parabolic type. Each can be derived from the mild slope equation given by Kirby(1984), with varying degrees of approximations. The current model is governed by the depth-integrated momentum and continuity equations, much the same as given by Ebersole and Dalrymple (1979).

In this paper, the emphasis is on evaluating wave models and their suitability for wave-current interaction modeling. Thus, the current condition is given as input rather than coupled with the circulation model. The evaluation of fully coupled models has been presented in Lee and Wang (1992).

## 2 Wave equations

The governing equations of the 5 models are all derivable from the linearized mild slope wave-current interaction equation given by Kirby (1984) as follows:

$$\frac{D^2\hat{\phi}}{Dt^2} + (\nabla \cdot U) \frac{D\hat{\phi}}{Dt} - \nabla \cdot (CCg\nabla\hat{\phi}) + (\sigma^2 - k^2CCg)\hat{\phi} = 0 \tag{1}$$

- where,  $\hat{\phi}$  is the surface velocity potential
- $C$  is the relative phase velocity ( $\sigma/k$ )
- $Cg$  is the relative group velocity ( $\partial\sigma/\partial k$ )
- $\sigma$  is the intrinsic angular frequency ( $\sigma^2 = gk \tanh kh$ )
- $\omega$  is the apparent angular frequency
- $k$  is the wave number
- $h$  is the water depth
- $U$  is the steady current velocity vector ( $u, v$ ).

The intrinsic frequency and wave number for progressive waves are determined by the Doppler equation

$$\omega = \sigma_d + U \cdot \mathbf{K}$$

where  $\sigma_d$  and  $\mathbf{K}$  are, respectively, the intrinsic angular frequency and wave number vector with the inclusion of diffraction effect. Ignoring the mean surface gradient in the above equation yields the conventional Doppler equation (see Eq.(9)). If any reflective wave exists in the current field, the intrinsic frequency and wave number of the reflected wave should be determined by a separate Doppler equation. Therefore, wave reflection effects may be included by superposition.

### 2.1 Hyperbolic-type model I (HM I) [Ohnaka et al., 1988]

The governing equations are a pair of first-order equations which constitute a hyperbolic system similar to the shallow water wave equations. Ito and Tanimoto (1972) first proposed the approach and Copeland (1985) completed the formulation through the application of the mild slope equation. Ohnaka et al. (1988) extended the formulation to a wave and current coexisting field to obtain:

$$\left[1 + \frac{\sigma}{\omega} \left(\frac{Cg}{C} - 1\right)\right] \frac{\partial\eta}{\partial t} + \nabla \cdot (U\eta) + \nabla \cdot \left(\frac{CCg\nabla\hat{\phi}}{g}\right) = 0 \tag{2}$$

$$\frac{\partial\nabla\hat{\phi}}{\partial t} + \omega g \nabla \frac{\eta}{\sigma} = 0 \tag{3}$$

The unknowns to be solved are the wave surface elevation,  $\eta$ , and the gradient of surface velocity potential,  $\nabla\hat{\phi}$ . It can be shown that in the presence of strong currents these equations will lead to conditions inconsistent with the conservation equation of wave action given by Bretherton and Garrett (1968).

### 2.2 Hyperbolic-type model II (HM II) [Yoo et al., 1986b]

In this second model the governing equations are based on kinematic and dynamic conservation equations of wave properties averaged over both a wave period and a wave length; they are of the following forms:

$$\frac{\partial \mathbf{K}}{\partial t} + (Cg \frac{\mathbf{K}}{k} + U) \cdot \nabla \mathbf{K} + \mathbf{K} \cdot \nabla U + \frac{k\sigma}{\sinh 2kh} \nabla h - \frac{CCg}{2a} \nabla [\nabla^2 (\frac{a}{\sigma})] = 0 \quad (4)$$

$$\frac{\partial}{\partial t} (\frac{a^2}{\sigma}) + \nabla \cdot [(Cg \frac{\mathbf{K}}{k} + U) \frac{a^2}{\sigma}] = 0 \quad (5)$$

Eqs.(4) and (5) are used to solve for  $\mathbf{K}$  and  $a^2/\sigma$ .

### 2.3 Elliptic-type model I (EM I)

The surface velocity potential is now assumed to be a harmonic function of time expressed as:

$$\hat{\phi}(\mathbf{x}, t) = \tilde{\phi}(\mathbf{x})e^{-i\omega t}$$

where  $\tilde{\phi}(\mathbf{x})$  is the surface potential in steady state. Substituting the above equation into Eq.(1) gives,

$$\begin{aligned} -i\omega \{2U \cdot \nabla \tilde{\phi} + \tilde{\phi}(\nabla \cdot U)\} + (U \cdot \nabla)(U \cdot \nabla \tilde{\phi}) + (\nabla \cdot U)(U \cdot \nabla \tilde{\phi}) \\ - \nabla \cdot (CCg \nabla \tilde{\phi}) + (\sigma^2 - \omega^2 - k^2 CCg)\tilde{\phi} = 0 \end{aligned} \quad (6)$$

The above equation together with the Doppler equation permits us to solve for  $\tilde{\phi}(\mathbf{x})$ .

### 2.4 Elliptic-type model II (EM II) [Jeong, 1990]

The surface velocity potential is approximated by wave-period and wave-length averaged quantity as,

$$\hat{\phi}(\mathbf{x}, t) = A(\mathbf{x})e^{i\psi} = A(\mathbf{x})e^{i(\int \mathbf{K} \cdot d\mathbf{x} - \omega t)} \quad (7)$$

Substituting the above equation into the linearized free surface boundary conditions, we obtain

$$A = -i \frac{g}{\sigma_d} a \quad (8)$$

$$\sigma_d^2 = \sigma^2 - \frac{g}{A} \nabla A \cdot \nabla \bar{\eta} \quad (9)$$

Where  $\sigma_d$  is the intrinsic angular frequency with diffraction effect as mentioned earlier, and  $\bar{\eta}$  is the mean surface elevation. The second term in Eq.(9) can be usually be neglected. Substituting Eqs.(7-9) into Eq.(1) and after some manipulation the real and imaginary parts yield two equations; the real part is the energy conservation equation of elliptic type,

$$\nabla \cdot [(Cg \frac{\mathbf{K}}{k} + U) \frac{a^2}{\sigma}] = 0 \quad (10)$$

and the imaginary part is the Eikonal equation,

$$CCg \frac{a}{\sigma} K^2 - \nabla \cdot (CCg \nabla \frac{a}{\sigma}) - k^2 CCg \frac{a}{\sigma} = 0 \tag{11}$$

Since there are 3 unknowns,  $a$ ,  $K_x$  and  $K_y$ , another equation expressing the irrotationality of wave number is introduced.

$$\nabla \times \mathbf{K} = 0 \tag{12}$$

2.5 Parabolic-type model (PM) [Winer, 1988]

The parabolic approximation to the elliptic-type equation of harmonic wave motion (Eq.6) is derived by 1) splitting the surface potential into two components ( $\tilde{\phi} = \tilde{\phi}^+ + \tilde{\phi}^-$ ) and 2) assuming that the waves are oriented in the x-direction, thus, allowing  $k_y \cong 0$ . There were several approaches with varying degrees of approximations to arrive at various terms of parabolic equation. The version suggested by Winer (1989) has the final form,

$$\begin{aligned} \sigma(Cg_x + u) \frac{\partial A'}{\partial x} + i(k_o - k_x)(Cg_x + u)A' + \frac{1}{2} \frac{\partial}{\partial x} [\sigma(Cg_x + u)]A' = \\ \frac{i}{2} \frac{\partial}{\partial y} (CCg \frac{\partial A'}{\partial y}) - \frac{\omega}{2} \frac{\partial v}{\partial y} A' - \omega v \frac{\partial A'}{\partial y} \end{aligned} \tag{13}$$

where

$$A' = \tilde{\phi}^+ e^{-ik_o x}, \quad Cg_x = Cg \frac{k_x}{k}$$

3 Numerical schemes

The numerical methods of all models fall under the category of finite difference method (FDM). Table 1 summarizes the numerical schemes as well as the unknowns of each model. The downwave and side boundary conditions are summarized in Table 2. A brief description of the numerical scheme of each model is given here.

Table 1

Model	Unknowns	Numerical scheme
HM I	$\eta$ and $\nabla \tilde{\phi}$	FDM on a staggered grid system
HM II	$a$ and $\mathbf{K}$	FDM on a staggered grid system
EM I	complex $\tilde{\phi}$	Combined Gragg's method-FDM
EM II	$a$ , $K$ and $\theta$	Generalized Lax-Friedrich FDM
PM	complex $A'$	Crank-Nicholson FDM

Table 2

Model	Downwave B.C.	Side B.C.
HM I	Method of characteristics	$\mathcal{D}_y \eta = ik_y \eta$
HM II	$\mathcal{D}_x a = 0, \mathcal{D}_x K_x = 0$	$K_y$ given by Snell's law
EM I	-	$\mathcal{D}_y \tilde{\phi} = ik_y \tilde{\phi}$
EM II	$\mathcal{D}_x a = 0, \mathcal{D}_x \theta = 0$	$\theta$ given by Snell's law
PM	-	$\mathcal{D}_y A' = ik_y A'$

$\mathcal{D}$ =finite difference operator



### 3.1 Hyperbolic model I

The numerical technique is based on Ohnaka et al. (1988). However, the technique of treating boundary conditions and calculating wave angles has been improved by the introduction of the complex variables as given in Table 2. For details see Lee and Wang (1992).

In the case of wave-current interaction, the determination of wave angle is very important because phase speed, group velocity and intrinsic frequency are determined through the dispersion equation which contains the scalar product of the current vector and the wave number vector. The wave angle is calculated at the center of each grid location by the approximation

$$\theta \cong \tan^{-1} \left[ \frac{\mathcal{R}e(\nabla_y \hat{\phi} / \eta)}{\mathcal{R}e(\nabla_x \hat{\phi} / \eta)} \right]$$

and the wave height is calculated by

$$H = 2\sqrt{\mathcal{R}e\{\eta\}^2 + \mathcal{I}m\{\eta\}^2}$$

### 3.2 Hyperbolic model II

The numerical scheme used here is the same as detailed in Yoo and O'Connor (1986a). The wave amplitude is specified at the center of the grid whereas the wave number vector is situated at the side of the grid.

The wave angle is calculated at the center of each grid location

$$\theta = \tan^{-1} \left( \frac{K_y}{K_x} \right)$$

where the wave number vector indicates the value at the center of each grid and the wave angle is measured from the x-axis.

### 3.3 Elliptic model I

The numerical scheme was developed by the authors. Here, Eq.(6) is treated as an ordinary differential equation in x while letting the y-direction differential operator,  $\mathcal{D}$ , be approximated by a finite difference scheme,

$$\begin{aligned} & (u^2 - CCg)\tilde{\phi}_{xx} + \{-2i\omega u + 2uu_x + u_y v + uv_y - (CCg)_x\}\tilde{\phi}_x \\ & + 2uv\mathcal{D}_y(\tilde{\phi}_x) + \{-2i\omega v + 2vv_x + uv_x + u_x v - (CCg)_y\}\mathcal{D}_y(\tilde{\phi}) \\ & + (v^2 - CCg)\mathcal{D}_{yy}(\tilde{\phi}) + \{-i\omega(u_x + v_y) + \sigma^2 - \omega^2 - k^2 CCg\}\tilde{\phi} = 0 \end{aligned}$$

in which subscripts indicate the differentiations.

The above equation is then converted into a pair of first-order equations by the simple expediency of defining the derivative as a second function.

$$\begin{aligned} \tilde{\phi}_x &= \tilde{\phi}_1 \\ \tilde{\phi}_{1x} &= \frac{1}{u^2 - CCg} \{ \{-2i\omega u + 2uu_x + u_y v + uv_y - (CCg)_x\}\tilde{\phi}_1 \\ & + 2uv\mathcal{D}_y(\tilde{\phi}_1) + \mathcal{F}(\tilde{\phi}) \} \end{aligned}$$

where

$$\mathcal{F}(\tilde{\phi}) = \{-2i\omega v + 2vv_x + uv_x + u_xv - (CCg)_y\} \mathcal{D}_y \tilde{\phi} + (v^2 - CCg) \mathcal{D}_{yy} \tilde{\phi} + (-i\omega(u_x + v_y) + \sigma^2 - \omega^2 - k^2 CCg) \tilde{\phi}$$

These ordinary differential equations are solved numerically using Gragg's method for which the main algorithm for a differential equation  $\phi'(x) = f(x, \phi(x))$  is given as

$$\begin{aligned} y_1 &= \phi_{i-1} + hf(x_{i-1}, \phi_{i-1}) \\ y_{j+1} &= y_{j-1} + 2hf(x_{i-1} + jh, y_j) \quad j = 1, 2, \dots, n-1 \\ \phi_i &\cong (y_n + y_{n-1} + hf(x_i, y_n))/2 \end{aligned}$$

where  $h$  is a subgrid space defined as  $h = \Delta x/n$ .

The upwave boundary condition is merely the specified complex  $\tilde{\phi}$  determined by the incident wave amplitude and wave angle. The side boundary conditions are either non-reflective or reflective. The non-reflective boundary condition can be specified by Snell's law in the absence of diffraction,

$$\tilde{\phi}_y = ik_y \tilde{\phi} \quad \text{where } k_y = k \sin \theta = k_o \sin \theta_o$$

The reflective boundary condition is expressed as

$$\tilde{\phi}_y = 0 \quad \text{i.e. } k_y = 0$$

If there is any reflective structure posed in the  $y$ -direction, the direction of the reflected waves is the mirror image of that of the incident wave. Since the unknown in this model is the complex surface potential, the reflected wave field can be easily specified as the conjugate by tracing the computation backward.

The wave angle is calculated by

$$\theta = \tan^{-1} \left( \frac{K_y}{K_x} \right)$$

where

$$K_x = \mathcal{I}m \left\{ \frac{\tilde{\phi}_1}{\tilde{\phi}} \right\}, \quad K_y = \mathcal{D}_y^\pm S$$

with

$$\begin{aligned} S &= \mathbf{K} \cdot \mathbf{x} = \tan^{-1} [\mathcal{I}m(\tilde{\phi})/\mathcal{R}e(\tilde{\phi})] \\ \mathcal{D}_y^\pm S &= [S_{j+1} - S_j]/\Delta y \quad \text{or} \quad [S_j - S_{j-1}]/\Delta y \end{aligned}$$

The wave height is calculated easily by

$$H = 2\sqrt{\mathcal{R}e\left\{\frac{\sigma}{g}\tilde{\phi}\right\}^2 + \mathcal{I}m\left\{\frac{\sigma}{g}\tilde{\phi}\right\}^2}$$

### 3.4 Elliptic model II

By introducing wave angle,  $\theta$ , Eq.(11) can be expressed as,

$$AK^2 - C = 0$$

where,

$$A = CCg\frac{a}{\sigma}, \quad C = \nabla \cdot (CCg\nabla\frac{a}{\sigma}) + k^2CCg\frac{a}{\sigma}$$

The solution of  $K$  is simply,

$$K = \sqrt{\frac{C}{A}}$$

The generalized Lax-Friedrich method is employed to solve Eqs.(10) and (12). Both unknown,  $\theta$  and  $a$ , are solved row by row using an explicit FDM (Ebersole et al. (1986) or Jeong (1990)).

**3.5 Parabolic model**

Eq.(13) is solved by the Crank-Nicolson scheme using a double sweep approach. The first sweep is required to approximate the x-directional component of group velocity.

The wave angle is calculated by

$$\theta = \tan^{-1}\left(\frac{K_y}{K_x}\right)$$

where

$$K_x \cong k\sqrt{1 - (K_y/k)^2}, \quad K_y = D_y^\pm S$$

with

$$S = \int K_x dx - k_0 x + K_y y = \tan^{-1}[\text{Im}(A')/\text{Re}(A')]$$

$$D_y^\pm S = [S_{j+1} - S_j]/\Delta y \quad \text{or} \quad [S_j - S_{j-1}]/\Delta y$$

The wave height is calculated by,

$$H = 2\sqrt{\text{Re}\left\{\frac{\sigma}{g}A'\right\}^2 + \text{Im}\left\{\frac{\sigma}{g}A'\right\}^2}$$

**4 Comparisons of wave models**

**4.1 Basic equation**

The nature and the exactness of the basic equations in each model are evaluated in terms of dynamics (energy conservation) and kinematics (Eikonal equation). The comparisons are summarized in Table 3. For details see Lee and Wang (1992).

Table 3

Model	Assumption	Energy eq.	Eikonal eq.	Violating cond.
HM I	$g\eta \cong i\sigma\phi$	approx.	exact	strong current
HM II	$\nabla(CCg) \cong 0$	exact	approx.	steep slope
EM I	-	exact	exact	-
EM II	-	exact	exact	-
PM	$k_y \cong 0$	approx.	approx.	wide angle

4.2 Computational difficulty

The degree of computational difficulty is measured in terms of stability as well as CPU time. The stability criteria given below are obtained for ideal cases only. Therefore, they are not general as well as not vigorous.

Table 4

Model	Stability
HM I	$\Delta t \leq T / [(L_{max} / \Delta x)^2 + (L_{max} / \Delta y)^2]^{1/2}$
HM II	$\Delta t \leq T / [(n_a L_{max} / \Delta x)^2 + (n_a L_{max} / \Delta y)^2]^{1/2}$
EM I	$\Delta y \geq L_{max} / \pi$ for central difference method
EM II	$\Delta y \geq L_{max} / \pi$ for $\tau = 0$
PM	stable

$n_a = Cg_a / C_a$  (with subscript *a* indicating the absolute)

The comparison for the computational time is also not general. Rather, a specific configuration as shown in Fig.1 is used as the test bench mark. This configuration is a circular shoal used by Ito and Tanimoto (1972) in their laboratory experiment to study combined diffraction and refraction. This configuration has been cited by many authors for verification purposes. Here, the same grids and same accuracy criteria are used in all models. Wave heights along three cross-sections as shown in Fig.2 are compared with the laboratory data of Ito and Tanimoto. The CPU time on a VAX-8350 computer and the values of the agreement parameter are given below.

Table 5

Model	CPU time	<i>d</i> (Sec.1)	<i>d</i> (Sec.2)	<i>d</i> (Sec.3)
HM I	15 min	0.98	0.97	0.95
HM II	12 min	0.97	0.97	0.96
EM I	24 sec	0.96	0.97	0.94
EM II	5 min	0.98	0.97	0.96
PM	17 sec	0.97	0.97	0.95

The agreement is based on an index, *d*, given here as an agreement parameter (Willmott, 1981):

$$d = 1 - \frac{\sum_i^N (P_i - O_i)^2}{\sum_i^N (|P_i - \bar{O}| + |O_i - \bar{O}|)^2}$$

where *P<sub>i</sub>* is the numerical value, *O<sub>i</sub>* is the theoretical or observed value and  $\bar{O}$  is the mean of the variates *O<sub>i</sub>*. The values for *d* vary between 0 and 1.0, with 1.0 indicating perfect agreement.

4.3 Wave shoaling and refraction

To test wave shoaling and refraction, numerical results were compared with the analytical solutions based on the energy conservation equation and Snell's law for waves propagating over a uniform slope. The input data are uniformly given to each model as follows:

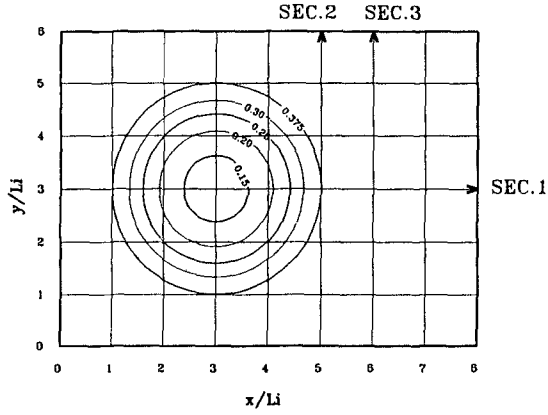


Figure 1: Shoal configuration for comparison of CPU time (concentric circular contours of  $h/L_i$ ).

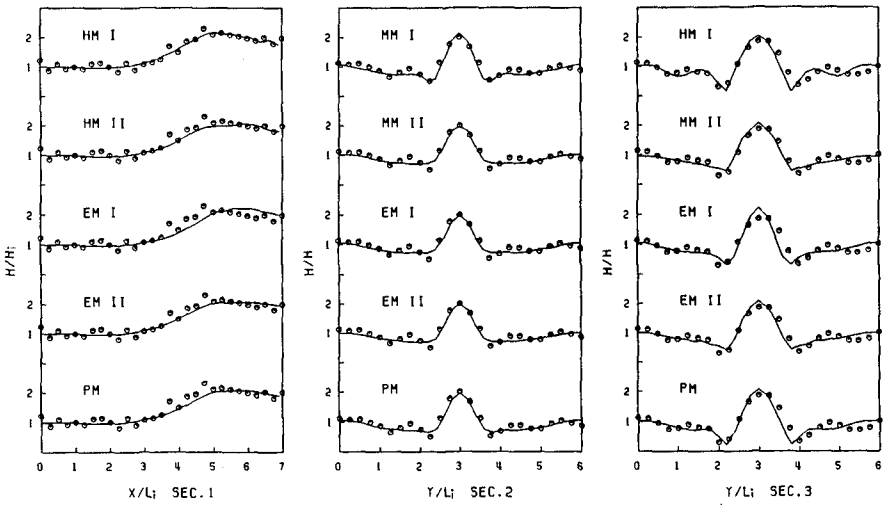


Figure 2: Comparison with the laboratory data of Ito and Tanimoto (1972).

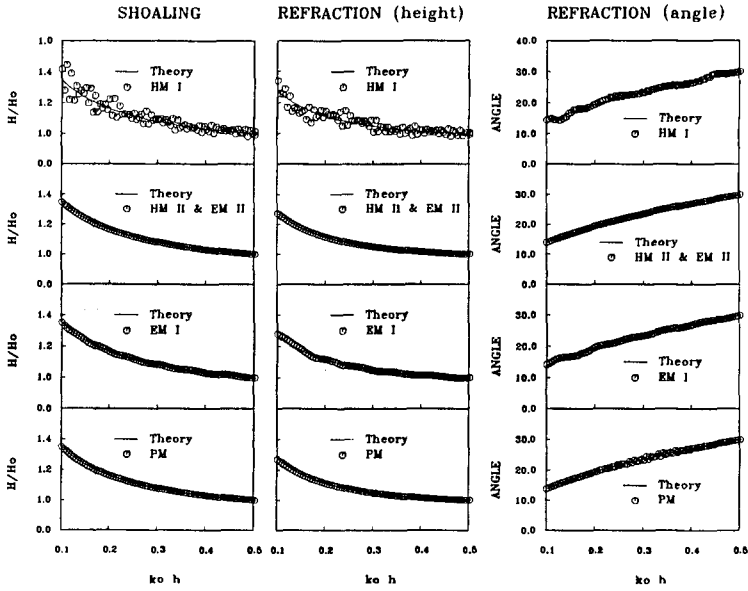


Figure 3: Comparison of wave shoaling and wave refraction.

NX	NY	$\Delta x(m)$	$\Delta y(m)$	T(sec)
101	21	0.02	0.14	0.8

The time step in the hyperbolic models is fixed at 0.01 sec.

As shown in Figure 3, all models except hyperbolic model I produce results of good agreement. Hyperbolic model I, on the other hand, induces periodical fluctuations. The numerical error appears to be related to the ratio of grid size to wave length. As the wave length shortens towards shoreline the error becomes larger and also propagates up-wave as time progresses. The numerical results were taken along a center grid line in x- axis.

#### 4.4 Wave diffraction

Wave diffraction was evaluated by comparing wave height with the analytical solution given by Wiegel (1962) for a semi-infinite breakwater. The input data are uniformly given as NX=91, NY=75,  $\Delta x=0.04 m (=0.1 L)$ ,  $\Delta y=0.08 m$  for  $T=0.511 sec$  except elliptic model II where NY=38 and  $\Delta y=0.16 m$  were used to avoid numerical instability. The time step is 0.01 sec in the hyperbolic models.

Figure 4 shows the comparisons for waves approaching normal to the breakwater axis. All models appear to agree well with the analytical result. For 30° angle to the normal, however, only hyperbolic model I and elliptic model II perform adequately (Fig.5). The performance in general can be improved by reducing  $\Delta y$ , except elliptic model II which is almost stable regardless the size of  $\Delta y$ .

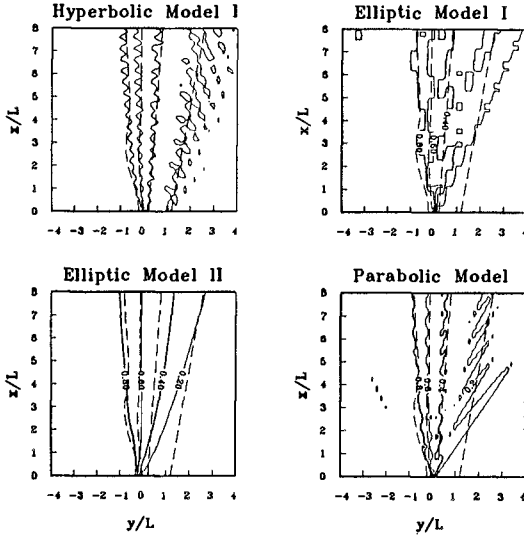


Figure 4: Comparison of wave diffraction for semi-infinite breakwater ( $0^\circ$ ) between analytic solutions (dotted line) and numerical solutions (solid contour line of 0.8, 0.6, 0.4 and 0.2 diffraction coeff. from left).

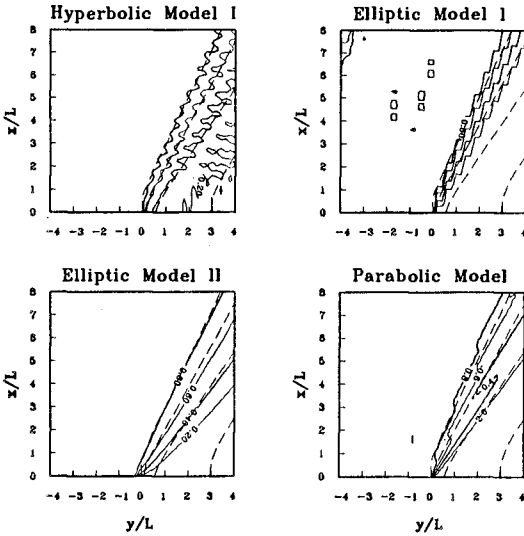


Figure 5: Comparison of wave diffraction for semi-infinite breakwater ( $30^\circ$ ).

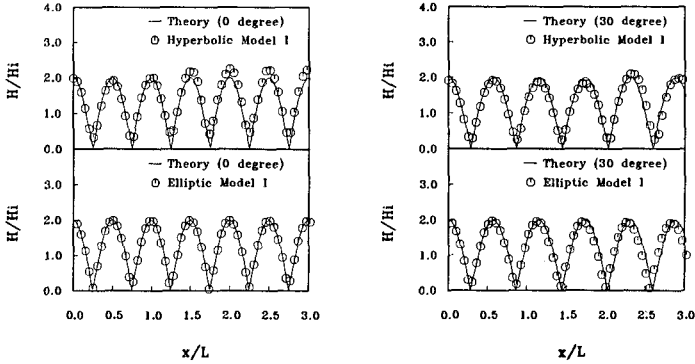


Figure 6: Wave reflection tests against wall.

4.5 Wave reflection

Wave reflection was tested for the case of waves approaching a seawall at 0° and 30° in constant deep water depth of 3 m, using the listed input conditions,

input data	NX	NY	$\Delta x(m)$	$\Delta y(m)$	$\Delta t(sec)$	$T(sec)$
HM	61	21	0.08	0.08	0.02	1.0
EM I	61	21	0.08	0.50	—	1.0

Owing to the finite grid size and time step a numerical error is also expected. Figure 6 shows that the numerical results, on the whole, agree well with theory for both 0° and 30° wave angles. The hyperbolic model tends to yield slightly larger error in wave height, whereas the elliptic model I produces slightly larger phase error.

The wave reflection against the bottom slope was also compared with the 3-dimensional numerical solution represented by Booij (1983). Both models run in this study give reasonably good agreement as shown in Fig.7.

4.6 Wave-current interaction

Wave-current interaction is compared for cases of colinear current and wave refraction due to the shearing current, both in constant deep water depth of 3 m. The analytic solution for the shearing current is given by Longuet-Higgins and Stewart (1961). The given wave conditions are  $H_i=0.1$  m at the upwave boundary and  $T=1$  sec. Waves are allowed to freely pass through the downwave boundaries. The input data are uniform with  $NX=101$ ,  $NY=21$ ,  $\Delta x=0.1$  m  $\Delta y=0.6$  m for the elliptic models and  $\Delta y=0.1$  m for the rest.  $\Delta t$ , whenever applicable, is taken as 0.01 sec.

The comparisons with analytical solutions are given in Fig.8. For the colinear case, all except hyperbolic model I performed adequately. For non-colinear case, hyperbolic model II and elliptic model II yield good results; the rest all produce varying degrees of inconsistency.



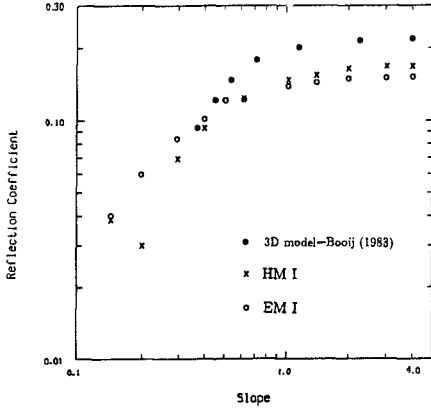


Figure 7: Wave reflection tests against bottom slope.

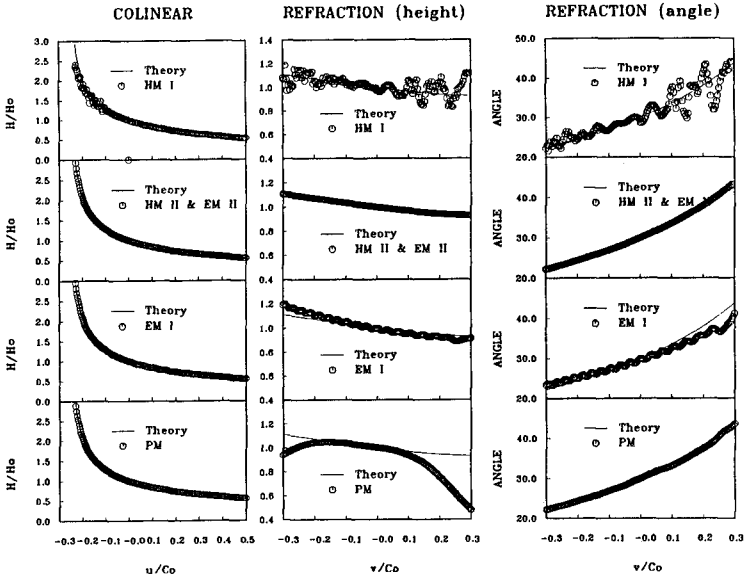


Figure 8: Wave-current interaction comparison.

4.7 Summary

Each model was evaluated or run on a number of bench mark cases. The final evaluations with assigned rankings are given in the following matrix:

Table 6

Case	HM I	HM II	EM I	EM II	PM
Governing equation	M	O	O	O	M
Programming ease	O	M	O	M	O
Numerical stability	M	X	X	X	O
Computational time	X	X	O	M	O
Shoaling	O	O	O	O	O
Refraction	M	O	M	O	M
Diffraction (normal)	O	O	O	O	O
Diffraction (oblique)	O	O	X	O	M
Reflection (vertical)	O	-	O	-	-
Reflection (slope)	O	-	O	-	-
Current (colinear)	M	O	O	O	O
Current (refraction)	X	O	M	O	X

O: good M: marginal X: bad -: not applicable

5 Conclusions

Five numerical wave-current interaction models were evaluated in a two-dimensional domain through mutual comparisons. The evaluation is limited in that the bench mark cases are restricted to those with either theoretical solution or accepted hydraulic model results. Within this context, the performance of each model is evaluated, and the comparisons are given in a matrix form. At this moment, there appears to be no single model that clearly outperforms the others. The selection of a model for application depends upon the intended purpose. Therefore, the present paper should serve as a useful guide line for model selection.

References

- [1] Berkhoff, J.C.W., 1972. "Computation of combined refraction-diffraction," Proc. 13th ICCE, ASCE, pp.471-490.
- [2] Booij, N., 1983. "A note on the accuracy of the mild slope equation," Coastal Eng., Amsterdam Netherlands, Vol. 7, pp.191-203.
- [3] Bretherton, F.P. and C.J.R. Garrett, 1969. "Wave trains on inhomogeneous moving media," Proc. Royal Society of London, London, England, Series A, Vol. 302, pp.529-554.
- [4] Copeland, G.J.M., 1985. "A practical alternative to the mild slope wave equation," Coastal Eng., Amsterdam Netherlands, Vol. 9, pp.125-149.
- [5] Dalrymple, R.A., K.D. Suh, J.T. Kirby and J.W. Chae, 1989. "Models for very wide-angle water waves and wave diffraction. Part 2. Irregular bathymetry," J. Fluid Mech. Vol. 201, pp.299-322.

- [6] Ebersole, B.A. and Dalrymple R.A., 1979. "A numerical model for nearshore circulation including convective accelerations and lateral mixing," Ocean Engineering Report No. 21, Dept. of Civil Eng., Univ. of Delaware, Newark, Delaware.
- [7] Ebersole, B.A., M.A. Cialone and M.D. Prater, 1986. "Regional coastal processes numerical modeling system," Report 1, RCPWAVE-A linear wave propagation model for engineering use, Technical report CERC-86-4, US Army Engineer WES, Vicksburg, Mississippi.
- [8] Ito, Y. and K. Tanimoto, 1972. "A method of numerical analysis of wave propagation-Application to wave diffraction and refraction," Proc. 13th ICCE, ASCE, pp.503-522.
- [9] Jeong, S.T., 1990. "Wave transformation in regions of slowly varying depths with currents", Ph.D dissertation, Dept. of Civil Engineering, Seoul National Univ., Seoul, Korea.
- [10] Kirby, J.T., 1984. "A note on linear surface wave-current interaction over slowly varying topography," J. Geophysical Research, Vol. 89, No. C1, pp.745-747.
- [11] Lee, J.L. and H. Wang, 1992. "Evaluation of wave models coupled with the circulation model," UFL/COEL-92/014, Coastal and Oceanographic Engineering Department, Univ. of Florida, Gainesville.
- [12] Longuet-Higgins, M.S. and R.W. Stewart, 1961. "The changes in amplitude of short gravity waves on steady non-uniform currents, J. Fluid Mech., Vol. 10, pp.529-549.
- [13] Noda, E., C.J. Sonu, V.C. Rupert and J.I. Collins, 1974. "Nearshore circulation under sea breeze conditions and wave-current interactions in the surf zone," Tetra Tech Report TC-149-4.
- [14] Ohnaka, S., A. Watanabe and M. Isobe, 1988. "Numerical modeling of wave deformation with a current," Proc. 21th ICCE, ASCE, pp.393-407.
- [15] Radder A.C., 1979. "On the parabolic equation for water-wave propagation," J. Fluid Mech., Vol. 95, pp.159-176.
- [16] Wiegel, R.L., 1962. "Diffraction of waves by a semi-infinite breakwater," J. Hydraulics Div., ASCE, Vol. 88, No. HY1, pp.27-44.
- [17] Willmott, C.J., 1981. "On the validation of models," Phys. Geog. Vol. 2, pp.184-194.
- [18] Winer, H.S., 1988. "Numerical modeling of wave-induced currents using a parabolic wave equation," Ph.D dissertation, Coastal and Oceanographic Engineering Department, Univ. of Florida, Gainesville.
- [19] Yan, Y., 1987. "Numerical modeling of current and wave interaction on an inlet-beach system," Technical Report No. 73, Coastal and Oceanographic Engineering Department, Univ. of Florida, Gainesville.
- [20] Yoo, D. and B.A. O'Connor, 1986a. "Mathematical modeling of wave-induced nearshore circulations," Proc. 20th ICCE, ASCE, pp.1667-1681.
- [21] Yoo, D. and B.A. O'Connor, 1986b. "Ray model for caustic gravity waves," Proc. 5th Congress of Asian and Pacific Division, IAHR, Vol. 3, pp.1-13.

## CHAPTER 32

### WAVE TRANSFORMATIONS OVER A SUBMERGED BAR: EXPERIMENTS AND THEORETICAL INTERPRETATIONS

Gianfranco Liberatore<sup>1</sup> and Marco Petti<sup>2</sup>

#### Abstract

Random wave tests were performed in a flume to investigate wave transformations above a submerged bar built on a horizontal bottom.

Wave data were analysed in the frequency and time domains. In the time domain, reference was made both to short ( $f > 0.5f_p$ ) and long waves (with  $f < 0.5f_p$ ). This allowed in particular investigation of transformations of long waves passing over the bar.

Experimental results were interpreted using a second-order analytical model, able to separate first- and second-order components from given (measured) variance spectra. The analytical method proved to be conveniently applicable as long as breaking phenomena are not too intense.

#### Introduction

As is well-known, the presence of a bar in domains of relatively shallow-water severely modifies the evolution of wave trains during their propagation from deep to shallow water.

At present, knowledge of wave transformations over submerged bars is not satisfactory and theoretical models are still not able to take into account adequately phenomena such as wave breaking occurring on a bar in shallow waters. The problem, certainly interesting from both the theoretical and engineering points of view, has recently been studied in several theoretical investigations aiming at a better mathematical description of wave transformations over a bar. In this regard, recent theoretical contributions deal, for example, with inclusion of breaking effects in Boussinesq-type equations (e.g., Schäffer et al., 1991, Brocchini et al., 1991) or in mild slope type equations (Rojanakamthorn et al. 1989). A number of experimental

---

<sup>1</sup>Associate Professor, Institute of Maritime Structures, University of Padova, Via Ognissanti, 39 – 35129 Padova (Italy)

<sup>2</sup>Researcher, Department of Civil Engineering, University of Firenze, Via S. Marta, 3 – 50139 Firenze (Italy)

investigations has also been conducted recently to improve understanding of wave transformations over bars and to calibrate numerical models (Thorkilsen et al., 1991, Liberatore and Petti, 1991, Battjes and Beji, 1992, Beji et al., 1992, Smith and Kraus, 1992).

The aim of the present paper is first to contribute via experimental investigations to better understanding of the phenomena occurring when a bar is present and, second, to interpret spectral transformations using a non-linear (second-order) theoretical model (Petti, 1991).

### Experimental apparatus and procedure

Investigations were carried out in a flume 33 m long, 1 m wide and 1.2 m deep. A smooth 30 cm high submerged bar, with offshore slope 1:20, inshore slope 1:10 and top width of 2 m was built on the horizontal (concrete) bottom of the flume. A spending beach with slope 1:10 (covered with absorbing mattresses) was also modelled in the flume (Fig. 1). Concrete was used to built both bar and beach.

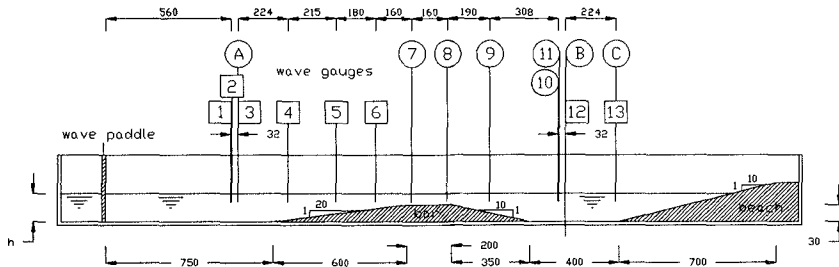


Fig.1 – *Experimental apparatus and location of wave gauges*

Waves were measured at thirteen measuring stations in the flume using eight parallel wire resistance wave gauges in two shifts. In Fig. 1, squared numbers correspond to group 1 (8 gauges, first shift) and circled numbers and letters to group 2 (second shift). Three of the measuring points (A, B and C) were common to the two shifts, enabling the repeatability of the two experiments to be checked. The gauges were set up so as to permit measurement of transformations of waves passing the bar, as well as reflections from both bar and spending beach.

Two offshore water depths of 40 and 50 cm were considered in the experiments; water depth above the bar was therefore 10 and 20 cm respectively.

For each water depth, three different random wave trains were generated. Their characteristics are shown in Tab.1.

Waves in the flume were produced by an hydraulically driven servo-controlled wave generator operated by a personal computer. A white noise filtering technique was used for wave generation. Every run lasted 1000 s. Sampling rate was 10 Hz.

Both short and long waves were analysed by filtering the signal and, considering the frequencies respectively higher and lower than  $0.5f_p$ , reconstructing the time domain signal (the basis for subsequent zero-crossing

analyses) using Inverse Fourier Transforms. This type of procedure was first proposed by Petti (1988).

Table 1 – *Characteristics of waves generated in flume.*

Test no.	$\alpha$	$f_p$ (Hz)	$H_{m_0}$ (cm)	$\gamma$	depth (cm)
1	0.0075	0.650	9.8	2.0	40
2	0.0081	0.781	7.9	3.0	40
3	0.0081	0.850	7.0	3.0	40
4	0.0075	0.650	11.6	2.0	50
5	0.0075	0.781	9.4	3.0	50
6	0.0081	0.850	8.2	3.0	50

Reflection coefficients in front of the bar and in front of the spending beach were also calculated using the method of Goda and Suzuki (1976).

For short waves, these coefficients ranged between 0.17 and 0.22 for the berm, and between 0.22 and 0.30 for the beach (lower values corresponding to shorter peak periods). For long waves, reflection coefficients were much higher, varying between 0.91 and 0.98 for the bar and between 0.62 and 0.70 for the beach.

### Results of experiments

As an example, Figs. 3a and 3b show profiles of short and long waves in the time domain obtained for gauges 1 and 6 during test 1. As the figures show, non-linearities and consequent long waves are definitely more pronounced for gauge 6, located at a shallower depth.

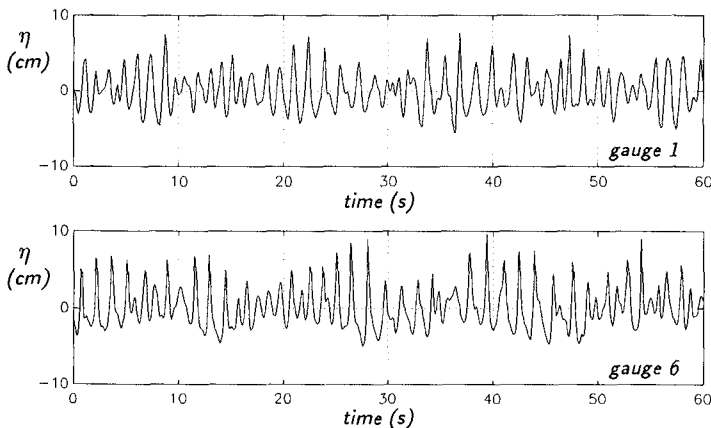


Fig. 3a – *Example of profiles of short waves in time domain (test 1).*

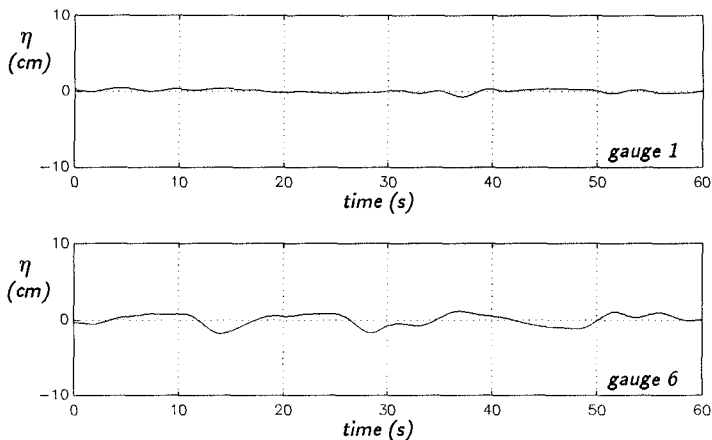


Fig. 3b – Example of profiles of long waves in time domain (test 1).

Spectral analyses generally reveal non-linear transformations of spectra on the seaside slope of the bar, with build-up of energy at low and high frequencies ( $f=2f_p$ ) due to shallow water effects. As a consequence of wave breaking processes on the bar, further transformations of spectra occur, leading to decreased energy depending on intensity of breaking. Behind the bar, rather broad, uniform spectra result.

Wave spectra computed during test 1 ( $h=40$  cm,  $f_p=0.65$  Hz,  $H_{m0}=9.8$  cm) are shown as examples in Figs. 4a and 4b.

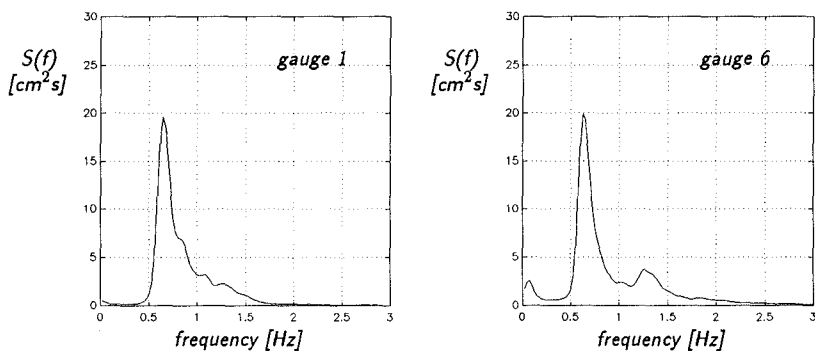


Fig.4a – Wave spectra obtained for test 1 (gauges 1 and 6).

Figs. 5 and 6 show trends for significant short wave heights  $H_s$  and for corresponding periods  $T_s$ , obtained for the two water depths of 40 and 50 cm, for all random wave trains generated during the experiments.

Figs. 5a show some increases in wave heights in the wave trains considered, due to shoaling effects, reaching a maximum on the seaside slope of the bar.

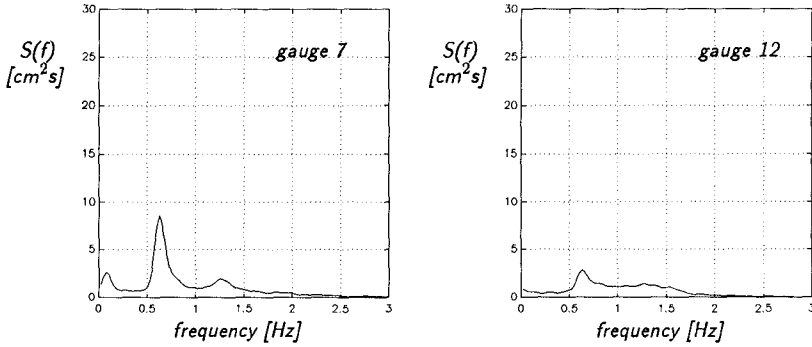


Fig.4b – Wave spectra obtained for test 1 (gauges 7 and 12)

Then decreases occur, due to breaking effects for waves passing the bar, with (nearly) constant wave heights for the three wave trains considered here.

Similar trends are observed for the greater water depth (50 cm; Fig. 6a), although in this case breaking processes are weaker and decreases in wave height are also less evident.

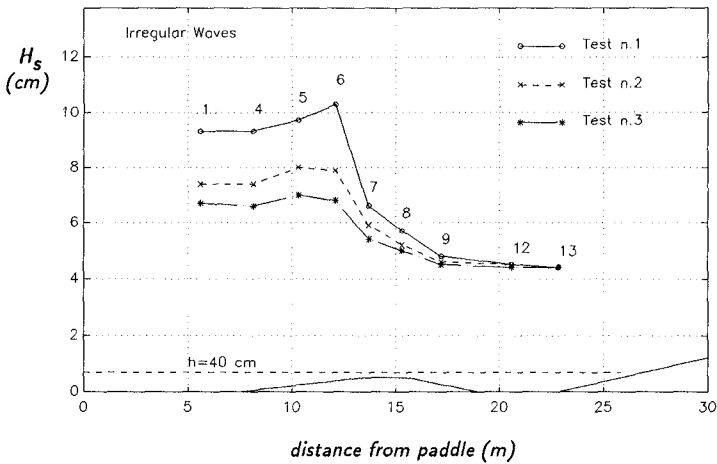


Fig. 5a – Significant wave heights of short waves calculated along flume for tests 1 – 3.

As regards wave periods, in the case of the 40 cm depth (Fig. 5b), after slight, rather uniform increases up to the top of the bar, decreases occur after the bar, and these are probably related to the intensity of breaking.

For the 50 cm water depth (Fig. 6b), periods are quite uniform with slight increases in the area of the bar.



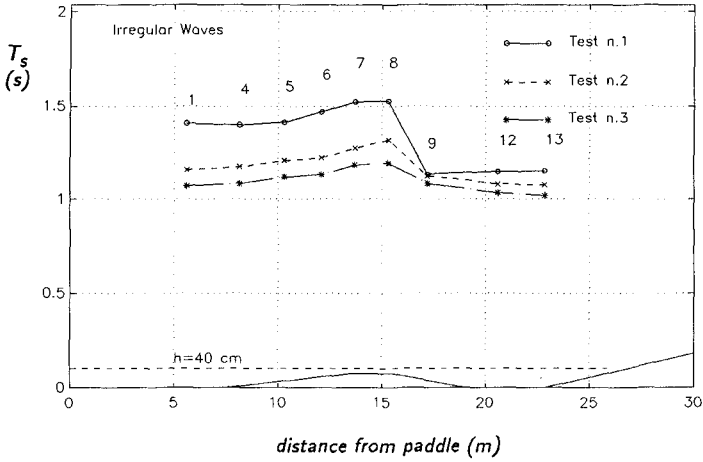


Fig. 5b—Significant periods of short waves calculated along flume for tests 1–3.

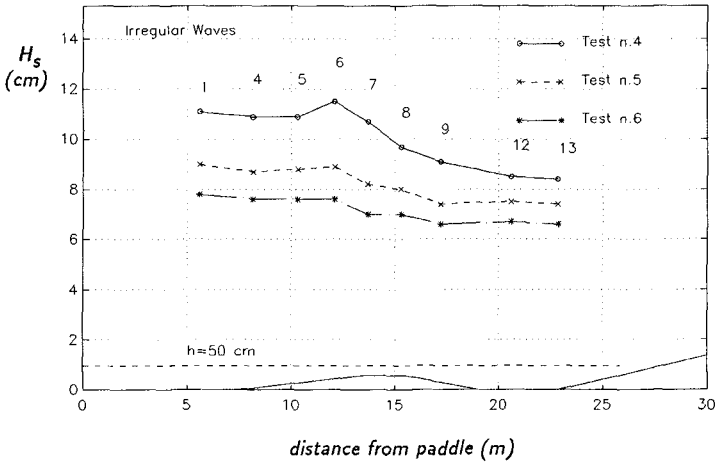


Fig. 6a—Significant heights of short waves calculated along flume for tests 4–6.

As regards long waves (Figs. 7a and 7b), in the case of the 40 cm water depth, their significant wave height initially increases, reaching a maximum on the top of the bar. After that, they rapidly decrease, although their height is still higher than offshore the bar.

This effect might at first sight be ascribed to flume seiches: this, however, would not explain wave height asymmetries with respect to the bar.

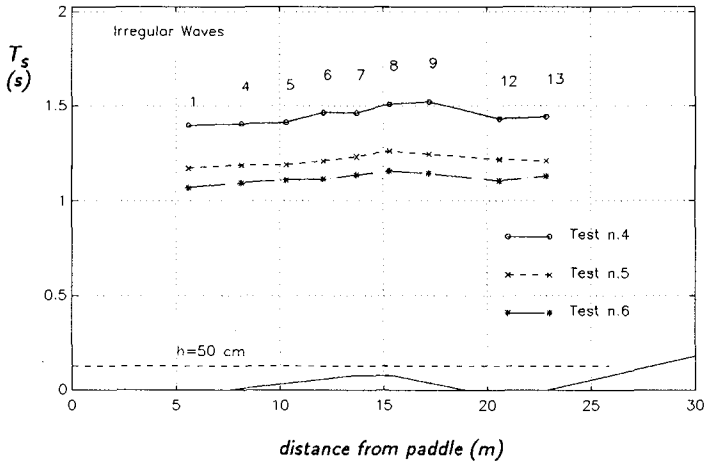


Fig. 6b—Significant periods of short waves calculated along flume for tests 4–6.

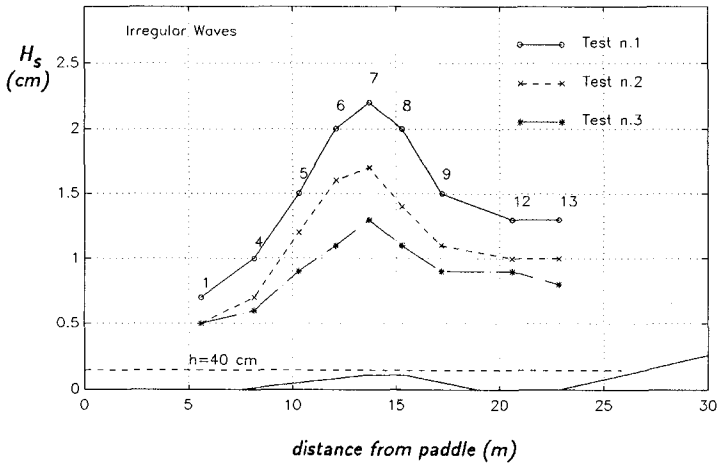


Fig. 7a—Significant heights of long waves calculated along flume for tests 1–3.

Instead, in our opinion, this phenomenon may more probably be ascribed either to seiches occurring between the bar and the spending beach or to partial persistence of the long waves generated above the bar.

Similar trends are also observed for the greater water depth (50 cm), although in this case breaking processes are weaker and decreases also less evident (Fig. 7b).

The significant periods of long wave ranged between 8 and 12 s.

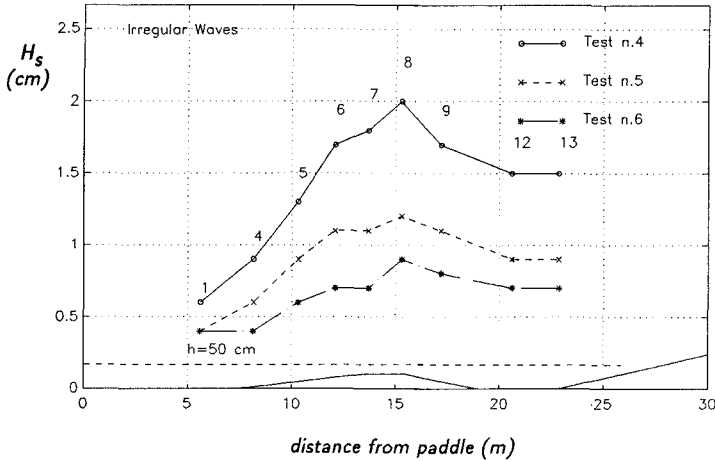


Fig. 7b – Significant heights of long waves calculated along flume for tests 4 – 6.

### Resumé of theoretical model

A non-linear theoretical model, able to separate first and second order components from a given non-linear (measured) spectrum, was utilised to interpret the experimental data. The model (Petti, 1991), is based on a systemic approach to sea wave behaviour and on some characteristic parameters which can be derived from the classic Stokes second-order solution. The method relies upon two fundamental assumptions: narrow-band spectrum and second order non-linearity. As a consequence of the last assumption, theoretical limits of the model should also be considered when applying the method. These may be expressed in terms of the generalised Ursell parameter or the "significant slope".

Let  $S_{\eta}(f)$  be a non-linear spectrum, as our spectrum measured at any location in the wave flume. Using the well-known Wiener-Khinchine relation (Bendat and Piersol, 1971) we can write:

$$B_{\eta}(\tau) = \int_0^{\infty} S_{\eta}(f) \cos(2\pi f\tau) df \quad (1)$$

Starting from Stokes' theory, it may be shown that the autocorrelation function  $B_{\eta}(\tau)$  of surface elevation may be written as:

$$B_{\eta}(\tau) = B_{\eta}^{(1)}(\tau) + B_{\eta}^{(2)}(\tau) \quad (2)$$

where  $B_{\eta}^{(1)}(\tau)$  and  $B_{\eta}^{(2)}(\tau)$  are respectively the first- and the second-order autocorrelation functions.

Second order contribution  $B_{\eta}^{(2)}(\tau)$  may in turn be expressed as function of first-order contribution  $B_{\eta}^{(1)}(\tau)$  as:

$$B_{\eta}^{(2)}(\tau) = 8 [f_2(k_0, h)]^2 [B_{\eta}^{(1)}(\tau)]^2 \quad (3)$$

where  $f_2(k_0, h)$  is a function of depth  $h$  and wave number  $k_0$  (relative to the peak frequency), equal to:

$$f_2(k_0, h) = \frac{k_0}{4} \left[ \frac{3}{\tanh^3(k_0 h)} - \frac{1}{\tanh(k_0 h)} \right] \tag{4}$$

Substituting (3) into (2) allows us to calculate  $B_\eta^{(1)}(\tau)$  as:

$$B_\eta^{(1)}(\tau) = \frac{-1 + \sqrt{1 + 32 [f_2(k_0, h)]^2 B_\eta(\tau)}}{16 [f_2(k_0, h)]^2} \tag{5}$$

while  $B_\eta^{(2)}(\tau)$  may then be obtained from (3).

Lastly, first- ( $S_\eta^{(1)}(f)$ ) and second- order ( $S_\eta^{(2)}(f)$ ) spectra may easily be obtained from corresponding autocorrelation functions  $B_\eta^{(1)}(\tau)$  and  $B_\eta^{(2)}(\tau)$  again using Wiener-Khintchine's relations.

Application of theoretical model: comparisons and discussion

Spectral wave transformations obtained in the laboratory were interpreted and compared with the results of above non-linear theory, by calculating first and second-order contributions for measured spectra.

As examples, measured and calculated spectra for tests 2 ( $h = 40$  cm,  $H_{m_0} = 7.9$  cm,  $T_p = 1.28$  s) and 5 ( $h = 50$  cm,  $H_{m_0} = 9.4$  cm,  $T_p = 1.28$  s) are shown in Figs. 8 and 9 for gauges 1, 6, 8 and 12. For better evidence of linear and second-order contributions, spectral densities are drawn on both linear and logarithmic scales.

Considering first the results for test 2, these show the very small contributions of second-order components for the offshore data (gauge 1).

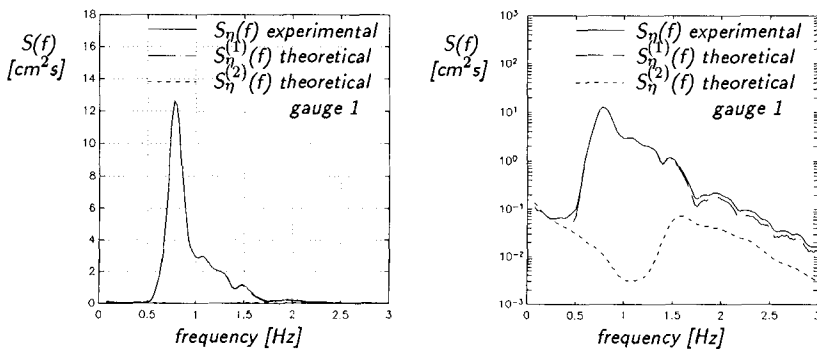


Fig. 8a – Example of wave spectra computed during test 2 (gauge 1) expressed in linear (left) and logarithmic scale (right).

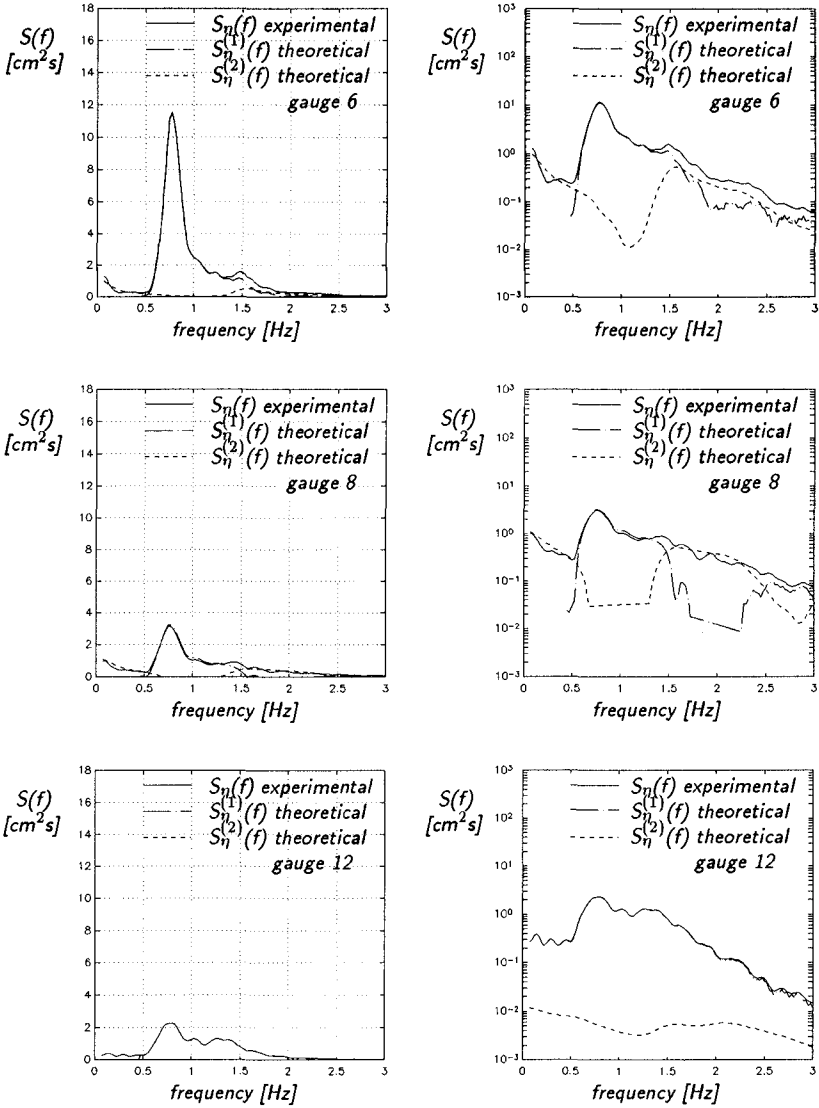


Fig. 8b – Example of wave spectra computed during test 2 (gauges 6, 8 and 12) expressed in linear (left) and logarithmic scale (right).

These become important with decreasing depths, as indicated by the results for gauge 6 (at the end of the offshore slope, near the top of the bar, just before intensive breaking occurs). In this case, second-order components at low and high frequencies are evident and may be predicted accurately by the

analytical model.

For gauge 8, the results do not appear very convincing, if only because the second-order components are in some cases greater than measured spectra. At the position of this gauge (above the top of the barrier, shoreside) intensive breaking occurs, and the measured spectrum is rather wide and therefore not suitable for analytic treatment, since this requires narrow banded spectra.

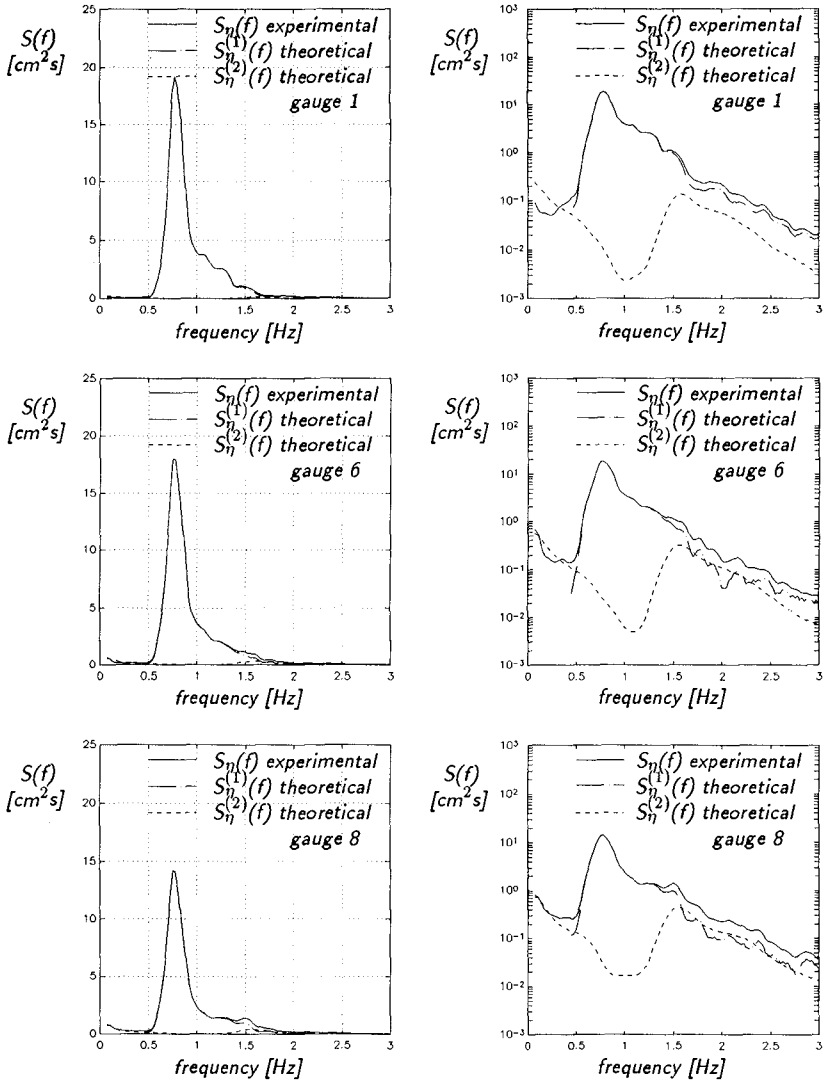


Fig. 9a – Example of wave spectra computed during test 2 (gauges 1, 6, and 8) expressed in linear (left) and logarithmic scale (right).

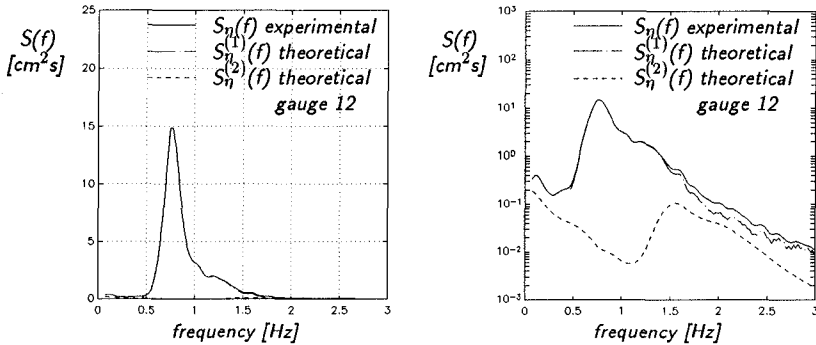


Fig. 9b – Example of wave spectra computed during test 2 (gauges 12) expressed in linear (left) and logarithmic scale (right).

Nevertheless, low frequency components may still be predicted quite well by the model.

Lastly, the spectrum measured at gauge 12 (shoreside of the bar) is quite broad and far beyond the applicability of the method; calculated second-order components are very small and not very meaningful.

For test 5 ( $h = 50$  cm,  $H_{m0} = 9.4$  cm,  $T_p = 1.28$  s) analytical results also appear satisfactory for shoreside gauges such as gauge 8. This is ascribable, in this case, to less intense breaking occurring above the bar (due to greater depths over it); measured wave spectra are still rather narrow and non-linear effects still pronounced.

In this case too, non-linearities become very small, due to greater water depths, for gauges located shoreside of the bar and therefore, again, the method cannot be properly applied.

### Summary and conclusions

Transformations of random waves over a submerged bar are investigated in this paper.

In particular, experimental results are analysed through zero-crossing analysis (including separation of short and long waves) and spectral analysis. In this regard, some features of the evolution of variance spectra above the bar were observed and the importance of non-linear effects and breaking on spectral transformations are highlighted and discussed.

Modified zero-crossing analysis allowed us to reveal some aspects of long wave behaviour over the submerged bar. A new and interesting problem observed during the experiments was the possibility of long waves resonances between the spending beach and the bar.

The influence of flume seiches on this phenomenon will be more fully investigated with new experiments to be carried in the near future using a longer flume. In these experiments, a new absorbing system recently installed on the flume will allow to investigate the influence of paddle re-reflection of waves on the observed phenomena.

A second order analytical method was applied to the data in order to

interpret non-linear transformations of spectra. As regards the procedure applied, which separates first- and second-order components for the measured spectra, the analytical method used seems conveniently applicable to describe non-linear effects, as long as breaking phenomena are not too intense.

### Acknowledgements

This work was undertaken within the framework of the MAST G6 Coastal Morphodynamics research programme. It was funded by the Commission of the European Communities, Directorate General for Science, Research and Development under contract no. 0035C.

The helpful comments received during this work from Mr M.W. Dingemans of Delft Hydraulics are gratefully acknowledged.

### References

- Battjes J.A. and Beji S. (1992). *Spectral evolution in breaking waves propagating over a shoal*. 23rd International Conference on Coastal Engineering, Venice.
- Beji S., Ohyama T., Battjes J.A. and Nadaoka K. (1992). *An experimental verification of a numerical model for nonlinear random waves*. 23rd International Conference on Coastal Engineering, Venice.
- Bendat J.S. and Piersol A.G. (1971). *Random Data: Analysis and Measurement Procedures*. Wiley - Interscience, New York.
- Brocchini, M., Cherubini, P. and Iovenitti, L. (1991). *An extension of a Boussinesq type model to the surf zone*. Extended abstract, MAST G-6 Morphodynamics Mid-Term Workshop, Edinburgh.
- Goda Y. and Suzuki, Y. (1976). *Estimation of incident and reflected waves in random wave experiments*. Proc. 15th Int. Conf. on Coastal Eng., ASCE, 828-845.
- Liberatore, G. and Petti M. (1991). *Random wave transformation over a submerged bar*. Extended abstract, MAST G-6 Morphodynamics Mid-Term Workshop, Edinburgh.
- Petti M. (1988). *Second Order Analysis of Shallow-Water Wave Spectra*, II Nuovo Cimento, Vol. 11 C, N. 5-6.
- Petti, M. (1991). *On the separation of second order components for non-linear wave spectra*, Proc. 2nd Int. Conf. on Computer Modelling in Ocean Engineering, Barcelona.
- Rojanakamthorn, S., Isobe, M. and Watanabe, A. (1990). *Modelling of wave transformation on submerged breakwater*. Proc. 22nd International Conference on Coastal Engineering, ASCE, 1061-1073.
- Schäffer, H.A., Deigaard, R. and Madsen P.A. (1991). *Incorporation of wave breaking in a Boussinesq model*. Extended abstract, MAST G-6 Morphodynamics Mid-Term Workshop, Edinburgh.
- Smith E.R. and Kraus N. C. (1992). *Laboratory study of wave transformation on barred beach profiles*. 23rd International Conference on Coastal Engineering, Venice.
- Thorkilsen, M., Rosing N. and Schäffer, H.A., (1991). *Experiments on waves breaking over a bar*. Extended abstract, MAST G-6 Morphodynamics Mid-Term Workshop, Edinburgh.



## CHAPTER 33

### Nonlinear Transformation of Irregular Waves in Shallow Water

Per A. Madsen<sup>1</sup>  
Ole R. Sørensen<sup>1</sup>  
Hemming A. Schäffer<sup>1</sup>

#### 1. Introduction

Propagation and shoaling of irregular wave trains in shallow water is a nonlinear process, where substantial cross spectral energy transfer can take place in relatively short distances. This process involves the generation of bound sub- and super-harmonics and near-resonant triad interactions, which are defined as the energy exchange between three interacting wave modes.

In the literature it is common practice to distinguish between bound waves and resonant free triads. The theory for bound waves is based on the assumption of a one way transfer of energy to generate higher and lower harmonics which are phase locked to the primary wave train. In reality, however, a feed back of energy to the primary frequencies will occur leading to near-resonant interactions.

This phenomena has previously been treated by e.g. Freilich and Guza (1984) on the basis of the classical Boussinesq equations. It turns out, however, that the accuracy of the linear dispersion relation for higher wave numbers is of major importance for the exchange of energy even in shallow water and for this reason we recommend as governing equations a special form of the Boussinesq equations. These were derived by Madsen et

---

<sup>1</sup> Danish Hydraulic Institute, Agern Allé 5,  
DK-2970 Hørsholm, Denmark

al. (1991a) on a horizontal bottom and here we shall extend these equations to a mildly sloping bottom.

The paper will contain a Fourier analysis of the inherent linear shoaling properties, transfer functions for bound sub and super-harmonics and a discussion of two cases of triad interactions.

## **2. New Boussinesq Equations**

The applicability of various forms of the Boussinesq equations expressed in terms of e.g. the bottom velocity, the surface velocity, the depth-averaged velocity and the depth-integrated velocity was discussed by Madsen et al. (1991a). With the objective of improving the linear dispersion characteristics a new set of equations were derived in two horizontal dimensions. As the first step an improved linear dispersion relation was obtained by combining a polynomial expansion of Stokes first order theory with Pade's approximant. As the second step the classical Boussinesq equations were modified by invoking the linear long wave approximation and using the method of operator correspondence.

The equations presented in this paper represent an extension of the approach by Madsen et al. (1991a), by including first derivatives of the sea bed. The result will be a set of two-dimensional equations which incorporate excellent linear dispersion characteristics and are applicable to irregular wave propagation on a slowly varying bathymetry from deep to shallow water.

The starting point for the derivation is the classical Boussinesq equations derived by Peregrine (1967). These equations, which are valid on a variable bathymetry, are reformulated in terms of depth-integrated velocity variables, i.e. flux components, and are simplified by neglecting higher derivatives and products of derivatives of the still water depth  $h$ . First derivatives of  $h$  are considered small but are included in the formulation.

It is a classical procedure to simplify higher order terms in the Boussinesq or KdV equations by introducing the linear long wave approximations (see e.g. Mei, 1983; Madsen et al., 1991a). As an example  $P_{xxt}$  type terms can be replaced by  $S_{xxx}$  type terms by the use of this method. In shallow water it makes no difference, but in deeper water the form of the Boussinesq terms is critical for the accuracy of the linear dispersion relation. Instead of replacing  $P_{xxt}$  with  $S_{xxx}$  type terms we use a different

approach. Spatial differentiations of the linear long wave equations lead to expressions containing the terms  $P_{xxt}$ ,  $P_{xyt}$ ,  $Q_{yyt}$  and  $Q_{xyt}$ . Since these expressions are effectively zero in shallow water we add them to the original Boussinesq equations and obtain the following new set of equations:

$$S_t + P_x + Q_y = 0 \quad (2.1a)$$

$$P_t + \left(\frac{P^2}{d}\right)_x + \left(\frac{PQ}{d}\right)_y + gdS_x + \psi_1 = 0 \quad (2.1b)$$

$$Q_t + \left(\frac{Q^2}{d}\right)_y + \left(\frac{PQ}{d}\right)_x + gdS_y + \psi_2 = 0 \quad (2.1c)$$

where subscripts x, y and t denote differentiation with respect to space and time, d is the total water depth, h is the still water depth, S is the surface elevation, P and Q are the depth-integrated velocity components, and  $\psi_1$  and  $\psi_2$  are the new Boussinesq terms defined by:

$$\begin{aligned} \psi_1 = & - \left(B + \frac{1}{3}\right) h^2 (P_{xxt} + Q_{xyt}) - Bgh^3 (S_{xxx} + S_{xyy}) \\ & - hh_x \left(\frac{1}{3}P_{xt} + \frac{1}{6}Q_{yt} + 2BghS_{xx} + BghS_{yy}\right) \\ & - hh_y \left(\frac{1}{6}Q_{xt} + BghS_{xy}\right) \end{aligned} \quad (2.2a)$$

$$\begin{aligned} \psi_2 = & - \left(B + \frac{1}{3}\right) h^2 (Q_{yyt} + P_{xyt}) - Bgh^3 (S_{yyy} + S_{xxy}) \\ & - hh_y \left(\frac{1}{3}Q_{yt} + \frac{1}{6}P_{xt} + 2BghS_{yy} + BghS_{xx}\right) \\ & - hh_x \left(\frac{1}{6}P_{yt} + BghS_{xy}\right) \end{aligned} \quad (2.2b)$$

Except for the slope terms proportional to  $h_x$  and  $h_y$ , these expressions are identical to the Boussinesq terms presented by Madsen et al. (1991a). B is the linear dispersion parameter, which will be determined in the following section. Further details concerning the derivation, and a description of the numerical method used to solve them, will appear in Madsen and Sørensen (1992b).

### 3. Linear dispersion relation and shoaling properties

A Fourier analysis of the linearized one-dimensional version of the new Boussinesq equations will be made with the objective of studying the linear dispersion relation and the linear shoaling gradient embedded in the new equations.

As a starting point for the analysis, the one-dimensional wave equation corresponding to (2.1a-c) combined with (2.2a-b) is derived. By using (2.1a) linear terms containing P are eliminated and secondly (2.1a) and (2.1b) are cross-differentiated and subtracted. This leads to:

$$\mathbf{L} = \mathbf{M} + \mathbf{N}_{xx} \quad (3.1a)$$

where

$$\mathbf{L} = \left[ S_{tt} - ghS_{xx} + Bgh^3S_{xxxx} - \left( B + \frac{1}{3} \right) h^2S_{xxtt} \right] \quad (3.1b)$$

$$\mathbf{M} = \left[ gS_x + (2B + 1)hS_{xtt} - 5Bgh^2S_{xxx} \right] h_x \quad (3.1c)$$

$$\mathbf{N} = \left[ \frac{1}{2} gS^2 + \frac{P^2}{d} \right] \quad (3.1d)$$

In the following linear analysis the non-linear operator  $\mathbf{N}$  is neglected and we shall look for solutions to (3.1a) on the form

$$S(x, t) = A(x) e^{i(\omega t - \varphi(x))} \quad (3.2)$$

where  $\omega$  is the cyclic frequency,  $A$  is the local wave amplitude and  $\varphi$  is the phase function, which is related to the local wave number by

$$\varphi_x = k(x) \quad (3.3)$$

The water depth, the wave number and the wave amplitude are considered to be slowly varying functions of  $x$  and consequently products of derivatives and higher

derivatives of these quantities will be neglected in the following.

The linear dispersion relation is obtained by inserting (3.2) into (3.1) and neglecting all x-derivatives of h, k and A,

$$-\omega^2 + ghk^2 + Bgh^3k^4 - \left(B + \frac{1}{3}\right) k^2h^2\omega^2 = 0 \quad (3.4)$$

Alternatively this can be formulated as:

$$\frac{c^2}{gh} = \frac{1 + Bk^2h^2}{1 + \left(B + \frac{1}{3}\right) k^2h^2} \quad (3.5)$$

where c is the wave celerity defined by  $c = \omega/k$ .

As shown by Madsen et al. (1991a) various classical formulations of the Boussinesq equations all lead to (3.5) with different values of B: using the surface velocity as dependent variable leads to  $B = -1/3$ , the bottom velocity leads to  $B = 1/6$  and the depth-averaged or depth-integrated velocity leads to  $B = 0$ . By far the best agreement with Stokes first order theory is obtained by using the value  $B = 1/15$ , which is determined by matching (3.5) with a Taylor expansion of the Stokes first order celerity combined with Pade's expansion technique. This value was originally suggested by Witting (1984). Madsen et al (1991a) analyzed the accuracy of (3.5) for the various possible values of B and concluded that the new Boussinesq equations combined with  $B = 1/15$  provide excellent linear dispersion characteristics for values of  $h/L_0$  as large as 0.5.

Proceeding with the Fourier analysis and collecting terms to the next order in (3.1) includes the terms proportional to the first derivatives of h, k and A. The frequency  $\omega$  is eliminated by the use of (3.4) and differentiation of this equation also makes it possible to eliminate terms proportional to  $k_x/k$ . After algebraic manipulations we get the expression:

$$\frac{A_x}{A} = -\gamma \frac{h_x}{h} \quad (3.6)$$

where  $\gamma$  is the linear shoaling gradient. The expression for  $\gamma$  reads:

$$\gamma = \frac{1}{4} \left[ 1 + (4B - 1)k^2h^2 + \left(6B^2 - \frac{2}{3}B\right)k^4h^4 + \left(4B^3 + \frac{1}{3}B^2 + \frac{1}{9}B\right)k^6h^6 + \left(B^4 - \frac{1}{9}B^2\right)k^8h^8 \right] \left[ 1 + 2Bk^2h^2 + \left(B^2 + \frac{1}{3}B\right)k^4h^4 \right]^{-2} \quad (3.7)$$

The reference linear shoaling coefficient based on Stokes first order theory is derived by using the concept of conservation of energy flux. After differentiation and algebraic manipulations this leads to:

$$\gamma_{Stokes} = \frac{2kh(\sinh 2kh) + 2k^2h^2(1 - \cosh 2kh)}{(2kh + \sinh 2kh)^2} \quad (3.8)$$

A comparison between (3.7) and (3.8) as a function of  $h/L_0$  requires that (3.7) is combined with the Boussinesq dispersion relation (3.4), while (3.8) is combined with Stokes dispersion relation. The result is presented in Fig. 1 and it can be concluded that the standard Boussinesq equations with  $B = 0$  lead to major discrepancies for  $h/L_0$  larger than 0.10, while  $B = 1/15$  has a remarkable effect and results in an excellent agreement with Stokes first order theory for  $h/L_0$  as large as 0.50.

#### 4. Bound waves in shallow water

Irregular wave trains travelling in shallow water can generate and sustain a considerable amount of bound harmonics, which travel phase-locked to the primary wave train. At locations, where drastic changes of the wave heights occur e.g. due to diffraction or wave breaking, the bound waves can be released and proceed as free waves. This may cause harbour resonance, drift motion of moored vessels and surf beats. The phenomena of bound waves has been discussed in numerous papers in connection with the reproduction of regular and irregular waves in physical wave flumes (e.g. Barthel et al., 1983 and Sand and Mansard, 1986). It has been concluded that linear boundary conditions often are insufficient and should be replaced by second order boundary conditions including the effect of bound sub- and super-harmonics. This problem is important for physical waves flumes and equally relevant for numerical models solving non-linear equations.

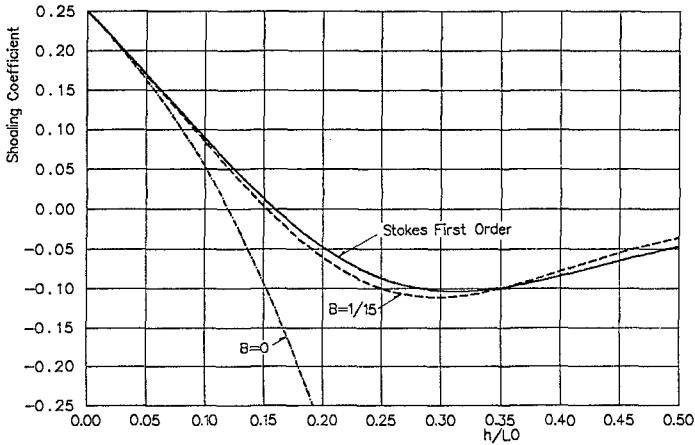


Fig. 1 Linear shoaling gradient,  $\gamma$  defined by (3.6), (3.7) and (3.8).

In this section transfer functions for second order bound sub and super-harmonics will be presented on the basis of the new Boussinesq equations. The derivation is straight forward and is based on a perturbation solution to the wave equation given in (3.1a-d). As a start we consider the forcing due to a simple first order wave group made up of just two frequencies  $\omega_n$  and  $\omega_m$  at a constant depth. Each of the two wave components are considered to be solutions to the linearized problem  $L\{S^{(1)}\} = 0$  where  $L$  is defined by (3.1b). The next step is to look for second order solutions to  $L\{S^{(2)}\} = N_{xx}\{S^{(1)}\}$  where  $N$  is defined by (3.1d). The first order bichromatic wave train will force a second order wave train consisting of four new frequencies: one sub-harmonic and three super-harmonics. The four second order wave numbers are determined from combinations of  $k_n$  and  $k_m$ , and they do not satisfy the linear dispersion relation, which implies that these waves are bound or phase-locked to the first order wave train. For general irregular wave trains consisting of many wave components, the contributions from all pairs of frequencies inherent in the wave train can be summed up (see Sand and Mansard, 1986).

The second order transfer function derived from the new Boussinesq equations reads:

$$G_p = \frac{ghk_p^2 (\sqrt{2} + \omega_n \omega_m / (ghk_n k_m))}{(\omega_p^2 - ghk_p^2 - Bgh^3 k_p^4 + (B + 1/3) h^2 \omega_p^2 k_p^2)} \quad (4.1)$$

where  $\omega_p = p\Delta\omega$  denotes the discrete sub or super-harmonic frequency receiving energy transfer from the primary frequencies  $\omega_n = n\Delta\omega$  and  $\omega_m = m\Delta\omega$ . For sub-harmonics (4.1) should be used with  $n = m + p$  and  $k_p = k_{m+p} - k_m$ . For super-harmonics  $n = p-m$  and  $k_p = k_{p-m} + k_m$ . Further details and the complete formulation of second order boundary conditions for irregular waves can be found in Madsen and Sørensen (1992a).

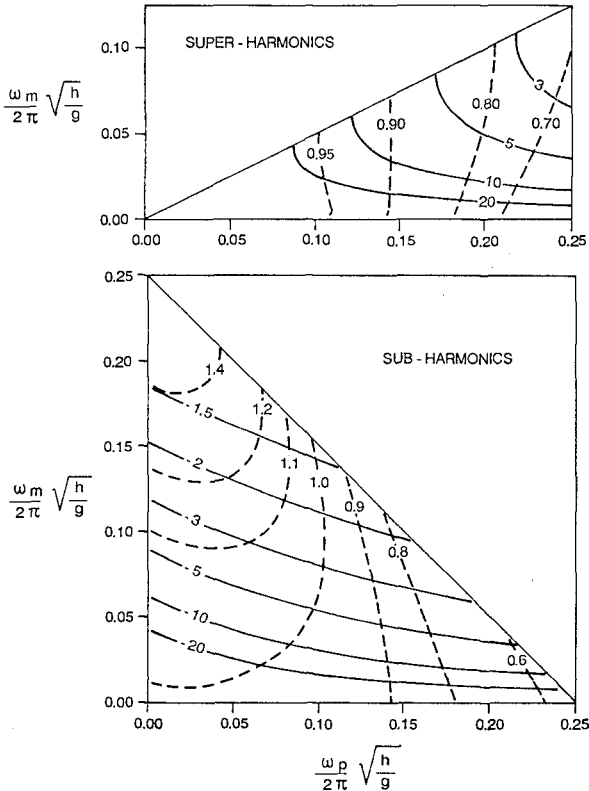


Fig. 2 Transfer Functions for super-harmonics and for sub-harmonics.

- Boussinesq transfer function determined by (4.1)  $B=1/15$
- Ratio between the Boussinesq transfer and the transfer function determined from the Laplace equation.

Fig. 2 shows the transfer function for the super-harmonics  $\omega_p$  generated by the interaction between  $\omega_m$  and  $\omega_{m+p}$ , and for the sub-harmonics  $\omega_p$  generated by the interaction between  $\omega_m$  and  $\omega_{m-p}$ .  $G^+$  and  $G^-$  determined by (4.1) are shown as full lines in Fig. 2, while the ratios



between  $G$  and the transfer functions derived from the Laplace equation (Sand and Mansard, 1986) are shown as dotted lines. Generally, the Boussinesq equations tend to underestimate the super-harmonics while the sub-harmonics can be underestimated as well as overestimated. Discrepancies up to 40% are noticed in the shown truncated spectrum, but typical errors are less than 10%.

An application of the theory is presented in Fig. 3, where time series of surface elevations are generated from a JONSWAP spectrum with  $\gamma = 3.3$ . The water depth is 10 m, the significant wave height is 2.0 m and the peak period is 9.0 s. The linear wave train is generated with random phases and with energy in the interval 0.05 Hz to 0.20 Hz. The maximum frequency corresponds to  $h/L_0 = 0.25$  which is within the range of application of the new Boussinesq equations. The bound sub-harmonics cover the interval the 0.001 Hz to 0.15 Hz, while the bound super-harmonics cover the interval from 0.10 Hz to 0.40 Hz.

The consequence of neglecting the bound wave components in the input time series will be the release of spurious free wave components of the same order of magnitude. In this situation the free sub-harmonics are by far the most critical, since they can penetrate, e.g. into harbours almost without being reduced in magnitude and result in harbour resonance or at least in a major overestimation of the local wave disturbance.

## 5. Triad Interactions

The theory of bound waves assumes an equilibrium situation where the non-linear wave train propagates without changing its form. In reality and especially in shallow water a substantial cross spectral energy transfer will take place due to triad interactions, which describe the exchange of energy between three interacting wave modes (see e.g. Freilich and Guza, 1984).

The simplest example of triad interactions occur, when first order monochromatic boundary conditions are applied in shallow water. This will unintentionally generate spurious free second order waves in addition to the bound second order waves, leading to an energy exchange between the primary wave frequency and its super-harmonics. A numerical example is presented in Fig. 4a, which shows the computed surface elevation at eight equidistant times within one wave period as a function of the distance from the open boundary. The corresponding spatial variation of the amplitudes of the

first three harmonics is obtained by FFT-analysis of the computed time series and is shown in Fig. 4b.

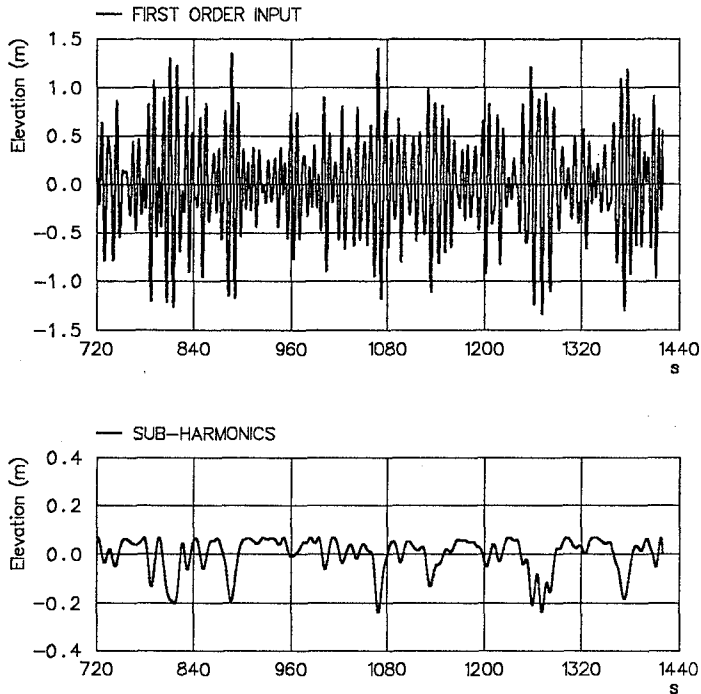


Fig. 3 First order irregular waves and their correspondingly bound sub-harmonics.

Boussinesq Eq. with  $B = 1/15$ . Water depth = 10 m.

JONSWAP SPECTRUM with  $H_s = 2.0$  m,  $T_p = 9.0$  s,  $\gamma = 3.3$ .

As discussed in Madsen et al. (1991b) the energy transfer can be shown to depend strongly on the phase mismatch, which is defined by:

$$\delta^+ \equiv k_m + k_{p-m} - k_p \tag{5.1a}$$

$$\delta^- \equiv k_{m+p} - k_m - k_p \tag{5.1b}$$

This calls for an accurate description of the linear dispersion relation and in connection with this it should be emphasized that even when the primary wave corresponds to very shallow water in terms of  $h/L_0$ , this is not necessarily the case for the higher harmonics. Hence, by using classical types of KdV or Boussinesq equations, the estimate of the phase mismatch may be rather inaccurate.

The new Boussinesq equations with  $B = 1/15$  improve the accuracy considerably and as an example Fig. 5 shows a comparison with the measurements of Chapalain et al. (1992). The agreement between the measurements and the FFT analysis of the time domain simulations is seen to be excellent, except for the beat length of the third harmonic, which is slightly underestimated. More examples of harmonic generation forced by linear monochromatic and bichromatic boundary conditions on a constant depth can be found in Madsen and Sørensen (1992a).

The final example is a study of non-linear refraction-diffraction on a semi-circular shoal. This was studied experimentally by Whalin (1971) for wave periods of 1, 2 and 3 seconds. We shall concentrate on a discussion of the case of 1 second waves, which has not previously been treated by the use of Boussinesq equations. The value of  $h/L_0$  varies from 0.29 at the toe of the shoal to 0.096 behind the shoal. An FFT analysis of time series in each grid point along the centre line has been made and the resulting spatial evolution of first and second harmonics is compared with Whalin's experimental data in Fig. 6. A considerable scattering in the data is seen in front of the shoal but behind the shoal the agreement between the data and the new Boussinesq equations with ( $B = 1/15$ ) is acceptable. Reasonable agreement is also found between the new Boussinesq equations and the results obtained by Liu and Tsay (1984), who solved the non-linear Schrödinger equation. Finally the classical Boussinesq equations (i.e.  $B = 0$ ) are seen to fail completely by predicting an unrealistic decrease of the first harmonic, a discrepancy which can be explained by the variation of the linear shoaling gradient in Fig. 2.

In fact this example demonstrates that Fig. 2 should be taken quite seriously as a measure of the range of application of different types of Boussinesq equations. A common mistake is that the accuracy of the wave celerity is taken as the practical measure, in which case a 5% error restricts the use of the standard Boussinesq equations to approximately  $h/L_0 = 0.22$ . However, according to Fig. 2 this is clearly much too optimistic in case of a variable bathymetry and the shoaling falsification increases rapidly for  $h/L_0$  exceeding 0.10. This emphasizes the importance of using the new Boussinesq equations presented in this paper, in which case  $h/L_0$  as large as 0.5 can be considered.

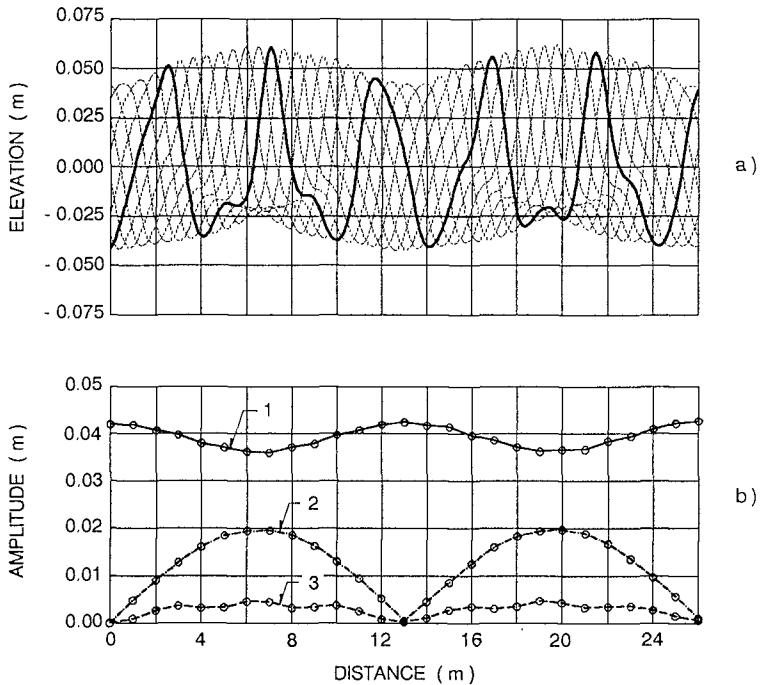


Fig. 4 Triad interactions due to first order monochromatic boundary conditions by time domain Boussinesq model with  $B = 1/15$ . Water depth = 0.40 m,  $T = 2.5$  s,  $H = 0.084$  m, grid size = 0.04 m, Time step = 0.01953 s.

a) Wave envelope

b) Spatial variation of the amplitudes for the first three harmonics.

1:  $f_1 = 0.40$  hz, 2:  $f_2 = 0.80$  hz, 3:  $f_3 = 1.20$  hz.

## 6. Conclusion

The paper presents a new set of Boussinesq equations applicable to irregular wave propagation on a slowly varying bathymetry from deep to shallow water. It can be concluded that the new equations are capable of describing the phenomenon of harmonic generation and triad interactions with an accuracy which is significant better than what can be obtained on the basis of the classical forms of the Boussinesq equations.

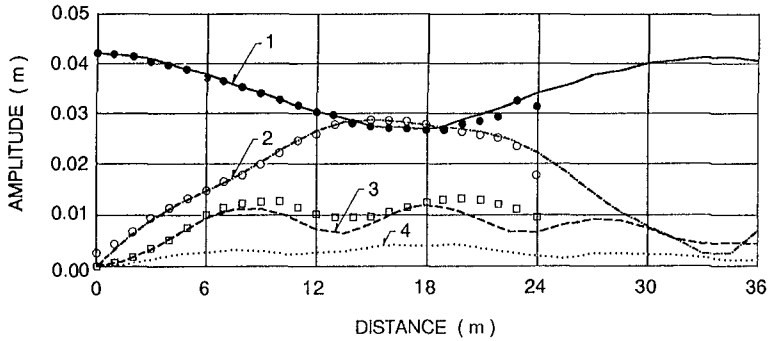


Fig. 5 Triad interactions due to first order monochromatic boundary conditions. Water depth = 0.40 m,  $T = 3.5$  s,  $H = 0.084$  m, Grid size = 0.06 m, Time step = 0.02734 s.

— Time domain Boussinesq model with  $B=1/15$ .  
 •, °, □ Measurement by Chapalain, Cointe and Temperville (1991).

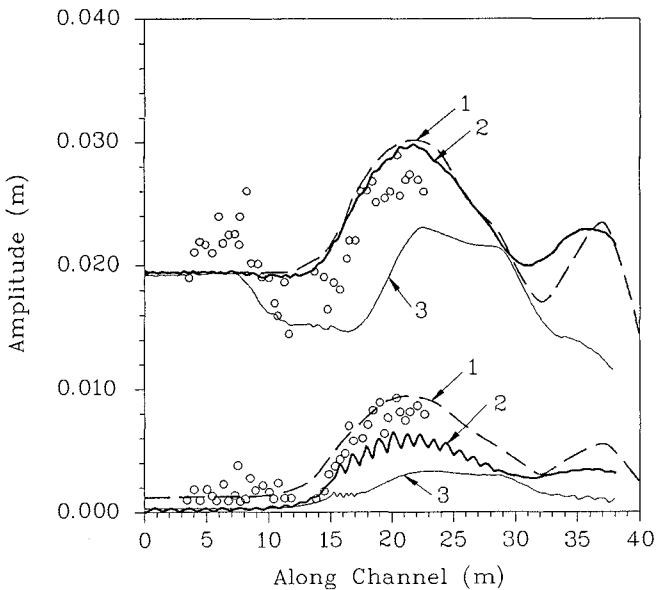


Fig. 6 Refraction-diffraction on a semi-circular shoal. Spatial variation of the amplitudes for the first three harmonics along the center line.  
 0: Experiment, Whallin (1971), 1: Liu and Tsay (1984), 2: Boussinesq  $B=1/15$ , 3: Boussinesq  $B=0$ .

**References**

- Barthel, V., Mansard, E.P.D., Sand, S.E. and Vis, F.C. (1983), "Group bounded long waves in physical models", *Journal of Ocean Engineering*, Vol. 10, No. 4, pp. 261-294.
- Chapalain, G., Cointe, R. and Temperville, A. (1992), "Observed and modelled resonantly interacting progressive water waves", *Coastal Engineering*, Vol. 16, No. 3., pp. 267-301.
- Freilich, M.H and Guza, R.T. (1984), "Nonlinear effects on shoaling surface gravity waves", *Phil. Trans. R. Soc. London, A* 311, pp. 1-41.
- Liu, P.L.-F. and Tsay, T.-K. (1984), "Refraction-diffraction model for weakly non-linear water waves", *Journal of Fluid Mechanics*, Vol. 141, pp. 265-274.
- Madsen, P.A. and Sørensen, O.R. (1990), "Extension of the Boussinesq equations to include wave propagation in deeper water and wave-ship interaction in shallow water", *Proc. 22 Int. Conf. on Coastal Engineering, Delft*, pp. 3112 - 3125.
- Madsen, P.A., Murray, R. and Sørensen, O.R. (1991a), "A new form of the Boussinesq equations with improved linear dispersion characteristics (PART 1)", *Coastal Engineering*, Vol. 15, pp 371-388.
- Madsen, P.A., Sørensen, O.R. and Yang Zhenyong (1991b), "Wave-wave interaction in shallow water", *Proc. XXIV IAHR Congress, Madrid, September 1991*, pp. B001-B011.
- Madsen, P.A. and Sørensen, O.R. (1992a), "Bound waves and triad interactions in shallow water", *Accepted for publication in Journal of Ocean Engineering*, March 1992.
- Madsen, P.A. and Sørensen, O.R. (1992b), "A new form of the Boussinesq equations with improved linear dispersion characteristics, PART 2: A slowly varying bathymetry", *Accepted for publication in Coastal Engineering*, June 1992.
- Mei, C.C. (1983), "The applied dynamics of ocean surface waves", *Wiley, New York, N.Y.* 740 pp.
- Peregrine, D.H. (1967), "Long waves on a Beach", *Journal of Fluid Mechanics*, Vol. 27, Parts 4, pp. 815-827.
- Sand, S.E. and Mansard, E.P.D. (1986), "Reproduction of higher harmonics in irregular waves", *Ocean Engineering*, Vol. 13, No. 1, pp. 57-83.
- Whalin, R.W. (1971), "The limit of applicability of linear wave refraction theory in a convergence zone", *Res. Rep. H-71-3, U.S. Army Corps of Engrs., Waterways Expt. Station, Vicksburg, MS.*
- Witting, J.M. (1994), "A unified model for the evolution of non-linear water waves", *Journal of Computational Physics*, 56, pp. 203-236.

## CHAPTER 35

### Hybrid Frequency-Domain KdV Equation for Random Wave Transformation

Hajime Mase<sup>1</sup>, M. ASCE, and James T. Kirby<sup>2</sup>, M. ASCE

**ABSTRACT:** This paper develops a hybrid model for random wave transformation by employing a modified spectral model of the KdV equation and a probabilistic bore-type wave breaking model, and compares the numerical predictions with experimental observations. Main results are as follows: 1) Original frequency-domain KdV equation overestimates energy densities, due to over-shoaling term by Green's law in the equation, even in a region where wave breaking is not seen; 2) Modification of the original KdV equation in order to represent shoaling for linear-dispersive component waves leads to better predictions in the non-breaking region; 3) Damping coefficients in the model equation, either estimated from measured spectral densities or the numerically predicted, are in inverse proportion to the water depth and in proportion to the square of frequency, similar to the viscous damping term of the Burgers equation; 4) The hybrid model developed here can predict transformations of random waves satisfactorily, as indicated by comparison of energy spectra, representative wave heights, periods, and crest heights.

#### INTRODUCTION

The Boussinesq equations include the effects of weak dispersion and nonlinearity under the condition of  $\mu^2 = (k_0 h_0)^2 \ll 1$ ,  $\varepsilon = a_0/h_0 \ll 1$ , and  $O(\mu^2) = O(\varepsilon)$  where  $k_0$ ,  $h_0$ ,  $a_0$  are the characteristic wave number, the water depth, and the wave amplitude (Peregrine, 1967; Madsen and Mei, 1969), and are a useful tool for predicting the transformation of shallow water waves. The Boussinesq type equations with a damping term introduced to simulate a turbulence dissipation can predict the change of monochromatic wave height both in the shoaling and the breaking regions (Karambas and Koutitas, 1992).

An efficient method to solve the Boussinesq equations is to deal with the equations in the frequency domain instead of the time domain. The resulting one-dimensional coupled mode equations considering only shoreward-propagating waves can predict the evolution of nearshore field wind waves (Freilich and Guza, 1984; Elgar and Guza, 1985), and the parabolic coupled mode equations can predict the transformation of periodic long waves over two-dimensional topography (Liu et al., 1985). An angular spectrum model of the Boussinesq equations can predict Mach reflection of cnoidal waves well (Kirby, 1990). The KdV equation is consistent with the Boussinesq equations when considering only shoreward-propagating waves. Although the Boussinesq equations and the KdV equation have only the lowest order of nonlinearity, the frequency-domain equations can estimate shoaled wave heights as well as wave

---

<sup>1</sup> Research Assoc., Department of Civil Engrg., Kyoto University, Kyoto, 606, Japan.

<sup>2</sup> Assoc. Prof., Department of Civil Engrg., Univ. of Delaware, Newark, DE 19716, USA.

profiles fairly close to the breaking point (Vengayil and Kirby, 1986). Extension of the Boussinesq equations and the KdV equation to improve their dispersion characteristics was studied by Madsen, Murray and Sørensen (1991) and Khangaonkar and LeMehaute (1991).

This paper develops a hybrid model for random wave transformation by employing a modified frequency-domain KdV equation and a probabilistic bore-type wave breaking model. The original frequency-domain (spectral) KdV equation is modified to reproduce the shoaling and the dispersion relation for linear component waves exactly. In order to include energy dissipation due to wave breaking, a damping term is introduced into the modified spectral KdV equation. A form for the coefficient of the damping term is first deduced by inspection of measured spectral energy densities together with calculated densities by the modified spectral KdV equation, and the coefficient is then formulated by using a probabilistic model of expected energy dissipation rate based on the bore model of Thornton and Guza (1983), taking into account the experimental characteristics.

The model equation developed here can be called a hybrid model, since it employs a spectral method and a probabilistic method (individual wave analysis method). Comparisons between experimental observations and numerical predictions by the hybrid model are carried out against energy spectra, representative wave heights, periods, and crest heights.

## MODEL EQUATION

Assuming a vertically two-dimensional case, small water depth variation such as  $O(|\nabla_h h|) \leq O(\mu^2)$ , and considering only shoreward-propagating waves (neglecting reflected waves), we reduce the Boussinesq equations to the KdV equation for variable depth as expressed by

$$\zeta_t + \sqrt{gh} \zeta_x + \frac{\sqrt{gh} h_x}{4h} \zeta + \frac{3\sqrt{gh}}{2h} \zeta \zeta_x + \frac{\sqrt{gh} h^2}{6} \zeta_{xxx} = 0, \quad (1)$$

$O(\epsilon) \qquad O(\mu^2)$

where  $\zeta$  is the surface displacement,  $h$  is the water depth,  $t$  is the time, and  $x$  is the horizontal coordinate. Substituting the Fourier series representation of surface displacement with complex amplitudes,  $A_n$ ,

$$\zeta = \sum_{n=1}^{\infty} \frac{1}{2} A_n e^{i n \left( \int k_1 dx - \omega_1 t \right)} + c. c. \quad (2)$$

into Eq.(1) yields the lowest-order frequency-domain KdV equation, equivalent to the consistent shoaling model of Freilich and Guza (1984):

$$\frac{dA_n}{dx} + \frac{h_x}{4h} A_n - \frac{1}{6} i n^3 k_1^3 h^2 A_n + \frac{3 i n k_1}{8h} \left[ \sum_{l=1}^{n-1} A_l A_{n-l} + 2 \sum_{l=1}^{N-n} A_l^* A_{n+l} \right] = 0; \quad n = 1, 2, \dots, N, \quad (3)$$

where  $dA_n/dx \sim O(\epsilon)$  is assumed. The procedure followed in deriving the above equation follows that of Freilich and Guza (1984), and Liu et al. (1985). The second



term on the left hand side of Eq.(3) represents shoaling by Green's law; that is, the equation for linear waves

$$\frac{dA_n}{dx} = -\frac{h_x}{4h} A_n \quad (4)$$

is integrated to

$$\frac{A_n(x)}{A_n(0)} = \left\{ \frac{h(x)}{h(0)} \right\}^{-1/4} \quad (5)$$

This can be compared to the component form of fully dispersive linear theory, which gives

$$\frac{dA_n}{dx} = -\frac{(C_{g_n})_x}{2C_{g_n}} A_n \quad (6)$$

The integrated form is then

$$\frac{A_n(x)}{A_n(0)} = \left\{ \frac{C_{g_n}(x)}{C_{g_n}(0)} \right\}^{-1/2} \quad (7)$$

which corresponds to the linear shoaling theory. The third term on the left hand side of Eq.(3) represents the effect of dispersion. For linear component waves in uniform depth, Eq.(3) reduces to

$$\frac{dA_n}{dx} - \frac{1}{6} i n^3 k_1^3 h^2 A_n = 0 \quad (8)$$

The resultant surface displacement is described by

$$\zeta = \frac{1}{2} a_n e^{i \left\{ \left( n k_1 + \frac{1}{6} n^3 k_1^3 h^2 \right) x - n \omega_1 t \right\}} + \text{c. c.} \quad (9)$$

From Eq.(9) the phase speed is given by

$$C_n = \frac{\omega_1}{k_1} \frac{1}{1 + (n k_1 h)^2 / 6} \quad (10)$$

where  $\omega_1/k_1 = \sqrt{gh}$ . Eq.(10) is an approximation in shallow water of the dispersion relation,

$$\frac{C_n}{\sqrt{gh}} = \sqrt{\frac{\tanh k_n h}{k_n h}} \quad (11)$$

where  $k_n$  is obtained from  $(n\omega_1)^2 = gk_n \tanh k_n h$ . When we adopt the equation given by

$$\frac{dA_n}{dx} - i n k_1 \left[ \sqrt{\frac{k_n h}{\tanh k_n h}} - 1 \right] A_n = 0 \quad (12)$$

instead of Eq.(8), we can provide the exact dispersion relation.

In summary a modified version of spectral KdV equation in order to provide exact shoaling and dispersion relation of each frequency mode is obtained by changing the shoaling and the dispersion terms:

$$\begin{aligned} \frac{dA_n}{dx} + \frac{(C_{g_n})_x}{2C_{g_n}} A_n - ink_1 \left( \sqrt{\frac{k_n h}{\tanh k_n h}} - 1 \right) A_n + \frac{3ink_1}{8h} \\ \times \left[ \sum_{l=1}^{n-1} A_l A_{n-l} + 2 \sum_{l=1}^{N-n} A_l^* A_{n+l} \right] = 0; \quad n = 1, 2, \dots, N. \end{aligned} \quad (13)$$

When energy dissipation is taken into account, a damping term  $\alpha_n A_n$  should be added to the left hand side of Eq.(13), where  $\alpha_n$  is a damping coefficient to be determined theoretically or experimentally:

$$\begin{aligned} \frac{dA_n}{dx} + \frac{(C_{g_n})_x}{2C_{g_n}} A_n - ink_1 \left( \sqrt{\frac{k_n h}{\tanh k_n h}} - 1 \right) A_n + \frac{3ink_1}{8h} \\ \times \left[ \sum_{l=1}^{n-1} A_l A_{n-l} + 2 \sum_{l=1}^{N-n} A_l^* A_{n+l} \right] + \alpha_n A_n = 0; \quad n = 1, 2, \dots, N. \end{aligned} \quad (14)$$

Depending on whether  $\alpha_n$  is real, image, or complex, change of energy only, phase only, or both energy and phase, respectively, can be introduced. Here we take  $\alpha_n$  to be real.

In shallow water the model equation with damping term is transformed to

$$\left( \sum_{n=1}^N |A_n|^2 \right)_x + \frac{h_x}{2h} \left( \sum_{n=1}^N |A_n|^2 \right) + 2 \sum_{n=1}^N \alpha_n |A_n|^2 = 0, \quad (15)$$

by adding the two equations of Eq.(14) multiplied by  $A_n^*$  and the complex conjugate of Eq.(14) multiplied by  $A_n$ . By using the relation of

$$E = \frac{1}{2} \rho g \sum_{n=1}^N |A_n|^2, \quad (16)$$

Eq.(15) is rewritten as in a form of an energy flux equation:

$$\left( E \sqrt{gh} \right)_x = - \rho g \sqrt{gh} \left( \sum_{n=1}^N \alpha_n |A_n|^2 \right). \quad (17)$$

It is confirmed from Eq.(17) that the  $\alpha_n$  is a kind of energy damping coefficient.

## EXPERIMENT ON RANDOM WAVE TRANSFORMATION

Random waves used here were simulated to have the Pierson-Moskowitz spectrum with  $f_p = 0.6$  Hz and  $f_p = 1.0$  Hz ( $f_p$ : the peak frequency), referred as Case 1 and Case 2, respectively. Dominated wave breaking type seen in Case 1 was plunging, while in Case 2 spilling breakers were dominated. Figure 1 shows a sketch of experimental setup. Water surface variation were measured by capacitance-type wave gauges (WG.1~WG.12) at water depths of 47 cm, 35 cm, 30 cm, 25 cm, 20 cm, 17.5 cm, 15 cm, 12.5 cm, 10 cm, 7.5 cm, 5.0 cm and 2.5 cm over a 1/20 plane beach. The data were recorded by a digital data recorder at the sampling interval of 0.025 see for about 30 min duration for Case 1 and 20 min for Case 2.

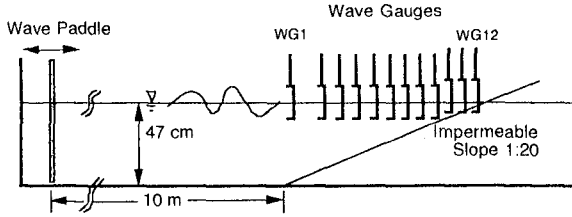


Fig. 1 Experimental Setup.

Figure 2 shows the change of measured energy spectra of Case 1 and Case 2. The data of water surface variations at each wave gauge were split into ten segments of 1024 points with the time interval of 0.1 sec. The energy spectrum of each segment was summed up and averaged. The ensemble averaged spectrum was smoothed by averaging three points. The degree of freedom is 60, and the resolution frequency is 0.03 Hz. The figures show the decay of energies around the initially peak frequency, the shift of peak frequency to the lower frequency, and the increase of energies in lower and higher frequency regions with decrease in the water depth. At the shallowest water of 2.5 cm (WG.12), the energy level of low frequency modes becomes almost the same as that around the initially peak frequency.

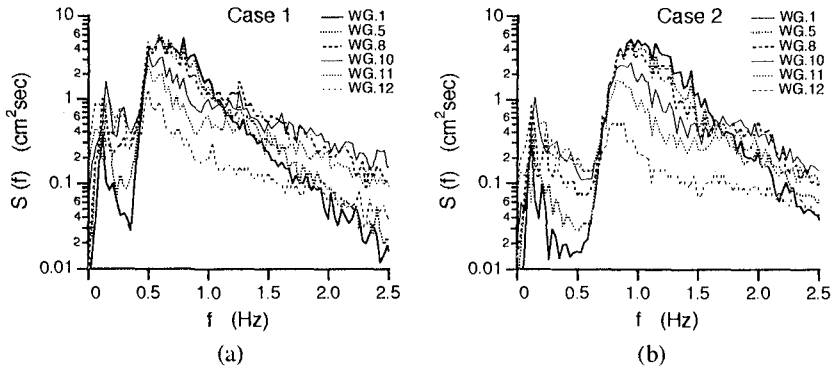


Fig. 2 Change of Measured Energy Spectra.

The calculated spectral energy densities by the original spectral KdV equation (Eq.(4)), the modified spectral KdV model without damping term (Eq.(14)), and the linear shoaling theory were compared with the measured energy densities, as shown in Fig.3. The 300 complex Fourier amplitudes at WG.1 ( $h = 47$  cm) were used as input data. The energy spectra were calculated for ten segments and were averaged as in the case of experimental data. The original KdV model overestimates the energy densities at WG.7 where wave breaking is very infrequent. The prediction by the modified KdV model agrees well with the observation at WG.7, but does not at WG.10 where energy dissipation due to wave breaking is important. The result means that since the Green's law is applied to all spectral components by the original KdV model, the overestimation occurs, and that the modified KdV model provides a better prediction outside the surf zone, but results in overestimation in the surf zone, due to the lack of a wave damping

term. The predictions by the linear shoaling theory differ from the observations in spectral shape.

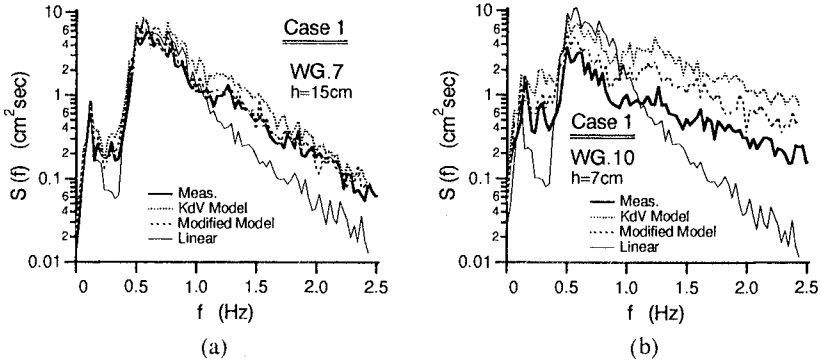


Fig. 3 Comparison between Calculated Results by the Frequency-Domain KdV Model, Modified KdV Model and Linear Shoaling Theory.

**DAMPING COEFFICIENT**

For constant water depth, the following equation for spectral densities is obtained from Eq.(15) multiplied by  $N\Delta t/2$ :

$$\sum_{n=1}^N \{ (S_n)_x + 2 \alpha_n S_n \} = 0 \tag{18}$$

When  $\alpha_n$  is nearly constant for short distance, the solution of Eq.(18) is

$$S_n(\Delta x) = S_n(0) e^{-2\alpha_n \Delta x} \tag{19}$$

and  $\alpha_n$  is expressed by

$$\alpha_n = - \ln \{ S_n(\Delta x) / S_n(0) \} / (2\Delta x) \tag{20}$$

The Taylor expansion of the above equation is

$$\alpha_n = [ 1 - \{ S_n(\Delta x) / S_n(0) \} ] / (2\Delta x) \tag{21}$$

However,  $\alpha_n$  estimated by Eq.(20) or Eq.(21), using the measured spectral energy densities, contains the effects of shoaling and nonlinear wave interaction. Some revision to remove such effects is required. Here the numerical results are utilized. Since the difference between the calculated spectral density at  $\Delta x$  downstream,  $S_n(\Delta x)_{Cal.}$ , and the measured density at a reference point,  $S_n(0)_{Meas.}$ , may be considered as the effects of shoaling and nonlinear interaction, the measured spectral density at  $\Delta x$  downstream,  $S_n(\Delta x)_{Meas.}$ , is modified as

$$S_n'(\Delta x) = S_n(\Delta x)_{Meas.} - \{ S_n(\Delta x)_{Cal.} - S_n(0)_{Meas.} \} \tag{22}$$

Since  $S_n'(\Delta x)$  takes negative value sometimes and the form of Eq.(20) is inconvenient, Eq.(21) is used as

$$\alpha_n = \left[ 1 - \left\{ S_n'(\Delta x) / S_n(0) \right\}_{Meas.} \right] / (2\Delta x) . \tag{23}$$

Another way is to obtain the  $\alpha_n$  so as to coincide  $S_n(\Delta x)_{Cal.}$  with  $S_n(\Delta x)_{Meas.}$  described by the following equation:

$$\alpha_n = - \ln \left\{ S_n(\Delta x)_{Meas.} / S_n(\Delta x)_{Cal.} \right\} / (2\Delta x) . \tag{24}$$

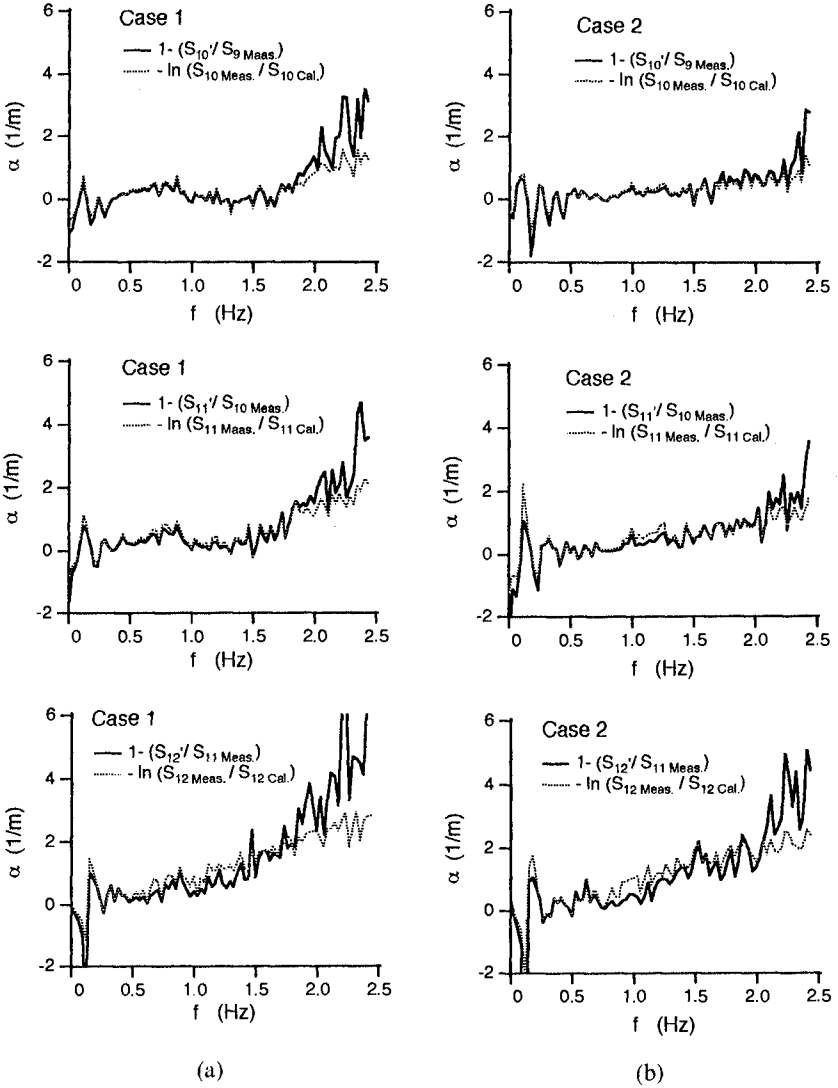


Fig. 4 Estimated Damping Coefficient.

Figure 4 shows the estimated  $\alpha_n$  using the data of consecutive wave gauges of WG.9 and WG.10, WG.10 and WG.11, WG.11 and WG.12, separated by 50 cm each other, in which the solid line is the result using Eq.(23) and the dotted line is by Eq.(24). The solid line and the dotted line are almost the same in a region of  $f < 2.0$  Hz. The  $\alpha_n$  at a given frequency becomes large with decrease in the water depth and appears to be proportional to  $f^2$  with a small constant value. The tendency is similar to that of the viscous damping term of the Burgers equation (given by  $-\nu \zeta_{xx}$  where  $\nu$  is the positive coefficient). The Fourier representation for  $-\nu \zeta_{xx}$ , using Eq.(2), results in  $\nu(nk_1)^2 A_n$ , which is rewritten as  $\nu(n\omega_1)^2/(gh) \cdot A_n$  using the relation of  $(nk_1)^2 = (n\omega_1)^2/(gh)$ ; that is,  $\alpha_n = \omega_n^2/(gh)$ . Because of the denominator  $gh$ , the  $\alpha_n$  becomes large with decrease in the water depth, and is proportional to the frequency squared. These results are used below to guide the choice of the distribution of damping on a frequency-by-frequency basis.

Thornton and Guza (1983) formulated the expected value of energy dissipation rate,  $\langle \epsilon_b \rangle$ , based on the probabilistic method (or individual wave analysis method), by using the Rayleigh distribution for wave height distribution, the specific weight function to represent the wave height distribution of broken waves, and an energy dissipation model of bore for each broken wave. The energy flux equation in shallow water is described by

$$\left( E\sqrt{gh} \right)_x = - \langle \epsilon_b \rangle, \tag{25}$$

$$\langle \epsilon_b \rangle = \frac{3\sqrt{\pi}}{16} \rho g B^3 \bar{f} \frac{H_{rms}^5}{\gamma^2 h^3} \left[ 1 - \frac{1}{\left\{ 1 + (H_{rms}/\gamma h)^2 \right\}^{5/2}} \right], \tag{26}$$

where  $B$  is a breaking coefficient,  $\bar{f}$  is the characteristic frequency,  $H_{rms}$  is the r.m.s. wave height,  $\gamma$  is the parameter to relate the  $H_{rms}$  with the water depth. Here we choose the parameter values to be

$$B = 1, \quad \gamma = 0.6, \quad \bar{f} = f_p, \quad H_{rms} = 2 \sqrt{\sum_n |A_n|^2}. \tag{27}$$

The right hand sides of Eqs.(17) and (25) should be equal to each other:

$$\begin{aligned} \sum_{n=1}^N \alpha_n |A_n|^2 &= \frac{3\sqrt{\pi}}{16\sqrt{gh}} B^3 \bar{f} \frac{\left( 2 \sqrt{\sum_n |A_n|^2} \right)^5}{\gamma^2 h^3} \\ &\times \left[ 1 - \frac{1}{\left[ 1 + \left\{ \left( 2 \sqrt{\sum_n |A_n|^2} \right) / \gamma h \right\}^2 \right]^{5/2}} \right] \equiv \beta(x) \sum_{n=1}^N |A_n|^2. \end{aligned} \tag{28}$$

Following Kirby et al. (1992),  $\alpha_n$  was determined to represent the experimental tendency as follows:

$$\alpha_n = \alpha_0 + (f_n / \bar{f})^2 \alpha_1 \tag{29}$$

$$\alpha_0 = F \cdot \beta, \quad \alpha_1 = (\beta - \alpha_0) \frac{\bar{f}^2 \sum_n |A_n|^2}{\sum_n f_n^2 |A_n|^2}. \tag{30}$$

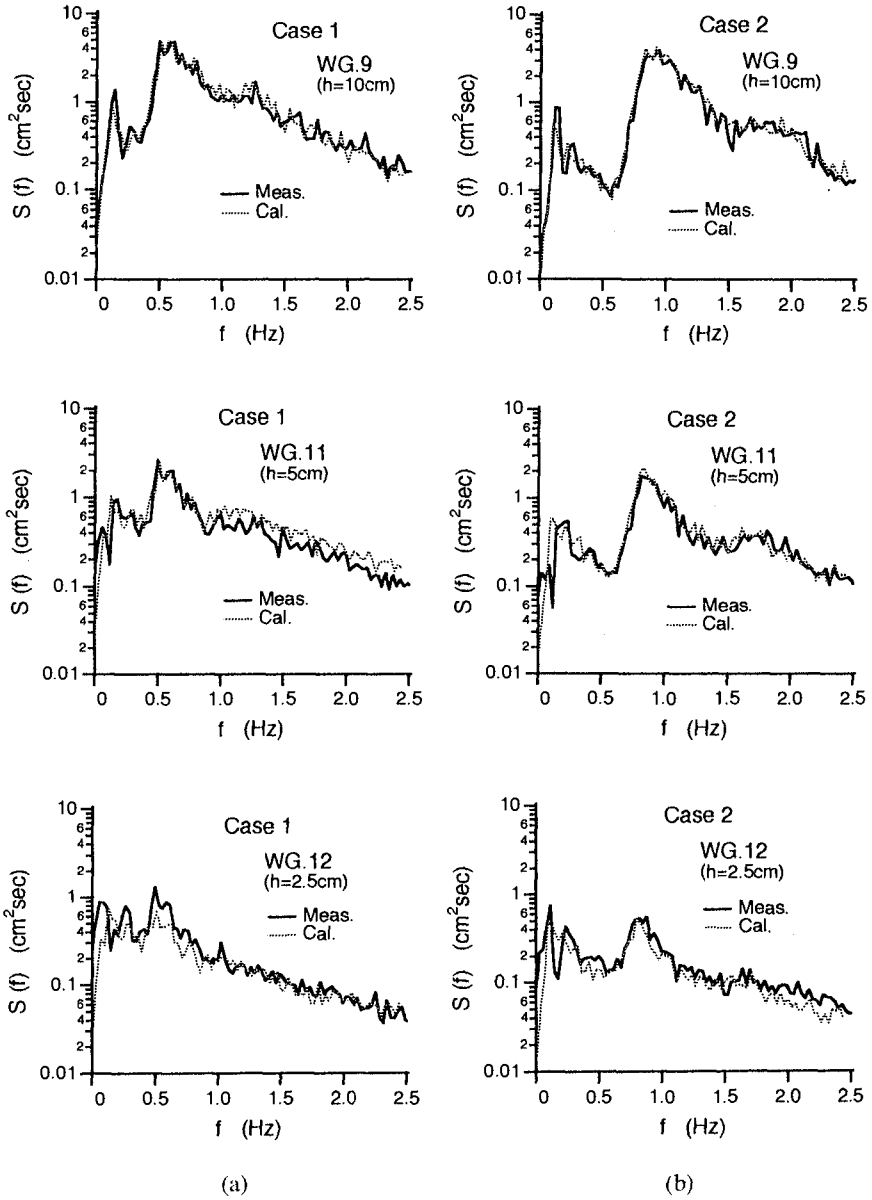


Fig. 5 Comparison between Measured Spectra and Calculated Ones by Hybrid Model Equation.

The first constant term of Eq.(29) represents uniform energy decay over all frequency components, and the second term is to express the  $f^2$  dependence. Here we chose as  $F = 0.5$ . Eq.(14) using  $\alpha_n$  determined by Eqs.(29) and (30) is the hybrid model equation used hereafter. The resulting model is integrated shoreward from the initial gauge position without any subsequent reference to use of measured data.

### COMPARISON BETWEEN EXPERIMENTAL OBSERVATIONS AND HYBRID MODEL PREDICTIONS

Figure 5 shows the comparisons of the measured spectra with the calculated ones by the hybrid model equation. Input data was given at WG.1 ( $h = 47$  cm). For Case 1, although there are slight differences in the region of  $f > 1.0$  Hz at WG.11 and  $f < 1.0$  Hz at WG.12, both results agree fairly well. The measured and calculated spectra of Case 2 also show good agreement. Predictions estimate the increase of energies in high and low frequency regions.

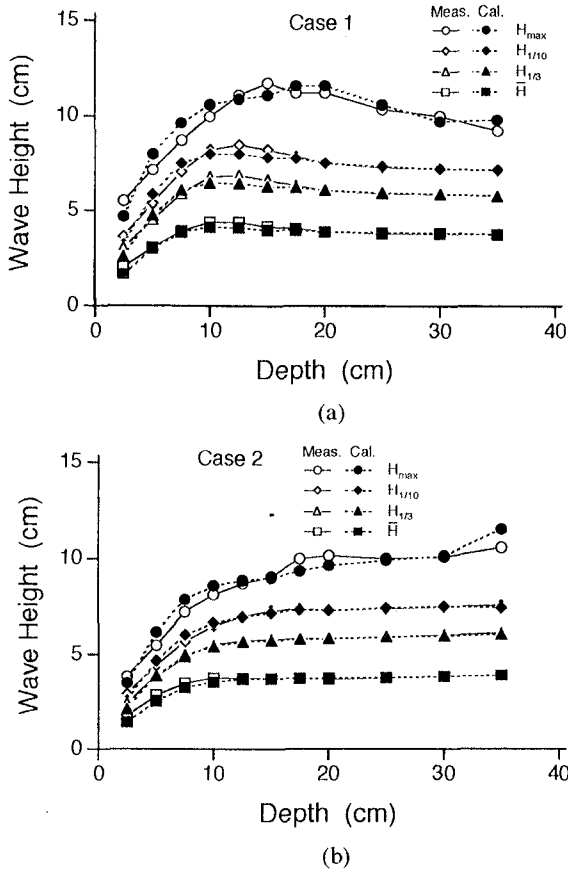


Fig. 6 Comparison between Measured and Calculate Representative Wave Heights.



Using the inverse FFT on the calculated  $A_n$ , we can obtain water surface variations from which wave characteristics such as wave heights, periods, crest heights, and so on, can be calculated. In the following comparisons, measured wave characteristics were calculated from the consecutive low-pass filtered (4.0 Hz) water surface variations with  $\Delta t = 0.025$  sec. Figure 6 shows the comparisons of the measured representative wave heights with the calculated ones for Case 1 and Case 2. It can be seen from the figures that the agreement between measured and calculated wave heights is good.

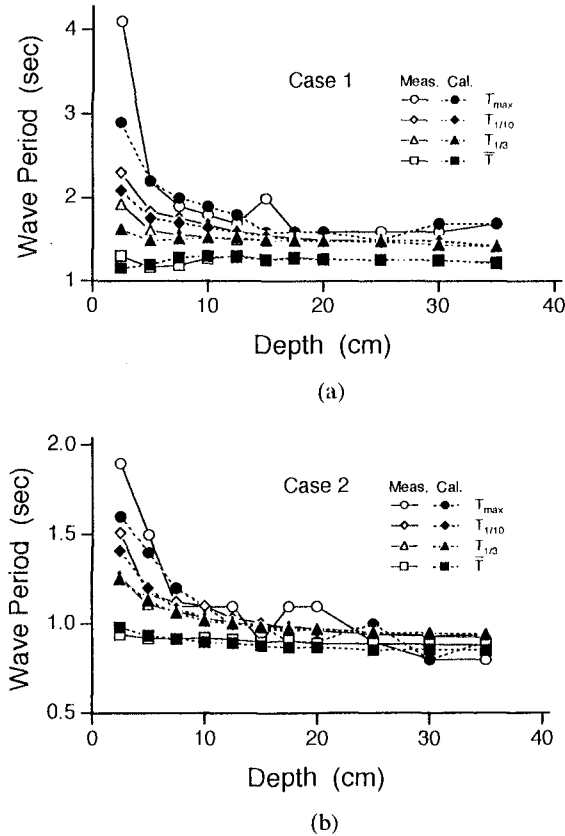


Fig. 7 Comparison between Measured and Calculated Representative Wave Periods.

Figure 7 shows the change of representative wave periods. Existing models based on the individual wave analysis model assume that the wave period is constant, or cannot deal with the change of wave period. Increase of energies of low frequency modes and decrease of energies around the initially peak frequency, according to Fig. 2, make the zero-upcrossing periods long compared to the incident wave periods. The present

hybrid model can estimate such change of wave periods, although a little differences can be seen at the shallowest water.

The wave crest height is an important factor for the design of the height of seawalls, platforms, and so on. Figure 8 shows the comparisons between the measured representative crest heights and the calculated ones. Although the predictions are a little smaller than the observations, satisfactorily good agreement is obtained. The representative normalized crest heights (each crest height was normalized by the wave height) are shown in Fig.9, which shows a little different tendency of change between the observations and the predictions. The values themselves agree fairly well.

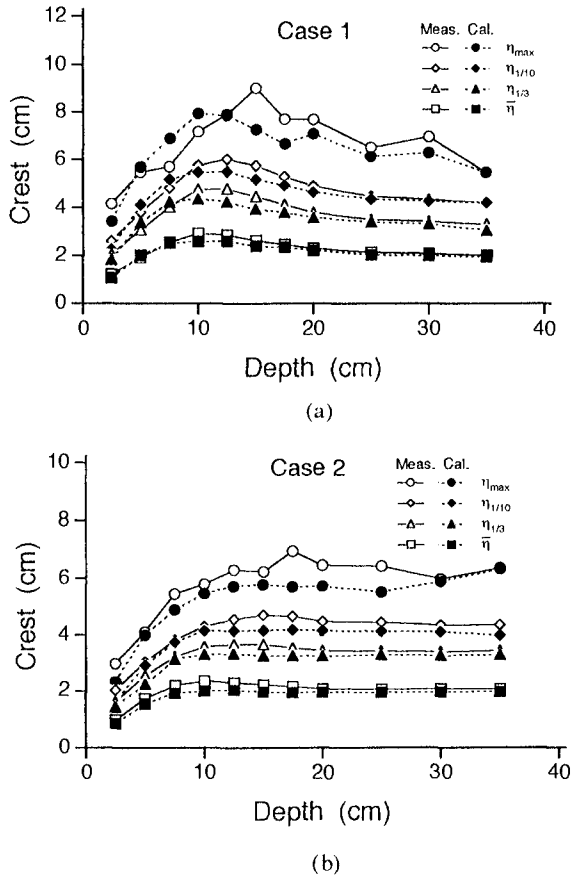


Fig. 8 Comparison between Measured and Calculated Representative Wave Crest Heights.

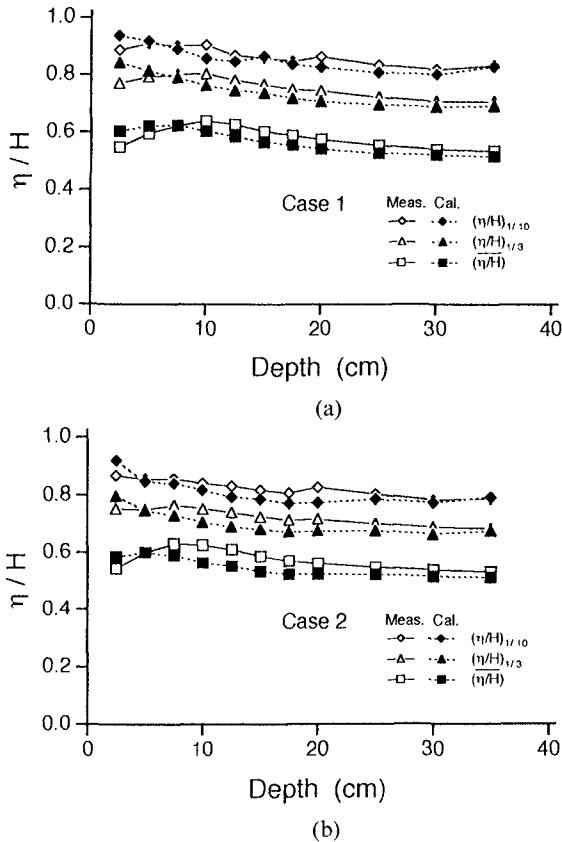


Fig. 9 Representative Normalized Wave Crest Heights.

## CONCLUSIONS

This paper proposed a hybrid model for random wave transformation, and compared the numerical predictions with the experimental observations. In the hybrid model a spectral model and a probabilistic model were employed: the former is the modified frequency-domain (spectral) KdV model to provide the shoaling and the dispersion relation for linear component waves with a damping term; the latter is a probabilistic model of energy dissipation due to wave breaking to formulate the coefficient of the damping term in the modified spectral KdV model.

The numerical predictions of energy spectra agreed well the experimental observations concerning the decay of energies around the initially peak frequency, the shift of peak frequency to the lower frequency, and the increase of energies in lower and higher frequency regions with decrease in the water depth. In addition to the energy spectra, the agreement between the predictions and the observation was satisfactorily

good against the representative wave heights, wave periods, wave crest heights. Thus, it was confirmed that the hybrid model developed here was useful as a vertically two-dimensional random waves over a uniform slope. The hybrid model should be further examined on the applicability to other situations such as multiple peak waves over a bar type topography.

## REFERENCES

- Freilich, M.II. and Guza, R.T. (1984). Nonlinear effects on shoaling surface gravity waves. *Phil. Trans. R. Soc. Lond.*, A311, pp.1-41.
- Karambas, Th.V. and Koutitas, C. (1992). A breaking wave propagation model based on the Boussinesq equations. *Coastal Engrg.*, Vol.18, Nos.1 & 2, pp.1-19.
- Khangaonkar, T.P. and LeMehaute, B. (1991). Extended KdV equation for transient axisymmetric water waves. *Ocean Engrg.*, Vol.18, No.5, pp.435-450.
- Kirby, J.T. (1990). Modelling shoaling directional wave spectra in shallow water. *Proc. 22nd Int. Conf. on Coastal Engrg.*, ASCE, pp.109-122.
- Kirby, J.T., Kaihatu, J.M. and Mase, H. (1992). Shoaling and breaking of random wave trains: spectral approaches. *Proc. 9th Engrg. Mech. Div. Specialty Conf.*, ASCE, College Station, pp.71-74.
- Liu, P.L.-F., Yoon, S.B. and Kirby, J.T. (1985). Nonlinear refraction-diffraction of waves in shallow water. *Jour. Fluid Mech.*, Vol.153, pp.185-201.
- Madsen, O.S. and Mei, C.C. (1969). The transformation of a solitary wave over an uneven bottom. *Jour. Fluid Mech.*, Vol.39, pp.781-791.
- Madsen, P.A., Murray, R. and Sørensen, O.R. (1991). A new form of the Boussinesq equations with improved linear dispersion characteristics. *Coastal Engrg.*, Vol.15, No.4, pp.371-388.
- Peregrine, D.H. (1967). Long waves on a beach. *Jour. Fluid Mech.*, Vol.27, pp.815-827.
- Thornton, E.B. and Guza, R.T. (1983). Transformation of wave height distribution. *Jour. Geophys. Res.*, Vol.88, No.C10, pp.5925-5938.
- Vengayil, P. and Kirby, J.T. (1986). Shoaling and reflection of nonlinear shallow water waves. *Proc. 20th Int. Conf. on Coastal Eng.*, ASCE, pp.794-806.

## CHAPTER 36

### BREAKING OF IRREGULAR WAVES ON A SLOPE\*

M. MIZUGUCHI<sup>1</sup>

#### ABSTRACT

Breaking condition of irregular waves on a slope is studied through a series of laboratory experiment of bichromatic waves. First, breaking condition of individual waves defined by zero-down crossing method is compared with breaking condition of regular waves. An empirical formula is proposed to take into account of the influence of both the depth and width of the following trough. Then it is shown that the breaking condition of regular waves can be applied successfully when the individual waves are properly defined by paying attention to the nature of the wave crests. Finally these results obtained from the laboratory experiment are tested against the field data with reasonable success.

#### 1. INTRODUCTION

Several studies have been already reported on the breaking of irregular waves on slopes. Goda (1973), Battjes and Janssen (1978), and Thornton and Guza(1983) dealt with probabilistic ( and somewhat heuristic ) methods to be incorporated into the transformation model of wave height distribution in the nearshore zone. Sugawara and Yamamoto (1978), Mizuguchi and Matsuda (1980), and Mase et al.(1986) constructed an irregular wave transformation model, in which wave breaking condition of individual waves are assumed to be the same as that of monochromatic waves.

---

\*) Part of this paper was published in Proc. of 35th Japanese Conf. on Coastal Eng. in Japanese( Mizuguchi et al., 1988)

<sup>1</sup>Professor, Dept. Civil Eng., Chuo Univ., Kasuga, Bunkyo-ku, Tokyo, JAPAN 112

There also have been presented some papers, which directly and experimentally investigated breaking conditions of individual waves in irregular wave trains either in laboratory or in the field (Iwagaki et al.;1977, Isobe et al.;1980, Hotta et al.;1984, Kimura and Seyama;1986, and Mizuguchi et al.;1987). One can summarize these papers as follows.

- 1) Local wave breaking condition of individual waves ( normally defined by zero-down crossing method ) shows considerably larger data scatter than that of monochromatic waves.
- 2) In average, individual waves in irregular wave trains tend to break more easily, that is, to break with smaller wave height compared with regular waves.
- 3) Adjacent waves, in particular, the depth of the following trough for the waves defined by zero-down crossing method, have some influence on its breaking.

In this paper, first, we look for a possible explanation for the cause of the data scatter as well as the tendency that irregular waves break more easily, taking into account of the influence of the neighbouring waves. In due course, we test the applicability of regular wave breaking criterion to irregular waves, and propose a way to relate the breaking criterions of irregular waves and regular waves. For that purpose, we conducted a series of laboratory experiment, using bichromatic waves, which essentially show a characteristic feature of the irregular waves that the neighbouring waves are not the same as is so for regular waves. An advantage to employ the bichromatic waves is that it is easy to measure the breaking waves by wave gauges, as they have limited number of fixed breaking points. Finally, we apply our results obtained from the laboratory experiments to the field data and discuss the improvement accomplished and problems remained.

## 2. LABORATORY EXPERIMENT

Experiment was carried out in a wave flume of 30 cm wide, 20 m long and 45 cm in height with glass side walls. Beach of 1/20 slope with painted plate was installed in one end. Wave maker in the other end was of an absorbing type. Water depth was 35.5 cm in the constant depth area.

Wave generating signal  $e$  was chosen as follows.

$$e = a \cos(2\pi t) + qa \cos(\pi t + \epsilon) \quad (1)$$

Here  $a$  is the amplitude of the primary waves of period 1 s. Various combinations of bichromatic waves were produced in the wave breaking area by varying the phase difference

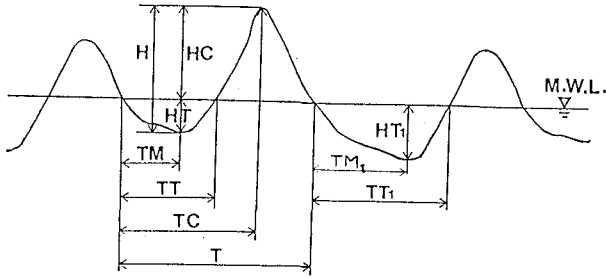


Fig. 1 Typical wave profile in time of two-wave train at one of breaking points. Various quantities to possibly influence the breaking condition are evaluated.

$\epsilon$  and the wave amplitude ratio  $q$ . This signal generates two-component waves also in terms of the time series, since the secondary wave has the half frequency of the primary waves. Hereafter we call this wave train as two-wave train. The amplitude  $a$  of the primary wave was set to be around 3 or 6 cm in the uniform depth area. The amplitude ratio  $q$  was varied as 0.1, 0.2, 0.3, and 0.5. Typical surface profile at a breaking point is shown in Fig. 1. Total of 160 runs of two-wave train experiment were conducted. In addition, 36 runs of regular wave experiment, which can be considered to be of the cases  $q=0$ , were also carried out in order to check the validity as well as the values of the experimental constants of the following Goda's breaking criterion (Goda; 1973).

$$H/d = A(L_0/d)[1 - \exp\{-Bd(1 + K\tan^s\beta)\}] + C \quad (2)$$

where  $H$ ,  $d$ , and  $L_0$  denote wave height, water depth, and deep-water wave length respectively.  $\tan\beta$  is the beach slope.  $A$ ,  $B$ ,  $K$ ,  $s$  and  $C$  are experimental constants and the originally proposed values are 0.17, 1.5, 15, 4/3 and 0 in its order. However, Eq.(2) with the original values of constants gives slightly larger breaking wave height as shown in Fig.2, as was also pointed out by Sugawara and Yamamoto(1978).  $A=0.158$ , with original values for other constants, is used in this paper, since it gives the better fitted curve to our regular wave experiment.

In the experiment, first, video-camera was used to determine the breaking points. Then capacitance-type wave gauges were placed at those breaking points ( normally two for two-wave trains ) to measure the surface profiles. The breaking points were defined visually as the position where significant white foams were observed. If not obvious, then the point of maximum wave height was searched by moving the

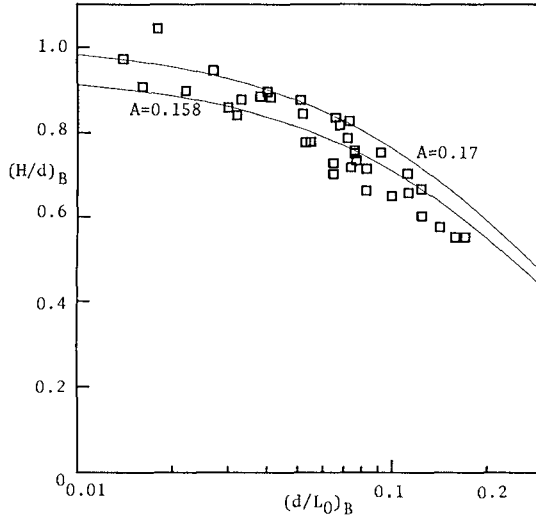


Fig. 2 Local breaking condition of regular waves on a uniform slope. Solid lines denote the experimental formula by Goda(1973) with specified values of A.

wave gauges in the cross-shore direction. The data was recorded on a digital tape recorder with sampling frequency of 50 Hz for the cases of  $a \approx 3$  cm and 100 Hz for both cases of  $a \approx 6$  cm and of regular waves. Data processing as well as signal making were done on a personal computer (Sord M343 SXII).

### 3. ANALYSIS OF LABORATORY DATA

The obtained data show small fluctuation of period 30 s, which is roughly the period of the first harmonics of the wave flume. The quantities defined for individual waves were averaged over 30 cycles of the primary wave. Positions of wave breaking also fluctuated within the horizontal distance of about 5 cm. This value gives rough estimate for the experimental error.

Zero-down crossing method was employed to define the individual waves, since this method takes the rise from the trough to the crest as the wave height as shown in Fig.1. This height is more appropriate for investigating the wave breaking condition than the fall height from the crest to the trough taken by the zero-up crossing method. As shown in Fig.1, various quantities associated with the defined wave, or more precisely with the shape of the troughs of both sides of the concerned crest, were also calculated in



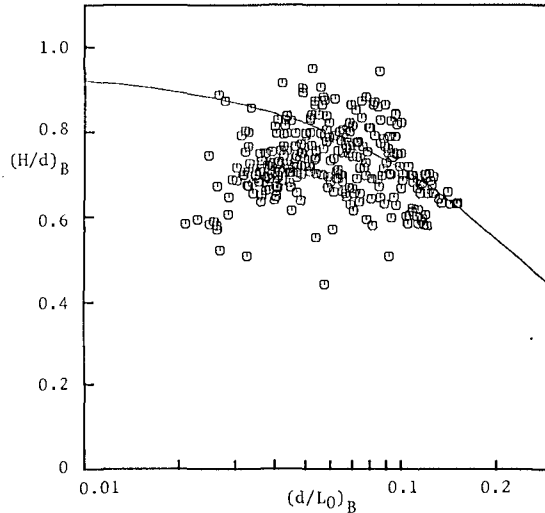


Fig. 3 Breaking condition of two-wave train waves. Goda's experimental formula for regular waves, Eq.(2), is denoted by a solid line.

order to study the influence of the adjacent waves, For the breaking depth, the still water depth at each location is employed. In this stage, a data-base of 196 cases of local wave breaking conditions is obtained.

### 3.1 Breaking Conditions of Waves Defined by Zero-Down Crossing Method and Regular Waves

Fig. 3 shows the local wave breaking condition in which  $(H/d)_B$  is plotted against  $(d/L_0)_B$ . Subscripts B indicates those evaluated at the breaking point. The distribution of the data is very similar to the case of irregular waves and the data scatter is much larger than that in Fig. 2 for regular waves. For irregular wave results in laboratory experiment, see Fig. 2 in Kimura and Seyama (1986).

Fig. 4 shows direct comparison of measured relative wave height,  $(H/d)_B$ , against that,  $(H/d)_R$ , given by Eq.(2). This figure shows that the waves break with wide range of relative wave height, 0.45-0.95, in spite of the expectation from the regular wave formula that they break with narrow range of relative wave height, 0.6-0.85. This may suggest that there are some other hidden parameters to control the breaking of irregular waves and also that the large data scatter in Fig. 3 can be reduced by playing with the definition of the water depth.

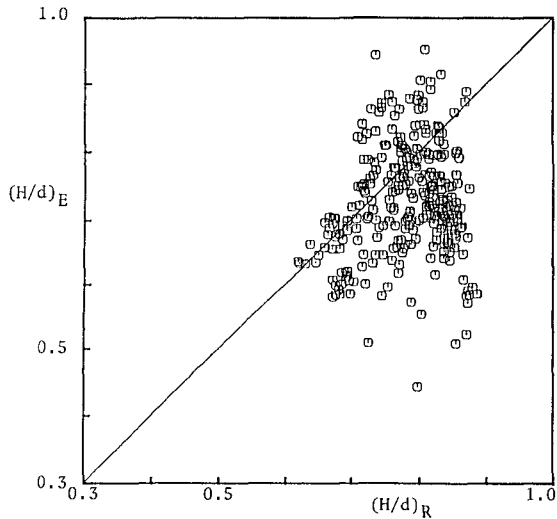


Fig. 4 Direct comparison of breaking wave condition for two-wave train waves with Goda formula.

Kimura and Seyama (1986) succeeded to reduce the data scatter by introducing a modified water depth  $d_m$ , that is the depth below the median level of wave crest and trough. However, the reduction may be largely due to the resulting nonlinear scaling in the vertical axis, i.e.  $H/d_m$ . Moreover, it is difficult to find physical meaning of  $d_m$  for the wave breaking.

Here, first, we assume that the large data scatter is brought in as a result of neglecting the difference of the adjacent waves. We plotted the ratio of measured relative wave height,  $(H/d)_E$ , to the relative height given by Eq.(2),  $(H/d)_R$ , against various parameters defined from the quantities shown in Fig.1. Then the ratio shows clear dependency on the following parameters,  $HU/H$  ( where  $HU = H - HT + HT_1$  ) and  $TU/T$  ( where  $TU = T - TT + TT_1$  ).  $HU$  and  $TU$  are, respectively, the wave height and period, defined by the zero-up crossing method for the concerned wave crest. This is very conceivable when one thinks of the fact that it is the wave crest that breaks. In Fig. 5, the ratio of  $(H/d)_E/(H/d)_R$  is plotted against  $HU/H$  with  $TU/T$  as a parameter. The data, as a whole, show monotonical increase, implying the tendency that the larger the  $HU/H$  is, i.e., the deeper the following trough is, the higher the breaking wave height is, as was pointed out by Isobe et al.(1980). However, once the length of the following wave trough is taken into account, the data show monotonical decrease, indicating that the waves which are followed by relatively

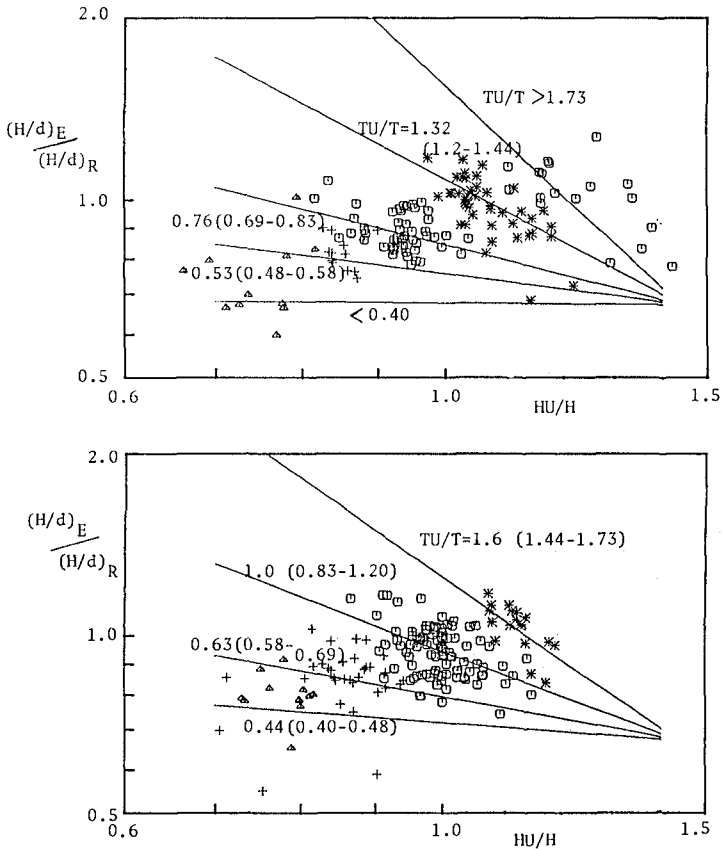


Fig. 5 Effect of the shape of the following trough on in individual wave breaking in two-wave trains. Upper and lower diagrams are for different values of the parameter  $TU/T$ .

deeper and shorter trough do break easily or with smaller wave height. In other words, the following deep trough, which is nearer to the wave crest, makes the crest break easily. This is reasonable as the situation means that the wave is sharp-crested and the actual water depth for the crest is shallow. The least square error method was applied to deduce the best-fitted curves, which are plotted with solid lines in Fig.5. They are expressed by the following equation.

$$\frac{(H/d)_E}{(H/d)_R} = 0.58(HU/H)^{-TU/T} \exp\{0.48(TU/T)\} \quad (3)$$

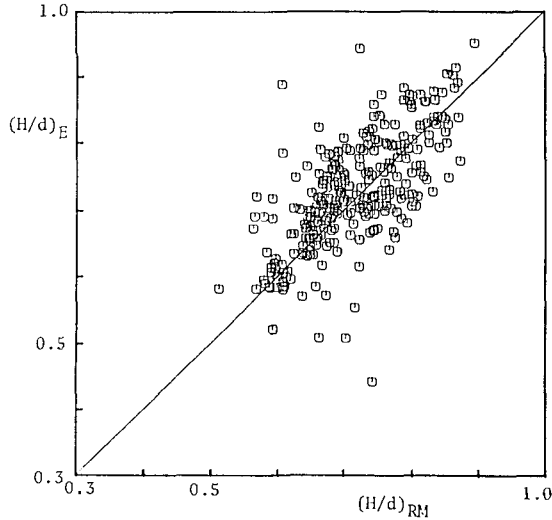


Fig. 6 Comparison of breaking conditions for two-wave trains after modification.

Equation (3) gives value of 0.94 for the ratio when  $TU/T=1$  and  $HU/H=1$ , although unit value may be expected as the conditions correspond to the regular waves. The irregular shape of the individual waves may be responsible for the easy breaking, although there is a possibility that the difference is within the experimental error. The data in Fig. 5 still show large scatter. In order to reduce the scatter, other parameters like  $TM_1$  to directly describe the shape of the trough could be better to be used. However we chose  $HU$  and  $TU$  to introduce the empirical formula, as they are the traditional quantities defined by zero-up crossing method.

Figure 6 shows comparison of measured relative wave height with that given by Eq.(2) with modification after Eq.(3). The improvement is obvious as the average tendency follows that of regular waves. The correlation coefficient in Fig. 6 is 0.68 and much larger than the value of 0.15 for Fig. 4. It may be possible to further reduce the data scatter by introducing another parameter to describe the irregular shape of the waves. However that sort of approach may not be productive.

### 3.2 Breaking Condition of Individual Wave Crest

In the preceding section a modification of regular wave breaking formula for the individual waves defined by zero-down crossing method was attempted. The results

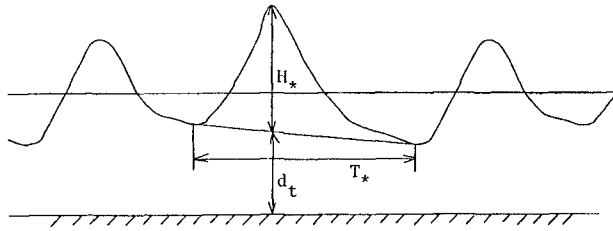


Fig. 7 Properties of an individual wave crest in bichromatic waves.

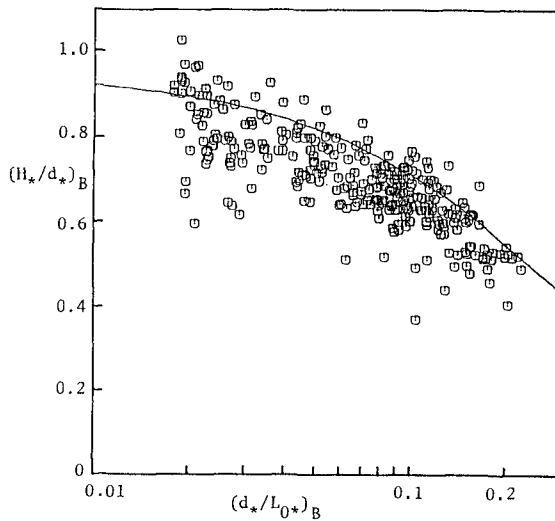


Fig. 8 Breaking condition of individual wave crests in two-wave train waves.

indicates that the properties of the wave crest are important to control the breaking. Now we look into the breaking condition of a wave crest in comparison with regular wave breaking. Here we define an individual waves by trough-to-trough method as shown in Fig. 7. For this individual waves, the height,  $H_*$ , is defined as the vertical distance between wave crest and the line drawn from the preceding trough to the following trough. Local water depth  $d_*$  is calculated by applying first order cnoidal wave theory ( Isobe;1985 ) as  $d_* = d_t + (\text{mean elevation of cnoidal waves over trough level})$ , with  $H_*$ , trough-to-trough period,  $T_*$ , and trough depth  $d_t$  given.

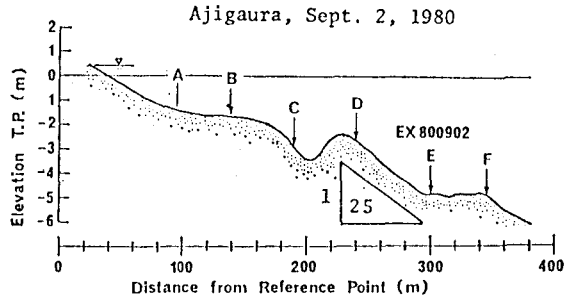


Fig. 9 Bottom topography of field observation site

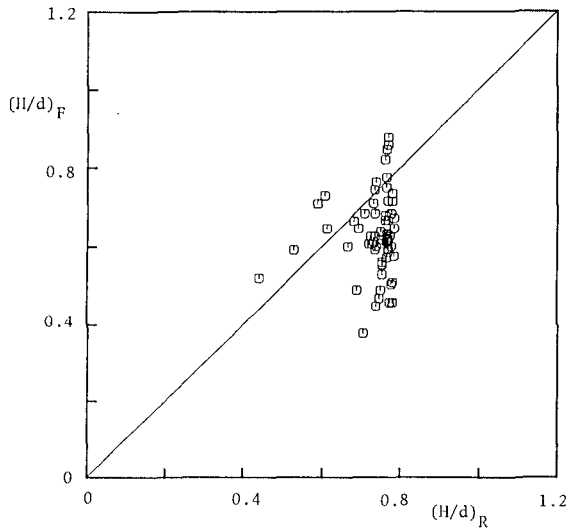


Fig. 10 Comparison of breaking condition of field waves defined by zero-down crossing method and regular waves.

Figure 8 shows local wave breaking condition for the individual wave crests. In contrast to Fig. 2, similarity with regular wave breaking is remarkable. There is still seen large data scatter, some of which may be of experimental error but most of which may be due to an artifice to approximate an individual wave by a regular wave. It is noted that the differences of wave period  $T$ , from the period  $T$  defined by zero-down crossing method are large and contribute quite significantly to move the data points in Fig. 7. In Fig. 7, average values of breaking height-depth ratio as well as their standard deviation could be evaluated for a given relative depth, as was done

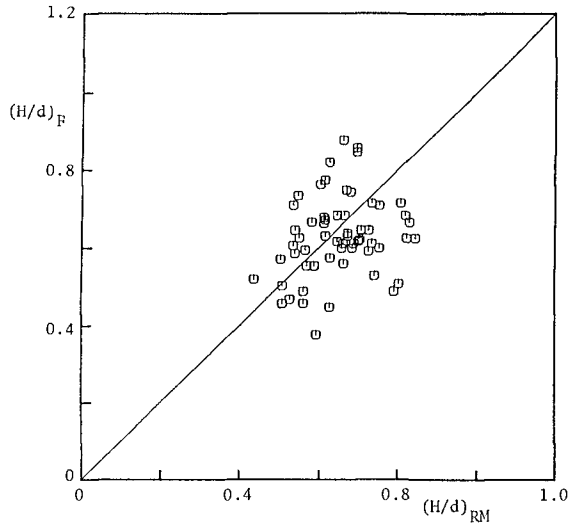


Fig. 11 Comparison of breaking condition of field waves after the modification.

by Kimura and Seyama(1986) for waves defined by zero-down crossing method with their modified depth  $d_m$ , yielding experimental formulae for the breaking condition, though not tried here.

#### 4. BREAKING CONDITION OF FIELD WAVES

16 mm camera movies, which shot the target poles in the nearshore zone were used to take out the waves, which are just breaking at the location. This film was already analyzed and the results for the zero-down crossing waves were reported by Mizuguchi et al.(1987). Here we re-analyze the film in the same way as we did for the laboratory data and calculated the quantities shown in Fig. 1. Fig. 9 shows the cross-shore bottom topography of the site. The data at position D is used. The mean water depth was 2.79 m. Numbers of just breaking waves at position D were 47 out of 1118 waves defined during the observation.

In Fig. 10, relative wave heights at the breaking point for field waves are compared with regular wave formula. For  $\tan\beta$ , value of  $1/25$  is used. Figure 10 is very similar to Fig. 4, showing that waves break with wide range of,  $H/d$ , values, although Eq.(2) gives narrow range of the values.

Figure 11 shows comparison of relative wave heights for field waves,  $(H/d)_F$ , with those of the breaking formula

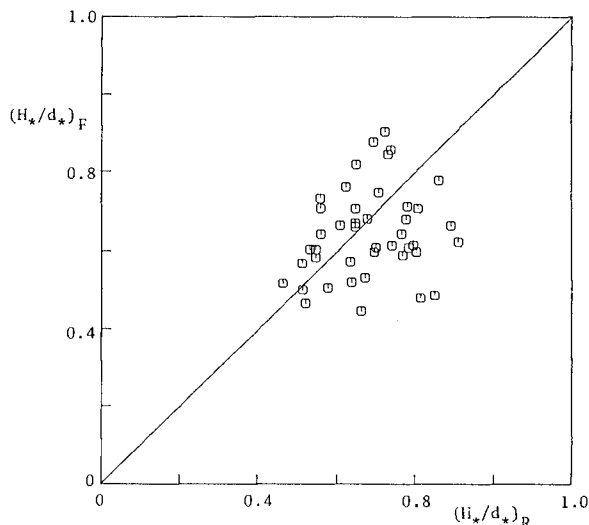


Fig. 12 Comparison of breaking condition of individual waves defined by trough-to-trough method for field waves.

modified with Eq.(3),  $(H/d)_{RM}$ . Figure 12 shows comparison of breaking condition of the wave crests,  $(H_*/d_*)_F$ , for field waves and regular waves. Both diagram show a linear trend though large data scatters are still observed. There is no tendency in Fig. 12 that the field values are smaller than those given by regular wave formula, in contrast to the results in Fig. 8. The linear trends proves that the present modifications are in the right direction to establish the wave breaking condition of the individual waves in the field waves. The data scatter may result from various complexities observed in the field, such as three dimensional feature of field waves and non-uniform bottom slope, in addition to the factors possible in laboratory data. Recently, Sato et al.(1990) looked into the effect of long period waves on the irregular wave breaking. Interaction between long period waves and wind waves may be partially responsible for the remaining data scatter.

## 5. CONCLUSIONS

We can conclude that the individual waves in an irregular wave train do, in average, break in a similar condition to that of the regular waves. However, conventional zero crossing methods may not be suitable to defining the breaking waves, for thus defined waves need the systematic modification as given by Eq.(3). Regular wave breaking condition can be applied reasonably well to



the waves defined by the trough-to-trough method.

One can also conclude that the average breaking height-depth ratio of two-wave train is slightly smaller (about 5 % ) than that of regular waves, although this tendency is not clear in field waves, and that some data scatter is inevitable when the regular wave formula is used for the individual waves. The irregular shape of the individual waves may be responsible for both of them.

Here only local wave breaking criterion is studied. It is necessary to develop a shoaling model for irregular waves as well as for two-wave trains, which is valid upto breaking point, in order to be able to predict both the breaking depth and wave height.

#### ACKNOWLEDGEMENTS

I would like to thank T. Watanabe, Y. Takemura, M. Itoh and T. Mori for their great help in carrying out this research. This research was financially supported by Grant-in-Aid of Ministry of Education and Culture, Japan.

#### REFERENCES

- Battjes, J.A. and J.P.F.M. Janssen(1978), Energy loss and set-up due to breaking of random waves, Proc. 16th ICCE, 559-587.
- Goda, Y.(1973), Irregular wave deformation in the surf zone, Coastal Eng. in Japan, Vol.16, 13-26.
- Hotta, S., M. Isobe, T. Izumiya and M. Enzawa(1984), Breaking criterion on a natural beach, Proc. 31st Japanese Conf. on Coastal Eng., 44-48 (in Japanese).
- Isobe, M.(1985), Calculation and application of first-order cnoidal wave theory, Coastal Eng., Vol.9, 309-325.
- Isobe, M., H. Nishimura and T. Tsuka(1980), Experimental study on breaking transformation of irregular waves, Proc. 27th Japanese Conf. on Coastal Eng., 139-142 (in Japanese).
- Iwagaki, Y., A. Kimura and N. Kishida(1977), Breaking of irregular waves on slopes, Proc. 24th Japanese Conf. on Coastal Eng., 102-106 (in Japanese).
- Kimura, A. and A. Seyama(1986), On the breaking condition of irregular waves on slopes, Proc. 33rd Japanese Conf. on Coastal Eng., 174-178 (in Japanese).
- Mase, H., A. Matsumoto and Y. Iwagaki(1986), Calculation

- model of random wave transformation in shallow water, Proc. JSCE, Vol. 375/II-6, 221-230 (in Japanese).
- Mizuguchi, M. and C. Matsuda(1980), Shallow water transformation of field waves, Proc. 27th Japanese Conf. on Coastal Eng., 134-138 ( in Japanese ). For English version, see Mizuguchi, M.(1982), Individual wave analysis of irregular wave deformation in the nearshore zone, Proc. 18th ICCE, 485-504.
- Mizuguchi, M., S. Hotta, T. Nakamura and T. Kawasaki(1987), On breaking condition of field waves, Proc. 34th Japanese Conf. on Coastal Eng., 152-156 (in Japanese).
- Mizuguchi, M., T. Watanabe, Y., Takemura and M. Itoh (1988), On breaking of irregular waves on a slope, Proc. 35th Japanese Conf. on Coastal Eng., 178-181 (in Japanese).
- Sato, S., M. Ozaki and T. Shibayama(1990), Breaking conditions of composite and random waves, Coastal Eng. in Japan, Vol. 33, No.2, 133-143.
- Sugawara, T. and M. Yamamoto(1978), Calculation model of wave transformation in shallow water, Proc. 25th Japanese Conf. on Coastal Eng., 80-84 (in Japanese)
- Thornton, E.B. and R.T. Guza (1983), Transformation of wave height distribution, J. Geophys. Res., Vol. 88(C1), 5925-5983.

## CHAPTER 37

### Oscillating Water Column Modelling

Iain G. Morrison <sup>1</sup> and Clive A. Greated<sup>2</sup>

#### Abstract

The development of a mathematical model to calculate the response of a simple oscillating water column wave energy device (OWC) to a known wave climate is described. The power available from the device is calculated and this is compared with results from model tests in a wave flume.

Particle Image Velocimetry (PIV) has been used to map the flow of water within the chamber of the device and vorticity maps have been calculated. The estimation of energy loss in vortices due to viscous dissipation is discussed in detail and is shown to account for as much as 8% of the total energy of an incident wave.

#### Introduction

The oscillating water column wave energy converter (OWC) is now a well established means of extracting useful energy from water waves both simply and cost effectively. It consists of a chamber with two orifices. One is open to the sea below the low water level and the other is typically at the top of the chamber and connects to a turbine. A water column is formed in the chamber and oscillates due to the force of the incident waves. This in turn forces air through the turbine thus generating electricity. Several devices are now in operation worldwide but these are single prototype units working at only a fraction of their true potential either due to turbine restrictions or to large scale dissipation of energy within the chamber itself.

---

<sup>1</sup>Research Student, Fluid Dynamics Unit, Physics Department, The University of Edinburgh, Edinburgh, EH9 3JZ, U.K.

<sup>2</sup>Director, Fluid Dynamics Unit, Physics Department, The University of Edinburgh, Edinburgh, EH9 3JZ, U.K.

This paper attempts to develop a mathematical model to predict the power available from a simple design of OWC and to use Particle Image Velocimetry (PIV) to study the characteristics of water flow in the chamber of a model of the same OWC. Analysis of the highly detailed velocity maps produced with PIV allows regions of energy dissipation to be identified and the magnitudes of these energy losses to be estimated.

The OWC under study here is a simplified  $\frac{1}{36}$ th scale model of the prototype designed by Whittaker[4] and now operational on the island of Islay off the west coast of Scotland. This working example utilises a self rectifying axisymmetric Wells turbine[3] for the conversion to electrical energy.

### The OWC model

The scale model measures approximately  $0.5\text{m} \times 0.5\text{m} \times 0.4\text{m}$  - the dimensions chosen to coincide with those of models built and tested at Queen's University, Belfast. The water depth shallows from a maximum of  $0.75\text{m}$  'offshore' to  $0.12\text{m}$  at the mouth of the OWC, the variation occurring steadily along a beach of slope 1:12 (figure 1).

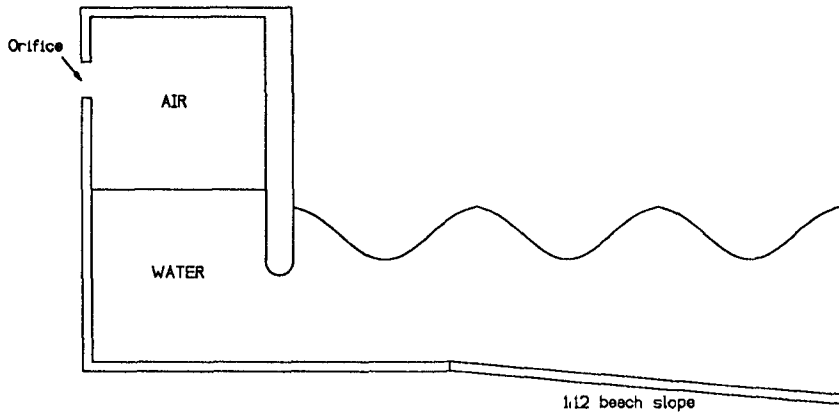


Figure 1: OWC model at top of 1:12 beach

### Mathematical modelling

It is important that an OWC and its turbine are capable of extracting the maximum amount of energy from the waves incident upon the chamber. In order to achieve this the natural frequency of the chamber must be chosen to be

close to that of the prevailing wave climate. Therefore it is useful to be able to predict theoretically the resonant frequency of an OWC chamber and the air pressure variations within it since it is these pressures which provide the force to drive the turbine. Linear wave theory is used as a first approximation here to model the typically low amplitude waves produced in the wave flume experiments.

It is assumed that the air column compresses adiabatically and the variation of the mass of this column due to air movement through the orifice is considered. It is further assumed that the air travels through the orifice with a velocity proportional to the excess pressure in the chamber. This yields a differential equation giving the rate of change of air pressure within the OWC:

$$\frac{dp}{dt} = \frac{\gamma p}{d - y} \left[ \frac{dy}{dt} - \frac{\kappa}{\rho_0 A} \left( \frac{p_0}{p} \right)^{\frac{1}{\gamma}} (p - p_0) \right] \quad (1)$$

where  $p$  is the air pressure in the chamber,  $y$  is the height of the water surface in the chamber above mean water level (MWL),  $\gamma$  is the ratio of the specific heat of air at constant pressure to that at constant volume,  $d$  is the length of the air column at MWL,  $p_0$  is atmospheric pressure,  $\kappa$  is a constant relating to the size of the orifice,  $\rho_0$  is the density of air at atmospheric pressure, and  $A$  is the cross sectional area of the air column.

Consideration of both the static and dynamic pressure under an incident wave and the upward force this exerts on the water column leads to the second differential equation :

$$\frac{d^2 y}{dt^2} = \frac{1}{\rho_w(L + y - d)} \left[ \rho_w g \left( a \sin \omega t - y - \frac{a \sinh k(h - b) \sin \omega t}{k(b - h) \cosh kh} + \frac{g a^2 k \sinh 2k(h - b)}{8 \omega^2 (b - h) \cosh^2 kh} \right) + p_0 - p \right] \quad (2)$$

where  $L$  is the chamber height,  $\rho_w$  is the density of water,  $h$  is the mean water depth at the OWC,  $b$  is the distance below mean water level of the lip of the front wall,  $a$  is the amplitude,  $k$  is the wavenumber and  $\omega$  is the angular frequency of the incident wave.

Equations (1) and (2) are insoluble analytically. They are solved numerically using a fourth order Runge-Kutta algorithm with a small time step. The program

which does this starts with deep water waves of known frequency and amplitude and calculates their amplitude and wavenumber in the shallower water at the mouth of the OWC before calculating the wave pressures at that point. This allows more reliable duplication of wave flume experiments where the amplitude and wavenumber of waves produced is only known accurately at their point of origin in deep water.

From calculated values of water elevation and chamber air pressure the instantaneous power is given approximately by :

$$P = A \frac{dy}{dt} (p_0 - p) \quad (3)$$

### The PIV system

PIV is a full field velocity measurement technique consisting of two distinct stages. First the displacement of small, neutrally buoyant, seeding particles in the flow is recorded on a photographic negative using a high quality medium format camera. Then the negative is analysed using the Young's fringe method to produce a detailed map of regularly spaced flow velocity vectors with a typical maximum error of the order of 5% of the maximum velocity magnitude.

The seeding particle displacements are recorded by illuminating the flow several times on a single frame with intense laser light. In the experiments carried out in Edinburgh the beam from a 15W continuous wavelength argon ion laser is scanned at high speed into the centre of the tank via a spinning mirror and a parabolic mirror which produce a 'sheet' of light illuminating a region about 1m wide.

One of the drawbacks of a PIV system is that although particle spacings on the film can be accurately determined the sense of direction of flow cannot. There is a 180° ambiguity in the direction of flow vectors which was overcome by the development of a rotating mirror image shifting system. This consists of a high quality front silvered mirror placed in a vertical plane and rotating on a turntable about a vertical axis through its centre. The turntable rotates at a constant known speed. The PIV pictures are then taken with the flow reflected in the mirror. The rotation effectively superimposes a known horizontal velocity on the flow. This is chosen to be large enough such that the sense of all the resulting velocity vectors can be inferred at the time of analysis. Finally the superimposed shift velocity is subtracted to give the true flow vectors.

The technique of PIV is discussed in greater detail by Gray & Greated[1] and

by Greated et al[2].

### Wave flume experiments

All wave flume experiments were carried out in a flume purpose built for PIV applications. The flume is 9.75m long, 0.4m wide and has a depth of 0.75m at mean water level. The walls and base of the tank are constructed from glass to allow unobstructed optical access from the base and sides of the tank. Waves are produced by a computer controlled hinged paddle with the capability to simultaneously produce waves and absorb reflections to minimise any seiche effects in the flume.

An OWC model was built entirely from perspex to allow access for the laser sheet from below and for photography from the side. The model was fitted with a high precision differential air pressure transducer. A resistance type wave gauge was fitted inside the chamber of the model and three further gauges were placed at different water depths on the sloping beach to measure the amplitudes of incoming and reflected waves. All five channels of data collection were sampled at a rate of 80Hz.

Building a scaled down Wells turbine for the model would not only be impractical but would also be unlikely to replicate the linear damping effect of a real turbine on the oscillation of the water column. Instead the square orifice of the model was closely packed with many small diameter tubes to reduce the Reynolds number of the airflow so that the flow would be laminar and thus proportional to the difference between chamber pressure and atmospheric pressure.

Wave gauge and air pressure records were taken for various amplitudes and frequencies of sinewaves and for nine different sizes of orifice ranging from a closed orifice to a maximum opening of 39mm  $\times$  39mm.

### Results

PIV was used to produce velocity vector maps of the flow within the OWC for various frequencies and amplitudes of forcing waves and several different orifice sizes. Each map contains about 2500 vectors with a resolution of about 5mm.

At frequencies below about 0.8Hz a strong vortex forms just within the lip of the front vertical wall of the model when water rushes in to the chamber. Figure 2 shows the flow of water into the OWC chamber just after the crest of a 0.6Hz, 15mm amplitude wave is incident. A vortex then forms as the water level rises in the chamber as shown in figure 3 and this is shed as the level drops again.

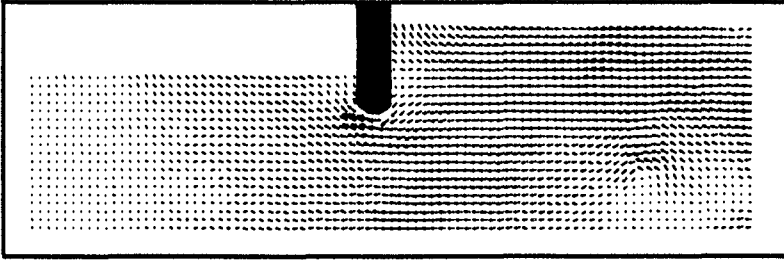


Figure 2: PIV vector map,  $f=0.6\text{Hz}$ , wave amplitude=15mm

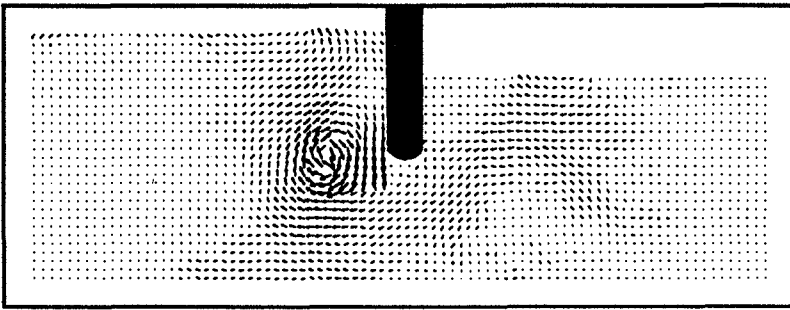


Figure 3: PIV vector map,  $f=0.6\text{Hz}$ , wave amplitude=15mm

Figure 4 shows the comparison of typical pressure and chamber water elevation results from theoretical and wave flume experiments. It can be seen that the theoretical results correctly predict the amplitude of oscillation of water in the column but underestimate the pressure variations. This may be due to the difficulty of determining the effective mass of water involved in the oscillations of the water column. However a more likely explanation is that the small diameter tubes placed in the orifice of the OWC model failed to lower the Reynolds number sufficiently to ensure laminar flow through them.

As a result of the underestimated pressure variations the theoretical model also underestimates the mean instantaneous power available from the device. The theoretical results in figure 5 suggest that the natural frequency of the OWC is about  $0.55\text{Hz}$  with an orifice of  $25\times 25\text{mm}$  whereas the experimental results suggest a lower value of less than  $0.5\text{Hz}$ . Unfortunately it was not possible to produce lower frequency sinusoidal waves in the flume. The experimental results in figure 6 show an optimum orifice size of about  $24\times 24\text{mm}$  whereas the the-



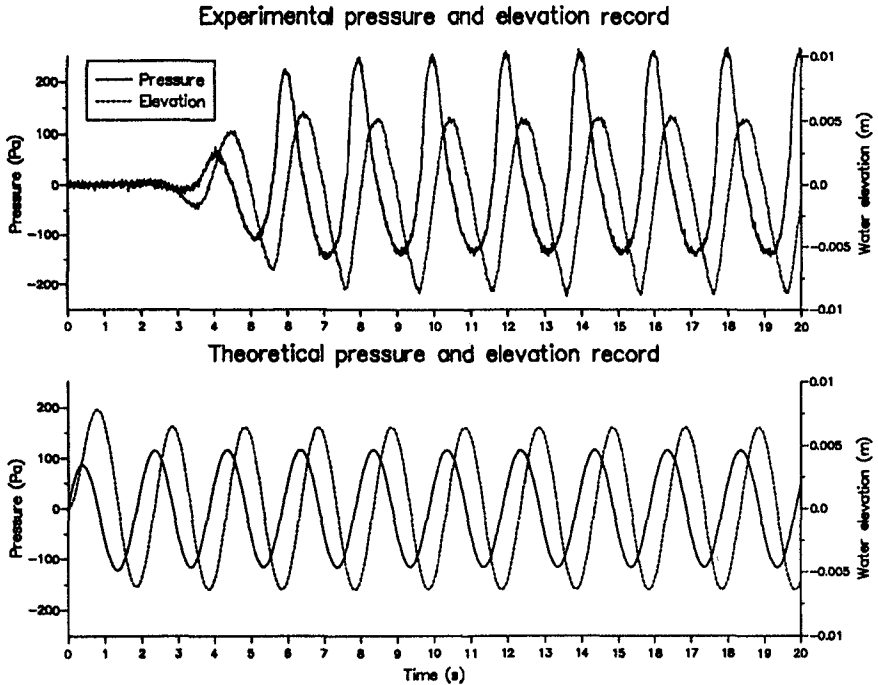


Figure 4: Air pressure and water elevation results,  $f=0.5\text{Hz}$ , wave amplitude=10mm, orifice=10x10mm

oretical results suggest an optimum size of  $22 \times 22\text{mm}$  at a frequency of  $0.5\text{Hz}$ . These dimensions compare remarkably well despite the large discrepancy in peak air pressures between the two sets of results.

### Vortex energies

Figure 3 shows a strong vortex within the chamber of the OWC. Much of the kinetic energy within the vortex is lost due to viscous dissipation. Therefore it is useful to attempt to calculate, from PIV vector maps, the kinetic energy contained in such a vortex.

For calculation of kinetic energies from PIV vector maps to be possible it is necessary to assume that the flow in the OWC is completely two dimensional i.e. in the plane of the PIV photographs. Although there is some movement through this plane it serves as good first approximation in this case.

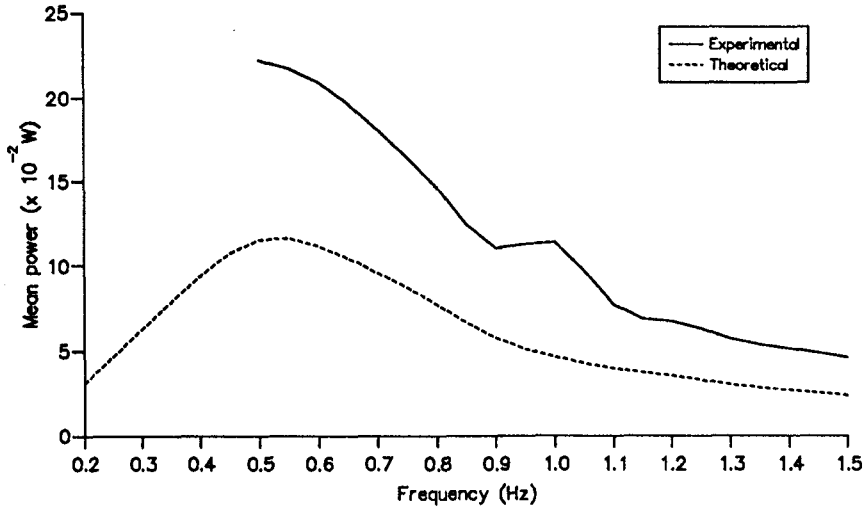


Figure 5: Calculated instantaneous power, orifice=25x25mm, wave amplitude=10mm

Each vector in the PIV velocity map is taken to lie at the centre of a cuboid of fluid with dimensions  $d_x \times d_y \times w$  where  $d_x$  and  $d_y$  are, respectively, the horizontal and vertical spacings of vectors and  $w$  is the width of the OWC model. The cuboid is assumed to have a translational velocity equal to that of the vector at it's centre and an angular velocity equal to half the magnitude of the calculated vorticity at that point. This allows the translational and rotational energies to be calculated and combined yielding a total kinetic energy  $E$  given by :

$$E = \frac{1}{2} \rho_w d_x d_y w (v_x^2 + v_y^2) + \frac{1}{96} \rho_w w d_x d_y \left( \frac{\partial v_y}{\partial x} - \frac{\partial v_x}{\partial y} \right)^2 \quad (4)$$

where  $v_x$  and  $v_y$  are the horizontal and vertical velocities respectively and  $\rho_w$  is the water density. These values can be summed to give the total kinetic energy within the frame of the PIV picture or the total kinetic energy of a vortex subject to the difficulty of determining it's size. This can be compared with the calculated energy of the wave transmitted by the wavemaker in order to estimate the proportion of wave energy dissipated by these vortices.

In figure 3 the kinetic energy of the water in the OWC chamber is calculated to be 0.21J with about 0.16J being contained within the vortex. This corresponds to about 8 % of the original wave energy. However it clearly accounts for a much

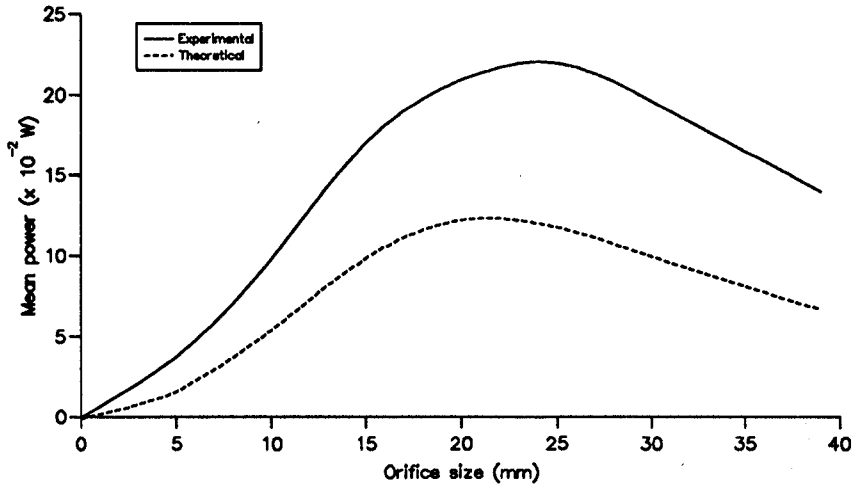


Figure 6: Calculated instantaneous power,  $f=0.5\text{Hz}$ , wave amplitude=10mm

higher proportion of the wave energy actually reaching the device since energy is dissipated as the wave travels from deep to shallow water. It should be noted that these energy calculations from PIV plots take no account of potential energy due to variations in water level.

### Conclusions

An attempt has been made to develop a theoretical model of an oscillating water column wave energy converter. It has been shown that although the model does not satisfactorily predict the pressure variations in the chamber it is able to approximate the optimum orifice size and the optimum frequency of power extraction. PIV vector maps of the flow into the chamber of the OWC have been used to calculate the energy trapped within a large vortex. This has been shown to account for more than 8% of the wave energy incident on the device.

These PIV experiments should enable future OWC wave energy converters to be designed with a more quantitative approach to reducing hydrodynamic losses within the device.

References

- [1] C. Gray and C.A. Greated. The Application of Particle Image Velocimetry to the Study of Water Waves. *Optics and Lasers in Engineering*, 9. 1988
- [2] C.A. Greated, D.J. Skyner and T. Bruce. Particle Image Velocimetry in the Coastal Engineering Laboratory. *Proc. 23rd Int. Conf. Coastal Eng.*
- [3] S. Raghunathan. The Wells Turbine. The Queen's University of Belfast.
- [4] T.J.T. Whittaker. Progress of the Islay shore-mounted oscillating water column device. In *UK - Ises Conference C57 - Wave Energy Devices*, November 1989.

## CHAPTER 38

### NEW APPROACH FOR ESTIMATING THE SEVEREST SEA STATE FROM STATISTICAL DATA

Michel K. Ochi\*

#### Abstract

This paper discusses a feature of the generalized gamma distribution which is particularly appropriate for statistical analysis of long-term significant wave height data. The agreement between the cumulative distributions of the data and the generalized gamma distribution is shown to be satisfactory. Methods to estimate the probable extreme sea state (significant wave height) expected in a specified time period as well as the extreme sea state for design consideration of marine systems are presented.

#### Introduction

Probabilistic estimation of the extreme sea state expected in 50 or 100 years provides information vital for the design of offshore and nearshore structures as well as for the stochastic analysis of various coastal processes such as wave-induced sediment transport.

Sea severity as evaluated from wave height measurements depends to a great extent on the geographical location where the data are obtained, since the crucial factors for sea severity are the frequency of occurrence of storms, water depth and fetch length. In addition, sea severity depends on the growth and decay stage of a storm even though wind speed is the same. Thus, there is no scientific basis for selecting a specific probability distribution function to represent the statistical distribution of sea state (significant wave height). Because of this, various probability distribution functions have been proposed which appear to best fit particular sets of observed data. These include (a) log-normal distribution [Ochi 1978a], (b) modified

---

\* Professor, Coastal & Oceanographic Engineering Department  
336 Weil Hall, University of Florida, Gainesville,  
Florida, 32611, U.S.A.

log-normal distribution [Fang and Hogben 1982], (c) three-parameter Weibull distribution [Burrows and Salih 1986] [Mathisen and Bitner-Gregersen 1990], (d) combined exponential and power of significant wave height [Ochi and Whalen 1980] and (e) modified exponential distribution [Thompson and Harris 1972], etc.

It is highly desirable that a more rational probability distribution be developed so that sea severity evaluated from data obtained anywhere in the world can be reasonably represented and analyzed by a specific distribution thereby permitting a direct comparison of data, including extreme values. To achieve this goal, this paper introduces a probability distribution called the generalized gamma distribution, and discusses a feature of the distribution which is particularly appropriate for analysis of long-term significant wave height data.

#### Statistical Trend of Long-Term Significant Wave Height Data

Prior to introducing a probability distribution to represent long-term significant wave height data, it may be well to examine the general trend of the statistical distribution. For this, significant wave height data obtained at various geographical locations as well as various water depths are analyzed in the present study.

Figures 1(a) through 1(g) show the cumulative distribution functions of significant wave height plotted on log-normal probability paper. These data were obtained at locations: (a) Norwegian coast [Mathisen and Bitner-Gregersen 1990], (b) North Sea [Bouws 1978], (c) North Pacific off Japan [Tomita 1988], (d) North Pacific off Canada [National Data Buoy Center 1990], (e) Atlantic Ocean off Georgia [National Data Buoy Center 1990], (f) Florida East Coast (shallow water area) [Coastal Data Network 1990] and (g) Gulf of Mexico (shallow water area) [Work 1992], respectively. Included also in these figures is a straight line which represents the cumulative distribution function by fitting the following log-normal probability distribution:

$$f(x) = \frac{1}{\sqrt{2\pi}\sigma x} \exp\left\{-\frac{1}{2}\left(\frac{\ln x - \mu}{\sigma}\right)^2\right\}, \quad 0 \leq x < \infty \quad (1)$$

As can be seen in Figure 1, the cumulative distributions of all significant wave height data show a consistent trend irrespective of geographical location and water depth. That is, at least 90 to 95 percent of each set of data is well represented by the log-normal probability distribution; however, the data diverge from the log-normal distribution for large significant wave heights which are extremely critical for estimating extreme values. The divergence is always consistent in such a way that the cumulative distribution function of the data converges to unity faster than that of the log-normal distribution. This implies that the log-normal distribution will overestimate the extreme significant wave height by a substantial amount.

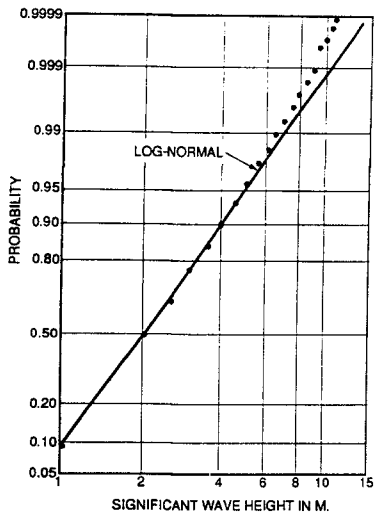


Figure 1(a): Long-term significant wave height data obtained off Norwegian coast plotted on log-normal probability paper (Data from Methisen & Bitner-Gregersen 1990)

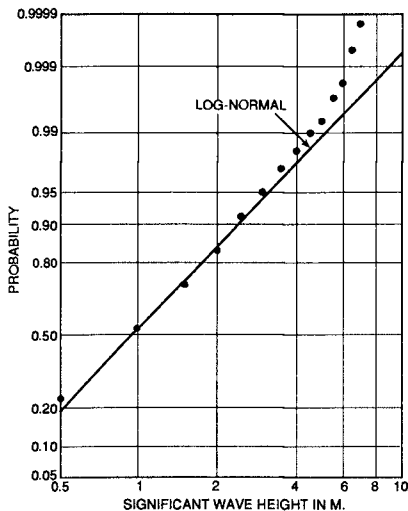


Figure 1(b): Long-term significant wave height data obtained in the North Sea plotted on log-normal probability paper (Data from Bouws 1978)

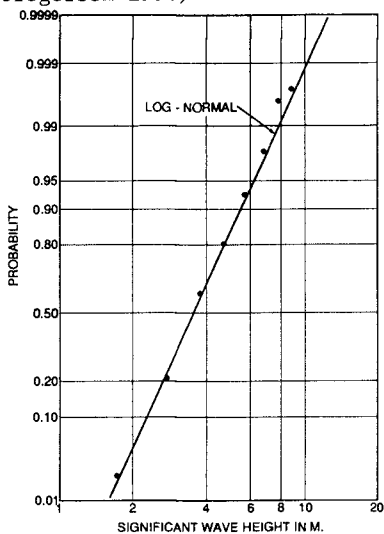


Figure 1(c): Long-term significant wave height data obtained in the North Pacific Ocean off Japan plotted on log-normal probability paper (Data from Tomita 1988)

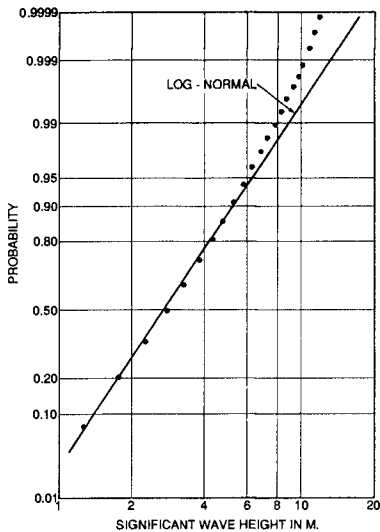


Figure 1(d): Long-term significant wave height data obtained in the North Pacific Ocean off Canada plotted on log-normal probability paper (data from Nat.Data Buoy Center 1990)

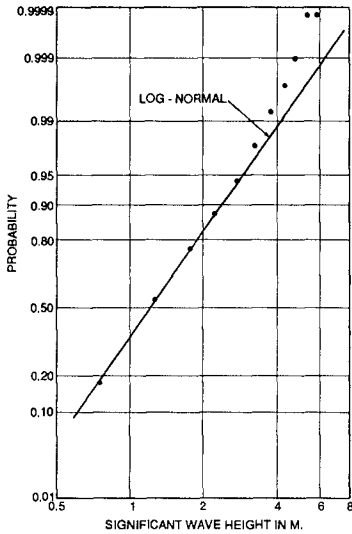


Figure 1(e): Long-term significant wave height data obtained in the Atlantic Ocean off Georgia plotted on log-normal probability paper (Data from Nat.Data Buoy Center 1990)

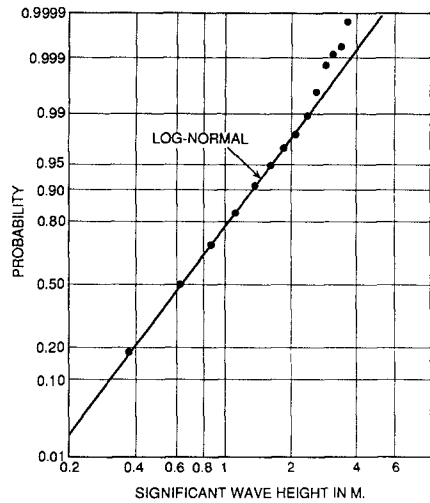


Figure 1(f): Long-term significant wave height data obtained off Florida East Coast plotted on log-normal probability paper (Data from Coastal Data Network 1990)

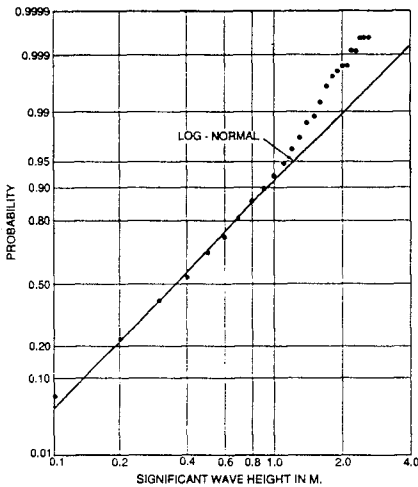


Figure 1(g): Long-term significant wave height data obtained in the Gulf of Mexico plotted on log-normal probability paper (Data from Work 1992)

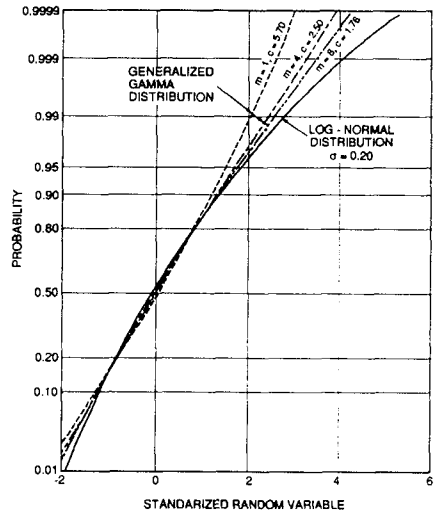


Figure 2: Comparison between the standardized cumulative distributions of (a) log-normal and (b) generalized gamma distribution for  $\sigma = 0.20$  and for various  $m$ -values



We may conclude from the results shown in Figure 1 that the statistical characteristics of long-term significant wave height can best be represented by a probability distribution whose cumulative distribution is by and large close to that of the log-normal distribution but converges to unity much faster than the log-normal distribution at higher values, say over 0.95.

### Generalized Gamma Probability Distribution

An extensive search was made to find an appropriate probability distribution which represents the cumulative distribution of significant wave height data. For this, various probability distribution functions were standardized so that a comparison of distributions could be made under the uniform condition of zero-mean and unit variance. Here, standardization was achieved through a change of random variables by subtracting the mean and dividing by the standard deviation of the original random variable. Let us define the standardized random variable as  $Z$  and its probability density function  $f(z)$ . The standardized log-normal distribution is given by

$$f(z) = \frac{1}{\sqrt{2\pi}\sigma} \frac{\sqrt{\alpha^2-1}}{\sqrt{\alpha^2-1}z+1} \exp \left\{ -\frac{\left( \ln \left\{ \alpha \left( \sqrt{\alpha^2-1}z+1 \right) \right\} \right)^2}{2\sigma^2} \right\}, \quad (2)$$

where  $-1/\sqrt{\alpha^2-1} \leq z < \infty$ ,  $\alpha = \exp\{\alpha^2/2\}$ .

Note that the standardized log-normal distribution has only one parameter  $\sigma$ , and its lower bound is a function of  $\sigma$ .

It was found that the following generalized gamma distribution (in the standardized form) appears to satisfy the conditions required for analysis of significant wave height data discussed in the previous section:

$$f(z) = \frac{c\sqrt{q}}{\Gamma(m)} \left( \sqrt{q}z+p \right)^{cm-1} \exp \left\{ -\left( \sqrt{q}z+p \right)^c \right\}, \quad (3)$$

where  $-p/\sqrt{q} \leq z < \infty$ ,  $p = \Gamma\left(m + \frac{1}{c}\right) / \Gamma(m)$ ,

$$q = \left[ \Gamma\left(m + \frac{2}{c}\right)\Gamma(m) - \left\{ \Gamma\left(m + \frac{1}{c}\right) \right\}^2 \right] / \left\{ \Gamma(m) \right\}^2.$$

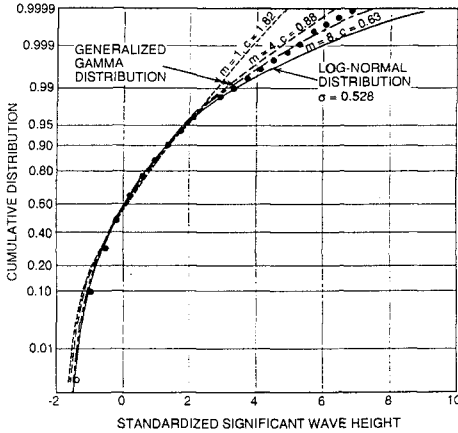


Figure 3: Comparison between the standardized cumulative distributions of (a) Norwegian data, (b) log-normal and (c) generalized gamma distribution for  $\sigma = 0.528$  and for various  $m$ -values

In order to elaborate on the above statement, let us compare the two standardized probability distributions given in Eqs. (2) and (3) for an arbitrarily chosen value  $\sigma = 0.20$  of the log-normal distribution and  $m = 1, 4$  and  $8$  of the generalized gamma distribution. Since the lower bounds of these two probability density functions are equal, we have a functional relationship between Eqs. (2) and (3). That is,

$$\exp\{\sigma^2\} = \Gamma\left(m + \frac{2}{c}\right) \Gamma(m) / \left\{ \Gamma\left(m + \frac{1}{c}\right) \right\}^2 \quad (4)$$

Hence, from Eq. (4), we can evaluate  $c = 5.70, 2.50$  and  $1.76$  for each  $m$ -value with  $\sigma = 0.20$ . A comparison of cumulative distribution functions of the log-normal and generalized gamma distributions (in standardized form) is shown in Figure 2. As can be seen in the figure, cumulative distributions are nearly equal up to  $0.90$ , but depending on the  $m$  and  $c$ -values in the generalized gamma distribution, the difference can become substantially large for cumulative distribution is greater than  $0.90$ .

For further confirmation of this feature, another comparison is shown in Figure 3 for  $\sigma = 0.528$  of the log-normal distribution evaluated from data obtained off Norwegian coast shown in Figure 1(a), and  $m = 1, 2$  and  $4$  of the generalized gamma distribution. Included in the figure is the cumulative distribution of the Norwegian data which is also standardized by using the mean and variance evaluated from the data. It can be seen in the figure that the values of significant wave height (standardized) for a specified cumulative distribution show little difference for the two probability distributions and they both agree well with data in the range of cumulative distribution up to  $0.95$ . However, the difference becomes substantially large for cumulative distribution greater than  $0.95$ . The cumulative distribution of the data is very close to the generalized gamma distribution with  $m = 8$  in this case.

This feature of the generalized gamma distribution shown in Figures 2 and 3 is considered to make its use advantageous in statistical analysis of significant wave height data. With this background, let us compare the cumulative distribution functions of measured data with the generalized gamma distribution (non-standardized) whose probability density function  $f(x)$  and cumulative distribution function  $F(x)$  are given as follows:

$$f(x) = \frac{c}{\Gamma(m)} \lambda^{cm} x^{cm-1} \exp\{-(\lambda x)^c\}, \quad 0 \leq x < \infty. \quad (5)$$

$$F(x) = \Gamma\left\{m, (\lambda x)^c\right\} / \Gamma(m), \quad (6)$$

where the numerator is the incomplete gamma function.

Figures 4(a) through 4(g) show comparisons of cumulative distributions of data with the generalized gamma distribution. Data in each figure correspond to those shown in Figures 1(a) and 1(g), respectively. Included also in each figure are the values of the three parameters of the distribution evaluated from the data. Methods to estimate the parameter values will be discussed in the next section. As can be seen in Figure 4, the long-term significant wave height data can be well represented by the generalized gamma distribution.

#### Estimation of Parameters of Generalized Gamma Distribution

Methods to estimate the three parameters involved in the generalized gamma distribution are discussed by Stacy and Mihram [Stacy and Mihram 1965]. They present a procedure based on two different approaches; one being the maximum likelihood method, the other the moment method. In both methods, the logarithm of the variables (significant wave height for the present problem) is used. In particular, the second method considers the following sample mean, variance and skewness:

$$\begin{aligned} \bar{u} &= \frac{1}{n} \sum_{i=1}^n u_i, \quad \text{where } u_i = \ln x_i \\ s_u^2 &= \frac{1}{n-1} \sum_{i=1}^n (u_i - \bar{u})^2 \\ g_u &= \frac{n}{(n-1)(n-2)} \frac{1}{s_u^3} \sum_{i=1}^n (u_i - \bar{u})^3 \end{aligned} \quad (7)$$

By equating Eq.(7) to the theoretical mean, variance and skewness (in logarithmic form), respectively, we may estimate the three

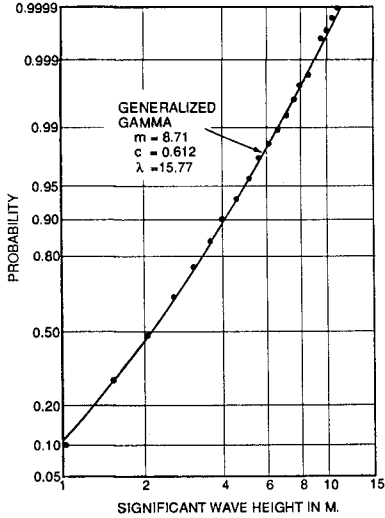


Figure 4(a): Comparison of cumulative distribution functions of data and generalized gamma distribution (Data from Mathisen and Bitner-Gregersen 1990)

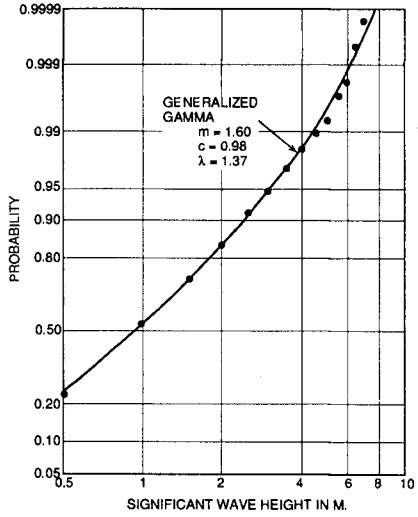


Figure 4(b): Comparison of cumulative distribution functions of data and generalized gamma distribution (Data from Bouws 1978)

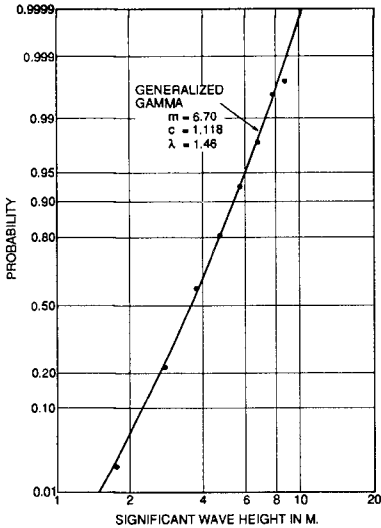


Figure 4(c): Comparison of cumulative distribution functions of data and generalized gamma distribution (Data from Tomita 1988)

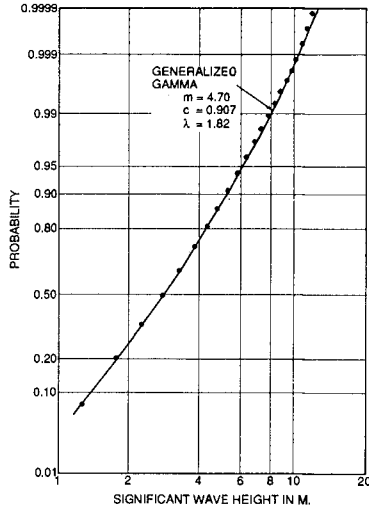


Figure 4(d): Comparison of cumulative distribution functions of data and generalized gamma distribution (Data from Nat. Data Buoy Center 1990)

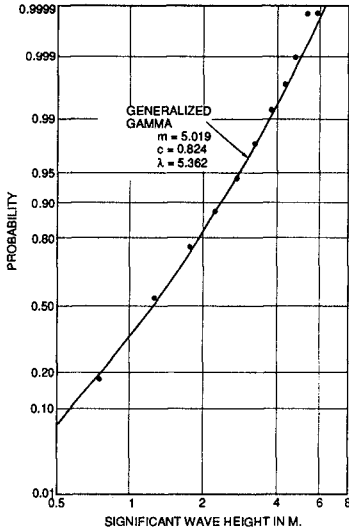


Figure 4(e): Comparison of cumulative distribution functions of data and generalized gamma distribution (Data from Nat. Data Buoy Center 1990)

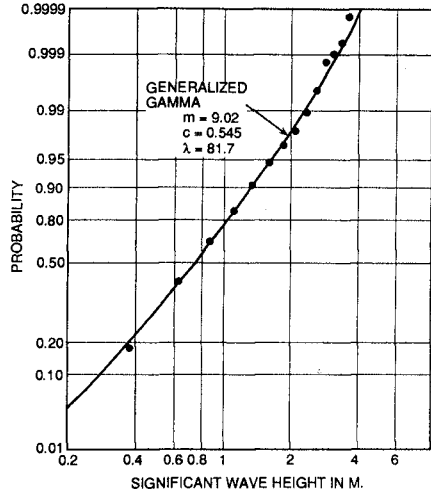


Figure 4(e): Comparison of cumulative distribution functions of data and generalized gamma distribution (Data from Coastal Data Network 1990)

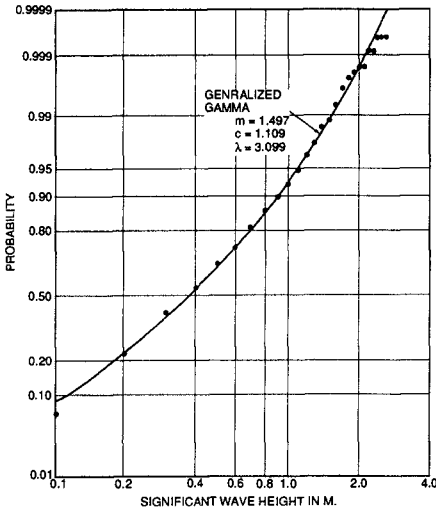


Figure 4(g): Comparison of cumulative distribution functions of data and generalized gamma distribution (Data from Work 1992)

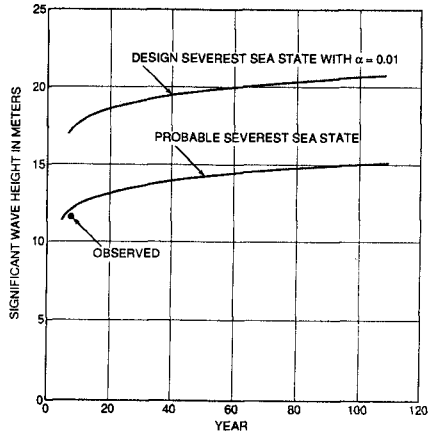


Figure 5: Probable extreme significant wave height and design extreme significant wave height with risk parameter  $\alpha = 0.01$  as a function of time (Data from Mathisen & Bitner-Gregersen 1990)

parameters. For example, the parameter  $m$  can be estimated from the following equation:

$$-|g_u| = \frac{\frac{d^3}{dm^3} \ln \Gamma(m)}{\left\{ \frac{d^2}{dm^2} \ln \Gamma(m) \right\}^{3/2}} \quad (8)$$

Although the Stacy and Mihram method is mathematically correct, some difficulty is often encountered in practice in solving Eq.(8) for certain set of data. It should be noted that in estimating the statistical properties of long-term significant wave height, the sample size of data is usually extremely large, on the order of several thousand. If this is the case, we may simply estimate the parameter values by equating the sample moments to theoretical moments. Here, the  $j$ -th moment of the generalized gamma distribution is given by

$$E[x^j] = \frac{1}{\lambda^j} \frac{\Gamma\left(m + \frac{j}{c}\right)}{\Gamma(m)} \quad (9)$$

Since the generalized gamma distribution has three unknown parameters  $m$ ,  $c$  and  $\lambda$ , we may consider a set of equations consisting of either the first three moments or the 2nd, 3rd and 4th moments; the latter places more emphasis on the higher order moments. It is found through statistical analysis of many data that the solution of a set of three moments consisting of the 2nd, 3rd and 4th moments yields the generalized gamma distribution which well represents the cumulative distribution of the observed data. The parameter values of the generalized gamma distributions given in each example in Figure 4 are all determined by this procedure. That is, from a set of three equations for  $j = 2, 3$  and  $4$  of Eq.(9), we can derive the following two equations by eliminating the parameter  $\lambda$ .

$$\frac{\{\Gamma(m)\}^{1/2} \Gamma\left(m + \frac{3}{c}\right)}{\left\{\Gamma\left(m + \frac{2}{c}\right)\right\}^{3/2}} = \frac{E[x^3]}{\{E[x^2]\}^{3/2}} \quad (10)$$

$$\frac{\Gamma(m) \Gamma\left(m + \frac{4}{c}\right)}{\left\{\Gamma\left(m + \frac{2}{c}\right)\right\}^2} = \frac{E[x^4]}{\{E[x^2]\}^2}$$

The parameters  $m$  and  $c$  are determined from the above equations.

### Estimation of Extreme Sea State

Estimation of the extreme sea state (significance wave height) expected to occur in a specified time period (50 years, for example) based on the generalized gamma distribution is discussed in this section.

#### (a) Probable Extreme Sea State

The probable extreme sea state refers to that most likely to occur in a specified time period which is the modal value of the probability density function of extreme values. It is essentially the value of the significant wave height which satisfies the equation of return period being equal to the number of significant wave heights in a specified time. In order to avoid possible confusion, the extreme value in  $N$ -observations is denoted by  $Y_N$ -value which satisfies the following equation:

$$\ln \left\{ 1 / \left[ 1 - \Gamma \left\{ m, (\lambda y_N)^c \right\} / \Gamma(m) \right] \right\} = \ln N \quad (11)$$

where  $N$  = number of significant wave heights expected in a specified time period.

Another approach for evaluating the probable extreme sea state is through application of Cramér's asymptotic extreme value statistics. This method was used for evaluating the extreme value of the generalized gamma distribution and therefrom the following equation to estimate the probable extreme values was derived [Ochi 1978b]:

$$\frac{1}{\Gamma(m)} u_N^{m-1} e^{-u_N} = \frac{1}{N} \left\{ 1 - \frac{1}{u_N} \left( m - \frac{1}{c} \right) \right\}, \quad (12)$$

where  $u_N = (\lambda y_N)^c$ .

The left-side of Eq.(12) is the gamma probability distribution, and hence solution of the equation with respect to  $u_N$  can easily be obtained for a given  $m$ ,  $c$  and  $\lambda$ . The asymptotic probable extreme value  $y_N$  can be evaluated from the extreme value of  $u_N$ . It is noted that the asymptotic probable extreme value thus obtained is very close to the value obtained as the solution of Eq.(11) when  $N$  is large.

#### (b) Extreme Sea State for Design Consideration

The probable extreme sea state discussed in the previous section is the modal value of the probability density function of  $y_N$ . However, the probability that the extreme value exceeds the probable extreme value is theoretically  $1 - e^{-1} = 0.632$ . Since this probability is very large, the probable extreme value should not be used for design of marine systems. For the design of marine systems, it

is necessary to consider an extreme value for which the probability of exceedance is a very small specified value,  $\alpha$ , called the risk parameter. It can be evaluated from the cumulative distribution function given in Eq.(6) as

$$F(x) = \frac{\Gamma\{m, (\lambda x)^c\}}{\Gamma(m)} = (1-\alpha)^{1/N} \quad (13)$$

Although Eq.(13) yields the exact solution numerically, we can derive the following equation for large  $N$  and small  $\alpha$ :

$$1 - \frac{\Gamma\{m, (\lambda x)^c\}}{\Gamma(m)} = 1 - (1-\alpha)^{1/N} \sim \frac{\alpha}{N} \quad (14)$$

Eq.(14) yields an equation in a form similar to that given in Eq.(11); and hence, the design extreme value with risk parameter,  $\alpha$ , can be obtained by finding the  $y_N$ -value which satisfies the following equation:

$$\ln \left\{ 1 / \left[ 1 - \Gamma\{m, (\lambda y_N)^c\} / \Gamma(m) \right] \right\} = \ln(N/\alpha), \quad (15)$$

where  $\alpha$  = risk parameter; namely, the probability that the extreme value exceeds the design extreme value.

The design extreme value can also be obtained as the solution of the following equation which has a form similar to that given in Eq.(12):

$$\frac{1}{\Gamma(m)} u_n^{m-1} e^{-u_n} = \frac{\alpha}{N} \left\{ 1 - \frac{1}{u_n} \left( m - \frac{1}{c} \right) \right\} \quad (16)$$

As an example of the estimation of extreme sea states, Figure 5 shows the probable and design severest sea states as a function of time using the Norwegian data shown in Figure 4(a). The estimations are made by Eqs. (12) and (16). As can be seen, the magnitude of the probable as well as that of the design extreme sea state with risk parameter  $\alpha = 0.01$  do not increase significantly with increase in time. However, the design extreme sea state with the risk parameter  $\alpha = 0.01$  is substantially larger (approximately 40 percent) than the probable extreme sea state in this example. The severest sea state observed in 7 years at this location agrees well with the estimated probable extreme sea state for this period.



### Conclusions

Results of statistical analysis of long-term significant wave height data obtained at various geographical locations and at various water depths show a consistent trend. That is, at least 90 to 95 percent of the cumulative distribution of each set of data is well represented by the log-normal probability distribution; however, the data diverge from the log-normal distribution for large significant wave heights. The divergence is consistent in such a way that the cumulative distribution of the data converges to unity faster than that of the log-normal distribution.

From comparisons of many probability distributions in standardized form, it is found that the generalized gamma distribution satisfies the condition that its cumulative distribution is by and large close to that of the log-normal distribution but it converges to unity much faster than the log-normal distribution at higher cumulative distribution values, say over 0.95. Comparisons of cumulative distribution functions of data and the generalized gamma distribution show satisfactory agreement. Methods for estimating the probable extreme sea state expected in a specified time as well as the extreme sea state for design consideration of marine systems are presented.

### References

- Bouws, E. (1978), "Wind and Wave Climate in the Netherlands Sector of the North Sea between 53° and 54° North Latitude", The Netherlands Meteorological Inst. Sci. Report WR78-9.
- Burrows, R. and Salih, B.A. (1986), "Statistical Modelling of Long-Term Wave Climates", Proc 20th Int. Conf. on Coastal Eng., Vol. 1, pp 42-56.
- Coastal Data Network (1990), "Wave Data Report 1984-1990", Univ. of Florida, CDN Report.
- Fang, Z.S. and Hogben, N. (1982), "Analysis and Prediction of Long Term Probability Distributions of Wave Heights and Periods", Nat. Mar. Inst. Report R146, Feltham, England.
- Mathisen, J. and Bitner-Cregersen, E. (1990), "Joint Distribution for Significant Wave Height and Zero-Up-Crossing Period", App. Ocean Res., Vol. 12, No. 2, pp 93-103.
- National Data Buoy Center (1990), "Climatic Summaries for NDBC Buoys and Stations, Update I".
- Ochi, M.K. (1978a), "On Long-Term Statistics for Ocean and Coastal Waves", Proc 16th Int. Conf. on Coastal Eng., Vol. 1, pp 59-75.
- Ochi, M.K. (1978b), "Generalization of Rayleigh Probability Distribution and its Application", J. Ship Res., Vol. 22, No. 4, pp 259-265.

Ochi, M.K. and Whalen, J.E. (1980), "Prediction of the Severest Significant Wave Height", Proc. 17th Int. Conf. on Coastal Eng., Vol. 1, pp 587-599.

Stacy, E.W. and Mihram, G.A. (1965), "Parameter Estimation for a Generalized Gamma Distribution", Technometrics, Vol. 7, No. 3, pp 349-358.

Thompson, E.F. and Harris, D.L. (1972), "A Wave Climatology for U.S. Coastal Waters", Proc. Offshore Tech. Conf., Vol. 2, pp 675-688.

Tomita, H. (1988), "Wave Characteristics of North West Pacific Ocean, Part 1. Analysis of Buoy Data", Ship Research Institute, Vol. 25, No. 5, pp 21-72. (In Japanese).

Work, P. (1992), "Sediment Transport Processes at a Nourished Beach", Ph.D. Dissertation, Univ. of Florida, Coastal and Oceano. Department.

## CHAPTER 39

### Modeling the Transformation of Nonlinear Waves Passing over a Submerged Dike

Takumi Ohyama <sup>1</sup> and Kazuo Nadaoka <sup>2</sup>

#### Abstract

The decomposition phenomenon of a nonlinear wave train passing over a submerged dike has been investigated by a previously developed numerical model. The model, based on the time-dependent boundary element method, employs an effective nonreflective open boundary treatment and can be applied to arbitrary nonlinear wave processes. The results for regular wave incidence indicate that the higher harmonics generated during passage over the dike are transformed into prominent free waves in the trailing side of the dike, revealing the essential mechanism of the observed decomposition phenomenon. The computed wave profiles at various locations agree favorably with experimental observations. The transformation of multicomponent random waves has also been investigated. The results show that a substantial amount of wave energy is transferred into higher frequency components. The power spectrum of the transmitted wave is found to be significantly influenced by the phase differences among the incident components as well as by the incident wave spectrum itself.

#### 1. Introduction

The decomposition phenomenon of waves passing over a submerged dike is directly related to the variation of wave spectrum and therefore of great importance for predictions of coastal wave fields and beach profile formation (Hulsbergen, 1974). This phenomenon is believed to be governed by both the nonlinearity and the dispersivity of wave fields.

The methods of numerical approaches to this phenomenon may be classified into the following groups. The first approach is based on shallow-water wave

---

<sup>1</sup>Institute of Technology, Shimizu Corporation, Etchujima 3-4-17, Koto-ku, Tokyo 135, JAPAN

<sup>2</sup>Department of Civil Engineering, Tokyo Institute of Technology, O-okayama, Meguro-ku, Tokyo 152, JAPAN

theories, such as Boussinesq's theory. However, because this approach relies on assumptions of both weak nonlinearity and weak dispersivity of wave fields it may not be valid especially for prediction in the trailing side of the dike, where higher harmonics may arise as deep-water waves. In fact, its applications have been restricted to the case of solitary wave evolution (Seabra-Santos et al., 1987). The incidence of periodic wave trains is taken into account in the second approach, which is based on the second-order Stokes' wave theory (Massel, 1984). However, because of the limitation of this wave theory, its application is restricted to the case of a deeply submerged dike in a weakly nonlinear wave field. Thus, the applications of these two approaches have been limited with respect to incident wave conditions and the submergence of the dike. In addition, these approaches cannot directly treat the evolution of random waves composed of multiple-frequency components.

By contrast, the time-dependent boundary element method may apply to a wave field of more general conditions, including an arbitrary nonlinear wave field, since the free-surface boundary condition can be fully incorporated without approximations. The lack of efficient open boundary treatments, however, has made it impossible to deal with the incidence of continuous wave trains and, therefore, in many cases solitary waves have been imposed instead (Cooker et al., 1990). Recently, the authors (Ohyama and Nadaoka, 1991) have successfully developed an idealized "numerical wave tank" model based on the boundary element method. This numerical model employs an effective nonreflective open boundary treatment so that it can be applied to arbitrary wave fields including nonlinear random waves. The present study investigates the decomposition of periodic and random wave trains passing over a rectangular submerged dike by using the previously developed numerical model.

## 2. Numerical Wave Tank Model

Numerical analyses have been performed by using a two-dimensional numerical wave tank model previously developed by the authors (Ohyama and Nadaoka, 1991). At both ends of the computational domain, numerical wave-absorption filters are installed as shown in Fig. 1. The filter is composed of a sponge layer to absorb the incoming shorter waves energy by frictional damping and a Sommerfeld-type radiation boundary at the lee side of the layer to transmit the outgoing longer waves. This numerical wave tank model additionally incorporates a nonreflective wave generator which combines a vertically distributed wave-making source ( $S_S$ ), introduced by Brorsen and Larsen (1987).

A decay term proportional to the velocity magnitude is added to the equation of motion in the sponge layers. Based on the potential theory, the dynamic

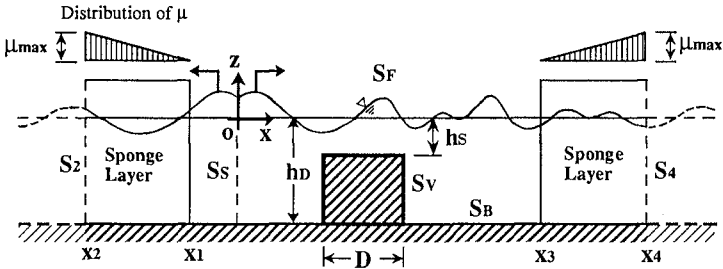


Figure 1. Numerical wave tank model used for the analyses.

condition on the free surface is consequently derived as

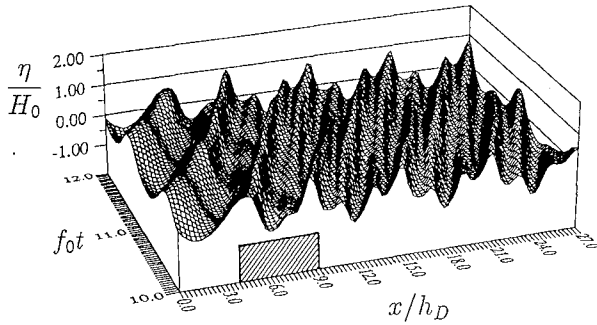
$$\frac{\partial \phi}{\partial t} + \frac{1}{2}(\nabla \phi)^2 + g\eta + \mu\phi - \int_{x_1}^x \frac{\partial \mu}{\partial x} \phi \Big|_{on S_F} dx = 0 \quad (on S_F), \quad (1)$$

in which  $\phi(x, z, t)$  is the velocity potential,  $\eta$  is the surface elevation from the mean water level, and  $\mu$  is the damping factor. The factor,  $\mu$ , is distributed linearly in the layers as shown in Fig. 1 in order to relieve the wave reflection at the leading side of the layers. Based on the results of the earlier study (Ohyama and Nadaoka, 1991), the maximum value of the damping factor in the sponge layers,  $\mu_{max}$ , is given as  $\mu_{max} \sqrt{h_D/g} = 0.25$  in the subsequent computations.

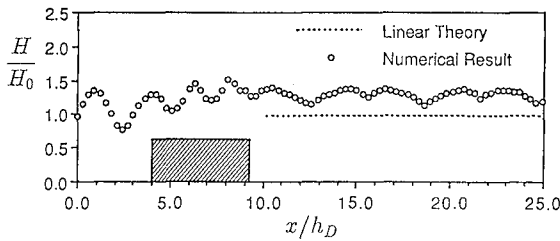
Since the governing equation for the velocity potential in the fluid domain  $\Omega$  is expressed by a Poisson equation, an integral equation is introduced by applying the second form of Green's theorem. All the boundary conditions except the dynamic condition on  $S_F$ , Eq. (1), are substituted into the integral equation. Another integral equation is derived by applying the method of weighted residuals to Eq. (1). These equations, which involve  $\phi$  (on  $S_F$ ,  $S_V$ ,  $S_2$  and  $S_4$ ) and  $\partial \phi / \partial t$ ,  $\eta$  and  $\partial \eta / \partial t$  (on  $S_F$ ) as unknown variables, are discretized spatially and solved simultaneously for successive time steps.

The nodal points on the free surface,  $S_F$ , are considered to move in a vertical direction with the time step advance. The unknown variables,  $\phi$ ,  $\partial \phi / \partial t$ ,  $\eta$  and  $\partial \eta / \partial t$ , can be rewritten by using  $\Delta \phi$  and  $\Delta \eta$ , which are the increments of  $\phi$  and  $\eta$ , respectively, during the time increment  $\Delta t$ . In this time-stepping procedure, nonlinear terms, which correspond to the spatial displacement of the nodal point on  $S_F$ , are taken into account for better accuracy (Ohyama, 1990). The linear algebraic equations to be solved for  $\Delta \phi$  (on  $S_F$ ,  $S_V$ ,  $S_2$  and  $S_4$ ) and  $\Delta \eta$  (on  $S_F$ ) are consequently obtained. The earlier paper (Ohyama and Nadaoka, 1991) provides a detailed description of the numerical procedure.

In the subsequent computations, the time increment,  $\Delta t$ , and the horizontal projection of distance between the surface nodes,  $\Delta x$ , are given to be 1/32 of



(a) Wave profile both in time and space.



(b) Wave height distribution.

Figure 2. Evolution of periodic wave for  $D/h_D = 5.25$ ,  $h_S/h_D = 0.4$ ,  $\sigma^2 h_D/g = 0.8$ ,  $H_0/h_D = 0.1$ .

incident wave period (or of significant wave period for the case of random waves) and 1/40 to 1/20 of incident wave length (or of significant wave length for the case of random waves), respectively. The initial condition for each case is the still-water condition, i.e.,  $\phi = \eta = 0$ , and numerical results 10 periods after the “cold” start are used for discussion.

### 3. Decomposition Phenomenon of Periodic Waves

Figure 2(a) shows a numerical example of the wave profile around the dike both in time and space, in which  $\sigma$  and  $H_0$  represent the angular frequency and the height of the incident waves. The conspicuous decomposition into the shorter waves occurs immediately after passage over the submerged dike, and the transmitted waves propagate as nonconservative waves composed of multiple-frequency components. The corresponding wave height distribution is indicated in Fig. 2(b), together with the linear solution for transmitted wave height (Ijima and Sasaki, 1971). Preliminary studies found that the linear theory accurately

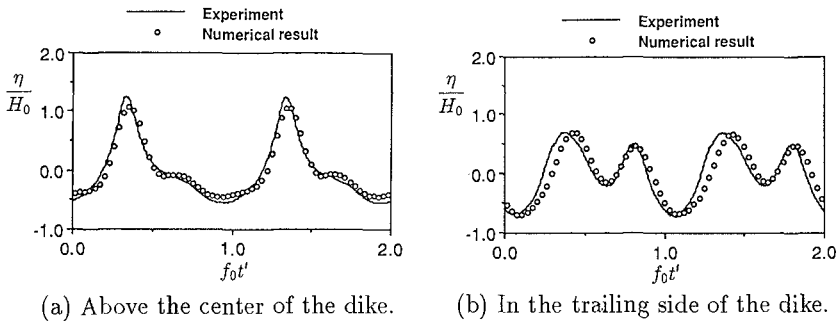


Figure 3. Comparison of computed wave profiles with experimental observations for  $\sigma^2 h_D/g = 0.97$ ,  $h_S/h_D = 0.3$ ,  $H_0/h_D = 0.1$ ,  $D/h_D = 4.0$ .

predicted reflected and transmitted wave energies, even when a conspicuous decomposition of wave trains occurs. As shown in Fig. 2(b), however, the predicted wave height in the trailing side of the dike is markedly greater than the corresponding linear solution, and varies in space since the transmitted waves propagate as nonconservative waves.

The wave evolution during passage through the dike, therefore, produces significant phenomena such as the transfer of a large amount of energy to higher frequency components along with the augmentation of wave height.

#### 4. Experimental Verification

Physical model experiments have been conducted to verify the present numerical method. The experimental wave tank is 17m long and 0.4m wide; the water depth,  $h_D$ , and the incident wave height,  $H_0$ , were set at 25cm and 2.5cm, respectively ( $H_0/h_D = 0.1$ ). The model of the submerged rectangular dike has a width of 100cm ( $D/h_D = 4.0$ ) and a height of 17.5cm ( $h_S/h_D = 0.3$ ). The wave profiles were measured at three locations: one over the center of the dike, and the others 125cm apart from the center of the dike on both sides.

Comparisons of wave profiles at a point over the center of the dike and at a point in the trailing side are given in Figs. 3(a) and 3(b), respectively, in which  $f_0$  represents the incident wave frequency ( $= \sigma/2\pi$ ). The computed wave profiles are found to agree favorably with the corresponding experimental observations, indicating the reliability of the present numerical model.

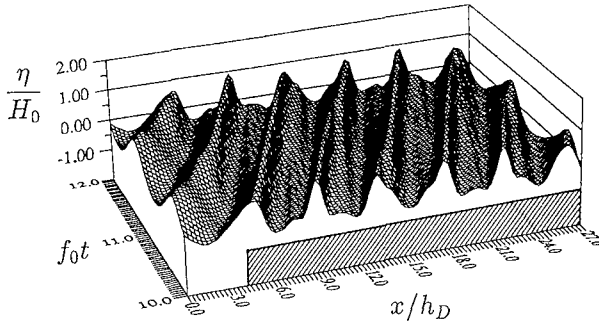


Figure 4. Wave profile both in time and space around stepped bottom for  $h_S/h_D = 0.4$ ,  $\sigma^2 h_D/g = 0.8$ ,  $H_0/h_D = 0.1$ .

### 5. Mechanism of the Decomposition Phenomenon

Figure 4 shows the computed wave profile for the case of a stepped bottom with  $h_S/h_D = 0.4$ . The incident wave conditions are identical to those of the previous case of the submerged dike (Fig. 2[a]). Figure 4 illustrates that a secondary wave appears at the trailing side of the primary wave as the wave crest propagates onto the step. It then gradually parts from the main crest and is overtaken by the following wave. These basic features of the wave deformation are similar to those of solitary wave disintegration over a stepped bottom (Madsen and Mei, 1969). As indicated in Fig. 2(a), by contrast, wave decomposition during passage over the dike occurs drastically, suggesting that its mechanism is quite different from that of the solitary-wave disintegration over the stepped bottom. Therefore, the wave field in the trailing side of the dike is compared with that over the stepped bottom in order to investigate the mechanism of wave decomposition.

The spatial evolutions of the lowest three harmonic amplitudes,  $|\eta_n|$  ( $n = 1, 2, 3$ ), are indicated in Figs. 5(a) and 5(b), in which  $|(\eta_0)_1|$  is the first harmonic amplitude of the incident wave. As shown in these figures, the second harmonic amplitude,  $|\eta_2|$ , is spatially modulated over the step, but is preserved in the trailing side of the dike. This modulation phenomenon over the step is explained by *nonlinear resonant interaction* based on the phase mismatch between the free and bound waves in the second harmonic (Mei and Ünlüata, 1972; Bryant, 1973).

Furthermore, in order to investigate the characteristics of the wave number (or celerity), spectral analyses in the wave number/frequency space have been performed for both the wave field over the stepped bottom ( $6.0 \leq x/h_D \leq 25.0$ ) and that in the trailing side of the dike ( $12.5 \leq x/h_D \leq 25.0$ ). The results are



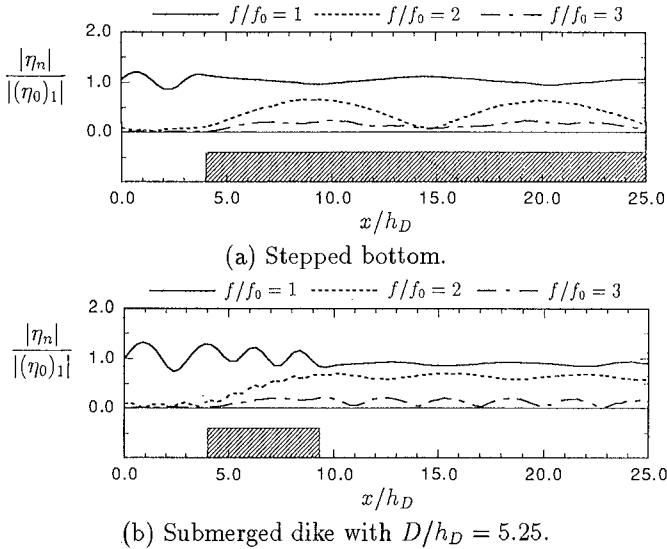
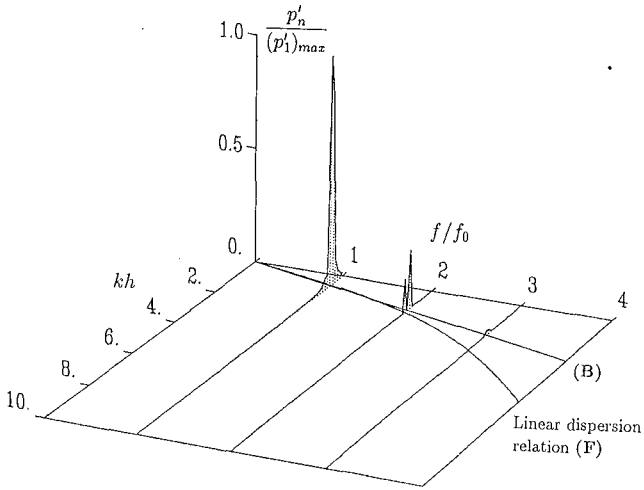


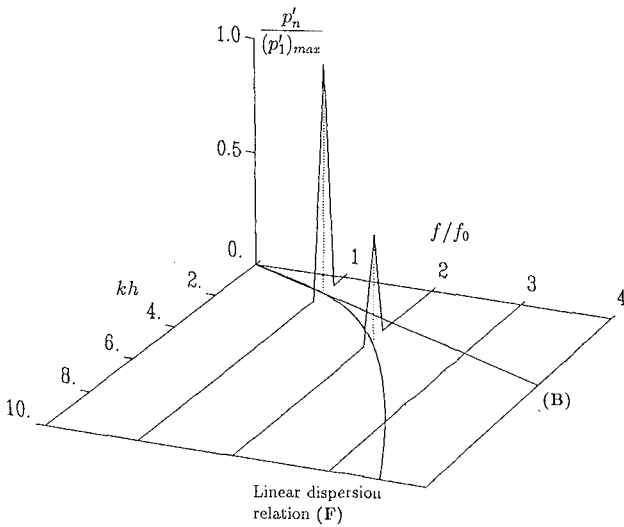
Figure 5. Distribution of each harmonic amplitude for  $h_S/h_D = 0.4$ ,  $\sigma^2 h_D/g = 0.8$ ,  $H_0/h_D = 0.1$ .

indicated in Figs. 6(a) and 6(b), respectively, in which  $k$  is the wave number and  $h$  is the water depth ( $h = h_S$  for the stepped bottom and  $h = h_D$  for the submerged dike). In the ordinates, the power spectrum for each component,  $p'_n$ , is divided by the maximum value of the spectrum in the first harmonic ( $p'_1$ )<sub>max</sub>. In each  $f/f_0 - kh$  plain, a curved line (**F**) represents the linear dispersion relation ( $k \tanh kh = 4\pi^2 f^2/g$ ), and a straight line (**B**) is drawn from the origin of direction to a point at which the spectrum for the first harmonic ( $f/f_0 = 1$ ) is at a maximum. The wave components on line (**F**) and those on line (**B**) correspond to the free waves and the bound waves, respectively. A larger difference in the celerity between the free and bound waves is found in the trailing side of the dike compared to the case of the stepped bottom. A comparison of the wave number spectra in the second harmonic is indicated in Fig. 7. In the shallow-water region over the stepped bottom, the amount of energy in the bound wave component is larger than that in the free wave component; whereas in the case of the submerged dike almost all the energy of the second harmonic exists as the free wave component.

The results of the spectral analyses yield the following description on the decomposition phenomenon: In the shallow-water region, both the free and bound waves in the higher harmonics result from wave nonlinearity. However, wave



(a) Shallow-water region over the stepped bottom.



(b) Deep-water region in the trailing side of the dike with  $D/h_D = 5.25$ .

Figure 6. Comparison of wave number-frequency spectrum for  $h_S/h_D = 0.4$ ,  $H_0/h_D = 0.1$ ,  $\sigma^2 h_D/g = 0.8$ .

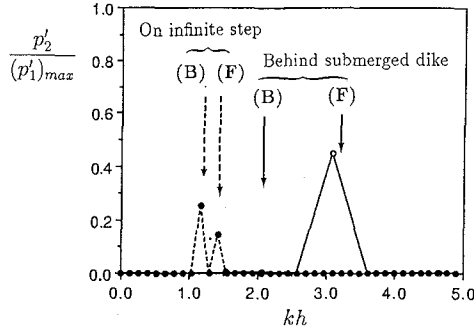


Figure 7. Comparison of wave number spectrum in second harmonic for  $h_S/h_D = 0.4$ ,  $H_0/h_D = 0.1$ ,  $\sigma^2 h_D/g = 0.8$ .

disintegration in this region emerges rather gradually because of the small difference between the celerities of the free and bound waves. When these waves propagate into the deep-water region where wave nonlinearity is so weak that the bound waves can no longer exist, a large amount of energy is transferred abruptly to the free waves in the higher harmonics. Since the celerities are significantly different among the primary wave and these free waves in the deep-water region, the wave disintegration phenomenon is conspicuous compared to the case of the stepped bottom.

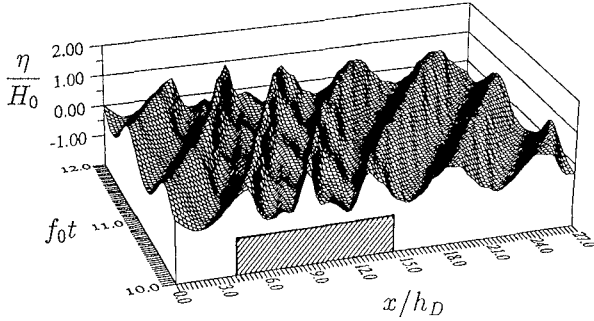
## 6. Variation in Decomposition Phenomenon According to Dike Width

As shown in Fig. 5(a), the second harmonic amplitude fluctuates spatially over the shallow-water region. Assuming the weak nonlinearity of a wave field, the beat length of  $|\eta_2|$ ,  $\lambda_2$ , can be expressed in the following form (Massel, 1983):

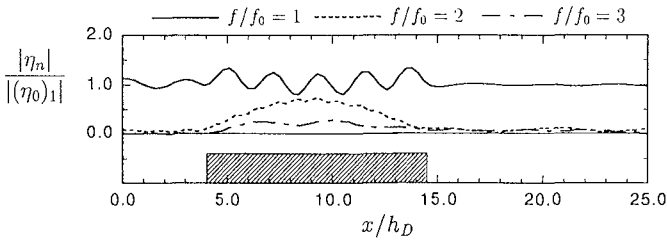
$$\lambda_2 = 2\pi/(k_2 - 2k_1), \quad (2)$$

where  $k_1$  and  $k_2$  represent the wave numbers of the free waves in the first and second harmonics, respectively. The beat length of  $|\eta_2|$  in Fig. 5(a) agrees favorably with the value calculated from Eq. (2).

According to the aforementioned mechanism of wave decomposition, it is expected that the amount of energy transferred into the free wave components varies appreciably with the dike width, and that the dike width relative to the beat length of  $|\eta_n|$ ,  $D/\lambda_n$ , is a definitive parameter, as suggested by Mei and Ünlüata (1972). The first numerical example indicated in Figs. 2(a) and 2(b) corresponds to the case of  $D/\lambda_2 = 0.5$  ( $\lambda_2/h_D = 10.5$ ), while Figs. 8(a) and 8(b) show the numerical results for  $D/\lambda_2 = 1.0$ , in which the dike width is twice as



(a) Wave profile both in time and space.



(b) Distribution of each harmonic amplitude.

Figure 8. Wave deformation around submerged dike for  $D/h_D = 10.5$ ,  $h_S/h_D = 0.4$ ,  $\sigma^2 h_D/g = 0.8$ ,  $H_0/h_D = 0.1$ .

large as in the first example. In this case of  $D/\lambda_2 = 1.0$ , the transmitted wave profile is almost sinusoidal and a negligible amount of energy is transferred to the higher frequency components during passage over the dike, although nonlinear effects such as steepened wave crests can be seen over the dike. Comparison of Fig. 8(b) with Fig. 5(a) reveals that the distribution of  $|\eta_2|$  over the dike is similar to that over the corresponding stepped bottom.

The variations in  $|\eta_2|$  and  $|\eta_3|$  of the transmitted waves, with  $D/\lambda_2$ , are indicated in Figs. 9(a) and 9(b) for the cases of  $h_S/h_D = 0.4$  and  $0.3$ , respectively. In the ordinates, the higher harmonic amplitudes are normalized with the first harmonic amplitude. Since  $|\eta_2|$  and  $|\eta_3|$  are slightly modulated even in the trailing side of the dike, spatially averaged values over each beat length are plotted in these figures. The results for  $h_S/h_D = 0.4$  (Fig. 9[a]) show that the maximum value of  $|\eta_2|$  appears at  $D/\lambda_2 = 0.5$  and the minimum value at  $D/\lambda_2 = 1.0$ , substantiating that the modulation of  $|\eta_2|$  over the dike is similar to that over the stepped bottom and its value at the trailing edge is preserved in the transmitted wave. In the case of  $h_S/h_D = 0.3$  (Fig. 9[b]), on the other

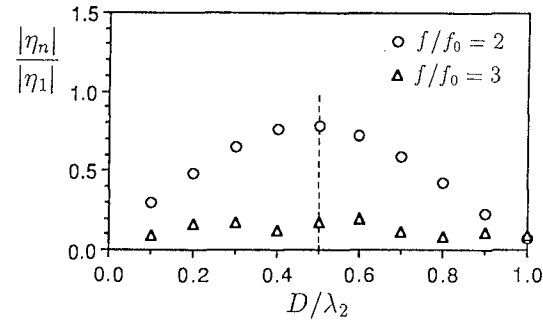
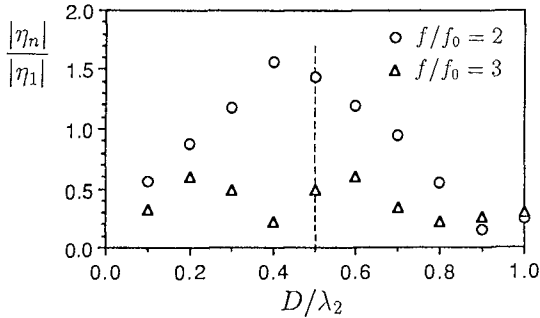
(a)  $h_S/h_D = 0.4$ .(b)  $h_S/h_D = 0.3$ .

Figure 9. Variation in  $|\eta_n|$  of transmitted waves with  $D/\lambda_2$  for  $\sigma^2 h_D/g = 0.8$ ,  $H_0/h_D = 0.1$ .

hand, the value of  $D/\lambda_2$ , where  $|\eta_2|$  attains its maximum, is smaller than 0.5. This may be because the wave nonlinearity over the dike is so strong that the use of  $\lambda_2$  obtained from Eq. (2) is no longer adequate. Furthermore, in this condition, since the beat length of  $|\eta_3|$  over the step is nearly one-half of  $\lambda_2$ ,  $|\eta_3|$  becomes the minimum at the location where  $|\eta_2|$  is at the maximum, and the peaks of  $|\eta_3|$  appear on both sides.

These results lead to the following conclusions: As inferred by Mei and Ünlüata (1972), each harmonic amplitude in the transmitted waves becomes remarkably larger when  $D/\lambda_n$  is nearly 0.5. When the water depth over the dike is very shallow, however, the stronger nonlinearity yields a shorter beat length of  $|\eta_2|$  than predicted from the weakly nonlinear solution.

## 7. Spectral Transformation of Random Waves

Lastly, this study investigates spectral transformation of random wave trains. The nonlinearity of the incident random waves considered here is so weak that they are expressed as a sum of multiple-frequency components:

$$\eta_{in} = \sum_n a_n \sin(k_n x - 2\pi f_n t + \varepsilon_n), \quad (3)$$

in which  $\eta_{in}$  is the surface elevation of the incident wave train, and  $a_n$ ,  $k_n$ ,  $f_n$  and  $\varepsilon_n$  represent the amplitude, the wave number, the frequency and the phase lag of each component, respectively.

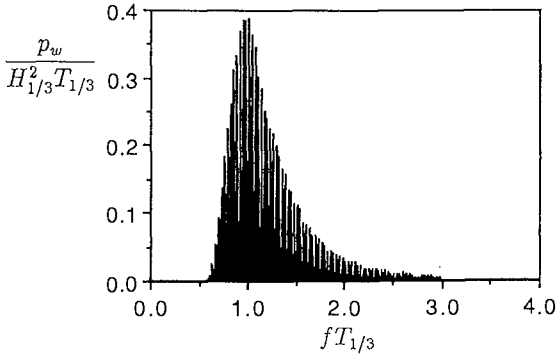
Figures 10(a) - 10(c) show the power spectrum of simulated random incident waves (10[a]), and their modifications through the transmission over a submerged dike with  $D/h_D = 4.0$  and  $h_S/h_D = 0.3$  (10[b] and 10[c]). The incident wave train considered here is composed of 96 wave components and the amplitudes of each component have been prescribed according to the spectrum of Bretschneider-Mitsuyasu (Mitsuyasu, 1970) with  $T_{1/3}\sqrt{g/h_D} = 8.0$ ,  $H_{1/3}/h_D = 0.07$ , in which  $T_{1/3}$  and  $H_{1/3}$  are the significant wave period and height, respectively. The power spectra of the water surface fluctuation were calculated from 4096 wave data at a point  $7h_D$  away from the center of the dike. The power spectrum of the incident waves was obtained from the computation for a flat-bed condition in which the dike does not exist.

In the transmitted wave spectra, several noticeable peaks arise in higher frequency components, indicating that a substantial amount of wave energy is transferred into the higher frequency components. This is of great importance because the augmentation of the wave energy for high frequency makes the significant wave period appreciably shorter. In addition, these spectral peaks are not located as the higher harmonics of the peak frequency of the incident wave spectrum.

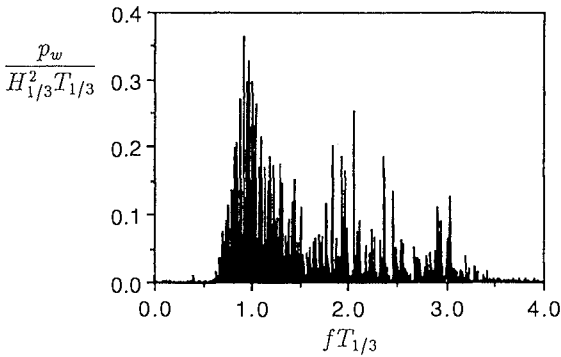
Figures 10(b) and 10(c) show the transmitted wave spectra for the incident waves with the same power spectrum (Fig. 10[a]), but with a different series of pseudo-random numbers for the specification of the phase lags among the wave components. The significant difference in the peak frequencies of the wave spectrum between these two cases indicates the importance of the phase difference among the wave components for the transformation of the random wave train.

## 8. Conclusions

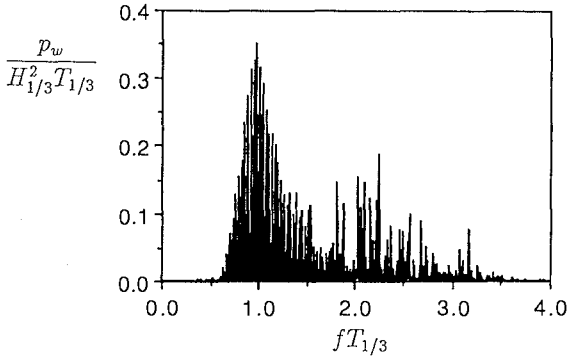
The previously developed numerical model has been applied to the analyses of wave decomposition during passage over a submerged dike. The computed wave profiles at various locations agree favorably with experimental observations.



(a) Incident wave composed of 96 components.



(b) Transmitted wave (CASE 1).



(c) Transmitted wave (CASE 2).

Figure 10. Power spectra of random waves for  $T_{1/3}\sqrt{g/h_D} = 8.0$ ,  
 $H_{1/3}/h_D = 0.07$ ,  $D/h_D = 4.0$ ,  $h_S/h_D = 0.3$ .

The higher harmonics generated over the dike are found to be transformed into prominent free waves in the trailing side of the dike, demonstrating the essential mechanism of the observed decomposition phenomenon. Further computations show that the occurrence of decomposition and its degree depend significantly on dike width. The results for random waves indicate that a substantial amount of wave energy is transferred into higher frequency components. Furthermore, the power spectrum of the transmitted wave is significantly influenced by the phase spectrum of the incident random waves.

## References

- Brorsen, M. and J. Larsen. (1987). "Source generation of nonlinear gravity waves with the boundary integral equation method." *Coastal Eng.*, **11**, 93-113.
- Bryant, P. J. (1973). "Periodic waves in shallow water," *J. Fluid Mech.*, **59**, 625-644.
- Cooker, M. J., D. H. Peregrine, and J. W. Dold. (1990). "The interaction between a solitary wave and a submerged semicircular cylinder." *J. Fluid Mech.*, **215**, 1-22.
- Hulsbergen, C. H. (1974). "Origin, effect and suppression of secondary waves," *Proc. 14th Coastal Eng. Conf., ASCE*, Chapt. 22, 392-411.
- Ijima, T. and Sasaki, T. (1971). "Theoretical studies on effects of a submerged breakwater 1. Impermeable breakwater," *Proc. 18th Japanese Conf. Coastal Eng., JSCE*, 141-147, (in Japanese).
- Madsen, O. S. and Mei, C. C. (1969). "The transformation of a solitary wave over an uneven bottom," *J. Fluid Mech.*, **39**, 781-791.
- Massel, S. R. (1983). "Harmonic generation by waves propagating over a submerged step." *Coastal Eng.*, **7**, 357-380.
- Mei, C. C. and Ü. Ünlüata. (1972). "Harmonic generation in shallow water waves." *Waves on Beaches*, edited by R. E. Meyer, Academic, New York, 181-202.
- Mitsuyasu, H. (1970). "Growth of the spectrum of wind-generated waves (2)," *Proc. 17th Japanese Conf. Coastal Eng.*, 1-7, (in Japanese).
- Ohyama, T. (1990). "A numerical method of solitary wave forces acting on a large vertical cylinder," *Proc. 22nd Coastal Eng. Conf., ASCE*, Chapt. 64., 840-852.
- Ohyama, T. and K. Nadaoka. (1991). "Development of a numerical wave tank for analysis of nonlinear and irregular wave field." *Fluid Dyn. Res.*, **8**, 231-251.
- Seabra-Santos, F. J., Renouard, D. P. and Temperville, A. M. (1987). "Numerical and experimental study of the transformation of a solitary wave over a shelf or isolated obstacle," *J. Fluid Mech.*, **176**, 117-134.



## CHAPTER 40

### Probabilistic Calculation Model of Directional Random Waves

Wi-Gwang Pae<sup>1)</sup>, Hajime Mase<sup>2)</sup>, M. ASCE  
and Tetsuo Sakai<sup>3)</sup>, M. ASCE

**ABSTRACT:** A probabilistic calculation model is developed, for the simplicity of inclusion of wave breaking and energy dissipation, to predict the transformation of directionally-spreading random waves by using parabolic refraction-diffraction equations. The numerical predictions are compared with the experimental observations of random wave transformation over an elliptic shoal by Vincent and Briggs (1989); the predictions agree well with the observations under the non-breaking condition, however, the agreement is poor under the wave breaking condition.

#### INTRODUCTION

Estimation of refraction and diffraction, shoaling and wave breaking deformation over complicated bathymetry is an important problem in coastal engineering. Although random sea state is usually approximated by a monochromatic wave equivalent to the significant wave, there are some differences between the actual sea state and the results of monochromatic representation.

There are mainly two methods to deal with transformations of random waves: that is, spectral and individual wave analysis methods. Here we employ the individual wave analysis method for the simplicity of inclusion of wave breaking and energy dissipation. Incident wave heights and incident angles of individual waves are given from probabilistic density functions of wave heights and angles, and periods are given depending on their wave heights. Model wave equations used here are two different parabolic refraction-diffraction equations depending on incident angles. The numerical predictions are compared with the experimental observations of wave transformations of directionally-spreading random waves over an elliptic shoal carried out by Vincent and Briggs (1989).

---

1) Consulting Engineer, Nikken Consultants, Inc., Shinagawa-Ku, Tokyo, 141, Japan.

2) Res. Assoc., and 3) Prof., Department of Civil Eng., Kyoto Univ., Kyoto, 606, Japan.

**NUMERICAL MODEL FOR DIRECTIONAL RANDOM WAVES**

**Input Wave Heights**

One-parameter Weibull distribution was adopted as an input wave height distribution (Mase and Kobayashi, 1991).

$$p(x) = \frac{m}{2\phi} h_{1/3}^m x^{m-1} \exp \left\{ -\frac{1}{2\phi} (h_{1/3} x)^m \right\}, \tag{1}$$

$$h_{1/3} = \frac{3m}{2\phi} \int_{(2\phi \ln 3)^{1/m}}^{\infty} h^m \exp \left( -\frac{h^m}{2\phi} \right) dh, \tag{2}$$

$$\phi = \frac{1}{2} \left[ \Gamma \left( \frac{m+1}{m} \right) \right]^{-m}, \tag{3}$$

where  $x$  is the wave height normalized by the significant wave height,  $H_0$ ,  $\Gamma$  is the Gamma function, and  $m$  is the shape factor related to the wave groupiness factor,  $GF$ , as described by

$$m = 3.44 - 1.99 GF, \tag{4}$$

according to Mase (1989) and Mase et al. (1990). Therefore, the effect of wave grouping is indirectly taken into account in the wave transformation model through Eq.(4).

From the Weibull distribution, representative individual wave heights were defined by dividing  $x$ , ranging from 0 to 2, into  $N$  ( $=20$ ) segments,  $x_i$  ( $i = 1, \dots, N$ ), and the corresponding occurrence probabilities,  $p_i$  ( $i = 1, \dots, N$ ) were calculated. A dimensional wave height is given by  $x_i * H_0$ .

**Input Wave Periods**

Considering that higher waves have longer periods and referring observed joint distributions of wave heights and periods (Goda, 1978), we set wave periods as

$$\left. \begin{aligned} T_i &= 0.6 T_0; & 0 < H_i \leq 0.5H_0, \\ T_i &= T_0; & 0.5H_0 < H_i \leq 1.5H_0, \\ T_i &= 1.2 T_0; & 1.5H_0 < H_i, \end{aligned} \right\} \tag{5}$$

in a simple manner, where  $T_0$  is the significant wave period.

An alternative way to give input wave heights and periods is to use a joint probability density function of wave heights and periods; however, this method results in more number of waves in the calculation of wave transformation than the present method, since several wave periods are defined for a given wave height.

### Input Incident Wave Angles

Here directional spreading of individual waves was considered as in the case of spectral method (Panchang et al., 1990). Directional distributions of individual waves were assumed to be described by the following function:

$$G(\theta) = G_0 \cos^{2S} \left\{ (\theta - \theta_0) / 2 \right\}, \quad (6)$$

where  $\theta_0$  is the principal (mean) direction against the  $x$  axis,  $S$  is the parameter representing the degree of directional concentration,  $G_0$  is the constant to make the integration of Eq.(6) unity. Eq.(6) was originally proposed for spectral components (Mitsuyasu et al., 1975); which was treated as a probability density function of incident angles here.

Assuming that the directional distribution of individual waves is narrow compared to that of spectral components, and since parabolic refraction-diffraction equations are employed as model wave equations, we limit the maximum absolute value of  $\theta$  to  $60^\circ$ . The representative incident wave angles,  $\theta_j$  ( $j=1, \dots, M$ ), were given by every  $10^\circ$  in the range between  $-60^\circ$  and  $60^\circ$ , and the corresponding occurrence probabilities,  $q_j$  ( $j=1, \dots, M$ ), were determined from Eq.(6).

The directional spreading function used by Vincent and Briggs (1989) was

$$G(\theta) = \frac{1}{2\pi} + \frac{1}{\pi} \sum_{j=1}^J \exp \left\{ -\frac{(j\sigma)^2}{2} \right\} \cos j(\theta - \theta_0). \quad (7)$$

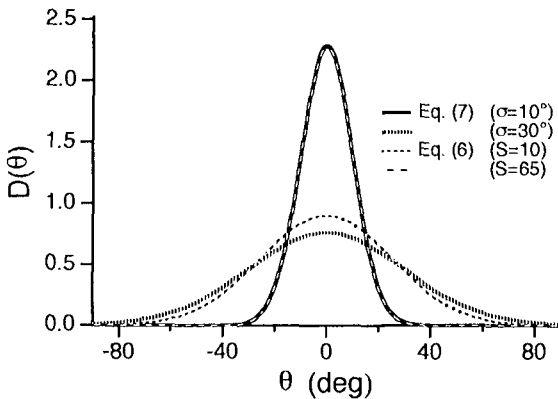


Fig. 1 Comparison of directional spreading functions.

If  $S$  in Eq.(6) is assigned to 400, 65, or 10, the directional distribution by Eq.(6) corresponds to that by Eq.(7) with  $\sigma = 0^\circ, 10^\circ$  or  $30^\circ$ , used as the experimental conditions of uni-directional, narrow-, or broad-banded directional spreading by Vincent and Briggs (1989). Figure 1 shows the comparison of the two directional distributions by Eqs.(6) and (7). It is seen from the figure that both almost agree.

**Model Wave Equation**

Transformations of all  $N^*M$  individual waves of wave heights  $H_i$ , wave periods  $T_i$ , and incident angles  $\theta_j$ , with the occurrence probabilities  $p_i^*q_j$ , were calculated by parabolic refraction-diffraction equations. The calculated results were superposed according to their occurrence probabilities. For waves with large incident angle  $|\theta_j| \geq 5^\circ$ , the minimax approximation model of Kirby (1986) was used:

$$\begin{aligned}
 A_x + i(\bar{k}-a_0k)A + \frac{C_{gx}}{2C_g}A + \frac{i}{\omega C_g} \left( a_1 - b_1 \frac{\bar{k}}{k} \right) (CC_g A_y)_y - \frac{b_1}{\omega k C_g} (CC_g A_y)_{yx} \\
 + \frac{b_1}{\omega} \left( \frac{k_x}{k^2 C_g} + \frac{C_{gx}}{2k C_g^2} \right) (CC_g A_y)_y - \left( a_1 - b_1 \frac{\bar{k}}{k} \right) \frac{W}{C_g} A \\
 + i b_1 \left( \frac{k_x}{k C} + \frac{C_{gx}}{2k C_g^2} \right) WA - \frac{i b_1}{k C_g^2} W_x A - \frac{i b_1}{k C_g^2} W A_x = 0 \quad , \quad (8)
 \end{aligned}$$

where  $A$  is the complex amplitude,  $\bar{k}$  is the wave number averaged over the  $y$  direction,  $k$  is the local wave number,  $C_g$  is the group velocity,  $\omega$  is the angular frequency,  $W$  is the damping coefficient described later, and  $a_0, a_1, b_1$  are the coefficients taken to be 0.9947, -0.8900, -0.4516. It is noted that the derivative of  $W$  was included in Eq.(8) compared to the original minimax model of Kirby (1986).

For waves with small incident angle  $|\theta_j| < 5^\circ$ , the following parabolic equation with an energy dissipation term was used:

$$A_x - i(K - \bar{k}_0)A + \frac{(K C C_g)_x}{2K C C_g} A - \frac{i}{2K C C_g} (C C_g A_y)_y = 0 \quad , \quad (9)$$

$$K^2 = k^2 + i \frac{kW}{C_g} \quad , \quad (10)$$

where  $\bar{k}_0$  is the wave number at the incident boundary averaged over the  $y$  direction. Eq.(9) is obtained from the mild slope equation with a damping term (Booij, 1981) by using the splitting matrix method (Radder, 1979; Dalrymple et al., 1984).

Incipient of wave breaking was estimated by a simple equation,

$$H_b/h_b = 0.85 (0.7 + 5 \tan \beta) \quad , \quad (11)$$

where  $H_b$  and  $h_b$  are the wave height and depth at the breaking point,  $\tan\beta$  is the bottom slope.

The damping coefficient in Eqs.(8) and (10) was formulated by a bore model (Battjes, 1986) as follows:

$$W = \frac{2B}{\gamma^3} \frac{1}{T} \left(\frac{H}{h}\right)^4, \tag{12}$$

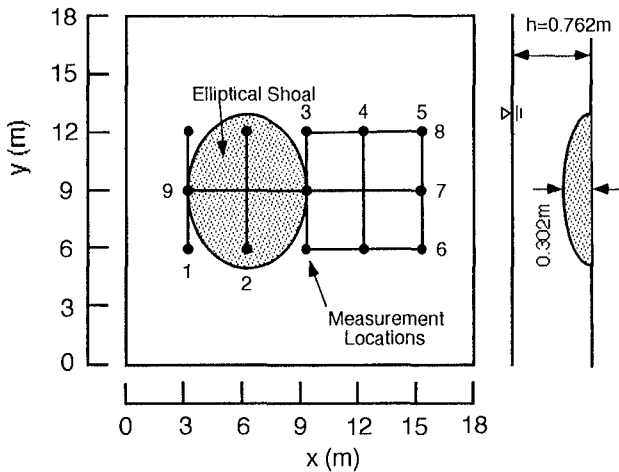
$$\gamma = 0.7 + 5 \tan\beta, \tag{13}$$

$$B = \begin{cases} 11-10 h/h_b, & 0.6 \leq h/h_b \leq 1.0 \\ 5, & h/h_b \leq 0.6 \end{cases} \tag{14}$$

Eq.(14) was used to represent the measured wave height change of monochromatic waves more accurate (Mase and Iwagaki, 1982). In the calculation, a treatment of the lateral boundary condition followed Yamamoto (1987).

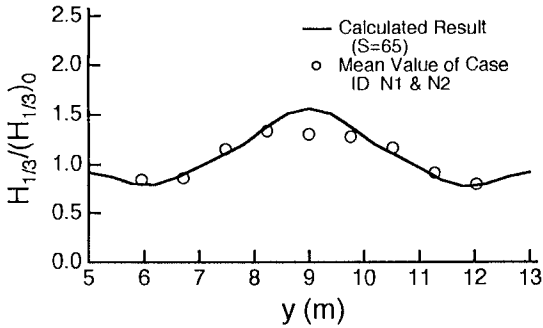
**COMPARISON BETWEEN NUMERICAL PREDICTIONS AND EXPERIMENTAL OBSERVATIONS**

Experiments of random wave transformations over a shoal were carried out by Vincent and Briggs (1989). Figure 2 illustrates the experimental layout of an elliptical shoal and measurement locations, but

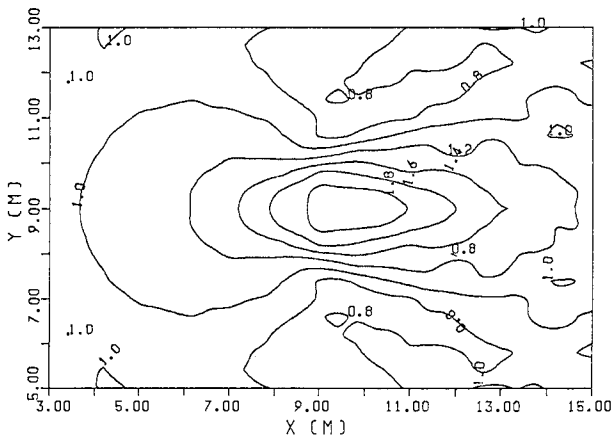


**Fig. 2 Experimental layout.**

the coordinates are rewritten so that the center of the shoal is located at  $(x, y) = (6\text{m}, 9\text{m})$ , for the convenience in the numerical calculations. The TMA spectrum was used as a target spectrum. Spectral peakedness was changed by two; that is, broad-banded and narrow-banded frequency spectra. In the present model, an energy spectrum was not given as input data, but given by a wave height distribution. As general, a narrow-banded spectral wave trains lead to the Rayleigh distribution of wave heights.



(a)



(b)

**Fig. 3 Spatial wave height distribution for narrow-banded directional spreading waves of Case N1 and N2.**

Figure 3 shows the comparison of measured and calculated wave heights along the measuring line #4 (figure (a)), and in a horizontal region (figure (b)), for the case of narrow-banded directional spreading waves with two different spectral peakedness of Case N1 and Case N2 in the paper of Vincent and Briggs (1989). Since the experimental results of N1 and N2 were almost the same, the experimental results were averaged and shown in Fig.3. In the calculation, the Rayleigh distribution ( $m = 2$  in Eq.(1)) was given as the input wave height distribution. Comparing wave heights along the measuring line #4, we see a fairly good agreement between both results, but the calculated wave heights around  $y = 9\text{m}$  are a little larger than the measured ones. One of the reasons of the discrepancy may be attributed to unsatisfactory smoothing due to inadequate number of division in both wave periods and incident angles in the calculation.

Figure 4 shows the comparison of wave heights along the measuring line #4 for the case of uni-directional random waves under the condition of non-breaking. In this figure, not only the significant wave height but also the one-hundredth maximum, the one-tenth maximum and the mean wave heights are plotted. Easiness to calculate such wave heights is one of the advantages of the present calculation method compared to spectral calculation methods. Experimental results of U3 and U4 were averaged in the figure. We can see a good agreement in this condition.

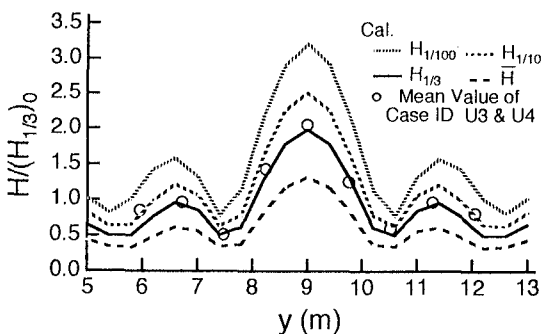
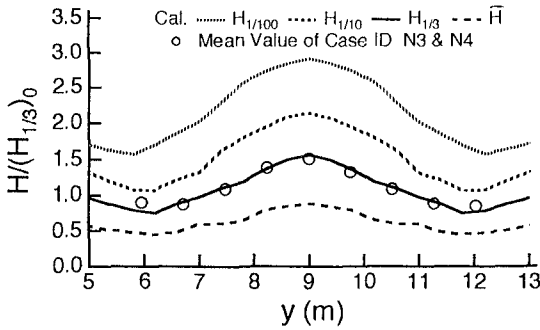


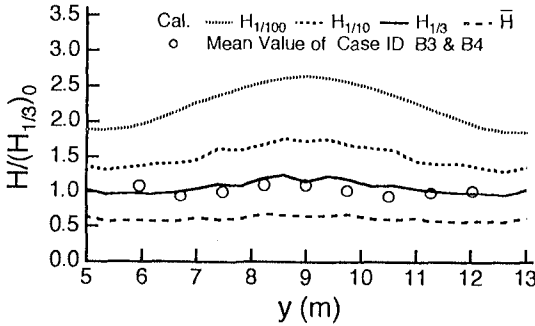
Fig. 4 Comparison of measured and calculated wave heights along the measuring line #4 for uni-directional random waves.

Figure 5 is the result of narrow-banded directional spreading waves of Case N3 and Case N4. Numerical predictions agree well with the observations.

Figure 6 shows the comparison for the case of broad-banded directional spreading random waves. The spatial wave height distribution along the measuring line #4 is very flat due to wide directional spreading. Averaged measured wave heights and calculated ones agree well. The



**Fig. 5 Comparison of measured and calculated wave heights along the measuring line #4 for narrow-banded directional spreading random waves.**

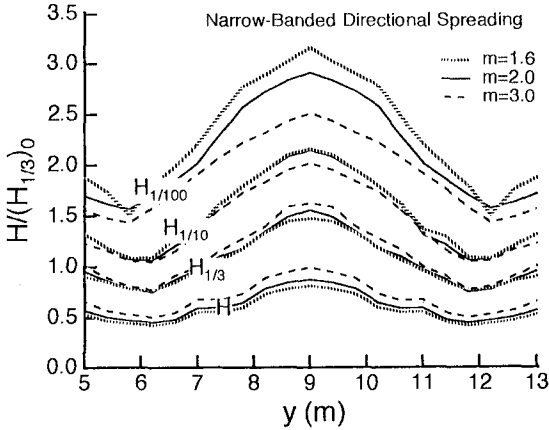


**Fig. 6 Comparison of measured and calculated wave heights along the measuring line #4 for broad-banded directional spreading random waves.**

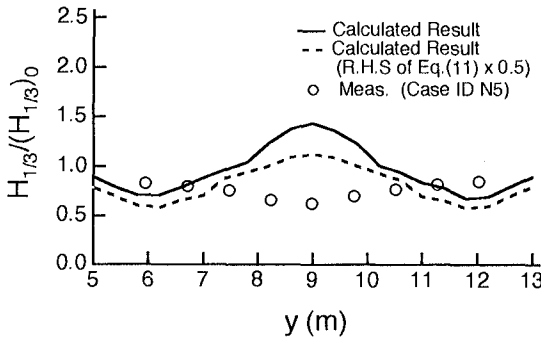
difference between the calculated one-hundredth and the mean wave heights around  $y = 9$  m is larger than that in both sides; that is, the wave height distribution around  $y = 9$  m becomes wider than that in both sides.

Figure 7 shows the effect of the shape factor of the Weibull distribution on the calculated wave heights along the measuring line #4. There is little difference in the significant wave heights, but we can see the difference for higher waves such as the one-hundredth maximum wave height. As the shape factor  $m$  becomes small, that is, the incident wave height distribution becomes wider, the one-hundredth maximum wave height becomes large especially around  $y = 9$  m.





**Fig. 7 Effect of incident wave height distribution on calculated wave heights along measuring line #4.**



**Fig. 8 Comparison of measured and calculated wave heights under the wave breaking condition.**

Figure 8 shows a result of the cases that wave breaking occurred over the shoal. The measured spatial wave height distributions along the measuring line #4 are different from the calculated ones. The observations become minimum around  $y = 9$  m, but the predictions are maximum. Even if the incipient condition of wave breaking was modified to make waves break at deeper water, by multiplying 0.5 to the original incipient condition, the shape of calculated spatial wave height distribution is unchanged, only resulting in smaller values (shown by broken line).

The following point should be noted. Experiments of uni-directional random wave transformations over a shoal were carried out by Lie and Tørum (1991). Even in the case that severe wave breaking occurred on the shoal, a concave wave height distribution along a transverse section, that is, being minimum of wave heights at the center of a transverse section cannot be seen, judging from contour maps of wave heights. The difference between the measured and the calculated wave heights under the wave breaking condition, and the difference between the measured results by different researchers may be attributed to the complexity of the breaking point and energy dissipation process over an arbitrary varying bathymetry.

## CONCLUSIONS

This study developed a probabilistic model to calculate transformations of directionally-spreading random waves, by using an incident wave height distribution, an incident angle distribution, and parabolic refraction-diffraction equations, for the simplicity of inclusion of wave breaking and energy dissipation. Other advantages of the present model were as follows: 1) the present model could estimate any representative wave heights including the significant wave height; and 2) could evaluate the effect of wave grouping through the relationship between the incident wave height distribution and groupiness factor. The experimental results of random wave transformations over an elliptic shoal by Vincent and Briggs (1989) agreed well with the predictions by the present numerical model in the case of non-breaking condition. In the case that wave breaking occurred on a shoal, the predictions were not in agreement with the observations. The shape of measured wave height distribution in a transverse section was concave, however, the calculated wave height distribution was convex. Therefore, one of the advantages of the present model, that is, the simplicity of inclusion of wave breaking process was not examined yet. The present model should be checked for other experimental observations over a shoal, since some of the observations showed a different pattern of wave height distribution.

## REFERENCES

- Battjes, J.A. (1986). Energy dissipation in breaking solitary and periodic waves. Communications on Hydraulic and Geotech. Eng., Delft Univ. of Tech., Delft, 18p.
- Booij, N. (1981). Gravity waves on water with non-uniform depth and current, Rep.81-1, Dept. of Civil Eng., Delft Univ. of Tech., Delft, 131p.
- Dalrymple, R.A., Kirby, J.T. and Hwang, P.A. (1984). Wave diffraction due to areas of energy dissipation. Jour. Waterway, Port, Coastal, and Ocean Eng., Vol.110, No.1, pp.67-79.
- Goda, Y. (1978). The observed joint distribution of periods and heights of sea waves. Proc. 16th Int. Conf. on Coastal Eng., ASCE, pp.227-246.

- Kirby, J.T. (1986). Rational approximations in the parabolic equation method for water waves. *Coastal Eng.*, Vol.10, No.4, pp.355-378.
- Lie, V. and Tørum, A. (1991). Ocean waves over shoals. *Coastal Eng.*, Vol.15, Nos.5&6, pp.545-562.
- Mase, H. (1989). Groupiness factor and wave height distribution. *Jour. Waterway, Port, Coastal, and Coastal Eng.*, ASCE, Vol.115, No.1, pp.105-121.
- Mase, H. and Iwagaki, Y. (1982). Wave height distribution and wave grouping in surf zone. *Proc. 18th Int. Conf. on Coastal Eng.*, ASCE, pp.58-76.
- Mase, H., Hayashi, K. and Yamashita, T. (1990). Wave group properties of coastal waves. *Proc. 22nd Int. Conf. on Coastal Eng.*, ASCE, pp.177-190.
- Mase, H. and Kobayashi, N. (1991). Transformation of random breaking waves and its empirical numerical model considering surf beat. *Proc. Coastal Sediments '91*, ASCE, pp.688-702.
- Mitsuyasu, H. et al. (1975). Observation of the directional spectrum of ocean waves using cloverleaf buoy, *Jour. Physical Oceanogr.*, Vol.5, No.4, pp.750-760.
- Panchang, V.G, Wei, G., Pearce, B.R. and Briggs, M.J. (1990). Numerical simulation of irregular wave propagation over shoal. *Jour. Waterway, Port, Coastal, and Coastal Eng.*, ASCE, Vol.116, No.3, pp.324-340.
- Radder, A.C. (1979). On the parabolic equation method for water-wave propagation. *Jour. Fluid Mech.*, Vol.95, pp.159-176.
- Vincent, C.L. and Briggs, M.J. (1989). Refraction-diffraction of irregular waves over a mound. *Jour. Waterway, Port, Coastal, and Ocean Eng.*, ASCE, Vol.115, No.2, pp.269-284.
- Yamamoto, A. (1987). Parabolic wave refraction-diffraction equation with dissipation and its applications. Master Thesis, Dept. of Civil Eng., Kyoto Univ., 103p.

## CHAPTER 41

### DIRECTIONAL WAVE MEASUREMENTS IN RIO DE JANEIRO COAST

C.E.Parente<sup>1</sup>, C.P Hansen<sup>2</sup>, R.M. Sampaio<sup>3</sup>,  
J.M. Lima<sup>4</sup>, J.L.B. Carvalho<sup>1</sup>

#### ABSTRACT

This paper presents the experience and results with a slope array of wavestaffs specially designed and built for directional wave measurements from an offshore platform off the Rio de Janeiro coast. We discuss the main features of the system, limitations and noise sources. A promising adaptive technique is introduced.

#### 1. INTRODUCTION

Having one of the biggest coastlines of the world, Brazil still lacks long term wave data, either in offshore areas or in the coast. In the last decade most of the oil production in the country is coming from offshore, and fields as deep as 1500 meters will be exploited in the incoming years. In this way, information on directional wave, wind and current, for the design of new huge structures to face such challenge, is mandatory. Besides that, an emerging consciousness in relation to the occupation, protection and management of coastal areas is also putting a big demand in environmental data.

Three directional wave measurement projects are going on in the Rio de Janeiro State coast (positions are shown in fig.1).

---

<sup>1</sup>Associate Prof. at UFRJ/RJ/Brazil and graduate student

<sup>2</sup>Researcher at Braz.Navy Hydrog.Office in Rio

<sup>3</sup>Researcher at INPH in Rio

<sup>4</sup>Researcher at CENPES/Petrobras in Rio

- A) A Directional Waverider buoy in front of Guanabara Bay (Rio de Janeiro city);

This instrument is being used in a joint project conducted by the Federal University of Rio de Janeiro and the Brazilian Navy Hydrographic Office (DHN), owner of the equipment (Melo et al, 1991). The main purpose is to characterise the wave climate along the famous Ipanema-Leblon beach that have been under severe erosion in the last years.

- B) A directional buoy built by CONSUB, a Brazilian company, for PETROBRAS, moored in 1500 meters of water.

This buoy sends via Imarsat satellite, meteorological and oceanographic data including directional wave data.

- C) An array of resistive wavestaffs mounted as a slope array in an offshore platform in waters 100 meters deep;

This paper describes the experience and results with this slope array.

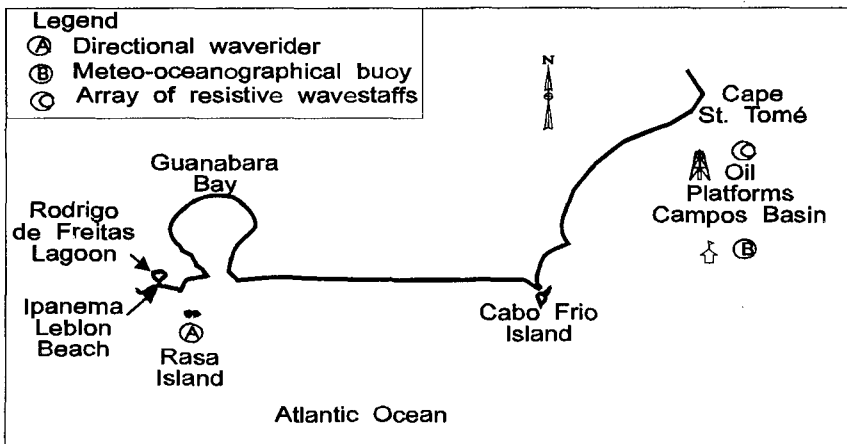


Fig.1 Rio de Janeiro coast with the locations of the directional measurements.

## 2. DIRECTIONAL MEASUREMENTS FROM AN OFFSHORE PLATFORM WITH A SLOPE ARRAY

The objective of this project is to simultaneously measure wave, current and wind in order to determine long term resultant forces in an offshore platform.

Directional wave measurements are made with arrays of resistive wavestaffs suspended from the platform.

Following the idea of Ford et al (1968), we built a slope array of resistive wavestaffs to be suspended from an offshore platform in the Campos basin. One array consists of four wavestaffs made with 0.25 mm stainless steel wire spirally wound around a 1.25 mm synthetic cable. The staffs are suspended from the platform, fixed in a light frame forming a square of 1.12 m each side. This configuration has shown several advantages in terms of handling, maintenance of vertical position and relative horizontal position among the staffs.

Due to safety reasons (protection against fishing boats) the array is mounted inside the platform; as we discuss later, this can be a source of noise.

The staffs are excited with CW signals in order to extend the life of the wires. All the signals are conditioned and processed in a central station producing surface elevation and two orthogonal surface slopes. We followed the processing techniques of Borgman (1982) and Kuik et al (1987) to get the one point spectrum, main direction and spread about the main direction. We can also calculate the wave number and compare with the value given by the linear theory.

Preliminary results have shown good agreement with visual observation (sea and swell) and measured data (wind and current).

The main characteristics of the slope array are:

**Requirements:** low drag and small weight in order to be easily placed by hand in the support base and keep good vertical position. In the beginning we have tried just single wires (very low drag), but the sensitivity was not enough for lower frequencies.

**Number of staffs:** 4 - mounted in a square of 1.12 m side.

**Sensor spacing:** 1.12 m. The spacing is a compromise between adequate sensitivity for slope measurements and spatial aliasing in high frequencies.

**Staff:** resistive. A stainless steel wire .25 mm in diameter is spirally wound in a 1.25 mm polypropylene wire.

**Resistance:** 135 ohms/meter.

**Weight:** Each staff has a 5 kg weight.

**Linearity:** 1.7 per cent.

**Length:** 12 meters.

**Excitation:** pulsed CW.

**Detection:** synchronous (sample/hold).

**Signal conditioning:** all the conditioning circuits are analog, the A/D conversion being done in the computer.

### 3. DATA ANALYSIS IN SITU

All the data (wave, current and wind) is transferred to a PC type computer and processed in real time; it is also send to Rio via satellite.

The software perform the following operations:

- data acquisition;
- data quality tests;
- time domain analysis;
- frequency domain analysis;
- directional wave analysis.

Raw data and calculated parameters are also send to shore via satellite.

We use the classical Fourier and the Borgman and Kuik techniques mentioned above to calculate the directional spectral parameters (main direction and spread); they are summarized below.

Elevation and slopes for a monochromatic wave ( $f, \theta$ ) are given by:

$$\eta = \alpha \cos(kx \cos \theta + ky \sin \theta - \omega t + \varepsilon) \quad (1)$$

$$\eta_x = -\alpha k \cos \theta \sin(kx \cos \theta + ky \sin \theta - \omega t + \varepsilon) \quad (2)$$

$$\eta_y = -\alpha k \sin \theta \sin(kx \cos \theta + ky \sin \theta - \omega t + \varepsilon) \quad (3)$$

Taking the origin at (0,0) and  $\epsilon=0$ ;

$$\eta = \alpha \cos \omega t \tag{4}$$

$$\eta_x = -\alpha k \cos \theta \sin \omega t$$

$$\eta_y = -\alpha k \sin \theta \sin \omega t \tag{6}$$

Now we Fourier transform and take cross spectra:

$$\eta \qquad \qquad \eta_x \qquad \qquad \eta_y \tag{7}$$

$$\alpha \cos \omega t \qquad -\alpha k \cos \theta \sin \omega t \qquad -\alpha k \sin \theta \sin \omega t \tag{8}$$

$$\begin{matrix} \downarrow & & \downarrow & & \downarrow \\ \cos \omega t & \sin \omega t & \cos \omega t & \sin \omega t & \cos \omega t & \sin \omega t \end{matrix} \tag{9}$$

$$\begin{matrix} \downarrow & & \downarrow & & \downarrow \\ \alpha & & -\alpha k \cos \theta & & -\alpha k \sin \theta \end{matrix} \tag{10}$$

$$\begin{matrix} \text{-----} & & \downarrow & & \downarrow & & \text{-----} \\ & & \alpha^2 k \cos \theta = a_1 & & \alpha^2 k \sin \theta = b_1 \end{matrix} \tag{11}$$

$$\text{main direction} \Rightarrow \theta = \text{atan}(b_1/a_1) \tag{12}$$

Kuik et al (1988) suggest that the energy distribution around the main direction,  $D(\theta)$ , can be associated to a probability distribution, the standard deviation representing the spread of energy.

$$\sigma = \sqrt{2(1 - m_1)} \ ; \ m_1 = \sqrt{a_1^2 + b_1^2} \tag{13}$$



Some data quality control are made comparing the measured wavenumber ( $k_m$ ) with the wavenumber given by linear theory ( $k_l$ ). For the same monochromatic case, taking the spectrum:

$$G_\eta = \alpha^2; G_{\eta_x} = \alpha^2 k^2 \cos^2 \theta; G_{\eta_y} = \alpha^2 k^2 \sin^2 \theta \quad (14)$$

and summing:

$$k_m = \sqrt{\frac{G_{\eta_x} + G_{\eta_y}}{G_\eta}} \quad (15)$$

We can see below an example from a fetch limited NE sea, typical of the Campos area. In fig. 2 the spectrum, in fig.3 main direction, in fig 4 spread and in fig. 5 comparison of wavenumbers.

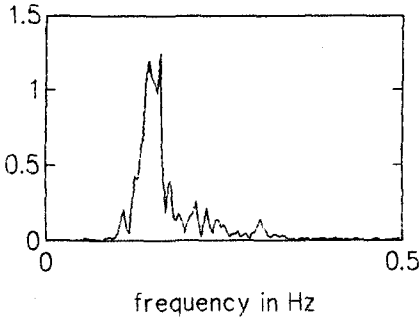


Fig.2 Spectrum of a NE sea

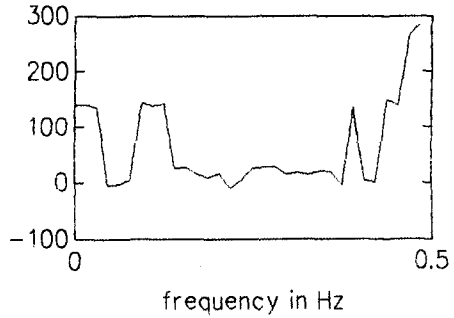


Fig.3 Main direction

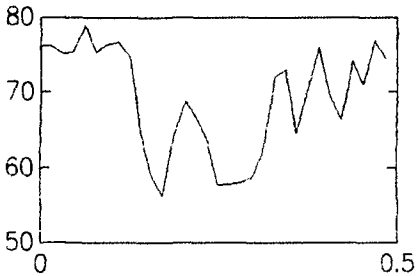


Fig.4 Spread

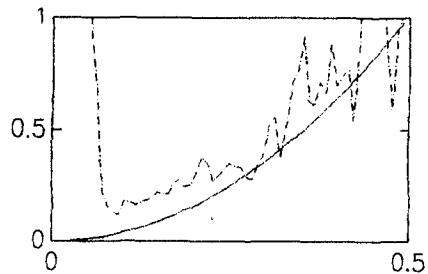


Fig.5 Wavenumbers ( $k_l$ ,  $k_m$ )

#### 4. DATA ANALYSIS ASHORE

Fig.6 shows the evolution of the spectrum for the peak frequency along the record, advancing one value of the series each time. We can notice regions of high and low values suggesting that possibly at a given moment the energy in the main direction is low but could be measurable at other directions.

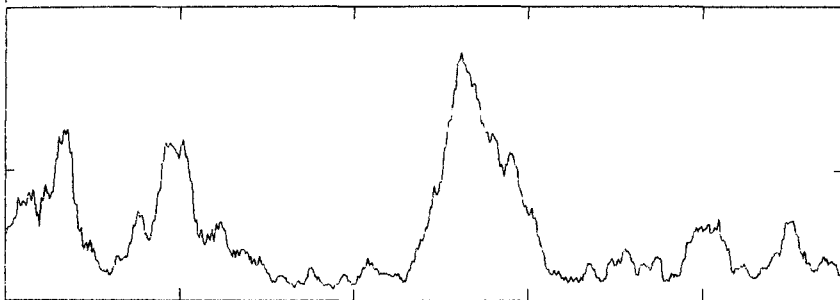


Fig.6 Spectrum (peak frequency) changing with time

We may consider that these ups and downs along the record are due not only to the fact that different frequencies, close together, combine in a constructive or destructive way but also to other factors, identified as noise, non-linearities, non-stationarity, inaccuracies, etc...

- limited number of sensors;
- non-linearities of staffs and circuitry;
- non verticality of staffs;
- influence of platform structure;
- non-stationarity of the wave field;
- finite sensor spacing and aliasing;

All this factors tend to contribute to the non-stationarity of the process along the recording time.

We can recall some basic principles of spectral analysis, quoting Gardner (1988):

The fundamental reason for interest in a statistical (e.g. time averaged) spectrum of some given data is a belief that interesting aspects of the phenomenon being investigated have spectral influences on the data that are masked by uninteresting (for the (purpose at hand) random effects and an additional belief (or, at least, hope) that these spectral influences can be revealed by averaging out the random effects. This second belief (or hope) should be based on the knowledge (or, at least, suspicion) that the spectral influences of the interesting aspects of the phenomenon are time-invariant, so that the corresponding invariant spectral features (such as peaks or valleys) will

**be revealed rather than destroyed by time averaging.**

The random combination or action of all the mentioned factors could destroy some features of the process rather than enhance if we average along the entire record, as mentioned by Gardner.

We could possibly select some recording periods where a given frequency band or directional sector is showing a better signal quality, wave grouping or other special feature. This is a kind of adaptive technique that we are trying now and we show here some results.

A possible criterium would consider how close are the wavenumber values (measured and from linear theory); another, perhaps, wave grouping. Using the first one, for each selected series (close values of  $k_l$  and  $k_m$ ) we collect spectrum and main direction. The result is a possible representation of the directional spectrum. If we sum, for each frequency, all the contributions in direction we approach the one point spectrum, whose area should agree with the mean square value of the process.

The technique could be resumed as follows:

1) For each sensor take series of  $m$  point at time, and calculate spectrum, main direction,  $k_m$  and spread. ( $m$  is typically 64, 128 or 256).

2) Take the average of all 4 sub-arrays (it is worth while to have some redundancy).

3) Select the series where  $ABS(k_m - k_l) < s \times k_l$ ;

$s$  between 0.05 and 0.2, for example.

4) Accumulate the spectrum value in the corresponding direction box.

We can see below some results. In Fig.7 we can see a 3D plot of the evolution of the spectrum value and main direction for the peak frequency along a given recording period. During this time we have enhancement of the spectrum value for different direction inside a given sector, changing in a well behaved way.

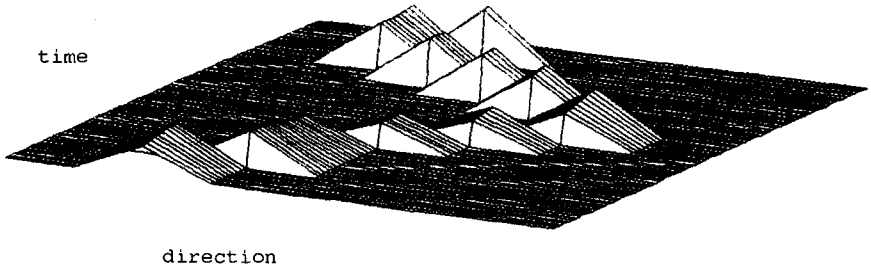


Fig. 7 Spectrum value and mean direction for the peak frequency changing along the time.

In fig. 8 a construction of  $D(\theta)$  for the peak frequency taking the contributions of all sub-arrays.

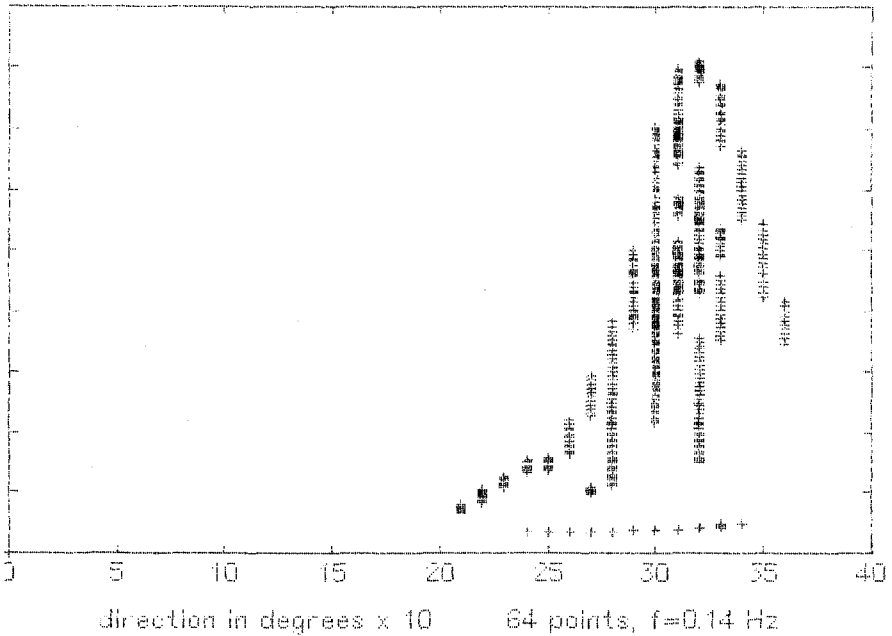


Fig.8  $D(\theta)$  for the peak frequency, using the contributions of all sub-arrays. Vertical axis is spectral density and horizontal axis is direction in degrees.

In fig. 9 we see a 3D plot of "directional spectrum" (frontal view). We have in the same graph two plots of the one-point spectrum. One is calculated using the entire record with 4 d.f. (dashed line); the other one is calculated summing the contributions of direction "boxes" for each frequency (continuous line).

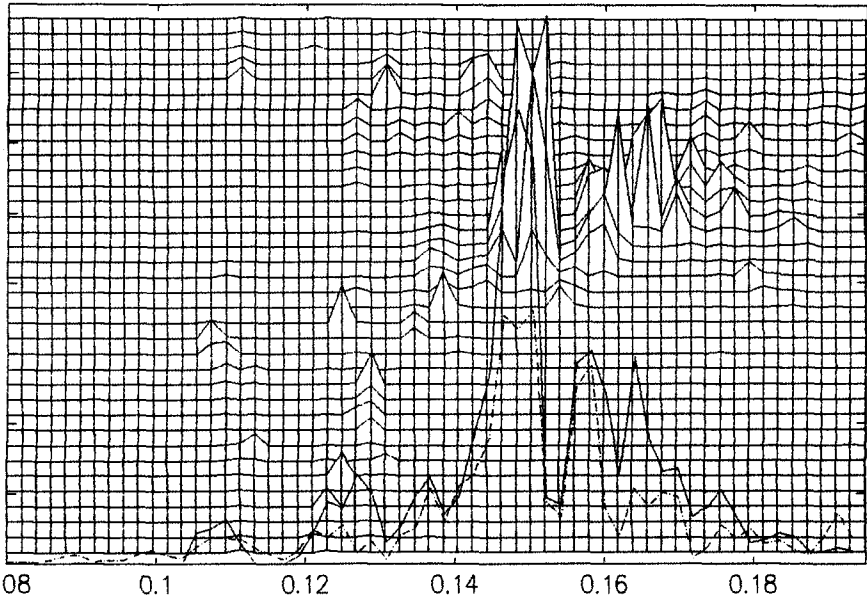


Fig. 9 3D plot of directional spectrum (frontal view). Vertical axis is direction and horizontal axis is frequency (axis z is spectral density). In the same graph one point spectrum.

In fig. 10 a 3D plot of the same data (side view). Vertical axis is frequency and horizontal axis is direction; z axis is spectral density.

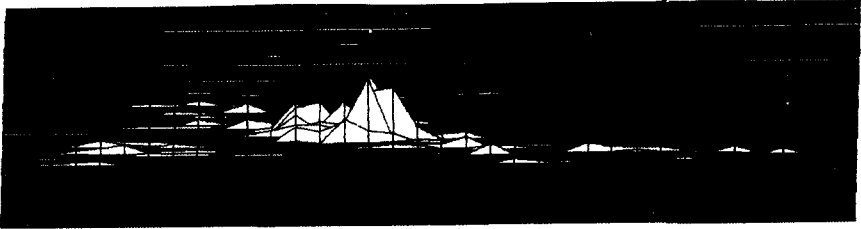


Fig. 10 3D plot of directional spectrum (side view). Horizontal axis is direction; vertical axis is frequency; z axis is spectral density.

## 5. CONCLUSIONS

The results are showing very good consistency compared with measured wind values and visual observations from the platform. As we would expect the resolution is relatively poor for low frequencies. We are about to use two arrays 30 m apart in an attempt to solve this problem.

The resistive wave staff have been used for many years and is a very cheap and reliable way to get wave data from an ocean fixed structure. Usually it is not very easy as one could expect to make oceanographic measurements from an offshore platform, mainly if it depends on divers, big cranks and special locations, just to mention a few problems. In this way, a small and light array suspended from the spider deck of a platform (the deck closest to the sea level) provided that the resolution is adequate for low frequencies, can be very useful not only as source of log term data but also for the day to day operation of the platform.

Work in progress is toward better resolution in low frequencies, simulations with artificial seas, combination of two or three arrays and the search for adaptive techniques.

## ACKNOWLEDGEMENTS

The slope array project is being supported by the Brazilian oil company, PETROBRAS.

**REFERENCES**

Borgman,LE (1982). Directional Wave Spectra from Wave Sensors. In Ocean Wave Climate, Plenum.

Ford,JR, RC Tim and A Trampus (1968). A New Method for Obtaining the Directional Spectrum of Ocean Surface Gravity Waves. IEEE Trans. Geosc. Electr. GE-6(4, november), pp. 190-197.

Gardner,WA (1988). Statistical Spectral Analysis. Prentice Hall,NJ, pp.68.

Kuik,AJ, GP Van Vledder and LH Holthuijsen (1968). A Method for the Routine Analysis of Pitch and Roll Buoy Wave Data. J. Phys. Ocean., 18, july, pp. 1020-1034.

Melo,E et al (1992). The erosion of the Ipanema-Leblon beach. Technical report (in portuguese). PENO/COPPE/UFRJ, Rio de Janeiro.

## CHAPTER 42

# ON THE ATTENUATION OF WAVES PROPAGATING WITH A CURRENT

Michio Sato\*

### Abstract

In this paper, the mechanisms which dissipate the energy of waves propagating on a current are considered. It is shown that the surface slope of an actual uniform current plays an important part for the variation of wave height attenuation rates with the intensity of the current. The surface slope enhances the attenuation of waves propagating on an opposing current and weakens it for a following current. It is also shown that, as the wave attenuation rate increases in stronger opposing currents, it affects the change in height of waves on a gradually varying opposing current to such an extent that we can not ignore the effect.

## 1 INTRODUCTION

When waves propagate on an opposing uniform current, the rate of wave height attenuation increases with the current velocity. Iwasaki and Sato (1972; hereafter referred to as IS) attempted to explain the increase of the wave height attenuation through the dissipation of wave energy due to the work done by internal and boundary shear stresses.

On the other hand, it has been pointed out that, when waves propagate on a following current, the wave attenuation rate decreases as the strength of the superimposed following current increases. Kemp and Simons (1983) and Simons et al. (1988) provided experimental results which showed the reduction of wave height attenuation rates on following currents.

The objective of this paper is to provide a theoretical explanation for the reduction of the wave attenuation rates on following currents together with the increase of ones on opposing currents.

---

\*Professor, Department of Ocean Civil Engineering, Kagoshima University, 1-21-40 Korimoto, Kagoshima-shi, 890 JAPAN



## 2 WAVE HEIGHT CHANGE ON A UNIFORM CURRENT

Problems on coexisting system of waves and currents have been treated frequently in an unrealistic situation of horizontal bed and uniform depth. However, when the bottom is horizontal, the depth of a flow changes in the flow direction and a uniform flow is not possible in real fluid.

Before going to the main subject, we consider the role of the mean surface slope in somewhat intuitive fashion through a thought experiment.

When waves propagate on still water of constant depth with a horizontal bottom, the wave energy fluxes and the wave heights at the sections I and II in figure 1(a) are equal unless the wave energy dissipates due to viscosity. Then, we consider the situation like (b) in figure 1 where waves go uphill assuming no wave energy dissipation due to viscosity. If waves propagate without change in height, there must be mass transports of the same intensity through the sections I and II. However, the potential energy of the mass transported through the section I is greater than the one transported through the section II by the quantity of the mass times the gravitational acceleration times the difference of mean surface elevations, and there are no energy sources which supply the potential energy other than wave energy. Therefore, the constant wave energy flux does not hold and wave height is expected to decrease as the waves propagate.

In the situation like (c) in figure 1, we can deduce that the wave height will increase as the waves propagate. This thought experiment suggests that the effect of surface slope be taken into consideration for the discussion of wave height change on a uniform current.

**WAVE ENERGY BALANCE** Now, we consider a two dimensional situation in which waves propagate on a current with uniform depth. The mean surface has the same inclination as the bottom slope. Choosing space coordinates  $x$  and  $y$  to be along and perpendicular to the mean water surface respectively (figure 2), equations of motion and continuity are

$$\frac{\partial u}{\partial t} + (U + u) \frac{\partial u}{\partial x} + v \frac{\partial (U + u)}{\partial y} = g \sin \theta - \frac{1}{\rho} \frac{\partial p}{\partial x} + \frac{1}{\rho} \frac{\partial \tau}{\partial y} \quad (1)$$

$$\frac{\partial v}{\partial t} + (U + u) \frac{\partial v}{\partial x} + v \frac{\partial v}{\partial y} = -g \cos \theta - \frac{1}{\rho} \frac{\partial p}{\partial y} \quad (2)$$

$$\frac{\partial u}{\partial x} + \frac{\partial v}{\partial y} = 0 \quad (3)$$

In IS, the term  $g \sin \theta$  in equation (1) was omitted on the assumption that the gradient of  $\tau_c$ , which was a part of  $\tau$  due to pure current, in  $y$  direction was compensated with this term when flow was uniform without waves. However, the mean surface slope of wave-current co-existing system differs from the surface slope of

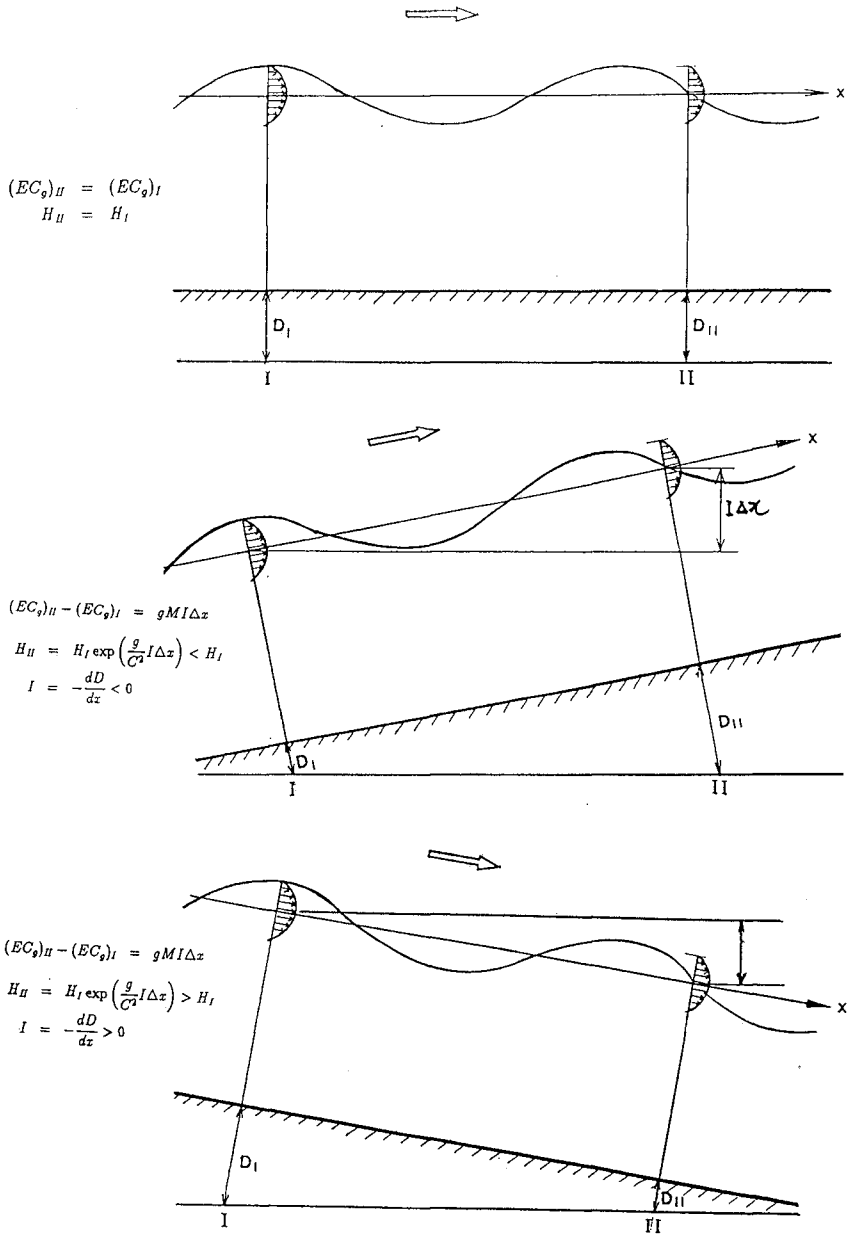


Figure 1: Energy balance of waves propagating over a still water with inclined surface

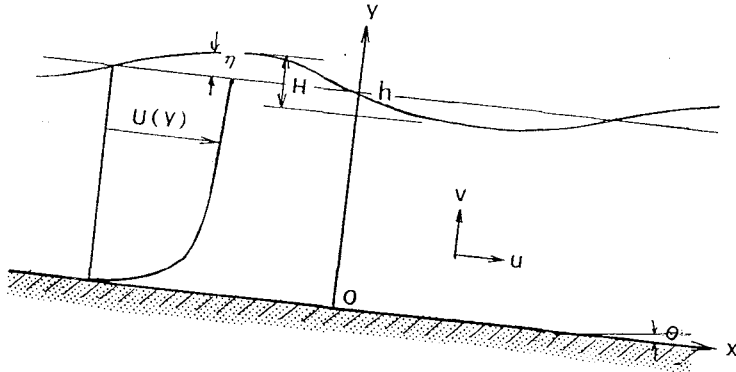


Figure 2: Definition sketch

pure current and this has been confirmed experimentally by Asano et al.(1986). The boundary conditions at the free surface  $y = h + \eta$  and at the bottom  $y = 0$  are

$$v = \frac{\partial \eta}{\partial x} + (U + u) \frac{\partial \eta}{\partial x} \quad \text{at } y = h + \eta \quad (4)$$

$$p = 0 \quad \text{at } y = h + \eta \quad (5)$$

$$v = 0 \quad \text{at } y = 0 \quad (6)$$

where  $u$  and  $v$  are the velocity components of wave motion in  $x$  and  $y$  direction,  $U$  is the current velocity and assumed to be a function of  $y$ ;  $\rho, p, g, \tau$  and  $\eta$  are density, pressure, gravitational acceleration, Reynolds stress and surface elevation.

Integrating the sum of equation (1) multiplied by  $\rho u$  and equation (2) multiplied by  $\rho v$  over the depth with respect to  $y$ , and making use of equations (3) to (6) together with the Leibnitz's rule, an equation for the balance of wave energy is obtained as follows after averaging over a wave period.

$$\begin{aligned} & \frac{\partial}{\partial t} \left[ \overline{\int_0^{h+\eta} \frac{\rho}{2} (u^2 + v^2) dy} + \frac{1}{2} \overline{\rho g \eta^2 \cos \theta} \right] \\ & + \frac{\partial}{\partial x} \left[ \overline{\int_0^{h+\eta} \left\{ \frac{\rho}{2} (u^2 + v^2) + p + \rho g (y - h) \cos \theta \right\} u dy} \right. \\ & \quad \left. + \overline{\int_0^{h+\eta} \frac{\rho}{2} (u^2 + v^2) U dy} + \frac{1}{2} \overline{\rho g \cos \theta \eta^2 U_{h+\eta}} \right] \\ & = \frac{1}{2} \overline{\rho g \cos \theta \eta^2 \frac{\partial U_{h+\eta}}{\partial x}} + \overline{\int_0^{h+\eta} u \frac{\partial \tau}{\partial y} dy} + \overline{\int_0^{h+\eta} (-\rho uv) \frac{dU}{dy} dy} \\ & \quad + \overline{\rho g \sin \theta \int_0^{h+\eta} u dy} \end{aligned} \quad (7)$$

Assuming that the slope is small enough for the following approximation to be valid

$$\cos \theta \approx 1 \quad \text{and} \quad \sin \theta \approx \tan \theta = I$$

and confining ourselves to the second order approximation of wave motion in the following discussion for the sake of simplicity, the wave energy balance equation becomes as follows

$$\frac{\partial E}{\partial t} + \frac{\partial F}{\partial x} = \int_0^h u \frac{\partial \tau}{\partial y} dy + \int_0^h (-\rho \bar{u} \bar{v}) \frac{dU}{dy} dy + \rho g I \int_0^{h+\eta} u dy \tag{8}$$

where E is the wave energy density and F is the wave energy flux given by

$$E = \int_0^h \frac{\rho}{2} (\overline{u^2 + v^2}) dy + \frac{1}{2} \rho g \bar{\eta}^2 \tag{9}$$

$$F = \int_0^h \bar{p} u dy + \int_0^h \frac{\rho}{2} (\overline{u^2 + v^2}) U dy + \frac{1}{2} \rho g \bar{\eta}^2 U_h \tag{10}$$

There appear three sources of wave energy in the righthand side of equation (8).

The first term gives energy dissipation due to viscosity. The second term shows the possibility of energy transfer between waves and a current through the mechanism similar to the energy transfer through the work done by Reynolds stress against flow strain in turbulent flow. This term vanishes for inviscid wave motion because of the phase difference of  $\pi/2$  between  $u$  and  $v$ . However, the existence of bottom wave boundary layer is expected, this term should be examined.

The last term stems from the existence of the inclination of surface on an actual uniform flow. As was mentioned previously, waves must do work against the gravity in order to maintain the mass transport over the inclined surface.

**WAVE HEIGHT CHANGE** Putting each terms of the righthand of the equation (8) as follows

$$\int_0^h u \frac{\partial \tau}{\partial y} dy = -2\alpha_1 F \tag{11}$$

$$\int_0^h (-\rho \bar{u} \bar{v}) \frac{dU}{dy} dy = -2\alpha_2 F \tag{12}$$

$$\rho g I \int_0^{h+\eta} u dy = -2\alpha_3 F \tag{13}$$

For monochromatic waves,  $\partial/\partial t = 0$  and equation (8) reduces to

$$\frac{d}{dx} F = -2(\alpha_1 + \alpha_2 + \alpha_3) F$$

Integrating this with respect to  $x$

$$\frac{F}{F_0} = \exp\{-2(\alpha_1 + \alpha_2 + \alpha_3)x\}$$

where the subscript  $_0$  denotes the quantities at  $x = 0$ , and the wave energy flux  $F$  is expressed using wave height  $H$  and wave energy transfer velocity  $C_g$ <sup>1</sup> as

$$F = EC_g = \frac{1}{8}\rho g H^2 C_g \quad (14)$$

For the uniform current under consideration,  $C_g = C_{g0}$ . Therefore, the change in height of the waves on a uniform current is given by

$$\frac{H}{H_0} = \exp\{-(\alpha_1 + \alpha_2 + \alpha_3)x\} = \exp(-\alpha x) \quad (15)$$

In order to obtain the attenuation coefficients  $\alpha$ , expressions relevant to the quantities on waves and currents must be given. In the following analysis, expressions in IS were used. They were derived on the assumption that the mean velocity profile was logarithmic for smooth bed and the prevailing part of eddy viscosity was due to the current and the contribution of waves to the eddy viscosity was small.

Examples of calculated results of the wave height attenuation rates are shown in figure 3. These results show that  $\alpha_1$ , defined by equation (11) and discussed in IS is positive and makes the base of the wave attenuation;  $\alpha_2$ , which is the part due to the Reynold's stress like stress induced by the wave orbital velocity components  $u$  and  $v$ , is small for a following current compared to the others, but this enhances the wave attenuation for a strong opposing current;  $\alpha_3$ , which is related to the slope of the mean water surface, is negative for a following current and positive for an opposing current and the absolute value increase with the current velocity.

Hence, the wave attenuation rate  $\alpha$  decreases with the velocity of the following current, and this seems to give a possible physical explanation for the experimental results of Simons et al. (1988).

When the velocity of a following current is small,  $\alpha_3$  is smaller than  $\alpha_1$  and the resultant  $\alpha$  gives wave attenuation. For a certain velocity of the following current,  $\alpha_1$  and  $\alpha_3$  cancel out and waves are expected to propagate without changing the height. And when the velocity exceeds the critical one,  $\alpha_3$  overcomes  $\alpha_1$ . In such situation as this, the resultant attenuation rate  $\alpha$  becomes negative and gives waves the growth in height.

On the other hand,  $\alpha_1, \alpha_2$  and  $\alpha_3$  all enhance the attenuation of wave height on opposing currents.

<sup>1</sup>To be exact,  $E$  is not necessarily equal to  $(1/8)\rho g H^2$  and wave energy transport velocity also does not necessarily coincide with group velocity defined by  $d\sigma/dk$  ( $k$ : wave number,  $\sigma$ : radian frequency) except the case in which the vertical velocity distribution is uniform. But the differences for the logarithmic flow are small.

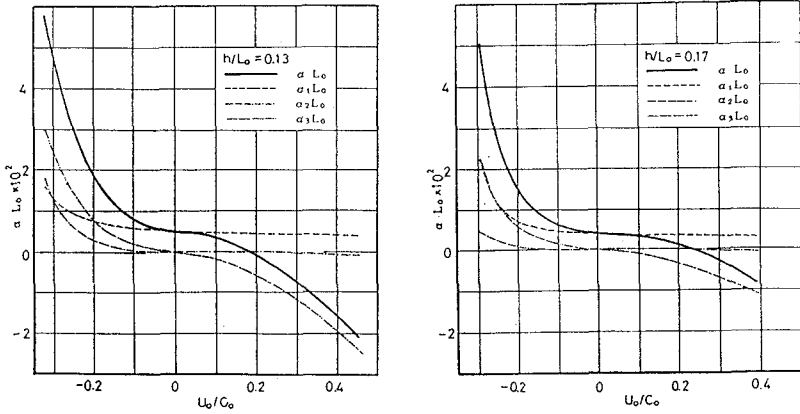


Figure 3: Calculated results of wave attenuation rate

The comparison between the calculated results and some experimental data is shown in figure 4. The agreement of the calculation with the experimental data is improved compared to IS. The experiment were conducted only for opposing currents since the experimental facilities were not available for following currents.

### 3 WAVES ON NON-UNIFORM CURRENTS

Next, the case in which both of water depth and velocity change along the direction of a current is considered (figure 5). In this case we choose space coordinates  $x$  and  $y$  along and perpendicular to a horizontal plane taken near the mean surface, respectively. Then, the basic equations and the boundary conditions are given by

$$\frac{\partial u}{\partial t} + (U + u) \frac{\partial (U + u)}{\partial x} + (V + v) \frac{\partial (U + u)}{\partial y} = -\frac{1}{\rho} \frac{\partial p}{\partial x} + \frac{1}{\rho} \left( \frac{\partial \sigma_x}{\partial x} + \frac{\partial \tau_{yx}}{\partial y} \right) \quad (16)$$

$$\frac{\partial v}{\partial t} + (U + u) \frac{\partial (V + v)}{\partial x} + (V + v) \frac{\partial (V + v)}{\partial y} = -g - \frac{1}{\rho} \frac{\partial p}{\partial y} + \frac{1}{\rho} \left( \frac{\partial \tau_{xy}}{\partial x} + \frac{\partial \sigma_y}{\partial y} \right) \quad (17)$$

$$\frac{\partial (U + u)}{\partial x} + \frac{\partial (V + v)}{\partial y} = 0 \quad (18)$$

$$V + v = \frac{\partial \eta}{\partial t} + (U + u) \frac{\partial \eta}{\partial x} \quad \text{at } y = \eta \quad (19)$$

$$p = 0 \quad \text{at } y = \eta \quad (20)$$

$$V + v = -(U + u) \frac{dh}{dx} \quad \text{at } y = -h \quad (21)$$

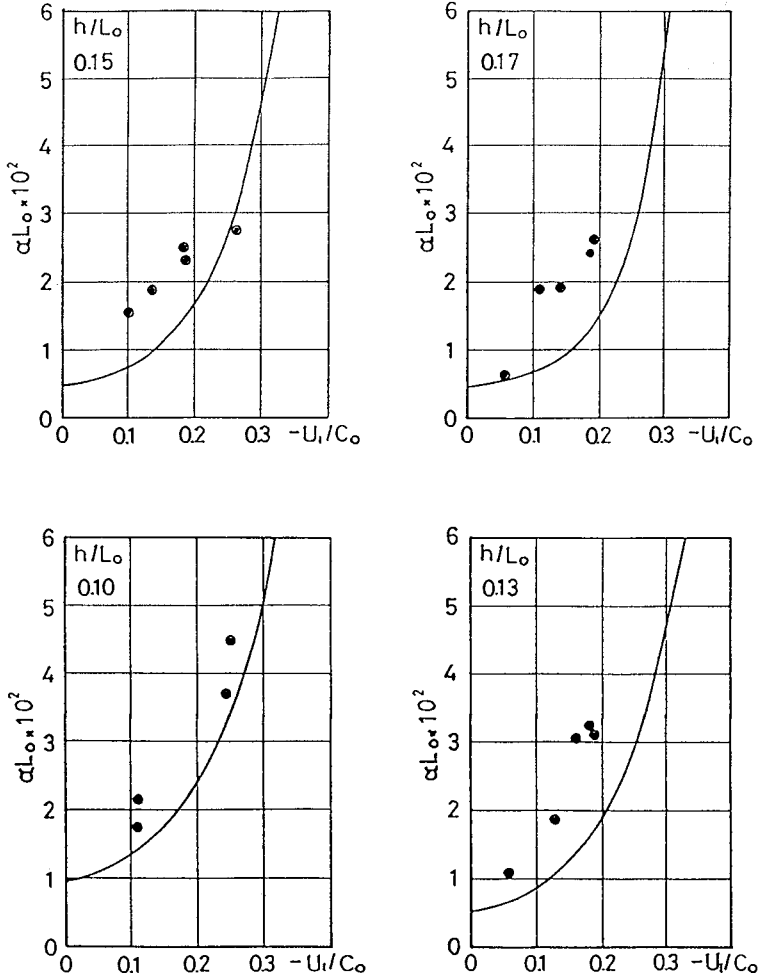


Figure 4: Comparison with experimental results for opposing currents

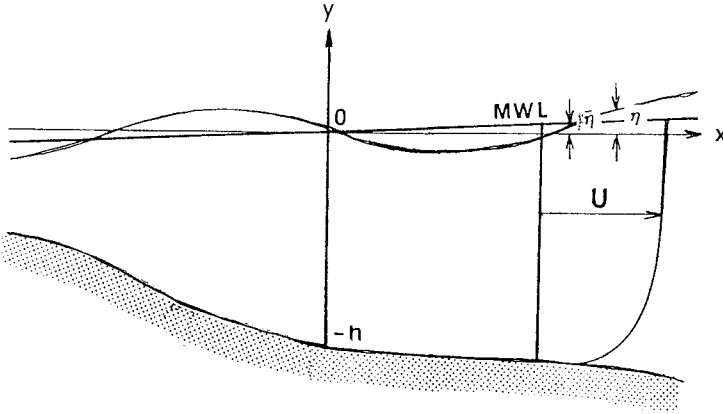


Figure 5: Definition sketch

where  $V$  is the vertical velocity component of the current and  $\sigma_x, \sigma_y, \tau_{xy}, \tau_{yx}$  denote stress component due to turbulence.

**WAVE ENERGY BALANCE** Based on these equations, we obtain an equation for wave energy balance in the same way as the case of uniform currents as

$$\begin{aligned}
 & \frac{\partial}{\partial t} \left[ \overline{\int_{-h}^{\eta} \frac{\rho}{2} (u^2 + v^2) dy} + \frac{1}{2} \overline{\rho g (\eta - \bar{\eta})^2} \right] \\
 & + \frac{\partial}{\partial x} \left[ \overline{\int_{-h}^{\eta} \left\{ \frac{\rho}{2} (u^2 + v^2) + p + \rho g (y - \bar{\eta}) \right\} u dy} \right. \\
 & \quad \left. + \overline{\int_0^{h+\eta} \frac{\rho}{2} (u^2 + v^2) U dy} + \frac{1}{2} \overline{\rho g (\eta - \bar{\eta})^2 U_{h+\eta}} \right] \\
 & = \frac{1}{2} \overline{\rho g (\eta - \bar{\eta})^2 \frac{\partial U_{h+\eta}}{\partial x}} - \overline{\int_{-h}^{\eta} \rho (U + u) u \frac{\partial U}{\partial x} dy} - \overline{\int_{-h}^{\eta} \rho (U + u) v \frac{\partial V}{\partial x} dy} \\
 & - \overline{\int_{-h}^{\eta} \rho (V + v) u \frac{\partial U}{\partial y} dy} - \overline{\int_{-h}^{\eta} \rho (V + v) v \frac{\partial V}{\partial y} dy} + \overline{\rho g (\eta - \bar{\eta}) \left[ V - U \frac{\partial \bar{\eta}}{\partial x} \right]_{\eta}} \\
 & + \overline{\int_{-h}^{\eta} u \left( \frac{\partial \sigma_x}{\partial x} + \frac{\partial \tau_{xy}}{\partial y} \right) dy} + \overline{\int_{-h}^{\eta} v \left( \frac{\partial \tau_{xy}}{\partial x} + \frac{\partial \sigma_y}{\partial y} \right) dy} - \overline{\rho g \frac{\partial \bar{\eta}}{\partial x} \int_{-h}^{\eta} u dy} \quad (22)
 \end{aligned}$$

where  $\bar{\eta}$  denotes mean water level.

In the righthand side of this equation, lots of sources of wave energy appear and rather complicated. For the sake of simplicity, we assume gradually varying flow. Then,  $(\partial U / \partial x)^2$  and  $V^2$  are small, and we may put  $-\rho v^2 = p - \rho g (\bar{\eta} - y)$ . Besides, we assume that  $(\partial \tau_{yx} / \partial y) \gg (\partial \sigma_x / \partial x), (\partial \sigma_y / \partial y), (\partial \tau_{xy} / \partial x)$  and  $(\partial U / \partial y) \gg (\partial V / \partial x)$ .



To the second order approximation, equation (22) reduces to

$$\frac{\partial E}{\partial t} + \frac{\partial F}{\partial x} = - \left[ \int_{-h}^{\eta} (\rho u^2 + p) \frac{\partial U}{\partial x} dy - \int_{-h}^{\bar{\eta}} p_0 \frac{\partial U}{\partial x} dy \right] + \int_0^h u \frac{\partial \tau}{\partial y} dy + \int_0^h (-\rho \bar{u} \bar{v}) \frac{dU}{dy} dy - \rho g \int_0^{h+\eta} u dy \frac{d}{dx} \left( \bar{\eta} + \frac{U^2}{2g} \right) \quad (23)$$

where E and F have been given by equations (9) and (10).

When  $U$  is independent on  $y$ , the part in the bracket of equation (23) becomes as follows

$$[\dots] = \left[ \int_{-h}^{\eta} (\rho u^2 + p) dy - \int_{-h}^{\bar{\eta}} p_0 dy \right] \frac{dU}{dx} = S_x \frac{dU}{dx} \quad (24)$$

where  $S_x$  is the radiation stress introduced by Longuet-Higgins and Stewart (1960). Therefore, the bracket can be considered to correspond to the radiation stress term in the case where current velocity varies not only horizontally but also vertically.

The last term of the righthand side corresponds to the one in equation (7). When we consider the head loss of the mean flow, we should take this term into consideration.

**WAVE HEIGHT CHANGE** Considering monochromatic waves and defining  $\alpha^*$  and  $\alpha$  as

$$-2\alpha^* F = \left[ \int_{-h}^{\eta} (\rho u^2 + p) \frac{\partial U}{\partial x} dy - \int_{-h}^{\bar{\eta}} p_0 \frac{\partial U}{\partial x} dy \right] \quad (25)$$

$$-2\alpha F = \int_0^h u \frac{\partial \tau}{\partial y} dy + \int_0^h (-\rho \bar{u} \bar{v}) \frac{dU}{dy} dy - \rho g \int_0^{h+\eta} u dy \frac{d}{dx} \left( \bar{\eta} + \frac{U^2}{2g} \right) \quad (26)$$

Equation (23) reduces to

$$\frac{d}{dx} F = 2\alpha^* F - 2\alpha F \quad (27)$$

Integrating this from  $x = 0$  to  $x$  with respect to  $x$

$$\frac{F}{F_0} = \frac{C_{g0}}{C_g} \exp \left( 2 \int_0^x \alpha^* dx \right) \exp \left( -2 \int_0^x \alpha dx \right) \quad (28)$$

Thus, wave height change is given by

$$\frac{H}{H_0} = \left( \frac{C_{g0}}{C_g} \right)^{1/2} \exp \left( \int_0^x \alpha^* dx \right) \exp \left( - \int_0^x \alpha dx \right) \quad (29)$$

We could calculate the change of wave height on non-uniform currents using this equation. However, it is rather complicated and laborious job to carry out the calculation.

When wave motion and currents are inviscid and vertical velocity distribution of the current is independent on  $y$ , equation (29) reduces to

$$\frac{H}{H_0} = \left( \frac{C_{g_{u_0}}}{C_{g_u}} \right)^{1/2} \exp \left( \int_0^x \alpha_u^* dx \right) \tag{30}$$

where subscript  $u$  denotes the expressions for waves on vertically uniform currents. So, equation(30) corrected by the factor  $\exp(-\int_0^x \alpha dx)$  was used in the following calculation.

The integrals in equation(30) were approximated using trapezoidal approximation for equally divides intervals of  $\Delta x$ . Then

$$\frac{H_n}{H_0} = \prod_{i=0}^{n-1} \frac{H_{i+1}}{H_i} = \prod_{i=0}^{n-1} \left( \frac{C_{g_{u_i}}}{C_{g_{u_{i+1}}}} \right)^{\frac{1}{2}} \exp \left\{ \frac{1}{2} (\alpha_i^* + \alpha_{i+1}^*) \Delta x \right\} \exp \left\{ \frac{1}{2} (\alpha_i + \alpha_{i+1}) \Delta x \right\} \tag{31}$$

Prior to the calculation of wave height, the depth and the velocity of the current and  $dU/dx$  were calculated at points  $i$  and  $i + 1$  by a conventional calculation method for a non-uniform current. Then, the wave height at each  $i$  was calculated.

Figure 6 is an example of calculated results for opposing currents. In this figure, subscript  $0$  denotes the quantities at  $x = 0$ .

As the bottom slope becomes smaller, the factor  $\exp(-\int_0^x \alpha dx)$  weaken the amplification effects due to the shoaling effect and the energy transfer through  $S_x (dU/dy)$  for the waves traveling over an opposing current. Figure 7 shows the comparison between experimental results and calculated ones. These results show that the dissipative effect of the factor  $\exp(-\int_0^x \alpha dx)$  plays an important role for the wave height change on a gradually varying opposing current.

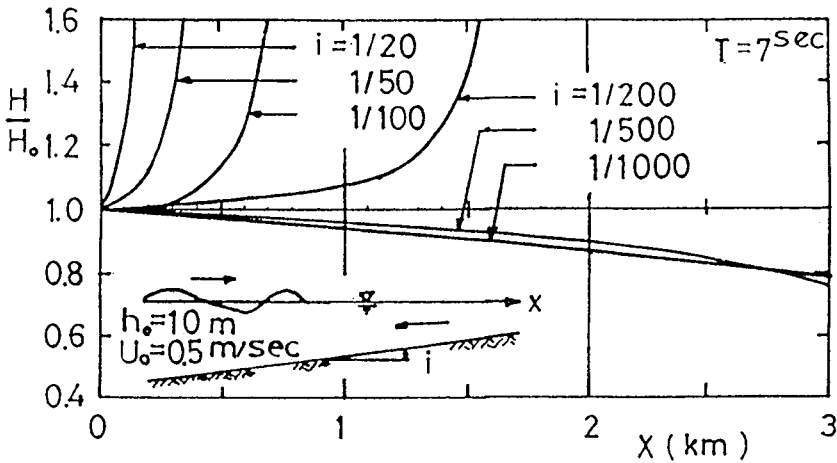


Figure 6: A model calculation results

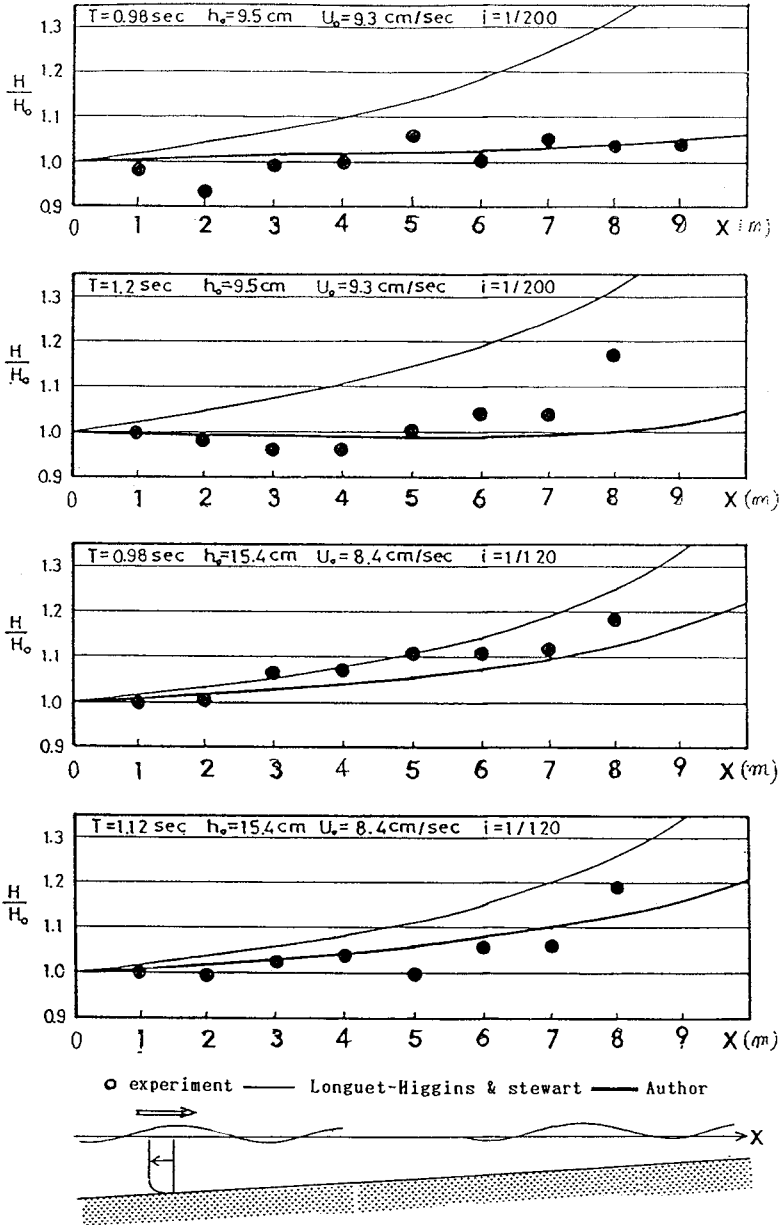


Figure 7: Comparison between measurements and calculated results

## 4 CONCLUSION

Waves propagating on a uniform current attenuate their height due to the effects of 1) viscosity, 2) Reynolds stress like wave stress induced by the orbital velocity in bottom wave boundary layer and 3) the existence of the inclination of the mean surface.

The effect of 1) makes the base of the wave attenuation rate. The effect of 2) is small for a following current, but this enhances the wave attenuation for a strong opposing current. And the effect of 3) gives positive attenuation rate for an opposing current and negative attenuation rate for a following current.

The combined effect of them increases the wave attenuation rate for an opposing current. But it decreases the attenuation rate as the velocity of a following current increases, and this seems to give a possible physical explanation for the experimental results of Simon et al. (1988).

As the wave attenuation rate increases with the velocity of an opposing current, it affects the change in height of waves on a gradually varying opposing current to such an extent that we can not ignore the effect.

## REFERENCE

- Asano T., Nakagawa M. and Y. Iwagaki, 1986 *Changes in Current Properties due to Wave Superimposing*, Proc. 20th ICCE., pp. 925-939
- Iwasaki T. and M. Sato, 1972 *Dissipation of wave energy due to opposing current*, Proc. 13th ICCE., pp. 605-622
- Kemp P.H. and R.R. Simons, 1983 *The interaction of waves and a turbulent current: waves propagating against the current*, J. Fluid Mech., 130, pp. 73-89
- Longuet-Higgins M.S. and R.W. Stewart, 1961 *The changes in amplitude of short gravity waves on steady non-uniform currents*, J. Fluid Mech. 10, pp. 529-549
- Simon R.R., Grass A.J. and A. Kyriacou, 1988 *The influence of currents on wave attenuation*, Proc. 21st ICCE., pp. 363-376

## CHAPTER 43

### A Two-Dimensional Surf Zone Model Based on the Boussinesq Equations

H. A. Schäffer<sup>1</sup>, R. Deigaard<sup>2</sup> and P. Madsen<sup>1</sup>

#### Abstract

A simple approach to wave breaking using the concept of surface rollers is introduced in a two-dimensional Boussinesq model. A surface roller represents a passive bulk of water riding on the front of a breaking wave and the vertical redistribution of momentum associated with the formation and change of surface rollers leads to additional terms in the Boussinesq equations. A simple geometrical method is used for the determination of the shape and location of these rollers at each time step in the simulation. This automatically results in a time-varying break point position in the case of irregular waves. Furthermore, breaking may well cease for example when waves reach a trough inshore of a bar.

Comparison between one-dimensional simulations and experiments shows good agreement for the variation of wave height and mean water surface as well as surface elevation time series throughout the surf zone for both regular and irregular waves. Simulations in two horizontal dimensions are still at the initial stage. A sample simulation is shown.

#### Introduction

The modelling of wave conditions in the surf zone is an important basis for the description of wave-driven currents and sediment transport.

Previously, waves breaking on a beach have been modelled by the non-linear shallow water equations. These predict that the front face of the wave will gradually become steeper until it is vertical. In such a model, the front of a break-

---

<sup>1</sup> Danish Hydraulic Institute, Agern Allé 5, 2970 Hørsholm, Denmark

<sup>2</sup> DTH, ISVA, DK-2800 Lyngby, Denmark

ing wave may then be represented by a jump condition in which mass and momentum are conserved. Thus only the integrated energy dissipation over the wave front is represented.

The details of the turbulent front of a bore were studied by Madsen (1981) and Madsen and Svendsen (1983) and Svendsen and Madsen (1984) using a two-layer model, and it was found that the energy dissipation can be represented in a depth-integrated model by taking the non-uniform velocity distribution into account in the momentum equation.

The main restrictions for the use of the non-linear shallow water equations are that they can only be used for very shallow water, and that they cannot describe a wave of constant form propagating over an even bottom. One consequence of this is that the offshore boundary must be very close to the surf zone and in some cases even within the surf zone. Another consequence is that once a wave has started breaking, it will continue to do so even if it enters deeper water, eg in a trough inshore of a bar. Due to these restrictions, it is of interest to develop a model for the surf zone based on the Boussinesq equations which has a wider range of applicability than the non-linear shallow water equations.

Boussinesq models for the surf zone have been developed by Abbott et al (1983), Karambas and Koutitas (1989, 1992) and Karambas et al (1990) using a depth-integrated one-or-two-equation turbulence model. Deigaard (1989) introduced the concept of surface rollers in Boussinesq modelling and estimated the surface roller geometry using ideas of Engelund (1981). The roller was taken to be a lump of water moving with the speed of wave propagation as in the models of Svendsen (1984, 1984a). The present work is an extension and modification of the model by Deigaard (1989).

## The Flow Description

The flow velocity in the surface roller is very large compared to the orbital motion, as the water in the roller travels with the wave celerity,  $c$ . Thus, the velocity distribution is very uneven in the presence of rollers. The breaking/broken waves are represented by including the effect of the surface rollers in the equations expressing the conservation of mass and momentum. The contribution from the rollers is determined by considering the momentum flux of the velocity profile shown in Figure 1. First, the one-dimensional case is considered. The orbital velocity,  $U_o$ , is taken to be uniformly distributed over the vertical, and the surface roller with a thickness  $\delta$  has the velocity  $c$ . The instantaneous water depth is  $h$ , the still water depth is  $D$ , and the water surface elevation is  $\eta$ .

The instantaneous depth-integrated flux in the  $x$ -direction  $p$  is then

$$p = \int_{-D}^{\eta} u \, dz = U_o (h - \delta) + c \delta = U_o h + (c - U_o) \delta \quad (1)$$

and the depth-integrated momentum flux,  $F_m$ , is

$$\begin{aligned} F_m &= \int_{-D}^{\eta} \rho u^2 dz = \rho U_o^2 (h-\delta) + \rho c^2 \delta \\ &= \rho U_o^2 h + \rho (c^2 - U_o^2) \delta \end{aligned} \quad (2)$$

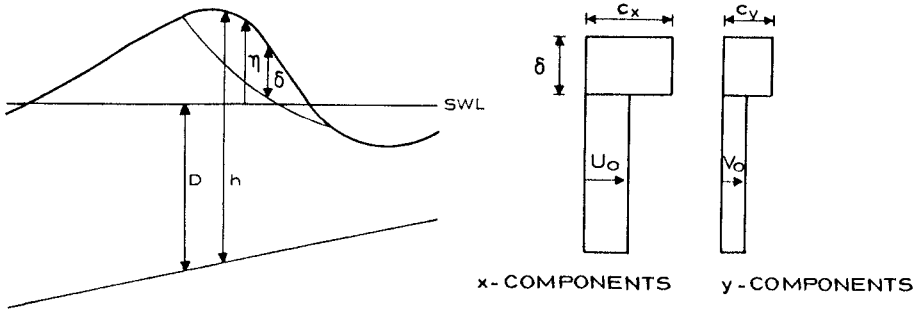


Figure 1. Cross-section and assumed velocity profile components of a breaking wave with a surface roller.

If no roller is present ( $\delta=0$ ), the momentum flux of the uniformly-distributed orbital velocity is given by

$$F_{m0} = \rho \frac{p^2}{h} \quad (3)$$

Retaining this expression for the momentum flux, even when rollers are present, a correction term must be included. This term (divided by  $\rho$ ) takes the form

$$\begin{aligned} R &= \frac{1}{\rho} (F_m - F_{m0}) \\ &= U_o^2 h + (c^2 - U_o^2) \delta - \frac{1}{h} (U_o h + (c - U_o) \delta)^2 \\ &= \delta (c - U_o)^2 \left( 1 - \frac{\delta}{h} \right) \end{aligned} \quad (4)$$

or with  $U_o$  determined from (1):

$$R = \delta \left( \frac{ch-p}{h-\delta} \right)^2 \left( 1 - \frac{\delta}{h} \right) = \delta \frac{\left( c - \frac{p}{h} \right)^2}{1 - \frac{\delta}{h}} \quad (5)$$

This contribution to the momentum flux from the rollers is then - together with  $F_{mo}$  - included in the full Boussinesq equation for conservation of momentum:

$$\frac{\partial p}{\partial t} + \frac{\partial}{\partial x} \left( \frac{p^2}{h} \right) + \frac{\partial R}{\partial x} + gh \frac{\partial \eta}{\partial x} + \frac{D^3}{6} \frac{\partial^3}{\partial x^2 \partial t} \left( \frac{p}{D} \right) - \frac{D^2}{2} \frac{\partial^3 p}{\partial x^2 \partial t} = 0 \quad (6)$$

The continuity equation is not affected by the presence of rollers:

$$\frac{\partial \eta}{\partial t} + \frac{\partial p}{\partial x} = 0 \quad (7)$$

When the flow equations are solved with the surface rollers at the wave fronts, the additional, third term in the momentum equation will cause an energy loss, which represents the energy dissipation in spilling breakers and broken waves.

The extension of this analysis to two dimensions is simple, and the three correction terms  $R_{xx}$ ,  $R_{xy}$  and  $R_{yy}$  are given by the expressions:

$$\frac{1}{\rho} F_{mxx} = \int_{-D}^{\eta} u^2 dz = \frac{p^2}{h} + \delta \frac{\left( c_x - \frac{p}{h} \right)^2}{1 - \frac{\delta}{h}} = \frac{p^2}{h} + R_{xx} \quad (8)$$

$$\frac{1}{\rho} F_{mxy} = \int_{-D}^{\eta} uv dz = \frac{pq}{h} + \delta \frac{\left( c_x - \frac{p}{h} \right) \left( c_y - \frac{q}{h} \right)}{1 - \frac{\delta}{h}} = \frac{pq}{h} + R_{xy} \quad (9)$$

$$\frac{1}{\rho} F_{myy} = \int_{-D}^{\eta} v^2 dz = \frac{q^2}{h} + \delta \frac{\left( c_y - \frac{q}{h} \right)^2}{1 - \frac{\delta}{h}} = \frac{q^2}{h} + R_{yy} \quad (10)$$

where  $c_x$  and  $c_y$  are the x- and y-components of the wave celerity vector, and  $q$  is the depth-integrated flux in the y-direction.  $\partial R_{xx}/\partial x + \partial R_{xy}/\partial y$  is then included in the equation for x-momentum and  $\partial R_{yy}/\partial y + \partial R_{xy}/\partial x$  is included in the equation for y-momentum. The equation for mass conservation is unchanged:

$$\frac{\partial \eta}{\partial t} + \frac{\partial p}{\partial x} + \frac{\partial q}{\partial y} = 0 \quad (11)$$



## Geometrical Determination of Surface Rollers

The consequence of the presence of surface rollers has now been established and it remains to determine their variation in space and time,  $\delta(x,y,t)$ . There is no appropriate theory available for this purpose, and we adapt the heuristic geometrical approach of Deigaard (1989) with some modifications.

As a shoaling wave approaches a shoreline, the local steepness of the front increases, the wave becomes unstable, and breaking initiates. Assuming that the local gradient of the front of a non-breaking wave has a maximum  $\tan\varphi$ , we simply take the wave to be breaking when this gradient is exceeded. Furthermore, we assume that the water above the tangent of slope  $\tan\varphi$ , to the water surface belongs to the roller as shown in Figure 2. This also implies that breaking ceases if the maximum of the local slope becomes less than  $\tan\varphi$ .

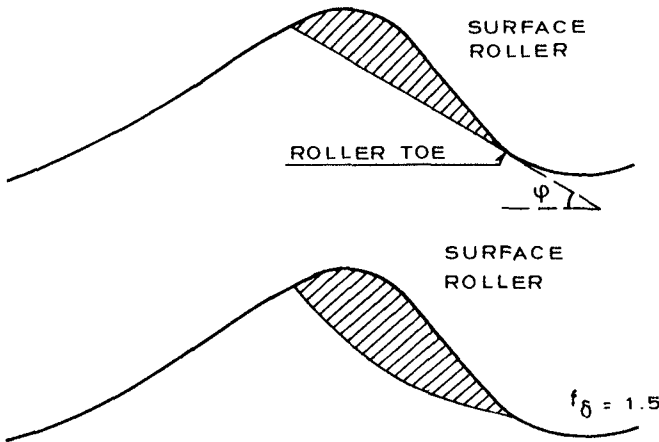


Figure 2. *a: Geometrical detection of surface roller (cross-section A-A in Figure 3), b: The same roller with  $f_{\delta} = 1.5$  applied.*

Engelund (1981) found that  $\varphi = 10^{\circ}$  was appropriate for weak hydraulic jumps, and using the bore/hydraulic jump analogy, we use this value in the inner surf zone. However, waves over a constant depth can be stable for much larger local slopes from which it is clear that  $\varphi = 10^{\circ}$  is inadequate near the break point. For this reason,  $\varphi$  is chosen to vary in time while being constant in space within each surface roller.

Breaking is initiated using  $\varphi = \varphi_B$ , which then gradually changes to the smaller terminal value  $\varphi = \varphi_0$ . Since breakers often transform rather quickly to the bore-like stage, an exponential transition of  $\tan\varphi$  is chosen: where  $t^*$  is the halftime for  $(\tan\varphi - \tan\varphi_0)$ . Thus, the roller is determined by the three parameters,  $\tan\varphi_B$ ,  $\tan\varphi_0$ , and  $t^*$ .

Furthermore, we introduce a roller shape parameter,  $f_{\delta}$ , to partially com-

$$\tan\varphi = \tan\varphi_0 + (\tan\varphi_B - \tan\varphi_0) \exp \left[ - \ln 2 \frac{t-t_B}{t^*} \right] \quad (12)$$

pensate for the primitive way of separating the surface roller from the rest of the flow. After the geometrical determination of the roller at each time step,  $\delta$  is simply multiplied by  $f_b$  before the influence of the roller is computed. Note that this has no direct influence on the roller determination.

In the 2D case, the toe of the roller becomes a curve (segment) instead of a single point, see Figure 3, and the cut-off line is a surface defined by the roller-toe curve and a set of generating lines. These generating lines are determined by the instantaneous local cut-off angle,  $\varphi$ , and the local direction of the maximum slope of the free surface.

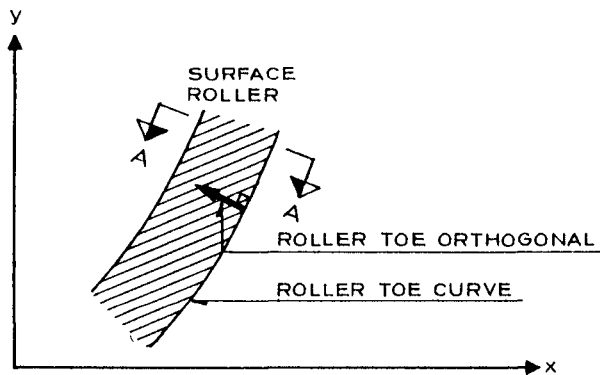


Figure 3. Plane view of a 2D surface roller. The cross vertical section A-A is shown in Figure 2.

The roller shape parameters,  $f_b$ , is maintained without difficulty. As in the 1D case,  $\varphi$  ( $\tan \varphi$  to be exact) is chosen to vary as given by (12). In the 2D case, however,  $\varphi$  is not constant in space within each surface roller (as in the 1D case), but only along a roller-toe orthogonal (see Figure 3), ie a lateral variation of  $\varphi$  within each roller is possible. This is because the age of different sections of the surface roller may vary: from the time of initial breaking, each roller section is traced along the roller-toe orthogonal and this provides a way of determining the age of each roller section. This age is then used for the determination of the local value of  $\varphi$ .

The detection procedure outlined above automatically allows for very different situations within the same surface roller. For example, for oblique incident waves on a beach, the bore-like stage in the inner surf zone is modelled using  $\varphi = \varphi_0$  simultaneously with initial breaking ( $\varphi \approx \varphi_B$ ) occurring in the seaward end of the roller.

## Numerical Results and Comparison with Measurements

In all numerical simulations shown below, three of the four parameters governing the instantaneous determination of the surface roller were kept constant using  $\varphi_0 = 10^\circ$ ,  $t^*/T_{(\varphi)} = 0.1$  where  $T_{(\varphi)}$  is the (peak) period, and  $f_b = 1.5$ . Furthermore,  $\varphi_\beta = 20^\circ$  was used in all tests but one, for which it was necessary to reduce the value to  $\varphi_\beta = 18^\circ$  in order to match the measured break point. At the seaward boundary, the depth-integrated velocity was specified, and at the shoreward boundary, the remaining waves were absorbed by a numerical sponge layer (Larsen and Dancy, 1983). The celerity was modelled by  $1.3\sqrt{gD}$  throughout.

Figure 4a shows the surface elevation at  $t = 24$  s including the rollers for a regular wave of  $T = 4$  s climbing a plane slope of 1:40. This computation was made with a time step of 0.1 s and a grid size of 0.4 m, using 37 CPU seconds on an IBM 4381 P12. The figure gives a first impression of the capability of the model to reproduce the wave decay and the development of asymmetric wave profiles resembling bores. Figure 4b shows the results when no surface-roller term is applied.

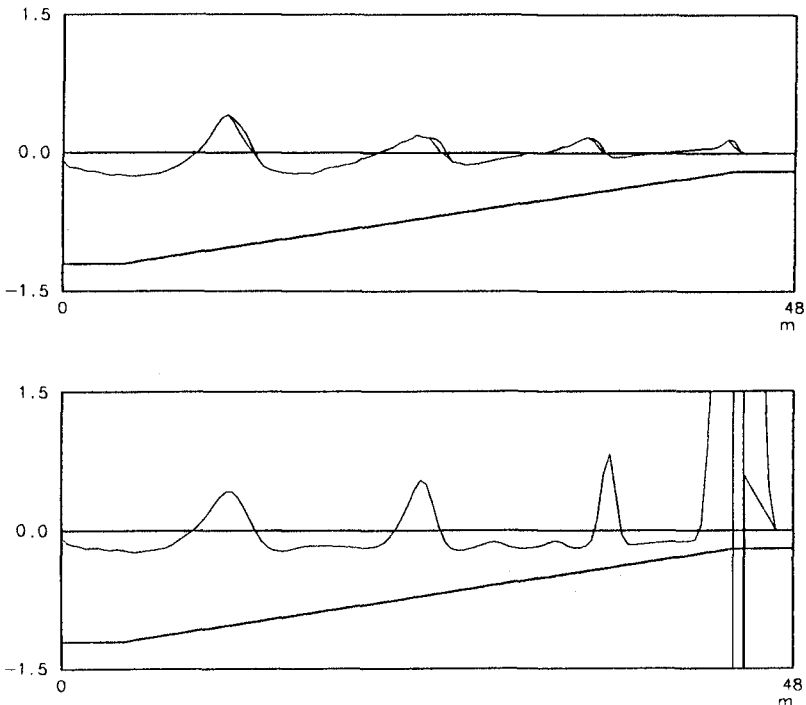


Figure 4. Instantaneous surface elevation of regular waves on a plane sloping beach. a: with surface rollers, b: without surface rollers.

In Figure 5, comparison of wave height,  $H$ , and mean water surface, MWS, with measurements from DHI (Thorkildsen et al, 1991) is shown. The beach profile has a bar with a depth of 0.10 m and the waves are regular with  $T = 1.6$  s and  $H_o = 0.12$  m (wave height at seaward boundary where the depth is 0.54 m).

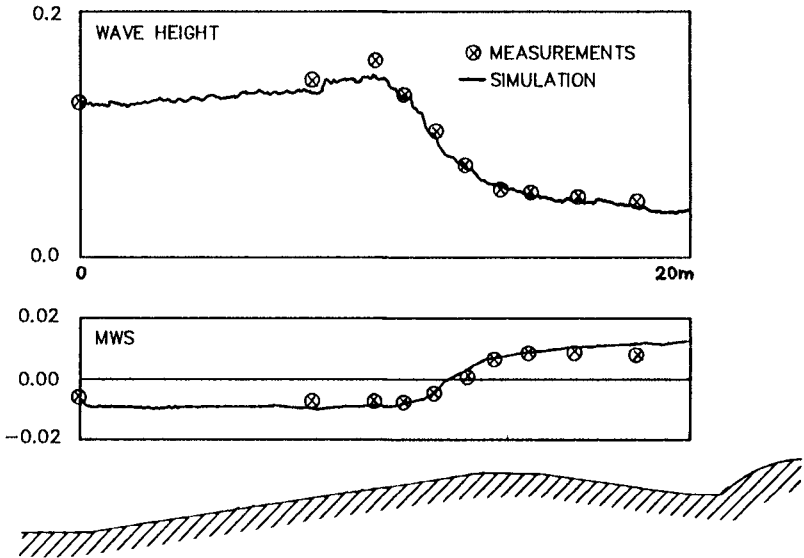


Figure 5. Comparison of wave height and mean water surface with DHI measurements for regular waves breaking over a bar (Thorkildsen et al, 1991).

Both the wave height and MWS compare very well with measurements. An interesting feature is that both measurements and numerical results exhibit the well-known 'delay' of the change of sign for the MWS-gradient relative to the breakpoint. This indicates that the model reproduces the effect of a rapid transformation of potential energy to kinetic energy and the change in the wave profile taking place in the initial breaking process. In Figure 6, surface elevation time series for another profile with a bar are compared with measurements from Hansen and Svendsen (1986). At the two locations shown, the depth was 70% and 42% of the breaker depth, respectively. The latter location is on the top of the bar where breaking has almost ceased, and the wave height is seen to be somewhat overestimated.

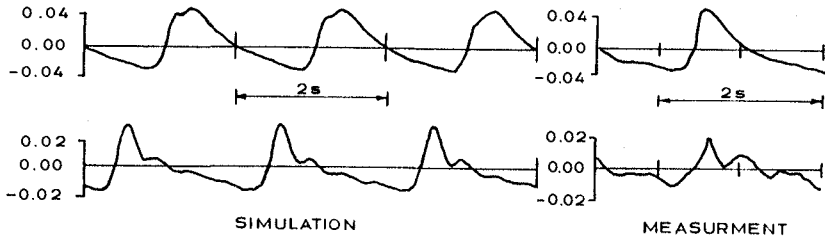


Figure 6. Comparison of surface elevation time series with measurements by Hansen and Svendsen, 1986.

We now turn to irregular waves bearing in mind that this only requires a change in the seaward boundary condition for the simulation and that no additional assumptions are needed regarding eg the variation of the break point position. Figures 7, 8 and 9 show results for incoming waves given by a JONSWAP spectrum with random phase assignment and a peak enhancement factor of 3.3. The incoming significant wave height is 0.14 m and the peak period is 1.8 s. The profile is the same as for the results shown in Figure 5 (Thorkildsen et al, 1991).

Figure 7 shows an instantaneous surface elevation and Figure 8 gives spatial variation of the RMS of the surface elevation as well as the MWS. Both quantities compare well with measurements, except for a general vertical shift between calculated and measured MWS-values. This, however, is explained by loss of water in the numerical sponge layer due to setup, and the problem is expected to disappear when a run-up condition is incorporated. Figure 9 shows time series of surface elevation at gauges nos 5 and 9 (indicated in Figure 8). The agreement is surprisingly good considering that the physical and numerical shoreline absorption are bound to be a little bit different.

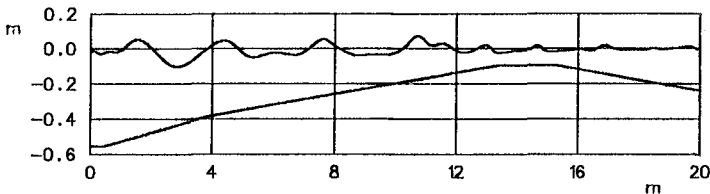


Figure 7. Instantaneous surface elevation of irregular waves breaking over a bar.

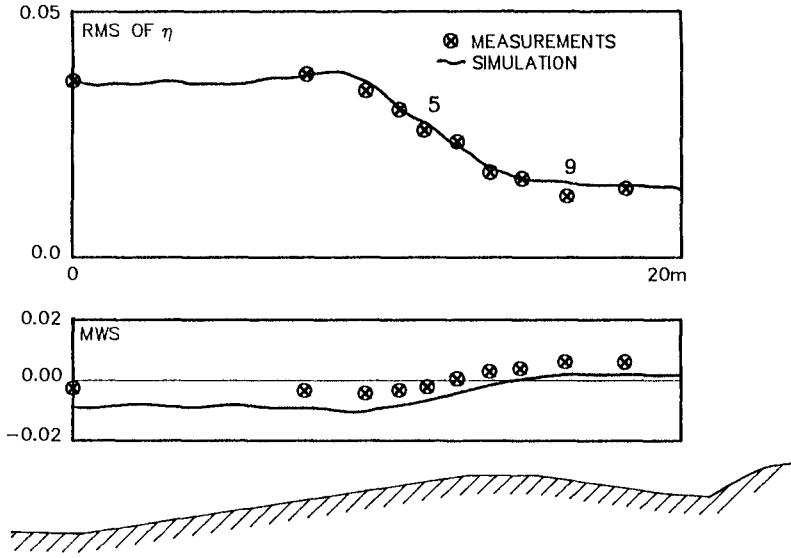


Figure 8. Comparison of RMS of surface elevation and mean water surface for irregular waves breaking over a bar with DHI measurements (Thorkildsen et al, 1991).

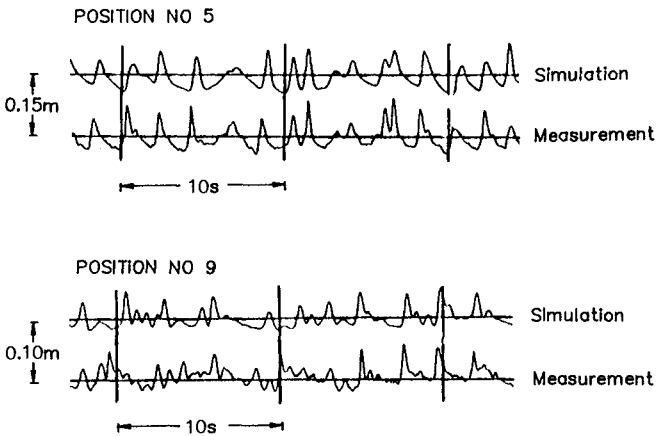
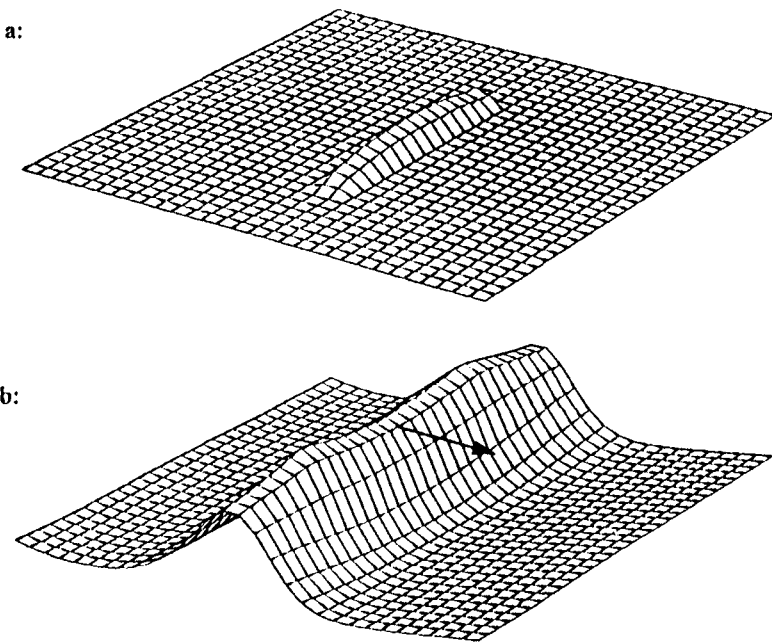


Figure 9. Comparison of time series of surface elevation for positions nos 5 and 9 in Figure 8.

Figure 10 shows a close-up of the instantaneous surface roller thickness and surface elevation for a two-dimensional simulation of a regular wave ( $H_o = 0.15$  m,  $T = 2$  s) breaking over a focusing shoal. The topography, known as the Whalin shoal, is given in Figure 11 where the close-up area is indicated by the square. The effects of breaking (Figure 10) have resulted in a decay of wave height in the central part of the wave. Without breaking, this part of the wave would have been the highest.



*Figure 10. Two-dimensional simulation of a wave breaking over a focusing shoal. a: surface roller, b: surface elevation.*

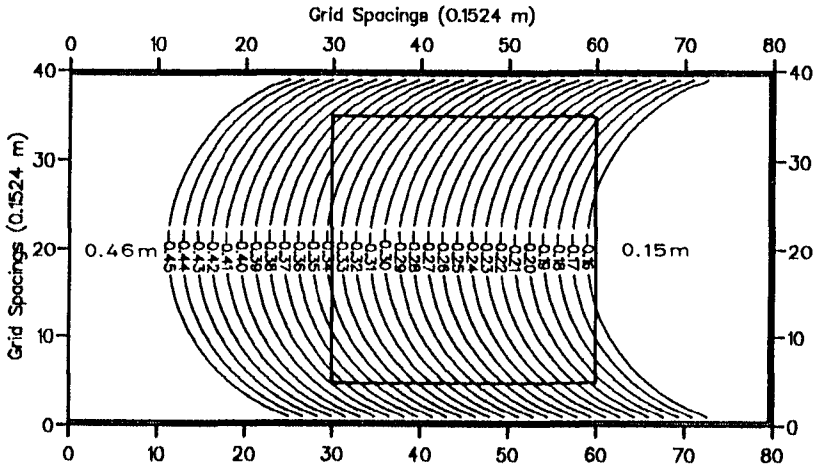


Figure 11. *Focusing shoal (Whalin topography).*

## Conclusion

Effects of wave breaking have been successfully incorporated in a Boussinesq model using the concept of surface rollers. Comparison with experiments shows that the model is capable of reproducing the variation of wave height and mean water surface for regular as well as irregular waves breaking in shallow water. Even details of surface elevation time series in the inner surf zone are reproduced quite well. The model has the potential to simulate irregular short-crested waves over a varying topography under surf conditions including phenomena like nearshore calculation and infragravity waves.

## Acknowledgements

This work was undertaken as part of the MAST G-6 Morphodynamics Research Programme. It was funded jointly by the Danish Technical Research Council (STVF) and by the Commission of the European Communities, Directorate General for Science, Research and Development under MAST Contract No 00-35.



## References

- Abbott, M.B., J. Larsen, P. Madsen, and J. Tao (1983), '*Simulation of wave breaking and run-up*'. Seminar on hydrodynamics of waves in coastal areas, Moscow, September 1983. Arranged by International association for hydraulic research in connection with the 20th congress of IAHR, Moscow, September 1983.
- Deigaard, R. (1989), '*Mathematical modelling of waves in the surf zone*'. Progress Report 69, pp 47-59. ISVA, Technical University, Lyngby, Denmark.
- Engelund, F. (1981), '*A simple theory of weak hydraulic jumps*', Progress Report 54, pp 29-32. ISVA, Technical University, Lyngby, Denmark.
- Hansen, J.B. and I.A. Svendsen (1986), '*Experimental investigation of the wave and current motion over a longshore bar*'. Proceedings 20th Int. Conf. Coastal Engineering, Taiwan, Vol 2, pp 1166-1179.
- Karambas, Th., Y. Krestenitis, and C. Koutitas (1990), '*A numerical solution of Boussinesq equations in the inshore zone*'. Hydrosoft, Vol 3, No 1, pp 34-37.
- Karambas, Th. and C. Koutitas (1990), '*Mathematical modelling of short waves in surf zone*'. In Water Wave Kinematics. A. Tørum and O.T. Gudmestad (eds), Kluwer Academic Publishers, pp 351-365.
- Karambas, Th. and C. Koutitas (1992), '*A breaking wave propagation model based on the Boussinesq equations*'. Coastal Engineering, Vol 18, pp 7-20.
- Larsen, J. and H. Dancy (1983), '*Open boundaries in short wave simulations - a new approach*'. Coastal Engineering, Vol 7, No 3, pp 285-297.
- Madsen, P.A. (1981), '*A model for a turbulent bore*'. Ph.D. thesis, Series paper 28, ISVA, Technical University, Lyngby, Denmark.
- Madsen, P.A. and I.A. Svendsen (1983), '*Turbulent bores and hydraulic jumps*'. Journal of Fluid Mechanics, Vol 129, pp 1-25.
- Svendsen, I.A. and P.A. Madsen (1984), '*A turbulent bore on a beach*'. Journal of Fluid Mechanics, Vol 148, pp 73-96.
- Svendsen, I.A. (1984), '*Wave heights and setup in a surf zone*'. Coastal Engineering, Vol 8, no 4, pp 303-329.
- Svendsen, I.A. (1984a), '*Mass flux and undertow in a surf zone*'. Coastal Engineering, Vol 8, no 4, pp 347-365.

Thorkildsen, M., N. Rosing, and H.A. Schäffer (1991), '*Experimental investigation of waves breaking over a bar*'. Extended abstract. Proc. of Mid-Term Workshop of the MAST G6-M Project, Edinburgh, September 1991.

## CHAPTER 44

### FIELD VERIFICATION OF NUMERICAL MODELS FOR CALCULATION OF NEARSHORE WAVE FIELD

Takuzo Shimizu <sup>1</sup>, Akiyuki Ukai <sup>1</sup> and Masahiko Isobe <sup>2</sup>

#### ABSTRACT

Field applicabilities of both the parabolic equation model and the energy flux equation model are verified through comparisons with field data. The results show that the parabolic equation model has fairly good accuracy for estimating the wave height distribution of the actual wave field over a complex bottom topography, but the transformation of directional wave spectra cannot be reproduced satisfactorily in the surf zone. It is also found that the energy flux equation model is applicable for practical use although its basic equation has a shortcoming of not taking into account the diffraction in a strict sense.

#### INTRODUCTION

In recent years, a numerical predictive model of three-dimensional beach topography change has been developed and applied to many practical problems in Japan. A few attempts have been made to demonstrate the practical applicability of the model through comparisons of the numerical predictions with the actual topographical changes around a harbor (e.g. Shimizu et al. 1990). In order to properly predict the beach evolution due to construction of a coastal structure, it is first of all important to evaluate the wave field with good accuracy. In a numerical model for estimating the wave field in the nearshore region, wave transformation such as shoaling, refraction, diffraction and wave breaking should be taken into account. Moreover, treatment of random waves is important for the field application. In this study, two calculation models are examined; namely,

---

<sup>1</sup>Penta-Ocean Construction Co. Ltd. , 2-2-8 Koraku, Bunkyo-ku, Tokyo 112, Japan.

<sup>2</sup>Professor, Dept. of Civil Eng., Univ. of Tokyo, 7-3-1 Hongo, Bunkyo-ku, Tokyo 113, Japan.

the wave energy flux equation model as described with the directional wave spectrum proposed by Karlsson(1969) and the parabolic-type equation model derived from the mild slope equation by using the wave ray-front coordinates proposed by Isobe(1987). We try to verify the field applicability of these two models quantitatively, through comparisons with the field measurement data. We shall also investigate the effects of the calculation results of the wave field on those of the wave-induced nearshore current field.

## FIELD INVESTIGATION

The field verification of the models has not been thoroughly discussed owing to difficulties of obtaining field data on nearshore waves and currents under severe wave conditions. The field observation was, therefore, carried out around the Tomioka Fishery Harbor, facing directly the Pacific Ocean, Fukushima Prefecture, Japan. The Tomioka Fishery Harbor is under construction and has been troubled with harbor shoaling since the construction started in 1986.

Fig. 1 shows the bottom topography of the investigation site and the locations of observation points. The calculation area is the same as shown in this figure and is about 2.5 km long in the alongshore direction and about 1.5 km long in the cross-shore direction. The calculated wave rays by Snell's law are also shown in this figure. The wave rays are calculated for the mean wave condition of storm waves which attacked during the observation. The significant wave period is 8.6 seconds and the direction of the crestline is 6 degree oblique to the shoreline. The bottom contours are complex and there exist some rocky shoals. In the southeast of the harbor entrance, the bottom contours extend offshoreward like a tongue and the wave rays converge and intersect with each other around this shoal.

At six points in the nearshore region with the water depth of about 5 m, waves and nearshore currents were measured by using a combination of an ultrasonic wave gauge and an electro-magnetic current meter with a pressure sensor. The incident wave conditions were also measured at Point 0 with the water depth of 12 m. Synchronized measurements of the water surface elevation and the two components of horizontal water particle velocities were conducted. The measuring instruments have the self-recording system and had been placed on the seabed during the observation. 10-minutes measurements with the sampling time of 0.5 seconds were recorded on the magnetic cassette tape every 2 hours for approximately one month.

The data obtained by an ultrasonic wave gauge during the storm waves beyond approximately 2 m are not normal because of intrusion of air bubbles due to wave breaking. The pressure fluctuations obtained by a pressure sensor are, therefore, converted into the water surface motion on the basis of the small amplitude wave theory. First, the pressure fluctuation profile is decomposed into a finite number of Fourier series components with the aid of the Fast Fourier Transform algorithm. The Fourier coefficients of the pressure fluctuations are converted into those of the water surface fluctuations on the basis of the linear wave theory. The wave profile is, then, reconstructed with these converted Fourier coefficients

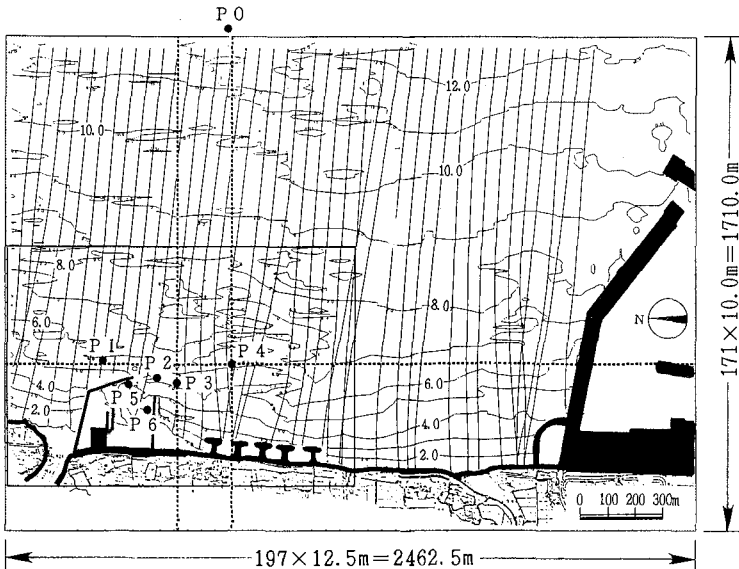


Fig. 1. Bottom topography of investigation site.

of water surface motion in the frequency range from 0.03 to 0.3 Hz. Moreover, the wave profiles estimated by using the pressure data are compared with those observed directly by the ultrasonic wave gauge during the relatively calm period when the simultaneous records of both data were obtained successfully.

The field observation was carried out over a period of approximately one month from September to November in 1990. During the observation, fortunately, storm waves greater than 3 m in significant wave height attacked twice. Our interests are focussed on the data obtained at Point 4 where the increase in wave height is a result of refraction and diffraction effects due to bottom topography, and at Point 5 where diffraction behind the breakwater occurs.

### CALCULATION METHOD

#### Energy Flux Equation Model (EFEM)

The wave energy flux equation model as described with the directional wave spectrum proposed by Karlsson(1969) has been widely used for refraction of random waves. In this study, the model with an additional term of energy dissipation is employed.

$$\frac{\partial}{\partial x}(Dv_x) + \frac{\partial}{\partial y}(Dv_y) + \frac{\partial}{\partial \theta}(Dv_\theta) = -f_D D \tag{1}$$

$$v_x = c_g \cos \theta, \quad v_y = c_g \sin \theta, \quad v_\theta = \left(\frac{c}{c_g}\right) \left(\frac{\partial c}{\partial x} \sin \theta - \frac{\partial c}{\partial y} \cos \theta\right) \tag{2}$$

where  $D(f, \theta)$  is the directional wave spectrum,  $c_g$  the group velocity,  $c$  the wave celerity and  $f_D$  the energy dissipation coefficient.

In this model, random waves are treated directly as the directional wave spectrum. Therefore, this model has an advantage of the computational time being relatively short in a wide region such as the actual field. On the other hand, this equation has a shortcoming of not taking the diffraction into account in a strict sense. But, this model gives an approximate estimation of diffracted wave height for practical applications, because diffraction of random waves can be explained mainly by the directional spreading.

### Parabolic Equation Model (PEM)

Many numerical models for calculation of the wave field under combined refraction and diffraction above a complex bottom topography have been developed on the basis of the mild slope equation. Approximate parabolic-type equations are often adopted because much computational time can be saved owing to the forward stepping scheme.

Isobe(1987) developed a parabolic equation model for the random waves transformation due to refraction, diffraction and wave breaking. Irregular waves are described as a superposition of component regular waves with different frequencies and directions. In order to improve the accuracy of calculating the wave transformation for a wide range of propagation directions of component waves, a curvilinear coordinate system is introduced and the parabolic equation is derived by taking into account the difference between directions of wave propagation and a pre-chosen coordinate. This coordinate consists of wave rays and fronts for modified bottom topography in which wave rays do not intersect with each other. In this model, the curvilinear coordinates are defined from the peak wave frequency and peak direction of the directional spectrum. In a shadow region, additional wave rays are radiated from the tip of the breakwater.

The following parabolic-type approximate equation was derived in the curvilinear coordinate system.

$$\frac{1}{Gh_\xi} \frac{1}{h_\eta} \frac{\partial}{\partial \eta} \left( G \frac{h_\xi}{h_\eta} \frac{\partial \phi}{\partial \eta} \right) + 2ik_\xi \frac{1}{h_\xi} \frac{\partial \phi}{\partial \xi} + \left\{ \frac{i}{Gh_\eta} \frac{1}{h_\xi} \frac{\partial(k_\xi Gh_\eta)}{\partial \xi} + (k^2 + k_\xi^2) + i \frac{\omega}{G} f_D \right\} \phi = 0 \quad (3)$$

where  $\phi$  is the complex amplitude of water surface fluctuation,  $G = cc_g$ ,  $\omega$  the angular frequency,  $k$  the wave number,  $k_\xi$  the  $\xi$ -direction component of the wave number vector, and  $h_\xi$  and  $h_\eta$  the  $\xi$ - and  $\eta$ -direction scale factors of the curvilinear coordinates, respectively.

### Energy Dissipation Model

As for the energy dissipation term due to wave breaking, the model proposed by Isobe(1987) is employed in both models. This energy dissipation model is divided into two phases. The first phase is the determination of breaking point

and the second is the evaluation of energy dissipation coefficient. The breaker index of an individual wave is expressed by the ratio of water particle velocity to wave celerity as follows.

$$\begin{aligned} \gamma'_b &\equiv (\dot{u}/c)_b \\ &= 0.53 - 0.3 \exp \left\{ -3\sqrt{d_b/L_0} \right\} + 5 \tan^{3/2} \beta \exp \left\{ -45 \left( \sqrt{d_b/L_0} - 0.1 \right)^2 \right\} \end{aligned} \quad (4)$$

where  $\gamma'_b$  is the criterion for regular waves,  $u$  the amplitude of horizontal water particle velocity at still water level,  $d$  the water depth,  $L_0$  the deepwater wavelength,  $\tan \beta$  the bottom slope, and the subscript  $b$  denotes quantities at the breaking point.

The ratio at the breaking point for individual waves of an irregular wave train was temporally taken as 0.8 times that for regular waves in the original paper. In this study, through comparisons with field measurement data, the coefficient is assumed to be 0.7. The breaker index for random waves,  $\gamma_b$ , is indicated as follows.

$$\gamma_b = 0.7\gamma'_b \quad (5)$$

The energy dissipation coefficient of irregular waves is given as the product of the probability of breaking waves and the energy dissipation coefficient of regular waves.

$$f_D = P_B f'_D \quad (6)$$

where  $f_D$  is the energy dissipation coefficient of irregular waves,  $P_B$  the probability of breaking waves, and  $f'_D$  the energy dissipation coefficient of regular waves.

$$f'_D = -\frac{5}{2} \sqrt{\frac{g}{d}} \sqrt{\frac{\gamma - \gamma_r}{\gamma_s - \gamma_r}} f_d(kd) \tan \beta \quad (7)$$

$$f_d(kd) = \sqrt{\frac{\tanh kd}{kd}} \frac{1}{2} (1 + s_2) \left\{ 1 - \frac{5(1 - s_2)(1 + s_2) + 2s_2(s_2 \cosh 2kd - 1)}{5(1 + s_2)^2} \right\} \quad (8)$$

$$s_2 = 2kd / \sinh 2kd \quad (9)$$

$$\gamma_s = 0.4 \times (0.57 + 5.3 \tan \beta) \quad (10)$$

$$\gamma_r = 0.135 \quad (11)$$

where  $\gamma_s$  and  $\gamma_r$  give the maximum values of  $\gamma$  on a uniform slope and in the wave recovery zone respectively. Eq.(7) to (9) are evaluated by using the significant wave as a representative wave.

On the assumption of the Rayleigh distribution, the probability of breaking waves is expressed as follows.

$$P_B = \left\{ 1 + 2.004 \left( \frac{\gamma_b}{\tilde{\gamma}_{1/3}} \right)^2 \right\} \exp \left[ -2.004 \left( \frac{\gamma_b}{\tilde{\gamma}_{1/3}} \right)^2 \right] \quad (12)$$

where  $\tilde{\gamma}_{1/3}$  is the value of  $\gamma$  without breaking dissipation corresponding to the significant wave. Both the energy equation model and the parabolic equation model are based on the small amplitude wave theory. However, the effect of wave nonlinearity cannot be neglected in the shallow water. Here, the nonlinearity effect is treated by multiplying a correction factor to the wave height. For non-breaking waves, the first-order cnoidal wave theory is used (Isobe, 1985) and for breaking waves, the correction factor is taken to be 1.25 on the basis of experimental results.

## COMPARISON OF WAVE HEIGHT AND DIRECTION

The parabolic equation method and the energy flux equation method were applied to reproduction of the observed wave field. In order to compare the calculations with the measurements, the measurement data obtained at Point 0 are classified into three cases in accordance with the wave height level. The wave direction is limited to the predominant direction, E. The numerical calculations are conducted for the mean significant waves of these three classifications, using the Bretschneider-Mitsuyasu frequency spectrum and the Mitsuyasu-type directional spreading function. The directional spreading parameter  $S_{max}$  is set to be 25, because the observed values at Point 0 were about 20 to 30 during the observation. The numbers of frequency and directional intervals with equal spacing are 10 and 15 respectively for calculation by the parabolic equation model, and 10 and 45 for that by the energy equation model.

Fig. 2(a) and (b) show the calculated wave fields for regular waves and for irregular waves by the parabolic equation model. The incident significant wave height is 2.9 m, the significant wave period is 8.5 s and the wave direction is E. As seen in Fig. 2(a) for regular waves, the extraordinary spatial variations in wave height are calculated owing to refraction over the complicated bottom topography. The calculation for random waves, on the other hand, show rather smooth wave height distribution because of presence of various directional and frequency components. Fig. 2(c) is the calculation result by the energy flux equation model. The spatial variation in wave height is even smoother than that of the parabolic equation model. Judging from these results, treatment of random waves is seemed to be inevitable for field application.

Fig. 3 shows the relationship between the incident wave height at Point 0 and that at the representative observation point in the nearshore region. The scattered plots are the measurements and the symbols are the calculations. At Point 3 near the harbor entrance, the significant wave height is almost the same as the incident wave height under relatively calm waves and becomes a little smaller owing to the wave breaking when the incident wave height is beyond 2 m. At Point 4 around the rocky shoal, the wave height increases owing to refraction over the shoal compared with the incident wave height, and the effect of wave breaking appear when the incident wave height becomes greater than 2 m. Although the conventional refraction analysis of regular waves gives the crossing of wave rays, both of the computed results by the parabolic equation model and by the energy flux equation model show good agreements with the measurements. As it was



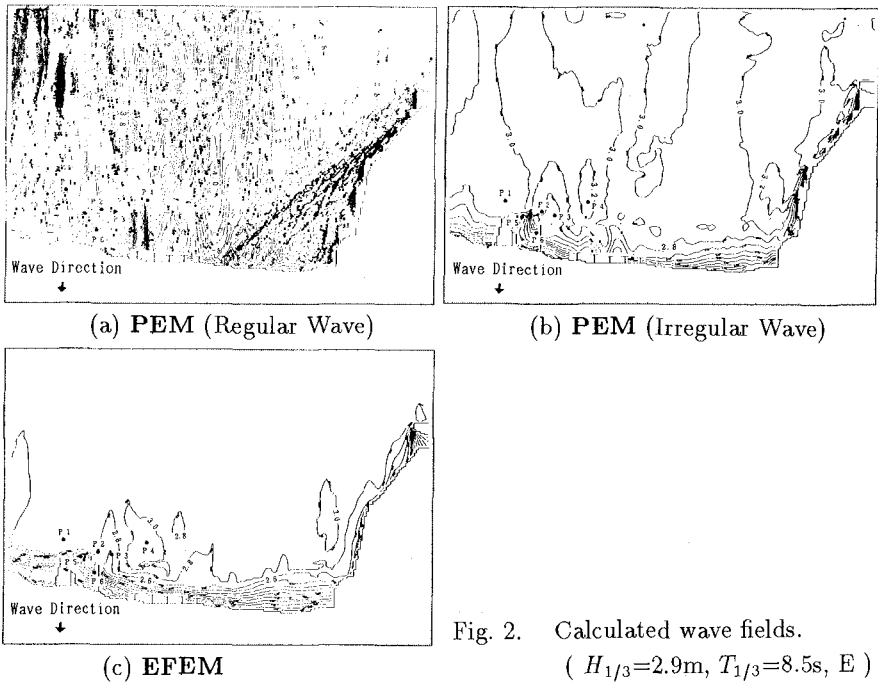


Fig. 2. Calculated wave fields.  
 (  $H_{1/3}=2.9\text{m}$ ,  $T_{1/3}=8.5\text{s}$ , E )

expected at Point 5, in the sheltering area behind the breakwater, the results calculated by the energy flux equation model underestimate the measurements. On the other hand, the calculated results by the parabolic equation model show fairly good agreements with the measurements.

Fig. 4 shows the comparisons between the measured and the calculated significant wave heights including data at Point 1 and 2. The calculations of the parabolic equation model agree with the measurements much better than those of the energy flux equation model.

Fig. 5 shows the comparisons between the measured and the calculated principal directions. The calculations of both the parabolic equation model and the energy flux equation model for irregular waves agree fairly well with the measurements.

## COMPARISON OF DIRECTIONAL WAVE SPECTRUM

### Measured Directional Wave Spectra

The directional wave spectra were estimated by the Maximum Entropy Method (MEP ; Kobune and Hashimoto, 1986). The Maximum Entropy Method has an

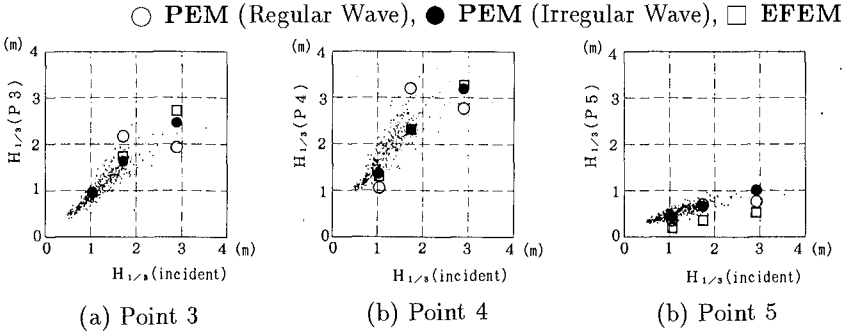


Fig. 3. Relationship between incident wave height at Point 0 and that at representative observation point.

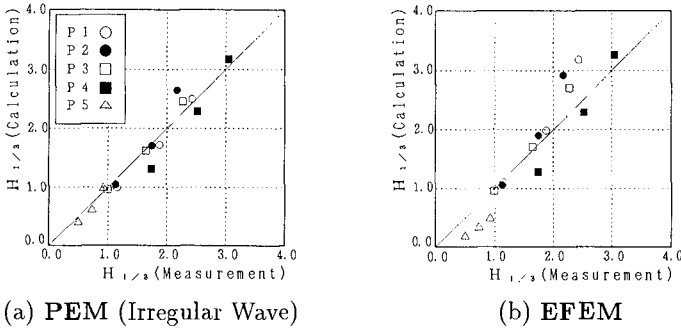


Fig. 4. Comparisons between the measured and the calculated significant wave heights.

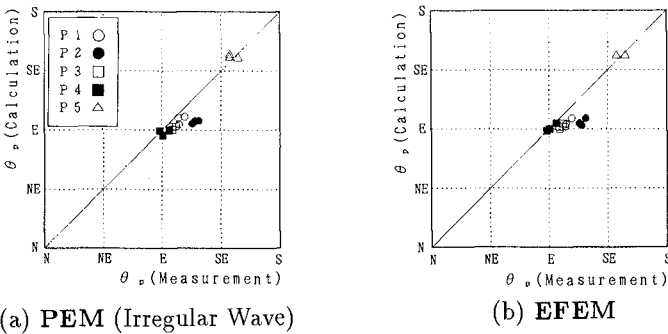


Fig. 5. Comparisons between the measured and the calculated principal directions.

extremely high resolution for a three sensor array. In this study, the pressure fluctuation measured by a pressure sensor and the two components of the horizontal water particle velocities measured by an electromagnetic current meter are used for estimating the directional wave spectrum. The directional spreading parameter  $S$  of the Mitsuyasu-type directional distribution function can be estimated as a function of frequency as follows (e.g. Isobe, 1988).

$$S(f) = \left( \frac{1}{\gamma(f)^2} - \frac{1}{2} \right) + \left( \frac{1}{\gamma(f)^4} - \frac{3}{4} \right)^{1/2} \quad (13)$$

The frequency-dependent longcrestedness parameter,  $S(f)$ , can be evaluated by eq.(14) and (15) and using the estimated directional spectrum.

$$\gamma(f) = \left\{ \frac{M_{20} + M_{02} - \sqrt{(M_{20} - M_{02})^2 + 4M_{11}^2}}{M_{20} + M_{02} + \sqrt{(M_{20} - M_{02})^2 + 4M_{11}^2}} \right\}^{1/2} \quad (14)$$

$$M_{pq}(f) = \int_{\theta_p - \frac{\pi}{2}}^{\theta_p + \frac{\pi}{2}} D(f, \theta) k^{p+q} \cos^p \theta \sin^q \theta d\theta \quad (15)$$

where  $\theta_p$  is the angle at the spectral peak.

Fig. 6(a) shows the observed frequency spectra and frequency-dependent directional spreading parameters under non-breaking wave condition with an incident significant wave height of 0.92 m and its period of 6.95 s, and (b) shows those under breaking wave condition with corresponding values of 3.21 m and 7.6 s. The frequency spectra observed at Point 3 and 4 in the nearshore region, have higher energy densities in both low and high frequency regions than those observed at Point 0. This tendency is remarkable under the severer wave condition as shown in Fig. 6(b). The high frequency fluctuations are due to wave breaking and the long-period motions are due to surf beats. Under the relatively calm condition, as shown in Fig. 6(a), the peakedness of directional wave spectrum increases owing to refraction at Point 3 near the harbor entrance compared with that at Point 0. On the contrary, as can be seen from Fig. 6(b), under the severe wave condition the peakedness does not increase. At Point 4 around the shoal, the peakedness does not increase owing to the intersection of wave rays under both conditions.

Fig. 7 shows the observed relations between the incident significant wave height and two ratios at the two points; one is the ratio of the significant wave height to the incident wave height and the other is the ratio of the directional spreading parameter of the peak frequency to that of the incident waves. Under the non-breaking condition where the significant wave height is below 2 m, at Point 3 near the harbor entrance as indicated schematically by the dash line, the peakedness of the directional distribution function increases owing to refraction compared with that of the incident wave. This can be usually seen in an area where the seabed topography has straight and parallel depth contours. At Point 4 around the shoal as illustrated by the solid line, the directional spreading parameter does not increase and is nearly equal to that of the incident wave, although

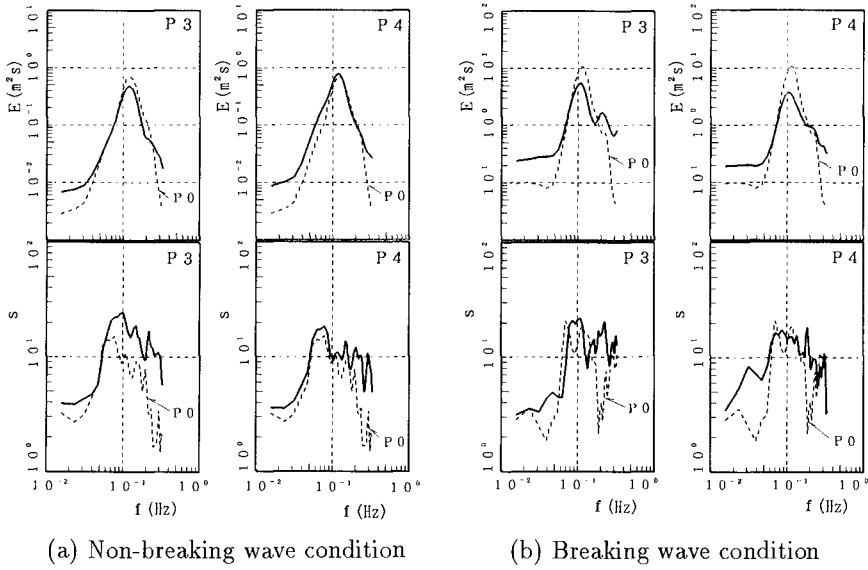


Fig. 6. Observed frequency spectra and frequency-dependent directional spreading parameters.

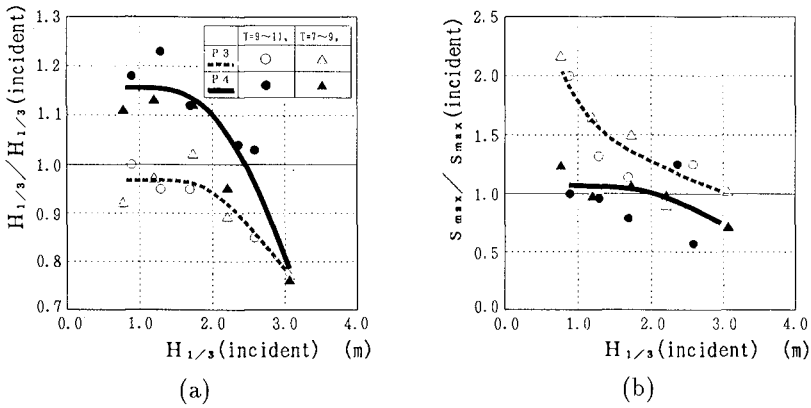


Fig. 7. Observed relations between incident significant wave height and two ratios; (a) the ratio of the significant wave height to the incident wave height and (b) the ratio of the directional spreading parameter of the peak frequency to that of the incident waves.

the wave height increases owing to refraction. In fact, because of the intersection of wave rays, the diffraction effect due to bottom topography occurs. Under the stormy wave conditions where the significant wave height is beyond 2 m, the directional spreading parameter at Point 3 decreases and is approximately equal to that at Point 4 around the shoal. This is supposed to be caused by wave breaking.

### Comparison between Calculations and Measurements

Fig. 8 shows comparisons between the measured and the calculated directional distribution functions which are integrated with respect to frequency. The calculations are conducted for the severest wave condition during the observation. The significant wave height is 3.5 m and the significant wave period 8.5 s. Under this condition, the observation points in the nearshore region were included in the surf zone. At Point 3 near the entrance of the harbor, both the results of the parabolic equation model and the energy flux equation model give larger peakedness than the measurements. At Point 4 behind the shoal, it is reproduced qualitatively that the calculated directional distribution functions have a smaller peakedness than those at Point 3. But the results of the energy flux equation model show better agreement with the measurements than that of the parabolic equation model. At Point 5 behind the breakwater, according to the results by the parabolic equation model, an extremely sharp directional distribution function is calculated of which the spectral peak direction is on a line from the tip of the breakwater to the observation point. The measured peakedness is, on the other hand, considerably dull and is close to the one calculated by the energy equation model. Although in the energy flux equation model diffraction cannot be taken into account, but the directional spreading is considered and there exists also a numerical diffusion especially in calculating the directional convection.

Fig. 9 shows the comparisons between the measured and the calculated frequency-dependent directional spreading parameter of the Mitsuyasu-type directional distribution function. Around the peak frequency of 0.12 Hz, the same tendencies are seen as shown in Fig. 8. It is a cynical result that the measured directional spectrum transformation in the nearshore region is reproduced seemingly better by the energy flux equation model, although the parabolic equation has theoretically good accuracy for calculating combined refraction and diffraction over a complicated bottom topography and behind a breakwater. There are some reasons for disagreement between the calculations by the parabolic equation and the field measurements in the surf zone. The first reason is that the parabolic equation model is based on the linear wave theory, but the actual waves are nonlinear in the surf zone. The second reason is that the energy dissipation model used in this study is a model for estimating the total energy transformation due to wave breaking and that the energy dissipation coefficient is assumed to be constant irrelevantly to the direction. Namely, it is assumed that the directional spectral shape does not change after wave breaking, which seems to be unrealistic. The other reason is that the method for estimating the directional wave spectrum is

$$G(\theta) = \int_0^\infty G'(f, \theta) df, D(f, \theta) = S(f) G'(f, \theta)$$

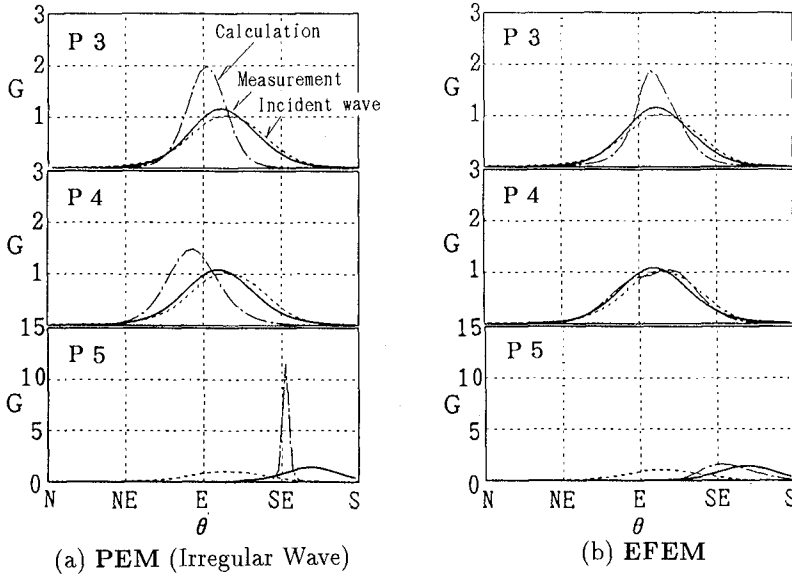


Fig. 8. Comparisons between the measured and the calculated directional distribution functions.

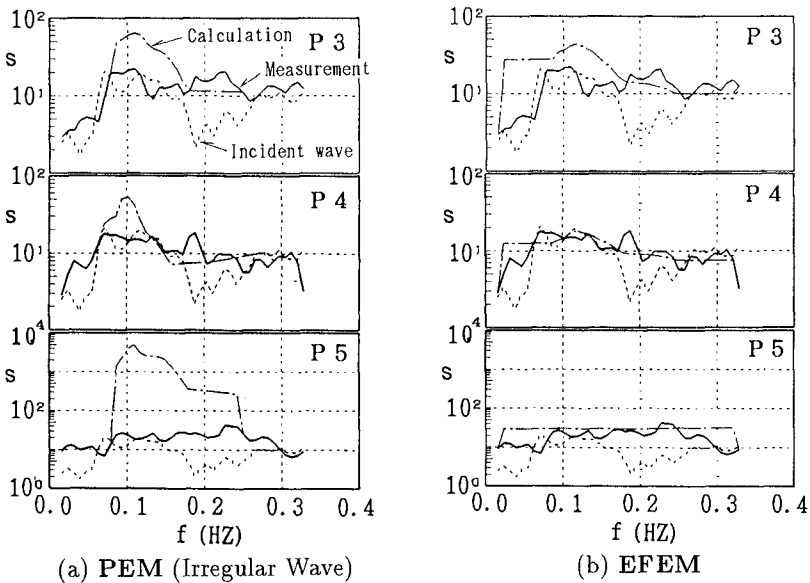


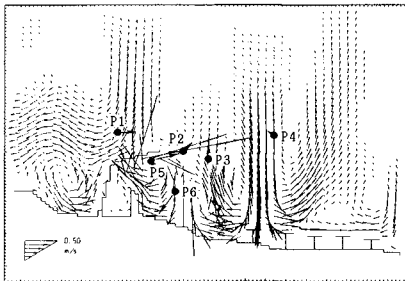
Fig. 9. Comparisons between the measured and the calculated frequency-dependent directional spreading parameters.

also based on the linear wave theory, and therefore, it does not have high resolution for data measured in the surf zone. Thus, there remains rooms for improving the estimation method of the directional spectrum by taking into account non-linearity of the actual sea state in the surf zone.

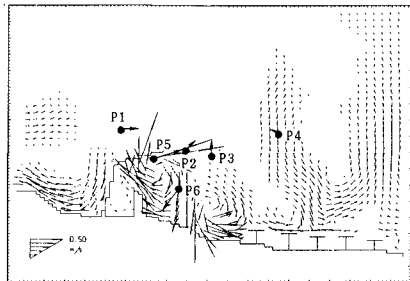
## INFLUENCES ON NEARSHORE CURRENT FIELD

Finally, we attempt to investigate the effects of the calculation results of the wave field on those of the wave-induced nearshore current field. Fig. 10 shows the results of the nearshore current calculations. The measured velocity vectors are also illustrated, but in a different scale from the calculated vectors. Fig. 10(a) and (b) show the results for regular waves and for random waves by the parabolic equation model and (c) shows the results by the energy flux equation model. In computing the nearshore current field of random waves, the radiation stress is evaluated as for a regular wave with the equivalent wave energy and the principal direction which are estimated from the calculated directional wave spectrum. The group velocity and the wave celerity are estimated by using the significant wave period.

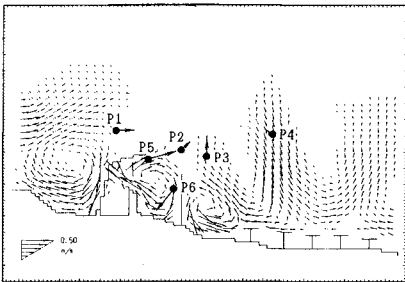
The result for regular waves gives an extremely large spatial variation and a strong shoreward current is calculated around the shoal in accordance with the spatial variation in wave height. On the other hand, the calculations by both



(a) PEM (Regular Wave)



(b) PEM (Irregular Wave)



(c) EFEM

Fig. 10. Calculated current fields.

models for random waves show relatively smooth current fields. The observed dominant current pattern is reproduced satisfactorily. Thus, the current field calculation results are not so sensitive to the difference in the wave field calculation results if random waves are treated in the wave calculation model.

## CONCLUDING REMARKS

The parabolic equation model and the energy flux equation model are applied to the calculation of the actual wave field over a complicated bottom topography and their field applicabilities are investigated through comparisons with the field data. As a result, it is found that both the parabolic equation model and the energy flux equation model are applicable for practical use and that the former has extremely good accuracy for estimating the wave energy transformation over a shoal, where the increase in wave height due to refraction and the diffraction effect due to bottom topography occur, as well as behind a breakwater. The transformation of directional wave spectra due to refraction and diffraction in the surf zone can be reproduced qualitatively by the parabolic equation model, but the observed directional spectra show smaller peakedness of the directional spreading function than the calculated ones. The observed spectra can be estimated better by the energy flux equation model. This is, however, a seeming agreement due to numerical diffusion. In order to properly estimate the transformation of directional wave spectra, it is necessary to accumulate further field data in the surf zone with good accuracy. It is also needed to develop a wave transformation model in which wave nonlinearity can be taken into account.

## REFERENCES

- Isobe, M., 1985: Calculation and application of first-order cnoidal wave theory, *Coastal Eng.*, Vol. 9, pp.309-325.
- Isobe, M., 1987: A parabolic equation model for transformation of irregular waves due to refraction, diffraction and breaking, *Coastal Eng. in Japan*, Vol. 30, No. 1, JSCE, pp.33-47.
- Isobe, M., 1988: Spectral description of irregular waves, *Nearshore Dynamics and Coastal Processes*, K. Horikawa (ed.), Univ. of Tokyo Press, pp.35-44.
- Kobune, K. and N. Hashimoto, 1986: Estimation of directional spectra from the maximum entropy principle, *Proc. 5th Offshore Mechanics and Arctic Eng. Symposium*, Vol. I, ASME, pp.80-85.
- Shimizu, T., H. Nodani and K. Kondo, 1990: Practical application of the three-dimensional beach evolution model, *Proc. 22nd Coastal Eng. Conf.*, ASCE, pp.2481-2494.



## CHAPTER 45

### Bottom Shear Stresses in the Boundary Layers under Waves and Currents crossing at Right Angles

Richard R.Simons<sup>1</sup>  
Tony J.Grass<sup>2</sup>  
Mehrdad Mansour-Tehrani<sup>3</sup>

#### Abstract

This paper describes a two year experimental research programme investigating the influence of non-linear wave-current interactions on wave and current characteristics. The tests focus on the mean and oscillatory velocity components and shear stresses within the bottom boundary layer over a rough bed for cases where waves propagate at right angles to the line of the current flow. Bed shear stresses have been measured directly by means of a novel shear plate device. The aim of the research is to generate a reliable data set for use by modellers.

Results show that currents experience a significant change both in mean bed shear stress and apparent bed roughness when waves are superimposed. However, the oscillatory, wave-induced, bottom shear stress has been shown to be insensitive to the addition of an orthogonal current.

#### Introduction

Recent years have seen the development of many mathematical models for predicting the boundary layer characteristics of combined wave-current flows and hence sediment transport along and across the coastline. However, the proliferation of models has not been matched

---

<sup>1</sup>Senior Lecturer, Civil & Environmental Engineering Dept, UCL

<sup>2</sup>Reader, Civil & Environmental Engineering Dept, UCL.

<sup>3</sup>Research Fellow, Civil & Environmental Engineering Dept,  
University College London, Gower Street, London WC1E 6BT.

by the availability of experimental results against which they can be validated, particularly at large scale and where waves propagate orthogonally or at arbitrary angles to the current.

Published field data which include combined wave-current conditions generally lack sufficient control over the main parameters to provide a reliable basis for model calibration. Laboratory experiments on wave-current interaction have most often considered only the case of colinear waves and current (for example, Bakker and van Doorn (1978); Brevik and Aas (1980); Kemp and Simons (1982), (1983); Simons et al. (1988)). This situation matches that found in estuaries and in some offshore regions, but contrasts with the condition frequently occurring along many coastlines where waves propagate directly on-shore, over a longshore current. Only Bijker (1967), and more recently Visser (1986), Arnskov et al. (1991), and Sleath (1990), have considered this more complex, but extremely important, orthogonal case. Bijker's tests were restricted to measurements of shear stress deduced from observations of water surface slope in an orthogonal wave-current field, and his instrumentation was unable to determine velocity profiles above the bed. Arnskov's tests were restricted to flows over a smooth boundary and are thus hard to extrapolate to real coastal engineering situations where the bed is invariably rough, and frequently rippled. Sleath's tests were performed over a variety of rough boundaries, and he simulated waves crossing a current at right angles by oscillating a section of roughened bed across the line of a unidirectional current flowing along a laboratory flume.

Another shortcoming of earlier data has been that shear stresses have had to be implied, from nearbed velocity profiles, water surface slopes, or wave attenuation, rather than from direct measurement. It is the aim of this paper to fill a gap in existing data by providing direct measurements of bottom stress and velocity field under laboratory conditions for a range of combined waves and currents crossing orthogonally.

### Wave Basin

The experiments were performed in a wave basin approximately 20 m square, designed for a water depth of 1.5 m but with a raised central test area, 9 m by 6 m, over which the still water depth was just 700 mm. This plateau area was installed specially for these tests, and was coated with a fixed layer of sand (nominal diameter of 2 mm) to produce a uniform rough boundary.

Ten ram-type wave generators were mounted along one

wall of the basin, the other three walls supporting permeable beach units 2.5 m long at a slope of  $15^\circ$ . Each ram could be operated under independent control to generate waves with periods between 1 s and 3 s, and with heights up to 300 mm.

Currents were introduced through a set of gate valves under the beaches in one of the side walls, flow being removed through a corresponding set of openings in the other side. The current strength was controlled by adjusting the speed of a pump which circulated water through a 2-compartment channel round the perimeter of the basin. For the tests described here, three current conditions were investigated: zero mean flow (wave alone), 125 mm/s, and 200 mm/s.

### Shear Plate Device

A vital element in the programme was the ability to make direct measurements of shear stress applied to the bed by the wave-current flow above. Very few attempts have been made to design such a device in the past, mainly because of the high sensitivity required to resolve the small forces involved, and the difficulty of reducing the wave-induced pressure gradient effect on the vertical faces of the structural elements. The most important results reported from such a device are those of Reidel & Kamphuis (1973), who measured friction factors for a rough boundary under a wide range of wave conditions in a two-dimensional laboratory flume. Oebius (1982) has also developed an instrument intended for deployment in the field under mobile bed conditions, while Arnskov et al. (1991) have used a hot film technique to measure shear stresses on a smooth bed.

The main criteria to be satisfied by the shear plate device during the present project were that it should be capable of measuring a 2-dimensional horizontal force vector varying rapidly in magnitude and direction, have sufficient sensitivity to resolve the relatively small shear stresses induced by the mean current, have the range to follow large wave-induced oscillatory stresses, have a surface area small enough relative to the length of a wave in the basin that spatial averaging would not significantly reduce the recorded peak oscillatory stress, have a sufficiently high natural frequency relative to the "forcing" wave frequency that inertial phase lag and resonant vibrations would be negligible, remain co-planar with the surrounding bed during test conditions, and tolerate the presence of sediment and debris in the water.

The design adopted consisted of a 0.9 mm thick, circular disc (250 mm diameter), supported on four tubular

columns, mounted flush with the surrounding bed, and deflecting sideways in a sway motion under the action of any lateral force. A clearance of under 0.5 mm was allowed between the circumference of the plate and the adjoining bed, imposing a physical constraint on the maximum possible deflection of the plate, and thus also on the measurable force for any given structural stiffness.

The horizontal displacement of the plate was measured by two eddy current transducers mounted orthogonally under the bed and positioned to monitor the movement of a small target block attached to the centre of the plate. These devices had a sensitivity of just over 0.1 microns, and operated with a working clearance of 1 mm.

Because of the finite length of the waves under test, there was a horizontal pressure gradient across the bed of the basin which exerted a significant force on the edge of the active shear plate. Although the plate was made as thin as possible to minimize the effect, pressure on the edge still contributed a significant proportion to the total force observed. The correction procedure adopted for these tests involved deducing the pressure gradient from direct measurements of orbital velocity (and hence acceleration) just above the oscillatory boundary layer. The edge force was calculated by dividing the plate into 1000 sectors, determining the radial force on each at discrete phases through the wave cycle, resolving this force into the direction of wave propagation, and integrating round the circumference.

To check whether the pressure correction was adequate, and to determine whether the shear plate was capable of measuring shear stresses to sufficient accuracy under oscillatory flow conditions, a set of preliminary tests was carried out in a wave flume. These tests were performed over a smooth bed, using a smooth active plate, for a range of wave periods between 1.0s and 1.35s. The smooth bed provided conditions for which there is a reliable theoretical solution for amplitude and phase of the bottom shear stress - calculated from the orbital velocity just outside the viscous-dominated oscillatory boundary layer.

The measured force was corrected for edge pressure, and the resulting shear stress plotted out with the theoretical shear stress and the orbital velocity through the wave cycle (**fig.1**). Bearing in mind that the edge pressure effect corrected for was generally far greater than the shear stress sought, there was remarkably good agreement between theory and experiment, with errors between 1% and 15%. This was felt to be satisfactory, as the shear stresses induced at the rough boundary in the main test programme were almost an order of magnitude

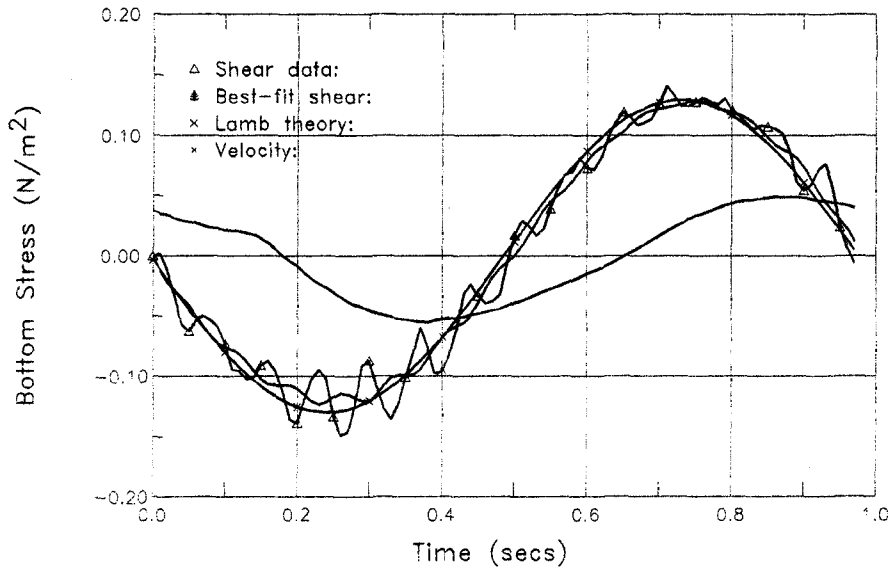


Fig.1 Pressure correction test for waves alone over a smooth bed: measured shear stress plotted with theoretical curve through a wave cycle.

greater than those at the smooth bed.

### Velocity Measurements

To determine the velocity field in the complex three-dimensional flow, measurements were made using an ultrasonic flow meter which yielded three velocity components simultaneously. The transmitters on this instrument "pinged" at 100Hz, giving a response time of 1/30s and a resolution of 1mm/s in a range up to 1 m/s. However, while it was ideal for determining the instantaneous velocity vector in the upper flow, its size (with a measuring volume 15 mm in diameter) meant that it was unable to provide detailed information within the relatively thin wave boundary layer.

Velocities close to the bed were measured with a fibre-optic laser anemometer supported by a vertical traversing device on the overhead gantry. The measuring volume was some distance away from the optical fibre probe, and thus provided a relatively non-intrusive means of determining velocities. Tests using the LDV had to be carried out twice in order to obtain all 3 velocity components. The main set of tests had the optical fibre

head set up pointing vertically downwards at the bed to measure the two horizontal components of velocity. Tests were then repeated with the optics pointing into the current, close to horizontal, so as to measure horizontal and vertical components of wave-induced velocity.

### Other Instrumentation

Wave characteristics were monitored by 16 resistance-type wave probes mounted in a rectangular grid pattern (spacing 0.5m by 0.66m) from an overhead gantry over the test area. Data from all the instruments (water surface, shear plate, anemometers) were recorded synchronously through a 32-channel data logger directly onto computer disc, together with a signal from the wave generators.

### Results

27 different wave/current conditions were tested from combinations of four wave periods [1.1s, 1.5s, 2.0s, 2.5s.], wave heights in the range 80 mm to 190 mm, and 700.

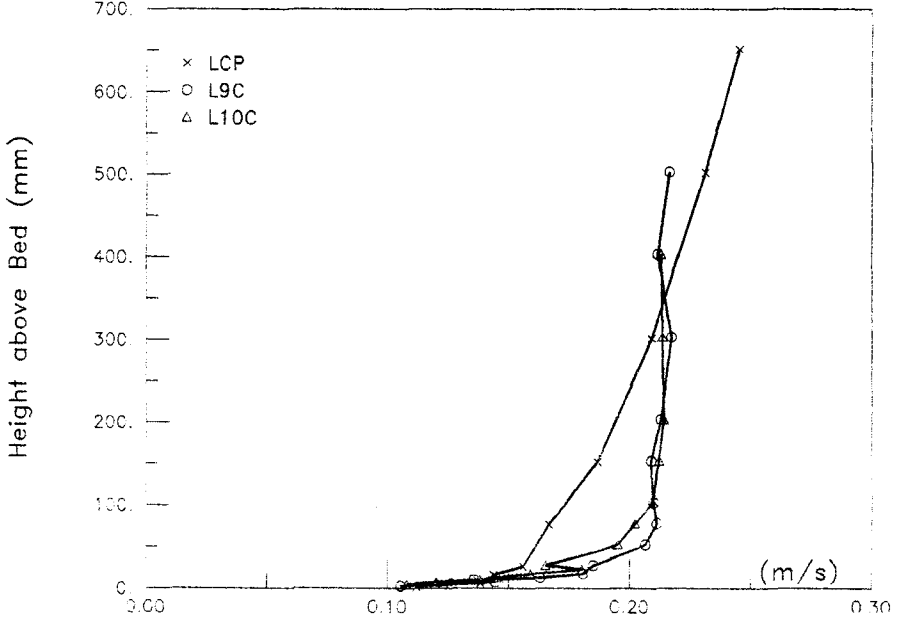


Fig.2 Mean velocity profiles for 2 cases of combined waves and current and for the same current alone.

three currents conditions [zero, 125 mm/s, 200 mm/s] running orthogonally to the waves. **Table 1** lists the general test parameters.

Run:	Wave Period s	Incident Wave Height mm	H at Plate mm	Reflex Coeff %	Current mm/s
W1P	1.49	136	125	11.8	0
W1C	1.49	135	125	25.9	200
L1CC	1.49	140	125	8.9	125
W2P	1.49	168	150	12.0	0
W2C	1.49	185	175	8.1	200
W3P	1.49	98	90	18.4	0
W4P	2.02	135	165	40.0	0
W4C	2.02	138	177	39.9	200
L4CC	2.02	145	176	37.9	125
W5P	2.02	160	190	31.0	0
W5C	2.02	172	209	34.9	200
L5C	2.02	168	202	37.2	200
L5CC	2.02	170	205	37.2	125
W7P	1.11	120	122	12.0	0
W7C	1.11	118	118	25.9	200
W8P	1.11	78	76	11.5	0
W8C	1.11	78	78	10.9	200
W9P	2.48	140	152	26.0	0
L9C	2.48	130	140	24.0	200
L9CC	2.48	140	147	24.0	125
W10P	2.48	183	200	24.6	0
L10C	2.48	184	191	22.0	200
W10CC	2.48	152	162	22.0	125
L10CC	2.48	182	195	22.0	125
W11P	2.48	123	130	25.0	0
W11C	2.48				200
W11CC	2.48	150			125

Table 1: General test parameters: water depth = 700mm.

Mean velocity profiles of the two currents on their own took a form typical of most turbulent boundary layers, following a logarithmic curve through the near-bed region (within 100mm of the bed), with velocities continuing to increase but more gradually above this level up to the water surface. However, when waves were superimposed, running orthogonally to the direction of flow, there was a significant reduction in mean velocity in the upper flow, matched in most cases by an increase in the lower half of the flow (**fig.2**). This effect was most pronounced for the waves with longest periods (1.5s, 2.0s, 2.5s) and greatest heights, whereas the 1.1s period waves showed little change in general profile shape.

When plotted out on log-linear axes, the profiles revealed that the apparent bed roughness  $z_A$  was increased, in some cases by more than a factor of 20 times its value for current alone. The mean bed shear stress was also increased by the addition of wave action (**Table 2**).

Run:	Orbital U <sub>max</sub> mm/s	Shear Vel. u, mm/s	$\tau_{\text{mean}}$ Pa.10 <sup>3</sup>	Apparent roughness z <sub>A</sub> mm	z <sub>A</sub> / z <sub>0</sub>
CCP	0	7.03	49.0	0.05	1.0
L1CC	157	7.82	61.0	0.10	2.0
L4CC	140	7.36	54.0	0.12	2.4
L5CC	164	6.53	43.0	0.08	1.6
L9CC	212	14.40	206.0	1.15	23.0
L10CC	287	12.50	157.0	0.90	18.0
LCP	0	9.81	96.0	0.05	1
L5C	164	11.9	141.0	0.30	6.0
L9C	212	17.7	313.0	0.45	9.0
L10C	303	17.1	291.0	0.55	11.0

Table 2: Wave-current tests: mean flow parameters

As the shear plate was set up during these tests to measure the large oscillatory shear stresses induced by the wave action, relatively small mean stresses caused by the mean current were difficult to determine precisely. Nevertheless, the values obtained from the combined wave-current tests, when substituted into the "Law of the Wall", suggest that the von Karman constant  $\kappa$  lies between 0.30 and 0.50 - a wide range, but probably acceptable in view of the experimental difficulties involved in measuring both



the mean velocities and the shear stress.

Table 1 listed the basic characteristics of the waves used for each test run. All the waves lay in the "intermediate" zone, although the 1.1s period waves were close to "deep water" conditions, and the 2.5s periods approached "shallow water" status. It should be noted that the reflexion coefficients were found to be very high in many of the tests - an inevitable consequence of using waves with a length far greater than that of the absorbing beaches round the perimeter of the basin.

The most interesting tests as far as the main objective of the research was concerned were those inducing significant shear stresses at the bed of the basin. These tended to coincide with tests involving waves with the longer wave periods and lengths, and hence also with high reflexions. However, this was not considered to be a serious problem, as the majority of wave-current theories are based on the interaction of a plane oscillatory flow with a current - and a standing wave pattern induces just such a plane oscillatory flow at the bed (albeit a spatially varied one).

Data analysis included a correction to the oscillatory shear stress measurements to account for the effect of wave-induced pressure gradients at the bed of the basin. Its effect is relatively greater for the short period waves. Sleath (1991) has pointed out that an equivalent force also acts on each sand grain at the bed, and this has been taken into account in the present work.

Results from the tests with wave alone (**fig.3**), and those with waves and currents combined (i.e. **fig.4**), both showed that the oscillatory shear stress, after correction, always peaked approximately  $30^\circ$  before the orbital velocity. Another important observation was that the maximum shear stress was relatively unaffected by the superposition of a turbulent current - either strong or weak (see **Table 3**). This contrasted with the significant effect the addition of waves had on the properties of the currents.

### Discussion

Considering first the changes caused to the mean current profiles by the superposition of waves, the additional resistance experienced in the upper flow is something that has been reported in earlier papers on wave-current interaction (Kemp & Simons, 1982; Bakker & van Doorn, 1978). However, it is an effect not included in any of the present generation of mathematical models purporting to describe the wave-current process. The most likely

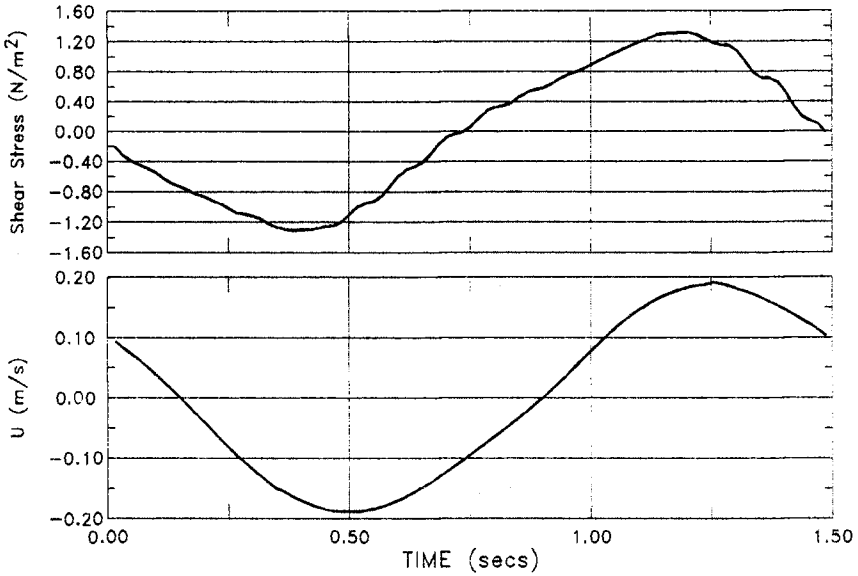


Fig.3 Ensemble averaged bottom shear stress and orbital velocity in line with direction of wave propagation: wave alone W2P:  $H = 168\text{mm}$ ;  $T = 1.49\text{s}$ ;  $U = 0\text{mm/s}$ .

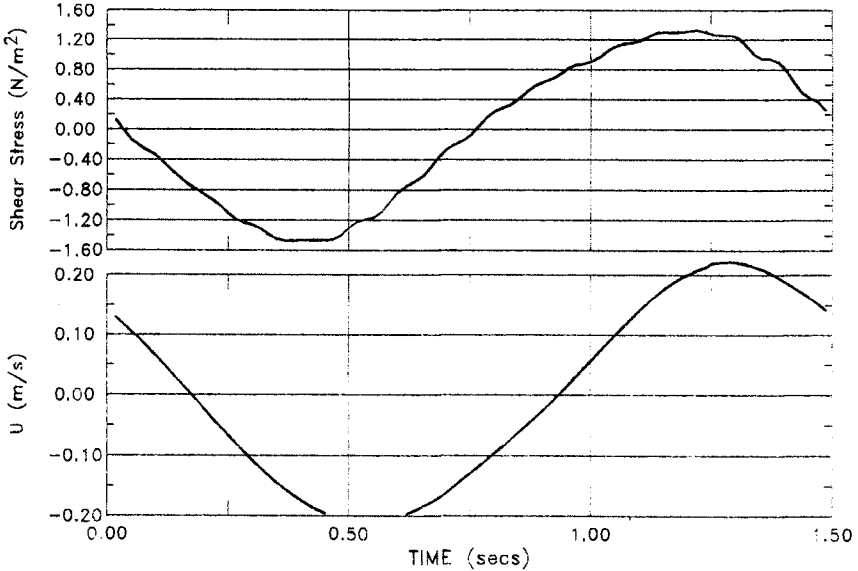


Fig.4 Ensemble averaged bottom shear stress and orbital velocity in line with direction of wave propagation: wave + current W2C:  $H = 185\text{mm}$ ;  $T = 1.49\text{s}$ ;  $U = 200\text{mm/s}$ .

Run:	Wave Period s.	Orb $U_{\max}$ mm/s	RE = $U_{\max}a/\nu$	$a/k_s$	$\tau_{\max}$ Pa	friction factor
W1P	1.49	142	4775	22	0.841	0.083
W1C	1.49	158	5910	25	0.902	0.072
L1CC	1.49	156	5761	25	0.792	0.065
W2P	1.49	189	8456	30	1.076	0.060
W2C	1.49	222	11562	35	1.066	0.043
W3P	1.49	104	2560	16	0.621	0.114
W4P	2.02	125	5112	27	0.626	0.080
W4C	2.02	114	4185	24	0.647	0.100
L4CC	2.02	131	5526	28	0.227	**0.027
W5P	2.02	173	9637	37	0.826	0.055
W5C	2.02	153	7538	33	0.815	0.070
L5C	2.02	163	8555	35	0.320	0.024
L5CC	2.02	164	8661	35	0.294	0.022
W7P	1.11	67	793	8	0.553	0.246
W7C	1.11	67	793	8	0.490	0.218
W8P	1.11	42	311	5	0.382	0.433
W8C	1.11	42	312	5	0.393	0.446
W9P	2.48	204	16440	54	0.435	0.021
L9C	2.48	214	18090	56	0.379	0.017
L9CC	2.48	212	17754	56	0.375	0.017
W10P	2.48	289	32992	76	0.672	0.016
L10C	2.48	300	35550	79	0.611	0.014
W10CC	2.48	260	26703	68	0.835	0.025
L10CC	2.48	277	30310	73		
W11P	2.48	177	12376	47	0.459	0.029
W11C	2.48	173	11851	46	0.485	0.032
W11CC	2.48	179	12657	46	0.436	0.027

Table 3: Oscillatory boundary layer parameters.

explanation is that additional Reynolds stresses are set up by the wave-induced orbital velocities, and these may be interacting with the mean current.

The increase in apparent bed roughness implied from the log-linear velocity profiles was qualitatively as predicted by all wave-current models, and, when compared with the predictions of Sleath (1991), there was good agreement in many cases. However, some of the values were found to be considerably lower than predicted by the theory, the greatest discrepancies occurring for waves with the shortest wave periods and the lowest amplitude Reynolds numbers.

Again, the increase in mean shear stress observed when waves were added to the current was as predicted by theory, and similar to that observed by Sleath (1990) in experiments on flow over an oscillating plate. It is also very much in line with that found by other researchers for a wide variety of test conditions including both field and laboratory tests.

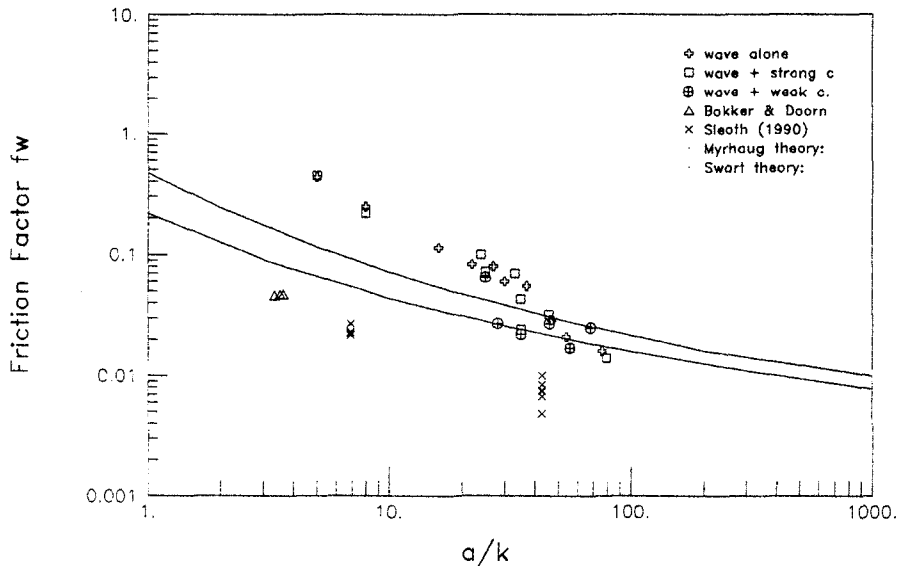


Fig.5 Variation of wave friction factor with relative bed orbital amplitude for different wave-current combinations.

Turning now to the effect the addition of currents has on the wave characteristics, the most important finding of the work is that the maximum oscillatory bed shear stress appears to remain virtually unaltered, irrespective of the strength of the superimposed current. This is demonstrated in **fig. 5**, where friction factors calculated from the maximum shear stresses under waves with and without currents are plotted out against relative orbital excursion at the bed,  $a/k$ . The tendency for observed friction factors to move above the theoretical predictions as  $a/k$  decreases may be due to some uncertainty about the velocity measurements by which they have been normalized. The effect may also relate to lower Reynolds numbers lying in the transitional rough regime where the Nikuradse roughness may vary from that determined in the tests on current alone.

The authors are presently analysing field data from a site off the south coast of Australia where conditions generally meet the criterion that waves propagate orthogonally across a coastal current (Black et al. (1992)). When available, those results will complement the present laboratory data.

### Conclusions

Currents experience a significant change both in mean bed shear stress and apparent bed roughness when waves are superimposed and propagate orthogonally across it. However, under the present test conditions, the oscillatory, wave-induced, bottom shear stress is insensitive to the addition of an orthogonal current.

### Acknowledgements

This work was undertaken as part of the MAST G6 Coastal Morphodynamics research programme. It was funded jointly by the Science and Engineering Research Council, and by the Commission of the European Communities Directorate General for Science, Research and Development under contract no. MAST-0035-C. The authors also acknowledge their gratitude to Hydraulics Research, Wallingford, for the use of their facilities.

### References

- Arnskov M.M., Sumer M. and Fredsoe J. 1991 Bed shear stress measurements in combined wave-current motion. Abstract from MAST G6-M Mid-Term Workshop, Edinburgh University, 16-20 September 1991.
- Bakker W.T. and van Doorn T. 1978 Near-bottom Velocities in Waves with a Current. Proc. 16th Int. Conf. on Coastal Engng, Hamburg, pp.1394-1413.

Bijker E.W., 1967 Some considerations about scales for coastal models with moveable bed. Delft Hydraulics Lab. Report 50.

Black K.P., Pattiarachi C., Rosenberg M., Simonds G. and Simons R.R. 1992 Measurements of the Wave, Current and Sea Level Dynamics of an Exposed Coastal Site. Proc. Int. Bienn. Conf. on Physics of Estuaries and Coastal Seas, Margaret River, W.Australia, 8-10 December 1992.

Brevik I. and Aas B. 1980 Flume experiments on waves and currents: rippled beds. Coastal Engineering, 3, pp149-177.

Kemp P.H. and Simons R.R. 1982 The interaction between waves and a turbulent current: waves propagating with the current. J.Fluid Mech., 116, pp.227-250

Kemp P.H. and Simons R.R. 1983 The interaction between waves and a turbulent current: waves propagating against the current. J.Fluid Mech., 130, pp.73-89

Oebius H. 1982 Laboratory and insitu bed shear stress measurements. Euromech 156: Mechanics of sediment Transport, Istanbul, 12-14 July 1982.

Reidel P.H. and Kamphuis J.W. 1973 A shear plate for use in oscillatory flow. J.Hydraulic Research, 11, No.2, pp.137-156

Simons R.R., Kyriacou A., Soulsby R.L. and Davies A.G. 1988 "Predicting the Nearbed Turbulent Flow in Waves and Currents". Proc. IAHR Symp. on Math.Modelling of Sediment Transport in the Coastal Zone, Copenhagen, Denmark, 1988, pp.33-47.

Sleath J.F.A. (1990) Velocities and bed friction in combined flows. Proc. 22nd Int. Conf. on Coastal Engng, Delft, Ch.35, pp.450-463.

Sleath J.F.A. (1991) Velocities and Shear Stresses in Wave-Current Flows. J.Geophys.Res., 96, C8, pp.15237-15244.

Visser (1986) Wave basin experiments on bottom friction due to current and waves. Proc. 20th Int. Conf. on Coastal Engng, Ch.61, Taiwan, pp.807-821.

## CHAPTER 46

### The Effect of Sheared Currents on Wave Kinematics and Surface Parameters

D.J.Skyner<sup>1</sup> & W.J.Easson<sup>2</sup>

#### ABSTRACT

Steep, steady non-linear waves have been generated onto strongly sheared currents. Quantitative, full-field velocity measurements have been made for a number of wave/current combinations using the method of Particle Image Velocimetry (PIV). For one of the combinations, the measured kinematics are compared to the estimate obtained by adding the stretched current profile to the predictions from irrotational theory. The steadiness of the conditions is assessed by calculating the vorticity distribution for different cycles in the wavetrain. Finally, the measured wavelengths for a range of wave frequencies are used to estimate the effective current.

#### INTRODUCTION

Knowledge of representative wave kinematics is crucial in the understanding of coastal processes and the design of offshore structures. Often, waves ride on top of steady currents, generated by the tides or the wind, and it is important that the combination of the kinematics in these cases can be understood and predicted.

High-order methods have been used for some time to predict the properties of steep waves, in the absence of current, and have been extensively verified by laboratory studies. On a uniform current the combined wave-current kinematics can be calculated by changing reference frame to one moving with the current and using a high-order model, after Doppler shifting the wave frequency. Several authors have recently tackled the problem of steep waves on currents of an arbitrary profile [Dalrymple and Heideman, 1989, Chaplin, 1990] and have implemented numerical models, but experimental studies are still rare.

Swan [1990] produced moderate amplitude waves on strongly sheared currents and addressed some of the difficulties posed by Dalrymple and Heideman in

---

<sup>1</sup>Research Associate, Dept Physics, the University of Edinburgh, Edinburgh EH9 3JZ, Scotland (D.Skyner@ed.ac.uk)

<sup>2</sup>Lecturer, Dept Mech Eng, the University of Edinburgh, Edinburgh EH9 3JL, Scotland

their cautionary note on tank testing. Other notable experiments include those of Thomas [1990], where good agreement was obtained between laboratory measurements and numerical predictions for weakly sheared currents, and Kemp and Simons [1983] whose study concentrated on the effects near the bed.

There is a severe experimental difficulty encountered when measuring currents with non-uniform profiles near the surface, in the presence of waves. Whichever end of the flume the currents are injected from, the wave action will ultimately disturb the formation of the upper part of the profile. One solution to this problem is to make the measurements of the combined kinematics during the short time window once the waves are established, but before the current formation is affected and reflected waves return. However, even with this approach the steadiness of the conditions must still be questioned.

## EXPERIMENTAL CONDITIONS

Experiments were performed in a purpose built wave flume, depth .75m, capable of producing forward or reverse currents with various profiles. The experimental arrangement is shown in figure 1.

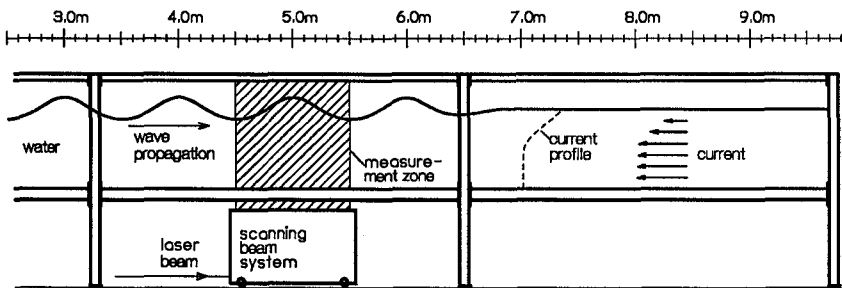


Figure 1: Wave flume used for the kinematic measurements

The main current profile required for the experimental programme was one which was strongly sheared in the direction of wave propagation. The current was generated by introducing a flow opposed to the waves along the bottom half of the flume. In the subsequent analysis, the bulk value of the current was altered to yield the desired profile in the chosen reference frame, and the wave frequency modified with the appropriate Doppler shift. If the frequency in a given frame is  $f_1$ , then the frequency measured in a second frame, moving with velocity  $u$  compared to the first, is given by

$$f_2 = f_1 - \frac{u}{\lambda} \quad (1)$$

The most strongly sheared current profile used in the tests is shown in figure 2, along with the rms turbulence level. The profile has an approximately linear form,



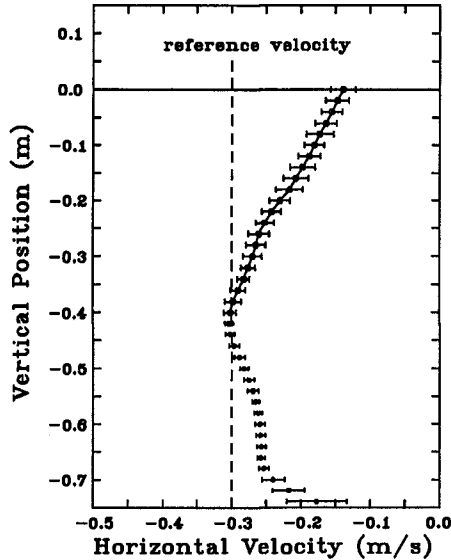


Figure 2: Current profile, sheared in the direction of wave propagation, used in the experiments

velocity gradient  $0.427\text{s}^{-1}$ , in the top half of the water depth and was shifted to a frame of reference moving at  $-0.3\text{ms}^{-1}$  when analysing the combined kinematics. The form of the current near the bed should be disregarded when assessing the profile, as the wave action in this region is small.

## EXPERIMENTAL MEASUREMENTS

In the experimental test sequence, steep waves were run onto the current and kinematic measurements made once the waves were steady and before reflections came back. In addition, estimates of the wavelength were obtained from wavelength records at different positions in the tank and from the photographs of the flow.

The combined kinematics were measured by the method of Particle Image Velocimetry (PIV), in which small seeding particles are multiply exposed by a pulsed light sheet in the flow and their images recorded onto film. From the separations of the images in each part of the film the local velocity at that location can be deduced, and hence the complete flow field established. Further details of the use of the technique in this and other hydrodynamic studies are described in Greated et al [1992].

A typical flow field measured in the study is shown in figure 3 as a vector

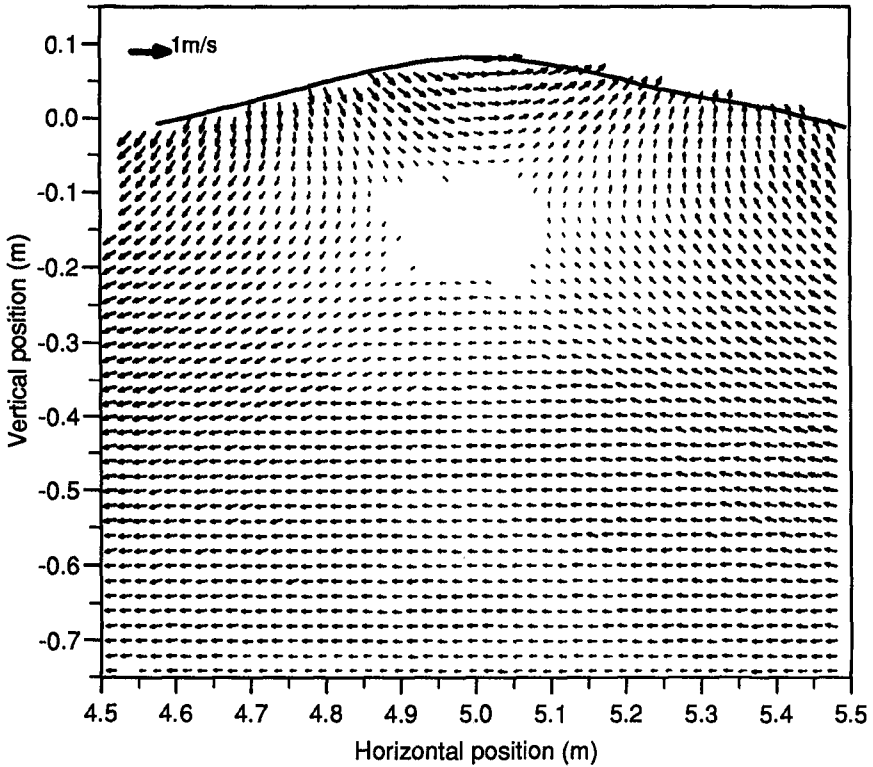


Figure 3: Internal kinematics of a wave on a sheared current measured with PIV

plot. Measurements were achieved up to the surface, and the measurement error was typically less than 2% of the maximum velocity, depending on the velocity gradients present. The missing data in the central part of the wave corresponds to a region of near-zero velocity in the flow, where the crest kinematics of the wave and the opposing current produce an instantaneous stagnation point. This results in overlapping particle images on the PIV photograph, whose separations cannot be resolved. Measurements could be made in this region by using an image shifting technique [Bruce,1992].

For the strongly sheared current, six wave conditions, were studied in detail. These wave cases covered a range of steepnesses ( $H/\lambda$ ) from .054 to .098, and a range of water depth to wavelength ratio ( $h/\lambda$ ) from .27 to .57. Results for these wave cases and other current profiles have been reported by the authors [Skyner,1992,1993]. The results presented here are for the central wave case on the strongly sheared current ( $H/\lambda=.0729, h/\lambda=.412$ ).

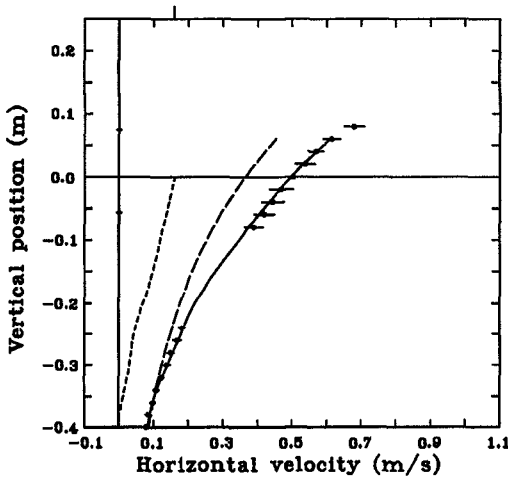


Figure 4: Horizontal velocity profiles under the crest, for a wave on a strongly sheared current. -●- experimental data, with scatter, - - - undisturbed current, — — irrotational numerical model, ——— prediction from numerical model and stretched current profile

## MEASURED KINEMATICS

The experimentally measured horizontal velocity profiles under the crest for the central wave condition, in the presence of the strongly sheared current is plotted in figure 4, along with numerical predictions. The graph contains the undisturbed current profile, the velocity profile under the crest for the combined flow, a numerically generated profile for an irrotational wave with the same height and wavelength, and the numerical data combined with the stretched current profile. The irrotational numerical data was generated by a program based on the Fourier approximation method of Riencker and Fenton [1981]

The method used for obtaining the combined kinematics was that recommended by the UK Department of Energy [1990], when a complete wave/current model is not available. The current value at a given height above the bed is moved to a new location by multiplying the distance from the bed by the factor  $(1 + C_N/h)$ , where  $C_N$  is the crest elevation, obtained numerically, and  $h$  the water depth. The recommendation is that no attempt be made to conserve the total mass flux of the current when stretching.

For wave case being considered, a composite vector map was constructed from flow records at different phases, in order to obtain information over a complete wavelength. From this data the average horizontal velocity component was obtained at various levels, and the results are plotted in figure 5. A significant reduction in the average shear is apparent, greater than that which would be

expected if the assumed current stretching applied over the whole wave, when the shear would decrease in the crest but increase in the trough, leading to an average value only slightly less than the undisturbed current value.

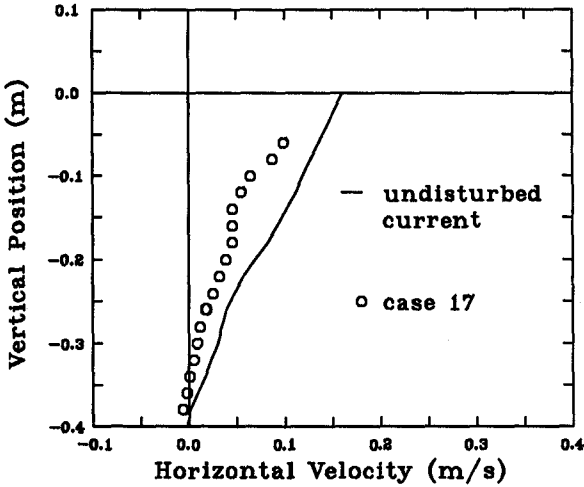


Figure 5: Mean horizontal velocities for medium steepness waves on a strongly sheared current.

### Derived Vorticity

Calculating vorticity from the experimentally measured flow fields is a profitable exercise because it separates the irrotational part of the motion, associated with the wave, from the rotational part, associated with the sheared current. It is possible to extract vorticity from the data obtained with PIV, because the velocity field is known over two spatial dimensions. The vorticity component perpendicular to the measurement plane is

$$\Omega_y = \frac{\partial u_z}{\partial x} - \frac{\partial u_x}{\partial z} \quad (2)$$

A reasonable estimate for the local vorticity can be obtained by numerically differentiating the velocity data, which is available on a regular grid. In order to reduce the effect of turbulence and reveal the underlying trends, the velocity fields obtained from a number of repeats of each wave phase were averaged before calculating the vorticity.

Figure 6 contains a shaded contour plot of vorticity, obtained from the repeats of the flow field illustrated in figure 3. Light areas corresponds to negative vor-

ticity (forward shear), and dark areas to positive vorticity. The blank area in the centre of the wave is due to missing data, no attempt been made to interpolate.

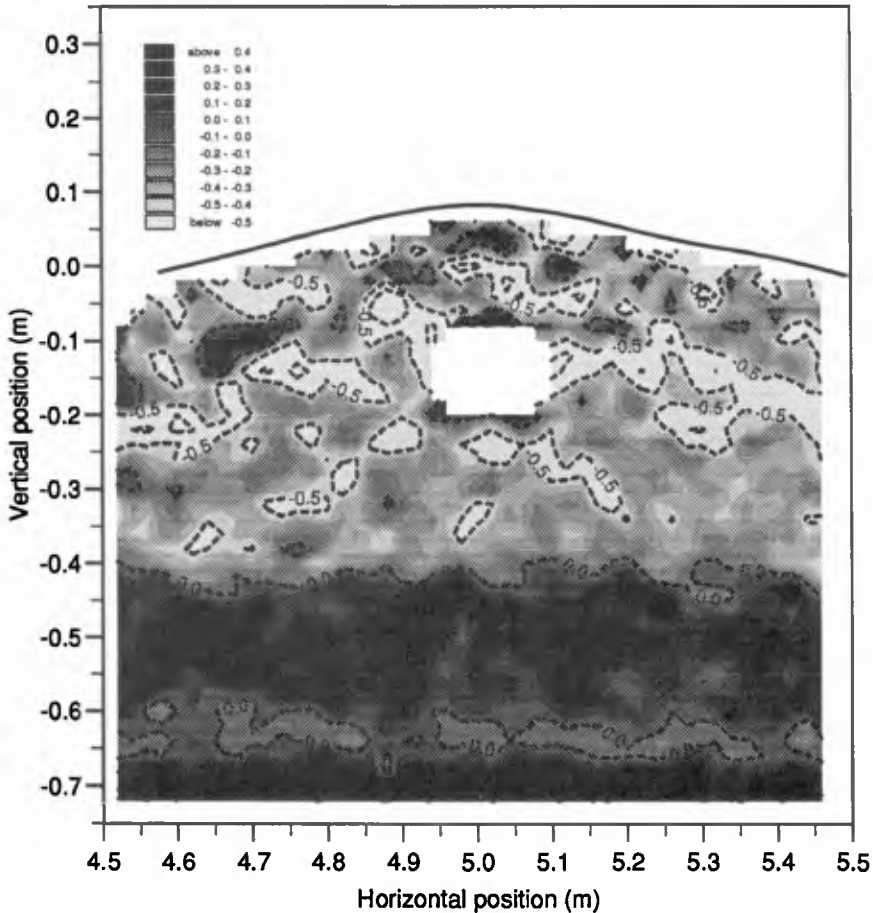


Figure 6: Vorticity contours for the average of 6 repeats of a medium amplitude wave on the strongly sheared current, *first* wave crest. Contour line interval:  $0.5s^{-1}$

Comparison with the undisturbed current profile shown in figure 2 reveals that the vorticity field has the expected features. The bed boundary layer is present as strip of high positive vorticity, and there is a major transition from positive to negative vorticity at around  $z = -0.4m$ . Apart from the small pockets of turbulence, the vorticity in the upper part of the wave is fairly constant with an average value between  $-0.3s^{-1}$  and  $-0.4s^{-1}$ .

The available time window for the kinematic measurements of the wave case

being considered corresponded to four wave periods. This portion of the wave elevation timeseries is shown in figure 9 as a continuous trace. The kinematic measurements presented here are for the first wave crest in this “steady portion” of the wavetrain at  $t = 12.4s$ . PIV measurements were also made for the third and fifth crests in this portion.

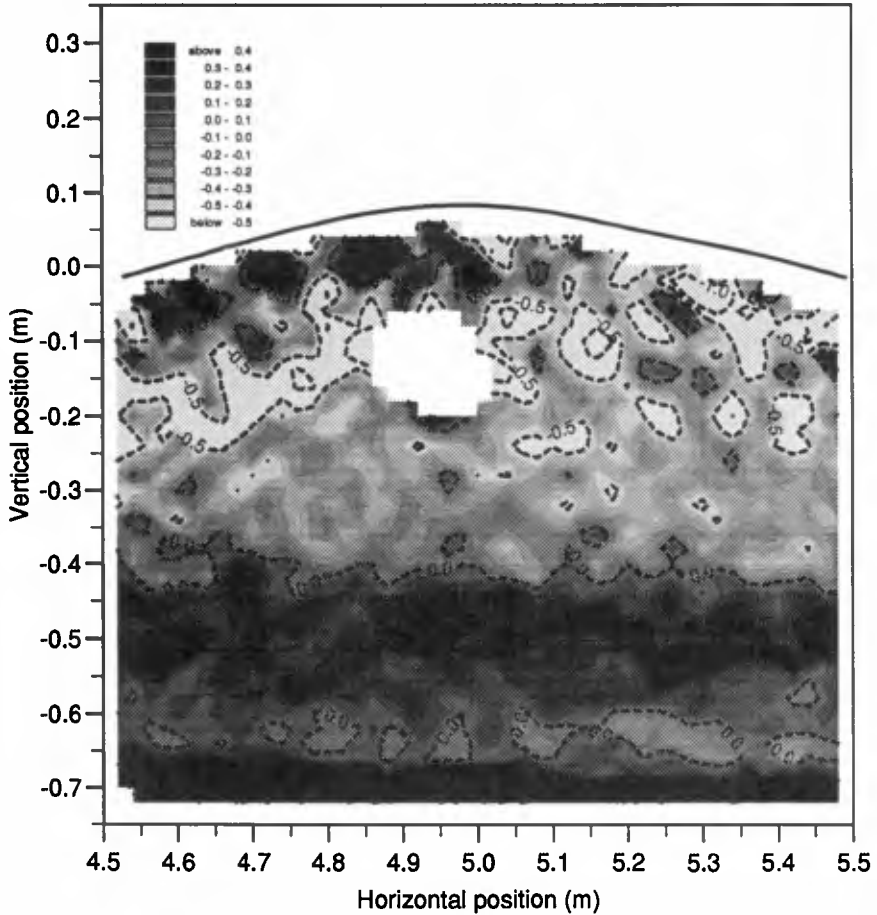


Figure 7: Vorticity contours for the average of 6 repeats of a medium amplitude wave on the strongly sheared current, *third* wave crest. Contour line interval:  $0.5s^{-1}$

Figure 7 contains the vorticity levels found in the third crest of the steady portion of the wave train. While the vorticity distribution is similar to the earlier cycle of the wave in the middle and lower parts, sizable areas of positive vorticity have appeared near the surface.

In figure 8 the areas of positive vorticity near the surface have increased still further compared to the previous cycles of the wave. The position of the crest is also noticeable retarded compared to its expected position in the middle of the plot.

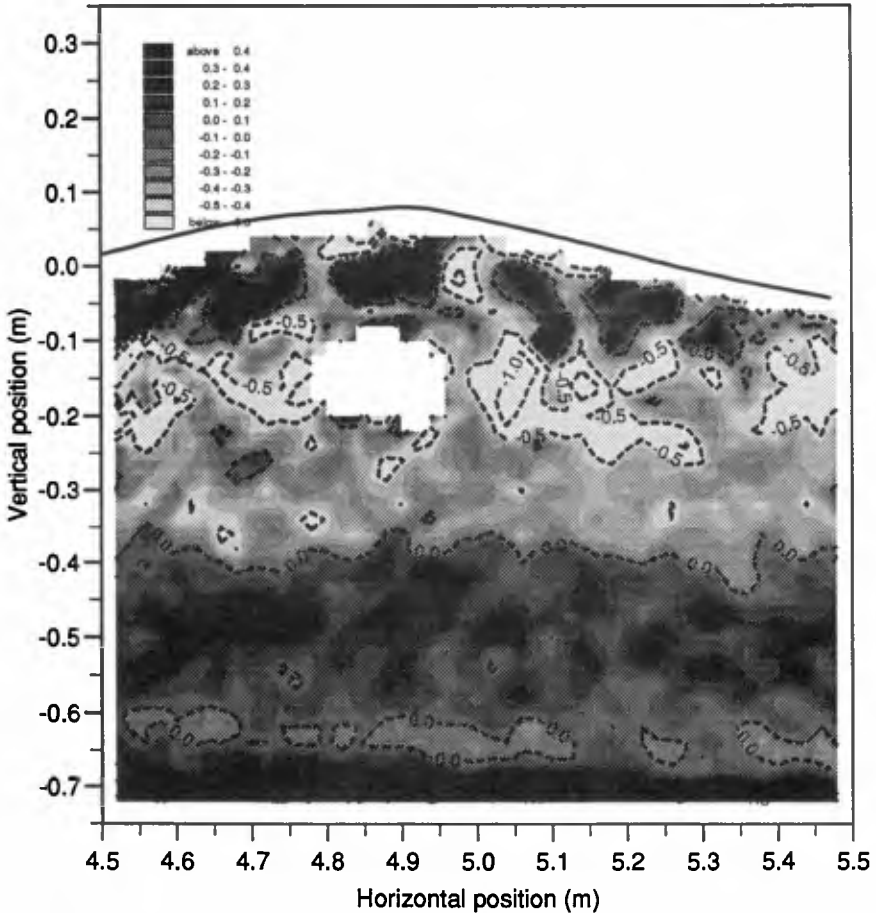


Figure 8: Vorticity contours for the average of 6 repeats of a medium amplitude wave on the strongly sheared current, *fifth* wave crest. Contour line interval:  $0.5s^{-1}$

Figure 9 also shows the average vorticity estimated for the top half of the wave (above  $z = -0.4m$ ). These values were calculated for each available wave crest by averaging the vorticity data, shown in figures 6 to 8, with no attempt being made to interpolate missing values. A clear trend is apparent, with the average vorticity moving away with time from the undisturbed current value towards zero.

This is equivalent to a decrease in the shear of the underlying current.

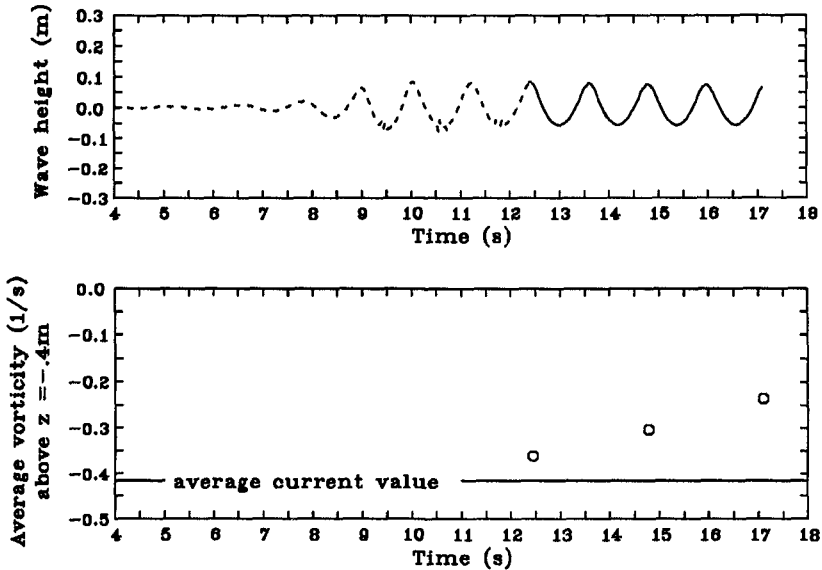


Figure 9: Average vorticity value obtained for different crests in the wavetrain, along with the wave elevation timeseries where the continuous trace represents the "steady" portion of the wave

## Wavelength

The measured wavelengths for the cases selected for the kinematic measurements were found to correspond, within experimental error, to those predicted from irrotational theory, given the wave height and wave frequency, after Doppler shifting the frequency to a frame moving with the surface current. From a sequence of tests, sweeping through a range of frequencies of small amplitude waves, the effective current was calculated from the measured wavelength using Doppler theory. The uniform current with the equivalent effect on the wavelength is plotted against wave frequency in figure 10. The values of the surface current and the current at half the depth are also shown.

## DISCUSSION

The estimate for the kinematics made by adding the stretched current to irrotational predictions assumed that the underlying current was not effected by the wave action, other than by being stretched according to the phase of the wave. However, calculation of the vorticity for different cycles in the "steady" portion



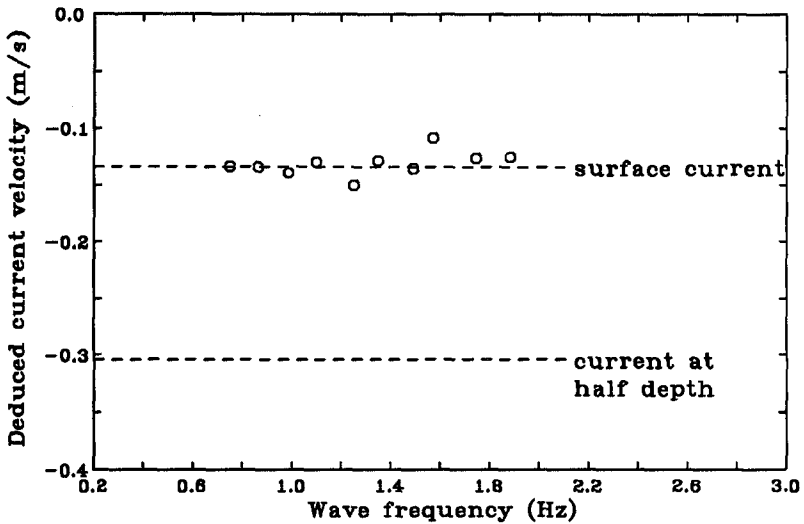


Figure 10: Equivalent uniform current velocity deduced using Doppler theory from measured wavelength on sheared current

of the wave train indicates that the rotational part of the fluid motion is changing with time. This may be due to the presence of turbulence influencing the wave/current interaction. However, the presented results should be viewed with some caution, as although care was taken in the experiments when establishing the wave train that the leading wave did not break, it is possible that interactions occurring at the front of the wave group may have been advected back to the measurement zone, effecting the later wave cycles.

## CONCLUSIONS

For the conditions considered, the kinematics in the crest were found to be well predicted by combining the results of an irrotational, high-order numerical model with the stretched current profile. In addition, it was found that the wavelength was accurately predicted using irrotational theory, after Doppler shifting the wave frequency to the frame of reference of the surface current. However, there was strong evidence that the conditions were not steady, particularly the change in the vorticity field between the cycles in the wave train.

## ACKNOWLEDGMENT

The authors would like to thank G. Klopman, of Delft Hydraulics for allowing the use of his numerical model in this study, and the UK Department of Energy who funded the majority of the work.

## References

- [1] Bruce T. and Easson, W.J. *The Kinematics of Wave Induced Flows Around Near-Bed Pipelines*. 1992. Proc. 23rd Int. Conf. on Coastal Eng., ASCE.
- [2] Chaplin, J.R. *The Computation of Non-Linear Waves on a Current of Arbitrary Non-Uniform Profile*. 1990. OTH 90 327, HMSO.
- [3] Dalrymple, R.A. and Heidemanm, J.E. *Non-linear Water Waves on a Vertically-Sheared Current Wave and Current Kinematics and Loading*. 1989. E&P Forum, Report No. 3.12/156, 69-92.
- [4] Department of Energy. *Offshore Installations: Guidance on Design, Construction*. 1990. 4th Edition, Section 11, Environmental considerations, 11.31-11.61, HMSO.
- [5] Greated, C.A, Skyner, D.J. and Bruce T. *Particle Image Velocimetry (PIV) in the Coastal Engineering Laboratory*. 1992. Proc. 23rd Int. Conf. on Coastal Eng., ASCE.
- [6] Kemp, P.H. and Simons, R.R. *The Interaction of Waves and a Turbulent Current: Waves Propagating against the Current*. 1983. Journal of Fluid Mechanics, 130, 73-89.
- [7] Rienecker, M.M, and Fenton, J.D. *A Fourier Approximation Method for Steady Water Waves*. 1981. Journal of Fluid Mechanics, 104, 119-37.
- [8] Skyner, D.J. and Easson, W.J. *Wave Kinematics on Sheared Currents*. 1993. Wave Kinematics and Environmental Forces, London.
- [9] Skyner, D.J, Easson, W.J. and Greated C.A. *The Internal Kinematics of Steep Waves on Sheared Currents — An Experimental Study*. 1992. OTH 92 366.
- [10] Swan, C. *An Experimental Study of Waves on a Strongly Sheared Profile*. 1990. Proc. 22nd Int. Conf. on Coastal Eng., ASCE, 1, 489-502.
- [11] Thomas, G.P. *Wave-current Interactions: an Experimental and Numerical Study, Part2: Non-Linear waves*. 1990. Journal of Fluid Mechanics, 216, 505-536.

## CHAPTER 47

### LABORATORY STUDY OF WAVE TRANSFORMATION ON BARRED BEACH PROFILES

Ernest R. Smith<sup>1</sup> and Nicholas C. Kraus<sup>2</sup>

**ABSTRACT:** In previously reported laboratory experiments, the authors found that incident waves with the same characteristics in deep water break differently on barred and plane-sloping beaches. For example, waves of greater steepness that plunge on plane beaches tend to collapse on barred beaches, and plunge distance on barred profiles is about half that on a plane sloping beach for a given wave steepness. In the present study, wave height transformation, reflection, and runup of monochromatic and random waves are investigated for barred and plane beach profiles in a wave tank, with deep-water wave steepness varied from 0.0085 to 0.09. For monochromatic and random waves, wave-height to water-depth ratios are higher for waves breaking on bars, whereas just seaward of breaking these ratios are lower than on a plane beach. For plane and barred beaches, the ratios unite in the inner surf zone, and the magnitude and shape of wave spectra are the same at fixed points outside and inside the surf zone, except just shoreward of the break point, where the spectrum on a barred profile has the same shape but contains less energy. Despite differences in breaker-related quantities on barred and plane beach profiles, runup, reflection, and wave height transformation in the surf zone on barred profiles are mainly controlled by the plane beach slope on which the bar or reef is located, with only minor influence by a bar, even for extremely-shaped obstacles such as reefs.

#### INTRODUCTION AND BACKGROUND

Most laboratory studies on wave transformation, runup, and reflection have been conducted on plane sloping beaches. In the field, however, linear bars are common, and waves will transform differently over barred profiles as compared to plane beaches. To elucidate these differences, the authors conducted an extensive laboratory study to examine breaking and broken wave properties on barred and terraced profiles, and the results were compared to those obtained for plane slopes. Results determined from video records were

---

(1) Research Hydraulic Engineer, and (2) Senior Scientist, U.S. Army Engineer Waterways Experiment Station, Coastal Engineering Research Center, 3909 Halls Ferry Road, Vicksburg, MS 39180-6199, USA.

presented in Smith and Kraus (1991) and in a report (Smith and Kraus 1990) that covers the experiment procedure and results. The present paper focuses on selected results determined from the digital wave gage data, and some analyses from the project report are extended.

As motivation, we consider breaker type and plunge distance on barred and plane slopes (Smith and Kraus 1991). Galvin (1968) expressed breaker type transition values in terms of beach slope  $m$ , wave height  $H$ , and wave period  $T$ . Battjes (1974) re-expressed the transition values in terms of the surf similarity parameter,  $\xi_o = m(H_o/L_o)^{1/2}$ , in which  $H_o$  and  $L_o$  are wave height and wavelength in deep water, respectively. Smith and Kraus observed different transition values of breaker type on single-bar profiles than determined by Battjes for plane slopes. Transition values between breaker types on barred profiles and plane slopes are shown as a function of  $\xi_o$  in Fig. 1. Transition values are lower for barred profiles, which means some waves that would spill on a plane slope plunge if a bar is present, and some plunging waves on plane slopes collapse on a barred profile.

Plunge distance  $X_p$  of breaking waves differs on plane and barred beaches (Smith and Kraus 1991). Fig. 2 plots plunge distance normalized by breaker height  $H_b$ , and the visually fit solid line for barred profiles as a function of  $\xi_o$ . The dashed line represents the predictive equation for plane slopes determined by Smith and Kraus. Plunge distance was 60 to 70 percent shorter over bars than over plane slopes. Differences in breaker height and depth, and splash distance between plane slopes and barred profiles were also found. On the basis of these findings, in the present work, the digital data of water surface elevation are examined to investigate wave transformation, runup, and reflection on barred and terraced (shelf) profiles, and the results are compared to those for plane sloping beaches.

## PROCEDURE

Data collection was conducted in a 45.70-m-long, 0.46-m-wide, and 0.91-m-high glass walled tank (Fig. 3). The tank contained a 1 on 30 smooth concrete-capped slope, which was separated from the wave generator by a 21-m-long horizontal section. Monochromatic and random waves were produced by an electronically controlled hydraulic system that drove a piston-type wave board. Water surface elevation was recorded at eight double-wire resistance-type gages. Gage 1 was located 9.1 m from the wave generator, Gages 2 and 3 were placed seaward of the bar and positioned to measure wave reflection according to the method of Goda and Suzuki (1976), Gage 4 was placed at the incipient break point, and Gages 5 through 8 were distributed through the surf zone. The water surface elevation was analyzed to obtain statistical wave heights and periods, and spectra.

Deep-water wave steepness  $H_o/L_o$  in part controls breaking wave characteristics. Therefore, it was desirable to generate waves with a wide range of steepnesses. A fixed water level (0.38 m) was maintained in all tests and allowed generation of relatively high waves while minimizing the effect of surface tension. Five design monochromatic wave conditions were selected ( $H_o/L_o = 0.09, 0.07, 0.05, 0.03, 0.0088$ ) through consideration of a diagram given by Galvin (1970, his Fig. 8) for delineating domains where periodic waves, single and multiple solitons, and breaking waves exist to obtain periodic breaking waves without contamination by soliton generation. Three random wave conditions were also developed from an input JONSWAP spectrum for spectral peak periods  $T_p$  of 1.0, 1.5, and 1.75 sec, with significant wave heights  $H_s$  of 11.3, 14.3, and 13.7 cm, respectively, in the horizontal section of the tank.

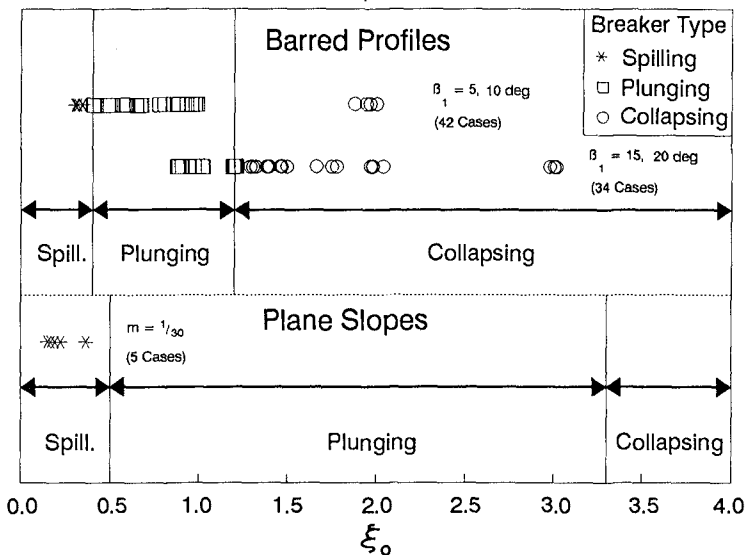


Fig. 1. Breaker type classification for plane and barred slopes (Smith & Kraus 1991)

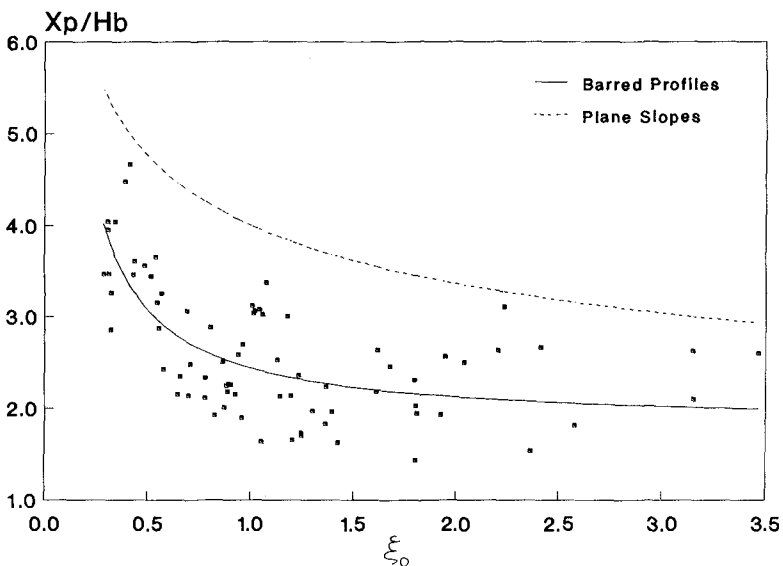


Fig. 2. Plunge distance on plane and barred slopes (Smith & Kraus 1991)

Submerged solid triangular-shaped objects were installed on the 1-on-30 slope to represent natural barred profiles, terraced profiles, and artificial reefs. The geometry of the objects was selected based on large wave tank studies and field measurements of bars (Larson and Kraus 1989). Seaward bar angles  $\beta_1$  varied from 5 to 40 deg, and shoreward angles  $\beta_2$  ranged from 0 deg (terrace) to 40 deg. The steeper seaward angles were included to observe breaking waves on shapes that approximate those of submerged breakwaters or reefs. The size and placement of the bars were determined based on findings of Larson and Kraus.

Bars used in the study were constructed of marine plywood, with the seaward and shoreward faces connected with strap hinges. For longer bars, legs were attached under the structure to minimize flexing of the faces due to wave action. Openings created at the crest by the seaward and shoreward faces and the sides of the bar against the tank wall were sealed to maintain a flush surface and minimize leakage. Steel plates were installed under the bar to prevent it from floating or moving when subjected to wave action.

Wave data were collected for 2 min at 50 Hz for monochromatic-wave tests, but only 15 successive waves were analyzed. The analyzed portion of the record began after waves reflected off the concrete slope and ended before reflected waves from the board had returned to the bar. This procedure eliminated contamination of the data by waves reflected off the board, yet simulated the natural reflection of waves by the beach and bar or reef. Random waves were recorded at 20 Hz and analyzed for 500 waves. Because the wave height and period varied, a long record was required to obtain a statistically strong confidence interval for the wave spectrum. Reflection and re-reflection between the beach and the wave board could not be avoided in the random-wave tests.

In summary, 108 tests were performed with regular waves, of which five tests were with a plane slope, and 12 tests were performed with random waves, of which three tests were with a plane slope. Table 1 summarizes the design test conditions. The table shows nominal values for design which were approximated in actual tests.

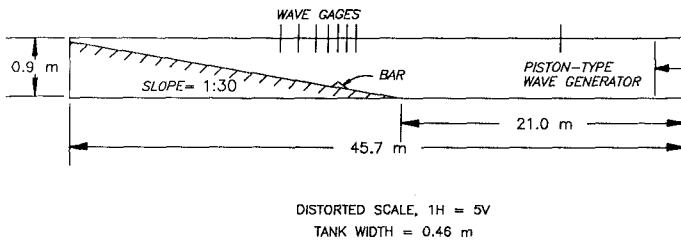


Fig. 3. Definition sketch for tank arrangement

Table 1. Test Design <sup>a</sup> Parameters				
Monochromatic Waves				
$H_o/L_o$	$T$ sec	$H$ cm	$\beta_3$ deg	$\beta_1$ deg
0.09	1.00	13.1	0, 20, 30, 40	5, 10, 15, 20, 30, 40
0.07	1.00	10.1	0, 20, 30, 40	5, 10, 15, 20, 30, 40
0.05	1.50	16.2	0, 20, 30, 40	5, 10, 15, 20, 30 <sup>b</sup>
0.03	1.75	13.7	0, 20, 30, 40	5, 10, 15, 20
0.0088	2.50	9.1	0, 20, 30, 40	5, 10, 15
Random Waves				
$(H_o/L_o)_o$	$T_o$ sec	$H_o$ cm	$\beta_3$ deg	$\beta_1$ deg
0.078	1.00	11.3	20	5, 10, 15
0.044	1.50	14.3	20	5, 10, 15
0.03	1.75	13.7	20	5, 10, 15
<sup>a</sup> Nominal values for design purposes which were only approximated (see Smith and Kraus (1990) for complete data listing) <sup>b</sup> One test conducted with $\beta_1 = 30$ deg, $\beta_3 = 20$ deg  Note: $H$ = wave height measured at the wave maker in depth of 0.38 m $H_o$ = significant wave height measured at the wave maker in depth of 0.38 m $T_o$ = peak wave period measured at the wave maker in depth of 0.38 m				

## RESULTS

### Wave Reflection

Miche (1951) developed a theoretical relation for the reflection coefficient  $K_r$  for smooth plane slopes. He assumed the reflected portion of wave energy corresponded to a critical deep-water wave steepness  $(H_o/L_o)_{cr} = (2\beta/\pi)(\sin^2\beta/\pi)$  in which  $\beta$  is the slope angle. Miche defined the quantity  $(H_o/L_o)_{cr}$  as the wave steepness to obtain complete reflection, and wave energy that exceeded this value was assumed to be dissipated. Wave reflection was expressed as  $K_r = (H_o/L_o)_{cr}/(H_o/L_o)$  if  $H_o/L_o > (H_o/L_o)_{cr}$ , and  $K_r = 1$  if  $H_o/L_o < (H_o/L_o)_{cr}$ . Miche stated that actual reflection coefficient values would be lower than theoretical values because of viscosity and roughness, and recommended a multiplicative factor of 0.8 to calculate reflection coefficients for smooth, plane slopes.

Battjes (1974) re-expressed the equation of Miche (1951) to obtain  $K_r$  as a function of the surf similarity parameter:

$$K_r = 0.1\xi_o^2 \quad (1)$$

Reflection coefficients calculated from wave data at Gages 2 and 3 are shown as a function of  $\xi_o$ , using  $\beta_1$  as input, in Fig. 4. Also shown are the predicted values of Miche and Battjes, using the reduction coefficient of 0.8. The data are scattered and show overlapping

of values for different seaward bar angles. Values obtained by the Miche equation produce a steep curve that approaches a perfectly reflected wave for bar and wave conditions if  $\xi_o \approx 1$ . The Battjes equation underpredicts the measured  $K_r$  at low values of  $\xi_o$  (including the plane slope data), and overpredicts  $K_r$  at higher  $\xi_o$  values. In general, the data show near constant reflection, whereas the Miche and Battjes equations give increasing values of  $K_r$  with increasing  $\xi_o$ . Measured  $K_r$  were also compared to the Miche and Battjes predictions using the 1/30 plane slope to calculate  $\xi_o$ , but both equations gave significantly lower values. Neither the equation of Miche nor that of Battjes estimates  $K_r$  well for barred profiles over the range of  $\xi_o$  values. These equations were developed for plane slopes and, as Fig. 5 illustrates, are not valid if the bottom topography is irregular.

Seelig and Ahrens (1981) developed an equation to determine  $K_r$  for plane smooth slopes, plane beaches, and breakwaters, as

$$K_r = \frac{\alpha}{1 + \frac{\chi}{\xi_o^2}} \quad (2)$$

in which  $\alpha$  and  $\chi$  are empirical coefficients, and equal to 1.0 and 6.2, respectively, for plane smooth slopes. The recommended values of Seelig and Ahrens were used in Eq. 2 to compare to the measured plane-slope  $K_r$  values, but the equation greatly underpredicted the measured values. However, for our data, Eq. 2 gave good predictions if values of  $\alpha$  and  $\chi$  were 0.22 and 0.02, respectively.

Reflection coefficients for barred profiles were grouped according to shoreward angle and plotted as a function of  $\xi_o$ , calculated using  $\tan\beta_1$  in place of  $m$  as the bottom slope. Linear regression was performed on the  $\alpha$  and  $\chi$  values that best fit the data for each group as a function of  $\tan\beta_1$ . The resulting equations for determining the empirical coefficients for use in Eq. 2 for barred profiles are  $\alpha = 0.19 + 0.07\tan\beta_1$  and  $\chi = 0.23 + 0.19\tan\beta_1$ . The correlation coefficients  $r^2$  of the regression analysis were 0.99 and 0.95 for  $\alpha$  and  $\chi$ , respectively. Fig. 5 shows predictions of Eq. 2 as a function of  $\xi_o$  using calculated  $\alpha$  and  $\chi$  values for the shoreward angles used in the study. Reflection coefficients differ by 5 percent for higher values of  $\xi_o$ , but are identical for lower values. Because reflection coefficients were found to be nearly constant, it is concluded that reflection on barred beaches is mainly dependent on the primary slope of the beach and the wave steepness, and only weakly dependent on seaward and shoreward bar angles.

### Wave Runup

Hunt (1959) gave an expression for wave runup  $R$  as a function of slope, wave height, and wave period, which was re-expressed by Battjes (1974) as a function of the surf similarity parameter, as

$$\frac{R}{H_o} = 1.0\xi_o \quad (3)$$



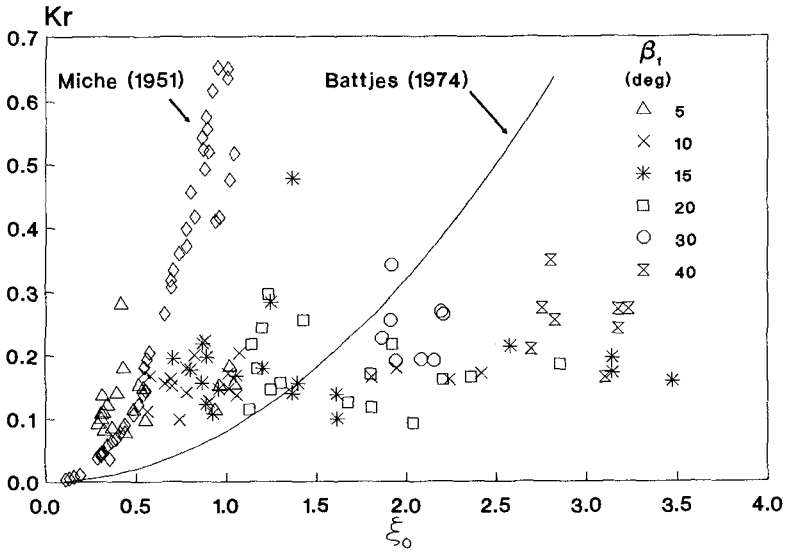


Fig. 4. Measured reflection coefficient vs. surf-similarity parameter

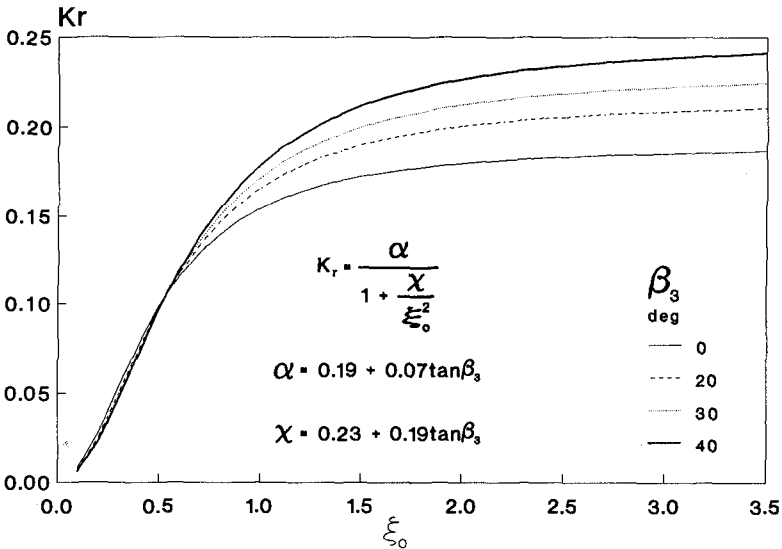


Fig. 5. Empirical curves for reflection coefficients for a 1/30 plane slope with a bar

in which the empirical coefficient value of 1.0 was determined from Hunt's results to be valid for plane, smooth slopes. (Runup is defined as the combination of a superelevated mean water level, called setup, and a time-dependent oscillation called swash.) Hunt recommended smaller values depending on slope roughness. Measured values of runup normalized by deep-water wave height display no dependence on surf similarity parameter if  $\xi_o$  was calculated using  $\tan\beta$ , as the primary angle. Runup normalized by wave height was plotted versus the surf similarity parameter using the 1/30 slope as the primary angle to determine  $\xi_o$  (Fig. 6). The data show increasing  $R/H_o$  with  $\xi_o$ . The line shown in Fig. 6 represents the average value of  $(R/H_o)/\xi_o$ , which was 0.76, and is approximately the value (0.78) given by Hunt for a 1.0-mm grain size slope. The discrepancy between Eq. 3 and measured values may be attributed in part to the slope used in the present study not being as smooth as the slope used by Hunt, but this hypothesis could not be confirmed.

Ahrens (1981) developed the following equation for average wave runup for random waves,

$$\frac{R}{H_{s_o}} = 0.84\xi_o \quad (4)$$

in which  $H_{s_o}$  is the significant deep-water wave height. Average runup for random waves and the calculated values by Eq. 4 were plotted as a function of  $\xi_o$ , calculated using  $\beta_1$ . Predictions by Eq. 4 estimate runup well for the plane-slope cases, but underpredict runup for cases with bars. Runup for barred profiles nearly equals that for plane slopes and is independent of  $\xi_o$ . However, Eq. 4 gives better results if the plane slope is used to calculate  $\xi_o$  (Fig. 7).

Holman and Sallenger (1985) analyzed field data of runup for a mildly barred beach. Although there was wide scatter in the data, they concluded that runup depended on  $\xi_o$ . However, the choice of slope with which to calculate  $\xi_o$  was unclear. The foreshore slope appeared to be appropriate for data taken at high tide and mid-tide, whereas the bar slope appeared to "have at least some influence" on setup at low tide. It is not evident if the bar was a major cause of wave breaking in their low-tide measurements. The present tests indicate that a bar has a very weak influence, if any, on runup if waves break on the bar. In agreement with Holman and Sallenger, the foreshore, or wide-area slope, appears to be the best quantity to use in correlating runup with  $\xi_o$ ; however, only one slope (1/30) was used in the present study, so this conclusion can only be tentative.

### Breaking Waves

Figures 8 and 9 show average wave height  $\bar{H}$  (monochromatic waves) and root-mean-square (rms) wave height  $H_{rms}$  (random waves), respectively, normalized by local still-water depth  $h$  as a function of distance from the shoreline at the still-water level. Wave decay for identical wave conditions is shown in each figure for plane (solid line) and irregular profiles (dashed lines). The tests conducted with bars show a significant increase of  $\bar{H}/h$  and  $H_{rms}/h$  over the bar. The increase results from shallower water at the bar and higher waves by (nonlinear) shoaling over the bar. Wave height to water depth decreases directly shoreward of the bar because the water is deeper, and a majority of the waves broke on the bar. The ratio increases as water depth decreases in the surf zone for all tests, including tests on the plane slope. The figures indicate that wave height does not decay uniformly through

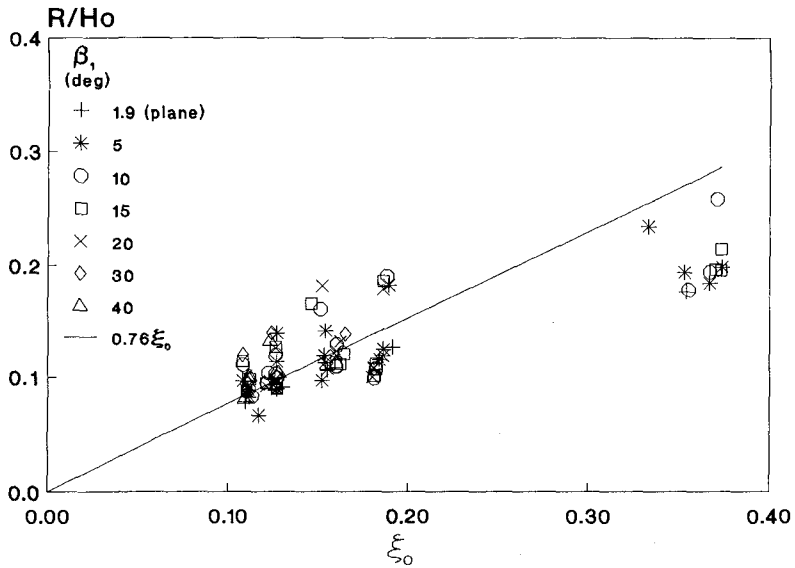


Fig. 6. Runup on barred and plane slopes (monochromatic waves)

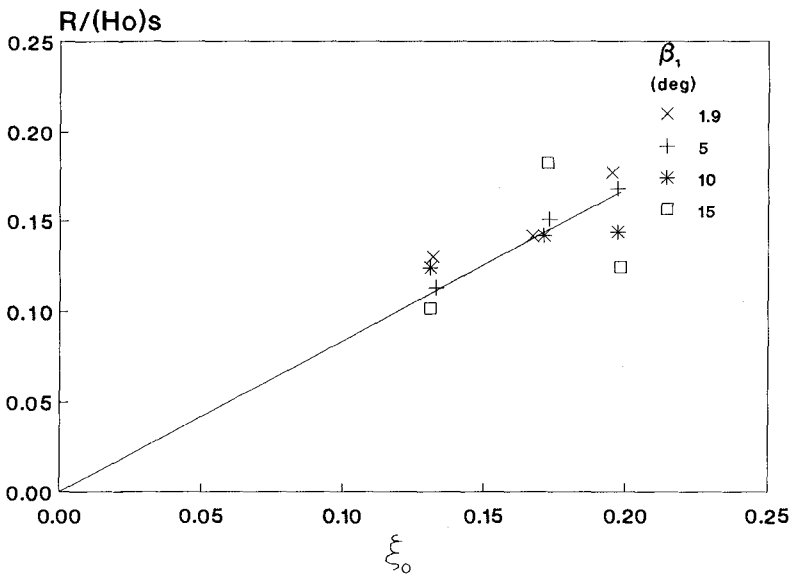


Fig. 7. Runup on barred and plane slopes (random waves)

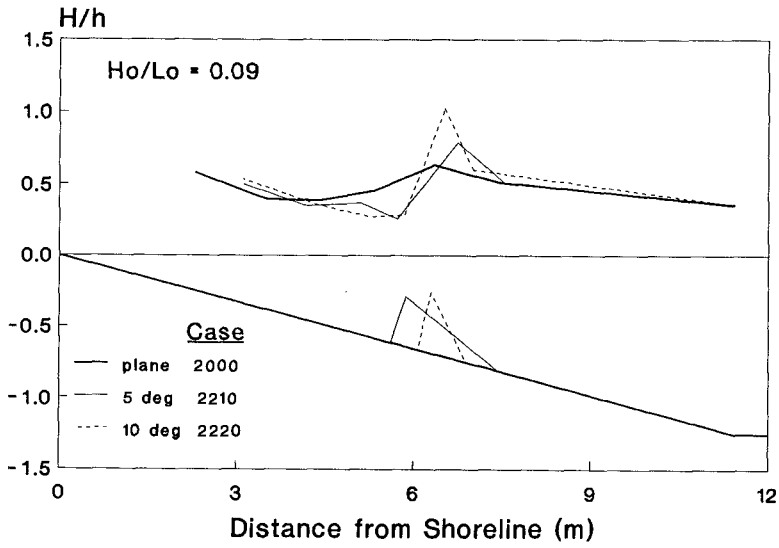


Fig. 8. Wave height on plane slope & two barred slopes,  $H_{so}/L_p = 0.09$  (mono. waves)

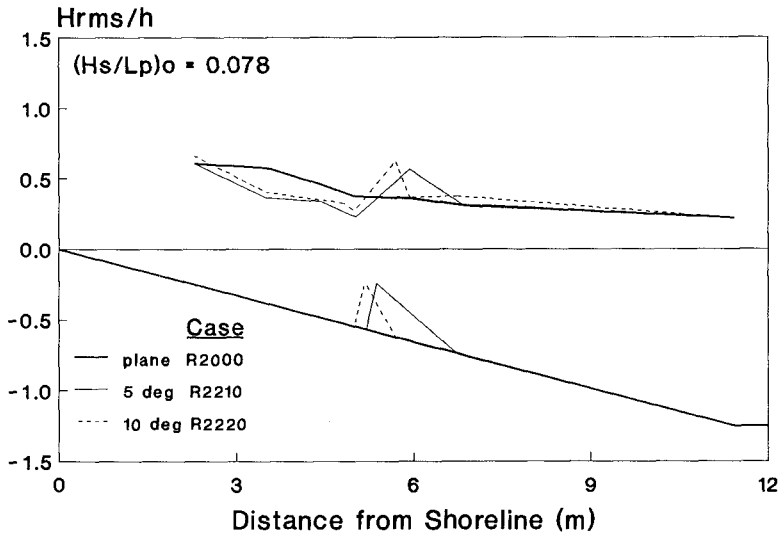


Fig. 9. Wave height on plane slope & two barred slopes,  $H_{so}/L_p = 0.078$  (random waves)

the surf zone for either barred profiles or plane-sloping beaches. Figs. 8 and 9 show that the wave height to water depth ratio is the same in the inner surf zone for barred profiles and plane slopes, despite appreciable differences near breaking. Although the ratio is identical in the inner surf zone, visual observations showed that for most tests broken waves on plane slopes remained as bores through the surf zone, whereas most broken waves on the barred profile reformed.

Maximum wave height  $H_{max}$ , significant wave height, and rms wave height were calculated from the time series of the random wave trains and were plotted versus distance from the still-water shoreline in Figs. 10 and 11. The deviation between  $H_{max}$ ,  $H_s$ , and  $H_{rms}$  decreased as the waves entered shallower water, indicating the waves become constant in height in the inner surf zone. This behavior has also been shown in other random wave studies, such as Thompson and Vincent (1984) for a plane-slope laboratory beach, and by Ebersole and Hughes (1987) for a barred profile in the field, and by Battjes and Beji (1992) for an irregular-bottom laboratory beach.

### Transformation of Wave Spectra

Wave spectra showed surprisingly little variation at fixed points along the profile for plane and barred slopes. Fig. 12 shows spectra for selected gages in two tests with the same gage locations and deep-water waves (random waves,  $H_s = 14.3$  cm,  $T_p = 1.5$  sec). The spectra were averaged over 16 frequency bands. Gage 2 was located in the shoaling zone seaward of significant breaking, Gage 4 was located in a region of significant breaking (on top of the bar in the case of the barred profile), Gage 6 was located shoreward of the bar in the outer surf zone, and Gage 8 was at the most shoreward measurement point in the inner surf zone where many waves had reformed. Two spectra are plotted for each gage, one for the barred slope and the other for the plane slope; these spectra are difficult to distinguish, having the same magnitude and shape, except for Gage 6, located directly shoreward of significant breaking. At Gage 6, energy in the vicinity of the peak frequency for the barred profile is greatly reduced, as is the energy of the low-frequency seiching mode. This result was pointed out in a different way in Figs. 8 and 9, as a decrease in rms wave height. (Note, in Fig. 12, the energy density is given in units of  $\text{ft}^2/\text{Hz}$ , where  $1 \text{ ft} = 0.3048 \text{ m}$ .)

### CONCLUSIONS

For monochromatic and random waves, wave-height to water-depth ratios were higher for waves breaking on bars than on plane slopes because of increased wave height and reduced water depth. Directly shoreward of breaking, the ratio for barred profiles was less than the plane slope. Wave-height to water-depth ratios increased in the surf zone for cases with and without bars and were identical in the inner surf zone. Although the wave height and spectra were approximately equal in the inner surf zone for both barred and plane beaches, broken waves on the plane slope tended to remain as bores through the surf zone, whereas most broken waves on barred profiles reformed. Maximum, significant, and root-mean-square wave heights of random waves became constant in height in the inner surf zone. Similarly, for the same deep-water wave condition, the energy content and shape of wave spectra were preserved from deep water to the inner surf zone, except in a region directly shoreward of the break point, where the spectra on barred profiles contained less energy than that on a plane slope.

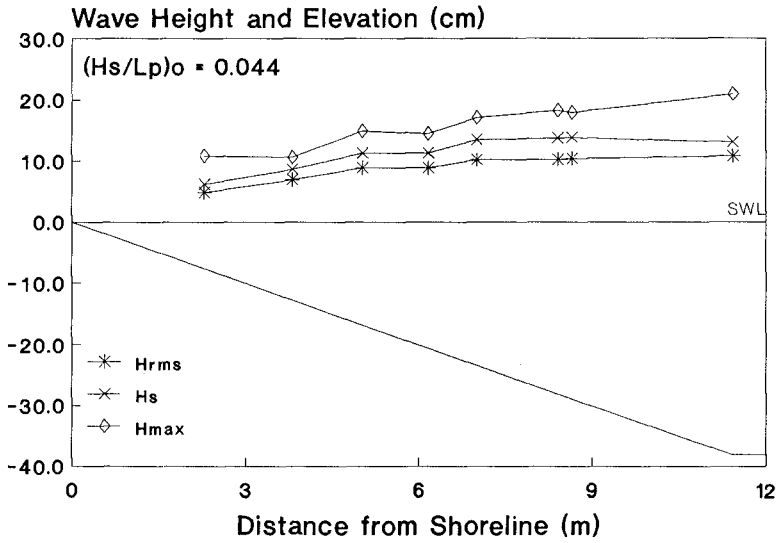


Fig. 10. Statistical wave heights on a plane slope,  $(H_s/L_p)_o = 0.044$  (random waves)

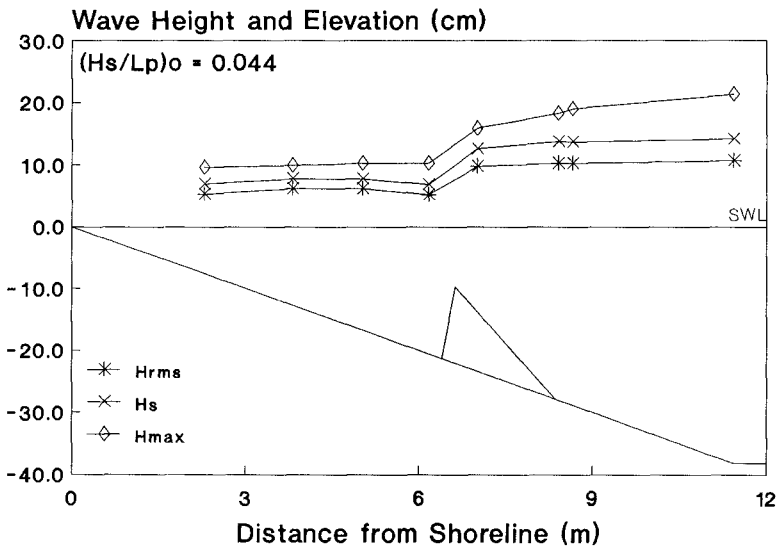


Fig. 11. Statistical wave heights on a barred slope,  $(H_s/L_p)_o = 0.044$  (random waves)

Reflection coefficients were found to be nearly constant across all tests. Reflection was controlled mainly by the plane bottom slope, and only weak variations in  $K_r$  were attributable to the seaward and shoreward bar angles. Barred profiles, including extreme bars or reefs, did not alter runup, which was controlled by the plane slope. For monochromatic waves, the measurements followed the runup equation of Hunt (1959) for beaches with 1.0-mm sand grain size. An equation of Ahrens (1981) well predicted average runup for random waves on barred profiles, with the bottom slope in the equation given by the plane slope. In summary, despite differences between breaker-related quantities on barred profiles and plane slopes, wave runup, reflection, and transformation in the inner surf zone on barred profiles were controlled by the plane bottom slope, with only minor influence by the bar, even for extreme (unnatural) bars.

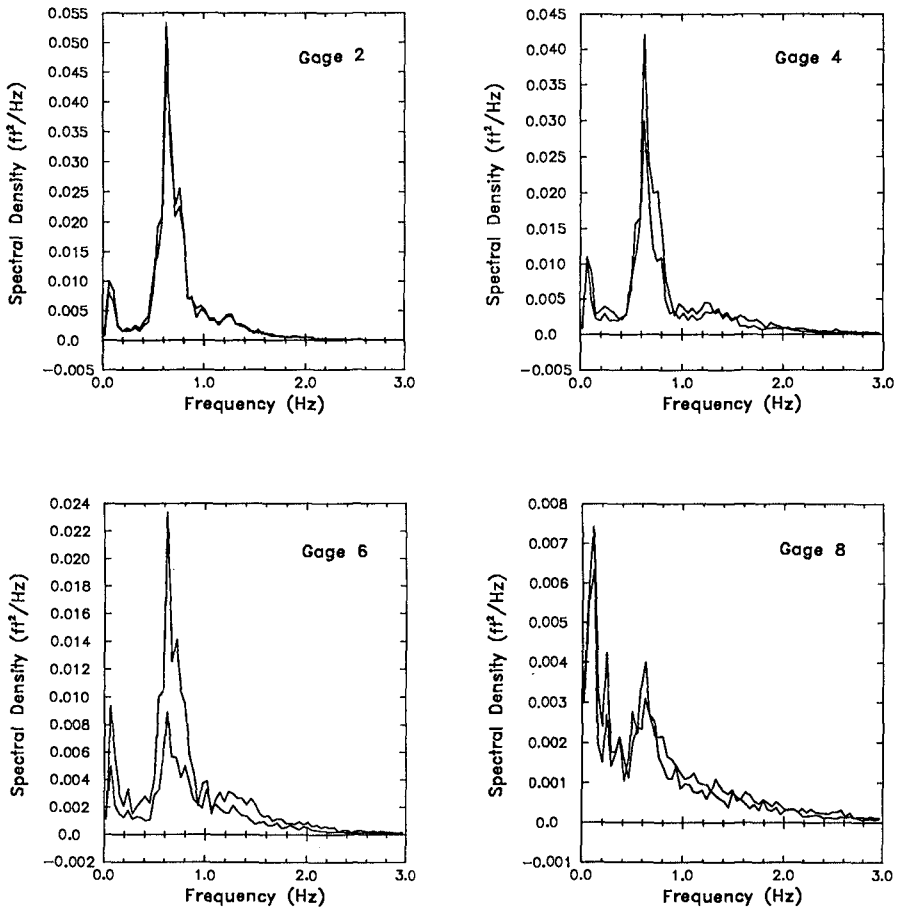


Fig. 12. Wave spectra on barred and plane slopes  $(H_s/L_p)_0 = 0.044$  (random waves)

## ACKNOWLEDGEMENTS

We thank Mr. George Kaminsky, former contract student, and Mr. John Evans, Engineering Technician, Coastal Engineering Research Center, for their assistance and advice in the laboratory. This study was performed as part of the activities of the Nearshore Waves and Currents work unit of the Shore Protection and Evaluation Program, Coastal Engineering area of Civil Works and Development. Permission was granted by the Chief of Engineers to publish this information.

## REFERENCES

- Ahrens, J. P., 1981. "Irregular Wave Runup on Smooth Slopes," *Coastal Engrg. Tech. Aid No. 81-17*, U.S. Army Engr. Waterways Expt. Station, Coastal Engrg. Res. Center, Vicksburg, MS.
- Battjes, J. A., 1974. "Surf Similarity," *Proc. 14th Coastal Engrg. Conf.*, ASCE, 466-480.
- Battjes, J. A. and Beji, S., 1992. "Spectral Evolution in Breaking Waves Propagating Over a Shoal," *23rd Coastal Engrg. Conf. Book of Abstracts*, ASCE, 57-58.
- Ebersole, B. A., and Hughes, S. A., 1987. "DUCK85 Photopole Experiment," Misc. Paper CERC-87-18, U.S. Army Engr. Waterways Expt. Station, Coastal Engrg. Res. Center, Vicksburg, MS.
- Galvin, C. J., 1968. "Breaker Type Classification on Three Laboratory Beaches," *J. Geophys. Res.*, 73 (12), 3651-3659.
- \_\_\_\_\_, 1970. "Finite-Amplitude, Shallow Water-Waves of Periodically Recurring Form," *Proc. Symp. on Long Waves*, 1-32.
- Goda, Y., and Suzuki, Y., 1976. "Estimation of Incident and Reflected Waves in Random Wave Experiments," *Proc. 15th Coastal Engrg. Conf.*, ASCE, 828-845.
- Holman, R. A., and Sallenger, A. H., Jr., 1985. "Setup and Swash on a Natural Beach," *J. Geophys. Res.*, 90 (C1), 945-953.
- Hunt, I. A., 1959. "Design of Seawalls and Breakwaters," *J. Waterways and Harbors Div.*, ASCE, 85 (WW3), 123-152.
- Larson, M., and Kraus, N. C., 1989. "SBEACH: Numerical Model for Simulating Storm-Induced Beach Change, Report 1, Empirical Foundation and Model Development," Tech. Rep. CERC-89-9, U.S. Army Engr. Waterways Expt. Station, Coastal Engrg. Res. Center, Vicksburg, MS.
- Miche, M., 1951. "Le Pouvoir Reflexissant des Ouvrages Maritimes Exposes a l'Action de la Houle," *Annals des Ponts et Chaussées*, 121e Annee, pp 285-319 (transl. Lincoln and Chevron, U. of Calif., Berkeley, Wave Res. Lab., Ser. 3, Issue 363, June, 1954).
- Seelig, W. N. and Ahrens, J. P., 1981. "Estimation of Wave Reflection and Energy Dissipation Coefficients for Beaches, Revetments, and Breakwaters," Tech. Paper No. 81-1, U.S. Army Engr. Waterways Expt. Station, Coastal Engrg. Res. Center, Vicksburg, MS.
- Smith, E. R. and Kraus, N. C., 1990. "Laboratory Study on Macro-Features of Wave Breaking Over Bars and Artificial Reefs," Tech. Rep. CERC-90-12, U. S. Army Engr. Waterways Expt. Station, Coastal Engrg. Res. Center, Vicksburg, MS.
- Smith, E. R. and Kraus, N. C., 1991. "Laboratory Study on Wave Breaking over Bars and Artificial Reefs," *J. Waterway, Port, Coastal, and Ocean Engrg.*, 117 (4), 307-323.
- Thompson, E. F., and Vincent, C. L., 1984. "Shallow Water Wave Height Parameters," *J. Waterway, Port, Coastal and Ocean Engrg.*, 110 (2), 293-299.



## CHAPTER 48

### ESTIMATION OF IRREGULAR WAVE KINEMATICS FROM A MEASURED RECORD

Rodney J. Sobey<sup>1</sup>

#### Abstract

This review of rational predictive methodologies for irregular wave kinematics confirms the crucial importance of the complete nonlinear free surface boundary conditions. Four methods, the global design wave method, the global linear superposition method, the local Wheeler stretching method and the local Fourier approximation method, have been compared for a very large measured wave from hurricane Camille. Free surface boundary condition errors are comparable to the wave height for the design wave and Wheeler stretching methods. They are sharply reduced by the local Fourier approximation method, though not eliminated. Linear superposition fails completely in the crest-trough region.

#### Introduction

The success that has been achieved in the theoretical prediction of regular wave kinematics is not immediately transferable to the prediction of surface and near-surface kinematics in irregular waves. Significant predictive difficulties have been encountered, especially near the crest.

In many situations, analysis is based on measured or simulated water surface time histories at a fixed location. Spatial measurements of the sea state are most rare and the vast majority of measured field and laboratory records are discrete water surface  $\eta(t)$  records from wave staffs or accelerometer buoys at a fixed location. The balance of the wave kinematics (velocities, accelerations and pressures) at the fixed location needs to be estimated from the known  $\eta(t)$  trace. A closely related problem arises in statistical simulation of a random sea state from the linear Gaussian random wave model. Considerable success is achieved in the prediction of the space and time varying water surface. Unfortunately, this

---

<sup>1</sup>Professor of Civil Engineering, Environmental Resources Engineering Group, University of California, Berkeley, CA 94720, USA

success does not carry through to the near-surface kinematics, where spurious predictions result from the increasing dominance of the higher frequency (but much smaller magnitude) spectral components.

Consideration here will be restricted to a subset of this problem where there is no  $y$  variation and the direction of both the wave motion and any coexisting Eulerian current coincides locally with the  $x$  axis.

Considerable attention has been given to this problem as water velocities, accelerations and dynamic pressures all reach their maximum magnitudes at the water surface. Unfortunately, predictive methodologies are most vulnerable at the water surface, as a direct consequence of approximations in the imposition of the nonlinear free surface boundary conditions. Any methodology for the prediction of irregular wave kinematics that is both rational and viable must give appropriate attention to the free surface boundary conditions.

Global and local methodologies are distinguished. Local methods do not compromise fidelity in the representation of the free surface boundary conditions in the global interest. Global methods, which closely follow regular wave theory, are less attractive for irregular wave kinematics. This paper will compare the predictive capabilities of two common global methods (the design wave approach and linear superposition), a common local method (Wheeler stretching) and the local Fourier approximation method. As interest in irregular wave kinematics inevitably centers on big waves, the comparison will be based on a measured wave segment from Hurricane Camille, Gulf of Mexico, 1969. The selected segment has the highest crest height in the sequence and is among the biggest waves ever recorded.

## BACKGROUND IN REGULAR WAVE THEORY

Common approaches to the prediction of irregular wave kinematics closely follow the pattern adopted in classical regular progressive wave theory. The discussion is simplified by recalling the basis of the classical theory.

Attention will be directed to the unsteady formulation of regular wave theory. With the velocity potential function  $\phi(x, z, t)$  as the dependent variable, the field equation is the Laplace equation

$$\frac{\partial^2 \phi}{\partial x^2} + \frac{\partial^2 \phi}{\partial z^2} = 0 \quad (1)$$

where the velocity components  $(u, w)$  in the fixed frame are  $(\partial\phi/\partial x, \partial\phi/\partial z)$ .

This field equation is subject to the following boundary conditions:

(i) Bottom boundary condition (BBC), representing no flow through the horizontal bed, is

$$w = 0 \quad \text{at } z = -h \quad (2)$$

where  $-h$  is the elevation of the bed.

(ii) Kinematic free surface boundary condition (KFSBC), representing no flow through the free surface, is

$$w = \frac{\partial \eta}{\partial t} + u \frac{\partial \eta}{\partial x} \quad \text{at } z = \eta(x, t) \quad (3)$$

where  $\eta(x, t)$  is the free surface.

(iii) Dynamic free surface boundary condition (DFSBC), representing constant atmospheric pressure on the free surface, is

$$\frac{\partial \phi}{\partial t} + \frac{1}{2}(u^2 + w^2) + g\eta = \bar{B} \quad \text{at } z = \eta(x, t) \quad (4)$$

where  $g$  is the gravitational acceleration and  $\bar{B}$  is the Bernoulli constant.

(iv) Periodic lateral boundary conditions (PLBC), imposing wave periodicity in space and time, are

$$\phi(x, z, t) = \phi(x + 2\pi/k, z, t) = \phi(x, z, t + 2\pi/\omega) \quad (5)$$

where  $k$  is the wave number and  $\omega$  is the wave frequency.

(v) Wave maintains a stable profile shape (or permanent form), requiring the wave profile to be symmetric in both  $x$  and  $t$  about the crest.

Because of conditions (iv) and (v), progressive waves of permanent form are steady in a frame of reference moving at the phase speed  $C = \omega/k$ . The space and time variations of the water surface must follow

$$\frac{d\eta}{dt} = \frac{\partial \eta}{\partial t} + C \frac{\partial \eta}{\partial x} = 0 \quad (6)$$

### Predictive Capability of Regular Wave Theory

Established regular wave theories (Stokes, Cnoidal, Fourier approximation) generally take advantage of the relative simplicity of the steady formulation where the independent variables are reduced to  $x - Ct$  and  $z$ . Basis function predictors of the dependent variable (typically the stream function) identically satisfy both the field equation and the bottom boundary condition, together with the permanent form constraint and the periodic lateral boundary conditions. Compatibility conditions designate the wave height and the co-flowing current.

The essential detail of the solution however is determined largely by the free surface boundary conditions, which must be satisfied along the complete water surface. The complexity of the gravity wave problem is manifested through these free surface boundary conditions, which introduce nonlinearity to the problem and are applicable at a free surface that is itself part of the solution. Different orders of the same wave theory are distinguished by the level of approximation to the free surface boundary conditions, higher orders providing enhanced fidelity.

A conflict is immediately identified between the predictive capabilities of regular wave theory and the nature of the solution field. Wave theory consistently predicts that peak magnitudes and response extremes in velocities, accelerations and dynamic pressures are located along the free surface. Unfortunately, this region of peak interest in the kinematics and dynamics exactly coincides with the

region of maximum uncertainty in the wave theory predictions.

Appropriate measures of theoretical error may be formulated from the free surface boundary conditions at the water surface. The kinematic and dynamic free surface boundary condition errors are respectively

$$K(x, t) = w(x, \eta, t) - \frac{d\eta}{dt} \quad (7)$$

and

$$D(x, t) = \frac{\partial \phi}{\partial t}(x, \eta, t) + \frac{1}{2}[u^2(x, \eta, t) + w^2(x, \eta, t)] + g\eta - \bar{B} \quad (8)$$

In application, these will be represented in length units, as  $K/\omega$  and  $D/g$  respectively, for direct comparison with the local water surface elevation.

For waves of even moderate height, the free surface boundary condition errors associated with the lowest order theory are significant. Predictive difficulties for near-surface kinematics must be expected from adoption of linear wave theory. They are indeed experienced. Nevertheless, there remains a reluctance to reject the simplicity and familiarity of the linear theory, and several measures have been proposed to mitigate the near-surface failings.

Higher order theories by definition do a much better job in satisfying the free surface boundary conditions. They have little theoretical difficulties in the prediction of near-surface kinematics in steady waves, though they may often impose a considerable computational burden. Irregular waves are not steady, but it is clear that fidelity in representing the free surface boundary conditions must have a crucial role in any rational predictive methodology for irregular wave kinematics.

Several unfavorable comparisons of regular wave theory and laboratory measurements have received considerable attention. The evidence however is not conclusive and closer scrutiny (Sobey 1989b) suggests that the predictive potential of regular wave theory remains sound. Errors both in measurement and in application of theory can be substantial and more than sufficient to negate any hasty conclusions.

The influence of current in particular is often not given the attention it deserves. This involves the specification of the appropriate definition (Stokes' first or second) of phase speed and the associated current. The differences are potentially significant and compounded by the fact that many published wave theories have automatically assumed Stokes' first definition of phase speed (and often also zero current) in the problem formulation. Current is assumed to be depth-uniform and any vertical structure is ignored<sup>2</sup>. The adoption of a higher order wave theory may not be realistic where due attention has not been given

---

<sup>2</sup>A Stokes theory with a linear velocity profile (i.e. constant vorticity) by Kishida and Sobey (1988) has suggested that vorticity has only a very minor influence. After subtracting out the current profile, the residual "wave" kinematics are little different from those that would have been predicted for a uniform current with the same depth-averaged magnitude. The generality of this observation is presently uncertain.

to the influence of tidal or other ocean currents on the wave kinematics. Alternatively, if the current is not known, higher order precision cannot and should not be expected.

Steady wave theory provides predictions of kinematics in long-crested regular progressive waves. Despite some unfortunate misinterpretation in the literature, steady wave theory does do a credible job where the waves correspond with the assumptions of the theory. The waves must be reasonably long-crested and steady, and the adopted wave theory must be consistent with the field or laboratory conditions. While the basis of wave theory is indeed sound, irregular waves clearly violate the permanent form and periodicity assumptions of the classical steady wave problem. Accordingly, there can be no strong expectation that regular wave theory will predict more than an outline of the kinematics in irregular waves.

### **Generalization to Irregular Waves**

The spatial and temporal complexity of irregular waves would initially appear to have little in common with the conspicuous order of regular wave theory. Nonetheless, much of the problem formulation remains appropriate. Irregular waves are by nature unsteady, so that an unsteady formulation is pertinent. The field equation (Eq. 1), the bottom boundary condition (Eq. 2) and both free surface boundary conditions (Eqs. 3 and 4) continue to be applicable; these make up the bulk of the mathematical physics. Neither the periodic lateral boundary conditions, nor symmetry about the crest in  $x$  and  $t$  are appropriate for irregular waves. Further, application of the KFSBC is inconsistent with the present reliance on measured water surface records at a fixed location, as spatial gradients  $\partial\eta/\partial x$  are not available from the measured record.

The crucial aspects of the mathematical physics of the regular wave problem are the nonlinear free surface boundary conditions. The close relationship between regular and irregular wave theory guarantees that the free surface boundary conditions will remain a crucial aspect of irregular wave theories.

### **GLOBAL APPROXIMATIONS**

Methodologies that seek to represent a complete irregular wave, from crest to following crest, from trough to following trough or from zero-crossing to following zero-crossing, are categorized as global. Among global methods, only the design wave and linear superposition methods will be considered here. Fourier-style methods (Dean 1965, Lambros 1981) and numerical field solutions (Forristall 1985) have also been proposed.

### **Design Wave**

An obvious candidate is to couple a trough to trough or zero-crossing identification of a wave height and a wave period for an individual wave record with an appropriate steady wave theory prediction for the same height, period, water depth and current. In principle, this is the essence of the design wave approach. As the dominant length and time scales are essentially correct, there

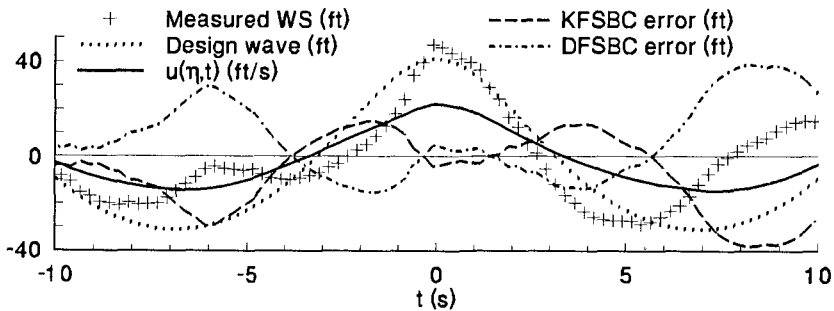
is an intuitive expectation that ensuing predictions of crest kinematics have the correct order of magnitude. There can be no expectation however that the predictive capability will consistently exceed order-of-magnitude precision. The associated regular wave theory will predict the water surface profile of the design wave. Regular and irregular wave profiles are unlikely to correspond, so that the free surface boundary conditions will not be satisfied on the actual water surface.

The nature of the design wave approximation is illustrated in Fig. 1, which is based on a measured water surface record from Hurricane Camille in the Gulf of Mexico in 1969. The record sequence is amongst the biggest waves ever recorded. The water depth is 340 ft (103.6 m). In selecting design waves from a measured record, trough to trough identification is often preferred because of its focus on the crest. The height and period are 72.1 ft (22.0 m) and 13.8 s respectively, so that this is a deep water wave. The solid line shows the steady wave theory (Fourier) prediction of horizontal velocity along the predicted water surface, located such that the crest time corresponds with the measured record. Also shown are the KFSBC and DFSBC errors along the measured water surface. These errors are of comparable order to the wave height. The design wave approach will certainly provide order of magnitude estimates of irregular wave kinematics, but consistently better predictions cannot be expected.

### Superposition of Linear Waves

A familiar alternative is the superposition of numerous freely-propagating Airy waves, whose amplitudes, frequencies and phases are determined from a discrete Fourier transform of the irregular water surface profile. Consistent kinematics are available from Airy wave theory.

As a direct consequence of the linear superposition approximation, the Fourier transforms all involve relatively simple transformations on the Fourier transform of the irregular water surface profile. The transfer functions (e.g.  $\omega CS(kz, kh)$  for horizontal velocity, where  $CS(kz, kh) = \cosh k(h+z)/\sinh kh$ ) are frequency, depth, (wave number,) and elevation dependent, where each of the component Airy waves separately satisfies the linear dispersion relationship. A



**Figure 1.** Design wave approximation to a measured deep water wave from hurricane Camille. Profile comparisons. horizontal velocity and free surface boundary condition errors along measured water surface.

discrete inverse Fourier transform will predict the time history of the field variable.

Using the FFT algorithm, the numerical procedure is tidy and efficient, but linear superposition does introduce some explicit assumptions regarding the nature of the irregular sea state and its spatial and temporal evolution. The adoption of Airy theory to characterize the separate components assumes that the irregular sea state is composed entirely of free modes, each component being a freely propagating Airy wave that separately satisfies the linear dispersion relationship. There are no bound modes and the FFT algorithm imposes a periodicity in time equal to the duration of the measured record.

In addition, considerable difficulties are encountered at elevations above the MWL, which is the strict upper bound of the Airy solution domain. The hyperbolic function quotients (CS, SS and CC) become exceptionally large for the high frequency (and high wave number) components. Where the record segment is a single irregular wave, the frequency resolution is  $\omega_0 = 2\pi/T$ , where  $T$  is the duration of the record and the approximate period. The frequency of the  $n$ th component is  $\omega_n = n\omega_0$  and the relative depth  $\omega_n^2 h/g = n^2 \omega_0^2 h/g$  rapidly increases with  $n$ . For  $\omega_n^2 h/g > 2.5$ , the CS( $k_n z, k_n h$ ), SS( $k_n z, k_n h$ ) and CC( $k_n z, k_n h$ ) hyperbolic function quotients approach  $\exp(k_n z)$  or  $\exp(n^2 \omega_0^2 z/g)$ . For large positive  $z$  in the crest region, these functions enormously magnify the influence of the high frequency components in the Fourier transform or variance spectrum. Kinematic predictions in the crest region become exceptionally large and clearly incorrect. They generally overflow the high number capacity of digital computer software, even in double precision. Any positive value of  $z$  is of course outside the strict Airy solution domain, and crest elevations are well above even the water surface of the smaller magnitude higher frequency components.

As these high frequency components generally contribute little to the total variance of the water surface record, low pass filtering of the Fourier transform is a potentially pragmatic response to this difficulty. An application to the Camille record segment is shown in Fig. 2. The fundamental frequency is  $\omega_0 = 2\pi/13.8 \text{ s}^{-1}$  or  $f_0 = 0.072 \text{ Hz}$  and the record Nyquist frequency is 2.0 Hz. Part (a) shows the measured water surface record together with the horizontal velocity prediction and the KFSBC and DFSBC errors at the measured water surface for a frequency cutoff at 0.1 Hz. This includes only a single frequency component  $\omega_0$ . It is effectively a design wave approximation using Airy theory, and the free surface boundary condition errors are broadly comparable to Fig. 1. Part (b) shows the same traces for a 0.15 Hz cutoff. This includes only two frequencies  $\omega_0$  and  $2\omega_0$ , yet predictive problems at the crest are already apparent. The predicted peak horizontal velocity has risen from 14.8 ft/s (4.5 m/s) to 59.6 ft/s (18.2 m/s) and the KFSBC error oscillates off scale. Including also  $3\omega_0$  increases the predicted peak horizontal velocity still further to 114.6 ft/s (34.9 m/s).

Clearly, Airy wave superposition, even with an arbitrarily determined cutoff frequency, has no credibility in estimating kinematics in the crest region (Forristall 1985). For elevations below the MWL, linear superposition may continue to provide credible predictions of the wave kinematics.

**LOCAL APPROXIMATIONS**

Methodologies that seek only to represent the local behavior of an irregular wave are categorized as local. Given that significant problems such as crest kinematics are strongly related to local errors in the free surface boundary conditions, there is evident attraction in such an approach. These methodologies compromise applicability in a global sense in an effort to achieve fidelity in a local sense. Note that this contrasts with the general approach of steady wave theory where local fidelity (especially near the wave crest) is perhaps sacrificed in the global interest.

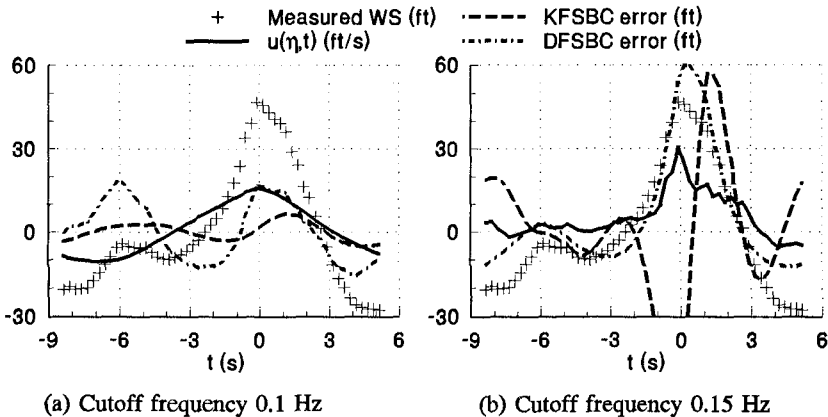
**Stretching Approximations**

One form of local approximation, the so-called 'stretching' method of Wheeler (1969), has found considerable favor as a pragmatic approach to the prediction of irregular wave kinematics. Recognizing that the failure of Airy superposition was contributed by extrapolation of the hyperbolic function quotients beyond the upper bound of the Airy solution domain, Wheeler introduced an empirical transformation on the local elevation such that it never exceeds the MWL. The horizontal velocity was predicted as

$$u(x, z, t) = \sum_j \omega_n \frac{\cosh \alpha k_n h}{\sinh k_n h} \eta_n(x, t) \tag{9}$$

where  $\alpha(x, z, t) = (h + z)/(h + \eta)$ , the transformation depending on the local water surface elevation  $\eta(x, t)$ . Though not defined by Wheeler, consistent definitions for the balance of the kinematics follow directly from the linear superposition approximations.

The stretching transformation shifts the instantaneous water surface to the MWL and avoids the spurious predictions of crest kinematics from direct linear



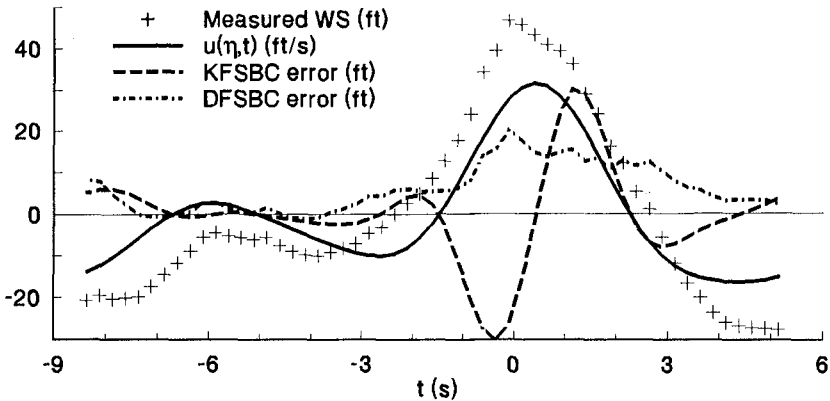
**Figure 2.** Linear superposition approximation to a measured deep water wave from hurricane Camille. Horizontal velocity and free surface boundary condition errors along measured water surface.



superposition. It also remains a linear superposition approximation and a linear spectral description of the kinematics. As such, it preserves access to the familiar methodologies of (linear) time series analysis in the time and frequency domains that are common practice in applications such as the dynamic structural analysis of offshore platforms.

Significant problems nonetheless remain. As a result of the stretching transformation, mass and momentum are no longer conserved by the predictive equations for the kinematics. The nature of the residual problems however remains best illustrated in the context of the free surface boundary conditions. The relocation of the local water surface to the MWL does sharply reduce errors in the free surface boundary conditions, as Airy theory imposes the free surface boundary conditions at the MWL. But the Airy theory does not impose the full free surface boundary conditions, and the omitted nonlinear terms are especially influential in the crucial crest region for the moderate to extreme waves that are common in design.

Smaller magnitude high frequency components in the Fourier transform remain troublesome and Wheeler (1969), for example, adopted a low pass cutoff frequency of 0.3 Hz. An application of the stretching methodology to the Camille record segment is shown in Fig. 3, which shows the measured water surface together with the predicted horizontal velocity, KFSBC and DFSBC traces at the measured water surface; frequencies above 0.3 Hz were excluded from the Fourier transforms. The 0.3 Hz cutoff includes the fundamental frequency  $\omega_0 = 2\pi/T$ , where  $T$  is the duration of the record segment (and the approximate period), together with the first three harmonics  $2\omega_0$ ,  $3\omega_0$  and  $4\omega_0$ . With direct linear superposition (as shown in Fig. 2), the horizontal velocity predictions in the crest region would be extremely large and well off scale, because of the influence the  $3\omega_0$  and  $4\omega_0$  frequencies on the hyperbolic function quotients in the crest region. The stretching approximation constrains these spurious contributions and



**Figure 3** Stretching approximation to a measured deep water wave from hurricane Camille. Horizontal velocity and free surface boundary condition errors along measured WS. Cutoff frequency 0.3 Hz.

provides a prediction of horizontal velocity at the water surface that is similar in magnitude to the design wave approximation in Fig. 1. Whether or not it is a superior approximation is unclear, as both have free surface boundary condition errors of significant magnitude.

The stretching approximation focuses on satisfying the linearized free surface boundary conditions at the measured water surface. This is done exactly for the KFSBC and approximately<sup>3</sup> for the DFSBC. But the nonlinear terms become significant, especially the KFSBC term  $u\partial\eta/\partial x$  in the crest region. Fig. 3 shows this error to be comparable in magnitude to the wave height.

### Local Airy Approximations

Airy wave theory has also been used with locally defined rather than globally defined parameters. Airy theory predicts that the water surface profile is

$$\eta(x,t) = a \cos(kx - \omega t + \theta) \quad (10)$$

where  $\theta$  is the phase. At a fixed location, the local parameters are the amplitude  $a$ , the frequency  $\omega$  and the net phase  $kx + \theta$ .

Nielsen (1986, 1989) localized the definition of amplitude, frequency and phase to a moving window of three consecutive water surface observations  $\eta_-$ ,  $\eta_0$  and  $\eta_+$ , spaced in time by  $\Delta t$ . Together with Eq. 10, these are sufficient to uniquely define the local amplitude, frequency and phase, as

$$\omega = \frac{1}{\Delta t} \cos^{-1}\left(\frac{\eta_+ + \eta_-}{2\eta_0}\right), \quad kx + \theta = \tan^{-1}\left(\frac{\eta_+ - \eta_-}{2\eta_0 \sin \omega \Delta t}\right), \quad a = \frac{\eta_0}{\cos(kx + \theta)} \quad (11)$$

respectively. The simplicity of this approach is immediately appealing, especially as it accommodates the irregularity by varying the local wave parameters and retains the familiarity and computational simplicity of the Airy wave theory. Unfortunately, Airy theory remains inadequate in the prediction of crest kinematics. Even with the addition of vertical coordinate stretching, it excludes the nonlinear terms in the free surface boundary conditions, especially the  $u\partial\eta/\partial x$  term, which are not small in the crest region of moderate and extreme waves.

In addition, Eqs. 11 fail frequently along the water surface on application to strongly irregular waves.  $(\eta_+ + \eta_-)/2$  is approximately  $\eta_0$ , so that the argument of the inverse cosine function in the predictive equation for the local frequency is approximately one. Arguments less than one are always encountered for an exactly linear profile. For a nonlinear wave of approximately permanent form, arguments in excess of one are computed in the neighborhood of the profile MWL crossings. A local frequency cannot be estimated; neither can the local phase and amplitude be estimated, as they depend on the frequency estimate. More significantly perhaps, similar problems are encountered at inflection points and around local minima and maxima in the crest and trough regions, such as are observed in the Camille trace.

---

<sup>3</sup>But exactly at the smoothed (i.e. after low pass frequency filtering) location of the water surface.

### Local Fourier Approximation

As outlined previously, a rational approximation to irregular waves should satisfy the field equation (Eq. 1), the bottom boundary condition (Eq. 2) and the complete form of both free surface boundary conditions (Eqs. 3 and 4); the permanent form and spatial and temporal periodicity constraints are not appropriate. Maximum advantage, at least from a theoretical viewpoint, can be made of a local approximation that does not compromise on these requirements, especially on the free surface boundary conditions along the actual water surface. However, measurements of  $\eta(t)$  at a fixed  $x$  location provide no information on  $\partial\eta/\partial x$ . Some compromise is necessary in representing this term, but it should not be allowed to dominate the solution methodology.

A local Fourier approximation (Sobey 1992) provides a pragmatic and rational response to these constraints. As a local approximation method, it enhances fidelity in representation of the crucial free surface boundary conditions and minimizes the influence of the necessary spatial evolution assumption. Further, it is a generalization of the widely successful (but global) Fourier approximation method for regular waves, which has almost universal applicability for both deep and shallow water waves and for coflowing uniform currents. The methodology is extended to complete irregular water surface profiles by means of a moving window of duration  $\tau$ , which is small in comparison with the local zero-crossing period.

The basis of the method is the representation of the velocity potential function within each window as

$$\phi(x, z, t) = U_E x + \sum_{j=1}^J A_j \frac{\cosh jk(h+z)}{\cosh jkh} \sin j(kx - \omega t) \quad (12)$$

This representation is familiar from global Fourier wave theory (e.g. Sobey 1989a), where  $U_E$  is the spatially-uniform Eulerian current,  $h$  is the water depth,  $A_j$  are the Fourier coefficients,  $k$  is the wave number,  $\omega$  is the wave frequency and  $(x, z)$  is the spatial position in the fixed frame. The current and the water depth define the local propagation medium and must be specified. In Fourier wave theory,  $\omega$ ,  $k$  and the  $A_j$ , together with the Bernoulli constant  $B$ , are a defining set of parameters that have unique values. In the local Fourier approximation method, the defining set of parameters is no longer constant but varies from window to window.

Within each window, the Eq. 12 basis functions exactly satisfy both the field equation throughout the fluid domain and the bottom boundary condition, whatever the numerical values of the defining set of parameters. The defining set of parameters is determined within each window to best satisfy the free surface boundary conditions at the measured elevations of the free surface within the window. In addition, the Bernoulli constant in the DFSBC is not a free parameter, being related to the other solution parameters through an exact integral relationship. In a global approximation, this constraint is implicit in imposition of the DFSBC along the entire water surface from crest to trough.

For each window solution, the given information is the local water depth

$h$  and the local coflowing uniform Eulerian current  $U_E$ , together with a set of water surface elevations  $\eta_i$ , where the  $i = 1, 2, \dots, J$  are distributed over the local window of duration  $\tau$ .

The temporal and spatial gradients of the water surface in the KFSBC equations remain to be specified. Temporal gradients can be estimated from the water surface time history. Cubic spline interpolation among the measured water surface nodes conveniently provides consistent and smoothly varying estimates of both  $\eta$  and  $\partial\eta/\partial t$ . The spatial gradient  $\partial\eta/\partial x$  is estimated from a locally steady assumption, which imposes Eq. 6 in each local window and relates the spatial and temporal gradients as

$$\frac{\partial\eta}{\partial x} = -\frac{1}{C} \frac{\partial\eta}{\partial t} \quad (14)$$

where  $C = \omega/k$  in the local window. The steady profile assumption is not imposed beyond the local window and does not dominate the solution methodology, as it does for example in the global Fourier-style methodologies.

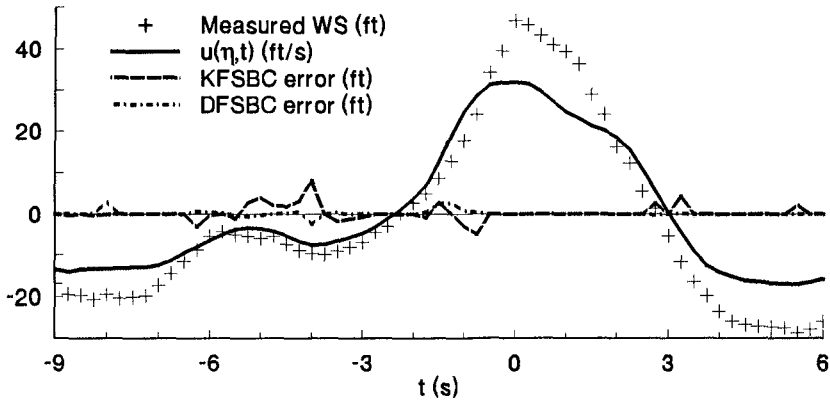
This equation set is nonlinear and implicit. The primitive unknowns in the local window are  $\omega$ ,  $k$ ,  $kx$  and the  $A_j$ , of which there are  $J$ . There are two independent equations potentially available at each of the  $\eta$  observations within the local window, of which  $M$  are selected for the numerical solution. The problem is uniquely defined for  $M = 3 + J$  and overspecified for  $M > 3 + J$ . In recognition of the certain existence of error bands about the measured water surface elevations, some overspecification is advantageous. Though significantly complicated by the error bands, numerical solution considerations are similar to those encountered in the Fourier steady wave theory; they are discussed in detail by Sobey (1992).

From a strictly numerical viewpoint, the only constraint on the choice of order  $J$  and the local window width  $\tau$  is the  $M \geq 3 + J$  requirement. There is a clear expectation however that an appropriate choice of these parameters will be dependent on the physical nature of the water surface time history together with the local resolution of the measured record. With cubic spline interpolation of the water surface record, the time location of individual windows is independent of the order and the window width. Nonetheless, adequate resolution must be provided to capture the temporal variation in the near-surface kinematics.

An application of this methodology to the Camille record segment is shown in Fig. 4. The free surface boundary condition errors are substantially reduced, especially in the crest region where interest is often centered. Overall, errors are small with respect to the wave height, but residual errors persist at profile zero-crossings and around local minima and maxima in the trough region.

### Local Polynomial Approximation

Fenton (1986) introduced a local polynomial approximation for the interpretation of submerged pressure records. With some changes to reflect the different context, the local polynomial methodology can be extended to irregular water surface records.



**Figure 4** Local Fourier approximation to a measured wave from hurricane Camille. Horizontal velocity and free surface boundary condition errors along measured water surface.  $J=1$ ,  $\tau=0.1$  s.

The wave field is assumed to be locally steady with local phase speed  $C$ , such that variations with  $x$  and  $t$  in the fixed frame can be combined in a locally steady frame as  $X = x - Ct$ , as in steady wave theory. The local solution is represented by a truncated polynomial series for the complex potential function

$$\Phi(X, z) + i\Psi(X, z) = \sum_{j=0}^M \frac{A_j}{j+1} [X + i(h+z)]^{j+1} \quad (15)$$

where the  $a_j$  polynomial coefficients are real. These basis functions satisfy the field equation and bottom boundary condition exactly. The polynomial coefficients would be determined numerically to best fit the kinematic and dynamic free surface boundary conditions at the known water surface nodes  $\eta_i$ , where the  $i = 1, 2, \dots, I$  are distributed over the local window of duration  $\tau$ .

The specific equations defining the window solutions closely parallel those for the local Fourier approximation. As  $\omega$  and  $k$  are involved in the local approximation, the local phase speed  $C$  is an explicit unknown. Given an estimate of the mean fluid speed in the locally steady frame, such as  $\Psi(0, 0)/h$  (Fenton 1986), the phase speed is estimated from a local dispersion relationship.

A polynomial variation in the vertical is a feature of the steady Cnoidal wave theory, and it would be expected that this approximation would be most appropriate in shallow water. It may be less satisfactory for deep water waves, where the vertical variation tends to exponential and local Fourier approximation may be more suitable. The local polynomial and Fourier approximations appear complementary.

## CONCLUSIONS

Even in regular wave theory, errors are centered on the free surface boundary

conditions. For irregular wave kinematics, a rational predictive capability should give particular attention to the complete nonlinear kinematic and dynamic free surface boundary conditions. Four approaches to irregular wave kinematics, the global design wave method, global linear superposition, local Wheeler stretching and the local Fourier approximation method, have been compared for a very large measured wave from hurricane Camille. Free surface boundary condition errors are comparable to the wave height for the design wave and Wheeler stretching methods. They are sharply reduced by the local Fourier approximation method, though not eliminated. Linear superposition fails completely in the estimation of surface and near-surface kinematics.

## REFERENCES

- Dean, R.G. (1965). "Stream function representation of nonlinear ocean waves," *Journal of Geophysical Research*, 70 4561-4572.
- Fenton, J.D. (1986). "Polynomial approximation and water waves." In *Procs., 20th International Conference on Coastal Engineering, Taipei*. Vol. 1., ASCE, New York, 193-207.
- Forristall, G.Z. (1985). "Irregular wave kinematics from a kinematic boundary condition fit (KBCF)," *Applied Ocean Research*, 7, 202-212.
- Kishida, N., and Sobey, R.J. (1988). "Stokes theory for waves on linear shear current," *Journal of Engineering Mechanics*, 114, 1317-1334.
- Lambrakos, K.F. (1981). "Extended velocity potential wave kinematics," *Journal of Waterway, Port, Coastal and Ocean Division, ASCE*, 107, 159-174.
- Nielsen, P. (1986). "Local approximations: A new way of dealing with irregular waves." In *Procs., 20th International Conference on Coastal Engineering, Taipei*. Vol. 1., ASCE, New York, 633-646.
- Nielsen, P. (1989). "Analysis of natural waves by local approximations," *Journal of Waterway, Port, Coastal and Ocean Engineering*, 115, 384-396.
- Sobey, R.J. (1989a). "Variations on Fourier wave theory," *International Journal for Numerical Methods in Fluids*, 9, 1453-1467.
- Sobey, R.J. (1989b). "Wave theory predictions of crest kinematics." In *Procs., NATO Advanced Research Workshop on Water Wave Kinematics, Molde, Norway*. (Eds. Torum, A. and Gudmestad, O.T.) Kluwer Academic Publishers, Dordrecht, 215-231.
- Sobey, R.J. (1992). "A local Fourier approximation method for irregular wave kinematics," *Applied Ocean Research*, 14, 93-105.
- Wheeler, J.D. (1969). "Method for calculating forces produced by irregular waves." In *Procs., 1st Annual Offshore Technology Conference, Houston*. Vol. 1., 71-82.

## CHAPTER 49

### ON SPECTRAL INSTABILITIES AND DEVELOPMENT OF NON-LINEARITIES IN PROPAGATING DEEP-WATER WAVE TRAINS

C.T. Stansberg <sup>1</sup>

#### Abstract

Modulation instabilities in surface waves on deep water are investigated. Experimental wave elevation records from laboratory tests are analysed, based on simultaneous records at different distances from the wavemaker. Initially monochromatic and bi-chromatic wave trains are seen to gradually change with the propagation, by splitting up into smaller groups. After further propagation, large individual waves, and wave breaking, may occur. Results from tests with irregular (random) waves indicate that the skewness of the record, which is mainly a measure of 2nd order nonlinearities, is closely connected to the wave steepness during the whole propagation, more or less independently of other wave processes going on. The non-linear wave group formation, however, which is related to higher-order instabilities, show a development during the propagation. This may lead to frequency down-shift of the wave energy, combined with energy dissipation and wave breaking.

#### 1. INTRODUCTION

Initially monochromatic wave trains (or more correctly: periodic Stokes waves) are unstable (Benjamin & Feir 1967). After a certain propagation distance, slow modulations will occur and grow with further propagation. This non-linear phenomenon, also known as side-band instabilities in the frequency domain, depends further on the wave steepness and is therefore coupled to the initial 2nd order (Stokes) non-linear component of the waves. The modulation itself, however, is a

-----  
<sup>1</sup>Principal Research Engineer, Norwegian Marine Technology Research Institute A/S (MARINTEK), P.O.Box 4125 Valentinslyst, N-7002 Trondheim, Norway

higher-order non-linear effect, and may be described by a 3rd order theory through the non-linear Schrödinger equation (Zakharov 1968). A 4th order correction is necessary in order to account for an asymmetric behaviour of the 2 sidebands (Dysthe 1979), resulting in a net frequency downshift of the wave energy, which is an important practical consequence of this phenomenon.

Such modulational instabilities will also occur in irregular (random) wave trains, although a complete theoretical description then may become rather complex. Tulin & Li (1991) have proposed a theoretical model where these effects are coupled to the development of large and breaking waves in wave groups, even in moderate sea states. Similar results have been shown by Cointe & Boudet (1991). These ideas may, together with experimental studies, lead to interesting contributions in the general problem of modelling random wave trains, and in particular problems like the prediction of the extreme wave of a given sea state.

The main purpose of the present work is to show some observations from laboratory tests with irregular waves, and thus provide experimental documentation of the nature of such higher-order non-linearities. The interpretation of the results will basically be done by spectral and statistical analysis of the measured wave elevation. Prior to the presentation of these results, however, results from an experimental verification of these modulational instabilities in monochromatic and bichromatic wave trains is given, as a first step to understand the problem.

## **2. INSTABILITES DEVELOPING IN MONOCHROMATIC AND BICHROMATIC WAVE TRAINS**

Results from laboratory tests with initially monochromatic & bichromatic waves are shown in the following. The monochromatic test was performed in MARINTEKs Ocean Basin, measuring 50mx80m, with the waves generated in the longitudinal direction. The bichromatic test was performed in MARINTEKs long towing tank, measuring 10mx270m. Wave elevation measurements were simultaneously made at a number of distances from the wavemaker, on the central longitudinal axis of the basin/tank. The water depth in the Ocean Basin tests was 2.8m, while for the long tank test it was 5.0m. These depths correspond to deep water for the tests considered. All input to the wavemakers were generated as linear wave signals.

The measured time series samples in fig. 1 as well as fig. 3 illustrate how the wave trains gradually develop from more or less undisturbed linear wave signals into wave trains breaking up into smaller groups with relatively large extreme waves.

Wave breaking was also observed at the largest distances from the wavemaker. The power spectra in figs. 2 & 4 show how the energy is spread out from the initial frequencies into neighbouring side bands. Some loss of energy is also observed.



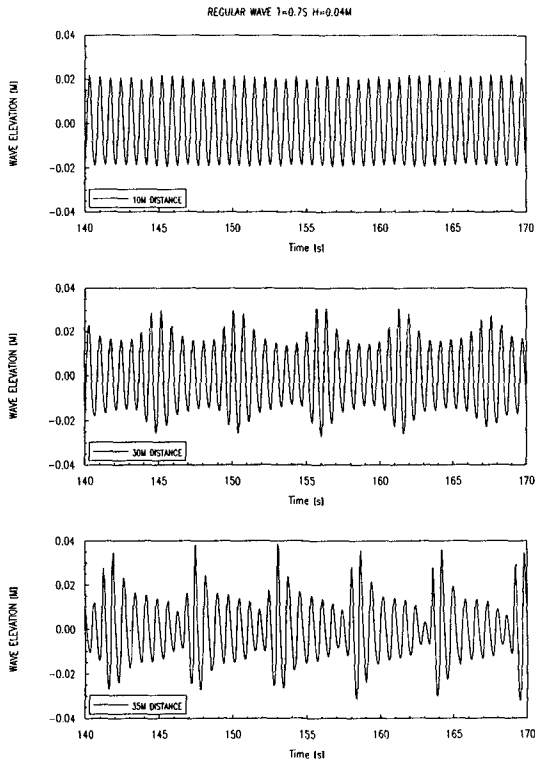


Figure 1. Time series samples of an initial monochromatic wave train, measured simultaneously at 3 locations.

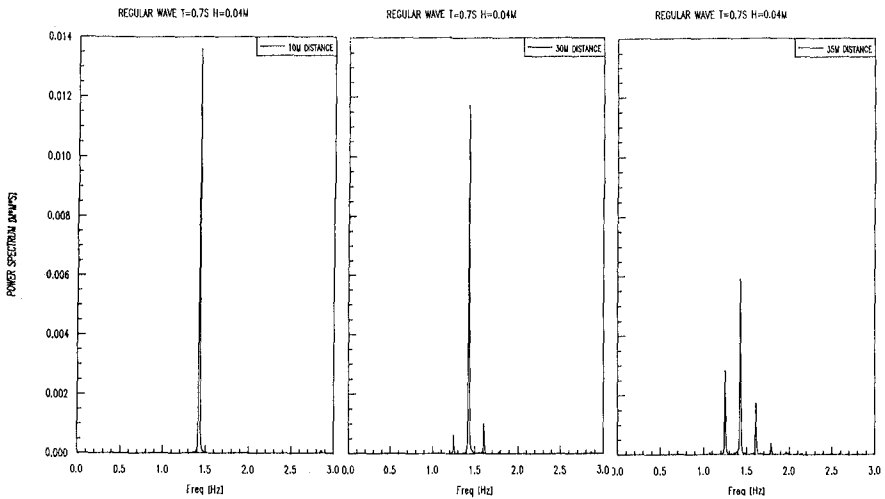


Figure 2. Power spectra of the wave records in figure 1.

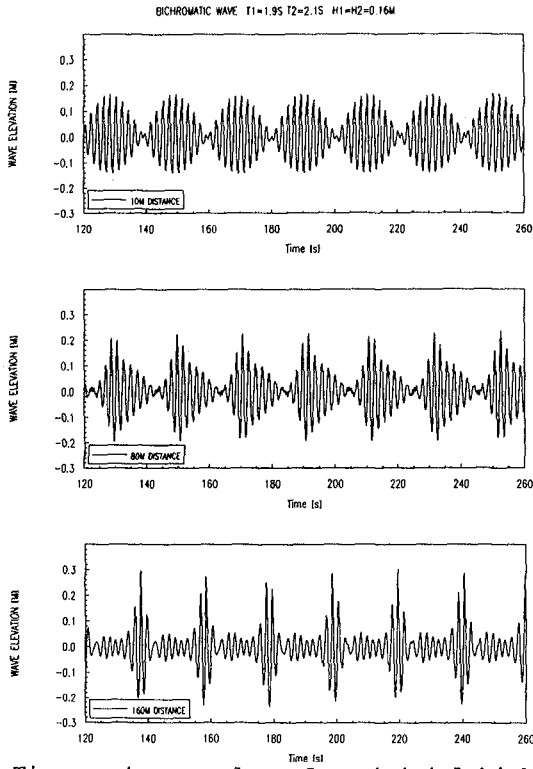


Figure 3. Time series samples of an initial bichromatic wave train, measured simultaneously at 3 locations.

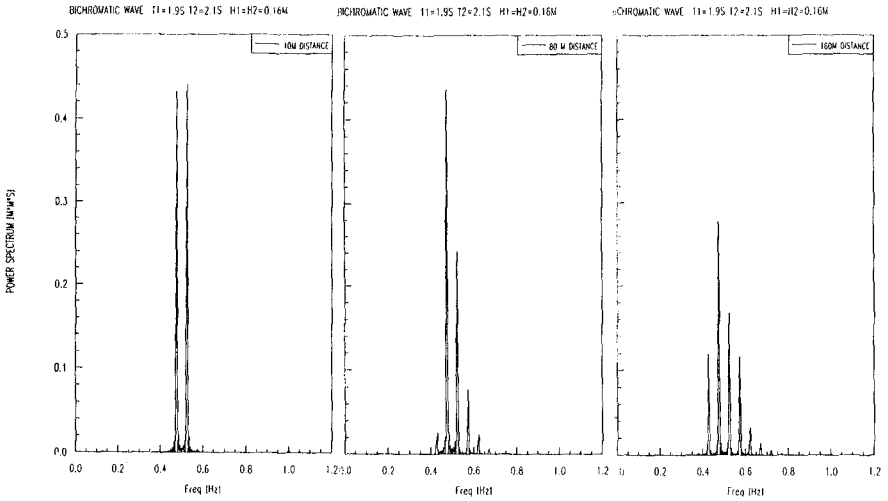


Figure 4. Power spectra of the wave records in figure 3.

### 3. SPECTRAL AND STATISTICAL PROPERTIES OF IRREGULAR WAVE TRAINS.

The influence from wave steepness and propagation length on the characteristics of longcrested irregular wave trains is experimentally investigated in the following. Measured records from laboratory tests in MARINTEKs Ocean Basin (size & depth: see Chapter 2) are used. The irregular input signal to the wavemaker was synthesized as a linear superposition of harmonic components by use of inverse Fast Fourier Transform with 4096 components. JONSWAP spectra with a peak enhancement factor, Gamma, equal to 3.0 were generated. A more detailed description of the irregular wave generation procedure is given in Stansberg (1990). Wave elevation measurements were made simultaneously at a number of distances from the wavemaker, in the same manner as described in Chapter 2. The total duration of each record was 20 minutes. In the analysis, we shall distinguish between the measurements made close to the wavemaker (only some wavelengths), and those made further away.

#### 3.1 Observations at short distances (< 10 wavelengths).

Fig. 5 shows selected time series samples from 2 tests with spectral peak period  $T_p=1.8s$ , both measured at 35m distance (i.e. 7 wavelengths) from the wavemaker. The selected time windows include the largest waves of the records. The 2 tests were run with the same input signal apart from a scaling factor of 2. The main difference observed is, apart from the scaling, the asymmetric and peaked shape of the extreme crests in the highest sea state. This is also reflected in the values obtained for the statistical skewness, based on the 3rd order statistical moment of the wave elevation record:

$$\text{skewness} = (1/N\sigma^3) \cdot \sum_{i=1}^N (x_i - \bar{x})^3 \quad (1)$$

(expected to be zero for a Gaussian process)

Here  $\bar{x}$  = mean value,  $\sigma$  = standard deviation, N = no. of samples.

It is seen that for the high sea state, the skewness value is twice the value for the low sea state. We may interpret this result as a direct result of steepness-induced 2nd order (Stokes) processes in the waves (Marthinsen & Winterstein 1992, Stansberg 1993). On the other hand, the values for the kurtosis, which is based on the 4th order statistical moment of the record:

$$\text{kurtosis} = (1/N\sigma^4) \cdot \sum_{i=1}^N (x_i - \bar{x})^4 - 3 \quad (2)$$

(expected to be zero for a Gaussian process)

is relatively low in both cases. The kurtosis is a measure of group formation, i.e. of enhanced modulation, in the signal. Thus an increased steepness of the waves does not seem to induce any increase in higher-order instabilities at this distance.

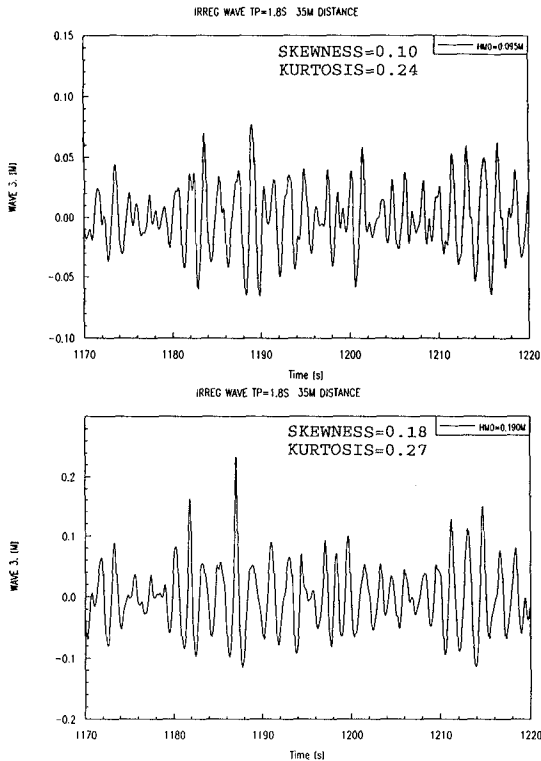


Figure 5. Time series samples from 2 irregular wave tests with  $T_p=1.8$ s. Significant wave heights  $H_{m0}$ : 0.095m and 0.19m. Both measured at 35m.

The influence from the wave steepness on the statistical skewness and kurtosis is also reflected in fig. 6, where results from several test runs are presented.

The power spectra in fig.7 show that a small part of the wave energy has dissipated at high frequencies for the steepest wave condition. No significant changes have taken place, however, in the frequency distribution of the energy.

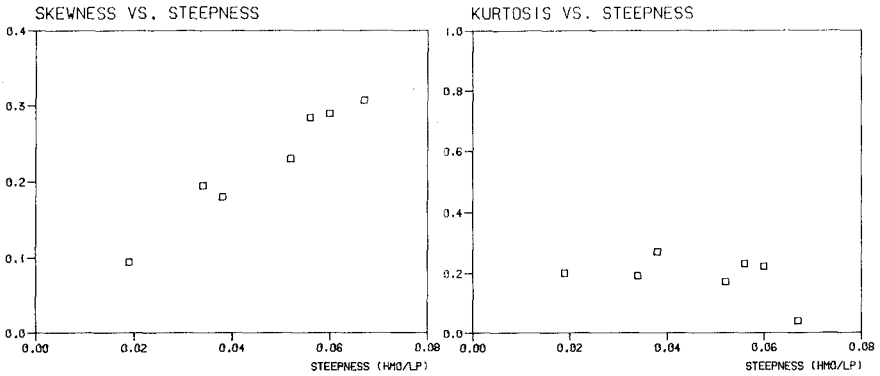


Figure 6. Measured skewness vers. wave steepness (Lp=wavelength of spectral peak frequency).

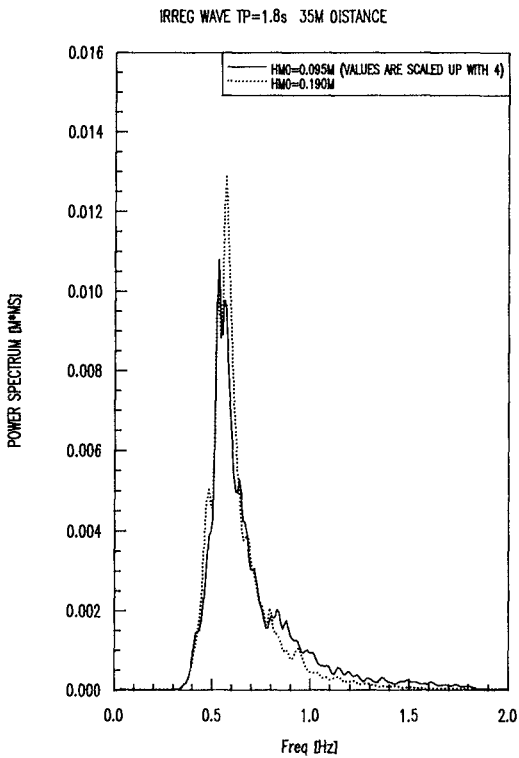


Figure 7. Power spectra of the waves in figure 5 (based on full 20 minutes records).

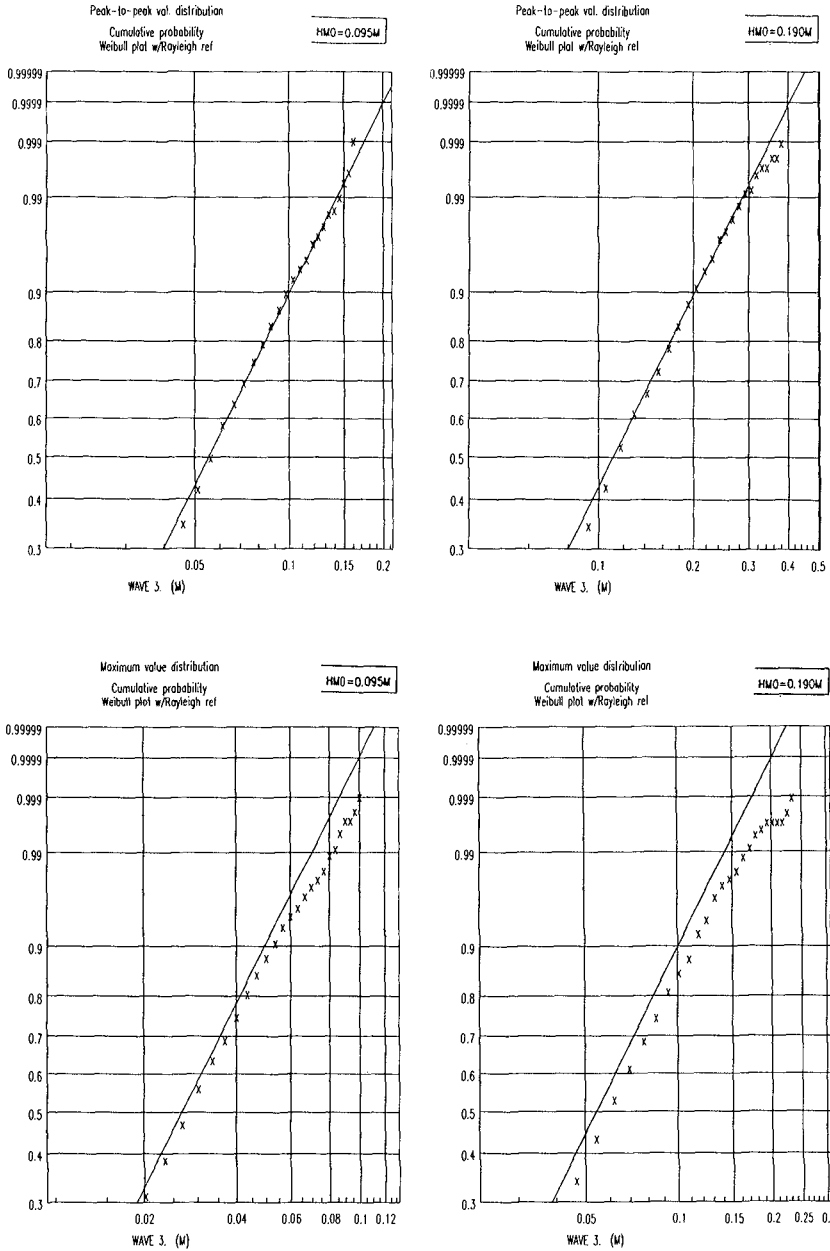


Figure 8. Cumulative distributions of wave and crest heights of the wave records in figs. 5 and 7.

The statistical distribution of wave and crest heights from the tests shown in figs. 5 & 7, are presented in fig. 8. In both wave conditions, the peak-to-peak wave heights seem to follow the commonly used Rayleigh model reasonably well, while the highest crests somewhat exceed the Rayleigh estimates. The latter observation is also discussed and reported in Stansberg (1991,1993), and is connected with 2nd order non-linearities commented on above.

### 3.2. Observations at a longer distance (>10 wavelengths).

The influence from the wave propagation on steep irregular waves is illustrated in fig. 9, where time series samples from a test with  $T_p=1.0s$  is shown. Wave elevation records measured simultaneously at 10m & 35 m distance (i.e. at 7 & 20 wavelengths, respectively) are shown. The selected samples include the largest waves of the records. The first location corresponds to the case discussed in section 3.1, while propagation-dependent effects may be observed in the latter. The shown samples illustrate how a wavetrain with steep, large waves may develop into a wavetrain

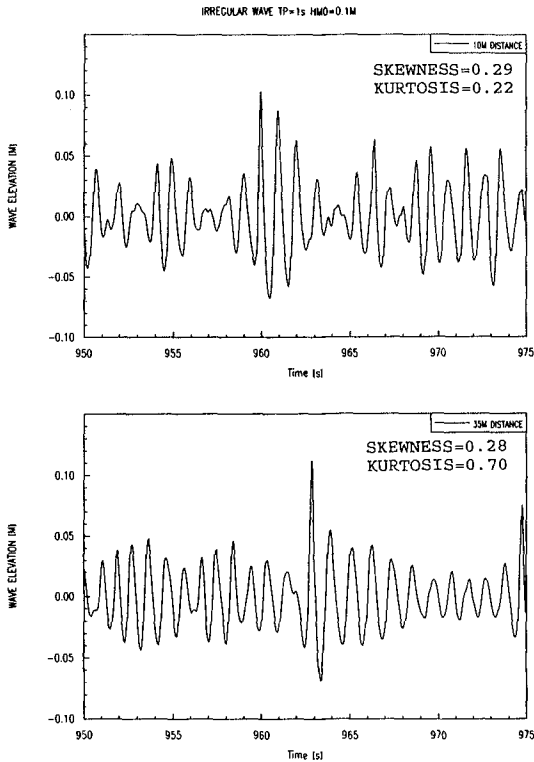


Figure 9. Time series samples recorded at 2 locations, for steep irregular wave with  $T_p=1s$ ,  $H_{m0}=0.1m$ .

with high group formation and a few particularly high waves. A similarity between the recorded extreme wave group and the unstable groups in Chapter 2 is observed. The increase in wave group formation may also be identified through the kurtosis value, which increases from 0.2 to 0.7 as the wave propagates. This development is additional to the 2nd order skewness effect seen in the previous section, and may probably be connected with the higher-order modulational instabilities demonstrated in Chapter 2. It is interesting to note that the skewness value is the same at both locations.

From the spectral plots in fig. 10, a net energy transfer from high to lower frequencies is observed. In addition, a 10% wave energy loss occurs due to dissipation by wave breaking and other processes.

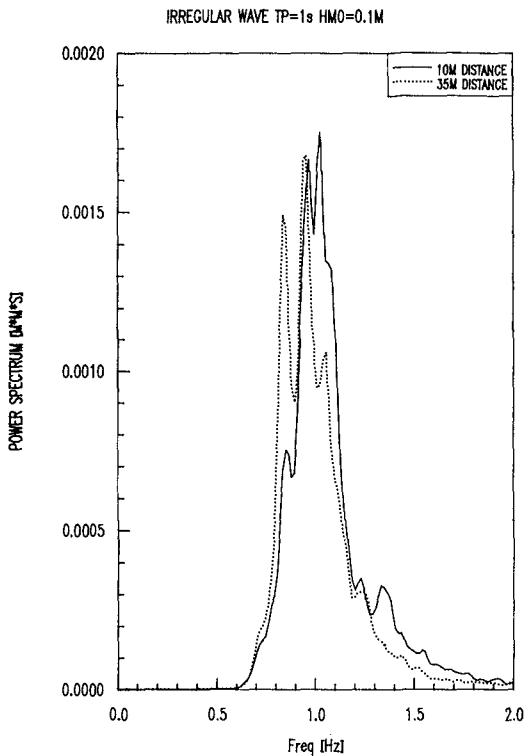


Figure 10. Power spectra of the wave in figure 9 (based on full 20 minutes record).

The influence from the propagation distance on the statistical wave parameters is shown in fig. 11, where results from several tests with different wave periods and wave heights are included. The propagating distance is normalized as  $D/L_p$ , where  $D$  is the distance from the wavemaker, and  $L_p$  is the "peak wavelength of the spectrum":



$$L_p = (g/2\pi) \cdot T_p^2 \quad (3)$$

It is seen that up to a certain point, the kurtosis (i. e. the non-linear wave group formation) increases with  $D/L_p$ . Then energy dissipation occurs by breaking etc., and the wave steepness decreases. A connected decrease in the kurtosis is then also observed at a far distance. The skewness, assumed to be related to 2nd order effects, seems to be given by the steepness (as in fig.6), regardless of the other higher-order wave processes.

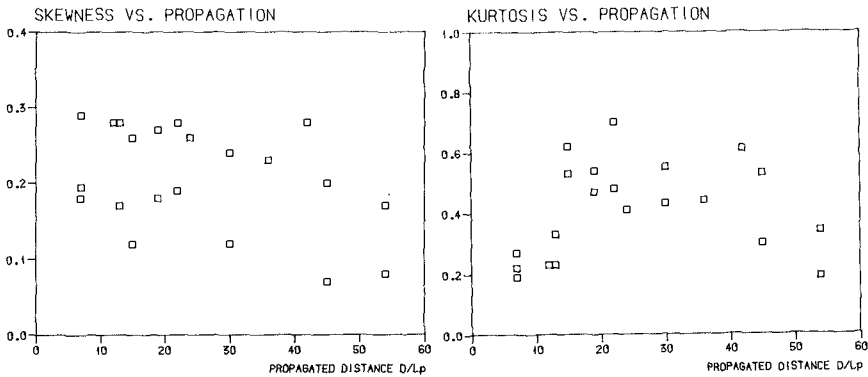


Figure 11. Measured statistical parameters vers. normalized propagation distance.

The statistical distribution functions of the full 20-minutes records illustrated in fig.9, are shown in fig. 12. As expected, the record closest to the wavemaker shows similar properties to the records in section 3.1, and may probably be described by 2nd order effects. At the far location, however, the increased modulation is observed through larger deviations from the Rayleigh estimates for large wave heights as well as large crest heights. This is connected with the high kurtosis value discussed above.

#### 4. DISCUSSION WITH CONCLUSIONS.

The tests with initially monochromatic and bichromatic waves verify the expected effects: After a certain propagation length ( $> 10$  wavelengths), the wave trains get unstable, and with further propagation they gradually form smaller groups. This may lead to groups with some asymmetric and pronounced individual waves. Wave breaking may also occur, even in wave trains with initially moderate steepness. The

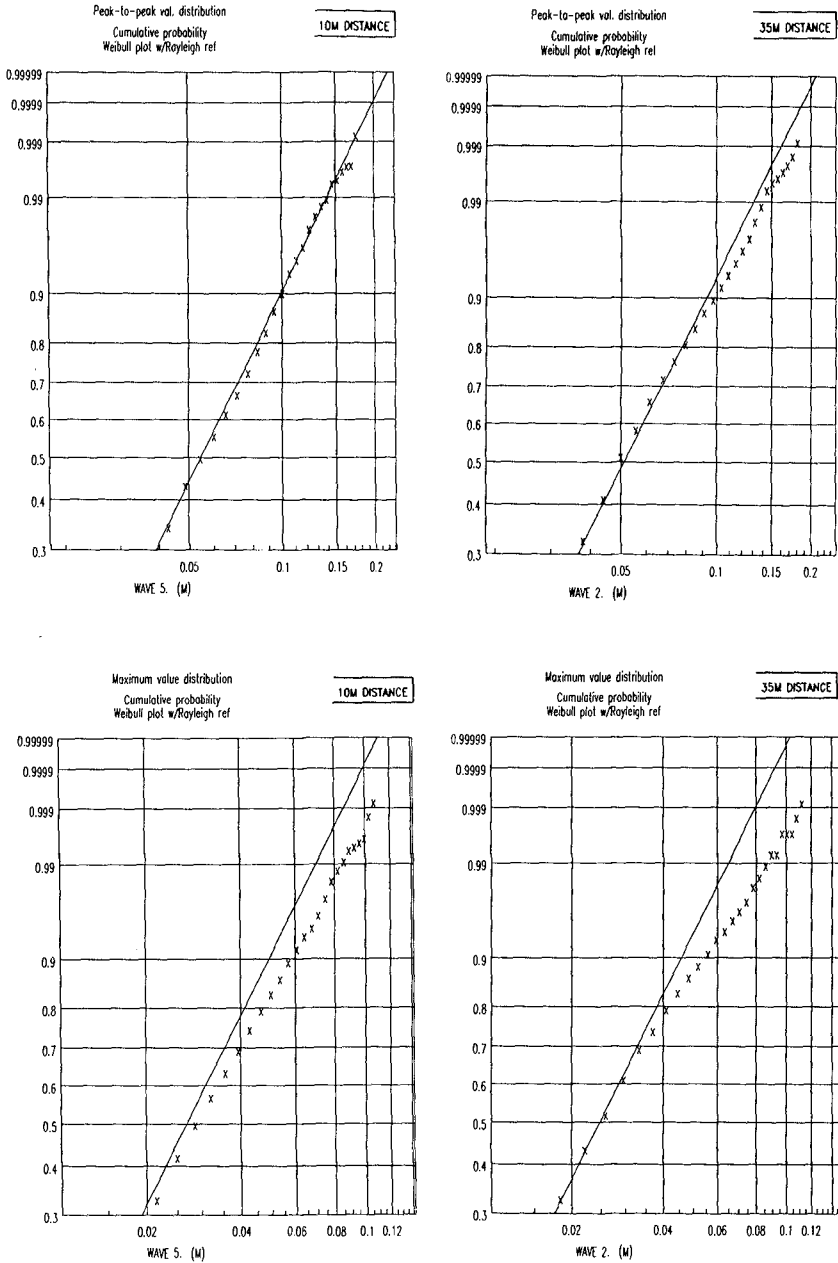


Figure 12. Cumulative distributions of wave 2 and crest heights of the wave records in figs. 9 and 10.

instabilities are connected with a continuous formation of side bands in the wave spectrum, i.e. the wave energy spreads out to lower as well as to higher frequencies. The net effect, as observed from a number of different tests (also including tests that are not shown in figs. 3 & 4), seems to be an energy transfer to lower frequencies, although the high-frequency side-bands seem to decrease rather slowly with the propagation. This confirms the results of Dysthe (1979) and others. Energy dissipation also occurs.

From the irregular wave tests it is observed that the statistical skewness of the records, interpreted as a consequence of 2nd order (Stokes) non-linearities, occurs already at a few wavelengths from the wavemaker. With further propagation, the skewness is still determined mainly by the steepness of the sea state. On the other hand, the statistical kurtosis, interpreted as a consequence of higher-order modulational instabilities, grows gradually with the propagation until the instabilities lead to energy dissipation (wave breaking and other processes) in the same manner as observed for monochromatic and bichromatic waves. The growth of the instabilities also seem to depend on the wave steepness, as expected. After the dissipation, however, the results seem to indicate that the wave train "reorganizes" to a more stable process with lower energy, lower skewness and lower kurtosis values.

For practical purposes, we may interpret the above results in the way that for proper future modelling of random wave fields, one should probably include at least 2nd order non-linearities, if the occurrence of large waves is an essential matter. Whether the higher-order instability effects should also be considered, is more uncertain, since the rise and decrease of such effects may possibly occur more as local events rather than permanent, homogenous properties. This is, however, a field where more studies are needed.

## 5. REFERENCES

- Benjamin, T.B. and Feir, J.E. (1967), "The Disintegration of Wave Trains in Deep Water. Part I. Theory", **Journal of Fluid Mechanics**, Vol. 27, pp.417-430.
- Cointe, R. and Boudet, L. (1991), "Non-Linear Breaking Waves in Bichromatic Wave-Trains: Experiments and Numerical Simulations", **Proceedings, the 1st ISOPE Conference**, Edinburgh, Scotland, August 1991, pp. 517-523.
- Dysthe, K.B. (1979), "Note on a Modification to the Nonlinear Schrödinger Equation for Application to Deep Water Waves", **Proc. Roy. Soc. Lond. A**, Vol. 369, pp. 105-114.

Marthinsen, T. & Winterstein, S. (1992), "On the Skewness of Random Surface Waves", **Proceedings, Vol. III, the 2nd ISOPE Conference**, San Francisco, USA, pp. 472-478.

Stansberg, C.T. (1990), "Extreme Waves in Laboratory Generated Irregular Wave Trains", in **Water Wave Kinematics**, ed. A. Tørum & O.T. Gudmestad, Kluwer Academic Publishers, Dordrecht, the Netherlands, pp. 537-589.

Stansberg, C.T. (1991), "Extreme Wave Asymmetry in Full Scale and Model Scale Experimental Wave Trains", **Proceedings, Vol. IA, the 10th OMAE Conference**, Stavanger, Norway

Stansberg, C.T. (1993), "Second-Order Numerical Reconstruction of Laboratory Generated Random Waves", submitted for presentation at the 12th OMAE Conference, Glasgow, Scotland.

Tulin, M.P. and Li, J.L. (1991), "On the Breaking of Energetic Waves", **Proceedings, the 1st ISOPE Conference**, Edinburgh, Scotland, August 1991, pp. 498-503.

Zakharov, V.E. (1968), "Stability of Periodic Waves of Finite Amplitude on the Surface of a Deep Fluid", **J. Appl. Mech. Tech. Phys. Vol. 2** (USSR), pp. 190-194.

## CHAPTER 50

### INTERACTION of NONLINEAR WAVE and CURRENT

S. Supharatid<sup>1</sup>, H. Tanaka<sup>2</sup>, and N. Shuto<sup>3</sup>

#### Abstract

A nonlinear wave-current model is developed to obtain the velocity and shear stress. The model employing an "empirical velocity deviation" which introduces the modification of the time-mean velocity caused by waves is proposed. With an application of a time-invariant linear eddy viscosity and making use of the truncated Fourier series, a boundary value problem is formulated and is solved numerically. Comparisons among many cases of measured and predicted results show reasonable agreements.

#### 1 Introduction

Knowledge on the combined wave and current in the boundary layer flows has been investigated theoretically and experimentally by many researchers. However, the modifications of the fundamental characteristics of the waves and current resulted from their interactions have been rarely mentioned.

At present, there are some numerical models which incorporate currents into their formulations. Dalrymple(1974) proposed a numerical perturbation while Teles da Silva and Peregrine(1988) used a boundary integral method to simulate the flow fields under waves with a linear shear current. Kishida and Sobey(1988) modified the Stokes theory to include the effect of a linear shear current. These wave-current model are still needed to be verified with experimental data or field measurements.

Recently, Tanaka(1989) extended his one-layer model to account for the nonlinear wave by a modifying Dean's stream function.(Dean, 1965) This model, however, does not succeed to predict the time-mean velocity near the water surface.

---

1 PTT Exploration and Production Co., Ltd., Bangkok, Thailand.

2 Assoc. Prof., Asian Institute of Technology, Bangkok, Thailand.

3 Prof., Disaster Control Research Center, Faculty of Engineering, Tohoku Univ., Sendai, Japan.

The present work was made by the incorporation of a modified current profile instead of the conventional log-current profile. The usual boundary value problem, with the application of the eddy viscosity approach and Fourier wave theory, is formulated in term of the stream function. The predicted velocity and bottom shear stress are compared with author's experimental data.

## 2 Boundary value problem

Prior to the formulation, the following assumptions should be made.

- 1) Waves propagate without change in form.
- 2) Wave height is known.
- 3) Current is uniform in the flow direction.
- 4) Flow is incompressible and fully turbulent.

Consider a two-dimensional periodic wave train propagating on a steady uniform current over a horizontal bottom(see Fig. 1). Equation of continuity is

$$\frac{\partial u}{\partial x} + \frac{\partial w}{\partial z} = 0 \quad (1)$$

where  $(u, w)$  are  $(\partial\psi/\partial z, -\partial\psi/\partial x)$  for the stream function

The boundary conditions to be satisfied in a moving reference frame with the wave celerity,  $c$  are as follows:

Non-slip condition at the bottom,

$$\frac{\partial \psi}{\partial z} = 0, \quad z = z_0 \quad (2)$$

No flow through the bottom,

$$\psi(x, z) = 0, \quad z = z_0 \quad (3)$$

No flow through the water surface(KFSBC),

$$\psi(x, z) = Q, \quad z = \eta(x) \quad (4)$$

Dynamic free surface boundary condition(DFSBC),

$$\frac{1}{2} \left( \frac{\partial \psi}{\partial x} \right)^2 + \frac{1}{2} \left( \frac{\partial \psi}{\partial z} \right)^2 + gz = R, \quad z = \eta(x) \quad (5)$$

Periodic lateral boundary condition with respect to wave length,  $L$

$$\psi(x+L, z) = \psi(x, z) \quad (6)$$

The mass conservation requires the invariant mean water level, on taking the x-co-ordinate with the origin at the wave crest,

$$\int_0^{L/2} \eta dx = D \quad (7)$$

The wave height, H is assumed known and is defined as the vertical difference between wave crest and wave trough.

$$\eta(0) - \eta(L/2) = H \quad (8)$$

where  $\eta$  = water surface elevation measured from the bottom  
 Q, R = constants  
 D = water depth  
 $z_0$  = bottom roughness height  
 H, L = wave height and wave length.

### 3 Stream function formulation

The stream function for a combined wave-current motion is expressed as

$$\psi = \psi_c + \psi_{WIR} + \psi_{WR} \quad (9)$$

where  $\psi_c$ ,  $\psi_{WIR}$ , and  $\psi_{WR}$  correspond to the stream functions for a steady current, irrotation(WIR) and rotation(WR) waves respectively.

#### 3.1 Stream function for a steady current

The stream function for a steady current,  $\psi_c$  is obtained from the normal momentum equation with the use of a time-invariant linear eddy viscosity,  $\tau_c / \rho = \kappa u_{*c} z \partial u_c / \partial z$ . However, with the introduction of an experimentally determined "velocity deviation,  $\Delta u_{cd}$ " as the water surface boundary condition, the final solution can be written in term of the time-mean velocity,  $u_c$  as

$$u_c = \frac{u_{*c} |u_{*c}|}{\kappa u_{*c}} \ln \frac{z}{z_0} \pm \Delta u_{cd} \frac{z - z_0}{D - z_0} \quad (10)$$

where  $u_{*c}$  = friction velocity for the steady current  
 $u_{*wc}$  = friction velocity for the combined flow  
 $\kappa = 0.41$ .

Symbols + and - are for waves with the following and opposing currents, respectively. Here,  $\Delta u_{c \pm}$  (see Fig. 2) is expressed empirically in term of the relative strength of waves to current,  $U_0/U_c$  by

$$\frac{\Delta u_{c \pm}}{|U_c|} = - \frac{1}{5} \frac{U_0}{U_c} \tag{11}$$

where  $U_0$  is the velocity amplitude at the bottom of the wave-induced motion (linear theory).  $U_c$  is the depth-averaged current velocity, symbol  $||$  means the absolute value.

It is clearly seen from Eq. (10) that the neglect of the second term on the right hand side reduces to a familiar log-current profile similar to that of the steady current alone.

3.2 Stream function for waves

Equations (12) and (13) represent the stream function for irrotational and rotational waves, respectively. For  $j = 1$ , they reduce to the fundamental forms of the first-order solution obtained by Fenton (1980) and Grant & Madsen (1979).

$$\psi_{WIR} = B_0(z-z_0) + \sum_{j=1}^n \frac{B_j \sinh(jk(z-z_0)) \cos(jkx)}{\cosh(jkD)} \tag{12}$$

$$\psi_{WR} = \frac{K_0 k}{\omega} \sum_{j=1}^n \frac{B_j}{R_{j0} \cosh(jkD)} F_j \tag{13}$$

where  $B_0, B_1, \dots, B_n =$  unknown constants

$$K_0 = \kappa u_{\infty c}, k = \text{Wave number}, \omega = \text{Angular frequency of wave}$$

$$R_{j0} = 2( \text{Ker}^2 \xi_{j0} + \text{Kei}^2 \xi_{j0} ) \quad \xi_{j0} = 2(j\omega z_0 / K_0)^{1/2}$$

$$\xi_j = 2(j\omega z / K_0)^{1/2}$$

$$F_j = \xi_j ( \text{Ker}' \xi_j \text{Kei} \xi_{j0} - \text{Kei}' \xi_j \text{Ker} \xi_{j0} ) \cos(jkx)$$

$$- \xi_j ( \text{Ker}' \xi_j \text{Ker} \xi_{j0} + \text{Kei}' \xi_j \text{Kei} \xi_{j0} ) \sin(jkx)$$

$$+ \xi_{j0} ( \text{Kei}' \xi_{j0} \text{Ker} \xi_j - \text{Ker}' \xi_{j0} \text{Kei} \xi_j ) \cos(jkx)$$

$$+ \xi_{j0} ( \text{Kei}' \xi_{j0} \text{Kei} \xi_j + \text{Ker}' \xi_{j0} \text{Ker} \xi_j ) \sin(jkx) .$$

$\text{Kei}, \text{Ker} =$  Kelvin functions of zero order.

Subscript "j" denotes the order of the finite Fourier expansions. Subscript "o" denotes values evaluated at the bottom except  $B_0$  which is one of unknown constants,  $B_j$ . Symbol " ' " means the 1st derivative of  $\text{Ker}$  and  $\text{Kei}$  with respect to  $\xi$ .



#### 4 Solution method

It is convenient to make variables dimensionless with respect to the mean water depth,  $D$ , and gravitational acceleration,  $g$  as shown Table 1.

The stream functions introduced above satisfy the equation of continuity, non-slip condition at the bottom, no vertical velocity at the bottom, and the periodicity with the wave length,  $L$ . Therefore, equations to be solved are kinematic and dynamic conditions at the free surface Eqs. (4) and (5), invariant condition for the mean water level Eq. (7), and the wave height Eq. (8).

Strictly speaking, the dynamic boundary condition at the free surface (Eq. (5)) is only applicable for an inviscid flow but not to the present case. This is because the flow under consideration inevitably yields the energy dissipation caused by viscous and turbulent motions. However, most of the energy dissipation occurs within the very thin region near the bottom, and outside this region the flow nearly behaves like an inviscid flow, making Eq. (5) applicable to the present case.

Now, we have  $(2n+4)$  equations for  $(2n+7)$  unknowns ( $u, w, c, B_0, k, Q, R, \eta_j (j=0, n)$ , and  $B_j (j=0, n)$ ). Therefore, three more equations are introduced as follows.

The value of  $u^*w_c$  has to be solved by iteration on an assumption of constant stress layer approximation near the bottom, i.e.

$$\tau_{wc} = \rho u^*w_c = \rho K_0 z_0 \left. \frac{\partial^2 \psi}{\partial z^2} \right|_{z=z_0} \quad (14)$$

where  $\tau_{wc}$  = maximum bottom shear stress for the combined flow.

The first definition of wave celerity,  $c$  is related to the time-mean velocity,  $\bar{u}$  and the Eulerian velocity,  $U_E$  as

$$U_E = c + \bar{u} \quad (15)$$

where

$$\bar{u} = \frac{1}{L} \int_0^L \frac{\partial \psi}{\partial z} dx = B_0 + \partial \psi_0 / \partial z \quad (16)$$

The  $z$ -dependent terms in Eq. (15) with Eq. (16) inserted should be balanced with each other. This yields

$$c = -B_0 \quad (17)$$

Now, the problem formulation provides  $(2n+7)$  non-linear equations for  $(2n+7)$  unknowns. The solutions are obtained by using the Newton-Raphson method. The solution flowchart is shown in Fig. 3

## 5 Results.

### 5.1 Time-mean velocity over a rough bed

The computed results are compared with the measurements conducted by authors in term of the time-mean velocity in Fig. 4. Modifications caused by waves are dependent on the flow direction, i.e. decrease and increase of the time-mean velocity near the free surface for waves with following and opposing currents. Introducing the "velocity deviation",  $\Delta u_0$  results in relatively good agreement above a height of about 100 mm.

In fact, discrepancies below this height may be caused by violent generation and transportation of vortices excited by triangular roughnesses on the bottom. With the use of the Nikuradse roughness to represent the bottom, the present model does not allow to predict such a 3-D phenomenon.

### 5.2 Ensemble-averaged velocity over a rough bed

Profiles of the ensemble-averaged velocity at phases of acceleration and deceleration are shown in Fig. 5(a)(following flow) and 5(b)(opposing flow). Agreements are reasonably well except in the vicinity of the bottom and the overshooting zone. However, the height of overshooting is well predicted. This near bottom phenomena, in fact, suggests that any model employing the closure assumption of a time-invariant eddy viscosity will suffer the same effect.

To improve the solution near the overshooting zone, it is necessary to adopt more realistic models such as the  $K-\epsilon$  model (Supharatid et. al., 1992). This certainly requires a considerably time-consuming computation.

### 5.3 Bottom shear stress over a smooth bed

The bottom shear stress for a smooth bed was measured directly using a hot-film sensor. Comparisons with the present theory are made in Fig. 6 for both waves with following and opposing currents. In the figure, two thin lines denote values of  $\langle \tau_b \rangle + \sigma_\tau$  and  $\langle \tau_b \rangle - \sigma_\tau$  of the measured data where  $\sigma_\tau$  is the standard deviation.

Throughout the wave cycle, the model generally gives satisfactory agreement, except for the results near the phase of wave trough in the case of waves with the opposing current. The distinct phase advance of the bottom shear stress is observed and predicted rather well by the model.

## 6 Conclusions

A model for nonlinear wave interacting with the steady current is developed to obtain the velocity as well as the shear stress. The effect of waves on the current is introduced in term of the "velocity deviation". The time-mean velocity, as a result, is given by a summation of logarithmic and linear profiles.

Good agreements are generally found between the predicted results and measured data. Velocity profiles are predicted rather well except in the vicinity of the "overshooting zone" where a time-invariant eddy viscosity assumed by the model is not applicable. Time histories of the bottom shear stress are also predicted reasonably well.

## References

- Darymple, R.A. (1974) Finite-amplitude wave on a linear shear current, *J. Geophys. Res.*, Vol. 79, pp. 4498-4504.
- Dean, R.G. (1965) Stream function representation of nonlinear waves, *J. Geophys. Res.*, Vol. 70, pp.4561-4572.
- Fenton, J.D. (1980) Accurate numerical solutions for nonlinear wave, *Proc. 17th ICCE*, pp. 50-69.
- Fenton, J.D. (1985) A fifth-order Stokes theory for a steady waves, *J. Waterway, Port, Coastal and Ocean Eng.*, Vol. 111(2), pp. 216-234.
- Grant, W.D. and Madsen, O.S. (1979) Combined waves and current interaction with a rough bottom, *J. Geophys. Res.*, Vol. 84(C4), pp. 1797-1808.
- Kishida, N. and Sobey, R.J. (1988) Stokes theory for waves on linear shear current *J. Eng. Mech.*, Vol. 114(3), pp. 1317-1334.
- Supharatid, S., Tanaka, H. and Shuto, N. (1992) Rough turbulent boundary layer under wave-current combined motions, *Proc. 36th Jap. Conf. on Hydr.*, JSCE, pp. 193-198.
- Tanaka, H. (1988) Bottom boundary layer under nonlinear wave motion, *J. Waterway, Port, Coastal and Ocean Eng.*, Vol. 115(1), pp. 40-57.
- Teles da Silva, A.F. and Pcregrine, D.H. (1988) Steep, steady surface waves on water of finite depth with constant vorticity, *J. Fluid Mech.*, Vol. 195, pp. 281-302.

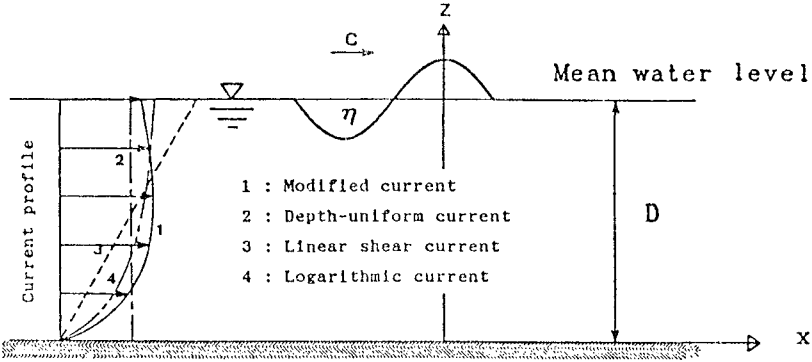


Fig. 1 Definition sketch

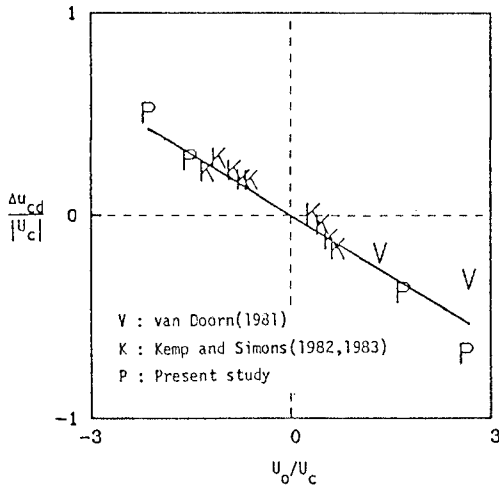


Fig. 2 Velocity deviation

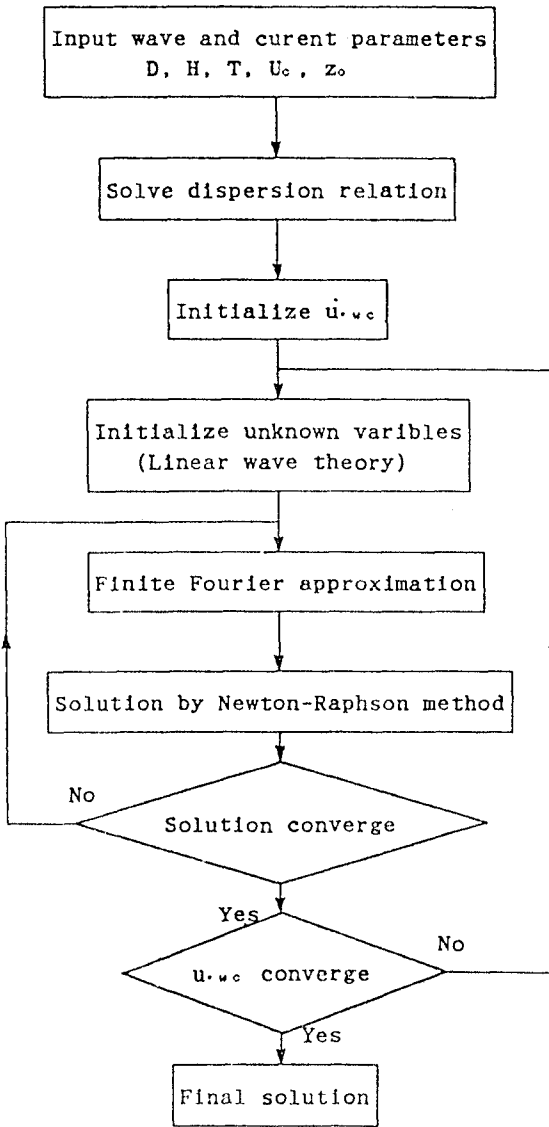
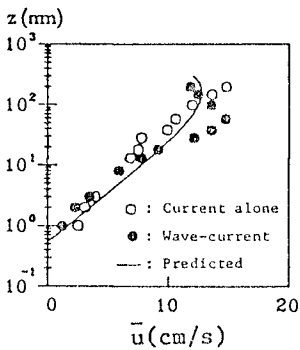


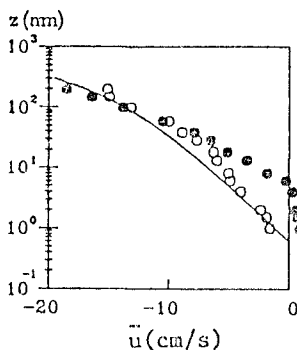
Fig. 3 Solution Flow chart

Table 1 Dimensionless variables

Dimensional variables	Dimensionless variables
x	$x/D$
z	$z/D$
$\eta$	$\eta/D$
$\psi$	$\psi / (gD^3)^{1/2}$
Q	$Q / (gD^3)^{1/2}$
R	$R/gD$
k	$kD$
c	$c / (gD)^{1/2}$
u	$u / (gD)^{1/2}$
w	$w / (gD)^{1/2}$

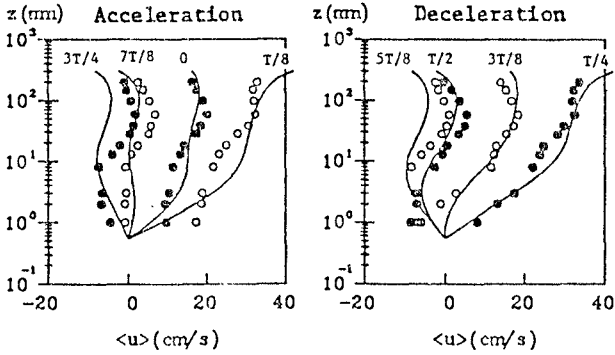


(a) Following flow  
 (D=0.30 m, H=9.4 cm,  
 T=1.3 sec,  $U_c=11.9$  cm/s)

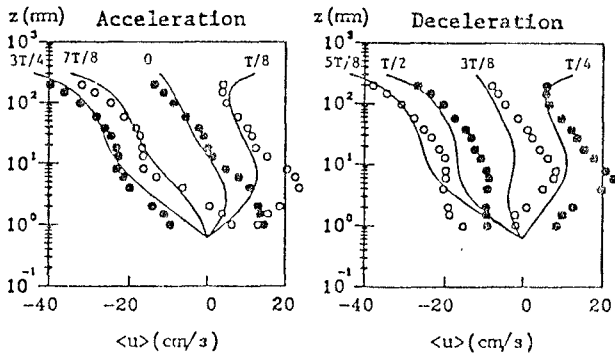


(b) Opposing flow  
 (D=0.30 m, H=9.7 cm,  
 T=1.3 sec,  $U_c=-14.7$  cm/s)

Fig. 4 Time-mean velocity(rough bed)

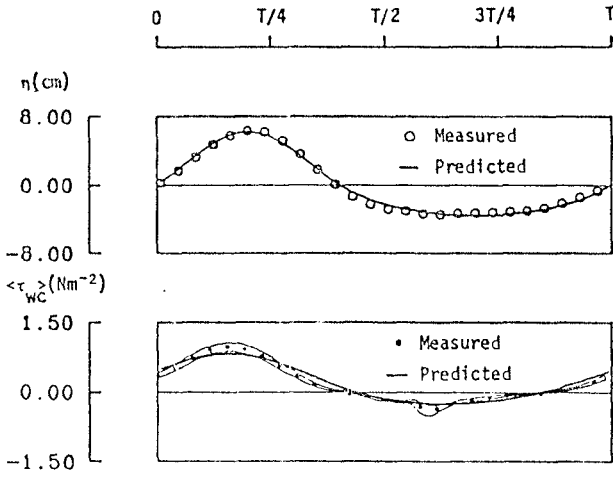


(a) Following flow  
 ( $D=0.30$  m,  $H=9.4$  cm,  $T=1.3$  sec,  $U_c=11.9$  cm/s)

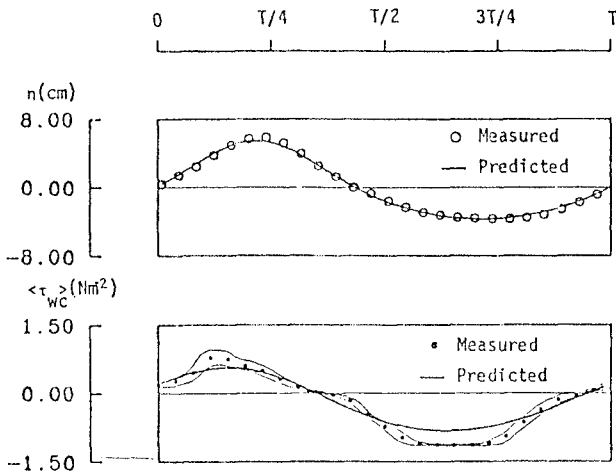


(b) Opposing flow  
 ( $D=0.30$  m,  $H=9.7$  cm,  $T=1.3$  sec,  $U_c=-14.7$  cm/s)

Fig. 5 Ensemble-averaged horizontal velocity(rough bed)



(a) Following flow  
 (D=0.30 m, H=9.4 cm, T=1.3 sec, U<sub>c</sub>=14.0 cm/s)



(b) Opposing flow  
 (D=0.30 m, H=9.5 cm, T=1.3 sec, U<sub>c</sub>=-14.9 cm/s)

Fig. 6 Time series of the bottom shear stress(smooth bed)



## CHAPTER 51

### A stream function solution for waves on a strongly sheared current.

Christopher Swan<sup>1</sup>

#### Abstract.

A perturbation analysis is presented in which a series of small amplitude progressive gravity waves interact with a strongly sheared current. The solution, which is extended to a second order of wave steepness, shows that if the time averaged vorticity distribution varies with depth the wave motion becomes rotational. An additional wave component, expressed in terms of the first harmonic, is identified at a second order of wave steepness. This does not arise within an irrotational solution and is quite distinct from the Doppler shift associated with the surface current. Explicit solutions are given for the dispersion equation and the wave induced kinematics. These are found to be very different from the existing irrotational solutions, and suggest that the non-linear wave-current interaction terms can become very important if the current profile is strongly sheared in the vicinity of the water surface. In such cases the underlying velocity field should not be predicted by an irrotational solution based upon an "equivalent" uniform current.

#### 1. Introduction.

The combination of waves and currents is an important feature of most marine environments. The present paper considers the fluid flow resulting from such an interaction once it has achieved a state of equilibrium. It will not consider the initial generation of waves on a strongly sheared current; nor will it consider the propagation of waves onto a strongly sheared current. The initial transfer of energy between the various components of the flow field,

<sup>1</sup> Lecturer, Department of Civil Engineering, Imperial College, London. SW7 2BU, UK.

and the resulting change in the wave height, forms part of a transient problem which has already been considered by a number of authors. These include Longuet-Higgins and Stewart (1960, 1961), Bretherton and Garrett (1968), and Brink-Kjær and Jonsson (1975). A full discussion of these matters is given in the review articles by Peregrine (1976) and Jonsson (1990).

It is well known that the equilibrium conditions associated with the interaction of waves and currents are strongly dependent upon the vertical distribution of the current velocity. In many practical cases it may be assumed that the current profile is approximately uniform with depth. Important examples of this type of behaviour are the large scale ocean currents, and the majority of tidal flows. Under these conditions, the wave motion remains irrotational and, in effect, the only interaction occurs within the associated dispersion equation. At a second order of wave steepness the dispersion equation for waves propagating on a uniform current ( $U=U_0$ ) is given by:-

$$c = \frac{\sigma}{k} - \left[ \frac{g}{k} \tanh(kh) \right]^{1/2} + U_0 \quad (1)$$

where  $c$  is the wave celerity,  $h$  is the water depth and  $g$  is the gravitational constant. The wave number ( $k$ ) and the wave frequency ( $\sigma$ ) are defined in the usual way so that  $k=2\pi/\lambda$  and  $\sigma=2\pi/T$ , where  $\lambda$  is the wave length and  $T$  is the wave period. This solution is often referred to as a "Doppler shifted solution" since it describes the wave form propagating on the surface current.

A second example which has been widely considered is that of waves on a linear shear current, or one in which the current velocity varies linearly with depth. Tsao (1959) considered this case and showed that the wave motion, or the oscillatory component of the flow field, will remain irrotational provided the vorticity is constant throughout the water depth. In this case the stream function ( $\psi$ ) can no longer be expressed in the form of a solution to Laplace's equation as would be the case in a classical Stokes' expansion (1847). The governing equation is thus expressed in the form of a Poisson equation:-

$$\nabla^2 \psi = \Omega_0 \quad (2)$$

where  $\Omega_0$  is the constant vorticity or the gradient of the linear shear current. Although the oscillatory motion remains irrotational, it is different from that which would be predicted in the absence of a current. If the current is assumed to be of a similar magnitude to the first order wave motion, an additional oscillatory term arises at a second order of wave steepness ( $O(a^2k^2)$ ). Kishida and Sobey (1988) identified this term as:-

$$\psi_{wc} = 2az\Omega_0 \frac{\sinh(kh+kz)}{\sinh(kh)} \cos(kx - \sigma t) \quad (3)$$

where  $a$  is the wave amplitude (or half the wave height,  $H$ ) and  $(x, z)$  are the Cartesian co-ordinates described below.

In many practical cases neither the current velocity or the vorticity distribution are uniform. For example, in the absence of significant vertical mixing, a wind driven current decays exponentially with depth. This creates a strongly sheared current with a concentration of vorticity near the water surface. To describe an interaction of this type has hitherto required a complex numerical model similar to that proposed by Chaplin (1989). The present paper will consider this case and presents a new analytical solution which is simple to use, and which provides a first approximation to the non-linear wave-current interaction which arises in the presence of a strongly sheared current profile.

## 2. Theory.

The new solution will take the form of a perturbation expansion in which a series of two-dimensional monochromatic waves, propagating in water of constant depth, interact with a strongly sheared current. To simplify the non-linear boundary conditions which must be applied at the water surface, the analysis will be conducted within an orthogonal curvi-linear co-ordinate system.

The Cartesian co-ordinates shown on figure 1a translate with the phase velocity ( $c$ ) to provide a steady ( $d/dt=0$ ) frame of reference. These axes are mapped onto the curvi-linear co-ordinates shown on figure 1b. To achieve this a sequence of transformations must be applied so that at each order of the perturbation (see below)  $\eta=0$  defines the free surface and  $\eta=-h$  the position of the impermeable bottom boundary. At a first order of approximation these transformations are similar to those applied by Benjamin (1959). The general form of the transformations are given by:-

$$\eta - z - \sum_{n=1}^N A_n \frac{\sinh(nkh+nk\eta)}{\sinh(nkh)} \cos(nk\xi) - B_n \tag{4}$$

$$\xi - x - \sum_{n=1}^N A_n \frac{\cosh(nkh+nk\eta)}{\sinh(nkh)} \sin(nk\xi)$$

where the subscript defines the order of the terms, and the unknown constants ( $A_n, B_n$ ), are dependent upon the water surface elevation ( $\zeta$ ). Since this cannot be known a priori an iterative approach is adopted in which an initial estimate of the surface profile is made, the co-ordinates are transformed, and a solution obtained as indicated below. This solution is then used in conjunction with the boundary conditions to define, where necessary, an appropriate modification of the surface elevation. In this way a unique solution can be identified which satisfies both the governing equation and the boundary conditions.

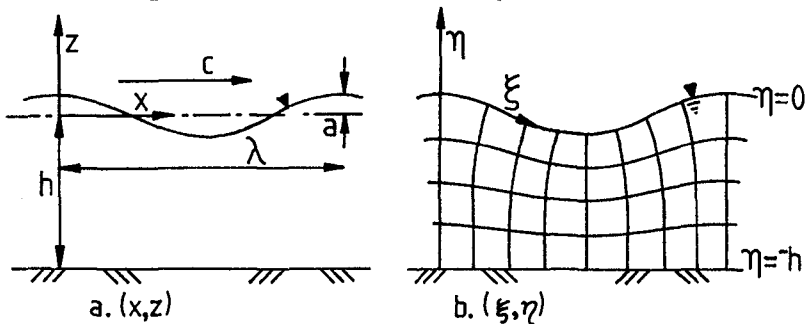


Figure 1. Co-ordinate arrangements.

To achieve this iterative approach the irrotational solution proposed by Stokes (1847) was used to provide an initial estimate of the surface elevation. If  $\zeta$  is measured relative to the still water level ( $z=0$ ), then the required second order expression is given by:-

$$\zeta = a \cos(\Phi) + a^2 k \cosh(kh) \frac{[2\sinh^2(kh) + 3]}{4\sinh^3(kh)} \cos(2\Phi) - \frac{a^2 k}{2\sinh(2kh)} \tag{5}$$

where  $\Phi$  is the phase angle ( $kx - \sigma t$ ). It is important to note that the surface elevation alone is being adopted as an initial estimate. No assumptions are made about the nature of the associated dispersion equation, and the flow is not assumed to be irrotational.

The transformations given above (4) are orthogonal, and the Jacobian  $J$  is defined by:

$$J = \frac{\alpha(\xi, \eta)}{\partial(x, z)} \quad (6)$$

Within the  $(\xi, \eta)$  co-ordinates the two dimensional vorticity equation for flow in an inviscid fluid is given by:

$$\frac{\alpha(\psi, \sqrt{\nabla^2 \psi})}{\partial(\xi, \eta)} = 0 \quad (7)$$

where the stream function ( $\psi$ ) is defined so that the total velocity components in the  $\xi$  and  $\eta$  directions are:-

$$(U+u)_\xi = J^{1/2} \frac{\partial \psi}{\partial \eta}, \quad u_\eta = -J^{1/2} \frac{\partial \psi}{\partial \xi} \quad (8)$$

In accordance with the arguments originally outlined by Stokes (1847) an exact solution of a two dimensional wave train does not exist. Consequently, a perturbation expansion must be employed in which the stream function ( $\psi$ ), the surface elevation ( $\zeta$ ), and the Jacobian ( $J$ ), are expressed in terms of a small expansion parameter ( $\epsilon$ ):

$$\begin{aligned} \psi &= \psi_0 + \epsilon \psi_1 + \epsilon^2 \psi_2 + \epsilon^3 \psi_3 + \epsilon^4 \psi_4 + \dots \\ \zeta &= \zeta_0 + \epsilon \zeta_1 + \epsilon^2 \zeta_2 + \epsilon^3 \zeta_3 + \epsilon^4 \zeta_4 + \dots \\ J &= J_0 + \epsilon J_1 + \epsilon^2 J_2 + \epsilon^3 J_3 + \epsilon^4 J_4 + \dots \end{aligned} \quad (9)$$

where the subscript again denotes the order of the term involved. In the present solution the wave steepness ( $ak$ ) is adopted as an appropriate expansion parameter, and the co-ordinate arrangement shown on figure 1b defines the following "zero order" terms:

$$\psi_0 = -c\eta, \quad J_0 = 1, \quad \zeta_0 = 0 \quad (10)$$

Substituting (9) and (10) into the governing vorticity equation and collecting powers of  $\epsilon$  gives the required expressions of the vorticity equation at successive steps in the perturbation:

$$c \frac{\partial}{\partial \xi} (\nabla^2 \psi_1) = 0$$

(11)

$$c \frac{\partial}{\partial \xi} (\nabla^2 \psi_2) = \frac{\partial (\nabla^2 \psi_1, \psi_1)}{\partial (\xi, \eta)} - c \frac{\partial}{\partial \xi} (J_1 \nabla^2 \psi_1)$$

Before discussing the boundary conditions we must define the characteristics of the current profile. Firstly, it should be noted that if the magnitude of the current velocity is close to the phase velocity (c), the vorticity equations (11) are indeterminate. Fortunately, this situation seldom arises within either a coastal or an ocean environment. Current velocities are typically much smaller than the phase velocity, and are generally more closely related to the magnitude of the first order wave motion ( $U=0.(ak)$ ). This assumption is adopted within the present formulation.

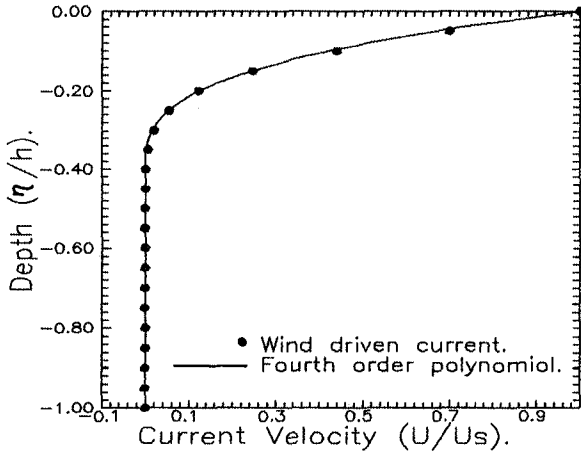


Figure 2. A strongly sheared current profile.

To ensure that an appropriate range of current profiles can be incorporated within the present solution, a polynomial representation is adopted to describe a current profile within the region  $0 \leq \eta \leq -mh$  where  $m$  is a constant within the range  $(0 \leq m \leq 1)$ . Hence:

$$U = (P + 2Q\eta + 3R\eta^2 + 4S\eta^3) \delta_s(\eta + mh) \tag{12}$$

Where  $\delta_s(\eta+mh)$  is the heavyside step function defined by:

$$\begin{aligned} \delta_s(\eta+mh) &= 1 & \text{if } (\eta+mh) \geq 0 \\ \delta_s(\eta+mh) &= 0 & \text{if } (\eta+mh) < 0 \end{aligned} \quad (13)$$

Figure 2 compares the current profile defined in (12) with a wind driven profile based on the lamina flow solution proposed by Lamb (1932).

The vorticity equations (11) must be solved within the confines of the following boundary conditions:

(a) If the bottom boundary is assumed to be both horizontal and impermeable, the vertical velocity at the bed must be zero:

$$-J^{1/2} \frac{\partial \psi}{\partial \xi} = 0 \quad \text{on } \eta = -h \quad (14)$$

(b) Since the water surface is a streamline the kinematic condition requires the velocity normal to the surface to be zero:

$$-J^{1/2} \frac{\partial \psi}{\partial \xi} = 0 \quad \text{on } \eta = 0 \quad (15)$$

(c) The dynamic free surface boundary condition further requires the pressure ( $p$ ) acting on the water surface to be constant. In general orthogonal co-ordinates the equations of motion are given by:-

$$\frac{\partial \underline{u}}{\partial t} + \frac{1}{2} \nabla(\underline{u}^2) - \underline{u} \times \omega = -\frac{1}{\rho} \nabla(p) + F \quad (16)$$

where the under-bar denotes a vector quantity,  $\omega$  is the vorticity distribution, and  $F$  is a body force. Taking the first component of (16) and applying the kinematic condition (15) gives the required dynamic condition:

$$\frac{\partial p}{\partial \xi} = F_\xi J^{1/2} - \frac{1}{2} \frac{\partial J}{\partial \xi} \left[ \frac{\partial \psi}{\partial \eta} \right]^2 - J \frac{\partial \psi}{\partial \eta} \frac{\partial^2 \psi}{\partial \eta \partial \xi} = 0 \quad \text{on } \eta = 0 \quad (17)$$

where  $F_{\xi}$  is the resolved component of the body force per unit mass in the  $\xi$  direction. If  $g$  is the gravitational constant, and  $\theta$  is the angle separating the  $z$  and  $\eta$  directions (figure 1), we obtain:

$$F_{\xi} = -g \sin(\theta) \tag{18}$$

(d) Finally the fluid motion must be continuous throughout the entire water depth. In the case of ( $m < 1$ ) the flow may be divided into two distinct regions which are characterised by the presence ( $0 \geq \eta \geq -mh$ ), or absence ( $-mh \geq \eta \geq -h$ ), of the current profile. If the governing equation (7) is to be consistent across this interface ( $\eta = -mh$ ) the time averaged vorticity must be zero at the lower edge of the current profile:

$$\lim_{(\eta \rightarrow -mh)}(\omega) = 0 \tag{19}$$

Furthermore, the value of the stream function and the velocity components must also be continuous across this region. If  $(\eta \rightarrow -mh)$  represents the limit taken in the negative  $\eta$  direction (from above) and  $(\eta \leftarrow -mh)$  represents the limit taken in the positive  $\eta$  direction (from below) the final boundary conditions are given by:

$$\begin{aligned} \lim_{(\eta \leftarrow -mh)}(\psi) &= \lim_{(\eta \rightarrow -mh)}(\psi) \\ \lim_{(\eta \leftarrow -mh)}\left(j^{1/2} \frac{\partial \psi}{\partial \eta}\right) &= \lim_{(\eta \rightarrow -mh)}\left(j^{1/2} \frac{\partial \psi}{\partial \eta}\right) \\ \lim_{(\eta \leftarrow -mh)}\left(-j^{1/2} \frac{\partial \psi}{\partial \xi}\right) &= \lim_{(\eta \rightarrow -mh)}\left(-j^{1/2} \frac{\partial \psi}{\partial \xi}\right) \end{aligned} \tag{20}$$

### 3. Results and discussion.

The perturbation analysis is extended to a second order of wave steepness. Since the current velocity is assumed to be of order  $ak$ , the solution will provide a first approximation to the wave-current interaction. The resulting stream function is given by:



$$\psi_0 = -c\eta$$

$$\psi_1 = (Q\eta^2 + R\eta^3 + S\eta^4) \delta_s(\eta + mh) - P\eta \delta_s(-\eta - mh)$$

$$\psi_2 = a(2Q\eta + 3R\eta^2 + 4S\eta^3 + \frac{6S\eta}{k^2} + F_a) \frac{\sinh k(h+\eta)}{\sinh kh} \cos(k\xi) \delta_s(\eta + mh) \quad (21)$$

$$+ a(-\frac{3R\eta}{k} - \frac{6S\eta^2}{k} + F_b) \frac{\cosh k(h+\eta)}{\sinh kh} \cos(k\xi) \delta_s(\eta + mh)$$

$$+ aF_c \sinh k(h+\eta) \cos(k\xi) \delta_s(-\eta - mh)$$

Where the heavyside function ( $\delta_s$ ) is defined in (13) and the terms  $F_a$ ,  $F_b$ , and  $F_c$  are constants for a given wave-current interaction (figure 3).

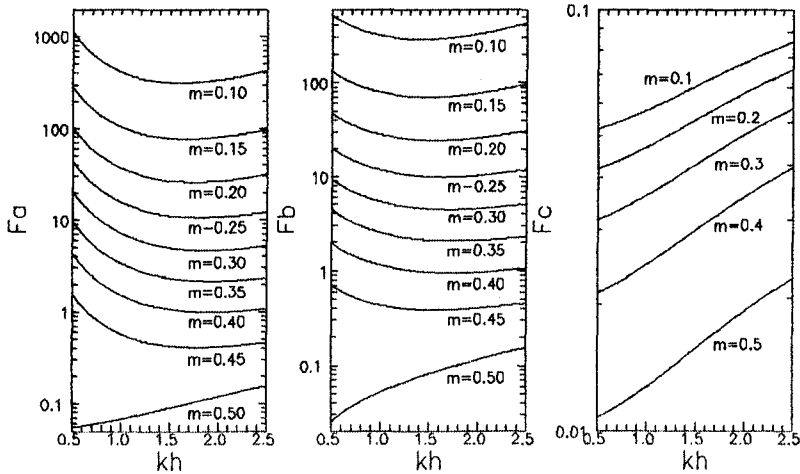


Figure 3. The constant coefficients ( $F_a$ ,  $F_b$ ,  $F_c$ ).  
(Defined for a cubic shear current).

The three terms within this series solution can be identified in the following way. The zero order term ( $\psi_0$ ), which arises due to the translation of the co-ordinate axes, may be used in conjunction with the Jacobian ( $J$ ) to define the irrotational velocity components within a classical Stokes expansion. The first order term ( $\psi_1$ ) provides a description of the current profile in a steady frame of reference, and the second order term ( $\psi_2$ ) defines the additional terms associated with the wave-current interaction.

To complete the required solution a dispersion equation describing the combined wave-current motion is required. At a second order of wave steepness the phase velocity measured relative to a stationary observer is given by:-

$$c = \frac{\sigma}{k} - \left( \frac{g \tanh(kh)}{k} \right)^{\frac{1}{2}} + P - \frac{Q \tanh(kh)}{k} + \frac{3R}{2k^2} - \frac{3S \tanh(kh)}{k^3} + \frac{F_a}{2 \cosh^2(kh)} \tag{22}$$

where P, Q, R and S are the constants used to define the current profile (12). Assessing these terms at the water surface ( $\eta=0$ ) we obtain:

$$P = (U)_{\eta=0} \quad , \quad Q = \frac{1}{2!} \left( \frac{dU}{d\eta} \right)_{\eta=0} \tag{23}$$

$$R = \frac{1}{3!} \left( \frac{d^2U}{d\eta^2} \right)_{\eta=0} \quad , \quad S = \frac{1}{4!} \left( \frac{d^3U}{d\eta^3} \right)_{\eta=0}$$

The effect of the surface vorticity ( $\omega_s$ ) is considered in figure 4. Convention dictates that a vorticity distribution is positive if it causes an anti-clockwise rotation of the fluid particles ( $\omega = -dU/d\eta$ ). Unfortunately, this definition results in a positively sheared current ( $dU/d\eta > 0$ ) having negative vorticity. To avoid confusion the horizontal abscissa on figure 4 is expressed in terms of ( $-\omega_s$ ) so that an increase in the positive x-direction indicates an increase in the positive shear.

Figure 4 considers a number of realistic current profiles in which a "favourable" current ( $U_s > 0$ ) has positive shear ( $-\omega_s > 0$ ) and an "adverse" current ( $U_s < 0$ ) has negative shear ( $-\omega_s < 0$ ). In all cases the vorticity distribution acts to reduce the effect of the Doppler shift associated with the surface current ( $U_s$ ). For example, if a series of waves propagate onto a "favourable" current the individual waves will be "stretched" thereby producing a reduction in the wave number. If however, the current profile is sheared ( $dU/d\eta > 0$ ) then the apparent change in the wave number is much reduced. Indeed, figure 4 indicates that a highly sheared current profile can entirely negate the wave length changes associated with the Doppler shift.

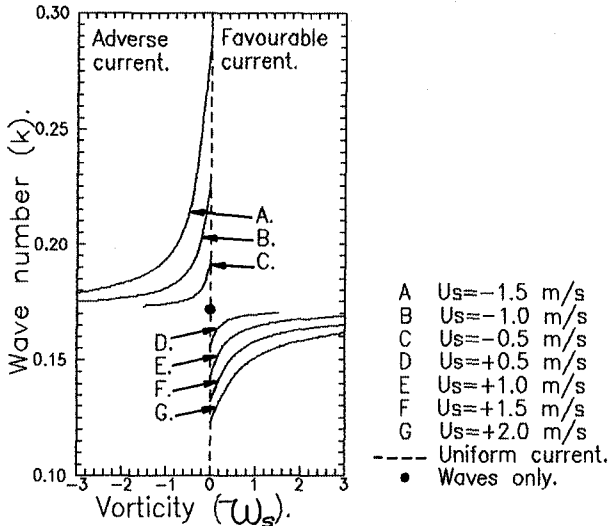


Figure 4. The wave number ( $k$ ).

This reduction in the apparent Doppler shift has led some authors to suggest that the interaction with a strongly sheared current can be described by an "equivalent" uniform current ( $U(\eta)=U_a$ ). Hedges and Lee (1992) define this "equivalent" uniform current as that which produces the same wave number ( $k$ ) as the actual depth varying current for a particular wave period, wave height, and water depth. This approach is considered in figures 5a-5b which respectively concern the interaction with a positively sheared "favourable" current and a negatively sheared "adverse" current. In each case the first figure provides a description of the current profile ( $U$ ), and the second figure describes the oscillatory velocity occurring beneath the wave crest ( $u$ ). Four different solutions of the wave induced velocity are presented: the first is a waves only solution which neglects the effect of the current profile; the second assumes that the surface current exists uniformly with depth ( $U(\eta)=U_a$ ); the third is based on the present solution for waves on a strongly sheared current, and the fourth is based on an "equivalent" uniform current.

Figures 5a and 5b show that the wave kinematics resulting from the interaction with a strongly sheared current are dependent upon two separate effects. The first corresponds to a change in the dispersive characteristics of the wave form given in equation (22), and the second is associated with the rotational wave components identified in equation (21). The dispersive characteristics are found to be dependent upon the magnitude of the surface current and

the time averaged vorticity distribution. In consequence the actual wave number falls between the values predicted by the waves only solution and the uniform current solution which is based upon the magnitude of the surface current ( $U_s$ ).

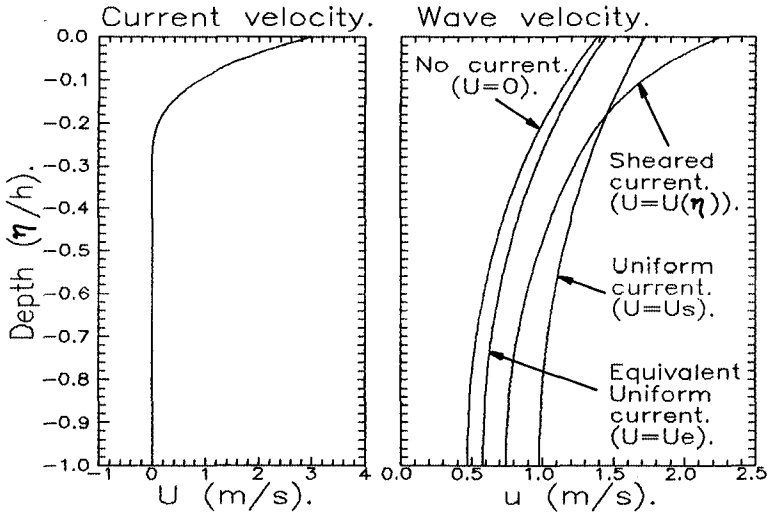


Figure 5a. Interaction with a "favourable" current. ( $T=5s$ ,  $h=10m$ ,  $H=2m$ ).

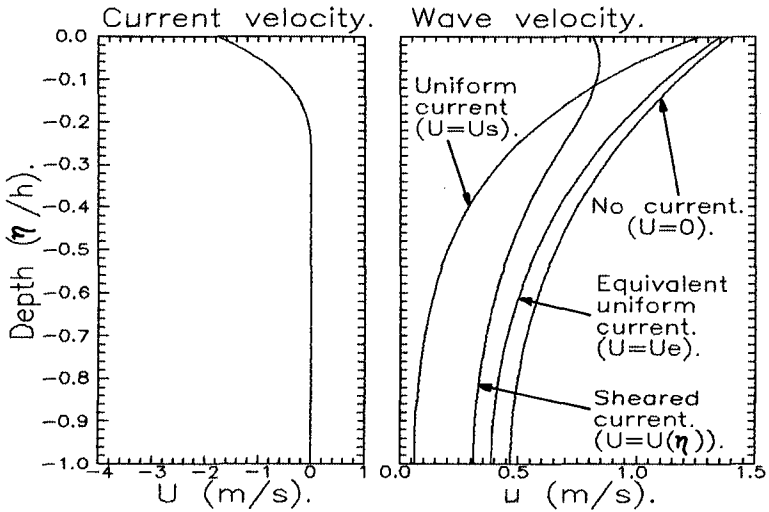


Figure 5b. Interaction with an "adverse" current. ( $T=5s$ ,  $h=10m$ ,  $H=2m$ ).

The "equivalent" uniform current will, by definition, correctly model the dispersive characteristics of the combined wave-current motion. However, this alone is not sufficient to describe the wave induced flow field in the presence of a strongly sheared current. Figures 5a and 5b clearly indicate that the wave kinematics are directly dependent upon the vorticity distribution. In the upper region of the flow field ( $0 \geq \eta \geq -mh$ ), where the current profile exists, figure 5a shows that a positively sheared "favourable" current produces a significant increase in the amplitude of the oscillatory velocity occurring near the water surface. In figure 5b a negatively sheared "adverse" current reduces the oscillatory velocity in this region. These changes are associated with the rotational wave component identified in equation (21). They are not related to the effective Doppler shift, and cannot therefore be predicted by an irrotational solution based on an "equivalent" uniform current.

It is interesting to note that even in the lower layers of the flow field ( $-mh \geq \eta \geq -h$ ) where no current profile exists, and consequently the flow must be irrotational, the solution based upon an "equivalent" uniform current again provides a poor representation of the wave kinematics. This arises because of the continuity conditions (20) which must be applied at the lower edge of the current profile ( $\eta = -mh$ ). This suggests that a wave-current interaction involving a non-uniform vorticity distribution will effect the entire wave field, even if, as in the present case, the vorticity profile is contained within a relatively narrow layer near the water surface.

#### 4. Conclusions.

An analytical solution has been presented to describe a series of two dimensional progressive gravity waves propagating on a strongly sheared current. The solution has been extended to a second order of wave steepness and shows that the wave motion becomes rotational if the vorticity distribution varies with depth.

The dispersion equation describing the combined wave-current motion is found to contain additional first order terms which are related to the vorticity distribution. These terms have a significant effect upon the predicted wave number, and in the case of a realistic current profile lead to a reduction in the apparent Doppler shift.

The oscillatory velocities associated with the wave motion are also shown to be very different from the existing irrotational solutions. In addition to the wave number effects discussed above, a favourable current with positive

shear produces a significant increase in the amplitude of the oscillatory motion, while an adverse current with negative shear reduces the amplitude of the oscillatory motion. These changes are associated with a rotational wave component which arises at a second order of wave steepness. This additional component is directly related to the vorticity distribution and does not therefore arise within a classical Stokes' expansion. As a result, the wave motion generated in the presence of a strongly sheared current cannot be predicted by an irrotational solution, even if this includes the effect of an "equivalent" uniform current.

## 5. References.

- Benjamin, T.B. (1959) "Shearing flow over a wavy boundary." J. Fluid Mech. Vol. 6 pp. 161-205.
- Bretherton, F.P. & Garrett, C.J.R. (1968) "Wave trains in inhomogeneous moving media." Proc. Roy. Soc. Ser. A Vol. 302 pp. 529-554.
- Brink-Kjör, O. & Jonsson, I.G. (1975) "Radiation stress and energy flux in water waves on a shear current." Tech. Univ. Denmark, Inst. Hydrodyn. and Hydraul. Eng. Prog. Rep. no. 36 pp. 27-32.
- Chaplin, J.R. (1989) "The computation of non-linear waves on a current of arbitrary non-uniform profile." Report to UK. Dept. of Energy.
- Hedges, T.S. & Lee, B.W. (1992) "The equivalent uniform current in wave-current computations" Coastal Engng. Vol. 16 pp. 301-311.
- Jonsson, I.G. (1990) "Wave-current interactions". The Sea Vol 9 Ocean Eng. Science. Chap. 1.1.3
- Kishida, N. & Sobey, R.J. (1988) "Stokes theory for waves on linear shear current." J. Eng. Mech. ASCE Vol. 114 pp. 1317-1334.
- Lamb, H. (1932) Hydrodynamics. Cambridge University Press. 6th edition.
- Longuet-Higgins, M.S. & Stewart, R.W. (1960) "Changes in the form of short gravity waves on long waves and tidal currents" J. Fluid Mech. Vol. 8 pp. 565-583.
- Longuet-Higgins, M.S. & Stewart, R.W. (1961) "The changes in amplitude of short gravity waves on steady non-uniform currents." J. Fluid Mech. Vol. 10, pp. 529-549.
- Peregrine, D.H. (1976) "Interaction of water waves and currents." Adv. Appl. Mech. Vol. 16 pp. 9-117.
- Stokes, G.G. (1847) "On the theory of oscillatory waves" Trans. Cam. Philos. Soc. Vol. 8 pp. 441-55.
- Taso, S. (1959) "Behaviour of surface waves on a linearly varying flow." Moskow. Fiz. Tech. Inst. Issl. Mekh. Prikl. Mat. Vol. 3 pp. 66-84.

## CHAPTER 52

### WAVE, TURBULENT AND MEAN MOMENTUM FLUXES ACROSS THE BREAKING WAVE TRANSITION REGION IN THE SURF ZONE

R. J. Thieke<sup>1</sup>, A.M. A.S.C.E.

#### ABSTRACT

This paper presents an application to the transition region of an integral momentum conservation model incorporating a Reynolds type decomposition for both wave and turbulent fluctuations. With simple parameterizations the model provides both a rough predictive capability for the limiting wave reduction across the transition zone and also an alternative means of examining the partitioning of flow momentum across the region.

#### INTRODUCTION

Historically, the quantitative prediction of many surf zone processes has suffered from a lack of sufficient understanding of the detailed hydrodynamics of the wave transformation, wave-induced circulation and turbulent velocity fluctuations across the nearshore zone. The processes of wave shoaling, wave breaking, subsequent wave decay in the surf zone, wave setup and wave induced cross-shore mean circulation occur simultaneously and are intimately interdependent. Their complexity has typically resulted in each process being studied in piecemeal fashion. While important advances have been made, there are notable regions where a thorough understanding is still lacking, particularly the transition region following breaking. The physical processes in the transition (or "outer") region play an important role in the establishment of the flow characteristics of the surf zone, however the dynamics of the region are not well understood quantitatively or qualitatively.

---

<sup>1</sup>Department of Coastal and Oceanographic Engineering, University of Florida, Gainesville, FL 32611, U.S.A.

The transition region begins at the breakpoint and extends shoreward, and it is characterized by a rapid decrease in wave height with almost no change in the setup of the mean water level (Svendsen, 1984). The end of the transition region (hereafter referred to as the transition point) is best defined by the point where the setup begins to increase, which is typically accompanied by a decrease in the rate of wave height decay. The entire region represents a relatively rapid reorganization of the wave motion.

The following analysis presents the application of an integral momentum rapidly varied flow analysis to the transition region. A Reynolds type decomposition for both wave and turbulent fluctuations is incorporated. In view of the lack of detailed experimental data within this region, the simplest possible parameterizations of the mean flow and wave properties are adopted. Nevertheless the model provides both a rough predictive capability for the limiting wave reduction across the transition zone and also an alternative means of examining the partitioning of flow momentum across the region.

## BACKGROUND

### Wave Height Decay and Rapidly Varied Flow

The rapid nature of change in the transition region render it largely unsuitable for a gradually varied flow analysis or a similarity approach. An example is provided by the energy flux conservation models for wave height decay in the surf zone. Such models solve the depth integrated energy and momentum conservation equations, and differ largely only in the chosen description of the breaking wave energy dissipation. Svendsen (1984) found very poor agreement with laboratory data when wave height decay computations were initiated at the breakpoint; agreement was substantially improved by starting the decay computations after the transition region following breaking, beyond which point surf zone waves are largely self-similar. Dally et al. (1985), found that a similar improvement in prediction could be achieved for certain of their comparisons with laboratory data by initiating decay computations after the transition region.

These observations suggest a simple analogy to jet flows: The transition region serves as the "zone of flow establishment" for the surf zone, while the inner surf zone is the "zone of established flow," in which similarity approaches have met with considerable success. The dynamics of these two regions appear quite dissimilar and warrant independent treatment.

### Transition Region "Paradox"

Another significant feature of the transition region is the "paradox" observed by Basco and Yamashita (1986) and Svendsen (1984). This paradox is evidenced by the simplified momentum balance in the x (onshore) direction:

$$\frac{dS_{xx}}{dx} + \rho g(h + \bar{\eta}) \frac{d\bar{\eta}}{dx} = 0 \quad (1)$$



where:  $S_{xx}$  = "radiation stress"  
 $\rho$  = mass density  
 $g$  = gravitational acceleration  
 $h$  = depth to still water level  
 $\bar{\eta}$  = mean water level setup

The paradox arises since  $S_{xx}$  ("the radiation stress") is known to be a function of wave height and hence is decreasing rapidly across the transition region. The first term in Equation 1 would appear to be finite and negative. Measurements indicate that the setup is constant, so the second term is approximately zero; the equality is not satisfied.

### Return Flow Modelling

Spatially varying wave height and setup fields have been used as input to a variety of return flow (or "undertow") models which solve for the distribution of the mean flow in the lower portion of the water column (for example Stive and Wind, 1986; Svendsen and Hansen, 1988). Such models follow the qualitative arguments of Dyhr-Nielsen and Sorensen (1970), wherein the return flow is driven by the vertical imbalance between the gradients of radiation stress and setup that is imbedded (but not explicit) in the depth integrated Equation 1. The models typically employ an eddy viscosity parameterization and differ in the description of the wave parameters (particularly the shoreward mass flux in the crest portion of the wave) and the boundary conditions. The mass flux in the crest region is observed to be substantially greater than that of a nonbreaking wave of equivalent height (Nadaoka and Kondoh, 1982) and is dynamically quite significant; the overall magnitude of the local return flow is largely determined by the value of the shoreward mass flux above the trough (which is entered as a "boundary condition"). Svendsen and Hansen (1988) particularly note that this feature of the flow is rather poorly understood.

The nature of the transition region paradox and the importance of this region to both wave height and return flow modelling and indeed to all surf zone processes suggests that additional analysis of this region is warranted. It should be noted that although these effects are sharply evident for the case of monochromatic waves, the "smearing" of the breakpoint in the random wave case tends to mask the importance of the transition region. However Nairn, et al. (1990) found that the inclusion of the lag effect of the transition region was crucial to the accurate modelling of both regular and random wave cases.

## INTEGRAL MOMENTUM CONSERVATION EQUATIONS

In the present context, emphasis is placed on the three hydrodynamic mechanisms which are locally crucial to the various surf zone processes of interest, namely, 1) the (generally nonlinear) wave orbital velocity, 2) the mean flow (often

wave induced), and 3) the residual turbulent velocity fluctuations. Throughout the breaking process and wave decay in the surf zone, the motion consists of complicated interactions between these three mechanisms, and the total available flow momentum is partitioned and exchanged between them. Consequently this analysis will include each of these component motions in a Reynolds type representation of the instantaneous velocity:

$$u = \bar{u} + u'' + u' \quad (2)$$

where the overbar indicates an average over the wave period (mean flow), and the double and single primes refer to the wave and turbulent fluctuations, respectively. This decomposition can be applied to the fundamental variables in the shorenormal (x) momentum conservation equation. Time averaging the resulting equation over a wave period and depth integrating produces the following integral equation:

$$\frac{d}{dx} \int_{-h}^{\eta_e} \rho \bar{u}^2 dz = -\rho g (h + \bar{\eta}) \frac{d\bar{\eta}}{dx} - \frac{d}{dx} \int_{-h}^{\eta_e} (s_{xx}'' + s_{xx}') dz - \tau_b \quad (3)$$

with the apparent stresses now retaining their depth variation and defined as:

$$\begin{aligned} s_{xx}'' &= \text{depth varying wave "radiation stress"} \\ s_{xx}' &= \text{depth varying turbulent "apparent stress"} \end{aligned}$$

The integral on the right hand side of Equation 3 is essentially equivalent to the conventional radiation stress  $S_{xx}$ , however in this instance it includes contributions from both wave and turbulent velocity fluctuations. The momentum flux associated with the mean flow is separated from the "radiation stress" and is represented by the integral on the left hand side of Equation 3.

By neglecting the bed shear stress  $\tau_b$ , Equation 3 can be used to reevaluate the transition region paradox. The paradox appears to stem partially from the conventional linear wave description of radiation stress in which the mean flow and turbulent fluctuations are neglected. Basco and Yamashita (1986) indicate that the paradox merely reflects the redistribution between the velocity and pressure parts of the radiation stress. The above decomposition explicitly including the mean flow further indicates that a reduction in wave height (and hence  $s_{xx}''$ ) in the absence of a setup gradient must be balanced by an increased mean flow and/or an increase in the turbulence intensity. The measurements of Nadaoka and Kondoh (1982) confirm that both the mean mass flux and turbulence intensity increase across the transition region. The success of the "surface roller" parameterization within the inner surf zone (Svendsen, 1984) also substantiates the requirement of an increase in mean flow.

The crucial objective in this region is thus to quantify the relative magnitudes of wave, mean flow and turbulent momentum fluxes from the point of incipient breaking to the end of the transition region. This breaking process sets up the entire flow in the inner surf zone, within which the previously mentioned gradually varied flow and similarity approaches may be more suitably employed.

### SIMPLE RAPIDLY VARIED FLOW MODEL

Further examination of the partitioning of flow momentum is accomplished by the development of a rapidly varied flow analysis of the transition region in direct analogy to the techniques used successfully for hydraulic jumps and bores in channel flows. Because the gradient of setup is zero, Equation 3 can be reduced to a momentum equality across a "shock" which can be considered short enough to neglect bottom friction:

$$\left[ \int_{-h}^{\eta_c} \rho \bar{u}^2 dz + \int_{-h}^{\eta_c} (s_{xx}'' + s_{xx}') dz \right]_b = \left[ \int_{-h}^{\eta_c} \rho \bar{u}^2 dz + \int_{-h}^{\eta_c} (s_{xx}'' + s_{xx}') dz \right]_t \quad (4)$$

The subscript b denotes the breakpoint and the subscript t denotes the transition point. To employ this relationship, a successful parameterization of the quantities in square brackets is necessary.

As a first approximation, the turbulent contributions to Equation 4 are neglected. For simplicity, linear wave theory is used to evaluate the radiation stress and mean flow. A two layer model dividing the flow at the wave trough level is adopted, following Thieke and Sobey (1990). However in this case the simplest possible "block-type" mean velocity profile is considered with the mean velocity considered uniform within each layer and estimated from linear theory for the upper layer (subscript 1) and the lower layer (subscript 2) respectively by:

$$\bar{u}_1 = \frac{ga^2k}{2\sigma H} = \frac{gHk}{8\sigma} \quad (5)$$

$$\bar{u}_2 = -\frac{ga^2k}{2\sigma h_r} = -\frac{gH^2k}{8\sigma h_r} \quad (6)$$

Where:

$h_r$  = water depth below wave trough level

$k$  = wave number

$\sigma$  = angular wave frequency

$a$  = wave amplitude

$H$  = wave height

Linear theory alone cannot capture the increased mass flux of surf zone waves, and guidance is accordingly sought from experimental evidence. The laboratory measurements of Nadaoka and Kondoh (1982) indicate that the mass flux in a surf zone wave is 2-3 times that of a linear wave of equal height. To accommodate this a constant mass flux correction  $Q$  is applied to the velocity profile at the transition point. The value  $Q = 2.5$  was selected to reflect the observations. It is recognized that the wave part of the radiation stress as predicted by linear theory is not a completely accurate representation, however the aerated flow in the surf zone has so far prevented any guidance from experimental evidence in this instance.

Substituting the aforementioned parameterizations into Equation 4 yields:

$$\begin{aligned} & \left[ \frac{\rho g^2 k^2}{64 \sigma^2} \left( H^3 + \frac{H^4}{h_r} \right) + \frac{\rho g H^2}{8} \left( 2n - \frac{1}{2} \right) \right]_b \\ & = \left[ Q^2 \frac{\rho g^2 k^2}{64 \sigma^2} \left( H^3 + \frac{H^4}{h_r} \right) + \frac{\rho g H^2}{8} \left( 2n - \frac{1}{2} \right) \right]_t \end{aligned} \quad (7)$$

Given the conditions at the breakpoint as known, substituting the appropriate parameters on the right-hand side of Equation 7 gives a single equation for the wave height at the transition point,  $H_t$ . An initial estimate of one-half the breaking height ( $H_t = 0.5 H_b$ ) is used together with a Newton-Raphson convergence procedure to solve for  $H_t$ .

## COMPARISON TO MEASURED DATA

The model was tested against the laboratory wave data of Hansen and Svendsen (1979). Measured conditions at the breakpoint are input to the model on the left hand side of Equation 7. The measured wave height at the transition point was obtained by determining the wave height corresponding to the sharp increase in the gradient of the setup of the mean water level. The controlling parameters for the various test conditions are given in Table 1.

The model results are shown graphically in Figure 1, which compares (in dimensionless fashion) the predicted wave height at the transition point with the corresponding measured values as a function of the breaking wave height.

Note that the predicted curve (which assumes all lost wave momentum is transmitted to the mean flow), provides an effective upper limit to the transition point wave height, and also explains a large portion of the observed behavior. This is shown schematically in Figure 2, where the departure of the predicted wave height from the best fit line through the measured data can be viewed as an approximate representation of the fraction of the wave momentum converted into turbulent momentum flux. The model indicates that the majority of the wave height reduction in the transition region is associated with the generation of the enhanced mean flow, with a smaller contribution toward the turbulent momentum flux.

Test No.	T (s)	$H_o$ (mm)	$H_b$ (mm)	$x_b$ (m)	$h_b$ (mm)	$\bar{\eta}_b$ (mm)
101101	1.0	100	105.1	22.56	132.9	-1.7
A10112	1.0	70	77.1	23.90	93.9	-1.64
081103	1.25	100	121.6	22.39	137.9	-2.36
A08102	1.25	70	86.8	23.82	96.0	-1.56
A08103	1.25	40	56.5	24.88	65.1	-0.98
061102	1.67	100	139.7	21.91	151.9	-2.74
061091	1.67	90	129.1	22.23	142.5	-2.26
061082	1.67	80	117.8	22.36	138.7	-1.94
061071	1.67	70	103.9	22.99	120.3	-1.80
051071	2.00	70	109.1	23.30	111.4	-2.40
051041	2.00	40	72.9	24.63	73.8	-1.62
041071	2.50	70	128.8	22.56	133.0	-2.30
041041	2.50	40	88.0	24.06	89.2	-1.30
031041	3.33	40	95.4	23.94	92.7	-1.48

Table 1: Wave conditions for various laboratory experiments of Hansen and Svendsen (1979) used as input for rapidly varied flow model simulations.

## REFINEMENT OF PARAMETERIZATIONS

### Higher Order Wave Theories

Accurate modelling of the transition region requires an adequate representation of the initial conditions, that is, the kinematics of incipient breaking waves. Such waves are highly nonlinear and are typically strongly asymmetric with time due to the effect of the sloping bottom. While the use of a steady wave theory (assuming a flat bottom) is strictly not consistent with these conditions, in the absence of any other practical analytical or hybrid numerical-analytical method such a theory can (if appropriately chosen) provide some predictive capability. Given the highly nonlinear nature of near-breaking waves and the obvious inappropriateness of linear wave theory for this region, it is natural to turn to a higher order wave representation.

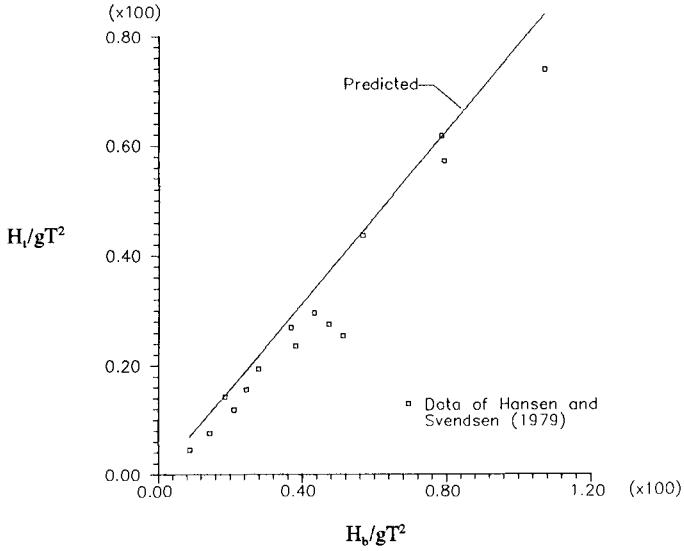


Figure 1: Dimensionless comparison of measured and predicted wave heights  $H_i$  at the transition point in terms of the breaking wave height  $H_b$ .

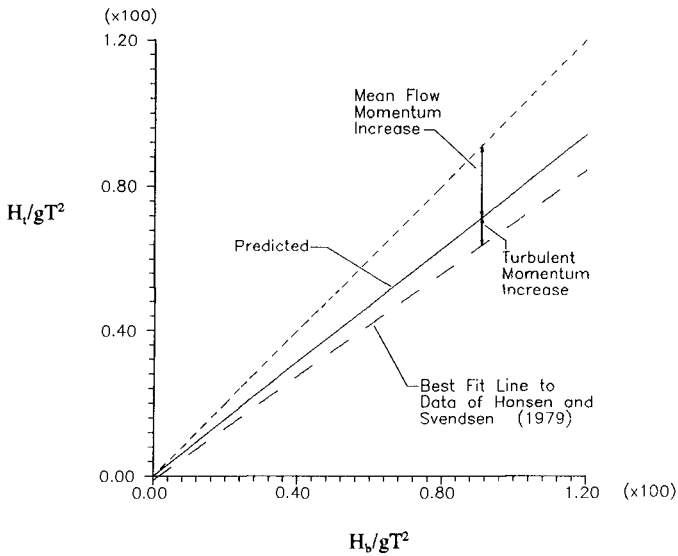


Figure 2: Schematic representation of the transition point partitioning of the increased mean flow and turbulent momentum flux resulting from wave height reduction.

Figures 3a and 3b compare velocity amplitudes measured in the laboratory for waves approaching breaking using a laser doppler anemometer (LDA) (Thieke, 1992), with those predicted by Stokes, Cnoidal and Fourier wave theories of varying order (following Sobey et al. 1987). In each case the velocities are measured at a point just seaward of the breakpoint. Figure 3a (for a relatively short wave) shows that the Fourier theory (to eighteenth order) predicts the positive velocity amplitude tolerably well and the negative amplitude slightly less so. The Stokes wave solutions are not at all useful; the higher order solution shows a clearly recurved profile. Figure 3b (for a somewhat longer wave) again shows that the Fourier wave theory predicts the velocity amplitudes quite well, while a Cnoidal II prediction is quite disparate from the measurements. Higher order Cnoidal predictions diverge quite rapidly under waves of this height ( $H/h$  greater than 0.5); Stokes wave solutions at this point were entirely divergent. The performance of the Fourier wave theory in each of these instances suggests that it should yield reasonable predictions of integral properties (mass flux, momentum flux) of waves approaching the breakpoint.

Although some difficulty is encountered in obtaining Fourier wave solutions at the maximum wave heights attained by waves breaking on a slope (which prevents the ready inclusion of such a parameterization in the model), it is generally possible to obtain informative solutions for all but the most extreme near breaking (albeit assumed steady) wave heights.

### **Evolution of Wave, Turbulent and Mean Momentum Fluxes**

The aforementioned predictions from Fourier wave theory, together with existing laboratory measurements in the surf zone, can be used to clarify the relative contributions of the wave, turbulent and mean motions to the total momentum flux as well as the spatial variation of these contributions. Figure 4 shows comparisons of Fourier wave predictions of Eulerian mean velocity with the laboratory LDA mean velocity measurements of Nadaoka and Kondoh (1982) for waves over a plane sloping beach. The example shown is for Case 1, a spilling breaker (wave period  $T = 1.32$  s) on a 1 on 20 slope. Comparisons are shown for three locations. Station P7 ( $h = 0.347$  m) is located just seaward of the breakpoint, while station P4 ( $h = 0.207$  m) is just inshore of the end of the transition region and station P2 ( $h = 0.107$  m) is well within the inner surf zone. The wave heights (scaled from trough and crest elevations) were 0.197 m (P7), 0.161 m (P4), and 0.065 m (P2), respectively. The setup was taken as zero since it was not measured in the experiments. The Fourier prediction of mean velocity in the near breaking wave is quite reasonable, despite the asymmetry and unsteadiness inherent in such a wave. However two observations are significant in the surf zone. The first is that the actual mean flow (as suggested earlier) grows to be much greater than that in a nonbreaking wave of similar height, leading to severe underprediction by the wave theory. Secondly, there are substantial mean vertical velocities present in the surf zone which do not exist outside the breakpoint. Note that these are essential for the maintenance of mass conservation in two dimensions due to the divergence of the horizontal velocity. They cannot be directly predicted by the wave theory.

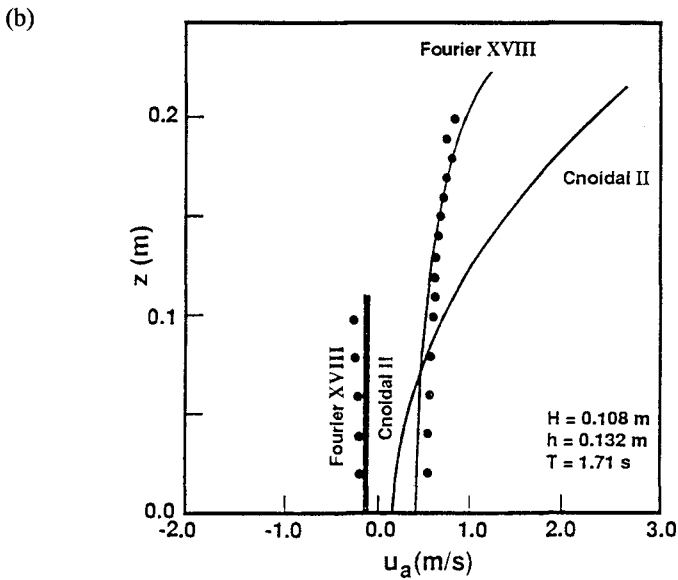
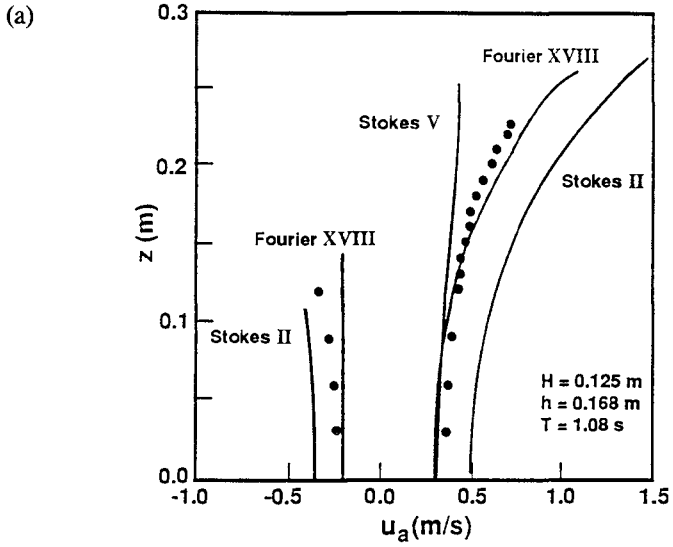


Figure 3: Comparison of LDA measured horizontal velocity amplitudes ( $\bullet$ ) with wave theory predictions ( $-$ ).



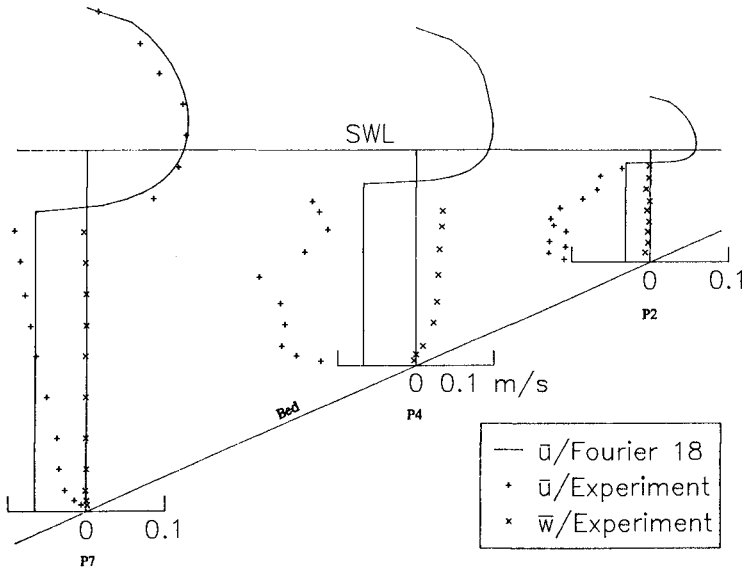


Figure 4: Profiles of predicted Eulerian mean velocities and comparison with data of Nadaoka and Kondoh (1982), Case 1.

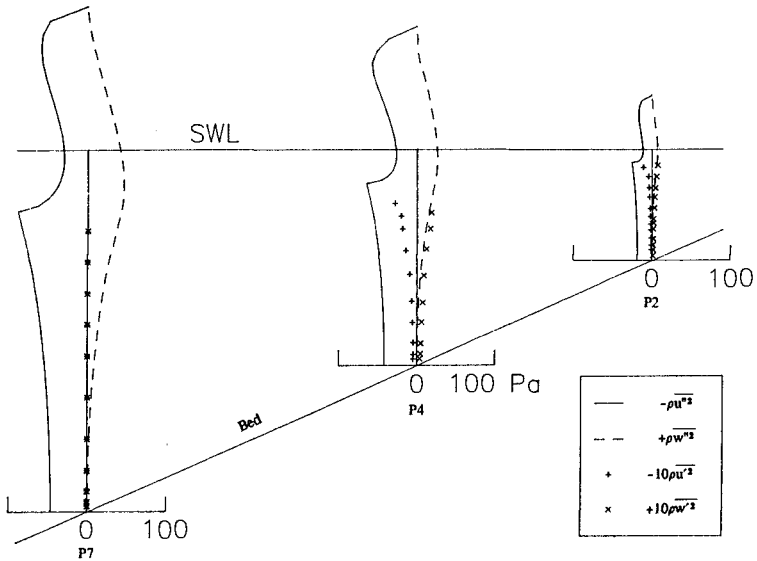


Figure 5: Profiles of predicted wave apparent stress and measured turbulent Reynolds stress from data of Nadaoka and Kondoh (1982), Case 1.

Similar comparisons are made for predictions of wave (double primed) momentum fluxes and laboratory (LDA) measurements of turbulent (single primed) momentum fluxes across the surf zone in Figure 5. It is seen that the turbulent intensities are essentially zero outside the breakpoint, but are "produced" through the transition region and then exhibit decay in the inner surf zone as the shoreline is approached. It is noteworthy that the wave momentum fluxes in the below trough region are approximately an order of magnitude greater than their turbulent counterparts. Although these measurements cannot cover the turbulent aerated crest region due to extensive air entrainment and LDA signal dropout, they indicate that over a large portion of the water column the dominant feature of the momentum balance is still the wave orbital motion, although it is clear that the mean flow has also taken on greater importance than it does outside the surf zone.

Flow Component	Depth Integrated Momentum Flux ( in N/m )	
	Station P7	Station P4
$\int_{-h}^{\eta_c} s_{xx}'' dz$	33.0	17.6
$\int_{-h}^{\eta_c} \rho \bar{u}^2 dz$	3.2	10.1
$\int_{-h}^{\eta_{tx}} \rho \overline{u^2} dz$	≈ 0	0.3
$\int_{-h}^{\eta_{tx}} \rho \overline{w^2} dz$	≈ 0	0.2

Table 1: Partitioning of total depth integrated momentum flux among wave, mean flow and turbulent components for the experimental test Case 1 (T = 1.32 sec) of Nadaoka and Kondoh (1982). (Mean flow and turbulent components inferred from measured data; wave apparent stress computed from Fourier wave theory)

Figures 4 and 5 together show the global trends of development of surf zone mean and turbulent momentum fluxes, with a limited predictive capability provided by Fourier wave theory. These results can be used to quantitatively analyze the partitioning of total momentum flux between the wave, mean flow and turbulence components across the transition region. For this purpose, locations P7 and P4 of

the previous Nadaoka and Kondoh example were again considered. The results of this exercise are given in Table 2. In this instance the wave radiation stress is evaluated from Fourier wave theory, while the turbulent apparent stresses are evaluated from the laboratory measurements and are limited to the below trough region. The depth integrated mean momentum flux is found by integrating the below trough measurements and inferring the remaining contribution through mass conservation constraints.

The wave radiation stress is clearly decreasing across the transition region, however it is in a large part balanced by an accompanying increase in the mean momentum flux. The below trough turbulent stresses are of little consequence. Complete closure is not possible due to the lack of information regarding the turbulent apparent stresses in the crest to trough region (a potentially larger contribution) and the neglect of bed shear. Nevertheless the measurements indicate that a substantial portion of the wave height reduction across the region is tied to an increase in mean flow momentum.

## CONCLUSIONS

A simple rapidly varied flow model of the breaking wave transition region provides insight into the mechanics of the region and a certain predictive capability, despite the relatively crude parameterizations employed. The model results support the arguments of Svendsen (1984) and Basco and Yamashita (1986) that only part other wave height reduction in the transition region is the result of energy dissipation (i.e. turbulence production). More specifically, the following conclusions may be drawn:

- a) A large portion of the wave height reduction across the transition region results from momentum being transferred to the mean flow, with a somewhat smaller reduction resulting from actual energy dissipation.
- b) Linear wave theory (with empirical adjustments) and the assumption of all momentum transfer to the mean flow provides a reasonable upper limit for the wave height at the transition point, despite the crude nature of the assumptions.
- c) The separation of the "velocity part" of the radiation stress permits the identification of the distribution of the total momentum flux to the wave, turbulent and mean flow contributions.
- d) Below the wave trough level the turbulence contributes minimally to the total balance of momentum (above the trough however the contribution is potentially larger and not well documented).
- e) The model described is not truly predictive but rather informative (i.e. the length of the transition region is not determined since the region is effectively compressed into a "shock"). Practical empirical measures for including the finite width of the

transition region in surf zone modelling are presented by Nairn, et al. (1990).

f) Detailed measurements of the wave, mean flow and turbulence characteristics in the trough-to-crest region are crucial to a complete understanding of the dynamics of the transition region.

## ACKNOWLEDGEMENTS

This material is based upon work supported by the National Science Foundation under Award No. CTS-9111076

## REFERENCES

- Basco, D.R. and Yamashita, T. (1986). Toward a simple model of the wave breaking transition region in surf zones. Proceedings 20<sup>th</sup> Coastal Engineering Conference, 2, 955-970.
- Dally, W.R., Dean, R.G. and Dalrymple, R.A. (1985). Wave height variation across beaches of arbitrary profile. Journal of Geophysical Research, 90,C6, 11917-11927.
- Dyhr-Nielsen, M. and Sorensen, T. (1970). Sand transport phenomena on coasts with bars. Proceedings 12<sup>th</sup> Coastal Engineering Conference, 2, 855-866.
- Hansen, J.B. and Svendsen, I.A. (1979). Regular waves in shoaling water, experimental data. Series paper no. 21, Institute of Hydrodynamics and Hydraulic Engineering, Technical University of Denmark.
- Nadaoka, K. and Kondoh, T. (1982). Laboratory measurement of velocity field structure in the surf zone by LDV. Coastal Engineering in Japan, 25, 125-145.
- Nairn, R.B., Roelvink, J.A. and Southgate, H.N. (1990). Transition zone width and implications for modelling surf zone hydrodynamics. Proceedings 22<sup>nd</sup> Coastal Engineering Conference, 1, 68-81.
- Sobey, R.J., Goodwin, P., Thieke, R.J. and Westberg, R.J. (1987). Application of Stokes, Cnoidal and Fourier wave theories. Journal of Waterway, Port, Coastal and Ocean Engineering, ASCE, 113, 6, 565-587.
- Stive, M.J.F. and Wind, H.G. (1986). Cross-shore mean flow in the surf zone. Coastal Engineering, 10, 325-340.
- Svendsen, I.A. (1984). Wave heights and set-up in a surf zone. Coastal Engineering, 8, 303-329.
- Svendsen, I.A. and Hansen, J.B. (1988). Cross-shore currents in surf zone modelling. Coastal Engineering, 12, 23-42.
- Thieke, R.J. and Sobey, R.J. (1990). Cross-shore wave transformation and mean flow circulation. Coastal Engineering, 14, 387-415.
- Thieke, R.J. (1992). Integral properties of steep and shoaling waves. (Manuscript).

## CHAPTER 53

### EFFECTS OF THE GULF STREAM ON WIND WAVES IN SWADE

Hendrik L. Tolman \*

#### ABSTRACT

Preliminary results of a numerical study of wave-current interactions in SWADE for 20 Oct. 1990 to 31 Oct. 1990 are presented. The results are obtained with the wave model WAVEWATCH, which incorporates both wave-current interactions and a full description of the dynamics wave growth and decay. It is shown that wave-current interactions are expected to be sufficiently strong to be observed in mean wave parameters, but that significant effects of interactions occur close to the Gulf Stream only. Furthermore, wave growth and decay are strongly influenced by the currents. Thus, modelling of wave-current interactions on the scales considered requires a comprehensive assessment of both (conservative) wave-current interactions and of the dynamics of wave growth and decay.

#### 1 Introduction

Effects of the Gulf Stream on wind waves are assessed in the light of the Surface Wave Dynamics Experiment (SWADE, Weller et al. 1991). This experiment took place during the winter 1990-1991 on the continental shelf at the East coast of the United States, north of Cape Hatteras. Due to the vicinity of the Gulf Stream (the Gulf Stream actually intruded into the measurement array in early March 1991), wave-current interactions are potentially important in analyzing experimental data. Furthermore, the SWADE data provides a unique opportunity to verify wave-current interaction models due to the above intrusion.

---

\* NRC Resident research Associate at NASA / Goddard Space Flight Center. Presently: NOAA/NMC21, World Weather Building, Washington, DC 20233, USA.

The wave-current interaction studies within SWADE consist of two parts. First, a mainly numerical assessment of wave-current interactions is made for the first Intensive Observation Period (IOP) of October 20 through 31 1990. The objective is to estimate effects of a realistic Gulf Stream on ocean wind waves using a full third-generation ocean wave model to provide a synthesis of all the idealized wave-current interaction studies performed so far. Such a study is the logical extension of Holthuijsen and Tolman (1990, 1991; henceforth denoted as HT). Secondly, an intercomparison of observations and model hindcasts will be made for part of the third IOP (March 3 through 5, 1991). The objective is to assess and verify present insights in wave-current interactions. In the present paper, preliminary results for the first part of the SWADE wave-current interaction studies will be presented.

## 2 Models

A cascade of nested models with increasing spatial resolution has been used, consisting of an Atlantic basin model ( $1^\circ \times 1^\circ$  longitude-latitude resolution), a regional model ( $1/4^\circ \times 1/4^\circ$ ) and the so-called SWADE model ( $1/12^\circ \times 1/12^\circ$ ) (see Weller et al. 1991, Fig. 11 and present Fig. 1). The Atlantic basin model is primarily used to provide boundary conditions for the regional model, and does not include currents. Because winds and waves outside the regional model proved irrelevant for the period considered, the Atlantic basin will not be considered in the following discussions. Gulf Stream surface currents for the regional and SWADE models (see Fig. 1) are obtained from feature models and the operational surface temperature analysis of NOAA/NMC. Wind fields for both models consist of high resolution SWADE wind analyses.

The results presented in this paper are obtained with the latest version of the model WAVEWATCH (Tolman 1991, 1992, 1993). In this model, the evolution of the action density spectrum  $N(\omega, \theta, \phi, \lambda, t)$  is calculated, where  $\omega$  is the absolute wave frequency (as observed in a fixed frame of reference),  $\theta$  is the wave direction,  $\phi$  is the latitude,  $\lambda$  is the longitude and  $t$  is the time. The action density spectrum  $N$  is directly related to the energy or variance density spectrum  $F(\omega, \theta, \phi, \lambda, t)$ ,  $N = F/\sigma$  (for brevity of notation dropping the dependence of  $N$  and  $F$  on  $\omega$ ,  $\theta$ ,  $\phi$ ,  $\lambda$  and  $t$ ), where  $\sigma$  is the intrinsic or relative frequency, as observed in a frame of reference moving with the mean current. The frequencies  $\sigma$  and  $\omega$ , the wavenumber vector  $\mathbf{k}$ , the depth  $d$  and the current velocity  $\mathbf{U}$  are interrelated in the combined Doppler-dispersion relation

$$\sigma = \sqrt{gk \tanh kd} = \omega - \mathbf{k} \cdot \mathbf{U} . \quad (1)$$

The balance equation for the action density spectrum  $N$  becomes (e.g., WAMDI group 1988, Tolman 1991):

$$\frac{\partial N}{\partial t} + (\cos\phi)^{-1} \frac{\partial}{\partial \phi} [c_{\phi} \cos\phi N] + \frac{\partial}{\partial \lambda} [c_{\lambda} N] + \frac{\partial}{\partial \omega} [c_{\omega} N] + \frac{\partial}{\partial \theta} [c_{\theta} N] = S, \quad (2)$$

where  $c_{\phi} = d\phi/dt$  etc. are the propagation velocities in the corresponding spaces (e.g., WAMDI group 1988, Tolman 1991), and where  $S$  denotes the net source term. The source term  $S$  consists of wind input (Janssen, 1989, 1991), nonlinear wave-wave interactions (Hasselmann and Hasselmann, 1985), energy dissipation due to whitecapping (Janssen, 1991) and energy dissipation due to bottom friction (Hasselmann et al., 1973). Thus, the present source terms are equivalent to those of cycle 4 of the WAM model (see, e.g., Mastenbroek et al., 1993). The source terms are corrected for effects of mean currents by applying them in a frame of reference moving with the mean current.

The numerics of WAVEWATCH as used in the present study incorporate a second order SHASTA propagation scheme and dynamic implicit source-term integration as described by Tolman (1992). The spectrum is discretized using 24 directions ( $\Delta\theta = 15^\circ$ ) and 33 frequencies (0.042 Hz through 0.88 Hz,  $f_{i+1} = 1.1f_i$ ). The time steps  $\Delta t$  are 450 s for the regional model and 240 s for the SWADE model.

In the final presentation of this part of the SWADE wave-current interaction studies, results of the WAM model (WAMDI Group, 1988) will also be included. These results are presently obtained by S. Hasselmann, H.C. Graber and R.E. Jenness. Note that cycle 4 of WAM (spring 1992) incorporates wave-current interactions for steady currents.

### 3 Meteorological conditions

On Oct. 20, winds in the regional model are weak with predominantly northeasterly directions, except for a fairly strong depression, which moves rapidly eastward over Nova Scotia. For the next few days, the entire region has weak northeasterly winds. On Oct. 24 a small depression develops over Cape Hatteras and starts moving in a northeasterly direction. On Oct. 25, this system is located south of Nova Scotia and on Oct. 26 it has left the regional model area. On the same day several systems develop around Cape Hatteras. These systems merge into a complex structure with strong northeasterly, northwesterly and southwesterly winds in the northwest, southwest and southeast quadrants respectively (wind speeds over 20 m/s). In the next two days this systems moves in a northeasterly direction and at Oct. 29 this

system has left the regional model. Finally, on this day a cold air outbreak occurs north of Cape Hatteras, and the associated depression moves over Nova Scotia on Oct 31.

#### 4 Results

Model calculations have been performed for the period of Oct. 15 1990 through Oct 31, 1990. The period of Oct 15 through Oct 20, 0000 UTC is used to initialize the models. For both the regional model and the SWADE model calculations have been performed with and without the Gulf Stream. Thus, effects of the Gulf Stream can be isolated by simply taking the difference between the two model runs. All weather systems described in section 3 are accompanied by a distinct wind sea system. Furthermore, all these systems generate swell traveling in northerly to easterly directions. The complicated structure on Oct 26 through 28, also radiates swell energy in southern directions.

Effects of wave-current interactions are found to vary on small space and time scales. This is illustrated in Fig. 2 with the maximum and minimum current-induced modulation of the significant wave height  $H_s$  and the mean wave length  $L$  for several models and areas.

$$H_s = 4\sqrt{E} \quad , \quad E = \iint F(\omega, \theta) d\omega d\theta \quad . \quad (3)$$

$$L = E \left( \iint 2\pi k^{-1} F(\omega, \theta) d\omega d\theta \right)^{-1} \quad . \quad (4)$$

The time scale of pronounced features in this figure is typically several hours to several days. A comparison of results for the SWADE model (solid lines) and the corresponding area in the regional model (dashed lines) shows qualitatively similar results. Due to the fairly limited resolution of the region model (a cross section of the Gulf Stream consists of no more that five grid points), the regional model shows less detail (figures not presented here) and consequently slightly different but similar extreme values for  $\Delta H_s$  and  $\Delta L$  (see Fig. 2). Consequently, one might expect the regional model to give a fairly accurate estimate of the wave-current interactions, in spite of the relatively poor resolution. Furthermore, Fig. 2 shows only limited effects of wave-current interactions in the overall quiet periods of Oct 20 through 23, Oct 25 and Oct 29. This might be expected because the wave heights in this period are generally less than 2 m. Finally, Fig. 2 shows that the largest impacts of wave-current interactions occur outside the SWADE area on Oct. 27 and 28.



To assess effects of wave-current interactions in more detail, the spatial distribution of effects of wave-current interactions will be discussed in some detail for Oct. 28, 0000 UTC. This time has been selected for the interesting interactions in the model. Note that, as discussed above, this time is not representative for the entire period considered. The discussion will concentrate on results for the regional model, because this model is expected to be sufficiently accurate to show the general features of the present Gulf Stream current field. In Fig. 3 the significant wave height  $H_s$  (obtained from a model including the Gulf Stream) and the current-induced modulation of the wave height  $\Delta H_s$  (model differences) are presented. Similarly, Fig. 4 shows the mean absolute period  $T_a$ , Fig. 5 shows the integral input source term  $S_{in,i}$  and Fig. 6 shows the integral dissipation (whitecapping) source term  $S_{ds,i}$ .

$$T_a = E \left( \iint 2\pi \omega^{-1} F(\omega, \theta) d\omega d\theta \right)^{-1} . \quad (5)$$

$$S_{in,i} = \iint S_{in}(\omega, \theta) d\omega d\theta . \quad (6)$$

$$S_{ds,i} = \iint |S_{ds}(\omega, \theta)| d\omega d\theta . \quad (7)$$

Figures 3 through 6 show that the space scales of current-induced modulations of the wave field are governed by the corresponding scales of the current and wind fields. Furthermore, such modulations are mostly confined to the immediate vicinity of the Gulf Stream and modulations can be large enough to be observed in the overall model results (i.e., without differencing models, figure panels a). However, it is nearly impossible to pinpoint the exact location of the Gulf Stream from such mean wave parameters only.

In the wave height and period fields presented in Figs. 3 and 4, several features can be observed.

First, swell trapping occurs south of Cape Hatteras. The trapped swell is identified by the significant increase of the wave height and the absolute period, which are closely confined to the Gulf Stream. The trapped swell was generated in the coastal area between Cape Hatteras and Cape Cod in the previous 36 hours. Note that the trapped swell is accompanied by a "shadow zone" just south of the Gulf Stream, as would be expected from straightforward energy conservation. Note furthermore the occurrence of two focal points of long wave energy on the coast south of Cape Hatteras (see Fig. 4). This current-induced modulation of swell energy around the Gulf Stream, and the location the Gulf Stream near the coast

suggest that swell penetration at coast south of Cape Hatteras can be influenced significantly by Gulf Stream (unlike coastal waves in most other areas).

Secondly, the combined wind-wave and swell field east of  $68^{\circ}\text{W}$  shows a complicated impact of the currents. Note the apparent reflection of wave energy south of the meander at  $39^{\circ}\text{N}$ ,  $56^{\circ}$ - $60^{\circ}\text{W}$  (Fig. 4). Given the predominant wave direction, such a reflection was expected from the results of HT for a straight section Gulf Stream. Furthermore, the meander at  $42^{\circ}\text{N}$ ,  $58^{\circ}\text{W}$  shows an impact similar to that of a ring for swell as shown by many authors.

Finally, several small and fairly weak rings in the area between the above two areas all show a the typical signature of a ring for swell fields, although the impact is typically small. Note that the rings identify the locally dominant swell direction.

As discussed by HT indirect effects of currents on the dynamics of wave growth and decay are expected to be important on the scale of the Gulf Stream. For a separate ring, such effects are easily isolated, due to the closed-system nature of the ring. For a meandering Gulf Stream, effects of modified growth dynamics can occur simultaneously with reflection and trapping of waves. Thus an assessment of current-induced modulations of wave-growth dynamics requires a detailed analysis of individual spectra. In the present paper, only the potential of such effects will be established by assessing the integral source terms  $S_{\text{in},i}$  (Fig. 5) and  $S_{\text{ds},j}$  (Fig. 6). These figures show current-induced modulations of  $S_{\text{in},i}$  and  $S_{\text{ds},j}$  of 20% to 50%, which agrees well with the results of HT for a ring. Considering the importance of current-induced modulations of the dynamics of wave growth in the latter case, a similar importance is expected here. The Gulf Stream, however, does show differences compared to the corresponding idealized cases of HT. The current-induced modulations of the input source term (Fig. 5) are centered on the currents (as in HT). This might be explained from the fact that the input winds (relative to the current) and local (conservative) interactions show similar modulations. The dissipation, however, changes both in and outside the Gulf Stream. In particular in the above mentioned reflection zone ( $39^{\circ}\text{N}$ ,  $56^{\circ}$ - $60^{\circ}\text{W}$ ) increased dissipation occurs at the edge of the Gulf Stream rather than at the center (in contrast to the results of HT).

One final remark should be made on the results of Figs. 3 through 6. The impacts of wave-current interactions as presented in these figures appear to occur mainly when the winds are decreasing, in other words, when the relative importance of wave growth decreases. This suggests that the dynamics of wave growth and decay dominate wave-current interactions in active growth conditions, which is another indication for the importance of incorporating the dynamics of wave growth and decay when considering wave-current interactions at the present scales.

## 5 Preliminary conclusions

The above preliminary results for numerical simulation of wind waves on the Gulf Stream lead to the following preliminary conclusions.

- Wave-current interactions induced by the Gulf Stream are sufficiently strong to be identified in wave height and mean period, but do not necessarily pinpoint the exact location of the Gulf Stream.
- Space (and time) scales of effects of wave-current interactions are relatively small and are governed by the corresponding scales of the wind field and the Gulf Stream.
- Effects of wave-current interactions are mainly confined to Gulf Stream and its direct surroundings, in particular for regions with active wave generation. Effects away from the Gulf stream are usually related to swell propagation and generally of moderate magnitude.
- The model indicates that trapping of swell can occur in realistic conditions. South of Cape Hatteras this might significantly influence swell penetration at the coast.
- In active generation conditions an interplay between conservative wave-current interactions and the dynamics of wave growth and decay occurs. Such an interplay is neglected in virtually all other wave-current interaction studies.
- The spatial resolution of regional model appears to be sufficient to assess wave-current interaction features of the Gulf Stream. The SWADE model, however, is expected to be significantly more accurate due to the better resolution.

## 6 Outlook

As stated in the introduction, this paper presents preliminary results of SWADE wave-current interaction studies. For the first part of the SWADE wave-current interaction study, the following work is in progress.

- The interplay between dynamics and kinematics are analyzed in more detail both by intercomparing spectra and by analyzing evolution of the net effect of wave-current interactions in space and time.
- Effects of different physical and numerical approaches are assessed by intercomparing results of the models WAVEWATCH and WAM.
- An assessment of effects of wave-current interactions with regard to remote sensing is being considered.

*Acknowledgements.* The author acknowledges with pleasure that H.C. Graber supplied the bottom grids for the present study. V.J. Cardone supplied the wind fields and S.M. Glenn and J.H. Clark supplied current data. The interaction with the SWADE group, in particular H.C. Graber, R.E. Jenssen, D.G. Duffy and S. and K. Hasselmann and the help of L. Rumburg in preparing the figures was greatly appreciated. Computer time was provided under the Air-Sea Interaction Studies grant, RTOP 461-31, funded by NASA Headquarters. This work was done while the author held a National Research Council - NASA Research Associateship.

## REFERENCES

- Hasselmann, K., T.P. Barnett, E. Bouws, H. Carlson, D.E. Cartwright K. Enke, J.A. Ewing, H. Gienapp, D.E. Hasselmann, P. Kruseman, A. Meerburg, P. Müller, D.J. Olbers, K. Richter, W. Sell and H. Walden, 1973: Measurements of wind-wave growth and swell decay during the Joint North Sea Wave Project (JONSWAP). *Ergänzungsheft zur Deutschen Hydrographischen Zeitschrift*, Reihe A (8) Nr. 12, 95 pp.
- Holthuijsen, L.H., and H.L. Tolman, 1990: Effects of the Gulf Stream on nearby coastal waves. *Proc. 22st Int. Conf. Coastal Eng.*, ASCE, Delft, 384-395.
- Holthuijsen, L.H., and H.L. Tolman, 1991: Effects of the Gulf Stream on ocean waves. *J. Geophys. Res.*, **96**, C7, 12755-12771.
- Janssen, P.A.E.M., 1989: Wave induced stress and the drag of air flow over sea waves. *J. Phys. Oceanogr.*, **19**, 745-754.
- Janssen, P.A.E.M., 1991: Quasi-linear theory of wind-wave generation applied to wave forecasting. *J. Phys. Oceanogr.*, **21**, 1631-1642.
- Mastenbroek, C., G. Burgers and P.A.E.M. Janssen, 1993: The dynamic coupling of a wave model and a storm surge model through the atmospheric boundary layer. *J. Phys. Oceanogr.*, in press.
- Tolman, H.L., 1991: A third-generation model for wind waves on slowly varying, unsteady and inhomogeneous depths and currents. *J. Phys. Oceanogr.*, **21**, 782-797.
- Tolman, H.L., 1992: Effects of numerics on the physics in a third-generation wind-wave model. *J. Phys. Oceanogr.*, **22**, 1095-1111.
- Tolman, H.L., 1993: User manual for WAVEWATCH-II, NASA technical report, in preparation.
- WAMDI group, 1988: The WAM model - a third generation ocean wave prediction model. *J. Phys. Oceanogr.*, **18**, 1775-1810.
- Weller, R.A., M.A. Donelan, M.G. Briscoe and N.E. Huang, 1991: Riding the crest: a tale of two wave experiments. *Bull. Amer. Meteor. Soc.*, **72**, 163-183.

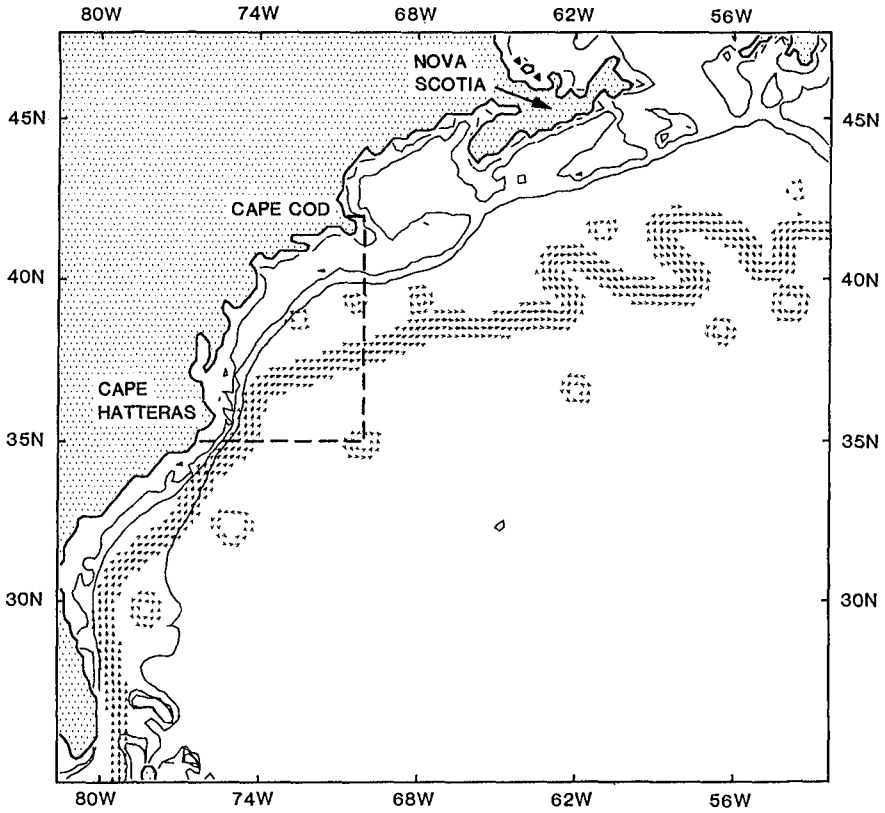


Fig. 1 Layout of the regional grid (entire figure) and SWADE grid (dashed lines). Depth contours for 25 m, 100 m and 1000 m. Vectors indicate location and direction of Gulf Stream ( $U > 0.5$  m/s only,  $U_{\max} \approx 2$  m/s for the Gulf Stream and  $U_{\max} \approx 1$  m/s for a typical ring).

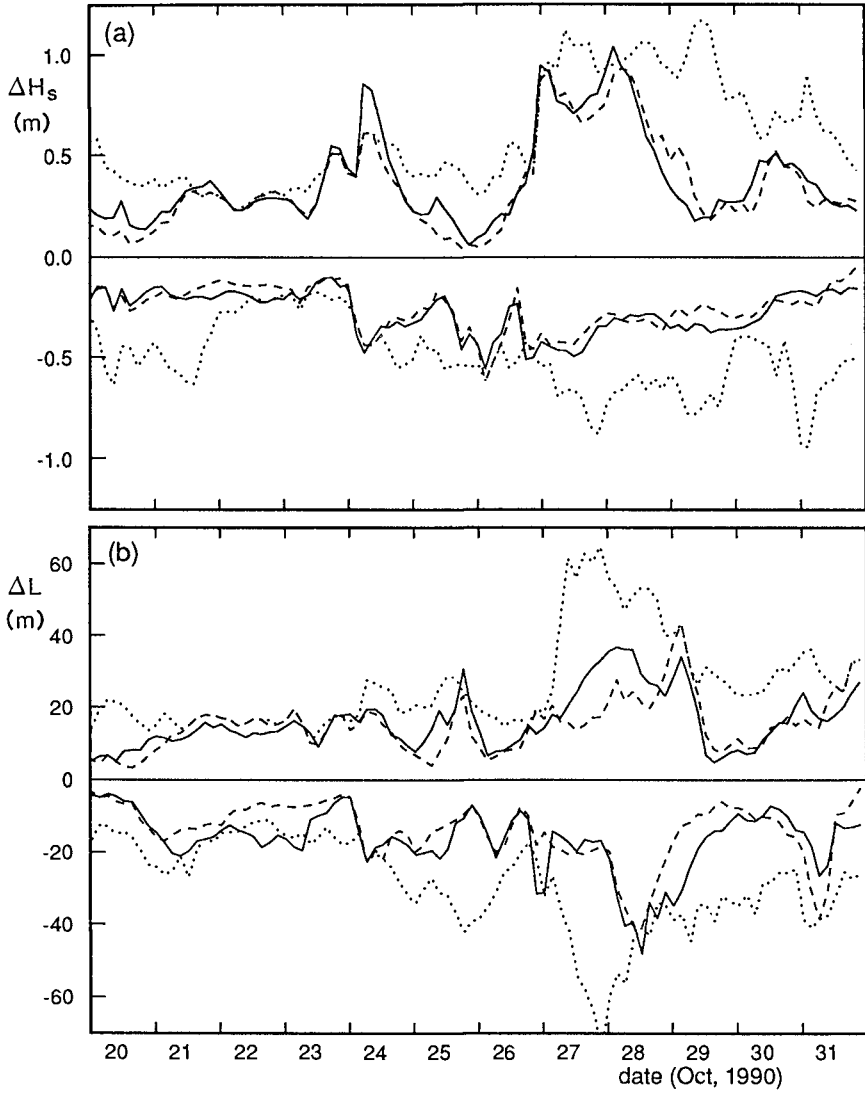


Fig. 2 Maximum and minimum current-induced modulation of the significant wave height ( $\Delta H_s$ , panel a) and the mean wave length ( $\Delta L$ , panel b) for the SWADE model (solid lines), the regional model (dotted lines) and the part of the regional model covering the SWADE model (dashed lines).

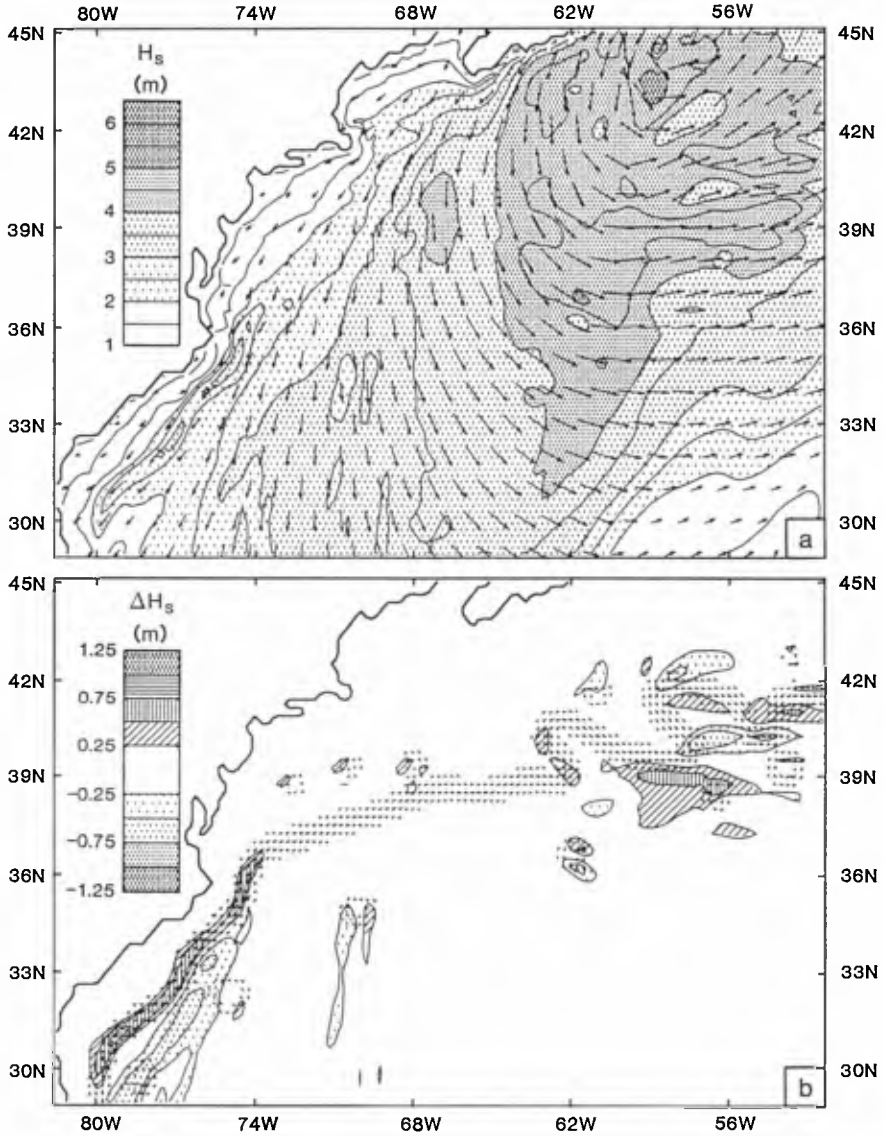


Fig. 3 The significant wave height ( $H_s$ , panel a), and its current-induced modulation ( $\Delta H_s$ , panel b) for part of the regional model on Oct. 28, 0000 UTC.

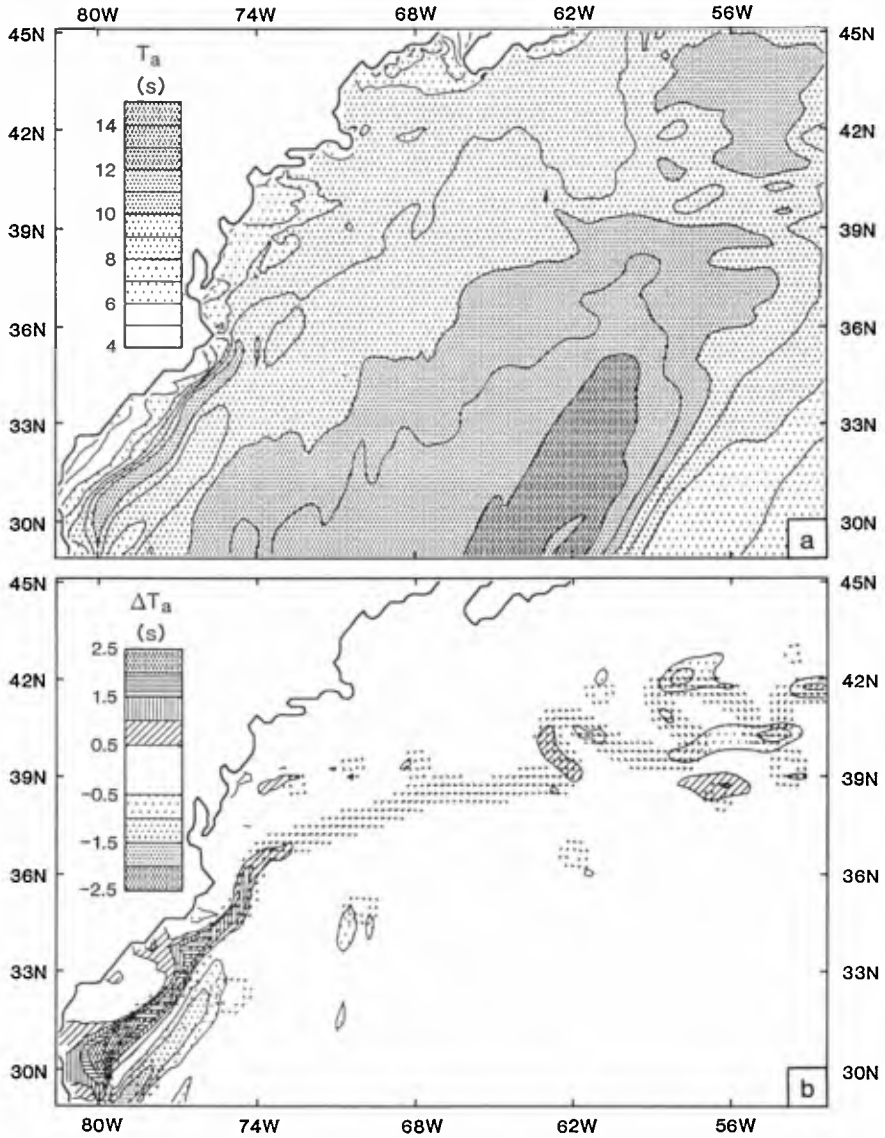


Fig. 4 Like Fig. 3 for the mean absolute wave period  $T_a$ .



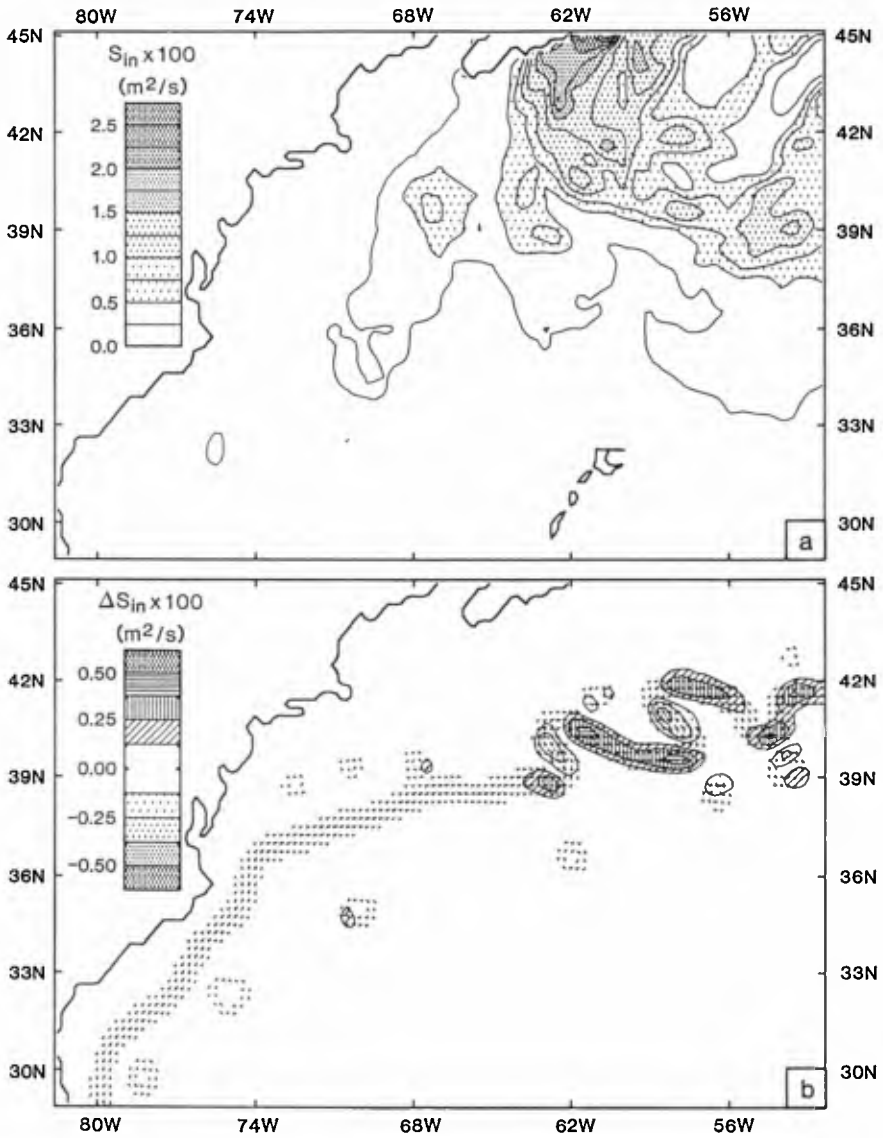


Fig. 5 Like Fig. 3 for integral input source term  $S_{in,i}$ .

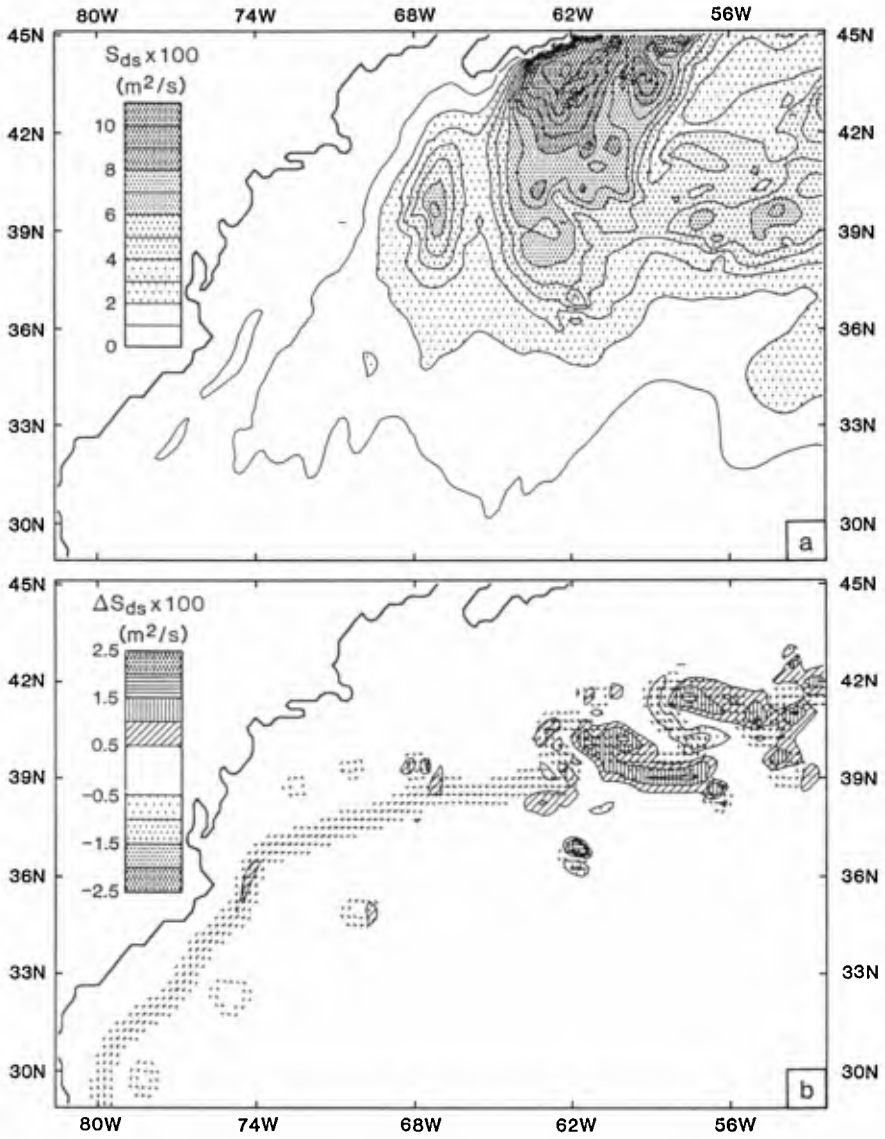


Fig. 6 Like Fig. 3 for integral dissipation (whitcapping) source term  $S_{ds,i}$ .

## CHAPTER 54

### AN IMPROVED ARRANGEMENT FOR THE PROGRESSIVE WAVE ABSORBER

S. W. TWU\* and C. C. LIU\*\*

#### Abstract

The progressive wave absorber discussed here in this paper contains several porous plates with different porosity. Four arrangements of progressive wave absorbers were compared in wave absorption. The results indicate that of the four arrangements examined, Arrangement 4 is the most effective at absorbing waves, for a relative water depth ranging from 0.05 to 0.5. The results also show that an eight-plate wave absorber is more effective than a six-plate wave absorber. When waves are well within the relative water depth ranging from 0.05 to 0.5, reducing the  $G$  value of the rear plates further may provide even greater wave absorption efficiency .

#### I. INTRODUCTION

Wave reflection by such structures as wharves, breakwaters, or boundaries in a wave basin is of concern to many investigators, due to the many problems reflected waves can create. Le Me' haute (1972) first presented the concept of a progressive wave absorber, in which the porosity decreases toward the rear of the wave absorber. He developed a theory on progressive wave absorption and conducted model tests on a wave absorber constructed of aluminum shavings, which became more compact in the direction of propagation of the incident waves. Relatively low reflection coefficients were measured and experimental results qualitatively demonstrated the validity of his theoretical development.

---

\*Professor, Dept. of Hydraulics & Ocean Engineering, National Cheng-Kung University, Tainan, Taiwan, R. O. C.

\*\*Research assistant, Tainan Hydraulics Laboratory, National Cheng-Kung University, Tainan, Taiwan, R. O. C.

Jamieson & Mansard(1987) conducted experimental studies on a progressive wave absorber constructed of multiple rows of perforated vertical metal sheets, with a progressive decrease in porosity toward the rear of the wave absorber. Their metal sheets were aligned normal to the direction of the incident wave propagation. They concluded that the upright wave absorber can be designed to provide low reflection coefficients (less than 5%) over a wide range of wave heights, wave periods, and water depths.

Twu & Lin(1991)developed a theory on a progressive wave absorber constructed of multiple rows of vertical porous plates, which were similar in structure to those of Jamiesons'. They conducted model tests to verify their theoretical solution and noted that the model test results agree fairly well with the theoretical solution. In their study,a dimensionless porous effect parameter,  $G = \rho\omega b/\mu K_0$  (Chwang and Dong,1984),was used to represent the porosity of the porous plates, in which  $\mu$  is the dynamic viscosity of the fluid,  $b$  is a material constant of the porous plate, having the dimension of length,  $K_0$  is the wave number,  $\omega$  is the circular frequency and  $\rho$  is the fluid density. Twu & Lin concluded that the progressive wave absorber should function better if the difference in  $G$  value between adjoining porous plates is larger for the front plates than for the rear plates. In Twu & Lin's study, the difference in  $G$  values between adjoining porous plates were progressively decreased, but the rate of decrease was arbitrarily selected. The goal of this paper is to determine exactly what decreased rate of  $G$  value should be adopted so that the progressive wave absorber will function more effectively, and if fewer porous plates can be installed without adversely affecting the wave absorption efficiency.

## II. CALCULATION PROCEDURE AND RESULTS

The progressive wave absorber used by Twu & Lin(1991) contained several porous plates, as shown in Figure 1. They assumed that the flow velocity passing through each porous plate obeys Darcy's Law. Defining the reflection coefficient,  $C_r$ , as the amplitude ratio of the reflected wave to the incident wave, they developed the following equations ( Twu & Lin 1991):

$$C_r = (A^2 + B^2)^{1/2} \quad (1)$$

in which

$$A = Re(M_1) \quad (2)$$

$$B = Im(M_1) \tag{3}$$

$$M_s = \frac{M_{s+1}(2G_s - 1) + \exp(-i2K_0L_{s-1})}{(2G_s + 1) - M_{s+1} \exp(i2K_0L_{s-1})} \quad s = 1, 2, 3, \dots (n-1) \tag{4}$$

$$M_n = \frac{F_1 + iF_2}{F_3 + iF_4} \tag{5}$$

where n is the number of porous plates used in the wave absorber.

$$\begin{aligned} F_1 &= (G_n - 1) \sin K_0 r_n \cos K_0 L_{n-1} + G_n \cos K_0 r_n \sin K_0 L_{n-1} \\ F_2 &= G_n \cos K_0 r_n \sin K_0 L_{n-1} - (G_n - 1) \sin K_0 r_n \sin K_0 L_{n-1} \\ F_3 &= -(G_n + 1) \sin K_0 r_n \cos K_0 L_{n-1} - G_n \cos K_0 r_n \sin K_0 L_{n-1} \\ F_4 &= G_n - \cos K_0 r_n \cos K_0 L_{n-1} - (G_n + 1) \sin K_0 r_n \sin K_0 L_{n-1} \\ G_s &= \frac{b_s \omega \rho}{\mu K_0} \quad (s = 1, 2, 3, \dots n) \end{aligned}$$

$G_s$  is a dimensionless porous-effect parameter of the plate "s".  $L_n$ ,  $L_{n-1}$  and  $r_n$  are indicated in Figure 1. According to Twu and Lin (1991), wave reflection by a progressive wave absorber is closely related to the spacing between the adjacent porous plates, as well as to the progression of  $G$  value of these plates. In this investigation a distance of 0.88 times the water depth has been adopted as the spacing between adjacent plates, as suggested by Twu and Lin. Four methods of reducing the  $G$  value along the direction of incident wave propagation are compared for both six-plate and eight-plate wave absorber. The  $G$  values of the first and

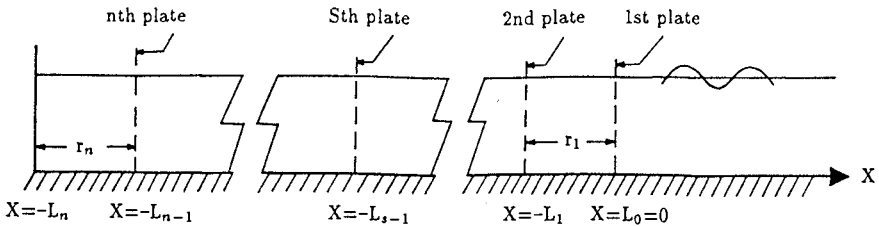


Fig.1 Schematic diagram of a progressive wave absorber

last plates are fixed at 16 and 1, respectively, for the first part of the study. The  $G$  values of the first and last plates were varied in the second part of the study.

The four arrangements of six-plate wave absorbers analyzed in this study were determined as follows:

1. The  $G$  values of the plates were evenly distributed, to obtain values of 16, 13,10,7,4 and 1, for plates 1 through 6, respectively.
2. The  $G$  value of each succeeding plate was reduced by the formula “16 exp (-x)”, with x ranging from 0 to 2.7726, yielding  $G$  values of 16, 9.19, 5.28, 3.03,1.74,and 1.
3. The  $G$  value of each succeeding plate was reduced by the formula “16/x”, with x ranging from 1 to 16, yielding  $G$  values of 16, 4, 2.28,1.6,1.23, and 1.
4. The  $G$  value of each succeeding plate was reduced by the formula “16/x<sup>2</sup>”, with x ranging from 1 to 4, yielding  $G$  values of 16, 6.25, 3.31, 2.04, 1.38 and 1.

The  $G$  values for each arrangement are summarized in Table 1.

Table 1.  $G$  Values for Six-Plate Wave Absorber

Arrangement number	Method of $G$ reduction	$G$					
		Plate number					
		1	2	3	4	5	6
1	linear	16	13	10	7	4	1
2	$16 \exp(-x_1)$	16	9.19	5.28	3.03	1.74	1
3	$16/x_2$	16	4	2.28	1.6	1.23	1
4	$16/(x_3)^2$	16	6.25	3.31	2.04	1.38	1

$x_1$  ranges from 0 to 2.7726

$x_2$  ranges from 1 to 16

$x_3$  ranges from 1 to 4

The reflection coefficient of these progressive wave absorbers were calculated over a relative water depth ranging from 0.05 to 0.5. The results are shown in Figures 2 through 5. The figures indicate that the reflection coefficient is higher for the first wave absorber (Figure 2) than for the last three. This verifies the conclusion reached by Twu and Lin, that the progressive wave absorber would function better if the difference in  $G$  values between adjacent porous plates is

larger in the front part than in the rear part of the wave absorber. These figures also indicate that Arrangement (4), shown in Figure 5, is most effective in wave absorption among these four arrangements.

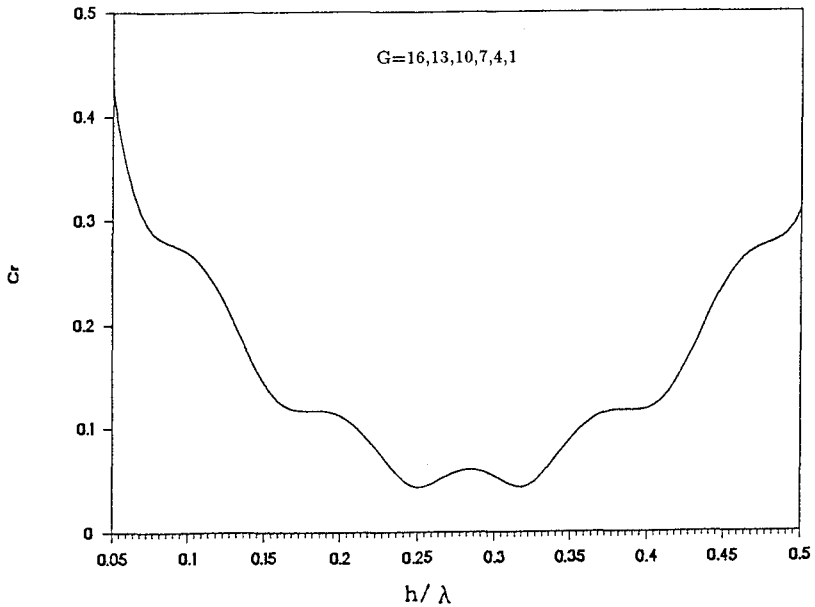


Fig.2 Wave reflection coefficient for the Arrangement (1) of six-plate wave absorber

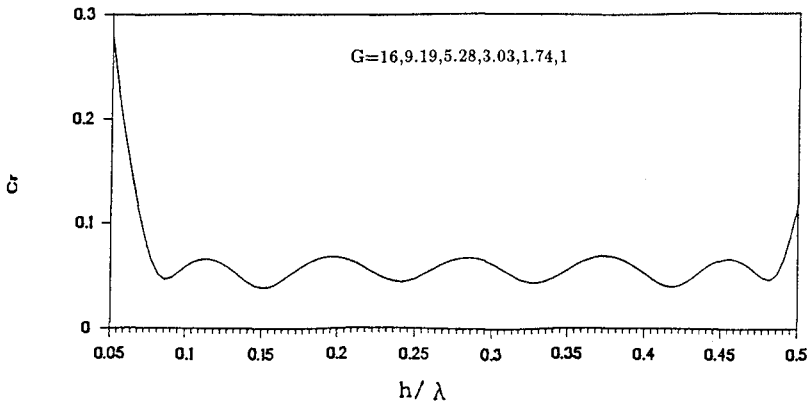


Fig.3 Wave reflection coefficient for the Arrangement (2) of six-plate wave absorber

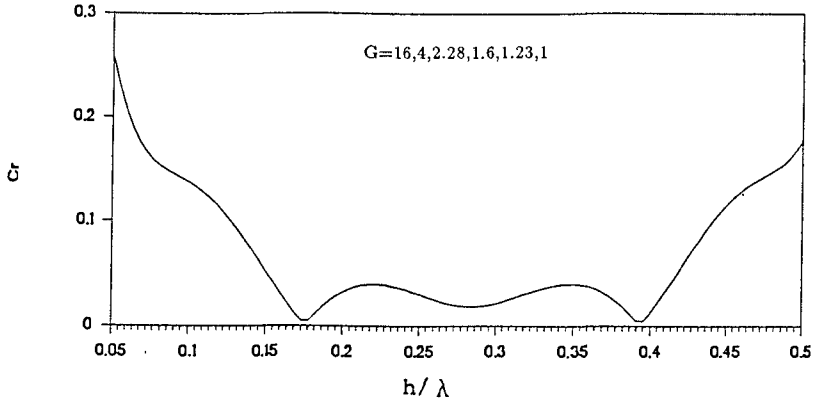


Fig.4 Wave reflection coefficient for the Arrangement (3) of six-plate wave absorber

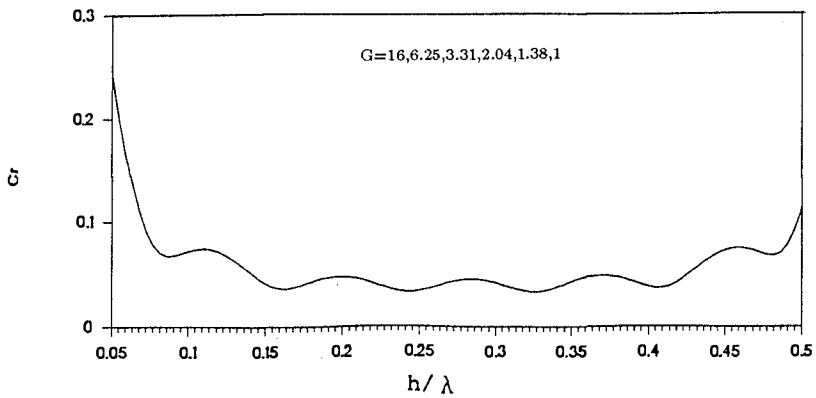


Fig.5 Wave reflection coefficient for the Arrangement (4) of six-plate wave absorber

The  $G$  values for each arrangement of the eight-plate wave absorber were determined by applying the same formulas used to determine the  $G$  values for the six-plate wave absorber.

The  $G$  values for each arrangement are presented in Table 2, and the results are plotted on Figures 6 through 9. These figures indicate that the wave reflection coefficient follows a similar trend for both six-plate and eight-plate wave absorbers,



and that Arrangement 4 again yields the most effective wave absorption over the considered range. This wave absorber maintains a wave reflection coefficient of less than .04 over the relative water depth ranging from 0.11 to 0.46, which satisfies the requirement for a wave basin wave absorber.

Table 2.  $G$  values of an Eight-Plate Wave Absorber

Arrangement number	Method of $G$ reduction	$G$							
		Plate number							
		1	2	3	4	5	6	7	8
1	linear	16	13.86	11.71	9.57	7.43	5.29	3.14	1.0
2	$16 \exp(-x_1)$	16	10.77	7.25	4.88	3.28	2.21	1.49	1.0
3	$16/x_2$	16	5.10	3.02	2.15	1.67	1.37	1.15	1.0
4	$16/(x_3)^2$	16	7.84	4.64	3.06	2.17	1.62	1.25	1.0

$x_1$  ranges from 0 to 2.7726

$x_2$  ranges from 1 to 16

$x_3$  ranges from 1 to 4

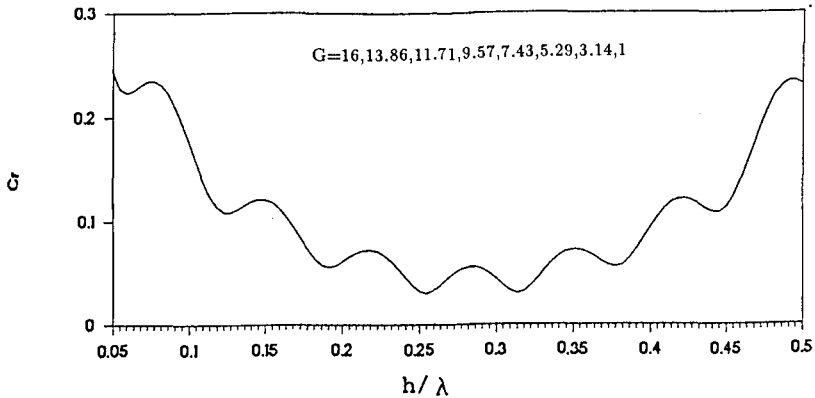


Fig.6 Wave reflection coefficient for the Arrangement (1) of eight-plate wave absorber

The next step was to analyze the effect on the reflection coefficient of varying the  $G$  value of the first and last plate. The best arrangement in the previous analysis, Arrangement 4, was selected for an eight-plate wave absorber. For the first case, the  $G$  value of the first plate was changed from 16 to 14 and from 16 to 20, while holding the  $G$  value of the last plate constant. The  $G$  values of the plates

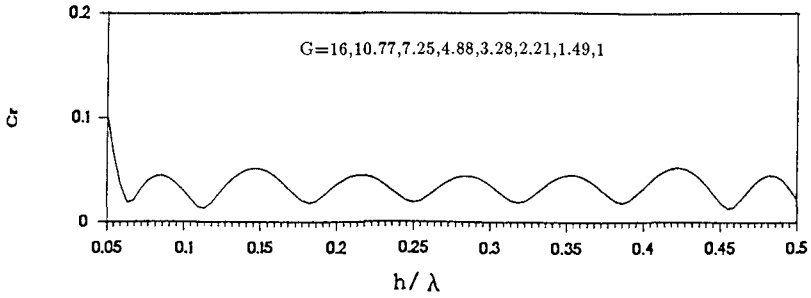


Fig.7 Wave reflection coefficient for the Arrangement (2) of eight-plate wave absorber

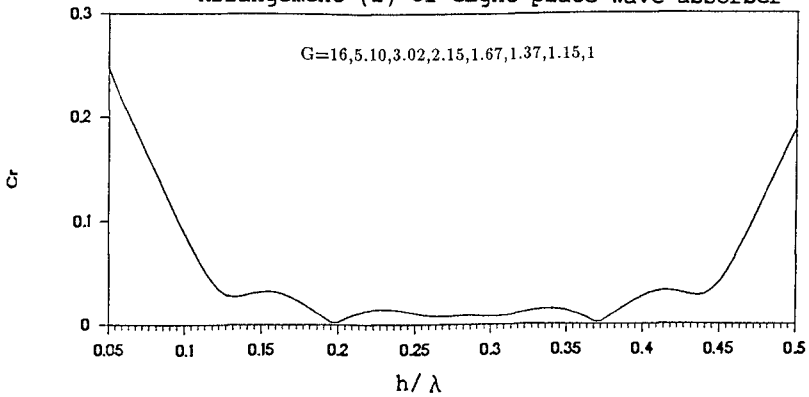


Fig.8 Wave reflection coefficient for the Arrangement (3) of eight-plate wave absorber

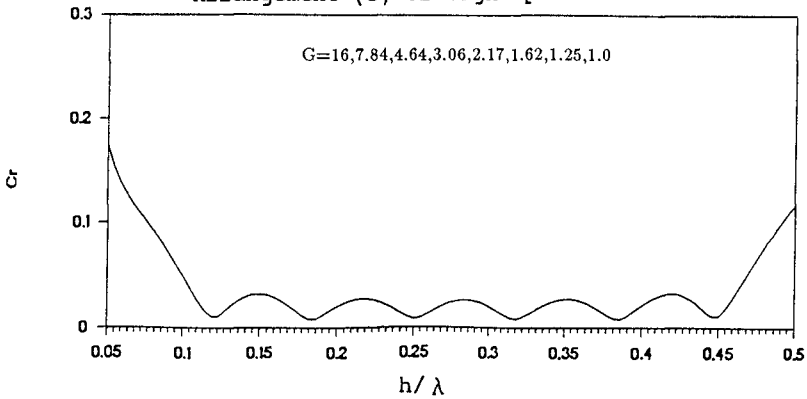


Fig.9 Wave reflection coefficient for the Arrangement (4) of eight-plate wave absorber

in between were determined from the formula  $G_1/x^2$  where  $G_1$  is the  $G$  value of the first plate. The results are plotted on Figures 10 and 11. A comparison of Figures 10 and 11 with Figure 9 indicates a slight increase in the reflection coefficient when the  $G$  values of all but last plate is either increased or decreased.

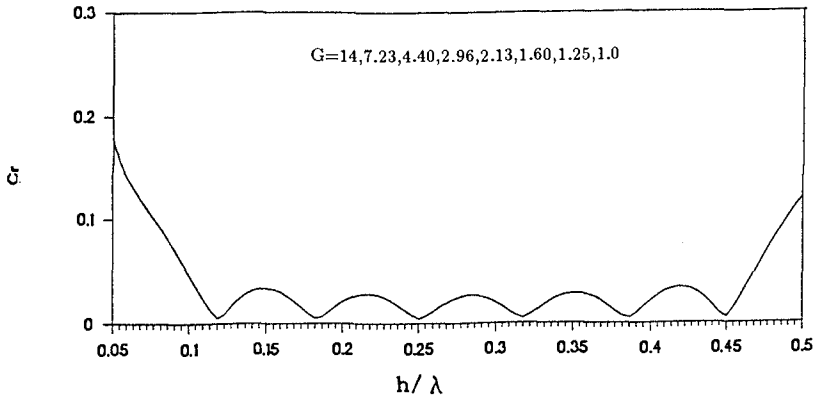


Fig.10 Wave reflection coefficient for the Arrangement (4) of eight-plate wave absorber with  $G$  value reduced for the front plates

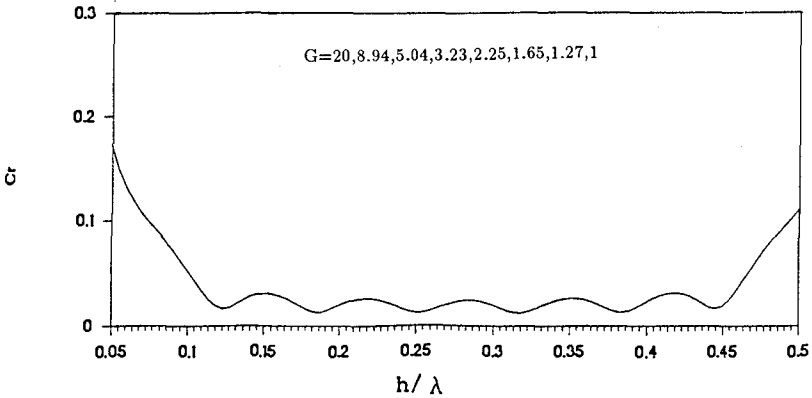


Fig.11 Wave reflection coefficient for the Arrangement (4) of eight-plate wave absorber with  $G$  value increased for the front plates

For the second case, the  $G$  value of the first plate is held at 16 and the  $G$  value of last plate changed to 0.5 and 2.0. The  $G$  values of the plates in between are modified relative to the  $G$  value of the last plate following the formula  $G_1/x^2$ . The results are plotted on Figures 12 and 13. A comparison of Figure 12 with Figure

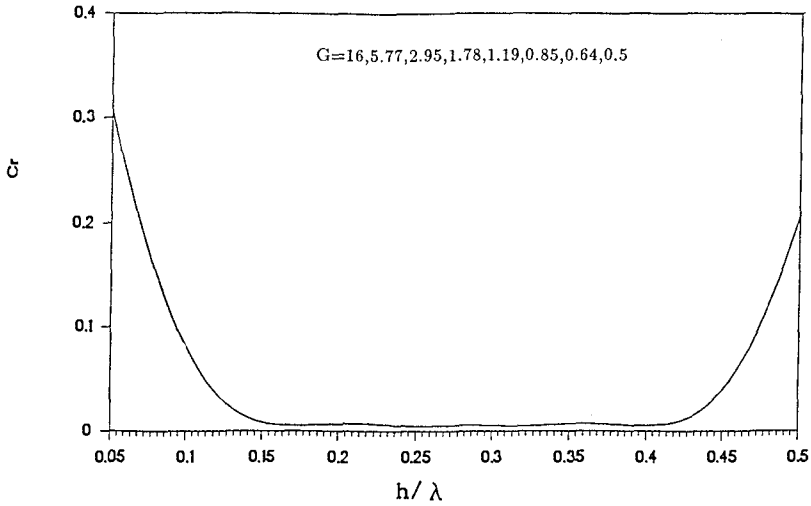


Fig.12 Wave reflection coefficient for the Arrangement (4) of eight-plate wave absorber with  $G$  value reduced for the rear plates

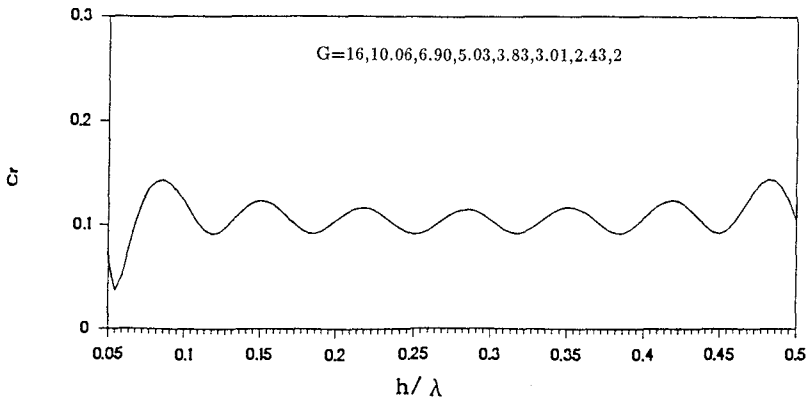


Fig.13 Wave reflection coefficient for the Arrangement (4) of eight-plate wave absorber with  $G$  value increased for the rear plates

9 indicates that, when the  $G$  value of the last plate is equal to 0.5 the reflection coefficient is lower for  $h/\lambda$  values between approximately 0.15 and 0.42, but higher for other  $h/\lambda$  values. Changing the  $G$  value of the last plate to 2.0 resulted in a larger reflection coefficient for most values of  $h/\lambda$ , as shown on Figure 13.

This comparison indicates that the reflection coefficient is more sensitive to the  $G$  values of the rear plates than the front plates of the progressive wave absorber. If waves which contain only a small range of wave lengths require damping, such as for  $0.15 < h/\lambda < 0.42$ , the  $G$  values of plates in the rear part of the wave absorber can be reduced.

### III. CONCLUSIONS

The wave absorption efficiency of a six-plate and eight-plate wave absorber was investigated mathematically to determine the most effective distribution of  $G$  values. The results indicate that of the four arrangements examined, Arrangement 4 is the most effective at absorbing waves, for a relative water depth ranging from 0.05 to 0.5. The results also show that an eight-plate wave absorber is more effective than a six-plate wave absorber. When waves are well within the relative water depth ranging from 0.05 to 0.5, reducing the  $G$  values of the rear plates further may provide even greater wave absorption efficiency.

### REFERENCE

1. Chwang A.T. and Dong Z. N. (1984). Wave-trapping due to a porous plate. Proc. 15th ONR Symp. Naval Hydrodynamics, pp.407-417.
2. Le' Mehaute Bernard (1972). Progressive wave absorber. J. Hydraulic Research, No.2, pp.153~169.
3. Jamieson W.W. and Mansard E. (1987). An efficient upright wave absorber. ASCE specialty conference on coastal hydrodynamics, pp.124~139.
4. Twu S.W. and Lin D.T. (1991). On a highly effective wave absorber. J. Coastal Engineering, 15: pp 389~405.

## CHAPTER 55

### Interrelation of Cnoidal Wave Theories

by Masataka Yamaguchi<sup>1</sup>

#### Abstract

The aim of this paper is to analytically clarify the interrelation among all of the existing cnoidal wave theories of the third order approximation. The result is that the Chappellear theory expressed with two expansion parameters is found to include the other theories. This means that they are able to be derived from the Chappellear theory by changing expansion parameters in the expressions of wave characteristics and integral properties and identifying the definition for wave celerity to be used in the theory. The expressions for the trajectory of a water particle, mass transport velocity and integral properties of waves are newly derived using these theories, and the wave characteristics and integral properties are examined based on the numerical computation and comparison with the experiments. As a result, use of the theory expressed with a single expansion parameter is recommended from a practical viewpoint. The figures describing a limiting range of wave parameters for the application of the above-mentioned theory are also provided by comparing wave characteristics and integral properties of the theory with those of Fenton's Fourier approximation wave theory.

#### 1. Introduction

Higher order solutions of cnoidal waves have been derived by Laitone(1960, 1965; the second order approximation, the second definition for wave celerity), Chappellear(1962; the third order approximation, the first definition), Fenton(1979; the ninth order approximation, the first definition), Tsuchiya & Yasuda(1985; the third

---

1 Prof., Dept. of Civil and Ocean Eng., Ehime Univ.,  
Bunkyocho 3, Matsuyama 790, Ehime Pref., Japan

order approximation, the third definition) and Isobe (1988; the third order approximation, the second definition). These solutions are different from each other in the definitions used for the derivation of wave celerity and the expansion parameters for the expression of wave characteristics.

Yamaguchi & Tsuchiya (1974) mathematically proved that the Laitone theory can be derived from the Chappelear theory within the second order approximation when the expressions of wave characteristics in the Chappelear theory are rewritten with the parameter in the Laitone theory under the condition that the same definition is applied for the derivation of wave celerity in each theory.

Now there are at least 4 kinds of third order cnoidal wave theories derived with different expansion parameters and definitions for wave celerity.

The aim of this paper is to mathematically clarify the interrelation among these third order solutions and to examine the wave characteristics and integral properties, and limiting conditions for practical application based on numerical computation and the comparison with experiments.

## 2. Theoretical Considerations

### (1) Definitions for wave celerity

Usually, either of the first and second definitions proposed by Stokes has been used for the determination of wave celerity, although Fenton(1990) recommends use of the term "approximation" in place of the term "definition". The first and second definitions for wave celerity are given respectively as

$$\overline{u^I} = 0 \quad \text{or} \quad c^I = \overline{\tilde{u}} \quad (1)$$

$$\int_{-D}^{\eta} \overline{u^{II}} dz = 0 \quad \text{or} \quad c^{II} = \int_{-D}^{\eta} \overline{\rho \tilde{u}} dz / \rho D \quad (2)$$

where  $c$  is the wave celerity,  $u$  the horizontal water particle velocity in a fixed frame of reference,  $\tilde{u}$  the horizontal water particle velocity in a moving frame of reference,  $D$  the water depth,  $\eta$  the surface displacement,  $z$  the ordinate taken vertically upward on the still water level, ' $\overline{\quad}$ ' the time-mean, and superscripts 'I' and 'II' indicate the first and second definitions respectively. The first definition means that time-averaged horizontal water particle velocity at a level under the trough in a frame of reference moving with a constant speed vanishes, and the second definition means that time-mean of depth-

integrated momentum in a frame of reference moving with a constant speed vanishes.

Tsuchiya & Yasuda have defined the wave celerity as gradient of the characteristics in  $x$ - $t$  space. In this case, the Bernoulli constant in wave field of the steady state  $C$  is equivalent to that in the coordinate system moving with wave celerity in still water.

$$C = gD + (c^{III})^2/2 \tag{3}$$

where  $g$  is the acceleration of gravity. This is tentatively termed the third definition for wave celerity, in which case superscript 'III' is used as the indication.

(2) The Chappellear theory

Chappellear derived a cnoidal wave theory with two expansion parameters  $L_0$  and  $L_3$ . The Bernoulli constant and horizontal water particle velocity in a moving frame of reference, wave celerity and horizontal water particle velocity in a fixed frame of reference based on the first definition are expressed respectively as

$$C = \{3/2 + L_0(1+x^2) + 3L_3 + (9/10)L_0^2(2+3x^2+2x^4) + 6L_0L_3(1+x^2) + (3/2)L_3^2 + (3/35)L_0^3(45+97x^2+97x^4+45x^6) + 9L_0^2L_3(2+3x^2+2x^4) + 15L_0L_3^2(1+x^2)\}gD \tag{4}$$

$$\begin{aligned} \bar{u}/\sqrt{gD} = & 1 + L_3 + L_0x^2\text{sn}^2\gamma\chi + \{L_0^2(1+x^2) + 5L_0L_3\}x^2\text{sn}^2\gamma\chi \\ & + L_0^2x^4\text{sn}^4\gamma\chi - (y/D)^2(3/4)L_0^2\{x^2 - 2(1+x^2)x^2\text{sn}^2\gamma\chi + 3x^4\text{sn}^4\gamma\chi\} \\ & + \{(1/5)L_0^3(7+19x^2+7x^4) + 9L_0^2L_3(1+x^2) + 10L_0L_3^2\}x^2\text{sn}^2\gamma\chi \\ & + \{(9/5)L_0^3(1+x^2) + 9L_0^2L_3\}x^4\text{sn}^4\gamma\chi + (6/5)L_0^3x^6\text{sn}^6\gamma\chi \\ & - (1/4)(y/D)^2\{3L_0^3x^2(1+x^2) + 15L_0^2L_3x^2 + 6\{L_0^3(-1+x^2-x^4) \\ & - 5L_0^2L_3(1+x^2)\}x^2\text{sn}^2\gamma\chi + 15\{-L_0^3(1+x^2) + 3L_0^2L_3\}x^4\text{sn}^4\gamma\chi \\ & + 30L_0^3x^6\text{sn}^6\gamma\chi\} + (3/16)(y/D)^4L_0^3\{-x^2(1+x^2) \\ & + (2+13x^2+2x^4)x^2\text{sn}^2\gamma\chi - 15(1+x^2)x^4\text{sn}^4\gamma\chi + 15x^6\text{sn}^6\gamma\chi\} \end{aligned} \tag{5}$$

$$\begin{aligned} c'/\sqrt{gD} = & 1 + L_3 + L_0(1-e) + 5L_0L_3(1-e) + (1/3)L_0^2\{5 \\ & + 4x^2 - 5(1+x^2)e\} + 10L_0L_3^2(1-e) + (1/25)L_0^3\{81 + 146x^2 \\ & + 58x^4 - (81 + 169x^2 + 81x^4)e\} + 3L_0^2L_3\{5 + 4x^2 - 5(1+x^2)e\} \end{aligned} \tag{6}$$

$$\begin{aligned} u'/\sqrt{gD} = & L_0(1-e-x^2\text{sn}^2\phi) + 5L_0L_3(1-e-x^2\text{sn}^2\phi) \\ & + (1/3)L_0^2\{5+4x^2-5(1+x^2)e-3(1+x^2)x^2\text{sn}^2\phi-3x^4\text{sn}^4\phi\} \\ & + (y/D)^2(3/4)L_0^2\{x^2-2(1+x^2)x^2\text{sn}^2\phi+3x^4\text{sn}^4\phi\} \\ & + 10L_0L_3^2(1-e-x^2\text{sn}^2\phi) + 3L_0^2L_3\{5+4x^2-5(1+x^2)e \\ & - 3(1+x^2)x^2\text{sn}^2\phi-3x^4\text{sn}^4\phi\} + (1/25)L_0^3\{81+146x^2+58x^4 \\ & - (81+169x^2+81x^4)e-5(7+19x^2+7x^4)x^2\text{sn}^2\phi\} \end{aligned}$$



$$\begin{aligned}
& -45(1+x^2)x^4\text{sn}^4\phi - 30x^6\text{sn}^6\phi + (3/4)(y/D)^2[L_0^3\{(1+x^2)x^2 \\
& - 2(1-x^2+x^4)x^2\text{sn}^2\phi - 5(1+x^2)x^4\text{sn}^4\phi + 10x^6\text{sn}^6\phi\} \\
& + 5L_0^2L_3\{x^2 - 2(1+x^2)x^2\text{sn}^2\phi + 3x^4\text{sn}^4\phi\}] \\
& + (3/16)(y/D)^4L_0^3\{(1+x^2)x^2 - (2+13x^2+2x^4)x^2\text{sn}^2\phi \\
& + 15(1+x^2)x^4\text{sn}^4\phi - 15x^6\text{sn}^6\phi\}
\end{aligned} \tag{7}$$

where  $x$  is the argument of elliptic function,  $e=E/K$ ,  $K$  and  $E$  are the complete elliptic integrals of the first and second kinds,  $\text{sn}$ ,  $\text{cn}$  and  $\text{dn}$  the Jacobian elliptic functions,  $y=D+z$ ,  $\gamma = \sqrt{3L_0}/2D$  and  $\phi = \gamma(x-c t)$ .

The relation between two expansion parameters is written as

$$\begin{aligned}
& 2L_3 + L_0(x^2+e) + L_0^2\{(1/5)(-1+6x^2+9x^4) + 2(1+x^2)e\} \\
& + 6L_0L_3(x^2+e) + L_3^2 + L_0^3\{(1/175)(-102+223x^2+944x^4+675x^6) \\
& + (1/25)(111+214x^2+111x^4)e\} + 2L_0^2L_3\{-1+6x^2+9x^4 \\
& + 10(1+x^2)e\} + 15L_0L_3^2(x^2+e) = 0
\end{aligned} \tag{8}$$

and the relation between wave height  $H$  and expansion parameters is expressed as

$$\begin{aligned}
H/D = x^2L_0\{1+(1/4)L_0(10+7x^2) + 6L_3 + (1/40)L_0^2(251+369x^2 \\
+ 151x^4) + (5/2)L_0L_3(10+7x^2) + 15L_3^2\}
\end{aligned} \tag{9}$$

Yamaguchi et al. (1990) confirmed that the Chappellear theory is correct except for some printing errors, and newly calculated the trajectory of a water particle and integral properties such as energy flux.

### (3) Relation with the Tsuchiya & Yasuda theory

Tsuchiya & Yasuda derived a cnoidal wave theory with a single parameter  $L_0$ .

If the parameter  $L_3$  in the Chappellear theory is expanded into the power series form of  $L_0$ ,  $L_3$  is expressed as

$$\begin{aligned}
L_3 = -(1/2)(x^2+e)L_0 + (1/40)\{4-24x^2+19x^4+10(-4+7x^2)e \\
+ 55e^2\}L_0^2 - (1/2800)\{-816+3884x^2-5048x^4+1375x^6+(8316 \\
- 21616x^2+10941x^4)e + 2625(-8+9x^2)e^2+14875e^3\}L_0^3
\end{aligned} \tag{10}$$

and the relation between wave height  $H/D$  and  $L_0$  becomes

$$\begin{aligned}
H/D = x^2L_0 + (1/4)x^2(10-5x^2-12e)L_0^2 + (1/8)x^2\{55-55x^2 \\
+ 13x^4 + 74(-2+x^2)e + 96e^2\}L_0^3
\end{aligned} \tag{11}$$

Substitution of  $L_3$  relation into the wave characteristics in the Chappellear theory yields the following expressions.

$$c^{III}/\sqrt{gD} = 1 - (1/2)(-2 + x^2 + 3e)L_0 + (1/40)\{64 - 64x^2 + 19x^4 + 90(-2 + x^2)e + 135e^2\}L_0^2 - (1/2800)\{-10448 + 15672x^2 - 7974x^4 + 1375x^6 + 21(2288 - 2288x^2 + 563x^4)e + 36225(-2 + x^2)e^2 + 36225e^3\}L_0^3 \quad (12)$$

$$\begin{aligned} \alpha^{III}/\sqrt{gD} = & (1 - e - x^2 \text{sn}^2 \psi)L_0 + [(1/2)\{3 - 2x^2 - (7 - x^2)e + 4e^2 \\ & - (2 - 3x^2 - 5e)x^2 \text{sn}^2 \psi - 2x^4 \text{sn}^4 \psi\} + (3/4)(y/D)^2\{x^2 - 2(1 + x^2)x^2 \text{sn}^2 \psi \\ & + 3x^4 \text{sn}^4 \psi\}]L_0^2 + [(1/200)\{688 - 842x^2 + 209x^4 - (2838 - 1888x^2 \\ & + 63x^4)e + 75(49 - 12x^2)e^2 - 1525e^3 + 5\{-76 + 148x^2 - 71x^4 \\ & + 10(38 - 37x^2)e - 375e^2\}x^2 \text{sn}^2 \psi - 180(2 - 3x^2 - 5e)x^4 \text{sn}^4 \psi \\ & - 240x^6 \text{sn}^6 \psi\} + (3/8)(y/D)^2\{x^2(2 - 3x^2 - 5e) + 2\{-2 + 7x^2 + 3x^4 \\ & + 5(1 + x^2)e\}x^2 \text{sn}^2 \psi - 5(2 + 5x^2 + 3e)x^4 \text{sn}^4 \psi + 20x^6 \text{sn}^6 \psi\} \\ & - (3/16)(y/D)^4\{-x^2(1 + x^2) + (2 + 13x^2 + 2x^4)x^2 \text{sn}^2 \psi - 15(1 + x^2)x^4 \text{sn}^4 \psi \\ & + 15x^6 \text{sn}^6 \psi\}]L_0^3 \end{aligned} \quad (13)$$

These expressions coincide perfectly with those in the Tsuchiya & Yasuda theory. Relation between  $L_0$  and the expansion parameter in the Tsuchiya & Yasuda theory  $\lambda$  is given as

$$\lambda = x^2 L_0 \quad (14)$$

(4) Relation with the Isobe theory

Isobe gave a third order solution of cnoidal waves expressed with relative wave height  $H/D$ .

If the expansion parameters  $L_0$  and  $L_3$  in the Chappellear theory are expanded into the power series of  $H/D$ ,  $L_0$  and  $L_3$  are written as

$$L_0 = (1/x^2)(H/D) - (1/4x^4)(10 - 5x^2 - 12e)(H/D)^2 + (1/8x^6)\{3(15 - 15x^2 + 4x^4) - 46(2 - x^2)e + 48e^2\}(H/D)^3 \quad (15)$$

$$\begin{aligned} L_3 = & -(1/2x^2)(x^2 + e)(H/D) + (1/40x^4)\{2(2 + 13x^2 - 3x^4) \\ & + 5(2 - 3x^2)e - 5e^2\}(H/D)^2 + (1/2800x^6)\{-584 - 2659x^2 + 2073x^4 \\ & - 150x^6 + (-511 + 4011x^2 - 861x^4)e + 1050(1 - x^2)e^2 - 175e^3\}(H/D)^3 \end{aligned} \quad (16)$$

and if these  $L_0$  and  $L_3$  relations are used, the wave characteristics in the Chappellear theory are transformed as

$$\begin{aligned} c^{II}/\sqrt{gD} = & 1 + (1/2x^2)(2 - x^2 - 3e)(H/D) + (1/40x^4)\{2(-8 + 8x^2 \\ & - 3x^4) + 5(2 - x^2)e + 15e^2\}(H/D)^2 + (1/2800x^6)\{1558 - 2337x^2 \\ & + 1079x^4 - 150x^6 - (2653 - 2653x^2 + 203x^4)e + 350(2 - x^2)e^2 \\ & + 175e^3\}(H/D)^3 \end{aligned} \quad (17)$$

$$\begin{aligned}
u''/\sqrt{gD} = & (1/x^2)(1-e-x^2\text{sn}^2\psi)(H/D) + (1/4x^4)[-2-x^2+x^2e \\
& + 2e^2 + (6+x^2-2e)x^2\text{sn}^2\psi - 4x^4\text{sn}^4\psi + 3(y/D)^2\{x^2-2(1+x^2)x^2\text{sn}^2\psi \\
& + 3x^4\text{sn}^4\psi\}](H/D)^2 + (1/x^6) \{ (1/200)[\{153+23x^2-71x^4+(-153-97x^2 \\
& + 47x^4)e + 25(-1+2x^2)e^2+25e^3\} + 5\{-101-27x^2+19x^4+10(10+x^2)e \\
& - 15e^2\}x^2\text{sn}^2\psi + 20(32+2x^2-15e)x^4\text{sn}^4\psi - 240x^6\text{sn}^6\psi] \\
& + (3/8)(y/D)^2\{-8+2x^2+7e\}x^2 + 2\{2(4+6x^2-x^4)-7(1+x^2)e\}x^2\text{sn}^2\psi \\
& + (-40-10x^2+21e)x^4\text{sn}^4\psi + 20x^6\text{sn}^6\psi\} + (3/16)(y/D)^4\{(1+x^2)x^2 \\
& - (2+13x^2+2x^4)x^2\text{sn}^2\psi + 15(1+x^2)x^4\text{sn}^4\psi - 15x^6\text{sn}^6\psi\} (H/D)^3 \quad (18)
\end{aligned}$$

These expressions are exactly the same as the Isobe theory.

#### (5) Relation with the Fenton theory

Fenton derived a cnoidal wave theory expressed with relative wave height  $H/h_t$ , in which  $h_t$  is the water depth under the trough,

If  $L_0$  and  $L_3$  are expanded into the power series of  $H/h_t$  and  $h_t/D$  relation is taken into account,  $L_0$ ,  $L_3$  and  $h_t/D$  are expressed as a function of  $H/h_t$ .

$$\begin{aligned}
L_0 = & (1/x^2)(H/h_t) + (1/4x^4)(-6+x^2+8e)(H/h_t)^2 + (1/8x^6)\{3(3+x^2) \\
& - 8(2+x^2)e + 8e^2\}(H/h_t)^3 \quad (19)
\end{aligned}$$

$$\begin{aligned}
L_3 = & -(1/2x^2)(x^2+e)(H/h_t) + (1/40x^4)\{2(2+3x^2+7x^4)-5(2-5x^2)e \\
& + 15e^2\}(H/h_t)^2 - (1/2800x^6)\{24+279x^2+307x^4+710x^6+7(53-153x^2 \\
& + 253x^4)e - 1050(1-2x^2)e^2+875e^3\}(H/h_t)^3 \quad (20)
\end{aligned}$$

$$\begin{aligned}
h_t/D = & 1 + (1/x^2)(1-x^2-e)(H/h_t) + (1/4x^4)\{2(1-3x^2+2x^4) \\
& - (6-7x^2)e + 4e^2\}(H/h_t)^2 - (1/400x^6)\{-66+399x^2-733x^4+400x^6 \\
& + 2(233-683x^2+458x^4)e - 200(4-5x^2)e^2+400e^3\}(H/h_t)^3 \quad (21)
\end{aligned}$$

Substitution of  $L_0$ ,  $L_3$ , and  $h_t/D$  relations into the wave characteristics of the Chappellear theory yields the following expressions, which agree exactly with those in the Fenton theory again.

$$\begin{aligned}
c^1/\sqrt{gh_t} = & 1 + (1/2x^2)(1-2e)(H/h_t) + (1/120x^4)\{- (13+2x^2+3x^4) \\
& + 10(4+x^2)e\}(H/h_t)^2 + (1/16800x^6)\{-2888+5697x^2-2689x^4+780x^6 \\
& + 4(392-1442x^2+917x^4)e\}(H/h_t)^3 \quad (22)
\end{aligned}$$

$$\begin{aligned}
 \bar{u}/\sqrt{gh_i} = & 1 + (1/2x^2)(-1 + 2x^2 - 2x^2 \text{cn}^2\gamma\chi)(H/h_i) + (1/40x^4)\{3(3 - 8x^2 \\
 & + 3x^4) + 10(4 - 5x^2)x^2 \text{cn}^2\gamma\chi + 40x^4 \text{cn}^4\gamma\chi\}(H/h_i)^2 + (3/4x^2)\{1 - x^2 \\
 & + 2(-1 + 2x^2) \text{cn}^2\gamma\chi - 3x^2 \text{cn}^4\gamma\chi\}(y/h_i)^2(H/h_i)^2 + (1/1120x^6)\{-88 + 167x^2 \\
 & + 181x^4 - 200x^6 + 4(-112 + 378x^2 - 133x^4)x^2 \text{cn}^2\gamma\chi \\
 & + 16(-119 + 133x^2)x^4 \text{cn}^4\gamma\chi - 1344x^6 \text{cn}^6\gamma\chi\}(H/h_i)^3 + (3/8x^4)\{-1 + x^4 \\
 & + 2(1 - 7x^2 + 4x^4) \text{cn}^2\gamma\chi + (19 - 29x^2)x^2 \text{cn}^4\gamma\chi + 20x^4 \text{cn}^6\gamma\chi\}(y/h_i)^2(H/h_i)^3 \\
 & + (3/16x^4)\{1 - 3x^2 + 2x^4 + (-2 + 17x^2 - 17x^4) \text{cn}^2\gamma\chi \\
 & + 15(-1 + 2x^2)x^2 \text{cn}^4\gamma\chi - 15x^4 \text{cn}^6\gamma\chi\}(y/h_i)^4(H/h_i)^3
 \end{aligned}
 \tag{23}$$

(6) Summary of the considerations

In short, substitution of these series forms for  $L_0$  and  $L_3$  into the wave characteristics and integral properties by the Chappellear theories based on three definitions for wave celerity yields the same expressions as those developed by the above-mentioned researchers in all the cases investigated. This means that all of the existing third order solutions of cnoidal wave theory can be derived from the Chappellear theory by properly changing expansion parameters when the definition for wave celerity is identified in each solution. Details of the wave characteristics and integral properties calculated are given in the series papers by the authors (Yamaguchi et al. 1990, 1991 and 1992).

Fig. 1 summarizes the interrelation established among the existing cnoidal wave theories.

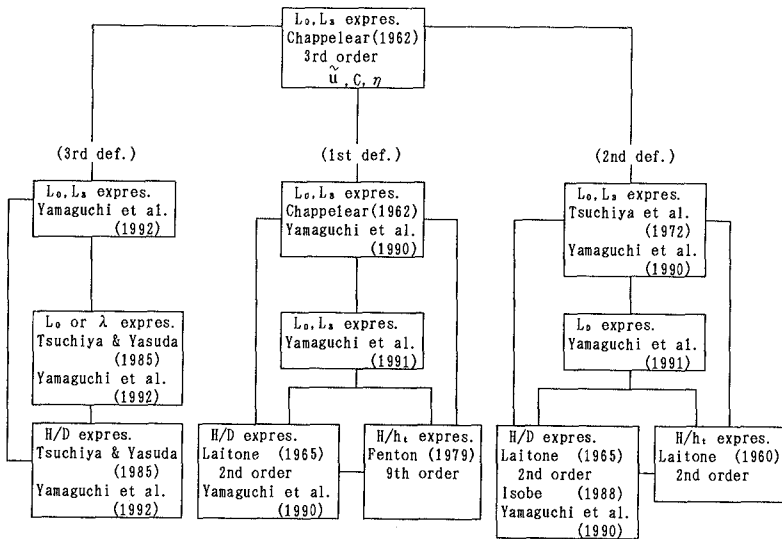


Fig. 1 Interrelation of cnoidal wave solutions.

3. Numerical Considerations

Fig.2 shows the vertical distributions of maximum horizontal water particle velocity  $u_c/\sqrt{gD}$  based on the cnoidal wave theories using the first definition with two parameters, one parameter and H/D parameter indicated by c-3-1, c-3-1M and c-3-1L respectively, in which T is the wave period. The theory with H/D parameter gives a more and more unrealistic distribution in the case of larger H/D values, and the theory with  $L_0$  parameter produces similar results to that with two parameters. But integral properties of the theory with two parameters do not show favorable behavior in the case of smaller  $T\sqrt{g/D}$ . Therefore, use of the cnoidal wave theory with  $L_0$  parameter is recommended for its practical application.

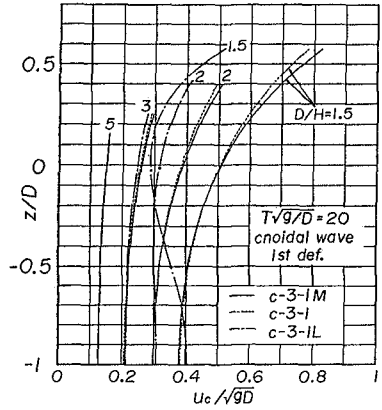


Fig. 2 Vertical distributions of maximum horizontal water particle velocity based on cnoidal wave theories with different parameters.

Examples of the comparison between computations with the experiments for wave celerity and maximum horizontal water particle velocity distribution are given in Fig. 3, which shows reasonable agreement between them. It is also

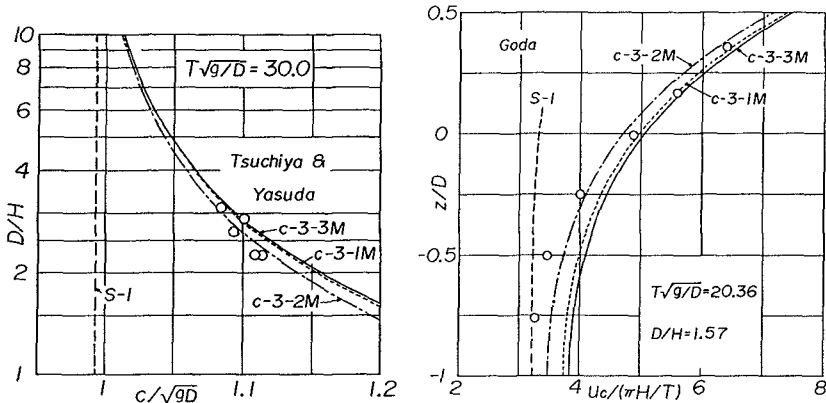


Fig. 3 Comparison between experiments and computations for wave celerity and vertical distribution of maximum horizontal water particle velocity.

seen that water particle velocity becomes larger according to the order of the theories with the second, first and third definitions.

Lagrangian velocity of a particular water particle is equal to Eulerian velocity at the position at time  $t$

$$dx/dt = u(x, z), \quad dz/dt = w(x, z), \quad x = x_0 + \xi(t), \quad z = z_0 + \zeta(t) \quad (24)$$

where  $(x_0, z_0)$  are the initial horizontal and vertical positions of a water particle, and  $(\xi, \zeta)$  the horizontal and vertical displacements of a water particle from its initial positions. Substitution of water particle velocities by cnoidal wave theory based on the first definition and use of a successive approximation method yield the trajectory of a water particle, in which case the initial conditions  $x=x_0$  and  $z=z_0$  at  $t=0$  are imposed. Horizontal and vertical displacements are written respectively as

$$\begin{aligned} x'/T\sqrt{gD} &= x_0/T\sqrt{gD} + (1/2K)\{[ea - E(\alpha)]L_0 \\ &+ [(1/6)\{2(1-x^2)[\alpha] + 2(-4+2x^2+3e)[E(\alpha)] + (4-5x^2-15e \\ &+ 6x^2\text{sn}^2\alpha)[ea - E(\alpha)]\} - (3/4)(y_0/D)^2x^2[\text{sn}\alpha\text{cn}\alpha\text{dn}\alpha]\}L_0^2 \\ &+ [(1/600)\{20(24-41x^2+17x^4)[\alpha] + 20\{-149+169x^2-34x^4 \\ &+ 5(52-29x^2)e-135e^2\}[E(\alpha)] + \{-256-244x^2+369x^4 \\ &+ 150(-32+25x^2)e+5625e^2\}[ea - E(\alpha)] + 200(1-x^2)x^2\text{sn}^2\alpha[\alpha] \\ &+ 200(-4+2x^2+3e)x^2\text{sn}^2\alpha[E(\alpha)] + 100(10-11x^2-27e \\ &+ 6x^2\text{sn}^2\alpha)x^2\text{sn}^2\alpha[ea - E(\alpha)] + 600x^2\text{sn}\alpha\text{cn}\alpha\text{dn}\alpha[ea - E(\alpha)]^2 \\ &- 8(1+x^2)x^2[\text{sn}\alpha\text{cn}\alpha\text{dn}\alpha] + 24x^4[\text{sn}^3\alpha\text{cn}\alpha\text{dn}\alpha]\} \\ &+ (1/40)(y_0/D)^2\{16(2-3x^2+x^4)[\alpha] + 32(-1+x^2-x^4)[E(\alpha)] \\ &- 30x^2\{1-2(1+x^2)\text{sn}^2\alpha+3x^2\text{sn}^4\alpha\}[ea - E(\alpha)] \\ &+ 30x^4\text{sn}\alpha\text{cn}\alpha_0\text{dn}\alpha_0[\text{sn}^2\alpha] + (-44+61x^2+105e)x^2[\text{sn}\alpha\text{cn}\alpha\text{dn}\alpha] \\ &- 60x^4\text{sn}^2\alpha_0[\text{sn}\alpha\text{cn}\alpha\text{dn}\alpha] - 18x^4[\text{sn}^3\alpha\text{cn}\alpha\text{dn}\alpha]\} \\ &+ (3/16)(y_0/D)^4\{- (1+x^2)x^2[\text{sn}\alpha\text{cn}\alpha\text{dn}\alpha] + 3x^4[\text{sn}^3\alpha\text{cn}\alpha\text{dn}\alpha]\}L_0^3 \end{aligned} \quad (25)$$

$$\begin{aligned} z'/T\sqrt{gD} &= z_0/T\sqrt{gD} - (3/2K\sqrt{3L_0})(y_0/D)x^2 \{ (1/2)[\text{sn}^2\alpha]L_0^2 \\ &- (1/8)\{2(-4+3x^2+7e-2x^2\text{sn}^2\alpha_0)[\text{sn}^2\alpha] - 8\text{sn}\alpha\text{cn}\alpha\text{dn}\alpha[ea \\ &- E(\alpha)] + (y_0/D)^2\{-2(1+x^2)[\text{sn}^2\alpha] + 3x^2[\text{sn}^4\alpha]\}\}L_0^3 \\ &+ [(1/240)\{80(1-x^2)\text{sn}\alpha\text{cn}\alpha\text{dn}\alpha[\alpha] + 80(4-2x^2 \\ &- 3e)\text{sn}\alpha\text{cn}\alpha\text{dn}\alpha[E(\alpha)] + 40(10-11x^2-27e+6x^2\text{sn}^2\alpha \\ &+ 6x^2\text{sn}^2\alpha_0)\text{sn}\alpha\text{cn}\alpha\text{dn}\alpha[ea - E(\alpha)] + 120\{1-2(1+x^2)\text{sn}^2\alpha \\ &+ 3x^2\text{sn}^4\alpha\}[ea - E(\alpha)]^2 + \{548-704x^2+213x^4+10(-200+133x^2)e \\ &+ 1665e^2\}[\text{sn}^2\alpha] + 60x^2\text{sn}^2\alpha_0(6-5x^2-11e+2x^2\text{sn}^2\alpha_0)[\text{sn}^2\alpha] \\ &- 24x^2(1+x^2)[\text{sn}^4\alpha] + 24x^4[\text{sn}^6\alpha]\} + (1/16)(y_0/D)^2\{8(1+x^2 \end{aligned}$$

$$\begin{aligned}
& -3x^2 \text{sn}^2 \alpha \text{sn} \alpha \text{cn} \alpha \text{dn} \alpha \left[ e\alpha - E(\alpha) \right] + 2\{4 - 8x^2 - 3x^4 \\
& - 7(1 + x^2)e\} \left[ \text{sn}^2 \alpha \right] + 2x^2 \text{sn}^2 \alpha_0 (8 + 8x^2 - 3x^2 \text{sn}^2 \alpha_0) \left[ \text{sn}^2 \alpha \right] \\
& + 3x^2 (7x^2 + 7e - 6x^2 \text{sn}^2 \alpha_0) \left[ \text{sn}^4 \alpha \right] - 8x^4 \left[ \text{sn}^6 \alpha \right] \\
& + 12x^2 \text{sn} \alpha_0 \text{cn} \alpha_0 \text{dn} \alpha_0 \left[ \text{sn} \alpha \text{cn} \alpha \text{dn} \alpha \right] + (3/160)(y_0/D)^4 \{ (2 + 13x^2 \\
& + 2x^4) \left[ \text{sn}^2 \alpha \right] - 15x^2(1 + x^2) \left[ \text{sn}^4 \alpha \right] + 15x^4 \left[ \text{sn}^6 \alpha \right] \} L_0^4
\end{aligned} \quad (26)$$

where  $\square f(\alpha) = f(\alpha) - f(\alpha_0)$ ,  $\alpha = 2K(x_0 - ct)/L$

$$\alpha_0 = 2Kx_0/L, \quad y_0/D = 1 + z_0/D, \quad (27)$$

and  $E(\alpha)$  is the Jacobian E function defined as

$$E(\alpha) = \int_0^\alpha \text{dn}^2 \alpha d\alpha \quad (28)$$

Mass transport velocity is calculated as time-averaged residual displacement of a water particle, and the distributions based on the solutions using three definitions are given respectively as

$$\begin{aligned}
U_m^I/\sqrt{gD} &= (1/3)\{-1 + x^2 + 2(2 - x^2)e - 3e^2\}L_0^2 + [(1/30)\{-24 + 41x^2 \\
& - 17x^4 + (149 - 169x^2 + 34x^4)e + 5(-52 + 29x^2)e^2 + 135e^3\} \\
& + (1/3)\{-1 + x^2 + 2(2 - x^2)e - 3e^2\}x^2 \text{sn}^2 \alpha_0 \\
& + (2/5)(y_0/D)^2\{-2 + 3x^2 - x^4 + 2(1 - x^2 + x^4)e\}]L_0^3
\end{aligned} \quad (29)$$

$$\begin{aligned}
V_m^I/\sqrt{gD} &= \underline{-(1/3\sqrt{3}L_0)L_0^4(y_0/D)x^2 \text{sn} \alpha_0 \text{cn} \alpha_0 \text{dn} \alpha_0\{-1 + x^2 \\
& + 2(2 - x^2)e - 3e^2\}}
\end{aligned} \quad (30)$$

$$U_m^{II}/\sqrt{gD} = (2/15)L_0^3\{1 - 3(y_0/D)^2\}\{2 - 3x^2 + x^4 + 2(-1 + x^2 - x^4)e\} \quad (31)$$

$$V_m^{II}/\sqrt{gD} = 0 \quad (32)$$

$$\begin{aligned}
U_m^{III}/\sqrt{gD} &= (1/2)\{-1 + x^2 + 2(2 - x^2)e - 3e^2\}L_0^2 + [(1/60)\{-66 \\
& + 109x^2 - 43x^4 + (421 - 461x^2 + 86x^4)e + 5(-146 + 79x^2)e^2 + 375e^3\} \\
& + (1/3)\{-1 + x^2 + 2(2 - x^2)e - 3e^2\}x^2 \text{sn}^2 \alpha_0 \\
& + (2/5)(y_0/D)^2\{-2 + 3x^2 - x^4 + 2(1 - x^2 + x^4)e\}]L_0^3
\end{aligned} \quad (33)$$

$$\begin{aligned}
V_m^{III}/\sqrt{gD} &= \underline{-(3/2\sqrt{3}L_0)L_0^4(y_0/D)x^2 \text{sn} \alpha_0 \text{cn} \alpha_0 \text{dn} \alpha_0\{-1 + x^2 \\
& + 2(2 - x^2)e - 3e^2\}}
\end{aligned} \quad (34)$$

When the initial conditions such as  $x=x_0$  and  $z=z_0$  at  $t=0$  are used, mass transport velocities based on the third order solutions of cnoidal waves using the first and third definitions depend on the initial horizontal position of a water particle, as denoted by underline. This may be due to the deficiency of the successive approximation method as in the case of Stokes wave theory. Thus,

$x_0$  is set to zero.

Fig. 4 illustrates the trajectory of a water particle and vertical distribution of mass transport velocity based on cnoidal wave theories using three definitions. None of the theories describe closed orbits, and all of them result in mass transport velocity distribution.

Wave energy  $\hat{E}$  and energy flux  $\hat{F}$  nondimensionalized by those of the small amplitude wave theory are shown in Fig. 5. Increase of  $T\sqrt{g/D}$  and decrease of  $D/H$ , that is to say, increase of wave nonlinearity, give rise to consistent and favorable reduction of dimensionless integral properties.

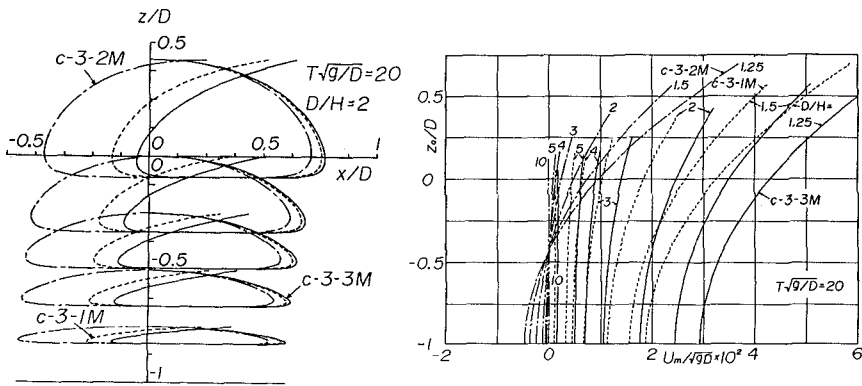


Fig. 4 Trajectory of a water particle and vertical distribution of mass transport velocity.

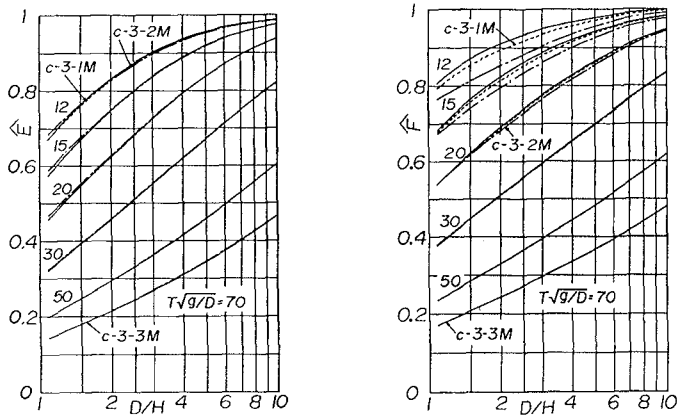


Fig. 5 Relation between integral properties and wave parameters.



#### 4. Limiting Range for Applicability

A limiting range for the application of cnoidal wave theory with a single expansion parameter is investigated by comparing wave characteristics and integral properties of cnoidal waves with those of Fenton's Fourier approximation theory, because the Fourier approximation theory gives the almost exact solution to water wave problem on a uniform depth.

Fig. 6 shows two examples of the comparison for vertical distribution of maximum horizontal water particle velocity and dimensionless energy flux, which shows that decrease of  $D/H$  and  $T\sqrt{g/D}$  gives rise to greater discrepancy between both theoretical results.

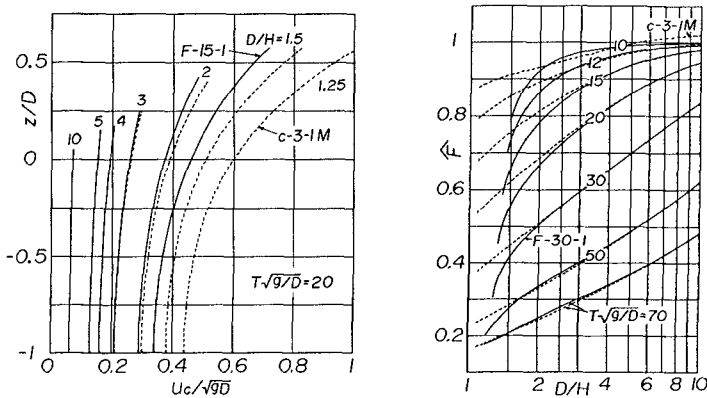


Fig. 6 Comparison between vertical distribution of maximum horizontal water particle velocity and dimensionless energy flux by cnoidal wave theory and those by Fourier approximation theory.

Fig. 7 illustrates a limiting range of wave parameters for the application of cnoidal wave theory, in which errors for wave celerity, horizontal water particle velocity and integral properties of cnoidal wave theory are less than 0.5 %, 5 % and 5 % respectively. In the figures, notations  $u_0$ ,  $u_5$  and  $u_b$  are the maximum horizontal water particle velocities at the still water level, middle point between still water level and bottom, and bottom,  $E_k$  and  $E_p$  the kinetic and potential energies,  $S_{11}$  and  $S_{22}$  the principal components of radiation stress and  $\overline{u_b^2}$  is the time mean of squared horizontal water particle velocity at the bottom. The range for individual wave characteristics and for integral property are different from each other. But roughly speaking, a limiting range of  $H/D$  for the third order solution is around 2.

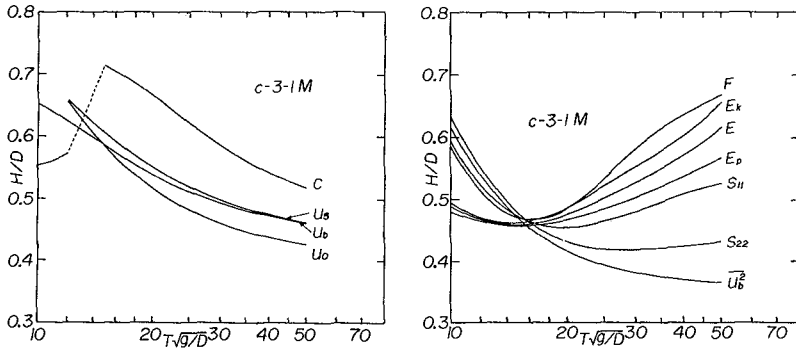


Fig. 7 Limiting range for application of the third order solution of cnoidal wave theory.

## 5. Conclusions

The main results are summarized as follows;

- 1) The interrelation among all of the existing cnoidal wave theories with the third order approximation is analytically established, in which case they can be derived from the Chappellear solution expressed with two expansion parameters by identifying the definition for wave celerity to be used in the theory and changing the expansion parameters in the expressions of wave characteristics and integral properties.
- 2) Based on the numerical computation of the wave characteristics and integral properties and the comparison with the experiments, use of the cnoidal wave theory expressed with a single parameter  $L_0$  was recommended from a practical viewpoint.
- 3) The figures describing a limiting range of wave parameters for the application of the cnoidal wave theory expressed with a single expansion parameter are provided by comparing wave characteristics and integral properties of the theory with those of the Fourier approximation theory.

## 6. Acknowledgements

A part of this study was accomplished with the support of the Science Research Fund (No. 01550408) of the Ministry of Education, for which the author expresses his appreciation.

## References

- Chappelear, J.E.(1962): Shallow-water waves, J. Geophys. Res., Vol. 69, No. 62, pp. 4693-4704.
- Fenton, J.D.(1979): A higher-order cnoidal wave theory, J. Fluid Mech., Vol. 94, Part 1, pp. 129-161.
- Fenton, J.D.(1990): Nonlinear wave theories, Part 1, Water Waves, in B. Le Mehaute and D. M. Hanes Ed., Ocean Engineering Science, The Sea, Vol. 9, Part A, John Wiley & Sons, pp. 3-25.
- Isoobe, M.(1988): Waves and nearshore currents, Chapter 2, Basic wave theories, in K. Horikawa Ed., Nearshore Dynamics and Coastal Processes-Theory, Measurement and Predictive Models-, Univ. of Tokyo Press, pp. 30-32.
- Laitone, E.V.(1960): The second approximation to cnoidal and solitary waves, J. Fluid Mech., Vol. 9, pp. 430-444.
- Laitone, E.V.(1965): Series solution for shallow water waves, J. Geophys. Res., Vol. 70, No. 4, pp. 995-998.
- Tsuchiya, Y. and T. Yasuda(1985): Cnoidal waves in shallow water and their mass transport, Advance in Non-linear Waves, Vol. 2, Research Notes in Mathematics, Pitman Press, p. 352.
- Yamaguchi, M. and Y. Tsuchiya(1974): Relation between wave characteristics of cnoidal wave theory derived by Laitone and by Chappelear, Bull. DPRI, Kyoto Univ., Vol. 24, Part 3, pp. 217-231.
- Yamaguchi, M. et al.(1990): A third order solution of cnoidal waves and its application to shoaling and refraction analyses, Memo. of Fac. of Eng., Ehime Univ., Vol. XII, No. 1, pp. 415-436(in Japanese).
- Yamaguchi, M. et al.(1991): A third order solution of cnoidal waves and its application to shoaling and refraction analyses(2), Memo. of Fac. of Eng., Ehime Univ., Vol. XII, No. 2, pp. 215-234(in Japanese).
- Yamaguchi, M. and O. Watanabe(1992): A third order solution of cnoidal waves and its application to shoaling and refraction analyses(3), Memo. of Fac. of Eng., Ehime Univ., Vol. XII, No. 3, pp. 197-222(in Japanese).

## CHAPTER 56

# FREAK WAVES IN UNIDIRECTIONAL WAVE TRAINS AND THEIR PROPERTIES

Takashi YASUDA\* , Nobuhito MORI\*\* and Kazunori ITO†

### ABSTRACT

This study aims to make clear the cause and occurrence condition of two-dimensional(2-D) freak waves by solving the hydrodynamic equations of 2-D irrotational flow for nonlinear waves with various spectra corresponding to swell from wind waves and describing the long-time evolution. As a result, it is shown that the third order resonant interaction causes the 2-D freak waves of which surface profiles are very similar with those observed in nature and multiplies the occurrence probability with the decreasing of the spectral bandwidth in deep water. Conversely, the feature of the freak waves —*single and outstanding wave height*— gets prominent with the broadening of the spectral bandwidth.

### INTRODUCTION

In recent years there has been a growing interest in single extreme waves referred as freak waves. Freak waves are individual high waves having severely damaging potential and are defined as waves with larger heights than two times of significant wave heights. There is no doubt on the occurrence of freak waves in nature because many reports are presented on their damages on offshore platforms at deck level and so on. However, the cause and properties of freak waves are still not so clear, although the state of the research on freak waves is already summarized at NATO Advanced Research Workshop in 1989[Peregrine,1990] and some explanations are suggested as their possible cause.

Laboratory measurement(Stansberg,1990) showed that a freak wave can be generated in a 2-D wave flume. This is a fairly strong evidence showing that some freak waves can actually occur in a unidirectional wave train without the effects of directional contents, wave focusing and currents. However, so definite explanation has not yet been suggested for its occurrence. In the case of

---

\*Prof., Dept. of Civil Engineering, Gifu Univ., 1-1 Yanagido, Gifu 501-11, Japan

\*\*Graduate Student, Dept. of Civil Engineering, Gifu Univ., 1-1 Yanagido, Gifu 501-11, Japan

†Research Engineer, Technology Research Center, Taisei Corporation, 344-1 Nasemachi, Totsuka-ku, Yokohama, Kanagawa 245, Japan

a quasi-monochromatic wave, Dold & Peregrine(1986) solved the fully nonlinear hydrodynamic equations for 2-D irrotational waves by using a boundary integral method and showed that a unidirectional wave train as gentle as  $ka=0.10$  undergoes a considerable modulation in its envelope and develops into breaking due to the nonlinear modulation. Their result suggests that the modulation due to resonant interaction might generate a freak wave in the 2-D domain. However, even if freak waves in nature could be treated approximately as long crested(2-D) waves, it remains unchanged that they must be treated as random waves having considerably broad spectral bandwidth. We hence are required to answer the question whether or not the resonant interaction can actually generate such freak waves as observed in nature in the 2-D wave trains having the broad band spectra similar with those in field.

In this study, we focus our interest on 2-D freak waves and make clear their cause and occurrence condition. For that purpose, we solve the hydrodynamic equations of 2-D incompressible and inviscid fluid for the waves having various spectra from swell to wind waves and perform intensive numerical simulations describing their long-time evolution. On the basis of the simulated results, we investigate relationships between their initial conditions and the time evolution and give an answer to the question whether or not 2-D freak waves can actually occur in random wave trains with arbitrary spectra. Furthermore, we make clear their cause and occurrence condition.

## COMPUTATIONAL METHOD

2-D vertical domain is assigned to be the usual spatial coordinates( $x, z$ );the origin is located at the mean water level,  $x$  the horizontal coordinate and  $z$  the vertically upward one. Boundary conditions at the free surface of the irrotational flow are rewritten into the evolution equations with regard to the free surface profile  $\eta(x, t)$  and the surface velocity potential  $\phi^s(x, t)$  at  $z = \eta$ ;

$$\eta_t + \phi_x^s \cdot \eta_x - (1 + \eta_x \cdot \eta_x) \phi_z = 0 \quad |_{z=\eta}, \quad (1)$$

$$\phi_x^s + g\eta + \frac{1}{2} \phi_x^s \cdot \phi_x^s - \frac{1}{2} (1 + \eta_x \cdot \eta_x) \phi_z^2 = 0 \quad |_{z=\eta}, \quad (2)$$

where the subscripts denote the partial differentiations with regard to  $t$  and  $x$ ,  $\phi_z$  the vertical gradient of the velocity potential  $\phi(x, z, t)$ ,  $t$  the time and  $g$  the acceleration due to gravity.

It is very difficult to solve eqs.(1) and (2) into the so-called Zakharov equation on the wavenumber space for waves having both the nonlinearity higher than the 3rd order and the arbitrary spectral bandwidth as far as based on the ability of present computer, although it was carried out for quasi-monochromatic waves by Yuen & Lake(1982). Hence, following Dommermuth & Yue(1987), we solve eqs.(1) and (2) on the physical space. Considering the nonlinear correction to  $\phi_z$  up to the  $M$ th order in the wave field composed of J-Fourier modes, we

formulate  $\phi_z$  so as to satisfy the Laplace equation,  $\nabla^2 \phi = 0$ , and the boundary condition on the flat bottom at  $z=-h$ ,  $\phi_z=0|_{z=-h}$ ;

$$\phi_z(x, \eta, t) = \sum_{m=1}^M \sum_{k=0}^{M-m} \frac{\eta^k}{k!} \sum_{j=1}^J \phi_j^{(m)}(t) \frac{\partial^{k+1}}{\partial z^{k+1}} \psi_j(x, 0), \tag{3}$$

$$\psi_j(x, z) = \frac{\cosh[k_j(z+h)]}{\cosh(k_j h)} \exp(ik_j x), \tag{4}$$

where  $k$  denotes the wave number,  $h$  the mean water depth,  $\phi_j^{(m)}(t)$  is derived by solving the following equations in order.

$$\begin{aligned} \phi^{(1)}(x, 0, t) &= \phi^s, \\ \phi^{(m)}(x, 0, t) &= - \sum_{k=1}^{m-1} \frac{\eta^k}{k!} \frac{\partial^k}{\partial z^k} \phi^{(m-k)}(x, 0, t) \quad (m = 2, 3, \dots, M). \end{aligned} \tag{5}$$

In this method, an approximation is made on the expression of  $\phi_z$  alone and eqs.(1) and (2) are solved directly in the physical space by using the pseudo-spectral method. While the spatial derivations of  $\phi^{(m)}$ ,  $\phi^s$  and  $\eta$  are evaluated in the spectral space, the nonlinear products are calculated in the physical space. The time evolution of  $\eta$  and  $\phi^s$  is made in the physical space by integrating eqs.(1) and (2) with the fourth-order Runge-Kutta-Gill method. An optimum FFT scheme for the vector operation in a super computer is used to delete the alising error generated in the computaion of the nonlinear terms and accomplish the fast computation.

### VALIDITY OF THE COMPUTATION

The accuracy and convergence of the computational model are tested by giving the exact Stokes waves as initial waves. The first check of the accuracy is provided by examining the maximum difference of the surface wave profile  $\varepsilon_1 = |k\{\eta_n(x, t) - \eta_e(x, t)\}|_{max}$  between the numerical solution  $\eta_n$  and the exact solution  $\eta_e$  during the propagation process from  $t/T=0$  to 100. Here,  $T$  is the wave period. Further, the accuracy and convergence of the numerical solutions are tested by defining the error to the conservation law of the total energy  $E(t)$  as  $\varepsilon_2 = |1 - E(t)/E(0)|$  and examining its time evolution.

Table 1 indicates the maximum values of  $\varepsilon_1$  and  $\varepsilon_2$  for the shallow water waves with  $ka=0.17$  and  $kh=1$  and for the deep water waves with  $ka=0.2$  and  $0.3$  when the numerical computations are made under the condition of the values of  $M=3$  and  $4$  and  $J=8$  and  $16$ . Here,  $a$  is the wave amplitude. Figure 1 describes the time evolution of  $\varepsilon_2$  for each numerical solution shown in Table 1. Both the error criteria,  $\varepsilon_1$  and  $\varepsilon_2$ , indicate finite values because the values of  $M$  and  $J$  employed here are not large enough for the numerical solutions to agree completely with the exact solution. However, the values of  $\varepsilon_1$  are still considerably

small after the long time evolution of  $t/T=100$ . Further, although the values of  $\epsilon_2$  grow with oscillation, their envelopes are almost constant independly of the values of  $kh, ka, M$  and  $J$  and their amplitudes are sufficently small. We can hence expect the sufficient accuracy and convergency for the obtained numerical solutions if solving eqs.(1) and (2) by the aforementioned method.

Table 1. Accuracy of the numerical solutions for the exact Stokes waves

$ka$	$kh$	$M$	$J$	$\epsilon_1 \times 10^3$	$\epsilon_2 \times 10^3$
0.17	1	3	8	0.43	1.33
0.17	1	4	8	0.37	0.85
0.20	$\infty$	3	8	0.42	0.72
0.20	$\infty$	3	16	0.42	0.72
0.20	$\infty$	4	8	0.42	0.70
0.30	$\infty$	3	8	3.05	5.75

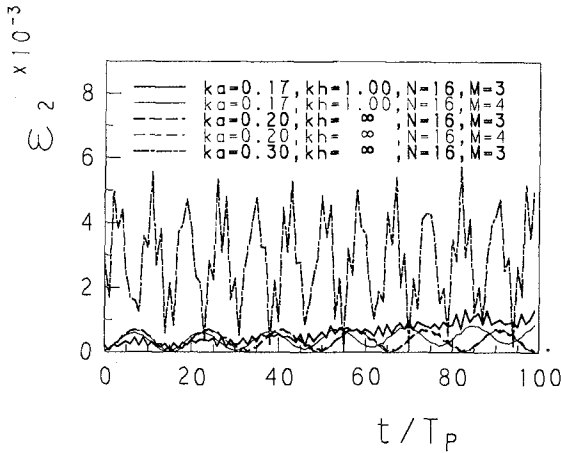


Figure 1. Time histories of the error criterion  $\epsilon_2$

**NUMERICAL SIMULATIONS**

Initial surface profiles  $\eta(x, 0)$  is given by

$$\eta(x, 0) = \sum_{n=1}^J \sqrt{2S(k_n)(2\pi/L_0)} \sin(k_n x + \epsilon_n) \tag{6}$$

where  $L_0$  is the total length of the simulated wave train,  $k_n$  the wave number of the  $n$ -th Fourier mode,  $\epsilon_n$  the phase constant of the Fourier mode given by a set of independent uniform random numbers uniformly distributed in the interval  $(0, 2\pi)$  radians and  $S(k_n)$  the desired wavenumber discrete spectrum into which the following Wallops continuous spectrum  $S(f)$  is transformed through the linear dispersion relation.

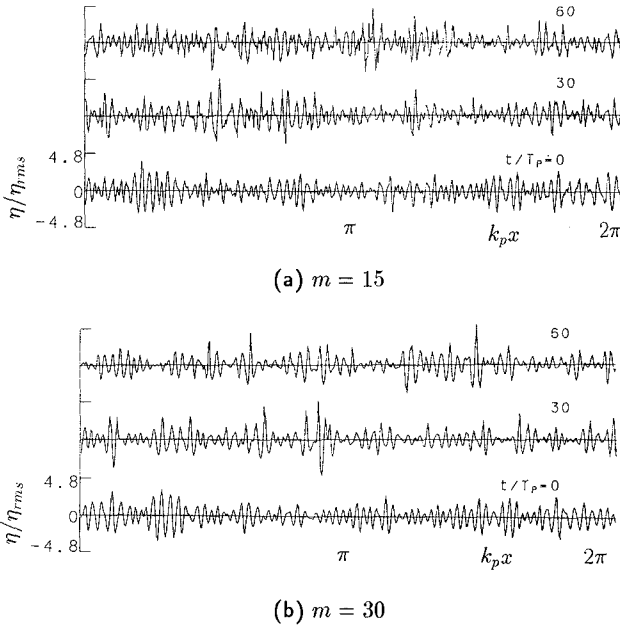


Figure 2. Spatial surface profiles of a simulated wave train at  $t/T_p=0, 30$  and  $60$  ( $k_p h=3.0, k_p a=0.17$ ).

$$S(f) = \alpha H_{1/3}^2 f^{(4-m)} (f/f_p)^{-4} \exp \left[ -0.25m (f/f_p)^{-4} \right], \tag{7}$$

where  $\alpha$  is a constant satisfying the relation,

$$H_{1/3} = 4.004 \left[ \int_0^\infty S(f) df \right]^{\frac{1}{2}}, \tag{8}$$

$f_p$  the spectral peak frequency,  $H_{1/3}$  the significant wave height and  $m$  the spectral bandwidth parameter. The value of  $m=5$  generally gives the spectrum of wind waves and those of  $m \geq 10$  swell spectra. Initial surface potential  $\phi^s(x, 0)$  is given here by the linear transformation of its conjugate  $\eta(x, 0)$ .

The numerical computations are made in the periodic space having the length of  $L_0 = 64L_p$  on the  $x$  coordinate; the subscript  $p$  denotes the quantity of the spectral peak mode. The values of  $M$  and  $J$  are fixed to 3 and 256, respectively. The time interval of the stepping is  $T_p/100$ . The simulations are performed with the accuracy of the energy error criterion  $\varepsilon_2$  of which value is always less than 0.05, under the initial statistics comprised of  $k_p h=1.04, 1.36, 1.72, 2.35$  and  $3.0, k_p a=0.17, m=5, 10, 15$  and  $30$ . The accuracy is accomplished without any consideration except for de-aliasing. This fact convinces us that



any breaking event does not occur during the propagation process because the breaking triggers the floating overflow error of the numerical solution.

Figure 2 shows the computed surface elevations for the waves with the initial statistics of  $k_p h = 3.0$ ,  $k_p a = 0.17$  and  $m = 15, 30$ . The free surface elevations at  $t/T_p = 20$  and 60 are considerably modulated in comparison with their initial ones and accompany single high waves characterized as freak waves because they are not part of a smooth wave group pattern and the crest heights clearly exceed those of their neighbours.

## NONLINEAR EFFECTS ON 2-D FREAK WAVES

### Surface profiles of 2-D freak waves

Figure 3 shows the temporal surface elevation of the typical freak wave observed in the North sea (Sandet *al.*, 1990). The wave profile definitely demonstrates the feature of a typical freak wave that is single —*not part of smooth wave group pattern*— and has remarkable horizontal asymmetry and the crest height clearly exceeding that of its neighbours.

Figure 4 indicates the spatial surface profiles of 2-D freak waves occurring in the simulated wave trains. The simulated wave profiles are easily found to be very similar with the observed wave profile shown in Fig.3, although there is a definite difference that the formers are spatial profiles in 2-D domain while the latter is temporal one in 3-D field. On the other hand, the wave profile of a linear freak wave shown in Fig.5 for comparison is mild and horizontally symmetric. We thereby notice that it is greatly differs from those shown in Figs.3 and 4 and very little possesses the aforementioned feature of the freak waves. This states that a linear combination of the Fourier modes cannot be probably the cause of the freak waves hitherto observed in nature even if it can generate the wave grouping containing a high wave of which height exceeds two times of  $H_{1/3}$ . On the contrary, the wave profiles shown in Fig.4 are very similar with that observed in nature (Fig.3) as mentioned. We could therefore say from the viewpoint of the similarity of both the wave profiles that freak waves can be generated by the 3rd order nonlinear interaction (resonant interaction) independently of the spectral bandwidth, that is, the 3rd order resonant interaction can be one of the causes of freak waves in nature. We should further notice that even if the occurrence of the freak waves might obey the Rayleigh distribution, which is based on the strict assumption of a narrow banded Gaussian process, the freak waves having the aforementioned feature —*single and outstanding*— never occurs from narrow banded linear wave trains.

Figure 6 describes the time evolution of the freak wave during the propagation process from its appearing to disappearing. Its appearing and disappearing times are denoted with the open arrows. The freak wave is not so unstable as it instantaneously appears and disappears, but so stable as it keeps the profile during about one period at least.

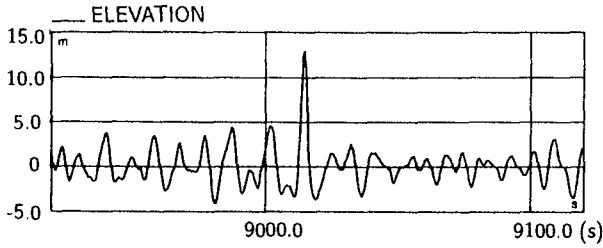
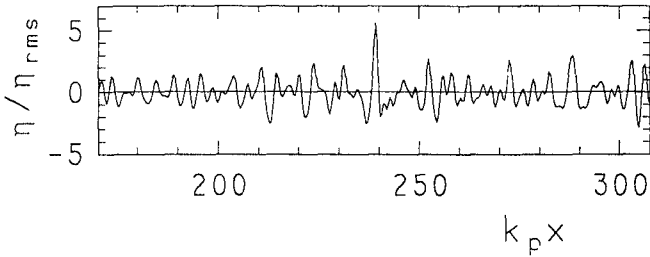
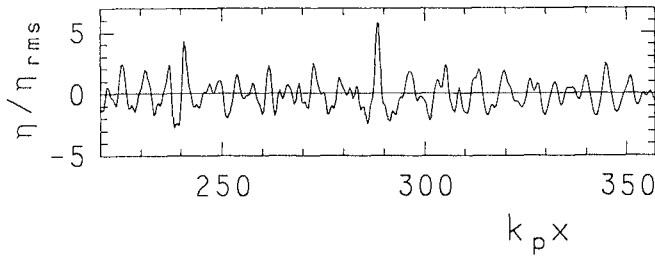


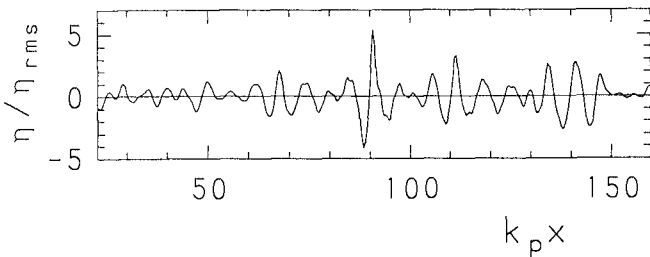
Figure 3. Temporal surface elevation of the freak wave observed in the North sea [Sand et al., 1990].



(a)  $m = 5$



(b)  $m = 15$



(c)  $m = 30$

Figure 4. Spatial surface profiles of the freak waves occurring in the simulated 2-D nonlinear wave trains ( $k_p h = 3.0, k_p a = 0.17$ ).

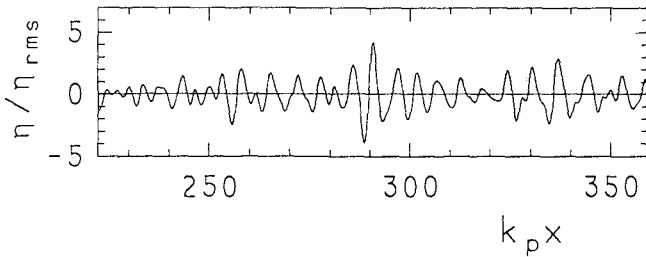
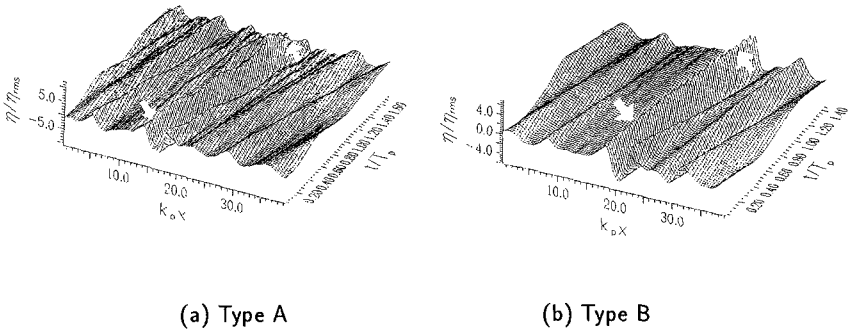


Figure 5. Spatial surface profile of a linear freak wave which occurs in a 2-D linear wave train( $k_p h=3.0, k_p a=0.17, m=15$ ).



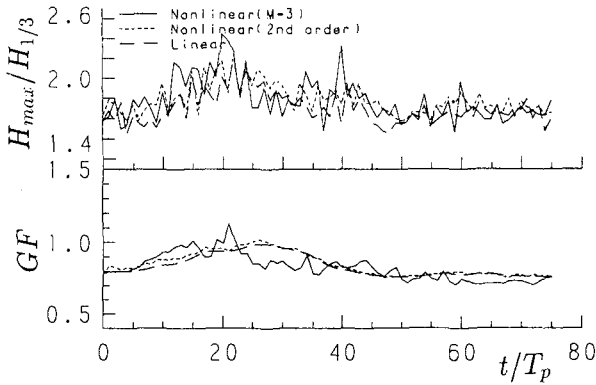
(a) Type A (b) Type B  
 Figure 6. Propagation process of the 2-D freak wave from its appearing to disappearing( $k_p h=3.0, k_p a=0.17, m = 30$ ).

**Nonlinear effects causing freak waves**

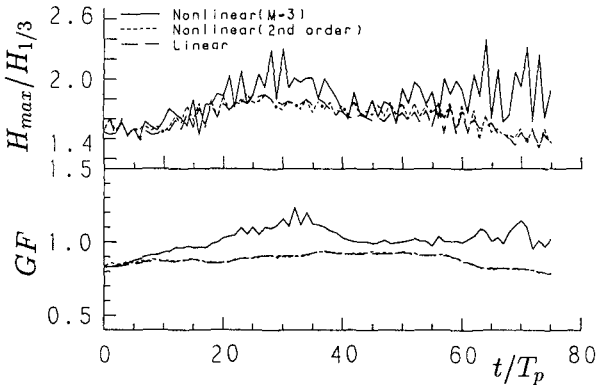
Figure 7 shows the time histories of the ratio  $H_{max}/H_{1/3}$  of the maximum wave height  $H_{max}$  to  $H_{1/3}$  and  $GF$ (Groupiness Factor) of the spatial surface profiles of the evolving simulated waves. For comparison, the results of linear waves and the 2nd order nonlinear waves are also shown. The 2nd order nonlinear wave solution is derived by solving not eqs.(1) and (2) but the original hydrodynamic equations in which the nonlinear terms more than the 3rd order are deleted. The 3rd order resonant interaction is not therefore taken into account in the 2nd order solution. It is found that nonlinear effects of the 2nd order are almost negligible on the values of  $H_{max}/H_{1/3}$  and  $GF$ , although it is well-known that they affects on the skewness of the free surface profiles. On the other hand, nonlinear effects of the 3rd order on those values are remarkable and grow with the narrowing of the spectral bandwidth. The time evolution of  $H_{max}/H_{1/3}$  corresponds well to

that of  $GF$  in the nonlinear( $M=3$ ) wave train. We could hence say that the 3rd order resonant interaction strongly modulates the envelope of the wave train so that it multiplies the values of  $GF$  and  $H_{max}$  and further causes the freak waves.

Figure 8 shows the amplitude modulation of the peak and its side-band Fourier modes of the nonlinear waves( $M=3$ ) shown in Fig.7. The time evolution of the amplitude modulation of the side-band modes clearly corresponds to both the time histories of  $H_{max}/H_{1/3}$  and  $GF$ . It should be noticed that the value of  $H_{max}/H_{1/3}$  exceeds 2 and the individual wave with  $H_{max}$  becomes a freak wave at the time when the side-band modes become dominant to the spectral peak mode independently of the spectral bandwidth( $m=15$  and 30) and that these occur. This result demonstrates that the 2-D freak waves are generated by the side-band instability due to the resonant interaction.



(a)  $m = 15$



(b)  $m = 30$

Figure 7. Time histories of  $H_{max}/H_{1/3}$  and  $GF$  for the evolving nonlinear wave trains( $M=3$  and the 2nd order) and the linear one( $k_p h=3.0, k_p a=0.17$ ).

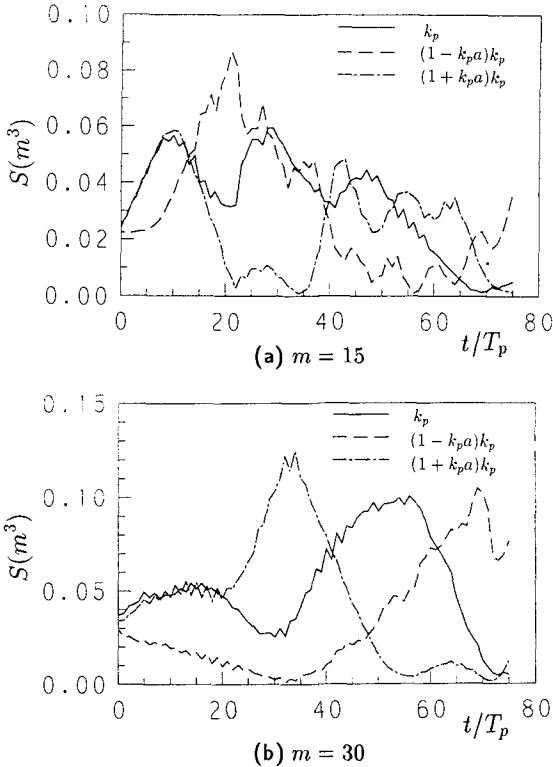


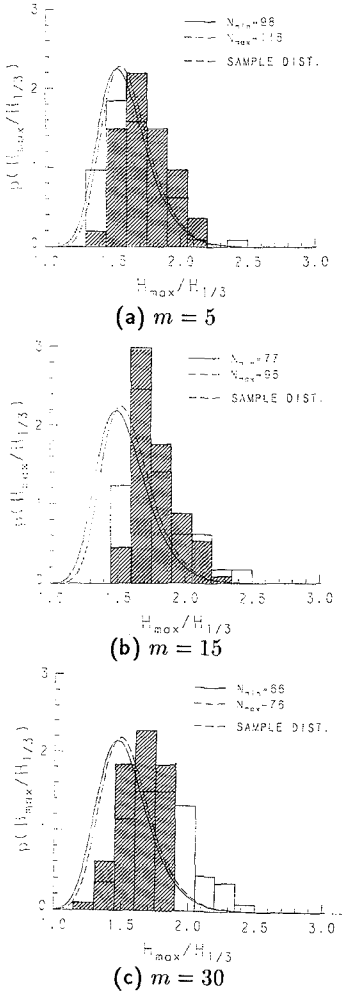
Figure 8. Time evolution of the modal energy  $S(k)$  of the spectral peak mode( $k_p$ ) and its both side-band modes( $k_p \pm k_p^2 a_{1/3}$ ) of the nonlinear waves( $M=3$ ) corresponding to the case reported in Fig.7( $k_p h=3.0, k_p a=0.17$ ).

**Nonlinear effects on the occurrence probability**

Figure 9 compares the frequency distribution of  $H_{max}/H_{1/3}$  obtained from the spatial surface profiles at every time step of  $\Delta t/T_p=1$  of the simulated waves during the propagation process from  $t/T_p=0$  to  $t/T_p=75$  with the following distribution  $p(H_{max}/H_{1/3})$  derived from the Rayleigh distribution,

$$p(x_{max}) = 2.832x_{max}\xi \exp(-\xi), \tag{9}$$

where  $x_{max}=H_{max}/H_{1/3}$ ,  $\xi=N \exp(-1.416x_{max}^2)$ .  $N_{min}$  and  $N_{max}$  in the Fig.9 denote the minimum value and the maximum one of the number of the zero-down crossing waves contained in the simulated waves during the propagation process. The frequency in the 2nd order nonlinear waves is not so influenced by the spectral bandwidth and is presumed to be almost same with that in linear waves because the 2nd order nonlinear interaction very little influences on the



**Fig.9.** Effects of the nonlinear interaction and spectral bandwidth on the frequency distribution of  $H_{max}/H_{1/3}$

On the contrary, the value of  $\mu$  in the nonlinear wave train largely exceeds that given by eq.(10) independently of the number of  $N$ . This suggests that the resonant interaction increases the occurrence probability of the 2-D freak waves 10 times ( $N=70$ ) from 5 times ( $N=500$ ) of that given by eq.(10).

wave height as mentioned above. The difference between both the frequencies (2nd and  $M=3$ ) thereby indicates the influence of the 3rd order resonant interaction on the frequency. It could hence be found from the difference that the influence of the resonant interaction is almost negligible in the case of  $m=5$  but becomes non-ignorable over the region of  $m \geq 15$ . We could thus say that the effects of the resonant interaction become pronounced and the occurrence probability of the freak waves accordingly increases as the spectral bandwidth becomes narrower.

Further, in order to investigate the influence of the number  $N$  of the zero-crossing waves on the exceedance probability  $\mu$  that the value of  $H_{max}/H_{1/3}$  is exceeds 2, that is, the occurrence probability of the 2-D freak waves, we compare the value of  $\mu$  obtained from the simulated wave train ( $M=3$ ) with that given by

$$\mu = 1 - \exp(-N/3041), \quad (10)$$

which is derived under the assumption that  $N$ -wave heights obey the Rayleigh distribution. The result is shown in Fig.10 for the waves with the number  $N$  of the zero-down crossing waves contained in the initial waves, 70, 150 and 500, respectively. The value of  $\mu$  in a linear wave train shown for comparison corresponds well to the solid line given by eq.(10) and the difference between both the results could be regarded to be within the region of statistical variation.

Figure 11 shows the relation between the frequency that the value of  $H_{max}/H_{1/3}$  of the simulated waves ( $M=3$ ) exceed 2 during their propagation process and the value of  $GF$  averaged over the propagation process,  $\langle GF \rangle$ . Symbols drawn with thick line indicate the values of the waves of which initial bandwidth parameter  $m$  equals to 30, those drawn with median line indicate the values with the initial statistics of  $m=15$  and those drawn with thin line denote the values with  $m=5$ . The mean number  $\langle N \rangle$  of the zero-down crossing waves in this case is about 80~100, so that if those wave heights obey the Rayleigh distribution, the theoretical value of  $p(H_{max}/H_{1/3} > 2)$  is about 0.026.

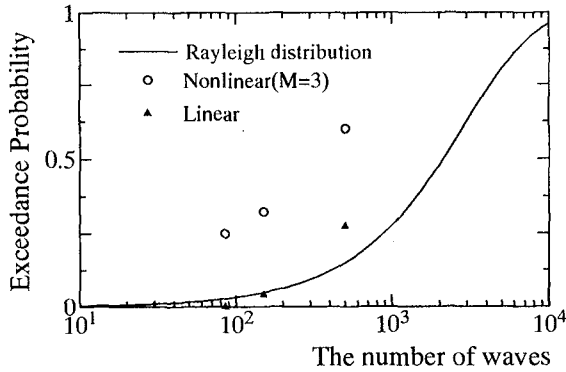


Figure 10. Influence of the number  $N$  of the zero-down crossing waves on the exceedance probability  $\mu(H/H_{1/3} > 2)$  [ $k_p h = 3.0, k_p a = 0.17, m = 30$ ]

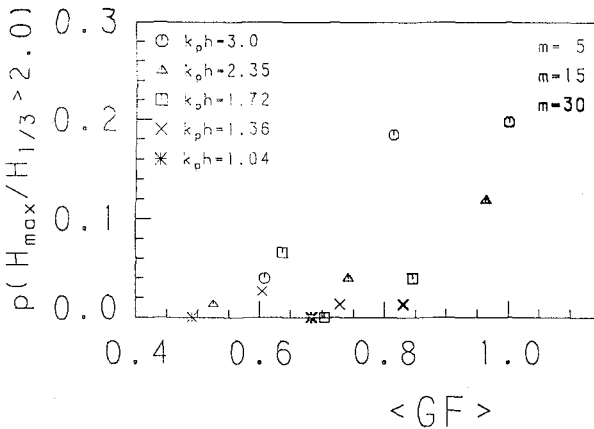


Figure 11. Relation of the occurrence probability of the 2-D freak wave during the propagation process and the averaged value of  $GF$  over the process.

Table 2 Relations of the initial statistics to the frequencies(%) of  $H_{max}/H_{1/3} > 2$ ,  $\kappa > 2$  and  $\chi > 0.65$ .

m		$k_p h$		
		3.0	1.72	1.04
5	$H_{max}/H_{1/3} > 2$	6.6 (1.3)	2.6(9.2)	0.0 (0.0)
	$\kappa > 2$	23.7(14.5)	5.2(7.9)	18.4(19.7)
	$\chi > 0.65$	19.7 (1.3)	11.8(5.3)	5.2 (1.3)
		2.6 (0.0)	0.0(0.0)	0.0 (0.0)
15	$H_{max}/H_{1/3} > 2$	22.3 (5.2)	1.3(0.0)	0.0 (1.3)
	$\kappa > 2$	34.2 (0.0)	19.7(7.9)	2.6 (0.0)
	$\chi > 0.65$	14.5 (0.0)	17.1(1.3)	7.8 (0.0)
		1.3 (0.0)	0.0(0.0)	0.0 (0.0)
30	$H_{max}/H_{1/3} > 2$	23.7 (0.0)	2.6(0.0)	0.0 (0.0)
	$\kappa > 2$	19.7 (0.0)	6.6(0.0)	0.0 (0.0)
	$\chi > 0.65$	13.2 (0.0)	9.2(0.0)	7.9 (0.0)
		0.0 (0.0)	0.0(0.0)	0.0 (0.0)

Although the value of  $p(H_{max}/H_{1/3} > 2)$ , that is, the occurrence probability of the freak wave is independent of the value  $\langle GF \rangle$  in the waves with the value of  $k_p h$  less than 1.72, the occurrence probability is multiplied with the increasing of the value of  $\langle GF \rangle$  in the waves with the value of  $k_p h$  over 2.35.

Following Klinting & Sand(1987), we calculate the frequencies that the ratio  $\kappa(=H_{i+1}/H_i)$  of the wave height to its neighbour exceeds 2 and that the ratio  $\chi(=\eta_{max}/H_{max})$  of the crest height  $\eta_{max}$  to the maximum wave height  $H_{max}$  exceeds 0.65, in addition to the frequency of  $H_{max}/H_{1/3} > 2$  and show the values of these frequencies to each initial statistics in Table 2. The numerical values on the fourth line the case of  $k_p h=3.0$  within the frame corresponding to each wave indicate the frequency satisfying simultaneously these three conditions,  $H_{max}/H_{1/3} > 2$ ,  $\kappa > 2$  and  $\chi > 0.65$ . The figures in parentheses indicate the values in linear waves with the same initial statistics. The frequency of  $H_{max}/H_{1/3} > 2$  increases as the spectral bandwidth gets to narrower. On the contrary, the conditions characterizing the freak waves, that is, the frequencies of  $\kappa > 2$  and  $\chi > 0.65$  increase large as the spectral bandwidth gets to narrower. We could hence say that the 2-D freak waves incline to occur in deep water because their cause —*resonant interaction*— is strengthened to the maximum extent in deep water. Furthermore, it should be noted that although the occurrence probability itself of freak waves defined by  $H_{max}/H_{1/3} > 2$  increase with the decreasing of the spectral bandwidth, the occurrence probability of the typical freak waves possessing the feature —*single and the crest height clearly exceed those of its neighbour*— with the increasing of the spectral bandwidth and becomes maximum under the broad band spectra corresponding to wind waves.



## CONCLUSIONS

The following major conclusions may be drawn from this study

- i) The 3rd order resonant interaction causes single extreme high waves typically characterized as freak waves in unidirectional wave trains with various spectra corresponding to wind waves from swell. On the other hand, the surface profile of a linear freak wave caused by a linear combination of the Fourier modes is mild and horizontally symmetric and is very different from those observed in nature. Since the resonant interaction is thus essential to cause the 2-D freak waves, its effects on the occurrence probability of the 2-D freak waves should be taken into account.
- ii) The resonant interaction multiplies the occurrence probability of the 2-D freak waves and its effects become pronounced as the water depth gets deeper and the spectral bandwidth gets narrower. However, the feature of the surface profile characterizing freak waves —*single, remarkably horizontal asymmetric and extreme high waves*— gets prominent with the broadening of the spectral bandwidth, that is, the feature is strengthened to the maximum extent under wind wave spectra in deep water.

## REFERENCES

- ◇ Dold, J.W. & D.H. Peregrine (1986), *Wave-wave modulation, Proc.20th Conf.on Coastal Eng.*, Vol.I, pp.163-175 .
- ◇ Dommermuth, D.G. & D.K.P. Yue (1987), *A high-order spectral method for the study of nonlinear gravity waves, JFM.*, Vol.184, pp.267-288 .
- ◇ Klinting, P. & S. Sand (1987), *Analysis of prototype freak waves, in Coastal Hydrodynamics*(ed.R.A.Dalrymple,ASCE), pp.618-632 .
- ◇ Sand, S.*et al* (1990), *Freak wave kinematics, in Water Wave Kinematics*(Eds. A.Tørum & O.T.Gudmestad,Kluwer Academic Pub.),pp.535-549 .
- ◇ Peregrine, D.H. (1990), *Report from the working group on breaking and freak waves, in Water Wave Kinematics* (Eds. A.Tørum & O.T.Gudmestad, Kluwer Academic Pub.),pp.17-20 .
- ◇ Stansberg, C.T. (1990), *Extreme waves in laboratory generated irregular wave trains, in Water Wave Kinematics*(Eds. A.Tørum & O.T.Gudmestad, Kluwer Academic Pub.), pp.573-589 .
- ◇ Yuen, H.C. & B.M. Lake (1982), *Nonlinear dynamics of deep-water gravity waves, Advances in Applied Mechanics*vol.22, pp.67-229 .

## CHAPTER 57

# A Method for Estimating Reflection Coefficient in Short-Crested Random Seas

Hiomune Yokoki<sup>1</sup>  
Masahiko Isobe<sup>2</sup>  
Akira Watanabe<sup>2</sup>

### Abstract

A method for estimating the reflection coefficient is developed for practical uses. In the method, a parametric expression of directional spectra is adopted and the parameters in it are estimated by the maximum likelihood method. The validity of the method is verified by applying it to simulated data. The method is also applied to field data, obtained at Oarai Port, Japan.

### 1 Introduction

The randomness of sea waves has recently become accounted for in the design of coastal and ocean structures. Directional spectra have often been used to describe multi-directional random sea waves. However, to evaluate the reflection coefficient of structures, a theory for uni-directional random waves has usually been applied with a slight modification. This is because a theory for multi-directional random waves has not yet been established for practical uses.

The purpose of this paper is to derive a method to estimate the reflection coefficient of structures for multi-directional random waves and to examine its validity by applying it to simulated and field data.

In various methods to estimate the directional spectrum, the maximum likelihood method (MLM) is the one which has a high resolution spectrum (Capon,

---

<sup>1</sup>Research Associate, Dept. of Civil Eng., Univ. of Tokyo, Bunkyo-ku, Tokyo, 113 Japan

<sup>2</sup>Professor, ditto

Table 1: Definitions of variables in Eq. (1)

$A(\mathbf{k}, \sigma)$	Amplitude (Eq. 1),
$A(d\mathbf{k}, d\sigma)$	Complex amplitude (Eq. 2)
$\mathbf{k}$	Wave number vector of incident waves
$\mathbf{k}_r$	Wave number vector of reflected waves
$\sigma$	Angular frequency
$\epsilon$	Phase

1969). Isobe and Kondo (1984) proposed the modified maximum likelihood method (MMLM) to estimate the directional spectrum in a combined incident and reflected waves field, taking into account the fact that there is no phase difference between the incident and reflected waves at the reflective wall. Recently for practical purposes, Isobe (1990) proposed a method to estimate the directional spectrum of a standard form in which the spectrum is expressed in terms of a few parameters. In this study, this method is modified to estimate the directional spectrum and reflection coefficient in an incident and reflected wave field.

## 2 Theory

### 2.1 Parametric expression of directional spectrum and cross-power spectrum

In a monochromatic wave field which consists of incident and reflected waves, the water surface fluctuation,  $\eta(\mathbf{x}, t)$ , at the position,  $\mathbf{x}$ , are represented by Eq. (1):

$$\eta(\mathbf{x}, t) = A(\mathbf{k}, \sigma) \{ \cos(\mathbf{k}\mathbf{x} - \sigma t + \epsilon) + r \cos(\mathbf{k}_r\mathbf{x} - \sigma t + \epsilon) \} \quad (1)$$

The definitions of the variables in the above equation are given in Table 1. We integrate Eq. (1) with respect to  $\mathbf{k}$  and  $\sigma$ , and get the expression of  $\eta(\mathbf{x}, t)$  for multi-directional random waves as Eq. (2):

$$\eta(\mathbf{x}, t) = \int_{-\infty}^{\infty} \int_{\mathbf{k}} A(d\mathbf{k}, d\sigma) \{ \exp [i(\mathbf{k}\mathbf{x} - \sigma t + \epsilon)] + r \exp [i(\mathbf{k}_r\mathbf{x} - \sigma t + \epsilon)] \} \quad (2)$$

where complex variables are introduced to represent the amplitude and phase. From Eq. (2), the directional spectrum ( wavenumber-frequency spectrum ),  $S(\mathbf{k}, \sigma)$ , is defined as Eq. (3):

$$S(\mathbf{k}, \sigma) d\mathbf{k} d\sigma = \langle A^*(d\mathbf{k}, d\sigma) A(d\mathbf{k}, d\sigma) \rangle \quad (3)$$

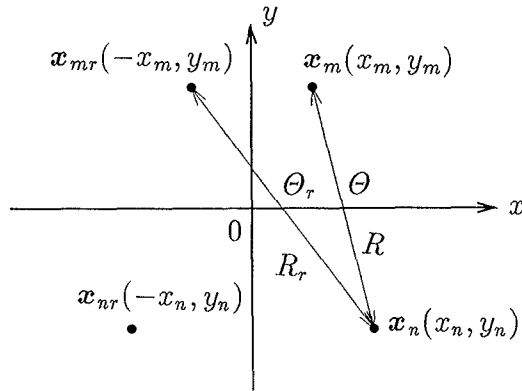


Figure 1: Definitions of variables

where  $\langle \rangle$  represents the ensemble average and  $A^*$  the complex conjugate of  $A$ . Then, the cross-power spectrum,  $\Phi_{mn}(\sigma)$ , can be defined by Eq. (4) (Horikawa, 1988, Isobe and Kondo, 1984):

$$\Phi_{mn}(\sigma) = \int_{\mathbf{k}} S(\mathbf{k}, \sigma) \{ \exp(i\mathbf{k}\mathbf{x}_m) + r \exp(i\mathbf{k}\mathbf{x}_{mr}) \} \times \{ \exp(-i\mathbf{k}\mathbf{x}_n) + r \exp(-i\mathbf{k}\mathbf{x}_{nr}) \} d\mathbf{k} \tag{4}$$

in which the variables are defined in Fig. 1.

In the present study, the directional spectrum,  $S(\mathbf{k}, \sigma)$ , is assumed to be expressed by using the directional spreading function proposed by Mitsuyasu *et al.* (1975). Then,  $S(\mathbf{k}, \sigma)$  is expressed by Eq. (5):

$$S(\mathbf{k}, \sigma) = P(f) \frac{2^{2s-1}}{\pi} \frac{\Gamma^2(s+1)}{\Gamma(2s+1)} \left[ \cos \frac{\theta - \theta_0}{2} \right]^{2s} \tag{5}$$

where  $P(f)$  is the frequency spectrum or the power spectrum,  $s$  the degree of directional concentration,  $\theta_0$  the peak wave direction and  $\Gamma$  the Gamma function.

We rewrite Eq. (4) by using the transformation of variables as follows. The definitions of variables are indicated in Fig. 1 as before.

$$\begin{aligned} \mathbf{k} &= (k \cos \theta, k \sin \theta) \\ \mathbf{x}_m - \mathbf{x}_n &= (R \cos \Theta, R \sin \Theta) & (= \mathbf{X}_1) \\ \mathbf{x}_{mr} - \mathbf{x}_{nr} &= (R \cos(\pi - \Theta), R \sin(\pi - \Theta)) & (= \mathbf{X}_2) \\ \mathbf{x}_{mr} - \mathbf{x}_n &= (R_r \cos \Theta_r, R_r \sin \Theta_r) & (= \mathbf{X}_3) \\ \mathbf{x}_m - \mathbf{x}_{nr} &= (R_r \cos(\pi - \Theta_r), R_r \sin(\pi - \Theta_r)) & (= \mathbf{X}_4) \end{aligned}$$

Table 2: Directional spectrum parameters

$s$	Degree of directional concentration
$\theta_0$	Peak wave direction
$r$	Reflection coefficient
$P(f)$	Frequency or power spectrum
$\varepsilon$	Ratio of the noise component to the power

Substituting Eq. (5) into Eq. (6) and using the above variables, Then we get the expression of the cross-power spectrum,  $\Phi_{mn}(\sigma)$ :

$$\Phi_{mn}(\sigma) = P(f) \frac{2^{2s-1} \Gamma^2(s+1)}{\pi \Gamma(2s+1)} \int_{\mathbf{k}} \left[ \cos \frac{\theta - \theta_0}{2} \right]^{2s} \times \left\{ \exp(i\mathbf{k}\mathbf{X}_1) + r^2 \exp(i\mathbf{k}\mathbf{X}_2) + r \exp(i\mathbf{k}\mathbf{X}_3) + r \exp(i\mathbf{k}\mathbf{X}_4) \right\} d\mathbf{k} \quad (6)$$

To rewrite Eq. (6) in a simpler form, we define a new function  $F_j$  as follows:

$$F_j(k, s, \theta_0, R_j, \Theta_j) = \frac{2^{2s-1} \Gamma^2(s+1)}{\pi \Gamma(2s+1)} \int_{-\pi}^{\pi} \exp [ikR_j \cos(\theta - \Theta_j)] \left[ \cos \frac{\theta - \theta_0}{2} \right]^{2s} d\theta \quad (7)$$

By using the above definition, Eq. (6) can be written as Eq. (8):

$$\Phi_{mn}(\sigma) = \begin{bmatrix} F_1(k, s, \theta_0, R, \Theta) \\ +r^2 F_2(k, s, \theta_0, R, \pi - \Theta) \\ +r F_3(k, s, \theta_0, R_r, \Theta_r) \\ +r F_4(k, s, \theta_0, R_r, \pi - \Theta_r) \end{bmatrix} \times P(f) \quad (8)$$

Here the noise component of the power spectrum is assumed to be  $\varepsilon P(f)$ ,  $\varepsilon$  being the ratio of the noise component to the power. Finally we get the expression of the cross-power spectrum in terms of the five parameters which are summarized in Table 2 and called the directional spectrum parameters in this paper:

$$\Phi_{mn}(\sigma) = \begin{bmatrix} F_1(k, s, \theta_0, R, \Theta) \\ +r^2 F_2(k, s, \theta_0, R, \pi - \Theta) \\ +r F_3(k, s, \theta_0, R_r, \Theta_r) \\ +r F_4(k, s, \theta_0, R_r, \pi - \Theta_r) \end{bmatrix} \times P(f) + \delta_{mn} \varepsilon P(f) \quad (9)$$

The integral on the right-hand side of Eq. (7) can be expressed by using the integral expression of the Bessel function of the first kind (*e.g.* Abramowitz and

Stegun, 1972):

$$F_j = a_0 J_0(kR_j) + 2 \sum_{n=1}^{\infty} \{(i)^n a_n J_n(kR_j) \cos n(\theta_0 - \Theta_j)\} \tag{10}$$

where  $J_n$  is the Bessel function of the first kind and  $a_n$  is defined as Eq. (11):

$$\begin{cases} a_0 = 1 \\ a_n = \left(1 - \frac{1}{s+1}\right) \times \left(1 - \frac{3}{s+2}\right) \times \dots \times \left(1 - \frac{2n-1}{s+n}\right) \end{cases} \tag{11}$$

In the present study, we use Eqs. (10) and (11) to calculate  $F_j$ .

**2.2 Definition of likelihood**

The maximum likelihood method is used to get the most probable values of the directional spectrum parameters. The likelihood,  $L$ , is defined as Isobe (1990):

$$\begin{aligned} L(A^{[j]}; \Phi) &= \{p(A^{[1]}) \times p(A^{[2]}) \times \dots \times p(A^{[J]})\}^{1/J} \\ &= \frac{1}{(2\pi \Delta f)^M |\Phi|} \exp\left(-\sum_{m=1}^M \sum_{n=1}^M \Phi_{mn}^{-1} \hat{\Phi}_{nm}\right) \end{aligned} \tag{12}$$

where  $p(A^{[j]})$  is a joint probability density function of the Fourier coefficients of the time series data,  $\Delta f$  the frequency interval, and  $|\Phi|$  the determinant of the matrix,  $\Phi_{mn}$ . The quantity  $\hat{\Phi}_{nm}$  which is represented by Eq. (13) corresponds to the periodogram with a rectangular filter and can therefore be called the power spectrum ( $n = m$ ) or the cross spectrum ( $n \neq m$ ) in the spectral analysis.

$$\hat{\Phi}_{nm} = \frac{1}{2J\Delta f} \sum_{j=1}^J \overline{A_n^{[j]}} A_m^{[j]} \tag{13}$$

where  $\overline{\phantom{x}}$  denotes the complex conjugate.

**2.3 The most probable values of the parameters**

In this Section, we show the procedure to estimate the directional spectrum parameters including the reflection coefficient by using the likelihood defined above.

The maximum likelihood method implies that the most probable values of  $\lambda_i$  are the solutions of the algebraic equation

$$\frac{\partial L}{\partial \lambda_i} = \sum_{k=1}^M \sum_{l=1}^M \frac{\partial L}{\partial \Phi_{kl}} \frac{\partial \Phi_{kl}}{\partial \lambda_i} = 0 \tag{14}$$

From Eq. (12), Eq. (15) is obtained.

$$\begin{aligned}
 \frac{\partial L}{\partial \Phi_{kl}} &= \frac{\partial}{\partial \Phi_{kl}} \left[ \frac{1}{(2\pi \Delta f)^M |\Phi|} \exp \left( - \sum_{m=1}^M \sum_{n=1}^M \Phi_{mn}^{-1} \hat{\Phi}_{nm} \right) \right] \\
 &= - \frac{1}{(2\pi \Delta f)^M |\Phi|^2} \exp \left( - \sum_{m=1}^M \sum_{n=1}^M \Phi_{mn}^{-1} \hat{\Phi}_{nm} \right) \frac{\partial |\Phi|}{\partial \Phi_{kl}} \\
 &\quad + \frac{1}{(2\pi \Delta f)^M |\Phi|} \exp \left( - \sum_{m=1}^M \sum_{n=1}^M \Phi_{mn}^{-1} \hat{\Phi}_{nm} \right) \\
 &\quad \times \left( - \sum_{m=1}^M \sum_{n=1}^M \frac{\partial \Phi_{mn}^{-1}}{\partial \Phi_{kl}} \hat{\Phi}_{nm} \right) \\
 &= -L \times \left( \frac{1}{|\Phi|} \frac{\partial |\Phi|}{\partial \Phi_{kl}} \right) + L \times \left( - \sum_{m=1}^M \sum_{n=1}^M \frac{\partial \Phi_{mn}^{-1}}{\partial \Phi_{kl}} \hat{\Phi}_{nm} \right) \tag{15}
 \end{aligned}$$

Also, the following relations are obtained from the theorem of the matrices.

$$\frac{\partial |\Phi|}{\partial \Phi_{kl}} = |\Phi| \Phi_{lk}^{-1} \tag{16}$$

$$\frac{\partial \Phi_{mn}^{-1}}{\partial \Phi_{kl}} = -\Phi_{ln}^{-1} \Phi_{mk}^{-1} \tag{17}$$

By using Eqs. (16) and (17), Eq. (15) is rewritten as follows:

$$\frac{\partial L}{\partial \Phi_{kl}} = L \times \left\{ -\Phi_{lk}^{-1} + \sum_{m=1}^M \sum_{n=1}^M \Phi_{ln}^{-1} \hat{\Phi}_{nm} \Phi_{mk}^{-1} \right\} \tag{18}$$

Substituting Eq. (18) into Eq. (14) and considering that  $L \neq 0$ , we obtain:

$$\sum_{k=1}^M \sum_{l=1}^M \left\{ -\Phi_{lk}^{-1} + \sum_{m=1}^M \sum_{n=1}^M \Phi_{ln}^{-1} \hat{\Phi}_{nm} \Phi_{mk}^{-1} \right\} \frac{\partial \Phi_{kl}}{\partial \lambda_i} = 0 \tag{19}$$

The directional spectrum parameters,  $\lambda_i$ , which satisfy Eq. (19) for all  $i$  ( $i = 1 \sim 5$ ) are the most probable values. Then the directional spectrum parameters, including the reflection coefficient, are estimated.

The solutions,  $\lambda_i$ , of Eq. (19) are obtained numerically by using the Newton-Raphson method. The left-hand side of Eq. (19) is first defined as a function of the directional spectrum parameters:

$$f_i(\lambda_{i'}) = \sum_{k=1}^M \sum_{l=1}^M \left\{ -\Phi_{lk}^{-1} + \sum_{m=1}^M \sum_{n=1}^M \Phi_{ln}^{-1} \hat{\Phi}_{nm} \Phi_{mk}^{-1} \right\} \frac{\partial \Phi_{kl}}{\partial \lambda_i} \tag{20}$$

In the Newton-Raphson method, the value of  $\lambda_i^{(j+1)}$  at the  $(j+1)$ -th iteration of the calculation is expressed in terms of the previous values,  $\lambda_i^{(j)}$ , in the following equation:

$$\lambda_i^{(j+1)} = \lambda_i^{(j)} - \left[ \sum_{i'=1}^I \left[ \frac{\partial f_i}{\partial \lambda_{i'}} \right]^{-1} f_{i'} \right]_{\lambda_i = \lambda_i^{(j)}} \tag{21}$$

Table 3: Values of the directional spectrum parameters

$s$	14.0
$\theta_0$	3.054 radian
$r$	0.4
$P(f)$	$0.1 \text{ m}^3/\text{Hz}$
$\varepsilon$	0.1

where  $\partial f_i/\partial \lambda_{i'}$  is expressed by Eq. (22):

$$\begin{aligned} \frac{\partial f_i}{\partial \lambda_{i'}} &= \sum_{k=1}^M \sum_{l=1}^M \left\{ -\Phi_{lk}^{-1} + \sum_{m=1}^M \sum_{n=1}^M \Phi_{ln}^{-1} \hat{\Phi}_{nm} \Phi_{mk}^{-1} \right\} \frac{\partial^2 \Phi_{kl}}{\partial \lambda_{i'} \partial \lambda_i} \\ &- \sum_{k'=1}^M \sum_{l'=1}^M \sum_{k=1}^M \sum_{l=1}^M \frac{\partial \Phi_{k'l'}}{\partial \lambda_{i'}} \frac{\partial \Phi_{kl}}{\partial \lambda_i} \\ &\times \left[ -\Phi_{l'k}^{-1} \Phi_{lk'}^{-1} + \left\{ \begin{array}{l} \Phi_{lk'}^{-1} \sum_{m=1}^M \sum_{n=1}^M \Phi_{l'n}^{-1} \hat{\Phi}_{nm} \Phi_{mk}^{-1} \\ + \Phi_{l'k}^{-1} \sum_{m=1}^M \sum_{n=1}^M \Phi_{ln}^{-1} \hat{\Phi}_{nm} \Phi_{mk'}^{-1} \end{array} \right\} \right] \end{aligned} \tag{22}$$

### 3 Application

#### 3.1 Application to simulated data

To verify the validity of the present method, we first created a set of  $\Phi_{mn}(\sigma)$  by Eqs. (9) and (10) for directional spectrum parameters given in Table 3. Then, the directional spectrum parameters,  $\lambda_i$ , were estimated by the present method.

However, since a converged solution of Eq. (19) could not be obtained for any set of initial values used, solutions were determined for various fixed values of  $r$  and  $\varepsilon$ .

Table 4 shows the results of the computations. It is seen that the likelihood,  $L$ , is maximum when  $\varepsilon = 0.1$ ,  $r = 0.4$ ,  $s = 13.3$  and  $\theta_0 = 3.1$ , which agrees closely with the given values. Hence, the directional spectrum parameters were estimated adequately by the present method.

#### 3.2 Application to field data

From November 7 to December 2, 1990, a field experiment was conducted at Oarai port in Ibaraki prefecture, Japan (Fig. 2). Four measuring points are arranged normal to the offshore breakwater as sketched in Fig. 3. An ultrasonic-



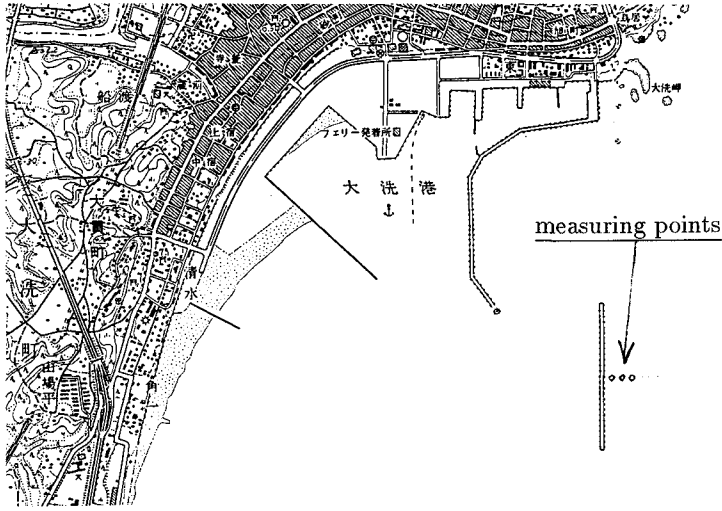


Figure 2: Map of Oarai port

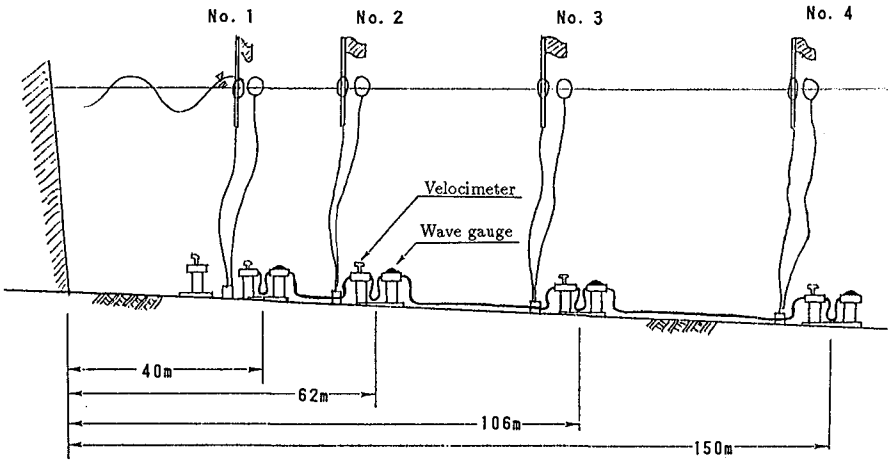


Figure 3: Sketch of measuring points

Table 4: Results of the estimation

$\varepsilon$	$r$	$s$	$\theta_0$	$\ln L$	$\varepsilon$	$r$	$s$	$\theta_0$	$\ln L$
0.00	0.2	4.570	3.141	19.944	0.10	0.2	12.378	3.139	20.660
0.00	0.3	5.694	3.139	20.504	0.10	0.3	12.753	3.139	20.824
0.00	0.4	6.476	3.139	20.706	0.10	0.4	13.311	3.140	20.862
0.00	0.5	7.088	3.139	20.722	0.10	0.5	13.875	3.140	20.818
0.00	0.6	7.601	3.139	20.651	0.10	0.6	14.367	3.140	20.728
0.05	0.2	8.079	3.141	20.387	0.15	0.2	15.504	3.140	20.708
0.05	0.3	8.587	3.142	20.702	0.15	0.3	15.670	3.140	20.813
0.05	0.4	9.130	3.141	20.798	0.15	0.4	16.135	3.140	20.826
0.05	0.5	9.648	3.140	20.775	0.15	0.5	16.654	3.140	20.776
0.05	0.6	10.109	3.140	20.690	0.15	0.6	17.127	3.140	20.687

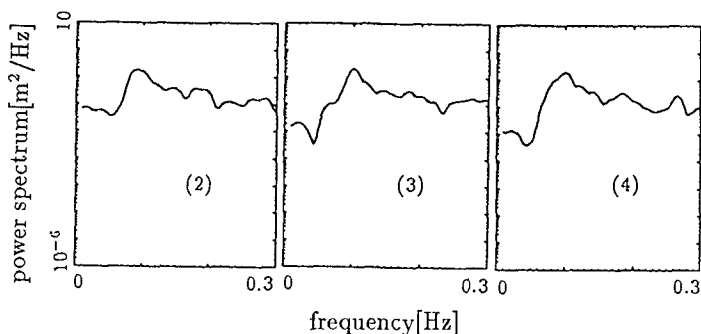


Figure 4: Power spectra

type wave gauge was installed on the sea bed of each measuring point. The four wave gauges were synchronized by a cable.

The sampling interval is 0.5 s and 2,046 time series data (about 17 min) were recorded every two hours. Because the wave gauge at the measuring point No. 1 did not work, the time series data at the three measuring points No. 2 to 4 were obtained and used.

The results of the spectral analysis are shown in Figs. 4 and 5. Time series data used were obtained at 14:00 on November 8. Figure 4 shows the power spectra at the measuring points, and Fig. 5 the cross spectra, the coherence squared and phase lag between the measuring points. In addition, the wave statistics at each measuring point are shown in Table 5.

Figures 4 and 5 indicate that both the power and cross spectra are maximum

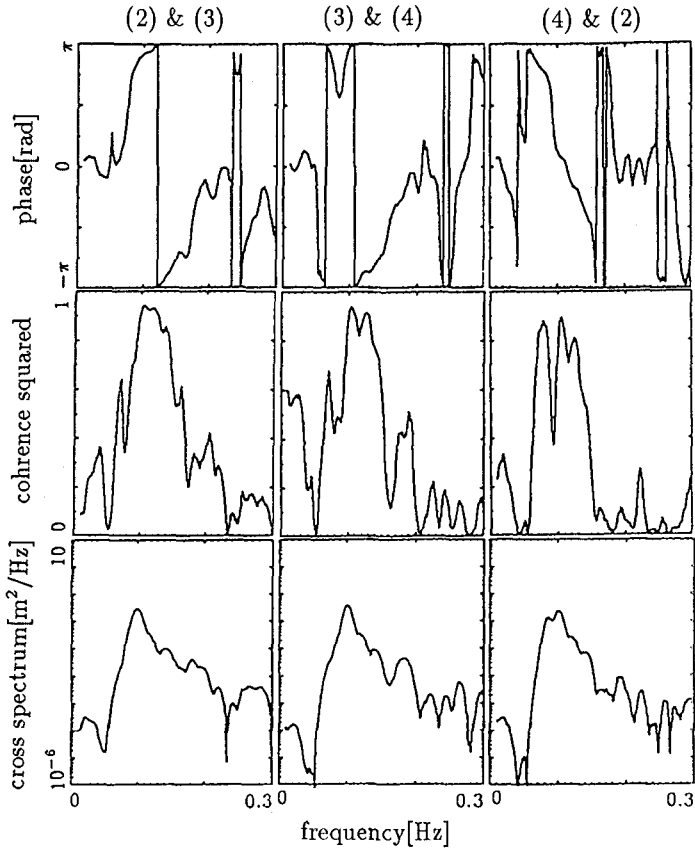


Figure 5: Cross spectra, coherence squared, phase

at the frequency of 0.1 Hz. Therefore, we calculated the directional spectrum parameters at this frequency.

The most probable values of the directional spectrum parameters as well as the likelihood are shown in Table 6. The parameters are estimated as  $\varepsilon \simeq 0.05$ ,  $r \simeq 0.4$ ,  $s \simeq 36$ ,  $\theta_0 \simeq 3.14$  rad. Since concrete blocks are installed in front of the breakwater, the reflection coefficient obtained is considered to be a reasonable value.

Table 5: Wave statistics

Measuring point No.	$h$ m	$H_{\max}$ m	$T_{\max}$ s	$H_{1/3}$ m	$T_{1/3}$ s	$H_{\text{mean}}$ m	$T_{\text{mean}}$ s
( 2 )	12.44	1.10	9.00	0.62	8.05	0.38	5.20
( 3 )	12.66	0.95	8.50	0.58	7.35	0.36	4.93
( 4 )	12.82	1.13	7.00	0.56	6.69	0.35	4.75
( 5 )	13.10	0.91	9.50	0.54	6.96	0.35	4.87

$h$  : water depth;

$H_{\max}$  : maximum wave height;  $T_{\max}$  : maximum wave period;

$H_{1/3}$  : significant wave height;  $T_{1/3}$  : significant wave period;

$H_{\text{mean}}$  : mean wave height;  $T_{\text{mean}}$  : mean wave period.

Table 6: Results of estimation

$\varepsilon$	$r$	$s$	$\theta_0$	$\ln L$	$\varepsilon$	$r$	$s$	$\theta_0$	$\ln L$
0.00	0.2	8.360	3.141	23.515	0.10	0.2	109.234	3.141	24.535
0.00	0.3	10.993	3.141	24.297	0.10	0.3	93.392	3.141	24.595
0.00	0.4	12.811	3.141	24.607	0.10	0.4	62.488	3.141	24.596
0.00	0.5	14.028	3.141	24.664	0.10	0.5	56.304	3.141	24.574
0.00	0.6	14.862	3.141	24.594	0.10	0.6	54.671	3.141	24.456
0.05	0.2	33.158	3.141	24.701	0.15	0.2	109.850	3.141	24.150
0.05	0.3	34.431	3.144	24.973	0.15	0.3	114.443	3.141	24.179
0.05	0.4	36.318	3.141	25.079	0.15	0.4	88.447	3.141	24.156
0.05	0.5	37.830	3.141	25.068	0.15	0.5	81.737	3.141	24.099
0.05	0.6	38.813	3.141	24.979	0.15	0.6	77.092	3.141	24.013

## 4 Conclusion

Based on the parametric expression of the directional spectrum, a method is proposed to estimate the directional spectrum parameters which include the reflection coefficient.

The validity of the method was confirmed by applying it to simulated data. The method was also applied to the data obtained by a field measurement at Oarai port. The result of estimation is considered to be reasonable.

## Acknowledgement

This study was financially supported by the Grant-in-Aid for Scientific Research, Ministry of Education, Science and Culture, Japan.

## Reference

- 1) Abramowitz, M. and I. A. Stegun, (ed.) (1972): Handbook of Mathematical Functions with Formulas, Graphs, and Mathematical Tables, Dover Pub. Inc., Chap. 9, p.360.
- 2) Capon, J. (1969): High-resolution frequency-wavenumber spectrum analysis, Proc. IEEE, Vol. 57, No. 8, pp. 1408-1418.
- 3) Horikawa, K. (ed.) (1988): Nearshore Dynamics and Coastal Processes, Univ. Tokyo Press, Part. V, pp. 407-411.
- 4) Isobe, M. and K. Kondo (1984): Method for estimating directional wave spectrum in incident and reflected wave field, Proc. 19th Int. Conf. on Coastal Eng., pp. 467-483.
- 5) Isobe, M. (1990): Estimation of directional spectrum expressed in standard form, Proc. 22nd Int. Conf. on Coastal Eng., pp. 647-660.
- 6) Mitsuyasu, H., F. Tasai, T. Suhara, S. Mizuno, M. Ohkusu, T. Honda and K. Rikiishi (1975): Observations of directional spectrum of ocean waves using a cloverleaf buoy, J. of Physical Oceanography, Vol. 5, pp. 750-760.

## CHAPTER 58

### Estimating Incident and Reflected Wave Fields Using an Arbitrary Number of Wave Gauges

J.A. Zelt<sup>†</sup> A.M. ASCE and James E. Skjelbreia<sup>†</sup> A.M. ASCE

#### 1 Abstract

A method based on linear wave theory is presented to decompose one-dimensional wave fields into left and right-travelling components using an arbitrary number of wave gauges. Results are presented to show that an increased accuracy is possible if more than three wave gauges are used. The technique uses a least squares scheme with variable weights. Results will also be presented that indicate a further improvement in accuracy is possible by an appropriate choice of the weighting coefficients.

#### 2 Decomposition Theory

The decomposition of general one-dimensional wave fields into component waves travelling in opposite directions is of fundamental importance in many experimental studies. Breakwater evaluation involves estimating reflection coefficients as a function of wave frequency, and the efficiency of wave-energy extraction devices can be quantified similarly. Reflection coefficients of shorelines are also important quantities since many beach processes are driven by the energy extracted from incident waves through wave breaking. For some studies it is sufficient to obtain the spectra of the incident and reflected waves, but the complete space/time description of these waves can also be important, especially in resonance studies.

Suppose that a one-dimensional wave field is observed by recording the surface elevation  $\eta_p(t)$  at a series of locations  $\{x_p\}$ ,  $p = 1, 2, \dots, P$ , as shown in Fig. 1. Using standard Fourier analysis techniques, the elevation can be expressed as

$$\eta_p(t) = \sum_{j=-N/2}^{N/2} A_{j,p} e^{i\omega_j t}, \quad (1)$$

where  $\omega_j = 2\pi j/T$ ,  $T$  is the length of the time series, and  $N$  is large enough to resolve adequately the frequencies of interest. The time  $t$  will be discrete for a

---

<sup>†</sup> Wave Technologies, PO Box 6043, 7003 Trondheim, Norway

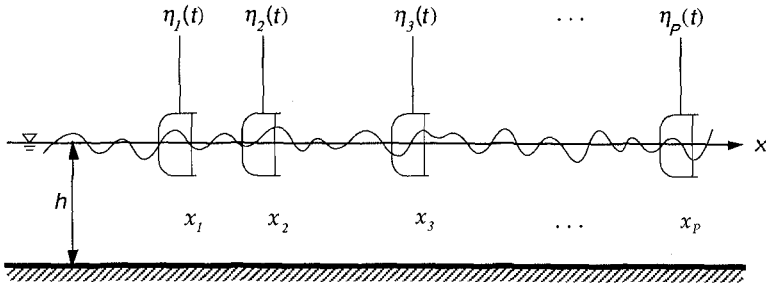


Figure 1. Measuring incident and reflected waves with  $P$  wave gauges.

sampled signal ( $t \rightarrow m\Delta t$ , for  $m = 0, 1, \dots, N - 1$ , with  $\Delta t = T/N$ ), but this will not be explicitly indicated here to simplify the notation.

Under the assumption that the waves are one-dimensional, dissipation is negligible, and that linear wave theory is valid, the wave field in Fig. 1 can be approximated by a Fourier sum of left and right travelling waves:

$$\eta(x, t) = \sum_{j=-N/2}^{N/2} a_{Lj} e^{i(k_j x + \omega_j t)} + a_{Rj} e^{i(-k_j x + \omega_j t)}, \quad (2)$$

where  $k_j = 2\pi/\lambda_j$ , and  $k_j$  is related to  $\omega_j$  through the linear dispersion relation:

$$\omega_j^2 = gk_j \tanh k_j h. \quad (3)$$

The still water depth is  $h$  and  $g$  is the acceleration of gravity. Evaluating  $\eta(x, t)$  at the location of wave gauge  $p$  yields

$$\eta(x_p, t) = \sum_{j=-N/2}^{N/2} \{a_{Lj} e^{i\phi_{j,p}} + a_{Rj} e^{-i\phi_{j,p}}\} e^{i\omega_j t}, \quad (4)$$

where  $\phi_{j,p} \equiv k_j x_p$ . The ultimate goal is to estimate the  $\{a_{Lj}\}$  and  $\{a_{Rj}\}$  as accurately as possible from the wave records  $\{\eta_p(t)\}$ . Equating the coefficients in Eqs. (1) and (4) yields the following equations:

$$A_{j,p} = a_{Lj} e^{i\phi_{j,p}} + a_{Rj} e^{-i\phi_{j,p}} \quad p = 1, 2, \dots, P \quad (5)$$

for each Fourier component  $j$ . If there are only two wave gauges, Eq. (5) can be solved exactly for  $a_{Lj}$  and  $a_{Rj}$  (Goda & Suzuki 1976). However, for  $P > 2$ , Eq. (5) is over-determined, and  $a_{Lj}$  and  $a_{Rj}$  must be estimated by an approximate technique. Mansard & Funke (1980, 1987) treated the case  $P = 3$  using a least squares approach with uniform weighting. Here, a weighted least squares approach will be described that is valid for *arbitrary*  $P$ . Instead of forcing strict equality in Eq. (5), the value of an appropriate 'merit' function will be minimized so that Eq. (5) holds *approximately* for each wave gauge  $p$ . Let

$$\epsilon_{j,p} = a_{Lj} e^{i\phi_{j,p}} + a_{Rj} e^{-i\phi_{j,p}} - A_{j,p}. \quad (6)$$

For a given choice of  $a_{Lj}$  and  $a_{Rj}$ ,  $\epsilon_{j,p}$  represents the error in matching the  $j^{\text{th}}$  Fourier coefficient  $A_{j,p}$  at wave gauge  $p$ . The merit function is chosen to be a weighted sum of the squares of the errors for each wave gauge:

$$E_j \equiv \sum_{p=1}^P W_{j,p} \epsilon_{j,p} \epsilon_{j,p}^*, \quad (7)$$

where  $W_{j,p} > 0$  is the weighting coefficient for wave gauge  $p$  at frequency  $\omega_j$ , and  $( )^*$  represents the complex conjugate of the enclosed quantity. At a given frequency specified by  $j$ , the reliability of the estimates of  $a_{Lj}$  and  $a_{Rj}$  depends on several factors, including the spacing between the wave gauges. The motivation of introducing nonuniform weighting is to make use of this information so that the errors associated with wave gauges that provide reliable estimates are weighted more than the errors associated with wave gauges that do not provide useful information for estimating  $a_{Lj}$  and  $a_{Rj}$ . The criteria for choosing the weights  $\{W_{j,p}\}$  will be discussed in §3. The minimum of Eq. (7) occurs at the point where  $E_j$  is stationary with respect to the real and imaginary parts of  $a_{Lj}$  and  $a_{Rj}$ . At this point the following relations hold

$$\begin{aligned} \sum_{p=1}^P W_{j,p} \epsilon_{j,p} e^{-i\phi_{j,p}} &= 0 \\ \sum_{p=1}^P W_{j,p} \epsilon_{j,p} e^{i\phi_{j,p}} &= 0. \end{aligned} \quad (8)$$

These are two complex equations for the two complex amplitudes  $a_{Lj}$  and  $a_{Rj}$ .



Substituting Eq. (6) into Eq. (8) yields the two equations

$$\begin{aligned} a_{Lj} S_j + a_{Rj} \sum_{p=1}^P W_{j,p} e^{-2i\phi_{j,p}} &= \sum_{p=1}^P W_{j,p} A_{j,p} e^{-i\phi_{j,p}} \\ a_{Lj} \sum_{p=1}^P W_{j,p} e^{2i\phi_{j,p}} + a_{Rj} S_j &= \sum_{p=1}^P W_{j,p} A_{j,p} e^{i\phi_{j,p}}, \end{aligned} \quad (9)$$

where  $S_j \equiv \sum_{p=1}^P W_{j,p}$ . Rather than work with the absolute phases  $\phi_{j,p}$ , it is more useful to consider phase *differences* between wave gauges. Let

$$\Delta\phi_{j,p} \equiv \phi_{j,p} - \phi_{j,1} = k_j(x_p - x_1) \quad (10)$$

denote the phase difference between wave gauges 1 and  $p$  for frequency  $\omega_j$ . Then the solution of Eq. (9) can be expressed as

$$a_{Lj} = \left[ S_j \sum_{p=1}^P W_{j,p} A_{j,p} e^{-i\Delta\phi_{j,p}} - \sum_{p=1}^P W_{j,p} A_{j,p} e^{i\Delta\phi_{j,p}} \sum_{q=1}^P W_{j,q} e^{-2i\Delta\phi_{j,q}} \right] \frac{e^{-i\phi_{j,1}}}{D} \quad (11a)$$

$$a_{Rj} = \left[ S_j \sum_{p=1}^P W_{j,p} A_{j,p} e^{i\Delta\phi_{j,p}} - \sum_{p=1}^P W_{j,p} A_{j,p} e^{-i\Delta\phi_{j,p}} \sum_{q=1}^P W_{j,q} e^{2i\Delta\phi_{j,q}} \right] \frac{e^{i\phi_{j,1}}}{D} \quad (11b)$$

where

$$D = S_j^2 - \sum_{p=1}^P W_{j,p} e^{2i\Delta\phi_{j,p}} \sum_{q=1}^P W_{j,q} e^{-2i\Delta\phi_{j,q}} \quad (12a)$$

The denominator  $D$  is a real quantity and can be simplified to

$$D = S_j^2 - \left( \sum_{p=1}^P W_{j,p} \cos 2\Delta\phi_{j,p} \right)^2 - \left( \sum_{p=1}^P W_{j,p} \sin 2\Delta\phi_{j,p} \right)^2 \quad (12b)$$

$$= 4 \sum_{p=1}^P \sum_{q < p} W_{j,p} W_{j,q} \sin^2 \Delta\phi_{j,pq} \quad (12c)$$

where

$$\Delta\phi_{j,pq} \equiv \Delta\phi_{j,p} - \Delta\phi_{j,q} = \phi_{j,p} - \phi_{j,q} = k_j(x_p - x_q) \quad (13)$$

is the phase difference between wave gauges  $p$  and  $q$  at frequency  $\omega_j$ . Equation (12b) is the most efficient form to compute  $D$  since it requires the fewest operations to evaluate; however, Eq. (12c) is more useful for showing the behaviour of the denominator. Since the weighting coefficients  $\{W_{j,p}\}$  are positive,

it is clear that the denominator can be zero at frequency  $\omega_j$  only if the wave gauges are placed such that  $\sin \Delta \phi_{j,pq} \equiv 0$  for all  $p$  and  $q$ . Clearly this is a condition to be avoided if possible, and this will be discussed further in §3.

Further manipulation of the numerators in Eq. (11) leads to the following formulae for  $a_{Lj}$  and  $a_{Rj}$

$$a_{Lj} = \sum_{p=1}^P C_{j,p}^* A_{j,p} \quad (14a)$$

$$a_{Rj} = \sum_{p=1}^P C_{j,p} A_{j,p} \quad (14b)$$

where

$$C_{j,p} = 2iW_{j,p} \frac{e^{i\phi_{j,1}}}{D} \sum_{q=1}^P W_{j,q} \sin \Delta \phi_{j,pq} e^{i\Delta \phi_{j,q}} \quad (15)$$

This form emphasizes that  $a_{Lj}$  and  $a_{Rj}$  are simply linear combinations of the  $\{A_{j,p}\}$ . For  $P = 2$  the results of Goda & Suzuki (1976) are reproduced, and for  $P = 3$  the decomposition formulae of Mansard & Funke (1980, 1987) are obtained.

### 3 Error analysis

The sensitivity of the decomposition formulae Eq. (11) or (14) to errors in measuring the Fourier coefficients  $\{A_{j,p}\}$  at a given frequency  $\omega_j$  depends on the choice of the weighting coefficients  $\{W_{j,p}\}$  as well as the spacing of the wave gauges relative to the wave length associated with  $\omega_j$ . Consequently, the weights and the wave gauge locations should be chosen appropriately to maximize the reliability of the decomposition estimates. To illustrate this, suppose that the elevation records obtained from the wave gauges can be expressed as the sum of two one-dimensional linear waves travelling in opposite directions plus a residual or error signal  $\mathcal{E}_p(t)$ :

$$\eta_p(t) = \sum_{j=-N/2}^{N/2} \left\{ A_{Lj} e^{i(k_j x_p + \omega_j t)} + A_{Rj} e^{i(-k_j x_p + \omega_j t)} \right\} + \mathcal{E}_p(t). \quad (16)$$

The residual signal  $\mathcal{E}_p(t)$  accounts for:

- 1) noise/nonlinearities in the wave gauges and data acquisition hardware.

- 2) nonlinear hydrodynamic effects (e.g. deviations from the linear dispersion relation).
- 3) two-dimensional wave motion (such as cross modes in a wave channel).
- 4) viscous effects.

With

$$\mathcal{E}_p(t) = \sum_{j=-N/2}^{N/2} \varepsilon_{j,p} e^{i\omega_j t}, \quad (17)$$

Eq. (16) can be expressed as

$$\eta_p(t) = \sum_{j=-N/2}^{N/2} \left\{ A_{Lj} e^{i\phi_{j,p}} + A_{Rj} e^{-i\phi_{j,p}} + \varepsilon_{j,p} \right\} e^{i\omega_j t}. \quad (18)$$

This is equivalent to Eq. (1) with  $A_{j,p} = A_{Lj} e^{i\phi_{j,p}} + A_{Rj} e^{-i\phi_{j,p}} + \varepsilon_{j,p}$ . Substituting this expression for  $A_{j,p}$  into the decomposition formulae Eq. (14) yields following estimates of the Fourier coefficients of the left and right travelling waves

$$a_{Lj} = A_{Lj} + \sum_{p=1}^P C_{j,p}^* \varepsilon_{j,p} \quad (19a)$$

$$a_{Rj} = A_{Rj} + \sum_{p=1}^P C_{j,p} \varepsilon_{j,p}. \quad (19b)$$

The "exact" coefficients are obtained if the residual signal is zero; otherwise, the error  $\varepsilon_{j,p}$  at wave gauge  $p$  is amplified by the coefficient  $C_{j,p}$ . The amplification of errors associated with wave gauge  $p$  can be represented by

$$\left| \frac{\partial a_{Lj}}{\partial \varepsilon_{j,p}} \right| = \left| \frac{\partial a_{Rj}}{\partial \varepsilon_{j,p}} \right| = |C_{j,p}| = \frac{2W_{j,p}}{D} \left| \sum_{q=1}^P W_{j,q} \sin \Delta\phi_{j,pq} e^{i\Delta\phi_{j,q}} \right|. \quad (20)$$

Since the residual signal will not, in general, be perfectly correlated between different wave gauges, large errors associated with different gauges will not cancel. If the residuals  $\varepsilon_{j,p}$  are uncorrelated between wave gauges, a measure of the reliability of the decomposition as a function of frequency can be estimated by summing the terms in Eq. (20) over all wave gauges. The worst case occurs when  $D = 0$ ; for  $P = 2$  (Goda & Suzuki 1976) this occurs for  $\Delta\phi_{j,12} = n\pi$ , i.e., for  $|x_2 - x_1| = n\lambda_j/2$  for any integer  $n$ . For arbitrary  $P$  this occurs if  $\sin \Delta\phi_{j,pq} = 0$  for all  $p$  and  $q$ , i.e., if  $2|x_p - x_q|/\lambda_j$  is an integer for each combination of  $p$  and

$q$ . Care should be taken when choosing the wave gauge positions to ensure that this criterion is not approached near frequencies of interest.

To choose the weighting coefficients  $\{W_{j,p}\}$  information must be available about the relative magnitudes of the residuals  $\varepsilon_{j,p}$ . If these error terms are the same for each wave gauge (at a particular frequency  $\omega_j$ ), then uniform weighting is appropriate. However, if this residual signal varies from gauge to gauge, variable weighting is appropriate. This may be the case if the primary source of the residual signal is the deviation from the linear dispersion relation due to finite amplitude effects. In this case it may be better to concentrate the weighting near one wave gauge (say gauge number 1) and reduce the weighting for distant gauges where the phase deviates from the linear prediction  $k_j(x_p - x_1)$ . This information might be obtainable from a cross-spectral analysis between the wave gauge elevation records. It might also be possible to make use of the sensitivity analysis in this section to help choose the weights. Other techniques for choosing the weights will depend on the particular sources of the errors and their statistical properties.

Preliminary results have been obtained by using an *ad hoc* scheme based on heuristic reasoning. For each frequency  $\omega_j$  being treated, a "goodness" function  $G(\Delta\phi_{j,pq})$  is defined that quantifies the desirability of the phase difference associated with the spacing between gauges  $p$  and  $q$ . Multiples of one-half the wave length are undesirable, and a large spacing relative to the wavelength is also undesirable. A function that reflects these characteristics is:

$$G(\Delta\phi_{j,pq}) = \frac{\sin^2 \Delta\phi_{j,pq}}{1 + (\Delta\phi_{j,pq}/\pi)^2}. \quad (21)$$

A large value of  $G$  indicates a better wave gauge spacing for frequency  $\omega_j$  than a smaller value of  $G$ . The weighting coefficient  $W_{j,p}$  for wave gauge  $p$  can then simply (and somewhat arbitrarily) be defined as

$$W_{j,p} = \sum_{q=1}^P G(\Delta\phi_{j,pq}). \quad (22)$$

## 4 Results

To illustrate the use of the decomposition theory presented, a simulated wave field in 2 m water depth was created consisting of 4096 points per wave gauge record with a 0.05 s time step. A Pierson-Moskowitz type spectrum was chosen with a spectral peak at 0.47 Hz (corresponding to a wavelength of 6.64 m in 2 m of water). The RMS height of the right travelling wave is 0.5 m, and the Fourier

components of the left travelling wave are exactly 10 % of the Fourier components of the right travelling wave, although with random phase shifts applied. Hence, the RMS height of the left travelling wave is 0.05 m, and the amplitude reflection coefficient is 0.1 for all frequencies. In addition, a 0.01 m RMS uncorrelated random noise signal was added on top of these two waves to simulate a wide variety of errors, noise, and other effects that cannot be simulated directly.

Eight wave gauge records were simulated at the locations  $x = 0, 0.016, 0.052, 0.130, 0.301, 0.679, 1.551$  and  $3.341$  m. These locations were chosen so that the minimum and maximum wave gauge spacings could resolve the minimum and maximum energy containing wavelengths of interest in the wave spectrum. A simple geometric telescoping factor was used to locate the intermediate gauges.

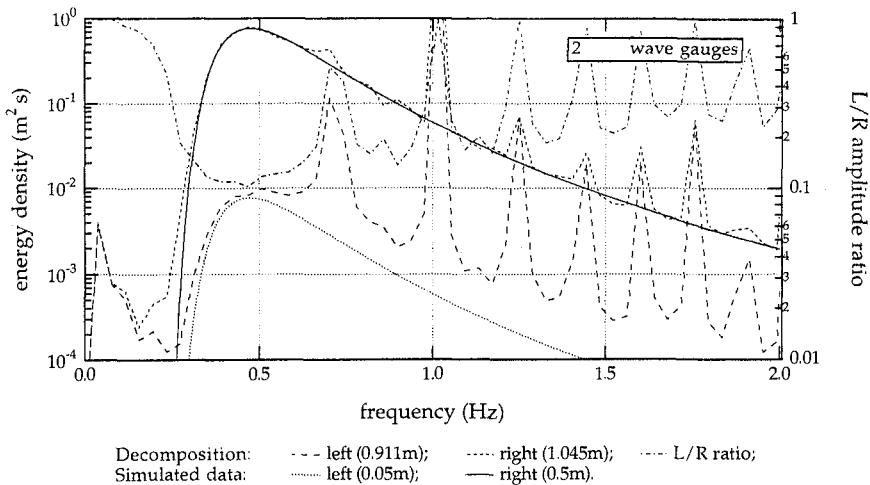


Figure 2. Energy density spectra and left/right amplitude ratios (RMS amplitudes in parentheses).

The energy spectra resulting from using only 2 wave gauges (located at  $x = 0$  m and  $x = 1.511$  m) are presented in Fig. 2. The data was partitioned into 15 segments each with 512 points with a 50% overlap. A Welch window was applied to each segment. The spectra of both the left and the right travelling simulated waves are compared with the estimated spectra obtained from the decomposition technique described here. The left/right amplitude ratio is also shown. As discussed above, it *should* be 0.1, but instead it deviates considerably from this value except near the peak of the spectrum since the wave gauge spacing was chosen to optimize the accuracy in this region. Uniform weights were used ( $W_{j,p} = 1$ ).

The results for 3 wave gauges (located at  $x = 0, 0.679$  and  $1.511$  m) and

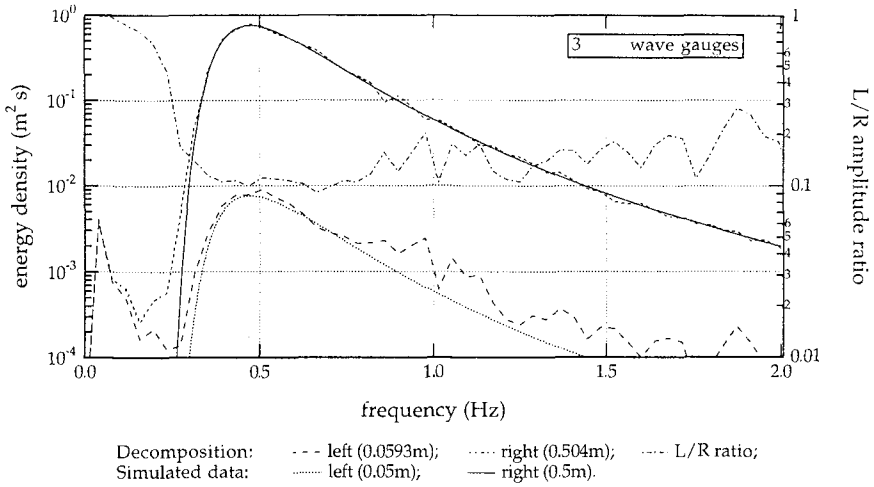


Figure 3. Energy density spectra and left/right amplitude ratios (RMS amplitudes in parentheses).

uniform weights are presented in Fig. 3. These results are considerably better than for only 2 wave gauges since they are not susceptible to the singularity that the 2-wave gauge arrangement is.

The results for all 8 wave gauges and uniform weights are presented in Fig. 4. These results are even better than for 3 wave gauges, although the improvement is perhaps not striking as the difference between the 2 wave gauge and the 3 wave gauge case.

However, in Fig. 5 the results for using 8 wave gauges and the *variable* weight scheme of § 3 are presented. A marked improvement is seen, with the left/right amplitude ratio very flat near 0.1 as it should be. It should be mentioned that the variable weight scheme described in § 3 yields exactly the same results for 2 wave gauges as for the uniform weight case. For 3 wave gauges, only a very slight improvement is obtained by using variable weighting coefficients, and the results do not differ appreciably from those displayed in Fig. 3.

The results in the time domain of the decomposition of with 8 wave gauges and variable weights are presented in Fig. 6. Here, only a small segment of the time record is displayed, but the relative amplitudes of the left and right waves as well as the noise signal can be seen. It should be noted here that the main source of the inaccuracy of the decomposition is due to the presence of the noise added to the left and right simulated waves. However, this noise signal does not cause significantly degrade the decomposition.

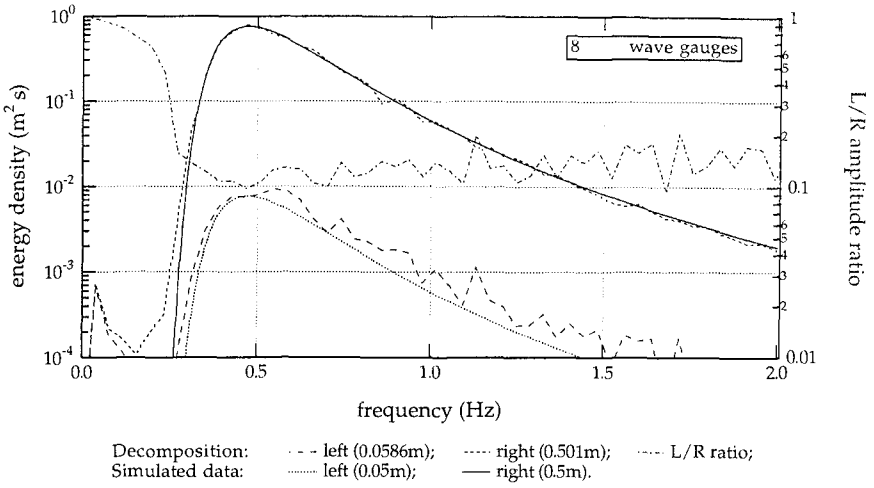


Figure 4. Energy density spectra and left/right amplitude ratios (RMS amplitudes in parentheses).

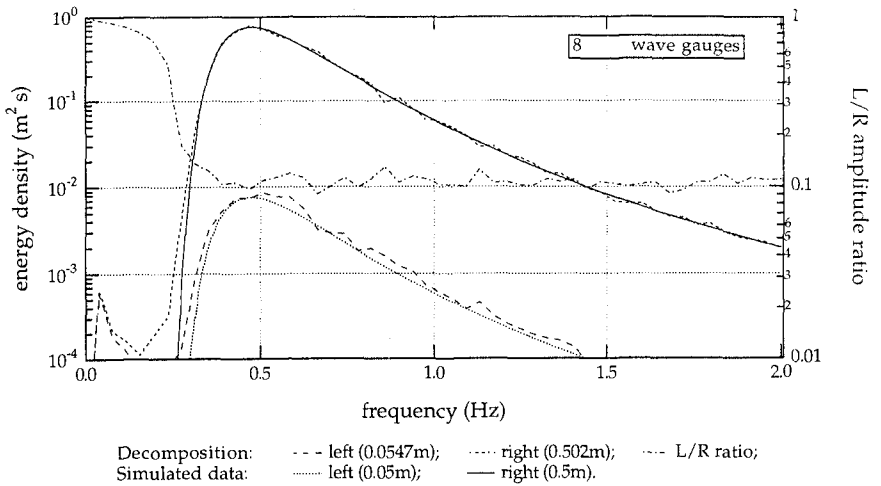


Figure 5. Energy density spectra and left/right amplitude ratios (RMS amplitudes in parentheses).

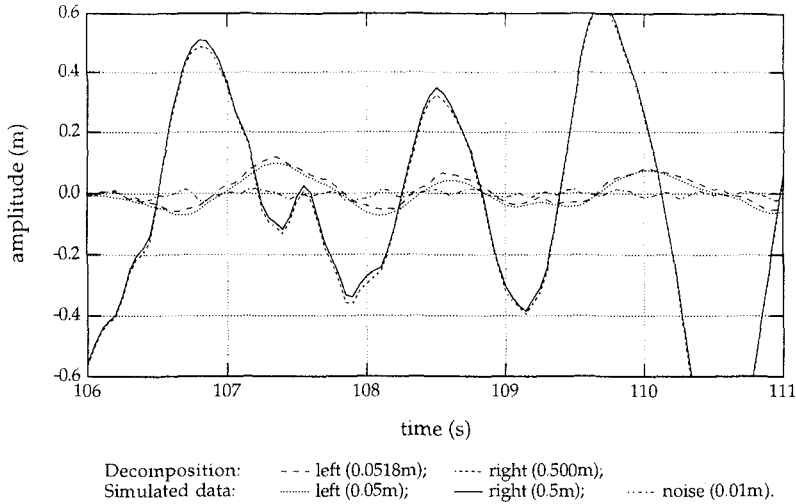


Figure 6. Left and right travelling waves (RMS amplitudes in parentheses).

## 5 Conclusions

A method based on linear wave theory has been presented to decompose one-dimensional wave fields into left and right travelling components using using an arbitrary number of wave gauges. Results were presented for simulated wave gauge data to show that an increased accuracy is possible if more than three wave gauges are used, especially for broad band wave spectra. Results were also presented to indicate that a further improvement in accuracy is possible by an appropriate choice of the least squares weighting coefficients.

*Acknowledgements.* The authors greatly appreciate the support of NTNF, Statoil, Amoco, Conoco, Exxon and Mobil.



## REFERENCES

- Goda, Y. & Suzuki, Y. 1976 Estimation of incident and reflected waves in random wave experiments. *Proc. 15th Conf. Coastal Engng.*, 828–845.
- Mansard, E.P.D. & Funk, E.R. 1980 The measurement of incident and reflected spectra using a least squares method. *Proc. 17th Conf. Coastal Engng.*, 154–172.
- Mansard, E.P.D. & Funk, E.R. 1987 *On the reflection analysis of irregular waves*. Tech. Rep. TR-HY-017, NRCC No. 27522, Nat. Res. Council of Canada. 38p.

## LIST OF SYMBOLS

$a_{Lj}$	estimate of the $j^{\text{th}}$ Fourier coefficient of the left travelling wave.
$a_{Rj}$	estimate of the $j^{\text{th}}$ Fourier coefficient of the right travelling wave.
$A_{Lj}$	hypothetical $j^{\text{th}}$ Fourier coefficient of the left travelling wave assuming there is no noise and that linear theory holds exactly.
$A_{Rj}$	hypothetical $j^{\text{th}}$ Fourier coefficient of the right travelling wave assuming there is no noise and that linear theory holds exactly.
$A_{j,p}$	$j^{\text{th}}$ Fourier coefficient of the wave amplitude time series recorded at wave gauge $p$ .
$C_{j,p}$	weighting coefficient for expressing $a_{Lj}$ and $a_{Rj}$ as linear combinations of the $\{A_{j,p}\}$ .
$E_j$	merit function whose minimum yields the amplitudes of the left and right travelling waves, $a_{Lj}$ & $a_{Rj}$ , at frequency $j$ .
$\mathcal{E}_p(t)$	residual elevation signal at wave gauge $p$ due to noise, nonlinear, viscous, and other effects.
$g$	gravitational acceleration.
$h$	still water depth.
$i$	$\sqrt{-1}$
$k_j$	wave number of the $j^{\text{th}}$ Fourier component: $2\pi/\lambda_j$
$P$	number of wave gauges used to record the composite wave spectrum
$S_j$	sum of the least squares weighting coefficients: $\sum_{p=1}^P W_{j,p}$ .

$T$	duration of wave gauge records $\{\eta_p(t)\}$ .
$W_{j,p}$	least squares weighting coefficient for probe $p$ at frequency $\omega_j$ .
$x_p$	location of wave gauge $p$ .
$\Delta\phi_{j,p}$	phase difference between probes 1 and $p$ for frequency $\omega_j$ : $\Delta\phi_{j,p} = \phi_{j,p} - \phi_{j,1} = k_j(x_p - x_1)$ .
$\Delta\phi_{j,pq}$	phase difference between probes $p$ and $q$ for frequency $\omega_j$ : $\Delta\phi_{j,pq} = \Delta\phi_{j,p} - \Delta\phi_{j,q} = \phi_{j,p} - \phi_{j,q} = k_j(x_p - x_q)$ .
$\epsilon_{j,p}$	the error in matching the $j^{\text{th}}$ Fourier coefficient $A_{j,p}$ at wave gauge $p$ using the least squares algorithm.
$\epsilon_{j,p}$	$j^{\text{th}}$ Fourier coefficient associated with the residual elevation signal $\mathcal{E}_p(t)$ .
$\eta_p$	wave elevation recorded at location $x_p$ .
$\lambda_j$	wavelength of the $j^{\text{th}}$ Fourier component.
$\phi_{j,p}$	absolute phase of the $j^{\text{th}}$ Fourier component at the $p^{\text{th}}$ wave gauge: $k_j x_p$
$\omega_j$	frequency of the $j^{\text{th}}$ Fourier component: $2\pi j/T$

### SPECIAL SYMBOLS

( )\* complex conjugate of the enclosed quantity.



## **PART II**

### **Long Period Waves, Storm Surges and Wave Groups**



*Tetrapods in Bari*

## CHAPTER 59

### LABORATORY TESTS ON THE INTERACTION BETWEEN NONLINEAR LONG WAVES AND SUBMERGED BREAKWATERS

Marco Petti<sup>1</sup> and Piero Ruol<sup>2</sup>

#### Abstract

This paper deals with the use of submerged detached breakwaters as beach protection, a use that today has become quite popular. This type of structure has been largely studied both theoretically and through experimental analyses in recent years, however its behaviour has not been completely understood, specially if related to the real irregular wave attacks. In particular some laboratory studies carried out by the authors have pointed out some interesting phenomena associated with the interaction between the nonlinearities of wave transformations in shallow water and submerged breakwaters.

Aiming at discerning between the phenomena related to the structure (beach and breakwater) and flume geometry, a new series of laboratory tests have been carried out in a 50 m long wave flume; these tests and the results obtained are described in this work. Besides the study of the behaviour of submerged structures related to the bounded-long-waves, some current velocities have also been measured during this research through directional micro-propeller fluid meters.

#### Introduction

Among the work aiming to protect ports and beaches the use of detached submerged breakwaters appears today of increasing interest. This is mainly related to the small environmental effects combined with the obvious aesthetic advantages of these structures and to their relatively low costs.

Even if the case of submerged structures have been given significant coverage in literature, certain aspects do not seem to have been treated in enough depth; for example only the first steps have been taken in studying the

---

<sup>1</sup>Researcher, Department of Civil Engineering, University of Firenze, Via S. Marta, 3 - 50139 Firenze (Italy)

<sup>2</sup>Researcher, Institute of Maritime Structures, University of Padova, Via Ognissanti, 39 - 35129 Padova (Italy)

behaviour of such structures under irregular wave attacks (Ahrens, 1989, Van der Meer, 1988, Petti and Ruol, 1991).

The difficulties connected to similar analytical or numerical studies (Kobayashi and Wurjanto, 1989) often lead to a physical analysis of the phenomena related to similar structures in measuring water level oscillations across the structure (Adams and Sonu, 1986, Hedges et al., 1985).

To explain some anomalous water level oscillations in front of the breakwater, which were measured during a similar approach (Petti and Ruol, 1991) the writers supposed that the mass transport, caused by the waves breaking on the structure, was able to create a current directed off-shore that was affecting the incoming wave characteristics.

In particular the authors found that the bounded long waves generated by the well-known non-linear modifications of the wave spectrum on a sloping bottom, problem recently solved also in analytical manner (Petti, 1991), seem to be greatly affected by the joint effect of the structure and by the current opposite to the incoming waves.

These experimental analyses were conducted in a wave flume using a submerged breakwater located on different fixed bottom configurations. These experiments were carried out in a 33 m-long wave flume reproducing a monotonously decreasing bottom profile initially and a barred profile later (Petti and Ruol, 1990, 1991).

In the present work, in order to have a better understanding of the physics of the problem, a new series of experiments carried out using the same structure but in a longer wave flume and with different bottom configuration are described. In particular during these experiments some velocity measures over the structure were also performed in order to estimate the current velocity field induced by the wave attacks in the regions close to the submerged breakwater. At present similar measures are the object of some interesting new research (Losada, 1992).

### Laboratory experiments

The series of experiments described in this paper were carried out in the wave flume of the Department of Civil Engineering which is 50 meters long, 0.8 m wide and 0.8 m deep. The analysed structure, located on a 1:50 fixed bottom slope, consisted of an impermeable submerged breakwater 14 cm high, 24 cm wide at the top and sloping 1:3.5 sea-ward and 1:1.5 shore-ward.

The wave transformations were first of all analysed considering the simple sloping beach without any structure and later considering a submerged breakwater located in a 20 cm local water depth at about 34 meters from the wave generator (Fig. 1).

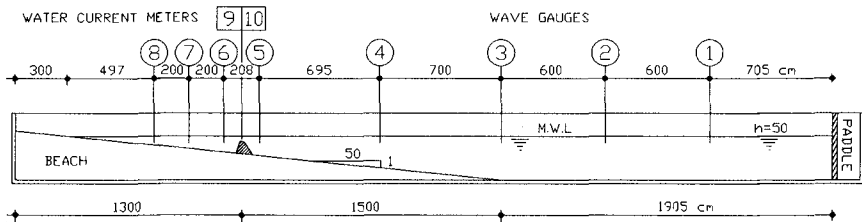


Fig. 1 – Experimental apparatus and scheme of the tested structure.

The wave characteristics in the flume were determined measuring water level oscillations with eight parallel wire resistance gauges. Besides these characteristics, reflection coefficient analyses and velocity measurements were also performed.

Both with and without the structure four different wave attacks, characterised by spectra of the JONSWAP type, were reproduced. Significant wave heights, the Phillips constant  $\alpha$ , the peak frequency  $f_p$  and the peakedness factor  $\gamma$  characteristic of each experiment are summarised in Tab. 1.

Table 1 – Characteristics of generated waves.

Test n.	$\alpha$	$f_p$ (Hz)	$H_{m0}$ (cm)	$\gamma$
1	0.0180	0.650	14.1	1.0
2	0.0100	0.650	11.7	2.0
3	0.0140	0.833	9.2	3.0
4	0.0180	0.833	8.6	1.0

### Test results and discussion

In Fig. 2a and 2b an example of the results obtained through the spectral analysis for both the case with submerged structure and without it is shown.

In these figures the wave spectra measured by the gauges located along the flume are compared; it does appear that in the first case (without structure) the non-linearities of the spectra (due to the shallow waters) are not evident in the deeper waters (gauges n. 1, 2, 3), while, as expected, the build-up of low-frequency and high-frequency components is evident in the shallow waters.

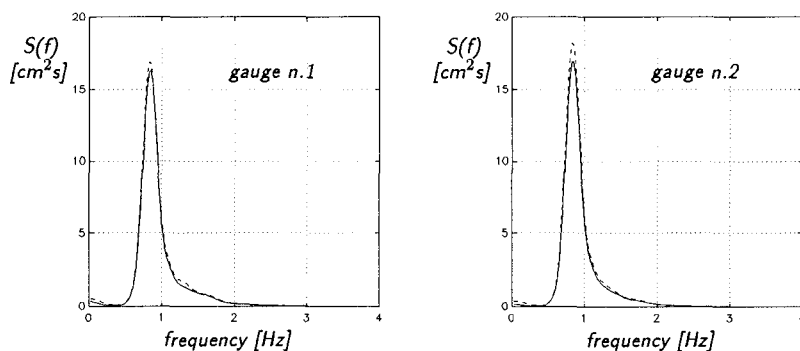


Fig. 2a – Comparison between spectral densities of the case with submerged structure (dotted line) and without it (solid line), for the test n.3 and gauges n. 1 and n. 2.

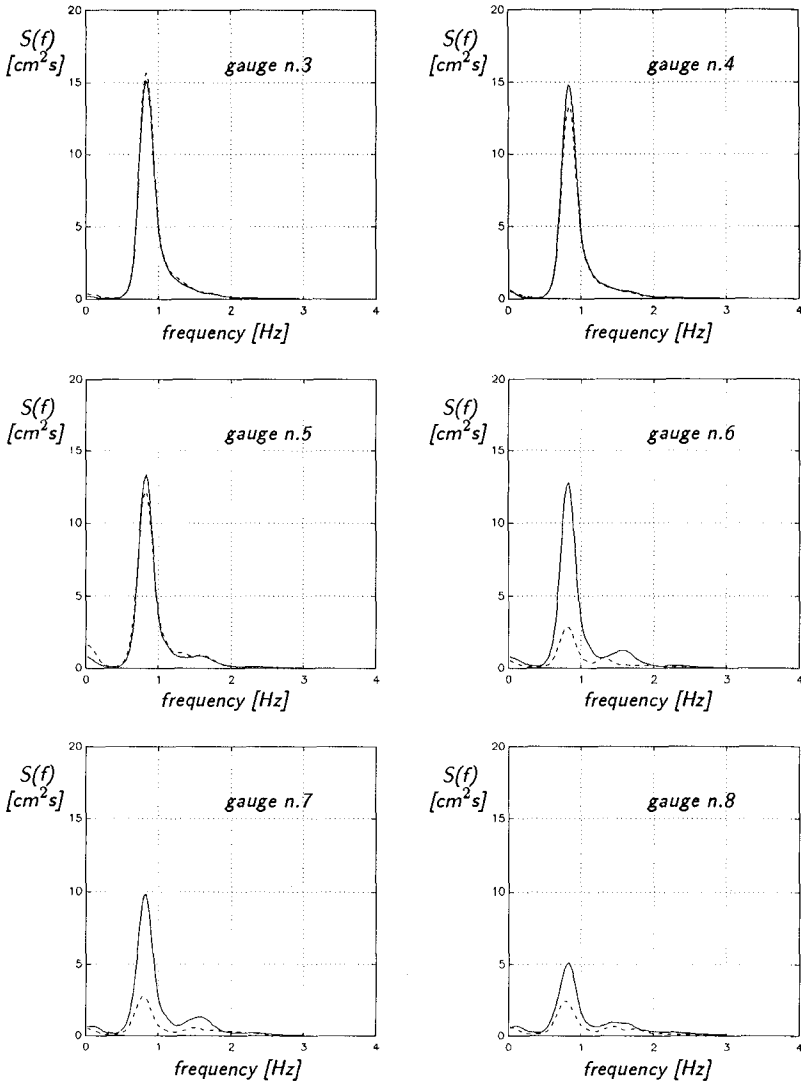


Fig. 2b – Comparison between spectral densities of the case with submerged structure (dotted line) and without it (solid line), for the test n.3 and gauges n. 3 ÷ 8.

In the second case also (with structure) the spectra referred to the deeper gauges show the absence of non linearities, while a considerable increase was found in the lower and higher frequency components just in front of the structure (gauge 5).



Of course the spectral densities decrease significantly after the impact of the breaking phenomenon located on the submerged breakwater and do not considerably change in the propagation towards the beach.

This typical non-linear phenomenon was studied in more detail dividing the long waves from the short ones: for this research the time domain records were analysed filtering the signal and considering the higher frequencies ( $f > 0.5 f_p$ ) and the lower ones ( $f < 0.5 f_p$ ) separately. An example of the results obtained through such wave data analyses referring to gauge n. 5 and lasting 60 s is shown in Fig. 3.

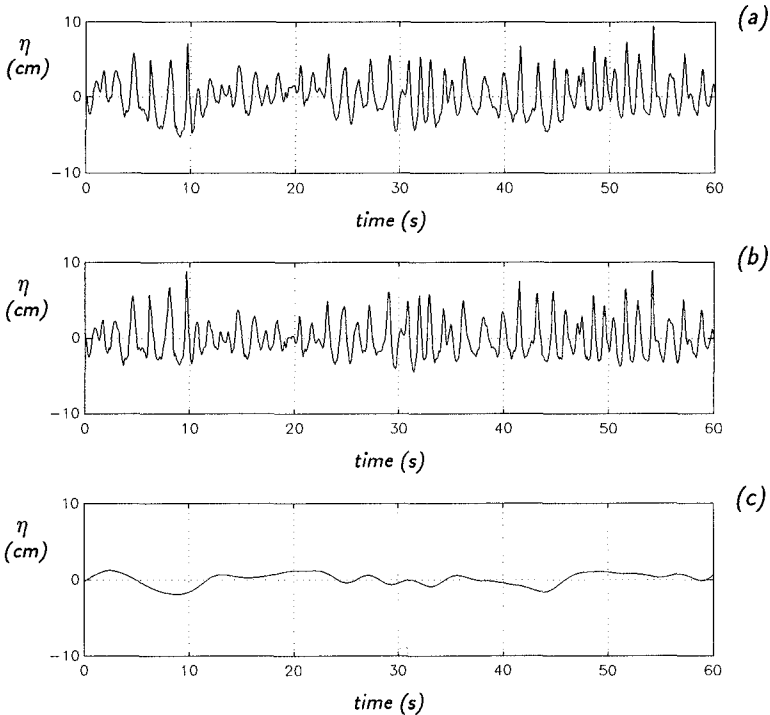


Fig. 3 – Example of water level oscillation data-recording (a), of the filtered signal with  $f > 0.5f_p$  (b) and with  $f < 0.5f_p$  (c) for test n. 2 and gauge n.5.

For both short and long waves previous analyses of the reflection coefficients (Goda and Suzuki, 1976) were performed in the case without the structure. These coefficients appeared to be close to 4% for short waves and 12% for long ones. The details of the results obtained by means of zero-(up)crossing analyses performed on the 4 reproduced tests are schematically drawn in Fig. 4a and 4b. In the figures significant short-wave heights  $H_s$  and periods  $T_s$  along the flume are reported.

As expected the periods perhaps appear constant along the flume, while the wave heights, as result of shoaling and breaking phenomena, decrease with decreasing water depths.

As already described, the same four tests were repeated with the submerged breakwater located on the bottom profile; the results obtained through experimental analyses are shown in Fig. 5a and 5b.

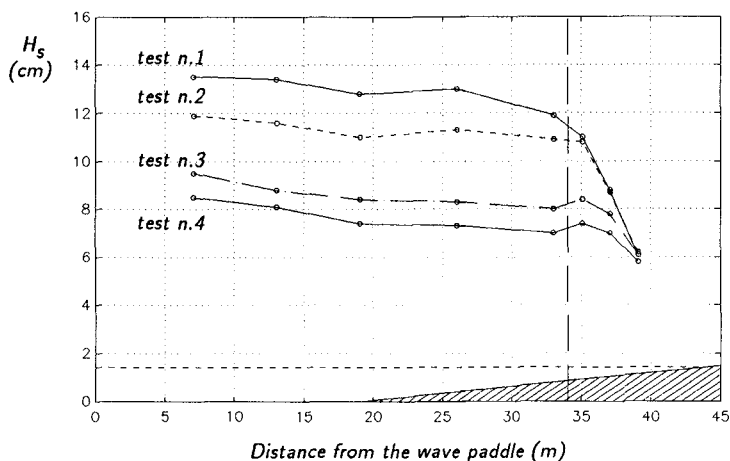


Fig. 4a – Significant wave heights for all gauges referred to short-waves zero-crossing analyses without the structure.

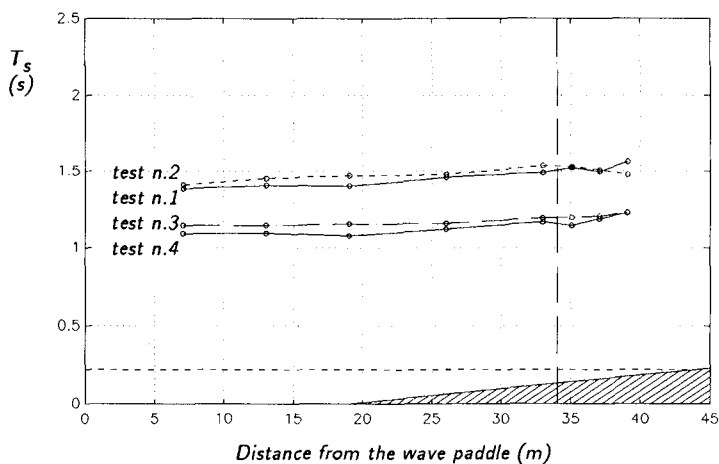


Fig. 4b – Significant wave periods for all gauges, referred to short-waves zero-crossing analyses without the structure.

In comparing Fig. 4a and 5a it does appear that in the off-shore region the wave heights do seem not to be greatly affected by the structure and this probably explains that, in the case analysed, the structure is not reflecting

waves significantly. Instead, wave heights following the breakwater are strongly affected by the structure itself and this is mainly related to the breaking of some waves over the structure.

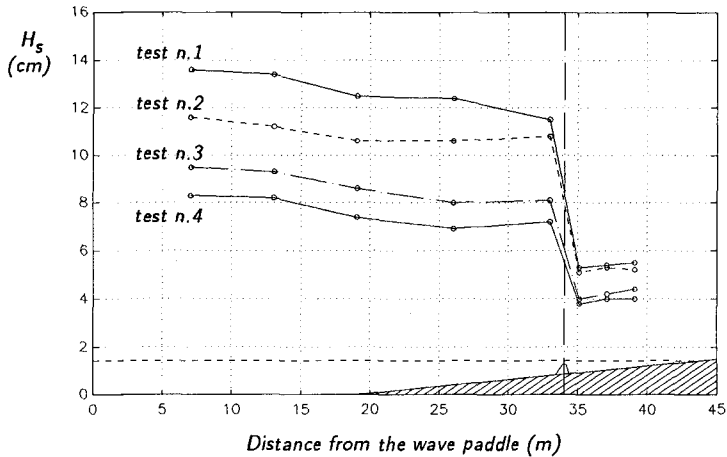


Fig. 5a—Significant wave heights for all gauges referred to short-waves zero-crossing analyses with the structure.

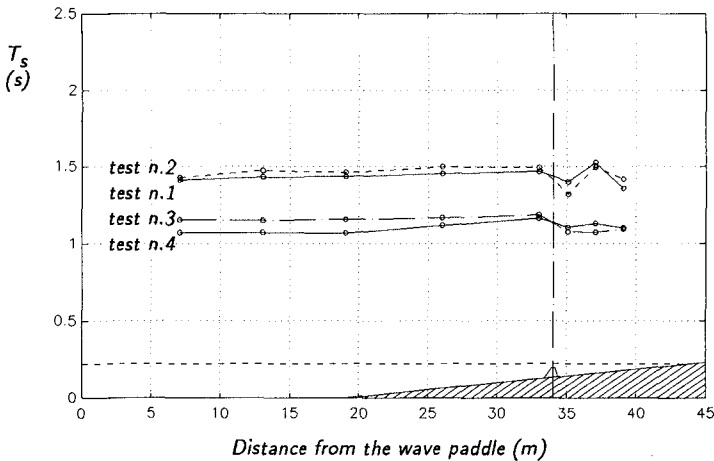


Fig. 5b—Significant wave periods for all gauges referred to short-waves zero-crossing analyses with the structure.

As far as periods are concerned (Figs. 4b and 5b) they do not seem to be greatly influenced by the structure, except for very weak instabilities around it.

However, the most interesting phenomenon that did appear is related to

the analysis of the bounded-long-waves and in particular to the difference induced by the placing of the submerged breakwater over the bottom profile. In Fig. 6a and 6b the long-wave significant heights evaluated for all gauges during each test are drawn.

It can be observed that a considerable increase of long wave heights just in front of the structure was measured; in fact the long wave heights within the structure were evaluated to be about 40% greater than without it.

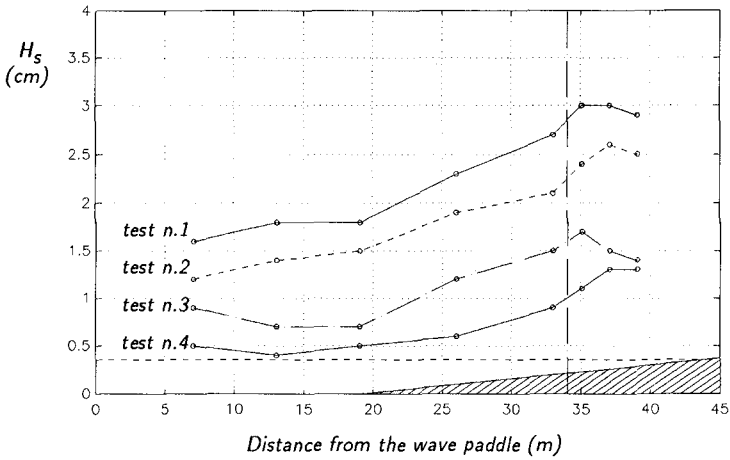


Fig. 6a – Significant wave heights for all gauges referred to long-waves zero-crossing analyses without the structure.

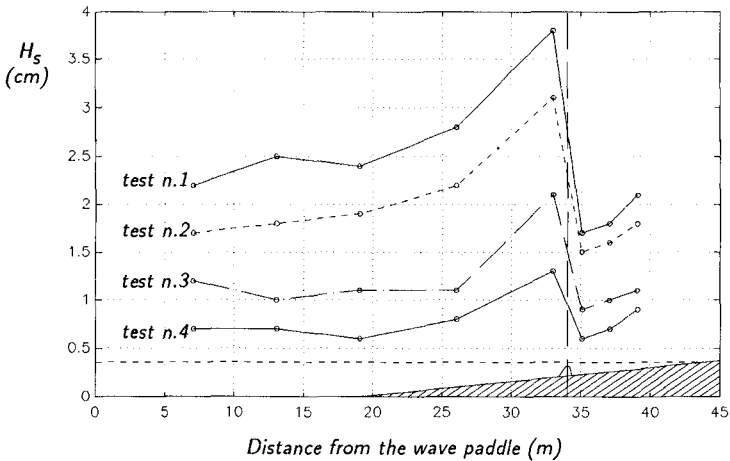


Fig. 6b – Significant wave heights for all gauges referred to long-waves zero-crossing analyses with the structure.

Similar results had already been found by the authors in previous experiments (Petti and Ruol, 1990, 1991) performed with the same structure but in a shorter flume and with different bottom configurations. This particular aspect lead to the thinking that the bottom configuration and the flume length affect only slightly the increasing of long wave heights in front of the structure.

As regards the length of the flume, probably some seiches were present because a non absorbing wave maker was used during the experiments. In the writers opinion, however, the results appear not to depend on them.

Firstly if the seiches were present they were very small because their reflection coefficient was small (12%). Secondly because eventual long wave oscillations should have been present in both the cases analysed: as a consequence the comparison of the results (e.g. the increase of the long wave heights) is not affected by the seiches themselves.

So as to be able to get more information about this interesting phenomenon, some velocity measurements over the structure were also performed.

A couple of water-fluid-meters (bi-directional micro-propeller) were located at 2.0 cm over the structure, one beside the other and three additional wave gauges were located in the same section in order to be able to associate the velocities with water levels (Fig. 7).

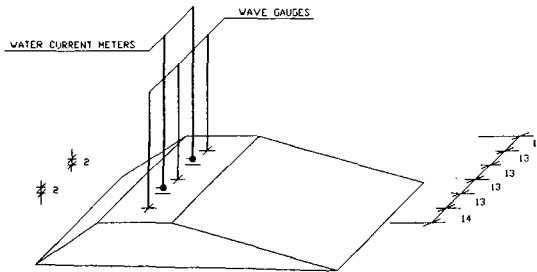


Fig. 7— Location of the micro-propellers and of the gauges over the structure.

An example of the velocity data registered during one test is reported in Fig. 8. As well as for the waves, the signal was also analysed considering the higher frequencies ( $f > 0.5f_p$ ) separately from the lower ones ( $f < 0.5f_p$ ). The results appear similar to ones referred to the wave gauge n. 5 located in front of the structure.

As regards the spectral analyses performed for velocity signals, in Fig. 9 the results relative to the four tests checked are reported.

It can be observed that while at the lower frequencies very high spectral values are present (due to nonlinear phenomena), at the higher frequencies they do not result all too evident. Moreover, while in the wave spectra calculated in front of the structure it was possible to find a frequency (about equal to  $0.5f_p$ ) dividing the low-frequency components from the high ones (Fig. 2), this was not possible for the velocity spectra.

Definitely a different behaviour of the velocity spectra compared to the wave spectra does appear: the frequency components in fact are strongly evolving towards the lower values and only weakly towards the higher values.

With regards to this, during the velocity analyses the mean values of the velocity pointing off-shore (a constant velocity distribution along the vertical was supposed) were also calculated: they were included in the range  $6 \div 14$  cm/s.

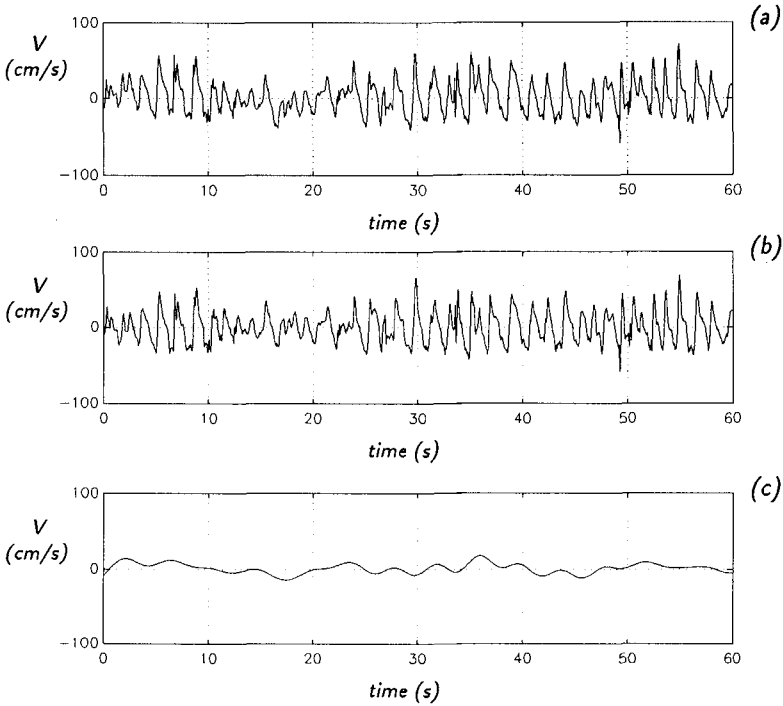


Fig. 8 – Example of velocity data-recording (a), of the filtered signal with  $f > 0.5f_p$  (b) and with  $f < 0.5f_p$  (c) for test n. 2.

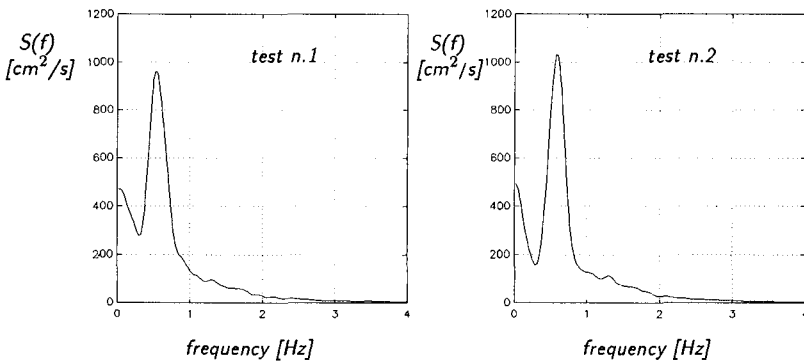


Fig. 9a – Spectral analyses of the velocities measured over the structure by a micro-propeller for tests n. 1 and 2.

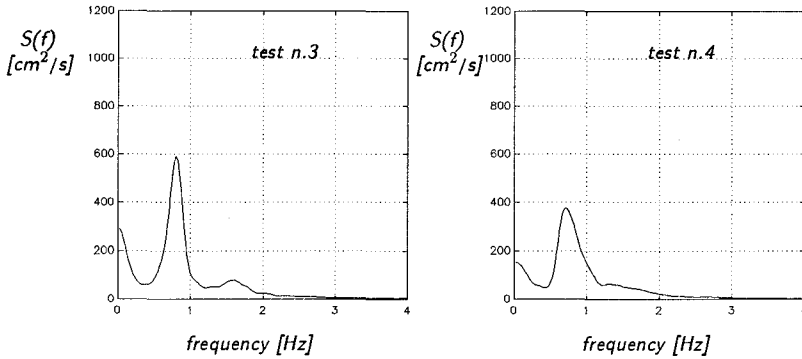


Fig. 9b – Spectral analyses of the velocities measured over the structure by a micro-propeller for tests n. 3 and 4.

In the authors' opinion these velocities, associated with the submerged breakwater presence, were able to affect the incoming bounded-long-waves; in fact the measured velocities appeared to be close to the theoretical long-wave orbital velocities (without structure) calculated, at first order, through linear theory (i.e.:  $u_{max} = 0.5H\sqrt{g/h}$ ). In conclusion, the incoming long wave really seems to be interfering with the opposite fluid discharge as if it were affected by a phenomenon similar to the interaction between waves and currents.

To corroborate this hypothesis the described mean velocity pointing offshore was related to the increase of long-wave heights due to the presence of the breakwater for each test (Fig. 10).

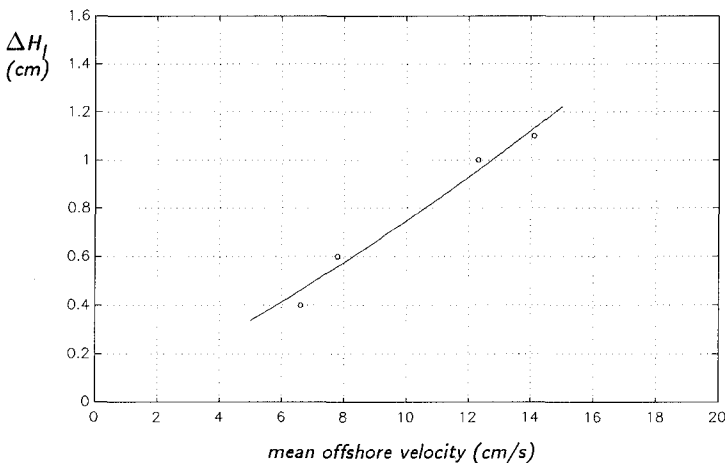


Fig. 10 – Increase of long wave heights in front of the structure (gauge n. 5) versus mean velocity measured over the structure.

As it does appear the greater the off-shore velocity over the breakwater the greater the increase of the long wave heights.

### Conclusive remarks

Some experimental studies carried out in a 50 m long flume on a submerged breakwater resulted in the definition of its behaviour under irregular waves attacks. In particular it was pointed out that the analysed structure was considerably affecting the bounded long wave heights: in fact the long wave heights were evaluated to be about 40% greater with the defence work rather than without it.

So as to be able to get more information about this phenomenon, some velocity measurements over the breakwater were performed: it did appear that greater the mean velocities pointing offshore (evaluated to be in the range  $6 \div 14$  cm/s), the greater the increase of the long wave heights in front of the structure.

Further experimental research with different submerged structures is asked for in order to determine analytical correlations between long wave height increases and geometrical characteristics.

### References

- Adams C.B. and Sonu C.J. (1986). *Wave Transmission across Submerged Near-Surface Breakwaters*. Proc. 20th Int. Conference on Coastal Engineering, ASCE, 1729 – 1738.
- Alrens J.P. (1989). *Stability of Reef Breakwaters*. Journal of Waterway, Port, Coastal and Ocean Engineering, ASCE, 221 – 233.
- Goda, Y. and Suzuki (1976). *Estimation of incident and reflected waves in random wave experiments*. Proc. of 15th Int. Conference on Coastal Engineering, ASCE, Houston.
- Hedges T.S., Anastasiou K. and Gabriel D. (1985). *Interaction of Random Waves and Currents*. Journal of Waterway, Port, Coastal and Ocean Engineering, ASCE, (111)2, 275 – 288.
- Kobayashi N. and Wurjanto A. (1989). *Wave Transmission over Submerged Breakwaters*. Journal of Waterway, Port, Coastal and Ocean Engineering, ASCE, (115)5, 662 – 680.
- Losada, M., Kobayashi, N. and Martin, F. (1992). *Armour stability on submerged breakwaters*. Journal Waterway, Port, Coastal and Ocean Engineering, ASCE, (118)2, 207 – 212.
- Petti, M. (1991). *On the separation of second order components for non-linear wave spectra*, Proc. of International Conf. on Computer Modelling in Ocean Engineering, Barcelona.
- Petti, M. and Ruol, P. (1991). *Experimental studies on the behaviour of submerged detached breakwaters*. Third Int. Conf. on Coast. and Port Eng. in Dev. Countries, Mombasa, Kenya, 167 – 178.
- Petti, M. and Ruol, P. (1990). "Indagine sperimentale sulla interazione tra il moto ondoso reale ed una barriera sommersa". XXII Conv. Idr. e Costr. Idr., pp.249-261.
- Van der Meer J.W. and Pilarczyk K.W. (1990). *Stability of low crested and reef breakwaters*. Proc. of 22nd Int. Conference on Coastal Engineering, ASCE, 1375-1388.



## CHAPTER 60

### Field Observation of Surf Beats Outside the Surf Zone

Tsunehiro Sekimoto<sup>1</sup>, Takuzo Shimizu<sup>2</sup>, Kosuke Kondo<sup>2</sup>  
and  
Yasuhiro Kubo<sup>3</sup>

#### Abstract

Field observations of waves were conducted inside and outside a harbor in order to study the behavior of surf beats. From the observations, it is confirmed that surf beats propagate as bounded long waves at depths of 13 to 15m, whereas they behave as free waves in the harbor. It is found that the amplitude of bounded long waves become 20% of the ordinary-wave amplitude when the ordinary-waves height is 5 m.

#### 1. Introduction

Since the surf beats, which are water surface fluctuations with long periods of 1 to 5 minutes, were first observed by Munk (1949) and Tucker (1950), their characteristics have been investigated by means of field measurements and laboratory experiments by many researchers, e.g. Hotta et al. (1981), Kimura (1984), Kostence (1984), List (1988), Mansard and Barthel (1984), Ottesen-Hansen (1978), Ottesen-Hansen et al. (1980), Sand (1982), Sharma and Dean (1979), Symonds et al. (1982), Symonds and Bowen (1984). It is pointed out that surf beat plays an important role in the sediment transport in the surf zone, the slow drift oscillation of a moored vessel, the resonant edge wave growth and the harbor resonance.

---

<sup>1</sup>Penta-Ocean Construction Co. Ltd., 1-11-25 Higashiohi, Shinagawa-Ku, Tokyo 140, Japan.

<sup>2</sup>Penta-Ocean Construction Co. Ltd., 2-2-8 Koraku, Bunkyo-Ku, Tokyo 112, Japan.

<sup>3</sup>Tokyo Electric Power Co. Inc., 1-1-3 Uchisaiwaicho, Chiyoda-Ku, Tokyo 100, Japan.

Outside the surf zone, it is suggested that surf beat exists as a bounded long wave (Longuet-Higgins and Stewart, 1962). However, few field data, which show that surf beats are bounded and how much the magnitude of bounded long wave is, have been observed. Moreover the behavior of the surf beat in an actual harbor is still unclear.

The aim of this study is to explain the characteristics of surf beat in the nearshore non-breaking zone and its propagation into the harbor on the basis of the field measurement data.

In this study the term of surf beat means long period fluctuation of mean sea level with 1 to 5 minutes periods irrespective of water depth.

## 2. Field investigations

Field investigations were conducted at two sites. One site was the port of Kashiwazaki-Kariwa nuclear power plant, Niigata prefecture, Japan, which is facing the Sea of Japan. This power plant was constructed in both Kashiwazaki city and Kariwa town, so we call it shortly Kashiwazaki-Kariwa. Another site was the port of Oharai, Ibaraki Prefecture, which is located at the Pacific Ocean side of Japan. The locations of these sites are shown in Figure 1.

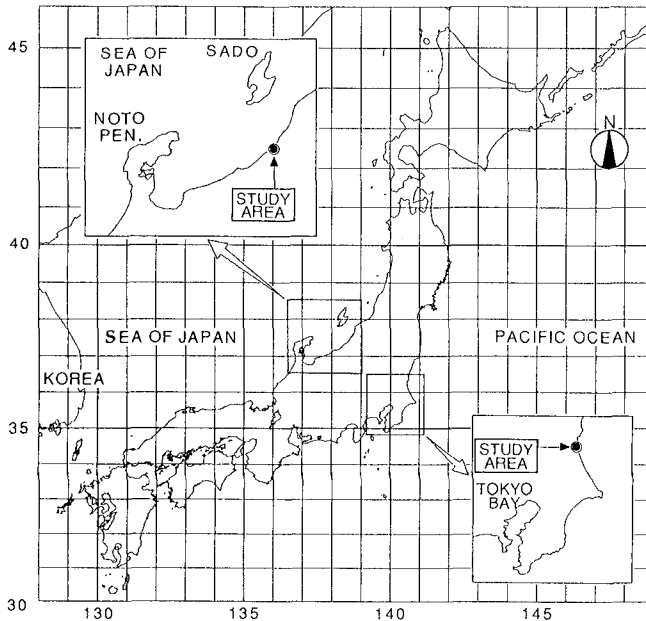


Figure 1. The location of the investigation site.

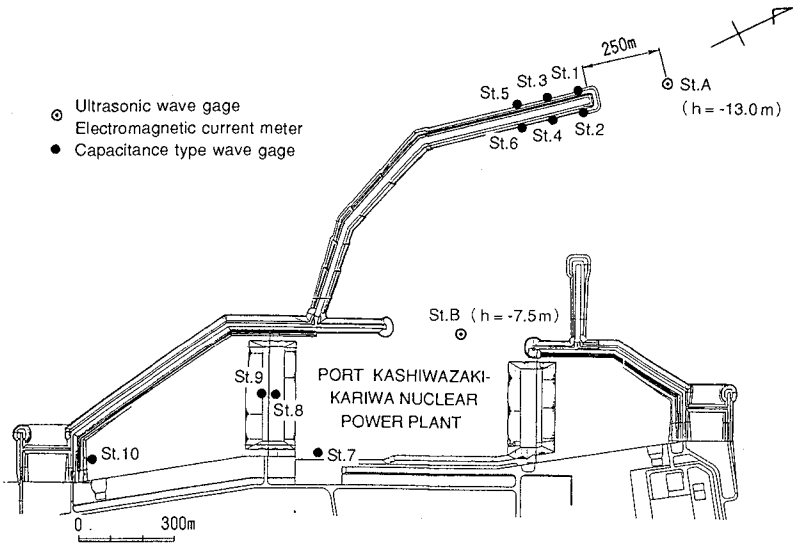


Figure 2. Location of observation points (Port of Kashiwazaki-Kariwa Nuclear Power Plant).

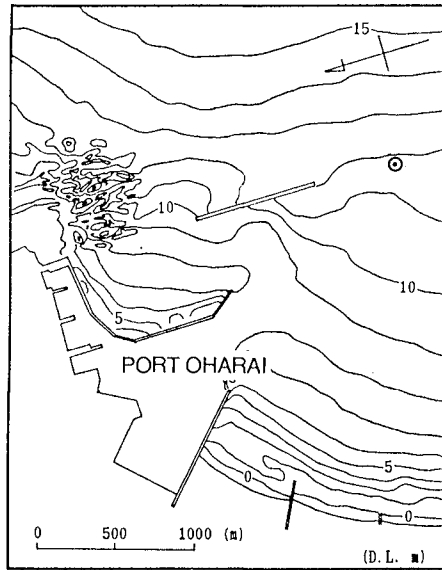


Figure 3. The location of observation point (Port of Oharai).

At Kashiwazaki-Kariwa site, field measurements were carried out inside and outside harbor from January through March of 1989. Figure 2 shows the port of Kashiwazaki-Kariwa nuclear power plant. The tip of main breakwater is located at 13m depth. The locations of measurement instruments are shown in this figure. At St. A and St. B the water surface elevation and two components of horizontal current velocity were measured using both ultrasonic wave gage and electromagnetic current meter. The water depths of St. A and St. B are 13.0m and 7.5m, respectively. At St. 1 through St. 10, the water surface elevation was measured by capacitance type wave gages. Since the waves higher than 2m were observed only a few times at Kashiwazaki-Kariwa during this observation, the wave data obtained in January and March of 1987 which are a part of a long term study by Tokyo Electric Power Co. Inc. were also analyzed. In this long term observation, ultrasonic wave gage is laid 1.5 km from the shore line.

At Oharai site, field observations were carried out outside the harbor, from November through December of 1990. Figure 3 is the general view of the Oharai port. The locations of measurement instruments are shown in this figure. An ultrasonic wave gage and an electromagnetic current meter with pressure gage were set at a point of 500 m away from the end of offshore breakwater.

The fluctuations of water surface level, and of pressure and two components of horizontal orbital velocities at the bottom were measured. At both sites, wave data were sampled at 0.5 second intervals and more than 300 records of time series of 20 minutes long and 150 records of 40 minutes long were obtained. The profiles of surf beat were extracted from

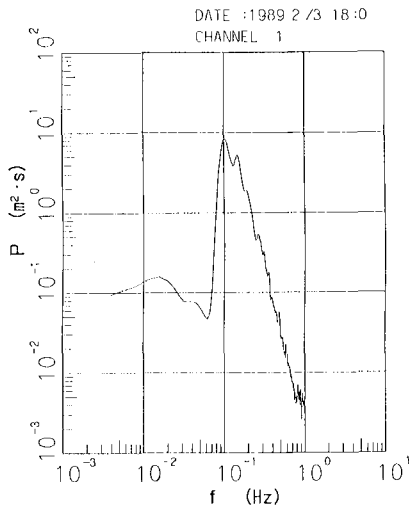


Figure 4. Typical wave spectrum at Kashiwazaki-Kariwa site.

those of water surface elevation and pressure by means of numerical filter. The cut off frequencies of numerical filter were 0.05 Hz for the data of Kashiwazaki-Kariwa and 0.04 Hz for the Oharai data which were determined from the results of power spectrum analysis. The extracted surf beats were used for various analyses. Typical wave spectrum at Kashiwazaki-Kariwa site is shown in figure 4. It is found that the peak frequency of ordinary-wave is about 0.1 Hz and the long wave energy is 2 orders below the peak energy of ordinary-wave.

### 3. Surf beats outside the harbor

Figure 5 shows the relationship between the significant wave height of ordinary-wave and that of surf beats at St. A. Under the condition of significant wave height higher than 1.5m, at the water depths of 13m the significant wave height of surf beats is proportional to the square of that of ordinary-waves. In this figure the calculation results estimated by unidirectional non-linear interaction theory (Ottesen-Hansen, 1978) and empirical relation proposed by Goda (1975) are also drawn.

The calculation by non-linear interaction theory is the average of 75 simulations of surf beat which are calculated from 75 simulated ordinary-waves using the procedure proposed by Sand (1982). In this calculation, the difference of the directions of ordinary-wave components is set to zero. The simulated 75 ordinary-waves were calculated from 3

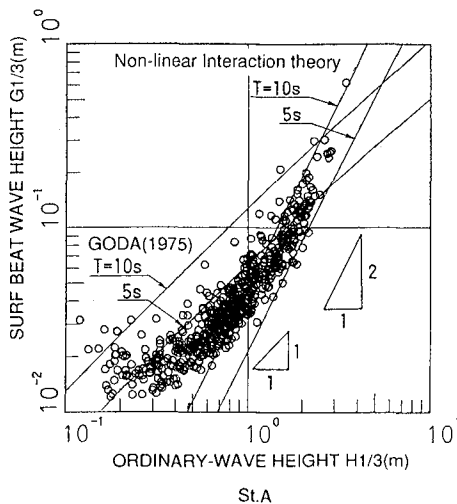


Figure 5. The relationship between the wave height of surf beat and that of the ordinary-wave height (St.A).

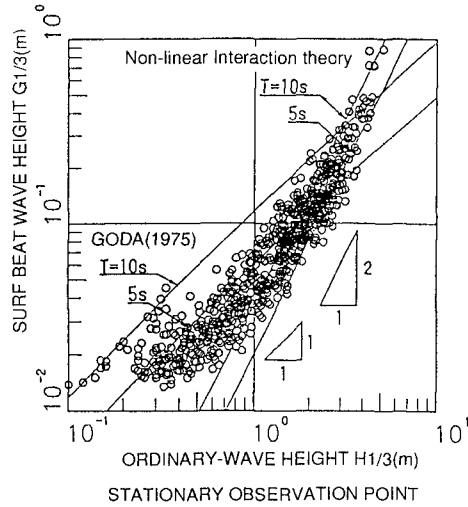


Figure 6. The relationship between the wave height of surf beat and that of the ordinary-wave height (Stationary observation point).

types of energy spectrum and 25 sets of phase angles of component wave. The calculation results estimated by non-linear interaction theories fit the field measurements very well. Figure 6 shows the relationship between the surf beat and the ordinary-wave height of long term observation by Tokyo Electric Power Co., Inc. It is confirmed that the relationship between surf beat and ordinary-wave is the same as the relationship which was found in figure 5.

The surf beat profile was simulated on the basis of the non-linear interaction wave theory proposed by Sand (1982) by using the observed ordinary-wave profile in the condition of approximately unidirectional wave. That is the difference of the directions of ordinary-wave components is set to zero.

$$\zeta = \sum_{i=1}^{\infty} \sum_{j=1}^{\infty} \sum_{m=1}^{\infty} \sum_{n=1}^{\infty} \xi_{ij}, \quad (1)$$

where

$$\xi_{ij} = a_i a_j G_{\eta \xi} \cos(\psi_i - \psi_j), \quad (2)$$

$$G_{\eta\xi} = \frac{1}{2h} \left[ \frac{G' - k_i h \cdot k_j h \cos \theta_{m_i n_j} - 16\pi^4 D_i^2 D_j^2}{4\pi^4 D_i^2 D_j^2} + 4\pi^2 (D_i^2 + D_j^2) \right], \tag{3}$$

$$G' = \left\{ (D_i - D_j) \left[ D_j (k_i^2 h - 16\pi^4 D_i^4) - D_i (k_j^2 h - 16\pi^4 D_j^4) \right] \right. \\ \left. + 2(D_i - D_j)^2 \left[ k_i h \cdot k_j h \cos \theta_{m_i n_j} + 16\pi^4 D_i^2 D_j^2 \right] \right\} / \\ \left\{ (D_i - D_j)^2 k_{ij}^- h \tanh k_{ij}^- h \right\}$$
(4)

$$\psi_i = \mathbf{k}_i \cdot \mathbf{x} - \sigma_i t + \varepsilon_i, \tag{5}$$

$$D_i = \sqrt{\frac{h}{g} \frac{\sigma_i}{2\pi}}, \tag{6}$$

$$\theta_{m_i n_j} = \theta_{m_i} - \theta_{n_j}, \tag{7}$$

$$k_{ij}^- = |\mathbf{k}_i - \mathbf{k}_j| \tag{8}$$

$$\mathbf{k}_i = (k_i \cos \theta_{m_i}, k_i \sin \theta_{m_i}), \tag{9}$$

and  $k_i$  and  $\sigma_i$  are the wave number and frequency respectively.

Figure 7 shows the directional spectra of wave which is used in surfbeat simulation. It is seen that the directional spectrum is very narrow.

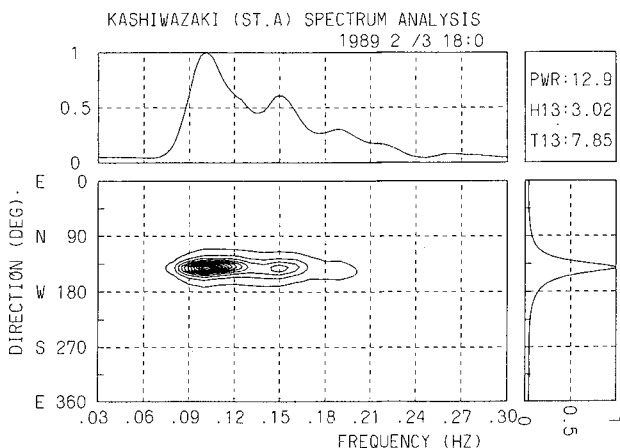


Figure 7. The directional spectra of wave which is used in surfbeat simulation.

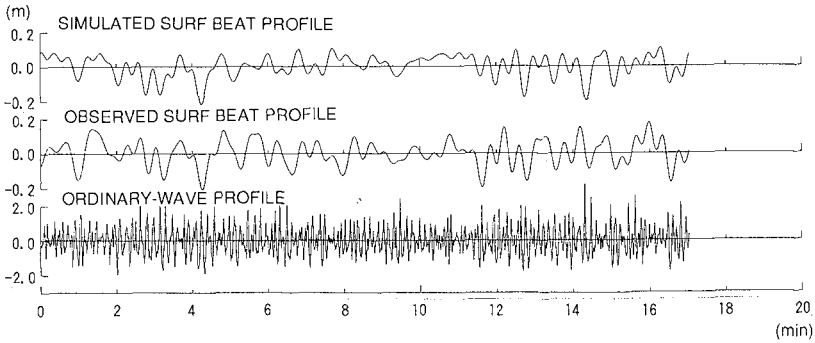


Figure 8. The comparison of the observed results with simulated surfbeat profile by non-linear interaction theory.

The comparison of observed surf beat with simulated surf beat is shown in figure 8. The observed surf beat profiles present a typical bounded long wave profile which is depressed beneath a group of high waves. The simulated profile shows good agreement with the observed one.

In order to investigate the correlation between the observed and simulated surf beat, cross-spectral analysis of these profiles was conducted. Figure 9 is the results of cross-spectral analysis. The figures are the phase function, square-root of ratio of powers, and coherence squared, respectively from top to bottom. Although the coherence squared is less

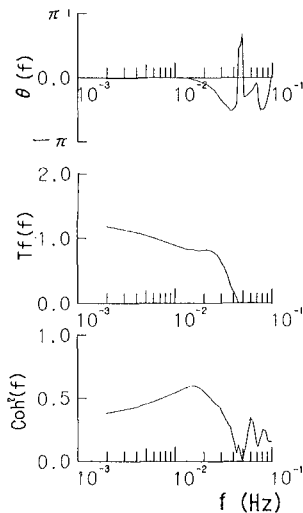


Figure 9. The results of cross-spectra (Phase function, square-root of ratio of power and coherence squared).



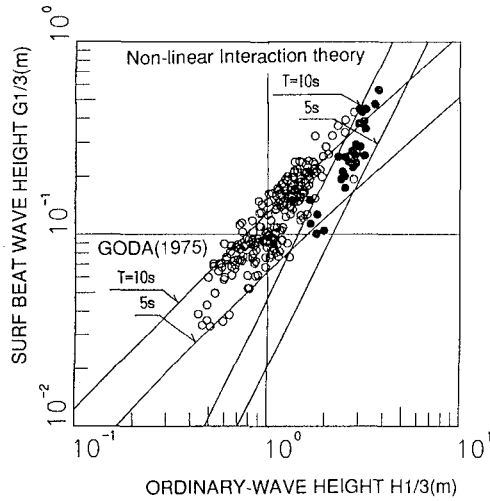


Figure 10. The relationship between the wave height of surf beat and the ordinary-wave height of Oharai wave data.

than unity but the phase function is nearly zero and transfer function is close to one. Considering that the coherence function is strongly affected by the fluctuation of phase difference in each component, it is concluded that the correlation is high and the observed surf beat is bounded.

Figure 10 shows the relationship between the wave height of surf

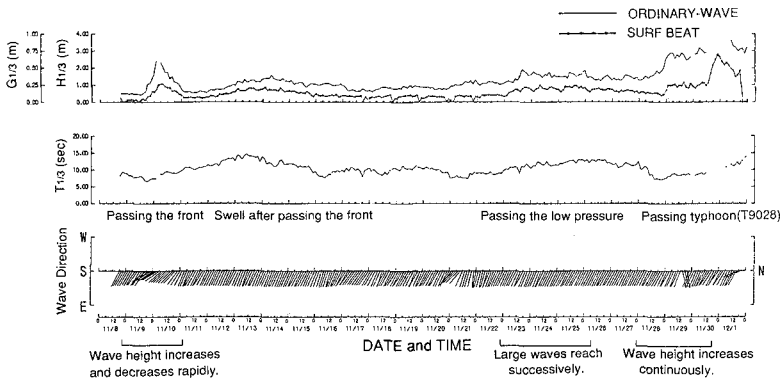


Figure 11. The variation of the ordinary-wave height and period and surfbeat wave height with the time.

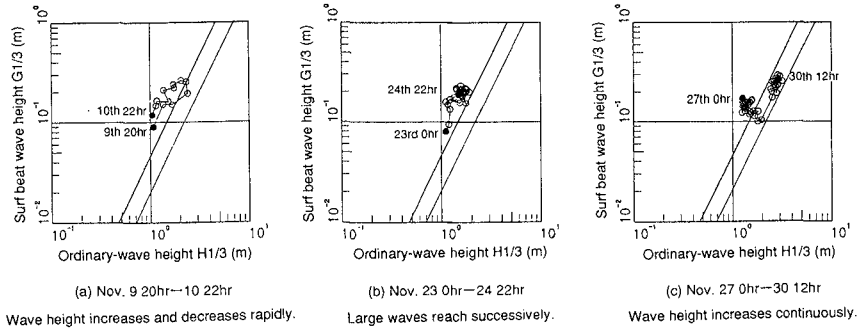


Figure 12. The relationship between the wave height of surf beat and the ordinary-wave height.

beat and the ordinary-wave height of Oharai wave data. In this figure, the relationship seems not the same as previous relation. In order to study the cause of this difference, we investigate this relation in detail.

Figure 11 is the variations of the ordinary-wave height and period, and the surf beat wave height with the time. Three intervals of typical sea state were selected for analysis. The first of these is the period of rapid wave height increase and decrease. The second is the interval which large waves arrive successively. The last is the period of continuous increase of wave height. Figure 12 is the plot of the relationships between the surf beat height and the ordinary-wave height corresponding to the above three periods of typical sea state. In this figure, black symbols indicate the start and end of plot.

Figure 12(1) is in the period of rapid wave height increase and decrease. In this period when the waves increase in height, surf beats fit the nonlinear interaction theory. In the period of the decay, however, surf beat wave heights decrease with relatively higher energy level than that of the increasing time.

Figure 12(2) is in the period of arriving large wave successively. The surf beat wave heights have a relatively large energy level. So, an energy other than that of bounded long waves may also exist in surf beat in this case. Because of the shape of the port, wave energy may trap by Oharai port.

Figure 12(3) is in the period of continuous increase of wave height. This figure shows that the increase of surf beat due to nonlinear interaction is preceded by a decrease in the surf beat wave height because of the decrease in the ordinary-wave period. Therefore, it is found that in the condition that wave height increase from calm, surf beats exist as bounded long waves.

In figure 10, the black symbols show the condition that wave height

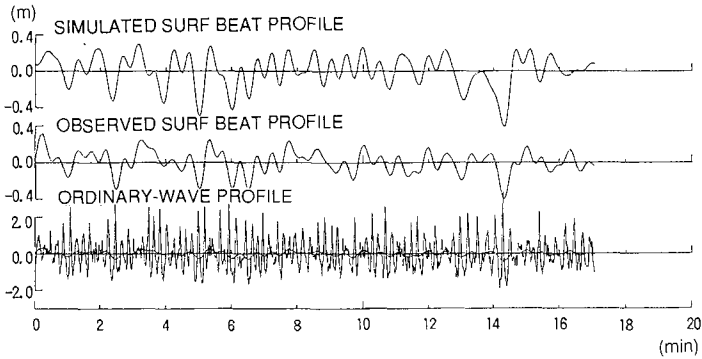


Figure 13. The comparison of the observed surfbeat with simulated surfbeat in the condition that wave height increase from calm.

increase from calm. It is seen that these fit the nonlinear interaction theory.

Figure 13 is the comparison of observed surf beat with simulated surf beat in the condition that wave height increase from calm. The simulated profile shows good agreement with the observed one. Thus it is concluded that the surf beats at the point of 13 m depth exist as bounded waves. According to both measurements and calculations, when the significant wave height of ordinary-waves is 5m, the wave height of surf beat is approximately 1m. This water surface fluctuation is not negligible to the design of maritime structures, because such a large long period fluctuation causes an increase in both hydrostatic pressure and buoyancy of the breakwater.

#### 4. Surf beats inside the harbor

Bowers (1977) investigated the long period wave behavior through theoretical and experimental study and concluded that the bounded long waves became free waves in a harbor. The surf beat behavior inside the harbor is investigated by using the field observation data. For this, wave data in Kashiwazaki-Kariwa are used. At the three points behind the breakwater, St. 2, St. 4 and St. 6, water surface elevations were measured along the direction of wave propagation. Figure 14 shows the result of cross spectral analysis between each two wave data. In figure 14, the solid curve means the phase difference which is calculated from the linear wave theory of progressive waves. From these results, it is confirmed that

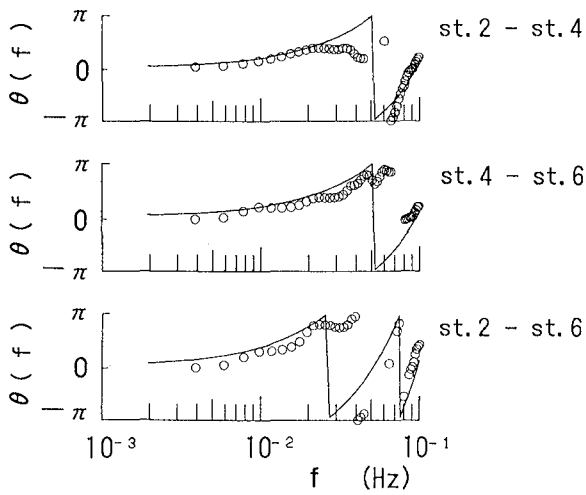


Figure 14. The results of cross spectra analysis between points of behind breakwater.

surf beats in the harbor propagate as free waves.

Figure 15 shows the relationship between the significant wave height of ordinary-wave and that of surf beats at St. B. In the harbor the

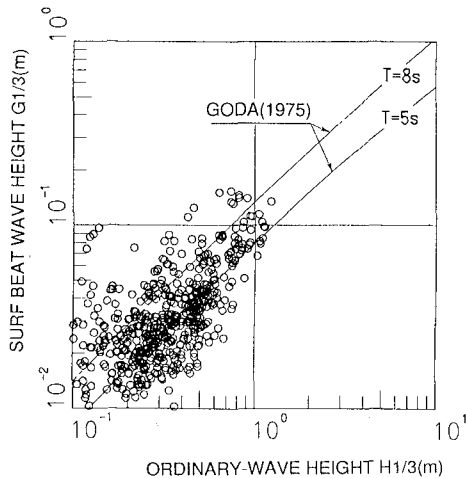


Figure 15. The relationship between the wave height of surfbeat and the ordinary-wave height (St.B).

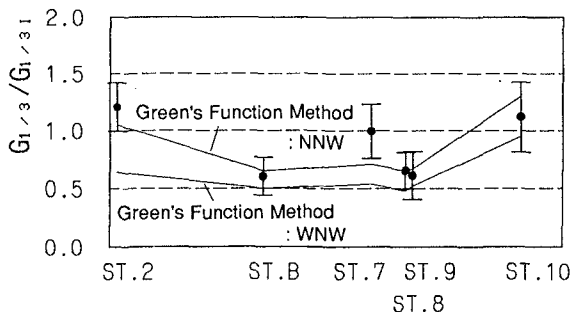


Figure 16. The comparison of the observation results with calculation results for wave height distribution inside the harbor by Green's function method.

clear relationship between the significant wave height of ordinary-wave and that of surf beats is not found because the degree of deformation of both depends on the wave direction and the wave period.

As the surf beats inside the harbor seem to be free waves, the wave height distribution of surf beat may be calculated by the method for ordinary-wave height. The wave height distribution of surf beat in the harbor was calculated, using Green's function method for ordinary-waves. The result of the comparison between the calculation and the observations is shown in figure 16. In this figure, the wave height ratio of surf beat is plotted for each observation point. Relatively good agreement was obtained between the calculation and the observation results except for St. 2 and St. 7. It is considered that the reason for these deviations are that the boundary condition of incident wave is not satisfied completely at St. 2 and the modeling of the shape of sea wall around the St. 7 is inadequate

## 5. Conclusions

Field observations of surf beat inside and outside a harbor were conducted and the characteristics of surf beat in the nearshore non-breaking zone were investigated. It was found that the surf beats exist as bounded waves outside the harbor. In the condition that wave height increase from calm, the height of surf beats may reach 20 % of ordinary-wave heights when the ordinary-wave height is 5m at the depth of 13 m. It was also confirmed that the surf beats exist as free waves inside the

harbor and the wave height distribution of surf beat inside the harbor may be calculated by the same method as that for ordinary-waves.

## References

- Bowers, E.C. (1977): Harbour resonance due to set-down beneath wave group, *J. Fluid Mech.*, Vol.79, part 1, pp.71-92.
- Hotta, S., M. Mizuguchi and M. Isobe (1981): Observations of long period waves in the surf zone, *Coastal Engineering Japan*, Vol.24, pp.41-76.
- Goda, Y. (1985): *Random seas and design of maritime structure*, University of Tokyo press, 323p.
- Kimura, A. (1984): Averaged two-dimensional low-frequency wave spectrum of wind waves, *Comm. on Hydraulics*, Dept. of Civil Engg. Delft Univ. of Tech., Report No.84-3, 54p.
- Kostence, J.K (1984): Measurement of surf beat and set-down beneath wave groups, *Proc. of 19th ICCE*, pp.724-740.
- List, J.H. (1988): Wave groupiness as a source of nearshore long waves, *Proc. of 21st ICCE*, pp.497-551.
- Languet-Higgins, M.S and R.W. Stewart (1962): Radiation stress and mass transport in gravity waves, with application to surf beat, *J. Fluid Mech.*, Vol.13, pp.481-504.
- Mansard, E.P.D. and V. Barthel (1984): Shoaling properties of bounded long waves, *Proc. of 19th ICCE*, pp.798-814.
- Munk, W.H. (1949): Surf beats, *Trans. Amer. Geophys. Un* 30(6), pp.849-653.
- Ottesen-Hansen, N.-E. (1978): Long period waves in natural wave trains. *Inst. Hydrodyn. and Hydraulic Engrg.*, Tech. Univ. Denmark, Prog. Rep. 46, pp.13-24.
- Ottesen-Hansen, N.-E., S.E. Sand, S.E. Lundgren, T. Sorensen and H. Gravesen (1980): Correct reproduction of group-induced long waves, *Proc. 17th Int. Conf. Coastal Eng.*, pp.784-800.
- Sand, S.E. (1982): Long waves in directional seas, *Coastal Engineering*, Vol.6, pp.195-208.
- Sharma, J.N. and R.G. Dean (1979): Development and evaluation of a procedure for simulating a random directional second order sea surface and associated wave force, *Ocean Engg. Rept. No.20*, Dept. Civil Engg., Univ. of Delaware, 139p.
- Symonds, G., D.A. Huntley and A.J. Bowen (1982): Two-dimensional surf beat: long wave generated by a time-varying break point, *J. Geophys. Res.*, Vol.87, No.C1, pp.492-498.
- Symonds, G. and A.J. Bowen (1984): Interaction of near shore bars with incoming wave groups, *J. Geophys. Res.*, Vol.89, No.C2, pp.1953-1977.
- Tucker, M.J. (1950): Surf beats: sea waves of 1 to 5 min. period, *Proc. Roy. Soc. London, Ser. A*, 207, pp.565-573.

## CHAPTER 61

### LOW FREQUENCY WAVES IN THE SURF ZONE

Gary Watson<sup>1</sup> and D. Howell Peregrine<sup>2</sup>

#### ABSTRACT

The generation of low-frequency waves (LFW, also known as ‘infragravity waves’) within a two-dimensional surf zone is investigated numerically using a short-wave resolving model. In this simplified model, based on the nonlinear shallow-water equations, breaking waves are represented by ‘bores’, at which there are jumps in both water depth and velocity. Some idealized trains of modulated waves are then used to investigate how LFW may be generated by forcing within the surf zone, as opposed to the mechanisms of bound wave reflection and moving break point forcing. In this way, the process of LFW generation may be examined in some detail. The model is also compared with some measurements of irregular waves in a flume: good agreement is obtained.

#### INTRODUCTION

Low-frequency waves (LFW) are generated by the transfer of energy from modulated high-frequency waves (short waves) when they propagate into shallow water near the shore (Hamm et al., 1993). The energy transfer may be thought of as being brought

---

<sup>1</sup>Research Associate, University of Bristol, Mathematics Department, University Walk, Bristol BS8 1TW, United Kingdom. (gary.watson@bristol.ac.uk)

<sup>2</sup>Professor of Applied Mathematics, Bristol (d.h.peregrine@bristol.ac.uk)

about by the variations in short-wave momentum flux (radiation stress) as the short waves of varying amplitude propagate over changes of water depth and break (Longuet-Higgins & Stewart, 1964). Past work on modelling LFW generation has used linear theory for the short waves and their radiation stresses. Empirical assumptions about wave amplitudes within the surf zone are used to estimate the radiation stress forces (Gallagher, 1971; Symonds et al., 1982; Nakaza & Hino, 1991; Schäffer, 1993; List, 1992; Roelvink et al., 1992).

Three particularly significant aspects of the generation process have been discussed:

(1) "Bound" LFW are generated with the short-wave groups and these grow as they propagate shorewards (Longuet-Higgins & Stewart, 1962; Agnon, 1993). The bound waves are released to propagate freely when the short waves lose their energy by breaking, or when they propagate over depth changes such as bars.

(2) Modulated short waves break in different depths. The radiation stress gradient is negative to shoreward of the break point and positive to seaward. LFW are generated as the break point moves (Symonds et al., 1982; Schäffer, 1993).

(3) Within the surf zone, the wave set-up fluctuates in response to fluctuations in incident wave amplitude. This rising and falling mass of water at the shoreline generates LFW. If the surf zone is saturated this effect is directly related to (2) but in general, modulations will penetrate into the surf zone and cause a complex time-varying radiation stress field (List, 1991).

These investigations have suffered from the disadvantage that questionable assumptions are made about the validity of linear theory for the propagation and radiation stresses of breaking waves within the surf zone. An alternative to this 'wave-averaged' approach is to use short-wave-resolving models to study the generation processes in more detail, without the need for such assumptions. Here we report studies of LFW generation using the nonlinear shallow-water equations. These are particularly appropriate in the inner surf zone, where the waves have formed into turbulent bores (Packwood, 1980) and they have been proved adequate for modelling breakers on a shallow beach (below, also Cox et al., 1992). It is in the surf zone that LFW have their largest amplitudes and the above generation mechanisms act. Other nonlinear equations such as the Boussinesq equations are only valid for non-breaking waves (although recent efforts have been made to extend their validity into the surf zone: see Schäffer et al., 1992). The shallow-water equations are thus best suited to the study of mechanism (3) above, and it is this which is discussed below.

Initially, our attention has been confined to one horizontal dimension and a



plane beach. The situation is thus simplified by the exclusion of edge waves and longshore currents. Bottom friction has been neglected, because it introduces an unnecessary empirical element into the model. Previous work has suggested that it has no qualitative effects, and that quantitative differences are mainly important in the very shallow swash zone (Packwood, 1980). Beach porosity has also been neglected for simplicity.

### MATHEMATICAL MODEL

The motion of a shallow layer of water, if the length scale of the motion is much greater than the water depth, may be described by the shallow-water equations for the conservation of mass and momentum,

$$d_t + (ud)_x = 0 \quad (1)$$

$$u_t + uu_x + g(d-h)_x = 0 \quad (2)$$

where  $u$  is the depth-averaged flow velocity,  $d$  the water depth,  $g$  the acceleration due to gravity,  $h(x)$  the undisturbed water depth and  $-h_x$  the local bottom slope (assumed small). Subscripts indicate differentiation. The surface elevation is  $\eta = d-h$ . The variables are illustrated in figure 1.

In appropriate conservation form, the equations are:

$$\frac{\partial}{\partial t} \begin{pmatrix} d \\ ud \end{pmatrix} + \frac{\partial}{\partial x} \begin{pmatrix} ud \\ u^2d + \frac{1}{2}gd^2 \end{pmatrix} = \begin{pmatrix} 0 \\ gdh_x \end{pmatrix} \quad (3)$$

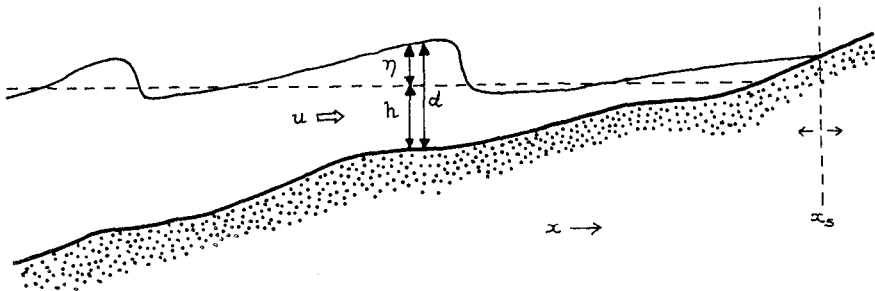


Figure 1: Sketch showing variables referred to in the text.

$$\text{or, } \underline{U}_t + \underline{F}_x = \underline{S}. \tag{4}$$

$\underline{U}$  is a vector of the conserved quantities mass and momentum,  $\underline{F}$  is the flux of those quantities and  $\underline{S}$  is a source term due to the bottom slope. These nonlinear, hyperbolic partial differential equations admit the development and propagation of discontinuities which represent bores at which both mass and momentum are conserved. These fundamental conservation properties are important to ensure that the basic physics is correct. They mean that no empirical terms are required, even for wave breaking, although this does not give a detailed model. The conservation of mass and momentum at a bore may be demonstrated mathematically by integration of eq. (4) to yield the hydraulic jump relations.

A useful way in which to write eqs. (1) and (2) is in the characteristic form. This is obtained by making the substitution  $c^2 = gd$  ( $c$  is the local long-wave speed), rearranging, and expressing in terms of time derivatives along certain trajectories:

$$\frac{d}{dt}(u+2c) = gh_x \quad \text{on} \quad \frac{dx}{dt} = u+c \tag{5}$$

$$\frac{d}{dt}(u-2c) = gh_x \quad \text{on} \quad \frac{dx}{dt} = u-c. \tag{6}$$

In terms of the Riemann invariants,  $R^+ = u+2c$  and  $R^- = u-2c$ , these are

$$R^+_t + (u+c)R^+_x = gh_x \tag{7}$$

$$R^-_t + (u-c)R^-_x = gh_x. \tag{8}$$

Eqs. (5) and (6), or (7) and (8), indicate that the quantities  $R^+$  and  $R^-$  propagate along the characteristics at speeds  $u+c$  and  $u-c$  respectively, changing at a rate  $gh_x$  as they do so.  $u+c$  and  $u-c$  are equal to the local long-wave speeds of shoreward- and seaward-propagating waves respectively, advected by the local flow velocity  $u$ .  $R^+$  and  $R^-$  thus specify the shoreward- and seaward-propagating waves, respectively, a fact which is very useful in analysing results. At bores, there are jumps in  $R^+$  and  $R^-$  (Peregrine, 1974).

The boundary conditions to be satisfied are as follows. The shoreline boundary conditions are that the water depth becomes zero and its position  $x_s(t)$  moves such that it has the same velocity as the water:

$$d(x_s[t], t) = 0, \quad u(x_s[t], t) = \frac{dx_s}{dt}. \quad (9)$$

The appropriate seaward boundary conditions depend on the particular situation being studied. For wave modelling on a real beach, we need to prescribe the incident waves and yet permit outgoing waves to escape without reflection. This is done using the Riemann invariants discussed above. As long as the flow is subcritical ( $|u| < c$ ) at all times,  $R^-$  propagates into the domain at speed  $u + c$  and  $R^+$  propagates out of it at speed  $u - c$ .  $R^-$  at the seaward boundary must thus be computed from the solution just inside, using eq. (8). Incident waves are specified by prescribing  $R^+(t)$ . In supercritical conditions, both  $R^+$  and  $R^-$  would be specified if  $u > c$ , but neither need be specified if  $u < -c$ . Supercritical conditions do not occur in the cases studied here.

For wave tank experiments, the correct seaward boundary conditions must be chosen to fit the data that are available. In the case discussed below, the water depth  $d(t)$  is set equal to that measured at a wave probe, with  $R^-$  computed as before. Unfortunately this permits non-physical reflections at the seaward boundary, which must be borne in mind when interpreting the results. If the entire flume is to be modelled, the mode of generation must also be modelled correctly.

## NUMERICAL METHOD

A new numerical scheme, the weighted average flux method, was adopted for the solution of these equations. Invented primarily for aerodynamics, it is a development of currently favoured methods such as Godunov's and Roe's. Toro (1989) introduced the method for a simple advection equation and for the Euler equations of compressible gas dynamics. Toro (1992) applied it to the shallow-water equations for water of uniform depth. Watson, Peregrine & Toro (1992) adapted it for use with a moving shoreline and variable depth.

The method is 'shock-capturing', in that discontinuities (bores) are automatically treated correctly without the need for a special tracking algorithm. Bores are followed very well and for a given accuracy less discretization points are required than with most methods. It is found to be more efficient and robust than previously used methods such as the Lax-Wendroff scheme used by Hibberd &

Peregrine (1979).

The essence of the method consists of solving the initial-value Riemann problem for the shallow-water equations in each cell, with constant data in each half of the cell and a jump at the mid-point. This is done analytically using Riemann invariants and the mass and momentum conditions at bores. In this way the average mass and momentum fluxes in each cell are estimated one half-timestep in advance. A Total Variation Diminishing (TVD) adjustment is then made to the flux average in order to eliminate spurious oscillations near bores. This is done by means of upwinding, using a flux limiter to reweight the flux average (hence the name, 'Weighted Average Flux'). The TVD procedure effectively makes the scheme somewhere between first and second-order, so as to achieve a compromise between accuracy and stability. An explicit finite difference scheme is used for advancing in time. Each time step  $\Delta t_n$  must be less than the time taken for the fastest wave in the solution to propagate one grid point (the 'CFL' condition).

The shoreline boundary conditions (9) are not solved explicitly, but are approximately satisfied in the model. Any negative values of  $d$  are reset to zero and a dry-bed Riemann problem is used at the next timestep (Toro, 1990). As the depth becomes very small near the shoreline, large errors would result if the unmodified scheme were used. This is because small errors in the momentum variable  $ud$  become large errors in  $u$  when divided by a small value of  $d$ . In order to avoid such errors, an alternative approximation is used for  $u$  wherever the depth is less than a suitable small depth tolerance  $d_{tol}$ . To plot the position of the moving shoreline, another small depth  $d_s$  is chosen and the position of that depth is plotted.

The seaward boundary conditions were implemented along the lines mentioned above, using a simple finite difference approximation to eq. (8). Note that it is necessary to check whether the flow is in fact subcritical before using this scheme.

## RESULTS

Before proceeding with more complicated cases, the numerical scheme was tested against an analytic solution for non-breaking shallow-water motion on a beach (Carrier & Greenspan, 1958). The test showed good agreement, except for a small error in velocity very close to the shoreline.

### *Some Idealized Illustrations.*

Figures 2 and 3 illustrate the generation of a single low-frequency cycle by an idealized wave group. The input  $R^+(t)$  consists of fully modulated sinusoidal waves cut off after one group of ten waves. Figure 2 shows a perspective view of the surface elevation solution in space-time. All variables are dimensionless, with the beach slope scaled out of the problem. In this example, a slope of 1/30 and an offshore depth of 1 m would correspond to a wave period of 5 s and a wave height of 0.8 m. The waves steepen into bores as they travel towards the beach, decreasing in amplitude and slowing down as they do so. In the first half of the group, each successively larger wave pushes more water up the beach face. As the wave amplitude decreases in the second half of the group, this water recedes back down the beach. The inertia of the backwash of these waves pulls the shoreline water level down beneath the still water level and it finally rises rather rapidly to its initial level. This rising and falling motion, on the time-scale of the wave group, shows up clearly in the shoreline position (thick line). It generates a low-frequency wave which propagates offshore, and which can just be seen in the latter half of the plot.

In figure 3 the incident and outgoing waves are separated by means of the Riemann invariants.  $2c \pm u$  ( $-R^\pm$ ) has been plotted rather than  $u \pm 2c$  so that higher values always correspond to deeper water. These are plotted at different offshore distances after subtraction of the undisturbed value. At  $x=0.2$  the beach is normally dry, but values become defined when a wave runs up past this position.

The incident invariant shows the waves steepening and decreasing in amplitude as they approach the shore, and the raising of the mean level in the middle of the group. This corresponds to the set-up which is forced by the wave group. It also shows the modulation of the group becoming weaker as the waves saturate. The outgoing invariant shows the almost complete absence of short waves travelling away from the beach, because they have dissipated their energy and are not reflected. An asymmetric low-frequency pulse is seen to propagate away from the beach, decreasing in amplitude as it does so. Note that at  $x=0$ , positive elevation is approximately in phase with the peak of the incident group (but this is expected to depend on group length).

The incident wave group used in figure 2 is not very realistic, since such large waves are not in reality sinusoidal. Also, large-amplitude sine waves have a net mass transport associated with them because the water is deeper when the velocity is

onshore (wave crest) and shallower when it is offshore (wave trough). This transport will be an increasing function of wave height and thus will cause a LFW to be generated by the group. Although a real wave group will have a mass transport associated with it, it will not necessarily be the same as that of these sine waves, and it may be thought of as being part of the bound wave driven by the group. In this example the LFW may thus be too large: an incident wave group is normally accompanied by a bound wave of depression, whereas ours is not. The bound wave

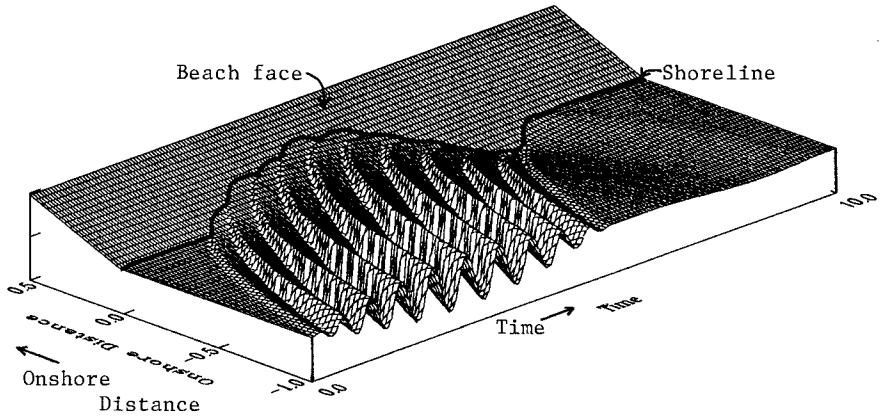


Figure 2: Response to a single wave group. Perspective view of space-time plot of surface elevation, including shoreline motion.

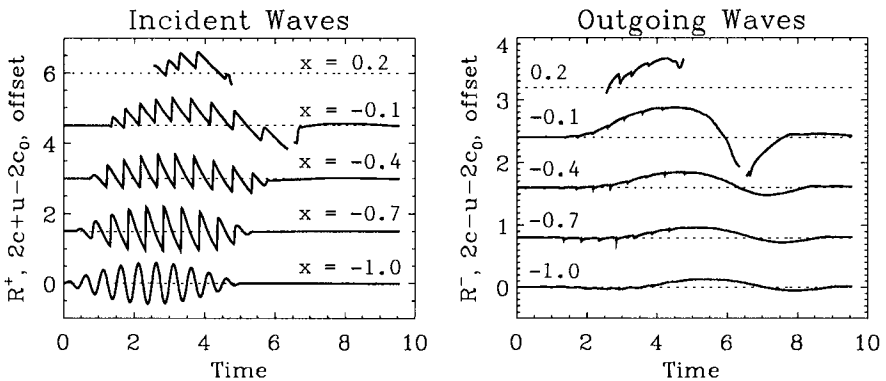


Figure 3: Plots of incident and outgoing wave signals (Riemann Invariants) at various distances offshore, for the waves in figure 2.

will depend on the offshore topography, in a way which is being investigated. A theory for bound waves in moderately shallow water, where the theory of Longuet-Higgins & Stewart (1962) fails, has recently been derived by Agnon (1993).

In the mean time we look to the other extreme and present an example where there is no mass transport associated with the wave group. The wave shape is also modified to the form of a 'sawtooth', representing waves which have already broken. The mass transport in each wave is forced to be zero by choosing appropriate values of the peak and trough water depths. The results from this wave group are shown in figures 4 and 5, which are equivalent to figures 2 and 3 and have the same scales.

In these results also, a similar LF pulse is generated. Its amplitude is about half that in the previous case. The trough of the wave is deeper, indicating that the

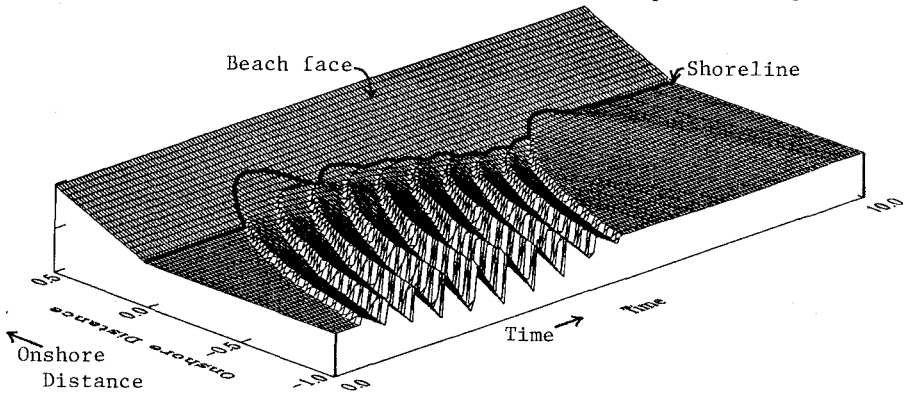


Figure 4: As figure 2, but for a group of breaking waves with no mass transport.

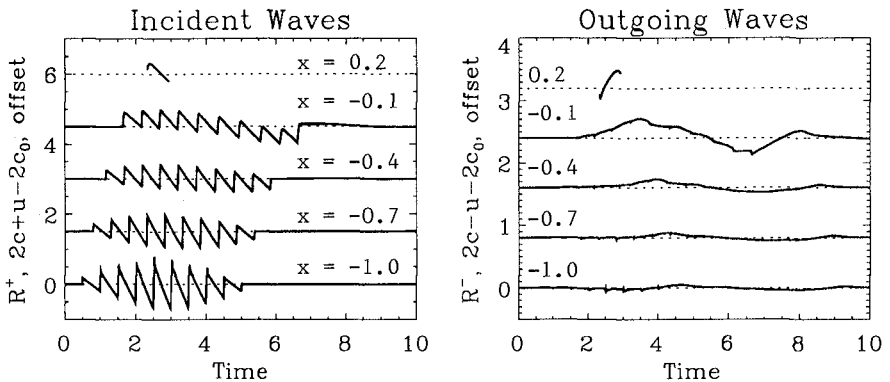


Figure 5: As figure 3, but for a group of breaking waves with no mass transport.

outgoing wave, like the incident wave, carries little mass. The phase of the pulse at  $x=0$  relative to the incident wave group is also slightly different, with the peak occurring about one fifth of a cycle ( $70^\circ$ ) earlier and being more sharply defined. Note that this corresponds closely to the different shape of the incident pulse at the still-water shoreline ( $x=0$ ). In both cases, the shape of the outgoing pulse is close to the shape of the low-frequency component of the incident group at this position.

We conclude that even for a wave group where the bound wave component is small, a significant LFW will be generated if the groupiness persists inside the surf zone. Note also that in both cases, the amplitude of the LF pulse is such that the propagation velocity of the incident short waves is modified significantly. This interaction is not usually treated in wave-averaged models, nor is the substantial shoreline excursion.

Experiments are under way to verify these results for single wave groups in a wave flume. The effect on the LFW of changes in incident wave amplitude, period and group shape remains a subject for further research.

#### *Comparison with Wave Flume Experiments.*

In order to assess the relevance of the model to real waves, comparison is made with data from some wave flume experiments. The measurements are supplementary to those reported by Hansen & Svendsen (1979), and were made in the same flume. The measurements consisted of a series of depth gauges within the surf zone on a slope of 1/34.26. Data from the furthest offshore of these gauges were used to specify the waves at the seaward boundary of the model. Since velocity measurements were not available, the incident Riemann invariant  $R^+$  could not be found exactly at the boundary. Instead, the boundary condition was approximated by setting the depth equal to the measured value, and using the outgoing invariant to compute the velocity. As already noted, this is not ideal.

The result from one such run is given in figure 6. Surface elevation is plotted against time, at each offshore distance where a wave gauge was located. The first wave reaches the offshore probe at about 20s after startup from rest. The measured data are plotted with a solid line and the model result with a dashed line. The two are identical at the furthest station offshore ( $x=-2.81$  m), which was the seaward boundary for the numerical model. As the shore is approached, differences begin to appear between the two.

Except for the two gauges closest to shore, these differences are small and the



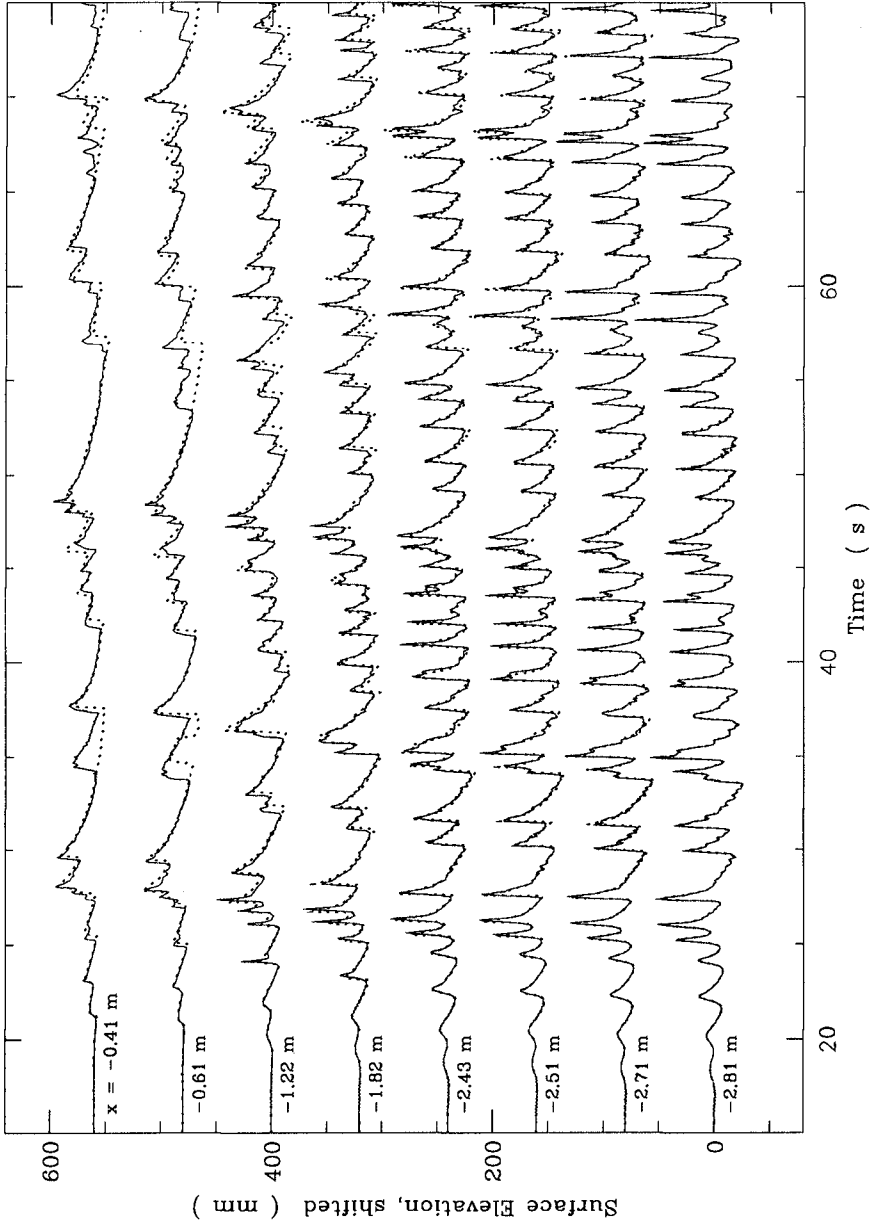


Figure 6: Comparison between measured and modelled surface elevation for irregular waves in a flume, data courtesy of J.B. Hansen and I.A. Svendsen.

agreement is very good. Propagation speeds, and changes in wave amplitude and shape, are reproduced well by the model. This is true even for the small waves at the beginning of the record. The onset of breaking is reproduced well by these equations, as was also found by Packwood (1980). At the two shallowest gauges, larger differences begin to appear. Some waves are missing altogether in the model result. This is because the waves did not reach this location in the experiment. At  $t=36\text{s}$  in the data from  $x=-0.61$ , there is a negative jump in surface elevation which was not present in the data. This results from a bore being forced to move back down the beach by the backwash from the preceding wave. The differences in this very shallow water may be due to the neglect of friction in the model. As in the above example, small changes in the position of a bore relative to a wave gauge may produce a large change in the time series at the gauge.

Despite these differences in high-frequency detail, the low-frequency component of the motion is very well reproduced in the shallow water. This manifests itself as changes in surface elevation on a timescale of about 10 seconds. This confirms that the nonlinear shallow-water equations used by the model contain all the essential components necessary for the LFW generation process to be modelled quite accurately.

## CONCLUSIONS

The nonlinear shallow-water equations have been shown to provide a good basis for the modelling of LFW generation in the surf zone. Comparison with wave flume data indicates a good reproduction of the long-wave motion everywhere, and of the short-wave properties except in very shallow water. Runs using idealized wave groups illustrate the process by which LFW are generated by forcing within the surf zone, as distinct from breakpoint forcing or bound wave reflection.

## ACKNOWLEDGEMENTS

This work was funded by the Commission of the European Communities under MAST contract 0035 as part of the G6M coastal morphodynamics program. We are grateful to E.F. Toro of Cranfield Institute of Technology for providing the constant-depth code, and for advising on its adaptation. The wave flume data were

kindly provided by J.B. Hansen and I.A. Svendsen, then at ISVA, Technical University of Denmark.

## REFERENCES

- Agnon, Y. (1993). On a uniformly valid model for surface wave interaction. *J. Fluid Mech.*, in press.
- Carrier, G.F. and H.P. Greenspan (1958). Water waves of finite amplitude on a sloping beach, *J. Fluid Mech.* **4**, 97-109.
- Cox, D.T., N. Kobayashi and A. Wurjanto (1992). Irregular wave transformation processes in surf and swash zones. *Proc. 23rd Int. Conf. Coastal Eng.*, paper 141.
- Gallagher, B. (1971). Generation of surf beat by nonlinear wave interactions. *J. Fluid Mech.* **49**, 1-20.
- Hamm, L., P.A. Madsen and D.H. Peregrine (1993). Wave transformation in the nearshore zone: a review, *Coastal Eng.*, in press.
- Hansen, J.B. and I.A. Svendsen (1979). regular waves in shoaling water experimental data. *Institute of Hydrodynamic and Hydraulic Engineering (ISVA), Tech. Univ. Denmark, Series Paper 21.*
- Hibberd, S. and D.H. Peregrine (1979). Surf and run-up on a beach: a uniform bore, *J. Fluid Mech.* **95**, 323-345.
- List, J.H. (1991). Wave groupiness variations in the nearshore. *Coastal Eng.* **15**, 475-496.
- List, J.H. (1992). Breakpoint-forced and bound long waves in the nearshore: a model comparison. *Proc. 23rd Int. Conf. Coastal Eng.*, paper 123.
- Longuet-Higgins, M.S. and R.W. Stewart (1962). Radiation stress and mass transport in gravity waves, with application to "surf beats", *J. Fluid Mech.* **13**, 481-504.
- Longuet-Higgins, M.S. and R.W. Stewart (1964). Radiation stresses in water waves: a physical discussion, with applications, *J. Fluid Mech.* **13**, 481-504.
- Nakaza, E. and M. Hino (1991). Bore-like surf beat in a reef zone caused by wave groups of incident short period waves. *Fluid Dynamics. Res.* **7**, 89-100.
- Packwood, A.R. (1980). Surf and run-up on beaches. *Ph.D. Thesis, University of Bristol, School of Mathematics.*
- Peregrine, D.H. (1974). Water-wave interaction in the surf zone, *Proc. 14th Int. Conf. Coastal Eng.*, 500-517.

- Roelvink, J.A., H.A.H. Petit and J.K. Kostense (1992). Verification of a one-dimensional surf-beat model against laboratory data. *Proc. 23rd Int. Conf. Coastal Eng.*, paper 122.
- Schäffer, H.A., R. Deigaard and P.A. Madsen (1992). A two-dimensional surf zone model based on the Boussinesq equations. *Proc. 23rd Int. Conf. Coastal Eng.*, paper 257.
- Schäffer, H.A. (1993). Infragravity waves induced by short-wave groups. *J. Fluid Mech.*, in press.
- Symonds, G., D.A. Huntley and A.J. Bowen (1982). Two-dimensional surf beat: long wave generation by a time-varying breakpoint. *J. Geophys. Res.* **87C**, 492-498.
- Toro, E.F. (1989). A weighted average flux method for hyperbolic conservation laws, *Proc. R. Soc. Lond. A*, **423**, 401-418.
- Toro, E.F. (1990). The dry-bed problem in shallow-water flows. *Cranfield Institute of Technology, College of Aeronautics Report 9007*.
- Toro, E.F. (1992). Riemann problems and the WAF method of solving the two-dimensional shallow-water equations. *Phil. Trans. Roy. Soc. Lond. A*, **338**, 43-68.
- Watson, G., D.H. Peregrine and E.F. Toro (1992). Numerical solution of the shallow-water equations on a beach using the weighted average flux method. *Computational Fluid Dynamics '92*, Ch. Hirsch et al. (eds.), Elsevier, 495-502.

## CHAPTER 62

### Low Frequency Waves in Intermediate Water Depths E C Bowers<sup>1</sup>

#### Abstract

This paper is concerned with calculations and field measurements of low frequency or infragravity waves associated with wave grouping (frequencies in the range of 0.005 to 0.04 Hertz). These waves have periods in excess of wind generated waves and they are assuming particular importance now due to the effect they are thought to have on sediment transport in and near the surf zone. However, the impetus for the work described here originated from a need to quantify the magnitude of these waves in intermediate depths typical of harbour entrances: it being generally accepted that long period waves excite harbour resonances and moored ship movements, leading to berth downtime.

#### 1. Introduction

In intermediate water depths the infragravity waves associated with wave grouping are expected to consist largely of an incoming component bound to groups of shoreward going (primary) waves, sometimes called set-down beneath wave groups, and a free long wave component which will be referred to as surf beat in this paper. In this context surf beat includes both "leaky" modes propagating offshore and trapped, high order, edge wave modes. A full description of set-down in terms of radiation stresses associated with wave grouping was first given by Longuet-Higgins and Stewart (1964) and, in the same paper, they suggested that surf beat was the reflection of the bound long wave which became free of wave groups in the surf zone: this to account for a time lag observed by Tucker (1950) in correlations between long waves measured offshore of a beach and the envelope of the incoming waves.

Subsequently, a description was provided by Symonds et al (1982) of another mechanism for the generation of free long waves or surf beat. Called the moving breakpoint mechanism, the authors showed that gradients in radiation stresses associated with breaking waves, as the break point moves onshore and offshore at wave group periods, would generate long waves. An extension of this mechanism has been developed by Watson and Peregrine (1992). Using non-linear shallow water equations they have shown that the grouping of broken waves, that remains within the surf zone may lead to additional free long wave energy. Schaffer and Jonsson (1990) have compared results from an analytical description of long wave generation, containing the moving break point mechanism and the reflection of the bound long wave, with results of flume experiments carried out by Kostense (1984) and obtained qualitative agreement. Time domain models (List, 1992 and Roelvink 1992) and a frequency space model (van Leeuwen and Battjes 1990) containing both mechanisms of surf beat generation have also been developed and comparisons made with flume and field data.

Free long waves can also be expected to be released by incoming wave groups as they propagate over seabed irregularities (see Mei and Bennisou, 1984, for example).

-----  
<sup>1</sup>Research Department, HR Wallingford, Wallingford, Oxon. OX10 8BA, UK.

From the above discussion it can be seen that two basic long wave populations associated with wave grouping can be distinguished: the incoming bound long waves and free long waves or surf beats generated via various mechanisms. In principle, the bound long waves can be calculated from a knowledge of the primary waves. Early flume experiments verified that the amplitude of the bound long wave could be predicted in intermediate water depths using a Stokes expansion of the basic wave equations taken to second order in wave amplitude (see Bowers, 1980, for example). This suggested that surf beats could be determined in field data by calculating the bound long wave component and subtracting it from the total long wave energy. With that in mind, a method of analysis of pressure sensor data was developed to separate out the surf beat and bound long wave components in the total long wave spectrum. This analysis was applied subsequently to a number of sites around the UK coast (water depths 4m to 19m) including Port Talbot on the south coast of Wales in 1984, Dover and Shoreham on the south coast of England in 1986, Barrow-in-Furness on the west coast of England in 1988 and Sunderland on the east coast of England in 1988. The method of analysis is outlined in the next section and the results from the 5 sites discussed in a following section.

Similar analyses of field data have been carried out recently by Okihiro et al (1992) and by Herbers et al (1992).

## 2. Method of analysis

The first point to make is that calculation of the bound long wave has to take the directional spread of primary wave energy into account (Sand 1982). This is well illustrated by flat bed wave basin results obtained recently at HR Wallingford using a shallow water multi-directional wave-maker. Figure 1 shows measured long wave spectra associated with primary waves representing a significant wave height of 8m, a spectral peak period of 15s and water depth of 40m. It can be seen that even a relatively narrow rms spread of  $22.5^\circ$  in short crested primary waves will almost halve the long wave height associated with long crested uni-directional (zero spread) waves. It is also of interest to note that the long wave height is not all that sensitive to the amount of directional spread, with a broad spread corresponding to a  $\cos^2\theta$  distribution ( $32^\circ$  rms spread) resulting in only slightly smaller long waves than those measured with a primary wave spread of  $22.5^\circ$ . These results indicate that once a small degree of directional spread exists in the primary waves, it produces a considerable reduction in the height of the bound long wave component but thereafter directional spread becomes a less sensitive parameter (see Equations (17) and (18) later). Of course, surf beats due to reflections of the bound long wave from the shingle beaches on the wave basin boundaries would also have been present in these experiments but they can be expected to be a fixed percentage of the bound long wave. Thus, the relative behaviour of the total long wave spectra in Figure 1 can be considered representative of the relative behaviour of just the bound long wave spectra in the model depth equivalent of 40m.

The second point to make is that relatively long wave records are required to reduce uncertainties in long wave magnitudes. For example, there would only be 10 waves of 2 minute period in a conventional wave record 20 minutes long with the result that large variations in the long wave height would occur from record to record even with a stationary sea state. This problem can be minimised by taking a long enough record for which a full range of different wave grouping patterns has had time to occur leading to representative bound long waves. For example, Bowers (1988) has demonstrated in flume work, with compensation for set-down at the wavemaker, that in moderately long experiments the spectrum of set-down or the bound long wave component in random seas will tend to an "expected" spectrum calculated without taking into account the phases of the primary waves. In short experiments, or short wave records, these phases become important because only certain patterns of wave grouping will have occurred leading to an unrepresentative long wave spectrum. To ensure long records in the field measurements a bottom mounted pressure sensor was programmed to take 2 hour records. This was done by sampling regularly for 5 minutes every 4 hours and when the significant wave height exceeded a present threshold level, a 2 hour record was taken. This technique ensured that long records were only taken at times of relatively high primary wave activity when the associated long waves were worth measuring.

In the measurements reported here, the specially programmed pressure sensor provided information about the one dimensional primary wave spectrum, but no information

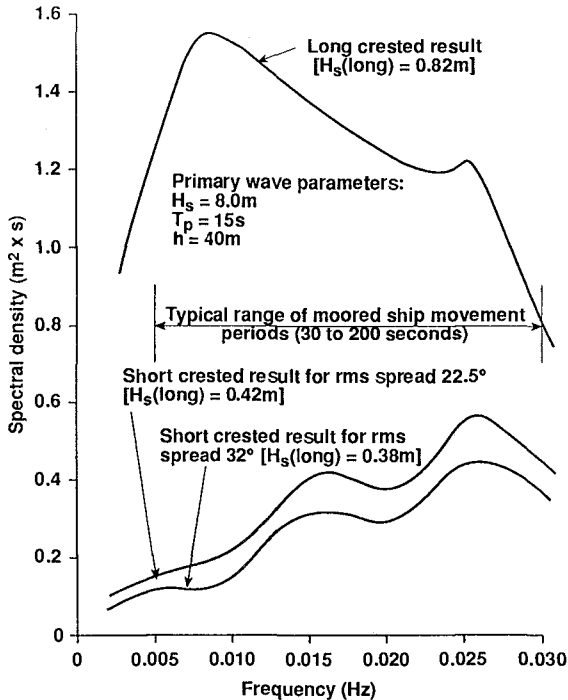


Figure 1 Wave basin long wave spectrum showing effect of short crestedness in primary waves

about directional wave properties. However, the (zero lag) correlation coefficient between the forced low frequency disturbance and the low frequency part of the square of the primary wave pressures is sensitive to the amount of directional spread in the primary waves, with narrow spreads producing higher correlations. Thus, by calculating the correlation coefficient for the total long waves from the pressure sensor data, it is possible to infer the mean directional spread in the primary waves (see Section 2.2). Armed with the one dimensional primary wave spectrum and a mean spread parameter, it is then possible to calculate the "expected" spectrum of the forced low frequency disturbance and subtract it from the measured long wave spectrum to leave the surf beat spectrum.

The bound long wave spectrum based on a second order Stokes expansion (see for example Sand 1982) really applies only to a flat seabed. If the seabed is sloping gently enough, so that the wave system has time to adjust itself to local depths, then the same calculation can be expected to apply to the real situation with the local water depth being used in the equations. While this assumption appears reasonable in most cases for the primary waves, it is less likely to apply to long waves where depth changes can be significant within a wavelength. In what follows, an allowance for seabed slope is made as a correction to the "flat bed" calculation of the bound long wave and it is found that an additional bound long wave component results which lags the main one by  $90^\circ$ . This may explain a lag in the total bound long wave component that has been reported by List (1992) in a numerical model of nearshore surf beat generation. However, for the seabed slopes and intermediate water depths applicable to the field measurements reported in this paper it is found that the additional bound long wave component remains a fraction of the "flat bed" bound long wave and, if included, alters resulting estimates of surf beat height by only a few percent.

2.1 Calculation of bound long waves

For convenience, we represent the seabed by straight parallel contours running perpendicular to the x axis of a right-handed orthogonal co-ordinate system where the x axis points offshore. The plane z = 0 is taken to be the water surface and we assume that a multi-directional sea approaches from offshore, with its mean direction parallel to the x axis. A constant seabed slope  $\alpha$  is taken so that water depth(h) is given by,

$$h = x \tan \alpha \tag{1}$$

We assume irrotational wave motion with fluid velocity  $\underline{q}$  derived from a velocity potential  $\phi$ ,

$$\underline{q} = (u, v, w) = -\nabla \phi$$

Incompressibility leads to the basic wave equation

$$\nabla^2 \phi = 0 \tag{2}$$

Solutions to (2) are sought subject to the following boundary conditions.

On the seabed z = -h, the normal velocity vanishes, i.e,

$$u \frac{dh}{dx} + w = 0 \tag{3}$$

and on the free surface z =  $\eta$  we have the kinetic condition

$$\frac{\partial \eta}{\partial t} + u \frac{\partial \eta}{\partial x} + v \frac{\partial \eta}{\partial y} - w = 0 \tag{4}$$

and Bernoulli's equation (with constant air pressure at the surface)

$$\frac{1}{2} \underline{q}^2 + g\eta - \frac{\partial \phi}{\partial t} = 0 \tag{5}$$

We solve the above equations by using a Stokes expansion, retaining linear terms in the equation in lowest order and bringing quadratic terms into next order. With in each order, flat bed solutions are obtained initially and then corrections obtained to allow for depth variations.

As the expressions for the final bound long wave spectrum are complex we consider just one component associated with two primary wave frequencies  $\omega_1$ , and  $\omega_2$  propagating at angles  $\theta_m$  and  $\theta_n$ , respectively, to the x axis,

$$\eta^{(1)} = a_{n2} \cos(\omega_2 t + \underline{k}_{n2} \underline{r} + \epsilon_{n2}) + a_{m1} \cos(\omega_1 t + \underline{k}_{m1} \underline{r} + \epsilon_{m1})$$

where

$$\begin{aligned} \underline{k}_{n2} \underline{r} &= k_2 \cos \theta_n x + k_2 \sin \theta_n y, \\ \underline{k}_{m1} \underline{r} &= k_1 \cos \theta_m x + k_1 \sin \theta_m y, \end{aligned}$$

Here,  $a_{n2}(x)$ ,  $a_{m1}(x)$  are the amplitudes of the two primary wave components and  $\epsilon_{n2}$ ,  $\epsilon_{m1}$  are their random phases, while each wave number satisfies the usual dispersion relationship in terms of the local water depth h(x),

$$\omega^2 = kg \tanh kh.$$

The depth variation can be shown to introduce an additional requirement on each primary component which expresses the conservation of wave energy during refraction over the varying seabed level,

$$\frac{d}{dx} (a^2 C_g \cos \theta) = 0$$



where  $c_g$  is the group velocity

$$c_g = \frac{\omega}{2k} \left( 1 + \frac{2kh}{\sinh 2kh} \right)$$

To next order in the Stokes expansion, the quadratic terms in (4) and (5) are expressed as products of the first order quantities and they lead to terms containing sum and difference frequencies  $\omega_2 \pm \omega_1$ . The bound long wave component has frequency  $\omega_2 - \omega_1$ , so we retain just the difference frequency component. Solutions to Laplace's equation (2) are sought for the second order potential  $\phi^{(2)}$  subject to boundary condition (3) on the seabed and the following surface condition obtained from (4) and (5),

$$\frac{\partial^2 \phi^{(2)}}{\partial t^2} + g \frac{\partial \phi^{(2)}}{\partial z} = \eta^{(1)} \left( \frac{\partial^2 w^{(1)}}{\partial t^2} \right) + g \frac{\partial w^{(1)}}{\partial z} + 2q^{(1)} \frac{\partial q^{(1)}}{\partial t} \tag{6}$$

Equation (6) shows how the surface perturbation on the right-hand side forces the bound long wave potential  $\phi^{(2)}$ . Following the pattern of solution outlined above for the primary waves, we calculate the bound long wave first of all neglecting depth variations and then consider the effect of variable depth as a perturbation on this solution. We denote the local depth solution for the bound long wave potential by  $\phi_o^{(2)}(x)$  and its correction for depth variation by  $\phi_1^{(2)}(x)$ . Thus,  $\phi_o^{(2)}(x)$  takes the form of the usual "flat bed" second order potential (see Sand, 1982 for example).

$$\phi_o^{(2)} = A_{mn} \cosh(|\underline{k}^-|(z+h)) \sin(\omega t + \underline{k}^- \cdot \underline{r} + \varepsilon) \tag{7}$$

where,

$$\begin{aligned} \varepsilon &= \varepsilon_{n2} - \varepsilon_{m1}, \\ \omega &= \omega_2 - \omega_1, \\ \underline{k}^- &= \underline{k}_{n2} - \underline{k}_{m1}, \end{aligned}$$

$$A_{mn} = \frac{1}{2} g^2 a_{n2} a_{m1} \left[ \frac{e^- + \frac{2k_1 k_2}{\omega_1 \omega_2} \omega^- (\cos(\theta_n - \theta_m) + \tanh k_1 h \tanh k_2 h)}{(\omega^-)^2 \cosh |\underline{k}^-| h - g |\underline{k}^-| \sinh |\underline{k}^-| h} \right]$$

$$e^- = \frac{k_2^2}{\omega_2 \cosh^2 k_2 h} - \frac{k_1^2}{\omega_1 \cosh^2 k_1 h}$$

To find  $\phi_1^{(2)}$  we consider solutions of (2) of the following form,

$$\phi_1^{(2)} = G_{mn}(x, z) \cos(\omega t + \underline{k}^- \cdot \underline{r} + \varepsilon) \tag{8}$$

where,

$$\begin{aligned} G_{mn} &= (B_{mn} + z E_{mn}) \sinh |\underline{k}^-|(z+h) \\ &+ (C_{mn} + z D_{mn} + z^2 F_{mn}) \cosh |\underline{k}^-|(z+h), \\ 2|\underline{k}^-| F_{mn} &= -k_x^- A_{mn} \frac{d}{dx} |\underline{k}^-| \\ |\underline{k}^-| D_{mn} &= -k_x^- A_{mn} \frac{d}{dx} |\underline{k}^-| d, \\ 2|\underline{k}^-| E_{mn} &= \frac{1}{A_{mn}} \frac{d}{dx} (k_x^- A_{mn}^2) + \frac{k_x^- h}{|\underline{k}^-|} A_{mn} \frac{d}{dx} |\underline{k}^-|, \end{aligned}$$

and,

$$k_x^- = k_2 \cos \theta_n - k_1 \cos \theta_m$$

The boundary condition (3) leads to a value for  $B_{mn}$

$$2|k^-|B_{mn} = -\frac{h}{A_{mn}} \frac{d}{dx} (k_x^- A_{mn}^2) + \frac{k_x^- h A_{mn}}{|k^-|} \frac{d}{dx} |k^-|,$$

and (6) leads to a value for  $C_{mn}$

$$C_{mn} [g|k^-| \sinh |k^-| h - (\omega^*)^2 \cosh |k^-| h] + gD_{mn} \cosh |k^-| h + gE_{mn} \sinh |k^-| h + B_{mn} [g|k^-| \sinh |k^-| h - (\omega^*)^2 \cosh |k^-| h] = H_{mn}.$$

Here,  $H_{mn}$  is the term on the right-hand side of (6) proportional to  $\cos(\omega^* t + k^- x + \epsilon)$ .

The above set of equations define the additional bound long wave component (8) due to a varying water depth. It can be seen that it has a 90° phase difference with the usual "flat bed" bound long wave (7).

The expressions derived so far relate to just a pair of primary wave components. To define the bound long wave associated with a multi-directional sea it is necessary to sum over all the pairs of wave components with amplitudes that can be defined in terms of the directional wave spectrum  $S_d$ , ie

$$a^{n2} = 2 S_d(f_2, \theta_n) df d\theta, \tag{9}$$

$$a_{m1}^2 = 2 S_d(f_1, \theta_m) df d\theta. \tag{10}$$

Finally, as measurements were made with a bottom mounted pressure sensor (with the diaphragm pointing upwards) we obtain an expression for the forced low frequency disturbance on the seabed from Bernoulli's equation,

$$\eta_s^{(2)} = \frac{1}{g} \left[ \frac{\partial \phi^{(2)}}{\partial t} - \frac{1}{2} (q^{(1)})^2 \right]_z = -h \tag{11}$$

### 2.2 Estimating directional spread

This was done using the correlation coefficient  $R_L$  (at zero lag) between the low frequency part of the square of the primary wave bed pressures, effectively the square of the seabed wave envelope, and the measured low frequency disturbance on the bed. Denoting the primary wave on the bed by  $\eta_p^{(1)}$  and the surf beat by  $\eta_b^{(2)}$  we have by definition,

$$R_L = \frac{\int (\eta_p^{(1)})^2 (\eta_s^{(2)} + \eta_b^{(2)}) dt}{(\int (\eta_p^{(1)})^4 dt)^{1/2} (\int (\eta_s^{(2)} + \eta_b^{(2)})^2 dt)^{1/2}}$$

Where  $\eta_s^{(2)}$  is defined in (11). The above quantity can be calculated from the measured pressure sensor data and examples of  $R_L$  are shown in Figure 2 for a range of lags and primary wave heights. It can be seen in all cases that a negative correlation coefficient occurs at zero lag, consistent with a set-down beneath groups of large waves. The Bernoulli pressure in (11) will contribute to this negative correlation but it is insufficient to explain the magnitude of the measured correlations. In all cases the recordings were made far enough offshore for us to assume that at zero lag surf beat is uncorrelated with both the square of the primary waves and the bound long wave so that  $R_L$  simplifies to,

$$R_L = \left( \frac{M_s}{M_L} \right)^{1/2} R_s \tag{12}$$

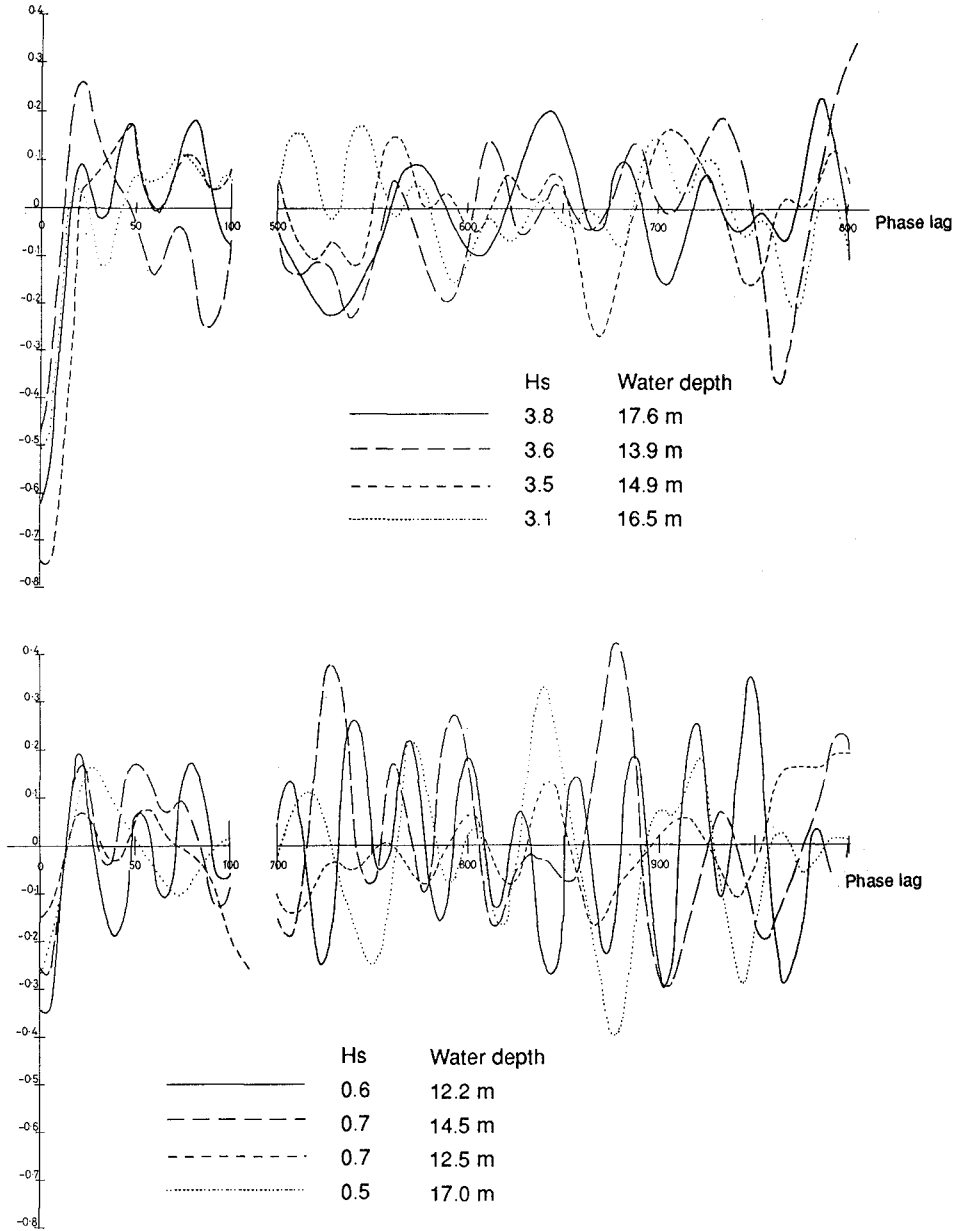


Figure 2 Correlation coefficients for large and small waves at Port Taibot

Where  $R_s$  is the correlation coefficient for the forced low frequency disturbance alone,

$$R_s = \frac{\int (\eta_p^{(1)})^2 \eta_s^{(2)} dt}{(\int (\eta_p^{(1)})^4 dt)^{1/2} (\int (\eta_s^{(2)})^2 dt)^{1/2}}$$

and

$$M_s = \frac{1}{T} \int_0^T (\eta_s^{(2)})^2 dt$$

In (12) the correlation coefficient  $R_L$  and the mean square of the total low frequency disturbance  $M_L$  can be obtained directly from the measurements, while the correlation coefficient ( $R_s$ ) and the mean square of the forced low frequency disturbance ( $M_s$ ) can be calculated in terms of the primary wave spectrum using (11), (7), (9) and (10). Only the "flat bed" component of the bound long wave defined in (7) is needed here because the 90° phase difference of the extra potential due to varying water depth means (8) does not contribute to the correlation coefficient at zero lag.

Clearly, both  $R_s$  and  $M_s$  are functions of the directional properties of the primary waves. We make the following assumption about the primary wave spectrum,

$$S_d(f, \theta) = \frac{1}{(\pi\theta_0)^{1/2}} \exp\left(-\frac{\theta^2}{\theta_0^2}\right) S(f) \tag{13}$$

where  $S(f)$  is the usual one dimensional wave spectrum and  $\theta_0$  defines a mean spread parameter for the primary waves. Different, and perhaps more familiar, forms for directional spread were tried in the analysis but the results were found to be insensitive to the exact form of the spreading function. The exponential form has the advantage that analytical integration is made possible (see next sub-section).

Equation (13) completes the expressions needed to define  $R_s$  and  $M_s$  in terms of the unknown  $\theta_0$ . This mean spread parameter can then be obtained making an initial guess for  $\theta_0$  and

iterating on this starting value until (12) is satisfied. Of course, even though the bound long wave quantities being used here relate to bed pressures they are expressed in terms of the spectrum  $S(f)$  of primary waves at the surface. This is obtained from the measured primary wave bed pressure spectrum by applying the square of the inverse of the (linear potential) depth attenuation factor, frequency component by frequency component. Also, in calculating the bound long wave, its "expected" value is obtained from the primary waves. This ignores the phases of the primary waves, as described above under method of analysis; a process that can be justified for long wave records.

**2.3 Calculation of the surf beat spectrum**

This spectrum is obtained by simply subtracting the calculated spectrum of the forced low frequency disturbance (11) from the measured long wave spectrum. In doing this, some estimate of the bound long wave due to a varying water depth is needed in addition to the "flat bed" bound long wave. We do this making the shallow water wave assumption,  $kh < 1$ , when evaluating expression (8). This is justified on the basis that this bound long wave component can be shown to be negligible for deep water waves. After much algebra we find its spectrum  $S_G(f)$  takes the form,

$$S_G(f) = \int S(f) S(f + f') I_G df' \tag{14}$$

where,

$$I_G = \left(\frac{h\pi}{2g}\right)^{1/2} \frac{0.0556g^5 \tan^2 \alpha}{\pi^9 h^7 \theta_0^7 f^{-4} (f + f')^4}$$

It is of interest to compare this spectrum with the spectrum  $S_F(f')$  of the "flat bed" bound wave calculated under the same shallow water wave assumption,

$$S_F(f) = \int S(f) S(f + f') I_F df \quad (15)$$

where

$$I_F = \left(\frac{h\pi}{2g}\right)^{1/2} \frac{0.2813g^2 f'}{\pi^3 h^4 \theta_0 f^2 (f + f')^2}$$

Both spectra in (14) and (15) can be evaluated and then integrated over difference frequencies  $f'$ . For typical parameters we find the ratio  $N$  of the bound long wave amplitude due to varying water depth, over the flat bed bound long wave amplitude is,

$$N = \frac{26.4 T_p^2 \tan \alpha}{h^{3/2}} \quad (16)$$

Where  $T_p$  is the spectral peak period of the primary wave spectrum and the constant has dimensions ( $m^{3/2} s^{-2}$ ). This shows immediately that effects of bed slope will only be important nearshore when the water depth is reduced. It must also be remembered that the Stokes expansions of the type being used in this paper are not valid in very shallow water when the waves become highly non-linear. This will limit the range of validity of the expressions given here. Nevertheless, it is of interest to use (15) to estimate the magnitude of the flat bed bound long wave. Defining the significant value as 4 times the standard deviation we find for a typical wave spectrum,

$$H_s (\text{bound long wave}) = 0.0413 \left(\frac{h^{1/2}}{\theta_0 T_p}\right)^{1/2} \frac{H_s^2 T_p^2}{h^2} \quad (17)$$

where  $H_s$  is the primary significant wave height and the constant has dimensions ( $m^{3/4} s^{-3/2}$ ). This compares with an equivalent expression for uni-directional primary waves,

$$H_s (\text{bound long wave}) = 0.074 \frac{H_s^2 T_p^2}{h^2} \quad (18)$$

where the constant has dimensions ( $ms^{-2}$ ). Expression (17) gives bound long waves that, typically, are half the height of those defined by (18) (see also Figure 1). Another difference between multi-directional seas and uni-directional seas is in the shape of the flat bed bound long wave spectrum. It is well known that, in theory, this spectrum has a finite value at zero frequency for uni-directional waves but (15) shows that in shallow water, the bound long wave spectrum in multi-directional waves tends to zero as the difference frequency tends to zero.

Although (17) and (18) are, in theory, limited to shallow water waves they appear, in comparisons with exact calculations, to give reasonable estimates of bound long waves even for  $kh \approx 1$ .

### 3. Field data

In applying the method of long wave analysis described in Section 2, exact calculations of the flat bed bound long waves were made using (7). The bound long wave due to varying bed level was then determined using (14). This resulted in only small corrections to the final estimate of surf beat thereby justifying the use of (a conservative) shallow water theory in deriving (14). Examples of these corrections are given for various sites in what follows.

#### 3.1 Port Talbot

In this deployment the pressure sensor was mounted about 4km from the shoreline at the seaward end of the navigation channel leading to the harbour of Port Talbot on the

south west coast of Wales. With the large tidal range at the site, depths at the sensor varied from 10m to 19m. Spectral peak periods ranged from 7s to 15s and, typically, significant wave heights were in the range of 1m to 2m but some large wave heights of 4m were measured. Such parameters indicated the main source of wave activity to be the Atlantic as shorter period waves would have been dominant if local fetches were applicable. The seabed slope in the vicinity of the wave recorder was about 1 in 600.

To illustrate the largest correction to the flat bed bound long wave due to a varying seabed level we take the record with the lowest depth. The parameters were,

$$H_s = 1.16\text{m}, T_p = 12.8\text{s}, h = 10.2\text{m}, H_s \text{ (long wave)} = 0.104$$

Exact flat bed analysis yielded,

$$H_s \text{ (bound long wave)} = 0.073\text{m with } \theta_o = 10^\circ, R_L = -0.60.$$

Here, and in what follows, the term bound long wave is taken to include the Bernoulli pressures in (11) although strictly speaking it should just refer to disturbances due to the second order potentials (7) and (8). Expression (14) leads to an additional bound long wave component with a significant height of 0.016m, ie 22% of the flat bed component. This percentage figure can also be obtained directly from (16). Thus, surf beat height is given by,

$$[(.104)^2 - (0.073)^2 - (0.016)^2]^{1/2} = 0.072\text{m}.$$

If we had neglected the additional bound long wave component our surf beat height would have been 0.074m and only a small error would have resulted. For the record with the largest water depth (18.9m) the additional bound long wave component was only 10% of the flat bed component and its neglect would have resulted in only a 0.05% error in surf beat height. Because of its small effect on estimates of surf beat it was decided to neglect the additional bound long wave component. However, it should be noted that such a component exists and, according to (16), can be expected to become more important nearer to the shore where it will tend to make the trough of total bound long wave lag behind groups of large waves: an effect also observed by List (1992).

The following table of some of the Port Talbot data gives an idea of the percentage contribution of surf beat to the total long waves measured. It can be seen that surf beat is dominant when primary waves are small but that the bound long wave component begins to dominate when primary wave heights are larger.

Table 1 Results from Port Talbot

Primary	Waves	Measured long waves	Calculated bound long waves	Surf beat
$H_s$ (m)	$T_p$ (s)	$H_s$ (m)	$H_s$ (m)	$H_s$ (m)
0.49	11.1	0.025	0.006	0.024
0.54	11.1	0.030	0.007	0.029
0.79	6.9	0.032	0.008	0.031
0.80	7.6	0.035	0.011	0.033
2.76	12.8	0.204	0.116	0.168
3.20	13.5	0.374	0.238	0.288
4.12	11.5	0.407	0.349	0.210
4.18	12.0	0.295	0.230	0.185

We know that the bound long wave component will increase with the square of wave height and period to the power 3/2 (see (17)). The above results (as well as those collected at the other sites) indicate that surf beat does not increase as rapidly with the severity of sea state. It is of interest for engineering studies to try and find an empirical relationship for the height of surf beat in terms of primary wave parameters. This was done with the powers of the following three parameters being chosen to minimise scatter in the data,

$$H_s \text{ (surf beat)} \propto H_s^\beta T_p^\alpha h^\delta$$

In the case of Port Talbot, the following relationship was found where wave height and water depth are in metres and wave period is in seconds.

$$H_s \text{ (surf beat)} = 0.0064 \frac{H_s^{1.32} T_p^{1.17}}{h^{0.34}} \quad (19)$$

Scatter in the data was judged by a normalised error parameter and it was found that this error parameter was larger when an empirical relationship of the above type was sort for the significant height of the total long wave component, i.e without first subtracting off the bound long wave energy. This result indicates that the assumptions made about the bound long wave in the method of analysis, are justified. Also, Herbers et al (1992) have provided evidence using bispectral analysis that the bound long wave spectrum in field measurements of long period disturbances, matches the bound long wave spectrum predicted by a second order Stokes expansion.

### 3.2 Shoreham Harbour

In this case, the pressure sensor was mounted about 2.5km from the shoreline, offshore of the entrance to Shoreham Harbour which lies on the south coast of England. Water depths ranged from 7m to 12m due to the tide and the wave climate consisted mainly of locally generated waves with spectral peak periods from 6s to 10s. Swell, which had propagated up the English Channel from the Atlantic was also present at times with significant heights generally under 1m and spectral peak periods of 12s to 18s.

The seabed in the vicinity of the wave recorder was very flat with a slope of about 1 in 700. The record with the largest slope induced bound long wave had the following parameters,

$$H_s = 0.6\text{m}, T_p = 15.5\text{s}, h = 8.8\text{m}, H_s \text{ (long wave)} = 0.055\text{m}.$$

The flat bed bound long wave was 0.024m which, ignoring the slope induced component, gave a surf beat of 0.0495m. Although slope induced bound long wave is 35% of the flat bed component, the inclusion of this component only reduces the surf beat estimate by 1.5% to 0.0488m. This justified neglect of the slope induced component in the other Shoreham records.

The following empirical relationship was found for the resulting surf beat heights,

$$H_s \text{ (surf beat)} = 0.0074 \frac{H_s^{0.93} T_p^{0.99}}{h^{0.06}} \quad (20)$$

### 3.3 Barrow-in-Furness

Here, the pressure sensor was deployed about 2.5km south of a sand spit, the Isle of Walney, which protects Barrow-in-Furness, on the north west coast of England. Water depths ranged from 4m to 12m due to the tide and locally generated waves occurred with significant heights of up to 2.4m and spectral peak periods of 5s to 8s. Occasional southerly swell from the Irish Sea was able to reach the recorder position with heights of under 1m and spectral peak periods of about 12s.

The seabed slope was very flat at about 1 in 600 and the record with the largest slope induced bound long wave (23% of the 0.10m flat bed component) had a surf beat height of 0.091m which was only 3% less than the surf beat height obtained ignoring the slope induced long wave. This justified neglecting the effect of the slope induced bound long wave.

The following empirical relationship was found for the resulting surf beat heights,

$$H_s \text{ (surf beat)} = 0.0024 \frac{H_s^{1.08} T_p^{1.59}}{h^{0.36}} \tag{21}$$

4. Discussion and results from other sites

Long wave recording was carried out at two other sites, Dover and Sunderland, but the separation into bound long wave and surf beat proved unsatisfactory in that scatter in the data increased after subtraction of the bound long wave. This may have been due to primary wave reflections from the vertically faced harbour breakwaters affecting the measurements. Ignoring such reflections (which could not be quantified) would tend to lead to overestimates of bound long wave energy under the assumptions made in the analysis and this in turn would under-estimate the surf beat. This problem did not arise for Port Talbot because the breakwaters were of rubble mound construction and highly absorbent of waves. At Shoreham the breakwaters were almost perpendicular to the coastline and directed reflections along and onshore rather than offshore towards the wave recorder while there was only a sandy beach at Barrow.

Averaging the powers of the primary wave parameters in (19), (20) and (21) suggests a variation,

$$H_s \text{ (surf beat)} = K \frac{H_s^{1.11} T_p^{1.25}}{h^{0.25}} \tag{22}$$

where the (dimensional) constant of proportionality K has the not dissimilar values of 0.0044, 0.0066 and 0.0041 for Port Talbot, Shoreham and Barrow, respectively. The largest scatter in surf beat heights occurred for the Barrow Data (see Figure 3).

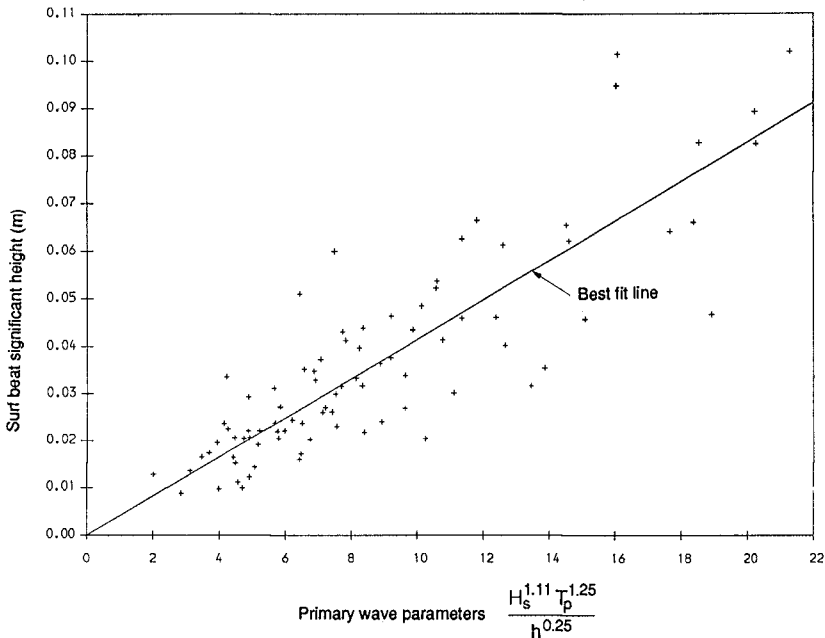


Figure 3 Surf beats off Barrow-in-Furness



This type of result is consistent with the near linear dependence of long wave height on primary wave height found by Tucker (1950) whose measurements appear to have been dominated by surf beat rather than bound long waves. Also, the inverse quarter power of depth (which could of course be fortuitous) is not inconsistent with inverse shoaling of free long waves and high order edge wave modes (Okhiro, 1982).

We can use (22) to predict long wave heights at Shoreham and Barrow for more extreme wave conditions than those measured. [In the case of Port Talbot we already have the data in Table 1]. Limiting primary wave parameters to those where a second order Stokes expansion can be expected to remain valid we obtain the following.

**Table 2** Extreme wave predictions for Shoreham in a depth of 12.4m

Primary waves Return period	$H_s(m)$	$T_p(s)$	Significant long wave height (m)		
			$H_s$ (bound long wave)	$H_s$ (surf beat)	$H_s$ (total)
10 times/yr	3.3	7.5	0.14	0.16	0.21
1/yr	4.0	8.4	0.27	0.23	0.35
1/10 yrs	4.7	9.2	0.45	0.31	0.55

**Table 3** Extreme wave predictions for Barrow in a depth of 13.1m

Primary waves Return period	$H_s(m)$	$T_p(s)$	Significant long wave height (m)		
			$H_s$ (bound long wave)	$H_s$ (surf beat)	$H_s$ (total)
10 times/yr	2.4	7.5	0.10	0.07	0.12
1/yr	4.0	9.2	0.32	0.16	0.36
1/10 yrs	4.8	10.0	0.53	0.22	0.57

These results, together with Table 1, show that surf beat dominates the total low frequency wave energy in frequently occurring conditions while bound long waves tend to dominate in more extreme conditions. Thus, surf beat probably consisting mainly of seaward propagating free long waves and along shore propagating high order edge wave modes, has been shown to be an important component of low frequency wave energy in intermediate water depths typical of harbour entrances. This means that both the bound long waves and surf beat need to be well represented in the modelling of harbour resonance and moored ship motions.

#### Acknowledgements

The author is grateful to Mr J M A Spencer for his help in the writing of the software used for analysis of the data, and to Dr P J Hawkes and Ms C E Jelliman for their help in applying the analysis program to data from the various sites. This work was funded in part by the UK Department of the Environment (CD) and in part by the EC sponsored MAST research programme, G6 Coastal Morphodynamics.

#### References

- Bowers E C (1980). Long period disturbances due to wave groups. 17th ICCE, Sydney, Vol 1, p610, ASCE.
- Bowers E C (1988). Wave grouping and harbour design. Proc. Instn. Civ. Engrs, Part 2, Vol 85, p237.
- Herbers T H C, Elgar S & Guza R T (1992). Longterm array observations of infragravity waves. 23rd ICCE, Venice, ASCE.
- Kostense J K (1984). Measurement of surf beat and set-down beneath wave groups. 19th ICCE, Houston, Vol 1, p724, ASCE.
- List J H (1992). A model for the generation of two-dimensional surf beat. J Geophys Res, Vol 97, C4, p5623.

- Longuet Higgins M S and Stewart R W (1964). Radiation stresses in water waves: a physical discussion with applications. *Deep Sea Research*, Vol 11, p529.
- Mei C C and Bennousa C (1984). Long waves induced by short wave groups over an uneven bottom *J Fluid Mech*, Vol 139, p219.
- Okihiro M, Guza R T & Seymour R J (1992). Bound infragravity waves. *J Geophys Res*, Vol 97, C7, p11453.
- Roelvink J A, Petit H A H & Kostense J K (1992). Verification of a one-dimensional surf beat model against laboratory data, 23rd ICCE, Venice, ASCE.
- Sand S E (1982). Long waves in directional seas. *Coastal Eng*, Vol 6, p195.
- Schaffer H A and Jonsson I G (1990). Theory versus experiment in two-dimensional surf beats. 22nd ICCE, Delft, Vol 2, p1131, ASCE.
- Symonds G, Huntley D A and Bowen A J (1982). Two dimensional surf beat: long wave generation by a time-varying breakpoint. *J Geophys Res*, Vol 87, C1, p492.
- Tucker M J (1950). Surf beats: sea waves of 1 to 5 min period. *Proc. Roy Soc*, Vol A202, p565.
- van Leeuwen P J and Battjes J A (1990). A model for surf beat. 22nd ICCE, Delft, Vol 1, p32, ASCE.
- Watson C & Peregrine H (1992). Low frequency waves in the surf zone. 23rd ICCE, Venice, ASCE.

## CHAPTER 63

### INFRAGRAVITY-FREQUENCY (0.005-0.05 HZ) MOTIONS ON THE SHELF

T. H. C. Herbers,<sup>1</sup> Steve Elgar,<sup>2</sup> R. T. Guza,<sup>1</sup> and W. C. O'Reilly<sup>1</sup>

#### ABSTRACT

Extensive field observations in depths between 8-204 m are used to investigate the sources and variability of infragravity-frequency (nominally 0.005-0.05 Hz) motions on the shelf. The predicted local forcing of 'bound' infragravity motions by difference-frequency interactions of swell and sea (Hasselmann, 1962) is verified with array measurements of sea floor pressure in 13 m depth. Observed forced infragravity energy levels agree well with theoretical predictions, but are consistently much lower than the observed total infragravity energy. Wavenumber estimates show that free waves, obeying the surface gravity wave dispersion relation, are frequently the dominant source of energy in the infragravity band. The observed directional properties and cross-shore decay of free wave energy show that refractive trapping, neglected in many current infragravity wave generation models, is of  $O(1)$  importance. Both free and forced wave energy levels generally increase with both increasing swell energy and decreasing water depth, but the observed dependencies of free and forced waves are different. The relative contributions of free and forced waves to infragravity energy on the shelf are therefore highly variable. Comparisons of observations in the same water depth at different sites suggest that free wave radiation is relatively stronger from broad, sandy beaches than from rocky, cliffed coasts.

#### 1. INTRODUCTION

Energy levels of surface elevation, velocity and pressure fluctuations at "infragravity" periods of 0.5-5 minutes, slightly longer than the 2-20 sec periods of typical wind-generated surface gravity waves, are generally weak in the deep ocean (Webb et al., 1991), but can be very energetic close to shore (surface elevation

---

<sup>1</sup> Center for Coastal Studies, 0209, Scripps Institution of Oceanography, La Jolla, California 92093-0209, U.S.A.

<sup>2</sup> Electrical Engineering and Computer Science, Washington State University, Pullman, Washington 99164-2752, U.S.A.

variances  $O(10^3) \text{ cm}^2$ ; e.g., Wright et al., 1982; Guza and Thornton, 1985). Although numerous field observations have shown that infragravity and swell energy levels are highly correlated (e.g., Munk, 1949; Tucker, 1950; Holman et al., 1978; and many others), the generation mechanisms of infragravity motions on the shelf are not well understood. Nonlinear interaction of two surface waves theoretically excites a forced secondary wave with the difference frequency (e.g., Longuet-Higgins and Stewart, 1962; Hasselmann, 1962). Field observations often exhibit the phase-coupling theoretically expected between groups of swell and forced infragravity motions (e.g., Hasselmann et al., 1963; Elgar and Guza, 1985; Okihira et al., 1992; Elgar et al., 1992). However, qualitative comparisons of theoretically predicted and observed infragravity energy spectra show that forced waves may contribute significantly to infragravity energy when swell and sea are very energetic (Sand, 1982), but account for only a small fraction of the infragravity energy when swell-sea energy is low (Okihira et al., 1992).

It has long been recognized that other contributions to the infragravity band may arise from the strong nonlinearities and wave breaking processes that occur close to shore. Based on early observations by Munk (1949) and Tucker (1950), Longuet-Higgins and Stewart (1962) suggested that, as the incident swells are dissipated in very shallow water through breaking, forced secondary waves may somehow be released as free waves and radiated from the nearshore. As these long-wavelength free waves travel seaward on a sloping beach refractive trapping may occur. Alongshore wavenumber spectra of infragravity motions in the surf-zone show clear evidence of topographically trapped low-mode edge waves (Huntley et al., 1981; Oltman-Shay and Guza, 1987; and others). Observed variations in infragravity energy across the continental shelf (Webb et al., 1991; Okihira et al., 1992) suggest that infragravity motions are predominantly trapped on the shelf with relatively weak radiation to the deep ocean. Various models have been developed that describe the generation of both leaky waves (radiating out to deep water) and edge waves at infragravity frequencies through nonlinear interactions and breaking of incident surface waves (e.g., Gallagher, 1971; Bowen and Guza, 1978; Foda and Mei, 1981; Symonds et al., 1982; Schäffer and Svendsen, 1988; Schäffer et al., 1990; List, 1992; Roelvink et al., 1992; Watson and Peregrine, 1992; and others).

In this paper, preliminary results are presented of a study of free and forced infragravity motions on the shelf, based on array measurements in 13 m depth and single-point measurements in depths ranging from 8-204 m. The field data are described in section 2. In section 3, bispectral analysis is used to decompose the observed infragravity energy in free and forced wave contributions, and the forced waves are compared to predictions of second-order nonlinear theory (Hasselmann, 1962). Wavenumbers and directional properties of free waves are discussed in section 4. The dependence of infragravity motions on water depth and incident wave conditions is examined in section 5, followed by a discussion and summary in section 6. A full account of the observations will be given in Herbers et al. (1992a,b).

## 2. FIELD DATA

The variability of infragravity motions on the shelf is investigated with single point pressure measurements at a variety of locations in both the Atlantic and Pacific oceans. Nine-months of bottom pressure data (September 1990-May 1991) were collected in 8 and 13 m depths, approximately 1 and 2 km offshore of Duck, North Carolina, respectively (Elgar et al., 1992). Three-month-long bottom pressure records were collected in 30-m depth during fall/winter of 1991/92 at 16 locations along the Southern California mainland coast and at 4 locations around Santa Rosa, an island in the Southern California Bight bordered with both steep vertical cliffs and shallow reefs (O'Reilly et al., 1992). Two representative coastal sites with gently sloping sandy beaches (Ventura and Redondo) and one of the Santa Rosa rocky island stations were selected for analysis here. Measurements in deeper water were obtained during a 6-month period in the fall/winter of 1991/92 from a pressure gauge mounted 16 m below the sea surface on Harvest Platform, located at the edge of the California shelf in 204 m depth (Seymour et al., 1985). More detailed results are based on data from a large aperture (250 x 250 m) array of 24 pressure sensors deployed in 13 m depth at Duck (Herbers et al., 1992a). The sample rates of the field data vary between 0.5 and 4 Hz. The data were divided into 170 minutes long records (137 minutes where longer continuous records were not available) for analysis.

The present study is focused on low frequency motions driven by surface waves. To exclude motions driven by other sources, the infragravity band was chosen to be the range in which spectral levels are strongly correlated with swell energy, 0.004-0.05 Hz for observations in the Atlantic and 0.004-0.04 Hz for observations in the Pacific (Herbers et al., 1992b). At frequencies below 0.004 Hz, weak correlations with swell energy suggest that the observed motions may be driven by atmospheric or other processes, not surface waves (e.g., Munk et al., 1956). The upper limit of the infragravity range was conservatively chosen to exclude contributions of low frequency swell.

## 3. FORCED WAVES

A perturbation expansion in weak nonlinearity shows that the interaction between two surface gravity waves with frequencies  $f$  and  $f + \Delta f$  excites a forced secondary wave with the difference frequency  $\Delta f$  (e.g., Longuet-Higgins and Stewart, 1962; Hasselmann, 1962). Accurate predictions of forced wave energy at infragravity frequencies require accurate estimates of the surface wave frequency-directional spectrum  $E(f, \theta)$ , information unavailable in previous studies that used single-point (Hasselmann et al., 1963; Sand, 1982) or pitch-and-roll type (Okhiro et al., 1992) measurement systems. Detailed estimates of  $E(f, \theta)$  for the dominant swell and sea ( $0.06 \text{ Hz} < f < 0.24 \text{ Hz}$ ), suitable for accurate predictions of forced wave energy, were extracted from the array measurements in 13 m depth at Duck. Predictions of the forced infragravity spectrum, based on Hasselmann's (1962) theory and the  $E(f, \theta)$  estimates, were obtained for 15 data runs spanning a wide

range of conditions (Herbers et al., 1992a). In all cases, predicted forced wave energy levels are much lower than observed infragravity energy levels (Figs. 1, 2a).

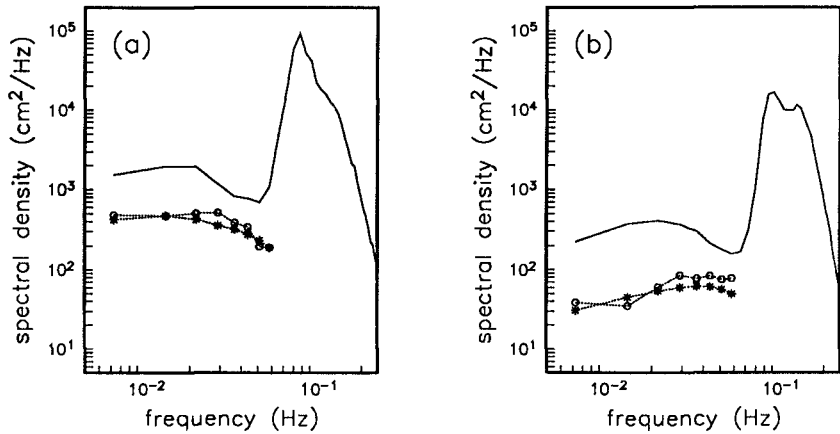


Fig. 1. Second-order nonlinear theory predictions (asterisks) and bispectrum-based estimates (circles) of the forced bottom pressure spectrum at infragravity frequencies. The observed (total) bottom pressure spectrum is indicated by a solid curve. (a) 26 October 1990. (b) 19 May 1991.

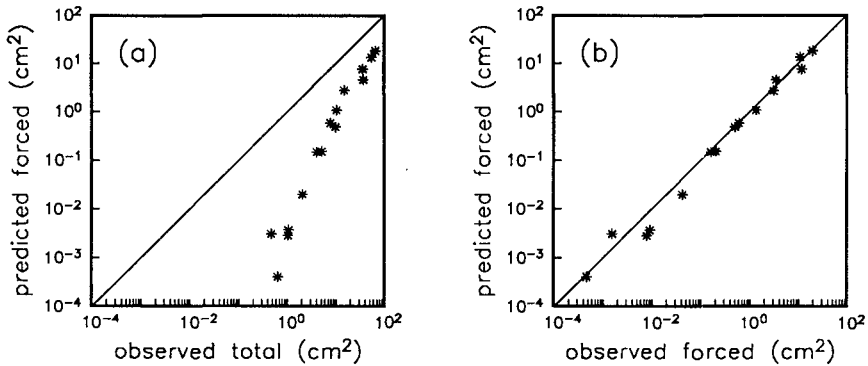


Fig. 2. (a) Predicted forced infragravity energy versus observed total infragravity energy. (b) Predicted versus observed (based on bispectral analysis) forced infragravity energy.

Bispectral analysis (frequency domain analysis of third-order statistics, Hasselmann et al., 1963) is used to estimate forced wave contributions to the infragravity band (Herbers et al., 1992a). Far from shore, free infragravity waves are statistically independent of the local swell-sea and thus do not contribute to the bispectrum. Nonzero bispectral values (i.e., nonGaussian statistics) result from phase-locking between forced waves and pairs of swell-sea components. Estimates of forced infragravity spectra, based on bispectral analysis, agree well with theoretical predictions, as illustrated in Fig. 1 (compare circles and asterisks) for two example cases with significant forced wave contributions to the infragravity band. For all 15 data runs, which span a variation of  $10^5$  in forced wave energy, (bispectrum-based) estimates and theoretical predictions of the total (integrated over the infragravity band) forced wave energy are in excellent agreement (typically within 30 %, Fig. 3b). The observed phase differences between forced waves and groups of swell are within a few degrees of the theoretical value  $180^\circ$  (Herbers et al., 1992a). Overall, the analysis shows that forced waves are accurately predicted by second-order nonlinear theory (Hasselmann, 1962), but their contribution to the infragravity band is relatively small (0.1-30 %, Fig. 2a).

#### 4. FREE WAVES

It has been suggested (e.g., Longuet-Higgins and Stewart, 1962; Symonds et al., 1982; and many others) that the surf-zone radiates seaward-travelling free waves at infragravity frequencies. The observed wavenumbers do indeed show that the remaining, not locally nonlinearly forced, infragravity energy in 13 m depth is caused by freely propagating surface gravity waves. An average wavenumber magnitude  $k_{rms}(f)$ , defined as

$$k_{rms}(f) \equiv \left[ \frac{\int_0^\infty dk \int_0^{2\pi} k d\theta k^2 E(f, k, \theta)}{\int_0^\infty dk \int_0^{2\pi} k d\theta E(f, k, \theta)} \right]^{1/2}, \quad (1)$$

with  $E(f, k, \theta)$  the frequency-(vector) wavenumber spectrum of sea floor pressure, was estimated from the 13-m depth array measurements at Duck (the technique will be described in a subsequent publication). Estimates of  $k_{rms}(f)$  are compared to the linear dispersion relation for surface gravity waves in Fig. 3 on three occasions with negligible forced wave contributions to the total infragravity energy (i.e., Fig. 2a). The observed wavenumbers in the infragravity band are in excellent agreement with the theoretical free-wave dispersion relation.

Both forced and free wave energies are expected to decrease with increasing water depth  $h$  owing to the weakening of nonlinearity and propagation effects, respectively. In shallow water forced infragravity energy is strongly amplified owing to near-resonances and approximately proportional to  $h^{-5}$  (Longuet-Higgins

and Stewart, 1962). On the other hand, the energy of leaky (radiating to deep water), free infragravity waves is approximately proportional to  $h^{-1/2}$  (e.g., Eckart, 1951; see also Elgar et al., 1992). In an earlier study, the observed ratio between total infragravity energy in 13 and 8 m depth at Duck was shown to be close to the theoretical value ( $h^{-1/2}$ ) for leaky free waves when incident swell energy levels are low, and to decrease systematically with increasing swell energy (Fig. 3 in Elgar et al., 1992). This trend was attributed to increasingly large forced wave contributions to the infragravity band with increasing swell energy. The bispectrum-based estimates of forced infragravity energy (section 3) allow for a more quantitative assessment of free wave decay with increasing depth. Free infragravity energy was estimated by subtracting the forced wave energy estimates from the total observed infragravity energy. The ratio  $R$  between free infragravity energy in 13 and 8 m depth is approximately independent of swell energy (Fig. 4), confirming that the trend observed by Elgar et al. (1992) was indeed caused by forced wave contributions. The observed  $R$  vary between 0.4 and 1, with the majority of the observations in the range 0.5-0.7, significantly lower than the theoretical value 0.8 for leaky waves. The observed low values of  $R$  indicate that a significant fraction (typically 10-50 %) of the free infragravity energy observed in 8 m depth is refractively trapped (i.e., has a turning point) between 8 and 13 m depth. According to Snell's law, free long waves travelling seaward at oblique angles greater than  $52^\circ$  in 8 m depth are trapped between 8 and 13 m depth. Hence, the observed low values of  $R$  imply that a significant fraction of free infragravity energy observed close to shore in 8 m depth is travelling at large oblique angles relative to the beach.

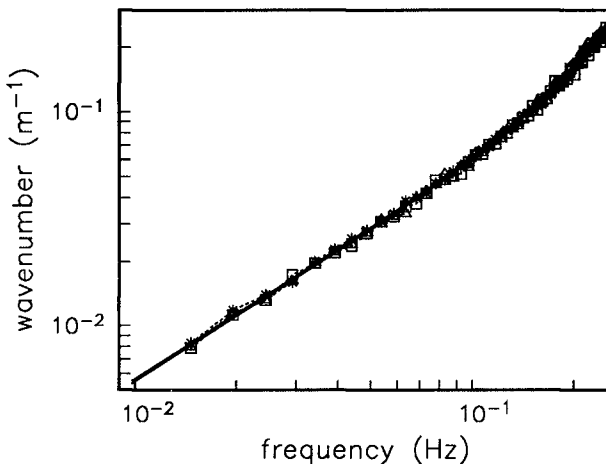


Fig. 3. Estimates of an average wavenumber magnitude  $k_{rms}(f)$  as a function of frequency (Eq. 1), obtained from array measurements in 13 m depth at Duck on 7 September (squares), 26 September (triangles) and 8 October (asterisks), 1990. The linear dispersion relation for surface gravity waves is indicated by a solid curve.



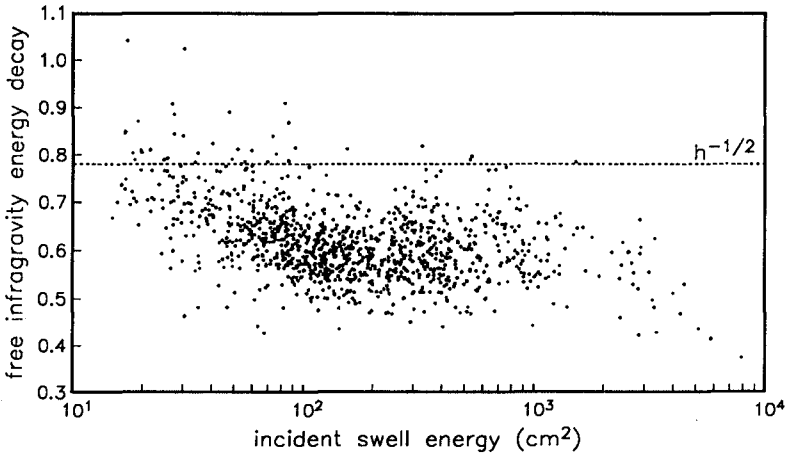


Fig. 4. Observed ratio  $R$  between free infragravity energy in 13 and 8 m depth at Duck versus incident swell energy (observed in 13 m depth). The dotted line labeled  $h^{-1/2}$  indicates the theoretical decay for leaky waves.

For swell energies larger than about  $50 \text{ cm}^2$ , the observations do not suggest a dependence of  $R$  on swell energy, but the relatively few cases with very small amplitude swell (variances  $< 50 \text{ cm}^2$ ) show weaker decay, closer to the theoretical value  $h^{-1/2}$  for leaky waves (Fig. 4). Possibly, these free infragravity motions are not generated at nearby shores but arrive from (and return to) the deep ocean. Observations by Webb et al. (1991) suggest that a small fraction of the free infragravity energy generated at coasts with energetic swell propagates off the shelf into deep water and radiates across ocean basins. These relatively weak background motions may be the dominant source of infragravity energy on the shelf when forcing by local swell is very weak.

Array measurements in 13 m depth confirm that free waves at infragravity frequencies are indeed directionally broad. Examples of estimates of directional distributions of energy at the infragravity (0.02 Hz) and swell (0.1 Hz) spectral peak frequencies, on a day with negligible forced wave contributions to the infragravity band, are shown in Fig. 5. In contrast to the directionally narrow, shoreward travelling swells, the directional distribution of infragravity energy is very broad with approximately equal amounts of energy travelling seaward and shoreward, and a maximum at  $90^\circ$ , corresponding to alongshore travelling waves. Note that although both swell and infragravity maxima correspond to waves travelling in the same upcoast direction there is significant infragravity energy travelling downcoast against the swell.

Consistent with earlier observations inside the surf-zone (e.g., Huntley et al., 1981, Oltman-Shay and Guza, 1987), the observed faster than  $h^{-1/2}$  energy decay with increasing depth and directionally very broad spectra show that refractive trapping is of  $O(1)$  importance to infragravity motions on a natural beach. The

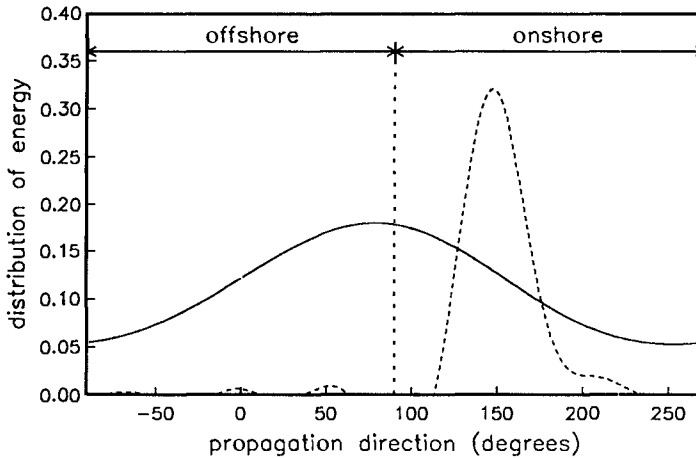


Fig. 5. Directional distributions of free infragravity energy (0.02 Hz; solid curve) and swell energy (0.1 Hz; dashed curve) observed in 13 m depth at Duck on 8 October 1990. The sector 90–270° corresponding to shoreward propagating waves, contains 98 % of the swell energy and 46 % of the infragravity energy.

assumption of uni-directional wave propagation used in current infragravity wave generation models (e.g., Symonds et al., 1982; Schäffer and Svendsen, 1988; Schäffer et al., 1990; List, 1992; Roelvink et al., 1992; Watson and Peregrine, 1992; and others) is inconsistent with the present observations.

## 5. SHELF-WIDE VARIABILITY

The mix of free and forced infragravity energy (Fig. 2a) observed on the inner North Carolina shelf (Duck) in 13 m depth is not necessarily representative of other sites, and is further investigated here using additional long-term bottom pressure measurements collected on the California shelf. Estimates of forced and free wave energy contributions to the infragravity band in 8, 30 and 204 m depth, based on bispectral analysis (section 3), are compared in Figs. 6a and 6b, respectively. Both free and forced infragravity energies are generally well correlated with swell energy (defined as the energy in the range 0.04–0.14 Hz for Pacific sites and 0.05–0.14 Hz for Atlantic sites). In all three depths forced wave energy is approximately proportional to the swell energy squared (Fig. 6a). This quadratic dependence is expected from second-order nonlinear theory because the amplitude of a forced secondary wave is proportional to the product of the amplitudes of the interacting swell components. Since the forced infragravity wave amplitude also depends on the frequencies and the difference in propagation direction of the interacting swell components, the scatter about the line with slope 2 is expected. As expected from theory, forced wave energies fall off rapidly with increasing depth. In 204 m depth

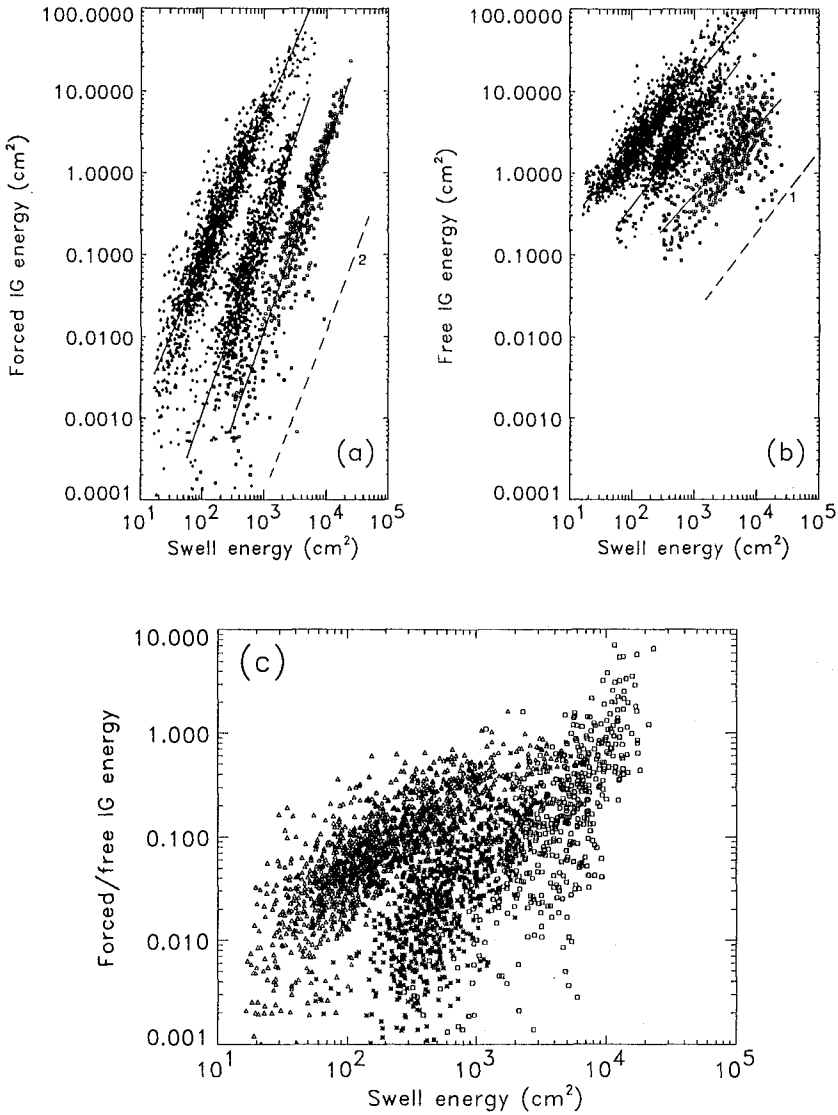


Fig. 6. Forced (a), free (b), and the ratio between forced and free (c) infragravity energies, observed in 8 m depth at Duck (triangles, upper clouds), in 30 m depth at Ventura (asterisks, middle clouds), and in 204 m depth at Harvest Platform (squares, lower clouds), are shown versus swell energy. Least-squares-fit curves to the logarithms of the observed energies are denoted by solid lines. Dashed lines labeled 1 and 2 indicate a linear and quadratic dependence, respectively.

the observed forced wave energy levels are typically smaller by a factor of  $10^2$ – $10^3$  compared to 8 m depth for comparable swell energy (Fig. 6a). The depth dependence observed for free infragravity energy (Fig. 6b) is weaker than observed for forced waves, but stronger than the  $h^{-1/2}$  dependence of leaky waves, consistent with significant refractive trapping of seaward propagating free waves.

In contrast to the strong (quadratic) dependence of forced wave energy on swell energy, in all three depths free wave energy is approximately linearly proportional to swell energy. The observed weak dependence of free infragravity energy on swell energy is not inconsistent with nonlinear generation and reflection at nearby shores, but suggests the importance of wave breaking in the generation process. If nonlinear transfer of energy from shoaling incident swell is the source of free infragravity motions, then the infragravity energy is expected to be roughly proportional to the square of the swell energy. However, the transfer of swell energy to lower frequencies may be arrested when the swell energy is dissipated through wave breaking. As larger amplitude swell break in deeper water farther from shore, the dependence of forced infragravity energy released in the surf-zone on incident swell energy is expected to be weaker than quadratic (Longuet-Higgins and Stewart, 1962). Alternative models (e.g., Symonds et al., 1982; and many others) assume that variations in set-up inside the surf-zone, rather than nonlinear interactions outside the surf-zone, drive free waves in the infragravity band. The solutions to these models (including standing waves within the surf-zone) are quite complicated, but since the driving set-up variations are linearly proportional to the incident swell amplitudes (Longuet-Higgins and Stewart, 1962), free infragravity energy generated inside the surf-zone is expected to be roughly linearly proportional to swell energy, qualitatively consistent with the present observations. A weaker than quadratic dependence of free infragravity energy on swell energy may also result from a nonlinear dependence of free wave damping (in the surf-zone or through bottom friction on the shelf) on swell energy.

The ratio of free to forced infragravity energy at the same three sites (Fig. 6c) is extremely variable, ranging from  $10^{-3}$  to 10. Owing to the different dependencies of free and forced wave energies on incident swell energy and water depth (e.g., compare Figs. 6a and 6b) the relative contribution of forced wave energy to the infragravity band generally increases with both increasing swell energy and decreasing water depth. Overall the present observations (including the sites not shown in Fig. 6, see Herbers et al., 1992b for further discussion) indicate that free waves are the dominant source of infragravity energy on the shelf (well outside the surf-zone). However, forced wave contributions are significant with energetic swell and sometimes dominate the infragravity band even in 204 m depth (e.g., the forced/free wave energy ratios  $> 1$  for swell energy  $> 10^4 \text{ cm}^2$  in Fig. 6c).

## 6. DISCUSSION AND CONCLUSIONS

Although differences in free infragravity energy levels measured in 8, 30 and 204 m depth (Fig. 6b) are qualitatively consistent with propagation (unshoaling and refractive trapping) effects, the observed energy levels may also depend on the

detailed characteristics of the nonlinear shoaling/surf-zone processes close to shore where the free waves are generated. Comparable (within roughly  $\pm$  a factor of 2) free wave energy levels observed in 30 m depth offshore of mildly sloping sandy beaches at various locations along the Southern California coast (not shown), do not indicate a strong sensitivity of the generation of free infragravity energy to the detailed, local beach morphology. However, free infragravity energy levels observed near rocky shores are much lower than observed near sandy beaches, as illustrated in Fig. 7 with comparisons of free and forced wave energy observed in 30 m depth offshore of a sandy beach at Redondo and in 30 m depth offshore of a rocky coast at Santa Rosa Island. The observed dependence of forced wave energy on swell energy is approximately the same at both sites, as expected for local nonlinear effects that depend only on the local water depth and wave conditions. However, for comparable incident swell conditions, free wave energy levels observed at Santa Rosa Island are typically an order of magnitude lower than observed at Redondo. Reflections of incident swell from steep cliffs and localized wave breaking on isolated reefs obviously affects the nonlinear shoaling and surf-zone processes at Santa Rosa Island, and may explain the observed low free infragravity energy levels. The dynamics are not understood but the observations strongly suggest that the generation and/or reflection of free infragravity motions is less efficient on rocky shores than on sandy beaches.

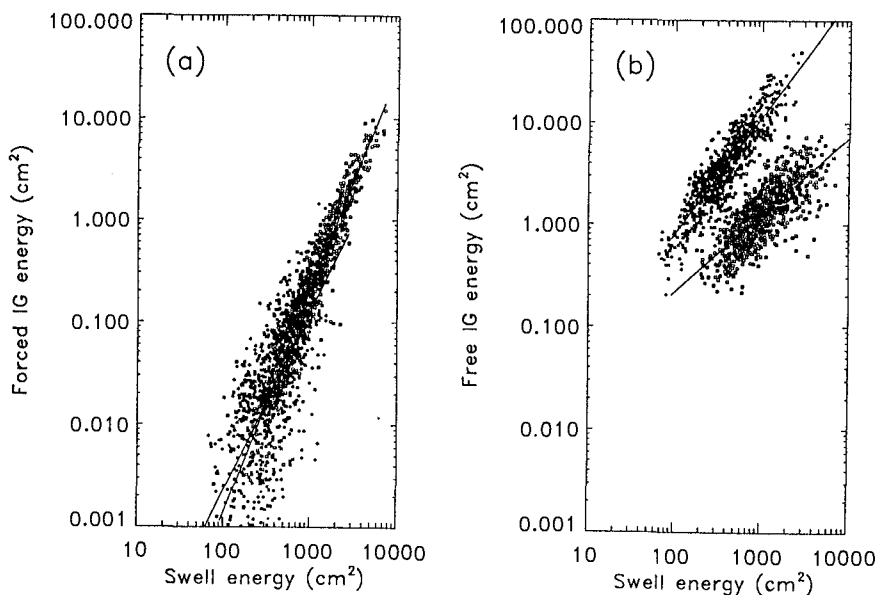


Fig. 7. Forced (a) and free (b) infragravity energies observed in 30 m depth, offshore of the sandy Redondo beach (asterisks, upper cloud in panel b) and offshore of the rocky Santa Rosa Island (squares, lower cloud in panel b), versus swell energy. Least-squares-fit curves to the logarithms of the observed energies are denoted by solid lines.

In summary, results of this study show that motions in the infragravity band (nominally 0.005-0.05 Hz) on the continental shelf are a mix of forced waves, phase-coupled to swell and sea, and free waves generated at nearby shores. The observed forced waves are accurately predicted by second-order nonlinear theory but the generation mechanism of free waves is not well understood. Both free and forced wave energies increase with increasing swell energy but, in contrast to the approximately quadratic dependence of forced wave energy on swell energy, the dependence of free wave energy on swell energy is approximately linear, qualitatively consistent with heuristic models of surf-zone dynamics (e.g., Longuet-Higgins and Stewart, 1962; Symonds et al., 1982; and others). Free and forced wave energies also decrease with increasing water depth owing to a weakening of local nonlinear effects and propagation effects, respectively. The observed free wave decay with increasing depth, although weak compared to the very strong forced wave decay, is much stronger than the decay theoretically predicted for leaky waves radiating to deep water. Refractive trapping of seaward travelling free waves, not included in many current infragravity wave generation models, is important on natural beaches. Very broad directional spectra at infragravity frequencies, with roughly comparable energy travelling seaward and shoreward, confirm that a large fraction of free wave energy radiating from the beach is refractively trapped on the shelf.

#### *Acknowledgements*

This research was sponsored by the Office of Naval Research Geology & Geophysics and Coastal Sciences programs, the Office of Naval Research Non-linear Ocean Waves Accelerated Research Initiative, and the California Department of Boating and Waterways. The pressure sensors in 13-m depth (North Carolina) and 30-m depth (California) were deployed by the staff of the Center for Coastal Studies, Scripps Institution of Oceanography. The data in 8-m depth (North Carolina) were collected by the U.S. Army Corps of Engineers Field Research Facility, Coastal Engineering Research Center, Duck, NC. The data in 204-m depth (Harvest Platform) were collected by the Coastal Data Information Program (supported by the U.S. Army Corps of Engineers and the California Department of Boating and Waterways). Excellent logistics support was provided by the U.S. Army Corps of Engineers Field Research Facility, Coastal Engineering Research Center, Duck, NC.

#### *References*

- Bowen, A. J., and R. T. Guza, 1978: Edge waves and surf beat. *J. Geophys. Res.*, 83, 1913-1920.
- Eckart, C., 1951: Surface waves on water of variable depth. *Wave Report 100*, 99 pp., Scripps Institution of Oceanography,

- Elgar, S., and R. T. Guza, 1985: Observations of bispectra of shoaling surface gravity waves. *J. Fluid Mech.*, 161, 425-448.
- Elgar, S., T. H. C. Herbers, M. Okihiro, J. Oltman-Shay, and R. T. Guza, 1992: Observations of infragravity waves. *J. Geophys. Res.*, 97, 15573-15577.
- Foda, M. A., and C. C. Mei, 1981: Nonlinear excitation of long-trapped waves by a group of short swells. *J. Fluid Mech.*, 111, 319-345.
- Gallagher, B., 1971: Generation of surf beat by non-linear wave interactions. *J. Fluid Mech.*, 49, 1-20.
- Guza, R. T., and E. B. Thornton, 1985: Observations of surf beat. *J. Geophys. Res.*, 90, 3161-3172.
- Hasselmann, K., 1962: On the non-linear energy transfer in a gravity-wave spectrum, Part 1. General theory. *J. Fluid Mech.*, 12, 481-500.
- Hasselmann, K., W. Munk and G. MacDonald, 1963: Bispectra of ocean waves, in *Times Series Analysis*, edited by M. Rosenblatt, pp. 125-139, John Wiley, New York. *J. Geophys. Res.*, 70, 1415-1427.
- Herbers, T. H. C., S. Elgar, and R. T. Guza, 1992a: Infragravity-frequency (0.005-0.05 Hz) motions on the shelf, Part 1. Local nonlinear forcing by surface waves. submitted to *J. Phys. Oceanogr.*
- Herbers, T. H. C., S. Elgar, R. T. Guza, and W. C. O'Reilly, 1992b: Infragravity-frequency (0.005-0.05 Hz) motions on the shelf, Part 2. Free and forced waves. to be submitted to *J. Phys. Oceanogr.*
- Holman, R. A., D. A. Huntley, and A. J. Bowen, 1978: Infragravity waves in storm conditions, in *Proceedings 16th Conference on Coastal Engineering*, American Society of Civil Engineers, New York, 268-284.
- Huntley, D. A., R. T. Guza, and E. B. Thornton, 1981: Field observations of surf beat, Part 1. Progressive edge waves. *J. Geophys. Res.*, 86, 6451-6466.
- List, J. H., 1992: A model for the generation of two-dimensional surf beat. *J. Geophys. Res.*, 97, 5623-5636.
- Longuet-Higgins, M. S., and R. W. Stewart, 1962: Radiation stress and mass transport in surface gravity waves with application to 'surf beats.' *J. Fluid Mech.*, 13, 481-504.
- Munk, W. H., 1949: Surf beats. *Eos Trans. AGU*, 30, 849-854.
- Munk, W., F. Snodgrass, and G. Carrier, 1956: Edge waves on the continental shelf. *Science*, 123, 127-132.
- Okihiro, M., R. T. Guza, and R. J. Seymour, 1992: Bound infragravity waves. *J. Geophys. Res.*, 97, 11453-11469.
- Oltman-Shay, J., and R. T. Guza, 1987: Infragravity edge wave observations on two California beaches. *J. Phys. Oceanogr.*, 17, 644-663.
- O'Reilly, W. C., R. T. Guza, B. W. Waldorf, M. R. Kirk, W. A. Boyd, and M. C. Clifton, 1992: Data Report, Southern California Wave Experiment. Scripps Institution of Oceanography, Reference Series No 92-14.
- Roelvink, J. A., H. A. H. Petit, and J. K. Kostense, 1992: Verification of a one-dimensional surfbeat model against laboratory data, to appear in *Proceedings 23rd Conference on Coastal Engineering*, American Society of Civil Engineers, New York.

- Sand, S. E., 1982: Wave grouping described by bounded long waves. *Ocean Eng.*, 9,(6), 567-580.
- Schäffer, H. A., and I. A. Svendsen, 1988: Surf beat generation on a mild slope beach, in *Proceedings 21st Conference on Coastal Engineering*, American Society of Civil Engineers, New York.
- Schäffer, H. A., I. G. Jonsson, and I. A. Svendsen, 1990: Free and forced cross-shore long waves, in *Water Wave Kinematics*, A. Torum and O. T. Gudmestad (eds.), 367-385.
- Seymour, R. J., M. H. Sessions, and D. Castel, 1985: Automated remote recording and analysis of coastal data, *J. Waterw., Port, Coastal Ocean Eng.*, 111, 388-400.
- Symonds, G., D. A. Huntley, and A. J. Bowen, 1982: Two-dimensional surf beat: long wave generation by a time-varying breakpoint. *J. Geophys. Res.*, 87, 492-498.
- Tucker, M. J., 1950: Surf beats: Sea waves of 1 to 5 minute period. *Proc. Roy. Soc. Lon.*, A202, 565-573.
- Watson, G., and D. H. Peregrine, 1992: Low frequency waves in the surf zone, to appear in *Proceedings 23rd Conference on Coastal Engineering*, American Society of Civil Engineers, New York.
- Webb, S. C., X. Zhang, and W. Crawford, 1991: Infragravity waves in the deep ocean. *J. Geophys. Res.*, 96, 2723-2736.
- Wright, L. D., R. T. Guza, and A. D. Short, 1982: Dynamics of a high-energy dissipative surf zone. *Mar. Geol.*, 45, 41-62.



## CHAPTER 64

### BREAKPOINT-FORCED AND BOUND LONG WAVES IN THE NEARSHORE: A MODEL COMPARISON

JEFFREY H. LIST

*U.S. Geological Survey, 600 4th St. S., St. Petersburg, FL 33701 U.S.A.*

#### ABSTRACT

A finite-difference model is used to compare long wave amplitudes arising from two group-forced generation mechanisms in the nearshore: long waves generated at a time-varying breakpoint and the shallow-water extension of the bound long wave. Plane beach results demonstrate that the strong frequency selection in the outgoing wave predicted by the breakpoint-forcing mechanism may not be observable in field data due to this wave's relatively small size and its predicted phase relation with the bound wave. Over a bar/trough nearshore, it is shown that a strong frequency selection in shoreline amplitudes is not a unique result of the time-varying breakpoint model, but a general result of the interaction between topography and any broad-banded forcing of nearshore long waves.

#### INTRODUCTION

Recent observations have shown that long period (30-300 sec.) waves often dominate the wave energy spectrum near the shoreline, especially during storms and on dissipative beaches. Despite the evident importance of these low frequency oscillations, also known as infragravity waves, much work is needed to understand the mechanisms by which these waves are generated. This paper concerns the generation of one form of these waves—the leaky modes, normally or near-normally incident long waves whose energy is radiated seaward after shoreline reflection.

Two primary models have been proposed for the generation of leaky modes, both of which depend on forcing by incident wave groupiness. Longuet-Higgins and Stewart (1962) showed that radiation stress gradients in unbroken wave

groups force a second-order sea-surface fluctuation in the form of a phase-locked or bound long wave. Although this concept has been substantiated in both field and laboratory observations (Sand, 1982; Kostense, 1985), it is clear that bound wave theory is not applicable in very shallow water where the Ursell number is large (Longuet-Higgins and Stewart, 1964, Okihiro et al., 1992).

Symonds et al. (1982) proposed an alternate model for leaky mode generation in which incident wave groups produce a forcing region associated with the time-varying position of the breakpoint. This model predicts a characteristic frequency selection in the amplitudes of the outgoing (seaward propagating) long waves. While substantiated by one laboratory experiment (Kostense, 1985), this frequency selection has never been observed in spectra calculated from field data. With an extension to a bar/trough topography, the time-varying breakpoint model also predicts a strong frequency selection in shoreline amplitudes (Symonds and Bowen, 1984), suggesting a resonant phenomenon. However, it has remained unclear whether this apparent resonance is a direct result of the time-varying breakpoint forcing, or just a natural outcome of the interaction between a bar/trough topography and any broad-banded long wave forcing.

In this study, a numerical scheme (List, 1988b, 1992) is used to investigate the relative magnitudes of the breakpoint-forced long wave (hereafter BFLW) and bound long wave (BLW), as well as the specific predictions of the breakpoint-forcing model described above.

## MODEL FORMULATION AND RUN PARAMETERS

List (1988b,1992) constructed a finite-difference solution to the equations of cross-shore ( $x$ -directed) continuity and momentum given by

$$\frac{\partial \eta}{\partial t} + \frac{\partial(hu)}{\partial x} = 0 \quad (1)$$

$$\frac{\partial u}{\partial t} + g \frac{\partial \eta}{\partial x} = -\frac{1}{\rho h} \frac{\partial S_{xx}}{\partial x} \quad (2)$$

where  $\eta$  and  $u$  are the time-averaged (over the incident wave period) sea-surface and vertically-integrated cross-shore current respectively,  $h$  is the water depth, and  $S_{xx}$  is the radiation stress in the cross-shore direction. An incident waves model provided non-steady  $S_{xx}$  gradients in both broken and unbroken waves through the surf zone over arbitrary topography. Incident waves were modeled as the wave envelope, which progressed over the bottom topography at the shallow water phase speed, shoaling and breaking as a function of the water depth. Long waves were generated throughout the nearshore by both the time-varying breakpoint and bound wave mechanisms. Long waves were reflected from a vertical wall near the shoreline, where the depth is  $\geq$  the long wave

amplitude. This mode of shoreline reflection crudely approximates natural reflection from a sloping beach, though the position of the shoreline is shifted seaward. (Although the depth at the reflection point can be a large fraction of the long wave amplitude, the model does not permit breaking.) Following shoreline reflection, waves propagate seaward and exit from the model through a radiative boundary condition. Support for the model came from an accurate simulation of the cross-correlation signal between groups and long waves from random wave records both inside and outside a natural surf zone. Key to the present study, a means of separating the BFLW and BLW components was demonstrated in which the model is run separately with BFLW forcing only, BLW forcing only, or total combined forcing.

Here, the model is run with both a plane beach (slope  $\tan \beta = 0.025$ , Fig. 2) and the idealized bar/trough topography of Symonds and Bowen (1984) (Fig. 3). Incident waves, again parameterized as the wave envelope, enter the model at depth  $h = 15$  m, requiring a minor extension to the model described above to allow for intermediate-depth phase speeds for wave groups. Model runs are conducted at a series of discrete group frequencies defined by the beating of incident wave pairs (Table 1). Except for runs generating only the BFLW, an incoming BLW at the boundary was specified following Ottesen Hansen et al. (1981). As shown in Table 1, this gives an input BLW magnitude that is almost negligible compared to long wave amplitudes generated by the model in shallower water.

For the plane beach case, the model was run with a distance step  $\Delta x = 7.5$  m, a time step  $\Delta t = 0.5$  sec., and a shoreline reflection depth  $h_o = 0.49$  m. Plane beach results other than for the conditions reported in Table 1 are given by List (1988b). For the bar/trough case, the model was run with  $\Delta x = 5.0$  m,  $\Delta t = 0.25$  sec., and  $h_o = 0.26$  m. The different choice of parameters for the bar/trough case was related to geometric constraints; as discussed by List (1992), the choice of time step has no significant influence on the results. Other model parameters were the same as used by List (1992).

Wave amplitudes reported below were found from model-generated time series of a length of at least one group period,  $T_g$ , after an initial interval for model stabilization. For the plane beach results, amplitudes were found from the interval  $t = 200 \rightarrow 400$  sec., while for the bar/trough results amplitudes were found from  $t = 700 \rightarrow 900$  sec.; the need for a much later start time for the bar/trough case will become apparent below.

## RESULTS

*Plane Beach*

Figure 1A gives the amplitude of the long waves at the shoreline ( $h_o = 0.49$  m reflection point) for model runs in BFLW, BLW and total forcing modes for the plane beach case. Except at the lowest frequencies, the BLW is predicted to be larger than the BFLW. Interestingly, the long waves generated in total forcing mode are lower at all frequencies than the sum of the BFLW and BLW. There is also a systematic variation in the degree to which the sum of the BFLW and BLW is destructive, with the total solution being less than either the BFLW or BLW at low frequencies, while at high frequencies the total solution amplitude is nearly identical to the BLW. An investigation of the phase between the envelope,  $A(t)$ , and the BLW seaward of the surf zone as well as between the BFLW and BLW near the shoreline, shown in Fig. 2, explains this model result. As the BLW progresses into shallow water, it lags behind the group structure, with higher frequencies showing a greater departure from the deepwater  $180^\circ$  relationship with  $A(t)$ . Higher frequencies are then closer to a  $90^\circ$  relation with the BFLW in the surf zone, resulting in a less destructive interference. This lag of the BLW behind  $A(t)$  has been shown previously by Elgar and Guza (1985) and List (1992).

Figure 1B shows the amplitude of the outgoing sea-surface component,  $\eta(off)$ , found by separating the onshore ( $\eta(on)$ ) and offshore ( $\eta(off)$ ) progressive long wave components following Guza et al. (1985). Model results are again shown for runs in BFLW, BLW, and total forcing modes, with the BLW now a free long wave after shoreline reflection. The BFLW clearly shows the frequency selection predicted by Symonds et al. (1982). The amplitude of the total solution relative to the BFLW and BLW indicates a highly variable phase relation between the BFLW and BLW for these outgoing waves. However, the net result is that the total solution amplitudes do not show a distinctive structure, apart from a general increase with increasing frequency.

*Bar/Trough Nearshore*

Figure 4 gives the amplitude of the long waves at the shoreline ( $h_o = 0.26$  m reflection point) for model runs in BFLW, BLW and total forcing modes over the bar/trough profile of Symonds and Bowen (1984) (Fig. 3). While the overall trends are similar to the plane beach case (Fig. 1A), there are now marked peaks at  $f_g = 0.0172$  Hz and  $f_g = 0.0309$  Hz for all forcing modes. Except for a frequency shift in the peaks due to a shoreline reflection point with  $h_o > 0$ , the structure is almost identical to that predicted by Symonds and Bowen (1984). The most striking result in Fig. 4 is that the shallow water

bound wave is just as likely to force the distinctive set of shoreline peaks as the breakpoint-forcing mechanism.

Because the above results suggested that the forcing mode is irrelevant to the generation of the peaked amplitude spectrum, a test was conducted in which all incident wave forcing was turned off, leaving only the solution to eqns. (1) and (2) with a small input long wave of variable frequency. For Figs. 5 and 6 the model was run in this mode at a series of discrete frequencies with  $\Delta x = 5.0$  m,  $\Delta t = 0.5$  sec, and an incoming long wave at  $x = 400.0$  m ( $h = 5.2$  m, Fig. 3) with amplitude  $A = 0.01$  m for all frequencies. Shoreline amplitudes were found at a reflection point with  $h_0 = 0.1$  m. These parameters were changed from the forcing-inclusive runs to improve model efficiency; the qualitative interpretation of the results is unaffected.

With the model configured in this way, the peaked shoreline amplitude structure is reproduced once more, as shown in Fig. 5 ( $t = 700$  sec. curve). (Note that the peak frequencies are again shifted due to a different depth of shoreline reflection,  $h_0$ .) This demonstrates that the Symonds and Bowen (1984) result can be reproduced by any model that generates a white spectrum of long waves incident to a bar/trough nearshore.

Symonds and Bowen (1984) suggested that these peak frequencies satisfy a "half-wave resonance" condition, in which an antinode in  $\eta$  corresponds with the bar crest. The characteristics of this potential resonance are investigated here by examining the time development of the amplitude structure. Fig. 5 shows long wave amplitudes found from group period length intervals starting at two different times:  $t = 110$  sec., or just after input long waves have reached the shoreline, and  $t = 700$  sec. after time for model stabilization. Except at the lowest frequencies, the amplitude of the  $t = 110$  sec. curve is almost invariant with frequency, at a level of about 0.05 m. This is the expected value for the shoreline amplitude of a standing wave, given shoaling of the  $A = 0.01$  m input wave from  $h = 5.2$  m to  $h = 0.1$  m. After 700 seconds there is a strong amplitude increase at the "half-wave resonance" frequencies, supporting the concept that these frequencies represent a resonant condition.

However, two other observations complicate this otherwise straightforward interpretation of a resonant phenomenon. First, as shown in Fig. 5, the non-resonant frequencies actually decrease in amplitude over time. Although this was also seen by Symonds and Bowen (1984) in a comparison between their bar/trough and plane beach results, the reason for this model result is not known. Second, the model as formulated using eqns. (1) and (2) contains no term for frictional dissipation; "resonant" peaks should continue to grow in amplitude until model depth limits are exceeded. However, as shown in Fig. 6, this is not the case; with time, peak and valley amplitudes reach a stable value. List (1988a) predicted the same shoreline structure using leaky mode solutions over the Symonds and Bowen profile, suggesting that the peak/valley result

relates more to an uneven distribution of wave energy across the nearshore than to a true resonance.

## DISCUSSION

The prediction of a strong, apparently linear, dependence of the BLW magnitude on the group frequency, shown in Fig. 1A, may be an artifact of the model simplifications, especially the lack of an energy balance between short and long waves. Field observations do not in general support this result. More recent models (e.g. Roelvink, 1991; Roelvink et al., this volume; Watson and Peregrine, this volume) may address this problem, although these models have not yet been directly tested in this respect. Thus the model result that the total outgoing wave will not show a distinctive frequency selection, as predicted by Symonds et al. (1982), is tempered by this problem.

In fact, some laboratory data do show a frequency selection in the outgoing wave (Kostense, 1985); this same pattern is reproduced, at least qualitatively, by the model of Roelvink et al. (this volume). However, modeling of a field data set (List, 1992) suggests that the BLW can be much larger than the BFLW, at least under certain conditions. In this case the outgoing long wave will not show a strong frequency selection. Consistent with this is the lack of supporting field observations showing a strongly peaked spectrum in the long waves offshore, despite a decade of nearshore field experiments since the Symonds et al. (1982) prediction. The results presented in this paper suggest that while the breakpoint-forcing mechanism may be valid and operative, the wave generated by this means has an amplitude and phase relation to the BLW such that a frequency selection in the outgoing wave will not be strong, explaining the lack of this type of field observation.

Although the bar/trough results clearly show that any white long wave forcing can result in a distinctly-peaked elevation spectrum at the shoreline, an explanation of this result as a resonant phenomenon, as suggested by Symonds and Bowen (1984), is subject to questions concerning the mechanism for lowering the amplitudes at non-resonant frequencies and for limiting the overall response. Clearly more work is needed to understand the nature of this interaction between topography and long wave dynamics.

## CONCLUSIONS

A possible explanation for the lack of field observations showing a strong frequency selection in the seaward propagating long waves, as predicted by the Symonds et al. (1982) model, is proposed. The breakpoint-forced long wave's relatively small size and phase relation with the wave originating as a bound wave may preclude this observation.

It is also shown that a strongly peaked elevation spectrum at the shoreline in the presence of a bar/trough topography (Symonds and Bowen, 1984) is not a unique result of the time-varying breakpoint model. It is demonstrated that any white forcing of long waves incident to a bar/trough nearshore can produce this result. Accounting for this frequency selection as a resonant phenomenon will require an explanation of several unusual observations related to the time development of this peak/valley structure.

#### ACKNOWLEDGEMENTS

Karen Monroe is thanked for preparing the figures. This study began at the Virginia Institute of Marine Science, Gloucester Point, Virginia, where L.D. Wright is thanked for encouraging and supporting this work.

#### REFERENCES

- Elgar, S., and R.T. Guza, 1985, Observations of bispectra of shoaling surface gravity waves, *J. Fluid Mech.*, 161, 425-448.
- Guza, R.T., Thornton, E.B., and Holman, R.A., 1985, Swash on steep and shallow beaches, *Proceed. 19th Internat. Conf. Coastal Eng., ASCE*, 708-723.
- Kostense, J.K., 1985, Measurements of surf beat and set-down beneath wave groups, *Proceed. 19th Internat. Conf. Coastal Eng., ASCE*, 724-740.
- List, J.H., 1988a, Leaky mode simulations over a bar-trough nearshore, *Abstracts, AGU Fall Meeting, EOS Transactions*, v. 69, n. 44, p. 1248.
- List, J.H., 1988b, Long wave generation by wave groups in the nearshore, *Ph.D. Dissertation, Virginia Institute of Marine Science, Gloucester Point, Virginia*.
- List, J.H., 1992, A model for two-dimensional surf beat, *J. Geophys. Res.*, 97, 5623-5635.
- Longuet-Higgins, M.S., and Stewart, R.W., 1962, Radiation stress and mass transport in gravity waves, with application to surf beats, *J. Fluid Mech.*, 13, 481-504.
- Longuet-Higgins, M.S., and Stewart, R.W., 1964, Radiation stress in water waves: a physical discussion, with applications, *Deep Sea Res.*, 11, 529-562.
- Okiihiro, M., Guza, R.T., and Seymour, R.J., 1992, Bound infragravity waves, *J. Geophys. Res.*, 92, 11453-11469.

- Ottesen Hansen, N.-E., Sand, S.E., Lundgren, H., Sorensen, T., and Gravesen, H., 1981, Correct reproduction of group-induced long waves, *Proceed. 17th Internat. Conf. Coastal Eng., ASCE*, 784-800.
- Roelvink, J.A., 1991, Modeling of cross-shore flow and morphology, *Proceed. Coastal Seds '91, ASCE*, 603-617.
- Roelvink, J.A., Petit, H.A.H., and Kostense, J.K., 1993, Verification of a one-dimensional surfbeat model against laboratory data, *this volume*.
- Sand, S.E., 1982, Long wave in directional seas, *Coastal Eng.*, 6, 195-208.
- Symonds, G., Huntley, D.A., and Bowen, A.J., 1982, Two-dimensional surf beat: long wave generation by a time-varying breakpoint, *J. Geophys. Res.*, 87, 492-498.
- Symonds, G., and Bowen, A.J., 1984, Interactions of nearshore bars with incoming wave groups, *J. Geophys. Res.*, 89, 1953-1959.
- Watson, G., and Peregrine, D.H., 1992, Low frequency waves in the surf zone, *this volume*.



$T_1$	$T_2$	$F_g$	Plane Beach Profile			Bar/trough Profile		
			$A_1$	$A_2$	$A_{BLW}$	$A_1$	$A_2$	$A_{BLW}$
11.32	10.70	0.0051	0.4	0.12	0.00957	0.2	0.06	0.00239
11.44	10.60	0.0070	0.4	0.12	0.00958	0.2	0.06	0.00240
11.55	10.50	0.0086	0.4	0.12	0.00959	0.2	0.06	0.00240
11.69	10.40	0.0105	0.4	0.12	0.00962	0.2	0.06	0.00241
11.81	10.30	0.0124	0.4	0.12	0.00963	0.2	0.06	0.00241
11.94	10.20	0.0143	0.4	0.12	0.00965	0.2	0.06	0.00241
12.08	10.10	0.0162	0.4	0.12	0.00968	0.2	0.06	0.00242
12.15	10.05	0.0172	--	--	--	0.2	0.06	0.00242
12.22	10.00	0.0181	0.4	0.12	0.00970	0.2	0.06	0.00242
12.39	9.90	0.0204	0.4	0.12	0.00975	0.2	0.06	0.00244
12.54	9.80	0.0223	0.4	0.12	0.00978	0.2	0.06	0.00244
12.72	9.70	0.0245	0.4	0.12	0.00984	0.2	0.06	0.00246
12.88	9.60	0.0264	0.4	0.12	0.00988	0.2	0.06	0.00247
13.06	9.50	0.0286	0.4	0.12	0.00993	0.2	0.06	0.00248
13.26	9.40	0.0309	--	--	--	0.2	0.06	0.00250
13.48	9.30	0.0334	--	--	--	0.2	0.06	0.00252
13.69	9.20	0.0356	--	--	--	0.2	0.06	0.00254
13.90	9.10	0.0379	--	--	--	0.2	0.06	0.00256

**Table 1.** Parameters used for plane beach and bar/trough profile model runs.  $T_1$  and  $T_2$  are the incident wave periods (in sec.),  $f_g$  is the resulting group frequency (Hz),  $A_1$  and  $A_2$  are the incident wave amplitudes (m), and  $A_{BLW}$  is the boundary condition bound wave given by Ottesen Hansen et al. (1981) (m).

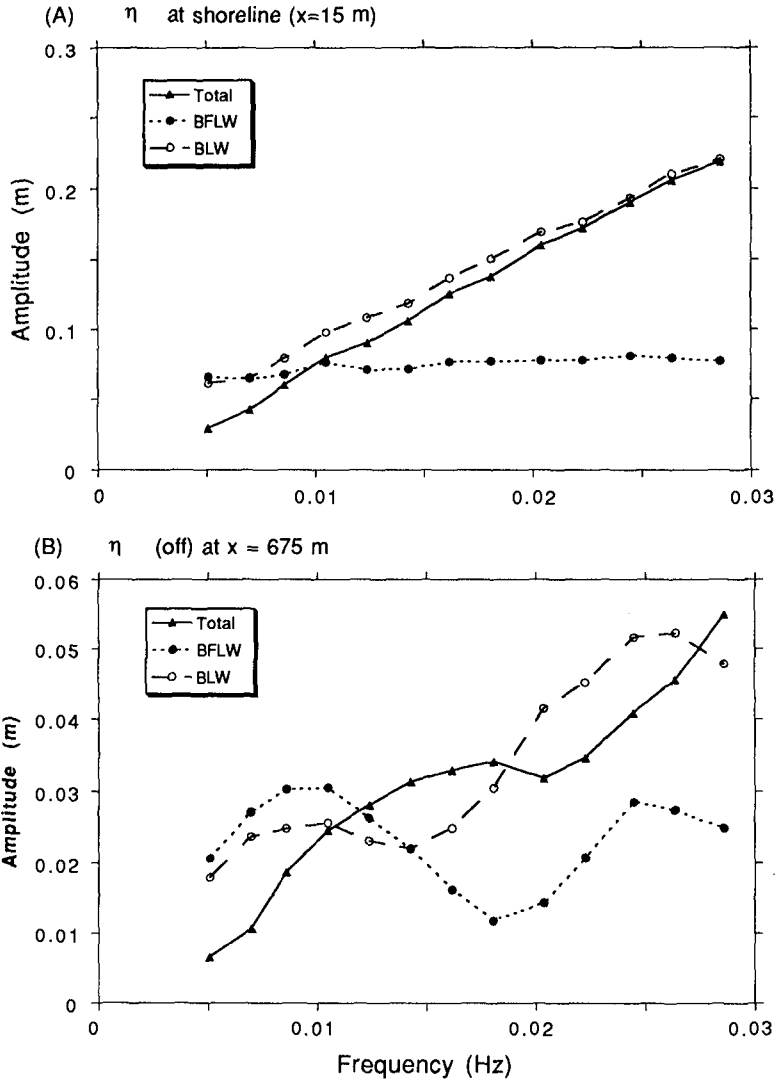
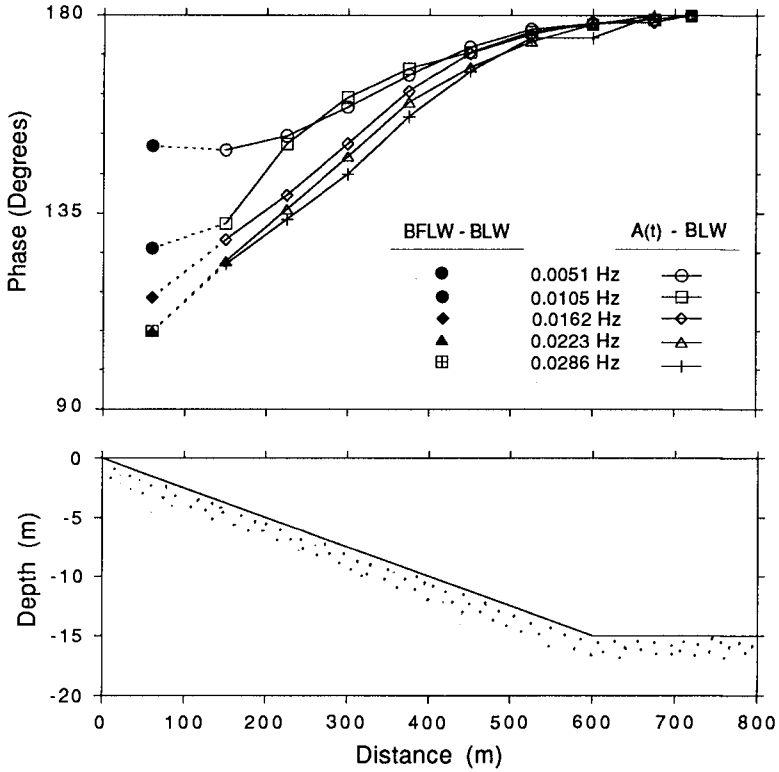
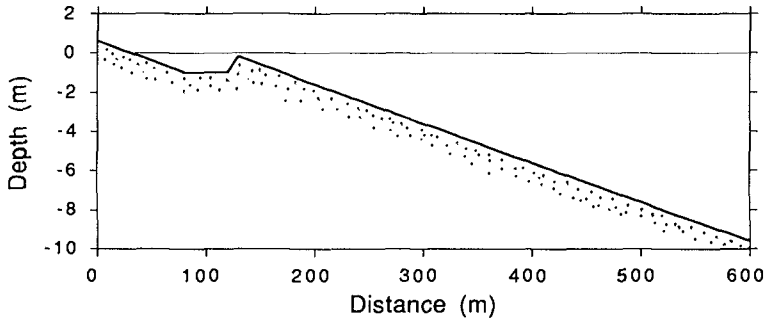


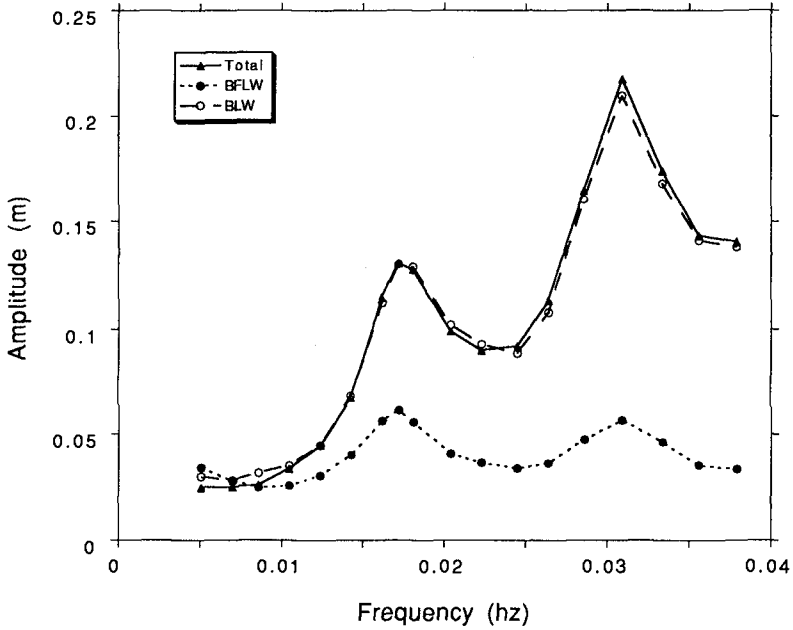
Figure 1. Model-generated long wave amplitudes of (A)  $\eta$  at the shoreline point of reflection and (B) offshore progressive component of  $\eta$  ( $\eta(off)$ ) at  $x = 675$  m over the profile shown in Fig. 2.



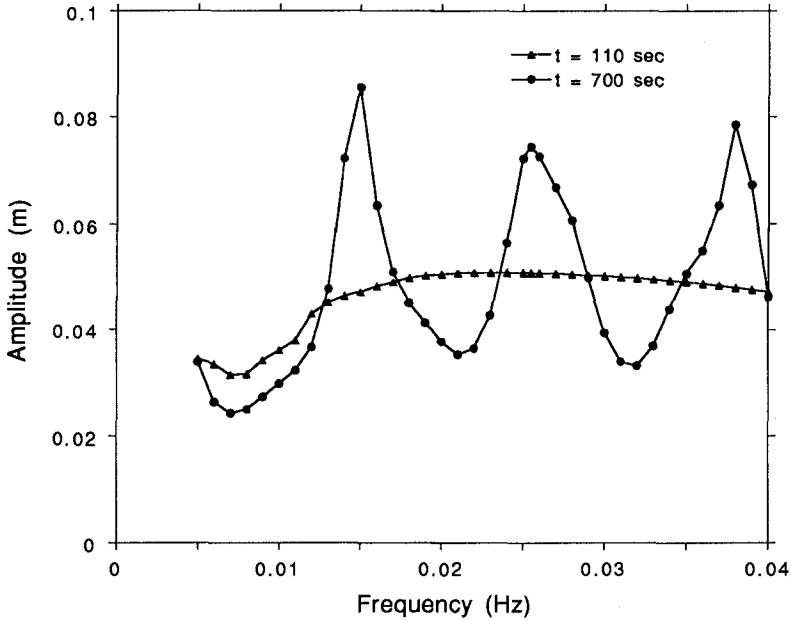
**Figure 2.** Phase between BFLW  $\eta(on)$  and BLW  $\eta(on)$  inside the surf zone (solid symbols) and between  $A(t)$  and BLW  $\eta(on)$  outside the surfzone (open symbols) for model-generated data at five group frequencies over the linear profile shown in the lower frame.



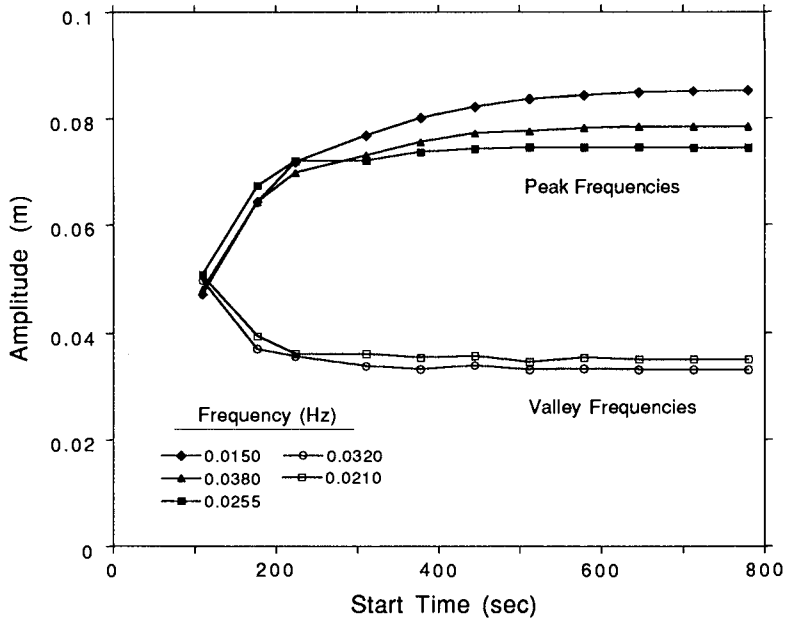
**Figure 3.** Bar/trough profile from Symonds and Bowen (1984). The profile used for model runs here (Figs. 4, 5) extends linearly to  $h = -15$  m, where wave groups enter the model over a constant depth segment as in Fig. 2.



**Figure 4.** Model-generated long wave amplitudes of  $\eta$  at the shoreline point of reflection using the bar/trough profile (Fig. 3).



**Figure 5.** Model-generated long wave amplitudes of  $\eta$  at the shoreline point of reflection using the bar/trough profile. Incident wave forcing has been turned off and long waves are input at the offshore boundary at a series of discrete frequencies, each with  $A = 0.01$  m. Long wave amplitudes were found by searching model-generated time series (obtained from independent model runs at each frequency) over an interval equal to the group period,  $T_g$ , starting at the times indicated.



**Figure 6.** Time development of three peak and two valley amplitudes shown in Fig. 5. Start time refers to the time at the beginning of the interval,  $T_g$ , for finding amplitudes from model-generated time series.

## CHAPTER 65

### The effect of waves on surges in the North Sea

C. Mastenbroek<sup>1</sup>

#### Abstract

Three effects of surface gravity waves on storm surges in the North Sea are studied with numerical models. The enhancement of the effective sea surface roughness due to growing waves causes the storm surge to build up more quickly. The maximum effect on the waterlevel along the English and Dutch coast is about 5 % of the total waterlevel elevation due to the storm. The effect of the radiation stress is opposite: it slows down the building up of the surge in the beginning of the storm. The maximum effect of the radiation stress is about 2 %. The enhancement of the bottom drag by swell in shallow water can be considerable. The lack of detailed insight in the local bottom roughness and the turbulence near the bottom defies a quantitative analysis.

## 1 Introduction

Waves influence both the generation and the decay of storm surges. In this paper three effects of waves on storm surges are discussed: the enhancement of the surface stress due to growing waves, the contribution of radiation stress and the enhancement of the bottom stress by swell in shallow water. During their generation, surface waves subtract this momentum from the atmospheric boundary layer. Some 60 to 90 % of the momentum transfer from the atmosphere to the currents goes via waves on the surface. This changes the structure of the atmospheric boundary layer. Until recently, the roughness of the sea surface was thought to be a function of the friction velocity only (Charnock, 1955).

---

<sup>1</sup>Royal Netherlands Meteorological Institute (KNMI), P.O. Box 201, 3730 AE de Bilt, the Netherlands

This leads to a drag coefficient which is roughly proportional to the windspeed. In recent years it has been shown by experiments, numerical simulations and analytical models that the sea state plays an important role in the transfer of momentum to the sea. If the waves extract a large amount of momentum from the atmosphere, which happens in the case of growing waves, the apparent roughness of the surface is enhanced. If on the other hand the phase speed of the waves is comparable to the windspeed and the waves do not grow, the roughness of the sea is relatively small. Since the growth of waves is concentrated in the first part of a storm, the generation of a storm surge will be enhanced during this period.

The second consequence of waves carrying momentum is that they are capable moving it around. In the equation for the total momentum balance, this gives rise to an additional advection term: the so-called radiation stress. At places where waves break or dissipate otherwise, this term can give rise to a wave set-up of several decimeters (Bertotti and Cavaleri, 1985) and long-shore currents (Battjes, 1974). Though this effect can be large locally, in this paper we will argue that on the scale of several tens of kilometres or larger it is of little significance. On that scale, to a very good approximation momentum goes directly from the atmosphere to the currents. This is caused by the fact that the waves carrying most of the momentum are short and dissipate quickly. Swell, which is capable of travelling a long way, carries little momentum compared to the short waves generated in the same storm.

Waves can also influence a storm surge via the bottom. If the depth of the water is comparable to the dominant wavelength, orbital wave motions reach to the bottom. This enhances the turbulent mixing near the bottom, which in its turn enhances the bottom friction felt by currents. The effect is largest in shallow regions which can be reached by swell from the open sea and where strong currents are present. In the North Sea this includes for instance the English Channel and the Bristol Channel. A few problems arise if we want to model this effect. The layer near the bottom where the orbital motions of the waves and the current interact is typically a few centimetres wide. No current measurements are available this close to the sea bed. This makes it impossible to verify theory directly. Another problem is the large variation in roughness of the seabed on the continental shelf. Compared to the errors made in the assumptions of these roughnesses the effect of the waves may be insignificant.

In the following sections the influence of waves on storm surges in the North Sea will be studied by numerical simulation. In section 2 the effect of growing waves on the storm surge elevations is discussed. The effect of the redistribution of momentum by waves is the subject of the following section. The last section focuses on the bottom roughness enhancement by long waves.



## 2 Effect of Waves on the Surface Stress

To simulate the elevations due to the tide and the storm a barotropic storm surge model of the continental shelf is used (Verboom et al, 1992). This numerical model solves the depth averaged Reynolds equation and the continuity equation with a resolution of 16 km. The waterlevels on the open boundaries, located in deep ( $> 200$  m) water, are prescribed by 10 tidal constituents. The surface stress is derived from the wind at 10 meter calculated by a regional meteorological model. In the standard version the wind is related to stress using the Charnock relation:  $z_0 u_*^2/g = \alpha$ , where  $z_0$  is the roughness length which determines the wind profile,  $u_*$  is the friction velocity,  $g$  is the gravitational acceleration and  $\alpha = 0.032$  is a constant found by tuning the model. The windprofile is assumed to be logarithmic:

$$u(z) = \frac{u_*}{\kappa} \ln\left(\frac{z}{z_0}\right), \quad (1)$$

where  $u(z)$  is the windspeed at height  $z$  and  $\kappa = 0.4$  is the von Karman constant. For given windspeed at a certain height these two equations yield  $u_*$  and  $z_0$ . The definition  $u_* = \sqrt{\tau/\rho_a}$  gives the windstress  $\tau$ .

To model the effect of waves on the momentum transfer the theory described by Janssen (1992) was used. In this theory, Janssen assumes that the momentum is transferred to the water by the turbulence and via the waves. To calculate the contribution of the waves a wave model is needed. In this research a regional implementation of the third generation WAM model was used (WAMDI, 1988). In fig. 1 an overview is given of the three models involved: the meteorological model, the wave model and the storm surge model. In the theory of Janssen, waves act to increase the effective roughness of the surface in the following way:

$$z_e = \frac{z_0}{\sqrt{1 - \tau_w/\tau}}, \quad (2)$$

where the roughness length  $z_0$  is given by the Charnock relation:  $z_0 = \tilde{\alpha} u_*^2/g$  with  $\tilde{\alpha} = 0.01$ . The windprofile is given by:

$$u(z) = \frac{u_*}{\kappa} \ln\left(\frac{z + z_e - z_0}{z_e}\right). \quad (3)$$

The total stress is now calculated in the following way. First, the wind at 10 meters  $u_{10}$  is obtained from a meteorological model. Using a wave model, the flow of momentum  $\tau_w$  to the waves is calculated with this wind. The equations (2), (3) and the Charnock relation give an implicit set of equations from which  $\tau$  (or  $u_*$ ),  $z_0$  and  $z_e$  can be obtained. Sometimes it is necessary to repeat this procedure, since the wave stress  $\tau_w$  depends on  $u_*$ . However, it converges very quickly and in practice no more than two iterations are required.

The coupled storm surge model has been compared with the standard version for several recent storm periods (Mastenbroek et al, 1992). Results from both versions have been compared with waterlevel measurements along the English

and Dutch coast. It is found that the elevations calculated with the coupled model are in good agreement with measurements. This is important because it means that the description of the flow of momentum according to Janssen is consistent with the momentum balance of the waves. A more detailed analysis reveals that the drag coefficient, defined as  $C_d = u_*^2/u_{10}^2$ , can vary a factor two depending on the sea state. Growing waves, dominant during the first part of the storm, enhance the drag considerably. This is illustrated in fig. 3. Due to this enhancement of the momentum transfer in the first part of the storm, the storm surge builds up more quickly. The maximum difference between elevations calculated with the coupled model and the reference model is about 10 cm, which is about 5 % of the total elevation due to the storm. This small difference disappears in the noise caused by measurement uncertainties and errors in the numerical model.

### 3 Transportation of Momentum by Waves

Due to the fact that propagating waves carry some momentum with them, an additional advection term arises in the balance equation for the total momentum, the so-called radiation stress term. The total momentum is the sum of the momentum of the depth averaged current and the momentum associated with waves. In terms of the wave spectrum  $F(f, \theta)$ , where  $f$  is the frequency and  $\theta$  the propagation direction, the radiation stress  $\tau_i$  in deep water is given by:

$$\tau_i = \rho g \nabla_j \int_{-\pi}^{\pi} \int_0^{\infty} \left\{ \frac{c_g}{c} \frac{k_i k_j}{k^2} + \left( \frac{c_g}{c} - \frac{1}{2} \delta_{ij} \right) \right\} F(f, \theta) df d\theta. \quad (4)$$

In the numerical experiment discussed here, the radiation stress is calculated from the wave spectrum of the regional WAM model mentioned above. It is then subtracted from the wind stress. The calculations show that the waves transport away less than 5 % of the total stress applied by the atmosphere. The rest either goes directly to the currents by means of a tangential turbulent stress or via waves that dissipate within one time interval (3 hours) between to consecutive windfields in the same gridbox where they were generated. In the case of the storm of 12/13 December 1990, dissipating waves exert a force on the water of up to 0.15 N/m<sup>2</sup> for a period as long as 12 hours on the Doggerbank. This corresponds to a windspeed of more than 10 m/s. This leads, in the case this storm, to an extra current of 3 cm/s to the South West on the Doggerbank and to an increase in the waterlevel along the English South East coast and the Dutch coast of 5 cm. During the storm of 13/14 February 1989, when the maximum winds were directed more to the East, the maximum force exerted by dissipating waves on the watercolumn occurred in the German Bight, raising the waterlevel a few centimetres along the German coast. Unfortunately these differences are small compared to the accuracy of the surge model and the measurements. The comparison of waterlevel measurements and calculations does not lead to conclusive evidence in favour or against the phenomenon discussed here.

## 4 Effect of Waves on the Bottom Stress

In most 2D storm surge models the bottom stress  $\tau_b$  is parametrised like  $\tau_b = \rho_w f_c \bar{u}^2$ , where  $\bar{u}$  is the depth averaged current. The bottom friction coefficient  $f_c \simeq 0.0025$  is constant. From recent experiments (Gross et al, 1992) it is known that waves have an important influence on this coefficient. A theoretical model of the effect of the orbital motions of waves on the turbulence near the bottom is given by Christoffersen and Jonssen (1985). For typical values for the North Sea, this theory predicts a significant variation of the bottom stress depending on the sea state. To model the effect of waves on the turbulence near the bottom, first an assumption has to be made for the turbulence in absence of waves. A convenient assumption is to parametrise the vertical exchange of horizontal momentum with an eddy viscosity  $\mu$ :

$$\tau = \rho_w \mu \frac{\partial u}{\partial z}. \quad (5)$$

The assumption that this eddy viscosity is proportional to the distance to the bottom  $\mu = \kappa u_* z$  leads to a logarithmic velocity profile  $u(z) = (u_*/\kappa) \ln(z/z_0)$ . The profile depends on an integration constant  $z_0$  which is usually associated with the roughness of the bottom. If the profile is integrated over the depth  $h$ , it can be found that the bottom friction coefficient equals:

$$f_c = \frac{\kappa^2}{(\ln(h/z_0) - 1)^2}. \quad (6)$$

Note that the assumption  $f_c = \text{constant}$  implies that the bottom roughness  $z_0$  is proportional to the water depth. The amplitude of the orbital motions at the bottom of a wave with amplitude  $a$  are  $u_w = (a\omega)/\sinh(kh)$ , where  $\omega$  is the angular frequency and  $k$  the wavenumber. This periodic motion causes an enhancement of the turbulent viscosity near the bottom in a region (the so-called *wave boundary layer*) which is typically a few centimetres wide. The apparent roughness felt by the current will be enhanced, leading to an enhancement in the bottom friction coefficient. In fig. 2 the bottom friction is given as a function of the wave height for a set of parameters which are typical for the North Sea.

In order to study the sensitivity of a storm surge model to a wave dependent bottom drag, a storm surge model (Flather, 1984) has been coupled to a wave model. If the results of this coupled model are to be compared with results from the conventional model, we have to assume that the roughness  $z_0$  is proportional to the depth. This is not based on a physical consideration, but it is implied by taking the bottom drag coefficient  $f_c$  constant in the conventional model. The calculations were performed for the storm surge which occurred 1 February 1983. Two regions on the continental shelf seem to be specifically sensitive to a wave dependent bottom drag: the English Channel and the Bristol Channel. Both of these regions are relatively shallow, have an open connection to the sea and sustain large currents. On the Doggerbank, which is shallow and experiences

large waves from the North, the drag coefficient is affected considerably. But on this location the currents are small, so the extra energy loss to the bottom due to the waves is small.

To make a quantitative analysis rather than a qualitative, several problems should be solved. First of all the modelling of the turbulence in the watercolumn in absence of waves should be made more sophisticated, specifically near the bottom. This will require a three dimensional model. Second, to test and calibrate theories such as the one discussed above, turbulence measurements near the bottom are needed. The interaction with ripples and other features on the bottom should be examined. Finally a bottom roughness map should be compiled for all relevant shallow areas.

## 5 Conclusions

- Growing wind sea enhances the wind stress in the beginning of the storm considerably. After a few hours this enhancement disappears. In the case of the North Sea, the maximum effect on the water level is about 5 % of total elevation due to the storm.
- In a growing sea, the radiation stress modifies the wind stress no more than 5 %. When swell generated in the Norwegian Sea reaches the shallow parts of the North Sea a radiation stress can be as large as  $0.15 \text{ N/m}^2$ . The maximum effect on the waterlevel along the English and Dutch coast is about 2 % of the total elevation due to the storm.
- The modification of the bottom stress by waves is important in shallow regions which can be reached by swell and which sustain large currents. Specific knowledge about the local bottom roughness and turbulence near the bottom is needed to make quantitative statements.

## References

- [1] Battjes, J.A. (1974) Computation of set-up, longshore currents, run-up and overtopping due to wind-generated waves, *Comm. on Hydraulics, Dept. of Civil Eng., Delft Univ. of Techn.*, No. 74-2.
- [2] Bertotti, L. and L. Cavaleri (1985) Coastal set-up and wave breaking. *Ocean. Acta*, **8**, No. 2, 237-242.
- [3] Christoffersen, J.B. and I.G. Jonsson (1985) Bed friction and dissipation in a combined current and wave motion. *Ocean Engng*, **12**, No 5, 387-423.
- [4] Flather, R.A. (1984) A numerical model investigation of the storm surge of 31 January and 1 February 1953 in the North Sea. *Quart. J. of the Royal Met. Soc.*, **110**, 591-612.

- [5] Gross, T.F. et al (1992) Estimation of stress and bed roughness during storms on the Northern California Shelf. *Cont. Shelf Res.*, **12**, No. 2/3, 389-413.
- [6] Janssen, P.A.E.M. (1992) Quasi-linear theory of wind wave generation applied to wave forecasting. *J. Phys. Oceanogr.*, **21**, 1631-1642.
- [7] Mastenbroek, C., G. Burgers and P.A.E.M. Janssen (1992) The dynamical coupling of a wave model and a storm surge model through the atmospheric boundary layer. *accepted for publication in J. Phys. Oceanogr.*
- [8] Verboom, G.K., J.G. de Ronde and R.P. van Dijk (1992) A fine grid flow and storm surge model of the North Sea. *Cont. Shelf Res.*, **12**, No 2/3, 213-233.

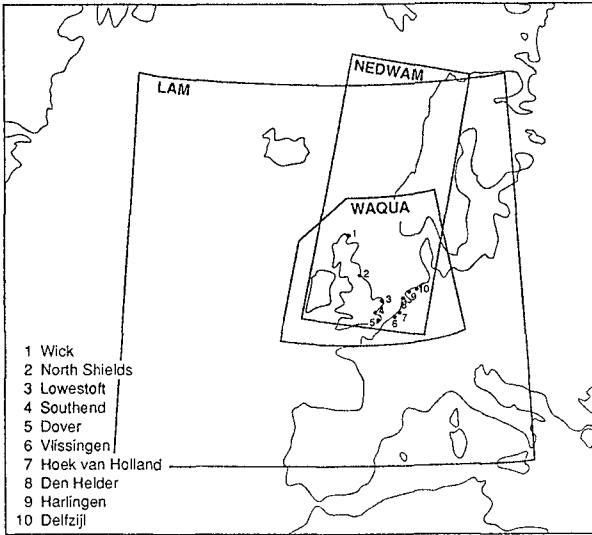


Figure 1: An overview of the areas covered by the meteorological model LAM, the wave model NEDWAM and the surge model WAQUA.

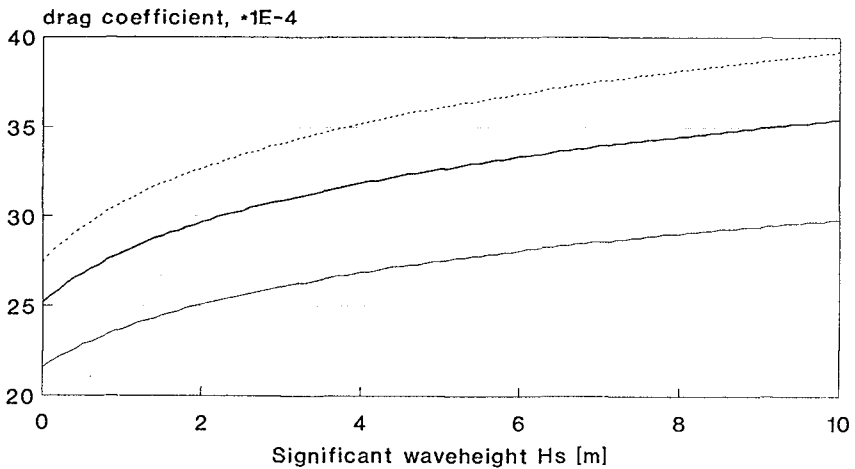


Fig. 3. Bottom drag coefficient  $f_c$  as a function of significant wave height for a typical North Sea case (depth is 40 m, wave period is 8 sec). The three line represent different sea bed roughnesses:  $z_0$  is 5, 3.3 and 1.7 mm from top to bottom.

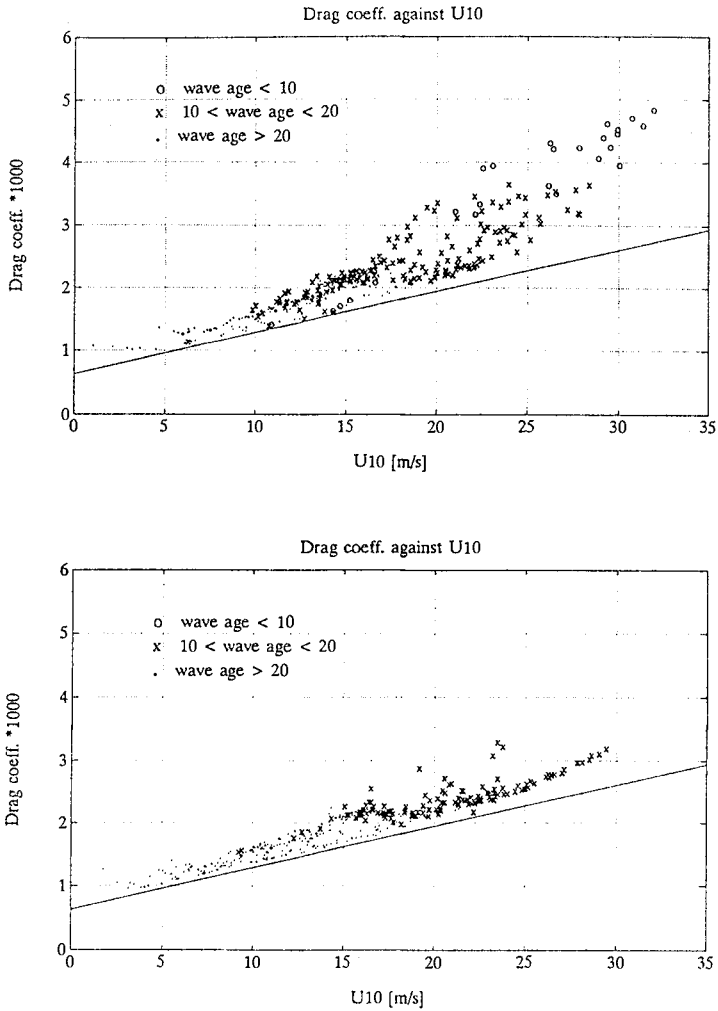


Figure 2: Scatter plots of the drag coefficient against windspeed at two different stages in the storm of 12 December 1990. Above, at the beginning of the storm, a lot of young sea is present. Below, 9 hours later, the waves are older. The wave age is defined as the phase velocity of the peak frequency divided by the friction velocity:  $c_p/u_*$ .

## CHAPTER 66

### DISTRIBUTION OF UNDERTOW AND LONG-WAVE COMPONENT VELOCITY DUE TO RANDOM WAVES

Akio Okayasu<sup>1</sup> and Hiroyuki Katayama<sup>2</sup>

#### Abstract

Laboratory measurements were performed on cross-shore velocity variations in the surf zone caused by random waves by using a laser Doppler velocimeter. Two-dimensional distributions of undertow and long-wave component velocity were obtained on a uniform slope bed and a bar-type beach. A model was presented to estimate undertow distribution due to random waves on an arbitrary beach topography.

#### 1. Introduction

In order to predict the sediment transport and the material diffusion in the surf zone, it is necessary to evaluate the velocity distribution of undertow with high accuracy. In the last decade, many detailed laboratory measurements related to the velocity distribution in the surf zone were performed under regular wave conditions [see e.g. Stive and Wind (1982), Nadaoka and Kondoh (1982) and Okayasu *et al.* (1986)]. In these researches, it was pointed out that the characteristics of waves and velocity fields change significantly around breaking or plunging points. The mass flux due to waves and vertical profiles of undertow also differ between the outer and inner region of the surf zone. On the basis of the experimental results, some theoretical and numerical models have been presented to estimate the undertow distribution by, such as, Svendsen (1984), Nadaoka and Hirose (1986), Tsuchiya *et al.* (1988) and Okayasu *et al.* (1990).

---

<sup>1</sup> Research Associate, Department of Civil Engineering, Yokohama National University, Hodogaya-ku, Yokohama 240, Japan

<sup>2</sup> Graduate Student, Department of Civil Engineering, Yokohama National University, Hodogaya-ku, Yokohama 240, Japan



However, the actual wave field is random. Velocity measurements under random wave conditions and models based on them are needed for practical use. Sato *et al.* (1988) performed laboratory measurements of near-bottom velocity in the surf zone under random wave conditions by using a laser Doppler velocimeter (LDV). Isobe (1983) and Mckee Smith *et al.* (1992) measured nearshore velocity in the field, then investigated the vertical distribution of cross-shore steady current. However, the number of measuring points was not enough for the quantitative discussion.

In the present study, laboratory experiments were performed for random wave conditions to measure cross-shore velocity in the surf zone by using LDV. The beach topographies were a 1/20 constant slope and a bar-type beach. Then a model was investigated to estimate the undertow distribution due to random wave breaking on an arbitrary beach topography by applying a model for regular wave conditions.

In recent years, the importance of long-wave component velocity on the sediment transport have been recognized in and near the surf zone, especially in terms of the suspended sediment transport. In this study, the velocity distribution of long-wave component in the surf zone is also investigated.

## 2. Experimental arrangements

The experiments were performed in a wave flume which was 17 m long and 0.5 m wide. A random wave generator with absorption control for reflected waves was equipped at one end of the flume. Beach topographies were a 1/20 uniform slope and a bar-type beach. The bar-type beach consisted of the first 5 m of 1/20, the next 1 m of  $-1/20$  and the last 4 m of 1/20 slopes. The bottom of the slopes were smooth. The figure 1 shows the side view of the flume with the bar-type beach.

Regular and random incident waves were used for the case of uniform slope beach to investigate the difference in the velocity field. The random waves (case 1) had the Bretshneider-Mitsuyasu spectrum and the significant wave height and period were planed to be almost same values as the wave height and period of the regular waves (case 2). In cases 3 and 4, velocity was measured on a bar-type beach for two random waves which had different significant wave heights and periods. The waves broke just before the top of the bar in case 3, and they began to break offshoreward away from the bar in case 4. The still water depths in the offshore regions,  $h_i$ , were 35.0 cm in cases of the uniform slope and 32.0 cm for the bar-type. The water depth at the top of the bar was 7.0cm. The experimental conditions are listed in Table 1. In the table,  $T$  is the wave period,  $H_i$  the wave height in the offshore region. For random waves, they are noted as the values for significant waves analyzed by using the zero-down cross method.

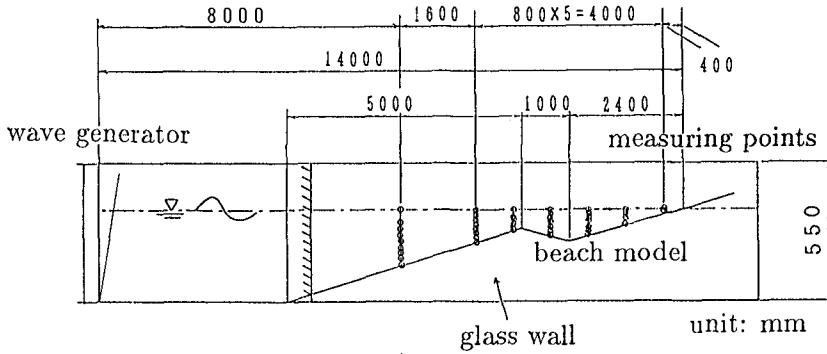


Fig. 1 Side view of the flume (bar-type beach).

Table 1 Experimental conditions

case	beach type	$h_i$ (cm)	$T$ (s)	$H_i$ (cm)	wave condition
1	uniform	35.0	1.20	7.85	regular
2	uniform	35.0	1.26	8.28	random
3	bar-type	32.0	0.945	5.67	random
4	bar-type	32.0	1.14	7.52	random

Seven vertical measuring lines were set on the beach model in each case, which covered the whole surf zone. Along these lines, several measuring points were arranged vertically from 2 mm above the bottom to the mean water level in every 3 to 40 mm. The distance from the points to the side wall of the flume was 16 cm. The total number of the measuring points were 49 for the uniform slope beach and 53 for the bar-type beach. The  $x$ -axis and  $z$ -axis were set to be onshoreward and vertically upward, respectively. The origin of the co-ordinates was the shoreline at the still water level.

An one-component LDV (15 mW, He-Ne) was used to measure the cross-shore velocity. The data of water surface elevation above the measuring point were also taken simultaneously by using a capacitance-type wave gage. The velocity and wave profile data were sampled every 20 ms and were stored in a digital data recorder.

For regular wave condition (case 1), the ensemble mean value of velocity was obtained as the average at the same phase of waves over 100 wave period. The steady current was calculated from those ensemble mean values. In case of random wave conditions, data were recorded for 5 minute (3 minute for case 2) after 3 minute of wave generating to make the wave field steady in every measurement. When the velocity was repeatedly measured at each point, the same incident signal for random waves was used in each case.

The long-term gradual fluctuation of the output voltage from the LDV system may seriously affect the precision of the velocity measurement, especially for the steady current, because the value of steady current is usually far smaller than the amplitude of the orbital velocity by waves. Therefore, the output signal from the LDV system in the still water condition was recorded for every measuring point and was used to compensate the zero level of the recorded velocity.

### 3. Experimental results

In random wave conditions, the cross-shore velocity  $u$  and the water surface elevation  $\eta$  can be divided into 4 components in terms of frequency  $f$ . They are, steady components  $U$  and  $\bar{\eta}$ , long-wave components  $u_l$  and  $\eta_l$ , short-wave components  $u_s$  and  $\eta_s$  and turbulence components  $u_t$  and  $\eta_t$ . In the present study,  $u_l$  and  $\eta_l$  were defined as  $f < 0.3$  (Hz),  $u_s$  and  $\eta_s$  as  $0.3 \leq f < 5$  (Hz) and  $u_t$  and  $\eta_t$  as  $5 \leq f$  (Hz). They were obtained by using numerical filters.

#### 3.1 Distribution of undertow

Figure 2 shows the results of steady current distribution on the uniform slope. The distributions for regular wave condition and that of random wave condition are shown together. In the figure, "b.p." denotes the breaking point by regular waves, "b.p.<sub>.1/3</sub>" denotes the significant breaking point due to random waves. Since these breaking points were determined on the measuring lines where the wave height or the significant wave height take their maximum values, the exact points of wave breaking may be different within the neighboring measuring lines. The mean water level due to regular waves is indicated in the figure.

In case of regular waves, the vertical profiles abruptly change a little after the wave breaking ( $x = -180$  to  $-120$  in Fig. 2). On the contrary, profiles near breaking point show gradual change in their forms for the random wave condition. The reason should be because that the positions of breaking have a variation in the cross-shore direction. The change already takes place from the breaking point in the case of random waves. This means that the influence by large waves in random condition cannot be neglected on the steady current distribution, although the frequency in appearance of the large waves is small.

No significant difference in the profiles is found in the inner region where almost all waves break. Vertically averaged values of undertow in random wave condition are 10 % or 30 % smaller than those by regular waves with equivalent wave heights.

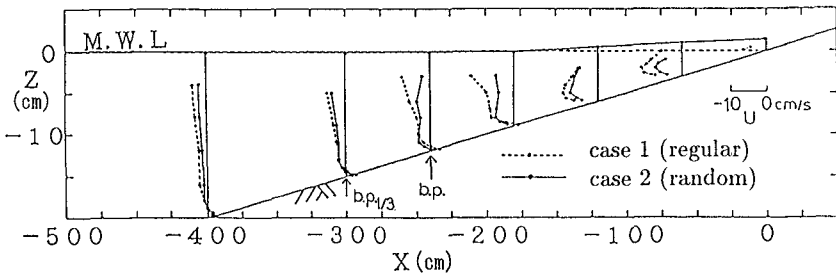


Fig. 2 Measured undertow due to regular and random waves (uniform slope).

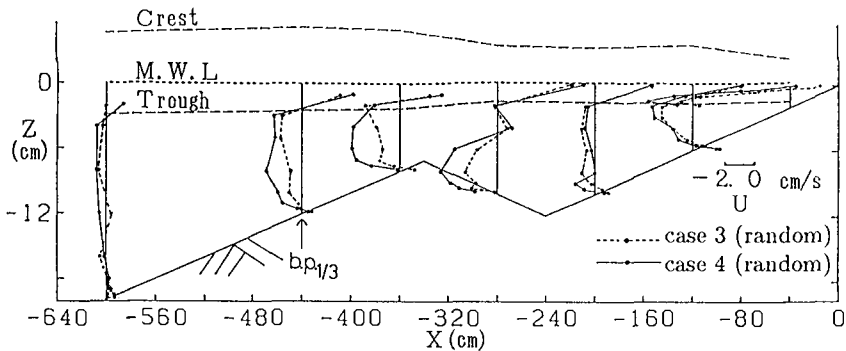


Fig. 3 Measured undertow due to random waves (bar-type).

Figure 3 gives the undertow distributions on the bar-type beach. In the figure, the mean water level for case 4 is shown. The crest and trough levels were obtained by averaging those of 1/3 maximum waves. In these cases, waves break around the top of the bar. At the onshore side of the bar, the distribution shows the typical profiles for inner region which has strong offshore directed current near the bottom.

After the first breaking, waves recover at the trough of the bar. The undertow profiles there become similar to the profiles outside the surf zone. The near-bottom velocity is offshoreward at the top of the bar, however, it comes onshoreward again at the trough. It can be considered that the bottom boundary layer develops at the trough of the bar.

**3.2 Distribution of long-wave component velocity**

Figure 4 shows the two-dimensional distribution of long-wave component of velocity, which was extracted by using a numerical filter from the time series of measured velocity. The root-mean-square value  $u_{l,rms}$  of the low frequency component velocity  $u_l$  on the uniform slope is given in the figure.

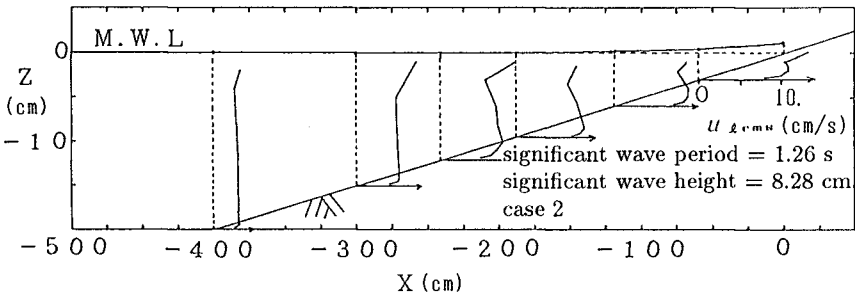


Fig. 4 RMS Value of long-wave component velocity (uniform slope).

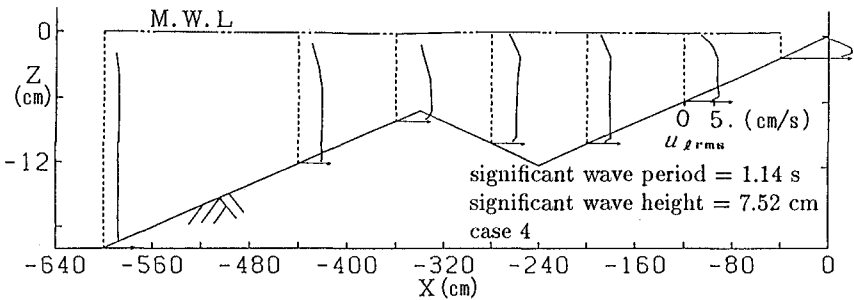


Fig. 5 RMS value of long-wave component velocity (bar-type).

The distribution of  $u_{l\text{rms}}$  on the bar-type beach is shown in Fig. 5. In both cases, the amplitudes of long-wave component are almost constant in vertical direction same as the distribution of the short-wave component, although the figures show maximum values around the elevation of 1 cm from the bottom. Below the level, the amplitudes considerably decrease. It should be due to the bottom boundary layer, but probably it is different from the ordinary turbulent oscillatory boundary layer because of the turbulence from the upper layer produced by wave breaking.

Figure 6 gives distribution of vertically averaged values  $u_{lm}$  of  $u_{l\text{rms}}$  on the bar-type beach. The variation of root-mean-square value  $\eta_{l\text{rms}}$  of low-frequency component of water surface elevation is shown together. Both of them take large values at the top of the bar, then decrease a little with increasing water depth in wave recovery zone, and then increase remarkably after second wave breaking. This result supports the previous researches for cross-shore variations of the long-wave components.

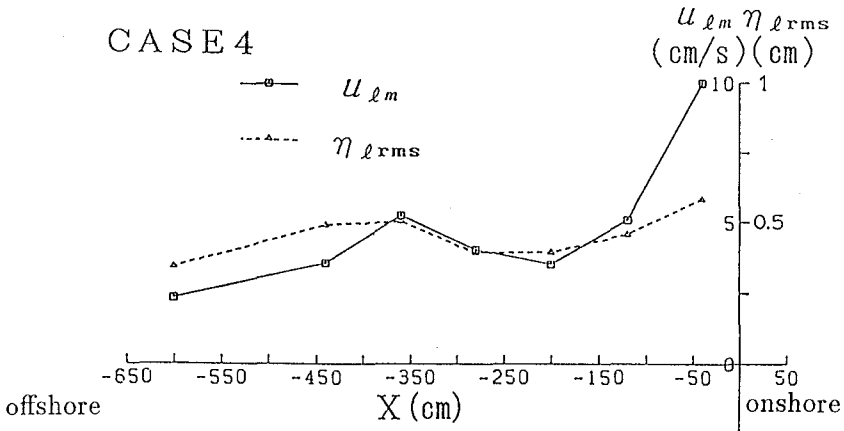


Fig. 6 Cross-shore variation of long-wave component velocity (bar-type).

#### 4. Undertow Model for Random Wave Condition

In random wave condition, the spatial distribution of breaking points cause gradual change of undertow profile around the break points as shown in the section 3.1. Therefore, in this case, good accuracy near the breaking points cannot be expected to undertow models developed for regular wave conditions.

In the present study, a model was investigated to estimate the undertow profile under random wave breaking by applying a model for regular waves.

In order to obtain the undertow distribution due to random waves by using a model for regular waves, it may be possible to estimate the distribution by superimposing the calculated values for every individual wave in the time series of random waves. However, it should not be practical because this way must need much computing time. Therefore, representative wave heights which were obtained by using the individual wave analysis was used in this study.

At first, individual offshore measured waves are classified into three groups which contain 1/10 of the highest, 7/30 of the next highest and 2/3 of the rest, that is the lowest waves. Then, the average wave heights  $H_1$ ,  $H_2$  and  $H_3$  for each group are calculated. The values  $H_1$ ,  $H_2$  and  $H_3$  are easily obtained by using the relations as shown below from the 1/10 maximum wave height  $H_{1/10}$ , the significant wave height  $H_{1/3}$  and the mean wave height  $\bar{H}$ .

$$H_1 = H_{1/10}$$

$$H_2 = \frac{10H_{1/3} - 3H_{1/10}}{7} = 1.429H_{1/3} - 0.429H_{1/10}$$

$$H_3 = \frac{3\bar{H} - H_{1/3}}{2} = 1.5\bar{H} - 0.5H_{1/3}$$

The each value is put into the undertow model presented by Okayasu *et al.* (1990) for regular wave conditions as the incident wave condition to evaluate the undertow distribution due to the representative waves.  $U_1$ ,  $U_2$  and  $U_3$  are calculated undertow value from  $H_1$ ,  $H_2$  and  $H_3$  with the significant wave period  $T$ . Contributions by the three representative waves were estimated by multiplying the factor of 1/10, 7/30 and 2/3 which are the frequencies of appearance of the each obtained values. Finally, the contributions are linearly superimposed and the undertow distribution due to the random waves is obtained. Figure 7 gives the flow chart of this process.

The calculated undertow distribution on the uniform slope is shown in Fig. 8 with the measured distribution. The calculated profile changes gradually around the breaking point.

Figure 9 shows the distribution on the bar-type beach. The overall agreement is good. The model can evaluate the profiles also in wave recovery zone, especially for onshore directed flow in the vicinity of the bottom. It can be said that the model is able to estimate the undertow distribution due to random waves.

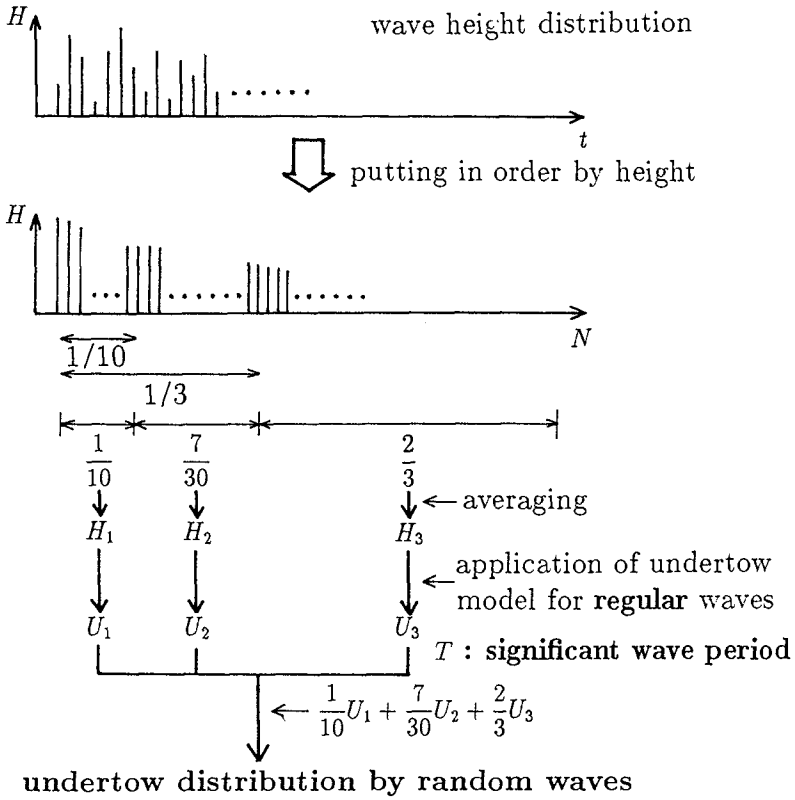


Fig. 7 Flow chart of the process of undertow evaluation.



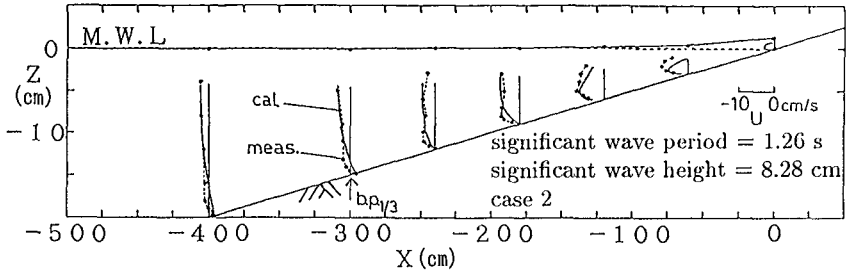


Fig. 8 Calculated and measured undertow (uniform slope).

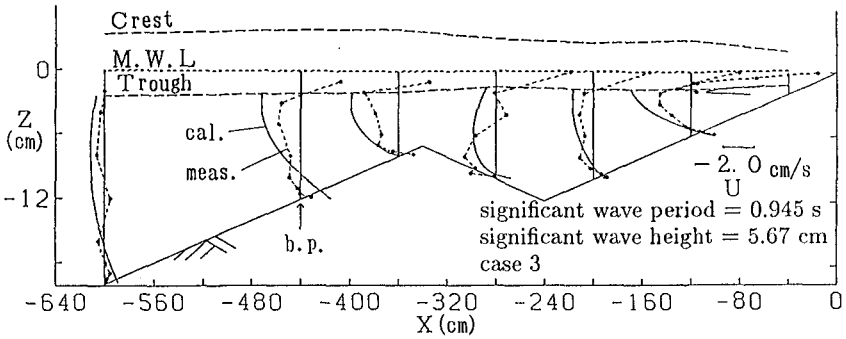


Fig. 9 Calculated and measured undertow (bar-type).

5. Conclusions

In the present study, laboratory experiments were performed for random wave conditions to measure cross-shore velocity in the surf zone on a 1/20 constant slope and a bar-type beach. Then a model was formulated to estimate undertow distribution caused by random wave breaking on arbitrary beach topographies from the offshore wave height distributions. The vertical distribution of long-wave component velocity was also investigated.

The conclusions obtained in this study are as follows.

- 1) The vertically averaged values of undertow due to random waves are 10 to 30 % smaller than those by regular waves. The change of vertical profiles of

undertow in the cross-shore direction around the breaking point is gradual under random wave conditions.

- 2) The amplitude of long-wave component velocity can be considered almost constant in vertical direction, although the influence by the boundary layer is obvious in the vicinity of the bottom.
- 3) The distribution of undertow caused by random waves can be estimated from three representative wave heights obtained from offshore wave height distribution. The distributions for the three representative wave heights calculated by using a model for regular waves are superimposed with factors depending on the frequencies of appearance.

### References

- Isobe, M., 1983: Field observation of vertical distribution of mean velocity in the nearshore zone, *NERC Rep.*, No.17, TR-82-1, pp.66-73 (in Japanese).
- Mckee Smith, J., I.A. Svendsen and U. Putrevu, 1992: Vertical structure of the nearshore current at DELILAH: measured and modeled, *Abstracts 23rd Int. Conf. Coastal Eng.*, pp.156-157.
- Nadaoka, K. and F. Hirose, 1986: A modeling of water particle dispersion under breaking waves in the surf zone, *Proc. 33rd Japanese Conf. Coastal Eng.*, pp.26-30 (in Japanese).
- Nadaoka, K. and T. Kondoh, 1982: Laboratory measurements of velocity field structure in the surf zone by LDV, *Coastal Eng. Japan*, JSCE, Vol.25, pp.125-145.
- Okayasu, A., T. Shibayama and N. Mimura, 1986: Velocity field under plunging waves, *Proc. 20th Int. Conf. Coastal Eng.*, pp.660-674.
- Okayasu, A., A. Watanabe and M. Isobe, 1990: Modeling of energy transfer and undertow in the surf zone, *Proc. 22nd Int. Conf. Coastal Eng.*, pp.123-135.
- Sato, S., M. Fukuhama and K. Horikawa, 1988: Measurements of near-bottom velocities in random waves on a constant slope, *Coastal Eng. Japan*, JSCE, Vol.31, No.2, pp.219-229.
- Stive, M.J.F. and H.G. Wind, 1982: A study of radiation stress and set-up in the near-shore region, *Coastal Eng.*, Vol.6, pp.1-25.
- Svendsen, I.A., 1984: Mass flux and undertow in a surf zone, *Coastal Eng.*, Vol.8, pp.347-365
- Tsuchiya, Y., T. Yamashita and M. Uemoto, 1988: A model of undertow in the surf zone, *Coastal Eng. in Japan*, Vol.30, No.2, pp.63-73.

## CHAPTER 67

### Occurrence Distribution of Maximum Wave Height including Wave Grouping Effect

Kosuke Kondo<sup>1</sup>, Tsunehiro Sekimoto<sup>2</sup>, Takuzo Shimizu<sup>1</sup>  
and  
Sumio Imai<sup>3</sup>

#### Abstract

The effect of wave grouping on the occurrence frequency distribution of maximum wave height was investigated on the basis of field observation data. The observed maximum wave height distribution fitted the distribution derived from Weibull distribution and was closely related with not only the wave grouping but also wave non-linearity. In the case of large degrees of wave grouping and wave non-linearity, it was found that the maximum wave height was greater than that estimated by the Rayleigh distribution.

#### 1. Introduction

Since the wave grouping may influence several important issues of coastal engineering, many researchers have been studying the characteristics of wave grouping. The first treatment of wave grouping was the analysis of statistical properties of run length (Goda, 1970; Kimura, 1980; Longuet-Higgins, 1984). The characteristics of run length of field data have been also studied (Goda, 1983). Besides the statistics of run length, the square of water surface elevation has been commonly used for wave grouping analysis (Funke and Mansard, 1979). Recently the concept of the modulational instability has been used for describing the wave

---

<sup>1</sup>Penta-Ocean Construction Co. Ltd., 2-2-8 Koraku, Bunkyo-Ku, Tokyo 112, Japan.

<sup>2</sup>Penta-Ocean Construction Co. Ltd., 1-11-25 Higashiohi, Shinagawa-Ku, Tokyo 140, Japan.

<sup>3</sup>Tokyo Electric Power Co. Inc., 1-1-83 Uchisaiwaicho, Chiyoda-Ku, Tokyo 100, Japan.

grouping process (Mase and Iwagaki, 1986) and the spatial change of wave group properties due to wave group propagation has been investigated (Ukai, 1990). Also, the relationship between wave grouping and occurrence frequency distribution of wave height has been studied by Mase(1989).

According to Mase's study, it was suggested that the frequency distribution of wave height becomes wider as the degree of wave grouping is higher. This result means that the wave grouping effect has to be considered when the maximum wave height is adopted as the design wave height because the maximum wave height becomes higher, when the occurrence frequency distribution becomes wider. This will be an important problem, especially for the design of deep water structures.

In this study, we aim to investigate the relationship between wave grouping and occurrence frequency distribution of wave height on the basis of field observation data, and to study the effect of wave grouping on the occurrence frequency distribution of the maximum wave height.

## 2. Field observations

Field observations were conducted at the port of Kashiwazaki-Kariwa nuclear power plant from January through March in 1989. This power plant was constructed in both Kashiwazaki city and Kariwa town, so we call it shortly Kashiwazaki-Kariwa. Figure 1 shows the location of observation site which is located in Niigata Prefecture in Japan and faces to the Sea of Japan. Along the WNW direction from this site, there is Noto peninsula and in the direction of N there is Sado island. Therefore the incident wave direction to this site is restricted to a range from WNW-direction to N-direction. Figure 2 shows the port of Kashiwazaki-Kariwa nuclear power plant. This port has an area of about 3 km wide along the shoreline and about 1.3 km long normal to shoreline. The wave height and direction were measured at the water depth of 13m by using ultrasonic wave gage and electromagnetic current meter. The locations of observation points are shown in this figure. More than 200 time series of wave data, 20 minutes each, were recorded every two hour. During this observation, the observed maximum significant wave had height of 3.45m and period of 8.3 s. However, waves higher than 2m were observed only a few times. Therefore wave data which were obtained in January and March in 1987, as part of a long term study by Tokyo Electric Power Co. Inc. were also analyzed. In this period, waves had relatively large height and maximum significant wave height was 5.13m with period of 9.9 s. In this long term observation, ultrasonic wave gage was laid 1.5 km far from the shoreline.

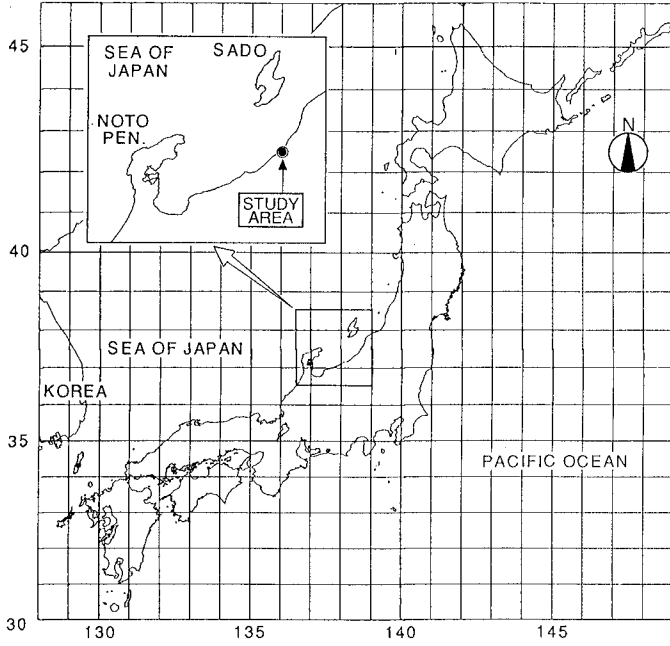


Figure 1. The location of the investigation site.

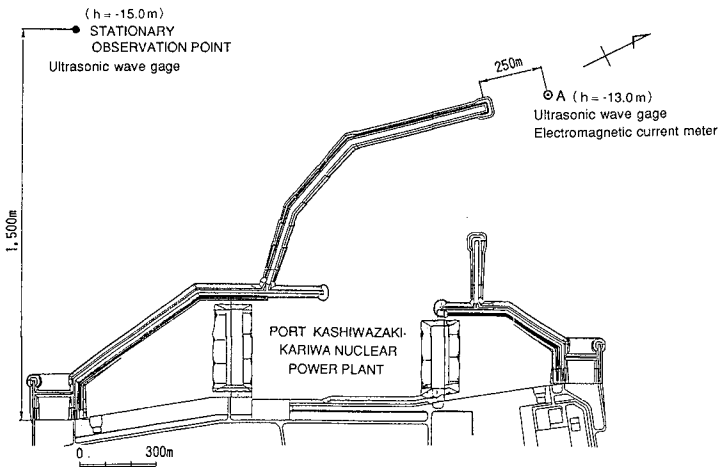


Figure 2. Location of observation points (Port of Kashiwazaki-Kariwa Nuclear Power Plant).

### 3. Wave Grouping

The wave grouping properties were discussed by using the groupiness factor,  $GF$ . The relationship between  $GF$  and the wave dispersion  $kh$ , non-linearity  $ka$ , and Ursell's parameter  $Ur$  were investigated, where  $k$  is the wave number,  $h$  the water depth and  $a$  the wave amplitude. The wave amplitude means half of significant wave height in this study.

Figure 3 shows the results of wave grouping analysis. Values of  $GF$  are plotted against the relative water depth,  $kh$ . The figures are classified for different ranges of the wave non-linearity,  $ka$ . From these figures, the so-called "shallow water effect", which is the phenomenon that  $GF$  becomes smaller as  $kh$  becomes smaller, can be confirmed. It is also confirmed that the non-linearity effect exists. In the case of large  $kh$ ,  $GF$  becomes large as  $ka$  becomes large and in the case of small  $kh$ ,  $GF$  and its scatter become smaller as  $ka$  becomes large.

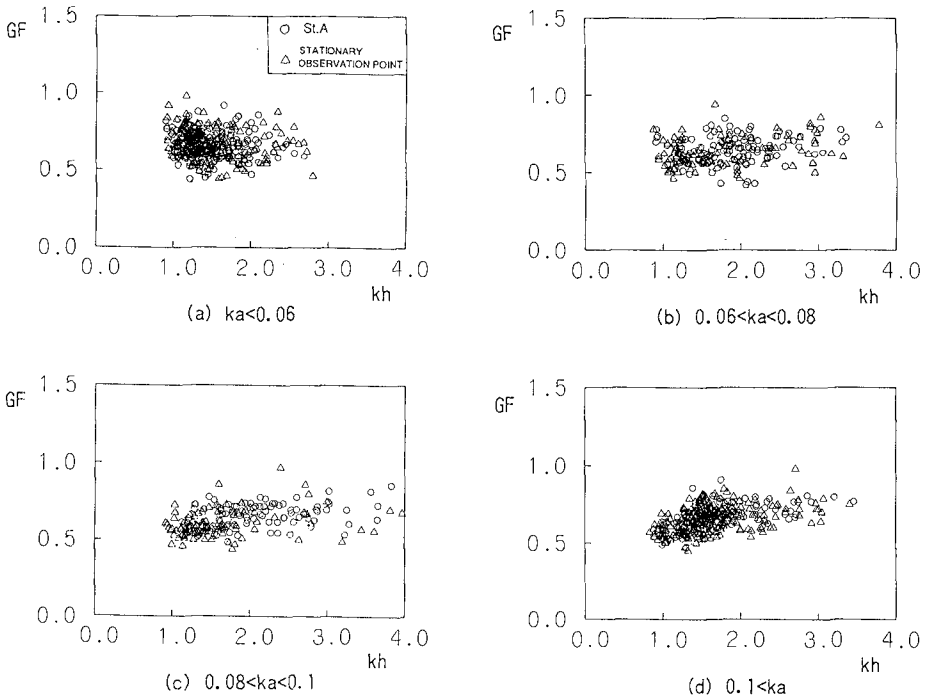


Figure 3. The relationship between relative water depth  $kh$  and groupiness factor  $GF$ .

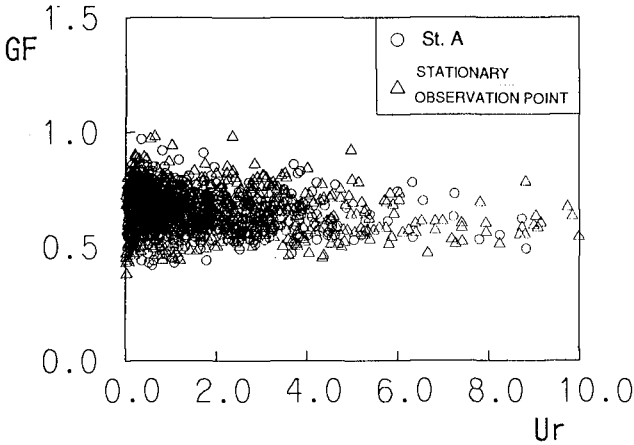


Figure 4. The relationship between Ursell's parameter  $Ur$  and groupiness factor  $GF$ .

Next, the relationship between  $GF$  and Ursell's parameter was investigated. Values of  $GF$  are plotted against Ursell's parameter in figure 4. This figure shows that  $GF$  becomes smaller and its distribution becomes narrower as the Ursell's parameter becomes larger. From these analyses of wave grouping, it was found that non-linearity of waves affects the wave grouping.

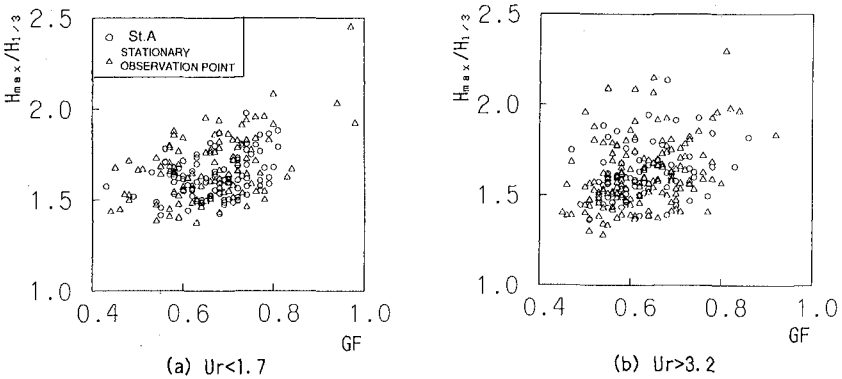


Figure 5. The relationship between groupiness factor  $GF$  and maximum wave height.

In this study, our main interest was in the occurrence distribution of maximum wave height. Therefore the relationship between maximum wave height and  $GF$  was investigated. Figure 5 shows this relationship. The ordinate is  $H_{max}/H_{1/3}$  and the abscissa is  $GF$  in this figure. It was found that weak correlation is available between  $GF$  and maximum wave height. In the case of large Ursell's parameter, distribution of maximum wave height is much broader. However, it was found that the lower limit of maximum wave height is almost the same in both, but the upper limit of maximum wave height is larger in the case of large Ursell's parameter. This results suggested that in the case of large Ursell's parameter higher maximum wave height occurs even if  $GF$  has the same value. Hence, also the occurrence frequency of maximum wave height is affected by the non-linearity of waves.

#### 4. Wave height distribution

Following the study of Mase(1989), the Weibull distribution was adopted to the observed wave heights. The Weibull distribution for ocean waves was given by Kimura(1981) and it's representation is

$$p(x) = \frac{m}{2\phi} x^{m-1} \exp\left(-\frac{x^m}{2\phi}\right) \quad (1)$$

where,  $\phi$  is the normalized factor, which is changed by a reference wave height, and  $x$  is the normalized wave height.  $\phi$  and  $x$  were expressed as follows.

$$\phi = \frac{1}{2} \left[ \Gamma\left(\frac{m+1}{m}\right) \right]^{-m} \quad (2)$$

$$x = \frac{H}{\bar{H}} \quad (3)$$

in which  $\Gamma(*)$  is the gamma function. The probability density is changed by the shape factor  $m$ . When  $m$  is small the distribution is wide and when  $m$  is large the distribution is narrow. The reference wave height employed here is the mean wave height  $\bar{H}$ .

The shape factor  $m$  of the observed waves was estimated by the maximum likelihood procedure proposed by Cohen (1960), which was also used by Mase (1989).



$$m = \frac{N_w}{\frac{1}{2\phi} \sum_{i=1}^{N_w} x_i^m \ln x_i - \sum_{i=1}^{N_w} \ln x_i} \tag{4}$$

where  $x_i$  means each wave height in a wave train normalized with the mean wave height and  $N_w$  is the number of waves.

The observed wave height distributions were shown in the form of histograms expressed in terms of probability density. Figure 6 presents an example of wave height distribution of an observed wave train. The fitted Weibull distribution is drawn as smooth curves in the figures. Figure 6(1) presents a very narrow distribution case and (4) is a very wide one. Figure

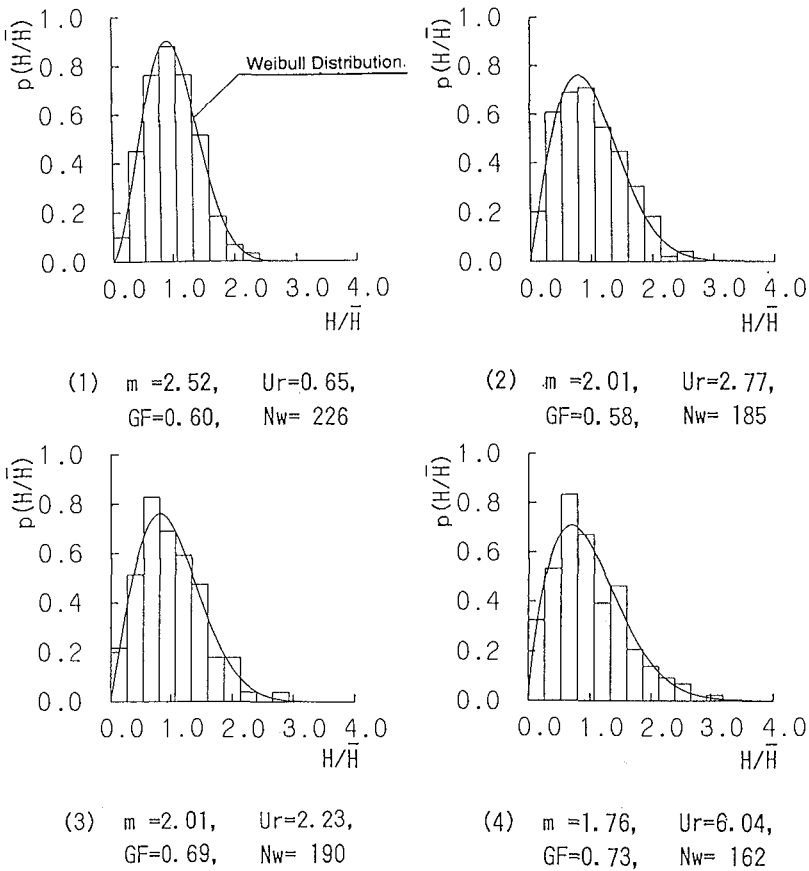


Figure 6. The occurrence distribution of wave height with Weibull distribution.

6(2) and (3) have the same shape factor. In these figures, the number of waves are 150 through 200. Considering the reliability of a small sample, the agreement between the observation results and fitted curve by means of Weibull distribution is good.

Since the application of Weibull distribution to observed wave height distribution was confirmed, the relationship between  $GF$  and shape factor  $m$  was investigated. Since  $GF$  is defined as the coefficient of variation of smoothed instantaneous wave energy history, distributions of wave height become broad as  $GF$  becomes large. Thus, it seems that a negative correlation should be available between the shape factor and  $GF$ . Mase(1989) proposed this relationship empirically.

$$m = 3.44 - 1.99GF \quad (5)$$

Figure 7(1) is the result of comparison between all observed data and the above empirical relation. It was confirmed that Mase's relationship seems to describe the mean of the observation data.

After careful analysis of the relationship between  $m$  and  $GF$ , it was found that the relationship between  $m$  and  $GF$  depends on Ursell's parameter. Figures 7(2), (3) and (4) show the case that  $Ur$  is less than unity, the case that  $Ur$  is from 1 to 3, and that  $Ur$  is greater than 3, respectively. For the same value of  $GF$ , the greater the Ursell's parameter is, the smaller  $m$  becomes. That is, in the case of larger Ursell's parameter, the occurrence frequency distributions of wave height become wider and therefore the maximum wave heights become larger, even if  $GF$  is the same. It should be mentioned that the wave height distributions become wider due to wave non-linearity.

According to these figures, even for the case of small Ursell's parameter, when  $GF$  is above 0.7 the shape factor  $m$  is less than 2.0. The Rayleigh distribution, which is often selected as the wave height distribution, has shape factor of 2. Therefore, the Rayleigh distribution underestimates the occurrence frequency distribution of higher wave heights, when  $GF$  is greater than 0.7.

## 5. Maximum wave height

Since the Weibull distribution successfully described the observed occurrence distribution, comparison was made between the occurrence distribution of maximum wave height derived from Weibull distribution and the observed one. Maximum wave height distribution on the basis of Weibull distribution can be expressed by equation (6). This equation is derived using the same manner proposed by Longuet-Higgins (1952), with the assumption of independence of each wave from others.

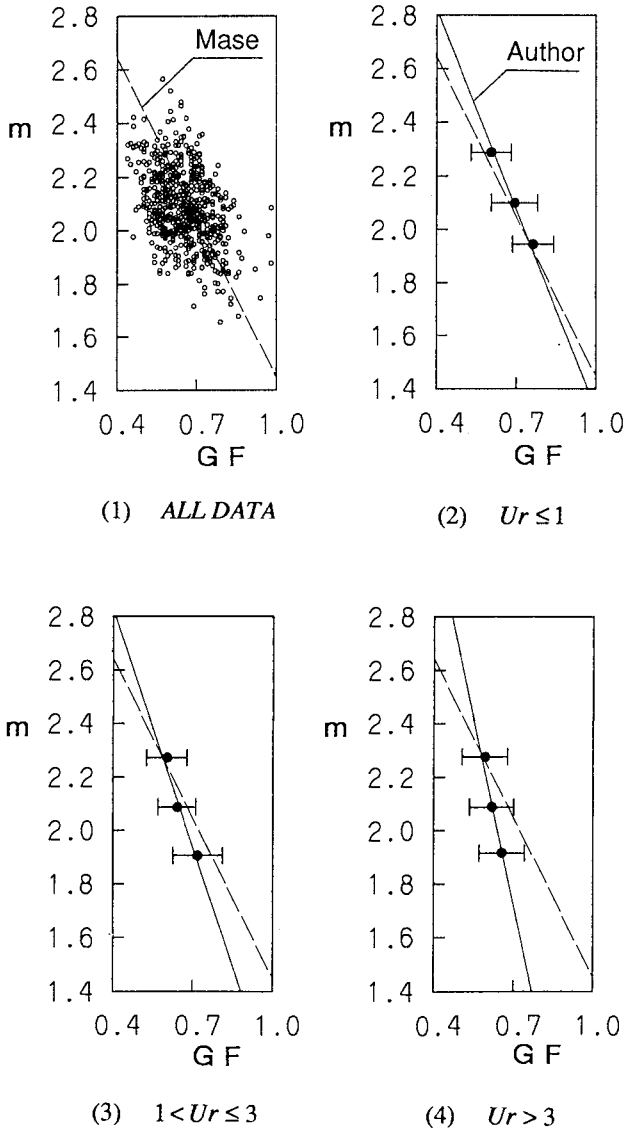


Figure 7. The relationship between groupiness factor  $GF$  and shape factor  $m$  of Weibull distribution.

$$p^*(X) = mN_w \beta (\beta X)^{m-1} \left[ 1 - \exp\{-(\beta X)^m\} \right]^{N_w-1} \exp\{-(\beta X)^m\} \quad (6)$$

$$\beta = (-\ln q)^{1/m} + \Gamma(1/m, -\ln q) / (qm) \quad (7)$$

$$X = H_{\max} / H_q \quad (8)$$

In these equations,  $\Gamma(*,*)$  is the incomplete gamma function of the second kind,  $H_q$  is a reference wave height and it is taken as the mean value of the highest  $qN_w$  waves, where  $q$  is less than or equal unity. When  $q$  is  $1/3$ ,  $H_q$  means significant wave height and  $q$  is  $1$ ,  $H_q$  means the mean wave height.

The results of the comparison between the observed maximum wave height and those predicted from Weibull distribution were described for four ranges of the shape factor. The lower part of figure 8 shows occurrence distribution of wave height with the Weibull distribution.

It was found that Weibull distribution fits these histograms very well. The upper part of the figure shows the distribution of the maximum wave height normalized by the significant wave height. In these figures, the three solid curves indicate the distribution derived from Weibull distribution with minimum, mean and maximum number of waves in the wave records. The occurrence frequency distribution of maximum wave height derived from Weibull distribution for the mean number of waves showed good agreement with histograms of the observed maximum waves except for the case of small value of the shape factor. When the shape factor is small,  $GF$  is large and the correlation between waves in a wave train is generally high. So, the agreement between the derived and observed distribution is not so good in this case.

Figure 9 shows the relationship between  $H_{\max}/H_{1/3}$  and  $m$ . The mean values of observed data are plotted by dots and their positive and negative standard deviations are described by lines. In this figure, the expected value of  $H_{\max}/H_{1/3}$  is drawn by dashed line. This expected value was calculated for 196 waves which is the mean number of waves in the observed records. Excluding the case that the shape factor is less than 2, calculation results described the observed data well. However, even in the case that the shape factor is less than two, the deviation between calculated results and observed results is small. Then, it may be concluded that the maximum wave height can be estimated by using the probability density derived from Weibull distribution. The shape factor of Weibull distribution may be estimated from  $GF$  and  $Ur$ .

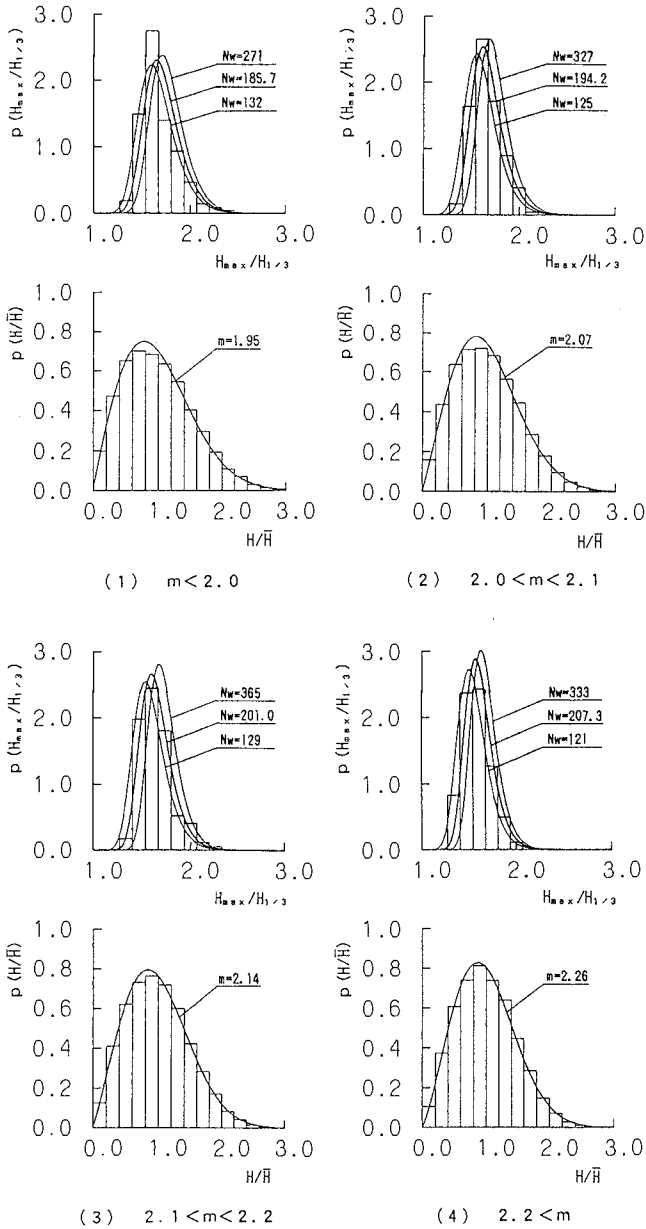


Figure 8. Comparison between the observed maximum wave heights and those predicted from Weibull distribution.

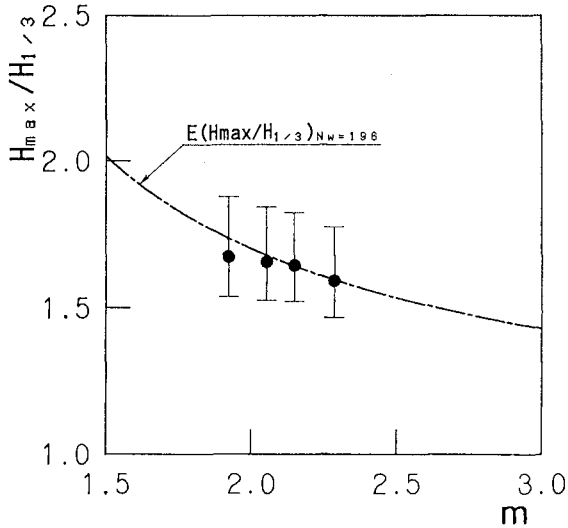


Figure 9. The relationship between shape factor  $m$  of Weibull distribution and maximum wave height.

## 6. Conclusions

The effect of wave grouping on the occurrence frequency distribution of maximum wave height was investigated through the field observations.

The conclusions of this study are summarized as follows.

- (1) Weibull distribution fits the observed wave height distribution very well.
- (2) The wave height distribution is affected by the wave groupiness.
- (3) The relationship between  $GF$  and the shape factor  $m$  of wave height distribution is affected by the Ursell's parameter.
- (4) Maximum wave height distribution derived from Weibull distribution fits the observed maximum wave height.
- (5) The maximum wave height can be estimated by the shape factor  $m$ . Then the maximum wave height is connected with the wave groupiness by using the shape factor with the Ursell's parameter.

## References

- Cohen,A.C.,Jr. (1965): Maximum Likelihood estimation in Weibull distribution based on complete and on censored samples, *Technometrics*, Vol.7, No.4, pp.579-588.
- Funke,E.R. and E.P.D.Mansard (1979): On the synthesis of realistic sea state in a laboratory Flume, Tech. Report, Hydraulics Laboratory, National Research council of Canada, LTR-Hy-66. 54p.
- Goda,Y. (1970): Numerical experiments on wave statistics with spectral simulation., Report of Port and Harbor Research Institute, Vol.9, No. 3.
- Goda,Y. (1983): Analysis of wave grouping and spectra of long-traveled swell, Rep. Port and Harbor Res. Inst., Vol.22, No.1, pp.3-41.
- Kimura,A. (1980): Statistical properties of random wave groups Proc. 17th ICCE, pp.2955-2973.
- Kimura,A. (1981): Joint distribution of the wave heights and periods of random sea waves, *Coastal Eng. in Japan*, Vol.24, pp.77-92.
- Longuet-Higgins,M.S. (1952): On the statistical distribution of the heights of sea state, *J. Marine Res.*, Vol.11, No.3, pp.245-266.
- Longuet-Higgins,M.S. (1984): Statistical properties of wave groups in random sea state, *Phil. Trans. Roy. Soc. London*, A312, pp.219-250.
- Mase,H. and Y.Iwagaki (1986): Wave grouping analysis of natural wind waves based on modulation instability theory, *Coastal Eng.*, Vol.10, pp.341-354.
- Mase,H. (1989): Groupiness factor and wave height distribution, *J. Waterway., Port, Coast., and Ocean Engrg.*, ASCE, No.15, Vol.1, pp.105-121.
- Ukai,A. (1990): Spatial variation of wave group statistics and representative wave-height of swell, Proc. 22nd ICCE, pp.812-825.

## CHAPTER 68

### AN EXPERIMENT AT SEA ON MECHANICS OF THE WAVE GROUPS

Paolo Boccotti (°), Giuseppe Barbaro (°°), Lucio Mannino (°°°)  
Department of Fluid Mechanics and Offshore Engineering  
University of Reggio Calabria

#### Abstract

Three field experiments were executed in the Straits of Messina starting in 1990 in order to verify the closed solution for the mechanics of the highest wave groups in a random wind generated sea state (Boccotti, 1984-88-89). The paper presents the first experiment which was concerned with the first part of the theory: the wave groups in an open sea. An array of nine wave gauges and nine pressure transducers supported by vertical piles provided space-time information on waves generated over a fetch of approximately 10 Km.

#### 1 Introduction

A wave with a given very large crest-to-trough height of  $H$ , in a random sea state assumed Gaussian, is expected to belong to a well defined wave group whose average configuration in space and time is specified in terms of the autocovariance of the random wave field,

$$\psi(\underline{X}, T) = \langle \eta(\underline{x}, t) \eta(\underline{x} + \underline{X}, t + T) \rangle \quad (1.1)$$

where  $\eta(\underline{x}, t)$  is the surface displacement. Specifically, if the crest of the given very high wave occurs at  $\underline{x}_o = (x_o, y_o)$  at time  $t_o$ , the mean surface configuration of the wave group is given by

$$\eta_c(\underline{x}_o + \underline{X}, t_o + T) = \frac{H}{2} \left\{ \frac{\psi(\underline{X}, T) - \psi(\underline{X}, T - T')}{\psi(\underline{O}, 0) - \psi(\underline{O}, T')} \right\} \quad (1.2)$$

-----  
(°) Professor of civil engineering, director of the Department, via E. Cuzzocrea 48, 89100 Reggio-Calabria, Italy

(°°) Assistant professor

(°°°) Engineer at the Department



where  $T^*$  is the abscissa of the absolute minimum of the autocovariance function, which is assumed to exist and to be the first minimum after  $T=0$ . The result (1.2), which was got by Boccotti (1984-1988-1989), assumes that  $H$  is very large compared with the mean wave height, or with  $\sigma = (\overline{\eta^2})^{1/2}$  for the wave field as a whole and, in effect, that the spectrum is narrow in the sense described by Longuet-Higgins (1984), so that  $\eta$  is a damped oscillatory function in  $\underline{X}$  and  $T$ . Superimposed on the deterministic form (1.2) is of course the "random noise" of the residual wave field whose r.m.s. surface displacement approaches  $\sigma$  as  $\underline{X}$  and  $T$  increase, but when  $H/\sigma$  is large, the variations in the actual sea surface configuration about  $\eta_c$  surrounding  $\underline{x}_o, t_o$  are small compared with  $\eta_c$  itself.

Associated with the configuration (1.2) is a distribution of velocity potential in the water, which to the lowest order in a Stokes expansion is given by

$$\phi_c(\underline{x}_o + \underline{X}, z, t_o + T) = \frac{H}{2} \left\{ \frac{\Phi(\underline{X}, z, T) - \Phi(\underline{X}, z, T - T^*)}{\Psi(\underline{O}, O) - \Psi(\underline{O}, T^*)} \right\} \quad (1.3)$$

where

$$\Phi(\underline{X}, z, T) = \langle \eta(\underline{x}, t) \phi(\underline{x} + \underline{X}, z, t + T) \rangle. \quad (1.4)$$

Note that the hypothesis that  $H/\sigma$  is large is not necessarily inconsistent with the use of the lowest order (linear) terms in the Stokes expansion, provided  $H$  remains small with respect to the wave length and the water depth. Note also that, if  $\eta$  and  $\phi$  are taken as solutions to the linear problem, then so are  $\eta_c$  and  $\phi_c$ . This can be demonstrated formally from (1.2) and (1.3).

The covariance functions in (1.2) and (1.3) can be expressed in terms of the spectra; for example

$$\Psi(\underline{X}, T) = \int_{-\pi}^{\pi} \int_0^{\infty} S(\omega, \theta) \cos(\underline{k} \cdot \underline{X} - \omega t) d\omega d\theta \quad (1.5)$$

where  $S(\omega, \theta)$  is the directional frequency spectrum and

$$\underline{k} \cdot \underline{X} = \frac{\omega^2}{g} (X \sin \theta + Y \cos \theta). \quad (1.6)$$

The substitution of (1.5) into (1.2) gives  $\eta_c$  as a function of position and time surrounding  $\underline{X} = 0, T = 0$  and leads to the sequence of configurations illustrated in Figure 1, representing a wave group moving along the  $y$ -axis, the dominant direction of the spectrum. The spectrum was taken as that used by Hasselmann et al. (1973) with the spreading direction function by Mitsuyasu et al. (1975). In deep water this has the form

$$S(\omega, \theta) = \alpha g^2 \omega^{-5} \exp \left[ -\frac{5}{4} \left( \frac{\omega_d}{\omega} \right)^4 \right] \exp \{ \ln(\gamma) \exp [ -(\omega - \omega_d)^2 / 2 S^2 \omega_d^2 ] \} \cdot \\ \cdot N(n) \left| \cos \frac{1}{2} (\theta - \theta_o) \right|^{2n}, \quad n = n_o \left( \frac{\omega}{\omega_d} \right)^5 \quad \text{if } \omega \leq \omega_d, \quad (1.7)$$

$$n = n_o \left( \frac{\omega}{\omega_d} \right)^{-2.5} \quad \text{if } \omega > \omega_d, \quad N(n) = \left[ \int_{-\pi}^{\pi} \cos^{2n} \frac{1}{2} \theta d\theta \right]^{-1}.$$

where the parameters  $\gamma, S$  and  $n_o$  are taken respectively as 3, 0.08 and 20, as Hasselmann et al. and Mitsuyasu et al. suggest ( $n_o=20$  applies

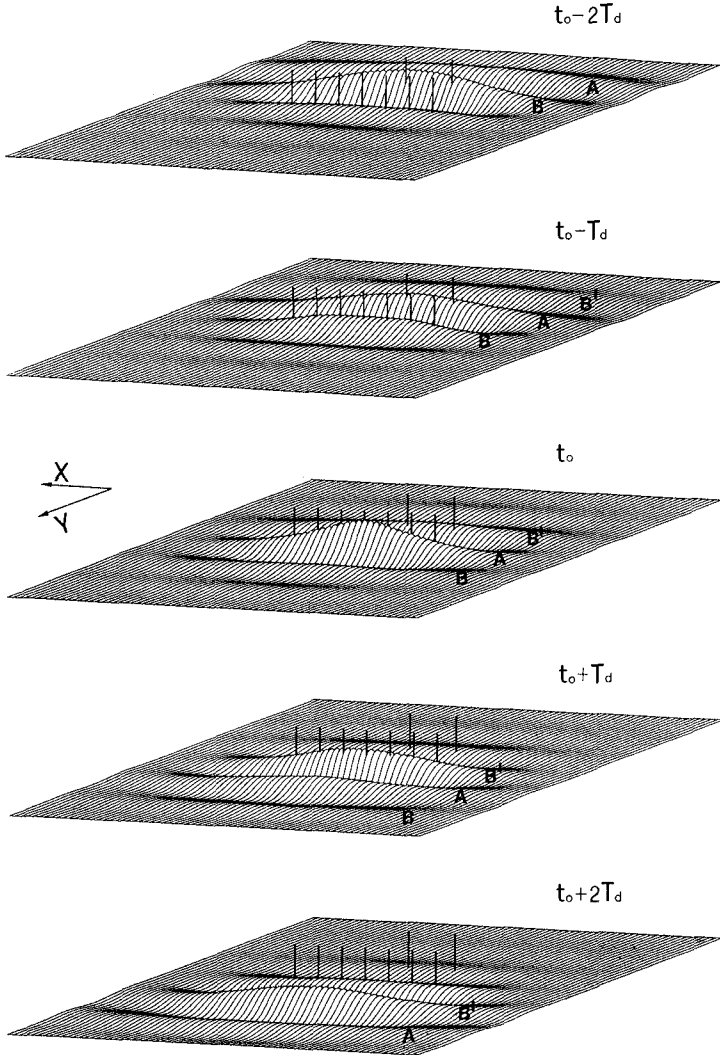


Fig.1 Quasi-determinism of the extreme wave events in a random wind generated sea state, assumed Gaussian, (Boccotti, 1989): an extremely high individual wave at a point  $x_0, y_0$  (center of the framed area), with a probability approaching 1, is produced by the transit of the wave group shown by the pictures. The water is deep, the spectrum of the sea state is that described in section 1. The time interval between two consecutive pictures is equal to one wave period  $T_d$  and the framed area is large  $3 L_d$  along x-axis and  $6 L_d$  along y-axis.

to the conditions of the experiment: fetch of 10 Km and wind speed of about 7 m/s).

The basic phenomena that occur during the course of evolution of the group are not dependent on the detailed shape of the wave spectra. First, the wave group has a development stage in which the height of the central wave grows to a maximum and the width of the wave front reduces to a minimum. Secondly, the individual waves have a propagation speed greater than the envelope. Each wave is born at the tail of the group and then dies at the head of the group, as illustrated by wave A in Figure 1. The wave with the given very large height  $H$  proves to be that at the center of the wave group at the apex of the development stage.

## 2 The field experiment

In order to test the predictions, a small scale field experiment was undertaken during May, 1990 at a location off the beach of Reggio-Calabria on the eastern coast of the Straits of Messina. Figure 2 shows the site of the experiment.



*Fig.2 The experiment was executed off the beach at Reggio-Calabria.*

An array of nine small towers was installed 20 m from the beach in the configuration shown in Figure 3. These rested on the sea bed and their bases (0.8 m squared) were ballasted by pig iron discs. The water depth ranged within 3 m at the inner row (numbered 1-7) and 4 m at the outer pair (8,9). Each tower supported an ultrasonic wave probe furnished by Delft Hydraulics Laboratory, having range 0.6-2.0 m, and a pressure transducer (full scale 0.175 bar) some 0.5 m below the water surface. The sampling rate was 10 Hz for each gauge and the data were stored in two personal computers. Since the station was equipped to receive data (wave elevation and pressure) from eight towers only, one of the nine had to be disconnected. During the experiment tower six was disconnected because its ultrasonic probe was damaged.

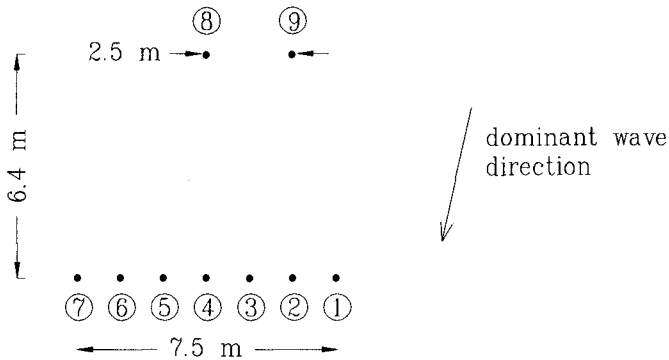


Fig.3 Plan view of the small towers which supported the gauges. The configuration of the towers is shown also in Figure 1 where the dominant wave length  $L_d$  is assumed to be 7.5m.

Suitable wind and wave conditions with a steady wind from the North West and the absence of southerly swells, were encountered 10 days after the array was installed. The experiment was conducted over a 12 hour period, starting at 8 AM on May 10, 1990. A total of 64 records was obtained, each of nine minutes duration and containing 280 to 360 dominant waves. The significant height ranged within 0.15 and 0.35 m and the dominant period of the spectrum ranged within 1.7 and 2.5 s, so that the water depth at the gauge locations was in effect deep.

### 3 Results of the experiment

#### 3.1 The surface displacement

The space-time covariances in equations (1.2) can be found from the measurements by cross-correlation of the time series obtained at the discrete measurement locations. The time series data of a record provide measured auto-covariances as a function  $T$  for the various gauge locations and these can be used on the right hand side of equation (1.2) to estimate the surface displacement at these locations in an extreme

wave. With  $x_0$  taken as the location of one of the gauges, the vectors  $X$  were specified by the relative locations of the other gauges.

A typical example of the result is shown in Figure 4 which was obtained from the time series data of record 30 without smoothing, with  $x_0$  taken as the location of gauge 4. Thus the figure represents the time histories of the expected surface configuration at the various gauge locations, if an extreme wave of given crest-to-trough height  $H$  is encountered at location 4. In this figure, A denotes the wave which is the highest at location 4, and B is the wave immediately before this one.

The direction of the wave can be estimated accurately since the front of wave A in the central position of the group along the traverse of locations 1-7 proves to be nearly straight. The relative phases indicate an angle of incidence of  $20^\circ$  - the front center before point 3 transits point 9, and this is consistent with the fact that in Figure 4, the wave group at point 9 is higher than at point 8.

Note that at locations 8, 9, wave B is slightly larger than A, but as it passes to the line 1-7, it decreases, passing from the center to the head of the group while the succeeding wave A grows because it replaces B at the group center. Note also that, in the course from location 9 to location 4, the period of wave B increases as it passes from the center to the head of the group, while the period of wave A decreases as it reaches its maximum height.

Similar calculations have been performed for all the records and the results are consistent with those described above. Specifically, there is an increase in period of the decreasing wave B, a decrease in the growing wave A and a local minimum period coupled to the maximum wave height.

Also Figure 5 shows the time histories of the expected surface waves at the various gauge locations, if an extreme wave of given crest-to-trough height  $H$  is encountered at location 4. In this case the auto-covariances in eq(1.2) were calculated from the theoretical spectrum (1.7), with the same dominant period and direction of record 30 ( $T_d = 2.17$  s,  $\theta_0 = 20^\circ$ ). We see that the result from the theoretical spectrum (Figure 5) is very close to that from the time series data (Figure 4): all the basic features described earlier are still evident.

### 3.2 The fluctuating pressure head at the transducer depth

The variations in pressure at a fixed depth are given by  $-\rho \partial \phi / \partial t$  or  $\rho g \zeta$  where  $\zeta$  is the fluctuating "pressure head" at this depth, so that the derivative of eq(1.3) with respect to  $T$  provides the following relation for the expected fluctuating pressure head at a fixed depth  $z$  below an extreme wave

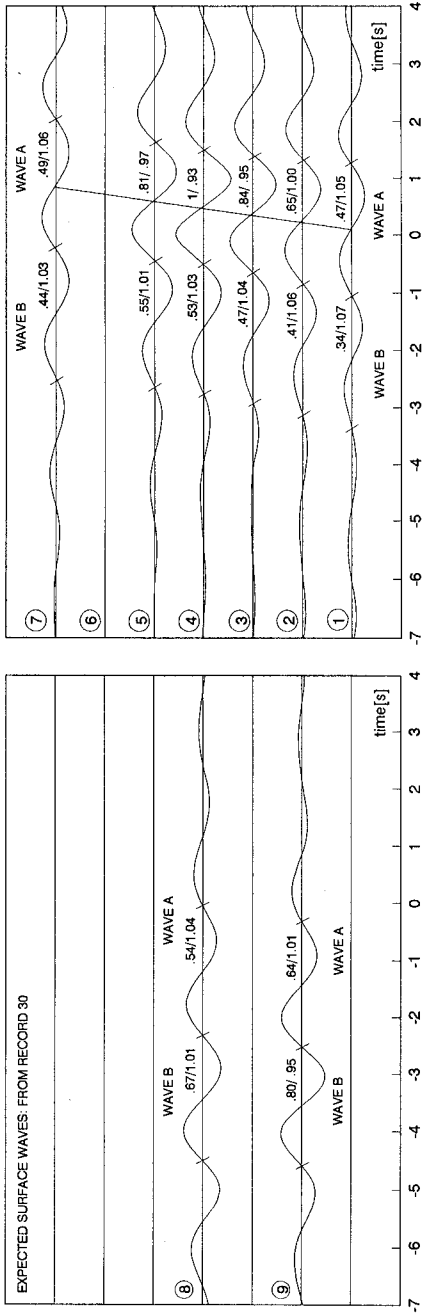


Fig.4 This picture was obtained from equation (1.2), using the time series data of the surface elevation of record 30, without smoothing. It shows the time histories of the expected surface waves at the locations of the gauges, if a wave with a very large height  $H$  is recorded at location 4. The first number over each wave denotes the crest-to-trough height, and the second number denotes the wave period; the wave height is scaled to given height  $H$  and the wave period is scaled to dominant wave period  $T_d$ .

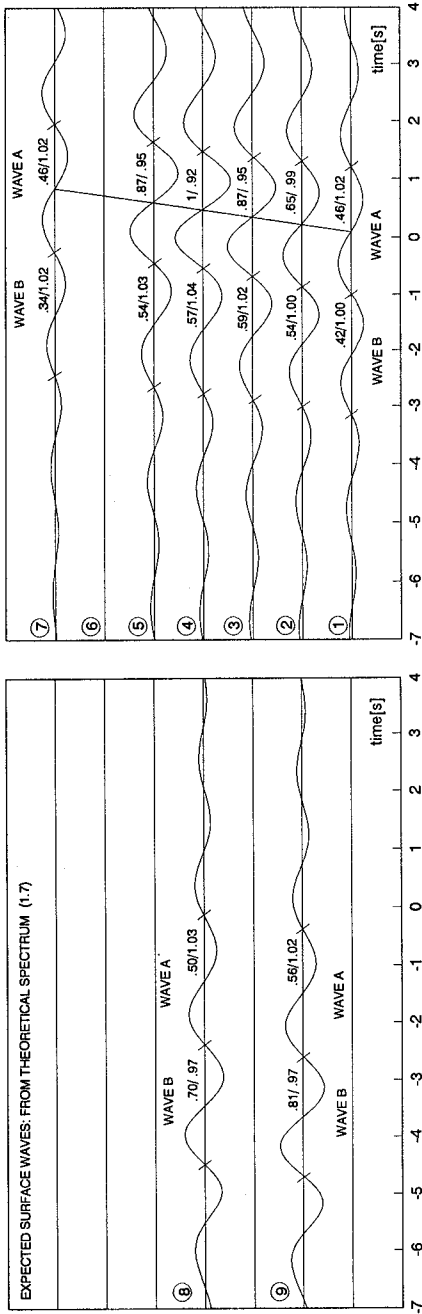


Fig.5 This picture was obtained from equation (1.2), with the auto-covariances calculated from the spectrum (1.7). Like Fig.4, it shows the time histories of the expected surface waves at the locations of the gauges, if a wave with a very large height H is recorded at location 4.

$$\zeta_c(\underline{x}_o + \underline{X}, z, t_o + T) = \frac{H}{2} \left\{ \frac{\Pi(\underline{X}, z, T) - \Pi(\underline{X}, z, T - T^*)}{\psi(0, 0) - \psi(0, T^*)} \right\} \quad (3.1)$$

where  $\Pi$  is the covariance of the surface displacement and the fluctuating pressure head, of the whole record

$$\Pi(\underline{X}, z, T) = \langle \eta(\underline{x}, t) \zeta(\underline{x} + \underline{X}, z, t + T) \rangle. \quad (3.2)$$

The time histories of the expected pressure head waves at the transducer depth at the various gauge locations, if a surface wave of given very large height  $H$  is encountered at location 4, were calculated by means of eq(3.1) from the time series data of the measured pressure and surface elevation of record 30. The results are shown in Figure 6. The overall similarity between this and Figure 4 gives confidence in the consistency of the measurements.

Note that the enhancement of wave A during its course from location 9 to location 4 is somewhat smaller at the transducer depth (Figure 6), than at the surface (Figure 4), and this is consistent with the reduction in period during this interval. Also, the abatement of the height of wave B from point 9 to point 4 is somewhat smaller at the transducer depth (Figure 6) than at the surface (Figure 4), which again is consistent with the increase in period between these two points. Finally, the wave direction estimated from the pressure head wave of Figure 6 is the same as that estimated from the surface measurements - the difference is smaller than  $1^\circ$ .

#### 4 Conclusive remarks

The comparison between the extreme wave groups and the predictions in terms of the measured space-time autocovariance, which was the goal of the experiment, is shown in the paper by Boccotti et al. (1992), which also gives a wider overall description of the experiment.

The experiment of May, 1990 revealed that it was possible to work off the beach of Reggio Calabria nearly like in a wave tank, because of the wave characteristics (pure wind waves with typical sizes of the laboratory tanks), of the very small tide excursion and the clearness of the water. That was because we decided to attempt some more complex experiments.

On May, 1991 a reflecting wall of 12x2.2 m was assembled on 1.6 m of water depth and thirty wave gauges were placed before the wall. The experiment essentially aimed to verify the theory of Boccotti (1988-89) as regards the nonhomogeneous wave fields. In particular, the theory shows that a very high wave at a wall forms because a well defined wave group like that of Figure 1, at the apex of the development stage, impacts the wall and is reflected mirrorwise. Also the significant wave height before the wall was analyzed through measurements at growing distances from the wall, like in the laboratory experiment of Hirakuchi et al. (1992). A preliminary illustration of the results was given by Boccotti (1992).

Finally, a third experiment dealing with the inertia loads on a big offshore platform has just been completed. The 1:50 scale model of a gravity platform was assembled in 2.5 m of water depth and two sets



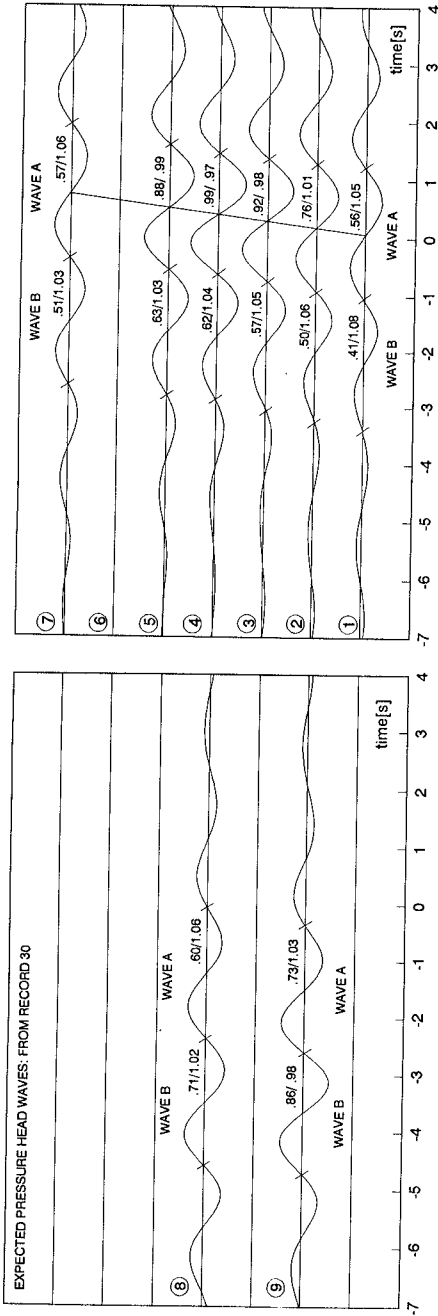


Fig.6 This picture was obtained from equation (3.1), using the time series data of the measured transducer pressure and surface elevation of record 30, without smoothing. It shows the time histories of the expected pressure head variations at transducer depths, if a wave with a very large height  $H$  is recorded at the surface at location 4. The wave heights are scaled to  $H(\zeta^2/\eta^2)^{1/2}$ . The periods are scaled to the dominant period of the surface waves.

of wave gauges and pressure transducers were placed at the platform and far from it, in order to compare the wave forces on the column and on an ideal mass of water with the same shape and volume.

### References

- Boccotti, P. (1984). Sea waves and quasi-determinism of rare events in random processes, *Atti Acc. Naz. Lincei, Rendiconti (Proc. Nat. Acc. Lincei)*, 76, 2, 119-127.
- Boccotti, P. (1988). Refraction, reflection and diffraction of irregular gravity waves, in *Excerpta of the Italian Contribution to Hydraulic Engineering*, Libreria Progetto Padova Publ., 47-89.
- Boccotti, P. (1989). On mechanics of irregular gravity waves, *Atti Acc. Naz. Lincei, Memorie (Trans. Nat. Acc. Lincei)*, 19, 5, 111-170.
- Boccotti, P. (1992). Quasi-deterministic mechanics of the highest waves in sea storms, *Lectures speciales, Journees Nationales Genie Cotier - Genie Civil*, Nantes, France.
- Boccotti, P., et al. (1992). A field experiment on the mechanics of irregular gravity waves, accepted for publication in the *Journal of Fluid Mech.*
- Hasselmann, K., et al. (1973). Measurements of wind wave growth and swell decay during the Joint North Sea Wave Project (JONSWAP), *Deut. Hydrogr. Zeit*, A-8.
- Hirakuchi, H., et al. (1992). Characteristics of absorbing directional wavemaker, *Proc. 23rd Int. Conf. on Coastal Engng.*, paper n°187.
- Longuet-Higgins, M.S. (1984). Statistical properties of wave groups in a random sea state, *Phil. Trans. R. Soc. London*, A312, 219-250.
- Mitsuyasu, H., et al. (1975). Observation of directional spectrum of ocean waves using a clover-leaf buoy, *J. Phys. Oceanography*, 5.

## CHAPTER 69

### Wave Group Modulations in Cross-shore Breaking Patterns

T. C. Lippmann<sup>1</sup> and R. A. Holman<sup>2</sup>

#### ABSTRACT

The principal aim of this work is to quantify the long period (group) time scales associated with incident wave breaking in the surf zone. A video based sampling technique is employed to distinguish those waves which are breaking from those which are not. The technique relies on the gray tone contrast between higher luminance of turbulent generated bubbles and foam associated with wave breaking, and the darker, unbroken surrounding water. Video image intensity time series,  $I(x,y,t)$ , are sampled across the width of the surf zone at 10 m increments, from just outside the shore break to the far offshore region of the wave breaking. Outside the point of minimum depth (at the bar crest), the width of the surf zone fluctuates over several hundred meters. In this region, low frequency oscillations in  $I$ , phase coupled to the crest of breaking incident waves, are associated with wave groups. Cross-shore phase relationships indicate a shoreward progressive group structure up to the crest of the bar. Landward of the bar crest in the trough, low frequencies in  $I$  are uncoupled from group modulations seaward of the bar. Video data also show that wave breaking does not cease immediately as waves propagate past the bar crest, but continues well into the deeper water of the trough.

#### INTRODUCTION

Modulations in wave height of incident sea and swell produce variations in the position of break points in the surf zone. These modulations are on the order of wave groups, with much longer periods than typical gravity waves. In the past two decades, considerable effort has been focused on understanding the importance of wave groupiness inside the surf zone.

---

<sup>1</sup>Department of Oceanography, Naval Postgraduate School, Monterey, CA 93943

<sup>2</sup>College of Oceanic and Atmospheric Sciences, Oregon State University, Corvallis, OR 97331-5503.

Previous estimates of breaking wave distributions in the surf zone were determined by visually identifying breaking waves in the time series of sea surface elevation on site during the collection of the data (Thornton and Guza, 1983; Whitford and Thornton, 1988). Breaking waves were defined as "when white water was observed passing the sled mast" (Whitford and Thornton, 1988). This method works well, although with tremendous logistical effort.

In this study, video-based data are presented which quantify the temporal evolution of breaking wave patterns on wave group time scales in a cross-shore transect across the width of the surf zone. In our methods, essentially the same determination of breaking waves is utilized but with a higher level of quantification, synchronous ground coverage over large spatial areas, and reduced logistical difficulty. The premise of the technique is based on contrast between the relatively low luminance of non-breaking water and the higher luminance of actively breaking waves and bores. An example snap shot of wave breaking is shown in Figure 1. The high intensity of the foam and bubbles created from active wave breaking contrasts with the darker non-breaking water. Local maxima in image intensity associated with the turbulent water motion of the breaker or roller is phase locked to a region near the crest of the wave (Figure 2).

Our principal aim is to quantify the time scales associated with modulations in incident wave breaking,  $\eta_b$ . We hypothesize that time series of image intensity,  $I(x,y,t)$ , can be used as a means to quantify the time (and space) scales of  $\eta_b(x,y,t)$  at given locations throughout the surf zone. Thus we assume

$$I(x,y,t) \propto \eta_b(x,y,t) \quad (1)$$

where  $x$  and  $y$  are the cross-shore and alongshore Cartesian coordinates, respectively. For this work we are only interested in the phase relationship and coherence in (1), not the absolute magnitude of  $I$ . This relationship has been shown to work well for estimating the phase speed and wave angle of breaking waves (Lippmann and Holman, 1991). An example time series of both  $I$  and  $\eta_b$  from the same position in the surf zone is shown in Figure 2 (taken from Lippmann and Holman, 1991). The passage of breaking waves is clearly identified in the video data. There are also waves which are not identified in  $I$ , indicating that not all the waves are breaking.

Quantification of images is accomplished using a real time image processing system. Video frames are digitized by the image processor into an array of 512 x 480 picture elements (pixels). Individual pixels store the value of light intensity (luminance) in gray shades from 0 (black) to 255 (white). Images are digitally enhanced to stretch the contrast in the image prior to analysis.



Fig. 1. Example photographic snap shot of wave breaking in the surf zone from October 13, 1990 at ~0900 EST. Breaking waves and bores are identified by the sharp contrast between breaking and non breaking waves.

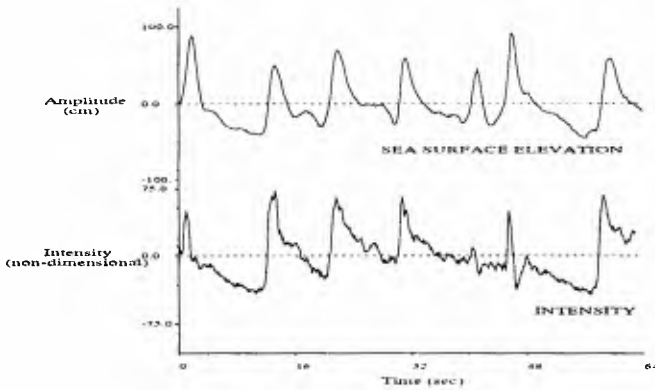


Fig. 2. Example co-located sea surface elevation (converted from pressure data; top) and video image intensity (bottom) mean-corrected time series from October 12, 1990 (from Lippmann and Holman, 1991).

Image locations of interest (for example the location of a fixed surf zone instrument) are determined using known photogrammetric transformation equations assuming the vertical coordinate to be the still water level (Lippmann and Holman, 1989). Time series at each location are then collected by sampling the corresponding pixel intensity at 6 Hz for the entire run (tape) length of ~2 hours. Resolution in image pixels is typically much less than 1 m in the cross-shore direction, and from ~0.5-2.5 m in the longshore direction.

A brief description of the field site and ancillary measurements used in the study is presented next. Analysis of wave breaking time series are then presented as a function of cross-shore distance. Results are then briefly discussed in terms of surf zone forcing models and cross-shore distributions in wave breaking patterns.

## FIELD METHODS

The data were collected as part of the DELILAH experiment in October of 1990, held at the Army Corps of Engineers Field Research Facility (FRF) on the Outer Banks of North Carolina near the village of Duck. A general description of the experiment and beach conditions at the FRF is given by Birkemeier, *et al.* (1991). The imaged area ranges from the dune crest to ~400 m offshore and begins ~180 m north of the FRF pier and extends alongshore ~350 m. The cameras were mounted on top of a 44 m high tower in weatherproof housings and hard wired to the FRF building for recording. Video time series were sampled along a cross-shore transect, from just outside the shore break ( $x = 135$  m) to the far reaches of the surf zone ( $x = 505$  m) with a spacing of 10 m.

Data are presented from October 13 at ~0645 EST, coinciding with swell generated by Hurricane Lily. Low tide (-0.21 m NGVD) occurred at ~0900 EST. A photographic snap shot from this day is shown in Figure 1. The offshore incident waves during this period were long crested and energetic, with  $H_s \approx 2.23$  m in 8 m depth. Directional spectra from an alongshore array of pressure gages in 8 m depth (Long and Olman-Shay, 1991) shows a very narrow banded swell at the peak frequency,  $f_p \approx 0.083$  Hz, approaching from an incident angle  $\alpha_o \approx 24^\circ$  CW from normal to the beach. The nearshore bathymetry consisted of a prominent linear bar ~100 m offshore (Birkemeier, pers. comm.). Cross-shore profiles at the position of the cross-shore transect from October 12, 13, and 14 are shown in Figures 3 and 5. For reference, the position of the shoreline is at  $x \approx 120$  m and the approximate bar crest is at  $x \approx 220$  m.

## RESULTS

The one-dimensional pattern of wave breaking is shown graphically by plotting together time series of  $I$  sampled along a cross-shore transect spanning the width of the surf zone. Figure 3 shows 38  $I$  time series, each of 120 minute duration, stacked vertically with offshore distance increasing toward the top of the figure. Intensity values are normalized to  $\pm 3$  standard deviations about the mean in each respective time series. Also shown on the right hand side is the approximate beach profile.

Seaward of the bar crest wave breaking distributions clearly show the arrival of wave groups, with breaking being more infrequent in the outer surf zone. The groupy modulations are destroyed by breaking in shallower depths. At the bar crest, nearly all of the waves are breaking. Interestingly, bores do not cease breaking immediately landward of the point of minimum depth over the bar, but continue to break well into the deeper water of the trough.

Example auto power spectra (with  $\sim 54$  degrees of freedom) of  $I$  are shown in the upper panels of Figure 4 for locations  $x = 188$  (in the landward slope of the bar) and  $x = 505$  m (in the outer surf zone). Both spectra show a prominent narrow peak at  $f \approx 0.08$  Hz, corresponding to the peak incident frequency ( $f_p \approx 0.083$  Hz). There is also considerable low frequency variance, as has been observed in previous video time series (Lippmann and Holman, 1991). This low frequency energy occurs at all locations sampled in the surf zone (not shown).

### *Low Frequency Modulations in Wave Breaking*

If modulations in the breaking wave field are associated with wave groups, with periods long compared to peak incident periods, then we expect low frequency energy in  $I$  to be coupled with incident frequencies. Coupling between frequencies in the power spectrum of any given time series are detected with the third order spectrum, the bispectrum (*e.g.*, Kim and Powers, 1979; Elgar and Guza, 1985a). The bispectrum is a measure of lowest order triad interactions between a pair of primary frequencies ( $f_1, f_2$ ) and a secondary frequency,  $f_3$

$$f_1 \pm f_2 = f_3 \quad (2)$$

Sum interactions in (2) generate harmonics which are phase-locked to the primary, and thus are not free and travel at the phase speed of the primary (Elgar and Guza, 1985b). Difference frequencies are associated with coupling between two signals of nearly the same frequency, and a secondary low frequency signal. In strongly amplitude modulated time series, lower frequency signals are phase-coupled to the primary frequencies, as in rectified signals commonly found in electrical engineering applications.

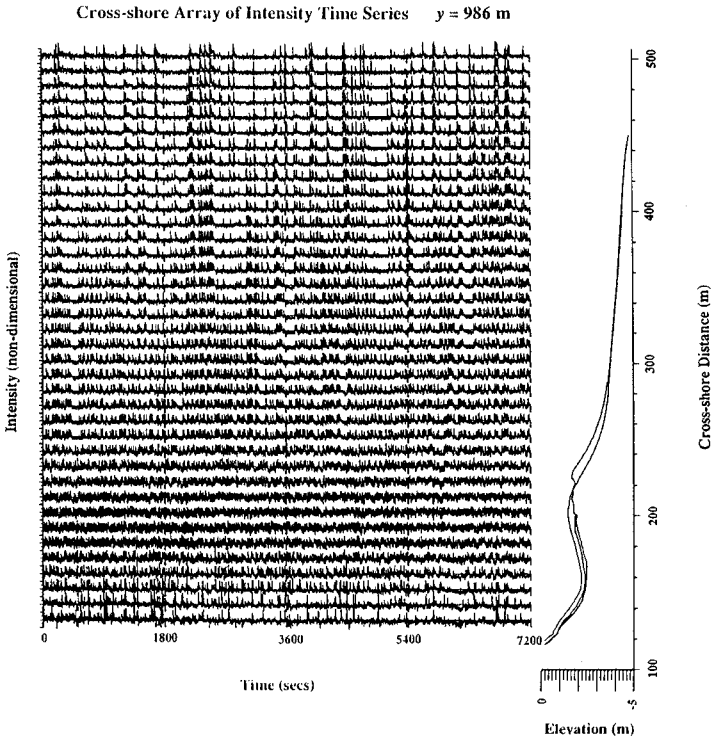


Fig. 3. Time series (120 minute records) of  $I$  sampled along a cross-shore transect at 10 m intervals, from just beyond the shore break to the outer surf zone. The vertical axis is nondimensional image intensity (mean corrected) scaled to  $\pm 3$  standard deviations. Time series are stacked vertically with offshore distance increasing toward the top. The beach profile along the transect is shown at the right.



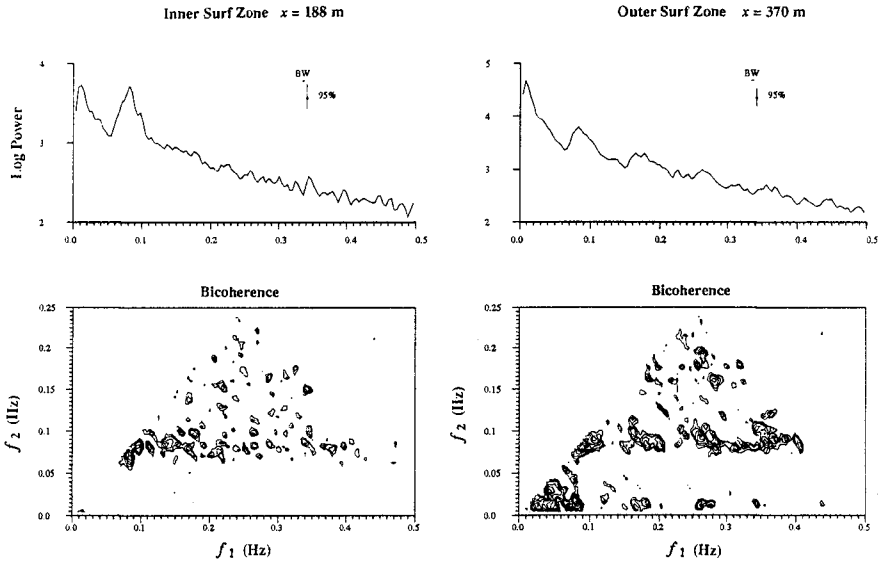


Fig. 4. Example power spectra (upper panels) and bicoherence (lower panels) for  $I$  sampled on the landward slope of the bar (left panels) and in the far offshore region of the surf zone (right panels). Bicoherences greater than the 95% significance level for 56 d.o.f. ( $b = 0.33$ ) are plotted in bi-frequency space with  $f_1$  along the horizontal axis and  $f_2$  along the vertical axis.

Bicoherence ( $b$ , normalized bispectrum) estimates from  $I$  sampled in the trough of the bar ( $x = 188$  m) and in the outer region of the surf zone ( $x = 370$  m) are shown in the lower panels of Figure 4. Only contours of bicoherence which are greater than the 95% significance level ( $b_{crit} = 0.33$ ) are plotted (at 0.5 increments). Due to its symmetry properties, only the unique portion of the bispectrum is shown (see Kim and Powers, 1979). Figure 4 shows strong coupling between the primary frequency (0.08 Hz) and the higher harmonics in both regions of the surf zone, arising from the sharp (non sinusoidal) peaks in the time series records. Strongest coupling occurs at the self-self interaction ( $f_p, f_p$ ),  $b \approx 0.61$  and  $b \approx 0.68$ , and the interaction between the primary and first harmonic ( $f_p, 2f_p$ ),  $b \approx 0.51$  and  $b \approx 0.55$ , for the inner and outer surf zone data, respectively.

There is a distinct lack of coupling between incident ( $f \geq f_p$ ) and lower frequencies ( $f \ll f_p$ ) in the trough of the bar, suggesting that  $I$  variance at infragravity frequencies in the trough is derived from free signals not directly associated with incident wave breaking. However, seaward of the bar crest, widespread bicoherence at low  $f$  reveals strong coupling to  $f_p$ . Highest coupling ( $b = 0.62$ ) occurs at  $(f_1, f_2) \approx (0.082, 0.015)$ . Low frequency spectral energy in  $I$  in this region is coupled to modulations in incident wave breaking patterns throughout the surf zone seaward of the bar.

#### *Phase Propagation of Breaking Wave Groups*

Wave group modulations also appear coherent across the surf zone up to the region near the bar crest (Figure 3). The phase propagation of the groups can be quantified using frequency domain (complex) empirical orthogonal functions (CEOF). In CEOF analysis, eigenvectors of the cross-spectral matrix are computed at each frequency (Wallace and Dickinson, 1972). Thus the data are decomposed into orthogonal factors representing the amplitudes and phases at each frequency as a function of cross-shore distance.

The first CEOF from the peak incident frequency ( $f_p \approx 0.082$  Hz), and also from the low frequency peak ( $f \approx 0.015$  Hz) observed in the power spectra (Figure 4) are shown in Figure 5. Only the first factor is shown since it contains the greatest proportion of the variance (63.7% at  $f_p$  and 45.9% at low  $f$ ), and because orthogonality constraints in the decomposition of the data make interpretation of higher modes unclear. CEOF phases are relative to cross-shore position (the absolute value of individual phase estimates is arbitrary), and amplitudes are normalized by the spectral power within each frequency band. Also shown are estimated (relative) phase relationships for phase speeds,  $C_p$ , predicted by shallow water (Solitary) wave theory

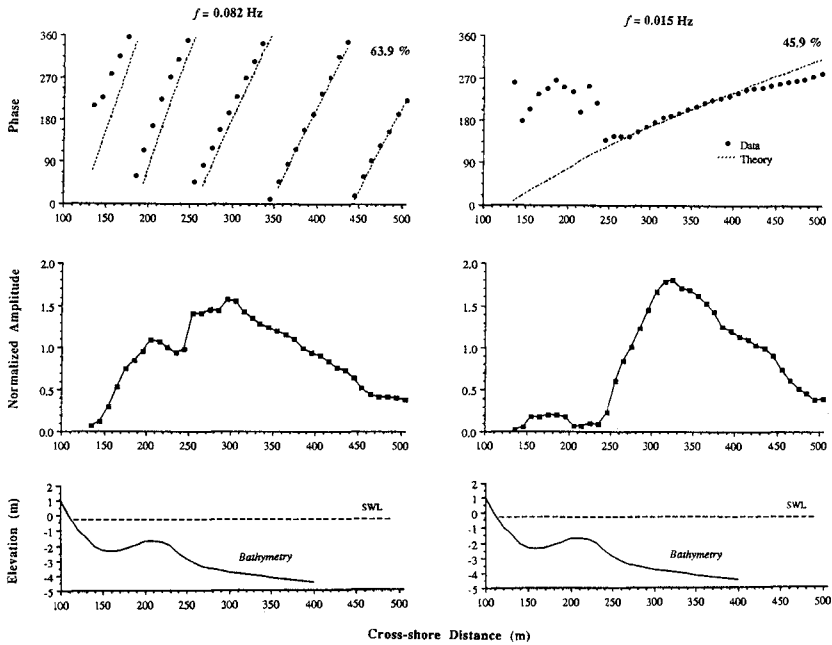


Fig. 5. Frequency domain empirical orthogonal functions (CEOF) from  $I$  at the peak frequency ( $f_p = 0.082$  Hz; left panel) and also the low frequency peak in the power spectra ( $f = 0.015$  Hz; right panel), plotted as a function of cross-shore distance. Phases are shown in the upper panels and normalized amplitudes in the middle panels. The approximate (smoothed) beach profile (from October 14) is shown in the lower panels for comparison. Predicted relative phase relationships (equation 4) are indicated with the dashed lines in the phase plots.

$$C_p = \sqrt{g(h + H_{\text{rms}})} \quad (3)$$

where  $H_{\text{rms}}$  is the root mean square wave height.  $H_{\text{rms}}$  across the surf zone was estimated using the random wave dissipation model of Thornton and Guza (1983), shown previously to well predict the energy decay of incident wave energy in the surf zone. The predicted phases,  $\phi(x)$ , in Figure 5 were computed by

$$\phi(x) \approx \frac{2\pi f \Delta x}{\bar{C}_p} \quad (4)$$

where  $\bar{C}_p$  is the mean phase speed of the peak incident waves over the distance  $\Delta x = 10$  m.

For  $f_p$ , predicted and observed phases are matched at the most seaward location to allow comparison across the surf zone. The first CEOF shows a clear negative phase ramp, indicating shoreward progressive (breaking) incident waves are coherent all the way through the surf zone. The data are reasonably predicted by (4), although near the bar crest and in the trough the theory systematically over predicts the observations (*i.e.*, steeper phase ramps), consistent with previous comparisons with video derived data (Lippmann and Holman, 1991).

At the low frequency peak ( $f \approx 0.015$  Hz), the cross-shore phase structure in the first CEOF also has a linear trend, but only seaward of the bar crest. In this region theoretical group phase speeds are in excellent agreement with the data (although deviates slightly in the far reaches of the surf zone,  $x > \sim 425$  m). Predicted phase relationships (4) are best fit to the data in the region of (approximately) constant celerity, between  $x \approx 255$ -425 m. The average phase speed between  $x = 255$ -425 m,  $\bar{C}_p \approx 7.3$  m/s, is very nearly the same as predicted by Solitary theory,  $\bar{C}_p \approx 7.5$  m/s. The phase relationships are consistent with a shoreward propagating group modulation in the breaking incident wave field traveling at the group velocity of the incident waves. Furthermore, the very small CEOF amplitudes over the bar crest indicate that low frequencies observed in this region are uncoupled to wave groups seaward of the bar, a consequence of widespread breaking over the bar destroying the group structure in the breaking wave field.

## DISCUSSION

In the surf zone, break point amplitudes are often taken as a linear proportion of the depth

$$H_b = \gamma h_b \quad (5)$$

where  $H_b$  is the height (twice the amplitude) of the breaking wave,  $h_b$  is the water depth at the break point, and  $\gamma$  is a constant of  $O(1)$  (e.g., Thornton and Guza, 1982). For a plane sloping bottom,  $h_b = x_b \tan \beta$ , breaking wave amplitudes can be expressed in terms of break point positions. Models based on forcing due to modulations in break point amplitudes can be distinguished by the behavior of  $\gamma$ . In one type (i.e., Foda and Mei, 1981; Schaffer and Svendsen, 1988), break point positions are assumed constant, and the group modulations are allowed to progress to the shoreline. Thus,  $\gamma$  in (5) is a temporal function of the amplitude modulation, in which  $\gamma$  is larger for the bigger waves. In the second type (i.e., Symonds, *et al.*, 1982),  $\gamma$  is assumed constant, and break point position is the parameter that fluctuates.

Our data indicates that the initial break points vary over large distances, ranging from far ( $> 400$  m) offshore for the largest waves to near the bar ( $\sim 100$  m offshore) for the smallest waves. Moreover, the group structure is substantially reduced by wave breaking in the inner surf zone, thus restricting group modulations to seaward of the bar. Thus constant  $\gamma$  more accurately describes the data, and is consistent with energy saturation in shallow depths (verified previously with field data; Thornton and Guza, 1982; Sallenger and Holman, 1985).

#### *Wave Breaking in the Trough*

Some recent models predicting longshore current profiles,  $V(x)$ , have been based on the ensemble distribution of incident wave dissipation,  $\langle \varepsilon_b(x) \rangle$  (e.g., Thornton and Guza, 1986; Whitford and Thornton, 1988). Incident wave breaking is assumed to decrease shoreward of the bar crest due to increasing depths in the trough. Thus model predictions over barred profiles suggest that longshore currents are strongest on the seaward flank of the bar where maximum incident wave dissipation occurs. However, recent observations of  $V(x)$  at Duck suggests that the maximum current often occurs in the trough, in direct conflict with the dissipation models (Whitford and Thornton, 1988; Howd, *et al.*, 1992).

The decay of wave height across a barred profile is well predicted by the model of Thornton and Guza (1983). However, the model assumes implicitly that no time lag exists between the production of turbulent kinetic energy by wave breaking and actual energy dissipation (a point made previously by Roelvink and Stive, 1989; Nairn, *et al.*, 1991). Our observations of wave breaking across the width of the surf zone (Figure 3) indicate that, although the initiation of breaking is confined to depths seaward of the bar, wave breaking does not cease immediately shoreward of the crest, but continues into the trough. The widespread presence of wave "rollers" and bores past the bar crest suggests that advecting turbulence away from the region of highest production over the bar, can be a viable mechanism for transporting momentum into the trough where often the maximum longshore current is observed.

## CONCLUSIONS

A video based technique is presented which accurately quantifies temporal modulations in wave breaking across the width of the surf zone. The technique is based on the gray tone (intensity) contrast between the lighter foam and bubbles created by actively breaking waves and bores, and the darker, surrounding non-breaking water. Thus video records of the surf zone contain visible-band time histories of wave breaking patterns. Quantification is accomplished with an image processing system, in which images are digitized at discrete pixels corresponding to defined field coordinates.

Data are presented from a very narrow banded ( $f_p \approx 0.083$  Hz), unidirectional day ( $\alpha_0 \approx 24^\circ$  CW) during the DELILAH experiment. In addition to energetic incident frequencies associated with the actively breaking incident waves, considerable low frequency variance was observed in all video time series, from the outer portions of the surf zone to the trough of the bar. In the outer surf zone wave breaking at incident frequencies is coupled to low frequency energy, indicating that fluctuations in break point patterns are associated with long period modulations in incident wave amplitudes. Group modulations propagate landward at the phase speed of the incident waves, consistent with simple shoaling expectations.

Finally, we observe the group structure in the wave field to be greatly reduced by breaking in the inner surf zone. All initiation of breaking occurs seaward of the crest, with generally larger waves breaking further offshore and a higher percentage of breaking waves in progressively shallower depths. This suggests that surf zone forcing models which assume a depth dependence on breaking amplitude are more in keeping with the data (*e.g.*, Symonds, *et al.*, 1982). Furthermore, breaking does not cease at the point of minimum depth at the crest, and in fact breaking is widespread in the trough of the bar. This suggests that lateral mixing of momentum across the surf zone, due to the advection of turbulence at the wave front (*e.g.*, Svendsen, 1984, Roelvink and Stive, 1989; Nairn, *et al.*, 1991, and others), could be an important mechanism for modeling longshore currents.

## ACKNOWLEDGEMENTS

This work was supported by the Office of Naval Research, Coastal Sciences program under grant number N00014-90-J1118. Additional funding for DELILAH was provided by CERC. Chuck Long computed the frequency-direction spectra. Ed Thornton provided the surf zone instrumentation for DELILAH. Appreciation is given to the hard working staff of the FRF who provided unparalleled support during the experiment. We wish to thank in particular Bill Birkemeier, Kent Hathaway, Todd Walton, and Todd Holland for aiding in the collection of the video data. The late Paul O'Neill was chief engineer for the OSU group, and without his efforts this

work would not have been possible. Over the past few years, Paul was instrumental in the development of all aspects of our video techniques and image analysis. He was a contemporary scientist, creative engineer, and a good friend.

#### REFERENCES

- Birkemeier, W. A., , DELILAH nearshore processes experiment: Data summary, miscellaneous reports, Coastal Eng. Res. Cent., Field Res. Facil., U. S. Army Eng. Waterw. Exp. Sta., Vicksburg, Miss., 1991.
- Elgar, S., and R. T. Guza, Observations of bispectra of shoaling surface gravity waves, *J. Fluid Mech.*, 161, 425-448, 1985a.
- Elgar, S., and R. T. Guza, Shoaling gravity waves: comparisons between field observations, linear theory, and a nonlinear model, *J. Fluid Mech.*, 158, 47-70, 1985b.
- Foda, M. A. and C. C. Mei, Nonlinear excitation of long-trapped waves by a group of short swells, *J. Fluid Mech.*, 111, 319-345, 1981.
- Howd, P. A., A. J. Bowen, and R. A. Holman, Edge waves in the presence of strong longshore currents, *J. Geophys. Res.*, 97(C7), 11357-11371, 1992.
- Kim, Y. C., and E. J. Powers, Digital bispectral analysis and its applications to nonlinear wave interactions, *IEEE Trans. Plasma Sci.*, PS-7(2), 120-131, 1979.
- Lippmann, T. C., and R. A. Holman, Quantification of sand bar morphology: A video technique based on wave dissipation, *J. Geophys. Res.*, 94, 995-1011, 1989.
- Lippmann, T. C., and R. A. Holman, Phase speed and angle of breaking waves measured with video techniques, in *Proceedings of Coastal Sediments '91 Specialty Conference*, pp. 542-556, American Society of Civil Engineers, New York, 1991.
- Long, C. E., and J. M. Oltman-Shay, Directional characteristics of waves in shallow water, Technical Report CERC-91-, Coastal Eng. Res. Cent., Field Res. Facil., U. S. Army Eng. Waterw. Exp. Sta., Vicksburg, Miss., 1991.
- Nairn, R. B., J. A. Roelvink, and H. N. Southgate, Transition zone width and implications for modeling surf zone hydrodynamics, in *Proceedings of the 22nd International Conference on Coastal Engineering*, American Society of Civil Engineers, 68-81, 1991.
- Roelvink, J. A., and M. J. F. Stive, Bar-generating cross-shore flow mechanisms on a beach, *J. Geophys. Res.*, 94(C4), 4785-4800, 1989.
- Sallenger, A. H., and R. A. Holman, Wave energy saturation on a natural beach of variable slope, *J. Geophys. Res.*, 90(C6), 11939-11944, 1985.

- Schaffer, H. A. and I. Svendsen, Surf beat generation on a mild-slope beach, in *Proceedings of the 21st International Conference on Coastal Engineering*, American Society of Civil Engineers, 1058-1072, 1988.
- Svendsen, I. A., Wave heights and set-up in a surf zone, *Coastal Engineering*, 8, 303-329, 1984.
- Symonds, G., D. A. Huntley, and A. J. Bowen, Two-dimensional surf beat: long wave generation by a time-varying breakpoint, *J. Geophys. Res.*, 87, 492-498, 1982.
- Thornton, E. B., and R. T. Guza, Energy saturation and phase speeds measured on a natural beach, *J. Geophys. Res.*, 87, 9499-9508, 1982.
- Thornton, E. B., and R. T. Guza, Transformation of wave height distribution, *J. Geophys. Res.*, 88, 5925-5938, 1983.
- Thornton, E. B., and R. T. Guza, Surf zone currents and random waves: Field data and models, *J. Phys. Oceanogr.*, 16, 1165-1178, 1986.
- Wallace, J. M., and R. E. Dickinson, Empirical orthogonal representation of time series in the frequency domain. Part I: Theoretical considerations, *J. Applied Meteor.*, 11(6), 887-892, 1972.
- Whitford, D. J., and E. B. Thornton, Longshore current forcing at a barred beach, in *Proceedings of the 21st International Conference on Coastal Engineering*, American Society of Civil Engineers, 77-90, 1988.



## CHAPTER 70

# PROBABILISTIC STRUCTURE OF RANDOM WAVE GROUPS

Ke Yu \*

### Abstract

This paper deals with the statistical properties of wave groups in a stationary ergodic normal process. For a narrowband Gaussian process, a method based on Kimura's theory is developed to estimate the characteristics of wave groups directly from the wave spectrum. For a non-narrowband Gaussian process with an arbitrary bandwidth, a new model is established to predict the formation of the wave groups by means of zero-upcrossing method. Thus the probabilistic structure of the wave groups in a Gaussian process with an arbitrary bandwidth can be determined. Using this model, the mean run length of the wave groups above any amplitude and the probability distribution of run length at any level can be obtained. On the other hand, a representative wave period of the wave group is suggested to describe the time intervals between two successive maxima. The computational data shows that the bandwidth parameter has a significant effect on the statistical properties of wave groups.

## 1 Introduction

A wave group can be conveniently defined as several successive waves which exceed a given amplitude level. The waves in the group have similar wave height and wave period. Wave groupiness is an important feature of stochastic wave processes. It has been proven that wave groups have significant effects on many ocean engineering problems, such as the resonance of offshore structures and the overtopping above coastal structures. Because of the importance of the groupiness phenomenon in naval, ocean and communication engineering, extensive studies have been made on this property of stochastic waves in the past twenty years, for example, Kimura (1980) and Funke *et al.* (1979). Using the Markov chain concept in expressing the relationship between two maximum points, Kimura (1980) derived the probability distributions about the runs of high waves, the runs of low waves, and the runs of resonant wave periods respectively. Funke *et al.* (1979) developed a different method, SIWEH, to describe a wave process. A parameter GF was defined to express the groupiness degree in a random wave process. Though SIWEH may have the advantages in describing non-Gaussian processes, the author appreciates Kimura's theory

---

\*Research engineer, Department of River and Harbor Engineering, Nanjing Hydraulic Research Institute, Nanjing 210024, P.R.China.

Current address: Center for Applied Coastal Research, Department of Civil Engineering, University of Delaware, Newark, DE 19716, U.S.A.

more for the wave group problem because it provides the information about the probabilistic structure of wave groups which is of concern by engineers and researchers.

However, there are some weaknesses in Kimura's theory. One is the adoption of the narrowband assumption. It is observed that most wave processes in the sea environment have spectrum bandwidth parameter values varying from 0.5 to 0.9, hence the application of Kimura's theory in this case may overestimate the correlation among successive maximum points. The other (Battjes *et al.*, 1984) is the inconvenience in deriving the statistical characteristics of wave groups. It is also worth mentioning that in previous studies, the wave period corresponding to a high wave run is neglected whereas the importance of this parameter is evident.

Therefore, the present study emphasizes the problem in assuming that the process is a stationary ergodic Gaussian process with an arbitrary bandwidth and that the maximum series is subject to the Markov chain condition. The author expects to derive the probabilistic structure of wave groups which include the probability distribution of wave runs above any given amplitude level and to provide some description about the representative wave amplitude and wave period at any given amplitude level.

## 2 Formation of the Probabilistic Structure of Wave Groups

### 2.1 Wave run and its probability distribution

Following Kimura (1980), we can consider a stationary ergodic Gaussian process  $x_1(t)$  with a zero mean and another random process  $x_2(t)$  which is essentially identical to  $x_1(t)$  but has a time shift  $\lambda$  prior to  $x_1(t)$ , i.e.,

$$x_2(t) = x_1(t + \lambda). \quad (1)$$

Assuming the successive maxima of  $x_1(t)$  and  $x_2(t)$  are subject to the Markov chain condition, the maxima of  $x_1(t)$  and  $x_2(t)$  are written as:  $A_1 = \{x_1(t), |x_1(t) \geq 0, \dot{x}_1 = 0, \ddot{x}_1 < 0\}$ ,  $A_2 = \{x_2(t), |x_2(t) \geq 0, \dot{x}_2 = 0, \ddot{x}_2 < 0\}$ . If the time interval  $\lambda$  is defined as the expected wave period between two successive maxima, the joint probability density function of two maxima  $f(A_1, A_2)$  becomes the probability density function of two successive maxima. The probability density function of  $A_1$  (or  $A_2$ ) is defined as  $f(A_1)$  and can be derived from  $f(A_1, A_2)$ .

Two states of wave height are defined. One state is  $S_0 = \{A_i, |A_i < A_L, i = 1, 2\}$ , the second is  $S_1 = \{A_i, |A_i \geq A_L, i = 1, 2\}$ . Hence, all the maxima of  $x_1(t)$  and  $x_2(t)$  can be classified into these two states according to their amplitude values and the given amplitude level  $A_L$ . The two states combined form a state space  $\Omega = \{S_0, S_1\}$ .

For this two state Markov chain, the one-step transition probability matrix is given by

$$P^{[1]} = P = \begin{bmatrix} P_{11} & P_{12} \\ P_{21} & P_{22} \end{bmatrix}, \quad (2)$$

where

$$P_{11} = Prob\{A_2 \in S_0, |A_1 \in S_0\} = \frac{\int_0^{A_L} \int_0^{A_L} f(A_1, A_2) dA_1 dA_2}{\int_0^{A_L} f(A_1) dA_1}, \tag{3}$$

$$P_{12} = Prob\{A_2 \in S_1, |A_1 \in S_0\} = \frac{\int_{A_L}^{\infty} \int_0^{A_L} f(A_1, A_2) dA_1 dA_2}{\int_0^{A_L} f(A_1) dA_1}, \tag{4}$$

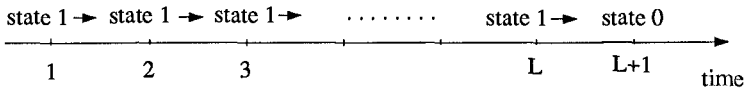
$$P_{21} = Prob\{A_2 \in S_0, |A_1 \in S_1\} = \frac{\int_0^{A_L} \int_{A_L}^{\infty} f(A_1, A_2) dA_1 dA_2}{\int_{A_L}^{\infty} f(A_1) dA_1}, \tag{5}$$

$$P_{22} = Prob\{A_2 \in S_1, |A_1 \in S_1\} = \frac{\int_{A_L}^{\infty} \int_{A_L}^{\infty} f(A_1, A_2) dA_1 dA_2}{\int_{A_L}^{\infty} f(A_1) dA_1}. \tag{6}$$

Because of the homogeneous feature and the Markov property of maximum point process, the N-step transition probability matrix can be easily obtained as follows

$$P^{[N]} = P^N. \tag{7}$$

The N-step transition probability matrix describes the probabilities of N-step transition through all possible paths. Now we consider a wave run which has a run length L. The transition path of this run must be the pattern as shown in the following figure .



The initial state probability distribution is taken as  $P_0 = [0 \quad 1]$ . The row matrix  $P_0$  means that the wave run starts when a wave exceeds the amplitude level  $A_L$  initially. The run ends when the Lth wave exceeds  $A_L$  at last.

The probability matrix after L-step transition can be expressed as

$$P_L = P_0 P^L = [0 \quad 1] \begin{bmatrix} P_{11} & P_{12} \\ P_{21} & P_{22} \end{bmatrix}^L. \tag{8}$$

From the above equation, the cumulative probability of a wave run which follows the mentioned pattern can be found as below

$$P(L) = P_{22}^{L-1} (1 - P_{22}), \tag{9}$$

where L is the length of the run . The mean run length of wave groups above some amplitude level can also be derived from equation (9) as follows

$$\bar{L} = \frac{1}{(1 - P_{22})}. \tag{10}$$

By a similar method, the probability distribution of a run of low waves and the distribution of the total wave run can be obtained. For conciseness, these results are not included in this paper.

## 2.2 Representative amplitude and period of wave groups

When an amplitude level is given the wave groups are defined. The global statistical properties of wave groups can be determined by using the method described above. However, in order to describe a wave group in detail, a wave amplitude  $A^*$  and a wave period  $T^*$  can be defined to represent the wave run.

$A^*$  could be defined as the expected amplitude value above the level  $A_L$

$$A^* = \frac{\int_{A_L}^{\infty} A_1 f(A_1) dA_1}{\int_{A_L}^{\infty} f(A_1) dA_1} \quad (11)$$

and  $T^*$  could be defined as the expected wave period under the condition of  $A = A^*$

$$T^* = \int_0^{\infty} T f(T, |A^*) dT, \quad (12)$$

where  $f(T, |A^*)$  can be derived from the joint probability density function of wave amplitude and wave period.

In addition to  $A^*$  and  $T^*$ , the characteristic extreme value of the maxima in a wave group with run length  $L$  can be calculated based on extreme value theory. For example, the probability density function of extreme values in a wave group can be expressed as

$$g(\xi) = L \{ f(\xi) [1 - P(\xi)]^{L-1} \} \quad (13)$$

and the required characteristic values of extreme value distribution can be evaluated from equation (13).

## 3 Wave Groups in a Narrowband Gaussian Process

### 3.1 The joint probability density function of two maxima

Suppose a narrowband Gaussian process  $x(t)$  has a zero mean and a spectrum  $S_X(\omega)$ . It is a well known fact that  $x(t)$  can be written as (Ochi, 1982)

$$x(t) = X_C(t) \cos(\omega_0 t) - X_S(t) \sin(\omega_0 t), \quad (14)$$

in which  $X_C$  and  $X_S$  are two orthogonal components which vary slowly with time and  $\omega_0$  is the central frequency. It can be proven that  $X_C$  and  $X_S$  are also the Gaussian processes which have the exact same mean and variance with  $x(t)$ . The auto-spectrum and co-spectrum of  $X_C$  and  $X_S$  can be expressed in terms of  $S_X(\omega)$  as

$$S_{X_C}(\omega) = S_{X_S}(\omega) = S_X(\omega - \omega_0) + S_X(\omega + \omega_0), \quad (15)$$

$$S_{X_C X_S}(\omega) = -S_{X_S X_C}(\omega) = i [S_X(\omega - \omega_0) - S_X(\omega + \omega_0)]. \quad (16)$$

An inverse Fourier transfer is applied to get the auto-correlation or correlation functions of  $X_C$  and  $X_S$  as follows

$$\begin{aligned} R_{X_C}(\lambda) &= R_{X_S}(\lambda) = \int_{-\infty}^{\infty} S_{X_C}(\omega) \exp\{i\omega\lambda\} d\omega \\ &= 2 \int_0^{\infty} S_X(\omega) \cos[(\omega - \omega_0)\lambda] d\omega, \end{aligned} \quad (17)$$

$$R_{X_C X_S}(\lambda) = -R_{X_S X_C}(\lambda) = \int_{-\infty}^{\infty} S_{X_C X_S}(\omega) \exp\{i\omega\lambda\} d\omega \quad (18)$$

$$= 2 \int_0^{\infty} S_X(\omega) \sin[(\omega - \omega_0)\lambda] d\omega,$$

where  $\omega_0 = \omega_p$  (peak frequency) and  $\lambda$  is defined as the expected period between two successive maxima estimated by following equation

$$\lambda = 2\pi \sqrt{\frac{m_0}{m_2}}, \quad (19)$$

where

$$m_i = \int_{-\infty}^{\infty} \omega^i S_X(\omega) d\omega, \quad i = 0, 2.$$

Alternatively, equations (17) and (18) can be expressed in terms of the one-side spectrum  $S(\omega)$

$$R_{X_C}(\lambda) = R_{X_S}(\lambda) = \int_0^{\infty} S(\omega) \cos[(\omega - \omega_0)\lambda] d\omega, \quad (20)$$

$$R_{X_C X_S}(\lambda) = -R_{X_S X_C}(\lambda) = \int_0^{\infty} S(\omega) \sin[(\omega - \omega_0)\lambda] d\omega, \quad (21)$$

where  $S(\omega) = 2S_X(\omega)$ .

If the spectrum is symmetric about  $\omega_0$ , then  $R_{X_C X_S}(\lambda) = R_{X_S X_C}(\lambda) = 0$ . It can be inferred (Middleton, 1960) that the two dimensional amplitude probability density function is given by

$$f(A_1, A_2) = \frac{A_1 A_2}{B} I_0 \left\{ \frac{\sqrt{R_{X_C}^2 + R_{X_C X_S}^2}}{B} A_1 A_2 \right\} \exp \left\{ -\frac{m_0(A_1^2 + A_2^2)}{2B} \right\}, \quad (22)$$

where  $B = m_0^2 - [R_{X_C}^2 + R_{X_C X_S}^2]$  and  $I_0(x)$  is the zeroth order Bessel function of the first kind.

After introducing two non-dimensional amplitudes,  $\xi$  and  $\eta$ , defined as

$$\xi = \frac{A_1}{\sqrt{m_0}}, \quad \eta = \frac{A_2}{\sqrt{m_0}}, \quad (23)$$

equation (22) can be rewritten as

$$f(\xi, \eta) = \frac{\xi \eta}{1 - \rho^2} I_0 \left\{ \frac{\rho \xi \eta}{1 - \rho^2} \right\} \exp \left\{ -\frac{\xi^2 + \eta^2}{2(1 - \rho^2)} \right\}. \quad (24)$$

The correlation coefficient  $\rho$  can be determined by the following formula

$$\rho = \frac{\sqrt{R_{X_C}^2(\lambda) + R_{X_C X_S}^2(\lambda)}}{m_0}. \quad (25)$$

The one dimensional amplitude probability density function can be derived from equation (22) as

$$f(A_1) = \frac{A_1}{m_0} \exp \left\{ -\frac{A_1^2}{2m_0} \right\} \quad (26)$$

and the dimensionless form of  $f(A_1)$  is

$$f(\xi) = \xi \exp \left\{ -\frac{\xi^2}{2} \right\}. \quad (27)$$

### 3.2 Representative amplitude and period of wave groups in a narrowband Gaussian process

Applying the maximum distribution into equation (11), the representative amplitude of a wave group above any given level  $\xi_L$  can be obtained as

$$\xi^* = \xi_L + \sqrt{2\pi} \exp\{\xi_L^2/2\} [1 - \Phi(\xi_L)], \quad (28)$$

where

$$\Phi(x) = \frac{1}{\sqrt{2\pi}} \int_{-\infty}^x \exp \left\{ -\frac{u^2}{2} \right\} du.$$

As for the representative wave period, the joint probability distribution of wave amplitude and period suggested by Longuet-Higgins (1975) is used to get the probability distribution of wave period under the condition of  $\xi = \xi^*$

$$f(\xi, \tau) = \frac{1}{1 - \Phi(-\xi/\nu)} \frac{1}{\sqrt{2\pi}} \xi^2 \exp \left\{ -\frac{\xi^2(1 + \tau^2)}{2} \right\}, \quad (29)$$

$$0 \leq \xi < \infty, \quad -\frac{1}{\nu} < \tau < \infty$$

where

$$\xi = \frac{A}{\sqrt{m_0}}, \quad \tau = \frac{T - \bar{T}}{\nu T}, \quad \nu = \sqrt{\frac{m_0 m_2}{m_1^2} - 1}, \quad \bar{T} = 2\pi \sqrt{\frac{m_0}{m_2}}.$$

$\Phi(x)$  is the error function and  $\nu$  is another bandwidth parameter which is determined by the spectral moments.

The conditional probability density function of the wave period is

$$f(\tau, |\xi^*) = \frac{f(\xi, \eta)}{f(\xi)} = \frac{1}{1 - \Phi(-\xi^*/\nu)} \frac{1}{\sqrt{2\pi}} \xi^* \exp \left\{ -\frac{1}{2} (\xi^* \tau)^2 \right\} \quad (30)$$

and the representative wave period can be calculated by equation (12)

$$\tau^* = \frac{1}{\sqrt{2\pi} \xi^* [1 - \Phi(-\xi^*/\nu)]} \exp \left\{ -\frac{1}{2} (\xi^* \tau)^2 \right\}. \quad (31)$$

Applying the two dimensional density function of two maxima presented by equation (22) and one dimensional density function expressed by equation (26) into equation (6), the probability  $P_{22}$  under the condition of a given amplitude level  $\xi^*$  can be determined. The  $P_{22}$  value can also be used to determine the probability distribution of wave runs which are above the level  $\xi_L$ . Equations (28) and (31) give the analytic expressions of representative wave amplitude and wave period of wave runs above a given amplitude level.

## 4 Wave Groups in a Non-narrowband Gaussian Process

### 4.1 The two dimensional maximum distribution

Given a stationary Gaussian process  $x_1(t)$  with a zero mean and an arbitrary spectral bandwidth and another process  $x_2(t)$  defined in equation (1), the time shift  $\lambda$  can be determined by the bandwidth parameter  $\epsilon$  and the moments of the spectrum

$$\lambda = 4\pi \frac{\sqrt{1 - \epsilon^2}}{1 + \sqrt{1 - \epsilon^2}} \sqrt{\frac{m_0}{m_2}}, \tag{32}$$

$$\epsilon = \sqrt{1 - \frac{m_2^2}{m_0 m_4}}. \tag{33}$$

It can be proven that the two processes  $x_1(t)$  and  $x_2(t)$  and their derivatives  $\dot{x}_1(t)$ ,  $\ddot{x}_1(t)$ ,  $\dot{x}_2(t)$ ,  $\ddot{x}_2(t)$  are subject to a six dimensional normal distribution ( Ochi, 1979). Their joint probability density function can be written as

$$f(X) = \frac{1}{(2\pi)^3 |\Sigma|^{1/2}} \exp \left\{ -\frac{1}{2} X \Sigma^{-1} X^T \right\}, \tag{34}$$

in which the row matrix X is

$$X = [ x_1(t) \quad \dot{x}_1(t) \quad \ddot{x}_1(t) \quad x_2(t) \quad \dot{x}_2(t) \quad \ddot{x}_2(t) ].$$

The covariance matrix can be expressed in terms of the spectral density function

$$\Sigma = \begin{bmatrix} m_0 & 0 & -m_2 & m_{0C} & -m_{1S} & -m_{2C} \\ 0 & m_2 & 0 & m_{1S} & m_{2C} & -m_{2S} \\ -m_2 & 0 & m_4 & -m_{2C} & m_{3S} & m_{4C} \\ m_{0C} & m_{1S} & -m_{2C} & m_0 & 0 & -m_2 \\ -m_{1S} & m_{2C} & m_{3S} & 0 & m_2 & 0 \\ -m_{2C} & -m_{2S} & m_{4C} & -m_2 & 0 & m_4 \end{bmatrix},$$

where

$$m_i = \int_0^\infty \omega^i S(\omega) d\omega \quad , \quad i = 0, 2, 4,$$

$$m_{iC} = \int_0^\infty \omega^i S(\omega) \cos(\omega\lambda) d\omega \quad , \quad i = 0, 2, 4,$$

$$m_{iS} = \int_0^\infty \omega^i S(\omega) \sin(\omega\lambda) d\omega \quad , \quad i = 1, 2, 3.$$

As mentioned before, the positive maxima of  $x_1(t)$  and  $x_2(t)$  must satisfy the conditions,  $x_i(t) \geq 0$ ,  $\dot{x}_i = 0$ ,  $\ddot{x}_i < 0$ ,  $i = 1, 2$ . The expected number of maxima

which are above the respective amplitude levels  $A_1$  and  $A_2$  per unit time can be evaluated by the following equation

$$\bar{N}_{A_1, A_2} = \int_{A_1}^{\infty} \int_{A_2}^{\infty} \int_{-\infty}^0 \int_{-\infty}^0 |\dot{x}_1| |\dot{x}_2| f(x_1, 0, \ddot{x}_1, x_2, 0, \ddot{x}_2) dx_1 dx_2 d\ddot{x}_1 d\ddot{x}_2. \quad (35)$$

Letting  $A_1 = A_2 = 0$  in equation (35), equation (35) can be rewritten as

$$\bar{N}_{0,0} = \int_0^{\infty} \int_0^{\infty} \int_{-\infty}^0 \int_{-\infty}^0 |\dot{x}_1| |\dot{x}_2| f(x_1, 0, \ddot{x}_1, x_2, 0, \ddot{x}_2) dx_1 dx_2 d\ddot{x}_1 d\ddot{x}_2 \quad (36)$$

and it can be used to estimate the expected number of maxima in  $x_1(t)$  and  $x_2(t)$  per unit time. The probability that the maxima in  $x_1(t)$  and  $x_2(t)$  exceed respective amplitude level  $A_1$  and  $A_2$  can be considered approximately as the ratio of these two expected numbers. Hence the joint probability density function of two maxima can be derived from the ratio  $\bar{N}_{A_1, A_2} / \bar{N}_{0,0}$

$$\begin{aligned} f(A_1, A_2) &= \frac{\partial^2}{\partial A_1 \partial A_2} \left( 1 - \frac{\bar{N}_{A_1, A_2}}{\bar{N}_{0,0}} \right) \\ &= \frac{\int_{-\infty}^0 \int_{-\infty}^0 |\dot{x}_1| |\dot{x}_2| f(A_1, 0, \ddot{x}_1, A_2, 0, \ddot{x}_2) d\ddot{x}_1 d\ddot{x}_2}{\int_0^{\infty} \int_0^{\infty} \int_{-\infty}^0 \int_{-\infty}^0 |\dot{x}_1| |\dot{x}_2| f(x_1, 0, \ddot{x}_1, x_2, 0, \ddot{x}_2) dx_1 dx_2 d\ddot{x}_1 d\ddot{x}_2}. \end{aligned} \quad (37)$$

Now, define two new Gaussian processes which are derived from  $x_1(t)$  and  $x_2(t)$

$$x'_1(t) = \frac{1}{\sqrt{m_0}} x_1(t) \quad , \quad x'_2(t) = \frac{1}{\sqrt{m_0}} x_2(t) \quad (38)$$

and two dimensionless maxima as before

$$\xi = \frac{A_1}{\sqrt{m_0}} \quad , \quad \eta = \frac{A_2}{\sqrt{m_0}}.$$

The two dimensional distribution of two dimensionless maxima  $\xi$  and  $\eta$  can be obtained simply by replacing  $x'_1, x'_2, \dot{x}'_1, \dot{x}'_2, \xi$  and  $\eta$  for the proper terms in equation (34) and (37). Note the covariance matrix  $\Sigma$  becomes  $\Sigma'$  and satisfies the following relation

$$\Sigma' = \frac{1}{m_0} \Sigma. \quad (39)$$

The probability density function of the maxima in process  $x_1(t)$  has the form

$$\begin{aligned} f(A_1) &= \frac{2/\sqrt{m_0}}{1 + \sqrt{1 - \epsilon^2}} \left[ \frac{\epsilon}{\sqrt{2\pi}} \exp \left\{ -\frac{1}{2\epsilon^2} \left( \frac{A_1}{\sqrt{m_0}} \right)^2 \right\} + \sqrt{1 - \epsilon^2} \left( \frac{A_1}{\sqrt{m_0}} \right) \right. \\ &\quad \left. \times \exp \left\{ -\frac{1}{2} \left( \frac{A_1}{\sqrt{m_0}} \right)^2 \right\} \left\{ 1 - \Phi \left( -\frac{\sqrt{1 - \epsilon^2}}{\epsilon} \frac{A_1}{\sqrt{m_0}} \right) \right\} \right], \quad (40) \\ &\quad 0 \leq A_1 < \infty \end{aligned}$$

and the non-dimensional form of equation (40) is as follows

$$\begin{aligned} f(\xi) &= \frac{2}{1 + \sqrt{1 - \epsilon^2}} \left[ \frac{\epsilon}{\sqrt{2\pi}} \exp \left\{ -\frac{\xi^2}{2\epsilon^2} \right\} + \sqrt{1 - \epsilon^2} \xi \right. \\ &\quad \left. \times \exp \left\{ -\frac{\xi^2}{2} \right\} \left\{ 1 - \Phi \left( -\frac{\sqrt{1 - \epsilon^2}}{\epsilon} \xi \right) \right\} \right]. \quad (41) \end{aligned}$$



## 4.2 The representative amplitude and period of wave groups in a non-narrowband Gaussian process

The representative dimensionless amplitude  $\xi^*$  can be estimated by equations (41) and (11).

For a non-narrowband Gaussian process, the joint probability density function of the maxima and the time intervals between two successive maxima can be used to calculate the representative wave period (Arhan *et al.*, 1976)

$$f(\xi, \tau) = \frac{2}{\sqrt{2\pi}} \frac{\alpha^3}{\epsilon(1-\epsilon^2)} \frac{\xi^2}{\tau^5} \exp \left\{ -\frac{\xi^2}{2\epsilon^2\tau^4} [(\tau^2 - \alpha^2)^2 + \alpha^4\beta^2] \right\}, \quad (42)$$

in which  $\xi = A_1/\sqrt{m_0}$ ,  $\tau = T/\lambda$ ,  $\alpha = 0.5(1 + \sqrt{1 - \epsilon^2})$ ,  $\beta = \epsilon/\sqrt{1 - \epsilon^2}$ .

The conditional probability density function of  $\tau$  can be expressed as

$$f(\tau, |\xi) = \frac{f(\xi, \tau)}{\int_0^\infty f(\xi, \tau) d\tau} \quad (43)$$

and the representative wave period  $\tau^*$  can be written as

$$\tau^* = \int_0^\infty \tau f(\tau, |\xi^*) d\tau. \quad (44)$$

Note that  $\tau^*$  is not a wave period according to the exact definition of a wave period by means of zero-upcrossing. It is just a time interval between two successive maxima. However, when the wave amplitude is large enough,  $\tau^*$  can be considered as a good approximation of wave period.

## 5 Computational Results and Discussions

In order to find the effect of the spectral bandwidth on the probability structure of wave groups, different  $\epsilon$  values should be applied in this computation. But the common wave spectra used in analysis and experiment, such as the JONSWAP spectrum and the Bretschneider spectrum, only have limited range of  $\epsilon$  values. Hence some typical wave records used in Ochi's study are used here again. The  $\epsilon$  values of these spectra vary from 0.46 to 0.8. A JONSWAP spectrum with  $\alpha = 0.05$ ,  $f_p = 0.1 Hz$ ,  $\gamma = 7.0$  and  $\epsilon = 0.685$  is applied to the computation. Table 1 displays the features of the spectra which include the bandwidth parameter  $\epsilon$  and the correlation coefficient  $\rho$  calculated by equations (33) and (25).

Table 1. Wave records and wave spectrum used in the computation

wave spectrum	spectral bandwidth parameter $\epsilon$	correlation coefficient $\rho$	peak frequency $\omega(2\pi * Hz)$
WS1	0.468	0.458	0.875
WS2	0.594	0.299	0.563
WS3	0.685	0.676	0.626
WS4	0.806	0.267	0.413

It is clear that the numerical integration in equation (37) is the major work in this computation. Here,  $2.401 \times 10^7$  discretizing points are used in calculating the quadruple integration in order to guarantee accuracy.

Figure 1 shows the relationship of  $P_{22}$  and  $\xi_L$ . For each spectrum, two  $\epsilon - \xi_L$  curves based on the non-narrowband and the narrowband theory respectively, are presented to compare the difference between two theories. It can be seen that the narrowband theory will give larger a  $P_{22}$  value when  $\epsilon$  is increased for fixed  $\xi_L$ . In this case it seems only the value of  $\epsilon$  will determine the  $P_{22} - \xi_L$  relation under the non-narrowband assumption. When  $\epsilon = 0.46$ , the two theories give almost the same results for small amplitude levels. For the wave spectra which have very small  $\epsilon$  values, the strong singularity of the co-variance matrix makes its determinant value approach zero and leads the elements in the inverse matrix  $\Sigma^{-1}$  to infinity. It will induce the non-existence of the joint probability density function expressed by equation (37). In this situation, the narrowband assumption could be applied to simplify the problem. We can also infer that when the value of  $\epsilon$  approaches zero, it is the correlation coefficient  $\rho$ , not the bandwidth parameter  $\epsilon$ , that will determine the  $P_{22} - \xi_L$  relation if  $\epsilon$  is very small. This estimation can be demonstrated by the one dimensional analytic distribution of wave amplitude in a non-narrowbanded Gaussian process which has a small bandwidth. From equation (41) it can be seen that the wave amplitude distribution with  $\epsilon$  value in the region  $0 < \epsilon < 0.5$  is almost the same with the Rayleigh distribution expressed by equation (27).

From equation (30) it can be seen that only the correlation coefficient  $\rho$  affects the joint distribution and finally determines the probability distribution of wave runs if the amplitude level remains constant. Employing equations (22) and (26) into equation (6), the probability distribution of wave runs can be obtained from equation (9). Figure 2 displays the relationship between the probability of wave run and its run-length with different  $\rho$  values.

Figure 2 also shows two probability distribution of wave groups based on narrowband theory and non-narrowband theory respectively. In the figure, the amplitude level  $\xi_L = 1.245$  represents the mean amplitude in a standard narrowbanded normal process. In figure 3, the level  $\xi_L = 2.005$  is just the significant amplitude in a narrowbanded normal process. By applying the two  $P_{22}$  values corresponding to a given amplitude level into equation (9), two probability distributions of the high wave runs above the amplitude level can be easily determined.

Applying equations (42) and (43) into equations (11) and (12), the dimensionless representative wave amplitude and wave period in a non-narrowband Gaussian process can be determined. Figure 4 displays the relation between the representative wave amplitude and the representative period with different  $\epsilon$  values. The curve noted as  $\epsilon = 0$  represents the  $\xi^* - \xi_L$  relation expressed by equation(28). Figure 5 shows the relationship of  $\tau^*$  and  $\xi$  with different  $\epsilon$  values. Within the narrowband theory, the representative wave period  $\tau^*$  calculated by equation (31) is zero when  $\xi^*$  takes its minimum value of 1.245. In other words, the expected wave period is considered to be the representative wave period in this case.

It is worthy to mention here that the present analysis and computation is in fact the extension of Kimura's theory to a more general case. We know from the previous analysis that two parameters, the bandwidth parameter,  $\epsilon$ , and the correlation coef-

ficient,  $\rho$ , decide the statistical properties of wave groups. For an ideal narrowband Gaussian process, the effect of the bandwidth parameter on wave groups reduces to zero and only the correlation coefficient determines the properties. For a non-narrowband Gaussian process with a large  $\epsilon$  value, the computational data shows the opposite result. The bandwidth parameter plays a major role in determining the probabilistic features of the wave groups. But for a small  $\epsilon$  value we do not know which parameter is more important. We expect to see that as  $\epsilon$  increases, the bandwidth parameter will gradually replace the correlation coefficient and dominate the statistical properties of wave groups. To see these effects more clearly, further numerical analysis is necessary with variance on the two parameters. For example, wave spectra having the same  $\epsilon$  value but different  $\rho$  values or having the same  $\rho$  value but different  $\epsilon$  values.

Another tricky problem arising in this study is the validity of the present theory when it is applied to a random process which tends to be white noise, i.e., the bandwidth parameter and the correlation coefficient approach to one and zero respectively. In this case the assumption that the successive maxima in the process subject to the Markov chain condition becomes questionable, since the successive maxima tend to be independent variables. To determine how far we can go with this model, more wave records and field data are necessary. It is definitely interesting and promising work to analyze and compare the experimental and field data about the random wave groups with the existing models. This will lead to a deeper understanding to the groupiness phenomenon in the real sea environment.

## 6 Conclusions

The following conclusions can be made from the above analysis:

1. When a stationary Gaussian process has a small bandwidth parameter, i.e.,  $\epsilon < 0.5$ , the narrowband assumption can be applied and the statistical properties of wave groups derived from the narrowband theory can be considered as a good approximation.
2. If the spectrum of a stationary Gaussian process is not assumed narrowbanded, i.e.,  $\epsilon \geq 0.5$ , the application of the narrowband assumption will overestimate the correlation between two successive maxima.
3. For a narrowband Gaussian process the correlation coefficient  $\rho$  will determine the statistical properties of wave groups. For a non-narrowband Gaussian process with large  $\epsilon$  value, it seems that the spectral bandwidth parameter will finally determine the probabilistic structure of wave groups.
4. Based on the formulas presented in this paper, the probabilistic structure of wave groups in a stationary ergodic Gaussian random process can be obtained directly from its wave spectrum.

## Acknowledgments

The author thanks Mr. Weidon Su for his meaningful insight which helped to start this work. In addition, the author expresses his appreciation to Dr. Jian Ye and Mr. Bingcan Din for their assistance in the numerical computation which was beneficial

to the development of this paper. The author also thanks Mr. Michael Poff and Mr. Daniel Cox who read this paper carefully and made many suggestions. Finally, the author's deep appreciation goes to Prof. Ib A. Svendsen, the head of Civil Engineering Department at University of Delaware, and Prof. Robert A. Dalrymple, the director of Center for Applied Coastal Research at University of Delaware, who provided a considerable financial aid for this trip. Their encouragement and support made this representation possible.

## Reference

- Arhan, M. K., Cavanié, A., and Ezraty, R. (1976). "Etude théorique et expérimentale de la relation hauteur-période des vagues de tempete," I.F.P. 24191. Centre National pour l'Exploitation des Oceans.
- Battjes, J. A. and Van Vledder, G. Ph., (1984). "Verification of Kimura's Theory for Wave Groups Statistics", *Proc. 19th Int. Conf. Coast. Engrng.*, ASCE.
- Funke, E. R. and Mansard, E. P. D., (1979). "On the Synthesis of Realistic Sea States in a Laboratory Flume", *Hydraulics Laboratory Report LTR-HR-66*, N.R.C., Ottawa, Canada.
- Kimura, A., (1980). "Statistical Properties of Random Wave Groups", *Proc. 17th Int. Conf. Coast. Engrng.*, ASCE.
- Longuet-Higgins, M. S. (1975). "On the Joint Distribution of the Periods and Amplitudes of Sea Waves", *JGR, J. of Geophys. Res.*, 80, No.18.
- Middleton, D., (1960). "An Introduction to Statistical Communication Theory", McGraw-Hill Book Company Inc.
- Ochi, M. K., (1979). "Extreme Values of Waves and Ship Responses Subject to Markov Chain Condition", *Journal of Ship Research*, Vol. 23, No. 3, Sept.
- Ochi, M. K., (1982). "Stochastic Analysis and Probabilistic Prediction of Random Seas", *Advances in Hydroscience*, Vol. 13-1982, Academic Press.

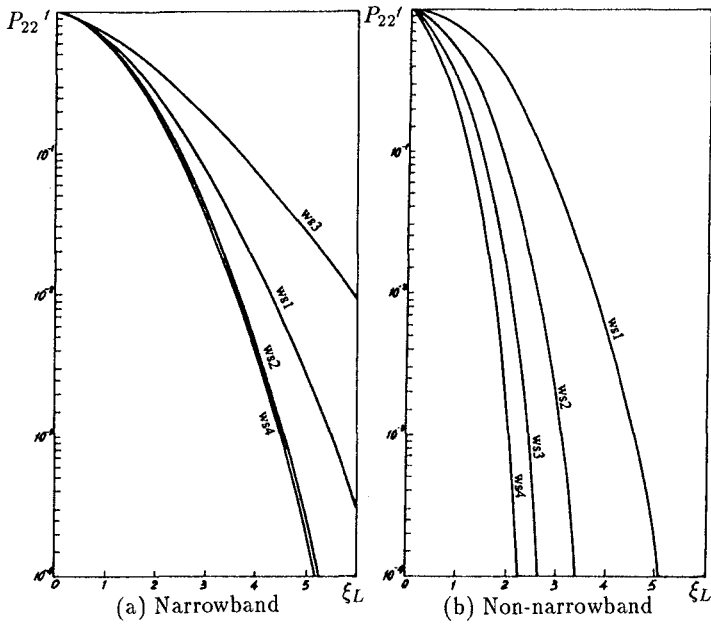


Fig. 1 Change of  $P_{22}$  value with amplitude level  $\xi_L$

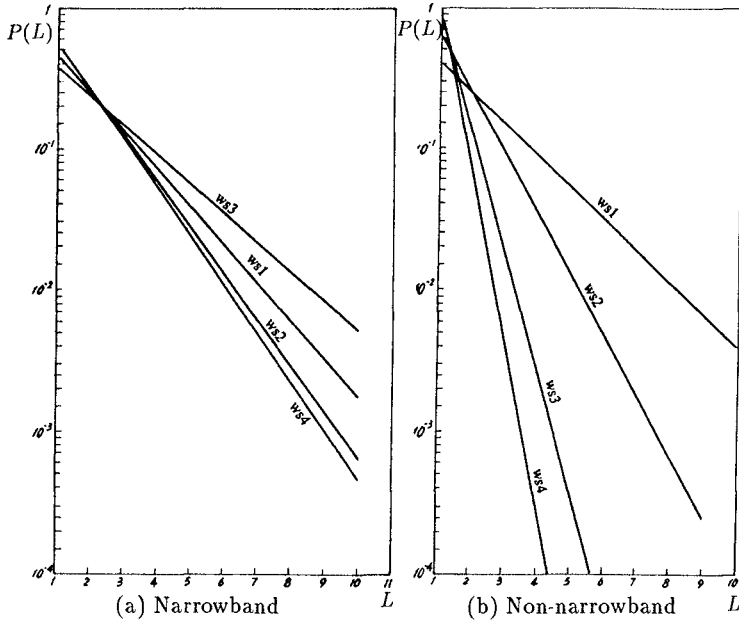


Fig. 2 Probability distribution of high wave runs ( $\xi_L=1.245$ )

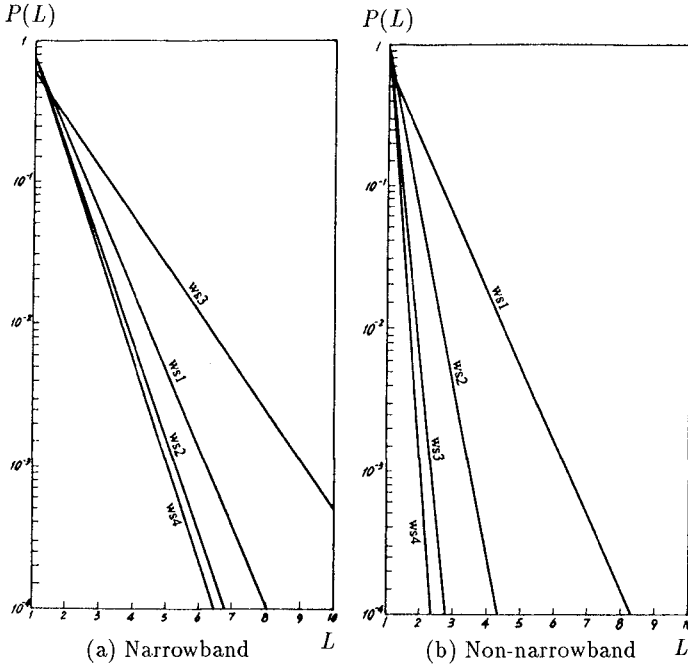


Fig. 3 Probability distribution of high wave runs ( $\xi_L=2.005$ )

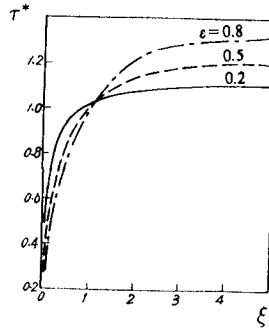
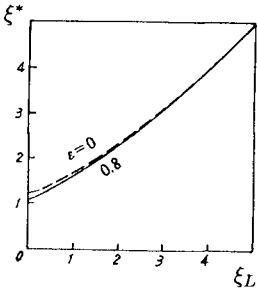


Fig. 4 Relationship between  $\xi^*$  and  $\xi_L$  Fig. 5 Relationship between  $\tau^*$  and  $\xi$

## CHAPTER 71

### Statistics of wave group parameters

Gerbrant Ph. van Vledder <sup>1</sup>

#### Abstract

The statistical properties of four spectral shape parameters ( $Q_p$ ,  $Q_e$ ,  $\kappa$  and  $\nu$ ) and the correlation coefficient between succeeding wave heights ( $\rho_{HH}$ ) are investigated using field data and numerically simulated data. The effects of spectral smoothing, integration range and duration of the data record on estimates of these parameters are discussed. The relation between spectral shape and wave grouping is discussed in relation to Kimura's theory for group length statistics. A group length distribution independent method for computing this mean group length is introduced. Further, a comparison is made between time and frequency domain estimates of the correlation coefficient between successive wave heights. Observed discrepancies between them are analyzed and an improved method for the spectral computation of this coefficient is suggested.

#### 1 Introduction

The statistical analysis of random wave groups has received much attention in the last years. These studies can be divided into analyses in terms of individual wave heights or in terms of wave envelopes. This paper concentrates on wave group analysis in terms of individual waves, where a wave group is defined as a sequence of waves all succeed a certain height. The most successful model for the statistical description of group lengths has been given by Kimura (1980). Principal parameter in this model is the correlation between successive wave heights. Various parameters have been developed to relate wave group length statistics to the spectral shape, e.g. the well known peakedness parameter  $Q_p$ , introduced by Goda

---

<sup>1</sup> Research Engineer, Delft Hydraulics, P.O. Box 152, 8300 AD Emmeloord, The Netherlands

(1970), or the  $\kappa$  parameter, used by Battjes and Van Vledder (1984). This  $\kappa$  parameter links the spectral width via the correlation coefficient  $\rho_{HH}$  between successive wave heights to group length statistics. Other measures for the spectral width are the parameter  $\nu$ , introduced by Longuet-Higgins (1975), or  $Q_e$ , introduced by Medina and Hudspeth (1987).

Most of these parameters lack a theoretical basis linking wave group statistics and spectral width. Only the  $\kappa$  parameter has such a basis, although it underestimates group lengths. Medina and Hudspeth (1990) have theoretically analyzed the relation between the spectral shape parameters  $Q_p$ ,  $Q_e$ ,  $\kappa$  and the correlation coefficient between successive wave heights  $\rho_{HH}$ . They used a three-axes representation to show that these parameters are interrelated. They argue, that because of this interrelationship, only one of these parameters is required in order to evaluate wave groupiness. Although they note the possible effect of statistical variability on the estimates of these parameters, they do not pursue the consequences of this variability on the interrelationship between these parameters.

The purpose of this paper is to analyze the statistical properties of four spectral shape parameters ( $Q_p$ ,  $Q_e$ ,  $\nu$  and  $\kappa$ ) and their usefulness in relation to wave grouping. Also, the effects of spectral smoothing, sensitivity to integration range and duration of the underlying wave record on estimates of these parameters are investigated. Finally, assumptions in the spectral computation of this coefficient are reviewed and improved where possible.

## 2 Wave group analysis in terms of individual waves

In this paper wave groups are defined in terms of individual zero-up crossing waves. A wave group is defined as a sequence of succeeding waves with heights that all exceed a preset threshold level (e.g. the mean wave height). The length of the wave group is equal to the number of waves in a group. The mean group length in a wave record is considered as the measure for the amount of wave grouping.

Models for the probability distribution of group lengths have been given by Goda (1970) and Kimura (1980). The model of Goda underestimates group lengths since it neglects the correlation between succeeding wave heights. As was shown by Rye (1974) and others, consecutive wave heights are positively correlated. This correlation is quantified by means of the coefficient of linear correlation:

$$\rho_{HH,t} = \frac{1}{\sigma_H^2} \frac{1}{N-1} \sum_{i=1}^{N-1} (H_i - H_m)(H_{i+1} - H_m) \quad (2.1)$$

in which  $\sigma_H$  is the standard deviation and  $H_m$  the mean wave height and  $N$  the number of waves in a record. The subscript  $t$  refers to time domain.



These correlations are considered in the model of Kimura (1980), in which it is assumed that succeeding wave heights form a Markov-chain. To compute the probability of a sequence of high waves with a certain length, Kimura used the conditional probability  $p_{22}$  that a wave height exceeds the threshold level,  $H_c$ , given that the previous wave also exceeds  $H_c$ :

$$p_{22} = \text{Prob} \{ H_{i+1} > H_c \mid H_i > H_c \} \tag{2.2}$$

The group length distribution function is:

$$P_1(j) = (1 - p_{22}) p_{22}^{j-1} \tag{2.3}$$

The mean group length can be computed as:

$$\bar{j}_1 = E\{j\} = \sum_{j=1}^{\infty} j P_1(j) = \frac{1}{1 - p_{22}} \tag{2.4}$$

and the standard deviation of group length can be computed as:

$$\sigma_1(j) = \{ E\{j^2\} - E\{j\}^2 \}^{1/2} = \frac{\sqrt{p_{22}}}{1 - p_{22}} \tag{2.5}$$

The probability  $p_{22}$  is computed from the joint probability density function  $p(H_1, H_2)$  of succeeding wave heights:

$$p_{22} = \int_{H_c}^{\infty} \int_{H_c}^{\infty} p(H_1, H_2) dH_1 dH_2 \mid \int_{H_c}^{\infty} \int_0^{\infty} p(H_1, H_2) dH_1 dH_2 \tag{2.6}$$

where  $p(H_1, H_2)$  is the bi-variate Rayleigh distribution:

$$p(H_1, H_2) = \frac{\pi^2}{4} \frac{H_1 H_2}{H_m^4 (1 - \kappa^2)} \exp \left( -\frac{\pi}{4} \frac{H_1^2 + H_2^2}{H_m^2 (1 - \kappa^2)} \right) I_0 \left( \frac{\pi}{2} \frac{\kappa}{(1 - \kappa^2)} \frac{H_1 H_2}{H_m^2} \right) \tag{2.7}$$

In Eq. (2.7)  $\kappa$  is a correlation parameter,  $H_m$  the mean wave height, and  $I_0$  the modified Bessel function of zeroth order. The relation between the correlation parameter  $\kappa$  and the coefficient of linear correlation is given by:

$$\rho_{HH} = \frac{E(\kappa) - \frac{1}{2}(1 - \kappa^2)K(\kappa) - \pi/4}{1 - \pi/4} \tag{2.8}$$

in which  $K$  and  $E$  are the complete elliptic integrals of the first and second kind, respectively. An accurate approximation of Eq. (2.8) has been given by Battjes (1974):

$$\rho_{HH} \approx \frac{\pi}{16 - 4\pi} \left( \kappa^2 + \frac{\kappa^4}{16} + \frac{\kappa^6}{64} \right) \tag{2.9}$$

The truncation error involved in approximation (2.9) is less than 0.1% for  $0 \leq \kappa < 0.7$  and less than 1% for  $0.7 \leq \kappa < 0.95$ .

The model of Kimura has been verified against field measurements by Goda (1983), Battjes and Van Vledder (1984), and others. The present study also supports Kimura's model for predicting the mean group length. To that end, numerically simulated data have been used, see section 7, Fig. 1, panel a).

### 3 The mean group length

The standard method of deriving the mean group length  $\bar{j}_1$  is via Eq. (2.4) on the basis of the theoretical group length distribution (2.3). The mean group length, however, is independent of this group length distribution (Van Vledder, 1983).

Consider a wave record with  $N_w$  waves of which  $N_h$  waves are higher than the threshold level  $H_c$ . Further, the wave record contains  $N_g$  groups of high waves. The mean group length  $\bar{j}_1$  can then be computed as:

$$\bar{j}_1 = \frac{N_g}{N_h} \tag{3.1}$$

The end of each wave group can be identified as a sequence of a high wave followed by a low wave. Consequently, the number of wave groups is given by:

$$N_g = N_w \times \text{Prob}\{H_i > H_c \wedge H_{i+1} \leq H_c\} \tag{3.2}$$

The number of high waves in the wave record is given by

$$N_h = N_w \times \text{Prob}\{H_i > H_c\} \tag{3.3}$$

Thus, the mean group length  $\bar{j}_1$  can be computed as:

$$\left. \begin{aligned} \bar{j}_1 &= \frac{\text{Prob}\{H_i > H_c\}}{\text{Prob}\{H_i > H_c \wedge H_{i+1} \leq H_c\}} \\ &= \frac{1}{1 - \text{Prob}\{H_{i+1} > H_c \mid H_i > H_c\}} \end{aligned} \right\} \tag{3.4}$$

which by virtue of Eq. (2.2) is equal to expression (2.4). This result implies that the mean group length  $\bar{j}_1$  is directly related to the correlation coefficient between successive wave heights  $\rho_{HH,t}$ , through the Eqs. (2.6), (2.7) and (2.8). It also implies that the mean group length does not depend on correlations between non-successive wave heights.

## 4 Spectral shape parameters

It is well known that the spectral width is related to the amount of wave grouping. Sea states with narrow spectra show a higher amount of wave grouping than those with broad spectra (Rye, 1974, and others). Below, four spectral width parameters ( $Q_p$ ,  $Q_e$ ,  $\nu$  and  $\kappa$ ) are described that have been suggested in relation to wave grouping. The  $Q_p$  parameter has been introduced by Goda (1970) as a measure for the peakedness of the wave spectrum. It is defined as:

$$Q_p = \frac{2}{m_0^2} \int_0^{\infty} f S(f)^2 df \quad (4.1)$$

in which  $S(f)$  the frequency spectrum and  $m_0$  its zeroth moment. The  $Q_p$  parameter is frequently used by many authors in relation to the amount of wave grouping of wind waves. Recently, Medina and Hudspeth (1987) proposed the spectral peakedness parameter  $Q_e$ , similar to Goda's peakedness parameter, it is defined as:

$$Q_e = \frac{2m_1}{m_0^3} \int_0^{\infty} S(f)^2 df \quad (4.2)$$

with  $m_0$  and  $m_1$  the zeroth and first spectral moment of  $S(f)$ , respectively. Another spectral width parameter was introduced by Longuet-Higgins (1975),

$$\nu = (m_0 m_2 / m_1^2 - 1)^{\frac{1}{2}} \quad (4.3)$$

and applied by Longuet-Higgins (1984) and Chandler and Masson (1992) to wave group statistics.

Above three parameters have been proposed on intuitive grounds rather than on theoretical ones. A fundamental approach to relate the spectral shape with the amount of wave grouping is based on Rice's (1944) theoretical results on envelope statistics. Rice (1944) has derived the joint probability of two values  $R_1$  and  $R_2$  of the wave envelope  $R(t)$  for a narrow-banded Gaussian process, separated by a time lag  $\tau$ . This distribution is the bi-variate Rayleigh distribution, given by Eq. (2.7), but with the parameters  $H_1$ ,  $H_2$  and  $H_m$  replaced by  $R_1$ ,  $R_2$  and  $R_m$ , respectively. This bi-variate Rayleigh distribution contains a correlation parameter that depends on the lag  $\tau$  and the spectral shape. The definition for this parameter has been rewritten by Battjes (1974) as:

$$\kappa^2(\tau) m_0^2 = \left[ \int_0^{\infty} S(f) \cos(2\pi f\tau) df \right]^2 + \left[ \int_0^{\infty} S(f) \sin(2\pi f\tau) df \right]^2 \quad (4.4)$$

For narrow spectra, Rice's result can be used to derive the joint distribution of two consecutive wave heights  $H_1$  and  $H_2$  by substituting  $H_1 = 2R_1$  and  $H_2 = 2R_2$ , and using

$\tau = T_m$ , where  $T_m$  is the mean wave period that can be computed from the wave spectrum (Arhan and Ezraty, 1978):

$$T_m = T_{m02} = \sqrt{m_0/m_2}. \quad (4.5)$$

Using relation (2.8) a frequency domain estimate of the correlation coefficient between successive wave heights can be obtained. Such an estimate is denoted by  $\rho_{HH,f}(\tau)$ .

## 5 Wave data and analysis

Field data were collected in the North Sea using a Waverider buoy in swell and wave growth situations. These data consist of 33 wave records and include some JONSWAP data as well as data from the severe storm of January 3, 1978 (Bouws, 1979). The wave records consist of time series of surface elevation (sampling rate 2 Hz) with a duration of approximately 20 minutes.

The random Fourier coefficient method (Tucker et al., 1984) was applied to generate relatively long time series of sea surface elevation. In this method, the sea surface  $\eta(t)$  consists of  $N$  values sampled at discrete times  $t_m$  with intervals  $\Delta t$ :

$$\eta(t_m) = \sum_{n=0}^{N/2} \{ a_n \cos(2\pi f_n t_m) + b_n \sin(2\pi f_n t_m) \} \quad (5.1)$$

in which  $f_n = n/(N\Delta t)$  and where the random Fourier coefficients,  $a_n$  and  $b_n$ , each are independent variables taken from a normal distribution with zero mean and variance  $S(f_n)\Delta f$  with  $S(f)$  the frequency spectrum. An inverse Fourier transform of the set of coefficients  $a_n$  and  $b_n$  then leads to the desired time series.

A total of 161 time series were generated, each with a time step of 0.5 s and a duration of 2 hours and 16 minutes. A JONSWAP spectrum was used to compute the random Fourier coefficients. The peak enhancement factor  $\gamma$  varied from 1.0 to 20 with a step of 0.125, and the peak period was 5.0 s. Typically, each wave record contained 2000 individual waves.

## 6 Sampling properties

It is well known that raw (unsmoothed) estimates of the spectral density  $S(f)$ , based on a single record, have a relatively large sampling variability. This is generally reduced by applying some smoothing at the expense of resolution. The four spectral parameters, considered here, all depend on integrals over the entire spectrum and therefore have a relatively small sampling variability (random error), regardless of the degree of smoothing. The same is true for the bias in the estimates of  $\nu$  and  $\kappa$ , because  $S(f)$  appears linearly in the integrals. For  $\kappa$  this is also because the cosine and sine terms in (4.4) vary slowly

compared to the unsmoothed estimate of  $S(f)$ . The parameters  $Q_p$  and  $Q_e$ , however, are proportional to an integral of the square of  $S(f)$ . Therefore, sampling variability in  $S(f)$  causes a positive bias in estimates of  $Q_p$  and  $Q_e$ .

As shown by Elgar et al. (1984), the expected value of  $Q_p$  is given by

$$E\{Q_p\} = Q_p(1 + 1/n) \quad (6.1)$$

in which  $n$  is the effective number of frequency bands. A similar analysis has been performed for the  $Q_e$  parameter, with similar result. The parameters  $\kappa$  and  $\nu$  are not affected by any smoothing of the spectrum, because they depend linearly on  $S(f)$ . For smoothly varying spectra (such as analytically expressed spectra),  $Q_p$  and  $Q_e$  are measures of peakedness in the sense of concentration of energy near a single frequency (which is the conventional interpretation), but for estimated spectra it is just as much a measure of all local peaks and thus of spectral roughness due to sampling variability. Therefore, the parameters  $Q_p$  and  $Q_e$  are no suitable spectral width parameters, and not even useful in relation to wave grouping (Van Vledder and Battjes, 1992).

The sampling properties of above parameters are given in Table 1, based on the analysis of a typical North Sea wind wave record.

$n$	$Q_p$	$Q_e$	$\kappa$	$\nu$
1	6.23	7.17	0.622	0.346
3	4.02	4.59	0.620	0.347
5	3.50	3.97	0.624	0.346
7	3.57	4.04	0.620	0.344
9	3.33	3.82	0.609	0.351

Table 1 Computed values of  $Q_p$ ,  $Q_e$ ,  $\kappa$  and  $\nu$  as a function of the number  $n$  of raw frequency bands used in the spectral smoothing.

The results confirm that estimates of the parameters  $\nu$  and  $\kappa$  are practically free of bias, whereas estimates of the parameters  $Q_p$  and  $Q_e$  are strongly biased. The results for the latter two parameters are nearly proportional to  $(1 + 1/n)$ , which is in agreement with the theoretical result of Elgar et al. (1984). The dependence of estimates of  $Q_p$  and  $Q_e$  on the amount of smoothing makes them unsuited as measure for spectral width, especially when the amount of smoothing is not known.

## 7 Effect of time series duration

Nelson (1987) and Medina and Hudspeth (1990) argue that long data records are required in order to reduce the variability in the estimates of wave group parameters to an acceptable level, since the standard deviation of group lengths is of the same order as their mean. Nelson (1987) recommends to use data records of at least 2 hours duration. Since such long data records are difficult to collect, time series of sufficient duration were generated numerically.

The effect of record duration on the variability of group length statistics was analyzed by using 153 simulated time series of 2 hours and 16 min duration, and by using 153 short time series with a duration of approximately 20 minutes. The results are shown in Fig. 1. Shown are the mean group lengths  $\bar{j}_1$  as a function of  $\rho_{HH,t}$ , together with the relation according to Kimura's theory.

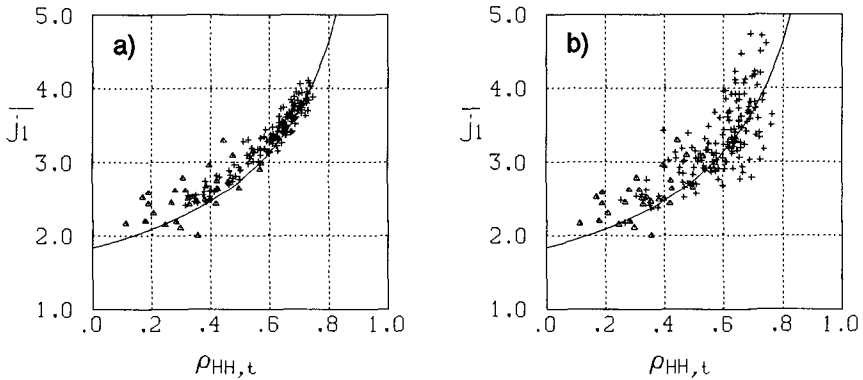


Fig. 1 Observed mean group lengths  $\bar{j}_1$  as a function of the correlation between successive wave heights  $\rho_{HH,t}$ . Triangles (field data), crosses (simulated data), solid line (relation 2.8). Panel a), simulated time series of 2 hour and 16 minutes duration, panel b) simulated time series of 18 minute duration.

These results show that long time series of surface elevation reduce the variability in estimates of the mean group length and correlation coefficient to an acceptable level (i.e. the data points cluster around the theoretical line). The results shown in panel b), are both based on time series of approximately 20 minute duration. As can be seen, the variability around the theoretical line is of the same order, both for field data and simulated data.

## 8 Effect of varying upper integration limit

The effect of changing the upper integration limit on the estimates of above four spectral parameters is shown in Fig. 2. Based on a simulated JONSWAP spectrum, the dimensionless upper integration limit  $f_{up}/f_p$  was varied over the range 1 to 4.

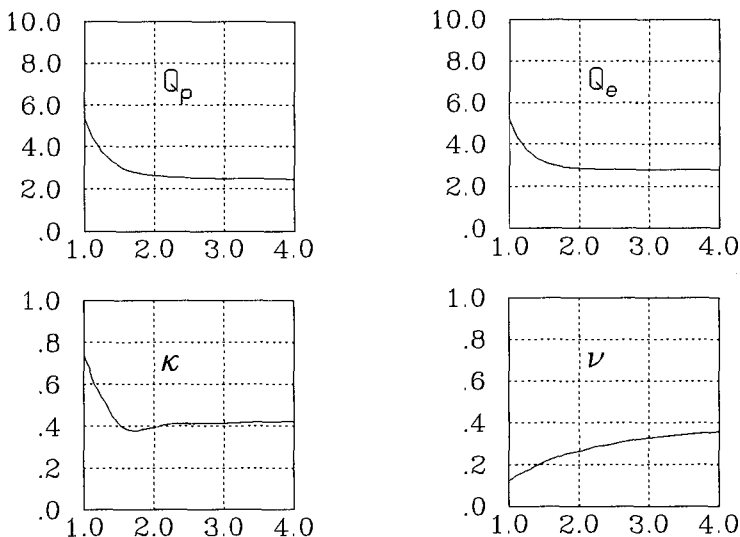


Fig. 2: Variation in the estimates of  $Q_p$ ,  $Q_e$ ,  $\kappa$  and  $\nu$  as a function of the dimensionless upper integration limit  $f_{up}/f_p$ .

The results indicate that for  $f_{up}/f_p > 2$  the  $\kappa$  parameter is converged to a limiting value, whereas for  $f_{up}/f_p > 3$  the  $Q_p$  and  $Q_e$  are converged to their final value. The  $\nu$  parameter, however, is still increasing for  $f_{up}/f_p = 4$ . These results indicate that the  $\kappa$  is least sensitive to the choice of the upper integration limit.

## 9 Spectral computation of correlation coefficient

As noted by Battjes and Van Vledder (1984), IAHR (1992), Chandler and Masson (1992), the spectrally computed coefficient of correlation between successive wave heights  $\rho_{HH,f}(T_{m0.2})$  is consistently smaller than its time domain estimate  $\rho_{HH,t}$ . This is illustrated in Fig. 3. Possible reasons for this underestimation have been considered by Stam (1988),

who identified 3 assumptions used in the derivation of the joint distribution of succeeding wave heights:

- 1 The underlying stochastic process is Gaussian,
- 2 the frequency spectrum is narrow, and
- 3 the joint distribution of two values of the amplitude envelope  $R(t)$  and  $R(t + \tau)$  is translated into the joint distribution of succeeding wave heights by defining succeeding wave heights as twice the values of  $R(t)$  and  $R(t + T_{m02})$ , respectively.

The first, Gaussian, assumption implies that the sea surface can be considered as a linear sum of mutually independent harmonic components. Possible non-linearities would increase the difference between the time and frequency domain estimates of the correlation coefficient. A possible effect of non-linearities has been investigated by Stam (1988) by analyzing wave flume experiments with different values of the ratio of water depth  $d$  over the deep water wave length  $L_0$ . These investigations indicate that non-linearities have a negligible effect. Thus, the linear assumption is not inconsistent with Stam's experiments. The linear assumption is also supported in the literature (e.g. Elgar et al., 1984; Chandler and Masson, 1992).

The second assumption is related to the existence of a well defined envelope. As argued by Battjes (1974), the assumption of a narrow spectrum is not necessary for the validity of the bi-variate Rayleigh distribution. The validity of this distribution was verified by computing the  $\kappa$  parameter directly in the time domain and comparing it with  $\rho_{HH,t}$ . As noted by Battjes (1974),  $\kappa^2$  is equal to the coefficient of linear correlation between squared succeeding wave heights:

$$\kappa_{HH,t}^2 = \frac{\frac{1}{N-1} \sum_{i=1}^{N-1} (H_i^2 - \bar{H}^2)(H_{i+1}^2 - \bar{H}^2)}{\frac{1}{N} \sum_{i=1}^N (H_i^2 - \bar{H}^2)^2} \tag{9.1}$$

The relation between  $\rho_{HH,t}$  and  $\kappa_{HH,t}$  is illustrated in Fig. 4, together with the theoretical relation (2.8). The agreement is good, which supports the validity of the bi-variate Rayleigh distribution.

The third assumption, a wave height is twice the amplitude at the time of a wave crest, is only valid for narrow spectra. For broader spectra, the use of wave envelope can underestimate, as well as over-estimate computed wave heights. This will affect the correlation between succeeding wave heights in case wave heights are based on wave amplitude values. Following Stam (1988), this was inspected by computing the correlation between succeeding wave crests (or maximum amplitudes). To that end the correlation coefficient between succeeding wave crests (or maximum amplitudes)  $\rho_{AA,t}$  was computed:



$$\rho_{AA,t} = \frac{\frac{1}{N-1} \sum_{i=1}^{N-1} (A_i - \bar{A})(A_{i+1} - \bar{A})}{\frac{1}{N} \sum_{i=1}^N (A_i - \bar{A})^2} \tag{9.2}$$

in which  $\bar{A}$  is the mean crest elevation. Estimates of this correlation coefficient have been compared with time domain estimates of the  $\kappa$  parameter, defined similarly as  $\kappa_{HH,t}$ , but now in terms of wave amplitudes:

$$\kappa_{AA,t}^2 = \frac{\frac{1}{N-1} \sum_{i=1}^{N-1} (A_i^2 - \bar{A}^2)(A_{i+1}^2 - \bar{A}^2)}{\frac{1}{N} \sum_{i=1}^N (A_i^2 - \bar{A}^2)^2} \tag{9.3}$$

Inspection of the relation between  $\rho_{AA,t}$  and  $\kappa_{AA,t}$  (not shown here) gives an even better agreement with theory (Eq. 2.8) than between  $\kappa_{HH,t}$  and  $\rho_{HH,t}$ . These results suggest that the bi-variate Rayleigh distribution is better suited to describe the joint distribution of succeeding wave amplitudes than of succeeding wave heights. Based on this notion, the relation between  $\rho_f(T_{m02})$  and  $\kappa_{AA,t}$  was investigated. The result thereof is shown in Fig. 5.

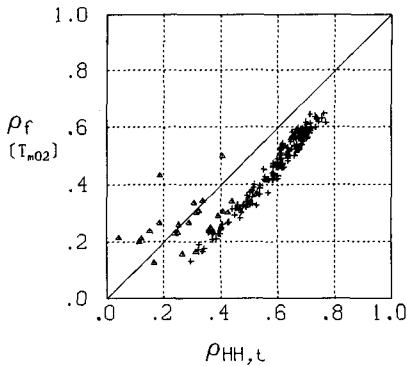


Fig. 3: Relation between  $\kappa_{HH,t}$  and  $\rho_{HH,t}$ . Crosses (simulation data), triangles (field data).

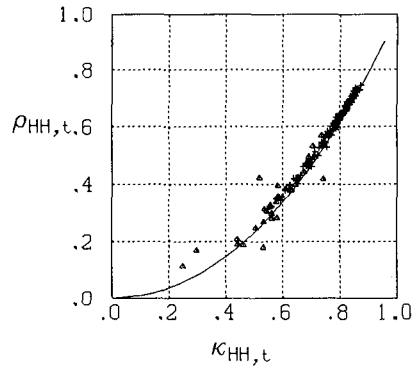


Fig. 4 Relation between  $\kappa_{AA,t}$  and  $\rho_f(T_{m02})$ , Crosses (simulation data), triangles (field data),

solid line (relation 2.8).

Fig. 4 shows good agreement between  $\kappa_{HH,t}$  and  $\rho_{HH,t}$  according to theory. The agreement between  $\kappa_{AA,t}$  and  $\kappa_f(T_{m02})$  is rather good which implies that theory of envelope statistics is applicable to wave heights, but not to wave heights. The difference between  $\kappa_{HH,t}$  and

$\kappa_f(T_{m02})$  can be attributed to the transformation of amplitudes to wave heights by a factor 2.

The assumption that the wave height is twice the value of the amplitude envelope at the time of a wave crest was considered by Tayfun (1990). An improved estimate of the wave height is to define a wave height as the sum of two values of the wave envelope separated by a time lag of half a wave period  $T$ :

$$H = A(t) + A\left(t + \frac{1}{2} T\right) \tag{9.4}$$

Substitution of Eqs. (9.4) into the definition of the correlation coefficient gives (Van Leeuwen, 1988):

$$\hat{\rho}_{HH} = \frac{\text{cov}\left(A(t_i) + A(t_i + \frac{1}{2}T), A(t_i + T) + A(t_i + \frac{3}{2}T)\right)}{\sigma\left(A(t_i) + A(t_i + \frac{1}{2}T)\right)\sigma\left(A(t_i + T) + A(t_i + \frac{3}{2}T)\right)} \tag{9.5}$$

Elaboration of Eq. (9.5) leads to:

$$\hat{\rho}_{HH,t} = \frac{\rho_{HH,f}\left(\frac{1}{2}T\right) + 2\rho_{HH,f}(T) + \rho_{HH,f}\left(\frac{3}{2}T\right)}{2 + 2\rho_{HH,f}\left(\frac{1}{2}T\right)} \tag{9.6}$$

In addition, the effect of finite bandwidth on the mean zero-crossing wave period is considered. Such a correction was given by Tayfun (1990):

$$\hat{T} = T_{m02}\left(1 - \frac{1}{2}v^2\right) \tag{9.7}$$

with  $v$  the spectral width parameter proposed by Longuet-Higgins (1975). Replacing the wave period  $T$  in Eq. (9.6) by the corrected expression of Eq. (9.7) gives:

$$\hat{\rho}_{HH,t} = \frac{\rho_{HH,f}\left(\frac{1}{2}\hat{T}\right) + 2\rho_{HH,f}(\hat{T}) + \rho_{HH,f}\left(\frac{3}{2}\hat{T}\right)}{2 + 2\rho_{HH,f}\left(\frac{1}{2}\hat{T}\right)} \tag{9.8}$$

The results of the improved method of computing the correlation coefficient between successive wave heights from the spectrum are shown in Fig. 6.

The effect of these corrections is to remove almost all of the bias in the spectral computation of the correlation coefficient between succeeding wave heights.

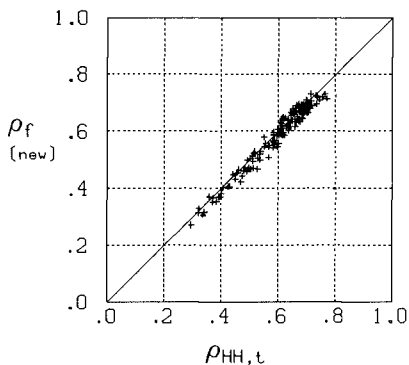
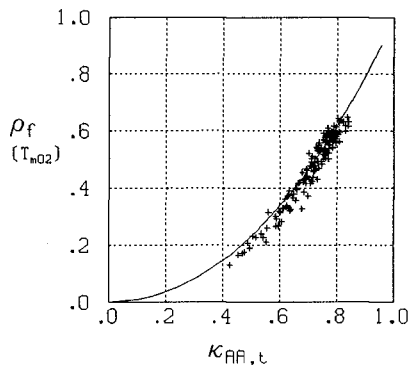


Fig. 5 Relation between  $\kappa_{AA,t}$  and  $\rho_f(T_{m02})$  Fig. 6: Relation between  $\rho_{HH,t}$  and  $\hat{\rho}_f$

## 10 Conclusions

- the mean group length is independent of the group length distribution.
- statistical variability distorts the inter-relationship between the parameters  $Q_p$ ,  $Q_e$ ,  $\kappa$  and  $\rho_{HH,t}$ , as proposed by Medina and Hudspeth (1990).
- the  $Q_p$ ,  $Q_e$  and  $\nu$  parameters are not suited as spectral group parameters.
- the  $\kappa$  parameter is a good parameter to relate wave grouping with the spectral shape.
- the  $Q_p$  and  $Q_e$  parameter are not suited as measures for the spectral width.
- long data records are necessary to decrease the variability in group length statistics to an acceptable level.
- the  $\kappa$  parameter is not sensitive to spectral smoothing, and least sensitive to the choice of the upper integration limit.
- the improved method of computing the spectral correlation coefficient removes practically all bias with respect to previous computations. This improved method enhance the applicability of the  $\kappa$  parameter in relation to wave grouping.

## References

- Arhan, M. and R. Ezraty, 1978: Statistical relations between successive wave heights. *Oceanologica Acta*, Vol. 1, 151-158.
- Battjes, J.A., 1974: Computation of set-up, longshore currents, run-up and overtopping due to wind-generated waves, Ph.D. thesis, Delft University of Technology.
- Battjes, J.A. and G.Ph. van Vliedder, 1984: Verification of Kimura's theory for wave group statistics. Proc. 19th Int. Conf. on Coastal Engineering, 642-648.

- Bouws, E., 1978: Spectra of extreme wave condition in the southern North Sea considering the influence of water depth. AREA Conference on sea climatology, Paris, 51-69.
- Chandler, P. and D. Masson, 1992: Wave groups in coastal waters, Proc. 3rd Int. Symp. on Wave Hindcasting and Forecasting, Montreal, 79-88.
- Elgar, S., Guza, R.T. and R.J. Seymour, 1984: Groups of waves in shallow water, J. Geophys. Res., Vol. 89, C3, 3623-3634.
- Goda, Y., 1970: Numerical experiments on wave statistics with spectral simulation. Rep. Port Harbour Res. Inst., Vol. 9, No. 3.
- Goda, Y. 1976: On wave groups, Proc. BOSS'76, Trondheim, Vol. 1, 115-128.
- IAHR working group, 1992: Closure by IAHR working group on wave generation and analysis, Journal of Waterway, Port, Coastal and Ocean Engineering, Vol. 118, 228-230.
- Kimura, A., 1980: Statistical properties of random waves, Proc. 17th Int. Conf. on Coastal Engineering, 2955-2973.
- Longuet-Higgins, 1975: On the distribution of the periods and amplitudes of sea waves, Journal of Geophysical Res., Vol. 86 (C5), 4299-4301.
- Longuet-Higgins, M.S., 1984: Statistical properties of wave groups in a random sea state. Phil. Trans. R. Soc. London. Ser. A, Vol. 312, 219-250.
- Medina, J.R. and R.T. Hudspeth, 1987: Sea states defined by wave height and period functions. Proc. IAHR Seminar Wave Analysis and Generation in Laboratory Basins, 22nd IAHR Congress, 249-259.
- Medina, J.R. and R.T. Hudspeth, 1990: Analyses of ocean wave groups, Coastal Engineering, Vol. 14, 515-542.
- Nelson, R.C., 1987: Wave groups - The length of a Piece of String, Proc. 8th Australasian Conference on Coastal and Ocean Engineering, Launceston, 1-4.
- Rice, S.O., 1944: The mathematical analysis of random noise, Bell Syst. Tech. Journal, Vol. 23, 282-332.
- Stam, C.J., 1988: The correlation parameter in the bi-variate Rayleigh probability density function of succeeding wave heights, a comparison of computation methods. Report M1983/H198, Delft Hydraulics, Delft Univ. of Technology (in Dutch).
- Tayfun, M.A., 1990: Distribution of large wave heights, Journal of Waterway, Port, Coastal, and Ocean Engineering, Vol. 116, No. 6, 686-707.
- Tucker, M.J., P.G. Challenor, and D.J.T. Carter, 1984: Numerical simulation of a random sea: a common error and its effect on wave group statistics. Applied Ocean Res., Vol. 6, No. 2, 118-122.
- Van Leeuwen, P.J., 1988: private communication, Delft University of Technology.
- Van Vledder, G.Ph., 1983: Verification of Kimura model for the description of wave groups. Report R/1983/6/H, Delft University of Technology, Department of Civil Engineering.
- Van Vledder, G.Ph. and J.A. Battjes, 1992: Discussion on 'List of sea state parameters', J. of Waterway, Port, Coastal and Ocean Engineering, Vol. 118, 226-228.

## CHAPTER 72

### VERIFICATION OF A ONE-DIMENSIONAL SURFBEAT MODEL AGAINST LABORATORY DATA

J.A. Roelvink, H.A.H. Petit and J.K. Kostense

DELFT HYDRAULICS, P.O. Box 152, 8300 AD Emmeloord

#### ABSTRACT

A mathematical model is presented which describes cross-shore low-frequency motions generated by shoaling and breaking of wave-groups on a beach. The numerical scheme is tested against known analytical solutions for standing waves on a plane beach. Model results are compared with laboratory experiments (Kostense, 1984) which refer to bichromatic carrier waves incident on a plane beach. It is shown that, apart from a good representation of the trends found in the experimental study, for realistic values of the breaking and friction coefficients the computational results also quantitatively agree surprisingly well with the experiments.

#### INTRODUCTION

Low-frequency motions on the time-scale of wave groups can have significant effects on cross-shore morphology, both in the inner nearshore region, where sometimes they even dominate over motions at wind-wave frequencies, and elsewhere in the nearshore region, through their interaction with the wave groups. Their effect on cross-shore morphology has been shown to be of the same order of magnitude as other mechanisms, such as return flow and wave asymmetry (Roelvink and Stive, 1989).

Several aspects of long-wave generation inside and outside the surf zone have been addressed in literature (e.g. Longuet-Higgins and Stewart, 1962; Symonds et al, 1982; Abdelrahman and Thornton, 1987; Schaeffer and Jonsson, 1990; List, 1992). The models presented in these references are strongly schematized in either the hydrodynamic equations or the bottom geometry and are not meant to be predictive models for arbitrary waves on an arbitrary profile. Some first attempts towards this were presented in Roelvink (1991), Symonds and Black (1991) and Sato (1991).

The purpose of the model presented here is to predict the cross-shore structure of the incident wave groups, the long waves generated inside and outside the surfzone, and their combined effect on sediment transport, for random waves incident perpendicular to a uniform beach of arbitrary profile. The model is

time-dependent on the time-scale of wave groups; the basic formulations have been described in Roelvink (1991).

In the paper we will discuss the model formulations; the numerical scheme will be outlined and tested against analytical solutions of parts of the problem. The model is then compared with experiments with bichromatic waves on a plane beach and the sensitivity of the model for the dissipation coefficients is investigated.

## MODEL FORMULATIONS

The model solves simultaneously a set of three short-wave averaged balance equations, viz. for momentum, continuity and wave energy. Closure relations which relate i.e. radiation stress to wave energy are derived from linear theory. Wave breaking is incorporated by means of an empirical formulation, which relates the dissipation rate to the local wave energy and the water depth.

The balance equations are: the momentum equation for the long waves,

$$\frac{\partial}{\partial t} Q_t + \frac{\partial}{\partial x} \left[ \frac{(Q_t - Q_w)^2}{h} + \frac{S_{xx}}{\rho} + \frac{1}{2}gh^2 \right] = gh \frac{\partial d}{\partial x} + \tau_b \quad (1)$$

the continuity equation for the long waves,

$$\frac{\partial}{\partial t} h + \frac{\partial}{\partial x} Q_t = 0 \quad (2)$$

and the wave action equation, reduced to a wave energy balance equation:

$$\frac{\partial}{\partial t} E + \frac{\partial}{\partial x} EC_g = -D \quad (3)$$

Here,  $h$  is the water depth,  $Q_t$  is the total flux,  $Q_w$  is the wave-induced flux,  $S_{xx}$  is the radiation stress,  $\rho$  is the density of the water,  $g$  is the acceleration of gravity,  $d$  is the still water depth,  $\tau_b$  is the bottom shear stress,  $E$  is the short wave energy and  $C_g$  is the group velocity of the short waves.

Additional equations are required to close the system of equations; very common ones are used here:

$$\tau_b = \frac{1}{2}\rho f_w \left| \frac{Q_t}{h} \right| \left| \frac{Q_t}{h} \right| \quad (4)$$

where  $f_w$  is a friction coefficient;

$$S_{xx} = \left[ 2 \frac{C_g}{C} - \frac{1}{2} \right] E \quad (5)$$

$$Q_w = \frac{E}{\rho C} \quad (6)$$

$$C = \frac{\omega}{k} \quad (7)$$

$$C_g = \frac{\partial \omega}{\partial k} = \frac{g}{2\omega} \left( \tanh(kh) + kh [1 - \tanh^2(kh)] \right) \quad (8)$$

Here,  $\omega$  is a representative angular frequency of the short waves and  $k$  is a representative wave number.

The short wave energy dissipation is modelled according to Roelvink (1992) as:

$$D = 2\alpha f E \left[ 1 - \exp \left[ - \left[ \frac{\sqrt{8E/\rho g}}{\gamma h} \right]^n \right] \right] \quad (9)$$

where  $f$  is a representative short wave frequency and  $\alpha$ ,  $\gamma$  and  $n$  are coefficients, with optimum values for random waves of 1.0, 0.55 and 10, respectively.

With the help of these additional equations, equations (1) through (3) are solved simultaneously for a given profile and boundary conditions for  $E$ ,  $Q_t$  and  $h$  at the seaward boundary.

#### NUMERICAL SCHEME

The differential equations are solved by a finite difference, second-order Richtmyer scheme on a nonequidistant moving grid of which the landward boundary moves up and down with the waterline. This is achieved by applying a transformation to the equations as described below.

The set of equations we want to transform can in Cartesian coordinates be described as:

$$\frac{\partial v}{\partial t} + \frac{\partial f(v)}{\partial x} = o(v) \frac{\partial p}{\partial x} + q(v) \quad (10)$$

where the functions  $f$  and  $q$  need not be linear in their arguments.

We now use a transformation to general time dependent coordinates of the following form:

$$\tau = t \quad (11)$$

$$\xi = \frac{\int_0^x W(\zeta) d\zeta}{\int_0^{x_0} W(\zeta) d\zeta} \quad (12)$$

This transformation transforms the interval in the  $x$ -domain:  $[0, X_r(t)]$  which depends on the time coordinate  $t$ , to the fixed interval  $[0, 1]$  in the  $\xi$  domain. The transformation to the  $\tau$  domain is trivial.

In order that the inverse transformation functions  $x(\tau, \xi)$  and  $t(\tau)$  exist the function  $W$  has to be chosen such that it does not change sign in the interval  $[0, X_r(t)]$ .

The function  $X_r(t)$  is the solution of an ordinary differential equation:

$$\frac{dX_r(t)}{dt} = S(v(t, X_r(t))) = u(t, X_r(t)) \quad (13)$$

In the new coordinate system the set of differential equations becomes:

$$\frac{\partial}{\partial \tau} (T_1(\tau, \xi) \hat{v}(\tau, \xi)) + \frac{\partial}{\partial \xi} (T_2(\tau, \xi) \hat{v}(\tau, \xi) + f(v(\tau, \xi))) = T_1(\tau, \xi) (o(\hat{v}(\tau, \xi)) \hat{p}_x(\tau, \xi) + q(\hat{v}(\tau, \xi))) \quad (14)$$

$$\frac{dX_r(\tau)}{d\tau} = \hat{u}(\tau, 1) \quad (15)$$

where,

$$T_1(\tau, \xi) = \frac{\int_0^{x(\tau, \xi)} W(\zeta) d\zeta}{W(x(\tau, \xi))}, \quad T_2(\tau, \xi) = - \frac{\xi W(X_r(\tau))}{W(x(\tau, \xi))} \frac{dX_r(\tau)}{d\tau}$$

$$\hat{v}(\tau, \xi) = v(\tau, x(\tau, \xi)) \text{ and } \hat{p}_x(\tau, \xi) = \frac{dp}{dx}(x(\tau, \xi)).$$

In the appendix a derivation of equation (14) is given.

Equation (14) can be written as:

$$\frac{\partial V}{\partial \tau} + \frac{\partial F(V, \tau, \xi)}{\partial \xi} = R(V, \tau, \xi), \quad (16)$$

so it has exactly the same structure as Eq.(10).

The discretization used to solve the set of differential equations (14) in the  $(\tau, \xi)$  domain is done on an equidistant grid:

$$\xi_i = \frac{i}{N} \text{ for } i=0(1)N.$$

The time steps are constant as well:  $\tau_j = j\Delta\tau$  and therefore  $t_j = j\Delta\tau$ .

In the physical domain  $(t, x)$  this introduces a non-equidistant grid with grid points  $x_i^j$  which satisfy the equation:

$$\xi_i = \frac{i}{N} = \frac{\int_0^{x_i^j} W(\zeta) d\zeta}{\int_0^{x(\tau_j)} W(\zeta) d\zeta} \quad \text{for } i=0(1)N \quad (17)$$



The weight function  $W$  can be chosen in such a way that near to regions where the physics becomes more interesting a grid refinement can be realized.

The scheme we use is Richtmeyer's predictor corrector scheme; the discretization of Eq.(16) now becomes:

Predictor:

$$V_{i+1/2}^{j+1/2} = \frac{1}{2}(V_{i+1}^j + V_i^j) - \frac{\Delta\tau}{2\Delta\xi}(F_{i+1}^j - F_i^j) + \frac{\Delta\tau}{4}(R_{i+1}^j + R_i^j) \tag{18}$$

where  $F_{i+1}^j = F(V_{i+1}^j, \tau_j, \xi_{i+1})$  ,  $R_{i+1}^j = R(V_{i+1}^j, \tau_j, \xi_{i+1})$  ,

$F_{i+1/2}^{j+1/2} = F(V_{i+1/2}^{j+1/2}, \tau_{j+1/2}, \xi_{i+1/2})$  and  $R_{i+1/2}^{j+1/2} = R(V_{i+1/2}^{j+1/2}, \tau_{j+1/2}, \xi_{i+1/2})$

$$X_r^{j+1/2} = X_r^j + \frac{\Delta\tau}{48}(34 \hat{u}(\tau_j, 1) - 14 \hat{u}(\tau_{j-1}, 1) + 4 \hat{u}(\tau_{j-2}, 1)) \tag{19}$$

$$x_{i+1/2}^{j+1/2} \text{ is solved from } \xi_{i+1/2} = \frac{i+1/2}{N} = \frac{\int_0^{x_{i+1/2}^{j+1/2}} W(\zeta) d\zeta}{\int_0^{X_r^{j+1/2}} W(\zeta) d\zeta} \text{ for } i=0(1)N-1.$$

Corrector:

$$V_i^{j+1} = V_i^j - \frac{\Delta\tau}{\Delta\xi}(F_{i+1/2}^{j+1/2} - F_{i-1/2}^{j+1/2}) + \frac{\Delta\tau}{2}(R_{i+1/2}^{j+1/2} + R_{i-1/2}^{j+1/2}) \tag{20}$$

$$X_r^{j+1} = X_r^j + \frac{\Delta\tau}{12}(23 \hat{u}(\tau_j, 1) - 16 \hat{u}(\tau_{j-1}, 1) + 5 \hat{u}(\tau_{j-2}, 1)) \tag{21}$$

$$x_i^{j+1} \text{ is solved from: } \xi_i = \frac{i}{N} = \frac{\int_0^{x_i^{j+1}} W(\zeta) d\zeta}{\int_0^{X_r^{j+1}} W(\zeta) d\zeta} \text{ , for } i=0(1)N.$$

The schemes that are used to solve Eq.(15) are (19) and (21), these are both third order Adams-Bashforth methods.

The linear stability condition for the Richtmeyer scheme is

$$\frac{\lambda\Delta\tau}{\Delta\xi} \leq 1 \tag{22}$$

where  $\lambda$  is the largest eigenvalue of  $\partial F/\partial V$  in absolute sense.

The largest eigenvalue of  $\partial f/\partial v$  in equation (10) can be approximated by  $u + \sqrt{gh}$  .

Since  $T_1$  and  $T_2$  are both scalar functions, the largest eigenvalue in the transformed problem (14) becomes:

$$\lambda = \frac{T_2}{T_1} + \frac{\hat{u} + \sqrt{gh}}{T_1}$$

Stability condition (22) can now be written as:

$$W(x(\tau, \xi)) \hat{u}(\tau, \xi) - \xi W(X_r(\tau)) \frac{dX_r}{d\tau} + W(x(\tau, \xi)) \sqrt{g \hat{h}(\tau, \xi)} \leq \frac{\Delta \xi}{\Delta \tau} \int_0^{X_r(\tau)} W(\zeta) d\zeta \quad (23)$$

The condition we use to replace Eq.(23) is:

$$W(x(\tau, \xi)) \sqrt{g(\hat{h}(0, \xi) + \epsilon)} \leq \frac{\Delta \xi}{\Delta \tau} \int_0^{X_r(\tau)} W(\zeta) d\zeta \quad (24)$$

here  $\hat{h}(0, \xi)$  is the still water depth and  $\epsilon$  is a small positive number. A convenient weight function now becomes:

$$W(x) = \frac{1}{\sqrt{g(h(0, x) + \epsilon)}}$$

With this choice the CFL stability condition (23) can now be replaced by:

$$\Delta \tau \leq \Delta \xi \int_0^{X_r(\tau)} \frac{1}{\sqrt{g(h(0, x) + \epsilon)}} dx \quad (25)$$

By replacing  $X_r(\tau)$  in Eq.(25) by a lower boundary of  $X_r(\tau)$  we found a constant value for  $\Delta \tau$ .

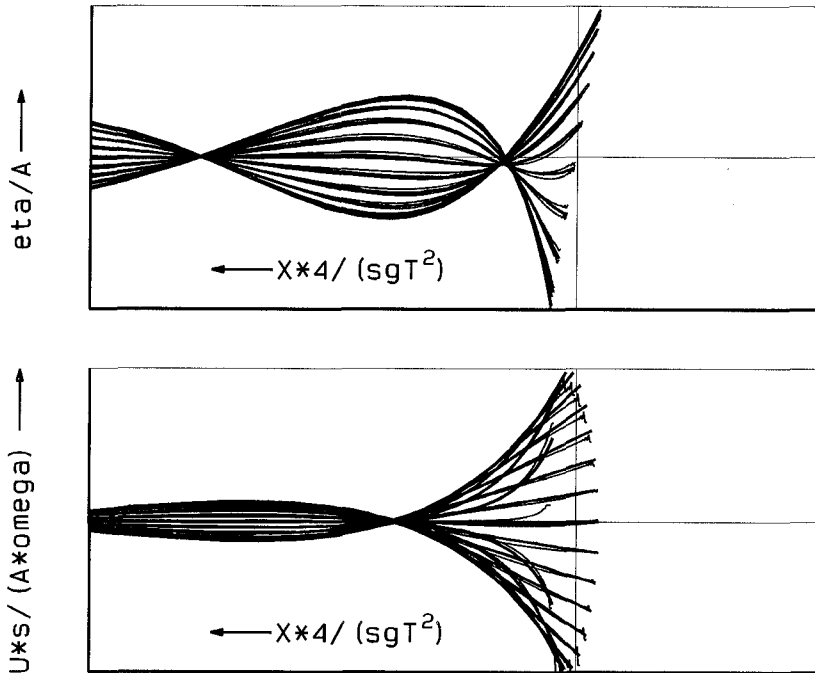
The scheme is compared with analytical solutions of standing long waves on a plane beach as given by Carrier and Greenspan (1957); an example is given in Figure 1. Very small deviations occur at the shoreline, which disappear with increasing number of grid points.

## MODEL RESULTS AND SENSITIVITY ANALYSIS

Model results are compared with laboratory experiments by Kostense (1984), which refer to wave channel tests of bichromatic waves on a plane beach. The experiments were carried out with active wave absorption and second order wave generation, enabling undisturbed, stable and accurate measurements. They cover a range of primary frequencies, group frequencies, amplitudes and modulation rates and are therefore well suited to verify the predictive ability of the model. The primary waves in these tests were made up of two frequencies generated in a water depth of 0.50 m and broke on a plane cemented beach of a 1:20 slope after travelling over a horizontal stretch. In Table 1 below, the ranges of frequency and amplitude of the primary waves are given. In series A, B and E, the effect of varying the difference frequency is studied for fixed primary wave amplitudes; in series C and D the effect of varying the primary wave amplitude is shown for a fixed difference frequency. Series A through D were carried out with weakly modulated waves; series E with strongly modulated primary waves.

For a given set of primary waves, the input boundary conditions for the numerical model are defined by:

$$E = \rho g \left[ \frac{1}{2}(\hat{\eta}_1^2 + \hat{\eta}_2^2) + \hat{\eta}_1 \hat{\eta}_2 \cos(\Delta \omega t) \right] \quad (26)$$



**Figure 1.** Comparison of numerical (thin lines) and analytical (thick lines) solution of standing long wave on a plane sloping beach; dimensionless elevation (top) and velocity (bottom).

Series	$\hat{\eta}_1$ (m)	$\frac{\hat{\eta}_2}{\hat{\eta}_1}$ (m)	$\omega_1$ (rad/s)	$\Delta\omega$ (rad/s)
A	0.055	0.2	3.1	0.3-0.9
B	0.055	0.2	4.1	0.3-0.9
C	0.035-0.080	0.2	4.1	0.77
D	0.030-0.055	0.2	3.1	0.61
E	0.035	0.8	4.3	0.3-0.9

**Table 1.** Ranges of primary wave parameters in Kostense experiment.

The accompanying bound long wave, which is also generated in the experiment, is given by Longuet-Higgins and Stewart (1964):

$$h - \bar{h} = - \frac{1}{\rho} \left[ \left( 2 \frac{C_g}{C} - 0.5 \right) / (gh - C_g^2) \right] \hat{\eta}_1 \hat{\eta}_2 \cos(\Delta\omega t) \tag{27}$$

$$Q_t = - \frac{C_g}{\rho} \left[ \left( 2 \frac{C_g}{C} - 0.5 \right) / (gh - C_g^2) \right] \hat{\eta}_1 \hat{\eta}_2 \cos(\Delta \omega t) \quad (28)$$

In order to prevent re-reflection of long waves at the seaward boundary, a weakly reflective boundary condition is used as described in Roelvink (1991).

The procedure to hindcast these the experiments is as follows. For a given set of primary waves, the model is run until a periodic solution is reached. The surface elevation time series are then split into three components, viz. the incoming bound wave, the reflected free wave and an incoming free wave. Incoming free waves are negligible since they are not generated and since the weakly reflective boundary condition allows waves reflected from the beach to propagate out of the model. The amplitudes of the incoming bound wave and the reflected free wave are determined by harmonic analysis. Per series A through E, approximately twenty such runs are carried out to cover the range of the free parameter for each series.

The numerical model contains empirical coefficients in the description of the dissipation of short waves by wave breaking, and of the dissipation of long waves by bottom friction. For random waves, a standard set of values for the wave breaking coefficients can be applied, as is shown in Roelvink (1992). A key factor here is the coefficient  $\gamma$ , which is proportional to the average breaking wave height over water depth ratio, and is set at 0.55 for random waves. For bichromatic waves, this ratio should be significantly higher; a reasonable estimate appears to be 0.75. Because of the uncertainty in this value, computations are performed for  $\gamma$ -values of 0.55, 0.75 and 0.90.

Since there is no accurate description of the bottom friction under combined short and long waves, the simplest possible formulation as in eq. (4) is applied. Computations are performed for three values of  $f_w$ : 0.00, 0.02 and 0.05. The variations in  $f_w$  are applied for a fixed  $\gamma$ -value of 0.75; the variations in  $\gamma$  for a fixed  $f_w$ -value of 0.02.

The results for series A through E are shown in Figures 2 through 6, respectively. In all cases, the bound long wave amplitude is predicted accurately; it does not depend on either of the coefficients. The increase in the bound wave amplitude for increasing difference frequency is due to the slight decrease in the mean of the primary frequencies. As expected, the bound wave amplitude increases quadratically with increasing primary wave amplitude.

The amplitudes of the reflected free waves show interesting interference patterns which are represented quite well by the model. Schaffer and Jonsson (1990) already concluded based on a comparison between their model and these data, that frictional effects must be important. Especially for the higher group frequencies this appears to be the case. A reasonable value for the friction factor of 0.02 appears to give acceptable quantitative agreement for all series.

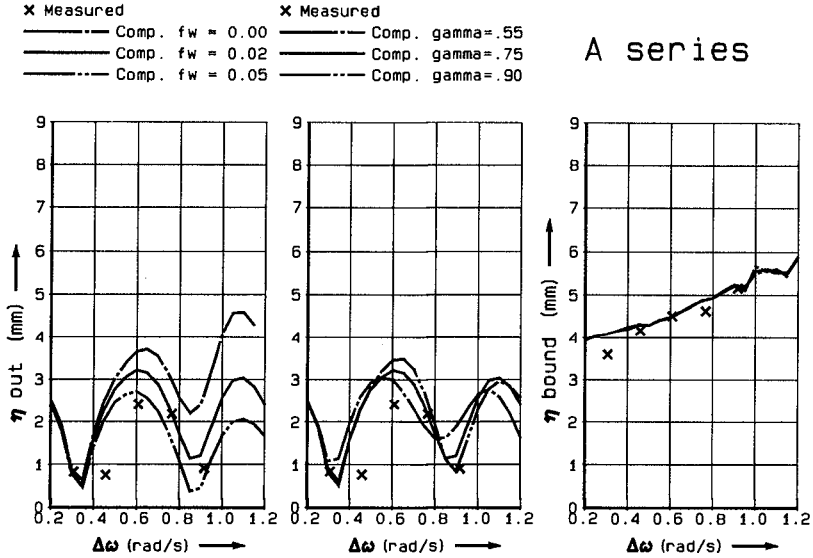


Figure 2. Measured and computed amplitudes of free reflected and bound long wave elevation against difference frequency  $\Delta\omega$ ; series A.

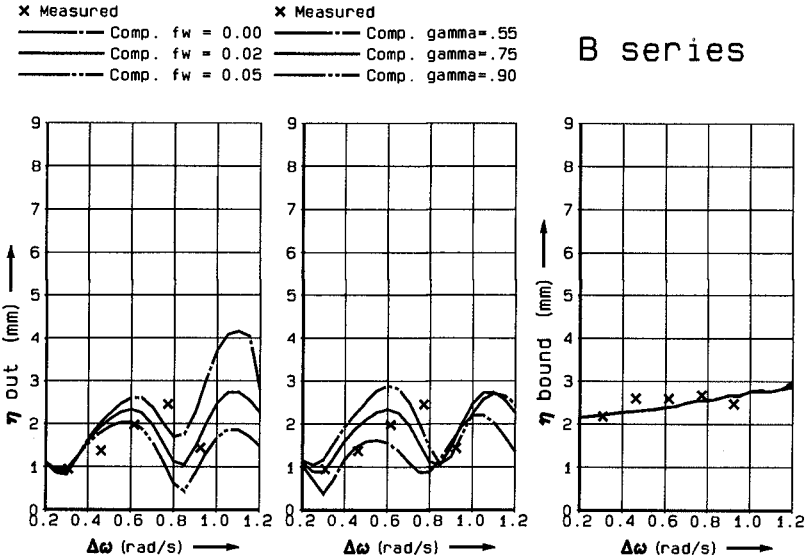
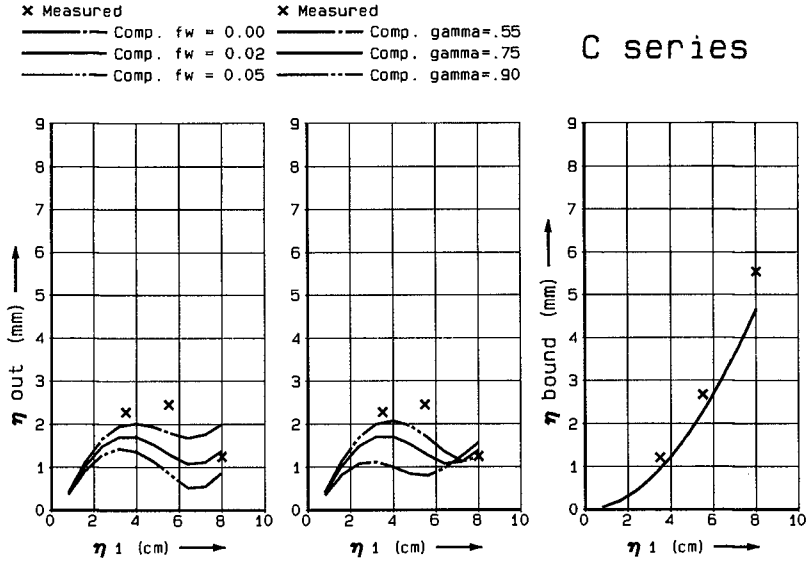
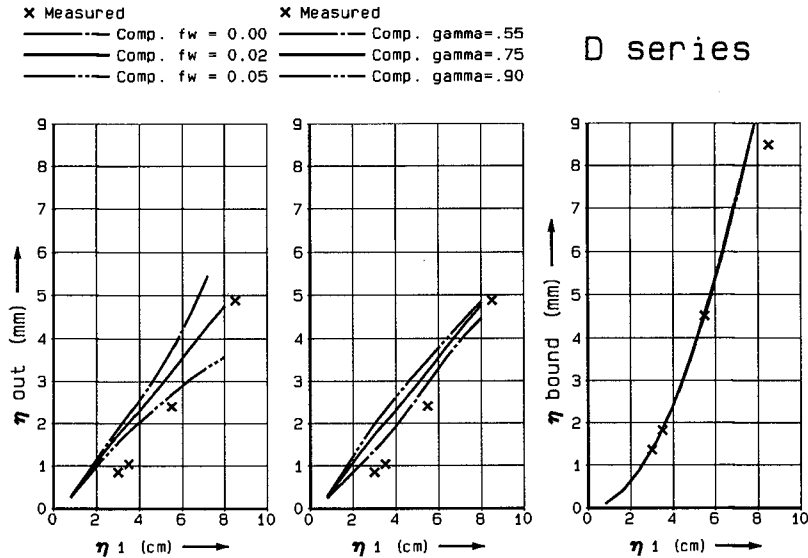


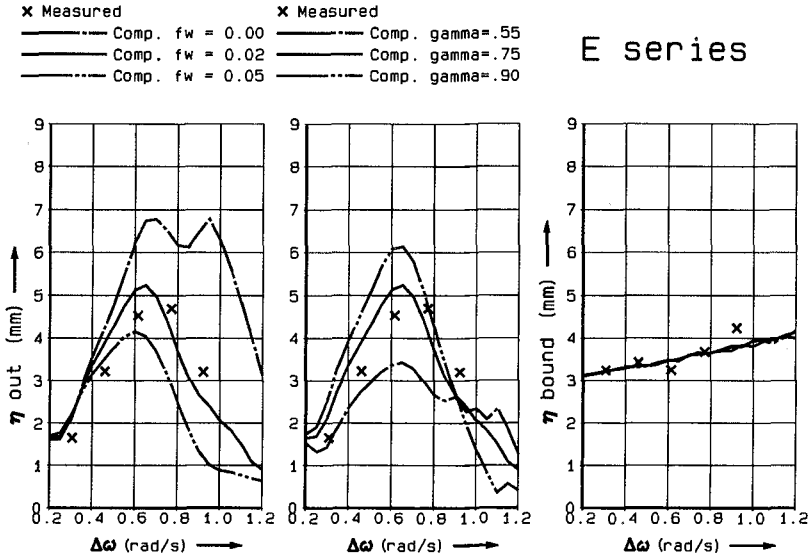
Figure 3. Measured and computed amplitudes of free reflected and bound long wave elevation against difference frequency  $\Delta\omega$ ; series B.



**Figure 4.** Measured and computed amplitudes of free reflected and bound long wave elevation against primary wave amplitude  $\hat{\eta}_1$ ; series C.



**Figure 5.** Measured and computed amplitudes of free reflected and bound long wave elevation against primary wave amplitude  $\hat{\eta}_1$ ; series D.



**Figure 6.** Measured and computed amplitudes of free reflected and bound long wave elevation against difference frequency  $\Delta\omega$ ; series E.

The model results are not extremely sensitive to variations in the breaker parameter  $\gamma$ . A reasonable value of 0.75 for these bichromatic waves gives acceptable results for all series.

The prediction of the reflected free wave amplitude for highly modulated waves in series E is quite accurate; no previous model results on this case have been presented in literature.

A disadvantage of this numerical model is, that it is not possible to separate different mechanisms of long wave generation, viz. the reflection of bound long waves, the break point mechanism or the shoreline set-up mechanism. Probably all of these mechanisms are important at times; the results indicate that no serious errors in the representation of any mechanism have been made.

**CONCLUSION**

The numerical model SURFBEAT appears to contain the necessary physics to predict long wave generation in the nearshore zone. Since it can be run with arbitrary boundary conditions over an arbitrary profile, it can be used to model realistic situations where cross-shore processes are dominant.

## ACKNOWLEDGEMENT

The work presented in this paper has been undertaken as part of the MaST G6 Coastal Morphodynamic Research Programme. It was funded partly by the Commission of the European Communities, Directorate General for Science, Research and Development under MaST Contract no. 0035-C and partly by the Tidal Waters Division of the Netherlands' Rijkswaterstaat, under the Coastal Genesis (Kustgenese) Programme.

## REFERENCES

- Abdelrahman, S.M. and E.B. Thornton (1987)**  
'Changes in the short wave amplitude and wave number due to the presence of infragravity waves'; Proc., Specialty Conf. Coastal Hydrodynamics, pp. 458-478, ASCE, New York, 1987.
- Kostense, J.K. (1984)**  
'Measurements of surf beat and set-down beneath wave groups'; Proc., 19th Int. Conf. Coastal Eng., Houston.
- List, J.H. (1992)**  
'A model for two-dimensional surfbeat'  
J. Geophys. Res., Vol. 97, pp. 5623-5635.
- Longuet-Higgins, M.S. and R.W. Stewart (1962)**  
'Radiation stress and mass transport in gravity waves, with application to "surf beats"'; J. Fluid Mech., 12, pp. 481-504, 1962.
- Roelvink, J.A. and M.J.F. Stive (1989)**  
'Bar generating cross-shore flow mechanisms on a beach'  
J. Geophys. Res., Vol. 94, no. C4., pp. 4785-4800, April 15, 1989.
- Roelvink, J.A. (1991)**  
'Modelling of cross-shore flow and morphology'; Proc. ASCE Conf. "Coastal Sediments '91", Seattle, pp. 603-617.
- Roelvink, J.A. (1992)**  
'Dissipation in random wave groups incident on a beach'  
*to appear in Coastal Engineering.*
- Sato, S. (1991)**  
'A numerical model of beach profile change due to random waves' Proc. ASCE Conf. "Coastal Sediments '91", Seattle, pp. 674-687.
- Schaffer, H.A. and I.G. Jonsson (1990)**  
'Theory versus measurements in two-dimensional surf beats'  
Proc. 22nd Int. Conf. Coastal Eng., Delft, pp. 1131-1143.
- Symonds, G. and K.P. Black (1991)**  
'Numerical simulation of infragravity response in the nearshore' Proc. 10th Australasian Conf. on Coastal and Ocean Engineering, Auckland, New Zealand, Dec. 1991, pp 339-344.
- Symonds, G., D.A. Huntley and A.J. Bowen (1982)**  
'Long wave generation by a time-varying breakpoint'  
J. Geophys. Res., Vol. 87, no C1, pp. 492-498, 1982.



APPENDIX

The transformation equations (11) and (12) are of the form:

$$\tau = t \tag{A1}$$

$$\xi = \xi(t, x) \tag{A2}$$

We can directly see that

$$\frac{\partial \tau}{\partial t} = 1$$

$$\frac{\partial \tau}{\partial x} = 0$$

The property  $\frac{\partial \tau}{\partial t} \frac{\partial \xi}{\partial x} - \frac{\partial \tau}{\partial x} \frac{\partial \xi}{\partial t} = \frac{\partial \xi}{\partial x} \neq 0$  implies that  $x(\tau, \xi)$  and  $t(\tau, \xi) (\equiv \tau)$  exist.

Obviously the inverse transformation has the property:

$$\frac{\partial t}{\partial \tau} = 1$$

$$\frac{\partial t}{\partial \xi} = 0$$

Since  $\frac{\partial t}{\partial \xi} = 0$  we find:

$$1 = \frac{\partial \xi}{\partial \xi} = \frac{\partial \xi}{\partial x} \frac{\partial x}{\partial \xi} + \frac{\partial \xi}{\partial t} \frac{\partial t}{\partial \xi} = \frac{\partial \xi}{\partial x} \frac{\partial x}{\partial \xi}, \text{ resulting in:}$$

$$\frac{\partial \xi}{\partial x} = \left(\frac{\partial x}{\partial \xi}\right)^{-1} \tag{A3}$$

Since  $\frac{\partial \tau}{\partial t} = 1$  and  $x$  and  $t$  are independent we have:

$$0 = \frac{\partial x}{\partial t} = \frac{\partial x}{\partial \xi} \frac{\partial \xi}{\partial t} + \frac{\partial x}{\partial \tau} \frac{\partial \tau}{\partial t} = \frac{\partial x}{\partial \xi} \frac{\partial \xi}{\partial t} + \frac{\partial x}{\partial \tau}, \text{ resulting in:}$$

$$\frac{\partial \xi}{\partial t} = -\frac{\partial x}{\partial \tau} \left(\frac{\partial x}{\partial \xi}\right)^{-1} \tag{A4}$$

The differential equation:

$$\frac{\partial v}{\partial t} + \frac{\partial f}{\partial x} = r,$$

which is one of the components of Eq.(1) to (3), can now directly be written as:

$$\frac{\partial \hat{v}}{\partial \xi} \frac{\partial \xi}{\partial t} + \frac{\partial \hat{v}}{\partial \tau} \frac{\partial \tau}{\partial t} + \frac{\partial \hat{f}}{\partial \xi} \frac{\partial \xi}{\partial x} + \frac{\partial \hat{f}}{\partial \tau} \frac{\partial \tau}{\partial x} = \hat{r},$$

where  $\hat{v}(\tau, \xi) = v(\tau, x(\tau, \xi))$  and  $\hat{f} = f(\hat{v}(\tau, \xi))$ .

With the use of Eqs.(A1),(A2),(A3) and (A4) this becomes:

$$-\frac{\partial x}{\partial \tau} \left( \frac{\partial x}{\partial \xi} \right)^{-1} \frac{\partial \hat{v}}{\partial \xi} + \frac{\partial \hat{v}}{\partial \tau} + \left( \frac{\partial x}{\partial \xi} \right)^{-1} \frac{\partial \hat{f}}{\partial \xi} = \hat{f}.$$

Multiplication with  $\frac{\partial x}{\partial \xi}$  yields:

$$-\frac{\partial x}{\partial \tau} \frac{\partial \hat{v}}{\partial \xi} + \frac{\partial x}{\partial \xi} \frac{\partial \hat{v}}{\partial \tau} + \frac{\partial \hat{f}}{\partial \xi} = \frac{\partial x}{\partial \xi} \hat{f},$$

which can be written as:

$$\frac{\partial}{\partial \tau} \left( \frac{\partial x}{\partial \xi} \hat{v} \right) + \frac{\partial}{\partial \xi} \left( -\frac{\partial x}{\partial \tau} \hat{v} + \hat{f} \right) = \frac{\partial x}{\partial \xi} \hat{f} \quad (\text{A5})$$

With the use of the expressions:

$$\frac{\partial \xi}{\partial t} = - \frac{\int_0^x W(\zeta) d\zeta}{x_{,0}} W(X_r(t)) \frac{dX_r}{dt}$$

$$\left( \int_0^x W(\zeta) d\zeta \right)^2$$

$$\frac{\partial \xi}{\partial x} = \frac{W(x)}{x_{,0} \int_0^x W(\zeta) d\zeta}$$

and the relations (A3) and (A4), equation (14) emerges from (A5)

## CHAPTER 73

### INCIDENT WAVE GROUPS AND LONG WAVES IN THE NEARSHORE ZONE

Y Foote<sup>\*</sup>, D Huntley<sup>\*</sup>, M Davidson<sup>\*</sup>, P Russell<sup>\*</sup>, J Hardisty<sup>†</sup> and A Cramp<sup>‡</sup>

#### ABSTRACT

Variations of the wave groupiness, cross-correlation between the incident wave envelope and long wave motion, and skewness of the near-bed velocity were measured on a macrotidal beach at Spurn Head, UK, as part of an experiment by the B-BAND (British Beach And Nearshore Dynamics) programme.

Wave groupiness persisted throughout the surf zone, and did not decay immediately at the breakpoint as is often assumed. The cross-correlation between the incident and long wavefields varied systematically across the nearshore, with negative values outside the surf zone and positive values near the shoreline. Offshore of the breakpoint, the skewness of the cross-shore current was dominated by three contributions - (i) the skewness of the incident waves, (ii) the interaction between the incident wave energy and the mean flow and (iii) the correlation between the incident and long waves. Onshore of the breakpoint, contributions (i) and (ii) remained important, along with the interaction between the long wave energy and the mean flow. The relative importance of these contributions to the skewness was unaffected by the incident wave characteristics.

#### 1. INTRODUCTION

Incident waves travelling towards the shoreline are known to have a groupy structure, with an alternating sequence of high waves and low waves. Longuet-Higgins and Stewart (1962, 1964), Larsen (1982) and Shi and Larsen (1984) proposed that associated with this incident wave 'groupiness' are gradients in the radiation stress generating a forced long wave (of infra-gravity frequency) where a depression of mean sea-level is correlated with groups of high waves and a rise in mean sea-level corresponds with groups of low waves. The radiation stress is proportional to the square of the amplitude of the incident waves.

<sup>\*</sup> University of Plymouth, Plymouth, PL4 8AA, UK

<sup>†</sup> University of Hull, Hull, HU6 7RX, UK

<sup>‡</sup> University of Wales, Cardiff, CF1 3YE, UK

Shi and Larsen (1984) suggested that the passage of a wave group and bound long wave over an erodible bed causes the re-suspension of sediments under high waves, which in conjunction with a negative long wave flow will result in net reverse sediment transport. Hanes (1988) observed the suspension of sand at both the incident wave frequency and at frequencies corresponding to wave groups. Whilst few studies have examined the variations in wave groupiness across the surf zone, where waves are radically transformed by the breaking process, it is generally understood that groupiness of ocean waves is an important characteristic of the climatology of waves both within and beyond the surf zone. Incident wave groupiness contributes significantly to the nearshore wave field. This is demonstrated through use of groupiness as a driving mechanism in models of long wave generation both in the offshore and nearshore zones, through its relationship with nearshore sediment transport and through its effect on coastal and marine structures (List, 1991).

This paper describes observations of incident wave groups and long waves from the large data set collected during the B-BAND (British Beach and Nearshore Dynamics) field experiment at Spurn Head, UK (Russell *et al*, 1991) in order to estimate the variation of wave groupiness across the nearshore zone over a range of wave and tidal conditions on a macrotidal beach and to investigate the theory that the long wave motion is forced outside the surf zone and that the short incident waves are modulated inside the surf zone.

In addition, this study describes the second stage of data analysis which involves the examination of cross-shore current data and certain velocity moments which are expected to determine sediment transport. Relatively recent studies (e.g. Bailard, 1981) of the processes which operate in the nearshore zone and the mechanisms which drive sediment transport, have shown the important role of velocity moments. Several field measurements of the velocity field on beaches have displayed features not explicitly present in many of the existing sediment transport models (Doering and Bowen, 1985). The examination of velocity moments, which are essentially current velocity components to some power, enables a more detailed understanding of the wave motion climatology and is vital to determining the processes which must be included in models of wave-driven coastal change.

Early models for nearshore sediment transport employed bulk empirical formulae based upon the general properties of the incident waves. Existing transport models are generally extensions to these theories, developed originally for the uni-directional conditions of aeolian or fluvial transport (Bagnold, 1963; Einstein, 1972; Yalin, 1972) and such models examine either bedload or suspended load transport. A more significant contribution to cross-shore sediment transport modelling has been provided, however, by those modellers who relate net sediment transport to the small deviations from symmetry which occur in the on-offshore fluid velocity field (Bowen, 1980; Bailard, 1981; Guza and Thornton, 1985; Roelvink and Stive, 1989). Theories such those by Bowen and Bailard generate a number of current velocity moments, but as yet the relative magnitudes of these moments is poorly known for field conditions. Guza and Thornton (1985) indicated that the

moment contributing most to the cross-shore suspended transport, for their particular wave and beach slope conditions, is the skewness. The present work examines the importance of several cross-shore velocity moments derived from the skewness (including mean, low-frequency and high-frequency components) within the nearshore zone, over a range of wave and tidal conditions.

## 2. FIELD SITE AND DATA COLLECTION

Field measurements were made at Spurn Head, Humberside, UK, during 16th to 25th April 1991 by the B-BAND (British Beach and Nearshore Dynamics) group. Ten tidal cycles of data in total were collected. This extensive data-set was collected on the eastern, seaward face of Spurn Head, a sand spit approximately 5km in length, which is located between the mouth of the Humber Estuary and the North Sea (Figure 1).

The beach at Spurn Head generally comprises a mobile shallow sand lens in conjunction with some superficial deposits of gravel which cover the underlying layers of boulder clay. The mean grain size of the predominant sand at the Spurn Head field site is 0.35mm. The beach profile at the field site (Figure 2) displays the characteristics of this East Coast beach, with a narrow sandy inter tidal terrace and a steep upper beach face and berm, backed by an extensive area of vegetated dune.

Gradients vary across the beach profile from 0.0230 over the inter tidal terrace, comprising well sorted sands and the underlying local glacial deposits, to a value of 0.0975 for the steeper high tide beach face which comprises fine to medium gravel (Figure 2). This range of beach slopes results in a morphodynamic regime which can alternate between dissipative at low water and reflective at high-water, but which can generally be considered to be intermediate (Wright and Short, 1984).

Wave conditions during the measurement period covered a wide range, from calm to the 2-year return period storm (with breaking wave heights in excess of 3m). The wave climate included not only the irregular and short period local wave motions, but also regular swell with pronounced groupiness characteristics. The tidal variation at Spurn Head is macrotidal and characterised by tidal currents which flood in a south-westerly direction parallel to the shoreline and ebb in a north-easterly direction.

Data logging occurred over 10 tidal cycles from 8 sensor rigs which extended to approximately 120m offshore. The four central A-Rigs (Figure 3), each comprising 3 electro-magnetic current meters spaced at heights of 0.10, 0.25 and 0.63m above the bed, 3 optical back-scatter sensors positioned at 0.04, 0.10 and 0.25m above the bed, plus one pressure sensor; formed the most detailed and comprehensive component of the instrumentation deployed (see Russell *et al.*, 1991).

## 3. DATA ANALYSIS

Data analysis in this study examines two complete tidal cycles, Tides 184PM and 234PM, in addition to Tide 164PM a partial tidal cycle. The data discussed here comes from a point source (Rig A2). Tide 164PM, comprising

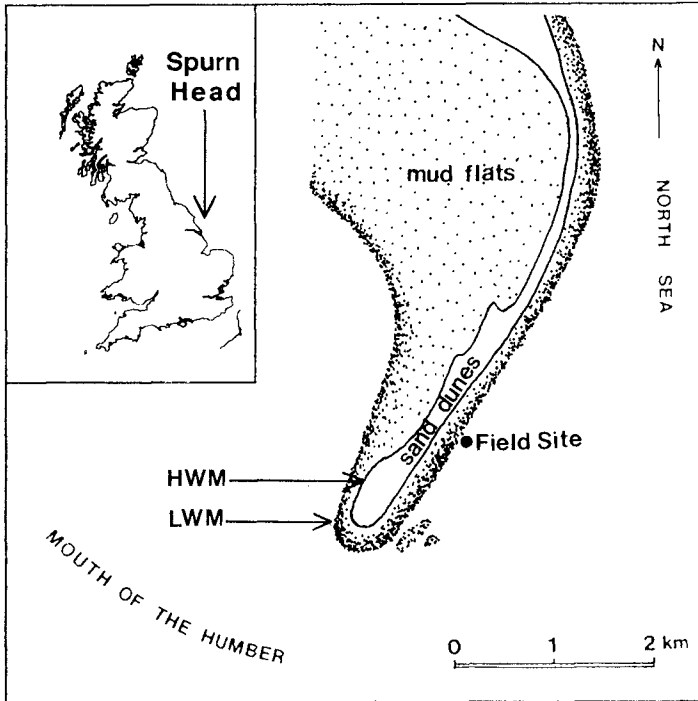


Figure 1. The location of the field experiment at Spurn Head

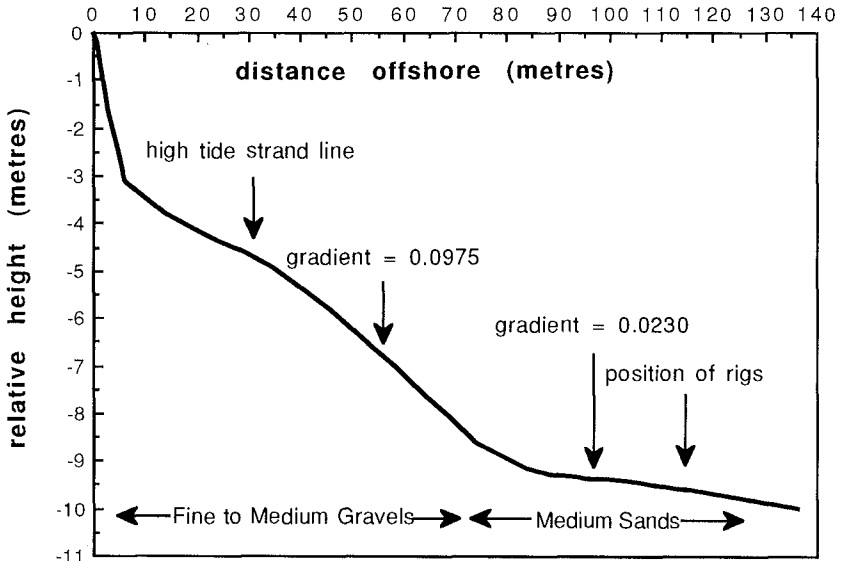


Figure 2. Beach Profile at Spurn Head Field Site, 18 April, 1991.

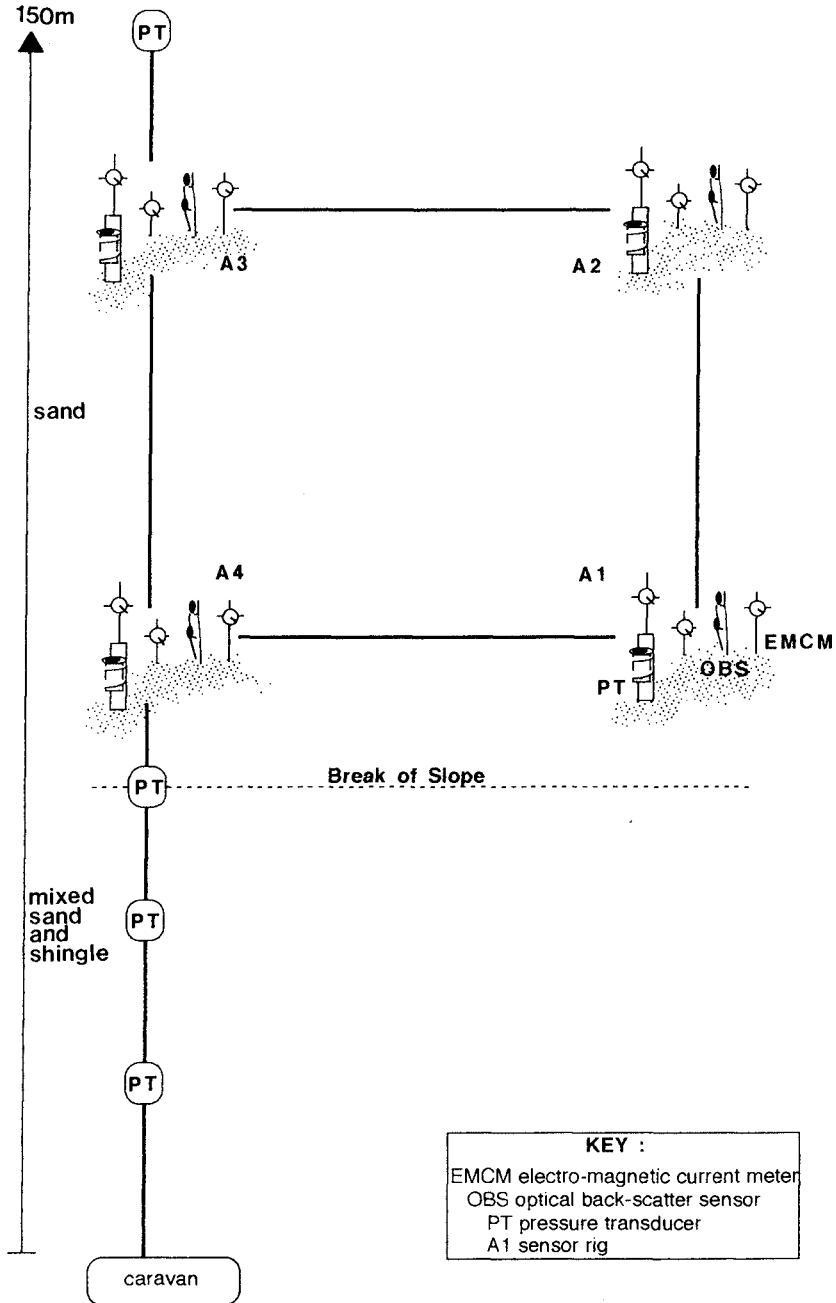


Figure 3. Field set-up used at Spurn Head, April 1991.

4 runs with each run containing 17 minutes or 1024 seconds of data, was logged on April 16th 1991 during a violent storm event with a very strong wind, a maximum  $H_s$  value of 1.6m and swell waves of up to 3m breaking height. (The significant wave height,  $H_s$ , is defined as  $4\sigma$  where  $\sigma^2$  is the total variance of the sea surface elevation data (Guza and Thornton, 1982)). Tide 184PM covers moderate swell and choppy conditions, maximum  $H_s$  of 1.1m, with a moderate wind, whilst Tide 234PM displays calmer conditions with smaller swell and chop waves and a maximum  $H_s$  value of approximately 0.8m.

### (i) ESTIMATION OF WAVE GROUPINESS AND CROSS-CORRELATION ANALYSIS

Following the selection of the three tides (Tides 164PM, 184PM and 234PM) all pressure data runs are examined for spikes, glitches or any other incongruous values, which have to be removed prior to analysis. The trend of the pressure sensor data is removed and the record is additionally 'demeaned'; such procedures help to exclude the possibility of any distorting effects upon the data by creating a quasi-stationary time series. The pressure signal is then converted to an approximate sea surface elevation record using a correction factor for the depth attenuation effect of the pressure transducer (e.g. Skovgaard *et al.*, 1974). Separation of the corrected data into both high- and low-passed components is achieved through use of a Kaiser-Reed (1977) digital filter. Spectral analysis of the pressure sensor time series indicates the presence of a trough near 0.05Hz between the incident wave peak and low frequency and sub-harmonic motion peaks and therefore, a cut-off value of 0.05Hz is applied to the separate low- and high-frequencies. The procedure for determining the incident wave groupiness involves the demeaning and squaring of the high-pass component of the surface elevation data, followed by application of the same filter used previously to produce high- and low-frequency wave height time series. The groupiness factor is then the square root of the root-mean-square of the wave envelope time series (Huntley and Kim, 1984).

The incident wave envelope time series is, therefore, used as the basis for estimating the groupiness factor. This has been determined for the three selected tides and plotted against depth (Figure 4) and significant wave height (Figure 5). Despite the examination of three very different tidal cycles the data exhibit a definite relationship whereby, outside the breakpoint, groupiness does not vary significantly (Figure 4), whilst shorewards from the breakpoint groupiness does not drop to zero but actually continues through the surf zone, decreasing to near zero only at the shoreline. Determination of the breakpoint position is achieved through examination of the current velocity mean and variance data (Davidson *et al*, 1992). As might be expected if wave heights obey a Rayleigh distribution, there is a linear relationship between wave height and the groupiness factor; Figure 5 suggests that this relationship persists to the shoreline. Thus whilst many numerical and laboratory models assume that groupiness decreases to zero at the breakpoint, the data analysed in this study based upon field results reveal a persistence of groupiness through the surf zone.



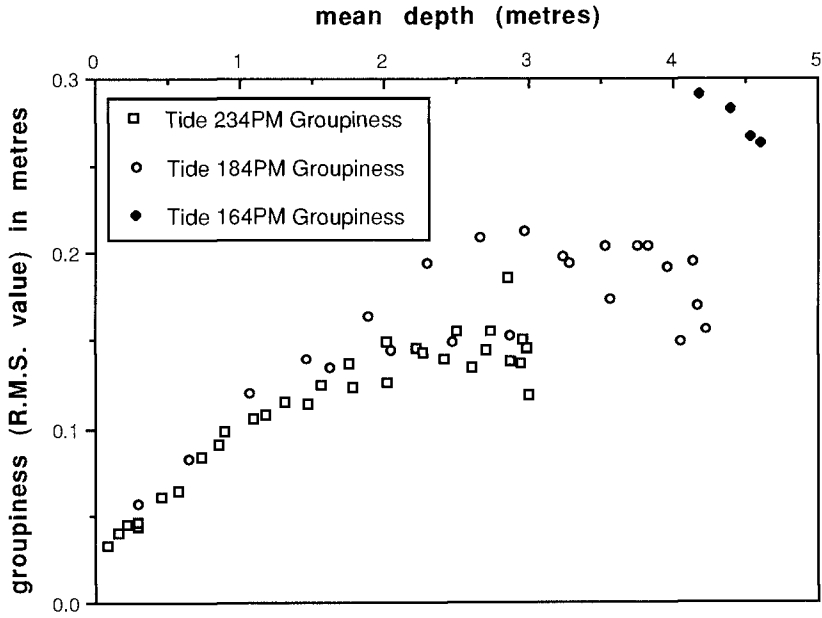


Figure 4. Variations in groupiness with depth across the nearshore zone.

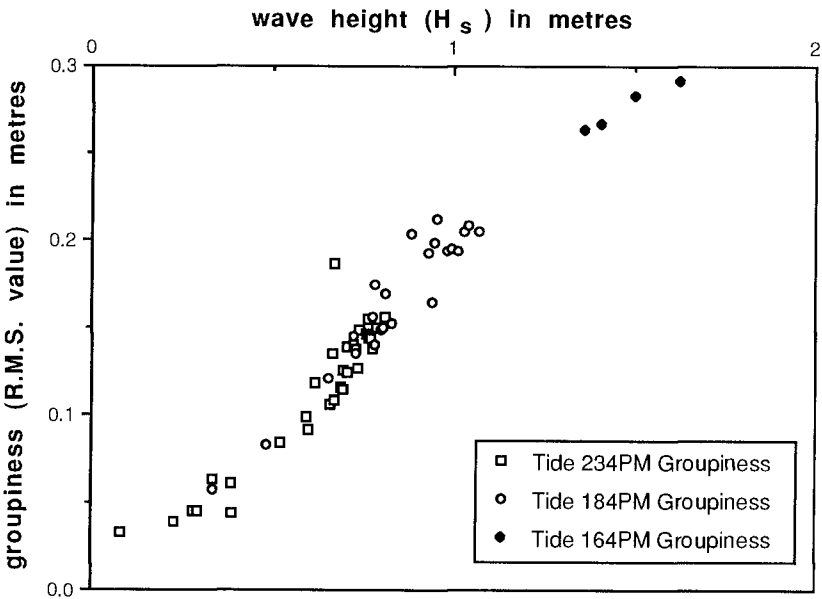


Figure 5. Variations in groupiness with wave height across the nearshore zone.

Cross-correlation coefficients between the incident wave envelope and the low-frequency motion are calculated for all data runs of three selected tidal cycles. The cross-correlation function,  $C_R$ , describes the degree of linear agreement between two data sets in the time domain thus :

$$C_R = \frac{\sum (x_i - \bar{x})(y_{i+k} - \bar{y})}{\sqrt{\sum (x_i - \bar{x})^2 \sum (y_i - \bar{y})^2}} \quad (1)$$

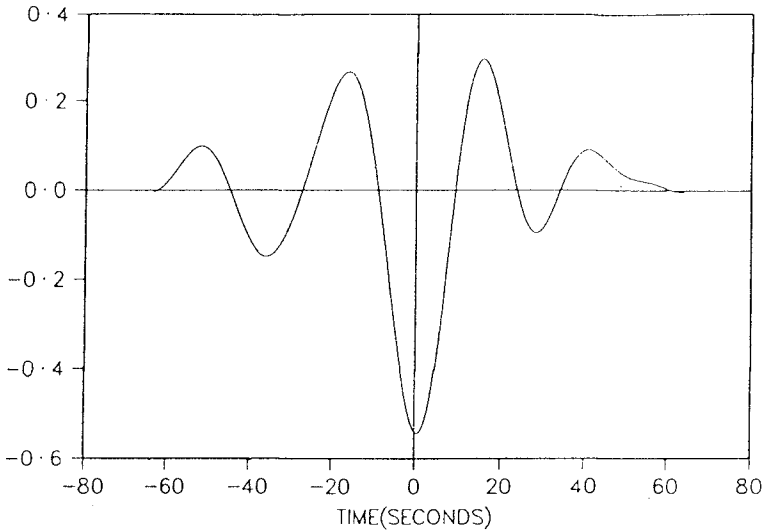
where  $\bar{\psi}$  and  $\psi_n$  are the mean and  $n$ th value of the  $\psi$  time series respectively, and  $\psi$  represents  $x$  or  $y$ .

Figure 6a illustrates the cross-correlation function between the incident wave envelope time series and the low-frequency motion time series for a high tide data run of Tide 234PM, whilst Figure 6b illustrates the equivalent cross-correlation function for a low tide data run, also from Tide 234PM. It is interesting to note in Figures 6a and 6b that for the large water depth of the high tide example, a large negative correlation value is obtained at zero time lag and for the shallower state of the low tide example, there is a considerable positive value. Values of the cross-correlation coefficient at zero time lag for all data runs are plotted in Figure 7 against depth. There appears to be a definite trend in the data. The positive cross-correlation values within the surf zone could be explained by the modulation of short wave breaker heights through the depth variations induced by long waves (Roelvink and Stive, 1989), although it is not known whether this depth-modulation is induced by the forced waves or the free waves. The negative correlation coefficient values outside the surf zone reflect the forcing of the long wave motion by the radiation stress of the incoming wave groups. Consequently, in agreement with other field data (Abdelrahman and Thornton, 1987) and laboratory data (Roelvink and Stive, 1989; Roelvink, 1991), there does appear to be significant direct coupling between the high- and low-frequency motions. The correlation near zero which occurs just inside the breakpoint may be explained by the occurrence of a standing long wave nodal point or by the competing effects of forced and free long wave energies. The fact that data from all three tides show the same trends, within the scatter, in both the cross-correlation and the groupiness suggests that both factors are independent of the offshore wave climate.

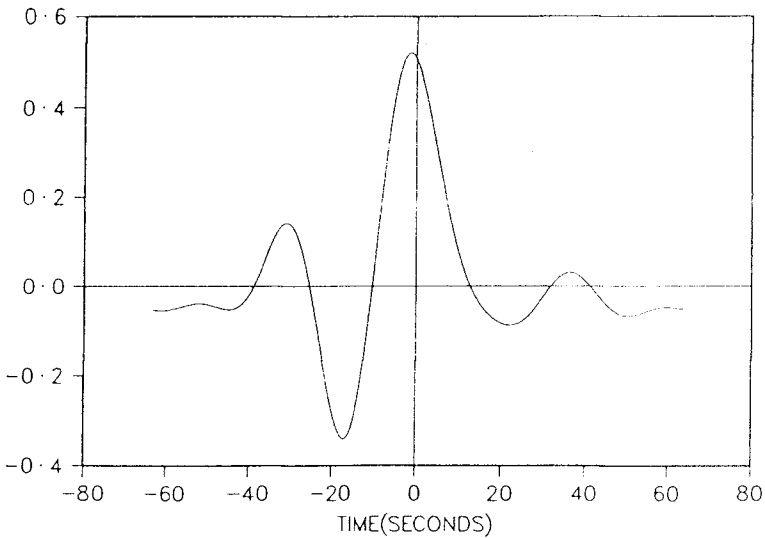
## (ii) VELOCITY MOMENT ANALYSIS

The process of examining velocity moments and attempting to establish the moments which contribute most significantly to nearshore sediment transport (Guza and Thornton, 1985), is adapted in this study for electro-magnetic cross-shore current velocity data (bottom sensor of Rig A2) from the B-BAND Spurn Head field experiment. The present study is concerned with cross-shore sediment transport and therefore only the cross-shore velocity ( $u$ ) is used. The cross-shore current velocity is assumed to comprise a mean flow ( $\bar{u}$ ), a high frequency wave component ( $u_s$ ) and a low frequency wave component ( $u_L$ ) thus:

$$u = (\bar{u} + u_s + u_L) \quad (2)$$



**Figure 6(a). Cross-correlation between wave envelope and low frequency motion near high tide**



**Figure 6(b). Cross-correlation between wave envelope and long wave motion near low tide.**

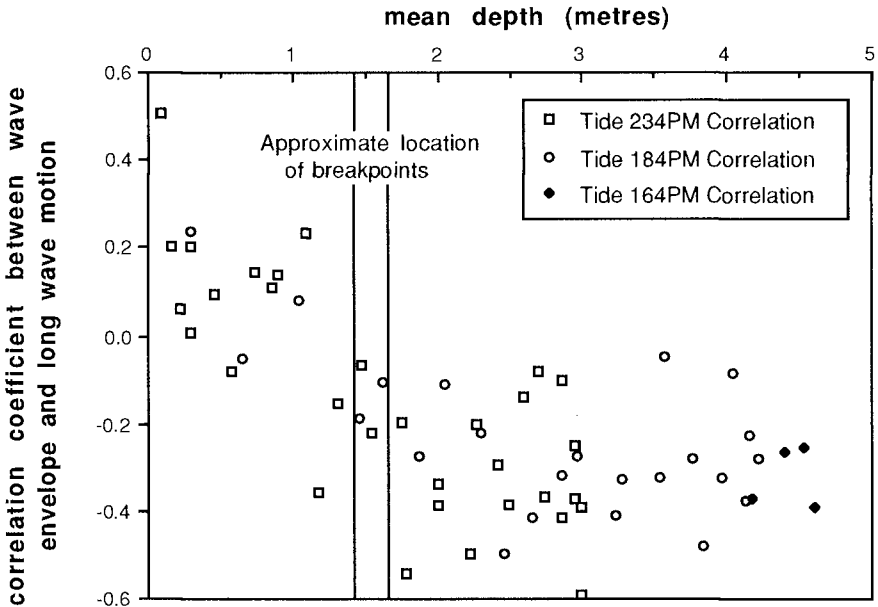


Figure 7. Correlation coefficient between wave envelope and long wave motion across the nearshore zone.

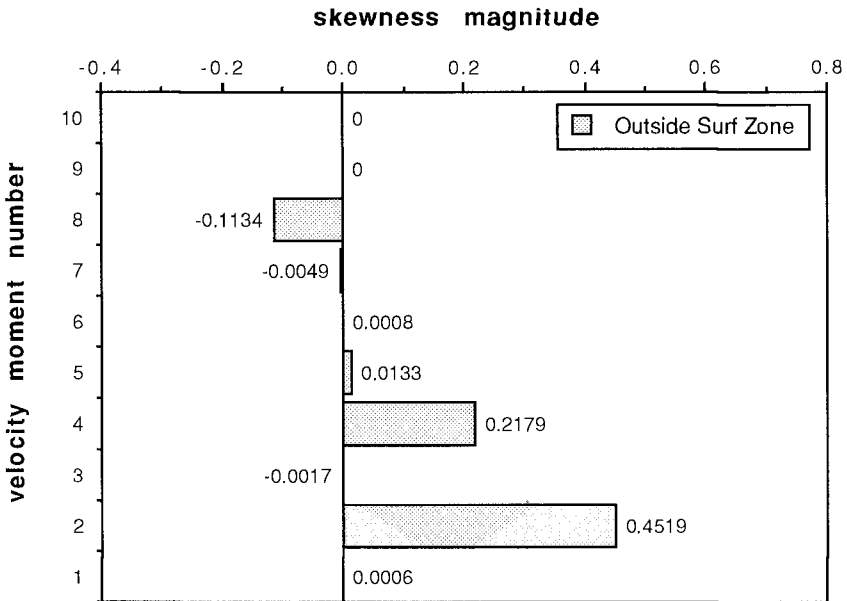


Figure 8(a). Tide 164PM skewness outside the surf zone.

When expanded in terms of these three components, the normalised cross-shore velocity skewness, defined as  $(u^3)/(u^2)^{3/2}$  consists of ten distinct terms since :

$$\overline{u^3} = (\overline{u + u_s + u_L})^3 \quad (3)$$

$$= \overline{u^3} + \overline{u_s^3} + \overline{u_L^3} + 3\overline{uu_s^2} + 3\overline{uu_L^2} + 6\overline{uu_su_L} + 3\overline{u_L^2u_s} + 3\overline{u_s^2u_L} + 3\overline{u^2u_s} + 3\overline{u^2u_L} \quad (4)$$

(Each of the above ten terms are normalised by dividing through by  $(u^2)^{3/2}$ ). These ten skewness terms describe various mechanisms which operate within the nearshore system as follows:

$\overline{u^3}$  = Term 1, mean flow cubed

$\overline{u_s^3}$  = Term 2, skewness of the short wave velocity component

$\overline{u_L^3}$  = Term 3, skewness of the long wave velocity component

$3\overline{uu_s^2}$  = Term 4, short waves mobilise sediment which then moves with the mean flow \*

$3\overline{uu_L^2}$  = Term 5, as Term 4, but with long waves mobilising sediment \*

$6\overline{uu_su_L}$  = Term 6

$3\overline{u_L^2u_s}$  = Term 7 } correlations between short and long wave components

$3\overline{u_s^2u_L}$  = Term 8 }

$3\overline{u^2u_s}$  = Term 9

$3\overline{u^2u_L}$  = Term 10

} will be near zero and will not be significant parameters

\*cf Inman and Bagnold (1963)

The three tidal cycles selected (Tides 164PM, 184PM and 234PM) for the groupiness analysis are also used for moment analysis. All current velocity data runs are examined for spikes or glitches which have to be removed before the moment analysis, in addition to the trend and mean prior to filtering. Each of the above ten terms is calculated for all three tidal cycles and averaged into measurements made seaward of the surf zone and measurements obtained within the surf zone.

The schematic representations of the ten terms outside and inside the breakpoint for the three tides examined can be seen in Figures 8 and 9 and indicate that particular velocity moment terms dominate through the nearshore zone. For all three tidal cycles, with varying characteristics, the following velocity moments appear to prevail :

Tide 164PM (Fig. 8a)	Seaward of the Surf Zone	Terms 2, 4 and 8 dominate
Tide 184PM (Fig. 8b)	Seaward of the Surf Zone	Terms 2, 4 and 8 dominate
Tide 234PM (Fig. 8c)	Seaward of the Surf Zone	Terms 2, 4 and 8 dominate

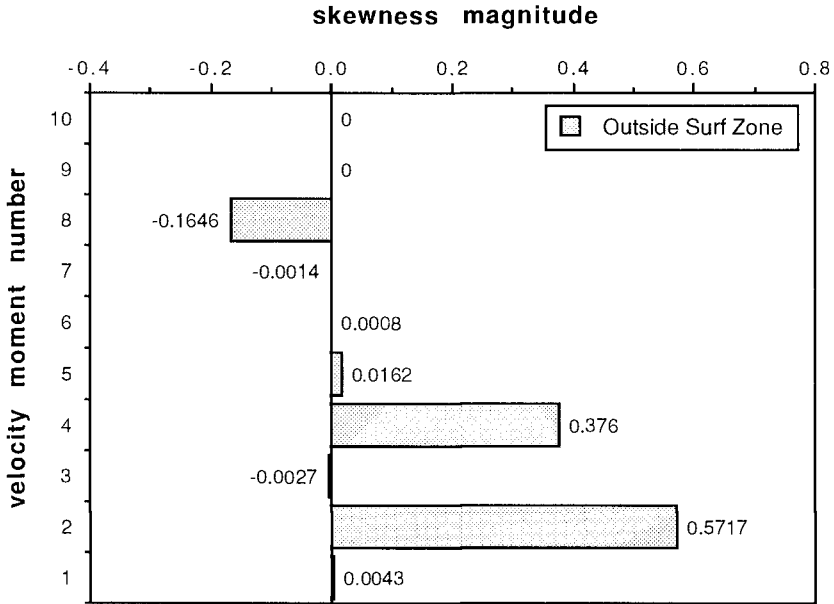


Figure 8(b). Tide 184PM skewness outside the surf zone.

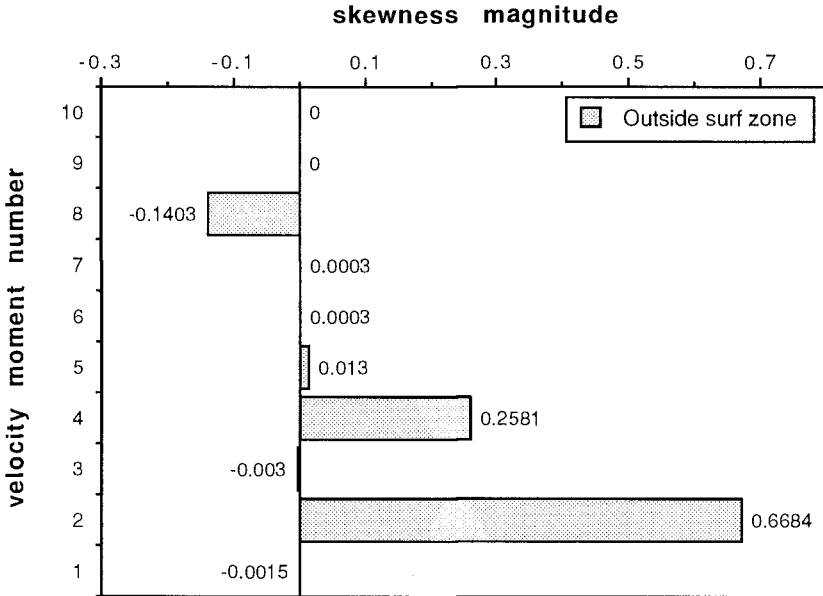


Figure 8(c). Tide 234PM skewness outside the surf zone.

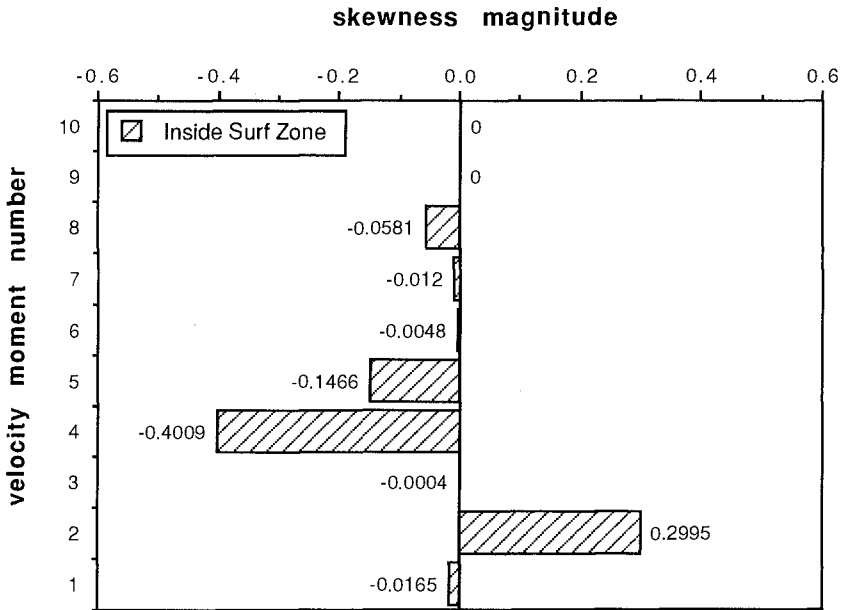


Figure 9(a). Tide 184PM skewness inside the surf zone.

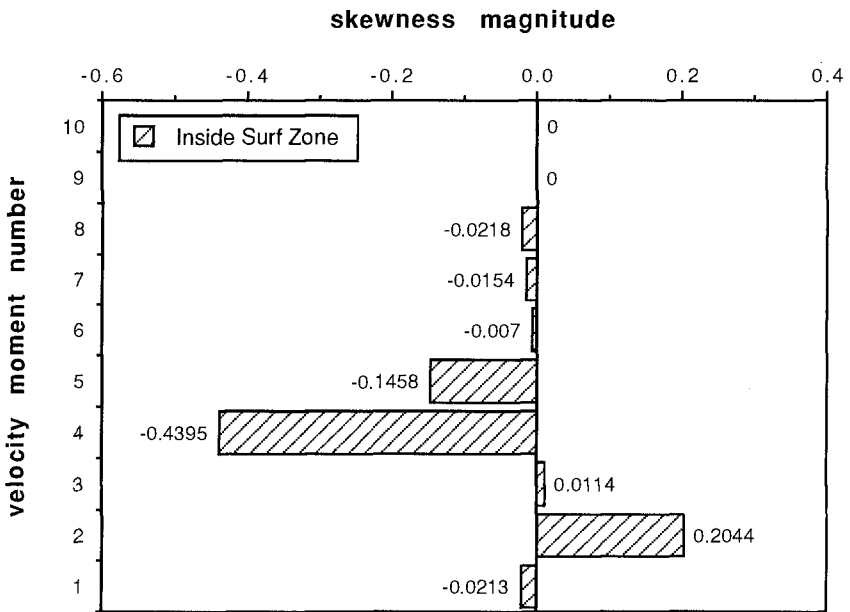


Figure 9(b). Tide 234PM skewness inside the surf zone.

Tide 164PM	Within the Surf Zone	No data collected*
Tide 184PM (Fig. 9a)	Within the Surf Zone	Terms 2, 4 and 5 dominate
Tide 234PM (Fig. 9b)	Within the Surf Zone	Terms 2, 4 and 5 dominate

\* Storm too violent so data logging stopped.

Seaward of the surf zone, the terms which dominate are, therefore, Term 2 (the skewness of the short wave velocity), Term 4 (the Inman/Bagnold-type term where short waves mobilise the sediment which is then moved by a mean flow) and Term 8 (the term describing the correlation between the short incident wave groups and the long wave motion). Inside the breakpoint, those terms which appear to dominate the very nearshore wave field are Terms 2 and 4 (described previously) and Term 5 (the Inman/Bagnold-type term which represents the mobilisation of sediment by long waves and the subsequent movement by a mean flow). The similarity of these terms for each of the tides, not only in direction but also in percentage contribution to the total skewness implies a remarkable degree of consistency, independent of incident wave conditions. It is also interesting to note the variation of Term 8 through the nearshore system since this reflects the earlier wave groupiness analysis; Term 8 describes the correlation between the incident wave envelope and the long wave motion and its behaviour supports the cross-correlation work which shows a large negative value occurs outside the breakpoint in the deeper water and a trend towards zero and then positive values as the shoreline is approached (Figure 8).

#### 4. CONCLUSIONS

The following conclusions can be drawn :

- (i) Outside the surf zone the cross-correlation between the long wave motion and the wave envelope has a constant negative value and is relatively insensitive to depth. At the breakpoint the correlation decreases towards zero, whilst within the inner surf zone positive correlation values occur. The interaction between long waves and short waves varies systematically through the surf zone.
- (ii) Wave groupiness does not decay immediately at the breakpoint. Instead there is a persistence of the groupiness through the surf zone. It is suggested that this might have important implications for modelling sediment response.
- (iii) The terms dominating skewness inside the surf zone are : the skewness of the incident waves, the correlation between the incident wave energy and a mean flow, and the correlation between the long wave energy and a mean flow.
- (iv) Outside the surf zone, the terms for the skewness of the short incident waves and the correlation between incident waves and a mean flow are dominant, in addition to the correlation between the wave envelope and the long wave motion.
- (v) It would appear that the relative importance of these skewness terms is almost insensitive to the incident wave conditions measured on this beach.



## 5. REFERENCES

- Abdelrahman, S. M. and Thornton, E. B., 1987. Changes in the short wave amplitude and wavenumber due to the presence of infragravity waves. Proceedings of the Speciality Conference on Coastal Hydraulics, American Society of Civil Engineers, New York, 458-478.
- Bagnold, R. A., 1963. Mechanics of marine sedimentation. In : The Sea , Ideas and Observations, Vol. 3, Interscience Publishers, New York, N.Y., 507-528.
- Bailard, J. A., 1981. An energetics total load sediment transport model for a plane sloping beach. Journal of Geophysical Research, 86 : 10938-10954.
- Bowen, A. J., 1980. Simple models of nearshore sedimentation; Beach Profiles and Longshore Bars. Coastline of Canada, Geological Survey of Canada, 21-30.
- Davidson, M. A., Russell, P. E., Huntley, D. A. and Hardisty, J., 1992. Tidal asymmetry in suspended sand transport on a macrotidal intermediate beach, Marine Geology (in press).
- Doering, J. C. and Bowen, A. J., 1985. Skewness *et al.*, the spatial distribution of some moments of the nearshore velocity field. Proceedings of the Canadian Coastal Conference, Newfoundland, 5-16.
- Einstein, H. A., 1972. A basic description of sediment transport on beaches. In : R. E. Meyer (editor); Waves on Beaches and Resulting Sediment Transport, Academic Press, New York, N.Y., 462pp.
- Guza, R. T. and Thornton, E. B., 1982. Swash oscillations on a natural beach. Journal of Geophysical Research, 87 (C1) : 483-491.
- Guza, R. T. and Thornton, E. B., 1985. Velocity moments in nearshore. Journal of Waterway, Port, Coastal and Ocean Engineering, 111 (2) : 235-256.
- Hanes, D. M., 1991. Suspension of sand due to wave groups. Journal of Geophysical Research, 96 (C5) : 8911-8915.
- Huntley, D. A. and Kim, C-S., 1984. Is surf beat forced or free? Proceedings of the 19th. Conference on Coastal Engineering, 9 : 1659-1676.
- Inman, D. L. and Bagnold, R. A., 1963. Littoral processes. In : The Sea, Ideas and Observations, Vol. 3, Interscience Publishers, New York, N.Y., 529-550.
- Kim, C-S., 1985. Field observations of wave groups and long waves on sloping beaches. Unpublished MSc. thesis. Dalhousie University, Halifax, Nova Scotia. 151 pp.
- Larsen, L. H., 1982. A new mechanism for seaward dispersion of midshelf sediments. Sedimentology, 29: 279-284.
- List, J. H., 1991. Wave groupiness variations in the nearshore. Coastal Engineering, 15: 475-496.
- Longuet-Higgins, M. S. and Stewart, R. W., 1962. Radiation stress and mass transport in gravity waves, with application to 'surf-beats'. Journal of Fluid Mechanics, 13 : 481-504.
- Longuet-Higgins, M. S. and Stewart, R. W., 1964. Radiation stress in water waves : a physical discussion, with applications. Deep Sea Research, 11: 529-562.

- Roelvink, J. A., 1991. Modelling of cross-shore flow and morphology. Proceedings of the Coastal Sediments '91 Conference, American Society of Civil Engineers, New York, pp. 603-617.
- Roelvink, J. A. and Stive, M. J. F., 1989. Bar-generating cross-shore flow mechanisms on a beach. *Journal of Geophysical Research*, 94: 4785-4800.
- Russell, P. E., Davidson, M. A., Huntley, D. A., Cramp, A., Hardisty, J. and Lloyd, G., 1991. The British Beach and Nearshore Dynamics (B-BAND) programme. Proceedings of the Coastal Sediments '91 Conference, American Society of Civil Engineers, New York, pp. 371-384.
- Shi, N. C. and Larsen, L. H., 1984. Reverse sediment transport induced by amplitude modulated waves. *Marine Geology*, 54: 181-200.
- Skovgaard, O., Svendsen, I. A., Jonsson, I. G. and Brink-Kjoer, O., 1974. Sinusoidal and cnoidal gravity waves formulae and tables. Institute of Hydrodynamics and Hydraulic Engineering (ISVA), Technical University of Denmark, Lyngby, Denmark, 8pp.
- Wright, L. D. and Short, A. D., 1984. Morphodynamic variability of surf zones and beaches: A synthesis. *Marine Geology*, 56 : 93-118.
- Yalin, M. S., 1977. *Mechanics of sediment transport*; (Second edition), Pergamon Press, Oxford, 290pp.

## ACKNOWLEDGEMENTS

The B-BAND project is funded by the Natural and Environment Research Council (NERC) (UK) research grant GR3/7128. The PhD research student, Yolanda Foote is funded by the Science and Engineering Council (SERC) (UK) and British Maritime Technology Ltd., (BMT Ceemaid Division, UK). The authors would like to thank Mr. P. Sims and Dr. T. O'Hare at the University of Plymouth, for their useful suggestions and help with this work.

## CHAPTER 74

# GENERATION OF INFRAGRAVITY WAVES IN BREAKING PROCESS OF WAVE GROUPS

Satoshi NAKAMURA<sup>1</sup> and Kazumasa KATOH<sup>1</sup>

### Abstract

To understand the cross-shore distribution of the wave groups and the infragravity waves in a storm, field observations have been carried out at the Hazaki Oceanographical Research Facility. The relationship between the wave groups and the infragravity waves is examined. The infragravity waves are generated in the wave breaking process of the wave groups. The observed heights of infragravity waves in the surf zone agree well with the predicted one by modified Symonds' model, in which a time delay of small wave breaking due to propagation is taken into consideration.

### 1 Introduction

Infragravity waves have been considered to be the main cause of abrupt beach erosion in a storm. For example, Katoh *et al.*(1990,1992) reported the field evidences of foreshore erosion due to the infragravity waves in the storms. Then, to predict the extent of abrupt beach erosions and to develop the effective countermeasures for them, it is important to estimate the magnitude of infragravity waves in a storm.

Although sea waves may look random, inspection of wave records indicates that high waves fall into groups rather than appear individually. This is called a wave groups. Concerning to the generation mechanism of infragravity waves, Symonds *et al.*(1982) showed the attractive theory by taking the wave groups into account. Nearly 10 years, however, have passed in a situation that their theory has not been verified with the field data.

The first purpose of this study is to carry out the simultaneous observation of the cross-shore changes of the wave groups and the infragravity waves in the storm, in order to understand their actual conditions. The secondary one is to modify the theory under certain circumstances for developing the more precise predictive model of infragravity waves in the surf zone.

---

<sup>1</sup>Port and Harbour Res. Inst., 3-1-1, Nagase, Yokosuka, Kanagawa, Japan

2 Field observations

2.1 Study site and method of observations

The site of field observations is a entirely natural sandy beach, being exposed to the full wave energy of the Pacific Ocean. On this beach, Port and Harbour Research Institute constructed the Hazaki Oceanographical Research Facility(HORF) for carrying out field observations in the surf zone under storm conditions(see Photo.1). A sediment research pier is 427 meters long.

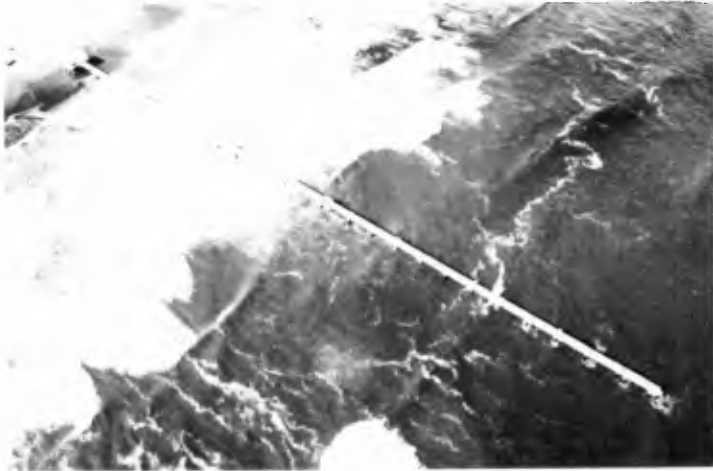


Photo. 1 Hazaki Oceanographical Research Facility(HORF).

Figure 1 shows the sea bottom profile and the locations where wave gages were set. Seven wave gages are permanently installed on the side of pier deck at the locations from No.1 to No.7 along the research pier. They emit supersonic waves downward and receive the supersonic waves reflected by the sea surface. At each location, wave profiles were measured continuously with a sampling time of 0.5 second. The data were sent to the laboratory at the base of research pier, where

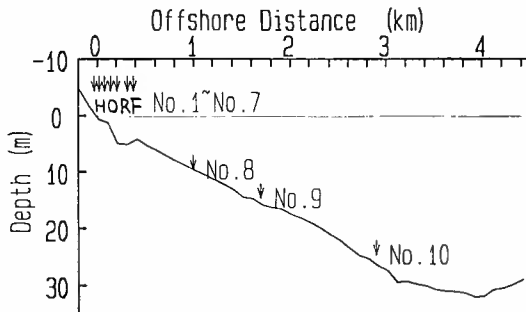


Figure 1 Beach profile and locations of measurement.

the signals were digitalized by a mini-computer and recorded on MT.

The other three wave gages at the locations from No.8 to No.10 were temporarily set on the sea bottom during storm, which were on the extension line of the pier. The water depths at these observation points were 9 meters, 14 meters and 24 meters respectively. At each location, waves were measured during 2 hours of every 6 hours with a sampling time of 0.5 second. The data were stored in a data cassette or an IC memory.

## 2.2 Wave conditions

The field observations were repeatedly carried out in the two different types of storm. Figure 2 shows the changes of offshore significant wave heights and periods, during the first observation from the 25th February to the 1st March in 1989. The maximum peak of wave height was 3.7 meters on the 26th February,

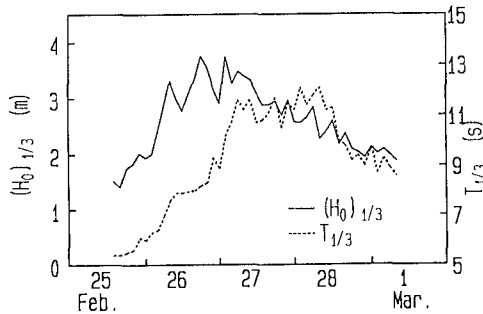


Figure 2 Changes of significant wave height and period in the first observation.

when the atmospheric depression passed through near the site. Figure 3 shows wave heights and periods during the second observation from the 5th to the 9th October in 1989. The maximum wave height was 4.6 meters on the 8th October, when the typhoon passed near the site.

Twenty-nine sets of ten wave records obtained during these two storms have been analyzed in this study. Figure 4 shows the cross-shore distribution of the spectral energy densities in two hours, when the significant wave height was 3.7

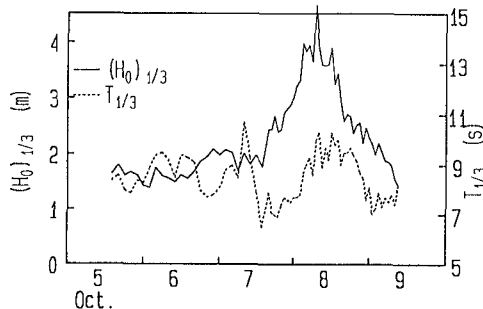


Figure 3 Changes of significant wave height and period in the second observation.

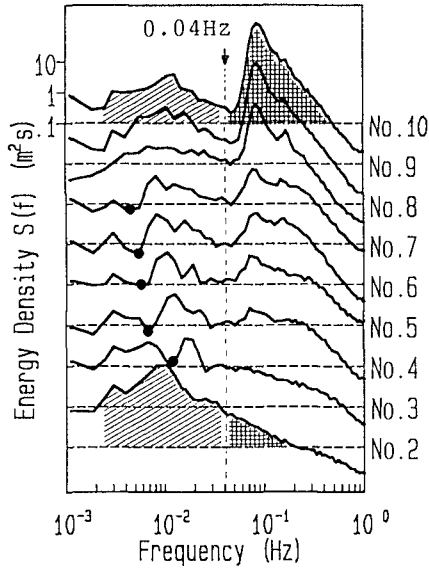


Figure 4 Cross-shore distribution of spectral energy densities.

meters in the offshore. The spectral energy density at the location of No.10 has two peaks. The first largest peak is at 0.1 Hz in frequency and second one is at 0.01 Hz. In addition, there is the minimum spectral density at the frequency of 0.04 Hz. The energy densities higher than 0.04 Hz in frequency are due to the incident wind waves, while those lower than 0.04 Hz are considered to be due to the infragravity waves. The former decreases due to the wave breaking with propagation to the shoreline in the surf zone, while the latter increases in the onshore direction. The height,  $H_L$ , and period,  $T_L$ , of infragravity waves have been estimated by calculating the 0th-order and 2nd-order moments of the spectral energy density in the frequency band from 0 to 0.04 Hz as follows;

$$H_L = 4 \int_0^{0.04} S(f)df, \tag{1}$$

$$T_L = \frac{\sqrt{\int_0^{0.04} S(f)df}}{\sqrt{\int_0^{0.04} f^2 S(f)df}}. \tag{2}$$

### 3 Data analysis on wave groups

#### 3.1 Analysis of wave groups

A new method has been introduced for analyzing the wave groups, which can be applied to irregular waves trains both in the offshore and in the surf zone. The new method of analysis is explained in Figure 5, by using the wave profile data measured in the surf zone. First of all, the low frequency components less than

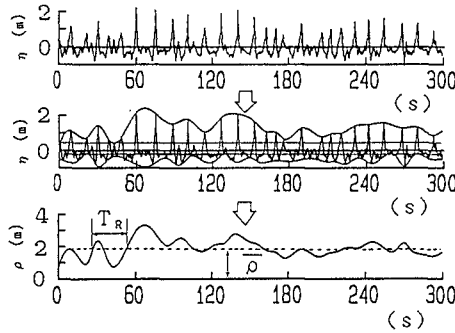


Figure 5 Method of wave groups analysis.

0.04Hz have been removed by using a numerical filter. The upper in Figure 5 is a high-pass-filtered wave profile. There are many small waves which are due to wave breaking and the non-linearity of waves. If individual waves are defined by the usual zero-crossing method, a wave number is greater in the surf zone than in the offshore. For removing small waves, a certain narrow band is established around the mean water level as shown in the middle of Figure 5. The small waves, whose wave height are less than the width of band, are neglected. The width of band has been determined so as to have the same wave number as that in the offshore.

After that, a natural cubic spline curve is fitted on each train of wave crests and wave troughs respectively. As the vertical width between the upper and the lower envelop curves corresponds to the wave height, the continuous wave height,  $\rho(t)$ , can be calculated as shown in the lower.

Based on this results, a mean wave height,  $\bar{\rho}$ , and a mean deviation around the mean wave height,  $\rho_{rms}$ , can be easily calculated by the following equations.

$$\bar{\rho} = \frac{1}{T_n} \int_0^{T_n} \rho(t) dt, \tag{3}$$

$$\rho_{rms} = \sqrt{\frac{1}{T_n} \int_0^{T_n} (\rho(t) - \bar{\rho})^2 dt}, \tag{4}$$

where  $T_n$  is total length of wave record.

If we adopt the Rayleigh distribution as the distribution of wave heights, the probability density function of  $\rho(t)$  is written as

$$p(x) = \frac{\pi}{2} x \exp\left(-\frac{\pi}{4} x^2\right) : x = \rho/\bar{\rho}. \tag{5}$$

By utilizing Eq.(5) and conducting a numerical integration, Eq.(4) can be rewritten as

$$\rho_{rms} = \bar{\rho} \sqrt{\int_0^{\infty} (1-x)^2 p(x) dx} = 0.52\bar{\rho}. \tag{6}$$

There is a well-known relation between  $H_{1/3}$  and  $\bar{H}$  (Goda, 1985), that is

$$H_{1/3} = 1.60\bar{H} (= 1.60\bar{\rho}). \tag{7}$$

By substituting Eq.(7) into Eq.(6),

$$\rho_{rms} \doteq \frac{1}{3}H_{1/3}. \tag{8}$$

Figure 6 shows the comparison of  $\rho_{rms}$  with  $H_{1/3}$  in the offshore. The data are plotted close to the dashed line which is the theoretical relation of Eq.(8).

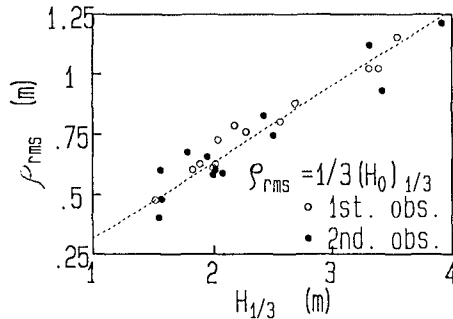


Figure 6 Comparison of  $\rho_{rms}$  with  $H_{1/3}$ .

A repetition period of wave groups is defined as an elapsed time from the time that wave height is excess of a threshold value to the time of its re-excess, that is to say, in the same manner as what is called a zero-crossing method. The individual repetition period of the wave groups and its mean value are denoted by  $T_R$  and  $\bar{T}_R$ , respectively, hereinafter. Several calculations of the mean repetition period,  $\bar{T}_R$ , have been done by changing the threshold value. Comparing the calculated mean repetition period in the offshore with the observed period of infragravity waves in the surf zone, it has been confirmed that the former agrees approximately with the latter when a highest one-tenth wave,  $H_{1/10}$ , is used as the threshold height. Figure 7 shows the histogram of the repetition periods of wave groups at the offshore in one record length of 2 hours when the significant wind wave height was 3.7 meters. The repetition periods of 60 wave groups are distributed in a wide range. Although there is no predominant peak of frequency in the distribution, the mean repetition period of  $\bar{T}_R$  is used as the representative value for convenience. Figure 8 shows a comparison of the mean repetition period of the wave groups with the significant wave period at the point of No.10. By means of the least square method, the increasing tendency of  $T_R$  can be expressed as

$$\bar{T}_R = 9.24T_{1/3}. \tag{9}$$



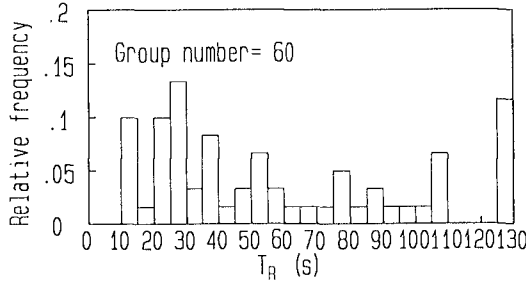


Figure 7 Histogram of repetition period.

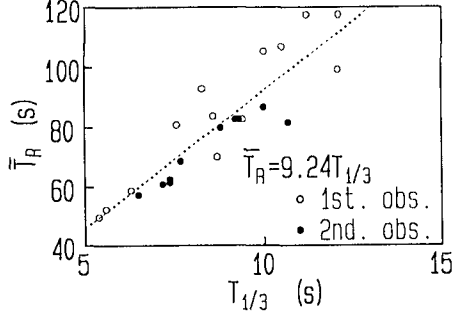


Figure 8 Comparison of significant wave period with mean repetition period.

**3.2 Relationship between wave groups and infragravity waves**

Figure 9 shows the cross-shore distribution of the mean repetition period of wave groups,  $\bar{T}_R$ , and the height of the infragravity waves,  $H_L$ , when the significant wave height was 3.7 meters. The mean repetition period of the wave groups decreased rapidly near the point of No.8, where the height of the infragravity waves increased. According to our visual observation, the incident wind waves broke in the area between the points of No.7 and 8. On the other hand, when the significant wave height was 1.8 meters in the offshore, which is not shown here,

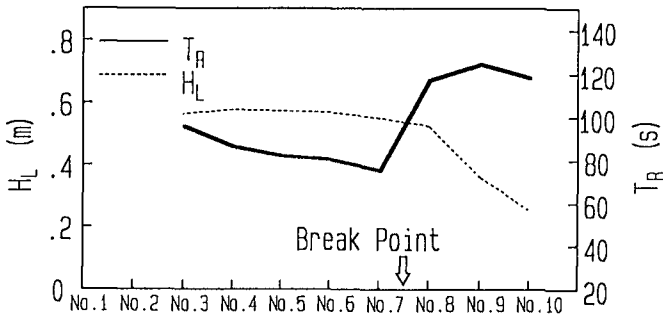


Figure 9 Distribution of  $\bar{T}_R$  and  $H_L$  in the storm.

the mean repetition period of the wave groups was not long in the offshore, and the height of infragravity wave increased slightly, being still small in the surf zone. Then, it is inferred from these evidence that infragravity waves are generated in the wave breaking process when the mean repetition period of wave groups is long.

#### 4 Modification of Symonds' model

##### 4.1 Applicability of Symonds' model

Symonds *et al.*(1982) showed that the time variation of the break point, which occurs when the incident waves are of varying amplitude, can generate waves at the group period and may be a significant source of infragravity wave energy. They used the non-dimensional, depth-integrated and linearized shallow water equations, that is,

$$\chi \frac{\partial U}{\partial t} + \frac{\partial \zeta}{\partial x} = -F(x, t), \tag{10}$$

$$\frac{\partial \zeta}{\partial t} + \frac{\partial(xU)}{\partial x} = 0, \tag{11}$$

$$\chi = \frac{\sigma^2 X}{g \tan \beta}, \quad \sigma = \frac{2\pi}{T_R}, \quad x = \frac{x'}{X}, \quad t = t'\sigma$$

where  $x'$  is a distance with the origin at the shoreline,  $\zeta$  is the sea surface,  $U$  is the depth-integrated velocity,  $a$  is the incident wave amplitude,  $X$  is the mean position of the break point,  $\tan \beta$  is the beach slope and  $g$  is the gravitational acceleration.

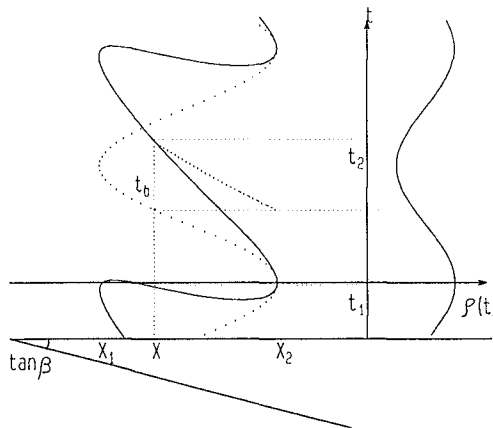


Figure 10 Schematic representation of Symonds' model.

To solve these equations, it is necessary to determine an analytic form for the forcing term on the right-hand side of Eq.(10). The value of the forcing term

depends on the position of the breakpoint,  $x_b(t)$ ,

$$F(x, t) = \frac{1}{2x} \frac{\partial(a^2)}{\partial x} = \begin{cases} 1 & x < x_b(t) \\ 0 & x > x_b(t) \end{cases} \tag{12}$$

The duration of the pulse of Eq.(12) is a function of  $x$ . For  $x$  located from  $x_1$  to  $x_2$ , the forcing term,  $F$ , defined by Eq.(12) tend to a series of pulses. For  $x$  located from 0 to  $x_1$ , it is unity for all time. Otherwise, it is zero for all time.

In the analytical treatment, after considering the result of pre-calculation in two cases of  $\chi$  from 1 to 5, Symonds *et al.* neglected the travel time,  $t_b$ . Then, by assuming that the break point varies sinusoidally with time as shown with the dotted line in Figure 10, they derived the analytical solution of the infragravity waves. By using the Symonds' model, the heights of infragravity waves in the surf zone had been calculated with the field data. In this calculation, we made some assumptions as follows:

a) Although there is the wide distribution of repetition periods as shown in Figure 7, the amplitude of incident waves varies sinusoidally with the observed mean repetition period of wave groups, that is,

$$\rho(t) = \bar{\rho} + \sqrt{2}\rho_{rms} \cos\left(\frac{2\pi}{T_R}t\right). \tag{13}$$

b) The slope of the bottom profile is constant, being  $\tan\beta = 1/140$  which is a mean slope around wave breaking points in the storms.

c) The wave breaking point is determined as the appearance point of the peak value of significant waves, employing the Goda's breaker indices(Goda,1985).

Figure 11 shows the comparison of the predicted height of infragravity waves with the observed one, where the dotted line indicates the relation of coincidence between them. The height of infragravity waves is defined as the mean value of the heights at the observation points in the surf zone. The predicted heights are about four times as large as observed ones. The large difference between them has

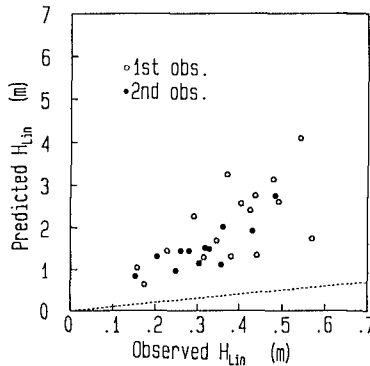


Figure 11 Comparison of observed infragravity wave height with predicted one (by the Symonds' model).

been considered to be caused by neglecting the travel time of small waves, because the conditions of their primary consideration  $\chi=25-100$  are far from our condition in the field observation. In the case of our condition, the trace of the break point has been extremely distorted sinusoidal curve, that is sawlike or overhanded, as shown with a solid line in Figure 10, even if the incident wave amplitude at the outside edge of the surf zone varies sinusoidally.

### 4.2 Modification of the Symonds' model

By taking the travel time into consideration, the Symonds' model must be modified. The position of the break point is given by

$$x_b = 1 + \Delta a \cos(t - t_b), \tag{14}$$

where  $\Delta a$  is a half width of dimension-less break point varying,  $t_b$  is the travel time required for a wave to propagate from  $x_2$  to  $x_b$ (see Figure 10), which is written as

$$t_b = 2\sqrt{\chi}(\sqrt{x_2} - \sqrt{x_b}), \tag{15}$$

according to the shallow wave theory. The forcing term,  $F$ , can be expressed as a Fourier series as follows;

$$F(x, t) = \frac{1}{2x} \frac{\partial(a^2)}{\partial x} = 2 \sum_{n=0}^{\infty} \{a_n(x) \cos nt + b_0(x) \sin nt\}, \tag{16}$$

$$a_0(x) = \frac{1}{4\pi} \int_{t_1(x)}^{t_2(x)} 1 dt, \quad b_n(x) = 0, \tag{17}$$

$$a_n(x) = \frac{1}{2\pi} \int_{t_1(x)}^{t_2(x)} \cos ntdt, \tag{18}$$

$$b_n(x) = \frac{1}{2\pi} \int_{t_1(x)}^{t_2(x)} \sin ntdt. \tag{19}$$

where  $t_1(x)$  and  $t_2(x)$  can be expressed with  $t_b$  defined by eq.(15) as follows:

$$t_1(x) = -\tau + t_b, \quad t_2(x) = \tau + t_b, \quad \tau = \arccos\left(\frac{x-1}{\Delta a}\right). \tag{20}$$

By substituting  $t_1(x)$  and  $t_2(x)$  into Eqs.(17),(18) and (19), we have

$$a_0(x) = \frac{\tau}{\pi}, \tag{21}$$

$$a_n(x) = \frac{\sin n\tau}{n\pi} \cos nt_b, \tag{22}$$

$$b_n(x) = \frac{\sin n\tau}{n\pi} \sin nt_b. \tag{23}$$

For the large value of  $\chi$ , the travel time becomes long, being  $t_b > \tau$ . In this case, the trace of breaking point is overhanded, then  $t_1(x)$  is given as

$$t_1(x) \doteq 0, \quad (24)$$

in place of Eq.(20). Under this condition, we also have  $a_0, a_n, b_n$  in the same way.

By combining Eqs.(10) and (11), the  $\zeta_0$  equation for  $n = 0$ , which is mean set-up, is simply given by

$$\zeta_0 = \begin{cases} -\frac{1}{\pi}\{(x-1)\tau - \sqrt{\Delta a^2 - (x-1)^2}\} & (x_1 < x < x_2) \\ \Delta a + (x_1 - x) & (0 < x < x_1) \end{cases}. \quad (25)$$

The  $\zeta_n$  equations for  $n > 1$  is of the following form

$$\chi \frac{\partial^2 \zeta_n}{\partial t^2} - x \frac{\partial \zeta_n}{\partial x} - \frac{\partial^2 \zeta_n}{\partial x^2} = \begin{cases} \frac{\partial(2F_n x)}{\partial x} & (x_1 < x < x_2) \\ 0 & \text{otherwise} \end{cases}, \quad (26)$$

where

$$F_n = a_n(x) \cos nt + b_n(x) \sin nt. \quad (27)$$

If we put

$$\zeta_n = \frac{V_n(x)}{x^{1/2}} \exp(int), \quad (28)$$

and by substituting Eq.(28) into Eq.(26), we have

$$\exp(int) \left[ \frac{\partial^2 V_n}{\partial x^2} + V_n \left( \frac{1}{4x^2} + \frac{\chi n^2}{x} \right) \right] = \begin{cases} -\frac{1}{x^{1/2}} \frac{\partial(F_n x)}{\partial x} & (x_1 < x < x_2) \\ 0 & \text{otherwise} \end{cases}. \quad (29)$$

The homogeneous solution of Eq.(29) is given by

$$V_n = P_n x^{1/2} Z_0(Q_n x^{1/2}), \quad (30)$$

where  $Z_0$  is the zero-th order Bessel function,  $J_0$ , or Neumann function,  $Y_0$ ,  $Q_n^2 = 4n^2\chi$ .

Outside the forcing region,  $0 < x < x_1$  and  $x_2 < x$ , the total solution is of the following form

$$\begin{aligned} \zeta_n &= \zeta_{nh}, \\ \zeta_{nh} &= \{A_n J_0(Q_n x^{1/2}) + B_n Y_0(Q_n x^{1/2})\} \cos nt \\ &\quad + \{C_n J_0(Q_n x^{1/2}) + D_n Y_0(Q_n x^{1/2})\} \sin nt, \end{aligned} \quad (31)$$

where  $A_n, B_n, C_n$  and  $D_n$  are the constants. In the forcing region,  $x_1 < x < x_2$ , the total solution is given by summing to following particular solution and eq.(31);

$$\begin{aligned} \zeta_n &= \zeta_{nh} + \zeta_{np}, \\ \zeta_{np} &= \{A_{np} J_0(Q_n x^{1/2}) + B_{np} Y_0(Q_n x^{1/2})\} \cos nt \\ &\quad + \{C_{np} J_0(Q_n x^{1/2}) + D_{np} Y_0(Q_n x^{1/2})\} \sin nt, \end{aligned} \quad (32)$$

$$\begin{aligned}
 A_{np} &= -\pi[2a_n(x)xY_0(Q_n x^{1/2})]_{x_1}^x - \pi \int_{x_1}^x a_n(x)Q_n Y_1(Q_n x^{1/2})dx, \\
 B_{np} &= \pi[2a_n(x)xJ_0(Q_n x^{1/2})]_{x_1}^x + \pi \int_{x_1}^x a_n(x)Q_n J_1(Q_n x^{1/2})dx, \\
 C_{np} &= -\pi[2b_n(x)xY_0(Q_n x^{1/2})]_{x_1}^x - \pi \int_{x_1}^x b_n(x)Q_n Y_1(Q_n x^{1/2})dx, \\
 D_{np} &= \pi[2b_n(x)xJ_0(Q_n x^{1/2})]_{x_1}^x + \pi \int_{x_1}^x b_n(x)Q_n J_1(Q_n x^{1/2})dx,
 \end{aligned}$$

where  $J_m$  is the m-th order Bessel function and  $Y_m$  is the m-th order Neumann function.

The constants are determined by setting the following conditions

- at  $x = 0$  with  $\partial\zeta_n/\partial x = 0$ ,
- at  $x = x_1$  and  $x = x_2$  with  $\zeta_n$  and  $\partial\zeta_n/\partial x$  continuous,
- at  $x = \infty$  with  $\zeta_n$  outgoing progressive.

After all, the  $\zeta$  solution is given by

$$\zeta = \sum_{n=0}^{\infty} \zeta_n. \tag{33}$$

Figure 12 shows the normalized amplitude at the shore line, which is calculated by the modified Symonds' model, as function of  $\chi$ . In this figure, the results calculated by the original model are also shown with dotted lines. For  $\chi$  smaller than 4, the modified model and the original model give the same results, while for  $\chi$  greater than 4, the results predicted by the modified model is smaller than that of the original model. In the case of  $n = 1$ , the amplitude at the shoreline increases with  $\chi$  up to  $\chi = 15$ , where the trace of break point begins to be overhanded, and it is decreases from here on.

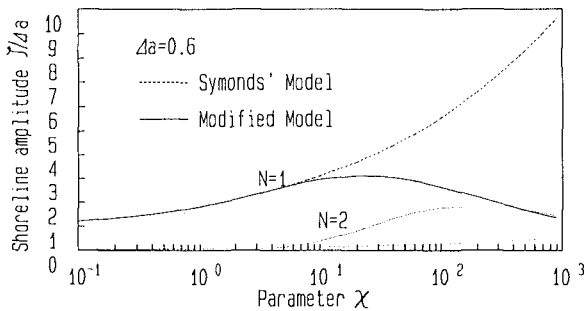


Figure 12 Normalized amplitude as a function of  $\chi$ .

### 5 Verification of modified model with the field data

In the case of our field observation, as the value of  $\chi$  is in range from 25 to 100, it is better to use the modified Symonds' model for estimating the height of infragravity waves in the surf zone. In the calculation, the assumptions described in the former section are employed, and the summation in Eq.(33) is conducted up to  $n = 3$ . Figure 13 shows the comparison of the observed infragravity wave heights in the surf zone with those predicted by the modified Symonds' model. Also in this case, the height of infragravity wave is the mean value of the heights

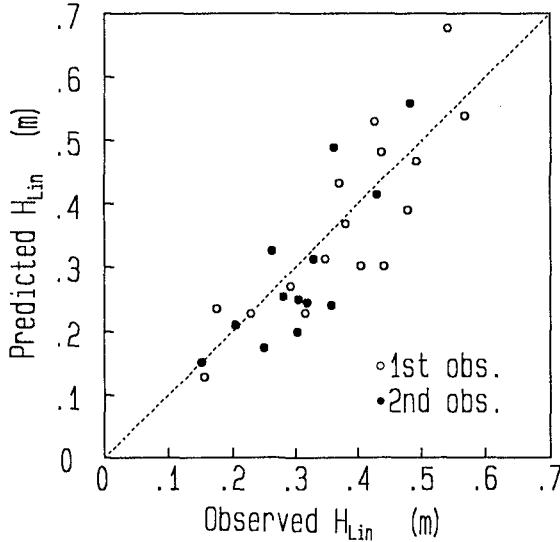


Figure 13 Comparison of observed infragravity wave height with predicted one (by the modified Symonds' model).

at the observation points in the surf zone. The data are plotted close to a dotted line, on which the observed height coincide with the predicted ones.

Next, let's do another verification of the modified Symonds' model. At the Port of Kashima located near the HORF, the waves and the currents are being permanently observed during 20 minutes of every two hours at the depth of about 24 meters. By utilizing these data, the value of  $\rho_{rms}$  and  $\bar{T}_R$  were estimated by Eqs.(8) and (9) respectively, and the heights of infragravity waves in the surf zone have been predicted by the modified Symonds' model. In the HORF, the heights of infragravity wave have been measured at the point from No.1 to 7 throughout the year.

Figure 14 shows the comparison of the predicted heights of infragravity waves with the observed ones in the HORF during one year of 1989, where the comparisons are made for the data obtained at 12 o'clock of every day. There is a close agreement between them.

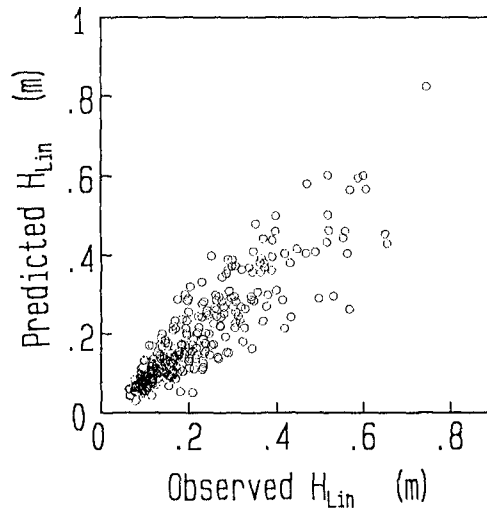


Figure 14 Comparison of predicted infragravity wave height by using the data of significant wave with observed one.

## 6 Conclusions

The main conclusions obtained in this study are as follows:

- a) The period of wave groups, which is long in a deep sea during the storm, decreases in the process of wave breaking, and the infragravity waves become large in the surf zone.
- b) The Symonds' theory has been modified by taking the effect of wave propagation into account. By means of this theory, the height of infragravity waves in the surf zone are estimated accurately with the representative value of wave groups,  $\rho_{rms}$  and  $\bar{T}_R$ .
- c) Even if the data of significant waves are only available, the heights of infragravity waves could be estimated by using the theoretical and the empirical relationships between the significant waves and the wave groups.

## References

- Katoh, K and S. Yanagishima** (1990): Berm Erosion Due to Long Period Waves, Proc. of 22nd ICCE, pp.2073-2086.
- Katoh, K and S. Yanagishima** (1992): Berm Formation and Berm Erosion, Proc. of 23rd ICCE.
- Symonds, G., D.A. Huntley and A.J. Bowen** (1982): Two-Dimensional Surf Beat: Long Wave Generation By a Time-Varying Breakpoint, J. Geophys. Res., Vol.87, No.C1, pp.492-498.
- Goda, Y** (1985): Random Seas and Design of Maritime Structures, University of Tokyo Press, 323p.





# **PART III**

## **Coastal Structures**



*Pozzallo (Sicily)*

## CHAPTER 75

### MONITORING MOUND BREAKWATERS. THE CASE OF SINES

F. ABECASIS<sup>1</sup> and C. PITA<sup>2</sup>

#### ABSTRACT

The aim of monitoring mound breakwaters is presented. Available techniques and Sines breakwaters monitoring program are described.

#### INTRODUCTION

It is normal that damage occur in mound breakwaters. However, in order to avoid the inoperationality of the structures or too expensive repairs, it is essential that these damages do not overpass certain thresholds. It is therefore necessary to carry out systematic monitoring of these structures; this will allow not only the opportune correction of any deficiency but also the diagnosis of the origin of this deficiency in order to its future correction. And it must not be forgotten that the monitoring is too a valuable source of knowledge for future designs of this kind of structures.

So, in the authors' opinion, the main scope of monitoring a breakwater is to foresee and to plan maintenance works; and it is important to take into account that any repair works of a breakwater are slow and only possible with relatively calm weather. This is why maintenance works must be planned without delay after the first signs of degradation and must be carried out in the next suitable opportunity.

As a matter of fact, the possible observation of a mound breakwater is the observation of its enveloping layers, namely of the position and integrity of the outer blocks. It is not difficult to observe in such a way the part of a breakwater above the sea level; this is not the

---

1 - Partner, HIDROTECNICA PORTUGUESA, Consulting Engineers

2 - Partner, WW, Consulting Engineers

same for the submerged part, in consequence of the turbulence and the low transparency of the water. However this is the most vulnerable zone of the structure, mainly the zone just below the sea level.

**TYPES OF DAMAGES**

The possible types of damages in mound breakwaters are the following (Per Bruun, 1982 and Pita, 1984), see figs. 1 and 2:

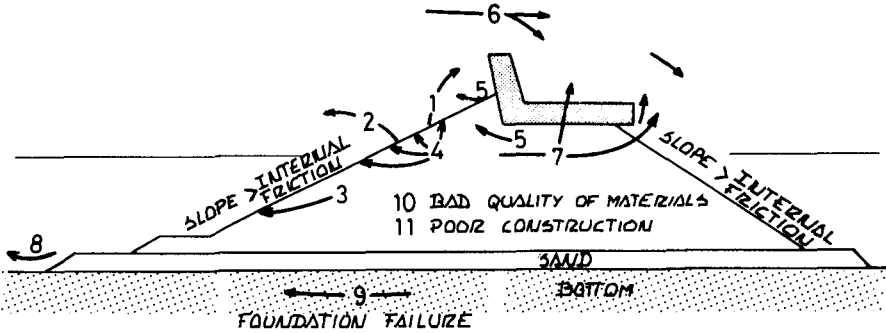


Figure 1

- 1 - Going out of armoring blocks due to plunging breaking of the waves on the outer slope, with subsequent displacement of blocks, generally upwards.
- 2 - Going out of armoring blocks due to underpressures caused by the combination of the effects of going down waves with incoming breaking waves and with hydrostatic forces of the water existing inside the mound.

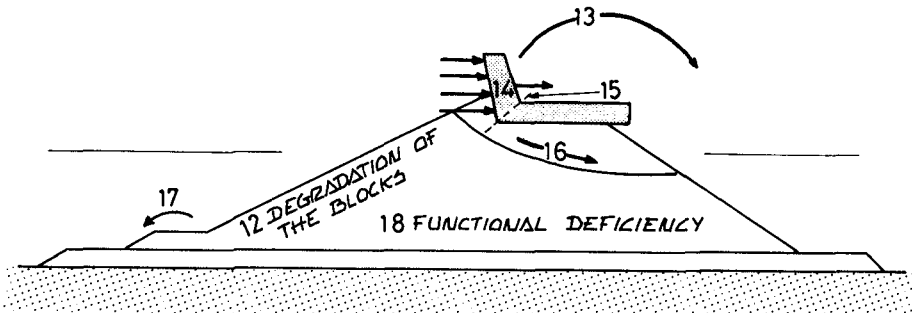


Figure 2

- 3 - Sliding of the armor layers. It happens often for very steep slopes or for very porous armor layers. It may be due to lack of support originated by berm deterioration (damages type 17).
- 4 - Falls or breakages of rocking blocks.
- 5 - Undermining of superstructure if it exists. The undermining may have several origins (differential settlements of the core, loss of fine elements, etc.).
- 6 - Instability of the top layers (and of the superstructure when it exists) and of the inner slope, due to overtoppings.
- 7 - Instability of the top layers (and of the superstructure when it exists) and of the inner slope, due to high underpressures. This may happen in consequence of too high porosity of filters and core.
- 8 - Bottom erosion in the base of the slope in consequence of wave action and/or currents.
- 9 - Rupture of the foundation.
- 10 - Damages provoked by bad quality of materials used.
- 11 - Damages originated by differences between the structure designed and the structure actually built, either in consequence of construction errors, or in consequence of adaptations of the design.
- 12 - Loss of weight and modifications in material properties due to chemical attack by sea water, to abrasion or to cavitation.
- 13 - Overturning of the curtain-wall, caused by the impact of waves.
- 14 - Sliding of the curtain-wall, caused by the impact of waves.
- 15 - Rupture of the superstructure, caused by wave action.
- 16 - Sliding of a wedge of the inner slope of the breakwater.
- 17 - Damages, by wave action, in the berm of support of the armor of both slopes (with possibility of damages of type 3).
- 18 - Functional deficiency of the structure, that is, loss (eventually temporary) of capacity of accomplishing its functions. This happens, for instance, when overtopping occur originating lack of shelter conditions inside the port.

## OBSERVATION TECHNIQUES

### General Comments

The approach used to monitor a mound breakwater is quite different from the approaches used in other structures.

A mound breakwater is a "collection" of thousands of blocks "randomly" placed, each one submitted to a different load and supported into a different way. It is impossible to identify a limited number of points representative of the stability of the breakwater, where forces, stresses and movements could be measured. To get these data, a large number of instrumented blocks would be required. Measurement devices acquisition and maintenance costs would be very high. Even if they were positioned, there would be a high probability of losing an important part of them if a major storm occurs.

It must be noted that to obtain relevant data, monitoring of a breakwater must be done on a permanent basis. In these conditions, simple and not expensive techniques must be used.

The information collected with a monitoring program should be completed by a wave and current measuring campaign, so that correlations between loads and breakwater behavior are possible. As the available measuring techniques for waves or currents are very well described in several documents, only the techniques of monitoring a breakwater are described in this paper.

### Available Techniques

#### **A - VISUAL OBSERVATIONS**

This technique is easy to perform frequently and regularly from the top of the structure or from a ship, specially in what concerns the emerged zone. Visual observation of the submerged zone is done by divers.

Anyway, this technique has some drawbacks:

- \* Damage is only detected when a certain level of it is reached;
- \* A detailed control of the submerged zone is difficult, due to turbulence and visibility problems.

The results of these observations can be influenced by the observer's criterion. To reduce this risk, a form must be fulfilled by the observer in accordance to the criteria presented in tables I and II. These criteria are adaptation of damage criteria used in model tests by Delft Hydraulics and by LNEC.

An important information collected easily and with sufficient accuracy by visual observations is the occurrence of overtoppings. In this case, it must be recorded:

- \* The date/hour at which overtopping begins and ends;
- \* Location of overtopping and its direction of propagation along the breakwater;
- \* Overtopping intensity and frequency, in accordance to classification presented in table III;
- \* Distance from the crownwall reached by the overtopping.

TABLE I  
REMOVED BLOCKS CLASSIFICATION

DEGREE	IDENTIFICATION	DESCRIPTION
0	Inexistent	There are not removed units or gaps in the armor layer.
1	Slight	Removed less than 1% of the units of upper layer of the armor. Gaps in this layer do not exceed 3 units.
2	Little	Removed less than 2% of the units of upper layer. Gaps in this layer do not exceed 3 units.
3	Moderate	Removed less than 3% of the units of upper layer. Gaps in this layer of 3 to 5 units.
4	Much	Removed more than 3% of the units of upper layer. Large gaps in this layer (more than 5 units).
5	Serious	Large gaps in the upper layer. Gaps in the second layer.
6	Destruction	The two armor layers were removed.

Note: Gap of X units: Removal of X adjacent blocks to positions distant from the original position more than a characteristic length.

TABLE II  
BREAKAGE CLASSIFICATION

DEGREE	IDENTIFICATION	DESCRIPTION
0	Inexistent	There are no broken units.
1	Hardly Any	Existing breakage has only a small effect on the weight and shape of armor units.
2	Slight	Broken units do not exceed 1% of the total number of units. No more than 3 adjacent broken units.
3	Small	Broken units do not exceed 2% of the total number of units. No more than 3 adjacent broken units.
4	Moderate	Broken units do not exceed 3% of the total number of units. The number of adjacent broken units is 3 to 5.
5	Many	Broken units do not exceed 5% of the total number of units. The number of adjacent broken units do not exceed 10
6	Serious	Broken units exceed 5% of total number of units. There are 10 or more adjacent broken units.

Note: Broken unit is a unit with a weight reduction of 10% or more of its original weight, or with an important change on its original shape.

TABLE III  
OVERTOPPING FREQUENCY AND INTENSITY

DEGREE	IDENTIFICATION	DESCRIPTION
0	Inexistent	No overtopping.
1	Hardly Any	Some waves produce a slight overtopping of "white water".
2	Little	Frequent overtopping of "white water". There is no "greenwater" overtopping.
3	Moderate	Some waves produce the passage of "green water" over the structure, but water quantities are not important.
4	Strong	Frequent overtopping of "green water", but water quantities are not important.
5	Very Strong	A few waves produce large overtopping water quantities.
6	Serious	Frequent overtopping of large water quantities.

#### B - PHOTOGRAPHY

Systematic photography of the breakwater at same scale and obtained from pre-defined points (to permit superposition of photos obtained at different observations) is an important tool to evaluate damage long term increase. These photos can be obtained from the crown of the breakwater or from a ship.

Photographic campaigns must be done in conditions that a photogrammetric treatment of the photos is possible, to evaluate the levels of the external surface of the breakwater.

#### C - TOPOGRAPHIC TECHNIQUES

Emerged area of the breakwater can be controlled by topographic record of the three coordinates (X,Y,Z) of selected points. As much as possible, the choice of these points must take into account the possibility of obtaining cross profiles of the breakwater (using sounding results for the submerged part).

#### D - SOUNDING

To quantify data on the behavior of the underwater part of the breakwater, sounding techniques must be used. The easier and less expensive technique is the manual sounding, done by a diver or from a ship. In both cases, the depths are measured in selected points located on lines perpendicular to the breakwater. The sounding with a diver has the advantage of visual observation and control of the actually sounded points (specially important in the case of a rubblemound breakwater, where the



sound can be done in the vertical of a unit or in the void between adjacent units).

More sophisticated sounding techniques involve the use of side scan sonar. They can be used to obtain cross profiles or 3-D restitutions of the underwater part of the structure. The use of 3-D scanning has difficulties, because measures are influenced by the effect of wind, waves and currents on the movement of the ship.

#### **E - AERIAL PHOTOGRAPHY**

Aerial photography is a very interesting complement of other techniques, specially because good restitutions of emerged zone can be obtained with photogrammetric treatment.

#### **F - UNDERWATER VIDEO RECORDING**

Underwater video recording has two main objectives:

- \* To record divers observations;
- \* When obtained from a remote operated vehicle (ROV), to permit the observation of areas not accessible to divers.

#### **G - TESTS OF THE MATERIALS**

To evaluate the deterioration of materials there are two possible kinds of tests:

- \* Non-destructive techniques, like the use of ultra-sounding equipment and sclerometers.
- \* Destructive techniques, where some samples are collected for laboratory tests.

### Identification and Quantification of Damages

No one of described techniques gives accurate information about the integrity of the breakwater. Anyway, with the simultaneous use of two or more techniques, it is possible to obtain reliable data to identify and quantify the several types of damages on mound breakwaters, described before. In table IV a synthesis of the use of these techniques for each type of damages is presented.

To make easier the treatment and analysis of collected data, the breakwater shall be considered split into small parts, with lengths of about 50 meters, each one being separately monitored.

### **THRESHOLDS FOR THE SEVERAL TYPES OF DAMAGES**

An attempt has been made to establish, for the several types of damages, thresholds above which it is considered necessary to carry out normal maintenance works, short term repair works (i.e. works to be carried out when the sea conditions or the constructive

TABLE IV  
OBSERVATION TECHNIQUES

DAMAGE	DESCRIPTION	POSSIBLE OBSERVATION TECHNIQUES
1 2	Removal of armor units	A - Visual observation (emerged and submerged zones).
3	Sliding of armor layers	B - Photography, eventually with photogrammetric treatment. C - Traditional topographic techniques.
4	Falls or breakages produced by rocking	D - Sounding techniques. E - Aerial photography, eventually with photogrammetry (emerged zone).
16	Sliding of a wedge of the inner slope	F - Submarine television.
5	Undermining of superstructure	A - Visual observation. B - Photography. C - Traditional topographic techniques. E - Aerial photography. G - Destructive tests
6 7 13 14 15	Instability of top layers and crownwall	A - Visual observation. B - Photography. C - Traditional topographic techniques. E - Aerial photography.
8	Bottom erosion	A - Visual observation (by divers).
9	Rupture of foundation	D - Soundings. F - Submarine television.
17	Damages in the berm of support of the armor of both slopes	
10	Bad mechanical properties of materials	A - Visual observation. G - Non-destructive tests. G - Destructive tests.
12	Physical and chemical deterioration of the materials	
18	Functional deficiency	Visual observations.

constraints allow) or as quick as possible repair works (even with provisional character and, therefore, designed for a very short life - only a few months).

These proposed thresholds, presented in table V, are based on the existing experience; as a matter of fact, they suffer very much from subjectiveness and therefore they will certainly require corrections and adjustments in the future.

TABLE V  
THRESHOLDS OF DAMAGES

Damage type	Description		Thresholds		
			Of normal maintenance	Of repair	
				Short term	As quick as possible
1 2	Going out of armor- ing blocks (outer and inner slopes)		Degree 1 falls or lacks of blocks	Degree 2 falls or lacks of blocks	Degree 3 or above falls or lacks of blocks
3	Sliding of the armor layers				
4	Falls or breakages of rocking blocks		Degree 1 falls or degree 2 fractures	Degree 2 falls or degree 3 fractures	Degree 3 or above falls or degree 4 fractures OR degree 2 falls and degree 3 fractures
5	Undermining of su- perstructure		If tendency to their occurrence is detec- ted, periodical recharges or repairs must be carried out	When detected	When detected, if if this detection happens in the beginning or during winter
6 13 14 15	Instability of top layers or of super- structure, due to the impact of waves or to overtoppings				
7	Too much porosity of filter layers or of core	Instability of top layers or of super- structure			
		Instability of inner slope	Degree 1 falls or lacks of blocks	Degree 2 falls or lacks of blocks	Degree 3 or above falls or lacks of blocks
8	Bottom erosion		-	If there is fear that foundation be affected	If the foundation is affected
9	Rupture of foundation		-	-	When detected (1)
10 12	Materials deterio- ration		When detected, even small	When the material strength of blocks or other important structural elements is reduced 30% or the weight of 3% of the blocks is reduced 40%	-
11	Differences between the structure de- signed and built		-	When detected, if the studies on the structure behavior show that the struc- ture actually built is not stable for the design wave	-
16	Sliding of a wedge of the inner slope		-	When detected	When detected, if this detection occurs in the beginning or during winter
17	Damages in the berm of support of the armor of both slopes		When detected, even small	If the support func- tion of the berm is affected	If the support function of the berm is seriously affected
18	Functional deficiency		If it causes draw- back to harbour operativeness	-	-

(1) - In this case immediate repair is required. This repair would probably be definitive.

**MONITORING SINES BREAKWATERS**Brief Description of the Breakwaters

Sines is an artificial harbor, with shelter conditions obtained with two large breakwaters.

Main breakwater, the so called West Breakwater, is also the harbor oil terminal and has several cross-profiles:

- \* **Type A** - Along 173 meters, it is characterized by a single layer armor of 40 tons Antifer cubes, with a slope 2:1. Top of the armor is at +14,0 m CD.
  - Concrete crown wall has a top level of +16 m CD with an external vertical face.
  - Design wave is  $H_s = 9$  m.
  
- \* **Type B** - Along about 317 meters, this profile is composed by a double layer armor of 40 tons Antifer cubes with a slope of 2:1. Armor top is at +17,5 m CD, with a 15 m wide berm. The toe is composed by a 10 meters wide berm of 40 tons Antifer cubes.
  - The superstructure has a crown wall, with an initial part with external vertical face and top at +16m CD, and a final portion with a curved parapet to reverse the run-up flow with a top level of +19 m CD.
  - Design wave height is  $H_s = 9$  meters.
  
- \* **Type C** - Along about 450 meters, this profile has a double layer armor of 90 tons Antifer cubes extending from levels +18 m CD to -20 m CD, with a composite slope:
  - From +18,0 m CD to -3,0 m CD → Slope 2:1
  - From -3,0 m CD to -5,0 m CD → Slope 8:1
  - From -5,0 m CD to -20,0 m CD → Slope 3:1.
  - Inner slope is composed by 3 - 6 tons quarry stones at 4:3, between levels +1,4 m CD and -15,0 m CD. Below this level, a quarry run material with a slope of 4:3 is used.
  - Superstructure is similar to the one described for the outer part of type B profile.
  - Design wave height is  $H_s = 14,0$  m.
  
- \* **Type D** - Along 500 meters, this section is composed by a composite slope of 2 armor layers of 90 tons Antifer cubes, reaching levels of +13,2 m CD at the top and -20,0 m CD at the bottom. Slopes are as follows:
  - Between +13,2 m CD and +5,84 m CD → 3:1
  - Between +5,84 m CD and -7,0 m CD → 2:1
  - Between -7,0 m CD and -11,0 m CD → 7:1
  - Between -11,0 m CD and -19,85 m CD → 3:1

- Inner slope is composed also by 2 layers of 90 tons Antifer cubes with a slope of 3:1 between levels +13,2 m CD and +9,0 m CD and 2:1 between levels +9,0 m CD and -1,0 m CD. Below level -1,0 m CD, 9 - 12 tons quarry stones were used with a slope of 3:2 until level -4,0 m CD and 2:1 between this level and the bottom.
- The head of the breakwater armor is composed by high density 105 tons Antifer cubes.

The initial West Breakwater was 2 kilometers long. The final part, between profile type D and the previous head, around 280 meters long, will be abandoned.

The second breakwater, East Breakwater, gives shelter conditions for the operation of a coal terminal, is about 1100 meters long in depths of about 25 to 30 meters in a sand bottom. This breakwater has a double layer armor of 60 tons Antifer cubes with a slope of 2,5:1, between +14,25 m CD and -11,75 m CD. At the toe, this armor is supported by a 9 - 12 tons quarry stones berm 10 m wide.

Inner slope is composed by a 60 tons Antifer cubes armor at 3:2 between levels +12,5 m CD and -5,0 m CD.

The top of this profile is 6,25 m wide and has an in situ concreted cap platform.

### The Monitoring Plan

First of all, it is recommended that the two breakwaters will be divided into reaches 30 m long.

The following observations of the two structures must be carried out:

#### A - Routine observations

##### A.1 - Visual observations

To be carried out monthly between October and April and in midsummer, in a total of 8 observations per year. They must be performed by walking on the crest of the breakwaters during low tide and recording the results. These observations must be complemented through identical procedure from a small boat, also during low tide, parallel to both slopes of the breakwaters.

Yearly (in the early spring) an observation of the submerged part of the breakwaters must be carried out. This observation will allow the completion of the program with data concerning the submerged part.

##### A.2 - Photography

In the beginning of spring and autumn, the visual observations from the crest and the boat referred to above must be complemented with local photos of each

reach. These photos must be obtained in low water, concerning only the outer slope and the superstructure.

Yearly, in early spring, general photos of the outer slopes must be taken, also during low tide, from a boat moving parallel to the breakwaters at a distance of 150 m. These photos must allow the obtention of amplifications at constant scale, not below 1:500, for superposition with other ones obtained previously, to identify block displacements. In the same occasion, local photos of the submerged part of the slopes must be obtained to illustrate eventual deficiencies of the armor.

In what concerns the inner slope, the general and local photos will be taken only every two years, unless if the visual inspection referred to in A.1 would have shown any damage; in this later case photos of the two types must be taken. However, taking into account that east breakwater and the reconstructed part of the west one will be overtopped frequently, the general and local photos of their inner slopes must be taken with the same frequency than for the outer slopes, that is to say, general photos yearly, in early spring, and local photos twice a year, in April and September.

#### **A.3 - Topographical techniques**

Twice a year, in April and September, it must be carried out the topographical control, with basis in points in land, of one point in each module (15 m long) of the superstructure of the West Breakwater. In East Breakwater, without superstructure, it is considered enough the topographical control of one point every 30 m.

These points, in both breakwaters, will serve for the location of cross-sections of the part above water level. It is recommended the obtention of these cross-sections, once a year (in April), 60 m apart.

#### **A.4 - Soundings**

Soundings must be carried out, by any of the procedures described before, prolonging as much as possible the sounding of the submerged part of the breakwaters, both near the water surface and seaward of the base of the slope (in this later case not less than 30 m beyond this base). These soundings must be carried out simultaneously with the cross-sections above water level.

#### **A.5 - Aerial photography**

It must be made yearly, in early spring, simultaneously, as much as possible, with the surveys and cross-sections referred to above. The aerial photography must be submitted to photogrammetric treatment, with the scope of obtaining breakwater plans to a scale not below 1:500.

**A.6 - Underwater TV**

If the observations referred to above show any local damages in the submerged part of the breakwaters, video-records of these damages must be obtained.

**B - Extraordinary observations****B.1 - Overtoppings**

When overtoppings occur, they must be observed.

**B.2 - Just after a storm with Hs exceeding 5 m in deep waters**

A visual observation of the A.1 type must be carried out; if this observation advises it, observations of the A.2 type must be carried out too.

**B.3 - After a storm with Hs exceeding 8 m in deep waters**

Besides the visual observation referred to in B.2, just after the storm, a complete observation using all the techniques referred to in A must be carried out as quick as possible; the distances between cross-sections of the emergent and submerged zones must be reduced to 30 m (or even less, locally, if it is necessary to a better characterization of the damages).

Obviously, after every big repair of the breakwaters, a complete observation of type A must be done (identical to the one carried out regularly in April). This observation may be eventually restricted to the repaired zone.

Besides the observation of the structures themselves referred to above, the actions on them - waves, tides, currents and winds, must obviously be regularly recorded. However it is not the scope of this paper to consider in detail these observations.

**First Results****• Wave Records**

At Sines there are two Datawell directional wave recorders, one of which in deep water [CD (-100 m)]. The wave recording program is being done since 1973, with some gaps due to wave buoy problems. Data are available in real time.

**• Breakwaters Monitoring**

Construction profiles of the underlayers and the armor are available. The results of the usual construction material tests are also in Administração do Porto de Sines files.

There are some profiles collected since 1980 on a non-regular basis of Type C zone of West Breakwater.

Included in the Systematic Monitoring Program, APS has done some work, consisting of:

- Several visual observations;
- Photographic reports;
- Topographic observation of selected points in the superstructures;
- An aerial photography and a photogrammetric restitution of the part of the West Breakwater above sea level.

APS monitoring program is included in a proposal to EC Marine Science and Technology Program (MAST II), in which obtained data will be compared with data collected at Zeebrugge harbor using the same techniques and also with the equipment installed at its northwest breakwater (which comprises the measurement of wave characteristics, tidal currents and orbital velocities, water levels and water pressure fluctuations at several points in front of the breakwater, in the armor layer and in the core, air pressures in the core, impact pressures on the faces of armor units and video observations of uprush and downrush).

#### ACKNOWLEDGEMENT

The monitoring plan of the Sines Breakwaters was prepared for the Administração do Porto de Sines. The authors are in debt to APS for the permission of preparing this paper.

#### REFERENCES

- PER BRUUN, 1982 - Stability and Fragility of Mound Structures, "The Dock and Harbour Authority", 736, Vol. LXIII, Mars 1982.
- PITA, C., 1984 - Dimensionamento de Quebra-Mares de Tálude e dos Seus Elementos Constitutivos, LNEC, May 1984.



## CHAPTER 76

### Rear Side Stability of Berm Breakwaters

O.H. Andersen<sup>1</sup>, J. Juhl<sup>1</sup> and P. Sloth<sup>1</sup>

#### Abstract

With the aim of providing improved methods for preliminary design of berm breakwaters, a series of physical model tests and a parameter study with special emphasis on the rear side stability of a trunk section have been carried out at the Danish Hydraulic Institute (DHI). The model tests included different geometries of the berm breakwater profile and a range of wave conditions. For each profile, the wave condition resulting in sea side and/or rear side damage was determined. As a hydrodynamic description of the overtopping waves would be very comprehensive, and at present is not available, a surf similarity approach in combination with a force balance for the armour stones has been chosen. A parametric expression for the rear side stability has been established and found to be in fairly good agreement with the model test results.

#### Introduction

Existing experience with berm breakwaters provides some insight in the behaviour of the various parts of a berm breakwater. Most research during the last ten years has concentrated on the sea side stability of the trunk section, ie the development of the berm profile. No systematic work on the rear side stability has previously been reported and hence a comprehensive study focusing on the rear side stability of the trunk section was carried out at DHI. As it is still not possible to give an adequate hydrodynamic description of the overtopping phenomenon, eg in the form of a numerical model, it was decided to carry out a series of physical model tests and an associated parameter study.

---

<sup>1</sup> Danish Hydraulic Institute, Agern Allé 5, 2970 Hørsholm, Denmark

In the present study, the rear side stability is treated as a traditional static stability phenomenon. Emphasis has been put on inclusion of a large number of physical parameters enabling the description to cover a variety of berm breakwater designs: wave height and steepness, crest height, rear side slope, effective sea side slope, stone diameter, relative density and natural angle of repose.

The stability criterion established has been compared to the results of the model tests carried out and in addition to an expression given by Van der Meer and Veldman.

## Model setup and procedure

A wave flume with a length of 65 m and a width of 1.8 m was used for model testing in four water depths of 0.67 m, 0.77 m, 0.87 m and 0.97 m. The profile tested is shown in Figure 1. Crushed stones were used both for the core,  $D_{50} = 0.011$  m (50% exceedance), and for the berm and armour layer,  $D_{n50} = 0.034$  m.  $D_{n50}$  is the nominal diameter given as  $(M_{50}/\rho_s)^{1/3}$ , where  $M_{50}$  is the mass of the stones (50% exceedance) and  $\rho_s$  is the density of the stones. The grading of the berm and armour material equalled  $D_{n85}/D_{n15} = 1.35$  and the relative density equalled  $\Delta = 1.68$ . The armour layer thickness on the crest and rear side was twice the value of  $D_{n50}$ . The model study covered variations in the following parameters:

- $w_c$ , width of the crest, 0.175 m and 0.30 m
- $R_c$ , freeboard of the crest, 0.20 m, 0.30 m and 0.40 m
- $f_h$ , width of the berm, 0.45 m, 0.65 m, 0.85 m and 1.05 m
- $f_v$ , freeboard of the berm, 0.10 m and 0.20 m.

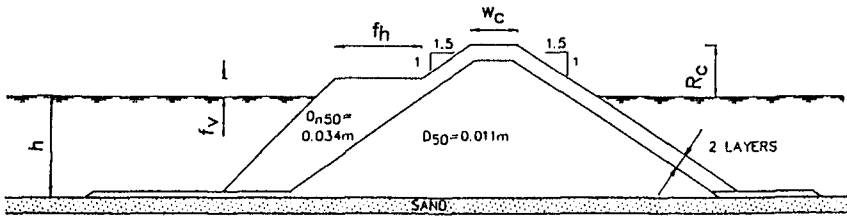


Figure 1. Test profile.

Tests were carried out in test series with successively increasing wave height,  $H_{m0}$ , and wave period,  $T_{02}$ , from test run to test run, with a fixed fictitious wave steepness  $s_{02} = 2\pi H_{m0}/gT_{02}^2$  equal to approximately 0.030 and 0.044 respectively. Each test series consisted of approximately 1,000 irregular waves. The incident wave characteristics in front of the berm breakwater,  $H_{m0}$  and  $T_{02}$ , and the reflection coefficient were calculated using a multi-gauge technique.

The berm profile was measured after each test run. Damage to the seaward side of the berm breakwater was defined to occur when the entire top of the berm was eroded. Rear side damage was defined as a settlement of the rear side armour layer which in some cases was followed by an exposure of the core.

Table 1 gives an overview of the 23 tested profiles for which rear side damage was observed prior to or coincident with damage of the sea side. The wave conditions,  $H_{m0}$  and  $T_{02}$ , resulting in rear side damage are also shown in Table 1.

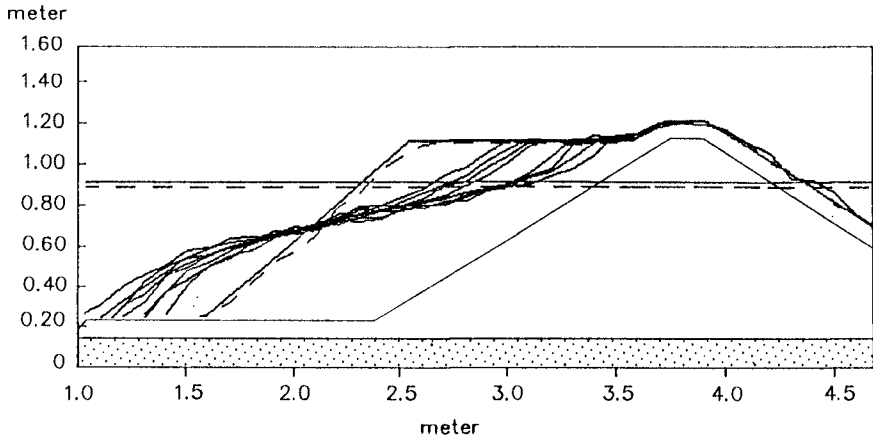
*Table 1. Rear side damages.*

Note: A is the berm area and  $\tan\alpha$  the effective sea side slope, as defined below.

wc (m)	Rc (m)	fh (m)	fv (m)	h (m)	A (m <sup>2</sup> )	$H_{m0}$ (m)	$T_{02}$ (s)	$s_{02}$	$\tan\alpha$
0.175	0.2	0.45	0.1	0.97	0.25	0.176	1.67	0.0404	0.39
0.175	0.2	0.85	0.1	0.77	0.59	0.228	1.84	0.0431	0.36
0.175	0.2	0.65	0.1	0.97	0.47	0.211	1.78	0.0427	0.37
0.175	0.2	1.05	0.1	0.77	0.76	0.228	1.84	0.0431	0.29
0.175	0.2	0.85	0.1	0.97	0.68	0.184	2.08	0.0272	0.43
0.175	0.2	1.05	0.1	0.97	0.89	0.202	2.13	0.0285	0.30
0.175	0.3	0.45	0.2	0.77	0.25	0.186	2.06	0.0281	0.45
0.175	0.3	0.65	0.1	0.77	0.41	0.209	2.11	0.0301	0.38
0.175	0.3	0.65	0.1	0.77	0.41	0.219	1.81	0.0428	0.36
0.175	0.3	0.45	0.2	0.87	0.25	0.184	2.00	0.0295	0.42
0.175	0.3	0.65	0.2	0.77	0.44	0.210	2.12	0.0299	0.39
0.175	0.3	0.85	0.1	0.77	0.59	0.228	2.20	0.0302	0.33
0.175	0.3	0.65	0.2	0.87	0.47	0.235	2.17	0.0320	0.37
0.175	0.3	0.85	0.2	0.77	0.64	0.256	1.93	0.0440	0.31
0.175	0.3	1.05	0.1	0.77	0.76	0.232	2.24	0.0296	0.29
0.175	0.3	1.05	0.1	0.77	0.76	0.270	1.99	0.0437	0.29
0.175	0.3	1.05	0.2	0.77	0.83	0.271	1.99	0.0438	0.29
0.3	0.2	0.65	0.1	0.97	0.47	0.207	1.71	0.0453	0.37
0.3	0.2	0.85	0.1	0.97	0.68	0.222	1.78	0.0449	0.32
0.3	0.2	1.05	0.1	0.97	0.89	0.241	1.83	0.0461	0.28
0.3	0.3	1.05	0.1	0.77	0.76	0.238	2.21	0.0312	0.27
0.3	0.3	1.05	0.2	0.77	0.83	0.248	2.19	0.0331	0.30
0.3	0.3	1.05	0.2	0.77	0.83	0.279	1.97	0.0460	0.28

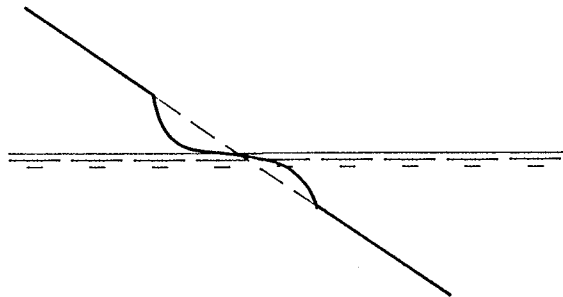
## Data Analysis

During the tests, it was observed that the developed sea side profile can be characterised as three slopes: an upper steep slope, a lower slope close to 1:4 or flatter and finally a steep slope intersecting the seabed, see Figure 2. This is a well known observation confirmed by several other researchers.



*Figure 2. Example of development of sea side profile.*

Rear side damage of a trunk section happens at almost fully developed sea side profile. A typical development is that a few stones just above still water level at the rear side are displaced downwards during a series of wave overtoppings (cf Figure 3), and after another few severe wave overtoppings, a settlement of the rear side armour layer occurs, possibly resulting in an exposure of the core.



*Figure 3. Initiation of rear side damage.*

The stability of the rear side depends on the sea side profile, crest height, crest width, rear side slope, stone diameter, relative density and natural angle of repose. It appears from the analysis of the present model test results that a variation with the crest width is not visible. New model tests with larger crest widths are presently being carried out in order to include this parameter as well. The following analysis is considered to be valid for the crests widths in Table 1, and hence  $w_c$  is not included in the analysis.

It is assumed that the speed of the overtopping water is the governing factor in determining the rear side stability. The speed at the crest,  $U_R$ , is chosen as a reference speed.

$U_R$  can be found by putting the potential at the crest equal to the potential at the still water level at the seaward side:

$$U_R^2 = 2g (R_{ui} - R_c) \quad (1)$$

where  $R_{ui}$  is the run-up on a hypothetical slope of the sea side, with index  $i$  indicating a fraction of the waves. The hydraulic parameters are defined in Figure 4.

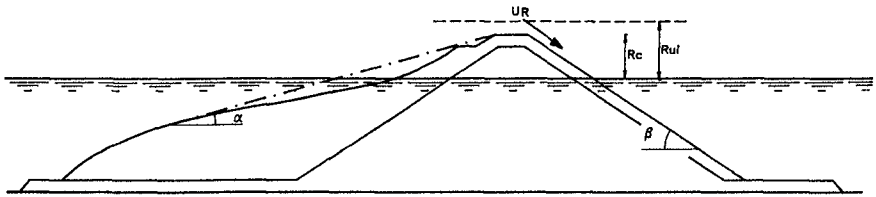


Figure 4. Definition of hydraulic parameters.

Pilarczyk (1990) applied the same reference velocity for the description of the rear side stability of dikes, resulting in a final stability criterion with large resemblance to the criterion derived below.

For the berm breakwater rear side, a traditional static stability criterion is applied. The stability of a single stone at still water level is expressed by a force balance parallel to the rear side slope, cf Figure 5:

$$F_D + W_s \sin\beta - \mu (W_s \cos\beta - F_L) < 0 \quad (2)$$

where  $F_D$  is the drag force,  $F_L$  is the lift force,  $W_s$  is the submerged weight, and  $\beta$  is the rear side slope angle. The resistance against rolling and sliding  $\mu$  can be found as  $\mu = \tan\phi$ , where  $\phi$  is the natural angle of repose.

This yields:

$$F_D + \mu F_L < W_s (\mu \cos\beta - \sin\beta) \quad (3)$$

The submerged weight equals:

$$W_s = \Delta \rho g D_{n50}^3 \quad (4)$$

where  $\rho$  is the density of water and  $D_{n50}$  is the nominal diameter.

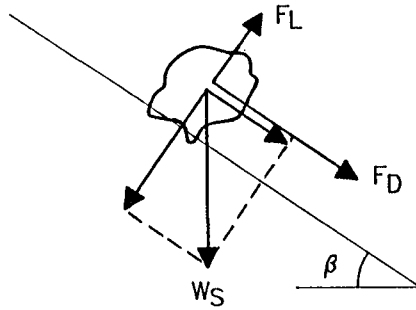


Figure 5. Forces acting on a single stone.

The left side can be expressed as:

$$F_D + \mu F_L = (C_D + \mu C_L) \frac{1}{2} \rho U_R^2 D_{nso}^2 \tag{5}$$

where  $C_D$  and  $C_L$  are force coefficients. For convenience, the nominal diameter is applied in the above expression. Combining (1), (3) (4), and (5) and re-arranging, the stability criterion now yields:

$$R_c > R_{ul} - \Delta D_{nso} \frac{\mu \cos \beta - \sin \beta}{C_D + \mu C_L} \tag{6}$$

For a relatively flat sea side slope, it is assumed that the run-up can be expressed as a function of the surf similarity parameter, cf CIRIA/CUR (1991):

$$R_{ul} = a \xi_{02} H_{mo} \tag{7}$$

where  $\xi_{02}$  is the surf similarity parameter (Iribarren number) given as:

$$\xi_{02} = \frac{\tan \alpha}{\sqrt{s_{02}}} \tag{8}$$

where  $\tan \alpha$  is the effective sea side slope and the factor  $a$  is a constant close to 1. In the following,  $a$  is kept equal to 1.

The effective sea side slope is for the present purpose defined as a straight line through the toe of the lower slope, where the influence of the breaking waves becomes significant, and up to the seaward face of the crest, cf Figure 4.

In general, the effective sea side slope represents the upper part of the berm area shaped by the incident waves. The effective sea side slope is considered to be

a good measure of the part of the berm area which is active in the wave deformation irrespective of the water depth in front of the structure.

For the specific test programme, the effective sea side slope for the cases with rear side damage has been plotted against the berm area, cf Figure 6. It is observed that the effective sea side slope decreases with the berm area.

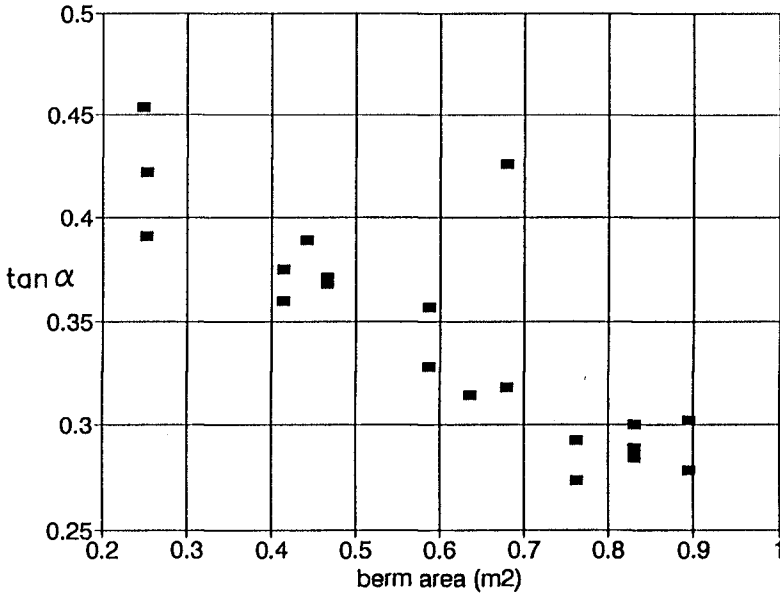


Figure 6. Effective sea side slope vs berm area for the cases with rear side damage.

Combining (6), (7) and (8) gives for the stability criterion:

$$R_c > \tan \alpha \frac{H_{mo}}{\sqrt{s_{02}}} - \Delta D_{n50} \frac{\mu \cos \beta - \sin \beta}{C_D + \mu C_L} \quad (9)$$

The above expression is made dimensionless by  $H_{mo} \sqrt{s_{02}}$ .

$$\frac{R_c}{H_{mo}} \sqrt{s_{02}} > \tan \alpha - \left( \frac{H_{mo}}{\Delta D_{n50}} \frac{1}{\sqrt{s_{02}}} \right)^{-1} \frac{\mu \cos \beta - \sin \beta}{C_D + \mu C_L} \quad (10)$$

For the observed rear side damages, the effective sea side slopes,  $\tan \alpha$ , have been divided into three equidistant intervals with the following limits: 0.27, 0.33, 0.39 and 0.45.

For the stone material applied,  $\mu$  equals 0.9. For this value, the expression (10) has been calibrated to fit the observations. The best agreement was obtained with  $(C_D + \mu C_L)$  equal to 0.08. Four different curves representing  $\tan\alpha = 0.27, 0.33, 0.39$  and  $0.45$  respectively have been drawn in Figure 7. For all curves, the rear side slope equals the value of the actual test programme:  $\tan\beta = 1:1.5$ .

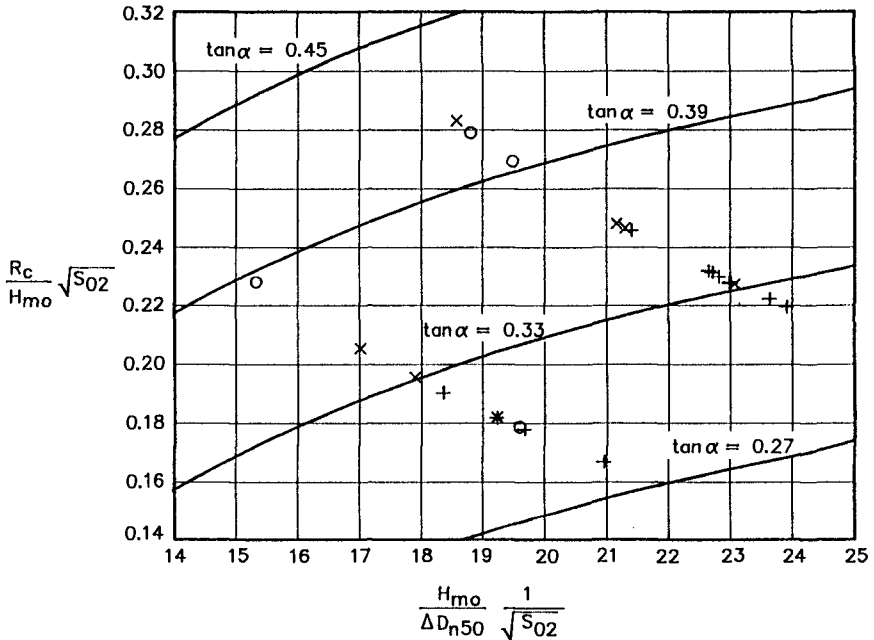


Figure 7. Stability of rear side.

Legend: Measurements:   
 +:  $0.27 < \tan\alpha < 0.33$ ,   
 x:  $0.33 < \tan\alpha < 0.39$ ,   
 o:  $0.39 < \tan\alpha < 0.45$

Full drawn curves show the stability criterion (10)

It is seen that a fairly good agreement between the measurements and the stability expression is obtained. The measurements show that  $R_c/H_{mo} \sqrt{s_{02}}$  increases with  $H_{mo}/\Delta D_{n50} / \sqrt{s_{02}}$ , which again shows that in the stability expression (10) the  $\tan\alpha$  term as well as the term including  $H_{mo}/\Delta D_{n50} / \sqrt{s_{02}}$  are of importance.

For a specified wave condition, the rear side stability can according to (10) be increased in several ways:

- increase of crest height,  $R_c$ , which is the most traditional method
- increase of stone diameter,  $D_{n50}$ . In Norway, a berm breakwater has been constructed with larger stones on the rear side than on the sea side, cf Tørum et al (1990)



- increase of relative density,  $\Delta$
- decrease of rear side slope,  $\tan\beta$

However, only the dependency on  $R_c$  has been studied experimentally.

The stability expression (10) bears some resemblance to the expression given by Van der Meer and Veldman (1992):

$$\frac{R_c}{H_s} s_{op}^{1/3} = K \quad (11)$$

- $H_s$  is the significant wave height  $\sim H_{mo}$   
 $s_{op}$  is the fictitious wave steepness based on the peak period  
 $K$  is a constant, which equals:  $K = 0.25$  for start of damage  
 $K = 0.21$  for moderate damage  
 $K = 0.17$  for severe damage

The above expression (11) is based on a parameter fitting procedure applied to two different sea side geometries (one of them in two different scale ratios). Comparing to the stability expression (10), the major difference is that in (11),  $R_c/H_{mo} s_{op}^{1/3}$  is constant, whereas the very similar quantity  $R_c/H_{mo} \sqrt{s_{02}}$  in (10) depends on  $H_{mo}/\Delta D_{n50} / \sqrt{s_{02}}$  and the effective sea side slope.

## Conclusions

- Model tests with a range of berm breakwater profiles have been carried out at DHI.
- A parametric expression for the rear side stability has been made, cf (10).
- The expression includes the wave height and steepness, crest height, rear side slope, effective sea side slope, stone diameter, relative density and natural angle of repose.
- The measurements show that the rear side stability increases with a decreasing effective sea side slope. A decrease in the effective sea side slope can be obtained by increasing the berm area.
- Applying the surf similarity approach for a bermed profile gives reasonably good agreement between the derived expression for the rear side stability and the model test observations.
- New model tests with different crest widths are being carried out in order to examine the variation of the rear side stability for a wider range of this parameter.

## Acknowledgements

The present study was carried out as a part of the research and technological development programme in the field of Marine Science and Technology (MAST) financed by the Commission of the European Communities, Directorate General for Science Research and Development, MAST I, Contract 0032, G6-S, Coastal Structures.

The authors wish to thank Mr Flemming John Andersen, Mr Christian Poulsen, Ms Bettina H. Sørensen and Mr Jakob Johannsen for carrying out the model tests, which were part of their B.Sc. dissertations at the Danish Academy of Engineering.

## References

- Burcharth, H.F. and Frigaard, P. (1988), '*On Three-Dimensional Stability of Reshaping Breakwaters*'. 21st International Conference on Coastal Engineering, pp 2284-2298.
- CIRIA/CUR (1991), '*Manual on the Use of Rock in Coastal and Shoreline Engineering*'. CIRIA Special Publication 83/CUR Report 154.
- Jensen, O.J. and Sørensen, T. (1987), '*Hydraulic Performance of Berm Breakwaters*'. *Berm Breakwaters: Unconventional Rubble Mound Breakwaters*, ASCE, pp 74-91.
- Pilarczyk, K.W. (1990), '*Design of Seawalls and Dikes - Including Overview of Revetments*'. In Pilarczyk, K.W. (Ed.), *Coastal Protection*, Balkema, Rotterdam, pp 197-288.
- Tørum, A., Mathiesen, M., Vold, S., Bjørdal, S., and Næss, S. (1990), '*Årviksand Fishing Port Breakwater Extension*'. 27th International Navigation Congress, PIANC, S.II-3, pp 99-105.
- Van der Meer, J.W. and Veldman, J.J. (1992), '*Singular Points at Berm Breakwaters: Scale Effects, Rear, Round Head and Longshore Transport*'. *Coastal Engineering*, 17, pp 153-171.

## CHAPTER 77

# Oblique wave attack on block revetments

Adam Bezuijen\* and Mark Klein Breteler†

November 12, 1992

### Abstract

The influence of the angle of the incoming wave on the stability of a placed block revetment on a filter layer has been investigated. A computer program is described to simulate the flow in the filter layer for various wave conditions. The flow in the filter layer together with the wave conditions determine the loading on the revetment. Two different boundary conditions have been studied, A schemed wave pressure distribution based on results obtained for wave loading perpendicular to the revetment and regular waves measured in a wave basin. The results show that for regular waves the influence of the angle of the incoming wave on the loading of a placed block revetment is small for a revetment with a leakage length equal or larger than the wave height. Oblique incoming waves can result in a considerable increase in loading when the leakage length is much smaller than the wave height and near transitions in the revetment.

## 1 Introduction

Model tests on placed block revetments are mostly carried out in a wave flume. In these tests the angle of the incoming waves is perpendicular to the revetment. In reality the incoming waves can make different angles with the slope. In the field the revetment will be loaded with oblique waves. A perpendicular wave loading will be an exception.

Until recently this was not considered to be a problem. The perpendicular wave loading was assumed to be the most severe wave loading on the revetment. However Gadd and Leidersdorf (1990) presented results of field observations which indicate that the loading on the revetment by oblique wave attack can be more severe than the loading by waves coming in perpendicular to the revetment. They found that a block mattress on a permeable core was damaged due to oblique incoming waves, while the same wave loading coming perpendicular to the revetment had not caused any damage.

---

\*Consultant, Delft Geotechnics, P.O. Box 69, 2600 AB Delft, the Netherlands.

†Head Coastal Structures group, Delft Hydraulics, P.O. Box 152, 8300 AD Emmeloord, the Netherlands.

The influence of oblique wave attack on the loading of a placed block revetment on a filter layer has been studied in a research programme commissioned by the Dutch Ministry of transport and public works (Rijkswaterstaat) and performed by Delft Geotechnics and Delft Hydraulics. Large scale experiments with oblique incoming waves are nearly impossible, because there are hardly facilities available for this type of research. On the other hand small scale experiments on placed block revetments cannot be done without scaling effects, Klein Breteler (1992). Therefore a small scale facility was used to measure only the wave pressures, the wave pressures apart from the wave impact can be measured without scaling effects and the wave impact is not the critical loading for the revetment. The filter flow in the revetment, the pore pressures and the loading on the revetment are simulated with a numerical finite difference program. The results of a comparable program for perpendicular wave attack are verified with the results of large scale model tests in a wave flume, Bezuijen et al. (1987). A comparable procedure, which combined the results of small scale model tests with the results of numerical simulations, is described by Bezuijen et al. (1988).

## 2 Description of numerical program STEEN3D

The numerical program is based on the STEENZET/1 program (Bezuijen et al., 1987; Bezuijen et al, 1990). The preliminary assumption, on which the STEENZET/1 program is based, is that the cover layer is relatively impermeable compared to the filter layer and that the flow through the base layer can be neglected. For most of the placed block revetments built in the Netherlands this appeared to be the case. In that case the pressure distribution can be described as a semi-confined aquifer. The flow in the filter layer is quasi-static. In the filter layer a mean potential  $\phi$  can be derived in a plane perpendicular to the slope assuming that the flow in the filter layer is in a plane parallel to the slope. Further the flow in the cover layer is assumed to be perpendicular to the slope. With these conditions the differential equation for the flow in the filter layer in two dimensions can be written as:

$$k_x \frac{\partial^2 \phi}{\partial x^2} + k_y \frac{\partial^2 \phi}{\partial y^2} = k' \frac{\phi - \phi'}{bD} \quad (1)$$

where:

$\phi$	: the mean piezometric head in the filter layer	(m)
$\phi'$	: the piezometric head on the cover layer	(m)
$x, y$	: co-ordinates, see figure 1	(m)
$k_x$	: the permeability of the filter layer in x direction	(m/s)
$k_y$	: the permeability of the filter layer in y direction	(m/s)
$k'$	: the permeability of the cover layer	(m/s)
$b$	: the thickness of the filter layer	(m)
$D$	: the thickness of the cover layer	(m)

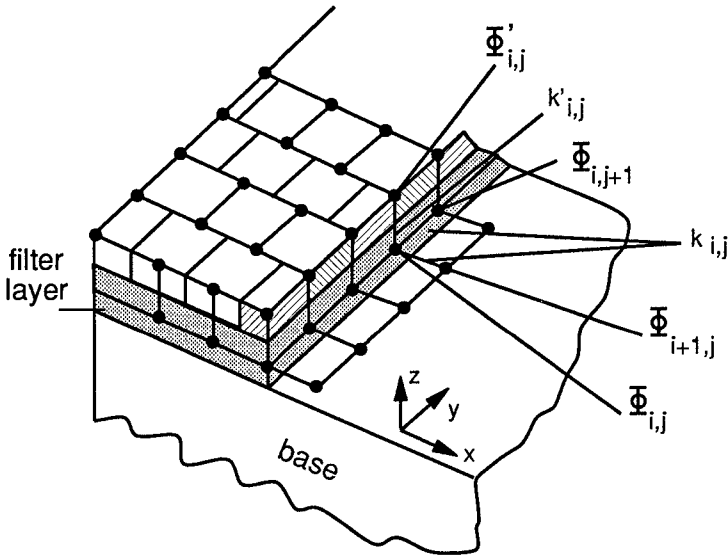


Figure 1: Finite difference scheme used.

In case of laminar flow with constant permeabilities  $k = k_x = k_y$  and  $k'$ , this leads to the more familiar equation:

$$\frac{\partial^2 \phi}{\partial x^2} + \frac{\partial^2 \phi}{\partial y^2} = \frac{\phi - \phi_t}{\Lambda^2} \tag{2}$$

where:

$\Lambda$  : The leakage length (m)

The leakage length or leakage factor is then defined as:

$$\Lambda = \sqrt{\frac{k b D}{k'}} \tag{3}$$

Analytical solutions of this equation, for 1 dimension ( $\partial\phi/\partial y = 0$ ) with a schemed wave pressure distribution as a boundary condition have been presented by Sellmeijer (1981) and Burger et al. (1990). A numerical approach as STEENZET/1 can use measured wave pressures as a boundary condition and turbulent flow can be included. To obtain a numerical solution equation 1 is written as a set of finite difference equations, using the points presented in figure 1 and the general relation:

$$\frac{\partial^2 y}{\partial x^2} \approx \frac{y_{i-1} - 2y_i + y_{i+1}}{(\Delta x^2)} \tag{4}$$

Where  $\Delta x$  is the distance between the points  $i$  and  $i + 1$ . In figure 1 it is shown that the distance along the X axis between two points in the finite difference scheme is L and it is B along the Y axis. It is also shown for what part of the cover layer the permeability is  $k'_{i,j}$  and where in the filter layer the permeability is  $k_{i,j}$ . With the equations 1 and 4 a set of equations for the points  $\phi_{i,j}$  can be obtained:

$$\phi_{i,j} = \frac{B^2(k_{i-1,j}\phi_{i-1,j} + k_{i,j}\phi_{i+1,j}) + L^2(k_{i,j-1}\phi_{i,j-1} + k_{i,j}\phi_{i,j+1}) + \kappa_{i,j}\phi'_{i,j}}{\kappa_{i,j} + B^2(k_{i-1,j} + k_{i,j}) + L^2(k_{i,j-1} + k_{i,j})} \quad (5)$$

Where:

$$\kappa_{i,j} = \frac{B^2 L^2 k'_{i,j}}{bD}$$

The filter layer is assumed to be impermeable at the boundaries of the revetment. This means that when a point on a boundary has to be calculated with equation 5, the value of  $\phi$  just outside the boundary (for example  $\phi_{i,j-1}$  when  $\phi_{i,j}$  is the lower boundary) is given the same value as the point just inside the boundary (the point  $\phi_{i,j+1}$  at the lower boundary). The situation is a bit different for the upper boundary. Here are two possibilities. It can be the same impermeable boundary as for the other boundaries, or it is the phreatic surface in the filter layer. It is assumed that when there is a phreatic surface it is located at the upper boundary because there is no need to simulate the revetment above the phreatic surface. If the upper boundary is the phreatic surface, then the piezometric head in the filter layer is not calculated with equation 5, but the piezometric head is given the same value as the height of that point. The program developed, which is called STEEN3D, is a static program. Up to now it does not include time effects. For a given wave pressure distribution at a certain moment the pore pressure distribution in the filter layer and the resulting loading on the revetment is calculated. Since it is a static program the phreatic surface is an input parameter, as in the analytic solutions mentioned before. The permeability of both the cover layer and filter layer is described with the Forchheimer relation:

$$i = aq + bq^2 \quad (6)$$

where:

- i : the hydraulic gradient (-)
- q : the specific discharge (m/s)
- a : linear Forchheimer coefficient (s/m)
- b : turbulent Forchheimer coefficient (s/m)<sup>2</sup>

The coefficients a and b for the cover layer, as well as the different coefficients for the filter layer are calculated from the width of the joints, the dimensions of the blocks and grain size and porosity of the filter layer as described by Bezuijen and Klein Breteler (1988). The hydraulic gradient in the cover layer is  $(\phi'_{i,j} - \phi_{i,j})/D$ . The permeability of the filter layer ( $k_{i,j}$ ) is assumed to depend

only on the value of the hydraulic gradient in the filter layer ( $i_f$ ), not on the direction of it, leading to:

$$i_f = \sqrt{\left(\frac{\phi_{i+1,j} - \phi_{i,j}}{L}\right)^2 + \left(\frac{\phi_{i,j+1} - \phi_{i,j}}{B}\right)^2} \quad (7)$$

Equation 5 needs the linearized permeability ( $k = q/i$ ), which can be derived from equation 6:

$$k = \frac{-a + \sqrt{a^2 + 4bi}}{2bi} \quad (8)$$

By using equation 8 to calculate the permeabilities non-linearity is introduced in the set of equations 5. Therefore an iterative solution method is used. The starting values of  $\phi_{i,j}$  is the hydrostatic pressure for long leakage lengths ( $\Lambda$ ) and the pore pressure distribution on the slope for small leakage lengths. With these starting values and the equations 5 new values of  $\phi_{i,j}$  are calculated and new permeabilities. This procedure is repeated until the maximum difference between two solutions of  $\phi_{i,j}$  is less than  $10^{-4}$  m. Using the Forchheimer relation, as given in equation 6, The leakage length (equation 3) depends on the hydraulic gradient. To characterize a revetment the leakage length is calculated for a gradient 1 over the cover layer and a gradient equal to the sinus of the slope angle in the filter layer.

### 3 Boundary conditions

#### 3.1 Schemed boundary condition

A schemed boundary condition has been developed to investigate the influence of the angle of the incoming wave on the flow in the filter layer. It is based on a pressure distribution proposed by Burger et al. (1990) for regular waves propagating perpendicular to the revetment. It was found that the moment of maximum loading on the revetment is present just before the wave impact. The pressure distribution for that situation can be schemed as is shown in figure 2. In case of oblique wave attack it is assumed that the maximum loading on the revetment is the same as in case of perpendicular wave attack, but on one side of the revetment the angle  $\beta$  (see figure 2) becomes less, on the other side the angle  $\beta$  remains the same and  $d_b$  and  $\phi_b$  decrease, as is shown in figure 2. The obliqueness of the incoming wave is represented with an angle  $\gamma$  which represents the deviation from perpendicular incoming waves.

#### 3.2 Measured boundary condition

The wave pressures have been measured in a 3 dimensional wave basin (the Vinjé basin). This wave basin is capable in generating regular and irregular waves with a wave height up to 0.2 m. The irregular waves can be long and short crested. In this study only regular waves were used. In the basin a

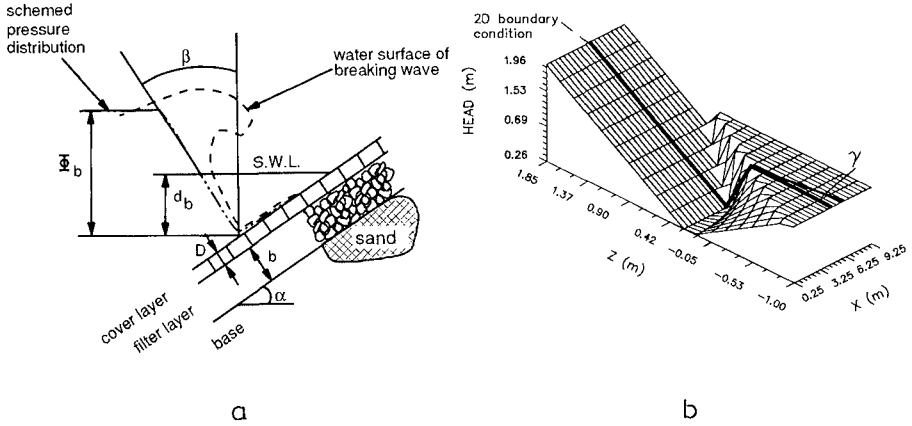


Figure 2: Schemed pressure distribution proposed by Burger et al. (a) and 3-dimensional proposal for oblique wave attack (b).

model was constructed with a slope 1:4. Tests have been performed with a wave steepness of 2 and 4%. The angle of incidence of the incoming waves varied between 0 and 50 degrees, where again 0 degrees means perpendicular incoming waves. The wave height was measured with 5 wave gauges. The wave height and direction were measured with 3 multi-directional wave gauges (These are combined wave gauges and 2-axis current meters). The wave pressures were measured at 10 positions on the slope on a line with a constant X position along the slope with varying depth. A top view of the model in the basin is presented in figure 3. The position of the pore pressure gauges is shown in figure 4. The pore pressure gauges were sampled with a sampling rate of 25 Hz and the results were stored in a computer. Since the velocity of the waves propagating along the slope is constant the wave pressure measured at one line can be transformed in a pressure field over the slope. When the origin of the X-axis (see figure 3) is chosen at the location of the wave pressure gauges, then the wave pressures measured at X=0 at a certain moment  $t_0$  can be transferred to the wave pressures that can be measured at a different position at a different moment according to the formula:

$$\phi'(x, y, t + T \frac{x \sin \gamma}{L_g}) = \phi'(0, y, t) \tag{9}$$



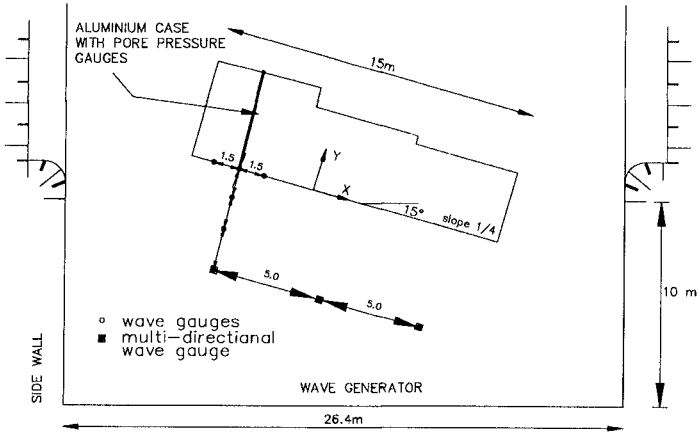


Figure 3: Top view of model in basin

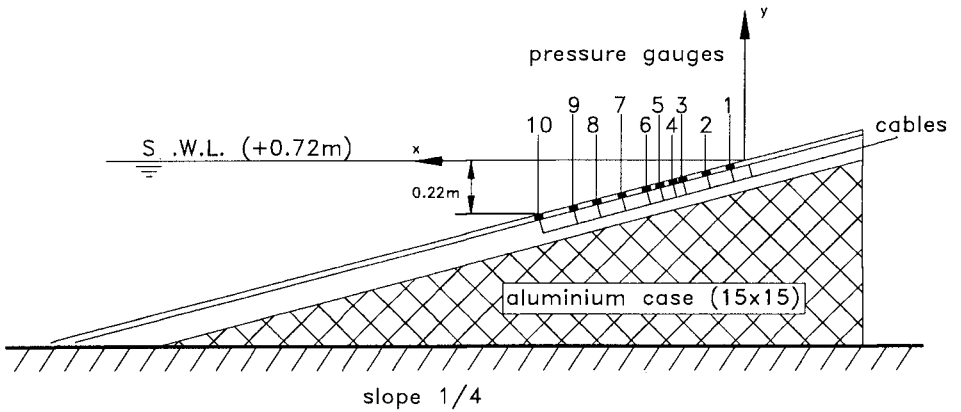


Figure 4: Pore pressure gauges on slope

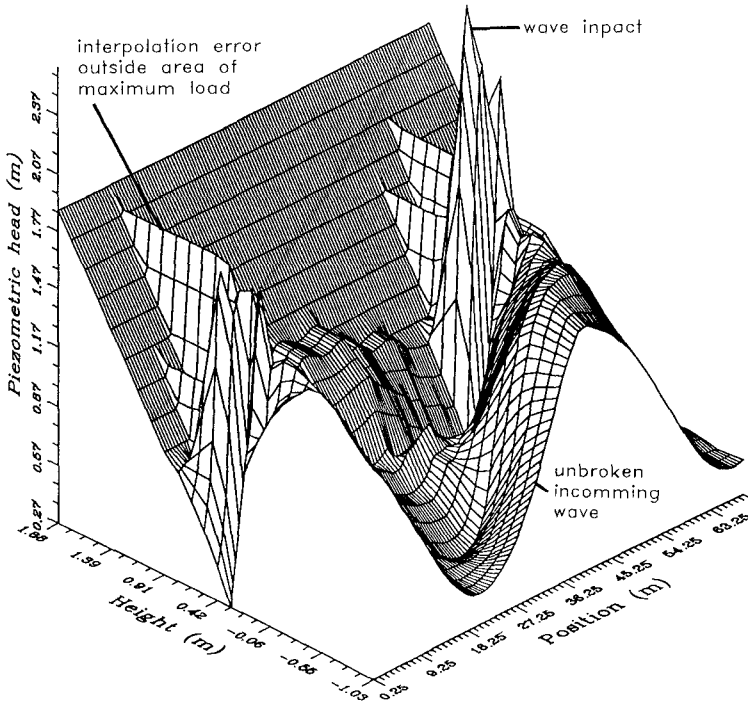


Figure 5: Wave pressure distribution under oblique wave attack on a slope 1:4 with wave height of 1.2 m and a wave period of 4.4 s. The angle of incidence of the incoming waves was 40 degrees (scaled up from a measured wave height of 0.12 m).

Where:

$L_g$  : the wave length in front of the slope (m)

$T$  : the wave period (s)

Figure 5 shows an example of a measured wave pressure distribution.

The plot shows the result of the fact that pore pressure gauges were present only below the still water level. The pressures higher on the slope were not measured. If a pressure was measured on the highest wave pressure gauge it is assumed that this pressure was present higher on the slope in a way that the piezometric head was constant. This leads to an interpolation error. However this error is only present higher on the slope and the maximum loading on the revetment is always well below the still water line.

From this plot it appeared that the schematisation used in the schemed boundary condition see figure 2 is reasonable for the area before wave impact. In that area there is clearly a steepening of the next incoming wave. The wave impact causes a pressure distribution very different from the schemed boundary

Parameter	Case 1	Case 2
top of revetment	2 m	1.5 m
toe of revetment	-1 m	-6.1 m
slope angle	18.43° and 14.03°	18.43° and 14.03°
block length and width	0.5 m	1.2 m
block thickness	0.2 m	0.23 m
width of joints	0.002 m	0.06 m
thickness filter layer	0.2 m	2 m
$d_{15}$ filter layer	0.02 m	0.001 m
porosity filter layer	0.4	0.35
leakage factor	1.1 m	0.92 m
still water level	1 m	0.0 m
wave height	1.2 m	3.3 m
wave angle $\gamma$	0 - 60	0 - 70
Wave steepness (measured)	0.04	0.04
$\phi_b$ in fig. 4 (schemed)	1.0 m	4.2 m
$d_b$ in fig. 4 (schemed)	0.8 m	2.78 m
$\beta$ in fig. 4 (schemed)	30°	46.5°

Table 1: Parameters used in the calculations

condition. Since the schemed boundary condition is reasonable in the area of maximum loading it still can be used for situations where no wave pressure recordings are available. However it should be taken into account that the angle of the wave on the revetment is less than the angle of the incoming wave due to refraction of the waves on the slope. For the wave shown in figure 5 with an angle of incidence of 40° for the incoming waves it was found that on the slope at a depth of 1.6 m below the still water level the angle of incidence of the wave pressures on the slope was approximately 25°, at 1 m below the still water line it was only 11°.

## 4 Results

The calculations were run with the parameters presented in table 1. Case 1 are the parameters of a revetment as can be expected in the Dutch estuaries. With the results of the field tests (see Stoutjesdijk et al., 1992) now available it must be stated that these are the parameters for a new revetment with no fine material in the filter layer and between the joints. The second case is an attempt to simulate the revetment described by Gadd and Leidersdorf (1990) at Northstar Island in the Beaufort Sea.

An example of a calculation with the schemed boundary condition presented in figure 2 is shown in figure 6, which showed the distribution of the difference in piezometric head over the blocks. A positive difference in this figure means

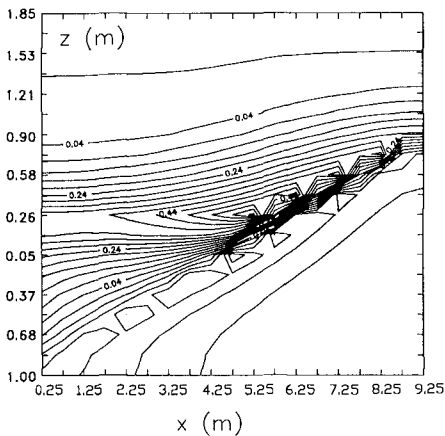


Figure 6: Contour plot of the calculated uplift pressure, schemed boundary condition  $\gamma = 30^\circ$ .

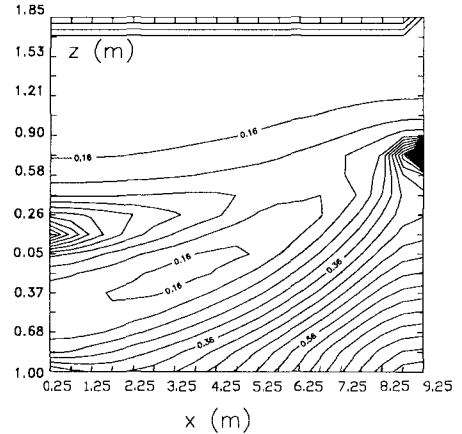


Figure 7: Contour plot of the calculated permeability in the filter layer.

that there is an uplift pressure over the blocks. If this uplift pressure is higher than the weight of the blocks and possible clamping forces blocks can be lifted from the revetment. In this calculation the parameters of case 1 in table 1 are used. Figure 7 showed the corresponding permeability in the filter layer. Due to turbulency the linearized permeability, see equation 8 is high in areas with a small hydraulic gradient and lower in area's with a higher gradient. It appeared from the calculations that using turbulency in the calculation leads to a slightly higher maximum uplift pressure than would result from a calculation with laminar flow. Comparing the calculated maximum uplift pressure with the boundary condition it appeared that the maximum uplift pressure can be found just before the impact of the next incoming wave as could be expected.

An example of the simulation results using a measured boundary condition for the revetment with the parameters of case 1 is shown in figure 8. It shows the difference in piezometric head as it is distributed over a placed block revetment at a certain time when loaded with oblique wave attack. The high values (the 'mountains' in the plot) correspond with a high uplift pressure. At these locations the blocks can be lifted out of the revetment. The difference in piezometric head is at maximum just in front of the areas of wave impact at X is approximately 9 and 50 m (the wave is propagating from high to low X values). Although the figure presents the result for an incoming wave angle of  $40^\circ$ , there is for each wave over a large part of the revetment only one Z value (one height on the revetment) with the largest difference in piezometric head and thus the

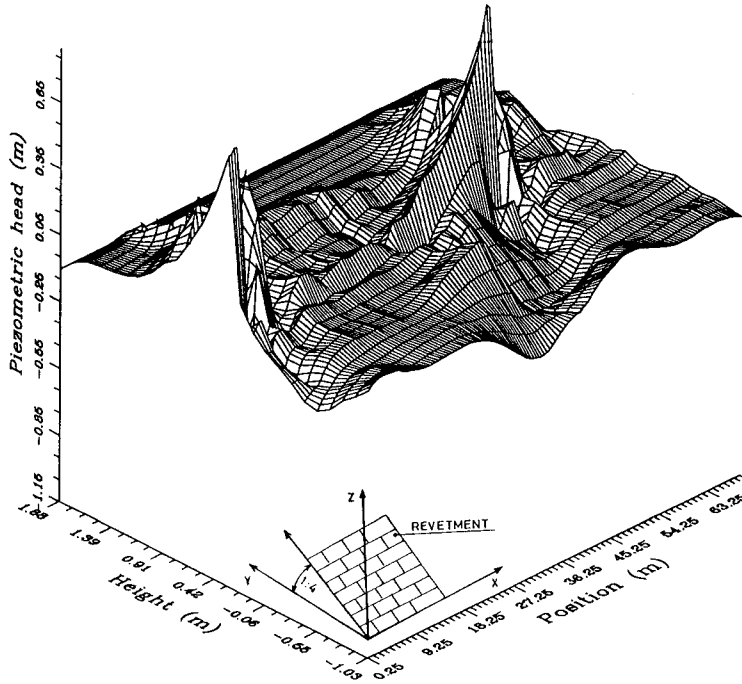


Figure 8: Example of calculated difference in piezometric head over the blocks. Calculation for a slope 1:4 by a wave attack of 1.2 m wave height, a period of 4.4 s and an incoming wave angle of  $40^\circ$ , the leakage length is 1.1 m.

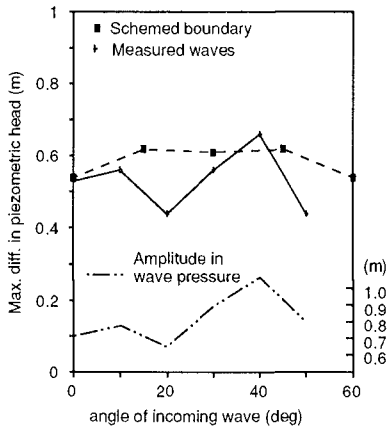


Figure 9: Calculated maximum difference in piezometric head as a function of the angle of the incoming wave, case 1.

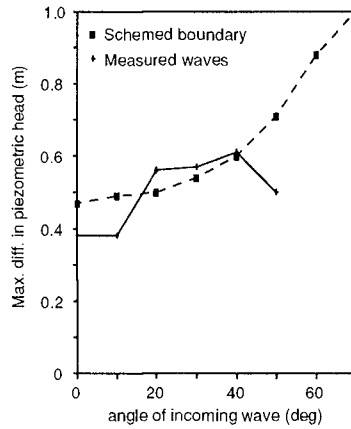


Figure 10: Calculated maximum difference in piezometric head as a function of the angle of the incoming wave, case 2.

maximum loading.

The influence of the angle of wave attack was tested by performing calculations for different angles of incoming waves. This was done for the schemed as well as the measured boundary conditions. For case 1 the results of the calculations are shown in figure 9 and for case 2 in figure 10. For case 1 it is clear that the influence of the angle of the incoming wave on the maximum calculated uplift pressure is small. The result shows that for angles of the incoming waves between 0 and 60° the maximum loading remains more or less the same. As is also shown in figure 9, differences found in the maximum uplift pressures for measured waves appear to correspond closely with differences in the amplitude of the piezometric head, measured with the lowest wave pressure gauge. These differences in amplitude correspond with small differences in wave height in front of the structure, which cannot be avoided in a wave basin. For case 2 there is an influence. The maximum calculated uplift pressure increases for measured as well as schemed boundary conditions. For schemed boundary conditions this increase goes on with an increasing angle of the incoming waves, for the measured boundary condition there seems to be a maximum for an angle of 40° for the incoming waves. In case 2 the ratio of the leakage length divided by the wave height of the incoming waves ( $\Lambda/H$ ) is much smaller than in case 1, see table 1. The results of the calculations show that in case  $\Lambda/H \approx 1$ , there is hardly any influence and this influence is larger for  $\Lambda/H = 0.33$ . It appears that for  $\Lambda/H = 0.33$  the loading is 50% higher for oblique incoming

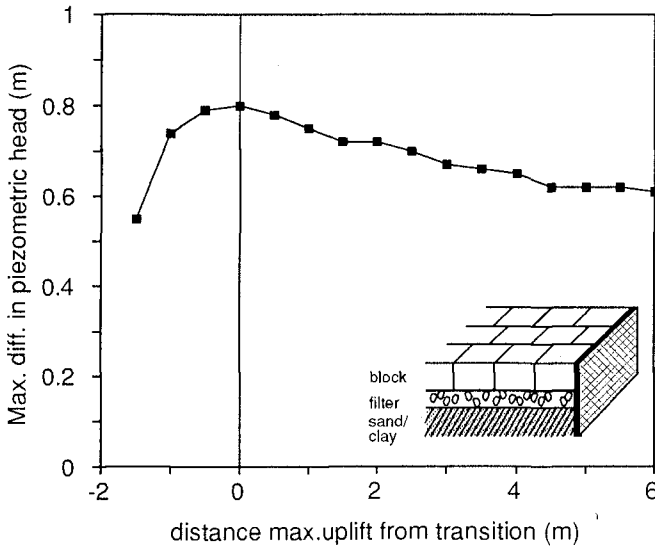


Figure 11: Maximum loading near an impermeable transition in the revetment, case 1, wave conditions as shown in figure 5. In the plot is a drawing of an example of an impermeable transition.

waves ( $\gamma = 40^\circ$ ) than for perpendicular incoming waves ( $\gamma = 90^\circ$ ). Further the influence of the transition in a revetment have been investigated. The locations where one type of revetment changes to another type. In the calculations the situation is simulated that at such a transition the filter layer is impermeable. Various calculations have been run to simulate the situation that the moment of maximum loading on a revetment reaches such a transition. This will always happen when a transition is present, because in case of oblique wave attack it looks as if the waves are travelling along the revetment. The results of the calculations are shown in figure 11. The results show that near a transition the uplift pressures on the revetment are higher than far from the transition. This is caused by changes in the flow in the filter layer near the transition.

Normally the strength of the revetment is less when there is transition in the revetment. The discontinuity present at the transition can cause a reduction of the clamping forces between the blocks and difficulties in densification of the subsoil during construction of the revetment, leading to uneven settlement later. This decrease in strength in combination with the calculated increased loading means that during oblique wave attack the edges of the revetment are especially vulnerable.

## 5 Conclusions

The results show that for oblique wave attack with regular waves the angle of the incoming waves have little influence on the maximum loading on the

revetment, as long as the leakage length is larger or equal than the wave height. When the leakage length of the revetment is much shorter, then oblique wave attack with can result in up to 50 % higher loading on the revetment. Further near transitions in the revetment the loading on the revetment is increased in case of oblique wave attack.

## 6 Acknowledgement

The authors wish to thank P.E. Gadd and C.B. Leidersdorf for stimulating discussion and supplying detailed information about the revetment on Northstar island, where they have observed failure from oblique wave attack.

## 7 References

Bezuijen A., Klein Breteler M., Bakker K.J., 1987. Design criteria for placed block revetments and granular filters. Proc. 2nd. COPEDEC, Beijing.

Bezuijen A., Laustrup C. and Wouters J., 1988. Design of block revetments with physical and numerical models. Proc. 21st Int. Conf. Coastal Engineering, Malaga. Bezuijen A., Klein Breteler M., and Burger A.M., 1990. Placed block revetments. Chapter in Coastal Protection, Pilarczyk (ed.), Balkema Rotterdam. ISBN 9061911273.

Burger A.M., Klein Breteler M., Banach L., Bezuijen A., Pilarczyk K.W. (1990) An analytical design method for relatively closed block revetments. J. of Waterway, Port Coastal and Ocean Engineering, vol. 116, No 5. ASCE. Gadd P.E., Leidersdorf G.B., 1990. Recent performance of linked mat armor under wave and ice impact. Proc. 22th int. Conf. Coastal Engineering, Delft.

Klein Breteler M., 1992. Scaling rules for placed block revetments (in Dutch). Report XX in the series Placed block revetments, Delft Hydraulics. Sellmeijer J.B. 1981. Uplift pressures by waves in placed block revetments (in Dutch). Delft Geotechnics report CO-255780

Stoutjesdijk Th., Rigter B.P. and Bezuijen A., (1992) Field experiments on placed block revetments. Proc. 23rd. Int. Conf. Coastal Engineering, Venice.



## CHAPTER 78

### THE PENETRATION OF SHORT-CRESTED WAVES THROUGH A GAP

N. Booij<sup>1</sup>, L.H. Holthuijsen<sup>1</sup> and P.H.M. de Lange<sup>1,2</sup>

#### Abstract

The propagation of long-crested and short-crested waves through a gap such as between two breakwaters is affected by diffraction. If the water depth is not uniform, refraction may also affect this penetration. It is shown with a navigation channel between two breakwaters (academic case and a realistic harbour case) that the effects of diffraction are small compared to those of refraction in regions where waves can penetrate with refraction only (e.g. where wave rays can penetrate). This region is relative large for short-crested waves. Outside these regions diffraction is dominant. With another example of waves penetrating through a tidal gap against a strong ebb current, it is shown that the short-crestedness of the waves destroys to a very large extent the waved guide effect of such currents. Both set of experiments show that the inclusion of short-crestedness in the wave computations causes some smoothing of the wave field, and that diffraction is a minor effect in regions with considerable wave motion. This is of some scientific and economic relevance as refraction can readily be combined in wave models with other physical phenomena such as wave generation and dissipation. Moreover, such models require less computer capacity than diffraction models which do not readily absorb wave generation and dissipation.

#### Introduction

To compute the propagation of waves through and beyond a gap between two obstacles such as breakwaters or islands, several aspects of the waves are important for modelling these waves numerically. As a boundary condition it is important to consider the waves as a harmonic, long-crested wave or as random, short-crested waves. In and beyond the gap several conservative and non-conservative processes should be considered. The conservative processes are: refraction, diffraction and

---

<sup>1</sup> Delft University of Technology, Stevinweg 1, 2628 CN Delft, the Netherlands

<sup>2</sup> Rijkswaterstaat, Division of Tidal Waters, the Hague, the Netherlands and College of Technology Enschede, Enschede, the Netherlands

reflection. The non-conservative processes are wave generation (by wind) and dissipation (by bottom friction and breaking, also during reflection). We are interested in these aspects from a modelling point of view because of the choice that has to be made between using a model for combined refraction-diffraction or a model for refraction only. A refraction-diffraction model requires considerable computing power, in particular for short-crested, random waves. Moreover, the inclusion of generation and dissipation is primitive or non-existent in such a model. A refraction model requires less computing power and is readily supplemented with generation and dissipation mechanisms, but it lacks diffraction. The question is, can a refraction model provide at least a reasonable estimate of a short-crested wave field in the absence of diffraction?

### Method of the study

To make a tentative step towards an answer, we consider three cases of waves propagating through a gap: (a) a fairly academic situation of waves propagating over a navigation channel between two breakwaters (b) a similar situation with a fairly realistic harbour beyond the gap and (c) an actual tidal inlet with a strong ebb-current.

We use the two different types of models mentioned in the introduction. The refraction-diffraction model is the PHAROS model of Delft Hydraulics (Kostense et al, 1988) and the refraction model is the HISWA model of Delft University of Technology (Holthuijsen et al, 1989). The major difference is that the refraction-diffraction model reconstructs the actual sea surface of an harmonic wave that is long-crested in deeper water by computing the phase and amplitude of the surface elevation whereas the refraction model computes the directional energy distribution of waves that are short-crested in deeper water. The short-crested cases are computed with the refraction-diffraction model by superimposing a number of computed harmonic waves. The long-crested cases are computed with the refraction model by considering a very narrow directional energy distribution in deeper water. For the interpretation of the results it is important to note that the HISWA model does not compute wave propagation in directions more than 60° at either side from a pre-determined direction (chosen as the initial wave directions in this study).

For economic reasons we consider only waves with one constant period. The waves that we consider are 10 s in period and either long-crested (PHAROS only) or short-crested with directional distributions of the type  $D(\theta) = A \cos^m(\theta)$  ( $m = 100$  for simulated long-crested waves in HISWA only or  $m = 4$  for simulated short-crested waves in PHAROS and HISWA).

We consider the similarities and differences in the results of the two models for the three cases mentioned above.

### The academic gap

The bottom topography for the situation with a navigation channel between two breakwaters is given in Fig 1.a. The channel originates in water of 15 m deep and the channel is maintained at that depth. Outside the channel the water depth decreases to a uniform depth of 11 m beyond the gap. The slope of the shoulders of the channel is 1:10 and the gap is 480 m wide (i.e. 5.5 wave lengths) The breakwaters and the circular boundary beyond the gap are fully absorbing. This means that the region beyond the gap may be interpreted as infinitely large.

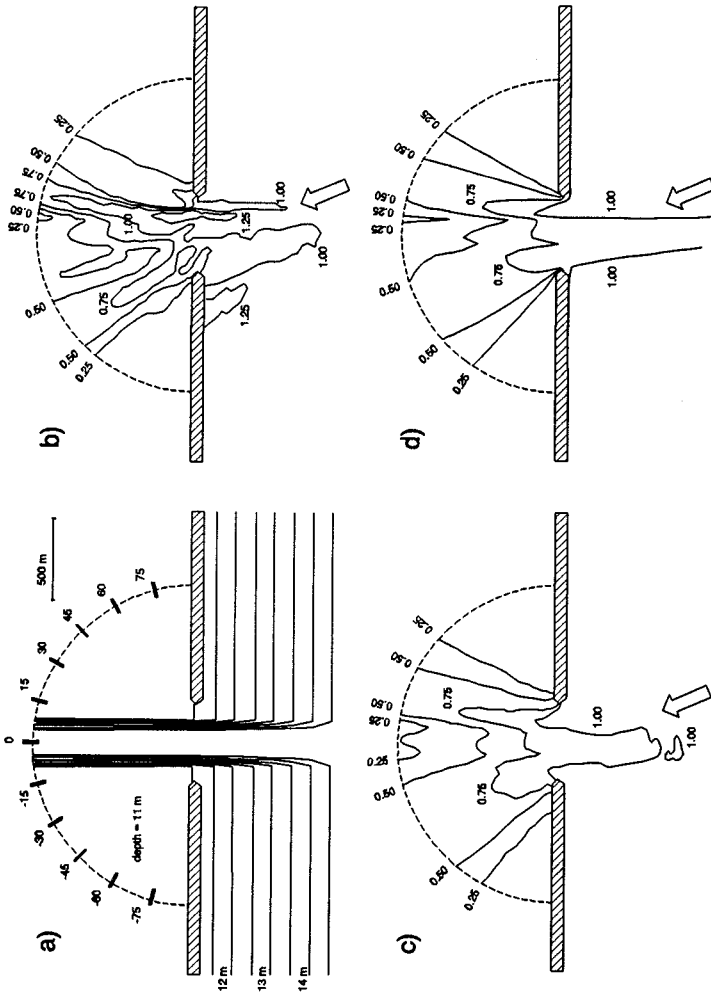


Fig. 1 The penetration of waves from  $24^\circ$  incidence with channel through a gap in terms of relative (significant) wave height  $H/H_0$ . Panel a) bottom topography and position indication along absorbing circle. Panel b) combined refraction and diffraction, long-crested waves. Panel c) combined refraction and diffraction, short-crested waves. Panel d) refraction only, short-crested waves.

We computed the wave situation with various initial wave directions and we found that the shoulders of the channel refract the waves such as to spread wave energy in fingers to the sides. From the initial (mean) wave directions of  $0^\circ$ ,  $12^\circ$ ,  $24^\circ$  and  $36^\circ$  (angle of incidence with the channel axis), we selected the results of the  $24^\circ$  case as representative. The effects shown next are slightly more extreme for the  $12^\circ$  case (the critical angle for reflection on the channel shoulder is appr.  $24^\circ$ ) and slightly less extreme for the  $0^\circ$  and  $36^\circ$  cases).

In Fig. 1.b the results are shown for the refraction-diffraction computations for long-crested waves (in terms of the local wave height  $H$  divided by the incident wave height  $H_i$ ). The finger pattern of the wave penetration is obvious with energy concentration slightly over 1.25 just beyond the gap. The pattern is smoothed somewhat by introducing short-crestedness as shown in Fig. 1.c where the finger pattern is still obvious but not as concentrated. The effect of removing diffraction from the short-crested waves situation is shown in Fig. 1.d where the results of the refraction computations are shown. Again the finger pattern is obvious and in fact not very different from that in Fig. 1.c where diffraction was included.

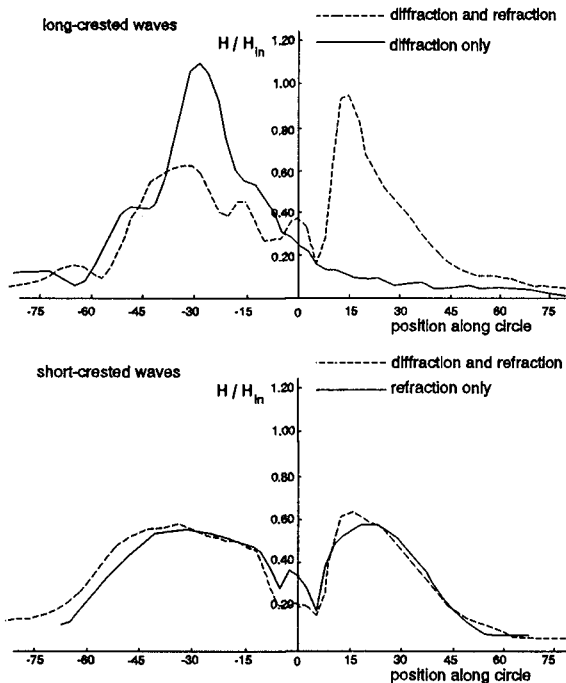


Fig. 2 The results of the computations of Fig. 1 along the absorbing circle. The results for the long-crested waves compared with the results for the short-crested waves for refraction only, diffraction only and combined refraction/diffraction. Diffraction only was achieved with constant water depth of 11 m.

A further comparison is made in Fig. 2. A pure diffraction computation for long-crested waves (obtained with the refraction-diffraction model with a uniform water depth of 11 m) is included (upper panel). Introducing the channel in these computations has the effect of splitting part of the energy propagation towards the right (looking down-wave, same panel, compare with Fig. 1.b). Adding short-crestedness in these computations gives a smoother distribution of the energy (lower panel of fig. 2, compare with Fig. 1.c). Using the refraction model instead of the refraction-diffraction model gives very similar results (lower panel), except where the refraction model does not compute (more than  $60^\circ$  from the incident wave direction), confirming the conclusion from Fig. 1.

### The harbour

The bottom topography for the harbour with a navigation channel very similar to the above is given in Fig. 3.a. The channel originates also in water of 15 m deep and the channel is maintained at that depth towards the deep basin in the harbour at the same depth. Beyond the deep basin, a shallow basin at 11 m depth is protected by a mole. The slope of the shoulders of the channel is 1:10 and the gap is 330 m wide (i.e. 4 wave lengths). For the purpose of this study the breakwaters and the quays are assumed to be fully absorbing.

We computed the wave situation with the initial (mean) wave direction along the channel axis and (of course) we again found that the shoulders of the channel refract the waves such as to spread wave energy in fingers to the sides.

In Fig. 3.b the results are shown for the refraction-diffraction computations for long-crested waves. The finger pattern of the wave penetration is obvious with energy concentration as high as 1 just beyond the gap and a fairly deep penetration behind the left breakwater. The pattern is smoothed considerably by introducing short-crestedness as shown in Fig. 3.c but the deep penetration behind the left breakwater is hardly affected. The effect of removing diffraction from the short-crested waves situation is shown in Fig. 3.d where the results of the refraction computations are shown. Again the pattern is obvious, including the deep penetration finger, and in fact not very different from that in Fig. 3.c. The patterns are nearly equal, although the penetration in the refraction-diffraction computations is slightly higher than in the refraction computation (5% difference where the finger behind the left breakwater touches the harbour contour). Again these computations demonstrate the marginal effect of diffraction in this case.

If reflection against breakwaters and quays is taken into account in the refraction-diffraction computation (not possible with the HISWA model) it appears that wave energy can penetrate virtually everywhere in the harbour and that diffraction remains relatively unimportant.

### Tidal inlet

To further illustrate the considerable effect of short-crestedness on the wave pattern, we compute the wave field in an actual tidal gap. It is the 3 km wide tidal entrance to the Wadden Sea between Den Helder and the island of Texel

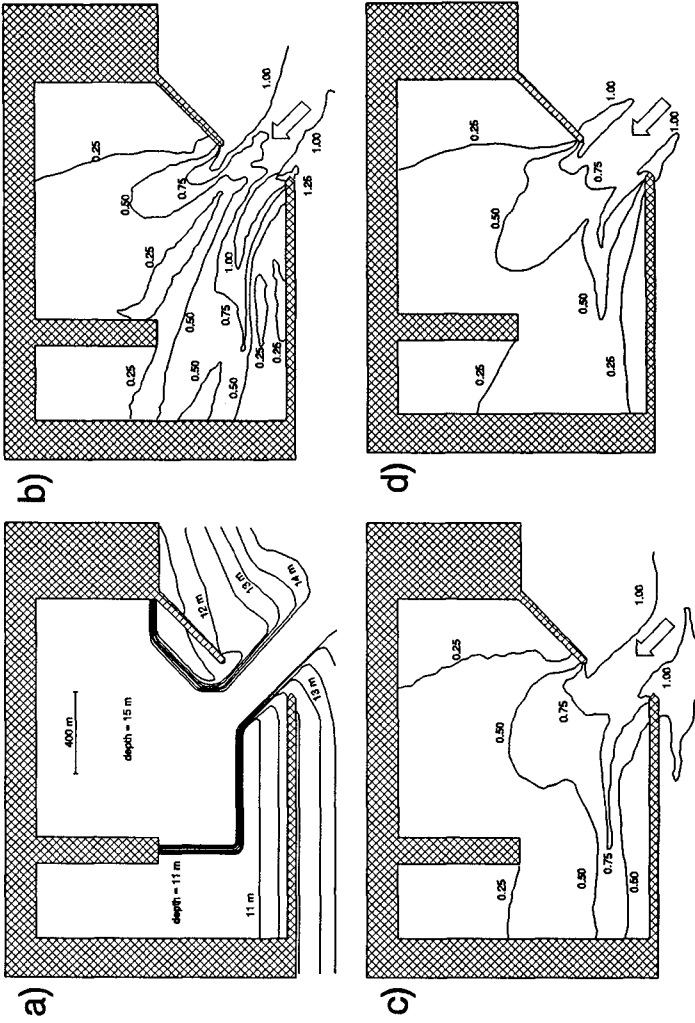


Fig. 3 The penetration of waves parallel to the navigation channel between two breakwaters in terms of relative (significant) wave height  $H/H_i$ . Panel a) bottom topography. Panel b) combined refraction and diffraction, long-crested waves. Panel c) combined refraction and diffraction, short-crested waves. Panel d) refraction only, short-crested waves.

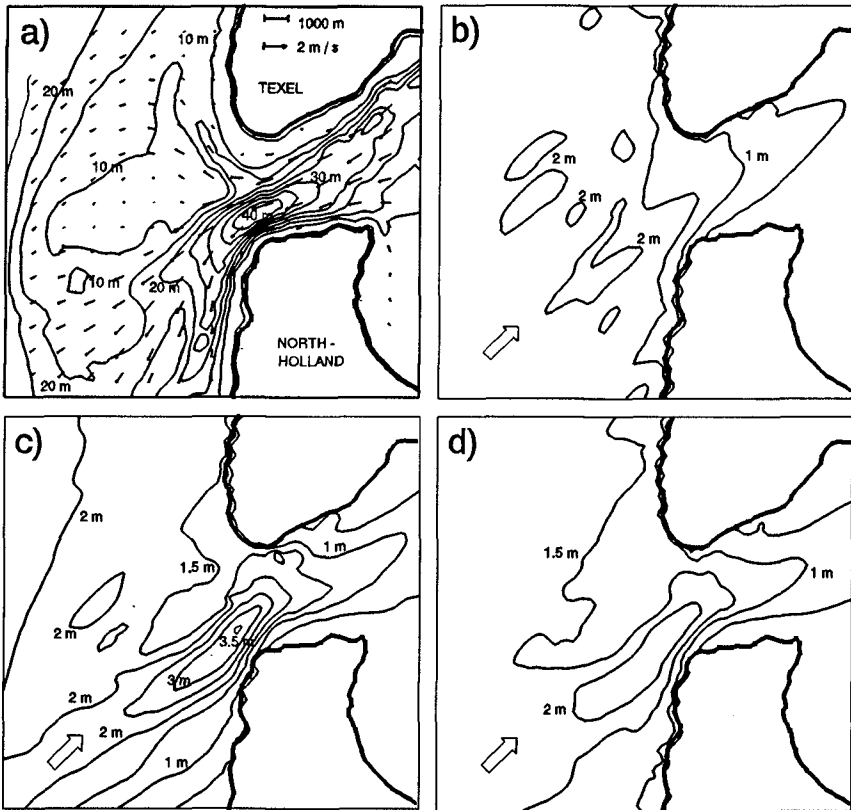


Figure 4. The penetration of waves into a tidal inlet computed with refraction model. Panel a) bottom topography and current velocity field. Panels b,c,d) isolines of significant waveheight. Panel b) long-crested waves without current. Panel c) long-crested waves with current. Panel d) short-crested waves with currents.

in the North of Holland. The bathymetry and the ebb-current pattern are given in Fig. 4.a. The current pattern has been computed with a two-dimensional nonlinear tidal model WAQUA (Leendertse et al., 1981 and Stelling, 1984) for a severe storm case. The waves that we consider propagate from deep water towards the gap from the South-west. The wave period is 6s and the significant wave height is 2m. For long-crested waves and no currents, the results of the refraction computations are shown in Fig. 3.b. Refraction-diffraction computations have not been carried out as the area is too large for that. The results show some increase in wave height before the waves reach the shallows (probably due to shoaling) and a considerable decrease at the shoal. Adding currents dramatically changes the results as the waves now increase just in front of the gap to 3.55 m (see fig. 3.c). This is almost certainly a wave guide effect,

that is, the waves are trapped by the counter current by current-induced refraction. However, adding short-crestedness to the computations destroys to a large extent the wave guide effect, resulting in dramatically lower waves (maximum 2.6 m, Fig. 3.d).

## Conclusions

From numerical experiments with a combined refraction-diffraction model and a refraction model, we come to the following conclusions.

Beyond a gap with a natural or dredged navigation channel, the shoulders of the channel may displace and focus waves in certain areas beyond the gap. This focussing is tempered by short-crestedness of the waves. In such cases and probably in similar cases, refraction computations without diffraction seem to provide a reasonable first estimate of the waves in those regions beyond the gap where waves can penetrate with refraction (e.g. where wave rays can penetrate). In other regions diffraction is essential.

In addition to these considerations of accuracy, the choice of using a refraction-diffraction model or a refraction model is one of convenience and economy. The computing power required for a refraction model without diffraction is considerably less than for a refraction-diffraction model (in the present study roughly a factor of 10). A refraction model without diffraction has the added advantage of readily combining other physical phenomena with the propagation of the waves, including current effects. Reflections (not considered in the present study) are relevant in harbours and can be included in both types of models. Reflection is included in the PHAROS model.

It further appears that diffraction models which assume a flat bottom are useless for any harbour with an entrance channel.

The above conclusions relate to wave computations in which short-crestedness is accounted for. The inclusion of the short-crestedness of waves also tends to smooth the wave guide effect of concentrated counter currents in a gap such as an ebb current between islands.

## Acknowledgements

We wish to thank Delft Hydraulics for its generous support and its permission to use the PHAROS model for this study. We are particularly grateful to J.K. Kostense for his guidance and assistance during this study.

## References

Holthuijsen L.H., N. Booij and T.H.C. Herbers (1989), "A prediction model for stationary, short-crested waves in shallow water with ambient currents". *Coastal Engineering*, 13, pp. 23-54.



Kostense, J.K., K.L. Meyer, M.W. Dingemans, A.E. Mynett and P. van den Bosch (1988), "Wave energy dissipation in arbitrarily shaped harbours of variable depth". *Proc. 20th Coastal Engineering Conference*, ASCE, Vol. 3, pp. 2002-2016.

Leendertse, J.J., A. Langerak, and M.A.M. de Ras (1981). "Two-dimensional models for the Delta Works", in *Transport models for inland and coastal waters* (ed. H.B. Fischer). Acad. Press, New York. pp. 408-450.

Stelling, G.S. (1984), "On the construction of computational methods for shallow water flow problems". *Comm. no. 35. Rijkswaterstaat*, the Hague.

## CHAPTER 79

# Design of Dolos armour units

Hans. F. Burcharth<sup>1</sup>    Zhou Liu<sup>2</sup>

### Abstract

The slender, complex types of armour units, such as Tetrapods and Dolosse are widely used. Many of the recent failures of such rubble mound breakwaters revealed that there is an imbalance between the strength (structural integrity) of the units and the hydraulic stability (resistance to displacements) of the armour layers.

The paper deals only with Dolos armour and presents the first design diagrams and formulae where stresses from static, quasistatic and impact loads are implemented as well as the hydraulic stability. The Dolos is treated as a multishape unit where the thickness can be adjusted to the strength needs.

### Introduction

Many of the recent dramatic failures of a number of large rubble mound breakwaters armoured with Dolosse and Tetrapods were caused by breakage of the units. Breakage took place before the hydraulic stability of intact units in the armour layers expired. Thus there was an imbalance between the strength (structural integrity) of the units and the hydraulic stability (resistance to displacements) of the armour layer.

The present paper deals only with Dolosse armour and presents the first design diagrams and formulae where stresses from static, quasistatic and impact loads are implemented as well as the hydraulic stability. Earlier publications only covered static and quasistatic stresses (e.g. Burcharth et al., 1991). The results are the outcome of a long-term research programme at Aalborg Hydraulic Laboratory (AHL), Aalborg University, which for the last three years has been coordinated with Dolosse research at CERC, Vicksburg.

Dolosse armour was chosen as research object because of its excellent hydraulic stability and because its structural strength can be adjusted by changing the waist ratio, cf. Fig. 1, which shows blocks with the three waist ratios applied in the experiments. By increasing the waist ratio in order to improve the structural behaviour the hydraulic stability will decrease somewhat. This must be taken into account in the design.

---

<sup>1</sup>Prof. of Marine Civil Engineering, Aalborg University, Denmark.

<sup>2</sup>Research Engineer, Aalborg University, Denmark.

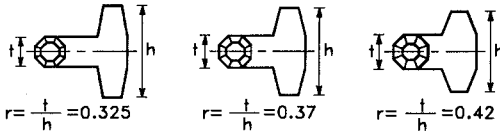
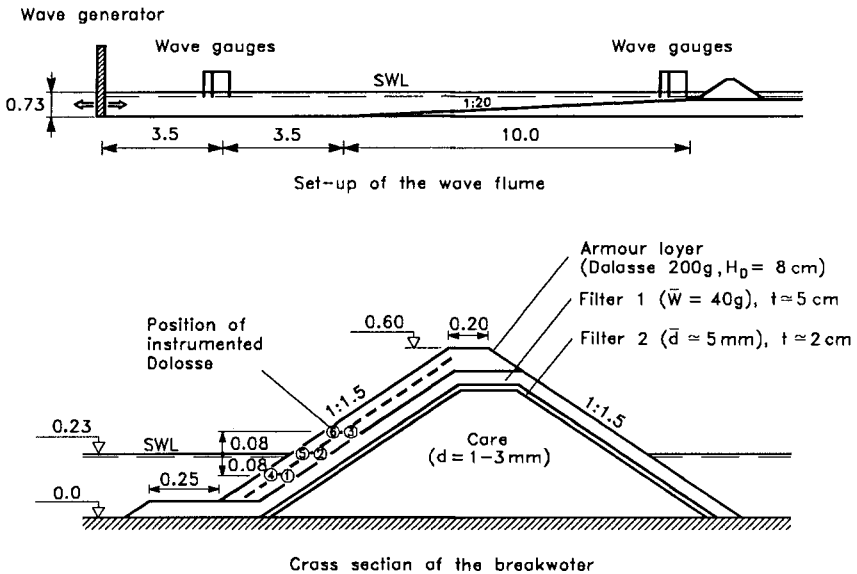


Fig. 1. Applied concrete Dolosse with different waist ratios but with equal mass.

**Description of the experiments**

A 1 : 1.5 slope armoured with 200 g concrete Dolosse of waist ratios as shown in Fig. 1 was exposed to irregular wave in a wave flume with a foreshore slope of 1 : 20. Fig. 2 shows the layout of the model and the cross section of the breakwater.



Measures and levels in meter

Fig. 2. Set-up of the wave flume and the cross section of the breakwater. Aalborg Hydraulic Laboratory (AHL) experiments.

To compensate for reflected waves two arrays of three wave gauges were installed. The incident wave spectrum was calculated by the least square method presented by Mansard et al., 1980.

The irregular waves were generated by a piston type paddle according to the five parameter JONSWAP spectrum. Table 1 lists the characteristics of the applied waves propagating towards the breakwater recorded at the paddle and at the toe of the breakwater.  $T_p$  is the spectral peak period,  $\xi_{m0} = \left(\frac{H_{m0}^2}{L_{p0}}\right)^{-0.5} \tan\alpha$ , where  $L_{p0}$  is the deep water wave length corresponding to  $T_p$ .

Table 1.  $H_{m0}$ ,  $T_p$  and  $\xi_{m0}$ .

$H_{m0}^p$	at the paddle (cm)	5 - 15
$H_{m0}^t$	at the toe (cm)	5.7 - 18.2
$T_p$	at the paddle (sec)	1.5 - 3
$\xi_{m0}$		3.23 - 11.7

The experiments were performed in series in which the wave height was increased step by step. The run time for each step was 5 minutes.

For each combination of  $H_{m0}$  and  $T_p$  the experiment was repeated 20 times in the study of the hydraulic stability and 3 times for each position of the instrumented Dolosse in the study of the stresses in Dolosse; all with the slope rebuilt.

In order to study the hydraulic stability of the Dolos armour layers a grid was put parallelly to the breakwater slope before and after wave attack and photos were taken. All displacements could then be visually registered.

The applied load cells are developed and produced by CERC. The load cell instrumented concrete Dolosse were calibrated for impact loaded conditions using prototype impact test data and were checked for dynamic amplification, cf. Burcharth et al. 1991. They were put in 6 positions on the slope as shown in Fig. 2.

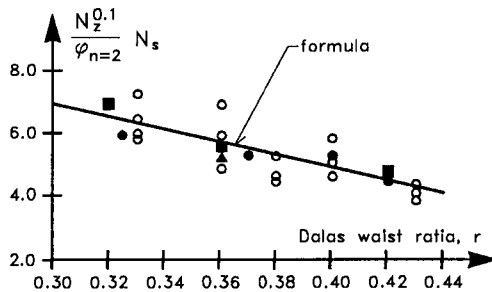
### Hydraulic stability of Dolos armour

The following formula for hydraulic stability of Dolos armour on slope 1 : 1.5 is based on the present test results and results by Brorsen et al. 1974, Burcharth et al. 1986, and Holtzhausen et al. 1990.

$$N_s = \frac{H_s}{\Delta D_n} = (47 - 72r) \varphi_{n=2} D^{1/3} N_z^{-0.1} \quad (1)$$

- where  $H_s$  significant wave height in front of breakwater  
 $\Delta$   $(\rho_{concrete}/\rho_{water}) - 1$ ,  $\rho$  is the mass density  
 $D_n$  length of cube with the same volume as Dolosse  
 $r$  Dolos waist ratio  
 $\varphi_{n=2}$  packing density  
 $D$  relative number of units within levels SWL  $\pm 6.5 D_n$  displaced one Dolos height  $h$ , or more (e.g. for 2% displacement insert  $D = 0.02$ )  
 $N_z$  number of waves. For  $N_z \geq 3000$  use  $N_z = 3000$ .

Fig. 3 shows the case corresponding to damage level of 2% displacement.



Legend:

Reference	$\varphi_{n=2}$	Repeated Na	Duration (min.)	$\xi_{m0}$
▲ Brorsen et al. (1974)	1 (App.)	2	60	2.49-5.37
■ Burcharth et al. (1986)	0.61-0.7	5 or 15	20	3.04-4.49
○ Holtzhausen et al. (1990)	1	3 or 8	60	2.91-7.6
● Burcharth et al. (1992)	0.74	20	5	3.23-11.7

Fig. 3. Hydraulic stability of two layer randomly placed Dolos armour on a slope of 1 : 1.5. Damage level,  $D = 2\%$  displaced units within levels SWL  $\pm 6.5D_n$ . Note that the data points are average of repeated tests, cf. the legend.

The formula (1) covers both breaking and non-breaking wave conditions, with the limits given by

$$0.32 < r < 0.43$$

$$0.61 < \varphi_{n=2} < 1$$

$$1\% < D < 15\%$$

The uncertainty of the formula is estimated to correspond to a variational coefficient of 0.2. If the PIANC partial coefficient system is used (Burcharth 1991) the design equation reads

$$\frac{1}{\gamma_z} \Delta D_n (47 - 72r) \varphi_{n=2} D^{1/3} N_z^{-0.1} \geq \gamma_{H_s} H_s^T \quad (2)$$

For the calculation of the partial coefficients  $\gamma_z$  and  $\gamma_{H_s}$ , the coefficient values  $k_\alpha = 0.025$  and  $k_\beta = 38$  should be used.

In the following is given a discussion of the dependency of the hydraulic stability of Dolos armour on various parameters.

*Test area* One of the reasons for the big scatter in the hydraulic stability test results from the various laboratories is the difference in the reference test area. Obviously, the bigger the reference test area, the higher the stability number.

Fortunately, the test areas seem always to be chosen large enough to cover the whole area where units are moving. Therefore the test results can be converted to results corresponding to a certain test area, e.g. to SWL  $\pm 6.5 \times D_n$ , as is done in the present paper.

*Breakwater slope* The effect of the slope angle of Dolos armour on hydraulic stability has been one of the most controversial points. Hudson's formula, which was developed for rock armour, where the main resistance to wave-induced movement is due to the gravitational force, cannot represent Dolos armour, the stability of which relies both on weight and interlocking.

With regard to the contribution of Dolos weight to the hydraulic stability, the milder the slope, the bigger the contribution, as expressed in Hudson's formula. But on the other hand, the interlocking ability of Dolos armour builds up with the increase of the slope (before the slope reaches its natural angle of repose, which is found to be around  $79^\circ$ , Gravesen et al. 1978). This means that there is an optimum slope which maximize the stability of Dolos armour as a whole. Price (1979) demonstrated in the on-land static stability test with Dolosse that the resistance to pull-out attained its maximum for slope angles around  $28^\circ$  ( $\cot\alpha = 2$ ).

In the hydraulic model tests, Brorsen et al. (1974) reported that the stability number of Dolosse is independent of the slope within the range of slope 1 : 1 ~ 1 : 2. Holtzhausen et al. (1990) concluded that Dolosse stability number decreases with steeper slope, but some of his test results also show the independence of  $N_s$  on slope, cf. Fig. 4.

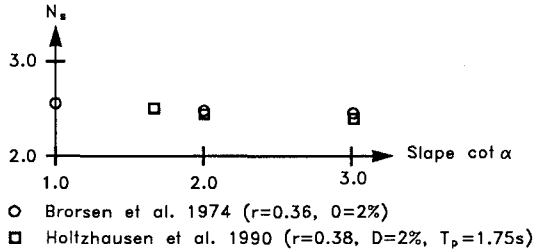


Fig. 4. Influence of slope on  $N_s$ .

**Wave period** The influence of the wave period on the stability of Dolos armour has been the subject of research over the years. HR Wallingford (1970) and Burcharth (1979) found that the stability number decreases with longer wave periods. Burcharth (1979) explained this tendency by *the reservoir effect of the voids* between the units.

The voids are filled with air during wave recession and with water during wave run-up. This reduces not only the wave run-up but also the overflow velocities. Armours with larger porosity, such as Dolosse, exhibit stronger reservoir effect which tributes to the higher hydraulic stability. However, the reservoir effect is reduced in the case of long waves, because such waves carry more water per wave onto the slope and, consequently, relative smaller portion of water can be stored in the voids. The result is higher overflow velocity and lower hydraulic stability of armour and, consequently, a relatively large reduction in stability for armour units with large porosity.

However, there are also some reports which predict increase of the stability number with the wave periods (Holtzhausen et al. 1990).

In the present test results there is no clear tendency about the influence of wave period on the hydraulic stability for which reason the wave period (or wave steepness or  $\xi$ ) is not included as an independent parameter in formula (1). This treatment of the wave period also reflects the fact that for a given design wave height there will be a range of wave periods anyway. The effect of wave period contributes to the uncertainty of the formula. This, however, is taken into consideration when the partial coefficient method is applied in the design.

**Packing density** Some research has been carried out previously to study the influence of Dolos packing density on the hydraulic stability.

Carver et al. (1978) collected data from different laboratories and depicted the Hudson formula stability coefficient  $K_D$  as a function of the packing density  $\varphi_{n=2}$ . If  $N_s = \frac{H_s}{\Delta D_n}$  is used instead of  $K_D$  an almost linear dependency of  $N_s$  on  $\varphi_{n=2}$  is seen.

Zwamborn (1978) first reported that the Dolos armour with three packing densities ( $\varphi_{n=2} = 0.83, 1$  and  $1.15$ ) displayed the same stability. But based on tests with a bigger packing density range ( $\varphi_{n=2} = 0.65, 0.83, 0.87, 1, 1.15$  and  $1.5$ ) Zwamborn et al. (1980) found a rather complicated relation between  $N_s$  and  $\varphi_{n=2}$ , with the general tendency that higher packing density increase the stability number.

A higher packing density gives more neighbour block support and interlocking and hence, fewer displaced units. Therefore, the increase of Dolos stability number with packing density is due to two effects, one is the reduction of displaced units, the other is the increase of total number of units. Eq (1) indicates that the Dolos stability number is linearly proportional to the packing density within the applied range ( $\varphi_{n=2} = 0.61 - 1$ ).

On the other hand a very high packing density ( $\varphi_{n=2} > 1$ ) might reduce the interlocking and the stability because limited space is available for legs to stick in between each other. Therefore, there exists an optimum packing density. SPM (1984) gives  $\varphi_{n=2} = 0.83$  while Zwamborn (1980) suggests  $\varphi_{n=2} = 1$ .

*Wave duration (number of waves  $N_z$ )* In the 50'ties and early 60'ties the storm duration parameter was not considered because the generated waves in laboratories were monochromatic waves, which are the same for every single wave. The equilibrium slope was reached in a short time.

In the case of irregular waves it takes longer time before a possible equilibrium state is reached. Font (1968) studied the effect of storm duration on the stability of rock armoured breakwater. He concluded that for mild wave climates, i.e. relative small  $\frac{H_s}{\Delta D_n}$  values, the duration of the storm is not important. However, the duration becomes relevant for more severe exposure.

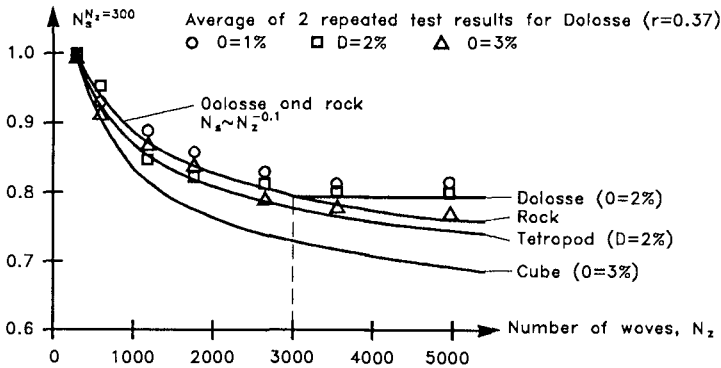


Fig. 5. Influence of wave duration on  $N_s$ .



In the present tests two identical tests with 5,000 waves were performed with Dolosse of waist ratio 0.37. Little difference in the ratio  $\frac{N_s}{(N_s)_{N_z=300}}$  was found for the damage levels  $D = 1\%$ ,  $2\%$  and  $5\%$ . Moreover, it was found that the Dolos armour reached an equilibrium state after  $N_z = 3,000$ . The relationship between  $N_s$  and  $N_z$  could be approximated by  $N_s \sim N_z^{-0.1}$  for  $N_z \leq 3,000$ .

In Fig. 5 the information on rock, cube and Tetrapod is from van der Meer (1988).

### Stresses in Dolosse under wave attack

*Sampling frequency* The natural frequency of the instrumented Dolosse was found to be app. 1,500 Hz by the impact calibrations. The sampling frequency in the wave flume test was 6,000 Hz, i.e. app. 4 times of the natural frequency of the instrumented Dolosse. Theoretical investigations showed that on average the sampled peak stresses were lower than the real ones by 10% due to the limit of the sampling frequency. This one sided bias has been corrected for in the data processing.

*Strain signal processing* The recorded strain signals were converted into signals of maximum principal tensile stress by

$$\text{max. principal tensile stress } \sigma_T = \frac{\sigma}{2} + \sqrt{\left(\frac{\sigma}{2}\right)^2 + \tau^2}$$

$$\text{normal stress } \sigma = \frac{M_c}{W_b}$$

$$\text{combined bending moment } M_c = \sqrt{M_x^2 + M_y^2}$$

$$\text{shear stress } \tau = \frac{T}{W_b/2}$$

where  $M_x$ ,  $M_y$  and  $T$  are the measured bending moments and torsion, respectively.  $W_b$  is the modulus of the strain-gauged cross section of Dolosse. For more detailed explanation see Burcharth et al. 1991.

The converted max principal tensile stresses were separated into (*static + pulsating*) and *impact* stresses. The static and pulsating stress contributions were converted into a range of prototype Dolos sizes using the valid linear scaling law, while the impact stress contributions were converted into the same prototype ranges using the non-linear scaling law for impinging solid bodies. The signals were then synthesized and a statistical analysis performed.

*Stresses from static, pulsating and impact loads in Dolosse* The relative importance of static, pulsating and impact stresses depends of the type and the size of the units, the slope angle, the position on the slope and the wave characteristics.

The Dolos stresses are treated as an extreme value problem. No distinction with respect to the Dolos position on slope was made because in practice the same type of units will be used over the whole height of the slope.

Table 2 indicates typical ratios between the various types of stresses for slender and bulky Dolosse on slope 1 : 1.5.

Table 2. Relative contribution to total stress from static, pulsating and impact stresses. 2 % exceedence probability values. Slope 1 : 1.5.

Waist ratio	Mass	$\frac{H_s}{\Delta D_n}$	$K_D$	$\sigma_{total} = \sigma_{static} + \sigma_{pulsating} + \sigma_{impact}$			
				$\sigma_{static}$	$\sigma_{pulsating}$	$\sigma_{impact}$	
0.325	10t	0.9	0.49	1	0.2	0	
		1.8	3.89	1	0.4	0.1	
		2.6	11.72	1	0.5	0.4	
	50t	0.9	0.49	1	0.2	0	
		1.8	3.89	1	0.4	0	
		2.6	11.72	1	0.5	0.1	
	0.42	10t	0.9	0.49	1	0.2	0
			1.8	3.89	1	0.4	0.4
			2.6	11.72	1	0.6	2
50t		0.9	0.49	1	0.2	0	
		1.8	3.89	1	0.4	0.1	
		2.6	11.72	1	0.6	1.3	

Note that the zeros in the  $\sigma_{impact}$  column does not mean that there is no impacts in the signal. It means that the impact portion of the stresses is smaller than the static+pulsating portion after scaled up to the given size. The tests showed that the variation in the stress ratios with the exceedence probability level is rather weak in the interval 1-5%.

The variation with the slope angle is not known in general. However, because static stresses show only small variations in the slope range 1 : 1.33 to 1 : 2 it is assumed that the stress ratios given in Table 2 are typical for this range of slopes. On the other hand the ratios are probably not valid for very steep slopes as it is known that the static stresses can be up to 100% larger for a 1 : 1 slope than for a 1 : 1.5 slope. For flat slopes of app. 1 : 4 to 1 : 6 it was found from

the Crescent City prototype study with 38 t instrumented Dolosse (Howell et al. 1990) that the ratio of the 10 % exceedence probability stress values,  $\sigma_{Static} : \sigma_{pulsating}$ , was app. 1 : 0.12 for  $N_s = 1.2 - 1.4$ . No impact stresses were recorded in this study, maybe due to the small  $N_s$ -values, cf. also the figures given in Table 2.

### Design diagrams for Dolosse

Based on the model tests at Aalborg University with instrumented Dolosse exposed to irregular waves, complete design diagrams for trunk sections of breakwaters are presented. The diagrams contain curves for stresses and displacements corresponding to different exceedence probability levels. The diagrams provides the relationship between all the following properties, expressed in statistical terms where relevant.

- Dolos waist ratio
- Dolos size
- Concrete tensile strength
- Concrete tensile stress
- Incident wave climate
- Strength exceedence probability (structural integrity)
- Relative number of displaced Dolosse (hydraulic stability).

Figs. 6 and 7 show examples of the design diagrams. The hydraulic stability in terms of displacements is obtained by Eq (1). The amount of rocking is not given explicitly in the design diagrams because the effect of rocking is relevant only to the breakage aspect which are dealt with specifically by the stress curves.

In Burcharth (1993) more diagrams can be found, also showing the strength exceedence probability as function of  $H_{mo}^t$ , Dolos mass, waist ratio and concrete strength.

All information related to the design diagrams refers to one shank cross section. However, for a Dolos there are 6 vulnerable sections (4 in the flukes and 2 in the shank). Because fluke failures contribute less to the failure probability than shank failures and because there exists some moderate correlation between the stresses in the sections it is recommended to adjust the exceedence probability levels for stress given in Figs. 6 and 7 corresponding to the mean of the simple upper and lower bounds. This means that app. 50 % should be added to the failure probability levels, i.e. 2 % should be interpreted as 3 %.

- Legend:
- Hydraulic stability limit ( $N_z=3000, \varphi=0.74, \Delta=1.29$ ) corresponding to relative number of displaced units  $P$ .
  - Tensile strength limit corresponding to strength exceedance probability  $P$ .
  - $H_{mo}^t$  Significant wave height at the toe of breakwater
  - $r$  Dolos waist ratio
  - $\sigma_T$  Concrete tensile strength
  - $P$  Strength exceedance probability and relative number of displaced units

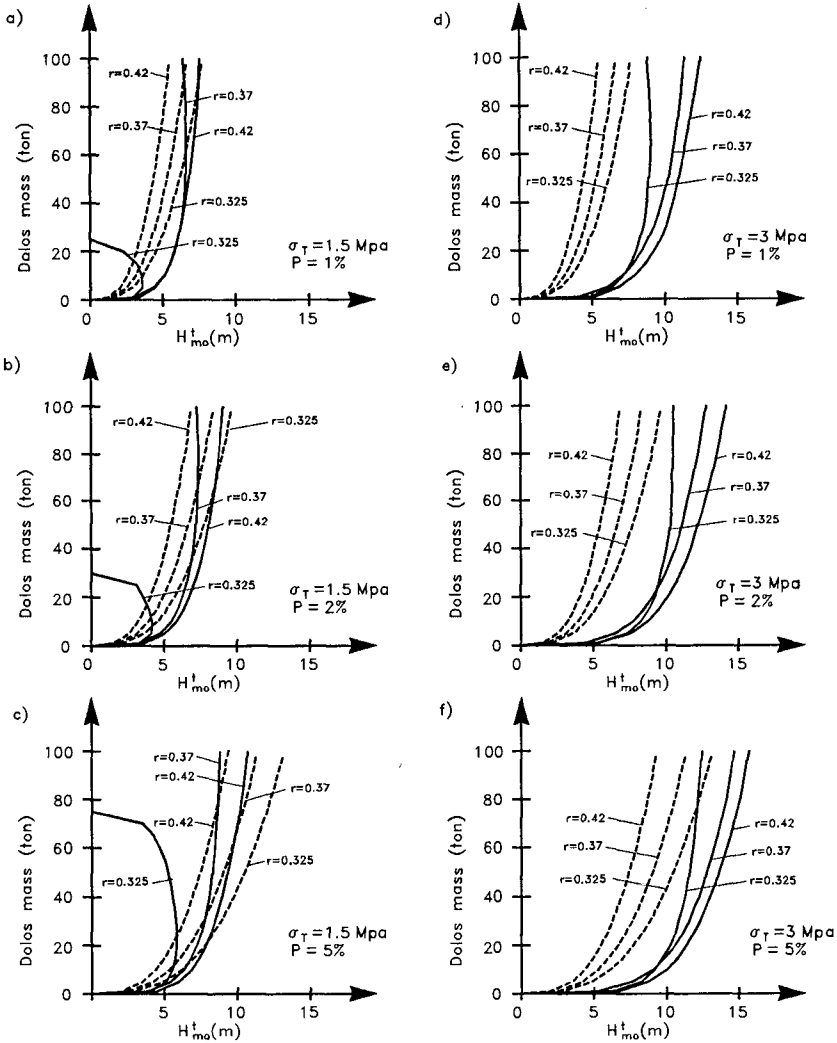


Fig. 6. Dolos design diagram (one shank cross section).  
 Input:  $H_{mo}^t$ , Dolos mass,  $\sigma_T$ ,  $P$ . Output:  $r$ .

- Legend:
- Hydraulic stability limit ( $N_s=3000$ ,  $\phi=0.74$ ,  $\Delta=1.29$ ) corresponding to relative number of displaced units  $P$ .
  - Tensile strength limit corresponding to strength exceedence probability  $P$ .
  - $H_{mo}^{\dagger}$  Significant wave height at the toe of breakwater
  - $r$  Dolos waist ratio
  - $\sigma_T$  Concrete tensile strength
  - $P$  Strength exceedence probability and relative number of displaced units

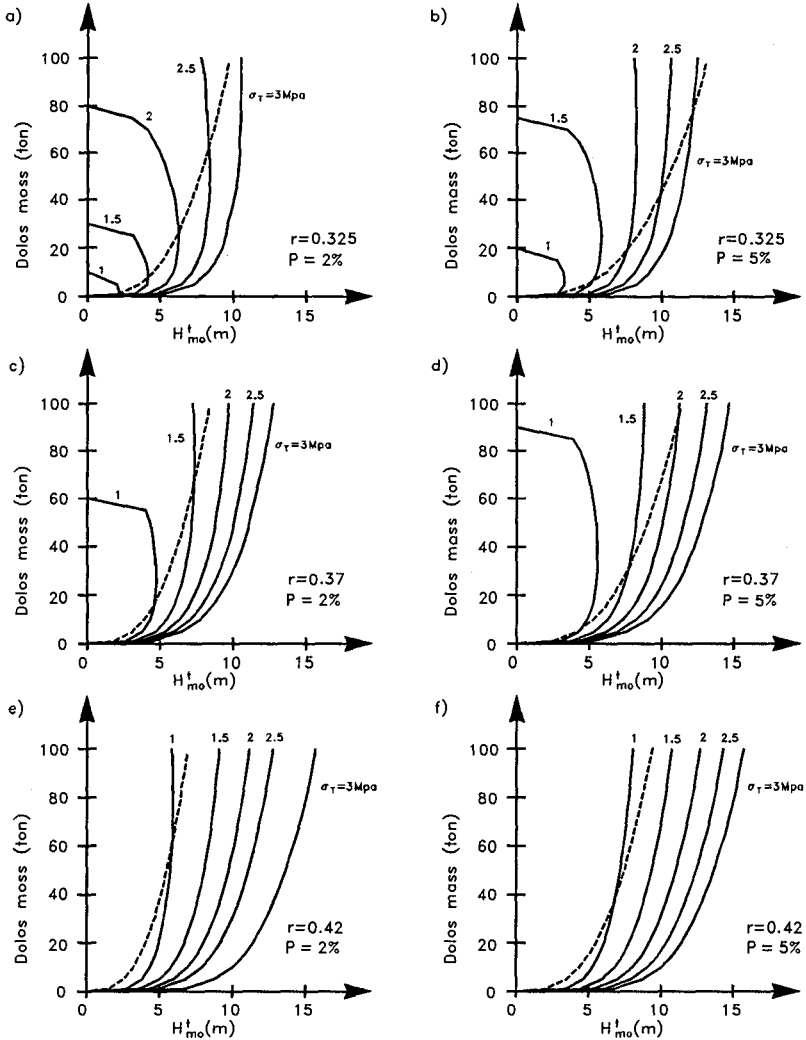


Fig. 7. Dolos design diagram (one shank cross section).  
 Input:  $H_{mo}^{\dagger}$ , Dolos mass,  $r$ ,  $P$ . Output:  $\sigma_T$ .

The design diagrams have been checked against observed behaviour of prototype Dolos breakwaters and good agreement was found, cf. Table 3.

Table 3. Prediction of damage of some Dolos breakwaters.

	Crescent City USA	Richards Bay SA	Sines  POR
$H_s$ (m)	10.7 <sup>(1)</sup>	5 <sup>(2)</sup>	9 <sup>(3)</sup>
slope	1:4	1:2	1:1.5
Dolos mass (ton)	38	20	42
Waist ratio	0.32	0.33	0.35
Dolos packing density	0.85	1	0.83
Concrete density ( $kg/m^3$ )	2500	2350	2400
Elasticity (MPa) <sup>(4)</sup>	40000	40000	40000
Tensile strength (MPa) <sup>(4)</sup>	1.5	1.5	1.5
Reported displacement	7.3%		
Reported breakage	19.7%		
Reported displacement+breakage	26.8%	4%	collapse
Predicted displacement	3.6%	0.6%	3.6 %
Predicted breakage <sup>(5)</sup>	> 10%	5.7%	> 10%

(1) depth limited in front of breakwater

(2) in front of breakwater

(3) offshore  $\approx$  in front of breakwater

(4) estimated values including some fatigue effect

(5) values 50 % higher than found for one shank cross section in Figs. 6 and 7

### Acknowledgements

Part of the study were funded by the Danish Research Council and by the U.S. Army Research, Development and Standardization Group, UK under the Contract DAJA 45-91-C-0010.

## References

- Brorsen, M., Burcharth, H.F., Larsen, T. (1974) : *Stability of Dolos Slopes*. Proceeding of the 14th International Conference on Coastal Engineering, Copenhagen, Denmark, June, 1974
- Burcharth, H.F. (1979) : *The effect of wave grouping on on-shore structures*. Coastal Engineering, 2 (1979).
- Burcharth, H.F. (1991) : *Introduction of partial coefficients in the design of rubble mound breakwaters*. Coastal structures and breakwaters. Proceeding of the conference organized by the Institution of Civil Engineers, London.
- Burcharth, H.F. (1991) : *The Design of Breakwaters*. Book to be published in 1993.
- Burcharth, H.F., Brejnegaard-Nielsen, T. (1986) : *The influence of waist thickness of dolosse on the hydraulic stability of dolos armour*. Proceeding of the 20th International Conference on Coastal Engineering, Taipei, Taiwan, 1986.
- Burcharth, H.F., Howell, G.L., Liu, Z. (1991): *On the determination of concrete armour unit stresses including specific results related to Dolosse*. Coastal Engineering, Vol. 15, 1991.
- Carver, R.D., Davidson, D.D. (1978) : *Dolos-armoured breakwaters: Special considerations*. Proceeding of the 16th International Conference on Coastal Engineering, Hamburg, FRG, July, 1978.
- Font, J.B. (1968) : *Effect of storm duration on rubble mound breakwater stability*. Proceeding of the 11th International Conference on Coastal Engineering, London, UK, September, 1968.
- Gravesen, H., Jensen, O.J., Sorensen, T. (1978) : *Stability of rubble mound breakwater*. Proceeding of the 16th International Conference on Coastal Engineering, Hamburg, FRG, July, 1978.
- Holtzhausen, A.H., Zwamborn, J.A. (1990) : *Stability of Dolosse with different waist thickness for irregular waves*. Proceeding of the 22nd International Conference on Coastal Engineering, Delft, Holland, July 1990.
- Price, W.A. (1979) : *Static stability of rubble mound breakwater*. Dock & Harbour Authority. Vol.LX (702), 1979
- Van der Meer, J.W. (1988) : *Stability of cubes, Tetrapods and Accropode*. Proceeding of Breakwaters '88, Eastbourne, UK
- Zwamborn, J.A. (1978) : *Dolos packing density and effect of relative block density*. Proceeding of the 16th International Conference on Coastal Engineering, Hamburg, FRG, July, 1978.
- Zwamborn, J.A., Bosman, D.E., Moes, J. (1980) : *Dolosse: past, present and future ?* Proceeding of the 17th International Conference on Coastal Engineering, Sydney, Australia, 1980.

## CHAPTER 80

# Results of Measurements on Large Model Tetrapods and Transfer to Prototype Units

Bürger, W.W. \*); Smidt, H.-J. \*\*); Partenscky, H.W. \*\*\*)  
University of Hannover, SFB 205, Franzius-Institut,  
Hannover, Germany

### Abstract

This paper intends to present results of the research work on structural stability of tetrapods done at the University of Hannover. The results are brought in accordance with interpretations from the hydraulic tests made in the large wave flume and prototype realisations. The analysis of the data are supposed to bring a clarification of the similitude problems related to the transfer of the measured impact strains to prototype conditions.

### 1. Introduction

Some breakwater failures, mainly caused by the breakage of armour units, have led to world wide activities in this field. Within an extensive basic research program on structural stability, performed at the University of Hannover, a number of hydraulic and dry tests were undertaken to simulate the most relevant loads on tetrapods. The main objective of these investigations is to develop one guidance for the design of unreinforced armour units with respect to their structural integrity.

Even if the fracture mechanism of concrete armour units in breakwaters are complex, several aspects are now known, like direct loads from wave action on tetrapods, possible displacement of tetrapod elements, strain due to movement (rocking and displacement) of tetrapod elements, relation wave height/degree of rocking, impact characteristics etc..

### 2. Description of the Research Program

The investigations on the structural behaviour of concrete armour units constitutes a part of an extensive basic research program on rubble mound breakwaters conducted at the University of Hannover and supported by the German Research Council (DFG) within the scope of the "Sonderforschungsbereich 205" (SFB 205).

---

\*) Dipl.-Ing., formerly Research Engineer at Franzius-Institut  
\*\*) Dipl.-Ing., formerly graduate student at Franzius-Institut  
\*\*\*) Prof. Dr.-Ing. Dr. phys., formerly Director of Franzius-Institut



Aside from the hydraulic test within the research program on structural behaviour of concrete armour units, a number of dry tests like static tests, pendulum tests, drop tests on model units as well on prototype units were performed (BÜRGER et al., 1990).

The main purpose of the hydraulic tests with respect to structural stability of the units was to determine the actual response of the units in a breakwater environment as a function of the incident waves and of the location of the units on the slope.

The results of the aforementioned experimental investigations, together with available results from basic research on impact and cyclic loading of concrete are intended to be used for the development of design criteria for the structural stability of the units.

### **3. Description of the Breakwater Model and the Instrumented Units**

The hydraulic tests described in the paper were conducted on a tetrapod armoured breakwater in the Large Wave Channel (GWK) (320.0 m \* 7.0 m \* 5.0 m) using 50 kg armour units and maximum wave heights up to 2.20 m. The instrumented tetrapods used in the hydraulic tests had a reduced cross-section in order to measure the wave-induced static loads, quasi-static loads and also dynamic loads. Fig. 1 shows the cross-section of the model investigated in the Large Wave Channel, Hannover.

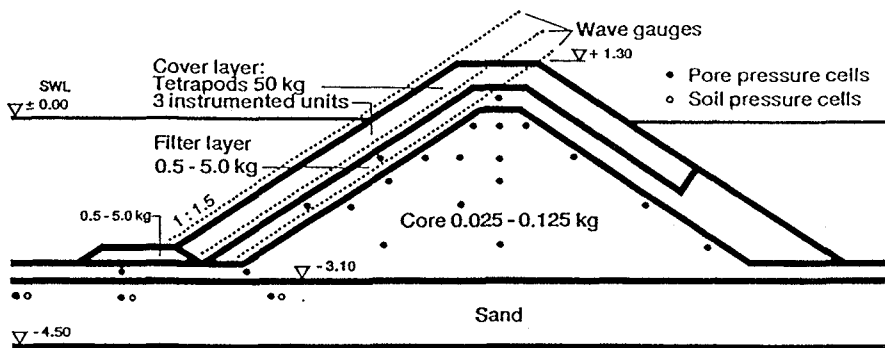


Fig. 1: Cross-section in the Large Wave Channel (GWK)

#### **4. Testing and Recording Procedures for the Hydraulic Tests**

The forces acting on a unit show a large variability based on the units location and the wave climate. To cover up all those variabilities, the instrumented tetrapods were placed at critical locations on the breakwater and the tests were performed with both regular and irregular waves, started with low wave conditions and increased in steps of 0.10 - 0.20 m until a significant unit movement was observed. After every test series, the cover layer was completely removed and reconstructed.

The measured data were recorded at a sampling frequency of 400 Hz and at the same time also registered at a sampling frequency of 11000 Hz by a Video Pulse Code Modulator (Video PCM).

Since the quasi-static and the dynamic load could not be measured separately, the recorded load signal should be splitted into a quasi-static and a dynamic part by a computer program developed for this purpose. (BÜRGER et al., 1990)

#### **5. Results from hydraulic tests**

In a reliable design of concrete armour units with respect to their mechanical strength all loads and environmental impacts should be required (BÜRGER et al., 1989). The most relevant loads, however, are induced by the combined action of waves and the weight of the units. That means the breakage of the single breakwater units is strongly connected with the hydraulic stability of the whole armour layer.

#### **Displacement**

The wave load on the breakwater resulted in rocking, displacement and strain in the tetrapods as the cover layer. Before and after every test, photographs were taken in order to determine the changes which occur in the whole armour layer and the instrumented units. After the development of the pictures, an enlarged positive and negative mask with the size of 0.18 \* 0.24 [m] was made.

For each test, the picture of the initial position of the test (positive mask) was superimposed with the picture of the final position of the same test (negative mask) and against a source of light, the changes of the position of the armour units could be seen. On a transparent sheet, a line starting from the initial position to the final position of the moved unit could be drawn.

Because of the model scale in the large wave channel the evaluation could be done very exactly. Due to the limitation of the tip of the isograph used for drawing only the differences of congruence which were smaller than 0.25 [mm] has to be neglected. Taking into account the transfer to different prototype units, for a 25 t tetrapod, this limitation is already equivalent to 0.07 [m]. The movements shown in

Table 1 are not theoretical values, but were measured from superposed photographs. This points to the importance of large scales also for hydraulic stability tests.

Movement	W [t]	Scale		Movement of the unit					
				[mm]	0.25	1.00	2.50	5.00	7.50
on the mask	-	3.5:1	[mm]	0.25	1.00	2.50	5.00	7.50	15.00
in the model	0.05	1:1	[m]	0.01	0.03	0.09	0.17	0.26	0.52
in prototype	17.5	1:7	[m]	0.06	0.24	0.61	1.21	1.82	3.63
in prototype	25.6	1:8	[m]	0.07	0.28	0.69	1.38	2.08	4.15
in prototype	36.5	1:9	[m]	0.08	0.31	0.78	1.56	2.34	4.67
in prototype	50.0	1:10	[m]	0.09	0.35	0.87	1.73	2.60	5.19

Table 1: Movement of Model Units Compared to Prototype Units

Table 2 shows the movements of the tetrapods for a significant wave height of  $H_S = 0.70$  [m] and a peak period of  $T_p = 4.5$  [s].

In this test more than 14 % of the units in an area  $0.75 * H_D$  (design wave height) above SWL moved about 0.09 [m]. Transferring these results e.g. to a 25 t tetrapod, it could be expected that, for the equivalent wave parameter, 14 % of the units move about 0.70 [m].

<b>Hydraulic Test 04118801</b>						
JONSWAP-Spectrum						
Wave Height $H_S = 0.70$ [m]						
Peak Period $T_p = 4.5$ [s]						
Movement of the 50kg unit [m]	0.01	0.03	0.09	0.17	0.26	0.52
Number of units (total 84)	21	34	12	8	4	1
Percentage	25.0	40.5	14.3	9.5	4.8	1.2
Movement of a 25 t unit [m]	0.07	0.28	0.69	1.38	2.08	4.15

Table 2: Movement of 50 kg Tetrapods and Comparison to 25 t Units

### Displacement and strain

The afore-mentioned displacement caused impact loading and strain in the legs of the displaced tetrapod itself (direct impact) or in the neighbour tetrapod (indirect impact). If the length of displacement and the dynamic strain are known it can be expected to find a relationship between these two values. A certain displacement could cause a certain strain like it was found in the drop test (BÜRGER et al., 1989).

The correlation between drop height and strain found in the drop tests cannot be transferred to the hydraulic test. There are many reasons. Two of them are:

- The distance measured from the overlaid pictures is the distance of the tetrapod before and after the whole hydraulic test. It cannot be proved if the tetrapod was displaced only ones or in more than one step.
- In a dry test the boundary conditions can be clearly defined. In the hydraulic tests the tetrapods are random placed and the impact points cannot be distinguished during and after the test.

### Strain

For the irregular wave tests, however, it is necessary to analyse the correlation between the single wave and the induced load. For the tests with more than one thousand waves the interaction between wave parameter and resulting load has to be described individually; i.e. separately for each wave.

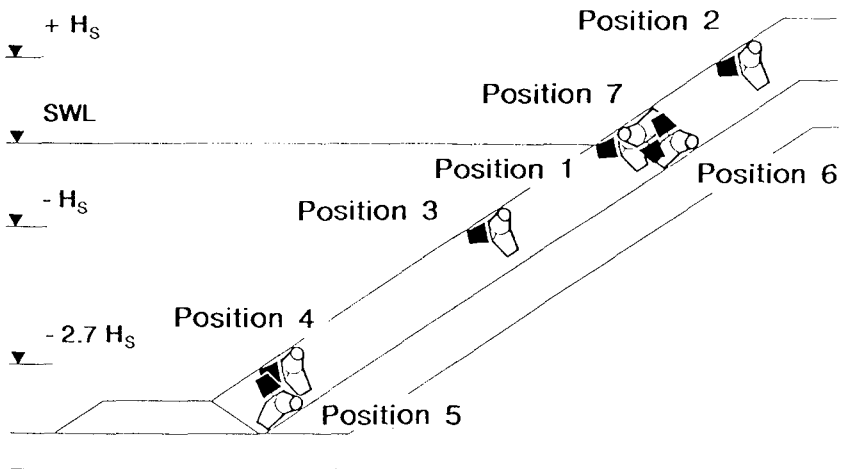


Fig. 2: Positions of the instrumented tetrapods (BÜRGER et al. 1990)

From the analysis of the data related to the location of the instrumented tetrapods, the highest wave-induced strain within the tetrapods generally occur at and slightly above the still water level (BÜRGER et al., 1989). For this the signals of the instrumented tetrapods in position 1 and position 7 (see Fig. 2) are evaluated.

Fig. 3a) shows values from all the tests with tetrapods in a stable position. For a stable position the strain increases linearly with increasing wave heights.

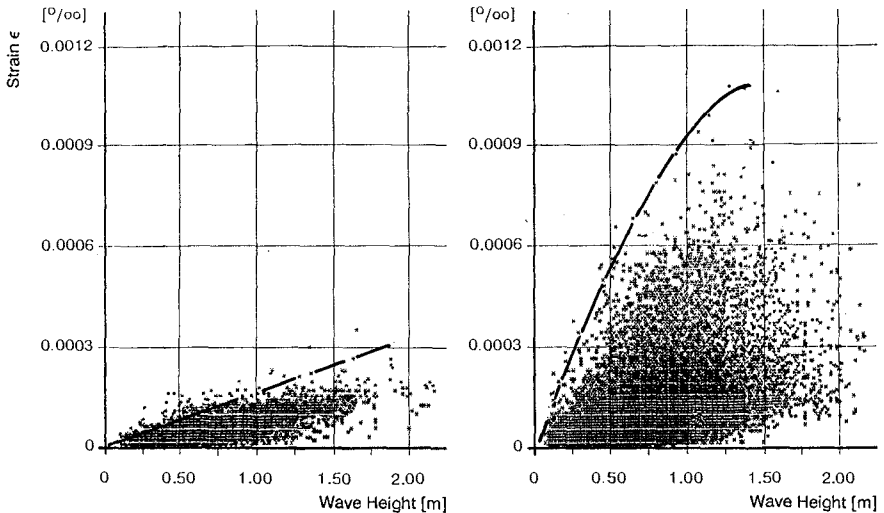


Fig. 3 Quasi-Static Strain induced in a 50 kg Tetrapod

a) in a stable position

b) in an unstable position

In Fig. 3b), all tests with tetrapods in an unstable position are combined and more than 28,000 values are plotted. It could be seen, that due to the large scatter of the data, an attempt to determine a relationship between those strains and corresponding incident wave parameters will not be successful, particularly for large wave heights. A better correlation could be obtained by considering only the maximum strain-values. The envelope curve shows that the quasi-static strain for unstable position is increasing rapidly with increasing wave height.

### **Breakage due to Rocking**

It is understood that fracture in large multilegged blocks is mainly caused by rocking motion induced by wave action (BURCHART, 1985). The porosity of armours of multilegged units is quite large and can reach values up to 60 %.

Therefore those units are able to rock between two extreme positions. This process due to weight and interlocking of units will be observed when the significant wave height exceeds a certain value. The rocking mode considered is a rotation of the unit to drag and acceleration forces, followed by an opposite rotation returning the unit to its original position.

If the rocking distance or the angle of rotation is large, the unit will possibly break itself or break one of the neighbour units. This will be intensified, when the combined action of flow and gravity will act.

For dynamic loads, a distinction cannot be made between units in an unstable position and units in a stable position because the measured strain could result either from the unstable unit or from the unstable neighbour unit hitting the stable unit. Even though, the strain is increasing rapidly with increasing wave height, but will not reach higher values after a certain wave height.

BONZEL (1986) gives reference values for bending tensile strain for critical load of concrete. After BONZEL strain will be already critical when the bending tensile stress will reach values between 65 and 90 % of the maximum stress  $\sigma_{\max}$ . Breakage will be expected when the stress  $\sigma_{\max}$  will be exceeded and the strain  $\epsilon_{\max}$  will reach values higher than 0.30 ‰.

The values after BONZEL (1986) are shown in Table 3.

Bending Tensile Stress	Tensile Strain [‰]
critical (65 - 90 % of $\sigma_{\max}$ )	$\epsilon_{\text{crit}} = 0.05 - 0.15$
maximum ( $\sigma_{\max}$ )	$\epsilon_{\sigma_{\max}} = 0.10 - 0.30$
$> \sigma_{\max}$ (breakage)	$\epsilon_{\sigma_{\text{br}}} = 0.30 - 0.60$

Table 3: Reference Values for unreinforced concrete after BONZEL (1986)

In some tests the measured strains in the 50 kg tetrapods are higher than 0.10 [‰], but are not plotted in Fig. 4. For those values the maximum stress  $\sigma_{\max}$  is reached (Table 4).

Wave Height $H_s$ [m]	$T_p$ [s]	Test	$\max \epsilon_{dyn}$ [‰]	Values after BONZEL (1986)		
				0,05 - 0,15	0,10 - 0,30	0,30 - 0,60
0.90	4.5	21118801	0.15		$\epsilon_{\sigma max}$	
1.00	4.5	11118801	0.12		$\epsilon_{\sigma max}$	
1.10	6.0	24118804	0.17		$\epsilon_{\sigma max}$	

Table 4: Maximum Strain measured in the Hydraulic Tests

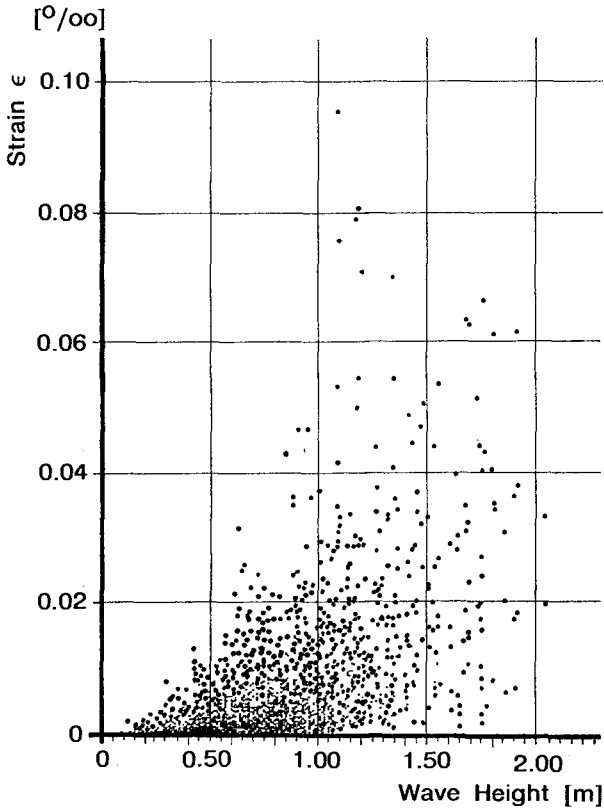


Fig. 4: Measured Dynamic Strain in a 50 kg Tetrapod

For dynamic strain especially the maximum values are most important. It was proved that the measured maximum dynamic strain values  $\epsilon_{\text{dyn}}$  in the hydraulic tests follow the distribution by GUMBEL. With increasing significant wave heights  $H_s$  also the possibility of occurrences of certain strain will increase. The extreme values of dynamic strain induced in a 50 kg tetrapod by waves of different significant wave heights plotted on GUMBEL paper is shown in Fig. 5.

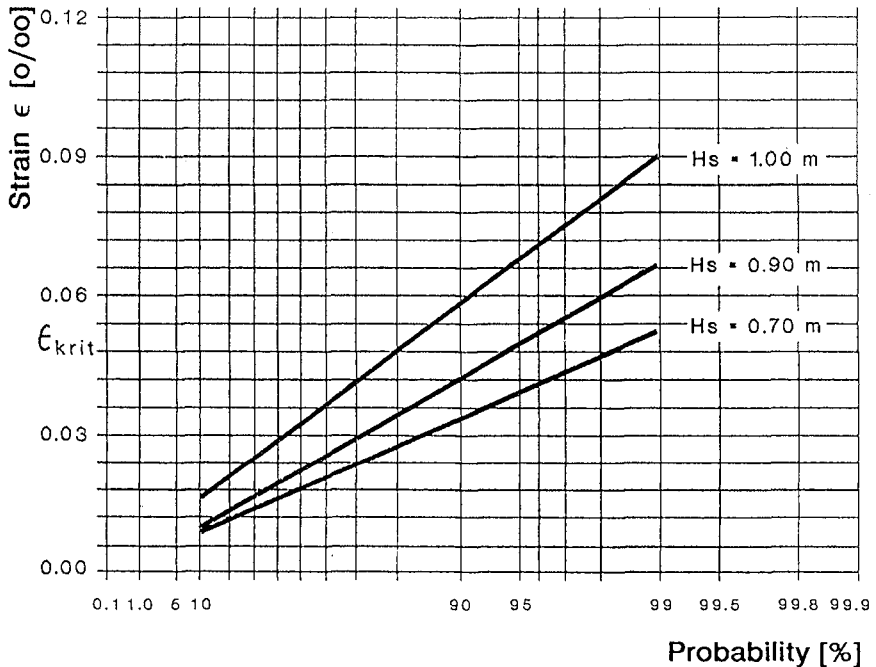


Fig. 5: GUMBEL Distribution for Extreme Values of Dynamic Strain in a 50 kg Tetrapod

The purpose is to find the possibility of occurrence from high strain values which could be higher than the strain for the concrete which will cause breakage of the unit.

Because of effects of other mechanisms not included the results of the probabilistic calculations must be regarded as still preliminary. The failure probability of the breakwater due to fracture of armour units as a consequence of production, placing procedures and so on has to be added. Those probabilities has to be based on engineering judgement.



Fig. 6 shows the preliminary design diagram. For the calculation of the weight of the armour unit the well known HUDSON formula is applied.

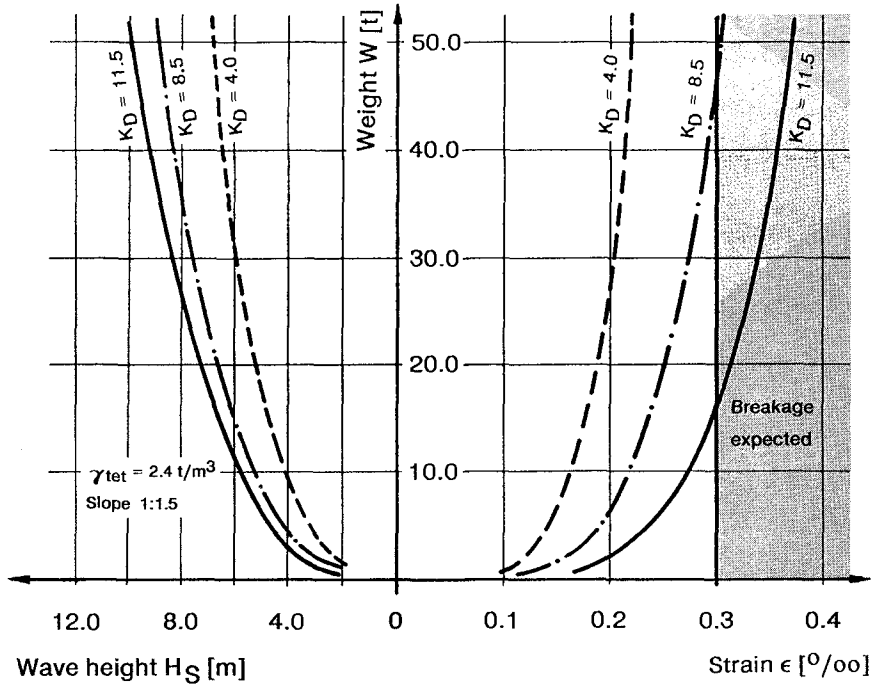


Fig. 6: Expected Strain for a Probability of 95 % and different  $K_D$ -Values

The design diagram combines the hydraulic stability with the structural stability. From the GUMBEL distribution for different sizes of tetrapods the calculated strain for a possibility of 95 % is plotted for these tested  $K_D$ -values. It is shown, that with higher  $K_D$ -values and higher waves the strain in the calculated unit will reach values higher than  $\epsilon = 0.3$  ‰ when breakage is expected.

Even if the design diagram is preliminary it can be concluded that the tetrapods with a certain weight are structural unstable for those conditions built in the large tests.

## **6. Perspectives**

The design procedure with respect to the structural stability of tetrapods has to be continued with an extensive study of concrete literature. Based on the experimental results and the results of the literature study the final design diagram will be presented.

## **7. Acknowledgements**

This study is a part of an extensive research programme within the Coastal Engineering Research Unit "Sonderforschungsbereich 205" at the University of Hannover which is supported by the German Research Council (DFG), Bonn.

## **8. References**

- BONZEI, J.                                Beton, Beton-Kalender 1986, Band I, Verlag Ernst & Sohn, Berlin, 1986 (in German)
- BURCHART, H.F.                        A design method for impact loaded slender armour units, ASCE Int. Convent New York, Bull. 18, Aalborg Univ., 1985
- BÜRGER, W.W.  
OUMERACI, H.  
PARTENSCKY, H.W.                    Geohydraulic Investigations of Rubble Mound Breakwaters, ASCE, Proc. 21st ICCE, Torremolinos, Spain, 1988
- BÜRGER, W.W.  
OUMERACI, H.  
PARTENSCKY, H.W.                    Impact Strain Investigations on Tetrapods: Results of Dry and Hydraulic Tests. Seminar on "Stresses in Concrete Armor Units", Vicksburg, Mississippi, U.S.A., 1989
- BÜRGER, W.W.  
OUMERACI, H.  
PARTENSCKY, H.W.                    Stresses in Tetrapods: Results of Large Scale Model Tests, Proc. 22nd Internat. Conference on Coastal Engineering, Delft, The Netherlands, 1990

## CHAPTER 81

### The Movement of Submerged Bodies by Breaking Waves

M.J. Cooker <sup>1</sup> & D.H. Peregrine <sup>2</sup>

#### Abstract

This paper describes a mathematical model of the large but short-lived forces exerted on submerged solid bodies by a wave impacting on a plane impermeable surface nearby. We consider the forces on a hemispherical boulder situated close to a wave impact on (i) a vertical wall and (ii) a steep slope. We show that for certain positions of the body and for a sufficiently strong wave impact the impulsive force on the body can be much greater than either the flow drag or the weight of the boulder. For a body which is free to move under the wave impulse we compute the body's initial velocity.

#### Introduction

This paper describes recent work on the mathematical modelling of the large sudden forces exerted on submerged bodies by breaking waves. See figure 1. When a wave breaks against a wall the peak pressure at a point in the fluid can be ten times greater than hydrostatic, and the pressure can rise and fall in milliseconds. Richert (1968) measured high pressures on both walls and slopes. Nagai (1960) reports measurements in which the maximum peak pressure occurs at the bottom of the wall; this may have occurred because the bed was exposed before impact.

Cooker and Peregrine (1990a,1992) have shown theoretically that when a wave breaks against a vertical wall the peak fluid pressure can be significant all the way down the wall and along the bed. Grilli et al (1992) have measured impulsive wave impact pressures along the bed in front of a vertical wall. The theory and measurements show that for a given wave impact the peak pressure decreases along the bed with increasing distance from the wall. Suppose a small boulder lies on the bed. During the short time of wave impact the boulder experiences high pressure on the side near the wall and

---

<sup>1</sup> Research Associate, <sup>2</sup> Professor of Applied Mathematics,  
Dept. of Mathematics, University of Bristol, Bristol BS8 1TW, UK.

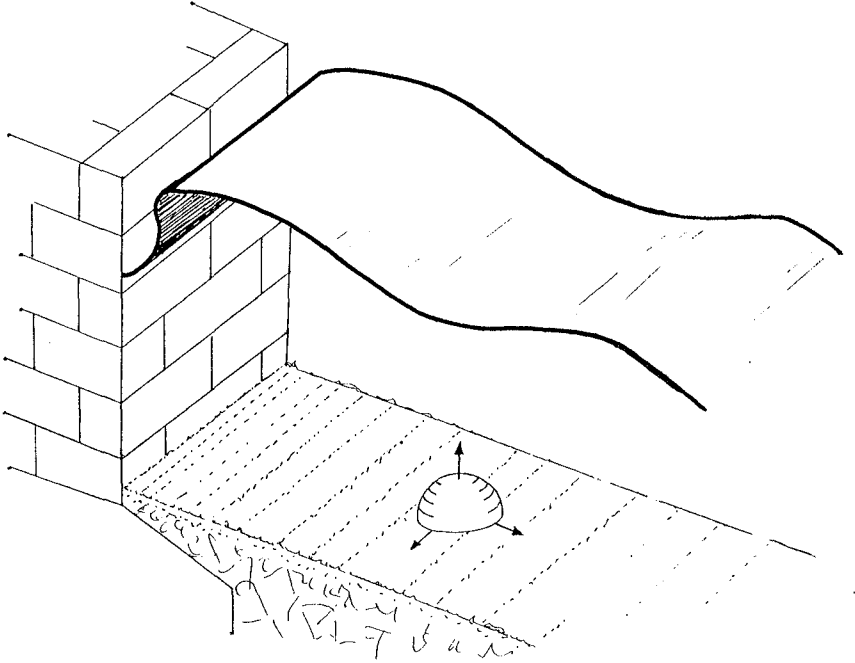


FIGURE 1: Sketch of a wave impact on a wall with a body on the bed.

lower pressure on the side away from the wall. This impulsive fluid pressure must be treated differently to hydrostatic pressure: in order to find the net impulsive load on the body we must carry out calculations similar to those for finding added mass.

In this work it is more convenient to work with the *pressure impulse* than the peak pressure. The pressure impulse,  $P(\underline{x})$ , at the point  $\underline{x}$  due to a wave impact which begins at time  $t_b$  and ends at time  $t_a$ , is defined to be the time-integral of the pressure  $p(\underline{x}, t)$ :

$$P(\underline{x}) = \int_{t_b}^{t_a} p(\underline{x}, t) dt. \quad (1)$$

For an incompressible liquid  $P$  satisfies Laplace's Equation (Lamb, 1932, §11). We expect the highest impact pressures to be generated when the fluid contains few air bubbles and so the water may be treated as incompressible.  $P$  is useful for finding the velocity after impact,  $u_a$ , from the velocity before impact,  $u_b$ :

$$u_a(\underline{x}) = u_b(\underline{x}) - \frac{1}{\rho} \nabla P(\underline{x}) \quad (2)$$

where  $\rho$  is the water density, and the flows  $u_a$ ,  $u_b$  can contain

vorticity. The peak pressure  $p_{pk}(x)$  is connected to the pressure impulse by the approximate relation

$$p_{pk}(x) = 2P(x)/\Delta t \quad (3)$$

where the impact duration  $\Delta t = t_a - t_b$  must be chosen appropriately.

The observed decrease in peak pressure with distance along the bed in front of a wall which is undergoing wave impact, corresponds to a decrease in the pressure impulse along the bed. In general, where the water contains a gradient of pressure impulse it can exert an impulse on a solid body. We show below that the impulse on the body is directly proportional to the product of the volume of the body and the size of the pressure impulse gradient. The direction of the net impulse can be quite different to the direction of the pressure impulse gradient. The size of the impulse on the body also depends on its shape, and whether it is fixed or free to move.

The calculation of the impulsive force on a body has two stages. First the pressure impulse  $P_1$  is calculated from a boundary-value problem (b.v.p.) appropriate to the shape and speed of the impacting wave at the instant it meets, for example, a vertical wall. A point  $\tilde{x}$  is chosen at which we will place a small body and there we find the pressure impulse gradient  $G = \nabla P_1$ . In the second stage we solve a second b.v.p. for  $P_2$ , which is the pressure impulse close to the body and which accounts for the disturbance to  $P_1$  caused by the presence of the body. Finally the net impulse is found from an integral of  $P_2$  over the surface of the body. If the body is free to move we can also find its initial velocity.

The analysis can be used to find the force on a body in front of a vertical wall (see Cooker and Peregrine, 1992) or a steep slope. The measurements of Richert (1968) show that when a slope is subjected to wave impact significant pressure impulse gradients can occur. The impulsive forces estimated in this paper can be briefly much greater than the forces of flow drag or body weight. This work may explain the movement of large blocks seaward away from steeply sloping and vertical sea defences, when these same blocks are unmoved by the drag from the water motion of waves.

## 2. Pressure Impulse: A comparison with experiment.

Figure 2(a) is a sketch of a wave impact on a plane vertical wall. The peak pressures are greatest when the incident wave crest is parallel to the wall at the instant of impact, so the flow may be modelled in a two-dimensional plane perpendicular to the shore. The idealized boundary-value problem (b.v.p.) for the pressure impulse,  $P$ , is shown in figure 2(b). The total height of water is  $H$  and for simplicity we suppose the wave face impacts the wall between  $y = 0$  and  $y = -\mu H$ , where  $\mu$  must be chosen between 0 and 1. The component of water velocity normal to the wall before impact is supposed the same at all points and denoted  $U_0$ . The bed and wall are impermeable.

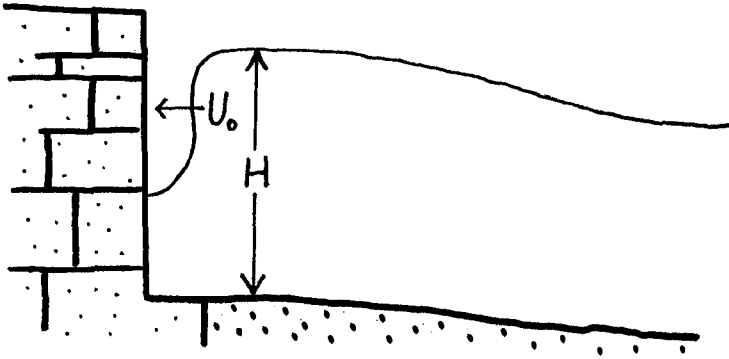


FIGURE 2(a): Sketch of the wave before impact on a vertical wall.

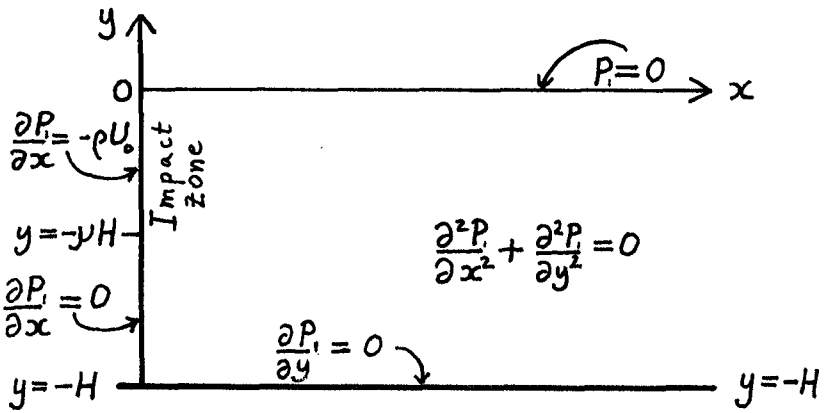


FIGURE 2(b): Boundary-value problem for pressure impulse  $P_1$ .

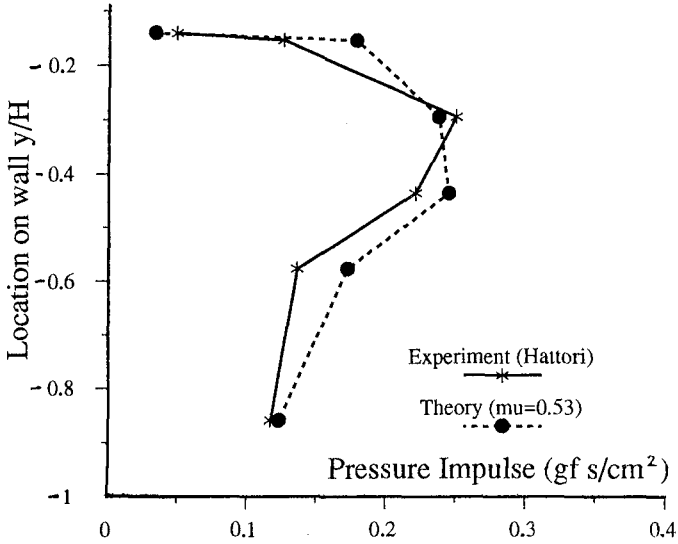


FIGURE 3(a): Comparisons of measured pressure impulse with theory, for impact as in figure 2.  $\mu = \frac{1}{2}$ ,  $U_0 = 1\text{m/s}$ ,  $H = 0.1\text{m}$ .

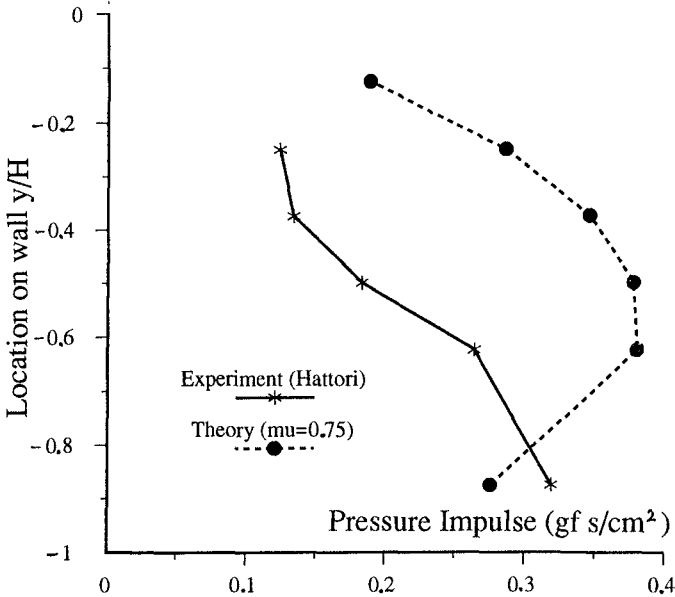


FIGURE 3(b): As fig. 3(a).  $\mu = \frac{3}{4}$ ,  $U_0 = 1\text{m/s}$ ,  $H = 0.1\text{m}$ . The disagreement may be due to the impact being more prolonged and less intense than in fig. 3(a): peak pressures are only  $\frac{1}{7}$  of those in fig. 3(a).

The b.v.p is solved by Cooker and Peregrine (1990a) and we compare this earlier result with the measurements of Hattori (1992). The values of  $\mu$ ,  $H$ ,  $U_0$  are estimated from high-speed video images:  $\mu = 0.53$ ,  $H = 0.1m$ , and  $U_0 = 1m/s$ . Figure 3 shows two comparisons between the theory (with parameters chosen from the video) and the pressure measurements of Hattori. The close agreement of figure 3(a) occurs for a wave impact of short duration with a very high maximum peak pressure of  $525gf/cm^2$ . The disagreement in figure 3(b) is interesting because it shows the pressure impulse with a maximum near the bed, indicating that  $P$  (and its gradient) may be significant along the bed. Also this second comparison corresponds to a low impact pressure maximum measured to be  $70gf/cm^2$ , so pressure impulse theory may be inappropriate for this less sudden impact. Further note that the values of pressure impulse in figure 3(a) and figure 3(b) are similar even though the maximum peak pressures differ by a factor of 7. This accords with the repeated wave experiments of Bagnold (1939) who observed the constancy of pressure impulse compared with the very wide variation of the peak pressures.

### 3. The Impulse on a Hemispherical Boulder: Vertical Wall.

Figure 4 shows the distribution of pressure impulse on the wall and along the bed for the solution  $P_1$  of the b.v.p. presented in figure 2(b). On the bed, the gradient of  $P_1$ , denoted  $\tilde{G}$ , is directed along the bed.  $|\tilde{G}|$  takes its greatest value of  $0.11\rho U_0$  at  $x = x_m = 0.48H$ , where  $x = 0$  is at the wall. We now place a boulder in the shape of a hemisphere on the bed at  $x = x_m$ , so that it can experience the greatest gradient of pressure impulse. Locally we can model the variation of  $P_1$  by a linear approximation:

$$P_1 = P_0 - G(x - x_m) \quad (4)$$

where  $P_0$  and  $G$  are the positive constants  $P_0 = P_1(x=x_m, y=-H)$  and  $G = \left| \frac{\partial P_1}{\partial x}(x=x_m, y=-H) \right|$ . We now compute the effect on  $P_1$  due to the presence of the boulder.  $P_2$  is the pressure impulse on and near the boulder. Let  $r, \theta, \phi$  be spherical polar coordinates centred on the hemisphere, where  $\theta$  is the angle subtended by the field point and the  $x$ -axis, at the centre of the hemisphere.  $P_2$  is harmonic and must match the variation of  $P_1$ , given by equation (4) (expressed in polar coordinates), at large distance from the boulder: i.e.

$$P_2(\tilde{x}) \longrightarrow P_1(\tilde{x}) = P_0 - G r \cos \theta \quad \text{as } |\tilde{x}| \equiv r \longrightarrow \infty. \quad (5)$$

On the boulder,  $r = a$ , we have the second boundary condition for  $P_2$ :

$$\frac{\partial P_2}{\partial r} = -\rho V \cos \theta \quad (6)$$

where  $V$  is the as yet unknown velocity component along the  $x$ -axis



FIGURE 4(a): The variation of pressure impulse up the wall for the wave impact illustrated in figure 2.  $\mu = \frac{1}{2}$ .

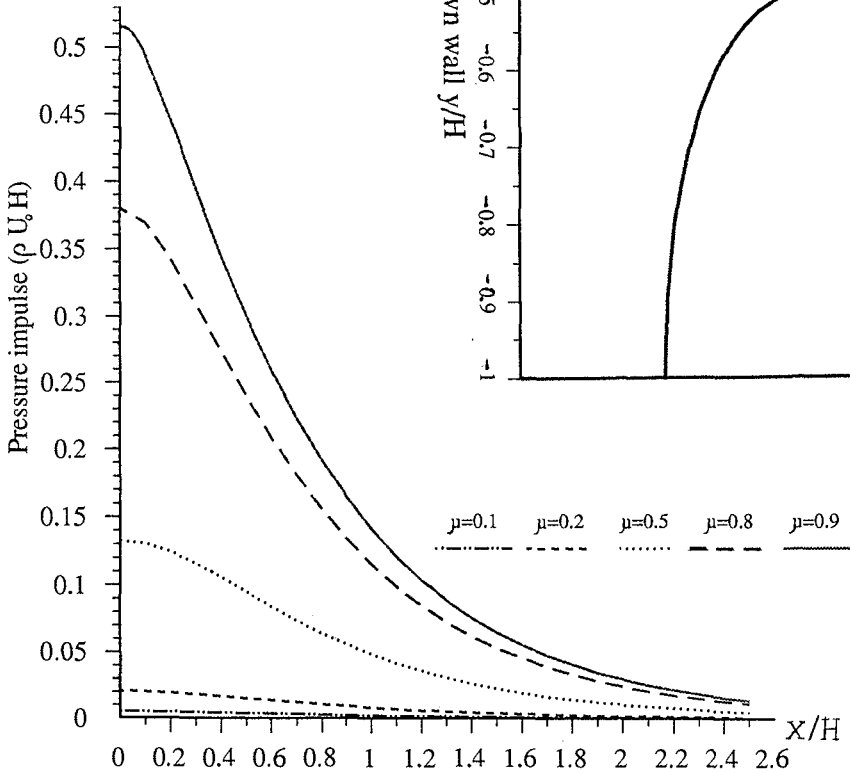
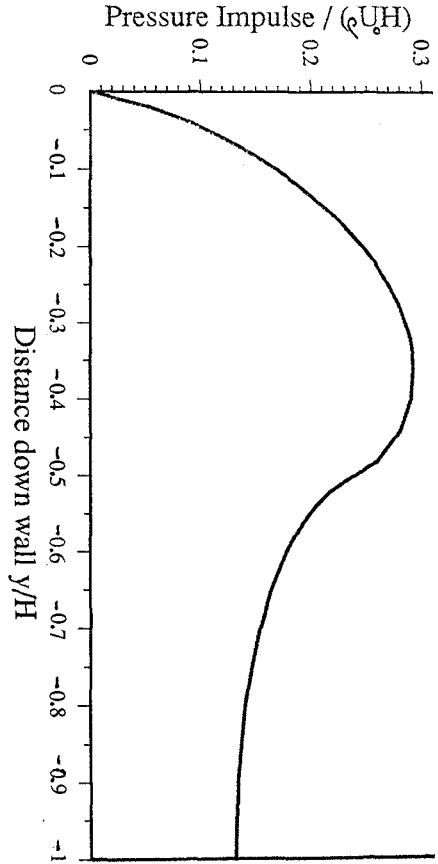


FIGURE 4(b): As figure 4(a). The pressure impulse on the bed for several values of  $\mu$ . At points where  $\partial P / \partial x$  is large the fluid can exert an impulsive load on a body.

acquired by the body due to the fluid impulse. Cooker and Peregrine (1992) show that the impulse on the hemisphere is

$$I = \frac{2}{3}\pi a^3 \left\{ 3G - \rho V \right\} . \tag{7}$$

For a free boulder we may equate the impulse I with momentum gained by the body: if  $\rho_b$  is the boulder's uniform density then the initial speed of unconstrained motion is

$$V = \frac{3G}{2\rho_b + \rho} . \tag{8}$$

If the body is fixed then  $V = 0$  in equation (7). If the body is free then equations (7) and (8) give

$$I = \frac{2}{3}\pi a^3 \left\{ \frac{3G\rho_b}{2\rho_b + \rho} \right\} . \tag{9}$$

Equation (3) suggests that the peak force is related to the impulse:

$$F = 2I/\Delta t. \tag{10}$$

EXAMPLE. Let  $H = 2m$  ,  $U_o = \sqrt{gH} = 4.4m/s$ , and  $\rho = 1035kg/m^3$ ,  $\rho_b = 2.7\rho$ . For impact on a vertical wall, with  $\mu = \frac{1}{2}$  , the position of maximum pressure impulse gradient is  $x_m = 0.48H = 1.2m$  from the wall.  $G = 0.1\rho U_o = 0.44\rho = 460$  Ns/m. Let the impact time  $\Delta t = 0.01s$ .

From equation (8)  $V = 0.21$  m/s and is the same for any hemisphere radius a.

From equation (9)  $I = 1.21 a^3$  kNs.

From equation (10)  $F = 240 a^3$  kN.

We estimate the flow drag, D, from that for a sphere for Reynold's numbers between  $10^4$  and  $10^6$  with a drag coefficient  $C_d = \frac{1}{2}$  and a typical flow speed of  $U_o$  (Batchelor, 1973, p341).

$$D = \frac{1}{2}C_d \left(\frac{1}{2}\pi a^2\right)\rho U_o^2 \tag{11}$$

$$D = 7.9 a^2 \text{ kN.}$$

Finally the dry weight  $W = \frac{2}{3}\pi a^3 \rho_b g$  (12)

Hence  $W = 57 a^3$  kN.

The following table compares the forces for several hemispheres of different radius, a, all much less than the local depth H.

a (m)	F (N)	D (N)	W (N)
0.05	30	19.7	7.2
0.1	240	79	57
0.2	1930	320	460

The impulsive force  $F$  is directed away from the wall and the drag  $D$  is directed toward the wall, at the instant of impact. In each case the impulsive force  $F$  is much greater than either the drag,  $D$ , or the dry weight,  $W$ . Also  $D$  is directly proportional to the cross-sectional area of the body, whereas  $F$  is directly proportional to its *volume*. So for larger bodies we expect the impulsive force to be even more important than the other forces acting. If the body is fixed then the impulsive force  $F$  is 19% greater than that tabulated.

#### 4. The Impulse on a Hemispherical Boulder: Steep Slope.

The effect of water impact is directly dependent on the inertia of the water, and during the short time of high impact pressures, gravity has no significant effect and so pressure impulse theory can be used for waves breaking directly onto a slope. For example figure 5 shows the distribution of  $P$  in a quarter-plane, adapted for a slope by simply turning it. We can choose any line  $P = \text{constant}$  as a free surface ( $\dot{P} = 0$ ), by subtracting the constant from the solution.

It is inadvisable to rely on pressure impulse theory near the impact region since the motion there is grossly simplified. Much energy is given to the small amount of water in the splash (see for example the jet flow computed in Cooker and Peregrine, 1990b). However, down the slope, the pressure impulse gradients are more reliably estimated. Proximity to the impact region leads to pressure impulse gradients which are much bigger than those on the bed in front of a wall.

In figure 5 the breaking wave face is modelled to strike the slope like a closing door which is hinged at  $y = -d$ , and has maximum speed  $U_0$  at  $y = 0$ . Figure 6 shows the variation on the slope of  $P$  and its derivative parallel to the slope. We place a hemisphere at  $y = -2d = -2m$  ( $d = 1m$ ), and we estimate  $U_0 = \sqrt{dg} = 3.13m/s$ . At the hemisphere position  $G = 0.065\rho U_0$ . The impact time  $\Delta t = 0.01s$ . From equations (9,10,11,12)

$$\begin{aligned} \text{The impulsive force is} & \quad F = 111 a^3 \text{ kN.} \\ \text{The flow drag force is} & \quad D = 4.0 a^2 \text{ kN.} \\ \text{The weight of the body is} & \quad W = 57 a^3 \text{ kN.} \end{aligned}$$

The following table compares the forces for several radii,  $a$ .

$a$ (m)	$F$ (N)	$D$ (N)	$W$ (N)
0.05	13.9	10	7.2
0.1	111	40	57
0.2	890	159	460

The impulsive force  $F$  is directed down the slope and the drag is directed up the slope. As  $a$  increases  $F$  becomes ever larger than the drag. The initial speed of each of the hemispheres is 0.09 m/s. The main difference between the two calculations of impulsive force on a body (in front of a wall and on a slope) is the value of  $G$ . Both  $F$  and  $V$  are directly proportional to  $G$ .

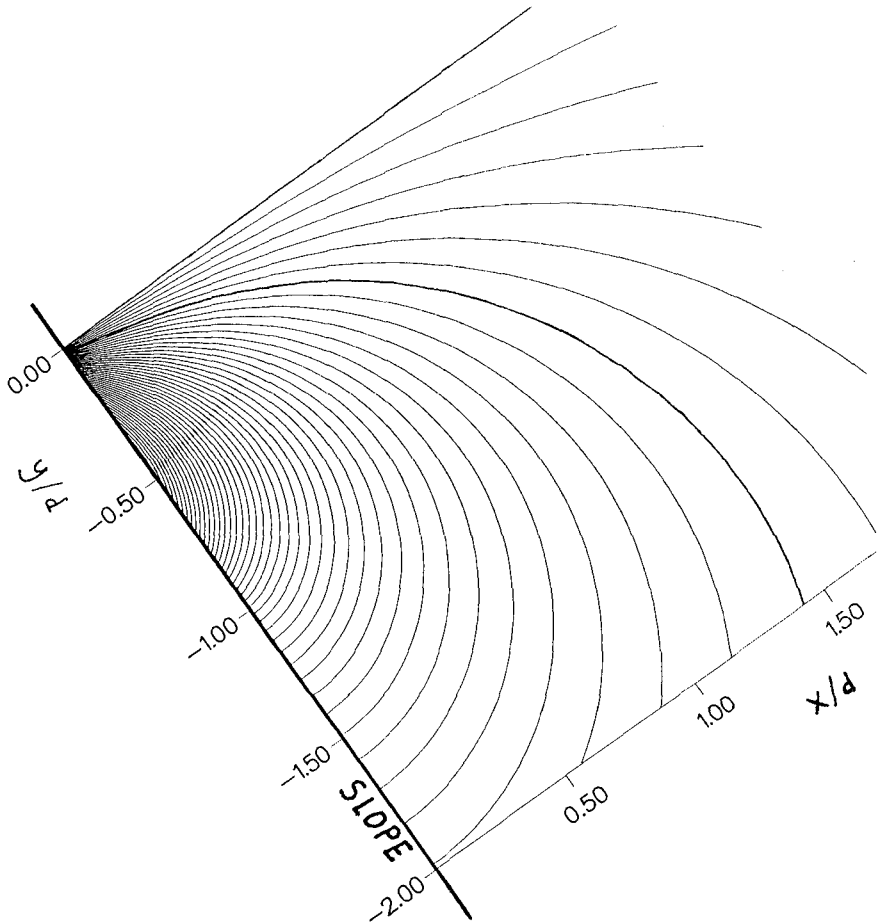


FIGURE 5: Contours of pressure impulse  $P$  for wave impact on a slope. A solution in a quarter-plane has been rotated to lie on the slope. By subtracting a constant from the solution a curved free surface can be obtained, (e.g. the bold contour shown). The impacting wave face is modelled as a closing door, hinged at  $y/d = -1$ , with speed  $U_0 = 1$  at  $y = 0$ . The contour increment is  $0.005 \rho U_0 d$ , with a maximum of  $0.240 \rho U_0 d$  on the slope at  $y/d = -0.4$ .

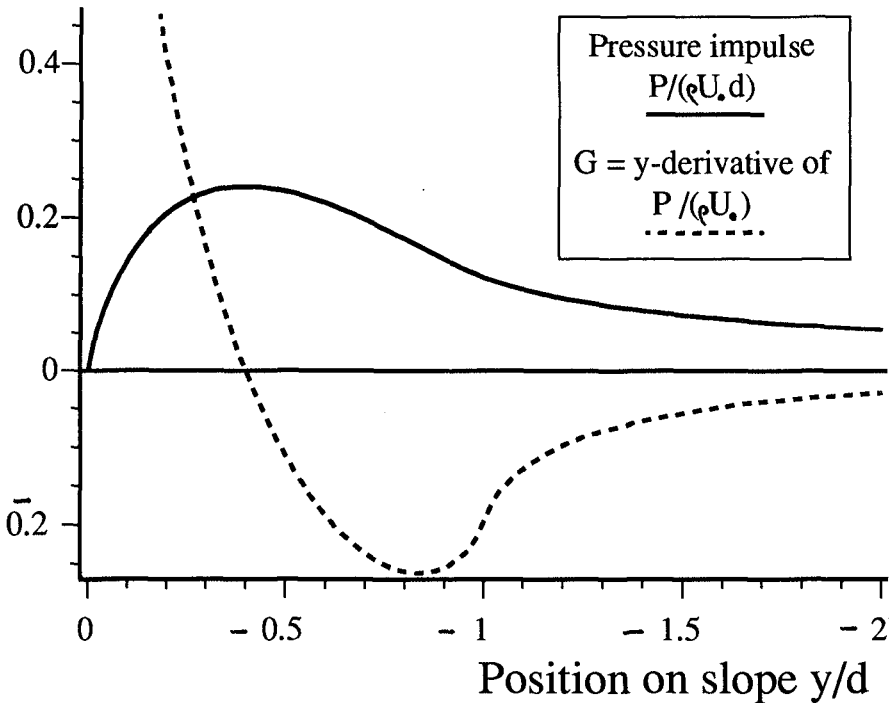


FIGURE 6: As figure 5. The distribution of  $P$  and its gradient on the slope. Note that  $G = \partial P / \partial y$  acts to thrust bodies down the slope below the impact zone (which lies between  $y/d = 0$  and  $y/d = -1$ ).

## 5. Conclusions

The hemisphere is an idealized boulder. Cooker and Peregrine (1992) discuss the impulsive force on a hemi-ellipsoid and they show that a body broadside on to an impact region receives a much larger impulse than a body pointing toward the impact region.

A hemisphere which is free to move may be expected to have a fluid layer between its base and the bed. If the layer has a narrow width  $h(x,y)$  then the pressure impulse obeys a certain partial differential equation:  $\nabla \cdot (h \nabla P) = 0$ . The distribution of pressure impulse in the layer may cause a net upthrust on the boulder. For the hemisphere, if the gap width is constant, it can be shown that the upthrust is equal and opposite to the downthrust on the upper curved surface. So in this special case there is zero net impulse normal to the bed (and hence no impulsive reaction between the boulder and

the bed due to friction). Nevertheless the pressure impulse distribution on the base of the hemisphere causes an impulsive overturning moment. In general the impulsive uplift and overturning moment depend in a complicated way on  $h(x,y)$  and the shape of the boulder, and is the subject of future study.

This work suggests that the impulsive pressure field created inside a wave when it impacts a solid surface may be large enough to move nearby bodies, such as armour units, and may explain some of the damage to the Sines breakwater which had a wall at its crest (see Baird et al, 1980). For a wave impact which is sufficiently high-speed and short-lived the impulsive loads on a hemisphere can be much greater than the flow drag or the weight of the body. Further, the impulse increases with the volume of the body, whereas the drag increases with its cross-sectional area. So we expect impulsive loading to be most important for the biggest boulders. The impulse is greater for a fixed body than one free to move (19% greater for a hemisphere).

The theory must be modified for a body which is so large that it alters the incident wave flow. Here a b.v.p in a domain containing both the wave and the boulder must be solved with modified boundary conditions. Despite the increased complexity we still expect the impulsive forces to be significant compared with the other types of load.

The solution for a body on a slope shows that a boulder can be thrust seawards down the beach if it is below the impact zone. Inside the impact zone the predicted pressure impulse gradients suggest they would force a body up the slope, but here we can be less certain of the applicability of pressure impulse theory.

**ACKNOWLEDGEMENTS:** Thanks to Prof M. Hattori of the Civil Engineering Department of Chuo University, Japan, for making available unpublished experimental results. Financial support for Dr Cooker by UK SERC through Grants GR/G 21032 and GR/F 28298 is acknowledged.

#### REFERENCES

- BAGNOLD, R.A. (1939) "Interim report on wave pressure research" *Journal of the Institute of Civil Engineers* (London), 12, 201-226.
- BAIRD, W.F., J.M. Caldwell, W.L. Edge, O.T. Magoon, D.D. Treadwell (1980) "Report on the damages to the Sines breakwater, Portugal" *Proc. 17th Intl. Conf. Coastal Engineering, ASCE*, 3063-3077.
- BATCHELOR, G.K. (1973) "An introduction to fluid dynamics" Cambridge University Press, 615pp.
- COOKER, M.J., D.H. Peregrine (1990a) "A model of the shock pressures from breaking waves" *Proc. 22<sup>nd</sup> Intl. Conf. on Coastal Engineering, ASCE*, 1473-1486.

COOKER, M.J., D.H. Peregrine (1990b) "Violent water motion at breaking wave impact", Proc. 22<sup>nd</sup> Intl. Conf. Coastal Engineering, Delft, ASCE, 164-176.

COOKER, M.J., D.H. Peregrine (1992) "Wave impact pressures and their effect upon bodies lying on the sea bed" Coastal Engineering (to appear), 25pp.

GRILLI, S.T., M.A. Losada, F. Martin (1992) "Wave impact forces on mixed breakwaters' ", Proc. 23rd Intl. Conf. Coastal Engineering.

HATTORI, M. (1992) Personal Communications.

LAMB, H. (1932) "Hydrodynamics" Cambridge University Press.

RICHERT, G. (1968) "Experimental investigation of shock pressures against breakwaters" Proc. 11<sup>th</sup> Conf. Coast. Eng. ASCE, 954-973.

## CHAPTER 82

### PLEA FOR THE PLACEMENT OF ARMOUR BLOCKS IN ORDERLY PATTERNS

Fernando Vasco Costa, F. ASCE (1)

#### Abstract

Just by placing hollow blocks in orderly patterns, all in the same direction and well interlocked among themselves, not only will their resistance against localized wave actions be greatly increased, but their resistance will vary little from one block to another. Furthermore, the risks of their breakage due to "rocking motions" and of the rapid spreading of damage once initiated, will be essentially eliminated.

To render possible the placement of blocks under the water surface in predetermined positions, in the presence of waves and currents, the blocks should be suspended simultaneously from three or four inclined cables.

#### Introduction

Blocks with a compact form, like quarry stones and cubic concrete blocks, were for a long time the only ones used in breakwater armours. Slender blocks, like tetrapodes and dolosse, came into use only after World War II. They were an improvement because they weighed much less and could be placed in steeper slopes. Hollow blocks, like Seabees and Diodes, were introduced quite recently, but primarily for use along river banks and for shore protection.

Different types of armour blocks should be compared, like alternative designs for any type of engineering structures, by taking into consideration the extreme high

- (1) Formerly Professor at Technical University of Lisbon, Consulmar, Rua Joaquim A. Aguiar, 27, 1000 Portugal.



actions their elements may be submitted to, the extreme low resistances some of the elements will not be able to oppose and how will the different modes and degrees of the failure of the elements affect the behaviour of the whole structure.

For compact blocks the more damaging wave actions will consist of pulling forces acting normal to the armour surfaces; for slender blocks the more damaging wave actions will consist of combinations of oblique forces and torques acting in particular orders and directions. The probability of occurrence of such combinations is very low, but it should not be ignored, especially in long breakwaters built in deep water.

The placing of hollow blocks in orderly patterns is advocated as a way to reduce the gravity of the consequences of wave actions, of reducing the dispersion of the resistance of the blocks and of reducing the risk of the rapid spreading of damage.

#### Oblique forces and torques as determining factors of the stability of armours of slender blocks

Static tests of several types of armour units have been described by Price (1979) and by Wang and Peene (1990). They showed that the mean value and the dispersion of the resistances of slender blocks against being pulled out by forces acting normal to the surface of the armours is not as much affected by the type of block as could be expected.

Had the slender blocks been submitted, during testing, to combinations of oblique forces and torques, not only would the average resistance of the blocks have been smaller but its dispersion would have been much greater.

Just by examining an armour of slender blocks, one can imagine the directions of the forces and torques that need to be applied in order to disentangle a particular block from its neighbours (Fig. 1). Sea waves can not see, or plan, but they can apply, for hours and days, a great variety of combinations of oblique forces and oblique torques. Once they succeed in removing the first block, neighbouring blocks, lacking the support of the block that left, will also start leaving the armour, one after the other, in a chain reaction (Vasco Costa, 1983).

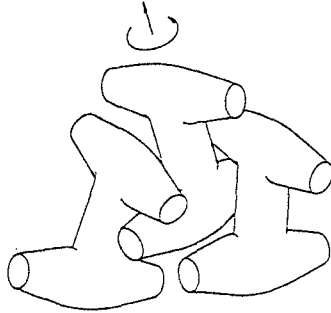


Figure 1 - Forces plus torques are required to disentangle dolosse blocks from an armour

The probability of even well interlocked blocks being submitted to the right (or wrong) combinations of forces and torques that can pull them out of an armour increases with the duration of a storm (Lousada and Guimenez - - Curto, 1981), with the number of the blocks in the armour (Burcharth, 1983) and with the range of directions of the waves (Christensen et al. 1984). The deeper the water in front of a breakwater the wider will be the variety of combinations of directions from which the waves will be able to reach the armour.

Tests run in narrow flumes, in which all waves come from the same direction, do not give an adequate picture of the behaviour of armours made of slender blocks. Such tests are conducive to the underdesign of armours of slender blocks. The recommendation to adopt values of the coefficient  $K_d$  for dolosse, in the Hudson formula, about 10 times larger than that for rough angular quarrrystones, was probably based on tests run in flumes that did not properly represent the variety of directions of forces and torques to which such blocks are subjected to in prototype (Shore Protection Manual, 1984).

How can a designer benefit from the advantages offered by blocks of slender form (the use of lighter blocks on steeper slopes), without incurring their disadvantages (wide dispersion of resistances, risk of breakage during "rocking motions" and the spreading of damage once initiated)? Just by placing the blocks in orderly patterns, all with the same orientation, well interlocked with their neighbours and without free spaces between them, so as to avoid "rocking motions".

Recently a new type of armour blocks has been developed; it consists of hollow blocks placed in orderly patterns, so as to avoid "rocking motions". Examples are the COB, the SEABEE, the SHED and the DIODE. As the porosity of

armours of hollow blocks is high, about twice that of armours of compact blocks, and well distributed, such armours resist heavy seas effectively. They are so stable that such blocks can be used in a single layer. They have been applied quite successfully in the protection of beaches and shores, where blocks can be placed above the water surface.

By providing the faces of such hollow blocks with ridges and grooves, the resistance of the blocks against occasional localized wave actions can be greatly increased (Fig. 2).

As the blocks need to be placed in quite precise positions below the water surface, even when the water is being submitted to the action of currents and waves, they should be suspended not just from a single cable, as is the current practice, but simultaneously from several inclined cables (Fig. 3).

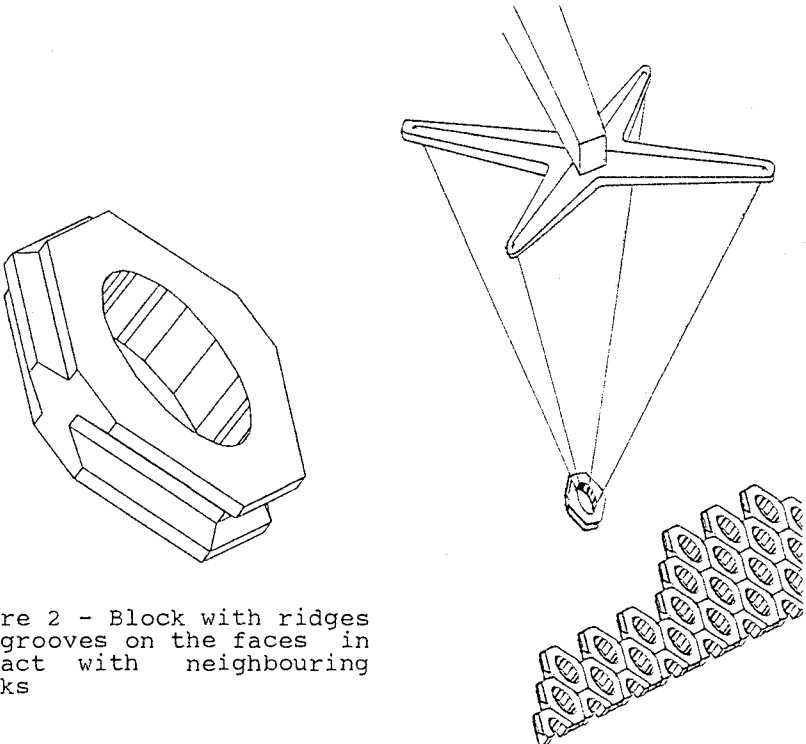


Figure 2 - Block with ridges and grooves on the faces in contact with neighbouring blocks

Figure 3 - The placing of blocks suspended from four cables

Importance of the blocks placing operation

Tetrapodes were a great success when they were first introduced because they permitted the use of lighter blocks in steeper slopes. Such success lasted as long as their use required the payment of patent rights to Sotramer. This company used to send technicians to the construction sites to instruct crane operators on how to place the tetrapodes so that the blocks would be well entangled with their neighbours. This procedure was essential not only to increase their average resistances against being pulled but, especially, to reduce the dispersion of such resistances.

In model tests conducted in narrow flumes, as all the blocks are submitted to almost the same flow conditions, the interlocking does not greatly affect their resistance against being pulled out. In prototype structures, however, the blocks are submitted to waves arriving from a great variety of directions and they can, now and then and here or there, exert strong localized actions on some of the blocks. The interlocking is then essential for the stability of the armour.

Dolosse were such a success when they were first used in their country of origin, South Africa, that they were promptly adopted for the armours of several long breakwaters built in the seventies in quite exposed locations. Such blocks did not behave as could be expected from the results of the model tests on which the design of the armours had been based. Because the larger a block the more brittle it becomes, plenty of large dolosse loosely placed broke during "rocking motions", even when submitted to relatively mild storms.

The natural periods of oscillation of suspended blocks have about the same order as those of sea waves. If, when entering the water, a block happens to move in the same direction the water is moving, the amplitude of oscillation is increased, and the risk of breakage during the placing operation is also increased (see Table I). In still water the oscillation would have been damped, but in moving water the oscillation of the suspended blocks can be greatly amplified.

Table I  
Period of Oscillation of a Suspended Block

$$T = 2 \pi \sqrt{l/g}$$

Lenght of the cable (l)	9m	16m	25m	36m	49m
Period of Oscillation(T)	6s	8s	10s	12s	14s

The placing operation is facilitated if the blocks have an octogonal form. The slanted faces will guide the blocks to occupy their proper position among other blocks; the horizontal faces will support the blocks weight; the vertical small faces will allow for minor deviations from the conventional pattern (Fig. 2).

Armours can have a behaviour approaching that of series systems or parallel systems

The way the failure of an armour spreads once a block breaks or leaves the armour needs be analyzed. Some armours fail like a chain, the classical example of a series system. As soon as its weakest link breaks, a chain is no longer useful. The wider the dispersion of the resistance of the links and the larger the number of links, the weaker a chain becomes. Engineers have tended, nevertheless, to base the design of all types of armours on the average resistance of the individual blocks, even when, as is the case with armours of slender blocks placed at random, their behaviour approaches that of a series system (Vasco Costa, 1983).

Armours composed of compact blocks that are placed at random, like natural stones and concrete cubes, can become more stable after being subjected to a few mild storms giving occasion to adjustments in the positions of poorly placed blocks. If a small percentage of the blocks leaves the armour during a storm, up to about 5%, the armour can still be regarded as sufficiently safe (Shore Protection Manual, 1984). As the leaving of a few elements does not imply that neighbouring blocks will also leave, and can even contribute to adjustments that will render such blocks more stable, armours of compact blocks can be regarded as having a behaviour approaching that of a parallel system (Fig. 4a).

The situation is quite different with armours composed of slender blocks, like tetrapodes and dolosse. Their resistances against being removed by strong wave actions exerted on particular blocks depends on how effectively each block is entangled with its neighbouring blocks. As soon as one block leaves its position, its neighbours, lacking the support of the block that left, are likely to leave also, one after the other, in a chain reaction. The larger the number of blocks, the less stable becomes an armour of slender blocks (Fig. 4b).

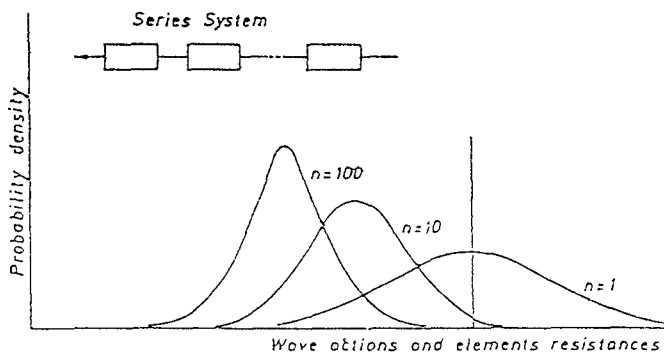
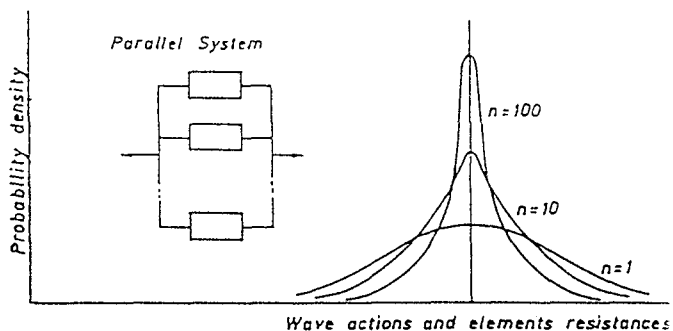


Figure 4 - Probability density of the failure of parallel and of series systems as affected by the number of the elements in a system.

Some of the accidents on very long breakwaters built in deep water during the seventies, with armours of large slender blocks, were attributed to the fragility of the blocks. They were due, however, at least in part, to the fact that the behaviour of their armours approached that of series systems.

The risk of the rapid spreading of the damage when a block occasionally breaks or leaves an armour will be greatly reduced in case of orderly placed and well interlocked blocks. If a block, of the type represented in Figure 5, breaks or leaves an armour, the six neighbouring blocks will lack its support on only one of their faces.

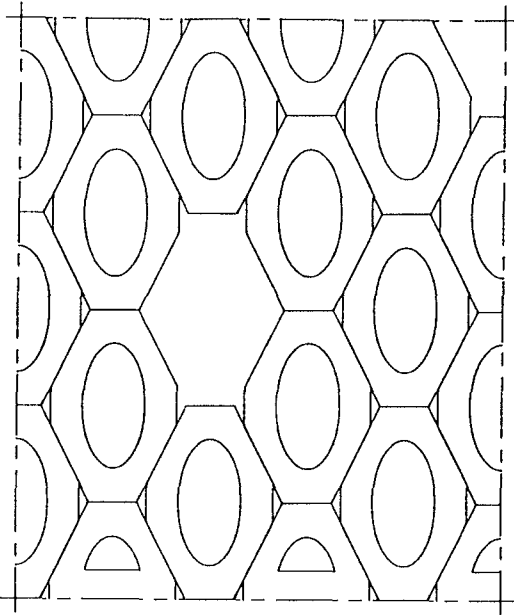


Figure 5 - Armour with a missing block

Side-scan sonar (SSS), already in use to detect damage under the water level of coastal structures, can also be used to guide and check the placement of blocks below the water surface (Kuckarski and Chauster, 1990).

#### Summary and Recommendations

Slender blocks have the advantage, over compact blocks, of opposing a much greater average resistance against being pulled out. Unfortunately such resistance, because it depends on how well each block is entangled with its neighbours, varies widely from one block to another. As the behaviour of armours of slender blocks approaches that of series systems, whenever a poorly placed block is submitted to strong localized wave actions, damage is likely to spread rapidly over the whole armour.

The placement of hollow blocks in orderly patterns, without clearances between blocks, helps to avoid "rocking motions". If their surfaces of contact are provided with ridges and grooves to assure a good interlocking, the blocks will present a great resistance against being removed and such resistance will be the same to all the blocks.

The placement of blocks in precise positions below the water surface will require the use of cranes especially built for the purpose, able to suspend the blocks simultaneously from three or four inclined cables, to avoid pendulation.

#### Acknowledgement

Prof. John S. MC Nown, visiting Professor of the Royal Institute of Technology, in Stockholm, and Carlos F. Abecasis, of Consulmar, read the manuscript and made valuable suggestions for its improvement.

#### References and Further Readings

Bruun, Per (1982). "Stability and Fragility of Mound Structures". The Dock & Harbour Auth. March.

Burcharth, Hans F., (1983) "The Way Ahead." Conf. on Breakwaters - Design and Construction, Inst. of Civil Eng. London.

Burcharth, Hans F., (1991) "Design Innovations, Including Recent Research Contributions", Coastal Structures and Breakwaters, Inst. of Civil Eng., London.

Christensen, F., Thumbo, F. C., Broberg, Stig E., and Tryde, F., (1984). "Behaviour of Rubble-mound Breakwaters in Directional and Uni-Directional Waves". Coastal Engineering, 8, pg 265-278.

"Behaviour of Rubble - Mound Breakwaters in Directional and Uni - Directional Waves. Coastal Engineering, 8 pg 265-278.

Clifford, J.E. (1991), "Breakwater Research: Single Layer Armour Units", The Dock of Harbour Auth. April. pg 349.

Golit, C.K. and Delok, H. (1976) "Large Scale Model Tests of Placed Stone Breakwaters". 15th Int. Conf. on Coastal Eng. Hawaii, pg 257.

Hettiarachchi, Sam and Holmes, P., (1988) "Performance of Single Layer Hollow Block Armours Units". Proc. Conf. of Breakwaters, ICE, Eastbourne, UK.



Kucharski, W.M., and Clausner, J.E., (1990) "Underwater Inspection of Coastal Structures Using Commercially Available Sonars". Technical Report REMR-CO-11, US Army Eng. Waterways Exp. Station, Vicksburg, MS.

Losada, M.A. and Gimenez-Curto, L.A. (1981) "Flow Characteristics on Rough, Impermeable Slopes under Waves Action". Coastal Engineering, 4 pg 187-206.

Oumeraci, H., Bürger, W. W., and Partensky, H. W. (1989) "Induced Pore Pressure in Rubble Mound Breakwaters - Results of Large Scale Model Tests", 22nd Int. Conf. on Coastal Engineering, Malaga, pg 195.

Price, W.A. (1979) "Static Stability of Rubble-mound Breakwaters". The Dock of Harbour Authority, May.

Shore Protection Manual, Volume II, (1984), Waterways Experiment Station, U.S. Army Corps Engineers, Vicksburg, USA.

Van der Meer, J. W. (1987), "Stability of Breakwater Armour Layers - Design Formulae". Coastal Engineering, Vol. II, pg 219-239.

Vasco Costa, F. (1983) "The Spreading of Damage in Breakwater Armours". The Dock and Harbour Auth. March.

Vasco Costa, F. (1984). "The Large Dispersion in Behaviour of Multilegged Armour Units". The Dock and Harbour Auth. May.

Vasco Costa, F. (1991), "Coastal Structures Design Taking into Consideration the Consequences of Possible Failures" Journal of Coastal Research, Vol. 7, pg 1175-1180.

Wang, Hsiang and Peene, Steven J., (1990). "A Probabilistic Model of Rubble Mound Armour Stability, Coastal Engineering, 14, pg 302-331.

## CHAPTER 83

### Nonlinear Wave Transformation Over a Submerged Permeable Breakwater

Eric C. Cruz<sup>1</sup>, Masahiko Isobe<sup>2</sup> and Akira Watanabe<sup>2</sup>

#### Abstract

A set of nonlinear vertically integrated equations has been derived to predict the transformation of waves over a submerged permeable breakwater on a one-dimensional topography. The square of the relative water depth is assumed to be of the same order as the wave height to water depth ratio and a set of second-order governing equations which are equivalent to the Boussinesq equations is derived. The equations have been applied to simulate non-breaking and breaking wave transformations obtained from laboratory experiments, in the latter incorporating a model for breaking wave energy dissipation. When breaking is nonexistent on the breakwater, the wave height as well as the wave profile is well predicted. However, the disintegrating character of the transmitted waves is weakly predicted. For breaking transformation, the wave profiles are predicted well prior to the lee of the breakwater where disintegration occurs.

#### 1 Introduction

In recent years, submerged permeable breakwaters have been constructed in coastal zones to provide protection against wave attack. This type of breakwater has become popular mainly because of its advantages on aesthetic and environmental considerations. Submergence below the water surface and the porosity of the breakwater cause part of the incident wave energy to pass through the structure. Although the structure allows a level of wave transmission into the protected zone, it dissipates wave energy considerable enough to protect a beach from erosion by generating turbulence in the porous medium and causing the waves to break over the structure.

---

<sup>1</sup>Graduate Student, Department of Civil Engineering, University of Tokyo, Hongo 7-3-1, Bunkyo-ku, Tokyo 113, Japan

<sup>2</sup>Professor, Department of Civil Engineering, University of Tokyo, ditto

A model describing wave transformation is an indispensable tool in coastal planning and design. For submerged permeable breakwaters, mathematical models have been developed so far on the basis of the linear sinusoidal wave theory (Rojanakamthorn et. al., 1980). However, since the nonlinearity of waves cannot be neglected on the breakwater, the models must be improved to predict the transformation accurately.

In this paper, a model of wave transformation that considers the nonlinearity of the waves, arbitrary bathymetry of the bed and nonlinear wave damping due to the porosity of the submerged breakwater is presented. Since the model equations are unsteady, they can be applied to irregular waves with suitable boundary conditions.

## 2 Basic Equations and Boundary Conditions

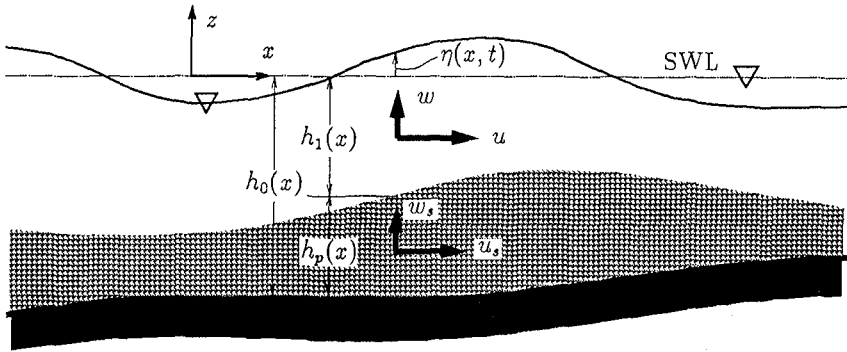


Figure 1: Definition of variables

The region of interest is shown in Figure 1. The depth of the free water layer is  $h_1(x)$  and that of the porous layer is  $h_p(x) = h_0(x) - h_1(x)$ . The horizontal and vertical components of fluid particle velocity and pressure are  $u$ ,  $w$ ,  $p$  in the water layer and  $u_s$ ,  $w_s$ ,  $p_s$  in the porous layer. The subscript  $s$  refers to seepage quantities representing the flow within the pores only. The water surface displacement due to wave motion is  $\eta(x, t)$ . The fluid in the water layer is assumed inviscid and Euler's equation of motion in two dimensions are used:

$$\frac{\partial u}{\partial t} + u \frac{\partial u}{\partial x} + w \frac{\partial u}{\partial z} = -\frac{1}{\rho} \frac{\partial p}{\partial x} \quad (-h_1 \leq z \leq \eta) \quad (1)$$

$$\frac{\partial w}{\partial t} + u \frac{\partial w}{\partial x} + w \frac{\partial w}{\partial z} = -g - \frac{1}{\rho} \frac{\partial p}{\partial z} \quad (-h_1 \leq z \leq \eta) \quad (2)$$

where  $\rho$  is the mass density of water and  $g$  the gravitational acceleration.

The flow within the porous layer is governed by Euler's equation if proper account is taken for the effect of the divergence and convergence of streamlines caused by the presence of solid particles and for the loss of momentum caused by laminar flow along the granular surfaces and momentum loss through turbulence within the pores. The first effect is that of the virtual mass and the second is that of friction between the fluid and the grains. For steady flow in large granular medium, the drop in piezometric head results from laminar viscous resistance for low-velocity flow and a turbulent friction resistance for the high-velocity regime:

$$-\frac{1}{\rho}\nabla(p_s + \gamma z) = \frac{\nu}{K_p}\epsilon\vec{u}_s + \frac{C_f}{\sqrt{K_p}}\epsilon^2|\vec{u}_s|\vec{u}_s, \quad (3)$$

where  $\vec{u}_s = (u_s, w_s)$ ,  $\nabla = (\partial/\partial x, \partial/\partial z)$ ,  $\gamma$  the unit weight of water,  $\nu$  the kinematic viscosity of water,  $K_p$  the intrinsic permeability,  $C_f$  a turbulent friction coefficient and  $\epsilon$  the porosity. The constant  $K_p$  (dimension: length<sup>2</sup>) and the coefficient  $C_f$  are determined from laboratory tests under standard conditions. The investigations of Shuto and Hashimoto (1970) showed that the resistance characteristics of steady and oscillatory flows do not significantly differ so that Eq.(3) can be applied to wave motion, which is under consideration here. The equations of unsteady motion for the porous layer ( $-h_o \leq z \leq -h_1$ ) therefore become

$$C_r \left( \frac{\partial u_s}{\partial t} + u_s \frac{\partial u_s}{\partial x} + w_s \frac{\partial u_s}{\partial z} \right) = -\frac{1}{\rho} \frac{\partial p_s}{\partial x} - \frac{\epsilon\nu}{K_p} u_s - \frac{\epsilon^2 C_f}{\sqrt{K_p}} u_s \sqrt{u_s^2 + w_s^2} \quad (4)$$

$$C_r \left( \frac{\partial w_s}{\partial t} + u_s \frac{\partial w_s}{\partial x} + w_s \frac{\partial w_s}{\partial z} \right) = -g - \frac{1}{\rho} \frac{\partial p_s}{\partial z} - \frac{\epsilon\nu}{K_p} w_s - \frac{\epsilon^2 C_f}{\sqrt{K_p}} w_s \sqrt{u_s^2 + w_s^2} \quad (5)$$

The effect of the virtual mass is expressed by the inertial coefficient  $C_r = 1 + (1/\epsilon - 1)C_M$ , where  $C_M$  is the added mass coefficient.

For the incompressible fluid assumed here, the divergence of the velocity vector, as required by continuity, must vanish:

$$\frac{\partial u}{\partial x} + \frac{\partial w}{\partial z} = 0 \quad (-h_1 \leq z \leq \eta) \quad (6)$$

$$\frac{\partial u_s}{\partial x} + \frac{\partial w_s}{\partial z} = 0 \quad (-h_o \leq z \leq -h_1) \quad (7)$$

The passage of a wave creates oscillatory motion in the two layers. This motion is subjected to the following boundary conditions:

- At the free surface, the usual dynamic and kinematic boundary conditions are enforced:

$$p = 0 \quad (z = \eta) \quad (8)$$

$$\frac{\partial \eta}{\partial t} + u \frac{\partial \eta}{\partial x} = w \quad (z = \eta) \quad (9)$$

- At the bottom of the porous layer, the usual kinematic condition is applied:

$$w_s + u_s \frac{\partial h_0}{\partial x} = 0 \quad (z = -h_o) \tag{10}$$

- The pressure and mass flux must be continuous at the water layer-porous layer interface, that is,

interface continuity of pressure:

$$p = p_s \quad (z = -h_1) \tag{11}$$

interface continuity of mass flux:

$$w + u \frac{\partial h_1}{\partial x} = \epsilon \left( w_s + u_s \frac{\partial h_1}{\partial x} \right) \quad (z = -h_1) \tag{12}$$

Equations (1), (2), (4) to (7) govern the unsteady, incompressible fluid motion in the water and porous layers subject to the boundary conditions Eqs.(8) to (12).

### 3 Nonlinear Equations for One-dimensional Wave Transformation on a Porous Bed

#### 3.1 Assumption

In theory, the governing equations together with the boundary conditions can be solved for the primitive variables  $u, w, u_s, w_s, p$  and  $p_s$ . Since both sets of equations are highly nonlinear and involve  $\eta$  which is not known *a priori*, this undertaking is a tremendous, if not an impossible, task. In order to reduce the number of unknowns in these equations, a vertical integration of the governing equations is performed considering the nonlinear nature of the terms.

Let  $l$  be a characteristic length of the wave motion and  $h$  a characteristic depth giving a characteristic velocity  $\sqrt{gh}$ . Dimensional coordinates are nondimensionalized by  $l$  and  $h$ , velocities by  $\sqrt{gh}$ , pressures by  $\rho gh$  and time by  $l/\sqrt{gh}$  giving the nondimensional (primed) quantities:

$$x' = x/l \quad z' = z/h \quad t' = t/(l/\sqrt{gh}) \tag{13}$$

$$u' = u/\sqrt{gh} \quad w' = w(l/h)/\sqrt{gh} \quad u'_s = u_s/\sqrt{gh} \quad w'_s = w_s(l/h)/\sqrt{gh} \tag{14}$$

$$p' = p/\rho gh \quad p'_s = p_s/\rho gh \tag{15}$$

Applying Eqs.(13) to (15) in the momentum equations, the following nondimensionalized equations of motion along  $z$  are obtained:

From equation (2),

$$\rightarrow \left(\frac{h}{l}\right)^2 \left(\frac{\partial w'}{\partial t'} + u' \frac{\partial w'}{\partial x'} + w' \frac{\partial w'}{\partial z'}\right) = -1 - \frac{\partial p'}{\partial z'} \tag{16}$$

From equation (5),

$$\begin{aligned} &\rightarrow \left(\frac{h}{l}\right)^2 C_r \left(\frac{\partial w'_s}{\partial t'} + u'_s \frac{\partial w'_s}{\partial x'} + w'_s \frac{\partial w'_s}{\partial z'}\right) = \\ &-1 - \frac{\partial p'_s}{\partial z'} - \left(\frac{h}{l}\right)^2 \frac{\epsilon \nu l}{K_p \sqrt{g h}} w'_s - \left(\frac{h}{l}\right)^2 \frac{\epsilon^2 C_f l}{\sqrt{K_p}} w'_s \sqrt{u'^2_s + (h/l)^2 w'^2_s} \end{aligned} \tag{17}$$

To describe waves in shallow water, the dispersion and nonlinearity should be taken into account. As in the case of the Boussinesq equations, the following assumption is made:

$$u' \sim w' \sim u'_s \sim w'_s \sim O(\epsilon) \sim (h/l)^2 \sim \delta^2 \tag{18}$$

### 3.2 First-order Approximation

To get a first-order formulation of the governing equations, terms of order  $\epsilon^2$  and higher in the nondimensional equations of motion are dropped from the corresponding dimensional counterparts invoking the assumption Eq.(18). Hence Eq.(16) gives the dimensional equation

$$0 = -g - \frac{1}{\rho} \frac{\partial p}{\partial z} \tag{19}$$

Integrating from  $z = \eta$  to  $z = z$  and applying the dynamic free surface condition, the last equation becomes

$$p = \rho g(\eta - z) \tag{20}$$

Similarly, integrating the first-order form of Eq.(5) and invoking the interface continuity of pressure and Eq.(24) give

$$p_s = \rho g(\eta - z) \tag{21}$$

The first-order form of Eq.(1) reduces to

$$\frac{\partial u}{\partial t} = -\frac{1}{\rho} \frac{\partial p}{\partial x}$$

and, invoking Eq.(20), becomes

$$\frac{\partial u}{\partial t} = -g \frac{\partial \eta}{\partial x} \tag{22}$$

Similarly, Eq.(4) reduces to

$$C_r \frac{\partial u_s}{\partial t} = -\frac{1}{\rho} \frac{\partial p_s}{\partial x} - \frac{\epsilon \nu}{K_p} u_s$$

and, using Eq.(21), gives

$$C_r \frac{\partial u_s}{\partial t} = -g \frac{\partial \eta}{\partial x} - \frac{\epsilon \nu}{K_p} u_s \quad (23)$$

From Eqs.(22) and (23),  $u$  and  $u_s$  do not depend on  $z$  (at least in the first order).

The kinematic boundary conditions are utilized after the continuity equations have been integrated. In the integration, Liebnitz rule is applied:

Integrating Eq.(7) from  $z = -h_0$  to  $z = z$ , the following is obtained:

$$0 = \frac{\partial}{\partial x} \int_{-h_0(x)}^z u_s dz + w_s|_z - \frac{\partial h_0}{\partial x} u_s|_{-h_0} - w_s|_{-h_0}$$

From the bottom boundary condition Eq.(10), the last two terms in the right-hand side vanish, giving

$$w_s(z) = -\frac{\partial}{\partial x} [u_s(z + h_0)] \quad (24)$$

Similarly, Eq.(7) is integrated from  $-h_0$  to  $-h_1$  and the bottom kinematic boundary condition is invoked, giving

$$w_{s,-h_1} + u_{s,-h_1} \frac{\partial h_1}{\partial x} = -\frac{\partial}{\partial x} [u_s(h_0 - h_1)] \quad (25)$$

Eq.(6) is integrated from  $-h_1$  to  $z$  resulting in

$$0 = \frac{\partial}{\partial x} [u(z + h_1)] + w(z) - \left( w_{-h_1} + u_{-h_1} \frac{\partial h_1}{\partial x} \right)$$

From the interface continuity of mass flux and Eq.(25), the parenthesized term becomes

$$w_{-h_1} + u_{-h_1} \frac{\partial h_1}{\partial x} = -\frac{\partial}{\partial x} [\epsilon u_s (h_0 - h_1)] \quad (26)$$

Finally, this gives

$$w(z) = -\frac{\partial}{\partial x} [u(z + h_1)] - \frac{\partial}{\partial x} [\epsilon u_s (h_0 - h_1)] \quad (27)$$

Integration of Eq.(6) from  $-h_1$  to  $\eta$  gives

$$0 = \frac{\partial}{\partial x} \int_{-h_1}^{\eta} u dz - \left( \frac{\partial \eta}{\partial x} u_{\eta} - w_{\eta} \right) - \left( \frac{\partial h_1}{\partial x} u_{-h_1} + w_{-h_1} \right)$$

Using the free surface kinematic boundary condition and Eq.(26) for the parenthesized terms, the last equation finally yields the continuity equation:

$$\frac{\partial \eta}{\partial t} = -\frac{\partial}{\partial x} [u(\eta + h_1)] - \frac{\partial}{\partial x} [\epsilon u_s (h_0 - h_1)] \quad (28)$$

### 3.3 Second-order Approximation

To get a second-order formulation of the governing equations, the results of the first-order equations for the vertical velocities and pressures are utilized. Neglecting terms of  $O(\varepsilon^3)$  and higher in the nondimensional equations and using the dimensional counterparts, the following results are obtained:

Equation (2):

$$\frac{\partial w}{\partial t} = -g - \frac{1}{\rho} \frac{\partial p}{\partial z}$$

Using Eq.(27), this becomes

$$-\frac{1}{\rho} \frac{\partial p}{\partial z} = g - \frac{\partial^2}{\partial t \partial x} [u(z + h_1)] - \frac{\partial^2}{\partial t \partial x} [\varepsilon u_s (h_o - h_1)] \quad (29)$$

Integrating Eq.(29) from  $z$  to  $\eta$  and applying the free surface dynamic boundary condition lead to

$$\frac{p(z)}{\rho} = g(\eta - z) - \frac{\partial^2}{\partial t \partial x} \left[ u \frac{1}{2} \{ (\eta + h_1)^2 - (z + h_1)^2 \} \right] - \frac{\partial^2}{\partial t \partial x} [\varepsilon u_s (h_o - h_1) (\eta - z)] \quad (30)$$

Equation (5):

$$C_r \frac{\partial w_s}{\partial t} = -g - \frac{1}{\rho} \frac{\partial p_s}{\partial z} - \frac{\varepsilon \nu}{K_p} w_s$$

The left-hand side is evaluated using the first-order form of  $w_s(z)$ , Eq.(24), resulting in

$$-\frac{1}{\rho} \frac{\partial p_s}{\partial z} = g - \frac{\partial^2}{\partial t \partial x} [C_r u_s (z + h_o)] - \frac{\partial}{\partial x} \left[ \frac{\varepsilon \nu}{K_p} u_s (z + h_o) \right] \quad (31)$$

Integrating from  $z$  to  $-h_1$  and invoking the interface continuity of pressure and Eq.(30), the last equation becomes

$$\begin{aligned} \frac{p_s(z)}{\rho} = & g(\eta - z) - \frac{\partial^2}{\partial t \partial x} \left[ \frac{u}{2} (\eta + h_1)^2 \right] - \frac{\partial^2}{\partial t \partial x} [\varepsilon u_s (h_o - h_1) (\eta + h_1)] - \\ & - \frac{\partial^2}{\partial t \partial x} \left[ C_r \frac{u_s}{2} \{ (h_o - h_1)^2 - (h_o + z)^2 \} \right] - \frac{\partial}{\partial x} \left[ \frac{\varepsilon \nu}{K_p} \frac{u_s}{2} \{ (h_o - h_1)^2 - (h_o + z)^2 \} \right] \end{aligned} \quad (32)$$

Equations (30) and (32) highlight the effect of the vertical velocity on the pressure distribution. The last four terms in the last equation are due to the inclusion of the local vertical velocity in the second-order formulation and show that in oscillatory flows where this component is nontrivial, the distribution of pressure in both water layer and porous layer is not hydrostatic.

Next, in consonance with the vertical integration of the equations for the pressures, a depth-integrated horizontal velocity  $U$  is defined in the water layer such that

$$u(x, z, t) = U(x, t) + u^*(x, z, t) \quad (33)$$



where

$$U = \frac{1}{h_1 + \eta} \int_{-h_1}^{\eta} u dz \quad (34)$$

and  $u^*$  is the horizontal velocity deviation along the vertical and is  $O(\varepsilon^2)$ . The velocity  $u$  can then be expanded as a power series in the parameter  $\varepsilon$ ,

$$u(x, z, t) = \varepsilon u_1(x, t) + \varepsilon^2 u_2(x, z, t) + \varepsilon^3 u_3(x, z, t) + \dots \quad (35)$$

From Eq.(34),

$$U = \varepsilon \hat{u}_1 + \varepsilon^2 \hat{u}_2 + \varepsilon^3 \hat{u}_3 + \dots \quad (36)$$

where

$$\hat{u}_1 = \frac{1}{h_1 + \eta} \int_{-h_1}^{\eta} u_1 dz \dots$$

The terms following  $\varepsilon \hat{u}_1$  in Eq.(36) are of  $O(\varepsilon^3)$  and higher and may be dropped out giving

$$U \approx \varepsilon \hat{u}_1 \quad (37)$$

Returning to the governing equations with Eqs.(35) and (37), the terms on the left-hand side reduce to the following:

$$\begin{aligned} \frac{\partial u}{\partial t} &= \frac{\partial U}{\partial t} + O(\varepsilon^3) + \dots \\ u \frac{\partial u}{\partial x} &= U \frac{\partial U}{\partial x} + O(\varepsilon^4) + \dots \\ w \frac{\partial u}{\partial x} &= O(\varepsilon^3) + \dots \end{aligned}$$

Substitution of these equations into Eq.(1), with the third-order and higher terms neglected, leads to the following:

$$\frac{\partial U}{\partial t} + U \frac{\partial U}{\partial x} = -\frac{1}{\rho} \overline{\frac{\partial p}{\partial x}} \quad (38)$$

where the overbar represents an averaging over the relevant depth. With the pressure  $p$  dependent on  $z$  and the left-hand side of Eq.(38) expressed in terms of depth-averaged values, Eq.(30) for the pressure  $p(z)$  is differentiated with respect to  $x$ , depth-averaged evaluating all integrals, then substituted in the last equation. This finally gives the horizontal momentum equation in the water layer:

$$\frac{\partial U}{\partial t} + U \frac{\partial U}{\partial x} = -g \frac{\partial \eta}{\partial x} + \frac{\partial^3}{\partial t \partial x^2} \left[ \frac{U}{3} (\eta + h_1)^2 \right] + \frac{\partial^3}{\partial t \partial x^2} \left[ \frac{\varepsilon U_s}{2} (h_o - h_1) (\eta + h_1) \right] \quad (39)$$

$U_s$  in Eq.(39) defined as

$$U_s = \frac{1}{h_o - h_1} \int_{-h_o}^{-h_1} u_s dz \quad (40)$$

was obtained from a similar development for the porous layer. Parallel developments for the terms on the left-hand side of Eq.(4) using Eq.(40) give, to second order,

$$C_r \left( \frac{\partial U_s}{\partial t} + U_s \frac{\partial U_s}{\partial x} \right) = -\frac{\overline{1 \partial p_s}}{\rho \partial x} - \frac{\overline{\epsilon \nu}}{K_p} u_s - \frac{\overline{\epsilon^2 C_f}}{\sqrt{K_p}} \sqrt{u_s^2 + w_s^2} u_s, \quad (41)$$

Using Eq.(32) for  $p_s(z)$ , the right-hand side of Eq.(41) is evaluated, integrating all terms with overbars. This finally gives the horizontal momentum equation in the porous layer:

$$\begin{aligned} C_r \left( \frac{\partial U_s}{\partial t} + U_s \frac{\partial U_s}{\partial x} \right) = & -g \frac{\partial \eta}{\partial x} + \frac{\partial^3}{\partial t \partial x^2} \left[ \frac{U}{2} (\eta + h_1)^2 \right] + \\ & + \frac{\partial^3}{\partial t \partial x^2} [\epsilon U_s (h_o - h_1) (\eta + h_1)] + \frac{\partial^3}{\partial t \partial x^2} \left[ \frac{C_r U_s}{3} (h_o - h_1)^2 \right] \\ & - \frac{\partial^2}{\partial x^2} \left[ \frac{\epsilon \nu}{K_p} \frac{U_s}{3} (h_o - h_1)^2 \right] - \frac{\epsilon \nu}{K_p} U_s - \frac{\epsilon^2 C_f}{\sqrt{K_p}} \sqrt{U_s^2 + W_s^2} U_s, \end{aligned} \quad (42)$$

The momentum equations (39) and (42) and the depth-integrated continuity equation (28), comprise a second-order formulation of the transformation of a surface disturbance in a depth-varying region with a porous layer, taking into account the effect of vertical acceleration, finiteness of the surface displacement and the momentum loss in the porous layer.

Under ordinary conditions,  $W_s$  in Eq.(42) is much less than  $U_s$ . By invoking the assumption that  $H/h \ll 1$  and noting that the interface and impermeable boundaries are rigid and that the porous layer has a homogeneous makeup, the second-order formulation can be simplified to the following set of nonlinear equations:

$$\frac{\partial \eta}{\partial t} + \frac{\partial}{\partial x} [U(\eta + h_1)] + \frac{\partial}{\partial x} [\epsilon U_s h_p] = 0 \quad (43)$$

$$\frac{\partial U}{\partial t} + U \frac{\partial U}{\partial x} + g \frac{\partial \eta}{\partial x} - \frac{h_1^2}{3} \frac{\partial^3 U}{\partial t \partial x^2} - \frac{\epsilon h_p h_1}{2} \frac{\partial^3 U_s}{\partial t \partial x^2} = 0 \quad (44)$$

$$\begin{aligned} C_r \left( \frac{\partial U_s}{\partial t} + U_s \frac{\partial U_s}{\partial x} \right) + g \frac{\partial \eta}{\partial x} - \frac{h_1^2}{2} \frac{\partial^3 U}{\partial t \partial x^2} - \left( \frac{C_r h_p^2}{3} + \epsilon h_p h_1 \right) \frac{\partial^3 U_s}{\partial t \partial x^2} \\ - \frac{\epsilon \nu}{3 K_p} \frac{\partial^2}{\partial x^2} [U_s h_p] + \frac{\epsilon \nu}{K_p} U_s + \frac{\epsilon^2 C_f |U_s|}{\sqrt{K_p}} U_s = 0 \end{aligned} \quad (45)$$

These equations can be applied in determining the wave field for progressive and oscillatory waves. Although wave motion is usually characterized by periodicity, this property is not a prerequisite in applying the equations since the time dimension has been explicitly included. Hence, these equations can be applied to both regular and irregular waves with suitable boundary conditions.

The assumption of order  $(h/l)^2$  in the nondimensionalized velocities precludes the application of the equations in deep water. In addition, consideration of the nonlinearity of the boundary conditions for the free surface conforms approximately to the region where finiteness of wave height is important. Therefore, the region of validity of the equation falls approximately where the cnoidal wave theory is valid. Lastly, the equations are applicable in a region where the only energy loss is through friction in the porous layer. When breaking is present, the additional energy dissipation must be considered.

#### 4 Breaking Wave Transformation

Wave breaking usually occurs on the breakwater upslope resulting in dissipation of wave energy. The amount of energy dissipated by this phenomenon has been related to the mass flux rate across a vertical section beyond the breaking point. For a submerged permeable breakwater, considering that the mass flux is due to flow across both water and porous layers, the energy dissipated is accounted for by adding an energy dissipation term per unit mass,  $f_D U$  in the water layer and  $f_D \epsilon U_s$  in the porous layer, to the left-hand sides of Eqs.(44) and (45).

The dissipation function  $f_D$  (dimension:  $\text{time}^{-1}$ ) for breaking on a sloping impermeable bed has been given by Watanabe and Dibajnia (1988). Recognizing the points of departure of the breaking dissipation over a submerged porous breakwater from that over an impermeable bed, the dissipation function was modified as

$$f_D = \alpha_D \tan \beta' \sqrt{\frac{g}{h'_1}} \sqrt{\frac{\varphi - \varphi_r}{\varphi_s - \varphi_r}} \quad (46)$$

where  $\alpha_D = 2.5$ ,  $\tan \beta'$  is the effective bottom slope at the breaking point,  $h'_1 = h_1 + \epsilon h_p$ ,  $\varphi = |\bar{\eta}|/h'_1$ ,  $\varphi_r = 0.4(|\bar{\eta}|/h'_1)_b$ ,  $\varphi_s = 0.5(0.57 + 5.3 \tan \beta')$ . The subscript  $b$  indicates values at the breaking point.  $|\bar{\eta}|$  is the effective amplitude defined as  $|\bar{\eta}| = 0.50(\eta_c - \eta_t)$  where  $\eta_c$  and  $\eta_t$  are the surface displacements of the crest and trough, respectively. A breaking criterion based on the experiments of Rojanakamthorn et. al. (1990) was used to locate the breaking point.

#### 5 Application and Results

In applying Eqs.(43) to (45) within a region where structures are present, the waves reflected from the structure are subtracted through the offshore boundary by considering an appropriate boundary condition. For one dimension, this is expressed by

$$\eta(x_o, t + dt) = \eta_I(x_o, t + dt) + [\eta(x_o + C_o dt, t) - \eta_I(x_o + C_o dt, t)] \quad (47)$$

where  $C$  is the celerity, subscript  $I$  refers to a prescribed incident wave and  $o$  refers to the offshore location. At the onshore boundary, complete transmission

of the transformed wave is enforced through the radiation condition:

$$\left. \frac{\partial \eta}{\partial t} \right|_{x=x_D} = -C_D \left. \frac{\partial \eta}{\partial x} \right|_{x=x_D} \tag{48}$$

where the subscript  $D$  refers to the onshore location. The velocity  $U$  is similarly prescribed.

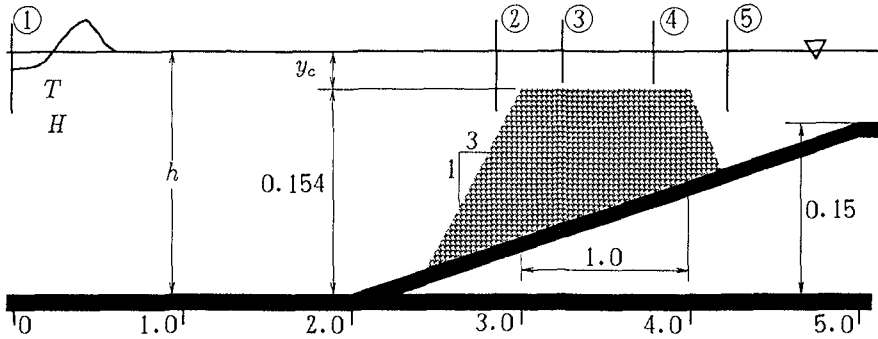


Figure 2: Submerged permeable breakwater

Equation (43) to (45) have been discretized for numerical computation using an eight-point finite-difference computational module on a staggered mesh. Calculation was carried out from still water conditions alternately for the velocities and  $\eta$ . The equations were tested for the case of monochromatic wave propagation on a horizontal bottom without any porous body by comparing with a theoretical solution for the spatial and temporal profiles of  $\eta$ . Calculation gives profiles that conform very well with those given by the second-order cnoidal wave theory.

Laboratory experiments were performed to examine the applicability of the nonlinear model to predicting wave transformation over a submerged permeable breakwater. The set-up is given in Fig. 2. One of the gauges was located beyond the structure to describe the disintegrated wave. In the calculations the properties of the fluid and porous material were:  $\nu = 1.3 \times 10^{-6} \text{m}^2/\text{s}$ ,  $\epsilon = 0.44$ ,  $K_p = 2.06 \times 10^{-8} \text{m}^2$ ,  $C_f = 0.428$ ,  $g = 9.8 \text{m/s}^2$  and  $C_r = 1.0$ . The porosity was measured directly in the laboratory and  $K_p$  and  $C_f$  are fixed by the size of the gravel used.

Figures 3 and 4 show the comparison of the wave profiles at different locations when no breaking was observed anywhere in the wave flume. In Fig. 3, the relative depth of submergence  $H/y_c$  is 0.29 and the relative depth  $h/L$  offshore is 0.073. It can be seen that the weak disintegration at the breakwater lee is predicted by the second-order equations. Using the nonlinear incident wave based on the experiments for the offshore boundary condition leads to a large reflection

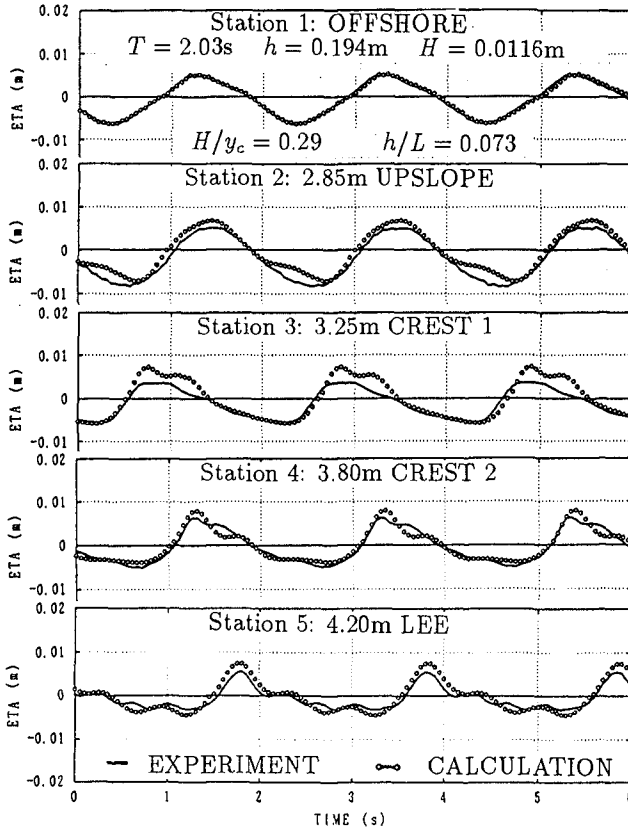


Figure 3: Wave Profiles (Case 1, Non-breaking transformation)

from the breakwater (Station 2) and a secondary peak at the first crest station. In Fig. 4, the water depth was reduced so that  $H/y_c$  becomes large, leading to a strong disintegration leeward. Although the high-frequency components of the disintegrated wave are not reproduced, the general pattern is predicted by the second-order equations.

For breaking transformation, the dissipation function is evaluated at all points beyond the breaking point using Eq.(46). Figure 5 shows a comparison of the wave profiles from calculation and experiments for a short period incident wave. The breaking point was located at  $x = 2.95\text{m}$  in both calculation and experiment. For this case, the wave height was increased so that  $H/y_c = 0.99$  and  $h/L = 0.136$ . It is evident that the model predicts the wave height distribution well. However, the second-order equations fail to yield the secondary component of the transmitted wave at the lee.

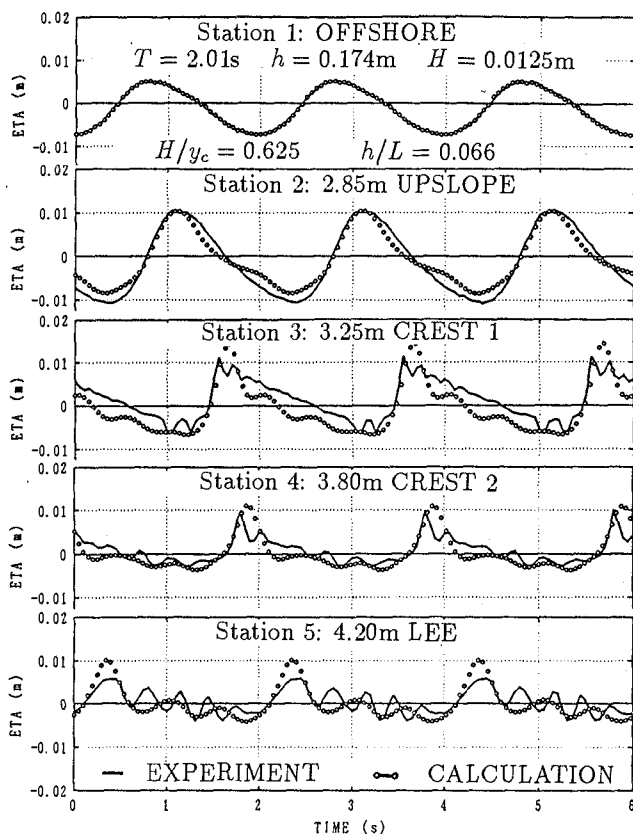


Figure 4: Wave Profiles (Case 2, Non-breaking transformation)

## 6 Conclusions

1. Basic equations of nonlinear wave transformation over a porous layer are derived.
2. For non-breaking transformation on the submerged permeable breakwater, the equations predict the wave height and the profile well. However, the disintegrating characteristic of the transmitted waves is weakly predicted by the second-order equations.

When  $H_i/y_c$  is less than about 0.29, the agreement is good while for higher ratios, the agreement is not good especially at the breakwater lee.

3. For breaking transformation, the wave profiles are predicted well prior to the region leeward of the breakwater where the waves disintegrate. Although the wave profile is not reproduced so well after breaking, the wave height distribution is predicted fairly well by the present model of wave breaking.

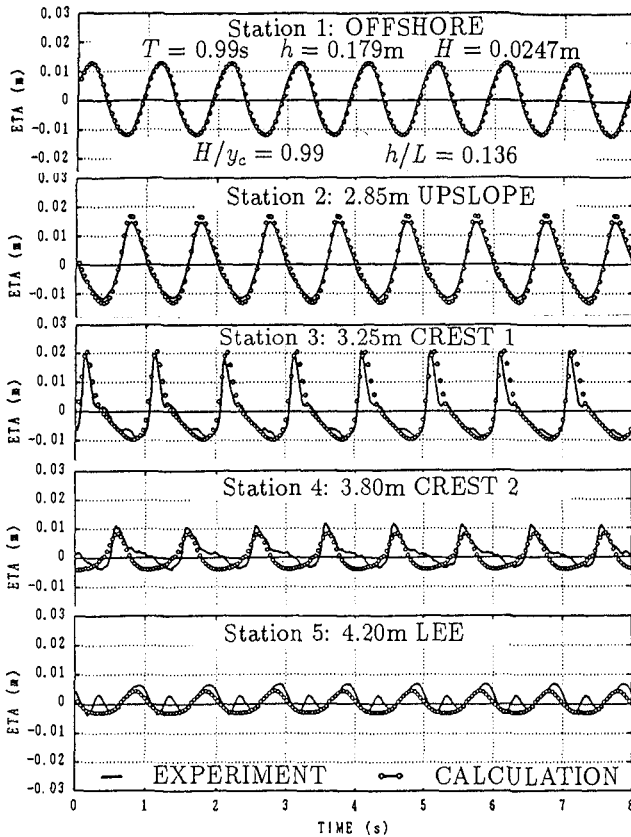


Figure 5: Wave Profiles (Breaking transformation)

## References

1. Rojanakamthorn, S., M. Isobe and A. Watanabe (1990): Modeling of wave transformation on submerged breakwater, Proceedings, 22nd Coastal Engineering Conference, ASCE, 1060-1073
2. Shuto, N. and S. Hashimoto (1970): Hydraulic resistance of artificial concrete blocks, Proceedings, 12th Coastal Engineering Conference, ASCE, 43-54
3. Watanabe, A. and M. Dibajnia (1988): A numerical model of wave deformation in the surf zone, Proceedings, 21st Coastal Engineering Conference, ASCE, 578-587

## CHAPTER 84

### MODEL TESTING OF WAVE TRANSMISSION PAST LOW-CRESTED BREAKWATERS

B. L. Davies<sup>1</sup> and D. L. Kriebel<sup>2</sup>

#### Abstract

Small-scale model tests were conducted to assess the wave transmission characteristics of low-crested breakwaters. The goals of this study are to quantify the wave transmission characteristics of these breakwaters for various structure heights, water depths, and wave conditions. The tests were conducted on cross-sections of solid and rubble breakwater models using both regular and irregular waves. A new parameter,  $(F-Ru)/H_i$ , is then proposed to represent transmission past a breakwater for all values of breakwater freeboard.

#### Introduction

Several recent studies have considered the wave transmission characteristics of low-crested breakwaters in which the armor stones were small enough to be remolded by the incident wave action, e.g. Ahrens (1987a) and van der Meer (1990). For such cases, Ahrens (1987a) has proposed that the breakwater porosity can be characterized by the Bulk Number, which represents the number of stones in the breakwater cross-section. These studies then provide wave transmission data for breakwaters with high Bulk Numbers, in the range of 200 to 600, and sometimes more.

In the United States, however, most low-crested breakwaters are not built with such small armor stones and Bulk Numbers in the range of 10 to 50 are most common. As a result, some of the recent data on wave transmission may not be applicable to realistic breakwater design conditions. In the present study, wave

---

<sup>1</sup>Graduate Program in Acoustics, The Applied Research Laboratory,  
The Pennsylvania State University, P.O. Box 30, State College, Pa., 16804

<sup>2</sup>Associate Professor, Naval Arch., Ocean and Marine Engineering Dept.,  
U. S. Naval Academy, 590 Holloway Rd., Annapolis, Md., 21401



transmission results from physical model tests are presented for low-crested breakwaters with Bulk Numbers in the range of 12 to 36. The breakwaters considered here are so-called statically-stable homogeneous breakwaters, e.g. van der Meer (1991), which contain a single uniform stone size selected in the traditional way according to the Hudson Formula to be stable under wave attack.

The overall objective of this study is to expand the existing database on wave transmission past low-crested breakwaters for conditions that would normally be encountered in design. Toward this goal, more than 250 small-scale physical model tests were carried out on two-dimensional solid and rubble breakwater cross-sections in the Coastal Engineering Wave Basin at the United States Naval Academy. This study was similar in scope to that of Seelig (1980). The primary goal was to investigate the parameters which affect the transmission of waves past the types of low-crested or reef breakwaters currently being constructed in the United States. Figure 1 illustrates the variables of interest.

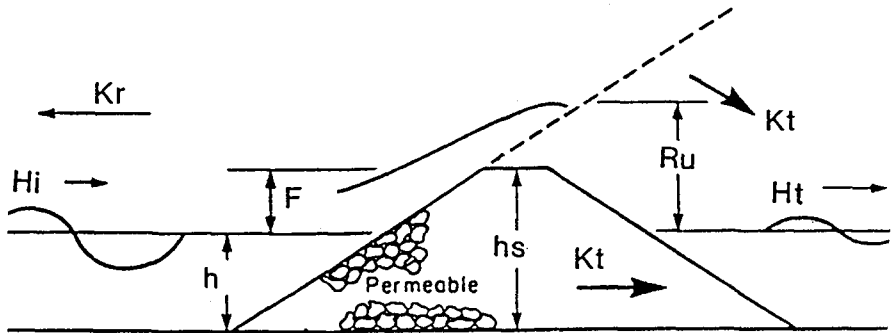


Figure 1. Reef Breakwater Definitions

### Experimental Setup

Laboratory tests were performed in the United States Naval Academy's Coastal Engineering wave basin. Figure 2 shows the side view of the test setup. The wave basin measured 16.61 meters long, and has a piston-type wavemaker that can generate either regular or irregular waves. The basin was then sub-divided by 2 plexiglass walls to form a test channel with a width of 0.61 meters. The test channel consisted of 3 segments. The first segment, 2.44 meters long, consisted of a 1:15 slope. The second segment, 4.88 meters long, was comprised of a level false bottom. In the final segment, 1.22 meters long, the false bottom was replaced by a wave absorbing gravel beach. Between the end of the channel and the back wall of the wave basin, there existed a 1.30 m wide space which prevented the ponding of water behind the breakwater test sections. A second wave absorbing

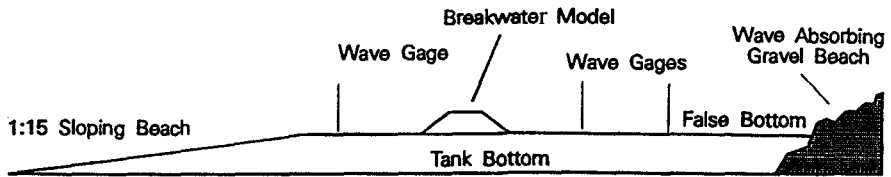


Figure 2. Side View of the Test Channel

beach was placed in front of the back wall of the tank. Numerous tests were conducted to document the effectiveness of the wave absorption system. In all cases studied, the value of wave reflection did not exceed 10%.

Capacitance wave gages were used to measure wave heights in front of and behind the breakwater. For the regular wave tests, three wave gages were generally used. Gages were placed 0.91 and 1.52 meters behind the breakwater and the results were averaged to yield the height of the transmitted wave, in a manner similar to Ahrens (1987b). The incident wave height was measured through the use of a single wave gage which was moved in front of the model from the base of the model to the top of the sloping beach. Through the movement of the gage, the incident and reflected wave heights were obtained from the partial standing wave envelope. The irregular wave tests utilized four wave gages, two in front of the model and two in the lee of the structure. Both pairs of these gages constituted a so-called Goda array, e.g. Goda and Suzuki (1976), which when analyzed has the capability of yielding the incident and reflected significant wave heights in front of and behind the breakwater at all frequencies in a random sea. The separation distance between these gages was 15.24 cm. The first pair of gages were located 76 cm in front of the breakwater while the lee pair were located 91 cm behind the model.

The breakwaters studied were two dimensional models, for which the transmission characteristics of different wave conditions and breakwater freeboards were of most interest. As a result, several design variables were held constant. The side slopes of the breakwater were built with a standard slope of 1:1.5, based on study of several recent reef breakwater projects in the United States. The weight of the armor stone was obtained through use of the Hudson (1959) equation. Despite the recent availability of alternate methods of sizing armor stone, the Hudson equation is still used to determine the size of the rock used in almost all current reef breakwater projects in the United States. For this model study, where limestone with a specific weight of  $2659 \text{ kg/m}^3$  was used, the Hudson equation yielded an armor stone weight of 0.18 kg and a diameter of approximately 5.1 cm, based on a maximum wave height of 10.2 cm in the test channel. Following this

analysis, the available stones were sieved and only rock that fell between the limits of 3.8 to 6.4 cm in diameter and 0.13 to 0.23 kg was accepted. Finally, the crest width was established from recommendations in the Shore Protection Manual of the U.S. Army Corps of Engineers (1984). The crest width used in this study was taken as 3 times the median stone diameter or 15.2 cm.

One unique aspect of these tests is that this design process yielded an order of magnitude smaller Bulk Numbers than the previous tests of Ahrens (1987a) or van der Meer (1990). Bulk Number is defined as:

$$B_n = \frac{A_t}{d_{50}^2}, \quad (1)$$

where  $A_t$  is the area of the breakwater cross section and where  $d_{50}$  is the median diameter of armor stone. The Bulk Number is therefore proportional to the number of stones in the cross-section. Based on the characteristics of the breakwater discussed above, the values of Bulk Number tested in this study ranged between 12 and 36, depending upon the breakwater crest height. Typical values for breakwaters built in the U.S. range from 10 to 50, e.g. Fulford (1985), so that values tested were within the range of recent prototype conditions.

Solid and rubble breakwaters were both tested during the course of this study. The solid models, which served as the limiting condition of zero permeability, were constructed of PVC to the same geometry specifications as the rubble structures. The crest heights tested for both types of models were 10.2, 15.2, and 20.3 cm tested in water depths of 10.2, 15.2, and 20.3 cm of water above the false bottom in the test channel. This produced a 3x3 test matrix. However, the two extreme cases were not tested, so that a 10.2 cm breakwater was not tested in 20.3 cm of water and likewise, a 20.3 cm breakwater was not tested in 10.2 cm of water. The purpose of this investigation was to study wave transmission past breakwaters at or near the still water line, with freeboards of +5.1 cm, 0.0 cm, and -5.1 cm.

The solid breakwater tests were conducted using regular waves only. Four frequencies were tested at each crest height and water depth combination. These frequencies were 0.55, 0.7, 0.9, and 1.1 Hz. In turn, at each of these frequencies four wave heights were generated. These wave heights extended up to heights which were close to breaking. The regular wave tests for the rubble breakwaters were run in exactly the same manner. The irregular wave tests were only conducted using the rubble models. These tests utilized the same combinations of crest height and water depth as did the regular wave study. With the irregular waves, JONSWAP spectral peak frequencies of 0.7 and 0.9 Hz were tested, and at each peak frequency, two significant heights were tested.

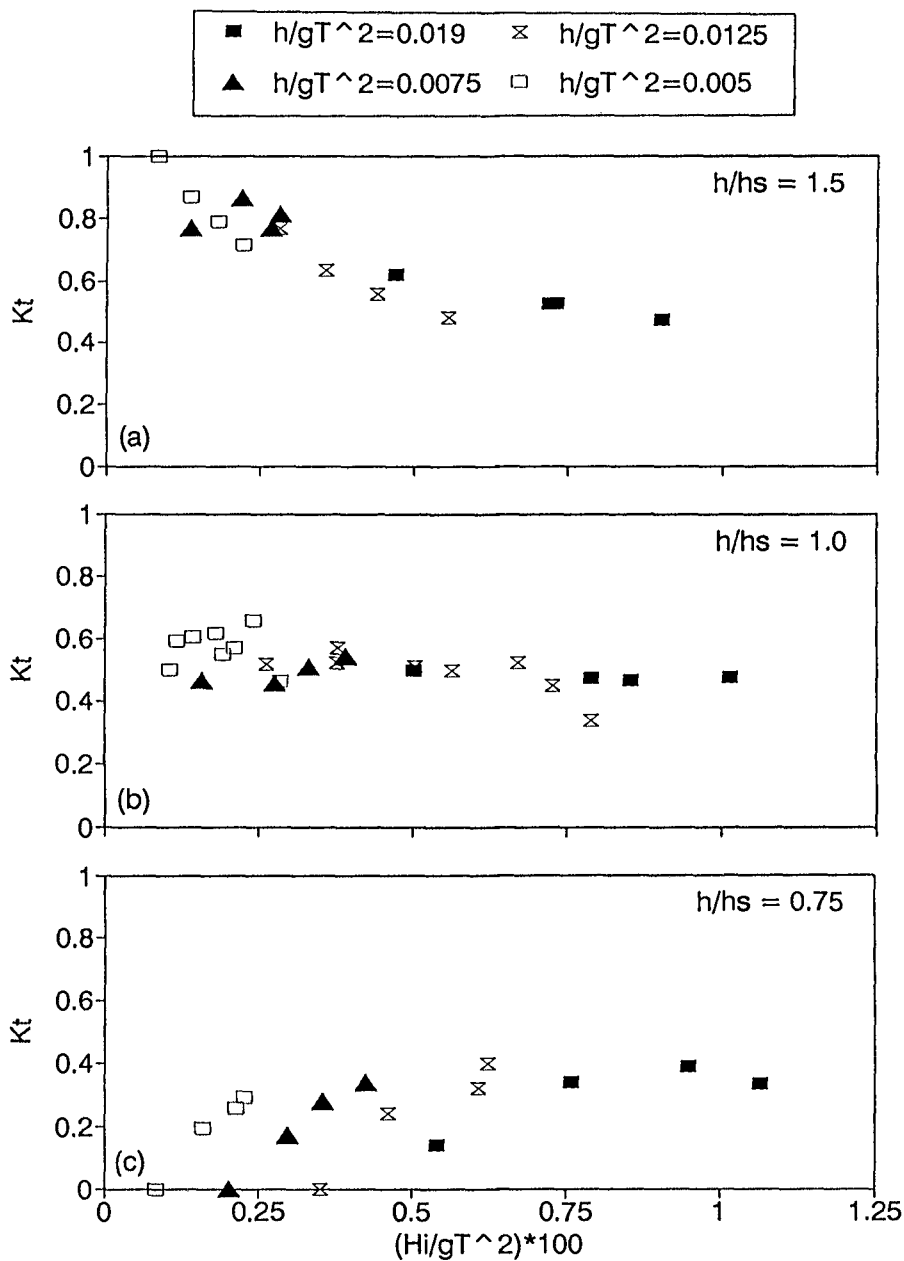
### Results--Regular Waves

Results for solid and rubble breakwaters subjected to regular waves are presented in Figures 3-6. Figures 3 and 4 illustrate the change in the wave transmission coefficient,  $K_t$ , or  $H_t/H_i$  for various wave steepness conditions,  $H_i/gT^2$ , breakwater geometries,  $h/h_s$ , (see Figure 1), and relative water depths,  $h/gT^2$ . These figures illustrate the dependence of wave transmission on wave steepness and relative water depth. They are especially valuable in illustrating the trends associated with various wave steepness conditions and breakwater freeboards where freeboard is defined as  $F = h_s - h$ .

Breakwaters with a high water depth to structure height ratio,  $h/h_s = 1.5$ , as shown in Figures 3a and 4a for solid and rubble breakwaters respectively, exhibit a trend of very high transmission for very low wave steepness, with diminishing values of  $K_t$  for very high steepness waves. This can be attributed to the fact that the breakwater, being below the still water level, allows waves of very low steepness to pass directly overhead with very little attenuation of the incident wave energy. Incident waves with very high steepness, on the other hand, are closer to breaking and the breakwater will succeed in "tripping" the wave, leading to energy dissipation. This situation is seen for both the solid and rubble breakwaters and  $K_t$  values are seen to approach about 0.5 for higher values of wave steepness.

The next conditions considered, in Figures 3c and 4c, are for breakwaters with a positive freeboard, where  $h/h_s < 0.75$ . The trend shown for this situation is different from that shown above for a breakwater with a negative freeboard and yields very different trends for the rubble and solid breakwaters. Figure 3c shows the case for the solid breakwaters studied. In this case, considering that the structure is impermeable, no wave energy will overtop the breakwater for very low steepness waves so that values of  $K_t$  are equal to zero in this portion of the graph. As the steepness of the waves increase, the wave runup will begin to overtop the breakwater and nonzero values of  $K_t$  are witnessed. As the wave steepness continually increases, the values for the transmission coefficient seem to approach a value between 0.4 to 0.5.

Rubble breakwaters, as shown in Figure 4c, illustrate a much different trend due to their porosity. Initially, even for very low steepness waves, there is transmission due to the flow through the permeable structure. The most interesting trend, however, is the fact that as wave steepness increases,  $K_t$  decreases, so that the breakwater is more effective in dissipating the energy of the steeper waves. In these cases, the waves are not able to run up the surface of the rubble structure to the same degree that they were able to run up the smooth surface of the solid breakwater. Thus, much less of the incident wave is able to overtop the structure, and instead must pass through the pores of the structure. In the process of passing through the structure, the higher steepness waves are not able to pass through the



**Figure 3.**  $K_t$  as a function of wave steepness for several structure geometries for solid breakwaters.

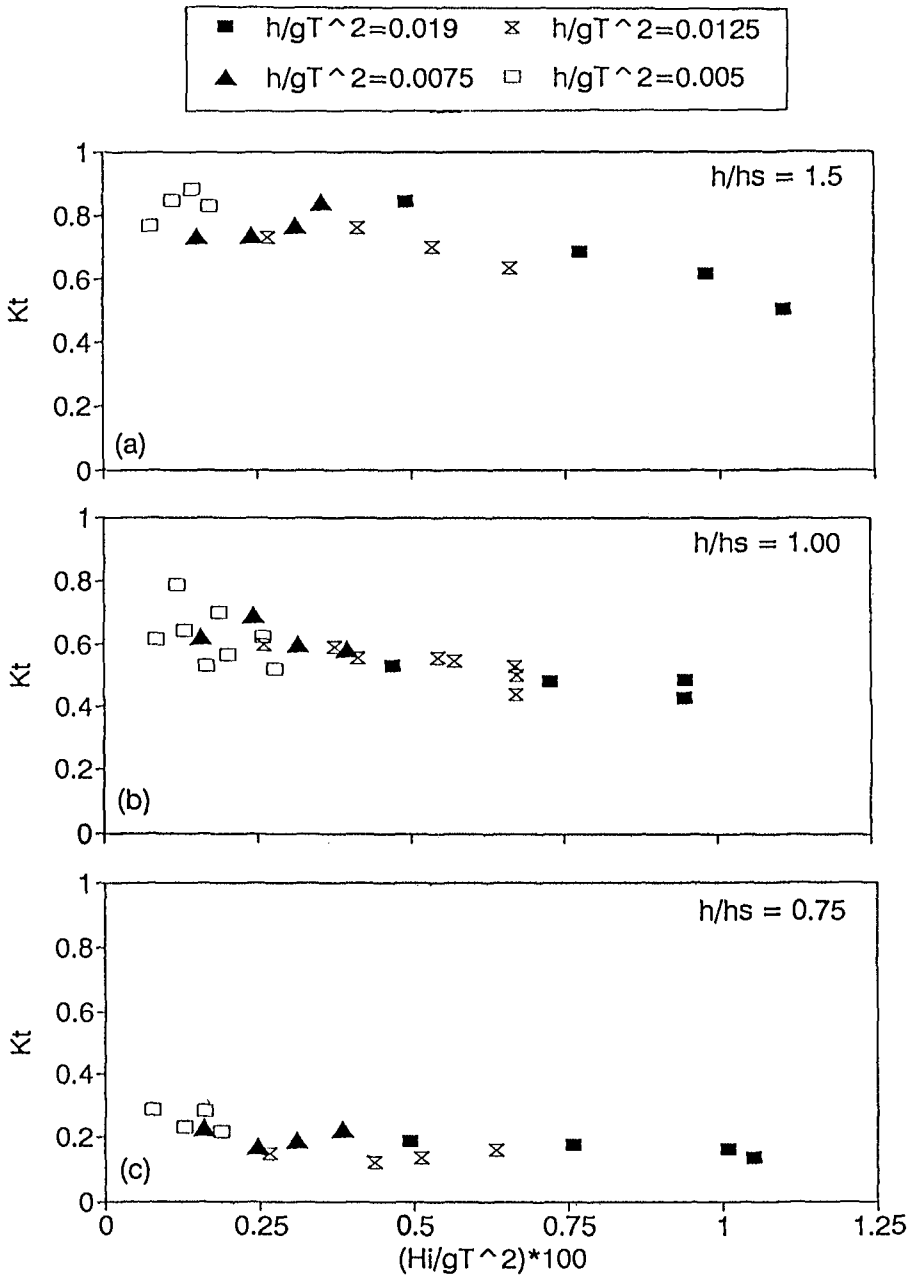


Figure 4.  $K_t$  as a function of wave steepness for several structure geometries for rubble-mound breakwaters.

breakwater as "cleanly" as are the low steepness waves. Within the breakwater, energy dissipation is likely related to the water particle velocities squared, much like head loss in turbulent fluid flow through pipes. Due to this, high steepness waves dissipate a greater percentage of their energy within the pores of the breakwater accounting for the downward trend in the data for steeper waves.

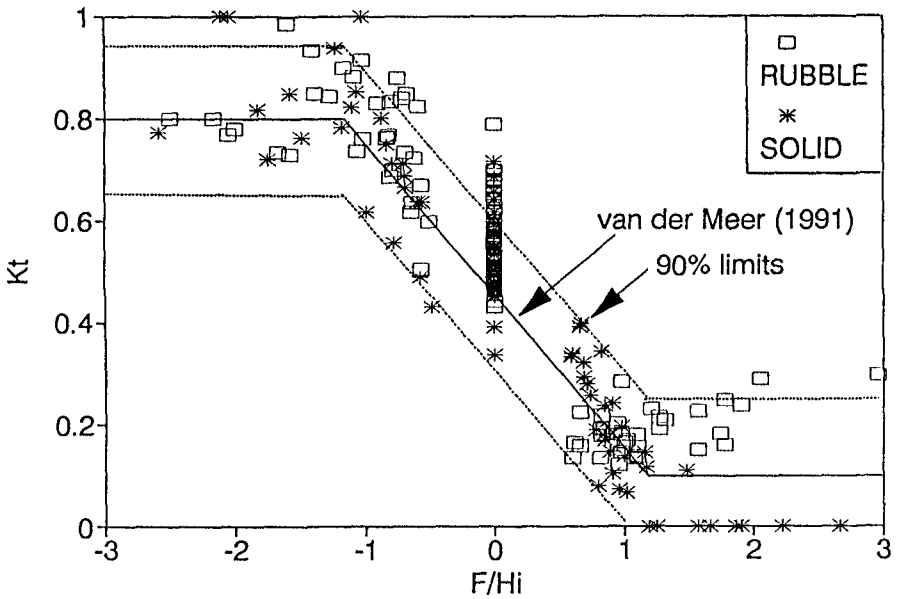
The final category of breakwaters considered are those with a zero freeboard, whose water depth to structure height ratio is equal to one. Figures 3b and 4b illustrate this case for solid and rubble breakwaters respectively. The trends shown in these figures are once again very similar for both solid and rubble breakwaters. As the wave steepness parameter increases,  $K_t$  seems to approach a limiting value of about 0.5. This limiting value appears to fit well within the trends established by Figures 3a, 3c, 4a, and 4c. Figures 3b and 4b also illustrate a weak transmission dependence upon relative water depth. For low values of relative water depth and low steepness waves, the transmission is greater than 0.5. As the steepness and relative water depth increase, however, there is less dependence upon relative water depth. In conclusion, Figures 3 and 4 show that values of  $K_t$  depend heavily upon wave steepness and breakwater geometry, and to a more limited degree on the relative water depth parameter,  $h/gT^2$ .

In addition to wave steepness, the relative freeboard parameter,  $F/H_i$ , was investigated as a controlling parameter for wave transmission. Figure 5 shows the values of  $K_t$  as a function of the relative freeboard parameter for both solid and rubble structures. The prediction equation of van der Meer (1991) is also superimposed along with its corresponding 90% confidence bands. Van der Meer's equation is defined as:

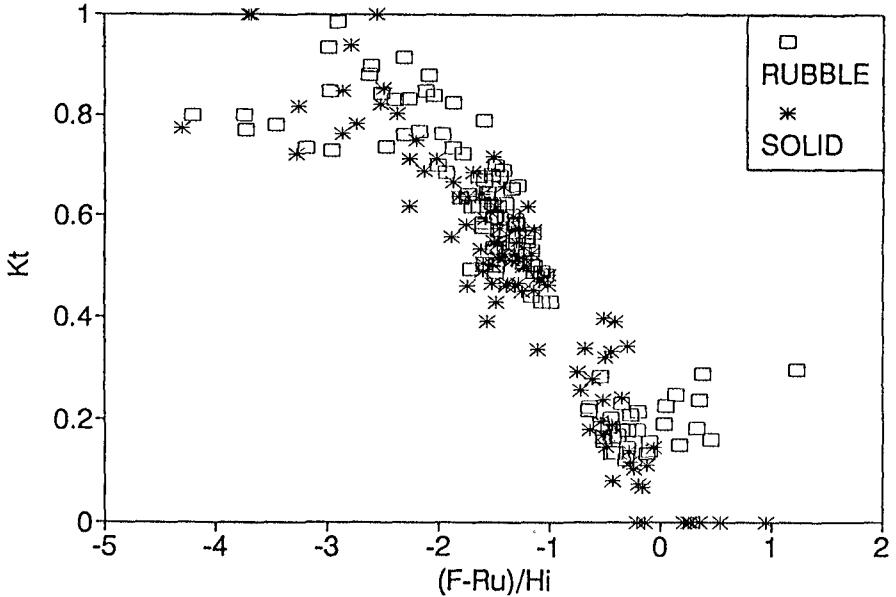
<i>Range of validity</i>	<i>Equation</i>
$-2.00 < F/H_i < -1.13$	$K_t = 0.80$
$-1.13 < F/H_i < 1.2$	$K_t = 0.46 - 0.3(F/H_i)$ (2)
$1.2 < F/H_i < 2.0$	$K_t = 0.10$ ,

and was meant originally for application to random wave transmission. The relative freeboard parameter has been the most widely studied of all parameters relating to wave transmission. Goda (1969), Seelig (1980), and Ahrens (1987a, 1987b) are just a few of the authors who correlate transmission past a breakwater to this parameter.

As illustrated by the data in Figure 5, when the relative freeboard of either a rubble or solid structure is negative, the transmission coefficient is relatively high. In these cases, the incident waves are able to pass over top of the structure with little interaction from the structure, especially for the lower steepness waves (small  $H_i$ ) as was illustrated above in Figures 3 and 4. In some cases for the solid breakwaters,  $K_t$  actually reaches a value of 1 for various cases of large negative relative freeboard. On the other hand, when the relative freeboard of the structure



**Figure 5.** Transmission of regular waves past solid and rubble breakwaters using traditional freeboard parameter.



**Figure 6.** Transmission of regular waves past solid and rubble breakwaters using new freeboard parameter.



is positive, the transmission coefficient is relatively low in both cases. In this extreme, however, the solid breakwater differs greatly from the rubble breakwater due to the latter's porous nature.

The solid breakwater in the positive extreme of the relative freeboard actually reaches a limiting value of zero since the structure only allows transmission once wave run up overtops the structure. The rubble breakwater, on the other hand, gives a minimum value of  $K_t$  at a relative freeboard value of about one. As the relative freeboard approaches higher positive values, the trend is once again back toward a larger  $K_t$  value due to flow through the structure. Since the highest value of freeboard was set at 5.1 cm, the controlling factor in these high values of  $F/H_i$  is the wave height. As a result, this parameter illustrates that the breakwater will allow significant transmission through the structure for very small waves even if the freeboard is much higher than the incident wave.

Relative freeboard is a good parameter for describing the transmission past breakwaters with either positive or negative freeboard, but for breakwaters with zero freeboard, it has some disadvantages. This is illustrated in Figure 5 where this parameter is unable to discriminate values of  $K_t$  for the cases of zero freeboard. For these cases, this parameter yields  $K_t$  values anywhere from 0.4 to 0.8 and lacks any dependence on the incident wave height. Despite this drawback, it is apparent that the predictive equation given by van der Meer for random waves does a reasonable job in predicting the trends in the data for regular waves, and a majority of the data taken in this study falls within the error boundaries established by van der Meer.

Because the relative freeboard parameter is not effective at zero values of freeboard, a new parameter is proposed in Figure 6 to describe the transmission past a reef breakwater at all values of freeboard. This new parameter,  $(F-Ru)/H_i$ , incorporates the potential vertical wave run up,  $Ru$ , (see Figure 1), based upon the Irribarren Number,  $\xi$ , and therefore contains an influence of wave steepness in a way similar to that proposed by Allsop (1983). This parameter is also similar to the overtopping parameter suggested by de Waal and van der Meer (1992). The potential wave run up used in this parameter was first proposed by Ahrens and McCartney (1975) in the form:

$$\frac{Ru}{H_i} = \frac{a\xi}{1 + b\xi}; \quad \xi = \frac{\tan\theta}{\sqrt{H_i/L_o}} \quad (3)$$

where  $L_o$  is the deep water wavelength and  $a$  and  $b$  are empirical coefficients which have the values of  $a = 0.775$  and  $b = 0.361$ , as proposed by Gunbak (1979).

As can be seen by Figure 6, this parameter does a better job in representing the data under all conditions of freeboard. Note that transmission past solid breakwaters is essentially zero when  $(F-Ru)/H_i$  equals zero, as is to be expected.

Transmission past rubble-mound structures is then minimized when  $(F-Ru)/H_i$  is approximately equal to zero, that is when the potential run up just equals the crest height. In the case of large positive values of the parameter, somewhat larger transmission is indicated. In general, these larger transmission values are again associated with the smallest incident wave heights tested at the lowest frequencies.

In conclusion, Figures 5 and 6 show that wave transmission does not significantly differ between the solid and rubble-mound structures, despite the low Bulk Numbers tested. Only for conditions where the breakwater crest is higher than the run up limit were results dramatically different, due to wave propagation through the porous rubble cross-section. Figure 6 illustrates that this transition will occur, for the conditions tested in this study, at a  $(F-Ru)/H_i$  value of approximately -0.4. Thus, below this value, solid breakwaters are shown to be a reasonable approximation of porous reef breakwaters when modelling wave transmission. In addition, these findings also show that the Bulk Number does not seem to be a primary parameter in determining wave transmission since impermeable structures yield similar transmission results as do extremely porous breakwaters.

### Results--Irregular Waves

Figures 7 and 8 present results obtained for rubble-mound breakwaters subjected to irregular waves, along with the earlier results for regular waves. For irregular waves, both the incident and transmitted wave heights are defined in terms of the significant height,  $H_s$ . Correlations were also performed using the root-mean-square wave height, but these results did not agree as well with the regular wave data. A possible reason behind this is that the energy dissipation and head losses in the porous structures are better modeled by  $H_s$ . Because the significant wave height represents the higher incident wave heights in random waves, it is more representative of the waves most affected by losses within the breakwater.

Both Figures 7 and 8 illustrate that the irregular waves tested followed the same trend and correlated well with the regular waves. Van der Meer's predictive equation for describing transmission as a function of  $F/H_i$ , again predicts the trend well and most of the random wave results fall within the suggested error bands. Once again, however the new  $(F-Ru)/H_i$  parameter is better able to discriminate  $K_t$  values for conditions with a zero freeboard, and the minimum wave transmission again occurs when this parameter is approximately equal to zero. This is shown to be the same for regular and irregular waves. Again, as was shown in Figure 6, the higher transmission for extreme positive and negative values of the new parameter are in all cases the result of very small waves of low frequency. Although the number of experiments performed with random waves was limited, the initial results indicate that regular wave results are useful for approximating the transmission of random waves defined by the significant height and peak frequency.

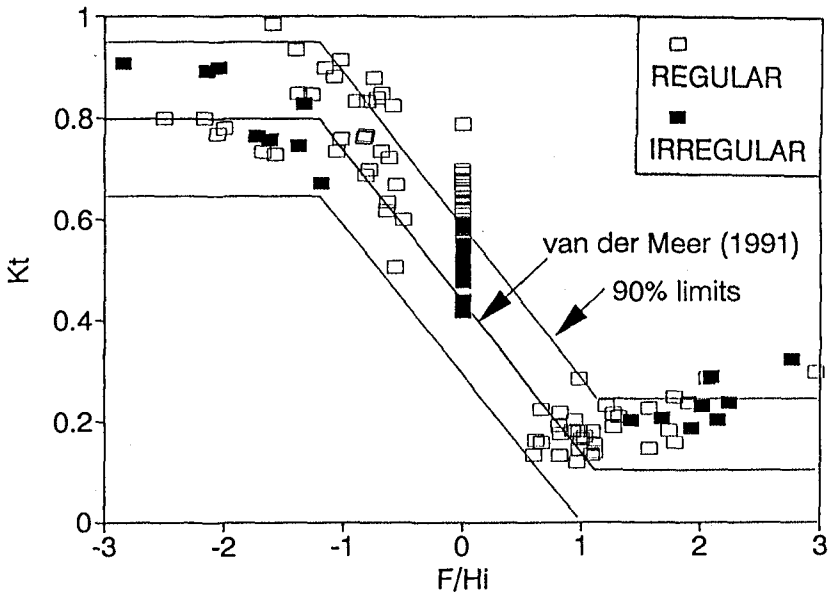


Figure 7. Transmission of regular and random seas past a rubble breakwater using traditional freeboard parameter.

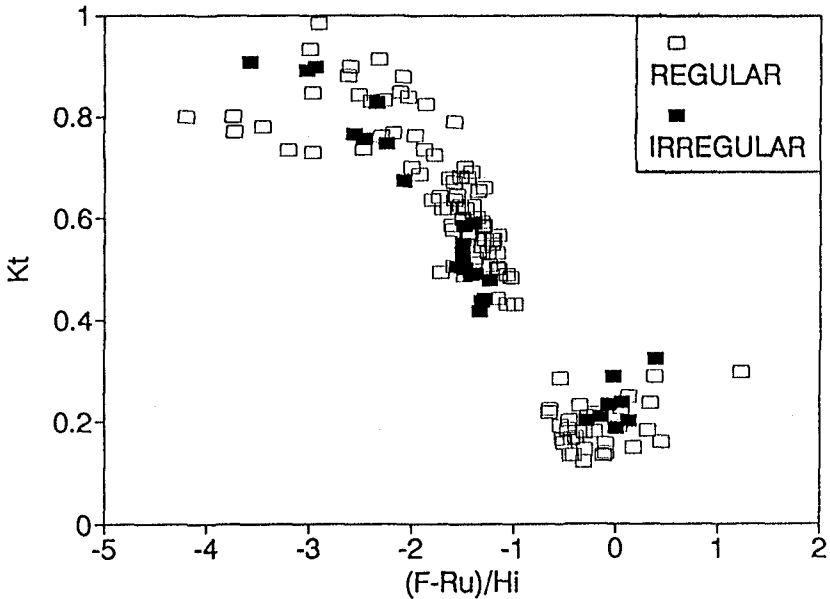


Figure 8. Transmission of regular and random seas past a rubble breakwater using new freeboard parameter.

## Conclusions

In general, this study found that breakwater freeboard, incident wave height, and wave run up, as a measure of wave steepness and potential overtopping, are the primary parameters determining transmission past low-crested breakwaters. A new parameter,  $(F-Ru)/H_i$  is proposed to describe the transmission characteristics of these structures. This parameter is able to spread the data for zero freeboard conditions, unlike the commonly used  $F/H_i$  parameter. In addition, solid breakwaters are shown to be a suitable approximation for transmission studies of rubble structures of values for  $(F-Ru)/H_i < -0.4$ ; and, regular wave results are shown to be a suitable approximation of irregular waves of similar significant height and peak frequency. Finally, comparisons of solid impermeable breakwaters to very porous rubble-mound structures shows that there are observable differences in transmission, but that the Bulk Number does not seem to exert a large influence on the wave transmission characteristics.

## Acknowledgments

The authors would like to thank John Ahrens for his assistance in planning the laboratory phase of this study and Louise Wallendorf for her invaluable assistance in the wave basin.

## References

- Ahrens, J., 1987a, "Reef Breakwater Response to Wave Attack," Proc. Conf. on Berm Breakwaters, ASCE, Ottawa, pp. 22-40.
- Ahrens, J., 1987b, "Characteristics of Reef Breakwaters," Tech. Rpt. CERC-87-17, Corps of Engineers, Waterways Experiment Station, Vicksburg, MS.
- Ahrens, J., and McCartney, B.L., 1975, "Wave Period Effect on the Stability of Riprap," Proc. of Civil Engineering in the Oceans/III, ASCE, pp. 1019-1034.
- Allsop, N.W.H., 1983, "Low-Crested Breakwaters, Studies in Random Waves," Proc. Coastal Structures '83, ASCE, Arlington, VA., pp. 94-107.
- De Waal, J.P., and van der Meer, J.W., 1992, "Wave Run-up and Overtopping on Coastal Structures," Proc. 23<sup>rd</sup> Intl. Conf. on Coastal Eng., ASCE, Venice, Italy.
- Fulford, E., 1985, "Reef Type Breakwaters for Shoreline Stabilization," Proc. Coastal Zone '85, ASCE, San Diego, CA., pp. 1776-1795.
- Goda, Y., 1969, "Reanalysis of Laboratory Data on Wave Transmission Over Breakwaters," Rpt. of Port and Harbor Research Institute, Japan, Vol. 18, No. 3.

Goda, Y., and Suzuki, Y., 1976, "Estimation of Incident and Reflected Waves in Random Wave Experiments," Proc. 15<sup>th</sup> Conf. on Coastal Engineering, ASCE, Vol. 1, pp. 828-845.

Gunbak, A., 1979, "Rubble Mound Breakwaters," Rpt. No. 1, Division of Port and Ocean Engineering, University of Trondheim, Trondheim, Norway.

Hudson, R., 1959, "Laboratory Investigation of Rubble-Mound Breakwaters," J. Waterways and Harbors Div., ASCE, as reprinted in "Classic Papers in Hydraulics," ASCE, 1982, pp. 610-659.

Seelig, W., 1980, "Two-Dimensional Tests of Wave Transmission and Reflection Characteristics of Laboratory Breakwaters," Tech. Rpt. CERC-80-1, Corps of Engineers, Coastal Engineering Research Center, Ft. Belvoir, VA.

van der Meer, J.W., 1990, "Data on Wave Transmission Due to Overtopping," Delft Hydraulics Lab., Report H986.

van der Meer, J.W., 1991, "Stability and Transmission at Low-Crested Structures," Delft Hydraulics Lab., Publ. No. 453.

U.S. Army Corps of Engineers, 1984, "Shore Protection Manual," Corps of Engineers, Waterways Experiment Station, Vicksburg, MS.

## CHAPTER 85

### GRAVITY DRAINAGE: A NEW METHOD OF BEACH STABILISATION THROUGH DRAINAGE OF THE WATERTABLE

Greg A. Davis<sup>1</sup>, David J. Hanslow<sup>1</sup>, Kevin Hibbert<sup>1</sup> & Peter Nielsen<sup>2</sup>

#### ABSTRACT

Beach nourishment to provide an erosion buffer and increase amenity is a well established coastal management option and is favoured because it is a relatively "soft" option with few aesthetic drawbacks. This paper describes how enhancement and stabilisation of the natural accretion processes may be achieved by a low-cost beach drainage system. The project described here shows that the watertable and shoreline can be lowered by a drainage system installed in the beachface. A prototype system was installed on Dee Why Beach, New South Wales, Australia in February–March 1991 and has been continuously discharging water until the present (November 1992). A number of minor storms have exposed and caused some damage to drainage material but the system continues to work.

Survey data are being collected at regular intervals to show the effects of the drainage system on the watertable and the morphology of the beach. Analysis of changes in morphology in both drained and undrained segments of the beach shows a significantly more stable beachface in the area of the drained beachface.

#### INTRODUCTION

Protection of coastal assets may be provided by seawalls while on coastlines with longshore littoral drift, groynes may provide both protection and a beach amenity. However, these hard structures may be aesthetically displeasing and may have adverse effects on adjacent areas of the coastline. Beach nourishment is not perceived to have these drawbacks. However,

- 
1. Coast & Rivers Branch, NSW Public Works Department, Sydney, Australia
  2. Department of Civil Engineering, University of Queensland, Brisbane, Australia

beach nourishment projects may have a limited life and therefore require further nourishment in the future. Recently a new technique of beach stabilisation through watertable drainage has been reported in the literature (eg, Parks 1989; Terchunion 1989; Bruun 1989; Ogden and Weisman 1991). This technique may extend the life of beach nourishment works thereby reducing the on-going costs.

Beach watertable drainage is thought to enhance sand deposition on wave uprush while diminishing erosion on wave backwash. The net result is an increase in subaerial beach volume in the area of the drain. Previous experimental work by Chappell et al. (1978) on a natural beach involving localised watertable drainage concluded that ". . . the evidence from these experiments very strongly supports the idea that beach aggradation can be induced by maintaining the beach watertable at a low level". The larger prototype drainage/pumping installations used by Terchunion (1989) in Florida; and Hansen (1986), Vesterby and Parks (1988) in Denmark also strongly suggest that beach aggradation may be artificially induced by beach watertable drainage. These installations have all employed systems of buried pipes and electrically powered pumps. The current paper describes an alternative to this technology. The idea is to achieve lowering of the watertable without pumps by enhancing the beach's own drainage capacity or hydraulic conductivity through the use of strip drains (Figure 1).

Duncan (1964) and Grant (1946, 1948) observed that beaches tend to erode as the tide falls and accrete as the tide rises. This is attributed to the effect of the watertable and its position relative to the offshore mean water level. As an incoming tide rises above the beach watertable, a proportion of the wave run-up infiltrates the beach face. This results in a reduction in the backwash volume and net beach accretion, particularly in the upper swash zone. As the tide falls, the beach watertable lags behind the offshore mean water level and thus contributes outflow to the swash zone. This contribution aids the backwash and causes net seaward movement of sediment. If this argument is correct, then it is the local watertable exit point

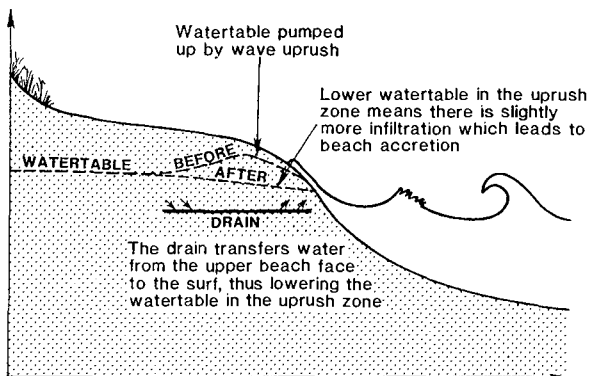


Figure 1 — Effect of the strip drain on the watertable

and its movement over a tidal cycle which is important for beach accretion and erosion and not the overall back beach watertable. Increasing the drainage capacity of the beach could be expected to decrease the time lag between oscillations of the beach watertable and the offshore mean water level and lower the watertable exit point within the wave run-up distribution of the beach.

This paper presents data relating to the effect of the drainage system on the beach watertable characteristics and some preliminary observations of the beach morphodynamics.

### STUDY AREA

The beach drainage system was installed in the central part of Dee Why Beach, which is an open coastal embayment approximately 14km north of Sydney's Central Business District (Figure 2). The beach faces the South East

which is the dominant direction of large swell waves from the Tasman Sea. The wave climate is highly variable and only weakly seasonal (Trenaman and Short, 1987). The tidal regime of the New South Wales coast is described by Easton (1970) as microtidal semidiurnal with a diurnal inequality, with a range up to 2m. Dee Why Beach occupies a drowned embayment and is flanked by rock headlands. The beach/barrrier system encloses a small lagoon which is only occasionally open to the ocean. The beach has undergone recession over recent geological time and this recession is thought to be continuing (Chapman et al. 1982).

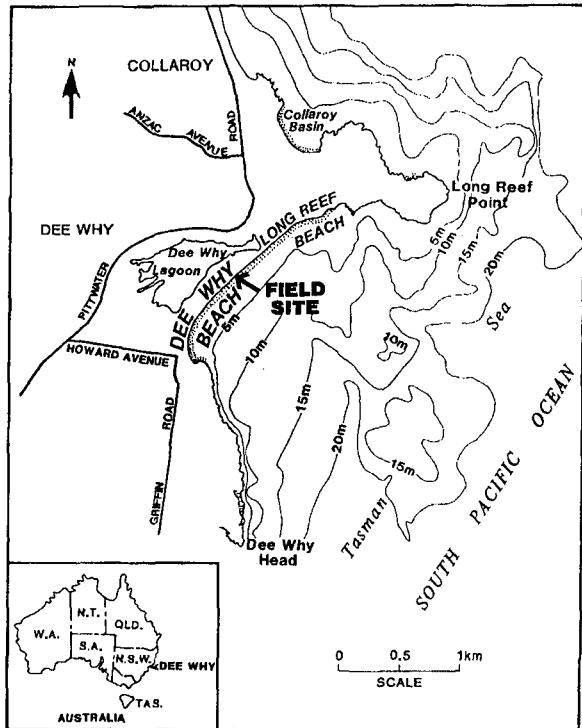


Figure 2 — Location diagram

and this recession is thought to be continuing



Mean swash zone grain size is of the order of 0.5mm. The surf zone is generally characterised by rhythmic topography with crescentic or transverse bars and regular rip channels. The beach may range between a reflective state with cusps after calm periods and a more dissipative bar/trough system after storms (Nielsen & Hanslow, 1991).

## MATERIALS AND INSTALLATION

The beach drainage system used in this installation incorporated an array of shore normal strip drains made of geotextile fabric enclosing a plastic core in an "egg-carton" configuration. The ends of the drains are covered with geotextile to prevent ingress of sand.

This type of drain is commonly used to drain ground-water from roads, parks and playing fields, etc. In these applications the drains are laid vertically. For the beach drainage system the drains were laid horizontally below the sand surface so as to minimise the risk of exposure during storms or rip formation. They were spaced from 5 to 15m apart and occupy 160m of the central part of Dee Why beach. A total of 18 drains were installed by 28 March, 1991. Drain installation was conducted during a period of spring low tides and small waves. A 27 tonne excavator was used to dig a series of 4 or 5 parallel trenches in the beach, finishing the job just before low tide. The drainage material was then laid and the trenches filled before the tide rose significantly. By this method, the seaward ends of the drains were buried to a level varying from -0.4m to -0.7m with respect to mean sea level (MSL).

The strip drain array was installed with the drains being parallel to one another and shore normal. This means that the landward ends of the drains have the greatest head due to elevated watertable and the seaward ends have the lesser head of the swash zone mean water level. Therefore, there is always a seaward flow potential. The location of the drains is indicated in **Figure 3**.

## WATERTABLE CHARACTERISTICS

### DATA COLLECTION

The impact of the drainage system on the beach watertable was assessed using the following techniques. All levels are to Australian Height Datum (AHD) which is approximately MSL.

Long-term watertable data were collected from a permanent beach well which housed a pressure transducer and data logging equipment. This well is in the drained area of the beach and located such that the sand elevation was approximately 3m AHD under normal conditions.

Short term observations of mean level were obtained using arrays of up to 95 stilling wells deployed in the beach. Water level inside the wells correspond to the local watertable. Levels were determined by surveying the well tops and then measuring the depth to the watertable. Wells were also used to determine the location of the shoreline in the drained and undrained sections of the beach. Wells were placed along a shore-normal transect with a spacing of between 2 to 5m.

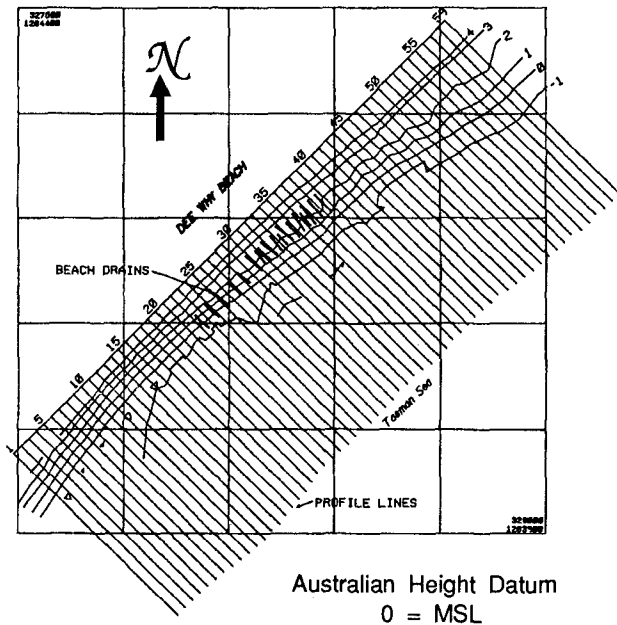


Figure 3 — Survey date 5–9–91. Location of beach drains and profiles for contour analysis

This spacing gives an accurate definition of the exit point of the watertable onto the beachface, and the intersection of mean water surface and the beachface, or shoreline.

The relative position of the shoreline or watertable exit point with respect to the run-up was determined by counting the number of waves running up past each of a number of beach wells or stakes marking points of known beach elevation. This was done over 20 minutes along drained and undrained transects, enabling calculation of the percentage of waves passing the watertable exit points on different sections of beach.

## RESULTS

### General

The drainage system has been deployed continuously in an open coastal beach for approximately 18 months. Observation of the treated intertidal beach shows, particularly at low tide, the marked seepage zones caused by outflow from the buried drains. Outflow from the drains has been observed to result in minor scour on very low tides. This scour appears to be limited by 'armouring' or increased coarseness of sediment around the drain ends. During

periods when the beach has been relatively wide, these effects have become less apparent. On the rising tide, the seepage zones apparent at low tide give way to infiltration zones as local infiltration directly over the drains is evidenced by marked narrowing of the zone of watertable outflow in those areas, extending over a width of 3 or 4m. The drains experienced some damage from rip-cell formations resulting in up to 4m of the drains having to be cut off in the swash zone. However, subsequent accretion has since covered the damaged drains and all have since continued to discharge water.

### Watertable Data

Figure 4 shows the response of the watertable at the permanent beach well before and after installation of the drains. The deep water wave height and tide record are also presented. This figure clearly shows that the placement of the drains immediately lowered the watertable and reduced the asymmetry of the tidal response. Table 1 shows comparison of lag times and rates of change of water levels deduced from analysis of months of watertable and tide records.

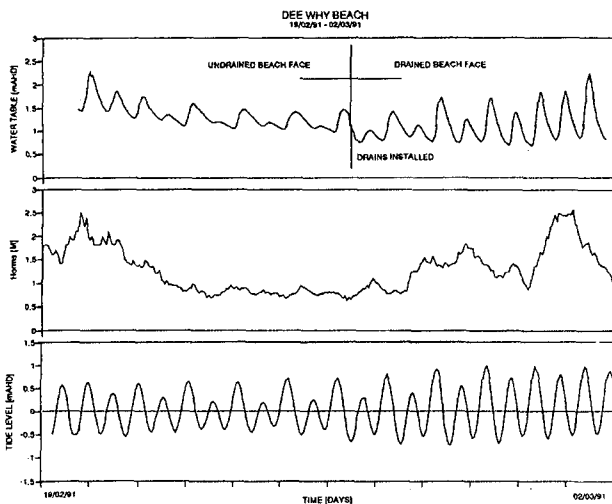
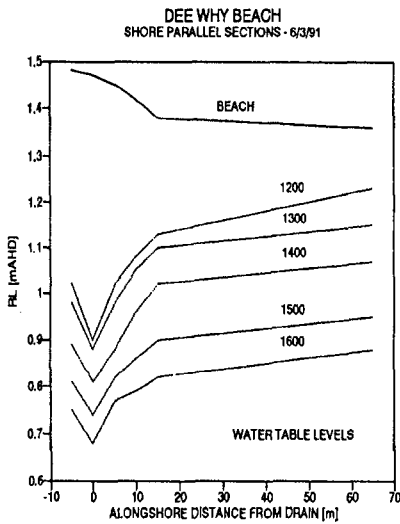
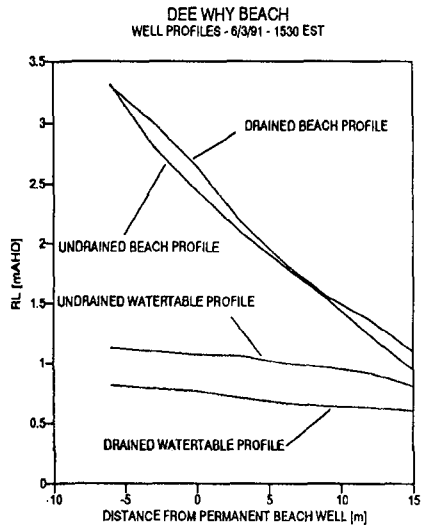


FIGURE 4 — Watertable record at permanent beach well and the deepwater wave height ( $H_{orms}$ ) and tide levels (between 20-2-91 and 2-3-91)

Figure 5 shows a shore-parallel section of the beach in which the effect of a single drain in the inter-tidal zone of the beachface was monitored over a half tide cycle. The watertable is lowered by about 0.3m at the location of the drain and the effect is seen to diminish with increasing distance from the drain. Figure 6 compares watertable profiles in two morphologically similar shore-normal transects, one in the drained section

**Table 1** — Relative lag time and rate of change in water level before and after installation of drains.

Lag Time (hrs)	Before Installation of Drains		After Installation of Drains	
	Low Tide	High Tide	Low Tide	High Tide
	4.10	1.50	3.30	1.10
Average Rate of Change in Water level (cm/hr)	Falling Tide	Rising Tide	Falling Tide	Rising Tide
	4	8	8	15

**Figure 5** — Effects of a single drain on the watertable at various times (EST)**Figure 6** — Watertable for a typical drained transect and a similar undrained transect

and another in the undrained section of the beach. Again, at the drain the watertable was lowered approximately 0.3m along the transect.

#### Beachface Watertable Exit Point

The point of emergence of the watertable onto the beachface is important because it influences the swash zone dynamic sediment budget which is the key to the success of the beach drainage technique. The comparison of the watertable exit point at high tide on 24 April, 1991 for the drained and undrained beach transects in relation to the wave run-up at the time is presented in **Figure 7**. On the drained transect 44% of waves transgressed the watertable exit point while 29% did so in the undrained section. This means that at high tide the

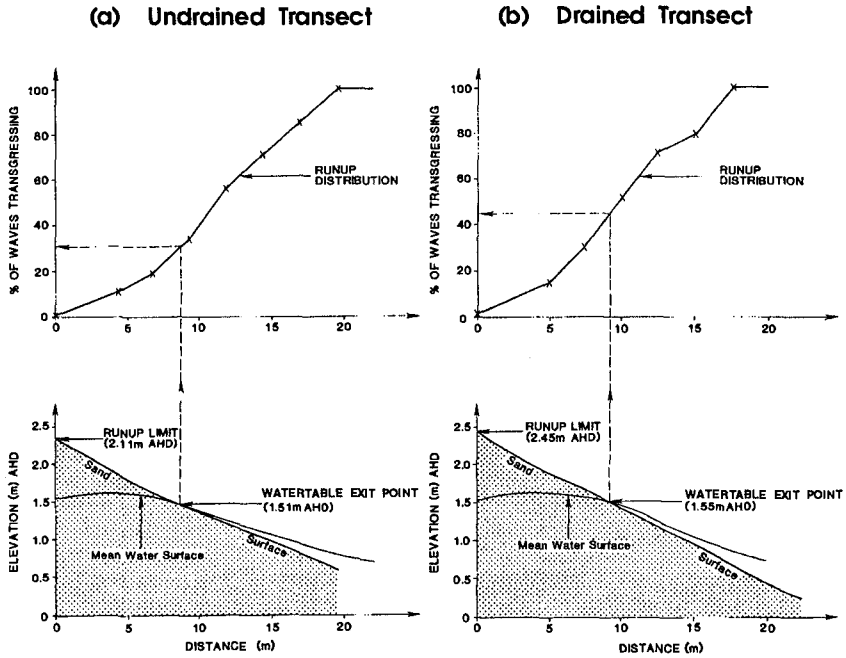


Figure 7 — Percentage of waves transgressing the watertable exit point on (a) Undrained and (b) Drained transects

watertable occurs lower within the run-up distribution on the drained section of the beach.

**BEACH MORPHOLOGY**

**DATA COLLECTION**

Variability of the location of the beach contours was used to assess the effects of the drainage system on beach morphology by comparing results for the drained and undrained section of the beach.

Pre-drainage beach morphology was determined using photogrammetric analysis of historical aerial photography. Fifteen dates of photography between 1961 and 1991 were analysed. Beach topography was contoured down to the water line using a Wild AC1 Stereo Restitution Instrument which plotted the position of the contours in plan view. A beach length of approximately 600m of the beach was contoured for each date of photography.

Post drainage beach surveys have been carried out every 10–15 days since drain installation. Again, the survey area comprised about 600m of beach centred about the drained section. Surveys were generally extended from the fence line (4.5m MSL) to approximately –1.5m MSL.

#### DATA ANALYSIS

Contour location data were determined for a series of parallel transects as shown in **Figure 3**. Distances from a base line to the 4m, 3m, 2m, 1m and 0m contours were measured along 60 transects for each beach survey taken since drain installation and for photogrammetric surveys prior to drain installation. These transects were spaced 10m apart and cover the drained section of the beach as well as equal portions of the undrained beach to the north and south. Measurements of contour location for each contour were compiled into data matrices consisting of distances at each profile and survey date.

#### BEACH STABILITY

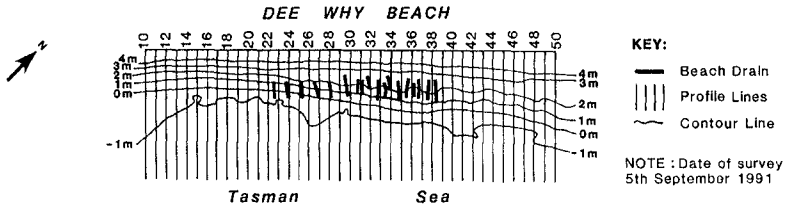
Variation in contour position over time was assessed by determining the mean and standard deviation of the contour location at each profile.

An indication of the relative stability of different portions of the beach both before and after drain installation is presented in **Figure 8**. Here the standard deviation of the 1m and 2m contours are presented for the photogrammetric (i.e. undrained) data, together with the standard deviation of the 0m, 1m and 2m contours for the survey data collected since drain installation. The standard deviations from the photogrammetric data set are generally higher. This is because a number of the photography sets used were taken specifically to record eroded post-storm beach (profiles 22–38) morphology. This figure also shows that the variance in contour position is lower in the drained section of the beach than the areas either side. This contrasts with the photogrammetric data which shows increasing variance in the 2m contour towards the north and rhythmic variation of the 1m contour.

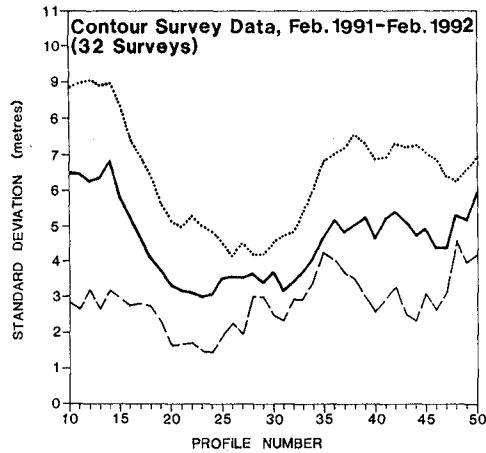
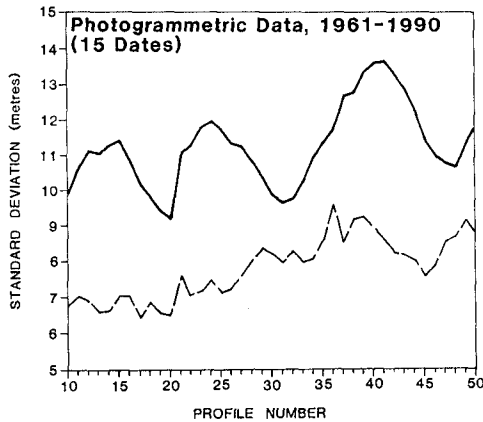
#### PRINCIPAL COMPONENTS

Beach morphology in the survey area since the installation of the drains has displayed considerable variability associated with both storm activity and rip current migration. For much of the time since the installation of the drains the beach has been characterised by rhythmic topography associated with rip cell formation and migration, this situation only changing during storms when the whole beach was cut back and assumed a more uniform shape.

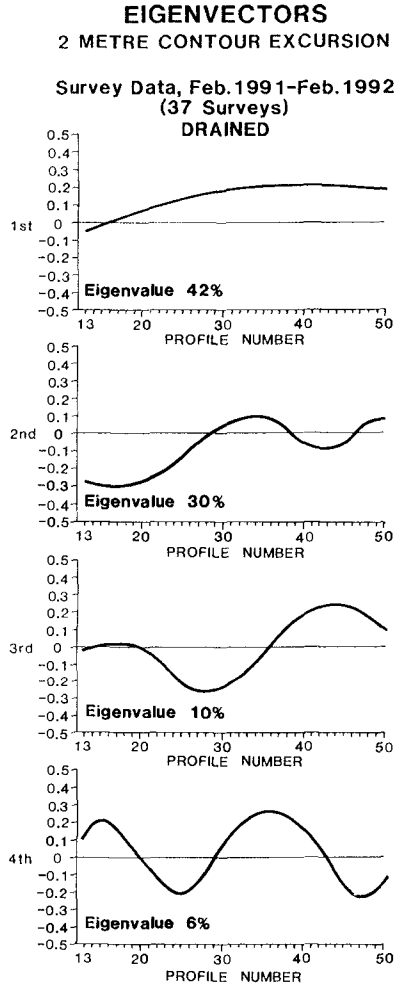
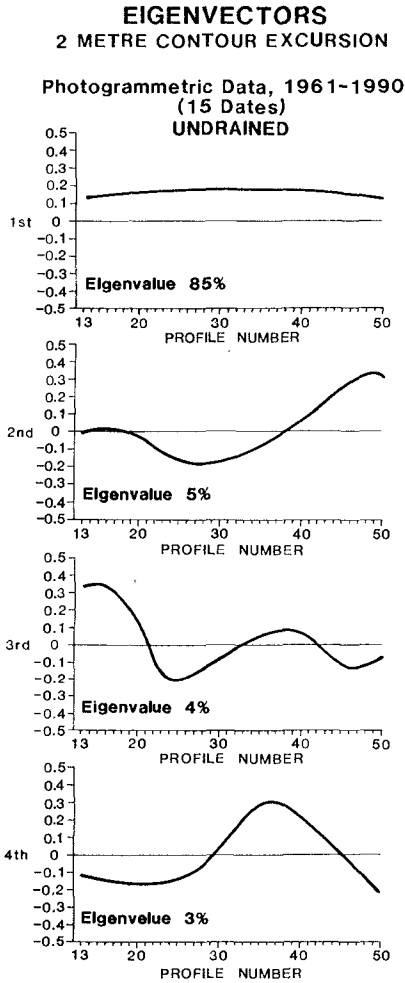
The results of the principal components analysis reflect this variation in beach morphology, showing several important components. Results are presented in **Figure 9** and **Figure 10** for the 2m contour. The first



**CONTOUR EXCURSION STANDARD DEVIATION**



**Figure 8** — Contour excursion standard deviation for photogrammetric data and survey data



**Figure 9** — Principal Components of the photogrammetric data

**Figure 10** — Principal Components of the survey data

component in each case reflects the onshore offshore sediment exchange associated with beach erosion/accretion. Subsequent components reflect the rhythmic topography produced by rips and seasonal longshore sediment exchange together with the effect of the drains.



Examination of the second component of survey data shows general stability (neither erosion nor accretion) in the region of the drains. This function is not found in the principal components of the photogrammetric survey data which appear similar to the subsequent components of the survey data. This component supports the contour variation analysis provided earlier which showed greater stability in the region of the drains and shows that the drains have added a significant morphological pattern to the beach behaviour. Principal Components 3 and 4 in the survey data and 2, 3, 4 in the photogrammetry reflect various rip conditions which are probably related to different incident wave conditions.

## CONCLUSIONS

The drainage material has been in place for approximately 18 months and is still performing well. There have been no operating or maintenance costs. Storm damage to the seaward ends of individual drains has reduced the efficiency of these drains but has not stopped the system from working. Although a general reduction in the watertable and shoreline levels sufficient to increase the stability of the beachface was achieved, a more closely spaced array of drains would be expected to increase these effects. In addition, a placement procedure providing a lower drainage system would reduce the potential for storm and rip damage without greatly reducing the draining capacity of the system.

It has been demonstrated that it is possible to alter the beach watertable by gravity drainage. Further, lowering the watertable by the method described has resulted in a stabilising of the beachface morphology in the local area.

If the nexus between watertable lowering and beach aggradation suggested by earlier researchers exists, then gravity drainage of the beachface watertable will prove to be a highly cost-effective means of beach stabilisation. It has the potential for significantly extending the life of beach nourishment programs.

## ACKNOWLEDGEMENTS

This project was initiated and funded by the New South Wales Public Works Department. The authors wish to thank the many members of the Coast and Rivers Branch who have contributed to the project. In particular, Rolyn Sario, Roderick Bowen and Alex Reed for their help with the data collection and analysis, Krystyna Starmach for the drafting and Caroline Harrington for the desktop publishing.

## REFERENCES

Bruun, P., (1989). The Coastal Drain: What Can It Do or Not Do. *Journal of Coastal Research*, Vol. 5, No.1, 123-125.

Chappel, J., Eliot, I.G., Bradshaw, M.P., & Lonsdale, E., (1979). Experimental Control of Beachface Dynamics by Water-table Pumping. *Engineering Geology*, Vol. 14, 21-41.

Chapman, D.M., Geary, M., Roy, P.S., & Thom, B.G., (1982). *Coastal Evolution and Coastal Erosion in New South Wales*. Report prepared for the Coastal Council of New South Wales. NSW Govt. Printer, 341p.

Clarke, D.J., & Eliot, I.G., (1982). Description of littoral, alongshore sediment movement from empirical eigenfunction analysis. *Journal of the Geological Society of Australia*, Vol. 29, 327-341.

Duncan, J.R., (1964). Effects of Watertable and Tide Cycle on Swash-Backwash Sediment Distribution and Beach Profile Development. *Marine Geology*, Vol. 2, 186-197.

Easton, A.K., (1970). *The Tides of the Continent Australia*. Horace Lamb Centre, Flinders University, Research Paper 37.

Grant, U.S., (1946). Effect of Ground-Water in Beach Erosion. *Bulletin of the Geological Society of America*, Vol. 57, 1252.

Grant, U.S., (1948). Influence of the Watertable on Beach Aggradation and Degradation. *Journal of Marine Research*, Vol. 7(3), 655-660.

Hansen, H.K., (1986). *Coastal Drain System: Full Scale Test at Thorsminditangen*, Summary Report No. 170-83322 Danish Geotechnical Institute, Lyngby, Denmark.

Nielsen, P., & Hanslow, D.J., (1991). Wave Run-up Distribution on Natural Beaches. *Journal of Coastal Research*, Vol. 7(4), 1139-1152.

Ogden, M.R., & Weisman, R.N., (1991). Beach Stabilisation Using Drains — An Experimental Model Study. *Coastal Sediments '91*, 1955-1969.

Parks, J., (1989). Beachface Dewatering: A New Approach to Beach Stabilisation. *The Compass*, Vol. 66, 65-72.

Terchunio, A.V., (1989). Performance of the STABEACH SYSTEM at Hutchinson Is. Florida. *Proceedings of 2nd Conference on Beach Preservation Technology*, Florida Shore & Beach Preservation Association, Feb. 89, 229-238.

Trenaman, N., & Short A.D., (1987). *Deepwater & Breaker Wave Climate of the Sydney Region, NSW 1971-1985*, University of Sydney Coastal Studies Unit, Technical Report No. 87/1.

Vesterby, H., & Parks, J., (1988). Beach Management with the Coastal Drain System, *Florida Shore & Beach Preservation Association Meeting*, Gainesville, Florida.

## CHAPTER 86

### Harmonic Generation and Transmission Past a Submerged Rectangular Obstacle

Andrew M. Driscoll <sup>1</sup>, Robert A. Dalrymple <sup>2</sup> and Stéphan T. Grilli <sup>3</sup>

**Abstract :** Experiments were conducted in a wave flume to study the harmonic evolution of a normally incident linear monochromatic wave train as it propagated over a submerged impermeable obstacle of rectangular cross-section. The reflection and transmission characteristics of the system were studied and compared to a linear scattering model, which was found to overpredict the transmission coefficients. The experiment was also simulated using the fully nonlinear model by Grilli *et al.* (1989), which performed well given its inviscid potential assumptions.

#### Introduction

The scenario of a linear wave train impinging on a submerged rectangular obstacle may be considered as a simplified representation of numerous physical phenomena, such as wave reflection and transformation over offshore reefs, bars and submerged breakwaters, which occur along actual coastlines. For this reason, the situation has been studied by numerous authors in the past 30 years, including Takano (1960), Mei and Black (1969), Losada (1991) and Rey *et al.* (1992), with the aim of analytically predicting the reflection and transmission characteristics for a given incident wave condition and obstacle geometry.

These authors have considered the problem completely in the linear context; an incident linear wave is partially reflected upon passing a submerged rectangular obstacle, with both transmitted and reflected energy propagating at the same frequency as the incident wave.

---

<sup>1</sup>Arctec Offshore Corporation, Escondido, CA 92025

<sup>2</sup>F. ASCE, Director, Center for Applied Coastal Research, University of Delaware, Newark, DE 19716

<sup>3</sup>M. ASCE, Department of Ocean Engineering, University of Rhode Island, Kingston, RI 02881

Such assumptions become suspect as  $\mu (= kh)$  becomes small and  $\delta (= a/h)$  becomes large over the obstacle. Under these circumstances, significant harmonic generation may occur over the obstacle, as has been observed by Seelig (1980) and Rey *et al.* (1992). The wave condition found downwave of the obstacle for such a nonlinear situation is likely to have energy distributed not only at the fundamental frequency, but at a number of higher harmonic frequencies as well.

The goals of this research are : (i) to perform a series of laboratory experiments to scrutinize the spectral transformation which occurs when a linear wavetrain passes over a submerged rectangular obstacle; (ii) determine the performance of the standard linear scattering theory for a situation where nonlinearity is significant over the obstacle; and (iii) to evaluate the ability of the fully nonlinear potential model by Grilli *et al.* (1989) to simulate the laboratory data.

## Experimental setup

The experiments were conducted in a precision wave flume with dimensions 30 m long by 0.6 m wide by 1 m deep. Repeatable wave trains were generated with a computer-controlled horizontal piston wavemaker, and a 1:35 impermeable slope at the opposite end of the tank functioned as a wave absorber. A submerged impermeable rectangular obstacle the width of the flume was fixed to the bottom of the tank 7.0 m from the wavemaker paddle. The water depth was  $h_o = 0.5$  m, and the obstacle depth was  $h_1 = 0.12$  m, so that the obstacle vertical aspect ratio is  $\frac{h_o - h_1}{h_o} = 0.76$ . The obstacle length was 0.78 m, i.e.,  $1.58h_o$  or slightly more than twice its height.

Two sets of experiments were carried out. In the first experimental set, a single sine wave condition (incident height  $H_i = 2.50$  cm, period  $T = 1.70$  s, with  $ka = 0.019$ ) was produced on seven occasions. By moving the position of four wave gages prior to each run, an array of 28 gage locations was created (fig. 1).

The second experimental set consisted of 12 additional runs with the same wave height but with wave periods ranging from 0.8 s to 1.9 s. A 3-gage array was placed between the obstacle and the wave generator, thereby allowing the reflection coefficient ( $K_r$ ) to be determined as a function of the incident wavenumber (fig. 2). Two additional gages were placed at locations downwave of the obstacle for redundant measurement of the transmission coefficient ( $K_t$ ).

## Experimental results

Spectral analyses of the 28 wave gage locations in the experimental data set yield the amplitudes of the individual harmonics, and reveal the nonlinear transformation undergone as incident linear waves pass over the obstacle (fig. 3). It is seen that significant harmonic generation occurs over the obstacle, and that

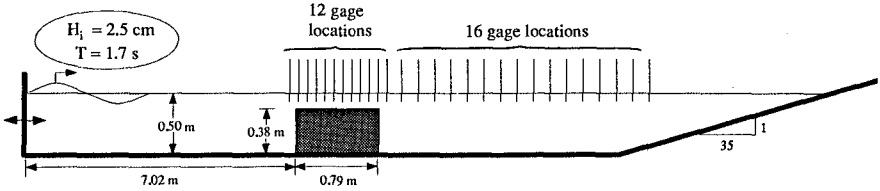


Figure 1: Experimental setup for spectral evolution portion of experiments.

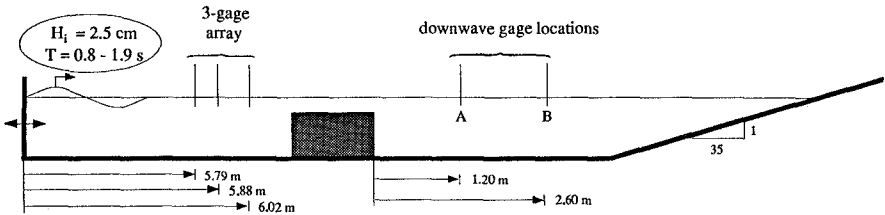


Figure 2: Experimental setup for reflection/transmission portion of experiments.

spatial amplitude modulation is present downwave of the obstacle. Such downwave amplitude modulations are certainly not due to reflection-induced partial standing waves, as reflection from the 1:35 slope is quite small (measured at less than 2 % at the first harmonic frequency). It must thus be concluded that the situation downwave of the obstacle is still quite dynamic with respect to harmonic evolution.

**Comparison: linear scattering model vs. experiment**

As the wave condition downwave of the obstacle has been shown to be both nonlinear and spatially varying, it is of interest to compare the experimentally measured values of  $K_r$  and  $K_t$  to those predicted analytically by a linear scattering model such as that of Losada (1991). The comparison, given in fig. 4, shows that the linear model predicts  $K_r$  quite well, but consistently overpredicts  $K_t$ . This overprediction is presumably due to the transfer of energy to the higher harmonics, and also to frictional and turbulent losses. From fig. 4, it is also seen that the measured value of  $K_t$  varied between gage location A and gage location B by as much as 5 % or more.

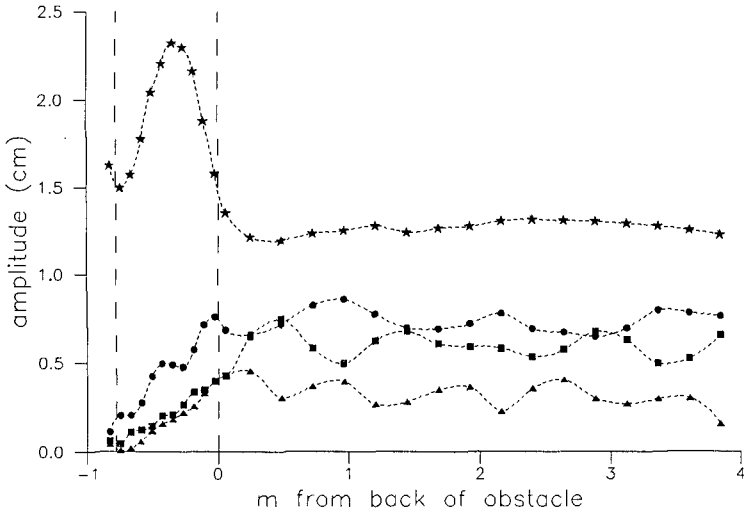


Figure 3: Spatial evolution of the first four harmonics in the experimental data; (★)=1st harmonic, (●)=2nd harmonic, (■)=3rd harmonic, (▲)=4th harmonic. Fine dashed lines are splines fit to data points, long dashed lines show boundaries of obstacle.

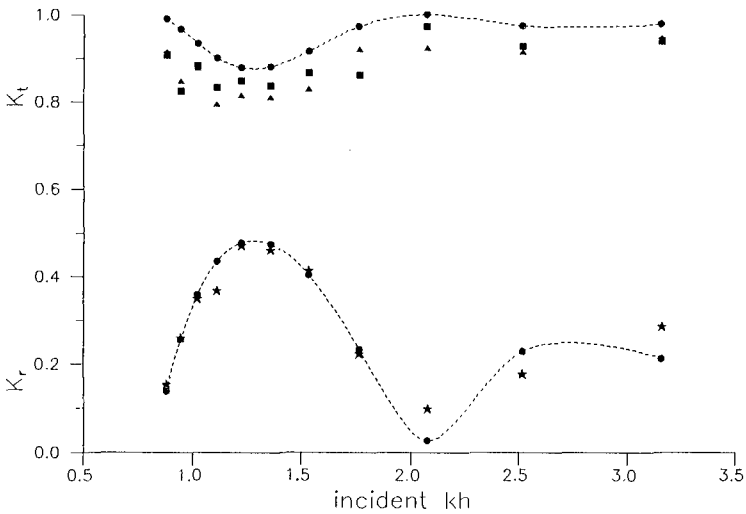


Figure 4: Comparison of  $K_r$  and  $K_t$  found experimentally and via the linear model of Losada (1991); (●)=results of Losada (1991) model, (★)=measured  $K_r$ , (▲)=measured  $K_t$  at gage A, (■)=measured  $K_t$  at gage B. Dashed lines are splines fit to Losada data.

## Boundary element method (BEM) model

The two-dimensional nonlinear potential model by Grilli *et al.* (1989,1990), and its most recent extensions, are used to compute wave propagation over the submerged obstacle. With the velocity potential being defined as  $\phi(x, t)$ , the velocity is given by  $u = \nabla\phi = (u, w)$ , and the continuity equation in the fluid domain  $\Omega(t)$  with boundary  $\Gamma(t)$ , is a Laplace's equation for the potential,

$$\nabla^2\phi = 0 \quad \text{in } \Omega(t) \quad (1)$$

Using the free space Green's function  $G(x, x_l) = -\frac{1}{2\pi} \log |x - x_l|$ , equation (1) is transformed into a Boundary Integral Equation (BIE),

$$\alpha(x_l)\phi(x_l) = \int_{\Gamma(x)} \left[ \frac{\partial\phi}{\partial n}(x)G(x, x_l) - \phi(x)\frac{\partial G(x, x_l)}{\partial n} \right] d\Gamma(x) \quad (2)$$

where  $x = (x, z)$  and  $x_l = (x_l, z_l)$  are position vectors for points on the boundary,  $n$  is the unit outward normal vector, and  $\alpha(x_l)$  is a geometric coefficient.

On the free surface  $\Gamma_f(t)$ ,  $\phi$  satisfies the full nonlinear kinematic and dynamic boundary conditions,

$$\frac{Dr}{Dt} = \left( \frac{\partial}{\partial t} + u \cdot \nabla \right) r = u = \nabla\phi \quad \text{on } \Gamma_f(t) \quad (3)$$

$$\frac{D\phi}{Dt} = -g\eta + \frac{1}{2}\nabla\phi \cdot \nabla\phi - \frac{p_a}{\rho} \quad \text{on } \Gamma_f(t) \quad (4)$$

respectively, with  $r$ , the position vector of a free surface fluid particle,  $g$  the acceleration due to gravity,  $\eta$  the vertical elevation of the free surface (positive upwards and  $\eta = 0$  at the undisturbed free surface),  $p_a$  the pressure at the surface, and  $\rho$  the fluid density.

No-flow conditions are prescribed along solid boundaries, and, in the present applications, cnoidal waves are generated on the boundary  $\Gamma_{r1}(t)$  by specifying a piston wavemaker motion, as in laboratory experiments (see Grilli & Svendsen 1990, for detail).

**The time integration :** The time stepping, follows the Eulerian-Lagrangian approach used by Dold & Peregrine 1984. It consists of integrating free surface conditions (3) and (4) at time  $t$ , to establish both the new position of the free surface  $\Gamma_f(t)$ , and the boundary conditions at time  $t + \Delta t$  ( $\Delta t$  denotes a small time step increment). Second-order Taylor expansions are expressed in terms of  $\Delta t$  and of the Lagrangian time derivative (as defined in (3)), for both the position  $r(t)$  and the potential  $\phi(t)$  on the free surface. Coefficients in the series

are calculated by solving two Laplace problems—for  $\phi$  and  $\frac{\partial\phi}{\partial t}$ —at each time step (see detail in Grilli, *et al.* 1989).

**Numerical implementation :** The BIE (2), equivalent to Laplace problems (1) for  $\phi$ , and the equivalent BIE problem for  $\frac{\partial\phi}{\partial t}$  are solved by a higher-order BEM, using a set of collocation nodes on the boundary, and elements to interpolate between collocation nodes. Quasi-spline elements are used on the free surface, and isoparametric quadratic elements elsewhere. Each integral in (2) is transformed into a sum of integrals over each boundary element. Non-singular integrals are calculated by standard Gauss quadrature rules. A kernel transformation is applied to the weakly singular integrals, which are then integrated by a numerical quadrature exact for the logarithmic singularity. Details of the numerical implementation can be found in Grilli, *et al.* 1990, along with a discussion of corner problems associated with surface piercing bodies such as wavemakers.

**Discretization and numerical parameters :** A limitation of the BEM model is that any wave breaking in the computational domain effectively halts the solution algorithm. An adjustment of tank boundaries, hence, had to be made to prevent breaking on the slope of the numerical wave flume. Tank boundaries were re-defined such that the most downwave portion of the slope made the transition to a shallow shelf just below the breaking depth. Fig. 5 shows the re-defined tank boundaries which includes a region of constant depth  $h_o = 1$  and length  $21h_o$ , and a 1:35 slope with a shelf of constant depth  $h_1 = 0.34$ , at the upper part of the slope, from  $x' = \frac{x}{h_o} = 44$  to 56. A rectangular bar of height  $0.76h_o$  and width  $1.58h_o$  is located with its axis at  $x' = 14.83$ . As a transmitting boundary condition was not available in the model, reflection off the back wall of the numerical wave flume became a limiting condition. The comparison of BEM model vs. experiments must thus be made in the time between the initiation of paddle motion and the arrival of back wall-reflected energy at the most downwave gage location in the BEM model ( $x' = 21$ ).

The free surface discretization is made of 224 quasi-spline elements, and there are 73 quadratic elements on the bottom and lateral boundaries. The interval between nodes on the free surface is 0.25, and 0.50 on the horizontal bottom, the slope, and the shelf bottom. To increase resolution and accuracy on and above the bar, this interval is reduced to about 0.20 along the bar three sides. The total number of nodes is 365. This corresponds to a CPU time of 7.63sec (IBM3090/300) per time step. Time step is automatically selected in the model, to ensure optimum accuracy and stability of calculations.

## BEM model vs. experiment

A comparison is made between computations and experiments, for which both experimental and numerical set-ups correspond to closely identical conditions, with the waves being generated from still water using a piston wavemaker in



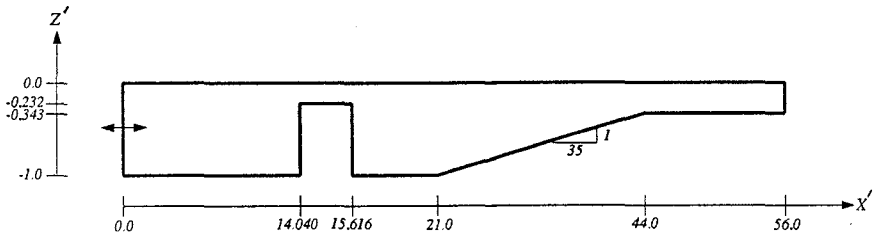


Figure 5: Geometry of the numerical wave flume, as re-defined for entry into BEM model. The shown axes are nondimensionalized with the water depth,  $x' = x/h$  and  $z' = z/h$ .

both cases. In the present case, a cnoidal wave of height  $H'_i = \frac{H_i}{h_o} = 0.05$ , and period  $T' = T\sqrt{\frac{g}{h_o}} = 7.52$  is generated at the leftward lateral boundary of the computational domain, and the corresponding incident wave profile is within 2% of a simple sine wave of length  $\frac{L}{h_o} = 6.75$ , as measured in the experiments. The model is run for over 20 wave periods, and no adjustment of time lag between both data sets is made before comparison. This, hence, represents a very demanding test of the model performance.

Fig. 6 shows a water surface comparison between the experimental and BEM results. A similar comparison is shown in fig. 7 for time series at locations 0.72 m and 1.92 m downwave of the obstacle. The BEM results are seen to deviate from the experimental results in both amplitude and phase. The nature of this deviation is better revealed by a frequency-domain comparison (fig. 8) which, due to the limitation of the non-breaking BEM requirement, is possible only for the first 8 waveforms following a 10-second startup period. The BEM model is shown to predict harmonics of similar amplitude to those observed in the experiments, with the exception of the first harmonic, which is overpredicted.

This discrepancy in first harmonic amplitude is likely due to the influence of flow separation as the wave-induced velocity oscillations interacted with the corners of the submerged obstacle. As such flow separation was observed in the experiments, the disagreement in the first harmonic amplitude between the BEM model and experiment is not surprising, given the inviscid potential flow assumptions of the model.

As a check, the flow separation loss incurred as a waveform passes the obstacle may be estimated with a crude analytical approach. A simple nonlinear friction representation is assumed,  $\eta_1 - \eta_2 = \frac{f}{2g}|u|u$ . If the obstacle is assumed thin in relation to the wavelength, quasi-steady flow is assumed, and frictional

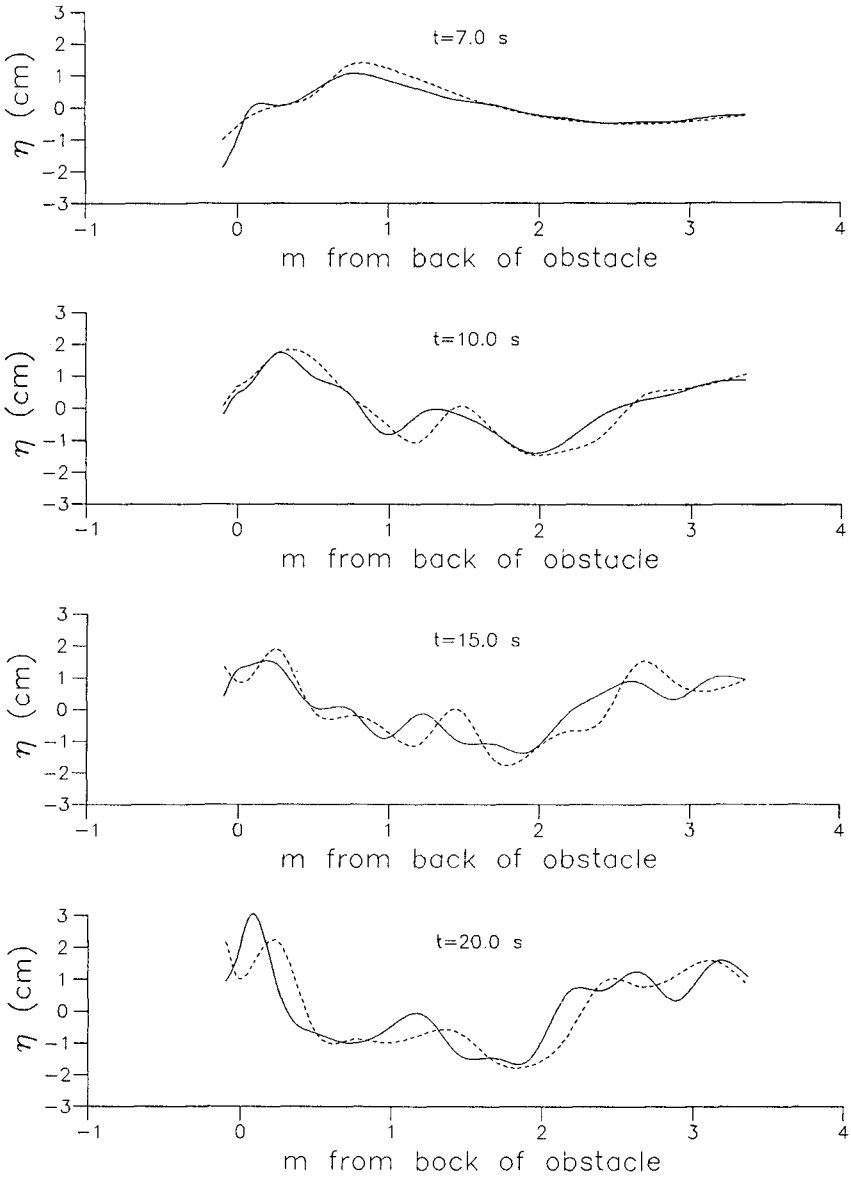


Figure 6: Water surface comparison of BEM model to experiment at  $t=7.0$  s,  $t=10.0$  s,  $t=15.0$  and  $t=20.0$  s after the initiation of paddle motion; (---)=BEM model, (—)=experiment.

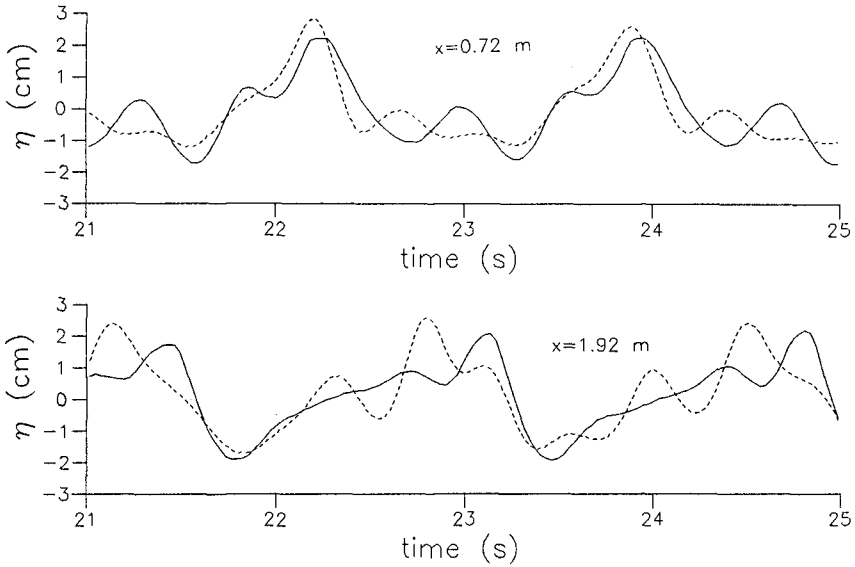


Figure 7: Time series comparison of BEM model data to experiment, at locations 0.72 m and 1.92 m downwave of obstacle; (---)=BEM model, (—)=experiment.

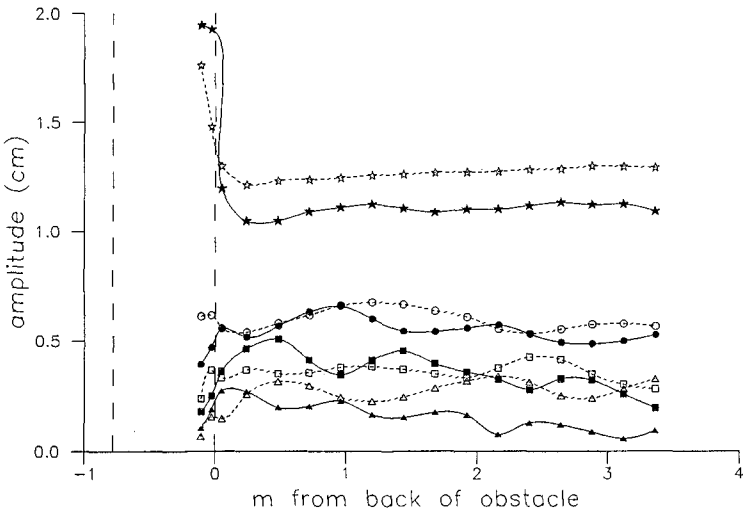


Figure 8: Comparison of spatial amplitude modulations, BEM model and experiment; (---)=BEM model, (—)=experiment, (★, ☆)=1st harmonic, (●, ○)=2nd harmonic, (■, □)=3rd harmonic, (▲, △)=4th harmonic.

effects are averaged over a wavelength, it may be shown that

$$\eta_1 - \eta_2 = \frac{4(h/h_o - 1)^2 a^2}{3\pi h_o^2 \omega^2 \cosh^2 kh} [\sinh kh - \sinh k(h - h_o)]^2 \quad (5)$$

where  $\eta_1$  and  $\eta_2$  are the water surface elevations prior to and after the obstacle,  $f$  is an empirical friction-loss coefficient,  $u$  is the amplitude of the depth-averaged velocity downwave of the obstacle,  $a$  and  $h$  are the amplitude and depth behind the obstacle and  $h_o$  is the depth on top of the obstacle. The friction coefficient  $f$  for this case is given by  $f = (h/h_o - 1)^2$ .

Introducing the downwave first harmonic amplitude from the BEM results ( $\sim 1.25$  cm) and the other relevant parameters into 5, we find  $\eta_1 - \eta_2 \simeq 0.16$  cm. This agrees well with the discrepancy between BEM and experimental amplitudes of approx 0.15 cm.

The downwave higher harmonic amplitude modulations are less pronounced in fig. 8 compared to fig. 3, when the tank was fully developed. Nonetheless, the BEM model does predict spatial amplitude modulations which are qualitatively similar to the experimental results. The degree of disagreement present is certainly also due to the influence of flow separation at the first harmonic frequency, as a misrepresentation of the first harmonic component will be passed on as erroneously simulated higher harmonics as well.

## Conclusions

The spectral evolution of an incident regular wave train has been traced as it propagated over a submerged rectangular obstacle, and comparisons have been made between the experimental data and both a traditional linear scattering model and a BEM model. The experimental data revealed the existence of spatial amplitude modulations downwave of the obstacle.

The linear model of Losada (1991) was shown to predict the reflection coefficient quite well, despite the high degree of nonlinearity present in the vicinity of the obstacle. However, it was seen that the transmission coefficient was consistently overpredicted due the linear model's omission of energy transfer to higher harmonics and energy dissipation. An implication of the above results is that the linear scattering approach may underestimate the effectiveness of a structure (ie, submerged breakwater) under highly nonlinear situations.

The BEM model by Grilli *et al.* (1989) was found to simulate downwave spatial amplitude modulations qualitatively similar to those found in the data. Comparisons, however, were hampered by the presence of flow separation in the experiments which could not be modelled in the BEM formulation. It is conjectured that the BEM model would have simulated the experiments more ac-

curately, had the obstacle depth been greater, thus inducing less flow separation.

## References

- Dold, J.W. and D.H. Peregrine (1984). Steep unsteady water waves: an efficient computational scheme. *Proceedings of the 19<sup>th</sup> International Coastal Engineering Conference*, ASCE, Houston, 955-967.
- Grilli, S.T., J. Skourup and I.A. Svendsen (1989). An efficient boundary element method for nonlinear water waves, *Engineering Analysis with Boundary Elements*, **6**, 97-107.
- Grilli, S.T. and I.A. Svendsen (1990) Corner Problems and Global Accuracy in the Boundary Element Solution of Nonlinear Wave Flows, *Engineering Analysis with Boundary Elements*, **7**(4), 178-195.
- Longuet-Higgins, M.S. and E.D. Cokelet (1976). The deformation of steep surface waves on water - I: a numerical method of computation, *Proceedings of the Royal Society of London*, **A350**, 1-26.
- Losada, I. (1991) Estudio de la propagacion de un tren lineal de ondas por un medio discontinuo, Ph.D. dissertation, University of Cantabria, Santander, Spain.
- Mei, C.C. and J.L. Black (1969). Scattering of surface waves by rectangular obstacles in waters of finite depth, *Journal of Fluid Mechanics*, **28**, 499-511.
- Rey, V., M. Belzons and E. Guazzelli (1991). Propagation of surface gravity waves over a rectangular submerged bar, *Journal of Fluid Mechanics*
- Seelig, W.N. (1980). Two-dimensional tests of wave transmission and reflection characteristics of laboratory breakwaters, Technical Report no. 80-1, USAE Coastal Engineering Research Center, Fort Belvoir, VA.
- Takano, K. (1960). Effets d'un obstacle parallepipédique sur la propagation de la houle, *La Houille Blanche*, **2**, 247-267.

## CHAPTER 87

### THE SUBMERGED PLATE AS A WAVE FILTER

#### THE STABILITY OF THE PULSATING FLOW PHENOMENON

Dr.-Ing. Kai-Uwe Graw \*\*

#### ABSTRACT

For many applications it is possible to reduce the wave motion in the protected area sufficiently using the submerged plate as a wave filter. The horizontal submerged plate, which hardly obstructs the cross-section of the flow, cannot be explained by the Wiegel approach at all. A strong pulsating flow opposite to the direction of the wave propagation originates beneath the plate during wave attack. New velocity measurements, carried out with an ultrasonic 3D-probe in the region below the plate, make it now possible to explain the principle much more in detail. They show that the flow phenomenon at the plate is very stable, the flow is nearly as strong if the region below the plate is partly closed.

#### 1. REASONS FOR THE INVESTIGATIONS

The protection of coastlines and harbours against wave attack is mainly achieved by the use of solitary breakwaters. Their negative features are that they hinder:

- a) the water exchange between the open sea and the protected area (diverted sediment transport, deteriorated water quality) and
- b) the view over the open sea.

Underwater breakwaters are not visible, but the water exchange does not increase as much as the efficiency decreases. One possibility to enhance the performance without hindering the water exchange is the use of a semi-submerged vertical wall which obstructs the energy flux near the surface. However, this leads to construction problems (destruction of the

---

\*\* Senior Research Engineer

Wasserbau und Wasserwirtschaft, Bergische Universität GH Wuppertal  
Pauluskirchstraße 7, 5600 Wuppertal 2, Germany

wall in large waves), and also in this case the structure is visible. The breakwater type which reduces all these secondary problems is the rigid horizontal submerged plate mentioned in this paper. The plate cannot be used to stop the wave motion in the protected area, but its efficiency is sufficient for many applications.

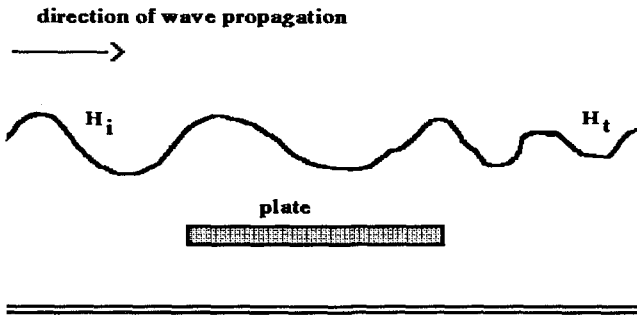


Figure 1: The submerged plate

## 2. THE SUBMERGED PLATE: THE WAVE FILTER

The performance of "normal" breakwaters can be explained by using the Wiegel approach. This means that the part of the wave energy in the regions covered by the structure is reflected, a very small part of the energy is dissipated at its surface and the other part passes by.

Figure 2 shows one series of the different measurements performed by Dauer [1984]. The figure shows the results for the shortest of the plates used (the length is only 1.333 times the water-depth,  $l/d=1.333$ ).

The performance of the plate is not adequate in two cases:

- ① All long waves ( $L/l > 6$ ) are not reduced sufficiently, the wave height reduction is approximately 25%.
- ② Furthermore it can be seen, that the plate which is submerged by more than one third (40%) of the water-depth does not really work.

All waves not longer than 3.5 times the plate length ( $L/l < 3.5$ ) are reduced by more than 50%. The largest value of the wave height reduction is approximately 80%.

The best results were obtained for the three smallest values, but one important reason for this is wave breaking above the plate, connected with large forces exerted on the plate. For a submergence depth between 20 and 30% of the water depth a sufficient wave height reduction was observed, not caused by wave breaking. These results were confirmed for

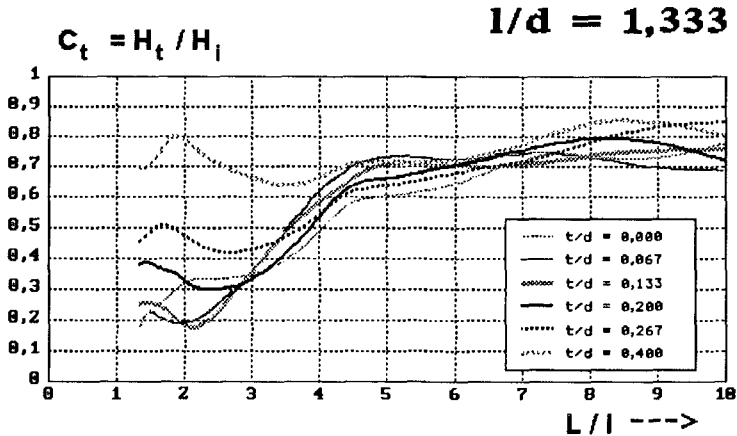


Figure 2: Wave height reduction at the plate [Dauer, 1984]

different plates longer than two times the wave length ( $l/d > 2$ ). The wave height reduction is relatively constant (50 - 70%) in the wave length range between  $L/l = 0.4$  and 4.

Examining a normal solitary breakwater, this principle is correct; looking at the semi-submerged vertical wall, it does not cover the whole problem but it is a good approximation. The horizontal submerged plate which hardly obstructs the cross-section of the flow cannot be explained by the Wiegel approach at all. For this reason, and as it performs well only in a particular region of the wave spectrum, it shall be called a wave filter from now on.

### 3. THE PULSATING FLOW

Dick [1968] noticed a flow around a horizontal plate submerged beneath waves, but he did not give any explanation for it. Analyses of the flow behaviour, based on flow visualization experiments [Graw, 1988; Graw, Kaldenhoff, Stieglmeier, 1989], and measurements of the wave height were presented by Hoeborn [1986]. She first gave an explanation based on a resonant flow behaviour. Continual experiments have shown that the dissipation of energy at the plate is caused in the wake behind the plate [Fischer, 1990; Fischer, Jirka, Kaldenhoff, 1991]. A finite element model gave us the possibility of calculating the energy equilibrium at the plate quite well, but the forecast of the flow was still uncertain. New velocity measurements, carried out with an ultrasonic 3D-probe in the region below the plate, make it now possible to explain the principle much more in detail. They show that the flow phenomenon at the plate is very stable, the flow is nearly as strong if the region below the plate is partly closed.



direction of wave propagation →

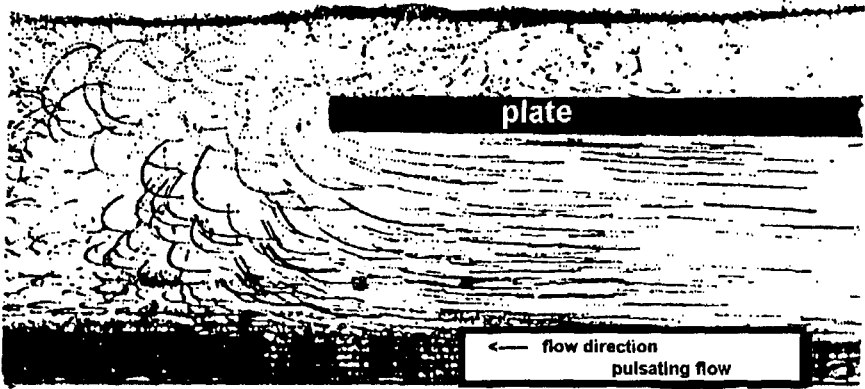


Figure 3 a: Pulsating flow beneath the plate

The physical principle of the plate as a wave filter can be explained as follows:

- ① The propagating water wave reaching the horizontal plate is divided into two parts: the energy flux above the plate is transformed into a new - shorter - gravity wave determined by the reduced water depth in this region, the one below the plate is a propagating pressure distortion travelling slower than the wave above.
- ② As soon as the first short gravity wave overflowing the plate reaches the region behind the plate, once more a new wave is formed, which travels away and has the same wave-length as the original wave, but less energy. Furthermore a part of the energy of the wave overtopping the plate also propagates into the region below the plate (backwards!).
- ③ If the length of the plate is such that at the same time there are a wave trough at the front edge and a wave crest at the end of the plate (resonance), and if the amount of this energy is relatively large compared to that travelling forward (no shallow water waves), a strong pulsating flow opposite to the direction of the wave propagation originates (figure 3).
- ④ The energy transferred back by this flow to the region before the plate makes it impossible for the pressure distortion caused by following waves to propagate into the region below the plate, the flow grows stronger. Thus a part of the energy is reflected by the structure. Figure 4 shows the particle orbits in front of the plate. It can be seen that the region below the plate is closed for the wave energy of the incoming wave.

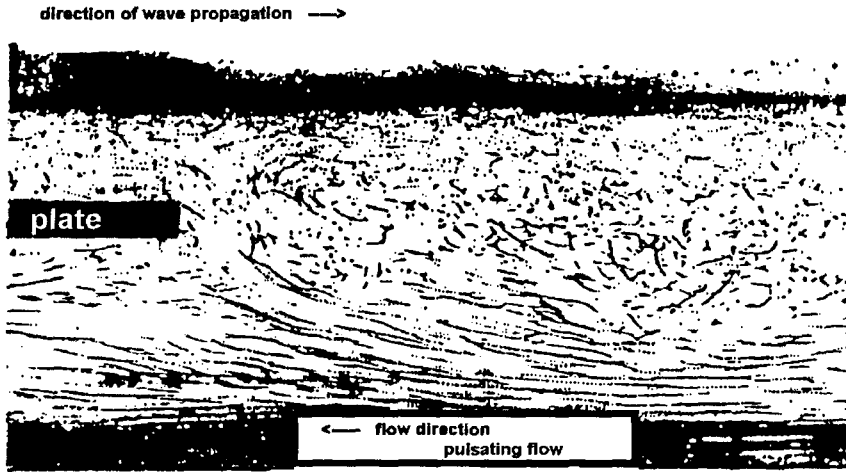


Figure 3 b: Pulsating flow beneath the plate

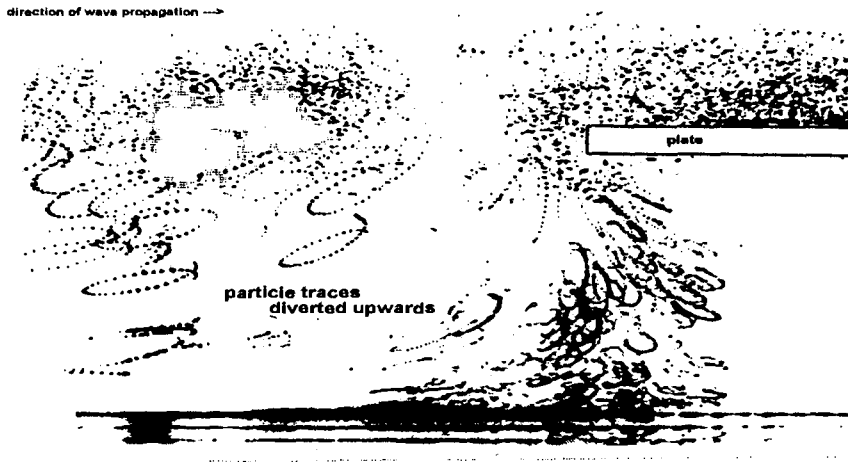


Figure 4: Diverted particle orbits in front of the plate

Figure 5 shows how the flow grows as the waves are passing by (in comparison with the undisturbed orbital motion). This flow is the physical reason why energy is reflected by this structure. As it depends on the energy equilibrium between the front and the rear below the plate, the plate acts as a wave filter. The mean parameters for the description of the performance are the ratio of wave-length ( $L$ ) to length of the plate ( $l$ ) and the relative immersion of the plate.

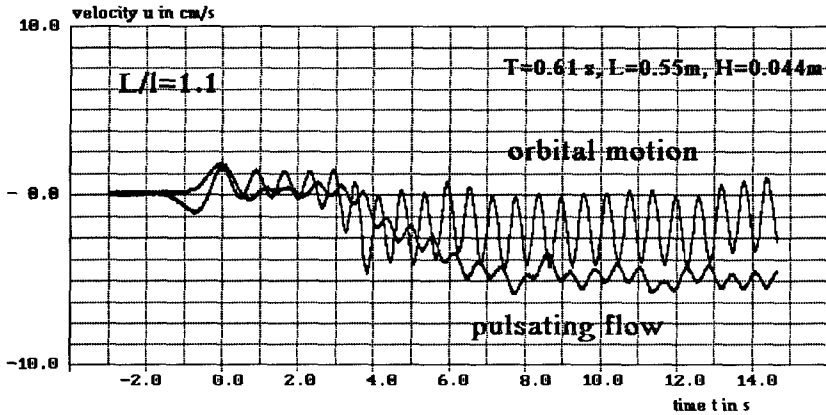


Figure 5: Development of the pulsating flow

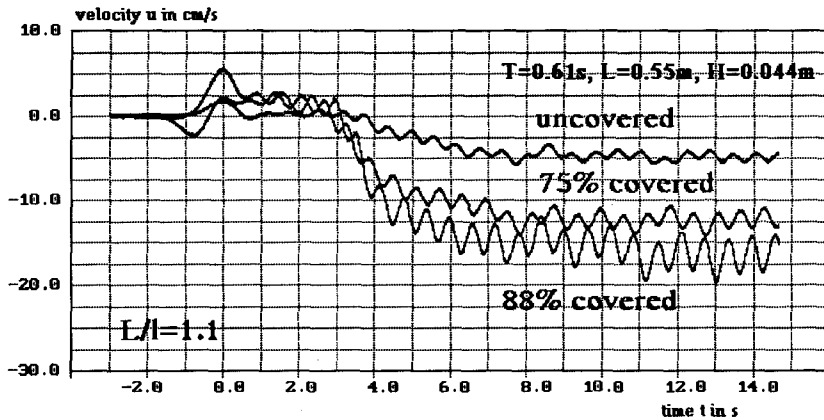


Figure 6: Pulsating flow with obstruction below the plate

In order to construct this wave filter it is necessary to build a connection between the plate and the bottom of the sea. The possibility of a durable realization increases if it is possible to build a very solid connection. The answer to the question if it is possible to partially obstruct the region below the plate without destroying the pulsating flow is given in figure 6. The kinetic energy of the three pulsating flows shown here is nearly the same.

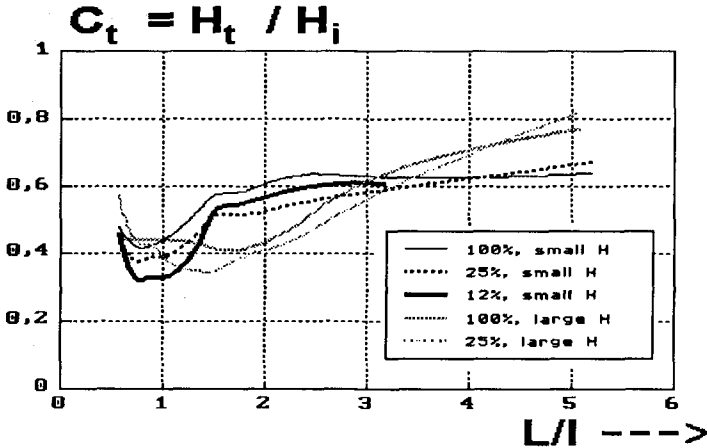


Figure 7: Performance of the breakwater

The phenomenon of the pulsating flow is not disturbed by the blockage and, connected with that, the performance of the wave filter is not reduced. Figure 7 shows the wave height reduction observed during the present experiments. The two measurements series shown were not performed with constant values of the wave height, accordingly they are named small and large waves. It is clearly visible that the wave height reduction also depends on the height of the incoming waves (and therefore on the depth distribution of the kinetic energy of the waves).

#### 4. CONCLUSIONS AND OUTLOOK

The experiments - that are presented here very briefly - show that the performance of the "plate as a wave filter" is a phenomenon which is stable even if the region below the plate is partly blocked up. This is a necessity because the plate has to be fastened to the ground of the sea somehow. As it is possible to build a solid construction, this way it seems possible to construct an economic, durable and strong breakwater.

The submerged plate as a wave filter is the only construction which allows to reduce the wave height without obstructing the flow region with the largest energy flux - the surface region - because a large amount of the wave energy is diverted into the deeper regions. This means that problems with the construction of common wave breakers as the destruction by very large waves, corrosion problems, etc, are reduced.

The diversion of energy also introduces a new principle for the construction of a wave energy converter. Today all known devices are placed somehow near the surface of the sea, including again all the problems mentioned above. The possibility of such a new wave energy device is being investigated at our institute at the moment.

## 5. LITERATURE

- [1] Dauer, L.; (1984); *Energietransport bei einer vertikalen Tauchwand, einer vertikalen Tauchwand mit einer horizontalen Platte und einer horizontalen Platte*; Berlin; Diplomarbeit am Institut für Wasserbau und Wasserwirtschaft, Technische Universität
- [2] Dick, T.M.; (1968); *On solid and permeable submerged breakwaters*; Kingston; Ph.D. Diss. at Queens University
- [3] Fischer, C.; (1990); *Scherschichtdissipation im Nachlauf einer getauchten horizontalen Platte unter dem Einfluß von Oberflächenwellen*; Wuppertal; Mitteilung Nr. 5, Wasserbau und Wasserwirtschaft, Bergische Universität
- [4] Fischer, C.; Jirka, G.H.; Kaldenhoff, H.; (1991); *Wave energy dissipation in the wake of a submerged horizontal plate*; Tokyo; Proc.: 4th Int. Conference. on Computing in Civil and Building Eng
- [5] Graw, K.-U.; Kaldenhoff, H.; Stieglmeier, M.; (1989); *An explanation of wave energy transmission around permeable breakwaters based on turbulence and resonance*; Ottawa; XXIII IAHR Congress
- [6] Graw, K.-U.; (1988); *Der Einsatz laseroptischer Verfahren zur Untersuchung von Geschwindigkeitsfeldern im wasserbaulichen Versuchswesen*; Berlin; Mitteilung Nr. 112 des Instituts für Wasserbau und Wasserwirtschaft, Technische Universität
- [7] Hoeborn, G.; (1986); *Einfluß einer starren horizontalen getauchten Platte auf Wellen*; Wuppertal; Mitteilung Nr. 2, Wasserbau und Wasserwirtschaft, Bergische Universität

## CHAPTER 88

### Wave impact forces on mixed breakwaters

Stéphan T. Grilli<sup>1</sup>, M. ASCE, Miguel A. Losada<sup>2</sup>, and Francisco Martin<sup>2</sup>

**Abstract :** Flat impact of a solitary wave on a mixed breakwaters is experimentally and numerically studied, using a 2D nonlinear potential flow model. Free surface profiles, internal velocities, instantaneous pressure and pressure envelope on the wall, and on the berm, are analyzed based on both measurements and calculations. Results show, a converging flow occurs above the berm, followed by a small vertical jet, with large acceleration, that is responsible for large impact pressure on the wall. Short duration peak pressures occur above SWL, and quite large pressures also occur on the berm, as far away as twice the local depth from the wall. Maximum pressure force and overturning moment on the wall reach up to 9 and 15 times corresponding hydrostatic values based on water elevation at the wall.

### Introduction

Mixed breakwaters are made of the combination of a vertical wall and a rubble mound berm (Fig. 1). Under wave action, they function as vertical walls during high tide, and as mound breakwaters during low tide. The design of mixed breakwaters requires that their upper part be safe against sliding and overturning due to wave impact pressure. Laboratory and field experiments show, impacts of normally incident breaking waves are the most severe (Goda, 1985). Geometrical parameters of the breakwater, such as berm depth,  $d = h - h_1$ , and length, in water of depth  $h$  (Fig. 1), control conditions under which impulsive breaking of incident waves of height  $H$  can occur on the wall.

Extensive experimental work was carried out over the past 50 years for the evaluation of the peak pressure on vertical seawalls. Results were analyzed mostly based on Bagnold's simple theory (Goda 1985). Kirkgöz 1991 (KIR), in his recent review of this experimental work, shows that the average maximum pressure on vertical walls,  $p_{max}$ , varies between 20 and 75 times  $\rho gH$  (where  $\rho$  is the water density, and  $g$  the acceleration of gravity), and that the highest maximum pressure can reach up to 220 times this value. Variations in maximum pressure depend on the incident wave type (periodic, solitary) and characteristics, on the experimental scale, and on the type and location of measuring devices. In addition, maximum

---

<sup>1</sup>Assistant Professor, Department of Ocean Engineering, University of Rhode Island, Kingston, RI 02881, USA, Ph.Nb.: (401) 792-2550

<sup>2</sup>Professor and Graduate Student, Departamento de Ciencias y Técnicas del Agua y del Medio Ambiente, University of Cantabria, Santander 39005, Spain

pressures on the wall vary with the bottom slope in front of the wall. Kirkgöz 1982, based on laboratory experiments, showed that greatest impact pressures are obtained with a 1/10 slope in front of the wall. KIR also showed that largest impact pressures are obtained for an inclined wall, with a 10° to 20° backward slope with respect to the vertical. Finally, as far as scale effects are concerned, Führböter 1985 showed that experimental pressures obtained in small-scale tests are larger than prototype pressures, due to increasing aeration effects at larger scale.

In the same line, Partensky 1988 showed, based on laboratory experiments with mixed breakwaters, that highest pressures are exerted on the wall when the colliding wave has an almost vertical face. In this case, the maximum impact force on the wall,  $F_{Hx}$ , can rise to more than 10 times the hydrostatic force,  $F_{Hx} = \frac{1}{2}\rho g(d + \eta)^2$ , based on wave elevation  $\eta$  at the wall.

In the experimental studies reported above, results were mostly analyzed, using statistical theories and semi-empirical methods. Few viable theoretical approaches indeed exist that can model waves close to breaking over an arbitrary bottom and structure geometry, and thus be used to analyze the magnitude of impact pressures as a function of the detailed incident wave flow. In fact, only two theoretical approaches have been developed so far, that have been successfully applied to calculating wave impact on vertical walls: (i) Solution of two-dimensional (2D) fully nonlinear potential flow equations, using a Boundary Integral Equation method (BIE) (e.g., Cooker and Peregrine 1991 (CP)); (ii) Solution of 2D Euler equations, using a Volume Of Fluid method (VOF) (e.g., Wang and Su 1992). The first method turns out to be very efficient and accurate in dealing with this problem, but is limited to prior to wave breaking first occurs. The second method is less accurate but is somewhat more efficient in dealing with wave breaking and discontinuities. Experimental results for wave impact on the wall can be classified into three types, that must be considered when developing theoretical or numerical models: (i) Non-breaking waves; (ii) Waves with flat impact on the wall (i.e., with an almost vertical front face); (iii) Waves with falling breaking jets, and imprisoned air under the wave (e.g., plunging breaker). Models based on satisfying continuity equation in the fluid, like the BIE method, can deal with cases (i) and (ii), in which very little or no air entrainment occurs, but they cannot deal with case (iii), further than the time the breaking jet impinges on the wall.

Experiments and calculations with non-breaking waves (case (i)) do not show occurrence of large impact pressures on the wall. The wave pressure and total wave force, instead, gently increase following the same pattern as wave runup on the wall. For sufficiently large incident waves, however, more complex pressure variations can be obtained, in the form of two successive pressure maxima, slightly before, and slightly after the time of maximum runup (see, results by Grilli and Svendsen 1991ab, using a BIE model and solitary waves). This double maximum is also supported by experiments. For flat impact of long waves on a vertical wall (case (ii)), calculations by CP confirmed experimental observations. Results showed, a maximum impact pressure of up to  $60\rho g d$  occurs at the wall, while a vertical jet starts forming, with

vertical velocity and acceleration of up to  $20\sqrt{gd}$  and  $8000g$ , respectively. CP also found, water compressibility does not play an important role in the process, provided no air is entrained, but suggested, wall and free surface roughness (not included in the calculations) are likely to be significant in reducing theoretical maximum pressures.

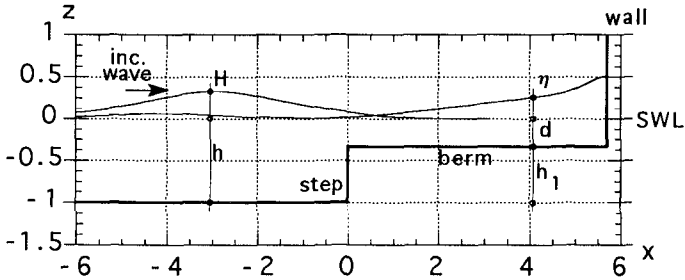


Figure 1: Sketch of a mixed breakwater, and main geometrical parameters.

In the present study, laboratory experiments are performed to measure wave impact pressure on the vertical wall of a mixed breakwater, in a similar case (ii) as above, for which incident wave front face is almost vertical at the time of impact, and there is no or very little air entrainment. Solitary waves are used as incident waves, both for simplicity, and because they are believed to have the largest impulse, impact force and runup on structures. They also represent a simplified tsunami model. Experimental results are compared with computational results obtained using the 2D fully nonlinear BIE potential model by Grilli *et al.* 1989, 1990 (GSS). Largest impact pressures on the wall are obtained for incident waves with large height to depth ratios. This was achieved in the calculations by CP, by introducing very high but quite arbitrary long waves into their model. Wave propagation over a flat bottom and impact on a vertical wall were then calculated. The present numerical model works for arbitrary geometry and incident wave conditions. Hence, this enables us to closely reproduce the experimental set-up in the numerical model (Fig. 2a), while studying a more realistic coastal structure.

## Laboratory experiments

Experiments are conducted in the 70x2x2m wave flume of the University of Cantabria. Solitary waves are generated using a computer-controlled hydraulic piston wavemaker, at one extremity of the flume. The wave generation method is similar to that of Goring 1978. The flume width is divided into two subsections, the smallest one, in which a plywood step is built on the bottom, being 0.9m wide. A vertical plate is fixed above the step, to complete the mixed breakwater. The distance from the wavemaker paddle to the breakwater step is approximately 45m. The step height is  $h_1 = 20\text{cm}$ , and the water depth in the flume is adjusted to  $h = 30\text{cm}$ , so that the step aspect ratio is  $h_1' = 0.667$  (primes denote nondimensional variables : length is divided by depth



$h$ , time by  $\sqrt{\frac{h}{g}}$ , and celerity by  $\sqrt{gh}$ ). The experimental set-up is illustrated in Figure 1.

A solitary wave is generated by the wavemaker at  $150h$  from the step, and propagates down the flume. The incident wave profile modifies its shape while propagating down the tank, mostly due to higher-order nonlinear effects not included in Goring's first-order solution (Grilli & Svendsen 1991b). The incident wave eventually stabilizes in the form of a slightly smaller solitary wave, after  $80h$  or so of propagation. Side-wall and bottom friction also lead to a small decrease in wave height. This was studied by Losada *et al.* 1989 (LVM), who found the decrease to be almost negligible when all tank surfaces are maintained smooth enough. To eliminate both of these (frictionless and friction) effects of amplitude reduction from the experimental results and thus make the comparison with the potential flow model more accurate, LVM measured incident wave height at a small distance in front of the bottom step. A similar procedure has been adopted in the present experiments, in which a solitary wave is generated in the tank, such that it has the height  $H = 9.67\text{cm}$ , or  $H' = 0.322$ , at  $x' = -7$ , where incident wave height is defined. Experiments are first realized without the vertical wall in the breakwater, thereby re-creating conditions of the study by LVM. In this case, the incident wave overturns over the step as a plunging breaker. The vertical wall is then added to the breakwater model and its horizontal position is adjusted to  $x' = 5.69$ , in order to make the incident wave impact the wall with an almost vertical front face. Hence, final length of the mixed breakwater berm is  $5.69h$ .

Water surface elevation is measured using wave gages placed at the tank center-line. Characteristics of the gages are : DHI capacitance gages type 202/60, with wave meter amplifiers 102/E (linearity better than 0.5%). Total water depth is recorded every 0.01s, over a period of about 10s for each experiment. Due to a limited number of gages (5), identical experiments are repeated several times, and gages, attached to a movable carriage, are moved to different locations until the full experimental region is covered. A one-gage overlap is maintained between successive repetitions, in order to check the repeatability of experiments. Experiments are discarded when differences in measured surface elevations are larger than 1.5mm, or 0.5% of the water depth, between two repetitions of an experiment. A very high degree of repeatability of experiments is found when applying this criterion, confirming the good control of all experimental procedures.

Flow velocities are recorded above the step, in front of the vertical wall, using a 6W LASER phase Doppler anemometer, Dantec 60x10 optical fibers, and a Dantec 58N20 particle dynamics analyzer. The positioning system is a Dantec 57H00 traversing system, that moves the optical fibers over a  $2.5 \times 2.5\text{cm}$  grid. The sampling frequency is variable, with burst detection (100-800Hz).

Dynamic pressure is measured using piezoelectric pressure gages that automatically eliminate hydrostatic pressure due to still water level (SWL). Corrected total pressure  $p$  is presented in the following. Characteristics of the gages are : transducer

type PDCR 830-201-Druck Limited, with strain amplifier DHI 106/E (linearity better than 0.1%), and the sampling frequency is 600Hz. Diameter of the pressure gages is about 15mm. The pressure is recorded at 11 locations along the vertical wall (Fig. 3), from  $z' = -0.23$  to  $z' = 0.77$ , and at 9 locations on the berm (Fig. 3), from  $x' = 4.69$  to  $x' = 5.62$ .

Experimental results are detailed in a following section.

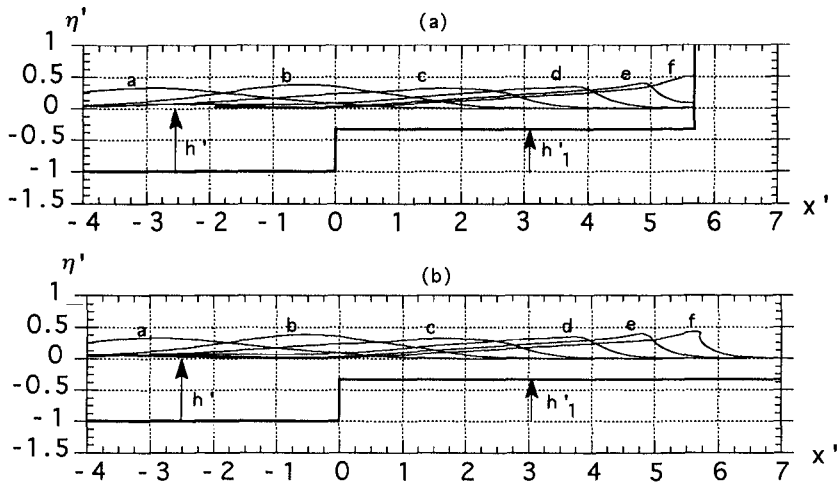


Figure 2: Computed surface elevations with  $H' = 0.322$ : (a) for the mixed breakwater, curves a-f,  $t' = 3.46, 5.73, 7.55, 9.03, 10.10, 10.70$ ; (b) for the step in the bottom, curves a-f,  $t' = 3.46, 5.70, 7.47, 8.93, 9.98, 10.77$ .

## Numerical experiments

The fully nonlinear 2D potential model by GSS, and its most recent extensions, are used in the numerical computations. In this model, continuity equation takes the form of a Laplace's equation, expressed in a BIE formulation discretized using a higher-order Boundary Element Method. Time integration is based on a second-order Taylor expansion, similar to that introduced by Dold & Peregrine 1986, expressed in a mixed Eulerian-Lagrangian representation. Both dynamics and kinematics free surface boundary conditions are exactly specified in the model, and no-flow conditions are prescribed along solid boundaries. Solitary waves are generated at the computational domain leftward boundary, as in laboratory experiments, by simulating a piston wavemaker motion according to Goring's 1978 procedure. It should be reminded, that computations based on potential flow theory are only valid up to the instant waves overturn and break, and that potential flow also implies, dissipations and flow separation cannot be modeled. Details of the numerical implementation can be found in GSS, along with a discussion of problems associated with surface piercing bodies such

as wavemakers. Details of the generation of solitary waves by a piston wavemaker are also given in Grilli & Svendsen 1990.

As already mentioned, computations closely reproduce the experimental set-up (Fig. 2a). To reduce computation time, however, the horizontal length of the computational domain in front of the berm ( $x < 0$ ) is reduced to  $20h$ , versus  $150h$  in the laboratory experiments. A solitary wave is generated in the model, and its initial height is adjusted in order to be  $H' = 0.322$ , at  $x' = -7$ , as in the experiments. The origin of time,  $t' = 0$ , for both experimental and numerical results corresponds to the instant, the crest of the incident wave crosses the point  $x' = -7$ .

Numerical data are selected to ensure good accuracy of the results, considering both the domain geometry and the incident wave condition. The discretization uses 161 nodes on the free surface, and 160 spline boundary elements. Other boundaries are discretized using 3-node quadratic elements. The total number of nodes is 256, which leads to a computing time of about 3s per time step (IBM 3090/300, including saving and postprocessing of results). The initial distance between nodes on the free surface is  $\Delta x' = 0.1606$ . Time steps are automatically selected, as in Grilli & Svendsen 1990, to ensure optimal accuracy and stability of the computations (constant mesh Courant number condition, starting with  $\Delta t' = 0.08$ ). The accuracy of the computations is checked by verifying conservation of wave mass above SWL, and total energy. With the selected numerical data, both of these stay constant to within 0.05% during most of the wave propagation. Slightly after maximum impact pressure occurs on the wall, however, a small jet starts forming at the wall (see next section), with very large vertical velocity and acceleration. Discretization nodes—identical to Lagrangian markers—tend to concentrate in this jet, and time step reduces accordingly. This makes numerical errors in wave mass and energy increase, and computations have to be stopped (shortly after the last surface profile shown in Fig. 2a). For the last computed wave profile, the time step has reduced to  $\Delta t' = 0.0012$ , and the numerical error on wave mass is 0.10%. Total number of time steps, however, is only about 300.

Computations with the step in the bottom and no vertical wall have also been made, using similar numerical data, to compare with the experimental procedure of selecting the position of the vertical wall in the mixed breakwater (Fig. 2b). Numerical results essentially agree with experiments. The incident wave overturns over the berm at  $x' = 5.56$ , with a local breaking index  $\frac{H_b}{d} = 1.31$  (curve f in Fig. 2b). Details of these computations and related problems can be found in Grilli *et al.* 1992.

Numerical results with the mixed breakwater are detailed in the next section.

## Results and discussions

Experimental and numerical results are presented and discussed in parallel in the following, for the case of Fig. 2a ( $H' = 0.322$ ).

**Free surface elevation.**— Figure 2a shows computed free surface elevations up to

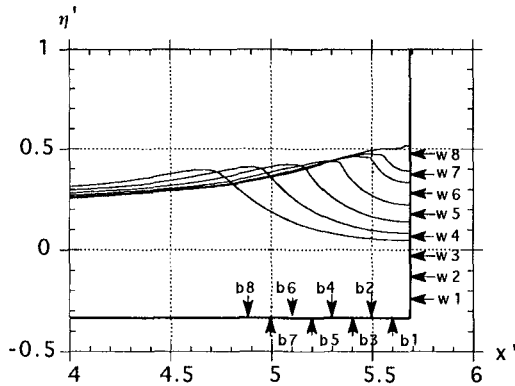


Figure 3: Blow-up of Fig. 2a, close to the wall ( $t' = 9.88, 10.10, 10.30, 10.47, 10.60, 10.65, 10.70$ , left to right), with location of pressure sensors (b1-b8) and (w1-w8).

the instant of maximum impact pressure on the vertical wall ( $t' = 10.70$ ), and Figure 3 shows a blow-up of these near the wall, over a period of 0.82 time unit.

Results in Fig. 2a show, wave height increases up to a maximum,  $H'_{max} = 0.384$  (curve b), upstream of the step, and decreases downstream of the step, to  $H'_{min} = 0.321$  (curve c). For larger  $x$ , wave height increases again, up to the instant of maximum impact on the wall. Computed free surface envelope is compared to measurements in Fig. 4. One sees, the agreement between both of these is quite good up to the step ( $x' = 0$ ). Downstream of the step ( $x' > 0$ ), the agreement is less good, and the model overpredicts maximum wave height by about 15%. This is due to energy loss by flow separation at the step, not included in the model (see LVM for detail).

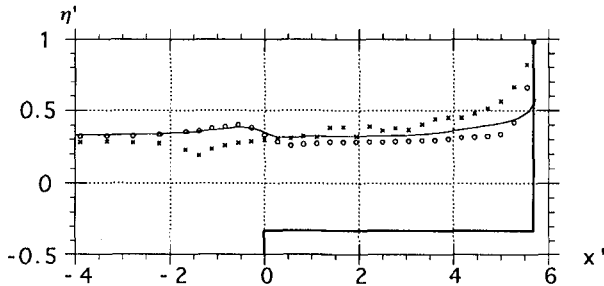


Figure 4: Free surface envelope of incident wave : (o) experimental; (—) numerical. Experimental envelope of reflected wave (x).

In Fig. 3, one also sees, a small jet starts forming close to the wall, in the last surface profile. Maximum water velocity and acceleration in the jet reach about

$20\sqrt{gd}$  and  $9800g$ , respectively, at this stage. These large values are similar to those obtained by CP, and provide a physical justification for the occurrence of large impact pressure on the wall. The internal velocity field (discussed in the next section) indeed shows, the wave flow strongly converges, in a jet-like manner, towards the upper part of the wall, while its horizontal momentum gradually transforms into vertical acceleration. This acceleration, in turn, is balanced by a large pressure gradient close to the wall (as can be seen from Euler equations).

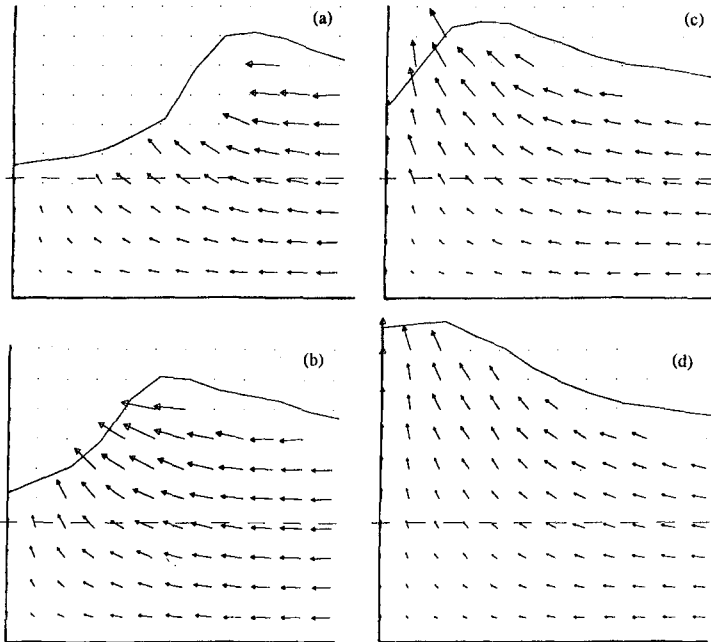


Figure 5: Internal velocity field at  $t' =$  : (a) 9.25; (b) 9.75; (c) 10.25; (d) 10.75.

**Internal flow velocity.**— Fig. 5a-d shows velocities measured over the berm. In (a), the incident wave approaches the wall with quite uniform and horizontal velocities under its crest. In (b), velocities start converging, and slightly increasing at the front face. In (c), the jet starts forming close to the wall, with vertical velocities larger than horizontal ones. From (c) to (d), a “flip through” motion occurs at the wall, i.e., the wave front face rotates, forward of a free surface point of approximate coordinates (5.23,0.42), and this upward motion has quite a large acceleration. These successive stages are also observed in calculations (Fig. 3). Maximum measured acceleration of the waterline at the wall is  $12g$ , and its maximum measured velocity is  $3\sqrt{gd}$ . Both of these occur close to stage (d). These are quite smaller, however, than the extrema found in the calculations.

**Instantaneous pressure on the wall.**— Figure 6 shows measured pressure at locations

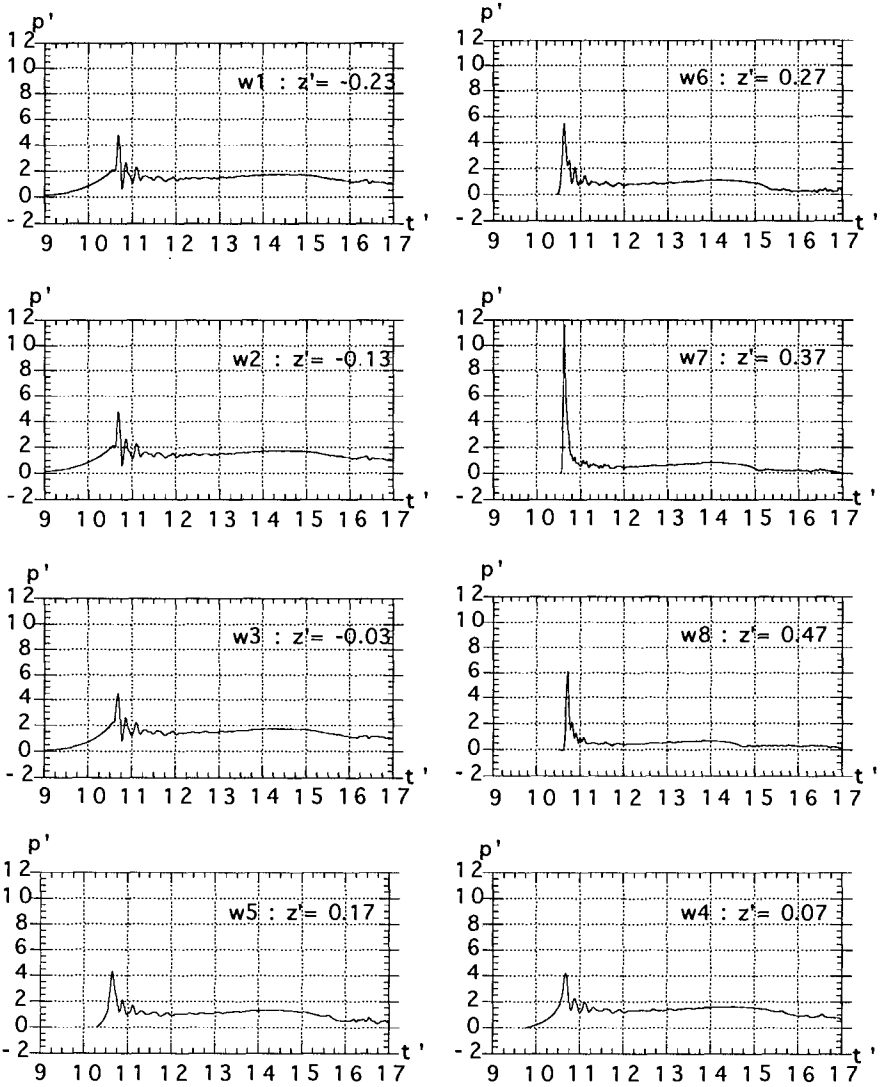


Figure 6: Pressure on the wall  $p'(t')$ , at  $x' = 5.69$ , as a function of  $z'$ .

(w1-w8) along the wall (Fig. 3). Dashes denote pressures that have been divided by the maximum pressure in still water,  $p_H = \rho g d$ . All pressure diagrams exhibit a peak of different magnitude, around time  $t' = 10.65$  (versus 10.70 in computations). This means, local pressures almost simultaneously reach their maximum, and the envelope of maximum pressure can be used to calculate the maximum impact force on the wall. This was also observed by KIR.

Maximum peak pressure is  $p'_{max} \simeq 12$ , at gage w7, i.e., at  $z' = 0.37$  above SWL. Peak pressure decreases both for larger and smaller values of  $z'$ , but stays quite constant under SWL, down to the bottom. All peak pressures are followed by small high frequency oscillations. Structural vibrations of the vertical wall model have been eliminated by using a stiff thick plate, and stiffeners. Thus, high frequency oscillations can be a sign, a small quantity of air is imprisoned between the wave and the wall during the impact. Based on pressure diagrams in Fig. 6, however, air entrainment seems to be quite minor.

**Instantaneous pressure on the berm.**— Figure 7 shows measured pressure at locations (b1-b8) on the berm (Fig. 3). All pressure diagrams exhibit a peak of decreasing magnitude when  $x'$  decreases, i.e., when moving away from the wall. Peak pressure is reached at, or close to  $t' = 10.65$ , for all locations. All peak pressures again are followed by small high frequency oscillations. Maximum peak pressure is  $p'_{max} \simeq 3.7$ , at  $x' = 5.62$ , i.e., very close to the wall.

Although it had been suggested earlier that peak pressures might be large on the bottom, it is, to our knowledge, the first time, comprehensive measurements of wave pressure on the berm of a breakwater have been made. The large impact pressures on the bottom, as far away as  $2.4d$ , require that they be considered when analyzing the berm stability, particularly for porous berms with large permeability (coarse granular media), in which significant pore pressures can transmit, and uplift isolated armour blocks. This is obviously a point for further study.

**Maximum pressure and force on the wall.**— Figure 8 shows instantaneous computed pressure distributions on the wall, for the same times as successive water profiles in Fig. 3 (solid lines). Symbols in Fig. 8 represent maximum pressure measured at each location, (w1-w9), during 9 repetitions of the experiment.

Results show, maximum computed and measured pressures reach 24 and 12 times  $p_H$ , respectively, and large pressures also occur down to the toe of the wall (as expected from Fig. 6 and 7 and discussion above). Maximum pressure is located above SWL, at  $z' = 0.39$  and  $0.37$ , in the computations and in the experiments, respectively. At these locations, the pressure increases from zero up to the maximum over  $\simeq 0.10$  time units. This can be seen from Fig. 6 for the experiments. Computed hydrostatic pressure is,  $\rho g(\eta - z) = 0.36p_H$ , at  $z' = 0.39$ , i.e.,  $1/66 p'_{max}$ . Global shape of the pressure diagram is well predicted in the numerical model. Maximum pressure, however, is overpredicted in the model. This could be due to the following few reasons : (i) the incident wave is about 15% smaller in the experiments, due to

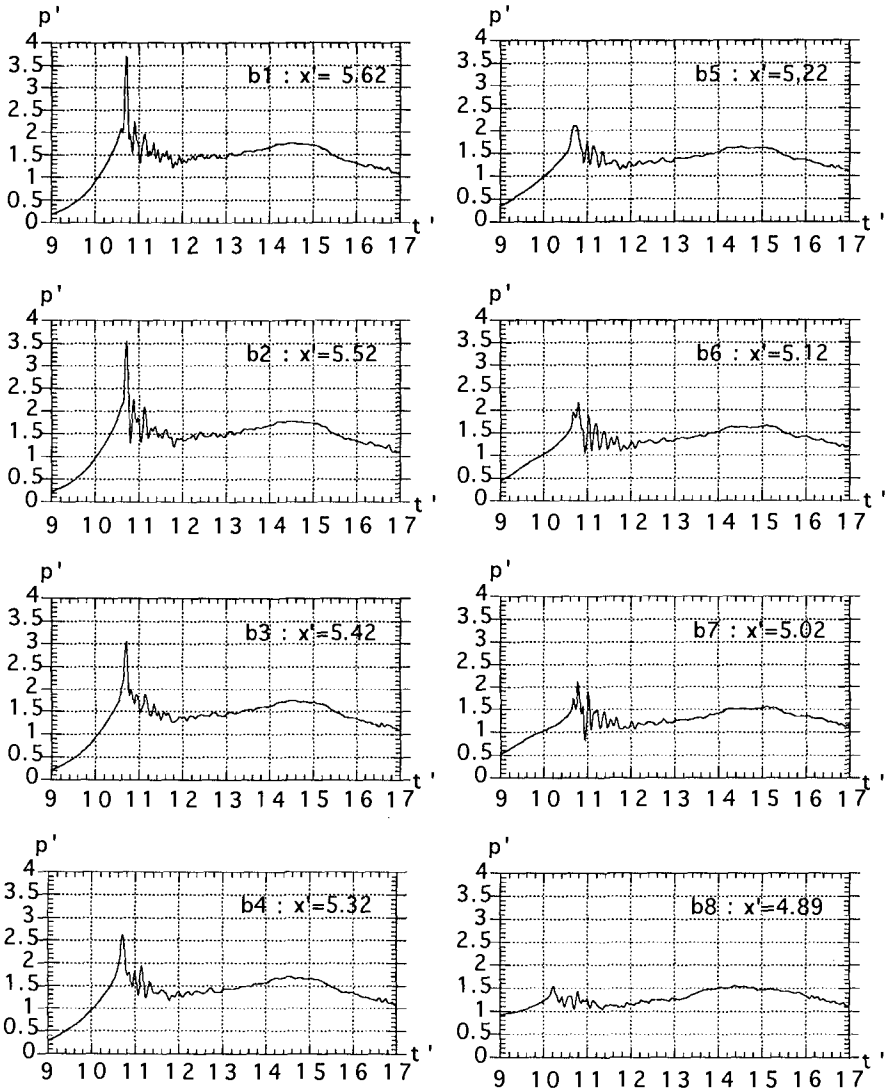


Figure 7: Pressure on the berm,  $p'(t')$ , at  $z' = -0.33$ , as a function of  $x'$ .



energy loss at the step. This leads to smaller impact pressures in the experiments; (ii) actual maximum pressures may have been "missed" in the measurements due to their very short time duration, and due to the size and location of pressure gages. The large dispersion of the measured pressure for  $z' > 0$  in nearly identical repetitions of experiments, tends to support this hypothesis; (iii) the roughness of the wall and of the free surface may limit the intensity of the jet formation in the experiments (i.e., accelerations and velocities) and, thereby, the magnitude of the maximum pressure (as suggested by CP). This is supported by the relatively low acceleration and velocity measured for the waterline along the wall in the experiments (see above).

As discussed above, maximum pressure envelope should be almost identical to instantaneous maximum pressure diagram (last solid profile in Fig. 8). Hence, it can be used for calculating maximum impact force. Figure 9 shows the instantaneous pressure force on the wall,  $F'_x$  (scaled by  $\frac{1}{2}p_H d$ ) as a function of time, in both experiments (solid line) and computations (chained line, up to maximum impact). The experimental force is simply based on integrating pressure diagrams in Fig. 6. Results show, numerical and experimental results quite well agree up to maximum impact. Computations, however, as could be expected from the pressures, overpredict maximum force.

As far as stability of the wall is concerned, Fig. 10 shows the time variation of computed force on the wall  $F'_x$ , and moment with respect to the toe of the wall  $M'_b$  (scaled  $\frac{1}{6}p_H d^2$ ), up to  $t' = 10.69$ . These are compared to hydrostatic force  $F'_{Hx}$  and corresponding moment  $M'_{Hb}$ , based on wave elevation  $\eta$  at the wall. Last force and moment shown on the figure are about 3 and 5 times larger than corresponding hydrostatic values, respectively. Peak impact pressures were obtained for a slightly later time,  $t' = 10.70$ , for which  $F'_x = 58.1$  and  $M'_{Hb} = 245.5$ , i.e. 9 and 15 times hydrostatic values, respectively.

## Conclusions

Present experimental and numerical results are bringing new light into the creation of large wave impact pressures on a vertical wall. Peak pressures on the wall have clearly been linked to a converging flow, and to the formation of a small scale jet, with large vertical velocity and acceleration. Large impact pressures have also been measured and calculated on the berm, as far away as twice the local depth from the wall. Such pressures might be of importance for the stability of porous berms. Water compressibility and air entrainment do not seem to be important factors in the present case. Computational results are well supported by experiments.

Based on these results, the numerical model can now be used for predicting wave pressure forces on breakwaters of various geometric configurations, keeping in mind the limitations of potential flow theory. Later studies will include: sensitivity analysis of impact pressure to the geometry (e.g., effect of streamlining); design implication for the sliding and overturning stability of the vertical wall, under wave impact pressure (a method based on wave impulse is being considered).

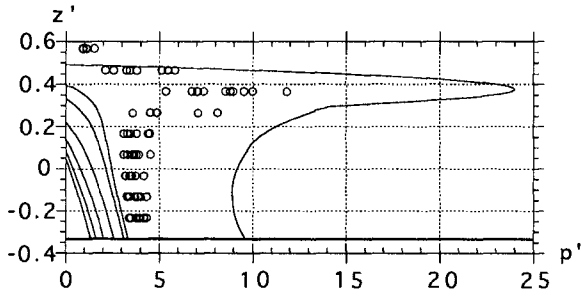


Figure 8: Impact pressure on the wall : (o)  $p'_{max}(z')$  in nine repetitions of experiments; (—) computed pressure  $p'(z')$  for surface profiles of Fig. 3.

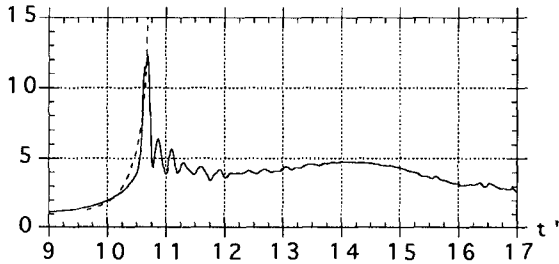


Figure 9: Impact force on the wall,  $F'_x(t')$  : (—) experiments; (- - -) computations.

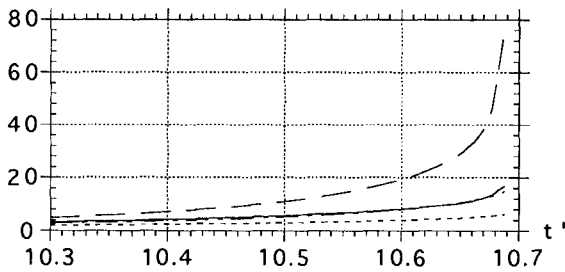


Figure 10: Computed impact force and moment on the wall : (—)  $F'_x$  total force; (- - -)  $F'_{Hx}$  hydrostatic force based on  $\eta$  at the wall; (—)  $M'_b$  total moment with respect to bottom; (- - -)  $M'_{Hb}$  total hydrostatic moment.

## Acknowledgments

The authors acknowledge financial support from the "NATO Research Grant No. CRG-901019", and the first author from the "NSF Grant No. BCS-9111827".

## References

- Cooker, M. and Peregrine, D.H. (1991) "Violent Water Motion at Breaking-Wave Impact." In *Proc. 22nd Intl. Conf. on Coastal Engineering (ICCE22, Delft, The Netherland, July 90)* Vol.1, 164-176, ASCE.
- Dold, J.W. & Peregrine, D.H. (1986) "An Efficient Boundary Integral Method for Steep Unsteady water Waves." *Numerical methods for Fluid Dynamics II* (ed. K.W. Morton & M.J. Baines), pp. 671-679. Clarendon Press, Oxford.
- Goda, Y. (1985). *Random Seas and Design of Maritime Structures*. Univ. of Tokyo Press.
- Führböter, A. (1985) "Model and Prototype Tests for Wave Impact and Run-up on a Uniform 1:4 Slope." *Coastal Engng.* **10** 49-84.
- Goring D.G. (1978) "Tsunamis - The Propagation of Long Waves onto a Shelf." *W.M. Keck Laboratory of Hydraulics and Water Resources, California Institute of Technology, Report No. KH-R-38*.
- Grilli, S, Losada, M.A. and Martin, F. (1992) "The Breaking of Solitary Waves over a Step : Modeling and Experiments" In *Proc. 4th Intl. Conf. on Hydraulic Engineering Software (HYDROSOFT92, Valencia, Spain, July 92)* (eds. W.R. Blain and E. Cabrera), Fluid Flow Modelling, pp. 575-586. CMP & Elsevier Applied Science.
- Grilli, S., Skourup, J. & Svendsen, I.A. (1989) "An Efficient Boundary Element Method for Nonlinear Water Waves." *Engineering Analysis with Boundary Elements*, **6** (2), 97-107.
- Grilli, S. & Svendsen, I.A. (1990) "Corner Problems and Global Accuracy in the Boundary Element Solution of Nonlinear Wave Flows." *Engineering Analysis with Boundary Elements* **7** (4), 178-195.
- Grilli, S. and Svendsen, I.A. (1991a) "Wave Interaction with Steeply Sloping Structures." In *Proc. 22nd Intl. Conf. on Coastal Engineering (ICCE22, Delft, The Netherland, July 90)* Vol. **2**, pps. 1200-1213, ASCE edition.
- Grilli, S. and Svendsen, I.A. (1991b) "The Propagation and Runup of Solitary Waves on Steep Slopes." *CACR, University of Delaware, Research Report 91-4*.
- Kirkgöz, M.S. (1982) "Shock Pressure of Breaking Waves on Vertical Walls." *J. Waterway, Port, Coastal, and Ocean Engng.* **108**, 81-95.
- Kirkgöz, M.S. (1991) "Impact Pressure of Breaking Waves on Vertical and Sloping Walls." *Ocean Engng.* **18** (1/2), 45-59.
- Losada, M.A., Vidal, C. and Medina, R. (1989) "Experimental Study of the Evolution of a Solitary Wave at an Abrupt Junction." *J. Geophys. Res.* **94** (C10), 14557-14566.
- Partenscky, H.-W. (1988) "Dynamic Forces Due to Wave Breaking at Vertical Coastal Structures." In *Proc. 2nd. Intl. Work. Coastal Zones*, pp. 4.1-4.15. Tech. Univ. of Athens.
- Wang, Y.X. & Su, T.C. (1992) "Numerical Simulation of Breaking Waves Against Vertical Wall." In *Proc. Offshore and Polar Engng. Conf. (ISOPE92, San Francisco, June 92)*.

## CHAPTER 89

### LOADS ON SLOPING SEADYKES AND REVETMENTS FROM WAVE-INDUCED SHOCK PRESSURES

JOACHIM GRÜNE <sup>1</sup>

#### ABSTRACT

This paper deals with detailed studies on wave-induced pressures on sloping seadykes and revetments. The presented results are found as well from extensive field measurements at the coast of the German Bight as from full - scale laboratory tests in the LARGE WAVE CHANNEL (GWK) at Hannover, Germany. Summaring the results, a generalisation of shock pressure occurrence with respect to deterministic and stochastic characteristics and a "dynamic" loading model is presented.

#### INTRODUCTION

Shock pressures occuring on sloping dyke surfaces are damped more frequently compared to those on vertical walls. Furthermore, especially under real sea state conditions, partly they are mixed with pressure components from waves and wave run-ups. This results in a more complex analysis of shock pressures.

The author has demonstrated (GRÜNE, 1988a and 1988b), that for detailed statements on the loads from shock pressures an analysis of pressure-time histories from high-speed records is necessary instead of a simple peak value analysis. A scheme for the definition of shock pressure-time history parameters ( anatomy parameters ) was presented ( Fig. 1 ) and its application was shown examplarily for compression domain with the pressure-time histories of individual breaking waves, measured in field. Furthermore first examples of some results from the anatomy parameter analysis have been presented. In this paper further results of the ongoing research work will be presented.

---

<sup>1</sup> Dipl.-Ing., senior researcher, deputy operation manager of the *Joint Institution LARGE WAVE CHANNEL ( GWK ) of the University Hannover and the Technical University Braunschweig*,  
Grosser Wellenkanal, Merkurstrasse 11, 3000 Hannover, Germany

## SHOCK PRESSURE ANALYSIS

As shown by GRÜNE (1988a and 1988b), the numberless different occurring shapes of pressure-time histories may be summarized by parameters ( anatomy parameters ) as defined in fig. 1, and divided into two domains:

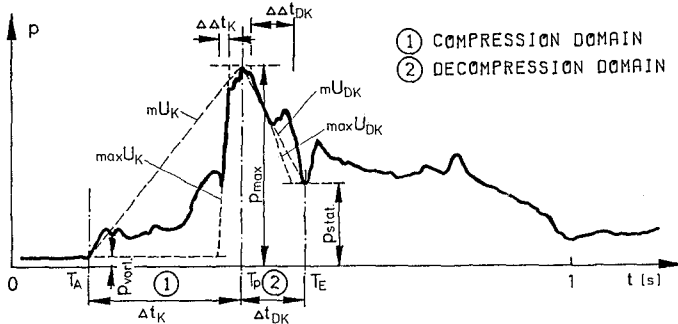


Fig. 1 Definition of anatomy parameters

- the compression domain ( Index K ) from the beginning up to the peak pressure
- the decompression domain ( Index DK ) from the peak pressure value to the minimum pressure at the beginning of the quasi-static domain, with the following anatomy parameters:

$P_{ws}$	[ $10^4$ Pa ]	- pressure at begin ( thickness of watersheet )
$P_{max}$	[ $10^4$ Pa ]	- maximum ( peak ) pressure value
$P_{stat}$	[ $10^4$ Pa ]	- min. pressure at begin of quasi-static domain
$\Delta t$	[ s ]	- total times
$\Delta \Delta t$	[ s ]	- minimum significant times
$M U$	[ $10^4$ Pa/s ]	- mean velocities
$Max U$	[ $10^4$ Pa/s ]	- maximum significant velocities

The application of this parameterizing mode is demonstrated in fig. 2 for both domains by an example of an individual shock pressure event, measured in field on a slope 1:4 in vertical steps of 9 cm. In this figure the local distributions of the anatomy parameters, analyzed from the measured pressure-time histories, are plotted versus  $\Delta D / H$  1/3, which is the vertical distance from stillwaterlevel related to significant waveheight  $H$  1/3.

From such distributons of single shock pressure events some general remarks may be stated: It is obviuos, that for the higher peak pressures  $P_{max}$  the rising times  $\Delta t$  tend to minimum values in the range of about 10 to 50 milliseconds and the corresponding rising velocities to maximum values of about 10 to 1000 m/s. Further higher peak pressures only occur, where the watersheet pressures  $P_{ws}$  are low or tends to zero, which demonstrates the wellknown damping effect of a watersheet (FÜHRBÖTER, 1986). Below the range of highest peak pressures on the dyke

COMPRESSION DOMAIN

DECOMPRESSION DOMAIN

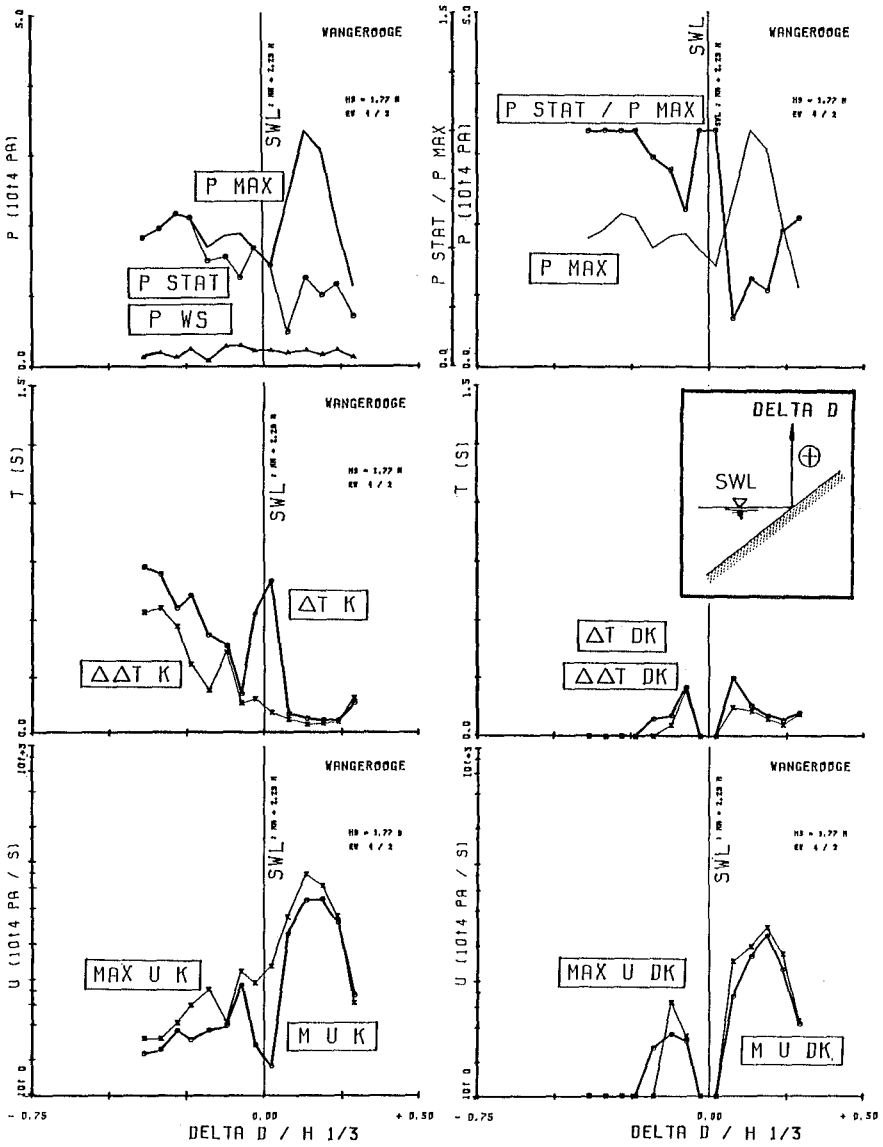


Fig. 2 Local distributions of anatomy parameters

surface, the decompression times and velocities have ( tend to ) zero values, where the pressures  $P_{stat}$  are equal to the ( tend to same value as ) the  $P_{max}$  ones.

It must be mentioned, that the selected example in fig. 2 is a typical one of the classic types and therefore it represents a certain generalisation. Nevertheless, also chaotic types show more or less similar elements, as demonstrated by GRÜNE (1988a). Thus such an analyzing method makes a distinctiveness in relation to real shock pressure occurrence possible.

### GENERALISATION OF SHOCK PRESSURE OCCURRENCE

In spite of all the different shock pressure types including the chaotic ones, it was possible to evaluate a generalized model of occurrence with respect to deterministic and stochastic characteristics. The deterministic parts of the model are represented by the local distributions of the anatomy parameters as given in fig. 3 for both domains. The x-axis  $\Delta D / H$  in fig. 3 is related to the point on the surface, where  $max P_{max}$  occur, instead of the stillwaterlevel in fig. 2. For the stochastic parts stand the superposition with the stochastic fluctuations of the anatomy parameters as shown in the following.

The local distributions in fig. 3 may be divided into five different local ranges, which in figs. 3 and 4 are marked from 1 to 5, each range represents a certain state during the wave breaking process on the slope surface ( fig. 4 ):

- Nr. 1 : This range represents the approaching steep wave front.
- Nr. 2 : At this range the steep wave front has its maximum height, which means the breaker point.
- Nr. 3 : This range gives the area between breaking wave front and the area, where the breaker tongue hits the slope surface. In this range the most chaotic pressure-time histories were found due to the enclosed air pockets with high turbulence.
- Nr. 4 : This is the range, where the breaker tongue hits the surface and thus where real significant shock pressures occur.
- Nr. 5 : This range represents the steep front of wave run-up.

Comparing the distributions of both domains in fig. 3, there are considerable differences for the time parameters. This is mainly due to the fact, that during the wave breaking process the compression times have substantial values except on the local range, where the breaker tongue hits the surface, whereas the decompression times mostly tend to zero values, either because the quasi-static pressures  $P_{stat}$  have the same magnitude as  $P_{max}$  or because the decompression shapes of the pressure-time histories have the same characteristics as the compression shape. This comes out more clearly by comparing the time distributions with the velocity distributions. Low time values and low velocity values indicate poor or no similarity between compression and decompression characteristic, whereas low times together with high

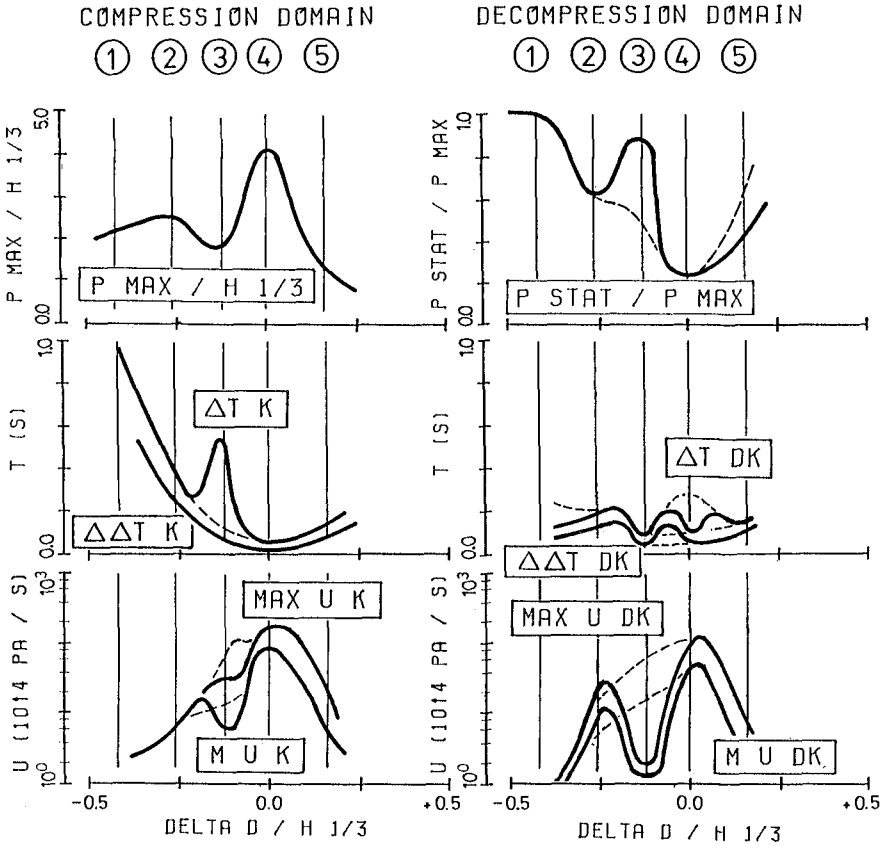


Fig. 3 Local distributions of deterministic parts of anatomy parameters

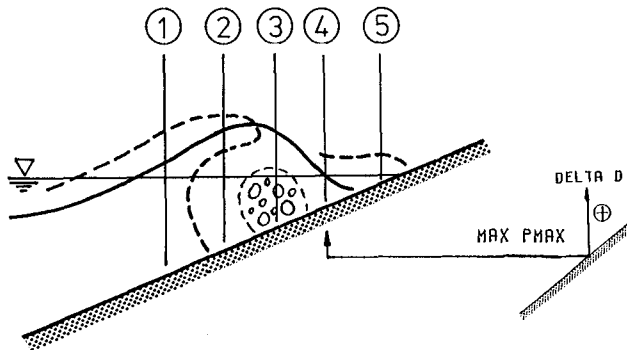


Fig. 4 Scheme of local ranges representing the wave breaking process



velocity values indicate a strong similarity between both domains. Furthermore the model demonstrates, that real shock pressures on slopes only are induced by the breaker tongue hitting on the the surface. Consequently for theoretical considerations the BAGNOLD piston model from the author's physical point of view cannot be used with respect to maximum pressure values on slopes.

### RELATIONS BETWEEN ANATOMY PARAMETERS

Due to the occurrence of numberless different shapes of pressure-time histories the data of the different anatomy parameters at a first sight spread like stars at the sky, but nevertheless there are some clear tendencies and some envelope conditions. There are many possibilities of relating the parameters among one another, in this paper all parameters are related to the peak values  $P_{max}$ .

In fig. 5 the parameter  $P_{ws}$ , which represents the thickness of the watersheet before the shock pressure occurrence, is related to  $P_{max}$ . The clear tendency comes out by the envelope curve and also by the density-distribution of the data cloud, that higher peak values  $P_{max}$  only occur with decreasing watersheet thicknesses.

Similar tendencies in dependence on higher peak values exist for some more parameters, for example in fig. 6 the time parameters  $\Delta T$  and  $\Delta \Delta T$  of both domains are plotted versus  $P_{max}$ . The ratios between both parameters gave no tendency. Differences between  $\Delta T$  and  $\Delta \Delta T$  may be found by the envelope curves and also be seen by the density distribution.

The mean velocities  $m U$  of both domains are plotted in fig. 7 versus  $P_{max}$ . The data have a wide range of spreading just as the maximum velocity ones. The ratios between the maximum and mean velocities  $max U / m U$  of both domains are given in fig. 8. From the density distribution it can be stated, that in most cases the maximum velocities are roughly in the same order of magnitude or only a few times higher than the mean velocities and furthermore, that there is less scatter for the decompression ratios. For higher peak pressures  $P_{max}$  the maximum velocity values may be roughly up to five times higher than the mean values.

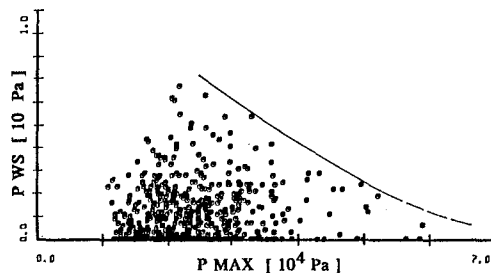


Fig. 5  $P_{ws}$  versus  $P_{max}$

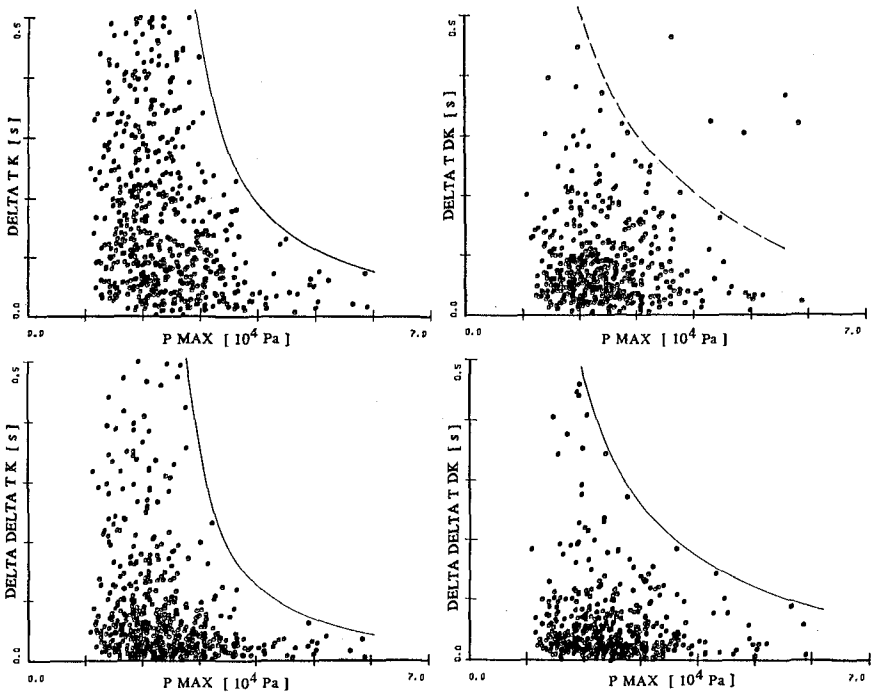


Fig. 6 Total and min. significant compression and decompression times versus  $P_{max}$

Comparisons between compression and decompression parameters are given in figs. 9 and 10. In fig. 9 the ratios for total and minimum significant parameters are plotted versus  $P_{max}$ . It is obvious, that in both domains generally the times can be shorter or longer compared to the other domain, but with higher peak pressures  $P_{max}$  the compression times decrease relatively more compared to the decompression times and thus the ratios tend to values around 1.0. The comparison of the velocity ratios

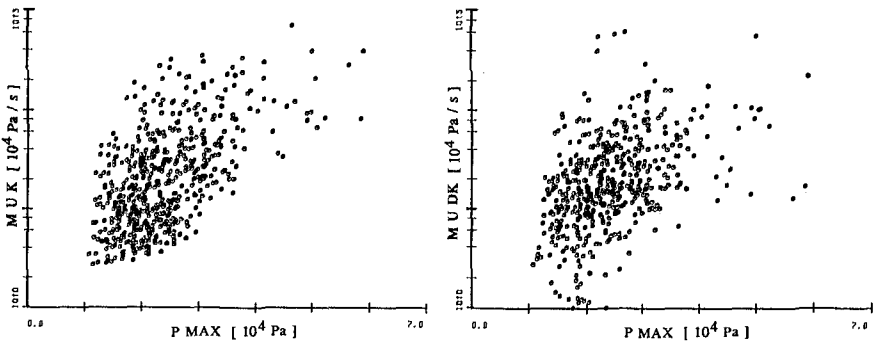


Fig. 7 Mean and maximum compression and decompression velocities versus  $P_{max}$

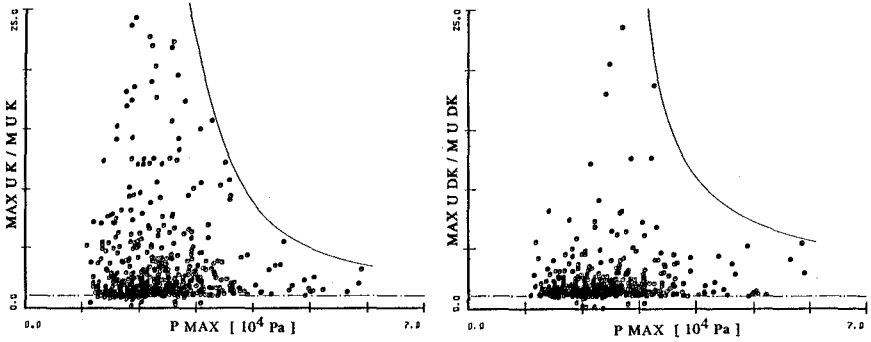


Fig. 8 Ratios between maximum and mean velocities of both domains versus *Pmax*

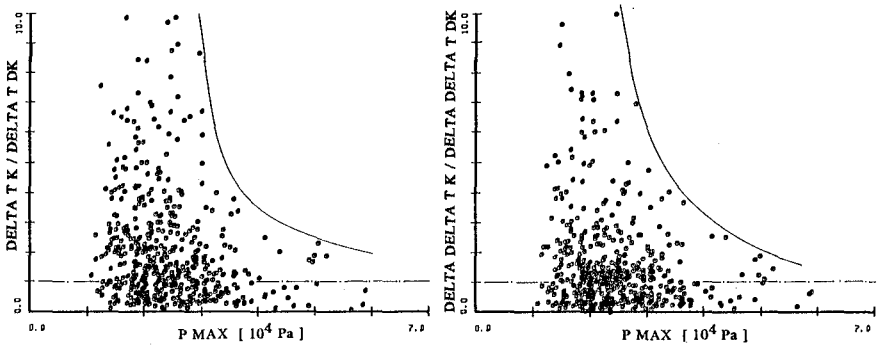


Fig. 9 Comparison between both domains for total and min. significant times

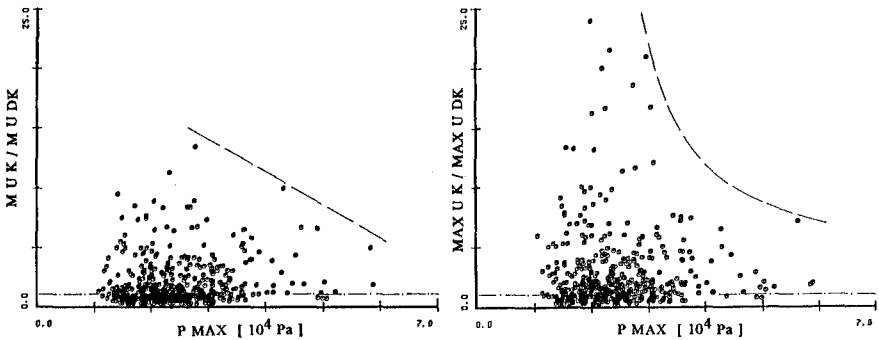


Fig. 10 Comparison between both domains for mean and maximum velocities

in fig. 10 shows more smaller ratio values for mean velocities *m U*. The density-distribution of the data indicate, that in most cases in both domains the velocity values are roughly in the same order of magnitude.

### COMPARISON OF PEAK PRESSURES FROM FIELD AND LABORATORY

The peak pressures measured in field were compared with those from large-scale laboratory tests, which have been done in the LARGE WAVE CHANNEL (GWK) of Universities at Hannover and Braunschweig, Germany (GRÜNE, FÜHRBÖTER, 1976). A research program is running since years, which includes investigations on shock pressures and wave run-up on different uniformly and combined sloped dykes. All dyke profiles have a sand core covered with an asphalt concrete layer ( same construction as used for field measurements ). The same types of shock pressure sensors and data recording systems were installed in the channel as used for the field measurements (GRÜNE, MALEWSKI, 1985). The first tests on slope 1:4 were done mostly with regular waves. The aim was to produce a collectiv of at least 200 single shock pressure events during each test for statistical considerations and to check the spatial width of pressure occurrence (FÜHRBÖTER, 1986).

For comparison of regular wave test data with field data some facts have to be considered:

- firstly one don't know, which wave height should be used. This problem is an old and suffering one, since tests were run in laboratories.
- secondly one have to notice, that regular waves have a more or less constant breaker point and thus the zone, where the breaker tongue hits the slope surface, is a rather narrow one. The thickness of the watersheets from the regular wave run-ups of the preceeding waves also are rather constant, mostly with a certain value (FÜHRBÖTER, 1986). Both conditions are contrary to irregular wave conditions, where the thickness together with the hitting zone of the breakertongue have a broad spreading characteristic. These conditions can be attenuated by the three-dimensionality of real sea state waves and by non oblique wave attack. This may result in higher

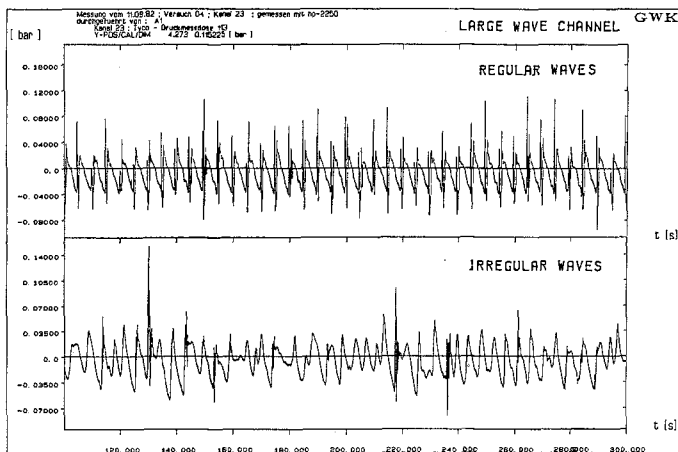


Fig. 11 Pressures on dyke surface induced by regular and irregular waves

shock pressures, if the breaker tongue of a high wave hits the slope surface at such a moment, when the watersheet is zero or tends to zero. Furthermore, as demonstrated in fig. 11 for the same pressure sensor and roughly the same waveheights, each regular wave gives a peak pressure value, which cannot be found for irregular waves. This leads to different statistical characteristics of the data (GRÜNE, 1988b).

In fig. 12 the statistical peak pressure values  $P_{99.9}$  from field and from GWK-tests with regular waves (FÜHRBÖTER, 1986) have been compared. Each value was derived from log-normal distributions of all peak pressures measured during one time interval on a slope 1:4 with all installed sensors. Both the data from field and laboratory are related to mean wave heights  $H_m$ . For all data the agreement is rather poor, but it must be mentioned, that there are also differences between the field data, due to different wave climate characteristics at the two locations. The wave characteristics of the laboratory tests were similar to those at Eiderdamm location. It is obvious,

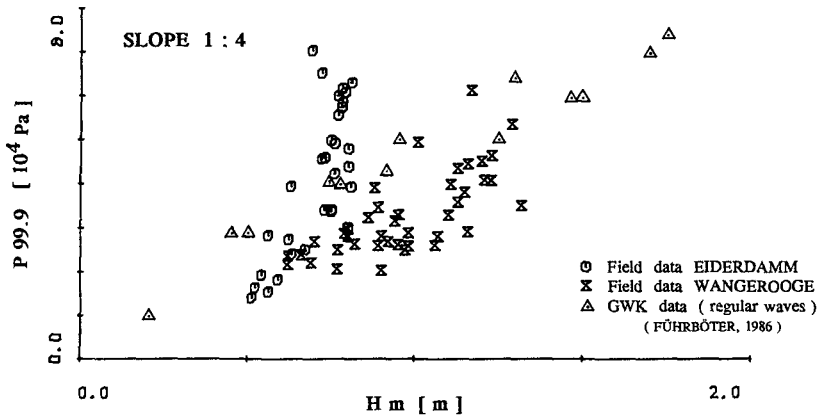


Fig. 12 Comparison between field and large scale test data with regular waves

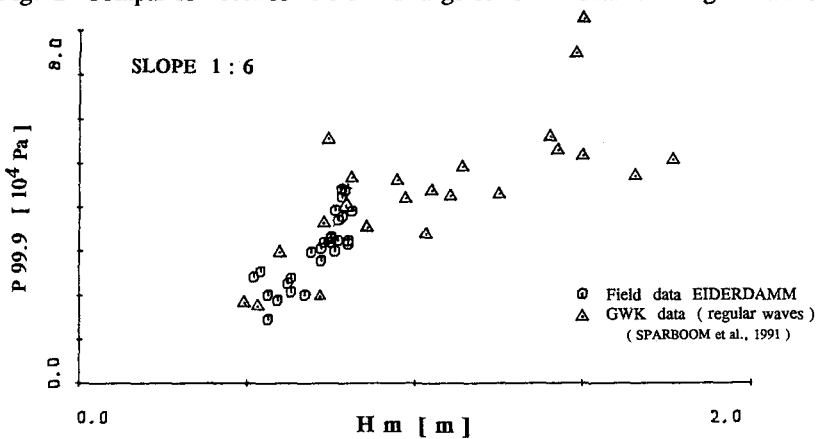


Fig. 13 Comparison between field and large scale test data with regular waves

that higher field pressure values were found. Further comparisons have shown, that even, if one relate the field data to significant waveheight  $H/3$ , there are some few higher pressure data. A comparison of field data for the slope 1 : 6 with GWK data (SPARBOOM et al., 1991) in fig. 13 shows a fairly well agreement. The differences of the GWK data between both slopes are rather small compared with those, found for field data (GRÜNE, 1988b).

Fig. 14 shows a comparison with a few GWK data, measured with irregular waves on slope 1:6. The data are as well related to mean waveheights  $H_m$  as to waveheights  $H/3$ . The agreement is much better compared to data measured with regular waves, nevertheless the laboratory data give the impression of a tendency to higher pressure values. If one use the actual measured maximum peak pressure values  $max P_{max}$  of each measured time interval or test, instead of the statistical values

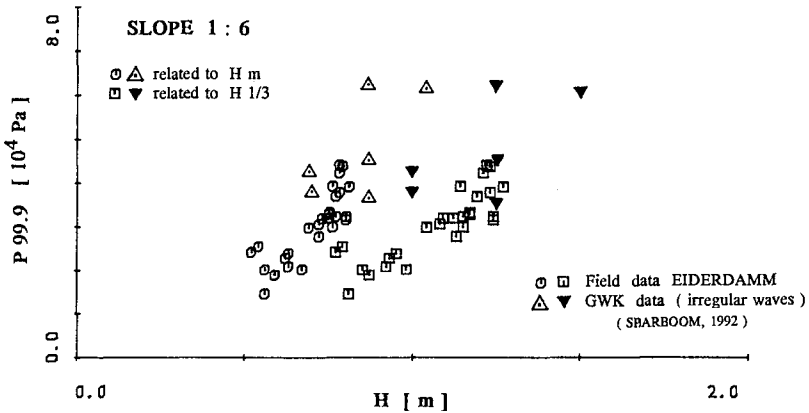


Fig.14 Comparison between field and large scale test data with irregular waves

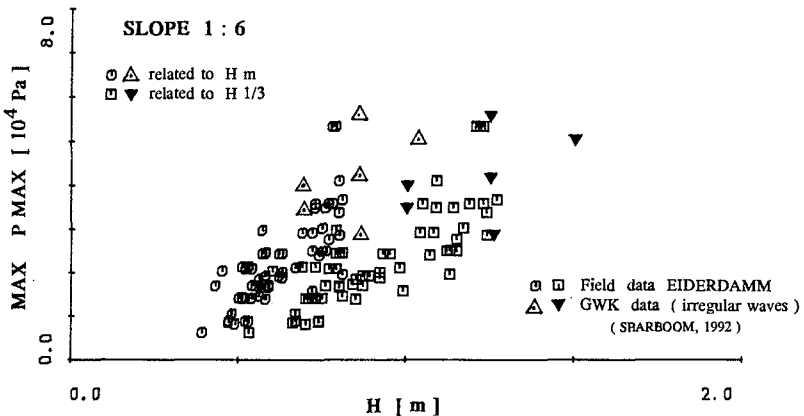


Fig. 15 Comparison between field and large scale test data with irregular waves

*P* 99.9, then the agreement between field and laboratory is quite well for these data as shown in fig. 15. Further comparisons have shown a quite well agreement with field data even for laboratory data from regular wave tests by using the *max Pmax* parameter related to *Hm*. From this results one may state, that comparison between field and laboratory data from regular waves tests both should be related to mean waveheight *Hm*, which is also the cleanest way from the definition point of view.

**A " DYNAMIC " LOADING MODEL**

A first approximation for a loading model has based on the local peak pressure parameter distributions, found for individual breaking wave events (GRÜNE, 1988b). Although the several values of these distributions have small phase lags mutually, they may give a realistic approximation of a worst-case loading model. The next developing step was, to evaluate actual synchronous pressure distributions without any phase lag from the recorded pressure-time histories.

On the lefthand in fig. 16 the pressure-time histories of one individual shock pressure event, measured with the sensors D8 to D21 in local steps on the surface, are plotted. The horizontal time axis is divided in 12 steps and for each time step the

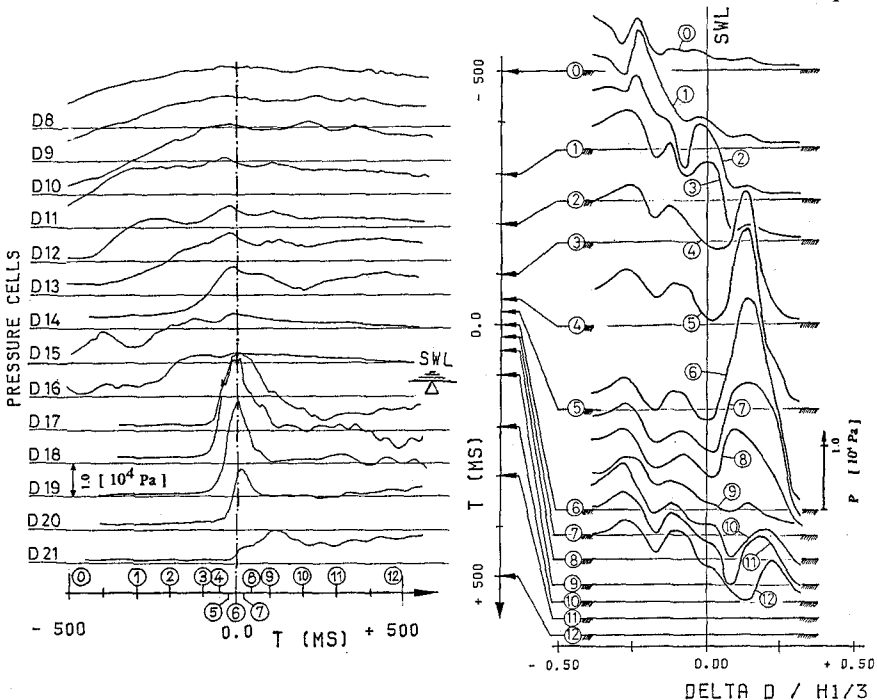


Fig. 16 Measured pressure-time histories (lefthand part) and evaluated actual pressure distributions (righthand part) for one individual breaking wave

pressure values at the certain levels were used to evaluate actual pressure distributions on the surface as plotted in the righthand part of fig. 16. There the time axis is the vertical axis, whereas the horizontal axis represents the slope surface, defined as the vertical distance from stillwaterlevel *SWL* related to  $H/3$ . From comparisons between the evaluated maximum actual pressure distributions and the local peak pressure distributions from the pressure-time histories it was found, that the actual distributions mostly are a bit narrower.

Based on such actual pressure distributions, a new version of the loading model was created, which is given in fig. 17. Compared with the first version the shape was modified with respect to linear geometrical pressure boundaries for simpler application. Each of these geometrical boundary conditions ( marked with a circled number in fig. 17 ), which are derived from the anatomy parameter results, have to be varied systematically within certain ranges ( listed in Table 1 ), to find out the

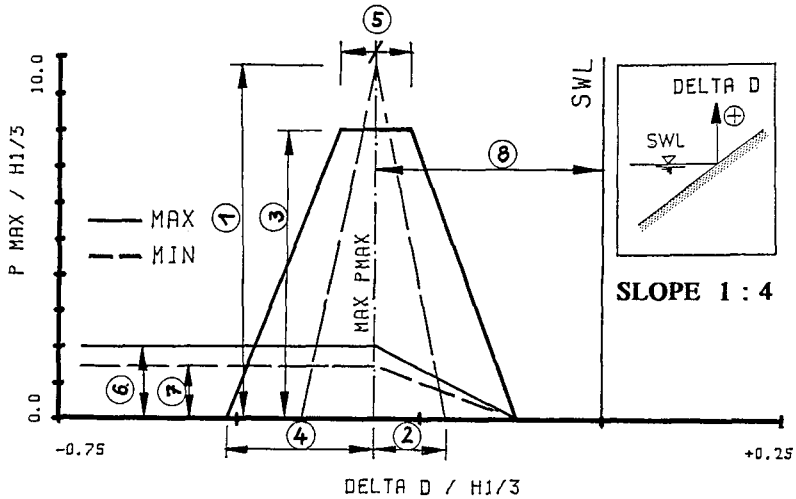


Fig. 17 "Dynamic" loading model for slope 1 : 4

			RANGE	
S	①	peakpressure	$3.0 \leq P_{max} / H1/3 \leq 10.0$	MIN
S	②	acting width	$0.10 \leq \Delta D / H1/3 \leq 0.25$	MIN
S	③	peakpressure	$3.0 \leq P_{max} / H1/3 \leq 8.0$	MAX
S	④	acting width	$0.15 \leq \Delta D / H1/3 \leq 0.30$	MAX
S	⑤	acting width	$0.05 \leq \Delta D / H1/3 \leq 0.10$	MAX
W	⑥	wavepressure	$P_{max} / H 1/3 \leq 2.0$	MAX
W	⑦	wavepressure	$P_{max} / H 1/3 \leq 1.5$	MIN
S	⑧	acting point	$-1.0 \leq \Delta D / H 1/3 \leq +0.5$	

Table 1 Ranges for boundary conditions of the loading model in fig. 17



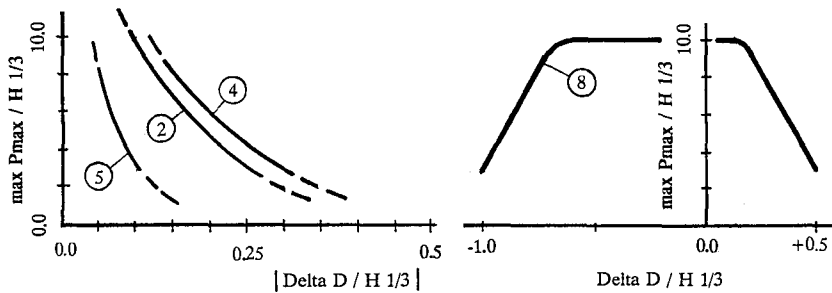


Fig. 18 Boundary conditions in dependence of  $\max P_{\max} / H^{1/3}$

worst case load. Fig. 18 shows the relations between the  $\max P_{\max} / H^{1/3}$  values and the different acting widths  $|\Delta D / H^{1/3}|$  (lefthand part) and the acting center line of the loading model related to the vertical distance  $\Delta D / H^{1/3}$  from stillwaterlevel *SWL* (righthand part). It must be mentioned, that the boundary conditions represent the worst case actual pressure distributions and thus most of recorded shock pressure events have smaller ones.

#### ACKNOWLEDGEMENTS

The research work partly was done by the SONDERFORSCHUNGSBEREICH 205 / A 1 ( supervision Prof. Dr.-Ing. Führbötter ) and has been supported by the GERMAN RESEARCH FOUNDATION ( DFG ).

#### REFERENCES

- FÜHRBÖTER, A. ( 1986 ). Model and prototype tests for wave impact and run-up on a uniform 1:4 slope. *Coastal Engineering*, 10, pp. 49-84.
- GRÜNE, J., FÜHRBÖTER, A. ( 1976 ). Large wave channel for "full-scale modeling" of wave dynamics in surf zones. *Proc. of Symp. on Modeling Techniques, San Francisco*, pp. 82-100.
- GRÜNE, J., MALEWSKI, W. ( 1985 ). Design and construction of a GWK 1:4 test slope for investigations on shock pressures and run-ups. *Technical report SFB 205/A1 ( in german )*, unpublished.
- GRÜNE, J. ( 1988a ). Anatomy of shock pressures ( surface and sand core ) induced by real sea state breaking waves. *Proc. of the Intern. Symp. on Modelling Soil-Water-Structure Interactions ( SOWAS 88 ), Delft*, pp. 261-270.
- GRÜNE, J. ( 1988b ). Wave-induced shock pressures under real sea state conditions. *Proc. of the 21st International Conference on Coastal Engineering ( ICCE '88 ), Malaga*, pp. 2340-2354.
- SPARBOOM, U., DEBUS, W. ( 1991 ). Local shock pressure distribution on a 1:6 slope in GWK (regular waves). *Technical report SFB 205/A1 ( in german )*, unpublished.
- SPARBOOM, U. ( 1992 ). Personal communication, manuscript for a *Techn. Report*.

## CHAPTER 90

### NUMERICAL MODELING FOR WAVE ENERGY DISSIPATION WITHIN POROUS SUBMERGED BREAKWATERS OF IRREGULAR CROSS SECTION

George Z. Gu<sup>1</sup> and Hsiang Wang<sup>2</sup>

#### Abstract

In the design of a porous submerged breakwater, the maximum wave energy dissipation within the breakwater is desirable. To calculate the energy dissipation, the process is simulated numerically in this study using the Boundary Integral Element Method (BIEM). The breakwater is idealized as a homogeneous porous medium and the flow inside the breakwater is modeled by a non-linear porous flow model which is linearized iteratively based on the equivalent energy principle in the numerical model. To fully explore the advantage of BIEM, a boundary integral expression for wave energy dissipation developed in an earlier work by the authors is used to replace the traditional domain integral expression. As a result, the efficiency of the numerical model is greatly increased. The numerical model was run for a number of cases and the results show that the maximum wave energy dissipation can be achieved at a practical permeability level (or stone size). The good agreement between the numerical results and the experiment data for non-breaking waves indicates that the wave energy dissipation within porous breakwaters can be adequately predicted by the numerical model.

#### Introduction

Due to increasing demand for beach protection in recreational areas, submerged breakwaters may become more and more popular over traditional sub-aerial ones. The advantages of submerged breakwaters as compared to sub-aerial ones are of low cost, aesthetics (they do not block the view of the ocean) and effectiveness in triggering early breaking of the incident waves. More general, a low crest sub-aerial breakwater may become submerged during storm surge or after being damaged.

---

<sup>1</sup>Dallas E & P Engineering, Mobil R & D Corp. 13777 Midway, Dallas TX 75244. Formerly with Coastal and Oceanographic Engineering Dept. University of Florida

<sup>2</sup>Professor, Coastal and Oceanographic Engineering Dept. of U. of Florida, Gainesville, FL, 32611

In the design of a porous submerged breakwater, one of the important aspects is to assess the energy dissipation within the structure due to turbulence and friction. Maximum energy dissipation (equivalently, minimum wave transmission) is usually desired.

The wave transmission, reflection and energy dissipation has been studied experimentally by Dick (1968), Dattatri (1978), Seelig (1980) and many other investigators. The measurements in these model tests were generally limited to the free surface oscillations on the weather and lee side of a submerged breakwater. As pointed out by Kobayashi et al. (1989), such measurements do not reveal the hydrodynamic processes over and within porous submerged breakwaters. In terms of theoretical modeling, a great deal of contributions have been made by Sollitt et al. (1972), Madsen (1974), Ijima et al. (1974), Sulisz, 1985 and others to the problem of wave interaction with sub-aerial porous breakwaters. Kobayashi (1989) successfully modeled the wave interaction with impermeable submerged breakwaters. However, the process of wave energy dissipation within porous submerged breakwaters has not been investigated thoroughly enough to guide practical designs.

In this paper, a numerical model using the Boundary Integral Element Method (BIEM) is developed to model wave interaction with porous submerged breakwaters. In general, wave attenuation over a porous submerged breakwater is affected by three mechanisms: reflection by the structure, breaking over the structure and damping due to percolation inside the porous structure. The wave energy dissipation are mainly caused by wave breaking and flow percolation. The main focus of this study is on the process of wave energy dissipation due to percolation.

The submerged breakwater is modeled as an infinitely long, shore parallel structure. The porous body of the structure is assumed to be a homogeneous porous medium, and described by the non-linear unsteady percolation model.

### Governing Equations and Boundary Conditions

The computation domain of the problem consists of two sub-domains, the fluid domain and the domain(s) of the submerged porous media (more than one porous domain if the breakwater has multiple layers). In the fluid domain, the water is considered inviscid and incompressible. The flow induced by gravity waves is assumed irrotational. Thus, the governing equation in this domain, for the velocity potential function  $\Phi$ , is the Laplace equation,

$$\nabla^2 \Phi = 0 \quad (1)$$

with fluid velocities being defined as

$$u = -\frac{\partial\Phi}{\partial x} \tag{2}$$

$$w = -\frac{\partial\Phi}{\partial z} \tag{3}$$

Further more we assume sinusoidal wave motion such that

$$\Phi = \phi e^{i\sigma t} \tag{4}$$

While in the porous domain, the viscosity of the fluid cannot be ignored since the flow is largely within the low Reynolds number region. The flow induced by sinusoidal linear waves can be described by the non-linear unsteady porous flow model used by Sollitt and Cross (1972)

$$-\frac{1}{\rho}\nabla P(x,y,z,t) = \sigma\left(\frac{1}{R} + i\beta + \frac{C_f}{\sqrt{\sigma\nu R}} |\vec{q}(x,y,z,t)|\right)\vec{q}(x,y,z,t) \tag{5}$$

or

$$-\frac{1}{\rho}\nabla p(x,y,z,t) = \sigma(f_1 + f_2 |\vec{q}|)\vec{q} \tag{6}$$

with

$$\Psi(x,y,z,t) = \psi(x,y,z)e^{i\sigma t}$$

$$f_1 = \frac{1}{R} + i\beta; \quad f_2 = \frac{C_f}{\sqrt{\sigma\nu R}}$$

where  $\Psi$  can be  $P$  or  $\vec{q}$  or any other wave field variable;  $P(x,y,z,t)$  is the pore pressure function inside porous media;  $\nu$  and  $\rho$  are the kinematic viscosity and the density of sea water, respectively;  $R$  is the permeability parameter defined as

$$R = \frac{\sigma K_p}{\nu}$$

$K_p$  is the intrinsic permeability of the porous media, measured under the conditions of steady flows; it is empirically related to particle diameter by (Engelund, 1953)

$$K_p = \frac{n^2 d_s^2}{a_0 (1-n)^3} \tag{7}$$

where  $a_0$  is an empirical constant and it is taken to be 570;  $n$  is the volumetric porosity;  $\sigma$  is the wave frequency;  $\beta$  is the inertial resistance parameter and  $C_f$  is a non-dimensional constant characterizing the non-linear resistance. In this study,  $\beta = 4.6$  and  $C_f = 1.0$ , as determined by a seabed experiment (Gu and Wang, 1990, Gu, 1990);  $\vec{q}(x,y,z,t)$  is the complex vector of discharge velocity in the porous medium.

Due to the mathematical difficulties in applying the non-linear model directly, the common practice is to linearize Eq.(6) such that

$$-\frac{1}{\rho}\nabla p = \sigma f_0 \vec{q} \quad (8)$$

where  $f_0$  is the linearized resistance coefficient which is a constant for a particular problem. This coefficient can be obtained by using the principle of equal energy dissipation, as will be discussed later. At this point, we assume that  $f_0$  is a known complex constant. Substitution of the above equation into the continuity equation gives the Laplace equation for  $p$ ,

$$\nabla^2 p = 0 \quad (9)$$

The boundary conditions for the fluid domain are:

$$\frac{\partial \phi}{\partial z} = \frac{\sigma^2}{g} \quad z = 0 \quad (10)$$

$$\frac{\partial \phi}{\partial n} = 0 \quad z = -h(x) \quad (11)$$

On the lateral boundary of lee side,  $x = l'$ ,

$$\frac{\partial \phi}{\partial n} = \frac{\partial \phi}{\partial x} = -ik'\phi \quad \text{with} \quad gk' \tanh k'h' = \sigma^2 \quad (12)$$

where  $h'$  is the water depth at  $x = l'$ .

While on the lateral boundary of weather side,  $x = -l$ ,

$$\frac{\partial \phi}{\partial n} = 2ik\phi_I - ik\phi \quad \text{with} \quad gk \tanh kh = \sigma^2 \quad (13)$$

in which  $\phi_I$  is the incident wave potential and  $h$  is the water depth at  $x = -l$ . For the porous domain(s),

$$\frac{\partial p}{\partial n} = 0 \quad \text{on impermeable surface(s)} \quad (14)$$

$$\left. \begin{aligned} \rho \frac{\partial \phi}{\partial t} &= p \\ \frac{\partial \phi}{\partial n} &= -\frac{1}{\rho \sigma f_0} \frac{\partial p}{\partial n} \end{aligned} \right\} \text{between fluid and porous domains} \quad (15)$$

$$\left. \begin{aligned} p_i &= p_j \\ \left(\frac{1}{f_0} \frac{\partial p}{\partial n}\right)_i &= -\left(\frac{1}{f_0} \frac{\partial p}{\partial n}\right)_j \end{aligned} \right\} \text{between two different porous domains} \quad (16)$$

where  $i$  and  $j$  refer to different porous domain.

Numerical Formulation of Boundary Integral Element Method

The boundary value problem stated in the previous section is solved numerically using the boundary integral element method (BIEM or BEM) owing to the irregular geometries of porous submerged breakwaters. The method has been proved to be a powerful and convenient method for problems governed by the Laplace equation.

Under the assumption of continuous and second order differentiable, the wave potential function  $\phi$  in the fluid domain  $D_1$  bounded by a closed boundary  $C_1$  can be expressed by

$$\alpha\phi(\mathbf{x}_0) = \oint_{C_1} [\phi(\mathbf{x}) \frac{\partial G}{\partial n}(\mathbf{x}_0, \mathbf{x}) - G(\mathbf{x}_0, \mathbf{x}) \frac{\partial \phi}{\partial n}(\mathbf{x})] ds \quad (17)$$

where  $G(\mathbf{x}_0, \mathbf{x})$  is a free space Green's function and  $\alpha$  is a coefficient depending on the position of point  $\mathbf{x}_0$ , ( $\alpha$  is  $2\pi$  when  $\mathbf{x}_0$  is an interior point and equals to the inner angle of the boundary when it is a boundary point);  $\mathbf{x}_0$  is a point in the domain  $D_1 \cap C_1$  and  $\mathbf{x}$  is a boundary point on  $C_1$ . The free space Green's function for normal incident wave is

$$G(\mathbf{x}_0, \mathbf{x}) = \ln r(\mathbf{x}_0, \mathbf{x}) = \ln \sqrt{(x_0 - x)^2 + (z_0 - z)^2} \quad (18)$$

Discretizing the boundary  $C_1$  into  $N$  segments, the Eq.(17) becomes

$$\alpha_i \phi_i(\mathbf{x}_{0i}) = \sum_{j=1}^N \int_{C_{1j}} \left[ \frac{\phi(\mathbf{x})}{r(\mathbf{x}_{0i}, \mathbf{x})} \frac{\partial r(\mathbf{x}_{0i}, \mathbf{x})}{\partial n} - \ln r(\mathbf{x}_{0i}, \mathbf{x}) \phi_n(\mathbf{x}) \right] ds \quad (19)$$

To evaluate the integrals, the curving segments  $C_{1j}$  are replaced by straightline segments. Each segment is then modeled by a linear element which assumes a linear variation of  $\phi$  and  $\phi_n$  over the segment. The line integration over each element can be carried out by introducing an auxiliary coordinate system (Liggett and Liu, 1983).

By applying the boundary conditions given in the previous section, Eq.(19) yields a set of linear algebraic equations with unknowns of  $\phi_i$  and  $\phi_{ni}$  ( $i=1,2, \dots N$ ). In matrix form, it can be expressed as

$$\begin{bmatrix} \mathbf{A}_1 & \mathbf{A}_2 \end{bmatrix} \begin{Bmatrix} \phi_f \\ \phi_c \end{Bmatrix} = \begin{bmatrix} \mathbf{B}_1 & \mathbf{B}_2 \end{bmatrix} \begin{Bmatrix} \phi_f \\ \phi_{nc} \end{Bmatrix} + \mathbf{b} \quad (20)$$

where  $\mathbf{A}_i$  and  $\mathbf{B}_i$  ( $i = 1, 2$ ) are the known matrices determined purely by boundary geometries,  $\phi_c$  and  $\phi_{nc}$  are the vectors of the unknown potential function and its normal derivative on the interface (common) boundary,  $\phi_f$  and  $\phi_{nf}$  are the vectors of the unknown potential function and its normal derivative along the boundaries other than the interface (common) boundary,

$\mathbf{b}$  is the known vector containing  $\phi_I$  resulting from the radiation boundary condition on the weather side lateral boundary.

In the porous domain, a similar expression can be derived by replacing  $\phi$  with  $p$  in Eq.(19). Introducing  $p_n = 0$  on impermeable boundaries and carrying out the same operations, the resulted matrix equation for  $p$  and  $p_n$  is

$$\begin{bmatrix} \mathbf{C}_{11} & \mathbf{C}_{12} \\ \mathbf{C}_{21} & \mathbf{C}_{22} \end{bmatrix} \begin{Bmatrix} \mathbf{p}_c \\ \mathbf{p}_b \end{Bmatrix} = \begin{pmatrix} \mathbf{D}_{11} \\ \mathbf{D}_{21} \end{pmatrix} \mathbf{p}_{nc} \quad (21)$$

where  $\mathbf{p}_c$  and  $\mathbf{p}_{nc}$  are the vectors of pressure function and its normal derivative along the common boundary and  $\mathbf{p}_b$  is the pressure vector on the impervious bottom of the porous domain.

Based on Eq.(21) and solving  $\mathbf{p}_{nc}$  in terms of  $\mathbf{p}_c$  by eliminating  $\mathbf{p}_b$ , a relationship between  $\mathbf{p}_{nc}$  and  $\mathbf{p}_c$  can be established

$$\mathbf{p}_{nc} = \mathbf{E} \mathbf{p}_c \quad (22)$$

with

$$\mathbf{E} = (\mathbf{D}_{11} - \mathbf{C}_{12} \mathbf{C}_{22}^{-1} \mathbf{D}_{21})^{-1} (\mathbf{C}_{11} - \mathbf{C}_{12} \mathbf{C}_{22}^{-1} \mathbf{C}_{21}) \quad (23)$$

Substitution of the matching conditions stated in Eq.(15) into Eq.(22) and then into Eq.(20) yields

$$\bar{\mathbf{A}} \phi = \mathbf{b} \quad (24)$$

with

$$\bar{\mathbf{A}} = [\mathbf{A}_1 - \mathbf{B}_1 \quad \mathbf{A}_2 + \frac{i}{f_0} \mathbf{E} \mathbf{B}_2]_{N \times N} \quad (25)$$

and

$$\phi = \begin{Bmatrix} \phi_f \\ \phi_c \end{Bmatrix}_{N \times 1} \quad (26)$$

This is a determinant equation with complex matrix elements and it can be readily solved by a complex equation solver if the linearized coefficient  $f_0$  for the resistances in the porous flow model is given. Unfortunately, it is still an unknown at this point and has to be determined by the linearization process.

#### Linearization of The Non-linear Percolation Model

The principle for the linearization is the equivalent energy dissipation by both linear and non-linear systems, i.e.

$$(E_D)_l = (E_D)_{nl} \quad (27)$$

For the energy dissipation  $E_D$  within a control volume (domain)  $V$  of porous medium during the time period  $T$ , the traditional expression (Sollitt et al, 1972, Madsen, 1974 and Sulisz, 1985) is

$$E_D = \int_V \int_t^{t+T} \vec{F} \cdot \rho \vec{q} dt dv \quad (28)$$

where  $\vec{F}$  is the dissipative resistance per unit volume of the porous medium, which is a function of the spatial coordinates and the time.

Since the domain integral in Eq.(28) is very awkward for a boundary element model, an equivalent expression in the form of boundary integration has been developed (Gu and Wang, 1991, Gu, 1990):

$$E_D = -\frac{T}{2} \int_C p^* u_n, ds \tag{29}$$

Where  $C$  is the common boundary of the fluid and the porous domains and  $p^*$  is the complex conjugate of  $p$  and  $u_n$  is the velocity normal to  $C$ , which is different for the linearized and for the non-linear systems. The ‘.’ sign is used here because  $E_D$  is considered as a positive value.

The physical explanation of Eq.(29) is that the energy dissipation inside the porous domain in one wave period  $T$  is equal to the net energy flux into the domain in the same time period. By expressing the energy dissipation in such a boundary integral, the advantage of BIEM can be well explored.

Equating  $(E_D)_l$  to  $(E_D)_{nl}$  and taking approximately  $|\vec{q}| \simeq |p_n / \rho \sigma f_0|$ , the linearized coefficient  $f_0$  can be found to be

$$f_0 = \frac{\int_C p_n p^* ds}{\int_C \frac{p_n p^*}{f_1 + f_2 |p_n / \rho \sigma f_0|} ds} \tag{30}$$

Equation (30) can be easily solved by iteration.

Numerical Results

As an example, two submerged breakwaters are computed with the model. One breakwater is made of concrete, therefore impermeable, and the other one is made of quarry stones of  $d_s = 0.4$  meters. The dimensions and the wave conditions are identical for both structures. The crest of the breakwater is 12 meters wide with 1.6 meter submergence in a water of 4.6 meters deep. The slopes are 1:1.5 on both sides. The wave envelopes and the waves at  $t=0$  are shown in Fig. 1. Comparing the two wave envelopes, it is obvious that the transmitted wave height by the permeable breakwater is less than that by the concrete one due to wave energy dissipation inside the breakwater. The dissipation is  $1.0 - K_T^2 - K_R^2 = 29\%$  of the total wave energy.

Fig. 2 illustrates the transmission and reflection coefficients for a submerged porous breakwater with a scale of 1:20 of the one in Fig. 1. In Fig. 2 the coefficients are plotted against the permeability parameter  $R$  for four



different wave heights,  $H = 2.0, 4.0, 6.0$  and  $8.0$  cm. The wave period is kept constant, at  $T = 1.2$ s. The transmission coefficient is shown to have a minimum value for each wave height for a particular stone size (around  $R \approx 1.0$ ,  $d_s \approx 1.6$  cm). A close examination of the resistances showed that this minimum transmission or maximum energy dissipation is achieved when the dissipative resistance (velocity related) is equal to the non-dissipative (acceleration related) resistance.

It can be observed in the figure that the permeability corresponding to the minimum transmission increases with increasing incident wave height, whereas the energy dissipation rate remains more or less the same. When the permeability (or equivalently the stone size) is greater than a certain value, say  $R = 10.0$  ( $\log R = 1.0$ ), the wave transmission decreases with increasing wave height. This means that larger stones are more effective for protection against storms. The curves in Fig. 2 also implies that the stone size (or permeability) should be large enough so that it will not fall to the left of the trough for the design wave height.

### Laboratory Experiment

The experiment was conducted in the Coastal Engineering Laboratory of Coastal and Oceanographic Engineering Department, University of Florida. The tank was 25 meters long, 0.6 meters wide and 1.7 meters deep with glass walls on both sides. The wave maker is of piston type furnished with an absorbing system which was designed to absorb the wave energy reflected back to the piston. The tank is also equipped with a motorized rail cart on the top to facilitate wave envelope measurements.

The model of the porous submerged breakwater was of trapezoidal shape made of river gravel of  $d_{50} = 0.93$  cm. It has the same configuration as the one shown in Fig. 1 with a scale factor of 1:20. The measurements were concentrated on wave reflection and transmission, although the wave envelope over the breakwater crest was also measured.

In the experiment, the measurements of transmission and reflection coefficients were carried out for 9 wave periods ranging from  $T = 0.642$  seconds to  $T = 1.778$  seconds with several different wave heights for each wave period. Both non-breaking and breaking waves were tested. Here 'breaking' refers to white caps over the breakwater crest, not breaking of incident waves.

It was observed in the experiment that higher order harmonics occur on the down wave side of the breakwater model, as opposed to monochromatic waves predicted by the numerical model. Fig 3 is the energy spectrum of a typical transmitted wave record. The data also showed that in general, the

wave energy of the first three modes accounts for more than 98% of the total transmitted wave energy.

In order to compare with the numerical results which is based upon the energy balance of the fundamental waves, an equivalent height for a transmitted wave was defined for the experimental data by summing the wave energy of the harmonics i.e.

$$(H_t)_{eq} = \sqrt{\sum_{i=1}^N (H_t)_i^2} \approx \sqrt{\frac{8}{\gamma} E} \quad (31)$$

where  $(H_t)_i$  is the wave height of the  $i$ -th order harmonic wave, which can be determined by the corresponding spike area of the spectrum diagram and  $E$  is the total energy per unit area of all the harmonics.

Figure 4 and 5 are the plots of the transmitted and reflected wave heights versus the corresponding incident wave heights. Also plotted are the predicted values by the numerical model. The agreement between the data and the prediction is reasonably good for transmitted waves before breaking occurs. Although the agreement for the reflected waves is not as good, it is not difficult to envision a good agreement for the energy dissipation ( $E_D = H_i^2 - H_t^2 - H_r^2$ ), because of small amplitude for the reflected waves. From Fig. 4 and 5, it is clear that the breaking occurs when the incident wave height is about  $H_i = 4.2$  cm. After the waves break over the crest, the numerical model limited to non-breaking waves apparently over estimates the transmitted wave heights. When the incident wave height is over the breaking threshold (4.2 cm for this case), the transmitted wave height in the experiment changes only slightly, if at all, with the increasing incident wave height. The reflected waves are not noticeably affected by the breaking over the crest.

In Fig. 6, the wave envelopes (normalized by the incident wave heights) predicted by the model are compared with those of measured in the experiment for the case of  $T = 0.856$  seconds; both non-breaking and breaking cases are shown. In the non-breaking case, although the measured wave envelope above the breakwater crest is shifted slightly upward, the numerical model is able to predict, with sufficient accuracy, both the variation patterns and the magnitudes of the wave heights (the distances between the two envelope profiles). Good agreement was also found for the non-breaking portion of the breaking wave cases. The upward shift of the mean water level in the data is believed to be caused by set-up over the crest.

### Conclusions

An efficient numerical algorithm using boundary integral method was developed to compute the energy dissipation inside submerged rubble-mound breakwaters of irregular cross sections. The porous flow model simulating the porous breakwaters includes both the velocity induced linear and non-linear resistances as well as the acceleration induced inertial resistance. The replacement of the domain integral expression for the energy dissipation—commonly required by the linearization of the porous flow model—by a boundary integral is a key element in achieving the efficient numerical algorithm.

The numerical results show that under a given wave condition the rate of energy dissipation in a porous structure has a well defined maximum when the dissipative (velocity related) resistance is equal to the non-dissipative (acceleration related) resistance. It is shown that porous submerged breakwaters, if designed properly, could be more effective than impervious ones with same dimensions. It is also shown that large stones (or high permeability) is more effective for protection against storms than small stones.

Laboratory experiments were also conducted under both non-breaking and breaking wave conditions. The energy dissipation and wave envelope over the crest predicted by the model agree well with the experiments for non-breaking cases and for the non-breaking portion of the breaking cases. For breaking waves, the crest submergence of the breakwater appears to play a dominant role in limiting the wave energy transmission.

### References

1. Dattatri, J., Raman, H., and Shankar, N.J., 1978, Performance Characteristics of Submerged Breakwaters, *Proc. 16th Coastal Eng. Conf.*, ASCE, 2153-2171.
2. Dick, T.M., and Brebner, A., 1968, Solid and Permeable Submerged Breakwaters, *Proc. 11th Coastal Eng. Conf.*, ASCE, 1141-1158.
3. Engelund, F., 1953, On the Laminar and Turbulent Flows of Ground Water Through Homogeneous Sand. *Trans. of the Danish Academy of Technical Sciences* **3**, No. 4.
4. Gu, Z., 1990, Water Wave Interaction with Porous Structures of Irregular Cross Sections. *PhD Dissertation, University of Florida*.
5. Gu, Z. and Wang, H, 1991, Gravity Waves over Porous Bottoms. *Coastal Engineering* **21**, 497-524.
6. Ijima, T., Chou., C.R., and Yoshida, A., 1976, Method of Analysis for Two-Dimensional Water Wave Problems, *Proc. 15th Coastal Eng. Conf.*, ASCE, 2717-2736.

7. Kobayashi, N. and Wurjanto, A., 1989, Wave Transmission over Submerged Breakwaters, *J. of the Waterways, Port, Coastal, and Ocean Engineering*, ASCE, Vol. 115, No.5.
8. Liggett., J.A., and Liu, P.L-F., 1983, *The Boundary Integral Equation Method for Porous Media Flow*, George Allen & Unwin Ltd.
9. Madsen, O.S., 1974, Wave Transmission through Porous Structures, *J. of the Waterways Harbors and Coastal Engineering Div.*, ASCE, Vol. 100, No.WW3.
10. Seelig, W.N., 1980, Two-Dimensional Tests of Wave Transmission and Reflection Characteristics of Laboratory Breakwaters, *Technical Report 80-1*, U.S. Army, Corps of Engineers, CERC., Ft. Belvoir, Virginia.
11. Sollitt, C.K., and Cross, R.H., 1972, Wave Transmission through Permeable Breakwaters. *Proc. 13th Coastal Eng. Conf., ASCE III*, 1827-1846.
12. Sulisz, W., 1985, Wave Reflection and Transmission at Permeable Breakwaters of Arbitrary Cross Section, *Coastal Engineering* Vol. 9, 371-386.
13. Wang, H. and Gu, Z., 1988. Gravity Waves over Porous Bottom. 2nd International Symp. on Wave Research and Coastal Engineering, pp. 1-21.

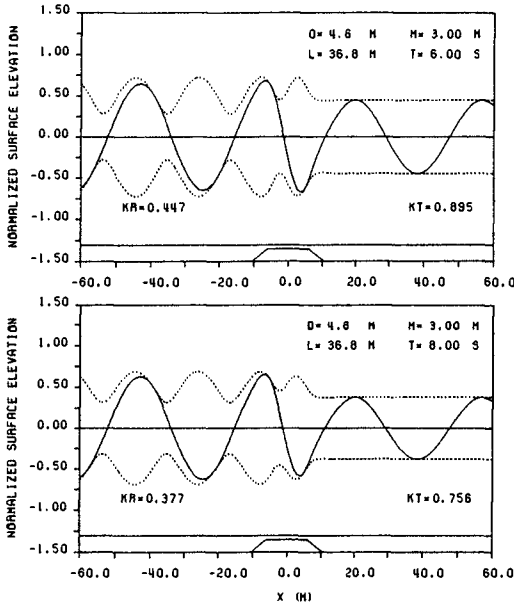


Figure 1. Wave field around Submerged breakwaters:  
 (a) Impermeable; (b) Permeable.

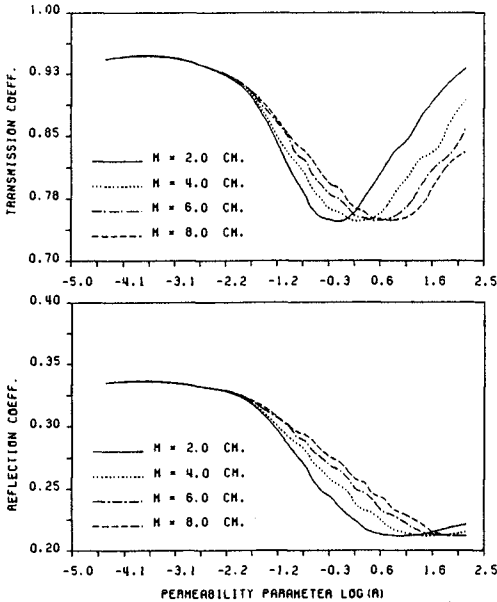


Figure 2. Transmission and reflection coefficients vs.  $R$ .  
 (a) Transmission coefficient; (b) Reflection coefficient.

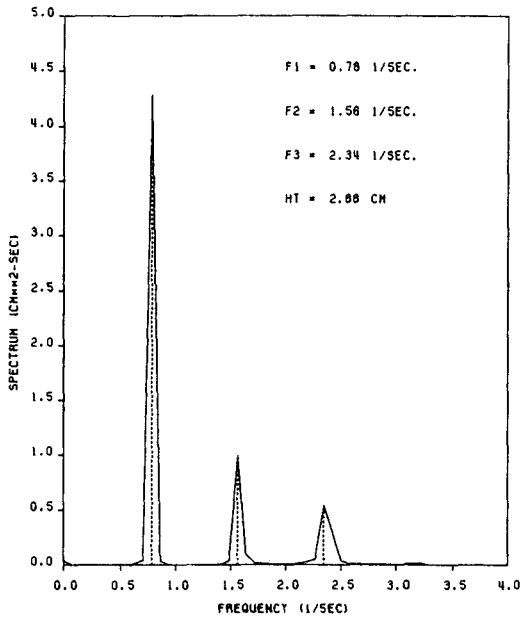


Figure 3. A typical power spectrum of transmitted waves

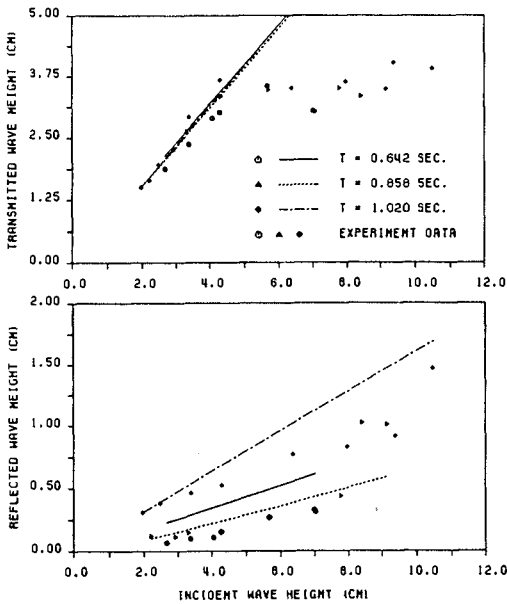


Figure 4. Transmitted and reflected wave height vs incident wave height.  
 (a) Transmitted waves; (b) Reflected waves.

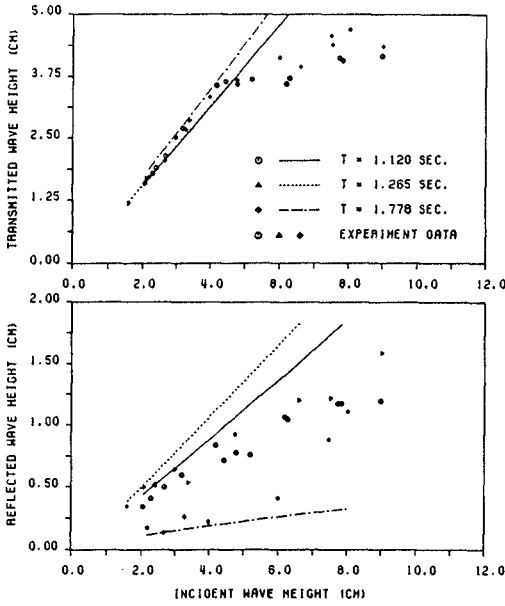


Figure 5. Transmitted and reflected wave height vs incident wave height. (a) Transmitted waves; (b) Reflected waves.

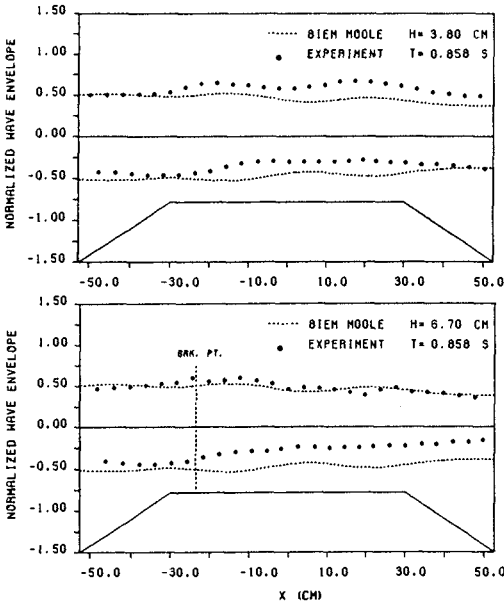


Figure 6. Comparison of measured and predicted wave envelopes. (a) non-breaking case; (b) breaking case

## SUBJECT INDEX

Page number refers to first page of paper

- Absorbers, 281, 726  
Access roads, 2745  
Accretion, 1129, 2205, 2233, 3260, 3357  
Accuracy, 212, 460, 590, 777  
Adaptive systems, 551  
Advection, 2500  
Aeolian sands, 3319  
Aerial photographs, 2332, 2450  
Aggradation, 4  
Air entrainment, 1639  
Air water interactions, 308  
Amplification, 3343  
Amplitude, 804  
Analog models, 1869  
Analysis, 267, 1414  
Analytical techniques, 737, 1341, 2122, 3343  
Application methods, 212  
Approximation methods, 644  
Armor units, 1053, 1091, 1285, 1341, 1400, 1679  
Atmospheric boundary layers, 874  
Attenuation, 563, 2786  
Australia, 240, 1129, 3319  
  
Backwashing, 2358  
Barges, 3149  
Barrier design, 1851, 2694  
Bars, 51, 2001, 2219, 2370, 2745  
Bathymetry, 391, 2242  
Bayesian analysis, 62, 281  
Beach cusps, 2205  
Beach erosion, 792, 1272, 1400, 1959, 2057, 2136, 2219, 2556, 2772, 3331, 3426  
Beach nourishment, 1129, 2043, 2265, 2464, 2474, 2581, 3305, 3319  
Beaches, 240, 630, 883, 974, 1461, 1924, 1973, 2219, 2358, 3357  
Bed load movement, 2084  
Bed movements, 2321, 2370, 2917  
Bed ripples, 2164, 2383, 2424  
Berms, 1161, 1203, 1448, 1651, 1758, 2136  
Blocks, 1091  
Boston, 3285  
  
Boulders, 1078  
Boundary conditions, 142, 644, 1030  
Boundary element method, 253, 526, 1189, 1327, 1461, 1599, 1799  
Boundary layer, 350, 2397, 2424, 2629, 2811, 3189  
Boundary shear, 1517  
Boundary value problems, 672  
Brazil, 551  
Breaking, 960, 990, 1461, 2001  
Breaking waves, 42, 89, 103, 156, 240, 253, 419, 488, 576, 698, 918, 1078, 1101, 1357, 1545, 1772, 1785, 1910, 1973, 2043, 2095, 2279, 2321, 2344, 2642, 3012  
Breakwaters, 170, 792, 1006, 1020, 1044, 1053, 1067, 1101, 1115, 1153, 1161, 1189, 1203, 1258, 1299, 1313, 1327, 1357, 1400, 1420, 1489, 1531, 1559, 1613, 1679, 1959, 3343, 3399  
Bubbles, 1639, 1785  
Buoyancy, 1867  
Buoys, 405, 1840  
  
Caissons, 1475, 1625  
Calibration, 76  
California, 1285  
Canada, 3230  
Channel improvements, 2724  
Channels, waterways, 2786, 2879, 3040  
Characteristics, 253, 281, 295  
Circulation, 2122  
Classification, 1545, 1896  
Closed form solutions, 907  
Cnoidal waves, 737  
Coastal engineering, 1  
Coastal environment, 3496  
Coastal structures, 1758, 1772, 1785, 2599, 2799  
Cohesive sediment, 3107, 3121  
Columbia River, 2893  
Comparative studies, 62, 76, 1651, 2108  
Computation, 89, 1734  
Computer models, 1420, 1448  
Computer programs, 3260  
Concrete blocks, 1573

**Vol. 1 1-1202 Vol. 2 1203-2410 Vol. 3 2411-3516**



- Consolidation, 2962
- Consolidation, soils, 2949
- Construction, 2029, 2599, 2926, 3149, 3285, 3305
- Correlation analysis, 378, 737, 946, 974
- Cost effectiveness, 1503
- Currents, 184, 563, 604, 618, 672, 684, 698, 712, 1938, 2015, 2500, 2528, 2542, 2567, 2613, 2629, 2680, 2724, 2799, 2811, 2839, 2867, 2893, 2937, 3093, 3163, 3246
- Curvature, 184
- Cylinders, 2867
  
- Damage accumulation, 1420
- Damage assessment, 1020, 1679
- Damage prevention, 1006, 1091
- Dams, 2669
- Data analysis, 1067, 1666, 1812, 1840, 1867, 1987, 2057, 2136, 2265, 2397, 2567, 2599, 2745, 2962, 3371
- Data collection, 1910, 2191, 2251
- Decomposition, 51, 526, 777
- Deep water, 184, 322, 364, 630, 658, 1231, 1625
- Depth, 4, 846
- Design, 1503, 1613, 2029, 2474, 2599, 3285
- Design criteria, 1115, 1217, 1385, 1489
- Design data, 1357, 1625
- Design improvements, 1053, 1371
- Design waves, 644, 1851
- Development, 1840
- Diffraction, 129, 1044
- Diffusion, 3202
- Dikes, 526
- Dimensional analysis, 1231
- Dispersion, 42, 2735, 2758, 3189
- Displacements, 1448
- Dissipation, 1613
- Distribution patterns, 103, 308
- Dolos, 1231, 1285, 1385
- Drainage systems, 1129
- Dredging, 2629, 2724
- Dunes, 2669
- Dynamic analysis, 1357, 1475
- Dynamic response, 1475
  
- Earthquake loads, 3343
- Ecosystems, 2710
- Efficiency, 726, 1371, 1613, 1959
- Eigenvectors, 62
  
- Elevation, 240
- Empirical equations, 1559
- Energy conservation, 1245
- Energy dissipation, 103, 308, 336, 502, 540, 563, 1101, 2786
- Energy losses, 1313, 1517, 3040
- Energy transfer, 336, 460, 526
- Entrainment, 308, 336, 2500
- Equations of motion, 76, 391, 474
- Equilibrium profile, 1973, 2556
- Equipment, 295
- Erosion, 4, 1812, 2205, 2265, 2464, 2669, 2937, 2976, 3260, 3273
- Erosion control, 1748, 2581, 3081, 3246, 3331, 3385, 3413
- Estimates, 62, 512
- Estuaries, 2542, 2745, 2879, 2962, 3054, 3121, 3371
- Evaluation, 432, 2043
- Evolution, development, 42
- Examination, 267, 1896, 2370, 3357, 3399
- Experimental data, 308, 378, 405, 447, 540, 604, 974, 1044, 1161, 1258, 1503, 1559, 1613, 1959, 2015, 2279, 2642, 2772, 2917, 3163
- Experimentation, 488, 576, 2358
  
- Failure modes, 1006
- Failures, investigations, 1053, 3343
- Fatigue, 1354
- Feasibility studies, 2581
- Fiber optics, 1327
- Field investigations, 2486, 2694, 2879, 2949
- Field tests, 240, 488, 590, 804, 832, 846, 894, 907, 946, 990, 1175, 1420, 1587, 1625, 1734, 1867, 1879, 1924, 1987, 2043, 2164, 2176, 2205, 2293, 2307, 2397, 2528, 2542, 3026, 3230
- Finite difference method, 860
- Finite element method, 1599, 1706, 2902, 3068
- Flexibility, 1613, 1748
- Flocculants, 3178
- Flood control, 1851
- Flooding, 3496
- Floods, 2917
- Florida, 2057
- Flow, 76, 2150, 2655
- Flow characteristics, 698, 3482

- Flow distribution, 1720  
 Flow patterns, 1938  
 Flow resistance, 1101, 1153  
 Flow simulation, 170, 1030  
 Fluid dynamics, 1938  
 Flumes, 142, 419, 447, 502, 818, 1067, 1142, 2108  
 Force, 1078  
 Forecasting, 116, 1826, 1865, 2057, 2176, 2242, 2293, 2513, 2825, 2902  
 France, 1414  
 Free surfaces, 89  
 Frequency, 364, 391, 832, 918, 1639  
 Frequency analysis, 156, 322, 447, 474, 846  
 Frequency distribution, 894  
 Friction, 350, 960, 1217, 2786  
 Full-scale tests, 1573, 1748, 2084  
  
 Gabions, 1748  
 Gaging stations, 295  
 Gas pipelines, 2029  
 Germany, 1573  
 Grain size, 2071, 2251, 2293  
 Gravity waves, 184  
 Great Britain, 1987  
 Great Lakes, 2976  
 Groins, structures, 2332, 3357  
 Growth projections, 2655  
 Gulf of Mexico, 2629  
 Gulfs, 712  
  
 Harbor engineering, 295  
 Harbors, 804, 832, 1044, 3081, 3216, 3230  
 Headwalls, 3426  
 Hurricanes, 644  
 Hydraulic models, 281, 1217, 1272, 1341, 1475, 1531, 1879  
 Hydraulic pressure, 1217  
 Hydraulic structures, 1693  
 Hydrodynamics, 1869, 2233, 3068, 3454  
  
 Impact forces, 1545, 1785  
 Impact loads, 1475  
 Impact tests, 1067  
 Instrumentation, 405, 1666, 2191  
 Intake structures, 3107  
 Integral equations, 142  
 Interactions, 184, 460, 604, 672, 712, 1924, 2710  
 Islands, 2450  
  
 Israel, 322, 3399  
 Italy, 1826, 1840, 1851, 1865, 1867, 1869, 3305, 3413  
  
 Japan, 2486, 3331, 3426  
 Jetties, 3040  
  
 Kinematics, 618, 644, 1327  
  
 Laboratories, 212, 281, 336, 488  
 Laboratory tests, 630, 658, 792, 883, 960, 1101, 1175, 1313, 1400, 1489, 1734, 1947, 2001, 2176, 2191, 2411, 2438, 2500, 2528, 2976, 3468  
 Lagoons, 4, 1812, 1826, 1851, 1865, 1867, 1869, 1879  
 Landfall, 2029  
 Lasers, 308  
 Least squares method, 777  
 Limiting factors, 551  
 Linear analysis, 184  
 Linear functions, 460  
 Liquefaction, 2937  
 Littoral currents, 2642, 2655, 2758, 2999, 3012  
 Long waves, 447, 792, 804, 832, 860, 883, 960, 974, 2438, 2999  
  
 Maintenance, 1006, 1693, 2745, 2926  
 Mass transport, 3093  
 Mathematical models, 502, 960, 1078, 1639, 1865, 1869, 1879, 2613, 2724, 2839  
 Measurement, 618, 792, 818, 974, 1587, 1651, 1758, 2084, 2279, 2321, 2358, 2383, 2542, 2825, 3026, 3178  
 Measuring instruments, 212, 295  
 Mechanical engineering, 1693  
 Meteorology, 116, 3496  
 Mining, 3331  
 Mixing, 1867, 2642, 2758, 2853, 2999, 3202  
 Model tests, 1020, 1115, 1231, 1245, 1434, 1489, 1545, 2669, 3454  
 Model verification, 2567  
 Modeling, 1947, 2893, 3121, 3202  
 Models, 42, 51, 116, 364, 474, 576, 698, 712, 860, 1203, 1812, 1973, 2108, 2122, 2150, 3012, 3054, 3081  
 Monitoring, 1006, 1285, 1420, 1666, 2332, 3305, 3319, 3385  
 Mooring, 3216

- Morphology, 1812  
 Mud, 2735, 2879, 2937, 2962, 3093  
 Nearshore circulation, 226, 364, 860, 2758, 2811, 2825  
 Netherlands, 2474, 2581, 2599  
 Network analysis, 1840  
 New York, State of, 3357  
 Nile River, 3246, 3260, 3273  
 Nonlinear analysis, 350  
 Nonlinear differential equations, 460  
 Nonlinear response, 156  
 North Carolina, 2219  
 North Sea, 874, 2029, 2307  
 Numerical analysis, 142, 322, 712, 1531, 2450  
 Numerical calculations, 540, 737, 946, 1161, 2424  
 Numerical models, 51, 62, 76, 89, 129, 170, 199, 350, 391, 419, 432, 526, 590, 672, 818, 874, 1189, 1299, 1599, 1651, 1772, 1799, 1840, 1938, 2057, 2150, 2344, 2411, 2438, 2513, 2556, 2825, 2879, 2949, 3093, 3107, 3305  
 Ocean disposal, 2735  
 Ocean waves, 2893, 3496  
 Offshore structures, 512, 551  
 Oil storage, 2724  
 One dimensional flow, 777  
 Optimization, 1503, 1693  
 Oregon, 2191, 2242, 2332  
 Oscillations, 502, 1639, 1826, 1865, 2655, 2990  
 Oscillatory flow, 604, 1896, 2122, 2424  
 Outfall sewers, 3285  
 Outwash, 2694  
 Overflow, 2669  
 Overtopping, 1758, 2694  
 Parameters, 765, 946  
 Particle full velocity, 212, 336, 1651  
 Pendulums, 1475  
 Permeability, 1299, 1517, 1531, 2962  
 Permeability tests, 1587, 1720  
 Perturbation, 684  
 Physical properties, 378, 1587  
 Pipelines, 2839, 2990, 3135  
 Planning, 1693  
 Pollution, 4  
 Pollution control, 3285  
 Pore pressure, 1706, 3135  
 Pore pressure measurement, 2962  
 Pore water, 2095  
 Pore water pressure, 2397  
 Porous materials, 170, 726, 1101, 1189, 1434, 1706  
 Porous media flow, 1772  
 Ports, 2926  
 Portugal, 2745  
 Potential flow, 89  
 Power plant location, 3413  
 Predictions, 474, 644, 932, 1189, 1420, 1938, 2219, 2464, 2556, 2724  
 Pressure distribution, 1545, 1599, 1706  
 Pressure measurement, 1573, 1785  
 Pressures, 1078, 1161, 1175, 2095  
 Probabilistic methods, 512  
 Probabilistic models, 540  
 Probability distribution, 103, 378, 932  
 Probability distribution functions, 2001  
 Profile measurement, 1559, 2513, 2694, 3260  
 Profiles, 2108, 2242, 2358, 2474, 3273  
 Progressive waves, 281, 684, 726  
 Prototype tests, 1067  
 Quality assurance, 1354  
 Quantitative analysis, 918, 1115, 2464, 2990  
 Random waves, 51, 447, 474, 526, 540, 630, 658, 751, 765, 883, 932, 1559, 1910, 1959, 2307, 2411, 2825  
 Rayleigh waves, 894  
 Reflection, 765, 777, 1142, 1625  
 Refraction, 129, 846, 1020, 1044  
 Regression analysis, 253  
 Rehabilitation, 1341  
 Reliability analysis, 1385  
 Research, 1987, 2937  
 Research and development, 1414  
 Resistance, 1091, 1371  
 Resonance, 751, 860  
 Rcvetmmts, 1030, 1175, 1299, 1573, 1587  
 Reviews, 2839, 2949  
 Reynolds number, 1720, 2015, 2122  
 Reynolds stress, 2424, 2853  
 Rheology, 3093  
 Risk analysis, 1341  
 Rivers, 240, 2486, 2772  
 Rock strength, 1448

- Roughness, 1758  
 Rubble-mound breakwaters, 1203, 1217,  
     1354, 1371, 1434, 1489, 1503,  
     1531, 1599, 1666, 1706, 1720,  
     1799, 3149  
 Safety analysis, 3216  
 Sand, 2599, 3331, 3426  
 Scattering, 1142, 1258, 3149  
 Scouring, 2799, 2839, 2867, 3482  
 Sea floor, 846, 2095, 2307, 2397, 2990,  
     3135, 3482  
 Sea state, 267, 512, 907  
 Sea walls, 1272, 1734, 1879, 1924  
 Seasonal variations, 2242, 2251, 2265,  
     2450  
 Sediment, 1812, 2205, 2251  
 Sediment concentration, 1910, 1947,  
     2321, 2613, 2680, 2853, 3026, 3202  
 Sediment discharge, 3054, 3202  
 Sediment transport, 832, 1272, 1865,  
     1896, 1910, 1947, 1973, 1987,  
     2015, 2071, 2084, 2108, 2150,  
     2164, 2176, 2191, 2307, 2344,  
     2370, 2411, 2450, 2486, 2500,  
     2513, 2528, 2542, 2567, 2613,  
     2629, 2669, 2680, 2867, 2879,  
     2902, 2917, 3121, 3189, 3273, 3385  
 Sedimentation, 2724, 2949, 3081  
 Sedimentology, 3399  
 Settling velocity, 2853, 3107, 3202  
 Shallow water, 267, 322, 364, 460, 818,  
     1613, 3068  
 Shear, 618, 684, 2642, 2655, 2999, 3189  
 Shear strain, 3163  
 Shear stress, 604, 672, 2164, 2176,  
     2917, 3012, 3093, 3107  
 Shearing, 184  
 Ship motion, 3216  
 Ships, 3216  
 Shoaling, 51, 199, 432, 460  
 Shore protection, 1272, 1414, 1879,  
     2710, 3413  
 Shoreline changes, 2233, 2265, 2332,  
     2772, 2976, 3246, 3273, 3305,  
     3399, 3413  
 Silts, 2879, 2926  
 Simulation, 62, 199, 576, 1101, 1142,  
     1772, 2307, 2902  
 Simulation models, 42, 405, 1531  
 Site selection, 2926  
 Skewness, 974  
 Slopes, 488, 1461  
 Solitary wave, 1161, 1327, 1461  
 South Africa, 3026  
 Spain, 2043, 2233, 2251, 2265, 3385  
 Spectral analysis, 364, 765, 777, 792,  
     1973  
 Spectral density function, 42  
 Speed changes, 199  
 Spits, coastal, 2233, 2694  
 Splitting, 658  
 Stability, 751, 1020, 1030, 1053, 1067,  
     1153, 1217, 1231, 1400, 1559,  
     1625, 1666, 1799, 2095, 2581, 3135  
 Stability analysis, 129, 658, 1573, 1679,  
     2071  
 Stability criteria, 1203, 2799  
 Stabilization, 1129, 2556, 3319, 3426  
 Static stress measurement, 1285  
 Stationary processes, 932  
 Statistical analysis, 512, 1231, 1545,  
     1924, 2474, 3149  
 Stones, 1354  
 Storm surges, 1851  
 Storms, 116, 990, 1748, 2136, 2370,  
     2450  
 Stratification, 2853  
 Stream function, 684  
 Stress, 1053  
 Stress analysis, 874  
 Stress measurement, 1385  
 Structural design, 1285, 1385, 1414  
 Structural failures, 1203  
 Structural materials, 170  
 Structural response, 1371  
 Structural stability, 1115  
 Structures, 765  
 Submerged jets, 1161  
 Submerging, 253, 1142  
 Subsidence, 4  
 Superstructures, 1217, 1489  
 Surf beat, 804, 846, 960  
 Surf zone, 76, 103, 156, 226, 308, 336,  
     576, 590, 698, 818, 832, 883, 918,  
     990, 1987, 2095, 2279, 2293, 2321,  
     2344, 2370, 2438, 2542, 2642,  
     2680, 2811, 2999, 3012, 3026  
 Surface properties, 563  
 Surface roughness, 1720  
 Surface waves, 405, 658, 3135, 3163  
 Surge, 874  
 Surveys, 2043, 2450, 2567, 3026  
 Surveys, data collection, 1129, 2029,

- 2136, 2219, 3260  
Suspended load, 1091, 2411  
Suspended sediments, 2150, 2279, 2293,  
2438, 2680, 3189
- Testing, 1354  
Tests, 226, 364, 447, 1910, 2383  
Theories, 737, 1258, 1313, 1693, 2071,  
2735, 2772, 2867, 3468  
Three-dimensional analysis, 3482  
Three-dimensional flow, 3454  
Three-dimensional models, 1679  
Tidal currents, 3054  
Tidal hydraulics, 1826  
Tides, 4, 3178, 3371  
Tides, astronomical, 1826  
Time dependence, 391, 419, 2464, 2513  
Topography, 129, 860  
Tracers, 2084  
Transformations, 51, 156, 474, 540, 630  
Transient flow, 142  
Transition points, 698  
Transport phenomena, 3068  
Transport rate, 2528  
Trenches, 2902  
Trends, 3371  
Turbidity, 1938, 2735, 3121, 3178  
Turbulence, 2279, 2383, 2424, 2629,  
2758, 2853  
Turbulent flow, 1517  
Turkey, 3081
- Undertow, 883, 2164  
United Kingdom, 2694, 3178, 3371  
Uplift pressure, 3135  
Uplift resistance, 1573  
U.S.S.R., 1357
- Validation, 1448, 3468  
Vector analysis, 2344  
Vegetation, 2710  
Velocity, 350, 604, 618, 672, 1078,  
1799, 1947, 2084, 2321, 2383,  
2486, 2990, 3054  
Velocity distribution, 883, 1153, 2811,  
3482  
Venezuela, 2724  
Verification inspection, 2867  
Vertical cylinders, 3482  
Videotape, 918  
Vortex shedding, 3163  
Vortices, 502
- Water circulation, 3068  
Water depth, 726, 832  
Water flow, 502, 1865, 1869  
Water level fluctuations, 1666  
Water pressure, 1666  
Water surface, 576  
Water table, 1129, 2136  
Water tanks, 2191  
Wave action, 1030, 1203, 1420, 1599,  
1706, 1799, 1896  
Wave attenuation, 1517  
Wave climatology, 267  
Wave crest, 199, 488  
Wave damping, 3040  
Wave diffraction, 419, 432  
Wave dispersion, 1434  
Wave energy, 336, 502, 1189, 1434,  
2528  
Wave forces, 1313, 1357, 1400, 1489,  
1639, 3454  
Wave generation, 818, 990, 2893, 3468  
Wave groups, 894, 907, 932, 946, 990,  
1503, 2411  
Wave height, 103, 253, 378, 512, 576,  
630, 751, 804, 894, 946, 1245,  
1734, 2001, 2486, 3230, 3385  
Wave measurement, 226, 322, 551,  
2205, 3230  
Wave propagation, 89, 129, 142, 226,  
391, 447, 460, 563, 658, 792, 1020,  
1044, 1142, 1153, 1461, 2500,  
2786, 2893, 3040  
Wave reflection, 630, 1299, 1327  
Wave refraction, 419, 432  
Wave runup, 156, 1245, 1299, 1461,  
1734, 1758, 1772  
Wave spectra, 378, 405, 590, 751, 765,  
2001  
Wave tanks, 226, 526  
Wave velocity, 2358  
Waves, 1175, 1258, 2015, 2071, 2542,  
2567, 2613, 2629, 2710, 2799,  
2811, 2839, 2937, 2976, 3093,  
3246, 3454, 3468, 3496  
Weather forecasting, 116  
Wind, 907  
Wind forces, 3496  
Wind speed, 1245  
Wind waves, 712  
Working conditions, 3230

## AUTHOR INDEX

Page number refers to first page of paper

- Abecasis, F., 1006  
Adami, Attilio, 1869  
Ahrens, J. P., 1354  
Alexis, Alain, 2949  
Allsop, N. W. H., 1599  
Andersen, O. H., 1020  
Arami, Atsusi, 1785  
Asano, Toshiyuki, 1896, 2710
- Baird, W. F., 1354  
Bakker, W. T., 2599  
Bale, A. J., 3178  
Barbaro, Giuseppe, 907  
Barkaszi, Stephen F., Jr., 1910  
Basco, David R., 103, 1924  
Bassoullet, Philippe, 2949  
Battjes, J. A., 42, 51  
Baumer, Joe, 103  
Bedford, Keith, 2629  
Beji, S., 42, 51  
Bellessort, B., 1414  
Bellomo, Douglas A., 1924  
Benoit, Michel, 62  
Berlamont, Jean, 2962  
Bertotti, Luciana, 116  
Bezuijen, Adam, 1030, 1587  
Bishop, Craig, 2976  
Blondeaux, Paolo, 2071  
Boccotti, Paolo, 907  
Boer, Sander, 3305  
Booij, N., 1044  
Bowers, E. C., 832  
Bradbury, A. P., 2694  
Breteler, Mark Klein, 1030  
Brocchini, M., 76  
Broekens, R. D., 1772  
Broeze, Jan, 89  
Brooks, P., 3285  
Brørs, Bård, 1938  
Bruce, T., 212, 2990  
Burcharth, H. F., 1354, 1720  
Burcharth, Hans F., 1489  
Burcharth, Hans F., 1053  
Bürger, W. W., 1067
- Cai, Maolong, 103  
Caielli, Alfredo, 1869  
Capobianco, Michele, 2464
- Carrion, Vicente, 3385  
Carson, Fulton C., 3357  
Carvalho, J. L. B., 551  
Castañeda, Ana, 3385  
Cavaleri, L., 1840  
Cavaleri, Luigi, 116  
Ceconi, Giovanni, 1869  
Chae, Jang Won, 129  
Chang, C., 1327  
Chen, Zhiwen, 1947  
Cheung, Kwok Fai, 142  
Chiaia, G., 1959  
Chian, Chimin, 3189  
Chow, K. Ander, 3230  
Chung, Yeong Chyang, 308  
Church, J. C., 2999, 3012  
Chyan, Jih Ming, 308  
Collado, F., 2811  
Converse, H. D., 1354  
Cooker, M. J., 1078, 1639  
Coppoolse, R. C., 3026  
Costa, Fernando Vasco, 1091  
Cox, D. T., 2397  
Cox, Daniel T., 156  
Cramp, A., 974, 1987  
Creed, Christopher G., 1973  
Cruz, Eric C., 1101  
Cuena, G., 2043
- Dally, William R., 1910  
D'Alpaos, L., 3068  
Dalrymple, R. A., 3468  
Dalrymple, Robert A., 1142, 1973, 3040  
Damiani, L., 1959  
d'Angremond, Kees, 1748  
Davidson, D. D., 1354  
Davidson, M., 974  
Davidson, M. A., 1987  
Davies, B. L., 1115  
Davis, Greg A., 1129  
De Boni, M., 1840  
De Girolamo, Paolo, 1851  
de Groot, M. B., 2599  
de Jager, Jan H., 1748  
de Lange, P. H. M., 1044  
De Rouck, J., 1666  
de Ruig, Joost H. M., 2581  
de Vriend, Huib J., 2150

- De Vriend, Huib J., 2464  
 de Waal, J. P., 1758  
 de Wit, P. J., 2937  
 Dean, R. G., 3260  
 Dean, Robert G., 2001  
 Debus, Wolf, 1573  
 Deguchi, Hiroshi, 2710  
 Deguchi, Ichiro, 1517, 2642  
 Deigaard, R., 576, 2344  
 den Adel, H., 1720  
 Dennis, W. A., 2332  
 Di Silvio, G., 1865, 1867  
 Dibajnia, Mohammad, 2015  
 Dodd, Nicholas, 2655  
 Drago, M., 76  
 Drapeau, G., 3054  
 Driscoll, Andrew M., 1142  
 Dumais, J. F., 3054  
 Dyer, K. R., 3178
- Easson, W. J., 618, 2990  
 Edge, B., 1354  
 Eide, A., 2029  
 Eidsvik, Karl J., 1938  
 Eisenberg, Y., 3285  
 Elgar, Steve, 846  
 Elwany, M. Hany S., 3273  
 Elzinga, Th., 3216  
 Endoh, Hiroshi, 1625
- Fanos, A. M., 3246, 3260  
 Fernández, A. J., 2043  
 Ferrante, Andrea, 3305  
 Fischer, M., 170  
 Fisher, J. S., 2332  
 Foote, Y., 974  
 Foster, Emmett R., 2057  
 Foti, Enrico, 2071  
 Fournier, Charles P., 3230  
 Franco, Leopoldo, 1879, 3305  
 Fredsøe, J., 2344, 2839  
 Fujima, Koji, 2450  
 Funke, E. R., 3454
- Gallagher, E. L., 2084  
 Galland, J. C., 2853  
 García, Reinaldo, 2724  
 Garzon, A., 3068  
 Gerber, Marius, 184  
 Goda, Yoshimi, 199  
 Gökçe, K. Tunç, 3081  
 Golik, A., 322
- Golik, Abraham, 3273  
 Gomez-Pina, G., 1679  
 Gordon, Angus D., 3319  
 Graber, H. C., 405  
 Grass, Tony J., 604  
 Graw, Kai-Uwe, 1153  
 Greated, C. A., 212  
 Greated, Clive A., 502, 2358  
 Grilli, S. T., 1461  
 Grilli, Stéphan T., 1142, 1161  
 Grüne, Joachim, 1175  
 Gu, George Z., 1189  
 Güler, İşikhan, 3081  
 Günbak, A. Rıza, 3081  
 Guza, R. T., 846
- Habara, Shin, 3426  
 Hall, Kevin R., 1203, 1217  
 Hamanaka, Ken-ichiro, 2424  
 Hamilton, David G., 1217  
 Hamm, Luc, 226, 2108  
 Hansen, C. P., 551  
 Hansen, E. A., 2344  
 Hanslow, David J., 240, 1129  
 Hara, Masanori, 253  
 Hardisty, J., 974, 1987  
 Harris, J. M., 2307  
 Hashida, M., 3331  
 Hatada, Yoshio, 267  
 Hatanaka, K., 2095  
 Hattori, A., 2095  
 Hattori, Masataro, 1785  
 Hayashi, Kenjiro, 2450  
 Hedegaard, Ida Brøker, 2108  
 Herbers, T. H. C., 846  
 Hibbert, Kevin, 1129  
 Hirakuchi, H., 281  
 Holman, R. A., 918  
 Holmes, P., 1448  
 Holthuijsen, L. H., 1044, 2893  
 Holtzhausen, A. H., 1231  
 Horikawa, Kiyoshi, 1734, 2122  
 Howell, Gary L., 295  
 Hughes, S. A., 1354  
 Huntley, D., 974  
 Huntley, D. A., 1987, 3178  
 Hurdle, David, 1851  
 Huynh, Trien N., 3093  
 Hwung, Hwung Hweng, 308
- Ikeno, M., 281  
 Imai, Sumio, 894

- Imberger, J., 1867  
Inman, D. L., 322  
Inman, Douglas L., 3273  
Iosilevskii, Ya. A., 322  
Iovenitti, L., 76  
Iribarren, J. R., 3216  
Irie, Isao, 2879  
Isaacson, Michael, 142  
Isobe, Masahiko, 419, 590, 765, 1101, 3093  
Ito, Kazunori, 751  
Iwata, K., 1400  
Iwata, Koichiro, 336
- Jaffe, Bruce, 2680  
Jensen, O. J., 3216  
Jeong, Shin Taek, 129  
Jorissen, R. E., 1693  
Juang, Jea-Tzyy, 1245  
Juhl, J., 170, 1020  
Jui, J., 1272
- Kaczmarek, Leszek M., 350  
Kaihatu, James M., 364, 1973  
Kajima, R., 281, 1531  
Kaku, Shuji, 1559  
Kakuno, Shohachi, 1258  
Kamphuis, J. W., 1272  
Kanayama, Susumu, 3107  
Kang, Yoon-Koo, 1503  
Karlikow, Nancy, 3121  
Kashiwagi, Mikio, 2438  
Katayama, Hiroyuki, 883  
Katoh, Kazumasa, 990, 2136, 2879  
Katoh, Ken, 2735  
Katopodi, Irene, 2150  
Katsui, Hidehiro, 2867  
Kawasaki, Masahiko, 3426  
Kawata, Yoshiaki, 2164, 3426  
Kendall, Thomas R., 1285  
Khafagy, A. A., 3246, 3260  
Khafagy, Ahmed A., 3273  
Kim, H., 2307  
Kim, Jong-Wook, 1503  
Kimura, A., 378  
Kimura, Akira, 3149  
Kirby, James T., 364, 391, 474  
Kitou, Nikos, 2150  
Kiyokawa, Tetsushi, 1613  
Kjeldsen, S. P., 405  
Klammer, P., 1475  
Klatter, H. E., 1693
- Klopman, G., 1772  
Kobayashi, Nobuhisa, 156, 1299, 1559, 2710  
Kobayashi, Tomonao, 3482  
Kochergin, Alexander D., 2176  
Kohlhase, S., 1475  
Komar, P. D., 3246  
Komatsu, T., 3331  
Kondo, Kosuke, 804, 894  
Kostense, J. K., 960  
Kos'yan, Ruben D., 2176  
Kotake, Yasuo, 419  
Kranenburg, C., 2937  
Kraus, Nicholas C., 630, 2191, 2219, 3357  
Kriebel, D. L., 1115  
Kriebel, David L., 1313, 1973  
Kroon, Aart, 2613  
Kubo, Yasuhiro, 419, 804  
Kuiper, H., 1693  
Kurata, K., 1400  
Kuroki, Keiji, 2205
- Lahousse, B., 2029  
Larson, Magnus, 2219  
Latteux, B., 2500  
Laurence, D., 2853  
Lavallée, D., 3054  
Le Hir, Pierre, 2949, 3121  
Lechuga, Antonio, 2233  
Lee, Changhoon, 391  
Lee, J. J., 1327  
Lee, Jongkook, 2629  
Lee, Jung L., 432  
Liang, Guoxiong, 2242  
Liberatore, Gianfranco, 447  
Ligteringen, H., 1341  
Lima, J. M., 551  
Lin, Li-Hwa, 2513  
Lippmann, T. C., 918  
List, Jeffrey H., 860  
Liu, C. C., 726  
Liu, Philip L.-F., 1258  
Liu, Zhou, 1053  
Losada, I. J., 2251, 2786  
Losada, M. A., 1679, 2251, 2786  
Losada, Miguel A., 1161, 2265
- Madsen, P., 576  
Madsen, Per A., 460  
Magda, Waldemar, 3135  
Magoon, O. T., 1354



- Malherbe, B., 2029  
 Mannino, Lucio, 907  
 Mansard, E. P. D., 1679, 3454, 3468  
 Mansard, Etienne, 142  
 Mansour-Tehrani, Mehrdad, 604  
 Marchi, Enrico, 4, 1869  
 Marinski, J. G., 1357  
 Martin, Francisco, 1161  
 Mase, H., 2397  
 Mase, Hajime, 474, 540  
 Mastenbroek, C., 874  
 Matsumi, Yoshiharu, 3149  
 Matsunaga, N., 3331  
 Matsunaga, Nobuhiro, 3163  
 McCabe, J. C., 3178  
 Medina, Josep R., 1371  
 Medina, R., 1679, 2251  
 Medina, Raúl, 2265  
 Medina Villaverde, José María, 2233  
 Mei, Chiang C., 3189  
 Melby, Jeffrey A., 1285, 1385  
 Memos, Constantine D., 3343  
 Mercanti, M., 2029  
 Miao, Gang, 2513  
 Miles, M. D., 3468  
 Miller, H. C., 2332  
 Mizuguchi, M., 488  
 Mizutani, N., 1400  
 Mizutani, Suguru, 2122  
 Mocke, G. P., 2279, 3026  
 Mol, A., 1812  
 Monadier, P., 1414  
 Mori, Nobuhito, 751  
 Morrison, Iain G., 502  
 Mulcahy, Michael W., 3230  
 Muraca, Alessandro, 1420  
 Murakami, Kazuo, 2879  
 Muttray, M., 1434  
  
 Nadaoka, K., 51  
 Nadaoka, Kazuo, 526, 2867  
 Naffaa, M. G., 3260  
 Nairn, Rob, 2976  
 Nakamura, Kazuo, 2293  
 Nakamura, Satoshi, 990  
 Nersesian, Gilbert K., 3357  
 Nicholls, Robert J., 2464  
 Nicholson, John, 2108  
 Nielsen, Peter, 240, 1129, 3202  
 Nishi, Ryuichiro, 2293  
 Nnadi, Fidelia N., 2917  
 Noli, Alberto, 1851  
  
 Norton, P. A., 1448  
  
 Ochi, Michel K., 512  
 O'Connor, B. A., 2307  
 Oda, Kazuki, 1258  
 Oebius, H. U., 2307  
 Ohta, T., 378  
 Ohyama, T., 51  
 Ohyama, Takumi, 526, 1613  
 Okayasu, Akio, 883, 2438  
 Oliveira, I. B. Mota, 2745  
 Oltman-Shay, J., 2999  
 Omata, Atsushi, 1613  
 Ono, Masanobu, 2642  
 O'Reilly, W. C., 846  
 Organizing Committee of the 23rd  
 International Conference on Coastal  
 Engineering, 3496  
 Osborne, Philip D., 2321  
 Ostrowski, Rafal, 350  
 Otta, Ashwini, 1461  
 Oumeraci, H., 1357, 1434, 1475, 1545,  
 1706  
 Overton, M. F., 2332  
  
 Pae, Wi-Gwang, 540  
 Parchure, Trimbak M., 2001  
 Parente, C. E., 551  
 Parle, Patrick, 3371  
 Partenscky, H. W., 1067, 1434, 1475  
 Partenscky, H.-W., 1545  
 Passacantando, Giancarlo, 1851  
 Pechon, Philippe, 2108  
 Pedersen, C., 2344  
 Pedersen, Jan, 1489  
 Peña, Carlos, 3385  
 Peregrine, D. H., 1078, 1639  
 Peregrine, D. Howell, 818  
 Petit, H. A. H., 960, 1772  
 Petrillo, A., 1959  
 Petti, Marco, 447, 792  
 Pina, G. Gómez, 2043  
 Pita, C., 1006  
 Pollock, Cheryl, 1924  
 Powell, K. A., 2694  
 Powell, Keith A., 2358  
 Protonotarios, John N., 3343  
 Pruszek, Zbigniew, 2370  
 Putrevu, Uday, 2758, 2825  
  
 Quinn, Paul A., 2358

- Rakha, K. A., 1272  
 Ramírez, J. L., 2043  
 Ramos, F. Silveira, 1341  
 Ranasoma, K. I. Mahesha, 2383  
 Rasmussen, Chris, 391  
 Rasmussen, E. B., 170  
 Rauw, C. I., 1354  
 Refaat, Hossam El-din A. A., 2772  
 Rigter, Ben, 1587  
 Rodriguez, A., 2811  
 Roelse, Piet, 2581  
 Roelvink, J. A., 960, 2108  
 Roldán, A. J., 2786  
 Roldan, Antonio J., 2265  
 Ropert, F., 1414  
 Rosen, D. S., 322  
 Rosen, Dov S., 3399  
 Rossi, Vito, 1420  
 Ruffin, T. M., Jr., 1400  
 Ruol, Piero, 792  
 Rusconi, A., 1840  
 Russell, P., 974  
 Russell, P. E., 1987  
 Ryu, Cheong-Ro, 1503  
  
 Saito, Eiichi, 2799  
 Sakai, T., 2095, 2397  
 Sakai, Tetsuo, 540  
 Sakakibara, Yukio, 253  
 Sakakiyama, T., 1531  
 Sallenger, Asbury, Jr., 2680  
 Sampaio, R. M., 551  
 Sánchez-Arcilla, A., 2811  
 Sato, Michio, 563, 2205, 2293  
 Sato, Shinji, 2411  
 Sato, Yukio, 2424  
 Sawaragi, Toru, 1517, 2642  
 Sayao, Otavio J., 3230  
 Schäffer, H. A., 576  
 Schäffer, Hemming A., 460  
 Schmidt, R., 1545  
 Schoonees, J. S., 3026  
 Sekimoto, Tsunehiro, 804, 894  
 Seymour, R. J., 2084  
 Seymour, Richard J., 2242  
 Shibano, Teruo, 3426  
 Shibayama, Tomoya, 2438, 2799  
 Shigemura, Toshiyuki, 2450  
 Shimizu, T., 281  
 Shimizu, Takuzo, 590, 804, 894, 3107  
 Shinohara, Tomoaki, 2205  
 Shirai, Toru, 2164  
  
 Shuto, N., 672  
 Shuto, Nobuo, 2486  
 Silva, P., 1812  
 Simonin, O., 2853  
 Simons, Richard R., 604  
 Skafel, Michael, 2976  
 Skjelbreia, James E., 777  
 Skyner, D. J., 212, 618  
 Sleath, J. F. A., 2383  
 Sloth, P., 1020  
 Smidt, H.-J., 1067  
 Smith, A. W. Sam, 1354  
 Smith, Ernest R., 630  
 Smith, G. G., 2279, 3026  
 Smith, Jane McKee, 2191, 2825  
 Smith, W. Gray, 1559  
 Sobey, Rodney J., 644  
 Sollitt, Charles K., 2191  
 Sørensen, Ole R., 460  
 Southgate, Howard, 2108  
 Sparboom, Uwe, 1573  
 Srinivas, Rajesh, 2001  
 Stansberg, C. T., 658  
 Steetzel, Henk J., 2669  
 Stive, Marcel J. F., 2464  
 Stoutjesdijk, Theo, 1587  
 Sulisz, Wojciech, 1799  
 Sumer, B. M., 2839  
 Sun, Z. C., 1599  
 Supharatid, S., 672  
 Svendsen, Ib A., 1461, 2758, 2825  
 Swan, Christopher, 684  
  
 Takahashi, Shigeo, 1625  
 Takehara, Kosei, 3163  
 Tanaka, H., 672  
 Tanaka, Hitoshi, 2486  
 Tanaka, Masahiro, 1613  
 Tanimoto, Katsutoshi, 1625  
 Teatini, P., 1865  
 Teisson, Ch., 2853  
 Teisson, Charles, 2949  
 Thieke, R. J., 698  
 Thornton, E. B., 2999, 3012  
 Thornton, Edward B., 2655  
 Tolman, Hendrik L., 712  
 Tomasicchio, Giuseppe R., 1879, 3413  
 Tomasicchio, Ugo, 1  
 Tomita, Takashi, 336  
 Toorman, Erik, 2962  
 Topliss, M. E., 1639  
 Tørum, Alf, 1651

- Toue, Takao, 2867  
Treadwell, D. D., 1354  
Tsuchiya, Yoshito, 2164, 2556, 2772, 3426  
Tsuruya, Hiroichi, 2879  
Turk, George F., 1385  
Twu, S. W., 726
- Uda, Takaaki, 1613  
Ueda, Y., 2397  
Ueki, Kazuhiro, 3107  
Ukai, Akiyuki, 590  
Uliana, Fiore, 3413
- Valera, Eduardo, 2724  
Van Damme, L., 1666  
van den Berg, Egbert J. F., 1748  
Van den Bosch, Lut, 2962  
van den Bosch, P., 1772  
van der Lem, J. C., 1341  
van der Meer, J. W., 1758, 1772  
van Gent, Marcel, 1651  
van Rijn, Leo C., 2613  
van 't Hoff, J., 2599  
van Vledder, Gerbrant Ph., 946  
Verhagen, Henk Jan, 2474  
Verhagen, L. A., 2893  
Vermeir, D., 1666  
Verwoert, H., 2599  
Vidal, C., 1679, 2251  
Vidal, Cesar, 2265  
Viguier, J., 1414  
Villaret, C., 2500  
Villoria, Carlos, 2724  
Vincent, Christopher E., 2321  
Visser, Paul J., 2669  
Vithana, S. Opatha, 2902
- Vittori, Giovanna, 1826  
Vrijling, J. K., 1693
- Walsh, G., 3054  
Wang, Hsiang, 432, 1189, 2513  
Watanabe, Akira, 419, 765, 1101, 2015, 2528, 3093  
Watson, Gary, 818  
White, Thomas E., 2242  
Whitehouse, Richard J. S., 2542  
Wibbeler, H., 1706  
Williams, A. F., 1599, 1720  
Williams, J. J., 2307  
Wilson, Kenneth C., 2917  
Winterwerp, J. C., 2599  
Won, Y. S., 2893  
Wong, Y. K., 2307  
Wurjanto, Andojo, 156, 1299
- Yamaguchi, Masataka, 267, 737  
Yamamoto, Yoshimichi, 1734  
Yamashita, Takao, 2556, 3426  
Yan, Yixin, 2926  
Yanagishima, Shin-ichi, 2136  
Yasuda, Takashi, 253, 751  
Yauchi, Eiji, 2735  
Yen, Kai, 2926  
Yokoki, Hiromune, 765  
Yu, Ke, 932
- Zeidler, Ryszard B., 2370  
Zelt, J. A., 777  
Zhuang, F., 1327  
Zimmermann, C., 1434  
Zwamborn, J. A., 1231  
Zyserman, Julio A., 2567

## CHAPTER 91

### Two Dimensional Effects in Modelling Berm or Reshaping Breakwaters

Kevin R. Hall  
Department of Civil Engineering  
Queen's University  
Kingston, Ontario, Canada

#### Introduction

In recent years, the failure of many large conventional type breakwater structures has led to a careful examination of the physical processes of wave-structure interaction. Although naturally armouring structures, which gain their stability as a consequence of profile readjustment due to wave action, have been around in various forms for hundreds of years, the high incidence of failure of conventional structures has led to their increased use in the past decade.

The interaction of an incident wave with a rubblemound breakwater results in complex flow patterns involving unsteady non-uniform flow (Hall (1987)). In most cases, it is desirable to construct a breakwater which works in harmony with the flow field; that is to construct a structure with a geometry and armour stone weight gradation which results in natural profile readjustment and subsequent minimization of the applied hydrodynamic loadings.

A reshaping or berm breakwater can be described as a mound of rock, often comprised of a wide range of stone sizes, which undergoes reshaping as a result of wave-structure interaction. As a consequence of this wave action, a stable profile is developed. Two major processes occur in the development of the stable profile. First, the overall geometry of the structure responds to the nature of the hydrodynamic loadings. Material is sorted and redistributed into a profile which acts to minimise the applied forces by altering the flow field kinematics. Secondly, this natural sorting leads to consolidation (densification) of the armour layer as stones that move eventually find voids into which the

nest.

This type of structure has been used extensively in the past decade and it has been found that these structures are significantly less expensive than more conventional breakwaters designed in accordance with guidelines given in design manuals such as the US Army Corps of Engineers Shore Protection Manual. The armour stones required are smaller than those required by conventional stability formulae and a much wider gradation can be used. This allows for the design to be based on the actual quarry output rather than some pre-conceived specification for stone for which a quarry must be found. Experimental studies have indicated that the reshaped breakwater profile can be closely predicted for the design wave conditions and the available material properties. This profile can be used as an initial design. Currently model studies are used to optimize the design and minimise the cost.

Limited research on the two dimensional stability of these breakwaters has been undertaken in the past decade; and although virtually no research has been undertaken with respect to the three dimensional stability of these structures, Hall et al. (1983), Hall (1987), and Burcarth and Frigaard (1987) have shown that significant three dimension effects can exist. These effects may be classified as purely three dimensional effects (due to attenuation of energy within the cross section) or effects resulting from the variation of the angle of wave attack, thus affecting the erosion prone areas (particularly the head of the breakwater). The later effects are typically what is thought of as being dominant; however, Hall et al. (1983) has shown that the difference between test results from narrow flumes and wider three dimensional test sections (for incident waves parallel to the trunk of the structure) can be substantial. The tests reported in this paper were designed to evaluate these effects, in particular to evaluate if the reshaping of these breakwaters is influenced by the flume width used in the tests.

#### Testing Programme

Experimental studies were undertaken using the facilities of the Coastal Engineering Research laboratory of Queen's University, Kingston, Canada. The studies were undertaken primarily to investigate the mechanism of reshaping of berm breakwaters and to evaluate the specific influence of the various parameters that may affect the reshaping process. These parameters include

wave height, wave period, wave groupiness, duration of each segment of the design storm, the gradation of the armour stones, and the percentage of rounded stones occurring in the gradation.

Tests were run in a 22 x 26 metre three dimensional basin where three separate "flumes" having widths of 1.2, 2,4 and 4.0 metres were constructed parallel to each other. Identical test structure were built in each of the flumes and were then subjected simultaneously to the same wave conditions. Basin layout is shown in Figure 1.

Profiles of the test breakwaters were measured at several locations along the structure following each segment of the design storm as shown in Figure 1. The profiler used to measure the three dimensional profiles was a trailing arm profiler which provided a continuous reading of the elevation of the breakwater with horizontal distance.

Tests undertaken in the three dimensional modelling programme utilized a core material shown in Figure 2. Two different gradations of armour were used having the following characteristics:

	$D_{50}$ (mm)	$D_{85}/D_{15}$	$D_{max}$ (mm)
Gradation 1	19	1.9	32
Gradation 2	14	2.0	27

Tests were undertaken on a berm breakwater whose general configuration is shown in figure 3. The basic geometry of the test structure was determined based on the large number of berm breakwaters tested at various institutions in Canada and abroad. This configuration has been found to be easy to construct in prototype. Five capacitance type water level transducers were placed just in front of the breakwater to measure the dynamic water level fluctuations. An additional water level transducer was placed immediately in front of the paddle to measure the deep water wave conditions.

Preliminary work was done before the breakwater was built to synthesize, generate and sample the waves and determine the appropriate span settings (settings that control the maximum excursion of the wave paddle) for the wave paddle. All the tests in subsequent experiments were then carried out using the same waves and same span settings. Additionally, the wave records measured during tests with the breakwater in place were separated into

incident and reflected components. In most cases, excellent agreement was obtained between results of the reflection analysis and those measured with no structure in the flume. The bounded long wave component resulting from the occurrence of wave groups was removed from the analysis using a software filter.

All tests were conducted with irregular waves synthesized using the GEDAP procedure of the National Research Council of Canada Hydraulic Laboratory. Jonswap spectra were generated having periods of peak energy density, ranging from 1 second to 2 seconds and significant wave heights from 6 cm to 14 cm.

The notation of a design storm consisting of several segments of specific wave height-period combinations, which altogether simulate the growth and decay of waves during a hypothetical design storm was utilized in the tests. A total of four design storms were utilized in the three dimensional tests and are detailed in Tables 1 to 4.

Table 4 Wave Climate # 1-3D

Segment	$H_s$ (m)	$T_p$ (s)	Duration (min)
1	.06	1.2	60
2	.08	1.4	70
3	.1	1.6	80
4	.12	1.8	90
5	.14	2.0	100
6	.12	1.8	90
7	.10	1.6	80
8	.08	1.4	70

Table 2 Wave Climate 2-3D

Segment	$H_s$ (m)	$T_p$ (s)	Duration (min)
1	.08	1.2	60
2	.10	1.4	70
3	.12	1.6	80
4	.14	1.8	90
5	.16	2.0	100
6	.14	1.8	90
7	.12	1.6	80
8	.10	1.4	70

Table 3 Wave Climate 3-3D

Segment	$H_s$ (m)	$T_p$ (s)	Duration (min)
1	.10	1.2	60
2	.12	1.4	70
3	.14	1.6	80
4	.16	1.8	90
5	.18	2.0	100
6	.16	1.8	90
7	.14	1.6	80
8	.12	1.4	70



Table 4 Wave Climate 4-3D

Segment	$H_s$ (m)	$T_p$ (s)	Duration (min)
1	.12	1.2	60
2	.14	1.4	70
3	.16	1.6	80
4	.18	1.8	90
5	.20	2.0	100
6	.18	1.8	90
7	.16	1.6	80
8	.14	1.4	70

Each segment of each storm was run for a time equivalent to 3000 waves attacking the structure. Profiles were measured before the test and after each segment of test. For certain tests, several intermediate profiles were measured after 500, 1000, 1500 and 2000 waves. To assess the long term reshaping process, some tests were carried out for a duration of 36000 waves with profiles measured every 3000 waves. These tests were used to assess the reshaping of breakwaters as a function of storm segment duration. The berm breakwater was considered to have failed when erosion of the berm progressed landward to the intersection of the horizontal berm with the upper 1:3 slope (see figure 3). A total of 12 series of tests were undertaken and are described in Table 5.

Table 5

Test Series	Wave Climate	Initial Berm Width (m)
1	1-3D	.40
2	1-3D	.45
3	2-3D	.50
4	2-3D	.50
5	2-3D	.60
6	3-3D	.60
7	3-3D	.70
8	4-3D	.70
9	4-3D	.60
10	2-3D *GF=0.2	.45
11	2-3D *GF=0.75	.45
12	2-3D *GF=1.2	.45

#### Test Procedures

The following general procedures were followed during each test:

- (1) A test was not commenced until the water surface in the flume was completely calm.
- (2) Predetermined settings on the hydraulic wave generator were used for all wave conditions.
- (3) The same number of samples of water level variations were taken. Sampling would start on the passage of the third wave.
- (4) The locations of the water level transducers did not vary for test to test.
- (5) Observations were made regarding stone movement resulting from wave attack, both initially and after the breakwater profile reached near equilibrium.

- (6) The breakwater was not rebuilt following each segment of wave attack. Rebuilding of the entire breakwater was done following the completion of a test storm and carried out under water, to simulate, as close as possible, prototype construction conditions.
- (7) The water level transducers and profiler were calibrated every 3 days and were found to remain stable over the duration of the testing programme.

### Results

It was found that the largest portion of berm erosion occurred during the attack of the first few relatively big waves in the wave train. The zone in which movement of stones occurred was located at the seaward edge of the berm. The stones moved by rolling about the slope. On passing of the first few waves, there was little sign of motion of stones in the landward region of the berm; the principal mode of reshaping was by rounding-off of the exposed corner of the berm.

After approximately five to ten big waves, there was very little mass movement, and subsequently, stones moved individually rather than "en masse". With time, the initial berm receded and armour stones were individually removed by the wave forces and deposited at some other location on the slope. With each impinging wave breaking on the berm, stones were removed from the outer edge of the berm and carried by uprush and downrush moving to and fro on the profile formed as a result of erosion. A net migration of stones offshore was observed from the profiles measured followed each section of the design storm. The reshaping process was usually too slow to be noticeable to the human eye (apart from the initial "shakedown" of the mound).

Figure 4 gives an example of average berm erosion (measured from the seaward edge of the structure) as a function of significant wave height for a particular test. In general comparable recession rates were observed in each flume over the course of the design storm. The net recession in each flume at the end of the test is typically within a range of 5-10%. Considering that on average 450 to 500 mm of erosion is experienced and given that  $D_{50} = 14\text{mm}$ , then  $\pm$  one stone would give a resolution of approximately 6%. Thus the range of 5-10% indicates no significant difference in the performance of each section.

Table 1 Example Wave Climate 4

Segment	$H_s$ (m)	$T_p$ (s)	Duration (min)
1	.12	1.2	60
2	.14	1.4	70
3	.16	1.6	80
4	.18	1.8	90
5	.20	2.0	100
6	.18	1.8	90
7	.16	1.6	80
8	.14	1.4	70

Correct interpretation of the data can only be carried out by analysis those data in which the berm structure were stable (in this case, a stable structure was one in which berm erosion did not progress landward of the upper 1:3 slope). Figure 5 provides an illustration of the relationship between flume width and  $B/H_{peak}$ , where B is the starting berm width (equal to the total amount of recession) and  $H_{peak}$  is the significant wave height at the peak of the design storm. In general,  $B/H_{peak}$  increases with increasing flume width (thus indicating more reshaping for all wave climates).

Figure 6 shows the influence of groupiness factor on relative shaping ( $B/H_{peak}$ ). For low values of groupiness, no significant difference in reshaping exists (as a function of flume width). As the groupiness factor is increased then the flume width becomes more important. The most significant difference in reshaping between the 4 m and the 1.2 and 2.4 m flumes occurs at the highest value of groupiness. Values of  $B/H_{peak}$  for flume widths of 1.2 and 2.4 m are relatively constant whereas  $B/H_{peak}$  shows an increase with increasing groupiness for the 4 m flume results. These findings are in agreement with Hall et al (1989) and leave questions regarding the validity of two dimensional tests to evaluate the stability of berm or reshaping breakwaters.

### Conclusion

A series of tests was undertaken utilizing various width "flumes" containing identical breakwaters simultaneously subjected to identical wave conditions. It was found that the extent of reshaping increased with increasing flume width. This effect was more pronounced when subjecting the structure to wave trains having a high groupiness factor.

This trend sheds doubt with respect to the validity of undertaking narrow flume two-dimensional tests of berms or reshaping breakwaters. At present, until further research can be undertaken, it is recommended that only fully three dimensional tests be undertaken when designing berm breakwaters, (even when incident wave conditions are parallel to the breakwater crest).

### References

Burcharth, H.F. and Frigaard, P. "Reshaping Breakwaters, On the Stability of Roundheads and Truck Erosion in Oblique Waves", Proceedings of workshop of Unconventional Rubble-mound Breakwaters, Ottawa, 1987, pp. 55-72.

Hall, K.R., "Experimental and Historical Verification of the Performance of Naturally Armouring Breakwaters". Proceedings of Workshop on Unconventional Rubblemound Breakwaters, Ottawa, 1987 pp 104-137.

Hall, K.R. and Rauw, C.I. and Baird, W.F. "Development of a Wave Protection Scheme for a Proposed Offshore Runway Extension", Coastal Structure 83, Washington 1983, pp 157-170.

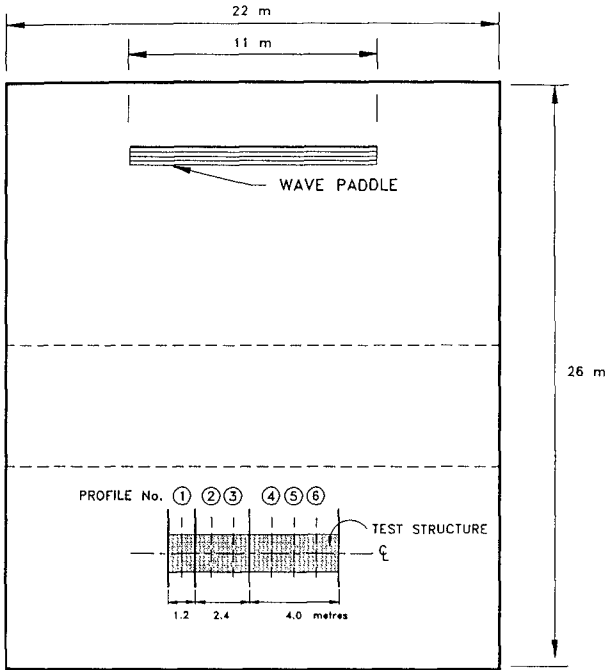


FIGURE 1 BASIN LAYOUT SHOWING FLUME LOCATIONS

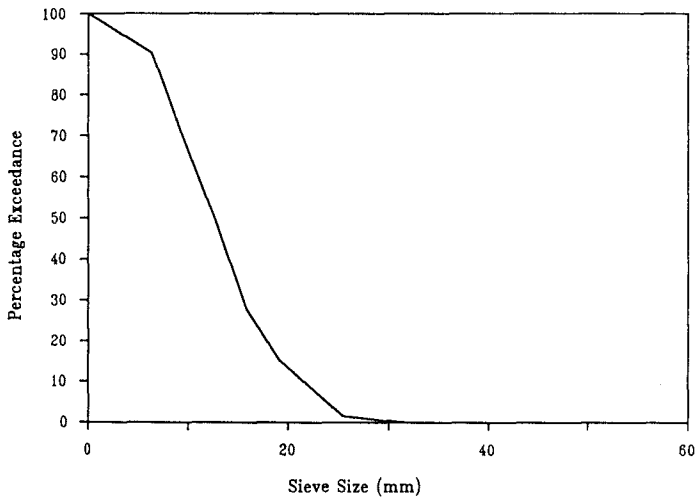


FIGURE 2 CORE MATERIAL GRADING

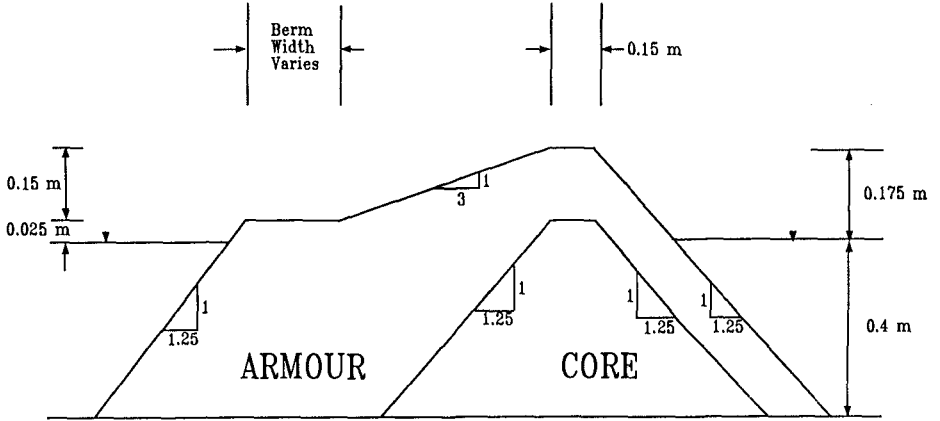


FIGURE 3 DIMENSIONS OF TEST STRUCTURE

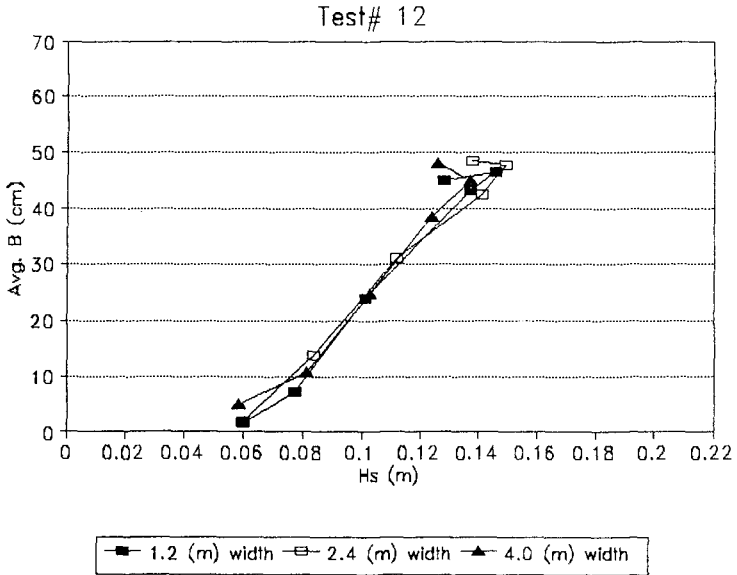


FIGURE 4 AVERAGE EROSION "B" RECORD DURING DESIGN STORM

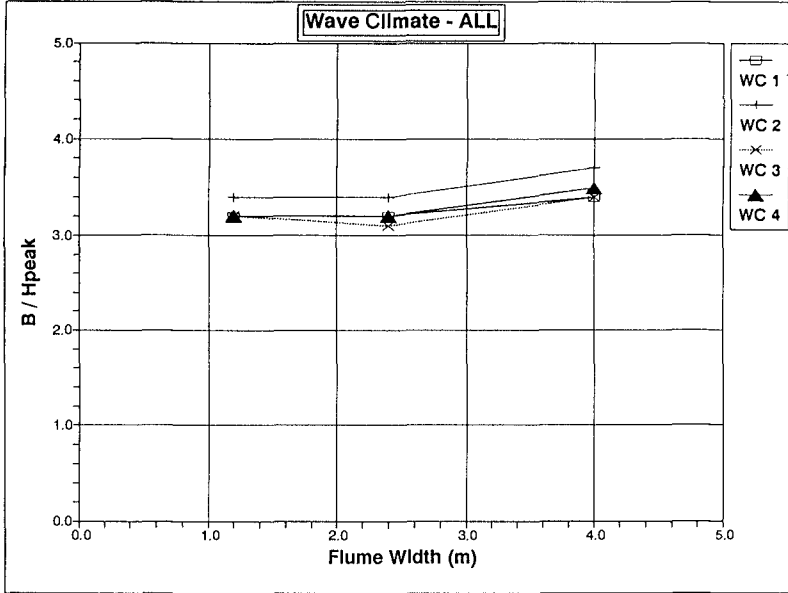


FIGURE 5 VARIATION OF TOTAL EROSION AS A FUNCTION OF WAVE CLIMATE



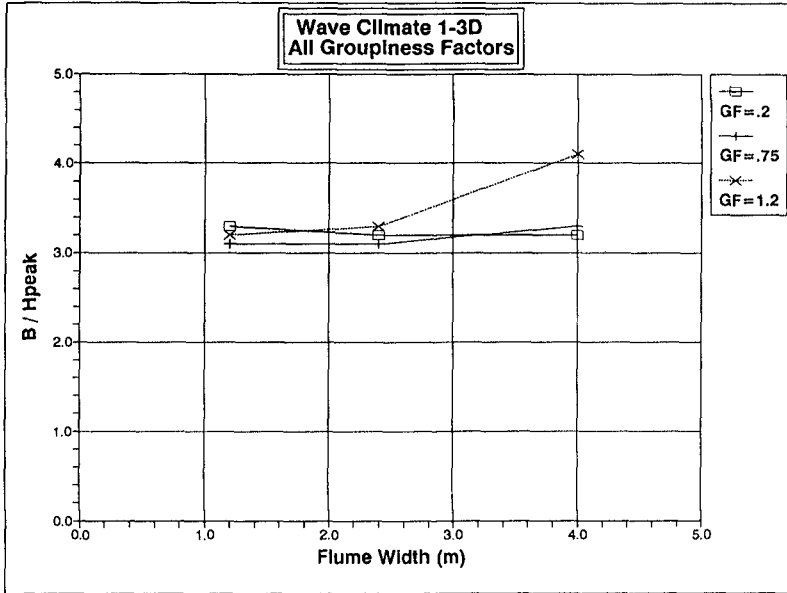


FIGURE 6 VARIATION OF TOTAL EROSION AS A FUNCTION OF GROUPINESS

## CHAPTER 92

### **Preliminary Analysis of the Stability of Rubblemound Breakwater Crown Walls**

by

David G. Hamilton<sup>1</sup> and Kevin R. Hall<sup>2</sup>

#### ABSTRACT

A series of two-dimensional hydraulic model tests was carried out to investigate the stability of rubblemound breakwater crown walls. The effect of seven design parameters on the minimum mass required for a crown wall to remain stable was studied: wave height, wave period, crown wall height, water level, front slope of the breakwater, position of the crown wall and length of stabilizing legs. Observations regarding the type of wave interaction, degree of overtopping, superstructure movement and overall hydraulic stability were studied. The coefficient of friction at the crown wall/breakwater interface was also measured. The crown wall superstructure was located on the crest of a conventional multi-layer breakwater and was subjected to both regular and irregular wave attack. Preliminary analysis of this data set is presented which shows trends established for each of the seven design parameters.

#### INTRODUCTION

Crown walls are designed, on a small scale, to provide pedestrian and vehicular access onto and along the crest of rubblemound breakwater structures. On a larger scale, crown walls support and protect pipelines and other services from the damaging forces of storm generated waves.

Crown walls are subjected to a complex set of forces including those resulting from direct wave impact and uplift pressure caused by the phreatic surface motion in the rubblemound. Since the physics of the hydrodynamic forces on crown walls is very complex, an accurate mathematical description of these forces, both spatially and temporally, along the front face and base of the crown wall is presently unattainable. Well designed hydraulic models are currently the only reliable design tool available, although these are subject to problems of scale effect due to the inability to obtain equality of Froude, Reynolds and Weber criteria. It is of paramount importance that the permeability of each layer is modelled correctly in order to minimize these scale effects.

---

1 Graduate Student, Department of Civil Engineering,  
Queen's University, Kingston, Ontario, Canada K7L 3N6

2 Associate Professor of Civil Engineering,  
Queen's University, Kingston, Ontario, Canada K7L 3N6

In one of the most comprehensive investigations of crown walls, Jensen (1983 and 1984) examined the forces on these structures by measuring the pressure distribution along the front face and base of the superstructure. A dimensionless empirical relationship was derived in order to predict the maximum horizontal wave force on the front face of a crown wall. Jensen's equation was calibrated to fit the model data using three sets of dimensionless coefficients which were valid for three specific crown wall configurations.

Bradbury et al. (1988) extended Jensen's work by modelling structures with different armour unit configurations fronting crown walls. The maximum horizontal force on the front face of the crown wall was measured for each of the crown wall/crest armour geometries using a system of strain gauges mounted inside a force table. By using an armour coefficient for a single wave climate, the authors extended Jensen's equation to six different crown wall/crest armour configurations. However, the authors point out that each of the two armour unit coefficients are only valid for a single random wave condition. They state that further studies are required to verify these armour unit coefficients over a wider range of incident wave conditions.

Although other studies of crown walls have been conducted, these two investigations are the most comprehensive. However, the results obtained from both of these studies could not be extrapolated with confidence to the range of breakwater/crown wall configurations of interest in this study.

This present study was undertaken in a two-dimensional wave flume at the Coastal Engineering Research Laboratory at Queen's University. The tests were developed to determine what influence seven design parameters had on the minimum mass for which a given crown wall configuration would remain stable: wave height, wave period, crown wall height, water level, front slope of the breakwater, position of the crown wall and length of stabilizing legs. Observations regarding the type of wave interaction, superstructure movement and overall hydraulic stability of the crown wall/breakwater were also studied. Finally, the hydraulic performance of each crown wall configuration was evaluated and classified as either an overtopping or a non-overtopping structure for a given design wave climate.

The testing programme consisted of 49 tests covering the range of breakwater/crown wall configurations and water levels presented in Table 1.

## EXPERIMENTAL SETUP

All experiments were carried out in a 0.9-m wide wave flume with an overall length of 47 m and an overall depth of 1.8 m. Tests were conducted with three different still water levels; 0.800, 0.850 and 0.875 m above the flume bottom. Both regular and irregular wave attack was used. A minimum of twelve combinations of wave height and wave period were used for each crown wall/breakwater configuration, as shown in Table 2. For some tests, as many as eight wave heights (for each wave period) were tested in order to better define trends in the stability data.

TABLE 1  
Test Summary

Test	F (mm)	H <sub>cw</sub> (mm)	BW Front Slope	P <sub>cw</sub>	L <sub>cw</sub> (mm)	Wave Type
RC1C01, RC1A01	25	40	1:1.5	C and A	N/A	Reg
RC1C02, RC1A02	50	40	1:1.5	C and A	N/A	Reg
RC1C03, RC1A03	100	40	1:1.5	C and A	N/A	Reg
RC1C04, RC1A04	25	70	1:1.5	C and A	N/A	Reg
RC1C05, RC1A05	50	70	1:1.5	C and A	N/A	Reg
RC1C06, RC1A06	100	70	1:1.5	C and A	N/A	Reg
RC1C07, RC1A07	25	100	1:1.5	C and A	N/A	Reg
RC1C08, RC1A08	50	100	1:1.5	C and A	N/A	Reg
RC1C09, RC1A09	100	100	1:1.5	C and A	N/A	Reg
RC1C10, RC1A10	25	100	1:3	C and A	N/A	Reg
RC1C11, RC1A11	50	100	1:3	C and A	N/A	Reg
RC1C12, RC1A12	100	100	1:3	C and A	N/A	Reg
RC2C01	25	100	1:1.5	C	10	Reg
RC2C02	50	100	1:1.5	C	10	Reg
RC2C03	100	100	1:1.5	C	10	Reg
RC2C04	25	100	1:1.5	C	30	Reg
RC2C05	50	100	1:1.5	C	30	Reg
RC2C06	100	100	1:1.5	C	30	Reg
RC2C07	25	100	1:1.5	C	50	Reg
RC2C08	50	100	1:1.5	C	50	Reg
RC2C09	100	100	1:1.5	C	50	Reg
RC2C10	25	100	1:3	C	10	Reg
RC2C11	25	100	1:3	C	30	Reg
RC2C12	25	100	1:3	C	50	Reg
RC3C01, RC3A01	25	N/A	1:1.5	C and A	N/A	Reg
RC3C02, RC3A02	50	N/A	1:1.5	C and A	N/A	Reg
RC3C03, RC3A03	100	N/A	1:1.5	C and A	N/A	Reg
RC3C04, RC3A04	25	N/A	1:3	C and A	N/A	Reg
IC1C01*	25	40	1:1.5	C	N/A	Irr
IC1C04*	25	70	1:1.5	C	N/A	Irr
IC1C07*	25	100	1:1.5	C	N/A	Irr
IC1C08	50	100	1:1.5	C	N/A	Irr
IC1C09*	100	100	1:1.5	C	N/A	Irr

C = On Core, A = On Armour

\*Only T = 1.75s

Ex. RC1C01 represents

R = Regular waves

C1 = Configuration 1 crown wall

C = Crown wall resting on Core layer.

01 = Test 1

The conventional multi-layer rubblemound breakwater consisted of a core layer (13-mm angular stone), a filter layer (40-mm angular stone) and an armour layer (two layers of 80-mm angular stone). Other characteristic properties are given in Table 3. All of the angular stone was assumed to have a specific gravity of 2.65.

Three types of crown walls were tested, as shown in Figure 1. Configuration 1 consisted of a vertical wall connected to a base plate. Crown wall heights of 40, 70 and 100 mm were tested. Configuration 2 was similar with the exception of an additional set of stabilizing legs penetrating the core layer. The objective of these legs was to increase the stability of the crown wall during wave attack. Three different pairs of stabilizing legs were constructed, with lengths of 10, 30 and 50 mm. Configuration 3 was used to simulate a walkway by removing the vertical crown wall and the stabilizing legs. Each structural member of the crown wall superstructure was fabricated using aluminum alloy having a specific gravity of 2.8.

The stability of the crown wall was tested in two positions. First, the crown wall was placed on top of the core at the breakwater crest, as shown in Figure 2a. It was assumed that for any future breakwater designs, the crown wall would be placed in this position. From a stability perspective, this was the ideal position since the crown wall is protected from direct wave impact forces during wave attack. As it was critical to isolate the horizontal resistance of the crown wall to frictional resistance, see Figure 2b, armour units were placed (seaward and landward of the structure) so that they added no additional stability to the crown wall.

In the second position, the crown wall was constructed on top of the armour layer along the breakwater crest (Figure 3). If crown walls could be designed to remain stable in this position, the armour units would not need to be removed to construct crown walls on existing breakwaters. However, installing the crown wall on top of the armour stone created two problems. First, it was difficult (if not impossible) to place the crown wall on top of the armour stones while maintaining the proper horizontal and vertical alignment along the breakwater crest. Secondly, the horizontal resistance created by friction between only a few armour stones and the base of the crown wall was considerably less than that found when the crown wall was constructed on the core of the breakwater. To resolve these two problems, a gravel bed was prepared along the crest of the breakwater by placing core material in the large voids between each armour stone. The crown wall was removed after completing each test and if any undermining or erosion had taken place, the gravel bed was reconstructed.

Preliminary studies were undertaken to determine the coefficient of friction at the breakwater/crown wall interface. A device was designed to enable the horizontal resistance of the crown wall to be measured over the range of crown wall mass which would be required during stability tests. Linear regression analysis resulted in a best fit line having a coefficient of friction,  $\mu = 0.51$ , as shown in Figure 4. This agrees with prototype estimates of  $\mu = 0.50$  to  $0.55$  (Jensen, 1984), and  $\mu = 0.60$  Goda (1985) between concrete superstructures and quarry stone.

The minimum wall and base thickness of prototype crown walls was assumed to be 0.20 m, as this thickness would provide adequate coverage for reinforcing steel within a crown wall. As this model was designed at a geometric scale of approximately 1:20, the minimum crown wall mass used throughout this study was approximately 6.5 kg, depending on the crown wall configuration.

TABLE 2  
Incident wave conditions for testing

Segment No.	T (s)	H (mm)	H/L <sub>o</sub>	$\xi = \tan\theta / [(H/L_o)^{1/2}]$	
				Slope 1:1.5	Slope 1:3
1	1.25	120	0.049	2.65	1.45
2	1.25	150	0.061	2.37	1.30
3	1.25	180	0.074	2.16	1.18
4	1.25	200	0.082	2.05	1.12
5	1.75	100	0.021	4.07	2.22
6	1.75	160	0.033	3.21	1.76
7	1.75	210	0.044	2.81	1.54
8	1.75	270	0.056	2.47	1.35
9	2.25	100	0.013	5.23	2.86
10	2.25	140	0.018	4.42	2.42
11	2.25	190	0.024	3.79	2.08
12	2.25	230	0.029	3.45	1.89

TABLE 3  
Summary of characteristic material properties

Material type	Nominal Diameter			Mass		
	Dmin (mm)	D50 (mm)	Dmax (mm)	Mmin (g)	M50 (g)	Mmax (g)
13 mm crushed gravel	9	13	30	1	3	35
39 mm crushed gravel	37	39	42	70	85	100
80 mm armour stone	70	80	90	500	680	1000

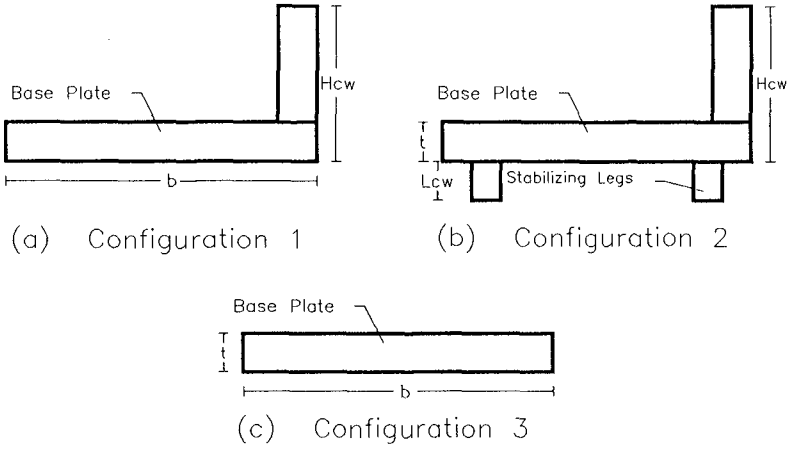


Figure 1 Configuration of 3 Crown Wall Test Sections

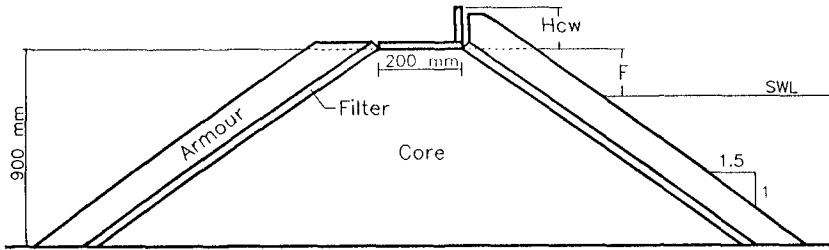


Figure 2a Crown Wall resting on Armour Layer

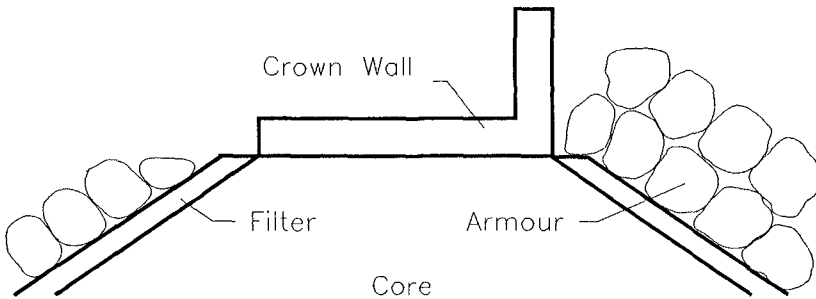


Figure 2b Placement of Armour Stone Adjacent to Crown Wall

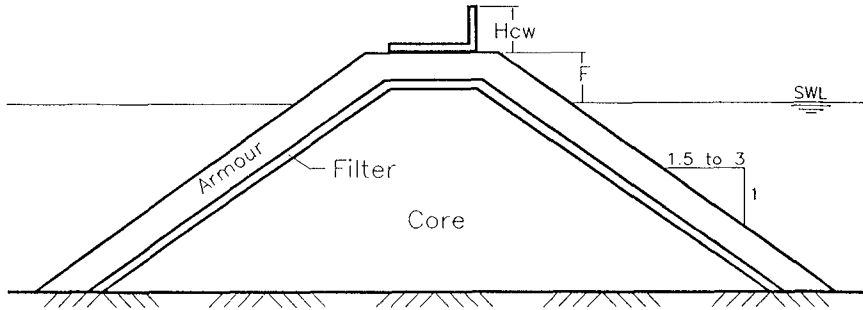


Figure 3 Crown Wall Resting on Armour Layer

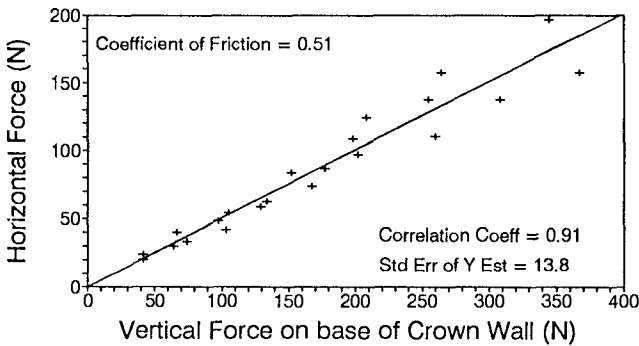


Figure 4 Coefficient of Friction at Crown Wall-Breakwater Interface

DETERMINATION OF MINIMUM STABLE MASS

Minimum stable mass (MSM) was defined as the minimum mass for which a given crown wall/breakwater configuration would remain stable while being subjected to certain design wave conditions. The MSM of a crown wall represented the point of limiting equilibrium between stable and unstable conditions. At this minimum mass, the crown wall could withstand a variety of complex and interactive forces resulting from direct wave impact, uplift pressure resulting from phreatic surface motion in the breakwater and forces associated with overtopping.

Results obtained from tests using Type 1 and 3 crown walls (Figure 1a and c) were classified into one of three categories; stable, unstable and minor displacements. The failure mode for each of these tests was found to be a sliding failure. A test was categorized as stable if the crown wall remained stationary during exposure to wave attack. In some tests vibrations of the crown wall were observed, although any resultant displacement would exclude such a result from

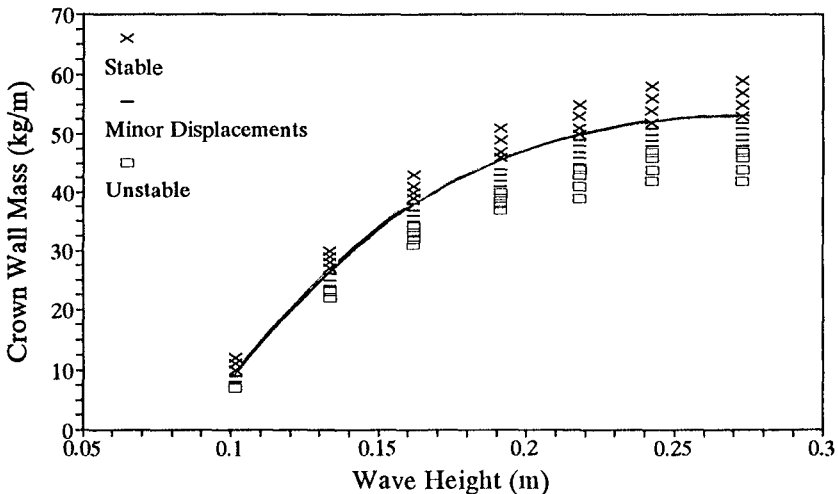


this category. Minor displacement test results were defined as tests in which the crown wall was displaced less than 10 mm during wave attack. This category included instances in which the crown wall would undergo a parallel slide, or alternatively, displacements of only one end of the crown wall. Test results in which the crown wall was displaced more than 10 mm were defined as an unstable. This category included three types of displacements of the crown wall. The two most common types of failures were displacements of the crown wall parallel to its original position or displacements of only one end of the crown wall. In some instances a catastrophic failure occurred in which the crown wall was forced over the landward side of the breakwater.

Test results for the Type 2 crown wall (Figure 1b) were classified as either stable or unstable. The mode of failure in each of these tests was found to be a quasi-overturning failure. The minor displacement failure category was not used for Type 2 crown wall tests since any measurable overturning of the crown wall was considered to be a failure.

Figure 5 is an example of typical test results from one test in the data set. The curve shown in the figure passes through the data points representing the minimum stable mass of the crown wall at different wave heights. This curve represents a reasonably accurate relationship between the mass of a crown wall and the incident wave height at the point of limiting equilibrium between stable and unstable conditions.

Test results presented later in this paper are based on the minimum stable mass of the crown wall. This will allow comparisons between different test results to be readily made.



$T = 1.75s, F = 0.025m, H_{cw} = 0.100m, \text{Slope } 1:1.5, \text{ On Core}$

Figure 5 Variability of Crown Wall Stability

## PRELIMINARY RESULTS

### *Wave height*

The following trends between incident wave height and minimum stable mass (MSM) were observed during preliminary analysis of the data set. Figure 6 shows typical test results.

Each test commenced with small waves and gradually the incident wave height was increased. When relatively small waves attacked the structure, the wave runup and internal phreatic surface would continue to fluctuate although no forces would be applied to either the base or the front face of the crown wall. Under these conditions a unit increase in the incident wave height had no influence on the stability of the crown wall.

Once the incident wave height was large enough for the wave runup and internal phreatic surface to reach the base elevation of the crown wall, a linear relationship between MSM and wave height was found. This agrees with results published by Jensen (1983 and 1984) and Bradbury et al (1988). This linear relationship continued until the waves were large enough to induce a significant amount of greenwater overtopping. At this point, the rate of increase of the MSM continued to decrease and a horizontal asymptote was approached.

### *Height of crown wall*

Figure 7 shows an example of the minimum mass required to ensure stability of a crown wall for three different crown wall heights. All of the available data consistently demonstrated that the stability of a crown wall increased with decreasing crown wall height. Three other conclusions were also worth noting. First, when the wave height was only 0.10 m, all three crown walls were found to have the same minimum stable mass (MSM). This was expected because for wave heights less than 0.10 m, no water overtopped the lowest crown wall (0.04 m high). Secondly, results of tests having a crown wall height of 0.040 m showed that the MSM remained constant once the incident wave height exceeded approximately 0.20 m. As stated earlier, this threshold wave height was directly related to the initiation of green water overtopping. Thirdly, the threshold wave height was found to increase with increasing height of the crown wall. This was also expected; a larger wave height was required to overtop a higher crown wall.

Eight tests were conducted using the Type 3 crown wall. All results demonstrated that this structure was substantially more stable than Configuration 1 and 2, under the same conditions. During most tests this crown wall was stable at the minimum mass. However, when the crown wall was on the armour layer and was subjected to very large waves, the stability of the structure increased with increasing wave period, decreasing water level and decreasing front slope steepness.

### *Freeboard*

The stability of each breakwater/crown wall configuration was evaluated for three different values of freeboard; 25, 50 and 100 mm. Tests consistently showed that the stability of a crown wall increased as the water level decreased.

### *Wave period*

The influence of wave period on the stability of a crown wall was tested for wave periods of 1.25, 1.75 and 2.25s. In general, the stability of a crown wall increased with decreasing wave period.

### *Breakwater front slope*

The front slope of the breakwater was also found to influence the stability of a crown wall. Two front slopes were tested,  $\text{Cot}\theta = 1.5$  and  $3.0$ , as these are the two extreme slopes usually found on prototype breakwaters. The data showed that, in general, the stability of a crown wall increased as the steepness of the front slope decreased.

### *Position of crown wall*

The influence of crown wall position was evaluated by conducting one set of tests with the crown wall resting on the core at the breakwater crest and another set with the crown wall resting on the armour layer. Figure 8 shows typical results from both sets of tests. The data demonstrated that for all wave conditions and breakwater/crown wall configurations, a crown wall was substantially more stable when resting on the core at the breakwater crest. These results seem reasonable when the following points are considered. First, when the crown wall rests on the core, the armour stones fronting the crown wall dissipate a significant amount of wave energy. Secondly, the armour units fronting the crown wall protect the superstructure from direct wave impact when the crown wall is resting on the core of the breakwater. Thirdly, the maximum elevation of the phreatic surface is lower when the crown wall is positioned on the core as compared with tests conducted with the crown wall on the armour layer, due to the difference in permeability of the two layers.

### *Stabilizing legs*

The influence of stabilizing legs on the stability of a crown wall is illustrated in Figure 9. Incorporating stabilizing legs into the design of a crown wall significantly increased the overall stability of the superstructure. However, the 30 and 50 mm stabilizing legs were no more effective at increasing the stability of a crown wall than 10 mm legs.

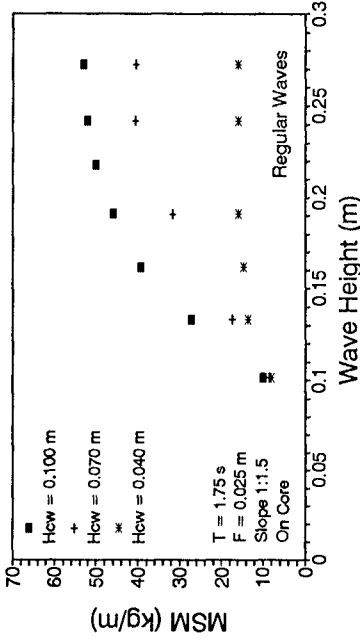


Figure 7 Influence of Crown Wall Height

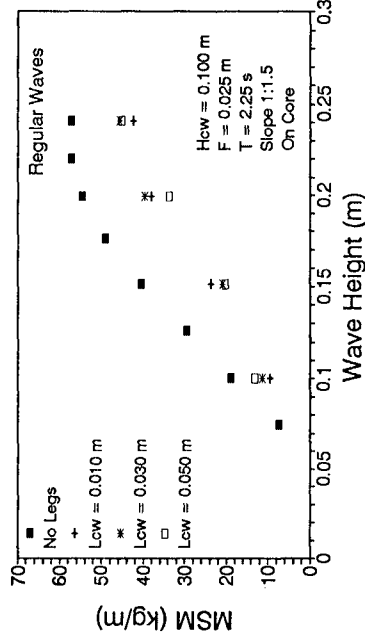


Figure 9 Influence of Stabilizing Legs

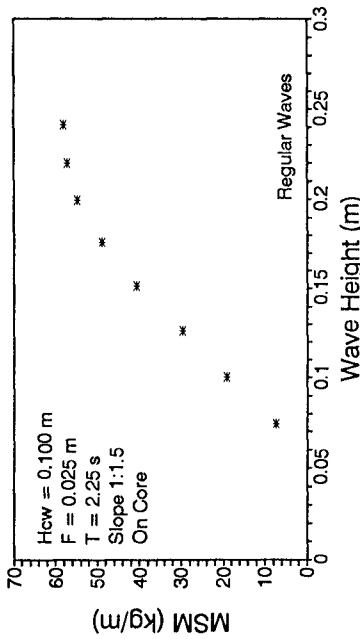


Figure 6 Influence of Incident Wave Height

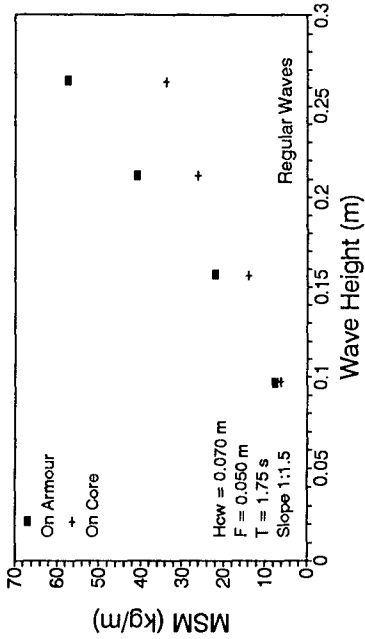


Figure 8 Influence of Crown Wall Position

Test results indicate that the use of stabilizing legs transformed what would otherwise be a purely sliding failure into a quasi-overturning failure. This change in failure mode occurred since less force was required to drag the seaward leg of the crown wall out of the core material (quasi-overturning failure) compared to the force required to cause a purely sliding failure.

## IRREGULAR WAVE TESTS

All of the results discussed above were obtained using regular sinusoidal waves. Five of these regular wave tests were repeated using irregular wave trains (see Table 1) to determine how the stability results of each set of tests could be correlated. A JONSWAP wave spectrum was synthesized using the National Research Council of Canada GEDAP laboratory control package.

Irregular wave test results were plotted as a function of regular wave test results, presented in Figure 10. Each data point indicates the irregular and regular wave height at which a specific crown wall configuration became unstable; the minimum stable mass. Assuming a irregular wave Rayleigh distribution, the irregular wave height,  $H_i$ , was defined using the equation,  $H_i = k\sigma$ . It was determined that  $H_i = 5.1\sigma$  gave the best correlation between the two sets of data. This represents the average wave height of the highest 10% of the waves,  $H_{10}$ , in the irregular wave train. Therefore, tests undertaken using irregular waves reproduced the same results as regular wave tests if  $H_{10}$  of the irregular wave train was equal to the wave height of the regular wave train.

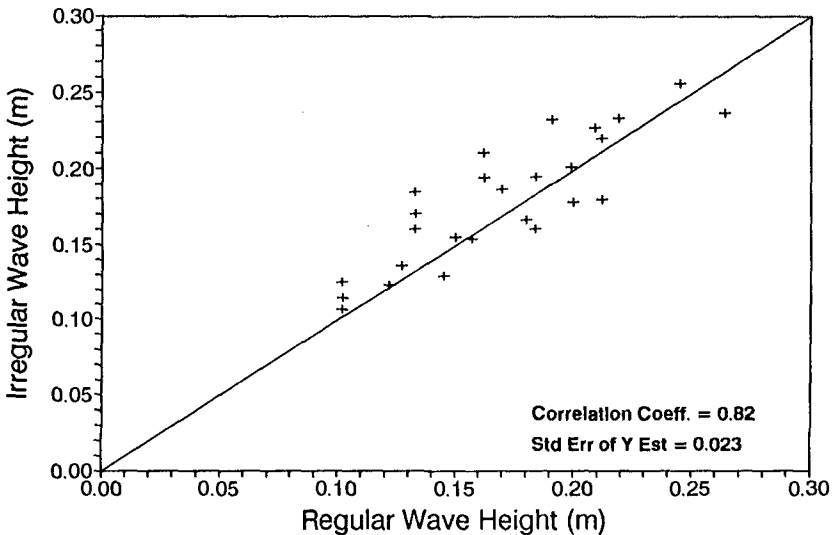


Figure 10 Irregular vs. Regular Wave Stability Tests  
(Irregular wave train defined by  $H_i = 5.1\sigma$ )

## CONCLUSIONS

Tests were conducted to evaluate the influence of seven design parameters on the hydraulic stability of crown walls. By determining the mass of each crown wall configuration at the point of limiting equilibrium between stable and unstable conditions (minimum stable mass), the following general trends have been established.

(1) During exposure to moderate wave climates, the magnitude of the wave forces on each crown wall configuration were found to be proportional to wave height. However, once the waves were large enough to induce greenwater overtopping, the wave induced forces approached a maximum. The data set showed that for each breakwater/crown wall configuration an upper limit exists, independent of wave climate, at which the destabilizing wave forces remain constant.

(2) The stability of each breakwater/crown wall configuration was found to increase with decreasing crown wall height, decreasing water level, decreasing wave period and decreasing front slope steepness.

(3) The forces exerted on a crown wall resting on the core of a breakwater were substantially less than those tests conducted with the crown wall resting on the armour layer. This demonstrated that the armour units fronting a crown wall dissipated a significant amount of wave energy and protected the superstructure from direct wave impact. It also demonstrated that decreasing the permeability of the material below the crown wall (core vs. armour material) significantly decreased the maximum elevation of the internal phreatic surface, and thereby reduced the uplift pressures.

(4) Stabilizing legs substantially increased the stability of each crown wall configuration. Short legs were found to be equally as effective as longer stabilizing legs.

(5) The coefficient of friction below the model crown wall was found to be similar to prototype estimates of the friction coefficient between a reinforced concrete superstructure and quarry stone.

(6) Irregular wave tests, simulating a JONSWAP spectrum, reproduced the same crown wall stability as regular wave tests, if  $H_{T0}$  of the irregular wave train was equal to the wave height of the regular wave train.

## ACKNOWLEDGEMENTS

The authors would like to express their appreciation to Public Works Canada, Marine H.Q. and Small Craft Harbours, Department of Fisheries and Oceans, Canada for providing financial support for this study.

LIST OF SYMBOLS

---

$D_{50}$	= Median diameter of stone gradation
$F$	= Freeboard
$H$	= Wave height of regular wave train
$H_{cw}$	= Height of the crown wall
$H_1$	= Irregular wave height
$L_{cw}$	= Length of crown wall stabilizing legs
$L_o$	= Deepwater wave length
$MSM$	= Minimum stable mass of crown wall
$M_{50}$	= Median mass of stone gradation
$P_{cw}$	= Position of crown wall
$t$	= Thickness of crown wall base
$T$	= Wave period of regular wave train
$\xi$	= Surf similarity parameter

---

## REFERENCES

- Bradbury, A P., Allsop N W H. and R V. Stevens (1988). Hydraulic Performance of Breakwater Crown Walls. Report No. SR 146, Hydraulics Research Wallingford, March 1988.
- Goda, Y. (1985). *Random Seas and Design of Maritime Structures*. University of Tokyo Press, Tokyo, Japan.
- Jensen, O.J. (1983). Breakwater Superstructures. Coastal Structures '83, Arlington, Virginia, U.S.A., March 1983.
- Jensen, O J. (1984). *A Monograph on Rubblemound Breakwaters*. Danish Hydraulic Institute, Horsholm, Denmark.

## CHAPTER 93

### NEW STABILITY FORMULA FOR DOLOSSE

<sup>1</sup>A H HOLTZHAUSEN and <sup>2</sup>J A ZWAMBORN

#### ABSTRACT

This paper describes the derivation of a stability formula for dolosse based on the physical model test results of Scholtz et. al. (1982) and Holtzhausen et. al. (1990). The derivation of the formula is based on dimensional analysis and subsequent curve fitting with a non-linear multi-variate regression model. The statistical treatment of the data made it also possible to estimate the confidence intervals.

Variables included in the formula are wave height, wave period, percentage displacement, dolos waist-to-height ratio, and armour unit density. Since not enough data were available to describe the effect of armour slope, only data for a slope of 1:1.5 were used. The test conditions and thus the derived formula represents deep water wave attack, that is, without a specific foreshore slope.

#### INTRODUCTION

A large number of model test results from tests carried out in South Africa over more than 10 years were used as a basis for the development of a new stability formula for dolosse. Since the tests included regular and irregular wave tests and were all done in the same test facility under identical conditions, their results provide an excellent basis for such a formula and also for the establishment of the variability in the stability which must be expected. Standard statistical analysis techniques were employed to achieve these results.

Although the new formula provides a useful tool for the initial design of dolos armouring, particularly for sensitivity and risk analyses, it must only be used for cases which are representative of the actual test conditions and which fall within the range of the variables used in the tests, that is , for deep water conditions, a 1:1,5 armour slope, dolos waist ratios between 0.33 and 0.40 and dolos unit densities from 1.8 to 3.0. Furthermore, the formula does not take into account

---

<sup>1</sup> Research Engineer, Division of Earth, Marine and Atmospheric Science and Technology, CSIR, P O Box 320, Stellenbosch, 7600, South Africa, and <sup>2</sup> Coastal and Hydraulic Engineer, 5 Province Avenue, Stellenbosch, 7600, South Africa.



the structural strength of individual units and it will therefore be representative of prototype conditions only for relatively small percentages damage.

## DESCRIPTION OF TEST PROCEDURES

### Model layout and Dolos Characteristics

The tests were done in the 127 m long (effective length), 3 m wide and 1,1 m deep wind-wave flume in Stellenbosch. The flume was divided into three 0,75 m wide test channels leaving two narrow dummy channels on either side. Identical breakwater test sections (except for the test dolosse) were constructed in each of the 0,75 m wide channels. The waves approached the dolos slope on a horizontal bottom with a depth of 0,8 m (Figure 1).

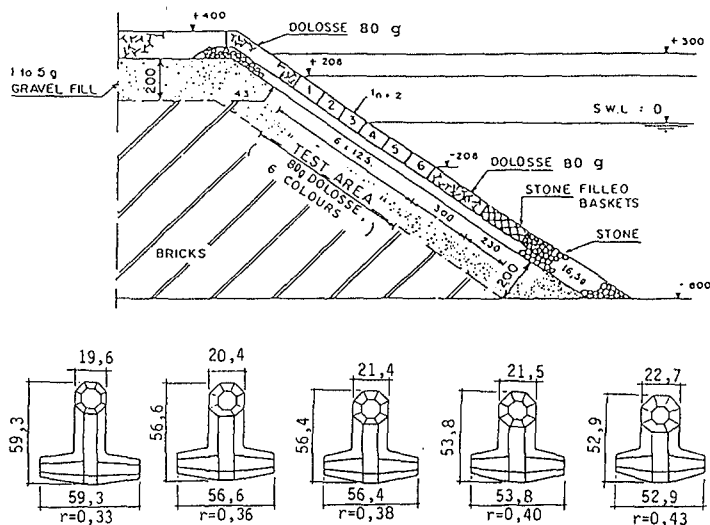


Figure 1. Section of model slope and model dolosse

The test areas were  $750 \times 750 \text{ mm}^2$  and the dolosse were placed in six 125 mm (about 2 h, where h is 'dolos height') wide bands of different colours, with three above and three below still-water level, that is, 208 mm below to 208 mm above the water level (about  $1,5 H_d$ , where  $H_d$  is the 'design wave height') (Zwamborn, 1980). A 'mean' packing density of  $\phi_{n=2} = 1.00$  was used. The underlayer consisted of 16,5 g selected stone and was 43 mm thick. The breakwater core was built of loose bricks covered with an approximately 200 mm thick layer of 1 to 5 g gravel (Holtzhausen et. al., 1990).

### Wave Generation and Measurement

Regular waves with a period of 1.75 s were used in the tests done to investigate the effect on stability of unit density (Scholtz et. al. 1982). The effect

of waist-to-height ratio ( $w_r$ ) and wave period were investigated with irregular waves generated by Seasim wavemakers (Holtzhausen et. al. 1990). These wavemakers are equipped with a wave absorption control unit making it possible to absorb reflections from the breakwater structure. Only results obtained with a Jonswap spectrum were used for fitting the stability formula.

Waves were measured by means of twin-wire resistance type probes. For the irregular wave tests three probes were positioned in each of the three channels at distances 5,55, 5,80 and 6,20 m from the model slope. These three sets of three probes were each used to separate the incident and reflected spectra. A three-point method using a least squares technique for decomposing the measured spectra from three known probe positions developed by Mansard and Funke (1980) was used.

The wave data calculated from the recordings made during the actual tests at the three probes in each channel (9 probes altogether) were used to calculate the mean incident wave height for each test.

### **Test procedures**

A test series consisted of 60 minutes of wave action (24 'bursts' of 2.5 minutes in the regular wave tests to avoid re-reflection, Scholtz et. al., 1983) for each wave height starting from the smallest wave height and increasing the wave height in steps of about 20 mm until failure occurred or until the biggest wave was reached (normally about 5 to 8 steps). Depending on the wave period, between 1800 and 2900 waves attacked the dolosse during each wave step.

The return period (55 to 80 minutes) of the input wave sequence used for the irregular waves was mostly longer than the actual test period used (60 minutes), with the result that the wave conditions mostly varied right through a test. All the repeat tests were started at the same position in the wave sequence, therefore the same section of the wave sequence was used for the different tests.

Dolosse of different densities or different waist-to-height ratios were tested side by side in the flume. To eliminate the effect of small differences in wave conditions in the three channels, the positions of the test dolosse were alternated in the three channels.

## **MODEL TEST RESULTS**

### **Available Test Data**

Results from the following tests were used in fitting the stability equation:

Regular waves,  $T=1.75$  s,  $w_r=0.33$ :

Density, $\rho_s$ (g/cm <sup>3</sup> )	Mass, W (g)	$D_n = (W/\rho_s)^{1/3}$ (mm)	Number of repeat tests
1.810	62	32.5	6
2.390	83	32.6	6
3.020	106	32.7	6

Irregular Waves with Jonswap spectrum:

Waist ratio $w_r$	Number of repeat tests for peak wave periods $T_p$			
	$T_p=1.25$ s	$T_p=1.50$ s	$T_p=1.75$ s	$T_p=2.00$ s
0.33	3	3	8	3
0.36	3	3	8	3
0.38	3	3	3	
0.40	3	3	7	3

Each test consisted of approximately 6 different wave heights which means that these data represent approximately 500 data points of damage versus wave height. Although tests were also carried out for  $w_r=0.43$  it was decided to leave out these results since this waist-to-height ratio becomes rather impractical (very low stability).

### Effect of Unit Density on Dolos Stability

Scholtz et. al. (1982) interpreted their results in terms of the Hudson formula which is given by:

$$W = \frac{\rho_s H^3}{K_d \Delta^3 \cot \alpha}$$

where, H is the wave height,  $K_d$  the stability number,  $\Delta$  the relative dolos density and  $\alpha$  the breakwater slope.

The effect of unit density on stability in this equation is given by  $W/\rho_s \propto 1/\Delta^3$  or  $V \propto 1/\Delta^3$  where V is the volume of a dolos. Scholtz et. al. found that this relationship did not apply to dolosse and modified it to:  $V \propto 1/\Delta^x$ . The following table from Scholtz et. al. (1982) shows the values found for the coefficient "x" at various levels of displacement:

Dolos displacements (%)	1	2	5	10
"x"	2.21	2.22	2.28	2.49
95 percent confidence limits	1.18 to 3.24	1.78 to 2.66	1.92 to 2.64	1.87 to 3.11

These results clearly show that "x" for dolosse is less than the value of 3 as suggested by the Hudson formula. The value of "x" for the stability formula was selected as 2.22 since this corresponds to a reasonable displacement level (approximately 1 to 5 percent) for design purposes. The effect of density on stability of dolosse for the formula presently being developed was therefore taken as:  $V \propto 1/\Delta^{2.22}$ . This reduced effect of density on dolos stability can be explained by the fact that interlocking contributes significantly to dolos stability.

It was decided to describe the size of an armour unit in terms of  $D_n$  (similar to Van der Meer, 1988) where  $D_n = V^{1/3}$ , since this simplifies the final equation. In terms of  $D_n$  the effect of unit density is therefore:  $D_n \propto 1/\Delta^{0.74}$ , compared to the Hudson formula which suggests an effect of unit density on armour size as  $D_n \propto 1/\Delta$ , representing no interlocking or friction between armour units.

### Effect of Unit Density on Rock Stability

Although rock stability does not affect the derivation of a stability formula for dolosse directly, comparisons with results obtained for rock can be useful. Brantzaeg (1966) reports on extensive tests (using regular waves) done by Kydland and Sodefjed to establish the effect of unit density on rock stability. The tests were done on slopes of 1:1.25, 1:1.5 and 1:2 for densities ranging from 1830 kg/m<sup>3</sup> to 4520 kg/m<sup>3</sup> and with a very narrow grading. It is stated specifically that any consistent differences in shape between different groups of rocks were avoided. Van der Meer (1988) also tested with different densities but concluded that no clear trends could be found in his results, essentially due to differences in the shape of rocks with different densities.

Sodefjed's results for "y" in the formula  $D_n \propto 1/\Delta^y$  are given in the following table:

cot $\alpha$	Value of y	
	1 % damage	10 % damage
1.25	0.71	0.73
1.50	0.70	0.71
2.00	0.91	0.96

This table shows that the effect of density was much the same on the 1:1.25 and 1:1.5 slopes while stability on the 1:2 slope was definitely more dependent on armour unit density. This is again due to the interlocking effect, also described by Price (1979). As the slope is made flatter, the interlocking between adjacent units decreases so that stability is more dependent on weight only.

According to Hudson's formula the value of "y" should be 1 if stability is only dependent on weight. The results of Sodefjed seem to indicate that for slopes of 1:2 (and most likely also for flatter slopes) the effect of density is correctly described in the Hudson formula (and therefore also the Van der Meer formula) for rocks. However, for steeper slopes the effect of density on stability is less and closely resembles that found for dolosse on a slope of 1:1.5. It can be expected that the effect of density on stability of dolosse will also be a function of the slope angle, although somewhat less than for rock due to the dolos interlocking shape.

## DERIVATION OF DOLOS STABILITY FORMULA

### Basic Assumptions

The result obtained by Scholtz et. al. (1982) on the effect of unit density on stability was assumed to apply also to irregular waves, different wave periods and different waist-to-height ratios. Although this assumption is not necessarily accurate for the full test range on which the final formula will be based, it was extensively tested (confirmed) whereas Hudson and Van der Meer based their estimate of the effect of unit density on theoretical considerations only.

### Selection of Dimensionless Variables

The variables considered in the present study are wave height,  $H_s$ , wave period,  $T_p$ , dolos size,  $D_n$ , dolos waist-to-height ratio,  $w_r$ , unit density,  $\rho_s$ , and dolos percentage displacement,  $N_{\%d}$  (displacements larger than dolos height,  $h$ ). Of these six variables both  $w_r$  and  $N_{\%d}$  are already dimensionless so that only the remaining four variables have to be grouped into dimensionless parameters. The relation between the damage number,  $N_o$  (Van der Meer, 1988), and  $N_{\%d}$  is given by:  $N_{\%d} = 4.32 N_o$ , based on the number of dolosse used in the CSIR tests. To enable the description of zero damage values with a power formula damage was defined as:  $N_{0.1} = N_{\%d} + 0.1$ .

Dolos unit density is expressed non-dimensionally with  $\Delta$ . As mentioned

before, Scholtz et. al. determined the effect of  $\Delta$  on  $D_n$  as:  $D_n \propto \Delta^{-0.74}$ . The effects of unit density, wave height and dolos size (for a slope of 1:1.5) can now be grouped into one parameter called the modified stability number,  $N_{sm} = H_s / (\Delta^{0.74} D_n)$ .

The wave period is normally expressed non-dimensionally as the wave steepness  $s_{op} = H_s / L_{op}$ , where  $H_s$  is the significant wave height at the toe of the structure and  $L_{op}$  is the deepsea wave length based on the peak wave period:  $L_{op} = T_p^2 g / (2\pi)$ , where  $g$  is gravitational acceleration. The wave period was also expressed as:  $T_{np} = (L_{op} / D_n)^{1/2}$ , where  $T_{np}$  is called the peak wave period number.  $T_{np} = T_p$  when  $D_n = g / (2\pi)$  i.e. the armour mass is approximately 9 000 kg (density of 2400 kg/m<sup>3</sup>).

The advantage of expressing  $T_p$  by  $T_{np}$  is that  $T_{np}$  changes only with  $T_p$  (for a specific dolos size) whereas  $s_{op}$  changes with both  $H_s$  and  $T_p$ .

**Basic Form of Equation**

The parameters with which to correlate the test data are thus the modified stability number,  $N_{sm}$ , either the wave steepness,  $s_{op}$  or the peak wave period number,  $T_{np}$ , the waist-to-height ratio,  $w_r$  and the adjusted percentage displacement,  $N_{0.1}$ . In terms of these parameters (using  $s_{op}$  to describe wave period) stability can be expressed as:

$$N_{sm} = f(N_{0.1}, s_{op}, w_r) \tag{1}$$

To comply with standard regression procedures  $N_{0.1}$  (the dependent variable) was made the subject of the formula and it was assumed that Equation 2 would adequately describe the trends found by Holtzhausen et. al. (1990):

$$N_{0.1} = A_1 N_{sm}^{B_1} s_{op}^{C_1} N_{sm}^{D_1} w_r^{E_1} s_{op}^{F_1} N_{sm}^{G_1} \tag{2}$$

where  $A_1$  to  $G_1$  are constants to be determined through regression. A non-linear regression (Statgraphics 1990) gave a regression coefficient of 0.86 (86 percent of variation in the data is described by the formula) and showed that the values of  $D_1$  and  $G_1$  were very close to zero. By setting these constants equal to zero, Equation 3 is obtained:

$$N_{0.1} = A_2 N_{sm}^{B_2} s_{op}^{C_2} w_r^{D_2} s_{op}^{E_2} \tag{3}$$

**Regression with respect to  $s_{op}$**

A regression of Equation 3 once again gave a regression coefficient of 0.86 suggesting that this equation is just as good as Equation 2. After rounding off some constants and doing another regression (which also gave an R-squared

value of 0.86), Equation 4 was obtained:

$$N_{0.1} = 26700 N_{sm}^{5.26} s_{op}^3 w_r^{20} s_{op}^{0.45} \dots(4)$$

The observed versus predicted values (316 data points) of this regression is shown in Figure 2.

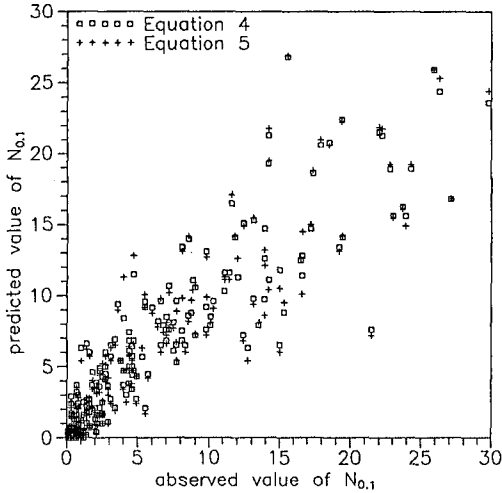


Figure 2. Predicted versus observed dolos stability

It is important to note that the effect of storm duration could not be addressed due to the test procedure that was followed. To apply the results to a specific design problem the equivalent prototype storm history can be obtained by scaling up the following values: dolos weight = 80 g, duration of each wave step = 1 hour, wave height increase for each step = 20 mm.

**Regression with respect to  $T_{np}$**

A similar regression to that done with Equation 4 was also carried out using  $T_{np}$  instead of  $s_{op}$  and the following result was obtained:

$$N_{0.1} = 0.109 N_{sm}^{6.57} T_{np}^{0.33} w_r^{1.20} T_{np}^{0.55} \dots(5)$$

As anticipated the R-squared value of Equation 5 was also 0.86 and the plot of observed versus predicted values was very similar to that obtained with Equation 4 (Figure 2).

If damage is calculated with Equation 5 a design condition is evaluated in which the wave period remains constant while the wave height is increased (in steps of 20 mm for 80 g units, each step lasting 1 hour).

**RELIABILITY OF EQUATIONS**

**Comparison of equations**

Figure 3 shows the effect of waist ratio on the adjusted percentage displacement,  $N_{0.1}$  over the range of wave period numbers used in the present tests for  $N_{sm}=2.75$ . Figure 4 shows the effect of  $N_{sm}$  on  $N_{0.1}$  over the same range of wave periods for  $w_r = 0,33$ . These figures show a good agreement in damage between Equations 4 and 5. Over all the data points used in fitting the equations, the average difference in  $N_{0.1}$  was less than 0.05 per data point. As stated before, the regression coefficients of these two equations were virtually identical (0.86) and therefore both equations can be applied with the same degree of confidence.

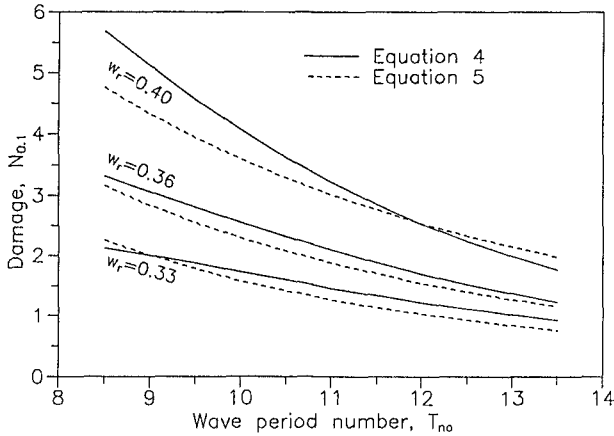


Figure 3. Comparison of the two equations for  $N_{sm} = 2,75$

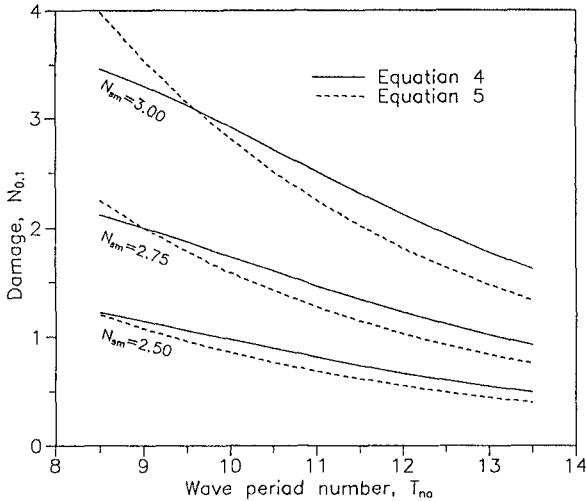


Figure 4. Comparison of the two equations for  $w_r = 0,33$



**Variation in Predicted Values**

Based on the test data, plots were made of the residuals, E, of the damage,  $N_{0.1}$ , (difference between observed and predicted values) of Equation 4 versus  $N_{sm}$ ,  $S_{op}$ , and  $w_r$ . It appeared that E was independant of all variables except the modified stability number,  $N_{sm}$ . The residuals were therefore divided into groups representing different values of  $N_{sm}$  and the mean and standard deviation of each group was determined. As expected the means were all very close to zero. The standard deviation of E versus  $N_{sm}$  is shown in Figure 5. A power fit to this data gave the following equation:

$$\sigma_E = 0.051 N_{sm}^{3.32} \quad \dots(6)$$

where  $\sigma_E$  is the standard deviation of the residuals.

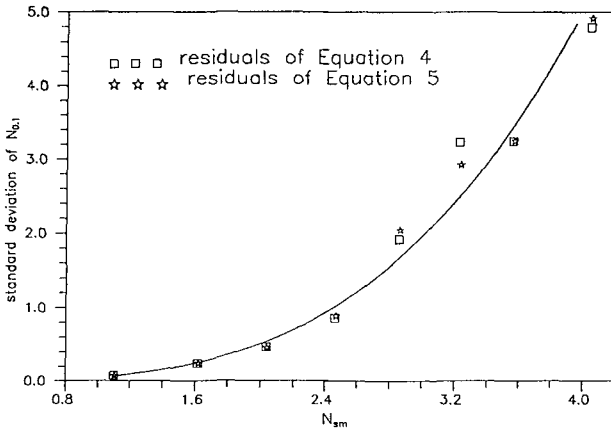


Figure 5. Standard deviation of damage ( $\sigma_E$ ) versus stability ( $N_{sm}$ )

The result obtained by analyzing the residuals of Equation 5 in the same way is also shown in Figure 5, from which it is obvious that the residuals of Equations 4 and 5 are virtually identical and that Equation 6 also applies to the variability of Equation 5. The reason that there is a big increases in  $\sigma_E$  as  $N_{sm}$  increase is due to the sharp increase in  $N_{0.1}$  with  $N_{sm}$  (see also Figure 7).

To obtain confidence intervals for Equations 4 and 5, the random variate E with zero mean and standard deviation  $\sigma_E$  as given by Equation 6, should be added to the right hand side of these equations. The best assumption on the type of distribution of E is that it is normally distributed. It should be remembered that this variation applies to a section of the breakwater of  $23D_n$  (width of test section) and assuming independence between different sections, the standard deviation of E over a width of "n" times  $23D_n$  could be decreased by  $\sigma_E/\sqrt{n}$  (equation for the standard deviation of the average of "n" identical independant normal variates).

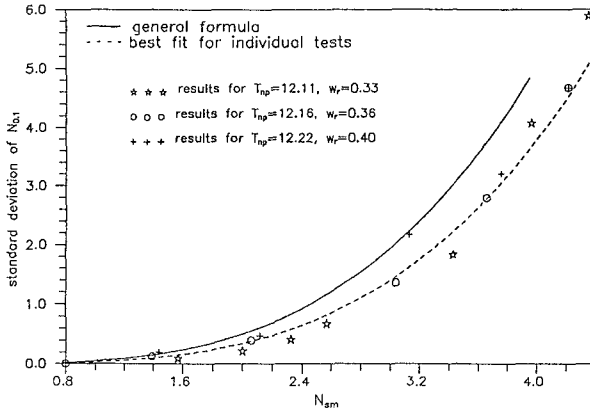


Figure 6. Comparison individual test variations with Equation 6

The variate E takes account of the natural variability of dolos stability (due to random packing) and of the errors due to possible imperfections in the stability Equation 5. To obtain an idea of the "natural variability", eight repeat tests done with a peak wave period of 1.75 s ( $T_{np} = 12$ ) and dolosse with waist ratios of 0.33, 0.36 and 0.40 were analyzed. The results of  $\sigma_E$  versus  $N_{sm}$  for each test, shown in Figure 6 together with a plot of Equation 6, show that the variability found for the full data set (Equation 6) is close to that found for individual tests. Figure 7 shows a plot of  $N_{0.1}$  versus  $N_{sm}$  (together with 90 percent confidence intervals) of tests done with  $w_r = 0.33$  and  $T_{np} = 12$ . The dotted lines represent a simple power fit of  $N_{0.1}$  versus  $N_{sm}$  as determined for the specific test condition while the solid lines are from Equation 5, by adding E from Equation 6. These Figures 6 and 7 show that the confidence limits based on Equations 4 to 6 compare well with those determined on the basis of one specific test condition.

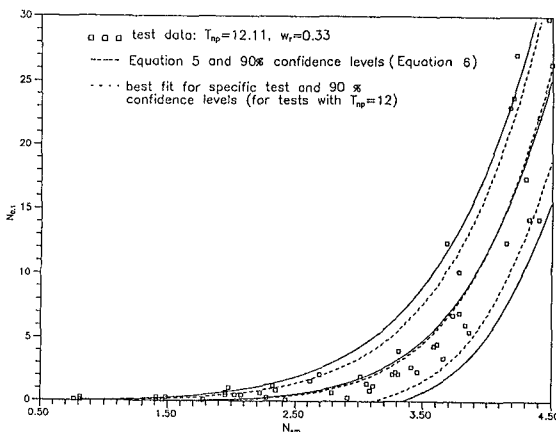


Figure 7. Comparison of confidence bands individual repeat tests versus stability equations

### Implication for Future Model Tests

If it is assumed that the standard deviation found in the present tests can also be expected in general for other similar tests, it is possible to estimate the required number of tests to ensure that the right conclusion is drawn from a limited number of physical model tests. If two armouring options ( $X_1$  and  $X_2$ ) are to be compared at an  $N_{sm}$  value of, say, 2.9, the required difference,  $\delta$ , in damage,  $N_{0.1}$ , to ensure that the most stable option is correctly identified is shown in the following table as a function of the number of repeat tests (each test representing a  $23D_n$  wide test section). In this table the probability of obtaining an incorrect results, that is, a more stable result from the option that has the lowest average stability, is set equal to 10 percent.

Number of repeat tests	$\delta$ difference in $N_{0.1}$	Typical values of $N_{0.1}$ for $X_1$ and $X_2$	
		$X_1$	$X_2$
1	3.07	2	5.1
2	2.18	2	4.2
3	1.78	2	3.8
4	1.54	2	3.5
5	1.38	2	3.4

$$* T_{no} \approx 12, w_r = 0.33$$

This shows that a difference,  $\delta$ , in mean damage of about 3 percent is needed if only one test is done but with four repeat tests this difference reduces to 1.5 percent. This table illustrates clearly why it is important to do repeat tests.

### Aspects related to Prototype Dolos behaviour

The real question in prototype is not only how many dolosse will be displaced, but rather what the real damage will be (displacements plus breakages). In previous studies (Holtzhausen et. al. 1990) it was reported that the number of dolosse rocking for more than one third of the time was approximately equal to the number of dolosse that had been displaced over a distance exceeding their own height,  $h$  (this was independant of the level of displacement). This suggests that, for the breakwater trunk, the percentage displacement is a good indication of the movement on the slope. Therefore, with further research it would most likely be possible to predict the number of broken dolosse based on the percentage displacement. Prototype tests done on dolos breakages (Zwamborn et. al., 1989) together with observations of damage on existing structures, confirm that total damage can be approximated as twice the number of displaced dolosse for dolosse weighing less than 25 t. However, the structural performance of slender type concrete armour units still require much research to reliably predict

armour breakages.

The range of Reynolds numbers ( $Re = D_n(gH_s)^{1/2}/\nu$ , where  $\nu$  = kinematic fluid viscosity) for the tests, the results of which were used to fit the stability equations, was from  $1,8 \cdot 10^4$  to  $4,4 \cdot 10^4$ . It is therefore possible that Reynolds scale effects influenced tests results, implying that the results could be slightly conservative.

**SUMMARY**

A large number of dolos test results have been summarised into two stability equations, giving the option to express wave period in terms of deepsea wave steepness,  $s_{op}$  (changes with wave height and wave period), or in terms of the peak wave period number  $T_{np}$  (changes only with wave period for constant  $D_n$ ):

$$N_{0.1} = 26700 N_{sm}^{5.26} s_{op}^3 w_r^{20} s_{op}^{0.45} + E$$

$$N_{0.1} = 0.109 N_{sm}^{6.57} T_{np}^{0.33} w_r^{1.20} T_{np}^{0.55} + E$$

where:  $N_{sm} = \frac{H_s}{\Delta^{0.74} D_n}$

- $s_{op} = H_s/L_{op}$
- $T_{np} = (L_{op}/D_n)^{1/2}$
- $L_{op} = T_p^2 g/(2\pi)$
- $T_p =$  peak wave period
- $w_r =$  dolos waist to height ratio
- $E =$  error term used to describe the random nature of dolos slope stability

The error term is assumed to be normally distributed with a mean of zero and a standard deviation of:

$$\sigma_E = 0.051 N_{sm}^{3.32}$$

The range of conditions covered by these equations is:

Parameter	Minimum	Maximum
$w_r$	0.33	0.40
$T_{np}$	8.6	14.0
$N_{sm}$	0.7	4.5
$N_{0.1}$	0.1	30.0
Reynolds no.	$1.85 \cdot 10^4$	$4.35 \cdot 10^4$

The range of wave steepnesses can be evaluated using  $T_{np}$ . Wave heights were increased in steps of approximately 0.6 times  $D_n$ , each wave height lasting 1 hour (model dolos mass = 80 g) and damage was cumulative. The wave period was kept constant as the wave height was increased. The water depth at the toe of the breakwater was 25 times  $D_n$ .

These above equations should only be applied to situations falling within this range of test conditions.

## REFERENCES

- BRAENTZAEG, A (1966). The effect of unit weights of rock and fluid on the stability of rubble mound breakwaters. Proceedings of 10th ICCE. Tokyo.
- HOLTZHAUSEN, A H and ZWAMBORN, J A (1990). Stability of dolosse with different waist thicknesses for irregular waves. Proceedings of 22nd ICCE. Delft.
- MANSARD, E P D and FUNKE, E R (1980). The measurement of incident and reflected waves in random wave experiments. Proceedings of 17th ICCE. Hawaii.
- PRICE, W A (1979). Static stability of rubble mound breakwaters. Hydraulics Research Station Wallingford. Oxon, England.
- SCHOLTZ, D J P, ZWAMBORN, J A and VAN NIEKERK (1982). Dolos stability. Effect of block density and waist thickness. Proceedings of 18th ICCE, Cape Town.
- SCHOLTZ, D J P and ZWAMBORN, J A (1983). Effect of the waist thickness on stability of dolosse. CSIR Research Report 556. Stellenbosch.
- VAN DER MEER, J W (1988). Stability of cubes, tetrapods and Accropode. Proceedings Breakwaters '88, Eastbourne, UK.
- ZWAMBORN, J A (1980). Measuring techniques, dolos packing density and effect of relative block density. CSIR Research Report 378. Stellenbosch.
- ZWAMBORN, J A and PHELP, D (1989). Structural tests on Dolosse. Proceedings, Seminar on Stresses in Concrete Armor Units, Vicksburg.

## CHAPTER 94

### Effect on Wind Speed to Wave Run-up

Jea-Tzyy Juang <sup>1</sup>

#### Abstract

In theoretical study, when the maximum run-up on sea wall was happened, the shape of the run-up wedge is assumed to be a parabola with its vertex at the bottom of the first wave trough. The another assumptions are the conservation of mass and momentum. In model test, four kinds of dyke slope (1:0.5, 1:1, 1:2, 1:3) were choiced and the tests of the wind speed from 0 to 16 m/s accompany with a range of wave steepness were completed. The experimental data shows that the general form of the equations to developed was correct. Comparison of the theoretical estimations and the experimental data are coincident very well. Besides, the relation coefficient between the exponential value  $n$  of the parabolic runup shape with the surf parameter ( $\xi$ ) was ranged in 0.19 to 0.65 in different kinds of dyke slope have been found also. At last, in general speaking, in spite of the strength of the wind speed, the relative run-up becomes the biggest when the dyke slope was 1:2.

#### Introduction

In case to determined the height of the sea wall, the height of the wave run-up is one of the most important factor. Parameters which will effect the run-up height

-----  
<sup>1</sup> Deputy Director, Institute of Harbour and Marine Technology,  
83, Lin-Hai Rd., Wu-Chi, Taichung Hsien, Taiwan 43501,  
Rep. of China.

was included not only the wave steepness, the relative depth before the toe of the coastal structure, but also the bottom slope. However, one of the most important parameter which always been neglected is the onshore strong wind speed. During the typhoon season, the seawall was attacked not only by the big waves which was propagate from the deep sea but also by the onshore strong wind speed which always induced a big increasing of wave run-up and produced an enormous amount of wave overtopping. Therefore, the study of the correlation between the onshore wind speed to the wave runup was need to understand.

Analytical Consideration

Based on the results of the dimensional analysis by Tsuchiya (1978), the correlation between the influence factors of wave run-up to the height of the relative run-up can be summarized as follows:

$$\frac{R}{H} = f_1\left(\frac{H}{L}, \tan \theta, \frac{h}{H}, \frac{d}{H}, \frac{\sqrt{K}}{H}\right) \dots\dots\dots(1)$$

- where H: Incident wave height
- L: Incident wave length
- θ : Angle of the slopping dyke to the bed
- h: Water depth before the toe of the slopping dyke
- d: Roughness on the surface of the slopping dyke
- K: Rate of percolation

Therefore, in case of the constant water depth, the smoothed slope dyke surface and the unpercolated dyke conditions, the above formula can be simplified as

$$\frac{R}{H} = f_2\left(\frac{H}{L}, \tan \theta\right) \dots\dots\dots(2)$$

When a wave run-up on a breakwater and at its maximum condition, the flow velocities are essentially zero and all the energy of this run-up water is in the form of potential energy. By knowing the shape and position of this hypothetical runup wedge, this potential energy can be calculated. Cross and Sollitt (1972) proposed that the shape of the runup wedge is assumed to be a parabola with its vertex at the bottom of the first wave trough as shown in Fig.1.

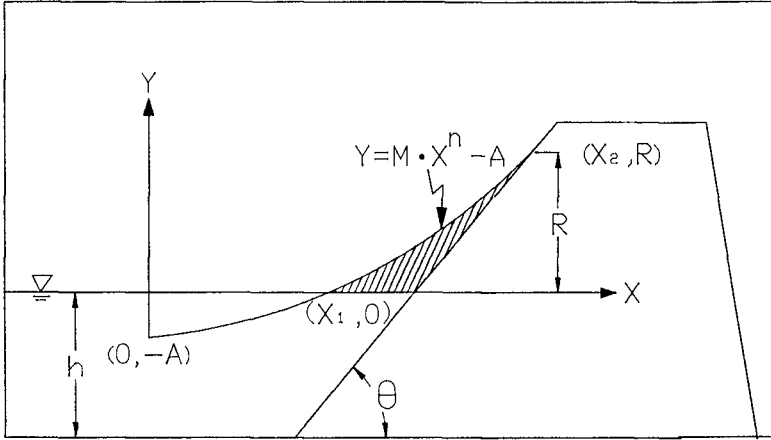


Fig.1 The shape of the runup wedge

The corresponding equation is

$$Y = M X^n - A \dots\dots\dots(3)$$

in which Y is the water surface elevation above the still water level; X is the distance from the trough shoreward; A is the amplitude at the trough and M, n are the shape parameter.

It follows directly that the potential energy of the run-up wedge at maximum runup is simply as

$$\begin{aligned}
 PE &= \rho g \left\{ \int_{x_1}^{x_2} \frac{Y^2}{2} dx - \frac{R^3}{6 \alpha} \right\} \\
 &= \frac{1}{2} \rho g \left\{ \int_{x_1}^{x_2} (M \cdot X^n - A)^2 dx - \frac{R^3}{3 \alpha} \right\} \\
 &= \frac{1}{2} \rho g \left\{ \frac{M^2}{2n+1} (X_2^{2n+1} - X_1^{2n+1}) - \frac{2 \cdot MA}{n+1} (X_2^{n+1} - X_1^{n+1}) \right. \\
 &\quad \left. + A^2 (X_2 - X_1) - \frac{R^3}{3 \alpha} \right\} \dots\dots\dots(4)
 \end{aligned}$$

Two boundary condition can be obtained when the parabola run-up curve run across to the sea water level at point X<sub>1</sub> and the maximum run-up R at X<sub>2</sub>. Therefore, from Eq.3 we know that:



$$R = M(X_2)^n - A \implies X_2 = \left(\frac{R+A}{M}\right)^{1/n}$$

$$0 = M \cdot X_1^n - A \implies X_1 = \left(\frac{A}{M}\right)^{1/n}$$

Substitute the above two boundary condition into Eq. 4, the potential energy of the wave run-up can be converted as

$$\begin{aligned} PE = & \frac{1}{2} \rho g \left\{ \frac{M^2}{2n+1} \left[ \left(\frac{R+A}{M}\right)^{(2n+1)/n} - \left(\frac{A}{M}\right)^{(2n+1)/n} \right] \right. \\ & - \frac{2MA}{n+1} \left[ \left(\frac{R+A}{M}\right)^{(n+1)/n} - \left(\frac{A}{M}\right)^{(n+1)/n} \right] \\ & \left. + A^2 \left[ \left(\frac{R+A}{M}\right)^{1/n} - \left(\frac{A}{M}\right)^{1/n} \right] - \frac{R^3}{3\alpha} \right\} \dots\dots\dots(5) \end{aligned}$$

As the water wave propagate across a fluid, it can transfer the energy flux. Based on the small amplitude wave theory, the average energy flux in unit width and over a wave period can be obtained as

$$TE = \frac{1}{8} \rho g H^2 \cdot L \cdot \left\{ \frac{1}{2} \left[ 1 + \frac{2kh}{\sinh(2kh)} \right] \right\} \dots\dots\dots(6)$$

By way of the assumption that the energy contained in the run-up wedge is evaluated from the net energy flux into a control volume which enclosing the runup wedge and the partial standing wave system, the related equation between the incident wave and the relative runup height can be expressed as

$$\begin{aligned} & \frac{M^2}{2n+1} \left[ \left(\frac{R+A}{M}\right)^{(2n+1)/n} - \left(\frac{A}{M}\right)^{(2n+1)/n} \right] - \frac{2MA}{n+1} \left[ \left(\frac{R+A}{M}\right)^{(n+1)/n} \right. \\ & \left. - \left(\frac{A}{M}\right)^{(n+1)/n} \right] + A^2 \left[ \left(\frac{R+A}{M}\right)^{1/n} - \left(\frac{A}{M}\right)^{1/n} \right] - \frac{R^3}{3\alpha} \\ & = C_e \cdot \frac{L}{4} H^2 \left\{ \frac{1}{2} \left[ 1 + \frac{2kh}{\sinh(2kh)} \right] \right\} \dots\dots\dots(7) \end{aligned}$$

where  $C_e$  indicate the coefficient of energy loss by the influence of surface and bottom frictions during the process of the wave run-up.

In accordance with the above mentioned equations, if the value of  $M$ ,  $n$  and  $C_e$  can be identified from surf parameter then by trial and error method, the height of the wave run-up can be computed.

On the heels of the effect on wind speed to wave run-up. The first thing must to determined was the additional wave which was induced by the strong wind that was blowing from the seaside to the shoreline during the typhoon season. Falvey (1974) using the momentum balance method over a control volume which includes the boundary layer of the air and the statistical relationship for the significant wave height. He suggested a correlated equation between the significant wave height, the wind speed and the fetch length as follows:

$$H_{1/3} = (3.1 \times 10^{-7} \cdot U_{10}^2 + 1.6 \times 10^{-3} \cdot U_{10}) \cdot \left( \frac{F}{g} \right)^{1/2} \dots\dots(8)$$

in which  $U_{10}$  is the onshore wind speed at the height of 10 meters from the still water level and  $F$  is the fetch.

If  $F$  is measured in kilometers,  $U_{10}$  in meters per second,  $H_{1/3}$  in meters and with  $g=981 \text{ cm/s}^2$ , the above equation becomes

$$H_{1/3} = (3.1 \times 10^{-4} \cdot U_{10}^2 + 1.6 \times 10^{-2} \cdot U_{10}) \sqrt{F} \dots\dots\dots(9)$$

At last, the work of the combination of the incident wave and the additional wave which was induced by the onshored strong wind must to determined. Due to the phenomenalism of wave-wave interaction is not so distinct. Therefore, the method of the linear addition of the wave energy was choiced to applied for temporary.

### Experimental Equipment and Procedures

Experiments were conducted in a wave tank 15 meters long, 40 cm wide and 80 cm deep. Both walls of the wave tank are constructed of strengthed glass throughout and the bottom is constructed of stainless steel of a plane surface. A blower was installed just upon the wave maker at one end of the tank while the sloping dyke model was constructed at the another end as shown in Fig.2.

The incident wave characteristics were measured using a capacitate wave gage at the location where the toe

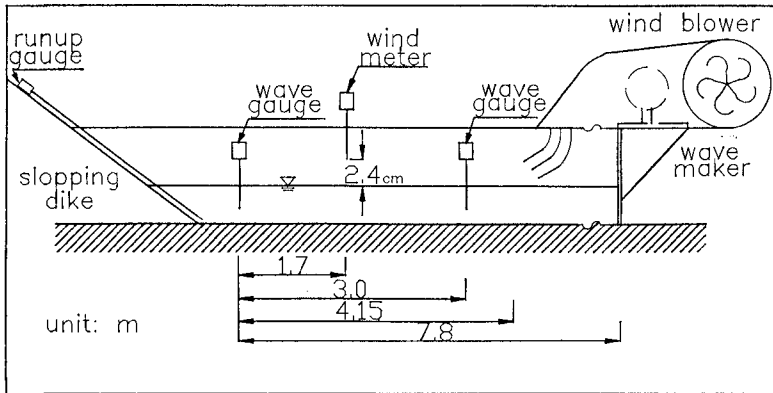


Fig.2 Diagram of Experimental Facility

of the structure was placed and the runup wave was measured on the inclined dike surface at the same way.

In experiment, the slope of the wave tank was maintained at horizontal and four kinds of dike slope (1:0.5, 1:1, 1:2 and 1:3) was choiced and the tests of the wind speed from 0 to 16 meters per second accompany with some range of wave steepness was completed.

### Results and Discussion

By way of the analysis to the wave run-up pictures which was taken from the experiments in different kind of conditions ( many kinds of dike slope and different kind of the incident wave steepness). We can find that the parabola shape of the wave runup was influenced by the surf parameter  $\xi$  ( $=\tan\theta / \sqrt{H/L}$ ). The correlation between the shape parameters of the parabola runup  $M$ ,  $n$  and the surf parameter  $\xi$  was shown in Fig.3 and 4 separately. From those figures, we can systematic out the following relationship between  $\xi$  to  $M$  and  $n$  in some kind of the dike slope.

$$\begin{aligned}
 (1) \quad S = 1:0.5 \quad ; \quad M &= 54.226 \xi^{-3.5} \\
 n &= 1.0075 \xi^{0.1909} \\
 (2) \quad S = 1:1 \quad ; \quad M &= 5.993 \xi^{-3.683} \\
 n &= 0.608 \xi^{0.5865}
 \end{aligned}$$

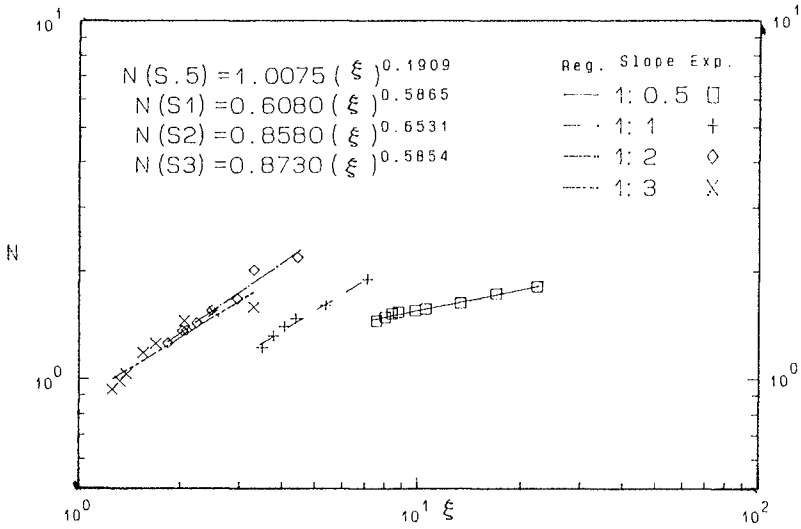


Fig.3 Correlation between M and  $\xi$

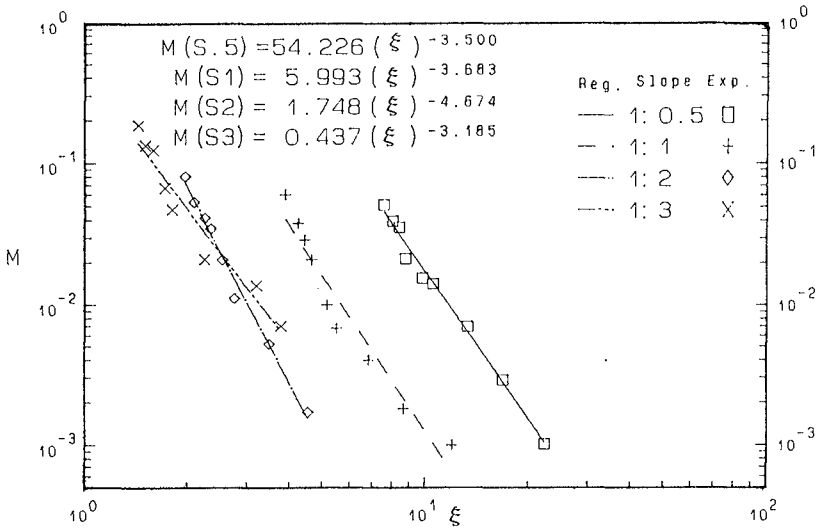


Fig.4 Correlation between n and  $\xi$

(3)  $S = 1:2$  ;  $M = 1.748 \xi^{-4.674}$   
 $n = 0.858 \xi^{0.6361}$

(4)  $S = 1:3$  ;  $M = 0.437 \xi^{-3.185}$   
 $n = 0.873 \xi^{0.5854}$

As to the effect on the onshore wind speed to the relative wave runup height, the results of the computation and the experiment was shown in Fig.5 (1)-(4). In those figures, we can find that in steep slope, for example when the dike slope is 1 to 0.5 and 1 to 1 with vertical to horizontal, the relative wave run-up will decreased first to some degree then increased when the value of the wind parameter ( $U/\sqrt{gH_0}$ ) was increased. But in gentle slope, that is the slope of the dyke is 1 to 2 and 1 to 3, the relative wave runup height was increased almost immediately when the value of the wind parameter was increased.

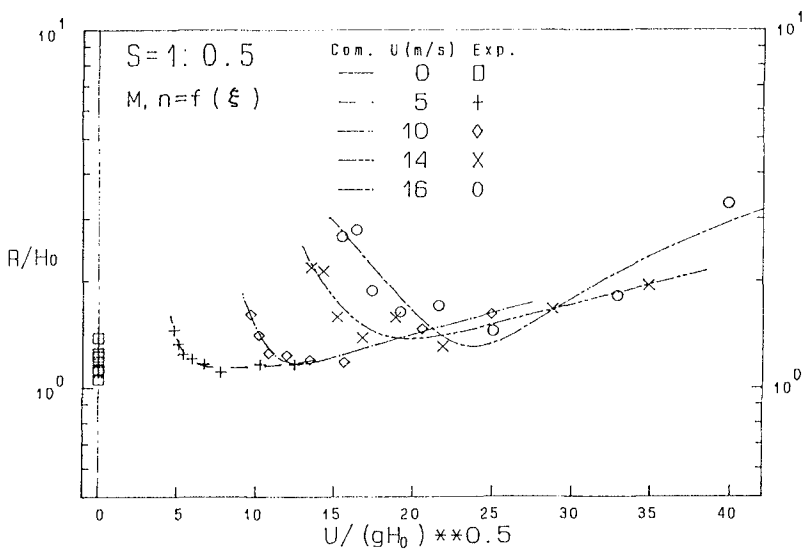


Fig.5 Correlation between the relative runup and the wind parameter (1)

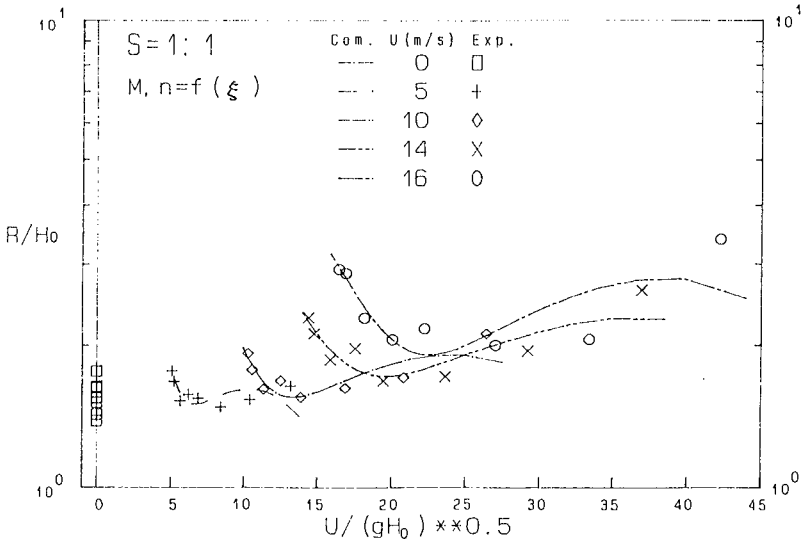


Fig.5 Correlation between the relative runup and the wind parameter (2)

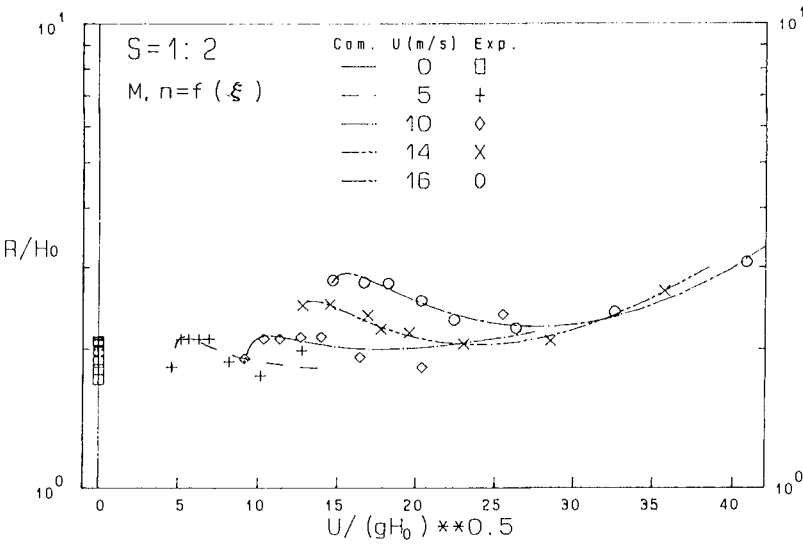


Fig.5 Correlation between the relative runup and the wind parameter (3)

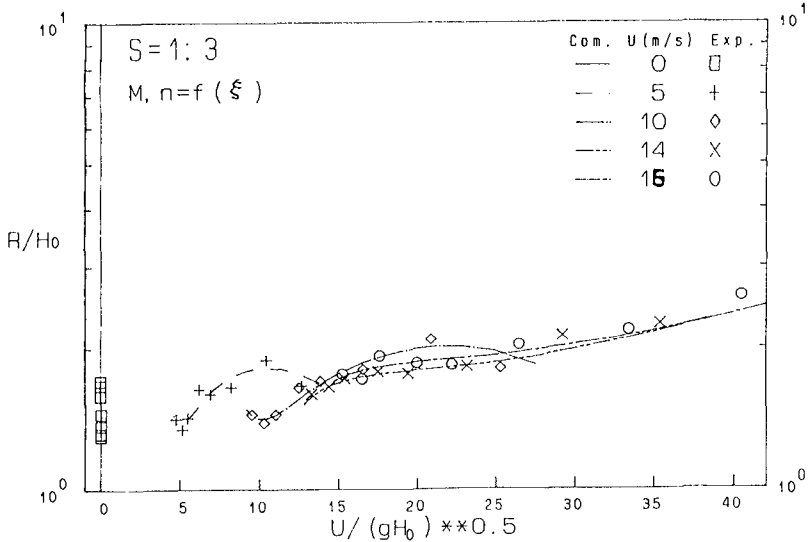


Fig.5 Correlation between the relative runup and the wind parameter (4)

If we pay the another attention to the incident wave steepness to stand for the wind parameter. The effect on the onshore wind speed to the relative wave runup height can be find as shown in Fig.6(1)-(4). From those figures, we can understand that the effect on the onshore wind speed to the relative wave runup height was more obviously in steeper slope ( $S=1:0.5, 1:1$ ) than in milder slope ( $S=1:2, 1:3$ ). However, the relative wave runup height will be increased when the onshore wind speed was increased are doubtless as shown in those figures. However, in general speaking, in spite of the strength of the wind speed, the relative run-up becomes the biggest when the dyke slope was 1:2.

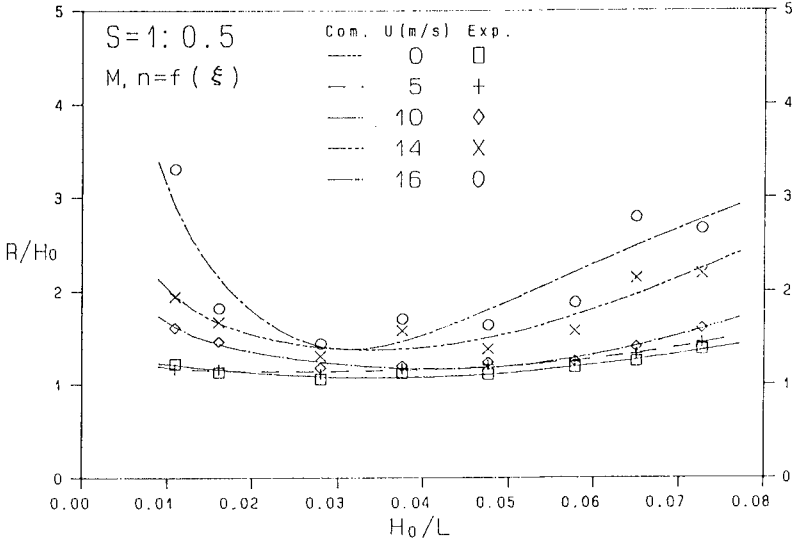


Fig.6 Correlation between the relative runup and the incident wave steepness (1)

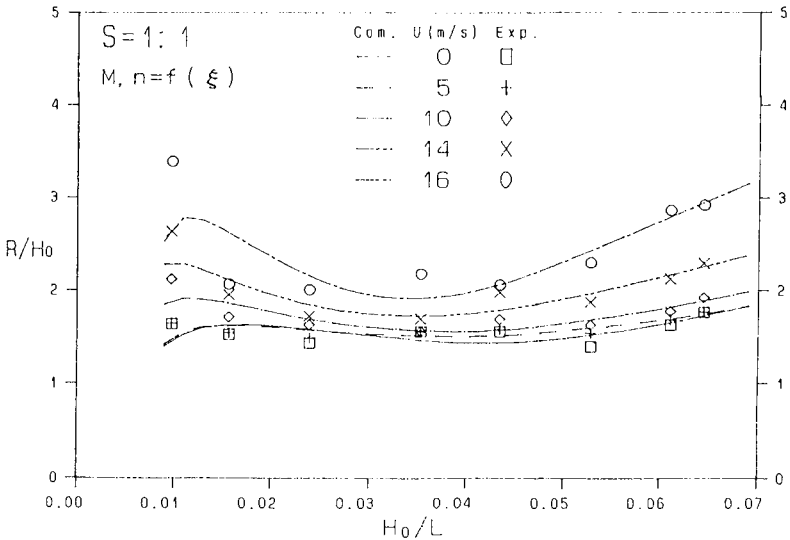


Fig.6 Correlation between the relative runup and the incident wave steepness (2)



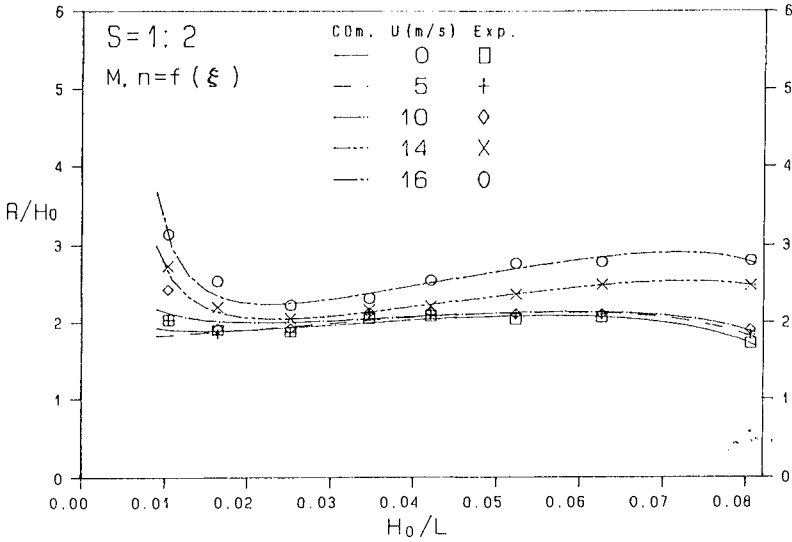


Fig.6 Correlation between the relative runup and the incident wave steepness (3)

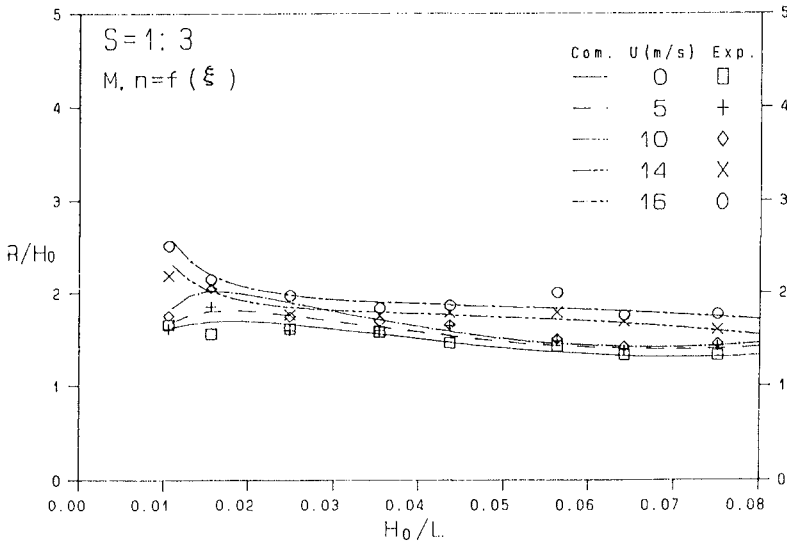


Fig.6 Correlation between the relative runup and the incident wave steepness (4)

### Conclusions

- (1) The parabolic shape of the wave runup was quite unsimilar in the condition of the different dyke slope and the incident wave steepness.
- (2) The exponential value in the relationship between  $n$  and the surf parameter  $\xi$  was between 0.19 to 0.65.
- (3) The effect on the onshore wind speed to the relative wave runup height was more obviously in steeper slope than in milder slope.
- (4) In general speaking, in spite of the strength of the wind speed, it is remarkable that the relative run-up becomes the biggest when the dyke slope was 1:2.

### Acknowledgement

This study was sponsored by the National Science Council of R.O.C. under Grant NSC 79-0410-E008-08. The author also wish to thank Mr.Y.C. Sun and Miss E.J. Chien for their assistance in experiment and preparing the manuscript.

### References

- Ahrens, J.P. and M.F. Titus (1985) : Wave run-up formulas for smooth slopes. *J. Waterway and Ocean Engineering*, ASCE, Vol.111, No.1, pp.128-133.
- Chue, S.H. (1980) : Wave run-up formula of universal applicability. *Proc. of the Institute of Civil Engineers, University of Malaya, Part 2, Vol.69*, pp.1035-1041.
- Cross, R. H. and C. K. Sollitt (1972) : Wave transmission by overtopping. *J. Waterway and Ocean Engineering*, ASCE, Vol.98, No.WW3, pp.295-309.
- Douglass, S. L. (1990) : Influence of wind on breaking waves. *J. Waterway and Ocean Engineering*. ASCE, Vol.116, No.6, pp.651-663.
- Falvey, H.T. (1974) : Prediction of wind wave heights. *J. Waterway and Ocean Engineering*, ASCE, Vol.100, No.WW1, pp.1-12.
- Raichlen, F. and J.L. Hammack, Jr. (1974) : Run-up due to Breaking and Non-breaking Waves. *Coastal Engineering*, Chapter 113, pp.1937-1955.
- Walton, T. L. J. and J. Ahrens (1989) : Maximum periodic wave run-up on smooth slope. *J. Waterway and Ocean Engineering*. ASCE, Vol.115, No.5, pp.703-708.

# CHAPTER 95

## SCATTERING OF WATER WAVES BY VERTICAL CYLINDERS WITH A BACKWALL

Shohachi Kakuno \*, Kazuki Oda\*, and Philip L.-F. Liu \*\*

### Abstract

The scattering of small amplitude water waves by an array of vertical cylinders with a solid vertical backwall is studied theoretically and experimentally. In the theoretical study, a method of matched asymptotic expansions is developed without considering real fluid effects. The energy loss due to flow separation near cylinders is modeled by introducing a complex blockage coefficient. The theories are compared with laboratory data.

## 1 Introduction

The slit-type breakwater consists of a vertically slitted front wall and a solid backwall as shown in Figure 1. The closely spaced cylinders cause flow separation and hence energy dissipation. This type of device is particularly effective in reducing wave action inside a harbor. It has gained popularity in many countries, where either the materials for building rubble-mounted breakwaters are lacking or usable water space is limited. Many studies for the slit-type breakwater have been performed since Jarlan's original work(1961). Most recently a semi-analytical approach has been reported by Fugazza and Natale(1992).

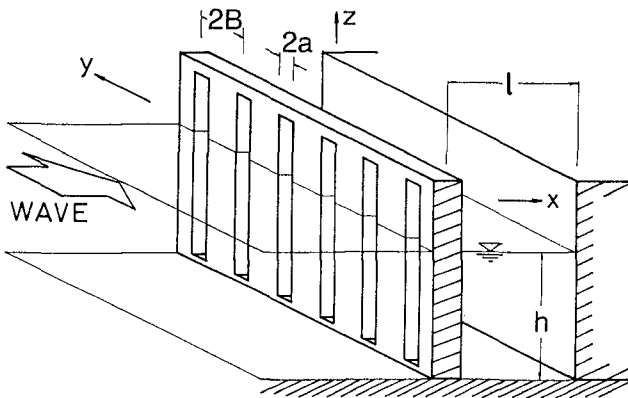


Figure 1. Slit-type breakwater.

\*Dept. of Civil Engrg., Osaka City University, Osaka, 558, Japan.

\*\*Joseph DeFrees Hydraulics Lab., School of Civil & Environmental Engrg., Cornell University, Ithaca, NY. 14853, USA.

The purpose of this study is to consider rigorously the mechanics of the interactions of water waves with the slit-type breakwater. The effects of the cross-section of the cylinders and energy dissipation caused by flow separation behind the cylinders are taken into consideration. The present work is the continuation of a previous study by Kakuno and Liu(1992) with additional consideration of the backwall.

## 2 Formulation of the Problem : Potential Flow Theory

A train of small amplitude monochromatic waves incidents normally upon an array of vertical cylinders with a vertical backwall. The distance between the centers of two adjacent cylinders is denoted as  $2B$  and water depth is a constant  $h$ . The distance between the center line of the array of cylinders and the backwall, we call it wave chamber width hereafter, is denoted as  $l$ .

Ignoring the possibility of flow separation in the vicinity of the cylinders, a potential flow theory is first formulated. Defining the velocity potential for the periodic wave motion as

$$\Phi(x, y, z, t) = \phi(x, y) \frac{\cosh k(h+z)}{\cosh kh} e^{-i\omega t} \tag{2.1}$$

where  $\omega$  is the wave frequency, and  $k$  the wave number which is the solution of the well-known dispersion relation

$$\omega^2 = gk \tanh kh. \tag{2.2}$$

The velocity potential on the still water level,  $\phi(x, y)$ , satisfies the Helmholtz equation

$$\nabla^2 \phi + k^2 \phi = 0, \tag{2.3}$$

in the flow domain with the no-flux boundary condition

$$\frac{\partial \phi}{\partial n} = 0, \tag{2.4}$$

on the perimeters of the cylinders and the backwall.

The incident waves propagate in the positive  $x$ -direction and their potential is expressed as

$$\phi_{inc} = e^{ikx}. \tag{2.5}$$

The scattered wave potential, which is the difference between the total wave potential  $\phi$  and the incident wave potential, must satisfy the radiation boundary condition at infinity. The radiation boundary condition, which requires the scattered waves be outgoing at infinity, can be stated as

$$\phi - \phi_{inc} \rightarrow Re^{-ikx}, \quad \text{as } x \rightarrow -\infty \tag{2.6}$$

where  $R$  is the reflection coefficient.

In the region of the wave chamber, two types of waves exist : waves propagating in positive and negative  $x$ -direction. Thus,

$$\phi \rightarrow T e^{ikx} + Q e^{-ikx}, \quad \text{as } 0 \ll x < l \quad (2.7)$$

where  $T$  and  $Q$  are the ratios of amplitudes of these waves to that of the incident wave, respectively. If we apply the no-flux boundary condition on the front line of the backwall to these two waves, we obtain

$$Q = e^{2ikl} T. \quad (2.8)$$

### 3 A Method of Matched Asymptotic Expansions

To find analytical solutions for the velocity potential,  $\phi$ , we develop a systematic procedure using a method of matched asymptotic expansions. First, the flow domain,  $0 < y < B$ ,  $-\infty < x < l$  is divided into two far-fields and a near-field. The near-field region is the flow domain in the vicinity of cylinders with the length scale of  $O(B)$ . The far-field regions are the flow domains far away from the cylinders, i.e.  $O(|x|/B) \gg 1$ , in which the length scale is the wave length. A method of matched asymptotic expansions is developed based on the assumption that  $kB = \varepsilon \ll 1$ .

#### 3.1 Far-Field Solutions

If we match the far-field solutions and the near-field solution far away from cylinders, so that  $O(|x|/B) \gg 1$  but  $O(|kx|) \ll 1$ , then evanescent modes can be discarded. In terms of the near-field coordinates  $(\bar{x}, \bar{y}) = (x/B, y/B)$ , (2.6) and (2.7) can be rewritten as:

$$\phi = e^{i\varepsilon\bar{x}} + R e^{-i\varepsilon\bar{x}}, \quad \bar{x} < 0 \quad (3.1a)$$

$$\phi = T e^{i\varepsilon\bar{x}} + e^{2ikl} T e^{-i\varepsilon\bar{x}}, \quad \bar{x} > 0. \quad (3.1b)$$

Expanding the reflection and the transmission coefficients in a power series of the small parameter  $\varepsilon$ , we have

$$R = \sum_{m=0}^{\infty} \varepsilon^m R_m, \quad (3.2a)$$

$$T = \sum_{m=0}^{\infty} \varepsilon^m T_m. \quad (3.2b)$$

Substituting (3.2) into (3.1), we obtain the inner expansions of the far-field solutions:

$$\begin{aligned} \phi &\sim (1 + R_0) + \varepsilon[R_1 + i(1 - R_0)\bar{x}] \\ &+ \varepsilon^2 \left[ R_2 - iR_1\bar{x} - \frac{(1 + R_0)\bar{x}^2}{2} \right] \\ &+ \varepsilon^3 \left[ R_3 - iR_2\bar{x} - \frac{R_1\bar{x}^2}{2} + \frac{i(R_0 - 1)\bar{x}^3}{6} \right] + \dots, \quad \bar{x} < 0 \end{aligned} \tag{3.3a}$$

$$\begin{aligned} \phi &\sim (1 + e^{2ikl})T_0 + \varepsilon[(1 + e^{2ikl})T_1 + i(1 - e^{2ikl})T_0\bar{x}] \\ &+ \varepsilon^2 \left[ (1 + e^{2ikl})T_2 + i(1 - e^{2ikl})T_1\bar{x} - \frac{(1 + e^{2ikl})T_0\bar{x}^2}{2} \right] \\ &+ \varepsilon^3 \left[ (1 + e^{2ikl})T_3 + i(1 - e^{2ikl})T_2\bar{x} - \frac{(1 + e^{2ikl})T_1\bar{x}^2}{2} - \frac{i(1 - e^{2ikl})T_0\bar{x}^3}{6} \right] \\ &+ \dots, \quad \bar{x} > 0. \end{aligned} \tag{3.3b}$$

The reflection and transmission coefficients,  $R_m$  and  $T_m$ , are to be determined by matching (3.3) with the outer expansions of near-field solutions.

### 3.2 Near-Field Solutions

In the near-field the potential function is also expanded in a power series of  $\varepsilon$ , i.e.

$$\phi = \sum_{m=0}^{\infty} \varepsilon^m \phi_m. \tag{3.4}$$

In terms of the near-field coordinates  $(\bar{x}, \bar{y})$  the governing equation, (2.3), can be rewritten as

$$\frac{\partial^2 \phi}{\partial \bar{x}^2} + \frac{\partial^2 \phi}{\partial \bar{y}^2} + \varepsilon^2 \phi = 0. \tag{3.5}$$

Substituting (3.4) into (3.5), we obtain a series of governing equations

$$\frac{\partial^2 \phi_m}{\partial \bar{x}^2} + \frac{\partial^2 \phi_m}{\partial \bar{y}^2} = 0, \quad m = 0 \text{ and } 1 \tag{3.6a}$$

$$\frac{\partial^2 \phi_m}{\partial \bar{x}^2} + \frac{\partial^2 \phi_m}{\partial \bar{y}^2} + \phi_{m-2} = 0, \quad m = 2, 3, 4, \dots \tag{3.6b}$$

The boundary condition requires that the no-flux condition be satisfied for all  $\phi_m$ , i.e.  $\partial\phi_m/\partial n = 0$  ( $m = 0, 1, 2, \dots$ ) along solid surfaces.

The solution of the Laplace equation and the homogeneous solutions of Poisson equation can be interpreted as a uniform flow passing an opening in a channel. The dimensional velocity potentials for the uniform flow,  $\phi'$ , can be written asymptotically as

$$\phi' \sim U'(x \pm C') + F' \quad x \geq 0 \quad (3.7)$$

in which  $U'$  is the velocity intensity,  $F'$  is an arbitrary constant and  $C'$  is the blockage coefficient. The blockage coefficient depends on the geometry of the cylinder and is independent of the wave characteristics. A brief discussion on the blockage coefficient for the circular and rectangular cylinders is given in Kakuno and Liu(1992). Rewriting (3.7) in a dimensionless form in terms of the near-field coordinates, we have

$$\phi \sim U \left( \bar{x} \pm \frac{C}{\varepsilon} \right) + F, \quad \bar{x} \geq 0 \quad (3.8)$$

in which

$$C = kC' \quad (3.9)$$

is the dimensionless blockage coefficient and is of order of magnitude of one or smaller. The scales in (3.8) and (3.9) are used so that the dimensional blockage coefficient,  $C'$ , can become large when the opening of the gap is small in comparison with the distance between two cylinders.

The velocity intensity  $U$  and the constant potential  $F$  are also expanded in terms of the small parameter,  $\varepsilon$ , i.e.

$$U = \sum_{m=0}^{\infty} \varepsilon^m U_m, \quad F = \sum_{m=0}^{\infty} \varepsilon^m F_m. \quad (3.10)$$

Substitution of (3.10) into (3.8) yields the outer expansions of the near-field potentials which are the solution of the Laplace equation.

### 3.3 Matching

After matching the far-field solutions of the leading order with the near-field solutions of the same order, the leading order coefficients may be obtained. The subsequent order coefficients may be calculated from the perturbation scheme with the known coefficients of the preceding order, that is,

$$U_0 = 0, \quad (3.11a)$$

$$F_0 = \frac{1 - iC(1 - e^{2ikl}) + e^{2ikl}}{1 - iC(1 - e^{2ikl})}, \quad (3.11b)$$

$$T_0 = \frac{1}{1 - iC(1 - e^{2ikl})}, \quad (3.11c)$$

$$R_0 = \frac{-iC(1 - e^{2ikl}) + e^{2ikl}}{1 - iC(1 - e^{2ikl})}, \quad (3.11d)$$

$$U_1 = i(1 - e^{2ikl})T_0, \quad (3.12a)$$

$$F_1 = \frac{-iM(iC - e^{2ikl} - 1)}{1 - iC(1 - e^{2ikl})}F_0, \quad (3.12b)$$

$$T_1 = \frac{(i + C)M}{1 - iC(1 - e^{2ikl})} F_0, \tag{3.12c}$$

$$R_1 = \frac{i[(1 + e^{2ikl}) - iC(1 - e^{2ikl})]M}{1 - iC(1 - e^{2ikl})} F_0, \tag{3.12d}$$

$$U_2 = \frac{e^{2ikl}M}{1 - iC(1 - e^{2ikl})} F_0, \tag{3.13a}$$

$$F_2 = \frac{(1 + e^{2ikl})T_2 + R_2}{2}, \tag{3.13b}$$

$$T_2 = \frac{(i + C)M}{1 - iC(1 - e^{2ikl})} F_1, \tag{3.13c}$$

$$R_2 = \frac{[i + C - (C - i)e^{2ikl}]M}{1 - iC(1 - e^{2ikl})} F_1, \tag{3.13d}$$

where  $2M$ , a net flux across the surface of the cylinder generated to compensate the flux by a symmetric part of the particular solution of the Poisson equation, is determined by

$$2M = - \int_{\Gamma} \frac{\partial}{\partial n} \left( -\frac{\bar{x}^2}{2} \right) ds = -\frac{S}{B^2} \tag{3.14}$$

where  $\vec{n}$  is pointing outward from the fluid region,  $\Gamma$  is the surface of the cylinder, and  $S$  is the half of the cross sectional area of the cylinder.

### 3.4 Reflection Coefficient

Up to the  $O(\varepsilon^2)$  the reflection coefficient can be expressed as

$$R = R_0 + \varepsilon R_1 + \varepsilon^2 R_2. \tag{3.15a}$$

The absolute value of the reflection coefficient of leading order is unity, which fulfill the energy conservation, regardless of the wave characteristics, the wave chamber width, and the porosity of the front wall, or  $C$ . The whole solution which includes higher-order terms, therefore, does not satisfy the energy conservation principle. In particular, the deviation of that solution from the principle become significant in the vicinity of region of  $l/\lambda = 0.5$ , where  $\lambda$  is the wave length.

### 3.5 Free surface displacement inside and outside the wave chamber

For design purpose, the free surface displacement in front of and behind the front wall, and in front of the backwall should be predicted. Knowing the phase difference in the free surface displacement inside and outside the wave chamber is helpful to get insight into the wave mechanics around the breakwater.

From the linear wave theory the free surface displacement can be related to the velocity potential  $\Phi$  through the free surface boundary condition



$$\eta = \Re e \left[ -\frac{1}{g} \frac{\partial \Phi}{\partial t} \right]_{z=0} \tag{3.16}$$

Substituting (2.1) into the above equation and collecting the real part of the resulting equation, we obtain

$$\eta = \frac{\omega}{g} \sqrt{\alpha^2 + \beta^2} \sin \left[ \omega t + \tan^{-1} \frac{\alpha}{\beta} \right] \tag{3.17}$$

where

$$\alpha = -\Im m[\phi(x, y)], \tag{3.18a}$$

$$\beta = \Re e[\phi(x, y)]. \tag{3.18b}$$

The phase difference in the free surface displacement inside and outside the wave chamber is, therefore,

$$\theta = \tan^{-1}(\alpha_O/\beta_O) - \tan^{-1}(\alpha_I/\beta_I) \tag{3.19}$$

where the subscript "O" and "I" stand for "outside" and "inside" of the wave chamber.

### 4 Energy Dissipation Model

As shown in (3.7) the outer expansions of the near-field solutions represent uniform flows with a difference in potential level. This difference denoted by the blockage coefficient,  $C'$ , can be related to the pressure drop between the front and the rear of the front wall. In the dimensional form, the dynamic pressure is defined as

$$P = -\rho \frac{\partial \Phi}{\partial t} = i\rho\omega\phi(x, y) \frac{\cosh k(h+z)}{\cosh kh} e^{-i\omega t} \tag{4.1}$$

Substituting (3.7) into the above equation, we obtain the dynamic pressures in front of and behind the wall

$$P = i\rho\omega[U'(x \pm C') + F'] \frac{\cosh k(h+z)}{\cosh kh} e^{-i\omega t}, \quad x \gtrless 0 \tag{4.2}$$

If we neglect terms whose order are higher than  $O(k^2)$ , the pressure difference between  $P_+$  and  $P_-$  is

$$\Delta P = P_- - P_+ = 2\rho C' \dot{U} \tag{4.3}$$

where

$$\dot{U} = \frac{dU}{dt}; \quad U = U' \frac{\cosh k(h+z)}{\cosh kh} e^{-i\omega t} \tag{4.4}$$

Therefore, the blockage coefficient  $C'$  plays a role of a coefficient of inertia resistance which is proportional to the acceleration of the oscillating flow  $U$ , (4.4).

To include the effects of energy dissipation due to flow separation in front of and behind the front wall, we assume that the flow separation is confined within the near field region. We assume that the energy dissipation causes an additional pressure drop, which is linearly proportional to the oscillating velocity  $U$ . Thus

$$\Delta P = 2\rho C' \dot{U} + 2\rho C'_i \omega U \tag{4.5}$$

in which  $C'_i$  can be considered as an empirical coefficient modeling the effects of energy dissipation. The simple model (4.5) can be derived in a different way. We introduce the blockage coefficient  $C'$  in (4.2) as a complex constant, i.e.

$$C' = C'_r + iC'_i \tag{4.6}$$

so that  $C'_r$  is the actual blockage coefficient based on the potential flow theory. Substituting (4.6) into (4.2), we can derive (4.5) with  $C'$  being replaced by  $C'_r$ . The significance of the simple relations stated in (4.5) and (4.6) is that when the energy dissipation is important, one can calculate the reflection coefficient (3.15) by replacing  $C$  by  $C'$ .

It is well known that the energy loss due to the flow separation is proportional to the square of the flow velocity through the opening, i.e.

$$\frac{\Delta P}{\rho g} = f' \frac{V^2}{2g} \tag{4.7}$$

where  $f'$  is the energy loss coefficient and  $V$  is the average velocity at the opening ( $x = 0$ ). Because the dissipation model introduced in (4.5) is linear in the velocity field, we must ensure that the same total energy loss (work done) over a wave period is determined by the quadratic resistance law and by the linear model. By equating the work done (energy loss) calculated from the linear model and the one calculated from quadratic resistance law, we get

$$\frac{C'_i}{B} = \frac{|\tau|(H/\lambda)f}{9\pi/4 (a/B)^2 (B/\lambda)} \left[ \frac{\sinh^2 kh + 3}{\sinh 2kh + 2kh} \right] \tag{4.8}$$

and

$$f = f' \gamma \tag{4.9}$$

in which "a" denotes the half-width of the opening, "H" is the incident wave height,  $\gamma$  is an empirical coefficient, and  $\tau$  is the ratio of the uniform velocity far away from the cylinder to the water particle velocity of the incident wave at the same position, and expressed as

$$\tau = (1 - e^{2ikl})T. \tag{4.10}$$

Equation (4.8) relates  $C'_i$  to the wave characteristics,  $H/\lambda$ ,  $\tau$ ,  $kh$ , and the geometry of the cylinder,  $a/B$  and  $B/\lambda$ . Only one dimensionless coefficient,  $f$ , need to be determined. The value of  $f$  may hold the same as that for the case without the backwall, say, 1.5 for rectangular cylinders.

## 5 Comparison Between Theoretical Solutions and Laboratory Data

To validate the theoretical models with the value of  $f = 1.5$  for rectangular cylinders, experimental data obtained in Osaka City University are compared with theoretical results.

The cylinders used are square. The experiments are performed in a wave tank, which is 1.0m wide, 50m long and 1.75m deep. The side lengths of the square cylinders are 15cm for the case of  $B/l = 0.129$  and 5cm for other cases. The water depth is kept constant at  $h = 50\text{cm}$ . The wave steepness  $H/\lambda$  varies slightly around 0.01. The wave heights are measured in front of and behind the front wall and in front of the backwall.

From Figure 2(a) to Figure 2(d), the laboratory data for the reflection coefficients are compared with the theoretical results obtained for  $f = 1.5$ , for different parameters,  $a/B$  (porosity),  $B/l$ , and  $h/B$ . The theoretical results obtained from the leading term only and from higher-order terms are shown in the figures. The discrepancy between these two types of the results is slight except the region of  $l/\lambda = 0.5$  where the higher-order solutions exhibit singular behavior. The agreement between data and theoretical results from the leading term only is good so that it is suffice for practical use to employ only the leading term. In Figure 3, the all experimental data of the reflection coefficients are plotted against the theoretical results. Both are in good agreement except for the region where the values are close to unity.

Figure 4 shows an example of the comparison in the free surface displacements at three locations inside and outside the wave chamber. The vertical displacements are normalized by the incident wave amplitude. Figure 5 plots the phase difference between the locations inside and outside the chamber. Both figures are the results based on the leading order approximation. The locations at which the free surface displacements are measured are indicated in the captions of each figure. The agreement between data and theory is again good for these results. Note that nodes appear behind the cylinders at a definite value of  $l/\lambda$ . Sudden jumps shown in the phase difference, which is about  $\pi$ , are because that the location of the wave gauge behind the cylinder ( $x_2$ ) is in the vicinity of a nodal point.

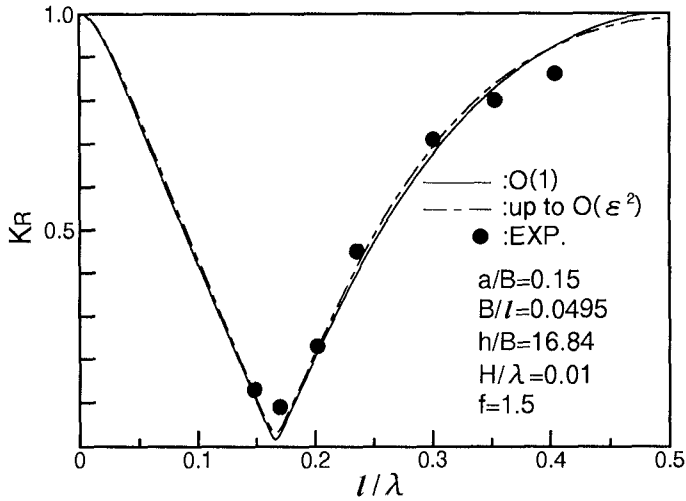


Figure 2(a). Comparison between theoretical and experimental data for reflection coefficient.

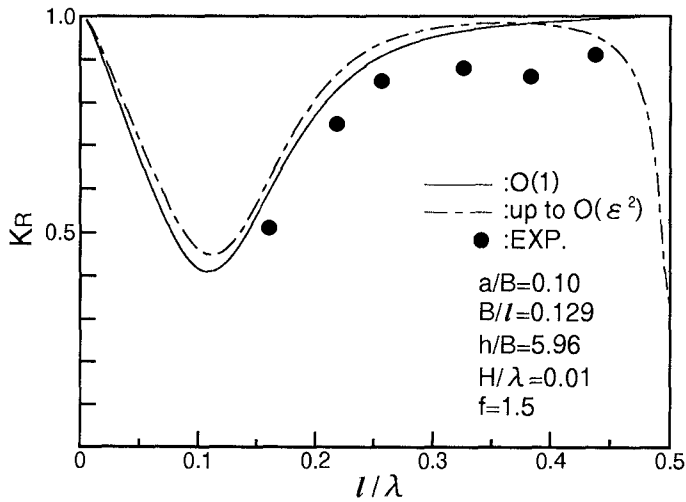


Figure 2(b). Comparison between theoretical and experimental data for reflection coefficient.

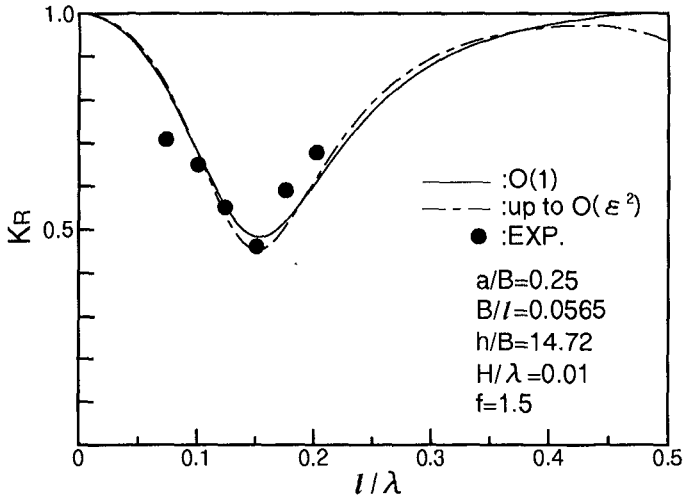


Figure 2(c). Comparison between theoretical and experimental data for reflection coefficient.

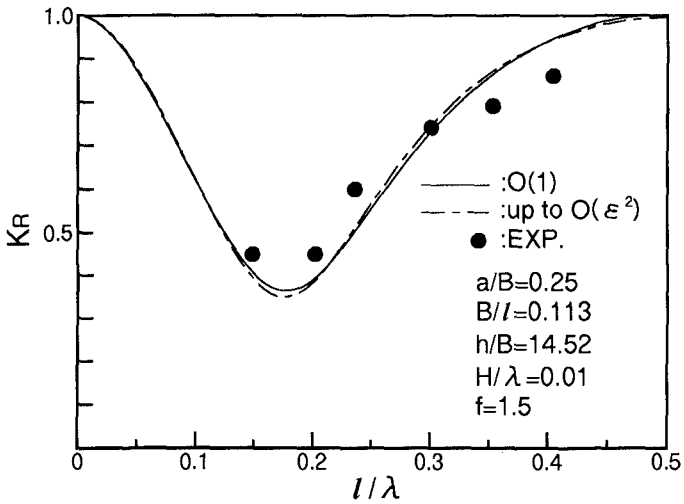


Figure 2(d). Comparison between theoretical and experimental data for reflection coefficient.

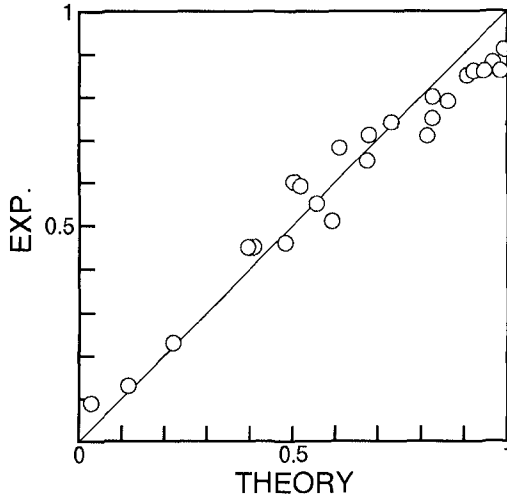


Figure 3. Comparison between measured and calculated reflection coefficients.

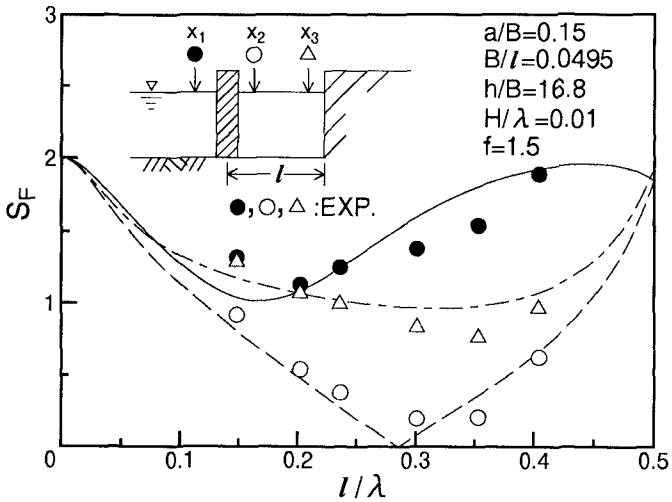


Figure 4. Comparison between theoretical and experimental data for free surface displacements,  $x_1/l = -0.125$ ,  $x_2/l = 0.125$ ,  $x_3/l = 0.917$ .

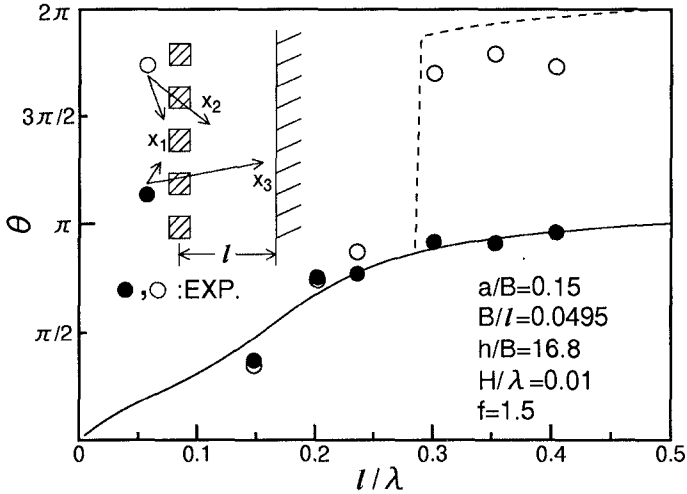


Figure 5. Comparison between theoretical and experimental data for phase differences between inside and outside the chamber,  $x_1/l = -0.125$ ,  $x_2/l = 0.125$ ,  $x_3/l = 0.917$ .

## 6 Conclusion

A modified method of matched asymptotic expansions has again been applied to study the wave interactions with a slit-type breakwater. The energy dissipation caused by the flow separation behind the cylinders is considered in the theory. Theoretical results with the empirical coefficient for square cylinders determined in the previous study are verified by experimental data. It is shown that the leading order solutions are accurate and can be used to calculate reflection coefficients and the wave action in the vicinity of the breakwater.

## 7 Acknowledgment

PLFL would like to acknowledge the support from New York Sea Grant Institute.

## 8 References

- [1] Fugazza, M., and L. Natale. (1992). Hydraulic design of perforated breakwaters, *J. Waterway, Port, Coastal, and Ocean Eng.*, ASCE, Vol.118, No.1, pp.1-14.

- [2] Jarlan, G. E. (1961). A perforated vertical wall breakwater, The Dock & Harbour Authority, VOL XLI, No.486, pp. 394-398.
- [3] Kakuno, S. and P.L.-F. Liu. (1992). Scattering of water waves by vertical cylinders, to be published in the J. Waterway, Port, Coastal and Ocean Engrg., ASCE.



## CHAPTER 96

### HYDRAULIC MODEL EXPERIMENTS ON SEAWALLS

by

J.W.Kamphuis<sup>1</sup>, K.A.Rakha, J. Jui.

#### ABSTRACT

The preliminary analysis of a set of three-dimensional tests on an infinite beach backed by a seawall is presented. The longshore sediment transport rate in front of the seawall was found to decrease as the beach in front of the seawall eroded. The location of the breaker peaks in the suspended and bed load sediment transport rate moved slightly offshore, and the bedload peak in the swash zone disappeared as the beach eroded. The local ratio of  $H/d$  approached a constant value as the beach eroded for most of the tests, however the erosion depth in front of seawalls cannot be simply related to offshore wave height.

#### INTRODUCTION

The function of a seawall is to protect the land behind it by fixing the land-sea boundary. It does not protect either the beach fronting it or adjoining unprotected beaches. Since seawalls are usually built along eroding rather than stable shorelines, they have commonly been perceived as causing or contributing to erosion rather than simply responding to a pre-existing erosion problem. When a seawall is constructed on an eroding coast, existing erosion processes will continue to decrease the size of the beach in front and eventually the beach in front of the seawall will disappear if there is inadequate sediment supply. The seawall protection solution prevents further recession of the coastline; it does not stop the physical processes which cause erosion. The extent to which a seawall affects the processes on

---

<sup>1</sup>Department of Civil Engineering  
Queen's University, Kingston, Ontario, Canada K7L 3N6

the fronting and adjacent beaches at any one time largely depends on the location of the seawall relative to the active shoreface and only indirectly on the level of wave action to which it is subjected.

Kraus (1988) presented an extensive review of approximately 100 technical papers on the effect of seawalls. Since most laboratory studies used wave flumes and investigated cross-shore sediment transport processes only, the effect of the seawall on the longshore sediment transport rate could not be deduced.

The set of experiments presented here was performed as a part of a comprehensive three-dimensional study of the effects of seawalls on the nearshore processes. The fundamental case of an infinite beach backed by a seawall is considered here. Wave heights, wave setup, longshore velocity distributions, longshore sediment transport rates, and longshore sediment transport distributions were measured. Preliminary analysis of the data is presented here.

## EXPERIMENTS

Five tests were carried out in a three-dimensional model basin (Figure 1). These tests are an extension of previous three dimensional sediment transport studies carried out in the same facility (Kamphuis, 1991a, 1991b, 1991c). A vertical seawall was constructed on a sandy beach of median grain size 0.12 mm. The test conditions are summarized in (Table 1). A time series of waves, simulating a Jonswap wave spectrum was used with a 10 degree incident wave angle, a peak period of 1.15 seconds and wave heights varying from 0.05 to 0.09 m. The random wave signal repeated itself after 200 waves.

A plane beach of initial slope 1:10 was first prepared for each test. This initial profile was allowed to reshape itself under wave action to approach equilibrium. The water level in the basin was chosen so that only about one percent of the incident waves impacted on the seawall at the top of the beach when the beach approached equilibrium, thus simulating a seawall well back on the beach. The water level was then raised in all tests except Test A to simulate storm surge. This resulted in the initial percentages of wave impact on the seawall as shown in Table 1. The tests were continued until a new equilibrium profile in front of the seawall was approached.

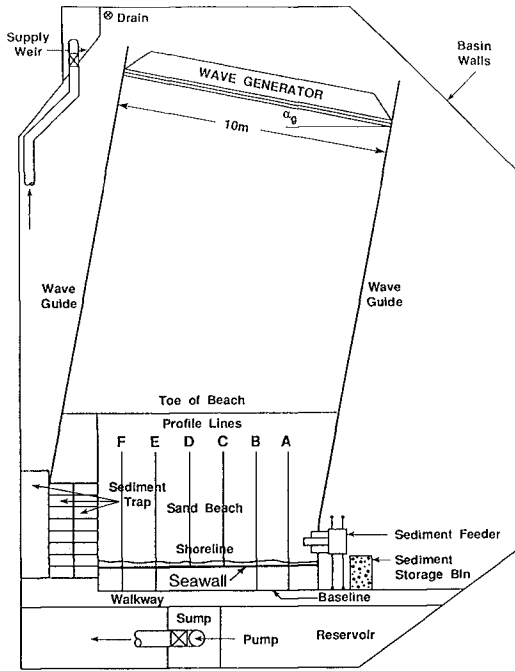


FIGURE 1 EXPERIMENTAL FACILITY

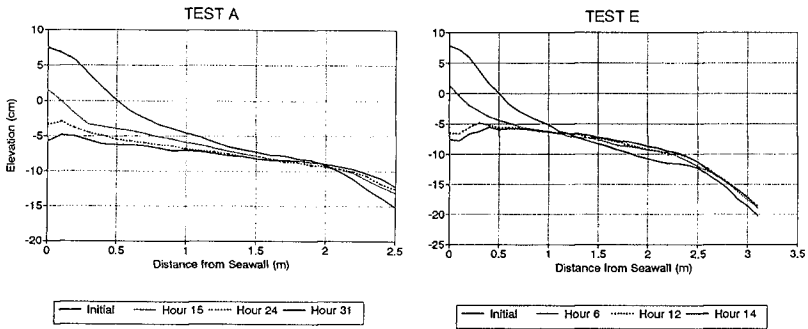


FIGURE 2 PROFILE DEVELOPMENT

TABLE 1  
TEST SUMMARY

TEST	GENERATED WAVE CONDITIONS			SURGE	TEST DURATION	
	Height Hs (cm)	Period Tp (sec)	Angle $\alpha$ (deg)	S (cm)	t (hr)	% touch
A	7	1.15	10.0	0.0	32	1.0
D	7	1.15	10.0	2.2	12	20
E	9	1.15	10.0	-	14	10
F	5	1.15	10.0	-	22	10
G	7	1.15	10.0	1.6	18	10

Each test consisted of a series of hourly segments. Wave heights, longshore velocity distributions, and beach profiles were measured during each segment. Wave heights were recorded using capacitance type wave gauges. One wave gauge was mounted offshore to record the incident wave height. Fifteen wave gauges were mounted on a horizontal beam at regular intervals of 0.2 m through the breaking zone. Longshore velocities were measured using a mini electro-magnetic current meter. Profiles of the beach in front of the seawall were measured along six parallel lines evenly spaced along the seawall. The profiles presented here are the average of profiles B,C,D, and E (Figure 1).

A sediment trap was located at the downdrift end of the beach but within the wave guides. It was designed to separate the bedload from suspended load and to measure their distributions across the swash and surf zone. Sediment Transport rates were measured every 15 minutes. Sediment transport distributions were measured every 4 hours. A detailed description of the sediment trap layout can be found in Kamphuis (1991c).

To represent an "infinitely long" beach, it is necessary to maintain parallel contours along the study area. For this purpose, sediment was supplied at the updrift end of the beach by a feeder at a rate comparable to the sediment transported along the beach.

## RESULTS

The tests essentially consist of two groupings. There are 3 tests with 7 cm high incident waves, with 1, 10, and 20 % of the waves directly impacting the seawall at the beginning of the test (Tests A,G, and D). Then there are 3 tests in which 10 % of the waves are initially incident on the seawall but in which the nominal incident wave height is 9, 7, and 5 cm (Tests E,G, and F). Test G is common to both sets. Figure 2 shows examples of the profile change with time. Figure 3 shows the initial and final profiles for all the tests.

The beach in front of the seawall gradually disappeared and the sand was eroded to well below the water level. The eroded sediment was deposited offshore, and a nearly horizontal plateau was formed. The horizontal plateau extended seaward to the breaker location. Very near the seawall a local scour hole was also observed in all the tests.

Figure 4 shows examples of the suspended, bed, and total longshore sediment transport rates as they evolved in time. All rates decreased as the foreshore eroded, because energy dissipation resulting from breaking decreased towards the end of the test. As the depths increased, more wave reflection and less breaking occurred. The longshore sediment transport rates tended toward equilibrium values.

Figure 5 shows an example of the development of the suspended and bed load distributions with time. The peaks of the distributions moved slightly offshore, following a slight offshore movement of the breaker location. As the test progressed the bedload peak in the swash zone disappeared and both distributions tended to have one single peak near the breaker location.

## PRELIMINARY ANALYSIS OF RESULTS

The present data set together with additional tests will be used to develop a Quasi-3D numerical model. This model will be an extension of the work of Briand (1990) by including wave reflection off the seawall. In the present paper a preliminary, general analysis of the data will be presented.

Figure 6 shows the wave height profiles at the ends of the tests. It is seen that the wave heights increase up to the breaking point and then decrease as wave energy dissipates. Up to breaking, the wave height profile is entirely predicted by combining small

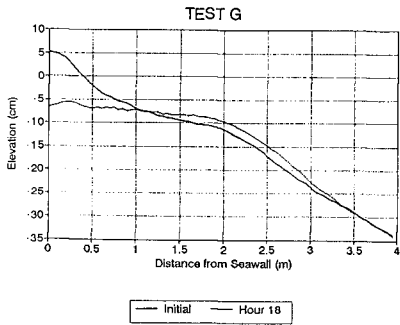
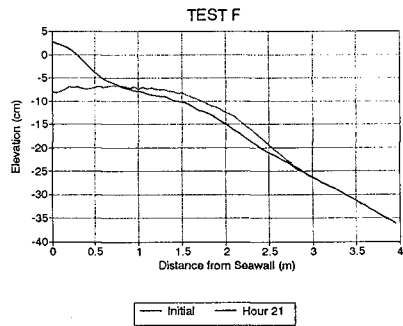
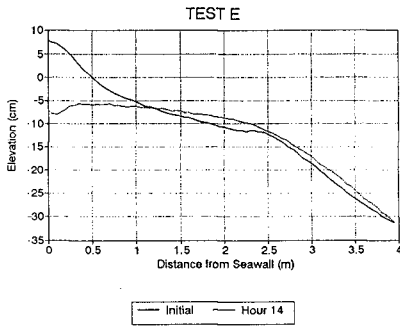
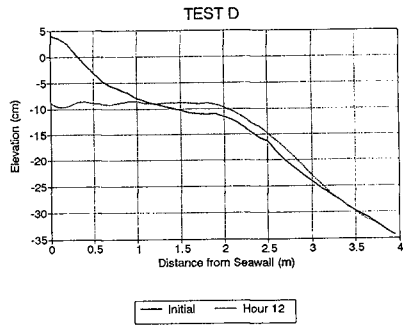
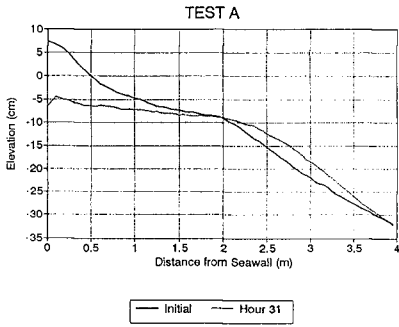


FIGURE 3  
INITIAL AND FINAL PROFILES

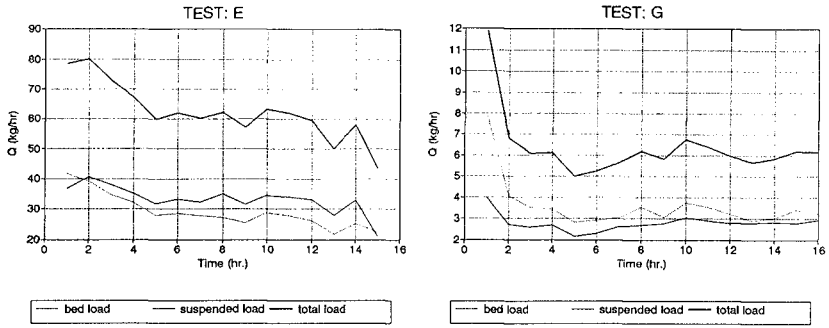


FIGURE 4 SEDIMENT TRANSPORT RATE

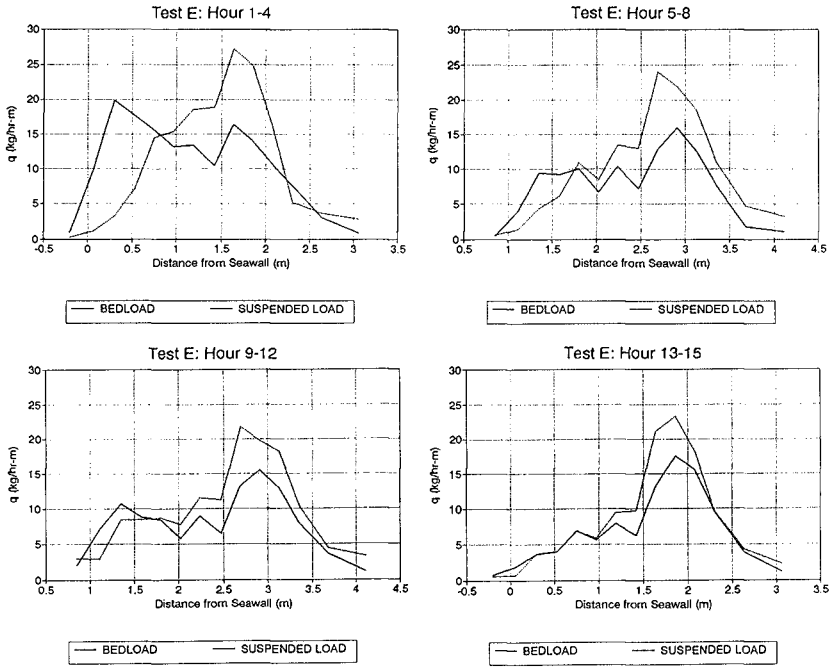


FIGURE 5 SEDIMENT TRANSPORT RATE DISTRIBUTION

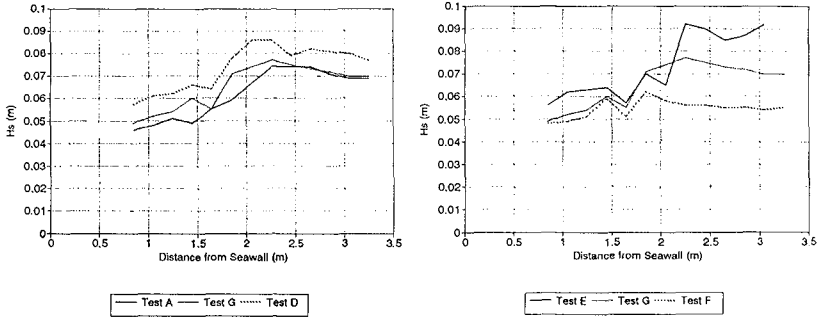


FIGURE 6

WAVE HEIGHT DECAY

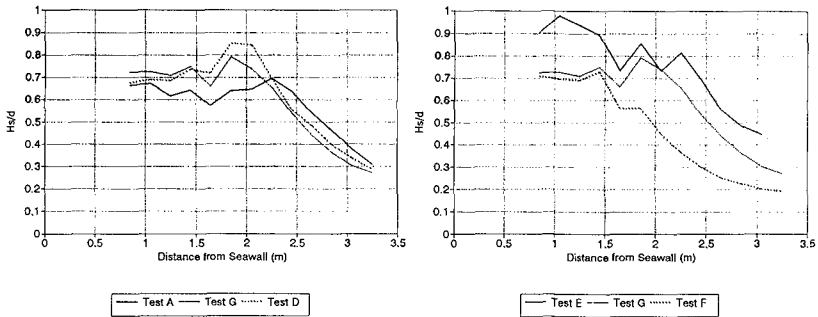


FIGURE 7

WAVE HEIGHT TO LOCAL DEPTH RATIO

amplitude shoaling theory, Snell's law and bottom friction (Kamphuis 1991a). Breaking is predicted by the incipient breaking criterion of Kamphuis (1991b) and the decrease in wave height is predicted by Kamphuis' (1993) adaptation of the energy dissipation rate proposed by Dally et al (1984). At about 1.5 m from the structure, however, the profile indicates a substantial reduction in wave energy dissipation rate. The remaining wave energy is simply reflected back to sea.



the simple ratio  $H_s/d$  and it is seen that near the structure water depth is indeed directly related to the wave height. In fact the ratio is about the same (0.7) for all tests except Test E (which is thought to contain a small error in depth measurement).

The average depth over the plateau from the seawall to the breaker ( $d_p$ ) is shown in Table 2.

TABLE 2  
SUMMARY OF PROFILE RESULTS

TEST	INPUT CONDITIONS			FINAL RESULTS		
	$H_s$ (cm)	$S$ (cm)	% touch	$H_{sb}$ (cm)	$X_b$ (m)	$d_p$ (cm)
A	7	0.0	1	7.4	2.5	7.4
G	7	1.6	10	7.7	2.3	7.7
D	7	2.2	20	8.7	2.2	9.2
E	9	-	10	9.2	2.6	7.7
G	7	1.6	10	7.7	2.3	7.7
F	5	-	10	6.2	1.9	7.5

For Tests A, G, and D, it was found to be approximately equal to the breaking significant wave height. This seems to support the idea that scour depth is related to incident deep water wave height (Kraus, 1988). For Tests E, G and F, however,  $d_p$  is almost constant, even though the wave height decreases from 9 to 5 cm. This would tend to indicate that depth is not related to wave height in a simple manner.

Depth of water over the plateau is actually a complex interaction between wave height, water level, the beach, and the seawall. This interaction may be explained using the conceptual model in Figure 8.

Assume that a beach profile is in equilibrium with the incident wave climate, as in Figure 8a. Its depth ( $d$ ) is defined everywhere out to a closure depth,  $d_c$ . If a storm surge ( $S$ ) raises the water level, the whole equilibrium profile will rise to follow the new water

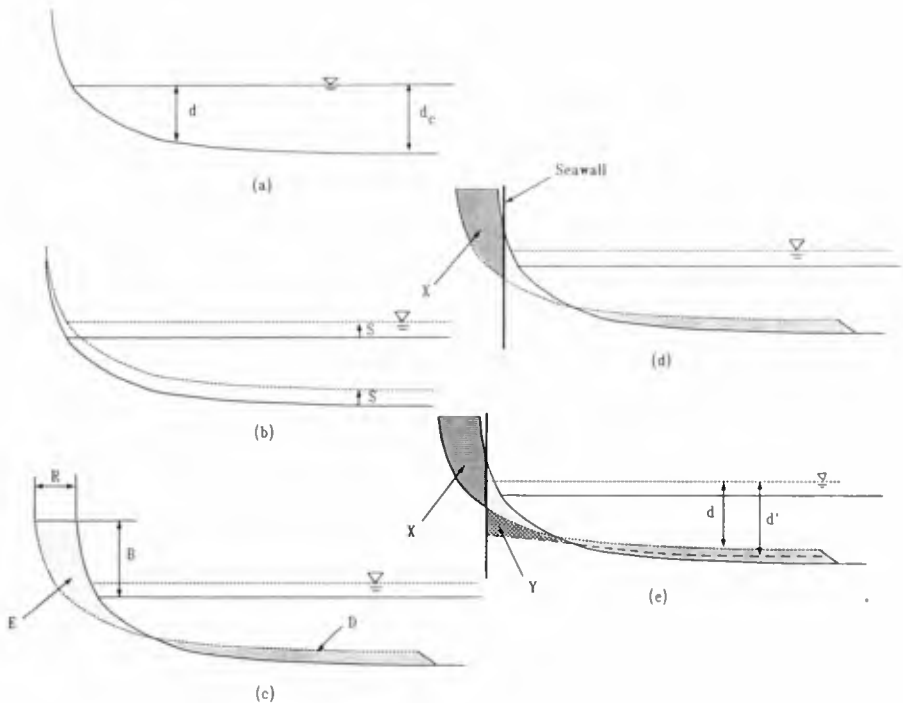


FIGURE 8 CONCEPTUAL MODEL OF EROSION NEAR A SEAWALL

level (Figure 8b). To raise the beach profile, however, requires additional sand and normally the existing profile must supply this, resulting in a profile recession ( $R$ ) as shown in Figure 8c. The eroded area ( $E$ ) must balance the area of deposition ( $D$ ) and hence  $R$  is a function of  $B$ , the berm or dune height above the water. This mechanism has been described by Bruun (1962) and others.

If a seawall is introduced (Figure 8d), a portion of the erosion zone ( $X$ ) is now no longer available to feed the deposition zone. The thickness of the deposition layer will be less and hence the water depth will be

greater. Reflection off the seawall, however, causes an increase in depth near the structure adding a volume of sand (Y) to the erosion volume. The total erosion volume with a seawall in place is therefore  $(E-X+Y)$ . Since Y is normally less than X, as shown for example by Barnett (1988),  $d'$  is normally greater than  $d$ . Storm surge therefore results in greater water depth near the structure (relative to the raised water level). Similarly, it may easily be shown that the depth increases when S increases.

Tests A,G and D began on the same equilibrium profile. Storm surge increased the depth over the plateau. Larger storm surge resulted in larger depths of water. This in turn permitted larger wave heights to occur over the plateau and interaction with these larger wave heights produced the final profiles.

Tests E,G and F began with different initial profiles; the wave height varied from 9 to 5 cm. The larger wave heights produced a larger runoff which means that the seawall was placed relatively further back in Figure 8. This implies that X was smaller and Y was larger, causing  $(E-X+Y)$  to be larger and the resulting water depth to be smaller. At the same time to increase the percent of waves impacting the structure from the 1% on the original equilibrium profile the test value of 10% required a larger storm surge for the larger wave heights. This caused the depths to be larger. Here we have two processes which compensated for each other in Tests E,G and F, resulting in the almost constant value of  $d_p$ .

The breaker location  $X_b$  moved further offshore for the larger wave heights (Table 2). This provided a longer distance for energy dissipation to occur. A calculation using the Kamphuis (1993) modification of the Dally et al (1984) wave dissipation model shows that a distance of 0.3 m is required to reduce the wave height from 9 cm to 7 cm in Test E, and 0.48 m to reduce the wave height from 7 cm to 5 cm in Test G. The actual differences between the breaker locations were found to be 0.3 m for Tests E and G, and 0.4 m for Tests G and F. Thus, a longer breaker distance permitted the higher offshore wave heights to reduce to the same heights close to the seawall, as shown in Figure 7. This resulted in similar depths over the plateau.

The depth of scour to wave height relationship is simple, but physically rather meaningless. Our research (not presented here because of page limits) has shown that scour depth can also be related to the wave climate

using energy dissipation and critical shear stress concepts.

To determine whether seawalls accelerate erosion, a comparison with beaches without structures is required. (Kraus, 1988). Long term tests are underway to make such comparisons. Preliminary results indicate that seawalls do not create disastrous increases in erosion rates, but this work is not complete at the present time.

#### CONCLUSIONS

The equilibrium profile developed in front of the seawall is a complex function of the initial profile, the storm surge, and the wave climate.

The longshore sediment transport rate decreased as the beach eroded in front of the seawall.

The location of the breaker peaks in the longshore suspended and bed load sediment transport rate distribution moved slightly offshore as the beach eroded. The bedload peak in the swash zone disappeared as the foreshore eroded.

The local depth was found to be closely related to the local wave height; the ratio  $H/d$  approached a constant value as the beach approached an equilibrium condition. However, average scour depth in front of a seawall can not be simply related to offshore wave height.

#### ACKNOWLEDGMENTS

This study was carried out under the Strategic Grants Program of the Natural Sciences and Engineering Research Council (NSERC) of Canada. The careful hydraulic testing was carried out by J. Kooistra and J. Jui.

#### REFERENCES

- Barnett, M.R., Wang, H. (1987). Effects of a vertical seawall on profile response. Proc. 21st Int. Conf. Coastal Eng., ASCE, Vol.2, pp.1493-1507.
- Bruun, P. (1962). Sea level rise as a cause of shore erosion. Waterway, Port, Coastal, and Ocean Eng., ASCE, Vol. 88, p.117.
- Dally, W.R., Dean, R.G., and Dalrymple, R.A. (1984). A model for breaker decay on beaches. Proc. 19th Int. Conf. Coastal Eng., ASCE, Vol.1, pp.82-98.

- Kamphuis, J.W. (1991a). Wave transformation. *Coast. Eng.*, Vol.15, pp.173-184.
- Kamphuis, J.W. (1991b). Incipient wave breaking. *Coast. Eng.*, Vol.15, pp.185-203.
- Kamphuis, J.W. (1991c). Alongshore sediment transport rate. *Waterway, Port, Coastal, and Ocean Eng.*, ASCE, Vol. 117, pp.624-640.
- Kamphuis, J.W. (1993). Wave height decay from deep water through the breaking zone. *Waterway, Ports, Coastal and Oceans Eng.*, submitted for publication.
- Kamphuis, J.W. (1993a). On the validity of two-dimensional beach profile tests. *Waterway, Port, Coastal, and Ocean Eng.*, submitted for publication.
- Kraus, N.C. (1988). The effects of seawalls on the beach: An extended literature review. *J. of Coastal Research*, Special issue No.4, pp.1-28.

## CHAPTER 97

### MOVEMENT AND STATIC STRESS IN DOLOSSE: SIX YEARS OF FIELD MONITORING AT CRESCENT CITY

Thomas R. Kendall, <sup>1</sup>M. ASCE  
and  
Jeffrey A. Melby, <sup>2</sup>A.M. ASCE

#### ABSTRACT

Breakwater failures have often been caused by or at least exacerbated by a structural failure of concrete armor units, especially when the units are the more slender type such as dolosse. To aid in the development of a structural design procedure for complex concrete armor units, post-construction monitoring of movement and stress in dolosse has been ongoing on the outer breakwater at Crescent City, California since its rehabilitation in 1986. This paper describes the significance of static stress in large (38-tonne) dolosse and documents the continued rapid growth of dolos static stress in a relatively nested shallow-water breakwater. New data from 1990, 1991 and 1992 have modified the previously suggested conclusion that dolos static stress was increasing at a decreasing rate (Kendall and Melby, 1989). These new data suggest that while dolos movement has continued to subside, static stress has been building approximately linearly.

This paper is divided into two basic sections:  
(1) general background on dolos design considerations and the monitoring program being carried out at Crescent City, including new techniques for the

<sup>1</sup>Civil Engineer, U.S. Army Corps of Engineers, San Francisco District, 211 Main Street, San Francisco, CA 94105-1905, USA

<sup>2</sup>Research Hydraulic Engineer, Coastal Engineering Research Center, U.S. Army Corps of Engineers, Waterways Experiment Station, 3909 Halls Ferry Road, Vicksburg, MS 39180-6199, USA

photogrammetric monitoring of armor unit displacement; and (2) breakage, displacement, and static stress results through the sixth year of monitoring.

## BACKGROUND

Following the rehabilitation of the Crescent City Outer Breakwater with dolosse in 1986, extensive field data were collected on incident waves, dolos loading and displacement. These data have been collected in support of a program whose objective is the development of a structural design procedure for dolosse based on breakwater design wave conditions. The procedures developed are intended to be applied to other armor types in addition to dolosse. The monitoring program and design procedure development are detailed in several publications, including Kendall, et al (1985), Howell (1986 and 1988), Kendall (1988), Howell and Melby (1991), Melby (1992 and in publication), Melby and Turke (1992), and Howell, et al (in publication).

The need for a dolos structural design methodology has been apparent in the United States since the early 1970's when the units were first introduced to the U.S. Dolosse were recognized for their excellent hydraulic stability and judged to be an economic armor unit choice for the severe wave climate of the northern California Coast. The north and south jetties at Humboldt, California were armored with two layers of 38-tonne dolosse around the head sections as part of their rehabilitation in 1971-1972 and 36-tonne dolosse were placed on the Crescent City Outer Breakwater as part of its rehabilitation in 1973-1974.

Uncertainty in the loading criteria applicable for any structural design of the dolosse led to two different approaches for the initial Humboldt and Crescent City dolos rehabilitations. The first dolosse at Humboldt were typically reinforced while those at Crescent City were unreinforced. Most of the Humboldt dolosse were reinforced with standard cage reinforcing using 40ksi (276MPa) steel rebar. Twelve No. 8 (2.5-cm diameter) longitudinal and four No. 4 (1.25-cm diameter) tie bars were placed in each fluke and shank under a 6-in (15-cm) concrete cover, representing 75 lbs of steel per cubic yard of mix ( $44\text{kg/m}^3$ ). However, analysis supported by field tests suggested that the quantity and strength of steel were not sufficient enough to contribute strength after concrete cracking. For the field tests, pairs of cage-reinforced, steel-fiber-reinforced, and unreinforced units were clamped together at the flukes

and then forced apart with hydraulic jacks operating on the opposite flukes. These test results plus the added cost of reinforcing led to the decision to experiment with exclusively unreinforced dolosse at Crescent City.

The majority of the unreinforced dolosse placed at Crescent City subsequently failed leading to the 1986 rehabilitation and monitoring program. Kendall and Melby (1989) provide more detail on these dolosse and their subsequent failure.

The second rehabilitation with dolosse at Crescent City was completed in September 1986 and monitoring began shortly thereafter. A total of 680 steel-fiber-reinforced 38-tonne dolosse were used in the repair. None of the original broken 36-tonne dolosse were removed as part of the rehabilitation. Fiber reinforcing (80 lbs of steel fiber per cubic yard of mix or  $47 \text{ kg/m}^3$ ) was used in the new dolosse, in part, as an experiment. Lab and field tests indicated that the fibers did not significantly increase the strength of the concrete, but did add toughness which would help hold the units together after fracture. The flexural strength of the concrete was measured at 984 psi (6.8 MPa) (Kendall and Melby, 1989).

The dolos section of the monitored breakwater (Figure 1) is located in 7.5 to 9 meters of water and is subjected to depth-limited breaking waves of up to 10.5 meters in height with peak periods between 15 and 20 seconds (Hales, 1985; Kendall, 1988).

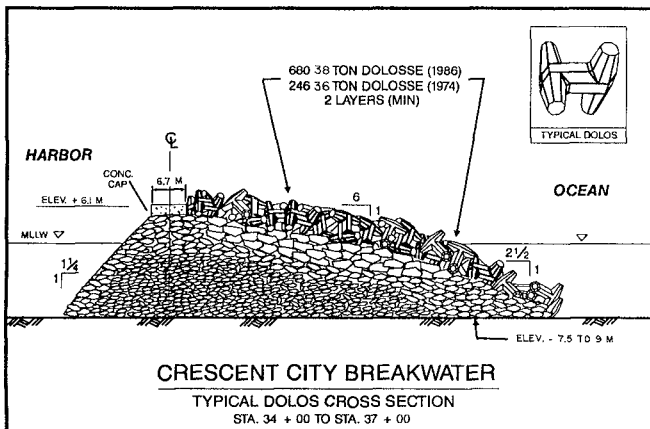


Figure 1 - Typical cross-section through the dolos section of the Crescent City Outer Breakwater



### Dolos Stress Monitoring

Dolos stress data have been derived from strains measured with gages internally mounted in select dolosse grouped together near the center of the dolos field. Twenty such dolosse were originally placed for the monitoring program. The strain signals are used to measure two moments and a torque at the shank-fluke interface of the dolos (Howell, 1988). Burcharth and Howell (1988) and Melby (1989) provide discussions on the computation of maximum principal tensile stress for a cross-section in the dolos shank and the comparison of that stress with concrete splitting strength as a failure criteria.

Two types of stresses have been recorded with the instrumented dolosse at Crescent City: wave-induced pulsating stresses and static stresses. Dolos stress data from the initial intensive monitoring period (1987-88) have been used to demonstrate that the mean over the sampled dolos field of the maximum wave-induced pulsating stress is linearly related to the average of the highest one-tenth of the waves in a 30-minute time series. Furthermore, the distribution about the mean of the maximum wave-induced pulsating stress is well described by the Rayleigh distribution (Howell and Melby, 1991). For the 38-tonne dolosse at Crescent City, however, these pulsating stresses were found to be nearly an order of magnitude lower than the recorded static stresses caused by self weight and settling-induced nesting or wedging forces. In many instances, the dolos static stress has consumed well over half of the concrete splitting strength.

Dolos static stress continues to be monitored from a diminishing sample of instrumented dolosse at Crescent City. Static moment data, which are reduced to principal stresses, are collected from the still functioning dolosse each summer. The data are sampled from each dolos at 1Hz for six minutes. Typically, with six functioning dolosse, the sampling rotates to each dolos once every hour. The minimum collection period is generally 24 hours. Only data passing a series of reliability tests are retained. These tests include verifying that the RMS error in each six-minute data file is within the range produced by environmental noise, i.e. temperature variations and small wave loads. If a single dolos repeatedly fails the reliability tests, then that dolos is dropped from the data acquisition system.

### Displacement and Breakage Monitoring

To better understand the overall behavior of the dolos field, the stress samples are supplemented by detailed surveys of dolos movement and breakage. Periodic aerial photography and low-altitude, high-resolution photogrammetry have been the primary tools used in this supplemental data collection. In addition, available nearby National Oceanic and Atmospheric Administration (NOAA) buoy records have been retrieved to track wave power offshore of Crescent City.

For the photogrammetric monitoring of displacement, targets were established on 26 dolosse. Eighteen of these are located in the instrumented section and eight are distributed uniformly throughout the remainder of the dolos field. Twenty two of these dolosse are located in the upper dolos layer and have been marked with three targets each; this allows their movement to be described with six degrees of freedom. The remaining four dolosse, which are located in the lower dolos layer of the test section, have only one clearly visible surface. Therefore, only a single target has been established on each of these.

In addition to the data collected from targeted dolosse, less precise data have been collected from dolosse which are not targeted. The detection and quantification of movement among non-targeted dolosse has been done both by using photo overlays (Kendall, 1988) and by using an application of time-lapse photography where the exposure from one flight is stereopaired with an exposure from a subsequent flight (Kendall and Melby, 1989).

Further details of the survey techniques used to supplement the instrumented dolosse measurements are provided by Kendall (1988), Kendall and Melby (1989), and Howell, et al (in publication). A recent improvement worthy of note is the use of extremely low-altitude photogrammetry acquired from a helicopter. This is discussed briefly in the following paragraphs.

#### Helicopter Photogrammetry

To improve the accuracy of photogrammetric data acquired at Crescent City, extremely low-altitude photogrammetry has been recently acquired by using a helicopter as the photo platform (Davis and Kendall, 1992). A mapping camera has been mounted on a helicopter in such a way that vibration- and

motion-free aerial mapping photography can be collected. The width of the breakwater literally fills the low altitude images allowing very rigid stereo models to be set. The flight line is now along the breakwater axis with the helicopter flying at an elevation of around 60m. Stereo images exposed from this low platform have scales on the order of 1:360 as compared to the 1:1200 scale obtainable from a fixed wing platform. The larger scale imagery does require that roughly five times as many models be set, but the ease of interpretation and increased accuracy easily compensate for this.

With a fixed wing platform, accurate readings to the nearest 3cm are possible. However, comparisons between all retained target readings generated from simultaneous ground and photogrammetric surveys of the dolosse indicated that agreement between the two methods had averaged just better than 5cm. With the helicopter as the photo platform, the total three-dimensional vectorial discrepancy never exceeded 2cm. A similar improvement is also being realized for the work with non-targeted dolosse.

Using the helicopter as the photo platform produced such scale and resolution that the roughly 8-cm wide cross-shaped targets originally established on the dolosse were simply too wide. To improve target definition, a smaller circular target divided into quadrants has been placed on top of each original target.

#### MONITORING RESULTS THROUGH THE SIXTH YEAR

This section summarizes the observations of dolos breakage, spatial distribution and types of dolos displacement, evidence of long-term nesting, evolution of static stress, and structural safety during the monitoring period between the fall of 1986 and summer of 1992.

##### Breakage

No above surface breaks nor significant movement of broken pieces have been observed since the second season; the breakage count remains that reported by Kendall (1988), i.e. seven post-placement broken dolosse, six of which broke during the initial nesting storm sequence. The majority of the breaks have occurred at a shank-fluke interface.

Refined measurements have been made of the

displacements experienced by broken dolosse. These measurements have shown that three of the broken dolosse experienced single-point displacements as large as 3m. However, these dolosse likely broke prior to experiencing the majority of the evident displacement and other broken dolosse clearly experienced minimal displacement while some unbroken dolosse experienced large displacements (Kendall, 1988). Therefore, the general conclusion remains that dolos breakage, while typically associated with some amount of movement, at least from adjacent units, is not necessarily associated with significant movement and vice versa.

Kendall (1988) suggested that, because of the high static stresses in many of these large dolosse, the magnitude of movement is not as significant in dolos breakage as the extent to which that movement causes a detrimental shift in boundary conditions (i.e. one that increases static loading). The build up of static stress with subtle movements and dolos wedging will be discussed more in subsequent discussions of long-term nesting and static stress history.

#### Spatial Distribution and Types of Dolos Displacement

The spatical distribution and types of dolos displacement have been described previously by Kendall (1988) and Kendall and Melby (1989). Generally speaking, the patterns have remained the same as those described earlier. With the exception of the only two dolosse observed to have moved during the sixth year, the dominant movement has continued to be upslope with slight settling plus rotation about the vertical or z-axis of the dolos (yaw).

Upslope movement has also been observed in the physical model for Crescent city and is believed to be an uprush dominated movement associated, at least in part, with the structures mild slope (Kendall, 1988; Jensen, 1984).

#### Evidence of Long-term Nesting

Long-term nesting has been documented by tracking the percent exceedence of single point displacements within the entire visible dolos field (approximately 400 dolosse) by season as shown in Figure 2. This necessarily includes untargeted dolosse so the measurement is limited to a determination of the magnitude of displacement experienced by a single identifiable point on each displaced dolos. This presentation clearly suggests that dolos movement has generally continued to subside with the possible

exception of the 1991-92 season.

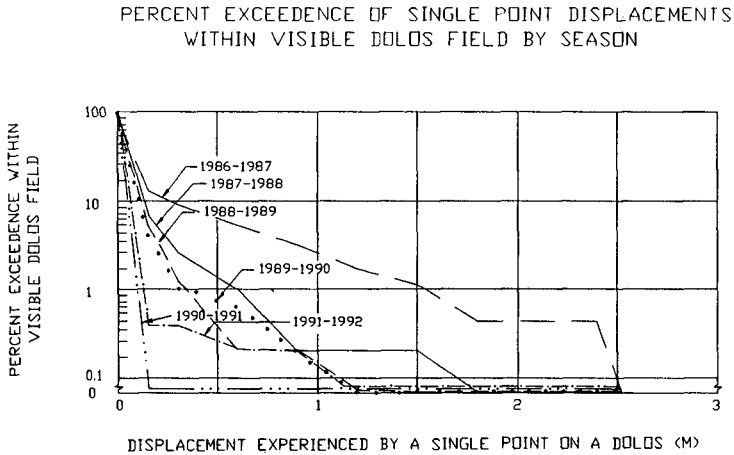


Figure 2 - Percent exceedence of single point displacements within the visible dolos field by season. Note the trend of generally fewer displacements in successive seasons with the exception of the 1991-92 season.

With few exceptions, once a unit moved it failed to register a significant subsequent displacement, i.e. the unit nested with the movement and appears to have remained relatively stable. When a previously displaced unit did experience further movement, it was typically displaced a distance equal to or less than the initial displacement experienced. Units which have been repeatedly displaced were rarely observed to do so in the same direction but tended to move in directions which were 90 to 180 degrees different than their original displacement direction, perhaps indicative of rocking.

Overall, the general trend reflects nesting, especially in light of the wave power history shown in Figure 3(a) which suggests that the first winter season, when most of the movement occurred, was actually one of the milder ones. The more extreme subsequent storms seasons have generally produced less movement.

During the monitoring period, a small percentage of individual waves is likely to have approached the depth-limited design height. However, the design storm which was used in the physical model has yet to be experienced at the site.

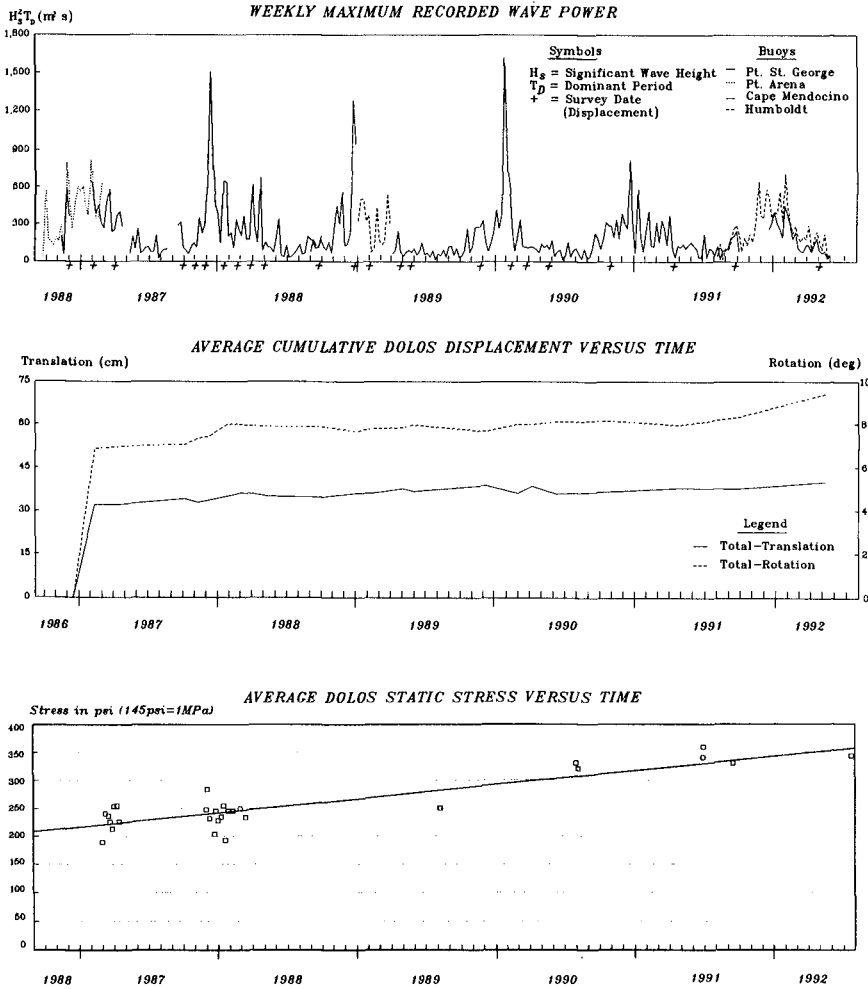


Figure 3 - (a) Timing of dolos displacement surveys relative to offshore wave power;  
 (b) time history of targeted dolos displacements;  
 (c) time history of dolos static stress; design splitting tensile strength is approx 700 psi.

The wave power history plot (Figure 3(a)) also indicates the timing of all targeted dolos displacement surveys; the results of these surveys are shown in Figure 3(b). For the targeted dolosse (about seven percent of the visible dolos field), the displacement history is resolved into translations and rotations.

The net or total rotation values shown represent the largest rotational displacement about the dolos centroid experienced by any point on the dolos surface. Because a more thorough sampling of surface points has recently been conducted, the resultant rotational displacement values shown here are slightly higher than those reported earlier by Kendall, Davis, and Leach (1987) and Kendall and Melby (1989).

The general pattern during the first few years also differs somewhat from that presented in 1989. As explained in the earlier paper (Kendall and Melby, 1989), the data set at that time contained some questionable readings which were still being verified. The subsequent filtering of many of these data has produced a slightly less patterned looking time series. The previously suggested trend of a summertime reversal in dolos field movement is no longer apparent.

The time series of Figure 3(b) tracks the average value of cumulative displacement of all targeted dolosse from their original location. This reflects gross trends created by similar displacements occurring throughout the targeted dolos field, and masks some types of displacement experienced by dolosse which have repeatedly displaced. While this produces a more smoothed time history, few dolosse have experienced repeated displacements of major significance and the plot is not considered misleading. Figure 3(b) again suggests that the bulk of the structure's nesting occurred during the first season and that only minor adjustments have occurred since then with the possible exception of the 1991-92 season.

The increased movement reflected in Figures 2 and 3(b) for the 1991-92 season has actually resulted from only two dolosse, both of which happen to be in the targeted population. These two units are located near the water line and were displaced downslope between .5 and 1m. This movement could be wave induced but downslope has not been a typical direction; most wave-induced displacements have been uprush dominated or upslope. Furthermore, the wave power, if responsible, was relatively low during the last year. Another potential explanation could be the 6.9 Richter

scale earthquake of April 1992 whose epicenter was approximately 150 km south of Crescent City. However, large earthquakes do not necessarily cause dolos movement. A 6.9 Richter scale earthquake which occurred about 100 km west of Crescent City in August 1991 failed to produce a noticeable response in the visible dolosse. Another scenario is that the supports were pulled out from beneath these units as a result of subsurface breaks. Sonar records cannot be used to confirm the suspected subsurface breakage but an observed pattern of increasing static stress with time does suggest that some breakage is to be anticipated. The static stress history is discussed further in the following section.

### Static Stress History

The history of average static stress is compared with the wave power and displacement histories in Figure 3(c). In less than six years, sampled stress levels have risen over 80% while the average cumulative displacement of targeted dolosse has risen about 30%. The 1990, 1991 and 1992 data have shed new light on the post-nesting growth of static stress. The best-fit curve is no longer suggestive of any tapering off of the post-nesting stress growth as indicated in 1989, but rather of a steady increase of about 26 psi (0.18 MPa) per year. The flexural strength of the concrete suggests a splitting tensile strength on the order of 700 psi (4.8 MPa). Therefore, the yearly increase reflected in the plot represents about 4% of the applicable concrete design capacity. Increasing static stress with time has been attributed to subtle dolos movements and unit-to-unit wedging (Kendall and Melby, 1989).

Its important to point out that the sample size for the static stress history has been variable and extremely small. The number of reporting dolosse has fallen off from 14 to six (i.e. as little as 1% of the dolos population placed in 1986). Each data point in Figure 3(c) represents the mean of all functional dolosse; an examination of just the six dolosse which have remained more or less faithful throughout the monitoring period suggests that the annual increase may be as much as 6% of the design capacity.

### Structural Safety

The structural factor of safety applicable to the Crescent City dolosse is already something less than unity when applying a conservative approach based on



field results (Melby, 1992). The pattern of increasing static stress with time is not yet factored into the design procedure. Incorporation of this pattern further reduces the safety of the structure.

The average reported static stress is now in excess of 350 psi (2.4 MPa) and one dolos is reporting static stresses in excess of 500 psi (3.5 MPa). This leaves little residual strength for continued static stress growth, pulsating wave loads, and impact loads. No impact loads have been recorded at Crescent City. However, the magnitude of pulsating loads has been reported to be as great as 70 psi (0.48 MPa) from the prototype data (Howell, et al, 1989) and as high as 110 psi (0.76 MPa) in the physical model (Markle, 1989).

## CONCLUSIONS

The procedures used to monitor movement and static stress in the dolosse at Crescent City have been revisited and updated and the monitoring results through the sixth year have been reported.

Helicopter photogrammetry has produced significant increases in the accuracy with which dolos displacements are measured.

Dolos movement has continued but at levels well below that experienced during initial nesting; static stress has been building approximately linearly as a result of subtle dolos movements and unit-to-unit wedging.

Static stress is the most significant design parameter for these large dolosse and the increase in static stress with time has reduced the structural safety of the armor layer.

Monitoring at Crescent City is scheduled to continue for at least the next three years. Future proposed work includes collecting cores from select dolosse to test for any reduction in concrete strength due to fatigue.

## ACKNOWLEDGMENTS

The work described in this paper has been conducted as part of the Crescent City Prototype Dolos Study and the Monitoring Completed Coastal Projects Program sponsored by the U.S. Army Corps of Engineers (USACE). The authors would like to acknowledge contributions

from the following individuals to this effort: Victor Liu, Len Madalon and Alicia Wong of USACE San Francisco District, the staff of Richard B. Davis Company, Eric Meindl of the National Data Buoy Center, and Dennis Markle of the Coastal Engineering Research Center, USACE Waterways Experiment Station.

## REFERENCES

Burcharth, H.F. and Howell, G.L., 1988. "On Methods of Establishing Design Diagrams for Structural Integrity of Slender Complex Types of Breakwater Armor Units," Seminaire International Entretien des Infrastructure Maritimes, Casablanca, Morocco.

Davis, R.B. and Kendall, T.R., 1992. "Application of Extremely Low Altitude Photogrammetry for Monitoring Coastal Structures," Proceedings of Coastal Engineering Practice, ASCE, New York, NY.

Hales, L.Z., 1985. Water Wave Refraction/Diffraction/Shoaling Investigation, Crescent City, California, Miscellaneous Paper CERC-85-3, U.S. Army Engineer Waterways Experiment Station, Vicksburg, MS.

Howell, G.L., 1986. "A System for the Measurement of the Structural Response of Dolos Armour Units in the Prototype," The Dock & Harbour Authority, Vol. 67 (779), pp.6-11.

Howell, G.L., 1988. "Measurement of Forces on Dolos Armor Units at Prototype Scale," Coastal Engineering, 1988 Proceedings of the International Conference, ASCE, New York, NY.

Howell, G.L., Rhee, J.P. and Rosati, J., III 1989. "Stresses in Dolos Armor Units Due to Waves," Proceeding of Stresses in Concrete Armor Units, Vicksburg, MS, ASCE, New York, NY.

Howell, G.L. and Melby, J.A., 1991. "Stochastic Estimation of Extreme Stresses in Breakwater Concrete Armor Units," Journal of Hydraulic Research, Vol. 29(6).

Howell, G.L., et al. (in publication). Crescent City Prototype Dolos Study, Technical Report CERC-93- , U.S. Army Engineer Waterways Experiment Station, Vicksburg, MS.

Jensen, O.J., 1984. A Monograph on Rubble Mound Breakwaters, Danish Hydraulic Institute, Agern Alle 5, DK-2970 Horsholm, Denmark.

Kendall, T.R., 1988. "Analysis of 42-Ton Dolos Motions at Crescent City," Coastal Engineering, 1988 Proceedings of the International Conference, ASCE, New York, NY.

Kendall, T.R., Howell, G.L. and Denes, T.A., 1985. "Prototype Measurement of the Structural Response of Dolos Armor Units," Proceedings: West Coast Regional Coastal Design Conference, Oakland, California, Coastal Engineering Research Center, U.S. Army Engineer Waterways Experiment Station, Vicksburg, MS, pp.288-299.

Kendall, T.R., Davis, R.B. and Leach, J., 1987. "Photogrammetric Measurements of 42-Ton Dolos Motions on the Outer Breakwater at Crescent City, California," Proceedings U.S. Army Corps of Engineers Sixth Remote Sensing Symposium, U.S. Army Corps of Engineers Water Resources Support Center, Fort Belvoir, VA.

Kendall, T.R. and Melby, J.A., 1989. "Continued Monitoring of 42-Ton Dolos Movements and Static Stresses at Crescent City," Proceeding of Stresses in Concrete Armor Units, Vicksburg, MS, ASCE, New York, NY.

Markle, D.G., 1989. "Crescent City Instrumented Model Dolos Study," Proceedings of Stresses in Concrete Armor Units, Vicksburg, MS, ASCE, New York, NY.

Melby, J.A., 1989. "Crescent City Dolos Structural Design Procedure," Proceedings of Stresses in Concrete Armor Units, Vicksburg, MS, ASCE, New York, NY.

Melby, J.A., 1992. "Application of a Dolos Structural Design Procedure," Proceedings of Coastal Engineering Practice, ASCE, New York, NY.

Melby, J.A. (in publication). A Dolos Design Procedure Based on Crescent City Prototype Dolos Data, Technical Report CERC-93- , U.S. Army Engineer Waterways Experiment Station, Vicksburg, MS.

Melby, J.A. and Turk, G., 1992. "Dolos Structural Response: Data Analysis and Design Considerations," Coastal Engineering, 1992 Proceedings of the International Conference, ASCE, New York, NY.

## CHAPTER 98

### IRREGULAR WAVE INTERACTION WITH PERMEABLE SLOPES

Nobuhisa Kobayashi<sup>1</sup>, and Andojo Wurjanto<sup>2</sup>

**ABSTRACT:** A one-dimensional, time-dependent numerical model is developed to simulate the flow over a rough permeable slope as well as the flow inside a permeable underlayer of arbitrary thickness for specified normally-incident irregular waves. The numerical model has been shown to be capable of predicting the time series and spectral characteristics of the reflected waves and waterline oscillations on a 1:3 rough slope with a thick permeable underlayer. The computed results are examined in detail to quantify the hydrodynamic processes which are difficult to measure in experiments. The computed results for the rough permeable and impermeable slopes are also compared to quantify the differences caused solely by the thick permeable underlayer.

#### INTRODUCTION

The permeability effects on wave run-up and reflection as well as armor stability have been regarded by previous researchers to be important for the design of highly permeable coastal structures such as berm breakwaters. Our quantitative understanding of the hydrodynamic processes involved with irregular wave interaction with permeable slopes is still rudimentary, although extensive hydraulic model tests have been performed.

Kobayashi and Wurjanto (1990) developed a numerical model for predicting the flow on a rough permeable slope as well as the flow in a thin permeable underlayer for normally incident irregular waves. This numerical model was limited to a thin permeable underlayer because it neglected the region landward of the waterline on the rough slope and the inertia terms in the horizontal momentum equation for the flow in the thin permeable underlayer. This numerical model turned out to be of limited practical use since the permeability effects of the thin permeable underlayer were found to be minor or negligible. Wurjanto and Kobayashi (1992) developed an improved numerical model by eliminating most of the shortcomings of the previous model as explained in the next section.

#### NUMERICAL MODEL FOR THICK PERMEABLE UNDERLAYER

Fig. 1 shows the symbols used in the improved numerical model where the prime indicates the dimensional variables. In Fig. 1,  $x'$  = horizontal coordinate taken to be positive landward with  $x' = 0$  at the toe of the slope;  $z'$  = vertical coordinate taken to be positive upward with

<sup>1</sup>Prof. and Assoc. Dir., Ctr. for Applied Coastal Res., Dept. of Civil Engrg., Univ. of Delaware, Newark, DE 19716.

<sup>2</sup>Lecturer, Dept. of Civil Engrg., Bandung Inst. of Tech., Jalan Ganesha 10, Bandung 40132, Indonesia.

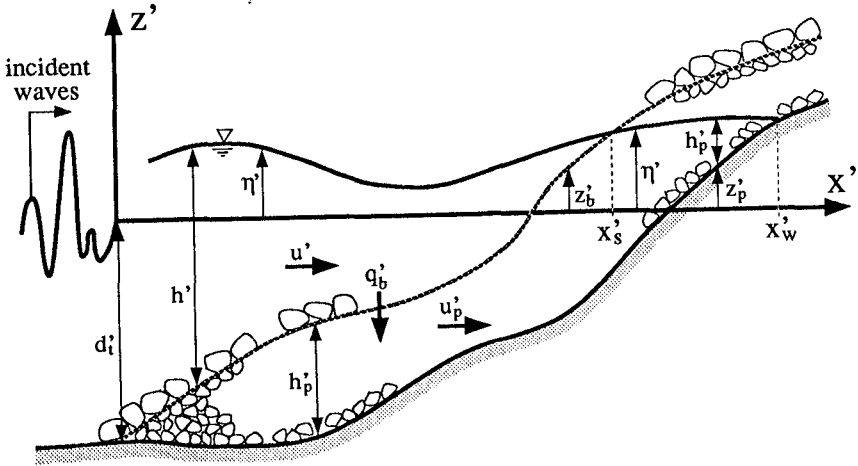


Figure 1: Definition Sketch for Numerical Model for Thick Permeable Underlayer

$z' = 0$  at the still water level (SWL);  $z_b' = z'$  - coordinate of the upper boundary of the permeable underlayer excluding the primary cover layer whose roughness effect is included by the bottom friction factor  $f'$  for the flow over the rough slope;  $z_p' = z'$  - coordinate of the lower boundary of the permeable underlayer which is assumed impermeable;  $d_t'$  = water depth below SWL at  $x' = 0$  where it is assumed that  $z_b' = z_p'$  at  $x' = 0$ ;  $\eta'$  = free surface or water table elevation above SWL;  $x_s' = x'$  - coordinate of the upper waterline defined as the location of  $\eta' = z_b'$ ;  $x_w' = x'$  - coordinate of the lower waterline defined as the location of  $\eta' = z_p'$ ;  $h'$  = water depth above the permeable slope given by  $h' = (\eta' - z_b')$  in the region  $0 \leq x' \leq x_s'$ ;  $u'$  = depth-averaged horizontal velocity above the permeable slope;  $h_p'$  = water depth inside the permeable underlayer given by  $h_p' = (z_b' - z_p')$  in the region  $0 \leq x' \leq x_s'$  and  $h_p' = (\eta' - z_p')$  in the region  $x_s' \leq x' \leq x_w'$ ;  $q_b'$  = volume influx per unit horizontal area into the permeable underlayer which is taken to be positive downward; and  $u_p'$  = vertically-averaged horizontal discharge velocity inside the permeable underlayer where the actual velocity is given by  $u_p'/n_p$  with  $n_p$  = porosity of the permeable underlayer.

Computation is performed using the dimensionless variables and parameters defined as

$$t = \frac{t'}{T'}; x = \frac{x'}{T'\sqrt{gH'}}; x_s = \frac{x_s'}{T'\sqrt{gH'}}; x_w = \frac{x_w'}{T'\sqrt{gH'}} \quad (1)$$

$$z = \frac{z'}{H'}; z_b = \frac{z_b'}{H'}; z_p = \frac{z_p'}{H'}; d_t = \frac{d_t'}{H'}; \eta = \frac{\eta'}{H'}; h = \frac{h'}{H'}; h_p = \frac{h_p'}{H'} \quad (2)$$

$$u = \frac{u'}{\sqrt{gH'}}; q_b = \frac{T'q_b'}{p_q H'}; u_p = \frac{u_p'}{p_q \sqrt{gH'}}; p_q = n_p p_u \quad (3)$$

$$p_u = \left[ \frac{n_p}{\beta_0(1-n_p)} \frac{d'_p}{T'\sqrt{gH'}} \right]^{1/2}; \quad \mu = \frac{\alpha_0(1-n_p)^2\nu}{\beta_0\rho_u d'_p \sqrt{gH'}} \quad (4)$$

in which  $t'$  = time;  $T'$  and  $H'$  = characteristic wave period and height used for the normalization, respectively;  $g$  = gravitational acceleration;  $p_q$  and  $p_u$  = dimensionless parameter expressing the order of magnitude of  $u'_p/u'$  and  $(u'_p/n_p)/u'$ , respectively;  $\nu$  = kinematic viscosity of the fluid;  $d'_p$  = characteristic stone diameter in the permeable underlayer;  $\alpha_0$  and  $\beta_0$  = empirical constant associated with the laminar and turbulent flow resistance, respectively (Madsen and White 1975); and  $\mu$  = dimensionless parameter expressing the order of magnitude of the laminar flow resistance as compared to the turbulent flow resistance.

The numerical model of Wurjanto and Kobayashi (1992) computed  $m = uh$ ,  $h = (\eta - z_b)$ ,  $q_b$  and  $m_p = p_u h_p u_p$  in the region  $0 \leq x \leq x_s$  where  $h_p = (z_b - z_p)$ , as well as  $m_p$  and  $h_p = (\eta - z_p)$  in the region  $x_s \leq x \leq x_w$  as a function of  $t$  and  $x$  using the one-dimensional, time-dependent equations of conservation of mass and  $x$ -momentum for the flow fields over and inside the permeable underlayer. It is assumed that  $m_p$  and  $h_p$  are continuous at  $x = x_s$ . The initial time  $t = 0$  for the computation marching forward in time is taken to be the time when the specified incident wave train arrives at  $x = 0$  and there is no wave action in the region  $x \geq 0$ . At the seaward boundary  $x = 0$  where  $h_p = 0$  is assumed, the normalized incident wave train,  $\eta_i = \eta'_i/H'$ , is prescribed as a function of  $t$  and the normalized reflected wave train,  $\eta_r = \eta'_r/H'$ , is computed as a function of  $t$  from the characteristics advancing seaward.

The numerical model is compared with the three test runs denoted by runs P1, P2 and P3 conducted by Cox (1989). The upper boundary of the permeable gravel underlayer was located at  $z'_b = (-d'_t + x' \tan \theta')$  with  $d'_t = 0.40$  m and  $\cot \theta' = 3$ . Its lower boundary was situated at  $z'_p = -d'_t$  for  $0 \leq x' \leq 0.566$  m and  $z'_p = -d'_t + (x' - 0.566) \tan \theta'$  for  $0.566$  m  $\leq x'$  where its thickness perpendicular to the impermeable base was  $0.566 \sin \theta' = 0.179$  m. The single layer of the gravel whose thickness was the median gravel diameter  $d'_p = 2.1$  cm is regarded as the primary cover layer. The other input parameters associated with (4) are taken as  $n_p = 0.48$ ,  $\nu = 0.01$  cm<sup>2</sup>/s at 20°C,  $\alpha_0 = 1140$  and  $\beta_0 = 2.7$ .

The significant wave height  $H'_s$  and the mean period  $T'_m$  of the zero upcrossings of the measured incident wave train are taken as the height  $H'$  and the period  $T'$  used for the normalization of the governing equations. The values of  $H' = H'_s$  and  $T' = T'_m$  for the three runs are listed in Table 1. The other values listed in Table 1 are as follows:  $\xi$  = surf similarity parameter based on  $H'$ ,  $T'$  and  $\cot \theta' = 3$ ;  $t_{max}$  = normalized duration of the measurement and computation;  $H_{m0}$  = spectral estimate of the normalized significant wave height;  $T_p$  = normalized spectral peak period;  $\xi_p$  = surf similarity parameter based on the spectral parameters  $H'_{m0} = H_{m0}H'$  and  $T'_p = T_pT'$ ; and  $f'$  = bottom friction factor estimated from the rough impermeable slope tests. The values of  $H_{m0}$  and  $T_p$  are obtained from the normalized incident wave spectrum  $S_i(f_*)$  with  $f_*$  = normalized frequency defined as  $f_* = f'_*T'$  computed from  $\eta'_i(t)$  for  $0 \leq t \leq t_{max}$  for each run. The frequency range of resolution of the measured incident and reflected waves based on three wave gages was  $0.12 < f_* < 1.6$  for run P1,  $0.15 < f_* < 2.0$  for run P2, and  $0.19 < f_* < 2.6$  for run P3 (Kobayashi et al. 1990). Table 1 also lists the values of  $p_q$  and  $\mu$  defined in (3) and (4). For these runs, the discharge velocity inside the permeable underlayer is generally small relative to the fluid velocity over the permeable slope, while the laminar flow resistance in the permeable underlayer is small as compared to the turbulent flow resistance.

Wurjanto and Kobayashi (1992) has shown that the numerical model can predict the time series and spectral characteristics of the measured reflected waves and waterline oscillations on the 1:3 permeable slope where the waterline meter measured the temporal variation of the elevation  $Z'_r$  above SWL of the intersection between the instantaneous free surface  $z' = \eta'$  and the straight line  $z' = (z'_b + \delta'_r)$  with  $\delta'_r \approx 2.75$  cm in the experiment. As a result, additional

Table 1: Three Test Runs Compared with Numerical Model

Run No.	$H'$ (cm)	$T'$ (sec)	$\xi$	$t_{max}$	$H_{mo}$	$T_p$	$\xi_p$	$f'$	$p_q$	$\mu$
P1	6.85	1.08	1.72	170.98	1.01	1.09	1.88	0.05	0.043	0.074
P2	5.35	1.36	2.44	268.98	1.03	1.56	3.75	0.05	0.041	0.088
P3	4.57	1.74	3.39	210.01	1.06	1.58	5.22	0.10	0.038	0.104

computed results are presented hereafter to elucidate the interaction processes of irregular waves with the rough permeable slope with the thick permeable underlayer. In the following, the computed results for run P2 are shown as typical results but the computed results for runs P1 and P3 are similar unless stated otherwise.

Fig. 2 shows the computed spatial variations of  $\eta$ ,  $u$ ,  $p_q q_b$  and  $m_p = p_u h_p u_p$  at  $t = 125.0$ , 125.5 and 126.0 where the shaded area shown with the variation of  $\eta$  corresponds to the permeable underlayer. Comparison of the variations of  $\eta$  and  $u$  reveals the sequence of water uprushing and downrushing on the permeable slope from  $t = 125.0$  to  $t = 126.0$ . The variations of  $p_q q_b$  indicate water flowing into the permeable underlayer during wave uprush and water outflow in the region below the trough of the free surface. The variations of  $m_b$  show the flux inside the permeable underlayer which appears to be driven mainly by the hydrostatic pressure gradient related to  $-\partial\eta/\partial x$  as is the case with the thin permeable underlayer (Kobayashi and Wurjanto 1990).

Fig. 3 shows the computed normalized spectra  $S_z^U$  and  $S_z^L$  of the upper and lower waterline oscillations, respectively. The upper waterline is taken as the normalized waterline elevation  $Z_r = Z'_r/H'$  on the permeable slope, whereas the lower waterline corresponds to the normalized elevation above SWL of the intersection between the instantaneous water table  $z = \eta$  and the straight line  $z = (z_p + \delta'_r/H')$  with  $\delta'_r = 2.75$  cm parallel to the impermeable slope  $z = z_p$ . Fig. 3 reveals that the permeable underlayer attenuates the high-frequency wave components significantly but damps the low-frequency wave components little as expected.

Fig. 4 shows the spatial variations of  $\bar{m} = \overline{uh}$ ,  $p_q \bar{q}_b$  and  $n_p \bar{m}_p = p_q \overline{u_p h_p}$  where the overbar indicates the time averaging over  $0 \leq t \leq t_{max}$ . The time-averaged volume flux per unit horizontal area,  $\bar{q}_b$ , is into or out of the permeable underlayer above or below the still waterline located at  $z_b = 0$ , respectively, where  $z_b = 0$  at  $x = 1.22$  for run P2. Correspondingly, the time-averaged volume flux  $\bar{m}$  and  $\bar{m}_p$  above and inside the permeable underlayer are landward and seaward, respectively, in the vicinity of the still waterline. The overall mass balance requires that  $\bar{q}_b$ ,  $\bar{m}$  and  $\bar{m}_p$  must approach zero at  $x = 0$ . In Fig. 4,  $\bar{m}$  approaches a very small negative value at  $x = 0$ . This implies that the numerical model may not predict the small time-averaged quantities very accurately partly because they are small relative to the corresponding time-varying quantities.

#### COMPARISON BETWEEN PERMEABLE AND IMPERMEABLE SLOPES

The additional computed results for the 1:3 rough permeable slope are presented hereafter in comparison with the computed results for the corresponding impermeable slope without the permeable underlayer. These runs corresponding to runs P1, P2 and P3 are denoted by runs I1, I2 and I3. The numerical model for impermeable slopes was shown to be capable of predicting the time series and spectral characteristics of the reflected waves and waterline oscillations on the 1:3 rough impermeable slope (Kobayashi et al. 1990). The measured reflected waves and waterline oscillations on the permeable and impermeable slopes were compared by Kobayashi et al. (1991) who found it very difficult to generate identical incident wave trains for the permeable

# Run P2

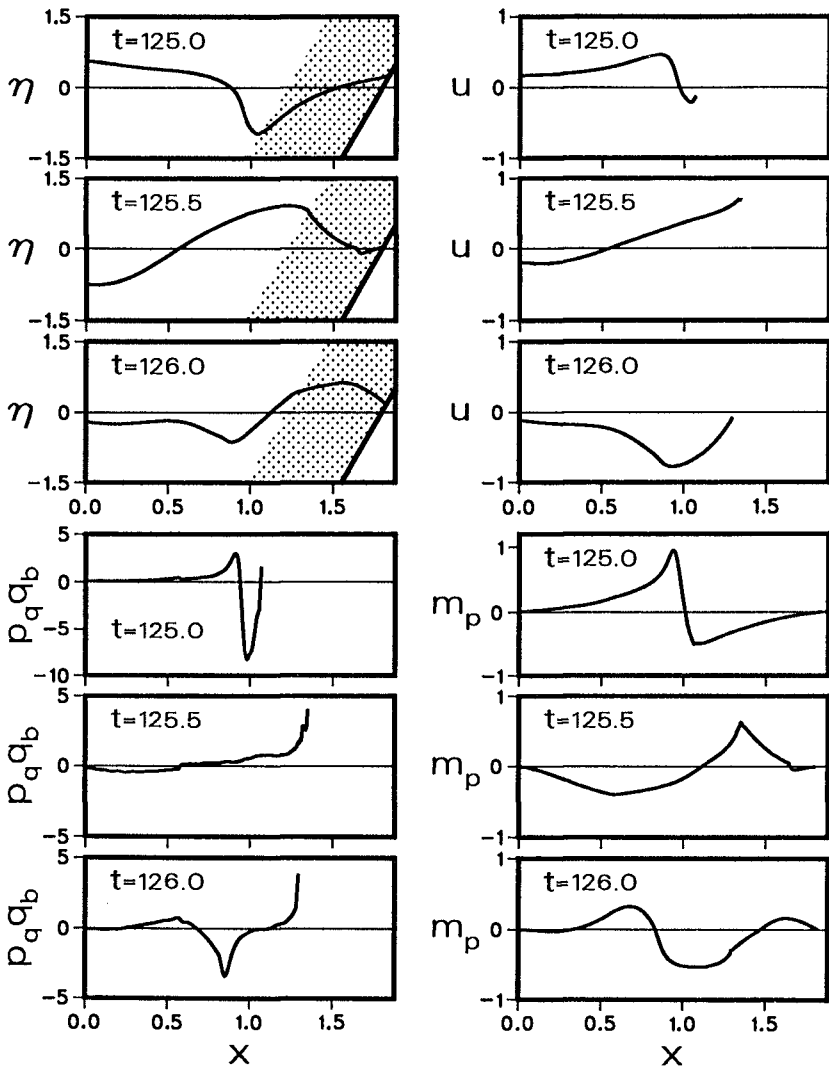


Figure 2: Computed Spatial Variations of  $\eta$ ,  $u$ ,  $p_q q_b$  and  $m_p = p_u h_p u_p$  at  $t = 125.0, 125.5$  and  $126.0$ .



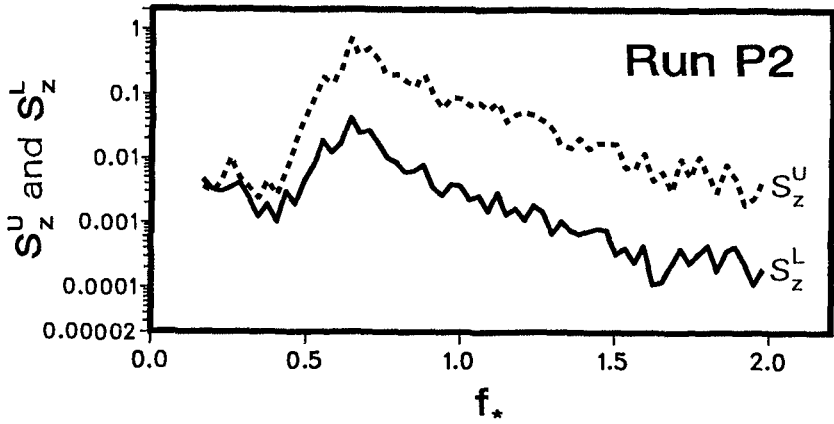


Figure 3: Computed Spectra of Upper and Lower Waterline Oscillations Denoted by  $S_z^U$  and  $S_z^L$ , Respectively.

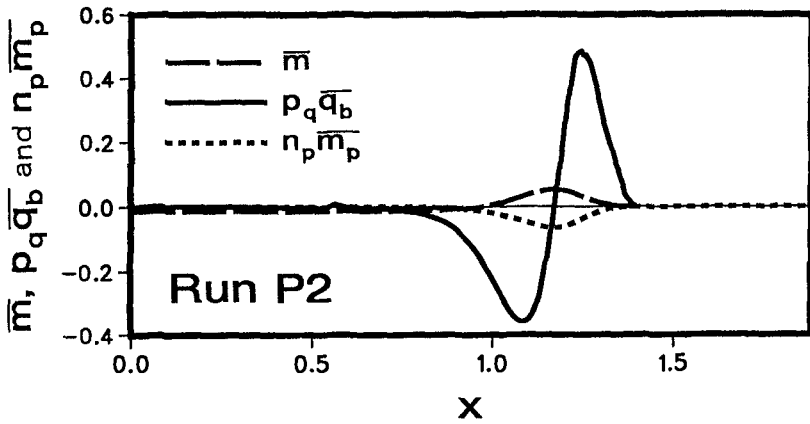


Figure 4: Time-Averaged Volume Fluxes  $\bar{m}$ ,  $\rho_q \bar{q}_b$  and  $n_p \bar{m}_p$

Table 2: Computed Values of  $\bar{r}$ ,  $\overline{Z_r}$ ,  $R_s$ ,  $R_{max}$  and  $N_{sc}$  for Permeable (P) and Impermeable (I) Slopes.

Run No.	$\bar{r}$		$\overline{Z_r}$		$R_s$		$R_{max}$		$N_{sc}$		$N_s$
	P	I	P	I	P	I	P	I	P	I	
1	0.09	0.20	0.06	0.12	0.57	0.91	1.01	1.48	1.16	0.49	2.29
2	0.15	0.55	0.05	0.14	0.78	1.52	1.11	2.20	1.49	0.38	1.78
3	0.26	0.66	0.05	0.11	0.94	1.72	1.85	3.24	1.43	0.45	1.52

and impermeable slope tests in a wave tank. In the present comparisons, the measured incident wave train for run PJ with J = 1, 2 and 3 is specified as input to the computation for run IJ so that the incident wave trains for runs PJ and IJ become identical. Moreover, the numerical models allow us to examine the permeability effects on the quantities which are very difficult to measure.

Fig. 5 compares the computed spatial variations of  $\eta_{max}$ ,  $\bar{\eta}$  and  $\eta_{min}$  as well as  $u_{max}$ ,  $\bar{u}$  and  $u_{min}$  for runs P2 and I2 where the subscripts *max* and *min* indicate the maximum and minimum values with respect to  $t$  over  $0 \leq t \leq t_{max}$ . The presence of the thick permeable underlayer reduces the vertical range of the free surface elevation  $\eta$  and the magnitude of the depth-averaged horizontal velocity  $u$  on the slope. The wave setup  $\bar{\eta}$  on the impermeable slope approaches  $\eta_{max}$  asymptotically since  $\bar{h} = (\bar{\eta} - z_b) > 0$  in the region reached by uprushing water during  $0 \leq t \leq t_{max}$ , whereas the wave setup  $\bar{\eta}$  on the permeable slope is connected to the wave setup inside the permeable underlayer. The negative value of  $\bar{u}$  on the impermeable slope is related to undertow on a beach (Kobayashi et al. 1989), whereas the time-averaged fluxes for the permeable slope shown in Fig. 4 result in the positive value of  $\bar{u}$  above the still waterline located at  $x = 1.22$  for runs P2 and I2. This suggests that the permeability may affect the net cross-shore transport of gravel and sand.

Fig. 6 shows the computed reflection coefficient  $r$  as a function of the normalized frequency  $f_*$  for runs P2 and I2 where  $r$  is defined as  $r = [S_r(f_*)/S_i(f_*)]^{1/2}$  with  $S_r$  = normalized reflected wave spectrum calculated from  $\eta_r(t)$  for  $0 \leq t \leq t_{max}$ . The computed values of  $r$  exceeding unity for run I2 may not be correct since  $r$  should not exceed unity unless additional waves propagating seaward are generated in the region  $x > 0$ . Fig. 6 indicates that the permeable underlayer dissipates the incident high-frequency wave components but damps the incident low-frequency wave components little. This is consistent with the computed results shown in Fig. 3. The average reflection coefficient  $\bar{r}$  may be defined as  $\bar{r} = [(m_o)_r/m_o]^{1/2}$  where  $m_o$  = zero moment of  $S_i(f_*)$ ; and  $(m_o)_r$  = zero moment of  $S_r(f_*)$ . The computed values of  $\bar{r}$  for the six runs listed in Table 2 increase with the increase of the surf similarity parameter  $\xi$  and  $\xi_p$  given in Table 1. Comparison of the values of  $\bar{r}$  for the permeable and impermeable slopes for given  $\xi$  and  $\xi_p$  indicates that the thick permeable underlayer reduced  $\bar{r}$  by a factor of more than two.

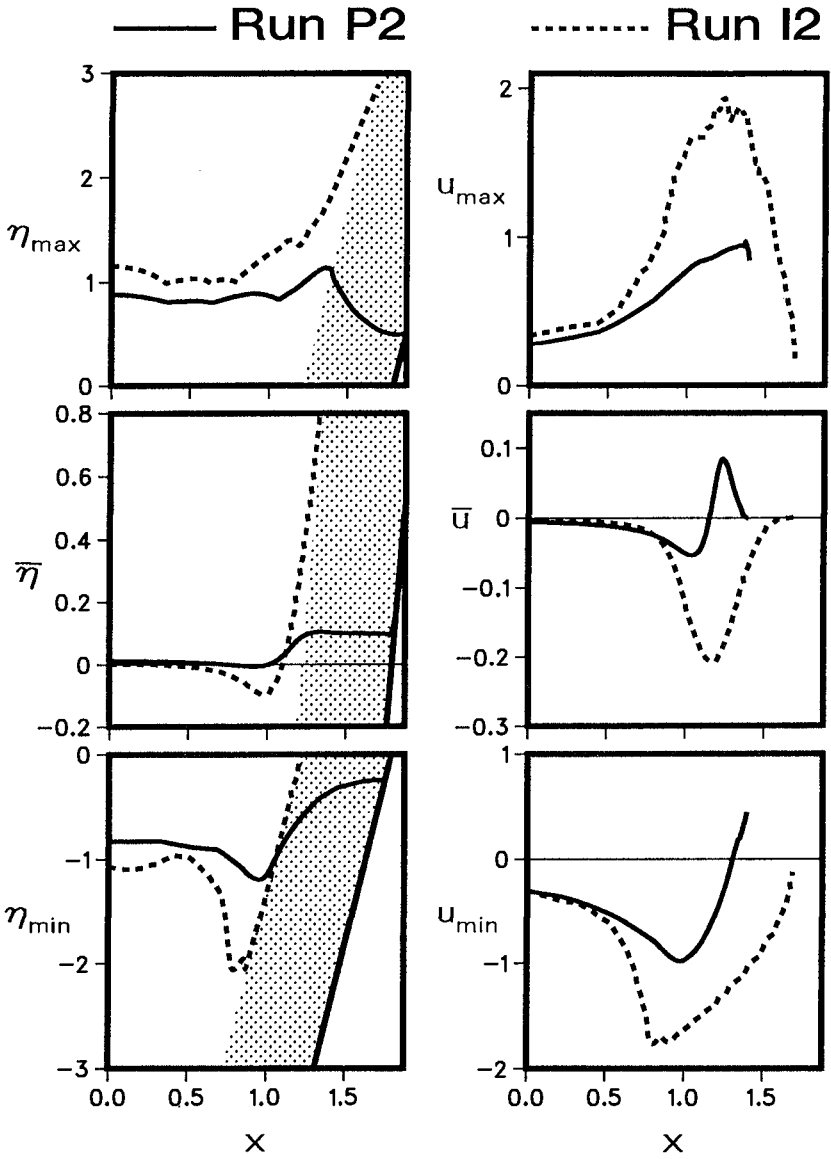


Figure 5: Computed Spatial Variations of  $\eta_{max}$ ,  $\bar{\eta}$  and  $\eta_{min}$  as well as  $u_{max}$ ,  $\bar{u}$  and  $u_{min}$ .

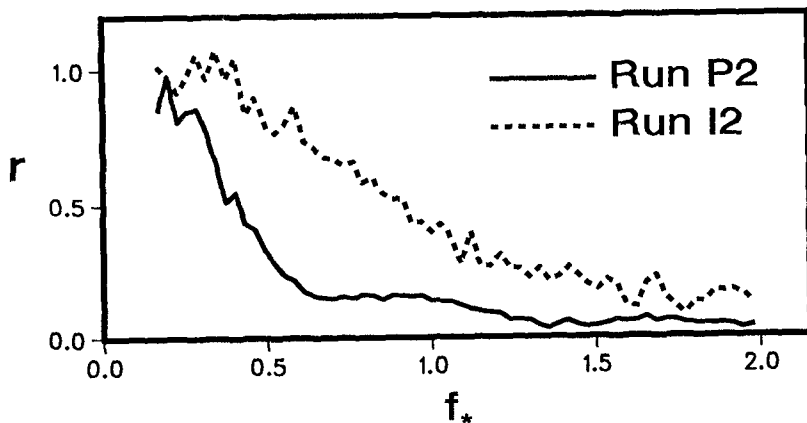


Figure 6: Reflection Coefficient  $r$  as a Function of Normalized Frequency  $f_*$ .

Fig. 7 shows the computed spectrum  $S_z^U$  of the normalized upper waterline elevation above SWL,  $Z_r(t)$ , for  $0 \leq t \leq t_{max}$ . The permeable underlayer reduces both high-frequency and low-frequency wave components unlike the computed results shown in Figs. 3 and 6. The interaction of uprushing and downrushing water on the impermeable slope seems to generate additional low-frequency wave components, whereas the permeable slope appears to absorb the incident waves with little water uprushing as shown in Fig. 2. The computed time series  $Z_r(t)$  for  $0 \leq t \leq t_{max}$  are also analyzed using the zero upcrossing method described by Kobayashi et al. (1990). Table 2 lists the computed values of  $\bar{Z}_r$ ,  $R_s$  and  $R_{max}$  for the six runs where  $\bar{Z}_r$  = time-averaged upper waterline elevation above SWL;  $R_s$  = normalized significant run-up defined as the average of the highest one- third run-up elevations above SWL; and  $R_{max}$  = maximum run-up elevation above SWL during  $0 \leq t \leq t_{max}$ .  $R_s$  and  $R_{max}$  increase with the increase of  $\xi$  and  $\xi_p$  given in Table 1. Moreover, the thick permeable underlayer reduces  $\bar{Z}_r$ ,  $R_s$  and  $R_{max}$  by a factor of slightly less than two. Fig. 7 also shows the exceedance probability  $P$  as a function of  $R_p/R_s$  with  $R_p$  = normalized run-up corresponding to the specific value of  $P$  together with the Rayleigh distribution. The probability distribution of the normalized run-up,  $R_p/R_s$  is affected little by the permeable underlayer whose effect on run-up may be accounted for by  $R_s$  only.

Fig. 8 shows the computed spatial variations of  $\bar{E}$ ,  $\bar{F}$ ,  $\bar{D}_p$  and  $\bar{D} = (\bar{D}_f + \bar{D}_B)$  for the flow over the permeable and impermeable slopes where  $\bar{E}$  = normalized specific energy;  $\bar{F}$  = normalized energy flux per unit width;  $\bar{D}_p$  = normalized energy flux per unit horizontal area into the permeable underlayer which is zero for the impermeable slope;  $\bar{D}_f$  and  $\bar{D}_B$  = normalized rate of energy dissipation per unit horizontal area due to bottom friction and wave breaking, respectively. The one- dimensional energy equations and associated quantities have been explained by Kobayashi and Wurjanto (1990) and Wurjanto and Kobayashi (1992). For the permeable slope as compared to the impermeable slope,  $\bar{E}$  does not increase much near the still waterline and the decrease of  $\bar{F}$  starts from  $x = 0$ , while  $\bar{D}_p$  is dominant as compared to  $\bar{D}$  calculated from  $\bar{D} = (-d\bar{F}/dx - \bar{D}_p)$ . For the impermeable slope with  $\bar{D}_p = 0$ , the comparison of  $\bar{D}_B$  and  $\bar{D}_f$  for runs I1, I2 and I3 indicates that  $\bar{D}_B$  is dominant for run I1 and  $\bar{D}_f$  is dominant for run I3, while  $\bar{D}_B$  and  $\bar{D}_f$  are equally important for run I2 as shown in Fig. 8.

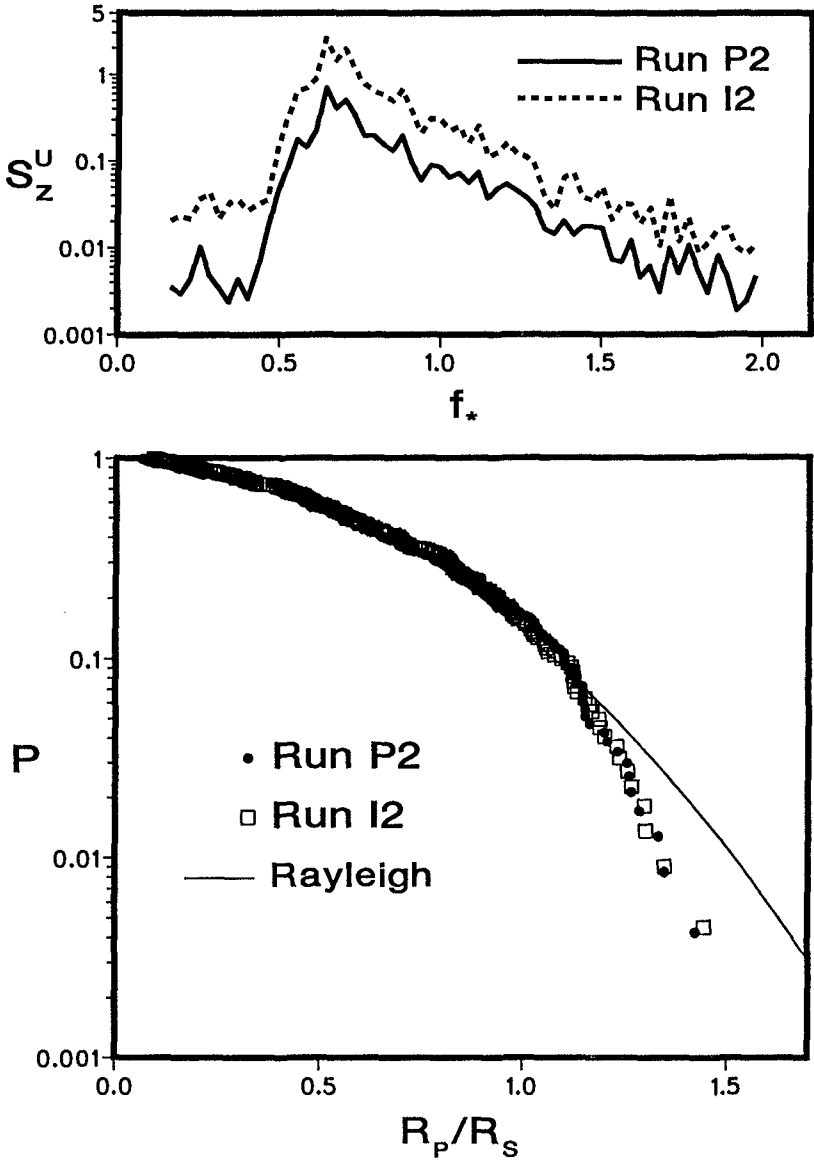


Figure 7: Computed Upper Waterline Spectrum  $S_z^U$  and Exceedance Probability  $P$  of Normalized Run-up  $R_p/R_s$  as Compared with Rayleigh Distribution.

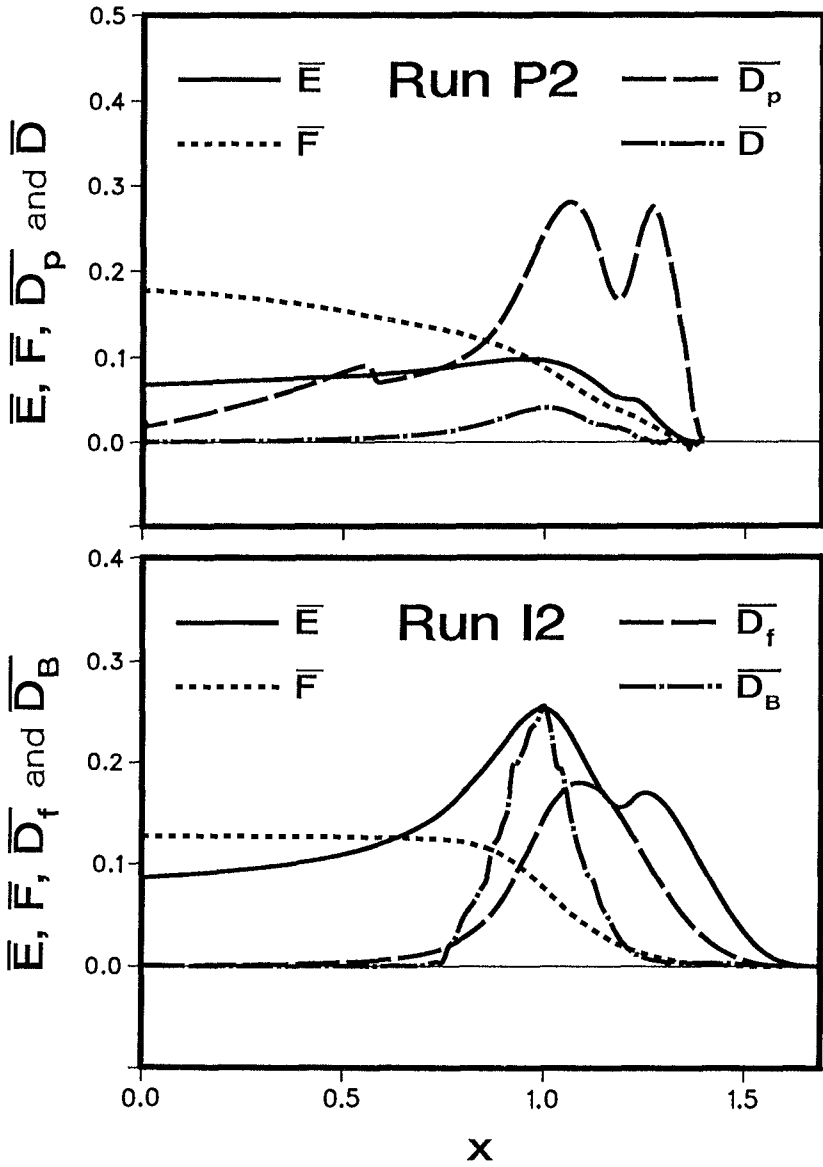


Figure 8: Time-Averaged Energy Fluxes and Dissipation Rates for Flow over Permeable and Impermeable Slopes.

Finally, the permeability effect on armor stability is examined. Kobayashi and Wurjanto (1990) expressed the hydraulic stability condition against sliding or rolling of an armor unit on a rough permeable slope in the form

$$N_s = H'(s-1)^{-1} (\rho s/W')^{1/3} \leq N_R(t, z_b) \quad (5)$$

where  $N_s$  = stability number;  $H'$  = characteristic wave height taken as the significant wave height  $H'_s$ ,  $s$  = specific density of the armor units;  $\rho$  = fluid density;  $W'$  = median mass of the armor units; and  $N_R$  = armor stability function varying with the normalized time  $t$  and the armor location on the slope represented by  $z_b$ . For the gravel used in the experiment,  $s = 2.7$ ,  $W' = 14.8$  g and  $(W'/\rho s)^{1/3} = 1.76$  cm. The values of  $N_R$  at given  $t$  are computed in the region  $h' \geq d'_p$  since the armor units are assumed to be fully submerged. The local stability number  $N_{sx}(z_b)$  is defined as the minimum value of  $N_R(t, z_b)$  at given  $z_b$  during  $0 \leq t \leq t_{max}$ . The critical stability number  $N_{sc}$  is defined as the minimum value of  $N_{sx}(z_b)$  for the region  $z_b \geq -d_t$ . Table 2 lists the computed values of  $N_{sc}$  for the six runs together with the measured value of  $N_s$  for each run. Fig. 9 shows the spatial variations of  $N_{sc}(z_b)$  for runs P2 and I2 with  $N_s = 1.78$ .

The numerical model predicts that the gravel units in the region  $N_{sx} < N_s$  should slide or roll. Cox (1989) observed that loose gravel units on the permeable slope remained at their initial locations, whereas those on the impermeable slope were dislodged during the tests. Fig. 9 indicates the intense movement of loose gravel units in the wide region of the impermeable slope but the limited movement of loose gravel units on the permeable slope. As a result, the computed results are qualitatively consistent with the observations and the empirical formula of van der Meer (1988), although the sliding or rolling of gravel units may not result in the dislodgement of the gravel units from their initial locations. Fig. 9 also shows the spatial variations of  $\eta$ ,  $u$ ,  $du/dt$  and  $N_R$  at the time  $t = t_{sc}$  when the minimum value of  $N_R$  with respect to  $z_b$  equals the critical stability number  $N_{sc}$ . For run I2 with  $t_{sc} = 91.83$ , the critical armor stability occurs during wave uprush when the landward fluid velocity and acceleration are very large. For run P2 with  $t_{sc} = 197.66$ , the critical armor stability occurs during wave downrush when the seaward fluid velocity and acceleration are large. It is noted that the stability analysis of Kobayashi and Wurjanto (1990) neglects the direct effect of  $q_b$  on the armor stability and may not be very accurate.

## CONCLUSIONS

The numerical model developed for predicting the flow over a rough permeable slope and the flow inside a permeable underlayer has been used to elucidate the interaction processes of irregular waves with a thick permeable underlayer. The computed results have also been compared with those for the corresponding rough impermeable slope to examine the differences caused solely by the permeable underlayer. The thick permeable underlayer has been shown to increase the armor stability considerably and reduce the wave reflection and run-up significantly. Most of the computed results presented herein have been observed visually or described qualitatively by previous researchers. The numerical models yield quantitative data with high spatial and temporal resolutions. The numerical models also allow one to perform sensitivity analyses easily by changing only one input parameter in each numerical simulation. For example, it may be important for the design of berm breakwaters to examine the sensitivity of the computed results to the thickness, porosity and stone diameter of the permeable underlayer.

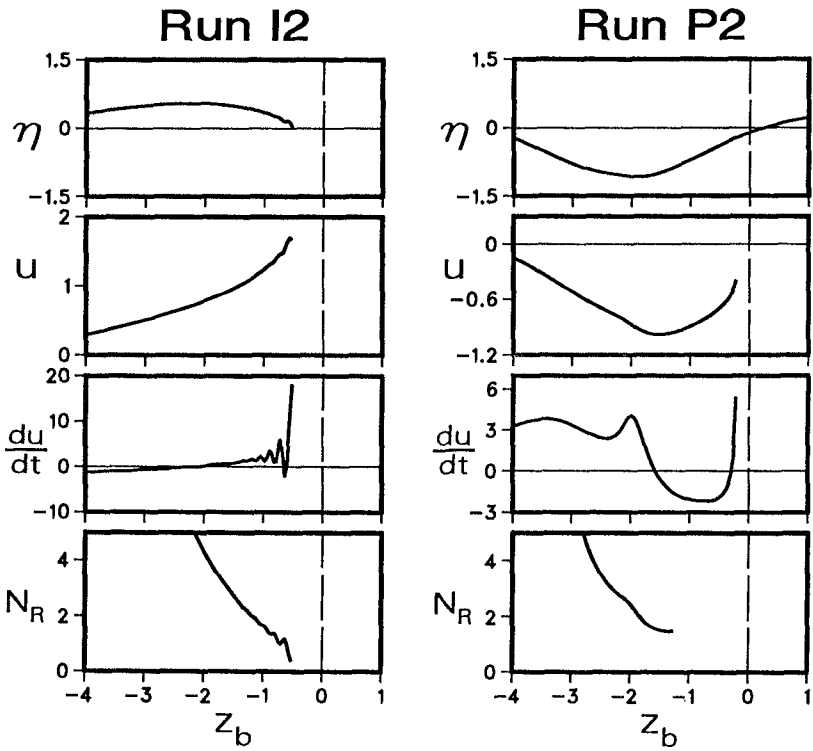
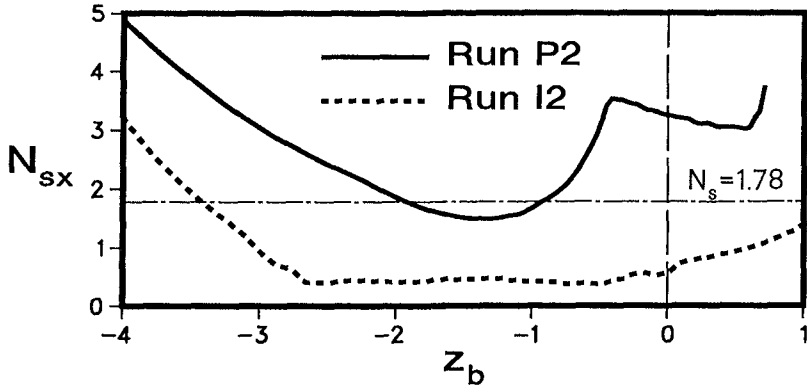


Figure 9: Spatial Variations of Local Stability Number  $N_{sx}$  and Flow Conditions at Time of Minimum Armor Stability.



ACKNOWLEDGMENTS

This work is a result of research sponsored by the National Science Foundation under grant CTS-8900640.

REFERENCES

- Cox, D.T. (1989). "Irregular wave reflection and runup on rough permeable slopes." Thesis for Master of Civil Engrg., Univ. of Delaware, Newark, DE.
- Kobayashi, N., Cox, D.T. and Wurjanto, A. (1990). "Irregular wave reflection and run-up on rough impermeable slopes." *J. Wtrwy., Port, Coast. and Oc. Engrg.*, ASCE, 116(6), 708-726.
- Kobayashi, N., Cox, D.T. and Wurjanto, A. (1991). "Permeability effects on irregular wave runup and reflection." *J. Coastal Res.*, 7(1), 127-136.
- Kobayashi, N., DeSilva, G.S. and Watson, K.D. (1989). "Wave transformation and swash oscillation on gentle and steep slopes." *J. Geophys. Res.*, 94(C1), 951-966.
- Kobayashi, N. and Wurjanto, A. (1990). "Numerical model for waves on rough permeable slopes." *J. Coastal Res.*, SI(7), 149-166.
- Madsen, O.S. and White, S.M. (1975). "Reflection and transmission characteristics of porous rubble-mount breakwaters." *Tech. Rept. No. 207*, R. M. Parsons Lab., Mass. Inst. of Tech., Cambridge, Mass.
- Van der Meer, J.W. (1988). "Rock slopes and gravel beaches under wave attack." Doctoral thesis, Delft Univ. of Tech., Delft, The Netherlands.
- Wurjanto, A. and Kobayashi, N. (1992). "Irregular wave reflection and run-up on permeable slopes." *J. Wtrwy., Port, Coast. and Oc. Engrg.*, ASCE (submitted).

## CHAPTER 100

### VERTICAL WAVE BARRIERS: WAVE TRANSMISSION AND WAVE FORCES

David L. Kriebel<sup>1</sup>

#### ABSTRACT

Wave interaction with a vertical slotted wave barrier, also called a wave screen or slit-type breakwater, is considered. A theoretical analysis is presented based on application of the continuity, momentum, and energy equations to flow through the slots in the breakwater, accounting for head losses associated with flow constriction and re-expansion. As a result, relatively simple expressions are found for the wave transmission coefficient and for the wave forces on the wall. These are then verified by laboratory experiments with regular waves.

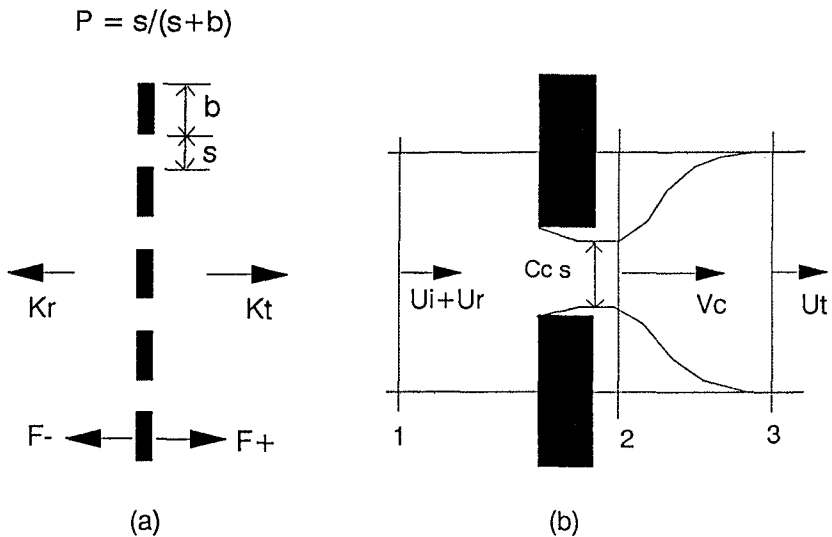
#### INTRODUCTION

Vertical-wall breakwaters are sometimes used to protect marinas and small boat harbors from both wind waves and boat wakes. These breakwaters encompass a variety of structures and have many names in the literature, including wave barriers, wave screens, and even wave "fences". In the Chesapeake Bay and other locations in the United States, these structures are most often built from marine lumber in the form of vertically-slotted walls extending to either full or mid-depth. Despite the growing use of such structures, however, relatively little comprehensive design information is available on either their wave transmission characteristics or on the wave forces that they would experience. As a result, these breakwaters have performed poorly in some instances, since even small gap spaces between the wall members allows a significant transmission of wave energy.

---

<sup>1</sup> Associate Professor of Ocean Engineering; Naval Architecture, Ocean, and Marine Engineering Dept.; United States Naval Academy; Annapolis, MD 21402

A definition sketch showing the plan-view of a slotted or slit-type vertical wave barrier with rectangular wall elements is shown in Figure 1. The primary variable defining the structure permeability is the porosity of the cross-section,  $P$ , defined as the ratio of the gap space,  $s$ , to the centerline-to-centerline spacing of the wall elements,  $s+b$ . Assuming that the wall is subjected to plane long-crested waves of height  $H_i$  with crests parallel to the wall, it is then of interest to describe the transmission coefficient,  $K_t = H_t/H_i$ , and the reflection coefficient,  $K_r = H_r/H_i$ , in terms of the porosity and in terms of the relative water depth and wave steepness. In addition, it is of interest to describe the wave force on one wall element,  $F$ , in either the positive or negative directions.



**Figure 1.** Definition sketch showing plan view of:  
(a) wall cross-section and (b) detail of flow through breakwater gap.

Vertical slotted or slit-type wave barriers have been actively studied for more than thirty years. Wiegel (1961), for example, estimated the transmission coefficient by assuming that the transmitted wave energy flux over width  $s+b$  was equal to that portion of the incident wave energy flux passing through the gap over width  $s$ . As a result, a simple expression for transmission was proposed as  $K_t = P^{1/2}$ . It is known, however, that this approach underestimates the transmission because it neglects the effects of wave reflection. In actuality, the pressure gradient across the wall is increased by the presence of the reflected wave and this drives more flow through the gap than is accounted for in Wiegel's method.

Recent analyses of these slit-type vertical wave barriers have been made using a variety of more complete analytical techniques. The most advanced solutions are based on potential flow methods and examples include the works of Kakuno (1983), Kojima et al. (1988), and Fugazza and Natale (1992). In these methods, the velocity potentials are found for the linear incident and reflected waves by applying both far field boundary conditions and matching conditions at the wall boundary. While solutions have been obtained for the wave transmission coefficient based on this approach, results have not been presented for the wave forces on the wall.

In contrast, simpler solutions based on fundamental hydraulics principles have also been proposed by Hayashi et al. (1966), Hayashi et al. (1968), Mei et al. (1974), Kondo (1979), and Urashima et al. (1986). These methods, also summarized by Mei (1983), have been developed for shallow water waves where wave pressures are hydrostatic and where flow velocities are uniform over depth. As a result, the equations for conservation of mass, momentum, and energy may be applied directly in two-dimensions in order to find the wave transmission coefficient. In most of these cases, solutions are also presented for the wave forces imparted on the wall by shallow water waves.

In the present paper, a hydraulic model similar to that of Hayashi et al. (1966) and Mei et al. (1974) is proposed for conditions of arbitrary water depth. It is assumed that both the wave transmission and wave forces are determined primarily by the strong horizontal fluid velocities that are driven through the breakwater gaps by the large pressure gradients that occur over the width of the wall. These maximum pressure gradients, and the associated maximum horizontal velocities, are largest during both the crest and trough phases of the wave. Because of this, it is assumed that the conservation equations can be applied first in horizontal layers and then depth-integrated to obtain the total wave transmission or the total wave force. Experimental verification of this simplified hydraulic theory is then presented based on recent laboratory experiments conducted at the U.S. Naval Academy.

## SIMPLIFIED HYDRAULIC THEORY

Consider the flow between two streamlines located along the centerline of adjacent wall elements and separated by width  $s+b$  as shown in Figure 1b. Conservation of mass requires the net discharge to be identical at each of the three sections shown in Figure 1b. As a result, the velocities at each of the three sections are related as:

$$u_i + u_r = C_c P V_c = u_t \quad (1)$$

where  $V_c$  is the velocity in the contraction and where  $C_c$  is the contraction coefficient, taken as  $C_c = 0.6 + 0.4P^3$  following Mei (1983). Based on linear wave theory, the velocities at the wave crest phase may then be given by

$$u_i = \sigma \frac{H_i}{2} Z_u \quad u_r = -\sigma \frac{H_r}{2} Z_u \quad u_t = \sigma \frac{H_t}{2} Z_u \quad (2)$$

where  $Z_u = \cosh(kh + kz) / \sinh(kh)$ ,  $k$  is the wave number,  $h$  is the water depth, and  $\sigma$  is the wave frequency. Because all velocities oscillate in time as  $\cos(\sigma t)$ , the wave heights are then related as

$$H_i - H_r - H_t \quad (3)$$

and the reflection and transmission coefficients are related as

$$K_r - 1 - K_t \quad (4)$$

Application of the momentum and energy equations then allows the pressure gradient across the wall to be determined. The momentum equation, applied between sections 2 and 3 in Figure 1b, is first used to find the pressure in the contraction in terms of the transmitted wave pressure and velocity. The energy equation, applied from section 1 to 2, is then used to relate the incident and reflected pressures to the pressure in the contraction. Combining these expressions, and using equation (1), finally yields the pressure drop across the wall as

$$p_i + p_r - p_t = \left(\frac{1}{C_c P} - 1\right)^2 \frac{1}{2} \rho u_t^2 \quad (5)$$

The right-hand-side of equation (5) represents the head loss through the gap as a quadratic function of the transmitted wave velocity. Following the method of equivalent linearization, e.g. Mei (1983), this may then be approximated as

$$p_i + p_r - p_t = K_{LOSS} \frac{4}{3\pi} \rho u_{tm} u_t \quad (6)$$

where  $u_{tm}$  is the magnitude of the transmitted wave velocity and where  $K_{LOSS}$  is the head loss coefficient. This is given as  $K_{LOSS} = ((1/C_c P) - 1)^2$  based on the flow constriction and expansion but will be modified later to account for other effects. As a result of the linearization, the velocities and pressures in equation (6) may be given by linear wave theory but the head loss on the right-hand-side will still retain a nonlinear effect of wave steepness.

**SOLUTION FOR WAVE TRANSMISSION**

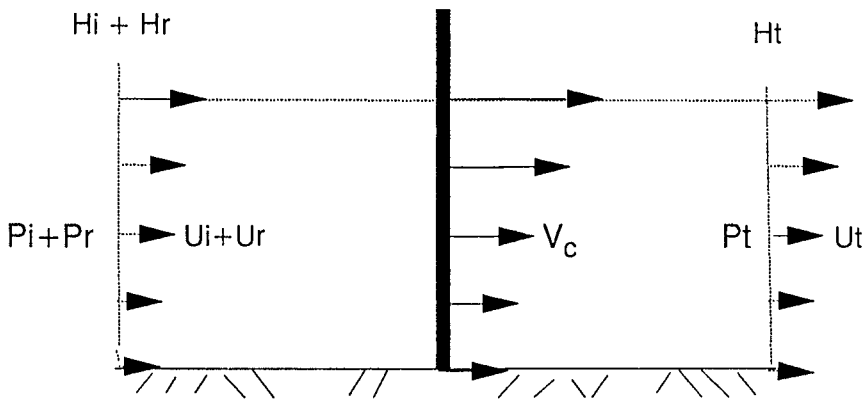
The results presented above may now be extended into three dimensions to allow for variable pressures and velocities over the water depth, and to determine the overall transmission coefficient. Referring to Figure 2, it is first assumed that equation (6) models the pressure drop across the wall in any horizontal layer. It is further assumed that the dynamic pressures at any elevation are given by linear wave theory as

$$p_i = \rho g \frac{H_i}{2} Z_p \quad p_r = \rho g \frac{H_r}{2} Z_p \quad p_t = \rho g \frac{H_t}{2} Z_p \quad (7)$$

where  $Z_p = \cosh(kh + kz) / \cosh(kh)$ . Substitution of these expressions into equation (6), making use of equations (2) and (3), and integrating over depth then gives the following expression for wave transmission

$$\rho g H_i (1 - K_p) \int_{-h}^0 Z_p dz - K_{LOSS} \frac{1}{3\pi} \rho \sigma^2 H_i^2 K_t^2 \int_{-h}^0 Z_u^2 dz \quad (8)$$

The vertical integrations in this expression, from the seafloor  $z = -h$  to the still water level  $z = 0$ , are consistent with linear wave theory and account for the variable head losses over depth. As may be seen in Figure 2, the head losses are much larger near the surface than at the seafloor. It is also noted that by integrating to  $Z = 0$ , the head losses are assumed to be identical during both the crest and trough phases.



**Figure 2.** Illustration of vertical distribution of pressure and velocity.

Carrying out the operations in equation (8) ultimately yields a simple quadratic equation for the wave transmission coefficient as

$$T_t K_t^2 + K_t - 1 = 0 \quad (9)$$

where the variable  $T_t$  may be termed the *transmission function* and is equal to

$$T_t = K_{LOSS} \frac{1}{6} \frac{H_i}{L} \frac{\sinh 2kh + 2kh}{\sinh^2 kh} \quad (10)$$

The solution for wave transmission in arbitrary water depth is then found to have a form similar to that given by Mei (1983) in shallow water as

$$K_t = \frac{-1 + (1 + 4T_t)^{1/2}}{2T_t} \quad (11)$$

The solution for  $K_t$  in equations (10) and (11) contains the effects of both the relative water depth and the wave steepness, in addition to the breakwater porosity as reflected in the head loss coefficient. Figure 3 shows the variation in  $K_t$  as a function of porosity and relative depth for a fixed value of wave steepness. This shows that transmission is lower in shallow water than in deep water, because of the uniform velocities and therefore larger head losses over depth in shallow water. In addition, the transmission is essentially equal to that in deep water once  $h/L > 0.3$  or so. Figure 4 then shows the variation with wave steepness for deep water conditions. This illustrates that the head losses increase, and that the transmission decreases, for waves of higher steepness.

The functional dependencies on wave steepness and porosity may be displayed more clearly by considering deep water conditions, consistent with the experimental phase of this study, where  $T_t = K_{LOSS} H_i / 3L_o$  and where  $L_o$  is the deep water wavelength. As shown by Mei (1983, p. 263), the solution for wave transmission may be simplified based on series expansions of equation (11). For small amplitude waves or large gap spaces (small values of  $T_t$ ), it is found that

$$K_t = 1 - T_t = 1 - K_{LOSS} \frac{1}{3} \frac{H_i}{L_o} \quad (12)$$

On the other extreme, for large amplitude waves and narrow gap spaces (large values of  $T_t$ ), it may be shown that

$$K_t = \left( \frac{1}{T_t} \right)^{1/2} = \left( \frac{3}{K_{LOSS}} \frac{L_o}{H_i} \right)^{1/2} \quad (13)$$

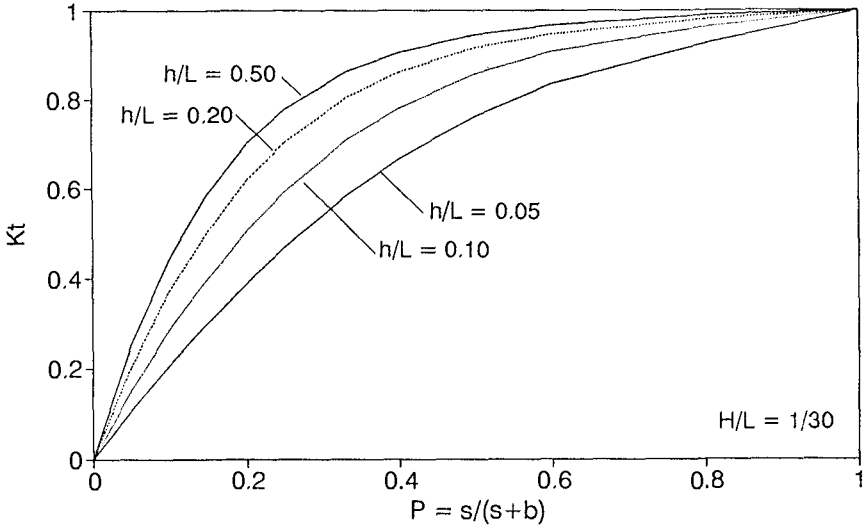


Figure 3. Example of wave transmission as a function of relative depth.

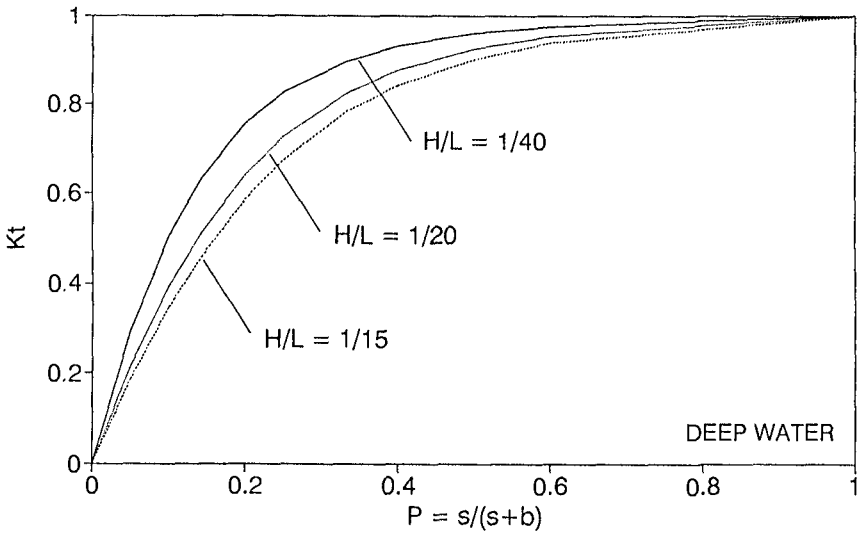


Figure 4. Example of wave transmission as a function of wave steepness.



## SOLUTION FOR WAVE FORCES

The wave force per unit length on one wall element,  $f$ , may be determined by applying the momentum equation from section 1 to 2 as shown in Figure 1b. Wave forces are then found from the differences in the specific forces on either side of the wall, assuming that the pressure in the contraction is impressed over the wake behind the wall. In water of arbitrary depth, this is applied to each fluid layer and the force per unit length is found to vary as

$$f = (p_i + p_r - p_t) (s+b) - \rho g H_i (1-K_r) Z_p (s+b) \quad (14)$$

Depth integration from the seafloor to the still water surface, consistent with linear wave theory, then gives the total force on one wall element,  $F$ , as

$$F = \rho g \frac{H_i}{k} \tanh(kh) (1-K_r) (s+b) \quad (15)$$

This expression is similar to the force exerted by linear standing waves on a solid wall of width  $b$ , denoted by  $F_o$  and given by

$$F_o = \rho g \frac{H_i}{k} \tanh(kh) b \quad (16)$$

As a result, the normalized force on one wall element of a slotted or slit-type vertical wave barrier may be expressed in the form

$$\frac{F}{F_o} = \frac{1 - K_r}{1 - P} \approx (1 - K_r)(1 + P) \quad (17)$$

where  $P$  is the wall porosity. According to equation (4), it is also found that the forces are directly proportional to the wave reflection coefficient. The maximum wave force reduces to the usual solution for linear standing waves when the wall porosity and the transmission coefficient approach zero. In general, however, the force on a permeable wall depends on the wall porosity, the relative depth, and the wave steepness, due to the dependence of the transmission coefficient on these parameters.

In the experimental phase of this study, wave forces were measured on walls with large gap spaces in some tests; and, in fact, some tests were performed on a single rectangular wall element placed in the center of the wave tank such that the porosity was essentially equal to unity. Under this extreme condition, the force on the wall element predicted by equation (17) is equal to zero. However, non-zero forces were measured and these measured forces were, as expected, well-represented by the Morison equation as the sum of drag and inertia forces.

Therefore, two empirical modifications of equation (17) were introduced. First, the inertia force on a rectangular wall element was included so that the total force on the wall was actually modelled as

$$\frac{F}{F_o} = (1-K_p)(1+P) \cos \sigma t - \pi C_m \frac{t}{L} K_t \sin \sigma t \quad (18)$$

where  $t$  is the wall thickness and  $C_m$  is the inertia coefficient, assumed to equal  $C_m = 1 + 0.325\pi b/t$  or 4.06 for rectangular members with a width-to-thickness ratio of 3 as used in this study. In addition, the head loss coefficient was modified as

$$K_{Loss} = \frac{3\pi}{16} C_D + \left( \frac{1}{C_c P} - 1 \right)^2 \quad (19)$$

where  $C_D$  is the viscous drag coefficient on a single rectangular element, assumed to equal two in this work. As the porosity approaches unity, the second term in equation (19) goes to zero and the first term then leads to the same drag force as would be found from the Morison equation, as may be shown based on the series expansion introduced in equation (12). On the other hand, as the porosity approaches zero, the second term governs and may be an order-of-magnitude larger than the first term.

## EXPERIMENTAL VERIFICATION

Verification of the theoretical results is based on physical model tests conducted at the United States Naval Academy Hydromechanics Laboratory in a wave tank 36.6 m long, 2.4 m wide, and 1.55 m deep, equipped with a flap-type wavemaker. A full-depth vertical wave barrier was constructed of wooden wall elements having a width,  $b = 7.62$  cm, and a thickness,  $t = 2.54$  cm. Five gap spacings were then tested, with  $s = 0.84, 1.27, 2.54, 3.81,$  and  $7.62$  cm. Single wall members were also tested. As a result, data is available for wall porosities  $P$  of 0.10, 0.14, 0.25, 0.33, 0.50, and 0.97.

Test were conducted using regular waves with four different wave frequencies, three of which produced deep water waves with  $h/L > 0.5$ . Deep water waves were considered here because many wave barriers are constructed in or adjacent to marinas or navigation channels where they are subjected to short-period wind waves or boat waves that are actually in deep water relative to their wavelength. At each frequency, up to three values of wave height were tested producing values of wave steepness of  $H/L = 1/40, 1/20,$  and  $1/15$ . Incident and transmitted waves were measured with fixed wave gages located near the wavemaker and 1 to 3 m behind the wall respectively. Wave forces were measured by attaching one of the vertical wall members, manufactured out of aluminum to provide additional stiffness, to a force gage.

## EXPERIMENTAL RESULTS

Examples of theoretical and experimental results for deep-water regular wave transmission are shown in Figure 5. In Figure 5a, transmission coefficients are shown for each of the four wave frequencies tested for a constant wave steepness of  $1/40$ . Figures 5b and 5c show similar results for a constant wave steepness of  $1/20$  and  $1/15$  respectively, although only three wave frequencies were actually tested at the higher steepness due to wavemaker limitations. As can be seen, the theory provides reasonable predictions of the transmission at all values of wall porosity and at all three values of wave steepness. In general, there was no discernable dependence in the data on wave frequency at a given value of porosity, consistent with the theoretical predictions. In addition, despite the linearizing assumptions made in the theory, predictions are quite good even for the higher wave steepness. One notable aspect of these results, however, is that for low steepness waves in deep water, wave transmission may be as high as 70 or 80 percent even for wall porosities of just 0.15 to 0.25.

Typical results for wave forces on the instrumented vertical wall element are shown in Figure 6. Figure 6a shows results for a wave steepness of  $1/40$  while Figure 6b shows results for a steepness of  $1/20$ . Measured forces reported here are actually the average of the positive and negative maximum forces, since the linear theory does not distinguish between force magnitudes at the crest or trough phase of the incident wave. The forces are then given in dimensionless form as the average measured force divided by the force predicted by linear standing wave theory. One result of this normalization, however, is that results differ for each wave frequency as porosity increases so that forces at different relative depths do not collapse to a single curve.

In Figure 6, it may be seen that the simplified hydraulic theory provides a reasonable estimate of measured forces for all values of porosity and for both values of wave steepness. Interesting features of the force predictions are that: (1) for very low values of porosity, predicted forces are mostly independent of relative depth and collapse to a single curve and that (2) once porosity exceeds about 0.5, dimensionless forces are nearly constant but differs for each relative depth. Reasons for this behavior may be seen in equation (18). At small values of porosity, the first term in equation (18) governs and, since the transmission coefficient is not a function of relative depth for these deep water conditions, the predicted dimensionless force is therefore the same for all frequencies tested. On the other hand, as the porosity becomes large, the second term in equation (18) governs and leads to a dependence of the dimensionless force on the wall thickness-to-wavelength ratio. It is noted that there is more scatter in the force data at the lower wave steepness since the measured forces for some of these conditions, particularly for  $h/L = 1.20$ , were very small and influenced by the sensitivity of the force gage

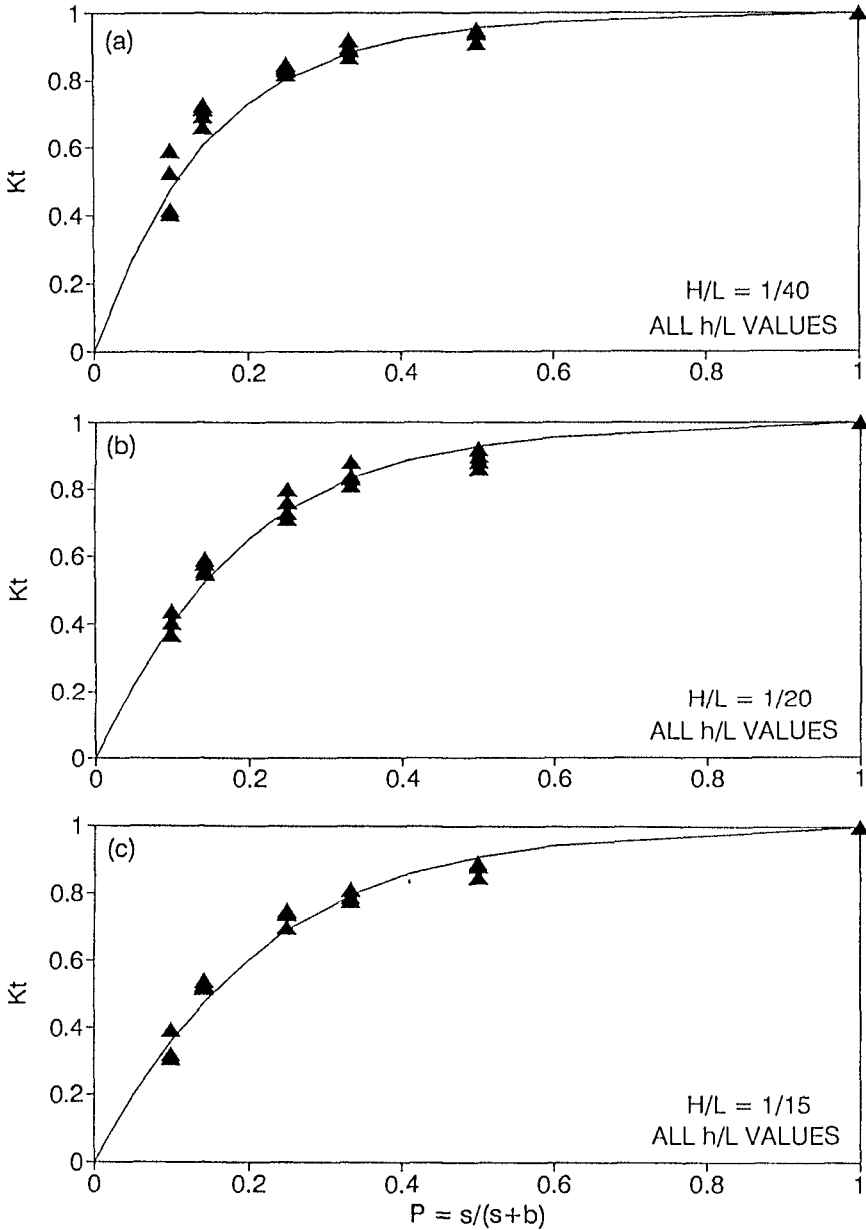
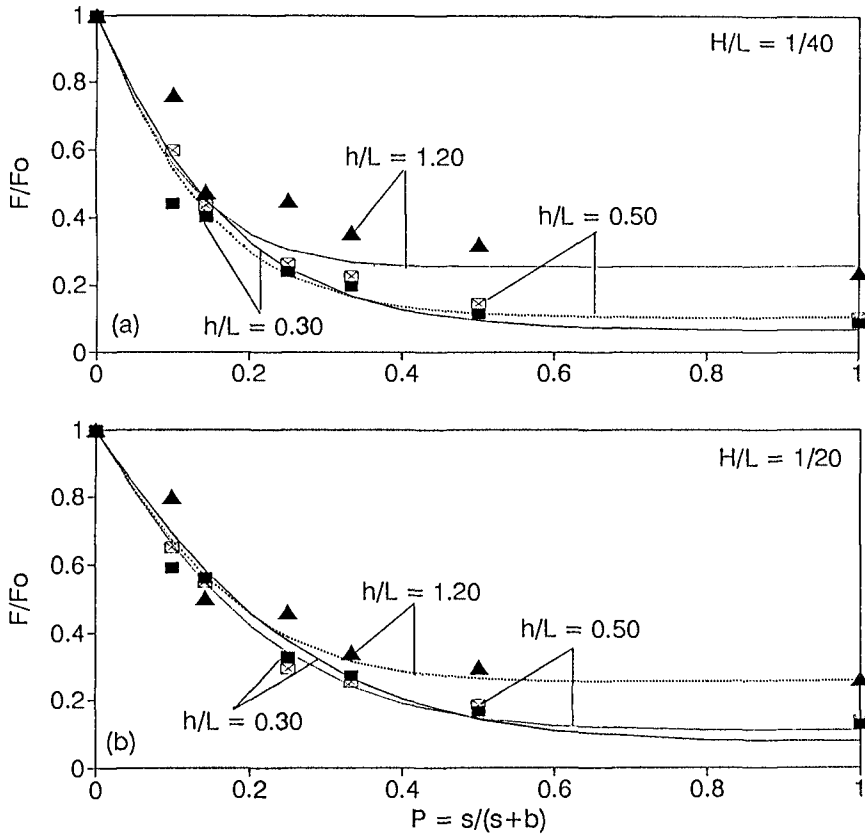


Figure 5. Comparison of measured and predicted deep water wave transmission. (a)  $H/L = 1/40$  and (b)  $H/L = 1/20$ , and (c)  $H/L = 1/15$ .



**Figure 6.** Comparison of measured and predicted deep water wave forces: (a)  $H/L = 1/40$  and (b)  $H/L = 1/20$ .

Some tests were also performed with random waves; however, space limitations prevent a complete discussion of these results. In general, it was found that the simplified hydraulic theory worked well for random wave transmission and wave forces when the significant wave height and peak wave period were used to characterize the random sea. As a single parameter, the significant wave height seemed to characterize the random sea better than the root-mean-square wave height. Apparently, the significant height gives a larger overall head loss that more closely approximates the actual head losses of the larger waves in a random sea.

## CONCLUSIONS

Methods presented in this paper allow a straightforward calculation of wave transmission and wave forces for a vertical slotted or slit-type wave barrier. As shown by both theory and experimental data, wave transmission decreases as the wave steepness increases and as the porosity decreases. However, wave forces increase under these same conditions. As a result, wave transmission can be decreased only at the expense of a large increase in the wave force on the wall. This trade-off between wave transmission and wave forces often leads to wall designs that are too porous and allow too much wave transmission in order to be economical to construct, particularly if the wall is to be attached to an existing pier as is often the case.

Under the assumption that both high wave transmission and high wave reflection are undesirable near marinas or entrance channels, the wall porosity associated with the maximum energy dissipation may be found. Based on an energy balance, the dissipated wave energy will equal

$$E_{DISS} = E_i - E_t - E_r = 2 E_i K_t (1 - K_t) \quad (20)$$

where equation (4) has been used to related  $K_r$  to  $K_t$ . As a result, it is found that the maximum wave energy dissipation occurs when  $K_t = 0.5$ . For values of wave steepness considered in this paper, and for deep water waves, this requires wall porosities in the range of 0.09 to 0.17 to maximize the energy dissipation. Based on constructed vertical wave barriers that the author has visited, porosities are generally larger than this by a factor of two or even three in some cases. Thus, the wave transmission coefficient is often more than 0.70 and is usually higher than intended or desired. Smaller gap spaces are therefore recommended when possible and where increased wave forces will not jeopardize the integrity of the supporting structure.

## ACKNOWLEDGEMENTS

This work was supported by the Ocean Technology Program of the National Science Foundation as part of a Presidential Young Investigator Award. The author would like to thank Louise Wallendorf of the Naval Academy Hydromechanics Laboratory and former students Laurie Wood, Troy McClelland, and Eric Thomas for carrying out the laboratory work. The author would also like to acknowledge several useful discussions with Robert G. Dean of the University of Florida who recently proposed a similar hydraulic model for wave transmission in an unpublished consulting report.

**REFERENCES**

- Fugazza, M., and Natale, L., 1992, "Hydraulic Performance of Perforated Breakwater," *Journal of Waterway, Port, Coastal, and Ocean Engr., ASCE*, Vol. 118, No. 1, pp. 1-14.
- Hayashi, T., Hattori, M., Kano, T., and Shirai, M., 1966, "Hydraulic Research on Closely Spaced Pile Breakwater," *Proc. 10th Intl. Conf. on Coastal Engr., ASCE*, pp. 873-884.
- Hayashi, T., Hattori, M., and Shirai, M., 1968, "Closely Spaced Pile Breakwater as a Protection Structure Against Beach Erosion," *Coastal Engineering in Japan*, Vol. 11, pp. 149-160.
- Kakuno, S., 1983, "Reflection and Transmission of Waves Through Vertical Slit-Type Structures," *Proc. Coastal Structures '83, ASCE*, pp. 939-953.
- Kojima, H., Ijina, T., and Yoshida, A., 1988, "A Numerical Method for Hydraulic Properties of a Slit-Type Breakwater Against Regular and Irregular Waves," *Proc. 6th Cong. Asian and Pacific Div. IAHR, Kyoto*, pp. 201-208.
- Kondo, H., 1979, "Analysis of Breakwaters Having Two Porous Walls," *Proc. Coastal Structures '79, ASCE*, pp. 962-977.
- Mei, C. C., 1983, "The Applied Dynamics of Ocean Surface Waves," John Wiley & Sons, New York.
- Mei, C., Liu, P., and Ippen, A., 1974, "Quadratic Loss and Scattering of Long Waves," *Journal of Waterways, Harbor, and Coastal Engr., ASCE*, Vol. 100, No. WW3, pp. 217-239.
- Urashima, S., Ishizuka, K., and Kondo, H., 1986, "Energy Dissipation and Wave Force at Slotted Wall," *Proc. 20th Intl. Conf. on Coastal Engr., ASCE*, pp. 2344-2352.
- Wiegel, R., 1961, "Closely Spaced Piles as a Breakwater," *Dock and Harbor Authority*, Vol. 42, No. 491, p. 150.

## CHAPTER 101

### INTERACTION OF NONLINEAR WAVES WITH COASTAL STRUCTURES

J.J. Lee <sup>1</sup>; C. Chang <sup>2</sup>; F. Zhuang <sup>2</sup>

#### ABSTRACT

Interaction of transient nonlinear waves (modeled by solitary waves with moderate wave height) with submerged breakwater has been studied both numerically and experimentally. The emphasis is on the comparison between the numerical solution and the laboratory experiments on the wave transformation and the water particle velocity of the induced flow field.

For the numerical analysis, the Boundary Element Method (BEM) has been used for analyzing the wave field induced by the coastal structure. For the laboratory experiments the wave profiles are obtained by resistance type wave gauge; the two dimensional water particle velocities are obtained by a four-beam Laser Doppler Velocimeter (LDV) equipped with frequency shifting and with a fiber optics system. The LDV measurements are directed to obtain the detail of the wave kinematic properties important for ascertaining the dynamics of the modified wave field in the vicinity of the submerged breakwater. This serves as a critical check for the validity of the numerical computations.

Results of the numerical model have been found to compare well with the experimental data for the conditions studied in both the wave profiles and the water particle velocities beneath the waves as they interact with the breakwater.

---

<sup>1</sup>Jiin-Jen Lee, Member, ASCE; Professor of Civil Engineering, Department of Civil Engineering, University of Southern California, Los Angeles, CA 90089-2531

<sup>2</sup>Chun Chang & Fei Zhuang, Graduate Research Assistants, Department of Civil Engineering, University of Southern California, Los Angeles, CA 90089-2531



# 1 Numerical Analysis

For the numerical analysis, the problem is formulated as a two-dimensional boundary value problems. The fluid in the solution domain is assumed to be incompressible and the flow irrotational, the viscous force is neglected. Potential theory is used for such flow condition and the Laplace's equation is obtained as the governing equation:

$$\nabla^2 \phi(\mathbf{x}, t) = 0 \quad \mathbf{x} \in \Omega(t). \quad (1)$$

The solution to the Laplace's equation is expressed as a boundary integral using the free space Green's function  $G(\mathbf{x}_i, \mathbf{x}_j) = -\frac{1}{2\pi} \log |\mathbf{x}_i - \mathbf{x}_j|$  and Green's theorem:

$$\alpha(\mathbf{x}_i) \phi(\mathbf{x}_i) = \int_{\Gamma(\mathbf{x})} \left[ \frac{\partial \phi}{\partial n} G(\mathbf{x}, \mathbf{x}_i) - \phi(\mathbf{x}) \frac{\partial G(\mathbf{x}, \mathbf{x}_i)}{\partial n} \right] d\Gamma(\mathbf{x}) \quad (2)$$

where  $\mathbf{x}_i$  and  $\mathbf{x}$  are position vectors for position on the boundary ( $\mathbf{x}_i$  can also be any where within the domain),  $\Gamma(\mathbf{x})$  is the boundary of the fluid domain  $\Omega$ ,  $\mathbf{n}$  the unit outward normal vector and  $\alpha(\mathbf{x}_i)$  a geometric coefficient.

The kinematic and the fully nonlinear dynamic free surface conditions are considered, i.e., on the free surface  $\Gamma_s$ ,  $\phi$  satisfies the following kinematic and dynamic boundary conditions:

$$\frac{D\mathbf{r}}{Dt} = \left( \frac{\partial}{\partial t} + \mathbf{u} \cdot \nabla \right) \mathbf{r} = \mathbf{u} = \nabla \phi \quad (3)$$

$$\frac{D\phi}{Dt} = -gy + \frac{1}{2} |\nabla \phi|^2 - \frac{p_a - p_o}{\rho} \quad (4)$$

with  $\mathbf{r}$  the position vector of a fluid particle at the free surface,  $g$  the acceleration due to gravity,  $y$  the vertical coordinate,  $p_a$  the pressure at the surface,  $p_o$  a reference pressure and  $\rho$  the fluid density.

The method used to update both the new position of the free surface and the potential function  $\phi$  on the free surface at the next time step was first suggested by Dold and Peregrine (1986). Similar procedure was also used by Grilli, Skourup & Svendsen (1989). Based on the Taylor expansion in a Lagrangian formulation (following a fluid particle on the surface), the explicit expressions for the position vector  $\mathbf{r}(t + \Delta t)$  and the potential function  $\phi(t + \Delta t)$  can be expressed as an infinite series as follows:

$$\mathbf{r}(t + \Delta t) = \mathbf{r}(t) + \sum_{k=1}^n \frac{(\Delta t)^k}{k!} \frac{D^k \mathbf{r}(t)}{Dt^k} + O[(\Delta t)^{n+1}] \quad (5)$$

$$\phi(\mathbf{r}(t + \Delta t), t + \Delta t) = \phi(\mathbf{r}(t), t) + \sum_{k=1}^n \frac{(\Delta t)^k}{k!} \frac{D^k \phi(\mathbf{r}(t), t)}{Dt^k} + O[(\Delta t)^{n+1}]. \quad (6)$$

The terms containing the material derivatives of  $\mathbf{r}$  and  $\phi$  in the above two equations are determined by first expressing them in terms of the potential function  $\phi$  and its time and spatial derivatives  $(\frac{\partial\phi}{\partial n}, \frac{\partial^2\phi}{\partial t\partial n}, \dots)$  and then solve the time and spatial derivatives by solving successions of Laplace's problems for the velocity potential  $\phi$  and its time derivatives. Each solution provides the nonlinear free surface boundary conditions for the next one. This is applicable because the Laplace's equation is indeed valid for all the time derivatives of  $\phi$ . The repeated solution of the Laplace's equation is actually quite simple after the coefficient matrix of the boundary element method has been formed and decomposed into an upper and a lower diagonal matrix. This is so because the coefficient matrix is only a function of the geometry and remain unchanged throughout the repeated solution process.

The Boundary Integral Equation is solved by using the so called Boundary Element Method which discretize the boundary into a finite number of elements. The boundary integration is performed on each element for a given  $\mathbf{x}_i, i = 1, 2, \dots, N,$

$$\alpha(\mathbf{x}_i)u(\mathbf{x}_i) = \sum_{k=1}^N \left\{ \int_{\Gamma_k} \left[ \frac{\partial u}{\partial n} G - u \frac{\partial G}{\partial n} \right] d\Gamma + \int_{\Gamma_k} \left[ \frac{\partial u}{\partial n} G - \bar{u} \frac{\partial G}{\partial n} \right] d\Gamma \right\}. \quad (7)$$

This produces a system of  $N$  linear algebraic equations for  $N$  unknowns. The integral equation is solved twice in the present study for both  $\phi$  and  $\partial\phi/\partial t$ . This gives a second order accuracy in the time marching scheme.

Interior solutions at the interior point  $x_j$  can be obtained using

$$2\pi\phi(x_j) = \int_{\Gamma} [\phi(x_i) \frac{\partial}{\partial n} (\ln r) - \ln r \frac{\partial}{\partial n} \phi(x_i)] ds \quad (8)$$

when all the potential values and normal potential derivatives on the boundary (for all  $x_i$ ) are known. Normally the value of the potential function inside the domain is not as important as its derivatives with respect to  $x$  and  $y$  because these values represent the velocity components at the interior points. The calculation of these velocity components can be performed by making direct derivatives of Equation 8 with respect to  $x$  and  $y$ , respectively,

$$2\pi \frac{\partial}{\partial x} \phi(x_j) = \int_{\Gamma} [\phi(x_i) \frac{\partial}{\partial x} (\frac{1}{r} \frac{\partial r}{\partial n}) - \frac{\partial}{\partial x} (\ln r) \frac{\partial}{\partial n} \phi(x_i)] ds \quad (9)$$

$$2\pi \frac{\partial}{\partial y} \phi(x_j) = \int_{\Gamma} [\phi(x_i) \frac{\partial}{\partial y} (\frac{1}{r} \frac{\partial r}{\partial n}) - \frac{\partial}{\partial y} (\ln r) \frac{\partial}{\partial n} \phi(x_i)] ds. \quad (10)$$

Only  $\phi$  at the interior point  $x_j$  is differentiated since that is where the derivatives are wanted. From Equation 9 & 10 it is seen that the values of  $\phi, \frac{\partial\phi}{\partial n}$  inside the integral are those on the boundary and they are not involved in the differentiation of the function.

## 2 Experimental equipment and experimental procedures

Experiments involving propagation of solitary waves over various submerged breakwater configurations are conducted in a wave tank 15.2 meter long, 39.4 centimeter wide, and 61 centimeter deep. The side-walls of the wave tank are made of glass and offer excellent transparency for laser beams. A programmable piston type wave generator is installed at one end of the tank and a sloping beach is installed at the other end of the wave tank.

Two different breakwater configurations are used in the experiment. The first breakwater is 45 inch wide, 4.5 inch high and is made of plywood. The second breakwater is of one third in width with the same height and is made of lucite. The breakwater is sunk and fixed to the bottom of the wave tank by adding lead weight.

The wave generating device is a piston type wave generator. It is powered by a hydraulic piston whose motion is controlled by a personal computer. The computer determines a voltage time history which defines the trajectory of the wave plate through a hydraulic-servo system. The wave generation program used by the computer allows motions of the wave machine to be prescribed for generating small amplitude periodic waves, finite amplitude periodic waves, and solitary waves.

Tap water is used to fill the wave tank to the desired depth. The depth is measured using a point gage which is mounted to a movable carriage traveling on a rail system installed at the top of both side walls of the wave tank. Resistance type wave gages are used to measure water surface elevations as a function of time. Three wave gages are installed at desired locations to make simultaneous wave profile measurements. The wave gages are connected to a Sanborn four channel oscillograph recorder which records the measurements on an oscillograph paper.

The water particle velocities are measured using a portable four-beam, two-component, fiber optic Laser Doppler Velocimeter (LDV) manufactured by TSI, Inc.. The LDV system used in the experiment consists of a 100 mW argon-ion laser, transmitting and receiving optics, a fiberoptic probe, frequency shifting and signal processing instruments. A multicolor beam separator separates the incident laser beam into four beams, two blue beams and two green beams. The four laser beams are focused into one point within the flow field to form a two-component system. Figure 1 provides a flow chart of the LDV system used for the present experiment. Two photomultipliers convert optical signals into electric signals. Two frequency shifters help attain accurate flow measurements in applications where high turbulence or flow

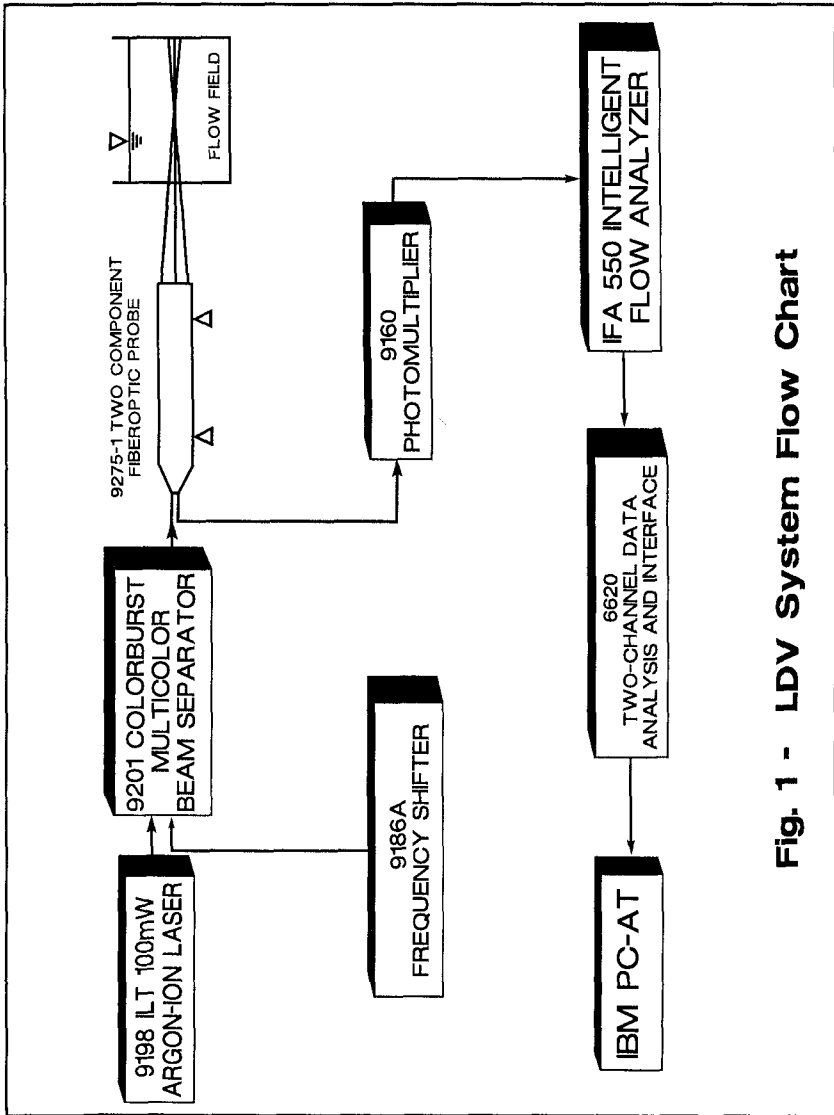


Fig. 1 - LDV System Flow Chart

reversals are anticipated. A fiberoptic probe which features focusing and receiving optics in one compact unit offer considerable ease for setting up the LDV system. Two IFA550 signal analysis systems are used for signal analysis. This is done by using a personal computer which manages the LDV measurements, stores velocity measurements, and displays the velocity-time history on the monitor. The whole LDV system is installed in a room close to the wave tank. When velocity measurements are needed, only the portable fiberoptic probe is moved to the measuring station and is mounted to a traversing mechanism which offers three dimensional positioning of the measuring point. Seeding is one of the key elements affecting the performance of the LDV measurements. Seeding particles must be small enough to move with the flow yet large enough to scatter sufficient light for ideal signal quality. Titanium Dioxide powder ( $\text{TiO}_2$ ) is used in the experiment and is proved to be a good seeding agent for water in the wave tank used for the present experiments.

### 3 Presentation and Discussion of Results

Figure 2 shows the wave profiles obtained from the numerical model at different time steps as the incident solitary wave propagates over a submerged breakwater which is at one-half of the water depth. The wave height/water depth ratio is 0.2, still water depth is 9 inches and the breakwater width is ten times the breakwater height. It should be noted that the vertical scale in Figure 2 is greatly distorted for easy visualization of the wave profiles. From Figure 2 it is seen that the frontal slope of the solitary wave is steepened when the propagating wave approaches the shallower water depth region. It is evident that the submerged breakwater acts to breakup the solitary wave with significant oscillatory tails.

Figure 3 shows the wave profiles computed at three locations: five water depth upstream, five water depth downstream, and on the top of the breakwater. The wave profiles computed from the present numerical model are compared with the wave profiles recorded from the present experiments. It should be noted that the wave profiles shown in Figure 2 are for the Lagrangian system and the time history of the computed wave profile shown in Figure 3 has been converted to the Eulerian reference system so that the computed wave profiles can be compared with the experimental wave profile directly. A comparison of the numerical results and the experimental wave profiles at the three locations shown in Figure 3 clearly demonstrate that the numerical model predicts the wave profile well. It is interesting to note that the peak amplitude of the transmitted solitary wave at the location five water depth downstream of the breakwater is actually larger than the amplitude of

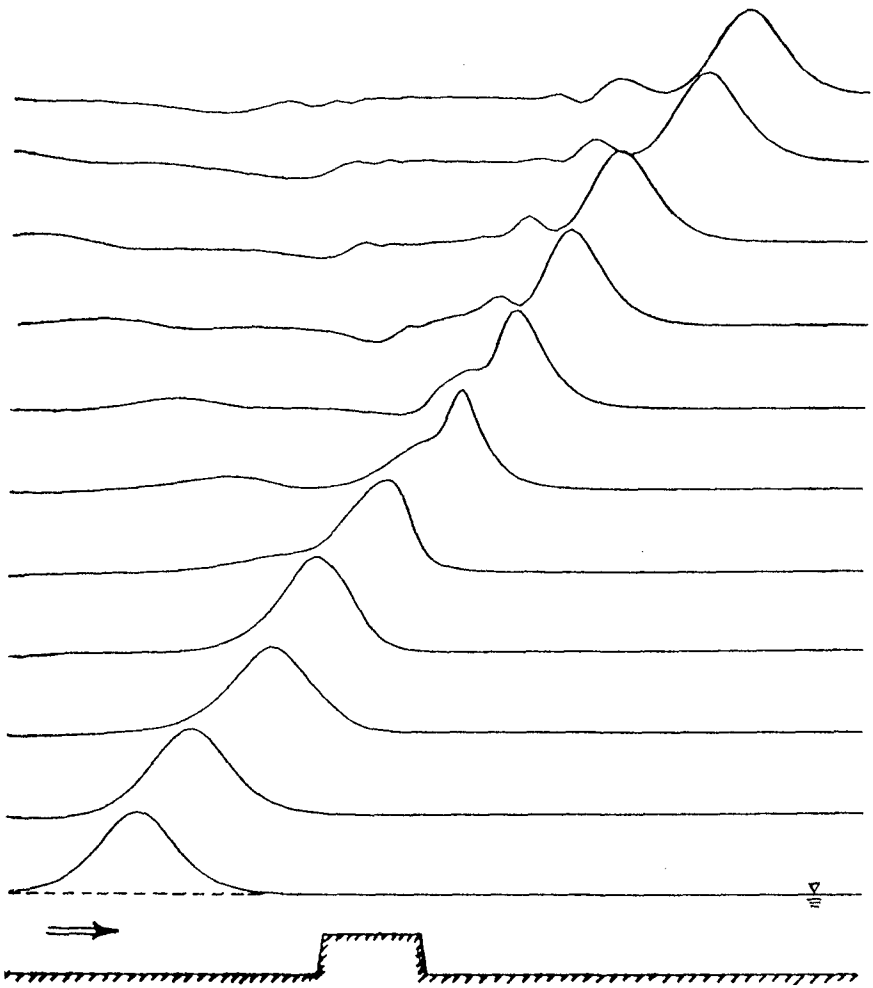


Figure 2: Transformation of solitary wave over submerged breakwater

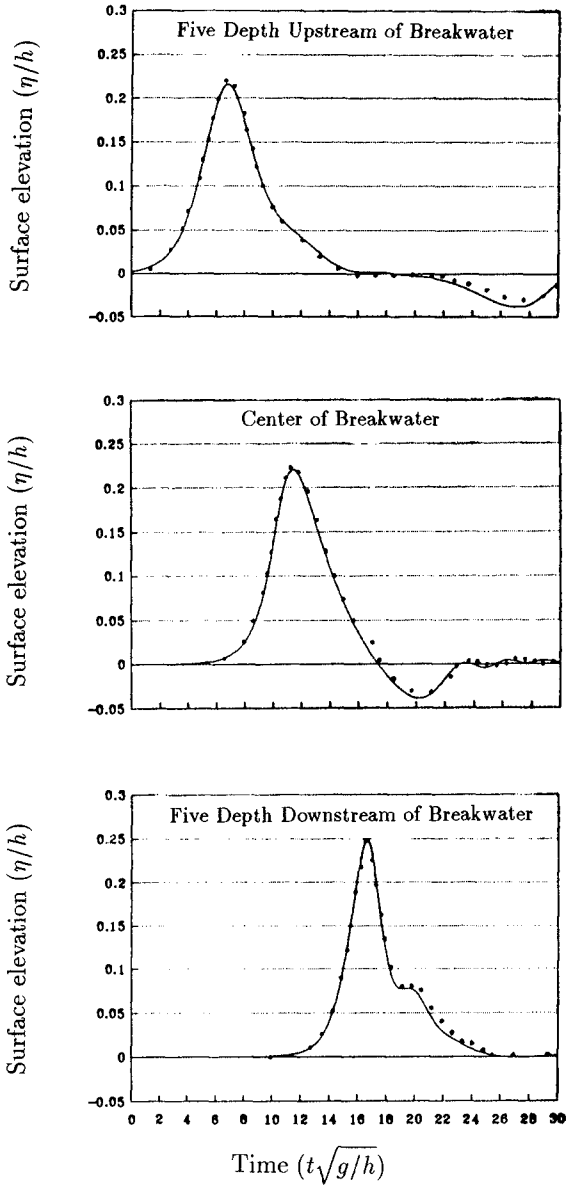


Figure 3: Comparison of wave profiles at three different locations (— present theory, ··· experiment)

the incident solitary wave before interacting with the breakwater. The shape of wave profile is different at the three locations showing the different degree of interaction with respect to transmission, reflection, and the varying water depths effect.

Figure 4 shows the numerical model and the experimental data on the horizontal and vertical water particle velocity at the same three horizontal locations and at 0.1 water depth below the still water level. In each of the three figures shown the horizontal velocities are significantly larger than the vertical velocities. Comparing the numerical and experimental results one can see that the agreement is quite good even though there is some scattering when the velocity is very small. The good agreement between the theory and experiment for the two components of the water particle velocities provides another critical check of the reliability of the numerical model.

Experiments for different water depths resulting in several cases for different relative submergence of the breakwaters have been conducted. LDV measurements for horizontal and vertical components of the water particle velocities have also been conducted at many different locations. However, space limitation does not permit presentation of these additional results.

Experiments have also been conducted for the case of breakwater crest height exactly at the still water level. Thus the incident solitary wave will travel across the top of the breakwater as if wave is traveling at zero water depth. A sketch of this series of experiments is shown in Figure 5. Wave profiles are measured at three stations: one at 10 water depth upstream of the breakwater (45" upstream), another at 3.33 water depth downstream of the breakwater (15" downstream) and the third station at 10 water depth downstream of the center of the breakwater (45" downstream).

The incident solitary wave height is  $H/h = 0.2$ . The measured wave profiles are presented in Figures 6-8. The ordinates of these three figures represent the wave height ( $H$ ) normalized with respect to the water depth ( $h$ ). The abscissa represents the real time in seconds.

From Figure 6 it is clear that the majority of the first wave represents the incident solitary wave and the second wave represents the reflected wave from the upstream edge of the breakwater. The shape of the reflected wave is quite similar to the solitary wave also. The wave profile shown in Figure 7 represents the transmitted wave profile at 15" downstream after the solitary wave has traveled above the breakwater crest region (at zero water depth). It shows that the primary wave is followed by a series of oscillatory tails. These oscillatory wave trains have been reformed into more regular oscillatory waves as they traveled further downstream as evidenced in the wave profile presented in Figure 8. It is interesting to observe the physical nature of the transmitted wave as it travels above the breakwater crest at



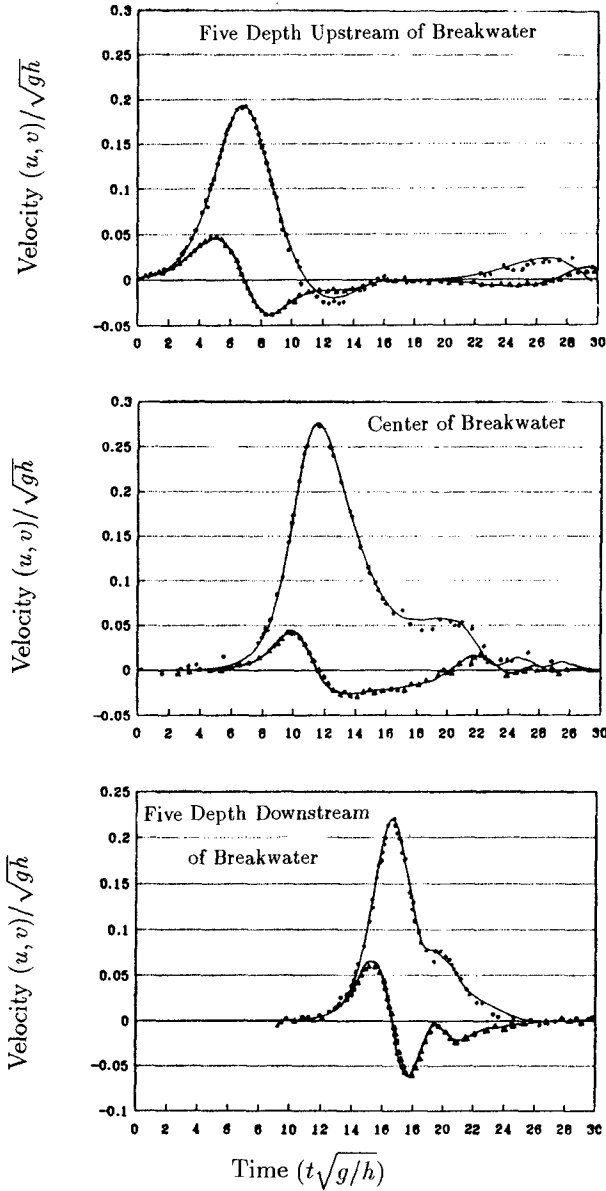


Figure 4: Comparison of water particle velocities at three different locations (— present theory; ··· experiment, u component; ▲▲▲ experiment, v component)

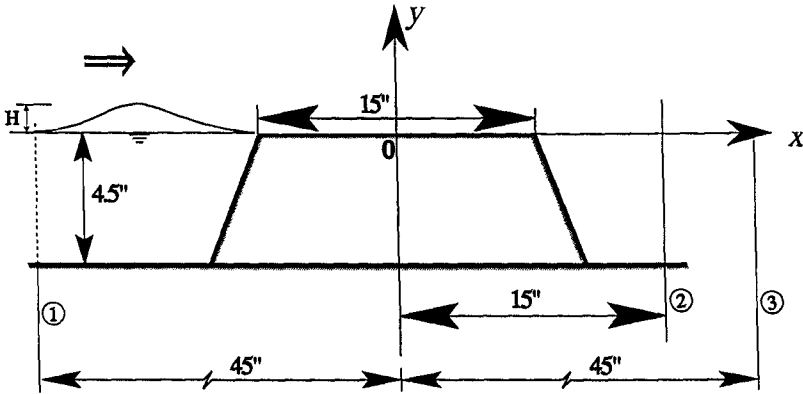


Figure 5  
 Sketch of an experimental set up showing the breakwater height, still water depth and locations of three wave profile measurement stations (not to scale)

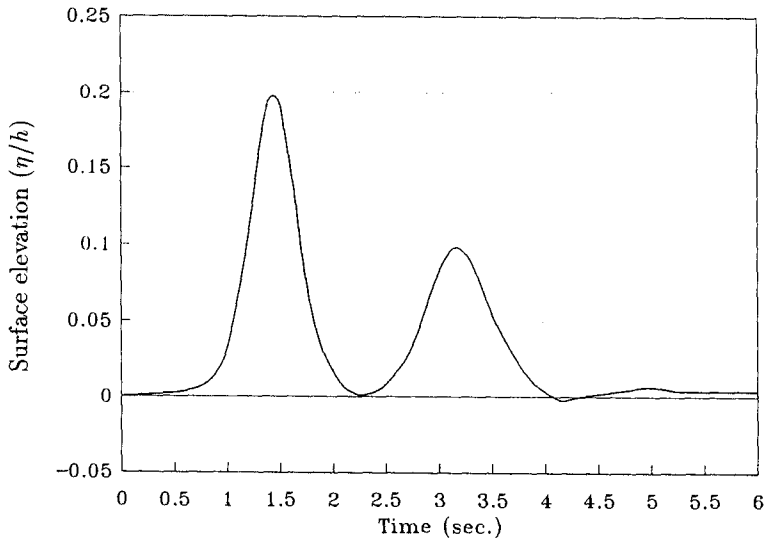
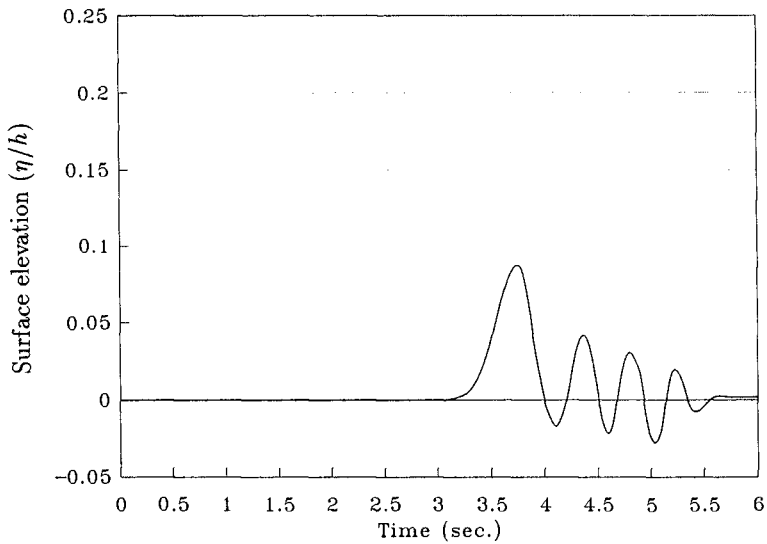
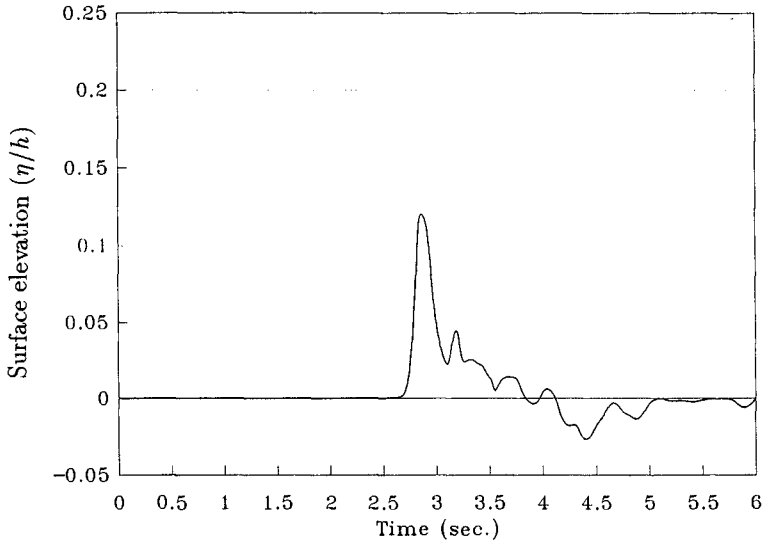


Figure 6: Wave record at 45" upstream of the center of breakwater (station 1)



zero depth. The jet like water mass is translated into the shoreward region of the breakwater. This water mass which is above the still water level then plunge into the shoreward region by the continuous effect of the gravity forces causing the water mass in the shoreward region to exhibit significant undulations. Velocity measurements in this region have also been performed but due to space limitation they are not presented herein. Comparing the wave profiles shown in Figure 6, 7, and 8, it is clear that the breakwater serves to break up the incident wave resulting in significant higher frequency wave components in the shoreward region. This physical phenomenon is significant for the assessment of basin response of the shoreward coastal region.

## 4 Conclusions

The interaction of solitary wave with submerged breakwater has been studied both experimentally and numerically using a boundary element method. For incident solitary wave with moderate wave height and when the breakwater is deeply submerged the numerical results have been compared with the experimental data. It is shown that the agreement between the numerical results and the experimental data has been excellent. The comparison was performed in terms of the wave profiles at various stations and the horizontal and vertical components of the water particle velocities in the vicinity of the breakwater. The LDV measurements of particle velocities are shown to be effective in resolving the velocity time history.

A series of experimental data is also presented for solitary wave interacting with the breakwater which has the same height as the still water depth. Only the experimental data is available for this aspect of the study. Since the incident wave actually travels in a certain region of zero water depth before propagating toward the shoreward region, the present numerical method would not be able to simulate this flow condition. The experimental data show that a series of higher frequency oscillatory tails is generated in the shoreward region. This transmitted wave is reformed to become a series of well defined oscillatory wave as they propagate further away from the breakwater.

## 5 Acknowledgment

The authors are grateful for the generosity of Dr. Fredric Raichlen for permitting them to conduct the experiments at Caltech's W.M. Keck Laboratory of Hydraulics and Water Resources. The LDV system used in this study was partially supported by an NSF grant to USC under grant No. 8906898.

Financial support from the USC Foundation for Cross-Connection Control and Hydraulic Research for this study is gratefully acknowledged.

## 6 Bibliography

- [1] Dold, J.W. & Peregrine, D.H. (1986) "An Efficient Boundary Integral Method for Steep Unsteady Water Waves." *Numerical Methods for Fluid Dynamics II* (ed. K.W. Morton & M.J. Baines), pp. 671-679. Clarendon Press, Oxford.
- [2] Grilli, S., Skourup, J. and Svendsen, I.A. (1989) "An Efficient Boundary Element Method for Nonlinear Water Waves." *Engineering Analysis with Boundary Elements*, 6(2), 97-107.

## CHAPTER 102

### Ponta Delgada Breakwater Rehabilitation Risk Assessment: with respect to Breakage of Armour Units

H. Ligteringen <sup>1</sup>, J.C. van der Lem <sup>1</sup>, F. Silveira Ramos <sup>2</sup>

#### Abstract

The outer portion of the Ponta Delgada Breakwater in the Azores was constructed in the sixties, applying an armour layer of 25 t Tetrapods on a slope of 3 in 4. After two decades of recurring damage and repairs, a redesign and rehabilitation were undertaken. An armour layer of 40 t Tetrapods on a slope 1 in 2 proved to meet the more severe design wave conditions established for the rehabilitation. This was the most attractive solution from cost and constructability viewpoint. To check the risk of breakage of these units under design conditions, the rocking was analysed both in hydraulic model and by means of an analytical simulation program. This allows to assess the actual impact velocities of rocking units and the percentage breakage under given wave conditions.

---

<sup>1</sup> Frederic R. Harris B.V., Badhuisweg 11, 2587 CA The Hague, The Netherlands

<sup>2</sup> Consulmar, Rua Joaquim A. de Aguiar 27, 1000 Lisbon, Portugal

## Introduction

Since the major failures of some large rubble mound breakwaters in the period 1978 - 1982 the importance of concrete strength of armour units has become evident. Research was undertaken into this aspect and a joint-industry research project in The Netherlands succeeded in developing algorithms for impact velocities of rocking armour units and the stresses in the concrete. A simulation program was developed to compute the percentage breakage in the armour layer, using these algorithms. (Ligteringen et al, 1990).

The simulation program ROCKING was validated on the basis of several failure cases. One of the first applications in design was for the rehabilitation of the Ponta Delgada breakwater and is presented in this paper.

After a description of the original design and the general approach followed for rehabilitation, the details of the ROCKING analysis are presented.

## Breakwater Extension at Ponta Delgada

The port of Ponta Delgada on the island of San Miguel in the Azores is protected by a breakwater of which the outer 1000m is located in over 20 m water depth (Figure 1). This new part was designed and built in the sixties as a rubble mound structure, using an armour layer of 25 t Tetrapods at a slope of 3 in 4 (Figure 2).

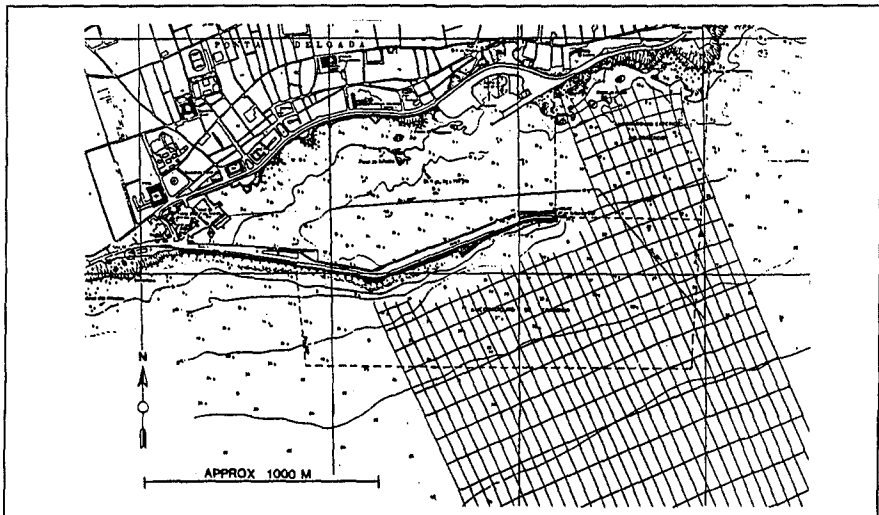


Figure 1. Ponta Delgada Breakwater Lay-out

The design wave height for the project was determined at  $H_s = 6.5$  m, having a return period of 50 year. Using a mass density of  $2.5 \text{ t/m}^3$  for the concrete, this meant a stability coefficient of 7.5, which is considered to be acceptable for a Tetrapod armour layer. The head of the breakwater was built as a vertical wall structure, composed of 5 caisson elements.

Unlike the older part of the breakwater, which had required relatively little maintenance, this new extension gave several problems, including displacement of Tetrapods, settlements of and cracks in the large superstructure, and settlements of the caissons at the head. Consecutive repair works were carried out in 1977/'78, 1983/'84 and in the period 1986 till 1988. It was after this rather extensive repair that the Portuguese Government ordered a detailed study into the causes of damage and the necessary improvements. This study was awarded to Consulmar in Portugal, with specialist assistance provided by Frederic R. Harris in the Netherlands.

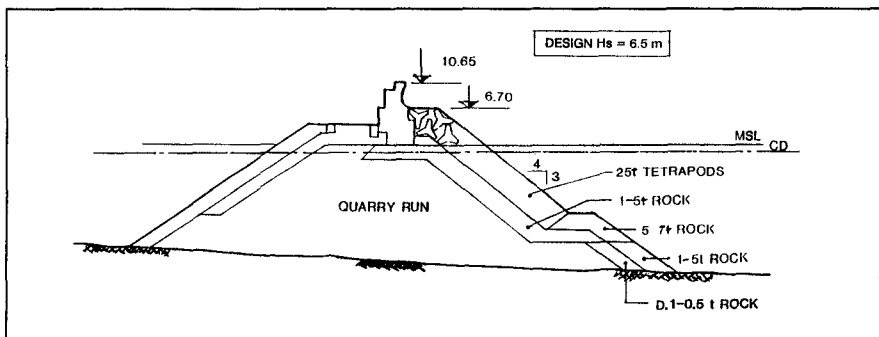


Figure 2. Original Breakwater Design

### Rehabilitation Study

The study comprised re-analysis of the wave climate at Ponta Delgada, assessment of the main causes of the damage to the existing structure, generation and evaluation of alternatives for rehabilitation and selection of the concept for detailed design and construction.

The deep-water wave climate at the Azores was established by using hindcast storm data for the area covering a period of 8 years, obtained from the U.K. Meteorologic Office, refraction computations and in-situ measurements by a wave buoy. Because the execution of the measurements was delayed, a two-step approach was followed: a preliminary wave climate was defined for the first phase of the study, while for the detailed design the wave measurements and additional hindcast computations would provide the final design conditions.



The preliminary results indicated the 100-years wave height at the site to be about  $H_s = 10$  m. Spectral periods could range from  $T_p = 10$  to 18s.

Relevant wave directions for Ponta Delgada were in the sector  $90 - 270^\circ$ . The refraction analysis did not show significant concentrations of wave energy. As an example one such computation has been shown on Figure 1.

The great difference with the original design wave height explained most of the damage. Since its construction the structure had seen several storms with wave heights at or above design level. Along the older part of the breakwater the water depth had provided a natural limitation of the wave height to levels at or below the original design value, but along the new part much higher waves could reach the structure. Hydraulic damage to the armour layer at the seaward and leeside slopes (due to overtopping), but also higher forces on the superstructure and on the end-caissons were the result.

The development of alternatives was based on the following criteria:

- small damage was acceptable for the 100-yrs wave conditions ( $H_s = 10$  m,  $T_p = 10-18$ s)
- run-up and overtopping should be reduced to avoid ongoing damage to the superstructure.
- minimum cost for the rehabilitation and improvement.

Four basic solutions were developed, as shown on Figure 3:

- A. A berm placed directly in front of the existing structure, with its crest at -5.0m CD and a small slope towards -10.0m CD.
- B. A submerged breakwater at 150m distance seaward of the existing structure.
- C. A strengthening of the seaward face of the existing breakwater, maintaining the slope of 3 in 4.
- D. A strengthening of the seaward face at a reduced slope of e.g. 1 in 2.

Preliminary designs were made for each solution, based on test data for comparable structures, e.g. alternatives studied for the Sines and San Ciprian rehabilitations. Also aspects of constructability and future maintenance were taken into account. The main results are indicated on Fig. 3. Subsequently cost estimates were prepared for each solution.

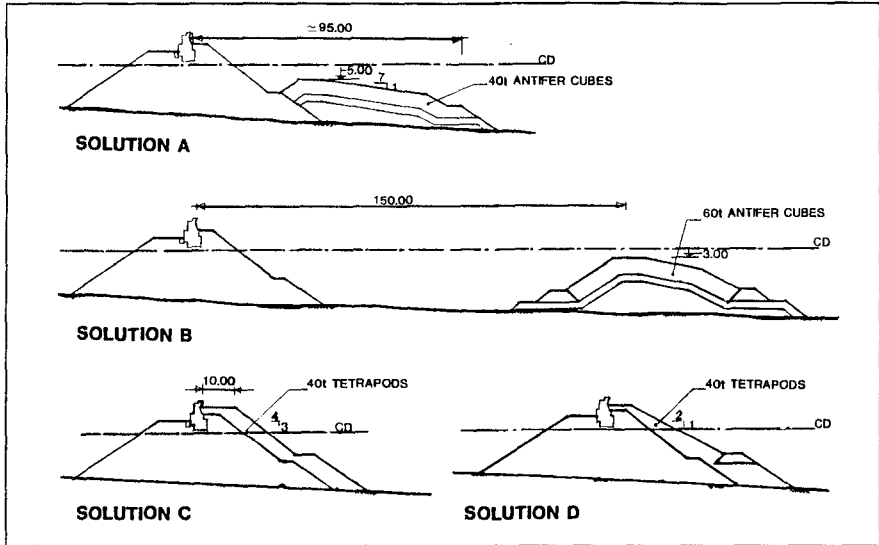


Figure 3. Basic Solutions

Comparison of the four solutions showed that A and B would be far more expensive than solution D, which in turn was slightly more expensive than solution C. Notwithstanding the latter price difference, the overall evaluation led to selection of solution D, for several reasons:

- (i) in both solutions the application of large size Tetrapods should be checked during detailed design on possible breakage of these units. In this respect Solution D gave some "reserve" strength, which Solution C did not have.
- (ii) the overtopping of Solution D was estimated to be lower, due to the larger volume of the seaward body.
- (iii) the new layer of Tetrapods will underwater be entirely placed on a new secondary armour and hence more reliable. Above water the preparation of the existing Tetrapod layer and placing of the new units could be achieved accurately.

A more detailed cross-section of the selected concept is given on Figure 4. The proposed solution for the head was to place a rubble mound structure around the caissons. For the primary armour of this rubble mound 70 to 80 ton Antifer Cubes were selected, because Tetrapods of this size were considered to be too vulnerable with respect to breakage.

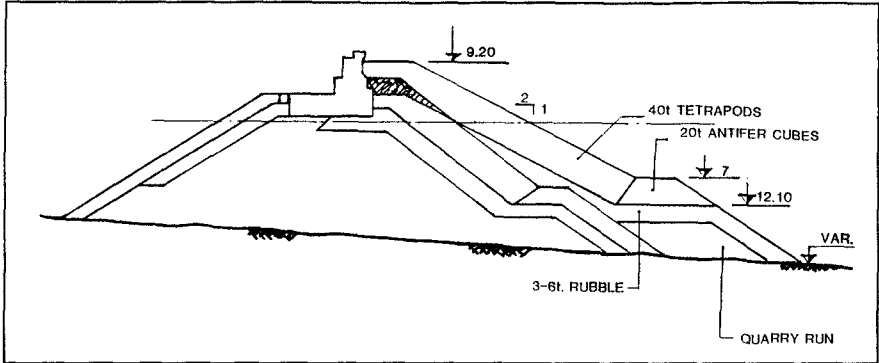


Figure 4. Selected Concept

### Detailed Design

Based on the selected concepts, the tasks for detailed design were to check and optimize both trunk and roundhead in modeltests, and to analyse the rocking and potential breakage of the 40 t Tetrapods on the trunk. The procedure followed during this phase of the project is given on Figure 5.

DETAILED DESIGN PROCEDURE	
WAVE ANALYSES	- 1 YEAR WAVE BUOY - HINDCAST MAJOR STORMS - COMPARISON BUOY/HINDCAST
MODEL TEST	- 2D AND 3D TESTS - HYDRAULIC STABILITY, ROCKING AND OVERTOPPING
TETRAPOD STRENGTH ANALYSIS	- ROCKING SIMULATION - COMPARISON MODEL/COMPUTER - BREAKAGE ASSESSMENT

Figure 5

As mentioned before the results of 1 year of buoy-recordings came only available during the detailed design. The final determination of the design

wave climate included the following analyses:

- from the measurement a total of 35 storm records were selected of which the highest reached a peak wave height of  $H_s = 9.0$  (December 1989).
- execution of additional hindcast computations by UKMO of the selected storm periods using the same model applied for the earlier hindcast analysis.
- comparison of measured and computed wave conditions, to evaluate the accuracy of the hindcast results and to correct for a possible bias in the computed wave climate.

It was fortunate for this analysis that some severe storms occurred during the year of measurements. The buoy kept functioning and an exceptional good basis for validation of the hindcast-model was obtained. The comparison between measured and computed wave heights for the most severe storm is shown on Figure 6, other records gave a similar good comparison. It could be concluded that the hindcast model gave an accuracy of the peak wave heights within 10%.

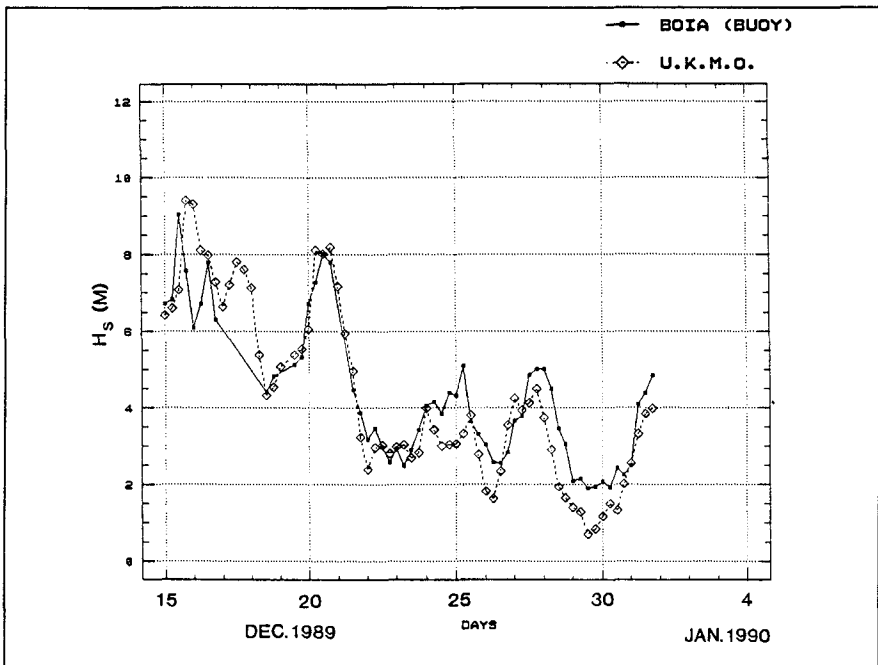


Figure 6. Comparison Measurements with Hindcast

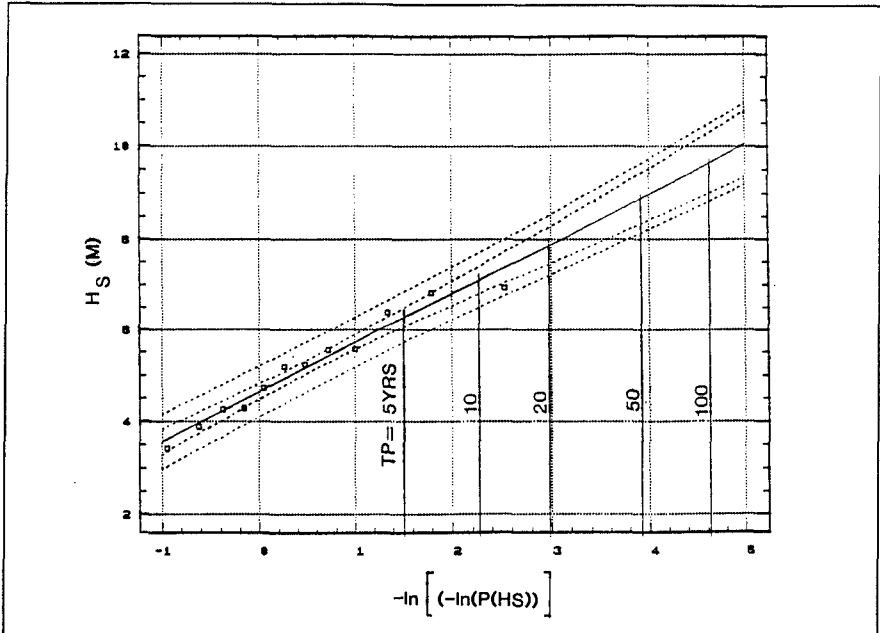


Figure 7. Gumbel distribution of extreme wave heights

The extreme values of wave heights at the breakwater location (original series and additional storms, including refraction effects) were analysed, using several distributions. The best fit was obtained from a Gumbel distribution. As shown on Figure 7, a 100-years wave height  $H_s = 9.6$  m is obtained. Taking into account the above mentioned uncertainty of the hindcast results the value  $H_s = 10.0$  m was maintained as the design wave height.

As the next step in the design process model tests were carried out at the Laboratório Nacional d'Engenharia Civil (LNEC) in Portugal. Two- and three-dimensional tests were carried out on a combined model of trunk and head, scale 1 to 58. The model was subjected to storm sequences, comprising runs with  $H_s = 4, 6, 8, 10$  and  $12$  m. Other parameters varied are the wave period:  $T_p = 10, 13$  and  $18$  s; and the water level: Lowest Low Water Level (0 m CD) and a high level due to tide and storm set-up (+2 m CD). Measurements included recording of wave conditions, hydraulic damage, overtopping and the rocking of armour layers and berms. The latter measurements were made by observations during the tests and by black-and-white photograph overlays after each test run.

The results of the tests on the trunk confirmed the preliminary design to be adequate, but for the level of the toe berm at the seaward face. This had

to be lowered to -10.0mCD.

Of importance for the evaluation of the design with respect to rocking and breakage of Tetrapods was the comparison of hydraulic model with the corresponding results of the simulation model, as presented below.

Rocking Analysis

A schematic representation of the simulation program ROCKING is given on Figure 8. Input parameters for the simulation are:

- (i) loads:  $H_s$ ,  $T_p$  and number of waves  $N$ .
- (ii) structural parameters: relative mass density  $\Delta$  and nominal diameter of the armour unit,  $D_n$ .
- (iii) concrete quality: characteristic tensile strength  $f$ .

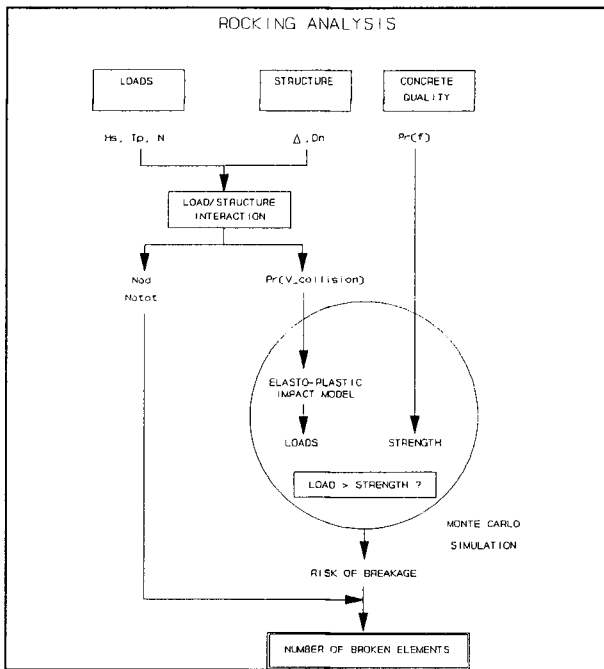


Figure 8. Schematic representation of ROCKING Analysis

For the determination of wave-structure interaction analytical formulae are used, which calculate the number of displaced units in the primary armour layer (Nod) for a given set of input parameters. Based on extensive tests on the correlation between hydraulic damage, rocking intensity and acceleration (Van der Meer and Heydra, 1990), the model generates the following results:

- (i) the sum of displaced and rocking units (Notot), from which the number of rocking units can be deduced.
- (ii) Impact velocity at collision of two adjacent units, given as a distribution function.

The latter distribution function is combined with the tensile strength of units (also given as a distribution function) in a stochastic determination of the risk of breakage for the applied input parameters. This is done by means of Monte Carlo simulation. For a large number of collisions the sampled value of impact velocity is translated into a peak-load exerted by the colliding units, applying a non-linear elasto-plastic impact model. (Van Mier and Lenos, 1991). Loads are converted into stresses, assuming at random one of a number of typical orientations for each of the two units. The calculated stresses are compared with the tensile strength, sampled from the distribution, and if the stress exceeds the actual tensile strength the unit is assumed to be broken.

The Monte Carlo simulation gives the percentages of rocking units, that will break in the pertaining wave conditions, or the risk of breakage. By multiplication with the number of rocking units the number of broken units, is obtained.

The actual simulation for the 40 t Tetrapods was carried out for the design wave conditions only, as shown on Figure 9. The concrete characteristics were taken in accordance with Portuguese standards, but for the relation between compression and tensile strength different expressions were applied, to test the sensitivity of the results for this value.

On Figure 10 a first comparison of measured results and computed displacement and rocking is presented. This gives a check on the validity of the empirical models for hydraulic displacements and rocking used in the simulation program.

The observed values show the range obtained from the model tests for the different wave periods. The percentage displaced units is very well predicted by the formula for Tetrapods, while the percentage rocking units is slightly overpredicted by the formula.

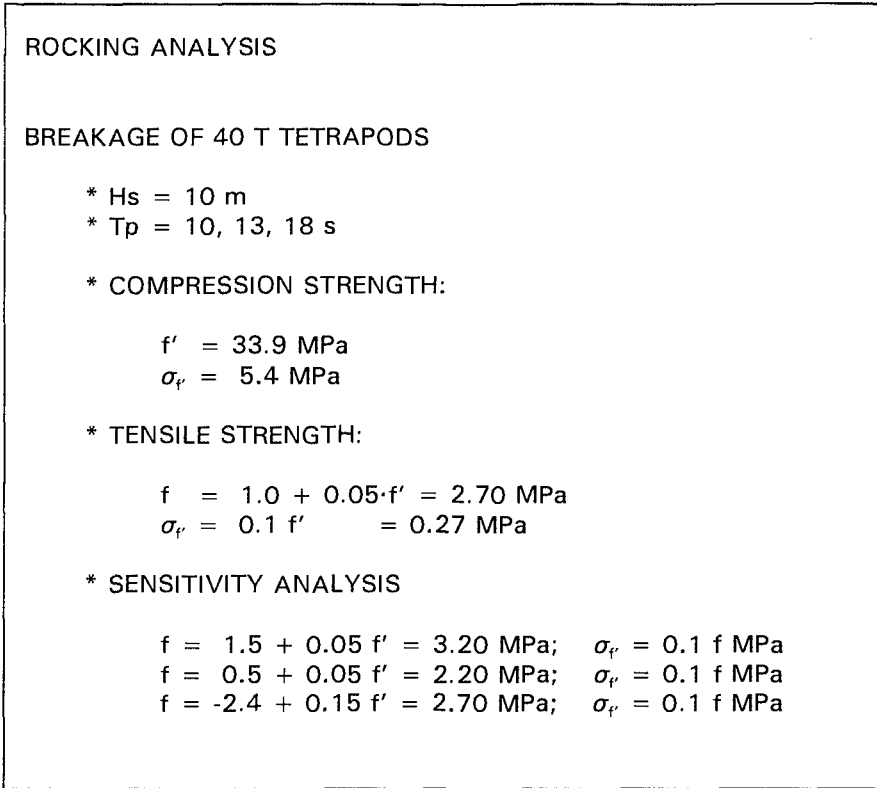


Figure 9. Boundary Conditions Rocking Analysis

The final results of the simulation are presented on Figure 11, depicting percentage of broken Tetrapods for  $H_s = 10$  m and the total damage, including the hydraulic damage given on Figure 10. The main conclusion is that the maximum percentage of total damage (3.5%) for the design wave condition is acceptable. Further it can be observed that the long wave periods are more critical for the hydraulic damage as well as for breakage. Finally the sensitivity of the results for the applied variations of the tensile strength is very limited (this does not mean that tensile strength is not important).



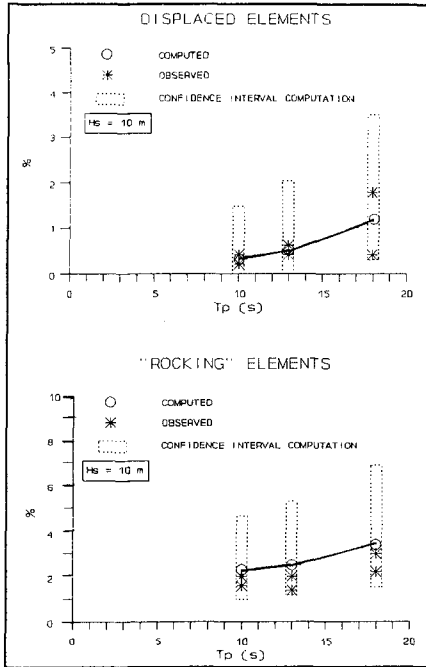


Figure 10. Comparison ROCKING results with test results

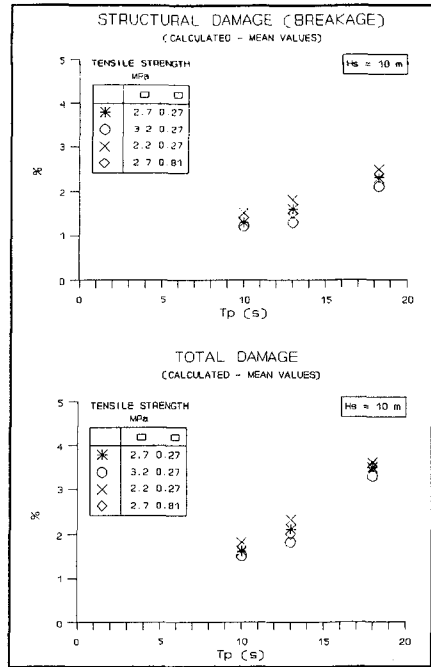


Figure 11. Results ROCKING analysis: risk of breakage.

Discussion of Results

The simulation program ROCKING allows to assess the additional damage to an armour layer due to breakage of the concrete units caused by rocking. The model proves to be a valuable design tool in cases such as presented in this paper, namely when the breakwater is protected by armour units of a size, which makes them susceptible to breakage.

The present version of ROCKING still has a number of limitations:

- (i) it can only handle primary armour layers comprising Cubes and Tetrapods.
- (ii) the empirical formulae describing wave-structure interaction are based on limited test data. Further testing is needed on influence of slope angle.
- (iii) the model assumes broken units to be eliminated from the slope, while in actual fact broken units may either cause further damage or

wedge themselves and contribute to the strength.

Further research will be needed to improve the range of application and the accuracy of the prediction.

Finally it is stressed that the model only describes breakage due to rocking. Other breakage may occur during placing or due to the static load on units, in particular those in the lower part of the armour layer.

### Acknowledgement

The program ROCKING was developed as the result of a joint-industry research project in The Netherlands, in which participated Frederic R. Harris B.V., F.C. de Weger International B.V., Royal Volker Stevin, Hollandsche Beton Groep N.V., Ballast Nedam Engineering B.V., TNO-Bouw, Delft University of Technology, Delft Hydraulics and Rijkswaterstaat.

### References

Ligteringen, H., Altink, H., and Van Oorschot, J.H., 1990. Strength of Concrete Armour Units; Stresses in Concrete Armour Units, ASCE, New York (1990).

Van der Meer, J.W. and Heydra, G. 1990. Impact Velocities of Rocking Armour Units; Stresses in Concrete Armour Units, ASCE, New York (1990).

Van Mier, J.G.M. and Lenos, S., 1991. Experimental Analysis of the Load-time Histories of Concrete to Concrete Impact. Jnl. Coastal Engineering, Vol. 15 (1991)

## CHAPTER 103

### DURABILITY AND TESTING OF STONE FOR USE IN RUBBLEMOUND STRUCTURES

O.T. Magoon,<sup>1</sup> W.F. Baird,<sup>2</sup> J.P. Ahrens,<sup>3</sup> B.Edge,<sup>4</sup> H.D.Converse,<sup>5</sup>  
D.D. Davidson,<sup>6</sup> S.A. Hughes,<sup>7</sup> H.F. Burcharth,<sup>8</sup> D.D. Treadwell,<sup>9</sup>  
C.I. Rauw,<sup>10</sup> and A.W. Sam Smith<sup>11</sup>

Rubblemound structures protected from wave action by a layer of quarried rock (stones) are the most common form of breakwaters. While extensive guidelines and procedures exist to select the size of stone there is very little information available on procedures to be followed to assure the quality of the in-place stone. This subject is not covered in depth in the principal breakwater design manuals such as the U.S. Army Corps of Engineers Shore Protection Manual (1984).

However, review of existing breakwaters show that deterioration of the stone is a common problem and some projects have experienced very serious difficulties in assuring the placement of durable stone.

Review of construction specifications used throughout the world shows considerable variability in testing procedures required to define properties of the stone and different criteria to measure acceptability of a stone.

In response to these issues a two-day seminar was held in Cleveland, Ohio on 22 and 23 May 1991, sponsored by the Rubblemound Structures Committee of the Waterways, Port, Coastal, and Ocean Division of the American Society of Civil Engineers. Cleveland was an important location because of the serious deterioration of some of the stones placed on the Cleveland breakwater.

---

1. President, American Shore & Beach Preservation Association, 2. Principal, W.F. Baird & Associates, 3. Engineer, Sea Grant Program, NOAA 4. Principal, Edge & Associates 5. Coastal Engineer, U.S. Army Corps of Engineers, 6. Engineer, U.S. Army Corps of Engineers, 7. Engineer, U.S. Army Corps of Engineers 8. Professor, University of Aalborg, 9. Principal, Treadwell & Rollo Inc., 10. Consulting Engineer, Creegan & D'Angelo, 11. Consulting Engineer

Contractors, researchers, geologists, and design engineers were invited to discuss their common concerns associated with the durability of quarried rock on a breakwater. The results of this seminar are presented in the conference proceedings by Magoon, et.al.(1)

Some initial observations by the participants were as follows:

- Problems associated with stone durability are relatively widespread, based on the number of problem breakwaters described.
- Problems of stone durability may be as much a result of blasting and handling practices as they are the result of weaknesses in the properties of the rock.
- There are no reliable, systematic procedures for assuring rock of acceptable durability exists on the completed structure (other than to involve a geologist or engineer with considerable experience both with the type of rock and its use in the marine environment, and with construction procedures).
- In general, specifications addressing stone quality, as well as the handling and placement of stones on the breakwater, vary considerably from project to project and, in some instances, are unsatisfactory. It appears that inspection and quality assurance has on many breakwater projects been unsatisfactory.

The experience of all the participants, as discussed at the seminar, represent an extremely valuable source of information.

Some of the principal conclusions and overall observations for this seminar are as follows:

- There are considerable differences between North American and European procedures for defining the quality of rock.
- For any given procedure, there is not demonstrated criteria that will assure acceptable quality of stones on a breakwater.
- The stone type is not necessarily a useful guide. There is considerable variability in the quality of a particular type of stone.

- Previous successful use at a quarry does not assure acceptable stone. Stone quality may vary within a quarry and different production practices may limit stone durability.
- There must be coordination between laboratory investigations, production procedures and the design effort, field inspections, in order to achieve acceptable quality for breakwater stone.
- Stone quality may be, in some instances, achieved by re-designing production procedures which may, in turn, require different designs. For example, cut stones can be produced in some locations relatively inexpensively and with minimum damage to the stone. However, a rubblemound structure design using cut stones in a regular pattern requires considerable attention and more information than exists in current literature.
- The subject of stone durability is receiving considerable attention for researchers at Queen Mary College, London, the U.S. Army Corps of Engineers, Ohio River Division Laboratory, Cincinnati, and the Waterways Experiment Station, Vicksburg, Mississippi. However, it will take time before field data will substantiate recommended procedures.

In summary, there needs to be as much care expended in determining the in-place quality/durability of stone as there is in designing the structure. Considerable guidance is provided by the various authors in the seminar proceedings on methods of selecting and producing durable stone for coastal structures. However, there is no completely reliable testing method to assure that the stone's performance will be satisfactory.

#### References

- (1) Magoon, Orville T., et.al. "Durability of Stone for Rubble Mound Structures"; published by the American Society of Civil Engineers, 345 East 47th Street, New York, NY; 264 pages; February 1992.

# CHAPTER 104

## Dynamic Response of Vertical Structures to Breaking Wave Forces - Review of the CIS Design Experience-

J.G. Marinski<sup>1)</sup>; H. Oumeraci<sup>2)</sup>

### Abstract

The necessity of a dynamic analysis and the dynamic approaches available in the CIS, formerly Soviet Union, for the stability of vertical structures subject to breaking wave impact loads are first briefly discussed. The different steps of the dynamic method recommended by the Russian Design Guidelines VNIIG-77 are presented. The results obtained by using the different static and dynamic methods for a numerical example are compared. Finally the effect of the nonlinear behaviour of the foundation of the structure under impact loads is discussed.

### Introduction

A large experience is available in the CIS, formerly Soviet Union, on prototype measurements, hydraulic model investigations and dynamic analysis of vertical breakwaters. The stability of these structures has long been recognised as being a purely dynamic problem when subject to breaking wave impact loads. In this case, the widely accepted (particularly in Japan and western countries) static approaches using static loads and static stability analysis is not sufficient and should be supplemented or replaced by dynamic approaches.

It is the main objective of this paper to review and discuss the CIS design experience in this field. Emphasis will particularly be put on dynamic analysis, as compared to the commonly used static analysis.

### Necessity of Dynamic Analysis

The failures experienced all over the world by vertical breakwaters have clearly shown that the traditional design approach (static stability analysis) can neither explain nor predict the most relevant failure modes and mechanisms observed in the field (OUMERACI et al., 1991).

Some of the further reasons for accounting for the effect of impulsive loading due to breaking waves in the stability analysis of vertical structures are given below.

In Fig. 1, wave loadings and accelerations of a caisson breakwater simultaneously measured in large-scale model tests are shown (OUMERACI et al., 1991).

---

<sup>1)</sup> Dr.-Ing., Senior Researcher, Bulgarian Academy of Sciences, Institute of Water Problems, Sofia, Bulgaria

<sup>2)</sup> Dr.-Ing., Senior Researcher, Franzius-Institut, University of Hannover, Germany

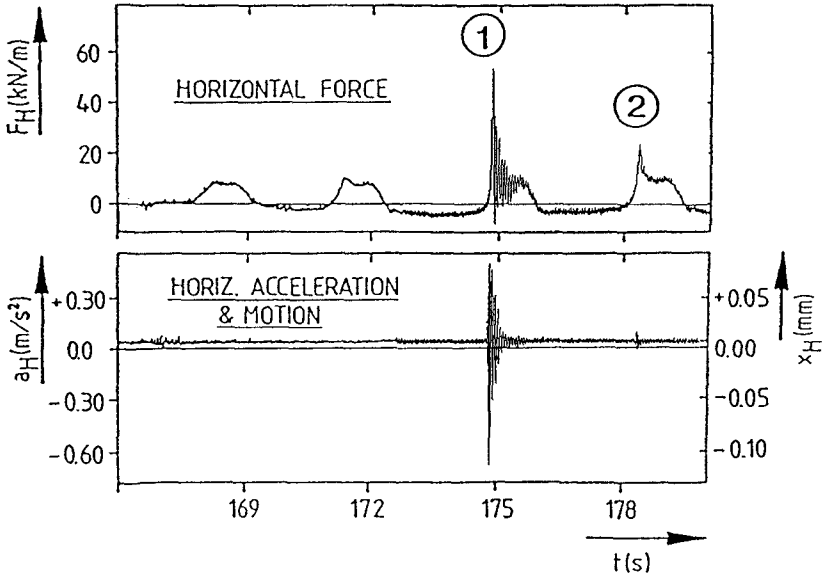


FIG. 1: EFFECT OF IMPACT FORCE ON CAISSON BREAKWATERS

By comparing the effect of impact force 1 and that of the quasi-static force 2 on the response of the structure, it is seen that the commonly suggested opinion that only quasi-static pressure forces are relevant for the stability of vertical structures cannot be confirmed.

On the other hand, the rocking motions of the caisson breakwater are transmitted to the rubble mound foundation and to the seabed which may result in an accumulation of irreversible deformations, and thus in the initiation of failure. These rocking motions are expected to be particularly high for breaking waves with large entrapped air pockets, since this generally results in force oscillations with periods in the range of the natural period of oscillations of the structure (OUMERACI et al, 1992).

Furthermore, the local impact pressures with high magnitude and relatively short duration may be important for the structural stability of the components of the structure in the impact zone.

### **Brief Review of Methods for Dynamic Analysis of Vertical Structures**

In the CIS, the application of dynamic methods for the stability analysis of vertical breakwaters subject to breaking wave loads already started in the fifties (PETRASHEN, 1956).

Most of the methods developed in the CIS for the dynamic analysis of vertical breakwaters are generally based on a lumped parameter model of a rigid

body on a homogenous, elastic and isotropic half space. The difference between the various methods mainly consists in the type of soil parameters used in the conceptual model.

By briefly reviewing the available literature in this field, three schools of thoughts appear to emerge which are represented by PETRASHEN, SMIRNOV and LOGINOV, respectively.

PETRASHEN (1956) was certainly the first to suggest dynamic methods for the stability analysis of vertical breakwaters. His first suggestion concerns a rigorous mathematical formulation which is difficult to apply to a practical problem. His second suggestion, however, was almost fully empirical (PETRASHEN, 1956). Since the latter was essentially based on the results of very small-scale model tests (empirical design diagrams), it was not accepted in the design practice.

In the model of SMIRNOV & MOROZ (1983), the vertical structure is considered as a rigid body with three degrees of freedom, and the elastic half space is described by the JOUNG Modulus  $E_S$  and POISSON'S ratio  $\nu$  of the foundation soil beneath the structure. This method has also found no acceptance in the design practice, although it generally leads to much larger stress and deformation in the soil than the static approach.

The model of LOGINOV (1962) is the only one which has been recommended for design practice by VNIIG-77. Since design guidelines and standards generally reflect to a great extent the state of the art in the related field and country, this method (called here "VNIIG Method") will be discussed below in more detail.

### VNIIG Method for Dynamic Analysis of Vertical Structures

As already mentioned, the dynamic analysis recommended in the Design Guidelines VNIIG (1977) is principally based on the method developed by LOGINOV (1962). The latter makes use of the

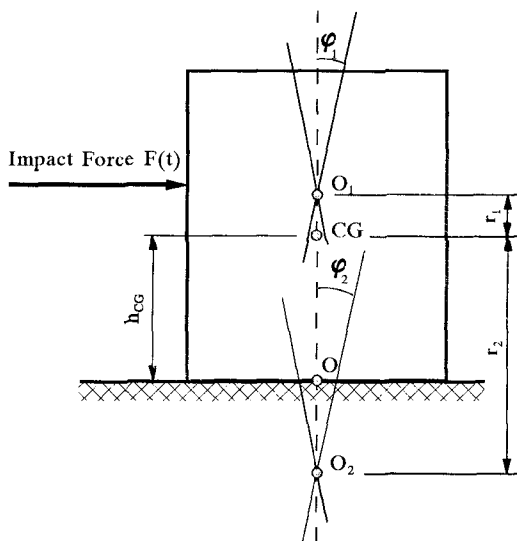


FIG. 2: DYNAMIC SYSTEM CONSIDERED BY VNIIG-77



large experience available in the field of the dynamics of machine foundation, particularly the methods introduced by SAVINOV (1955) and BARKAN (1948). In these methods, the subsoil is considered as an elastic half space. This means that the structure on an elastic foundation described by coefficients of subgrade reaction according to SAVINOV (1955) exhibits horizontal and rocking motions. The vertical motions which is assumed to be uncoupled is not considered.

In addition, the damping is neglected in the equations of motion, since only the first maximum amplitude is considered to be of interest for the stability of the structure. The dynamic system considered is given by Fig. 2, showing that the structure may rotate around point  $O_1$  and  $O_2$  located on the vertical axis through the centre of gravity  $C$  of the structure; i.e. the rotating and swaying motions have been replaced by the rocking motions around  $O_1$  and  $O_2$ . The different steps of the procedure recommended by VNIIG (1977) are described below.

**Step 1: Evaluation of Force Impulse and Load Durations**

The typical impact pressure history is schematised in Fig. 3 where  $t_r$  is the rise time up to  $p_{max}$ ,  $t_D$  the duration of the impact pressure and  $p_s$  the maximum quasi-static pressure.

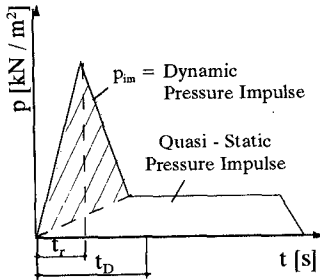


FIG. 3: TYPICAL PRESSURE HISTORY

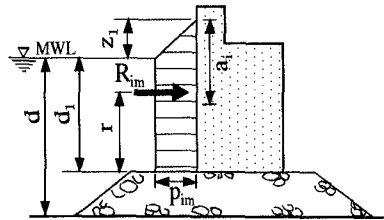


FIG. 4: PRESSURE IMPULSE DISTRIBUTION

The distribution of the pressure impulse on the structure front is given in Fig. 4 where:

$$z' = (0.55d_3 + 0.1H) \tag{1}$$

$$p_{im} = \frac{k_p}{\pi^2 \cdot g} \cdot \gamma_w \cdot a' \cdot v = 0.065 a' v \tag{2}$$

- with  $g$  = acceleration of gravity [ $m/s^2$ ]
- $k_p$  = 6.17 empirical coefficient [-]
- $\gamma_w$  = specific weight of water [ $t/m^3$ ]
- $v$  = velocity of the impinging wave [ $m/s$ ] according to the following formula:

$$v = 1.2 \sqrt{g \cdot d_3} \tag{3}$$

$a'$  = height of the wave impact zone [m] which is defined by the relationship:

$$\frac{a'}{H} = 1.6 \tanh \left( \frac{2H}{d_3} - 1.34 \right) \sin \frac{8\pi H}{L} = \leq 1.1 \tag{4}$$

$H$  = wave height [m]

$L$  = wave length [m]

$d_3$  = water depth at the wall [m]

The force impulse  $R_{im}$  [ts/m] is then obtained by:

$$R_{im} = k'_a \cdot p_{im} \left( d_2 + \frac{1}{2} z' \right) \tag{5}$$

where  $k'_a$  = empirical coefficient which accounts for the irregularity of the distribution of the pressure impulse along the wall (length  $l_C$ ):

$$k'_a = \frac{k_a \cdot a' + 1.3 k_a (d_2 + z' - a')}{d_2 + z'} \tag{6}$$

$$k_a = 0.55 + 0.15 \tanh \frac{H}{l_C} \tag{7}$$

$l_C$  = length of the caisson [m]

The point of application of the resultant force impulse  $R_{im}$  is located at a distance  $r_{im}$ :

$$r_{im} = \frac{d_2^2 + z' d_2 + z' \cdot \frac{2}{3}}{2d_2 + z'} \tag{8}$$

from the caisson base (Fig. 4).

The relative rise time  $t_r$  and the relative impact duration  $t_D/T$  of the resultant force corresponding to the impulse  $R_{im}$  is obtained from Fig. 5 as a function of the relative depth  $d_3/a$  ( $T$  = wave period).

**Step 2: Calculation of Natural Periods of Oscillations**

The swaying and rotating motions of the structure are combined to give rocking motions around  $O_1$  and  $O_2$  located above and under the centre of gravity  $C$ , respectively (Fig. 2).

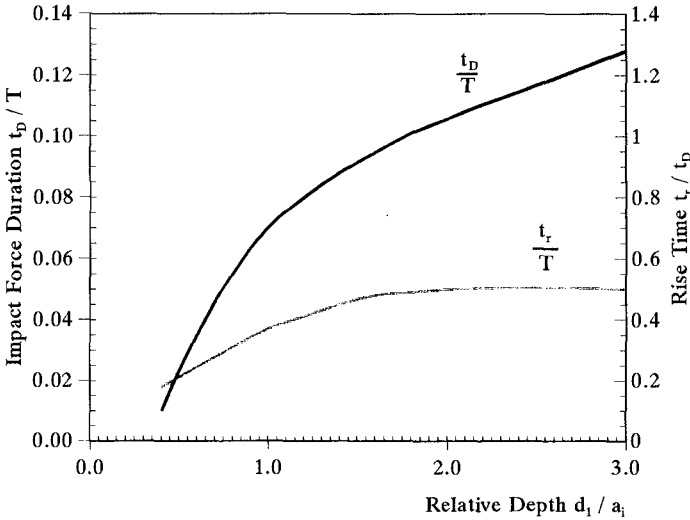


FIG. 5: IMPACT DURATION AND RISE TIME OF HORIZONTAL FORCE

The points  $O_1$  and  $O_2$ , located at a distance  $r_1$  and  $r_2$  from the centre of gravity  $C$ , are determined according to the following formula:

$$r_{1,2} = \frac{h_0 \omega_x^2}{\omega_x^2 - \omega_{1,2}^2} \tag{9}$$

where:  $h_0$  = distance of the centre of gravity from the caisson base

$\omega_{1,2} = \frac{2\pi}{T_{N_{1,2}}}$  angular frequency of the free oscillation around  $O_1$  and  $O_2$ , respectively [rad/s] which is determined by:

$$\omega_{1,2} = \frac{1}{2\vartheta} \left[ (\omega_x^2 + \omega_\varphi^2) \pm \sqrt{(\omega_x^2 + \omega_\varphi^2)^2 - 4\vartheta(\omega_x^2 + \omega_\varphi^2)} \right] \tag{10}$$

where:

$$\vartheta = \frac{\theta_C}{\theta_0} \tag{11}$$

$\theta_C$  = mass moment of inertia around the centre of gravity  $C$  [ $\text{tm}^2$ ]  
 $\theta_0 = \theta_C + mh_0^2$  = Mass moment of inertia around the centre of caisson base  $O$  [ $\text{tm}^2$ ]

$$\omega_\varphi = \sqrt{\frac{C_\varphi \cdot I}{\theta_0}} \tag{12}$$

$$\omega_x = \sqrt{\frac{C_x \cdot A_f}{m}} \tag{13}$$

- where:  $m$  = mass of the structure  
 $A_f$  =  $a \cdot l_C$  = Area of the caisson base [m<sup>2</sup>]  
 $l_C$  = length of the caisson [m]  
 $I$  = moment of inertia of surface  $A_f$  [m<sup>4</sup>]  
 $\omega_\varphi$  = natural angular frequency of rotation around centre of caisson base O [rad/s]  
 $\omega_x$  = natural angular frequency of swaying motion [rad/s]  
 $C_x$  = coefficient of subgrade reaction for swaying motion [t/m<sup>3</sup>] which is defined according to SAVINOV (1955):

$$C_x = 0.7 \cdot C_z \tag{14}$$

with

$$C_z = C_o \left[ 1 + 2 \frac{a + l_C}{A_f} \right] \sqrt{\frac{W'}{2a}} \tag{15}$$

- where:  $C_z$  = coefficient of subgrade reaction for vertical motion [t/m<sup>3</sup>]  
 $a$  = width of the caisson base [m]  
 $l_C$  = length of the caisson [m]  
 $W'$  = submerged weight of the caisson [t/m]  
 $C_o$  = coefficient of subgrade reaction determined from field measurements or from Tab. 1 as a function of the thickness of the rubble mound foundation  $d_r$ , the width of the caisson base  $a$  and the type of the subsoil [t/m<sup>3</sup>]  
 $C_\varphi$  = coefficient of subgrade reaction for rotational motion [t/m<sup>3</sup>] according to SAVINOV (1955):

$$C_\varphi = C_o \left[ 1 + 2 \frac{a + 3l_C}{A_f} \right] \sqrt{\frac{W'}{2a}} \tag{16}$$

**Step 3: Calculation of Maximum Amplitude of Oscillations**

The angle of rotation around  $O_1$  and  $O_2$  are  $\varphi_1$  and  $\varphi_2$ , respectively. These angles and the resulting horizontal motion  $\delta$  at the base of the caisson are shown in Fig. 6.

$$\varphi_1 = \frac{2 k_{d_1} \cdot M_{im,1}}{\vartheta_{O_1} \cdot \omega_1^2 \cdot t_D} \quad [ rad ] \tag{17}$$

Characteristics of foundation		$C_o$ [kN/m <sup>3</sup> ]
1	<ul style="list-style-type: none"> <li>Rubble with small thickness <math>d_r/a \leq 0.25-0.30</math> on sandy subsoil, silty clay, peaty clay, peat or very soft clay</li> <li>on silty sand or very soft clay</li> </ul>	1250 - 1500
2	<ul style="list-style-type: none"> <li>Rubble with small thickness <math>d_r/a = 0.25-0.30</math> on sand or relatively stiff clay</li> <li>Rubble with medium thickness <math>d_r/a = 0.35-0.40</math> on soft soil (clay and sand)</li> </ul>	2000 - 3000
3	<ul style="list-style-type: none"> <li>Rubble with medium thickness <math>d_r/a \approx 0.40</math> on relatively compact subsoil (sand and clay)</li> </ul>	2500 - 4000
4	<ul style="list-style-type: none"> <li>Rubble with large thickness <math>d_r/a \geq 0.45</math> on subsoil with medium stiffness (sand and clay)</li> </ul>	4000 - 6000
5	<ul style="list-style-type: none"> <li>Rubble mound with large thickness <math>d_r/a \geq 0.45</math> on compact soil (gravel, compact sand, hard clay)</li> </ul>	6000 - 8000
6	<ul style="list-style-type: none"> <li>Concrete bags or concrete blocks</li> </ul>	11000 - 13000
7	<ul style="list-style-type: none"> <li>Rock</li> </ul>	30000 - 50000

TAB. 1: EVALUATION OF COEFFICIENT OF SUBGRADE REACTION  $C_o$

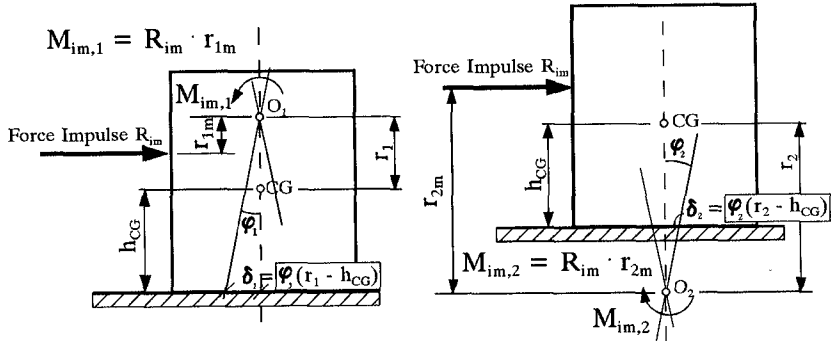


FIG. 6: DEFINITION OF ROTATION ANGLE  $\phi_I$  AND  $\phi_{II}$  AND DISPLACEMENT  $\delta$

$$\phi_2 = \frac{2 k_{d_2} \cdot M_{im,2}}{\delta_{O_2} \cdot \omega_2^2 \cdot t_D} \quad [ rad ] \quad (18)$$

The horizontal motion at the base of the caisson is given by:

$$\delta = \varphi_2 (r_2 - h_0) - \varphi_1 (r_1 + h_0) \tag{19}$$

where  $M_{im, 1}, M_{im, 2}$  = moment of the force impulse around  $O_1$  and  $O_2$ , respectively [t·m/m]

The dynamic coefficient  $k_{d1}$  and  $k_{d2}$  are obtained from response curves like those shown in Fig. 7 as a function of the ratio  $t_D/T_{N1,2}$  and  $t_r/t_D$ .

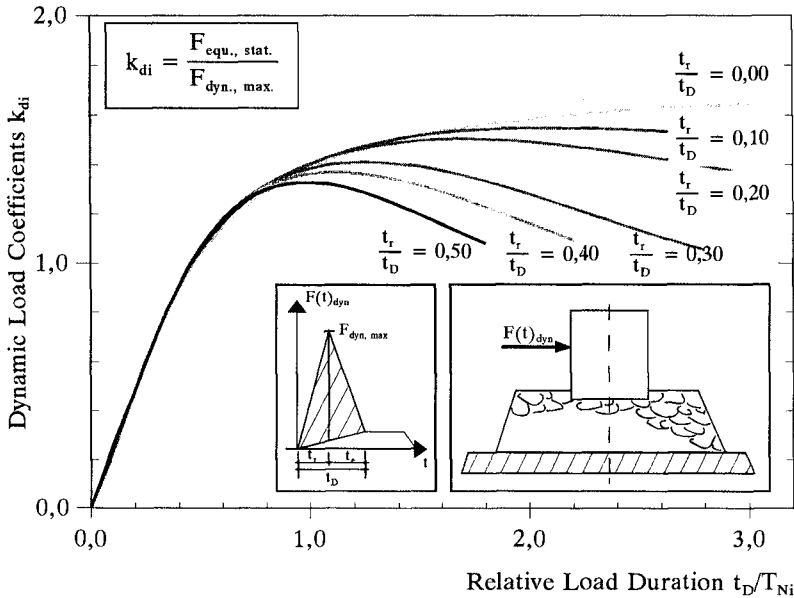


FIG. 7: RESPONSE CURVES AND DYNAMIC COEFFICIENT  $k_D$

**Step 4: Evaluation of Stability against Sliding**

The safety coefficient  $\eta_{SL}$  against sliding of the caisson is given by:

$$\eta_{SL} = \frac{(W' - n R_u) \mu}{R_s + n R_u} \tag{20}$$

- where  $\mu \approx 0.6$  friction coefficient (concrete - rubble mound)
- $R_u$  = uplift force [t/m]
- $W'$  = submerged weight of the caisson [t/m]
- $R_s$  = shear resistance [t/m]:

$$R_s = C_x \cdot \delta \cdot a \tag{21}$$

$$n = t_1 / T_N \leq 1$$

$t_1$  = time of occurrence of the maximum amplitude of motion [s],  $t_1$  is obtained from Fig. 8 as a function of  $t_D / T_N$  and  $t_r / t_D$

$t_D$  = impact force duration

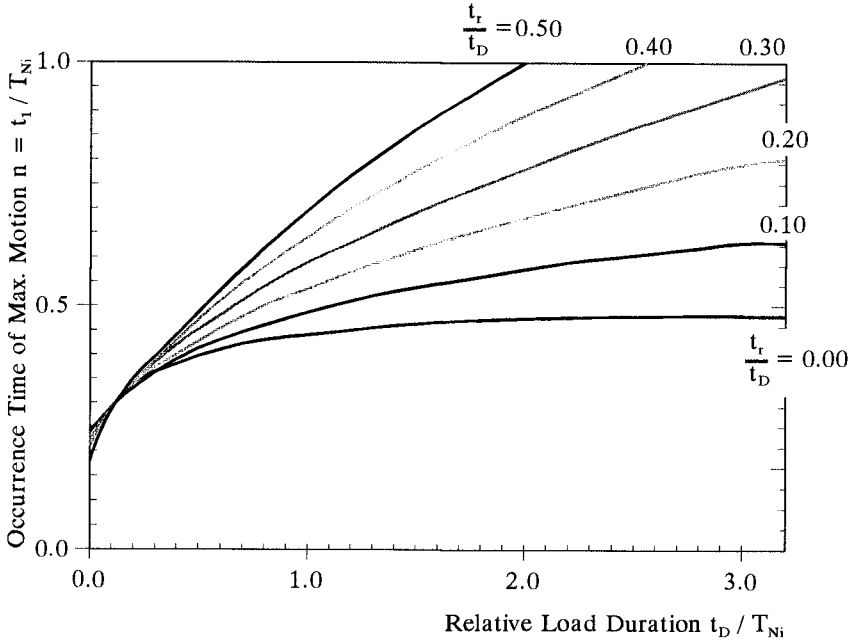


FIG. 8: TIME OF OCCURRENCE OF MAXIMUM OSCILLATION

**Step 5: Evaluation of Maximum Normal Soil Stress**

The normal soil stress induced by the oscillation of the caisson in the foundation is given by:

$$\sigma_{1,2} = \frac{W' - nR_u}{a} \pm \left[ (\varphi_1 + \varphi_2) \cdot \frac{a}{2} \cdot C_\varphi + \frac{n \sum M}{W_r} \right] \tag{22}$$

where:  $W_r = a^2/6$  [m<sup>3</sup>]

$\sum M$  = moments around the centre O of the caisson base due to  $W'$ ,  $R_u$  and  $R_p$

$n = t_1 / T_{Ni}$  from Fig. 8

$\sigma_{1,2} = \text{max. normal soil stress under the caisson edges}$  ( $\sigma_1 = \text{shoreward}$  and  $\sigma_2 = \text{seaward}$ )

### Discussion of the Methods

#### a) Comparison of Existing Standard Design Methods

In order to compare the existing standard methods for the analysis of the stability of vertical breakwaters, the numerical example and the structure shown in Fig. 9 are considered.

Wave Conditions:  $H = 5.0\text{m}$ ;  $T = 7.8\text{s}$

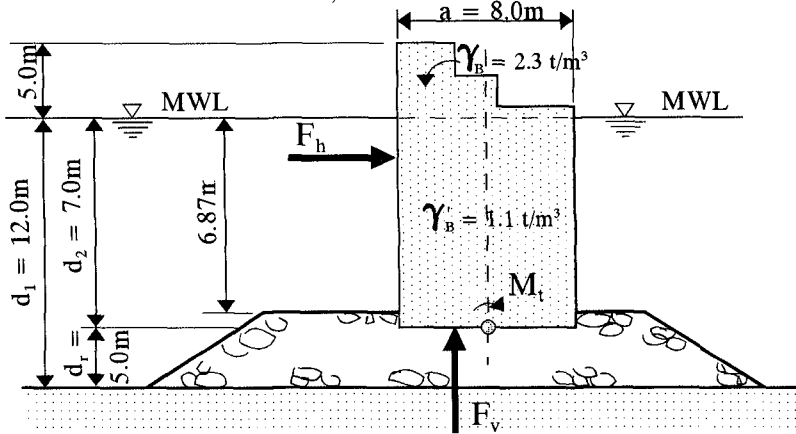


FIG. 9: STRUCTURE FOR COMPARISON OF STANDARD DESIGN METHODS

The results of the calculation by using the methods of SNIP-82 (static approach), VNIIG-77 (static and dynamic approach), PETRASHEN (dynamic approach) and GODA (static approach) are summarized in Tab. 2 showing that:

- GODA method appears to be more conservative than the existing standard methods in the CIS with respect to the bearing capacity of the rubble mound foundation.
- The static approach of SNIP-82 appears to be the most conservative method with respect to the stability against sliding.

#### b) Comparison of Linear and Nonlinear Calculation

A model which accounts for the nonlinear behaviour of the foundation of a vertical structure subject to breaking wave impact loads has been suggested by LOGINOV (1969). In order to compare the results obtained by this model and the dynamic approach of VNIIG-77, the structure and the numerical example shown in Fig. 10 are considered.



Method	SNIP-82 (1982)	VNIIG-77 (1977)	PETRASHEN (1956)	GODA (1974)
Dynamic Force [kN/m]	-	316	1045	-
Rise Time [s]	-	0.39	0.075	-
Static Force [kN/m]	610	496	620	495
Uplift Force [kN/m]	120	140	71.4	140
$p_{\max}$ [kN/m <sup>2</sup> ]	76.5	62.4	220.0	52.0
$M_h$ [kNm/m]	3254	2730	-	3400
$M_u$ [kNm/m]	640	746	380	746
$M_t$ [kNm/m]	3894	3476	-	4166
$\eta_{sl}$ [-]	1.07 <sup>*)</sup>	1.30 <sup>*)</sup> 1.58 <sup>**)</sup>	1.10 <sup>*)</sup>	1.30 <sup>*)</sup>
$\eta_{ov}$ [-]	1.24 <sup>*)</sup>	1.39 <sup>*)</sup>	-	1.17 <sup>*)</sup>
$\sigma_1$ [kN/m <sup>2</sup> ]	509 <sup>1)</sup>	320 <sup>1)</sup>	-	646 <sup>1)</sup>
$\sigma_2$ [kN/m <sup>2</sup> ]	-165	32	-	-380
$\phi$ [rad]	-	$1.69 \cdot 10^{-3}$	-	-
$\delta_{\max}$ [mm]	-	3.5	-	-
$T_N$ [s]	-	0.56 0.14	1.35	-
<sup>*)</sup> According to static analysis	<sup>1)</sup> Admissible stress 500 kN/m <sup>2</sup>			
<sup>**)</sup> According to dynamic analysis	$\eta_{ov} =$ Safety coefficient for overturning stability			

TAB. 2: RESULTS OF COMPARISON BETWEEN STANDARD DESIGN METHODS

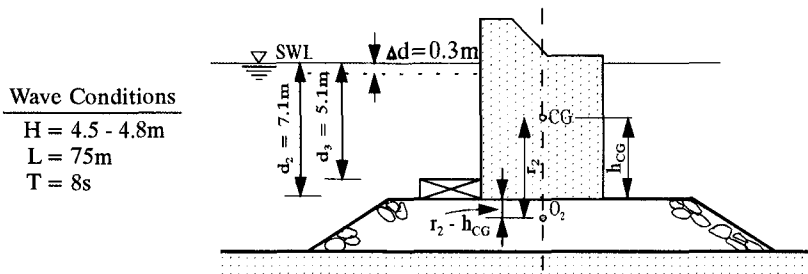


FIG. 10: STRUCTURE FOR COMPARISON OF LINEAR AND NONLINEAR CALCULATIONS

The results of this comparison are summarized in Tab. 3, showing that much larger amplitudes of oscillations of the structure (and thus larger soil deformations) and slightly larger periods of oscillations are obtained by using a linear model instead of a nonlinear one.

Description of Parameters		RESULTS		
		Prototype Measurements	Nonlinear Calculations (LOGINOV, 1969)	Linear Calculation (VNIIG 77)
$R_{im}$	kNs/m	130	102	102
$P_{im}$	kNs/m	14.5 - 16.5	15	15
$F_{h,max}$	kN/m	715	497.3	497.3
$P_{max}$	kN/m <sup>2</sup>	160	62.4	62.4
$(r_2 - h_{CG})$	m	1.50	1.67	1.34
<b>Periods of oscillations</b>				
$T_1$	s	-	0.155 **)	0.158 **)
$T_2$	s	-	0.50 **)	0.55 **)
$t_D$	s	1.0	1.0	1.0
$t_r$	s	0.4	0.5	0.5
$\varphi$	rad	-	$0.541 \cdot 10^{-3}$ **)	$0.733 \cdot 10^{-3}$ **)
$\delta$	mm	1.0 - 1.1	1.2 *)	1.63 *)
*) By using static calculations $\delta = 4$ mm				
**) linear description yields overestimated results for deformations (by +35%) and oscillation periods (by up to +10%) as compared to nonlinear description				

TAB. 3: RESULTS OF LINEAR AND NONLINEAR CALCULATIONS

### Concluding Remarks

As the stability of vertical breakwaters against sliding and the bearing capacity of the rubble mound foundation are concerned, GODA method and further standard static methods used in the CIS are more conservative than the dynamic approach recommended by the Russian Design Guidelines VNIIG-77. However, this so-called "dynamic approach" appears to have some limitations which may be due to a) uncertainties in the impact load characteristics used for the calculations and b) uncertainties of the measurement (prototype and model tests) of the structure motions used for model validation (low natural frequency of the accelerometers).

Furthermore, it is suggested that nonlinear behaviour of the foundation of vertical structures should be accounted for in the case of breaking wave impacts for which soil deformations larger than 0.1 mm are expected. However, the use of linear model appears to yield conservative results with respect to soil deformations.

### **Acknowledgements**

This study has been conducted at the University of Hannover (SFB 205/TP B3) and is mainly supported by the German Research Council (DFG). Additional support provided by the European Community within MAST G6- 0032 is also gratefully acknowledged.

### **References**

- BARKAN, D.D.: Dynamics of bases and foundations. Stroymorizdat, Moscow, 1948, 412p.(in Russian). Also published in English by Mc Graw Hill Book Co., 1962, 434p.
- GODA, Y.: New wave pressure formulae for composite breakwaters. ASCE, Proc. 14th ICCE'74, 1974, pp.1702-1720.
- LOGINOV, V.N.: Evaluation of the pressure impulse of on vertical structures subject to breaking waves. Trudy Soiuzmorniiproekta, Vyp. 2, 1962, pp. 47-59 (in Russian).
- LOGINOV, V.N.: Nonlinear oscillations of vertical breakwaters subject to wave impact loads. Trudy Soiuzmorniiproekta, Vyp. 27, 1969, pp. 67-75 (in Russian).
- OUIMERACI, H., PARTENSCKY, H.W.; TAUTENHAIN, E.; NICKELS, H.: Large-scale model investigations: a contribution to the revival of vertical breakwaters. Inst. Civil Engineers, Proc. Conf. Coastal Structures & Breakwaters, London 1991.
- OUIMERACI, H.; PARTENSCKY, H.W.; TAUTENHAIN, E.: Breaking wave loads on vertical gravity structures. Proc. 2nd Int. Conf. Offshore & Polar Eng., ISOPE'92, Vol. III, San.Francisco, 1992, pp.532-539.
- PETRASHEN, V.I.: Action of breaking waves on vertical structures. Sbornik trudov VNIIGs, 7, pp. 75-110 (in Russian).
- SAVINOV, O. A.: Machine foundations. Stroizdat, Leningrad, 292p., 1955 (in Russian)
- SMIRNOV, G.N.; MOROZ, L.R.: Oscillations of gravity protective structures of a vertical wall type. IAHR, Proc.20th Congress, Vol. 7, pp. 216-219.
- SNIIP-57-82: Technical Standard: Loads and actions on maritime structures. SNIIP-57-82, Gosstroj, Moscow, 39p., 1982 (in Russian).
- VNIIG-77: Guidelines for the evaluation of the loadings and effects on maritime structures. VNIIG Vedeneev, Leningrad, 1977, 316 p. (in Russian)

## CHAPTER 105

### A ROBUST ARMOR DESIGN TO FACE UNCERTAINTIES

Josep R. Medina,<sup>1</sup> Member ASCE

#### ABSTRACT

A new rubblemound breakwater cross section design named D-armor breakwater is presented. The D-armor cross section shows a significantly larger active armor area than the conventional cross section. The D-armor breakwater shows a similar resistance to the initiation of damage, but a significant increase of resistance to total failure. The observed structural response has a wave height range about 30% wider than the range corresponding to the conventional breakwater; the new section reshapes to an efficient S-shape armor near the total failure point. The D-armor breakwater appears to be a reasonable first step towards a convenient evolution from the conventional breakwater to more efficient designs; the wider structural response makes it appropriate for construction sites with large uncertainties in the estimation of the worst wave conditions in its lifetime.

#### INTRODUCTION

During the last decades, a continuous effort has been developed towards a better understanding of the structural and hydrodynamic factors affecting the stability of rubble-mound breakwaters. There are two main goals of the research effort: a) New calculation procedures for a more reliable and accurate estimation of the structural response in lifetime to optimize the designs; and b) New designs to reduce the construction cost, maintenance and risk of failure in its lifetime.

The design waves of a variety of maritime projects can only be decided assuming large uncertainties (see Goda, 1988). On the other hand, there are still significant differences in the calculation procedures proposed by different authors to estimate the structural response of conventional breakwaters for given wave

---

<sup>1</sup>Profesor Titular, Director del Laboratorio de Puertos y Costas, Dep. Transportes, Univ. Politécnica de Valencia, Camino de Vera s/n, 46022 Valencia, SPAIN.

conditions (see SPM, 1984; Van der Meer, 1988; Bruun et al., 1990; Teisson, 1990; and Medina et al., 1990). Additionally, a number of concrete armor unit designs have been proposed and used in conventional cross sections; however, some of the most costly failures involved the use of special concrete armor units (Sines, San Ciprián, Tripoli, Arzew, Giona Tauro, etc.). Finally, some new breakwater cross sections are being proposed to reduce construction cost or to increase armor resistance; however, some failures have been reported recently (St. Paul berm breakwater) with only a few unconventional breakwaters actually built. This paper focuses the attention on a new breakwater cross section which may be considered a rational alternative design to allow a safe evolution from the conventional section used worldwide to more economically efficient unconventional designs.

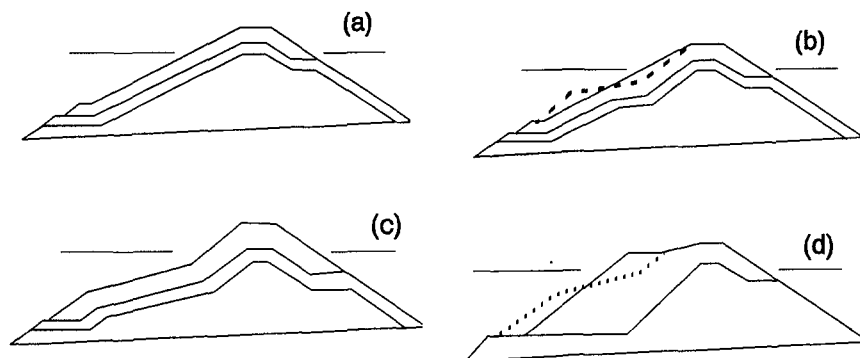
A variety of alternative designs to the conventional rubblemound breakwater cross section have been proposed; the S-shape and berm type breakwaters are the most popular unconventional designs. In spite of the limited number of prototypes built according to these new designs, there is an increased number of laboratory results which indicate some of their advantages. However, the current practice for the design and construction of mound breakwaters is conservative; the frequent breakwater failures, and the unknown risks associated with designs that lack experimental verification, may explain the general opposition of designers to adopt radical changes in the classic mound breakwater cross section.

This paper describes a new rubblemound breakwater design: the D-armor breakwater. A comparative tentative analysis of the functional performances of the conventional, the S-shape, the berm, and the D-armor breakwater cross sections is given. The D-armor design appears to incorporate most of the best features of the different alternatives. It has a failure function that covers a wider range of wave heights than the conventional breakwater making the new design a robust solution to face large uncertainties associated with long term wave actions at a construction site.

## **D-ARMOR: A ROBUST DESIGN**

From a structural point of view, the D-Armor breakwater is similar to a conventional design with a significant increase of the armor thickness in the area where the mean water level crosses the external armor profile of uniform slope. Figs. 1-a and 1-b show the cross sections corresponding to the conventional and D-armor breakwaters. Before damage, the external profile is the same; however, when armor erosion increases the D-armor design progressively transforms to an S-shape breakwater (see Fig. 1-c). Because of this characteristic, the structural performance is similar to the conventional breakwater at low levels of armor erosion, but the reshaping process significantly increases the resistance capacity as an S-shape breakwater. Therefore, the D-armor design has the large structural response flexibility required to face the high levels of uncertainty usually associated with the design wave storms. Contrary to the conventional or S-shape breakwaters, the D-armor breakwater may be designed to reshape significantly during its lifetime.

Although the D-armor design is expected to reshape in its lifetime, it is totally different than the berm or reshaping breakwater illustrated in Fig. 1-d. The berm type breakwaters also have failure functions covering a wide range of wave heights and extremely high acceptable armor erosion levels. However, the berm breakwaters have large rock movements along the breakwater which are not present in the D-armor breakwater. The armor elements may be compacted in the reshaping process, but the rock displacements in the D-armor design are very short in comparison with the displacements observed in berm breakwaters.



**Figure 1.- Rubble-Mound Breakwater Cross Sections: a) Conventional; b) D-Armor; c) S-Shape; and d) Berm Type.**

The methodology used by Medina et al.(1990) to study the stability of the armor layer of rubble-mound breakwaters has been applied to experiments in the wave flume at the Universidad Politécnica de Valencia (30x1.2x1.2 m). The wave flume was divided in two parts to check simultaneously a conventional and a D-armor breakwater cross section. The stability of a deep water model with  $W_{50}=130g$  was analyzed and a preliminary test result using regular waves is given in Fig. 2, and compared to the data provided by Ergin et al.(1989), by Torum and Naess(1988), and by the SPM(1984). The D-armor breakwater shows a start of damage limit similar to a conventional breakwater. It shows an acceptable damage limit (reshaping) similar to the S-shape breakwater. The D-armor design is more resistant to total destruction than a conventional breakwater, it is more flexible than the S-shape breakwater, and it shows far shorter rock displacements in the reshaping process than the berm type breakwater.

Most breakwaters are built at a construction site where the long term wave climate or the maximum water depth (MSL to sea bed) can only be estimated with large uncertainties. In those cases, low risk and economically-efficient solutions demand robust designs with a flexible structural response having a wide margin

between start of damage and total destruction. To face large uncertainties in wave action, economic optimization leads to very conservative and expensive designs for brittle structural responses, and to less expensive and safer designs for flexible structural responses.

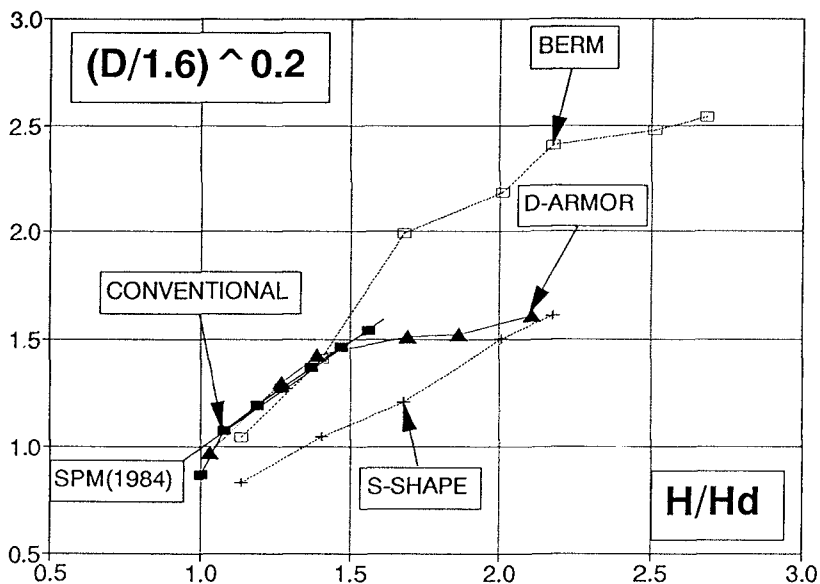


Figure 2.- Normalized Failure Functions Corresponding to Conventional, D-Armor, S-Shape, and Berm Breakwaters.

## DESCRIPTIONS OF EXPERIMENTS

In order to analyze the structural performance of the D-armor breakwater, series of 2-D experiments were conducted at the UPV wave flume (30x1.2x1.2 m), divided in two parts to test simultaneously a conventional and a D-armor cross section. A transparent glass divider was used for the verification of the same wave attack on the two cross sections during the experiments. Two capacitance wave gauges were placed in front of the model to analyze the incident and reflected wave train using a modified version of the method of Goda and Suzuki(1976). Fig. 3 shows the longitudinal cross section and plan view of the wave flume used in the experiments. The piston type wave paddle, hydraulically controlled with a servomechanism, was able to move according to the desired time series given by a PC used for the wave generation, recording, and analysis.

Fig. 4 shows the cross section of the conventional and D-armor breakwaters used for the experiments. Fig. 4a describes a typical deep water conventional section similar to that proposed by SPM(1984), with a cap on the top of the structure to

minimize overtopping. On the other hand, Fig. 4b describes a deep water D-armor section in which the armor thickness has been significantly increased in the area where the MWL crosses the armor, while the maximum armor water depth has been reduced from  $2H_d$  to  $1.5H_d$ .

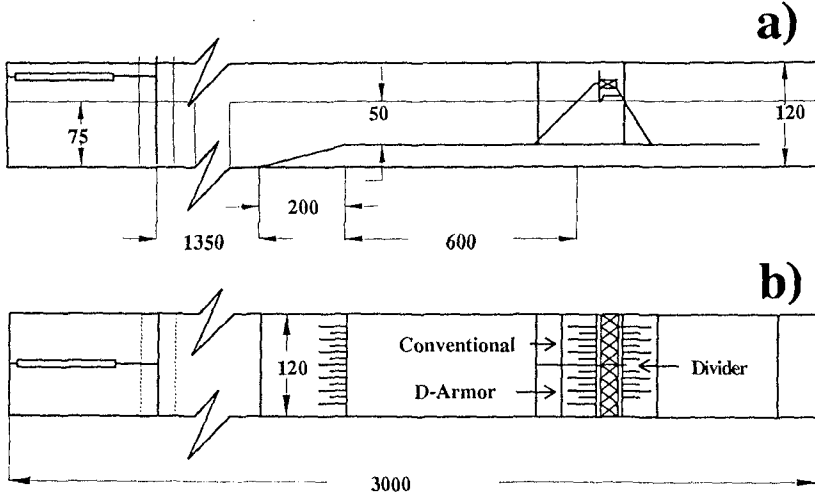


Figure 3.- UPV Wave Flume: a) Longitudinal Cross Section, and b) Plan View.

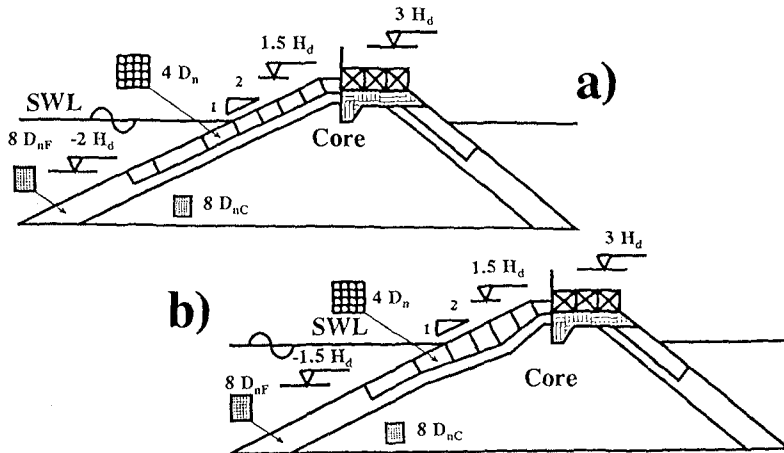


Figure 4.- Breakwater Model Cross Sections: a) Conventional, and b) D-Armor.

The armor was built of angular quarrystones with a uniform gradation, a median weight of  $W_{50}=130$  g, and a maximum deviation of 25% according to the SPM recommendations. The mean mass density was  $\rho_r=2.65$ , the slope was 2/1, and the zero-damage design wave height according to SPM(1994) was  $H_d=12$  cm



( $K_D=4$ ). The mean weight of the filter material and core was  $W_F=7.5$  g and  $W_C=4.3$  g, respectively; the corresponding equivalent cube sizes (Iribarren's terminology) or nominal diameters (Van der Meer's terminology) were  $D_n=(W_{50}/\rho_r)^{1/3}=3.66$  cm,  $D_{nF}=(W_F/\rho_r)^{1/3}=1.42$  cm, and  $D_{nC}=(W_C/\rho_r)^{1/3}=1.18$  cm. The armor thickness was  $2D_n$  in the conventional section, while it varied from  $2D_n$  to  $3.5D_n$  in the D-armor section. The filter thickness was about  $3.5D_{nF}$  in both sections. The stability of the cap was not analyzed, but its stability was guaranteed using extra lead ingots to avoid cap displacements. The stones of the armor were painted with different colors and placed in five bands of  $3D_n$  width above the SWL, and two bands of width  $4.5D_n$  and  $7.5D_n$  below SWL. The conventional section had an additional stone band to complete the armor section.

## Regular Waves and Random Waves

To evaluate the structural response of the D-armor breakwater, 10 tests with regular waves and 10 tests with random waves were conducted in the UPV wave flume from the no damage level to the total failure point of both the conventional and the D-armor breakwater models. The conventional section reached the total failure point first in all the tests; therefore, it was necessary to protect the destroyed conventional armor to continue the test with the D-armor model, in order to avoid a total collapse of the overall conventional structure. Once both armors were destroyed, all the armor stones were removed and classified by colors, to rebuild the profiles of both filter layers to put the armor units in their corresponding place for a new test.

The tests with regular waves were planned to be free of paddle reflected waves. The Iribarren's number ( $Ir=[\tan \beta]/[2\pi H/gT^2]^{0.5}$ ) was kept constant for all the runs of each test; different values of  $Ir$  were used for each test in the range  $1.7 < Ir < 4.2$ . Starting from the zero-damage design wave height,  $H_d=12$  cm, the wave height was increased 10% each run ( $H=H_d [1.1]^k$ ;  $k=0,1,2,\dots$ ) until total failure of the armor layer. Only a few waves were generated each run to avoid reflections on the paddle; therefore, the run of each energy level was repeated many times until an equilibrium profile was obtained in both breakwater models.

The tests with random waves were planned for not being free of paddle reflected waves. Seven minutes of random wave generation of JONSWAP spectra ( $\gamma=1$  and  $\gamma=10$ ) using the DSA-FFT method produced between 200 and 300 waves depending on the  $Ir$  value of the run. An Iribarren's number for random waves defined as  $Ir=[\tan \beta]/[2\pi H_{m0}/gT_{02}^2]^{0.5}$  was constant for all the runs of each test; different values of  $Ir$  were used for each test in the range  $2.2 < Ir < 3.5$ . Starting from the zero-damage design wave height,  $H_{10}=H_d=12$  cm, the wave height was increased 10% each run ( $H_{10}=H_d [1.1]^k$ ;  $k=0,1,2,\dots$ ) until total failure of the armor layer.

The measured characteristics of the incident wave trains do not exactly fit the desired waves; therefore, the results shown in this paper refer to the wave

characteristics actually measured and not the theoretical characteristics indicated as generated waves. According to the planned experiments, each test should keep constant the Iribarren's number ( $Ir$ ); however, the measured value of  $Ir$  for each run in each test showed small variations about the mean value, most of them in the interval  $\pm 1\%$ . The mean value of the measured  $Ir$ , of all the runs of each test, was taken as the actual measured  $Ir$  of the test.

## EXPERIMENTAL OBSERVATIONS

For a first evaluation of the D-armor versus the conventional breakwater, 10 tests with regular waves were carried out with  $1.7 < Ir = [\tan \beta] / [2\pi H / gT^2]^{0.5} < 4.2$ . Fig 5 shows the stability numbers ( $N_s = H / \Delta D_p$ ) corresponding to the start of damage and total failure point for both sections. SPM(1984) indicates a stability number for start of damage of  $N_s = 2$  ( $K_D = 4$ ), and a stability number for maximum damage (40% to 50%) of  $N_s = 3.12$ ; the  $N_s$  values suggested by SPM(1984) are near to the minima of the stability curves represented in Fig. 5, in agreement with the fact that the design method proposed by the SPM(1984) does not take into consideration the design wave period. The D-armor breakwater shows a start of damage curve similar to the conventional breakwater, but the total failure curve is qualitatively different, showing in all the cases analyzed a significantly higher resistance to total failure.

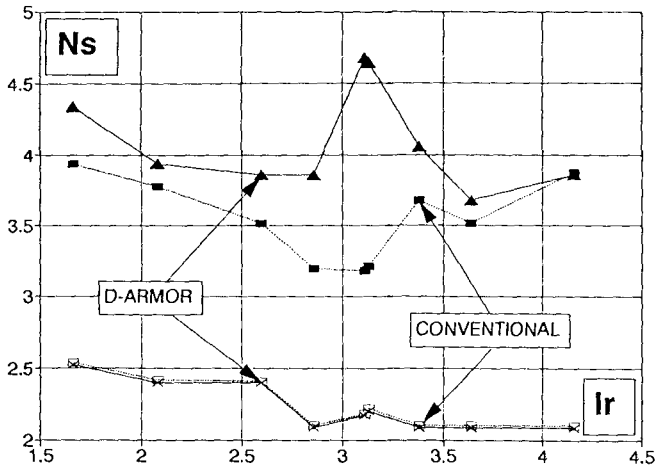


Figure 5.- Stability Numbers for start of Damage and Total Failure Corresponding to the Conventional and D-Armor Breakwaters.

According to the structural performance characteristics represented in Fig. 5, the D-armor breakwater shows a minimum stability number for total failure 15% higher than that corresponding to the conventional breakwater. However, the sea wind waves are not regular waves but irregular waves; a more realistic analysis of the structural response may be achieved using random waves.

## Criteria for the Measurement of Armor Damage

There are significant discrepancies in the literature about the quantitative definitions of the start of damage, the partial damage, and the total failure criteria. Therefore, it is convenient here to define first the concept of armor damage used in this paper.

Iribarren(1965) used the equivalent cube size,  $(W/\rho_r)^{1/3}$ , to normalize armor damages. Iribarren defined the total failure point as the erosion of the armor section affecting 100% of (his definition) the active zone, which had an area of  $9 D_n^2$ . Van der Meer(1988) also used the same concept re-named as nominal diameter,  $D_n=(W/\rho_r)^{1/3}$ , to normalize the measurements of the erosion of the armor layer. The erosion corresponding to the failure criterion given by Van der Meer(1988) was  $8 D_n^2$  (filter layer visible, slope:  $\cotan(\beta)=2/1$ ). On the other hand, SPM(1984) defined the damage as a percent of the armor units displaced from its breakwater active zone. However, while Iribarren(1965) defined his active zone as  $9(W/\rho_r)^{2/3}$  (two layer armor), SPM(1984) defined its active zone as that one which "extends from the middle of the breakwater crest down the seaward face to a depth equivalent to one zero-damage wave height below the still water level". Therefore, Medina et al.(1992) found that the total failure criterion is equivalent to an erosion of the armor layer of  $8 D_n^2$ ,  $9 D_n^2$ , or  $14 D_n^2$ , depending of who is the author in the above referred publications. On the other hand, Medina et al.(1990) presented a large scale experiment with partial armor damages higher than  $20 D_n^2$ . It is evident that the total failure point is quite subjective in the literature. In this paper, the total failure point is defined as the level of armor erosion which suddenly shows a sharp decrease of armor resistance with significant displacement of stones from the filter layer.

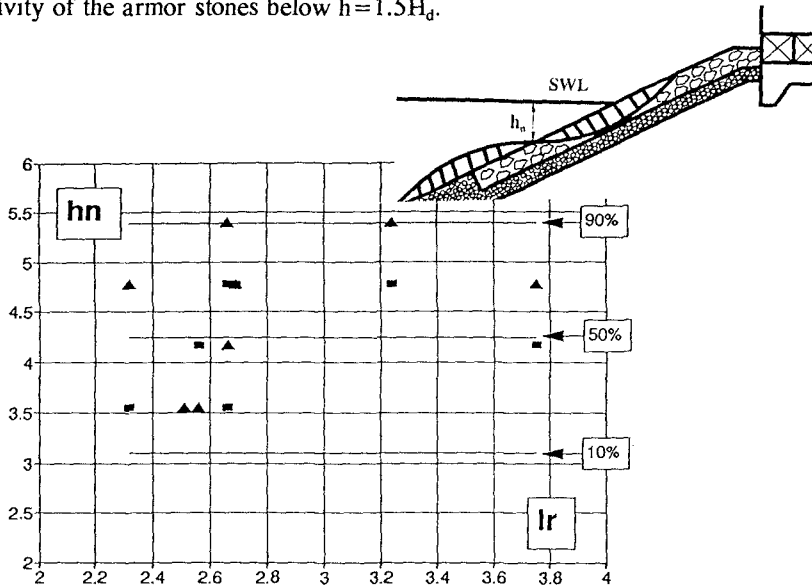
The start of damage point is also difficult to define. Van der Meer(1988) considered the start of damage point as an erosion of  $2 D_n^2$ ; however, SPM(1984) indicates an erosion of 0 to 5% of the active armor zone (0 to  $1.6 D_n^2$ ) as a no-damage condition. In this paper, the start of damage is defined as the point with a minimum, but detectable erosion of the armor. After 20 subjective evaluations of start of damage points, it was found that  $1.0 D_n^2$  is a reasonable estimation of the minimum detectable damage: the start of damage point. This quantitative definition of the start of damage point is in agreement with the no-damage condition in SPM(1984) because  $1.0 D_n^2 \approx 3\%$  of the active armor zone.

Between the start of damage and the total failure points, the armor damage was calculated as the eroded area of the armor profiles corrected for errors and settlement. Single profiles centered in both the conventional and the D-armor models were obtained using rods separated  $1.25 D_n$  with articulated circular feet having a diameter of  $0.75 D_n$ . A flexible aluminum chain mat was placed on the eroded armor to regularize the penetration of the rods into the armor. The distances in the profiles were normalized by  $D_n=(W/\rho_r)^{1/3}$ . The origin of coordinates was located at the waterline where the SWL crossed the original armor profile. The normalized dimensionless profiles obtained in this experiment were similar to those shown by

Medina et al.(1990) from the large scale experiment conducted in the O.S.U. Wave Research Facility. For the lower damage levels, damages were estimated counting colored stones moving among bands of different color (assuming 38% porosity), and high levels of damage were estimated from the rod profiles.

**Experimental Results**

In this experiment, and in the large scale experiment described by Medina et al.(1990), the erosion profiles show an almost constant neutral point between the erosional and the accretional armor areas. The water depth of that neutral point,  $h_n$ , was observed to be about  $h_n = H_d$  independently of the level of armor damage. Fig. 6 shows the maximum depth of the neutral points,  $h_n$ , for both D-armor and conventional breakwaters. The depth of the neutral points appears to be independent of  $Ir$  with an 80% confidence band covering the range  $0.8H_d$  to  $1.5H_d$ . The D-armor breakwater was built with filter stones below  $h = 1.5H_d$ , and no significant movement of those small stones were observed during the tests; therefore, there seems to be no activity of the armor stones below  $h = 1.5H_d$ .



**Figure 6.- Maximum Depth of the Neutral Point.**

Fig. 7 shows the maximum damage measured,  $D_{max}$ , in both the conventional and D-armor breakwaters. The maximum damage seems to be independent of  $Ir$ ; the D-armor breakwater showed  $D_{max}$  larger than the conventional breakwater, and the difference roughly corresponds to the increase of the D-armor thickness (area:  $11.8D_n^2$ ). The extra volume of armor stones used to increase the armor thickness of the D-armor breakwater appears to be fully active during the armor erosion process

before the total failure of the structure, contrary to the armor stones placed below  $h=1.5H_d$  (area:  $7.3D_n^2$ ) in the conventional section, which appear to be inactive during the erosion process. From both Figs. 6 and 7, the inefficiency of the conventional breakwater is apparent, as is the possibility of improving the breakwater cross sections by concentrating the volume of armor stones in the active zones where the wave action is more intense.

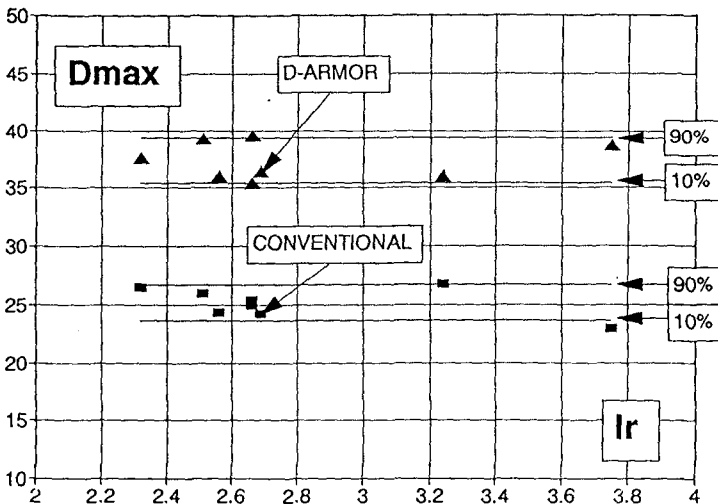


Figure 7.- Maximum Armor Damages Measured During the Experiment.

Although it is evident that the D-armor breakwater has as many as 50% more active armor stones than the conventional breakwater, it is convenient to present the measured failure functions with random waves, in order to give an appropriate description of both structural responses. The first problem to be solved concerns the definition of variables in the representation of failure functions of breakwaters under random waves. A simple representation of damage versus  $H_{m0}=4[m_0]^{0.5}$  is not appropriate because it is well known that the damage depends also on the number of waves in the run, the value of  $I_r$ , etc. Therefore, it is necessary first to normalize the variables used in the representation of failure functions.

In this paper, the damage  $D$  is a dimensionless variable of the armor erosion because the magnitudes of lengths and distances have been normalized by the nominal diameter  $D_n$ . Taking into consideration the fifth power relationship between damage and wave height shown by the failure functions given by SPM(1984), Van der Meer(1988), and Medina et al.(1990) for conventional breakwaters, the ordinates in the failure functions of this paper have been transformed using the expression  $[D/1.6]^{0.2}$ . According to Medina et al.(1992), the failure function suggested by SPM(1984) for rough quarrystones fits the line

$$\frac{H_{10}}{H_d} = \left[ \frac{D}{1.6} \right]^{\frac{1}{5}} \quad (1)$$

The runs of random waves had different number of waves,  $N_w$ , Iribarren number,  $Ir$ , and groupiness parameter,  $\alpha$ . In order to normalize the characteristic wave heights (abcisa), the formulas of Van der Meer(1988) and the preliminary conclusions given by Medina et al.(1990) were used. According to Van der Meer(1988), the damage  $D$  is proportional to  $H_{m0}^5$ ,  $[N_w]^{0.5}$ , and  $[Ir]^{2.5}$  if  $Ir \leq 3.5$ . The minimum armor stability using the Van der Meer's formulae is obtained for  $Ir=3.5$ ; if  $N_w=1000$  and  $Ir=3.5$ , the estimation of damage provided by this formulae is fairly coincident with the estimation given by the SPM(1984). On the other hand, according to Medina et al.(1990), the damage  $D$  is proportional to  $H_{m0}^5$ , and  $[\alpha]^{0.5}$ , in which  $\alpha$  is the envelope exceedance coefficient used by Medina et al.(1990) to characterize the wave groupiness of irregular wave trains attacking rubblemound breakwaters. Therefore, the standard characteristics of the irregular wave train to represent failure functions were:  $N_w=1000$ ,  $Ir=3.5$ , and  $\alpha=1$ .

In the conditions for normalization given above, the failure functions of the conventional breakwater fairly showed the expected fifth power relationship between dimensionless damage and wave height for the complete wave height range, but the observed mean stability numbers for all the damage levels were about 7% lower than the stability number predicted by the Van der Meer's formula. On the other hand, the D-armor breakwater showed two radically different parts in the failure functions: a)A fairly fifth power relationship between damages and wave heights for low and moderate damages up to 50%  $D_{max}$ , and b)A higher resistant upper tail of the failure function. The stability numbers of the start of damage point, and the low levels of damage, appear to be 5% to 10% smaller than the conventional breakwater; however, the stability number corresponding to the total failure point is 10% to 15% higher than the conventional breakwater.

Analyzing the results obtained from the tests using regular and random waves, the global structural response patterns are clear. In all the cases tested, the D-armor was significantly more resistant to total failure than the conventional breakwater. The difference in resistance to total failure depends on  $Ir$  for regular waves, and is relatively constant for random waves. The stability number of the D-armor for total failure and random waves is 10% to 15% higher than the conventional breakwater. In most cases tested, the D-armor was less resistant to the start of damage point and to low levels of damage. The stability number of the D-armor for the start of damage point and low damage levels appears to be 5% to 10% lower than the conventional breakwater.

The above described behavior of the D-armor breakwater suggests an alternative definition of armor damage, appropriate for these kind of structures with as much as 50% more armor erosion capability before total failure. One could

consider only "initiation of damage" the identifiable damage levels below the extra active armor area of the D-armor section ( $11.8 D_n^2$  in this experiment), which approximately corresponds to the difference between the maximum damage of the D-armor and the conventional breakwaters. The new definition of the armor damage applicable to D-armor breakwaters in this experiment is  $D^* = D - 11.8$ . One could also reduce the stability numbers corresponding to the D-armor breakwater by a factor of 1.15 to fit the total failure point of both breakwaters, which is equivalent to a reduction of the weight of the armor stones by a factor of 2/3. With this new definition of armor erosion to equalize the maximum armor damage, and with the reduction of median armor mass to equalize the total failure point, the new failure functions are those represented in Fig. 8.

Using lighter armor stones (factor 2/3), and the definition of damage which equalizes the maximum armor erosion, the D-armor breakwater shows fairly the same failure function as the conventional breakwater. This D-armor breakwater would show identifiable minor damages ( $D^* = [D - 11.8] < 0$ ) for values of  $H_{10}$  in the range:  $0.65H_d < H_{10} < 1.15H_d$ ; and the same structural response until total failure as the conventional breakwater with heavier stones. Therefore, a prototype based on the D-armor concept is expected to be significantly cheaper than the conventional breakwater with the additional advantage of having a wider wave height range of acceptable minor damages. These properties make the D-armor breakwater a cost-efficient design especially indicated for construction sites with large uncertainties on the design wave condition.

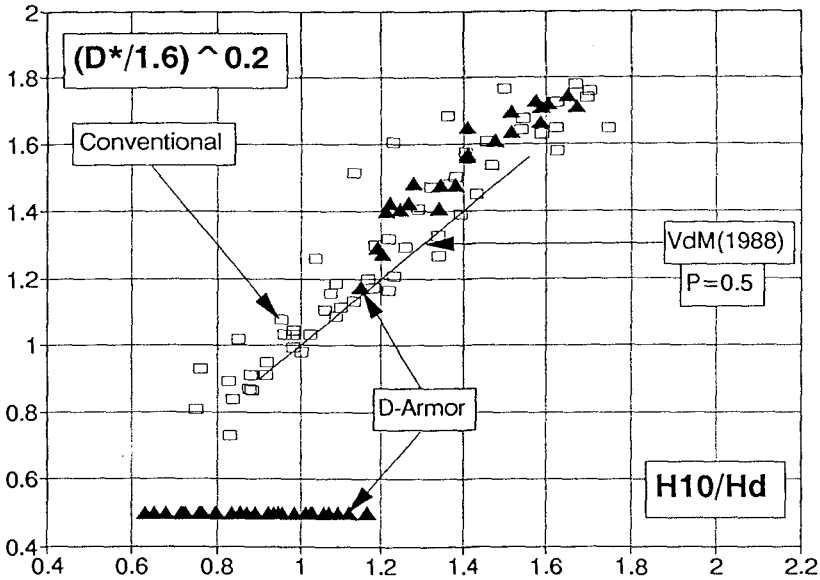


Figure 8.- Equalized Failure Functions Corresponding to the D-Armor and the Conventional Breakwaters.

All the cases were tested with approximately constant mean water level; therefore, appropriate designs for construction sites with large tide ranges may require a modification of the D-armor breakwater shown in Fig. 4b. On the other hand, the results are consistent with the intuitive concept on which the D-armor design is based: it is structural and cost efficient to concentrate the armor volume in the area where maximum erosion is expected. Therefore, the first tentative D-armor design shown in Fig. 4b should be adapted to the specific tidal range and overtopping conditions to get full advantage of the new concept. As a matter of fact, some preliminary tests not shown in this paper indicate that a D-armor breakwater may be extremely cost-efficient with respect to conventional breakwaters, if significant overtopping is acceptable for the design conditions.

## CONCLUSIONS

A D-armor mound breakwater cross section is presented and conceptually compared with conventional, S-shape, and berm breakwaters. A systematic comparison between a conventional and the corresponding D-armor design is given. The UPV wave flume (30x1.2x1.2 m) was divided in two parts to test simultaneously both sections with exactly the same wave attack. The results were obtained from 10 tests with regular waves and 10 tests with random waves, all of them developed from the no damage level to the total failure of the armor layer. The observed damages are consistent with the interpretation that the increase of the armor volume near the SWL fairly corresponds to the increase of the active volume of the armor layer. Considering this extra volume of armor stones as an acceptable erosionable part of the D-armor (minor, but identifiable damages), the D-armor structural performance is similar to the conventional breakwater with two clear advantages: 1<sup>st</sup>) A 15% higher stability number for moderate and high levels of armor erosion, and 2<sup>nd</sup>) A 50% wider wave height range of acceptable damages about the SPM design wave condition. The first advantage allows the design of a cheaper armor layer in prototypes using lighter stones and achieving the same stability; the second advantage makes the design appropriate to face large uncertainties in the design wave action in its lifetime.

The global view of the results noted above points out the inefficient design of the conventional breakwater. The deep water cross section proposed by SPM(1984) indicates the use of armor stones in inactive areas ( $h > H_d$ ), while critical armor areas near the MWL are only protected by a  $2D_n$  thick armor layer. New structural and cost-efficient breakwater cross sections are necessary to surpass the old conventional design. However, any unconventional design implies new and unknown risks due to new problems like control of construction versus design, new and unexpected modes of failure, etc. The uncertainty to new and unknown risks due to any new design, and the reasonable aversion to risk of most designers, constructors, and decision makers, breaks down the application in practice of new laboratory tested efficient designs. Therefore, the migration from the conventional design to new cost-efficient designs will be an step by step process, in which each step does not imply an excessive jump on the generally accepted designs. The D-



armor breakwater is a new concept which has shown in the laboratory to have significant economic advantages over the conventional design, and does not appear to be an excessive conceptual and constructive jump from the conventional breakwater.

As noted above, the D-armor breakwater may be a reasonable first step for a safe migration from the inefficient conventional breakwater to new structural and cost-efficient designs. It shows less inactive armor area, and 50% more active area with a wide acceptable wave height range of minor damages (initiation of damage) and 15% higher stability number for high damage levels up to total failure. It appears to have the same or low construction cost with higher stability. On the other hand, it has a reasonably low risk to unknown aspects. The D-armor design shows a structural response with extremely high flexibility, making it appropriate to face high uncertainties in the design wave conditions at the construction site; therefore, it seems to be a reasonable economically-efficient alternative to the conventional design in both deep and shallow waters.

#### ACKNOWLEDGMENTS

The author gratefully acknowledges the financial support provided by the Dirección General de Investigación Científica y Técnica, under Grant PB90-0744.

#### REFERENCES

- Bruun, P.; Hedar, P.A.; Losada, M.A., and Medina, R.; Medina, J.R., and McDougal, W.G. (1990).** Discussions of "Deterministic and Probabilistic Design of Breakwater Armour Layers", by J.W. Van der Meer. *J. of Waterway, Port, Coastal and Ocean Engrg.* 116(4):502-516.
- Ergin, A., Gunbak, A.R., and Yanmaz, A.M.(1989).** Rubble-Mound Breakwaters with S-Shape Design. *J. of Waterway, Port, Coastal and Ocean Engrg.* 115(5):579-593.
- Goda, Y., and Suzuki, Y.(1976).** Estimation of Incident and Reflected Waves in Random Wave Experiments. *Proc. 15<sup>th</sup> ICCE.* ASCE. 828-845.
- Medina, J.R., Fassardi, C., and Hudspeth, R.T.(1990).** Effects of Wave Groups on the Stability of Rubble Mound Breakwaters. *Proc. 22<sup>nd</sup> ICCE.* ASCE. 1552-1563.
- Medina, J.R., Hudspeth, R.T., and Fassardi, C.,(1992).** Breakwater Armor Damage Due to Wave Groups. *J. Waterway, Port, Coastal and Ocean Engrg.* (in review).
- Shore Protection Manual(1984).** Coastal Eng. Res. Center, Dep. of the Army, Waterways Exp. Stat., Vicksburg, Miss.
- Teisson, C.(1990).** Statistical Approach of Duration of Extreme Storms: Consequences on Breakwater Damages. *Proc. 22<sup>nd</sup> ICCE.* ASCE. 1851-1860.
- Torum, A., and Naess, S.(1988).** On Berm Breakwaters. *Proc. 21<sup>st</sup> ICCE.* ASCE. 1997-2012.
- Van der Meer, J.W. (1988).** Deterministic and Probabilistic Design of Breakwater Armor Layers. *J. Waterway, Port, Coastal and Ocean Engrg.* 114(1):66-80.

## CHAPTER 106

# Dolos Design Using Reliability Methods

Jeffrey A. Melby and George F. Turk \*

### Abstract

Historically, concrete armor unit design has not included conventional structural design methods. The primary reason is the lack of knowledge of the loads and the resulting structural response. Also, complex and random boundary conditions and wave loading made the engineering problem difficult. With recent advances in concrete armor unit stress prediction and measurement methods, we can begin to utilize conventional structural design methods in concrete armor design. This paper adapts conventional structural reliability design methods in the Load and Resistance Factor Design (LRFD) format to allow a unified approach to both reinforced and unreinforced dolos design. Stress prediction methods are validated for several well known structures. Then LRFD methods are described and applied generically for both unreinforced and reinforced dolos design. The reliability methods described herein are adaptable for general concrete armor unit design.

## 1 Reliability Methods

Conventional land-based concrete structures are typically designed using Load and Resistance Factor Design (LRFD) methodology. It has been argued that conventional structural design methods are not applicable to the dolos structural design problem because the random and highly variable wave loading and boundary conditions cannot yet be specified. With recent advances in concrete armor unit stress prediction and measurement methods, the reliability methods appear to be readily adaptable to concrete armor design. The primary advantages of the LRFD format are:

- follows conventional structural engineering practice
- provides measures of the uncertainty for both the loads and the strength
- permits robust, unified unreinforced and reinforced concrete design

The LRFD methods are particularly appropriate for breakwater armor design because the large uncertainties associated with breakwater armor hydraulic and structural response can be quantified and presented in a familiar format. Also, historically, breakwater armor designers often put structural steel reinforcement in armor without knowledge of the loads or internal response and without reasonable analysis methods. Typical concrete armor designs were therefore not economical when designed with reinforcement. But even with current dolos stress prediction methods, efficient reinforcement design

---

\*Research Hydraulic Engineers, Coastal Engineering Research Center, U. S. Army Engineer Waterways Experiment Station, Vicksburg, MS, 39180

could not previously be done because of the need to specify component forces. But conventional structural engineering techniques provide the means to distribute this armor layer design stress to the component forces. The existing armor layer stress prediction methods along with the component force relations enclosed within the LRFD framework, therefore, provide a complete procedure for concrete armor design.

The LRFD methods outlined herein are based on reliability methods as described in Ellingwood, et al (1980). The balanced LRFD design equation can be expressed as the equilibration of a factored load with a factored strength or

$$\gamma Q_n = \phi R_n \quad (1)$$

where  $\gamma$  and  $\phi$  are the load and strength factors and  $Q_n$  and  $R_n$  are the nominal load and resistance, respectively. The strength coefficient and load factor take into account the appropriate uncertainties.

The loads on breakwater armor units are difficult to determine due to the complexity and randomness of both hydrodynamics and boundary conditions. Therefore, the methods currently used to describe the loads on concrete armor units are indirect, specifying the maximum armor layer stress as a function of environmental parameters such as wave height, structure slope, and armor weight. Previous publications show methods for determining the design stress level using probability of exceedance curves and expected levels of exceedance (Howell and Melby 1991). To couple these previously described methods and the LRFD method, the load factor is chosen so as to preserve the design probability of exceedance as follows.

$$E = \Phi(-\beta) \quad (2)$$

where  $\Phi$  is the unit normal cumulative distribution and  $\beta$  is the reliability index. The load factor can be determined as

$$\gamma = \phi \frac{R_n Q_m}{R_m Q_n} \exp \left[ -\Phi^{-1}(E) \sqrt{V_R^2 + V_Q^2} \right] \quad (3)$$

where  $Q_m$  and  $R_m$  are the mean load and resistance and  $V_Q$  and  $V_R$  are the load and resistance coefficients of variation, respectively. The limit states are given by ACI (1989) and Ellingwood (1980) as  $\phi = 0.85$ ,  $R_m/R_n = 1$ , and  $V_R = 0.2$  for torsion and  $\phi = 0.90$ ,  $R_m/R_n = 1.05$ , and  $V_R = 0.11$  for flexure (ACI 1989).

In this report, previously published dolos stress prediction methods are used to preliminarily define the loads. The stress is distributed to the component forces which are then used as the loads in the LRFD formulation. The result is a comprehensive design methodology for dolosse that includes strength enhancement specification and conforms with present structural engineering design practice. The methods allow the designer to compare the economies of different strength enhancement options including high strength concrete, shape modification, and steel bar reinforcement in a unified format to achieve the most efficient dolos design. The basic methods outlined herein are general and can be adapted to any armor unit shape.

## 2 Design Stress Prediction

Concrete armor unit design has progressed a great deal during the last few years. This rapid progress is, in large part, due to the prototype dolos structural response data set

and associated research accomplished under the Crescent City Prototype Dolos Study (CCPDS). Figure 1 shows 38-tonne dolosse being placed on the breakwater at Crescent City. In the prototype study, dolos structural response data and numerical models were



Figure 1: 38-tonne Dolosse at Crescent City, CA

used to link design parameters such as dolos size, shape, and material specifications to the measured stress statistical moments. Using these methods, the Crescent City stress distributions could be extended to other structure geometries (Howell and Melby 1991). The dolos small-scale-model load cell was verified as a tool to measure pulsating stresses in the physical model (Markle 1990). The CCPDS has been widely reported and other primary publications include Howell (1988), Melby and Howell (1989), Kendall and Melby (1990), and Rosati and Howell (1990).

The dolos stress prediction methodology is based on stochastic methods because of the random nature of both the loading and the boundary conditions. Separate distributions for static and pulsating stresses have been generated and are combined using the methods that follow. The result is a single maximum design stress for the armor layer for a specified probability of occurrence.

In general, the static stress will be much larger than the pulsating stress (Melby and Howell 1989). The static nondimensional stress log-normal distribution is given in Equation 4 with mean and standard deviation given in Equation 5 and 6 and shift parameter given in Equation 7 (Howell and Melby 1991). The original distribution based on measured stress statistics has been extended for the general design case by modifying the statistics for the dolos size, density, waist ratio, and stacking depth. The waist ratio is the ratio of the depth of the shank (center section) to the length of a fluke (end

sections).

$$p(\sigma'_s) = \frac{1}{\sigma'_s \beta \sqrt{2\pi}} \exp \left[ -\frac{1}{2} \left( \frac{\ln \sigma'_s - \alpha}{\beta} \right)^2 \right] \quad (4)$$

$$\alpha = \ln[k_r(\alpha_{cc} + a)] - \beta/2 \quad (5)$$

$$\beta = \sqrt{\ln \left( \frac{\beta_{cc}}{\alpha_{cc} + a} \right)^2 + 1} \quad (6)$$

$$a = S_L \left[ \frac{1}{\gamma} (N_L - 1) - \frac{1}{\gamma_{cc}} \right] \quad (7)$$

In the above equations,  $\alpha_{cc} = 26$  and  $\beta_{cc} = 12$  are the Crescent City prototype nondimensional mean and standard deviation, being nondimensionalized by the product of fluke length and weight density,  $\gamma_{cc} = 2456 \text{ kg/m}^3$  is the Crescent City dolos weight density, and  $N_L$  is the number of armor layers. The waist ratio coefficient, given by

$$k_r = 5.14 - 28.74r + 66.07r^2 - 52.08r^3 \quad (8)$$

was determined using a fully deterministic FEM analysis with several representative boundary and loading conditions.

The maximum pulsating or wave-induced stress is a function of the design wave height,  $H_n$  and a wave stress constant,  $k_{ps}$ . The Rayleigh distribution of the form

$$p(\sigma_p) = \frac{\pi \sigma_p}{\bar{\sigma}_{pmax}^2} \exp \left[ -\frac{\pi}{4} \left( \frac{\sigma_p}{\bar{\sigma}_{pmax}} \right)^2 \right] \quad (9)$$

best describes the dolos pulsating response. The mean of the maximum pulsating stress, which is linearly related to the average of the highest one-tenth of the waves can be expressed by the empirical relationship

$$\bar{\sigma}_{pmax} = k_{ps} H_{1/10} \quad (10)$$

where

$$k_{ps} = 0.036 \text{ MPa} \quad (11)$$

per meter of wave height and  $H_{1/10}$  is computed using the zero-downcrossing method of analysis, i.e., the difference between the maximum and the preceding minimum between two successive zero downcrossings in a time series. Note that during the prototype data acquisition period, the maximum pulsating stress was approximately  $\sigma_1 = 1 \text{ MPa}$ , which occurred during a design event.

The modified static and pulsating distributions are convolved, assuming they are independent, to get a combined stress distribution which is integrated to get a stress exceedance distribution. This distribution is used along with a design probability of exceedance,  $E$ , to determine a design stress. This stress is interpreted as that which will be exceeded in  $E$  percent of the armor units. Note that this is a hydraulically stable design stress because the impact stress is not yet included in the calculations. We do not include impact stresses because of the unknown scale effects in the instrumented impact tests and because of the uncertainties associated with uninstrumented drop test results. All of the calculations for stress prediction are performed within a PC computer-based program called CAUDAID.

Extensive physical model tests utilizing the small-scale load cell instrumentation were used to validate the static log-normal distribution (Melby 1992). But, as noted by Melby, the mean for the prototype data is significantly greater than that of the scaled physical model data. There are several reasons for this difference including the flat slope of the prototype breakwater, surface friction scale effects, and overly stiff instrumented cross sections in the small-scale units. Utilization of the modified prototype static distribution, rather than the load cell measured results, is likely to be conservative. But as shown later in this paper, these modified prototype distributions appear to predict the design stresses well.

The data reported in Burcharth et al. (1991) and Anglin et al. (1990) are based, for the most part, on scale model results utilizing the load cell structural instrumentation scheme. The results published by these two authors were accomplished through careful laboratory examinations and their results appear to be very reliable. As noted above, this load cell instrumentation scheme has also been employed by the present authors but has only been validated for pulsating response. Scale effects in both static and impact load cell measured responses may introduce unconservativeness in the dolos load prediction process. Thus the load cell measured results are not included in this paper.

## 2.1 Application of Maximum Stress Prediction Methods

The stress predictions described in the previous section have been applied to several dolos armored breakwaters (Table 1). The LRFD methods were not used in this section so that actual computed stress levels could be shown clearly. Each example breakwater, with the exception of Cleveland and Sines was physically surveyed by the authors within the last 6 months. Cleveland and Sines breakwaters have been thoroughly studied by others and therefore provide excellent examples. The 1974 rehabilitation of the Crescent City breakwater was not used as an example because many of the dolosse were broken due to storms that occurred during construction. In Table 1,  $Age$  is the difference in years between original construction and the last survey;  $H$ , the wave height in meters;  $W$ , the weight in tonnes;  $N$ , the number of dolosse placed;  $S$ , the specific gravity;  $r$ , the waist ratio;  $\cot(\alpha)$ , the breakwater slope;  $E$ , the probability of exceedance used in the calculation of the design stress, which is the surveyed number of broken dolosse as a percentage of the total number of dolosse placed;  $\sigma_1$ , the maximum principal stress as computed in CAUDAID in MPa; and  $f_t$ , the concrete tensile strength in MPa.

Each structure has its own design peculiarities which effect the design stress as follows.

- Crescent City: Flat structure slope makes structure extremely stable and limits breakage; conservative stress estimates will always be high.
- Humboldt: Conventional reinforcement adds approximately 20% to resistive capacity as reflected in high  $f_t$ .
- Nawiliwili: No peculiarities; relatively simple application of stress prediction methods.
- Waianae: Wide fronting reef limiting wave energy;  $E = 1$  does not include 170 construction related breaks.

Table 1: Application of Design Methods

SITE	Age	H	W	N	S	r	$\cot(\alpha)$	$E$	$\sigma_1$	$f_t$
Crescent City	7	11	38	680	2.46	0.32	5	1	8.1	7.0
Humboldt	10	12	38	4772	2.46	0.32	2	1	8.5	8.4
Nawiliwili	15	7	10	485	2.30	0.32	2	8	3.6	3.8
Waianae	13	4	1.8	6633	2.30	0.32	2	1	3.5	3.8
Honolulu, H	16	8	5.5	4516	2.30	0.32	2	4	3.5	3.0
Honolulu, T	16	8	3.6	13790	2.30	0.32	1.5	4	3.0	3.0
Cleveland	5	4	1.8	29500	2.30	0.32	2.0	4	2.4	2.5
Sines	1	14	42	19000	2.55	0.35	1.5	5	6.2	5.0

- Honolulu: Wide fronting reef; estimated concrete strength is low by U.S. construction standards.
- Cleveland: Estimated concrete strength is very low.
- Sines: Damage primarily due to single storm, long slope, deep water.

Given no peculiarities, the stress prediction methods will reasonably predict long-term cumulative damage of a relatively stable structure (Nawiliwili) but will overpredict short term damage (Sines) and damage on an extraordinarily stable structure (Crescent City). Although the stress prediction methods do not include impact response, the conservativeness in the predicted stress appears to allow enough safety to account for all loading over the structure life. Because the design goal is to achieve an armor layer design that does not require periodic rehabilitation and has an extremely low probability of catastrophic failure during its design life, the stress prediction program is appropriate for conservative design load determination and it was used as input to the following LRFD methods.

### 3 LRFD - Optimizing Design Methods

#### 3.1 Strength Enhancement Options

As shown in Table 1, the design stress for the large dolosse at Crescent City exceeds the tensile strength. Also, because these dolosse were built without significant reinforcement and because the average stress level is increasing over time (Kendall and Melby 1990), the dolos breakage is expected to continue and a rehabilitation will likely be required before the design life is reached. For the Crescent City breakwater, a strength enhancement of the design dolosse is required. Melby (1992) showed that, as a general rule, for dolosse exposed to design wave heights above 7m, the stress exceeds the commonly used concrete strength of 3.6 MPa and strength enhancement is required. The designer has several strengthening options including fiber reinforcement, increased concrete strength, modified shape, and steel reinforcement.

Metal fiber reinforcement was used in Crescent City and Humboldt, California dolosse. The Crescent City dolos tensile rupture strength was very high (Kendall and Melby 1990) using approximately 1 % fibers; but this high strength is likely attributable to the concrete mix characteristics and not the fiber. With approximately 50 kg of steel added per cubic meter of concrete, a mere seven percent tensile strength increase was reported from tests conducted during trial mix designs. One of the major problems encountered during prototype casting was the tendency for the steel fibers to congregate or "ball up" during concrete mixing. Recent evidence indicates that fiber reinforcement is not likely to increase the strength enough to make it economical.

Increasing the concrete tensile strength can be practical in the U.S. because high strength concrete is now commonly used. Also, recent tests of high strength silica fume concrete indicate that the ratio of tensile to compressive strength is maintained for compressive strengths up to about 107 MPa (Saucier 1984). But the compressive strength can only be increased economically to about 70 MPa at this time. The corresponding tensile strength of this concrete mix is approximately 7 MPa.

For armor unit design, the primary design input site parameters include directional wave energy, water depth, breakwater slope, and position on breakwater. The designer is free to optimize the design by varying the dolos weight, shape, density, packing density, and material strength. In practice though, the dolos shape and concrete properties are fixed, with a waist ratio of  $r = 0.32$ , a packing density of  $k_{\Delta} = 0.94$ , a specific weight of approximately 2.3, and a compressive strength of  $f'_c = 36$  MPa. This leaves only the dolos weight as a variable. But in order to achieve an optimized design, none of these parameters should be fixed. Also, for some designs it may be more economical to reinforce slender dolosse than use unreinforced stout dolosse.

Utilizing the previous stress prediction methods, it is a simple process to minimize the stress level by varying the dolos shape, packing density, and material properties. For a given waist ratio, incorporating reinforcement in the optimizing process is straight forward, as will be shown. But our ability to fully optimize the dolos design by maximizing dolos strength and hydraulic stability is limited because knowledge of dolos stability and stress versus waist ratio is still needed. Also, no research has been done to determine the response of very slender dolosse ( $r \leq 0.31$ ). Yet with efficient reinforcement schemes, slender reinforced dolosse may be a viable option because the amount of concrete is reduced and the wave energy dissipation of the armor layer is increased. Integrating reinforcement, shape modification, and stability analysis into a general optimizing design procedure using existing knowledge is therefore a great challenge.

In order to explore the advantages of shape modification on stability, previous research results were used. Zwanborn et al. (1988) provided stability results for dolos waist ratios of 0.33, 0.36, 0.38, and 0.40. In the following analyses, these stability data were highly simplified by averaging multiple curves for various surf similarity parameters and extrapolating to slender waist ratios. Figure 2 shows the resulting Hudson (1958) stability coefficient versus waist ratio curve. This curve is simply used in the general optimization process herein and is not intended for design purposes.

### 3.2 LRFD Formulation

The design stress is a result of combined bending and torsion loads. To resist combined loading, the strength due to torsion is generally different than the strength due to flexure.



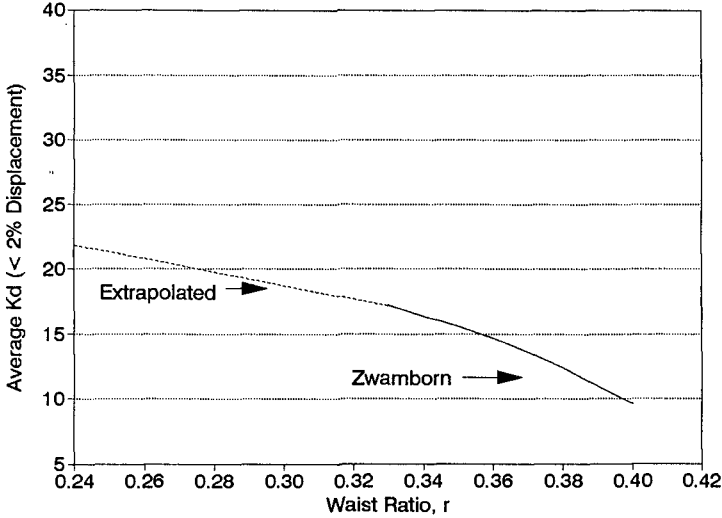


Figure 2: Hydrodynamic Stability from Zwamborn et al.(1988)

Also, reinforcement schemes must be designed for torsion and flexure separately in order to maximize efficiency. Therefore, a strength failure criterion in the form of a moment-torque circular interaction curve has been adopted for both unreinforced and reinforced dolos design, i.e.,

$$\left(\frac{T_c}{T_{cr}}\right)^2 + \left(\frac{M_c}{M_{cr}}\right)^2 = 1 \tag{12}$$

$M_{cr} = S_M f_{ct}$  is the flexural cracking moment in the absence of torsion and  $T_{cr} = S_T f_{ct}$  is the torsional cracking moment in the absence of flexure. Here  $S_M$  and  $S_T$  are the flexural and torsional section moduli and  $f_{ct}$  is the tensile splitting strength.  $M_c$  and  $T_c$  are the respective moments at failure in the presence of combined bending.

The principal stress as computed by CAUDAID can be used as the loading criterion if the statistical variability of the torsional and flexural contributions to this principal stress are known. For this analysis, we assumed  $M = S_M k_M \sigma_1$  and  $T = S_T k_T \sigma_1$ , where the torsional and flexural section moduli are given by  $S_T = 0.2105(rC)^3$  and  $S_M = 0.10526(rC)^3$ , respectively. Here  $C$  is the fluke length and  $r$  the waist ratio. The stress contribution factors are taken from Crescent City prototype data as  $k_T = 0.6$  and  $k_M = 0.6$ . These values require further refinement and will be addressed in the future.

Using Equation 12, the torsional and flexural concrete strength in combined loading can be expressed as

$$T_c = \frac{T_{cr}}{\sqrt{1 + 4 \left(\frac{M_c}{T_c}\right)^2}} \tag{13}$$

$$M_c = \frac{M_{cr}}{\sqrt{1 + 0.25 \left(\frac{T_c}{M_c}\right)^2}} \tag{14}$$

With  $k_T$  and  $k_M$  equal to 0.6,  $M_c/T_c = 0.5$ , and the combined loading torsional and flexural strengths are 70 % of the respective pure torsional and flexural strengths. Also, design fluke stress levels are conservatively estimated to be equivalent to those in the shank, although they are assumed to be created from pure flexural loading. This is perhaps overly conservative but is done here in order to illustrate the general analysis procedure.

The load factor in Equation 1 has been determined using Equation 3 and the values given in Section 1 for the limit states. The load factor was found to range from 1.0 to 1.2 over a range of typical values of the exceedance probability. A value of  $\gamma = 1.0$  was used herein because of the conservativeness inherent in the calculation of the design stress. With the strength and loading defined, the LRFD balanced equation,  $\gamma Q = \phi R$ , becomes for torque

$$\gamma S_T k_T \sigma_1 = \phi 0.7 T_{cr} \quad (15)$$

$$1.0(0.6)\sigma_1 = 0.85(0.7)f_{ct} \quad (16)$$

$$\sigma_1 \approx f_{ct} \quad (17)$$

and for moment

$$\gamma S_M k_M \sigma_1 = \phi 0.7 M_{cr} \quad (18)$$

$$1.0(0.6)\sigma_1 = 0.9(0.7)f_{ct} \quad (19)$$

$$\sigma_1 \approx f_{ct} \quad (20)$$

The approximation is done in order to show the basic methodology as simply as possible in this brief format.

### 3.3 Unreinforced LRFD

The preceding stress prediction methods, shape modification and high-strength concrete, waist ratio stability and combined loading strength reduction have all been incorporated into the LRFD design formulation above to determine the optimal unreinforced dolos weight for a given design wave height. For the unreinforced dolos analysis, stable dolos weights were computed for several waist ratios using the Hudson equation with a given wave height, structure slope of  $\cot \alpha = 2$ , specific gravity of  $S = 2.34$ , packing density of  $K_\Delta = 0.94$ , and  $K_D$  of half the value shown in Figure 2 (i.e., no-rocking). These stability coefficients were chosen to be conservative. Using the Hudson stable weight, the design maximum principal stress, which is the load side of the LRFD Equations 17 and 20, was computed using CAUDAID with  $E = 5\%$ . On the resistance side of the LRFD formulation, concrete splitting tensile strengths were estimated using compressive strengths of 35 MPa and 70 MPa and the ACI splitting strength recommendation of  $f_{ct} = 6\sqrt{f'_c}$ . Note that the strengths and loading moments were reduced for combined loading in Equations 13, 14, 15, and 18 but the final LRFD equations reduced to equating the design stress to the splitting tensile strength (Equations 17 and 20).

Figure 3 shows the hydraulically and structurally stable weight for unreinforced dolosse as a function of wave height for the three waist ratios and two concrete strengths. Note that the maximum wave height that can be successfully resisted for unreinforced dolosse over the design life of the structure is approximately 7.5m using high strength

concrete. For larger wave heights it is necessary to reinforce with structural steel. The effects of waist ratio can be clearly seen in this figure. The more slender the dolos, the less the required weight. But the figure shows that, for a given wave height, high strength concrete might be required for a more slender design dolos while not for the stouter dolos. It is clear that dolos design optimization could save a considerable amount of money through minimizing the concrete costs.

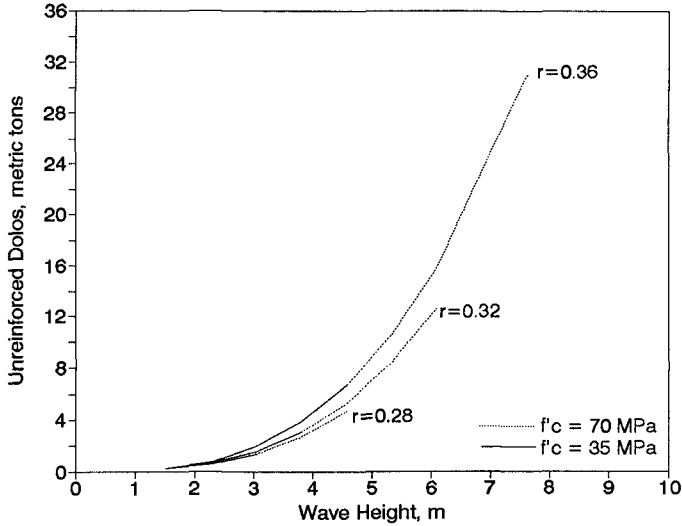


Figure 3: Unreinforced Structurally and Hydraulically Stable Dolos

### 3.4 Steel Reinforced LRFD

Two options exist for the steel reinforcement; deformed bars and prestressed tendons. In the U.S., the Corps of Engineers has placed conventionally reinforced dolosse on the Humboldt, Ca. Jetties; Manasquan Inlet, N.J. Jetties; and on several Hawaiian breakwaters. In most cases, no information was available about the magnitude of flexural and torsional loading. This resulted in inadequate hoop steel to resist torsional moments and improperly sized longitudinal reinforcing. With appropriate information about the nature of the loading, proper amounts of steel can be used to greatly strengthen dolosse.

Conventional reinforcement corrosion can be a significant problem. As a unit is loaded, tensile stresses within the concrete are transferred to the steel dowels along their development length only after the concrete cracks. Depending on the nature and severity of the loading condition, these cracks often extend through the concrete cover layer. Also, if the steel bars deform outward during concrete pouring then the amount of bar cover can be reduced. In the marine environment, cracks provide a conduit for seawater intrusion and subsequent chloride ion attack. This results in corrosion of the steel, and ultimately the eventual failure of the unit.

For the moderate to severe wave climate, prestressed concrete offers a solution for

strengthening dolosse that would otherwise crack. Prestressed concrete also has an enhanced ability to resist impact loads and fatigue.

### 3.4.1 Conventional Steel Bar Reinforcement Design

With conventional steel bar design, the torsional steel is specified first, and then the flexural steel. As per ACI (1989), resistance to torsional loading is computed as  $T_n = T_c + T_s$ , where  $T_n$  is the nominal torsional strength, and  $T_c$  and  $T_s$  are the nominal concrete and steel torsional strengths, respectively. Thus, the torsional resistance provided by the hoop steel is computed by

$$T_s = \frac{\gamma k_T T_u - \phi T_c}{\phi} \quad (21)$$

and the area of steel by  $A_s = T_s / R_h f_y$  where  $R_h$  is the distance from the center of section and  $f_y$  is the steel yield strength. To offset pure torsional forces, an equivalent amount of longitudinal steel is placed in the spacing between hoops as is contained in a single hoop.

Contrary to the preceding torsional reinforcement design, resistance offered by the concrete tensile strength is not considered in flexure. Nominal strength is reached when a crushing strain at the extreme fiber occurs as the tension steel yields. Strains in the steel and concrete are assumed directly proportional to the distance from the neutral axis. Unlike conventional structures where ductile failure indicates imminent collapse, armor unit design benefits from a brittle failure where a high steel-to-concrete ratio reduces crack width and formation under service loading. Although the stress-strain distribution across the section is nonlinear, a rectangular distribution is used to facilitate design. A concrete stress intensity of  $0.85f'_c$  is assumed to be uniformly distributed across an equivalent compressive zone. With the compressive force defined, an equivalent tension force comprised of the sum of forces generated by symmetrically placed steel is assumed. These forces become the components of a moment couple dependent on an unknown neutral axis location, requiring an iterative solution. The procedure to specify flexural steel is straight forward and the reader is referred to ACI (1989).

Using the aforementioned conventional reinforcement analysis methods, it was found that the reinforcement scheme of 12 equally spaced #6 bars in 16-ton dolosse at Manasquan, NJ provided approximately a 20% increase in flexural capacity and little increase in torsional capacity.

Figure 4 shows the results of a more general analysis with the weight of reinforcing steel required within a stable dolosse versus design wave height.  $f_s$  is the steel yield strength. Note that while the packing density is held constant, the porosity of the armor layer varies with waist ratio. Therefore to permit comparison of differing strengthening schemes, the amount of steel is given per  $100m^2$  of breakwater surface. Again, the effects of waist ratio can be clearly seen. The more slender the dolos, the less the number required to armor the breakwater. This significantly offsets the increase in steel required for slender units. Also note that, although high strength concrete was analyzed, the resulting curves are not shown because they do not differ significantly from those of normal strength concrete. This is because most of the resistance in a conventionally reinforced dolos comes from the steel. It must be noted that even though a substantial

amount of steel is specified, conventionally reinforced dolosse are still susceptible to cracking and, hence, a possible reduction in service life.

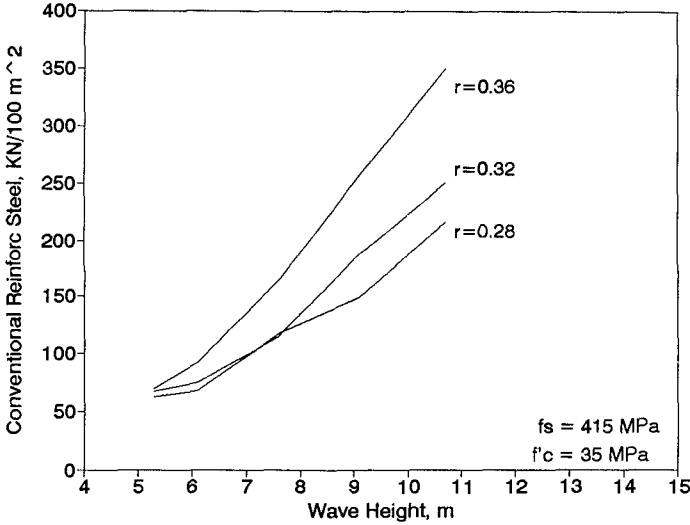


Figure 4: Conventional Reinforcing Steel Required

**3.4.2 Prestressed Steel Reinforcement Design**

Prestressing is a means of applying a precompression load to a structural member regardless of the dead or live loads acting on the structure. For the plane stress assumption, as precompression is added, the failure plane becomes more vertical and the section less susceptible to pure shear related inclined cracking.

Prestressed concrete design methodology differs from that of conventional reinforcement because both the torsional and flexural tensile strength of the concrete must be considered. Prestressing acts to directly apply an axial compressive force. The magnitude of the prestressing force is governed by the loading mode. The principal stress reduction factor as a function of a given precompression stress is

$$\xi = 0.5 \left( k_M - \lambda + \sqrt{(k_M - \lambda)^2 + 4k_T^2} \right) \tag{22}$$

where  $\lambda$  is the ratio of applied precompressive stress to design principal stress, as computed by CAUDAID, and  $k_M$  and  $k_T$  are 0.6. Substituting the moment-torque interaction relation into Equation 1 yields

$$\gamma \xi k_T \sigma_1 = 0.5 \phi \sqrt{\frac{f'_c}{1 + 4 \left( \frac{k_M S_M}{k_T S_T} \right)^2}} \tag{23}$$

for torsion with a similar relation for flexure. Again, ACI (1989) standard design practice methods were used to determine the amount of steel required.

Figure 5 shows the amount of steel required for the given design wave for the same  $100m^2$  of breakwater surface as used in the conventional reinforcement design.  $f_{pu}$  is the steel strength. Again, the slender reinforced dolos appears to be more efficient than the stouter one. Comparing Figures 4 and 5 shows that the prestressed dolos made with normal strength concrete requires slightly less steel than the conventionally reinforced dolos. But, using high-strength concrete, it is clear that the combination of prestressing and high-strength concrete is a much more efficient than conventional reinforcement.

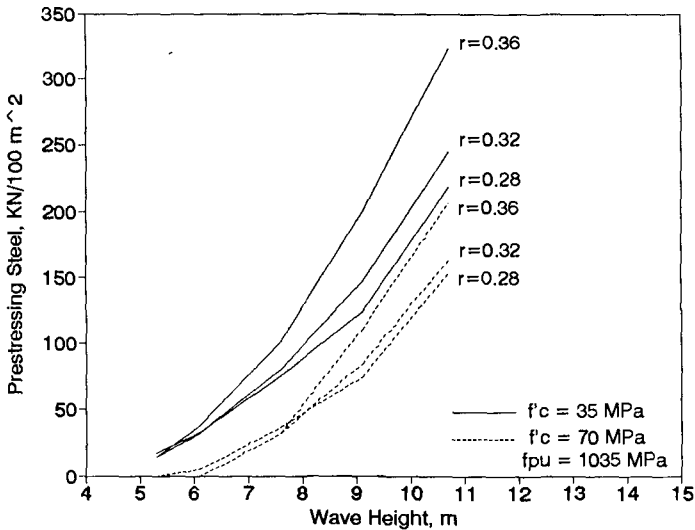


Figure 5: Prestressed Steel Required

## 4 CONCLUSIONS

In this paper conventional structural reliability methods have been adapted to the design of dolos. The loading was specified using a PC-based stochastic stress prediction algorithm incorporating Crescent City prototype dolos stress distributions. These site specific static and pulsating stress distributions are modified in the program according to the user specified dolos weight, armor unit density, number of layers, waist ratio, and wave height. The static and pulsating stress distributions are combined to get a design distribution which is used along with a design probability of exceedance to get a maximum probable stress level for the design armor layer. The LRFD methods are formulated so as to preserve this exceedance probability or the expected amount of breakage on the breakwater over the design life. It is shown that these methods predict the stress levels in dolos armored breakwaters well. The LRFD methods are further employed to allow the design of steel bar reinforcement.

The new design methodology is used to compare various strength enhancement options for dolosse including shape modification, high strength concrete, conventional steel

rebar reinforcement, and high strength prestressed reinforcement. It is shown that for wave heights below about 7.5m stouter dolosse and high strength concrete can be used effectively. Steel bar reinforcement may be required in dolosse for wave heights above 7.5m. It is shown that in some cases it may be economical to use slender dolosse with reinforcement than to use stouter dolosse without reinforcement. Finally, prestressing was found to be slightly more efficient than conventional steel bar reinforcement when used with normal strength concrete but superior when used with high strength concrete.

## 5 ACKNOWLEDGEMENT

The work described in this paper was conducted as part of the Coastal Research and Development Program of the Coastal Engineering Research Center, Waterways Experiment Station, US Army Corps of Engineers. Permission to publish this paper was granted by the Chief of Engineers.

## 6 REFERENCES

- American Concrete Institute (1989) "Building code requirements for reinforced concrete." ACI 318-89 and commentary ACI 318R-89, Detroit, MI.
- Anglin, C.D., Scott, R.D., Turcke, D.J., Turcke, M.A. (1990) "The development of structural design criteria for breakwater armour units." *ASCE/WPCO Sem. on Stres. in Conc. Ar. Un.*, ASCE, NY, NY.
- Burcharth, H.F., Howell, G.L., Liu, Z. (1991), "On the determination of concrete armour unit stresses including specific results related to dolosse," *Coastal Engineering*, 15 (1991) 107-165.
- Ellingwood, B., Galambos, T., MacGragor, J., Cornell, C. (1980), "Development of a probability based load criterion for ANS A58." US National Bureau of Standards SP577, US Govt. Printing Off., Wash., DC.
- Howell, G.L. (1988), "Measurements of forces on dolos armor units at prototype scale." *Proc. 21st ICCE ASCE*, NY, NY.
- Howell, G.L., Melby J.A. (1991), "Stochastic estimation of extreme stresses in breakwater concrete armor units," *J. of Hyd. Res.* V .
- Hudson. R.Y. (1958), "Design of quarry stone cover layers for rubble-mound breakwaters," Research Report No. 2-2, Jul 58, USACE, WES, Vicksburg, MS.
- Kendall, T.R., Melby, J.A. (1990), "Continued monitoring of 42-ton dolos movements and static stresses at Crescent City." *ASCE/WPCO Sem. on Stres. in Conc. Ar. Un.*, ASCE, NY, NY.
- Markle, D.G. (1990), "Crescent City instrumented dolos model study." *ASCE/WPCO Sem. on Stres. in Conc. Ar. Un.*, ASCE, NY, NY.

- Melby, J.A. (1992), "Application of a dolos structural design procedure." *Proc. Coastal Engineering Practice '92 Conf.*, ASCE, NY, NY.
- Melby, J.A., Howell, G.L. (1989), "Incorporation of prototype dolos static response in a dolos design procedure." *Proc. IAHR XXIII Congress*, Ottawa, Canada.
- Melby, J.A., Rosson, B.T., Tedesco, J.W. (1990), "An analytical investigation of static stresses in dolosse." *ASCE/WPCO Sem. on Stres. in Conc. Ar. Un.*, ASCE, NY, NY.
- Rosati, J., Howell, G.L. (1990), "Field measurements of structural response in break-water concrete armor units." *ASCE/WPCO Sem. on Stres. in Conc. Ar. Un.*, ASCE, NY, NY.
- Saucier, K.L. (1984), "High-strength concrete for peacekeeper facilities." MP SL-84-3, USAE WES, Vicksburg, MS.
- Zwamborn, J.A., Scholtz, D., Classens, H. (1988), "Stability and structural behaviour of strength improved dolosse." *Proc. 21st ICCE ASCE*, NY, NY.



## CHAPTER 107

### LABORATORY INVESTIGATION ON THE STABILITY OF A SPHERICAL ARMOR UNIT OF A SUBMERGED BREAKWATER

N. MIZUTANI,<sup>1</sup> K. IWATA,<sup>2</sup> T. M. RUFIN JR.,<sup>3</sup> and K. KURATA<sup>4</sup>

#### Abstract

The stability of the armor unit in relation to the wave force acting on a spherical armor unit of a submerged breakwater was discussed experimentally in this paper. Stability models were derived to relate the stable weight of the spherical armor unit with the wave forces acting. The proposed models were in good agreement with the experimental results. And the vicinity around the leading crown-edge was revealed to be the most critical location of the submerged breakwater.

#### 1. INTRODUCTION

The submerged breakwater is one type of coastal structure that can compensate the demerits of a detached breakwater in the prevention of beach erosion. In the design of submerged breakwater, stable weight of the armor unit must be properly evaluated. The critical stable weight of the armor unit depends largely on an accurate estimation of the wave forces and on a complete understanding of its generating mechanism and the wave characteristics; thus, it is necessary to estimate the stability in relation to wave forces in assessing the overall effectiveness of such structure. A number of researches has been conducted on the stability of armor units and many estimation methods have been proposed, such as Hudson (1959) and Van Der Meer (1987). Uda et al. (1989) developed an estimation method of stable weight of armor units of an artificial reef based on the laboratory experiment of armor stability. However, previous researches show that very few studies about wave force acting on armor units have been conducted; although there has been some study on wave forces acting on an armor rubble of a rubble-mound slope breakwaters (Iwata et al., 1985), still its wave force characteristics are not fully clarified. Hence, this paper aims to present experimentally the stability of a spherical armor unit of a submerged breakwater in relation to the wave forces acting on it.

---

<sup>1</sup>D. Eng., Assoc. Professor, Dept. of Civil Eng., Nagoya Univ., Nagoya 464-01, JAPAN

<sup>2</sup>M. ASCE, D. Eng., Professor, Dept. of Civil Eng., Nagoya Univ., Nagoya, JAPAN

<sup>3</sup>M. Eng., Graduate Student, Dept. of Civil Eng., Nagoya Univ., Nagoya, JAPAN

<sup>4</sup>D. Eng., Researcher, Toyo Construction Co. Ltd., Nishinomiya 663, JAPAN

2. EXPERIMENTAL PROCEDURE

The stability tests and the laboratory observations of wave forces acting on a spherical armor unit on a submerged breakwater were carried out using an indoor wave tank (25 m long x 0.7 m wide x 0.9 m deep). The submerged breakwater, as shown in Fig. 1, was installed on a horizontal bed. The model of the breakwater was prepared using spheres, diameter  $D = 0.03$  m, to exclude complexities due to shape complexity of natural stones. The porosity of the submerged breakwater was 26%. Two separate sets of experiments under different water depths were performed in this study, hereafter to be referred to as EXPT90 and EXPT91 respectively.

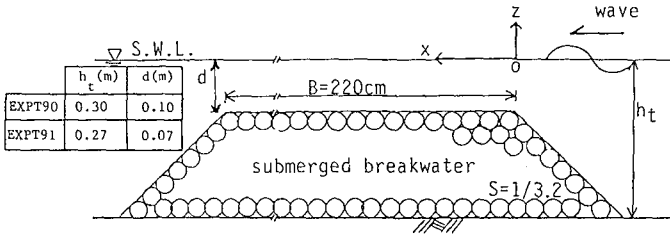


Fig. 1 Schematic diagram of submerged breakwater.

2.1 Stability Measurement

Eight and 12 samples of spheres of the same diameter but varying in weight were prepared for EXPT90 and EXPT91, respectively. Regular waves with different wave periods (EXPT90:  $T = 1.0, 1.41, 1.60$  s; EXPT91:  $T = 1.0, 1.4, 1.80$  s) were generated in this experiment. For every designated locations on the submerged breakwater, the critical wave height of each sample in each period were determined. Critical wave height is defined as the minimum wave height required to move a given sample of sphere. The determination was made by generating series of experimental trials with different values of wave height until the critical wave height is attained. Then, the corresponding water surface elevations and horizontal and vertical water particle velocities ( $u$  and  $w$ ) were measured with electric capacitance-type wave gauges and an electromagnetic-type velocimeter. For EXPT91, wave forces in horizontal and vertical directions ( $F_x$  and  $F_z$ ) were also measured with cantilever-type wave force meters. Measurements were conducted for both embedded and non-

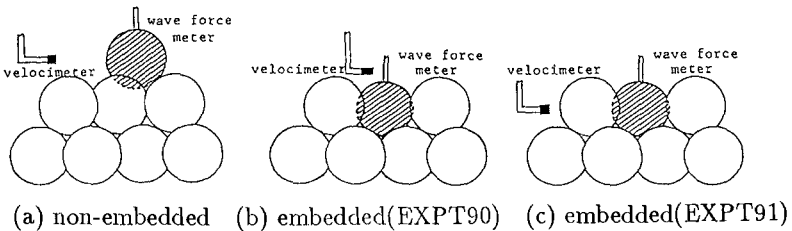


Fig. 2 Methods of wave force and velocity measurements.

embedded conditions and the methods of stability measurement for each set of experiment are given in Fig. 2. However, the half-embedded condition was adopted in EXPT90 since few movements in embedded conditions were observed.

## 2.2 Wave Force Measurement

Wave force measurements were also performed in this study to determine the fundamental characteristics of wave forces under a given wave conditions. Regular waves with the same periods as in the stability measurements were generated. Four different values of wave height ( $H_I = 0.03, 0.05, 0.07, 0.10$  m) which include both non-breaking and breaking wave conditions were assigned in this experiment. For each wave condition, the water surface profile, horizontal and vertical water particle velocities and wave forces were measured for both non-embedded and embedded conditions using the same instruments as in the previous experiments. The methods of wave force and velocity measurement are shown in Fig. 2.

Figure 3 shows the schematic illustration of the wave force meter devised for this experiment. It consists of a supporting rod and a cantilever with a sensing sphere on its head. The cantilever was covered with shield of appropriate shape to minimize the flow-turbulent effect. The wave force acting on the sphere causes strain on the cantilever and the output signal of the strain gauge on the cantilever together with the calibration table gives the magnitude of the wave force. The natural frequencies of wave force meters are more than 10Hz, which are much higher than the incident waves but its effect on wave forces is negligible and is removed using a low pass filter. The same diameter of sensing sphere was chosen for the non-embedded condition, however, a smaller diameter,  $D = 0.025$  m, of sensing sphere was used for the embedded condition in order to prevent contact with the surrounding spheres.

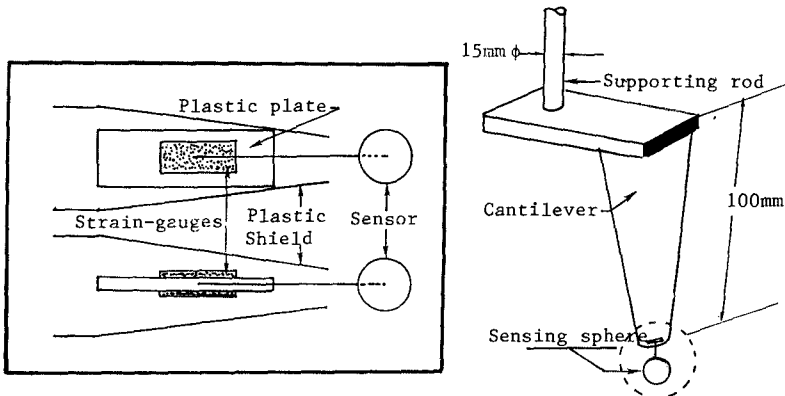


Fig. 3 Schematic diagram of cantilever-type wave force meter.

### 3. Stability of the Armor Unit

The relationship between the dimensionless critical stable weight of the armor unit  $W'_c/\rho g D^3$  and the dimensionless maximum velocity  $u_m/\sqrt{gd}$  is shown in Fig. 4, where  $W'_c$  is the critical stable weight of the armor unit in water,  $\rho$  is the density of water,  $g$  is the gravitational acceleration and subscript  $m$  indicates the maximum value. In the figure, the dimensionless maximum velocities corresponding to  $KC_x$  number equal to 10 and 20 are also indicated, where  $KC_x = u_m T/D$  is the Keulegan-Carpenter number. It is shown that the dimensionless critical stable weight is proportional to the velocity when  $KC_x$  is less than 10. On the other hand, it is proportional to the maximum velocity squared for  $KC_x$  larger than 10.

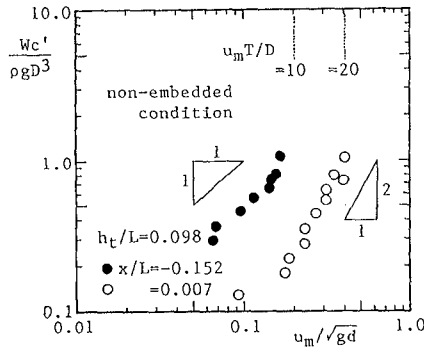
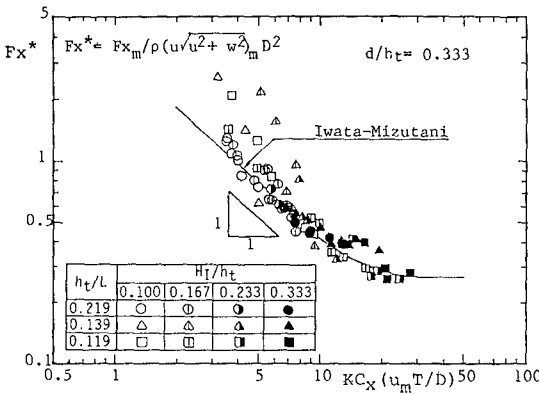


Fig. 4 Relationship between  $W'_c/\rho g D^3$  and  $u_m/\sqrt{gd}$ .

Figure 5 shows the relationship between the dimensionless maximum wave force  $F x_m/\rho(u\sqrt{u^2+w^2})_m D^2$  and  $KC_x$ . In the figure, the mean value obtained for an isolated sphere (Iwata and Mizutani, 1989) is also plotted. It can be observed that  $F x_m/\rho(u\sqrt{u^2+w^2})_m D^2$  is inversely proportional to  $KC_x$  when



(a) non-embedded(EXPT90)

Fig. 5 Relationship between  $F x_m/\rho(u\sqrt{u^2+w^2})_m D^2$  and  $KC_x$ .

$KC_x < 10$ . The inclination becomes mild when  $10 < KC_x < 20$  and it approaches a constant value when  $KC_x > 20$ . These tendencies are quite similar to those of isolated spheres. This clearly shows that the drag force is dominant over the inertia force when  $KC_x > 20$ ; conversely, the inertia force is a significant component when  $KC_x < 20$ , especially when  $KC_x < 10$ . And this causes the difference in the inclination of variation as given in Fig. 4. Thus, it can be concluded that the inertia force is also an important force component for the stability of the armor unit. Furthermore, this result suggests that a more accurate estimation of stable weight of an armor unit will be attained if it is expressed in terms of the wave forces acting rather than by its velocity.

**4. STABILITY MODEL**

In all stability trials, the motion of all samples was observed to be a rotating-type. This signifies that the spherical armor units starts to move when the overturning moment overcomes the restoring moment. Thus, the relationship between the stable weight and the wave force acting is obtained from the equilibrium state of moments. The force components considered in the system are the wave forces, gravitational force, buoyant force and frictional force. However, the frictional force between spheres is not considered in the analysis; since, the contact area between spherical armor units is very small and its contribution is considered to be negligible as compared to the other forces. This treatment, however, leads to a conservative estimation in the engineering point of view. The schematic diagram of the equilibrium state is shown in Fig. 6, and the following equations are obtained from this balance of moments.

For the non-embedded condition:

$$\frac{W_c}{\rho g D^3} = \left( \frac{2\sqrt{2}}{\cos \theta - 2\sqrt{2} \sin \theta} \right) \frac{F p_m}{\rho g D^3} + \frac{B_F}{\rho g D^3} + \frac{F n_m}{\rho g D^3} \tag{1}$$

For the embedded condition:

$$\frac{W_c}{\rho g D^3} = \frac{F z_m}{\rho g D^3} + \frac{B_F}{\rho g D^3} + \frac{F x_m}{\rho g D^3} \tag{2}$$

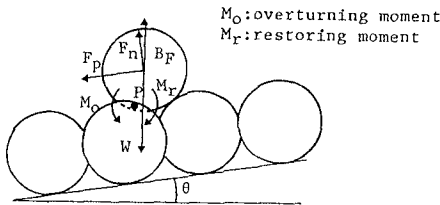


Fig. 6 Balance of moment and force.

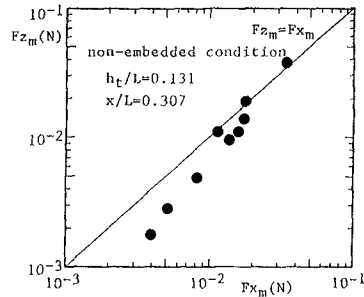


Fig. 7 Relationship between  $Fz_m$  and  $Fx_m$ .

where  $Fp_m$  and  $Fn_m$  are the maximum tangential and normal components of wave force, respectively, and  $B_F$  is the buoyant force.

In the given equations, the third term should be the instantaneous value when the wave force component in the first term becomes maximum. However, based on the experimental results, there are cases that the normal and tangential wave forces or vertical and horizontal wave forces attain its maximum values almost instantly. This phenomenon corresponds to the most dangerous condition of armor stability; thus, the maximum values instead of the instantaneous values are adopted in the third term of the given equations.

However, for easier evaluation of the stable weight, the given equations should be expressed in terms of one wave force component. Figure 7 shows an example of the relationship between  $Fz_m$  and  $Fx_m$ . From the figure, the orthogonal wave forces are correlated by a linear relationship as given in the following equation.

$$Fn_m = \phi Fp_m \quad Fz_m = \phi Fx_m \quad (3)$$

where  $\phi$  is the coefficient determined by least square method and varies with the settlement condition (non-embedded or embedded) and location on the submerged breakwater.

Substitution of Eq.(3) into Eqs.(1) and (2) yields the final form of the stability model and are given as follows:

For the non-embedded condition:

$$\frac{W_c}{\rho g D^3} = \left( \frac{2\sqrt{2}}{\cos \theta - 2\sqrt{2} \sin \theta} + \phi \right) \frac{Fp_m}{\rho g D^3} + \frac{B_F}{\rho g D^3} \quad (4)$$

$$\phi = 1.0$$

For the embedded condition:

$$\frac{W_c}{\rho g D^3} = \left( \frac{1 + \phi}{\phi} \right) \frac{Fz_m}{\rho g D^3} + \frac{B_F}{\rho g D^3} \quad (5)$$

$$\phi = 0.7 \text{ for armor units on the crown}$$

$$\phi = 1.6 \text{ for armor units on the slope}$$

The proposed model, hereafter to be referred as MODEL A, expresses the stable weight in terms of two wave force components together with the buoyant force. Some of previous research, however, considered only one wave force component which is in the direction of movement. This type of condition is also considered in this paper, another model without the third term of Eqs. (1) and (2) is derived as given in Eqs. (6) and (7) and hereafter to be referred as MODEL B.

For the non-embedded condition:

$$\frac{W_c}{\rho g D^3} = \frac{2\sqrt{2}}{\cos \theta - 2\sqrt{2} \sin \theta} \frac{F_{p_m}}{\rho g D^3} + \frac{B_F}{\rho g D^3} \tag{6}$$

For the embedded condition:

$$\frac{W_c}{\rho g D^3} = \frac{F_{z_m}}{\rho g D^3} + \frac{B_F}{\rho g D^3} \tag{7}$$

The comparisons between experimental results and the proposed models are given in Fig.8, from which an excellent agreement between the calculated value of MODEL A and the experimental value is revealed. On the other hand, MODEL B underestimates the stable weight as shown in Fig.8(b) and (c). This implies that the normal component of wave force for the non-embedded condition and the horizontal component for the embedded condition are both

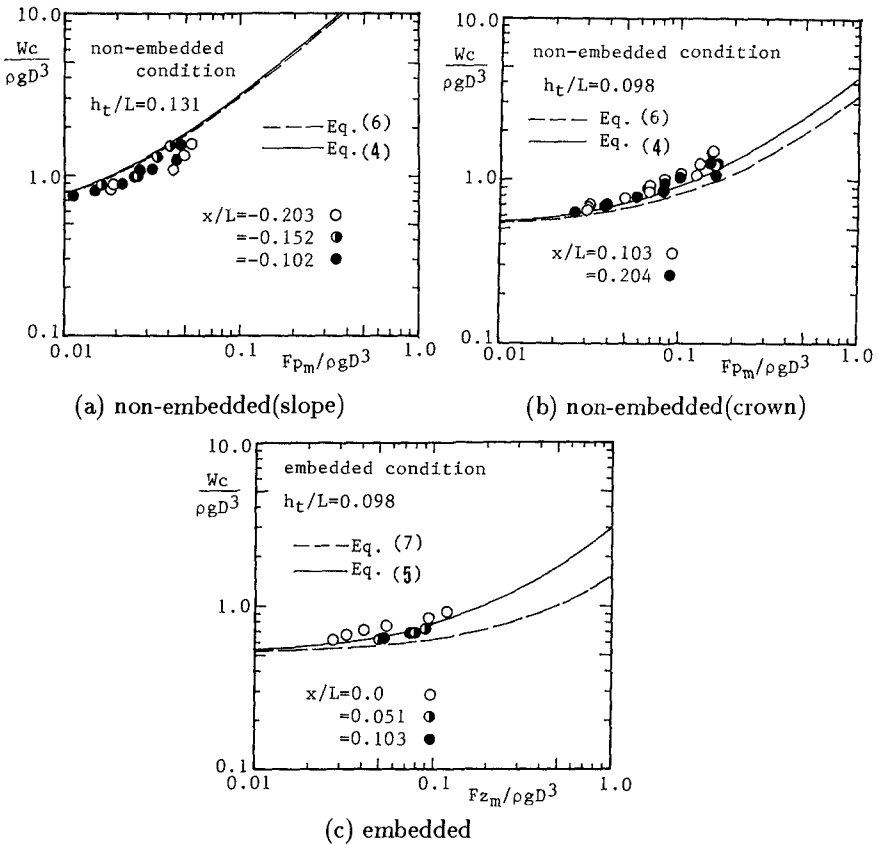


Fig. 8 Relationship of  $W/\rho g D^3$  with maximum dimensionless wave force.

significant in the armor stability. The normal component of wave force enlarges the upward force, thereby, making the non-embedded armor unit more unstable. Whereas, the horizontal force enlarges the overturning moment of the embedded armor unit.

Based on these two models, it is shown that the third terms are very important in a precise estimation of the armor stability. Thus, it can be concluded that both wave force components should be taken into account for an accurate estimation of stable weight of an armor unit. Very small difference between MODEL A and MODEL B is obtained for the non-embedded armor unit on the sloping part; since, in this situation, the tangential component of wave force is dominant over the normal component.

### 5. Maximum Wave Force

The proposed models express the stable weight of an armor unit in terms of the maximum wave forces acting on it. Therefore, an accurate estimation of wave force is required in the evaluation of stable weight.

Figures 9 and 10 show the variations of the dimensionless maximum wave forces,  $Fx_m/\rho gHD^2$  and  $Fz_m/\rho gHD^2$  with dimensionless distance from the leading crown-edge,  $x/L$ , as obtained from the wave force measurement experiments, where  $x$  is the horizontal distance measured from the leading crown-edge and  $L$  is the wavelength. Regardless of  $h_t/L$ , where  $h_t$  is the still water depth at the toe of the submerged breakwater, the variations under the same  $H_I/h_t$  value are quite similar. However, different variations of  $Fx_m/\rho gHD^2$  are obtained between non-breaking and breaking conditions. In Fig. 9, a typical variation of non-breaking and breaking wave conditions are shown with broken and solid lines, respectively.

For the non-embedded condition,  $Fx_m/\rho gHD^2$  increases with  $x/L$  on the slope and it reaches a maximum value near  $x/L = 0.0$ , regardless of wave breaking. On the crown,  $Fx_m/\rho gHD^2$  under breaking wave condition first decreases rapidly with increasing value of  $x/L$ , then takes a very large value when breaking waves attack the armor unit; and then finally decreases again. Under the non-breaking wave condition,  $Fx_m/\rho gHD^2$  decreases gradually with  $x/L$ , but a very large value at  $x/L = 0.7$  is again attained. In general,  $Fx_m/\rho gHD^2$  on the crown under the non-breaking wave condition is larger than that of the breaking wave condition except in the vicinity of the crown-edge.

For embedded condition, the variation of  $Fx_m/\rho gHD^2$  with  $x/L$  is smaller as compared to the non-embedded condition, because the variation of its velocity is also small.

The variation of  $Fz_m/\rho gHD^2$  with  $x/L$  is shown in Fig.10; however, the values of  $Fz_m/\rho gHD^2$  and its variation with  $x/L$  and  $H_I/h_t$  are smaller than those of  $Fx_m/\rho gHD^2$ . The quantity  $Fz_m/\rho gHD^2$  for both embedded and non-embedded conditions show no significant difference in magnitude except at  $x/L = 0.0$  where it becomes large under the non-embedded condition.



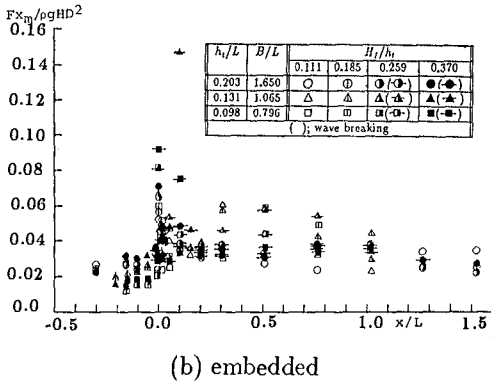
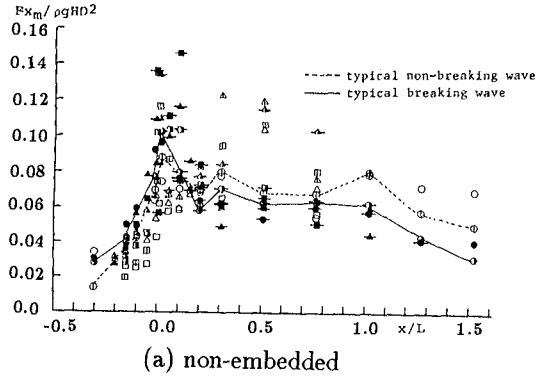
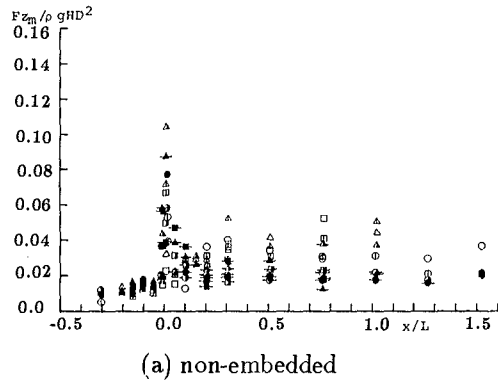


Fig. 9 Relationship of  $F x_m / \rho g H D^2$  with  $x/L$ .

The relative crown depth,  $d/h_t$  also has a significant effect on wave force, where  $d$  is the depth of water from the crown. Experimental results show that a smaller  $d/h_t$  results in a larger wave forces, although the figures corresponding to larger  $d/h_t$  are not shown in this paper (Iwata et al. 1991,1992, Mizutani et al., 1991, Rufin, 1992).



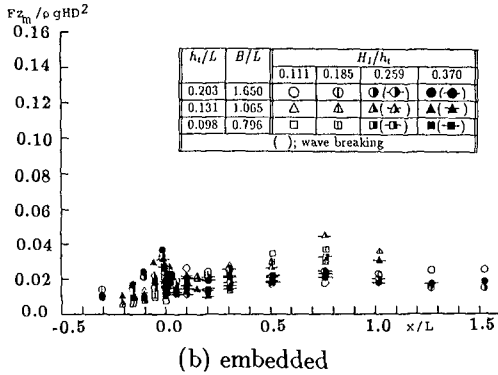


Fig. 10 Relationship of  $Fz_m/\rho g H D^2$  with  $x/L$ .

The relative crown depth,  $d/h_t$  also has a significant effect on wave force, where  $d$  is the depth of water from the crown. Experimental results show that a smaller  $d/h_t$  results in a larger wave forces, although the figures corresponding to larger  $d/h_t$  are not shown in this paper (Iwata et al. 1991,1992, Mizutani et al., 1991, Rufin, 1992).

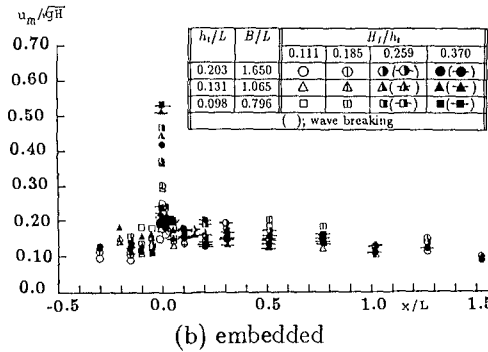
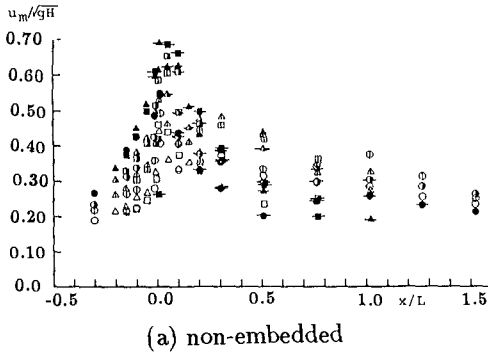


Fig. 11 Relationship of  $u_m/\sqrt{gH}$  with  $x/L$ .

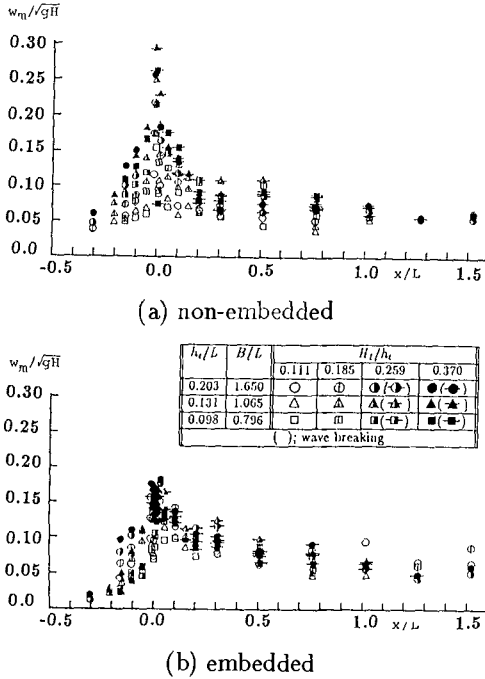
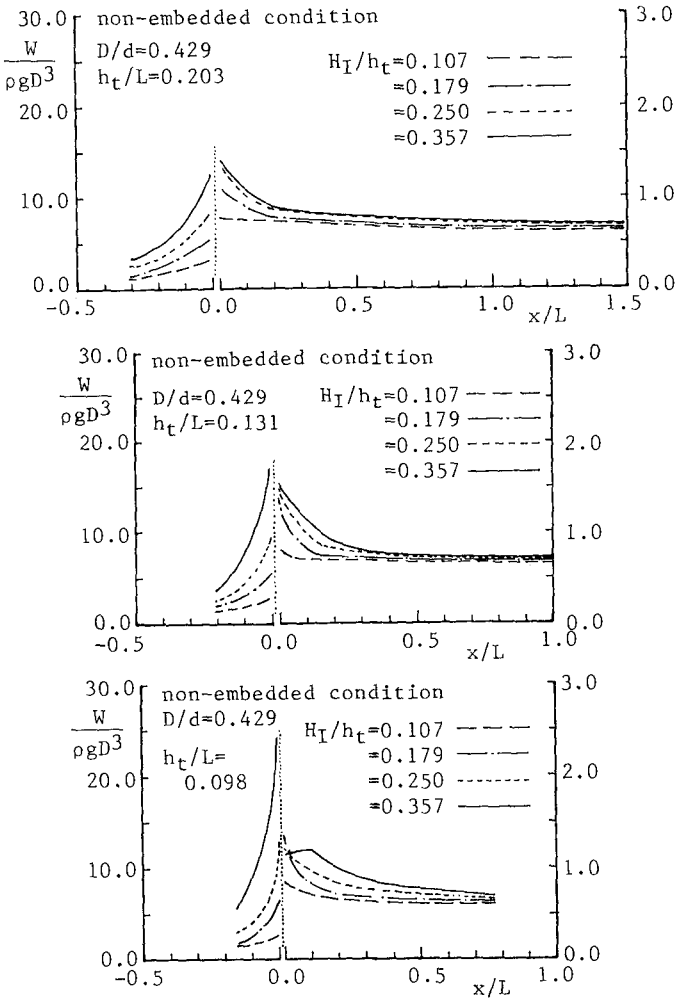


Fig. 12 Relationship of  $w_m/\sqrt{gH}$  with  $x/L$ .

These characteristics of wave forces are well correlated with the water particle velocities. The variation of dimensionless maximum particle velocities  $u_m/\sqrt{gH}$  and  $w_m/\sqrt{gH}$  with  $x/L$  are given in Figs. 11 and 12. On the slope, the velocity becomes larger with increasing  $x/L$ , due to wave shoaling, then attains a maximum value at the crown-edge. On the crown, the dimensionless maximum velocity decreases with  $x/L$  because of energy loss due to friction in the permeable structure and also due to wave breaking. A clear difference between the non-embedded and embedded conditions is observed in the horizontal component; however, no significant difference in the vertical component is observed. With regards to the effect of  $d/h_t$ , it was revealed that the dimensionless maximum velocity increases as  $d/h_t$  decreases (Iwata et al. 1991,1992, Mizutani et al., 1991, Rufin, 1992). These tendencies are similar to the dimensionless maximum wave forces. This means that the variation of dimensionless maximum wave forces is largely attributed to the velocity characteristics.

**6. STABLE WEIGHT OF SPHERICAL ARMOR UNIT**

Substituting the variation of maximum wave forces into Eqs. (4) and (5), the stable weight of the armor unit along the submerged breakwater is obtained. A plot showing the variations of the dimensionless stable weight of the spherical armor unit with  $x/L$  is given in Fig. 13. The discontinuity of the distribution at the leading crown-edge of the non-embedded condition is attributed to the significant contribution of the gravitational force. On the crown, the gravitational force acts only as a restoring force; however, some part of it acts as an overturning moment on the slope.



(a) non-embedded

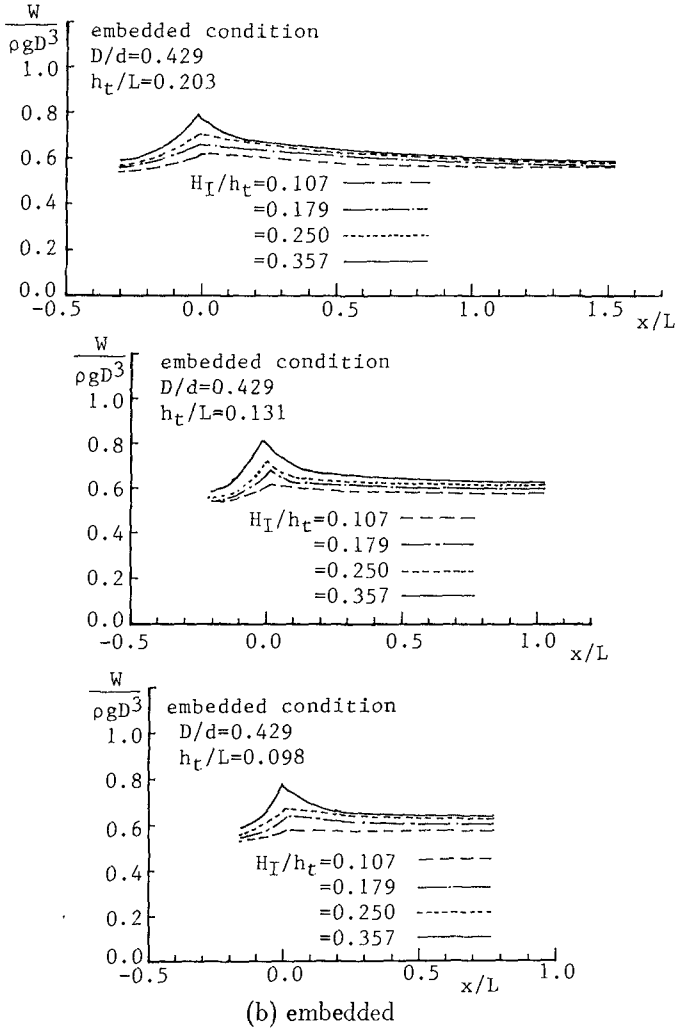


Fig. 13 Variation of  $W/\rho g D^3$  with  $x/L$ .

It is confirmed from the figures that the stable weight increases with increments of wave height on the slope where wave breaking does not occur. And the stable weight is greater around the vicinity of the crown-edge and at the location where wave breaks or where the horizontal roller and oblique-down vortex attack the armor units. Except at the vicinity of the crown-edge, there is a very little difference in the stable weight of the armor unit on the crown.

**7. CONCLUSION**

Results obtained from this study can be summarized as follows:

- (1) The vicinity around the crown-edge is revealed to be the most critical lo-

cation on the submerged breakwater.

- (2) A breaking wave greatly affects the stability of armor units.
- (3) Both horizontal and vertical or tangential and normal wave forces should be taken into account in the estimation of stable weight of armor units.
- (4) Stability models are derived to relate the stable weight of the armor unit with the wave forces acting. Also, the variations in the stable weight of spherical armor units on the submerged breakwater are given graphically.

#### ACKNOWLEDGMENT

The study presented was supported by Grant-in-Aids for Scientific Research from the Ministry of Education, Science and Culture of Japan, under Grant No. 03201138 (Head: Professor M. Hattori, Chuo University) and Grant No. 04201140 (Head: Professor Y. Iwagaki, Meijo University). The scholarship awarded by Offshore Mechanics and Polar Engineering Council and the International Society of Offshore and Polar Engineers to Mr. Teofilo Monge Rufin, Jr., one of the authors, is deeply appreciated.

#### REFERENCES

- [1] Hudson, R. Y.(1959): Laboratory Investigation of Rubble Mound Breakwaters, *Proc. ASCE*, Vol.85, WW3, pp.93-121.
- [2] Iwata, K., N. Mizutani, T.M. Rufin Jr., N. Totsuka (1992): Laboratory Analyses on Wave Forces Acting on a Spherical Armor Unit and the Stability of the Submerged Breakwater, *Tech. Report, Toyo Const. Co. Ltd.*
- [3] Iwata, K., N. Mizutani and T.M. Rufin Jr. (1991): Experimental Study on Wave Force Acting on a Spherical Unit of an Artificial Reef, *Tech. Report, Toyo Const. Co. Ltd.*
- [4] Iwata K. and N. Mizutani (1989): Experimental Study on Wave Force Acting on Submerged Sphere, *Proc. 8th Int. Conf. on OMAE, ASME*, Vol.2, pp.145-152.
- [5] Iwata, K., Y. Miyazaki and N. Mizutani (1985): Experimental Study of the Wave Force Acting on Armour Rubble of a Rubble-Mound Slope, *Proc. Natl. Disaster Science*, Vol.7, No.2, pp.29-41.
- [6] Mizutani, N., K. Iwata, T.M. Rufin Jr. and K. Kurata (1991): Experimental Study on Wave Forces Acting on an Spherical Armor Unit of the Submerged Breakwater. *Proc. Intl. Symposium on Natural Disaster Reduction and Civil Engineering.*, pp.107-115.
- [7] Rufin, T. M. Jr. (1992): Laboratory Analyses on Stability and Wave Forces Acting on a Spherical Armor Unit of a Submerged Breakwater. *Master Thesis, School of Engineering, Nagoya University.*
- [8] Uda, T., T. Omata and T. Saito (1989): Design Formula for the Weight of Armor Unit for an Artificial Reef, *Proc. Coastal Eng., JSCE*, Vol.36, pp.648-652 (in Japanese).
- [9] Van Der Meer, J.W. (1987): Stability of Breakwater Armor Layers- Design Formulae, *Coastal Eng. Elsevier Sci. Pub.*, pp.219-239.

## CHAPTER 108

New types of shore protection. Possibilities of application along the coast of France

P. Monadier\*, F. Ropert\*, B. Bellessort\*\*, J. Viguier\*\*

### ABSTRACT

The first part of this article gives an overview of the development works that have been carried out to date along the French coast, covering types, operating principles and impacts. A "philosophy" is identified with regard to the schemes implemented so far and those recommended for the future: rather than static structures that resist the action of the sea, it would often be preferable to substitute dynamic structures and schemes that work in harmony with it. Much research is being carried out on designs of this type. An analysis and summary of this work is given in the second part of this article. Most such work is currently at the experimental stage and no "miracle" solution has been found so far. Local conditions must be examined carefully before deciding to use any of the new alternatives being proposed.

### 1. INTRODUCTION

Until now, shore protection works on the French coast have usually involved the use of:

- rockfill, for transverse structures (groynes) and longitudinal structures on the upper beach (sea walls) or at sea (breakwaters),
- masonry or concrete structures (groynes, sea walls),
- beach nourishment, sometimes combined with stabilisation works (groynes, breakwaters).

The side-effects of these structures are not without drawbacks (for example, beach erosion), while blending them into the environment may pose problems.

---

\* SCTPMVN, 2 boulevard Gambetta, 60321 Compiègne, France

\*\* SOGREAH, 6 rue de Lorraine, 38130 Echirolles, France

In order to combat these negative features, various new solutions have been proposed in outline and even implemented in different parts of the world.

The Service Central Technique des Ports Maritimes et des Voies Navigables (SCTPMVN) commissioned SOGREAH firstly to carry out bibliographical research into the various new types of protection and to make an objective critical analysis of them, and secondly to examine the possibilities of applying them along the coast of France.

The operating principles of the various processes have been grouped under five headings: action on the hydraulic medium, use of geotextile, artificial seaweed, gentle methods, miscellaneous.

## 2. THE FRENCH COAST: TYPES OF SCHEME - OPERATION

### 2.1 The need for development works

Coastal development works (other than at ports) have various aims:

Natural processes:

- protection against sea erosion (e.g. cliffs in the Caux region),
- protection of low-lying areas against flooding (e.g. Ile de Ré),
- protection against changes in shoreline (e.g. La Coubre spit),
- reclamation and polder construction (e.g. Mont Saint Michel).

Human activities:

- Development linked directly with tourist and resort activities, namely sea fronts (e.g. La Baule, Royan, Les Sables d'Olonne) or artificial beaches (e.g. Prado, Mourillon, Larvotto).

- Coastal defence works (sea walls, dikes, groynes).

### 2.2 Overview

The French coast comprises 3300 km of soft terrain (i.e. 59% of the total, including 2000 km of beaches and 1300 km of marshland) and 2300 km of rocky formations.

The structures built along the coast include:

- 1300 transverse structures (groynes), totalling 125 km,
- 800 longitudinal structures (sea walls and bulkheads), totalling 375 km.

The total length (500 km) represents about 10% of the entire coastline (5500 km), i.e. a mean density of 50 m/km. On the basis of 5000-10 000 French francs per linear metre, the present cost of these works would be 3-5 billion francs.



The greatest density of structures is found in regions where loose formations are prevalent and where there is intense resort development, for example 175 m/km in Lower Normandy and 155 m/km in Languedoc-Roussillon and the central Atlantic coast. It is lowest in regions with loose formations but little development, such as Aquitaine (85 m/km) or a broken rocky coastline, such as Brittany (63 m/km). In Provence, where the coast consists mainly (75%) of hard rocks, the density of 100 m/km corresponds to a great extent to artificial beaches.

### 2.3 Operation

It is particularly important and instructive to analyse the operation of these schemes. Indeed, such an analysis must form the basis for future designs and justify the use of new methods.

The schemes may be divided into two basic categories, namely static ("hard" structures, such as bulkheads and sea walls that are "opposed" to the sea) and dynamic works (consolidation, by-passing, dune development, which are an attempt at compromise). Until recently, static methods were the ones most commonly used. They have often had negative impacts connected with two main factors:

- insufficient knowledge of the natural phenomena involved, resulting in inappropriate, wrongly sized or badly situated schemes,
- consideration of problems at the wrong scale, i.e. by taking into account administrative and not sedimentological areas.

The following points should be stressed in particular:

- Longitudinal structures have broken the beach-dune links that helped to regulate beach evolution and contribute to beach nourishment. They have disturbed both transverse and longitudinal balances by introducing resistant points that have finished by creating protrusions which then suffer preferential wave attack.

- Sea walls and bulkheads are often located too close to the sea and have given rise to erosion as a result of wave reflection and breaks in the natural equilibrium profile of the sea bed.

- There are serious problems of erosion on the down-current side of groyne because of a shortage of sediment supply. This problem is never solved correctly.

Structures of this type have therefore often produced erosion processes requiring other types of remedial work. This all has a snowball effect. A few examples may be given:

- On the regional scale, the coastal regime in the Seine-Somme area has been strongly affected by the various harbour works implemented over the last 200 years and by widespread pebble extraction. What was once a

continuous stretch of coast 150 km long is now segmented by harbours, while the stock of sediment (pebbles) has been impoverished.

- On the local scale, most large beaches developed inside bays are being eroded, mainly on account of the negative effects of coastal development works (as at La Baule, Les Sables d'Olonne and Royan).

- Numerous small harbours have produced localised disruptions, in particular when they are situated inside bays, as at Bormes-les-Mimosas, Cavalaire or Pornichet.

Until now, dynamic (or so-called "gentle") methods have been used relatively infrequently, for two main reasons:

- They do not provide any "universal" solution. The more active the coastal regime, the more difficult it is to contemplate using them. For example, they would be well suited to many small bays in Brittany but unacceptable on the coast of Aquitaine.

- In addition to the initial investment required, they usually involve maintenance, which is rarely appreciated by local and regional authorities.

### 3. NEW METHODS

Over the past two or three decades, the financial aspects involved (protecting 1 km of coast now costs 5-10 million francs) and increasing environmental awareness have favoured the use of "gentle" methods and at the same time encouraged research into new ones, mainly of the dynamic type. The various methods now being considered, experimented or studied may be grouped into five broad categories:

- action on the hydraulic medium,
- use of geotextiles,
- artificial seaweed and planting,
- gentle methods,
- miscellaneous.

#### 3.1 Action on the hydraulic medium

##### a. Modifications in wave propagation

Investigations have concerned:

- the recomposition of waves following artificial creation of a phase shift, the result of which is a transmitted wave carrying less energy than the incident wave: oscillating wall of water (PRINCIPIA),

- recomposition of cone-diffracted waves producing a wave front parallel to the coast (SOGREAH-LCHF study),

- reflection of waves on artificial bars (sand-filled geotextile tubes) according to the Bragg principle (NCEL).

These processes have all remained at the experimental stage as far as shore protection is concerned.

b. Attenuation of wave energy

Research in this field has concentrated more on various types of breakwater:

- submerged breakwaters,
- submerged moored floating breakwaters (Japan),
- pneumatic breakwaters (Great Britain, CIS),
- discontinuous pile-mounted breakwaters (CIS),
- miscellaneous types of breakwaters: tyres, cement pontoons, articulated breakwaters (Cornic, C1000).

Most of these studies have remained at the experimental stage. Often, the structures only operate correctly under specific hydrographic and oceanographic conditions.

c. Slightly reflecting structures

The function of these structures is to stabilise the coastline by limiting wave reflection and the formation of surf, which cause coastal erosion: Jarland caissons, Igloo blocks, ARC chambers (SOGREAH), Delta breakwaters (Berger Staemfli).

The results obtained are generally satisfactory.

### 3.2 Use of geotextiles in beach protection

The main types of mattress that have been tested are Armorflex, Nidaplast and Enkamat. The various procedures involving structures with a geotextile envelope are Longard, Sandtex, Robusta and Cornic. Most of these procedures are derived from those used in rivers or lakes and there have been many drawbacks in using them in a maritime context, such as stability and fragility of the textiles, damage of human origin, etc.

### 3.3 Artificial seaweed - planting

a. Artificial seaweed

So far, there have been no convincing results, although many tests have been carried out throughout the world.

### b. Planting (in particular Posidonia)

Planting Posidonia is now well understood, but there are still problems with this technique in the field of coastal protection, including growth time and area of planting.

### 3.4 Gentle methods

Gentle methods are meant to work in harmony with the sea. Usually, they should be considered not as a basic solution but as a complementary measure. The main types include:

- development of dunes (a new solution includes stabilisation using a gel),
- the creation of artificial coastal strips (Maguelo),
- beach nourishment, which is an attractive solution that is still little used in France and which poses certain problems in terms of the quantity and quality of material used and maintenance,
- by-passing; this technique is virtually unused in France so far; there are problems in terms of installation, maintenance and cost price.
- acceptable coastline retreat; this solution can only be envisaged under well-defined coastal conditions (in particular geographic and economic). It must be acceptable to the authorities and persons concerned.

### 3.5 Miscellaneous

This heading covers many different methods, many of which are still at the experimental stage, for instance:

- drainage of the foreshore (Stabeach system),
- artificial reefs created by electrolysis,
- planting on clay breakwaters (using geotextiles),
- cylindrical groynes and breakwaters (SOGREAH).

## 4. CONCLUSIONS

Many solutions are currently at the experimental stage. There would appear to be no "magic" solutions. In fact, it would seem rather a case of looking at the positive aspects of developing and adapting systems that already exist but that are sometimes "forgotten" because of technical or financial problems (e.g. beach nourishment, by-passing).

## CHAPTER 109

### FIELD ANALYSIS OF WAVE ACTION ON BREAKWATER

Alessandro Muraca (\*) - Vito Rossi (\*\*)

#### Abstract

Field analysis of breakwater damage progression has been performed using monitoring programs which included both photographic and topographic surveying. Reliable information on cover blocks displacement were obtained using a metric camera and a digitizer. Measured damage was compared with those estimated using empirical formulae.

A computer model, capable of predicting damage progression, has been also calibrated using in site collected data. Predicted damage has been satisfactory also for long time interval period.

#### Introduction

Field measurements have been carried out on a breakwater built up to protect a water intake dockyard for the power plant of Montalto di Castro (Tyrrhenian Sea, Italy). Cover consists of two strata of rocks, randomly placed by land based equipment, whose average diameter is equal to about 1 meter. The weight of primary armour ranges from 2 to 4 tons and the seaward slope is 1:2. The water depth in front of the structure is about 5 m. The structure is faced by one Waverider Datawell and one Wave-Track directional Endeco: the first installed in 1978, the second in 1986. From December 1991 Wave Track Endeco was replaced by a directional wave rider Datawell .

A field analysis of breakwater behaviour is necessary to evaluate the capability of commonly used design formulae for predicting the damage level ,due to wave attacks, attained by mound structure. Photogrammetric techniques combined with adequate ground control represents a common method for monitoring breakwater damage progression (Ackers, 1983; Gebert, 1984; Kluger, 1982; Pope, 1983; CETN, 1984).

-----  
(\*) Faculty of Engineering - Viale Ungheria, 43 - Udine, Italy

(\*\*) ENEL-CRIS Servizio Idrologico - Mestre (Venice), Italy

Accurate field investigations relied upon the use of photography, supported by topographic measurements. Both metric and non metric cameras were used to photograph the breakwater cover layer. Metric photographs were analysed using a stereoscope; this allowed both a better evaluation of cover blocks movements and a good estimation of the rotation of visible stones.

An accurate time and frequency domain study was made on recorded wave climate; moreover wave grouping aspects, its statistical properties and possible affects on breakwater stability were analysed. Recorded wave parameters were introduced in four commonly used stability theories. Comparison between the empirical design methods and prototype behaviour were made and found to be satisfactory.

Analysis of wave records and results of field inspections were also used to calibrate a computer program for predicting breakwater damage progression. By this model damage progression can be estimated as a function of real sea state records.

### Theoretical Damage Prediction

Breakwater stability analysis has been made over the past 30 years by using the Hudson formula (Hudson 1959). In recent years experiments in large wave flumes with irregular waves and careful analysis of prototype damage have led to the formulation of new theories which comprehend also random wave characteristic effects. Losada and Gimenez-Curto developed an exponential model as a function of surf similarity parameter to represent rubble-mound breakwater stability (Losada and Gimenez-Curto, 1980). This stability function is given by :

$$P = \frac{H_s^3 \cdot \gamma}{(S-1)^3} \cdot A(I - I_b) \cdot \exp[B(I - I_b)] \quad (1)$$

A and B are coefficients whose value is the function of foreshore slope and type of cover layer block. In plane H, T expression (1) could be plotted as an "interaction curve", equal to a set of the points which produce the same value of armour unit weight (Losada, 1980).

More recently Sawaragi and Ryu (Sawaragi, 1983) have analyzed in detail group effects on mound stability. These authors have discovered that a strong correlation exists between Goda spectral peakedness parameter  $Q_p$  and the energy sum of grouped waves  $E_{sumj}$  (Sawaragi and Ryu, 1985).

This relationship is expressed as follows:

$$E_{sumj} = H_s (0.042 Q_p + 0.125) \quad (2)$$

For an exact significance of  $E_{sumj}$  the reader is referred to Sawaragi, 1985. The linear relationship between sum energy of grouped waves ( $E_{sumj}$ ) and the spectrum peakedness parameter ( $Q_p$ ) has been verified using wave data recorded at Montalto di Castro. Both parameters have been evaluated at wave rider depth. Computed values of  $E_{sumj}$  were very similar to those estimated using eq. 2. The comparison is reported in Fig. 1.

Irregular wave experiments showed that the percentage of damage suffered by breakwater ( $D\%$ ) is a function of the above mentioned parameters according to the following expressions:

$$D\% = 153.8 \cdot \left[ \frac{E_{sumj}}{\gamma \cdot l a^2} \cdot \frac{tg \alpha}{tg \phi} \right] - 30.1 \quad (3)$$

$$D\% = \left[ \frac{\gamma a \cdot H_s^2}{\frac{1}{\gamma^3}} \cdot \frac{tg \alpha}{tg \phi} \cdot \frac{6.15 Q_p + 20}{P^{\frac{2}{3}}} \right] - 30.1 \quad (4)$$

Sawaragi defines the degree of damage as the percentage of destroyed volume with respect to the total volume of cover layer. According to Sawaragi a displacement takes place when armour units are moved over a distance greater than the overall size of blocks (Sawaragi, 1983).

More than 300 experiments were done by Van der Meer to analyse the effect of storm duration, wave period, group characteristics and spectral shape (Van der Meer, 1987, 1988). The effect of cover layer and sub layer permeability were also carefully investigated. Surprisingly group effects were not found to have a significant effect. More recently, stone shape and layer thickness influence were also analyzed using an expression comparable with Van der Meer formulation (Bradbury, Lothan, Allsoy, 1990) and new stability formulae were found for both overtopped and submerged breakwaters (Van d. Meer 1991). Van der Meer found two different relationships to determine stable rock block dimensions, for plunging and surging waves.

**Plunging waves** (I z < I c)

$$\frac{H_s}{\Delta \cdot D} \cdot \sqrt{Iz} = 6.2 \cdot p^{0.18} \cdot \left( \frac{d}{\sqrt{n}} \right)^{0.2} \quad (5)$$

**Surging waves** (I z ≥ I c)

$$\frac{H_s}{\Delta \cdot D} = \bar{p}^{0.13} \cdot \left( \frac{d}{\sqrt{n}} \right)^{0.2} \cdot \sqrt{\cot \alpha} \cdot (Iz)^p \quad (6)$$

Transition from plunging to surging is given by the following expression:

$$Ic = \left( 6.2 \cdot p^{0.31} \cdot \sqrt{tg \alpha} \right)^{1/(p+0.5)} \quad (7)$$

Using Van der Meer theory a mathematical method capable of describing revetment damage progression has been calibrated.

This analysis is possible by introducing a parameter that can be referred to as "equivalent sea state". This is equal to a time parameter describing the duration of a fixed sea state capable of causing the same amount of damage of different wave climate conditions (Muraca, 1989). Rearranging formulas (5) and (6) "equivalent sea state" results equal to :

$$D_1 = a \cdot \left( \frac{d \cdot p^{0.9}}{Iz^5} \right)^2 \cdot \left( \frac{\Delta^5 \cdot D^5}{H_s} \right)^2 \cdot T_m \quad (8)$$



$$D_2 = b \cdot \left( \frac{d}{p^{0.65}} \right)^2 \cdot \left( \frac{I_z^p \cdot \cot \alpha}{H_s^2} \right)^5 \cdot (\Delta^2 \cdot D^2)^5 \cdot T_m \quad (9)$$

where  $D_1$  and  $D_2$  are for plunging and surging waves respectively and  $a$  and  $b$  are dimensional coefficients depending on the units used in the above formulas.

The following steps were used to implement the stability model:

- 1) Evaluation of data from gauge records and calculation of wave parameter at the front of the structure depth;
- 2) Computation of minimum sea state capable of causing significant damage to the structure, in order to attain a lower limit below which the wave data recorded can be disregarded;
- 3) Interpolation between sea states and computation of Van der Meer 's damage parameter with free interval time steps.

All these operations have been implemented on a Vax Digital Computer.

Superimposition of the effects of a sequence of sea states, such as those registered by wave gauges, and the damage description starting from whatever revetment condition is thus modelled.

#### Site investigation

The investigated breakwater is provisional and undergoes large damage during severe storms. From autumn 1984 the structure has been regularly surveyed by contractors. An accurate zonation of cover layer according to the degree of suffered damage and the number of blocks necessary to rebuild the original sections have been registered at the end of each major event. From 1988, a more accurate survey of damage has been programmed. Two stretches measuring about 15 meters of the structures have been delimited by permanent rods and more visible blocks at different levels have been marked by water resistant paints. Once in two months three pictures were taken of each of the selected parts and the exact position of marked blocks was surveyed using topographical instruments. These operations were also repeated at the end of storms, when the structure was subjected to significant damage.

Cover layer photographs have been analyzed using direct linear transformation, a method developed by Abdel Aziz and Marzan and Karara at Illinois University (Abdel, 1971, 1974; Marzan, 1975). This technique is applicable after measurement by topographic instruments of the position of seven marked blocks, visible in each picture. Using a computer program and a digitizer has allowed a satisfactory precision in the estimation of the movement of cover layer blocks.

The computer program was based on direct linear transform method of Marzan. The lowest movements estimated with this technique were within the range of five to ten

centimetres and the possible errors in predicted position only seldom were over 0.5 meter. From autumn 1989 metric camera and digital photogrammetric stereo workstation was also applied for inspection. The photographs have also been viewed in pairs under a stereoscope: this provided a three dimensional image of the breakwater primary layer and good estimation of rotation of all visible blocks. A higher degree of accuracy in cover blocks displacements estimation was possible by using the photogrammetric workstation ; this was an appreciable advantage for the evaluation of global damage.

Since no underwater inspection was scheduled the following considerations refer only to the above water level part of the structure. However it is believed that this information provide a reasonable indication of the general condition of the breakwater cover layer.

Field survey were made on the following dates:

<b>Topographic</b>	<b>Photographic</b>
June 21 1988	June 21 1988
July 14 1988	July 14 1988
Sept 23 1988	Aug. 25 1988
Nov. 02 1988	Nov. 05 1988
Jan. 11 1989	Jan. 27 1989
Mar. 06 1989	Mar. 15 1989
May 02 1989	May 02 1989
June 12 1989	
July 06 1989	July 07 1989
Nov. 15 1989	Oct. 21 1989
Jan. 10 1990	Jan. 10 1990
June 26 1990	
July 09 1991	July 20 1991
July 16 1992	July 18 1992

The strongest storms were recorded in January and November 1987 and at the end of March 1988. The cover layer, which was seriously damaged, was repaired at the end of these storms.

Frequency and zero up-crossing time domain analysis of wave gauge records were made. An accurate study was also carried out to analyse wave grouping aspects registered by Datawell Waverider.

The length of runs were determined for two threshold values: the significant wave heights and average heights of the highest one-tenth waves. Possible resonance conditions were analyzed according to Sawaragi and Bruun and Gunbak theories (Sawaragi, 1985; Bruun Gunbak, 1978). Thus a continuous knowledge of structure behaviour and wave regime was available.

### Results and Discussion

The sea state characteristic of the major storms registered have been treated with the above mentioned methodology. Bathymetry is regular in front of the structure and bottom slope is equal to 1:80. Goda technique for random sea waves was applied for transforming Waverider information from deep to shallow water (Goda, 1975, 1985). A comparison between predicted and measured damage was done for the major storms registered. Hudson, Losada, Sawaragi and Van der Meer theories has been applied to compute theoretical damage level. Two severe events were registered in January 1987 and March 1988. The results of analysis of wave records, for March 1988 storm, are shown in Tab.1.

DATE	HOUR	H1/10 (cm)	T1/10 (s)	H1/3 (cm)	T1/3 (s)	Qp
30-03-88	18	307	6.8	253	6.9	2.2
	21	356	8.1	302	7.8	2.9
31-03-88	0	396	7.5	310	7.5	2.9
	3	537	8.0	415	8.0	2.4
	6	642	8.9	501	8.9	2.9
	9	508	8.9	405	8.8	2.4
	12	426	7.6	351	8.0	2.5
	15	425	7.8	312	7.5	2.5
	18	394	7.7	310	7.5	2.7
21	344	7.3	268	7.5	2.5	
01-04-88	0	265	7.0	206	6.6	2.6

Tab.1 Wave statistics from Waverider data - 30 March through 1 April 1988 (significant wave heights below 2.5 m are disregarded).

In both cases the structure suffered very severe damage.

Run lengths of groups exceeding significant and average of highest one-tenth waves were analyzed. During the March 1988 storm nearly all groups with heights over significant ones were within Sawaragi critical region and the breakwater suffered the highest observed damage: part of the filter was discovered and large portions of cover blocks were carried away. Tab. 2 shows damage estimations according to Hudson, Sawaragi and Van der Meer theories.

EVENT	Measured damage			Predicted damage		
	Hudson	V.d.Meer	Sawar.	Hudson	V.d.Meer	Sawar.
Jan.87	20	6.5-7	60	15-20	6.8	46
Mar.88	30	8	100	20-30	7.8	87
<b>PERIOD</b>						
Ja.-Ap.89		2.5			3	
Jul.90-92		4			5.2	

Tab. 2 Comparison of measure and predicted damage in selected events.

In June 1987 the damages were, in the same order mentioned previously, 20, 60 and 7 (Tab. 2). The maximum significant wave height and average height of the highest one-tenth waves, both computed in front of the structure, were introduced using Hudson formula. Predicted damage was closer to measured one using significant wave height.

Interaction and breaking limit curves for the Montalto breakwater have been plotted and compared with wave characteristic estimated in front of the structure. Interaction curve separates on plane (H, T) stability and instability zones (Losada, 1980). Significant wave characteristics, estimated at structure depth, for the March 1988 storm were compared with interaction curve. All significant waves were found to fall inside the stability area. To attain the instability region the average height of one tenth of waves should be used.

In shallow water this wave parameter seems more suitable for comparison between wave attacks and Losada stability function. For Sawaragi theory the maximum value of  $D\%$  parameter has been considered. For each wave gauge record significant wave heights at structure depth were computed with the theory of Goda while  $Q_p$  was estimated directly from Waverider records (eq. 4). No theory is available to transfer  $Q_p$  parameter at different depths (Mansard, 1987, 1988). However, because of the complexity of the shoaling mechanism, an exact transfer of wave data, especially those referred to wave grouping, from deep to shallow water depth is not possible through the existing theories (Mansard and Funke, 1988; Nelson, 1988).

Recently an application based on the TMA and Doneland models was used to transfer wave frequency spectrum from deep to shallow water, and results seem promising (Rebaudengo, 1992).

However all these methods are not applicable if there are significant non linearities. Since the variability of  $Q_p$  is not predictable, the peakedness value introduced in Sawaragi formula was estimated at wave rider depth. This could explain the higher differences between measured and predicted damage levels (Tab. 2). However

bathymetry is regular in front of the structure and bottom slope lower than 1:80 ; as a consequence  $Q_p$  computed at the Waverider depth is believed to be comparable with that in front of the structure (Rye, 1982).

To find out the degree of variability of  $Q_p$  parameter with water depth, some wave records at different depths were carefully analyzed. Data are referred to different Italian sites where two or more wave-riders are located at different depths, but aligned orthogonally to the coastline.

As shown in Fig. 2 the range of  $Q_p$  variability seems to be not significant in the range 13 to 50 meters of depths. An attempt to transfer the Esunj parameter from deep to shallow water was made using different shoaling theories for a single wave registered in time domain ; however results were not satisfactory.

The stability model was applied to determine the damage using the Van der Meer theory. Significant wave heights below 2.5 m were disregarded. After many computer trials and in site measurements to calibrate the program, this value of wave height value was found to be the minimum below which the estimated damage using the Van der Meer method, for a three hours wave attack, is negligible (Muraca, 1989).

The computer model allowed, in all examined events, a reliable prediction of breakwater damage due to wave attack ( see Tab. 2 for January 1987 and March 1988 storms ).

In 1988 the breakwater cover layer was repaired. During the first four months of 1989 the structure suffered only a slight damage. At the end of April 1989 the measured damage according to Van der Meer theory was equal to 2.5.

To test the capability of computer program in reproducing damage evolution, wave data of January-April 1989 were inserted as input. The test result was completely satisfactory since the final predicted damage was very close to the measured damage (Fig. 3).

A lengthy duration test was made inserting recorded wave data from July 1990 till June 1992. Also for the two year period the predicted damage was very closed to the measured damage (Fig. 4).

A continuous description of damage level evolution, based on Van der Meer's theory, then seems possible with satisfactory approximation. Nevertheless, some indetermination remains in estimation of wave parameter at shallow water depth, although the site measurements and wave data were carefully analysed.

### Conclusion

Photographic and topographic surveying have been applied for monitoring the stability of a rubble mound breakwater. Reliable estimation of cover blocks displacements can be obtained using non metric camera and direct linear transform method of analysis.

The use of a metric camera and digital photogrammetric workstation has allowed a high degree of accuracy.

A comparison between in site measured and predicted damage for a prototype breakwater has been made applying four different theories. A mathematical model for continuous damage description, based on Van der Meer stability analysis, has been calibrated with in site measured data.

This model describes superimposition of different sea states and evaluates the damage starting from different structure conditions. Predicted damage with stability model has been satisfactory also for very long simulation period.

A knowledge of the response of the structure for a real or project sequence of sea states can be helpful in programming maintenance or to decide if damage attained can be critical for the whole stability of the structure.

### LIST OF SYMBOLS

d	= Van der Meer damage level
D	= median diameter of stones of armour layer
D%	= Sawaragi damage index
Esumj	= Energy sum of grouped waves
H	= wave height
Hs	= significant wave height
I	= Iribarren number
Ic	= transition Iribarren number
Ib	= Iribarren number for breaking condition
Iz	= Iribarren number using Rice average wave period and Hs
la	= average dimension of armour stone
m <sub>n</sub>	= spectral moment of n order
n	= number of waves
Qp	= Goda spectral peakedness parameter
p	= Van der Meer permeability parameter
P	= weight of stable stone
S	= specific gravity of armour rock ( $\gamma / \gamma_a$ )
Tm	= average wave period ( $\sqrt{m_0 / m_2}$ )
$\alpha$	= angle of seaward slope of the structure
$\gamma$	= specific weight of stone
$\gamma_a$	= specific weight of water
$\phi$	= natural angle of repose of stone
$\Delta$	= relative mass density (S - 1)

MONTALTO DI CASTRO - WAVE DATA 1987

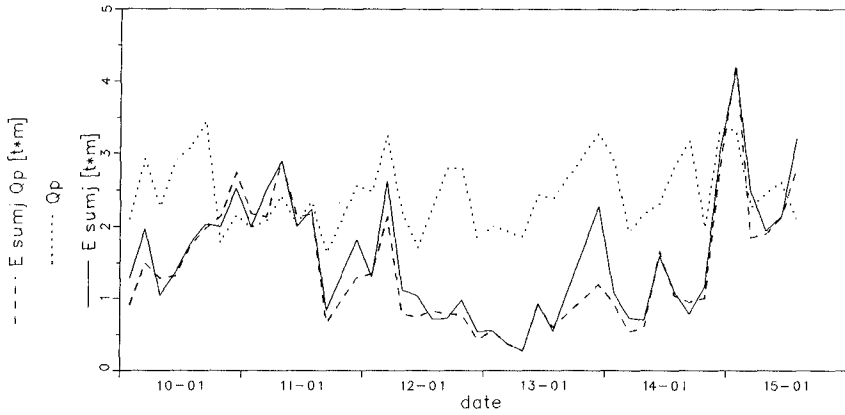


Fig. 1 - Comparison between energy sum of grouped waves calculated from Qp (Esumj(Qp)) and measured by waverider record(Esumj)

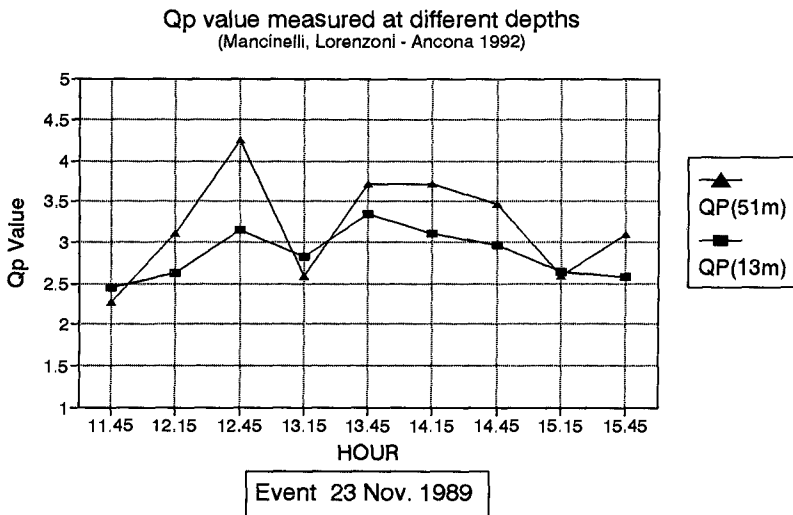


Fig. 2 - Range of Qp variability at different depths.

MONTALTO – JAN. APRIL 89 – MEASURED AND PREDICTED DAMAGES

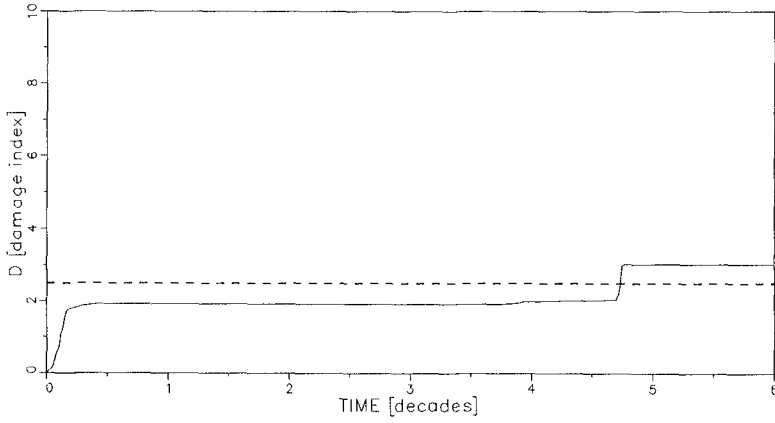


Fig. 3 - Damage index evolution (period January–April 1992).

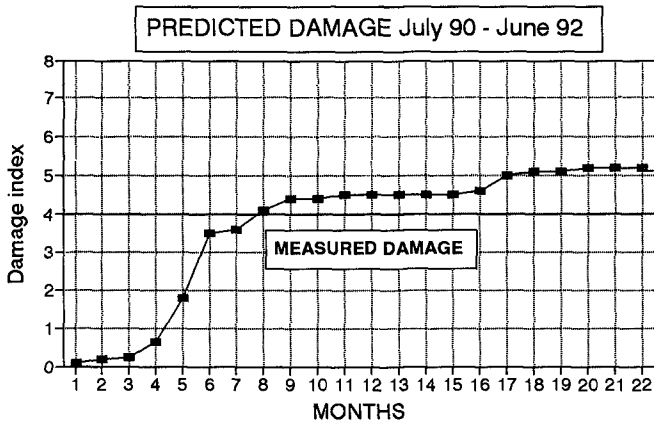


Fig. 4 - Damage index evolution ( July 1990 - June 1992 ).



REFERENCES

- Abdel-Aziz Y.L. and Karara H.M., 1971 "Direct Linear Transformation from Comparator Coordinates into Object-space Coordinates". In: Close Range Photogrammetry, American Society of Photogrammetry, Falls Church, Virginia.
- Abdel-Aziz Y.L. and Karara H.M., 1974 "Photogrammetric Potentials of Non-metric Cameras". In: Civil Engineering Studies, Photogrammetry Series n. 36, University of Illinois, Urbana.
- Ackers P., Pitt J.D., 1983 "Field scale studies of riprap", Proc. ICE Conf. on Breakwater, London.
- Bradbury A.P., Lotman J.P., Allsoy N., 1990 "Rock armour stability formulae - Influence of stone shape and layer thickness" Proc. 22th Coast. Eng. Conf., Malaga
- Bruun P., 1985 "Design and construction of mounds for breakwater and coastal protection", Developments in Geotechnical Engineering, 37, Elsevier, Amsterdam.
- Bruun P., Gunbak A.R., 1978 "Stability of sloping structures in relation to the  $\xi$  criteria in design", Coast. Eng., Vol. II, Elsevier.
- CETN-III-21, 1984 "Monitoring Rubble-mound Coastal Structures with Photogrammetry", U.S. Army Engineering Waterways Experiment Station, Coastal Eng. Res. Center, Vicksburg, MS.
- Gebert J., Clausner V., 1984 "Photogrammetric monitoring of dolos stability, Manasquan inlet, New Jersey", Proc. 19th Coast. Eng. Conf., Houston.
- Goda Y., 1975 "Irregular wave deformation in the surf zone", Coast. Eng. in Japan, Vol. 18.
- Goda Y., 1985 "Random seas and design of maritime structures", University of Tokyo Press.
- Hudson R.Y., 1959 "Design of Quarry-Stone Cover Layers for Rubble-mound Breakwaters", U.S. Waterways Experiment Station, Miscellaneous Paper n. 2-296, Vicksburg, Mississippi.
- Kluger J.W., 1982 "The monitoring of rubble-mound breakwater stability using a photographic survey method". 18th Conf. on Coast. Eng., Cape town.
- Losada M.A., Gimenez-Curto L.A., 1980, "Mound breakwater under wave attack", Dept. Ocean Eng., University of Santander, Rep. SR 1-80.
- Mancinelli A., Lorenzoni C., 1992 " Verifiche sperimentali sulla trasformazione di onde di mare in profondità finita " XXIII Convegno di Idraulica e Costruzioni Idrauliche, Firenze.
- Mansard E.P.D., Funke E.R., Readshaw J.S., Girard R.K., 1988 "On the transformation of wave statistics due to shoaling", 21st Coastal Eng. Conf., Malaga.
- Mansard E.P.D., 1988 "Toward a better simulation of sea states for modelling of coastal structures", Proc. Berm Breakwater ASCE Spec. Conf., Canada.

- Mansard E.P.D., Funke E.R., 1987 "Experimental and analytical techniques in wave dynamics - A comparative study", IAHR Seminar on Wave Analysis and Generation in Laboratory Basins, Lausanne.
- Marzan G.T. and Karara H.M., 1975 "A Computer Program for the Direct Linear Transformation Solution of the Collinearity Condition and some applications of it". In: Close-range Photogrammetric Systems, American Society of Photogrammetry, Falls Church, Virginia.
- Muraca A., 1989 "Field scale analysis of wave action on breakwater", Proc. XXIII Congress IAHR, Ottawa.
- Nelson R.C., Treolar P.D., Lawson N.U., 1988 "The Dependency of inshore long waves on the characteristic of offshore short waves", *Coast. Eng.*, Elsevier, Vol. 12.
- Pope J.M., Clarke D., 1983 "Monitoring of a dolos armour cover, Cleveland", *Coast. Structure* 83, Spec. ASCE Conf.
- Rebaudengo Landò L., Scarsi G., Taramasso A. C., 1992 " The transfer of the Donelan et al. spectrum in shoaling water " Proc. Computer Modelling of Seas and Coastal Regions, CMP Press.
- Rye H., 1982 " Ocean Wave Groups ", Report UR-82-18 , Dep. Marine Tech., Un. Trondheim.
- Ryu C., Sawaragi T., 1986 "A new design method of rubble mound structures", Proc. 20th Coast. Eng. Conf., Taiwan.
- Sawaragi T., Ryu C., 1983 "Consideration of the destruction mechanism of rubble mound breakwaters due to resonance phenomenon", Proceeding 8th Int. Harb.
- Sawaragi T., Ryu C., Kusumi M., 1985 "Destruction mechanism and design of rubble mounds structures by irregular waves", *Coast. Eng. in Japan*, Vol. 28.
- Tayfun M.A., 1981 "Distribution of crest-to-trough wave heights", *Journal Wat. Harb. Div.*, ASCE.
- Van der Meer J.W., 1987 "Stability of breakwater armour layer design formulae", Seminar on Unconventional Rubble-Mound Breakwaters, Ottawa, Canada.
- Van der Meer J.W., 1988 "Deterministic and probabilistic design of breakwater armour unit", *Journal Wat. Port. Coast. Eng. Div. ASCE*, Vol. 114, n. 1.
- Van der Meer J.W., 1988 "Rock Slopes and Gravel Beaches under Wave Attack", *Delft Hydraulics Communication* n. 396.
- Van der Meer J.W., 1991 " Stability and transmission at low-crested structures " *Delft Hydraulics Communication* n. 453.

# CHAPTER 110

## Wave Energy Dissipation on and in Rubble Mound Structures

M. Muttray<sup>1)</sup>, H. Oumeraci<sup>2)</sup>, C. Zimmermann<sup>3)</sup>, H. W. Partenscky<sup>4)</sup>  
University of Hannover, SFB 205, Franzius-Institut, Hannover/ Germany

### Abstract

The results of large-scale model tests are presented on the wave energy dissipation in the various layers of an Accropode armoured mound breakwater and on the interaction between external and internal wave motion. An attempt is also made to describe the "discontinuity" of the waterline at the boundary between layers of different porous materials. Wave reflection coefficients of the structure as well as dissipation and transmission coefficients through the different layers are evaluated as a function of the incident wave parameters.

### Introduction

In a previous paper it was shown that a) an improvement of the evaluation of the reflected wave energy is required as it represents an important portion of the incident wave energy, b) most of the incident wave energy is dissipated within the armour and underlayer and that a better description of the wave-induced flow in these regions is needed and (c) a good knowledge of the external flow and its interaction with the internal flow is needed as this represents a prerequisite for the development of a mathematical/numerical model for the internal flow field (OUMERACI & PARTENSCKY, 1990).

In this respect, further large-scale model tests have been performed in the Large Wave Flume (GWK), Hannover. The main objectives of these tests consist in the study of a) the interaction of the external and internal wave motion and b) the energy dissipation within the various layers of the structure, especially that dissipated in the first layers (high turbulent flow).

The present paper principally intends to present and discuss the first results of these tests which will certainly have some implications for the simulation of the wave-induced flow on and in rubble mound structures by using small-scale model tests and mathematical/numerical models (WIBBELER & OUMERACI, 1992).

### Experimental Set-up and Test Conditions

The experimental set-up in the Large Wave Flume (GWK) of Hannover is given in Fig. 1, showing

---

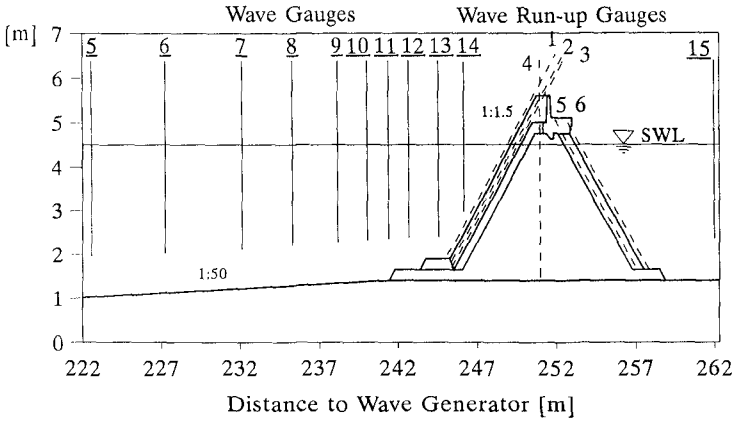
<sup>1)</sup> Dipl.-Ing., Research Engineer, SFB 205

<sup>2)</sup> Dr.-Ing., Senior Researcher, SFB 205

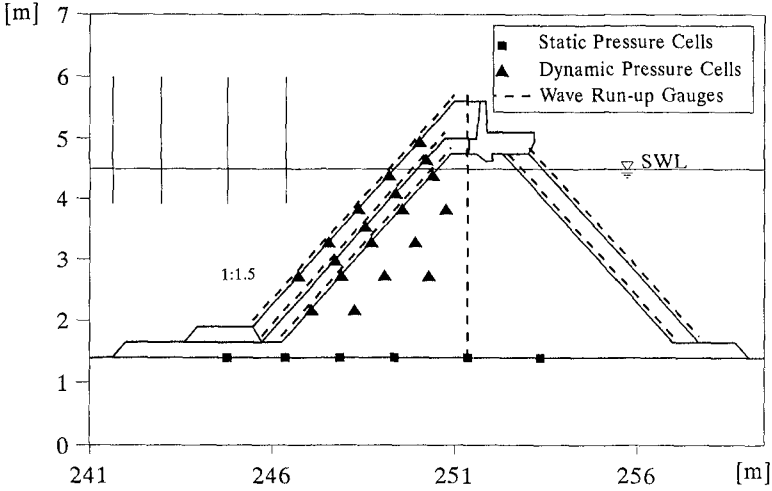
<sup>3)</sup> Prof. Dr.-Ing., Managing Director Franzius-Institut

<sup>4)</sup> Prof. Dr.-Ing. Dr.-Phys., formerly Managing Director Franzius-Institut

- a) the cross-section of the model with the position of the pressure and "wave run up" gauges on and within the structure and
- b) the location of the wave gauges in front of and behind the structure.



a) Location of Wave Gauges



b) Location of Pressure Cells and 'Wave Run-up' Gauges

FIG. 1-EXPERIMENTAL SET-UP IN THE LARGE WAVE FLUME (GWK)

Four wave gauges in deeper water are used to determine the incident and reflected wave by using the 3-wave-gauge-procedure (MANSARD & FUNKE, 1987). Ten wave gauges on the foreshore are installed to analyse the wave field in front of the structure. The positions of these gauges are shown in Fig. 1a.

A cross section of the breakwater model with the position of the pressure cells and the wave run-up gauges is shown in Fig. 1b. Six wave run-up gauges and six static pressure cells were used to record the surface elevation on and in the structure. In order to measure the pressure variation in the most turbulent zone, 19 dynamic pressure cells were placed within the first layers of the structure.

The mean grain size of the core material (crushed stones) is  $d_{50}=4\text{cm}$  and the uniformity coefficient  $U=d_{60}/d_{10}=2.2$ . The underlayer is made of crushed stone of 0.5-5.0 kg ( $d_{50}=12\text{ cm}$ ), whereas the armour is composed of a single layer of 40kg Accropodes.

Regular waves with heights  $H=0.20\text{-}1.80\text{m}$  and periods  $T=3.0\text{-}12.0\text{s}$ , and irregular waves (TMA Spectra) with significant heights  $H_s=0.20\text{-}1.20\text{ m}$  and peak periods  $T_p=3.0\text{-}12.0\text{s}$  were used. Most of the wave spectra had a groupiness factor  $GF=0.77$ . However, some tests were carried out with groupiness factors  $GF=0.6\text{-}0.9$  in order to examine the effect of the groupiness factor on the results. The water depths in the wave flume was varied from  $d=4.20\text{m}$  to  $d=4.80\text{m}$ .

In the results presented below only non-overtopping test conditions are considered, i.e. regular waves with  $H=0.20\text{-}0.85\text{m}$  and  $T=3.0\text{-}12.0\text{s}$  and irregular waves with  $H_s=0.20\text{-}0.70\text{m}$  and  $T_p=3.0\text{-}12.0\text{s}$

For the conditions tested, REYNOLDS numbers (related to the grain size of the core material) in the range of  $10^5$  to  $10^6$  are expected within the core material; i.e. no scale effects due to the dissimilarity of viscous forces will occur.

## Discussion of Experimental Results

### **General Considerations**

As already mentioned, only tests with non-overtopping wave conditions are considered. In addition, no wave breaking occurs in front of the structure. In this case, the incident wave energy is splitted up into reflected, dissipated and transmitted wave energy.

$$E_i = E_r + E_d + E_t \quad (1)$$

The wave reflection coefficient ( $K_r$ ), the dissipation coefficient ( $K_d$ ) and the transmission coefficient ( $K_t$ ) are correlated by the relationship:

$$K_r^2 + K_d^2 + K_t^2 = 1 \quad (2)$$

$$\text{with } K_r = \sqrt{\frac{E_r}{E_i}}, \quad K_d = \sqrt{\frac{E_d}{E_i}} \quad \text{and} \quad K_t = \sqrt{\frac{E_t}{E_i}}$$

and where  $E_i$ ,  $E_r$ ,  $E_d$  and  $E_t$  are the incident, reflected, dissipated and transmitted (through the structure) wave energy components, respectively. Each of these energy components is considered to be expressed by the corresponding wave height squared ( $E_i \sim H_i^2$ ). The total dissipated wave energy  $E_d$  may be divided into the dissipated energy component on and in the armour layer ( $E_{da}$ ), on and in the underlayer ( $E_{du}$ ) and in the core ( $E_{dc}$ ),

$$E_d = E_{da} + E_{du} + E_{dc} \tag{3}$$

so that the following relationship for the corresponding local dissipation coefficients will result:

$$K_{da}^2 + K_{du}^2 + K_{dc}^2 = 1 \tag{4}$$

with  $K_{da} = \sqrt{\frac{E_{da}}{E_d}}$  ,  $K_{du} = \sqrt{\frac{E_{du}}{E_d}}$  and  $K_{dc} = \sqrt{\frac{E_{dc}}{E_d}}$

Eqs. (2) & (4) build the principal basis for the analysis and discussion of the experimental results . The porous structure and its geometry being given, the quantities involved in Eqs. (2) & (4) are determined by the prevailing water depth and incident wave parameters. The relative water depth ( $d/L$ ) and the wave steepness are expected to be the most relevant influencing parameters, since they strongly affect the shapes and kinematics of the waves at the structure. Since the latter are commonly described by the surf similarity parameter, its application to characterise the prevailing breaker types in the case of relatively high reflection coefficients and high velocity currents during the wave run down process on steep slopes is briefly discussed.

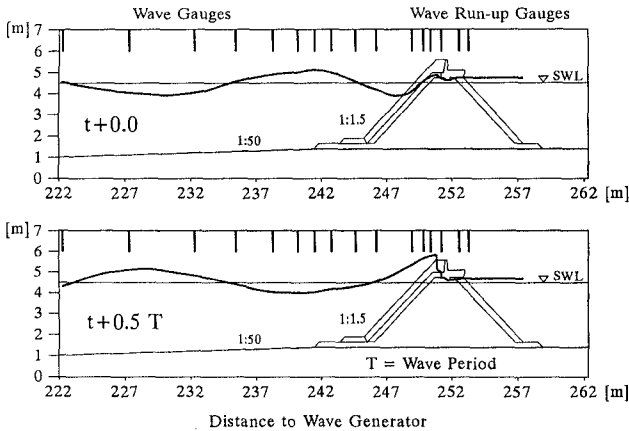


FIG.2 WAVE MOTION OUTSIDE AND INSIDE THE BREAKWATER

### Interaction Between External and Internal Wave Motion

Based on the wave motion simultaneously recorded at wave gauges 5-14 (Fig.1a) and "run-up gauges" 1-6 (Fig.1b), a detailed description of the external wave motion and the wave motion in the different layers of the breakwater is given, illustrating how the internal and external flow field influence each other.

The wave motion in front of the structure is described by using video records and the wave gauges located in that area. These records are intended to be used for the description of the breaker types, the volume and the velocity of the waves.

An example of the temporal variation of the surface elevation outside and inside the breakwater is shown in Fig.2 for an incident wave period  $T=4.5s$ , a wave height  $H=0.82m$  and a water depth  $d=4.50 m$ .

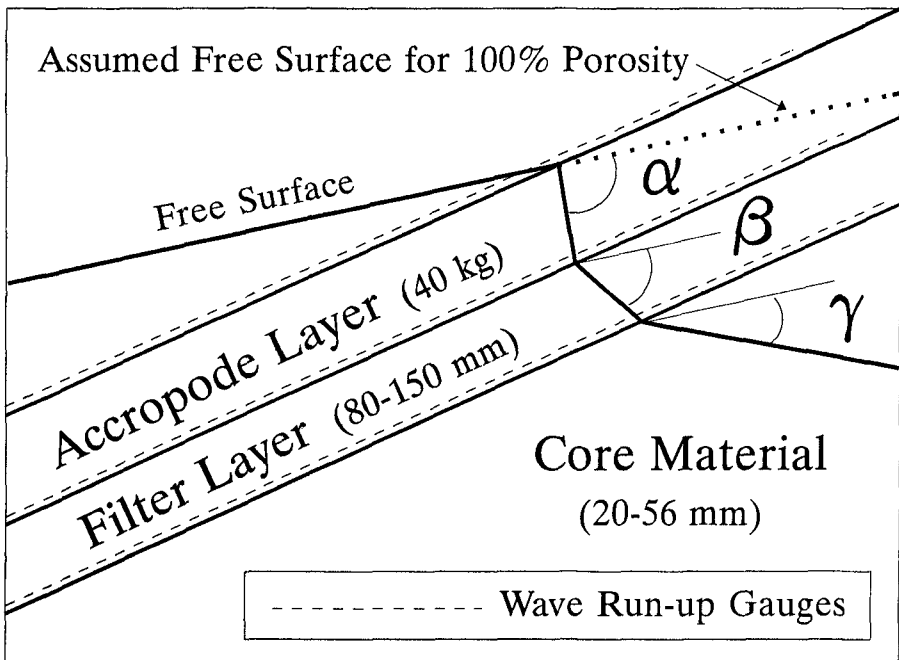


FIG.3 PRINCIPLE SKETCH FOR DISCONTINUITY ANALYSIS

An attempt is made below to partially describe the "discontinuity" of the waterline at the boundary between two layers of different porous materials. A

discontinuity of the waterline is generally expected at the boundary of two layers with different hydraulic resistance. Even by using the wave run-up gauges as shown in Fig.1b this discontinuity can not be described accurately. Despite the limitations resulting from this measurement procedure, an attempt is made to get an approximate description of the waterline within the first layers during the wave run-up and run-down process. For this purpose three angles  $\alpha$ ,  $\beta$ ,  $\gamma$  are defined in Fig.3. The definition of these angles is based on the assumption, that the free surface at the outer slope would continue to be represented by a *straight line* if the first layers had 100% porosity and no hydraulic resistance. It is therefore suggested that the deviation of the waterline from its straight course is caused by the relative difference in hydraulic resistance between two successive layers. Angles  $\alpha$ ,  $\beta$  and  $\gamma$  describe this deviation at the boundaries between the outer slope (Accropode layer), filter layer and core material, respectively. It is suggested that the analysis of the relationship between these angles and the wave parameters should lead to an approximate description of the discontinuity of the waterline at the boundary between two adjacent layers.

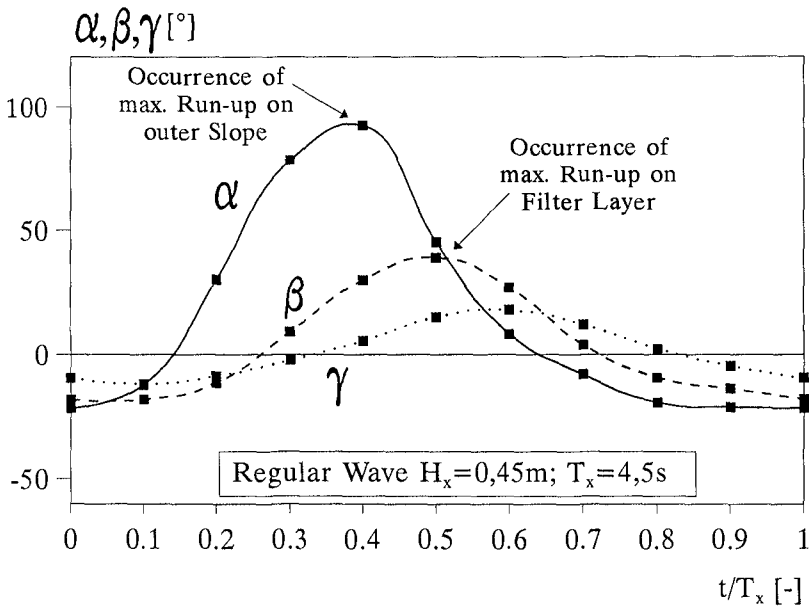


FIG.4 TEMPORAL RELATIVE VARIATION OF ANGELS  $\alpha$ ,  $\beta$  AND  $\gamma$

The temporal relative variation of the three angles  $\alpha$ ,  $\beta$  and  $\gamma$  during one wave period starting with the wave run-down at its lowest elevation is shown in Fig.4. Angle  $\alpha$  reaches a maximum at the highest run-up on the armour layer,  $\beta$  and  $\gamma$  at the highest run-up on the underlayer and on the core material, respectively. It is seen



that the maximum value of angle  $\gamma$  occurs later than that of angle  $\beta$  and that the occurrence of the maximum value of angle  $\beta$  is much more delayed as compared to that of angle  $\alpha$ .

In addition, it is found that the variation of  $\alpha$ ,  $\beta$  and  $\gamma$  strongly depends on the wave height. This is shown by Fig.5 illustrating the increase of angle  $\alpha$  with incident regular wave heights. This increase was expected, since angle  $\alpha$  was supposed to describe the hydraulic resistance of the Accropode layer and thus represents a measure of the hydraulic loss (dissipated energy). The same trend is also found for angles  $\beta$  and  $\gamma$ , but the effect of the wave height is less pronounced than for angle  $\alpha$ .

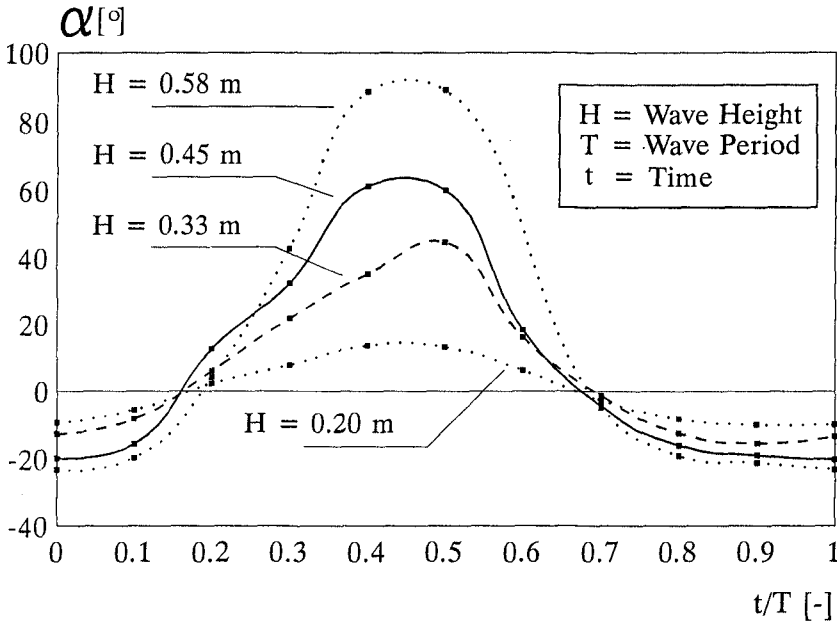


FIG.5 EFFECT OF WAVE HEIGHTS ON ANGLE  $\alpha$

### Wave Reflection Coefficients

The separation of induced and reflected wave components from the measured partial standing wave system taking place in front of a sloping porous structure still represents one of the most difficult tasks in hydraulic model tests. In Fig.6, the partial standing wave in front of the structure is shown for different wave conditions.

Due to non-linearities, cross-wave phenomena and measurement inaccuracy, simultaneous wave records at more than two different locations in the wave flume (in the direction of wave propagation) is required. Therefore, four wave gauges with different spacing in front of the structure are used. Depending on the prevailing wave periods, three wave probes are optimally selected for the reflection analysis. Details of the reflection analysis used in this study are given by MANSARD & FUNKE (1987).

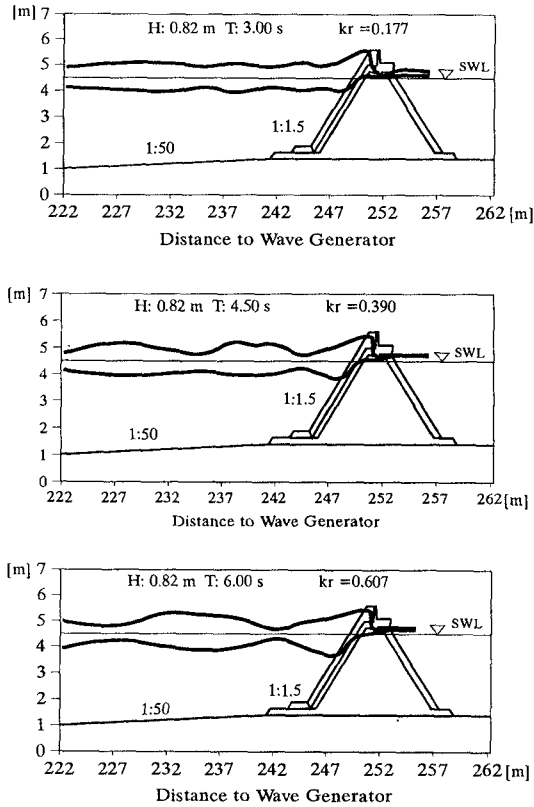


FIG. 6 PARTIAL STANDING WAVE IN FRONT OF THE BREAKWATER

Reflection coefficients  $K_r$  are determined as a function of relative depth  $kd$  ( $k=2\pi/L$ ), wave period  $T$ , wave height  $H$ , wave steepness  $H/L$  and onshore surf similarity parameter  $\xi$  ( $= \tan \alpha / (H/L)^{0.5}$ ).

Fig.7 shows the relationship between wave period and reflection coefficient  $K_r$ , which is stronger for irregular waves than for monochromatic waves. The wave periods on the x-axis refer to prototype conditions in which  $H_s=1.60-6.60\text{m}$  and  $H/L=.005-0.063$  were considered for this figure. For large values of the wave period, reflection coefficients of more than 50% may result and the reflection coefficient for regular waves is about up to 10% larger than for irregular waves.

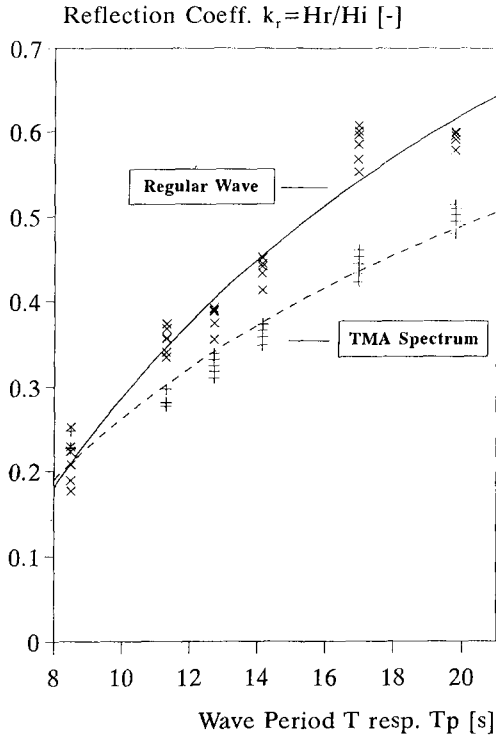


FIG. 7 REFLECTION COEFFICIENT VS. WAVE PERIOD

The reflection coefficient for Accropode armour is also found to be nearly the same as for Tetrapod armour (Fig.8). The large scatter shown in Fig.8 also indicates that the surf similarity parameter does not represent an optimal mean for the description of the reflection process.

**Dissipation and Transmission Coefficients**

Wave-induced pressures have also been measured along the outer slope (seaward), so that the inflow boundary conditions may be described by both pressure (dynamic) and surface elevation (static).

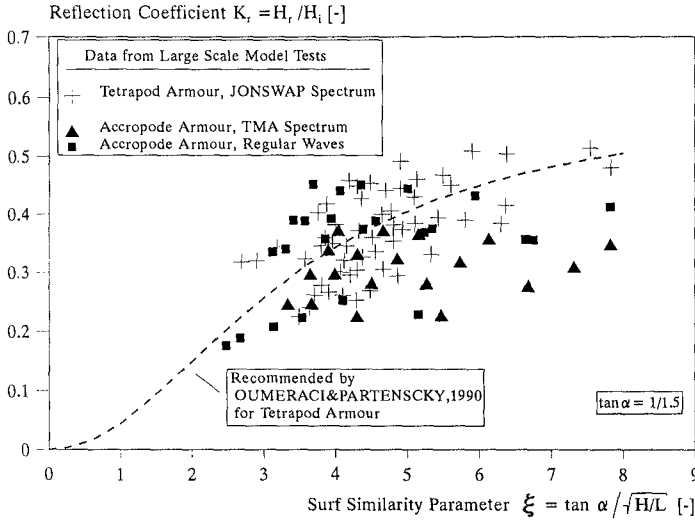


FIG. 8 REFLECTION COEFFICIENT VS. SURF SIMILARITY PARAMETER

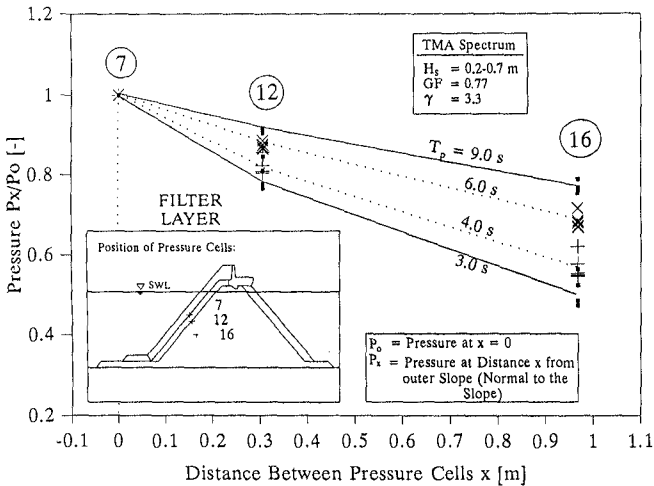


FIG. 9 PRESSURE DISSIPATION WITHIN THE FIRST LAYERS (LOWER ELEVATION, FAR FROM SWL)

The damping rates of the wave-induced pressure in a direction normal to the outer slope is plotted for different wave parameters. The related pressure gradients are evaluated as a function of the wave height, wave period and wave steepness.

Fig.9 illustrates for instance how the dynamic pressures are damped along the line through the locations of the pressure cells 7, 12 and 16. The pressure dissipation in the underlayer is a little higher than that inside the core. The damping rate is related to the wave period. At shorter wave periods ( $T=3.0$  s), the damping in the first layer is about 2.5 times higher than at longer periods ( $T=9.0$  s). Inside the core, however, it is only about 1.75 times higher. Comparing the damping along the line through the pressure gauges 8, 13, 17 and 19 (Fig.10) and along the line through the gauges 7, 12 and 16 (Fig.9) it can be seen that there is a slight increase of the damping rate for all wave conditions when the location of the line considered becomes closer to still water level (turbulent zone).

By considering a direction normal to the outer slope, the pressure gradients within the armour layers may reach values which are more than twice of those in the underlayer and more than four times of those in the first layers of the core material.

By assuming that the wave energy is proportional to the squared wave height ( $E \sim H^2$ ), the reflected, dissipated and transmitted wave energy components are analysed according to Eqs.(1)&(3) and as a function of the incident wave parameters. For this analysis the data recorded by wave gauges and wave run-up gauges has been used.

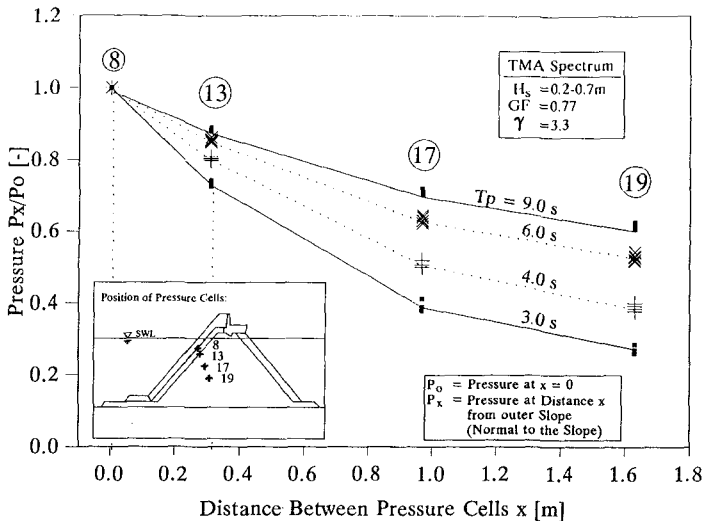


FIG.10 PRESSURE DISSIPATION WITHIN THE FIRST LAYERS (HIGHER ELEVATION, CLOSE TO SWL)

For instance, the results in Fig.11 illustrate the variation of the various energy components as a function of the wave period  $T_p$  for irregular waves with significant wave heights  $H_s=0.2-0.7m$ . The wave parameters in Fig.11 correspond to wave conditions in the Large Wave Flume (GWK). As expected, the reflected and transmitted part of the wave energy increases with increasing wave period while the dissipated energy decreases. In order to better examine the variation of the different components of the dissipated energy described by Eq.(3), Fig.12 has been prepared. It shows in more detail the variation of the dissipated energy in the armour layer, in the filter layer and in the core material as a function of wave period  $T_p$  and for the same wave conditions as in Fig.11. It is seen that the effect of the wave period on the wave energy dissipation is stronger in the outer layers and that in the core material almost no effect can be identified.

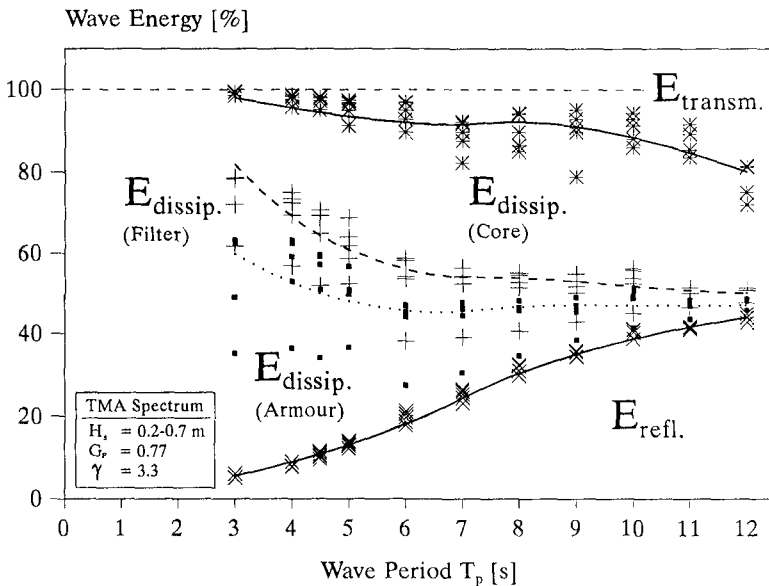


FIG. 11 WAVE ENERGY COMPONENTS VS. WAVE PERIOD

**Concluding Remarks**

The knowledge of reflected waves is determinant for the evaluation of the further dissipated and transmitted wave energy components. Therefore, particular attention has been devoted to the separation of the reflected waves from the measured partial standing wave system. This problem is, however, not definitely solved and the evaluation of reflected waves still remains an estimate.

A further topic which has been particularly dealt with, is the interaction of the wave motion outside the structure and the internal wave-motion. The results which have been reached so far, are expected to contribute to the better understanding of

the coupling mechanisms between external and internal flow which can generally not be satisfactorily described by small-scale model simulation and by existing numerical codes (WIBBELER & OUMERACI, 1992).

The attenuation of wave height and wave-induced pressure in the direction of wave propagation inside the structure is very fast within the first layers. The rate of attenuation tends to strongly increase with increasing wave height.

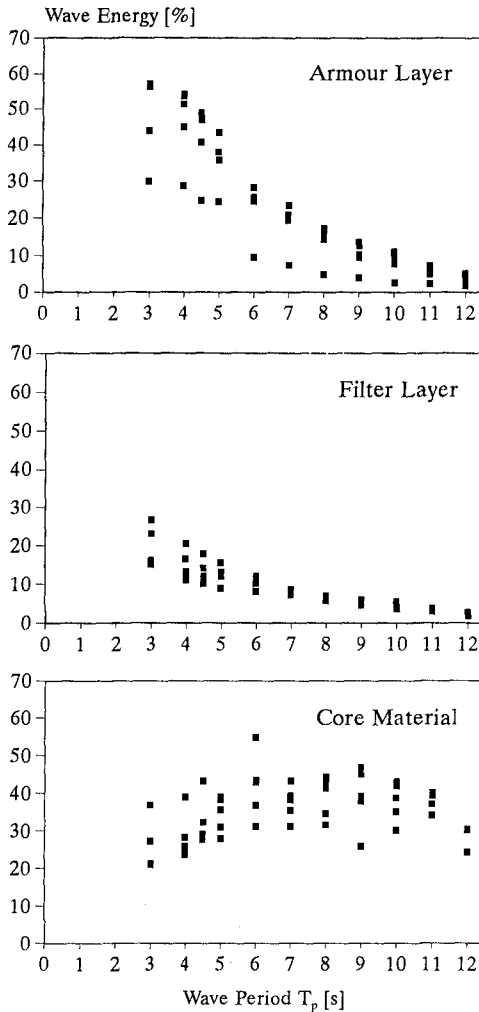


FIG. 12 WAVE ENERGY DISSIPATION IN DIFFERENT LAYERS VS. WAVE PERIOD

As expected, less wave energy is dissipated by a single armour layer (Accropodes) than by a double armour layer (Tetrapods). Consequently, more wave energy has to be dissipated within the underlayer of the Accropode armour than within the underlayer of the Tetrapod armour; i.e. particular effort should be devoted to the design of the underlayer when a single armour layer is used.

It is hoped that the results presented in this paper will eventually contribute :

- (a) to get a better insight into the geohydrodynamic processes affecting the overall stability of the structure as well as the stability of the armour units and further structure components;
- (b) to improve the description of the wave-induced flow on and in the structure and thus to evaluate properly the actual forces on the armour units and further elements of the structures;
- (c) to improve the commonly used simulation tools (small-scale models and numerical codes) by providing reliable data for their validation.

Further research is directed to developing a theoretical method for the approximate evaluation of the dissipated wave energy components in the structure as a function of the wave parameters and the hydraulic properties of the porous media.

### **Acknowledgements**

This study is supported by the German Research Council (DFG), Bonn. It is part of a research programme on breakwaters within the Coastal Engineering Research Unit (SFB 205) at the University of Hannover, Germany.

### **References**

- MANSARD, E.P.D.; FUNKE, E.R.: On the Reflection Analysis of Irregular Waves, National Research Council Canada, Hydr. Labor., Techn. Rep. TR.-HY 011, Ottawa, Canada, 1987.
- OUMERACI, H.; PARTENSCKY, H.W.: Wave-Induced Pore Pressure in Rubble Mound Breakwaters. ASCE, 22nd ICCE'90, Delft, The Netherlands, 1990.
- WIBBELER, H.; OUMERACI, H.: Finite Element Simulation of Wave-Induced Internal Flow in Rubble Mound Structures. ASCE, submitted to 23rd ICCE'92, Venice, Italy 1992.



## CHAPTER 111

### Armour Displacements on Reshaping Breakwaters

P.A. Norton<sup>1</sup> and P. Holmes<sup>2</sup>

#### Abstract

A computer simulation model for the reshaping of dynamically stable breakwaters under normally incident, monochromatic waves has been developed. The proposed model is used to simulate initial reshaping as well as transport on the developed profile. Preliminary validation of the model has been carried out by comparison with data obtained from experimental tests on a berm breakwater.

#### Introduction

The concept of reshaping breakwaters has recently received a significant amount of attention although such structures have been in existence for many years. Potential design problems associated with reshaping breakwaters concern the extent of initial profile reshaping and the implications of rock degradation on overall structural integrity. Rock durability has been the subject of a number of investigations including the work of Latham (1988) and more recently Magoon (1992) although there is no model relating incident wave conditions to stone mobility on the seaward slope.

Van der Meer (1990) developed a computational model, based on empirical equations, which can be used to

---

<sup>1</sup> Researcher,

<sup>2</sup> Professor of Hydraulics,

Dept. of Civil Eng., Imperial College, South Kensington,  
London, SW7 2BU, UK.

predict profile changes. The need for more detailed information, without physical model testing, has led to the development of a numerical model which includes some representation of individual elements of the structure.

A reshaping simulation model has been developed by combining a numerical description of both wave loading and the particulate structure of a breakwater armour layer. A one-dimensional model is used to describe wave-induced velocities on the seaward slope. Rock armour units within the armour layer are represented by equivalent spherical particles. A force model is used to assess armour stability and initiate displacements on the slope. With a good calibration procedure it is possible to simulate rock displacements resulting from exposure to given wave conditions.

### Particulate Structure

The armour layer of a breakwater is numerically represented by a random assembly of spherical particles. From a specified grading curve for the rock material, the equivalent spherical diameter is calculated for each stone class. The proportion of each size of spheres is also determined followed by random selection and finally placement within the packing volume. The structure is built-up in a series of horizontal layers of variable thickness to form the required initial profile.

Placement involves a vertical drop, from an appropriate location in the horizontal plane, followed by a rolling sequence until a statically stable position of minimum energy is found. If necessary, it is possible to achieve increased packing density by using a more selective placement procedure. For static stability, the centre of gravity of the object sphere must lie within the triangle formed by the three contact points in the horizontal plane. The following geometric equations must be simultaneously satisfied for the object sphere to be in contact with three supporting spheres,

$$(x_0 - x_1)^2 + (y_0 - y_1)^2 + (z_0 - z_1)^2 = (r_0 + r_1)^2 \quad (1)$$

$$(x_0 - x_2)^2 + (y_0 - y_2)^2 + (z_0 - z_2)^2 = (r_0 + r_2)^2 \quad (2)$$

$$(x_0 - x_3)^2 + (y_0 - y_3)^2 + (z_0 - z_3)^2 = (r_0 + r_3)^2 \quad (3)$$

in which  $x$ ,  $y$  and  $z$  are the co-ordinates of the sphere centre,  $r$  is the radius and the subscript 0 indicates the object sphere whilst the subscripts 1, 2, 3 identify the three supporting spheres. Longitudinal and transverse

sections through the numerically constructed armour layer of the berm breakwater are illustrated in figure 1. There are approximately 3000 spherical particles in total. The transverse section shows the structure width to be 0.3m (or  $9D_{n50}$  where  $D_{n50} = (M_{50}/\rho_s)^{1/3}$  in which  $M_{50}$  is the average stone mass and  $\rho_s$  is the mass density of the stone) which is sufficient to minimize the influence of the side-wall boundaries. Above the berm it can be seen that there are two layers of spheres which correspond to two layers of rock in the physical model. This layer is extended beyond the crest level of the physical model as the numerical wave model is not able to simulate overtopping by waves.

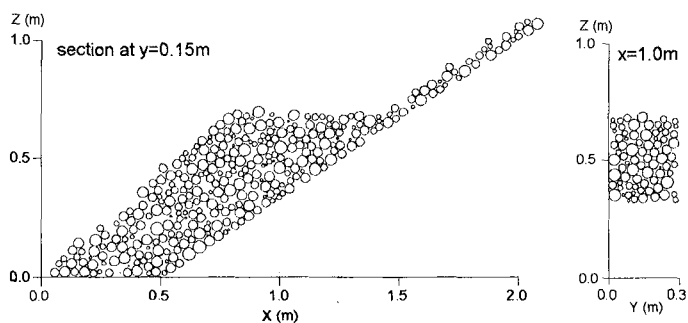


Figure 1. Numerically Constructed Armour Layer

### Wave Loading

A mathematical wave model is used to calculate the water particle velocities and accelerations on the seaward slope. Figure 2 provides a definition sketch for the wave model.

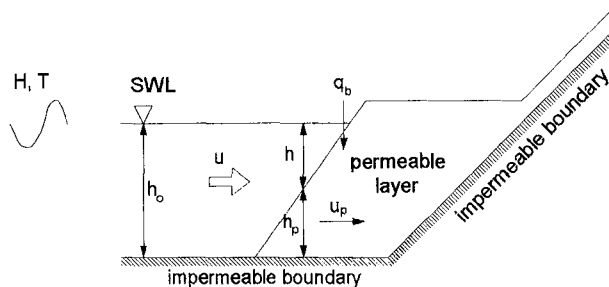


Figure 2. Definition Sketch

The governing differential equations, as derived by Kobayashi (1990), for the flow on and within a permeable slope are given for:

(i) external flow:

$$\frac{\partial h}{\partial t} + \frac{\partial(hu)}{\partial x} = -q_b \tag{4}$$

$$\frac{\partial(hu)}{\partial t} + \frac{\partial(hu^2)}{\partial x} = -gh \frac{\partial \eta}{\partial x} - \frac{1}{2} f_w u |u| - u_b q_b \tag{5}$$

in which  $h$  is the water depth,  $u$  is the depth-averaged velocity,  $g$  is gravitational acceleration,  $f_w$  is a wave friction factor,  $q_b$  is the discharge into permeable layer and  $u_b$  is the horizontal discharge velocity at interface

(ii) internal flow:

$$\frac{\partial(h_p u_p)}{\partial x} = q_b \tag{6}$$

$$\frac{\partial(h_p u_p)}{\partial t} + \frac{1}{n} \frac{\partial(hu_p^2)}{\partial x} - u_b q_b = -gnh_p \frac{\partial \eta}{\partial x} - gn h_p (a + b |u_p|) u_p \tag{7}$$

in which  $h_p$  is the depth of permeable layer,  $u_p$  is the discharge velocity in permeable layer,  $n$  is the porosity of armour layer,  $\nu$  is the kinematic viscosity of fluid and further:

$$a = \frac{\alpha(1-n)^3 \nu}{n^2 g D_{n50}} \quad b = \frac{\beta(1-n)}{n^3 g D_{n50}^2} \tag{8}$$

A preliminary verification of the permeable slope wave model has been carried out with velocity measurements on the seaward slope of a reshaped berm breakwater.

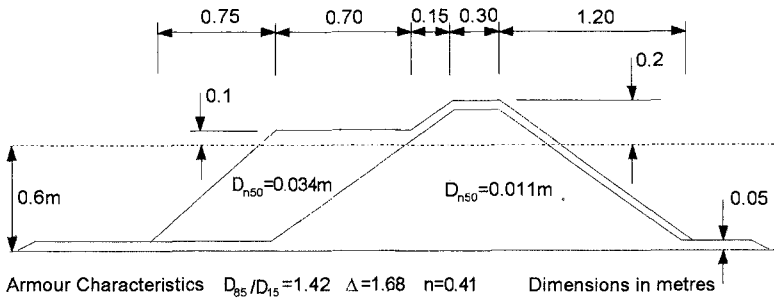


Figure 3. Model Berm Breakwater

The initial profile of the berm breakwater is illustrated in figure 3. The berm breakwater was reshaped using 4000 irregular waves from a Pierson-Moskowitz type spectrum with a significant wave height,  $H_s=0.180\text{m}$  and mean period,  $T_M=1.93\text{s}$ .

Maximum uprush (positive) and downrush (negative) velocities, measured using a MINILAB ultrasonic current meter, can be compared with calculated values in figure 4 for the specified regular wave conditions. The velocities are measured at mid-depth and the calculated values are depth-averaged values. Calculated maximum downrush velocities appear to be in relatively good agreement with measured values although the calculated velocities are consistently greater. There are more significant differences observed with the uprush velocities. The measured uprush velocities are much lower than expected and are not considered reliable due to poor performance of the current meter in highly aerated flows as observed during the uprush phase.

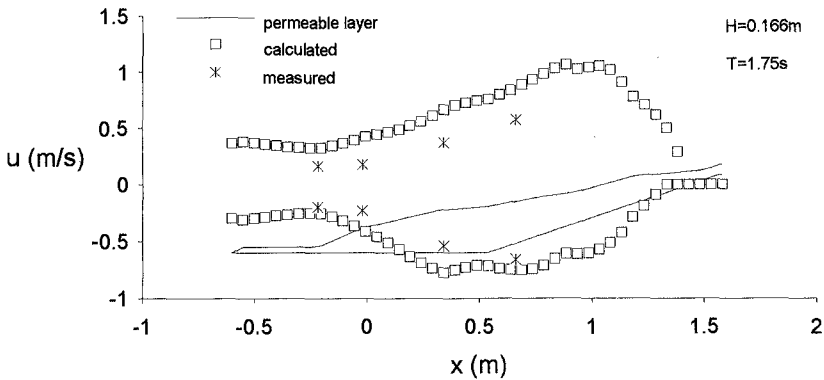


Figure 4. Measured and Calculated Maximum Velocities

The wave model requires the estimation of three input parameters which may be adjusted for calibration purposes. Some guidance for the selection of a suitable wave friction factor,  $f_w$  in equation 5, can be given by the formula developed by Madsen (1975) although a value of  $f_w=0.3$  was adopted after calibrating the model against observed maximum run-up levels. For the internal flow resistance, the laminar and turbulent flow coefficients,  $\alpha$  and  $\beta$  in equation 8, must be specified for the rock material. Values of  $\alpha=8000$  and  $\beta=2.4$  were selected based on the results of experimental investigations by Burcharth (1991).

Armour Initiation

To assess the stability of individual elements on the surface layer of the seaward slope, a failure mode must first be assumed. The most common displacement mechanism for single stones can be observed in the laboratory to be of a rotational nature. Den Breker (1985) found that almost 90% of rock armour displacements could be characterized by a rolling motion as opposed to sliding or lifting. For initiation it is thus appropriate to consider disturbing and restoring moments acting about a possible point or axis of rotation.

Disturbing forces resulting from the hydrodynamic wave loading are determined using a Morison-type equation including drag,  $F_D$ , inertia,  $F_I$ , and lift,  $F_L$ , force components given as:

$$F_D = 0.5\rho_w C_D (C_{SD} \frac{\pi}{4}) D^2 u |u| \tag{9}$$

$$F_I = \rho_w C_M (C_{SI} \frac{\pi}{6}) D^3 \frac{du}{dt} \tag{10}$$

$$F_L = 0.5\rho_w C_L (C_{SL} \frac{\pi}{4}) D^2 u^2 \tag{11}$$

in which  $\rho_w$  is the mass density of water and D is the particle diameter. The values selected for the force coefficients are based on the results obtained by Tørum with a drag coefficient,  $C_D=0.35$  and an inertia coefficient,  $C_M=0.20$ . For the lift coefficient,  $C_L=0.15$  is chosen although there is no guidance on suitable values. The resultant in-line force,  $F_x (=F_D+F_I)$ , is assumed to act through the centre of gravity of the projected area which is exposed to the surface flow. The vertical component of force,  $F_z (=F_L)$  perpendicular to the direction of the flow is assumed to act through the centre of gravity of the body.

The coefficients,  $C_{SD}$ ,  $C_S$  and  $C_{SL}$  are included to take into account the influence of partial submergence which may be necessary for particle locations between the maximum run-up and run-down levels. The submergence coefficients,  $C_{SD}$  and  $C_{SL}$  represent the reduction in projected area in the vertical and horizontal planes respectively, whilst  $C_S$  is associated with the reduced volume.

In addition to the hydrodynamic loading, the buoyancy force resulting from the displaced fluid must also be considered. The buoyancy force,  $F_B$ , acts through

the centre of gravity of the body in a direction perpendicular to gradient of the local, instantaneous free-surface as previously considered by Brandtzaeg (1966). The magnitude of the force can be calculated using the following expression:

$$F_B = \rho_w g (C_{SI} \frac{\pi}{6}) D^3 \quad (12)$$

The buoyancy force is separated from the particle weight as information concerning the gradient of the free surface is available from the wave model. The force is normally assumed to act vertically upwards. Restoring forces resisting movement comprise of the weight of the body:

$$W = \rho_s g \frac{\pi}{6} D^3 \quad (13)$$

as well as friction and interlocking forces.

Previous research by Wang (1990) indicates that friction and possibly interlocking forces can be directly related to the weight of the particle. In an attempt to include the combined influence of friction and interlocking, a coefficient,  $C_{FI}$ , is introduced. The selection of suitable values for  $C_{FI}$  is discussed further in the section describing the reshaping simulation model. The following condition must be satisfied during the specified duration to ensure initiation of movement:

$$e_1 F_{ZX} > e_2 (C_{FI} W) - e_3 F_B \quad (14)$$

in which  $F_{ZX}$  is the resultant wave force ( $F_{ZX} = \sqrt{F_X^2 + F_Z^2}$ )  $e_1$ ,  $e_2$  and  $e_3$  are the moment arms for the wave loading, effective particle weight and buoyancy force respectively. The moment arm for each component of force is found by calculating the perpendicular distance from the line of action of the applied force to the point or axis of rotation. A diagram of the system of forces, for a simplified particle geometry, considered for initiation is given in figure 5.

The wave loading is calculated for each particle and during a single wave cycle, based on calculated local depth-averaged velocities and accelerations. If the disturbing moments exceed the restoring moments for a specified minimum duration,  $t_{MN}$ , then movement is initiated in the direction under consideration. Usually, three possible directions of movement are considered

which are defined by the relative position of the supporting particles.

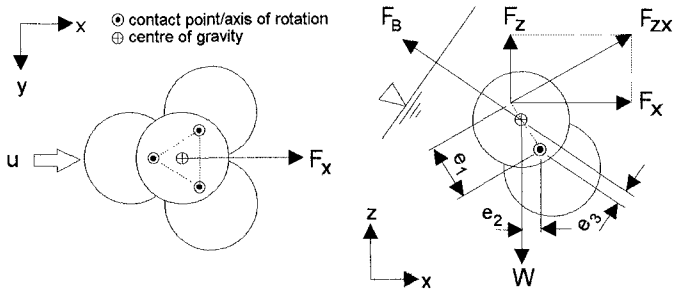


Figure 5. Forces Applied to Single Particle

For the purposes of predicting forces on individual particles it is more appropriate to consider a velocity outside the boundary layer. This is consistent with the measurements made by Tørum (1992) in which velocities and forces were measured on a berm breakwater slope from which force coefficients have been derived.

Reshaping Simulation

The reshaping simulation involves the application of two separate models which are linked by an iterative procedure. Initially, the surface of the armour layer is numerically profiled and an average profile is obtained from three longitudinal sections with measurements at intervals of  $D_{150}$ . To provide input to the wave model, a greater resolution of profile measurements will be required. Additional data is obtained by linear interpolation between points of the average measured profile.

Once a converged solution has been obtained from the wave model, temporal variations of water depth, velocity, acceleration and gradient of the free surface during a complete wave cycle are stored for 25 *sampling stations* along the slope.

One limitation of the displacement model is that only surface particles which are exposed to the external flow are considered to be potentially mobile. These particles are identified by having contact with only three supporting particles.



The stability of each surface particle is considered in turn commencing with particles nearest the toe of the slope. The wave-induced horizontal and vertical components of force are calculated using the data from the wave model. Velocities and accelerations at the precise particle location are obtained by interpolation of data stored for the two nearest sampling stations.

The magnitude of the discrete displacement,  $d_{MN}$ , must be small enough to provide a good resolution of particle displacements but sufficiently large to minimize computational times. For the simulations carried out,  $d_{MN} = 5D_{150}$  was found to be adequate.

If threshold conditions are obtained, the particle is given a discrete displacement of length  $d_{MN}$  in the direction selected as the path of least resistance. This is the direction which is associated with the maximum ratio of disturbing to restoring moments. Periodic boundary conditions are applied; thus if a particle passes through the sides of the computational domain, it is re-introduced at the opposite side. By this means any sidewall effects are eliminated. After displacement, a rolling sequence is used until the particle is relocated in a statically stable position.

After all surface particles are considered and displaced if hydrodynamically unstable, the process is repeated a further four times. The adjusted slope is then re-profiled for new input to the wave model followed by further displacement of surface particles. The complete iterative procedure described is repeated until there is negligible profile change from two successive particle relocation operations although there may be oscillatory displacements on the slope.

The process of particle *nesting*, particularly with berm breakwaters, has been observed in the laboratory whereby smaller material fills voids within the berm resulting in a highly interlocked layer and increased stability. This process has, to some extent, been incorporated into the simulation model by checking the location of surrounding elements after a particle is relocated on the slope. If the particle is sheltered from the surface layer from the external flow, an increased coefficient of  $2C_n$  is applied to the particle weight which generally prevents further movement. If the surrounding elements are subsequently moved, the coefficient reverts back to its normal value and further displacement is possible. Particle nesting of undersize material was not found to be a dominant factor for stability of the reshaped slope which may be attributed to the relatively narrow material grading ( $D_{85}/D_{15}=1.42$ ).

### Application to Berm Breakwater

The berm breakwater illustrated in figure 3 was reshaped with the irregular wave conditions previously described. The numerically constructed breakwater was reshaped by regular waves with the same waveheight and period as the irregular wave parameters,  $H_s$  and  $T_M$ , therefore  $H=0.18\text{m}$  and  $T=1.93\text{s}$ . The damage was expected to be more extensive with the regular wave conditions as there will be few waves greater than  $H_s$  in the irregular wave series.

The main calibration factor required by the reshaping simulation model is the combined friction-interlocking coefficient,  $C_R$ . An artificially high value of  $C_R=5.0$  results in an almost statically stable structure whereas a low value,  $C_R=0.5$  produces a highly mobile structure for which all particles are unstable. In the absence of suitable data relating to the rock material, a trial and error procedure is required in order to determine a suitable value for which the predicted profile matches the experimental profile. Once established, reshaping under other wave conditions can be studied as the value of  $C_R$  is also expected to be a property of the packed material and independent of the wave conditions. The value of  $C_R$  is expected to be a function of the structure slope although the chosen constant value of  $C_R=1.6$  was found to be adequate for the simulation presented.

Results from the reshaping simulation, for the initial structure, are presented as an average reshaped profile. A measured and predicted reshaped profiles are shown in figure 6. An intermediate profile is also included although the simulation is not time-dependent and only included to provide an illustration of how the profile evolves.

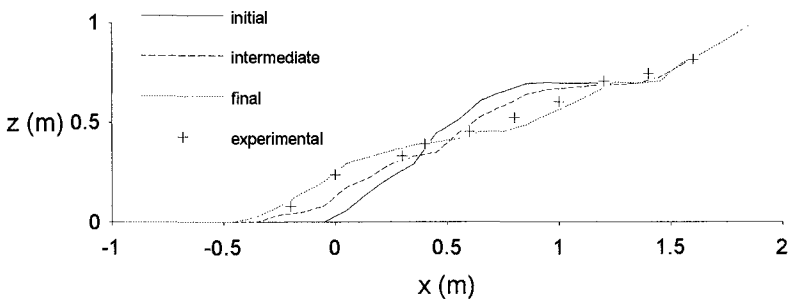


Figure 6. Measured and Predicted Average Profiles

The predicted profile shows an increased degree of erosion from the upper part of the slope with a corresponding increased amount of accretion below SWL. The toe of the reshaped profile does not consist of material at its natural angle of repose but there is still some influence of the hydrodynamics which produces a relatively smooth transition to the horizontal bed. A section through the numerically reshaped structure is presented in figure 7.

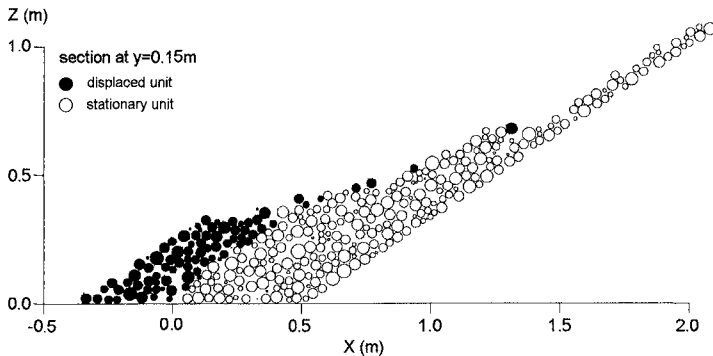


Figure 7. Section Through Reshaped Berm Breakwater

After initial reshaping of the model breakwater, further tests were carried out in which individual stone displacements were observed as described by Tomasicchio (1992). By painting the reshaped profile in zones across the width of the flume, damage to the surface layer defined by the number of displaced stones was determined. Wave conditions with progressively increasing stability number,  $N_s$  ( $N_s = H / \Delta D_{n50}$ , where  $\Delta = (\rho_a - \rho_w) / \rho_w$ ), but constant wave steepness, were used and an assessment of the cumulative damage made after each test. Most of these tests were conducted with irregular waves although some data is available for displacements under regular waves. Due to the differences in the measured and predicted profiles, quantitative results from physical and numerical experiments are not compared. Figure 8 shows results from a typical simulation of displacements on the reshaped slope presented as a plan view of surface particles before and after exposure to regular waves with  $H = 0.166\text{m}$  and  $T = 1.86\text{s}$ . The particles are shaded according to their position on the reshaped slope before displacement.

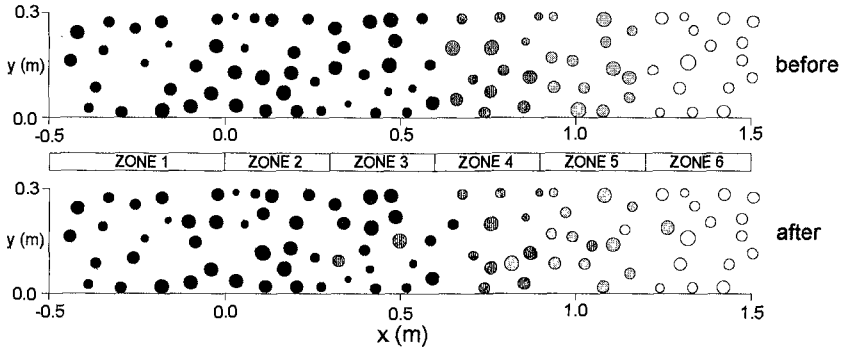


Figure. 8 Surface Particle Displacements

### Conclusions

A reshaping simulation model, using a deterministic approach, which includes detail of individual armour displacements is shown to provide a qualitatively good prediction of profile development. Predictions of transport on the reshaped profile can also be made with the calibrated model although the results have not been validated against experimental data.

The influence of variability within the random structure of the armour layer can be investigated by repeating the numerical experiments on a modified structure. A different structure, with the same material grading and initial profile, can be numerically constructed by providing different seed values to the random number generator used to select particles for placement.

Modifications towards a more probabilistic model should include the variability of particle shape. This would require a distribution of projected area/volume, wave force and friction-interlocking coefficients rather than applying a single value as used in the present model.

Further improvements to the component models are possible although the associated increase in computational time should be taken into consideration. The simulation of initial reshaping with the present model can take up to 8 hours on a 50MHz 486 machine.

### Acknowledgements

This work was carried out within the research and technological development programme in the field of Marine Science and Technology (MAST) financed by the Commission of the European Communities.

### References

- Brandtzaeg, A. (1966) The effect of unit weights of rock and fluid on the stability of rubble mound breakwaters. *Proc. 10<sup>th</sup> Int. Conf. on Coastal Engineering*, 991-1021.
- Burcharth, H.F. and Christensen, C. (1991) On stationary and non-stationary porous flow in coarse granular material. *Proc. 1<sup>st</sup> MAST G6-S Project 3B workshop*.
- Den Brecker, R.C. and Vries, M. (1985) Stability of top-layer elements (in Dutch, translation by M.R.A. van Gent). *Report S 467 (4), Delft Hydraulics*.
- Kobayashi, N. and Wurjanto, A. (1990) Numerical model for waves on rough permeable slopes. *Journal of Coastal Research*, SI 7, 149-166.
- Latham, J-P. and Poole. A.B. (1988) Abrasion testing and armourstone degradation. *Coastal Engineering*, 12, 233-255.
- Madsen, O.S. and White, S.M. (1975) Reflection and transmission characteristics of porous rubble-mound. *Technical report No. 207, R.M. Parsons Laboratory, M.I.T., Cambridge, Massachusetts*.
- Magoon, O.T., Baird, W.F., Ahrens, J.P., Edge, B., Converse, H.D., Davidson, D.D., Hughes, S.A., Burcharth, H.F., Treadwell, D.D., Rauw, C.I. and Sam Smith, A.W. Durability and testing of stone for use in rubblemound structures. *23<sup>rd</sup> Int. Conf. on Coastal Engineering*.
- Tomasicchio, G.R., Andersen, O.H. and Norton, P.A. (1992) Measurement of individual stone movements on reshaping breakwaters. *Proc. final MAST G6-S overall workshop*.
- Tørum, A. (1992) Wave induced water particle velocities and forces on an armour unit on a berm breakwater. *Report STF60 A92104, Norwegian Hydrotechnical Laboratory*.
- Van der Meer, J.W. and Koster, M.J. (1988) Application of computational model on dynamic stability. *Design of Breakwaters, Proc. Breakwaters '88 Conf., Institution of Civil Engineers, London, 333-342*.
- Wang, H.S. and Peene, S.J. (1990) A probabilistic model of rubble mound armor stability. *Coastal Engineering*, 14, 307-331.

## CHAPTER 112

### THE BREAKING AND RUN-UP OF SOLITARY WAVES ON BEACHES

Ashwini Otta<sup>1</sup>, Ib A. Svendsen<sup>2</sup>, and S. T. Grilli<sup>3</sup>

#### ABSTRACT

A high accuracy boundary element method is used to compute the propagation of solitary waves from a constant depth region onto a plane slope. Initial wave heights range from  $H/h = 0.06$  to  $0.775$ , slopes between  $1:35$  and  $1:1.73$  ( $30^\circ$ ) have been investigated. The prebreaking shoaling shows very different characteristics on gentle slopes ( $1:20$  and less) and on steeper slopes.

A diagram constructed on the basis of a large number of numerical experiments gives a simple limit between which waves break on which slopes and which not. Typical examples of the range of wave behavior are shown. Waves that do not break at run up often break during run down. The velocity fields for the two types of breaking are compared and found to be very different. A simple explanation for this is offered.

#### 1. INTRODUCTION

The shoaling, run-up and breaking of solitary waves is of interest in connection with the analysis of the behavior of tsunamis in coastal regions.

A significant amount of literature has been published which analyses long wave propagation on slopes using the non-linear shallow water (NSW) equations or Boussinesq approximations. Thus, analytic solutions to periodic problems were obtained by Carrier & Greenspan (1958), Carrier (1966) and to the solitary wave problem by Synolakis (1987). Numerical solutions have been developed by Hibberd and Peregrine (1979), Pedersen & Gjevik (1983), and Zelt (1991). Furthermore, Kim et al. (1983) used a boundary integral formulation to analyze the problem. Experimental results for run-up were obtained by Ippen & Kulin (1954), Camfield & Street (1969) and recently, by Synolakis (1987). In particular

---

<sup>1</sup>Delft Hydraulics Laboratory, De Voorst, Postbus 152, 8300 AD, Emmeloord, The Netherlands

<sup>2</sup>University of Delaware, Department of Civil Engineering, Newark, DE 19716

<sup>3</sup>The University of Rhode Island, Department of Ocean Engineering, Kingston, RI 02881

Synolakis, comparing results from the NSW equations with experimental run-up, finds some deviations in the surface profiles in the final stages when the waves get steep. Papanicolaou & Raichlen (1987) give a few results for breaker heights on very gentle slopes ( $< 1:50$ ). Finally, Svendsen & Grilli (1990) found using a high accuracy boundary element method (BEM) that when solitary waves of steepness up to 0.50 run-up on a relatively steep slope, the velocity profiles would differ quite significantly from the depth uniform velocity which is intimately linked with the NSW-equations. Similarly, the run-up of non-breaking waves, while in accordance with experimental results, would differ from the NSW predictions by as much as 75%.

Synolakis also developed a criterion for whether the waves would eventually break during the run-up and concluded that as the slope angle becomes small, the theory is only valid for small  $H/h$  whereas for steep beaches, he estimated the theory would be valid for relatively large  $H/h$ .

In the present paper we apply the version of the BEM method developed by Otta, Svendsen & Grilli (1992) to analyze the development of solitary waves on beaches. The wave heights initially (on the constant depth region in front of the slope) have height to depth ratios  $H/h$  from a moderate 0.10 to 0.775, the latter being almost equal to the steepest stable solitary wave on a horizontal bottom. The beach slopes are between 1.35 and  $1/1.73$  ( $30^\circ$ ). Both the shoaling behavior and the question of whether the waves break (and how) are addressed.

## 2. PROBLEM FORMULATION

The situation considered is described in Fig. 1. Solitary waves generated with initial height  $H_0$  in a region of constant depth  $h_0$  propagate towards a plane beach with slope angle  $s$ . Hence the only independent parameters of the problem are  $H_0/h_0$  and  $s$ . The motion is assumed irrotational and hence can be described by a velocity potential  $\phi$ . Hence the velocity field  $\vec{v}$  is given as

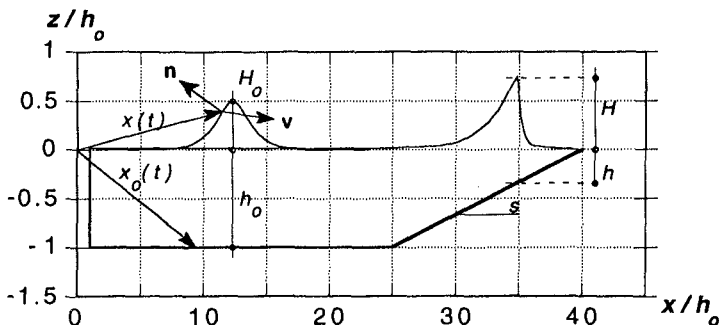


Figure 1: Definition Sketch

$$\vec{v} = \nabla\phi \tag{1}$$

and in the entire flow region  $\phi$  satisfies the Laplace equation

$$\nabla^2\phi = 0 \tag{2}$$

subject to the boundary conditions

$$\frac{\partial\phi}{\partial n} = 0 \text{ at the bottom } z = -h_0(x) \tag{3}$$

$$\frac{D\phi}{Dt} = \frac{1}{2}|v|^2 - g\eta \tag{4}$$

at the free surface  $z = \eta(x, t)$

$$\frac{D\eta}{Dt} = \vec{v} \tag{5}$$

where  $D/Dt = \partial/\partial t + (\vec{v} \cdot \nabla)$  represents the total derivative following a fluid particle. The geometrical quantities are shown in Fig. 1 and we have assumed a constant pressure along the surface.

To achieve the necessary accuracy in the computations, the solitary waves are generated initially by a method described by Tanaka (1986). At  $t = 0$ , we assume such a wave present in the computational wave tank with crest sufficiently far from the toe of the beach to be essentially undisturbed by the beach. Similarly, the seaward boundary is placed sufficiently far away not to disturb the computations with its reflection.

### 3. METHOD OF SOLUTION

The exact equations described in section 2 are solved by transforming the Laplace equation (2) into a Boundary Integral Equation which reads

$$\alpha(\vec{x}, t)\phi(\vec{x}, t) = \int_{\Gamma} \frac{\partial\phi}{\partial n} G(\vec{x}, \vec{x}_0) - \phi(\vec{x}_0) \frac{\partial G(\vec{x}, \vec{x}_0)}{\partial n} d\Gamma(\vec{x}_0) \tag{6}$$

$\Gamma$  represents the (closed) boundary of the computational domain given by the bottom and slope, the entire free surface and the seaward boundary (see Fig. 1).  $\vec{x}$  and  $\vec{x}_0$  indicate points on the boundary curve,  $\vec{x}_0$  being the point with respect to which the integral is performed. A free space Greens function is used for  $G(\vec{x}, \vec{x}_0)$ . (6) is an exact representation of the original equation (2) which was exact too.

The solution of (6) at each time step is found numerically at modal points on the boundary. These nodes divide the boundary  $\Gamma$  into  $M$  segments  $\Gamma_j$  each spanning over an element. Thus, (6) can be written

$$\alpha(\vec{x}, t)\phi(\vec{x}, t) = \sum_{j=1}^M \int_{\Gamma_j} G(\vec{x}, \vec{x}_0) \frac{\partial\phi}{\partial n} d\Gamma - \sum_{j=1}^M \int_{\Gamma_j} \phi(\vec{x}_0) \frac{\partial G(\vec{x}, \vec{x}_0)}{\partial n} d\Gamma \tag{7}$$



which is still exact. Hence, the solution is reduced to the question of expressing the two types of integrals in (7) in terms of  $\phi$  and  $\frac{\partial\phi}{\partial n}$  at the nodes.

The details of this technique, which also includes upgrading to the next time step the boundary values of  $\phi$  and  $\partial\phi/\partial n$  at each point using the boundary conditions (3) and (4) are described by Grilli et al. (1989), Grilli & Svendsen (1990a,b).

The approach used for the computations reported here differ from previous versions of the method in the way the derivatives along the boundary and integrals in (7) have been computed. A third order polynomial based on four nodes has been used, centrally positioned around each interval (termed midinterval approximation).

This turns out to yield a substantial improvement in accuracy over the spline approximations used earlier. Fig. 2 shows a comparison of results for  $H/h$  and the maximum error in the normal velocity  $\partial\phi/\partial n$  for the propagation of a very steep solitary wave ( $H/h = 0.775$ ) on a horizontal bottom. This is close to highest wave of  $H/h = 0.78$  that remains stable according to Tanaka (1986).

Ideally, we should expect each of the quantities in these computations to stay constant during the propagation. Initially, however, the wave undergoes minor changes before settling down to a largely constant value. These adjustments are caused by the fact that the numerical representation of the wave in our computations is based on different node position and also uses interpolation between nodes that differ (slightly) from the interpolation used in the computation of the initial wave (at  $t = 0$ ) by Tanaka's method.

In all, however, the constancy of the parameters in Fig. 2 shows the substantial improvement over previous versions of the method, which were not quite able to cover the propagation of waves with heights so close to the maximum stable wave height. The figure represents propagation over approximately 30 water depths.

#### 4. SHOALING OF SOLITARY WAVES

The tool thus developed has been used for numerical experiments with the shoaling and breaking of solitary waves on beaches with slopes varying from 1/35 to approximately 1/2.

Fig. 3 shows computations on a slope of 1/35 of waves with steepness between 0.10 and 0.40. The local value of  $H/h$  on the slope is plotted against  $x/h_0$ , the distance from the initial position of the wave crest.

The variation is essentially the same for all value of  $H/h$  and all waves in the figure end up breaking. Noticeable is the fact that the value of  $H/h$  at the breaking point almost independent of the initial height of the wave. The smaller waves just travel to smaller depths before they break. This pattern was already

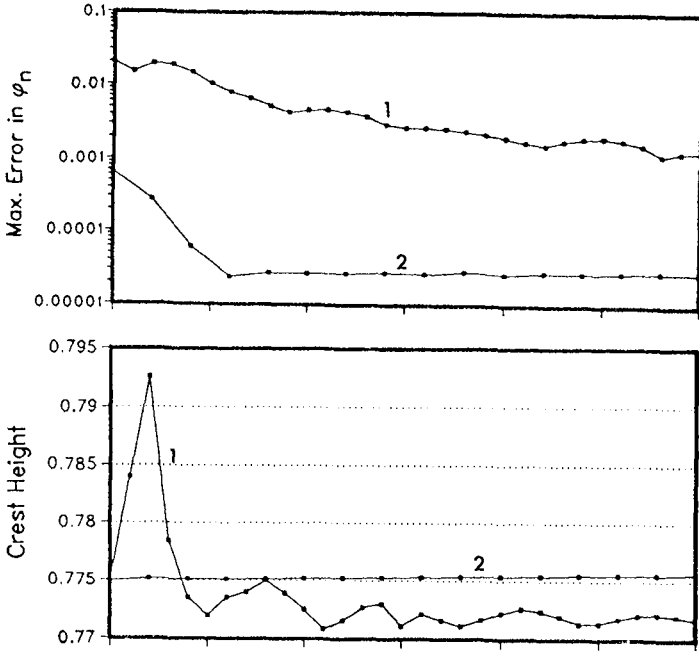


Figure 2: Accuracy of Computations for Very Steep Solitary Wave ( $H/H = 0.775$ ) on a Constant Depth. 1) Quasi-spline interpolation. 2) Cubic mid-interval approximation.

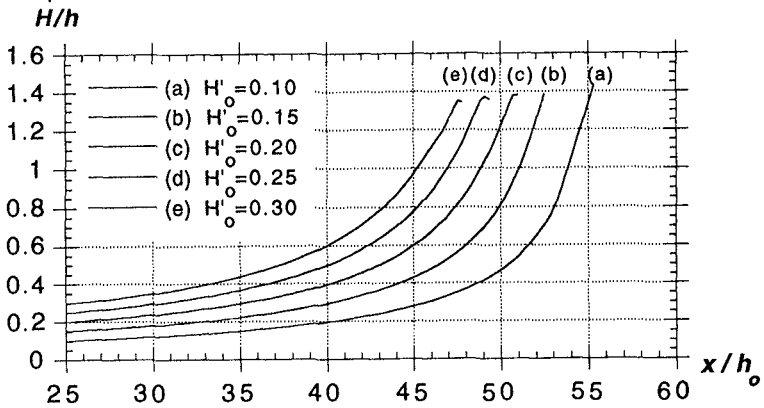


Figure 3: Shoaling of Solitary Waves of Different Initial Height  $H_o/h_o$ , on a slope  $1/35$ .  $H/h$  on the Slope versus  $x/h_o$ . Slope Starts at  $x/h_o = 25$ .

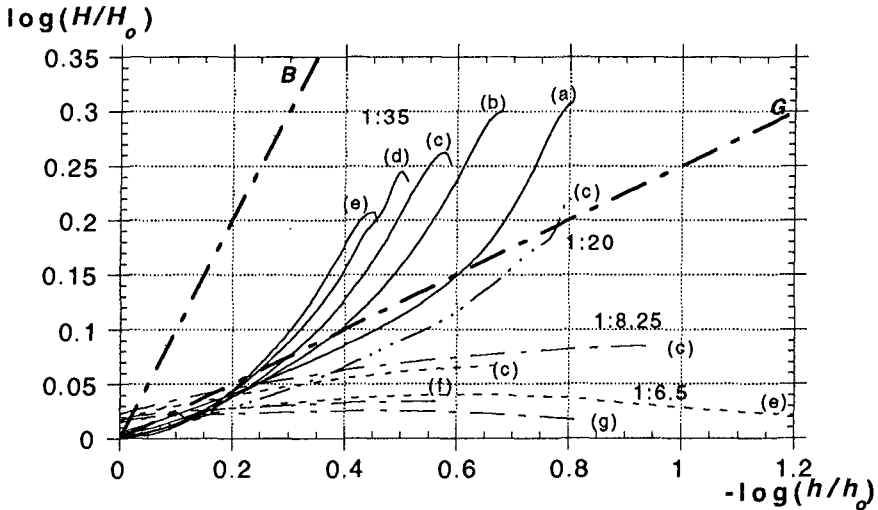


Figure 4: Shoaling of Solitary Waves of Different  $H_o/h_o$  on Different Slopes.

observed experimentally by Ippen & Kulin (1954). It is also worth noticing that the  $H/h$  value of breaking for all the waves is 1.35–1.45, i.e., dramatically above the height 0.78 or 0.8 of the highest stable wave. The reason for this is of course that the (in)stability of a high symmetrical wave on a constant depth has little to do with unsymmetrical deformation to breaking of a wave on a gradually decreasing water depth.

The absolute change in the height of the waves can not be deduced from Fig. 3. Fig. 4, however, shows the variation of wave height  $H$  relative to the original height  $H_o$ . This figure also includes a sample of results for a number of steeper slopes (1/20, 1/8.25, 1/6.5). We observe in this figure a substantial difference in the behavior on different slopes of waves initially of the same height. Whereas the waves on a 1/35 slope studied in the previous figure increase in height by generally a factor of 2 ( $\log H/H_o \sim 0.3$ ), the same waves on the steeper slope of 1/8.25 or 1/6.5 propagate on the slope essentially without change in absolute height. It even turns out that on a slope with steepness 1/6.5, only the initially steepest of those waves reach breaking (see below).

The figure also shows that non of the two theoretical laws proposed in the literature for the variation of the height of shoaling long waves are particularly satisfactory. Green's law  $H \propto h^{-1/4}$  (represented by line G in Fig. 4) clearly has some merit during the initial stages of waves on the slope of 1/35 as one should expect from its derivation based on small amplitude waves on gentle slopes. More surprising perhaps is that the relation  $H \propto h^{-1}$  predicted by the Boussinesq theory (line B in Fig. 4) can be said to approximate the later part

of the wave height development towards breaking as judged from the fact that  $H/H_0$  curves for waves on a 1/35 slope have the same slope in that region. These features were discussed by Synolakis (1991) on the basis of experimental results. On the steeper slopes, however, even 1/20, none of these laws will apparently provide accurate predictions for the wave height variations. In fact, the steepest wave of 0.40 (curve g) on a 1/6.5 slope even decreases slightly in height as it climbs the slope.

## 5. WAVE BREAKING ON SLOPES

### Variation with slope angle and wave height

The second problem addressed in the present paper is the question of which waves break on which slopes.

Fig. 5 shows the propagation of the same wave, a very steep solitary wave with initial height  $H_0/h_0 = 0.75$ , on three different slopes,  $30^\circ$ ,  $7.12^\circ$  (1/8),  $3.81^\circ$  (1/15). The three figures illustrate the range of behavior described in section 4, and we particularly see that even a wave initially close to the maximum stable steepness does not break if the slope is too steep. It turns out that a wave of nearly maximum steepness will only break if the slope angle is smaller 1:4.

We also see the radical difference between the behavior of the same wave on a  $30^\circ$  and a  $7.12^\circ$  slope. Where the crest in the first case essentially rushes up the slope with a total runup of close to three times the initial wave height the wave on a  $7.12^\circ$  slope hardly changes height at all and mainly undergoes a rapid deformation that ends with breaking.

On a  $7.12^\circ$  slope, the front of the wave becomes an almost vertical wall at the point of breaking and the breaking occurs violently as the entire wall tumbles over. On the gentler slope of  $3.81^\circ$  the wave breaking is a classical plunging breaker although the size of the jet is relatively small.

In Fig. 6 is shown the influence (or lack of influence) of wave height on the breaking on a fairly gentle slope ( $3.81^\circ$ ). Each of the four waves with initial heights of  $H_0/h_0 = 0.3, 0.45, 0.6$  and  $0.7$  have shapes at the point of breaking that virtually are scaled versions of the others. Only the height to depth ratios  $H/h$  are slightly different as indicated in section 4 with the smaller wave reaching the largest  $H/h$ -value before it breaks.

### Breaking criterion

Based on a sufficient number of such calculations as numerical experiments, we are then able to construct the diagram shown in Fig. 7 which shows which waves break, which do not. The axes are  $\log 1/s$ , ( $s = h_x$  being the slope) and  $\log(H_0/h_0)$ ,  $H_0$  the original wave height on the constant depth  $h_0$ . The full line in the diagram separates the waves that break before or during run-up on

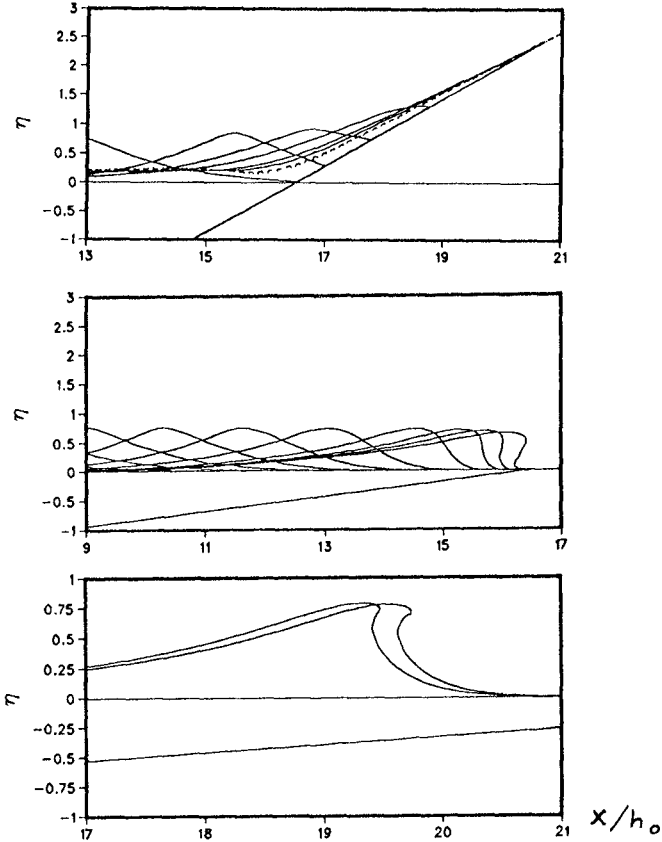


Figure 5: The Breaking of the Same Wave ( $H_o/h_o = 0.75$ ) on Three Different Slopes: a)  $30^\circ$ , b)  $7.18^\circ$  (1:8), c)  $3.81^\circ$  (1:15).

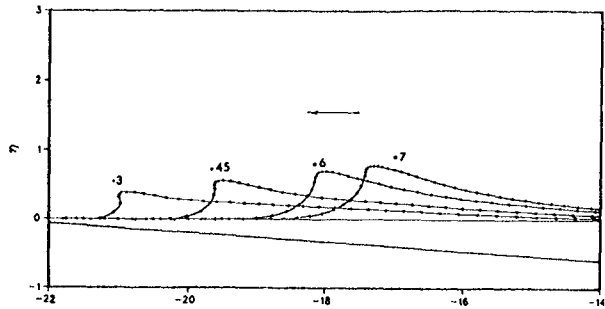


Figure 6: Breaking of Four Different Waves ( $H_o/h_o = 0.3, 0.45, 0.6$  and  $0.7$ ) on the Same (relatively gentle) Slope  $3.81^\circ$  (1:15).

a given slope. We see that the line indicates that waves with

$$\frac{H_0}{h_0} > 8.4 s^{15/9} \quad (8)$$

will break sometime during run-up on a slope.

The question of which waves break on a slope was also addressed by Synolakis (1987). Using the non-linear shallow water equations (NSW), he found that waves would eventually break on the slope if  $H_0/h_0 > 0.825^{10/9}$ . This criterion is indicated by the dashed line in Fig. 7.

We see that only for waves initially of noticeable steepness the NSW equations predict, that much smaller waves will break, than is found by the present more accurate method. Since run-up is greatly reduced if the waves break, this will also result in the NSW equations predicting much less run-up for the class of waves that actually do not break.

It could be argued that for waves initially of very small height (such as Tsunamis), the extrapolation of the two lines in the figure will meet. This happens for  $H_0/h_0 = 0.0078$  (corresponding to  $s = 0.015$ ), so that for that set of parameter values, the two methods give the same limit for which waves break and which do not.

However, in the first place it is not clear in advance that the formula (8) can be extrapolated to such small values of  $H_0/h_0$ . We have not at the present time performed any numerical experiments with so small wave heights on such gentle slopes.

Secondly, even such small waves will become quite steep when they approach breaking. The fact that the NSW equations fail to correctly predict breaking of the initially steeper waves may indicate that their prediction of the behavior of waves close to breaking is generally deficient, no matter how those waves start out. This would be in accordance with the general knowledge that near breaking the deviations from the hydrostatic pressure imbedded in the NSW equations is important.

#### Surging breakers

One of the interesting phenomena to look for in the numerical experiments is what happens to the waves that almost break, or only just break. Those are the waves around the full line in Fig. 7. If they break, this would presumably correspond to a so-called surging breaker. Fig. 8 shows computations for very steep waves on a slope of 1/4. The initial wave heights are 0.65, 0.68 and 0.75, and according to Fig. 7 these waves should not break but, particularly the 0.75 case should be very close to breaking. The figure is undistorted in scales so we can judge the development.

We notice that these waves show all the characteristics found from experi-

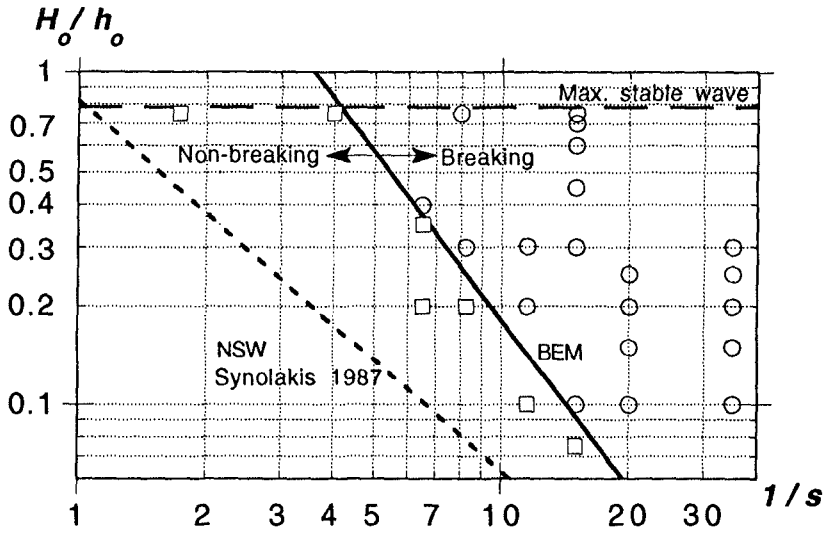


Figure 7: Wave Breaking Criterion

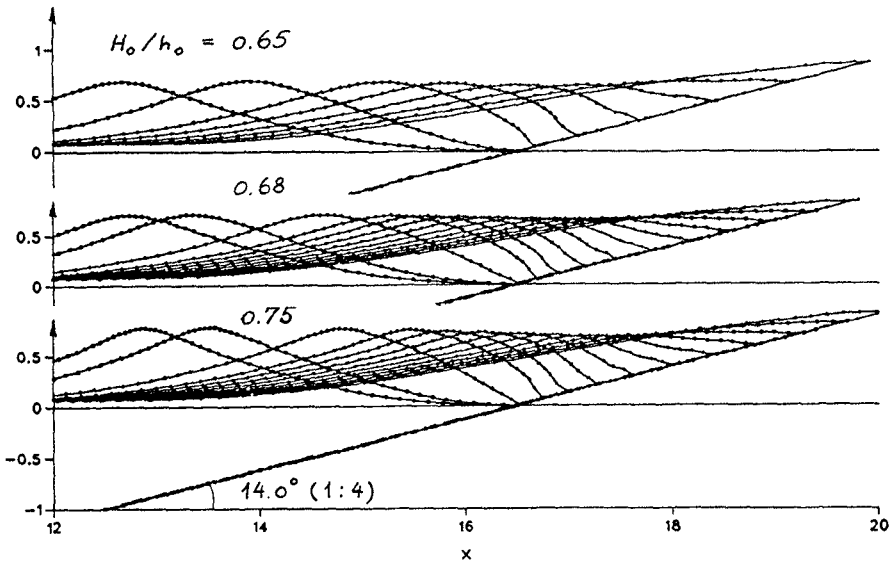


Figure 8: Waves Close to a Surging Breaking

ments for surging breakers. The front, with no water ahead of it, steepens to about  $75^\circ$  and the steepest surface slope is at very bottom of the front. At a certain point, the steepness stops, however, and the toe of the front shoots forward into a run-up while the wave crest behind collapses. Clearly, a very significant part of the potential energy plus the kinetic energy built into the wave crest at the instant of maximum slope is transferred into kinetic energy causing the run-up.

Though we have not tested this through more extensive experiments, we would expect this pattern to apply for a wide range of wave/slope combinations along the line given by (8). The question remains open however, how gentle the slope can be and how nearly breaking waves behave on really gentle slopes such as  $1/50$ .

#### Wave breaking in the backwash

It turns out that waves that do not break during run-up may still do so during run-down. This was already seen in the computations on steep slopes by Svendsen & Grilli (1990) and Grilli & Svendsen (1991) who also described the velocity fields.

Fig. 9 shows an example of the breaking of a wave during run-down. At the period following maximum run-up (approximately position 1), the water starts rushing down the slope at rapidly increasing speed. The water level nearly parallel to the bottom indicates the acceleration is close to  $g \sin \alpha$  where  $\alpha$  is the slope angle. Close to the slope, the water level drops well below undisturbed SWL while staying well above SWL a little further out. This creates a front, as of a new incoming wave, which rapidly breaks shoreward. The whole sequence, in particular the breaking, takes place so swiftly that under laboratory conditions it can hardly be followed with the naked eye. After the breaking, the SWL is restored at the shoreline while smaller reflected wave propagates away. This phase can only be reproduced by the present method when the wave does not reach breaking in the downrush.

It is worth noticing that although it looks like the down-wash breaking is equivalent to a new incoming wave front, the velocity field in this breaker is radically different from the velocity field in an ordinary shoreward propagating breaker. Fig. 10 shows a comparison between the two situations. It seems that due to the strong downward water flow on the slope meeting the backward breaker, this wave is held in an almost stationary position while it turns over. The strong outward going particle velocities confirms this impression.

## 6. CONCLUSION

Summarizing the results described, we conclude that

- The wave height variation of solitary waves shoaling on plane slopes depends far more radically on the slope than on the initial wave steepness.



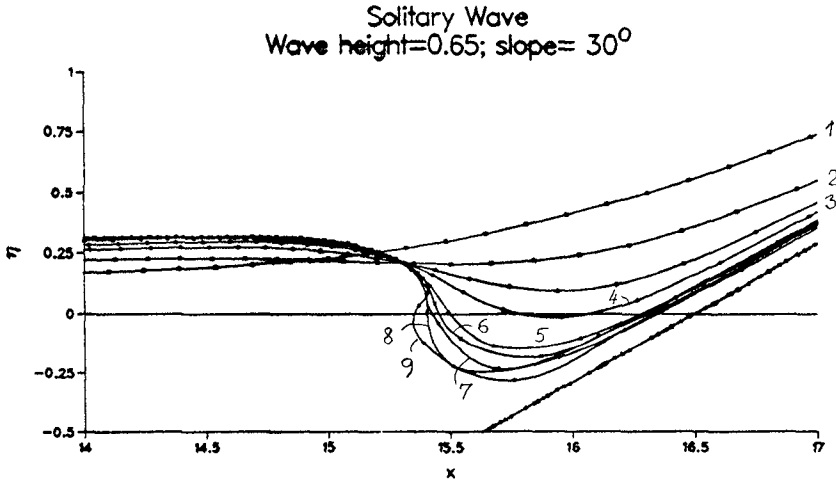


Figure 9: Breaking During Run Down.

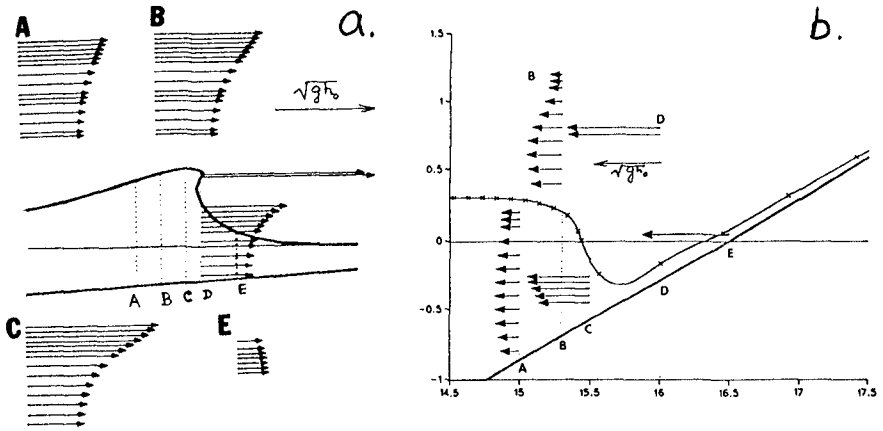


Figure 10: Velocity Profiles Under Forward & Backward Breaking Waves.

On gentle slopes ( $< 1:20$ ), the wave height grows monotonously, slowly at first, towards breaking nearly as  $h^{-1}$ .

On steeper slopes, the wave height stays almost constant over the slope.

- For all slopes investigated (1:35 being the gentlest), the wave height to water depth ratio at breaking is well above the limit of approximately 0.78 of the steepest stable wave on constant depth. For the moderately steeper slopes, the waves may break even at the shoreline (and the value of  $H/h$  then is infinite).
- No waves that can propagate stably on a constant depth break on slopes steeper than  $12^\circ$ .
- Waves that do not break during run up may still generate a (backward) wave breaking during run down. The velocity field in such a breaking is very different from the breaking of a progressive wave. It resembles the velocity field of a (second) shoreward moving wave which is arrested by the downrush. The wave deforms to breaking without propagating.

## 7. REFERENCES

- Camfield, F.E. and R.L. Street (1969). Shoaling of solitary waves on small slopes. *ASCE*, **95**, WW1, 1–22.
- Carrier, G.F. (1966). Gravity waves on water of variable depth. *J. Fluid Mech.*, **24**, (4), 641–659.
- Carrier, G.F. and H.P. Greenspan (1958). Water waves of finite amplitude on a sloping beach. *J. Fluid Mech.*, **4**, (1), 97–110.
- Dold, J.W. and D.H. Peregrine (1986). An efficient method for steep unsteady water waves. In *Numerical Methods for Fluid Dynamics II*, K.W. Morton and M.J. Baines (eds.)
- Grilli, S., J. Skourup and I.A. Svendsen (1989). An efficient boundary element method for nonlinear water waves. *Engineering Analysis with Boundary Elements*, **6**(2), 97–107.
- Grilli, S.T. and I.A. Svendsen (1990a). Corner problems and global accuracy in the boundary element solution of nonlinear wave flows. *Engineering Analysis with Boundary Elements*, **7**, 4, 178–195.
- Grilli, S.T. and I.A. Svendsen (1990b). Long wave interaction with steeply sloping structures. *Proc. 22 Int. Conf. Coast. Eng.*, Delft, Chap. 90, 1200–1213.

- Grilli, S. and I.A. Svendsen (1991). The runup and reflection of solitary waves on steep slopes. *Research Report No. CACR-91-04*, Center for Applied Coastal Research, Univ. of Delaware.
- Hibberd, S. and D.H. Peregrine (1979). Surf and run-up on a beach: A uniform bore. *J. Fluid Mech.*, **95**, 323-345.
- Ippen, A.T. and G. Kulin (1954). The shoaling and breaking of the solitary wave. *Proc. 5th Int. Conf. Coast. Eng.*, Grenoble, Sept. 1954.
- Otta, A.K., I.A. Svendsen and S.T. Grilli (1992). Unsteady free surface waves in a region of arbitrary shape. *Research Report No. CACR-92-10*, Center for Applied Coastal Research, Univ. of Delaware, 153 pp.
- Papanicolaou, P. and F. Raichlen (1987). Wave characteristics in the surf zone. *Proc. Coastal Hydrodynamics*, (R.A. Dalrymple, ed.), Newark, June 1987, 765-780.
- Pedersen, G. and B. Gjevik (1983). Run-up of solitary waves. *J. Fluid. Mech.*, **135**, 283-299.
- Svendsen, I.A. and S. Grilli (1990). Nonlinear waves on steep slopes. *J. Coastal Research*, **SI7**, 185-202.
- Synolakis, C.E. (1987). The runup of solitary waves. *J. Fluid Mech.*, **185**, 523-545.
- Synolakis, C.E. (1991). Green's law and the evolution of solitary waves. *Phys. Fluids*, **A3(3)**, 490-491.
- Tanaka, M. (1986). The stability of solitary waves. *Phys. Fluids*, **29**, 3, 650-655.
- Zelt, J.A. (1991). The run-up of non-breaking and breaking solitary waves. *Coastal Engineering*, **15**, 205-246.

# CHAPTER 113

## Impact Loading and Dynamic Response of Caisson Breakwaters

### - Results of Large-Scale Model Tests -

H.Oumeraci<sup>1)</sup>, H.W. Partenscky<sup>2)</sup>, S. Kohlhas<sup>3)</sup>, P. Klammer<sup>4)</sup>

#### **Abstract**

The results of large-scale model tests on impact loading and dynamic response of a caisson breakwater are presented.

Hydraulic model tests are performed in which the impact loading is induced by breaking waves on the structure. Horizontal impact forces, uplift forces and the related overturning moments are determined. The transmissibility of the impact loads and the accelerations of the structure are investigated (dynamic response).

The hydraulic model tests are supplemented by pendulum tests on the same caisson breakwater model used in the hydraulic model tests in order to determine the characteristics of the structural model itself. The added mass of water oscillating with the structure, the stiffness of the foundation and the damping ratio are evaluated from these tests.

#### **Introduction**

Based on the lessons drawn from past failures and on a literature review, a research programme on monolithic structures subject to breaking waves has been established (OUMERACI et al, 1991). The main objective of this programme is the development of design guidelines as well as the evaluation of counter-measures for increasing the overall stability of the structure and its foundation. In fact, the stability of vertical and composite breakwaters has been yet approached by the existing codes of practice and design methods of different countries as a static problem (GODA, 1985). Therefore, the underlying philosophy of these investigations is to show that a caisson breakwater/foundation system is a purely dynamic problem which cannot be simply treated statically. For this purpose, large-scale hydraulic model tests and pendulum tests on a caisson breakwaters were performed, supplemented by a dynamic analysis of the structure. The paper is principally intended to present and discuss some of the most relevant results of the hydraulic and pendulum tests. The results of the dynamic analysis of caisson breakwater by using a simple numerical model, together with the experimental results, will be presented in a further paper (OUMERACI & KORTENHAUS, 1993).

---

<sup>1)</sup> Dr.-Ing., Senior Researcher, SFB 205, University of Hannover, Appelstr. 9A, 3000 Hannover

<sup>2)</sup> Prof. Dr.-Ing., Dr.-Phys., formerly Managing Director Franzius-Institut

<sup>3)</sup> Prof. Dr.-Ing.habil., Franzius-Institut

<sup>4)</sup> Dipl.-Ing., Research Engineer, SFB 205

### Experimental Set-up and Test Conditions

Hydraulic model tests and pendulum tests have been performed in the Large Wave Flume (GWK) in Hannover on a caisson breakwater, with a rubble mound foundation lying on a sand bed.

#### a) Hydraulic Model Tests

The hydraulic model tests were conducted by using regular and irregular waves with wave heights and periods up to 1.20m and 7s, respectively. The measurements were simultaneously performed on two independent caisson structures. Total forces were measured on the first caisson. The second caisson was installed on a rubble mound foundation lying on a 1.4 m-thick sand layer (Fig. 1).

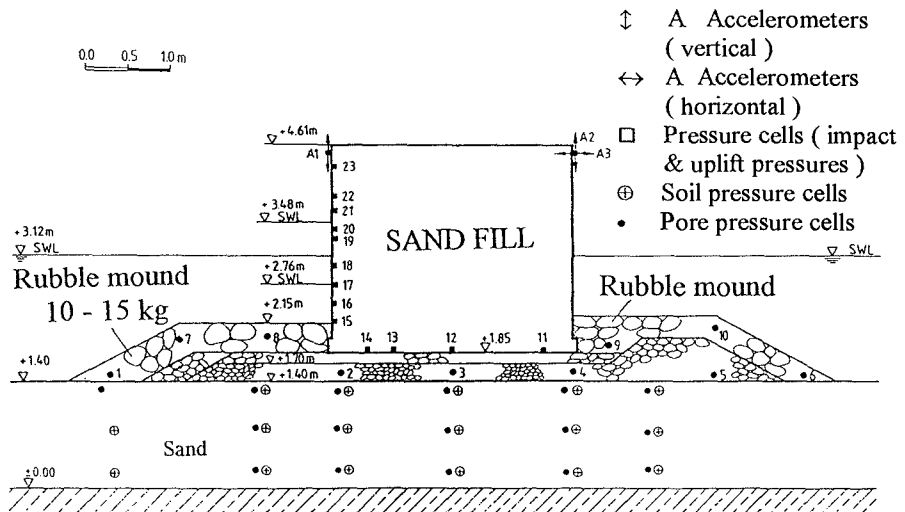


FIG. 1: CAISSON BREAKWATER TESTED IN THE LARGE WAVE FLUME (GWK)

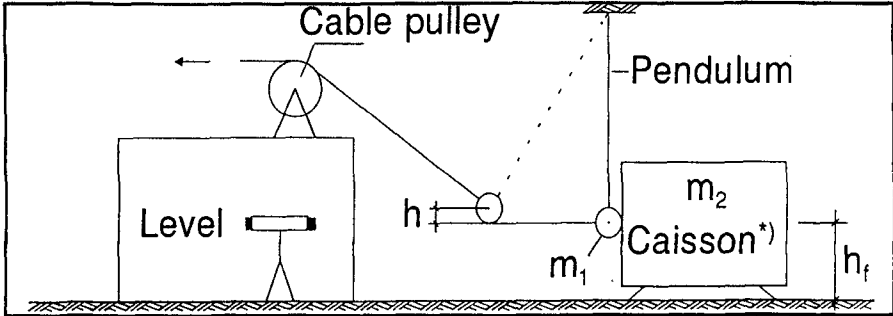
Simultaneous measurements of the following items were carried out:

(a) incident and reflected waves, (b) impact pressure on the caisson front, (c) uplift pressure, (d) wave-induced pore-water pressure in the foundation, (e) total wave-induced stress in the sand layer, (f) dynamic response of the caisson (accelerations) and (g) total forces.

Pressure and load transducers with high natural frequencies were used. Sampling rates up to 11kHz were adopted for impact pressures and forces.

**b) Pendulum Tests**

The hydraulic model tests were supplemented by pendulum tests (Fig. 2) using the same caisson/foundation model (Fig. 1) in different water depths.



\*) Same Model as shown in Fig. 1

FIG. 2: EXPERIMENTAL SET-UP FOR PENDULUM TESTS

The impulsive loads induced by the pendulum and the response of the structure and its foundation were simultaneously recorded. The main objective of these tests was to determine the hydrodynamic mass as well as the damping and the subgrade reaction coefficients to be considered in a dynamic analysis of the caisson/foundation system. Two test series were conducted on the caisson part lying on the rubble mound foundation: Tests under dry conditions and tests with different water depths.

**Discussion of Results of Hydraulic Model Tests**

**a) Impact Pressure Histories and Distribution**

The characteristics of the impact pressure histories simultaneously recorded at nine elevations of the caisson front are strongly related to the types and kinematics of the waves breaking on the structure (OUMERACI et al, 1993). Spatial pressure distributions on the caisson front for time steps as small as  $\Delta t = 0.1\text{ms}$  can be plotted from the measured data, and the related total forces are calculated from pressure integration. An example of such pressure distributions resulting from a breaking wave with  $H = 0.85\text{m}$  and  $T = 4\text{s}$  is given in Fig. 3 for  $\Delta t = 6.3\text{ms}$ .

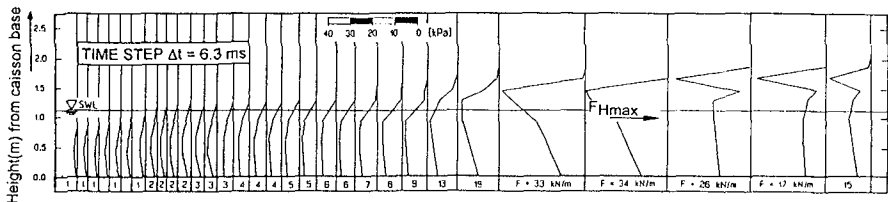


FIG. 3: PRESSURE DISTRIBUTION ON CAISSON FRONT

These pressure distributions, together with the simultaneously measured pressure histories at different wall elevations not only give a complete picture of the impact process, but also allow us to identify the most relevant characteristics of the shape of the breakers impinging on the wall.

**b) Uplift Pressure Histories and Distributions**

Uplift pressures are subject to much less variation in time than the pressures on the caisson front (OUMERACI et al, 1991). For waves breaking on the caisson, the recorded uplift pressure histories exhibit a dynamic shape, even if much less sharper than that of the impact pressure on the caisson front. In this case, the uplift pressure is not linearly distributed and not equal to zero at the rear edge of the caisson, as usually assumed. This is shown for instance by Fig. 4 which represents the uplift pressure distribution at the instant of wave breaking ( $H = 0.85\text{m}$ ,  $T \approx 4.0\text{s}$ ).

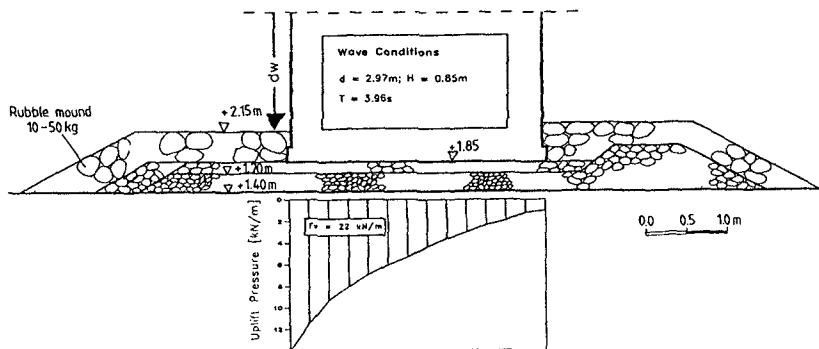


FIG. 4: UPLIFT PRESSURE DISTRIBUTION FOR BREAKING WAVES

**c) Total Forces and Overturning Moments**

The total horizontal and uplift forces were obtained by spatially integrating the impact pressures measured on the caisson front (horizontal force  $F_h$ ) and the uplift pressure (vertical force  $F_v$ ). An example of the total horizontal force  $F_h$  and its overturning moment  $M_h$  around the rear edge of the caisson is shown in Fig. 5. It can also be seen that during the impact process, the location of the point of application of  $F_h$  is almost constant and slightly under still water level.

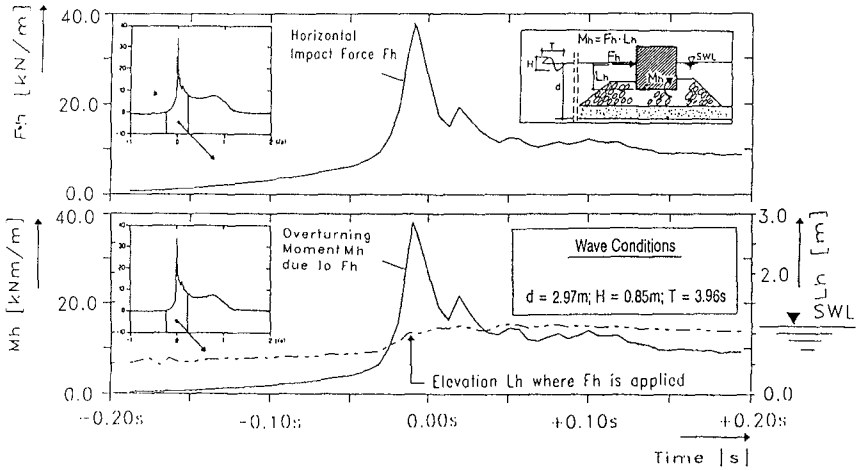


FIG. 5: HORIZONTAL FORCE AND INDUCED OVERTURNING MOMENT

The uplift force and related overturning moment which are caused by the same wave which induced the force and moment in Fig. 5 are also shown in Fig. 6. It can be seen that the point of application of the uplift force during impact is located rather at  $\frac{1}{4}$  than  $\frac{1}{3}$  of the caisson width from the seaward edge, due to the non-linear uplift pressure distribution as shown in Fig. 4. This will result in a larger contribution of the uplift force to the total overturning moment. In fact, depending on the caisson size, the water depth, the thickness of the rubble mound foundation, the breaker type and the magnitude of the horizontal force, this contribution may be higher than that of the horizontal impact forces (Fig. 7).

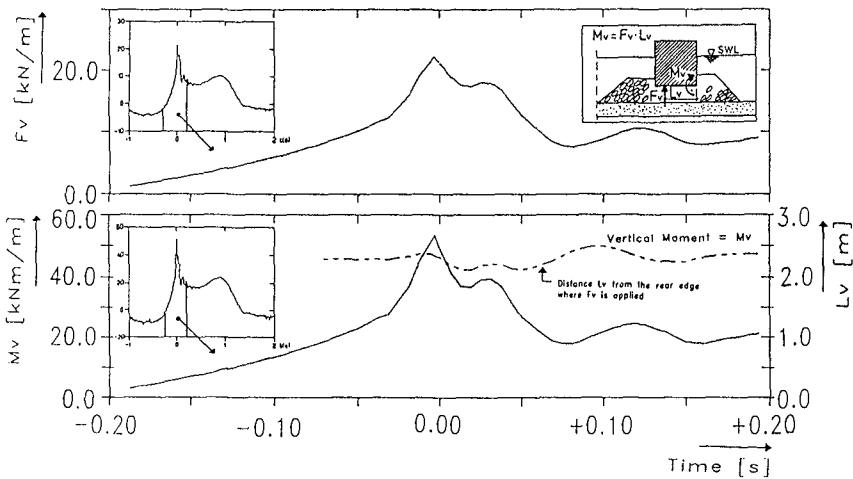


FIG. 6: UPLIFT FORCE AND INDUCED OVERTURNING MOMENT



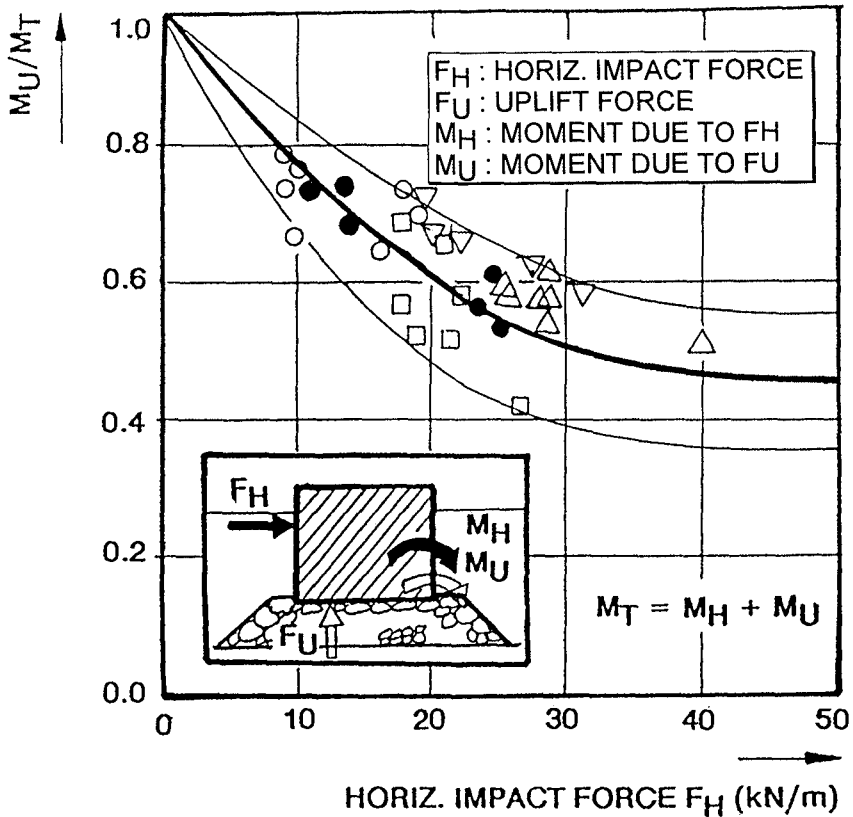


FIG. 7: CONTRIBUTION OF UPLIFT FORCE TO THE TOTAL OVERTURNING MOMENT

#### d) Dynamic Response of the Structure

##### Transmissibility of Impact Loads

The dynamic response of the first part of the model caisson behind which the total horizontal reaction force was measured is described by the transmissibility of the impact load. This transmissibility is defined as the ratio of the reaction force measured behind the caisson to the total impact force on the caisson front obtained by pressure integration over the front area. An example of the results obtained is given in Fig. 8.

This and further similar results show that for the conditions tested, the transmissibility of the impact forces is in the range of 0.10 to 0.80 whereas the transmissibility of the force impulses is about twice the transmissibility of the related peak forces. This, however, strongly depends on the shape of the impact force history which is known to be primarily determined by the shape of the breaker impinging on the wall (OUMERACI & KORTENHAUS, 1993).

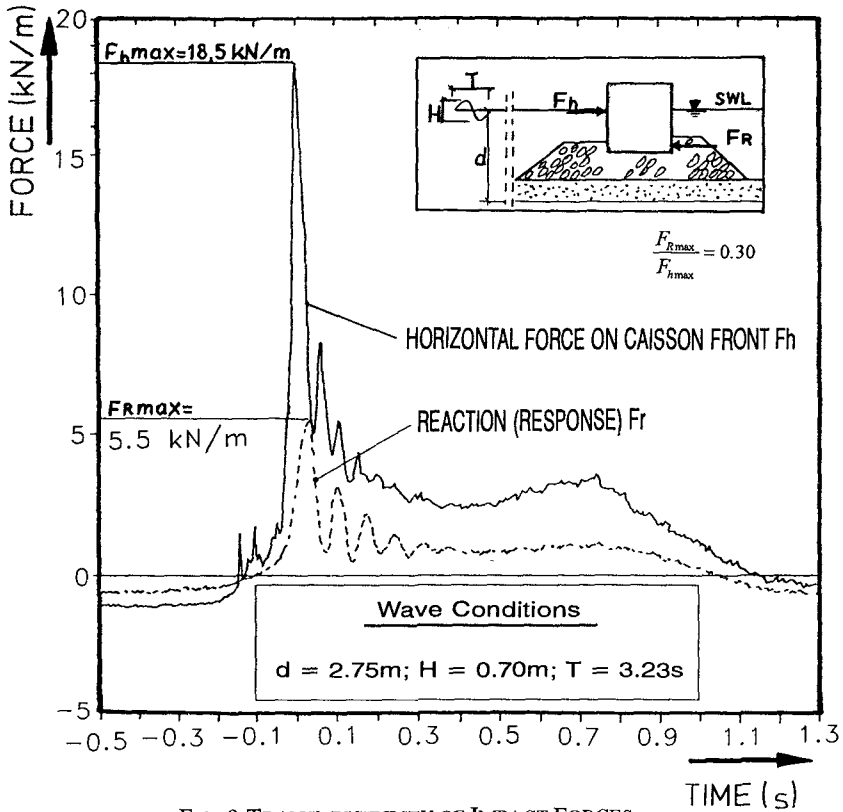


FIG. 8 TRANSMISSIBILITY OF IMPACT FORCES

Accelerations of the Structure

The response of the second caisson part is described by the accelerations of the caisson (vertical and horizontal direction at the rear top and horizontal direction at the front top of the caisson). A typical horizontal acceleration trace is given in Fig.9, showing that accelerations in the order of some decimeters/s<sup>2</sup> may occur. It is also seen that the structure oscillates with periods  $T_s \approx 0.06 - 0.08\text{s}$ .

Pore Water Pressure in Rubble Mound Foundation and Sand Layer

Pore-water pressure in the foundation and total stress in the sand layer induced by waves and wave impacts on the caisson represent further means to characterize the response of the foundation. The pore pressures in the rubble mound foundation are found to have peak values which are an order of magnitude lower than those of the impact pressure on the caisson front (OUMERACI, 1991).

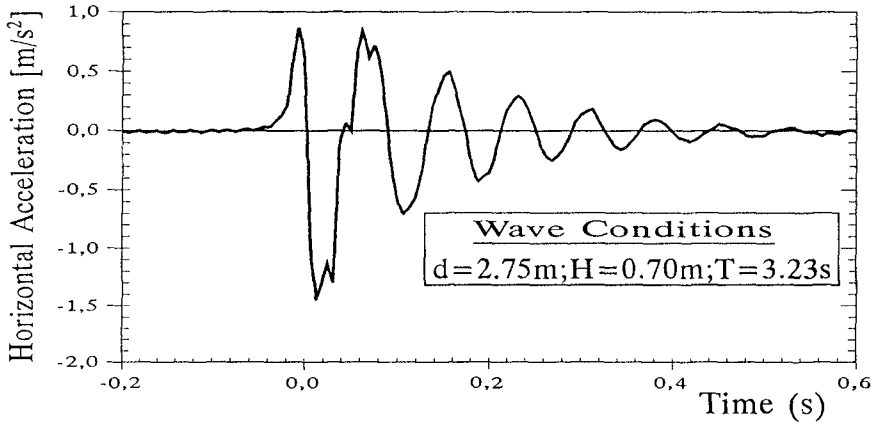


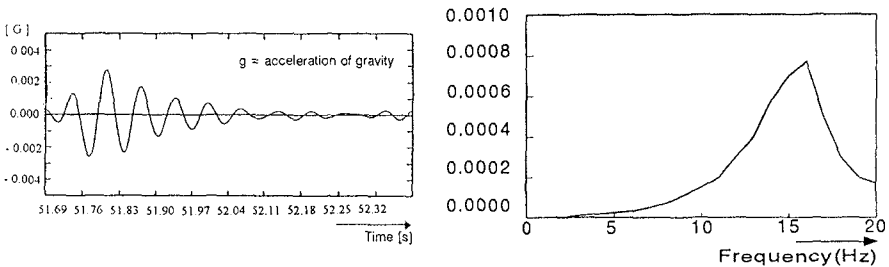
FIG. 9: HORIZONTAL ACCELERATIONS AT THE REAR TOP OF THE CAISSON

The pore pressure histories in the sand foundation exhibit a shape which is almost similar to that of the pressure induced by a partial clapotis. The corresponding total stress is characterized by the sharp peaks at both the seaward and shoreward bottom edges and by low frequency oscillations after the peak which correspond to the rocking motions of the caisson recorded by the accelerometers.

**Results of Pendulum Tests**

**a) Tests under Dry Conditions**

An illustrative example for the results related to the rocking motions of the caisson subject to pendulum impact under dry conditions (without any water in the flume) is given in Fig. 10a showing the time series, and Fig. 10b showing the corresponding spectral representation. This means that the natural frequency of the structure under dry conditions is  $f_n^* \approx 15\text{Hz}$ .



a) Time Series

b) Spectral Representations

FIG. 10: ACCELERATION OF STRUCTURE OSCILLATIONS (DRY CONDITIONS)

The damping of the structure oscillations under dry conditions is shown by Fig. 11 where the oscillation amplitude  $A$  is plotted against dimensionless time corresponding to the number of oscillation cycles.

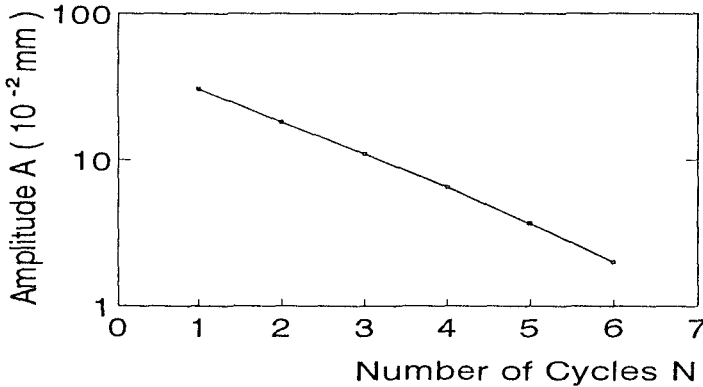


FIG. 11: DAMPING OF STRUCTURE OSCILLATIONS (DRY CONDITIONS)

From Fig. 11 and further similar results, the logarithmic decrement

$$\delta = \frac{1}{n} \left[ \frac{A(t)}{A(t+n \cdot T)} \right] = \frac{2 \pi D}{\sqrt{1-D^2}} \quad (1)$$

has been determined to  $\delta = 0.446$  which leads to a damping ratio  $D = 0.071$ . Since:

$$f_n = f_n^* \left[ \sqrt{1-(D)^2} \right] \quad (2)$$

where  $f_n^*$  is the natural frequency of the undamped oscillations, it can be assumed that  $f_n = f_n^*$  and that the logarithmic decrement  $\delta = 2\pi D$ .

### b) Tests with Different Water Depths

The pendulum tests were conducted for different water depths under the same loading conditions as for the tests under dry conditions.

As already mentioned, the main objective of these tests was to determine the dynamic parameters needed for dynamic analysis, namely :

- the added mass of water which is forced to oscillate with the structure subject to impact loads,
- the damping ratio of the oscillating structure,
- the stiffness of the foundation.

Added Mass of Water

The hydrodynamic mass is generally calculated by using the following formulae derived on the assumption of an incompressible and irrotational potential flow (OUMERACI & KORTENHAUS, 1993):

$$m_{ad,hor.} = 0.543 \cdot \rho_w \cdot d_w^2 \tag{3}$$

$$m_{ad,rot.} = 0.218 \cdot \rho_w \cdot d_w^2 \tag{4}$$

where:

$m_{ad,hor.}$ ,  $m_{ad,rot}$  = added mass of water for horizontal and rotational motion of the structure, respectively  $[kg/m]$

$\rho_w$  = density of water  $[kg/m^3]$

$d_w$  = water depth at the wall  $[m]$

Since the frequency of oscillations  $f_n$  of the structure is directly related to the total mass of the oscillating system  $M_t = M_c + m_{ad}$  ( $M_c$  = caisson mass /m), the added mass of water for each water depth  $d_w$  can be determined from the corresponding measured frequency  $f_n$  by the following relationship:

$$\frac{M_c + (m_{ad})_2}{M_c + (m_{ad})_1} = \left( \frac{f_{n1}}{f_{n2}} \right)^2 \tag{5}$$

where indices 1 and 2 are related to water depth  $d_{w1}$  and  $d_{w2}$ , respectively.

The variations of the frequency of oscillations for which the relative water depth  $d_w/d_h$  obtained from the pendulum tests is shown in Fig. 12. By using Eq. (5), the relationship between the added mass and the water depth can be found.

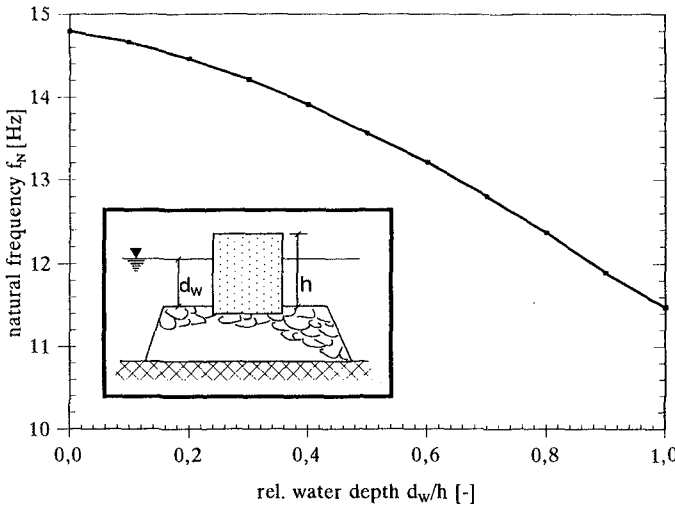


FIG. 12: EFFECT OF WATER DEPTH ON OSCILLATION FREQUENCY

Generally, the added mass calculated by using Eqs. (3) & (4) are slightly underestimated as compared to the experimental results (OUMERACI & KORTENHAUS, 1993).

Stiffness of Foundation

The stiffness coefficient related to the horizontal motions ( $K_x$ ) and to the rotational motions ( $K_\phi$ ) have also been determined from the results of the pendulum tests for different water depths. These results are compared to the approximate method of SAVINOV in Fig. 13 ( see MARINSKI & OUMERACI, 1992).

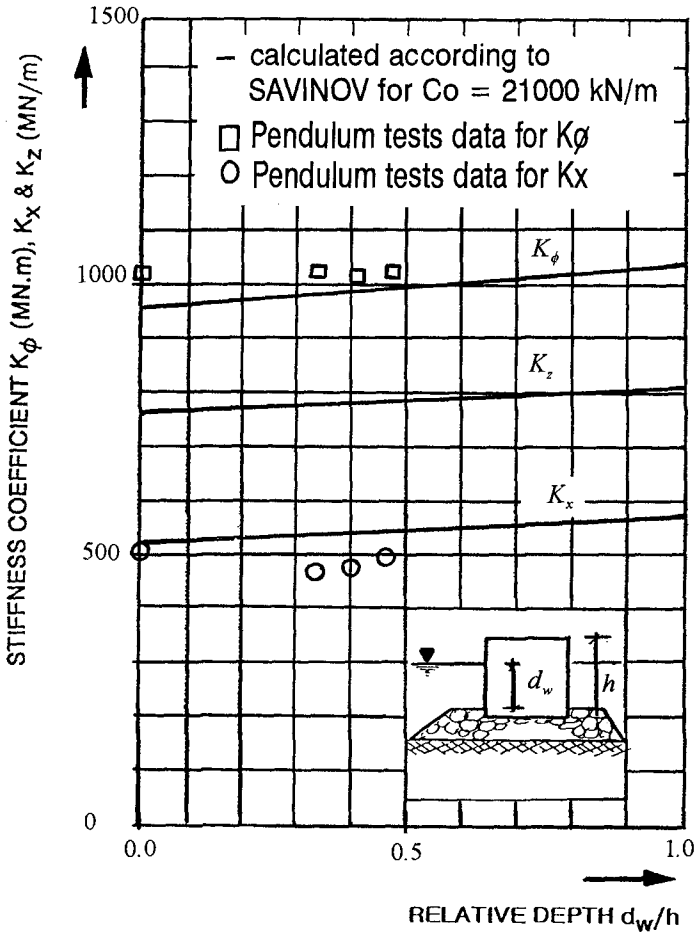


FIG. 13 - STIFFNESS COEFFICIENTS VS. WATER DEPTH

It is seen from Fig. 13 that the experimental results do not exhibit any variation with water depth, but show a relatively good agreement with the approximate method of SAVINOV.

**Damping Ratio**

The damping ratio  $D_x$  and  $D_\phi$  (for horizontal and rotational motions, respectively) have been determined for different water depths  $d_w$  at the caisson front by using the following relationships:

$$D_{x,\phi} = \sqrt{\left(\frac{\delta_{x,\phi}}{4\pi^2 + \delta_{x,\phi}^2}\right)} \tag{6}$$

where:

$\delta_x, \delta_\phi$  = logarithmic decrement for the horizontal and rotational motion, respectively:

$$\delta_x = \ln\left[\frac{x(t)}{x(t+T_x)}\right] \tag{7}$$

$$\delta_\phi = \ln\left[\frac{\phi(t)}{\phi(t+T_\phi)}\right] \tag{8}$$

$x(t), \phi(t)$  = amplitude of horizontal and rotational oscillations, respectively

$T_x, T_\phi$  = period of horizontal and rotational oscillations, respectively

$t$  = time

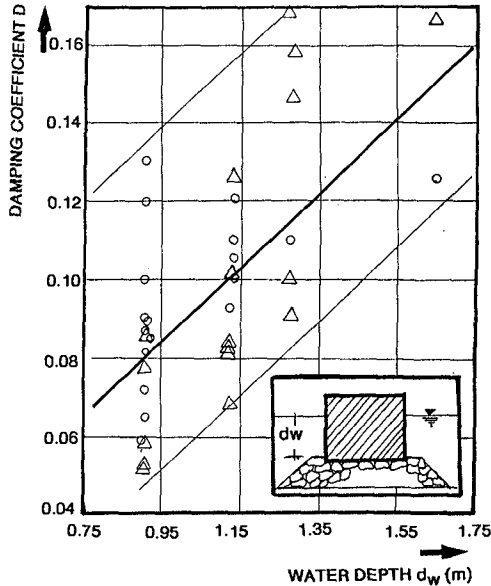


FIG. 14: DAMPING COEFFICIENT VS. WATER DEPTH

The damping ratio  $D_x$  and  $D_\phi$  obtained from the pendulum tests are plotted in Fig. 14 against water depth  $d_w$ .

It can be seen that the experimental D-values show a large scatter, but there is a clear tendency for the damping coefficient to increase with water depth.

### **Summary of Results, Concluding Remarks and Perspectives**

The results achieved so far in the hydraulic model tests, supplemented by the pendulum tests on the same model may be summarized as follows.

The suggestion commonly found in the literature that the effect of impact pressures on the stability of caisson breakwaters is not significant, could not be confirmed by the present study. In fact, the occurrence of a sharp force peak followed by a quasi-static load generally leads to a higher response of the structure than that of the quasi-static force alone (MARINSKI & OUMERACI, 1992).

The shape of the wave breaking on the structure primarily governs the characteristics of the impact load. Double-peaked impact forces which are induced by well-developed plunging breakers are found to be the most critical loads (OUMERACI et al, 1992).

Dynamic uplift pressures caused by wave impacts are not linearly distributed and appear to be important for the dynamic stability analysis of the structure.

Free damped nonlinear oscillations of the structure foundation system are essentially induced by the impulsive load due to breaking waves. This nonlinearity is probably due to the plastic deformations of the foundation as well as the hydrodynamic mass and geodynamic mass which both increase with the amplitudes of the oscillations of the structure.

The oscillations of the structure are transmitted to the foundation. The total stress recorded in the foundations shows a sharp peak, followed by smaller oscillations corresponding to the free rocking oscillations of the structure.

The total stresses recorded in the sand layer beneath the caisson structure and its rubble mound foundation are of two types: one is caused by the shock wave propagation into the soil foundation and the other one by the free oscillations of the structure following the impact.

The logarithmic decrement of the free oscillations of the structure-foundation system subject to breaking wave impact loads ranges from  $\delta = 0.35$  to 1.1 (average value of  $\delta$  is 0.62).

Accounting for the added mass of water oscillating with the structure may result in an increase up to 25 % of the natural frequency of the rocking motions, depending on the loads, the water depth and the size of the structure.

The stiffness coefficients ( $K_x$  and  $K_\phi$ ) determined by the pendulum tests agree relatively well with those determined by the approximate method of SAVINOV.



The damping coefficients determined by the pendulum tests exhibit a wider variation ( $D= 0.08 - 0.16$ ) than the subgrade reaction coefficients.

The results of these investigations can be used, together with a numerical model for the simulation of the dynamic response of the structure, in order to perform a sensitivity analysis of the most relevant parameters (shape and different characteristics of the loading, added mass, damping and stiffness coefficients etc.) of the system (OUMERACI & KORTENHAUS, 1993).

In the ongoing further analysis of the data from both hydraulic and pendulum tests, more effort is being concentrated on :

- the dynamic response of the foundation as related to the caisson oscillations;
- scaling problems related to the loading and response of the structure;
- providing a complete set of reliable data for the validation of numerical models.

### **Acknowledgements**

This study is part of an extensive research programme within the Coastal Engineering Research Unit "SFB 205" which is supported by the German Research Council (DFG), Bonn. Additional support is provided by the European Community within the Research Program MAST G6-0032.

### **References**

- Goda, Y.: Random seas and design of maritime structures, University of Tokyo Press, 1985
- Marinski, T.; Oumeraci, H.: Dynamic response of vertical structures to breaking wave forces-Review of the CIS design experience, ASCE, ICCE 92, Venice, Italy, 1992 (these Proceedings)
- Oumeraci, H.; Partenscky, H.-W.; Tautenhain, E.; Nickels, H.: Large-scale model investigations: a contribution to the revival of vertical breakwaters - ICE, Proc. Conf. in Coastal Structures and Breakwaters, 1991, pp. 207-220.
- Oumeraci, H.; Klammer, P.; Partenscky, H.-W.: Classification of breaking wave impact loads on vertical structures. ASCE, J. Waterway, Port, Coastal and Ocean Eng. Div. (To appear 1993).
- Oumeraci, H. :Dynamic loading and response of caisson breakwaters - Result of Large-scale model tests. MAST G6-S/ Research in Coastal Structures/ Project 2, Res. Rep. Sept. 1991, pp. 33 + Appendices
- Oumeraci, H.; Kortenhau, A.: Analysis of the dynamic response of caisson breakwaters . Paper submitted to "Special Issue on Vertical breakwaters" in Coastal Engineering, Elsevier Amsterdam, 1993
- Oumeraci, H.; Partenscky, H.-W.; Tautenhain, E.: Breaking wave loads on vertical gravity structures. Proc. 2nd Int. (Conf. Offshore & Polar Eng., ISOPE 92, Vol III, San Francisco, 1992 pp. 532 - 539.

## CHAPTER 114

# WAVE FORCES ON CROWN WALLS

Jan Pedersen<sup>1</sup>

Hans F. Burcharth<sup>2</sup>

### Abstract

This paper presents some of the results from a large parametric laboratory study including more than 200 long-duration model tests. The study addresses both the wave forces imposed on the breakwater crown wall as well as the performance of the structure in reducing the wave overtopping. The testing programme includes variations of the sea state parameters and of the geometrical configuration of the breakwater and crown wall. Basic relations between forces/overtopping and the varied parameters are examined and preliminary design guidelines for structures within the tested range of variations are proposed.

### Introduction

A rubble mound breakwater is very often constructed with a crown or parapet wall at its crest, since such a superstructure contributes to the effectiveness of the breakwater in reducing the amount of overtopping water. Furthermore, a wall will in most cases reduce the necessary crest height of the rubble structure and thereby decrease the amount of rubble material. The superstructure often functions also as service and traffic road.

Although crown walls are very popular and have been used worldwide for decades, there still does not exist any general applicable guidelines or design criteria for these structures. This is in sharp contrast to some of the other modes

---

<sup>1</sup>Ph.D., Department of Civil Engineering, Aalborg University, Sohngaardsholmsvej 57, DK-9000 Aalborg, Denmark

<sup>2</sup>Prof. of Marine Civil Engineering, Department of Civil Engineering, Aalborg University, Sohngaardsholmsvej 57, DK-9000 Aalborg, Denmark

of failure for rubble mound breakwaters where today's design procedures includes fairly reliable calculations of the probability of failure within the lifetime of the structure, see fx. [2, Burcharth 1991a] and [3, Burcharth 1991b]. Such calculations requires as basis a well documented design equation which for example for failure of the main armour layer is fulfilled by the Hudson formula or the stability formulae by [10, v.d. Meer 1988]. The uncertainties related to existing general formulae for wave wall stability and overtopping are very large. The design of crown walls therefore relies on site specific hydraulic model studies or careful extraction and interpretation of the research results presented in the literature, see fx. [1, Bradbury et. al. 1988], [7, Jensen 1983] and [8, Jensen 1984].

Looking at the stability of the crown wall, several modes of failure have to be considered as shown in Fig. 1.

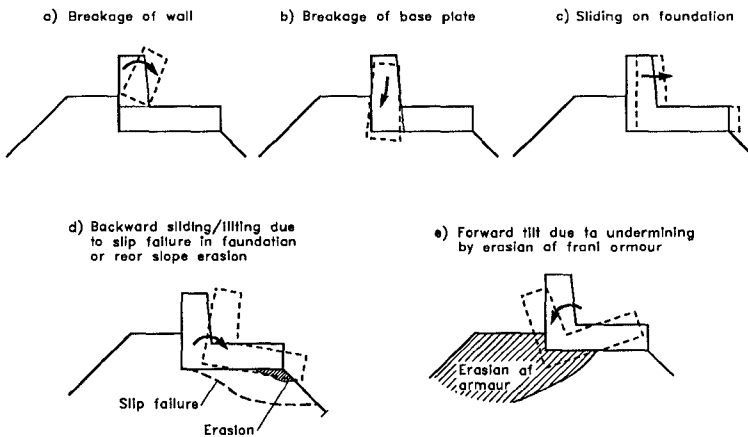


Fig. 1 - Possible failure modes for crown walls. From [4, Burchart 1993]

Only the failure modes a) and b) depends exclusively on the strength of the superstructure and the wave loading, whereas failure modes c), d) and e) are much more complex involving the properties of the underlying soil and failures of other parts of the structure. The problem of stability must in all cases be treated dynamically due to the dynamic behaviour of the wave loading. This imposes other problems since the transmissibility or relative amount of load transmitted to the rubble structure may be very different for the different failure modes. In the present investigations this dampening effect is not studied. All results relates to the pressures recorded on the stiff wave wall. The corresponding forces might be very conservative design measures especially for failure modes

c) and d), since these combined structure-soil failure mechanisms have relatively low transmissibility coefficients for short duration force actions. For a caisson breakwater [9, Oumeraci 1991] found a transmissibility coefficient in wave impact tests of 0.2-0.6 depending on the actual force history applied.

Model Tests

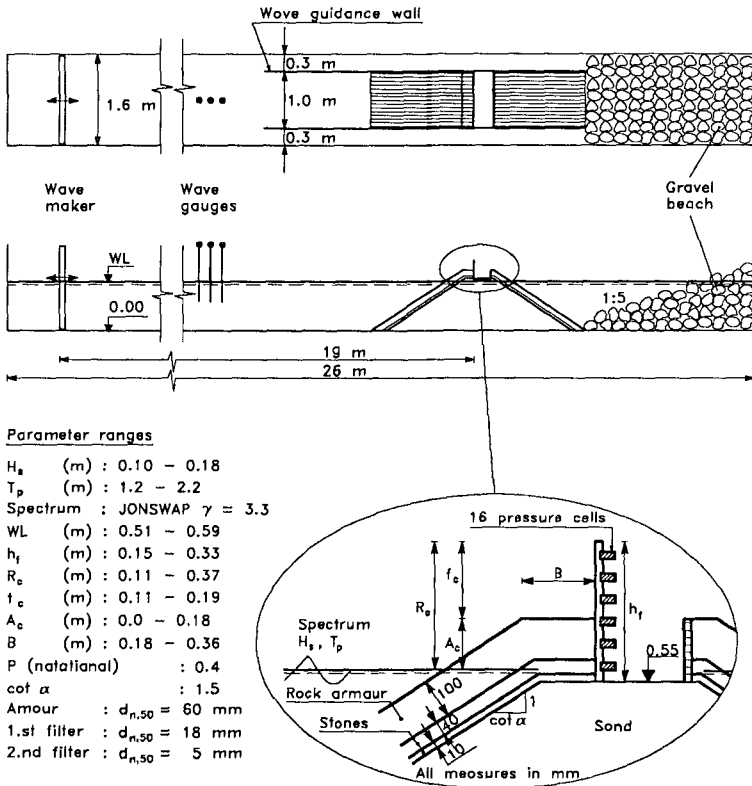


Fig. 2 - Experimental setup and parameter ranges.

Figure 2 shows the experimental setup used in the parametric laboratory study in one of the wave channels at Aalborg University. The channel is 1.6 m wide, 26 m long and is equipped with a piston type wave paddle. For the present study the wave channel was divided into a mid-section of 1 m width and two small side channels each of a width of 0.3 m. All varied parameters and their ranges

are given in Fig. 2. Waves are generated using a white noise filtering technique where it has been verified that the random number generator does not repeat itself, which is essentially for the probabilistic estimates of the measurements. Each of the over 200 performed test-runs consists of 4000-10000 waves, corresponding to 2-4 hours of run, in order to reach low exceedence probability levels with a high degree of reliability. Wave conditions are measured just in front of the breakwater and are separated in incident and reflected waves by a combination of the methods suggested by [6, Goda 1974b] and [5, Funke & Mansard 1980]. This separation is important since reflection amplitude coefficients of 20-30 % are registered.

The wave forces on the crown wall are measured using 16 Phillips P13 OEM 18 mm diameter pressure transducers mounted into the front face of the crown wall. In order to minimize the influence from local pressure disturbances the pressure cells are placed in 2-4 columns, dependent on the height of the used wave wall. Each column is displaced one diameter or less from the adjacent transducer columns, to get the best possible vertical resolution of the pressure field.

The wall itself consists of a 5 mm thick steel plate, supported several places along the width to ensure a stiffness large enough to prevent dynamic disturbances from movements and deformations. Preliminary tests using a strain gauge instrumented force table showed that this setup was unable to register the high frequent parts of the loading without introducing dynamic amplification and thereby blurring the measurements with signals from natural oscillations of the force table itself.

Sampling rates of 128 and 256 Hz were used depending on the actual geometric configuration. Only wave pressures on the front face of the wall were measured. The uplift pressure at the base plate was not recorded because of the uncertainty in correct scaling of the pore pressure in the underlying core material. Also, the forces from the armour units being in contact with the wall are not included in the present study.

From the pressure records the following force components (cf. Fig. 3) were calculated:

- The total horizontal force  $F_h$ .
- The base pressure  $P_b$  in the front base point.
- the overturning moment  $M_h$  around the front base point.
- The second order moment of pressures  $m_2$  around the front base point.

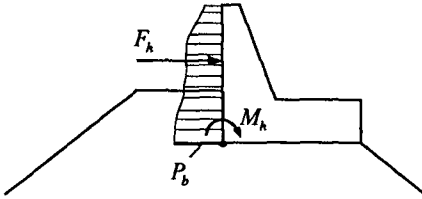


Fig. 3 - Calculated force components.

Forces

A typical example of the measured pressures on the crown wall is shown in Fig. 4. From left to right the figure illustrates the pressure evolution when a wave approaches the breakwater slope, hits the wall and starts to rush down. The timestep between each frame is 7.8 ms.

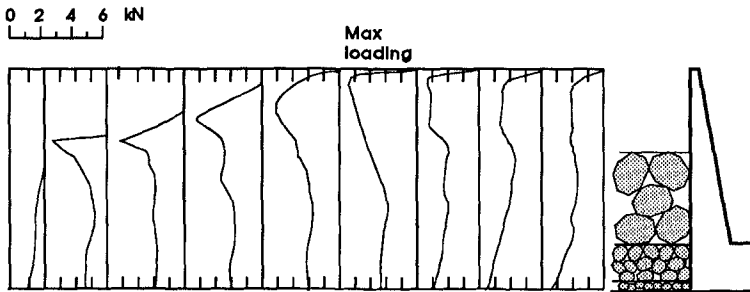


Fig. 4 - Example of typical pressure evolution on crown wall.  
Timestep between each frame is 7.8 ms.

High local pressures are observed in a narrow region just above the crest of the armour in the same moment the water hits the wall. This phenomenon happens because the water velocities outside the porous stone layers are higher than inside. The maximum loading occurs a little later when the porous layers are fully saturated and the water pressure is acting over the full height of the wall. The pressure decay during the down-rush has a much longer duration (in the order of half a wave period) than the pressure rise which occurs within 0.02-0.05 seconds, i.e. in the order of 1-3 % of the wave period.

By spatial integration of the pressure recordings the horizontal force and the overturning moment are obtained. Examples of time series of these force

components are shown in Fig. 5, which also illustrates the afore mentioned time scales for pressure rise and decay.

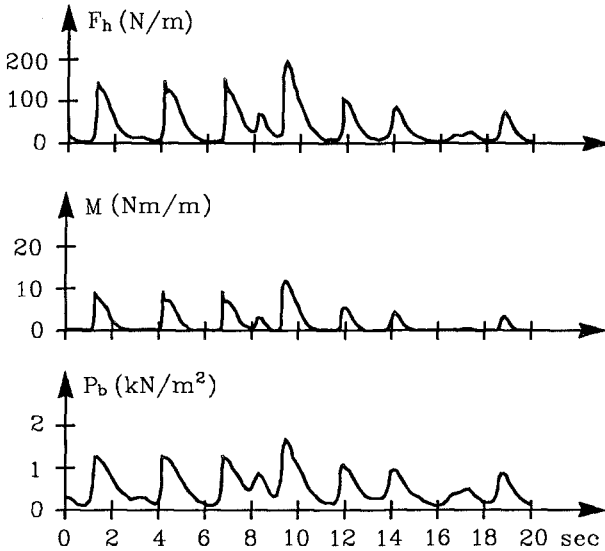


Fig. 5 - Examples of typical time series of force components. Obtained for lowest wall ( $h_f = 0.15$  m).

For the further processing the time series are analysed and probabilistic estimates for each of the force components are extracted. For simplicity only  $F_{0.1\%}$ , being the horizontal force which has an exceedance probability of 0.1%, will be used in the following. Also, unless otherwise stated, all results discussed in the following are obtained for a high wall, where practically no overtopping occurs.

#### Influence of parameters

To represent the sea state conditions the significant wave height  $H_s$  and the spectral peak period  $T_p$  (or the corresponding wave length  $L_p$ ) are used. For changes in water level [8, Jensen 1984] used the vertical distance  $A_c$  from the still water level to the armour crest and he showed that together with  $H_s$  it constitutes an important dimensionless parameter in predicting the wave forces on the crown wall. The influence of the width  $B$  of the armour crest and the height of the wave wall have also been examined. In Figs. 5-8 these different parameters are plotted against  $F_{h,0.1\%}$ .

Since the maximum forces are impulse forces (fig. 4 and 5) which are proportional to  $mv^2$ ,  $m$  being the mass of water hitting the structure and  $v$  the water velocity in the up-rush, which is proportional to  $\sqrt{gH}$ , it must be expected that the loading is proportional to  $H$ . The test results verify this, showing a clear linear dependency between  $H_s$  and  $F_{h,0.1\%}$ , Fig. 6. This is also in agreement with results by [1, Bradbury et. al 1988].

Like for  $H_s$  an increase in wave period and thereby wave length gives an increase in the wave load on the structure. Although the scatter is larger than for  $H_s$  Fig. 7 shows that the horizontal force is proportional to the wave length  $L_p$ . This result was also obtained by [8, Jensen 1984] whereas [1, Bradbury et. al 1988] found proportionality between the mean zero upcrossing wave period and the loading.

The parameter  $\frac{H_s}{A_c}$ , which incorporates variations in both wave height, water level and armour crest elevation, is in fig. 8 plotted against  $F_{h,0.1\%}$ , showing excellent linear dependency with nearly no scatter around the fitted lines.

In fig. 9 the results for different widths  $B$  of the crest berm are shown. Compared to the other investigated parameters, the influence of  $B$  is surprisingly small. As expected, the overall tendency is that the wave load on the wall decreases with increasing berm width, though when extending the width from  $3d_{n,50}$  to  $4d_{n,50}$  a small increase in the load is observed. No general conclusions of the influence of  $B$  on  $F$  can be drawn without examining the conditions for various force probability exceedence levels and various wave periods.

The last investigated parameter is the crown wall height  $h_f$ . From Fig. 10, where  $h_f$  is plotted against  $F_{h,0.1\%}$  for five different values of  $\frac{H_s}{A_c}$ , it is seen that for small values of  $h_f$  and relative large values of  $\frac{H_s}{A_c}$  an increase of the wall height results in an increase in the wave loading. Unfortunately, only two wall heights are situated in this part of the figure, but by using the point  $(h_f, F) = (0,0)$  it is possible to get an idea of the relation between  $h_f$  and  $F_{h,0.1\%}$ . As seen in Fig. 10 this relation is quite non-linear. When the wave wall height is extended above a certain level, an upper limit, exclusively depending on sea state and water level, is reached. From this upper limit the wave force will no longer depend on  $h_f$ . For very low walls the influence of the sea state more or less vanishes and the horizontal force only depends on the height of the wave wall. This situation is caused by excessive overtopping where a large part of the up-rushing water spills over the structure without causing significant impulse loads.



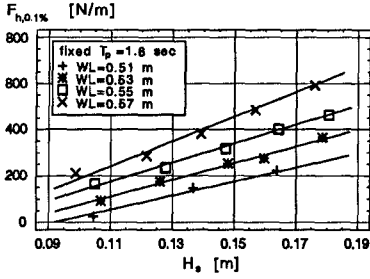


Fig. 6 - Influence of  $H_s$

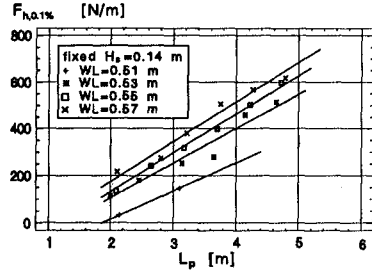


Fig. 7 - Influence of  $L_p$

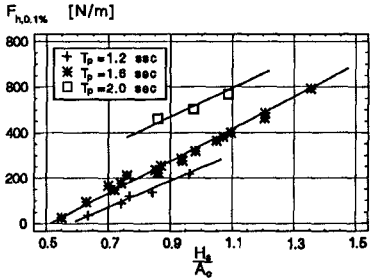


Fig. 8 - Influence of  $\frac{H_s}{A_c}$

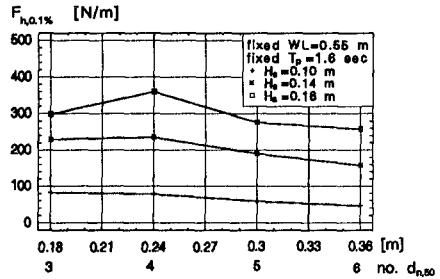


Fig. 9 - Influence of berm width  $B$

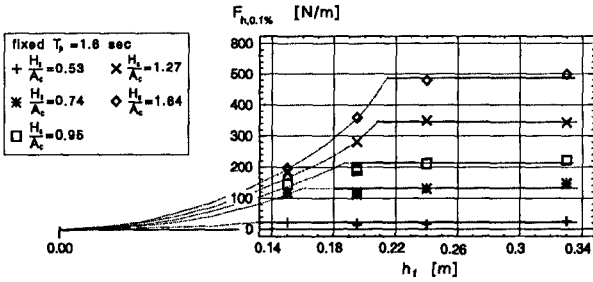


Fig. 10 - Influence of  $h_f$

Guidelines for calculation of horizontal wave force

At present the only way to determine the horizontal wave loading on a crown wall accurately is by means of physical model tests. Based on such tests [8, Jensen 1984] proposed the following empirical relationship between  $F_{h,0.1\%}$  and some of the parameters also examined in the present study :

$$\frac{F_{h,0.1\%}}{\rho g h_f L_p} = a \left( \frac{H_s}{A_c} + b \right) \tag{1}$$

where  $\rho$  is the water density and  $a$  and  $b$  are dimensionless empirical coefficients. Although the method by which the different parameters have been non-dimensionalised is not fully correct, the main features of the formula are verified by the current study. Figs. 6 and 7 show the same linear influence of  $H_s$  and  $L_p$  respectively as expressed in eq. 1. The influence of the wall height  $h_f$  however, which in eq. 1 also is expressed as proportional to  $F$ , can not be confirmed. Although slightly unreliable due to the relative few wall heights tested the current study shows that  $h_f$  should enter the formula in a power larger than 1. Assuming that the major part of the load is caused by hydrostatic water pressure, one finds that the horizontal force is a function of  $h_f^2$  which, although the forces are merely caused by impact pressures, supports the present observations.

In Fig. 11 the ratio  $\frac{H_s}{A_c}$  is plotted against the left hand side of equation 1 for model test results obtained from [8, Jensen 1984], [1, Brabury et. al 1988] and the present study.

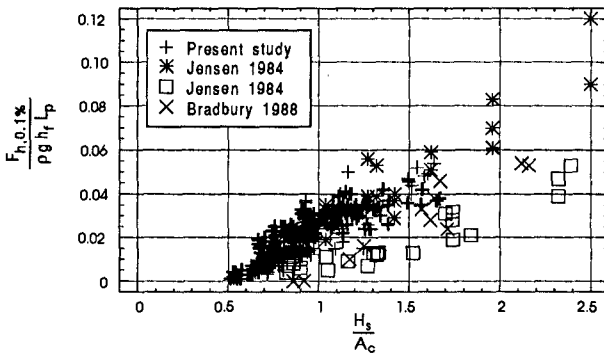
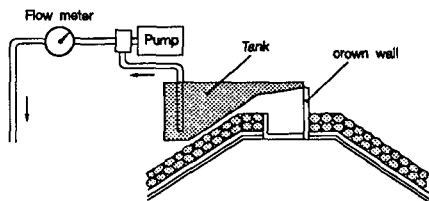


Fig. 11 - Different model test results plotted according to eq. 1.

Although not fully explaining the influence of all relevant parameters, and showing quite a lot of scatter compared to the model test results, eq. 1 still provides a satisfactory first estimate on the wave loading on the crown wall.

## Overtopping

In all model tests performed also the mean overtopping rate  $Q_m$  was measured. An 0.5 m wide tank for collection of the water discharged over the crown wall was installed in the middle of the test section and fitted to the top of the wall. From the tank the water was automatically pumped through a flow meter and back into the flume. Reading of the flow meter was taken after each test. Fig. 12 illustrates the used setup.



*Fig. 12 - Sketch of setup for overtopping measurements.*

Like for the study of the wave forces the overtopping results are used to examine the influence of the different sea state and geometrical parameters on  $Q_m$ .

## Influence of parameters

Fig. 13 shows the significant wave height plotted against  $Q_m$  for fixed wave period, wall height and berm width but for different water levels. As seen the influence from  $H_s$  on  $Q_m$  is very large.  $Q_m$  is approximately proportional to  $H_s^5$ . In Fig. 14 the influence of changes in water level and wall height is shown.  $R_c$  being the distance from the still water level to the top of the wave wall, is able to incorporate the variations of both parameters. The ratio  $\frac{H_s}{R_c}$  is seen to constitute an important dimensionless parameter expressing the influence of both the wave height and the vertical distance to the top of the structure.

Several examinations of how the wave period alters  $Q_m$  were carried out, showing no general dependency for nor  $T_p$  or  $L_p$ . The ratio  $\frac{L_m^2}{T_m^2}$  (or  $c_m L_m$ ) where  $T_m$  is the mean zero upcrossing period and  $L_m$  and  $c_m$  the corresponding wave length and wave celerity, offers a very fine expression for the influence of the period cf. Fig. 15. This figure shows, with nearly no scatter around the fitted lines, that

$Q_m$  depends linearly on  $\frac{L_m^2}{T_m}$ .

Finally also the influence of the armour berm width  $B$  on the mean overtopping rate has been investigated. As expected Fig. 16 shows that when  $B$  increases the amount discharged over the wall decreases.  $Q_m$  is approximately proportional to  $\frac{1}{B}$ .

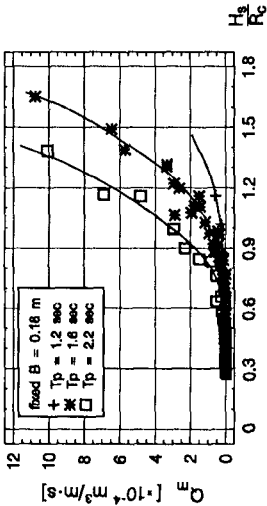


Fig. 14 - Influence of  $\frac{H_s}{R_c}$

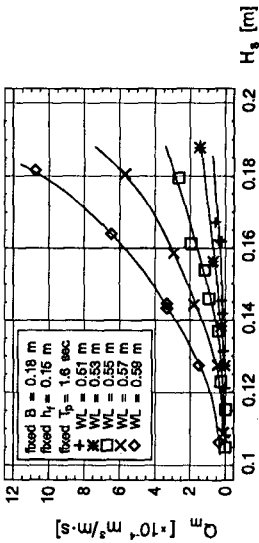


Fig. 13 - Influence of  $H_s$

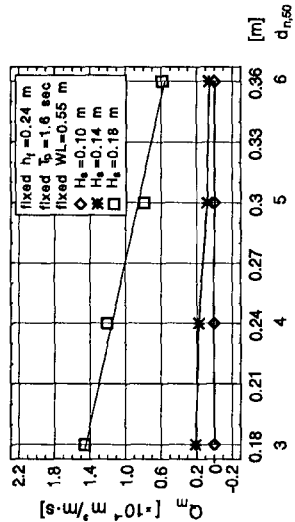


Fig. 16 - Influence of berm width  $B$

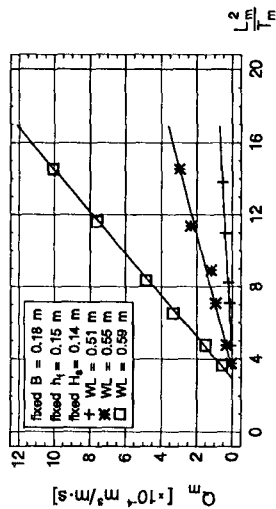


Fig. 15 - Influence of  $\frac{L_m^2}{T_m}$

Guidelines for calculation of mean overtopping rates

Several researchers have studied the subject of overtopping of coastal structures. Probably the most comprehensive work concerning crown walls on rubble mound breakwaters is found in [1, Bradbury et. al 1988]. Based on a large model study the authors suggest the following expression for calculation of the mean overtopping rate :

$$Q^* = \alpha (F^*)^\beta \quad (2)$$

where

$$Q^* : \text{dimensionless discharge} = \frac{Q_m}{T_m g H_s}$$

$$F^* : \text{dimensionless freeboard} = \left( \frac{R_c}{H_s} \right)^2 \sqrt{\frac{s_p}{2\pi}}$$

$\alpha, \beta$  : empirical coefficients depending on breakwater  
and wave wall geometries

In Fig. 17  $\ln(F^*)$  is plotted against  $\ln(Q^*)$  for the model test results obtained in the present study. For all results shown the armour berm width was kept constant at 0.18 m ( $3d_{n,50}$ ). Though some scatter is observed eq. 2 generally predicts the overtopping rates very well. For the actual case  $\alpha$  and  $\beta$  was fitted to  $7.4 \cdot 10^{-8}$  and  $-2.58$  respectively.

Based on the analysis of the influence of the different examined parameters on  $Q_m$  (cf. Figs. 13-16) the following alternative relationship for prediction of the overtopping rates was developed :

$$\frac{Q_m T_m}{L_m^2} = \alpha \left( \frac{H_s}{R_c} \right)^\beta \quad (3)$$

where  $\alpha$  and  $\beta$  are empirical dimensionless coefficients.

As in eq. 2 the influence of the armour berm width must be included in  $\alpha$  and  $\beta$ , since a general non-dimensional expression for this parameter has not yet been found. Also, the effects of permeability, slope angle and slope roughness have to be included in  $\alpha$  and  $\beta$  just as for eq. 2. In Fig. 18 logarithmic values of both sides of eq. 3 are plotted for a fixed armour berm width of 0.18 m ( $3d_{n,50}$ ). Compared to Fig. 17 the scatter around the fitted line is a little smaller.  $\alpha$  and  $\beta$  are fitted to  $1.26 \cdot 10^{-5}$  and 5.2 respectively.

It must be concluded that both models, eq. 3 slightly better than eq. 2, are able to predict the amount of water overtopping the wave wall with quite good accuracy.

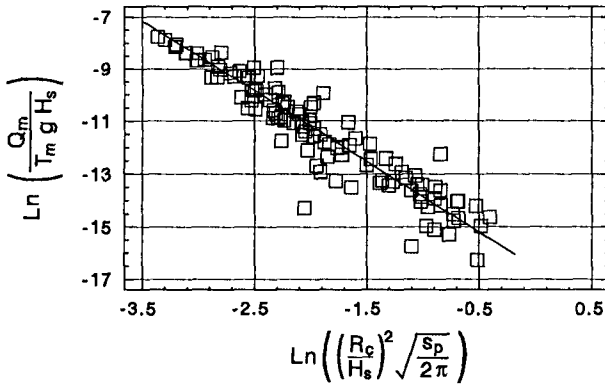


Fig. 17 - Plot of  $\ln(F^*)$  against  $\ln(Q^*)$  from eq. 2.

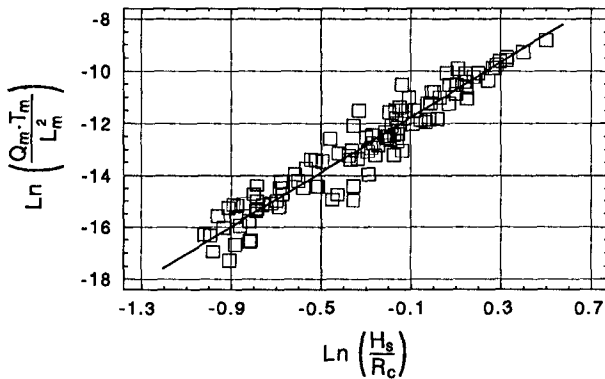


Fig. 18 - Plot of  $\ln\left(\frac{Q_m T_m}{L_m^2}\right)$  against  $\ln\left(\frac{H_s}{R_c}\right)$  from eq. 3.

### Conclusions

Some of the results obtained from an extensive parametric model study concerning wave forces and overtopping on rubble mound breakwater crown walls have been presented.

The analyses more or less confirm the relationship suggested by [8, Jensen 1984] for prediction of the horizontal wave forces, though some discrepancies are observed. Until more work has been carried out on this subject the formula by

Jensen serves well as a first estimate in assessing the wave load.

Concerning wave overtopping a new formula has been developed, which, although not fully complete, is able to predict the mean overtopping rate on the wave wall with quite good accuracy. The relationship proposed by [1, Bradbury et.al] has also been analysed and shows an almost similar accuracy in estimating the amount of water discharged over the crown wall.

## References

- [1] Bradbury A. P., N. W. H. Allsop, R. V. Stevens. *Hydraulic performance of breakwater crown walls*. Hydraulics Research, Wallingford, Report SR146, 1988.
- [2] Burcharth H. F. *Development of a partial coefficient system for the design of rubble mound breakwaters*. PIANC Working Group 12, Subgroup-F report, 1991.
- [3] Burcharth H. F. *Recommendation of a partial coefficient system for the implementation of predetermined safety in the design of rubble mound breakwaters*. PIANC, PTC II, Working Group 12 report, 1991.
- [4] Burcharth H. F. *The design of rubble mound breakwaters*. Aalborg University, In print, to be published, 1993.
- [5] Funke E. R., E. P. D. Mansard. *The measurement of incident and reflected spectra. Using a least squares method*. Proc. Coastal Engineering Conf., 1980.
- [6] Goda Y., Y. Suzuki. *Estimation of incident and reflected waves in random wave experiments*. Proc. Coastal Engineering Conf., Copenhagen, 1976.
- [7] Jensen O. J. *Breakwater superstructures*. Proc. Coastal Structures Conf., Arlington, 1983.
- [8] Jensen O. J. *A monograph on rubble mound breakwaters*. Danish Hydraulic Institute, 1984.
- [9] Oumeraci H. *Dynamic loading and response of caisson breakwaters - Results of large-scale model tests*. MAST G6-S, Project 2 research report, Franzius Institut, 1991.
- [10] van der Meer J. W. *Rock slopes and gravel beaches under wave attack*. Delft Hydraulics, 1991.

## CHAPTER 115

### Optimal Design of Rubble Mound Structures under the Irregular Wave

Cheong-Ro Ryu<sup>1</sup>, Yoon-Koo Kang<sup>2</sup> and Jong-Wook Kim<sup>3</sup>

#### Abstract

A design algorithm for the optimal cost effective rubble mound structures is developed considering extreme wave statistics and wave control functions as well as the stability under the irregular wave attack. In the algorithm, the conventional deterministic design method and the optimization technique, SUMT (Sequential Unconstrained Minimization Techniques) are used to evaluate the minimum cross section of the structure.

The applicability and design sensitivity of the algorithm is examined using experimental data on stability, run-up / overtopping and reflection under the various irregular waves that have different wave grouping characteristics. The field conditions not only the construction method but also the costs can be introduced in the cost estimation subroutine.

#### 1. Introduction

Cost effectiveness is an important factor in the optimal design concept of coastal structures as well as the stability and wave control functions of the structures are. In the design, uncertainty of extreme waves and/or design waves, allowable damage considered destruction process, and various wave control functions of the structures in irregular wave field should be considered, however, these effects were not introduced systematically in the conventional design process (Hudson, 1959; CERC, 1984; Ryu and Sawaragi, 1986; Smith, 1987; Van der Meer, 1987).

In this study, conventional deterministic design method and a new optimization technique, SUMT are used simultaneously and/or as a dual system to develop a systematic design algorithm for the rubble mound structures considering those effects and cost effectiveness. In the construction of the algorithm, previous experimental works on stability, run up / overtopping and reflection by irregular waves with different wave

---

<sup>1</sup> Professor, Dept. of Ocean Eng., National Fisheries University of Pusan, Pusan 608-737, Korea

<sup>2</sup> Graduate Student, Dept. of Civil Eng., Nagoya Univ., Nagoya, Aichi 464, Japan

<sup>3</sup> Researcher, Maritime Research Institute, Hyundai Heavy Industries Co., Ulsan 682-792, Korea



grouping characteristics are applied to the present problem of setting up the modules for design constraints.

To discuss some aspects of the usefulness of the algorithm, we first analyze the reliability of the well known conventional design methods for regular and irregular waves. Next, check the design sensitivity due to the irregularity and the uncertainty of extreme waves, as well as construction field conditions and by introducing design concept of allowable damage and wave control functions.

## 2. Construction of the Optimal Design Algorithm

The algorithm is constructed with the modules for 1) extreme wave probability analysis, 2) structural stability analysis, 3) considering of wave run up, overtopping and reflection problems for wave-structural interaction analysis as the wave control functions, 4) total cost minimizing during life time, 5) drawing the structural dimensions.

In the construction of each module, the up-to-date research results including experimental results carried out in the study and conventional well known results are used simultaneously to study comparatively. In the design process, the conventional deterministic and the optimal design methods are used to calculate the structural dimensions and the total cost.

Figure 1 shows the flow of the optimal cost effectiveness design process. As shown in the figure, the calculation starts with the defined initial total cost ( $TCM_{max}$ ), allowable damage steps (N), return period steps (NN). The total cost for every step can be estimated in the every iteration step, and the cross sectional dimensions for the minimum total cost condition is found as the optimal cost effective design.

## 3. Optimization of the Cross-Section of Structures

### 3.1 Design Variables

Design variables for rubble mound structures with uniform and composite slopes defined as following equation in relation to Figure 2 and Figure 3.

$$X = (X_1, X_2, X_3, X_4, X_5, X_6, X_7, X_8, X_9, X_{10})^T \quad (1)$$

where  $X_1, X_2, \dots, X_n$  are the characteristic length scales of the structure as shown in Figure 2, 3,  $X_5$  in the uniform slope and  $X_8$  in the composite slope are the specific length of the revetment armor, and  $h$  the water depth.

### 3.2 Application of the Optimization Technique

In the development of design algorithm, to minimize the cross-sectional area efficiently, the conventional deterministic design method is applied to calculate initial design variables, and the optimization technique such as Sequential Unconstrained Minimization Techniques (SUMT) are used shown as Figure 1.

The optimal design concept can be expressed as the finding problem of design variables under the condition of minimizing the objective function and satisfying the constraint functions as;

$$\text{Find } X = (X_1, X_2, \dots, X_n)^T \quad (2)$$

$$\text{Minimize : } f(X) \quad (3)$$

$$\text{Subject to : } g_j(X) \leq 0, \quad j=1, \dots, m \quad (4)$$

$$h_k(X) = 0, \quad k = 1, \dots, l \quad (5)$$

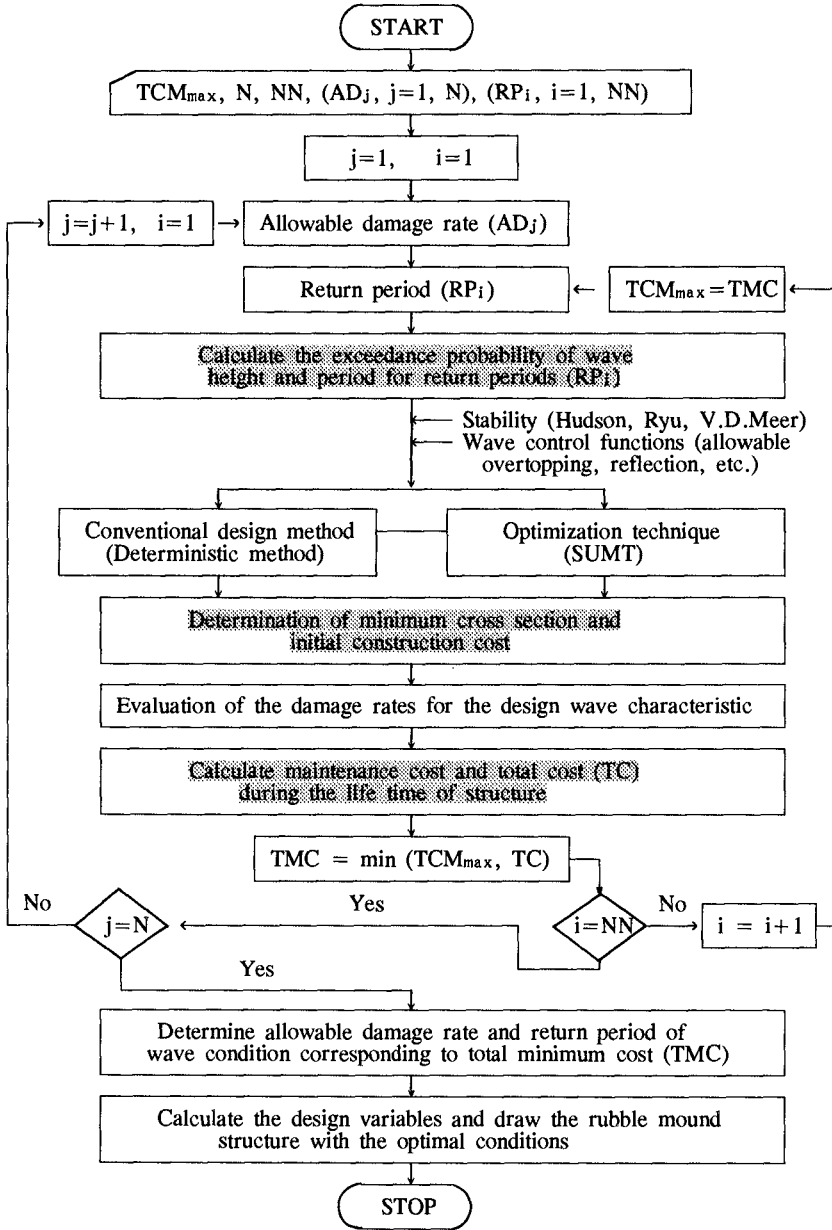


Figure 1. The flow of the optimal design process.

where  $f(X)$  is objective function,  $X$  design variable vector,  $g_j(X)$  the inequality constraints functions, and  $h_k(X)$  the equality constraint functions.

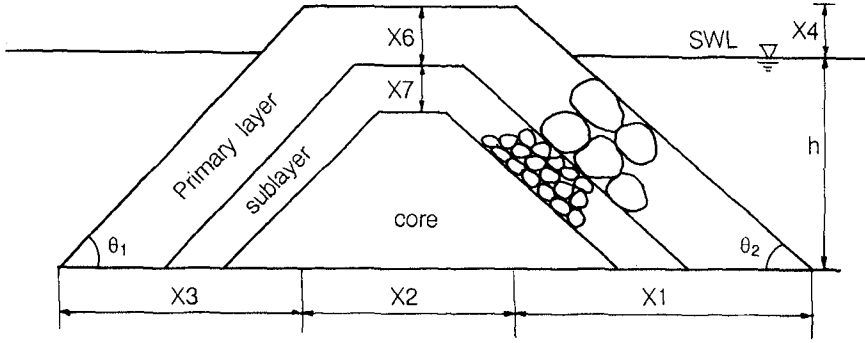


Figure 2. Definition of design variables and sectional area of the rubble mound breakwaters with uniform slope.

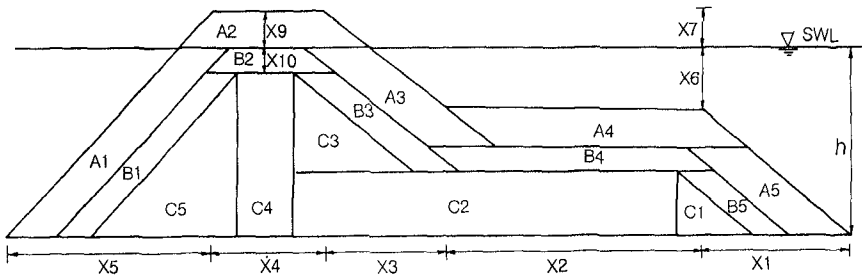


Figure 3. Definition of design variables and sectional area of the rubble mound breakwaters with composite slope.

3.2.1 Objective function

The objective function of cross-sectional area is estimated by following equations for the uniform slope.

$$\begin{aligned}
 f(X) &= A + B + C \\
 &= A_1 + A_2 + A_3 + B_1 + B_2 + B_3 + C_1 + C_2 + C_3
 \end{aligned}
 \tag{6}$$

where,

$$\begin{aligned}
 A1 &= X6 / \sin\theta1 * (h + X4 - X6) \\
 A2 &= (X2 + X2 + X6 / \tan\theta1 + X6 / \tan\theta2) * X6/2 \\
 A3 &= X6 / \sin\theta2 * (h + X4 - X6) \\
 B1 &= X7 / \sin\theta1 * (h + X4 - X6 - X7) \\
 B2 &= [(X2 + X6 / \tan\theta1 + X6 / \tan\theta2 - X6 / \sin\theta1 - X6 / \sin\theta2) \\
 &\quad + (X2 + X6 / \tan\theta1 + X6 / \tan\theta2 - X6 / \sin\theta1 - X6 / \sin\theta2) \\
 &\quad + X7 / \tan\theta1 + X7 / \tan\theta2)] * X7/2 \\
 B3 &= X7 / \sin\theta2 * (h + X4 - X6 - X7) \\
 C1 &= (h + X4 - X6 - X7) * (h + X4 - X6 - X7) / (2 * \tan\theta1) \\
 C2 &= [X2 - (X6 / \sin\theta1 - X6 / \tan\theta1) - (X7 / \sin\theta1 - X7 / \tan\theta1) \\
 &\quad - (X6 / \sin\theta2 - X6 / \tan\theta2) - (X7 / \sin\theta2 - X7 / \tan\theta2) \\
 &\quad * (h - X6 - X7) \\
 C3 &= (h + X4 - X6 - X7) * (H + X4 - X6 - X7) / (2 \tan\theta2)
 \end{aligned}$$

The cross-sectional area for the composite slope can also calculate by the same conception in relation to Figure 3 as

$$\begin{aligned}
 f(X) &= A + B + C \\
 &= A1 + A2 + A3 + A4 + A5 \\
 &\quad + B1 + B2 + B3 + B4 + B5 \\
 &\quad + C1 + C2 + C3 + C4 + C5
 \end{aligned} \tag{7}$$

where  $A$ ,  $B$  and  $C$  are the area of cover layer, sublayer and core layer respectively.

### 3.2.2 Design Constraint Functions

#### (1) Estimation of Extreme Wave Conditions

Using the relation between the return period (RP) and non-exceedance probability,  $P(X \leq x)$  and considering Weibull distribution for the extreme storm wave heights and wave periods for design can be estimated by the following equations.

$$RV = [ - \ln\{ 1 - P( X \leq X_{m, n} ) \} ]^{1/k} \tag{8}$$

$$X = a_0 RV + b_0 \tag{9}$$

where  $RV$ : transformed variable for the non-exceedance probability,  $m$ : order of data,  $n$ : number of data,  $X$ : variables (wave height & period),  $k$ : parameter of extreme value distribution function,  $a_0$ ,  $b_0$ : regression constants.

The uncertainties of the extreme waves are defined by the reliability analysis, and the design waves with confidence interval can be expressed as

$$H_{1/3} = H_{1/3}' \pm \sigma H_{1/3} \tag{10}$$

$$T_{1/3} = T_{1/3}' \pm \sigma T_{1/3} \tag{11}$$

in which  $H_{1/3}$  is the significant wave height,  $T_{1/3}$  is the significant wave period, superscript ' denotes the value from the regression formular equation (2),  $\sigma H_{1/3}$  and  $\sigma T_{1/3}$  are the uncertainty parameter for extreme wave height and period respectively, and (+) and (-) signals denote the upper and the lower confidence level.

The extreme / design wave characteristics for the return periods ( $RP_i$ ;  $i=1, NN$ ) can be estimated from the equations (9), (10), (11).

## (2) Stability Analysis of Rubble Mound Structure

Among the many well known conventional design formulas, Hudson (1959) and CERC (1984) for the regular wave, and Ryu & Sawaragi (1986) and Van der Meer (1987) for the irregular waves are applied for the stability check in the algorithm.

For the uniform slope structures:

$$W_H = \frac{\gamma_r H^3}{K_D \cot \theta (S_r - 1)^3} \quad (12)$$

by Hudson (1959) & CERC (1984)

$$W_R = \left[ \frac{\gamma_w (6.15 Q_p + 20.0) \tan \theta}{\gamma_r^{1/3} (D_R + 30.1) \tan \phi} \right]^{3/2} H_{1/3}^3, \quad (13)$$

by Ryu and Sawaragi (1986)

$$W_V = \frac{\xi_z^{3/2}}{\{6.2 P^{0.18} (D_V / \sqrt{N})^{0.2} \xi_z^{0.5}\}^3} \frac{H_{1/3}^3 \gamma_r}{(S_r - 1)^3} \quad (14)$$

for plunging wave

$$= \frac{1}{\{P^{0.13} (D_V / \sqrt{N})^{0.2} (\cot \theta)^{0.5} \xi_z P\}^3} \frac{H_{1/3}^3 \gamma_r}{(S_r - 1)^3} \quad (15)$$

for surging wave by Van der Meer (1987)

For the composite slope structures:

$$W_R = \left[ \frac{\gamma_w (5.46 Q_p + 17.73) \tan \theta'}{\gamma_r^{1/3} (D_R + 36.3) \tan \phi} \right]^{3/2} H_{1/3}^3 \quad (16)$$

by Ryu and Sawaragi (1986)

where  $W$  is the rubble unit weight, subscripts  $H$ ,  $R$  and  $V$  are the weight by Hudson, Ryu and Sawaragi, and Van der Meer respectively,  $H$  the design wave height,  $K_D$  the empirical stability coefficient,  $\theta$  the angle from horizontal of seaward slope of the structure,  $\gamma_r$  the unit weight of armor unit,  $S_r$  the specific gravity of armor unit,  $Q_p$  the wave spectrum peakedness parameter,  $\tan \phi$  the friction coefficient,  $D_R$  the allowable damage level by Ryu's definition,  $D_{n50}$  the nominal diameter,  $T_z$  the average wave period,  $D_V$  the damage level by Van der Meer's definition,  $P$  the permeability of core,  $\xi_z$  the surf-similarity parameter with average wave period, and  $\theta'$  the equivalent slope of the composite structures.

These stability equations can rearrange to inequality constraint functions for the optimization formulation as

$$g_1(X) = X_5^3 \gamma_r - [ \gamma_r / \cot \theta (K_D (S_r - 1)^3) ] H_{1/3}^3 \geq 0 \quad (12')$$

$$g_1'(X) = X_5^3 \gamma_r - \left[ \frac{\gamma_w(6.15 Q_p + 20.0)}{\gamma_r^{1/3} (D_R + 30.1)} \frac{\tan\theta}{\tan\phi} \right]^{3/2} H_{1/3}^3 \geq 0 \quad (13)'$$

$$g_1''(X) = X_5^3 \gamma_r - \frac{\xi_z^{3/2}}{\{6.2P^{0.18}(D_V/\sqrt{N})^{0.2}\xi_z^{0.5}\}^3} \frac{H_{1/3}^3 \gamma_r}{(S_R - 1)^3} \geq 0 \quad (14)'$$

for plunging wave

$$= X_5^3 \gamma_r - \frac{1}{\{P^{0.13}(D_V/\sqrt{N})^{0.2}(\cot\theta)^{0.5}\xi_z^P\}^3} \frac{H_{1/3}^3 \gamma_r}{(S_R - 1)^3} \geq 0 \quad (15)'$$

for surging wave

$$g_1'''(X) = X_8^3 \gamma_r - \left[ \frac{\gamma_w(5.46 Q_p + 17.73)}{\gamma_r^{1/3} (D_R + 36.3)} \frac{\tan\theta'}{\tan\phi} \right]^{3/2} H_{1/3}^3 \geq 0 \quad (16)'$$

### (3) Wave Control Functions

In considering with function and purpose of the structures, the following equations are used as the design constraints for wave control functions in relation to wave overtopping and reflection (Takada, 1973; Ryu and Kang, 1990; Ryu, 1984).

$$g_2(X) = AQ - Q \geq 0 \quad (17)$$

$$g_3(X) = AR - K_r \geq 0 \quad (18)$$

$$Q = 0.5a(R_u - H_c)^2 (X_0/R_u - \cot\theta) \quad (19)$$

$$a = 7.6 (\cot\theta)^{0.73} (H_0/L_0)^{0.83} \quad (20)$$

$$R_u = [1.17 \xi_{1/3}/(1 + 0.8 \xi_{1/3})] \times H_{1/3}, \text{ for the uniform slopes} \quad (21)$$

$$K_r = 0.5 \left[ \frac{(\xi_{1/3} - 2.65 \tan\theta)}{4.3} \right]^{0.7}, \text{ for the uniform slopes} \quad (22)$$

where  $AQ$  is the allowable overtopping rate,  $Q$  the overtopping rate,  $AR$  is the allowable wave reflection and  $K_r$  the wave reflection coefficient,  $R_u$  is run-up height,  $\xi_{1/3}$  is significant surf-similarity parameter,  $H_c$  is the crest height,  $X_0 = L_0/4$ , and  $L_0$  and  $H_0$  are deep sea wave length and height respectively.

For the composite slopes, the same inequality constraints are used as equations (17) and (18), however the run-up and the wave reflection characteristics on the composite slope are considered referred to the analysis results with phase interaction mechanism on the composite slope face by Ryu et al. (1986) instead of equations (21) and (22).

Crest width, slope stability and other design constraints can also be included from necessity.

## 4. Optimal Cost Effectiveness

### 4.1 Initial Construction Cost (ICC)

Initial construction cost is very different by field by field, however, the cost changes can be defined to be proportional to the cross-sectional area and material scales. The relation simply can express as following equation.

$$ICC = \alpha_a A + \alpha_b B + \alpha_c C \quad (23)$$

The weight functions  $\alpha_a$ ,  $\alpha_b$  and  $\alpha_c$  should be change with the field conditions, construction facilities and techniques, and other a lot of constraints. Where  $A$ ,  $B$ , and  $C$  are the unit costs of the cover layer, sublayer and core layer respectively.

#### 4.2 Maintenance Cost

To estimate the maintenance cost, the probability of failure occurrence should be considered as denoted as following equation.

$$dF = (1 - (1 - \Delta P))^\lambda \quad (24)$$

where  $dF$  denotes the probability of failure occurrence per a year,  $\Delta P$  is the exceedance probability of wave conditions, and  $\lambda$  the total number of wave events per a year to destruct. If it can be assumed that the maintenance work will be immediately made after damage is accrued, the total maintenance cost during life time of structures ( $TMY$ ) is given by

$$TMY = \int_L^U [\alpha_f (EDR \times ICC)] dRP \quad (25)$$

where  $dRP$  is considered interval of the return period,  $U$  and  $L$  are the upper and lower limit of the return period,  $EDR$  is the equivalent damage rate, and  $\alpha_f$  the weighting value for repair compare to the initial construction cost.  $\alpha_f$  in the equation is one of the sensitive constant in the maintenance cost estimation. It is very changeable parameter by field by field, and the value in the  $[\alpha_f (EDR \times ICC)]$  means the maintenance cost per a year.

#### 4.3 Total Cost (TC) Minimization

Total cost during the life time ( $TC$ ) can be written as the sum of initial construction cost ( $ICC$ ) and total maintenance cost ( $TMY$ ). The maintenance cost  $TMY$  is required every year, and the cost can be changed to the present value considering interest / discount rate and the other effects.

The typical total cost change is shown in Figure 4, and it can be written as

$$TC = ICC + P_{wf} (TMY) \quad (26)$$

$$P_{wf} = \frac{(1+i)^n - 1}{i(1+i)^n} \quad (27)$$

where  $P_{wf}$  denotes the present value exchange rate,  $i$  the discount rate,  $n$  the life time of the structure. In the above equation,  $i$  is an important and effective parameter in the  $TC$  calculation, and it is changeable by the economic conditions.

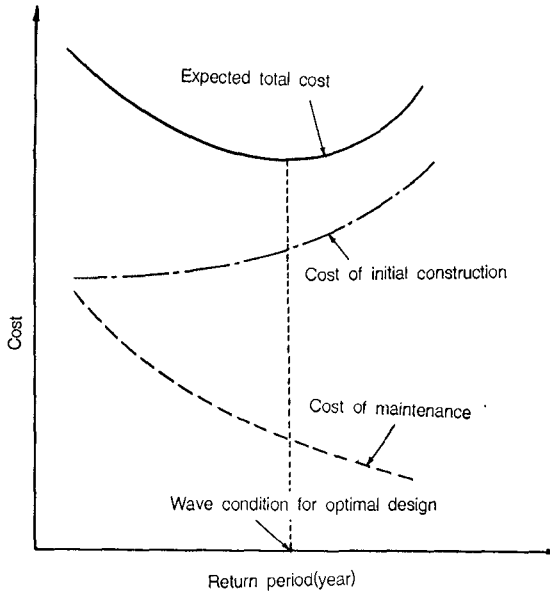


Figure 4. Construction, maintenance, and total costs as functions of wave conditions.

If those effective parameters such as  $i$ ,  $\alpha_f$ ,  $\alpha_a$ ,  $\alpha_b$  and  $\alpha_c$  can be introduced reasonably in the cost estimation, the minimum cost condition can be found easily by the conception as shown in Figure 4.

## 5. Application of the Design Algorithm

### 5.1 Variation of the Cross-Section for Uniform Slope

Using the wave observed data at the east coast of Korean Peninsula, the extreme wave characteristics can be derived as

$$\left. \begin{aligned} H_{1/3} &= 1.01 RV + 1.93 \\ T_{1/3} &= 2.50 RV + 6.66 \end{aligned} \right\} \quad (28)$$

where the symbols are same as equations (8) and (9). The unit construction cost and other design constraints are also referred to G-port in Korea

From the equation (28), extreme / design wave characteristics by return periods can be easily estimated, and can get the cross-sectional dimensions by the algorithm. Figure 5(a) shows the cross-sectional variation characteristics due to the select of return period for the design waves. Figure 5(b) indicates the effect of allowable reflection of waves on the cross-section. The detail dimensions are illustrated in the Figures. From the Figures, it can be remarkably said that the allowable reflection very sensitively affect to the slope angle and total cross-sectional area, and the change of design waves



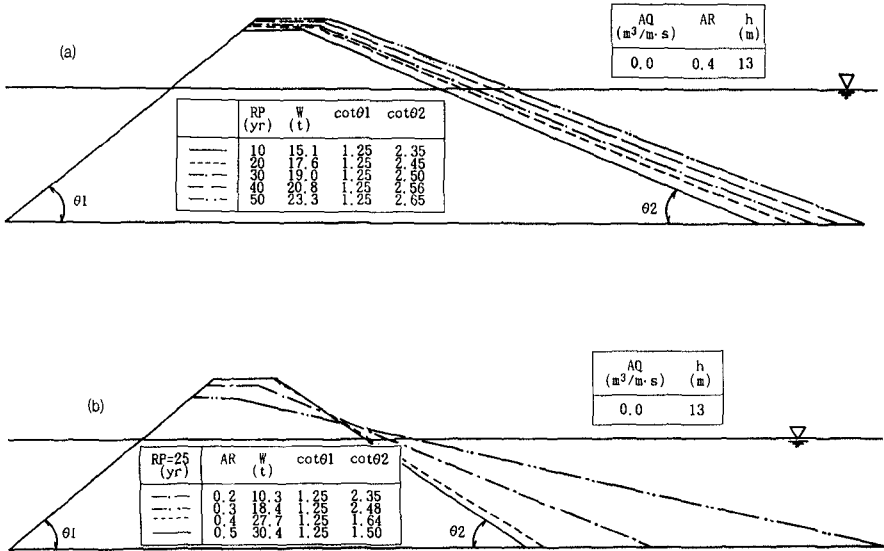


Figure 5. The cross-sectional variation characteristics due to the select of return period for the design waves and the effect of allowable reflection of waves on the cross-section.

affects to the weight of cover layer armor unit. Figure 6 shows the cross-sectional and the crest height changes as well as the rubble weight and the slope angle variations due to the allowable overtopping rate as a function of return period of design waves.

In the calculation the allowable reflection coefficient  $AR$  is considered to  $0.3$ , and Ryu and Sawaragi's formula is applied to the stability analysis with allowable damage rate  $D_R = 60\%$  and spectral peakedness parameter of irregular wave  $Q_p = 2.0$ . From the figures it can be concluded that allowable overtopping rate affects sensitively on the change of crest height. As the result the cross-sectional area is also changed by the rate as a function of the return period.

Figure 7 shows the effects of the spectral peakedness parameter of irregular design waves. In the figure, it is also found that the effects can not be neglected in the design as neglected in a lot of conventional design formulas.

### 5.2 The Cross-Section Changes of Composite Slope

The optimal design results for the composite slope structures are listed in Table 1. In this case, the reflection control functions are considered with the reflection coefficient at boundary 1, berm front, to be less than  $0.4$ , and the overtopping is not allowed. In the table, it can understand that the design variables are sensitively affected by the extreme wave statistics (RP). The berm width and depth are especially sensitive with a small change of design waves. These may will be more changeable if the allowable reflection is considered as a function of the wave statistics with a conception of environmental wave control in a sea area.

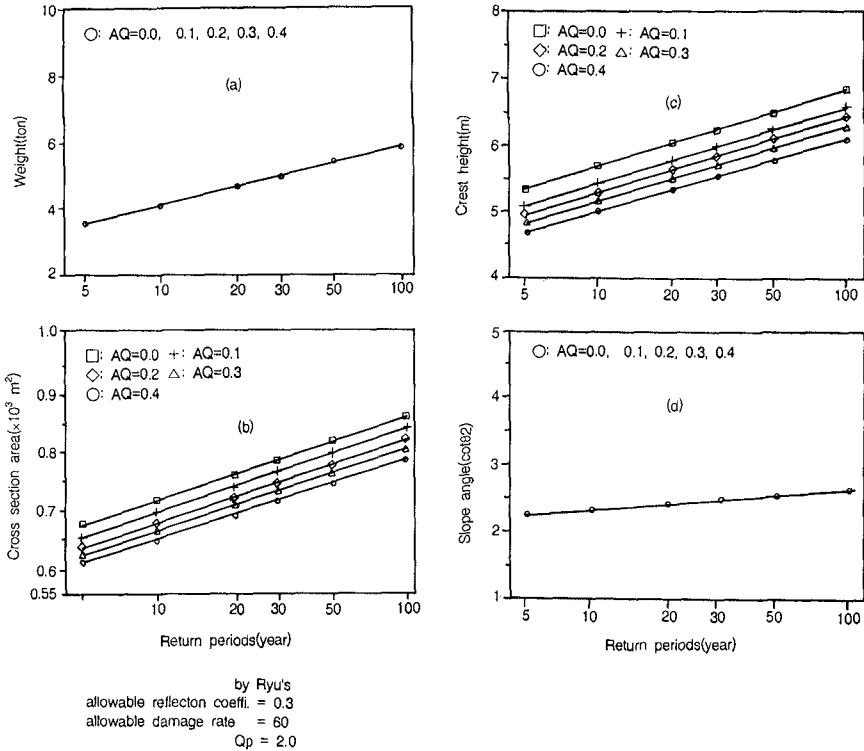


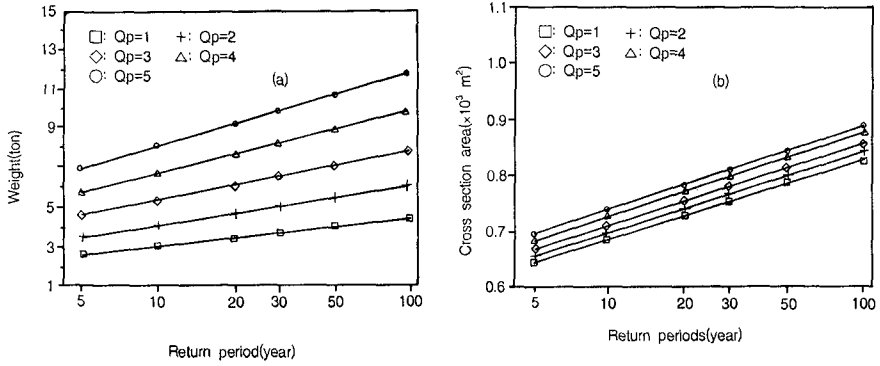
Figure 6. The variations of design variables according to the allowable overtopping rates.

Table 2 shows the results of the design variables change due to the allowable damage. The rubble weight, X8 has a decreasing tendency with increasing of allowable damage  $D_R$ , however, we can not find a typical cross sectional area in the table.

From these results, it is emphasized that the algorithm can be applied to the design of composite slope structures.

### 5.3 Total Cost Variations

Figure 8 is the final results on unit total cost calculation by the algorithm. It changes according to the return period and the other design constraints listed in the figure, and we can easily find the minimum cost point by the design conditions. Although, it is a special application example and the result can be changed by field by field, it can be emphasized that the minimum point take place in some region of medium return periods shorter than 50 years. It means that the optimal design concept is a reasonable design method for the systematic and cost effective coastal developments.



by Ryu's  
 allowable overtopping rate = 0.3  
 allowable reflection coeff. = 0.3  
 allowable damage rate = 60

Figure 7. The effects of the spectral peakedness parameter of irregular design waves.

Table 1. Optimal design variables for the composite slope according to the return period of the waves

RP (year)		1	5	10	20	30	40	50	100
$H_{1/3}$ (m)		3.15	3.90	4.23	4.55	4.75	4.88	4.99	5.31
$T_{1/3}$ (sec)		13.17	15.40	16.36	17.32	17.88	18.29	18.59	19.55
Dimensions of the section	X1	18.58	17.69	17.22	16.85	16.61	16.60	16.45	16.13
	X2	54.14	74.03	83.55	93.64	99.79	104.42	107.88	119.31
	X3	8.64	10.32	11.03	12.09	12.09	12.41	12.63	13.18
	X4	2.06	2.30	2.39	2.46	2.51	2.54	2.68	2.62
	X5	30.94	31.49	31.70	31.87	31.99	32.15	32.22	32.23
	X6	3.15	3.90	4.23	4.55	4.75	4.88	4.99	5.31
	X7	2.60	2.97	3.11	3.22	3.30	3.37	3.39	3.46
	X8	0.66	0.68	0.71	0.79	0.81	0.81	0.82	0.84
	X9	1.32	1.47	1.53	1.58	1.61	1.63	1.64	1.68
	X10	0.61	0.68	0.71	0.73	0.75	0.76	0.76	0.78

Table 2. Variation of the design variables according to the allowable damage rate D% for the composite slope structure

D (%)		20	40	60	80	DATA
Dimensions of the section	X1	16.60	16.60	16.60	16.60	$H_{1/3} = 4.88$ m
	X2	104.42	104.42	104.42	104.42	$T_{1/3} = 18.29$ sec
	X3	12.41	12.41	12.41	12.41	$Q_p = 2,5$
	X4	2.54	2.34	2.13	1.98	$h = 18$ m
	X5	32.15	32.16	32.16	32.16	
	X6	4.88	4.88	4.88	4.88	
	X7	3.37	3.35	3.35	3.35	
	X8	0.81	0.75	0.68	0.64	
	X9	1.64	1.50	1.36	1.27	
	X10	0.76	0.70	0.63	0.59	

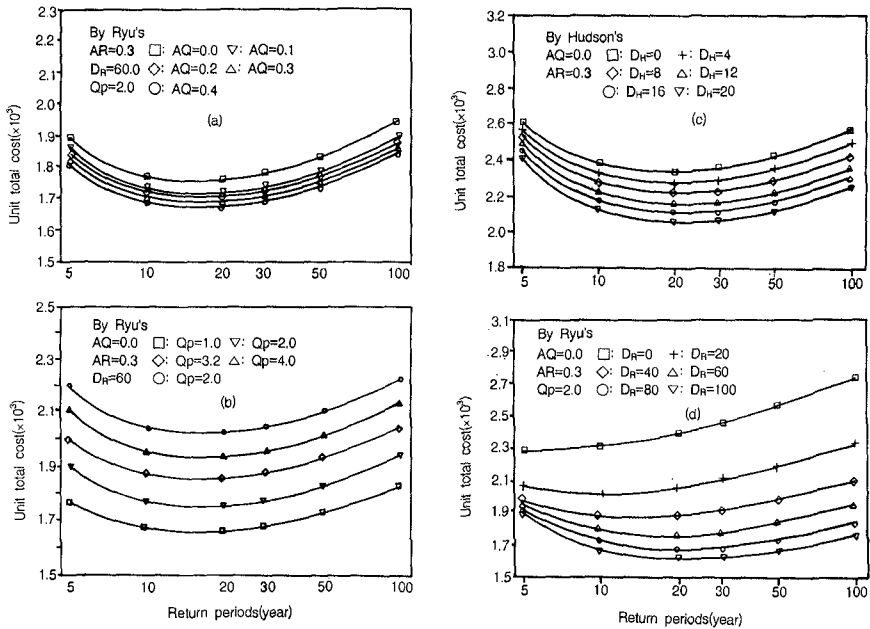


Figure 8. The final results on unit total cost calculation in the algorithm according to the return period and the other design constraints.

## 6. Conclusions

The conclusions obtained herein are as follows:

A cost-effective design algorithm of rubble mound structure with various slope shapes has been developed considering the uncertainty and irregularity of design waves / the return period of extreme waves, allowable damage ( $D_R$ ), and wave control functions.

The reliability of the design results can be directly estimated using the algorithm. It means that the design algorithm can overcome the design fault because of the design wave selection problems in the extreme waves. In considering the allowable ranges of the design constraints and irregularity of the design wave, the design sensitivity can easily be checked also by using the algorithm.

In order to examine the applicability of the algorithm, the design sensitivity for the structural dimensions and total costs are analysed and compared with those of conventional methods using design examples. From the results of comparative studies, the algorithm is found to be applicable, and it will be more useful and powerful algorithm for the design of rubble mound structures under the more complex design conditions, design constraints, and cost functions.

## Acknowledgements

Part of this work has been financially supported by RCOID, National Fisheries Univ. of Pusan. The authors wish to thank Professor N. Kobayashi, Univ. of Delaware, USA and Professor T. Sawaragi, Osaka Univ., Japan for their fruitful comments.

## References

- Hudson, R. Y.(1959): Laboratory investigation of rubble mound breakwaters, J. Waterway, Port, Coastal and Ocean Engineering, ASCE, Vol. 85, 93-121.
- Ryu, C. R. and Kang, H. Y. (1990): A prediction model of irregular wave run-up height on coastal structures, Proc. 22nd ICCE, ASCE, 371-383.
- Ryu, C. R. and Sawaragi T. (1986): A new design method of rubble mound structures, Proc. 20th ICCE, ASCE, 2188-2202.
- Smith, O.P. (1987): Cost effectiveness of breakwater cross section, J. of Waterway, Port, Coastal and Ocean Engineering., ASCE, Vol. 113, 447-460.
- Van der Meer (1987): Stability of breakwater armor layer design formulae, Coastal Engineering, Vol. 11, 219-239.
- C.E.R.C.(1984): Shore Protection Manual, 4th ed, Vol.II, 7-202-243.
- Takada, A.(1973) : On the relation between run-up wave shape and overtopping rate, Proceedings of JSCE, 212, 25-39.
- Ryu, C.R. (1984): On the optimal design of the rubble mound breakwaters, Ph.D. Thesis, Dept. of Civil Engineering, Osaka University, 167 p.
- Ryu, C.R. and Sawaragi, T. (1986): Wave control functions and design principles of composite slope rubble mound structures, Coastal Engineering in Japan, Vol. 27, 227-240.

## CHAPTER 116

### Numerical simulation of nonlinear wave interacting with permeable breakwaters

T.Sakakiyama<sup>1</sup> and R.Kajima<sup>2</sup>

#### Abstract

A fully nonlinear simulation model was developed to predict the wave transformation interacting with a permeable breakwater. The present model was applied to simulate wave transformations due to a rubble-mound breakwater and due to a caisson breakwater covered with armor units and verified by hydraulic model tests. Numerical experiments were also performed to interpret the stability of armor units and the wave-induced pressure on the caisson through the pile of armor units.

#### 1. INTRODUCTION

Numerical models to predict wave motions near and inside of a rubble mound breakwater have been recently developed. Since some models are based on the linear wave theory (Hölscher *et al.*, 1989), they provide only a change of amplitude of a sinusoidal wave. Others are nonlinear but one-dimensional models, *i.e.*, they are based on the depth-integrated equations (Wurjanto and Kobayashi, 1992). Ohyama and Nadaoka (1991) developed a fully nonlinear model to simulate wave transformation on an impermeable bottom based on the potential theory. No fully nonlinear model including the effect of permeability is developed yet.

The purpose of this paper is to develop a fully nonlinear two-dimensional numerical model to predict the wave transformation in the field which is partially occupied by a permeable structure. The interaction between waves and structures is expressed by the resistance forces in the structures, the drag and inertia forces. In this paper, analyzed are the wave transformations due to a rubble-mound breakwater and due to a caisson breakwater covered with armor units both in

---

<sup>1</sup> Senior research engineer, Central Research Institute of Electric Power Industry, 1646, Abiko, Abiko-city, Chiba, 270-11, Japan.

<sup>2</sup> Senior research fellow, ditto.

front and at back. The computations are compared with hydraulic experimental results. Numerical experiments are also carried out to investigate the wave force acting on the armor units and the wave-induced pressure on the caisson through the pile of armor units.

## 2. Numerical simulation method

### 2.1 Governing equation

Sha *et al.*(1977) derived the quasi-continuum governing equations for conservation of mass, momentum and energy called the porous body model(PBM). Their purpose was to apply these equations to the flow in a class of systems, such as heat exchangers and fuel-rod bundles in a nuclear reactor.

The governing equations of PBM for incompressible two-dimensional flow are modified to apply it to the wave field(Sakakiyama,1991). The inertia and the drag forces are introduced into the horizontal and vertical components of the momentum equations, and rearranging them yields the following equations:

Continuity equation

$$\frac{\partial(\gamma_x u)}{\partial x} + \frac{\partial(\gamma_z w)}{\partial z} = 0, \quad (1)$$

Momentum equation

$$\lambda_v \frac{\partial u}{\partial t} + \lambda_x u \frac{\partial u}{\partial x} + \lambda_z w \frac{\partial u}{\partial z} = -\gamma_v \frac{\partial \phi}{\partial x} - R_x + \frac{1}{\rho} \left\{ \frac{\partial(\gamma_x \tau_{xx})}{\partial x} + \frac{\partial(\gamma_z \tau_{zx})}{\partial z} \right\}, \quad (2)$$

$$\lambda_v \frac{\partial w}{\partial t} + \lambda_x u \frac{\partial w}{\partial x} + \lambda_z w \frac{\partial w}{\partial z} = -\gamma_v \frac{\partial \phi}{\partial z} - \gamma_v g - R_z + \frac{1}{\rho} \left\{ \frac{\partial(\gamma_x \tau_{xz})}{\partial x} + \frac{\partial(\gamma_z \tau_{zz})}{\partial z} \right\}, \quad (3)$$

where

$$\left. \begin{aligned} \lambda_v &= \gamma_v + (1 - \gamma_v) C_M \\ \lambda_x &= \gamma_x + (1 - \gamma_v) C_M \\ \lambda_z &= \gamma_z + (1 - \gamma_v) C_M \end{aligned} \right\} \quad (4)$$

and  $\lambda_v$  is the volume porosity and  $\lambda_x$ ,  $\lambda_z$  the horizontal and vertical components of the surface permeability, respectively.  $\phi = p/\rho$  is the ratio of the pressure  $p$  to the density of the fluid  $\rho$  and  $u$ ,  $w$  the velocity components in the  $x$ - and  $z$ -direction respectively,  $g$  the acceleration due to gravity,  $\tau$  the viscous stress acting on the surface of the control volume. The drag forces are modeled by Eq. (5) and Eq. (6),

$$R_x = \frac{C_D}{2\Delta x} (1 - \gamma_x) u \sqrt{u^2 + w^2} \quad (5)$$

$$R_z = \frac{C_D}{2\Delta z} (1 - \gamma_z) w \sqrt{u^2 + w^2} \quad (6)$$

Unknown are the inertia and drag coefficients  $C_M$ ,  $C_D$ , which are experimentally determined.

### 2.2 Boundary conditions

The continuity equation Eq. (1) and the momentum equations (2) and (3) are numerically solved with appropriate boundary and initial conditions.

A kinematic boundary condition on the free surface is expressed as:

$$\frac{\partial \eta}{\partial t} + u_s \frac{\partial \eta}{\partial x} = w_s \tag{7}$$

where  $\eta$  is the free surface displacement,  $u_s$  and  $w_s$  are the horizontal and vertical components of the velocity on the free surface  $\eta$ , respectively.

A dynamic boundary condition at the free surface is represented by the following:

$$p = 0 \quad \text{on} \quad z = \eta \tag{8}$$

At a bottom boundary, a free slip condition is imposed. When a water depth is uniform, the slip conditions for the velocity  $u$ ,  $w$  and the pressure  $p$  are expressed as follows:

$$\frac{\partial u}{\partial z} = 0 \tag{9}$$

$$w = 0 \tag{10}$$

$$\frac{\partial p}{\partial z} = -\rho g \tag{11}$$

The boundary condition on the pressure given by Eq. (11) is led by substituting Eq. (10) into the vertical component of the momentum equation, Eq. (3). In the case that a boundary contains an impermeable vertical wall, the similar free slip condition is imposed at the impermeable boundary.

An inflow boundary works as a wavemaker. Perturbation solutions of the nonlinear wave theory by Isobe *et al.*(1978) are used to give the inflow boundary conditions. The nonlinear wave theory applied to the inflow boundary condition depends on the following wave condition:

$$\left. \begin{array}{l} \text{Stokes wave 5th-order solution} \\ \text{cnoidal wave 3rd-order solution} \end{array} \right\} \begin{array}{l} U_s \leq 25 \\ 25 < U_s \end{array} \tag{12}$$

where  $U_s$  is the shallow water Ursell parameter defined with the long wave length  $L = T\sqrt{gh}$  in the Ursell parameter  $U_r = HL^2h^3$ ;

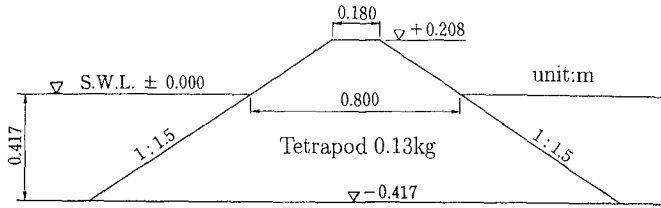
$$U_s = \frac{gHT^2}{h^2}. \tag{13}$$

At an outflow boundary, Sommerfeld's radiation condition is imposed:

$$\frac{\partial F}{\partial t} + C \frac{\partial F}{\partial x} = 0 \tag{14}$$

where  $C$  is the wave celerity and  $F$  denotes the variable  $\eta, u, w$  or  $p$ . Eq. (14) indicates that the variable  $F$  progresses with the phase speed  $C$ .



Fig. 1 Rubble-mound breakwater( $\lambda = 1/60$ )Table 1 Experimental conditions for rubble-mound breakwater( $\lambda=1/60$ )

wave period $T$ (s)	wave height $H$ (m)	water depth $h$ (m)	Tetrapod		
			$W$ (kg)	$b$ (m)	$\epsilon$
1.50	0.015-0.275	0.417	0.13	0.059	0.53

The initial condition is set as the still water state. The surface displacement  $\eta$  at  $t = 0$  is null for a whole computational region as well as  $u = w = 0$ . The pressure  $p$  at  $t = 0$  is given by the hydrostatic pressure.

The Poisson equation for the pressure is iteratively solved by the successive over-relaxation(SOR) method with the given boundary and initial conditions mentioned above. The dynamic boundary condition on the free surface given by Eq. (8) is exactly satisfied in an iterative process of the pressure computation by applying the "irregular star" method(Chan and Street,1970).

### 3. Rubble-mound breakwater

#### 3.1 Experiments

The experiments were performed by using a laboratory wave flume (78m long, 1.2m high and 0.9m wide). The model breakwater was a conventional trapezoidal rubble-mound breakwater as shown in Fig. 1. The rubble-mound breakwater consists of single size of Tetrapods(weight  $W = 0.13$ kg) for the simplicity to analyze experimental results. The *In Situ* porosity of the breakwater is  $\epsilon = 0.53$ . Slopes of the breakwater surface are 1 on 1.5 for both the seaward and landward side surfaces. Table 1 shows the experimental conditions. The model scale is supposed as  $\lambda = 1/60$ . Water depth at the breakwater is  $= 0.417$ m in the model scale and uniform depth  $h = 0.737$ m. Wave period was  $T = 1.5$ s. Wave height ranges from  $H = 0.015$ m to  $0.275$ m. The maximum ratio of the wave height to the water depth  $H/h$  was up to about 0.65. The nonlinearity of the waves generated was remarkable but wave breaking was not included in the present experimental conditions.

The reflection coefficient was estimated with the method for resolving incident and reflected waves proposed by Goda(1985). The displacements of a transmitted wave were measured at five locations. The averaged values of the five transmitted wave heights are used in the following analysis.

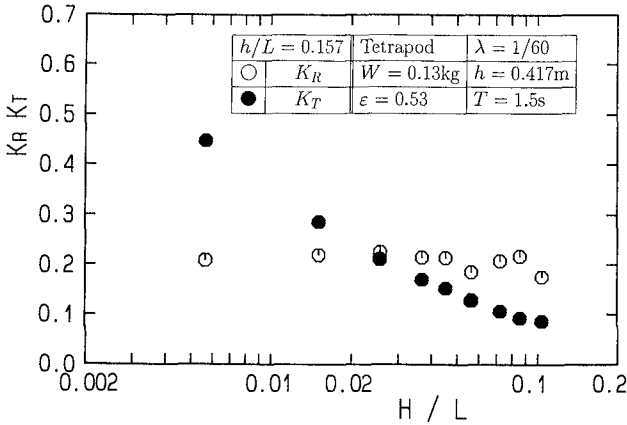


Fig. 2 Reflection and transmission coefficients of rubble-mound breakwater

Table 2 Calculation condition for rubble-mound breakwater

$H(\text{m})$	$T(\text{s})$	$h(\text{m})$	$L_I(\text{m})$	$\Delta x/L_I$	$\Delta z/h$	$\Delta t/T$	cal. region
0.15	1.5	0.417	3.20	1/71.1	1/13.89	1/200	$8.63 \times L_I$

In Fig. 2, the experimental results of the reflection coefficient  $K_R$  and the transmission coefficient  $K_T$  are shown as a function of the wave steepness  $H/L$ , where  $L$  is the wave length at the breakwater ( $h = 0.417\text{m}$ ) estimated by the linear wave theory. As the wave steepness  $H/L$  increases, the transmission coefficient  $K_T$  decreases remarkably but the reflection coefficient  $K_R$  is almost constant. Basically, the wave reflection depends on the porosity and slightly on the inertial resistance. The wave transmission depends on the energy dissipation in the permeable structure. An amount of the energy dissipation is proportional to the product of the friction factor and the velocity squared.

### 3.2 Simulation of wave transformation

The computation was carried out under the wave condition as shown in Table 2. The wave period is  $T = 1.5\text{s}$  and the progressive wave height at the breakwater  $H = 0.15\text{m}$  ( $H/h = 0.36$ ). The horizontal distance of the calculation region was  $8.63 \times L_I$ , where  $L_I$  is the incident wave length at the uniform depth ( $h_I = 0.747\text{m}$ ) obtained from the nonlinear wave theory. The wave lengths are  $L_I = 3.20\text{m}$  at the uniform depth and  $L = 2.68\text{m}$  at the breakwater. The space increments are  $\Delta x = 0.045\text{m}$  ( $\Delta x/L_I = 1/71.1$  and  $\Delta x/L = 1/58.9$ ) horizontally and  $\Delta z = 0.03\text{m}$  ( $\Delta z/h = 1/13.89$ ) vertically. The time increment is  $\Delta t = T/200$ . It took about one hundred minutes with the main frame computer HITAC 680H to calculate 4000 time steps (20 cycles  $\times$  200 steps per wave period) to reach steady state wave motion near the rubble-mound breakwater.

The inertia coefficient  $C_M$  and the drag coefficient  $C_D$  were estimated so that

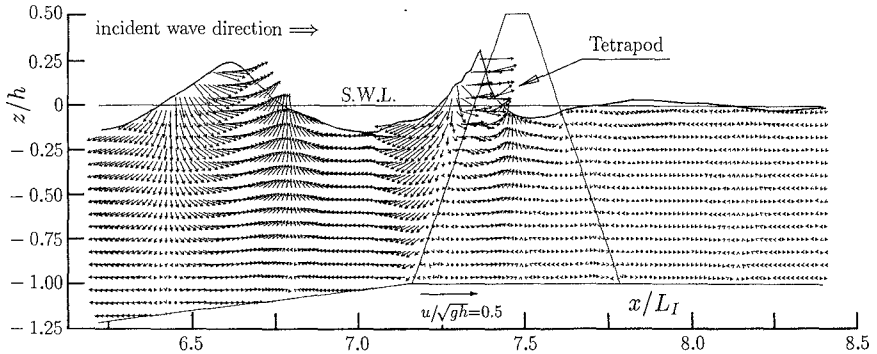


Fig. 3 Simulated result of wave transformation due to rubble-mound breakwater

the reflection and transmission coefficients obtained in the computation might agree well with those in the experiment, respectively. The reflection and transmission coefficients obtained in the computation are  $K_R = 0.15$  and  $K_T = 0.14$ . The corresponding experimental results are  $K_R = 0.18$  and  $K_T = 0.14$ , respectively. The values of  $C_D = 1.2$  and  $C_M = 1.7$  are obtained by best fitting the computation to the experimental result.

Fig. 3 shows one of the computed wave velocity fields near and within the rubble-mound breakwater. Although a partial standing wave is formed at the windward side of the breakwater, the wave profile and its velocity field are rather similar to those of a progressive wave. It is because of a small reflection coefficient ( $K_R = 0.15$  in the computation). Comparing with the profile of partial standing wave, that of wave run-up on the breakwater slope is deformed and becomes steep. The wave attenuation in the permeable breakwater and the wave propagation through it are reasonably simulated.

### 3.3 Wave force acting on armor units

One of the most important physical phenomenon to investigate the stability of armor units is the movement of wave run-up on a breakwater slope. However, it is quite difficult to measure the velocity and acceleration along the slope during the wave run-up and -down in a hydraulic experiment. Numerical simulation is one of the most useful tools to investigate the wave run-up cooperating with hydraulic experiments. A well-calibrated numerical simulation method helps us interpret that phenomenon.

Fig. 4 shows the hodographs of the wave run-up velocity at the two elevations along the armor layer. The vertical heights of the wave run-up and run-down are  $R_{max}/h = 0.209$  and  $R_{min}/h = -0.128$ , respectively. The circles on the curves are time scale, which indicate the moments at every one eighth of the wave period. Arrows show the mean velocity vectors of the wave run-up velocity. The slope of armor layer of the breakwater is indicated with the dashed line. Above the elevation of the wave run-down, the hodographs are not closed. The direction of the mean flow at  $z/h = 0.043$  is into the body of the permeable

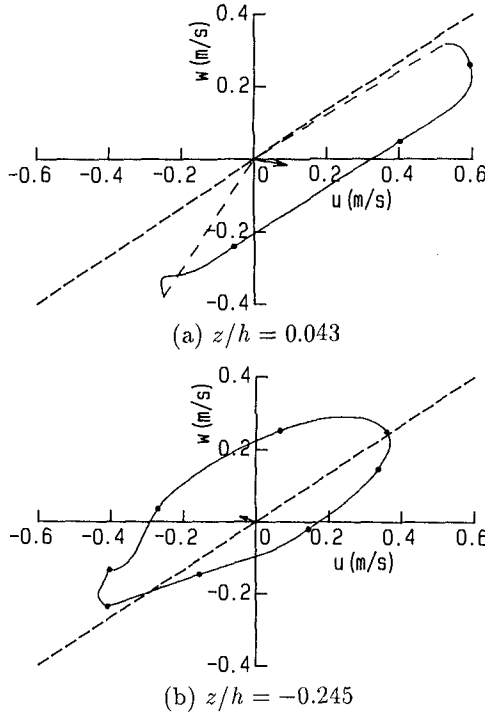


Fig. 4 Velocity hodograph

breakwater. The positive(upward) velocity perpendicular to the slope of the breakwater occurred below  $z/h = -0.101$ . Below the level of the wave run-down,  $z/h < R_{min}/h = -0.128$ , velocity hodographs are closed and make ellipses as shown in Fig. 4(b)  $z/h = -0.245$ , and the apsis of the velocity hodograph is parallel to the slope of the breakwater. Getting close to the bottom, the ellipse becomes flat. The velocity hodograph is affected by the impermeable flat bed.

With the results of the numerical simulation, we discuss wave force action on armor units placed on the slope of the rubble-mound breakwater. Wave force acting on the armor units are estimated by using the Morison equation given by Eq. (15) with the velocity field near the armor layer.

$$\begin{aligned}
 F(x, z, t) &= F_D(x, z, t) + F_I(x, z, t) \\
 &= \frac{1}{2} \rho C_D A u_s(x, z, t) |u_s(x, z, t)| + \rho C_M V \alpha_s(x, z, t) \quad (15)
 \end{aligned}$$

where  $F_D$  is the drag force and  $F_I$  the inertia force. The drag and inertia coefficients  $C_D$ ,  $C_M$  of the single Tetrapod were obtained by Sakakiyama and Ka-

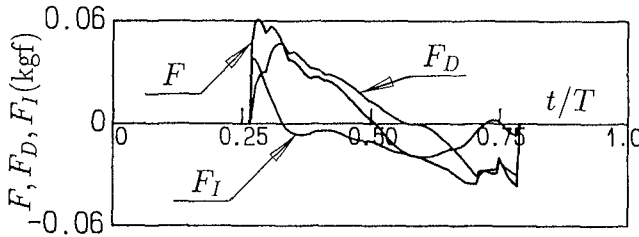


Fig. 5 Time histories of total wave force  $F$ , inertia force  $F_I$  and drag force  $F_D$

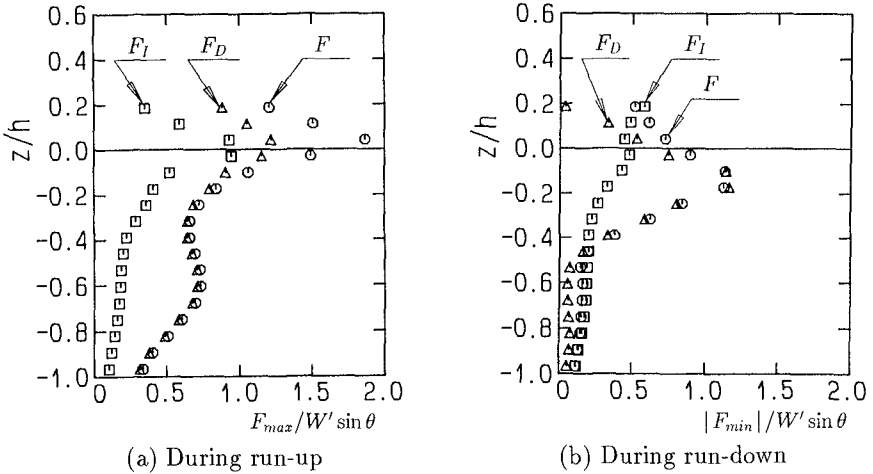


Fig. 6 Vertical profile of wave force on armor units

jima(1990). They show the relationship between  $C_D$ ,  $C_M$  and the Reynolds number with a parameter of  $KC$  number.

Fig. 5 shows the time histories of the wave forces. The drag and inertia coefficients are determined as  $C_D = 1.0$  and  $C_M = 1.0$ , respectively referring to the results by Sakakiyama and Kajima(1990). The time history of the total wave force is very similar to the measured one obtained by Sakakiyama and Kajima(1990) except that the total wave force in Fig. 5 does not contain the buoyant weight of the armor unit. From the time history of the calculated wave force, the inertia force  $F_I$  works for a short time with a large peak behaving like a slamming force. The drag force  $F_D$  has longer duration than the inertia force. It is considered that the slamming force is not dangerous for the stability of the armor units because that force works into the body of the breakwater. However, the breakage of slender and fragile concrete armor units is due to this type of wave force causing the armor units to be rocking (Burcharth *et al.*,1991).

Fig. 6 shows the profiles of the wave force along the slope of the breakwater. The symbols indicate the peak values of the inertia, drag and total forces both

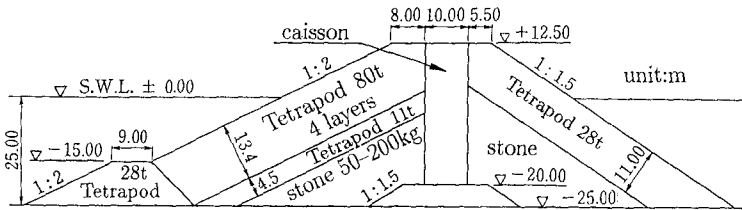


Fig. 7 Caisson breakwater( $\lambda = 1/60$  and  $1/15$ )

Table 3 Experimental conditions for caisson breakwater in prototype

wave period $T(s)$	water depth $h(m)$	wave height $H(m)$	
		$\lambda = 1/60$	$\lambda = 1/15$
15.5	25.0	1.08-17.64	1.08-16.92

during the wave run-up in Fig. 6(a) and during run-down in Fig. 6(b). The axis of abscissa indicates the ratio of the wave force to  $W' \sin \theta$ , where  $W'$  is the buoyant weight of an armor unit,  $\theta$  the angle of breakwater slope. The ratio of the value of unity means the incipient condition of the armor unit when the friction force between armor units is neglected. The computational results shows that the profiles of the drag, inertia and total forces have the maximum values near the still water level during the wave run-up. During the wave-run down, the maximum value of the total wave force is found close to that of the drag force at  $z/h \simeq -0.2$ . It agrees with the fact that the armor units near the still water level are the most unstable as we have experienced in hydraulic experiments.

## 4. Caisson breakwater covered with armor units

### 4.1 Experiments

The experiments on a caisson breakwater covered with armor units were performed by using both a large wave flume(205m long, 6.0m deep and 3.4m wide) and a small one(78m long, 1.2m deep and 0.9m wide). The model scales were  $1/15$  and  $1/60$ , respectively. Fig. 7 shows the prototype breakwater of which models were used in the scale model experiments. A narrow caisson is placed in the breakwater body to reduce transmitted waves. The core material consists of stones( $W = 50\text{kg}$  to  $200\text{kg}$  in prototype scale) of which porosity is estimated as  $\epsilon = 0.4$ . The weights of armor units are  $W = 80\text{t}$  in the armor layer at the windward side,  $W = 11\text{t}$  in the filter layer and  $W = 28\text{t}$  in the armor layer at the leeward side. The corresponding weights of the armor units in the  $1/15$ -scale experiment were  $20\text{kg}$ ,  $6.8\text{kg}$  and  $10.0\text{kg}$ . Those used in the  $1/60$ -scale experiment were  $0.37\text{kg}$ ,  $0.054\text{kg}$  and  $0.13\text{kg}$ . The *In Situ* porosity of armor and filter layers in the breakwater is  $\epsilon = 0.50$ . The armor layer at the leeward side is placed to reduce multi-reflected waves in a harbor.

Table 3 shows the experimental conditions indicated in equivalent prototype

Table 4 Calculation condition for caisson breakwater

$H$ (m)	$T$ (s)	$h$ (m)	$L_I$ (m)	$\Delta x/L_I$	$\Delta z/h$	$\Delta t/T$	cal. region
9.00	11.6	25.0	191.24	1/114.7	1/15.0	1/200	$8.48 \times L$

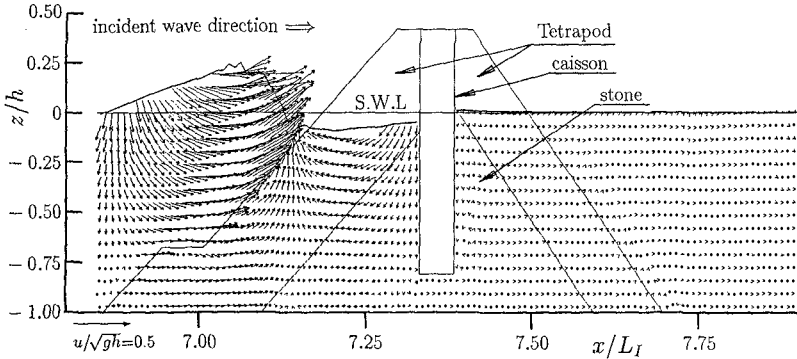


Fig. 8 Simulated result of wave transformation due to caisson breakwater

values. The reflection and transmission coefficients for various wave conditions (prototype wave conditions of incident wave height  $H = 1\text{m}$  to  $17\text{m}$ , period  $T = 15.5\text{s}$  and water depth  $h = 25.0\text{m}$ ) were obtained in the same way.

Measurements include also wave pressures on the seaward wall of the caisson covered with the permeable structures at 10 points in the large-scale experiments and at 6 points in the small-scale experiments.

#### 4.2 Simulation of wave transformation

The computation was carried out under the wave conditions of the small scale-experiment such as the wave period  $T = 1.5\text{s}$ , the wave height at the breakwater  $H = 0.15\text{m}$  ( $H/h = 0.36$ ). Difference between the small- and large-scale conditions is the values of the inertia and drag coefficients which are functions of the Reynolds number and by which the scale effect is considered in the numerical simulation.

The computational condition is shown in Table 4 indicated in the prototype values. The horizontal distance of the calculation region was  $8.48 \times L_I$ , where  $L_I$  is the incident wave length at the uniform depth ( $h_I = 44.2\text{m}$ ) obtained from the nonlinear wave theory. The wave lengths are  $L_I = 191.24\text{m}$  at the uniform depth and  $L = 161.16\text{m}$  at the breakwater. The space increments are  $\Delta x = \Delta z = 1.667\text{m}$  ( $\Delta x/L_I = 1/114.7$  and  $\Delta x/L = 1/96.7$  horizontally,  $\Delta z/h = 1/15.0$  vertically). The time increment is  $\Delta t = T/200$ . It took about four hours with the main frame computer HITAC 680H to calculate 4000 time steps (20 cycles  $\times$  200 steps per wave period) to gain the steady state wave motion near the caisson breakwater.

The reflection and transmission coefficients obtained in the calculation for the

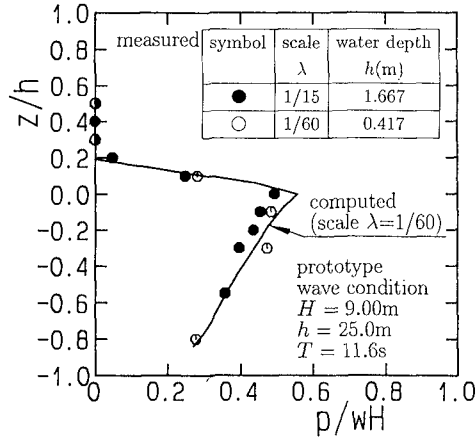


Fig. 9 Comparison of wave pressure between calculation and experiment

small-scale model are  $K_R = 0.18$  and  $K_T = 0.010$ . The corresponding small-scale experimental results are  $K_R = 0.21$  and  $K_T = 0.015$ , respectively. The computation which reproduced the experiment best gives  $C_M = 1.2$  and  $C_D = 0.9$ .

Fig. 8 shows the computed wave velocity field and the surface profile for the small-scale model when the wave runs up on the slope at the windward side of the permeable breakwater. The wave surface profile is deformed on the slope of the armor layer resulting in a steeper surface at the leeward side than that at the windward. Velocity of the wave front just outside the armor layer is increased according to the wave deformation. The velocity inside the armor layer is small and discharge also smaller than that outside the armor layer. The difference of the velocity between inside and outside the armor layer is large and the flow is concentrating to the surface of the armor layer. It is concluded that the velocity field is reasonably simulated as a whole.

The inertia and drag coefficients  $C_M$  and  $C_D$  in the computation were estimated so that the reflection and transmission coefficients obtained by the experiment might agree well with the those obtained by the computation, respectively. In order to verify the present method, it is necessary to compare other values between the experiment and the computation. Thus a wave-induced pore pressure is compared between the computed and measured results as shown in Fig. 9, where  $w$  is the specific weight of fluid. It is found that the quantitative agreement of the computed pressure profile with the measured one is very good for the small-scale experiment. The large-scale experimental result is also shown in Fig. 9. The scale effect on the pressure will be discussed in the following subsection.

#### 4.3 Scale effect of wave transformation and pressure

Fig. 10 shows the results of the reflection and transmission coefficients obtained through the large- and small-model scale experiments. The factor of the model scale according to the Froude law is 4 (the large-model scale is 1/15 and the small



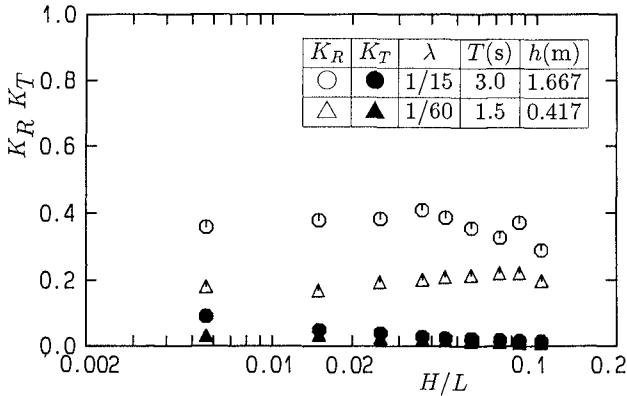


Fig. 10 Scale effect of reflection and transmission coefficients

one 1/60). It is found that the reflection coefficients of the large-scale experiments are larger than the small ones. The transmission coefficients of the large-scale experiments are larger than small-scale one, although the difference is very small. Consequently, the energy dissipation rate of the large-scale experiments is less than that of the small-scale ones.

The tendency of the scale effect on the wave pressure is opposite to that on the wave reflection as shown in Fig. 9 on the pressure profiles comparing between the experimental results with the large- and small-scale models. That is, the wave pressures in the small-scale hydraulic experiments are larger than those in the large-scale one.

It is concluded from the results of the scale effects on the wave reflection and the wave pressure that the wave pressure is small when the wave reflection is large. It is very natural and explained as follows: When the reflection coefficient is large, a small amount of wave penetrates in a permeable structure and onto the caisson. As the result, the wave pressure becomes small.

The scale effects on the wave reflection and wave pressure mentioned above is explained with the following numerical experiments. Fig. 11 shows the effect of the inertia coefficient on the wave pressure, when the drag coefficient is constant as  $C_D=0.9$ . The computation are performed by varying the inertia coefficient  $C_M$  with 1.2, 1.5 and 1.7. As the inertia coefficient  $C_M$  increases the wave pressure decreases. On the other hand, the reflection coefficient increases as the inertia coefficient  $C_M$  increases. The transmission coefficient decreases very slightly. The reflection and transmission coefficients are less sensitive to the change of the inertia coefficient  $C_M$  than the wave pressure.

As the inertial resistance described by the factor  $\lambda_v = \gamma_v + (1 - \gamma_v)C_M$  defined as Eq. (4) increases, the wave reflection from the armor and filter layers increases. Consequently, the less part of wave transmits in the permeable structure and the wave pressure decreases. As the Reynolds number increases under the condition

that  $KC$  number is constant, the inertia coefficient increases according to the Froude law for scaling.

Fig. 12 shows the effect of drag coefficient on the wave pressure, while the inertia coefficient is constant as  $C_M = 1.5$ . The drag coefficient  $C_D$  is selected as  $C_D = 0.3, 0.6$  and  $0.9$ . As the drag coefficient increases, the wave pressure decreases. It is caused by an increase of the wave energy dissipation in the permeable structure.

As explained above, both the drag and inertia coefficients influence the scale effect on the wave reflection, transmission and also the pressure. These scale effects are reflected to the numerical model through  $C_M$  and  $C_D$  which are functions of the Reynolds number.

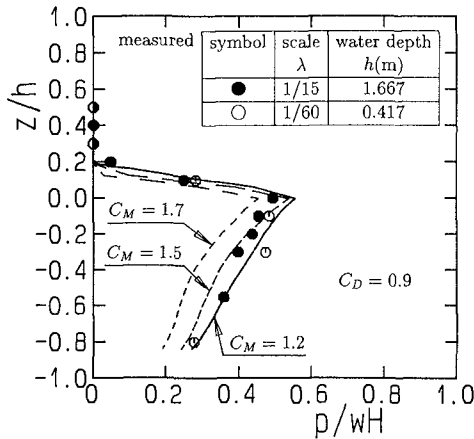


Fig. 11 Wave pressure depending on inertia coefficient ( $C_D = 0.9$ )

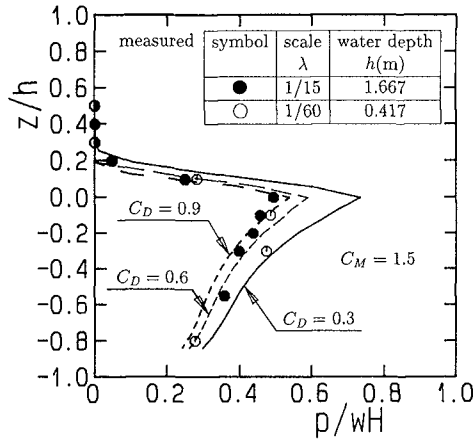


Fig. 12 Wave pressure depending on drag coefficient ( $C_M = 1.5$ )

## 5. Conclusions

A fully nonlinear numerical model has been developed to simulate the wave motion near and in a permeable breakwater. The simulated results were compared with hydraulic experimental ones using two types of permeable breakwaters, a rubble-mound breakwater and a caisson breakwater covered with armor units. The present model can reproduce the wave reflection and transmission, and also the pressure on the caisson. Wave profiles and velocity fields near and in the permeable breakwaters were realistically simulated. Wave force acting on armor units was estimated by Morison equation with the computed velocity. The maximum wave force was found near the still water level during wave run-up.

The scale effects on the wave reflection, transmission and wave-induced pore pressure were demonstrated by the hydraulic experiments. Computation interprets these scale effects. As model scale increases the drag coefficient decreases and the inertia coefficient increases. As the result, the wave energy dissipation due to the drag force decreases while the wave reflection increases due to the inertial resistance. Consequently, the scale effect on the wave-induced pore pressure is canceled by two opposite effects of fluid resistance.

The drag and inertia coefficients were determined so that the reflection and transmission coefficients of the experiment fit with those of the computation, respectively. A fundamental experiment, an oscillation flow test using U-tube tank, for instance will be required to estimate the inertia and drag coefficients.

## REFERENCES

- Ohyama, T and K. Nadaoka(1991): Development of a numerical wave tank for analysis of nonlinear and irregular wave field, *Fluid Dynamics Res.*, 8, pp.231–251.
- Burcharth, H.F., G.L.Howell and Z.Liu(1991): On the determination of concrete armour unit stresses including specific results related to Dolosse, *Coastal Engineering*, 15, pp.107–165.
- Chan, R.K.C. and R.L.Street(1970): A computer study of finite-amplitude water waves, *J. Computational Physics*, 6, pp.68–94.
- Hölscher, P., de Groot, M. P. and J.W. van der Meer(1989): Simulation of internal water movement in breakwater, *Modelling Soil-Water-Structure Interaction*, pp.427–433.
- Wurjanto, A. and N. Kobayashi(1992): Irregular wave prediction and run-up on permeable slope, *J. Waterway, port, coastal and ocean Engineering*, ASCE, (submitted).
- Sakakiyama, T. and R.Kajima(1990): Scale effect of wave force on armor units, *Proc. 22nd Coastal Engineering Conf.*, ASCE, Vol.2, pp.1716–1729.
- Sakakiyama, T(1991): Nonlinear-wave interaction with permeable breakwaters, *Extended Abstract of 4th Int. Conf. Computing in Civil and Building Engineering*.
- Goda, Y.(1985): Random seas and design of maritime structures, University of Tokyo Press, 323p.

## CHAPTER 117

### WAVES ON PERMEABLE LAYERS

Toru Sawaragi<sup>1)</sup> and Ichiro Deguchi<sup>2)</sup>

#### **Abstract**

To analyze a wave attenuation on a permeable layer, we first examined the applicability of Forchheimer type equation to the fluid motion in the permeable layer through permeability tests in steady and unsteady flows. Then, we investigated the effects of a boundary shear on the surface of the permeable layer on the wave attenuation by solving boundary layer equations around the surface of the layer.

It is found that the permeability and the turbulent drag coefficient in the Forchheimer type equation in the unsteady flow are different from those in the steady flow. We showed that the Forchheimer type equation could linearize by using an equivalent linear drag coefficient formulated empirically through the permeability test. The effect of the boundary shear on the wave attenuation on the permeable layer was small compared with the effect of energy loss in the permeable layer if the thickness of the layer was relatively large.

It is also found that we can predict the wave attenuation on the permeable layer exactly when the incident wave has a strong linearity.

#### **Introduction**

When we analyze a wave deformation through a structure with permeability, we often apply a Forchheimer type equation to a fluid motion in the permeable layer. A non-linear turbulent resistance term in the equation is usually replaced by a linear resistance term based on a so-called Lorentz's law of equivalent work. Also we can linearize the equation by using a newly defined equivalent linear drag coefficient through permeability tests.

However, the wave deformations on the permeable layer that were analyzed by these methods do not always agree well with the measured wave deformation. The followings are the conceivable reasons for this disagreement:

1) Errors in the evaluation of empirical coefficients in the Forchheimer type equation in unsteady flow. Several experimental results were reported about the permeability, an additional mass coefficient and a turbulent drag coefficient of a constitution material of the permeable layer in unsteady flow. Those are obtained from the experiments under very limited conditions.

1) Professor and 2) Associate Professor, Dept. of Civil Engineering, Osaka University, Suita-city, Osaka 565, Japan

2) Disregard of the boundary shear on a surface of the permeable layer. The continuity of vertical velocity on the surface of permeable layer is satisfied in the analysis of the wave deformation of conventional potential approach. However, the continuity of horizontal velocity is not satisfied and we can not evaluate exact boundary shear.

3) Non-linear behavior of incident waves.

Objectives of this research are as follows:

- 1) To investigate the influence of unsteady property of fluid motion on coefficients in the Forchheimer type equation through unsteady and steady permeability tests. Based on the experimental results, we formulate an equivalent linear drag coefficient.
- 2) To evaluate boundary shear on the permeable layer by using a horizontal water particle velocity that is a solution of a boundary layer equation near the surface of permeable layer. We examine the influence of the boundary shear on wave attenuation.
- 3) To examine the effect of nonlinear property of incident waves on wave attenuation by carrying out a Fourier analysis of surface displacement measured on the permeable layer.

**Waves on permeable layer**

First of all, we give brief explanation of an expression of wave on the permeable layer based on the potential approach. We suppose the wave of a period  $T$  and height  $H$  propagating in the positive  $x$  direction on the permeable layer. Figure 1 illustrates a definition sketch where  $D$  is the thickness of the permeable layer,  $h$  is the depth on the permeable layer,  $(u, w)$  are the water particle velocity in  $x$  and  $z$  directions,  $\phi$  and  $p$  is the velocity potential and the pressure. We attach a subscript  $d$  to the quantity in the permeable layer.

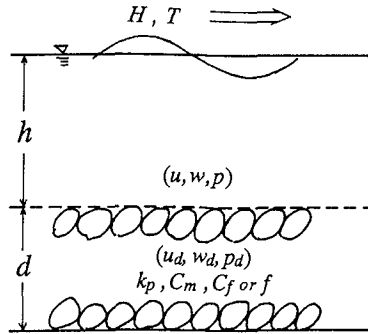


Fig.1 Definition sketch of wave on permeable layer

We can treat a fluid motion on the permeable layer as a potential flow. If we apply Forchheimer type equation to the fluid motion in the permeable layer that is expanded to the unsteady flow by Sollitt et al.(1970), we can express the fluid motion in the permeable layer as follows:

$$S \frac{\partial q}{\partial t} = -\frac{1}{\rho} \nabla p - \frac{v}{K_p} q - \frac{C_f \lambda}{\sqrt{K_p}} q^2 \tag{1}$$

$$S = \{1 + (1 - \lambda) C_m\} / \lambda$$

where  $q$  is the sectional averaged infiltration velocity (macroscopic velocity) in the permeable layer,  $\nabla p$  is the pressure gradient,  $K_p$  is the permeability of the permeable layer,  $g$  is the gravity acceleration,  $\nu$  is the kinematic viscosity of the fluid,  $C_m$  and  $C_f$  are the added mass and the turbulent drag coefficients of the rubble of the permeable layer, and  $\lambda$  is the void ratio of a permeable layer.

There are two methods to linearize the non-linear resistance term in Eq.(1). One is to determine an equivalent linear permeability by applying the Lorentz's law of equivalent work to the each layer of the horizontally divided permeable layers. We can determine a unique equivalent linear permeability  $K_{pe}$  through the whole sublayer by iterative calculations so that the total energy loss during one wave period becomes the same as that of the non-linear resistance term. However, we have to determine the values of  $C_m$ ,  $C_f$  and  $K_p$  before we find out the equivalent linear permeability and linearize Eq.(1). This method also requires large CPU time.

Another method is to use an equivalent linear drag coefficient  $f$ , which brings the same energy dispersion as that of Eq.(1) in one wave period, instead of the permeability and the turbulent drag coefficients to evaluate drag force in Eq.(1). We have to determine the value of  $f$  before we linearize Eq.(1) through the unsteady permeability test which I will mention later in detail in a next section. Anyway, in both methods, we can linearize Eq.(1) as Eq.(2) with the relation between  $K_{pe}$  and  $f$  given by Eq.(3):

$$S \frac{\partial q}{\partial t} = -\frac{1}{\rho} \nabla p - f \sigma q \quad \text{or} \quad S \frac{\partial q}{\partial t} = -\frac{1}{\rho} \nabla p - \frac{\nu}{K_{pe} \sigma} q \quad (2)$$

$$f = \gamma / (K_{pe} \sigma) \quad (3)$$

We normalize the quantities in the following manner:

$$\begin{aligned} (x', z', h', D') &= (\sigma^2/g)(x, z, h, D), \quad t' = \sigma t, \quad K_p' = \sigma K_p / \nu \\ (u', w, 'u_d', w_d') &= (1/\alpha a_0)(u, w, u_d, w_d) \\ (p', p_d') &= (1/\rho g a_0)(p, p_d), \quad (\phi', \phi_d') = (\sigma/g a_0)(\phi, \phi_d) \end{aligned} \quad (4)$$

where,  $\sigma$  is the angular frequency and  $a_0$  is the amplitude of surface displacement of a fundamental frequency component.

Then the fundamental equations to be solved are shown below.

On the permeable layer:

$$\nabla^2 \phi' = 0 \quad (5)$$

$$\text{where, } u' = \partial \phi' / \partial x', \quad w' = \partial \phi' / \partial z' \quad (6)$$

In the impermeable layer:

$$\nabla^2 \phi_d' = 0 \quad (7)$$

$$\text{where, } u_d' = \xi (\partial \phi_d' / \partial x'), \quad w_d' = \xi (\partial \phi_d' / \partial z') \quad (8)$$

$$\text{and } \xi = K_{pe} \sigma / \nu = 1 / f \quad (9)$$

The pressure on and in the permeable layer is expressed as follows:

$$p' = - \left[ \frac{\partial \phi'}{\partial t'} + \frac{g}{\alpha a_0} z + \frac{\sigma^2 a_0}{2g} \left\{ \left( \frac{\partial \phi'}{\partial x'} \right)^2 + \left( \frac{\partial \phi'}{\partial z'} \right)^2 \right\} \right] + \frac{C_1}{g a_0} \quad (10)$$

$$p_d' = -\phi_d' - \xi S \frac{\partial \phi_d'}{\partial t'} + C_2 \quad (11)$$

where,  $C_1$  and  $C_2$  are the constant.

The velocity potential in and on the permeable layer has to satisfy the following boundary conditions:

Kinematic boundary condition on the free surface:

$$\frac{\partial \eta'}{\partial t'} = -\frac{\sigma^2 a_0}{g} \frac{\partial \phi'}{\partial x'} \frac{\partial \eta'}{\partial x'} + \frac{\partial \phi'}{\partial z'} \quad : z' = \eta \quad (12)$$

Dynamic boundary condition on the free surface:

$$\eta = -\frac{\partial \phi'}{\partial t'} - \frac{\sigma^2 a_0}{2g} \left\{ \left( \frac{\partial \phi'}{\partial x'} \right)^2 + \left( \frac{\partial \phi'}{\partial z'} \right)^2 \right\} \quad : z' = h' \quad (13)$$

Continuity of the pressure on the surface of permeable layer:

$$p' = p_d' \quad : z' = -h' \quad (14)$$

Continuity of the vertical (macroscopic) velocity on the surface of permeable layer:

$$w' = w_d' \quad : z' = -h' \quad (15)$$

No vertical flux from the bottom:

$$w_d' = 0 \quad : z' = -(h' + d') \quad (16)$$

These equations are solved by the same way as finding the solution of Stokes waves. The author et al.(Deguchi,1988) have already derived the 2nd order solution corresponding to the Stokes 2nd order theory of the order of  $(\sigma^2 a_0/g)$ . Here we show the result of the 1st order solution for the sake of restricted space.

The dispersion relation for a sinusoidal wave with an amplitude  $a_0$ , which is expressed by Eq.(17) is given by Eq.(18).

$$\eta = \exp\{i(k' x' - t')\} \text{ or } \eta = a_0 \exp\{i(kx - \sigma t)\} \quad (17)$$

$$\sigma^2 = gk \frac{(\xi S + i) \sinh kh \cosh kd + \xi \cosh kh \sinh kd}{(\xi S + i) \cosh kh \cosh kd + \xi \sinh kh \sinh kd} \quad (18)$$

Equation (18) is correct to the 2nd order and is expressed here in a dimensional form. When the angular frequency  $\sigma$ , the water depth on permeable layer  $h$  and the thickness of permeable layer  $d$  are given, we can find the wave number on permeable layer from Eq.(18). If the wave number is a complex with a positive imaginary part, i.e.  $k = \alpha + i\beta$  and  $\beta > 0$ , the value of  $\beta$  becomes an attenuation factor of the wave on the permeable layer and we can express the surface profile of the wave as follows:

$$\eta = a_0 \exp(-\beta x) \exp\{i(\alpha x - \sigma t)\} \quad (19)$$

Figure 2 illustrates the dependency of the attenuation factor  $\beta$  on the non-dimensional permeability  $\xi$  and the value of  $d/h$ . These results are calculated by applying Lorentz's law of equivalent work to Eq.(1). The values of the coefficients in E(1) are shown in the figures.

We can see from Fig.2(a) that the attenuation factor becomes the maximum when the value of  $\xi$  is in the range of 0.2 and 0.4. This means that the optimum permeability exists to attenuate incident waves on the permeable layer. Figure 2(b) shows that the attenuation factor increases with the increase of the relative thickness of the permeable layer  $d/h$ . However, the rate of increase of the attenuation factor is small when  $d/h > 1$ . It is also found that the turbulent drag coefficient  $C_f$  also gives influence on the attenuation factor.

From these results, we can judge that the values of the coefficients in Eq.(1) (or Eq.(2)) play very important roles in the attenuation of wave on the permeable layer.

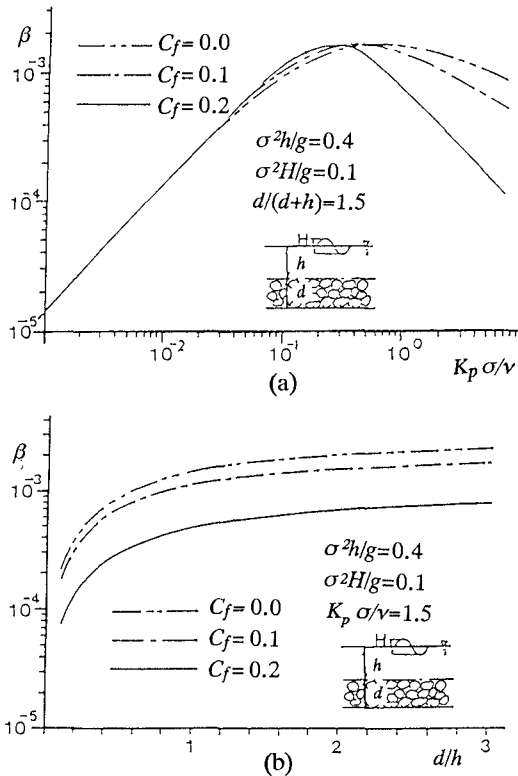


Fig.2 Dependency of attenuation factor  $\beta$  on nondimensional permeability  $\xi$  (Fig(a)) and  $d/h$  (Fig.(b)).

**Unsteady permeability test**

The author et al.(1988) have already carried out the unsteady permeability tests of rubble stones of mean grain diameter  $D=3.18cm$  and  $1.35cm$  under various flow conditions of velocity amplitude  $\hat{q}$  and period  $T$ . We found from the results that the value of  $f$  increases with the increase of K-C number ( $KC=\hat{q}/(\sigma D)$ ) and proportional to  $-1/2$  power of Reynolds' number ( $R_d=\hat{q}D/\nu$ ) when K-C number is small. It is also found that the permeability  $k_p$  in unsteady flow is almost the same as that in steady flow. However, a turbulent flow drag coefficient consists is even more small a value in unsteady flow. The added mass coefficient becomes 0 to 1.8.

However, a wave height attenuation on the permeable layer depends deeply on these coefficients. Therefore, we conducted another series of steady and unsteady permeability tests under a more extensive conditions by using rubble stones ( $D=4.50cm, 3.07cm,$  and  $1.80cm$ ). We measured a permeability  $K_p$ , added mass coefficient  $C_m$ , turbulent drag coefficient  $C_f$  and equivalent linear drag coefficient  $f$ . We also examined their dependencies on the values of  $KC, R_d$  and so on.



The equivalent linear drag coefficient is determined from the following equation by using measured pressure gradient  $\nabla p(t)$  and sectional averaged velocity  $q(t)$  in the unsteady permeability tests:

$$f = \frac{\rho \int_t \left( -S \frac{\partial q}{\partial t} - \frac{\nabla p}{\rho} \right) q dt}{\rho \sigma \int_t q^2 dt} \quad (20)$$

An experiment was carried out by using a U-tube wave tunnel that has a straight part of 3m (0.2m wide and 0.3m high). We filled up rubbles in the middle of the straight part for 1.2m length. The amplitude of depth-averaged velocity  $\hat{q}$  and the period  $T$  of generated oscillatory flow were  $2\text{cm/s} < q < 10\text{cm/s}$  and  $5\text{s} < T < 12\text{s}$ . The corresponding ranges of  $KC$  and  $R_d$  were  $0.4 < KC < 10$  and  $360 < R_d < 4500$ .

The results are summarized as follows:

- 1) The permeability in Eq.(1) obtained from unsteady test is not always coincides with that obtained from the steady test in the region where the value of is large ( $KC > 4$ ). The former is usually larger than the latter by 20 to 50%.
- 2) The turbulent drag coefficient becomes 0 to 0.2 in the unsteady flow. This value is smaller than that in the steady flow.
- 3) The added mass coefficient becomes the maximum (1.8) when the relative acceleration defined by  $\hat{q}\sigma/g$  is about 0.01. In the region where  $\hat{q}\sigma/g$  is nearly 0 and greater than 0.04, the added mass coefficient can be regarded to be almost 0.
- 4) An equivalent linear drag coefficient does not rely on the value of  $R_d$  when the value of  $KC$  is larger than 2. The result is shown in Fig.3. It can be expressed by a unique function of  $KC$ . We can find the following empirical relation between  $f$  and  $KC$  from Fig.3.

$$f = 0.1 + 1.8 \{ \hat{q} / (\sigma D) \} \quad (21)$$

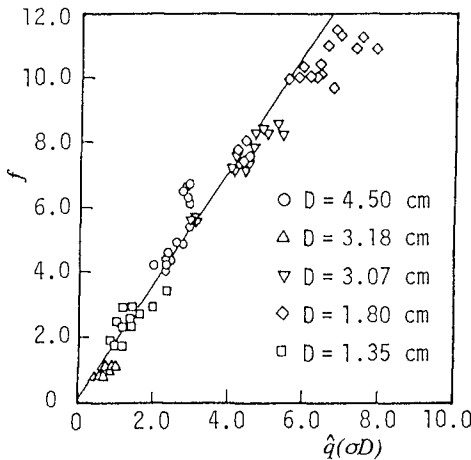


Fig.3 Relation between equivalent linear drag coefficient and K-C number

As I mentioned before, if we intend to evaluate fluid motion in the permeable layer more precisely, we should use Eq.(1) by applying the Lorentz's law of equivalent work. However, this procedure requires large CPU time until we find the

equivalent linear permeability coefficient. Also, we cannot formulate the permeability and the turbulent drag coefficient in the unsteady flow. Therefore, we use Eq.(2) together with Eq.(21) to construct boundary layer equation on and inside the permeable layer.

**Boundary shear stress on the surface of permeable layer**

(1) Boundary layer equation on and inside the permeable layer

The former analysis of the wave deformation on a permeable layer is based on a potential wave theory. Accordingly, the continuities of the pressure and vertical discharged velocity are satisfied by the imposed boundary conditions. However, the continuity of horizontal velocity is not satisfied. On the surface of the rubble on the permeable layer, a so-called non-slip condition has to be applied. A Hell-Shaw approximation is usually applied in the analysis of the steady flow on the permeable layer. However, there is no guarantee that the same approximation can apply to the unsteady fluid motion on the permeable layer.

Here, we suppose the existence of the boundary layer on and inside the permeable layer where the macroscopic horizontal velocity and the vertical gradient of horizontal velocity continue smoothly. We construct the boundary layer equations by applying Couette flow approximation in the boundary layer. Based on the analyzed results, we evaluate the boundary shear on the surface of the permeable layer and examine their effect on the wave attenuation on the permeable layer.

Figure 4 illustrates the coordinate system where,  $u_p$  and  $u_{dp}$  are the potential velocities on and in the permeable layer,  $u$  and  $u_d$  are the horizontal velocities inside the boundary layer.

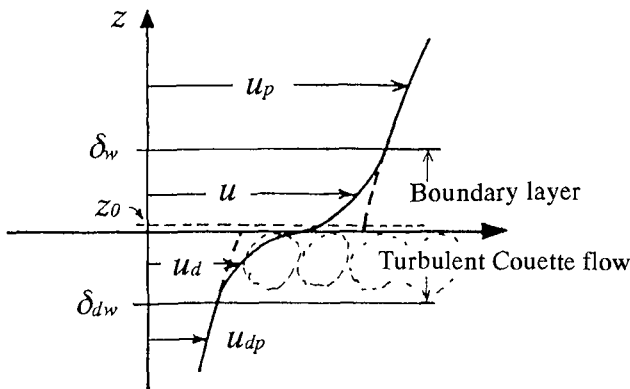


Fig.4 Coordinate system

We also assume that the thicknesses of the boundary layers on and in the permeable layer are  $\delta_w$  and  $\delta_{dw}$ , respectively and that the zero adjusting height is  $z_0$ . We need not adjust velocity distribution on the surface of the permeable layer. However, we use the expression of  $z_0$  considering the contrast of a rough turbulent boundary layer on an impermeable layer.

Then the boundary layer equations on and inside the permeable layer are expressed as follows:

The upper boundary layer,  $z_0 < z < \delta_w$ :

$$\frac{\partial U}{\partial t} = K_z \frac{\partial^2 U}{\partial z^2} \tag{22}$$

The lower boundary layer,  $-\delta_{dw} < z < z_0$ :

$$S \frac{\partial U_d}{\partial t} = -f \sigma U_d + K_{dz} \frac{\partial^2 U_d}{\partial z^2} \tag{23}$$

$$U = u - u_p, U_d = u_d - u_{dp} \tag{24}$$

where,  $K_z$  and  $K_{dz}$  are the eddy viscosity on and inside the layer.

Boundary conditions for these boundary layer equations are given by the following equations:

$$U = 0 \text{ or } u = u_p \text{ at } z = \delta_w \tag{25}$$

$$U_d = 0 \text{ or } u_d = u_{dp} \text{ at } z = \delta_{dw} \tag{26}$$

$$\partial U / \partial z = \partial U_d / \partial z \text{ or } \partial u / \partial z = \partial u_d / \partial z \text{ at } z = z_0 \tag{27}$$

$$U - U_d = u_{dp} - u_p \text{ or } u = u_d \text{ at } z = z_0 \tag{28}$$

We borrow the following expression for the kinematic eddy viscosity in Eq.(22) from the rough turbulent boundary layer theory:

$$K_z = \kappa u^* z \text{ in } z_0 < z < \delta_w \tag{29}$$

where  $u^*$  is the shear velocity on the permeable layer and  $\kappa$  is Karman's constant.

On the other hand, we express the kinematic eddy viscosity in the lower boundary layer assuming that the mixing length in the permeable layer is regulated by the scale of the void (Yamada et al.,1982):

$$K_{dz} = \gamma Du^* \text{ in } -\delta_{dw} < z \leq z_0 \tag{30}$$

where,  $\gamma$  is an empirical constant.

Through the continuity of the kinematic eddy viscosity, the order of  $\gamma$  is estimated to be as follows from Eqs.(29) and (30):

$$\gamma = \kappa z_0 / D \sim 0.4/30 \approx 0.0133 \tag{31}$$

Also, we assume that the boundary layer thicknesses of upper and lower boundary layer are expressed as follows based on the analogy of the rough turbulent boundary layer on the impermeable layer:

$$\delta_w = \delta_{dw} = \alpha \kappa u^* / \sigma \tag{32}$$

We conducted preliminary calculation as for the empirical constant  $\alpha$  and it is found that the border shearing stress becomes almost constant in the region where  $\alpha > 3$ . Therefore, we use the value  $\alpha = 4$  in the following calculation.

(2) Velocity distribution and boundary shear stress

The horizontal water particle velocities obtained as solutions to the upper and lower boundary layer equations are expressed as follows:

$z_0 < z$ :

$$u = \left[ -\beta_1 \left\{ \frac{\ker q_w + i \keiq_w}{\ber q_w + i \beiq_w} (\ber q + i \beiq) - (\ker q + i \keiq) \right\} + \beta_2 \right] \exp(-i\sigma t) \tag{33}$$

$z < z_0$ :

$$u_d = \left[ \beta_3 \exp \left\{ \frac{(a^2 + \sigma^2)^{1/4}}{b^{1/2}} \exp \left( \frac{i}{2\theta} \right) z \right\} + \beta_4 \right] \exp(-i\sigma t) \tag{34}$$

Where,

$$q_w = 2\{\delta_w \sigma / (ku \cdot)\}^{1/2}, \quad q = 2\{z \sigma / (ku \cdot)\}^{1/2}$$

$$a = f \sigma / S, \quad b = \gamma Du \cdot / S, \quad \theta = \tan^{-1}(-\sigma / a).$$

(ber, bei) and (ker, kei) are the real and the imaginary parts of the 1st and 2nd kinds of Bessel function. The integral constants  $\beta_1$ - $\beta_4$  are determined from the boundary conditions Eqs.(25) to (28).

The boundary shear stress on the surface of the permeable layer  $\tau(t)$  and the amplitude of the shear velocity  $u^*$  corresponding to the maximum shear stress  $\tau_{max}$  are evaluated by using the results.

$$\tau(t) = \rho \kappa u \cdot z_0 \frac{\partial u}{\partial z} \Big|_{z=z_0} \quad (35)$$

$$u \cdot = (\tau_{max} / \rho)^{1/2} \quad (36).$$

We can decide the water particle velocity in the boundary layers and the shear stress on the permeable layer by carrying out the same iterative calculation as in the boundary layer theory on the impermeable bed using these relations.

Figure 5 shows an example of the calculated phase variation of vertical distribution of horizontal water particle velocity in the case of J-6 that will be mentioned latter. The calculation conditions are shown in the figure.

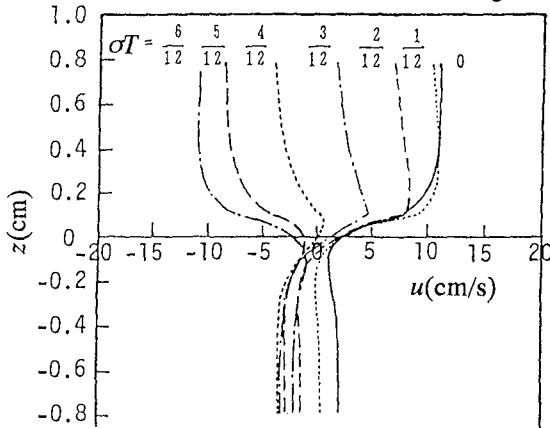


Fig.5 Example of the calculated velocity distribution

Figure 6 illustrates the effects of nonlinearity on incident waves and permeability of the layer on the boundary shear stress. The horizontal axis  $gHT^2/h^2$  of Fig.6(a) is the nondimensional parameter proposed by Shuto(1976) to show the nonlinearity of the waves of height  $H$  and period  $T$  at the depth of  $h$ . The horizontal axis of Fig.6(b) is the nondimensional permeability  $K_{pe} \sigma / \nu = 1/f$ . A calculation condition is shown in figures.

From Fig.6(a) it is found that the boundary shear stress increases in proportion to the increase of  $gHT^2/h^2$ . However, it decreases with the increase in  $1/f$  (or  $K_{pe} \sigma / \nu$ ) and becomes constant in the region of  $1/f = K_{pe} \sigma / \nu > 3$ . This region of  $1/f$  corresponds to the region where the influence of the permeability on wave attenuation decreases rapidly (see Fig.2(a)).

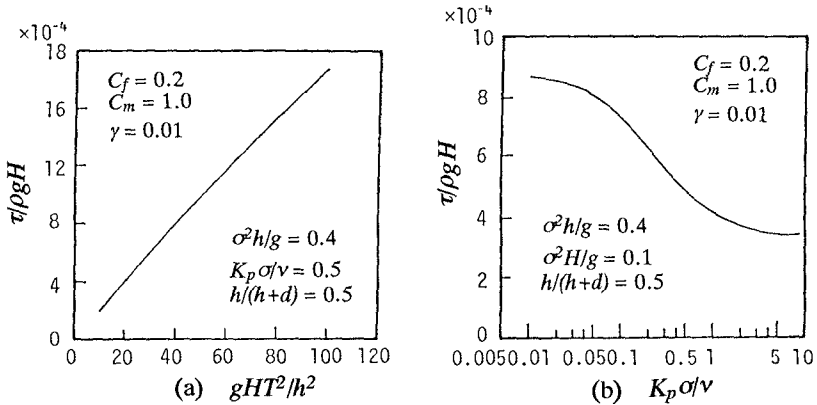


Fig.6 Effect of nonlinear property of incident wave (a) and permeability (b) on boundary shear stress

Furthermore, we examined the influence of the turbulent drag coefficient and the added mass coefficient on the boundary shear stress. As a result, the non-dimensional shear stress increases with the increases of the turbulent drag coefficient and the added mass coefficient. As for the rate of increase one of the former is big. Accordingly, that border shearing force is relying strongly on a turbulent flow drag coefficient more an addition mass coefficient was understood.

### Effect of boundary shear stress and nonlinearity of incident waves on wave attenuation on permeable layer

#### (1) Experiment on wave attenuation and velocity distribution on permeable layer

We carried out experiments concerning attenuation of waves propagating on the permeable layer to investigate the effects of the boundary shear and nonlinear effect of incident waves on wave transformation on the permeable layer. The experiments were carried out on the permeable layer in the two-dimensional wave tank of 30m long, 0.7m wide and 0.9m high. The permeable layer was made on the horizontal bottom in the wave tank and the length was 3.5m and the thickness was 15cm. The water depth on the permeable layer was 15cm. Two kinds of rubble stone whose mean diameter were 3.07cm and 1.80cm were used to construct the permeable layer. Experimental conditions are summarized in Table-1.

In the experiment, We measured the water height attenuation through the permeable layer and particle velocity at the center of the permeable layer. Wave height was measured by capacitance type wave gauges at the interval of 25cm and water particle velocity was measured by an electromagnetic current meter and a hydrogen bubble method. The measured time series of surface displacement was analyzed by FFT to investigate the frequency component of wave motions. We also measured the phase difference of the water particle velocity near the boundary at the center of the permeable layer by a tuft method in 6 cases. Vertically distributed 6 pieces of silk yarn glued on the side wall of the wave tank were used as tufts.

Table-1 Experimental conditions

Case	$d$ (cm)	$h$ (cm)	$T$ (s)	$H$ (cm)	$gHT^2/h^2$
J-1	3.07	15.0	1.50	6.32	62
J-2				3.58	35
J-3			1.25	6.03	43
J-4				3.96	27
J-5			1.00	5.87	26
J-6				3.58	16
K-1		25.0	1.50	6.78	34
K-2				3.66	13
K-3			1.25	6.32	16
K-4				3.85	9
K-5			1.00	6.92	11
K-6				4.08	6
L-1	1.80	15.0	1.50	6.52	64
L-2				3.67	37
L-3			1.25	6.41	44
L-4				3.80	26
L-5			1.00	5.72	25
L-6				3.15	14
M-1		25.0	1.50	6.53	23
M-2				3.66	13
M-3			1.25	6.20	15
M-4				3.57	9
M-5			1.00	6.33	10
M-6				3.45	5

(2) Change in wave height on permeable layer

We calculated the deformation of the waves that were propagating on the permeable layer in the positive  $x$  direction by the following method: Let the wave heights at  $x=j\Delta x$  and  $(j+1)\Delta x$  be  $H_j$  and  $H_{j+1}$ , respectively. The wave attenuation rate  $k_p$  between  $x=j\Delta x$  and  $(j+1)\Delta x$  caused by the permeability of the permeable layer is expressed as follows:

$$k_p = \exp(-\beta\Delta x) = H_{j+1}/H_j \tag{37}$$

where,  $\beta$  is the imaginary part of the complex wave number that is the solution to the dispersion relation Eq.(18).

On the other hand, the wave attenuation rate at the same distance  $\Delta x$  caused by the boundary shear stress ( $K_t$ ) is calculated from the following equation:

$$K_t = \left[ \frac{E_t \Delta x}{H_j} \left\{ \frac{1}{16} \left( 1 + \frac{2kh}{\sinh 2kh} \right) \frac{\rho g \sigma}{k} \right\} + 1 \right]^{1/2} \tag{38}$$

where,  $E_t$  is the energy dissipation that is evaluated by using the boundary shear stress on the surface of the permeable layer as follows:

$$E_t = \frac{2}{T} \int_0^{T/2} \tau u|_{z=z_0} dt \quad (39)$$

Wave height at  $x=(j+1)\Delta x$  is calculated by using  $K_p$  and  $K_t$  from the wave height at  $x=j\Delta x$  by the following relation:

$$H_{j+1} = k_p k_t H_j \quad (40)$$

Figure 7 shows two examples of comparisons of measured and calculated wave attenuation in different cases. A full line is the result calculated by considering only the influence of the permeable layer by using the equivalent linear drag coefficient ( $Kt=1$ ). A broken line is the calculated result that includes both effects of the boundary shear and the permeability.

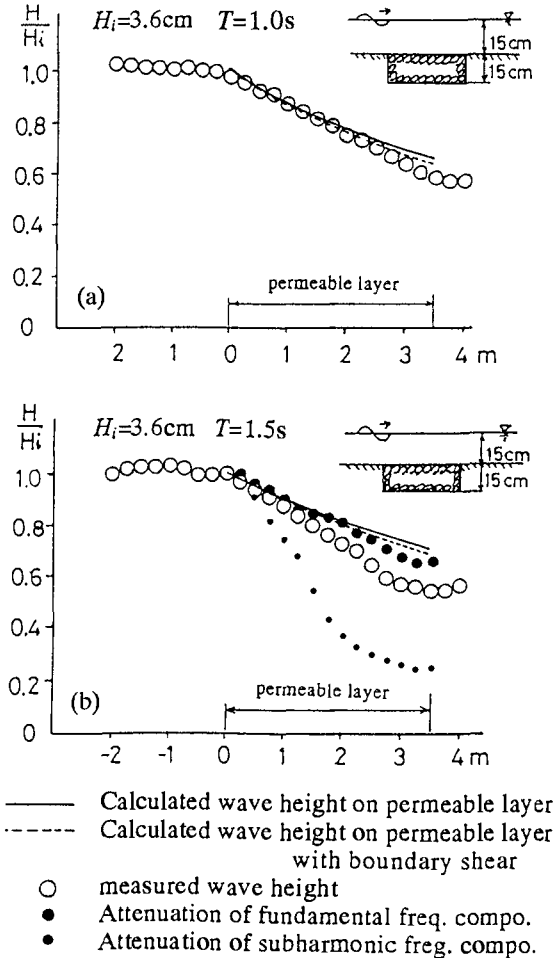


Fig. 7 Wave attenuation on a permeable layer((a):Case J-5,(b):CaseJ-2)

Figures 7(a) and (b) are the results of Case J-6( $T=1.0s$ ) and Case J-2 ( $T=1.5s$ ). Experimental conditions are shown in each figure. We used the value of the added mass coefficient in Eq.(22) obtained from the unsteady permeability tests.

First, the influence of the boundary shear on the wave attenuation, that is shown by the difference of the solid and broken lines in the both figures, is very small and can be negligible as compared with the effect of the permeability.

From Fig.7(a), it is found that measured wave height on the permeable layer (shown by the open circles) coincides fairly well with the calculated wave height when the wave period of incident waves is somewhat short. When the period is relatively long, the results of which is shown in Fig.7(b), the decrease of measured wave height on the permeable layer is larger than that of calculated one.

We investigated this reason by examining fundamental frequency and subharmonic frequency components obtained from a Fourier analysis of the measured surface displacement around the permeable layer. The energy of the subharmonic component at the offshore side of the permeable layer was less than 5% of that of the fundamental frequency component in Case J-6. On the other hand, the energy of the subharmonic component in Case J-2 was more than 30% of that of the fundamental frequency band at the offshore of the permeable layer.

In Fig.7(b), the decrease of the amplitudes of fundamental frequency and subharmonic frequency components obtained from the Fourier analysis are shown by large and small closed circles. The decrease of the amplitude of fundamental frequency component on the permeable layer agrees well with the calculated wave attenuation based on the linear wave theory. However, the decrease of the subharmonic component is larger than the predicted wave attenuation. Therefore, the difference of the measured and calculated wave heights of case shown in Figure 6 comes from the fact that a large subharmonic component was included in the incident waves.

We have already reported that the decrease of the subharmonic component in a bound wave like Storks 2nd order wave is twice as first as the decrease of the fundamental frequency component (Deguchi, et al.,1988). However, the incident waves in the case of J-2 included a larger subharmonic component that cannot be explained by the Stokes wave theory. Also, the analysis method of the wave deformation on the permeable layer based on a non-linear wave theory has been proposed (Isobe, et al.,1991). Here, we examine applicability of the linear wave theory to the wave transformation on the permeable layer.

Figure 8 illustrates errors of the calculated wave heights in the 24 cases shown in Table 1.

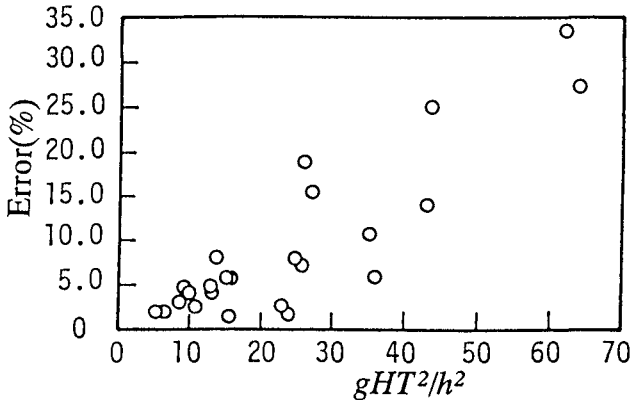


Fig. 8 Estimated error of wave attenuation on permeable layer



The horizontal axis is the parameter  $gHT^2/h^2$  concerning the nonlinearity of incident waves (Shuto, 1973). The error was defined by using the difference of measured and calculated wave attenuation rate,  $K_m$  and  $K_c$ , at the onshore end of the permeable layer as follows:

$$\delta = |K_m - K_c|/K_c * 100 \quad (26)$$

It can be seen from Fig.8 that the error becomes more than 10% when the value of  $gHT^2/h^2$  is larger than 30, i.e., the nonlinear property of incident waves is large. When the value of  $gHT^2/h^2$  is less than 10, the error remains within 5%.

## **Conclusion**

The main results obtained in this study are summarized as follows:

- 1) The turbulent drag coefficient and the permeability in the Forchheimer type equation in the unsteady flow are different from those in the steady flow. In the unsteady flow, they depend on K-C number, and the relative acceleration. We proposed the empirical relation between the equivalent linear drag coefficient and K-C number through the unsteady permeability tests.
- 2) The wave attenuation on the permeable layer is caused mainly by the energy loss in the permeable layer. The effect of the boundary shear on the surface of the permeable layer on the wave attenuation is negligibly small when the thickness of the layer is relatively large.
- 3) The linear wave theory can apply to the analysis of wave decay on the permeable layer when the value of  $gHT^2/h^2$  is smaller than 10. When the value of  $gHT^2/h^2$  is greater than 30, the non-linear property of the incident waves becomes significant. In such case, the wave attenuation on the permeable layer is larger than that predicted by the linear wave theory. We can explain this reason by the fact that the amplitude of subharmonic component included in the incident waves is faster than that of the fundamental frequency component.

## **References**

- Deguchi, I., Sawaragi, T. and Shiratani, K., 1988, "Applicability of non-linear unsteady Darcy law to wave deformation on permeable layer", Proc. 36th Japanese Conf. on Coastal Eng., pp.487-491.(in Japanese)
- Isobe, M., Shiba, K. and Watanabe, A., 1991, "Non-linear wave transformation through permeable submerged breakwater", Proc. 38th Japanese Conf. on Coastal Eng., pp.551-555.(in Japanese)
- Shuto, N., 1973, "Shoaling and deformation of non-linear long waves", Coastal Eng. in Japan, Vol.16, pp.1-12.
- Sollitt, C. K. and Cross, R.H., 1972, "Wave reflection and transmission at a permeable breakwater", Rept. Ralf Parson'S Lab., MIT, No.147.
- Yamada, M. and Kawabata, N., 1982, "Theoretical study on the resistance law for the flow on the permeable layer", Proc. JSCE, Vol.325, pp.69-80.(in Japanese)

## CHAPTER 118

### IMPACT LOADS INDUCED BY PLUNGING BREAKERS ON VERTICAL STRUCTURES

Schmidt, R.<sup>1)</sup> ; Oumeraci, H.<sup>2)</sup> ; Partenscky, H.-W.<sup>3)</sup>

#### Abstract

Results of large-scale model tests on impact loading of a vertical wall by using waves up to 2 m height and 9.4 s period are presented. A classification of the breaker types tested and breaking criteria for waves in front of a vertical wall are suggested. Impact pressure distributions, forces and force impulses induced by plunging breakers on a vertical wall are discussed. The statistical distributions of the impact pressures and forces for different breaker types are also given. Some aspects of the generation mechanisms of impact pressures and the role of air content and its statistical distribution in the impact process are outlined.

#### Introduction

It has often been suggested in the literature that impact pressure induced by breaking waves has no structural significance, and hence should not be used for design purposes. One of the main reasons for this view point may certainly be explained by the static approach yet used to study the stability of vertical structures. The results of a study on vertical breakwater failures (OUMERACI et.al., 1991) together with the results of more recent investigations on the effect of impact loads on a vertical breakwater (OUMERACI et.al., 1992; TAKAHASHI et.al., 1992) have shown that impact pressure has not only a very localized effect, but may also be detrimental for the stability of the structure components as well as for the overall stability of the structure, including the foundation; i.e. the stability

---

1) Dipl.-Ing., Research Engineer, GROSSER WELLENKANAL (GWK)

2) Dr.-Ing., Senior Research Engineer, Sonderforschungsbereich 205

3) Prof. Dr.-Ing. Dr.-Phys., Formerly Managing Director Franzius-Institut

of monolithic structures subject to breaking waves is of purely dynamic nature and cannot be simply reduced to a static problem.

For the dynamic stability analysis, detailed spatial and temporal pressure distributions with the corresponding force histories are required. However, reliable laboratory measurements in the impact area generally represent a very difficult task due to the highly transient and complex nature of the two-phase flow and pressure field involved, as well as to the scale effects related to air entrainment/entrapment. Therefore, a detailed large-scale model study on impact pressures due to breaking waves on a vertical wall has recently been performed in the Large Wave Flume (GWK) of Hannover. It is the main purpose of the paper to discuss some of the results of this study.

**Experimental Set-Up and Test Conditions**

The hydraulic model tests were performed in the Large Wave Flume of Hannover (320x5x7 m) by using regular and irregular waves up to 2 m height and 9.4 s period. The experimental set-up is given in Fig. 1, showing a) a sloping seabed 1:20 terminated by a vertical stiff wall of 6 m height instrumented with 28 high resolution pressure transducers ( $f_N > 35$  kHz), and b) the locations of eleven wave gauges installed in front of the wall.

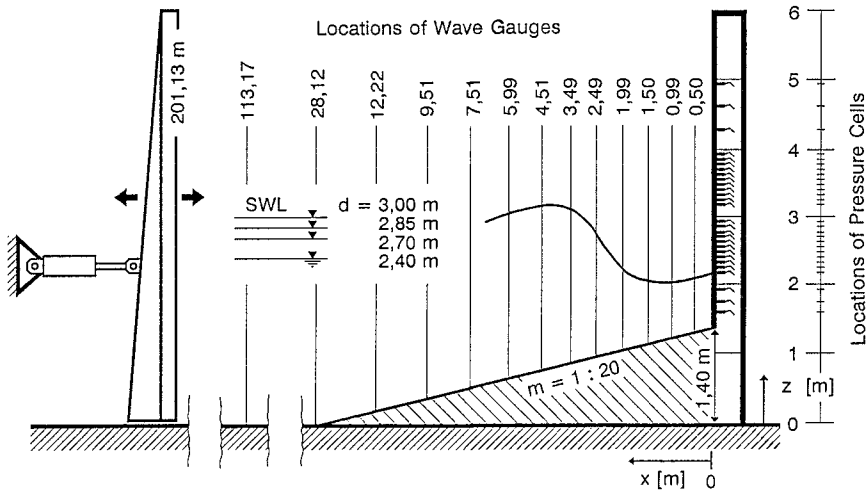


Fig. 1. Experimental Set-Up in the Large Wave Flume (GWK)

Water depths in the flume up to 3.0 m (1.6 m at the wall) were used for the tests. Most of the waves used in the tests arrive at the wall as plunging breakers, the maximum breaker heights obtained are in the range of  $H_b = 1.15 \cdot d_b$ , where  $d_b$  is the breaking depth measured from SWL.

**Breaker Types and Kinematics**

*Breaker Types*

A strong correlation exists between the shapes of the breaking waves at the vertical wall and the trapped air. On the other hand, the latter is known to considerably affect the magnitude as well as the spatial and temporal distribution of the impact pressure. Therefore, an attempt was first made to classify the breaker types obtained for the conditions tested, before any further analysis of the results was undertaken. In fact, different breaking wave conditions in comparison to those on an unobstructed beach are expected (GALVIN, 1968). For this purpose, video records as well as wave profiles obtained from wave gauge measurements were used. Depending on the value of  $H_b/d_w$  and on further parameters, seven types of breaking and broken waves – five for the plunging and two for the spilling breaker – in front of the vertical wall were obtained (Fig. 2). The water depth  $d_w$  directly at the vertical wall corresponds to the breaking depth  $d_b$  measured from SWL by the linear relationship  $d_w = 0.80 \cdot d_b$  (average from 705 breaking waves and correlation coeff. of 0.84).

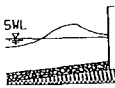
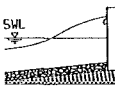
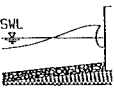
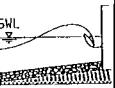
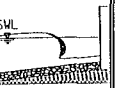
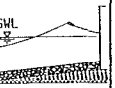
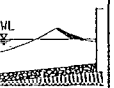
Plunging breaker					Spilling breaker	
upward deflected	well developed		broken		well developed	broken
$\frac{H_b}{d_w} = 0,92$	$\frac{H_b}{d_w} = 0,99$	$\frac{H_b}{d_w} = 1,06$	$\frac{H_b}{d_w} = 1,14$		$\frac{H_b}{d_w} = 0,99$	$\frac{H_b}{d_w} = 1,14$
						
Type 1	Type 2	Type 3	Type 4	Type 5	Type 6	Type 7

Fig. 2. Breaker Types Observed during Tests in GWK

In the following, however, special emphasis was put on the analysis of the results related to plunging breakers.

*Breaking Criteria*

Existing formulae for the prediction of the maximum breaker height  $H_b$  (or of the breaking depth  $d_b$ ) as a function of the wave period  $T$  and the beach slope  $m$  (see for instance Eq. (2.92) in C.E.R.C., 1984) are related to waves on an unobstructed beach slope. Due to a full obstruction by a vertical wall in the flume, waves with  $H_o/L_o = 0.0075 - 0.013$  were found to break in a depth  $d_b$  which is about 30 % higher than those predicted by the C.E.R.C. - formula. This is shown for instance by Fig. 3 in which the results of WEGGEL (1968) have also been plotted for comparison.

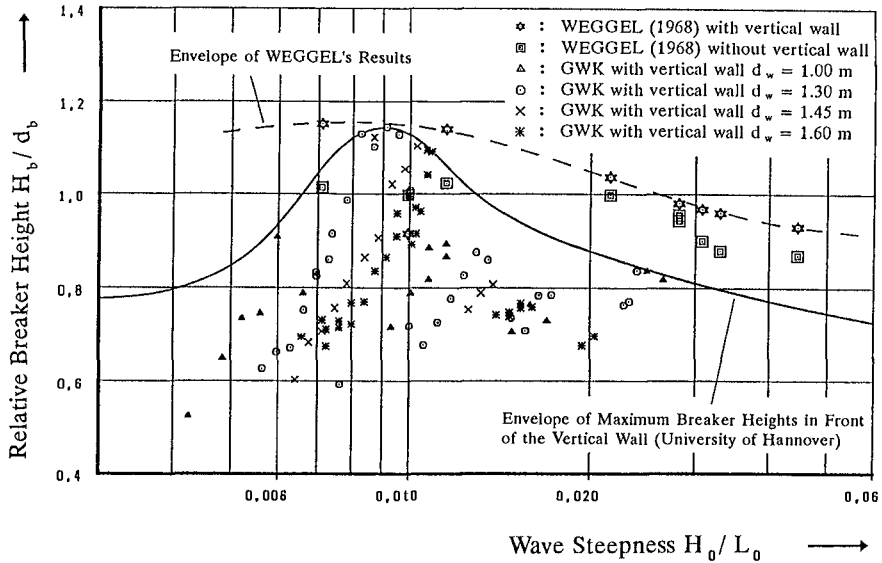


Fig. 3. Maximum Breaker Heights in Front of a Vertical Wall

It is seen that in the presence of a vertical wall, a maximum breaker height  $H_b$  may occur which is almost 20 % larger than the breaking depth  $d_b$ . The corresponding deep water wave steepness is about 0.009.

*Velocity and Volume of Wave at Breaking*

The wave profiles in front of the vertical wall recorded by the wave gauges and video are shown for different time steps in Fig. 4. The

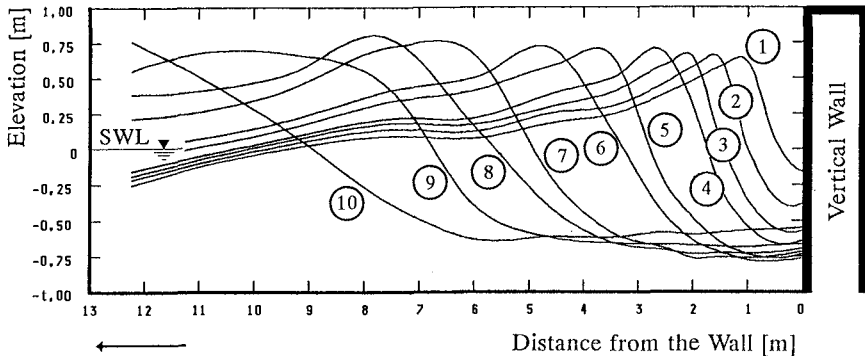


Fig. 4. Wave Profiles in Front of a Vertical Wall at Different Time Steps

velocities and the volume of the wave at the instant of breaking are determined from such wave profile developments like those in Fig. 4 and compared to those predicted by different wave theories (linear wave theory, modified linear wave theory by GODA (1964) and solitary wave theory). It was found that for both the velocities  $u_s$  and the volume of the wave  $V_s$  at breaking, the solitary wave theory provides the best approximation:

$$u_s = \sqrt{g \cdot (d_b + H_b)} \quad (1) \qquad V_s = \sqrt{\frac{16}{3} \cdot H_b \cdot d_b^3} \quad (2)$$

where  $d_b$  is the breaking depth measured from SWL and  $H_b$  the breaker height, respectively. This is an important result as the momentum transferred by a breaking wave to the wall may be approximately evaluated directly by using Eqs. (1) and (2). A comparison of such an approximation with the related force impulse obtained from pressure measurements will be shown later in Fig. 10.

## **Impact Loads**

### *Influence of Sampling Frequency on measured Impact Loads*

The first step when measured highly dynamic processes generally consists in evaluating the proper sampling rate. Therefore, the effect of the sampling frequency  $\Delta f$  on the peak pressures, peak forces and impulses has been investigated for  $\Delta f = 0.1 - 11$  kHz. The results obtained show particularly that:

- a) For the pressure peaks, sampling rates of  $\Delta f = 2, 1$  and  $0.175$  kHz result in a reduction of 2, 7 and 50 %, respectively;
- b) For the force peaks, sampling rates of  $\Delta f = 2, 1, 0.175$  and  $0.1$  kHz result in a reduction of 2, 3, 20 and 37 %, respectively;
- c) For the force impulses, no significant changes results even if the sampling rate is reduced to  $0.1$  kHz.

### *Impact Pressures and Forces*

For each of the breaker types in Fig. 2, the following results can be obtained:

- a) Simultaneous pressure histories at the 28 wall elevations by using a sampling frequency of  $11$  kHz;
- b) Pressure distributions along the wall for time steps  $\Delta t = 0.09 - 10$  ms.

For instance, some pressure distributions are given in Fig. 5 (breaker height  $H_b = 1.57$  m and wave period  $T = 6.75$  s) at eleven different time steps. The horizontal force  $F_h$  per linear meter obtained from pressure integration is also given. Fig. 5 also illustrates that impact pressures are not only limited to small local areas but may also occur simultaneously over a large height (in a range up to the wave height!) of the vertical wall.

Particularly in the case of well-developed plunging breakers with large entrapped air pocket, the spatial integration of the impact pressures generally leads to a total force with a duration which may be much larger than usually assumed. In fact, the duration of total impact forces may reach 5 to 10 times that of the corresponding impact pressures. Since the latter is generally in the range of 0.05 – 0.02 s (in the model), the duration of the total impact force may reach values in the range of 0.05 – 0.2 s corresponding to values of 0.15 – 0.6 s in prototype; i.e. values which may be in the same range or higher as the natural period of oscillations of common prototype caisson breakwaters:  $T_N = 0.2 - 0.4$  s (MURAKI, 1966).

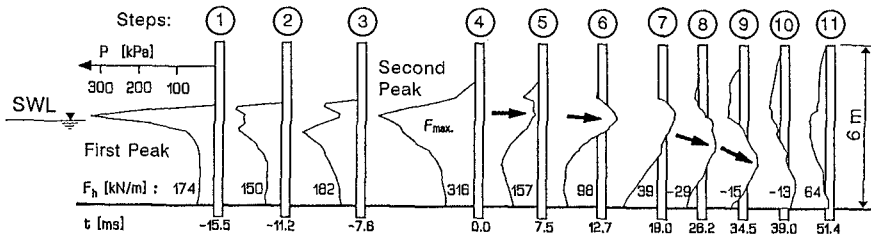


Fig. 5. Pressure Distributions at Different Time Steps ( $H_b=1.57$  m ;  $T=6.75$  s)

The origin of negative pressure (see Fig. 5, steps 6–10) can also be explained by the fact that the trapped air is compressed so much that in re-expanding it throws the water mass back with such a velocity that the pressure drops below the atmospheric pressure value. The pressure distributions in Fig. 5 clearly characterize the impact of a plunging breaker with a large air pocket entrapped between the breaker front and the wall.

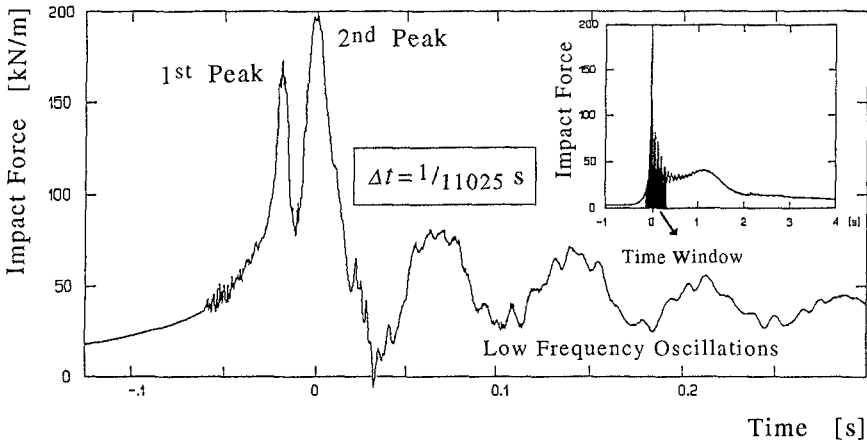


Fig. 6. Horizontal Force History Resulting from Pressure Integration

Typically, two force peaks (time step 1+4) occur which are also seen in the related force history shown in Fig. 6. A further important characteristic of this type of impact (well-developed plunging breaker with entrapped large air pocket) is the presence of the relative low frequency oscillations after the force peak (see Fig. 6). The latter are caused by the cyclic compressions and expansions of the entrapped air pocket under the highly transient pressure fields, and are hence related to the size of the entrapped air pocket. The equivalent diameter  $D_o$  of the air pocket at its initial stage can be determined from the period  $T_{osc}$  of the force oscillations by the following relationship (OUMERACI et.al., 1992):  $D_o = k_a \cdot T_{osc}$  where  $k_a = 5.35$  m/s. This means that the force oscillations with  $T_{osc} = 0.075$  s in Fig. 6 corresponds to a trapped air pocket of  $D_o = 0.40$  m in the large-scale model. The period of the force oscillations transferred to prototype conditions may also lie in the range of the natural period of prototype caisson breakwaters:  $T_N = 0.2 - 0.4$  s (MURAKI, 1966). These force oscillations may lead to near resonance excitation.

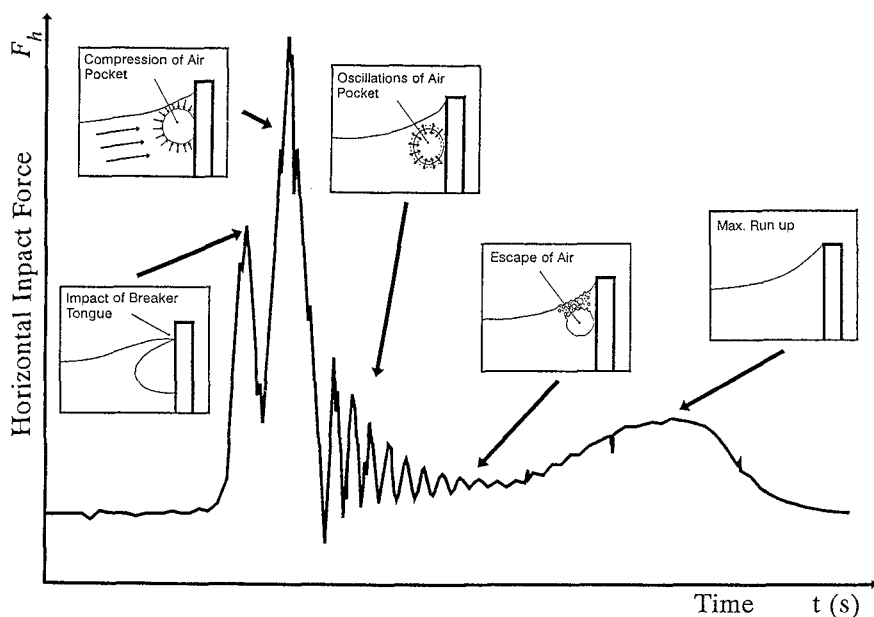


Fig. 7. Characteristics of Impact Forces and their Origin

The typical features of a force history caused by the impact of a breaker plunging on a vertical wall and entrapping a large air pocket are schematically summarized in Fig. 7 which also illustrates the origin of each of these characteristics.



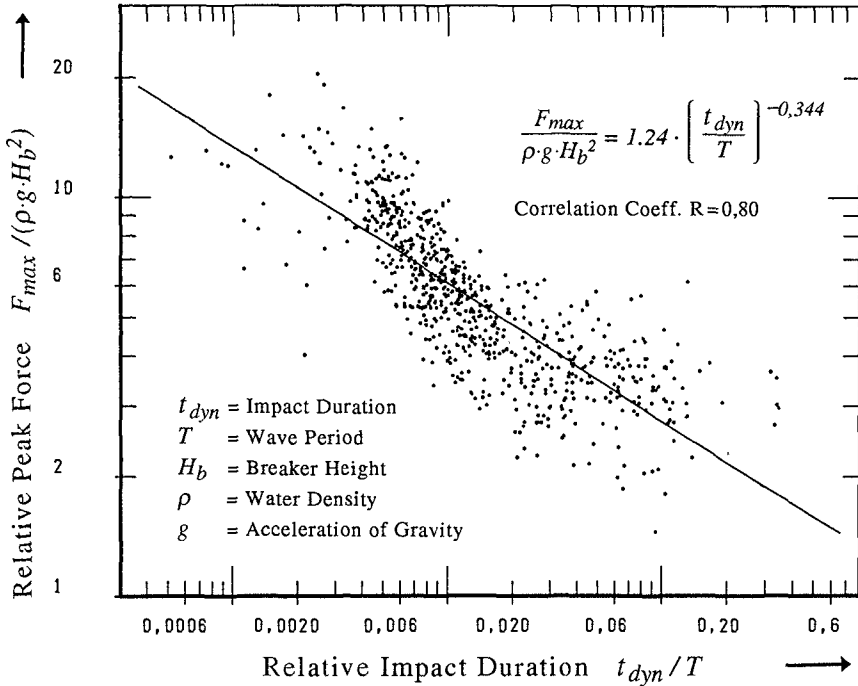


Fig. 8. Duration of Impact Force

#### *Duration of Impact Forces*

Since the duration of the total impact force  $t_{dyn}$  constitutes an important characteristic of the dynamic loading, a relationship between  $t_{dyn}$  (related to wave period  $T$ ) and the dimensionless maximum peak force  $F_{max}$  (related to the squared breaker height  $H_b$ ) has been determined in Fig. 8, showing that  $t_{dyn}$  is almost inversely proportional to  $F_{max}^2$ . The extreme values of  $F_{max}$  generally occur for a deep water wave steepness  $H_o/L_o \approx 0.005$ . For lower or larger values of  $H_o/L_o$ ,  $F_{max}$  decreases abruptly. For the force impulse, however, the extreme values occurs for  $H_o/L_o \approx 0.0075$ .

#### *Force Impulses*

The "dynamic" and "quasi-static" components  $I_{dyn}$  and  $I_{stat}$  of the force impulse have been determined separately. These are defined in Fig. 9 where the point  $M$  of maximum wave run-up is also shown. By assuming the conservation of momentum, the force impulse  $I_w = I_{dyn} + I_{stat}$  should be equal to the momentum of the wave with a mass  $m_w = \rho \cdot V_s$  impinging on a wall with a horizontal velocity  $u_s$ . The momentum of the wave was also

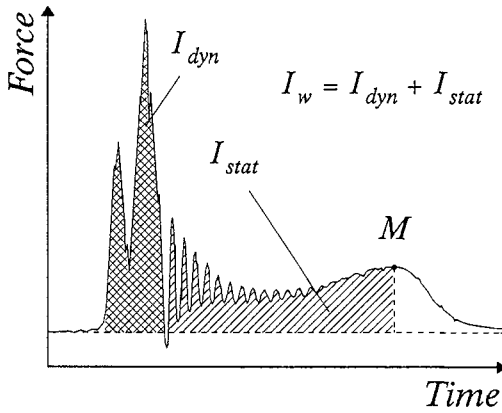


Fig. 9. Force-Impulse Definition Sketch

calculated by using Eqs. (1) and (2) and compared to the force impulse  $I_w$  in Fig. 10. It is seen that despite the large scatter, the solitary wave theory still represents a good mean for the approximate evaluation of the loading of vertical structures induced by breaking waves. In average, the wave momentum was slightly larger (7%) than the force impulse  $I_w$  ( correlation coeff. = 0.83 ).

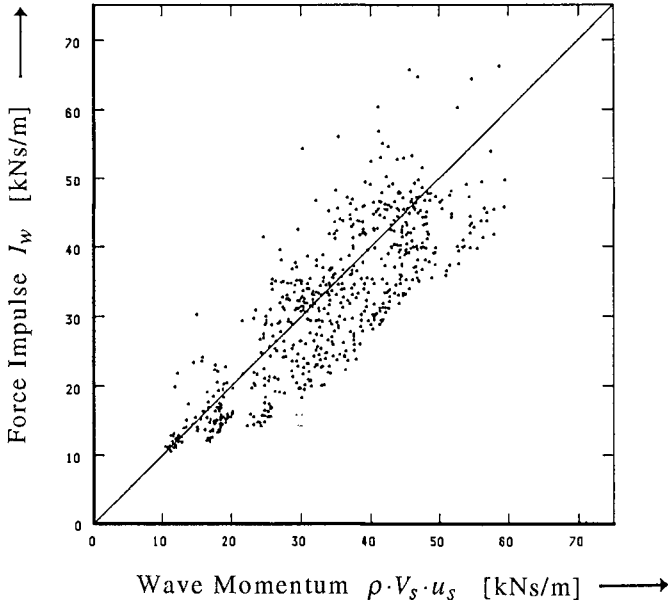
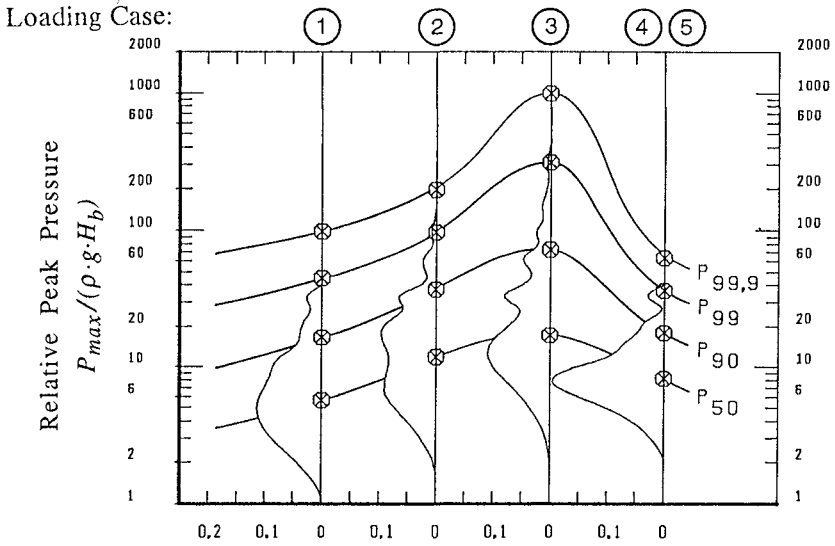


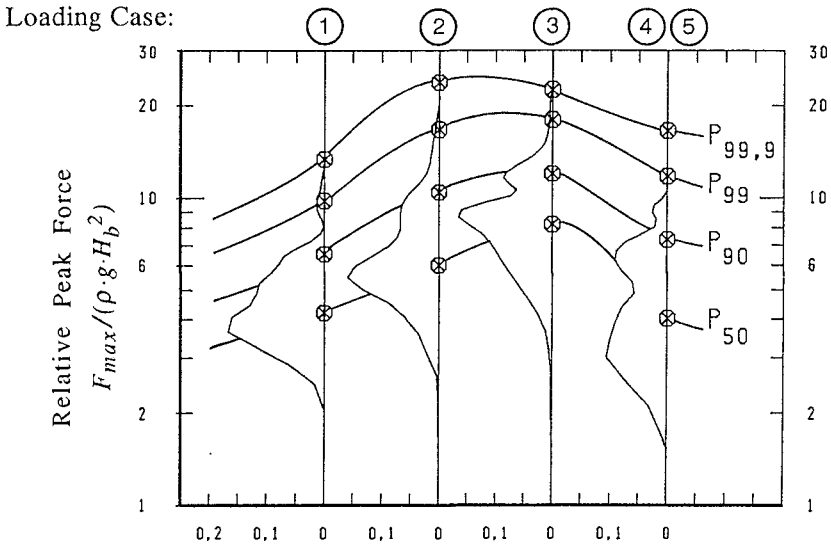
Fig. 10. Force Impulse vs. Wave Momentum

*Statistical Analysis of Impact Pressures and Forces*

A statistical analysis of the impact pressures and forces recorded for the different loading cases defined in Fig. 2 has been performed for almost 1000 breaking wave impacts. Although this analysis still proceeds, some of the first results may already be discussed below.



a) Impact Pressures: Relative Frequency of Occurrence (36 Classes)



b) Impact Forces: Relative Frequency of Occurrence (30 Classes)

Fig. 11. Statistical Distribution of Impact Pressures and Forces for the Different Loading Cases of the Plunging Breaker (see Fig. 2)

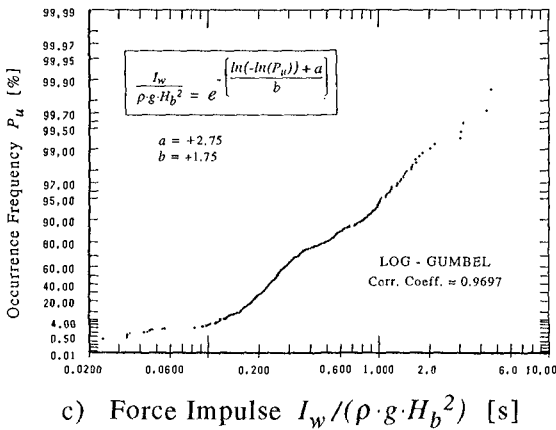
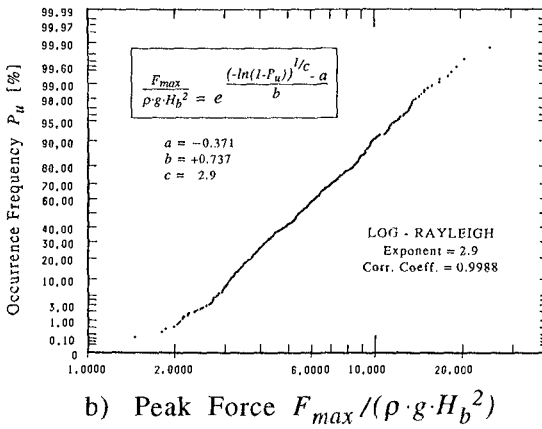
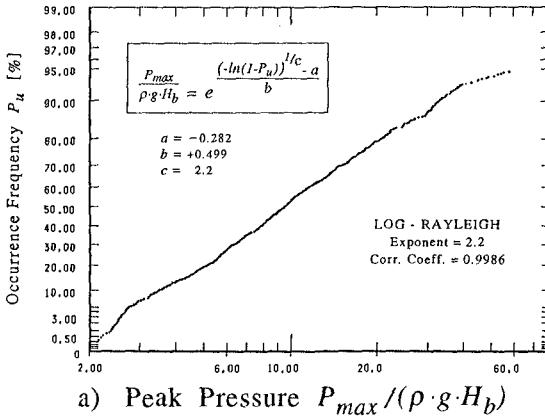


Fig. 12. Statistical Distribution of Impact Loads (n=717 Breaking Waves)

In Fig. 11 the frequency of occurrence of the dimensionless peak pressures and forces is plotted for the different loading cases of the plunging breaker shown in Fig. 2. It is clearly seen that the highest impact pressures occur for loading case 3. On the other hand, the differences between the loading cases are more pronounced for the distribution of impact pressures (Fig. 11a) than for that of the impact forces (Fig. 11b). Further results have also shown that the maximum impact pressures, forces and overturning moments are best described by a LOG-RAYLEIGH distribution whereas the corresponding impulses follow a LOG-GUMBEL distribution (Fig. 12).

### Air Content

The air content of the air-water mixture and the air dynamics involved

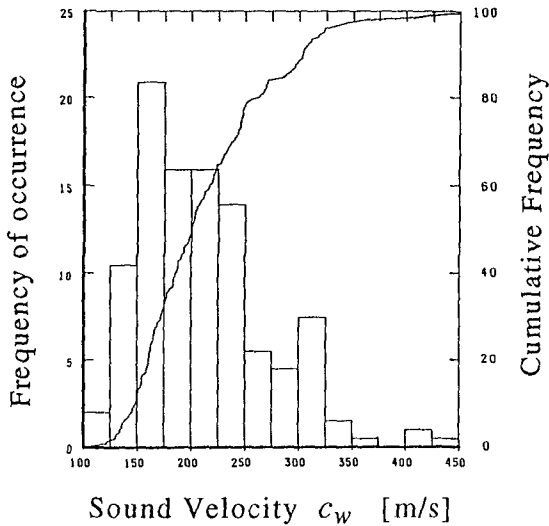


Fig. 13. Statistical Distribution of Sound Velocities in Air-Water Mixture during Impact

ward the wall) of a perturbation in the impact pressure traces and distributions (Fig. 5). The identification of the same perturbation at different pressure cells and the phase shifts have been determined from the detailed pressure histories (sampled at 11 kHz) of the pressure gauges under still water level by using FFT-techniques (SCHMIDT, 1993).

The results obtained by using this procedure for 201 breaking waves impacting directly on the wall are given in Fig. 13 showing the statistical distribution of the investigated sound velocity  $c_w$ , i.e.  $c_w$  values between 100 m/s and 450 m/s with an average value of  $\bar{c}_w = 212$  m/s occur,

in the impact process represent a further important factor in the generation mechanisms of impact pressures. However, the entrained air could not be directly measured in the model tests. Nevertheless, an attempt is made to use the detailed impact pressures measured at 28 different elevations along the wall for the approximate statistical evaluation of the air content involved in the impact process. This has been done through the sound velocity  $c_w$  in the air-water mixture which is evaluated by following the propagation (down-

corresponding to air contents  $\alpha = 0.04 - 1.0 \%$  ( $\bar{\alpha} = 0.2 \%$ ). These velocities actually correspond to speeds at which a perturbation propagates downwards within the air-water mixture. Detailed shock pressure measurements performed by HATTORI and ARAMI (1992) have also shown that this propagation essentially develops within the air-water mixture.

### **Concluding Remarks**

Despite more than 80 years of research work on impact loading of vertical structures subject to breaking waves there are still two basic attitudes related to the design of such structures.

The first attitude consists in simply assuming that impact pressures are not important and thus should not be adopted in the design. The inadequacy of this approach has been demonstrated by the results of the more recent investigations (OUMERACI et.al., 1992; TAKAHASHI et.al., 1992).

The second attitude is to skip the problem of evaluating the design impact load by assuming that the structure can be designed in such a way that impact pressure will not occur. The existing standard design pressure formulae implicitly reflect this attitude. However, it is not advisable to design vertical breakwaters only by applying such formulae, since most of vertical structures will certainly be subject to all conditions of breaking waves during their lifetime.

In fact, the worst loading case for a vertical structure and its foundation is induced by a well-developped plunging breaker. In this respect, the results to be presented in this paper intend to help in assessing the worst impact loads to be considered in a dynamic analysis of the structure and its foundation.

### **Acknowledgements**

This study is a part of a research programme within the Coastal Engineering Research Unit "SFB 205" which is supported by the German Research Council (DFG), Bonn. Additional support by the European Community within the Research Programme MAST G6-0032 is also gratefully acknowledged by the second author.

### **References**

- C.E.R.C. : Shore Protection Manual. Vol. 1, 1984
- GALVIN, C. : Breaker type classification on three laboratory beaches. Journal of Geophysical Research, Vol. 73, No. 12, 1966, pp. 3651-3659

- GODA, Y. : Wave forces on a vertical cylinder: Experiments and a proposed method of wave force computation. Report of the Port and Harbour Technical Research Inst., No. 8, 1964
- GODA, Y. : Random seas and design of maritime structures. University of Tokio Press, 1985
- HATTORI, M. ; ARAMI, A. : Impact breaking wave pressures on vertical walls. ASCE, Proc. 23rd ICCE, Venice, 1992 (these proceedings)
- MURAKI, Y. : Field investigations on the oscillations of breakwaters caused by wave action. Coastal Engineering in Japan, Vol. 9, 1966
- OUMERACI, H.; PARTENSCKY, H.-W.; TAUTENHAIN, E.; NICKELS, H. : Large-scale model investigations: a contribution to the revival of vertical breakwaters. Inst. Civil Engineers, Proc. Conf. Coastal Structures & Breakwaters, London, 1991
- OUMERACI, H. ; PARTENSCKY, H.-W. ; TAUTENHAIN, E. : Breaking wave loads on vertical gravity structures. Proc. 2nd Int. Conf. Offshore & Polar Eng., ISOPE'92, Vol. 3, San.Francisco, 1992, pp.532-539
- OUMERACI, H. ; KLAMMER, P. ; PARTENSCKY, H.-W. : Classification of breaking wave loads on vertical structures. ASCE, Journal of the Waterways, Port, Coastal and Ocean Eng. (paper accepted), 1993
- SCHMIDT, R. : Druckschlagbelastung senkrechter Wellenschutzbauwerke. Ph.D-Thesis, University of Hannover, 1993 (in German)
- TAKAHASHI, S. ; TANIMOTO, K. ; SHIMOSAKO, K. : Experimental study on impulsive pressures on composite breakwaters. Report of the Port and Harbour Tech. Research Inst., Vol. 31, No. 5, 1992
- WEGGEL, J. R. : The impact pressures of breaking water waves. Ph.D-Thesis, University of Illinois, 1968

## CHAPTER 119

### PROFILE CHANGES OF ROCK SLOPES BY IRREGULAR WAVES

W. Gray Smith<sup>1</sup>, Nobuhisa Kobayashi<sup>2</sup>, Shuji Kaku<sup>3</sup>

#### Abstract

Experimental data has been obtained to test the abilities and limitations of existing and new empirical predictive methods for breakwater profile changes under random waves. The thirty data points obtained within this study describe a structure that is neither solely statically nor dynamically stable, and have indicated the difficulties of empirical formulas in accounting for the complex wave and structural interactions affecting breakwater profile development. Data analyses have indicated that current empirical formulas are not able to predict the profile changes very accurately for the data obtained herein. However, qualitative understanding can be obtained based upon the application and adjustment of the formulas to the structure tested herein.

#### Introduction

Design of conventional and berm breakwaters requires the prediction of structural profile changes caused by irregular waves. These changes can be defined by the damage suffered by a statically stable structure or through the description of the structural profile evolution experienced by a dynamically stable structure. This paper examines experimental profile changes for structures overlapping the dynamic/static stability boundary, and evaluates the predictive capabilities of existing and new empirical formulas tested in comparison to profile change data obtained through specific model tests. The new data set is used to clarify the abilities and limitations of the current design methods, and possibly lend insight into the development of an improved method of design for the structures of interest. An attempt is also made to elucidate similarities and differences existing between rock slopes and sand beaches since different formulas

---

<sup>1</sup> Hydraulic Engineer, Coastal Engrg. Res. Center, U.S. Army Engrg. Waterways Exp. Stn., 3909 Halls Ferry Rd., Vicksburg, MS 39180-6199, formerly Graduate Student, Dept. of Civil Engrg., Univ. of Delaware, Newark, DE 19716.

<sup>2</sup> Prof. and Assoc. Dir., Center for Applied Coastal Res., Univ. of Delaware.

<sup>3</sup> Civil Engrg., CTI Engrg. Co., Ltd., 4-9-11 Nihonbashi Honcho, Chuo-ku, Tokyo 103, Japan.



proposed for different sizes of cohesionless materials should be synthesized and generalized.

### New Static Stability Formula

van der Meer (1987) conducted extensive irregular wave tests and proposed an empirical formula for the static stability of uniform rock slopes, for which only minor profile changes are allowed under design wave conditions. This formula yields a prediction of the damage suffered by a structure under a given wave climate, where damage is qualitatively described as the displacement of armor stones. This damage level,  $S$ , is defined as the cross-sectional eroded area,  $A$ , normalized by the square of the nominal armor unit diameter based on a median stone mass,  $D_{n50}$ , as  $S=A/D_{n50}^2$ . van der Meer's formula can be arranged to express the structural damage level,  $S$ , as a function of  $\cot \alpha = \cotangent$  of the structural slope angle  $\alpha$ ,  $N = \text{number of individual waves}$ ,  $P = \text{empirical permeability coefficient}$ ,  $\xi_m = \text{surf similarity parameter based on the significant wave height, } H_s$ , and the mean wave period,  $T_m$ , and  $N_s = \text{stability number defined as } N_s = H_s/[(s-1)D_{n50}]$  where  $s = \text{specific density of the armor unit}$ . This stability number may be used to classify structures as either statically or dynamically stable, where  $N_s = 1 - 4$  was the range van der Meer prescribed for his static stability formula. It is noted that this classification system contains a transition from static to dynamic stability, where dynamic stability was defined with  $N_s \geq 3$ . It is evident, therefore, that for certain structural types such as berm breakwaters it can be difficult to select design methods, specifically whether to design the structure as dynamically or statically stable. This formula for static stability assumes that  $S$  is proportional to  $N^{0.5}$  and  $S > 0$  as long as  $N_s > 0$ . This implies that the damage level does not approach an equilibrium value,  $S_e$ , with the increase of the duration,  $NT_m$ , of the wave action. This is in disagreement with the evolution of the berm breakwater which is initially dynamic, but may eventually reach a stage of static stability similar to sand beaches approaching equilibrium for given wave conditions. Moreover, the formula does not account for the threshold condition of initiation of armor movement.

Kaku *et al.* (1991) found that van der Meer's static stability formula provided reasonable estimates of the stability number for specified damage levels, but failed to yield predicted damage levels with an adequate level of confidence. Therefore, using the data sets of van der Meer (1988), and Ryu and Sawaragi (1986), Kaku *et al.* (1991) proposed a new empirical formula to estimate the damage level of a statically stable structure under design conditions. This data set included 665 data points with the stability number,  $N_s$ , ranging between 0.9 - 3.9. By assuming that the damage level approaches an equilibrium value,  $S_e$ , asymptotically with time, the damage level,  $S$ , is expressed as (van der Meer, 1988)

$$S = S_e(1 - e^{-KN}) \quad (1)$$

where  $S_e = \text{equilibrium damage level}$  and  $K = \text{empirical parameter related to the number of waves required to establish an approximately equilibrium slope profile}$ . For example,  $S = 0.95S_e$  at  $N = 3/K$ . A similar equation was employed by Kriebel and Dean (1985) to express time-dependent beach and dune erosion.

The data sets used in the development of the formula suggest that  $K$  be given by

$$K \approx \frac{a_1}{S_e^{b_1} + c_1} \quad (2)$$

where  $a_1 = 0.01$ ,  $b_1 = 0.8$ , and  $c_1 = 7$  are empirical constants. The similarity between the stability number,  $N_s$ , and the Shields parameter used for sediment transport allowed Kaku *et al.* to include the initiation of armor movement in their formula. A critical stability number,  $N_c$ , was defined by modifying van der Meer's formula for very small damage levels, with the structure assumed to be totally stable below this critical value. This critical stability number was given as

$$N_c = C \frac{6.2P^{0.18}}{\sqrt{\xi_m}} \quad \xi_m < \xi_c \quad (3a)$$

$$N_c = C \xi_m^P \frac{\sqrt{\cot \alpha}}{P^{0.13}} \quad \xi_m > \xi_c \quad (3b)$$

with  $C = 0.4$ , the surf similarity parameter  $\xi_m$ , and the critical value  $\xi_c$ , given as

$$\xi_m = \frac{\tan \alpha}{\sqrt{\frac{2\pi H_s}{gT_m^2}}} \quad \xi_c = [6.2P^{0.31} \sqrt{\tan \alpha}]^{\frac{1}{P+0.5}} \quad (4)$$

The equilibrium damage level was then expressed as

$$S_e = a_2(N_s - N_c)^{b_2} \quad N_s > N_c \quad (5a)$$

$$S_e = 0 \quad N_s \leq N_c \quad (5b)$$

with  $a_2 = 12$  and  $b_2 = 1.3$ .

van der Meer's formula and the new stability formula are compared with the data sets used to develop these formulas in Figures 1a and 1b, where the comparison is the measured damage level against the empirical damage level. The predicted and measured damage levels can vary by a factor of two for these data sets with significant scatter evident for higher damage levels, which indicates a structure approaching a more dynamic classification. Consequently, larger errors would be expected for other data sets.

## Experiment

The experiment was organized to obtain detailed data on macro-scale armor unit

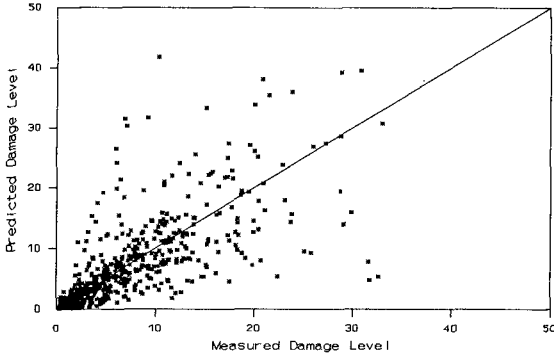


Figure 1a: Comparison with van der Meer's Formula (1987)

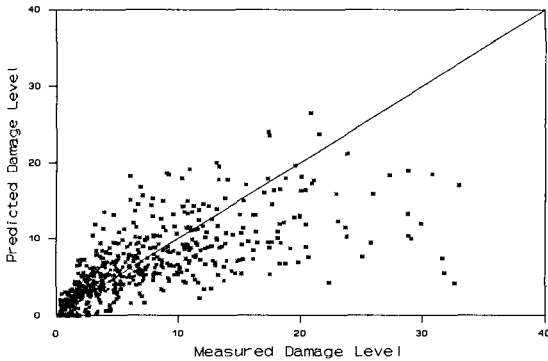


Figure 1b: Comparison with New Formula

movement in the laboratory by measuring altered breakwater profiles under random wave action. A concise summary of the experimental results and analyses from Smith (1991) is presented in the following. The experiment was conducted in a wave tank using a 20 cm thick layer of gravel,  $D_{n50} = 1.8$  cm and a specific density of  $s = 2.7$ , placed on top of a 1:3 glued gravel slope (Figure 2a). Evaluation of the armor unit distribution showed an essentially uniform gravel distribution, where the gradation ratio,  $D_{85}/D_{15}$ , was approximately equal to 1.25. The wave generation was conducted using a piston-type paddle driven by a hydraulic system, and made use of a TMA spectrum as explained by Kobayashi *et al.* (1990). The random signal typically repeated itself after approximately 200 waves. Six irregular wave signals were prepared by varying  $H_s$  and  $T_m$ .

Free surface displacement measurements taken at three locations seaward of the slope were separated into incident and reflected wave trains, where the setup of the

gages is shown in Figure 2a. A surface profiler, shown in Figures 2a and 2b, was constructed to measure the structural profile automatically using three vertically mounted survey probes, located relative to the structure as shown in Figure 2b. The horizontal and vertical motion of the profiler was controlled automatically and produced structural changes relative to the initial profile. It is also noted that the lateral variability of the profile response was negligible and profile change was essentially two-dimensional.

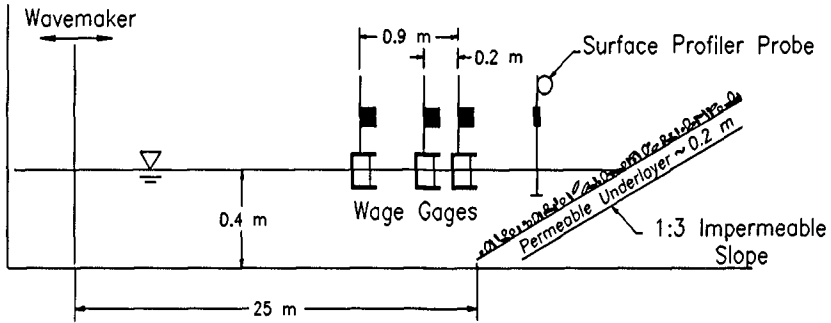


Figure 2a: Experimental Setup

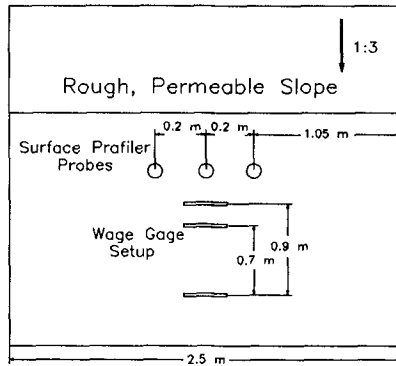


Figure 2b: Plan View of Wave Gage and Surface Profiler Locations

Six tests were performed, with each test consisting of six structural profile measurements at  $N = 0$  and  $N = 200, 400, 600, 800,$  and  $1000$ , where  $N$  is the number of individual waves from the beginning of each test. Each of the six tests hence consisted of five runs with the measured incident and reflected waves as well as the slope profile relative to the initial profile for each run. The data from the thirty runs are summarized in Table 1. Figure 3 depicts a typical result obtained for the wave measurements. Figure 3 shows the incident versus reflected wave spectrum, where wave reflection from the structure was minimal. It was also observed that the incident wave

train proved reproducible and that the reflected waves during each test were observed to remain essentially the same, thus being insensitive to profile changes. The measured average reflection coefficient,  $r$ , as defined by Kobayashi *et al.* (1990), is listed for each run in Table 1.

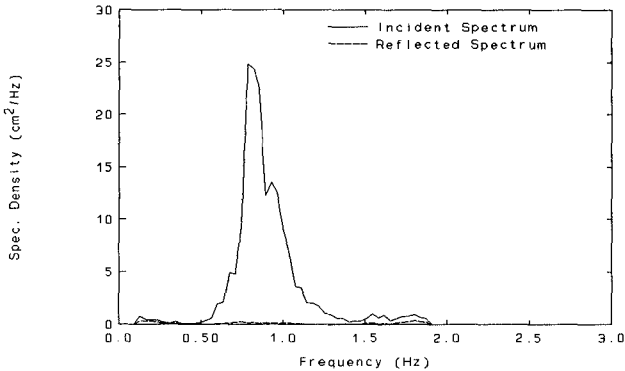


Figure 3: Incident and Reflected Spectrum

The slope geometry of the breakwater structure was obtained for each of the thirty test runs. Figure 4 depicts a typical measured altered profile, where the initial slope is included in an effort to indicate the degree of profile change. Qualitative assessment of the data showed erosion of the profile near the still water level (SWL) at profile elevation zero, with areas of deposition located both above and below the erosional area, corresponding to the transition between accretional and erosional profiles for sandy beaches. The increase of  $S$  with the increase of  $N$  followed the assumed exponential form as given by Eq. 1 fairly well, where significant alteration of the profile occurred during the first few hundred waves with much less profile change associated with the later stages of each test run. This implies that the profile change is sensitive to the degree of profile deviation from the equilibrium profile. It is also noted that the effects of the wave period proved important as shown in Table 1. In summary, the test runs with  $N_s = 2.69 - 3.67$  and  $S = 6.3 - 38.1$  were close to the upper limit of applicability of the static stability formulas.

### Comparison with Static Stability Formulas

The static stability formula proposed herein and that of van der Meer (1987) are compared with the thirty new data points obtained from the present experiment. Before the comparison was completed the validity of the application of the formulas was ensured using the parameter ranges described by van der Meer (1988), including the stability number, wave steepness, surf similarity parameter, and initial profile slope. It was found that the values for the present experiment were within the ranges established by van der Meer (1988) for his static stability formula.

Table 1: Governing Parameters for 30 Test Runs

Run #	$N$	$H_s(cm)$	$T_m(sec)$	$N_s$	$\xi_m$	$S$	$r$	$cot \alpha$
L1A	199	10.07	1.11	3.28	1.40	12.6	0.17	3.13
L1B	402	10.17	1.10	3.31	1.38	15.0	0.18	
L1C	601	10.22	1.10	3.33	1.38	18.1	0.18	
L1D	800	10.25	1.10	3.33	1.37	16.9	0.18	
L1E	995	10.25	1.11	3.34	1.39	20.5	0.19	
S1A	195	9.65	1.13	3.14	1.41	6.3	0.17	3.23
S1B	392	9.75	1.12	3.18	1.39	9.1	0.18	
S1C	593	9.78	1.12	3.19	1.39	10.1	0.18	
S1D	792	9.78	1.12	3.19	1.39	13.7	0.18	
S1E	996	9.76	1.11	3.18	1.38	13.1	0.19	
L2A	194	9.83	1.34	3.20	1.60	10.3	0.23	3.33
L2B	380	10.02	1.37	3.26	1.62	16.3	0.24	
L2C	567	10.09	1.38	3.29	1.63	19.7	0.25	
L2D	756	10.13	1.38	3.30	1.63	22.4	0.26	
L2E	948	10.15	1.37	3.31	1.61	23.5	0.26	
S2A	190	8.26	1.37	2.69	1.79	10.9	0.23	3.33
S2B	386	8.68	1.35	2.83	1.81	15.5	0.22	
S2C	576	8.75	1.36	2.85	1.72	18.3	0.24	
S2D	767	8.79	1.36	2.86	1.72	18.7	0.24	
S2E	959	8.82	1.36	2.87	1.72	20.0	0.24	
L3A	202	11.14	1.61	3.63	1.81	18.8	0.34	3.33
L3B	401	11.20	1.62	3.65	1.82	34.5	0.39	
L3C	600	11.21	1.63	3.65	1.83	33.5	0.37	
L3D	794	11.25	1.64	3.67	1.83	37.3	0.36	
L3E	988	11.26	1.65	3.67	1.84	38.1	0.35	
S3A	215	8.53	1.51	2.77	1.81	11.8	0.27	3.57
S3B	421	8.56	1.54	2.79	1.84	14.5	0.27	
S3C	624	8.60	1.56	2.80	1.86	17.4	0.28	
S3D	829	8.61	1.57	2.81	1.87	18.8	0.28	
S3E	1036	8.63	1.57	2.81	1.87	19.8	0.29	

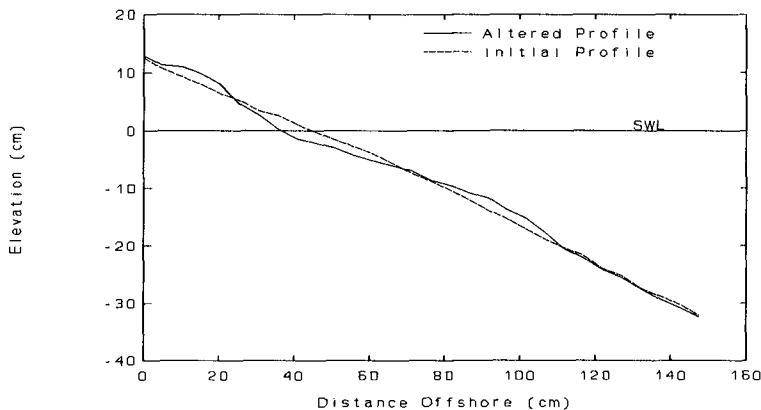


Figure 4: Typical Measured Altered Breakwater Profile

Figures 5a and 5b graphically depict the accuracy of van der Meer's formula, where different permeability coefficients are used in an effort to improve the agreement. The permeability of a structure has been shown to affect the structural response, where in general impermeable structures suffer greater erosion than do permeable structures subject to the same wave conditions. Examining the structure studied herein, a permeability coefficient  $P = 0.4 - 0.5$  seemed appropriate based on van der Meer's recommendations. However, calculations have been conducted using a range of permeability coefficients. Figure 5a indicates that the damage level is being underestimated by roughly a factor of two, using the permeability coefficient,  $P = 0.4$ , with the error increasing for the higher levels of damage. Decreasing  $P$  to a value of 0.1 caused the predicted damage level to increase as shown in Figure 5b. It can be seen from Figures 5a and 5b that the damage prediction improves for the lower permeability coefficient. However, the lower permeability coefficients are unrealistic for the structure used in the experiment. These observations seem to be in agreement with the data analyses presented by Kaku *et al.* (1991), where it was shown that the formula predicted poorly for higher damage levels. Interpretation of these results indicate that this formula might be sufficient when applied to structures with low stability numbers, but is not accurate enough for structures approaching dynamic stability.

Figures 6a and 6b depict the capability of the new formula in predicting the damage levels, using various empirical coefficients in an attempt to improve the agreement. Figure 6a represents the new formula, using the empirical coefficients as fitted to the data sets of van der Meer (1988), and Ryu and Sawaragi (1986), and displays results similar to those shown in Figure 5a. It is noted that the permeability coefficient was again adjusted for this new formula, however, it provided relatively insignificant improvement in the formula's prediction. Hence  $P = 0.4$  is assumed for the new formula. Two alternative approaches were undertaken toward the improvement of the agreement for Kaku *et al.*'s formula. First, it was observed that the equilibrium damage level, predicted by Eq. 5, was only slightly higher than most of the damage levels

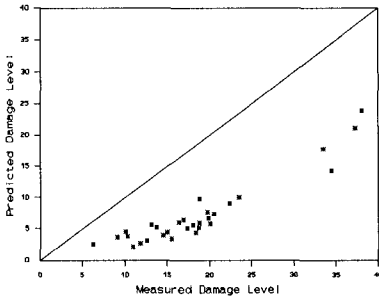


Figure 5a: Comparison with van der Meer's Formula ( $P = 0.4$ )

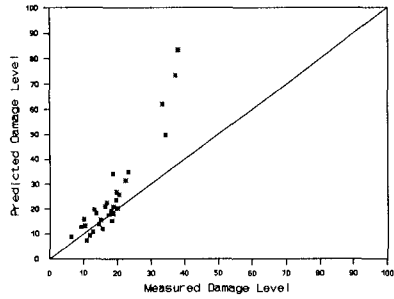


Figure 5b: Comparison with van der Meer's Formula ( $P=0.1$ )

suffered by the structure following 1000 waves. It was not anticipated that the structure would reach equilibrium over this amount of time, therefore, the value of the equilibrium damage level was increased in an effort to obtain higher damage level estimates. This increased equilibrium damage level caused a decrease of the exponential growth factor,  $K$ , as predicted by Eq. 2. The lower value of  $K$  in Eq. 1 offset the increase of the equilibrium damage level and little improvement was obtained from this adjustment.

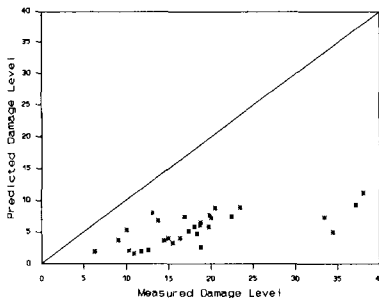


Figure 6a: Comparison with New Formula ( $a_1 = 0.01$  &  $b_2 = 1.3$ )

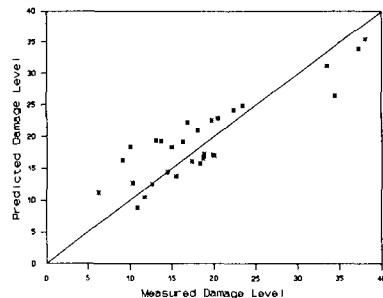


Figure 6b: Comparison with New Formula ( $a_1 = 0.08$  &  $b_2 = 1.5$ )

Secondly, it was observed that approximately half of the damage was occurring during the first 200 waves, thus indicating that this profile would possibly approach equilibrium more rapidly than anticipated. Kaku *et al.*'s formula, however, predicts a much smoother rise towards equilibrium, with the initial damage level increase much less than that observed during the experiment. Adjustment of the exponential growth



parameter  $a_1$  for  $K$  in Eq. 2 caused the damage levels to be predicted more accurately, while the increase of the equilibrium damage level by adjusting the parameter  $b_2$  in Eq. 5 also allowed for improved prediction of the higher damage levels. These two empirical parameters,  $a_1$  and  $b_2$ , were fitted to the present data set. Figure 6b depicts the improved results of the new formula, where  $a_1 = 0.08$  and  $b_2 = 1.5$  are the parameters fit to the new data set. This adjustment has improved the performance of Kaku *et al.*'s method for the data described herein. However, any conclusive results will require more data in order to properly calibrate the parameters. Nevertheless, better agreement is achieved with the adjusted formula of Kaku *et al.* in comparison with van der Meer's formula. Also, it is important to point out the adjustment of van der Meer's formula required unrealistic permeability coefficients. The framework of Kaku *et al.*'s formula may be more realistic, for it adjusts the time scale of profile development, which is not fully defined by any previous work.

In summary, the damage levels predicted by the empirical formulas of van der Meer (1987) and Kaku *et al.* (1991) failed to accurately predict the damage suffered by the structure in this experiment. However, it is expected that the formula due to Kaku *et al.* is more adjustable to various conditions. Moreover, the necessity of the adjustments of the empirical parameters suggest that these simple formulas are not sufficiently accurate partly because they do not account for detailed irregular wave and structural characteristics.

#### Comparison with Dynamic Stability Formulas

In addition to the previous static stability approach to profile evolution prediction, the range of  $N_s = 2.69 - 3.67$  associated with the new data set may allow for the evaluation of dynamic profile prediction methods. Dynamic stability allows for significant alteration of the structure from the initial profile configuration, thus requiring the prediction of the actual evolved profile shape. van der Meer and Pilarczyk (1986) studied the dependency of the evolved profile on various wave and structural parameters, and developed an empirical formula that predicts the locations of abrupt profile changes on an assumed profile shape. This formula connects these points with straight lines and curves, which are described by power functions similar to those used to express the equilibrium profile for sandy beaches. Their formula is applicable to structures with  $N_s$  between 3 and 200 with arbitrary initial profile configurations, and the new data set corresponds to the lower limit of applicability for this dynamic stability formula.

A typical result of van der Meer and Pilarczyk's formula is shown in Figure 7, where the predicted profile is plotted with the measured altered structural slope. It is evident that the formula overpredicts the response of the breakwater. It is noted that this result was anticipated due to the low stability associated with the data set in relationship to the data used to develop the dynamic stability formula. It can be seen that the accretion of the berm was greatly overpredicted, and that a large area of erosion was predicted below the SWL. In general, the formula predicts accretion above the SWL and erosion below, which is in contrast to the data which depicts more of an S-shape, where erosion is restricted to the area around the SWL with areas of accretion both above and below the SWL as shown in Figure 4. The damage levels associated with the predicted profiles were also calculated in order to quantify the predictive capabilities

of the formula when applied to the structure tested herein. It was found that the damage level obtained for the predicted profiles is overestimated by roughly a factor of two as shown in Figure 8, where application of this method might be used to define an upper limit of damage for a static/dynamic structure.

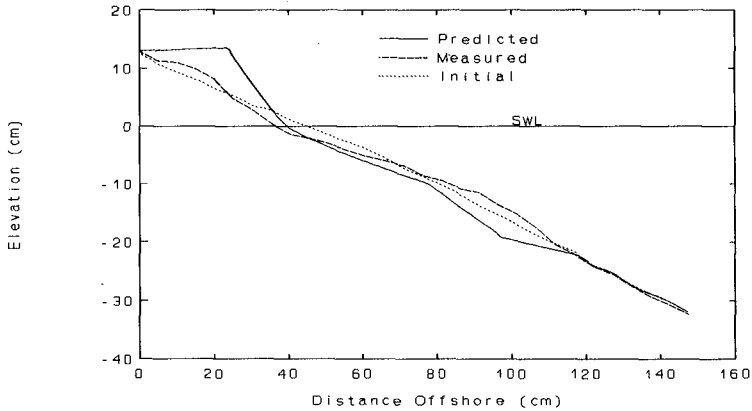


Figure 7: Predicted Dynamic Profile(van der Meer and Pilarczyk, 1986)

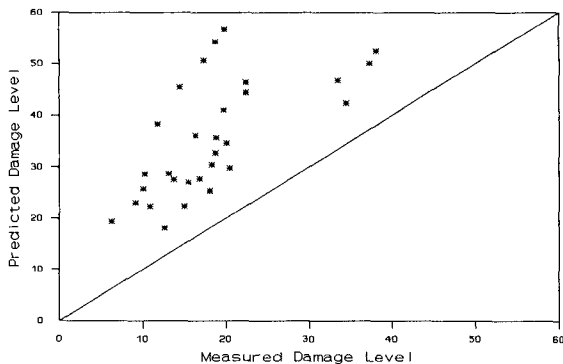


Figure 8: Comparison with Formula of van der Meer and Pilarczyk (1986)

van der Meer (1992) reanalyzed the data set used previously to develop the dynamic stability formula of van der Meer and Pilarczyk (1986), with emphasis placed on berm breakwaters which pass through stages of dynamic stability and eventually develop an essentially stable profile. The data set contained structures with  $N_s$  between 3 and 500, but a new formula was developed for the data set concentrating on structures with  $N_s < 6$ . The modified method notes the probability of a more rapid increase in the damage

level than that predicted for statically stable structures and may be applied for  $N = 250 - 10,000$  with alterations to the profile taking place even after significant durations. The effects of the initial slope are discussed by van der Meer (1992) where it is noted that for  $N_s < 10$  the initial slope largely affects the final profile, much as is the case with statically stable structures. This lead to the inclusion of a definition of an equivalent slope profile to be used with the modified formula, which would prove important for a typical berm breakwater profile. The present experiment, however, used a uniform slope of approximately 1:3, and the qualitative assessment of the profile development as discussed by van der Meer (1992) agrees with the observed profile evolution within the experiment.

The modified formula has been applied to the new data set described herein, where comparisons are made between the measured and predicted slope profiles and corresponding damage levels. A typical result of the new formula is shown in Figure 9. Figure 9 depicts that the predicted slope underestimates the berm accretion both in volume and in the height to which the berm is developed, also the erosion around the SWL and the accretion below the SWL are poorly predicted. van der Meer (1992) encountered similar problems with the prediction of the size of the structural crest when the formula was applied to the data of Ahrens and Heimbaugh (1989), and suggests that the limited data did not allow for calibration of the parameter related to this structural feature. However, the trend of the profile seems to agree with the present data, because the formula predicts accretional areas both above and below the SWL, and an erosional area near the SWL. Despite the appropriate profile shape, profile development is insufficient due to the relatively small alteration of the initial profile as predicted by the formula. This observation was also noted quantitatively when calculating the damage levels of the predicted profiles, where the damage was found to be underpredicted by roughly a factor of two as shown in Figure 10. In analyzing the results it is anticipated that an improved prediction of the berm crest would allow better agreement to be realized since this would in turn upgrade the erosive portion about the SWL, thus improving overall results for the entire predicted profile.

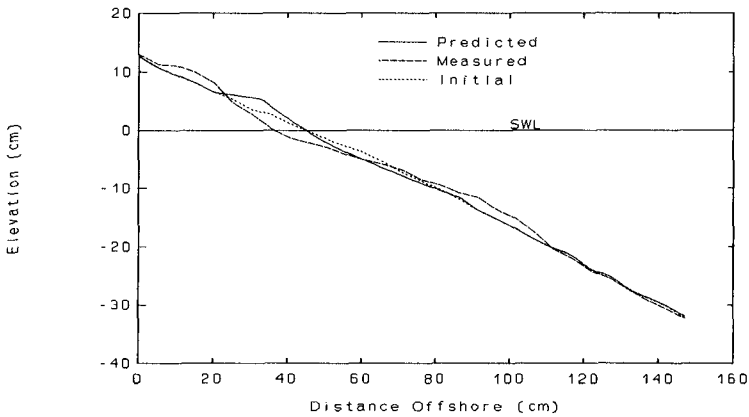


Figure 9: Predicted Dynamic Profile(van der Meer, 1992)

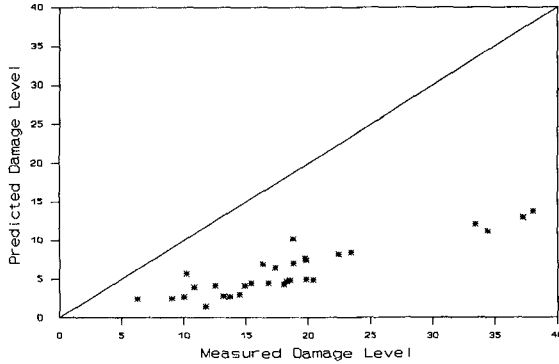


Figure 10: Comparison with Formula of van der Meer (1992)

## Conclusions

It has been shown that for the new data set with a structural classification that is neither strictly statically or dynamically stable, current design methods are insufficient in predicting profile response with any consistent accuracy. The static stability formulas of van der Meer (1987) and Kaku *et al.* (1991) failed to accurately predict the damage suffered by the structure, where the formulas underestimated the damage. This result is not surprising in that the formulas were developed with data that included numerous structures with low damage levels. The flexibility of the static stability formulas was tested for the new data set with the adjustment of the empirical permeability coefficient and the empirical parameters contained within the formula due to Kaku *et al.* (1991). van der Meer's formula improved with the decreasing permeability coefficient, however, the results were dependent on what appears to be an unrealistic value for the permeability coefficient. Kaku *et al.*'s formula showed improved accuracy with the adjustment of the time scale for profile development, which occurred at a higher rate for the more dynamic structure studied herein. It appears, therefore, that the formula due to Kaku *et al.* is more versatile and allows for adjustments to be made dependent upon the structural type of interest. More data will be required to properly calibrate this formula. It seems that the previous investigators tried to describe too varying a range of structural types with simple formulas, where it is not plausible given the wide variety of influences to which different structural types are subjected.

Secondly, the dynamic stability formulas of van der Meer (1992), and van der Meer and Pilarczyk (1986) were evaluated using the new data set. The data tested the ability of the formulas to predict the actual profile response and damage levels suffered. van der Meer (1992) revised the stability formula for structures close to the static stability boundary. The revised formula provided good qualitative results in that the profile shape was predicted relatively well despite a repeated underprediction of the amount of actual profile response. It is anticipated that this formula is a step in the right

direction, but requires additional data in order to produce more accurate results. van der Meer and Pilarczyk's (1986) dynamic stability formula repeatedly overpredicted profile response. In summary, the existing dynamic formulas seem to be insufficient for the specific structures studied within this study.

### Acknowledgement

This work is a result of research sponsored by the National Science Foundation under grant number CTS-89000640. The study was conducted by the first author as a graduate student at the University of Delaware preceding the author's association with the U.S. Army Corps of Engineers. Permission to publish this work was granted by the Chief of Engineers.

### References

- Ahrens, J.P. and Heimbaugh, M.S. (1989). "Dynamic stability of dumped riprap," *Proc. of Coast. Zone '89*, Charleston, ASCE.
- Kaku, S., Kobayashi, N., and Ryu, C.R. (1991). "Design formulas for hydraulic stability of rock slopes under irregular wave attack," *Proc. of 38<sup>th</sup> Japanese Coast. Engrg. Conf.*, JSCE, 661-665 (in Japanese).
- Kriebel, D.L. and Dean, R.G. (1985). "Numerical simulation of time-dependent beach and dune erosion," *Coast. Engrg.*, 9, 221-245.
- Kobayashi, N., Cox, D.T., and Wurjanto, A. (1990). "Irregular wave reflection and runup on rough impermeable slopes," *J. Wtrway. Port, Coast., and Oc. Engrg.*, ASCE, 116(6), 708-726.
- Smith, W.G. (1991). "Experiments on armor stability and movement on rough permeable slopes," thesis submitted to Univ. of Delaware for degree of Master of Civil Engrg., Dept. of Civil Engrg., Univ. of Delaware, Newark, DE.
- Ryu, C.R. and Sawaragi, T. (1986). "A new design method of rubble mound structures," *Proc. 20<sup>th</sup> Coast. Engrg. Conf.*, ASCE, 2188-2202.
- van der Meer, J.W. and Pilarczyk, K.W. (1986). "Dynamic stability of rock slopes and gravel beaches," *Proc. 20<sup>th</sup> Coast. Engrg. Conf.*, ASCE, 1713-1726.
- van der Meer, J.W. (1987). "Stability of breakwater armor layers-Design formula," *Coast. Engrg.*, 11, 219-239.
- van der Meer, J.W. (1988). "Rock slopes and gravel beaches under wave attack," thesis submitted for the degree of Doctor of Philosophy, Delft University of Technology, Delft, The Netherlands, 1988.
- van der Meer, J.W. (1992). "Stability of the seaward slope of berm breakwaters," *Coast. Engrg.*, 16, 205-234.2

## CHAPTER 120

### Wave-Induced Uplift Characteristics on Concrete Block Slope Revetments

Uwe Sparboom<sup>1</sup> and Wolf Debus<sup>2</sup>

#### Abstract

The paper deals with full-scale wave attack on concrete block slope revetments. The tests were carried out in the research facility LARGE WAVE CHANNEL, Germany. The blocks were placed on a filter layer (granular and/or geotextile) preventing the failure of the sandy sub-soil. Stability results are reported. Pressure measurements at special testblocks were used to investigate uplift characteristics of the blocks. Furthermore, the measurements were applied for verifying analytical design procedures.

#### Introduction

Permeable dyke revetments are preferably applied for coastal protection works at the German coast. An economical solution for the sloping cover layer on dykes with a sandy core can be realized by the use of prefabricated concrete blocks placed on a filter layer preventing failure of the sandy sub-soil. The filter layer can be constructed by a quasi three-dimensional granular filter, by a quasi two-dimensional geotextile filter or by a combination of both filter types. In the past, wave attack at storm surge conditions frequently caused failures of such dyke revetments. With the new full-scale laboratory LARGE WAVE CHANNEL a fundamental research project was started in order to investigate dyke revetments under prototype conditions. The main dimensions of this research facility are: depth 7.0 m, width 5.0 m and length 324 m. Regular waves and random seas are produced mechanically by a wave generator. The maximum wave height is 2.5 m. Details about the channel were published by Grüne and Führböter (1975); design criteria and technical works were reported by Grüne and Sparboom (1982).

---

<sup>1</sup> Dr.-Ing., Senior Research Engineer, Large Wave Channel, Coastal Engineering Research Group SFB 205, University of Hannover, Merkurstrasse 11, 3000 Hannover 21, Germany

<sup>2</sup> Dipl.-Ing., Civil Engineer, Coastal Engineering Research Group SFB 205, University of Hannover

### Test Set-Up

The core of the 1 to 4 sloping sea dyke was made by sand with a mean diameter of  $d_{50} = 250 \mu\text{m}$ . The area of the highest expected wave attack was subdivided into two testfields each of 10 m in length and 2.5 m in width. Both testfields were separated by a concrete wall of 1 m in depth. A cross-section of the revetment is given in Figure 1. The whole prototype revetment can be seen in Figure 2. The testfields are shown in Figure 3. The concrete blocks were placed in stretcher-bond equivalently to usual method in practice. The investigated structure types are drawn in Figure 4.

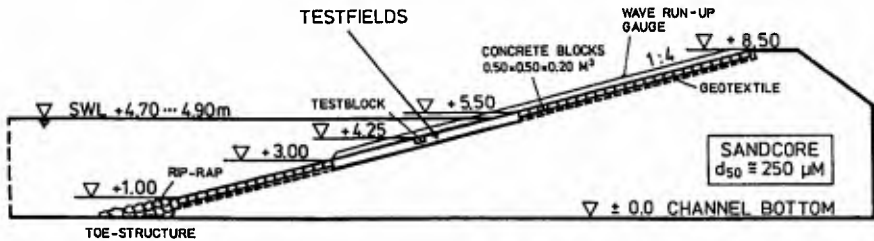


Figure 1. Cross-Section of the Prototype Dyke Revetment



Figure 2. 1 to 4 Sloping Dyke Revetment in the Large Wave Channel



Figure 3. Testfields of the Prototype Dyke Revetment

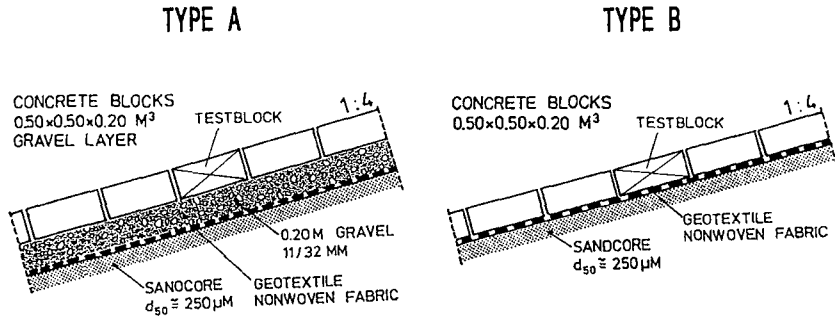


Figure 4. Investigated Structure Types of the Prototype Dyke Revetment

The testblocks which contained measuring devices were installed nearly 0.5 m below SWL in each teststructure or testfield. The measuring equipment was designed to registrate the following electrical signals synchronously:

- wave parameters (height and period) at the toe of the dyke revetment and
- wave pressures acting on the testblocks at the top and bottom side.

The waves were generated regularly applying an integrated absorption control system. The minimum wave number for each test was 200. After very first block failure which was observed by visual control the test was interrupted. A damaged teststructure was replaced by a more stable one being able to increase the wave parameters as far as the second teststructure was damaged. This is the reason why synchronous measurements at both structures (Type A and B) are only available for testserie 1. Testserie 2 was carried out with the structure of Type B only.

### Stability Investigations

Designing blocks of sea dyke revetments it is very useful to consider the breaker parameter which contains the influence of the wave period (as part of the wave steepness) and the slope angle (Bruun,1985). The stability parameter proposed by Pilarczyk, 1987 is given with a non-dimensional quantity which is calculated by the ratio wave height to block thickness multiplied with the relative block density.



Breaker Parameter  $\xi_0 = \frac{1}{n \cdot \sqrt{H_M / L_0}} ; L_0 = \frac{g T_M^2}{2 \pi}$  (1)

- $\xi_0$  (-) breaker number in deep water
- $n$  (-) front slope 1 : n
- $L_0$  (m) wave length in deep water
- $T_M$  (s) wave period (regularly generated)
- $H_M$  (m) wave height (regularly generated)
- $g$  (m/s<sup>2</sup>) acceleration due to gravity

Stability Parameter  $\chi = \frac{H_M}{\Delta d_B} ; \Delta = \frac{\rho_b - \rho_w}{\rho_w}$  (2)

- $\chi$  (-) stability parameter
- $H_M$  (m) wave height (regularly generated)
- $\Delta$  (-) relative block density
- $\rho_b$  (kg / m<sup>3</sup>) density of concrete blocks
- $\rho_w$  (kg / m<sup>3</sup>) density of water
- $d_B$  (m) block thickness

In Führböter and Sparboom, 1988 there can be found stability results for various types of block structures. In this paper tests with wave parameters very close to failure conditions are focussed. In testserie 1 the failure - very first block lifting out of the revetment - occurred at wave parameters  $H_M = 0.8$  m and  $T_M = 6.0$  s (Type A, Figure 5) whereas in testserie 2 the failure

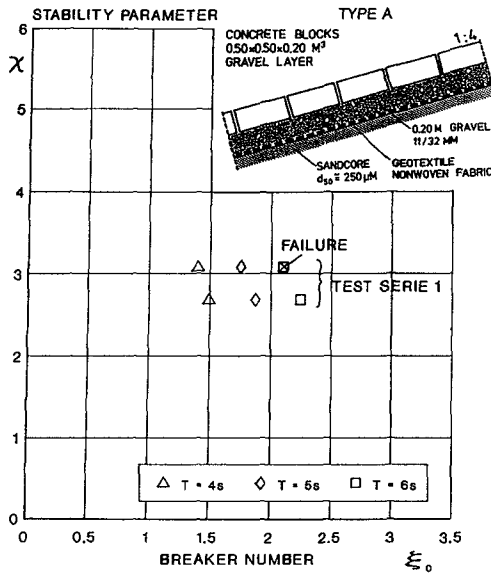


Figure 5. Stability Results Under Critical Wave Conditions - Granular Filter (Testserie 1)

occurred at wave parameters  $H_M = 1.2$  m and  $T_M = 5.0$  s (Type B, Figure 6). The structure of Type B remained stable under test conditions of testserie 1.

For both structure types the failure position was found nearly  $0.5 H$  beneath SWL. The very first block lifting occurred just before wave breaking (foto Figure 7).

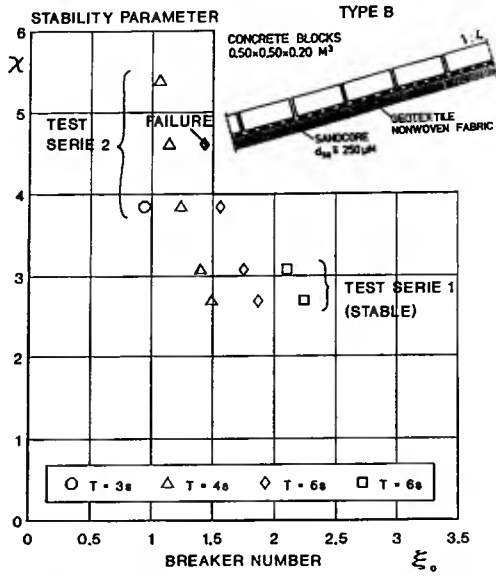


Figure 6. Stability Results Under Critical Wave Conditions - Geotextile Filter (Testseries 1 and 2)

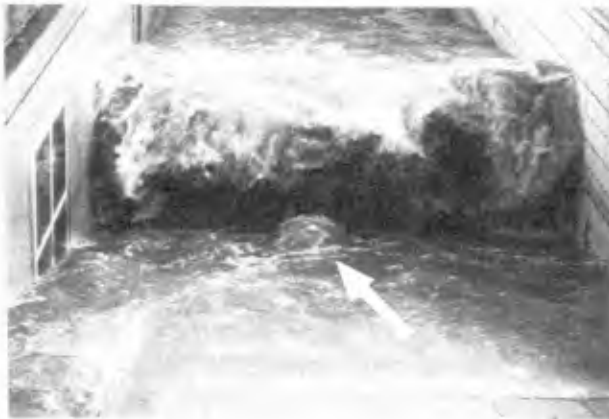


Figure 7. Very First Block Failure

Block Lift Forces

In order to investigate pressure variations causing block lifting special testblocks (see Figure 3) were supplied with pressure transducers at top and bottom side. An example of these measurements is plotted in Figure 8. The pressure differences  $\Delta p$  of top and bottom side just before wave breaking were evaluated. Additionally, the reaction times  $T_{pos}$  with uplift characteristic (from zero to maximum) were recorded.

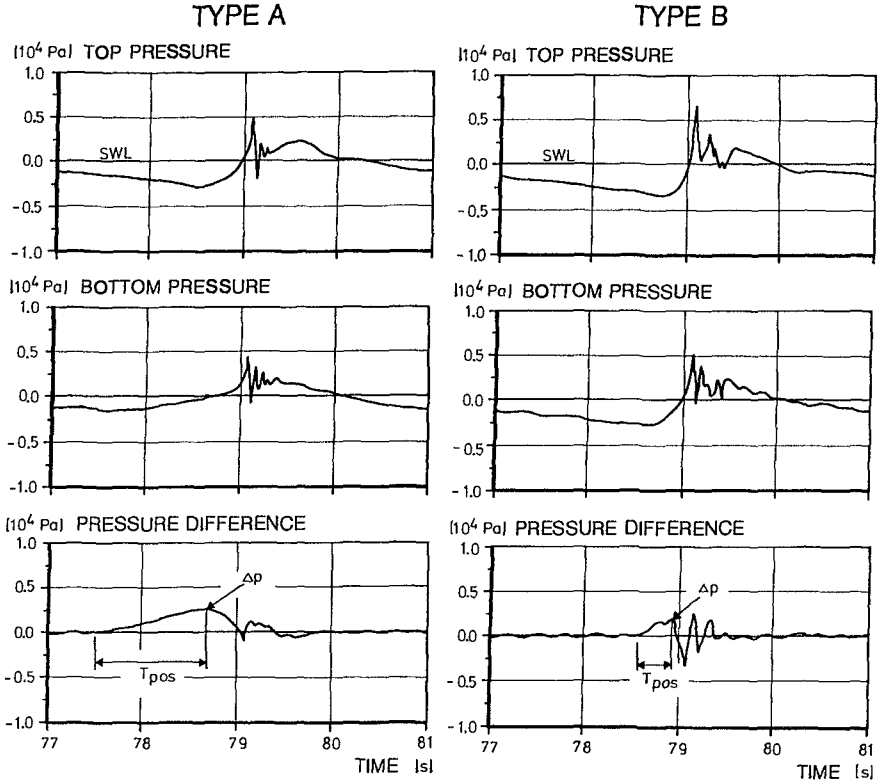


Figure 8. Example of Synchronous Pressures Acting on the Testblocks (Testserie 1)

Estimating the uplift forces (Sparboom and Debus, 1990) the uplift pressures were integrated over the plane of the testblock. For the critical damage tests the development of the uplift forces - evaluated for several waves in each test - can be seen in Figures 9 and 10. Both structure types were damaged in nearly 10 minutes. The maximum uplift force amplitudes are of nearly equal amount for both structure types.

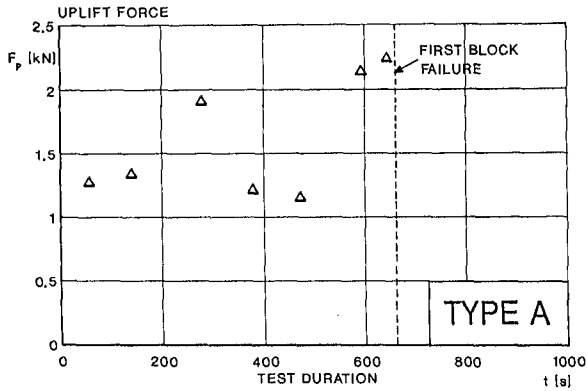


Figure 9. Block Failure Testserie 1; Waves:  $H_M = 0.8$  m,  $T_M = 6.0$  s

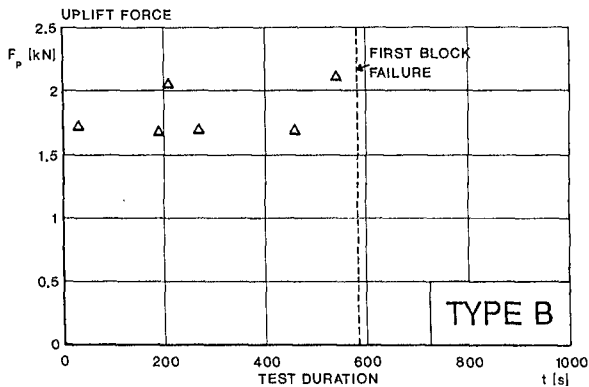


Figure 10. Block Failure Testserie 2; Waves:  $H_M = 1.2$  m,  $T_M = 5.0$  s

For the testseries 1 and 2 a representative set of parameters defined in Figure 8 were evaluated. The uplift forces  $F_p$  were found by integrating the pressure differences over the testblock. These force values  $F_p$  were related to the block weight under water  $F_w$  (weight force minus buoyant force). The reaction times  $T_{pos}$  were related to the wave period  $T_M$  of the corresponding test. In the case of a granular filter the uplift force works in the range 0.10 to 0.45 of the period ratio (Figure 11). For comparison in the case of a geotextile filter the main range lies between 0 and 0.15 (Figure 12). But there are also period ratios in the range 0.3 to 0.4. It can be assumed that uplift forces acting under such conditions cause block failures.

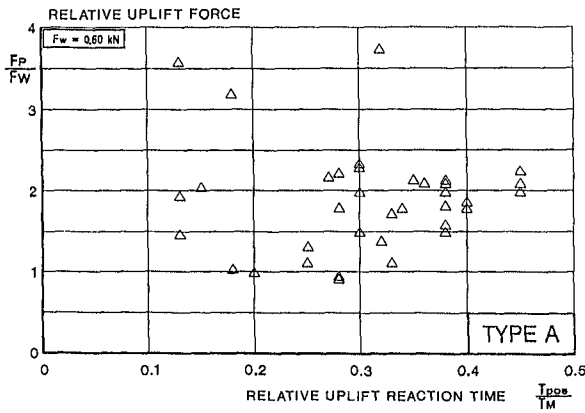


Figure 11. Uplift Forces vs. Reaction Time for Testserie 1 - Granular Filter

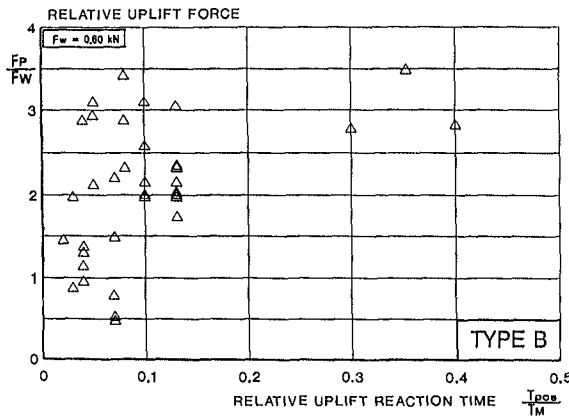


Figure 12. Uplift Forces vs. Reaction Time for Testserie 2 - Geotextile Filter

From Figures 11 and 12 it may be assumed that block failures occur if the uplift forces are acting in a time interval with a duration of at least 1/3 of the wave period (Führböter and Sparboom, 1988). Uplift forces causing block movements roughly amount 2 to 4 times of the block weight force under water.

Verification Analysis

Experimental full-scale data on block revetments are especially helpful verifying theoretical evaluations. Burger et al., 1990, Bezuijen et al. 1990 and Klein Breteler and Bezuijen, 1991 published analytical procedures for the design of block revetments placed on a granular filter layer. In Figure 13 a definition sketch of the used parameters is given.

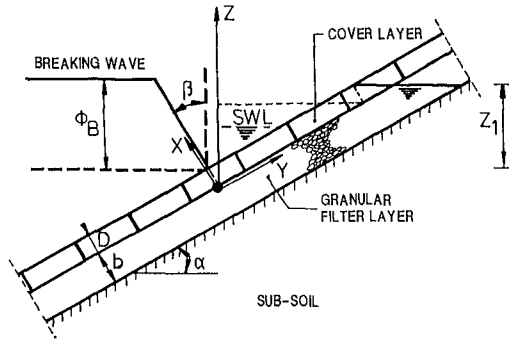


Figure 13. Definition Sketch of the Analytical Solutions on Waves Acting on Block Revetments

It was assumed that - with respect to full-scale failure mechanism - the maximum pressure over the revetment occurs just before wave breaking. The following equations were used (see also Figure 13):

BURGER et al., 1990 and BEZUIJEN et al., 1990

$$\Phi_w = \left[ \frac{\lambda}{2 \tan \alpha \tan \beta} * \left( 1 - e^{-\tan \alpha \tan \beta \Phi_B / \lambda} \right) + \frac{\lambda}{2} \right] * \left[ 1 - e^{-2 Z_1 / \lambda} \right] \quad (3)$$

- $\Phi_w$  (m) maximum uplift pressure over the revetment
- $\lambda$  (m) vertical leakage factor
- $\alpha$  ( $^\circ$ ) slope angle
- $\beta$  ( $^\circ$ ) angle of the wave front
- $Z_1$  (m) height of the phreatic surface in the filter layer
- $\Phi_B$  (m) height of the wave pressure front

$$\lambda = \sin \alpha * \sqrt{\frac{k * b * D}{k'}} \quad (4)$$

- $k$  (m/s) permeability of the filter layer
- $k'$  (m/s) permeability of the cover layer
- $b$  (m) thickness of the filter layer
- $D$  (m) thickness of the cover layer

BURGER et al., 1990

$$\Phi_B = H * ( 0.17 * \cot \alpha + 0.07 ) * \xi^{(-0.125 * \cot \alpha + 1.22)} \quad (5)$$

- $H$  (m) incoming wave height (regularly generated)
- $\xi$  (-) breaker number

$$\beta = ( 26.6 + 2.45 \cot \alpha ) * \xi^{(-0.215 * \cot \alpha + 0.73)} * \left( \frac{d}{H} \right)^{( 0.05 * \cot \alpha + 0.06 )} \quad (6)$$

$d$  (m) water depth

BEZUIJEN et al., 1990

$$\Phi_B = 0.36 H \left( \frac{\tan \alpha}{H / L_0} \right)^{0.5} ; \frac{\tan \alpha}{H / L_0} \leq 37 \tag{7}$$

- H (m) incoming wave height (regularly generated)
- L<sub>0</sub> (m) wave length in deep water ( $g * T^2 / 2\pi$ )
- g (m/s<sup>2</sup>) acceleration due to gravity
- T (s) wave period (regularly generated)

$$\tan \beta = \frac{0.17}{\sqrt{H / L_0}} \tag{8}$$

KLEIN BRETELER, BEZUIJEN, 1991

$$\Phi_W = \Lambda * [ 0.43 * (H / \Lambda)^{0.6} * (H / L_0)^{-0.2} * (\tan \alpha)^{0.5} ] \tag{9}$$

- Φ<sub>W</sub> (m) maximum uplift pressure over the revetment
- Λ (m) leakage factor

$$\Lambda = \sqrt{\frac{k * b * D}{k'}} \tag{10}$$

The relative uplift pressures evaluated for waves of testserie 1 are plotted in Figure 14. Since these measured uplift pressures belong to the structure type with a granular filter layer they are comparable to calculated uplift pressures using the formulae (3) to (10).

As also remarked by Bezuijen et al., 1990 it was very difficult to estimate real cover layer permeabilities. The joint width between the blocks of the investigated revetment differed from close contact to 10 mm wide gaps (mean 5 mm). For comparison, three various cover layer permeabilities were

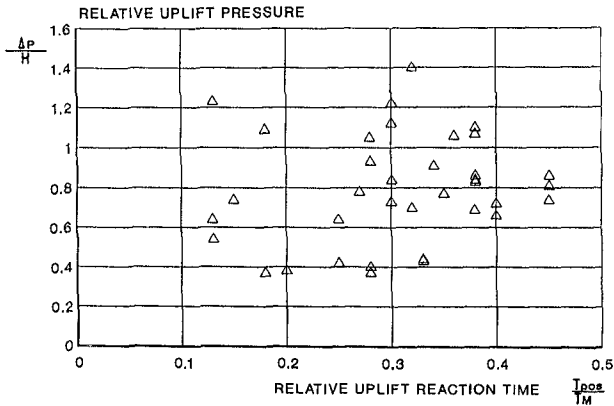


Figure 14. Measured Uplift Pressures With Wave Parameters of Testserie 1; Structure Type A With a Granular Filter Layer

estimated. It was assumed that the relative reaction time of the calculated uplift pressures would have been as long as in the experiments. Results of the calculations are shown in Figure 15.

Comparing the results of Figures 14 and 15 it can be seen that theoretically calculated uplift pressures are much smaller than the highest pressures measured in full-scale. In the case of 5 mm joint width the maximum measured pressure is nearly 75 % underestimated. On the one hand the analytical approach seems to be affected by semi-empirical assumptions based on small-scale modelling, especially the description of the pressure due to the breaker process and the description of the permeabilities of the cover layer as well as of the filter layer. On the other hand real uplift pressures are larger due to friction or clamping forces between single blocks. It is very difficult to estimate these resistant forces theoretically. It is proposed to combine the theoretical design for loose block revetments with results of full-scale experiments with naturally placed blocks using transfer factors from theoretical to prototype conditions. In Figure 16 theoretically calculated uplift pressures of the different procedures are compared with measured uplift pressures. For the special structure considered here such transfer factors could be expected in the range between 2 (small gaps) and 4 (wide gaps). This means that theoretically calculated maximum uplift pressures for a loose block should be increased at least 2 to 4 times being able to estimate the total uplift pressure causing block failure.

### Concluding Remarks

According to earlier results reported by Führböter and Sparboom, 1988 it is expected that placed concrete blocks (relative density  $\Delta = 1.3$ ) protecting a slope 1 to 4 remain stable under the following assumptions:

$d_B \geq 1/3 H$  case of granular filter on sandy sub-soil,

$d_B \geq 1/5 H$  case of geotextile filter on sandy sub-soil.

Failure occurrence of such structures is expected at breaker numbers  $\xi_0$  ranging from 1 to 2. The failure location was found nearly  $0.5 H$  below SWL.

From time history records of pressure measurements at top and bottom side of testblocks it was found that block movements occur if uplift forces are acting at least  $1/3$  of the wave period. Uplift forces may cause block movements if the amplitude is 2 to 4 times higher than the block weight force under water.



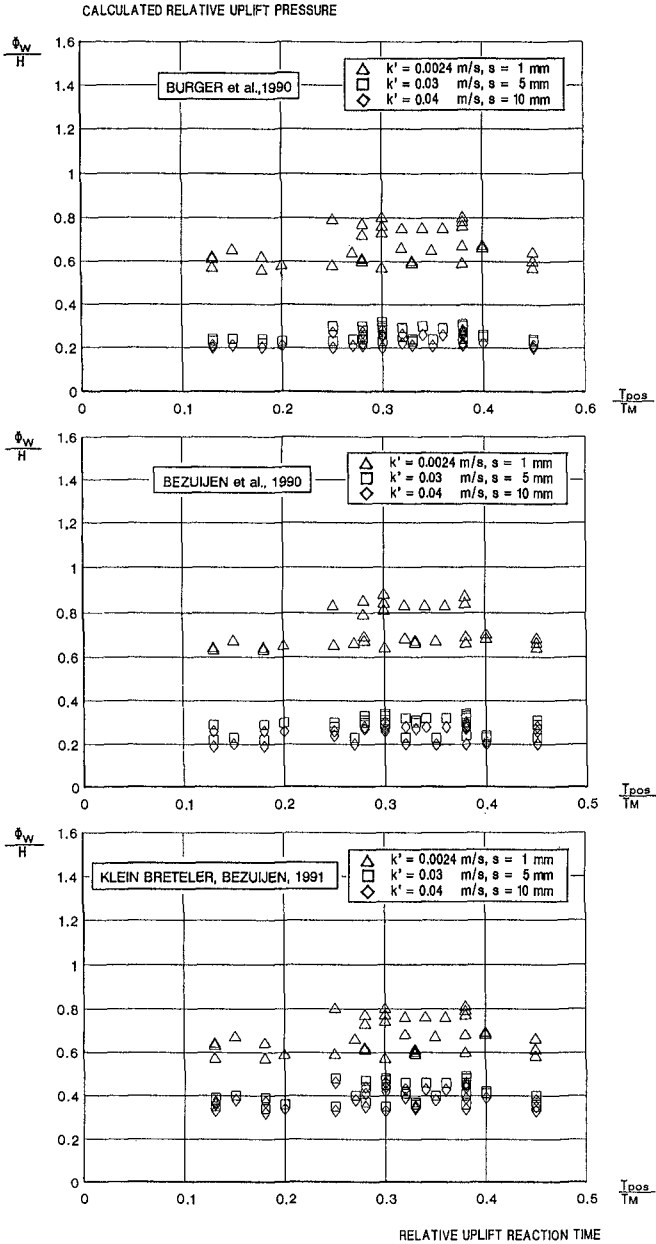


Figure 15. Calculated Uplift Pressures for Various Cover Layer Permeabilities Related to Wave Parameters of Testserie 1, Structure Type A With a Granular Filter Layer

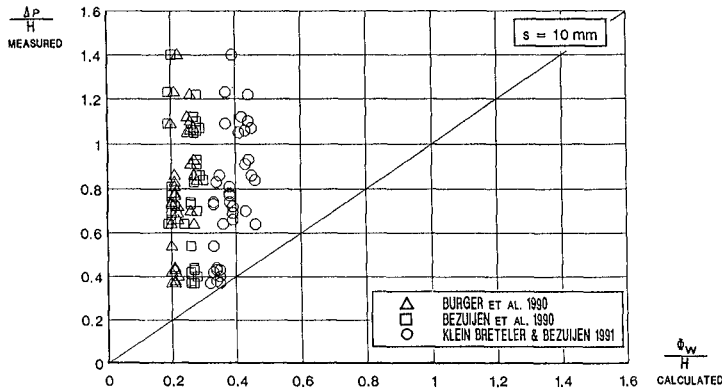
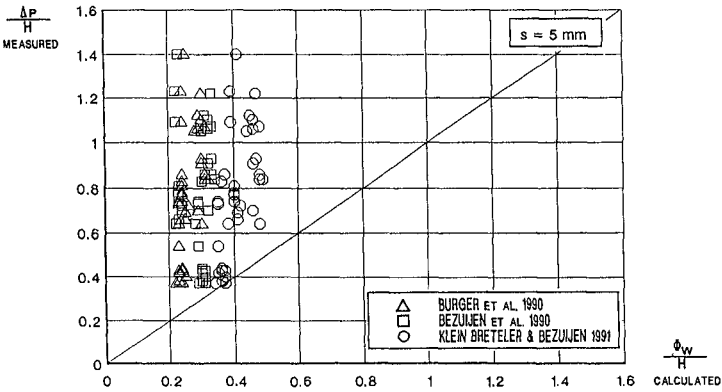
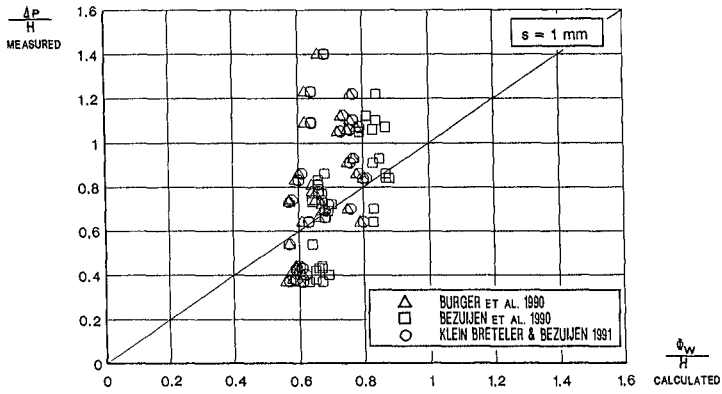


Figure 16. Measured Versus Calculated Relative Uplift Pressures for Joints With a Width of 1, 5 and 10 mm

For an economical design on placed block revetments it is recommended to select structural permeabilities increasing from sub-soil to filter layer and from filter layer to cover layer.

Verifying analytical approaches on placed block revetments it was found that calculated uplift pressures in the case of loose blocks are definitely smaller than measured uplift pressures in the naturally placed revetment. The physical mechanism of wave breaking together with the response of a more or less permeable and flexible block revetment is a very complex domain. In the opinion of the authors full-scale laboratory experiments as well as field investigations are inevitably necessary to study breaking wave attack of sea dykes and revetments. Results of such experiments are especially useful to verify theoretical solutions or to calibrate numerical models.

### Acknowledgements

Sponsoring the research program on safety and reliability of dykes and revetments for coastal protection (SFB 205/A1) the DEUTSCHE FORSCHUNGSGEMEINSCHAFT is gratefully acknowledged.

### References

- Grüne, J. and Führböter, A.: Large Wave Channel for "Full Scale Modelling" of Wave Dynamics in Surf Zones. Proc. Symp. on Modelling Techniques, San Francisco, 1975
- Grüne, J. and Sparboom, U.: Großer Wellenkanal - Problemstellung und Lösung aus versuchstechnischer und konstruktiver Sicht. Techn. Bericht, SFB 79, Universität Hannover, 1982 (in German)
- Bruun, P.: Design and Construction of Mounds for Breakwaters and Coastal Protection. Elsevier, Amsterdam, 1985
- Pilarczyk, K.W.: Sea Defences-Dutch Guidelines on Dike Protection. Report WB-NO-87110, Rijkswaterstaat, Delft, 1987
- Führböter, A. and Sparboom, U.: Full-Scale Wave Attack of Uniformly Sloping Sea Dykes. Proc. 21st Int. Conf. on Coastal Eng., ASCE, Malaga, 1988
- Sparboom, U. and Debus, W.: Wellenbelastung von Deichdeckwerken mit gesetzten Betonblöcken - Versuche im Großen Wellenkanal. Techn. Bericht, SFB 205, Universität Hannover, 1990 (in German)
- Burger, A.M., Klein Breteler, M., Banach, L., Bezuijen, A. and Pilarczyk, K.W.: Analytical Design Formulas for Relatively Closed Block Revetments. Journal of Waterway, Port, Coastal and Ocean Eng., ASCE, Vol. 116, 1990
- Bezuijen, A., Klein Breteler, M. and Burger, A.M.: Placed Block Revetments. Coastal Protection, Ed. K.W. Pilarczyk, Balkema, Rotterdam, 1990
- Klein Breteler, M. and Bezuijen, A.: Simplified Design Method for Block Revetments. Proc. Conf. on Coastal Structures and Breakwaters, Institution of Civil Engineers, London, 1991

# CHAPTER 121

## FIELD MEASUREMENTS ON PLACED BLOCK REVETMENTS

Theo Stoutjesdijk, MSc<sup>1</sup>  
Ben Rigter, MSc<sup>2</sup>  
Adam Bezuijen, MSc<sup>1</sup>

### Abstract

A report is given on a field measurement campaign on placed block revetments. Four types of measurement are described. Typical results are presented and discussed. The entire campaign shows a consistent image of changing physical properties in the field.

### Introduction

Placed block revetments are a type of coastal protection commonly used in the Netherlands and Germany. Extensive research has been carried out on this type of construction, including small and large scale model tests (Burger et al, 1990, Sparboom and Führböter, 1990). Analytical and numerical design methods are available (Burger et al, 1990 and Bezuijen et al, 1987). However, until recently little field data of this type of construction in marine conditions has been reported. Therefore, Rijkswaterstaat, the Dutch Ministry of Public Works, has initiated a field measurement campaign. The scope of this work was to compare the results of model tests and calculation models with the physical behaviour of revetments in the field.

### Some theory on placed block revetments

Shown in figure 1 is a common construction in the Netherlands. You see a top layer of carefully placed blocks and a permeable filter layer underneath.

The theory behind this type of revetment can be simplified into four statements:

- first, wave action causes pressures on the top layer.
- in the filter layer a reaction to these pressures takes place. This reaction depends largely on the permeabilities of top layer and filter layer. This can be characterized by one

---

<sup>1</sup>DELFT GEOTECHNICS, P.O. Box 69, 2600 AB Delft, The Netherlands

<sup>2</sup>RIJKSWATERSTAAT, P.O. Box 5044, 2600 GA Delft, The Netherlands

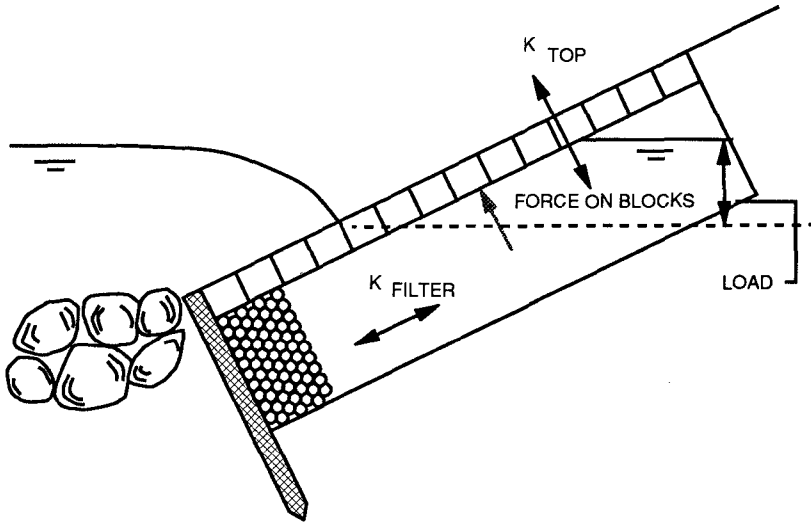


Figure 1 Placed block revetment

parameter; the leakage length. This parameter can be expressed as:

$$\Delta = \sqrt{\left(\frac{b \cdot D \cdot k}{k'}\right)} \quad [1]$$

with:  $\Delta$  = leakage length [m]  
 $b$  = thickness of filter layer [m]  
 $D$  = thickness of top layer [m]  
 $k$  = permeability of filter layer [m/s]  
 $k'$  = permeability of top layer [m/s]

- the load on the top layer is the difference in pressures on top and underneath the top layer.
- the load on the top layer can be compared to the strength. A certain force is required to push a block out of the revetment.

In the analytical and numerical models wave pressures, permeabilities and leakage length are used to calculate the reaction in the filter layer and consequently the load on the top layer. The load is compared to the strength, which is expressed in terms of one or more times the block weight.

#### Overview of performed measurements

The same factors as mentioned above return in the overview of performed measurements. Four types of measurement are discussed, respectively:

1. Permeability tests  
It is clear that the permeability of the top layer is an important factor. This can be measured directly in the permeability test. The amount of water that disappears from a reservoir is measured. This can be linked to the permeability of the top layer.
2. Infiltration tests  
The reaction in the filter layer to an imposed water-column is measured in the infiltration test. As this reaction is a function of the leakage length, the leakage length can be predicted.
3. Wave and pore pressure tests  
In the wave and pore pressure test the wave pressure on the top layer and the pore pressure beneath the top layer are measured simultaneously. The difference is the load on the top layer. The results are used to hindcast the leakage length.
4. Pull-out tests  
Blocks are pulled out of the revetment. The force required to do this is measured. This gives an impression of the strength of the top layer.

#### Permeability test

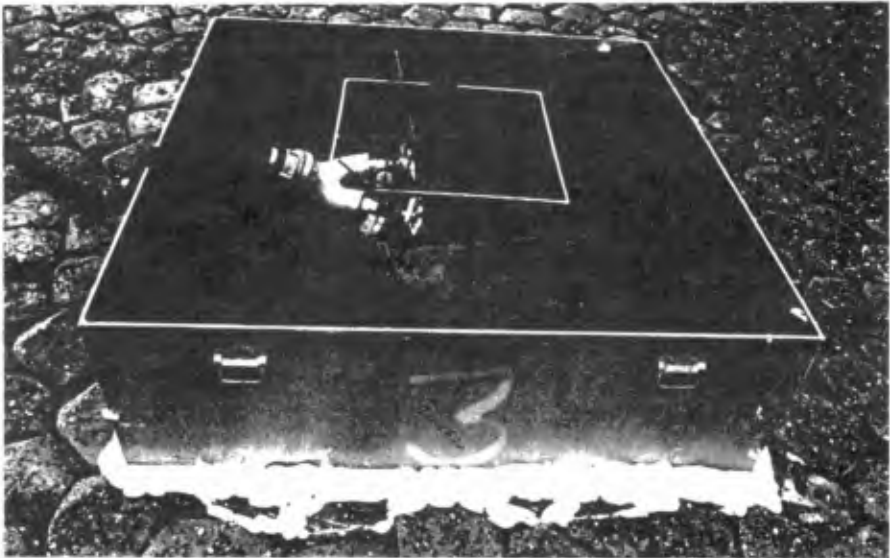


Figure 2 Set-up of permeability test

As shown in figure 2, the permeability of the top layer is measured by placing a reservoir with a known surface of the open bottom on the top layer. Leakage through the gaps between the top layer and the reservoirs is reduced to a minimum by applying foam around the sides. A second reservoir is placed around the inner reservoir to make sure that the flow through the top layer is as one

dimensional as possible. Next, the reservoirs are both filled with water. The amount of water disappearing in a fixed period of time from the inner reservoir through the top layer is measured. This can be linked to the permeability of the top layer.

#### Results of permeability test

Measurements of the permeability of the top layer are performed at different heights.

Roughly, three zones can be distinguished:

- the tidal zone with a permeability of  $5 \cdot 10^{-7}$  m/s.
- the zone between high water level and high high water level, with a permeability 100 times higher than in the tidal zone.
- the storm surge level, again with a permeability which is again 100 times higher than the zone below.

The conclusion is, that the permeability in the tidal zone has decreased with a factor 10,000 during the lifetime of the construction. This permeability is also much lower than normally found in model tests. The reason for this sharp decrease in permeability was found when some blocks were lifted. The joints between the blocks are completely filled with sand and other fine material. Especially in the tidal zone, biological growth can influence the permeability. The filter layer, which originally consisted of gravel, is now a mixture of gravel and sand. However, as the decrease in permeability of the filter layer is less dramatic than the decrease in permeability of the top layer, inevitably the leakage length increases. As a large leakage length yields larger loads this is unfavourable.

#### Infiltration test

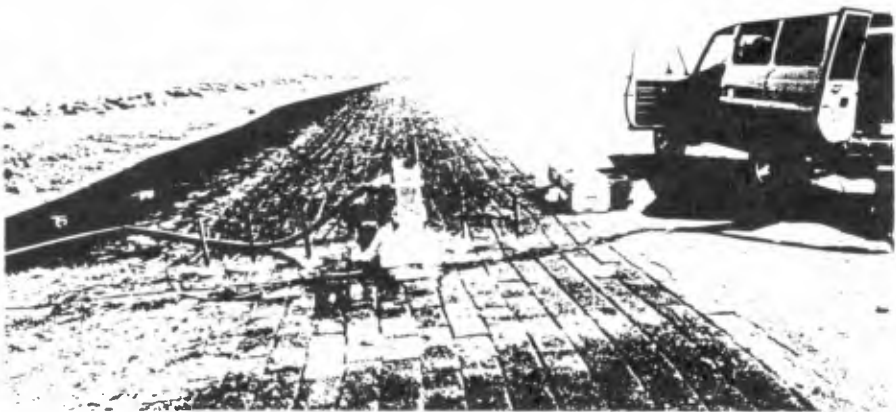


Figure 3 Infiltration test, measurement set-up

The next type of test presented here is the infiltration test. This test is used to determine the leakage length. The state of the art in modelling allows us to calculate the reaction in the filter layer to a given load, if only the leakage length is known. Therefore, some elements of the top layer are removed and a box of 1 m height is placed in the hole. Water is pumped into the box to a certain, constant, level, so that the local load on the filter layer is known. The decrease in pore pressure, as a function of distance from the location where the load is applied is measured.

A long leakage length means that the permeability of the top layer is relatively small compared to the permeability of the filter layer (see also equation [1]). Therefore the decrease in pore pressure with increasing distance from the infiltration point is small. A short leakage on the other hand means that the permeability of the top layer is relatively large. The decrease in pore pressures takes place over a limited distance.

Figure 3 shows the measurement set-up. An infiltration reservoir is placed on the top layer. Bore holes are made through the top layer. This enables the placement of pore pressure transducers in the filter layer. Next, the reservoir of 1 m height is filled to overflow level and kept there until a stationary situation is obtained. At that moment the pore pressures in the filter layer are determined.

#### Results infiltration test

Shown in figure 4 is the measured decrease in pore pressure as a function of height. Schematically drawn are also the revetment, the infiltration reservoir, and the measured pore pressures. In a one-dimensional situation, that can be reached with several infiltration points in a horizontal row with laminar flow, an analytical solution is possible.

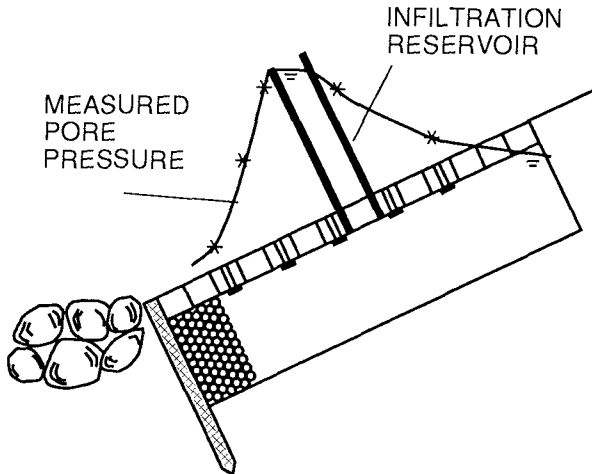


Figure 4 Result of infiltration test



In practice however, only one or two infiltration points are used, and around the infiltration points turbulent flow is dominant. This means two dimensional flow has to be dealt with to determine the leakage length. Calculations are performed with the same numerical model that is used to investigate the influence of oblique wave attack on revetments (Bezuijen et al, 1992). The result of a calculation with this model can be seen in figure 5.

Shown is the calculated piezometric head for a two dimensional situation. The leakage length in this case is relatively short, about 0.8 m. The drawn lines are lines of equal pore pressure. Vertically is set out the height on the revetment (not the distance along the surface of the slope), horizontally the horizontal distance. The calculation is performed on a dry slope; the tidal level is below the toe of the revetment.

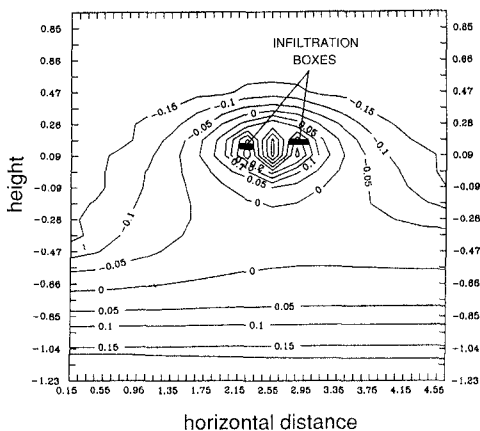


Figure 5 Result of calculation model

Around the infiltration point the water flows down the slope in a kind of umbrella shape. If the pore pressure is measured in several points, this can be compared to the calculated piezometric head in figure 5. Shown is the difference in piezometric head over the cover layer. A negative value means, that the water level lies below the cover layer at that position. Only if this value is positive, water will flow through the cover layer out of the construction. The minus 0.15 m-line represents the phreatic surface in the filter layer. The positive values on the bottom of the graph represent a build-up of difference in piezometric head that is caused by an impermeable toe construction. Good agreement is found, provided the right leakage length is chosen.

#### Wave and pore pressure test

In the wave and pore pressure test, a measuring beam with a length of six to nine metres is placed on the top layer, as shown in

figure 6. On top of the measuring beam 12 wave pressure transducers are fixed. Along the measuring beam 3 bore holes are made through the top layer. Through the bore holes pore pressure transducers are placed in the filter layer.

Measurements are only useful when there is enough wind to generate waves of some height. Measurements are possible up to Beaufort 7 to 8. During fairly stormy weather the wave pressures on the top layer and the pore pressures beneath the top layer are measured simultaneously. The difference between them is the load on the top layer. Therefore, the wave and pore pressure test is a direct measurement of the load on the top layer.

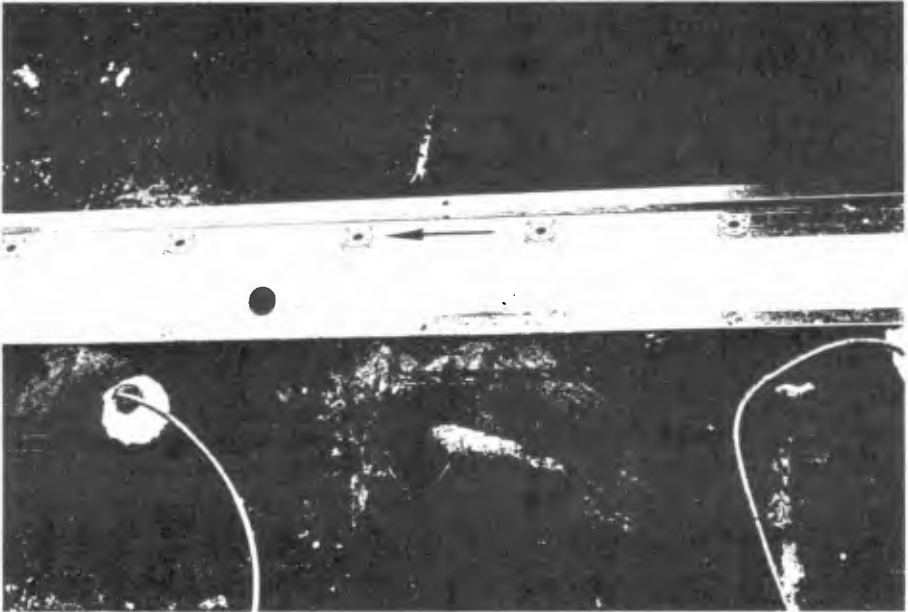


Figure 6 Measurement beam and bore holes

#### Results of wave and pore pressure test

Shown in the graph in figure 7 are the measured wave pressure, the measured pore pressure and the difference between these two, which is the load on the top layer.

The wave height on the spot of the pore pressure transducers is some 20 cm, the reaction in the filter layer is about 2 cm. This reaction in the filter layer is much smaller than expected, because the permeability of the cover layer in the tidal zone is much lower than expected. The result of such a small reaction in the filter layer is, that a wave height of one fifth of the design wave height will be sufficient to cause a load on the top layer that is equal to the weight of the blocks. The same theory, however, also explains that with permeabilities that are very low, little water can reach

the critical point. A much higher load is required to actually cause damage.

According to the theory on placed block revetments the reaction of the pore pressures to the wave pressures is determined by the leakage length. The wave and pore pressure test therefore can also be used to make a hindcast of the leakage length.

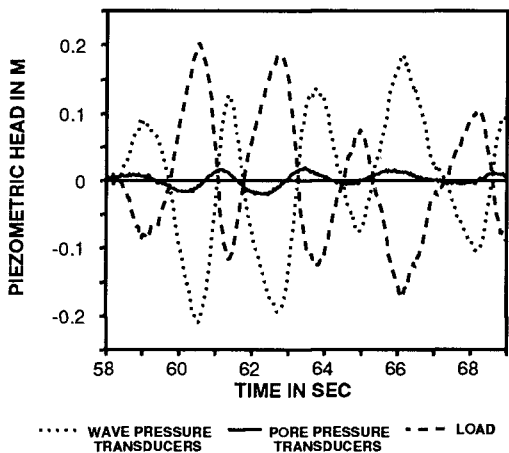


Figure 7 Result of wave and pore pressure test

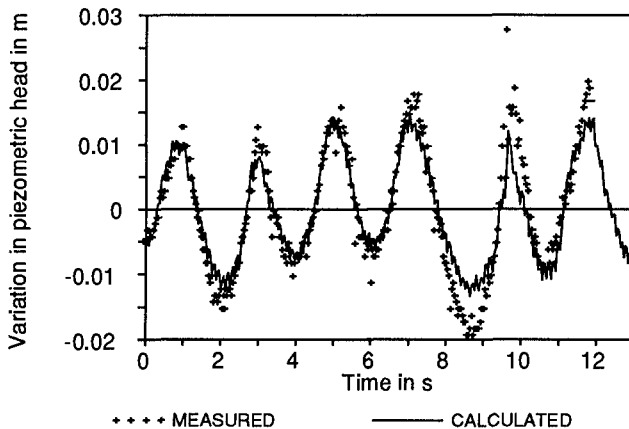


Figure 8 Simulation of pore pressures

This hindcast is performed done with a numerical calculation model STEENZET/1. The measured wave pressures are used as input for

the model. The pore pressures in the filter layer are calculated and compared to the measured pore pressures. A good correspondence between measured pore pressures and calculated pore pressures can be found, provided the right leakage length is chosen. In figure 8 both these properties are given.

The leakage length used for this simulation is 13 m. This is 10 to 20 times larger than usually found in model tests. As a long leakage length yields large loads, this is unfavourable.

A different aspect is found when we take a look at the phreatic surface in the filter layer. The test is repeated at different tidal levels. This information can be used to compare the phreatic surface in the filter layer with the mean sea water level. Because of the small permeability of the top layer, the phreatic surface does not respond instantaneously to a change in tidal level. This difference in water levels can cause a considerable extra load on the top layer if the tidal level drops and the phreatic surface does not react accordingly, as shown in figure 9.

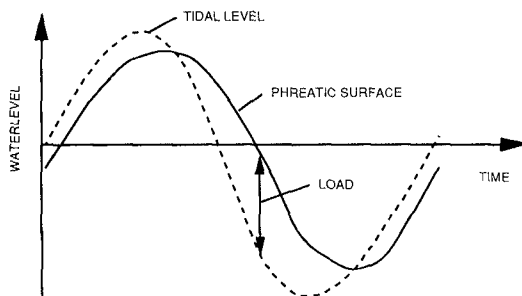


Figure 9 Phreatic surface and tidal level

So far this phenomenon has never been observed in model tests, simply because these tests are performed on newly made constructions. Therefore, also in calculation models it is always assumed that the mean water level in and outside the construction is more or less equal. This proves to be a dangerous assumption.

#### Pull-out test

So far only the load on the top layer has been considered. As it is shown in the previous paragraphs that this load can be much larger than expected, it is important to compare this load to the strength of the top layer.

An impression of the strength of the revetment can be obtained by pulling blocks out of the revetment and registering the force required to do this.

Shown in figure 10 is a pulling unit, consisting of a trailer which is fixated on the top layer with four supports. On board of the trailer a computer-controlled system is mounted that is able to lift a block over a vertical distance of 2.5 cm by exerting a

hydraulically controlled pulling force of about 6 times the block weight. The maximum pull-out force is about 10 kN.

A large number of blocks (over one thousand) was pulled out, ensuring that a statistical evaluation of the results is valid. The aim of the test was to answer the question how many blocks are loose blocks that can be lifted easily during wave attack.

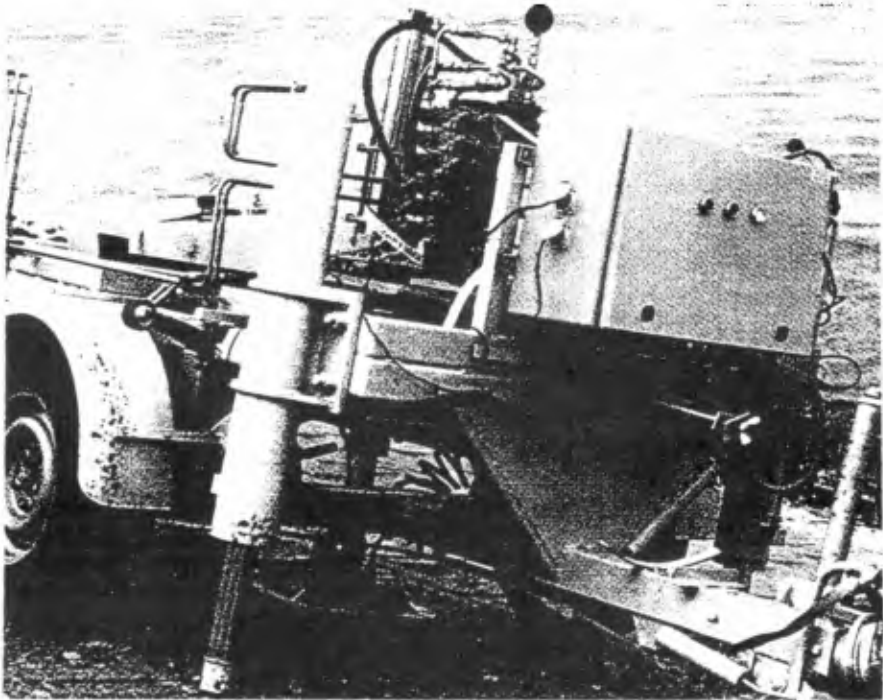


Figure 10 Pulling unit

#### Results of pull-out tests

Shown in figure 11 are the results of pull-out tests on three different levels.

Three things can be read from this graph:

- the influence of the height is evident: the lower on the revetment the higher the strength of the construction.
- at a pull-out force equal to the block weight less than one percent of all the blocks is pulled out
- the percentage of blocks that is not pulled out of the revetment, even at a pull-out force of 6 times the block weight is considerable. Depending on the level, only 15, 30 or 70 percent of the blocks was lifted.

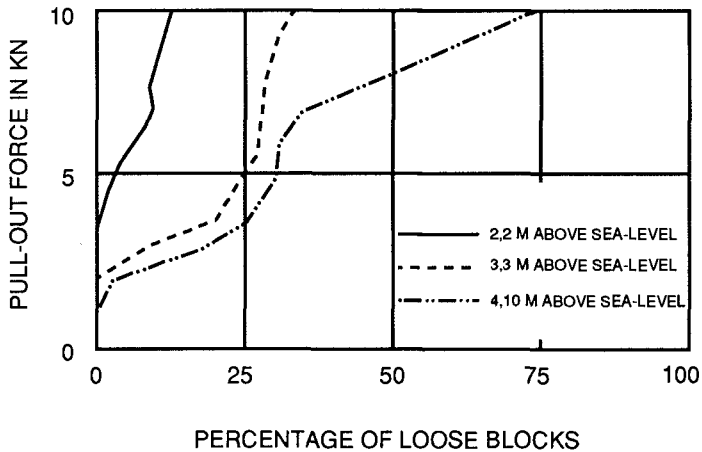


Figure 11 Results of pull-out tests

Not shown in this graph is the fact that in the tidal zone no blocks could be pulled out. In general, the required pull-out force is higher than expected. This is caused by friction forces and clamping forces in case of a slight rotation of the block. It is stressed that, during wave attack, the load on the blocks can be different than the schematized load of the pull out tests. Also, it is possible that more than one block at a time will move. Still, the strength of older placed block revetments with a low permeability of the cover layer can be considered higher than the strength of loose blocks.

### Conclusions

The entire campaign of field measurements shows a consistent image from which the following conclusions can be safely made:

- first, it is clear that physical properties in the field, especially permeabilities, can differ dramatically from properties in model tests. This means that existing revetments can show physical behaviour that differs from the behaviour found in model tests.
- in time permeabilities decrease due to biological activity and migration of sand and fine material.
- in the tidal zone this influence is larger than in the zones above it. Properties vary with height.
- if the permeability of the cover layer decreases more than the permeability in the filter layer, the load on the top layer increases. At the same time however, also the strength seems to increase.

Existing design methods are based on the concept of loose blocks. The methods have been verified in model tests, and therefore they are valid for revetments with relatively large permeabilities

and short leakage length. Usually, a revetment is designed on the properties as expected directly after construction.

In the measurement campaign it is shown, that the concept of loose blocks is valid at storm surge level, but not necessarily in the tidal zone. Also, it is shown, that permeabilities decrease, the leakage length grows and consequently the load on the top layer increases. Permeabilities in the tidal zone can decrease to a degree that, even if there is a large uplift pressure, still no block movement will occur, as no water can flow towards the attacked block. In practice, also the pull-out force can be much higher than expected.

As a consequence for the design of placed block revetments the change in physical behaviour with time should be anticipated for the entire lifetime of the construction.

### References

Bezuijen, A., M. Klein Breteler and K.J. Bakker (1987). Design criteria for placed block revetments and granular filters. Proc. 2nd Int. COPDEC, Beijing.

Bezuijen, A. and M. Klein Breteler (1992). Oblique wave attack on block revetments. Proc. 23rd ICCE '92, Venice.

Burger, A.M., M. Klein Breteler, L. Banach, A. Bezuijen and K.W. Pilarczyk (1990). An analytical design method for relatively closed block revetments. ASCE Journal, Harbour and Port Engineering.

Führbötter A. and U. Sparboom (1988). Full scale investigation on the stability of concrete block slope revetments. Proc. Int. SOWAS Symposium Delft.

## CHAPTER 122

# Numerical determination of wave induced flow in rubble mound breakwaters.

Sun ZC<sup>1</sup>, Williams AF<sup>2</sup>, Allsop NWH<sup>2</sup>

### 1 ABSTRACT

This paper describes a numerical model of wave action onto and into a rubble mound breakwater. The model is constructed of two parts, the wave action on the exterior of the mound in which a boundary element method is used and flow inside the rubble mound in which a finite element method is used. The two parts of the model are coupled by demanding continuity of flow through the front face of the breakwater. The predicted pressures within the core of the rubble mound are compared with data collected from physical model tests.

### 2 INTRODUCTION

The problem is that of wave action onto and into a rubble mound breakwater as illustrated in Fig(1). External wave action on the breakwater induces wave action within the porous material of the rubble mound. The stability of both the rubble mound core and the external armour layers is dependent on the pore water pressures within the structure. Our aim is to model the wave motion within the rubble mound, and calculate the instantaneous pore pressures as they change under wave action.

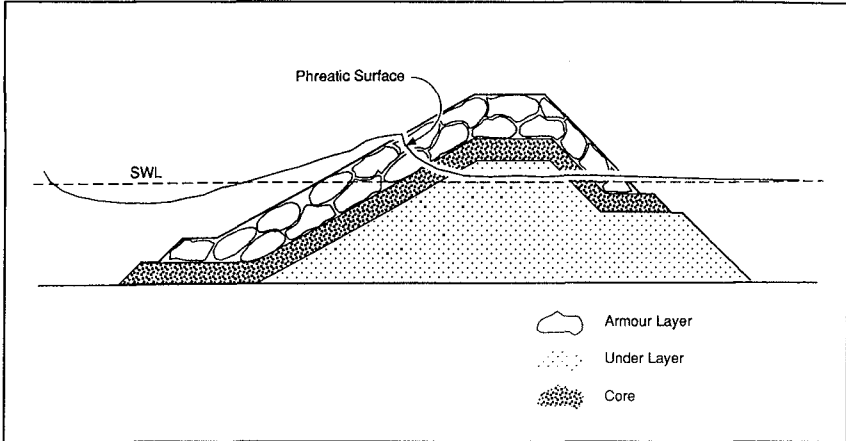
A complete model needs to incorporate all of the following physical processes: Random wave motion external to the breakwater and uprush onto the breakwater face. Energy dissipation caused by wave breaking and friction at the breakwater surface. The transport of water through the front face of the breakwater. The flow of water through the porous material of the breakwater core. Here the flow is non-Darcy or turbulent and the flow rate is unsteady. The effect of entrained air in the flow of water through the porous material. A complete model must also be able to deal with complex breakwater geometries, such as berms and layers of armour and filter

---

<sup>1</sup>Dalian University of Technology, Dalian, China.

<sup>2</sup>Coastal Structures section, Hydraulics Research, Wallingford, OX10 8BA, UK.





**Figure 1** Wave action on a rubble mound breakwater.

materials.

No model is presently able to incorporate all of these processes. Analytical solutions such as that proposed by Sollitt & Cross (1972) by necessity require the geometry to be simplified to a homogeneous rectangle with vertical faces. Madsen & White (1976) also developed an analytical solution which uses assumptions of rectangular geometry and linear periodic wave theory. They improved the range of application of their model by representing multi-layered trapezoidal breakwaters with a "hydraulically equivalent" homogeneous rectangular structure. Predictions of wave reflection and transmission can be made using analytical models of this type. Unfortunately the simplifying assumptions and averaging processes necessary to arrive at an analytical solution make it impossible to calculate local instantaneous water velocities or pressures.

To find the local instantaneous velocities and pressures required for the investigation of breakwater stability, a method is required that does not make gross assumptions about the structure geometry or involve integration of the solution over a wave period. These requirements may only be met by use of a numerical model. McCorquodale & Nasser (1974), Nasser (1974) and Hannoura (1978) have all developed numerical models for flow with the porous material of the breakwater. A hybrid finite element/difference model is described by Hannoura & McCorquodale (1985), in which the time integration is carried out by a finite difference method and the space integration is solved by use of a finite element method. The model is restricted in its application as it only simulates the flow within the breakwater, and requires the boundary condition on the seaward face of the breakwater to be supplied from empirical data or an alternative numerical model.

A more comprehensive model is at present in development under the European MAST G6-S project (Meer et al. (1992)). This model utilises the

volume of fluid (VOF) technique similar to the SOLA-VOF developed by Nicholas, Hirt & Hotchkiss (1980). VOF methods are the most promising way forward to a complete model which includes the effects of wave runup and breaking. Unfortunately VOF models are computationally intensive and at present a main frame computing facilities are required for implementation. The model being developed under MAST still requires further work and it may be several years before a fully working VOF model is available.

At Wallingford we have developed an intermediate numerical model which divides the problem into two parts:- a). The external wave action which produces pressures on the outer surface of the breakwater. (The external flow field). b). The internal flow within the breakwater driven by the pressures induced by the external flow field. (The internal flow field). The internal flow field (b) is modelled by the use of a finite element method. The external flow field (a) is calculated by use of a boundary element method. These two models are then coupled by allowing water to flow through the shared boundary. The ability to model the wave action on the exterior face of the breakwater means that support from physical model tests, as is necessary for the implementation of the Hannoura & McCorquodale (1985) model, is not required.

### 3. THE EXTERNAL FLOW FIELD

Here the wave motion is calculated in two dimensions by use of a boundary element method. The program used is a variation of the program developed by Shih (1989), from the method described by Vinje & Brevig (1981).

#### 3.1 GENERAL PRINCIPLES

The fluid is assumed to be both incompressible and irrotational. Such a two dimensional flow field can be described by either one of the pair of orthogonal functions termed the velocity potential  $\phi$  and stream function  $\psi$ . Both the velocity potential and the stream function are solutions of the Laplace equation with some specified boundary condition. In this way the Laplace equation relates the values of these functions in the interior of the computational domain to values at the boundary of the domain. If the stream function or the velocity potential is specified at all points on the boundary, then the stream function inside the boundary can be found and hence the complete flow field computed. This is convenient as in our problem the boundary condition at the free surface of the material is most easily phrased in terms of the velocity potential  $\phi$ , while the conditions at the other boundaries of the domain are most easily specified by the stream function  $\psi$ . For the purposes of the numerical model the boundary is specified at discrete points  $z_k$  as shown in Fig (2).

If suitable boundary conditions can be specified for the whole domain, then the complete flow field may be calculated. The only remaining problem is that of finding the position of the free surface. The position of the free surface is continually re-calculated by tracking the movements of points on the surface. The motion of these points is given by the most recently computed values of the flow field at these points.

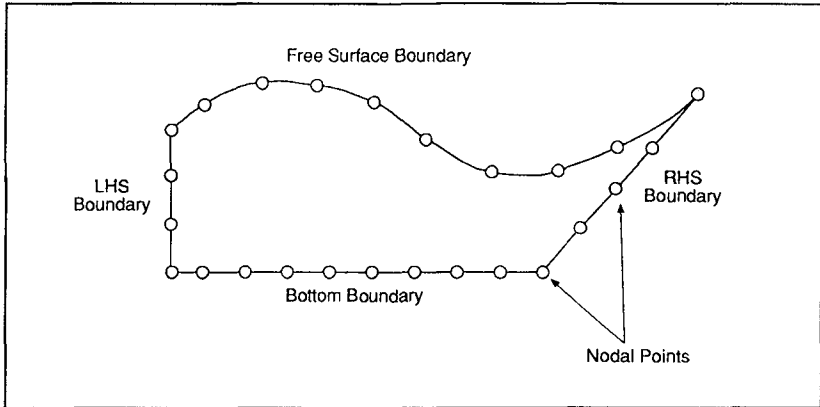


Figure 2 The computational domain.

### 3.2 MATHEMATICAL FORMULATION

The orthogonal function defined by the velocity potential  $\phi$  and stream function  $\psi$  may be combined to form the complex potential;

$$\beta(z, t) = \phi(z, t) + i\psi(z, t) \quad (1)$$

In which  $z$  is a complex variable which describes the position in the computational domain;  $z = x + iy$  and  $t$  is the time variable.

As  $\phi$  and  $\psi$  both satisfy the Laplace equation,  $\beta$  must be an analytical function within the boundary of the fluid. For such an analytical function the value of  $\beta$  within the boundary can be related to the values of  $\beta$  at the boundary by use of the Cauchy integral theorem. If  $z_k$  is some point inside the boundary  $C$  then:

$$f(z_k) = \frac{1}{2\pi i} \oint_C \frac{f(z)}{z - z_k} dz \quad (2)$$

We are interested in the case when  $z_k$  also lies on the boundary. In this case if the boundary  $C$  is smooth, then  $z_k$  is related to all other points on the boundary by:

$$-i\pi\beta(z_k, t) + \oint_C \frac{\beta(z, t)}{z - z_k} dz = 0 \quad (3)$$

Equating the real and imaginary parts of Equ(3) produces two equations for the conditions where either  $\phi$  or  $\psi$  is known at the boundary point  $z_k$ :

$$\pi \psi(z_k, \hat{t}) + \operatorname{Re} \oint_C \frac{\beta(z, \hat{t})}{z - z_k} dz = 0 \quad (4)$$

for  $z_k$  lying on the boundary for which  $\phi$  is known

$$\pi \phi(z_k, \hat{t}) + \operatorname{Re} \oint_C i \frac{\beta(z, \hat{t})}{z - z_k} dz = 0 \quad (5)$$

for  $z_k$  lying on the boundary for which  $\psi$  is known

For purposes of the numerical calculation, the boundary is divided into discrete points. By assuming a linear variation of  $\beta$  between the points, the integral around the boundary can be expressed in terms of a summation over an influence function. The set of equations formed by this summation for each point is then assembled into a matrix. The matrix is solved by Gaussian elimination to produce  $\phi$  and  $\psi$  at each point on the boundary.

### 3.3 BOUNDARY CONDITIONS

There are four boundaries on which conditions must be specified.

**THE IMPERMEABLE BOTTOM BOUNDARY:** Here the condition is no flow normal to this boundary, which results in:

$$\psi = \text{constant}$$

In our case the constant = 0

**THE LEFT HAND BOUNDARY:** This boundary condition is supplied by the wave maker and the simple theory of wave generation proposed by Galvin (1964) is used. The wave maker is simulated as a piston that produces flow normal to this boundary, hence at this boundary  $\psi$  is specified. In addition to the original model developed by Shih, this boundary has been modified to allow wave energy to exit the computational domain.

**THE RIGHT HAND BOUNDARY:** This is the interface with the internal flow model. Flow normal to the boundary is given by the seepage flow from the internal model at this interface. Here  $\psi$  is again specified.

**THE FREE SURFACE BOUNDARY:** At this boundary two conditions are required, one to specify the velocity potential and another to describe how this boundary should move between time steps.

The velocity potential is given by the dynamic condition:

$$\frac{\partial \phi}{\partial t} = ww^* - gy - \frac{p_s}{\rho} \quad (6)$$

Where  $w = u - iv$  the conjugated complex velocity,  $g$  = acceleration due to

gravity,  $y$  = the vertical position of the boundary point,  $p_s$  = the pressure at the surface (in most cases  $p_s = 0$ ),  $\rho$  = density of the fluid

Hamming's fourth order predictor-corrector method is used to determine  $\phi$  from Equ(6) with the exception of the first three time steps of a calculation when the Runge-Kutta method is used.

The new position of the boundary is calculated from the kinematic condition:

$$\frac{Dz}{Dt} = \frac{D}{Dt}(x+iy) = w^* \quad (7)$$

Where  $z$  = the complex position of the boundary point (which has coordinates  $x$  and  $y$ ). This allows the new position  $z$  of the boundary to be calculated for the next time step by an integration over time  $t$ .

#### 4. THE INTERNAL FLOW FIELD

As in the external flow model the internal flow model is two-dimensional, with the breakwater cross section forming the computational domain. Wave motion is caused by the variation of the pressure on the seaward face of the structure and fluid flow through the structure. The front face of the breakwater forms the interface of the two models. The pressures on this external face are supplied by the external flow model.

##### 4.1 THE GENERAL PRINCIPLES

The problem is one of seepage flow through a porous granular medium, with a free surface within the medium. The granular material of the breakwater is of sufficient size that the flows within the medium are turbulent and may not be described by Darcy's linear law. The existence of an exact relationship between hydraulic gradient  $i$ , and the bulk flow velocity  $u$ , is in this case uncertain, however recent research by Williams, Burcharth, & den Adel (1992) indicates that the Forchheimer equation forms the best fit to the empirical data available at present. The unsteady flow form of the Forchheimer equation is:

$$i = au + bu^2 + \frac{(1+C)}{g} \frac{\partial u}{\partial t} \quad (8)$$

Where  $a$  and  $b$  are the Forchheimer coefficients which are dependent on the granular material. Separate layers of filter material within the breakwater result in  $a$  and  $b$  being functions of position.  $C$  is the virtual mass coefficient and is also dependent on the material. Means of determining values for  $a$ ,  $b$  and  $C$  are discussed in the paper by Williams et al. (1992).

The assumption that the fluid is incompressible provides the continuity equation in the form

$$\nabla u = 0 \quad (9)$$

The Forchheimer equation and the equation of continuity with adequate boundary conditions are sufficient to allow the flow field to be solved uniquely.

The flow field is calculated by use of a finite element method where the computational domain is defined by the breakwater cross section and the phreatic surface of the water. The phreatic surface rises and falls with the wave motion. As a result the size and shape of the computational domain is also a function of time. The position of the phreatic surface must therefore be calculated at each time step and the finite element mesh re-fashioned to fit the new computational domain.

## 4.2 MATHEMATICAL FORMULATION

It is useful to phrase the Forchheimer equation in terms of the piezometric head  $P_p$ .

$$-\nabla P_p = (a+b|\bar{u}|)\bar{u} + \frac{(1+c)}{g} \frac{\partial \bar{u}}{\partial t} \quad (10)$$

the piezometric head is related to the pressure  $p$  by:-

$$P_p = \frac{p}{\gamma} + y \quad (11)$$

where  $y$  is the some vertical coordinate.

The time domain is dealt with by the use of finite differences. Writing:

$$\frac{\partial \bar{u}}{\partial t} = \frac{(\bar{u}|_{t+\Delta t} - \bar{u}|_t)}{\Delta t} \quad (12)$$

Substituting Equ(12) into Equ(10) gives:

$$\bar{u}^{t+\Delta t} = K \left( \Delta(P_p)|_{t+\Delta t} - \frac{1+c}{g\Delta t} \bar{u}^t \right) \quad (13)$$

where

$$K = \frac{1}{a+b|\bar{u}| + \frac{(1+c)}{g\Delta t}} \quad (14)$$

is the conductivity of the rubble material. Note that  $K$  is a function of  $u$ .

Substituting Equ(14) into the continuity equation (Equ(9)) yields the governing equation for the piezometric head:

$$\Delta( K \Delta P_p ) = 0 \quad (15)$$

For the purposes of the numerical simulation this equation is re-phrased as the requirement that:

$$\chi = \iint_A K \left[ \left( \frac{\partial P_p}{\partial x} \right)^2 + \left( \frac{\partial P_p}{\partial y} \right)^2 \right] dx dy \quad (16)$$

should be a minimum for the given boundary conditions and the integration is carried out over the whole of the computational domain. Finite element discretization of this equation is carried out using triangular mesh elements. The minimisation technique produces a set or matrix of equations that can be solved to give the piezometric head and flow velocities for the specified boundary conditions.

### 4.3 BOUNDARY CONDITIONS

For the internal flow the boundary conditions are specified in terms of the piezometric head  $P_p$ . There are four relevant boundaries:

**THE BOTTOM BOUNDARY:** This boundary is impermeable so the condition of no flow normal to this boundary gives:

$$\frac{\partial P_p}{\partial y} = 0 \quad (17)$$

where  $y$  is the vertical coordinate.

**THE HARBOUR SIDE BOUNDARY:** At present, this boundary has been kept simple by specifying that the water level behind the breakwater remains constant at  $y=d$ . Hence:

$$P_p = d \quad (18)$$

**THE SEAWARD BOUNDARY:** This is the interface between the internal and external models. Here the boundary condition is supplied by the pressure distribution given by the external model.

$$P_p = \frac{\rho}{\gamma} + y \quad (19)$$

Continuity of flow through this boundary is achieved by the coupling technique described in the next section.

THE PHREATIC SURFACE BOUNDARY: Since this boundary moves, two boundary conditions are required.

The kinematic boundary condition:

$$\frac{Dx}{Dt} = u, \quad \frac{Dy}{Dt} = v \quad (20)$$

where  $x$  and  $y$  are the coordinates of the boundary point and  $u$  and  $v$  at the flow velocities at these points.

The dynamic boundary condition:

$$P_p = \gamma \quad (21)$$

At time  $t = 0$ , the initial conditions are:

$$P_p = \text{const.} \quad \bar{u} = 0 \quad (22)$$

## 5 COUPLING OF THE INTERNAL AND EXTERNAL FLOW MODELS

The external flow model is coupled to the internal flow model by demanding continuity of flow and pressures through the shared boundary. This is achieved by use of a trial and error technique as shown in the flow chart in Fig(3).

It is this coupling of the external and internal flow regimes that makes the completed model unique. This technique allows the wave motion onto and through the breakwater to be simulated without the need for additional data to be supplied from physical model tests.

## 6 PHYSICAL MODEL TESTS

Work carried out at Wallingford for the Single Layer Armour Unit Research Club has provided an excellent opportunity to obtain empirical data against which the numerical model can be tested. The study involved the construction of a model rubble mound which was armoured with model units.

The rubble mound was constructed with the geometry as shown in Fig (4). The core material was crushed limestone ranging in size from 4-6mm, the underlayer consisted of 10-14mm limestone. The armour units were simulated by a plastic frame work of the appropriate porosity or by model units of the correct density. During construction care was taken to carefully weigh all the core and filter material used in the model so that the porosity of the relevant layers could be determined. These porosities must be known to allow the correct determination of the Forchheimer coefficients  $a$  and  $b$  used in the numerical model.

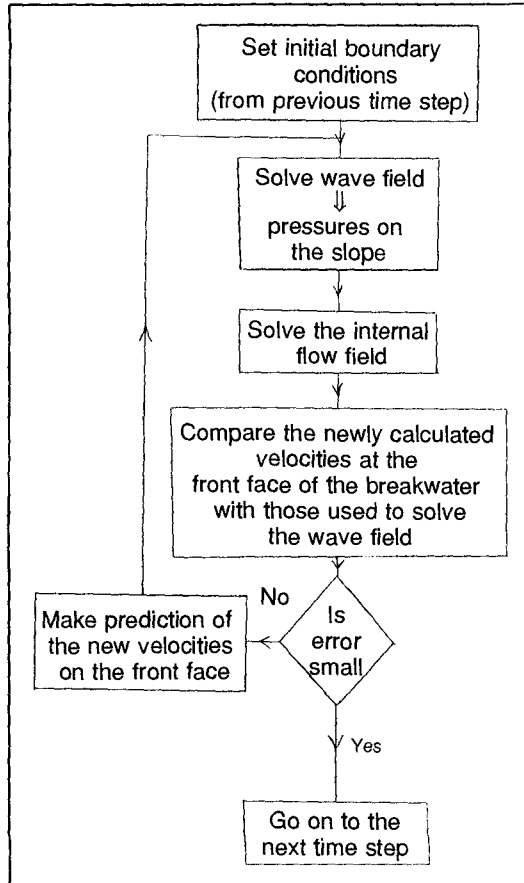
During the construction the pressure transducers were buried in the positions



shown. The cables of these transducers exited the rear of the mound and connected to the appropriate equipment to allow the pressures to be monitored by computer.

In order to make the comparison of the numerical simulation and the physical model test data as simple as possible, only data from regular wave conditions have been investigated. The wave conditions tested ranged in height from 0.11 to 0.2m and in period from 1.6 to 2.8s. The piezometric heads measured by the pressure transducers were logged by computer for each test condition.

The numerical model was run for a structure with the same geometry and material properties as the physical model. The values of the Forchheimer coefficients  $a$  and  $b$  were determined by comparison of the core and filter material with material whose permeability had previously been measured at HR, (see Williams et al. (1992)). The piezometric head at the positions of the pressure transducers was determined from the internal flow model and compared to the physical model data as described in the next section.

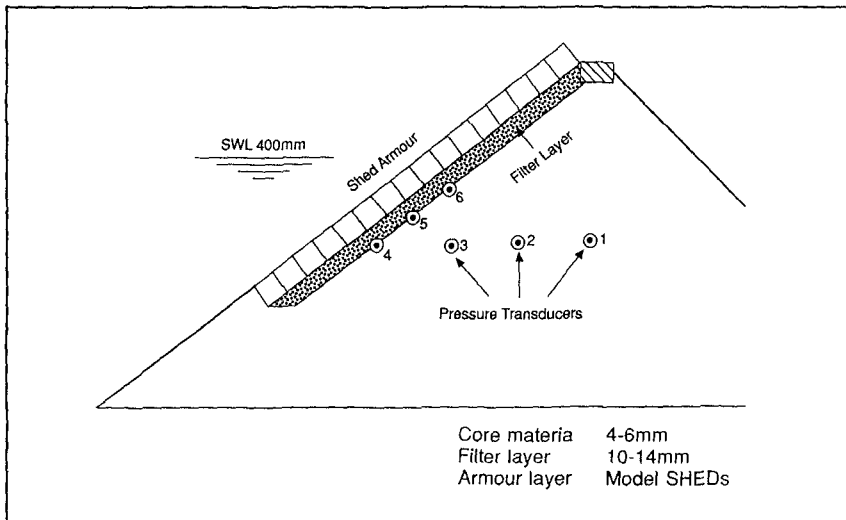


**Figure 3** Linkage of Wave and Internal Flow Models.

## 7 RESULTS

The flow of fluid within the mound is illustrated as a velocity plot in Fig. (5.a-d). The wave height is 0.14m with a period of 2.4s. It is seen that the majority of the fluid flow occurs within the armour and filter layers. This is expected as the armour and filter layers are several orders of magnitude more permeable than the core of the breakwater. Points on the phreatic surface are marked  $\circ$ .

In Fig.(6.a-e) show the predicted and observed pressures at the positions of

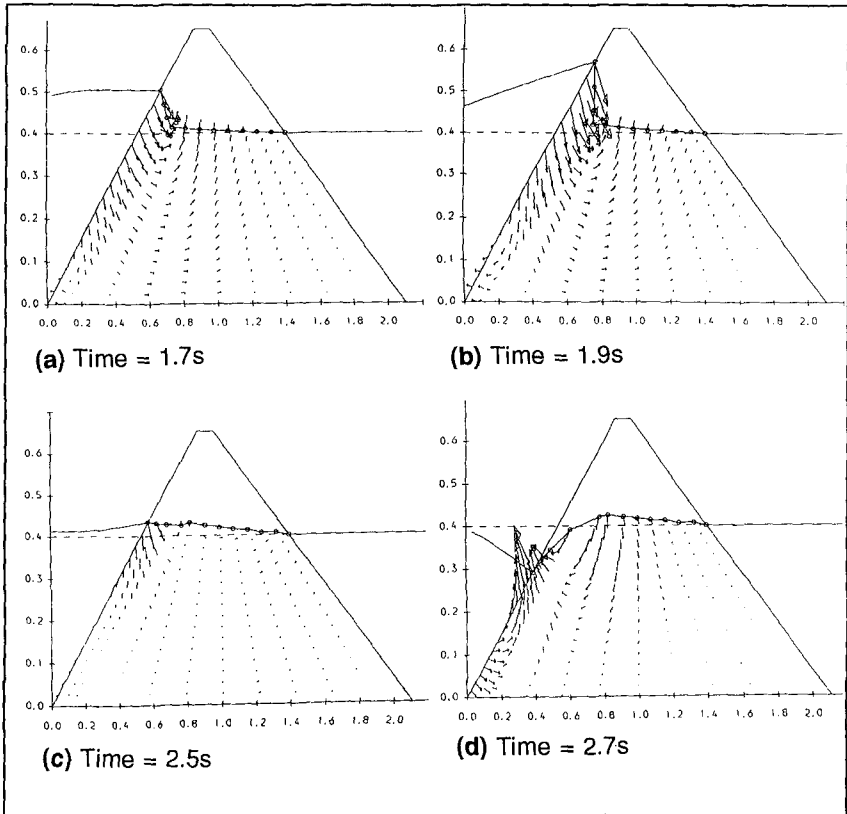


**Figure 4** Locations of the pressure transducers.

the pressure transducers within the mound. The close match between the empirical data and numerical results is very encouraging. The discrepancy between the observed and predicted pressures for positions deep within the mound is probably the result of the boundary condition, of constant water level behind the mound imposed on the internal flow model. Replacement of this boundary condition would allow wave motion behind the breakwater, and reduce the amount of predicted of wave attenuation within the mound. It may be possible to model the wave motion behind the breakwater, by applying the boundary element method to this region and demanding continuity of flow through the rear face of the breakwater as for the front face.

The discrepancies between observed and predicted pressures for high wave conditions may be the result of the effects of wave breaking that cannot be modelled with the boundary element technique described. The use of empirically derived correction factors might be of use in reducing this error, however this would require an extensive series of physical model tests. Such a series of tests would circumvent the advantages of this model over the internal flow model developed by Hannoura & McCorquodale (1985).

The model at present is sometimes unstable. Problems may be encountered in establishing continuity of flow across the external/internal interface with sufficient accuracy. This may be due to the fundamental differences in the models used to calculate the external and internal flows, and the assumptions that these models are based upon. The boundary element model used for the external flow requires the assumption that the flow is irrotational. No such restriction is placed on the internal finite element model. Such inconsistencies of formulation may well be the source of the observed inability to match the



**Figure 5** Velocities within the mound

flow through the interface. The nature of the instability requires further study so that the conditions that lead to it may be predicted. Until this time the model must be used cautiously and the results interpreted with care.

## 8 CONCLUSIONS

There is a good agreement between predicted and observed pressures near the front face of the breakwater mound for waves of moderate height. The accuracy of the model declines when significant a degree of wave breaking and air entrainment occurs.

The model under predicts the amount of wave action deep within the mound. This is almost certainly due to the effects of an unrealistic boundary condition applied to the harbour side of the breakwater. Correction of this boundary condition should significantly improve this aspect of the model.

The full modelling of wave action that includes wave breaking and the

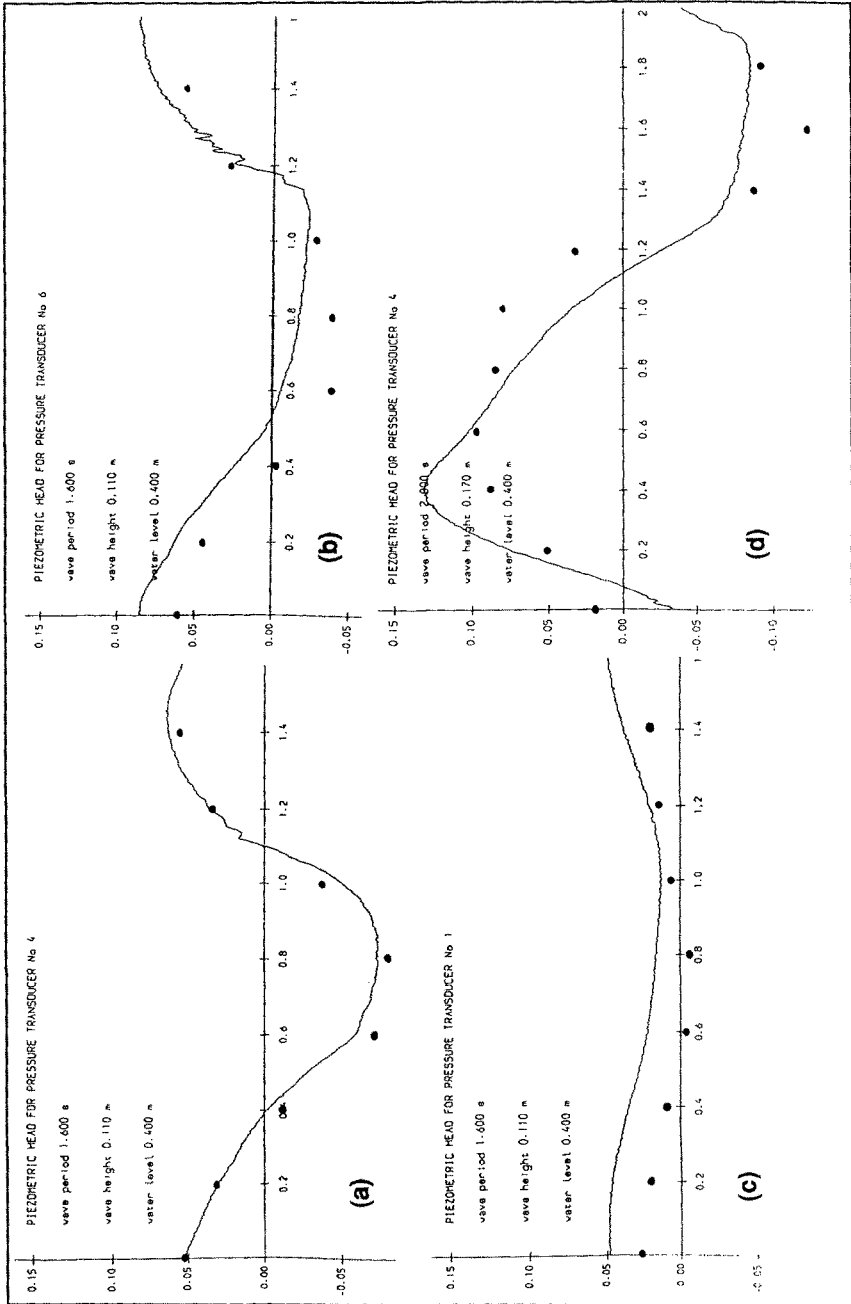


Figure 6 Predicted • and observed pressures within the mound.

entrainment of air must wait for the development of volume of fluid methods as described in the introduction. Until VOF models are available for implementation on small computers, composite models such as this will continue to provide valuable insight into the nature of flows within the cores of rubble mound breakwaters.

## 9 ACKNOWLEDGEMENTS

The collection of physical modelling data and the comparison of this data with the numerical model described in this paper was supported by Single Layer Armour Unit Research Club, co-funded by the Department of the Environment Construction Industry Directorate. Work on the development of the numerical model was funded by Dalian University Of Technology, the British Council and HR Wallingford. The presentation of this paper was supported by HR Wallingford.

## 10 REFERENCES

- Galvin,C.J. "Wave height prediction for wave generators in shallow water". Tech. Memo 4, U.S. Army, Coastal Engineering Research Centre, Mar. 1964.
- Hannoura,A.A. "Numerical and experimental modelling of unsteady flow in rockfill embankments". PhD Thesis, University of Windsor, Windsor, Canada, 1978.
- Hannoura,A.A. & McCorquodale,J.A. "Rubblemounds: numerical modelling of wave motion". Journal of Waterway, Port, Coastal and Ocean Engineering, Volume III, Number 5, September 1985. pp 800-816.
- Madsen,O.S. & White,S.M. "Wave transmission through trapezoidal breakwaters", Proc. 15<sup>th</sup> International Conf. on Coastal Engineering, 1976. Chap 153.
- McCorquodale,J.A. & Nasser,S.M. "Numerical methods for unsteady Non-Darcy flow". Proc. International Symposium on Finite Element Methods in Flow Problems, University of Wales, United Kingdom, January 1974. pp 545-551.
- van der Meer,J.W., Petit,H.A.H., van der Bosch,P., Klopman,G., & Broekends,R.D. "Numerical simulation of wave motion on and in coastal structures". Proc. 23<sup>rd</sup> International Conf. on Coastal Engineering, 1992.
- Nasser,M.S. "Theoretical and experimental analysis of wave action in rockfill structures". PhD Thesis, University of Windsor, Windsor, Canada, 1974.
- Nichols,B.D., Hirt,C.W., & Hotchkiss,R.S. "SOLVA-VOF: A solution algorithm for transient fluid flow with multiple free boundaries". Report LA-8355 Los Alamos Scientific Laboratory, Univ. of California. 1980.
- Shih,R.W.K. "Wave induced uplift pressures acting on a horizontal platform". PhD thesis, University of London, 1989.
- Sollitt,C.K., & Cross,R.H. "Wave transmission through permeable breakwaters", Proc. 13<sup>th</sup> International Conf. on Coastal Engineering, 1972. Chap 103.
- Vinje,T., & Brevig,P. "Numerical simulation of breaking waves". Advanced Water Resources 4, pp 77-82, 1981.
- Williams,A.F, Burcharth,H.F, & den Adel,H. "The permeability of rubble mound breakwaters. New measurements and new ideas". Proc. 23<sup>rd</sup> International Conf. on Coastal Engineering, 1992.

## CHAPTER 123

### Characteristics of Wave Dissipation by Flexible Submerged Breakwater and Utility of The Device

Masahiro Tanaka<sup>1)</sup>  
Takumi Ohshima<sup>1)</sup>  
Tetsushi Kiyokawa<sup>2)</sup>  
Takaaki Uda<sup>3)</sup>  
Atsushi Omata<sup>3)</sup>

#### **Abstract**

A flexible submerged breakwater called "flexible mound", made of an elastic membrane bag filled with water, has been developed for wave control in shallow water as an advanced alternative to the conventional rigid submerged design. Experimental studies were carried out to compare the characteristics of the wave dissipation by flexible mound with those by rigid models. The appropriate ranges of important parameters affecting the efficiency of the flexible type were identified. Numerical studies were also conducted to investigate the mechanism of wave absorption by the flexible structure. To verify the stability and utility of the flexible mound, additional experimental studies were performed using a prototype model. A design concept involved in an actual field construction of the flexible breakwater is also presented.

#### **Introduction**

With more than 30,000 km of coastlines surrounded by rough seas, detached breakwaters, made of concrete blocks, are commonplace in the coastal scenery of Japan. Although these structures serve the intended purpose of shore protection, their undesirable effects on the scenic value of shorelines have been questioned recently. For development of marine recreational zones, there is a particularly strong demand for invisible yet safe and effective wave control methods. Conventional submerged rigid dikes could partially meet this need if it is made very wide with its height close to the water surface. However, it is often too massive for general

---

1) Institute of Technology, Shimizu Corp., Koto-ku, Tokyo 135, Japan

2) Ohsaki Research Inst., Shimizu Corp., Chiyoda-ku, Tokyo 100, Japan

3) Public Works Research Inst., the Ministry of Construction, Tsukuba, Ibaraki 305, Japan

applications, and breaking waves and fast currents around the structure could be dangerous to swimmers and small boats. In response to this demand, and as an alternative to the rigid submerged design, the authors have devised a submerged flexible breakwater called "flexible mound", made of an elastic membrane bag filled with water. Earlier studies by Tanaka et al. (1987) and Kiyokawa et al.(1987) have shown that characteristics of wave dissipation by the flexible mound are substantially different from those by a rigid model, and that the flexible mound can effectively dissipate waves even when the submergence ratio is greater than 0.4. The authors have also identified some important parameters and their appropriate ranges for optimum performance of the flexible design.

The objective of the present study is to investigate the mechanism of wave absorption by the flexible mound by physical and numerical model analyses. Experimental studies using a prototype model are also carried out to verify stability and utility of the flexible submerged breakwater.

**Modeling Approach**

The concept of the flexible mound and the definition of parameters used in the present study are shown in Figs.1 and 2, where  $p_0$  is the static internal added pressure;  $\rho$  : the fluid density;  $g$  : the gravitational acceleration;  $\rho_m$  : the membrane density;  $e$  : the membrane thickness; and  $E$  : Young modulus of the membrane.

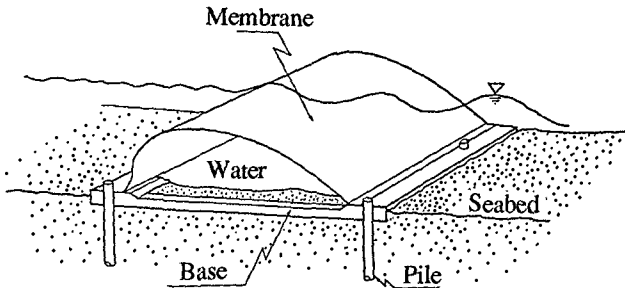


Fig.1 Concept of Flexible Mound (FLM)

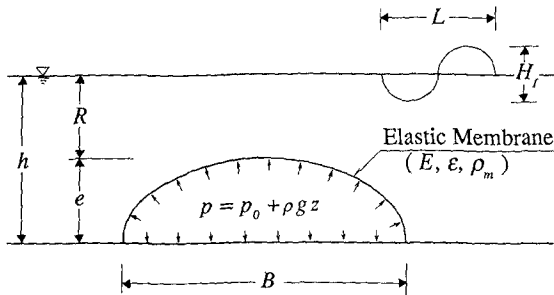


Fig.2 Definition sketch & modeling using lumped-mass method

Since numerical model has been described in detail by Ohyama et al. (1989), only an outline of the numerical analysis is presented here. In this modeling approach, the elastic membrane is discretized into small elements using the lumped-mass method as shown in Fig.3. Forces acting on  $j$ -th nodal point are shown in Fig.4; where  $F_j$  is the hydrodynamic force caused by the pressure difference between the interior and the exterior of the membrane,  $f_j$  and  $f_{j-1}$  are the tensions acting on  $j$ -th and  $j-1$ -th spring, and  $f_0$  is the net weight of the mass in the water. These forces can be represented by using the velocity potentials on the surfaces of the membrane and amplitudes of the membrane motions for all elements. In addition to the assumption inherent in the velocity potential, the motions of the fluid and the membrane are assumed to be sufficiently small, so that the linear theory can be applied. The boundary value problem for the potentials can be transformed into boundary integral equation by applying Green's function and Green's formula. Discretizing the integral equations into finite elements, linear equations for the velocity potentials and the amplitudes of the membrane are obtained.

Wave transmission coefficient,  $K_T$ , and reflection coefficient,  $K_R$ , are obtained from the potential values on the free surface sufficiently apart from the structure.

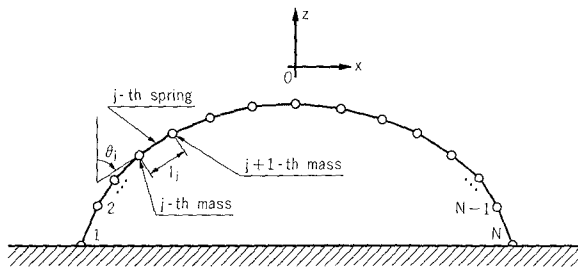


Fig.3 Modeling by the lumped-mass method

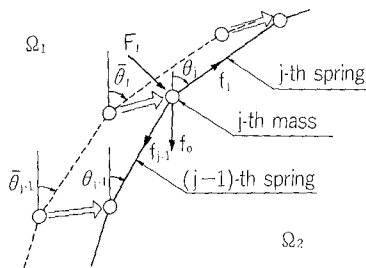


Fig.4 Forces acting on  $j$ -th nodal point



## Experiments

Physical model experiments were carried out in a wave tank, 40 m long, 0.6 m wide and 1.3 m deep as shown in Fig.5. Two models of the flexible mound were made of reinforced rubber membrane fiber with Young modulus,  $E=5800 \text{ N/cm}^2$ , density,  $\rho_m=1.2 \text{ g/cm}^3$ , and thickness,  $\epsilon=1.5 \text{ mm}$ . The models were then hermetically sealed, filled with water and installed on the bottom of the wave tank. A rigid model was also examined for comparison of mobility effects on wave dissipation. The model configuration and the wave conditions are listed in Tables 1 and 2. During the experiments, it was observed that the stationary component of the internal pressure  $p_0$  shifts steadily upward by  $\Delta p_0$  as a train of waves traverses over the flexible model. Therefore,  $p_0' = p_0 + \Delta p_0$  is the virtual internal pressure during experiments.

A comparison between the experimental and the numerical results for the frequency dependence of the transmission and the reflection coefficients,  $K_T$  and  $K_R$ , is shown in Fig.6, in which  $B$  is the base width of the model, and  $L$  is the incident wave length. Some discrepancies between the numerical and the experimental results are attributable to the fact that the energy loss by the structure's motion in the experiments was not taken into account in the numerical analysis. Nonetheless, this numerical model can qualitatively evaluate governing parameters and their effects on wave dissipation by the flexible mound.

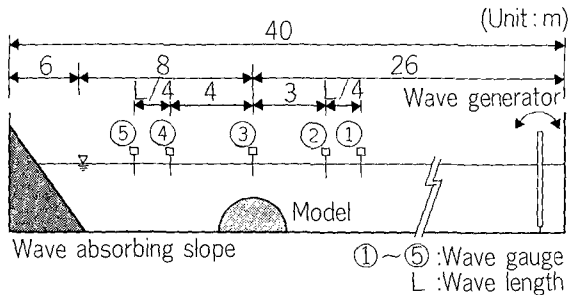


Fig.5 Wave tank layout

Table 1 Model cases

Model type	Width B (cm)	Height e (cm)	Case	Internal pressure $p_0$ (Pa)	Crown depth R (cm)	B/h	R/h	$p_0/\rho gh$
Flexible A	160	40	A - 1	657	27	2.34	0.4	0.10
			A - 2	329	27	2.34	0.4	0.05
Flexible B	80	19	B - 1	172	16	2.29	0.46	0.05
Rigid C	160	36	C - 1		9	3.56	0.20	

Table 2 Wave conditions

No.	Wave depth h (cm)	Wave height H <sub>1</sub> (cm)	Wave periods T (sec)	Length ratio B/L	Note
1 - 1	45	4.5	1.01 ~ 2.65	0.3 ~ 1.05	for B = 1.6 m
1 - 2	45	11.3	1.01 ~ 2.65	0.3 ~ 1.05	
2 - 1	67	4.0	0.93 ~ 3.26	0.2 ~ 1.2	
2 - 2	67	8.0	0.93 ~ 3.26	0.2 ~ 1.0	
3 - 1	35	22 ~ 35	1.01 ~ 4.37	0.1 ~ 0.55	for B = 0.8 m

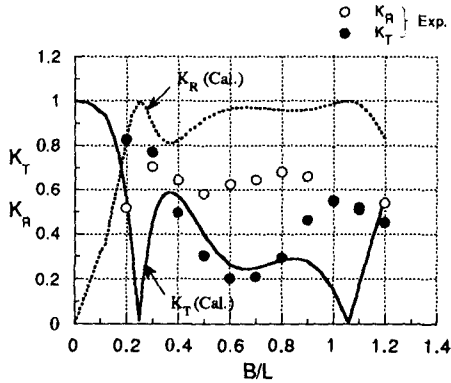


Fig.6 Comparison between numerical and experimental results for wave transmission and reflection characteristics (Case A - 1 : R/h = 0.4, B/h = 2.34, p<sub>0</sub>/ρgh = 0.1)

**Characteristics of wave dissipation**

According to the customary dimensional reasonings, K<sub>T</sub> and K<sub>R</sub> may be expressed by the following dimensionless parameters:

$$K_T, K_R = f(B/L, B/h, R/h, R/H_1, p_0/\rho gh, E/\rho_m gh, \rho_m/\rho, \epsilon/h) \tag{1}$$

A preliminary study (Ohyama et al., 1989) has indicated that, among the eight dimensionless parameters in the group, three parameters, E/ρ<sub>m</sub>gB, ρ<sub>m</sub>/ρ, and ε/h are insignificant in the practical range of application. The rest of the parameters, dimensionless frequency, B/L; width to water depth, B/h; submergence ratio, R/h; relative internal added pressure, p<sub>0</sub>/ρgh; and crown depth to incident wave height, R/H<sub>1</sub>, have influence on the performance of wave control by the flexible structure.

A previous study (Tanaka et al., 1990) has shown that the appropriate ranges of the

parameters,  $B/h$ ,  $R/h$  and  $p_0/\rho gh$ , in order to obtain good performance for a wide range of  $B/L$  are  $B/h : 1.5 \sim 3.0$ ,  $R/h : 0.3 \sim 0.5$ , and  $p_0/\rho gh : 0.03 \sim 0.1$ . These values are used in the subsequent discussion.

Significant factors in the wave dissipation by the flexible mound are found to be 1) interaction between radiation waves and scattering waves, 2) breaking waves over the structure, and 3) energy loss other than the breaking waves. Since the mechanism of the energy loss has not been analyzed in detail, the first two factors are investigated by comparison with the characteristics of wave dissipation by a rigid breakwater. Fig.7 shows the numerical results of the transmission and the reflection coefficients,  $K_T$  and  $K_R$ , versus the parameter,  $B/L$ , for the rigid and the flexible models. The flexible mound can markedly reduce the transmitted wave heights because of the phase interaction between the radiated and diffracted waves, whereas the transmission coefficient is nearly 1.0 in the case of the rigid model. In Fig.7, there

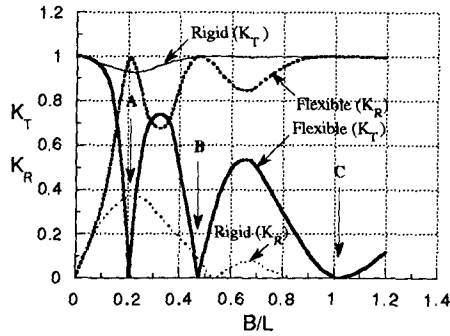


Fig.7 Comparison of  $K_T$  characteristics between for a rigid model and a flexible model

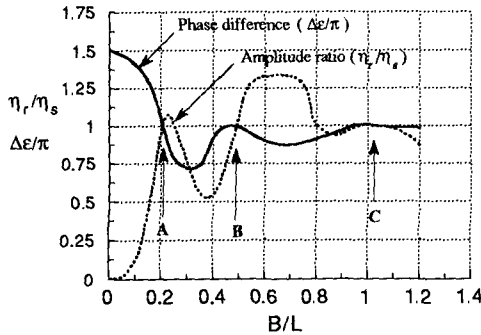


Fig.8 Amplitude ratio and phase differences of radiation wave to scattering wave.

are wave periods, A, B and C, at which  $K_T=0.0$ . At these points, the scattering and the radiation waves have the same height but are in the inverse phase as seen in Fig.8. Thus, it is concluded that the phase interaction between the radiation and the scattering waves plays the primary role for wave dissipation by the flexible mound. The points where no waves transmit may be related to the natural periods of the flexible mound.

Fig.9 shows the experimental results of  $K_T$  versus  $B/L$  for the rigid and the flexible models under breaking wave conditions. The parameters,  $R/H_1$  and  $B/L$ , are important for the wave dissipation for the rigid model. As is well-known, when  $R/H_1$  is greater than 2.0 or  $B/L$  is less than 0.3, a rigid model cannot reduce the transmitted wave heights because the incident waves propagate over the structure without breaking (Nagai et al., 1977). The breaking waves may also play an important role in wave dissipation by flexible dikes when  $R/H_1$  is small. As shown in Fig.9, however, the characteristics of wave dissipation for the flexible model are different from those for the rigid model under the condition of wave breaking. This indicates that the transmitted waves for the flexible model may be reduced not only by the wave breaking but also by the wave interaction.

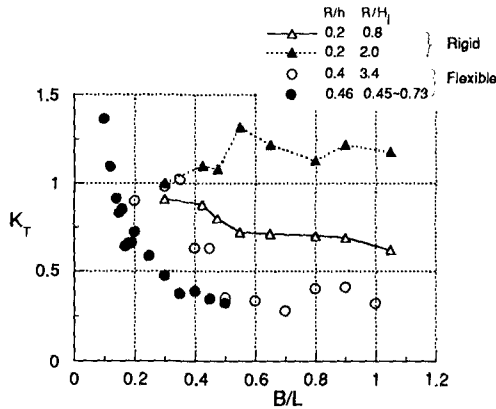


Fig.9 Effect of wave breaking on transmission coefficients by experiments  
 (Case A - 2 :  $R/h = 0.4$ ,  $B/h = 2.34$ ,  $p_0/\rho gh = 0.5$ , Case B - 1 :  $R/h = 0.46$ ,  $B/h = 2.29$ ,  $p_0/\rho gh = 0.5$ , Case C - 1 :  $R/h = 0.2$ ,  $B/h = 3.56$ )

Since a flexible mound is a kind of multi-degree-of freedom oscillation system, it is expected to respond sensitively to the wave periods. Therefore, it is important for practical design of the flexible breakwater to evaluate the effects of irregularity of wave field on the wave dissipation. Fig.10 shows the experimental results for regular and irregular waves for which the incident wave heights,  $H_1$  and  $H_{1/3}$ , are 8cm and between 6.2 and 8cm, respectively. Bretschneider-type spectra (Bretschneider, 1968), with the significant periods, 1.24, 1.43 and 1.63, were used for irregular waves. The performance of  $K_T$  for irregular waves is insensitive to  $B/L$  compared to the results for the regular waves, a desirable feature for practical applications.

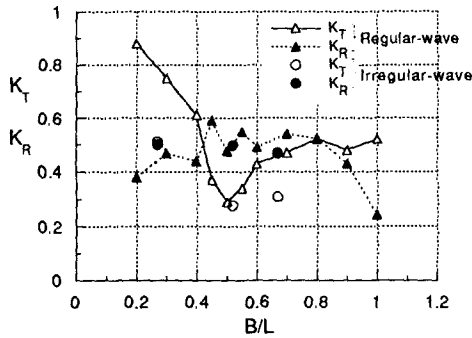


Fig. 10 Comparison between regular & irregular waves (exp.)

**Utility and Application of the flexible mound**

A prototype model of the flexible mound, which has a 4 m-wide base and is 1.2 m high, was designed according to the aforementioned experimental and numerical studies. The layout of the setup is shown in Fig.11. Experimental study was carried out to verify the effectiveness of wave control, the durability of the membrane, and the stability of the seabed around the structure under the conditions;  $h = 2\text{ m}$ ,  $R/h = 0.4$ ,  $p_0/\rho gh = 0.05$  and  $B/h = 2.0$ . Fig.12 indicates an example of the characteristics of  $K_T$  versus  $B/L$  when  $R/H_I$  varies from 0.89 to 3.1. The prototype model achieved transmission coefficients of less than 0.5 in broad ranges of  $R/H_I$  and  $B/L$ . Figs.13 and 14 show experimental results of scouring around the structure and evolution of beach profile behind the structure. The maximum depth of scouring around the structure is about 30% of incident wave height even under storm surge condition, an insignificant factor in general application. The evolution of beach profile behind the flexible mound is also the same level as those of conventional submerged breakwaters. The durability of the membrane and the stability of the structure's base have also been verified in this experiment.

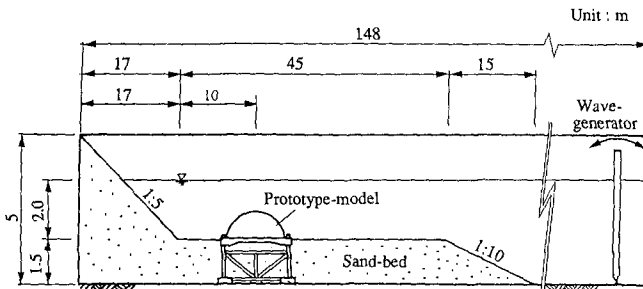


Fig.11 Layout of prototype model test

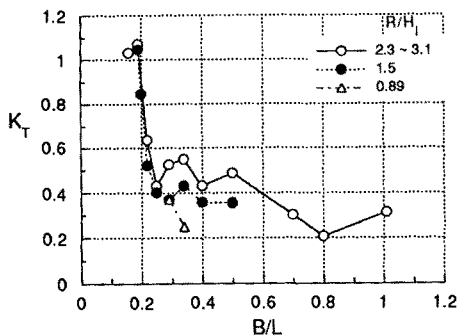


Fig.12 Wave transmission characteristics by a prototype model ( $B/h = 2.0$ ,  $R/h = 0.4$ ,  $p_0/\rho gh = 0.05$ )

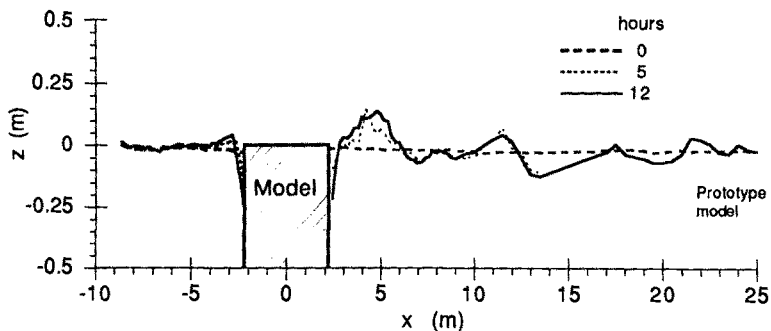


Fig.13 The scoring profile around the flexible mound

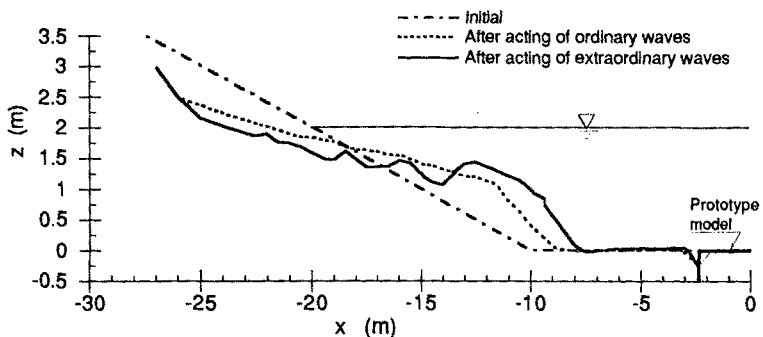


Fig.14 The evolution of the beach profile behind the flexible mound

The flexible mound is not only useful as an improved alternative to the ordinary submerged breakwaters but is also effective as an emergency breakwater, that can be inflated only during a storm passage. Two units of the flexible mound, 9 m wide, 40 m long and 3 m high, have been installed recently at an entrance of a small harbor shown in Fig.15. The units are normally deflated, flush with the sea floor with water-supply-drainage system so that passenger liners can pass over the structure. During a storm surge, the mounds are inflated by the water and serve as emergency breakwaters. Photo.1 shows a inflated membrane at a construction yard. Before the installation, it has been verified by 3-dimensional model tests that the flexible structures can reduce transmitted wave heights to less than 50 % of incident wave on average.

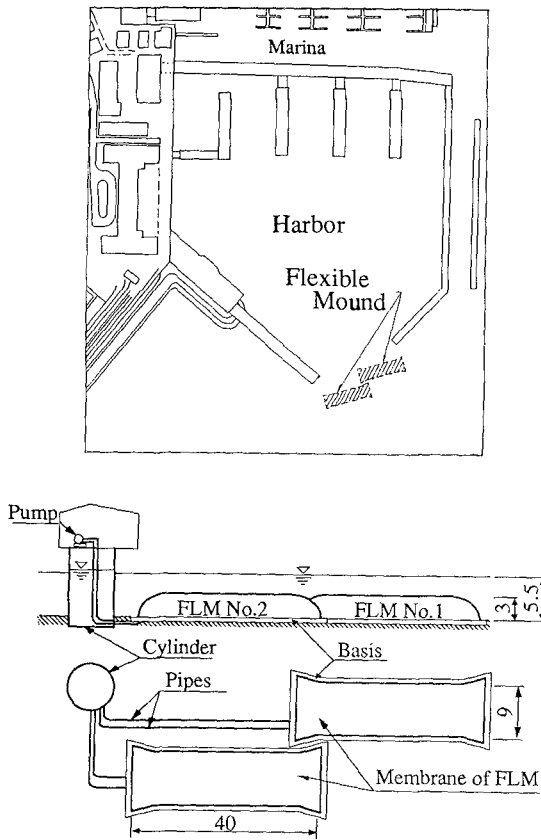


Fig.15 The equipments and their layout of the applied flexible mound as an emergency breakwater



Photo 1 Inflated Membrane

## **Conclusions**

A flexible submerged breakwater, composed of a thin membrane bag filled with water, has been developed for wave control in shallow water as an alternative to the conventional rigid type. The flexible dike can be made more compact compared to the rigid type, and controls waves without sacrifice to the scenic value of the coastal landscape. A noteworthy feature of the flexible design is that it utilizes the interaction of incident and scattering waves with radiation waves generated by the membrane's motion.

Major findings are summarized as follows:

- (1) Three factors, 1) wave interaction, 2) wave breaking over the structure and 3) energy loss other than breaking waves, are related to the mechanism of wave dissipation by the flexible breakwater. The interaction of the scattering waves with the radiation waves, generated by the membrane's motion, plays the most important role in wave dissipation. The performance of the wave interaction is effective when the scattering and the radiation waves have the similar height but in the inverse phase. In addition to the interaction, the wave breaking is also important for the dissipation of the wave energy when the crown depth to incident wave height,  $R/H_1$ , is small. The energy loss excluding wave breaking also has some significance. Its mechanism is currently being investigated by writers.
- (2) Although the flexible dike consists of a multi-degree-of freedom oscillation system, characteristic of wave dissipation for irregular waves is not sensitive to wave periods.
- (3) The effectiveness of wave dissipation by the flexible mound, the durability of the membrane and the stability of the structure were verified by a prototype model test for a wide range of wave conditions.



- (4) The flexible mound is not only useful as an improved alternative to the conventional submerged breakwaters but is also effective as an emergency breakwater, that can be inflated only during a storm passage. Two units of flexible mound have been installed at an entrance of a harbor as a emergency dike, recently.

## REFERENCES

- Bretschneider, C. L. (1968): Significant waves and wave spectrum, Ocean Industry, pp. 40 - 46.
- Kiyokawa, T., M. Mitsumata, M. Tanaka and T. Ohyama (1987): Wave Control by Radiation Wave Generator (in Japanese), Proceedings of 34th Japan Conference on Coastal Engineering, JSCE, pp. 472 - 476.
- Nagai, S., K. Kurata and K. Hasegawa (1977): Effect of crown width on wave dissipation by submerged breakwaters (in Japanese), Proceedings of 24th Japan Conference on Coastal Engineering, JSCE, pp. 303 - 307.
- Ohyama, T., M. Tanaka, T. Kiyokawa, T. Uda and Y. Murai (1989): Transmission and Reflection Characteristics of Waves over a Submerged Flexible Mound, Journal of Coastal Engineering in Japan, Vol. 32, No. 1, pp. 53-68.
- Tanaka, M., M. Mitsumata, T. Ohyama, T. Kiyokawa, T. Uda and Y. Murai (1987): Experimental Study on Wave Control by a Flexible Submerged Dike (in Japanese), Proceedings of 34th Japan Conference on Coastal Engineering, JSCE, pp. 492 - 496.
- Tanaka, M., T. Ohyama, T. Kiyokawa, T. Uda and A. Omata (1990): Wave Control by Flexible Underwater Mound, Proceedings of Offshore Technology Conference, Vol. 3, pp. 551-558.

## CHAPTER 124

### FIELD EXPERIMENTS ON A DUAL CYLINDRICAL CAISSON BREAKWATER

\* Katsutoshi TANIMOTO\*, Hiroshi ENDOH\*\*, Shigeo TAKAHASHI\*\*\*

#### INTRODUCTION

A deepwater caisson breakwater as shown in Fig.1 has been developed by the Ministry of Transport, Japan. The new breakwater is a composite breakwater with a cylindrical caisson named as dual cylinder caisson. The caisson has dual cylindrical walls and its outer cylinder has a perforation in the fore half of the upper portion, forming a wave chamber of a doughnut shape bounded by its inner impermeable cylinder.

A series of laboratory experiments had been carried out at the Port and Harbour Research Institute from 1985 to 1988<sup>1)3)</sup>. According to the laboratory experiments, the caisson was found to have advantages of low reflection and high stability. The design method of the caisson was proposed through intensive laboratory studies in 1988.

Prototype experiments of the dual cylindrical caisson breakwater have been conducted in order to verify its proposed design method against waves at Sakai Port by the Third District Port Construction Bureau, since 1989. A distinguished attempt in the field experiments was tried to measure the displacement of caisson as well as wave pressures during sliding due to high waves. This attempt was accomplished by a storm occurred on February 17, 1991.

Photo 1 shows a scene of the test breakwater after the storm. The middle caisson was slid and fallen down from the rubble mound. The middle caisson is the test caisson which was designed against a

---

\* Professor, Faculty of Engineering, Saitama University, Japan

\*\* Former Director General, Kobe Investigation and Design Office, The third District Port Construction Bureau, Ministry of Transport

\*\*\* Chief, Maritime Structures Laboratory, Port and Harbour Research Institute, Ministry of Transport

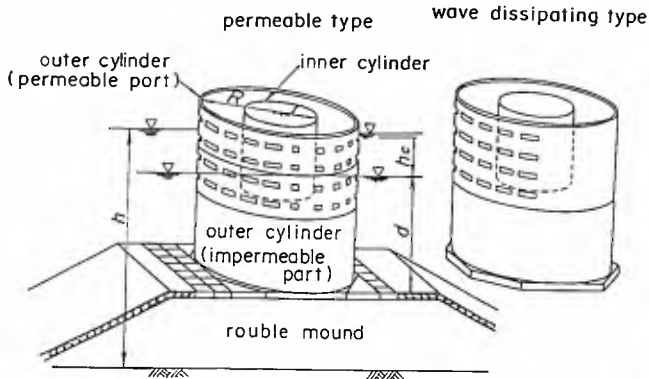


Fig. 1 Conceptual Figure of Dual Cylindrical Caisson



Photo. 1 Slid Caisson in Sakai Port

design wave with one year return period, while the other two caissons were designed with the 50-years return period wave.

After the field test of sliding, model experiments with a scale of 1/21 were performed in a wave basin to reproduce the field situation and investigate the details of the phenomena. The present paper describes both results of field and laboratory experiments, especially on the wave forces and the sliding stability of the caisson in comparison with the proposed design method<sup>4</sup>).

#### DESIGN OF TEST CAISSON AND MEASURING SYSTEM

##### Calculation Method of Design Wave Force

The proposed method to calculate design wave forces and the design of the test caisson for the sliding test are explained here before showing the experimental results.

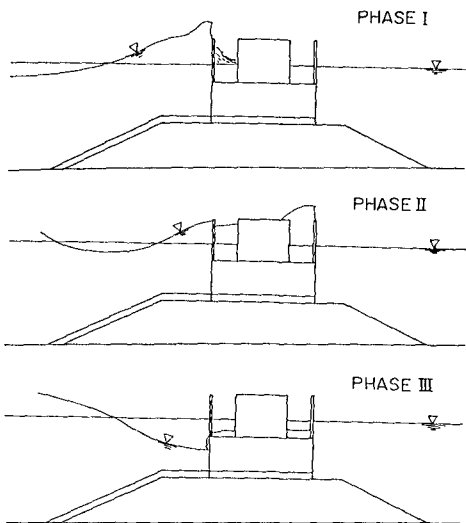


Fig. 2 Three Phases of Wave Action

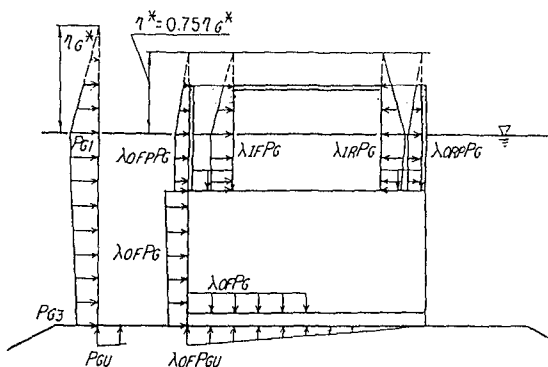


Fig. 3 Distribution of Wave Pressure

Figure 2 demonstrates three phases of wave action which must be considered in the caisson design against waves. The phases I indicates the phase when the wave force on the front side of the outer cylinder peaks. At this phase the resultant upward vertical force  $F_V$  mostly has its peak during one cycle of wave action and the horizontal wave force on the caisson  $F_H$  is large. Consequently, the stability against sliding is most critical at this phase.

The phase II indicates the phase when the wave pressure in the wave chamber is predominant. At this instant, the horizontal wave force  $F_H$  peaks, but the vertical force  $F_V$  is generally small due to a large amount of seawater in the wave camber. The phase III is when the water surface in front of the caisson is the lowest. The horizontal force has its negative peak (maximum to the showered) at this phase. The phase II and III are important for the design of the structural strength of the caisson.

A general distribution of the design wave pressure for the phase I and II is shown in Fig. 3. The intensity of wave pressure on each structural member can be obtained from the Goda pressure formula<sup>1)2)</sup> with each modification factor, which had been obtained from the model experiments<sup>3)</sup>. It should be noted that the pressure on the upper half of the outer cylinder in Fig.3 is defined as the difference between the pressures of outer and inner faces of the perforated wall and that the wave pressure is assumed to exert up to the elevation of  $0.75 \eta_{G^*}$  above the still water level.

The basic pressure distribution is calculated by the Goda pressure formula with  $\alpha_2 = \theta$  as follows:

$$\eta_{G^*} = 0.75(1 + \cos \beta) H_D \tag{1}$$

$$p_{G1} = 0.5(1 + \cos \beta) \alpha_1 W_0 H_D \tag{2}$$

$$p_{G3} = p_{G4} = \alpha_3 p_{G1} \tag{3}$$

where  $\alpha_1 = 0.6 + 0.5 \left[ \frac{4\pi h}{L_D} / \sinh(4\pi h / L_D) \right]^2$  (4)

$$\alpha_3 = 1 - (h'/h) [1 - 1/\cosh(2\pi h / L_D)]$$
 (5)

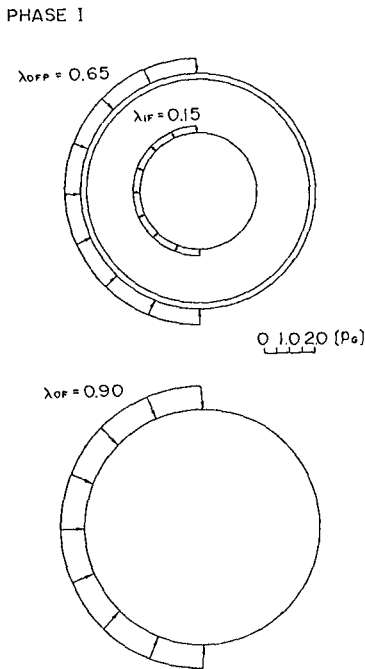


Fig. 4 Wave Pressure Distribution in Horizontal Sections at Phase I

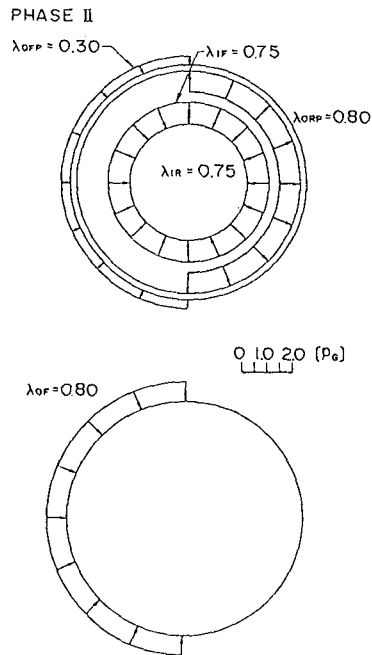


Fig. 5 Wave Pressure Distribution in Horizontal Sections at Phase II

$\beta$  : the angle of wave approach measured from a line normal to the breakwater alignment,  $H_D$ ,  $L_D$  : the wave height and length applied to the calculation of design wave forces,  $w_0$  : the specific weight of seawater,  $h$  : the water depth in front of the breakwater,  $h'$  : the distance from the design water level to the bottom of the caisson.

The wave pressure distribution in the horizontal sections and values of the modification factors are shown in Fig. 4 for the phase I. The wave pressure is assumed to act uniformly on the fore half of cylinders for the action of non-breaking waves. The modification factor  $\lambda_{OF}$  for the perforated wall is 0.65, and the modification factor  $\lambda_{OF}$  for the lower impermeable part of the outer cylinder is 0.9. The modification factor  $\lambda_{IF}$  for the front half of the inner cylinder is 0.15. The modification factors at the phase II are similarly shown in Fig. 5.

The negative wave pressure at the phase III can be obtained appropriately according to the fourth order approximation of a finite amplitude standing wave theory. The residual water level in the wave chamber, however, must be separately given as  $\eta^- = 0.25 H_D$ . The pressures in the wave chamber is the hydrostatic water pressure corresponding to the difference between the water level and the still water level.

#### Design Condition and Safety Factor Against Sliding

The design wave with a return period of one year was selected for the sliding test caisson. The design conditions are as follows:

$$\begin{aligned} H_1/3 &= 2.6 \text{ m}, H_D = H_{MAX} = 4.7 \text{ m}, \\ \beta &= 0, \text{ Design tidal level} = + 0.4 \text{ m} \end{aligned}$$

Figure 6 shows a cross section of the sliding test caisson. The caisson is a reinforced concrete caisson with the outer diameter of 16.2 m and the height of 10.4 m. The opening ratio of the perforated wall is 0.25. The inside of caisson is filled with only water to reduce the caisson weight for the sliding test. The caisson weight deducted the buoyancy in seawater is 860 tf.

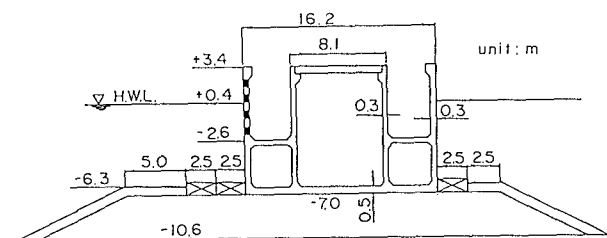


Fig. 6 Cross Section of Sliding Test Caisson

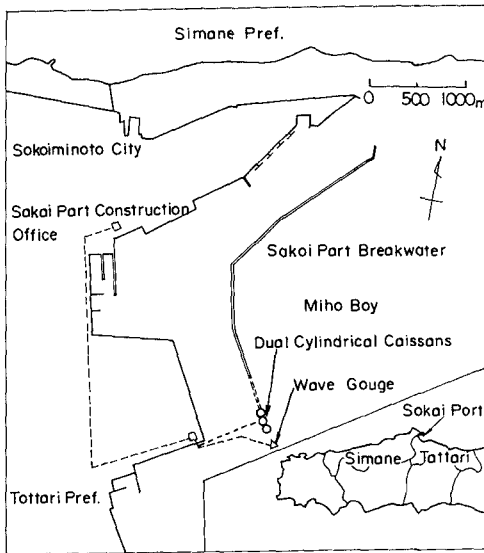


Fig. 7 Test Caissons in Sakai Port

The safety factor  $SF_s$  against sliding is defined by the following relation:

$$S F_s = \mu (W_0 - F_v) / F_H \quad (6)$$

where  $\mu$  is the friction coefficient between the bottom slab of caisson and the rubble mound foundation, and it is taken as 0.6 according to the design standard of breakwaters. The safety factor of the test caisson is 0.98 against the calculated wave force.

### Measuring System

Figure 7 shows the plan of Sakai Port and the location of the test breakwater. The test breakwater is isolated one consisting of three units of caissons. The middle caisson is the sliding test caisson.

The wave profile and wave direction were measured by a set of wave gauges and velocity meters which located at the position 250 m away from the test breakwater as in the figure. Thirty four pressure transducers were attached to the sliding test caisson to measure the wave pressure distribution and to calculate the resultant wave force. Six displacement meters of wire type were equipped at the top and the bottom of the caisson. They were fixed on the neighboring caissons and on armor concrete blocks for the rubble mound foundation. The data of the pressures and displacements were recorded continuously during storms by a computer in an on-land observation house.

## SOME RESULTS OF FIELD EXPERIMENTS

Example of Analogue Records

Figure 8 shows an example of field records obtained during the storm in February 17, 1991. The top record indicates the water surface oscillation measured by the wave gage. The middle record indicates the wave pressure profile at the impermeable front wall. It is noticed that the time profile of the pressure is well correlated to that of the water surface elevation. This is because the incident waves to the breakwater are diffracted waves by a peninsula (Zizou-misaki Cape of Shimane Peninsula) and have relatively long crests and the wave angle is almost zero. The bottom record shows the horizontal displacement of the caisson measured at the bottom. The first sliding is not included in this figure and the displacement from the second to the fifth sliding is shown in the figure. The capacity of the displacement meters was

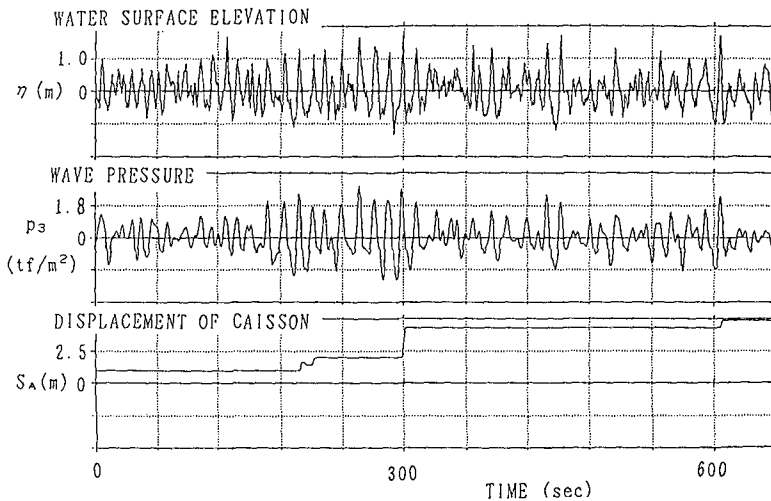


Fig. 8 Sample Record during the Storm on the 17th of February 1991

Table 1 Waves and Sliding Distances

TIME	$H_{max}$ (m)	$H_{1/3}$ (m)	$T_{1/3}$ (s)	$S_a$ (m)	$\Delta S$ (m)	
2:45-3:00	3.15	2.05	14.1	1.06	1.06	once
3:00-3:15	2.77	1.72	13.1	1.06	0	no
3:15-3:30	3.19	2.03	12.7	4.32	3.26	thrice
3:30-3:45	2.92	2.05	12.6	4.87	0.55	once
3:45-4:00	3.17	2.23	13.4	>5		



5 m and therefore, the wires of the meters were cut off when the sixth sliding occurred.

Wave Conditions and Sliding Distances

The first sliding was recorded at 02:50:40 on February 17 and the sixth sliding was occurred at 03:53:47 on the same day. Observed waves were analyzed for every 15 minutes from 02:45:00 to 04:00:00. The results are shown in Table 1 together with data of the sliding distances, in which  $S_A$  denotes an accumulated sliding distance and  $S$  denotes the sliding distance during each 15 minutes. For the first 15 minutes, the maximum wave height is 3.15 m, the significant wave height and period are 2.05 m and 14.1 s, and the first sliding occurred which distance was 1.06 m. The tidal level is observed as 0.31 m above the datum level at this time. This sliding distance by one wave is considerably large due to the non breaking wave action having a relatively long wave period in this case.

Measured Wave Pressure Intensity

Figure 9 demonstrates the order of the magnitude of the wave pressure measured at several points of the caisson. In this figure, the representative positive wave pressure intensities like  $P_{max}$ ,  $P_{1/10}$ , and  $P_{1/3}$  are plotted against the corresponding representative wave heights like  $H_{max}$ ,  $H_{1/10}$ , and  $H_{1/3}$ . Relatively large pressure intensities appear at the most rear part in the wave chamber, but the intensity is less than  $1.0 w_0H$ .

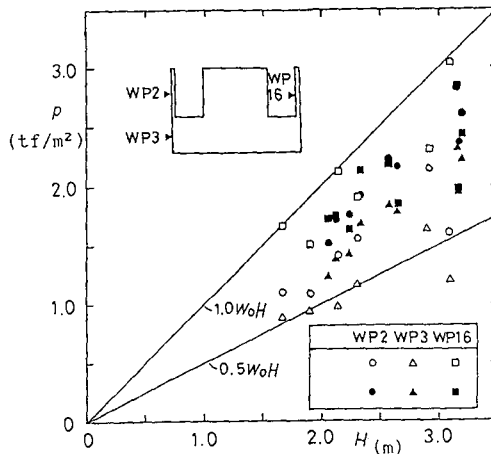


Fig. 9 Pressure Intensities in the Field Experiments

## LABORATORY EXPERIMENTS AND COMPARISON WITH FIELD DATA

Wave Conditions

Laboratory experiments were carried out to reproduce the field experiment in a wave basin with a model scale of 1/21 using uni-directional irregular waves. Seven kinds of laboratory waves having different wave heights and periods were used in the experiments. Two of them are corresponding to the November storm waves and others are corresponding to the February storm waves, which wave conditions are listed in Table 1. The November storm is a short and small storm just after the completion of the caisson installation. For each of them five different wave trains were prepared. Representative wave parameters according to the zero-upcrossing method are presented in Table 2 with the mean value and the standard deviation for five wave trains. The duration time of one wave train is 15 minutes. The wave direction is perpendicular to the breakwater alignment.

The wave spectra for the November storms are represented by the Modified Bretschneider-Mitsuyasu (MBM) spectrum. For the February storm, however, the MBM spectrum is not applicable, because the observed spectrum is very sharply peaked. Therefore, the JONSWAP type is applied as the target spectrum of the February storm. The peak parameter in the JONSWAP spectrum can be selected so that the realized spectrum coincides with the spectrum observed in the field as much as possible. Figure 10 shows the comparison of the wave spectra in the field and in the laboratory.

Table 2 Waves in Laboratory Experiments

	Field			Laboratory		
	$H_{max}(m)$	$H_{1/3}(m)$	$T_{1/3}(s)$	$H_{max}(m)$ (mean, S. D.)	$H_{1/3}(m)$ (mean, S. D.)	$T_{1/3}(s)$
II A	2.91	1.90	7.1	2.56~3.02 (2.84, 0.165)	1.87~1.93 (1.89, 0.021)	7.0~7.2
II B	3.09	1.67	6.4	2.47~2.87 (2.64, 0.153)	1.65~1.68 (1.66, 0.011)	6.3~6.5
II C	2.62 (3.15) <sup>*</sup>	2.05	14.1	2.76~3.05 (2.86, 0.103)	1.99~2.09 (2.05, 0.032)	14.0~14.2
II D	2.50 (2.77) <sup>*</sup>	1.72	13.1	2.30~2.72 (2.53, 0.135)	1.69~1.76 (1.72, 0.028)	13.1~13.3
II E	2.61 (3.19) <sup>*</sup>	2.03	12.7	2.75~2.93 (2.84, 0.062)	2.03~2.05 (2.04, 0.006)	12.6~12.7
II F	2.74 (2.92) <sup>*</sup>	2.05	12.6	2.73~3.19 (2.95, 0.156)	2.02~2.08 (2.04, 0.023)	12.5~12.6
II G	2.91 (3.17) <sup>*</sup>	2.23	13.4	3.12~3.35 (3.26, 0.091)	2.18~2.29 (2.22, 0.036)	13.2~13.3

<sup>\*</sup>(zero crossing down)

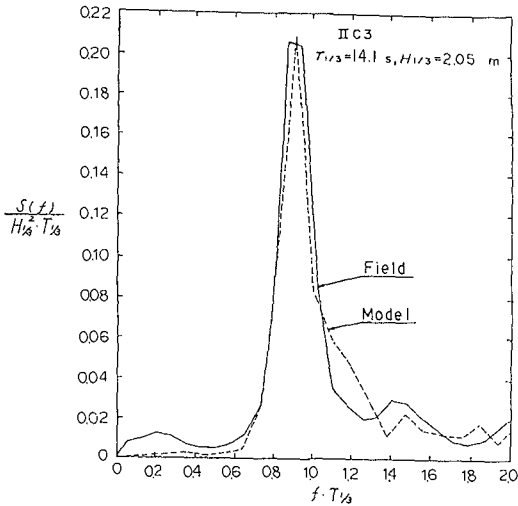


Fig. 10 Wave Spectra in the Field and Laboratory

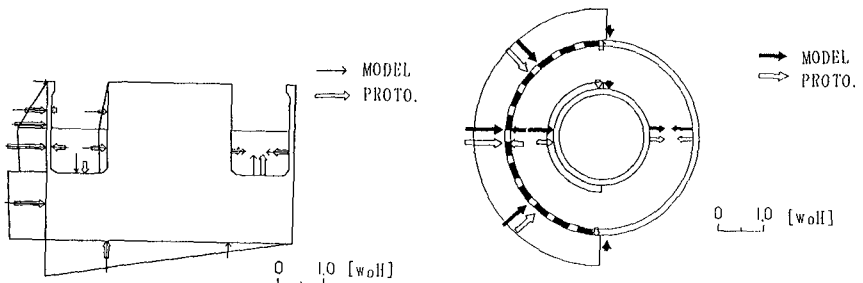


Fig. 11 Measured Instantaneous Pressure Distribution

Wave Pressure Distribution

Figure 11 shows an example of the instantaneous distribution of wave pressures when the wave force at the phase 1 is the largest during the action of random waves. Both data measured in the field and the laboratory are shown together with the distribution calculated by the proposed method. Although the measured wave pressure are considerably larger than the calculated ones at the front of the inner cylinder, it can be said that the proposed method predicts well the wave pressure distribution as a whole. The resultant wave forces are calculated from such an instantaneous distribution of the wave pressures by considering application areas of caisson walls shared by respective measuring points.

Horizontal and Vertical Wave Forces

Peak values of measured and calculated wave forces for the

phase I are compared in Figs. 12 and 13. In the figures, the ordinate indicates the measured force and the abscissa indicates the calculated force. The horizontal wave forces are shown in Fig. 12, where the measured wave forces in the laboratory experiments are generally larger than the calculated ones, but the laboratory data agree well the field data. Data of the vertical wave forces in Fig. 13 are widely scattered. The main reason is that the amount of water in the wave chamber at the phase I varies considerably depending on the wave periods and wave trains.

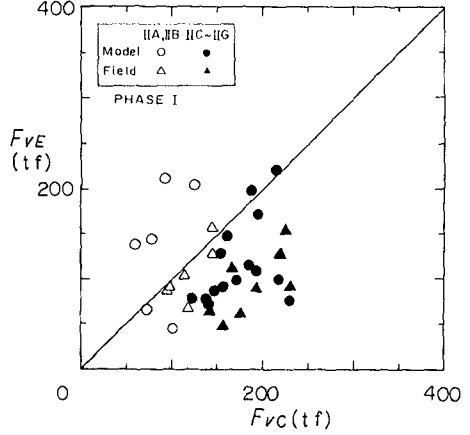
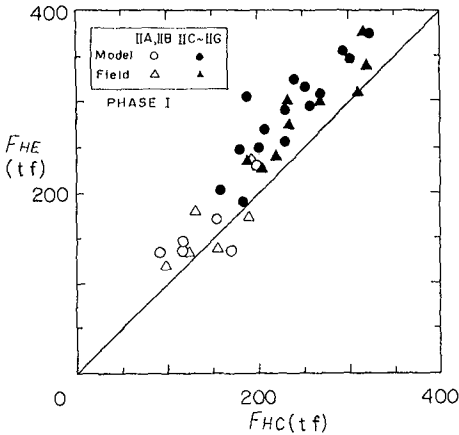


Fig. 12 Horizontal Wave Forces Fig. 13 Vertical Wave Forces

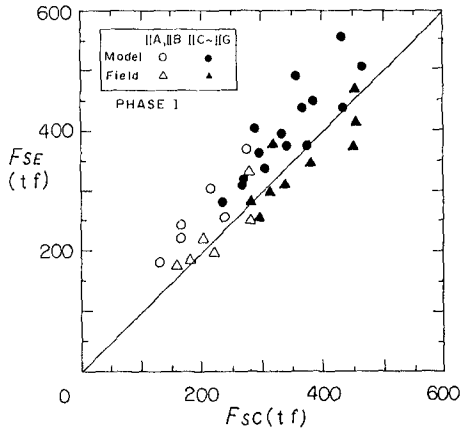


Fig. 14 Equivalent Sliding Forces

Figure 14 shows the peak values of calculated and measured equivalent sliding forces which are equal to  $(F_H + \mu F_V)$ . The ordinate indicates the measured force and the abscissa indicates the calculated force. The equivalent sliding forces in the laboratory experiments are generally larger than the calculated ones, as the horizontal forces in Fig. 11. However, it should be noted that the equivalent sliding forces measured in the field are a little lower than those in the laboratory and are almost the same as the calculated ones. The measured wave forces scatter significantly in the figures. This is because the wave profile varies even though the wave height is the same. Therefore, this may be the reason of the difference between the values in the laboratory and the field.

Relation between Safety Factor and Sliding Distance

In the laboratory experiments, the horizontal displacement was measured for two possible weights of the sliding test caisson. The one is corresponding to the design weight, and the other is the weight assumed that the water level inside the inner caisson lowers to the tidal level. They are denoted by  $W_1$  and  $W_2$ , respectively.  $W_2$  is calculated as 781 tf in a still water and is 90% of  $W_1$ . Because it is difficult to prevent the leakage of water from the inner cylinder, the weight  $W_2$  is presumably the weight during sliding.

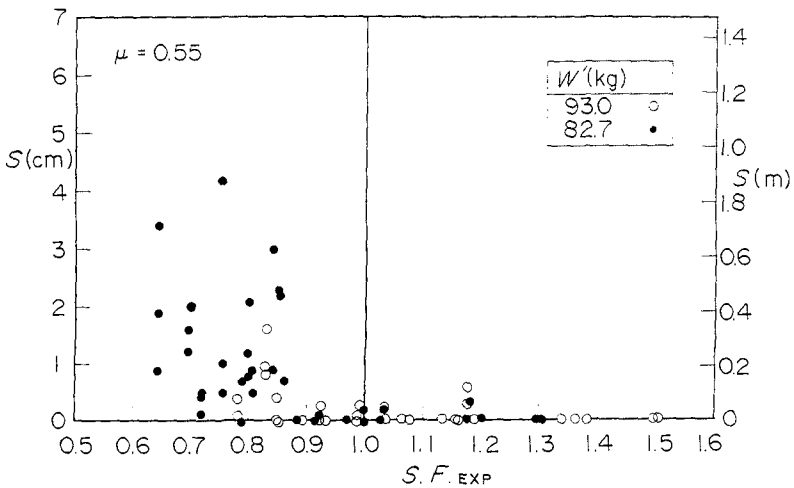


Fig. 15 Safety Factor and Sliding Distance

In the laboratory experiments, the friction coefficient was also measured. Since the sliding in the field occurred only three months after its installation and no large storms attacked the caisson until the sliding occurred, the compaction of the rubble mound by the caisson movements was not enough to get the ordinary friction factor of 0.6. The measured friction coefficient without the compaction of the rubble mound were about 0.55 in the laboratory experiments.

Figure 15 shows the results of sliding tests in the laboratory. The ordinate indicates the maximum sliding distance by one wave during the action of irregular waves. The abscissa indicates the safety factor against sliding, which is calculated for the measured wave forces, the caisson weight ( $W_1$  or  $W_2$ ), and the friction coefficient of 0.55. The results shows that the caisson slides in most cases having the safety factor less than 1.0. Thus, the results of laboratory experiments suggests that the occurrence of the sliding can be judged by the safety factor.

#### Safety Factor against Sliding for the Field Data

The safety factor against sliding which is calculated according to the measured wave forces is shown in Table 3 for the condition of the first sliding in the field. The caisson slid by 1.06 m during the first sliding. The safety factor is 0.93, less than 1.0, when the friction factor is assumed to be 0.55 and the caisson weight is  $W_2$ . Even if the caisson weight is  $W_1$  and the friction factor is 0.6, the safety factor is less than 1.2. Therefore, it can be concluded that the caisson sliding can be judged by its safety factor also in the field experiments.

Table 3 Safety Factor against Sliding

$w_0$ (tf)	$\mu$	S. F.
895	0.60	1.19
895	0.55	1.10
781	0.60	1.01
781	0.55	0.93

The safety factor using the calculated wave forces, the caisson weight of  $W_2$  and the friction coefficient of 0.55 is 0.87. Because the measured wave forces in the field are almost the same as the calculated wave forces, the safety factor against sliding using the calculated wave forces is close to that using the measured wave forces.

#### CONCLUDING REMARKS

Slidings of a prototype dual cylinder caisson were successfully measured in the field verification experiments. The slidings of the caisson were reproduced in laboratory experiments. The major conclusions in this study are as follows:

1) The sliding of the caisson can be judged by its safety factor

- using the measured wave forces, the caisson weight and the friction factor both in the field and in the laboratory.
- 2) The measured wave forces acting on the caisson in the field were almost the same as the calculated wave forces. Therefore, the sliding of the caisson in the field can be judged also by the safety factor using the calculated wave forces.
  - 3) The measured wave forces in the laboratory are larger than those in the field as a whole. However the difference is not significant and this is because of the wide variation of the laboratory data.

#### ACKNOWLEDGMENTS

The field experiments have been conducted under the guidance of the advisory committee chaired by professor Y. Goda. The experiments were carried out by the collaboration with many engineers especially of the Sakai Port Construction Office and the Kobe Design and Investigation Office of the Third District Port Construction Bureau, MOT. The authors wish to express their sincere gratitude to all the people.

#### REFERENCES

- 1) TANIMOTO, K., TAKAHASHI, S., and KIMURA, K. : Structures and Hydraulic Characteristics of Breakwaters, - State of the Art of Breakwater Design in Japan-. Rept. of Port and Harbour Res. Inst., Vol. 26, No. 5. 1987, pp. 11-55.
- 2) GODA, Y. : Random Seas and Design of Maritime Structures, University Tokyo Press, 1985, 323 p.
- 3) TANIMOTO, K., et al. : Hydraulic Characteristics and Design Wave Forces of Double-Cylindrical Caisson, - A Study on Development of Deepwater Breakwater (part 4) - , Tech. Note of Port and Harbour Res. Inst., No. 600, 1987, pp. 1-21, (in Japanese).
- 4) TAKAHASHI, S., Ken'ichirou SHIMOSAKO, and Hitoshi SASAKI : Experimental Study on Wave Forces and Sliding of Dual Cylinder Caisson - Reproducing Experiment of Field Sliding Test in Sakai Port-. , Tech. Note of Port and Harbour Res. Inst., No. 742, 1992, (in Japanese).

## CHAPTER 125

# Pressure Oscillations during Wave Impact on Vertical Walls

M.E.Topliss\*    M.J.Cooker†    D.H.Peregrine‡

### Introduction

This area of study concerns wave impact pressure on vertical structures. Severe damage can be inflicted on coastal defences during storms and numerous laboratory experiments have been undertaken to gain an understanding of the physical processes. This paper gives a mathematical description of high frequency pressure oscillations which are observed in measurements of water-wave impacts; particularly impact against a vertical wall. Our ultimate aim is to trace the physical origins of the pressure fluctuations which are related to the understanding of the role of fluid compressibility in breaking wave impact pressure. It has been suggested by some authors that the recorded pressure oscillations are due to the vibrations of air-filled gas bubbles, for example Weggel & Maxwell (1970) model some details of acoustic wave propagation. In addition, it is well known that the compressibility of a small volume fraction of air in water dramatically reduces the velocity of sound in the mixture. We investigate possible cases by simplifying the geometry and finding the frequency of free oscillations. We ignore the main flow of water since it has a longer time-scale. Our initial model considers compressible aerated water near the wall and compressible non-aerated water with a much higher sound speed further away. This is compared with a simple example of an air pocket trapped against a wall in incompressible water. Comparisons with three experimental results are encouraging.

---

\*Research Student, School of Mathematics, Bristol University, Bristol BS8 1TW

†Research Assistant, School of Mathematics, Bristol University, Bristol BS8 1TW

‡Professor of Mathematics, School of Mathematics, Bristol University, Bristol BS8 1TW



### Bubbly mixture near a wall

This model applies to the instances when a wave has broken creating a volume of water with many small bubbles next to the impact wall. This is now a compressible mixture.

Consider a region of uniform bubbly mixture (region 1) with a gas fraction  $\alpha$  next to a vertical wall, and non-aerated water on the other side (region 2) as shown in figure 1.

We treat the solid wall and solid bed as rigid so that the component of displacement normal to these boundaries vanishes. As there is a large density contrast between the fluid and the air above, we take the pressure to vanish at the free surface. For linearised theory and sinusoidally varying velocity potential  $\phi(x, y) e^{i\omega t}$  this implies  $\phi$  may be taken to be zero on the free surface.

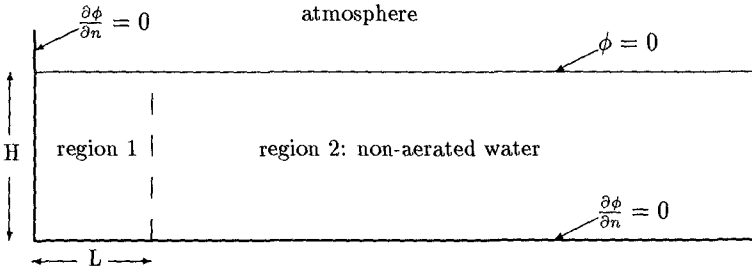


Figure 1. Limited volume of bubbly water

Sound waves are weak pressure disturbances which propagate at high speed through a fluid. The sound velocity in air is approximately 340 metres per second; that in water is approximately 1500 metres per second. In a mixture of air and water however, the speed of sound is dramatically reduced. The density in region 1 is taken to be  $\rho_1 = (1 - \alpha)\rho_2$  where  $\rho_2$  is the density in region 2. We have taken the speed of sound in region 1 as derived by Hsieh & Plesset (1961) to be

$$c_1^2 = \frac{\gamma p}{\rho_1 \alpha (1 - \alpha)},$$

where  $p$  is the atmospheric pressure,  $\rho_1$  is defined above,  $\gamma$  is the ratio of specific heats,  $\alpha$  is the gas fraction. For example 1 percent, 4 percent and 10 percent aeration give sound speeds of 120 m/s, 60 m/s and 40 m/s respectively, and this accords with experimental measures. The expression for  $c^2$  is a good empirical rule provided  $\alpha$  is not too near 0 or 1.

Viscosity and gravitational effects will be ignored. The reduced wave equation,

$$(\nabla^2 + k_i^2) \phi_i = 0$$

where the subscripts  $i = 1, 2$  refers to regions 1, 2 respectively and  $k_i = \omega/c_i$  where  $\omega = 2\pi f$ , is solved by separation of variables.

As the free surface and the rigid bed are totally reflecting surfaces the fluid can be considered as an acoustic plane waveguide and a standing wave field results, which has a cut-off frequency  $\omega_n$  for each mode of oscillation, below which no propagation occurs. In region 2 the sound speed is very much higher and therefore  $\omega$  maybe less than the cut-off frequency and there is no propagation. The velocity potential for the bubbly mixture in this instance is:

$$\phi_1 = A_1 e^{\sqrt{k_1^2 - \gamma_n^2} L} \cos(\gamma_n y) \cosh \left[ \sqrt{k_1^2 - \gamma_n^2} (x + L) \right] e^{i\omega t}$$

and for the non-aerated water outside the bubbly mixture is

$$\phi_2 = A_1 e^{\sqrt{k_1^2 - \gamma_n^2} L} (1 - \alpha) \cos(\gamma_n y) \cosh \left[ \sqrt{k_1^2 - \gamma_n^2} L \right] e^{-\sqrt{\gamma_n^2 - k_2^2} x} e^{i\omega t}$$

where  $c_2 =$  the speed of sound in non-aerated water,  $\gamma_n = n\pi/2H$ ,  $n = 1, 3, 5, \dots$ ,  $H$  is the depth of the fluid,  $L$  is the width of the bubbly layer,  $A_1$  is a constant.

Assuming pressure and normal velocity are continuous across the interface between region 1 and region 2, we find an expression for the frequency of modes of oscillations trapped in region 1:

$$(1 - \alpha) \sqrt{\gamma_n^2 - k_2^2} = \sqrt{k_1^2 - \gamma_n^2} \tan \left[ \sqrt{k_1^2 - \gamma_n^2} L \right]$$

For a fixed width and air content, a high free surface will give a low frequency as illustrated in figure 2. Figure 3 shows that, for a fixed amount of air and depth, a wider region will have a lower frequency. Conversely a very narrow band of bubbles against a rigid wall will produce very high frequencies. Both figures show higher frequencies with a lower aeration level.

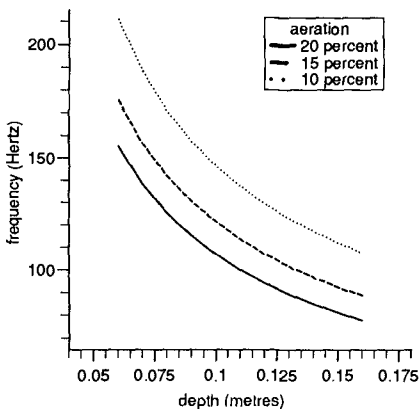


Figure 2. Variation of  $f$  with  $H$

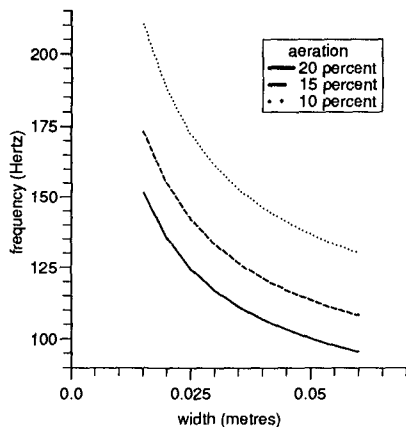


Figure 3. Variation of  $f$  with  $L$

### A trapped air pocket

To model of a trapped air pocket against a vertical wall we now have to take into account a) the presence of the free surface, b) the cylindrical geometry of the gas pocket, c) the presence of the rigid wall.

Suppose the bubble contains air at atmospheric pressure and that it's centre is submerged a distance  $h$  below the free surface and lies a distance  $d$  above the seabed as shown in figure 4. The water is taken to be incompressible.

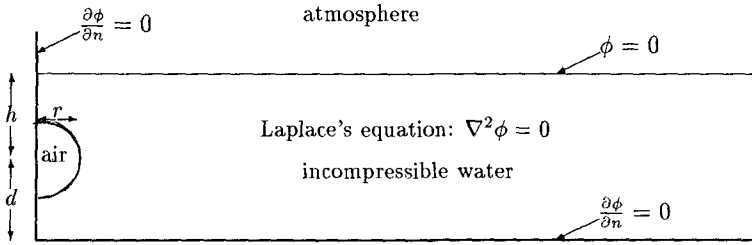


Figure 4. Trapped air pocket at the wall

We model the vibrations of the trapped air pocket by considering the radial oscillations, translation and shape oscillations of a single two dimensional bubble with semi-circular cross-section of radius  $r$ . As this study concerns only relatively large bubbles, surface tension effects can be neglected as they are only significant for small radii. During the short time in which the bubble oscillates regularly we suppose that the free surface moves very little so that we may again ignore the flow in the impacting wave. We take an image of the bubble above the free surface to be oscillating in anti-phase with respect to the bubble, an image below the rigid bed to be oscillating in phase, and a third image below, oscillating in anti-phase, to ensure symmetry as shown in figure 5. These images then extend above and below to produce an infinite series which is summed analytically. The potential for this model is

$$\phi = -\alpha_0 \log \left[ \frac{\cosh(\lambda z) - \cos(\lambda d)}{\cosh(\lambda z) + \cos(\lambda d)} \right] + \frac{\alpha_1}{(z - z_0)} + \frac{\alpha_2}{(z - z_0)^2}$$

where  $\lambda = \pi/2(d + h)$ ,  $z_0$  = the position of the bubble,  $i = \sqrt{-1}$ ,  $\alpha_0, \alpha_1, \alpha_2$  are constants. Figure 6 shows the pressure contours from a two dimensional bubble.

The logarithmic term, which is the dominant term, represents the radial oscillations. The second term, evaluated on the bubble surface,

$$\frac{\alpha_1}{(z - z_0)} = -\alpha_0 \frac{\lambda r}{2} [\cot \lambda d + \tan \lambda d] \sin \theta ,$$

represents translational motion and the third term, evaluated on the bubble

surface,

$$\frac{\alpha_2}{(z - z_0)^2} = \alpha_0 \frac{\lambda^2 r^2}{8} [4 + \tan^2 \lambda d - \cot^2 \lambda d] (2 \cos^2 \theta - 1) ,$$

represents a first approximation to shape oscillations.

We calculate the time-harmonic irrotational flow induced by the semicircular two dimensional bubble and the frequency of the small oscillations is given by

$$\omega^2 = - \frac{2\gamma p [1 + \frac{1}{2}\lambda^2 r^2]}{\rho r^2 [\log(\frac{1}{2}\lambda r \tan \lambda d) + \frac{1}{4}\lambda^2 r^2]}$$

$p$  is the atmospheric pressure,  $\rho$  is the density of water. As figure 7 shows, for fixed  $h + d$ , an air pocket nearer the rigid bed will have a lower resonant frequency than an air pocket nearer the free surface. The size of the air pocket is inversely proportional to the frequency as illustrated in figure 8. This corresponds to the previous model for the bubbly mixture which showed high frequencies are obtained for lower aeration.

i) as  $h$  becomes large,

$$\omega^2 = - \frac{2\gamma p}{\rho r^2 \log [2rd/R]},$$

the frequency for a single two dimensional bubble in the vicinity of a rigid boundary, where  $R$  is a large number representing a boundary far away. This is to ensure boundary conditions in the far field are satisfied.

ii) as  $d$  becomes large,

$$\omega^2 = - \frac{2\gamma p}{\rho r^2 \log [r/2h]},$$

the frequency for a single two dimensional bubble in the vicinity of a free boundary (Topliss 1991).

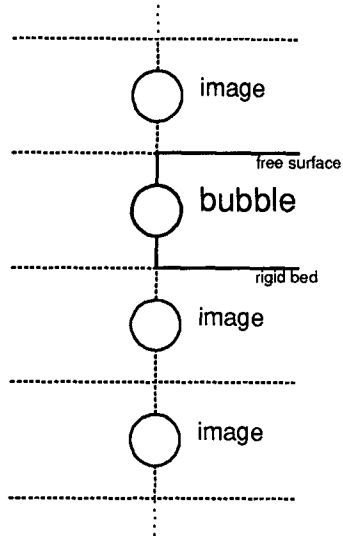


Figure 5. Bubble and three images

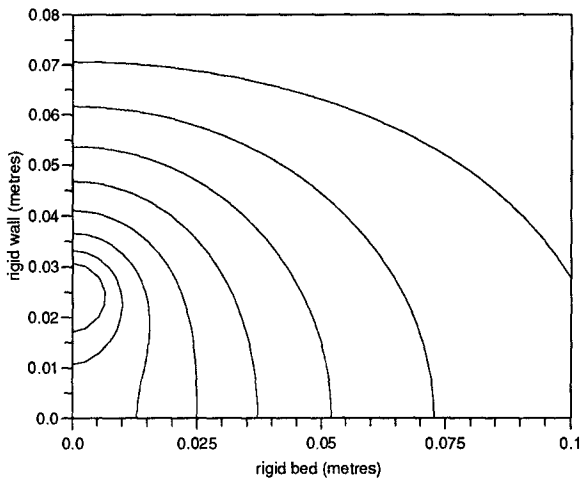


Figure 6. Pressure contours from single bubble on wall

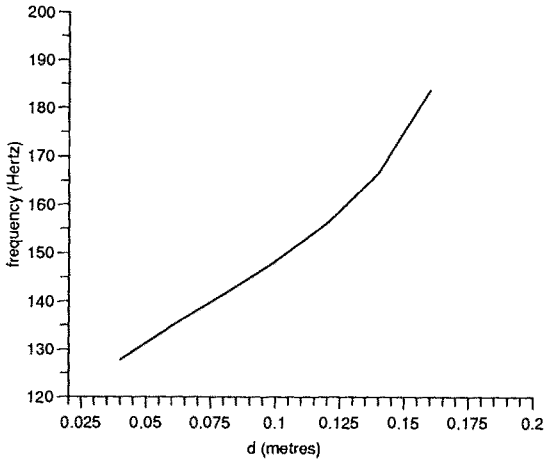


Figure 7. Variation of frequency with d  
h+d fixed at 0.2 m, r=0.01 m

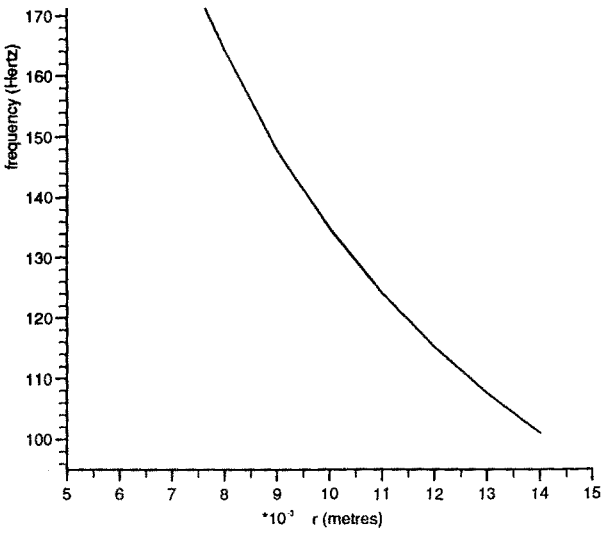


Figure 8. Variation of frequency with radius  
h+d fixed at 0.2 m, h=0.14 m, d=0.06 m

## Comparisons with experiments

We have considered three experimental studies for comparison with these theoretical results:

I) Hattori & Arami (1992); Chuo University, Japan

Hattori & Arami have provided us with many details of their experiments which investigate the importance of an air pocket between the breaking wave and the wall. The experiments were undertaken in a small wave tank (still water depth at the wall of five centimetres) and high-speed video frames were taken of waves as they impact on a vertical wall and some waves appear to trap a cylinder of air against the wall. Records from six pressure gauges of one centimetre diameter are available.

The histories of the pressure, measured at the wall, for these waves exhibit three stages. Initially the pressure rises to a peak value and is followed by an interval of regular smooth oscillations, of decreasing amplitude. These oscillations are displayed with the same frequency in all six pressure gauges. Clearly this decay requires further modelling. This finally develops into a more confused signal, consisting of higher frequencies with lower amplitudes, and which carries on for an indefinite time.

As the wave advances towards the impact structure, it begins to curl over, entrapping an air pocket against the wall. In the video frames following the impact, it can be seen that the free surface rises and a thin jet of water shoots up the wall. We neglect this since it is usually much thinner than the bubble until a later stage and assume a flat surface in our models. For each experiment we have considered, we have taken measurements from the first three frames at the beginning of the oscillations and compared the frequency calculated for that geometry with the frequency given by the pressure gauges. The theory compares particularly well for large air pockets, see table 1.

II) Witte (1988); Leichtweiss-Institut, Germany

Witte describes a wave impact against a vertical wall and observed an air pocket trapped against the impact wall. The wave tank had a still water depth at the wall of sixteen centimetres and fourteen pressure cells. Full details are given of one case (example no.13, figure 6.3, type II). Regular oscillations are recorded in all cells of period 12 milliseconds, or a frequency of 83.3 Hertz. If we choose  $h = 0.22$  m and  $d = 0.05$  m (no photographs are given but the description given by Witte suggests that the air pocket is nearer the bed than the free surface) then, from figure 9 below where the variation of frequency with size of air pocket is presented, a bubble of radius 0.0155 m would give a frequency of 83 Hertz. Although no photos are available, the statistics presented in Witte (1988) for this type of impact give scope for further study.

description				Topliss	Hattori
	distance $d$ (metres)	distance $h$ (metres)	radius $r$ (metres)	frequency $f$ (Hertz)	frequency $f$ (Hertz)
data No.1-031-3					
frame 715	0.06	0.016	0.011	235	210
frame 720	0.06	0.017	0.011	228	210
frame 725	0.061	0.017	0.011	228	210
data No.172-3					
frame 815	0.031	0.038	0.007	233	210
frame 820	0.032	0.04	0.007	231	210
frame 825	0.033	0.042	0.007	229	210
data No.132-3					
frame 295	0.031	0.024	0.008	241	190
frame 300	0.031	0.04	0.008	207	190
frame 305	0.031	0.044	0.008	202	190
data No.178-3					
frame 320	0.027	0.025	0.02	142	104
frame 325	0.029	0.041	0.02	106	104
frame 330	0.029	0.043	0.02	104	104
data No.152-6					
frame 015	0.029	0.044	0.024	93	100
frame 020	0.03	0.047	0.024	90	100
frame 025	0.03	0.05	0.024	87	100
data No.2-255-4					
frame 330	0.032	0.037	0.02	113	99
frame 335	0.032	0.044	0.02	104	99
frame 340	0.032	0.049	0.02	99	99

Table 1. Comparison of experimental data and theory. The frames are separated by a timestep of five milliseconds and  $f = \omega/2\pi$



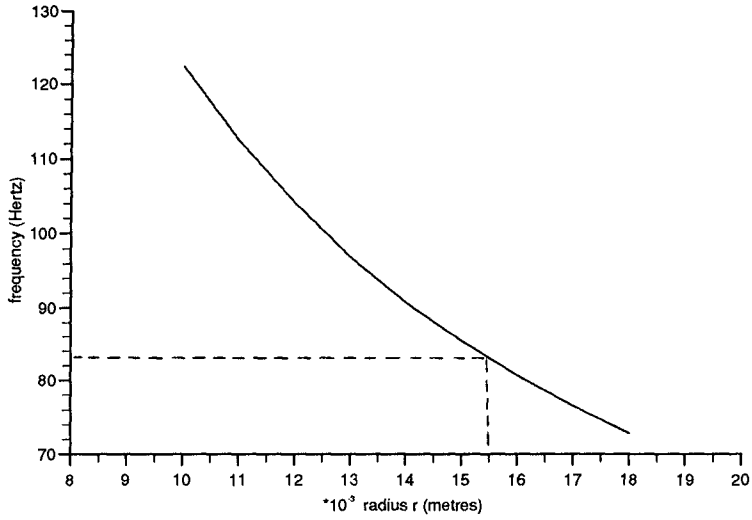


Figure 9. Comparison of theory with data

$h = 0.22$  m,  $d = 0.05$  m

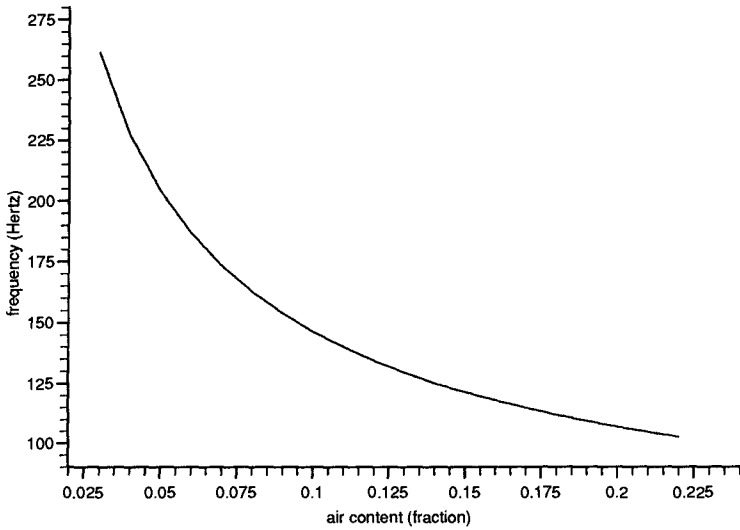


Figure 10. Comparison of theory with data

## III) Graham &amp; Hewson (1992); Plymouth University, England

Graham & Hewson have carried out model-scale experiments of waves breaking against a vertical wall, with three pressure transducers and one aeration gauge in order to investigate aeration levels of a wave impacting upon structures. No previous work (to our knowledge) has been carried out on aeration measurements and with the kind permission of Graham & Hewson we are able to compare our theoretical work with the preliminary work carried out at Plymouth. Video frames are not yet available.

After impact the pressure transducers show both rapid fluctuations and an underlying frequency of approximately 30-40 Hertz. Although we have been unable to find an example which would give a frequency this low, the rapid fluctuations are in the range of 100-300 Hertz which is consistent with other experiments. The levels of aeration shown range between 4 percent and 20 percent. If we estimate the depth of the water at the wall to be 0.1 metres and the width of the bubbles to be 0.04 metres we can expect frequencies of between 100 and 260 Hertz, as illustrated in figure 10. These are within the range of frequencies measured in the experiments.

## Discussion

We have not yet been able to compare the theory with large scale experiments, although studies are been undertaken in Hannover (Schmidt, Oumeraci & Partensky 1992), where double peak forces have been recorded along with negative pressures. Table 2 gives examples of how scale effects could vary the frequencies according to the size and position of an air pocket trapped. We have taken an example from table 1 (data No.132-3) and altered the geometric parameters.

	radius $r$ (metres)	distance $d$ (metres)	distance $h$ (metres)	frequency $f$ (Hertz)
	0.008	0.031	0.040	207
x 5	0.04	0.155	0.2	42
x 10	0.08	0.31	0.4	21
x 50	0.4	1.55	2.0	4.2
x 100	0.8	3.1	4.0	2.1

Table 2. Variation of geometries for a trapped air pocket

For a wave which breaks giving a bubbly mixture, table 3 gives examples of frequencies which could be obtained in a larger volume. Here we have taken the gas fraction to be 0.1.

	height H (metres)	width L (metres)	frequency $f$ (Hertz)
	0.1	0.04	146
x 5	0.5	0.2	106
x 10	1.0	0.4	14.6
x 50	5.0	2.0	10.6
x 100	10.0	4.0	1.46

Table 3. Variation of geometries for a bubbly mixture

Table 2 and 3 show that the frequency varies linearly with the geometric parameters, a property easily deduced from the equations. For the lowest frequency shown above, a typical compressible length = wavelength /  $2\pi$  which is approximately 160 metres in pure water but only 5 metres for 10 percent aeration indicates that for the largest waves that trap air, sound propagation is important as has been noted by Schmidt, Oumeraci & Partenscky.

This work has only studied free oscillations. The initial forcing, amplitude and damping of the oscillations all require further study. The decay of the regular oscillations, well illustrated by the experiments of Hattori & Arami (1992), are due to damping which could be the result of several mechanisms: viscous damping, thermal damping or acoustic radiation. There are also radiating modes which need investigation.

The financial assistance of SERC is gratefully acknowledged.

## References

- GRAHAM, D.I & HEWSON, P.J: (1992) Measurement of aeration in model-scale breaking waves. *Mast G6-S/Project 2*, Informal Internal Report.
- HATTORI, M & ARAMI, A: (1992) Impact breaking wave pressures on vertical wall. *23rd Int. Coastal Engineering Conf.*, Venice, Italy.
- HSEIH, D.Y & PLESSET, M.S: (1961) Theory of rectified diffusion of mass into gas bubbles. *J. Acoust. Soc. Am* **33** no. 2
- SCHMIDT, R., OUMERACI, H & PARTENSCKY, H.-W: (1992) Impact Loads Induced by Plunging Breakers on Vertical Structures. *23rd Int. Coastal Engineering Conf.*, Venice, Italy.
- TOPLISS, M.E: (1991) *Mathematical description of air bubbles in water*. M.Sc Thesis, Bristol University.
- WEGGEL, J.R & MAXWELL, W.H.C: (1970) Numerical Model for wave pressure distributions. *J. Waterways, Harbors & Coastal Engineering Div*, Proc. ASCE **96** pp 623-642.
- WITTE, H.-H : (1988) Wave-induced impact loading in deterministic and stochastic reflection. *Mitteilungen*, Leichtweiss Institut für Wasserbau, Tech. University Braunschweig, **102** pp ix-227.

## CHAPTER 126

### WATER PARTICLE VELOCITIES ON A BERM BREAKWATER

Alf Tørum <sup>1</sup> and Marcel van Gent <sup>2</sup>

#### ABSTRACT

Water particle velocities in waves running up and down a berm breakwater have been measured for several wave heights and wave periods with a Laser Doppler Velocimeter (LDV).

The measured water particle velocities have been compared with velocities computed with the numerical model ODIFLOCS. There is a fair agreement between the calculated and measured velocities.

#### 1 INTRODUCTION

It is the velocity field on a breakwater front that is the main governing factor with respect to the stability of the armour cover blocks. This velocity field and the forces on a cover block have been poorly known.

The different formulae that have been presented on the required block weight, e.g. Iribarren (1938), Hudson (1985) and Hedar (1960) have been based on some approximate concept of the velocities and the forces, leading to formulae with a single unknown coefficient. The value of this coefficient has been determined from model tests.

One of the first attempts to calculate and measure the velocities for downrush on a rubble mound breakwater model was made by Brandtzæg and Tørum (1966), Brandtzæg, Tørum and Østby (1968). They measured velocities

---

<sup>1</sup>SINTEF Norwegian Hydrotechnical Laboratory/Norwegian Institute of Technology, 7034 Trondheim, Norway.

<sup>2</sup>Delft Technical University, Department of Civil Engineering, Hydraulics and Offshore Engineering Division, POB 5048, GA 2600, Delft, The Netherlands.

with a micro propeller. The measurements were made at one height above the slope and gave no details about the velocity variation from the slope face and up towards the water surface. There was a fair agreement between the measurements and the simple mathematical model that was derived to calculate the velocities in downrush.

Sawaragi et al. (1982) measured particle velocities on the breakwater slope by filming particles made of sponge with the same specific mass as water introduced in the water. The point to point movement of the particles was recorded on 16 mm colour films taken by a high speed film camera (50 frames per sec). From the film the particle velocities were obtained by superposition of projected film frames to give a distance and a time interval of movement. Sawaragi et al. found that the non-dimensional maximum velocity was a function of the surf similarity parameter and the ratio of the wave height to the water depth. Sawaragi et al. did not compare their velocity measurements with any theoretical results.

Kobayashi et al. (1987) and Kobayashi and Wurjanto (1989) developed a numerical model for the computation of the water particle velocities on an impervious rubble mound slope. This model is based on the finite amplitude shallow water wave equation. By use of this model they can calculate the vertically averaged horizontal velocities as well as run up and run down. They compared the calculated run up with measurements, which showed fair agreement, but did not make any comparisons between calculated and measured velocities.

Breteler and van der Meer (1990) report the measurement and computation of wave induced velocities on a smooth slope. The measurements were made with an electromagnetic current meter. The computations were made with the computer program developed by Kobayashi and Wurjanto (1989). Breteler and van der Meer concluded that there was a fair agreement between the measurements and the computations with respect to run up levels and run down velocities, the results for run up velocities were a little worse and the results for pressures and run down levels were bad.

Laser doppler velocity meters (LDV) offers the possibility to make good velocity measurements without any interference with or disturbance of the fluid. Since no detailed velocity measurements have been carried out as the waves run up and down a berm breakwater slope it was decided to carry out such measurements. The results have been compared with results obtained by the computer program ODIFLOCS, van Gent (1992).

## **2 TEST SET UP AND MEASUREMENT SYSTEMS**

### **2.1 Wave flume and berm breakwater model**

The measurements were carried out in a wave flume with the berm breakwater

as shown in Figure 1. The width of the flume was 1.0 m.

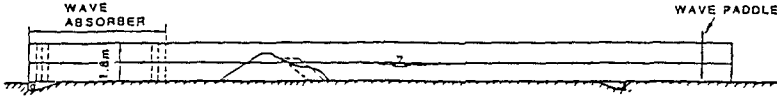


Figure 1 The wave flume with the breakwater model.

The breakwater cross section is shown in Figure 2. The shown section of the reshaped breakwater was obtained by using waves with heights up to 0.25 m.

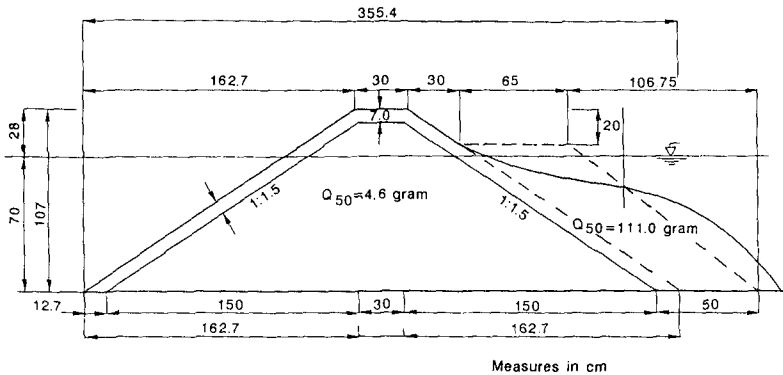


Figure 2 Berm breakwater cross section.

## 2.2 Laser Doppler Velocimeter (LDV)

The water particle velocities were measured with a Laser Doppler Velocimeter (LDV). The LDV system is a two component system based on the forward scatter mode. This LDV system was built in-house for a study of the kinematics of irregular water waves (potential flow). The noise to signal ratio was too large for this instrument to give any meaningful measurements of turbulence. The measurements were taken with a rate of 100 samples per second. In the analysis the data have been smoothed by using a gliding average of 11 data points.

The velocities were taken at several of the points shown in Figure 3. The main reason for concentrating the velocity measurement points in the area shown in Figure 3 was that less air entrainment due to breaking waves was expected in this area

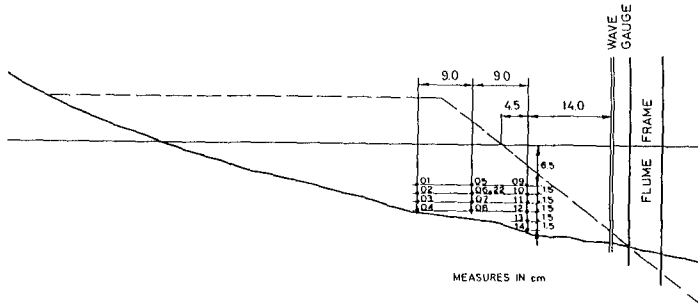


Figure 3 Velocity measurement points.

than closer to the breakwater crest. Air entrainment causes drop outs of the LDV measurements. Another reason is that it may be expected that the destructive velocities and forces downslope are largest in this region where the breakwater slope is flattest.

The berm breakwater profile shown in Figure 3 gives an average profile along the glass panel wall of the flume. The distance between this profile and the lowest measuring point is not necessarily representative for the distance between the measurement point and the closest stone. The measurement points are located approximately in the middle of the wave flume. The LDV system was orientated such that the velocities in horizontal and vertical direction was measured. However, during the analysis the instantaneous velocities in any direction could be obtained. In this paper velocities parallel and normal to the breakwater slope are given. Positive parallel velocities mean uprush while positive normal velocities mean velocities away from the slope.

### 2.3 Wave measurements

The waves were measured with wave gauges of the conductivity type. Prior to the velocity measurement runs the waves were calibrated in the wave flume. During the wave calibration runs the waves were measured in an area approximately 5 m ahead of the breakwater model. All the tests during the water particle velocity measurements were carried out with regular waves. Hence the waves were calibrated by moving a wave gauge along the wave flume to obtain the maximum and minimum wave heights. The height of the incoming wave was then set as the average of the maximum and minimum wave height.

During the velocity measurement runs the waves were measured close to the velocity measurement points, Figure 3. The main purpose of this gauge is to give phase information between the wave elevation and the velocity measurements. The wave elevation measurements at this gauge may be inaccurate, partly because of the shallow water and partly by air entrainment during the breaking of the largest waves.

### 3 VELOCITY MEASUREMENTS - ANALYSIS AND RESULTS

Water particle velocities have been measured primarily at the measurement points, see Figure 3: 08, 09, 10, 11, 13 and 22 for the three wave periods  $T = 1.5, 1.8$  and  $2.1$  s for several wave heights for each wave period. Not all data have been analysed, but we will present some main features of the analysis. Figure 4 shows waves measured at the location of the reference wave gauge shown in Figure 3. Figures 5 and 6 show parallel and normal velocities in point 08 measured simultaneously with the waves. Figure 7 shows a time expanded diagram of the wave and the parallel and normal velocity at point 08. The time reference is the same as in Figures 4, 5 and 6. Further details on the measurements are given by Tørum (1992).

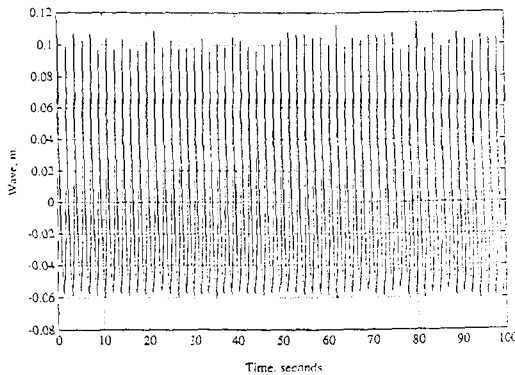


Figure 4 Measured wave at the location of the reference wave gauge shown in Figure 3.

Although the waves are "regular" there are slight variations in their heights at the reference gauge. In this case the waves broke after they passed the wave gauge and the measurements are not influenced by any air entrainment.

There are also slight variations in the parallel velocities. It is though not necessarily such that a high wave generate a large uprush velocity. The normal velocities are more irregular than the parallel velocities.



The maximum, mean and minimum velocities measured in the points 08, 09, 10, 13 and 22 are shown in Tables 1 and 2 for uprush and downrush. Point 9 "went dry" during downrush. Hence no "maximum" downrush velocities were taken for this point.

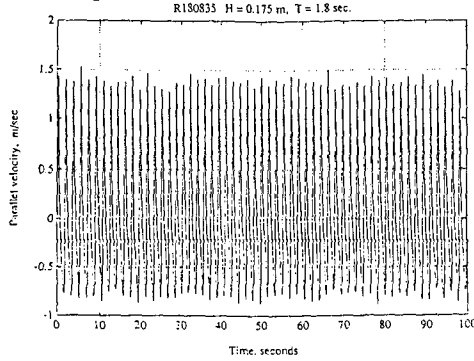


Figure 5 Measured parallel velocity at point 08. Positive velocity means uprush.

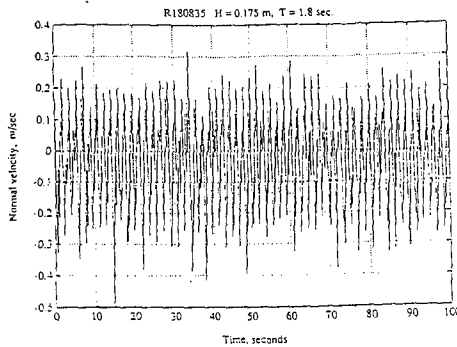


Figure 6 Measured normal velocity at point 08. Positive velocity means velocity away from the slope.

There is a tendency that the maximum parallel velocities in uprush are largest closest to the berm breakwater slope. This might be due to amplification effects close to cover stones or overshoot effects in the wave boundary layer.

Since the velocities were not measured simultaneously in the different points it is not possible to draw a "true" velocity profile through the measurement points 09, 10 and 13. An order of magnitude analysis indicates that the boundary layer thickness is 0.01 - 0.015 m during maximum velocities.

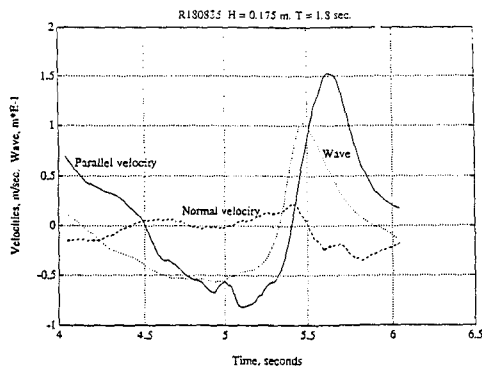


Figure 7 Measured velocities in point 08 and wave at reference wave gauge. Positive velocity means uprush.

Table 1 Minimum, mean and maximum parallel velocities in m/sec during uprush and downrush.  $H = 0.175$  m,  $T = 1.8$  sec.

Measure- ment point	$u_{up}$			$u_{down}$		
	min	mean	max	min	mean	max
09	0.6	1.0	1.25	-	-	-
10	0.6	0.9	1.1	0.75	0.8	0.90
13	1.15	1.20	1.30	0.7	0.8	1.0
08	1.25	1.4	1.55	0.7	0.75	0.8
22	0.95	1.05	1.15	0.85	0.9	1.0

Table 2 Minimum, mean and maximum normal velocities in m/sec.  $H = 0.175$  m,  $T = 1.8$  sec.

Measure- ment point	$v_{up}$			$v_{down}$		
	min	mean	max	min	mean	max
09	0.6	0.65	0.7	0.20	0.30	0.4
10	0.40	0.45	0.50	0.25	0.30	0.35
13	0.20	0.22	0.25	0.20	0.23	0.25
08	0.13	0.20	0.31	0.21	0.25	0.41
22	0.4	0.45	0.5	0.12	0.18	0.25

## 4. COMPARISON OF MEASUREMENTS WITH THE NUMERICAL MODEL ODIFLOCS

### 4.1 Description of the numerical model ODIFLOCS

The model ODIFLOCS (One Dimensional Flow on and in Coastal Structures) describes the wave motion on and in several types of structures. The model takes various phenomena into account. For instance reflection, permeability, infiltration, desorption, overtopping, varying roughness along the slope, linear and non-linear porous friction (Darcy- and turbulent friction), added mass, internal set-up and the disconnection of the free surface and the phreatic surface are all implemented. The model couples a hydraulic model to a porous flow model. Kobayashi et al. (1987 and 1989) proved that long wave equations can be used for the description of the external flow. The way in which the wave front is treated is also done in a similar way as by Kobayashi et al. (1987 and 1989). In the model ODIFLOCS long wave equations are applied for the internal flow as well. Long wave equations use hydrostatic pressures and imply a simulation of a breaking wave like a bore. The external flow and the internal flow are computed in two layers, a hydraulic layer and a porous layer, that partially overlap. The flow between both layers is determined by the pressure gradients. This flow has a maximum caused by the equilibrium of the pressure gradient and the friction. The pressure gradient in the vertical direction is assumed not to be larger than one. For a detailed description of this aspect and the model in general, see Van Gent (1992).

### 4.2 Comparison of measurements with the numerical model ODIFLOCS

The model can deal with only one porous layer. For a berm breakwater with a core, the choice has to be made whether the breakwater will be modelled as a homogeneous structure or as a structure with an impermeable core. The permeability of the core was very much the same as the material of the berm itself. Therefore, modelling as a homogeneous structure has been applied. The friction factor, depending on the roughness of the surface and the flow characteristics, was derived by using the empirical formula for fully rough turbulent flow on a uniform sloping breakwater by Madsen and White (1975):

$$f_w = 0.29 \left( \frac{d}{d_s} \right)^{-0.5} \left( \frac{d}{R \cot \alpha} \right)^{0.7}$$

The depth in front of the structure  $d_s$  was 0.79 m; for the size of the armour unit,  $d$ , the  $D_{n50}=0.034$  m was taken; the run-up  $R$  is about equal to the

wave height for which 0.175 was used and for the angle of the slope, the angle from the berm section was taken ( $\cot\alpha=5$ ). This gives a friction factor  $f_w=0.15$ . For the porosity, 0.35 was used. For the simulation added mass was not included. It might be inappropriate to compare calculated depth-averaged velocities with measured velocities in one point. However, an approximation of the maximum boundary layer thickness gives 0.01-0.015 m. This is rather low compared to the local water depth. Measured velocities in points above the boundary layer are assumed to be representative for the depth-averaged velocities. Measured velocities in different points above the slope, but in the same cross section, show differences in the order of magnitude of 20%.

For comparisons, two measuring points have been selected. The velocities measured in point 8 and 10, both above the berm and about 0.1 m away from each other, were used. Point 8 was positioned very close to the bottom and point 10 was about 0.07 m above the slope. Wave heights were measured above the berm and a comparison of those wave heights has been made as well, although the measured wave heights may be inaccurate as explained before. The simulated wave conditions were the nine combinations of wave heights of about 0.10, 0.15 and 0.20 m and wave periods of 1.5, 1.8 and 2.1 s. The combination  $H=0.175$  m and  $T=1.8$  s was added. Measuring point 8 is about at the level of the boundary thickness for these wave conditions. Point 10 is assumed to be above the boundary layer.

The calculated velocities are the horizontal velocities while the given measured velocities are the velocities along the slope. In principle the given measured velocities should be slightly larger than the calculated velocities.

The calculated velocities are the depth averaged velocities while the given measured velocities are velocities in a point. It is though believed that the measurement points are outside the boundary layer, except point 8.

The results of the comparisons of measured surface elevations with output from the numerical model, are summarized in Table 3.

The differences are rather low. A comparison between the maximum and minimum surface elevation is made to exclude the influence of a slightly different water level. The numerical model underestimates the fluctuation of the surface elevation with an average of 12.6 % difference (about 0.02 m) with the measured elevations. The wave condition  $T=1.5$  s and  $H=19.5$  cm gives a difference (10.9%) in the same order of magnitude as the average difference (12.6%). Therefore this computation is supposed to give a representative impression of the differences, see Figure 8.

Table 3 Differences between measured and calculated surface elevations.

Surface elevation (H in cm)		Measured		ODIFLOCS		Difference (in %)
		max	min	max	min	
T=1.5	H=11.7	32.0	14.9	28.8	14.7	17.5
	H=15.0	35.0	15.0	31.0	14.5	17.5
	H=20.8	36.0	13.5	37.0	13.0	-6.7
T=1.8	H= 9.7	25.9	17.5	26.1	17.5	-2.4
	H=14.0	30.8	16.8	29.2	15.8	4.3
	H=19.8	34.5	14.5	33.0	14.0	5.0
T=2.1	H= 9.9	26.2	16.4	24.8	18.2	32.7
	H=14.2	30.7	15.0	27.0	16.8	35.0
	H=19.5	32.1	12.8	29.0	11.8	10.9
Average						12.6

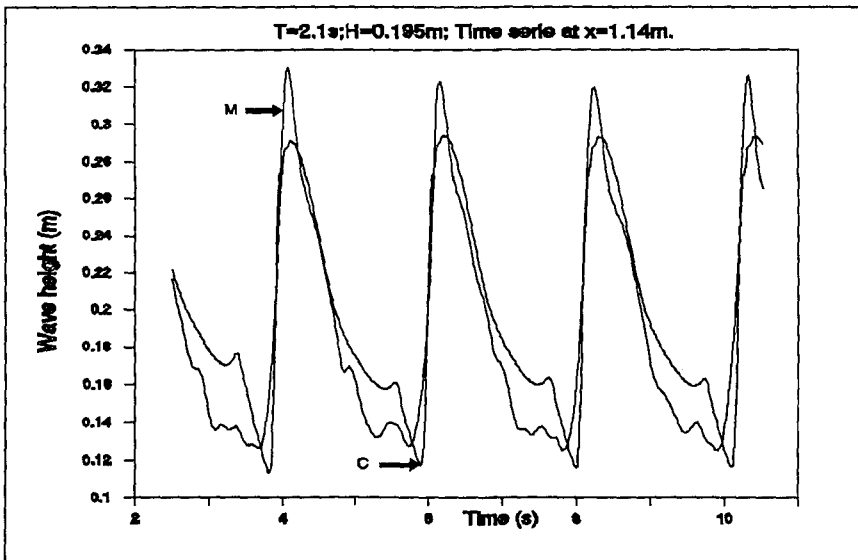


Figure 8 Comparison of the measured surface elevation with ODIFLOCS results.

The comparison of simulated depth-averaged velocities with the measured (point) velocities are summarized in Table 4 and Table 5. Two measurements in point 8 were not carried out. Differences for point 8 were to

be expected because this point is so close to the bottom that the influence of the boundary layer is present here. However, an underestimation of the measured velocities with an average of 15.3% (maximum uprush velocity + maximum downrush velocity) is not so bad regarding the assumptions made for comparisons. The velocities in the direction of the breakwater (max) show an average underestimation of 18.4%. The velocities in the opposite direction give an average underestimation of 8.4%.

Table 4 Differences between measured and calculated velocities in point 8.

VELOCITIES point 8 (H in cm)		Measured		ODIFLOCS		Difference (in %)		
		max	min	max	min	mx-mn	max	min
T=1.5	H=20.8	1.19	-0.80	0.92	-0.92	7.5	22.7	-15.0
T=1.8	H= 9.7	0.75	-0.44	0.52	-0.35	26.9	30.7	20.5
	H=14.0	1.12	-0.63	0.70	-0.60	25.7	37.5	4.8
	H=19.8	1.31	-0.82	0.90	-0.88	16.4	31.3	-7.3
T=2.1	H= 9.9	0.90	-0.62	0.62	-0.38	34.2	31.1	38.7
	H=14.2	1.15	-0.85	0.92	-0.66	21.0	20.0	22.4
	H=19.5	1.20	-1.02	1.18	-0.90	6.3	1.7	11.8
Average						15.3	18.4	8.4

Table 5 Differences between measured and computed velocities for point 10.

VELOCITIES point 10 (H in cm)		Measured		ODIFLOCS		Difference (in %)		
		max	min	max	min	mx-mn	max	min
T=1.5	H=11.7	0.38	-0.43	0.42	-0.40	-1.2	-10.5	7.0
	H=15.0	0.55	-0.55	0.52	-0.60	-1.8	5.5	-9.1
	H=20.8	0.90	-0.83	0.73	-0.88	6.9	18.9	-6.0
T=1.8	H= 9.7	0.34	-0.34	0.47	-0.33	-17.6	-38.2	2.9
	H=14.0	0.58	-0.56	0.64	-0.55	-4.4	-10.3	1.8
	H=19.8	0.94	-0.83	0.92	-0.90	-2.8	2.1	-8.4
T=2.1	H= 9.9	0.52	-0.54	0.57	-0.38	10.4	-9.6	29.6
	H=14.2	1.05	-0.90	0.77	-0.60	29.7	26.7	33.3
	H=19.5	1.42	-1.20	1.05	-0.90	25.6	26.1	25.0
Average						5.0	1.2	8.5

Comparisons with data from measuring point 10 give better results than for point 8. As mentioned before, the relatively higher differences for point 8 are probably due to the overshoot effect in the boundary layer. The average underestimation is now 5% (average of max. uprush velocity + max. downrush velocity) of the measured velocity. The average difference independent of whether an underestimation or an overestimation is found, is higher than 5%. The average (absolute) deviation of the sum of the maximum velocities in both directions is 11.1% (max-min). The average deviation is 16.4% in the direction towards the breakwater and 13.7% in the direction away from the breakwater. Table 4 shows that the underestimation is relatively high for the combination with high wave heights and long wave periods. For these cases, the boundary layer may be relatively thick. Measuring point 10 may be influenced by the higher velocities of the boundary layer. In general, the predicted velocities show differences with the measured velocities in the same order of magnitude as the differences which appear between measured velocities at different positions above the slope in the same cross section. The results prove that the numerical model ODIFLOCS predicts velocities rather good although differences of about 35% occurred sometimes. Figure 9 and 10 show the results of two comparisons. Figure 11 shows differences for a wave height of 0.099 m and a period of 2.1 s in measuring point 10. This combination gives a difference with the measurement of 10.4% which gives a representative impression of the deviations.

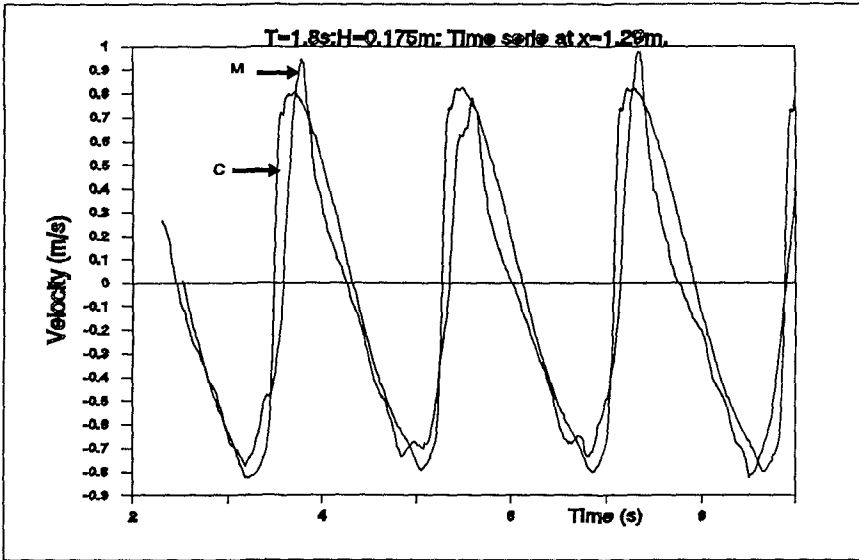


Figure 9 Comparison of the measured velocity with ODIFLOCS results - point 10.

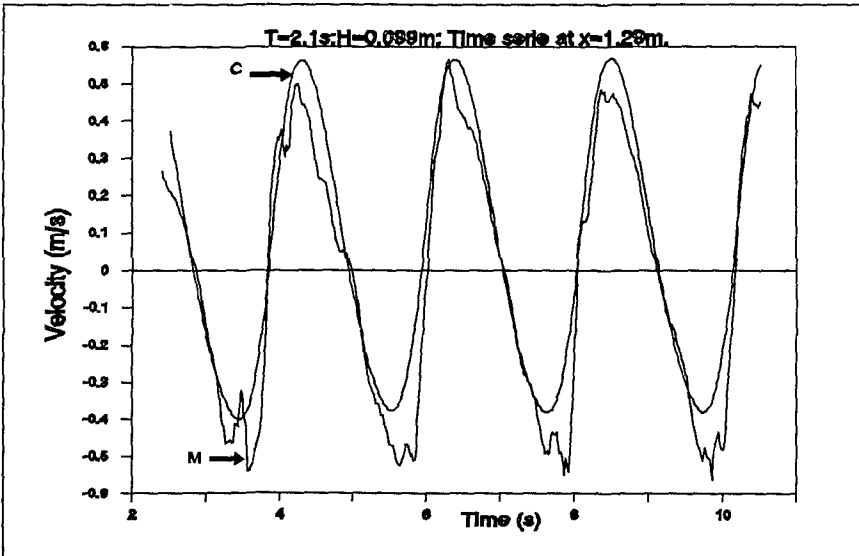


Figure 10 Comparison of the measured velocity with ODIFLOCS results - point 10.



### 4.3 Calculated extreme velocities

The comparison between the measured velocities and the calculated velocities give a fair agreement. Therefore, it is interesting to compute the

MAXIMUM VELOCITIES					
T	H	U <sub>max</sub>	U <sub>min</sub>	x-U <sub>max</sub>	x-U <sub>min</sub>
1.5	0.117	1.33	-0.52	-0.03	-0.03
	0.150	1.61	-0.69	-0.03	0.00
	0.208	2.01	-0.92	-0.03	-0.48
1.8	0.097	0.94	-0.50	-0.03	-0.09
	0.140	1.55	-0.71	-0.09	-0.06
	0.198	2.02	-0.93	-0.06	-0.69
2.1	0.099	0.87	-0.49	0.03	-0.12
	0.142	1.53	-0.70	-0.12	-0.09
	0.195	2.02	-0.95	-0.12	-0.81

Table 6 Maximum velocities with the positions along the slope.

found further down the slope. For these three cases local maximums occurred just below still water level.

maximum velocities appearing somewhere along the slope. The calculated maximum velocities show that the maximum upward velocities (U<sub>max</sub>) are higher than the maximum downward velocities (U<sub>min</sub>). These extreme velocities appeared to be just below the still water level. Only for the computations with the relatively high wave heights, the extreme velocities U<sub>min</sub> were

## 5 CONCLUSIONS

Although the measurements were carried out for "regular" waves, there were variations in the heights of consecutive waves and also in the maximum velocities for each wave.

On this background the conclusion from the few comparisons we have made between the ODIFLOCS calculations and the measurements are that there is a fair agreement between the measurements and the calculations except in measurement point 08. The velocities in measurement point 08 are as previously remarked possibly influenced by proximity to the stone cover layer.

## ACKNOWLEDGEMENT

This project was carried out under the European Communities Research Programme Marin Science and Technology, EC MAST. More specifically the project was a subproject under EC MAST Coastal Structures. The project was funded partly by EC and partly by the Norwegian Coast Directorate. We appreciate very much this financial support.

The authors are also grateful to the participants of the EC MAST - Coastal Structure project for discussions and comments during workshops.

## REFERENCES

Brandtzæg, A. and Tørum, A. (1966): A simple mathematical model of wave motion on a rubble mound breakwater front. Proceedings Xth International Conference on Coastal Engineering, Tokyo, Japan. ASCE.

Brandtzæg, A., Tørum, A. and Østby, O.R. (1968): Velocities in down-rush on rubble mound breakwaters. Proceedings XIth International Conference on Coastal Engineering, London, Great Britain. ASCE.

Gent, M.R.A. van (1992): Numerical model for wave action on an in coastal structures, Communications on Hydraulic and Geotechnical Engineering, ISSN 0169-6548 No. 92-6, Delft University of Technology.

Hedar, P.A. (1960): Stability of rock-fill breakwaters. Dr. Thesis No 26, Chalmers Technical University, Akademieförlaget Gunnverts, Goteborg, Sweden.

Hudson, R.Y. (1958): Design of quarry-stone cover layers for rubble mound breakwaters. U.S. Waterways Experiment Station, Research report No 2-2, Vicksburg, USA.

Iribarren, Cavanilles, R. (1938): Una formulae para el calculo de los diques de escollera, Panjes (1938).

Kobayashi, N., Otta, A.K. and Roy, I. (1987): Wave reflection and run-up on rough slopes. J. of WPC&OE, ASCE, Vol. 113, No 3.

Kobayashi, N. and Wurjanto, A. (1989): Numerical model for design of impermeable coastal structures. Research Report No CE-89-75, Center for Applied Coastal Research, Department of Civil Engineering, University of Delaware.

Madsen, D.S. and White, S.M. (1975): Reflection and transmission characteristics of porous rubble mound breakwaters. Report No 207, Ralph M. Parsons Laboratory, Department of Civil Engineering, Massachusetts Institute of Technology, Cambridge, Mass.

Sawaragi, T., Iwata, K. and Kobayashi, N. (1982): Conditions and probability of occurrence of resonance on steep slopes of coastal structures. Coastal Engineering in Japan, Vol. 25, 1982.

Tørum, A. (1992): Wave induced water particle velocities and forces on an armour unit on a berm breakwater. SINTEF Norwegian Hydrotechnical Laboratory, Report No STF60 A92104, ISBN 82-595-7417-3, 24 Sep 1992.

Van der Meer, J.W. and Breteler, M.K. (1990): Measurement and computation of wave induced velocities on a smooth slope. Proceedings of 22nd International Conference on Coastal Engineering, Delft, The Netherlands, 2 - 6 July 1990. ASCE.

## CHAPTER 127

# RUBBLE-MOUND BREAKWATER STABILITY : RESULTS OF IN-SITU MEASUREMENTS

ir. L. Van Damme <sup>1</sup>  
dr. ir. J. De Rouck <sup>2</sup>  
ir. D. Vermeir <sup>3</sup>

### ABSTRACT

When the construction of the Zeebrugge Outer Harbour was finished a full scale monitoring system was realized as a part of the global monitoring and inspection programme.

The monitoring system was designed to follow the water level- and the water pressure fluctuation inside and in front of the breakwater.

A general description is given of the instrumentation of a section of the NW-breakwater followed by a global overview of the data-acquisition system and off-line data processing.

Results from the primary analysis of the raw data of relevant storm measuring sessions are presented.

### 1. INTRODUCTION

In 1989 the construction of the breakwaters of the Zeebrugge Outer Harbour was finished. The breakwaters are of the rubble-mound type with open crest (without a concrete parapet wall). Figure 1 shows a typical cross-section. Some quantities involved in the construction of the breakwaters are approximately : willow mattresses : 1.1 Mm<sup>2</sup> ; quarry stones : 11 Mtons ;

---

<sup>1</sup> Ministry of Public Works, Coastal Department, Ostend, Belgium

<sup>2</sup> Harbour and Engineering Consultants HAECON N.V., Ghent - Ghent University, Belgium

<sup>3</sup> Harbour and Engineering Consultants HAECON N.V., Ghent, Belgium

concrete cubes 25 t - 30 t : 60,000 units ; Haros®  
15 ton : 11,000 units.

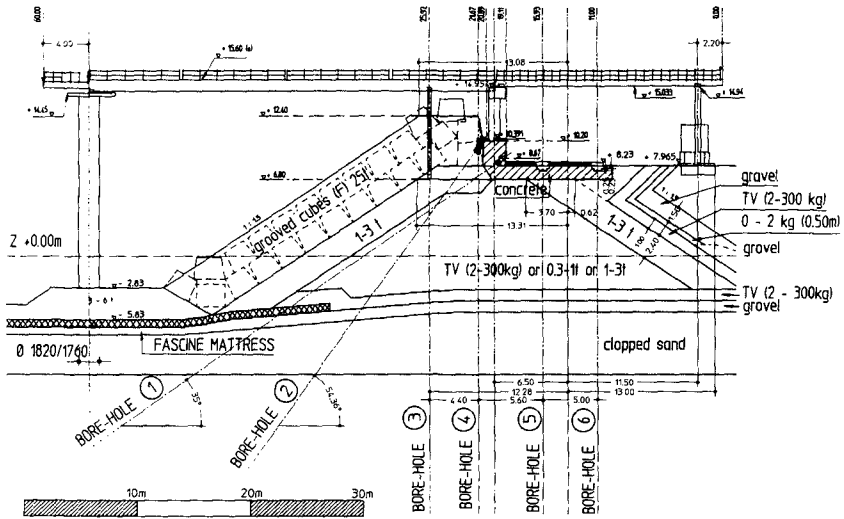


Figure 1. Cross-section of the breakwater

Once the construction of the breakwaters was finished, the principal organized an inspection, monitoring and maintenance programme of the new breakwaters. Such a programme is a standard rule in the management policy of the Ministry of the Flemish Community regarding major infrastructure works.

The monitoring and inspection programme is based on a complete design file and is composed of the following parts :

- (a) visual control of the armour layer, the crest of the breakwater and the filter construction next to the road ;
- (b) topographic measurements ;
- (c) bathymetric soundings of the different zones surrounding and inside the harbour ;
- (d) aerial remote sensing of the armour units ;
- (e) side scan sonar recordings of the underwater armour layer and the wave breaking carpet and berms ;
- (f) evaluation of the hydraulic design conditions on the basis of data collected by five measurement

- stations and seven wave-buoys in the surroundings of the harbour ;
- (g) evaluation of some design hypothesis by means of an instrumentation of a section of the NW-breakwater.

The last item of this programme, the NW-breakwater instrumentation, makes it possible to collect reliable prototype measurement-data. As such, it is an important step forward to a more reliable design of rubble-mound breakwaters.

## 2. AIM OF THE NW-BREAKWATER INSTRUMENTATION PROGRAMME

The whole infrastructure was designed to measure, to follow the water level- and water pressure fluctuation inside and in front of the breakwater. Knowledge of these phenomena are important on the one hand with regard to the stability of the armour layer and on the other hand with regard to the overall slope stability of the breakwater.

At several occasions the importance of water pressures inside the armour layer on the hydraulic stability of the armour units has been emphasized. To our knowledge less attention has been paid to the influence of the water pressure fluctuation on the overall slope stability. We will focus our attention to this item.

With regard to the water level fluctuation and especially the influence on the slope stability one has to distinguish between two loading situations :

- A. slope only subjected to tides (e.g. inner slope of a breakwater)
- B. slope subjected to tides and waves.

For case A one can assume that the pore pressure is hydrostatic with regard to the still water level (S.W.L.). Regarding the high permeability of the breakwater material the S.W.L. in the core will be the same as in front of the breakwater. The low water situation is the most critical one.

For case B (tide and waves) the water level in front of the breakwater varies over several meters in a few seconds. As a result hydrodynamic pore-pressures will be generated in the armour layer, under-layer and breakwater core. Harlow E.H. (1980), Barends F.B.J. et al. (1983) and others state that these hydrodynamic pressures played an important role in the destruction of some bigger rubble-mound breakwaters (such as Sines, Bilbao, Tripoli, Arzew, ...).

Literature review revealed only limited information with regard to research work on the water pressure fluctuation inside the breakwater : some researchers have tried to solve the problem using mathematical modelling, others worked on physical models.

Before discussing in more detail the results of the modelling we draw the attention on the set-up which occurs in the breakwater core (fig. 2). This set-up is predominantly caused by the geometry of the slope : inflow of water through AC (at maximum run-up), outflow through AB (at maximum run-down). This difference in surface, together with the longer way which has to be passed through by the water particles during outflow cause a surplus of water with an internal set-up of the water level as a consequence.

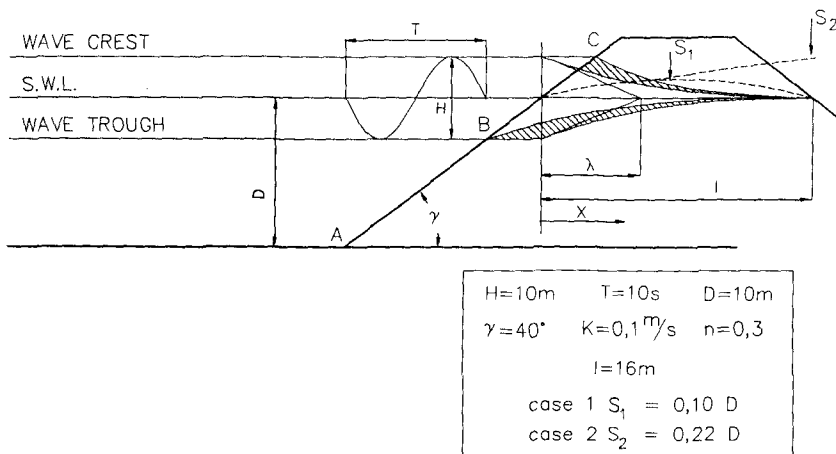


Figure 2. Internal set-up due to wave action (Barends, 1985)

#### a) Mathematical models

The water level fluctuation inside a breakwater is determined by the still water level S.W.L., the internal set-up and an internal wave. The S.W.L. is defined by the design conditions.

The internal set-up depends on the permeability of the materials and the width of the breakwater at the S.W.L. Barends F.B.J. (1985) finds a set-up up to 0.25 D (D = water depth in front of the breakwater). The set-up becomes important, especially when a sand fill has been placed at the inner side of the breakwater. Barends F. B.J. et al. (1983 and 1985) and Hannoura A.A. et al.

(1985) present the model HADEER : this model calculates the horizontal water movement in and through the coarse core-material, caused by regular waves acting on the seaward slope of the breakwater. The main results of the published data are :

- the finer the core material, the higher the set-up and the higher the damping (= the lower the wave amplitude at the leeside) ;
- the higher the incoming wave, the higher the set-up ; the damping is not influenced by the magnitude of the incident wave.

#### b) Physical models

Depending on the scale of the physical model one can distinguish models with normally applied scale (scale model less than 1,0 m high) and the so-called big scale models.

Considering scale models with normally applied scale, the most relevant results were found in Günbak A.R. (1976) and Simm J.D. et al. (1988).

The main results of Günbak's experiments are :

- mean water level inside the breakwater core is clearly higher than S.W.L. .
- the water level fluctuation decreases while moving to the centre of the core;
- the water pressure inside the core increases when finer core material has been used.

Simm J.D. et al. find :

- the set-up is proportional to  $H^2T$ , so closely related to the wave energy ;
- the damping of the fluctuation inside the core ;
- the pore pressure in the middle of the breakwater varies almost hydrostatically.

Considering the so-called big scale models, Burger W. et al. (1988 and 1990) report the results of tests carried out in the Groszen Wellen Kanal (G.W.K.) at Hannover. In the G.W.K. they have built a breakwater of ca. 4.00 m high on a sandbed of ca. 1,50 m thick.

When analyzing into detail one finds that the results of Burger et al. confirm some results of Simm et al. : the water pressure varies almost hydrostatically in the centre of the breakwater core.

To our knowledge only few attempts have been made to measure the pore water pressure fluctuation in a breakwater on site, e.g. Hakimi et.al. (1984) describe the instrumented breakwater at Jorf Lasfar (Morocco).

Only preliminary results are available. They find a rather high damping even in the seaward borehole, which is located close to the axis of the breakwater. However they have used open pipes instead of pressure transducers.

The foregoing emphasizes the lack of results, especially full-scale results, with regard to the water level and pore water pressure fluctuation inside a breakwater. By reviewing some literature we focussed on data which are useful to analyze the overall slope stability. We assume that a review focussed on the armour layer stability will lead to a comparable conclusion.

Yet, in 1983, at the opening session of the "Coastal Structures Conference" held in Washington D.C., A.W. Price stated that the common approach for the design of rubble mound breakwaters (based on mathematical and physical modelling) was not sufficiently funded on measurements on full scale operational breakwaters and that there was a serious lack of knowledge about the real phenomena of energy dissipation inside the different parts of the rubble-mound breakwater.

The main final objectives of the herein presented instrumentation programme are :

- 1) Acquire a better understanding of the geo-hydraulic phenomena and parameters affecting the overall stability and behaviour of the armour layer of rubble-mound breakwaters subjected to random wave attack.
- 2) Development of simulation techniques of these phenomena on physical models, leading to higher reliability in model tests.
- 3) Particular attention will be paid to the determination of the real forces acting on the amour units and the real hydraulic pressure set-up in the breakwater core and foundation layers.

These goals can't be achieved all at once. So in a first phase, we intend to collect data, interpret and implement these data in order to be able to provide basic full scale data for :

- the calibration of mathematical models ;
- the elaboration of a more comprehensive and adequate scaling method in physical modelling.

### 3. INFRASTRUCTURE

A measurement jetty of ca. 70 m long has been built on a steel pile at the toe of the breakwater and on a support on top of the breakwater (fig. 1).



Six boreholes have been drilled : four vertical boreholes (3, 4, 5 and 6) in the core and partially in the armour layer and two oblique boreholes (1 and 2) in the core, underneath the armour layer. Galvanized steel casings are placed in these boreholes. These casings are perforated in order not to disturb the overall permeability. In these casings part of the instruments are placed.

The casings reach the clapped sand. Doing this way it is possible to place pore water pressure transducers in the clapped sand underneath the breakwater toe. Knowledge of the variation of the pore water pressure in this area is very important for the overall slope stability.

The results of a measurement campaign and an evaluation of their influence on the overall slope stability can be found in De Rouck (1991).

A data acquisition system confined in an airconditioned 20' container is placed on the lee-side of the jetty at the landward side of the service road.

The steel pile and the bridge over the armour layer, is used to install measuring equipment.

#### 4. MEASURING EQUIPMENT

The main considerations kept in mind during the selection of instrument layout and instruments themselves were :

- good reliability to marine environment and wave action ;
- good accessibility for instrument installation and maintenance ;
- provision of reliable power supply.

The instrumentation was directed to the measurement and observation of the following phenomena :

- wave characteristics in front of the breakwater up to 250 m seaward, and at greater distances (ca. 3 km) ;
- tidal currents and orbital velocity (3 axes) at the toe of the armour layer ;
- water level and water pressure fluctuation at several points in front of the breakwater, in the armour layer and in the core ;
- air pressure in the upper part of the boreholes underneath the service road of the breakwater ;
- impact pressure on all faces of armour units ;
- video observation of the uprush and downrush of the waves on the armour layer.

The following equipment has been installed :

- wave-rider buoys : 2
- infra-red wave height sensor : 1
- pressure transducers : 11
- electrical analog step-gauge : 3
- electrical digital step-gauge : 1
- video camera : 2
- 3D ultrasonic current meter : 1
- temperature meter : 1

The location of the sensors is indicated on fig. 3.

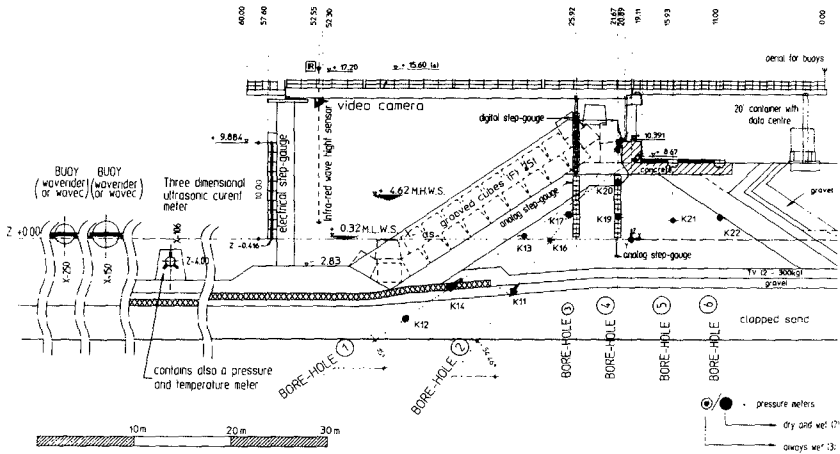


Figure 3. Location of the sensors in the measurement jetty

All instruments are controlled by a data acquisition system and scanned at variable frequencies, with a maximum of 50 for the dynamic wave impact on the armour units. The system permits a visual control of the signals and dumps the accumulated data into a hard disc memory. After a measuring session the data are transferred to tape cassettes for further off-line data processing.

Fig. 4 is giving a global overview of the data-acquisition system and the off-line data processing.

DATA-ACQUISITION  
SYSTEM FOR  
MEASUREMENTS IN-SITU

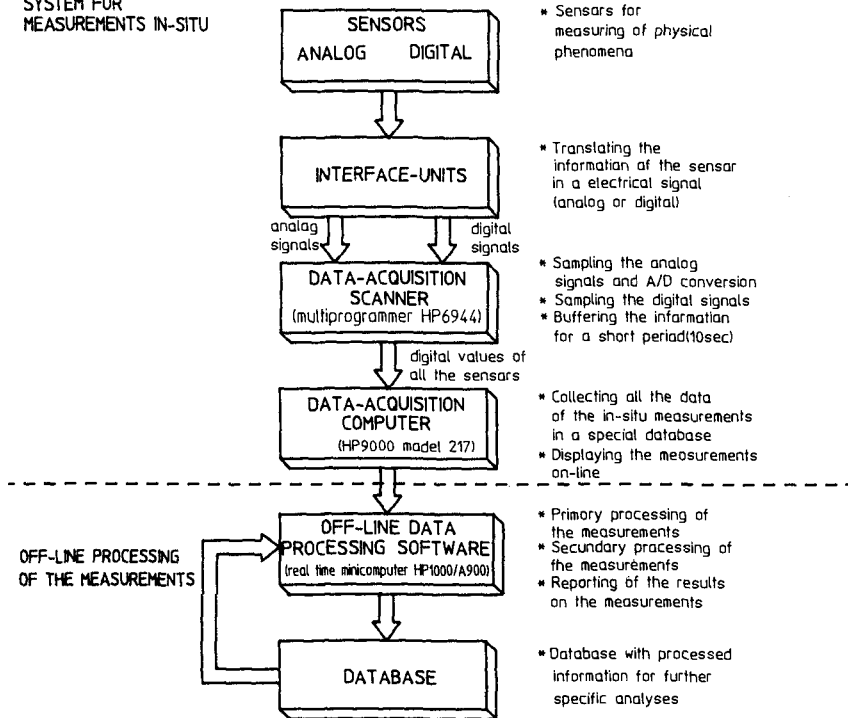


Figure 4. Global overview of the data-acquisition system and off-line processing

A basic software package has been established to reorganize the data in an appropriate database, to calibrate and scale the raw data, to produce graphical output (time plots and instant profiles) and to perform the specific analysis of some variations in selected significant time intervals. Experience has shown that this basic package has to be revised and upgraded continuously in parallel with the interpretation, further analysis of the results and orientation of the research.

In normal weather conditions a watch-dog programme is running continuously on the computer system to check all sensors. In order to be aware of major storm weather conditions a special prewarning procedure has been elaborated. The oceanographic hydro-meteo station at Zeebrugge is making special forecasts with a preavis

(stand-by) of 48, 24, 12 and 6 hours to the responsible scientist. At this moment the decision is taken to measure or not. In the positive case the programme is loaded for the start of a continuous measuring session during maximum 17 hours.

## 5. RESULTS

Relevant storm measuring sessions were performed during the storm periods of March 1988, March-April 1989 and January-February 1990.

These sessions did provide the raw data for a primary analysis which revealed very promising results. All data and results were stored in a well structured database and are partially reported. A primary interpretation did reveal some interesting phenomena, e.g. about the components of the waves in front of the rubble-mound breakwater and the damping of these waves in the core.

As an example : on 26.01.1990 measurements were carried out for several hours during a storm. An excerpt of the measurements is given on fig. 5. The wave height of the incident wave was 3.30 m. From this figure it can be concluded that the incoming wave is propagated into the core of the breakwater at least to sensor K19 which is installed in borehole 4. Even the signals registered by sensor K21 (borehole 5) and K22 (borehole 6) show some damped wave action.

To detect any damping of the waves with increasing distance from the slope of the breakwater the double amplitudes  $A_{Ki}$  of the measured waves at each location are compared with the wave height of the incident wave  $A_{inc.w}$ . The mean results are given in table 1 and are represented on fig. 6.

Sensor	$A_{Ki}$ (m)	$\frac{A_{Ki}}{A_{inc.w}}$
K13	1.90	0.58
K16	1.30	0.39
K17	1.27	0.38
K19	0.50	0.15
K21	ca. 0.30	0.09
K22	ca. 0.20	0.06

Table 1 : Damping ratio of sensors placed in the six boreholes

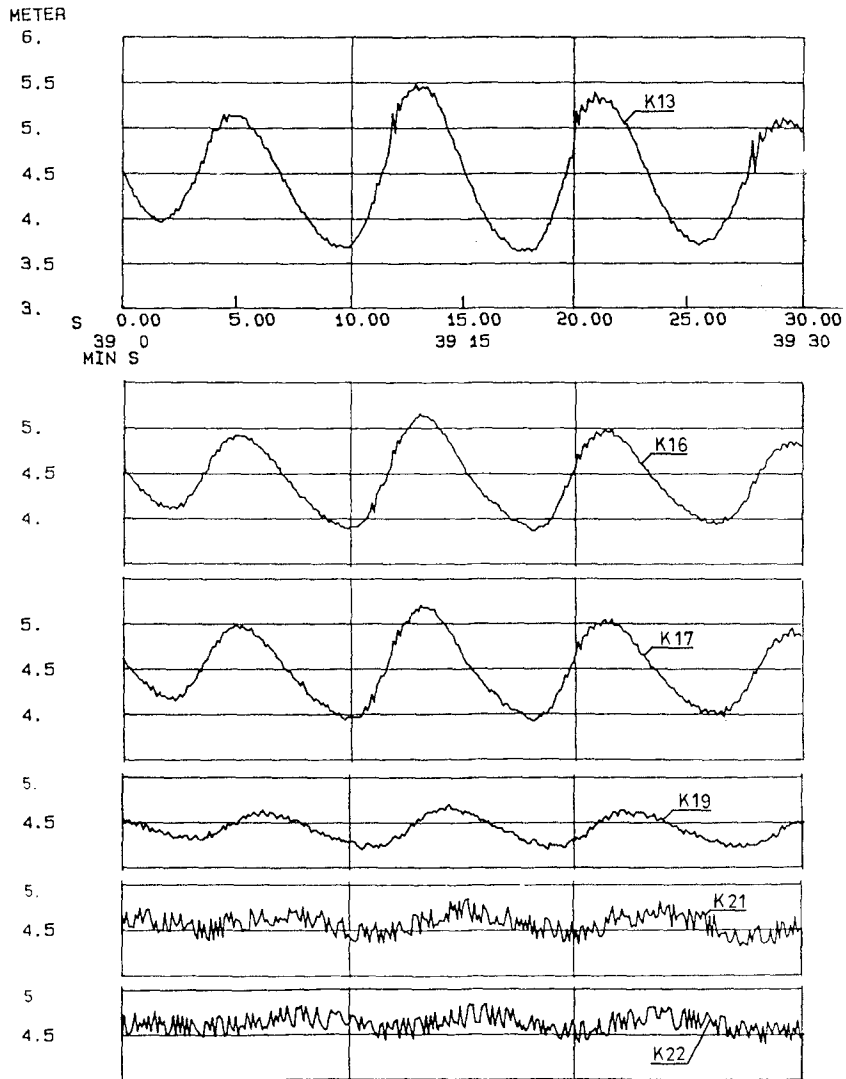


Figure 5. Example of propagation of an incident wave into the core of the breakwater

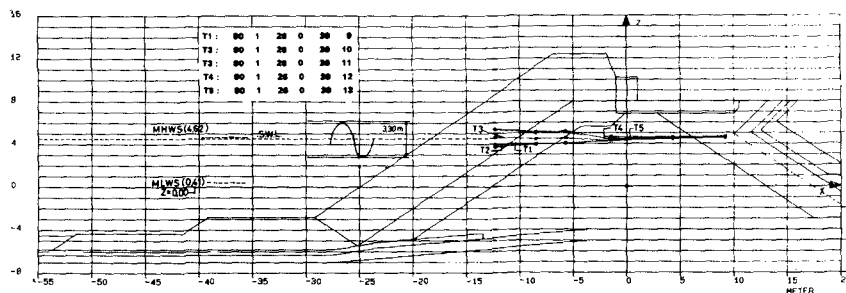


Figure 6. Cross-section of instrumented breakwater and example of wave damping

Pressure meter K13 is placed at the LW-level and approximately on the interface between the 1-3 ton filter layer and the core. At the location of K13 the amplitude has decreased to ca. 1.90 m, due to damping in the armour layer and underlayer.

## 6. CONCLUSIONS AND PERSPECTIVES

The first results of the breakwater instrumentation have proved the reliability of the system to collect full scale data. However more elaboration and interpretation is needed to clearly identify and extract the basic information.

The complexity of the phenomena and the considerable investments involved make it necessary to look for future international cooperation.

As the available infrastructure in Zeebrugge is unique, it can also be used for testing of marine instruments and measuring sensor packages actually under development.

## REFERENCES

Barends F.B.J., Van Der Kogel H., Uijtewaal F.J. and Hagenaar J. (1983) : West Breakwater Sines : Dynamic geotechnical stability of breakwaters. Proc. conf. on Coastal Structures, Arlington, 1983, pp. 31-44.

Barends F.B.J. (1985) : Geotechnical aspects of rubble-mound breakwaters. Proc. of the Conf. on Breakwaters, Institution of Civil Engineers, London, October 1985, pp. 155-174.

Burger W., Oumeraci H. and Partenscky H.W. (1988) : Geohydraulic investigations of rubble-mound breakwaters. Proc. 21st I.C.C.E., Malaga 1988, pp. 2242-2256.

Burger W., Oumeraci H. and Partenscky H.W. (1990) : Stresses in tetrapods : results of large scale model tests. Book of abstracts, 22nd I.C.C.E., Delft 1990, pp. 513-514.

De Rouck J. (1991) : De stabiliteit van stortsteengolfbrekers : Algemeen glijdingsevenwicht - Een nieuw deklaagelement. Thesis submitted to the Catholic University of Leuven in fulfillment of the degree of doctor in applied sciences, 525 pages.

Günbak A.R. (1976) : The stability of rubble-mound breakwaters in relation to wave breaking and run-down characteristics and to the  $\xi \cong \text{tg } \alpha \cdot T / \sqrt{H}$  number. Thesis submitted to the University of Trondheim, The Norwegian Institute of Technology, Division of Port and Harbour Engineering. In partial fulfillment of the requirements for the Doctor of Engineering Degree, June 1976, 230 pp.

Harlow E.H., (1980) : Large rubble-mound breakwater failures. Journal of the Waterway, Port, Coastal and Ocean division, A.S.C.E., Vol. 106, no. WW2, May 1980, pp. 275-278.

Simm J.D. and Hedges T.S. (1988) : Pore pressure response and stability of rubble mound breakwaters. Proc. on Breakwaters 1988, Thomas Telford Limited, London, pp. 47-57.

## CHAPTER 128

### A UNIVERSAL ANALYSIS FOR THE STABILITY OF BOTH LOW-CRESTED AND SUBMERGED BREAKWATERS

C. Vidal<sup>1</sup>,  
M.A. Losada<sup>1</sup>,  
R. Medina<sup>1</sup>,  
E.P.D. Mansard<sup>2</sup>  
G. Gomez-Pina<sup>3</sup>

#### Abstract.

Three-dimensional physical models of detached rubble-mound breakwaters have been built with separate Total Section, Front Slope, Crest and Back Slope sections. The stability responses of the armor units of this sections have been tested using irregular waves and different freeboards.

The stability curves relating the level of damage, the stability number,  $N_s$ , and the freeboard, have been obtained for each one of the different sections defined on the breakwaters. A distinct behaviour of the different sections have been found. The curves that plot the stability number against the freeboard for a given level of damage shows a minimum for an intermediate freeboard for the Crest and Back Slope sections. The total section stability response is a combination of the response of each one of its components. As a consequence, relative minimums of stability may appear for intermediate freeboards, due mainly to the contribution of the Crest failure to the total stability.

---

<sup>1</sup> Ocean & Coastal Research Group, Santander, Spain.

<sup>2</sup> National Research Council, Ottawa, Canada.

<sup>3</sup> Dirección General de Costas, M.O.P.T., Madrid, Spain.



## Introduction.

Low-crested and submerged breakwaters are designed to allow the transmission of a significant amount of wave energy due to overtopping. Conventional breakwaters have the traditional multi-layer cross-section. Reef breakwaters are low-crested or submerged breakwaters composed by a homogeneous rubble.

Because of the overtopping, the flow over the front slope section of the breakwater attenuates as the freeboard decreases and the weight of the armour stones on the front slope can be significantly reduced, as proposed by Van der Meer (1988). However, the crest and back slope armour units may need increased weight to withstand the wave forces caused by overtopping. The combination of increasing stability on the front slope and the decreasing stability on the crest and back slope can lead to stability minimums in intermediate positive freeboards, as suggested by Ahrens et al. (1990). Losada et al. (1992) used experimental velocity data and analytical values, obtained from Kobayashi et al. (1987, 1990), to show that the minimum stability of crest units occurs when the crest is at the mean water level. Experimental studies of the U.S. Army (1965), Raichlen (1972), Magoon et al. (1975) and Walker et al. (1976), suggested that the Back Slope section of low-crest breakwaters is more susceptible to damage than the seaward slope.

The aim of this paper is to establish that the different sections of the breakwater trunk have very diverse stability response to a sea state condition and that the behavior of the Total Slope section, (generally the only probed in two-dimensional model tests), reflects the stability response of each section component of the breakwater trunk. A complete description of this study is described in Vidal et al. (1992).

## Damage criteria.

The average erosion area,  $A_e$ , and the number of displaced units,  $N$  are usually used to describe the damage in the breakwater tests. The values of these variables do not give complete information of the state of damage of the breakwater, because they depend upon the geometry of the study sections. To relate the state of damage of a section of the structure with the values of these variables, it is necessary to define some general damage criteria.

Losada et al. (1986) defined three different degrees of armour damage that can be recognized by visual

assessment. These are: Initiation of Damage, (ID), Iribarren's Damage, (IR) and Destruction, (D). Recently, Vidal et al. (1991) proposed an additional damage level called Start of Destruction, (SD). These global damage definition will be used in the following. Relations between the S parameter and the damage level will also be given (see Table 3) in this paper for the different sections tested.

### Experimental set-up and data analysis.

#### Experimental set-up.

The physical tests were carried out at the Hydraulics Laboratory of the National Research Council, Ottawa, Canada.

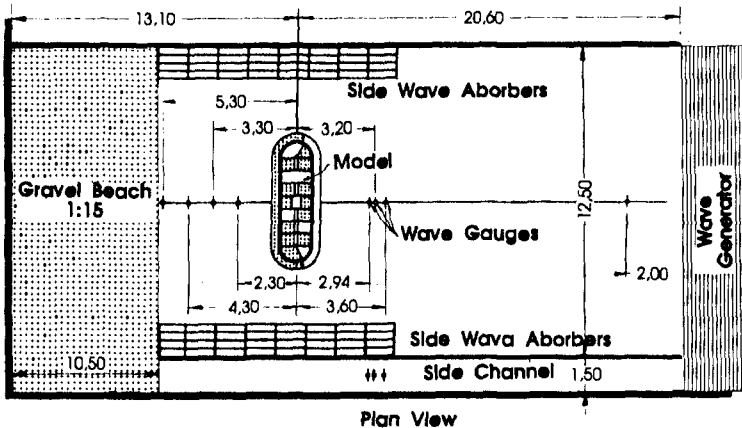


Figure 1.

The net area used in the facilities was  $34 \times 14 \text{ m}^2$ . Figure 1 shows a plan view of the experimental set-up. A 1.5 meter-wide channel was constructed on one of the sides of the basins. In the side walls near the model heads, five modules of upright wave absorbers were placed in order to dissipate the diffracted energy from the model. On the side opposite the wave board, a 1/15 sloped gravel beach was built in order to ensure an efficient dissipation of wave energy. Excluding the gravel beach, the bottom in all the testing area was kept horizontal. The models were placed with their longitudinal axis parallel to the wave board. A distance of approximately 5 m between the rear toe of the

breakwater and the front toe of the rear gravel beach was available to monitor the transmitted and diffracted wave energy.

Figure 2. shows a plan view of the models. A steel frame covering the upper 0.35 m of the breakwater was built. Using this frame, the structure was subdivided into six components, four trunk- and two head-sections. The trunk sections, 0.5 m long each, were: Front Slope, (FS), Back Slope, (BS), Crest, (C) and Total Slope, (TS). The remaining parts of the breakwater sections, which were not included in these sectors were covered with a steel mesh having square openings of 1x1 cm in size. This prevented any motions or damage to these parts without changing the flow characteristics through and over the structure.

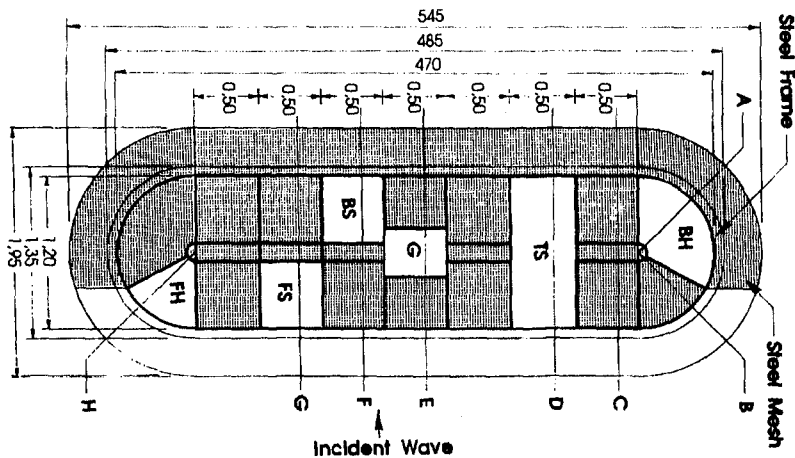


Figure 2.

The breakwater cross-section was composed of a permeable core armoured with two layers of rocks which were carefully selected in term of weight. Some main characteristics of the armour and core stones are provided in Table 1. In order to assure easy tracking of the armour units displacement, a colour coding was deployed. All the slopes of the trunk and heads were 1:1.5 and the crest width was equivalent to  $6 \cdot D_{h50}$  and therefore, approximately 0.15 m. The water surface elevations of sea states were measured at eleven different locations as shown in Figure 1.

Before and after every test profiling, VCR pictures and color photographs were taken in order to assess the

damage. During the wave generation period of each test, VCR pictures were taken to survey the evolution of the damage. The profiling of the breakwater cross-sections was performed using an electro-mechanic profiler. Nine profiles, 0.05 m apart, were taken for each trunk sector.

PARAMETER	ARMOUR	CORE
$D_{n15}$ cm	2.37	1.64
$D_{n50}$ cm	2.49	1.90
$D_{n85}$ cm	2.64	2.24
$\rho_r$ g/cm <sup>3</sup>	2.65	2.65
$P_s$	0.45	0.44

**TABLE 1: Model rubble characteristics**

The one hour time series were synthesized using the Random Phase Spectra Method. The synthesized time series had JONSWAP spectra with two different peak periods ( $T_p = 1.4$  and  $1.8$  s) having a peak enhancement factor of  $c = 3.3$  and variable zero-moment wave height  $H_{m0}$ .

TEST NUMBER	$d_s$ cm	$h_c$ cm	$T_p$ sec	$H_{m0}$ cm
1, 4, 5, 2, 3	40	40	1.4	5, 8, 8, 10, 13
13	60	60	1.4	15
9, 6, 7, 8	45	40	1.4	8, 10, 13, 15
14, 15	65	60	1.4	15, 18
12, 10, 11	38	40	1.4	8, 10, 12
16, 17	58	60	1.4	5, 18
18, 19, 20, 21, 22, 23	56	60	1.4	5, 8, 10, 13, 16, 19
24, 25, 26, 27, 28, 29	54	60	1.4	6, 8, 10, 12, 14, 16
30, 31, 32, 33	58	60	1.8	6, 9, 12, 15
34, 35	54	60	1.8	8, 11

**TABLE 2: Target parameters for the stability tests.**

A total of 35 tests were carried out. The relevant target parameters of these tests are summarized in Table 2. The damaged breakwater sections were rebuilt after each test.

#### Data analysis.

The wave data from the probes was subjected to spectral, SIWEH, zero crossing and probability distribution analysis. The data collected from the three probes in front of the sea side of the test structure was subjected to reflection analysis.

The global damage figure for each part of the breakwater was obtained from the visual inspection of the model after the test. The final figures for the relation between the global damage levels and the S parameter was obtained after the tests and is given in Table 3. To assess the number of units displaced during each test, still colour photographs and video pictures were taken before and after the test.

SECTION DAMAGE	TS	C	BS	FS
ID	1.5	1.0	0.5	1.0
IR	2.5	2.5	2.0	2.5
SD	6.5	5.0	3.5	4.0
D	12.0	10.0	---	9.0

**TABLE 3: Approximate 'S' minimum threshold values for the different definitions of damage and breakwater trunk sectors.**

If  $N_{ex}$  is the number of units displaced in a trunk sector of length  $X$  and porosity  $P_s$ , the following expression, was used to translate this number into an equivalent visual damage parameter,  $S_v$ :

$$S_v = N_{ex} \cdot D_{n50} / ((1 - P_a) \cdot X) \quad (1)$$

Using the data from the mechanical profiler the average profile for each section of the breakwater before and after each test was calculated and the eroded average area,  $A_e$ , was derived. The adimensional damage parameter ' $S_p$ ' was evaluated from this eroded area,  $A_e$ , using the expression:

$$S_p = A_e / (D_{n50})^2 \quad (2)$$

Using the indicated procedure, four values of  $S_p$  and  $S_v$ , corresponding to the four trunk sectors were obtained for each test.

### Discussion of stability results.

To represent an overall dimensionless sea state parameter, the stability number,  $N_s$ , was used:

$$N_s = H_s / (\Delta \cdot D_{n50}) \quad (3)$$

Where  $\Delta = (\rho_r - \rho) / \rho$ . It was decided to classify the results according to the values of the adimensional freeboard,  $F_d = F / D_{n50}$ , where  $F$  is the breakwater freeboard,  $F = h_c - d_s$ . For a given breakwater, water depth, time domain characteristics of incident waves and sea state duration, the damage should be a function of the stability number and the adimensional freeboard:

$$S = f(N_s, F_d) \quad (4)$$

For fixed damage levels,  $S = S_o$ , this function can be represented in a bidimensional plot relating the stability number for this damage level,  $N_{so}$ , with the freeboard:

$$S = f_o(F_d) \quad (5)$$

If this function has a minimum for a given freeboard, this freeboard will give the minimum stability for the corresponding section of the breakwater.

### **Comparison between damage levels.**

In the following plots of the stability results  $F_d - N_s$  for each one of the trunk sections will be presented. Each set of data will be related to a global damage level.

#### **- Front slope section 'FS':**

Figure 3 plots the stability results for the 'FS' section. The lines drawn at the right correspond to the limiting  $N_s$  values for each line, taken from Van der Meer's (1988) data of non-overtopped breakwaters.

The curves fitted to each set of data in Figure 3 are straight lines suggesting a linear relation between the freeboard and the stability number for each damage level. The minimum value for a given damage level always corresponds to the non-overtopped breakwater. The values of  $N_s$  for initiation of damage and destruction are closer for the positive than for the negative freeboard or that the section is more brittle for the positive freeboards. The

freeboard of minimum stability increases as the level of damage increases. This is because the minimum stability corresponds to the non-overflowing condition and if the wave height increases to attain bigger damages, the freeboard for non-overflowing must also increase.

### FRONT SLOPE SECTOR

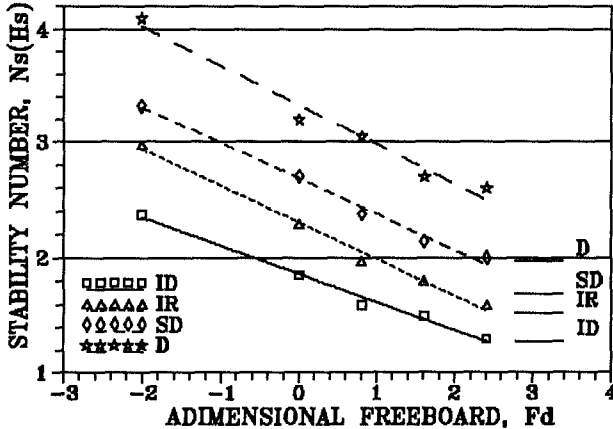


Figure 3.

Any damage in the breakwater that decreases the freeboard will cause better stability conditions in the 'FS' section. As the deformation of the 'FS' section due to damage also improves its stability, the result is that the 'FS' section in low-crested breakwaters is always in a stable condition (any damage increases the stability of the section).

#### - Crest section, 'C'.

Figure 4 depicts the results for the 'C' section. The curves that fit the data are 2<sup>nd</sup> order parabolas.

For a given damage level, the freeboard of minimum stability is found slightly below the zero freeboard. The minimum of stability moves somewhat to the negative freeboards as the damage level increases, indicating the effect of the increasing wave height. The slope of the curves for positive freeboard is higher than for negative freeboard. That implies that the 'C' section increases its stability faster with the increase of positive freeboard than with the decrease of the negative freeboard. When the freeboard is positive, the armour units removed from the

Crest section by the waves are mainly carried with the forward movement of the waves to the 'BS' section. When the freeboard is negative, a higher proportion of armour units are carried to the front slope with the backward movement of the waves, due to the increase of the symmetry of the flow over the crest as the freeboard decreases. The proportion of units that moves to the FS or to the BS depends also on the wave height.

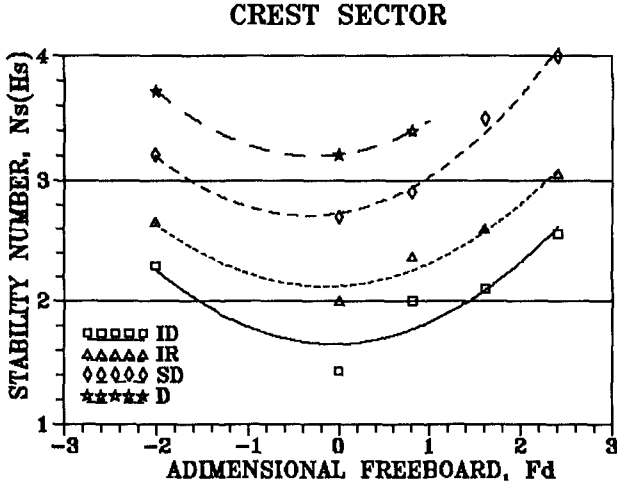


Figure 4.

Taking into account only the freeboard, the Crest section is in an unstable situation for positive freeboards: when the damage reduces the freeboard, the stability decreases. Figure 4 shows that the crest section is not more brittle for positive than for negative freeboards. The factors that compensate the decrease in stability due to de reduction of the crest height should be the increase of the width of the crest and the change in the crest slope that results from this reduction of crest height.

- Back slope section, 'BS'.

Figure 5 plots the results for the 'BS' section. Due to the high stability of this section, only the Initiation of Damage has enough information to show the complete trend. The fitted curve is a 2<sup>nd</sup> order parabola that has its minimum in a  $F_d$  value between 1 and 2. The other curves for higher levels of damage must have their minimums for higher freeboards and stability numbers. Extrapolating the trend



of the curves for Iribarren's Damage and Starting of Destruction, and assuming that they are parabolas it can be concluded that the a high brittleness could be expected.

The behavior of the 'BS' section can be explained by the characteristics of the flow over the armour. For negative freeboards, the waves go over the crest and break (backward and forward) on the water that protect the back slope armour units. When the crest emerges, the water jet starts to impinge over the back slope armour units and the stability continues to decrease because the flow works with gravity to move the armour units. With the crest emerged, a minimum  $N_s$  is necessary for the initiation of overtopping and the origin ( $S=0$ ) of the line  $N_s-S$  moves to higher  $N_s$ .

**BACK SLOPE SECTOR**

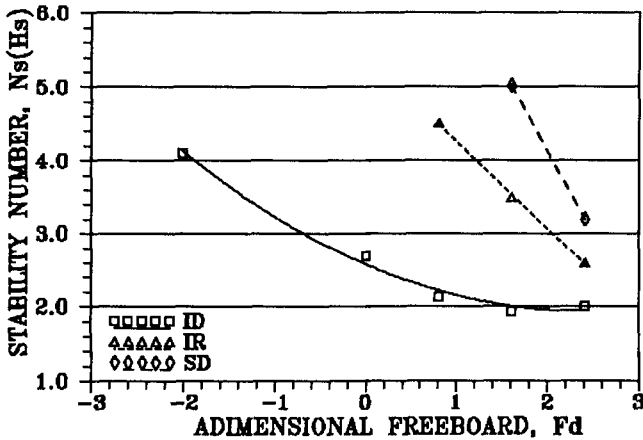


Figure 5.

The distribution of damage in the 'BS' section is more irregular than in the other sections. The shape and concentration of the water jet that impinges over the 'BS' creates areas where the damage is concentrated. Because of that, the values of  $S$  for a given damage level are smaller in this section than in the others (see Table 3).

**- Total slope section, 'TS'.**

Figure 6 shows the results for the 'TS' section. The horizontal lines at the right of the figure indicates the values of  $N_s$  for the different damage levels corresponding to the non-overtopping case, obtained from Van der Meer (1988). Instead of the straight lines of the 'FS' section

(Figure 3), the best fits are 2<sup>nd</sup> order parabolas with a minimum corresponding to the freeboard of non-overtopping. The interaction between the damage on the sections, particularly between the Crest and the Front Slope, produces relative minimums in the curve  $F_d-N_s$ . This complex behavior is the cause of controversy about which is the  $F_d$  of minimum stability.

TOTAL SLOPE SECTION

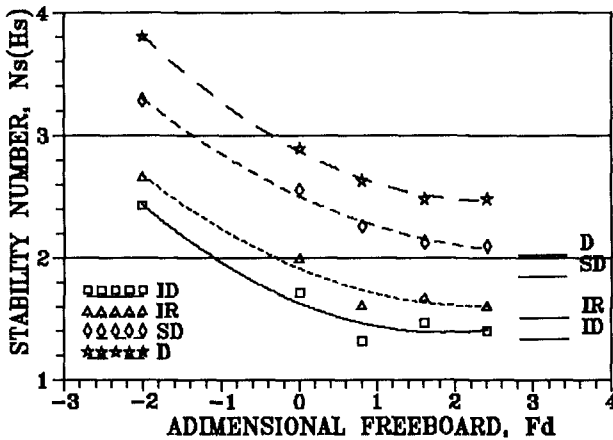


Figure 6.

The separation between the curves for the different damage levels is slightly minor in the positive freeboard range. This is due to the increase of brittleness for the positive freeboards in the Front Slope section. This brittleness is maximum for the non-overtopping case.

Comparison between sections.

The comparison between sections can be performed for fixed damage levels. As a representative example, the comparison for Iribarren's damage is discussed here.

Figure 7 plots the stability results  $F_d-N_s$  for Iribarren's Damage. Each set of data represents a different breakwater trunk section. The fitted curves are the same as used in Figures 3 to 6.

The 'FS' section is the least stable for  $F_d \geq 0.5$ . For  $F_d \leq 0.5$ , the 'C' section is the least stable of the trunk sectors. The Back Slope section is the most stable section of the breakwater for  $F_d \leq 2.0$ . For  $F_d \geq 2.0$ , the Crest section

is the most stable. For this reason, if the freeboard is high and the armour of the Crest is the same as the Back Slope, the damage can start in the Back Slope and desegregate the Crest.

### IRIBARREN'S DAMAGE

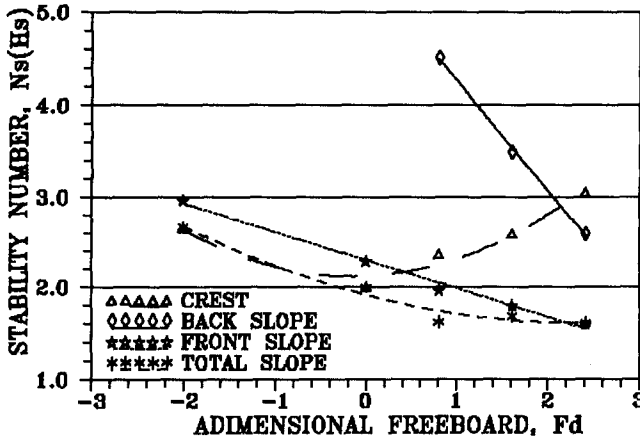


Figure 7.

The curve corresponding to the 'TS' section reflects the influence of the damage in all its components: for high positive freeboards, it behaves like the 'FS' section and for negative freeboards, it approaches the 'C' curve. Because the Crest section is more stable than the Front Slope for  $F_d \geq 0.5$ , the damage produced on the crest region of the 'TS' section is mainly caused by the spreading of the damage from the seaward slope to the crest. Several tests with positive freeboards have reported Destruction of the crest region of the 'TS' section while the Crest section had only Initiation of Damage. This damage on the crest region of the 'TS' was also attained for high positive freeboards due to the spread of the damage in the landward slope, because in these cases, the crest region is more stable than the back slope region.

### Conclusions and recommendations.

The damage in a low-crest or submerged breakwater is the response to the different flow and stability conditions that support the armour units in the different sections of the breakwater. The different sections of the breakwater have distinct stability responses to a sea state condition. The behavior of the Total Slope section, (generally tested

in conventional model tests), reflects the stability behaviour of each section component of the breakwater trunk. If the objective of the model tests is to optimize the armor weight to obtain a similar security condition in each part of the breakwater, the stability curves for each section should be determined.

The stability of low-crested rubble-mound breakwaters is very dependent on the freeboard. This implies that, any comparative evaluation of breakwater stability should be based on low levels of damage such as Iribarren's Damage or lower. Higher level of damage could affect the crest level of the structure, thereby, affecting the stability and performance characteristics.

More experimental and theoretical work is necessary to establish the influence of other variables held constant in these tests: slope angles, crest width, type of armour units, etc. The high stability of the Back Slope section has impeded the completion of the stability curves for high levels of damage.

#### **Aknowledgements.**

The authors are grateful to the Hydraulics Laboratory of the National Research Council of Canada for generously providing the facilities for these experiments and also to the Dirección General de Puertos y Costas, the University of Cantabria and the Dirección General de Investigación Científica y Técnica of Spain for their support of the work.

#### **Bibliography**

Ahrens, J.P. and Cox, J., 1990. "Design and Performance of Reef Breakwaters". Journal of Coastal Research. Spring 1990.

Kobayahi, N. and Otta, A.K., 1987. "Hydraulic Stability Analysis of Armor Units". ASCE, Journal of Waterway, Port, Coastal and Ocean Engineering, 113(2), 171-186.

Kobayashi, N., Wurjanto, A. and Cox, D.T., 1990. "Irregular Waves on Rough Permeable Slopes". Journal of Coastal Research, SI#7, 167-184.

Losada, M.A., Desire, J.M. and Alejo L.M., 1986. "Stability of Blocks as Breakwater Armor Units". Journal of Structural Engineering, ASCE, 112(11), 2392-2401.

Losada, M.A., Kobayashi, N. and Martin, F.L., 1992. "Armor Stability on Submerged Breakwaters". Journal of Waterway, Port, Coastal and Ocean Engineering. Vol 118, No.2, March/April.

Magoon, O.T., Sloan, R.L. and Foote, G.L., 1975. "Damages to Coastal Structures". Proc. 14th Conf. on Coastal Eng., ASCE, Copenhagen, 1975.

Mansard, E.P.D. and Funke, E.R., 1987. "On the Reflection Analysis of Irregular Waves". National Research Council of Canada, Hydraulics Laboratory Technical Report, TR-HY-017.

Raichlen, F., 1972. "Armor Stability of Overtopped Breakwaters". Journal of Waterways, Harbors and Coastal Engineering Division, Proceedings of ASCE, WW2, Vol. 98, May, 1972, Discussion of Paper 8138, pages 273-279.

U.S. Army Engineering District, Los Angeles Corps of Engineers, (1965). "Dana Point Harbor, Dana Point, California". General Design Memorandum No.1, September, 1965.

Van der Meer, J.W., 1988. "Rock Slopes and Gravel Beaches under Wave Attack". Doctoral thesis, Delft University of Technology. Also: Delft Hydraulics Communication No. 396.

Vidal, C., Losada, M.A. and Medina, R., 1991. "Stability of Mound Breakwater's Head and Trunk". Journal of Waterway, Port, Coastal, and Ocean Engineering, ASCE, Vol. 117, No. 6. Nov/Dec, 1991.

Vidal, C. and Mansard, E.P.D., 1982. "On the Stability of Reef Breakwaters". National Research Council of Canada. Hydraulics Laboratory Technical Report. In preparation.

Walker, J.R., Palmer, R.Q. and Dunhan, J.W., 1976. "Breakwater Back Slope Stability". Civil Engineering in the Oceans.

## CHAPTER 129

### THE MAINTENANCE OF HYDRAULIC STRUCTURES

prof. J.K.Vrijling, Delft University of Technology, The Netherlands.

H. Kuiper, Grabowsky & Poort Engineers, The Hague, The Netherlands.

R.E.Jorissen, Ministry of Transport, Public Works and Water Management, The Netherlands.

H.E. Klatter, Ministry of Transport, Public Works and Water Management, The Netherlands.

#### 1.0 INTRODUCTION

With the completion of the Eastern Scheldt storm surge barrier the Delta plan was realized. Herewith a period of the construction of large hydraulic engineering structures ended more or less. Therefore the interest in the optimal maintenance of the existing structures is growing and efforts are made to develop a theoretical basis for the planning of maintenance.

In the field of mechanical engineering considerable progress has been made. Maintenance is defined as consisting of two activities inspection and repair. Inspection implies the observation of the state of the structure and repair the restoration of the structure to it's original state.

Two main classes of maintenance are discerned: corrective and preventive maintenance. In this classification only the last subclass contains inspection besides repair. When a corrective maintenance strategy is applied, the structure will be repaired after failure. In a preventive maintenance scheme the structure will be repaired at specified intervals defined in time or operational hours before failure occurs. In a more refined strategy the state of the structure is inspected at such intervals. On the basis of the inspection result the decision to repair is taken.

The optimal cycle of inspection and repair is found by minimization of the present value of the sum of failure costs, inspection costs and repair costs. In these optimization models simple probability distributions for the time to failure as the exponential distribution are frequently applied. Some times this constant failure rate model is refined by the use of a "bathtub" curve for the failure rate.

Generally in mechanical engineering the failure rate is not related to the environmental conditions or loads. This paper studies if these theories can be applied directly to the maintenance of hydraulic structures like dikes, dunes, breakwaters, bottom protections or that further refinement is required.

## 2.0 THE MAINTENANCE OF HYDRAULIC STRUCTURES

The design of hydraulic structures is among others based on the analysis of the ultimate and the serviceability limit states (ULS and SLS respectively) that are typical for the structure at hand. Beside one class of ULS two classes of SLS can be discerned.

ULS models the failure of the structure under extreme loads  $S$

SLS describes the deterioration the resistance  $R$  of the structure under the ever present loads.

SLS analyses the functional performance of the structure under the ever present loads (e.g. limiting wave transmission for a breakwater.

When maintenance is studied the first mentioned type of SLS needs special attention. As the deterioration due to SLS leads in many cases to an increased likelihood of the occurrence of the ULS over the lifetime [3] and thus to failure. The deterioration may be regularly redressed by systematic repair. The regular heightening of dikes in the Netherlands to neutralize the effects of settlement and sea level rise is an example.

In hydraulic engineering the corrective maintenance strategy is generally not advised in view of the great risks involved when a dike, a breakwater or a bottom protection reaches an unsafe state due to ULS failure. The corrective maintenance strategy can only be applied to relatively unimportant parts of the structure that do not initiate overall failure. The maintenance of dike revetments in Holland gives an example. Every year during major storms minor parts of the dike revetment

are washed away. This poses no threat to the hinterland protected by the dike as a considerable reserve strength is hidden in the clay layers on which the revetments are mostly placed. After the storm the damage will be repaired before the next extreme high water occurs. In hydraulic engineering only preventive maintenance is advised in view of the high failure costs associated with the breach of a dike, the interruption of harbour activities due to breakwater failure.

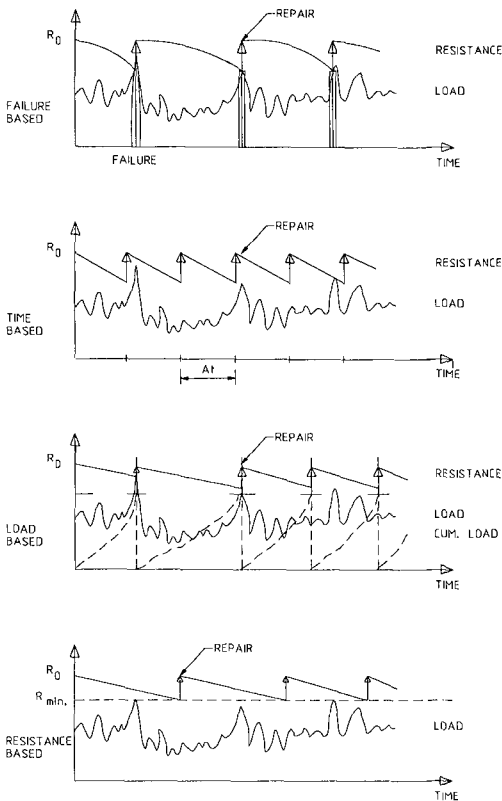


Fig. 1 Corrective maintenance and preventive maintenance governed by various triggers

Several types of triggering preventive maintenance can be imagined (Fig. 1). The simplest alternative is time based maintenance which implies that the structure is repaired at fixed intervals. Use based maintenance is a



second alternative. Here the structure is repaired after a certain number of uses. A spillway can be repaired after a specified number of spills.

Connected to this type is the load based strategy. Here repair is triggered if e.g. the sum or cumulative effect of the loads exerted on the structure over time exceeds a specified level. In the resistance based strategy the resistance or the state of the structure is inspected and repair is due when this variable falls below a specified minimum level.

Due to the spatial vastness of hydraulic structures, the high cost of inspection and the often poor resolution of the (underwater) observations a strategic approach to inspection is necessary. The decision to start a thorough inspection of the state of the structure is based on the outcome of an observation of variables that provide an indication of the state to be expected in case of a full inspection. The observation of these proxy-variables is called monitoring. Monitoring of the time, the use, the cumulative load or the state will precede an expensive and elaborate inspection of the exact state of the structure. This principle is shown in Fig.2.

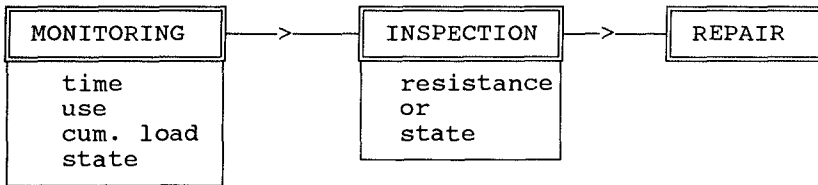


Fig.2 Preventive maintenance with monitoring and inspection

The steel gates of the Eastern Scheldt Storm Surge Barrier provide an example. The cumulative effect of the wave loads is monitored on a continuous basis. When the cumulation exceeds a certain level the nodes of the steel frame, supporting the water retaining surface of the gates, are inspected to measure growth of fatigue cracks.

The way to choose between corrective and preventive maintenance and the various strategies comprised under the latter is depicted in Fig 3. If the consequences of failure are grave preventive maintenance is preferred. The second question is if a description of the deterioration process is known. Without such a

deterioration model continuous monitoring and subsequent inspection of the state is the only viable solution. If a good deterioration model is available and if it contains the effect of loading on the process, the monitoring of strategies the cumulative

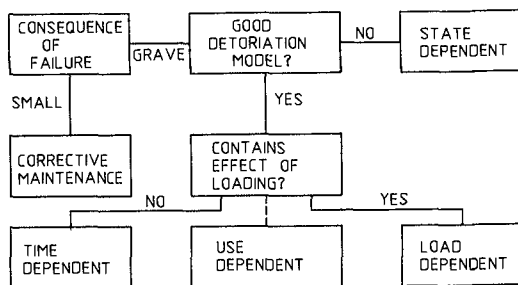


Fig. 3 Choice between maintenance strategies

the cumulative load as a precursor to full inspection of the state seems the right alternative. If there is no clear relation between the loads and the deterioration the monitoring of time forms the only basis for the scheduling of inspections. The use based inspection strategy lies between these extremes. Many specialists assume that deterioration models for various hydraulic structures do not yet exist. Some reflection however shows that with slight adaptation the equations used in the SLS analyses provide excellent deterioration models. The calculation of the settlement of a dike, of the erosion of a bottomprotection, of scour behind a structure, of long shore transport on a berm breakwater, provide examples. The scour behind the bottomprotection of a discharge sluice can be predicted as a function of time via the current velocity, the turbulence and the  $D_{50}$ , see [5]. The relatively slow scour process is however only a threat insofar it may cause an instability of the foundation of the discharge sluice via a slide flow (ULS). The slide flow is initiated by a steep upper slope of the scour hole as is shown in fig.'s 4 and 5. The steep upper slope may be redressed by the dumping of gravel or sand as a maintenance measure.

The value of inspection was analyzed for two types of SLS behaviour common in hydraulic engineering (Fig.6). The first type is characterized by a deterioration of the resistance  $R$  linear with time, as is the case with settlement and sea level rise. The derivative with respect to time is constant but uncertain. If an inspection is performed the derivative can be accurately estimated and a precise prediction of the resistance  $R(t)$  at some moment in the future can be provided. The value of the inspection is that the wide p.d.f. of  $R(t)$  existing before changes into a very narrow one after.

The behaviour of a dune under the continuous action of waves and wind, that is conveniently described by a random walk model [3], constitutes the second type. Now the inspection provides the position of the dunefoot at  $t_i$ . Due to the random walk character of the process the position of the dune foot at some future moment can only be predicted in terms of a fairly wide p.d.f.

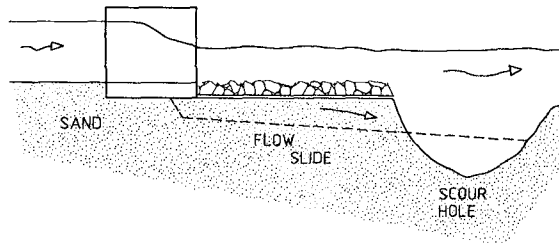
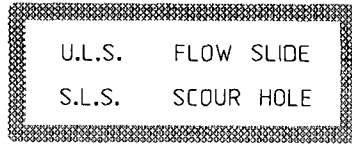


Fig. 4 Scour hole (SLS) leading to a flow slide (ULS) threatening the foundation

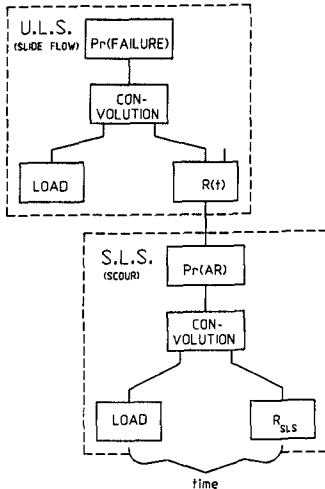


Fig. 5 Relation SLS-ULS

Quite narrower however than before inspection. So generally speaking inspection reduces the standard deviation of the prediction of the state of the structure in the future, for instance the planned moment of repair.

The optimal intervals of inspection and repair can be evaluated by minimizing the expected value of the present value of the total cost. The total cost comprises the cost of inspection, the cost of repair and the risk defined as the product of the probability of failure and the consequential damage  $D$ . Moreover the

expected value of the present value of the total cost has to be taken as the various costs are stochastic variables. In the literature decisions are based on

expected values neglecting the variance of the total cost. Most decisionmakers are however risk averse. Therefore the study of the variance might be of interest for future studies.

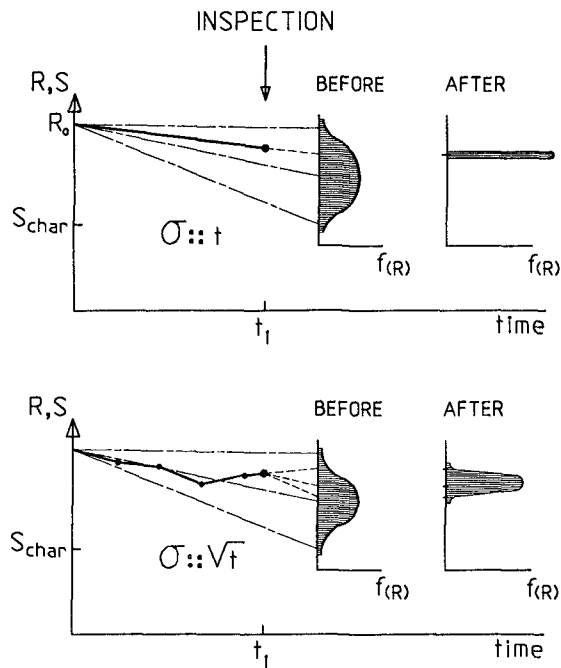


Fig. 6 The value of inspection for two types of degradation processes

### 3.0 EXAMPLES

Some examples that were solved successfully elsewhere where already mentioned. The linear degradation of the dikeheight by sea level rise and the regular heightening was studied in [2]. For the settlement of the dike, a logarithmic function of time, an analysis is given in [6]. The optimal interval of beach nourishment to combat the erosion of a dune, that can be modelled as a random walk process was studied in [3] and [7].

A fourth type describes the gradual deterioration of a bed protection or a berm breakwater that loses once in every year an uncertain amount of material due to the extreme load. Given the threshold character of the transport relation the transported amount is in many years zero and has some years a positive value causing erosion. The p.d.f. of the significant wave height and

the consequent p.d.f. of longshore transport is given in Fig. 7.

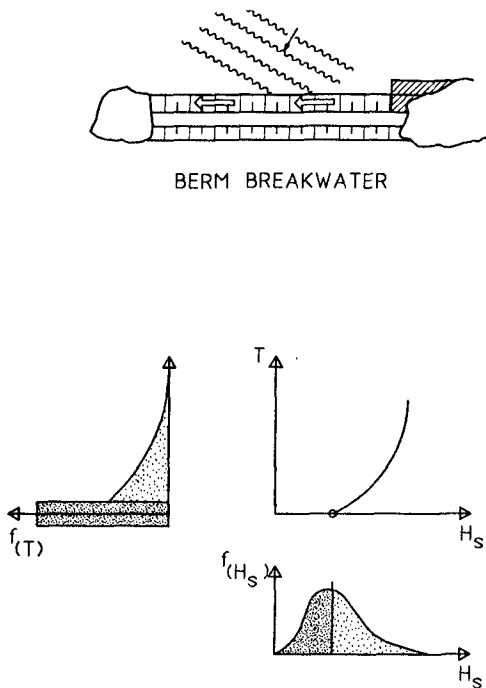


Fig. 7 Longshore transport  $T$

In this paper a similar process leading to the degradation of the bottom protection (BP) behind a discharge sluice will be studied. The BP consists of a sand tight cloth ballasted by a layer of rock. The layer of rock is gradually eroded over time by extreme discharges. This leads in due time to one of two failure modes (Fig.8): either the cloth is exposed to the current and fails or the weight of the rock layer becomes insufficient to withstand the uplift pressure, that is a fraction of the head difference, when the sluice is closed.

The uplift pressure follows a Gumbel-distribution with parameters of 1.55 and 0.78 kN/m<sup>2</sup> for mode and width.

The maximal current velocity  $U$  is normally distributed with a mean of 2 m/s and a standard deviation (s.d.) of 0.4 m/s.

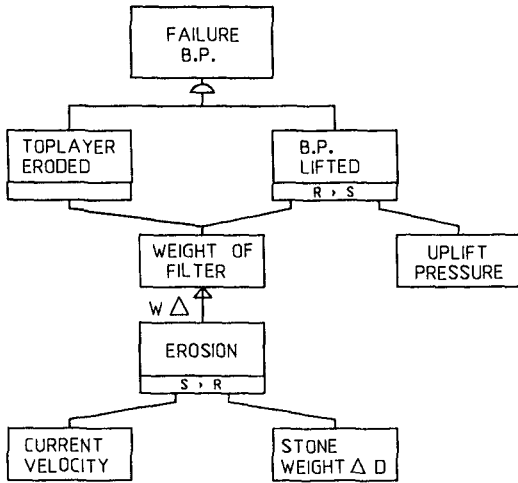
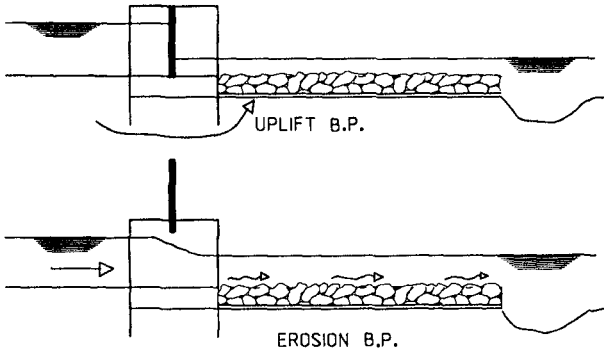


Fig. 8 The two failure modes of the bottom protection

The transport relation has the following form  $T = 1260 (U - 2)^2$  kg/m<sup>2</sup> per year for  $U > 2$  m/s and  $T = 0$  elsewhere.

The conditional p.d.f. of the transport per year if transport occurs is derived as:

$$f_T(X|X>0) = \frac{1}{\sqrt{5040 * X}} * e^{\frac{-X}{403.2}}$$

The probability of transport is 0.5 and equal to the probability of no transport. Numerically the mean and the s.d. of the transport per year are calculated at 101 and 226 kg/m<sup>2</sup>. The degradation as a function of time is the sum of the yearly erosion. The p.d.f. of the degradation after 5, 10, 20 and 40 year is given in Fig. 9.

Next the probability of uplift is calculated for every year and the probability of total erosion leading to the exposure of the filter cloth. In the area (I) near the sluice the latter is the deciding mechanism and in the areas further away (II & III) erosion forms the main failure cause. The  $p_f$  is given as a function of time in Fig. 10.

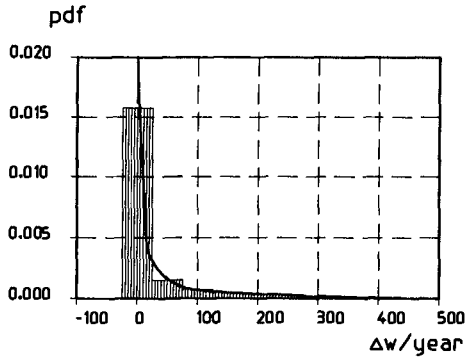


Fig. 9 The p.d.f. of degradation of the B.P. after 5, 10 20 40 years

$f(t)$  [1/year]

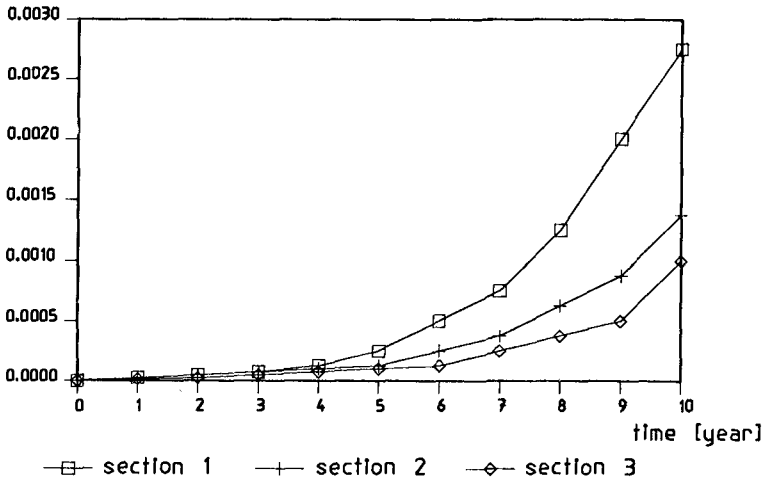


Fig. 10 The failure rate  $p_f$  as a function of time

The present value of the risk is written as follows:

$$\sum (D * f(t) * \frac{\Delta T}{(1+r)^t})$$

The cost of repair is based on the expected value of the erosion, which equals  $101 \cdot t$  kg/m<sup>2</sup> after  $t$  year for area I. The present value of the total cost of repair at  $t$  is given by:

$$\frac{C + c * (101 * t)}{(1+r)^t}$$

Now the present value of the cost of repairs and the risk between repairs has to be added over the life time of the structure. This defines the objective function that has to be minimised with respect to  $t$ , the repair interval.

For the numerical evaluation the following values have been assumed:

$$\begin{aligned} D &= 40 \text{ Mfl} \\ C &= 10 \text{ kfl} \\ c &= 100 \text{ fl.m}^2/\text{kg} \quad (\text{equal to } 50 \text{ fl/ton}) \\ r &= 0.04 \end{aligned}$$

The present value of the total cost as a function of the repair interval is given in Fig. 11. The optimal interval is 4 year if the three areas of the B.P. are repaired at the same time. The calculation was also performed for separate intervals for each of the three areas of the B.P. With the reasonable assumption that the mobilization cost  $C$  has to be paid only once when the repairs for the areas coincide and three times when not, the minimum cost is reached at 4 yearly interval for all areas. If inspection of the state of the B.P. is introduced the p.d.f. of the resistance  $R(t)$  will be replaced by the result of the inspection the deterministic value  $R_i$ . Ex ante the value of  $R_i$  is uncertain and follows the p.d.f. of  $R(t)$ . To find the value of the inspection under the assumption of instantaneous repair, we have to integrate over all possible results of the inspection with their respective probabilities given by the p.d.f. of  $R(t)$ .



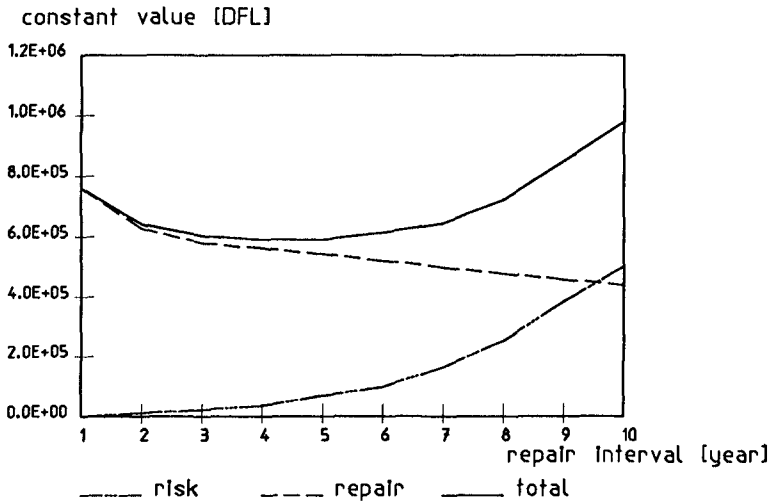


Fig. 11 Total expected cost as a function of the repair interval

#### 4.0 CONCLUSIONS

The maintenance theory developed in mechanical engineering has to be adapted and refined to account for the typical problems of hydraulic engineering. A probabilistic approach proves to be highly effective and necessary in the approach of the problem. Moreover the serviceability limit state (SLS) equations used in the design of hydraulic structures may be easily adapted to serve as degradation models.

The advantage of the use of rigorous maintenance models is that the risk of deferred repair and the value of inspection can be objectively assessed. Therefore the theory can assist managers of coastal structures in the definition of optimal maintenance strategies.

However all decisions in the described model are based on expected values of the costs. The limitations imposed by the omission of the variance of the cost has to be further explored.

#### REFERENCES

- [1] Hahn, G.J., Shapiro, S.S., Statistical models in Engineering, Wiley & Sons, New York, 1967.

- [2] Vrijling, J.K., Beurden, J. van, Sea level rise; a probabilistic design problem, Proc. 22d ICCE, Delft, 1990.
- [3] Bakker, W.T. and Vrijling, J.K., 1980. Probabilistic Design of Sea Defenses, Proc. 17th ICCE Sydney, 1980.
- [4] Vrijling, J.K., 1991, Berm breakwater design; the longshore transport case, a probabilistic approach, Coastal structures and breakwaters '91, London.
- [5] Jorissen R.E. and Vrijling, J.K., Local scour downstream hydraulic constructions, IAHR XXII congress, 1989, Ottawa
- [6] Kuiper, H., Onderhoud in de waterbouwkunde, Delft University of Technology, 1992. [In Dutch]
- [7] Verhagen, H.J., Method for artificial beach nourishment, Proc. 23rd ICCE Venice, 1992

## CHAPTER 130

### Finite Element Simulation of Wave-Induced Internal Flow in Rubble Mound Structures

H. WIBBELER<sup>1)</sup> and H. OUMERACI<sup>2)</sup>

University of Hannover, Sonderforschungsbereich 205,  
Coastal Engineering, Hannover/Germany

#### Abstract

A Finite Element Model for the simulation of the wave-induced flow in a porous structure is presented and applied to three types of structures: homogeneous vertical structure, homogeneous trapezoidal structure and traditional multilayered rubble mound breakwater. The obtained results are related to the motion of the phreatic surface, the pore pressure histories and distributions within the structure as well as to the internal velocity field induced by wave action. The problems to be solved in order to get an improved numerical model are discussed.

#### Introduction

Rubble mound breakwaters still represent the most commonly used type of structure for the protection of coastal areas, harbours and further facilities against wave action. The traditional approach to study the stability of such structures still consists in the use of physical wave models with scales ranging from 1:30 to 1:50. For such scales the REYNOLDS numbers of the wave-induced flow in the core material of the model are generally smaller than the critical value  $Re_D = 10^4$ . For lower  $Re_D$ -values scale effects due to higher viscous forces start to occur. The latter will in turn affect the flow field in the armour and underlayer, so that the hydraulic stability may also be subject to scale effects. Due to the oscillatory nature of the flow and to the large variation of the hydraulic gradients, the tentative approach using distortion factors in the FROUDE scaling of the core material is not satisfactory. On the other hand, the performance of large-scale model tests in a wave flume is too costly and time consuming when used for design purposes or basic research including a large variation of the relevant parameters. For this reason, a research strategy has been adopted which consists in using numerical codes calibrated by experimental data obtained from a limited number of large-scale model tests (WIBBELER / OUMERACI, 1992).

---

1) Dipl.-Ing., Res.Eng., Sonderforschungsbereich 205, Callinstr. 34

2) Dr.-Ing., Senior Researcher, Franzius-Institut, SFB 205, Nienburger Str. 4  
3000 Hannover 1 / Germany

These calibrated codes are used as research tools for further parameter studies, the final objective being, however, the development of analytical solutions. Since the early seventies several models for the simulation of the wave-induced flow on and in rubble mound breakwaters have been developed. Both analytical solutions and numerical models were described. Despite the relatively high number of existing numerical models, no model exists which has been calibrated by reliable data covering all relevant flow phenomena involved. This paper will first briefly review some of the mathematical/numerical models available and then discuss the results of a Finite Element Model developed at the University of Hannover for the simulation of the wave-induced flow in a rubble mound breakwater.

### Review of Existing Mathematical/Numerical Models

An exhaustive review of the existing mathematical/numerical models for the simulation of wave-induced internal flow in rubble mound structures would be beyond the scope of this paper. Therefore, only a very brief review is given below. As illustrated by Fig. 1, one may distinguish analytical and numerical models. The latter are in turn divided in a) Finite Difference Models (FD), b) Finite Element Models (FE) and c) Hybrid Models using Finite Elements and Finite Difference Techniques (FD/FE).

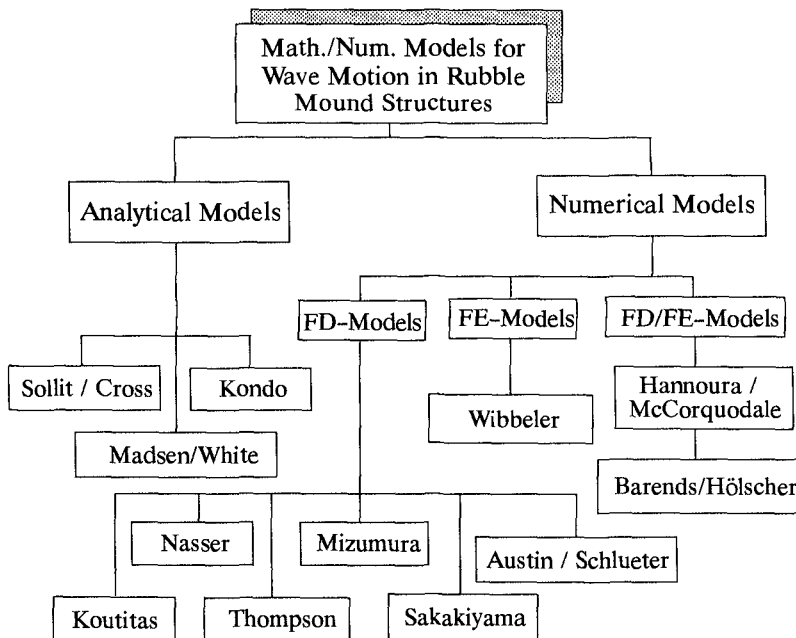


Fig. 1: Existing Models for Wave Motion in Rubble Mound Structures

However there are still a number of problems to be solved in order to come up with a reliable model which can properly simulate the interaction between waves and rubble mound structures, especially the wave-induced internal flow. Among these problems the following may be mentioned:

a) *Description of the external flow field:* The present knowledge on the wave kinematics in front of a rough permeable structure is almost nil.

b) *Interaction between external and internal flow:* Almost nothing is available on the physical processes involved at the boundary between two layers of different porous materials (discontinuities) and their mathematical formulation (coupling problem).

c) *Energy dissipation on the slope:* The question on how to account for this dissipation in case of breaking is still an unresolved problem.

d) *Porous flow equation:* It is still not clear whether a FORCHHEIMER-type equation will apply for the flow in the armour layer and filter layer.

e) *Air entrainment:* The air entrained by waves breaking on the structure is expected to strongly affect the internal flow. No attempt has yet been made to account for this effect in a numerical model.

f) *Internal stability of the porous medium:* Generally the porous matrix is assumed to be fixed. Actually, however, this is not the case.

As a conclusion, there is still a long way to go before a reliable numerical model can be developed which can account for all these aspects. Meanwhile, a relatively simple Finite Element Model for the simulation of wave-induced internal flow in a rubble mound breakwater has been developed at the University of Hannover. This model and some of the computational results obtained so far are discussed below.

### **Description of the Finite Element Model**

#### **Porous Flow Equations**

For the description of the fluid flow within the rubble mound structure non-linear constitutive equations of the FORCHHEIMER-type :

$$i = (a + b|v|) v \quad (1)$$

or of the exponential-type :

$$i = c |v|^{m-1} v \quad (2)$$

can be used, where :

- $v$  velocity vector
- $a$  FORCHHEIMER constants
- $b$  FORCHHEIMER constants
- $i$  hydraulic gradient ( $i = -grad h$ )
- $c, m$  constants of exponential law

The FORCHHEIMER constants and the constants of the exponential law are mainly dependent on the grain size and shape, the roughness of the grain surface and the porosity of the material. These constants have to be determined experimentally. Such experimental studies have been performed for instance by (SHIH, 1990) and (HANNOURA / McCORQUODALE, 1985). From the latter study the following equations can be evaluated:

$$a = 70.0 \frac{\nu}{g n \delta^2} \quad (3)$$

$$b = 0.54 \frac{(0.5 + 0.5f_r)}{g \sqrt{n} \delta} \quad (4)$$

$$\delta = \frac{n d}{6(1-n)S_f} \quad (5)$$

- $a, b$  FORCHHEIMER constants
- $d$  particle diameter
- $\delta$  effective pore hydr. diameter
- $f_r$  roughness factor
- $g$  acceleration due to gravity
- $n$  porosity
- $\nu$  kinematic viscosity
- $S_f$  particle shape factor

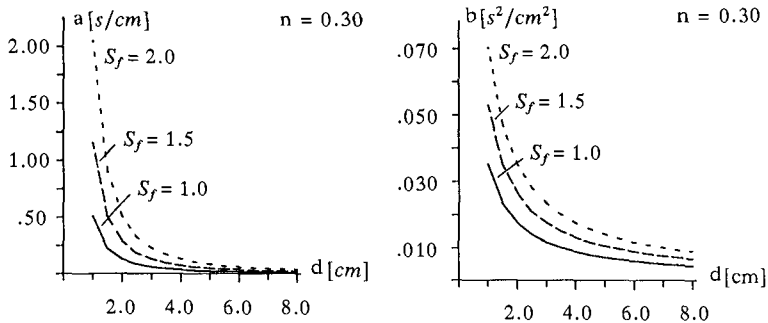


Fig. 2: Effect of Size and Shape of Grain Particles on FORCHHEIMER constants

Furthermore, the velocity vector  $v$  is expressed as a function of the permeability tensor  $K$ . Using a relative permeability coefficient  $k_r$ , the following general linearized constitutive equation is obtained which is used in the computations to evaluate the velocity in the porous media:

$$v = - k_r k_n K i \quad (6)$$

where  $k_n$  is a non-linear permeability coefficient.

### Finite Element Formulation and Evaluation of the Phreatic Surface

In the present Finite Element Model the piezometric heads  $h$  are used as degrees of freedom ( $h$ -model). The transient motion of the phreatic surface, which is defined by the condition  $p=0$  (pressure head), is described by the following differential equation:

$$\phi \gamma \frac{\partial S}{\partial p} \frac{\partial h}{\partial t} - k_r k_n \operatorname{div} ( K \operatorname{grad} h ) - q = 0 \quad (7)$$

$\gamma$	specific weight	$k_r$	relative permeability
$h$	piezometric head	$\phi$	porosity
$K$	permeability tensor	$q$	discharge
		$S$	saturation

A Finite Element formulation of Eq. (7) leads to following equation:

$$\left( \frac{1}{\Delta t} S_e + \Theta K_e \right) h_{n+1} = \left( \frac{1}{\Delta t} S_e - (1 - \Theta) K_e \right) h_n - Q \quad (8)$$

with:

		$B$	derivatives of shape functions
		$\Delta t$	time step
$K_e = \int_{\Omega} B^T K B \, d\Omega$	(9)	$K_e$	element matrix
		$N$	shape functions
$S_e = \int_{\Omega} S_0 N^T N \, d\Omega$	(10)	$Q$	vector of nodal flows
		$S_e$	saturation matrix

Eq. (8) is solved by using a  $\Theta$  - method.

The position of the phreatic surface must be evaluated by an iterative procedure. For these calculations, the domain of the structure is divided into two parts. These are the wet part beneath and the dry part above the phreatic surface. During the iteration, the permeability of the structure above the phreatic surface is set to a very small value, so that it behaves as almost impermeable. In each iteration step the element matrices must be calculated by using the new position of the phreatic surface. This procedure has to be continued until the position of the phreatic surface remains constant. The convergence of the iteration can be improved by use of a transition area between the permeable and impermeable domain (RANK / WERNER, 1986). This transition area is also used to calculate the saturation matrix  $S_e$ . Matrices of elements which are intersected by the phreatic surface have to be calculated by a special integration method (WIBBELER / MEISSNER, 1992).

### The Finite Element Mesh

One of the most important steps of a Finite Element calculation is the discretization of the structure. For the present model, an automatic mesh generator is available. This mesh generator is able to create meshes according to the different layers of the breakwater and the position of the phreatic surface. The reliability of the results can be controlled by the evaluation of an error estimator (MEISSNER / WIBBELER, 1990). The distribution of the approximation error allows the mesh generator to create an improved mesh either by a complete remeshing or by local refinements (adaptive discretization).

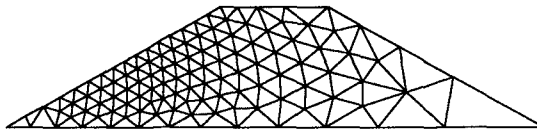


Fig 3: Adaptive Discretization of a Breakwater

### Simulation of Wave Motion

The wave motion in front of the structure and at the seaward slope of the breakwater can be described by using any wave theory or a numerical model as well as by using the wave data directly recorded from hydraulic model tests. The pressure at each boundary slope is prescribed by the function  $h(t)$  where  $h$  denotes the piezometric head (Fig. 4).

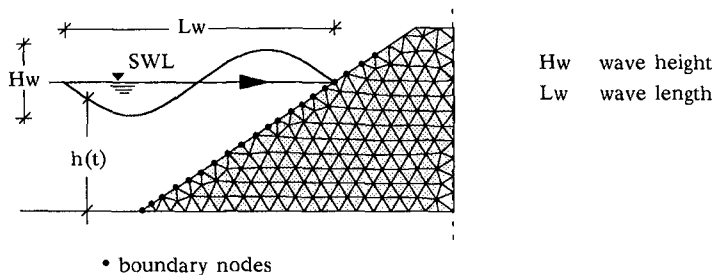


Fig.4: Simulation of Wave Motion

### Flowchart of the Finite Element Model

The main components of the present Finite Element Model are described by the flowchart in Fig. 5.



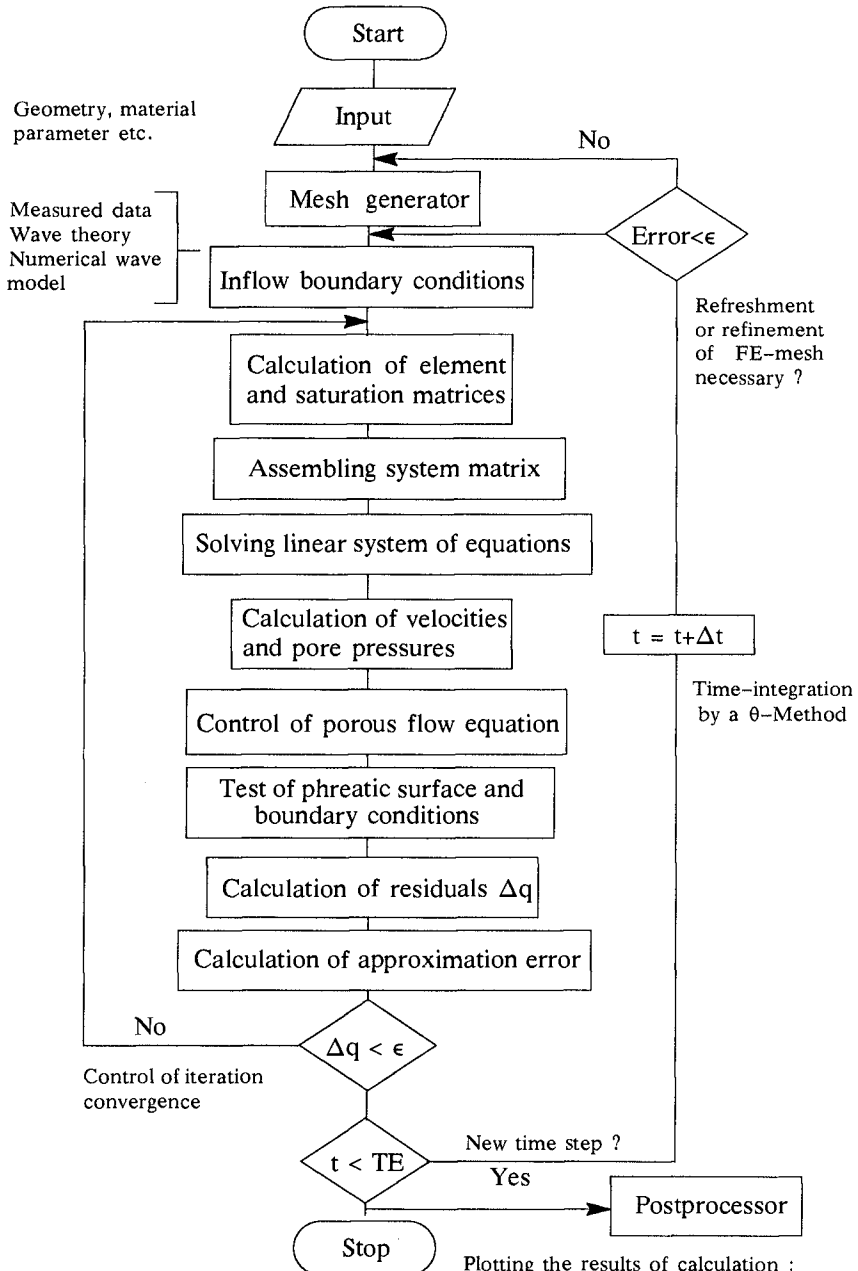


Fig. 5: Flowchart of the Numerical Model

Plotting the results of calculation : Velocity vectors, contours of pore pressure, pore pressure histories etc.

### Computational Results

The simulation using the FE-Model described above is demonstrated on three types of porous structures: on a homogeneous vertical structure, a homogeneous trapezoidal structure and a multilayered traditional breakwater.

#### a) Homogeneous Vertical Structure

The actual vertical structure and its FE-discretized counterpart are shown in Fig. 6.

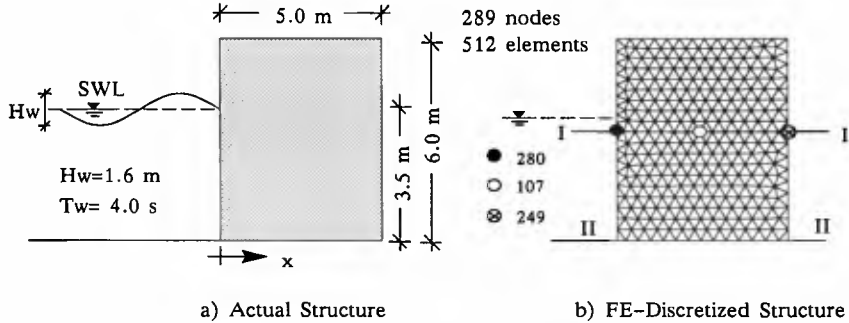


Fig. 6: Homogeneous Vertical Porous Structure

The instantaneous velocity fields and isobars at four successive time steps  $\Delta t = T_w/4$  ( $T_w = \text{Wave Period}$ ) are shown in Fig. 7, providing a good insight in the flow processes within the structure during a wave cycle.

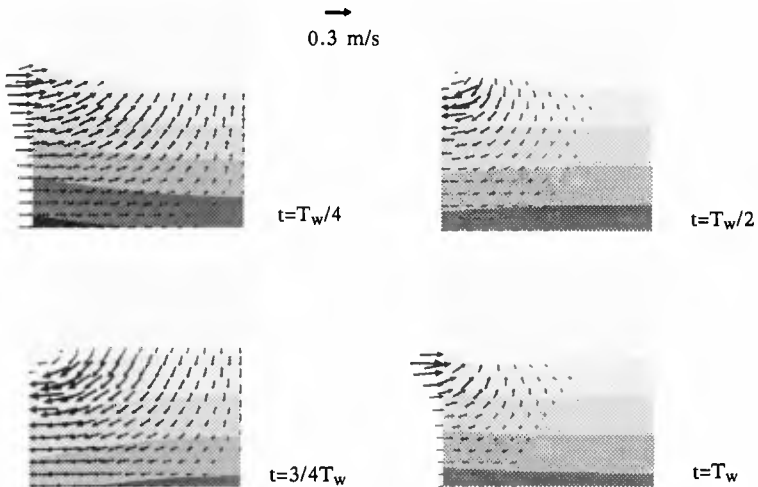


Fig. 7: Velocity Fields and Isobars within the Vertical Structure  
( Wave Conditions see Fig. 6)

Pore pressure histories at two different elevations under still water level are given in Fig. 8, showing a) the rate at which the wave motion is damped at different levels as the wave propagates into the structure and b) the phase shift of the pressure histories at different locations in the direction of wave propagation.

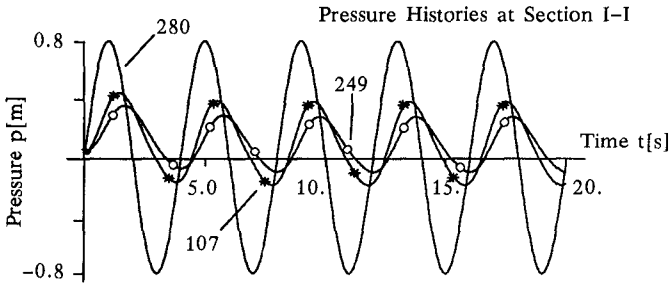


Fig. 8: Pore Pressure Damping and Phase Shift  
(Wave Conditions see Fig. 6a)

The spatial pore pressure distribution at section II-II during maximum wave run-up and maximum wave run-down are given in Fig. 9, showing the possible range of pressure variation within the structure during one wave cycle.

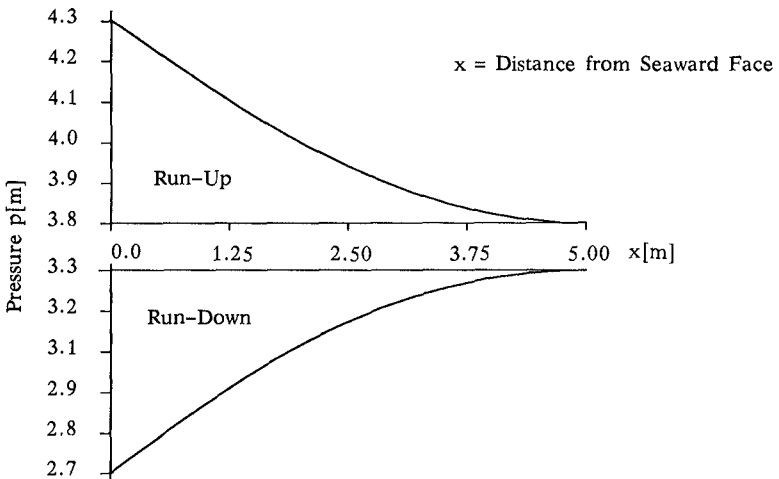


Fig. 9: Pore Pressure Distribution at Section II-II during  
Max. Wave Run-Up and Max. Run-Down

**b) Homogeneous Trapezoidal Breakwater**

Both the actual and discretized homogeneous trapezoidal breakwater are shown in Fig. 10 where also the incident wave conditions used for the computation are given.

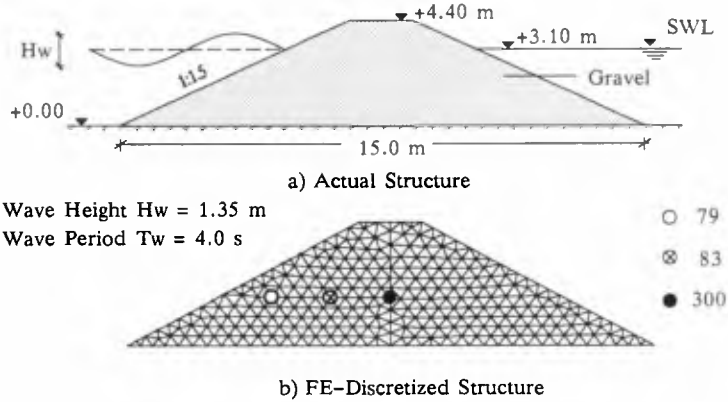


Fig. 10: Homogeneous Trapezoidal Breakwater

In the same manner as for the homogeneous vertical structure, instantaneous velocity fields and isobars at different time steps of the wave cycle can be determined (Fig. 11).

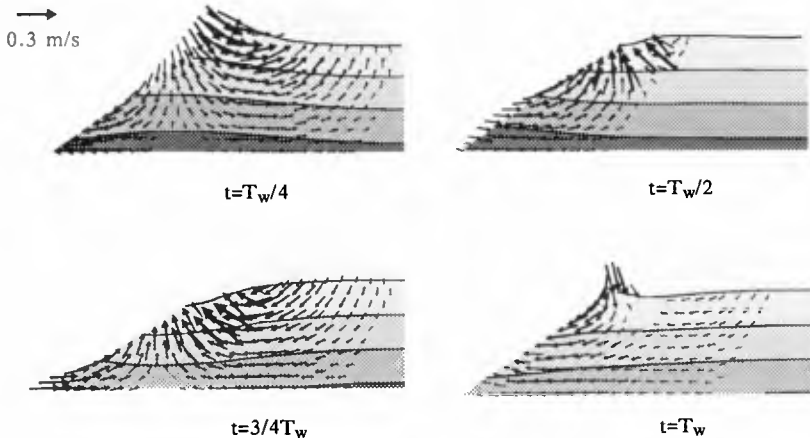


Fig. 11: Velocity Fields and Isobars within the Homogeneous Trapezoidal Structure (Wave Conditions see Fig. 10)

This kind of results is particularly important for the study of the flow-induced forces on the armour units as well as for the stability of the armour layer and breakwater toe. For instance, it is seen from Fig. 11 that not only run-down but also run-up may exert large forces on the armour units. A number of results of numerical tests of this kind can be analysed in order to improve the understanding of the flow processes leading to failures and to enable an analytical description of the forces involved.

The simultaneous pore pressure histories obtained at the three different locations (79,83 and 300 in Fig. 10b) in the breakwater also well illustrate the damping of the wave motion and the phase shift of the pore pressure histories at the different locations in the direction of wave propagation (Fig.12).

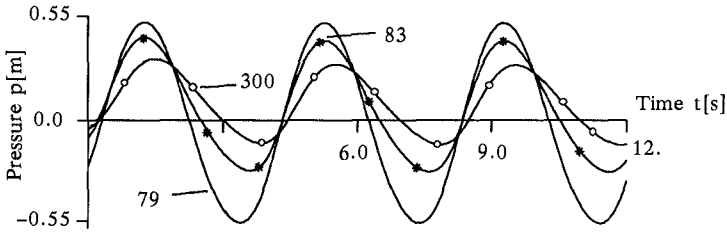
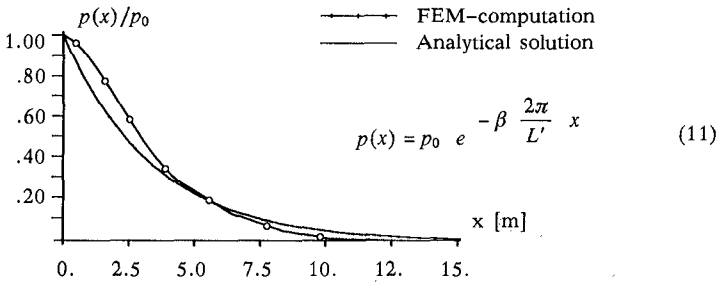


Fig. 12: Simultaneous Pore Pressure Histories  
(Wave Conditions see Fig. 10)

The relative pore pressure  $p(x)/p_0$  distribution in a horizontal plane located slightly below SWL is given for instance in Fig. 13, showing a relative good agreement with the results of large-scale model tests and the analytical solution given by (OUMERACI/PARTENSKY, 1990).



- $p_0$  : pore pressure at the seaward slope ( $x=0$ )
- $L'$  : wave length in the breakwater
- $\beta$  : damping coefficient which is strongly depth dependent

Fig. 13: Horizontal Distribution of Wave-Induced Pore Pressure

**c) Traditional Multilayered Breakwater**

The actual structure which has been tested in the Large Wave Flume (GWK) in Hannover and its discretized counterpart are given by Fig. 14,

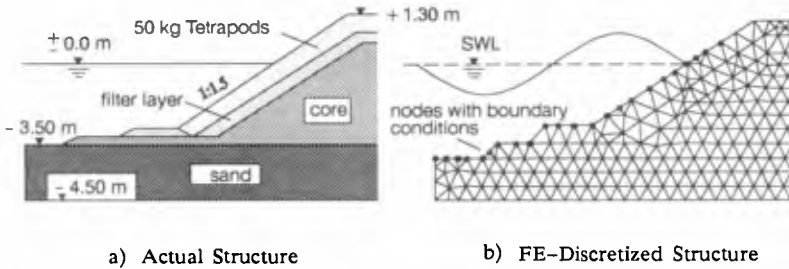


Fig. 14: Traditional Multilayered Breakwater

where only half of the structure is represented (second half is symmetrical to the represented part). In the same manner as for the previous homogeneous structures, the velocity fields in the structure during four steps ( $t=T_w/4$ ,  $T_w/2$ ,  $3/4T_w$ , and  $T_w$ ) of the wave cycle  $T_w$  are obtained in Fig. 15,

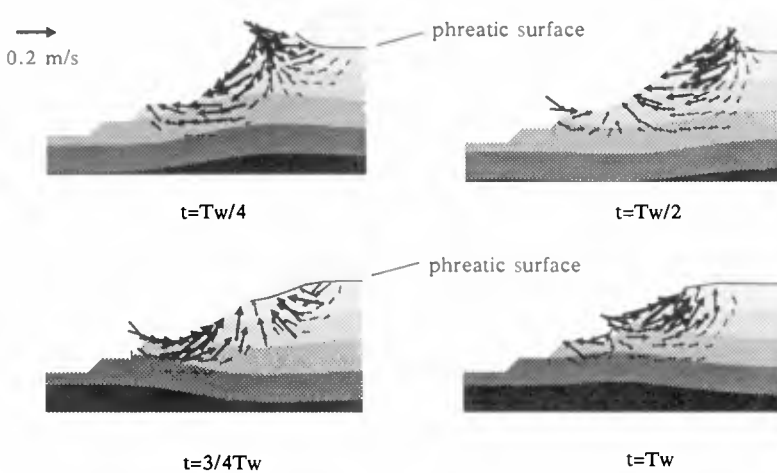


Fig. 15: Velocity Field and Isobars in the Multilayered Structure  
(Wave Conditions see Fig. 14)

which may give some indications on possible critical locations for the stability of the armour layer and the toe of the structure.

Further results of the computation as compared to the experimental data from the large-scale model tests are given in a further paper (WIBBELER / OUMERACI, 1992 ) showing a relatively good agreement between computed and measured wave-induced pore pressures within the structure.

### **Concluding Remarks and Perspectives**

The results of the FE-Model applied to three types of porous structures subject to wave action have shown that:

- a) the wave-induced pore pressure histories at different locations within the structure,
- b) the motion of the internal water table,
- c) the internal velocity field during a wave cycle

can be satisfactorily simulated, despite the simplicity of the model used. This has also been shown more clearly in a further paper (WIBBELER / OUMERACI, 1992 ).

The reasons for some discrepancies between numerical and experimental results are essentially due to air entrainment, singularities due to abrupt changes, unsteadiness of the flow and high turbulence within the first layers. Although the computation yields acceptable results for engineering purposes, there is a considerable need to improve and extend the FE-Model. This concerns particularly the coupling of the internal and external flow field, the improvement of the inflow boundary conditions, the consideration of the virtual mass effects and the simulation of the two-phase flow.

The research within the next years will be directed toward the development of an integrated numerical model for the simulation of the wave-induced flow processes on, at and in the rubble mound structure. The final result will be a reliable research tool for the study of the hydraulic stability of rubble mound structures, including all hydrodynamic effects of internal and external flow.

### **Acknowledgements**

This study was part of a research programme within the Coastal Engineering Research Unit SFB 205 at the University of Hannover, supported by the German Research Council (DFG).

### **References**

Austin D.I., Schlueter R.S.: A Numerical Model of Wave/Breakwater Interaction, Proceedings of 18th Coastal Eng. Conf., Cape Town, 1982.

- Hannoura A., McCorquodale J. A.: Rubble Mounds: Hydraulic Conductivity Equation, *Journal of Waterway, Port, Coastal and Ocean Engineering*, Vol. 111, No. 5, 1985.
- Hölscher P., Barends F.B.J.: Finite Difference Scheme for Wave Transmission in a Rubble Mound Breakwater, *International Journal for Numerical Methods in Engineering*, Vol. 30, pp. 1129–1145, 1990.
- Kondo H.: An Analytical Approach to Wave Transmission through Permeable Structures, *Coastal Engineering in Japan*, Vol. 13, 1970.
- Koutitas Ch.: A Numerical Model for Rubble Mound Breakwater Stability, *Proceedings of Symposium on Engineering in Marine Environment*, Brügge, 1982
- Madsen O. S., White S. M., Reflection and Transmission Characteristics of Porous Rubble Mound Breakwaters, Techn. Report No. 207, R. M. Parsons Laboratory, Dept. Civil Eng., Massachusetts Inst. of Techn., 1975.
- Meißner U., Wibbeler H.: A-Posteriori Errors of Finite Element Models in Groundwater and Seepage Flow, *Comp. Methods in Subsurface Hydrology, Comp. Mech. Publications / Springer-Verlag*, pp. 83–101, 1990.
- Mizumura K.: Flow Analysis in Idealized Rubble Mound Breakwater, *Journal of Waterway, Port, Coastal and Ocean Engineering*, Vol. 110, No. 3, 1984.
- Oumeraci H., Partenscky H.W.: Wave-induced Pore-Pressure in Rubble Mound Breakwaters, 22nd International Conference on Coastal Engineering, Delft, 1990.
- Rank E., Werner H.: An Adaptive Finite Element Approach for the Free Surface Seepage Problem, *Int. Journal for Numerical Methods in Engineering*, Vol. 23, 1986.
- Sakakiyama T.: Nonlinear-Wave Interaction with Permeable Breakwaters, *Extended Abstracts of Fourth International Conference on Computing in Civil and Building Engineering*, Tokyo, 1991.
- Shih R.W.K.: Permeability Characteristics of Rubble Material – New Formulae, *Proceedings of the 22nd International Conference on Coastal Engineering*, Delft, 1990.
- Wibbeler H., Oumeraci H.: Wave-induced Flow in Rubble Mound Breakwaters – Numerical Simulation vs. Measurements, *Proc. Conf. Interaction of Computation and Measurement in Hydraulics and Hydrology, HYDROCOMP' 92*, Budapest, 1992.
- Wibbeler H., Meißner U.: FEM-Model for Seepage Flow through Rubble Mound Breakwaters, *IX International Conference on Computational Methods in Water Resources*, Denver, 1992



## CHAPTER 131

# The permeability of rubble mound breakwaters. New measurements and new ideas.

Williams AF<sup>1</sup>, Burcharth HF<sup>2</sup>, den Adel H<sup>3</sup>

### 1 ABSTRACT

The results of an extensive series of permeability experiments originally analysed by Shih (1990) are reinterpreted in the light of new experiments. It is proposed that the Forchheimer equation might not fully describe flow at the high Reynolds numbers found in the interior of rubble material. A new series of tests designed to test for deviations from the Forchheimer equation and investigate the effects of material shape are described. While no evidence can be found to indicate a deviation from the Forchheimer equation a dependency of permeability and the surface roughness the material is demonstrated.

### 2 INTRODUCTION

This work forms part of a study under the MAST project G6 Coastal Structures, funded by the European Community, to develop a package of techniques to model wave action on rubble mound breakwaters. An important parameter necessary for such models is the permeability; HR Wallingford of the UK, Aalborg University of Denmark and Delft Geotechnics of the Netherlands. The major part of the testing has been carried out at HR Wallingford, by Williams, while contributions to the analysis have been made by Burcharth and den Adel.

Traditionally, permeability of the material in rubble mounds has been a difficult

---

<sup>1</sup>Coastal Structures Section, HR Wallingford, UK.

<sup>2</sup>Department of Civil Engineering, University of Aalborg, Denmark.

<sup>3</sup>Department of Marine Structures, Delft Geotechnics, The Netherlands.

parameter to measure. Prototype size experiments are not feasible due to the large scale of the material involved. The problem is compounded by uncertainties about the way small scale experiments may be scaled to prototype size. Before the start of this study a large amount of work had already been carried out on permeability at Wallingford. A large range of material sizes (4-60mm) were tested so that the effects of material size could be investigated. Shih (1990) carried out the first analysis of the results and looked for the desired scaling effects. Here further ideas about the interpretation of these experiments are discussed and a further set of measurements designed to look at the effects of material shape are described.

Following the analysis by Shih and similar work carried out at Aalborg, it became apparent that there were uncertainties about the interpretation of the data. Burcharth & Christensen (1991) suggested that there might be several distinct flow regimes possible in rubble material and that the transition from a laminar flow pattern to a turbulent flow pattern would be described by a Reynolds number. If this was the case then it would effect attempts to scale permeability measurements made at model scale to prototype size.

Further experiments were required to investigate the transition from laminar to turbulent flow regimes. In order to do this the permeameter at Wallingford was modified to increase the maximum possible flow rate and, thus enable a wider range of Reynolds number, for each single material size, to be investigated.

In addition to looking for flow regime changes, these new tests also provided the opportunity to investigate the effects of material shape on permeability. It was possible to obtain samples of material that had been carefully prepared according to shape. This material had been analysed using an image processing technique, by Latham et al. (1988).

### 3 FLOW EQUATIONS

The most common interpretation of permeability of a material is as a measure of the pressure gradient required to produce a given flow rate of fluid through the material. This was formulated into an equation by Darcy,

$$u = ki \quad (1)$$

where  $u$  is the discharge velocity, and  $k$  is the effective permeability

The linear form of Darcy's law makes it easy to deal with, and has proved very successful in the modelling flows through pores materials when the flow

rate or Reynolds number is low. However, at higher Reynolds number the inertia of the fluid becomes important and the relationship between  $i$  and  $u$  can no longer be expressed in this linear form. The size of the rubble material within a breakwater and the flow rates induced by wave action result in flows with typically large Reynolds numbers (>500). This means that to model correctly the breakwater behaviour requires a non-linear expression within the flow equation.

The exact form that such a non-linear flow law should take is at present unclear, for the purposes of these experiments the equation suggested by Forchheimer (and described by Engelund (1953)) shall be used.

$$i = au + bu^2 \quad (2)$$

In this equation the permeability is described by the two coefficients  $a$  and  $b$  which are intended to be independent of the discharge rate  $u$ .

It is generally considered that the two terms on the right hand side of Equ(2) independently describe the laminar and turbulent flow regimes. The first term  $au$  describes the laminar flow and is dominant at small values of  $u$ . In laminar flow the viscous terms in the Navier stokes equation dominate and hence the coefficient,  $a$  should be dependent on the viscosity of the fluid  $\nu$ . Conversely the second term,  $bu^2$  is dominant at large values of  $u$  and is attributed to the turbulent flow regime, indicating that  $b$  must be independent of the fluid viscosity.

The Forchheimer equation is the most widely used in the analysis of permeability data, however it may not fully describe the complex flows that occur in the large porous material of a rubble mound. If the Forchheimer equation is our chosen flow equation, the question is now one of determining the form of the coefficients  $a$  and  $b$ .

#### 4 THE $a$ AND $b$ COEFFICIENTS

Engelund (1953) suggests that the relevant parameters are the porosity of the porous medium  $n$ , and some measure of the grain size  $D$ . By demanding that the coefficients remain dimensionally correct he obtained the best fit to his data with the expressions:-

$$a = \alpha \frac{(1-n)^3}{n^2} \frac{\nu}{gD^2} \quad (3)$$

These expressions provide the permeability in terms of only two simply-determined parameters, by the incorporation of the two dimensionless

$$b = \beta \frac{(1-n)}{n^3} \frac{1}{gD} \quad (4)$$

coefficients  $\alpha$  and  $\beta$ . Ideally  $\alpha$  and  $\beta$  would be constants however even Engelund recognised that they may be dependent on other properties of the material, such as shape or grain size distribution. This means that there is a wide range in the possible values for  $\alpha$  and  $\beta$  which must be determined for the material under consideration.

Engelund chose his coefficients to provide the best possible fit to his data. It has been pointed out by Burcharth & Christensen (1991), that Engelund's data set is restricted to results from material with very small particle sizes, and hence low Reynolds number flows. Burcharth goes on to suggest a new formula for the laminar coefficient,  $a$ , based on arguments of dimensional analysis and geometry of the voids in a porous material. Burcharth's new coefficient takes the form:-

$$a = \alpha_B \frac{(1-n)^2}{n^3} \frac{v}{gD^2} \quad (5)$$

This results in the new dimensionless coefficient  $\alpha_B$ . It should be noticed that in the range of experimental observation of  $n=0.3$  to  $n=0.45$  the general form of Engelund's laminar coefficient and Burcharth's new coefficient are so similar as to be indistinguishable.

Shih (1990) analysed the large amount of data collected in previous experiments at Wallingford in terms of the Engelund coefficients. This data set contained measurements for a wide range of material sizes and gradations. The  $\alpha$  and  $\beta$  values were investigated for any dependence on grain size ( $D_{15}$ ). For material with a narrow grain size distribution laminar constant  $\alpha$  was found to increase with  $D_{15}$  in the way illustrated in Fig.(1). The turbulent constant  $\beta$  was found to decrease exponentially with  $D_{15}$ , as shown in Fig.(1). These results suggested that Engelund's expressions for  $a$  and  $b$  could be modified to provide a scaling law for the permeability. The coefficients  $a$  and  $b$  for the Forchheimer equation become.

$$a = \left[ \alpha_1 + \alpha_2 \left( \frac{g}{v^2} \right)^{\frac{2}{3}} D_{15}^2 \right] \frac{(1-n^3)}{n^2} \frac{v}{g D_{15}^2} \quad (6)$$

where  $n$  = porosity  $\alpha_1 = 1683.71$ ,  $\alpha_2 = 3.12 \times 10^{-3}$ ,  $v$  = kinematic viscosity of water  $\approx 1.14 \times 10^{-6} \text{ m}^2 \text{ s}^{-1}$ ,  $g$  = gravitational acceleration =  $9.81 \text{ ms}^{-2}$

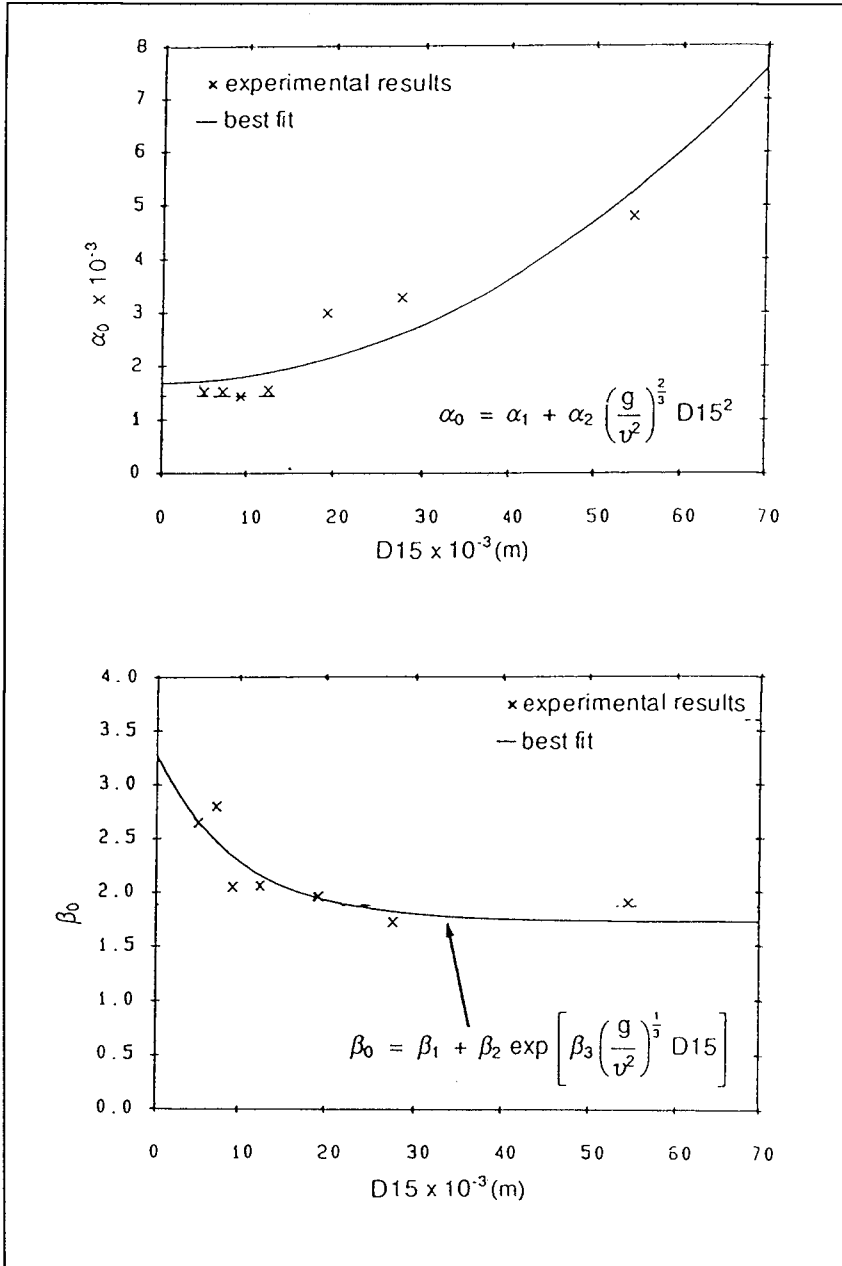
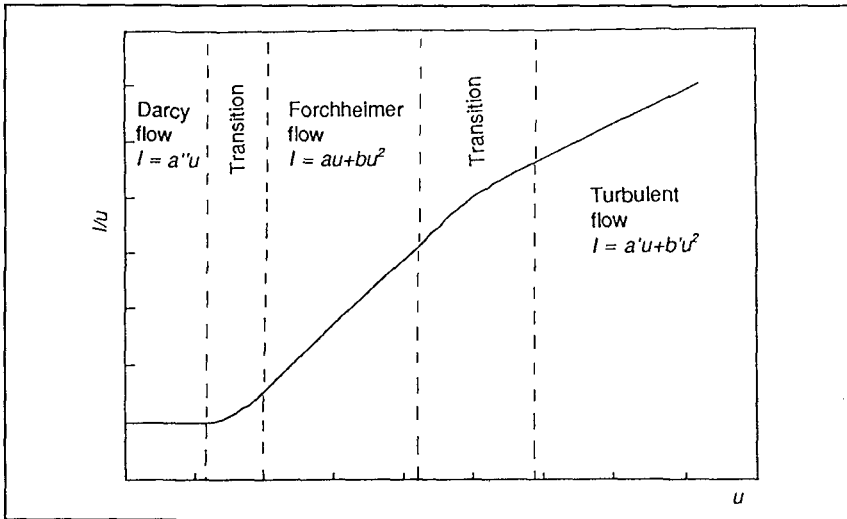


Figure 1 Shih's variation of  $\alpha$  and  $\beta$  with  $D_{15}$

$$b = \left\{ \beta_1 + \beta_2 \exp \left[ \beta_3 \left( \frac{g}{v^2} \right)^{\frac{1}{3}} D_{15} \right] \right\} \left\{ \frac{(1-\eta)}{n^3} \frac{1}{g D_{15}} \right\} \quad (7)$$

A similar analysis was carried out on the data from material with a wider size grading and a formula for an equivalent  $D_{15}$  is proposed for use in these formulae.

Following the analysis by Shih and inspection of data collected at Aalborg University, Burcharth & Christensen (1991) suggests that the Forchheimer equation does not accurately model the behaviour of the flow through porous media. He proposes that a plot of  $l/u$  against  $u$  does not have the linear form



**Figure 2** Flow regimes suggested by Burcharth

demand by the Forchheimer equation, but has the form shown in Fig.(2). The extreme portions of the graph represent laminar and turbulent flow regimes as indicated, while between these two extremes lies a transition region modeled by the Forchheimer equation.

Burcharth interprets the trends in  $\alpha$  and  $\beta$  as the result of differing flow regimes in the separate tests. The intercept and gradient of the line in Fig(2) is a measure of  $\alpha$  and  $\beta$  respectively. For tests conducted with small material the flow is describe by the Forchheimer equation and yields small values of  $\alpha$  and large values of  $\beta$ . Conversely of large material the flow regime is

turbulent and has correspondingly large values for  $\alpha$  and small values for  $\beta$ .

This would mean that the Forchheimer equation could not be used to extrapolate from small scale tests to prototype material. At this stage this hypothesis could not be confirmed as no single experiment had been conducted over sufficiently wide a range of Reynolds number to allow any deviation from the Forchheimer equation to be observed.

In addition to this interpretation there are further doubts about the validity of the scaling formulae proposed by Shih. The accuracy of the measurements of the  $\alpha$  and  $\beta$  coefficients are both functions of material size in just the form required to produce the trends reported by Shih.

## 5 THE PERMEAMETER EXPERIMENTS

To test Burcharth's hypothesis the permeameter at Wallingford was modified to approximately double its maximum flow rate. This would allow measurements to be made over a larger range of Reynolds number and thus increase the opportunity of finding deviations from the Forchheimer equation.

To test for the effects of shape five types of material were tested and were classified according to shape in the following manner:

- TABULAR: The maximum/minimum dimension was greater than two. Flat and elongate material was included. Selection was by eye.
- CUBIC: The maximum/minimum dimension was less than two and there was at least one pair of parallel faces. Selection was by eye.
- FRESH: The angular material left after the tabular rock had been removed.
- SEMI-ROUND: Fresh material was rounded by abrasion to achieve a 5 to 10% weight loss.
- ROUND: Fresh material was rounded by abrasion to achieve a 20 to 25% weight loss.

The source material was crushed Carboniferous limestone which had been sorted into the above classifications for a previous study on the effects of material shape on stability. The  $D_{50}$  of the material in each group  $\approx$  50mm. A full description of the material preparation is given by Bradbury et al. (1988).

The above material was tested in the large permeameter at Wallingford. This permeameter consists of a large cylinder of 0.6m diameter and 1m long, which is mounted with its axis vertical. The material is loaded into the permeameter and water is pumped into the bottom of the cylinder and allowed to flow freely out from the top. The pressure gradient is measured across the material by two pressure tappings 0.5m apart attached to a differential pressure cell. The corresponding flow rate is measured by a magnetic

flowmeter mounted in the entry pipe.

## 6 SHAPE ANALYSIS

The material used in the tests with the modified permeameter had previously been analysed by Latham, at Queen Mary College, University of London, and a full description of the technique is given in Latham et al. (1988).

A sample of each type of stone was placed on a light table and an image of its silhouette obtained with a video camera. The resulting image was then digitised and passed on to a computer. Both a Fourier transform and a fractal technique were used in the analysis of the results.

### 6.1 Fourier transform analysis

Once the digital form of the stone's silhouette has been obtained on the computer, it is a simple task to obtain the coordinates of the silhouette outline. From these coordinates the centre of the projected area or "centre of gravity" of the silhouette may be calculated and this is then used as a centre reference point. The outline may then be described in polar coordinates  $(r, \theta)$

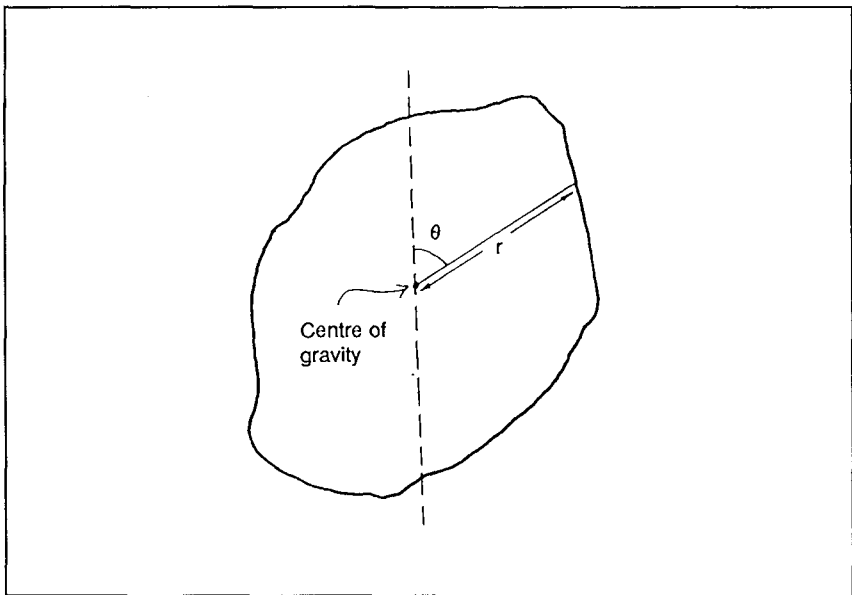


Figure 3 Coordinate system for shape analysis

using the centre of gravity as the origin (see Fig.(3)). A Fourier analysis was



carried out on the normalised radius vector of the outline. The outline was be described by a Fourier series in the following manner:

$$r(\theta) = C_0 + \sum_{n=1}^{\infty} C_n \cos(n\theta - A_n) \quad (8)$$

where  $C_n$  is the amplitude coefficient of the  $n^{\text{th}}$  harmonic,  $A_n$  is the phase angle of the  $n^{\text{th}}$  harmonic,  $n$  is the harmonic order,  $\theta$  is the polar angle measured from an arbitrary reference line.

The gross shape of the outline is described by the lower harmonics in the series, while the higher harmonics provide information on the degree of surface roughness.

The problem now remains of choosing suitable parameters from the resulting harmonic amplitude coefficients. It is useful to first define a coefficient  $Q$  which provides a flexible quantitative index which can be computed over all or a chosen range of harmonics and is defined as:

$$Q = (0.5 \sum C_n^2)^{0.5} \quad (9)$$

The following parameters are suggested by Latham & Poole (1987)

Symbol	Range of n	Name
$P_n$	1 to $\infty$	Fourier noncircularity
$P_C$	1 to 10	Fourier shape factor
$P_R$	11 to 20	Fourier asperity roughness factor

In their report Latham & Poole (1987) choose to give the results of the shape analysis in terms of  $P_C$  and  $P_R$ , and these results are presented in Table (1). Along with the mean values the 15, 50 and 85% exceedance values, are also given to provide an indication of the degree of spread within a sample.

## 6.2 FRACTAL SHAPE DESCRIPTION

A better measure of the convolution or roughness of a stones outline may be provided using the concepts of fractal geometry, described by Mandelbrot (1982). The concept is centred on the way the measured perimeter of the silhouette image changes as a function of the scale of the measuring instrument. In our case the perimeters of the silhouette were measured by stepping around the outline with a "hypothetical" pair of dividers set at a given step length. This process was then repeated many times with differing step

SHAPE	GROSS SHAPE Fourier Shape Contribution Factor $P_c$				ROUGHNESS Fourier Asperity Roughness $P_r$				SURFACE TEXTURE Fractal Coefficient $F_d$	
	Mean	$P_{c50}$	$P_{c85}$	$P_{c95}$	Log Mean	$P_{r50}$	$P_{r85}$	$P_{r95}$	Mean	$F_d$
TABULAR	2.67	3.03	1.82	4.65	.0165	.0180	.0125	.0325	.014	.017
EQUANT	1.43	1.52	1.00	2.21	.0117	.0124	.0085	.0166	.015	.018
FRESH	1.88	2.08	1.38	3.06	.0188	.0150	.0107	.0216	.016	.019
SEMIROUND	1.89	2.13	1.22	3.19	.0097	.0121	.0080	.0153	.010	.012
VERY ROUND	1.55	1.80	1.05	2.64	.0046	.0053	.0035	.0092	.008	.009

Table 1 Shape analysis of rubble material

lengths so that the variation of measured perimeter with step length could be studied. A Mandelbrot-Richardson plot was then made of the log perimeter measured against the log step length. The gradient of the resulting plot is a measure of the roughness of the outline and is the negative of the fractal shape coefficient  $F$ . The resulting values of  $F$  are given in Table (1).

## 7 RESULTS

The data from each test was plotted as  $i/u$  against Reynolds number and a linear regression made to obtain values for  $b$  from which  $\beta$  was determined. It should be noted that for the size of material used in these tests the flow was always predominately turbulent so no attempt was made to measure the lamina coefficient  $a$  and  $\alpha$ .

Each data set was investigated for variations from the Forchheimer equation as proposed by Burcharth. No variation larger than the typical experimental error was observed for any of the data sets.

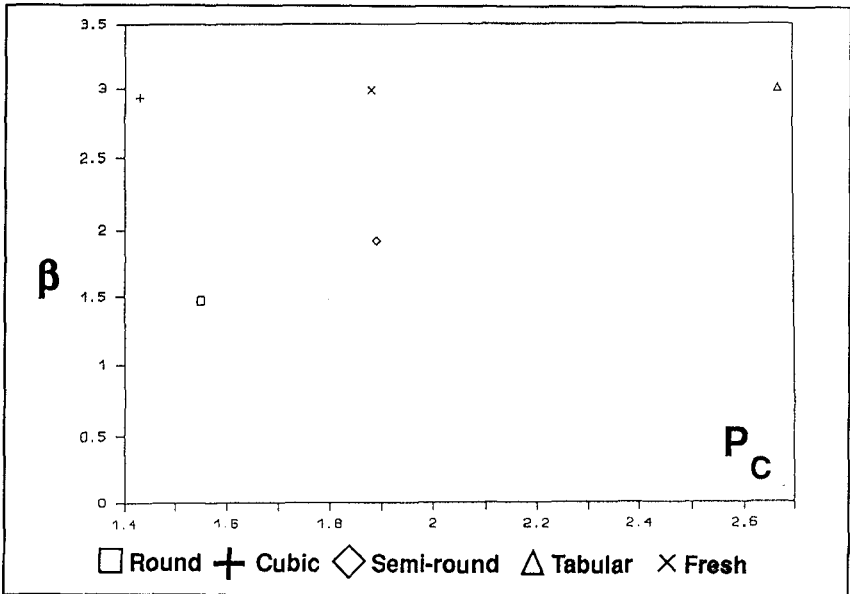


Figure 4  $\beta$  plotted against the Fourier shape contribution factor  $P_C$

The  $\beta$  values of each test have been plotted against each of the shape parameters described in Section 6, Fig(4,5 & 6). No trend can be seen for the Fourier shape contribution factor  $P_C$ . The Fourier asperity roughness and

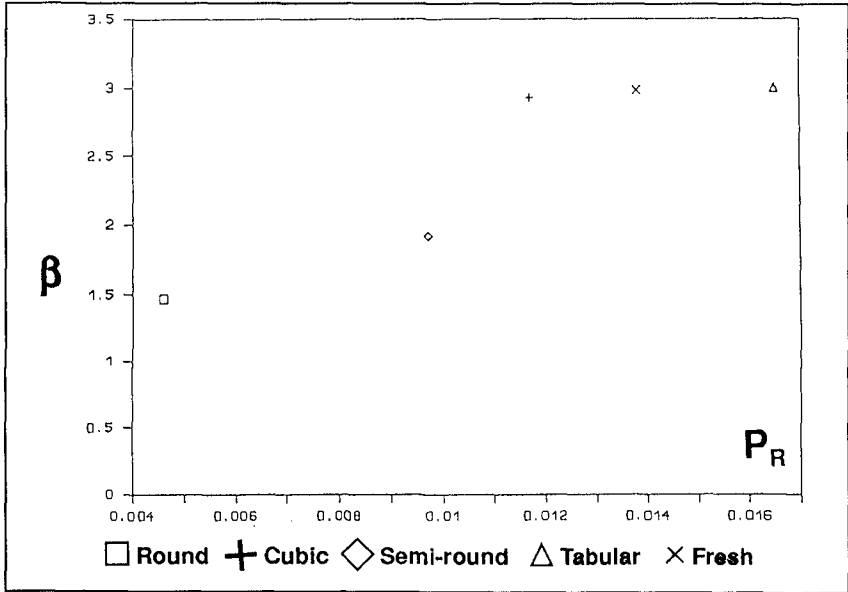


Figure 5  $\beta$  plotted against the Fourier asperity roughness  $P_R$

the fractal coefficients both show  $\beta$  as a decreasing function. The Fourier asperity roughness and fractal coefficient are a measure of the surface roughness. It may be concluded that the nature of the surface of the test material is more important than the overall shape of the material in the determination of the turbulent coefficient  $b$ .

It should be stressed that the range of tested material was small (only five groups), so the form of  $\beta$  as a function of the  $F$  or  $P_R$ , can not be determined. Figs (4,5 & 6) show that this material forms only two distinct groups in terms of surface roughness. The equant, tabular and fresh rock all have very similar surface properties, which are essentially those of freshly crushed rock. The preparation of the round and semi-round material produces a smooth surface which behaves in a different way to turbulent flows.

The intention of these tests was to investigate the suitability of the shape analysis parameters, rather than to produce enough data to derive the form of  $\beta$  as a function of these parameters. It is hoped that these experiments will point the way for further tests, which will make use of these shape description techniques.

## 8 CONCLUSIONS

The Forchheimer equation has been used in the analysis of permeability data

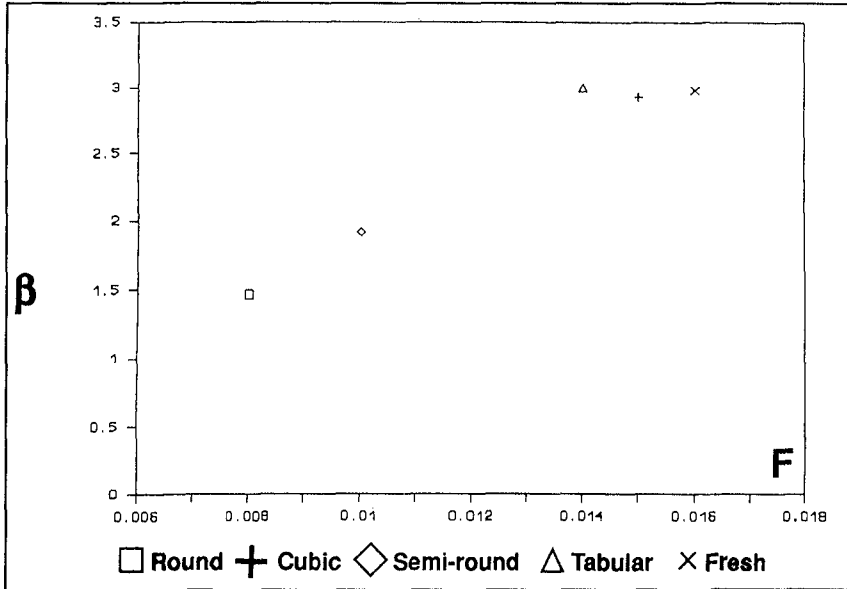


Figure 6  $\beta$  plotted against the fractal coefficient F

for many years and up to data there has been no significant evidence to suggest that it is not applicable over the whole range of possible flow rates. The data collected in these experiments supports this view, in that within the accuracy of the experiments no deviation from Equ.(2) could be found. The question still remains that the range of Reynolds numbers tested for a single sample might not be large enough to demonstrate a deviation from the Forchheimer equation. If this is the case then some caution must be used in the scaling up of laboratory tests to larger prototype material.

The material tested with the modified permeameter at Wallingford was made up of samples of narrow size grading of around 50mm, which had been hand graded with respect to shape. This material was analysed for shape by the use of a video imaging technique. The shape is described by three parameters, the gross shape of the material is provided by the Fourier shape contribution factor  $P_C$ , the surface roughness is described by the Fourier asperity roughness  $P_R$  and the fractal coefficient  $F$ . The value of  $\beta$  shows no distinguishable trend as a function of the Fourier shape contribution factor  $P_C$ , however  $\beta$  is a function of both the asperity roughness,  $P_R$  and the fractal  $F$ . These results indicate that the turbulent coefficient  $\beta$  is a function of the surface texture of the rubble material, rather than the overall gross shape of the material. The data set from these experiments was small and far more data is required over a wider range of material surface textures before the dependency of  $\beta$  can be determined.

## 9 ACKNOWLEDGEMENTS

This paper describes work carried out under the MAST programme of the European Community.

## 10 REFERENCES

- Burcharth, H.F. & Christensen, C., (1991). "On stationary and non-stationary porous flow in coarse granular materials." MAST G6 Project 1. University of Aalborg, Denmark.
- Bradbury, A.P., Allsop N.W.H., Latham, J-P., Mannion, M.B. & Poole, A.B., (1988). "Rock armour for rubble mound breakwaters, sea walls and revetments: recent progress." Report No SR 150, HR Wallingford, the U.K.
- Engelund, F., "On the laminar and turbulent flows of groundwater through homogeneous sand." Trans. Danish Academy of Technical Sciences, Vol. 3, 1953, No 3.
- Latham, J-P., & Poole, A.B.,(1987) "The application of shape descriptor analysis to the study of aggregate wear." Quarterly Journal of Engineering Geology, London. Vol. 20, pp 297-310.
- Latham, J-P., Mannion, M.B., Poole, A.B., Bradbury, A.P. & Allsop N.W.H., (1988). "The influence of armourstone shape and rounding on the stability of breakwater armour layer." Report 1, Coastal Engineering Group, Queen Mary College, University of London, U.K.
- Mandelbrot, B.B., (1982). "The fractal geometry of nature." W.H.Freeman, San Francisco, California., U.S.A., 406 pp.
- Shih, R.W.K., (1990) "Permeability characteristics of rubble material - New formulae." Proc. 22nd ICCE, Delft. Available as HR Published paper No. 38, HR Wallingford, the U.K.

## CHAPTER 132

### NEW METHODS TO EVALUATE WAVE RUN-UP HEIGHT AND WAVE OVERTOPPING RATE

Yoshimichi Yamamoto<sup>1</sup>  
Kiyoshi Horikawa<sup>2</sup>

#### Abstract

Recently, waterfront development and the mean sea level rise due to greenhouse effect have been noticed, and it has become important to develop a practical method to calculate wave run-up height or wave overtopping rate.

This paper presents new methods for calculating the wave run-up height on and the wave overtopping rate over a seawall located on a complicated bottom profile of sea coast. The proposed methods were tested both in the laboratory and in the field. The predicted results coincide well with the available data.

#### Introduction

Waterfront development has extended rapidly over recent years. Governmental agencies are also seriously concerned about the mean sea level rise due to greenhouse effect. The mean sea level is expected to be risen some 20cm to 110cm by the year of 2030. Under such circumstances, precise evaluation of the wave run-up height or of wave overtopping rate is of extreme importance for the future planning of coastal preservation.

Many conventional methods to calculate the wave run-up height and the wave overtopping rate exist, but the scope of applicability of these methods is limited (refer to Herbich, 1991). For example, Saville's nomograph (1957) for calculating the wave run-up height can not evaluate the difference of bottom profiles from the breaking point to the extent of maximum wave run-up. Goda's nomographs (1970a) for calculating the wave overtopping rate are graphs for the condition of vertical seawalls. Battjes' calculating method (1974) for the overtopping rates over sloped structures does not consider the influence

---

1 Graduate student, Saitama University, 255, Shimo-Okubo, Urawa, Saitama, 338, Japan.

2 President, Saitama University, ditto.

of bottom profiles. Thus this method is applicable only for non-breaking waves. Therefore it is important to develop methods that can be applied to a wide range of conditions such as complicated bottom profiles and arbitrary sloped seawalls.

Kobayashi et al.(1989) developed a numerical model for the calculation of the wave overtopping rate. In their study, shallow water long wave theory was used and a finite difference method was applied. However the effects of wave breaking on wave overtopping were not taken into account in the above model. Mizuguchi et al.(1988) considered the effects of wave breaking on wave run-up height by using a set of an energy equation including a term of energy dissipation by wave breaking and a time-averaged integral momentum equation. Although the wave run-up height can be obtained by using the above method, but the wave overtopping rate can not be obtained. These numerical models should be keenly promoted in order to develop suitable calculating methods.

On the other hand, it is also important to develop methods that can be easily applied to complicated coastal profiles on site using a personal computer. Therefore in this paper characteristics of wave run-up profile were investigated and new methods consisting of experimental equations were proposed.

### New Method for the Evaluation of the Wave Run-up Height

#### (1) For Breaking Waves

It is assumed that the influence of the complicated coastal profile on the wave run-up height can be evaluated by introducing a hypothetical single slope angle  $\alpha$  proposed by Nakamura et al.(1972) as follows:

$$\alpha = \tan^{-1} (R + h_b)^2 / 2A \quad (1)$$

where  $R$  is the wave run-up height,  $h_b$  is the breaking water depth and  $A$  is the shaded area from the depth at the breaking point to the extent of maximum wave run-up, as shown in Figure 1.

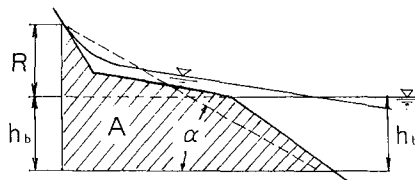


Figure 1. Hypothetical single slope angle (Nakamura et al.,1972).

By considering the balance between the potential energy of maximum wave run-up and the kinetic energy of waves on a shoreline, the wave run-up height can be expressed as follows:



$$R = (1 - k) U_s^2 / 2g \tag{2}$$

where,  $k$  is a coefficient of energy loss caused by sea-bed friction,  $U_s$  is the fluid velocity at the shoreline and  $g$  is the acceleration of gravity. According to Iwagaki et al.(1966),  $U_s$  can be expressed by Eq.(3).

$$U_s = C \sqrt{g \bar{\eta}_s} \cos \alpha \tag{3}$$

where,  $C$  is a coefficient dependent on the sea-bed topography in surf zone and  $\bar{\eta}_s$  is the wave set-up at the shoreline. Substitution of Eq.(3) into Eq.(2) gives

$$R = 0.5(1 - k) C^2 \bar{\eta}_s (\cos \alpha)^2 \tag{4}$$

If Eq.(4) is valid, the value of  $R / \bar{\eta}_s$  should be constant in case of the coasts with the same coefficients  $k, C$ . In the laboratory experiment against the same sea-bed, the wave set-up was measured at a shallow point near the shoreline by a servo-type waterlevel gauge. It was assumed that this measured value of the wave set-up corresponds to the value of  $\bar{\eta}_s$  and the relationship between the value of  $R / \bar{\eta}_s$  and the deep water wave steepness was investigated. Figure 2 shows the result of this investigation. From this figure, it is remarkable that Eq.(4) is applicable with the conditions of the experiment. Equation (4) indicates that the wave set-up is important for the evaluation of the wave run-up height for breaking waves.

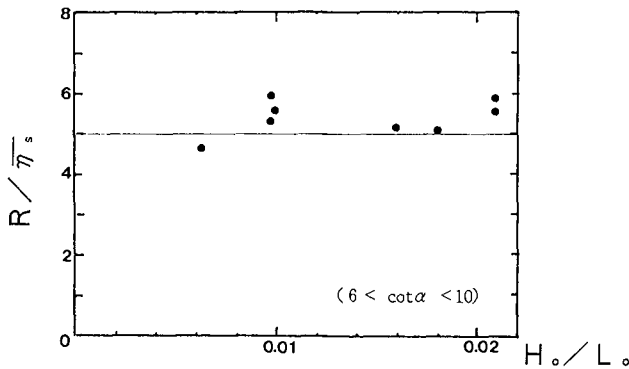


Figure 2. Relation between  $R / \bar{\eta}_s$  and wave steepness.

Yamamoto (1988) obtained the following empirical equation:

$$\bar{\eta}_s = H_s / [2.4(\tan \alpha)^{0.3}] = 0.8(\tan \alpha)^{0.6} H_b \tag{5}$$

where  $H_s$  is the wave height at the shoreline and  $H_b$  is the breaking wave height. Sunamura (1983) obtained the following equation for  $H_b$ :

$$H_b = (\tan \alpha)^{0.2} (H_o / L_o)^{-1/4} H_o \tag{6}$$

where  $H_0$  and  $L_0$  are the wave height and the wavelength in deep water respectively. From Eqs.(4), (5) and (6), the following equation can be obtained:

$$R = 0.4(1-k)C^2 (\cos\alpha)^2 (\tan\alpha)^{0.8} (H_0/L_0)^{-1/4} H_0 \quad (7)$$

The coefficient  $(1-k)C^2$  is formulated by comparison of Eq.(7) with data of Nakamura et al.(1972) against several types of seawalls located on complicated bottom profiles as follows:

$$(1-k)C^2 = 3.125(\tan\alpha)^{-0.2} \quad [1/3 \geq \tan\alpha \geq 1/50] \quad (8)$$

Now, the wave run-up height  $R$  and the hypothetical slope  $\tan\alpha$  can be determined by using Eqs.(1), (7) and (8). Since the relationship between  $R$  and  $\tan\alpha$  is nonlinear, an iterative scheme is used.

First, the breaking water depth is evaluated by using the nomograph for non-overtopping by Goda (1970b). The reduction of the breaking water depth due to wave overtopping is ignored in order to simplify the treatment. The comparison of the breaking water depths and the breaking wave heights obtained from wave overtopping tests in this study with those for non-overtopping by Goda (1970b) is presented in Figure 3. This figure shows that the breaking water depth during wave overtopping is smaller than that for non-overtopping.

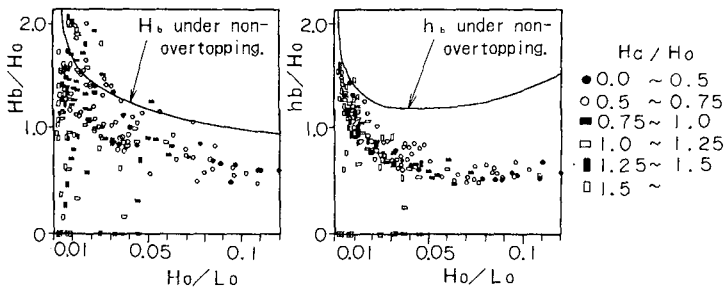


Figure 3. Breaking wave height and breaking water depth during wave overtopping.

Second, the wave run-up height is assumed and an approximate value of  $\tan\alpha$  is obtained by using Eq.(1).

Third, the wave run-up height is calculated by Eq.(7) with the evaluated  $\tan\alpha$ . The procedure is repeated until the difference between successive solutions of the wave run-up height  $R$  and  $\tan\alpha$  is less than some prescribed tolerance.

The wave run-up heights calculated by using Eqs.(1), (7) and (8) agree well with those obtained by using the nomograph presented by Nakamura et al.(1972) as shown in Figure 4. The comparison of calculated values with field data is shown in Figure 5.

Usually, the assumption that the influence of the seabed profile on the wave run-up height is small for non-breaking wave is acceptable. Thus the following equation of Sainflou (1928) was used to evaluate the wave run-up height.

$$R = (1.0 + \pi (H/L) \coth(2\pi h/L)) H_o \tag{9}$$

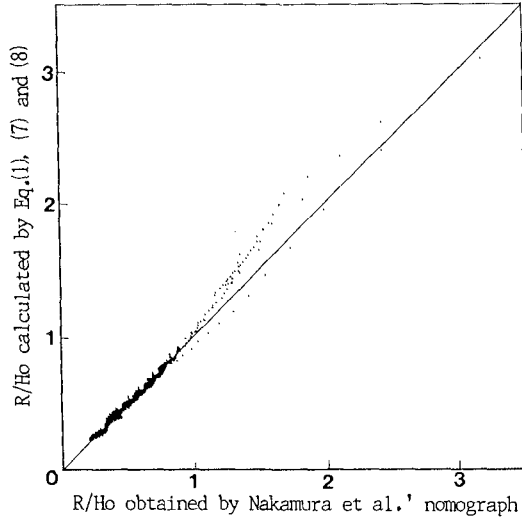


Figure 4. Comparison of R/Ho calculated by using Eq.(7) with R/Ho obtained by nomograph presented by Nakamura et al.

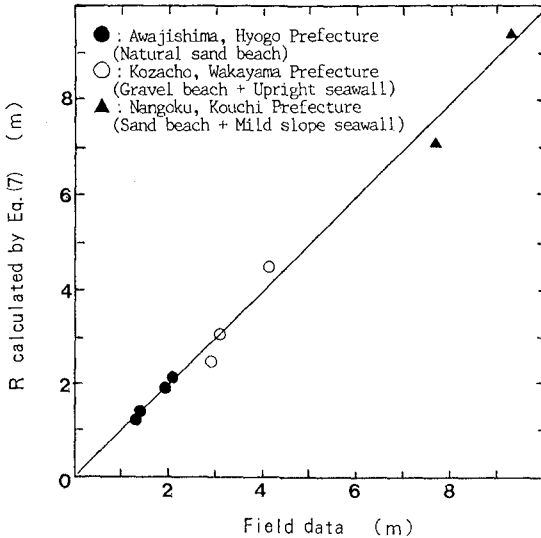


Figure 5. Comparison of R calculated by using Eq.(7) with field data.

New Method for the Evaluation of the Wave Overtopping Rate

(1) For Breaking Waves

The actual shape of the wave run-up profile is presented in Figure 6(a). Takada(1977) assumed that it could be approximated by the one presented in Figure 6(b) and studied the wave overtopping rate over one wave period  $T$ . He found that this value is proportional to the shaded area  $A$  in Figure 6(b). That is,

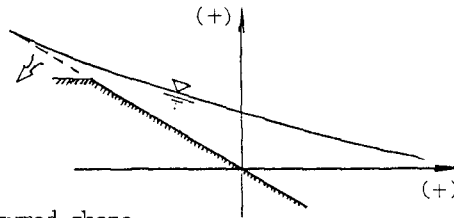
$$q \propto A \quad (10)$$

where  $q$  is the wave overtopping rate over one wave period ( $m^3/m/T$ ) and  $A$  is a hypothetical area above the seawall crown in a wave run-up profile shown in Figure 6(b) and obtained by the following equation.

$$A = (R - H_c) \times [(X_o/R) - \cot \alpha] (R - H_c) / 2 \quad (11)$$

where  $H_c$  is the freeboard above SWL and  $X_o$  is the horizontal length of the shape of the wave run-up profile.

(a) Actual shape



(b) Assumed shape

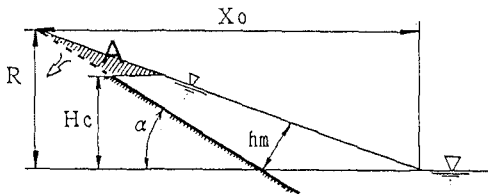


Figure 6. Actual shape and assumed shape of wave run-up profile.

From Eqs.(10) and (11), the overtopping rate  $q$  can be predicted by the following equation:

$$q = c [(X_o/R) - \cot \alpha] (R - H_c)^2 / 2 \quad (12)$$

where  $c$  is a overtopping coefficient which can be determined from experiment.

In Figure 6, the upper part of the actual shape of the wave run-up is thinner than that of the assumed shape, and the value of  $X_o$  in the actual shape is longer than that of the assumed shape. Thus if the

value of  $X_0$  of the actual shape is used, the resultant evaluation of the area  $A$  will be extremely exaggerated. Therefore the value of  $X_0$  of assumed shape is used. It is calculated by using the following equation obtained from geometrical relationship.

$$X_0/R = \cot[\alpha - \tan^{-1}(hm/R/\sin\alpha)] \quad (13)$$

where  $hm$  is the maximum thickness of the water tongue shown in Figure 6(b).

The expression for  $hm$  can be found by the following procedure: By using the long wave theory, the wave run-up profile on the uniform slope can be obtained as follows:

$$\eta = \frac{H_a}{2} J_0\left(-\frac{\omega}{2ig}\sigma\right) \sin\left(-\frac{\omega}{2ig}\lambda\right) - \frac{2gH_a^2}{\sigma^2} J_1^2\left(-\frac{\omega}{2ig}\sigma\right) \cos^2\left(-\frac{\omega}{2ig}\lambda\right) \quad (14)$$

where  $\eta$  is the water surface elevation above SWL,  $H_a$  is the wave height at the point where there is no energy loss by the breaking waves and the average water level  $\bar{\eta}$  nearly equals 0,  $\omega$  is the angular frequency ( $= 2\pi/T$ ),  $J_0$  and  $J_1$  are the Bessel functions of the zeroth and first order respectively,  $\sigma = 4\sqrt{g(iX + \eta)}$ ,  $\lambda = 2(u - g i t)$ ,  $i$  is the bottom slope ( $= \tan\alpha$ ),  $x$  is the spatial coordinate directed from shore towards offshore,  $u$  is the horizontal component of the water particle velocity and  $t$  is the time.

Next the simplified form of the energy equation proposed by Izumiya and Horikawa (1983) is solved in order to obtain the relationship between the wave height  $H_a$  and the breaking wave height  $H_b$ .

$$\frac{d\gamma}{dx} + \frac{5\gamma}{4x} - \frac{1}{400i} \frac{\gamma^2}{x} - \frac{9}{80i} \frac{\gamma^3}{x} \left(1 - \frac{0.072}{\gamma^2}\right)^{1/2} = 0 \quad (15)$$

Bottom friction term                      Breaking wave term

The coordinates used here is the same as that in Figure 6(a) and  $\gamma$  is the wave height - water depth ratio. By performing a Taylor expansion on the breaking wave term in Eq.(15) with respect to  $0.072/\gamma^2$  and omitting small terms at the position where the variable  $x$  is reasonably large, the remained term of the energy loss is the only that by the breaking waves. The integration of this simplified energy equation under the condition of  $\gamma = \gamma_b$  at the breaking point  $x = x_b$  results in Eq.(16).

$$\gamma = 1 / \left\{ \left( \frac{1}{\gamma_b^2} - \frac{9}{100i} \right) \left( \frac{x}{x_b} \right)^{5/2} + \frac{9}{100i} \right\}^{1/2} \quad (16)$$

Experimentally it can be assumed that the position where the average water level  $\bar{\eta}$  nearly equals 0 is expressed by  $x_a \approx 0.8x_b$ . Therefore  $H_a (\approx \gamma \times 0.8x_b i)$  is obtained by Eq.(17).

$$H_a = (0.8H_b/\gamma_b) / \left\{ 0.572 \left( \frac{1}{\gamma_b^2} - \frac{9}{100i} \right) + \frac{9}{100i} \right\}^{1/2} \quad (17)$$

If the maximum value of  $\eta$  at  $X=0$  is derived by the differential calculation of Eq.(14) and the wave set-up at the shoreline is considered by using Eq.(5), the following equation can be obtained as an approximation for  $hm$ .

$$\frac{hm}{H_b} = \frac{1}{2} \frac{H_a}{H_b} \cdot J_0 \left( \frac{4\pi H_b}{\sqrt{gTi}} \sqrt{\frac{hm}{H_b}} \right) + 0.8i^{0.6} \tag{18}$$

The results of the calculations by using Eq.(18) are shown as the dotted lines in Figure 7. The plotted data are the measured values of the experiment for non-overtopping. The length, width and height of the two-dimensional flume used were 18m, 40cm and 75cm respectively, while the slope of the seabed was 1/10. The front slopes of the sea-walls were 1:4, 1:2, upright. The wave height, period and water depth were variously changed.  $H_b$  was obtained by using Eq.(6). The values calculated by using Eq.(18) are larger than the measured values. It takes long time to calculate the Bessel function  $J_0$  in Eq.(18). Therefore the use of the approximate expression of the Bessel function and the substitution of realistic values for  $hm$  induce the following equation:

$$\frac{hm}{H_b} \approx 0.7 \left[ \frac{0.375}{\pi^{3/4}} \left( \frac{i}{\sqrt{0.8H_b/L_0}} \right)^{1/2} + 0.8i^{0.6} \right] \tag{19}$$

The results of the calculations by using Eq.(19) are shown as the solid lines in Figure 7.

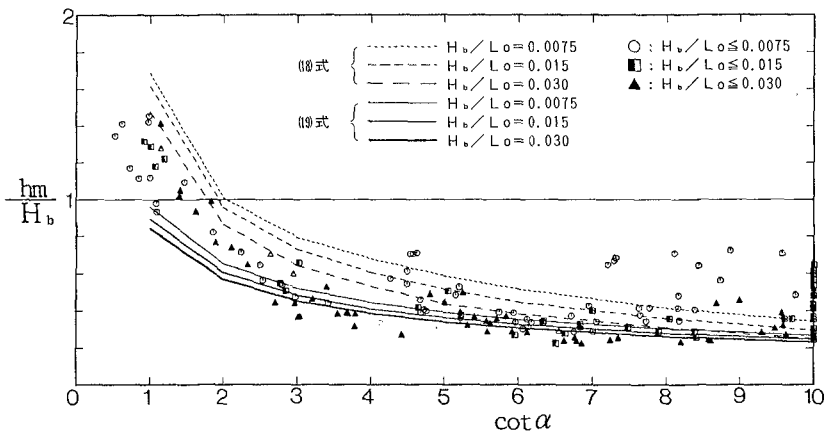


Figure 7. Relation between the maximum thickness of the water tongue and the bottom slope.

Finally the overtopping coefficient  $c$  was investigated. The overtopping coefficient represents the percentage of the imaginary area of the wave run-up profile that passes over the sea wall crown and that actually reaches the inland side. It can be assumed that the overtopp-

ing coefficient increases with the increase of the lateral component of the water block movement of the wave run-up. Therefore this coefficient increases as the front slope angle of the seawall or the wave steepness becomes smaller. Because of this, the two parameters  $(\cos \theta + \cos \alpha) / 2$  and  $(L_o / H_b)^{1/3}$  were considered, and the relationship between the non-dimensional wave overtopping rate and these parameters was investigated. In the above expression,  $\theta$  is the front slope angle of the seawall. The experiment for overtopping was conducted by using the same flume and models that were used for the experiments of non-overtopping. The wave height, period and water depth were variously changed. The experimental results are shown in Figure 8 which indicates that the non-dimensional wave overtopping rate increases as the two parameters increase. By substituting experimental data into Eqs.(12), (13) and (19), Eq.(20) for the coefficient  $c$  can be obtained.

$$c = 0.1(L_o / H_b)^{1/3} (\cos \theta + \cos \alpha) / 2 \tag{20}$$

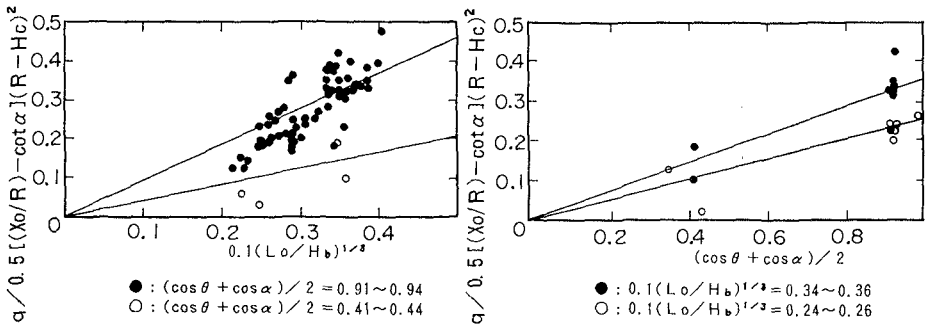


Figure 8. Relation between the wave overtopping rate and the wave overtopping coefficient.

Figure 9 depicts the comparison between the calculated values of  $q$  by Eqs.(12), (13), (19) and (20) and the experiment data. This figure suggests that there is a good fit between the calculated values of  $q$  and the measured ones. Figure 10 depicts the comparison of the values of  $q$  computed by using Eq.(12) with the ones computed by using the equation proposed by Kikkawa et al.(1967). Figure 11 is the same comparison between the values obtain by Eq.(12) and the experiment data for a compound bottom profile by Inoue et al.(1972). However the breaking water depths for non-overtopping were used for these calculations.

(2) For non-breaking waves

It can be assumed that the effect of the seabed profile on the wave overtopping rate is small for non-breaking waves. Therefore the following experimental equation by Takada(1977) was used.

$$q = 0.65 (R - H_c)^2 \tag{21}$$

where  $R$  is the wave run-up height determined by Eq.(9).

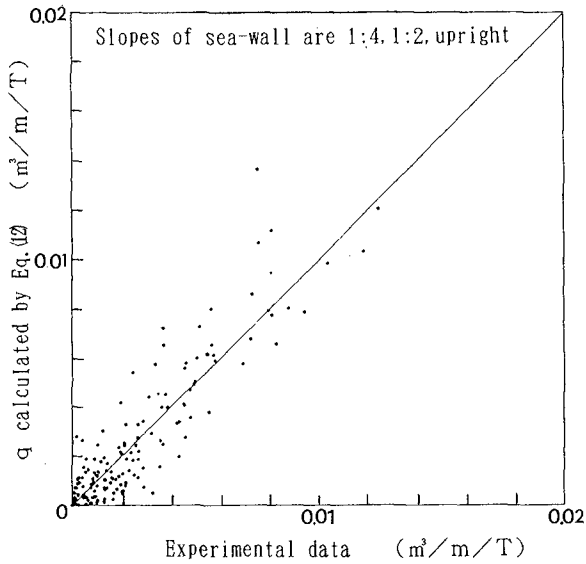


Figure 9. Comparison of  $q$  calculated by Eq.(12) with experimental data (regular waves).

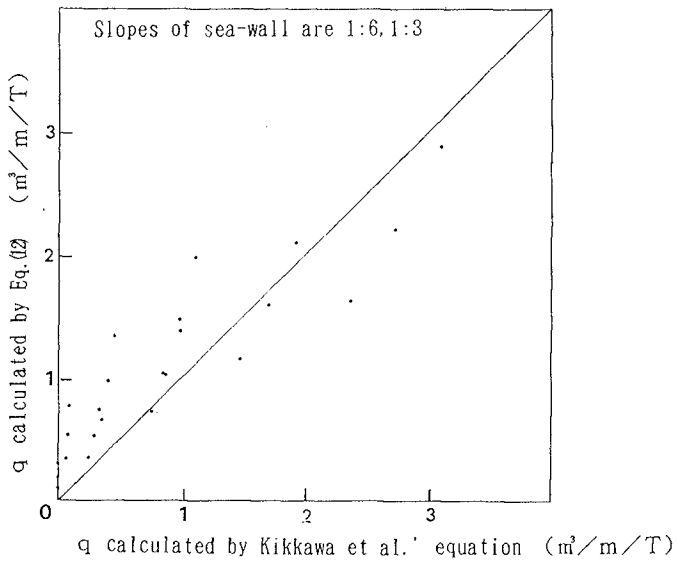


Figure 10. Comparison of  $q$  calculated by Eq.(12) with  $q$  calculated by the Kikkawa et al.' equation (regular waves).



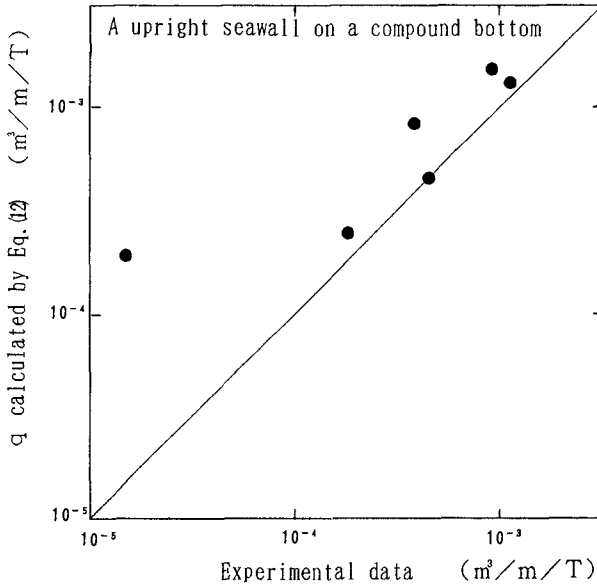


Figure 11. Comparison of  $q$  calculated by Eq.(12) with experimental data (regular waves).

(3) For irregular waves

The wave overtopping rate for irregular waves can be calculated by the following equation:

$$Q = \int_0^\infty \int_0^\infty q \cdot p \, dH \, dT \tag{22}$$

where,  $Q$  is the overtopping rate of irregular waves,  $p$  is the joint distribution function of wave heights and wave periods,  $q$  is the overtopping rate of the component waves and  $H$  and  $T$  are the wave height and the wave period of the component waves respectively. The term  $p$  proposed by Watanabe et al.(1984) can be expressed as follows:

$$\left. \begin{aligned} p &= p(\tau) p(\chi_f | \tau) / \chi_m(\tau), \\ p(\tau) &= \frac{\nu \sqrt{1 + \nu^2}}{1 + \sqrt{1 + \nu^2}} \frac{\nu^2}{[\nu^2 + (\tau - 1)^2]^{3/2}}, \\ \nu &= \sqrt{(m_0 m_2 / m_1^2) - 1}, \\ p(\chi_f | \tau) &= (32 / \pi^2) \chi_f^2 \exp[-4 \chi_f^2 / \pi], \\ \chi_f &= \chi / \chi_m(\tau), \\ \chi_m(\tau) &= \sqrt{S(f) f} / \int_0^\infty \sqrt{S(f) f} p(\tau) d\tau \end{aligned} \right\} \tag{23}$$

where  $\chi = H / \bar{H}$ ,  $\tau = T / \bar{T}$  (the overbar indicates an average value),  $f$  is the frequency,  $m_k$  is the  $k$ th order moment of the spectrum and  $S(f)$  is the Bretschneider-Mitsuyasu Spectrum.

The overtopping rate for breaking waves is calculated by using Eqs.(1), (7), (8), (12), (13), (19) and (20). That for non-breaking waves is

calculated by using Eqs.(9) and (21).

Figure 12 is comparison of the calculated values by this method with the prototype data. From this figure, it is remarkable that this method is applicable for the prototype conditions.

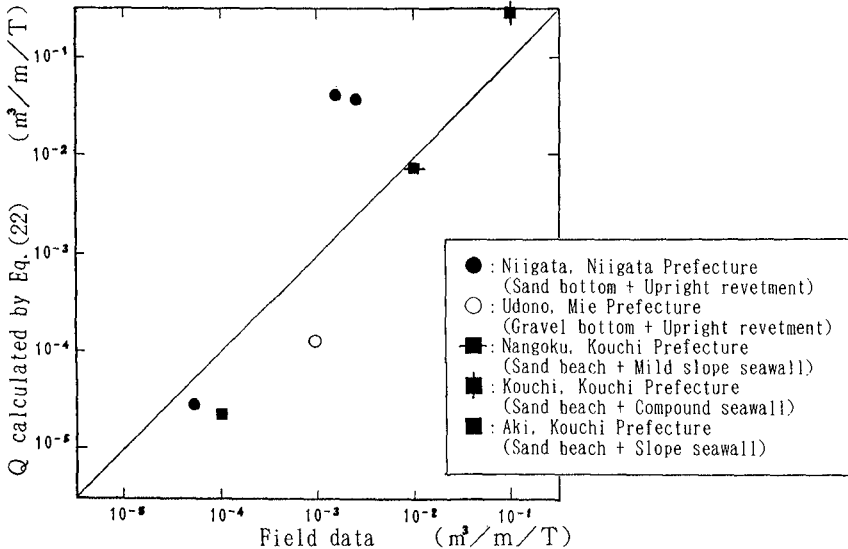


Figure 12. Comparison of  $Q$  calculated by Eq.(22) with field data. (irregular waves)

#### Application of The Present Method to Predict The Overtopping Rate in Case of The Mean Sea Level Rise Due to Greenhouse Effect

If the lapse-rate of air temperature is assumed to increase by greenhouse effect in future, there is a possibility that the intensity of typhoon becomes stronger. Manabe et al.(1990) predicted that the lapse-rate of air temperature is increased by this effect in the zone where many typhoons are generated. Therefore it is important to investigate the effect of the increment of the typhoon intensity on the wave overtopping rate in addition to the mean sea level rise.

Emanuel(1987) stated that 3° C increment in sea surface temperature leads to 30~40% increase in the maximum pressure drop of tropical cyclone and 15~20% increase in the maximum wind speed.

Now if these conditions are applied to a typhoon model (radius of the isopressure line 1000mb is 600km and central pressure 930mb), a remarkable increase in the wave overtopping rate were predicted by the present method and the results are shown in Figure 13. In this figure, type A is the case when there is a seawall of 10m height on the uniform sea bottom of 1/10 slope and type B is the case when there is the same seawall on the compound sea bottom of 1/10 and 1/100 slopes.

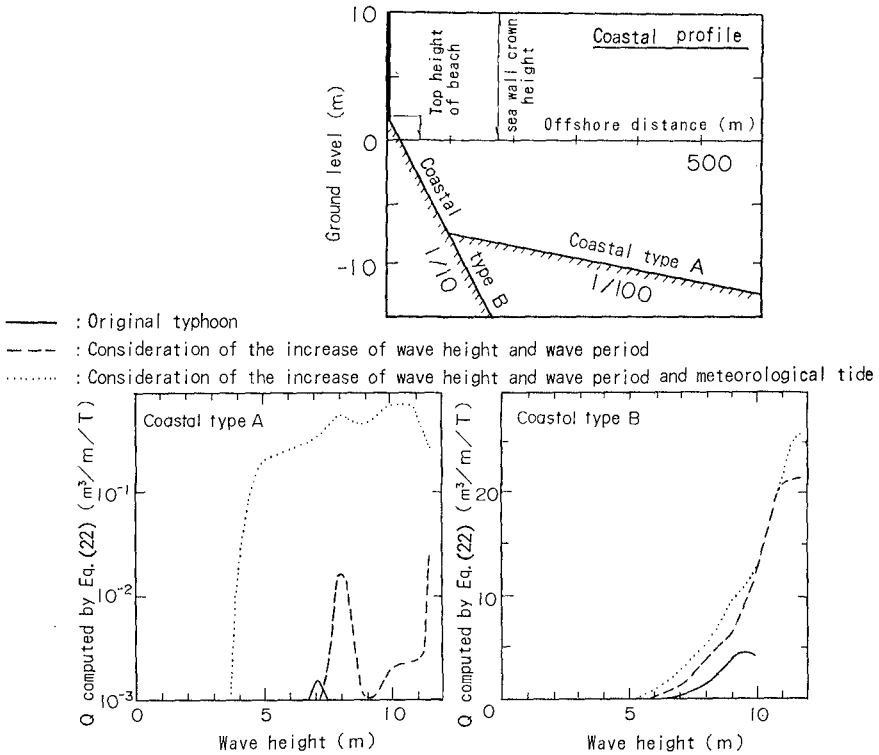


Figure 13. Increase in wave overtopping rate due to a typhoon.

Conclusions

- (1) The proposed methods have been checked with the laboratory data as well as the field data. The agreement between the calculated values and the available data is favourably good.
- (2) If the intensity of typhoon becomes stronger by the greenhouse effect, the rate of wave overtopping may increase remarkably by the small increment of the typhoon intensity.

In case the bottom slope of sea is mild, the heights of infra-gravity waves become large in the surf zone, and the wave overtopping rates by these waves cannot be ignored. This problem should be a subject of the future study.

Acknowledgement The authors are grateful to Dr. Katsutoshi Tanimoto, Mr. Hiroaki Nakamura and Mr. Thane Ca Vu of Saitama University for their useful suggestions.

References

1. Battjes, J.A. (1974). Computation of set-up, longshore currents, run-up and overtopping due to wind-generated waves. Report No.74-2, Delft University of Technology, Dept. of Civil Engineering, Delft, the Netherlands.
2. Emanuel, K.A. (1987). The dependence of hurricane intensity on climate. NATURE, Vol.326, pp.483~485.
3. Goda, Y. (1970a). Estimation of the rate of irregular wave overtopping of seawalls. Port and Harbour Research Institute, Japan, Vol.9-4, pp.3~41 (in Japanese).
4. Goda, Y. (1970b). A synthesis of breaker indices. Proc. Soc. Civil Eng., JSCE, Vol.180, pp.39~49 (in Japanese).
5. Herbich, J.B. (1990). Wave run-up and overtopping. Handbook of Coastal and Ocean Engineering, Vol.1, GULF, pp.727~834.
6. Inoue, M. and S.Kikuoka (1972). Influence of bottom profile in front of seawall on wave overtopping. Proc. 19th Japanese Conf. on Coastal Eng., JSCE, pp.283~288 (in Japanese).
7. Iwagaki, Y., M.Inoue and K.Oohori (1966). Experimental study on the mechanism of the wave run-up on a sloped bottom. Proc. 13th Japanese Conf. on Coastal Eng., JSCE, pp.198~205 (in Japanese).
8. Izumiya, T. and K.Horikawa (1983). Modeling of wave energy equation in surf zone. Proc. 30th Japanese Conf. on Coastal Eng., JSCE, pp.15~19 (in Japanese).
9. Kikkawa, H. H.Shiigai and F.Kouno (1967). Fundamental study on the wave overtopping over seawall. Proc. 14th Japanese Conf. on Coastal Eng., JSCE, pp.118~122 (in Japanese).
10. Kobayashi, N. and A.Wurjanto (1989). Wave overtopping on coastal structures. P.C.O. Engrg., ASCE, Vol.115, No.2.
11. Mizuguchi, M. and Y.Okubo (1988). Transformation of wave and wave set-up, and wave run-up on beaches with complicated bottom profiles. Proc. 35th Japanese Conf. on Coastal Eng., JSCE, pp.133~137 (in Japanese).
12. Nakamura, M., Y.Sasaki and J.Yamada (1972). A study on wave run-up on compound profile. Proc. 19th Japanese Conf. on Coastal Eng., JSCE, pp.309~312 (in Japanese).
13. Sainflou, G. (1928). Essai sur les diques maritimes. Annales des Ponts et Chaussees, Paris, France, Vol.98, No.1, pp.5~48.
14. Saville, T., Jr. (1958). Wave run-up on composite slopes. Proc. 6th Conf. on Coastal Eng., Chapter41, pp.691~699.
15. Sunamura, T. (1983). Determination of breaker height and depth in the field. Ann. Rep., Inst. Geosci., Univ. Tsukuba, Japan, No.8, pp.53~54.
16. Takada, A. (1977). Wave run-up and wave overtopping. Proc. 13th Hydro-eng. Summer Course, JSCE, B-2 (in Japanese).
17. Watanabe, A. and T.Kawahara (1984). Relation between spectrum and distribution of wave height-wave period in irregular waves. Proc. 31st Japanese Conf. on Coastal Eng., JSCE, pp.153~157 (in Japanese).
18. Yamamoto, Y. (1988). On the wave run-up height after wave breaking on a complicated nearshore profile. Proc. Civil Eng. in the Ocean, JSCE, Vol.4, pp.295~299 (in Japanese).

## CHAPTER 133

### USE AND BEHAVIOR OF GABIONS IN COASTAL PROTECTION

Kees d'Angremond<sup>1</sup>, M.ASCE  
Egbert J.F. van den Berg<sup>2</sup>  
Jan H. de Jager<sup>3</sup>

#### Abstract

To limit erosion during severe storms, it is considered to apply a hard core in a dune, prior to beach nourishment. One of the potential structural alternatives is a gabion protection. The behavior of gabions was studied. It appeared that the rigidity is a factor that cannot be neglected in model investigations. Full scale tests have been carried out to establish the flexibility in prototype. A model material was developed to reproduce the flexibility on model scale.

#### Introduction

Erosion of sandy coasts is a well known phenomenon. It may be an ongoing process, caused by a gradient of the longshore transport, or it may be an alternating process, mostly caused by the cross section adapting itself to varying wave conditions. In many instances, the erosion will be noted first by a narrowing of the beach. Subsequently, the dunes along the beach will erode as well. In densely populated areas, or areas with a high recreational value, this process leads inevitably to loss of infrastructure and property and to a cry for remedial measures.

---

<sup>1</sup> Professor of Coastal Engineering, Delft University of Technology, Faculty of Civil Engineering, P.O.Box 5048, 2600 GA Delft, The Netherlands.

<sup>2</sup> Msc. Student, Delft University of Technology.

<sup>3</sup> Koninklijke Wegenbouw Stevin, Celciusstr. 6, 1704 RW Heerhugowaard, The Netherlands.

Over the years, landowners have tended to choose for the most direct way of protection through the construction of seawalls and revetments. The latter method is not always favored by the coastal engineers because of the risk of undermining of the foundation in case of ongoing erosion. A wide variety of technical solutions is available nowadays, ranging from the construction of (offshore) breakwaters and groins to extensive beach nourishment schemes. Especially the option of beach nourishment has the advantage that the recreational function of the beach is maintained in the best possible way. Landowners, however, keep their reservations with respect to this method as it is mostly not a permanent solution and needs to be repeated from time to time. Extreme weather conditions short before a planned replenishment may still cause erosion of the dune face, and may consequently lead to damage of property.

In the Netherlands, this type of damage causes little concern with the Central Government, as the function of the dune as sea defense is not jeopardized. Local authorities and landowners, however, would like to prevent too frequent occurrence of such damage. The cost of remedial measures must therefore be low. For this reason, it is frequently considered to construct a hard element inside the dune when the coast is being restored (Figure 1).

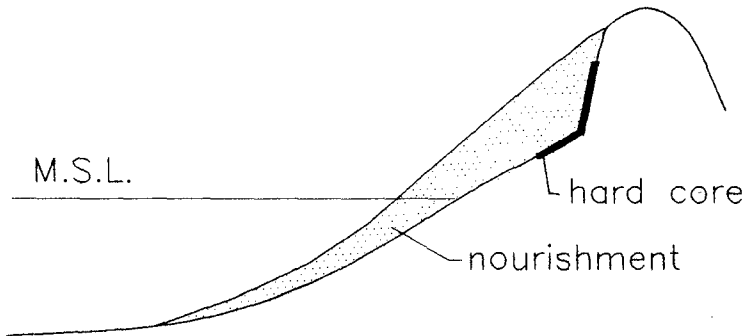


Figure 1. Hard core in dune.

In future storms this core may prevent erosion to make rapid progress. The core is not supposed, however, to survive extreme storms and to protect the hinterland from flooding under the most extreme conditions. Examples of such structures are available (or rather hidden under the sand) at various locations along the Dutch coast. Here again, however, the main risk is the undermining of the toe of such structures.

### Flexible Toe Protection

To prevent this erosion of the toe it is good engineering practice to provide an anti scour apron in front of the toe. The apron is constructed at the actual beach level, or slightly below, to prevent large quantities of excavation during construction. When the apron gets exposed, it should settle along with the erosion of the beach in front of it, and thus prevent the scour hole to reach the actual structure. It is evident that both, the apron and the structure must be flexible enough to follow the settlements, and that it should be heavy enough to resist the wave forces. Asphalt, fascine mattresses, geotextile covered with riprap are known materials for this kind of application. They all have their specific advantages and disadvantages. Recently, also the use of gabions has been suggested for this purpose in the Netherlands, as this may lead to considerable savings with respect to the cost of armor. Although there are examples of a satisfactory performance of gabions in other countries, not all reports were favorable. Therefore, it was considered useful to study the behavior of gabions once more. One of the most important questions was in how far the gabions would settle along with the deformation of the seabed directly in front. Model investigations into this effect are hampered till now by the impossibility to scale down the flexibility of the gabion mattresses. The flexibility of the gabions may influence at the same time the stability under wave attack.

### Flexibility of Gabions

To obtain insight into the flexibility of gabions, full scale tests have been performed on mattresses with varying fill rate. The dimensions of the mattresses were 4.00 m x 2.00 m x 0.5 m (L x W x t). A single test was carried out on a mattress of 0.3 m thick.

The gabions proper consisted of steel wire mesh, twisted in a hexagonal pattern as shown in Figure 2. The characteristic size D amounted to 8 cm. The steel wire had a diameter of 2.7 mm, and was coated with PVC, resulting in a gross diameter of 3.8 mm. The tensile strength of the wire material amounted to 380-500 N/mm<sup>2</sup>.

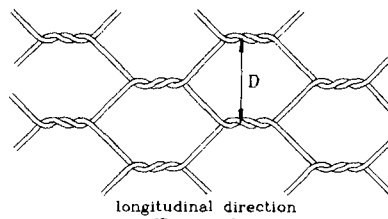


Figure 2. Wire mesh.

The gabions were filled with gravel with a density of  $2600 \text{ kg/m}^3$ , and dimensions between 80 and 120 mm. The bulk density was measured and amounted to  $1550 \text{ kg/m}^3$ , resulting in a porosity of about 40 %. The fill rate was determined by weighing the fill material and converting the weight into volume by using the measured value of the bulk density. The fill rate is defined as the ratio between the volume of the fill material and the nominal volume,  $L \times W \times t$ . The test conditions are summarized in Table 1.

Test no.	Thickness (mm)	Fill rate (%)
1	500	105
2	500	105
3	500	110
4	500	110
5	500	110
6	500	100
7	500	95
8	500	85
9	300	110

Table 1. Test Conditions

The stiffness was determined by lifting the mattresses in longitudinal direction, and measuring the curvature. Results of the tests have demonstrated the very high flexibility (or low stiffness). Originally, it was envisaged to derive a stiffness (EI) from the tests, and to relate the value of E to the fill rate of the gabions. The deformations, however, were so large that the normal theory of elastic bending could not be applied any more (Figure 3).

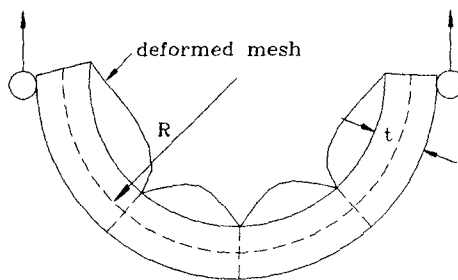


Figure 3. Deformation during lifting.

From the test results, it appeared that the gabions when lifted adapted with a reasonable accuracy to a circular shape. The diameter of the circles showed a direct relation to the fill rate (Figure 4).



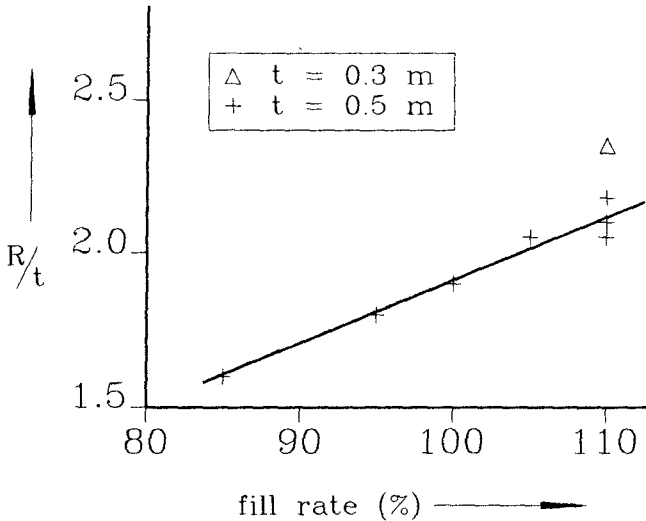


Figure 4. Results stiffness test.

### Scaling

In order to prepare scale model tests with gabions in a dune base, one should analyze which effects need to be reproduced in the model, and which effects can be neglected for the time being. The main design aspects are:

- stability under wave attack
- erosion at the toe
- deformation of the toe
- sand tightness

When testing the stability under wave attack, one should ascertain the wave climate at the toe of the structure. This wave climate is fully determined by the water depth in front of the dune, and as such determined to a large extent by the (eroded) level of the foreshore. Unfortunately, erosion of the foreshore is not reproduced adequately under the scales that are usually applied for stability tests. The eroded level of the foreshore is therefore determined with the aid of the mathematical model DUROSTA, which in turn is based on large scale model experiments. Steetzel, 1990). For the actual stability tests, thus, a fixed bed model can be used with a calculated bottom profile. A similar procedure can be followed when stability is calculated on the basis of a Hudson-type formula. When selecting the scale for stability tests, proper attention shall be paid to the permeability in the model. To avoid complications in the transition between laminar and turbulent conditions inside the gabions, model material should preferably be larger than 1 cm diameter, which leads to model scales in the order of 1:10 to 1:20.

The erosion process at the toe of the structure is largely affected by the ratio between orbital velocities and the fall velocity of the sediment. This effect causes strict limits for model scales to be applied, as the grain size of the model material can not be reduced infinitely. Traditionally, this problem is solved by accepting distorted model scales. In case of a combination of morphological and stability problems, application of distorted models is not well possible, since distortion leads to different slopes in model and prototype. Proper reproduction of both phenomena in the same model necessitates model scales in the order of 1:5 to 1:10.

Deformation of the toe itself is a complicated process, which is initiated by erosion creeping forward under the edge of the structure. The extent of this process depends on the capability of the structure to follow the deformation without losing its coherence. It is evident that the flexibility of the structure should be similar in model and prototype. On the basis of the experiments described above, it is necessary that model gabions demonstrate a similar deformation when lifted. In general, model gabions tend to be far too rigid. Initially, two different model materials have been developed. One is consisting of model gabions made out of fabric, and filled with small size gravel. The flexibility is adjusted by manipulation of the fill rate. The other consists of a (fabric) base material of the proper flexibility, covered with artificial ballast. Before making a final choice, it was realized that another process influences the deformation, i.e. loss of base material through the voids of the structure. Although the idea of losing base material seems against the proper functioning of the structure, a closer look leads to a different judgement. By a controlled loss of material, it will be easier to achieve a condition where the toe structure will slowly follow the eroding bed, and eventually bring the erosion to a halt.

It is clear now that requirements for sand tightness must be defined in two different ways for the main body of the structure and for the toe. As sand tightness is ensured in prototype by the application of geotextile under the gabions, this can be done in model as well. The quality of the geotextile can be tested separately. The model scales are therefore hardly affected by considerations of absolute sand tightness. To reproduce the controlled loss of material from the deforming toe, it must be attempted to keep the ratio between base material and filter material constant. This leads to model scales in the order of 1:5 to 1:10, and to the selection of model gabions instead of a base with fixed ballast.

### Design

Before any model tests could be carried out, a preliminary design had to be made. It was decided to select a frequent problem area along the Dutch coast near Egmond as an example. The deep water design wave height was estimated to be around 8 m. Taking into account the erosion in front of the core and the storm surge level, wave heights up to about 2.5 m height could be expected just at the toe of the structure.

For reasons of hydraulic and soil mechanical stability, the main slope was designed under 1:3 between a level of M.S.L. + 2.5 m to M.S.L. + 8.0 m. This part of the slope should be sand tight and statically stable. Sand tightness is achieved by the application of geotextile under the gabions. To avoid local fluidization and micro loss of stability it is considered necessary to apply a layer of gravel in between gabion and geotextile. (Negative experiences reported elsewhere may be due to omission of such layer).

In front of this slope a toe is foreseen under a slope 1:10. As it is the purpose that this part of the structure will follow deformation of the sand bed, sand tightness is deliberately reduced here by leaving out both, geotextile and granular filter.

To initially assess the required thickness of the gabions, use was made of model experiments reported by Brown (1979). According to his studies the stability can be expressed in a Hudson-type stability formula:

$$H/\Delta t = C(1-n) (\cot(\alpha))^{1/3}$$

wherein

H	=	Wave Height in m
t	=	Thickness of gabion in m
C	=	Coefficient
n	=	Porosity
$\alpha$	=	Slope Angle
D	=	Relative Density

It must be noted, however, that derivation of stability on the basis of mechanical analysis would lead to the use of  $(1-n)^{1/3}$  instead of  $(1-n)$ . Fortunately, the variation in the porosity  $n$  is limited.

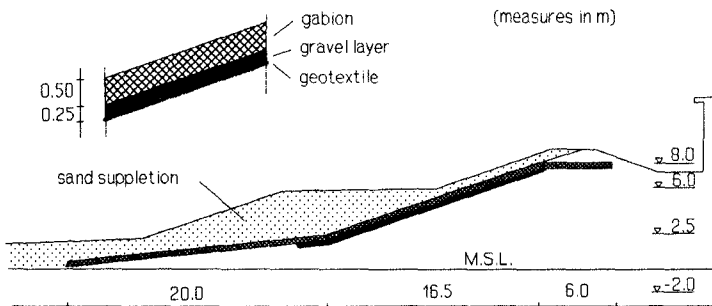


Figure 5. Design of dune core.

Pilarczyk et al(1987) have converted the Brown formula for irregular waves, leading to the expression:

$$H_g / \Delta t = 4 (1-n) (\cot(\alpha))^{1/3}$$

Here again,  $(1-n)$  is used instead of  $(1-n)^{1/3}$ .

Under the prevailing design conditions this leads to a value of 0.5 m for  $t$ , the thickness of the gabions. A schematic design of the cross section is given in Figure 5.

### Model Tests

Due to space limitations, it was not yet possible to carry out model tests on the structural design according to the preferred model scale 1:10. Instead, preliminary tests had to be performed on a linear scale 1:20. The prototype sand diameter of 0.24 mm was reproduced in model by a material with a grain size of 0.11 mm. Conditions in the flume could be reproduced in such a way that a scour hole of about 2.5 m deep developed right in front of the toe, well in line with the calculated scour depth. As can be noticed from Figures 6 and 7, the toe of the gabion structure was able to follow the erosion and thus to prevent undermining of the actual 1:3 slope.

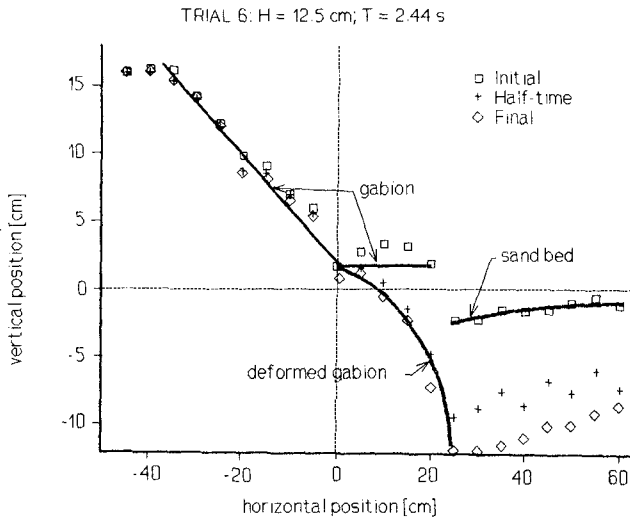


Figure 6. Erosion at flexible toe.

### Further Research

The results of the investigations so far have demonstrated the possibility to design a satisfactory structure using gabions. The tests will have to be continued on a larger scale to further analyze problems of sand tightness and stability. These tests shall also make clear why in some cases gabion structures did not perform



Figure 7. View of scour test.

satisfactorily where they certainly did in other conditions. It is the present preliminary conclusion that failure in some cases was due to (micro) loss of stability due to the absence of a granular layer between gabions and geotextile.

**References**

- Brown, C.T., 1979. Gabion Report. The University of New South Wales Water Research Laboratory, Manly Vale, N.S.W., Australia.
- Pilarczyk, K.W., et al., 1987, Guidelines for the Design and Construction of Flexible Revetments incorporating Geotextiles for inland waterways, PIANC working Group I/4, Supplement to Bulletin no. 57, ISBN 2/87223/000/9, Brussels.
- Steetzel, H.J., 1990, Cross-Shore Transport during Storm Surges, Proc. 22nd Int. Conference on Coastal Engineering, Delft.

## CHAPTER 134

### WAVE RUNUP AND OVERTOPPING ON COASTAL STRUCTURES

J.P. de Waal<sup>1)</sup> and J.W. van der Meer<sup>2)</sup>

#### Introduction

Delft Hydraulics has recently performed various applied research studies in physical scale models on wave runup and overtopping on various structures. Runup has extensively been measured on rock slopes. Runup and overtopping have been measured on smooth slopes, including the influence of berms, roughness on the slope, shallow water, short crested waves and oblique (long and short crested) waves. The paper gives an overall view of the final results, such as design formulas and design graphs.

#### Reference conditions

The slope of the structure which will be used as a reference for all kind of influences has a value between 1:1.5 and 1:8. The surface of the slope is smooth, for example concrete or asphalt. Wave conditions are according to common situations in nature. Only irregular waves with a spectrum like Pierson-Moskowitz or Jonswap are considered. The wave conditions are characterized by the significant wave height  $H_s$  of the incident waves at the toe of the structure and the peak period  $T_p$ . The significant wave height and the peak period are combined in the (dimensionless) wave steepness  $s_p$ :

$$s_p = H_s / \left( \frac{g}{2\pi} T_p^2 \right) \quad (1)$$

where:

$H_s$  = significant wave height, average of highest one-third (m)

$T_p$  = peak period (s)

$g$  = gravitational acceleration ( $m/s^2$ )

The wave conditions cover the range  $0.010 \leq s_p \leq 0.045$ . Under reference conditions the water depth  $h$  at the toe of the structure is at least  $3 H_s$ , which means that the wave height is assumed to be Rayleigh distributed.

---

1) Project engineer, 2) Deputy division director.

Delft Hydraulics, P.O. Box 152, 8300 AD Emmeloord, The Netherlands

The runup on the slope under the irregular wave conditions is characterized by the 2% runup  $R_{u2\%}$ .  $R_{u2\%}$  is defined as the level with respect to SWL which is exceeded by two per cent of the number of incident waves.

Wave runup on plane smooth slopes

Runup is one of the aspects of the behaviour of waves on a slope and can be characterized by the breaker parameter (also called surf similarity parameter)  $\xi_p$ . This breaker parameter is defined as:

$$\xi_p = \frac{\tan\alpha}{\sqrt{s_p}} \tag{2}$$

where:  $\tan\alpha$  = slope (-)

The general formula for the 2%-runup  $R_{u2\%}$  is shown in Fig. 1 and has been described by Van der Meer and Stam (1992). It is given by:

$$R_{u2\%}/H_s = 1.5 \xi_{op} \text{ with a maximum of } 3.0 \tag{3}$$

It is usual to include some safety (about one standard deviation) which gives the following recommended design formula:

$$R_{u2\%}/H_s = 1.6 \xi_{op} \text{ with a maximum of } 3.2 \tag{4}$$

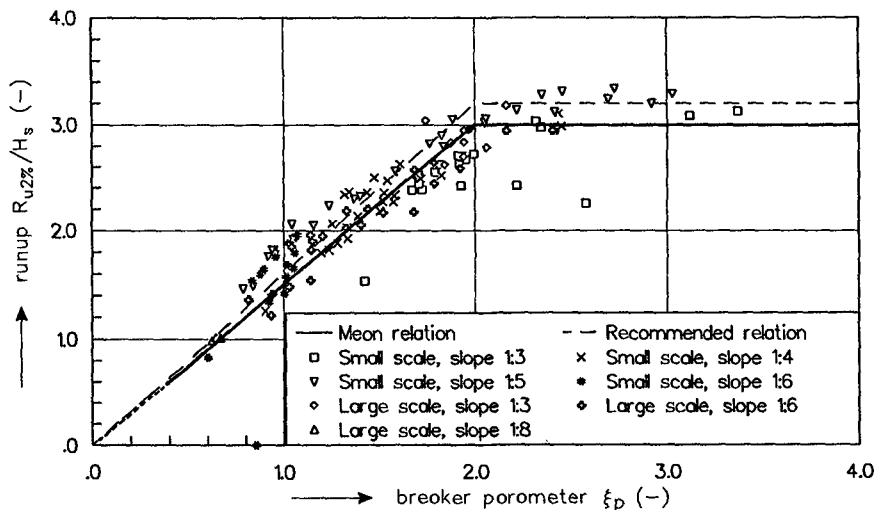


Figure 1 Runup in reference conditions

Eq. 3 and 4 are well known, except for the quantitative aspects of the influence of a berm, roughness, shallow water and oblique wave at-



tack. In order to take these influences into account the runup formula is adapted. (In this paper the influence factors are only introduced in Eq 3. For design purposes these factors should be used in a similar way in Eq. 4.) The adapted version of Eq. 3 is:

$$R_{u2\%}/H_s = 1.5 \gamma_r \gamma_h \gamma_\beta \xi_{p,eq} \quad \text{with a maximum of } 3.0 \gamma_r \gamma_h \gamma_\beta \quad (5)$$

where:

$\gamma_r$  = influence factor for roughness

$\gamma_h$  = influence factor for shallow water

$\gamma_\beta$  = influence factor for oblique wave attack

$\xi_{p,eq}$  = breaker parameter based on an equivalent slope

The influence factors  $\gamma_r$ ,  $\gamma_h$  and  $\gamma_\beta$  are defined as the ratio of runup on the specific slope to the runup in the reference situation with identical values of  $H_s$ ,  $T_p$  and  $\tan\alpha$  (TAW, 1974). The influence of a berm in the structure is taken into account by defining an equivalent slope which yields an equivalent breaker parameter  $\xi_{p,eq}$ . The influence factors will be described in the next sections.

#### Influence of a berm

A berm in the structure is characterized by the berm width  $B$  and the berm depth (with respect to SWL)  $d_B$ , see Fig. 2.

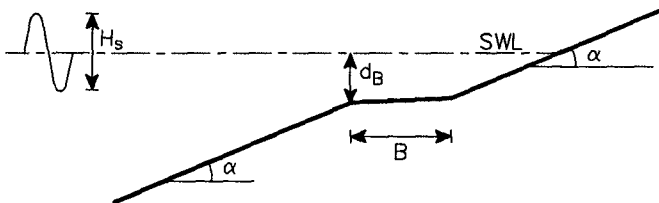


Figure 2 Berm parameters

About 120 tests have been performed on structures with a berm. The variation of the relevant parameters in the model investigation on the influence of a berm is given in Table 1.

$\tan\alpha$	(-)	1:3, 1:4
$s_p$	(-)	0.01, 0.02, 0.03, 0.04, 0.05
$H_s$	(m)	0.10 - 0.20
$B$	(m)	0.40, 0.60, 1.00
$d_B$	(m)	-0.08, 0.00, 0.08, 0.16

Table 1 Parameters in test programme for berms

In case of a berm in the structure an equivalent slope can be defined, which should be used to determine the equivalent breaker parameter  $\xi_{p,eq}$  in Eq. 5.

$$\xi_{p,eq} = \gamma_b \xi_p \tag{6}$$

where:  $\gamma_b$  = influence factor for a berm

The influence factor  $\gamma_b$  is defined as the ratio of the equivalent slope which takes account of the berm ( $\tan\alpha_{eq}$ ) to the average slope of the structure excluding the berm ( $\tan\alpha$ ). The combined influence of the berm width and berm depth is given by the following formula for  $\gamma_b$ :

$$\gamma_b = 1 - r_B(1 - r_{dB}) \quad \text{with} \quad 0.6 \leq \gamma_b \leq 1.0 \tag{7}$$

where:

$r_B$  = reduction of the average slope ( $\tan\alpha$ ) caused by the berm width B (a structure without berm yields  $r_B = 0$ )

$r_{dB}$  = reduction of the influence of a berm caused by the berm depth  $d_B$  (a berm at SWL yields  $r_{dB} = 0$ )

The average slope of a structure with a berm can be defined by drawing a straight line through the points on the slope excluding the berm at  $1 H_s$  above and  $1 H_s$  below SWL, see Fig. 3. The equivalent slope of a structure with a berm can be defined by drawing a straight line through the points on the slope including the berm at  $1 H_s$  above and  $1 H_s$  below the berm. The optimum value of  $1 H_s$  was a result of the analysis. This procedure results in the following formula for  $r_B$ :

$$r_B = \frac{B/H_s}{2 \cot\alpha + B/H_s} \tag{8}$$

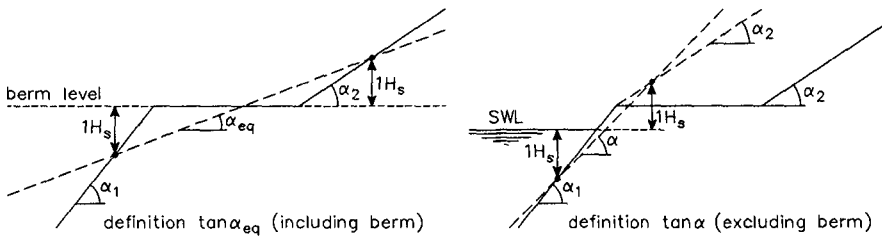


Figure 3 Definition equivalent and average slope

A berm at SWL ( $d_B = 0$ ) is most effective in the reduction of the runup. In that case  $r_{dB} = 0$  and  $\gamma_b = 1 - r_B$ . For  $d_B \neq 0$  the influence of the berm will be less so that  $\gamma_b$  will be closer to 1. The influence of the berm on runup is negligible when the berm is about  $1.5 H_s$  above or below SWL. In that case  $r_{dB} = 1$  and  $\gamma_b = 1$ . This reduction of the influence of the berm caused by the berm depth can be expressed by the following formula for  $r_{dB}$ :

$$r_{dB} = \frac{1}{2} \left( \frac{d_B}{H_s} \right)^2 \quad \text{with } 0 \leq r_{dB} \leq 1 \quad (9)$$

The influence factor  $\gamma_b$  has a lower limit of 0.6. This implies that in a situation where  $\gamma_b = 0.6$  an increase of the berm width will not lead to a further reduction of the runup. For a berm at SWL an optimum berm width is given by the following formula, derived from Eq. (7) with  $\gamma_b = 0.6$  and  $r_{dB} = 0$ :

$$B = \frac{4}{3} H_s \cot \alpha \quad (10)$$

Fig. 4 gives in the upper graph the runup versus the breaker parameter  $\xi_p$ , based on the average slope, excluding the berm. The lower graph shows the results when Eq. 7 to 9 are used to determine the equivalent breaker parameter  $\xi_{p,eq}$ . The results show a good agreement with the formulas.

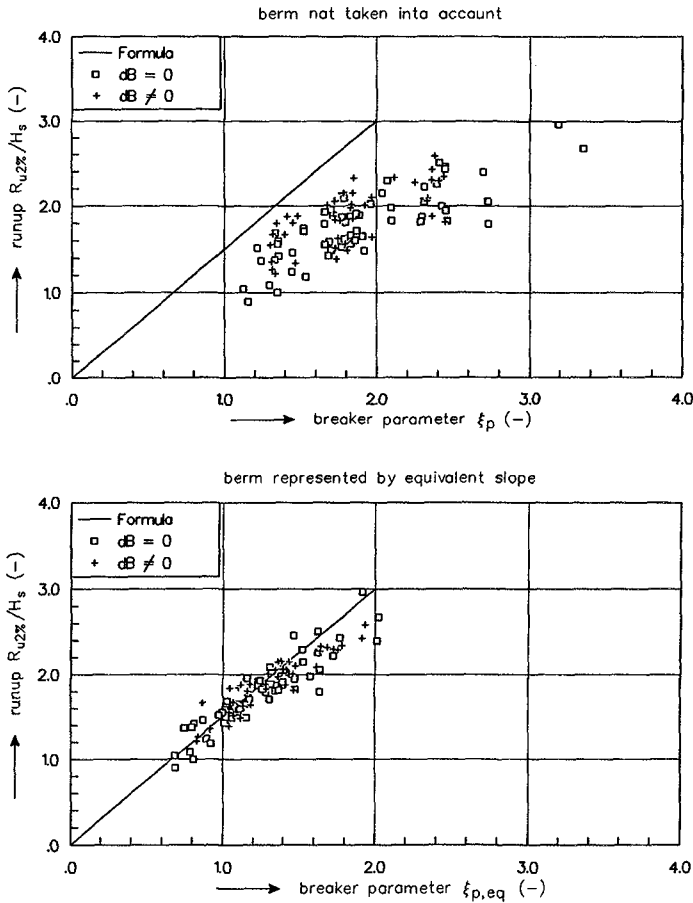


Figure 4 The influence of a berm on runup

Influence of roughness

The influence of roughness on runup is described in Table II.5.5 in TAW (1974) or the similar Table 7-2 in the Shore Protection Manual (CERC 1984). However, these tables have been based on regular waves. In this paper results of tests with irregular waves are discussed.

The influence of roughness has been investigated for various types of surface coverings in small scale as well as full scale tests. For impermeable structures the results of the investigations are summarized in Table 2 which gives recommended values for the influence factor  $\gamma_f$ . This table can be seen as an update of Table 7-2 in the Shore Protection Manual (CERC 1984). In total 20 tests have been performed.

Surface covering				Influence factor $\gamma_f$
Smooth, concrete, asphalt				1.00
Impermeable smooth block revetment				1.00
Grass (3 cm)				0.90 - 1.00
Ribs on smooth slope (l=9b)		l = length b = width h = height		0.60 - 0.70
h/b	b/H <sub>s</sub>	covering		
1.00	0.12-0.19	1/7.5		
Blocks on smooth slope (l=b)				0.70 - 0.75 0.75 - 0.85 0.85 - 0.95 0.85 - 0.95 0.75 - 0.85
h/b	b/H <sub>s</sub>	covering		
0.88	0.12-0.19	1/9		
0.88	0.12-0.24	1/25		
0.44	0.12-0.24	1/25		
0.88	0.12-0.18	1/25 (above SWL)		
0.18	0.55-1.10	1/4		
Rock				0.55 - 0.60 0.50 - 0.55
one layer		(H <sub>s</sub> /D = 1.5 - 3.0)		
two or more layers		(H <sub>s</sub> /D = 1.5 - 6.0)		

Table 2 Influence factor for roughness ( $1 < \xi_p < 4$ )

The parameters l, b and h in this table respectively stand for the length (parallel to the structure axis), the width along the slope (perpendicular to the structure axis) and the height of artificial roughness elements (blocks or ribs). The value for the covering stands for the relative area of the slope which is covered by the roughness elements. Finally the parameter D stands for the diameter of the rock. The recommended values of  $\gamma_f$  can be applied for  $1 < \xi_p < 4$ . For larger values of  $\xi_p$  (surging waves) the values of  $\gamma_f$  will slowly increase to 1.

The results for two or more layers of rock on a structure are only an average value. During his extensive test series on the stability of

rock slopes Van der Meer (1988) simultaneously measured wave runup. The results have been described by Van der Meer and Stam (1992). Preliminary results have also been published by CIRIA/CUR (1991). Two methods for the prediction of wave runup have been described by Van der Meer and Stam (1992). First, formulas were derived for various runup levels (2%, significant, etc.) as a function of wave height and surf similarity parameter. A second set of formulas gave the wave runup as a Weibull distribution.

Influence of shallow water

About 40 small scale tests have been performed on structures with a 1:100 foreshore in front and relatively shallow water at the toe. In addition the development of the wave conditions on the foreshore has also been investigated intensively in tests without a structure, in order to have accurate information about the incident waves in the situation with a structure. Table 3 gives global values of the relevant parameters in the investigations.

$\tan\alpha$	(-)	1:3, 1:4
$s_p$	(-)	0.01, 0.02, 0.03, 0.04, 0.05
$H_s$	(m)	0.10 - 0.20
$h$	(m)	0.18, 0.29, 0.33, 0.41, 0.60

Table 3 Parameters in test programme for shallow water

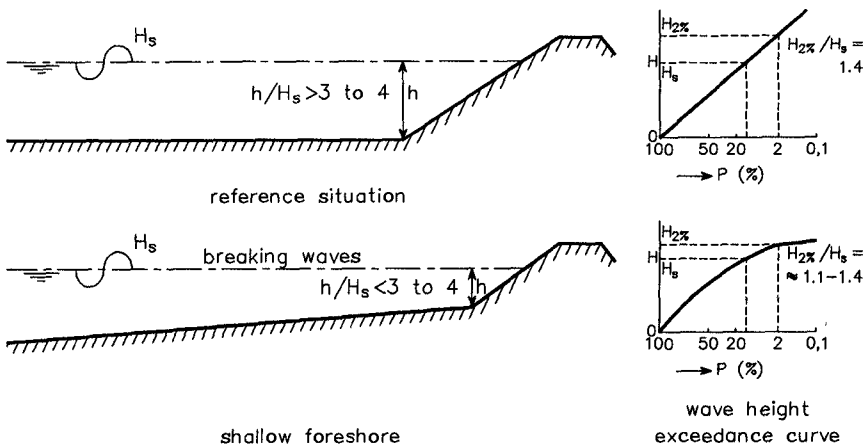


Figure 5 Wave height distribution in shallow water

In general the 2% runup  $R_{u2\%}$  is related to both the significant wave height  $H_s$  (which should be used to determine the breaker parameter) and the 2% wave height  $H_{2\%}$  which characterizes the higher waves. However,

in Eq. 5  $R_{u2x}$  is only related to  $H_s$ . This relation is therefore only valid for situations in which the wave height is Rayleigh distributed because then the ratio of  $H_{2x}$  to  $H_s$  is constant (equal to 1.4).

In situations with a shallow foreshore the higher waves will break before they reach the structure. Then the wave height at the toe of the structure is no longer Rayleigh distributed, see Fig. 5. In these situations the influence factor  $\gamma_e$  for shallow water can be described by the following simple formula:

$$\gamma_h = \frac{H_{2x}}{1.4H_s} \tag{11}$$

For a gentle foreshore slope of 1:100 the ratio of  $H_{2x}$  to  $H_s$  has been investigated which led to the influence factor  $\gamma_e$  (including the relative water depth) which is given in Fig. 6 and the following formulas:

$$\gamma_h = 1 - 0.03 \left(4 - \frac{h}{H_s}\right)^2 \quad \text{for } 1 \leq \frac{h}{H_s} \leq 4 \quad \text{and} \tag{12}$$

$$\gamma_h = 1 \quad \text{for } \frac{h}{H_s} \geq 4.0 \tag{13}$$

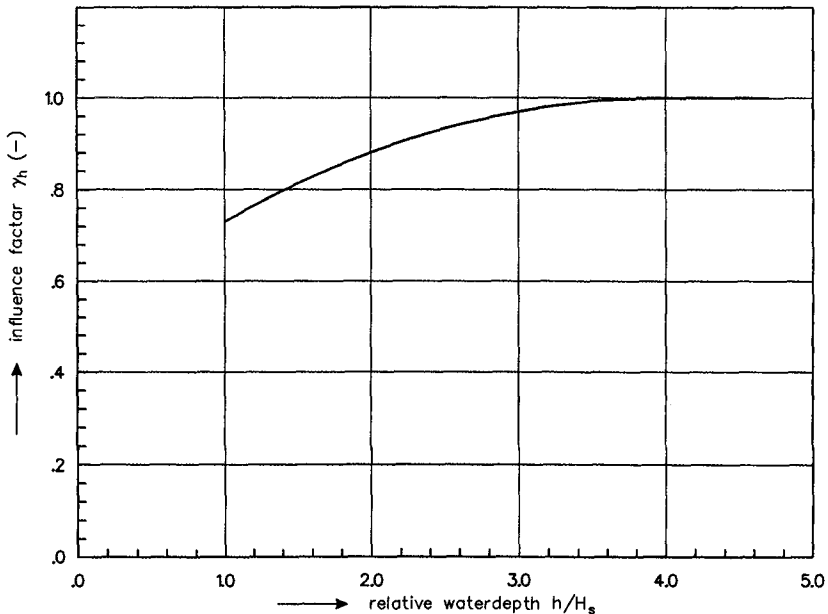


Figure 6 Influence factor for shallow water for a 1:100 foreshore

Influence of the angle of wave attack (for long and short crested waves)

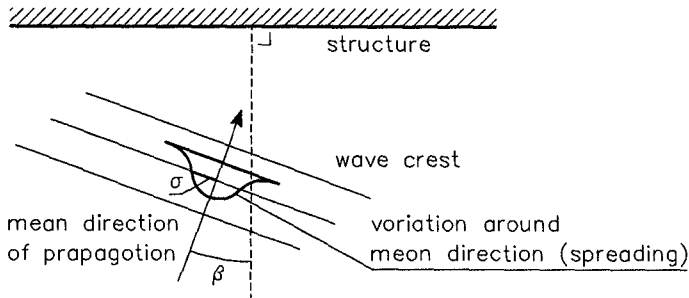


Figure 7 Angle of wave attack

The definition of the angle of wave attack  $\beta$  is given in Fig. 7. The directional spreading parameter  $\sigma$  is defined as the standard deviation of the direction of wave propagation.

About 160 tests were performed in a multi-directional wave basin on wave runup and overtopping. The structure was 15 m long and was divided in 3 sections with different crest levels, see also Van der Meer (1989). Overtopping was measured at two sections and runup at the other. Smooth plane 1:2.5 and 1:4 slopes were tested and a 1:4 slope with a berm at SWL. The range of the main parameters is given in Table 4.

$\tan\alpha$	(-)	1:2.5, 1:4, 1:4 with berm
$s_p$	(-)	0.01, 0.02, 0.03, 0.04, 0.05
$H_s$	(m)	0.06, 0.12
$\beta$	( $^\circ$ )	0, 10, 20, 30, 40, 50, 60, 70, 80
$\sigma$	( $^\circ$ )	0, 12, 25, 32, 45

Table 4 Parameters in test programme for oblique waves

Short crested *perpendicular* wave attack gives similar results on both wave runup and overtopping as long crested perpendicular wave attack. The results are different when the wave attack on the structure is oblique ( $\beta > 0^\circ$ ), see Fig. 8.

The effect of oblique wave attack on runup on a 1:6 slope with regular waves has been studied by Tautenhain et al. (1982). Their results suggest that runup for normal wave attack ( $\beta = 0^\circ$ ), can be exceeded for small angles (say,  $\beta = 10-30^\circ$ ). Fig. 8 shows that the measured influence factor for these small angles is only higher than 1 for a few tests. The average trend shows no increase of the runup for small angles.

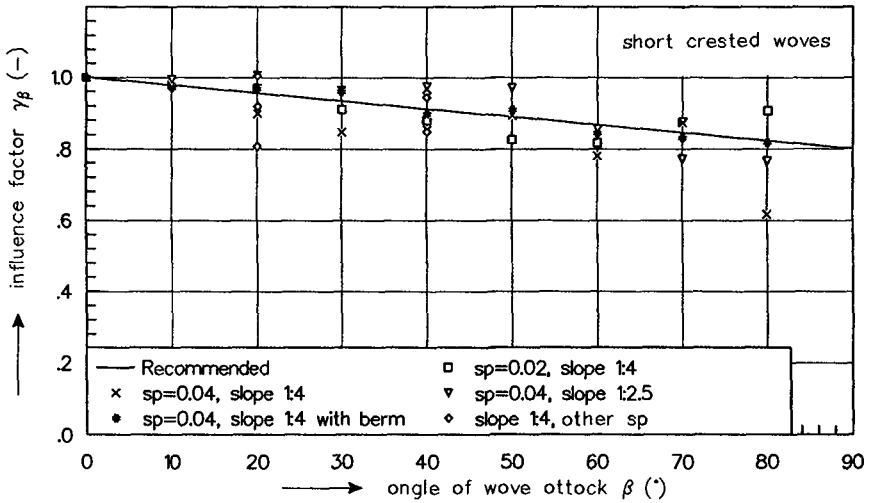
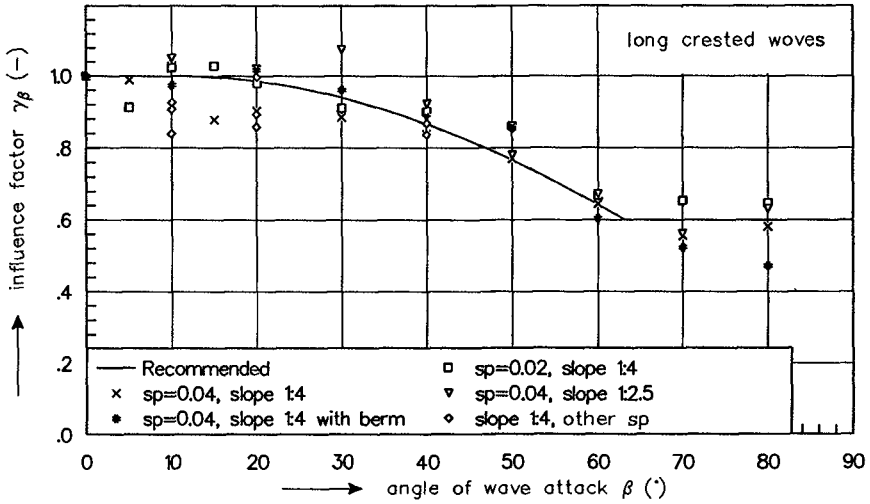


Figure 8 Measured influence factor for oblique wave attack

Long crested waves give an influence factor  $\gamma_\beta$  which is almost equal to 1 for  $\beta < 30^\circ$ , then decreases to 0.6 for  $\beta = 60^\circ$  and remains constant for  $\beta > 60^\circ$ . Short crested oblique waves, more similar to nature, give a different picture. The influence of the angle of wave attack on runup is much less than for long crested waves. This is due to the fact that even for large angles a number of waves arrive at smaller angles, giving a higher runup. For  $\beta$  increasing from  $0^\circ$  to  $90^\circ$  the runup influence factor decreases linearly from 1.0 to 0.8. The spreading of the multi-directional sea itself has no influence on the



results. As long as  $\sigma > 10^\circ$  the results are similar (and therefore different from long crested waves).

Wave overtopping is given per meter structure width. With oblique wave attack less wave energy will reach this meter structure width and therefore influence factors for oblique wave attack are smaller for overtopping than for runup. The recommended values for the influence factor  $\gamma_\beta$  are shown in Fig. 9 and are given in the following formulas ( $\beta$  in degrees):

Long crested waves (exceptional in nature)

Runup:

$$\gamma_\beta = \cos(\beta - 10^\circ); \quad (\gamma_\beta \geq 0.60 \text{ and } \gamma_\beta = 1.0 \text{ for } 0^\circ \leq \beta \leq 10^\circ) \quad (14)$$

Overtopping:

$$\gamma_\beta = \cos^2(\beta - 10^\circ); \quad (\gamma_\beta \geq 0.60 \text{ and } \gamma_\beta = 1.0 \text{ for } 0^\circ \leq \beta \leq 10^\circ) \quad (15)$$

Short crested waves (common in nature)

Runup:

$$\gamma_\beta = 1 - 0.0022 \beta \quad (16)$$

Overtopping:

$$\gamma_\beta = 1 - 0.0033 \beta \quad (17)$$

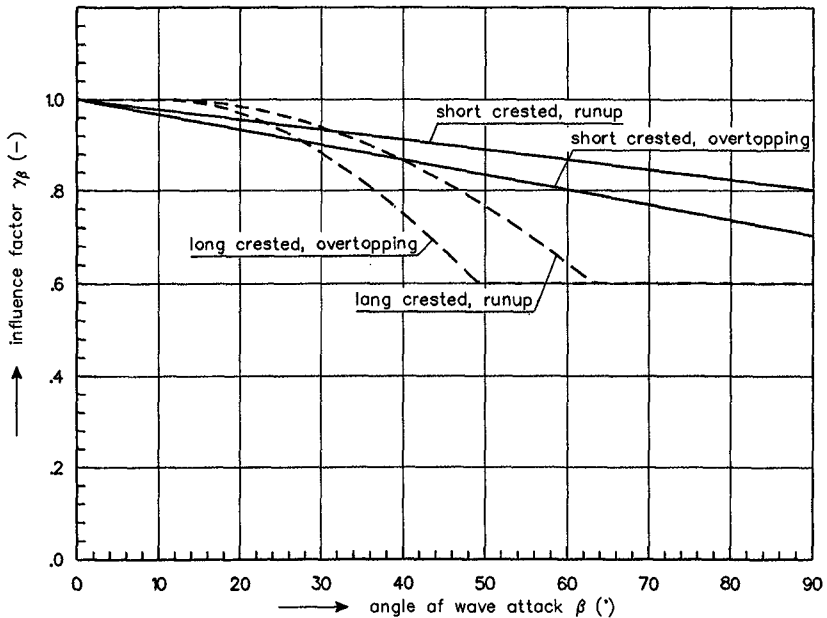


Figure 9 Recommended influence factors for oblique wave attack

Wave overtopping

The wave overtopping  $q$ , given as the mean overtopping discharge in  $m^3/s$  per  $m$  width, is strongly determined by the crest freeboard  $R_c$  which is defined as the crest level with respect to SWL. The relation between  $q$  and  $R_c$  given by TAW (1974) has been compared with the relations for several slopes given by Owen (1980). A generalized version has been derived from the exponential functions given by Owen (1980) and showed a good agreement with a large set of overtopping data, including the latest measurements. However, this relation turned out to be only valid for plunging (breaking) waves. For surging (non-breaking) waves another formula with different dimensionless parameters should be applied. In order to avoid this set of two different overtopping formulas a different approach has been followed which will be described here. The approach described above, according to Owen (1980) will be given elsewhere.

In the new approach the crest freeboard  $R_c$  is related to an expected runup level on a non-overtopped slope, say the  $R_{u2\%}$ . This "shortage in crest height" can then be described by:

$$\frac{R_{u2\%} - R_c}{H_s}$$

Eq. 5 can be used to determine  $R_{u2\%}$ , including all influences of berms, etc.

The most simple dimensionless form of the overtopping discharge is:

$$\frac{q}{\sqrt{gH_s^3}}$$

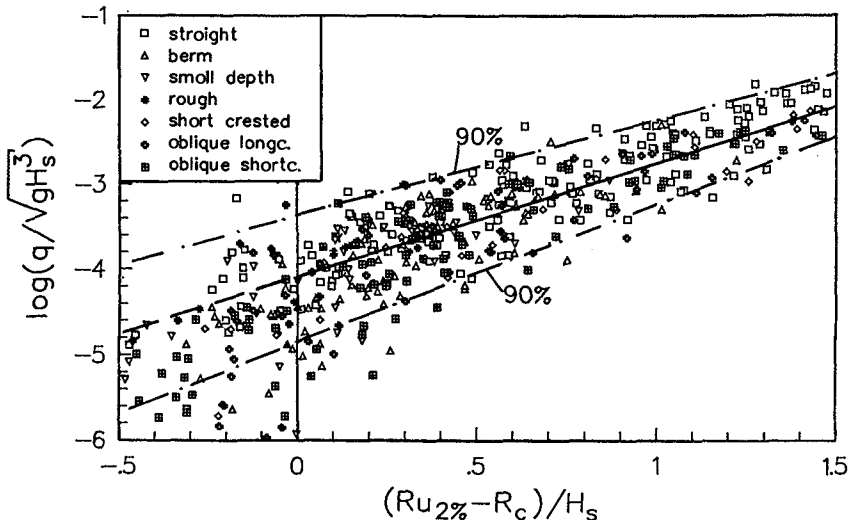


Figure 10 Overtopping formula and data

Fig. 10 shows the final results on overtopping and gives all available data, including data of Owen (1980, only plane slopes), Führböter et al (1989) and various tests at Delft Hydraulics. The horizontal axis gives the "shortage in crest height". For the zero value the crest height is equal to the 2% runup height. For negative values the crest height is even higher and overtopping will be very small. For a value of 1.5 the crest level is 1.5  $H_s$  lower than the 2% runup height and overtopping will obviously be very large. The vertical axis gives the logarithm of the mean dimensionless overtopping discharge.

Fig. 10 gives about 500 data points. The formula that describes more or less the average of the data is given by an exponential function:

$$\frac{q}{\sqrt{gH_s^3}} = 8.10^{-5} \exp \left[ 3.1 \frac{R_{u2\%} - R_c}{H_s} \right] \quad (18)$$

The reliability of Eq. 18 can be given by assuming that  $\log(q/\sqrt{gH_s^3})$  has a normal distribution with a variation coefficient (the ratio of the standard deviation to the mean value) of 0.11. Reliability bands can then be calculated for various practical values of mean overtopping discharges. The 90% confidence bands for two wave heights and four overtopping discharges are given in Table 5.

Mean discharge (l/s per m)	90% confidence band (l/s per m)	
	$H_s = 1$ m	$H_s = 2.5$ m
0.1	0.015 - 0.65	0.012 - 0.83
1.0	0.23 - 4.3	0.18 - 5.5
10.0	3.5 - 28.2	2.8 - 36.1

Table 5 90% confidence band for some overtopping discharges

Limitations of Eq. 18 are that for  $R_c/H_s < 1$  and also for cases (in nature) where  $q > 10$ -50 l/s/m and where an influence factor is applied, the reliability is small and in these cases Eq. 18 is not recommended.

### Conclusions

About 200 tests have been performed in a wave flume and about 160 in a wave basin for the investigation of the influence of a berm, roughness, shallow water and oblique (long and short crested) wave attack on wave runup and overtopping. The results of former investigations and investigations carried out by other institutes have been added to these data. Based on this large set of data design formulas for runup and overtopping are recommended which can be used under a very wide range of circumstances.

Acknowledgement

The Dutch Rijkswaterstaat and the Technical Advisory Committee for Water Defenses (TAW) are acknowledged for their support. The authors gratefully acknowledge Mr. Owen and Hydraulics Research Wallingford for their kind supply of useful data.

REFERENCES

- CIRIA/CUR (1991). Manual on the use of rock in coastal and shoreline engineering, CIRIA Special Publication 83, London, CUR Report 154, Gouda, The Netherlands.
- Coastal Engineering Research Center (1984). Shore Protection Manual. US Army Corps of Engineers, WES, Vicksburg.
- Führböter, A., Sparboom, U. and Witte, H.H. (1989). Großer Wellenkanal Hannover: Versuchsergebnisse über den Wellenauflauf auf glatten und rauhen Deichböschungen mit der Neigung 1:6. Die Küßte. Archive for Research and Technology on the North Sea and Baltic Coast.
- Owen, M.W. (1980). Design of seawalls allowing for wave overtopping. Hydraulics Research Station, Wallingford, England. Report EX 924b.
- TAW, (1974). Wave runup and overtopping. Technical Advisory Committee on protection against inundation. Government publishing office, The Hague, The Netherlands.
- Van der Meer, J.W. (1988). Rock slopes and gravel beaches under wave attack. Doctoral Thesis, Delft University of Technology. Also Delft Hydraulics Publication No. 396.
- Van der Meer, J.W. (1989). Measurement and analysis of directional seas in a basin. Proc. 23rd IAHR Congress, Ottawa.
- Van der Meer, J.W. and Stam, C.J.M. (1992). Wave runup on smooth and rock slopes of coastal structures. Journal of Waterway, Port, Coastal and Ocean Engineering, Vol. 118, No. 5, September/October 1992.
- Tautenhain, E., Kohlhase, S. and Partenscky, H.W. (1982). Wave runup at sea dikes under oblique wave approach. Proc. 18th ICCE, ASCE.

## CHAPTER 135

### NUMERICAL SIMULATION OF WAVE MOTION ON AND IN COASTAL STRUCTURES

J.W. van der Meer<sup>1)</sup>, H.A.H. Petit<sup>1)</sup>, P. van den Bosch<sup>1)</sup>, G. Klopman<sup>1)</sup>  
and R.D. Broekens<sup>2)</sup>

#### Abstract

A 2-dimensional program for simulation of wave motion on coastal structures is described. The program is based on the Volume Of Fluid method and is able to describe fully plunging waves on all kind of structures.

#### Introduction

Simulation of wave motion on coastal structures, such as dikes and breakwaters, has traditionally been done by using physical small scale models. Most phenomena in these models reproduce nature fairly well. But phenomena such as porous flow, wave impacts and viscous effects, can not be modelled correctly. Furthermore, measurement of flow fields in breaking waves on a slope is difficult and may be easier to calculate by a numerical model.

The numerical simulation of wave motion on coastal structures will be presented in this paper. Most literature on this subject describes the 1-dimensional "bore approach", i.e. breaking waves are not modelled correctly. Kobayashi and Wurjanto (1989) described such a model. Verification of that model by Van der Meer and Klein Breteler (1990) showed that wave runup and depth-averaged velocities were simulated fairly well and that wave rundown and wave pressures on a slope could not be predicted. A similar and improved model, including porous flow, is given by Van Gent (1992).

Other 2-dimensional models are based on potential flow theory, such as described by Klopman (1987). These kind of models can simulate an overturning wave tongue, but calculations stop before the wave tongue hits the water or a structure.

---

1) Delft Hydraulics, P.O. Box 152, 8300 AD Emmeloord, The Netherlands  
2) Rijkswaterstaat, P.O. Box 5044, 2600 GA Delft, The Netherlands

This paper will deal with a 2-dimensional description of the complete wave motion.

### The method

The 2-dimensional program SAVOF, developed by the National Aerospace Laboratory in The Netherlands, computes incompressible flow with a free surface in a closed container. The flow is described by the Navier-Stokes equations and the program is based on the program SOLAVOF, presented by Nichols and Hirt (1981). The programs use the volume of fluid (VOF) method which is, in contrast to surface tracking methods, capable to compute free surface flow when the fluid domain becomes multiply connected, i.e. when for example an overturning breaking wave hits the free surface. SAVOF has been modified and became the code as mentioned above. The new name for the code became SKYLLA.

The fluid is treated as incompressible and the resulting equation for the pressure is treated implicitly where in the original code artificial compressibility or limited compressibility was used in combination with an explicit solver. The results of a first calculation with the original SAVOF-program are shown in Fig. 1. The closed container was put on a slope of 1:4 and the calculation started with a "block" of water in the edge. Plots 5-10 show more or less a plunging breaker on a slope and the subsequent runup.

### Possible applications

Various applications can be considered when a numerical simulation of wave motion in and on coastal structures is possible.

- Wave motion on impermeable (smooth or rough) slopes, giving water velocities, accelerations, pressures and runup levels.
- Wave overtopping on impermeable low-crested structures, giving water velocities and overtopping discharges.
- Wave motion on a submerged impermeable structure, giving wave transmission.
- Wave motion on and in a porous rubble structure, giving the same parameters as for an impermeable structure, but also the porous flow, phreatic line and wave transmission.
- Wave motion on vertical structures as caissons, giving wave forces and overtopping.
- Simulation of wave-current interaction on sloping beaches including bars.

### Development of the research code SKYLLA

A feasibility study was performed (Broekens and Petit, 1991) on the modifications required or relevant for the application of SKYLLA on the simulation of wave motion on and in coastal structures. The main modifications were:

- prescription of incident waves and a weakly reflecting boundary condition
- description of an impermeable slope
- description of porous flow

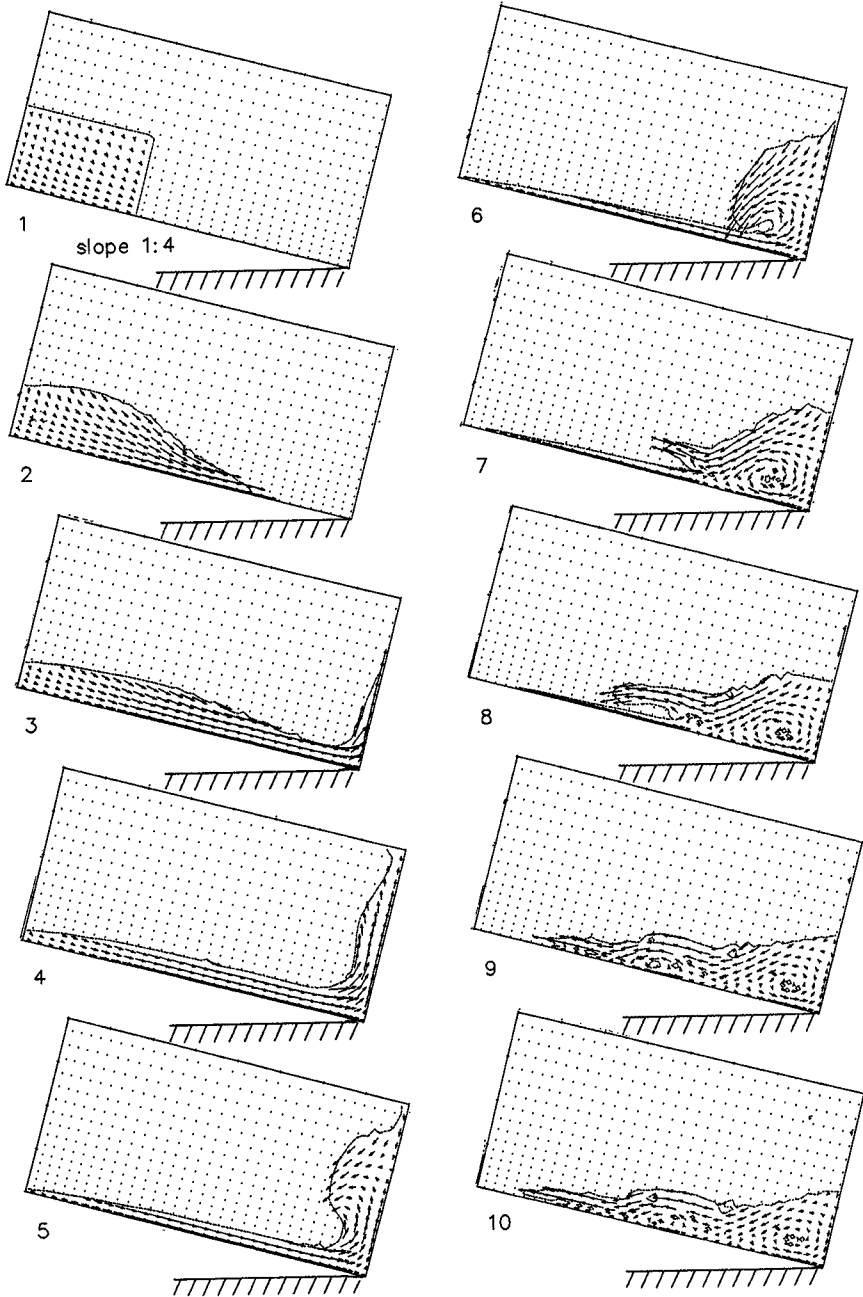


Figure 1 First calculations with SAVOF

The first two modifications will be summarized here and are more fully described in Petit and Van den Bosch (1992).

#### Weakly reflecting boundary condition

In order to give an idea of how a weakly reflecting boundary condition and an impermeable slope were implemented in the SKYLLA model first the pressure equation for the VOF method will be derived. The Navier-Stokes equations for the momentum in x and y direction respectively are:

$$\frac{\partial u}{\partial t} + u \frac{\partial u}{\partial x} + v \frac{\partial u}{\partial y} = - \frac{\partial P}{\partial x} + \nu \nabla^2 u \quad (1)$$

$$\frac{\partial v}{\partial t} + u \frac{\partial v}{\partial x} + v \frac{\partial v}{\partial y} = - \frac{\partial P}{\partial y} + \nu \nabla^2 v - g \quad (2)$$

where u and v are velocities in the x and y direction respectively and P denotes the reduced pressure  $P = p/\rho$ , with p = pressure and  $\rho$  = mass density of the fluid. Conservation of mass is, for constant  $\rho$ , expressed by:

$$\frac{\partial u}{\partial x} + \frac{\partial v}{\partial y} = 0 \quad (3)$$

By discretizing the momentum equations in time the following equations are found:

$$\frac{u^{n+1} - u^n}{\Delta t} + u^n \frac{\partial u^n}{\partial x} + v^n \frac{\partial u^n}{\partial y} = - \frac{\partial P^{n+1}}{\partial x} + \nu \nabla^2 u^n \quad (4)$$

$$\frac{v^{n+1} - v^n}{\Delta t} + u^n \frac{\partial v^n}{\partial x} + v^n \frac{\partial v^n}{\partial y} = - \frac{\partial P^{n+1}}{\partial y} + \nu \nabla^2 v^n - g \quad (5)$$

Notice that the pressure is taken at the new time level n+1 while both the convection and the viscous terms are taken at the old time level n. Furthermore, the conservation of mass at the new time level n+1 is required:

$$\frac{\partial u^{n+1}}{\partial x} + \frac{\partial v^{n+1}}{\partial y} = 0 \quad (6)$$

From these equations the pressure Poisson equation can be derived by differentiating Eq. (4) to x, Eq. (5) to y and use Eq. (6) to eliminate the velocities at the time level n+1. The result is:

$$\begin{aligned} \nabla^2 P^{n+1} = & \frac{1}{\Delta t} \left( \frac{\partial u^n}{\partial x} + \frac{\partial v^n}{\partial y} \right) + \frac{\partial}{\partial x} \left( -u^n \frac{\partial u^n}{\partial x} - v^n \frac{\partial u^n}{\partial y} + \nu \nabla^2 u^n \right) \\ & + \frac{\partial}{\partial y} \left( -u^n \frac{\partial v^n}{\partial x} - v^n \frac{\partial v^n}{\partial y} + \nu \nabla^2 v^n - g \right) \end{aligned} \quad (7)$$



In space the VOF method uses a staggered grid like given in Fig. 2, where the velocities are given at the centre of the cell faces and the pressure is given at the cell centre. At the cell centre also the F value is given which indicates the fraction of the cell which is filled with fluid.

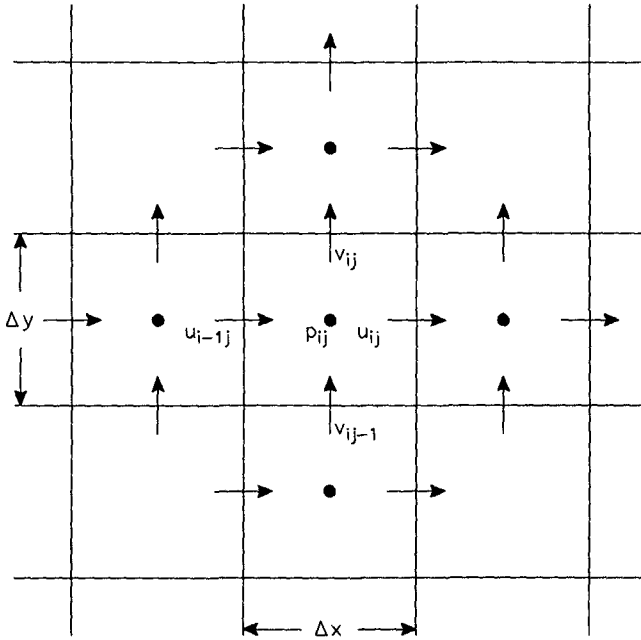


Figure 2 Staggered grid with velocities and pressures

By also discretizing in space the Navier-Stokes equations can be written (here, for simplicity, in the case of an equidistant grid in both x and y direction) as:

$$u_{ij}^{n+1} + \Delta t \frac{P_{i+1j}^{n+1} - P_{ij}^{n+1}}{\Delta x} = \tilde{u}_{ij} \quad (8)$$

$$\text{where } \tilde{u}_{ij} = u_{ij}^n + \Delta t \text{DISU}_{ij} \left( -u^n \frac{\partial u^n}{\partial x} - v^n \frac{\partial u^n}{\partial y} + \nu \nabla^2 u^n \right) \quad (9)$$

and  $\text{DISU}_{ij}$  stands for an operator that discretizes at the U velocity point.

$$v_{ij}^{n+1} + \Delta t \frac{P_{ij+1}^{n+1} - P_{ij}^{n+1}}{\Delta y} = \tilde{v}_{ij} \quad (10)$$

$$\text{where } \tilde{v}_{ij} = v_{ij}^n + \Delta t \text{DISV}_{ij} \left( -u^n \frac{\partial v^n}{\partial x} - v^n \frac{\partial v^n}{\partial y} + \nu \nabla^2 v^n - g \right) \quad (11)$$

Here  $\text{DISV}_{ij}$  is an operator that discretizes at the V velocity point.

The discretized version of Eq.(6) is given by:

$$(u_{ij}^{n+1} - u_{i-1j}^{n+1})\Delta y + (v_{ij}^{n+1} - v_{ij-1}^{n+1})\Delta x = 0 \tag{12}$$

By using this equation the velocities at time level n+1 can be eliminated and the discretized version of the pressure Poisson equation is found:

$$\frac{P_{i+1j}^{n+1} - 2P_{ij}^{n+1} + P_{i-1j}^{n+1}}{\Delta x^2} + \frac{P_{ij+1}^{n+1} - 2P_{ij}^{n+1} + P_{ij-1}^{n+1}}{\Delta y^2} = \frac{1}{\Delta t} \left( \frac{\tilde{u}_{ij} - \tilde{u}_{i-1j}}{\Delta x} + \frac{\tilde{v}_{ij} - \tilde{v}_{ij-1}}{\Delta y} \right) \tag{13}$$

The velocity arrows which are shown in Fig. 2 indicate all the velocities that are used in the discretization of the right hand side of Eq. (13). At an impermeable boundary, which coincides with a gridline, the velocity at the boundary at time-level n+1 can be left out in Eq. (12) and the velocities outside the flow domain, which are needed to calculate DISU or DISV at the boundary, can be chosen such that e.g. a free slip boundary condition is met. These velocities are called virtual velocities.

Once the pressure equation is solved Eq. (8) and (10) can be used to find the velocities at the new time level.

In Fig. 3 the situation at a left boundary is sketched. The velocities  $v_{0j}^n$  and  $v_{0j-1}^n$  are virtual velocities.

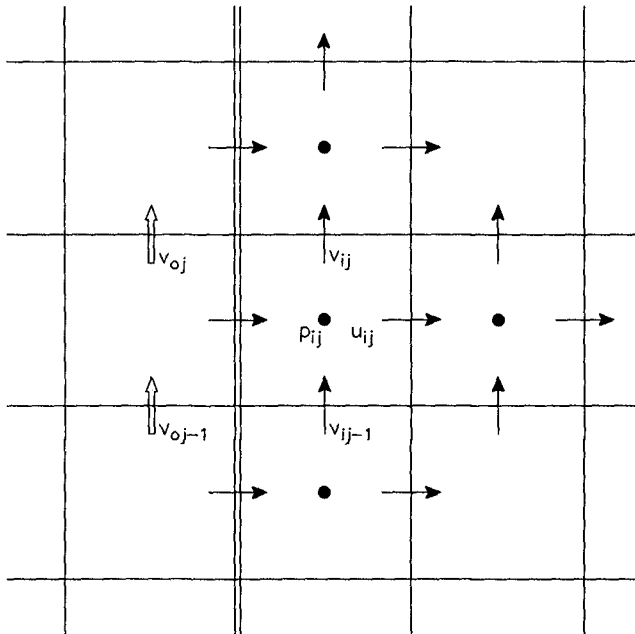


Figure 3 Left side boundary

In order to allow waves to enter and leave at the left boundary, the following equations were discretized:

$$\frac{\partial u}{\partial t} - c \frac{\partial u}{\partial x} = \frac{\partial u_{in}}{\partial t} - c \frac{\partial u_{in}}{\partial x} \quad (14)$$

$$\frac{\partial v}{\partial t} - c \frac{\partial v}{\partial x} = \frac{\partial v_{in}}{\partial t} - c \frac{\partial v_{in}}{\partial x} \quad (15)$$

$$\frac{\partial \eta}{\partial t} - c \frac{\partial \eta}{\partial x} = \frac{\partial \eta_{in}}{\partial t} - c \frac{\partial \eta_{in}}{\partial x} \quad (16)$$

The discretization of Eq.(14) was done upwind for the outgoing waves to yield an explicit expression for  $u_{0j}^{n+1}$ . Note that the right hand side of this equation involves the incoming wave and is supposed to be known. Eq. (15) was discretized implicitly using timelevels  $n$  and  $n-1$ , yielding an explicit expression for the virtual velocity  $v_{0j}^n$ . Equation (16) was also discretized upwind for the outgoing waves and explicitly in time where  $\eta$  in Eq. (16) can be related to the  $F$  values in the first two columns by:

$$\eta_i^n = \sum_{j=2}^{j_{s1}} F_{ij}^n \Delta y_j \quad \text{for } i = 1, 2 \quad (17)$$

where  $j_{s1}$  has the property:

$$F_{ij} = 1 \quad \text{for } j = 1(1)j_{s1} - 1$$

$$0 < F_{ij_{s1}} < 1$$

$$F_{ij} = 0 \quad \text{for } j > j_{s1}$$

Here it was implicitly assumed that near to the weakly reflecting boundary the surface is a single valued function of  $x$ .

#### Impermeable slope

Again, by setting virtual velocities, an impermeable free-slip slope could be included in SKYLLA, where the slope is allowed to intersect the grid arbitrarily. In Fig. 4 the four possible cell intersections of a climbing slope with pressure cells is shown. Cases where the slope intersects the cell at a corner can numerically be treated as one of the four cases. For each of the cases 2), 3) and 4) two virtual velocities were defined such that the velocity stencil given in Fig. 2 can be used at each cell which contains fluid. These virtual velocities are defined such that a free- or a no-slip boundary condition is satisfied at a given location point on the slope in the intersected cell.

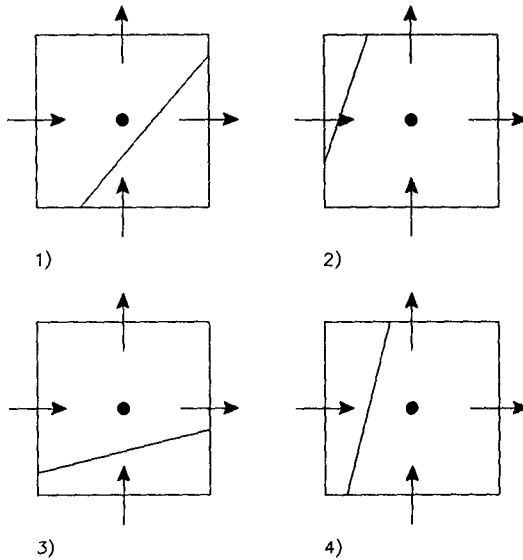


Figure 4 Cells with an impermeable slope

The advantage of this approach over the pressure-velocity iteration technique (Viecelli, 1969), is that an elliptic solver (e.g. Conjugate Gradient Squared (CGS)) can be used to solve the pressure equation instead of the (Successive Over Relaxation (SOR) like) process of artificial compressibility needed for the pressure-velocity iteration technique. Since solving the pressure equation is by far the most time consuming process in the VOF solver, the use of versions of the CGS method that were specially built for vector computers meant a significant improvement of the performance of SKYLLA.

In order to achieve a more accurate free surface update after new velocities are determined the FLAIR method (Ashgriz and Poo, 1991) was adopted. Updating the fluid domain near the position where the free surface meets the slope proved to be rather difficult however.

#### Computational results

Various calculations have been done with SKYLLA on smooth impermeable structures in order to test the flexibility and the robustness of the program. Results of one calculation will be given here. No validation tests have been performed until now which means that the results are only output of a computer program and the correspondence with nature has not been verified.

The calculations showed that the grid size is of paramount importance to the results especially when breaking waves occur. The result is that in order to describe breaking waves on a slope small cells and time steps are required. This is not a drawback of the VOF-method as used in SKYLLA, but a direct result from the fact that a nonlinear highly instationary process is simulated.

Fig. 5 gives the cross-section of a dike with a berm. The upper and down slopes are 1:4 and the berm with a length of 5 m has a slope of 1:15 and is located just beneath the still water level. The water depth is 3.4 m at the toe of the structure. This cross-section was used for computation. The generated wave had a wave height of 1.2 m and a wave period of 4.5 s.

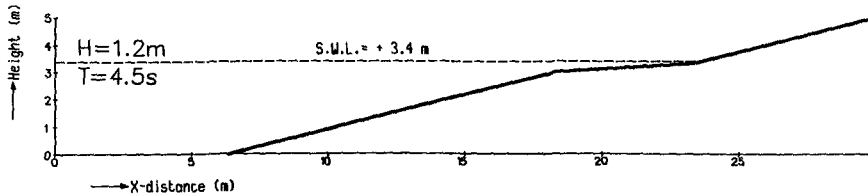


Figure 5 Cross-section used for computations with SKYLLA

In total 350 cells were used in the x-direction with a decreasing cell size from left to right from 0.101 m to 0.050 m. In the y-direction 69 cells were used with a refinement near the still water level (range: 0.041 m to 0.258 m). The basic time step was 0.025 s and the minimum time step needed was 0.0015 s (at 8.6 s, see Fig. 6). In total 17 s wave motion was simulated which required 5977 s of cpu time on a CONVEX C3820.

Figs. 6-9 show results of the calculations at 4 different time steps. Each Fig. has 3 subfigures. At the top the F function is shown where the black colour corresponds with cells that are completely filled with fluid ( $F = 1$ ) and white cells that are empty ( $F = 0$ ). The middle plot shows the velocity field in the wet domain. The lowest plot gives the tangential velocity at the free-slip slope as a function of the x-coordinate.

In Fig. 6, at  $t = 8.6$  s, the overturning wave tongue is about to fall on the backwash, thereby multiply connecting the region of the filled cells. Fig. 6c gives the location of the separation point. Fig. 7 gives the result 0.2 s later at  $t = 8.8$  s. The wave tongue has hit the water surface and a horizontal jet emerges from this process. The downstream velocity under the enclosed cylinder of "vacuum" increased. At about  $x = 18$  m the velocity has changed to a shoreward direction.

In reality the enclosed cylinder of air will change to large air-bubbles and escape rapidly upwards out of the fluid. Fig. 7 does not show this escape due to the fact that vacuum was modelled and not air. This is certainly a difference with nature.

Fig. 8 shows the results 2.3 s later when another wave arrives at the toe of the structure and steepens its slope, partly due to the back wash from the previous wave. Further on the slope the breaking goes on which is caused by the nearly horizontal berm and the up and back rushing water. Runup velocities are about 1 m/s. In Fig. 9 the wave starts to break again.

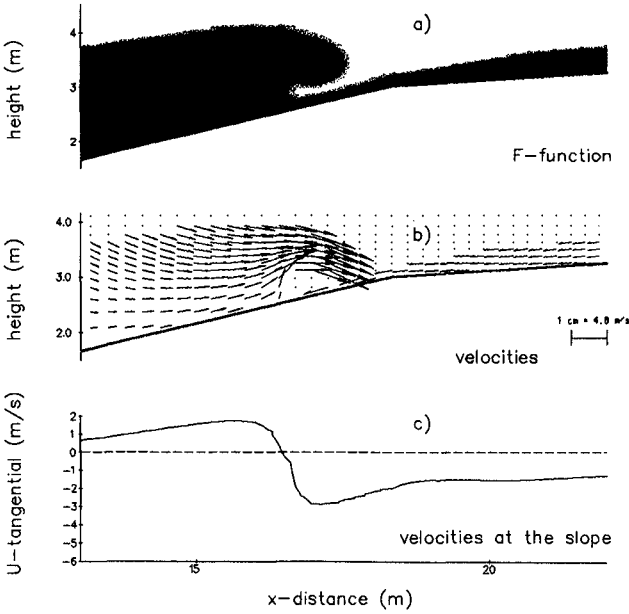


Figure 6 SKYLLA results at  $t = 8.6$  s

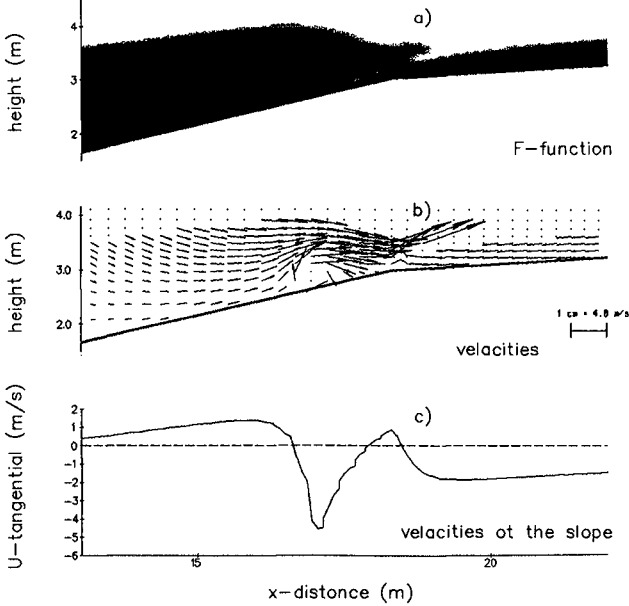


Figure 7 SKYLLA results at  $t = 8.8$  s

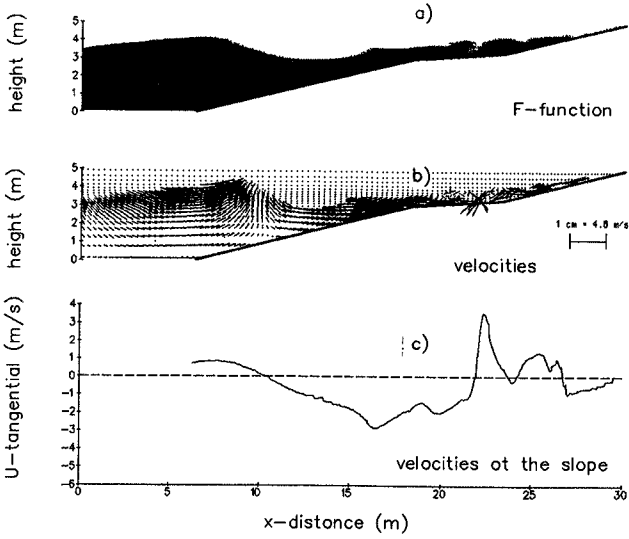


Figure 8 SKYLLA results at  $t = 11.1$  s

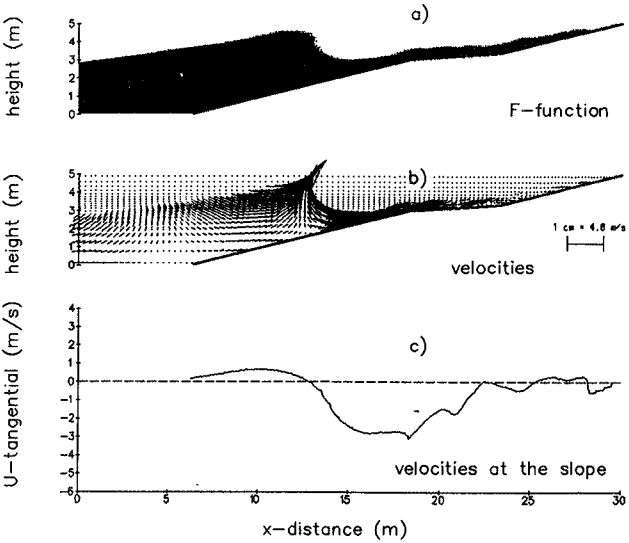


Figure 9 SKYLLA results at  $t = 12.0$  s

### Conclusions and recommendations

The results of the computations show that it is possible to simulate breaking waves on a slope. The next step, however, is to perform physical model tests in order to validate the accuracy of the results. The wave profiles at various time steps can then be compared and possibly the whole velocity field using a Partical Image Processing technique.

Attention has to be paid to the effect that vacuum "bubbles" do not escape from the water.

Calculations are still costly. By applying better solvers for solving the Poisson equation on a vector computer the SKYLLA-code has already become 4 times faster than the original code. With the expected increase in calculation speed of supercomputers in the (very) near future and the better solvers that are being developed it is expected that computation time will become less important.

The existing program can be developed further to cope with the possible applications which were mentioned earlier. Wave overtopping can be included and also a porous medium like a breakwater. Recent research on porous flow modelling (the same MAST research, see Acknowledgement) can easily be included, and suggestions to adjust the Navier-Stokes equations for a porous medium have been given in Broekens and Petit (1991). It seems well possible and even straight forward to add extra terms to the momentum equations and to include these in a VOF-method.

### Acknowledgements

The work has been performed under a project of the Commission of the European Communities, called MAST - G6 Coastal Structures, project 0032 and was further funded by the Dutch Public Works Department (Rijkswaterstaat) and Delft Hydraulics. Institutes and universities from Denmark, Greece, United Kingdom and The Netherlands were involved in the project.

The objective of the MAST-project was: the development of a physically based numerical formulation of the water motion on a smooth slope (runup, rundown, overtopping, water velocities, water pressures, wave breaking), and a formulation of the same water motion on, but also in a porous rubble structure (phreatic line, pressures and porous flow).

The authors are grateful to A. van der Ploeg who supplied us with a vectorizable preconditioner for the CGS method that was used to solve the pressure equation.

### References

Ashgriz, N. and Poo, J.Y. (1991). Axisymmetric Liquid Sloshing under low-g Conditions: Numerical Simulation Method. National Aerospace Laboratory Report NLR TR 86057 L, The Netherlands.



- Broekens, R.D. and Petit, H.A.H. (1991). SKYLLA: wave motion in and on coastal structures. Feasibility study on the application of SAVOF. Delft Hydraulics Report H 1351.
- Hirt, C.W. and Nichols, B.D. (1981). Volume of fluid method for the dynamics of free boundaries. Journ. of Computational Physics 39, 201-225.
- Klopman, G. (1987). Numerical simulation of breaking waves on steep slopes. Coastal Hydrodynamics, ed. R.A. Dalrymple.
- Kobayashi, N. and Wurjanto, A. (1989). Numerical model for design of impermeable coastal structures. Research Report No. CE-89-75. University of Delaware.
- Petit, H.A.H and Van den Bosch, P. (1992). SKYLLA: Wave motion in and on coastal structures. Numerical analysis of program modifications. Delft Hydraulics Report H 1351.
- Van der Meer, J.W. and Klein Breteler, M. (1990). Measurement and computation of wave induced velocities on a smooth slope. Proc. ASCE, 22nd ICCE, Delft, The Netherlands.
- Van Gent, M.R.A. and Engering F.P.H. (1992). The modelling of wave action on and in coastal structures. Proc. Final workshop MAST G6S, Lisbon.
- Viecelli, J.A. (1969). A Method for Including Arbitrary External Boundaries in the MAC Incompressible Fluid Computation Technique, J. Comp. Phys. 4, 543-551.

## CHAPTER 136

### IMPACT BREAKING WAVE PRESSURES ON VERTICAL WALLS

Masataro HATTORI<sup>1)</sup> and Atsusi ARAMI<sup>2)</sup>

#### ABSTRACT

Impact wave pressures acting on a vertical wall were discussed by simultaneous measurements of the pressure and wave shapes at impact.

Experiments confirmed the principal role of adiabatic processes of trapped air bubbles to the generation of impact pressures. The most severe impulsive pressure was observed when breaking waves hit the wall with trapping small air bubbles or a very thin lens-shaped air pocket. The larger the amount of the entrapped air, the lower the magnitude of the impact pressures. Due to the pulsation of the air pocket, damped pressure oscillations were observed immediately after the impact pressure.

A predictive model, taking account of the adiabatic compression processes of the trapped air pocket, predicts fairly well the maximum impact pressure and the frequency of the damped pressure oscillation, in the case when plunging breakers collide against the wall.

#### 1. INTRODUCTION

Impact pressures have been considered unlikely to be effective for sliding and overturning massive structures seawalls. Nevertheless, some studies (Weggel and Maxwell, 1970; Mogridge and Jamieson, 1980; Arami and Hattori, 1988) and recent field observations pointed out a clear evidence that such pressures can cause severe local damages to vertical wall type structures, and that the resulting damages would develop owing to successive attacks of breaking waves and cause sudden failures of the structures.

Since Bagnold (1939) proposed an air pocket model for the physics of the high impulsive wave pressure, many experimental studies have been performed to explicate the physics of wave-

---

1) Department of Civil Engineering, Chuo University, Tokyo

2) Ishikawajima-Harima Heavy Industries Co., Ltd., Tokyo

impact processes. However, published data from the various studies provide very wide and different views on the wave-impact physics. Therefore, more detailed and reliable examinations on this process are absolutely necessary to the development of physical models predicting for the impact pressure. The principal aims of this study are as follows;

1. To explicate the difference of the wave-impact processes under various colliding conditions of breaking waves onto the wall,
2. To examine aerodynamic contributions of the entrapped air to the generation of the impact pressure, and
3. To propose a predictive model, taking account of adiabatic compression processes of the air pocket entrapped between the structure and wave.

## 2. EXPERIMENTAL EQUIPMENT AND PROCEDURES

### 2.1 EXPERIMENTAL EQUIPMENT

General arrangement of the experimental equipment is shown in Fig. 1. Experiments were carried out in a glass-walled wave flume, 0.30 m wide, 0.55 m high, and 20 m long, in which a steel beach of 1/20 slope was installed. Regular waves were produced by a reflection-absorbing wave maker of flat type.

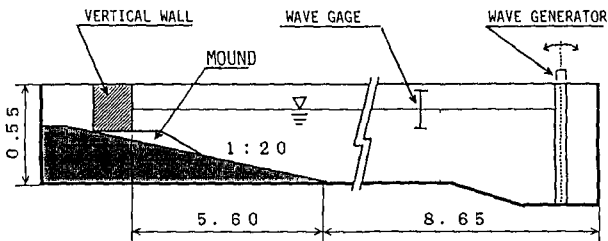


Fig. 1 General arrangement of the experimental equipment. (Units:m)

Vertical plane wall of a 35 mm thick plastic plate (0.30 m wide and 0.50 m high) was shored up with steel frames. The wall complex, having a natural frequency of 1.2 KHz in water, was mounted rigidly on a plastic mound with a foreshore slope of 1/10. Incident wave properties were detected by a capacitance-type wave gauge installed at the uniform water depth.

### 2.2 PRESSURE MEASUREMENTS

Impact pressures were measured by semi-conductor type transducers of 10mm in diameter. The pressure transducers have operational capacity of 100 gf/cm<sup>2</sup> and 200 gf/cm<sup>2</sup>, with 100% overload capability. Their natural frequency in water is 9.6 KHz and the frequency response range DC to 4.8 KHz.

Four pressure transducers were located vertically along the centerline of the wall at an interval of 2.0 cm. The maximum impact pressure is occurred most likely in the vicinity of the still

water level. Hence, two additional pressure transducers were set at 1.0 cm below and above the still water level and 5.0 cm apart from the centerline.

### 2.3 RECORDING THE IMPINGING BREAKING WAVE PROFILE

High-speed videos were simultaneously taken at 200 frames/s with the measurements of impact pressures. Photo. 1 is an example of the picture of wave shape at impact. Number of the last three digits in millisecond after the start of a test run. White arrows on the left hand side show the locations of the pressure transducers. Real-time pressure record from the pressure transducer ( $P_4$ ) at the still water level is monitored on the left hand side of the still. The synchronization between the pressure records and sequential stills was made by using the pressure monitor within an accuracy of 0.1ms.

Length measurements were made using a 1.0 cm square grid system, attached on the sidewall glass. The breaking wave height, the size and shape of trapped air pocket, the forward and upward velocities of wave surface at and in front of the wall were read from the pictures projected on a 29-inch video-screen.

### 2.4 EXPERIMENTAL PROCEDURES

In the repeated tests, impact pressures vary significantly owing to the instability of the wave breaking and the high reflection of the wall. We employed the two following procedures to ensure the repeatability of the experiments; (1) Every test run was made after the free surface disturbance due to the preceding test run was well subsided, and (2) The wave generator was controlled by a programmed analogue signal yielding a regular wave train.

Outputs of the impact pressures were recorded on digital recorders over six wave periods at a sampling frequency of 5 KHz for extensive processing by computer. Data analyses were made for four subsequent breaking waves preceded by some non-breaking waves.

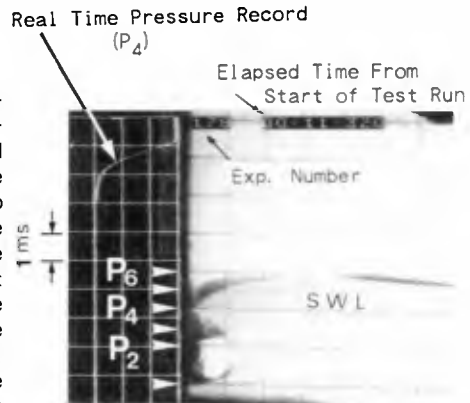


Photo. 1 Example of the video picture.

### 3. EXPERIMENTAL RESULTS OF THE IMPACT PRESSURE CHARACTERISTICS

Since wave-impact processes depend closely on the wall location relative to the wave breaking position (Chen and Melville, 1988), it is reasonable to characterize them by the development of wave breaking at the wall, or the colliding conditions. In this study, we will examine into the essential characteristics of

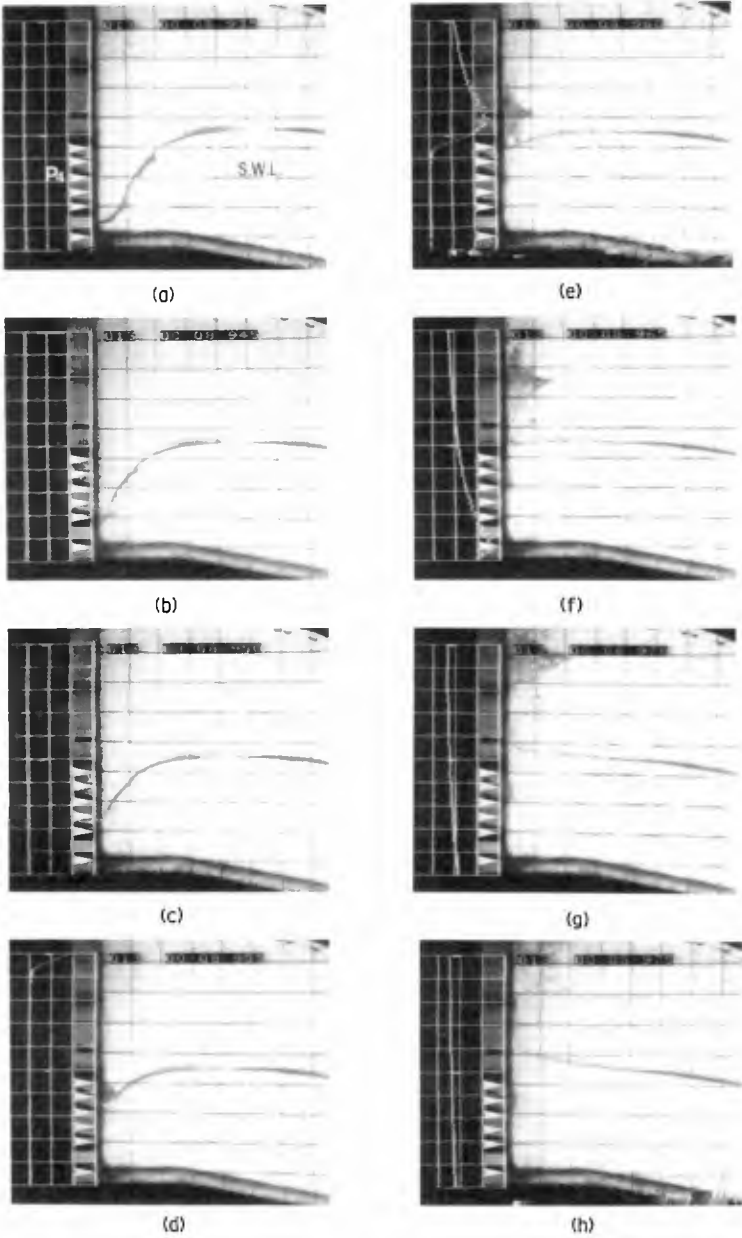
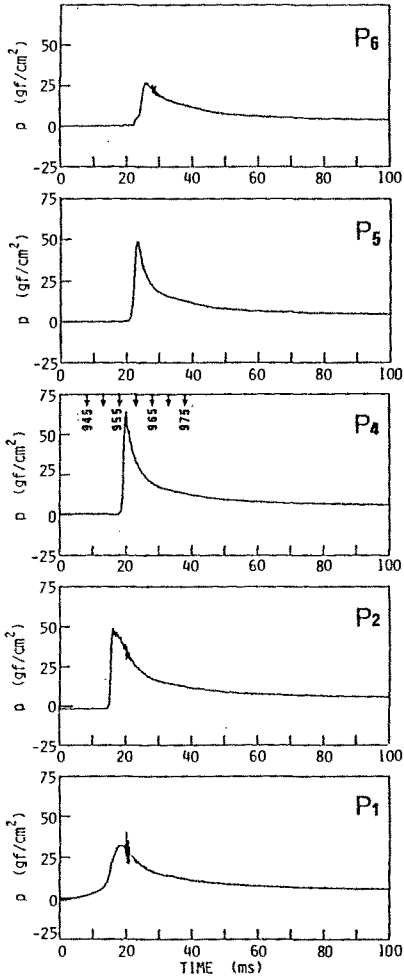


Photo. 2 Sequence of the still pictures of the wave surface. (Flip-through condition)



WAVE PRESSURE RECORDS (No. 013-3)  
FOR THE FLIP-THROUGH IMPACT.

$H_i = 4.7 \text{ cm}, \quad T = 1.7 \text{ s}$

$H_b = 5.7 \text{ cm}, \quad \bar{\gamma} = 0$

$h_d = 2.5 \text{ cm}.$

$P_{\max} / \rho g H_b = 11.2$

Fig. 2 Wave pressure records (Flip-through condition)  
( $H_b=5.7\text{cm}, T=1.7\text{s}$ )

impact pressures for the four following conditions, somewhat similar to Oumeraci, Klammer, and Partenscky (1991):

- (1) " Flip-Through" condition with no air bubbles,
- (2) Collision of the vertically flat wave front with entrapping small air bubbles -- single peak pressure --,
- (3) Collision of plunging breakers with a thin air pocket -- damped pressure oscillations with high frequencies --, and
- (4) Collision of fully developed plunging breakers with a thick air pocket-- damped pressure oscillation with low frequencies --.

### 3.1 FLIP-THROUGH COLLISION WITH NO AIR BUBBLES.

Impact process due to the " flip-through" action (Cooker and Peregrine, 1991) is observed when incident waves break as upward deflected breaker near the wall. Photo 2, consisting of 8 still pictures, gives the wave shape changes during the collision on the wall. We notice from the sequential pictures that the wave shapes change a very similar process to the computation by Cooker and Peregrine (1991). The corresponding pressure records at various elevations are given in Fig. 2, in which 20 ms on the time axis refers to the time of the maximum peak pressure recorded at  $P_4$ , on the still water level. Thick arrows on the top of the pressure record at  $P_4$  represent the shooting instant of the pictures.

Although the resultant peak pressures are not so high in the magnitude ( $p_{\max, 4}/\rho g H_b = 11.2$ ), the pressure record at  $P_4$  shows that an impact is occurred without a clear hit of the wave front.

### 3.2 COLLISION OF VERTICALLY FLAT WAVE FRONT WITH SMALL AIR BUBBLES -- SINGLE PEAK IMPACT PRESSURE --.

Collision of breaking waves with vertical or slightly curled front brings about extremely high impact pressures ( $p_{\max, 4}/\rho g H_b = 109.6$ ), as seen in Photo. 3 and Fig. 3. However, even the highest impact at  $P_4$  is much lower than that due to a water hammer process.

The pictures about the instant of collision (Photo. 3 (e) and (f)) do not show apparently the air entrainment. But we can find out dark image indicating a group of small air bubbles trapped over the hitting region of wave crest (Photo. 3 (g) and (f)). The pressure records in this region (Fig. 3  $P_1 - P_3$ ) exhibit clear pressure fluctuations with very high frequencies of about 1,000 Hz during the impact. The peak pressures occur simultaneously at various elevations, but their magnitudes decrease remarkably with the distance from the hitting point of the wave crest.

If a small air pocket in a form of very thin lens is trapped in the vicinity of the impinging region of the wave crest, the pocket is collapsed into small air bubbles at impact. This also results in a single peak impact pressure. Occasionally we observed a fact that a fraction of the air bubbles was released upwards with wave splash. This results in noticeable reduction of the peak pressure and causes variability in the pressure magnitude. The experiments, however, confirm an important role of the trapped air bubbles to generation of the impact pressures.

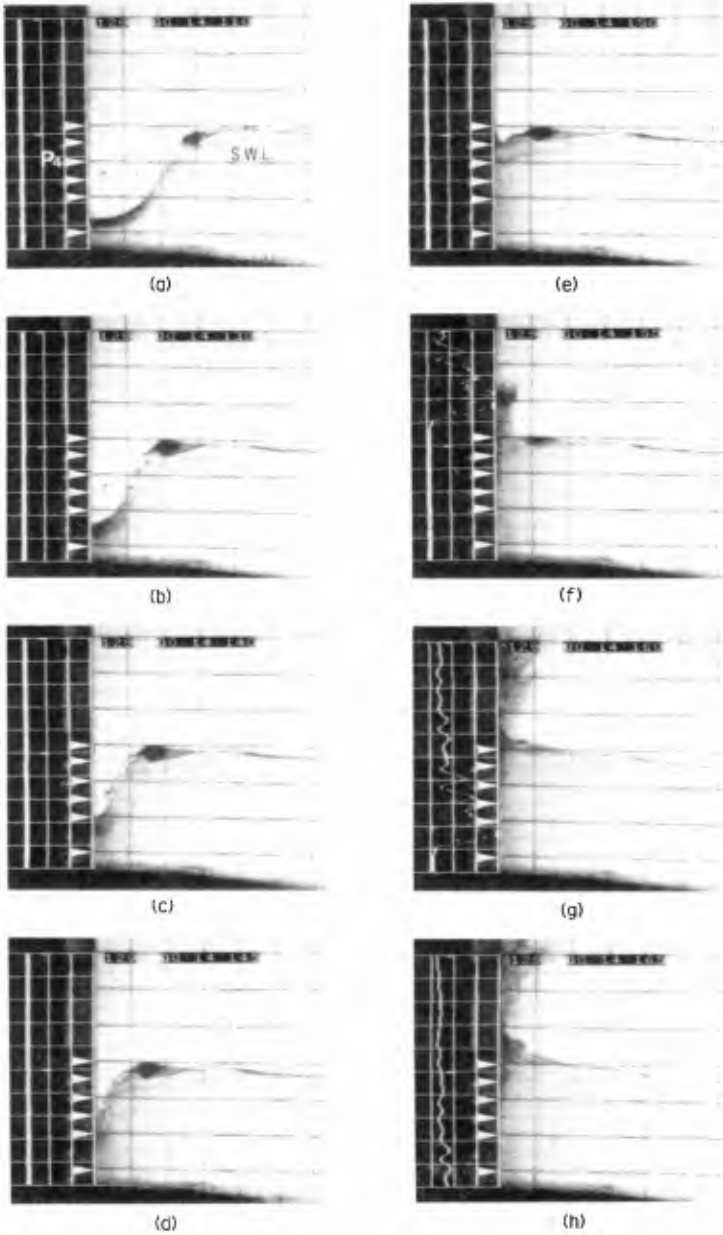
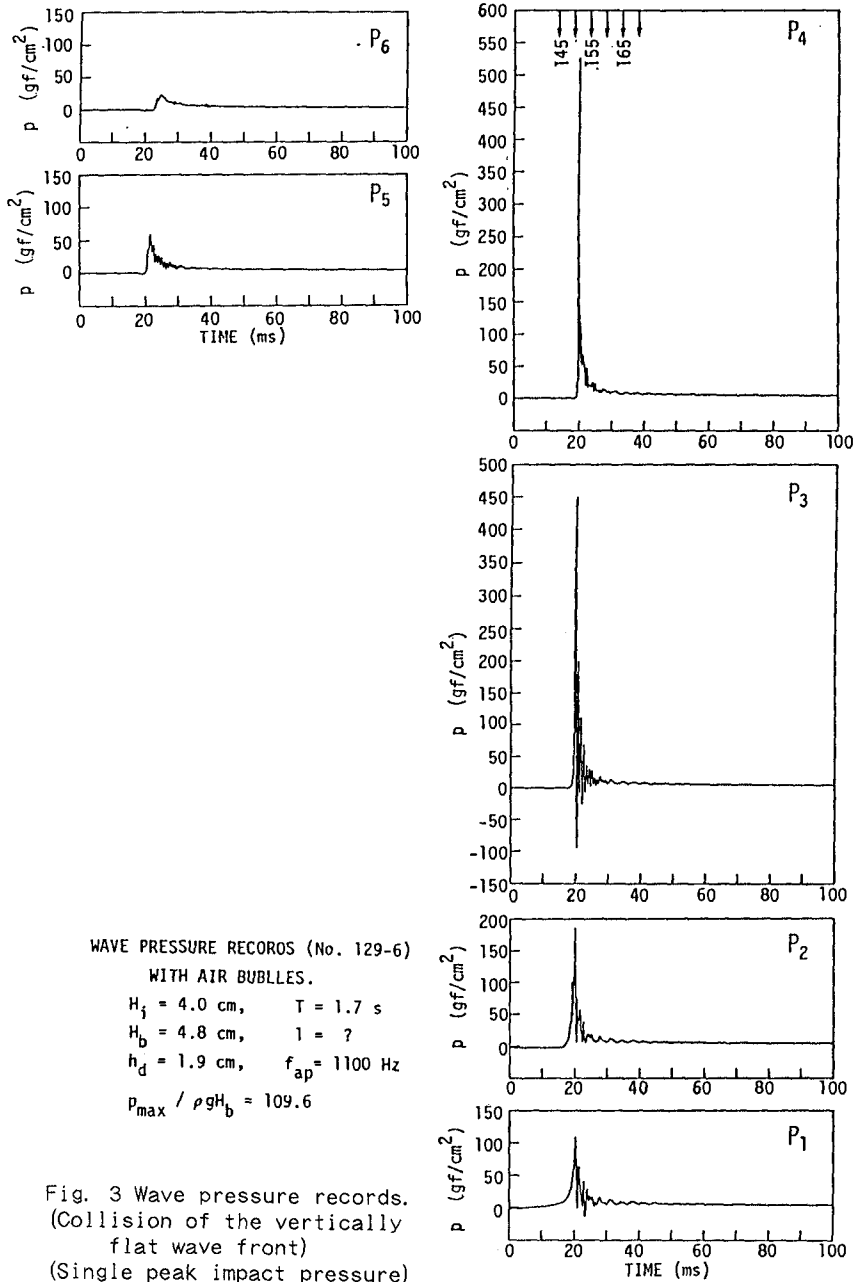


Photo. 3 Sequence of the still pictures of the wave surface.  
 (Collision of the vertically flat wave front)





### 3.3 COLLISION OF PLUNGING BREAKERS -- DAMPED PRESSURE OSCILLATIONS OF HIGH FREQUENCIES --

Photo. 4 gives the trapping process of a two dimensional air pocket between the wall and wave. The pressure records at various elevations in Fig. 4 show that the adiabatic action of the air pocket gives rise not only to relatively high impact pressures on the wall ( $p_{\max, 4} / \rho g H_b = 51.9$ ), but also to damped oscillations with a high frequencies of 250 Hz, immediately after a rapid pressure drop. The pressure records in the air pocket zone ( $P_1-P_3$ ) exhibit almost the same variations both in magnitude and in phase. This indicates repeated compression and expansion of the air pocket. Immediately after the collision, the air pocket transforms into a group of air bubbles, in which the bubbles rotate violently (Photo. 4 (f)), and this will likely play some role in the reduction of pressure oscillations (Cooker and Peregrine, 1991). We can not yet specify any dominant process of the energy dissipation due to the violent motion of the air bubbles.

From the simultaneous records of the pressure and wave, we found an evidence that damped pressure oscillations continue until the air bubbles start to escape through the wave surface.

### 3.4 COLLISION OF FULLY DEVELOPED PLUNGING BREAKERS -- DAMPED PRESSURE OSCILLATIONS OF LOW FREQUENCIES --

As plunging and curling of the breaking wave are developed, a large cylindrical air pocket will be trapped and confined between the wall and wave. As shown in Figs. 5 and 6, an increase of the air pocket thickness  $l$ , or the trapped air amount results in a decrease both in the peak pressure  $p_{\max}$  and in the frequency of damped pressure oscillation,  $f_{ap}$ . Both  $p_{\max}$  and  $f_{cap}$  are inversely proportional to  $l$ . However, the other principal characteristics of the impact pressure are almost the same as those for the plunging breaker collision.

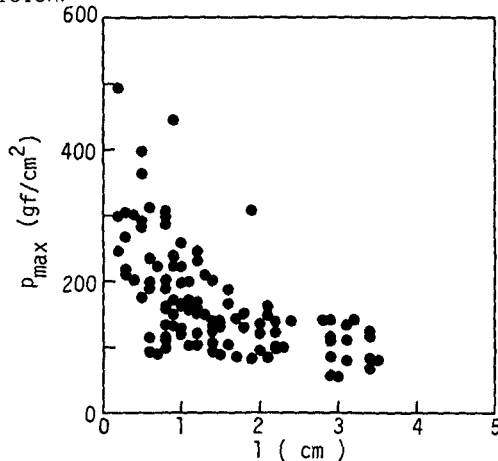


Fig. 5 Relation between  $p_{\max}$  and  $l$ .

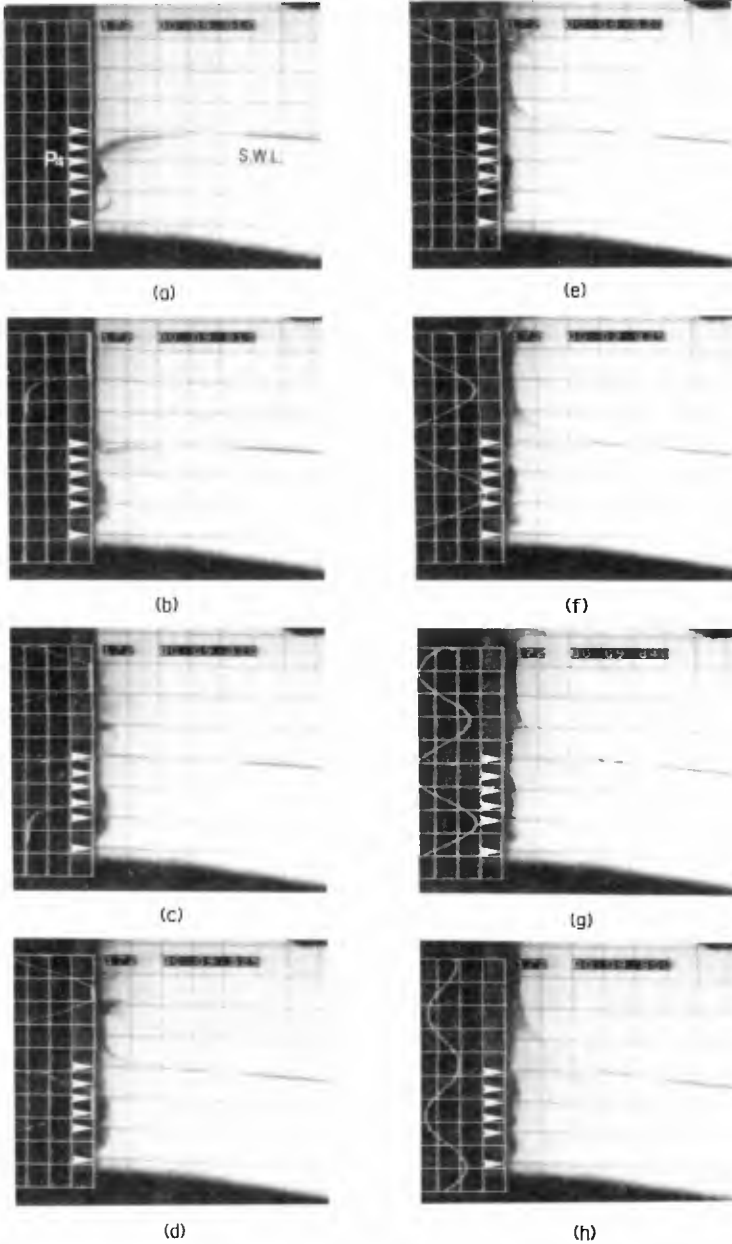
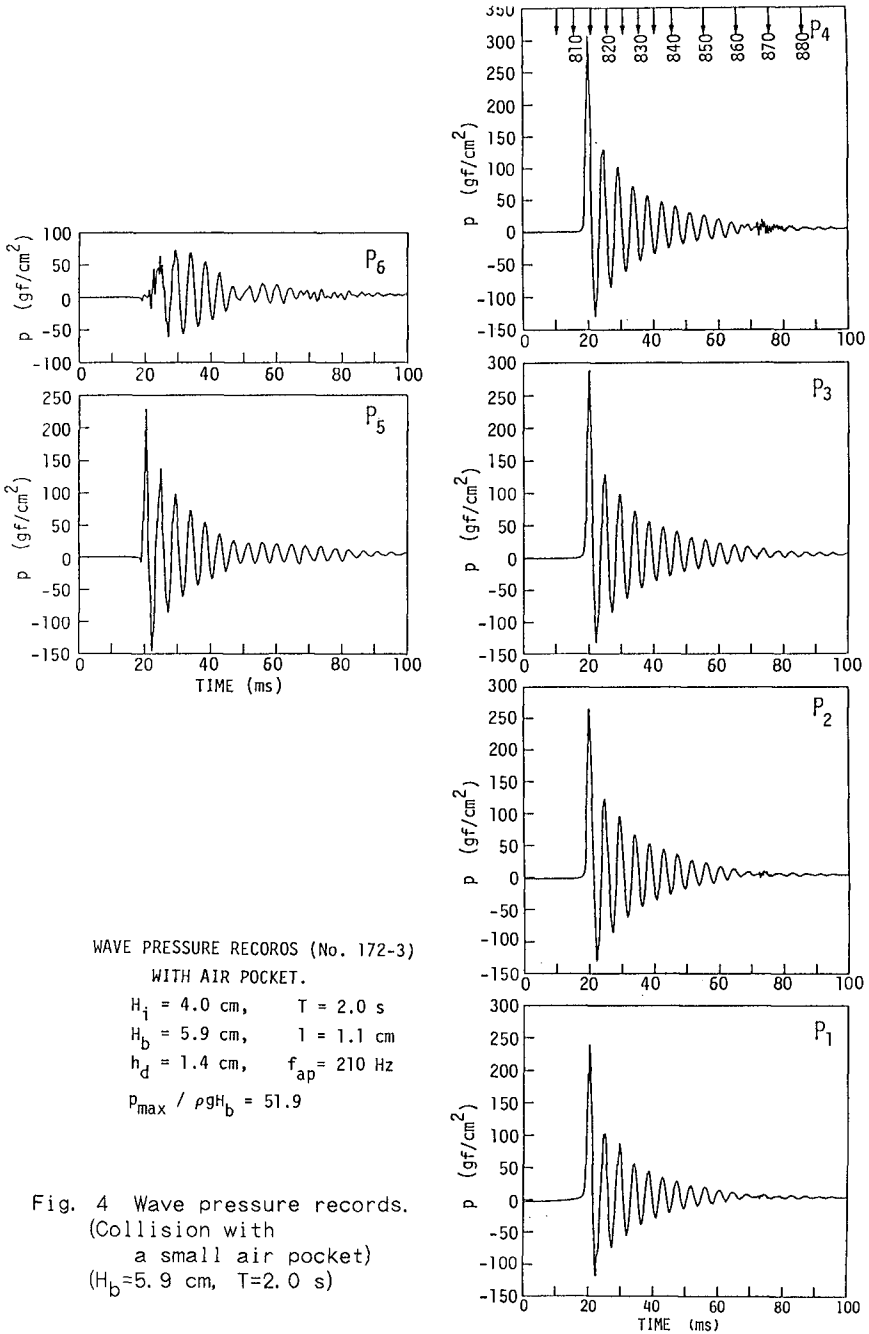


Photo. 4 Sequence of the still pictures of the wave surface.  
(Collision with entrapping a small air pocket)



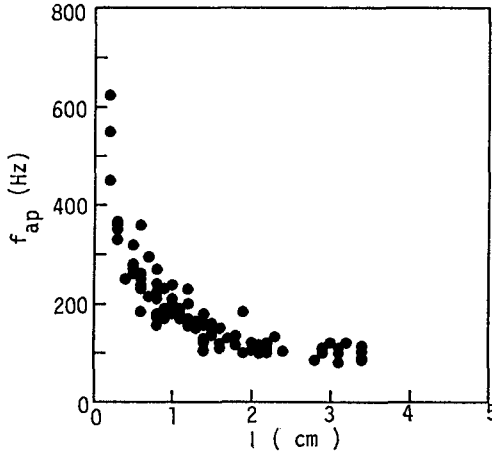


Fig. 6 Relation between  $f_{ap}$  and  $l$ .

6. PREDICTIVE MODEL

Predictive model for the impact pressure is developed under the following assumptions:

- (1) The two dimensional air pocket can be substituted by a square pillar of width  $B$ , height  $d$ , and thickness  $l$ ,
- (2) The adiabatic process of the air pocket is represented by an equivalent spring system, as shown in Fig. 7, having apparent spring constant  $k$ , and
- (3) Radial oscillation and energy dissipation of the air pocket are ignored.

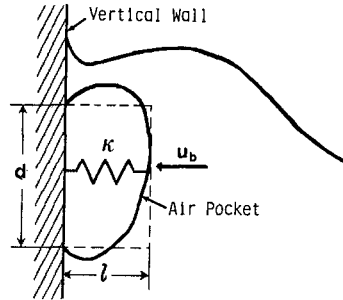


Fig. 7 Model of the air pocket.

The spring constant of the replaced air pocket can be written as  $k=(Ed/l)E_v$ , in which  $E_v(=1.4 p_{atm})$  is the bulk modulus of air and  $p_{atm}$  the atmospheric pressure. By introducing the virtual mass length  $K$  contributing the wave impact pressure (Bagnold, 1939), the maximum impact pressure  $p_{max}$  and the resonant frequency of the air pocket  $f_{ap}$  are obtained as

$$p_{max}=(\rho_w K E_v / l)^{1/2} u_b \tag{1}$$

and

$$f_{ap}=(E_v / \rho_w K l)^{1/2} \tag{2}$$

, in which  $\rho_w$  is the density of the water, and  $u_b$ : forward velocity of the breaking wave front. The virtual mass length can be evaluated by measurements of impact pressure  $p$ , the rising time  $\tau$ , and the forward velocity of wave front  $u_b$  (Bagnold, 1939):

$$K=\int_0^\tau p dt / \rho_w u_b \tag{3}$$

Figs. 8 and 9 show the agreements between the model and measurement,  $p_{max,M}/p_{max}$  and  $f_{ap,M}/p_{ap}$ , with respect to the air pocket thickness  $l$ , or the trapped air amount. Subscript M denotes the prediction. As seen in Fig. 8, due to the high variability in

measurement is not so good, especially when the air pocket is thin,  $l < 1$  cm. The agreement, however, becomes better with increasing the pocket thickness. From investigations of the measured data, we can specify the following main factors causing the high variability ; (1) The peak pressure region is much smaller than the diaphragm of pressure transducer, (2) The irregularity of the wave front changes the trapped air amount, and (3) The hitting location of wave crest tip is always shifted by high reflection of the wall. On the other hand, the model predicts reasonably well the frequency of the pressure oscillation, taking account of that the frequency should be lowered by boundary effects of the free surface, the bottom, and the wall (Topliss, Cooker, and Peregrine, 1992; Oumeraci and Partenscky, 1991).

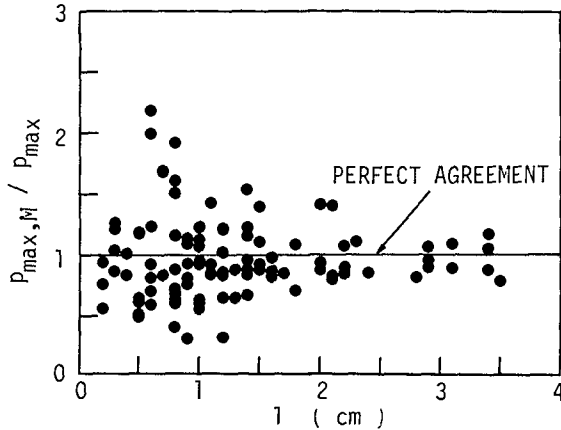


Fig. 8 Comparison between the predicted and measured maximum pressures.

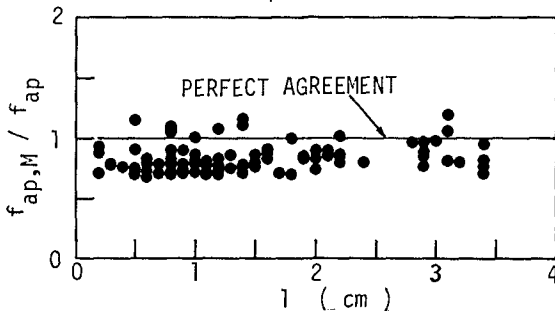


Fig. 9 Comparison between the predicted and measured frequencies of the damped pressure oscillation.

## 5. CONCLUDING REMARKS

Simultaneous measurements of the impact pressure and the wave shape change clarify that air bubbles and air pocket entrapped between the wall and the wave plays a predominant role to the occurrence of the high impact pressure. The wave-impact process is

occurrence of the high impact pressure. The wave-impact process is characterized by the development of the wave breaking at impact, because of that the entrapped air amount depends critically on the impinging front shape of breaking waves onto the wall. The larger air amount trapped gives the lower impact peak pressure and the longer period of damped pressure oscillations immediately after the impact. The damped oscillation continues until the compressed air in the pocket starts to escape through the free surface.

The model proposed describes the wave-impact process and predicts the maximum pressure and the frequency of damped pressure oscillations, when the air pocket of two dimensional form is trapped between the wall and the wave. High variability in the wave-impact process deteriorates validity of the model.

#### ACKNOWLEDGEMENTS

We are grateful to Messrs. T. Yui and H. Sakai, students of the post graduate course of Chuo University, for their help in the experiment and data analyses. A part of this study is supported financially by the Ministry of Education, Japan.

#### REFERENCES

- Arami, A. and M. Hattori (1988): Experimental study on shock pressure of breaking waves, Proc. of Coastal Eng., JSCE, Vol. 36, pp. 579-583. (in Japanese)
- Bagnold, R. A. (1939): Interim report on wave pressure research, Jour. of ICE, Vol. 12, pp. 202-225.
- Chen, E. S. and W. K. Melville (1988): Deep-water plunging wave pressures on a vertical plane wall, Proc. of Royal Soc. London, A 417, pp. 95-131.
- Cooker, M. J. and D. H. Peregrine (1991): Wave breaking and wave impact pressures, Developments in Coastal Eng., Univ. of Bristol, pp. 47-64.
- Mogridge, G. R. and W. W. Jamieson (1980): Wave impact pressures, Proc. of 17th Conf. on Coastal Eng., pp. 1829-1848.
- Oumeraci, H. and H. W. Partenscky (1991): Effect of entrapped air on structure response, MAST G6-S Project 2, Proc. 1st project workshop, Hannover.
- Oumeraci, H. P. Klammer, and H. W. Partenscky (1991): Classification of breaking wave impact loads on vertical structures, Submitted to ASCE, Jour. Waterways, Port, Coastal and Ocean Eng. Div.
- Topliss, M., M. Cooker, and Peregrine (1992): Pressure oscillations during wave impact on vertical walls, Proc. 23rd ICCE, Venice, ASCE.
- Weggel, J. R. and W. H. Maxwell (1970): Numerical model for wave pressure distributions, Proc. ASCE, Jour. of Waterways, Harbors and Coastal Eng. Div., No. WW3, pp. 623-641.

## CHAPTER 137

### NUMERICAL MODELLING OF THE STABILITY OF RUBBLE BASES

By

Wojciech Sulisz<sup>1</sup>

#### ABSTRACT

A numerical model is developed to predict the stability of rubble bases exposed to wave action. A boundary element method is applied to solve the problem of wave interaction with a caisson and its rubble base, and to calculate the velocity field. The predicted velocities are used to determine the destabilizing forces on individual stones. Theoretical results reveal two local minima in stability: in very shallow water and at intermediate depths. The rubble base stability increases with decreasing incident wave height, the rubble base height and the bench width. Preliminary results also show that the stability depends on the damping properties and that the stability increases with increasing permeability.

#### INTRODUCTION

A rubble base exposed to a wave action has to satisfy several requirements. The design of a rubble base requires an estimation of the weight of stones used to build the rubble base which is one of the most important design parameters. These stones have to provide stability of the rubble base during large waves.

There are several empirical formulae for the determination of the stability of a rubble base. The empirical formulae are mainly a result of some modifications of the classical Iribarren or Hudson equations. However, it is a well known fact that the empirical formulae have a number of limitations. Additionally, an analysis of various parameters involved in the stability based on laboratory experiments is very time-consuming and expensive. Moreover, some conclusions regarding the stability

---

<sup>1</sup>Chalmers University of Technology, Department of Hydraulics, 41296 Gothenburg, Sweden; on leave from IH PAS, Gdańsk.



based on laboratory experiments may be severely contaminated by scale effects. An alternative method for the analysis of the effect of various parameters on the stability is still a widely recognized need.

A numerical modelling of the stability of rubble mounds seems to be the alternative method. This method has been given more and more attention recently (McDougal and Sulisz 1990; Sulisz and McDougal 1991). The numerical modelling is employed in the present work by modelling theoretically the interaction of water waves with a caisson and its rubble base and then employing predicted flow fields in a stability model to determine the required stone size. A similar approach was applied to determine the stability of rubble mounds beneath caissons by Sulisz and McDougal (1991). However, they used a constant value of the damping coefficient, which may underestimate or overestimate damping properties of the rubble base.

**NUMERICAL MODEL**

The model for waves interacting with a caisson and its rubble foundation is based on the unsteady Forchheimer equation of motion in the pores of a coarse, granular medium (Sulisz 1983; Sulisz 1985). The wave flow in the porous domain  $\mathbf{R}$  and the adjacent wave field is governed by the following equations

$$\nabla^2\Phi = 0 \quad , \tag{1a}$$

$$S \frac{\partial\Phi}{\partial t} + \frac{1}{\rho} P + gz + f\omega\Phi = 0 \quad , \tag{1b}$$

where the damping coefficient  $f$ , is

$$f = \frac{1}{\omega} \frac{\int_{\mathbf{R}} d\mathbf{R} \int_t^{t+T} \epsilon^2 \left( \frac{vV^2}{K} + \frac{C_f \epsilon}{\sqrt{K}} |V| V^2 \right) dt}{\int_{\mathbf{R}} d\mathbf{R} \int_t^{t+T} \epsilon V^2 dt} \quad , \tag{1c}$$

and  $S$  is the inertial coefficient,  $\rho$  is the density of fluid,  $g$  is the acceleration due to gravity,  $v$  is the kinematic viscosity,  $\epsilon$  is the porosity,  $K$  is the intrinsic permeability,  $C_f$  is the turbulent damping coefficient,  $T$  is the wave period,  $P$  is the pressure,  $\Phi$  is the velocity potential, and the velocity vector  $V = V [\Phi_x, \Phi_z]$ .

The above model, Eqs. (1), has successfully been applied to describe the interaction of waves with a rubble-mound breakwater (Sulisz 1985), a composite

breakwater (Sulisz & McDougal 1988; Sulisz 1992b) and a rubble toe protection (Sulisz *et al.* 1989). The boundary element method has been used to determine  $\Phi$ . Various results from the theoretical model have been confirmed by experimental data.

Velocity fields determined by a solution of the problem of wave interaction with a composite breakwater (Sulisz 1992b) are used as the input data for a stability model. Forces acting on an individual stone are computed tangential and normal to the slope from the following Morison-type equations

$$F_s = \frac{1}{2} C_{Ds} \rho A_s V s |V \cdot s| + C_{Ms} \rho \nabla \frac{\partial V}{\partial t} s \pm \frac{1}{2} C_{Ls} \rho A_n (V \cdot n)^2, \quad (2a)$$

$$F_n = \frac{1}{2} C_{Dn} \rho A_n V n |V \cdot n| + C_{Mn} \rho \nabla \frac{\partial V}{\partial t} n \pm \frac{1}{2} C_{Ln} \rho A_s (V \cdot s)^2, \quad (2b)$$

where  $s$  and  $n$  are the tangential and normal unit vectors with respect to the slope, respectively;  $(C_{Ds}, C_{Dn})$ ,  $(C_{Ms}, C_{Mn})$ ,  $(C_{Ls}, C_{Ln})$  are the drag, inertia and lift force coefficients in the direction of  $s$  and  $n$ , respectively;  $A_s$  and  $A_n$  are the cross-sectional areas of the stone in the direction of  $s$  and  $n$ , respectively;  $\nabla$  is the volume of the stone.

The velocity vector in Eqs. (2) is calculated at various positions along the slope from a velocity potential corresponding to a fluid domain rather than rubble base domain. Due to uncertainties in determining the direction of the lift forces it is assumed that the lift forces maximize the instability.

Stability is based on the static equilibrium of the stone by examining lifting, sliding or rolling. An analysis shows that for a nearly spherical stone, the stability condition for rolling is the most critical. The detailed analysis of the static equilibrium of a sphere located on a layer of spheres in contact, shows that the critical condition for rolling is

$$W_B (\tan \beta - \tan \alpha) \cos \alpha < F_n \tan \beta - F_s \quad (3)$$

where  $W_B$  is the stone weight in water,  $\beta$  is the angle associated with location of spheres in relation to each other, and  $\alpha$  is the slope angle.

Several parameters like density, size, shape and placement scheme of the armor unit are involved in the stability model. Of course, the stability is also a function of the wave period, wave height, caisson shape, rubble base shape, porosity, permeability and turbulent damping properties of the rubble base. The model makes possible a detailed examination of the contribution of various parameters on the overall stability. Because calculations can be conducted on personal computers, the model may provide engineers with a useful tool for examining a variety of cases at a very low cost.

## RESULTS

The described model is first employed to calculate the flow field for a problem of interaction of water waves with a caisson founded on a rubble base (Fig. 1). The boundary element method is used to solve a boundary-value problem and to determine the velocity potential in the rubble base and in the vicinity of the caisson and its rubble base. The caisson of the width  $2b/h = 0.5$  is analyzed. The rubble base of the caisson is considered to be of trapezoidal cross-section and of various widths and heights, but of fixed slopes 1:2. Additionally, it is assumed that the inertial coefficient  $S = 1$ , porosity  $\epsilon = 0.4$ , and that the damping coefficient is known for each analyzed wave frequency ( $0.04 \leq kh \leq 4$ ). The calculations are conducted for a constant value of a dimensionless coefficient  $\hat{f}$  which is related to the damping coefficient  $f$  via the following relation

$$f = \hat{f} / (kh \tanh kh)^{0.5} \quad (4)$$

where  $k$  is the wave number and  $h$  is the water depth.

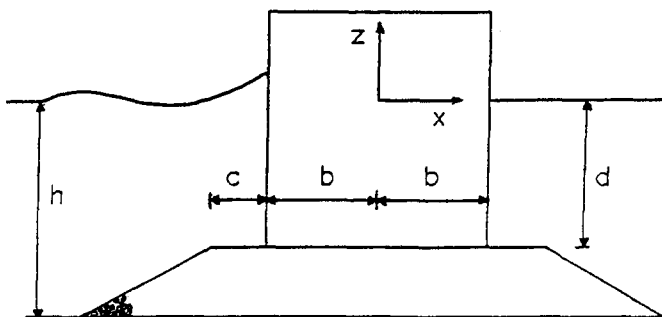


Fig. 1. Definition sketch

A presentation of the results based on Eq. (1b) may be confusing and their analysis difficult to follow if the damping coefficient  $f$  is kept constant over a wide range of wave frequencies, as is stressed by Sulisz (1992a). This is because the damping coefficient  $f$  is a function of the wave frequency even in a case where a pure Darcy motion law is applicable ( $C_f = 0$ ). Further analysis shows that the calculations based on a constant value of the damping coefficient usually underestimate rubble mound damping properties in shallow water or overestimate them for waves of intermediate lengths and in deep water. Of course the dimensionless coefficient  $\hat{f}$  is still a function of wave frequency which is evident from Eq. (1c) and Eq. (4). However, in a case of a pure Darcy flow the coefficient  $\hat{f}$  is directly related to a Darcy coefficient and the wave frequency is not involved in the relation. This implies that a presentation of the results versus a function of

wave frequency, based on a constant value of the dimensionless coefficient  $\hat{f}$ , properly reflects features of a case with the pure Darcy flow in a rubble mound. The presentations of the results versus a function of wave frequency for different values of  $\hat{f}$  also provide insight into a significance of the nonlinear damping term included in Eq. (1c) for an analyzed quantity.

A predicted flow field is used to calculate the required stone size of the rubble base. The calculations are conducted for the drag force coefficient  $C_{Ds} = C_{Dn} = 0.7$ , the inertia force coefficient  $C_{Ms} = C_{Mn} = 0.5$ , the lift force coefficient  $C_{Ls} = C_{Ln} = 0.5$ . These values of the force coefficients are chosen based on the results of some previous works on the stability problem. Of course the force coefficients are parameters of the stability model and they require further research based on experimental verifications.

The stability number,  $N_s$ , is used to present the output of the calculations conducted to estimate the required stone size of the rubble base. The stability number is defined as follows

$$N_s = \frac{(6/\pi)^{1/3} H_d}{(S_r - 1) D} \quad , \quad (5)$$

where  $S_r$  is the relative stone density,  $H_d$  is the incipient damage wave height, and  $D$  is the equivalent spherical stone diameter.

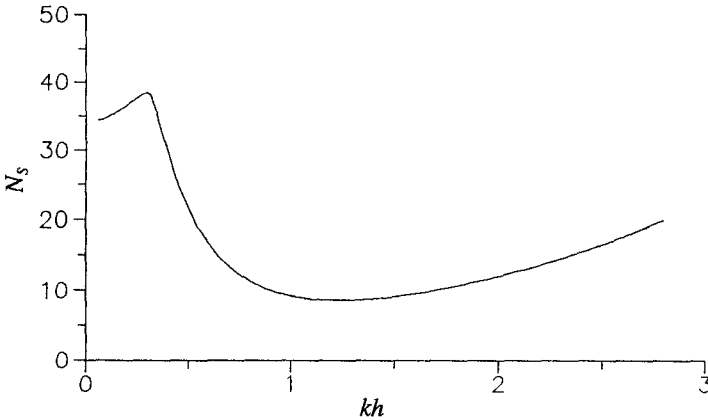
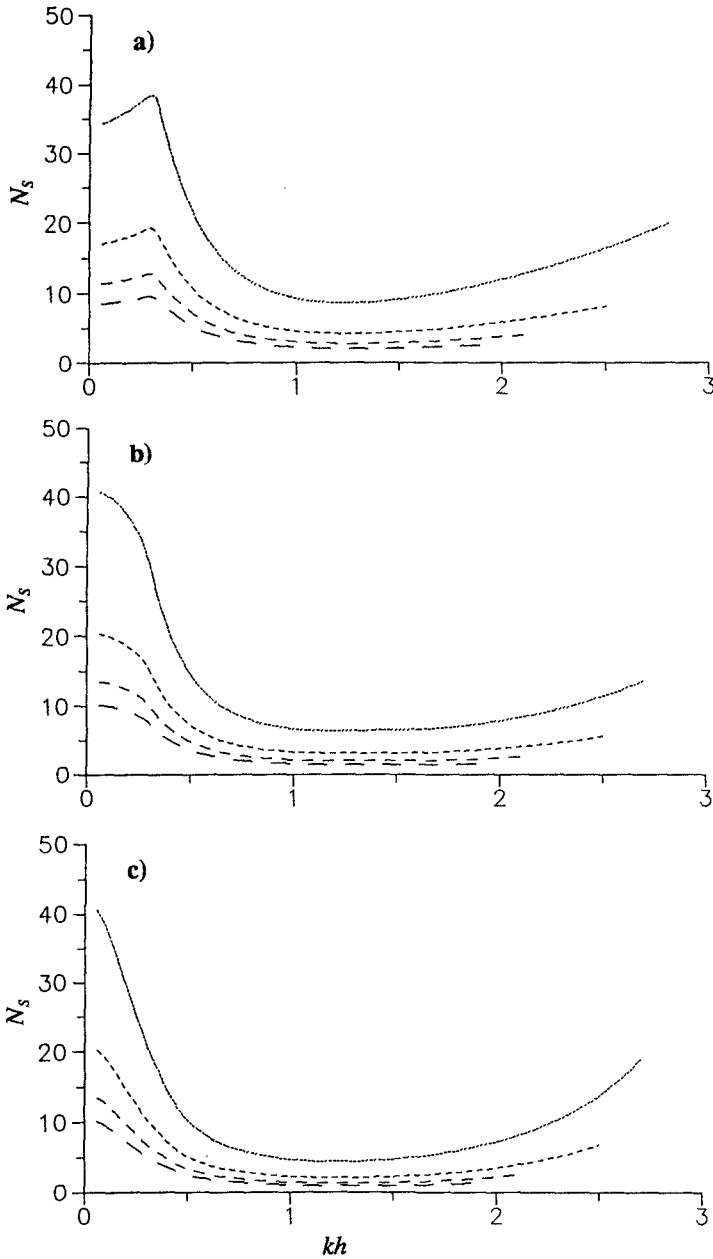


Fig. 2. Stability number versus  $kh$ ;  $d/h = 0.6$ ,  $c/h = 0.2$ ,  $H/h = 0.1$ ,  $\hat{f} = 1$ .

A typical dependency of the stability number on dimensionless wave number,  $kh$ , is presented in Fig. (2). In general, for relatively low rubble bases analyzed here, two local minima in stability may occur: a local minimum in very shallow water and a local minimum at intermediate depths. The local minimum in very shallow water is of interest only for rubble bases of small damping properties



**Fig. 3. Stability number versus  $kh$ ;  $d/h = 0.6$ ,  $\hat{f} = 1$ ,  $\cdots$   $H/h = 0.1$ ,  $- -$   $H/h = 0.2$ ,  $- \cdot - \cdot$   $H/h = 0.3$ ,  $- - -$   $H/h = 0.4$ ,  $- - -$   $H/h = 0.4$ , a)  $c/h = 0.2$ , b)  $c/h = 0.4$ , c)  $c/h = 0.6$ .**

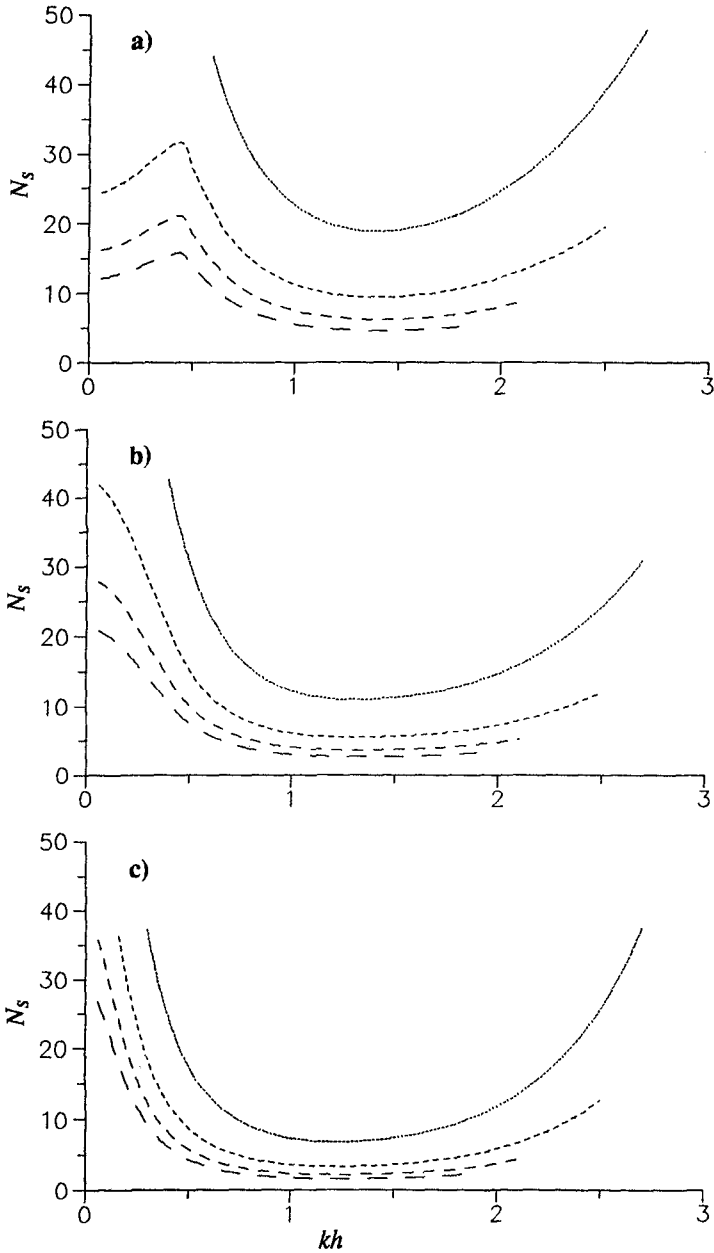
where it may become a global minimum of the stability number. The local minimum in stability at intermediate depths is, in a majority of cases, our main interest, because this minimum is usually a global minimum of the stability number and requires further investigation. Of course in some cases, the plots of the stability number versus the dimensionless wave number may become more complex and additional minima may occur.

The results presented in Fig. (2) show that the incident wave length is essential to predict the stability number. An additional parameter involved in the stability that belongs to a group of parameters associated with wave excitation properties, is the incident wave height ( $H$ ). Figs. (3)-(4) show the stability number plotted versus dimensionless wave number for four ratios of the incident wave height to the water depth ( $H/h = 0.1, 0.2, 0.3, 0.4$ ). Some plots for the steepest waves are omitted because the corresponding parameters of the incident waves exceed the breaking limits for progressive waves. Breaking may still occur for some waves included in Figs. (3)-(4) due to large reflection from a composite breakwater.

The results in Figs. (3)-(4) are intuitive and the general conclusion follows that reported by Sulisz (1992a). The stability increases with decreasing incident wave heights. However, it is necessary to point out that the calculations are conducted for a constant value of the dimensionless coefficient  $\hat{f}$ . Thus the presented results correspond to a case of the pure Darcy flow in the rubble base. Although, a contribution from the nonlinear damping term in the motion equation that is included in Eq. (1c) is expected to be rather small due to large reflection, some changes in the presented results may occur if the incident wave height is additionally included in the calculations of velocities via Eq. (4) and Eq. (1c). The main changes are expected in shallow water where a contribution from the nonlinear damping term may be significant and where the stability model is sensitive to the rubble base damping properties.

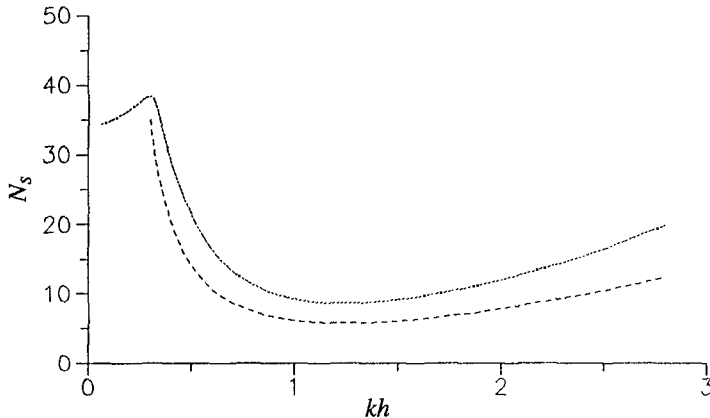
The results presented in Figs. (3)-(4) also enable us to examine some parameters from a second group of parameters affecting the rubble base stability. This group is associated with the shape of the composite breakwater. The stability number is plotted versus dimensionless wave number for six rubble bases. An effect of the rubble base height and the bench width on the rubble base stability is investigated. The results show that deeper rubble bases are more stable. This conclusion is fairly well supported by experimental data (Brebner and Donnelly 1962). A somewhat surprising result refers to the effect of the bench width on the rubble base stability. The plots indicate an increase in stability with decreasing the bench width. This is observed for both analyzed rubble base heights.

The local minimum of the stability number in very shallow water was reported by Sulisz and McDougal (1991), who presented the stability number versus the dimensionless wave number based on a constant value of the damping coefficient. Since the damping coefficient is a function of wave frequency, the calculations based on a constant value of the damping coefficient usually, as is pointed out above, underestimate media damping properties in shallow water, or overestimate them at intermediate depths and in deep water. Further calculations conducted by applying the present approach with  $\hat{f} = \text{constant}$ , confirm an occurrence of the local



**Fig. 4.** Stability number versus  $kh$ ;  $d/h = 0.8$ ,  $\hat{f} = 1$ , ....  $H/h = 0.1$ , - -  $H/h = 0.2$ , - · -  $H/h = 0.3$ , —  $H/h = 0.4$ , a)  $c/h = 0.2$ , b)  $c/h = 0.4$ , c)  $c/h = 0.6$ .

minimum in very shallow water for rubble bases of small damping properties, however, this local minimum does not occur for rubble bases of significant damping properties as is shown in Fig. (5).



**Fig. 5. Stability number versus  $kh$ ;  $d/h = 0.6$ ,  $c/h = 0.2$ ,  $H/h = 0.1$ ,  $\dots \hat{f} = 1$ ,  $- - \hat{f} = 10$**

The results presented in Fig. (5) also show the importance of the rubble base damping properties for the stability of the rubble bases. Several conclusions may be drawn from the results presented in Fig. (5). A preliminary analysis indicates that if the damping property of the analyzed rubble base decreases, the minimum stability number increases. It has already been pointed out that in a case of a pure Darcy flow, the coefficient  $\hat{f}$  is directly related to the Darcy coefficient. The results in Fig. (5) indicate that for a pure Darcy flow in the analyzed rubble base, the stability of the rubble base increases with increasing its permeability. This conclusion is drawn on a base of the minimum stability number at intermediate depths which is our main interest. An opposite conclusion may be drawn in very shallow water. Additionally, the results indicate the importance of the nonlinear damping term included in the present approach in Eq. (1c) for the stability analysis. The analysis shows that this term is of relatively minor importance for the minimum stability number associated with intermediate depths, but may be of major importance in shallow water.

## CONCLUSIONS

A theoretical analysis of the stability of rubble bases is conducted, applying an approach based on numerical modelling. The flow in the rubble base of a caisson-type breakwater is described by a linearized Forchheimer equation of motion. The boundary element method is applied to solve the problem of wave interaction with



the caisson and its rubble base, and to calculate the velocity field. The predicted velocities are used in a Morison-type equation to determine the destabilizing forces on individual stones.

The stability is shown to depend on several parameters. There are three or even four groups of parameters involved in the stability analysis. The detailed analysis is conducted to investigate the parameters associated with incident wave properties and rubble base shapes. Preliminarily examined are some parameters associated with hydraulic properties of the rubble base.

The incident wave properties are shown to be essential to predict the stability number. Theoretical results reveal two local minima in stability: a local minimum in very shallow water and a local minimum at intermediate depths, but in some cases additional minima may occur. The local minimum at intermediate depths is usually becoming a global minimum. The stability, as intuitively expected, is also a function of the incident wave height and the stability increases with decreasing wave height. The rubble base shape belongs to the second group of parameters involved in the stability. The results show that the stability increases with decreasing rubble base height and the bench width. The preliminary results indicate the necessity of including damping properties in the stability analysis and show that for the analyzed rubble base the minimum stability number increases with increasing permeability.

## ACKNOWLEDGEMENTS

This work was supported by *Hydro-Alpha*, Gdańsk. The presentation of the results was supported by University of Bologna, Department of Hydraulics; Dynomar AB, Gothenburg; Chalmers University of Technology, Department of Hydraulics, Gothenburg; and the Swedish Institute. The support is acknowledged.

## REFERENCES

- Brebner, A. and Donnelly, P. 1962. Laboratory study of rubble foundations for vertical breakwaters. Proc. of the 8th Coastal Engineering Conference, ASCE, 408-429.
- Mettam, J. D. 1980. Can we develop new breakwater armor formulae. Proc. of the 17th Coastal Engineering Conference, ASCE, 2304-2323.
- Sulisz, W. 1983. Transmission of waves through permeable breakwaters of arbitrary cross-sections. Ph. D. Thesis, Polish Academy of Sciences, Institute of Hydroengineering, Gdańsk.
- Sulisz, W. 1985. Wave reflection and transmission at permeable breakwater of arbitrary cross-section. Coastal Engineering, 9, 371-386.
- Sulisz, W. & McDougal, W. G. 1988. Wave interaction with a composite breakwater. Proc. of an International Conference on Computer Modelling in Ocean Engineering, Venice, 715-721.

- Sulisz, W., McDougal, W. G. and Sollitt, C. K. 1989. Water wave interaction with rubble toe protection. *Ocean Engineering*, 16, 463-473.
- Sulisz, W. & McDougal, W. G. 1991. Wave interaction with a composite breakwater. *Proc. of the Second International Conference on Computer Modelling in Ocean Engineering*, Barcelona, A. A. Balkema, 715-721.
- Sulisz, W. 1992(a). Stability analysis for multilayered rubble bases. Manuscript in preparation.
- Sulisz, W. 1992(b). Wave loads on a caisson founded on a multilayered rubble base. Manuscript in preparation.



# **PART IV**

## **The Venetian Coast**



*San Giorgio Island and Venice Lagoon*



*Test Section of Venice  
Barrier being Transported to Lido Inlet*

## CHAPTER 138

### DEVELOPMENT OF THE VENICE MORPHOLOGICAL SYSTEM

P.SILVA(\*) and A.MOL(\*\*)

(\*)Technital S.p.A. (Verona, Italy)

(\*\*)Grabowsky & Poort (The Hague, Holland)

#### ABSTRACT

The paper discusses the morphological development of the Venice Lagoon since 1850 and, on the basis of analyses of the system, presents models to simulate large scale development of the lagoon and of various sub-basins.

The morphological development consists mainly in a continuous erosion of the salt-marshes and shallow areas, and the filling of canals. Also a general loss of sediment from the lagoon was observed. The main causes were identified in engineering structures like jetties, dredging of artificial canals and maintenance dredging.

These works resulted in a disequilibrium of the natural hydraulic system. In addition, loss of biological protection in shallow areas, due to pollution, has contributed.

Models were prepared on basis of time and partially averaged concentrations of sediment in shallow areas and canals. Averaging was carried on over a full year.

This approach facilitated the building of models of various complexity, which were found to be useful tools in the analysis of the effectiveness of remedial measures.

#### 1. HISTORICAL BACKGROUND

The lagoon of Venice is a salt water basin connected to the Adriatic Sea by three inlets (see fig. 1). Sediments range from silt in the inner areas to fine sands close to the inlets. The conditions in the present lagoon have been heavily influenced by man; since the Middle Ages significant human intervention has changed the brackish estuary into a saline lagoon which interacts only with the Adriatic Sea. This saline system was in relative equilibrium in the period 1600-1850.



Fig.1 - MAP OF 1970



Fig.2 - MAP OF 1810

Since 1850 engineering works including inlet control structures, dredging and land reclamation (fig. 2) and changes in the ecological system due to urban, agricultural and industrial discharge, have brought the system to a state of disequilibrium which, in the last 20 years, has accelerated changes in the lagoon.

Significant erosion is observed in the shallow area, while natural channels are silting up. Salt marshes are disappearing at an increasing rate (compare fig. 1 and 2). The ecological system is out of balance as indicated by excessive algal growth and the disappearance of many species.

The changes of the morphology also determine negative consequences on human activities, causing difficulties to navigation in natural channels and an heavier wave attack against the defences of villages and agricultural land (fig. 3).

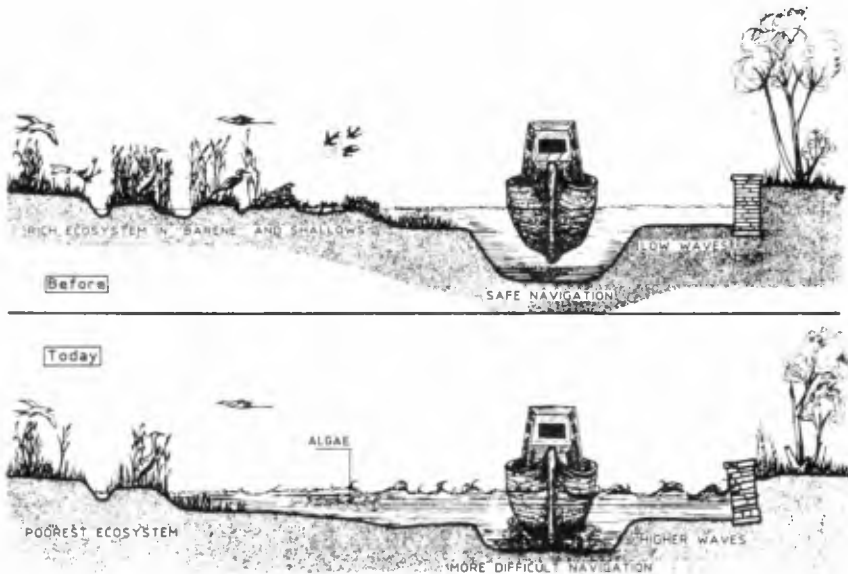


Fig. 3 - EFFECTS OF MORPHOLOGICAL CHANGES

Erosion and sedimentation patterns for the lagoon are available from 1900 onwards and information on inlets and coastline since 1800. The morphological changes over these time periods correlate well with significant engineering works such as inlet control structures and dredging of navigation channels. Figure 4 presents the main findings on the basis of analyses of bathymetric maps.

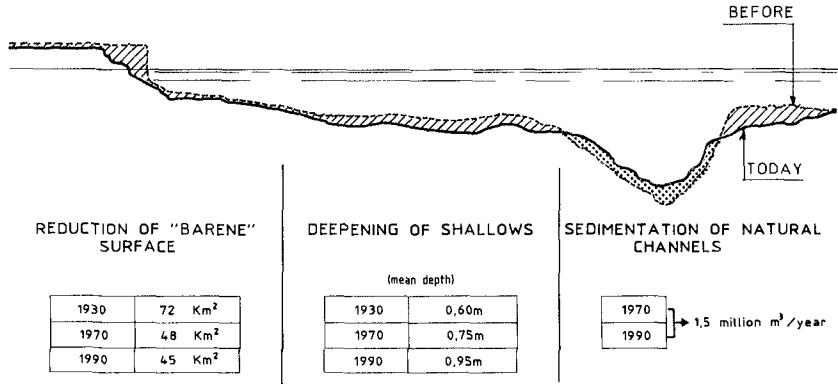


Fig. 4 - MAIN PHENOMENA

## 2. ANALYSIS OF CAUSES

Section 1 described a significant change of the geometrical parameters of the lagoon, due to change in the morphological equilibrium. These changes have been caused by an imbalance of the total sediment budget of the lagoon (input-output, see fig. 5) and by an internal sediment redistribution (fig. 6). A detailed analysis, comprising all possible phenomena, followed by order of magnitude estimates, has resulted in the following most probable causes.

The first historical change to the sediment balance was caused by the diversion of rivers directly to the sea between 1500-1600 which reduced the sediment input by roughly 700,000 m<sup>3</sup>/year.

The main reason for this diversion was siltation of the lagoon. Since that period, the lagoon found a relative equilibrium, with only a slow reduction of the area of salt marshes (being former river deltas). From 1850 the jetty construction has reduced sediment input from the sea. Estimated reduction was 300,000 m<sup>3</sup>/year.

Particularly since 1970 there is evidence that the average sediment content of outflowing water has increased. The reasons are: the reduced resistance forces due to pollution (disappearance of biological protection) and the increase of active forces (shipping, fishing).

"Apparent" sediment loss was caused by subsidence of lagoon bottom due to water exploitation close to Marghera. This has been stopped since 1970.



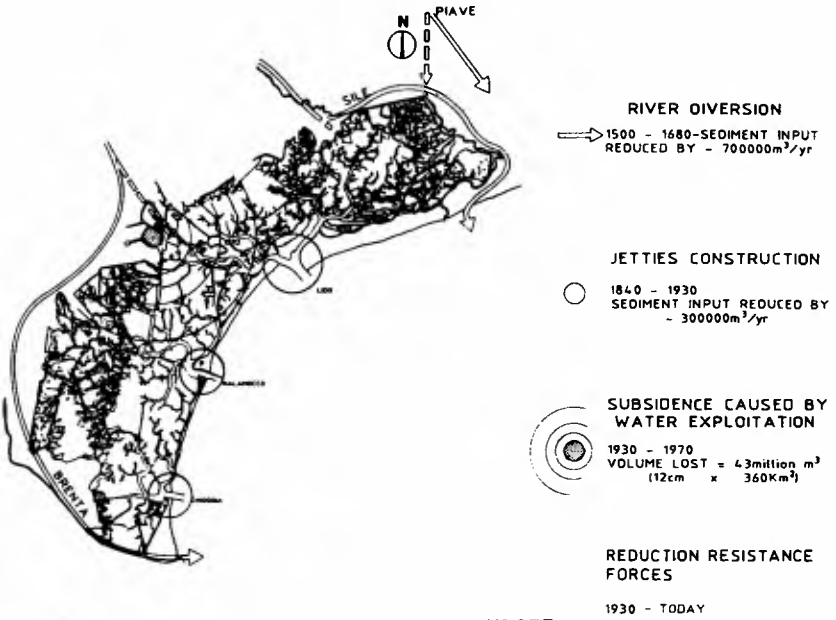


Fig.5-MAIN CAUSES : GLOBAL "VOLUMETRIC" BUDGET

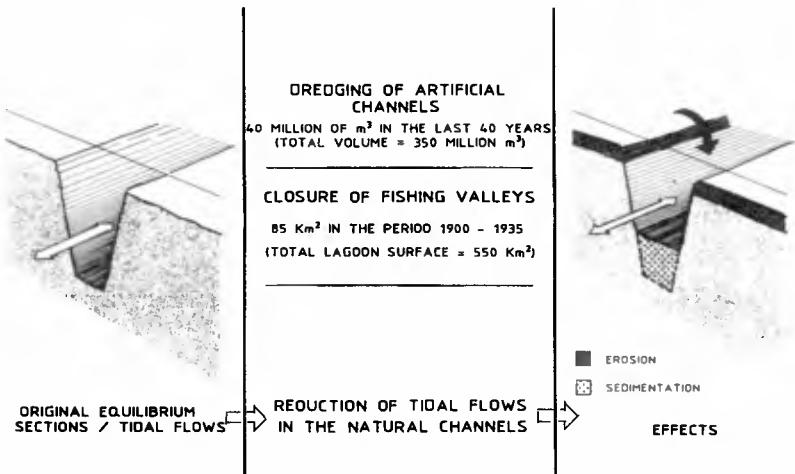


Fig. 6 - INTERNAL SEDIMENT REDISTRIBUTION

Another important element is the redistribution of sediment in the lagoon: erosion of shallow water areas and saltmarshes at the same time as sedimentation of natural and artificial channels have been found.

The main phenomena are:

- imbalance of hydraulic system due to dredging of artificial channels, increasing velocity in shallow areas and reducing velocity in natural channels;
- closure of fishing valleys reducing tidal volume, and then the velocities in the channels.

As a result the channels function today as sediment traps (see fig. 6).

### 3. STABILITY OF LAGOON CHANNELS

The lagoon channels have been remarkably stable since 1600 after the rivers were diverted. Comparison of maps available since 1910 show only slight changes due to natural causes. Meandering and geometrical profile characteristics (depth-width ratios) are noticeably similar. Total cross-section generally depends upon tidal volumes flowing through the cross-section, according to relations resembling similar laws for tidal inlets (see References (3) and (5)). An analysis was carried on following an approach developed by Marchi (Ref. (4)), who analytically developed a formulation equal to the Jarret relation for inlets.

This relation allows the introduction of the bottom characteristics using the Strickler coefficient. As the bottom characteristics of the various channels were measured, the relation between discharge and cross section was calculated. It was found that, since smaller channels had a smaller  $D_{50}$  of bottom sediment, on a logarithmic paper the new relation was within a similar band to the Jarret relation. Table 1 presents both relations, while figure 7 shows empirical plots of lagoon channels; the discharges were calculated using a finite elements hydraulic model.

In the Lido area (where no artificial dredging has been carried out) channels were found to follow the theoretical relation according to Marchi. The other lagoon channels, were found to have too large cross sections. This historical development however should a gradual decline towards the theoretical equilibrium, following the Marchi approach.

Hence, also for lagoon channels a general relation exist between tidal volume and cross section, or, as a general hypothesis one may say: lagoon tidal volume has a direct relation to volume of lagoon channels.

Table 1 - Discharge/section relations

$$\text{Jarrett (1976)} \quad \Omega = K1 Q^{K2}$$

$$K1 = 9 \times 10^{-4}$$

$$K2 = 0,85$$

Q = mean max discharges in a spring tide

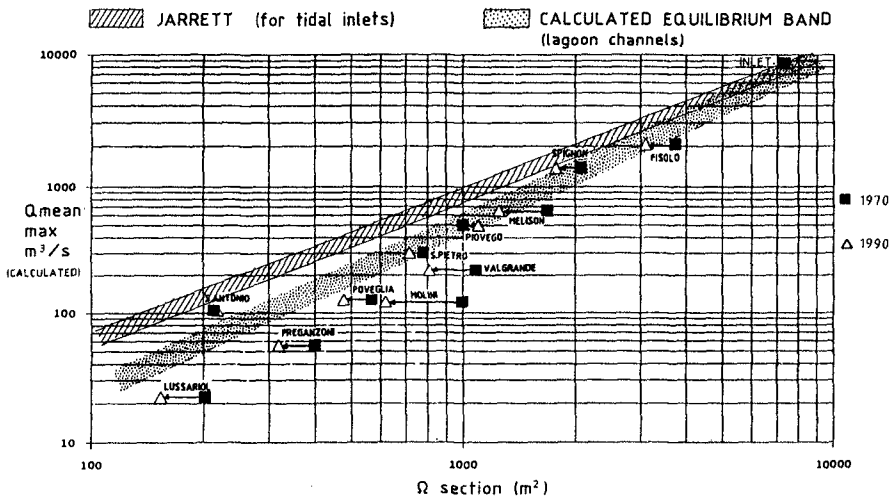
$\Omega$  = cross-sections

$$\text{Marchi (1989)} \quad \Omega = [n^2 \gamma b^{1/3} / Ks T^2 \tau_{CR}]^{3/7} \times Q^{0.857}$$

b = channel width

Ks = Strickler coefficient

T = tidal period

Fig.7 - Q/ $\Omega$  RELATIONS, EXTRAPOLATED TO INTERNAL CHANNELS

#### 4. MEASUREMENTS AND ANALYSIS

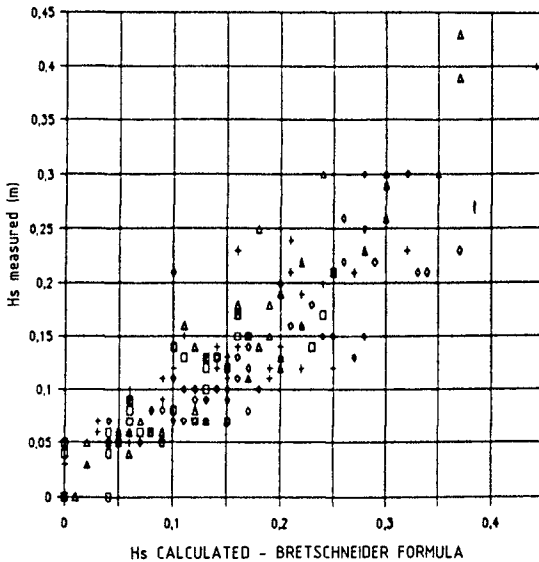
In order to verify various hypotheses a measurement campaign was carried out. It was performed by Danish Hydraulic Institute and Ecomar on behalf of Consorzio Venezia Nuova. The main objectives were to assess:

- relation between wind, waves and meteorological component of water levels;
- relation between sediment concentration and waves/currents;
- effects of shipping upon sediment concentration.

Three fixed stations with sensors (to measure wind, velocity, waves) and sediment samples were installed in shallow areas and used for a period of one year. During the same period, a campaign was carried out by boat to establish the spatial variation of parameters, and to analyse the conditions in the channels.

The analysis of results lead to the following conclusions:

- wind-waves relation were similar to Brethschneider relations (fig. 8);
- sediment-wave/current relations (figures 9 and 10) could well be correlated using the Bijker formula, reducing in the lagoon the found concentration by a factor 5 to consider the conditions of not breaking waves and the silty to fine sand environment.



Note: The different symbols are referred to different areas of measurements.

Fig.8 - WAVE HEIGHT IN THE LAGOON: MEASURED VS. CALCULATED DATA

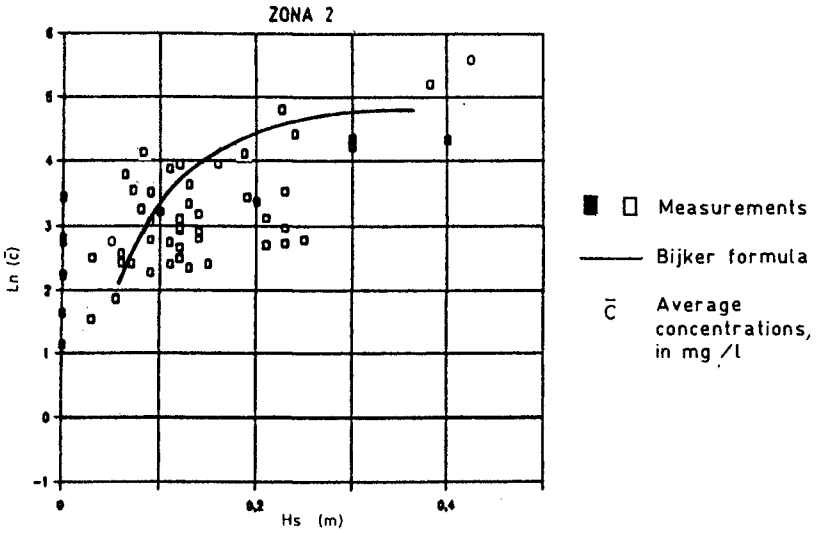


Fig.9 - SUSPENDED SEDIMENT CONCENTRATION IN THE SHALLOWS MEASURED VS. CALCULATED DATA

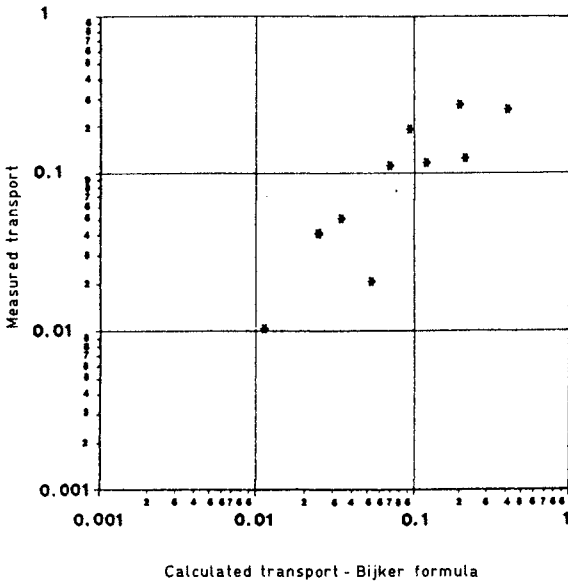


Fig.10 - LITTORAL TRANSPORT IN FRONT OF THE INLETS: MEASURED VS. CALCULATED DATA

5. MODELLING OF SEDIMENT BUDGET

As morphological processes have a large time scale a schematisation was proposed averaging the tide and wind effects over a full year, following the approach of Di Silvio (Ref. (2)). Yearly averages were calculated of all parameters affecting the sediment budget model (see Table 2). Velocities were calculated on the basis of a finite element tidal model of the lagoon. The yearly averaged concentrations were calculated on the basis of the Bijker formula. It was found that in the canals the velocity was the driving force, and in the shallows the wave action. After the calculation of the wave statistics from wind statistics, and the subsequent calculation of the sediment concentration statistics on the basis of Bijker, it was found that an approximate linear relation existed between mean sediment concentration and the mean water depth.

For modelling purposes a rooted vegetation coefficient was added to model biological protection by seagrasses and benthic fauna.

A first schematization was prepared on basis of a three cell model for each of the three basins Chioggia, Lido and Malamocco (see fig. 11).

Computer simulations showed that the 3-cell model was a useful tool capable of simulating main events utilizing calibration of parameters which were considered realistic on the basis of measurements (figure 12).

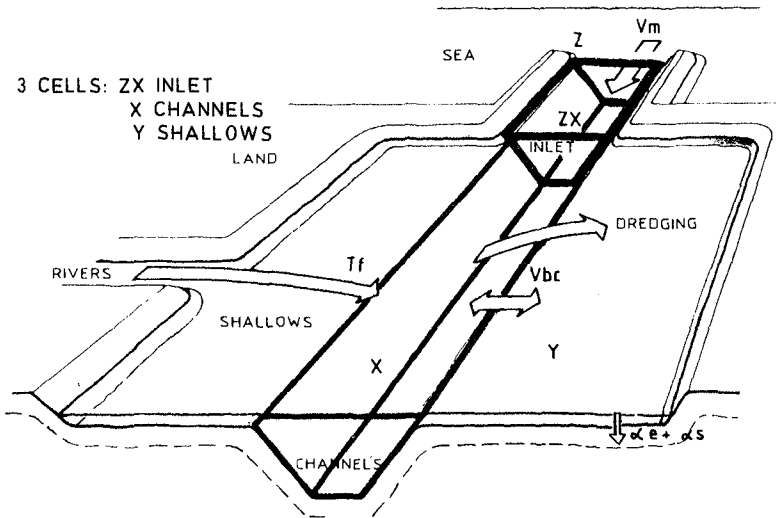


Fig.11 - THREE CELLS BALANCE MODEL

<b>Table 2 - Balance model</b>	
Hydraulic flows	<--- 2D finite element model
Bottom variations	<--- hydraulic flows x differences in mean concentration + volumetric changes for subsidence and eustatic rise + direct effects (dredging-river input)
Mean concentrations (averaged in space and in time)	<--- channels $x = C_1/d [C_2 (Q_{med}/b \cdot d)]^4$
	shallows $y = C_w \cdot C_v/d$
	$C_w$ = wave energy coefficient $C_v$ = rooted vegetation coefficient

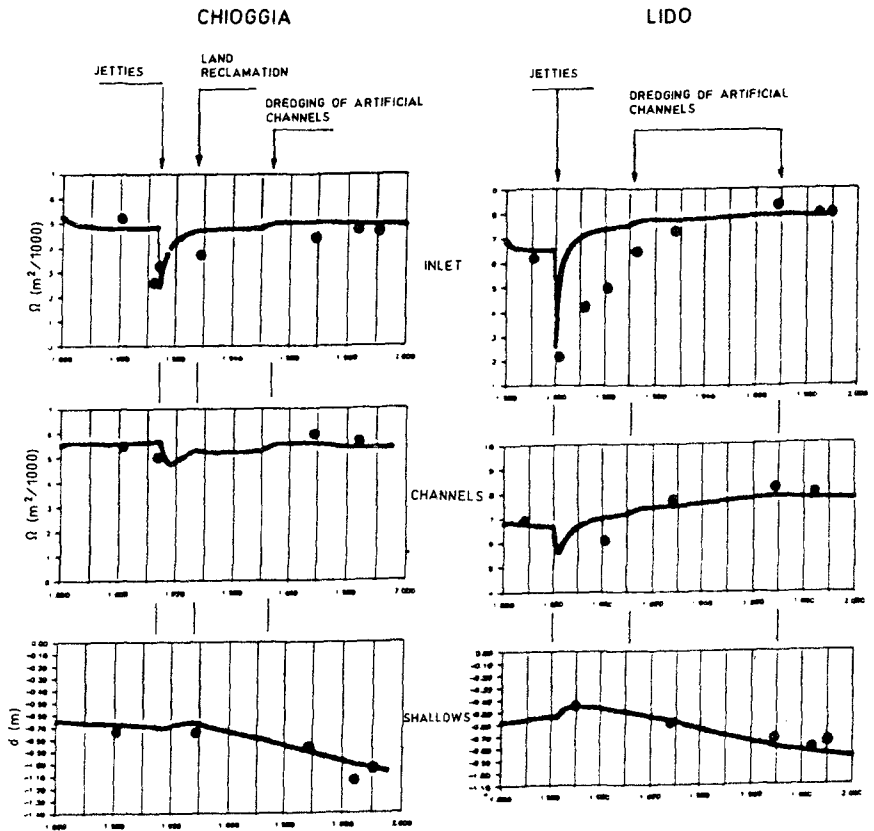


Fig.12 - 3 CELLS MODEL EXAMPLE OF RESULTS

In addition, a finite elements model was built dividing the lagoon into approximately 90 cells, to study the effects of the remedial measures, such as filling of artificial canals, nourishment of sediment, increase of biological protection, etc. Calibration of the model was carried out utilizing maps of 1970 and 1990. Parameters to be applied were within the range as measured during the field campaign, except for some complicated cells which were nodal points in the canal system around Venice.

Figure 13 presents the validation, demonstrating that the trend on virtually all cells is in agreement with reality. Figure 14 presents a forecast, without any measures, and with filling of artificial canals.

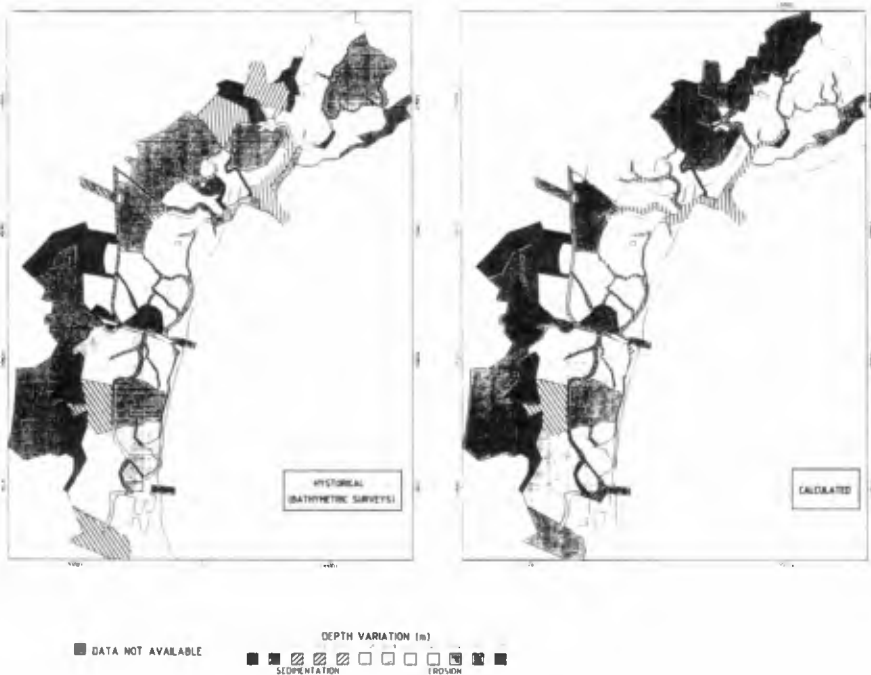


Fig.13 - MULTICELL BALANCE MODEL - VALIDATION





Fig.14 - MULTICELL BALANCE MODEL - PREDICTION

6. DISCUSSION

1. It is believed that the causes of the morphological disequilibrium in the lagoon have been identified. Nevertheless the effects of the huge algal growth in lagoon is not investigated in detail. The main occurrence is in the Lido basin, where it may have a stabilizing effect or even reduce depths due to deposits of organic material.
2. A major uncertainty is the effect of biological protection (benthic fauna, seagrass). The loss of this protection in large parts of the lagoon is undoubtedly due to pollution (biological, chemical) but also due to intensive illegal fishing. Although no figures are available, there are signs that large areas of the lagoon are frequently disturbed by heavy systems installed on fishing boats, destroying all biological protection and increasing mean sediment concentration.

3. The schematizations are all based upon granular material. However, in the lagoon stirring-up and deposit conditions will be different, and the models are not necessarily able to forecast adverse developments.
4. The models may oversimplify certain phenomena and are not able to include effects such as asymmetric tides. Nevertheless, calibration was easy and it is believed that the dominant phenomena are modelled.

#### 7. REFERENCES

- (1) Bruun P. (1978). "Stability of Tidal Inlets - Theory and Engineering". Elsevier Publ. Co.
- (2) Di Silvio G. (1989). "Modelling the morphological evolution of tidal lagoons and their equilibrium configurations". 23rd IAHR Congress, Ottawa (Canada).
- (3) Jarret J.T. (1976). "Tidal Prism-Inlet Area Relationships". GITI Report 3, US Army Coastal Engineering Research Center, Ft. Belvoir, VA.
- (4) Marchi E. (1989). "Sulla stabilità delle bocche lagunari a marea". Presented at Accademia dei Lincei, 9/12/1989.
- (5) O'Brien M.P. (1969). "Equilibrium Flow Area of Inlets on Sandy Coasts". Journal of Waterways and Harbours Division. American Society of Civil Engineers.

## CHAPTER 139

### On the Chaotic Structure of Tide Elevation in the Lagoon of Venice

Giovanna Vittori <sup>1</sup>

#### Abstract

Sea level oscillations related to astronomical and meteorological tides in the Lagoon of Venice are analysed in order to find evidence of a possible chaotic nature of the phenomenon. On the basis of the analysis of the signal spectrum and by considering the values of the correlation dimension and of the largest Lyapunov coefficient of the attractor of the system, it is possible to infer that tidal oscillations inside the Lagoon of Venice are the result of deterministic dynamics, i.e. of a chaotic system characterized by few degrees of freedom. In the second part of the paper, taking advantage of the chaotic nature of the system, Farmer & Sidorowich's (1987) algorithm is used in order to make predictions of the time development of the system.

#### Introduction

The time development of dynamic variables of natural systems often shows random oscillations which sometimes are superimposed on a regular and predictable signal. Such behaviour can be the result either of a stochastic or deterministic non-linear process, highly influenced by initial conditions known in literature as "deterministic chaos". In the latter case, the time development of the system is somehow similar to that of a stochastic process even though from a mathematical point of view its dynamics are entirely deterministic.

From a practical point of view, the main difference between a stochastic process and a process showing deterministic dynamics is the different number of degrees of freedom necessary to describe the state of the system. In fact, when a system shows a chaotic behaviour, its dynamics can be described using a limited number of degrees of freedom. In other words, the time development of the system can be obtained by integrating a small number of ordinary differential

---

<sup>1</sup>Researcher, Istituto di Idraulica - Università di Genova - Via Montallegro, 1 - 16145 - Genova.

equations. This result is not applicable to the behaviour of stochastic systems which are characterized by an infinite number of degrees of freedom. The detailed description of such systems is extremely complex and stochastic or statistical methods are recommended for the study of the time development of the system.

Recent studies have shown the existence of deterministic chaos in the time development of climate variables such as wind velocity (Tsionis & Elsner (1989)), atmospheric pressure (Henderson & Wells (1988)), rainfall (Sharifi, Georgakakos & Rodriguez-Iturbe (1990)). Those studies have opened up new fields for the study of the predictability of natural events.

In this paper, the time oscillations of water elevation at Venice are considered, depurated from the contribution due to sea waves, to obtain information about "high waters" and in particular about their frequency and their predictability.

Tidal levels recorded at Punta della Salute and Diga Sud Lido between 1975 and 1984 and published by the "Consorzio Imprese Veneto-Emiliane" are considered. The study is based on recent measurements, however a preliminary investigation performed on data recorded at the beginning of the century has shown similar results.

Because extreme events are of more practical interest, the analysis is performed also for the signal envelope of maxima which is obtained starting from the knowledge of diurnal and semidiurnal tidal oscillations.

The procedure used in the rest of the paper is the following: first the time oscillations of the water level in the lagoon of Venice are analysed by studying both the hourly measurements and the 'envelope' of maxima recorded during one year for different years. The presence of a predictable periodic component and of an irregular component is shown. Indeed, the Fourier spectra of the signals relative to the hourly measurements show peaks related to the diurnal, semidiurnal and moon tide and a broad band part, which is characteristic of random and/or chaotic systems. Moreover, the intensity of the continuous part of the spectra turns out to be of the same order of magnitude as the peaks. Then the dynamic behaviour of the system is analyzed in the pseudo-phase space where the attractor is reconstructed by means of the time-delayed coordinate technique. The characteristics of the attractor are evaluated and in particular the correlation dimension, which gives indications of the degrees of freedom of the system, is computed along with the largest Lyapunov coefficient which is a measure of the sensitivity of the system on initial conditions. The results obtained give strong indications of the presence of chaotic dynamics. For this reason, an attempt to predict the time development of the system by using the deterministic algorithm by Farmer & Sidorowich (1987) is made. The success in predicting the future time development of the system on the basis of historical records by means of deterministic methods is a further indication of the presence of deterministic chaos.

### Signal and spectrum of tidal elevation

It is widely recognized that the understanding of the dynamics of currents and sea level oscillations is extremely important in most coastal regions and particularly in estuaries and lagoons. Typically, sea level oscillations related to the astronomical tide are the most significant even if sometimes meteorological factors such as wind, a non uniform distribution of atmospheric pressure and storms can induce sea level oscillations of the same order of magnitude as tidal oscillations.

Indeed, in Venice, "high" waters are often caused by the simultaneous presence of high tide and meteorological factors. While tidal oscillations, being the result of the periodic motion of celestial bodies, are deterministic and thus predictable, the effect of meteorological events is aperiodic and thus not easily predictable.

In fact, the astronomical tide is caused by spatio-temporal variation of the gravitational field due to the relative motion of the earth with respect to other celestial bodies. An analysis of the phenomenon taking into account all the possible influences is extremely complex. However, considering the order of magnitude of gravitational forces induced on the earth's surface by different celestial bodies, it can be inferred that in order to study sea level rise due to the astronomical tide it is sufficient to consider the relative motion of the earth, the moon and the sun. Usually tidal oscillations are decomposed into a number of sinusoidal time components, each with its own periodicity. Five basic periods are usually taken into account: 1 day due to the earth's rotation, 29.53 days due to the rotation of the moon around the earth, 365.24 days due to the rotation of the earth around the sun, 8.847 years due to the motion of the moon perigee and 18.616 years due to the rotation of the orbital plan of the moon.

Since in the present work we study sea level oscillations when meteorological factors prevail, the time scale of interest to us is of one week and thus periodicities of 365.24 days, 8.847 and 18.616 years can be ignored. In other words, we will assume that the sea level oscillates with periodicities of 1 and 29.53 days around a mean level slowly varying with moderate excursions during one year.

The periodic nature of the astronomic component of the tide is evident in figure 1 where the tidal levels ( $\eta$ ) recorded during the months of August and September 1981 are plotted. Similar results are obtained considering different years. During summer and spring, the influence of wind, storms and other meteorological events on sea level oscillations is usually negligible. On the other hand, aperiodic meteorological events become relevant in autumn and winter. In figure 2 the tidal curve relative to November and December 1981 is reported in order to show the aperiodic character of exceptional events. The aperiodic character of extreme events is still more evident by looking at figure 3 where the envelope of maxima is shown for the years 1980-1984.

The spectrum of the signal, shown in figure 4(a) for the year 1981, supports this argument showing two peaks related to the periodicities of 12 and 24 hours

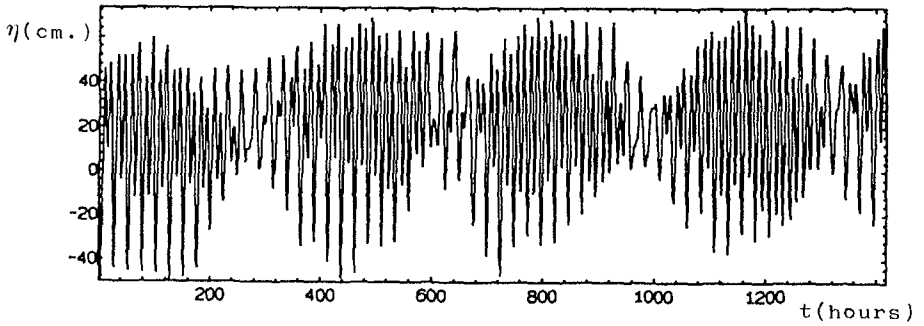


Figure 1: Tidal levels recorded at Punta della Salute during August and September 1981.

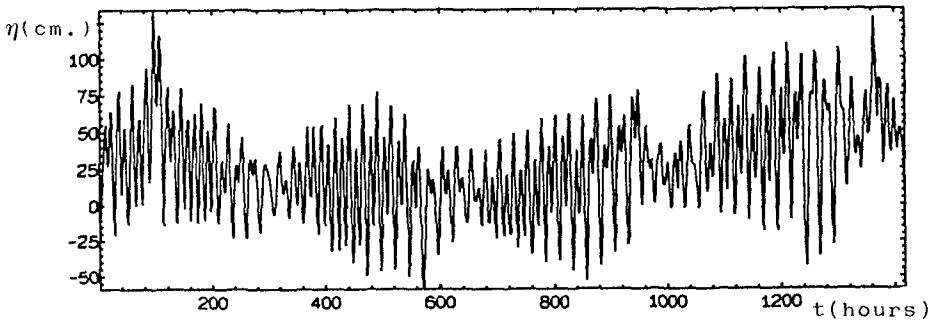


Figure 2: Tidal levels recorded at Punta della Salute during November and December 1981.

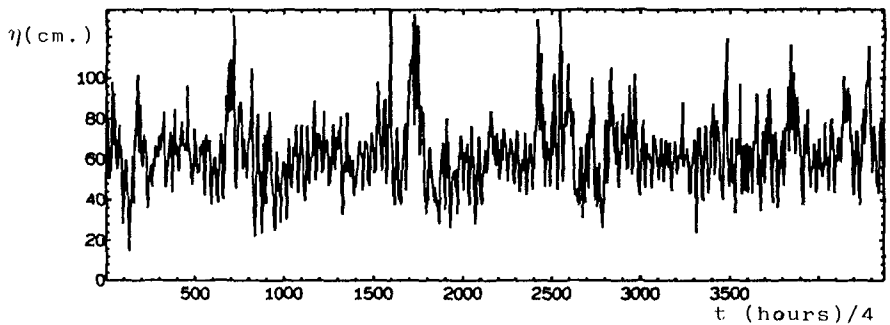


Figure 3: Envelope of maxima for the years 1980, 1981, 1982, 1983 and 1984.

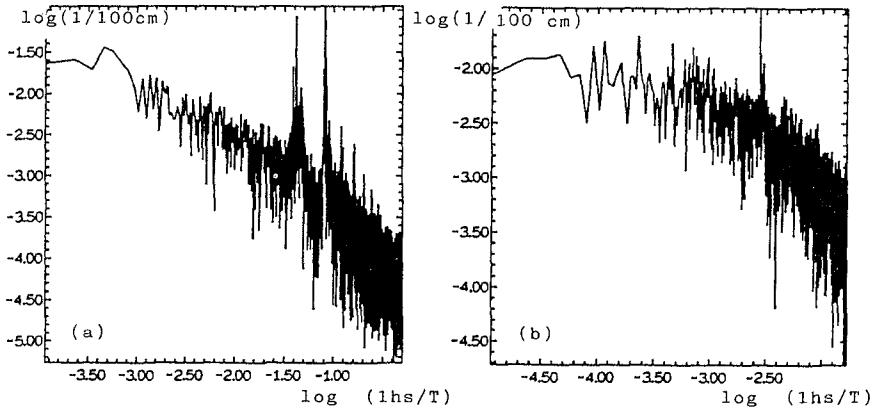


Figure 4: a) Spectra for the year 1981, b) Spectra of the 'envelope of maxima' for the years 1980, 1981, 1982, 1983 and 1984.

and a broad band part with the same order of magnitude.

The intensity of the broad band part varies when different years are considered: in fact, it is larger for years which have experienced more "high waters". However, considering different years, no relevant differences are found. The spectrum of the 'envelope' of maxima (see figure 4(b)) shows no peaks since the periodicities of 12 and 24 hours have been removed from the time sequence and the broad band part is larger and stronger with respect to that of the original signal.

So far, we have shown evidence of the non-periodic nature of sea level oscillations inside the lagoon of Venice; in the following we will investigate the nature of such oscillations. In fact, they could either be the result of a stochastic system, i.e. a dynamic system with a high number of degrees of freedom or the result of a chaotic system with few degrees of freedom.

### The Chaotic Character of Tidal Elevation

In order to study the aperiodic character of tidal oscillations, it is necessary to perform a quantitative study of the attractor of the system. As suggested by Takens (1981) the trajectory of the system is reconstructed into a "pseudo-phase" space by using the time sequence of the values attained by one physical variable characteristic of the phenomenon. More specifically the  $N$ -dimensional vectors  $\vec{s}$ , describing the trajectory of the system in the pseudo-phase space, are obtained on the basis of the measurements  $f(t)$  of the tidal level performed at the stations of Punta della Salute and Diga Sud Lido:

$$\vec{s}(t) = [s_1, s_2, \dots, s_N] = [f(t), f(t - \tau), \dots, f(t - (N - 1)\tau)] \quad (1)$$

where  $f$  is the water level as a function of time and  $\tau$  is an arbitrary time delay.

Takens (1981) showed that an attractor topologically equivalent to that of the original system, is obtained independently of the value of  $\tau$  if  $N$  is sufficiently large. However, for computational reasons, it is necessary to accurately choose these parameters in order to have an accurate estimate of the characteristics of the attractor. In fact, if  $\tau$  is too small, the attractor collapses along the line  $s_1 = s_2 = s_3 = \dots$  and the computation of the characteristics of the attractor becomes inaccurate.

In literature, it is suggested that the value of  $\tau$  as the time delay relative to the first zero of the autocorrelation function be chosen. According to Battiston & Zambella this procedure gives a value of  $\tau$  equal to 20 hours. However, in the following we have used values of  $\tau$  equal to 50, 100 and 200 hours because these values have led to a better estimate of the Lyapunov exponent and of the correlation dimension. As far as the value of  $N$  is concerned, we have computed the characteristics of the attractor for increasing dimensions of the pseudo-phase space until non relevant differences were observed between  $N$  and  $N + 1$ .

It is well-known that a chaotic attractor possesses a geometric structure called fractal attractor which has a finite and generally non integer dimension. To establish the nature of the aperiodic oscillations of the tidal wave, it is necessary first to evaluate the dimension of the attractor. In order to obtain a quantitative estimate of the possible fractal structure of the attractor, we computed the correlation dimension as defined by Grassberger & Procaccia (1983). As suggested by Takens (1981), the trajectory of the system into the pseudo-phase space is represented by a set of  $M$  points  $\vec{s}_i$  defined by (1) and their relative distance is computed using the Euclidean distance. Then the correlation function is defined as the limit for  $M$  tending to infinity of the number of pairs with a relative distance  $d_{ij}$  less than  $r$  divided by  $M^2$ .

$$C(r) = \lim_{M \rightarrow \infty} \frac{1}{M^2} \{\text{Number of pairs } (\vec{s}_i, \vec{s}_j) \text{ such that } d_{ij} < r\} \quad (2)$$

Grassberger & Procaccia (1983) showed that for many attractors the correlation function for  $r$  tending to zero behaves like a power law, i.e.

$$\lim_{r \rightarrow 0} C(r) = ar^d \quad (3)$$

The correlation dimension is then defined as the exponent  $d$  of the power law, which can be expressed as:

$$d = \lim_{r \rightarrow 0} \frac{\log_{10} C(r)}{\log_{10} r} \quad (4)$$

In figure 5, the correlation function relative to the signal of tidal elevation is plotted for the years 1980 and 1982 and for a few dimensions  $N$  of the embedding ( $r_{max}$  denotes the maximum linear extent of the attractor). It is possible to observe that in both cases, by increasing  $N$ , the slope of the correlation function



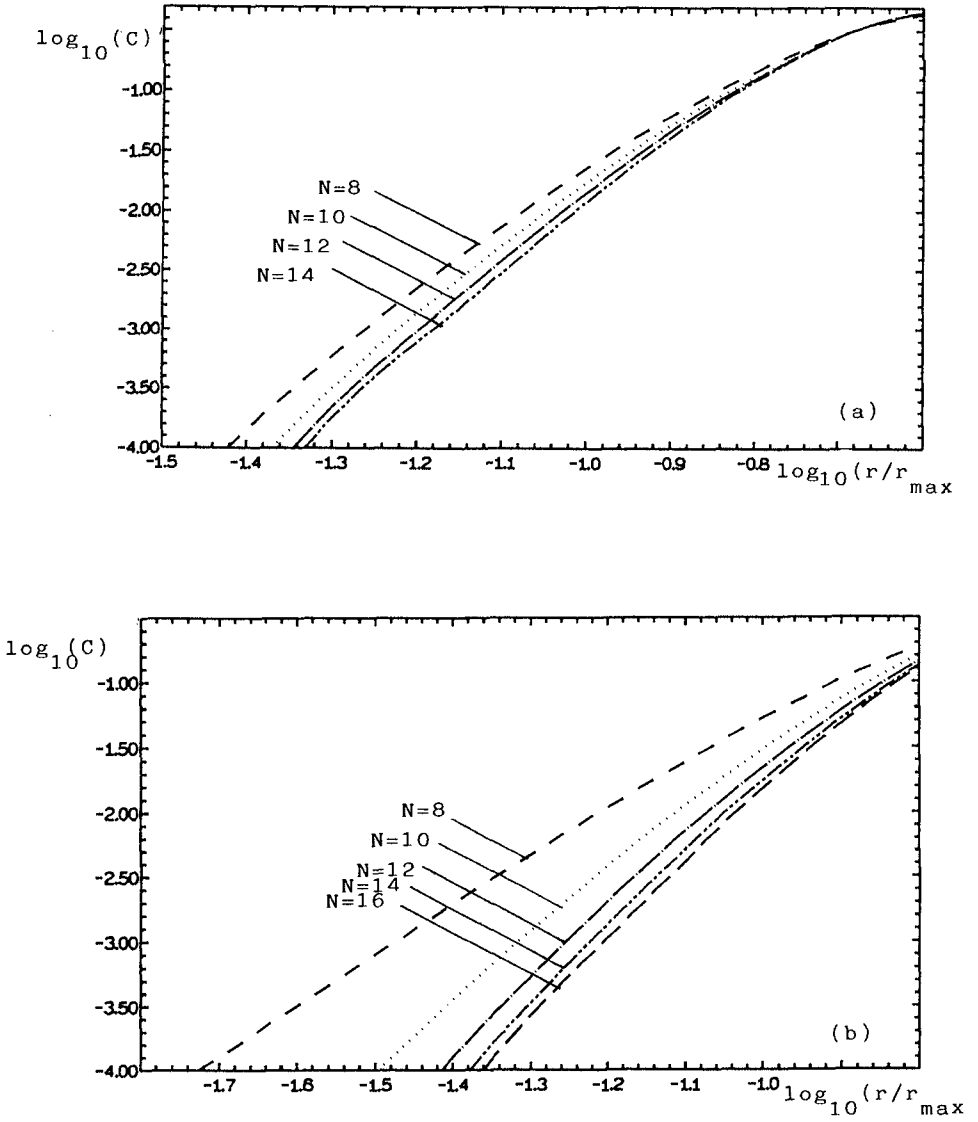


Figure 5: Correlation function for the years a) 1980  $\tau = 200$ ; b) 1982  $\tau = 200$ .

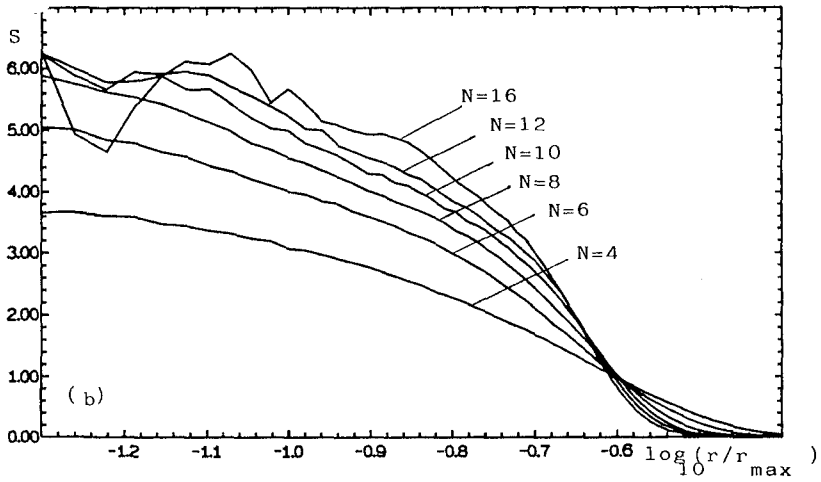
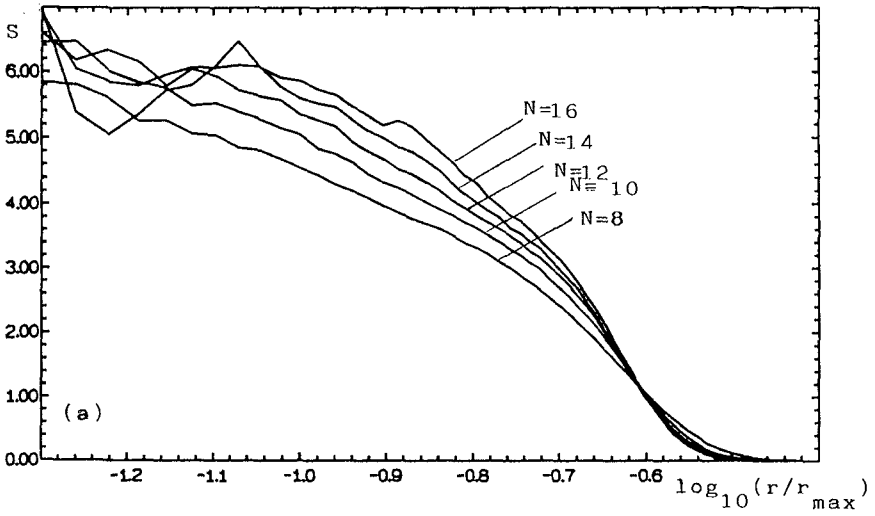


Figure 6: Slope of the correlation function for the years a) 1980  $\tau = 200$ ; b) 1982  $\tau = 200$ .

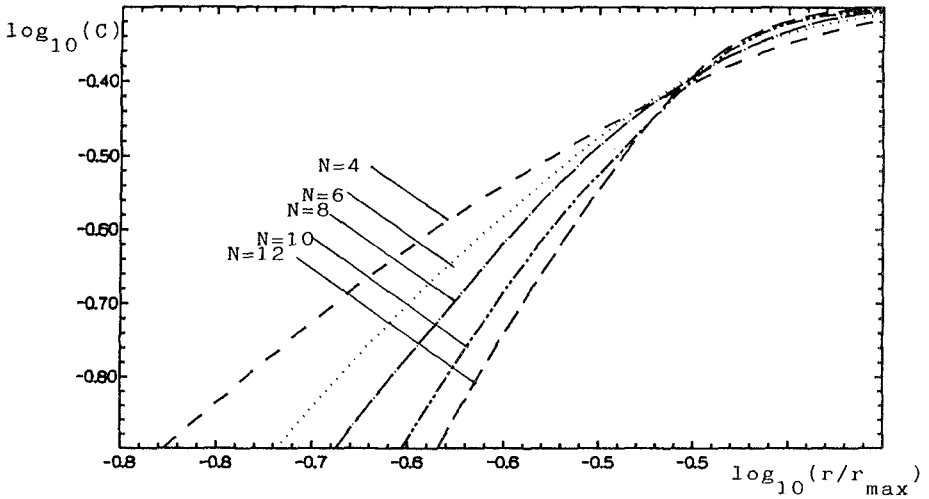


Figure 7: Correlation function for the 'envelope of maxima' relative to the years 1980, 1981, 1982, 1983 and 1984  $\tau = 40$ .

reaches a limiting value for small but finite values of  $r$  where the limit defined by (4) can be evaluated and in the meantime boundary effects can be ignored. The value of the correlation dimension can best be estimated by looking at figure 6 where the function  $S(r)$ , corresponding to the slope of the correlation function, is plotted as a function of  $\log_{10}(r/r_{max})$  for the same years as in figure 5.

It can be seen that for sufficiently large values of  $N$  and for small values of  $\log_{10}(r/r_{max})$ ,  $S$  attains a constant non integer value close to 6. This value can be regarded as an approximation of the correlation dimension  $d$ .

A smaller value of the correlation dimension is obtained considering the attractor relative to the envelope of maxima. In figure 7, where the slope of the correlation function relative to the envelope of maxima is plotted for different values of  $N$  it can easily be seen that for small  $r/r_{max}$  the correlation dimension tends to a constant non integer value close to 2. The fact that the correlation dimension of the envelope of maxima is lower than that of the original signal is reasonable since by extracting the envelope of maxima a number of degrees of freedom related to the astronomic tide have been removed. As we shall see in the following, the lower dimension of the envelope of maxima turns out to be an advantage when making predictions of the temporal development of the system.

From the results shown so far, it is possible to conclude that sea level oscillations inside the lagoon of Venice are the result of a chaotic dynamic system since the number of degrees of freedom of the attractor is limited. Hence, in principle, it would be possible to predict the time development of tidal elevation

by integrating a limited number of ordinary differential equations.

The following step is to determine the time interval within which a trajectory of the system can be predicted with a given uncertainty starting from an initial state known with an assigned error. It is well-known that chaotic attractors show an exponential divergence of the trajectories in the phase space. After some time, two states initially close to each other develop into two states far apart. Thus, the prediction of the time development of a given state, known with a given uncertainty, can be obtained only for a time interval which depends on the rate of divergence of the trajectories in the phase space. This rate of divergence is expressed by the largest Lyapunov coefficient.

Lyapunov coefficients can be defined by considering the time development of a hypersphere lying on the attractor reconstructed into the pseudo-phase space. Due to the chaotic nature of the system, the hypersphere will develop into an ellipsoid. The  $i$ -th Lyapunov coefficient is defined in terms of the length of the  $i$ -th principal axis of the ellipsoid ( $p_i$ ) by means of the following relationship:

$$\lambda_i = \lim_{(t_1 - t_0) \rightarrow \infty} \frac{1}{t_1 - t_0} \log_2 \frac{p_i(t_1)}{p_i(t_0)} \quad (5)$$

where the values of  $\lambda_i$  are ordered in ascending order and  $t_1 - t_0$  is the time interval during which the computation is performed.

Thus, the Lyapunov coefficients are related to the average expansion or contraction of the hypersphere in the different directions of the phase space. Axes which expand on average originate positive values of  $\lambda_i$  while axes which on average contract give rise to negative values.

In the present paper the procedure suggested by Wolf et al (1985) to compute the largest Lyapunov coefficient is employed.

In table 1 the values obtained for the largest Lyapunov exponent ( $\lambda_1$ ) are reported for the years ranging between 1980 and 1984.

TABLE 1

year	1980	1981	1982	1983	1984
$\lambda_1$ (hours <sup>-1</sup> )	0.025	0.024	0.026	0.023	0.026

Similar values are obtained by taking into account the 'envelope of maxima'.

The values obtained for  $\lambda_1$  would lead to the conclusion that sea level oscillations inside the Lagoon of Venice could be predicted for long periods, at least from a theoretical point of view. However, it should be considered that the use of a finite number of experimental data does not allow the desired infinitesimal length scales of the attractor to be tested. These scales are also inaccessible due to the presence of noise on finite length scales. Therefore, also taking into account that the chaos-producing structure of the attractor might be of small spatial extent, the estimate of the largest Lyapunov exponent of the system and thus of the timescale on which the system dynamics becomes unpredictable may be

affected by a significant error. This fact can cause an underestimate of the largest Lyapunov coefficient.

### The Predictions

Even though the characteristics of its attractor could not be quantified accurately due to the knowledge of a finite number of data, from the results previously described it is possible to infer that the system has a chaotic nature. Therefore, the prediction of the time development of the system can be attempted by using algorithms which take advantage of the deterministic nature of the system.

Even though the extreme sensitivity of the time development of the system on initial conditions poses some limits to the possibility of predicting its future time development, it is possible to make accurate predictions for small times and, at least in principle, to give an estimate of the error affecting the predictions.

In the present paper use has been made of the method proposed by Farmer and Sidorowich (1987). As a first step, a time sequence of data is used to represent a state on the attractor in the pseudo-phase space by means of (1). Secondly, a functional relationship between the current state  $\vec{s}(t)$  and the future state  $\vec{s}(t+\Delta t)$  is assumed to exist:

$$\vec{s}(t + \Delta t) = f_{\Delta t}(\vec{s}(t)) \quad (6)$$

Due to the chaotic nature of the system, the function  $f_{\Delta t}$  is certainly non-linear. To obtain an approximation to  $f_{\Delta t}$ , Farmer & Sidorowich (1987) suggest using the knowledge of the time development of a number of points on the attractor which are near to  $\vec{s}(t_0)$ , i.e. to the state whose time development we want to predict. Let us consider the  $P + 1$  points of the attractor ( $\vec{s}(t_j)$ ,  $j = 1, 2, \dots, P + 1$ ) which are the nearest to  $\vec{s}(t_0)$ . A local approximation of  $f_{\Delta t}$  is obtained on the basis of the values  $\vec{s}(t_j + \Delta t)$  attained by the  $P + 1$  points. The easiest procedure would be a zero order approximation where  $P = 0$ . In this case  $\vec{s}(t_1 + \Delta t)$  could be assumed to be the approximation of  $f_{\Delta t}$ . A better approximation is obviously obtained assuming  $P + 1$  larger than  $N$  and determining, by means of the least square method, the coefficients of the linear relationship  $a * \vec{s}(t_j) + \vec{b}$  which best approximate  $\vec{s}(t_j + \Delta t)$ .

After the values of the matrix  $a$  and  $\vec{b}$  have been obtained, the prediction can easily be performed:

$$\vec{s}(t_0 + \Delta t) = a * \vec{s}(t_0) + \vec{b}.$$

The results obtained are presented in figures 8 and 9 where predicted and measured levels are plotted as a function of time both for tidal levels and for the envelope of maxima. The measurements of tidal elevations during the years 1980, 1981, 1982 and 1983 have been used to reconstruct the attractor and the

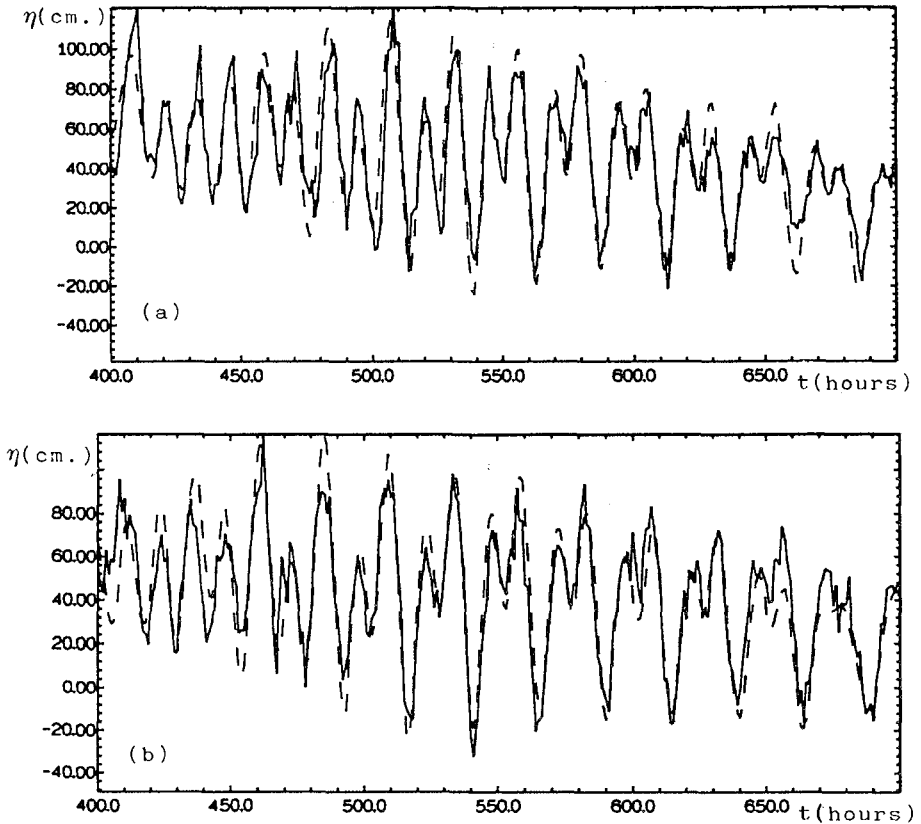


Figure 8: Predictions (—) and measurements (- - -) of tidal elevations at Punta della Salute in the last months of 1984. a)  $\Delta t = 2$  hours; b)  $\Delta t = 24$  hours.

prediction of tidal levels has been made for the last three months of 1984 when there were some exceptional events.

In figure 8 the observed (- - -) and the predicted (—) tidal levels are shown for November 1984 when three events of high water were observed. In figure 8(a) the prediction 2 hours into the future is shown while in figure 8(b) the prediction 24 hours into the future is presented. In figure 9(a) and (b) the predictions of the envelope of maxima are shown for 12 and 24 hours into the future respectively.

It is possible to see that the predictions relative to the envelope of maxima are more accurate than those of the original signal; this fact can be explained on the basis of the lower correlation dimension of the signal envelope of maxima with respect to that of the signal of tidal elevations.

As expected, by increasing  $\Delta t$  the predictions are less accurate both for the

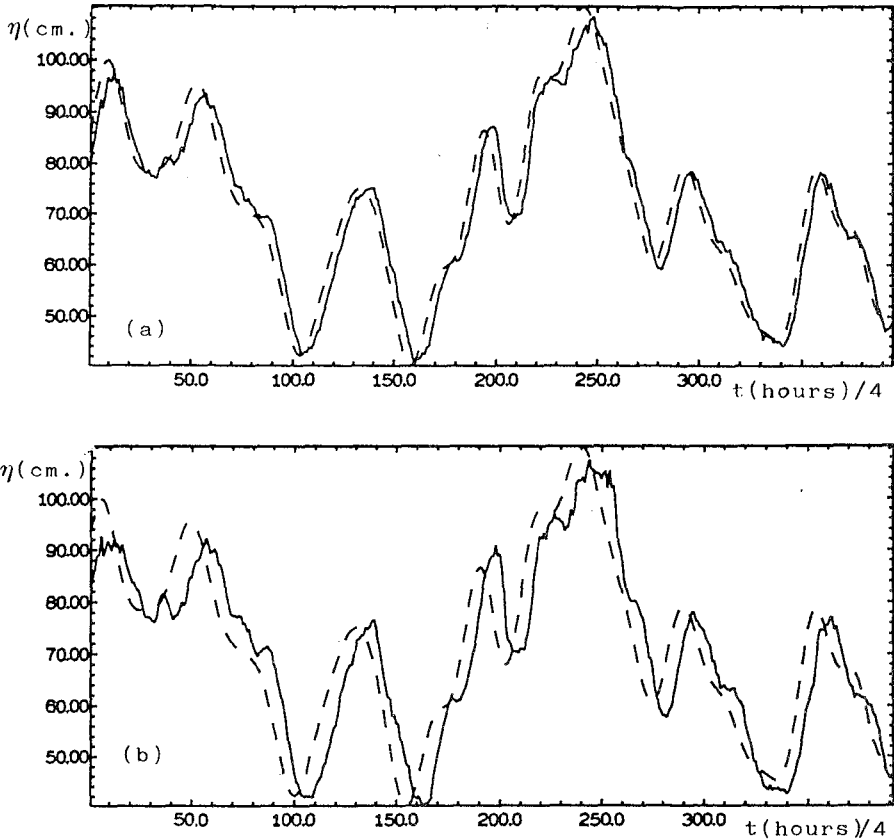


Figure 9: Predictions (—) and envelope of maxima (- - -) at Punta della Salute in the last months of 1984. a)  $\Delta t = 12$  hours; b)  $\Delta t = 24$  hours.

original signal and for the envelope of maxima.

However, the prediction could be improved by considering larger data set to reconstruct the attractor and by using a higher order approximation to obtain the local predictor  $f_{\Delta t}$ . In order to evaluate the performance of the proposed model it is necessary to take into account that, as reported by different authors (Battiston & Zambella (1981), Cecconi et al (1992)), the error of the statistical methods for predictions for a time in the future less than 15 hours ranges between 10 to 15 cm.

### Acknowledgements

Many thanks are due to Prof. Tomasin of "Istituto per la Dinamica delle Grandi Masse" of C.N.R. who kindly provided some of the data used in the paper.

### References

- Battiston, L. and Zambella, D. (1991). "Noise driven intermittency in tidal dynamics". Manuscript.
- Cecconi, G., Buzzi, A., Canestrelli, P., Vieira, J. (1992). "Feasibility study for improving the Venice flood warning system". Book of Abstract 23rd Int. Conf. Coastal Eng.
- Farmer, J.D. and Sidorowich, J.J. (1987). "Predicting chaotic time series". Phys. Rev. Lett., 59(8) 845-848.
- Grossberger, P. and Procaccia, I. (1983). "Characterization of strange attractors". Phys. Rev. Lett., 50 346-349.
- Henderson, H.W. and Wells, R. (1988). "Obtaining attractor dimensions from meteorological time series". Adv. Geophys., 30 205-237.
- Sharifi, M.B., Georgakakos, K.P. and Rodriguez-Iturbe, J. (1990). "Evidence of Deterministic Chaos in the Pulse of Storm Rainfall". J. Atmos. Sci. 47(7), 888-893.
- Takens, F. (1981). "Detecting strange attractors in turbulence". Lecture Notes in Mathematics, 898, Springer-Verlag.
- Tsionis, A.A. and Elsner, J.B. (1989). "Chaos strange attractors and weather". Bull. Amer. Meteor. Soc. 70(1), 14-23.
- Wolf, A., Swift, J., Swinney, H.L. and Vastano, J. (1985). "Determining Lyapunov exponents from a time series". Physica 16D, 285-317.



## CHAPTER 140

### THE ITALIAN WAVES MEASUREMENT NETWORK

M. DE BONI<sup>1</sup>, Manager; L. CAVALERI<sup>2</sup>, Researcher;

A. RUSCONI<sup>3</sup>, Manager

#### 1. INTRODUCTION

The Rete Ondametrica Nazionale (RON) - the Italian Wave Measurement Network - is a system for recording directional wave motions along the Italian coasts, operational since 1st July 1989. The network includes eight wavec directional wave Datawell buoys and the corresponding land-based receiving stations.

Following an international tender, the Ministry of Public Works appointed TEI SpA for the design and management for the network and for data processing. Following the reorganization of the National Technical Services, the responsibility for the network and its activities has been transferred to the Italian Hydrographic and Tidal Service ("Servizio Idrografico e Mareografico, (SIM)"- under the aegis of the "Presidenza del Consiglio dei Ministri" (President of the Ministries Council), a special parliamentary body.

After three years of continuous operations (1989-1992), it is now possible to make a preliminary general account of the venture, analysing in particular the following aspects:

- Reliability of the technical solutions and efficiency of the network management system;
- Scientific and technological applications of statistical data;
- Use of the data in wind-waves numerical modelling for the Mediterranean Sea;
- Prospectives of development and follows-up.

---

<sup>1</sup> TEI Environmental Engineers, via Paleocapa, 6 - 20121 Milano, Italy

<sup>2</sup> Istituto Studio Dinamica Grandi Masse, San Polo 1364 - 30125 Venezia, Italy

<sup>3</sup> Presidenza del Consiglio dei Ministri Servizio Idrografico e Mareografico Nazionale Direzione Centrale, via Nomentana, 2 - 00198 Roma, Italy

2. TECHNICAL DESCRIPTION

The Italian Wave Measurement Network (henceforth referred to as RON) includes eight stations, whose position is shown in Fig. 1.

The choice of the locations has been done with the aim of:

- a) monitoring the sea conditions in areas of intense wave activity;
- b) optimizing the distribution of wave measurement around Italy, given the already existing instruments (see Fig. 1).

Preliminary activity started in early 1989 and the network became operational on 1st July, 1989. In this section we give a compact description of the measuring instruments, of the network and of the data processing.

MEASURING INSTRUMENTS

Each station (see Fig. 2) includes a Wavec buoy, manufactured by Datawell, and a receiving station. The buoy has been amply described in the literature and we give here only a very compact description of it (see e-g, Manual of direc receiver, Manual of wavec buoy from Datawell B.V. Haarlem).

The buoy, moored using a flexible system that allows maximum freedom of movements, is of the surface following type.

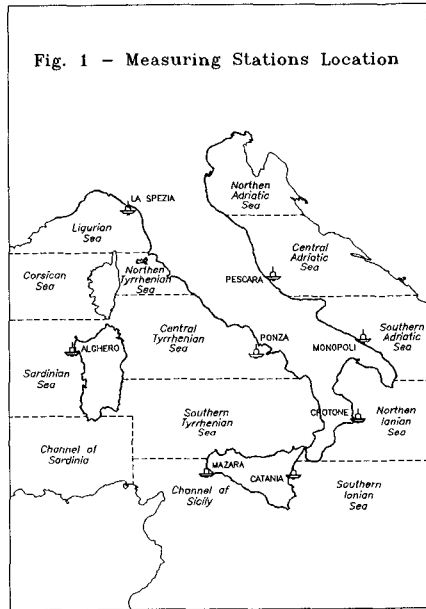


Fig. 1 - Measuring Stations Location

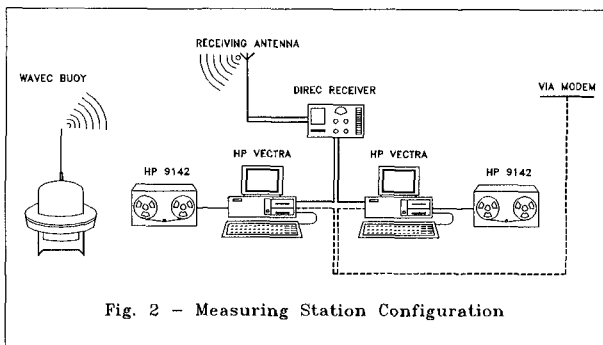


Fig. 2 - Measuring Station Configuration

Vertical acceleration, pitch and roll of the buoy, and relative components of the earth magnetic field are measured and used to deduce the heave and slopes (in North and South direction) of the local sea surface.

Each parameter is sampled at 128 Hz frequency and the data are continuously transmitted by radio to the receiving station located on the main land.

Each buoy is located far enough from the main land to allow full representativeness of open sea conditions.

The mooring depth varies from 80 to 100 m. The buoys are powered by self-contained batteries, with an autonomy of 10 months.

The system for the acquisition and processing of data, of which the Direc receiver is an integral part, is made up of two AT compatible HP Vectra ES 12 Personal Computers.

The PCs are connected by means of serial ports to the MAIN and UAX gates of the Direc; the second serial port is connected to a telephone modem used for tele-servicing and real-time remote control. Through the MAIN computer, it is possible to program the Direc receiver for the functions of sampling time, time, type of data output from the AUX port (monitor, real-time, CQ), and the  $H_s$  above which the system must sample continuously. This PC is also used to store the processed data, and the directional spectra are displayed every 30 minutes, as well as a set of data on the functioning characteristics of the buoy such as tilt, platform offset, compass offset, battery voltage, and water temperature, and a report on the quality of the signals received in the previous half-hour.

As already noted, the AUX PC is used only for the acquisition of data (monitor, real or CQ) sent from the AUX port of the Direc receiver. To minimize the risk of loss of data due to hardware failures in the two computers, each day the data recorded on the hard disk are downloaded to the streaming tape as a sequential file, and then at the end of the month both the physical copy on the hard disk and the daily recordings on tape for each computer are saved.

A detailed description of the network organization and all the technicalities involved is given by Rusconi et al (1990, 1992).

#### DATA PROCESSING

The combined analysis of heave, pitch and roll of the sea surface at a given location, pioneered by Longuet-Higgins et al (1962), provides estimates of:

- a) the one-dimensional wave frequency spectrum  $E(f)$ , and related quantity as significant wave heights  $H_s$ , mean and peak period  $T_m$  and  $T_p$  respectively;

b) directional distribution of energy at each frequency represented by mean direction  $\theta(f)$ , second mean direction  $\theta_2(f)$ , skewness and kurtosis, and the deduced mean spectral direction  $\theta_m$ .

## MANAGEMENT

The degree of reliability of the technical solutions adopted and the efficiency of the Network Management System set is demonstrated by the percentage of valid data which, for each recording station, is supplied every three months to the SIM (Table 1).

	S 89	A 89	W 90	S 90	S 90	A 90	W 91	S 91	E 91	A 91	W 92	TOT
La Spezia	91,30	99,70	86,00	96,40	96,70	93,30	97,10	95,40	94,20	95,40	91,10	94,24
Alghero	94,80	98,90	96,70	95,90	98,50	94,60	97,10	86,70	99,70	93,60	98,80	95,92
Pescara	95,60	100,00	99,90	93,30	89,80	85,20	93,50	96,10	96,70	93,30	99,90	94,85
Monopoli	99,00	96,10	89,90	99,00	98,90	96,30	96,30	99,90	96,00	86,00	97,50	95,90
Ponza	95,90	94,00	86,20	97,50	98,60	90,80	85,10	99,30	98,80	98,80	90,40	94,13
Crotone	96,20	99,70	96,50	85,00	96,70	95,00	99,90	92,00	96,60	92,50	95,50	95,05
Catania	89,80	86,40	85,40	89,80	97,80	96,10	95,70	98,40	94,80	91,20	92,90	92,57
Mazara d.V.	93,30	99,50	86,80	94,60	95,00	85,20	88,80	93,50	88,30	99,60	95,50	92,74
Totale	94,49	96,79	90,93	93,94	96,50	92,06	94,19	95,16	95,64	93,80	95,18	94,42

The following considerations can be made:

- the global reliability of 94,4% is considerably above the minimum limit of 85% required by the SIM;
- this degree of reliability, following a preliminary phase, has been maintained at a level more or less constant thanks to the Management System and to the use of the Argos satellite. This service started in 1990, and it is used for remote control of the position of the buoys;
- no substantial variations of reliability have been noted with the seasons (2% lower than the mean value), which confirms that the technological choice was correct and that reliability depends only to a limited extent on weather conditions;
- loss of data is basically the result of fishing activities: it is a random event more frequent in certain southern areas.

Two activities of considerable technological importance have been implemented to guarantee these reliability levels:

- connection of all the buoys to the Argos satellite in order to check the positioning of the measuring system;
- a star-shaped telecommunications connection via modem between the peripheral recording stations and the central interrogation system.

A permanent Assistance Service has been organized for the RON network to fully exploit these technological supports. It has the twin tasks of an immediate intervention and both a preventive and ordinary maintenance.

## PREVENTIVE AND ORDINARY MAINTENANCE

These activities comprise:

- Downloading to streaming tape and monthly checking of data.
- processing and checking of the quality of the data received (the task of TEI Data Processing Centre), which issues a monthly bulletin, for use by the Assistance Service, on the quality of functioning of the sensors and the percentage of valid data. These activities provide a concise statistical picture of the functioning of the equipment and make it possible to establish in advance the ordinary and special maintenance interventions required.
- Maintenance support activities, for each peripheral site corresponding to a wave gauge station, carried out by two local operators: one for the sea parte, providing immediate nautical intervention in the event of equipment breakdowns; the other for the land part, having the task of carrying out preventive maintenance and the monthly downloading of data.
- Monthly checks on the state of the wave gauge equipment, the relative photographic documentation, underwater inspections to check the moorings, and the preparation of a service report to be delivered to the Data Processing Centre.
- Monthly checks of the equipment on land, with an evaluation of the degree of wear of components such as processors, aerials, cables, ecc.
- Calibration of the wave meters taken out of service for maintenance, using the "Ferris Wheel" system and preparation of the relative certificates.

These preventive activities make it possible to guarantee replacements with a maximum delay of 48 hours for the breakdown of any component on land, and a similar facility within 48-72 hours of notification for incidents involving a wave gauge buoy at sea, using personnel and tenders available on site.

## ALARMS MANAGEMENT

This activity consists of:

- Checking of daily reports supplied via modem by the Argos service, concerning the correct positioning of each buoy.  
If a buoy is found a drift out of its area of action (which is calculated on the basis of the length of the mooring cable), its movement is continuously tracked and repeated via telex or modem to the centre, where the specialist control team will forward the required instructions to the people on site in order to rapidly recover the buoy and to ensure that it is immediately repositioned or replaced.  
This system, based on equipment for the transmission of signals to the Argos satellite, is installed on the wave gauge buoy. It has produced

excellent results and it is certainly one of the reasons that has guaranteed the high percentages for recorded data.

- Daily activation of the automatic interrogation procedure of the peripheral stations, making it possible to check at any moment the functioning of the individual stations/components and to transfer concise wave data.

#### 4. RESULTS

The availability of large quantities of data allows some basic analysis of the wave conditions around Italy, both for basic physical problems as for engineering applications.

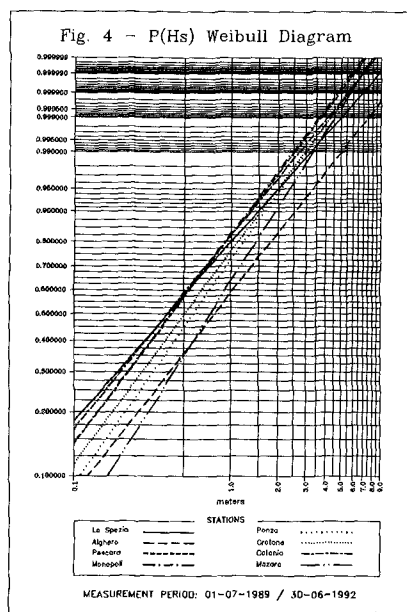
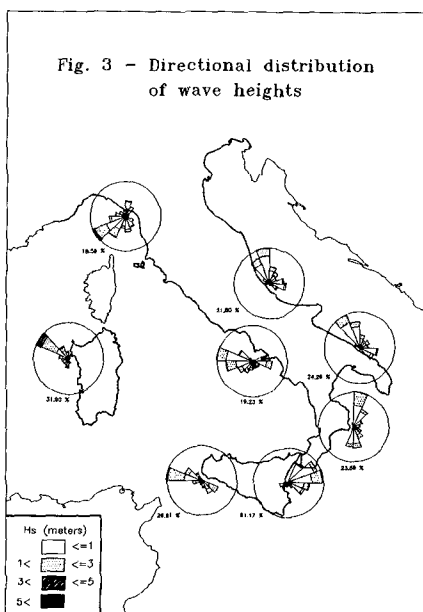
##### A) Wave climate

From the statistical point of view, a number of specific analyses are usually carried out for each station concerning:

- the statistical distribution of  $H_s$ ;
- the combined distributions ( $H_s, T_m$ ), ( $H_s, \theta_m$ );
- the seasonal variability of the above distributions.

Fig. 3 shows, in synoptic form, the directional distribution of the wave height, evaluated on all the data so far collected.

Fig. 4 shows the distribution functions  $p(H_s)$  relative to all the data recorded for the various stations.



The figure highlights the various energy levels corresponding to the different sites, and also the existence of different slopes for the various curves. These distributions cannot be considered conclusive because three years of data are by far a too short period for the deduced statistics to be significant. Besides, the data show a clear yearly variability that depends on the general meteorological pattern of the period. Hence the above statistics should be considered with much care. Because the data collection is continuing, updated statistics will be published as soon as available.

#### B) Extreme waves analysis

A further consideration more concerned with engineering is the selection of the extreme events recorded in the three year period under consideration. Table 2 shows, for the various stations, the maximum values of  $H_s$ ,  $T_p$ ,  $T_z$  and the corresponding mean direction evaluated during the most violent storms at each station.

Undoubtedly the area most exposed to wave motion is the west coast of Sardinia: for this station, in correspondance with the storm of 20th December 1991, a significant wave height of 8.92 m has been recorded.

STATION	$H_s$ (m)	$T_p$ (s)	$T_M$ (s)	MeanDir( $^{\circ}$ N)
La Spezia	6.60	11.10	8.00	60
Alghero	8.92	12.50	9.50	135
Pescara	5.10	9.10	6.00	170
Monopoli	4.40	9.10	7.00	233
Ponza	5.70	12.50	5.40	94
Crotone	5.60	11.10	8.10	302
Catania	5.20	11.10	8.10	275
Mazara	5.50	12.50	8.30	105

## 5. APPLICATION TO NUMERICAL MODELLING

One of the most interesting applications for the data collected by the wave gauge network is the validation of numerical models for the calculation of wave motion.

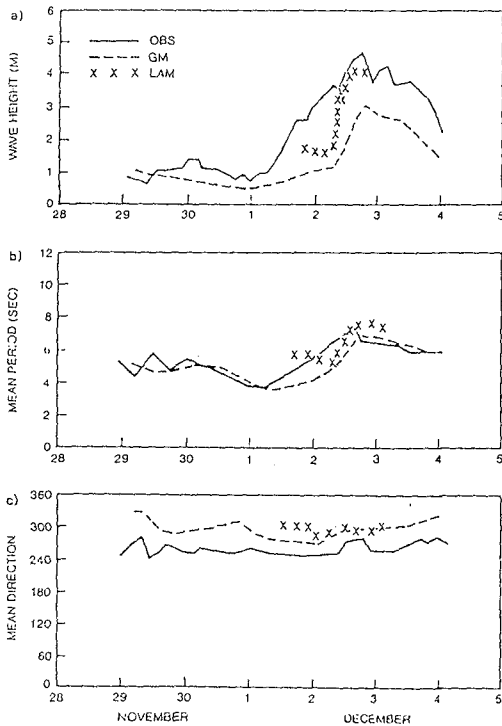
Models at various levels of complexity have been repeatedly applied in the Mediterranean Sea, and the results improve as the approach becomes more sophisticated. Presently one of the most advanced model is WAM, the product of the coordinated work of a large group of specialists in the field (WAMDI Group, 1988). This model has been repeatedly applied in the Mediterranean basin (Cavaleri et al., 1991).

The main result has been to assess the difficulty of correctly representing the field of surface wind in the basin, and consequently the wave field associated with it. An error of 20% in wind speed leads to an error of the significant wave height  $H_s$  of 30-40%, and consequently to an error of 70-100% for the energy of the wave motion, which is the variable of most practical interest in engineering applications. Errors of this level are unacceptable!! We must recognize, however, that different meteorological models, with different solutions, give wind fields that can differ well over 20%. It is also very difficult to thoroughly test a wind model, as the complicated orography of the basin, particularly along the Italian coasts, can affect the local wind field in a drastic way and the stations of interest are located on the coast.

This makes any comparison between a detailed item of measured data (typically wind speed and direction) and the results of a meteorological model of limited significance, when the latter cannot take orographical details into account.

The solution, although neither complete nor definitive, may come from an analysis of the results of the wave field. The conditions of wave motion in a given location represent an effect, integrated in time and space, of the wind field on the entire basin. The recorded wave conditions provide therefore a validation of the combined meteorological and wave models.

Because the performance of a wave model is not affected by the geometry of the surrounding orography, particularly in areas like the Mediterranean Sea, recorded wave data, combined with the models results, can provide useful indications



[Fig. 5 Comparison between recorded and computed wave heights by using the ECMWF (GM) and LAM models]

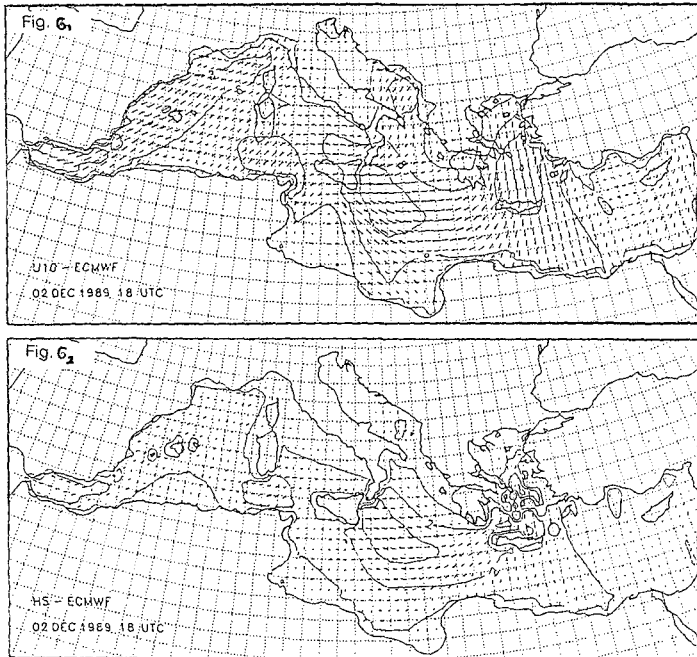


on the accuracy of the input wind fields.

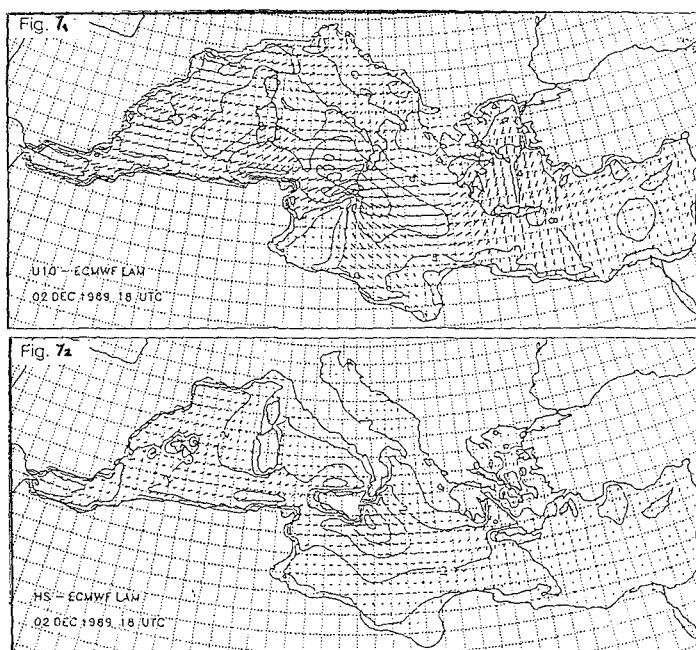
The Mediterranean Sea is characterized, as well as by large-scale events, also by events of a smaller scale, and yet extremely violent. An example is provided by the storm that hit the Malta area on 2nd December 1989 during the meeting between Presidents Bush and Gorbachov. A detailed study of this event has been made by Dell'Osso et al. (1992). The storm was characterized by the development of a deep pressure on the Ionian Sea, characterized by very strong winds with an extremely high spatial gradient. Results of the computation of the wave field by the WAM model have been compared with the experimental data recorded at Catania (Fig. 5). While the direction of the field is correct, there is a considerable underestimate of the wave height, a strong suggestion that the wind has been underestimated.

This led to repeating the meteorological simulation with a finer mesh (40 km, compared with the 125 km resolution of the global model of the ECMWF).

The results, in terms of wind and wave fields, are shown in Fig. 6). There is a strong increase and concentration of the wind in the area of Capo Passero, with a consequent increase of the wave height in the Catania area. Fig. 7 shows the obvious consequent improvement in the wave model results.



[Fig. 6 Windfield (6<sub>1</sub>) computed by ECMWF model and associated waves field (6<sub>2</sub>)



[Fig. 7 Windfield (7a) computed by ECMWF model and associated high resolution waves field (7b) computed by LAM model]

In general, the results of the modelling exercise indicate that a resolution of 125 km, such as that in the operative model of ECMWF until the end of September 1991, is not sufficient to provide the necessary accuracy of the wind field. A 70 km resolution, as that corresponding to the new model of ECMWF (T213), seems the minimum required for a sufficient reliability of the wave model results.

## 6. PRESENT SITUATION AND FUTURE DEVELOPMENTS

In view of the high reliability of the RON System, the Hydrographic and Tidal Service has decided to proceed with the monitoring activities for three more years, appointing once more TEI for the management of the project.

To improve the system the following additional activities have been added:

- connection in real-time of the existing eight stations with the central station at TEI in Milan;
- transfer of the data to a workstation located at the Rome Centre of the Hydrographic and Tidal Service;

- display of the recorded data, in real-time, using the RAI (Italian Broadcasting Corporation) Televideo Service.

Future expected activities include:

- the extension of the present network to four more stations;
- the distribution of the wave data collected and analysed in real time to the GTS - This will allow the assimilation of the wave data in the present Mediterranean Sea wave forecasting system (Cavaleri and Bertotti, 1992) with a consequent improvement of the wave forecast in the basin.

## BIBLIOGRAPHY

- Cavaleri L., L. Bertotti and P. Lionello (1991), "Wind wave cast in the Mediterranean Sea", *J. Geoph. Res.*, 96 (C6), pp 10739-10764.
- Cavaleri L., L. Bertotti (1992), "The Mediterranean Sea wave forecasting system", *Proc. 23rd International Conference on Coastal Engineering*, 4-9 October 1992, Venice, in these proceedings.
- Dell'Osso L., Bertotti L., and C. Cavaleri (1992), "The Gorbush storm in the Mediterranean Sea - atmospheric and wave simulation". *Monthly Weather Review*, 120 n. 1, pp. 77-90.
- Janssen P., P. Lionello and M. Reistad (1989), "Hindcasts and data assimilation studies with the WAM model during the Seasat period", *J. Geoph. Res.*, 94 (C1), pp. 973-993.
- Rusconi A., M. De Boni and G.F. Grancini (1990), "La rete Ondametrica Nazionale: risultato del primo anno di gestione". *La Marina Italiana*, LXXXVIII, pp.30-39.
- Rusconi A., L. Cavaleri and M. De Boni (1992), "Rete Ondametrica Nazionale. Risultati del primo triennio di funzionamento e gestione della rete, analisi di affidabilità del sistema e selezione di eventi eccezionali - Prospettive di sviluppo", *Proc. III convegno AIOM*.
- The WAMDY Group (1988), "The WAM model - a third generation ocean wave prediction model", *J. Physic. Ocean*, 18 pp. 1775-1810.

# CHAPTER 141

## EVALUATION OF DESIGN WAVES ALONG THE COAST AND AT THE INLETS OF THE VENICE LAGOON

Paolo De Girolamo(\*), Giancarlo Passacantando(\*\*)  
David Hurdle(\*\*\*) and Alberto Noli(\*)

### Abstract

The prevention of flooding inside the Venice lagoon requires a system to disconnect the North Adriatic sea and the lagoon hydraulically in order to control water level. This paper describe the method followed to define design wave conditions to support the design of the new storm surge barriers. The derivation of design waves was not straightforward because of the presence of an extended continental platform and irregular geografic boundaries.

### 1.Introduction

The prevention of flooding inside the Venice lagoon (Fig.2) requires a system to disconnect the North Adriatic sea and the lagoon hydraulically to control water level. One of the most feasible ways to achieve this is to use a system of moveable storm surge barriers (Varisco 1992).

Definition of the wave and water level conditions is required for the associated design activities. This paper describes the work carried out in order to define the design waves for normal and extreme conditions. The emphasis is on the statistical methodology to derive the extreme conditions and on the appropriate modelling approach for the simulation of the wave behaviour close to the inlets. A number of numerical models were evaluated to select the appropriate one for the preliminarily and design phases. The derivation of the conditions at the outside boundary of these models is discussed by Hurdle et al.(1993). This paper also discusses the special characteristics of the North Adriatic sea (in particular the extended continental shelf) and the predominant wind conditions. For the purposes of this paper, it is sufficient to know that three wind types are important for the design conditions: the Scirocco wind (from the South East), the Levante wind (from the East) and the Bora wind (a cold wind from East North East).

---

(\*) University of Rome "La Sapienza"-Via Eudossiana,18 - 00184  
Rome (ITALY).

(\*\*) Technital S.p.a.-Via Carlo Cattaneo,20 - 37121 Verona (ITALY).

(\*\*\*)Delft Hydraulics-P.O. Box 152, - 8300 AD Emmeloord (THE  
NETHERLANDS).

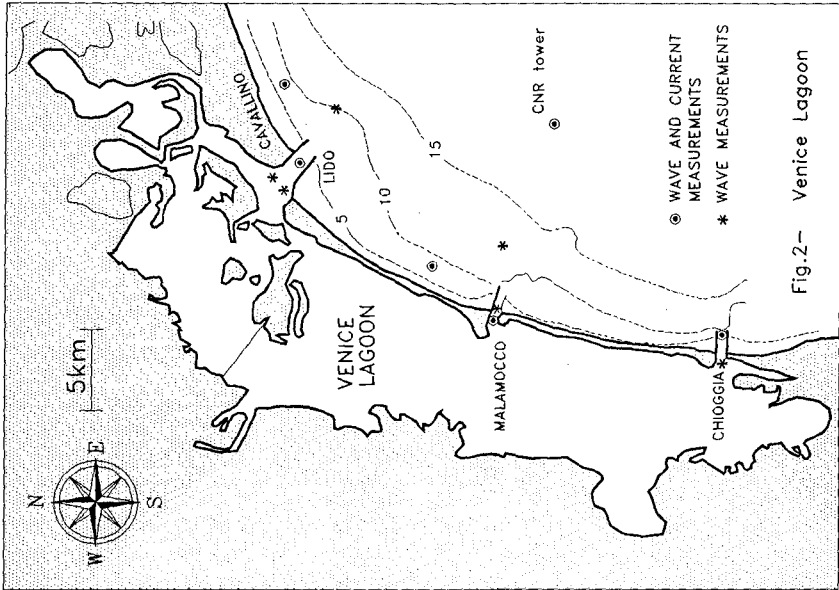


Fig.2- Venice Lagoon

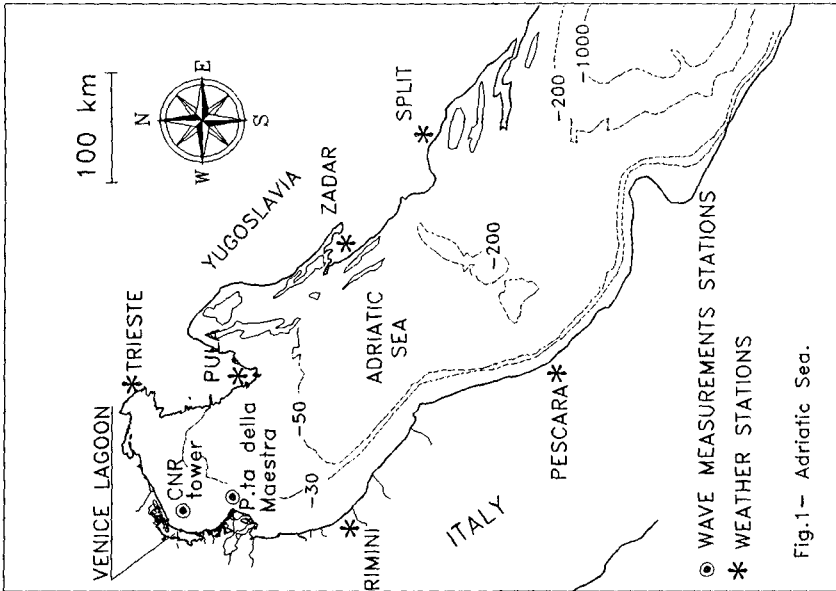


Fig.1- Adriatic Sea.

Even in the preliminary phase, the design of the moveable storm surge barriers required a careful evaluation of the extreme wave conditions in front of the barriers. In fact, initial studies using simple numerical models indicated that a moveable storm surge barrier would not be feasible without the construction of offshore detached breakwaters to reduce the wave penetration. Such structures would have affected the delicate morphological balance of the surrounding coasts. However, the application of a more sophisticated wave model showed that the offshore breakwaters are not necessary; an important result giving both environmental and economical advantages.

## 2. Methodology to derive extreme design conditions.

Extreme wave conditions are required for the following purposes:

- design of the moveable storm surge barrier (extreme wave conditions, high water levels only, inside inlets);
- design of the associated fixed structures (extreme wave conditions, all water levels, inside inlets).

In principle there are two fundamental ways to obtain extreme wave and water level conditions. These are illustrated in Fig. 3.

In the first method, illustrated by the clockwise route in Fig.3, the input data is the history of meteorological conditions in the area. These are then statistically extrapolated to get a nominal extreme storm (meteorological condition). Wave and flow models are then applied (modelling phase) to predict the extreme wave and water level conditions at the locations of interest. This method has the following drawbacks:

- It is very difficult to define "extreme meteorological conditions". This can be done in a schematised way by obtaining the extreme wind speed in a number of direction classes and assuming stationary and uniform wind conditions.

- It is unlikely that it will be sufficient to model only one condition, since it is not known which combination of extreme conditions gives the most severe results (e.g. if the meteorological conditions are defined by the extreme wind speed in each direction sector, runs will have to be made for several direction sectors);

- The final results depend on the performance of the models used to predict the extreme wave and water level conditions. The models used must therefore be validated for some real cases.

In the second method, (anti-clockwise route in Fig. 3), the basic data is the same set of meteorological conditions. A series of the most severe events is selected and models are used to hindcast the required parameters at the site of interest. These parameters may then be converted to a damage factor of some kind (e.g. significant wave height) which can be statistically extrapolated to obtain the extreme damage. Alternatively, an analysis can be carried out to obtain the joint extreme statistics of the required parameters. This method has the following drawbacks:

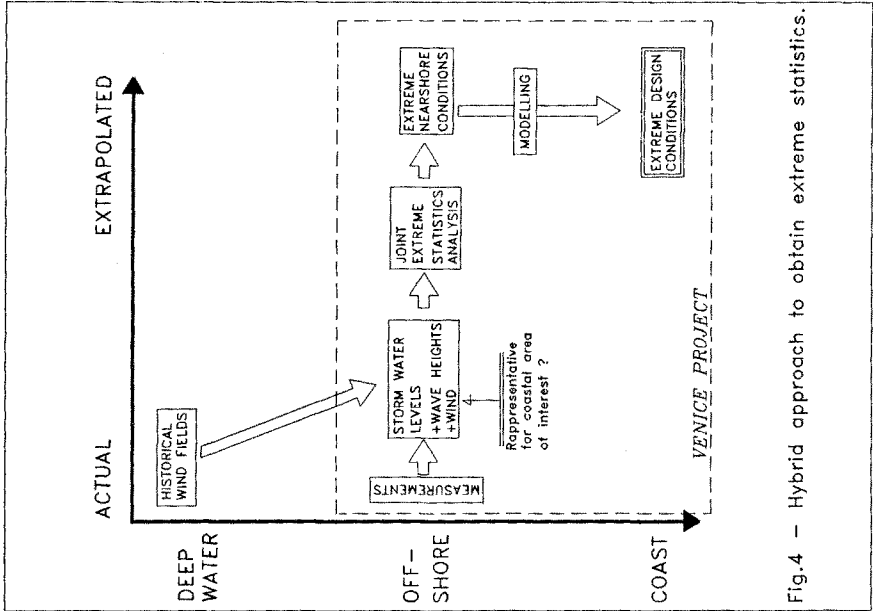


Fig.4 - Hybrid approach to obtain extreme statistics.

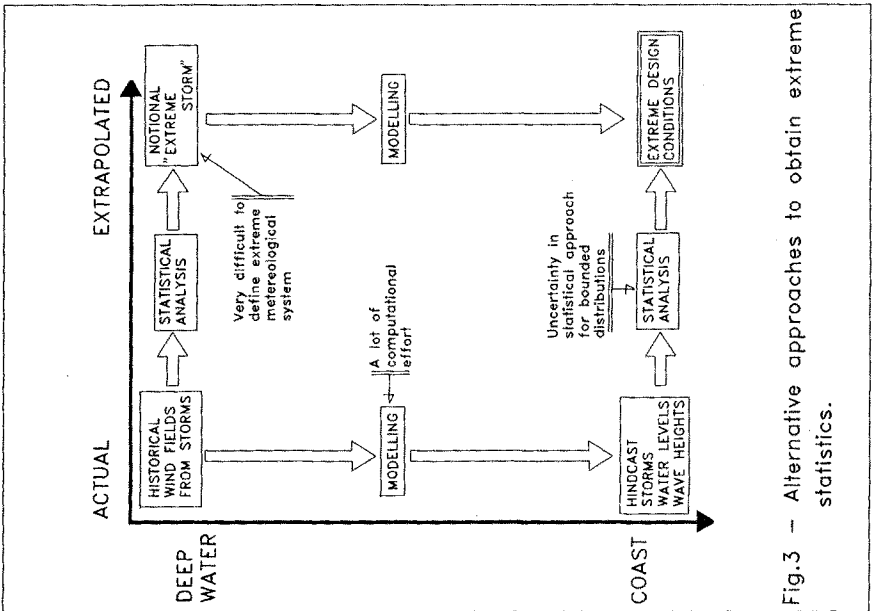


Fig.3 - Alternative approaches to obtain extreme statistics.

- It is difficult to make a restricted and correct selection of the most severe events. For example, if water level and wave height are the parameters of interest, the conditions which give the highest wave height may be very different from those which cause the highest water levels.

- The distribution of parameters at the site of interest is often bounded (e.g. wave height in shallow water). The prediction of the extreme values of such distributions is difficult and often sensitive to errors.

A practical solution to these problems is to use a hybrid approach between the two methods with or without the additional use of measurements of relevant parameters at an intermediate station. Such an approach is illustrated in Fig. 4. In this approach the physical processes are separated into two phases, between which the statistical extrapolation is carried out. The phases are:

- A wave generation phase in which depth limitation plays a minor role but in which the wind field is treated as non-stationary and non-uniform in any modelling. Any modelling is large scale and does not have to include accurate representation of the coastal area. Modelling of water levels and currents in this phase is also on a large scale and applies non-uniform non-stationary wind fields.

- A wave propagation phase in which refraction, shoaling and dissipation by bottom friction and by breaking play an important role. However, the area being modelled is sufficiently small to be able to consider wind fields and incident wave conditions to be stationary.

Real storms are modelled in the first phase, thus avoiding any problems of characterising the non-stationary and non-uniform wind fields. Sometimes, this modelling phase can be omitted when a sufficient period of measured values is available. Otherwise, measurements may be used to calibrate the models. The results of the first phase (wave height, period and direction, water levels and wind speeds and direction) are then statistically analysed to get design values which can be applied as stationary boundary conditions for the modelling of the second phase. The application of this method poses some questions about which combinations of extreme values give the most onerous design conditions at each site of interest. In practice the most onerous design scenario is likely to depend on what is being designed (e.g. breakwater, storm surge barrier, refuge harbour) and where it is located. There is therefore no single combination of the design boundary conditions which can be considered to give the design scenario for all purposes.

In the Venice project three design scenarios were considered according to the wind direction in the Venice gulf (Bora, Levante or Scirocco). Each of them has been characterized only by one wave condition according to the wind direction. For each of these scenarios the design wind and wave conditions were taken to be fully dependent. This restricted the number of design scenarios which had to be considered to three (Bora, Levante, Scirocco). The relationship between the extreme water levels and the extreme wave conditions was derived on the basis of a joint probability analysis carried out only for Scirocco/Levante storms. For Bora storms lower



levels were considered. Of course, some sensitivity studies were carried out to examine the effect of changes in the boundary conditions for the modelling of the second phase.

The activities carried out to derive the extreme wave conditions at the barriers are shown by Fig. 5. The boundary conditions at the outer boundary of the models of the wave behaviour in the inlets for each scenario (significant wave height  $H_B$ , peak period  $T_p$ , diectional spreading, and water level  $h_w$ ) were derived from measurements and wave modelling in the offshore area is described by Hurdle et al. (1993).

### 3. Selection of the wave mathematical models.

There is no mathematical model capable of simulating all the relevant physical phenomena over the entire generation and propagation area. Therefore the governing processes were itemized and the area in which they act determined. The area was then divided into sub-area and numerical models selected for each sub-area to model the relevant phenomena to give the degree of accuracy required for each design phase. Relevant physical phenomena and the area on which they act are shown in Table 1.

Although the Table provides a valuable insight into the relevant phenomena, it should be noted that it is generally not possible to account for the phenomena in isolation because of the way they interact. The selected sub-areas are an offshore (OUT) and coastal area (CST) and the three lagoon inlets and the channels leading to them (INL) as it is shown by Fig. 6. In the offshore and coastal area, the wave propagation is dominated by depth refraction, shoaling and external energy effects. In the inshore areas the wave propagation is dominated by refraction, shoaling and diffraction. For extreme waves, wave breaking is also of some importance in these areas.

Apart from the wave dissipation processes, the most interesting non-linear wave aspects are those which give rise to the generation of free long waves from the short wave field. These long waves will not have a significant effect on the short wave propagation but may be of interest in themselves. For example, they may have an onerous effect on the efficiency of the storm surge barriers or may excite long waves resonances in the inlets. Such non-linear effects could play a role throughout the area between the CNR tower and the coast.

In all areas, a correct representation of the directional spectrum of the wave field is of importance because of the role that this plays in the wave propagation. A correct transfer of information about the directional spectrum on the boundaries between the areas is also very important.

The criteria applied for the selection of the model for the offshore and coastal area were that the directional spectrum should be properly represented and that refraction, shoaling and external energy effects should be modelled. The wave model applied will be called "spectral wave refraction model" (SRM) (see Hurdle et al. 1993).

In the inner area, different models were applied at different design phases. All the applied models accounted for refraction, shoaling and reflection effects while diffraction was accounted for

Property of model	Importance for Venice			Numerical wave model				PM
	OUT	CST	INL	SRM (1)	RDR (1)	MSM (1)	BM (1)	
<b>LINEAR PROPAGATION AND INTERACTION WITH STRUCTURES</b>								
Shoaling	+	+	+	*	*	*	*	*
Depth refraction	+	+	+	*	*	*	*	*
Current refraction	-	-	+	*	* 2	*		*
Diffraction	-	-	+		* 3	*	*	*
Reflection	-	-	+		*	*	*	* 4
Transmission	-	-	-		* 2	*		* 4
<b>NON-LINEAR PROPAGATION</b>								
Long waves from wave groups	-	?	+				*	* 5
long waves from surfbeat	-	?	+					* 5
diffraction	-	-	-				*	*
refraction	-	-	-				*	*
<b>DISSIPATION AND GROWTH</b>								
bottom friction	+	+	+	*	*	*	*	* 4
breaking	+	+	+	*	*	*	?	* 4
generation by wind	+	0	0	*				
<b>DESCRIPTION OF THE WAVE FIELD</b>								
directional spreading of energy	+	+	+	*	*	*	*	* 2
frequency spreading of energy	-	-	6	* 2	* 2	* 2	*	*
<b>AREA TO BE MODELLED</b>								
Area (km x km)	100	20	5	100	100	5	5	5
	x	x	x	x	x	x	x	x
	100	5	5	100	100	5	5	5
<b>Other limitations</b>								
	n/a	n/a	n/a				7	4 5

**LEGEND**

**Areas:**  
 OUT - outer area  
 CST - coastal area up to depth of 15 m excluding inlets  
 INL - area in and around inlets and access channel

**Models:**  
 SRM - spectral refraction model  
 RDR - Ray model with diffraction based on analytical sol.  
 MSM - mild-slope model  
 BM - Boussinesq model  
 PM - Physical model in wave basin

**Key:**  
 + Important  
 - Not important  
 0 Limited importance  
 \* included in the model  
 1 depth integrated model  
 2 not applied for Venice project  
 3 adaptation for structures diffraction using analytical sol., no bottom diffraction  
 4 at small scales, breaking, bottom friction, reflection and transmission not properly reproduced  
 5 long wave resonance of wave basin?  
 6 spectral form required at storm surge barrier  
 7 only valid in shallow or shallow/intermediate depth water

Tab.1

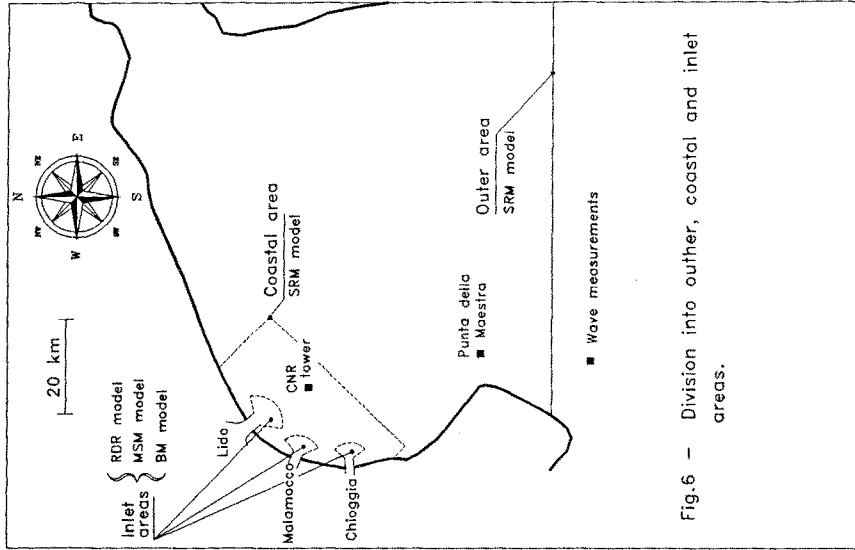


Fig.6 - Division into outer, coastal and inlet areas.

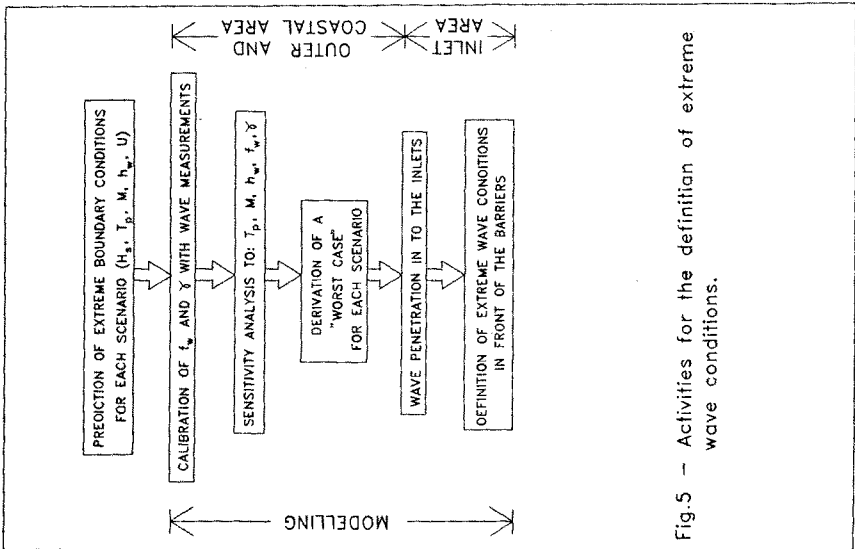


Fig.5 - Activities for the definition of extreme wave conditions.

either approximately or exactly. The models were a refraction-diffraction ray model (RDR), a mild-slope model (MSM) and a Boussinesq model (BM). Table 1 shows also the capability of reproducing the physical phenomena for each numerical model. All of the models are depth integrated and the only non linear model is the Boussinesq model.

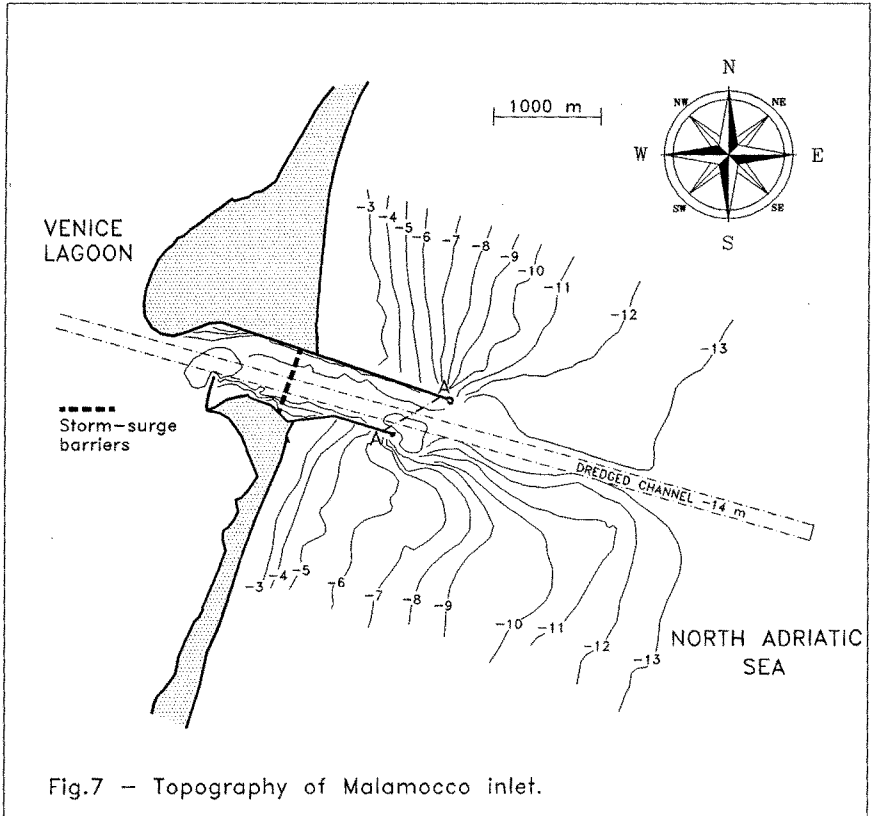
Some elucidation of the comments in the table about the limitation of physical models is now given. In general, the porosity and roughness of structures are difficult to reproduce at small scales and surface tension effects, which do not play a role at full scale, become increasingly important for waves of small height and length. This results in reduced energy transmission and increased reflection by porous structures at model scale. Further it is difficult to distinguish long wave resonances which results from the wave basin from those occurring in reality.

#### 4. Wave penetration into the inlets.

The three inlets which connect the North Adriatic sea to the lagoon (Lido, Malamocco and Chioggia, Fig. 2) are protected by breakwaters of length between 1.5 + 2 km. The bottom topography of the inlets is characterised by the presence of navigational channels maintained by the effect of the tidal current and periodic dredging works. As an example Fig. 7 shows the bottom topography of Malamocco inlet. The new storm surge barriers have been located inside the inlets at 1.5 + 2 km far from the breakwater heads so that they are sheltered from wave activity by the breakwaters.

As mentioned in the introduction, a careful evaluation of the extreme wave conditions at the barriers was required even in preliminary design phase. This is because the feasibility of a solution using floating barriers is very sensitive to the wave conditions due to the loads acting on their foundations and decrease in their efficiency for high incident wave conditions and wave overtopping.

As it is shown in Tab.1, almost all of the wave propagation phenomena become relevant close to and inside the inlets. When the waves approach the navigational channel the concave shape of the bottom causes refraction of waves out of the channel and the concentration of wave energy on the shallow areas bounding the channel. This spreading effect (sometimes known as channel refraction), due to the bottom refraction, is balanced by bottom diffraction which tends to increase the wave energy inside the channel. The concentration of wave energy over the shallows is limited by wave breaking. The tidal current, which increases inside the inlets, influence the wave propagation through a refraction effect. The combined action of waves and current interferes with the floating flap gates during the closing operations of the inlets. During surge events the barriers are subjected to both short and long wave actions. Long waves are associated with wave groups and surf-beat along the beaches located outside the inlets and can excite natural modes of oscillation of the floating flap gates.



Due to the complexity of the physical phenomena involved, a preliminary study was carried out in order to analyse the importance of each phenomenon for the wave penetration of the inlets and the capability of the numerical models to reproduce them.

A first analysis was carried out in order to understand the effects and the importance of frequency and directional spreading of the energy spectrum and of non-linear interactions among wave components. With this purpose a Boussinesq model was applied to the Malamocco inlet for three different wave conditions:

Case 1: long crested monochromatic waves;

Case 2: long crested irregular waves;

Case 3: short crested irregular waves.

All of the mentioned cases were run with the same significant wave height  $H_g$  and peak period  $T_p$ . The results obtained showed that the wave penetration inside the inlet increases considerably with the inclusion of energy directional spreading (Case 3). The effect of frequency spreading (Case 2) does not give important differences with respect to monochromatic waves (Case 1).

It is to be noticed that at the time of the work the available Boussinesq models did not include the effect of wave breaking which is still a research subject. Due to the importance of wave breaking for extreme wave conditions inside and around the inlets, it was decided to study whether linear models, for which the inclusion of wave breaking has proved to be successful (De Girolamo et al. 1988), could be applied. A mild-slope model (MSM) was then applied with the inclusion of directional spreading and compared to the Boussinesq model. The results showed that a proper reproduction of directional spreading was enough to guarantee a correct wave field inside the inlets and that the effect of non-linear interference between wave components was of secondary importance for the purposes of the study.

The reproduction of directional spreading in the MSM was obtained by using the superposition principle for a number of wave direction components. Due to the fact that wave breaking introduces a non-linear condition in the model, this was run using an iterative approach. Fig. 8 shows some results obtained for a point located at the site of the storm surge barriers inside the Malamocco inlet. The continuous line shows the obtained amplification coefficients for different offshore directions of incoming unidirectional waves. The spreading effect (channel refraction) due to the concave bathymetry of the inlet increases as the waves approach the navigation channel with a direction close to the inlet axis. This effect causes a strong reduction of wave height at the barriers. The effect of including directional spreading is clearly shown in the Figure by the square points and is stronger for the waves coming along the channel axis for which the wave height can increase by up to three times.

Some applications for the Chioggia inlet including wave breaking using the Batjjes and Janssen (1978) formulation are presented in De Girolamo et al. (1988). Fig. 9 shows an example of the verification of the computation of the wave penetration of the Malamocco inlet during ebb and flood tidal conditions. In this case the model was run simulating current refraction effects (Kostense et al. 1988).

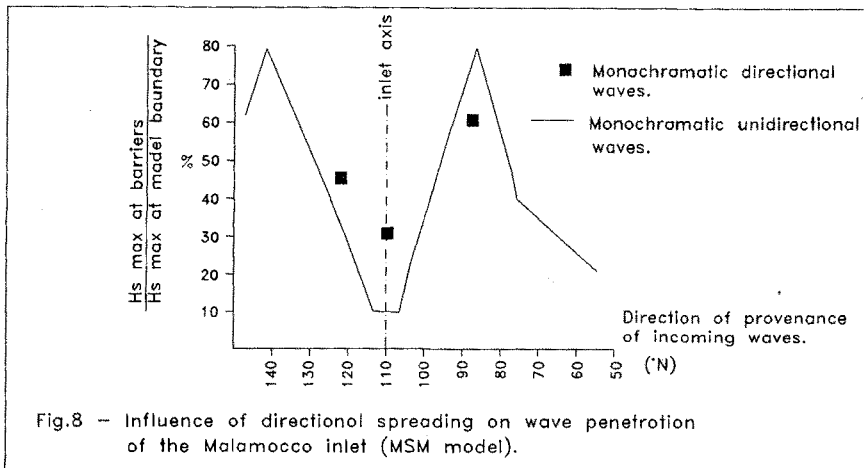


Fig.8 - Influence of directional spreading on wave penetration of the Malamocco inlet (MSM model).

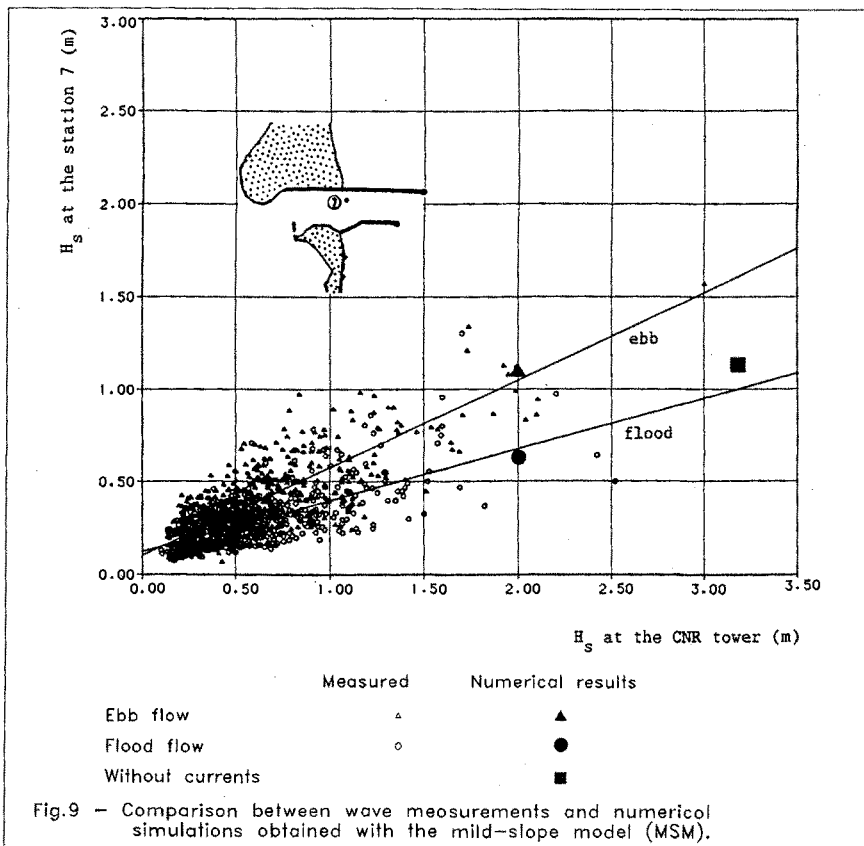


Fig.9 - Comparison between wave measurements and numerical simulations obtained with the mild-slope model (MSM).

The preliminary design required the study and the comparison of a number of different layouts for each inlet. For this reason it was important to distinguish a simple numerical model which could be used, as an alternative to the MSM, as a practical tool for such a work.

A very efficient and simple tool was found in a refraction-diffraction ray model (RDR see Tab.1 - Southgate 1985). The model simulates the diffraction effects around obstacles using an analytical approach but neglects bottom diffraction. Further it can be easily run with directional spreading. Even if the model cannot be used in some situations for a correct quantitative analysis (De Girolamo et al. 1989) it can give insight into the wave paths and can be used to compare different layouts. The most important limitation of the model is the neglect of bottom diffraction which in presence of an undersea channel plays an important role in containing the energy spread due to the refraction effects.

Summing up the numerical work was split into two phases using the more suitable model for each of them.

In the first phase the existing situation (before the construction of the new structures) was analysed and various alternative layouts were studied. The simple RDR model was used in order to carry out the large number of required simulations.

For the second phase the more complex models (MSM and BM) were used in order to study the selected layouts for each inlet. The large extent of the inlet areas required up to 150.000 computational grid points for the MSM model. The most important result obtained with the MSM was to show that the construction of new offshore detached breakwaters was not necessary.

For the final design of the structures, physical models in wave basin, reproducing the real topography of the inlets, have been used. The work, which is still being carried out, requires a scale ratio ranging from 1:60 to 1:80 in order to minimize the limitations mentioned at Paragraph 6 for physical models. The maximum modelled area is 11.000 m<sup>2</sup>. The models will be used in order to reproduce the effective hydrodynamics of the area including the interference by waves and tidal currents with the floating flap gates, already tested in a three dimensional basin (Varisco 1992) using a constant water depth. The translation waves caused by the closure of the floating flap gates during surge events will also be investigated. Due to the large extent of the modelled area, directional wave spectra will be not reproduced. Consequently the results obtained using uni-directional waves will be analysed and interpreted with the support of the results for short crested waves obtained using numerical models.

##### 5. Concluding remarks.

The definition of design waves for the Venice project was not straightforward. Diverse models (numerical and physical) have been used to derive the design waves. Simple models were valuable in the feasibility phase and sophisticated models in later phases.



Because of the diverse limitations of both physical and numerical models it was necessary to distinguish three distinct areas where different physical phenomena are dominant: the outer area, the coastal area and the area in and around the inlets.

In the inlet areas directional spreading has an important influence on the wave penetration of the inlets while frequency spreading is less important.

The ebb tidal current, with the barriers open, increases the wave height for normal conditions while the height of extreme waves is limited by wave breaking.

Refraction of uni-directional waves propagating parallel to the access channels leading to the inlets gives a strong reduction in the wave height. The effect of bottom diffraction and directional spreading reduce this effect. The mentioned effects and wave dissipation by breaking limit energy concentration inside the inlets which can take place for other incoming wave directions.

In spite of the very large width of the inlet entrances (ranging from 460 m to 900 m) the significant wave height,  $H_g$ , in front of the barriers does not exceed 3+3.7 m for the 1000 year return period. The three dimensional wave basin simulations showed a satisfactory behaviour of the floating flap gates under these wave conditions.

#### Acknowledgements.

The studies presented in this paper were carried out for Consorzio Venezia Nuova under the coordination of Technital. Consorzio Venezia Nuova is concessionary for the studies and works related to the Venice protection project on behalf of the competent Italian state authority Magistrato alle Acque.

The numerical studies were carried out by Danish Hydraulic Institute, Delft Hydraulics, HR Wallingford and TEI; the physical models by Protecno and field measurements by Ecomar.

The authors are grateful to CNR and ENEL for the supply of wave data measured in the Venice gulf.

#### References.

- Battjes, J.A. & Janssen, J.P.F.M. (1978). "Energy Loss and Set-up due to Braking of Random Waves". Proc. 16<sup>th</sup> Int. Conf. Coastal Eng., ASCE, New York, U.S.
- De Girolamo, P., Kostense, J.K. & Dingemans, M.W. (1988). "Inclusion of Wave Breaking in a Mild-slope Model". Computer Modelling in Ocean Engineering, Ed. Schrefler & Zienkiewicz, Venice, Italy.
- De Girolamo, P., Nicolai, L. & Noli, A. (1989). "Wave Propagation along Undersea Canals". Proc. 2<sup>nd</sup> AIOM Congress, 15-17 Nov. 1989, Neaple, Italy.
- Hurdle, D., De Girolamo, P. & Pellegrini, G. (1993). "Evaluation of Design Waves along the Adriatic Coast of the Venice Lagoon". Submitted for special issue on Coastal Engineering on HISWA applications.
- Konstense, J.K., Dingemans, M.W & Van den Bosch, P. (1988). "Wave Current Interaction in Harbours". Proc. 21<sup>st</sup> Int. Conf. Coastal Eng., ASCE, Malaga, Spain.
- Varisco, D. (1992). "Interaction between Flap Gates and Tidal Currents and Waves". Proc. 23<sup>rd</sup> Int. Conf. on Coastal Eng., ASCE, Venice, Italy.

## CHAPTER 142

### Effects of non-uniform sediment grainsize in the long-term evolution of tidal lagoons

G. DI SILVIO\* and P. TEATINI\*\*

\*Istituto di Idraulica «G. Poleni», Università di Padova, Via Loredan, 20 - 35131 Padova, Italy

\*\* Dipartimento di Metodi e Modelli Matematici per le Scienze Applicate  
Università di Padova, Via Belzoni, 8 - 35131 Padova, Italy

#### 1. INTRODUCTION

Long-term coastal processes [9, 10] usually consist in slight net morphological changes that result from large positive and negative oscillations occurring to a much shorter time-scale. As soon as one is not interested in these short-term variations, one may perform a preliminary time averaging of the basic waterflow and sediment transport equations in order to obtain a much simpler and manageable model for long-term simulations [6].

Long-term mathematical models, in fact, not only require much less computer time, but can run without knowing the detailed time - history of all the boundary conditions (which on the contrary is absolutely needed by short-term mathematical models).

Averaging of non-linear equations, on the other hand, produce residual terms that either may be neglected or should be expressed, in some convenient way, as a function of the averaged quantities. The procedure, indeed, is analogous to the averaging of the Navier-Stokes equations in order to eliminate turbulence pulsations, where the Reynolds stresses should be conveniently expressed in terms of averaged velocity.

In the case of long-term morphological models of tidal lagoons, semi-empirical expressions of the residual terms can be found. The relative calibration coefficients may be then identified by comparison with field data and/or with a limited number of simulations carried out on short-term models.

In some previous papers, long-term morphological models of a tidal lagoon have been developed with different space-resolution (zero-dimensional [4] and two-dimensional [5] approach) by considering only one equivalent (uniform) sediment grainsize. The zero-dimensional procedure, in particular, has been applied to the Lagoon of Venice [8].

In the present paper the two-dimensional model is re-considered and extended to the case of particles with different grainsize, ranging from sand to silt.

#### 2. TWO DIMENSIONAL LONG-TERM MODEL

The  $n$  two-dimensional balance equations for the sediments belonging to the  $i$ -th grainsize class ( $i = 1, 2, \dots, n$ ) are written as:

$$\frac{\partial T_{x_i}}{\partial x} + \frac{\partial T_{y_i}}{\partial y} = E_i \quad (1)$$

where  $T_{x_i}$  and  $T_{y_i}$  are the long-term sediment transport (averaged over a long period of time) in the direction  $x$  and  $y$  respectively and  $E_i$  is the long-term rate of removal from the lagoonal surface.

The following expression for the "net" sediment transport are obtained by integrating the suspended transport equations over a long period of time:

$$T_{x_i} = h \left( C_i U - D_x \frac{\partial C_i}{\partial x} \right) \quad (2)$$

$$T_{y_i} = h \left( C_i V - D_y \frac{\partial C_i}{\partial y} \right) \quad (3)$$

where  $h$  is the average water depth and  $C_i$  the average sediment concentration of the  $i$ -th class over the water column. The components of the residual currents,  $U$  and  $V$ , are mainly due to the inland water input but also to the (eulerian) net circulation produced by the asymmetry of tidal flow. Even with a symmetrical tidal flow, however, a large amount of net transport is due to the intertidal dispersion produced by the irregular morphology of the lagoon; dispersion coefficients  $D_x$  and  $D_y$  result in fact being quite large (hundreds of  $m^2/s$ ), as recently confirmed by experiments in the lagoon of Venice [7]. The quantities  $U$ ,  $V$ ,  $D_x$  and  $D_y$  may be provided by a tidal model.

The long-term evolution of the water depth,  $h$ , is given by adding up the bottom erosion rate  $\Sigma E_i$  (removal of all the grainsize classes), the eustatism rate  $\alpha_c$  (rise of mean sea level) and the subsidence rate  $\alpha_s$  (settlement of ground surface):

$$\frac{dh}{dt} = \Sigma E_i + \alpha_c + \alpha_s \quad (4)$$

A first-order reaction equation is assumed for the bottom erosion rate:

$$E_i = w_i (\beta_i C_{ji} - C_i) \quad (5)$$

where  $C_{ji}$  is the equilibrium concentration of the  $i$ -th grainsize class,  $\beta_i$  is the percentage of the same class present in the bottom and  $w_i$  a parameter that, for fine particles, coincides with the fall velocity of the particle with a diameter  $d_i$ . Eq. (5) shows that the equilibrium concentration of the  $i$ -th class in a certain place is the average sediment concentration over the water column which would yield neither erosion or deposition, should the bottom be composed by that grainsize ( $\beta_i = 1$ ). Equilibrium concentration  $C_{ji}$  depends on the grainsize diameter  $d_i$ , on the local hydrodynamics (waves and currents) and on the local depth, as it will be discussed in the subsequent section.

The mathematical model should also include the balance equation of the  $i$ -th class in the bottom:

$$\frac{d(\beta_i \delta)}{dt} = - E_i + \beta_i^* \Sigma E_i \quad (6)$$

where  $\delta$  is the thickness of the "mixing layer" (i.e. the amplitude of the bottom variation during the annual cycle) and

$\beta_1^*$  is the grainsize percentage in the mixing layer (if  $E_1 < 0$ ) or below it (if  $E_1 > 0$ ).

The numerical integration of eqs. (1) to (6) provide the evolution of water depth, sediment transport and grainsize composition all over the lagoon, provided that initial and boundary conditions are duly prescribed.

### 3. EQUILIBRIUM CONCENTRATION

The expressions of the equilibrium concentration,  $C_{ij}$ , constitute the crucial link coupling hydrodynamics, sediment transport and morphology of a lagoon. These expressions are obtained by integrating over a long period of time (say, one year) any transport formula of sediments by currents and waves. By assuming a plausible statistical distribution for wave climate and tidal flow and by treating residual terms with necessary simplifications, one comes to a formulation of this type:

$$C_{ij} = C_{ji}(W, Q, d_i, h) \quad (7)$$

which is in principle different for channels ( $C_{ij} \equiv C_{ci}$ ), shoals ( $C_{ij} \equiv C_{si}$ ), and tidal flats ( $C_{ij} \equiv C_{fi}$ ), where  $w$  and  $Q$ , respectively, are quantities related to the local wave climate and tidal flow; coefficients in eq. 7 are to be determined via calibration against morphological and sedimentological data.

An approximate form of eq. (7) is a simple monomial expression; however, if one considers a threshold-value for the waves and currents capable of picking-up the sediment from the bottom (incipient motion), one comes to more complicated expressions that can explain various interesting features of the lagoon's morphology and sedimentology.

### 4. CONCLUSIONS.

Grainsize distribution in estuaries and tidal lagoons is generally far from being uniform. In the Lagoon of Venice, for

example, a systematic survey [1, 2, 3] shows that sediments tend to be sandy near the inlet sand to decrease towards the periphery, especially in the northern-eastern part, where silt and clay definitely prevail (Fig. 1). Another distinction, although less clear, exists between a channel and the adjacent shoals where sediments are generally finer.

In a lagoon with negligible sediment input by rivers and moderate eustatism and soil subsidence, this typical pattern is essentially due to the "threshold effect" of the pick-up function by currents and waves. Indeed, as the net transport through the lagoon should be practically zero, the average concentration of each grainsize class in the water column should be almost the same all over the lagoon. Consequently, shoals that are less subject to wave action result to have a smaller depth and a finer bottom composition; in this way all the particles here are put in suspension less frequently but with a higher concentration with respect to the particles in more exposed shoals.

In general, however, grainsize distribution is also controlled by the sediment net fluxes towards the sea (by river input) or towards the periphery (by eustatism and soil subsidence), as well as by any long-term evolutionary process. The relative importance of the various mechanisms in the transport of non-uniform grainsize particles in estuaries and tidal lagoons can be assessed and discussed by the mathematical model described above.

### BIBLIOGRAPHY

1. Barillari, A. (1977-78). Prime notizie sulla distribuzione dei sedimenti superficiali nel bacino centrale della Laguna di Venezia. *Atti Ist. Veneto di SS.LL.AA.*, 136, Venezia.
2. Barillari, A. (1980-81). Distribuzione dei sedimenti superficiali nel bacino meridionale della Laguna di Venezia. *Atti Ist. Veneto di SS.LL.AA.*, 139, Venezia.
3. Barillari, A. e Rosso, A. (1975). Prime notizie sulla distribuzione dei sedimenti superficiali del bacino settentrionale della Laguna di Venezia. *Mem. Biogeogr. Adriatica*, 9 (suppl).
4. Di Silvio, G. (1989). Modelling the morphological evolution of tidal lagoons and their equilibrium configurations. *XXIII Congress IAHR*, Ottawa.
5. Di Silvio, G. and Gamholati, G. (1990). Two-dimensional model of the long-term morphological evolution of tidal lagoons. *VII Int. Conf. on Computational Methods in Water Resources*, Venice.
6. Di Silvio, G. (1991). Averaging operations in sediment transport modelling: short-step versus long-step morphological simulations. *Int. Symposium on the Transport of Suspended Sediments and its Mathematical Modelling*, Florence.
7. Imberger, J. and Di Silvio, G. (1992). Mixing processes in a shallow lagoon. *ICCE 1992*, Venice.
8. Silva, P. and Mol, A. (1922). Development of Venice morphological system. *ICCE 92*, Venice.
9. Terwindt, J.H.J. and Battjes, J.A. (1991). Research on large-scale coastal behaviour. *Proc. 22nd Int. Conf. Coastal Eng.*, Delft.
10. Terwindt, J.H.J. and Wijnberg, K.M. (1991). Tought on large-scale coastal behaviour. *Submitted to "Coastal Sediments 91"*, Seattle.

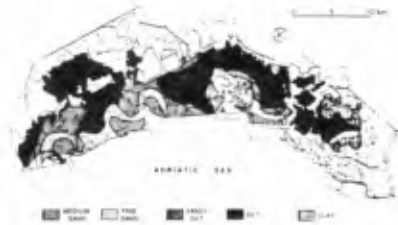


Fig. 1: Grainsize distribution of the bottom in the Lagoon of Venice.

## CHAPTER 143

### Mixing processes in a shallow lagoon

J. IMBERGER\* and G. DI SILVIO\*\*

\*Centre of Water Research, University of Western Australia

\*\*Istituto di Idraulica, Università di Padova, Italy

#### Introduction

Lagoons are enclosed water basins at the boundary between the land and the ocean; they usually have one or a number of streams entering around the perimeter and are open to the ocean at one or a number of entrances. Lagoons are shallow and the motion of water within them is governed by a delicate balance between tidal forces, wind stresses, bottom friction and density induced pressure forces. In general, ocean water enters a lagoon via deeper channels whereas the river inputs enter through alluvial fans. The freshwater, being lighter, overflows the lagoon waters whereas the entering ocean water, being heavier, underflows. This leads to a strong vertical stratification in the main channels and a general horizontal stratification in the shallows. Much work has been done on estimating the net horizontal mixing in large water bodies and, in general, it is assumed that the water column is fully turbulent and the horizontal scales of motion range from the size of the lagoon to millimetres and vertical scales from the depth to millimetres. Under such conditions it is assumed that there is a cascade of energy similar to normal turbulent shear flow (Tennekes and Lumley, 1972). For water bodies which have dimensions in the tens of kilometres, it is found both by fitting the results from numerical models (Di Silvio and Fiorillo, 1981) and from large scale field comparisons (Dronkers *et al.* 1981) that a horizontal diffusion coefficient of the order of 50 to 500 m<sup>2</sup> s<sup>-1</sup> is applicable.

This logic, however, ignores two major recent findings. First, in shallow waters, Wolanski *et al.* (1984) have found that the bottom friction is usually sufficient to overcome the horizontal inertial forces so that the *effective* Reynolds number of the flow can be as low as 30 or 40. Numerous cases have now been documented where the wake behind islands, flows over undulating topography or past headlands. All appear to shed eddy structures which are reminiscent of slow viscous flow rather than of an inertial turbulent regime. Second, with recent remote sensing techniques and fast fine-scale sampling (Luketina and Imberger, 1987) it has been revealed that lagoons and coastal waters are partitioned by a complicated network of fronts. These fronts form a mosaic of lenticular structures which move under the influence of the tide, the wind field and baroclinic forces. The role of the fronts is to enhance mixing at small scales through shear flow dispersion, but they appear to inhibit the natural cascade of energy from the larger scales through the intermediate scales to the smaller scales of the horizontal eddy structures. Thus both bottom friction and the presence of fronts prevents an energy cascade and the development of a full turbulent velocity spectrum. It therefore remains to be explained why the net horizontal eddy diffusion coefficients in shallow lagoons are comparable to the open ocean values summarised by Okubo (1974).

#### Field Campaign

Two field campaigns (respectively commencing 11th June 1990 and 2nd March 1991) were carried out in the Lagoon of Venice, involving detailed fine-scale temperature and conductivity measurement surveys. The aim of these experiments was to assess the role and influence of the buoyancy introduced around the perimeter, by freshwater inputs, on the dispersion in the lagoonal waters. A portable fine-scale profiler was used both in a vertical profiling mode and in horizontal tow mode. The fine-scale profiler was equipped with SeaBird conductivity and temperature sensors and a Digiquarts pressure transducer (Fozdar *et al.* 1985). The resolution of these sensors was 10<sup>-4</sup> Sm<sup>-1</sup>, 10<sup>-3</sup> °C, and 10<sup>-3</sup> m respectively. In addition to these fine-scale measurements, in the winter experiment some temperature and conductivity microstructure was also gathered in order to estimate the turbulent kinetic energy dissipation (Imberger and Ivey, 1991). During both experiments velocity estimates were obtained using bucket drogues, drogued to different depths.

During the summer experiment, most of the data collection was in the area influenced by the Dese River (Figure 1). By comparison, the winter experiment concentrated on the Venice Lagoon as a whole in order to obtain a broader overview (Imberger, 1991).

The investigations showed the following major features:

- (a) The tidal flow in the canal system is a mixture of barotropic and baroclinic flows; the degree of baroclinicity being dependent on the phase of the tide and on the salinity difference within the canals and was strongest in the areas which had direct freshwater input. However, the measurements show that sufficient salinity differences existed almost everywhere for baroclinicity to be important.
- (b) The water masses on the shoals appeared to be formed in an orderly explicable way. As the water rose in the channels and reached a point where the water breached the shoals, the salinity of the inflowing water was completely determined by the surface salinity at the point of breach in the tidal channel. A shoal may thus be envisaged as a region of land with a perimeter where water of increasing salinities is ejected on the rising tide. It appeared that these injections formed well-defined lenticular structures which were separated by stable fronts, leading to a patchwork of water masses over the shoal at high tide which retained their identity throughout the tidal cycle but which were moved by the tidal motion and the surface wind stresses. These lenticular structures, observed throughout the whole lagoon, originate from buoyant jets at the river mouths and move over the shoals and along the channels with little tendency to decay. The shallowness of the water of the shoals led to a pseudo potential flow.

### Large Scale Flushing

In Figure 1 we show a typical set of salinity isohalines contoured over the whole Venice Lagoon. The data shown is depth averaged salinity and clearly shows that there was a major freshwater inflow into the Venice Lagoon in the northern and southern regions, but that the lagoon as a whole had a horizontal gradient of salinity from the perimeter to the three entrances. A bulk estimate of the horizontal diffusion coefficient may be obtained by equating the flushing time  $V_f/Q_f$  to an average horizontal mixing time  $L^2/\epsilon_x$ , where  $Q_f$  is the total freshwater input into the lagoon,  $V_f$  is the total volume of freshwater in the lagoon,  $L$  is a typical horizontal length scale of the lagoon and  $\epsilon_x$  is an average horizontal diffusion coefficient. There are numerous other ways of estimating an average diffusion coefficient and we have calculated the estimate  $\epsilon_x$  by a number of different techniques. Using the data collected in the campaign, the various methods gave a typical flushing time of approximately three tidal cycles and a horizontal diffusion coefficient ranging from 100 to 400  $m^2 s^{-1}$ . These values were compared against more detailed estimates obtained in two canals by fitting a horizontal advection diffusion model to the documented inter-tidal gradient of salinity. This techniques yielded estimates in the same range.

In summary, therefore, the fine-scale measurements in the Venice Lagoon yielded global dispersion coefficients averaged over many days (averaged over tidal and wind motions) of the same magnitude as found in open deep water.

### Lenticular Structures

The mechanisms by which freshwater entered a particular shoal was investigated in considerable detail during the winter experiment. In Figure 2, we show a typical salinity plot at the commencement of the falling tide and it is clearly seen that the freshwater outflow produced a plume of fresher water extending a distance of 2 or 3 km from the mouth and being swept alongshore by the prevailing tidal current. A similar exercise was conducted in the central part of the lagoon (Figure 3) which shows that even in the middle of the lagoon, far removed from the direct influences of the fresh river inputs, lenticular structures with horizontal length scales of the order of 1 to 2 km could be clearly identified. As seen from Figure 3, the salinity differences associated with the lenticular structures, even in the central part of the lagoon, are comparable to those found at the perimeter near the entrance inflowing river plumes (Figure 2). Lastly a series of drogues released in this latter study area showed that even over a period of three to four hours, drogues placed in close proximity remained together. Thus, the horizontal dispersion was always minimal until some drogues pass from channel to shoal or viceversa. Only at this point did the drogues in the shoal lag behind those in the channel. The same is true for lenticular structures that are moved around the lagoon by the tidal motion and the wind induced stresses. These lenticular structures thus only mix across fronts and by vertical entrainment over channels. No evidence was found of large scale eddy type structures.

### Conclusions

These and other findings lead to the conclusion that mixing in the lagoon operates at different scales:

(i) Large structures, with scales determined by the morphology and of under  $10^4 - 10^3 m$  are responsible for the global

horizontal dispersion; they control the flushing of the lagoon as well as the distribution and the shape changes of the lenticular structures, but not the mixing.

(ii) Intermediate and small scale turbulence of the order of 10 metres and less control the mixing over the depth and the weak horizontal dispersion during the tidal cycle. This is responsible for the slow annihilation of the lenticular structures.

### References

- Di Silvio, G. and Fiorillo, G. (1981). Modeling of Lagoons: The experience of Venice. *Transport Models for Inland and Coastal Waters*. Academic Press, 1981, 112-138.
- Dronkers, J. van Os, A. G. and Leendertse, J. J. (1981). Predictive salinity modeling of the Oosterschelde with hydraulic and mathematical models. *Transport Models for Inland and Coastal Waters*. Academic Press, 1981, 451-482.
- Fozdar, F. M., Parker, G. J. and Imberger, J. (1985). Matching temperature and conductivity sensor response characteristics. *J. Phys. Oceanogr.*, 15, 1557-1569.
- Imberger, J. (1991). Dynamics of the Venice Lagoon. CWR, University of Western Australia Ref. ED 605 JI.
- Imberger, J. and Ivey, G. N. (1991). On the nature of turbulence in a stratified fluid. Part 2: Application to Lakes. *J. Phys. Oceanogr.*, 21, 659-680.
- Luketina, D. A. and Imberger, J. (1987). Characteristics of a surface buoyant jet. *J. Geophys. Res.*, 92, 5435-5447.
- Okubo, A. (1974). Some speculations on oceanic diffusion diagrams. *Rapp. P.V. Reun. Cons. Int. Explor. Mer.*, 167, 77-85.
- Tennekes, H. and Lumley, J. L. (1972). *A First Course in Turbulence*. Massachusetts Institute of Technology Press.
- Wolanski, E., Imberger, J. and Heron M. (1984) Island wakes in coastal waters. *J. Geophys. Res.*, 89, 10553-10569.

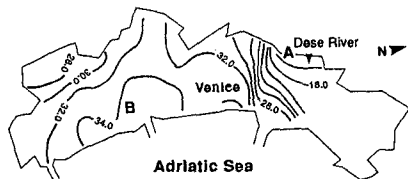


Fig 1. Averaged salinity in the Venice lagoon.

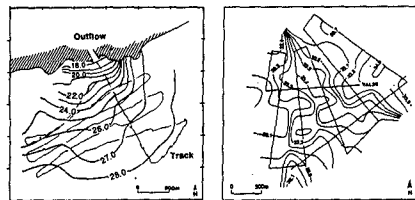


Fig 2. Plume of fresh water near the coast (joint A in Fig 1)

Fig 3. Lenticular structures in the middle of the lagoon (joint B in Fig 1)

## CHAPTER 144

### WATER FLOW MODELLING OF THE VENICE LAGOON

Enrico Marchi <sup>(1)</sup>  
Attilio Adami <sup>(2)</sup>  
Alfredo Caielli <sup>(3)</sup>  
Giovanni Cecconi <sup>(4)</sup>

#### Abstract

The paper describes the relevant set of analogical, mathematical and physical models used to simulate the hydrodynamics phenomena of the Venice lagoon. The various models are divided in two classes, depending on the scale: the great scale models, to examine the problems interesting the entire lagoon, and the little scale models for the problems localized near the inlets, where the barrages will be built to control the lagoon water level.

#### 1 - Foreword

In 1984 the Italian Government commissioned the "Consorzio Venezia Nuova" to undertake what had been called the "Venice Project"; this project comprised a number of works necessary for the safeguarding of the city of Venice and its lagoon. Amongst these, by far the most expensive and technically difficult task was the project for the deployment of flapgates across the three lagoon entrances for the control of high tides within the lagoon.

It was evident straight from the start of works that such a large and complex project would have to be supported by a series of model tests in order to investigate the various project hypotheses.

It was also evident that one model only would not have been enough, and that due to the many different problems studied, the project would have to avail itself of investigative means that were in keeping with the different aspects to research.

For the purpose of the research, the project-related phenomena were classified in two categories: the large scale phenomena, which concern the general behaviour of the

---

(1) Full professor, Institute of Hydraulics, Genoa University, via Montallegro 1, Genova

(2) Full professor, Institute of Hydraulics, Padua University, Via Loredan 20, Padova

(3) Chief Engineer Safeguard Office of Venice, Magistrato alle Acque, Palazzo X Savi, Rialto, Venezia

(4) Director of Studies Office of Consorzio Venezia Nuova, Palazzo Morosini, Campo S. Stefano, Venezia

lagoon, and the small scale phenomena, which concern the phenomena in the immediate vicinity of the flapgates.

When the New Venice Consortium became operational in 1987 the following models of the Venice lagoon already existed, so they were also adopted for the new activities: the general physical model of the lagoon, the specific physical model of the Lido entrance and the unidimensional mathematical model of the entire lagoon itself.

Alongside these models a new set of models were prepared, a description of which follows hereafter.

## 2-1 Large Scale Models

### 2,A - General Model of the Lagoon

The model (refer to Fig. 1) reproduces the entire lagoon to a planimetric scale of 1:250 and an altimetric scale of 1:20. The area occupied by the model is approximately 12,000 sq.m. Its distortion ratio of 12.5, which is typical for maritime models — in this case with a morphology consisting of canals and shoals — creates problems with regard to the roughness of the walls, which generally appear too smooth. The model is equipped with a tide generator for each of the three entrances; the three generators operate automatically and are controlled by a computer.

Due to the size of the model and the encumbrance of test handling, typical of physical models, the general model was not widely used in the engineering work concerning the lagoon entrance flapgates; thus it was often replaced by the mathematical models discussed hereafter. Nonetheless, it is the best means of investigating the phenomena that take place in the innermost parts of the lagoon where continuous contouring is a fundamental characteristic. Refer to [1] for a more detailed description of the possible uses of the model.

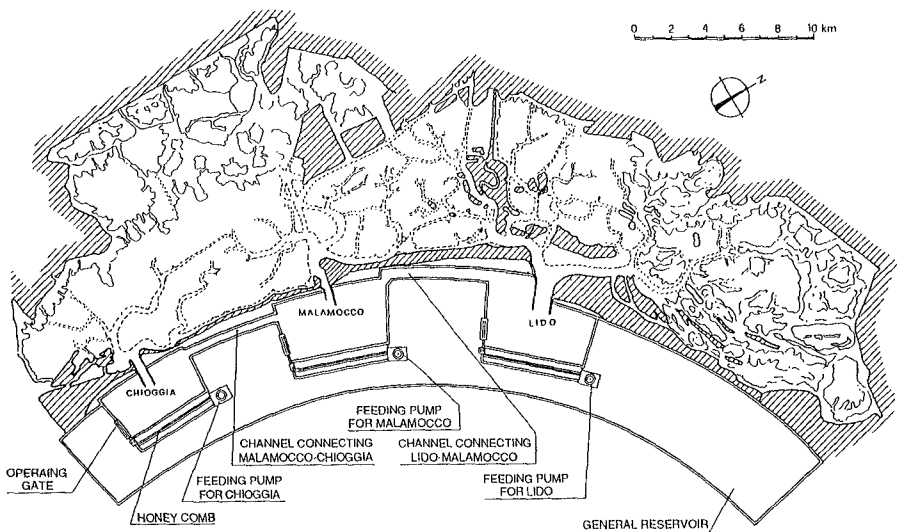


Fig. 1 - General plants of the model of the entire lagoon of Venice.

## 2,B - Mathematical Models

From a historical point of view the first mathematical model of the lagoon that was ever made is the one that mapped the lagoon with its network of interconnected canals alongside which are the shallow areas whose main function is that of providing storage capacity. This lay-out features the great advantage of simplicity and a reduced number of unknown quantities (unlike other lay-outs); but it requires an in-depth knowledge of the actual phenomena to be able to trace an illustrative network of canals and therefore work out the shallow water basin on both sides of each canal. Today this 1D model is still employed in a recent version (i.e. the fourth generation) whose network is shown in Fig. 2.

More recently, a 2D model has been developed using the finite element technique whose mesh is shown in Fig. 3, and another 2D finite difference model whose mesh is shown in Fig. 4, which also shows a stretch of sea opposite the entrances. This model blocks out the lagoon with a mesh having a 300 m pitch, and has the advantage of being able to zoom in on areas of limited surface area by reducing the spatial grid to 50 m.

Table 1 compares the characteristics of the three adopted models.

At present, in the engineering work, all three models are used depending on their different characteristics and on the phenomenon that is to be investigated. In fact, the finite difference model has proved to be the best in representing lagoon hydrodynamics in the areas closer to the entrances by depicting both the adjoining stretch of sea and the somewhat flat bathymetry of the area (with very wide canals and deeper shoals). The finite element models have instead proved to be very versatile in reproducing phenomena in the intermediate area of the lagoon where canals and shoals are clearly

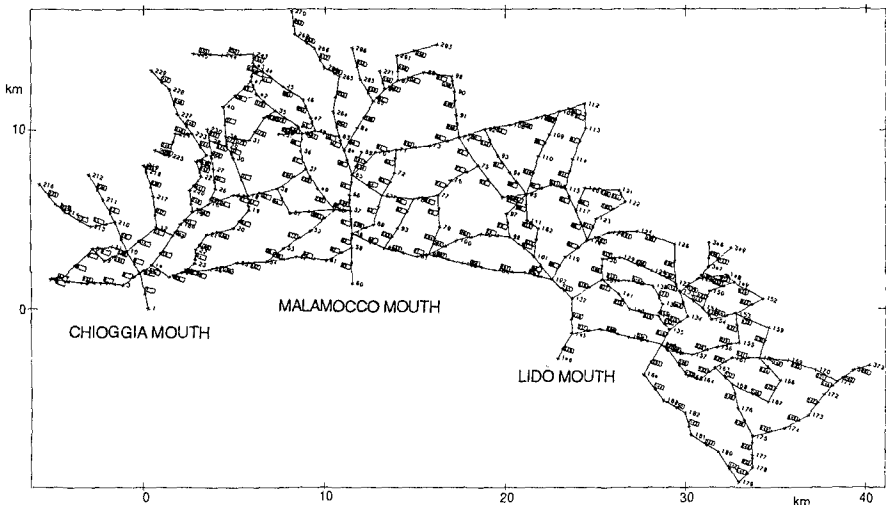


Fig. 2 - The channel net of the 1 D, mathematical model.



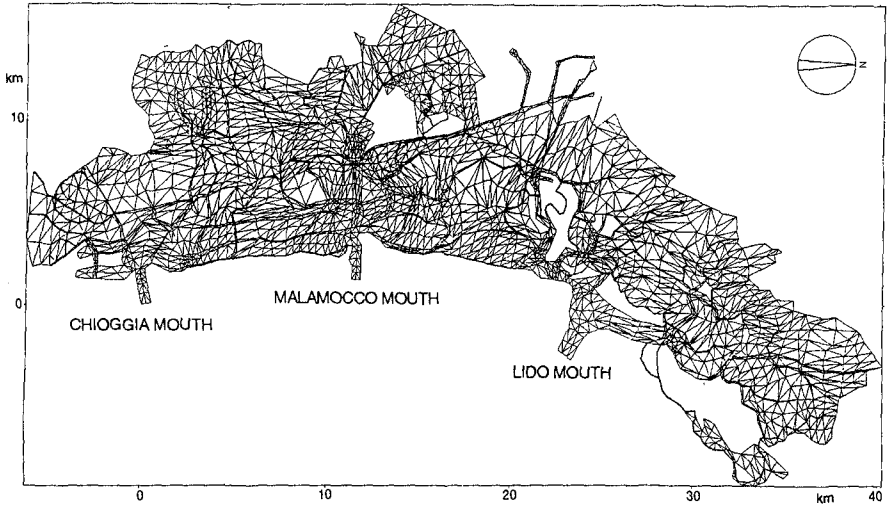


Fig. 3 - The mesh of the 2 D, finite elements mathematical model.

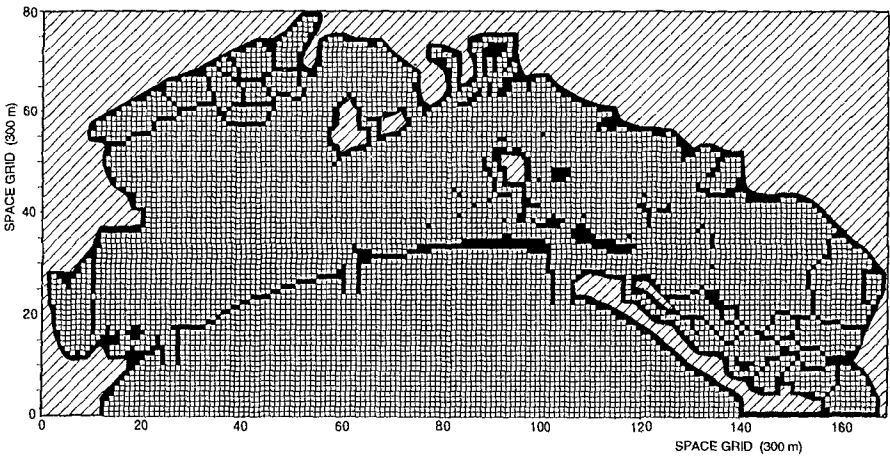


Fig. 4 - The mesh of the 2 D, finite differences mathematical model.

Table 1

	1 dimension	2 dimension Finite elements	2 dimensions Finite difference
Type of mesh and number of elements	323 multiconnected branches	2580 vertices and 4528 triangular elements	Square grid with 13,851 vertices
Dimension of elements	1000 - 2000 m	Distance between two vertices 100 - 1000 m	Squares 300 x 300 m
Average number of elements for km <sup>2</sup> of lagoon	0.9	7	11
Roughness coefficient	Chezy C=50m <sup>1/2</sup> /s	Strickler k=30,25,20 m <sup>1/3</sup> /s in channel and shallows	Strickler k=28 m <sup>1/3</sup> /s
Time step	600 s	300 s	90 s
Resolution method	Implicit with iterations	Two level time scheme, semi-implicit	Algorithm of alternate direction, implicit
Time to simulate 24 h of tide with a VAX 8600	6 minutes	60 minutes	75 minutes

distinguishable. Finally, the unidimensional model is still considered the best for the reproduction of phenomena in the innermost area of the lagoon where the tidal flow takes place nearly exclusively along the narrow submerged canals — a phenomenon that is hardly reproducible in the other lay-outs. A factor in favour of the unidimensional model is the calculation time which is nearly one order of magnitude less than that required for the other two models.

More detailed information about these models and the algorithms used can be found in [4].

### 3 - Small Scale Models

This name has been attributed to those models detailing the port entrances; they have allowed the study of localised phenomena that take place in the vicinity of the new barrage structures. The models that were used are described below.

#### 3,A - Aerodynamic Models

These types of models are not widely used in current techniques; but in this case they were found to be a very effective means of research. Obviously, in aerodynamic

models the water flow is replaced by an air flow and the flow must take place in a confined field. For this reason the free surface of the water is replaced by a solid plate which acts as a covering lid for the model. The result is a double approximation of a top contour of the flow with a horizontal plain and a zero speed. At any rate, in this case the differences in level between the sea and the inside of an entrance are maximum 20/30 cm over a depth that may vary from 8 to 15 metres; this means a percentage level variation of less than 10%; consequently, the above mentioned approximations appear acceptable, especially if one researches data not in the absolute sense but merely as a parametric value, i.e. to highlight what happens in the presence or absence of a certain modification to the flow contours. A critical appraisal about these types of models can be found in [2].

The scales used in the models have been 1:3000 in planimetry and 1:1000 in altimetry; the models reproduced (refer to Fig. 5) the inlet, the initial tract of the lagoon canals that stem from the entrance, and a sufficient stretch of open sea. A further simplification was introduced in these models; this consisted in the fact that, unlike the real case, the flow was permanent. Given the extent of complexity to correctly reproduce the periodical variations of current, a decision was taken to represent in the model a certain configuration of the flow, usually the one at peak flow rate, and to maintain it steady throughout the time needed to take the measurements. The model boundary conditions, i.e. the flow rate at the entrance and in the adjacent canals, were provided by the mathematical models.

It is understood that by reproducing a stationary flow the model does not reproduce the forces linked to temporal accelerations, but this is acceptable if one bears in mind that under maximum speed conditions these forces are practically null.

The information elicited from these models concerned the course of the water levels by drawing up an analogy between Euler's number of the model and Froude's number of the real flow, velocity distribution, paying special regard to the areas of current separations and to wakes. The great advantage of these models is the rapid and economical reproduction and study of the inlet flapgates layout, immediately indicating their major defects.

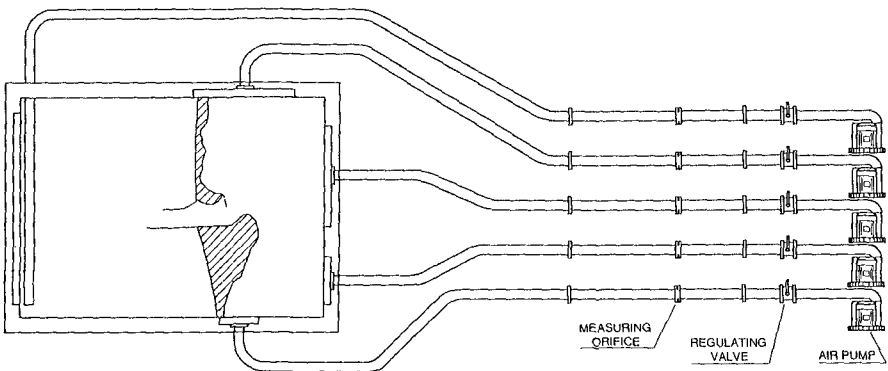


Fig. 5 - The general scheme of the aerodynamical model of the Malamocco mouth.

### 3,B - The Mathematical Models of the Mouths

These derive from the finite difference bidimensional model of the lagoon, already mentioned previously, where it was possible to perform close-ups reducing the mesh size to only 50 m. For the "mouths" (refer to Fig. 6) a rotation of the mesh was performed which was different for each entrance, so that one direction of the two axes would coincide with that of the breakwaters that project into each entrance — this was done to reproduce the contours of tidal flow in the best possible way.

Of course the boundary conditions were provided by the general mathematical model of the lagoon; thus flood and ebb tides were correctly represented.

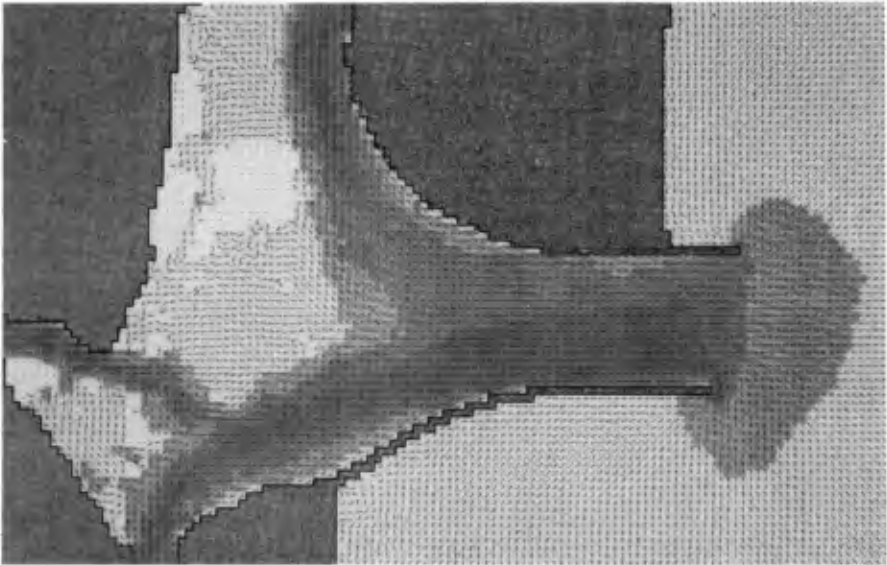


Fig. 6 - A typical flow field of the 2 D mathematical model of the Lido mouth with a 50 m space grid.

### 3,C - Detailed Physical Models

As already stated, the first detailed model of Lido mouth had been constructed far back in 1972 for a number of studies that were then being conducted on the hydrodynamics of that entrance. The model was made to a scale of 1:60, undistorted. This model, like the aerodynamic ones previously mentioned, is not equipped with a tide generator, so it was used for permanent tide flow by reproducing a certain tide flow condition and keeping it steady throughout the whole test.

Thanks to the experience gained with that model, the New Venice Consortium built similar models on the same scale for the other two lagoon mouths, Chioggia and Malamocco. The three models have a fixed bottom, but the facility to reproduce a movable bottom in limited areas is featured, and this is where the flapgates will be deployed. These models can accommodate a wave generator as wide as 20 m which enables hydrodynamic studies to be combined together with those about the penetration of wave motion from the sea into the entrances. Fig. 7 shows a planimetry of the Chioggia mouth model, in which one may notice the large area of sea reproduced; this allows the simulation of heavy seas heading from the principal sectors of the prevailing winds. The other two models are absolutely similar.

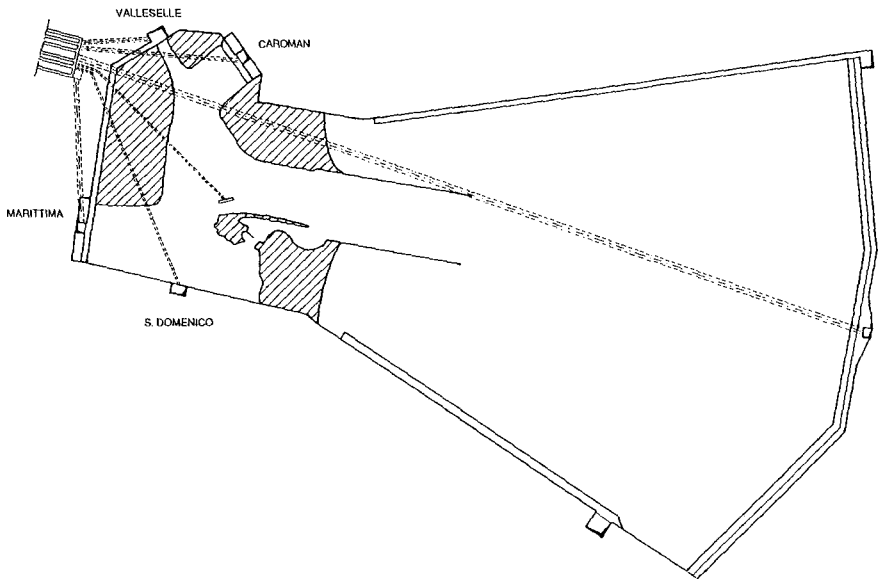


Fig. 7 -The map of the particular model of Chioggia mouth in scale 1:60.

The three models have been constructed at the Experimental Centre of Voltabarozzo in Padua, adjoining the shed that houses the physical model of the entire lagoon. The shed also houses the aerodynamic models, so that all the physical models in question have been concentrated in the same location for practical purposes. Fig. 8 shows an aerial photograph of the centre at Voltabarozzo which illustrates the various locations of the models.



Fig. 8 - Aerial view of the Voltabarozzo Center with the models of the three mouths.

#### 4 - Use of the Models

In the research work about the inlet flapgates, Project REA (environmental recovery) [3] the following procedure was adopted:-

- Literally starting off at the drawing board, the engineers designed all the planimetric configurations of the flapgates that were deemed feasible: eventually six possible lay-outs were produced for Lido mouth, seven for Chioggia mouth and as many as twelve different lay-outs for Malamocco mouth.

- All of these feasible solutions were reproduced and studied on the aerodynamic models, out of which were rejected those that caused an excessive current contraction, which meant speeds unacceptable for navigation and large areas of separation and vorticity.

- The solutions that passed the first test were studied on the mathematical models of the entrances in order to have more detailed information about the distribution of speeds, with special emphasis laid upon its transversal components which are the most hazardous for navigation.

- The information elicited from these models also allowed the correct reproduction of these lay-outs on the general mathematical models so that the large scale effects following their construction could be assessed.

- Finally, the solution that was judged to be the best for each mouth is currently undergoing study on the detailed physical models to allow a more in-depth study and to proceed with optimisation of the configuration of the flapgates.

## 5 - Conclusions

To proceed with the design of the "mouth" flapgates for the control of the high tides in the Venetian lagoon, the New Venice Consortium has constructed a set of physical, analogic and mathematical models for the reproduction of lagoon hydrodynamics, discriminating between models for large scale phenomena and models for small scale phenomena.

For the study of large scale phenomena three mathematical models of the entire lagoon, having different characteristics, were used; for the small scale phenomena, i.e. for those localised in the lagoon entrances, an extra small scale aerodynamic model, a mathematical model and an undistorted physical model were used.

These models are used in sequence with different retroactions, in the sense that the mathematical models of the lagoon create the boundary conditions of the aerodynamic models and undistorted physical models; these produce information that allows to improve the performance of detailed mathematical models of the inlets and of the general mathematical models of the lagoon. To sum up, the end result has been a complex hybrid system of models that together enact maximum verisimilitude of incoming results.

## REFERENCES

- [1] A. Adami: Alcuni aspetti idrodinamici legati all'apertura delle valli da pesca rilevati sul modello fisico della laguna. Proceedings of the Symposium organized by "l'Istituto Veneto si SS.LL.AA. in occasione del bicentenario della conterminazione", Venezia, 15 ottobre 1991, pag.102-115.
- [2] A. Adami, G. Alfonsi, L. Da Deppo: Su un'applicazione di un modello aerodinamico in scala molto piccola. L'Energia Elettrica, n° 11, 1981, pag. 3-8.
- [3] Consorzio Venezia Nuova: Progetto R.E.A. Riequilibrio e ambiente, vol. I,II,III,IV 1989.
- [4] C. Datei: Esame comparato delle caratteristiche dei modelli matematici della laguna di Venezia. Proceedings of the Symposium organized by "l'Istituto Veneto si SS.LL.AA. in occasione del bicentenario della conterminazione", Venezia, 15 ottobre 1991, pag.95-101.

## CHAPTER 145

### HYDRAULIC AND MATHEMATICAL MODELLING OF HISTORICAL AND MODERN SEAWALLS FOR THE DEFENCE OF VENICE LAGOON

Leopoldo Franco<sup>1</sup> and Giuseppe R. Tomasicchio<sup>2</sup>

#### Abstract

This paper gives an overview of the development of design and construction of coastal defence works in Venice. In fact shore protection is one of the tasks of the present large project for the safeguard of Venice lagoon. A brief description is given of the most interesting steps of the new design supported by extensive field measurements and interactive model testing. An introductory review of the old historical structures for the defence of the lidos (in part still existing) is also given to underline the important links with the past experience and the unusual constraints of the present designs.

#### Introduction

The lagoon of Venice is connected to the Adriatic Sea by three tidal inlets (the port entrances of Lido, Malamocco and Chioggia) which divide a system of barrier islands and sand beaches (Fig.1). These thin strips of land, named "lidi", extend for some 40 km and have long since been representing vital natural barriers to defend the physical integrity of the lagoon and even the military safety of Venice. Therefore, the protection of the littorals has always been a fundamental issue for Venetian Authorities and has been dealt with by a special Water Committee (Magistrato alle Acque) managed since 1501 by elected hydraulic experts. Despite their efforts, progressive shore erosion has been taking place after the diversion of the river mouths to avoid the lagoon siltation and after construction of the inlet jetties to ease navigation.

---

<sup>1</sup> Professor of Coastal Engineering, Department of Hydraulic, Environmental and Surveying Engineering, Politecnico di Milano, P. Leonardo da Vinci 32, Milan

<sup>2</sup> Researcher, Hydraulic Institute, University of Perugia, Pian di Massiano, 06100 Perugia, Italy



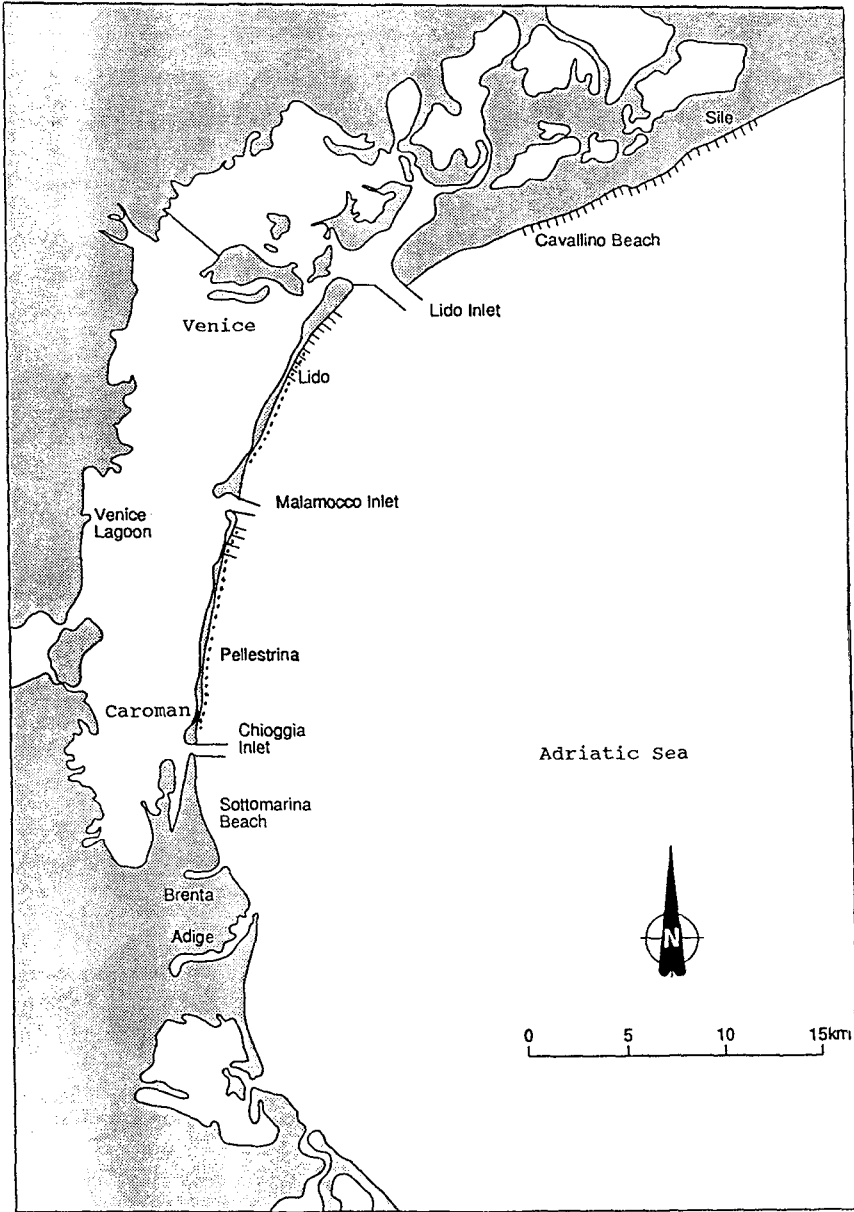


Fig. 1 Map of Venice lagoon and littorals including location of the existing "murazzi" (denoted by dots) and groynes.

### Historical evolution of sea defence works in Venice

Interesting information on historical sea defences in Venice can be found in a nice book by Grillo (1989). Written reports of local shore protection works date back as early as 537 a.C., when wicker faggots were used to hold the earth dykes reinforcing the sandy dunes formed from river supply, wind and wave action.

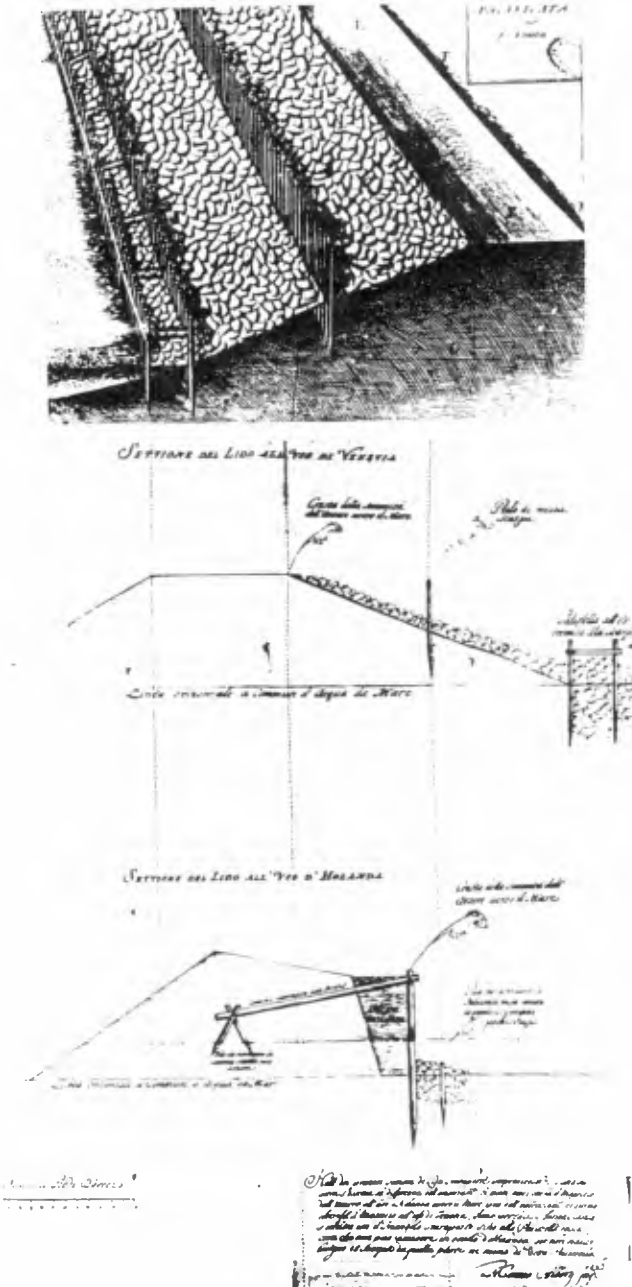
Strict environmental regulations were issued since the 13th century to preserve the littoral defences, such as prohibiting the transit of cattle upon the dykes, the removal of sand or vegetation and the export of materials useful for shore protection. These were mainly timber and rock, often combined in a sort of cribwork.

The typical seawall in the 17th century was made by rows of longitudinal fences of timber piles half embedded along the dyke outer slope and at the toe which contained a few layers of stones (as shown in fig.2 in the drawing of 1692 by M.Alberti in comparison with the Dutch standards). The timber piles however had only few years lifetime and excessive maintenance work was needed.

Therefore the Authorities, around 1700, sought for innovative designs: various technical solutions were experimented at the own risk of consultants and contractors (who might get paid only after the proved effectiveness of the work!). Coastal protection works included either seawalls and revetments (made with riprap, gabions, smooth marble blocks linked with mortar and steel, flexible steel strips, regularly placed stepped limestone blocks and various elements to increase the slope roughness) or groynes (made with timber and steel piles, often filled with rock).

Finally around 1740 a durable monolithic seawall structure was proposed by the mathematician B. Zandrini which worked successfully until today (Fig.3): the so called "murazzi" are composed by a smooth white flagstone revetment supported at toe and crest by massive walls. The innovative technology was in fact represented by the effective block bonding with "pozzolana" mortar (a lavatic powder hardening in water, shipped from Naples). The "murazzi" have been maintained and repaired in the last 250 years: the existing structure was reinforced in the middle of past century with a toe rock revetment and recently even with diaphragms and anchor piles (Fig. 4).

Rock groynes have also been built along the beaches of Lido, Cavallino and Pellestrina even in front of the "murazzi". The construction of the inlet jetties (Malamocco 1856, Lido 1887 and Chioggia 1914) and the dredging of navigation channels changed the sediment transport conditions along the littoral. Sand has been trapped by the long end jetties with accretion taking place in the lee areas (especially against the jetties at north Lido and south Chioggia), whereas strong erosion kept occurring in central Lido and Pellestrina beaches. Shoreline retreat has been enhanced in the last 40 years due to sea level rise (mainly because of subsidence) and to the reduction of river sediment supply, partly lost offshore during ebb tidal flows.



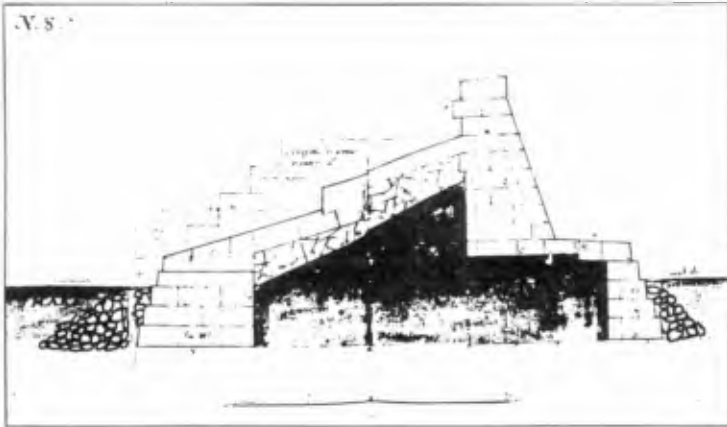


Fig.3 The original "murazzi" seawall at Caroman in a drawing by B.Zendrini (1743) (Grillo,1989)

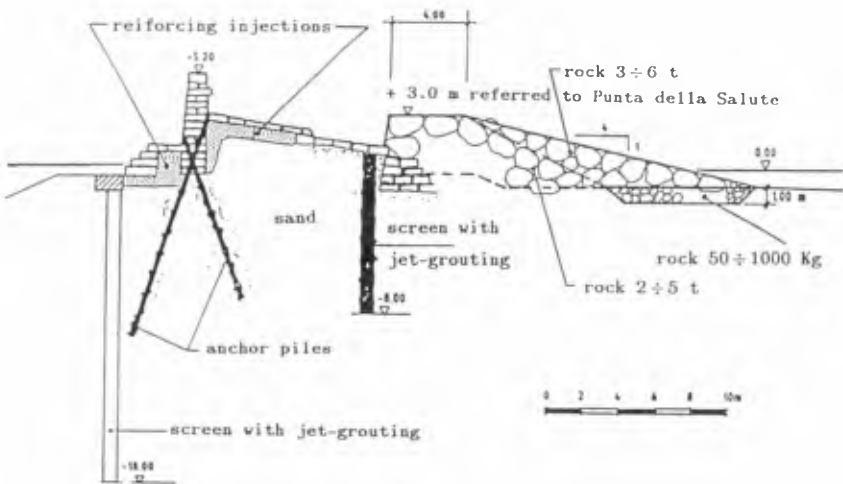


Fig.4 The present reinforced murazzi seawall at Caroman

The disappearance of the emerged beach and the erosion of the submerged seabed profile (with deposition occurring at depths below -8 m), results in larger waves reaching the seawall with increased overtopping and reduced stability of the rock protection. In fact a large breaching took place during the severe storm of 4 November 1966, when an extreme water level of nearly +2.0 m M.S.L. was recorded.

Therefore, within the present large project for the safeguard of Venice, new sea defence works have been designed in order to preserve not only the valuable coastal strips, but also the existing monumental old defence works themselves, without any negative aesthetical impact.

#### New design of coastal defence works with model studies

An accurate design process has been undertaken by TECHNITAL on behalf of the CONSORZIO VENEZIA NUOVA. The main design efforts have been devoted to the most vulnerable Pellestrina littoral and included detailed field investigations on the coastal morphology and dynamics and a large set of advanced physical and mathematical model studies for the design optimization.

At the basic design stage an extensive series of small scale (1:30) model tests was carried out in the 42.5 m long random wave flume at the hydraulic laboratory of the Magistrato alle Acque in Voltabarozzo (Padua). The tests were conducted and reported by PROTECNO (1990) with the assistance of DHI (Denmark) for the weakest "murazzi" sections at Pellestrina (first phase) and Caroman (second phase).

The following measurements were made in each test of 6 hours duration (prototype) with five Jonswap wave spectra (up to  $H_s=4.5$  m and  $T_p=11.0$  s) and four water levels (0,+1.0,+1.5,+2.0 m MSL) : wave heights and reflection coefficient, wave overtopping discharge, rock armour stability (by counting the coloured displaced stones), forces on the old vertical wall (by a strain gauge), pressures inside the rubble mound (by two transducers), toe scour of the mobile seabed (Fig.5). The beach profile, with a slope of 1:100, was modelled to a depth of -8 m MSL.

Initial testing of the existing structure showed unacceptable overtopping rates and damage of the 2-5 t rock armour under the design conditions (sea level +2.0 m).

For the "murazzi" at Caroman (the area at the southern border of Pellestrina strip) four alternative defense schemes with submerged berms with variable width and elevation were tested. The design choice was to extend the rubble mound toe underwater to avoid any visual impact, whereas a beach nourishment was not regarded as a cost-effective option due to the particular convex coastline planshape. The model tests showed that a satisfactory reduction of wave forces on the old vertical wall, overtopping discharge, and armour damage was obtained with a berm crest at -0.5 m to m.s.l. extending offshore for 30 m, whilst no further benefits related to the forces on the wall were found by increasing the berm width to 40 m. The scheme shown in fig. 6 (together with the local existing section) was then adopted for

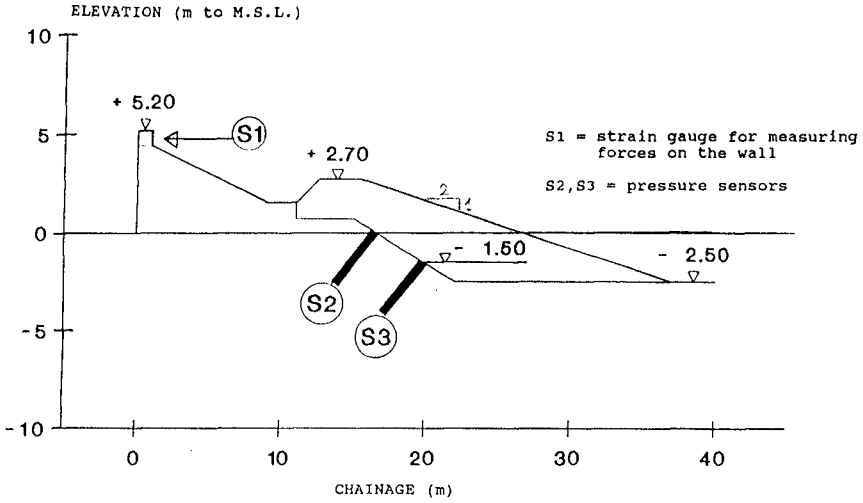


Fig. 5 Model set-up of existing "murazzi" at Pellestrina

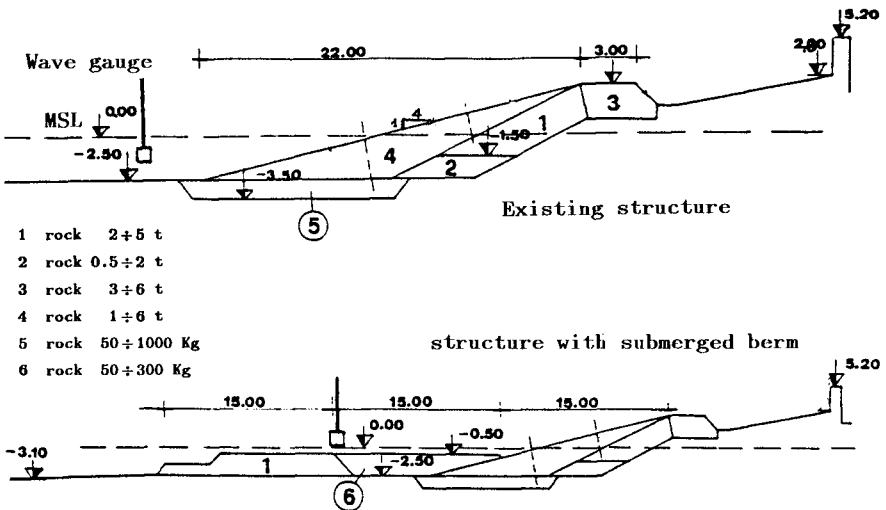


Fig. 6 Model test sections for the Caroman murazzi

the final protection design at Caroman. The stability of the submerged rock berm was also checked by profiling along two longitudinal axes after each test.

For the "murazzi" at Pellestrina several alternative reinforced structures have been tested, following the "environmental requirement" that crest elevations could not be increased. The remedial works mainly consisted in larger and heavier rock revetments (even including proper underlayers) and beach nourishment. The results showed a significant decrease of the overtopping discharge and of the cumulated damage of the main armour (always reduced below 2%). The most effective solution turned up to be a combination of a larger rubble seawall and a beach nourishment protected by submerged rock barriers.

The final design of the protection scheme for Pellestrina was recently optimized with the support of an interactive system of both 2-D and 3-D mathematical and hydraulic mobile-bed models performed by HR, Wallingford (1992). The main conclusions of the study allowed an inshore displacement of the submerged rock sill and a larger spacing of the rock groynes, partly submerged, which confine the artificial beach with just a 2-3% yearly volume loss of sand (provided a borrow fill material with D<sub>50</sub> in excess of 0.1 mm). The final and optimized design schemes are shown in fig. 7.

At present detailed geophysical surveys and vibrocore sampling are being undertaken to verify the exploitation of ancient sand deposits in depths of 17-22 m off the Malamocco inlet, to be dredged and pumped ashore. It may be interesting to remark that even this "modern" scheme of artificial beach nourishment was among the shore protection solutions proposed three centuries ago, when primitive dredgers were in use to excavate the channels of Venice lagoon!

#### Comparison of model results with formulae of static stability

The above studies demonstrate the great efficiency of a combined use of physical and mathematical models to verify the complex sea-structure interactions in the coastal zone. Generally the laboratory tests can be used to study small scale processes and to calibrate the numerical model tests, which in turn can be quickly repeated to investigate the influence of many parameters and extend the analysis to a larger temporal-spatial scale. Model tests can also be useful to calibrate practical empirical design formulae which can then be easily applied for a greater number of hydraulic and geometric conditions.

It was then believed useful to make a comparison between the results obtained from the application of some well known formulae of armour stability against the observed damage of the existing murazzi rock revetment. The count of the displaced stones at the end of each test enables to determine the numerical value of the damage parameter  $S = A_e/D_{n50}^2$ , where  $A_e$  is the erosion area in a cross section,  $D_{n50}$  is the nominal diameter of the stones. The damage parameter  $S$  is physically the number of cubic stones with a side of  $D_{n50}$  eroded within a  $D_{n50}$  wide strip of the structure.

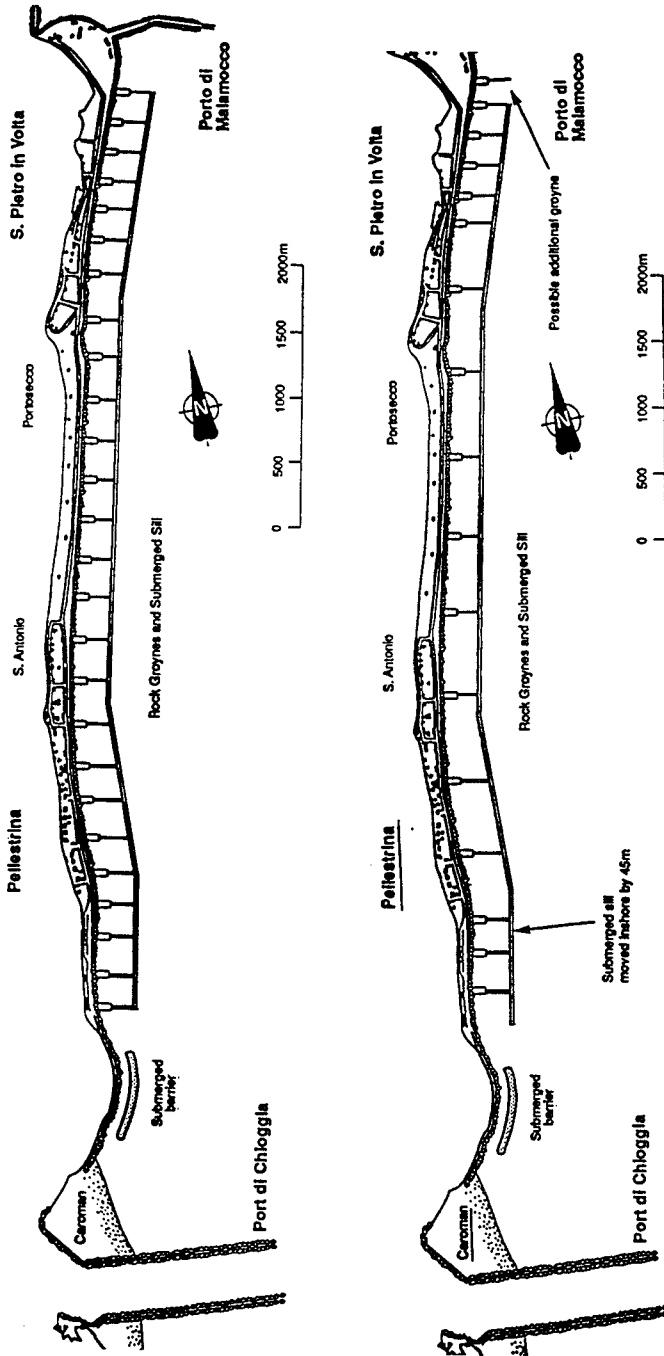


Fig. 7 New defence of Pellestrina littoral: basic design plan and final optimized design



The parameter S can be related to the actual number of displaced stones ( $N_d$ ):

$$S = N_d * D_{n50} / [B * (1-n_v)] \quad \text{where:}$$

B = length of modelled seawall;

$n_v$  = porosity of the mound.

S = 2 signifies start of damage, S = 8 means that the underlayer is visible (slope 1:2).

Two well known equations for static stability have been considered: the one proposed by Van der Meer (1988) for plunging waves :

$$H_s / \Delta D_{n50} * \sqrt{\bar{\epsilon}_m} = 6.2 P^{0.18} (s/\sqrt{N})^{0.2} \quad (1)$$

and the Hudson formula given in SPM (1984) and modified by Van der Meer (1988):

$$H_s / \Delta D_{n50} = 0.70 (K_D \cot \alpha)^{1/3} s^{0.15} \quad (2)$$

$N = 2500-4000$  is the number of waves in the various test series.

$P = 0.4$  is the assumed value of the permeability factor

$T_m = T_p/1.25$  is the assumed average wave period in each test.

Eq. (1) and (2) were obtained for not overtopped structures. The test conditions and some results are given in tabs.1, 2 for the two slopes and in figs. 8, 9. The high rate of wave overtopping on the "murazzi" influences the observed damage. The results may also be affected by the depth limited wave conditions at the seawall. This analysis enables to verify the reliability of the two proposed formulae for static stability when predicting the rock armour damage of the existing "murazzi" seawalls. Van der Meer's formula was used to predict the cumulated damage for all the considered water level conditions and the results show a good agreement with the observed damage up to a water level of +1.5 m MSL, with a slight expected overestimation (see Fig.8 for the 1:2 slope). The application of the modified Hudson formula (with  $K_D = 2$  for breaking waves) does not describe the cumulated damage and produces unreliable results for both slopes of the "murazzi". A stability factor  $K_D=5$  should be used in this case to match the experimental results.

For all the tests with water levels up to +1.5 m MSL a good correlation was found between the measured overtopping discharge and the difference of the computed ( $S_{vdM,cum}$ ) and the observed ( $S_{obs}$ ) damage as shown in fig. 9. Only for the highest water level, near to the seawall crest (+2.0 m), the data is more dispersed. In the figure data from both Pellestrina and Caroman test series is plotted.

This analysis confirms the correlation between the stability of the front armour and the overtopping rate of a low-crest coastal structure. It also shows that the Van der Meer formulae can give acceptable conservative results even for low seawalls in shallow waters.

murazzi at Pellestrina  $W_{50} = 2.45 t$  slope 1:2

$H_s$ [m]	$N_s$	$T_m$ [s]	$S_{obs}$	$S_{VdM cum}$	$S_{Hudson}$	Sea Level [m]	$Q$ [m <sup>3</sup> /s/m]
1.90	1.04	5.60	0.0	0.20	0.66	1.50	—
2.40	1.41	6.64	0.87	0.91	4.88	1.50	$1.46 \cdot 10^{-4}$
2.57	1.51	7.36	1.49	1.68	7.36	1.50	$7.21 \cdot 10^{-4}$
2.60	1.52	7.00	1.61	2.15	8.33	1.50	$1.56 \cdot 10^{-3}$
3.20	1.88	8.00	2.86	4.79	33.26	1.50	$7.08 \cdot 10^{-3}$
3.20	1.88	8.88	4.23	6.70	33.26	1.50	$5.82 \cdot 10^{-3}$
2.10	1.23	6.16	0.0	0.46	2.00	2.00	$3.63 \cdot 10^{-4}$
2.70	1.58	7.20	0.80	1.69	10.71	2.00	$5.26 \cdot 10^{-3}$
3.00	1.76	8.00	2.36	3.43	21.63	2.00	$2.16 \cdot 10^{-2}$
2.80	1.64	8.48	2.86	4.30	13.65	2.00	$1.63 \cdot 10^{-2}$
2.80	1.64	8.88	3.23	5.16	13.65	2.00	$2.99 \cdot 10^{-2}$
3.10	1.82	8.88	3.23	6.63	26.92	2.00	$4.38 \cdot 10^{-2}$
1.90	1.11	7.20	0.24	0.30	1.02	0.00	0.00
2.00	1.17	8.48	0.37	0.59	1.44	0.00	0.00

Table 1

Sea level to msl

$S_{obs}$  = observed damage

$S_{VdM cum}$  = cumulated damage calculated using BREAKWAT (Van der Meer, 1988)

$S_{Hudson}$  = damage calculated using Hudson formula with  $K_D = 2$

murazzi at Caroman  $W_{50} = 2.9t$  slope 1:4

$H_s$ [m]	$N_s$	$T_m$ [s]	$S_{obs}$	$S_{VdM cum}$	$S_{Hudson}$	Sea Level [m]	$Q$ [m <sup>3</sup> /s/m]
2.53	1.49	7.20	0.0	0.34	2.48	1.00	$1.54 \cdot 10^{-5}$
2.57	1.51	8.00	0.0	0.56	2.76	1.00	$6.75 \cdot 10^{-5}$
2.47	1.45	8.88	0.0	0.73	2.11	1.00	$1.95 \cdot 10^{-4}$
2.70	1.59	7.20	0.13	0.43	3.88	1.50	$4.58 \cdot 10^{-4}$
2.70	1.59	8.00	0.17	0.69	3.83	1.50	$1.01 \cdot 10^{-3}$
2.75	1.62	8.88	0.24	0.99	4.33	1.50	$2.90 \cdot 10^{-3}$
2.79	1.64	7.20	0.55	0.49	4.77	2.00	$3.30 \cdot 10^{-3}$
3.07	1.81	8.00	0.68	1.01	9.03	2.00	$9.10 \cdot 10^{-3}$
3.24	1.91	8.88	0.92	1.65	12.94	2.00	$2.24 \cdot 10^{-2}$

Table 2

Sea level to msl

$S_{obs}$  = observed damage

$S_{VdM cum}$  = cumulated damage calculated using BREAKWAT (Van der Meer, 1988)

$S_{Hudson}$  = damage calculated using Hudson formula with  $K_D = 2$

Tabs. 1-2 Comparison of observed and calculated armour damage  
( $H_s$  = significant wave height at the toe in depth of -2.5 m MSL)

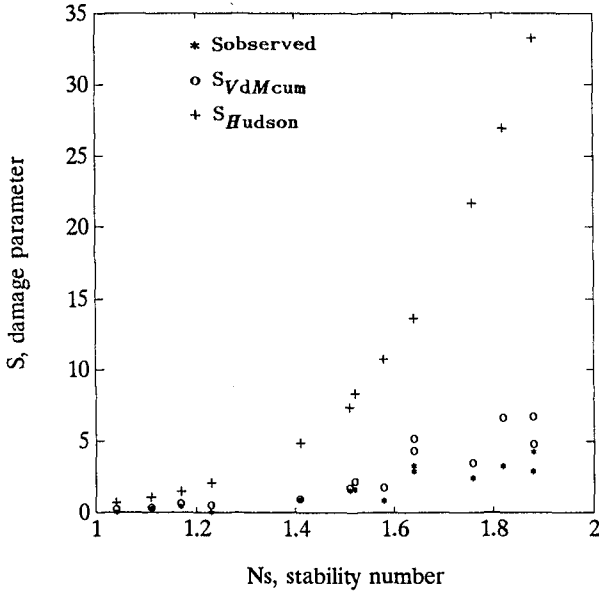


Fig.8 Comparison of observed and calculated armour damage for the murazzi at Pellestrina ( $N_s = H_s / \Delta D_{50}$ )

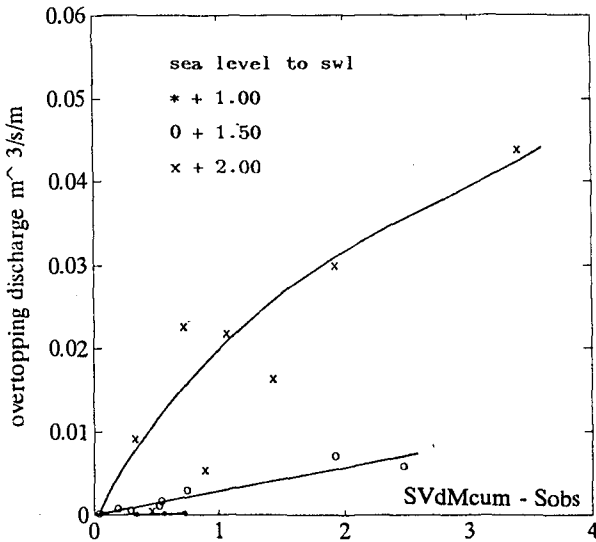


Fig.9 Correlation between damage and overtopping for the murazzi seawall

### Final remarks

The development of an effective system of coastal defence works plays an important role within the present large project for the safeguard of Venice lagoon. Careful studies have been carried out to optimize a modern design in harmony with the past experience, in order to ensure the required level of structural stability and environmental protection. The chosen solutions, a confined beach nourishment at Pellestrina and submerged berm at Caroman, are compatible with the conservation of the historical "murazzi" seawall and the former one also with the increasing touristic use of the beach. Since the sediment available for beach nourishment is very fine, the design of the longitudinal and transversal structures for the sand containment required extensive simulations with advanced interactive mathematical and physical models. Results from model tests have also been used to check the efficiency of two popular formulae for armour static stability in depth-limited wave conditions. The equations by Van der Meer seem to give reasonable conservative predictions in the case of the low crest "murazzi" seawall and the difference between the computed and observed damage is in fact fairly correlated with the overtopping discharge.

### Acknowledgements

The authors wish to thank Mr P. Silva and Mr. F. Galante of TECHNITAL, Verona, design engineers of Venice coastal defences, and Mr A. Venuti of PROTECNO, Padua, model engineer, for the kind supply of useful information. The model studies have been conducted for the Consorzio Venezia Nuova, concessionary for the studies and works related to the Venice project on behalf of Magistrato alle Acque.

### References

- Grillo, S., (1989). Venezia, le difese a mare. Arsenale Editrice, Venezia.
- HR Wallingford, (1992). Model tests for the Pellestrina littoral. Report EX 2524.
- Protecno,(1990). Prove su modello fisico dei Murazzi di Pellestrina, I e II fase, Padova.
- U.S.Army CERC (1984). Shore Protection Manual, Washington
- Technital, (1990). Interventi di difesa del litorale veneziano dal fiume Brenta al fiume Sile. Progetto di massima, Verona.
- Van der Meer, J. (1988). Rock slopes and gravel beaches under wave attack., Ph.D. thesis, Delft



Photo 1-2 Views of the existing murazzi at Pellestrina  
(in some areas with macro-roughness elements)



PROVE SU MODELLO FISICO  
 DEI MURAZZI DI PELLESTRINA  
 PADOVA 25 GEN 89  
 SITUAZIONE ATTUALE

PROVA N. 2A  
 LIVELLO +2.00 m s m  
 H 2.0 m

Photos 3-4 Views of the model section of the "murazzi" at Pellestrina with evidence of rock armour displacements



## **PART V**

### **Coastal Processes and Sediment Transport**



*“T” Groins and Nourishment  
Protecting Coastal Railway*



## CHAPTER 146

### OBSERVATIONS OF GRANULAR-FLUID MIXTURE UNDER AN OSCILLATORY SHEET FLOW

by

Toshiyuki Asano<sup>1</sup>

#### 1. Introduction

Sediment transport due to wave action has been classified into three modes; bed load over a practically flat bed under small tractive force, suspended load over a rippled bed under moderate shear stress, and sheet flow under high shear stress where ripples are washed out. Studies of the sheet flow have recently received much attention because a large amount of sand is transported under this mode. However, sheet flow is a grain-fluid mixture flow of high concentration, thus the mechanism is more complex than that of the other two modes. In the sheet flow region where several layers of grains are mobilized, grain to grain collision performs a main role in the momentum exchange. The relationship between the applied stress and the bulk deformation is not a Newtonian, and depends on the grain concentration and the rate of deformation.

Hanes - Bowen(1985) have proposed a granular - fluid model to describe intense bed - load transport in an uni-directional flow. In their model, the flow is divided into two regions; grain collision dominated granular fluid region, and fluid stress dominated fluid shear region. They have derived a relation mathematically between the grain transport rate and applied shear stress.

Shibata - Mei(1986) have proposed another granular - fluid model in so-called macro viscous region where the shear rate is low and granular friction is as important as granular collision. Mathematical expressions to describe velocity profiles and granular discharge have been deduced.

These studies provide physical insight into the mechanism of sheet flow, however, the results are not able to be applied directly because the oscillatory sheet flow is a dynamic process under an unsteady flow.

---

<sup>1</sup>Dept. of Ocean Civil Engineering, Kagoshima University, Korimoto 1-21-40, Kagoshima, 890, Japan

The author (1990) has proposed a two-phase model for oscillatory sheet flow based on the conservation of mass and momentum for fluid and sediment. The model provides the quantitative description on the sheet flow properties, however, reliable experimental data are essentially required to examine the validity of the model. Since the mechanism of time varying grain densely mixed flow is highly complicated, clear experimental understandings have not sufficiently been obtained.

Even for macroscopic properties, there is much difference among reported results. For example, Horikawa et al.(1982) reported that their data on sediment transport rate agree well with Madsen - Grant formula in which the sediment transport rate is proportional to the 3rd power of the Shields number. Meanwhile, Sawamoto-Yamashita(1986) reported to the 1.5 power relationship between the sediment transport rate and Shields number.

In the present paper, detailed measurements on the intrusion depth of the sheet flow, sediment transport velocity and concentration etc. are carried out in order to obtain basic data which are useful to investigate the flow mechanism of oscillatory sheet flow.

## 2. Experimental Apparatus

An oscillatory flume capable of generating oscillatory sheet flows was constructed. The flume illustrated in Fig.1 is 8.0m long for horizontal section and 2.5m high for vertical section. The total length of the water column when the flume is filled is 10.2m including the joint section. The natural frequency of the oscillation calculated by the total length is 4.53sec. The horizontal section was made of clear acrylic which allows direct visual observation, and has a 15cm × 15cm square cross-section. The bottom of the central section is depressed to form a bed material container which is 1.8m long and 5.0cm deep. The oscillatory flows were generated via a piston driven by an electric servo motor and a drive shaft.

For the convenience of video frame tracing analysis, large and light plastic particles, 4.17mm in diameter and 1.24 in specific gravity, were used. Some parts of the particles were painted in various colors, and the water in the flume was also dyed in order to obtain clear pictures. Motion of the particles under oscillatory flows was taken with a high speed video camera at an exposure speed of 1/1000 sec, and also taken with a 35mm motor-driven camera as an auxiliary.

During one experimental run, special attention is paid to maintain the upper surface of the particle assembly flat and uniform in the flow direction. Keeping it uniform over a long time was found to be difficult because a large amount of particles is moved under sheet flow condition. Consequently, an oscillatory flow was generated just for 2 periods for each run, the data from the second half to the fourth half period in which uniformity of the flow had been assured was used for the analysis.

Table 1 shows the experimental conditions. The Shields number,  $\Psi$  in the table was tentatively calculated by assuming a friction factor  $f=0.01$ , since the movable bed friction under oscillatory flows is not sufficiently understood yet.

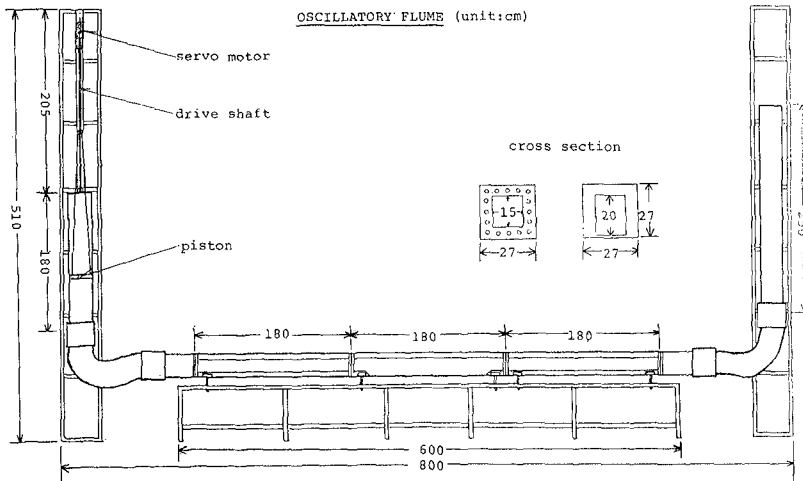


Figure 1: Oscillatory Flume

Table 1: Experimental Conditions

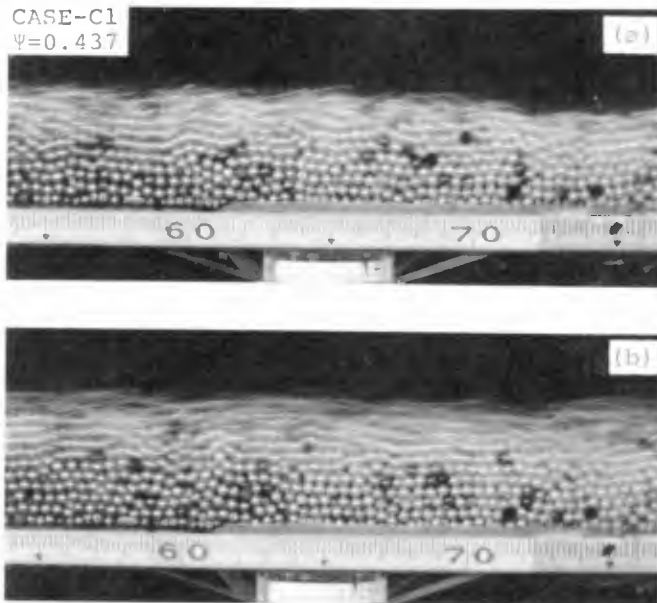
	T (sec)	$\hat{U}$ (cm/s)	$\Psi$
CASE-1	4.64	73.94	0.279
CASE-2	4.64	96.85	0.478
CASE-3	4.98	101.25	0.523
CASE-4	5.28	83.04	0.352
CASE-5	5.44	63.07	0.203
CASE-6	4.35	76.35	0.297
CASE-C1	4.64	92.60	0.437
CASE-C2	4.64	85.04	0.369
CASE-C3	5.01	54.43	0.151
CASE-C4	4.28	63.72	0.207

### 3. Experimental results

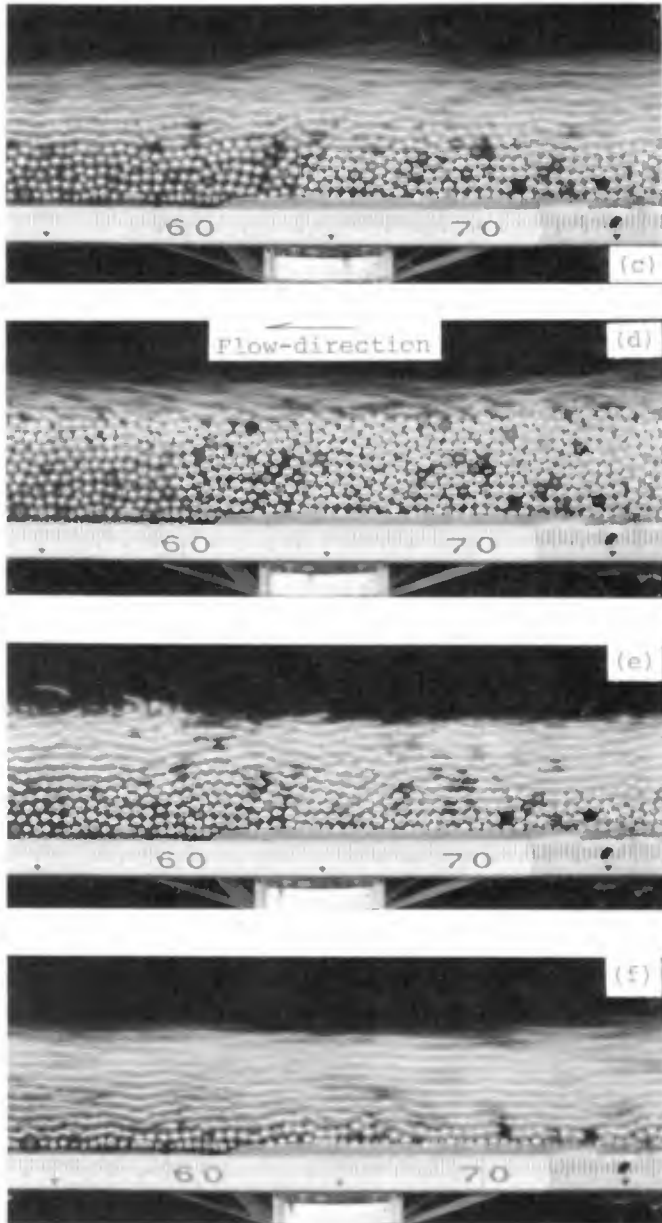
#### (a) particle motion

Picture-1 shows the behavior of the particles every 0.5sec. The period of this run(Case-C1) is 4.64sec, so that these six pictures cover over a little more than half a period. The indicator attached beneath the bottom shows the water surface level in the right vertical flume section.

The indicator in Picture (a) shows that the water level in the right vertical section rises to the maximum. In this phase, the flow velocity becomes zero, and the pressure gradient is the maximum. The particles have already started to move due to the pressure gradient. In the phase (b), the thickness of the sheet flow grows larger and moving velocity also increases. The particles move in saltation mode in the flow region  $z > 0$ , and move in sheet flow mode in the region  $z < 0$ , where a datum level ( $z=0$ ) is taken as an upper surface of the particle assembly under still water condition. Although the flow velocity increases toward phase (c) and takes the maximum between phases (c) and (d), the particle velocity starts to decrease in the sheet flow layer  $z < 0$ , meanwhile the particles maintain large velocity in the saltation layer  $z > 0$ .



Picture-1 Sheet Flow and Saltation Motion under an Oscillatory Flow (CASE-C1)



Picture-1 Sheet Flow and Saltation Motion under an Oscillatory Flow (CASE-C1) (Continued)

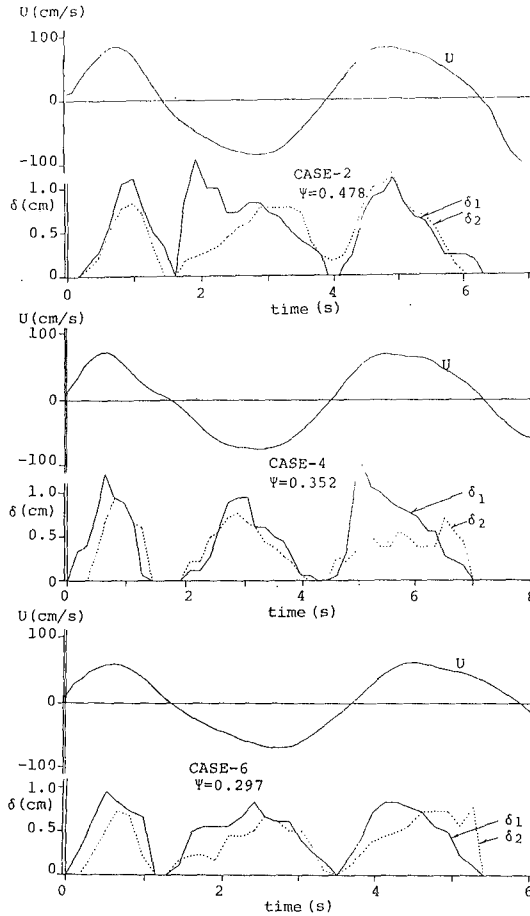


Figure 2: Temporal variations of thickness of sheet flow layer  $\delta_1$  and saltation layer  $\delta_2$

In the phase (e), particles in the sheet flow layer turn the direction to the right due to the pressure gradient although the mean stream velocity still moves from right to left. Some particles near  $z=0$  are found to rotate because the flow direction may change there. In the phase (f), the thickness of the sheet flow layer starts to increase again.

In brief, the particle motion shows remarkable phase precedence from mean stream flow due to pressure gradient in the sheet flow layer, but relatively small phase precedence in the saltation layer.

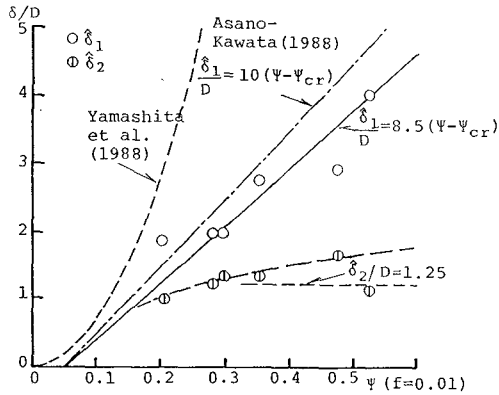


Figure 3:  $\hat{\delta}_1, \hat{\delta}_2$  vs Shields number  $\Psi$

(b) Thicknesses of Sheet flow layer and Saltation layer

A sheet flow layer thickness  $\delta_1$  is determined by an intrusion depth of moving particles below the datum level ( $z=0$ ), and the saltation layer thickness  $\delta_2$  is defined by the maximum jumping height upward from  $z=0$ . Fig. 2 shows the phase variation of  $\delta_1$  and  $\delta_2$ .

Fig. 3 shows the measured maximum thicknesses during half an oscillatory period  $\hat{\delta}_1$ , and  $\hat{\delta}_2$  in relation to the Shields number  $\Psi$  for CASE- 1 ~ 6. The sheet flow layer thickness  $\hat{\delta}_1$  increases almost linearly with the Shields number, and shows good agreement with the relation which the author proposed (1990). The relation that  $\hat{\delta}_1$  is proportional to the applied shear stress has been confirmed by Hanes and Bowen (1985) and Wilson (1984), although their data were obtained in uni-directional flows.

Meanwhile, the maximum saltation layer thickness  $\hat{\delta}_2$  increases gradually with the Shields number. The rate of increase is, however, small compared to results of stationary saltation for uni-directional flows (for example; Tsuchiya 1969). The reason why the difference arises is explained as follows: The momentum of a successively saltating particle increases with the number of times of saltation, however, the number is restricted under an oscillatory flow because the change of flow direction forces a saltating particle stop every half a period. Moreover, under sheet flow condition, the bed itself, on which a saltating particle collides and rebounds, moves as a sheet flow layer, so that a colliding particle does not receive enough momentum at the collision.

The thickness of the sheet flow layer might be governed by the dynamic Coulomb yield criterion which states the proportion between a shear stress

and a normal stress acting on a plane. The normal stress which consists of static pressure of the particle lattice, dispersive pressure due to particle collision and pore-fluid turbulence stress, balances not instantaneously but time-averagingly with the immersed weight of grains above. Applying the criterion at the boundary between mobile and immobile layers yields the following relation.

$$\tau_{-\delta_1} = \int_{-\delta_1}^0 \rho g(s-1)c \, dz \tan \phi_r \tag{1}$$

in which,  $\phi_r$  is the critical dynamic angle of internal friction. For the simplicity, the profile of sediment concentration  $c$  is herein assumed to be uniform throughout a sheet flow layer. After some algebra of Eq.(1), the thickness of the sheet flow layer is given as a function of the Shields number  $\Psi = u_*^2/\{g(s-1)D\}$  as follows.

$$\frac{\delta_1}{D} = \frac{\Psi}{\bar{c} \tan \phi_r} \tag{2}$$

In an oscillatory sheet flow, the angle of internal friction may be varied between an initial yield angle and an dynamic yield angle reflecting the flow unsteadiness. Tentatively adopting  $\phi_r = 26.5^\circ$  constant over a period, and  $\bar{c} = 0.40$  provides,

$$\frac{\delta_1}{D} = 5.0\Psi \tag{3}$$

This coefficient 5.0 is found to be the same order as the value 8.5 obtained in the experiment in Fig. 3.

(c) Sediment Transport Velocity

The profiles of the horizontal particle velocity when the velocity becomes the maximum are shown into a non-dimensional form in Fig. 4. The figure shows that the velocity profile is upward convex, and approximately expressed by 1.5 power of  $z/\hat{\delta}_1$ .

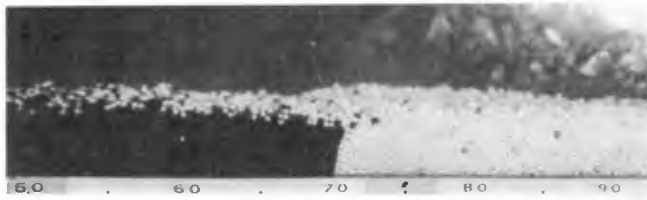
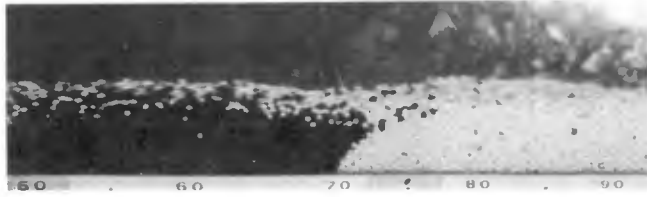
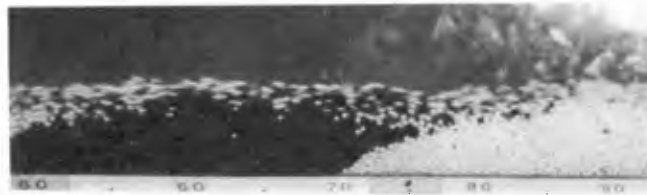
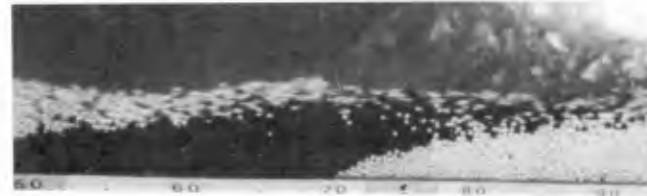
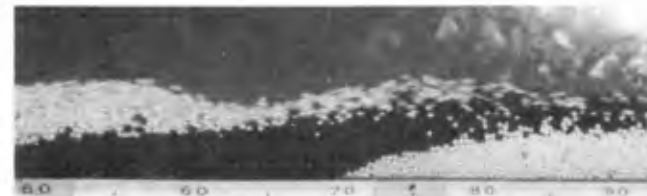
To visualize the velocity profile, additional experiments are performed in which white and red painted granulars are placed separately before generating an oscillatory flow. Picture-2 shows the results. The boundary is found to be upward convex, which coincides with the property of velocity profile illustrated in Fig. 4.

Fig. 5 shows the phase variations of the sediment transport velocity and mean stream velocity.

(d) Particle concentration

Instantaneous particle concentration was measured by counting the particles adjacent to the side wall within vertically divided grids. Fig. 6 shows the profiles of particle concentrations at the phase when mean stream velocity



 $t^* = 0.00s$  $t^* = 0.25s$  $t^* = 0.50s$  $t^* = 0.75s$  $t^* = 1.00s$ 

Picture-2 Particle Movements in a Sheet Flow Layer  
(CASE-B5,  $T=4.60\text{sec}$ ,  $\hat{U} = 91.3\text{cm/sec}$ ,  $\Psi = 0.425$ )

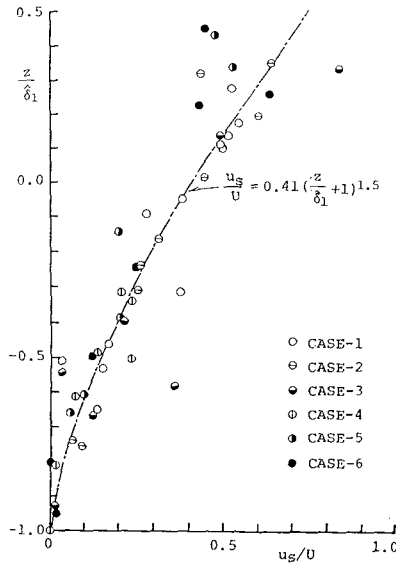


Figure 4: Profiles of Sediment Transport Velocity

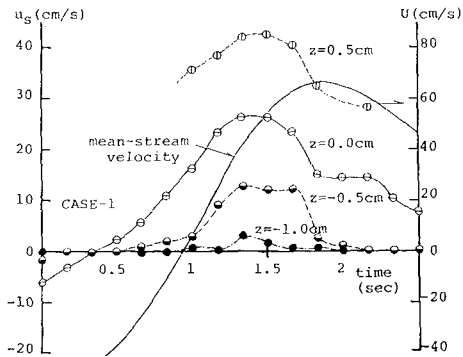


Figure 5: Phase Variations of Sediment Transport Velocity

becomes the maximum. The profiles are approximately expressed by upward convex curves in the sheet flow layer and by exponentially decay curves in the saltation layer. The curves in Fig. 6 show calculated concentrations using Eqs.(9) and (10) described later.

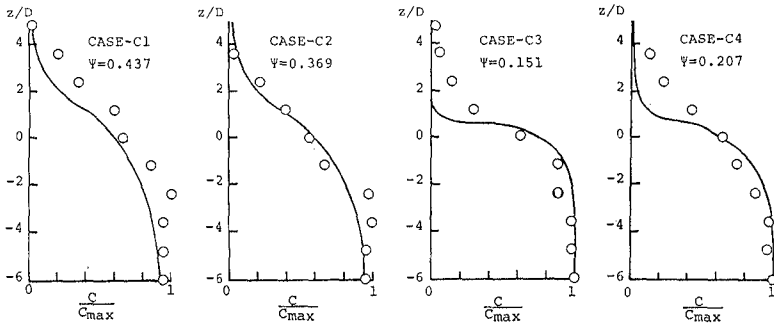


Figure 6: Profiles of Sediment Concentration at phase  $\pi/2$

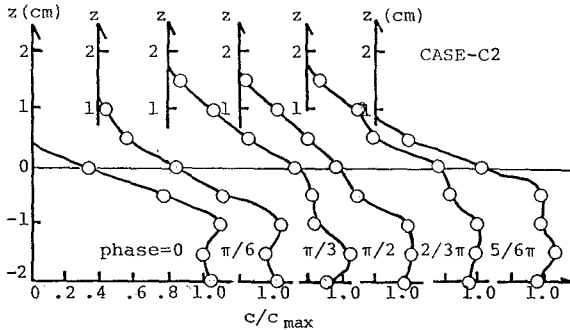


Figure 7: Phase Variation of Sediment Concentration Profile

The phase variations of the profiles are illustrated in Fig. 7.

Fig. 8 shows that the phase variation of the concentration at the boundary between the sheet flow layer and saltation layer;  $z=0.5\text{cm}$ . The reason why  $z=0.5\text{cm}$  is adopted here as the boundary is that the dilatancy of the particle assembly raises the boundary by around one particle diameter. This large dilatancy results from relatively large spheres used in the experiments as the bed material. If ordinary sea bed sand is used, the dilatancy effect would not arise so noticeably. Estimated concentration according to Englund-Fredsoe(1976) formula is also drawn in the figure, which is originally proposed for an uni-directional flow.

#### 4. Sediment Transport Rate

In this section, the relation between sediment transport rate  $Q$  and the Shields parameter  $\Psi$  is considered by synthesizing the above results.

The non-dimensional sediment transport rate during a half cycle is calculated as follows.

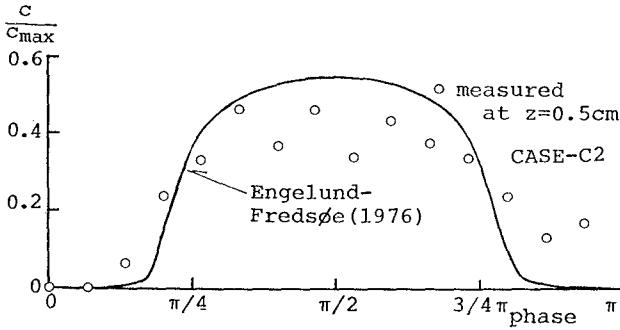


Figure 8: Phase Variation of Sediment Concentration at  $z=0.5\text{cm}$

$$Q = \frac{q}{w_0 D} = \frac{\hat{U}}{\pi w_0} \int_0^\pi \int_{-\delta_1(t)/D}^{\hat{\delta}_2/D} c(z, \theta) \frac{u_s(z, \theta)}{U} dz^* d\theta \quad (4)$$

where,  $w_0$  is the fall velocity of a particle,  $z^*$  is  $z/D$ ,  $\hat{U}$  is the amplitude of mean stream fluid velocity expressed as a function of  $\Psi$  as follows.

$$\hat{U} = \sqrt{2(s-1)gD\Psi/f} \quad (5)$$

First, based on the results in Fig. 3, the thicknesses of the sheet flow layer  $\delta_1(t)$  and saltation layer  $\hat{\delta}_2$  are assumed to be given by,

$$\delta_1(t)/D = 8.5[\Psi(t) - \Psi_{cr}] = 8.5[\Psi \sin^2 \sigma t - \Psi_{cr}] \quad (6)$$

$$\hat{\delta}_2/D = 1.25 \quad (7)$$

According to the results in Fig. 4, the sediment transport velocity  $u_s$  is given by,

$$\frac{u_s(t)}{U} = 0.41 \left( \frac{z}{\delta_1(t)} + 1 \right)^{1.5} \sin \sigma t \quad (8)$$

Concerning the particle concentration, the following profiles are assumed.

$$c = c_{max} - \{c_{max} - c_B(t)\} \exp(\alpha_1 z^*) \quad z^* < 0 \quad (9)$$

$$c = c_B(t) \exp\{-\alpha_2 z^*\} \quad z^* > 0 \quad (10)$$

in which,  $z^* = z/D$ ,  $\alpha_1 = D/\delta_1(t)$ ,  $\alpha_2 = D/\hat{\delta}_2$ , and  $c_{max}$  is the maximum concentration (here, 0.65 is used). The time dependent concentration  $c_B(t)$  at the datum level is given by Engelund - Fredsøe formula. The calculation of Eq.(4) is carried out using the present experimental condition;  $s=1.24$ ,  $D=4.17\text{mm}$ . The friction factor is given by constant 0.01.

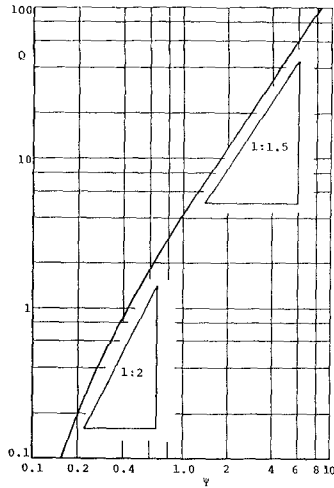


Figure 9: Calculated Non-dimensional Sediment Transport Rate

The calculated sediment transport rate  $Q$  shown in Fig. 9 is found to be proportional to the  $3/2$  power of the Shields number if  $\Psi$  is greater than around 0.8, and the power approaches to 2 with decrease of  $\Psi$ . This result is explained as follows. The sheet flow layer thickness  $\delta_1(t)$  which occupies most of the integral range is found to be proportional to  $\Psi$ , and  $u_s/U$  does not show clear dependence on  $\Psi$ , so that  $u_s \sim U \sim \Psi^{1/2}$ . Consequently, the sediment transport rate  $Q$  is approximately proportional to the Shields number  $\Psi$  raised to the  $3/2$  power. According to Engelund-Fredsoe formula  $C_B$  also varies with  $\Psi$ , however, the dependence on  $\Psi$  is little if  $\Psi$  is greater than around 0.8.

## 5. Conclusions

- (1) The particle motion is characterized by two modes; saltation mode above the datum level and sheet flow mode below that. The phase precedence of the particle motion against mean stream motion is becoming noticeable with entering downward in the sheet flow layer.
- (2) The maximum thickness of the sheet flow layer is found to increase linearly with the Shields number, which is assured by simple kinematic model. Meanwhile, the maximum thickness of the saltation layer increases gradually with the Shields number.
- (3) The profiles of the horizontal particle velocity at the phase of the maximum mean flow velocity are expressed by upward convex curves expressed

by 1.5 power of  $z/\hat{\delta}_1$ .

(4) The particle concentration is approximately described by a simple profile proposed here, where the concentration at datum level is given by Engelund-Fredsøe formula.

(5) Summarizing the above results, a semi-empirical relation between sediment transport rate  $Q$  and the Shield number  $\Psi$  is proposed. The sediment transport rate is found to be proportional to  $\Psi$  raised to the 1.5 power for large tractive force  $\Psi > 0.8$ .

### ACKNOWLEDGEMENT

The author wishes to express his appreciation to Mr. Kazuo Nakamura, technician of Dept. of Ocean Civil Engrg., Kagoshima Univ. for designing and fabricating the electronic driving unit of oscillatory flow. The author also expresses his thanks to Mr. Yasuhiro Nakano and Mr. Toshimitsu Takazawa, former students; and to Mr. Kenji Tamai, graduate student of Ocean Civil Engrg., Kagoshima Univ. for their help in performing experiments and data analyses.

This research is partly sponsored by the Grant-in Aid for Scientific Research of the Japanese Ministry of Science, Culture and Education.

### REFERENCES

- Asano T. (1990): Two-phase flow model on oscillatory sheet flow, Proc. of 22nd ICCE, pp.2372-2384.
- Engelund F. and J. Fredsøe (1976): A sediment transport model for straight alluvial channels, Nordic Hydrology, Vol.7, pp.293-306.
- Hanes D. M. and A. J. Bowen (1985): A granular-fluid model for steady intense bed-load transport, J. of Geo. Res., Vol.90, No. C5, pp.9149-9158.
- Horikawa K, A. Watanabe and S. Katori (1982): Sediment transport under sheet flow condition, Proc. 18th ICCE, pp.1335-1352.
- Sawamoto M. and T. Yamashita (1986): Sediment transport rate due to wave action, J. of Hydrosience and Hydraulic Engineering, Vol.4, No.1, pp.1-15.
- Shibata M. and C. C. Mei(1986): Slow parallel flows of a water - granule mixture under gravity, Part I and II, Acta Mechanica, Vol. 63, pp.179-216.
- Tsuchiya Y. (1970): On the mechanics of saltation of a spherical sand particle in a turbulent stream, Proc. 13th Cong. IAHR, Vol.2, pp.191-198.
- Wilson K.C. (1984): Analysis of contact load distribution and application to deposit limit in horizontal pipes, J. of Pipelines, Vol.4, pp.171-176.

## CHAPTER 147

### FINE-SCALE MEASUREMENT OF SEDIMENT SUSPENSION BY BREAKING WAVES AT SUPERTANK

Stephen F. Barkaszi, Jr.<sup>1</sup> and William R. Dally<sup>2</sup>; M. ASCE

#### ABSTRACT

During the SUPERTANK data collection project, a mobile, vertical array of five Optical Backscatterance Sensors was used to measure sand suspension in the outer surf zone. Test conditions included both regular and random waves, and two different wave energy levels. Examination of the data reveals significant cross-shore variation in both the structure of the time-dependent concentration, as well as mean suspended load.

#### INTRODUCTION

A primary element of sediment transport in the nearshore is the process of sand entrainment by breaking waves and the resulting suspended load that is available to be carried by currents. Field measurements of Hanes (1988) outside the surf zone and Beach (1989) inside the surf zone indicate that sand suspension often occurs on a wave-by-wave basis; i.e., important phase information may be lost when transport is calculated based upon the long-term mean concentration. Most field measurement efforts have been limited to documenting the mean suspended load and its distribution with depth; however, temporal and spatial detail of the initiation, movement, and settling of sand clouds has not been examined.

The SUPERTANK Data Collection Project (Kraus, Smith, and Sollitt, 1992) provided the opportunity to make high-resolution measurements of sediment suspension by breaking waves in a controlled laboratory setting at large scale. Hydrodynamic data, consisting of fluid velocity and free surface displacement, were also collected. The experiments were designed to study the behavior of sand suspension under breaking waves, measured at high spatial and temporal resolution, with the aim of developing and verifying quantitative models for sand

---

<sup>1</sup>Graduate Student, <sup>2</sup>Associate Professor, O/OE/EVS Dept, Florida Institute of Technology, 150 W University Blvd, Melbourne, FL 32901

transport. The two data sets selected are an initial investigation of the substantial amount of concentration measurements obtained near the break point during the SUPERTANK project.

**EQUIPMENT**

Tests were conducted at the large wave channel operated at the O.H. Hinsdale Wave Research Laboratory, Oregon State University. A 76-m long beach of well sorted quartz sand was placed in the channel at the beginning of the SUPERTANK project. Figure 1 is a plot of the fall speed distribution for the sand used during the SUPERTANK project. Data obtained in the settling tube analysis also provided grain size distributions from the fall speed of the sand grains.

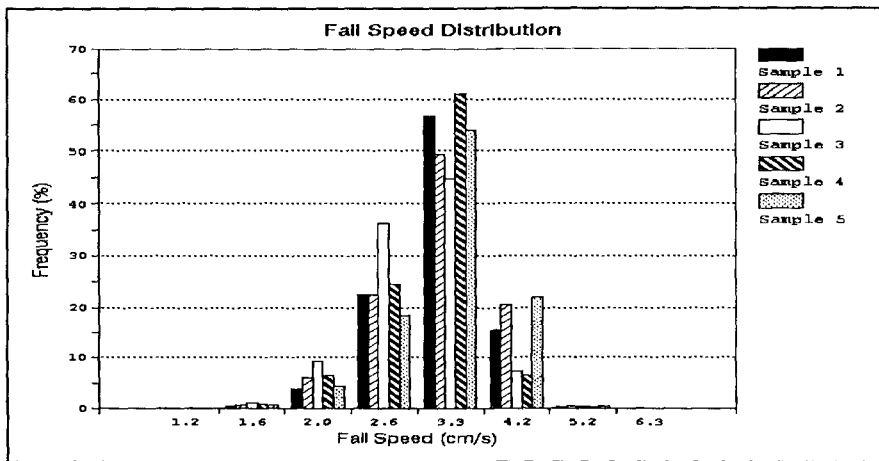


Figure 1 Fall speed distribution of the sand used during the SUPERTANK project.

The median grain diameter determined from the fall speed distribution was 0.25 mm. Result of these analyses are similar to those obtained by other SUPERTANK participants using mechanical sieve analysis.

Suspended sediment concentration was determined using five Optical Backscatterance Sensors (OBS), whereas free-surface displacement was obtained with a capacitance wave gage. The vertical and cross-shore components of the fluid motion were measured with four electromagnetic current meters (EMCM). A 8mm-format video camera was used to visually record the waves as they passed by the instruments. From this, qualitative, macro-characteristics of each passing wave could be determined.

The OBS were mounted to an aluminum sailboat mast, with the sensor beam axis oriented parallel to the wave crests. The array could be



adjusted vertically using a pulley and winch system, to accommodate changes in bed elevation. The wave gage was mounted to a second sailboat mast and could also be moved vertically, to compensate for changes in the water level under different test conditions.

The EMCs were mounted on an aluminum strut, with the instruments evenly spaced in the vertical, and oriented so that the vertical and cross shore components of the fluid velocity would be detected.

The three arrays were mounted on the shoreward side of a self-propelled carriage, which spanned the walls of the wave channel. The cross-shore position of the sensors could be changed with relative ease by moving the carriage.

## PROCEDURE

SUPERTANK was a collection of tests dedicated to cross-shore processes in a large wave channel. Each of the major tests were broken into runs which were short periods of continuous wave activity. The mobile OBS array was utilized in a total of 179 runs during the SUPERTANK project. The data presented in this paper are from four runs out of the test series labeled ST 20, second out of a total of twenty tests. Two of the runs were with regular waves, and two were with random waves. In all runs, the breakers were of the plunging type.

Data collection began approximately 45 sec before the start of a run so that still-water offsets for the OBS array could be determined. The video camera was manually started at the beginning of the run and did not require further adjustment. While a run was underway, the sensors could be monitored by viewing graphical displays.

In the two regular wave runs, the carriage was moved across the region of incipient breaking, pausing at five locations which ranged from 6 m seaward of the break point to just shoreward of the plunge point. Data were collected for approximately five minutes at each position. The entire procedure was repeated for a second 40-minute run with different wave conditions.

OBS must be calibrated for the sand at the project site due to variations in optical properties. Calibration was accomplished by immersing each sensor into a tank containing a sand/water mixture. The mixture was stirred continually to ensure a constant mean concentration in the region of the sensor.

Fig. 2 presents the calibration curves for the five OBS. It can be seen that the OBS were linear, therefore the sensor output can be converted to engineering units by applying the appropriate gain and offset.

The measurements records were found to contain occasional spikes which are attributed to electronic noise and not actual fluctuations in sediment concentration. All of the SUPERTANK OBS data were filtered

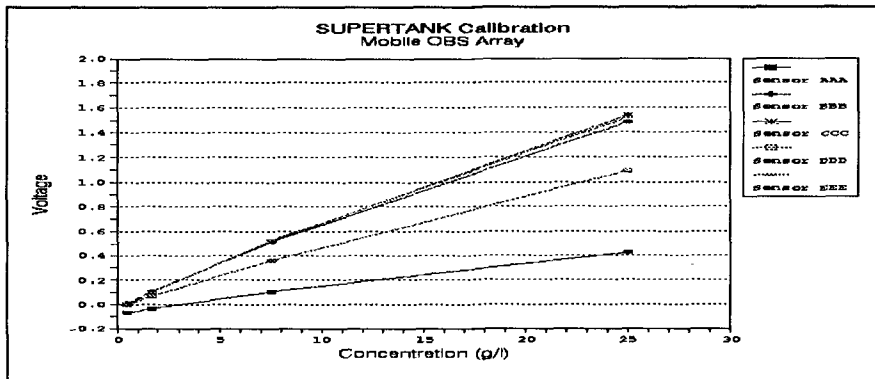


Figure 2 Calibration curves for OBS used during SUPERTANK.

by a program which removes outlying points, replacing the value with one interpolated between the preceding and succeeding points.

**REGULAR WAVES: TIME SERIES**

The following time series plots pertain to the sensor closest to the bed under regular waves. In most cases the sensor at the bottom of the array detected the greatest concentrations and most clearly displayed the event-based structure that is of interest.

Regular Wave Run #1

Fig. 3 presents the OBS time series for a sensor approximately 8 cm from the bed, with a cross-shore position 6 m seaward of breaking. Offshore conditions for this run were a wave height of 0.6 m and period of 3 s. At this location the waves were just beginning to strongly shoal, and the OBS record showed only a small amount of suspension near the bed.

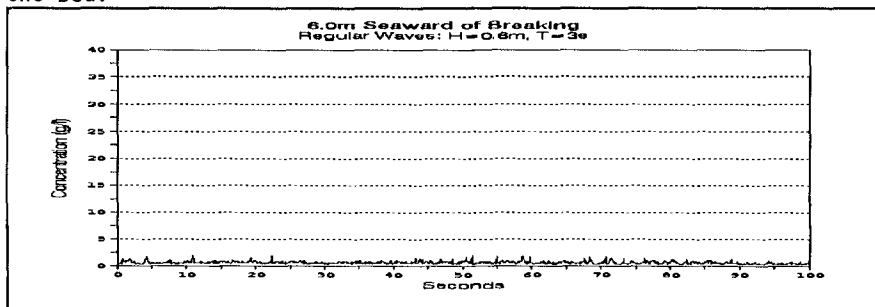


Figure 3 OBS time series 7.8 cm from the bed

Fig. 4 presents data from a position 4 m seaward from the break point, and is an example of concentration fluctuation that is directly correlated to the 3 sec oscillatory motion. The sensors indicate regular changes from a low background concentration to relatively high concentration within one wave period.

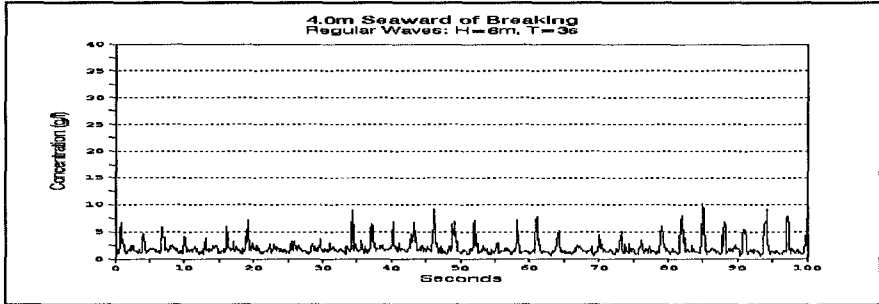


Figure 4 OBS time series 7.5 cm from the bed

Moving to a position 2 m from the breakpoint, the background concentration increased from 1 g/l to 2-3 g/l as seen in Fig. 5. The events at this position are regular, but are not as sharply peaked as those found 4 m from the breakpoint. The complete time series for this run contains a noticeable long period oscillation, part of which can be seen in this 100-sec segment, and may be caused by seiche in the channel.

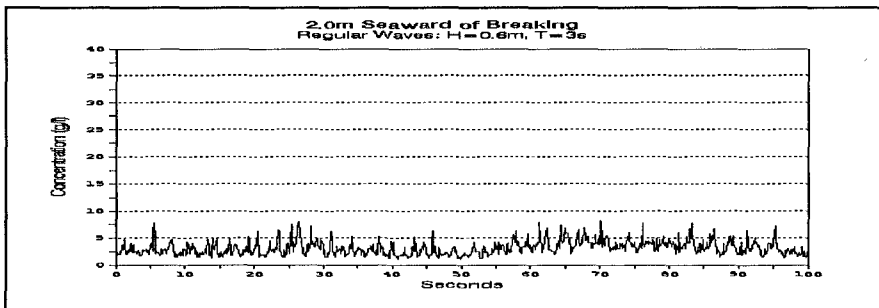


Figure 5 OBS time series 6.8 cm from the bed

At the break point (Fig. 6), the background concentration increased to nearly 5 g/l, and some peak concentrations lie above 10 g/l. The oscillatory structure is absent and peak concentrations are no longer strongly linked to the wave period.

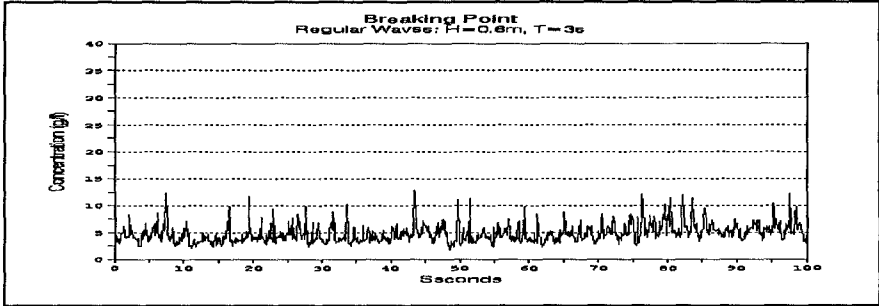


Figure 6 OBS time series 6.8 cm from the bed

In Fig. 7, which corresponds to a location 2 m shoreward of the break point and just shoreward of the plunge point, the most noticeable feature in the OBS record is that the background concentration has dropped to about 2 g/l. However, the peak concentrations remain relatively high. This time series shows no indication of wave-correlated structure, with the peaks in sediment concentration not following a distinguishable pattern.

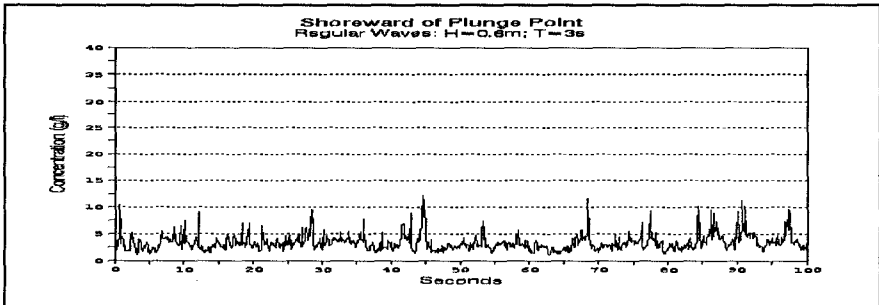


Figure 7 OBS time series 6.8 cm from the bed

These records indicate the temporal and spatial structure of the boundary between the relatively clear water outside the surf zone, and the cloud of sediment entrained and maintained by the intense turbulence levels induced by breaking. As the boundary advected back-and-forth in the oscillatory flow, it was visually observed to drift offshore several meters from its origin near the breaking point. A sharp gradient in suspended sediment concentration defined the boundary between the cloud and the surrounding water.

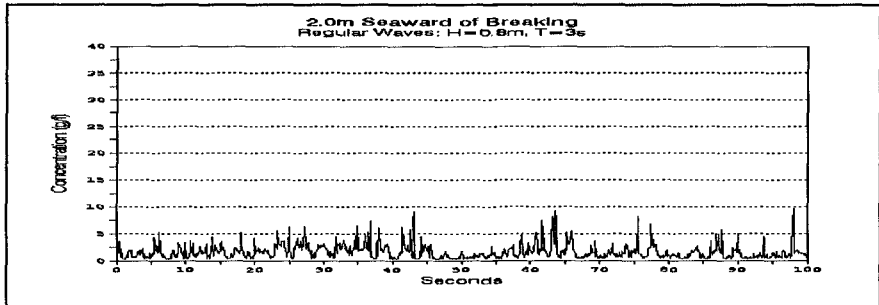


Figure 8 OBS time series 7.5 cm from the bed

### Regular Wave Run #2

In this second run, the offshore wave height was increased to 0.8 m, whereas the wave period remained at 3 sec. The position of the break point shifted approximately 4 m offshore from the previous run. Fig. 8, corresponding to a position 2 m seaward of this break point, shows that the magnitude of the sediment concentration in this time series oscillated regularly, much like in the previous run (Fig. 5); however, the background concentration was notably less with the larger wave conditions.

As seen in Fig. 9, by moving only half a meter closer to the breakpoint the peak concentrations increased, indicating deeper penetration into the sediment cloud as the boundary advected past the sensor. Suspension peaks were regular but not all of the same magnitude.

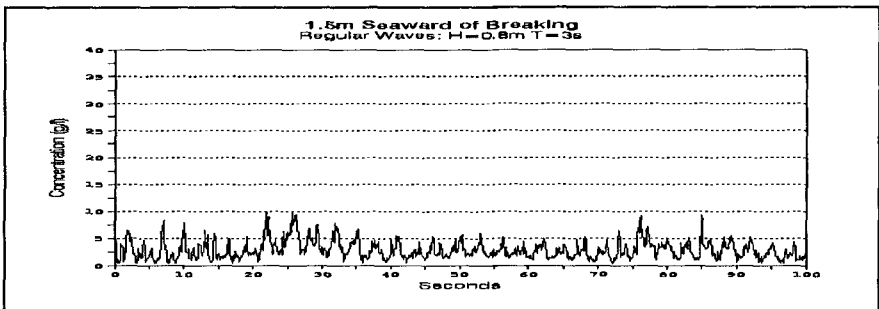


Figure 9 OBS time series 8.4 cm from the bed

At the break point (Fig. 10), there was a notable increase in the amount of sediment in suspension. Peak concentrations ranged from 15 to 20 g/l, and the background concentration was about 5 g/l, which are significantly greater than was observed at the break point in the first run.

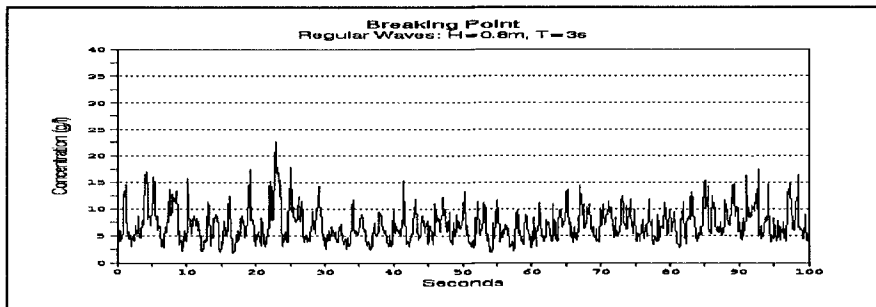


Figure 10 OBS time series 8.4 cm from the bed

Fig. 11 displays data that were collected 0.8 m inside the point of incipient breaking, which was still seaward of the plunge point. In this region, the highest peak concentrations of suspended sediment and greatest suspended load were found. No regular structure is apparent in the time series, and only in a few instances can 3-sec period events be observed.

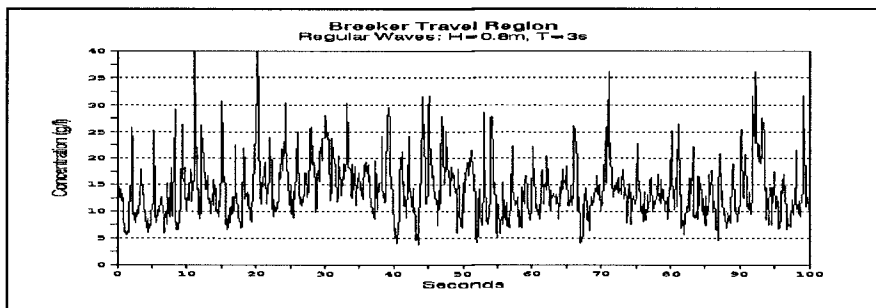


Figure 11 OBS time series 8.4 cm from the bed

4.3 m shoreward of the break point (Fig. 12), the background concentration drops to approximately 3 g/l and the peaks are reduced to the 5 to 10 g/l range. Fluctuations in sediment concentration appear to be considerably more random after the plunge point. The shoreward boundary of the sediment cloud is not as well defined as the seaward boundary, indicating more efficient cross-shore mixing in the broken wave region as would be expected.

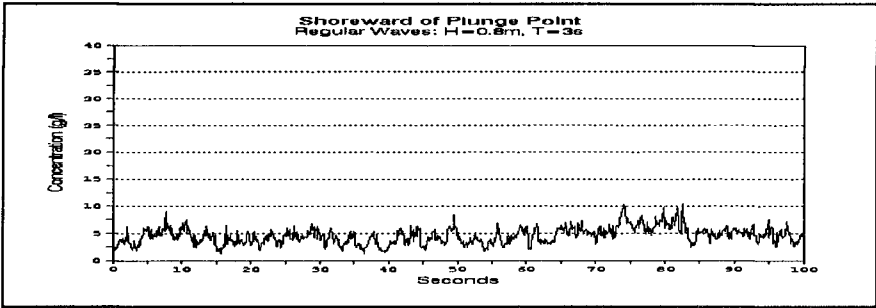


Figure 12 OBS time series 7.5 cm from the bed

**REGULAR WAVES: MEAN CONCENTRATION PROFILES**

Fig. 13 and Fig. 14 present mean concentration for all five OBS in the vertical array, for the two regular wave conditions discussed above. Mean concentration was calculated from the entire record that was collected at each station. Sensor elevations ranged from 7 to 34 cm above the bed.

Regular Wave Run 1

Fig. 13 displays the mean concentration profiles at the five cross-shore positions identified in Fig. 3 through Fig. 7. The profiles are labeled 1 through 5, with Profile 1 being the most seaward and Profile 5 being the most shoreward.

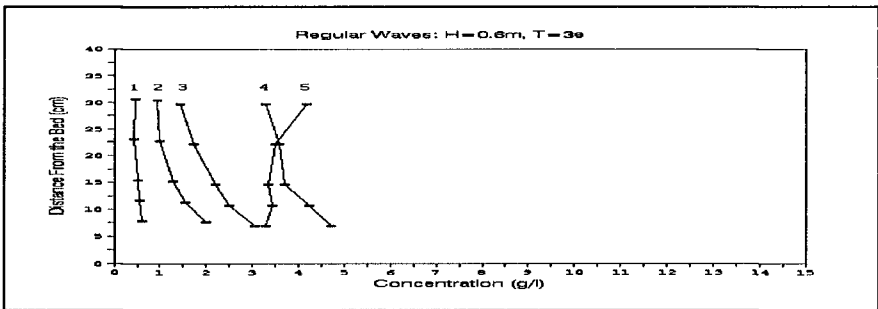


Figure 13

The first curve is for the cross-shore position 6-m seaward of the break point, where there was little suspended material as indicated by the low mean concentrations and the absence of vertical structure. The second curve, which is 2-m closer to the break point, shows an exponential decrease in concentration with distance from the bed. Profile 3 is 2 m seaward of the break point, where the curve is similar in shape to the previous, but with an increase in the amount of suspended material.

Profile 4, which was taken at the position where the wave crest began to curl over the front face, the concentration nearly doubled from the previous location. Here the profile is no longer smooth, but has a noticeable kink. After breaking (Profile 5) there is a distinct inversion in the mean sediment concentration profile.

### Regular Wave Run 2

Fig. 14 displays the mean concentration profiles at the five cross-shore positions identified in Figs. 8-12. The mean concentration profiles are numbered 1 through 5 as in Fig. 13.

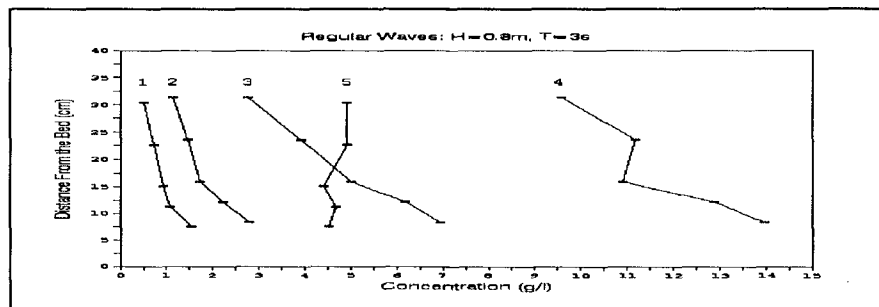


Figure 14

Seaward of the break point, the mean concentration profiles again show an exponential shape similar to those in Fig. 13. Profile 2 shows that the amount of suspended material was nearly twice of that in Profile 1, even though these locations were only 0.5 m apart. At the break point (Profile 3), the vertical structure loses its exponential character, as in Profile 4 of the previous run.

The highest mean concentrations measured at any cross-shore position are found in Profile 4, which was located between incipient breaking and the plunge point. Here the profile has an irregular shape, but concentration still decreases with distance from the bed. Even though this profile was taken less than 1 m landward of the previous position, mean concentrations doubled. Profile 5, which is shoreward of the plunge point, the concentration profile was inverted, but not to the degree observed in the first regular wave case.

### RANDOM WAVES: TIME SERIES

Most of the tests during the SUPERTANK project dealt with random waves. Unfortunately, there were no runs with random wave conditions during which the OBS array was shifted to different positions in the surf zone. However, for comparison of random and regular waves, two random wave runs were identified that had similar energy levels and



breaking conditions as the two regular wave runs. All four runs were conducted in immediate succession, so that the bottom profile underwent only slight change.

### Random Wave Run 1

The design wave conditions were 0.6-m significant height and 3-sec peak period. For the entire 40 min run, the OBS array was positioned about 5.4 m seaward of breaking, 0.6 m shoreward of the first position for the regular wave case.

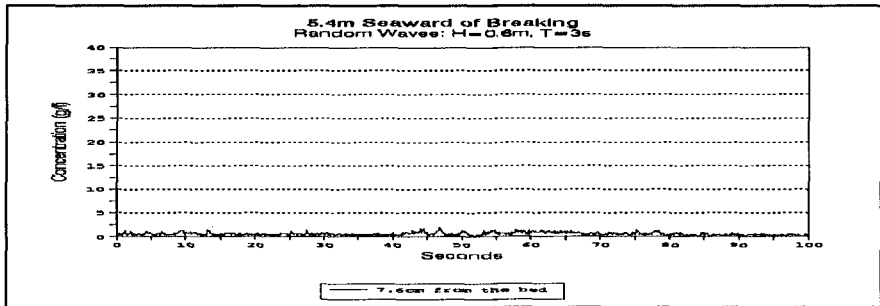


Figure 15 OBS time series 7.6 cm from the bed

Fig. 15 presents a 100-sec segment of the 40 min run. Concentrations measured at this position under random waves were comparable to those measured in the first regular wave case (Fig. 3). Background concentration was low and the suspension events were sparse during both runs.

### Random Wave Run 2

The offshore conditions for the second random wave case were 0.8-m significant wave height and 3-sec peak period. The OBS array was positioned about 2.1 m seaward of breaking, nearly the same as the first position for the 0.8-m regular wave case.

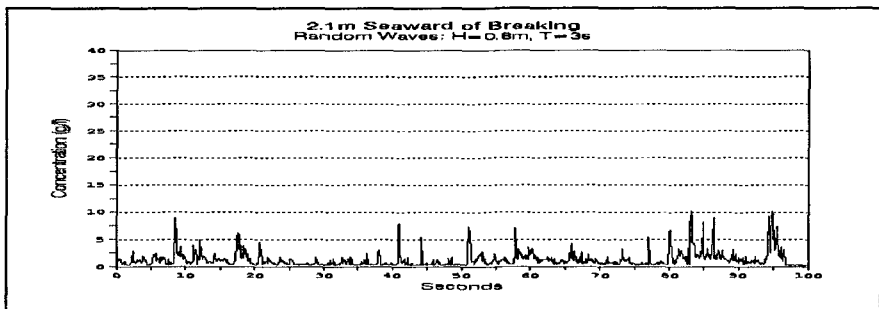


Figure 16 OBS time series 7.5 cm from the bed

In Fig. 16 it can be seen that with random waves the sediment suspension events are intermittently spaced and the peak concentrations are less uniform than those in the regular wave run (Fig. 8). There are also sections where little suspension occurs; however, no new structure (i.e. structure that was not encountered at some location in the regular wave run) is evident. Visual observations confirmed that smaller waves produced a sediment cloud of smaller dimensions and lower concentration.

### RANDOM WAVES: MEAN CONCENTRATION PROFILES

Average concentrations for each of the sensors in the OBS array were calculated and the mean concentration profiles were generated for the random wave cases. Since data were available at only one cross-shore position for the two random wave tests, the random wave profiles are plotted together with a concentration profile from a comparable position during the regular wave runs.

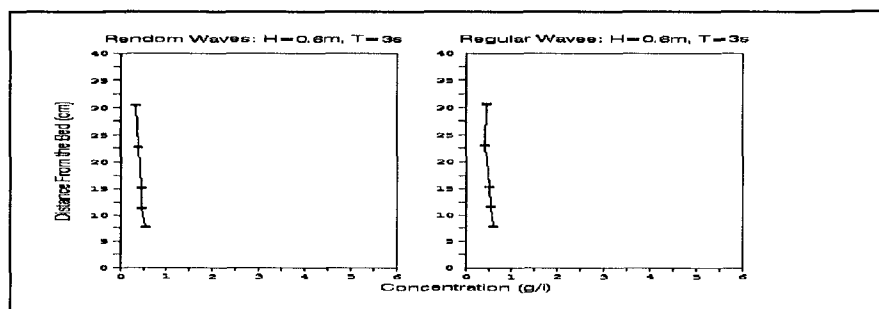


Figure 17 Mean Concentration Profiles

Fig. 17 shows the mean concentration profiles for the two types of waves at positions nominally 6 m seaward of breaking. The position of the array in the regular wave case was 0.6 m seaward of the random wave case. The shape of the curves and magnitude of the concentration are nearly identical.

Fig. 18 shows sediment concentration profiles under comparable regular and random wave conditions, but from a location nominally 2 m seaward of breaking. They display very similar exponential decay in concentration with distance from the bed. The mean suspended load for the random wave case is slightly lower than in the regular wave case. The consistent amount of energy available on a wave-by-wave basis for regular wave conditions may generate this higher background concentration.

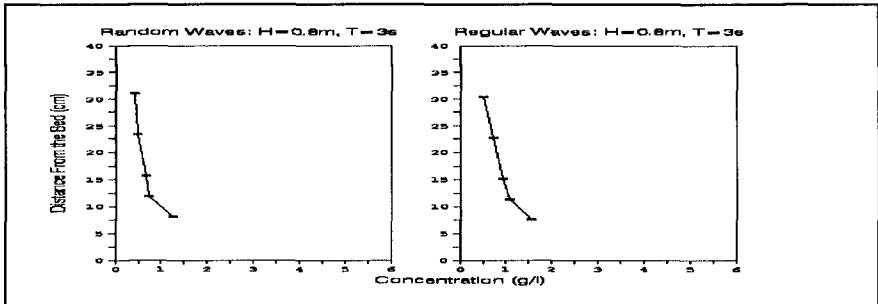


Figure 18 Mean concentration profiles

## CONCLUSIONS

The temporal behavior of suspended sand concentration, as well as the mean suspended load, changes dramatically as one moves through the outer edge of the surf zone. Suspension just outside the breaking region is characterized by a relatively well-defined boundary between clear water and sediment in suspension. The position of this boundary oscillates with the motion of the waves and drifts offshore with the mean cross-shore current, resulting in a concentration that varies regularly with the wave period. Mean concentration profiles in this region display the classical exponential shape.

The highest concentrations of suspended sediment are found in the region of initial breaking, where the sand cloud originates. Here much of the oscillatory structure in the time series is lost, with peaks in concentration occurring randomly, even for regular waves. Mean concentration adopts a profile that decays roughly linearly with distance from the bed. Just shoreward of the region of initial breaking the profile of mean concentration inverts.

For random waves, suspension is more irregular and intermittent, as should be expected. However, the mean concentration profiles are similar in both magnitude and shape as for regular waves.

## ACKNOWLEDGEMENTS

Appreciation is given to Dr. Nicholas C. Kraus for encouragement and discussions. This work was partially funded by the Dredging Research Program of the US Army Corps of Engineers' Coastal Engineering Research Center.

**REFERENCES**

Beach, R., 1989, Suspended Sediment Transport in the Surf Zone. Ph.D. Dissertation, University of Washington, Seattle, WA, 134p.

Beach, R., and Sternberg, R., 1991, Infragravity Driven Suspended Sediment Transport in the Swash, Inner and Outer-Surf Zone. Proceedings Coastal Sediments '91, ASCE, pp 114-128.

Nielsen, P., 1991, Combined Convection and Diffusion: A New Framework for Suspended Sediment Modelling. Proceedings Coastal Sediments '91, ASCE, pp 419-431.

Hanes, D., 1988, Intermittent Sediment Suspension and Its Applications to Sand Tracer Dispersal In Wave Dominated Environments. Jour. Geology, v. 81, pp 175-183.

Kraus, N., McKee Smith, J., and Sollitt, C., 1992, SUPERTANK Laboratory Data Collection Project. Proceedings 23rd International Conference on Coastal Engineering, ASCE.

## CHAPTER 148

### STATISTICALLY SIGNIFICANT BEACH PROFILE CHANGE WITH AND WITHOUT THE PRESENCE OF SEAWALLS.

David R. Basco<sup>1</sup>, Douglas A. Bellomo<sup>2</sup>, and Cheryl Pollock<sup>3</sup>

#### Abstract

The interaction of beaches and seawalls is a highly controversial subject today. Many of the arguments both "for" and "against" the construction of seawalls have been speculative. Few are based on actual field or laboratory measurements. This paper is part of a continuing study at one location, which intends to shed some light on this controversy using statistical analysis of real field data.

#### 1. Introduction

Sandbridge, Virginia (USA) is the site for an ongoing investigation of seawall and beach interaction. The study area lies on the east coast of the United States. Sandbridge is located south of the Chesapeake Bay and north of the Virginia-North Carolina border, as depicted in Figure 1. The beach is used by local property owners, residents, and tourists as a recreational area.

The long term shoreline recession rate (Everts et al., 1983) has been shown to vary at Sandbridge from 1.1 m/yr at the north end, to 2.9 m/yr at the south end. For this reason, many beach front private property owners have acted to protect their investments by constructing timber, steel or concrete seawalls (bulkheads). The protection of septic tanks, concrete slabs, and other property at ground level are a few reasons for their construction. The majority of homes in the area are on piles above the one percent chance storm surge event.

A few wall sections were constructed as early as 1978; however, most were erected in the mid to late 1980's. Fifteen sections of wall presently exist totaling 4816 m, roughly 60 percent of the 7.7 km study length (See Figure 1, insert). In general these sections lie about 46 m seaward of our baseline, Sandfiddler Road. Some sections, particularly those south of profile 162, are located within the daily tidal range. During storm events, the beach berm, seaward of the walls, is submerged at all locations. This allows waves to break at or near the walls.

---

<sup>1</sup>Professor, Coastal Engineering Program, Old Dominion University, Norfolk, VA (USA), 23529-0241, <sup>2</sup>Graduate Student, Coastal Engineering, and

<sup>3</sup>Coastal Engineer, Coastal Engineering Research Center, WES, Vicksburg, MS (USA)

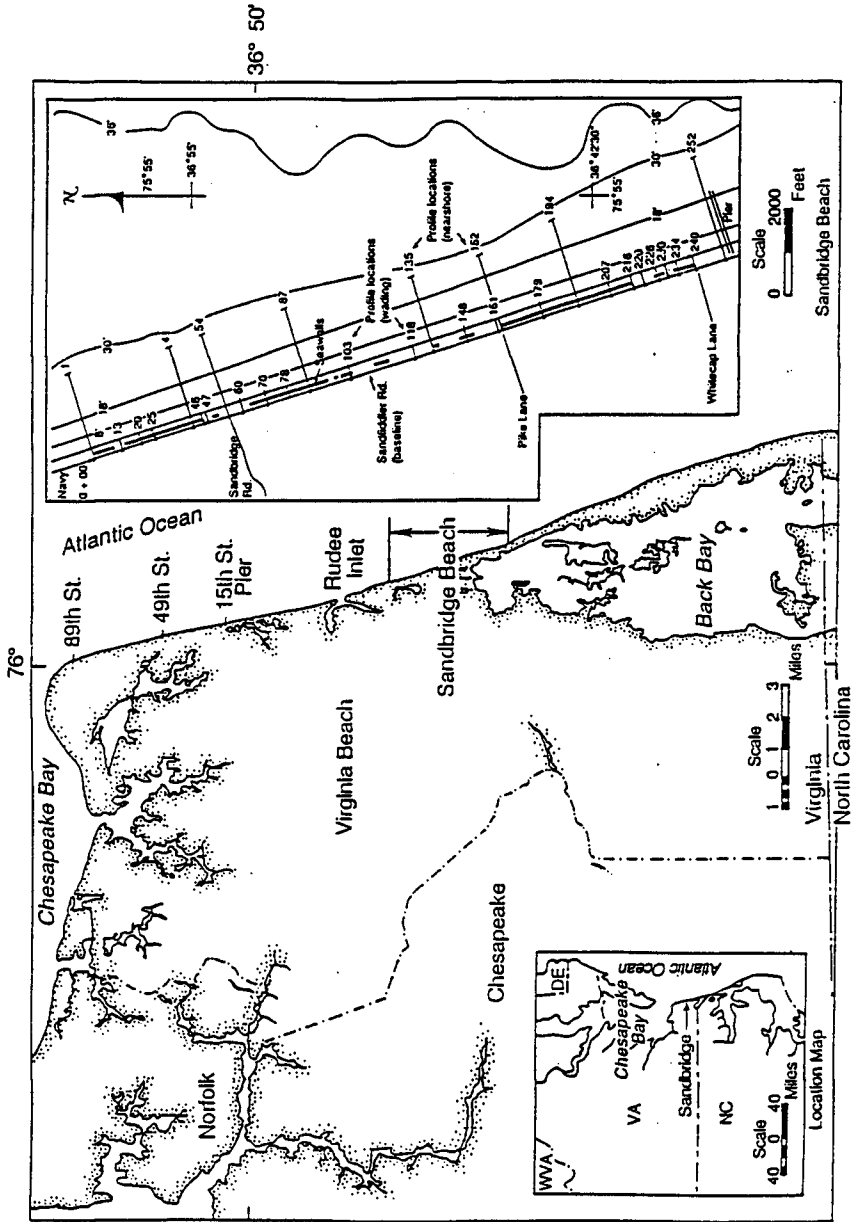


Figure 1 Location Map

The effects seawalls have on beaches, and their overall performance as a shoreline protection strategy, is the subject of much controversy today. The Journal of Coastal Research's 1988 Special Issue Number 4 entitled, "The Effects of Seawalls on the Beach", was specifically devoted to this topic (Kraus and Pilkey, 1988 Editors). Of the eight articles in this issue, none contained a rigorous statistical analysis of beach profile "change".

Profile data has been collected at Sandbridge since 1980, and continues to be collected today. Using this data, long term trends can be observed. These trends can then be used to determine statistical differences in walled and non-walled profiles. This statistically based information will help determine if the seawalls are responsible for altering the existing "natural " variations in beach profile data.

## 2. Field Efforts and Data Base

In August of 1990 Old Dominion University (ODU) began collecting monthly profile data at 28 locations along Sandbridge Beach. The project, sponsored by the Corps of Engineers' Coastal Engineering Research Center (CERC), has been extended through 1995. Of the 28 profile locations, 12 contain walls, 10 are across dunes, and 6 are located near wall ends, as shown in Figure 1. Profiles are taken out to low tide wading depths (-0.6 m), extending seaward about 122 m from the baseline.

The City of Virginia Beach began survey work in 1980 with profiles at roughly 305 m intervals. Most profiles extend only out to wading depths, however, some nearshore profiles (ie. to depths of -8 meters) have been taken. The time between City surveys varies over the past 12 years.

Other agencies, for instance the Corps of Engineers and the Virginia Institute of Marine Science, have also sponsored survey work at Sandbridge.

Compiling all the data from all the sources, 78 profile locations have been established. Today over 1600 separate profile lines have been taken at these 78 locations. At some locations 80 separate surveys have been taken, and by 1995 many will have over 100 surveys, spanning a 15 year period. Each profile has been archived to a common vertical and horizontal datum in CERC's Interactive Survey Reduction Program (ISRP). Using this data, statistical statements can now be made regarding the "differences" in beach profile response at walled and non-walled locations.

## 3. Quantification of Profile Change, Five Parameters

To quantify profile "change" we have adopted five parameters as depicted in Figure 2.

### 3.1 Profile Section Volumes

There are three section volume parameters, namely: landward volume ( $V_L$ ), seaward volume ( $V_S$ ), and total volume ( $V_T$ ), each carrying units of  $m^3/m$ . The

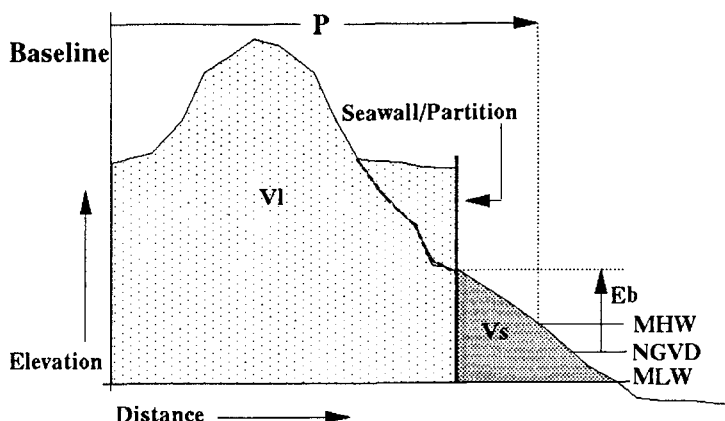


Figure 2 Definition Sketch

area between the profile and the MLW line is calculated using the trapezoidal rule. To obtain a volume, this area is then multiplied by a unit length parallel to the beach. The different volumes (landward, seaward, and total) are calculated using different right and left hand boundaries. Landward volume is bounded on the left by the survey baseline. For a walled profile, the right hand boundary for landward volume is the wall itself. However, for a dune/beach profile, an imaginary partition is used as the landward right hand boundary. This imaginary partition is located at the same distance from the baseline as the nearby seawalls. Seaward volume is bounded on the left by the imaginary partition or seawall, and on the right by the intersection of the profile and the MLW line. The total volume is simply the sum of the landward and seaward volumes. Figure 2 graphically depicts these definitions.

### 3.2 Berm Elevation

The berm elevation ( $E_b$ ) is measured in meters above the vertical datum. It is simply defined as the elevation of the profile at the seawall or imaginary partition, as shown in Figure 2.

### 3.3 Shoreline Position

The shoreline position ( $P$ ) is also shown in Figure 2. It is defined as the distance from the baseline, to where the profile intersects the MHW line. The MHW vertical datum has been chosen here to be consistent with map and aerial photograph data.

In Figure 3, the heavy solid line represents the shoreline position at Old Dominion University's 28 profile locations in August 1990. The heavy dotted line represents the shoreline position two years later in August 1992. The shoreline change, over that two year period, is indicated by the light solid line. Profile locations are depicted as short vertical lines at the bottom of Figure 3, and the



horizontal lines represent the walled sections. Notice how close the shoreline is to the baseline ( $P=0$ ) for profile numbers greater than 162. It is easily seen, that the long term receding shoreline poses an immediate threat to home and property owners.

#### 4. Methods of Data Analysis

##### 4.1 Jack Knife (JK) Technique

The Jack Knife (JK) technique (Dolan et al., 1991) has been used to determine a linear relationship between a given profile parameter and time. The first step in this method is to linearly regress all of the data points for one parameter versus time. This produces one slope and one intercept. Then by linear regression of all the points except the first, another slope and intercept can be calculated. Regressing all points except the second gives a third slope and intercept, ect. Given  $X$  surveys at one location, a "family" of  $X+1$  slopes and intercepts can be generated using this method. From this "family" of slopes, the average slope, as well as the standard deviation associated with that average slope, can be computed. Two methods of data analysis have been employed using the Jack Knife technique.

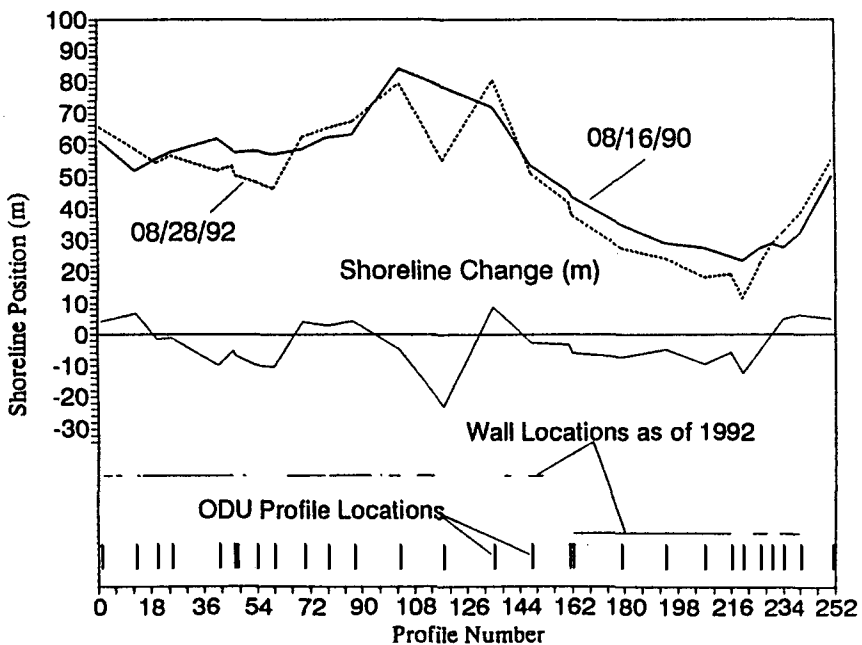


Figure 3 Shoreline Position

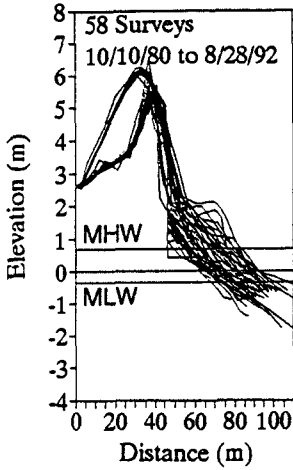


Figure 4a Profile 0

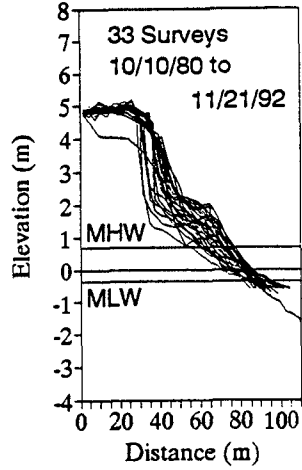


Figure 4b Profile 25

4.2 Compare Nearby Locations (CNL) Method

In this method, four profile pairs were selected at various locations along the beach. Each pair consists of a dune/beach profile and a seawall profile. Seawall profiles 25, 74, 194 and 205 were paired with dune/beach profiles 0, 60, 161, and 220, respectively. The variation in the long term shoreline recession rate along the study length, coupled with the availability of data dating far enough back in time, played a role in the selection of these pairs.

Figures 4a and 4b are envelope plots for profiles 0 and 25, respectively. Each profile line represents the beach cross section at a particular time. From each of these lines the five parameters  $V_L$ ,  $V_s$ ,  $V_T$ ,  $E_B$ , and  $P$  can be calculated. Each parameter can then be plotted versus time. Figure 5 shows each of the three section volumes versus time for the dune/beach profile 0. Figure 6 is the same type of plot for the walled section, profile 25, 760 m south of profile 0.

In Figures 5 and 6, the data has been divided into three groups: those points prior to October 1988 (dotted), those after October 1988 (dashed), and all the points inclusive (solid). The data has been divided at October 1988 simply because this is when the nearby wall at profile 25 was constructed. The JK technique was then employed on all three data groups for each profile. Statistics for the other two parameters,  $E_B$  and  $P$ , were calculated in a similar fashion. In Figures 7 and 8, the x's represent parameter values for profile 25, and the o's represent parameter values for profile 0. The light lines are the JK lines through profile 25 data, and the darker lines are those through profile 0 data. These types of calculations were made for all four profile pairs selected (0/25, 60/74, 161/194, 205/220).

At this point, the null hypothesis test was used to determine if any statistical

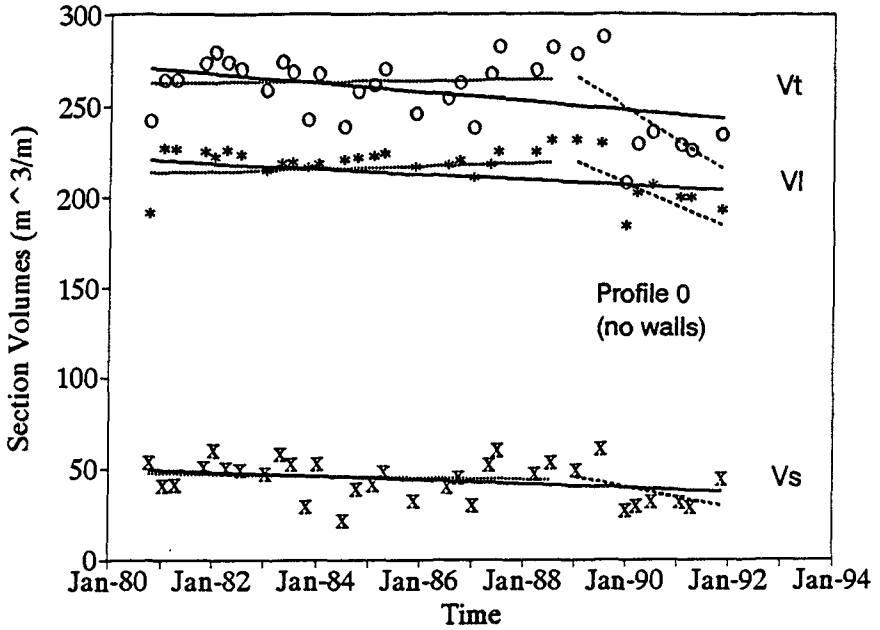


Figure 5 Section Volumes Profile 0 (dune/beach)

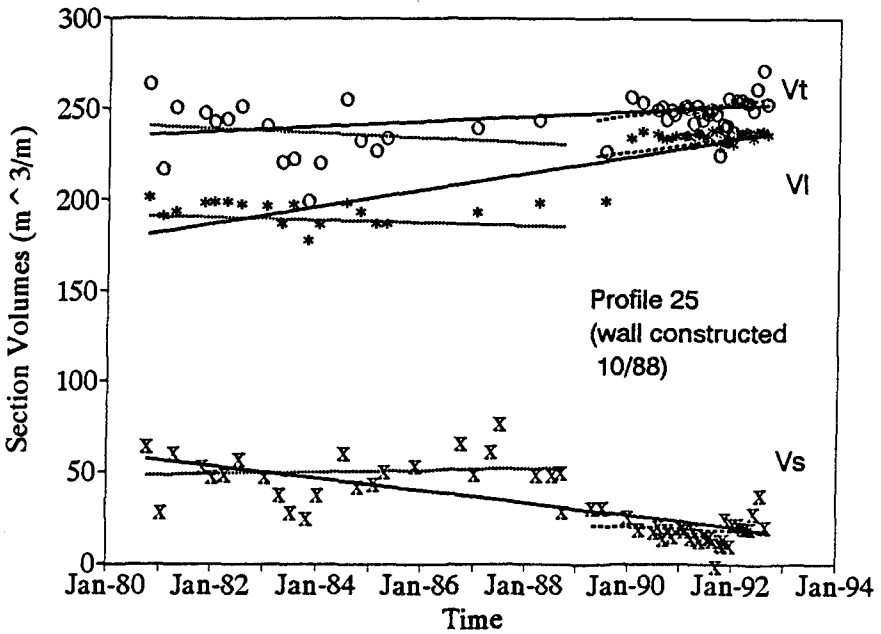


Figure 6 Section Volumes Profile 25 (seawall)

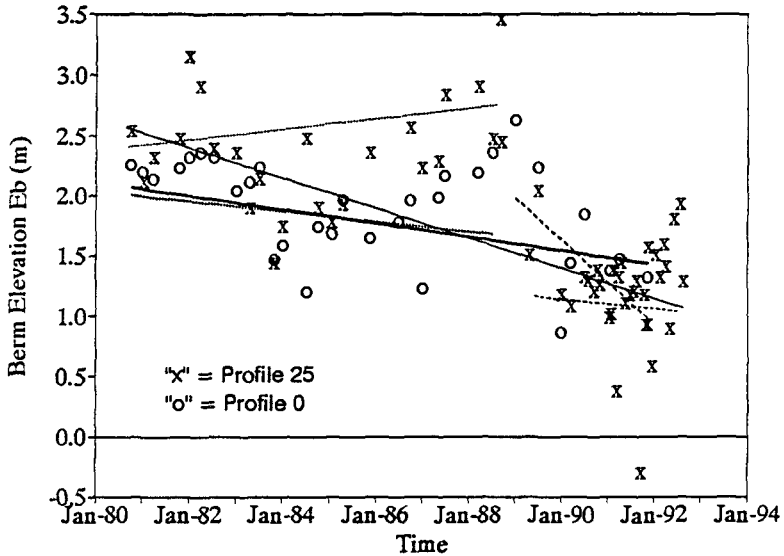


Figure 7 Berm Elevations Profile 0 and 25

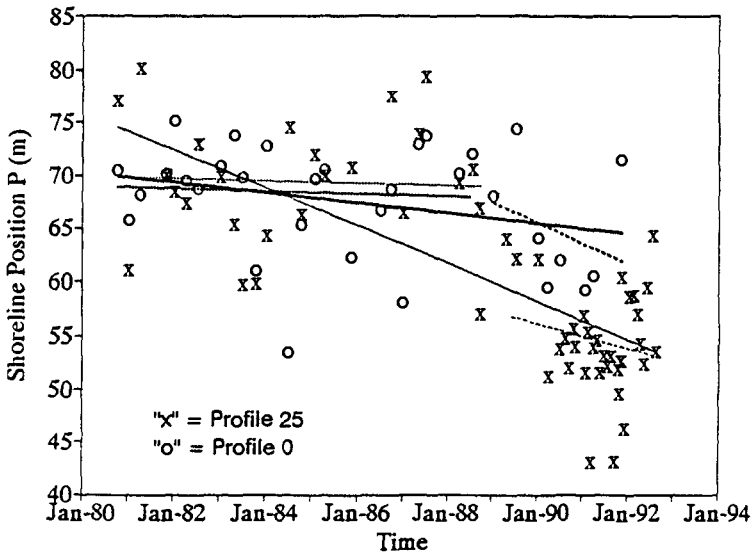


Figure 8 Shoreline Positions Profile 0 and 25

differences existed between the dune/beach and seawall line slopes generated by the JK technique. This was done for all 3 groups (prior to wall construction, after wall construction, and all data inclusive) and all four pairs. A five percent signifi-

cance level or 95 percent confidence was used for the null hypothesis. Since large degrees of freedom existed (ie. more than 29 slopes generated), a standard normal curve was used (Scheaffer and McClave,1990). The results found using this technique are discussed in Section 5 and summarized in Table I.

#### 4.3 Weighted Average (WA) Method

The second of the two data analysis techniques used is the Weighted Average (WA) method. Carefully distinguishing between walled and non-walled sections, each of the five parameters were integrated along the beach. The integrated values were then divided by a representative length, resulting in a weighted average parameter value. For example,  $V_L$  was calculated at various walled locations along the beach. These values were then used to integrate  $V_L$  along each of the fifteen walled sections. At this point an estimate of the total volume of sand in cubic meters, behind the walls was known. The weighted average  $V_L$  for the seawall sections was then calculated by dividing this total cubic volume by the entire wall length. Similar computations were made to calculate the total volume of sand behind an imaginary partition for the dunes.

To carry out this technique, data was collected monthly at 28 specific profile locations for a two year period. As mentioned earlier, Figure 3 shows the location of the 28 profiles (vertical lines), and walled sections (horizontal lines). Of the entire study length, roughly 4600 meters (60 percent) is walled and 3100 meters (40 percent) is duned. Note that not all walled sections nor duned sections have profiles running through them. These sections, however, make up only 14 percent of the study length. For this small percentage, parameter estimates were obtained using nearby profile data.

Calculating the seawall and dune/beach weighted average volumes for each of the monthly surveys, and plotting them versus time, results in Figure 9. Again we have  $V_L$ ,  $V_s$ , and  $V_T$  versus time as in the CNL method. The time span, however, is only 2 years in this case. In Figure 9, an "x" represents the weighted average parameter value for the seawall sections, and an "o" represents the weighted average parameter value for the dune/beach sections. The dashed and solid lines represent the Jack Knife line through the seawall and dune/beach data, respectively. Figure 10 shows the weighted average berm elevation ( $E_B$ ) versus time, and Figure 11 the weighted average shoreline position (P) versus time.

Again the null hypothesis test was used to determine if any statistical differences could be found in the slopes generated by the JK technique. The results are discussed in section 5, and are summarized in Table II.

#### 4.4 Littoral Drift Effects

One of the major concerns with this type of analysis is the independence between the two populations (seawall and dune/beach slope "families"). Two truly independent populations must exist; otherwise, it is impossible to make any valid statistical statements using the null hypothesis technique. If the sediment transport was strictly in the onshore-offshore direction, there would be no problem in

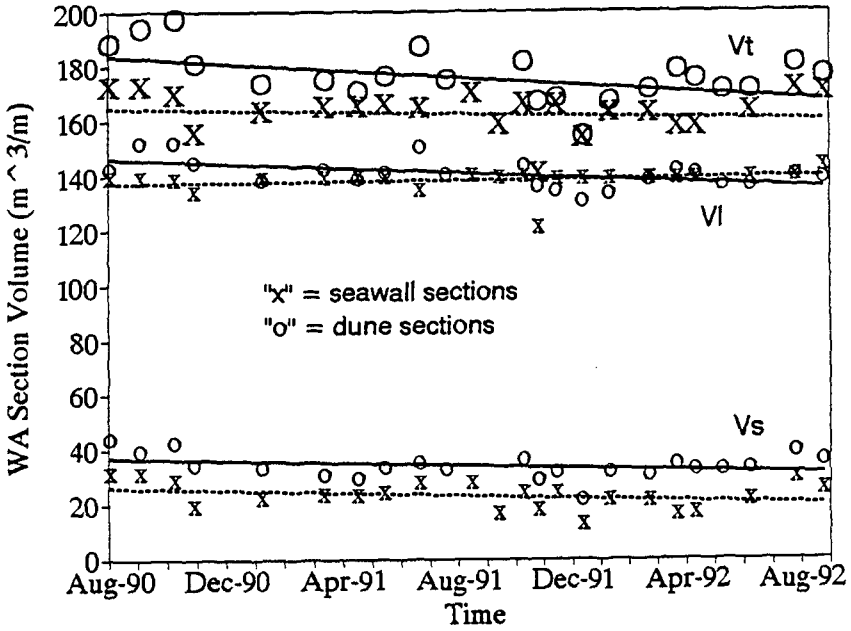


Figure 9 Section Volumes WA method

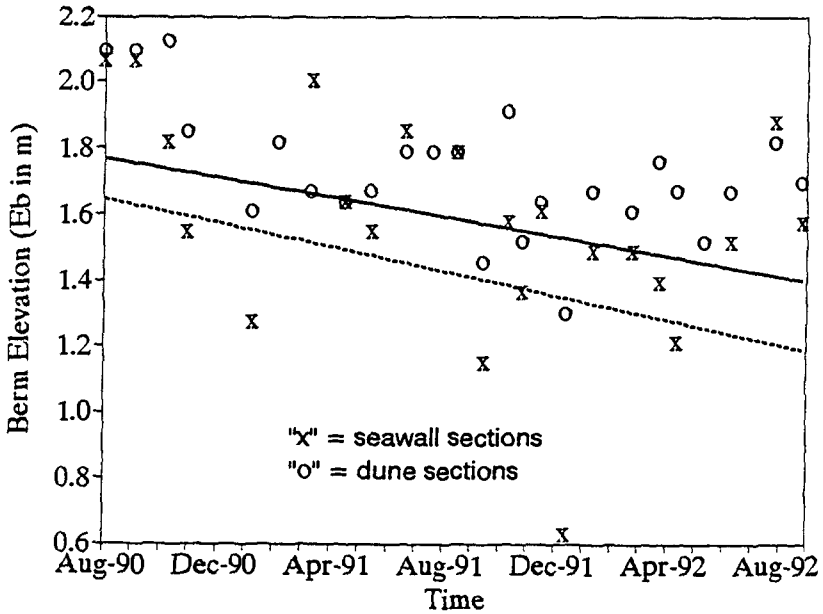


Figure 10 Berm Elevations WA method

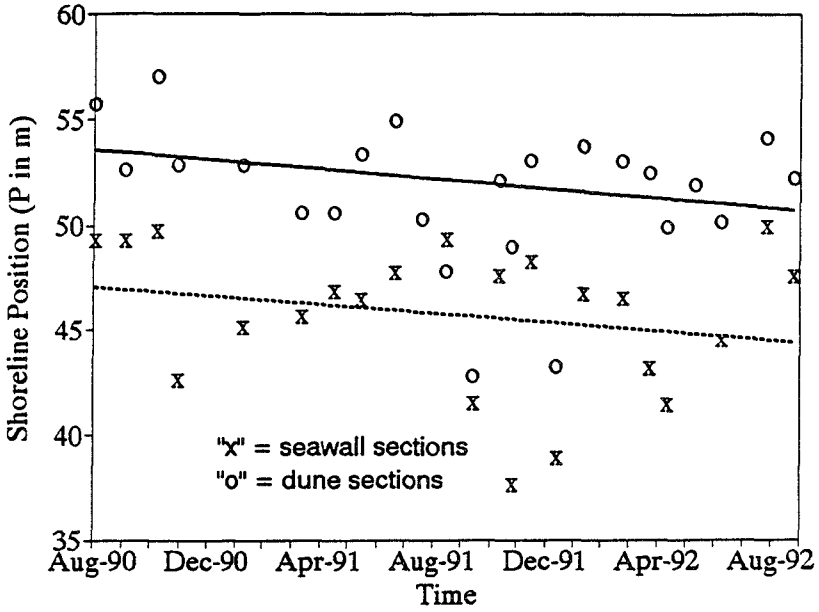


Figure 11 Shoreline Positions WA method

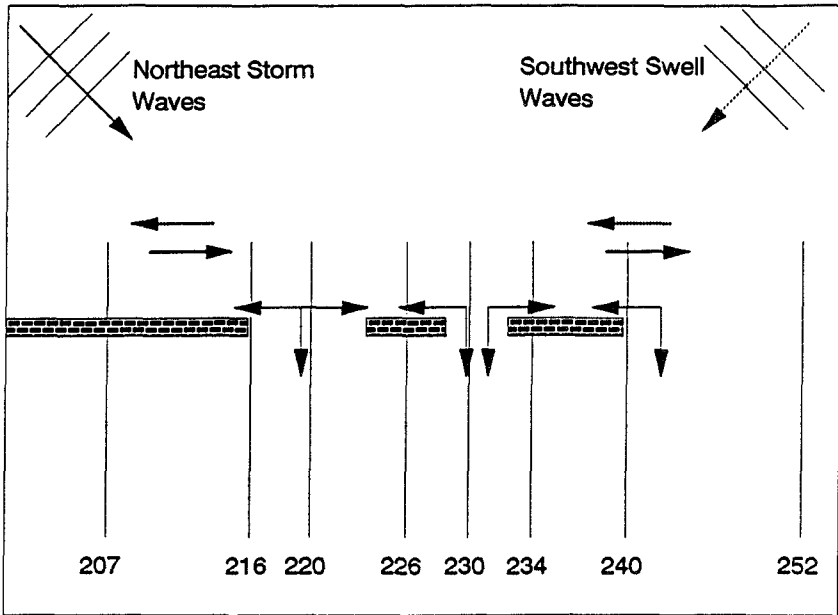


Figure 12 Littoral Drift Effects

making the independence assumption. However, this is not the case since longshore transport does exist.

In Figure 12 we depict to scale the seawall and profile locations at the southern end of the study area. Also shown are the directions for the northeast storm waves and the southwest swell waves. These produce a longshore sediment transport in the southerly (solid arrow) and northerly (dotted arrow) directions, respectively. Sand is moved from walled areas to dune/beach areas and vice-versa during the time periods corresponding to the reversals in wave direction. This is also shown schematically in Figure 12.

For the *long-term* trends analysis discussed herein, both the CNL and WA methods have tacitly assumed that the lateral transport processes **balance each other out over long periods of time**. In other words, sand moves locally from in front of walls to adjacent dune/beach areas, and in the reverse direction in approximately balanced quantities, **over the long term**. This assumption will be investigated as part of the overall project in the future, when the focus will be on end-of-wall effects on adjacent beaches, and storm induced changes over short time intervals.

## 5. Results

### 5.1 Compare Nearby Locations (CNL) Method

The five parameters  $V_L$ ,  $V_s$ ,  $V_T$ ,  $E_B$ , and  $P$  were tested on all four profile pairs. Each profile pair consisted of six JK lines, three for the dune/beach, and three for the seawall. Recall that these three lines were generated by dividing the data at the date when the local wall in the particular area was constructed. One line used data points before wall construction, the second used points after wall construction, and the third JK line used all the data points.

The results using the null hypothesis test on the slopes generated from the JK technique are found in Table I. The first column in the table states the hypothesis being tested. Columns two, three, four, and five represent profile pairs 0/25, 60/74, 161/194, 205/220, respectively. An "x" in a column means that the pair agreed with the hypothesis (i.e., both seawall and dune/beach regression slopes came from the same population). If no "x" exists, the hypothesis was found to be false. Column six is the number of profile pairs out of four in agreement with the hypothesis.

The trends are clearest for Group 1 (i.e., all the data is regressed). Seawalls retain sand behind them, therefore, the higher volume loss rate for the dune/beach sections behind the imaginary partition is to be expected. This also contributes to the higher loss rate for the total volume,  $V_T$  of a dune/beach section. The volume loss rate **seaward** of the partition was shown to be **higher** for the seawall in three of the four profile pairs. Berm elevation and shoreline position comparisons were inconclusive, since two pairs exhibited one trend and two, another.

The results for Groups 1 and 2 (i.e., before and after wall construction) are



Hypothesis	Profile Pair				Number in agreement
	0 25	60 74	161 194	205 220	
<b>Group 1: All Data</b>					
Vt loss rate is higher for dune/beach.	x	x	x	x	4
VI loss rate is higher for dune/beach.	x	x	x	x	4
Vs loss rate is higher for seawall.	x	x	x		3
Eb loss rate is higher for seawall.	x	x			2
P loss rate is higher for seawall.	x	x			2
<b>Group 2: Data Before Wall Construction</b>					
Vt loss rate is higher for seawall.	x	x			2
VI loss rate is higher for seawall.	x		x		2
Vs loss rate is higher for seawall.		x			1
Eb loss rate is higher for seawall.		x	=		1
P loss rate is higher for seawall.	=	x			1
<b>Group 3: Data After Wall Construction</b>					
Vt loss rate is higher for dune/beach.	x	x		x	3
VI loss rate is higher for dune/beach.	x	x		x	3
Vs loss rate is higher for seawall.	=		x		1
Eb loss rate is higher for seawall.			x		1
P loss rate is higher for seawall.			x		1

Table I Results CNL method

Profile Change Parameter	Dune/Beach		Seawall		Result
	Average Slope	Stdev	Average Slope	Stdev	
Vt	-8.20	0.650	-2.58	0.604	Dune weighted average Vt loss rate is higher.
VI	-5.34	0.359	+0.58	0.203	Dune weighted average VI loss rate is higher.
Vs	-2.86	0.406	-3.24	0.449	Seawall weighted average Vs loss rate is higher.
Eb	-0.17	0.014	-0.22	0.024	Seawall weighted average Eb loss rate is higher.
P	-1.40	0.174	-1.30	0.266	Weighted average P loss rates are same.

Table II Results WA method

less conclusive. We are investigating other profile pairs to expand the number used in the CNL method.

5.2 Weighted Average (WA) Method

All five parameters were tested over the 2 year period from August 1990 to August 1992. Two JK lines were calculated for each of the 5 parameters. One line was calculated using the dune/beach WA method values and the other used seawall WA method values. The results using the null hypothesis test on the slopes generated from the JK technique are found in Table II. Column one shows the profile change parameter being tested. Column two shows the average slope calculated using dune/beach WA method values, and the JK technique. Column three represents the standard deviation associated with the average slope in column two. Columns four and five are similar to two and three, only they were calculated using seawall WA method values. Column six states the result of the null hypothesis test.

The integrated, weighted average results for total and landward volume loss rates, again show that seawalls hold more sand in the profile. These are the same results a for the CNL method. Also, the volume loss rate seaward of the partition

(or wall) was higher for the seawalls. The averaged seaward volume loss rate was  $-2.86 \text{ m}^3/\text{m}$  (per year) for all the dune areas compared to  $-3.24 \text{ m}^3/\text{m}$  (per year) for all the seawalled sections. The standard deviations of all the slopes determined by the JK technique were similar (0.406 versus 0.499) for this estimate. The WA method also shows that the berm elevation loss rate is higher for the seawalls than for the dune/beach sections.

Despite these results for weighted average seaward volumes and berm elevation at the partition (seawall), statistical evidence does not permit a similar conclusion to be drawn regarding the shoreline position change rate over the two year study period.

## 6. Conclusions

The seawalls were installed at Sandbridge as an effort to protect the land and other property behind them from the encroaching sea. This study has shown, that at seawalled sections, the landward loss of sediment was much lower, and the seaward loss was slightly higher. Because of the volume held behind the walls, total loss of sediment was lower. It was also shown that the berm lowering rate, is slightly larger at seawalled sections in comparison to dune/beach sections. However, no strong statistical evidence was found to support the claim that seawalls have caused higher shoreline recession rates at Sandbridge. These results include the assumption that the lateral transport rates are in balance over long time periods.

These results are based upon 12 years of data for the CNL method and 2 years for the WA method. They are reflective of one 7.7 km stretch of East Coast shoreline in the United States. At the end of the study in 1995, we should have significantly more data for the WA method to make stronger conclusions. These results are applicable to the Sandbridge site with the complicated number of short seawall segments. The extrapolation of these results to other locations should be used with caution. Future efforts to sort out the end-of-wall and short term storm effects will aid in determining the validity of the "lateral transport balance" assumption. This will also help to determine if these results can be generalized and applied to other locations.

## 7. References

- Dolan, R., Fenster, M.S., and Holme, S.J. (1991) "Temporal Analysis of Shoreline Recession and Accretion", *Journal of Coastal Research*, Vol. 7, No.3, Summer.
- Kraus, N.C. and O.H. Pilkey (editors), (1988) "The Effects of Seawalls on the Beach", *Journal of Coastal Research*, Spec. Iss., No.4, Autumn.
- Everts, Craig H., et al. (1983) *Shoreline Movements: Cape Henry, Virginia to Cape Hatteras, North Carolina, 1849-1980*, Rept. No.1, Tech. Rept, CERC-83-1, WES, Vicksburg, MS, July, 123p.
- Scheaffer, R.L. and McClave J.T., (1990) *Probability and Statistics for Engineers*, 3rd Ed.

## CHAPTER 149

# PREDICTION OF TURBIDITY CURRENTS WITH BOUSSINESQ VISCOSITY AND SECOND-MOMENT CLOSURE MODELS.

Bård Brørs<sup>1</sup> and Karl J. Eidsvik<sup>1</sup>

### ABSTRACT

Sediment auto-suspension criteria (specifying the limit between eroding, self-accelerating flow and depositing, decelerating flow depending on the slope angle and particle settling velocity) differ by two orders of magnitude for different models in use. Experiments suggest that the results from ordinary density currents are applicable to turbidity currents. In the present study, models based upon well-known turbulence closures are applied in order to obtain a realistic description of turbidity currents:

A two-equation ( $k-\varepsilon$ ) model predicts phase plane behaviour in accordance with results from theoretical work reported in the literature, and with limits for auto-suspension within the range of conventional estimates. However, by its design, this model and simpler gradient diffusion models are unable to produce turbulent diffusion of sediments up through the level of the velocity maximum.

A model with second-moment Reynolds stress turbulence closure is applied. This model proves to overcome the problem of vanishing turbulent diffusivity in the velocity maximum and give plausible results for vertical distribution of flow parameters in turbidity currents.

### INTRODUCTION

Turbidity currents belong to the class of flows called gravity currents. A turbidity current is forced by the down-slope component of the gravitational acceleration acting on the soaring sediment grains, which in turn are kept in suspension by the turbulence generated by the current itself. Turbidity currents on the sea-bottom are known to have travelled hundreds of kilometers at speeds of more than 25 m/s and to have left turbidites (sediment deposits) of over 100 km<sup>3</sup>. The present study considers the portion of the flow well behind the advancing front, where horizontal gradients of flow variables may be ignored. Figure 1 shows a sketch

---

<sup>1</sup>Norwegian Hydrotechnical Laboratory, N-7034 Trondheim, Norway.

of the situation with suggested mean velocity and mean concentration profiles. As long as the slope is sufficiently steep and sediments are available, the flow increases its height, velocity and amount of sediments in suspension. For this

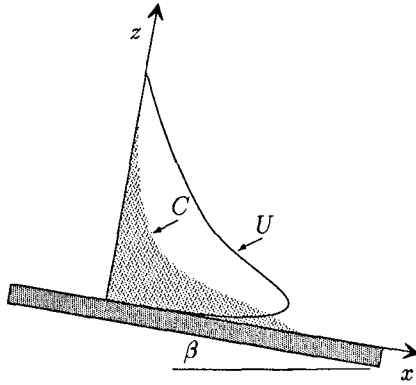


Figure 1: Turbidity current sketch.

shallow near-to-uniform flow, the thin shear layer approximation can be made, the equations for the mean velocity  $U$  and mean sediment concentration  $C$  may be written

$$\frac{\partial \rho U}{\partial t} = \frac{\partial \tau}{\partial z} + (\rho_s - \rho_f) C g \sin \beta, \tag{1}$$

$$\frac{\partial C}{\partial t} = -\frac{\partial}{\partial z} (\overline{cw} - w_T \cos \beta C). \tag{2}$$

Here,  $\rho_s$  and  $\rho_f$  are the solid and fluid densities and  $w_T$  is the particle settling velocity (positive downwards) and  $g$  is the gravitational acceleration.

Sediment auto-suspension criteria differ by two orders of magnitude for different models in use (Seymour, 1986). It is a limited supply of data for model verification, but experiments suggest that results from ordinary density currents are applicable to turbidity currents (Simpson, 1982). In the present study, several models based upon well-known turbulence closures are applied in order to obtain a realistic description of turbidity currents.

## MODELS

The equations for  $U$  and  $C$  given above contain two additional unknowns, the turbulent shear stress  $\tau$  and the turbulent sediment flux  $\overline{cw}$ . The shear stress may be expressed as  $\tau = -\rho \overline{uw} + 2(\rho_s - \rho_f)(w_T \cos \beta)^2 C + \rho_s w_T \cos \beta C U$ , and turbulence closures are needed for the normal-the-slope fluxes of turbulent momentum  $\overline{uw}$  and sediment concentration  $\overline{cw}$ .

### Boussinesq viscosity model

In Boussinesq viscosity models, the turbulent fluxes are expressed in terms of the mean flow gradients and some specified diffusivity. The results to be reported here are obtained with the use of the well known ( $k$ - $\epsilon$ ) model. Dynamic equations are solved for the turbulent kinetic energy  $k$  and the rate of dissipation  $\epsilon$  of turbulent kinetic energy:

$$\frac{\partial k}{\partial t} = \frac{\partial}{\partial z} \left( \frac{\nu_T}{\sigma_k} \frac{\partial k}{\partial z} \right) + P + G - \epsilon, \quad (3)$$

$$\frac{\partial \epsilon}{\partial t} = \frac{\partial}{\partial z} \left( \frac{\nu_T}{\sigma_\epsilon} \frac{\partial \epsilon}{\partial z} \right) + \frac{\epsilon}{k} (C_{\epsilon 1} P + C_{\epsilon 3} G - C_{\epsilon 2} \epsilon). \quad (4)$$

The fluxes are expressed in terms of  $k$ ,  $\epsilon$  and the mean flow gradients as

$$-\overline{uw} = \nu_T \frac{\partial U}{\partial z}, \quad -\overline{cw} = \frac{\nu_T}{\sigma_c} \frac{\partial C}{\partial z}. \quad (5)$$

The diffusivity  $\nu_T$  (often termed the eddy viscosity) is expressed as  $\nu_T = C_\mu k^2/\epsilon$ . The coefficients of the model are  $(C_\mu, C_{\epsilon 1}, C_{\epsilon 2}, C_{\epsilon 3}, \sigma_c, \sigma_k, \sigma_\epsilon) = (0.09, 1.44, 1.92, 0, 1.0, 1.0, 1.22)$ . Further details of this model is given in (Eidsvik and Brørs, 1989) and (Brørs, 1991).

### Reynolds stress model

In Reynolds stress models, dynamic equations are solved for  $\overline{uw}$  and  $\overline{cw}$ , and there is no need for an eddy viscosity. However, several additional unknowns emerge in the Reynolds averaging process. It is the Reynolds normal stresses  $\overline{u^2}$ ,  $\overline{v^2}$ ,  $\overline{w^2}$ , the concentration flux  $\overline{cw}$  and the variance of the concentration fluctuations,  $\overline{c^2}$ . With the  $\epsilon$  equation, this adds up to an eight equation model:

$$\begin{aligned} \frac{\partial \overline{u^2}}{\partial t} &= \frac{\partial}{\partial z} \left( C_s \overline{w^2} \frac{k}{\epsilon} \frac{\partial \overline{u^2}}{\partial z} \right) - \frac{\epsilon}{k} \left( C_1 (\overline{u^2} - \frac{2}{3} k) - C'_1 f \overline{w^2} \right) \\ &\quad - \left( 2 - \frac{4}{3} C_2 + \frac{2}{3} C_2 C'_2 f \right) \overline{uw} \frac{\partial U}{\partial z} + \left( 2 - \frac{4}{3} C_3 + \frac{2}{3} C_3 C'_3 f \right) \overline{cw} g' \sin \beta \\ &\quad - \left( \frac{2}{3} C_3 - \frac{4}{3} C_3 C'_3 f \right) \overline{cw} g' \cos \beta - \frac{2}{3} \epsilon, \end{aligned} \quad (6)$$

$$\begin{aligned} \frac{\partial \overline{v^2}}{\partial t} &= \frac{\partial}{\partial z} \left( C_s \overline{w^2} \frac{k}{\epsilon} \frac{\partial \overline{v^2}}{\partial z} \right) - \frac{\epsilon}{k} \left( C_1 (\overline{v^2} - \frac{2}{3} k) - C'_1 f \overline{w^2} \right) \\ &\quad - \left( \frac{2}{3} C_2 + \frac{2}{3} C_2 C'_2 f \right) \overline{uw} \frac{\partial U}{\partial z} + \left( \frac{2}{3} C_3 + \frac{2}{3} C_3 C'_3 f \right) \overline{cw} g' \sin \beta \\ &\quad - \left( \frac{2}{3} C_3 - \frac{4}{3} C_3 C'_3 f \right) \overline{cw} g' \cos \beta - \frac{2}{3} \epsilon, \end{aligned} \quad (7)$$

$$\begin{aligned} \frac{\partial \overline{w^2}}{\partial t} &= \frac{\partial}{\partial z} \left( C_s \overline{w^2} \frac{k}{\varepsilon} \frac{\partial \overline{w^2}}{\partial z} \right) - \frac{\varepsilon}{k} \left( C_1 (\overline{w^2} - \frac{2}{3} k) + 2 C_1' f \overline{w^2} \right) \\ &\quad - \left( \frac{2}{3} C_2 - \frac{4}{3} C_2 C_2' f \right) \overline{w w} \frac{\partial U}{\partial z} + \left( \frac{2}{3} C_3 - \frac{4}{3} C_3 C_3' f \right) \overline{c u} g' \sin \beta \\ &\quad - \left( 2 - \frac{4}{3} C_3 + \frac{8}{3} C_3 C_3' f \right) \overline{c w} g' \cos \beta - \frac{2}{3} \varepsilon, \end{aligned} \tag{8}$$

$$\begin{aligned} \frac{\partial \overline{w w}}{\partial t} &= \frac{\partial}{\partial z} \left( C_s \overline{w^2} \frac{k}{\varepsilon} \frac{\partial \overline{w w}}{\partial z} \right) - \frac{\varepsilon}{k} \left( C_1 + \frac{3}{2} C_1' f \right) \overline{w w} \\ &\quad - \left( 1 - C_2 + \frac{3}{2} C_2 C_2' f \right) \overline{w^2} \frac{\partial U}{\partial z} + \left( 1 - C_3 + \frac{3}{2} C_3 C_3' f \right) \overline{c w} g' \sin \beta \\ &\quad - \left( 1 - C_3 + \frac{3}{2} C_3 C_3' f \right) \overline{c u} g' \cos \beta, \end{aligned} \tag{9}$$

The closed equations for the scalar fluxes and half the variance of the scalar fluctuations are:

$$\begin{aligned} \frac{\partial \overline{c u}}{\partial t} &= \frac{\partial}{\partial z} \left( C_{cs} \overline{w^2} \frac{k}{\varepsilon} \frac{\partial \overline{c u}}{\partial z} \right) - \overline{w w} \frac{\partial C}{\partial z} - \frac{\varepsilon}{k} C_{c1} \overline{c u} - (1 - C_{c2}) \overline{c w} \frac{\partial U}{\partial z} \\ &\quad + (1 - C_{c3}) \overline{c^2} g' \sin \beta, \end{aligned} \tag{10}$$

$$\begin{aligned} \frac{\partial \overline{c w}}{\partial t} &= \frac{\partial}{\partial z} \left( C_{cs} \overline{w^2} \frac{k}{\varepsilon} \frac{\partial \overline{c w}}{\partial z} \right) - \overline{w^2} \frac{\partial C}{\partial z} - \frac{\varepsilon}{k} (C_{c1} + C_{c1}' f) \overline{c w} \\ &\quad - (1 - C_{c3} + C_{c3} C_{c3}' f) \overline{c^2} g' \cos \beta, \end{aligned} \tag{11}$$

$$\frac{\partial \frac{1}{2} \overline{c^2}}{\partial t} = \frac{\partial}{\partial z} \left( C_c \overline{w^2} \frac{k}{\varepsilon} \frac{\partial \frac{1}{2} \overline{c^2}}{\partial z} \right) - \overline{c w} \frac{\partial C}{\partial z} - \varepsilon_c. \tag{12}$$

The model equation for turbulence energy dissipation is

$$\frac{\partial \varepsilon}{\partial t} = \frac{\partial}{\partial z} \left( C_\varepsilon \overline{w^2} \frac{k}{\varepsilon} \frac{\partial \varepsilon}{\partial z} \right) + \frac{\varepsilon}{k} (C_{\varepsilon 1} P - C_{\varepsilon 2} \varepsilon + C_{\varepsilon 3} \max(0, G)). \tag{13}$$

The dissipation of scalar variance is approximated from an assumed constant ratio  $R$  between the scalar and dynamic turbulent time scales:

$$\varepsilon_c = \frac{1}{2R} \frac{\varepsilon}{k} \overline{c^2}. \tag{14}$$

In the equations,  $P$  and  $G$  denote the generation rate of turbulent kinetic energy by the mean velocity gradient and by gravitational effects:

$$P = -\overline{w w} \frac{\partial U}{\partial z}, \tag{15}$$

$$G = \overline{cu} g' \sin \beta - \overline{cw} g' \cos \beta. \quad (16)$$

The function  $f$  is a damping function for the wall echo effect on the pressure strain correlations. It is normalized to a value of one near the wall and is expressed by the turbulent length scale  $\ell$ :

$$f \propto \left(\frac{\ell}{z}\right), \quad \ell \equiv \frac{k^{\frac{3}{2}}}{\varepsilon}. \quad (17)$$

The present model is equivalent to the one presented by Gibson and Launder (1977) and the same set of coefficients is used. Further details are given in Brørs (1991) and Brørs and Eidsvik (1992). The model takes into account the proximity or "echo" effect of the bottom on the turbulent stresses. All coefficients with primes in equations (6) to (13) indicate terms with this purpose.

## RESULTS

The two-equation ( $k$ - $\varepsilon$ ) model predicts phase plane behaviour in accordance with results from theoretical work reported in the literature, and with limits for auto-suspension within the range of conventional estimates (Eidsvik and Brørs, 1989). However, by its design, this model and simpler gradient diffusion models are unable to produce turbulent diffusion of sediments through the level of the velocity maximum. This feature is considered to be important for the development of turbidity currents, and should be reproduced by a proper model. Modifications of the ( $k$ - $\varepsilon$ ) model with algebraic stress models and algebraic length-scale expressions are made but do not solve this problem. Use of second-moment Reynolds stress turbulence closure (Brørs, 1991, Brørs and Eidsvik, 1992) proves to overcome the problem of vanishing turbulent diffusivity in the velocity maximum, and plausible results for vertical distribution of flow parameters in turbidity currents are obtained. Predictions with the full, eight-equation Reynolds stress model mentioned here compare favourably with available data for this type of flow.

Figure 2 (a) and (b) shows predicted normal-to-the-slope profiles for a turbidity current on a  $\beta = 0.05$  radians slope. The flow has been allowed to develop for  $t = 320$  seconds, from a 0.3 m high stationary cloud. The sediment grain diameter is 50  $\mu\text{m}$  and the settling velocity is 0.15 cm/s. The initial concentration is  $C = 0.3$ . At the time shown, the flow has reached a height of about 7 m. The ( $k$ - $\varepsilon$ ) and Reynolds stress models are seen to produce nominally nearly identical velocities, although the former predicts a very pointed velocity maximum. The Reynolds stress model predicts a fuller  $C$  profile.

The turbulent kinetic energy  $k$  and eddy viscosity  $\nu_T$  are shown in Figure 2 (c) and (d). For the Reynolds stress model, an eddy viscosity is back-calculated from the prediction using the expression  $\nu_T = C_\mu \overline{w^2} k / \varepsilon$ , with  $C_\mu$  being a constant equal to 0.263 and  $\overline{w^2}$  the variance of the velocity fluctuations normal to the slope. The dashed line shows the  $\nu_T$  profile for the ( $k$ - $\varepsilon$ ) model. The eddy viscosity is seen to be zero at the level ( $z \sim 0.2$  m) of the mean velocity maximum. Here, the turbulence energy production  $P = \nu_T (\partial U / \partial z)^2$  in (3) is zero. The velocity

minimum inhibits the transport of sediments to the outer part of the flow, and a strong density gradient is created at this level. The steep density gradient causes a large negative value for the bouyancy production term  $G = g'(\nu_T/\sigma_c)(\partial C/\partial z)$ . This reduces  $k$  further, it eventually approaches zero, and so does  $\nu_T$ .

In zero-equation models it is usual to omit the problem by using a so-called "linear bridge", that is by exchanging the portion around the minimum of the  $\nu_T$  profile with a straight line connecting the maxima on either side. An approach like this has been applied on the present ( $k$ - $\epsilon$ ) model, both to  $\nu_T$  and to  $k$ . The dashed-dotted lines in Figure 2 show predicted profiles when the dip in the  $k$  profile is replaced with a value 0.15 times the near-bottom  $k$  maximum value. Although the  $k$  bridge is seen to give  $U$  and  $C$  profile shapes similar to those produced by the full Reynolds stress model, it causes a large (about 50% for the velocity) nominal increase in the values. This could possibly be corrected by changing the model coefficients, although this has not been attempted.

Figure 3 shows a prediction of one of the laboratory saline gravity currents of Ellison and Turner (1959). The profiles are normalized, and  $z_{1/2}$  is the level in the outer layer where the velocity is reduced to one half the profile maximum  $U_m$ . The Reynolds stress model is seen to be superior to the ( $k$ - $\epsilon$ ) model in representing this experiment.



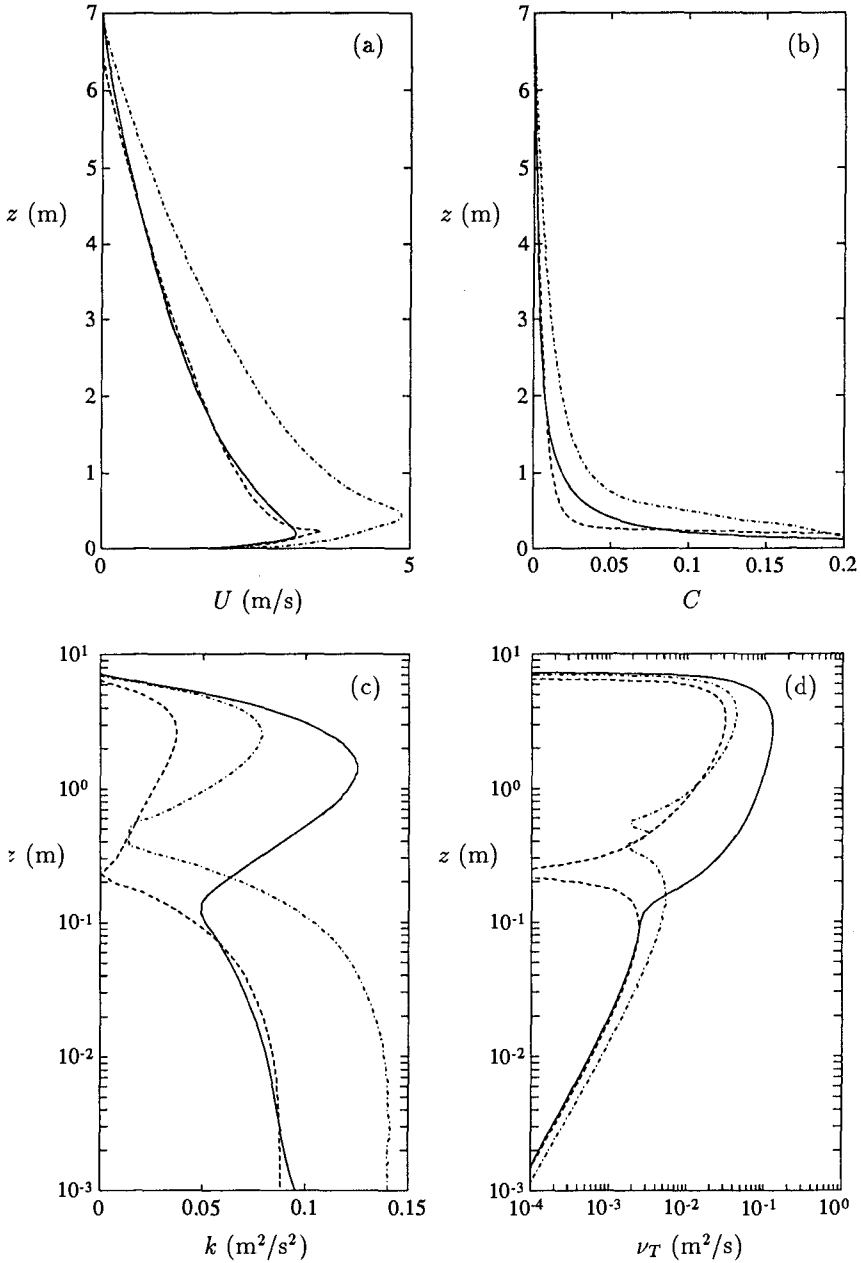


Figure 2: Predicted profiles for self-accelerating turbidity current. Full line; Reynolds stress model, dashed line;  $(k-\epsilon)$  model, dashed-dotted line;  $(k-\epsilon)$  model with bridge across the  $k$  profile dip.

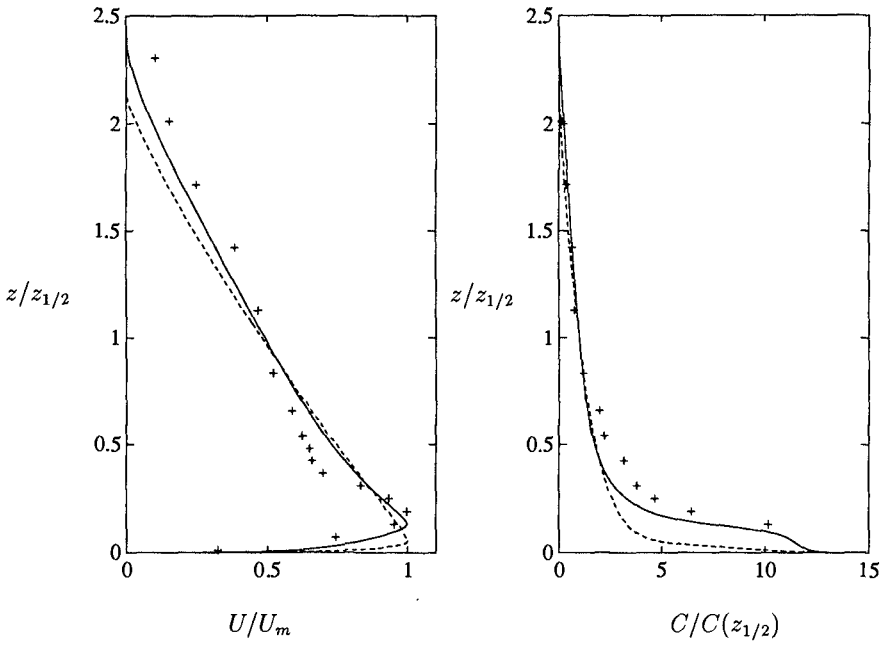


Figure 3: Predicted mean flow profiles for saline gravity current. Symbols represent laboratory experiments by Ellison and Turner (1959). Line types as in Figure 2. The slope is  $\beta = 0.24$  radians.

**REFERENCES**

- Brørs, B. (1991). *Turbidity current modelling*. Dr.ing. thesis, The Norwegian Institute of Technology, Trondheim, Norway. 164 pp.
- Brørs, B. and K. J. Eidsvik (1992). Dynamic Reynolds stress modelling of turbidity currents. *J. Geophys. Res.*, *97*, (C6), 9645-9652.
- Eidsvik, K.J. and B. Brørs (1989). Self-accelerated turbidity current prediction based upon  $(k-\varepsilon)$  turbulence. *Cont. Shelf Res.*, *9*, 617-627.
- Ellison, T. H and J. S. Turner (1959). Turbulent entrainment in stratified flows. *J. Fluid Mech.*, *6*, 432-448.
- Gibson, M.M. and B. E. Launder (1977). Ground effects on pressure fluctuations in the atmospheric boundary layer. *J. Fluid Mech.*, *86*, 491-511.
- Seymour, R. J. (1986). Nearshore auto-suspending turbidity flows. *Ocean Engineering*, *13*, 435-447.

## CHAPTER 150

### CROSS-SHORE TRANSPORT MODELLING IN TERMS OF SEDIMENT CONCENTRATIONS AND VELOCITIES

Zhiwen Chen<sup>1</sup>

#### ABSTRACT

The fluctuations of sediment concentration and velocity during a wave period may play an important role in cross-shore sediment transport. In this study, the contribution of the fluctuations was estimated by measuring time-varying sediment concentration and velocity under laboratory conditions. The results showed that the contribution can only be neglected if the mean flow is relatively strong compared to the wave orbital motion.

#### 1. INTRODUCTION

The phenomenon of cross-shore transport has been widely investigated for a long time. The solution of many real life problems relies on a proper description of the cross-shore transport mechanism [e.g., beach and dune erosion during storm surges; beach profile response to global sea level rise]. Many beach evolution models start by calculating the cross-shore transport distribution along a beach profile.

The cross-shore transport rate through a vertical plane with unit width can be

---

<sup>1</sup> Assistant researcher, Dept. of Civil Engineering, Delft University of Technology, Stevinweg 1, 2600 GA, Delft, The Netherlands.

expressed in principle by:

$$q = \int_0^{h+\eta} \overline{u(z,t) * c(z,t)} dz \quad (1)$$

Where:

- $q$  : cross-shore transport rate, [kg/ms]  
 $u(z,t)$  : instantaneous cross-shore velocity at level  $z$ , [m/s]  
 $c(z,t)$  : instantaneous sediment concentration at level  $z$ , [kg/m<sup>3</sup>]  
 $h$  : water depth, [m]  
 $\eta$  : maximum water surface elevation, [m]  
 $z$  : elevation above the bed level, [ $z = 0$  at the bottom], [m]  
 $t$  : time, [s]  
 overline : time-average

Eq.(1) offers a proper description of cross-shore transport. However, the direct use of Eq.(1) has been proved very difficult because of our entirely insufficient knowledge of the parameters  $u(z,t)$  and  $c(z,t)$ . This holds especially inside the surf zone, the most active part of a beach profile. For this reason, coastal engineers in the past have often used more or less integral approaches to calculate cross-shore transport [e.g., Swart (1974) and Dean (1982)].

Recent models for cross-shore transport have attempted to consider a greater degree of detail in the internal mechanism of cross-shore transport [i.e., velocity multiplied by concentration]. For example, those of Bowen (1980) and Bailard (1981) estimated cross-shore transport on the basis of velocity fluctuations alone, indicating that some function of velocity fluctuations is used as a model for concentration variations; those of Stive and Battjes (1984) and Steetzel (1990) calculated cross-shore transport from the product of time-averaged velocities  $\overline{u}(z)$ , and time-averaged concentrations  $\overline{c}(z)$ , by assuming that sediment transport due to the fluctuations of concentration and velocity is negligible. In the latter case,  $\overline{u(z,t) * c(z,t)}$  can be approximated by  $\overline{u}(z) * \overline{c}(z)$ . The aim of this paper is to study some fundamental aspects of cross-shore transport modelling in terms of sediment concentrations and velocities, with an emphasis on:

- The temporal behaviour of sediment concentration under waves and a current on an intra-wave scale.

- The relative importance of the fluctuations of sediment concentration and velocity in cross-shore transport.

A description of the experiments is given in Chapter 2. The experimental results are presented in Chapter 3. Conclusions of this study are given in Chapter 4.

## 2. EXPERIMENTAL SET-UP

The experiments for this study were performed in a small-scale wave flume in the Hydromechanics Laboratory of the Civil Engineering Department of the Delft University of Technology. Regular waves were generated in the flume. A current, directed against the wave propagation, was superimposed on the waves in order to 'simulate' a return flow as caused by wave breaking under field conditions. Measurements of local time-varying sediment concentration and velocity were obtained using an optical concentration meter (OPCON) and an electro-magnetic flow meter (EMS) at a number of elevations above the bottom. The experiments were conducted first over a fixed bed and then over a sandy bed. Five tests were carried out, three under waves and a current and two under waves only.

In the fixed bed tests, artificial triangular ripples were used over the horizontal flume bottom. The ripple height was 20 mm and the ripple length was 80 mm. The measuring cross-section was located in the middle of the flume. During the tests, sediment was fed constantly upstream of the measuring cross-section. The increase in the volume of sediment downstream of the measuring cross-section was measured during a test to check whether a 'steady' sediment transport condition was achieved. A 'steady' condition was required because it took a rather long time to perform the velocity and concentration measurements at many elevations over the water depth. It was found that the transport rate kept approximately constant.

In the sandy bed tests, the middle part of the flume was filled with sand. No sand feeding was applied. The bed level change during a test was measured. Consequently, the net sediment transport rate through the measuring cross-section was computed.

The main characteristics of the tests are listed in Table 1.

test	condition	$H$	$T$	$h$	$\bar{u}$	$\eta$	$\lambda$	$D_{50}$
A	w+c, fixed bed	0.065	1.76	0.25	-0.08	0.02	0.08	0.18
B	w+c, fixed bed	0.065	1.76	0.25	-0.08	0.02	0.16	0.20
C	w, fixed bed	0.065	1.76	0.25	0	0.02	0.08	0.20
D	w+c, sandy bed	0.065	1.76	0.25	-0.08	0.01	0.07	0.20
E	w, sandy bed	0.065	1.76	0.25	0	0.01	0.07	0.20

**Table 1** Characteristics of the tests

Where:

w+c : under waves with a current

w : under waves only

$H$  : wave height, [m]

$T$  : wave period, [s]

$h$  : water depth, [m]

$\eta$  : ripple height, [m]

$\lambda$  : ripple length, [m]

$\bar{u}$  : depth-averaged current velocity, [m/s]

$D_{50}$  : diameter, 50% by weight is finer, [mm]

### 3. RESULTS

#### 3.1 THEORETICAL CONSIDERATIONS

If a periodic water motion is assumed, the velocity and concentration at height  $z$  above the bed in a wave period can be described as:

$$u(t) = \bar{u} + u_1 \cos(\omega t - \alpha_1) + u_2 \cos(2\omega t - \alpha_2) + \dots \quad (2)$$

$$c(t) = \bar{c} + c_1 \cos(\omega t - \beta_1) + c_2 \cos(2\omega t - \beta_2) + \dots \quad (3)$$

Where:

$u_n, c_n$  : amplitudes of the harmonic components  
 $\alpha_n, \beta_n$  : phase angles of the harmonic components  
 $\omega$  : wave frequency, [s<sup>-1</sup>]

The sediment transport at height  $z$  is then given by:

$$\overline{u(t) * c(t)} = \bar{u} * \bar{c} + \frac{1}{2} u_1 c_1 \cos(\beta_1 - \alpha_1) + \frac{1}{2} u_2 c_2 \cos(\beta_2 - \alpha_2) + \dots \quad (4)$$

The total cross-shore transport can be found by integrating Eq.(4) over the water depth. As shown in Eq.(4), the transport rate can be decomposed into a number of components. The  $\bar{u} * \bar{c}$  term represents the contribution due to the mean flow. The sum of the other terms on the right hand side of Eq.(4) represents the contribution due to the fluctuations.

Under wave action, large  $u_1$  and  $c_2$  components can be expected. Due to wave asymmetry, the  $u_2$  component usually has a large magnitude. Till it can be proved that the  $c_1$  component is very small or that  $\beta_1 - \alpha_1$  is in the order of 90° [similar remarks can be made to the third and higher terms in the right hand side of Eq.(4)], one has to be very careful in neglecting the contribution due to the fluctuations.

## 3.2 TEST RESULTS

Some preliminary results were described by Chen and Van de Graaff (1991). A more extensive description is given below.

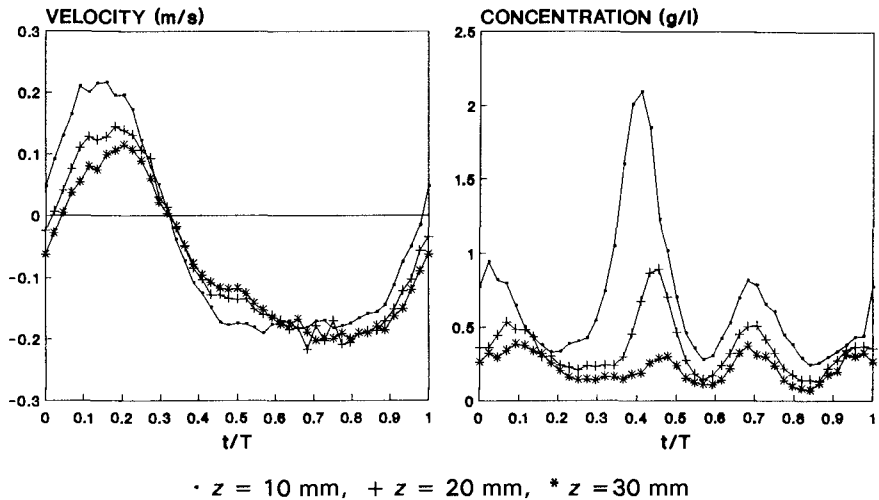
### Temporal Behaviour of Sediment Concentration

The measured time-varying sediment concentration and velocity data were first used to study the temporal behaviour of sediment concentration in a wave period. The test results showed that the concentration at a point varies strongly in time



at the wave cycle scale. The concentration fluctuations do not repeat in time from one wave period to another. This means that the concentration fluctuations consist of a periodic component and a random component. [However, the random components are of little importance to the net sediment transport, as will be further discussed below].

An example of the periodic fluctuations of sediment concentration, measured over the ripple crest in Test A, is given in Fig.1,



**Fig.1** Velocity and concentration in a wave period [measured over ripple crest, Test A]

As shown, near the bed, three concentration peaks can be found in a wave period. Two are related to the vertical ejections of the high concentration clouds departing from the ripple crest when the flow reverses. The other one is due to the wave orbital motion which carries the high concentration at the flow reversal horizontally from a ripple crest to the neighboring one. In the upper column of the water depth, the concentration fluctuations become insignificant.

The test results under other conditions showed that the time-variations of sediment concentration in a wave period depend very much on the local bed geometry and local flow conditions. A mathematical description is very difficult. This implies that the cross-shore transport modelling based on the separate

descriptions of velocity and concentration as a function of time cannot be accomplished at this stage. In the following discussion, only the product of velocity and concentration [i.e., sediment transport rate] will be considered. Emphasis will be placed on the relative roles played by different forcing agents in sediment transport, especially the mean flow versus the fluctuations.

## Sediment Transport Due to Mean Flow and Fluctuations

**Role of the random components:** The measured time-varying sediment concentration and velocity data were decomposed into period components and random components. It was found from the results that the random components, though relatively large compared to the periodic fluctuations, do not contribute much to the sediment transport.

**Role of the higher harmonic components:** With the periodic fluctuating components, harmonic components were calculated with Eq.(2) and Eq.(3). Consequently, the transport due to each harmonic component was calculated with Eq.(4). The calculation results showed that the harmonic components with a frequency higher than  $2\omega$  together with the random components contribute less than 5% of the total transport.

**Role of the first and second harmonic components:** The transport contributions due to these components, as indicated in Eq.(4), depend on the amplitudes of the harmonic components the phase differences. The test results showed that the  $c_1$  and  $c_2$  components at a level are not small compared to the  $\bar{c}$  component at the level. Since  $u_1$  and  $u_2$  are larger than  $\bar{u}$ , the magnitude of  $\frac{1}{2}u_1c_1$  and  $\frac{1}{2}u_2c_2$  is not negligible compared to with  $\bar{u}\bar{c}$  [see Fig.2]. This implies that the phase differences may play an important role in the resulting sediment transport.

It was found that significant phase lags occur between the concentration and velocity fluctuations. The distributions of the phase lag over the water depth exhibit, in some cases, fairly distinct trends. The magnitude of  $\beta_1 - \alpha_1$  decreases with height above the bottom. Under waves with a relatively strong current, the  $\beta_1 - \alpha_1$  values are approximately  $90^\circ$  close to the bottom, suggesting that the transport due to the  $u_1$  component close to the bottom is small. Under waves alone, the  $\beta_1 - \alpha_1$  values close to the bottom increase [order of magnitude over

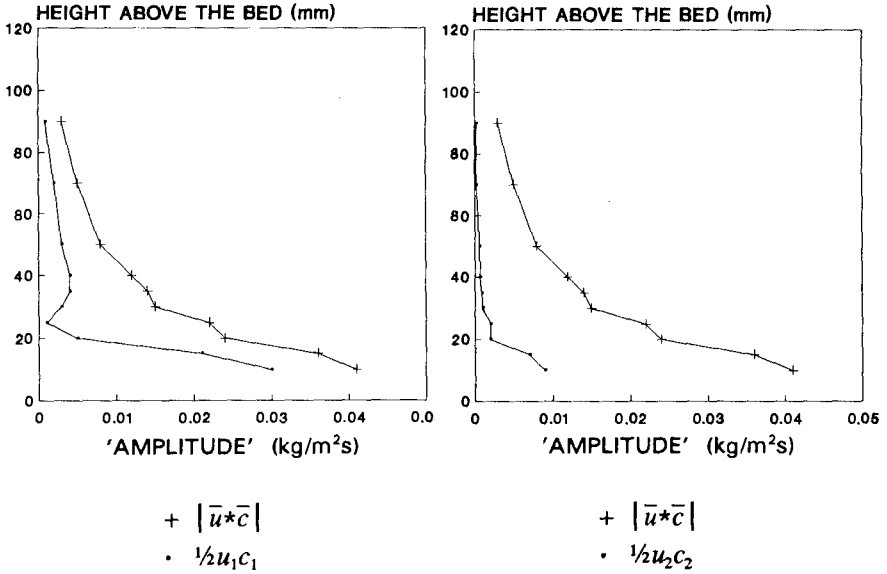
100°], resulting in an increase in the transport due to the  $u_1$  component, see Fig.3.

Taking both the contributions of the  $u_1$  and  $u_2$  components into account, the sediment transport due to the fluctuations was determined. The test results showed that the transport due to the fluctuations relative to that due to the mean flow may vary over the water depth, both in magnitude and direction. In general, both transports at a level are in the same order. Under the specific wave conditions for this study, the transport due to the fluctuations and due to the mean are in the same direction close to the bottom and in opposite direction in the upper column of the water depth. Therefore, in some cases, the depth-integrated transport due to the fluctuations may be negligible compared to the transport due to the mean flow, even though both transports may be well-matched in magnitude at a specific level above the bed.

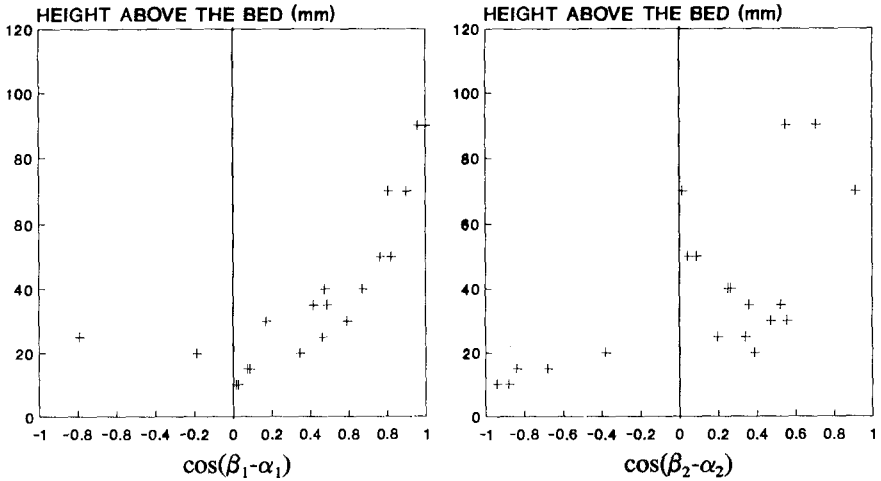
**Role of the mean flow:** It appeared from the test results that an increase in the magnitude of the current velocity may alter the relative contributions due to the fluctuations and due to the mean flow [see also Fig.4 and Fig.5, a negative value means that the transport is opposite to the direction of the mean flow]. If the mean flow is relatively weak, both contributions are of the same order of magnitude. If the mean flow becomes strong, the transport by the mean flow may play a dominant role, in that case, the transport due to the fluctuations may be neglected.

#### 4. CONCLUSIONS

The test results indicate that, in general, the contribution due to the fluctuations of velocity and concentration should be considered in cross-shore transport calculations. However, under some specific conditions - for example, in a surf zone where the mean flow may be strong due to wave breaking - the contribution of the fluctuations may be neglected as a first order of approximation.



**Fig.2** Vertical distributions of  $\frac{1}{2}u_1c_1$ ,  $\frac{1}{2}u_2c_2$  and  $\bar{u}^*\bar{c}$  over the water depth [measured over ripple crest in Test A]



**Fig.3** Vertical distributions of  $\cos(\beta_1 - \alpha_1)$  and  $\cos(\beta_2 - \alpha_2)$  over the water depth [measured over ripple crest in Test A]

test	positions	$q(\bar{u})$	$q(\bar{u})$	$q(\bar{u})+q(\bar{u})$	$q$
A	C&T	1.21	0.03	1.24	1.22
B	C	0.84	0.36	0.48	0.40
	T	0.46	0.05	0.51	
C	C	0.31	0.15	0.46	
D	C&T	0.42	0.12	0.54	0.31
E	C&T	0.08	0.07	0.15	0.13

**Table 2** Sediment transport rates in absolute values

Where:

$q(\bar{u})$  : transport due to the mean flow, [g/ms]

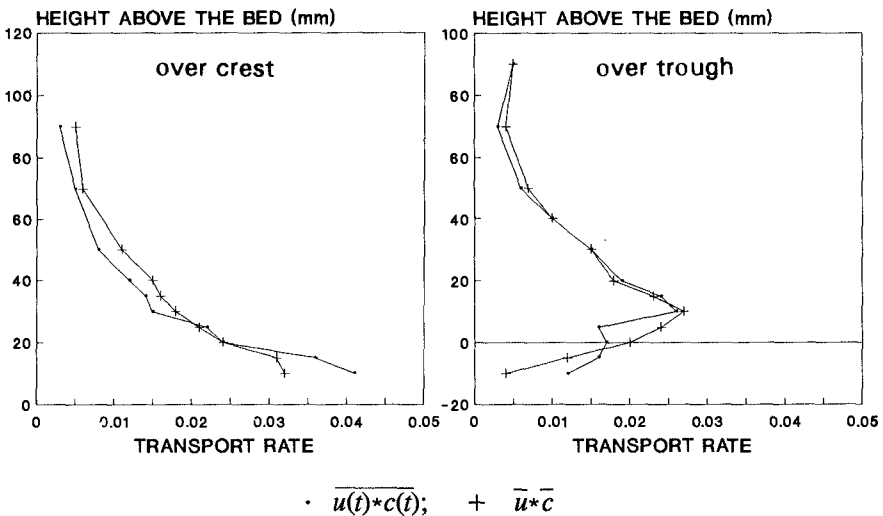
$q(\bar{u})$  : transport due to the fluctuations, [g/ms]

$q$  : transport rate obtained from the mass conservation technique, [g/ms]

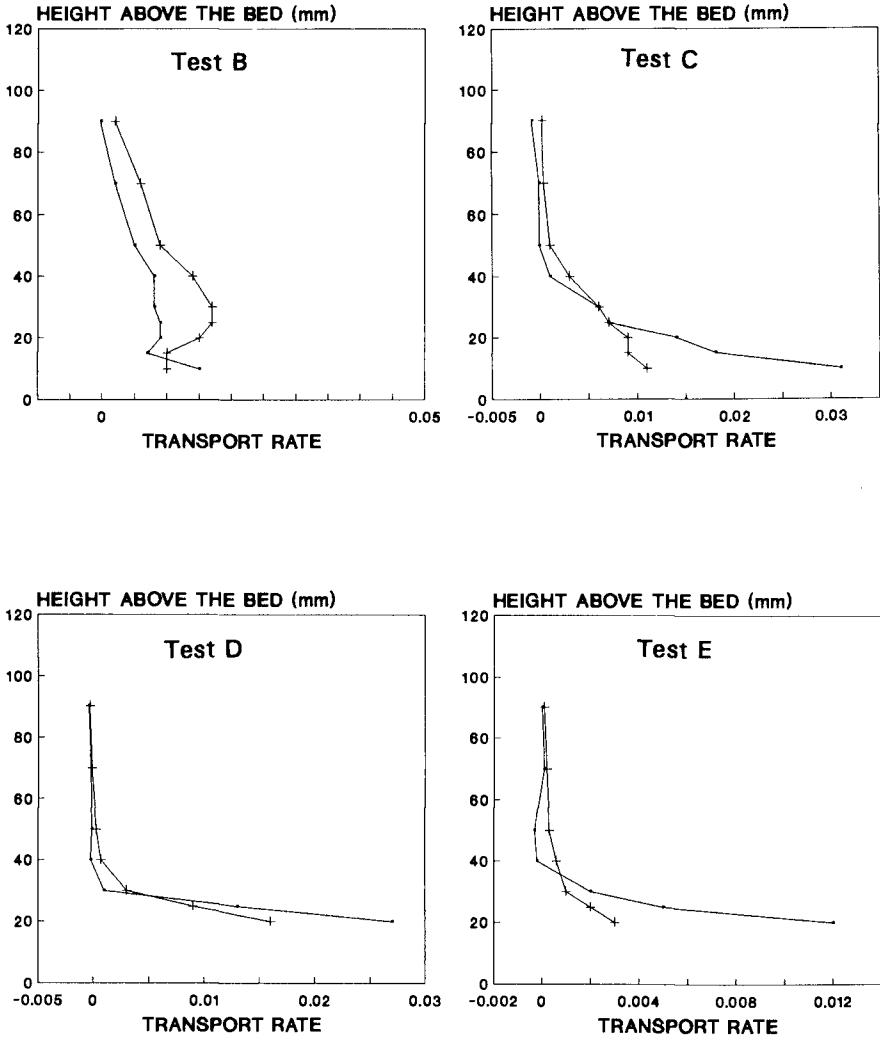
C : measurement over ripple crest

T : measurement over ripple trough

C&T : average of measurements over crest and over trough



**Fig.4** Vertical distributions of transport rate, in kg/m<sup>2</sup>s, results of Test A



$$\cdot \overline{u(t) * c(t)}; \quad + \quad \overline{u} * \overline{c}$$

**Fig.5** Vertical distributions of transport rate at ripple crest, in kg/m<sup>2</sup>s, results of Tests B, C, D and E

**REFERENCES**

- Bailard, J.A. (1981).  
An Energetic Total Load Sediment Transport Model for a Plane Sloping Beach. *J. of Geophy. Res.*, Vol.86, No.c11.
- Bowen, A.J. (1980).  
Simple Models of Nearshore Sedimentation; Beach Profiles and Longshore Bars. *The Coastline of Canada*, S.B. MacCann, ed., Geological Survey of Canada, Paper 80-10.
- Chen, Z. and J. van de Graaff (1991)  
Modelling of Cross-Shore Transport. *Proc. Coastal Sediments '91*, ASCE, Seattle.
- Dean, R.G. (1982).  
*Models for Beach Profile Response*. Technical Report, No.30, University of Delaware, Newark.
- Steezel, H.J. (1990).  
Cross-shore Transport During Storm Surges. *Proc. 22nd Int. Conf. on Coastal Engineering*, ASCE, Delft.
- Stive, M.J.F. and J.A. Battjes (1984).  
A Model for Offshore Sediment Transport. *Proc. 19th Int. Conf. on Coastal Engineering*, ASCE, Houston.
- Swart, D.H. (1974).  
*Offshore Sediment Transport and Equilibrium Beach Profiles*. Ph. D. Thesis, Delft University of Technology.

## CHAPTER 151

### EVOLUTION OF A BEACH WITH AND WITHOUT A SUBMERGED BREAKWATER: EXPERIMENTAL INVESTIGATION

G. Chiaia, L. Damiani, A. Petrillo\*

#### Abstract

In the present report experimental results about the efficiency of a submerged structure are presented. The experiment, carried out with random waves, covered about 2500 hours until equilibrium profile was reached. The most significant results are the good behaviour of the tested breakwater as a sand holding structure and its slowing effect produced on the shoreline backing, whereas the final position of the shoreline was nearly the same with and without breakwater.

#### 1. INTRODUCTION

In coastal areas where tide excursions are limited, submerged breakwaters can be used to protect the beaches from the strong eroding wave action. This choice mostly depends on the better water exchange between the inner and outer zones of the submerged breakwater, which reduces the waterlogging area. Moreover it doesn't disfigure the seascape and allows to better enjoying the beach for all touristic activities, unlike emerged structures. Submerged breakwaters are also used to protect beach nourishment works. Many Italian researchers are involved in the study of this kind of structures (Aminti et al., 1983; Lamberti et al., 1981; Lamberti et al., 1984). This paper presents an experimental investigation about the cross-shore evolution of an unprotected beach subjected to random waves, as compared to the evolution of the same beach, protected by a submerged breakwater.

Trials showed significant results about the long-term evolution of a beach under the action of different wave attacks, and about the behaviour of each attack.

---

\* Hydraulics and Hydraulic Constructions  
Polytechnic of Bari - Via E. Orabona, 5 - 70125 BARI (ITALY)



## 2. EXPERIMENTAL SET-UP

Tests were performed in the wave channel of the Hydraulics and Hydraulic Constructions Institute of Bari Polytechnic. The channel is about 45 m long, 1 m wide and 1.2 m high (fig. 1). It was longitudinally divided into two equal parts by a thin glass wall, in order to simulate an unprotected beach on the first half of the channel and a protected beach with a submerged breakwater on the other half. Eighty gauging cross-sections, numbered from the shoreline to the wave generator paddle are located along the channel. The wave maker consists of a flat paddle which receives a rotatory-translational motion through a kinematic mechanism, able to reproduce any kind of waves.

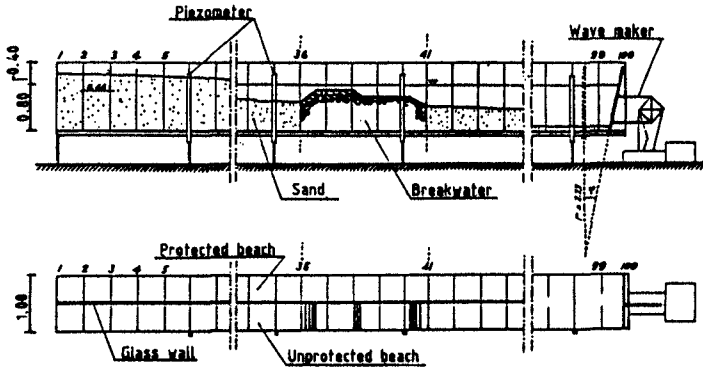


Figure 1. Experimental channel.

A beach of the Middle Adriatic coast was reproduced in the channel, in Froude Number similitude with undistorted 1:10 scale. The channel bottom is covered with a sandy layer of a pretty uniform size with  $d_{50} = 0.15 \text{ mm}$ , and fall velocity  $w = 0.018 \text{ ms}^{-1}$ . The mean water level in the channel was kept constant during the tests and the depth near the paddle was equal to 0.80 m.

Five wave attacks were chosen to simulate the sea wave conditions; they were characterized by JONSWAP energy density spectra with  $\gamma = 3.3$  and  $w = 0.07$  for  $f < f_p$  and  $w = 0.09$  for  $f > f_p$ . The wave attack characteristics, near the paddle, and their duration are reported in Table 1.

In the trials the attacks were grouped in a six-storm cycle with sequence 1-2-3-1-4-5 to simulate different energy sea conditions. The duration of the two attacks number 1 of the cycle was assumed equal to half the time reported in Table 1. The experiment covered 17 cycles over about 2400 hours, when the equilibrium profile was reached in both sides of the channel.

<i>ATTACK</i>	$m_o$ [ $m * 10^{-4}$ ]	$f_p$ [ $s^{-1}$ ]	$t$ [ $h$ ]
1	3.0	0.63	88.0
2	15.5	0.47	12.5
3	6.0	0.47	32.2
4	30.5	0.38	5.5
5	15.0	0.38	11.2

Table 1. Wave attack characteristics and their duration.

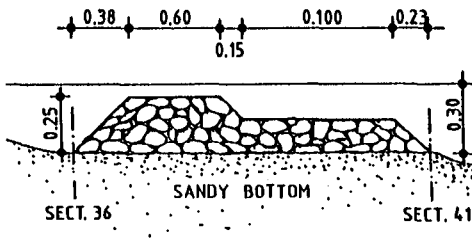


Figure 2. Tested submerged breakwater.

On the left side of the channel the submerged breakwater was located between sections 36 and 41; this position, with the characteristics of the selected wave attacks, is just outside the breaking zone and only the highest waves of attack n. 4 break offshore the structure. The breakwater face slope is about 1/1.5 and the submergency ( $h/d$ ) is 0.17 (fig. 2).

The first results of the here presented trials were already discussed in previous papers (Lamberti et al., 1985; Chiaia et al., 1990).

### 3. PROFILE EVOLUTION IN THE LONG PERIOD

The starting profile (fig. 3) in the experiment was far from equilibrium so as to simulate an artificial filling action.

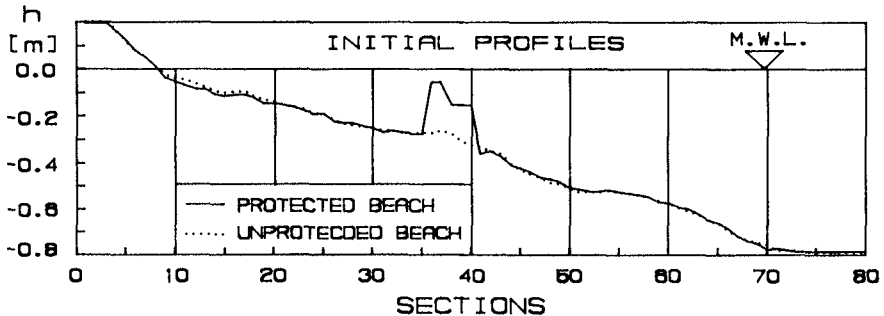


Figure 3. Comparison between protected and unprotected beach profiles.

Basically three constant slope zones may be observed: the first from section 70 to section 40 with  $1.8^\circ$  slope, the second between sections 40 and 13 with  $1.08^\circ$  slope and the third from section 13 to the shoreline with  $2.33^\circ$  slope. The zone close to the shoreline was concave with a maximum slope of about  $5^\circ$ . The initial profile, shown in figure 3, was obtained after the action of a low energy level wave attack, in order to simulate a sand compaction closer to reality.

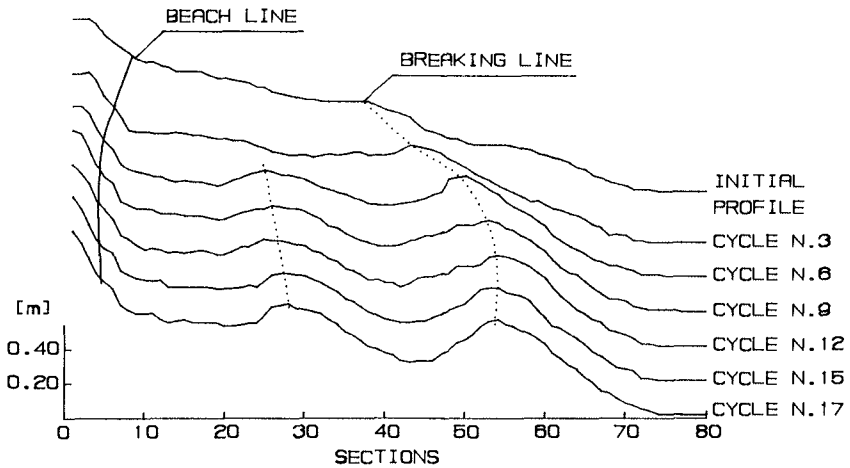


Figure 4. Unprotected beach evolution.

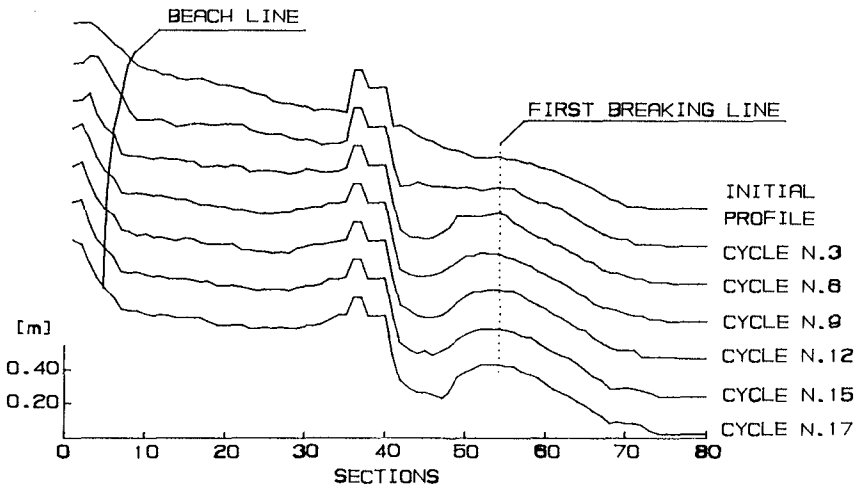


Figure 5. Protected beach evolution.

The global evolution both in the protected and unprotected beach are reported in figures 4 and 5 in which the backing of shoreline and the formation and migration of bars are clearly shown in both configurations.

The efficiency of the tested submerged breakwater was firstly studied by comparing the profiles observed both on the unprotected and protected beach at the end of each wave attack. The beach profiles obtained at the end of some cycles are shown in next figures.

The behaviour of the two beach profiles starts becoming substantially different at the end of the first storm cycle (fig. 6). A notable offshore transport is observed in the unprotected beach resulting in a sharp backing of the shoreline and the formation of a bar.

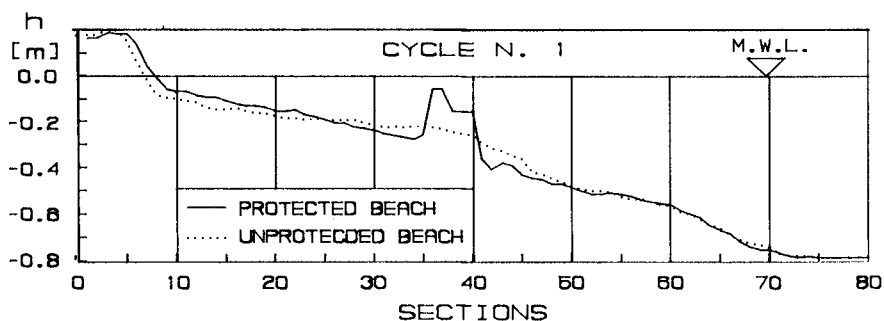


Figure 6. Comparison between protected and unprotected beach profiles.

Sand transport is far less marked in the protected beach, although its characteristics are the same as in the unprotected one (shoreline backing and offshore transport). However, the action of the submerged breakwater in reducing the offshore transport is noticeable since the beginning.

Such a behaviour is clearly shown in fig. 7, in which the profiles at the end of the 4th cycle are reported.

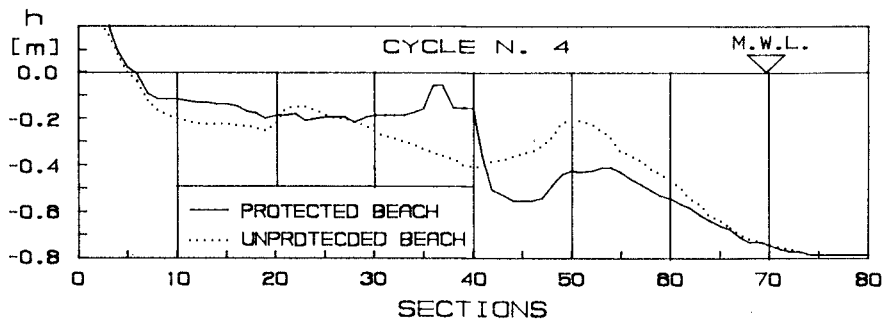


Figure 7. Comparison between protected and unprotected beach profiles.

The surf-zone in the protected beach is, on the average, less deep if compared to the unprotected one and a deposit area forms just at the back of the breakwater which increases until equilibrium conditions are reached. This behaviour confirms the efficiency of the breakwater in reducing the offshore transport.

Figures 6 and 7 show an erosive trough at the toe of the structure which tends to become deeper and to stabilize when the equilibrium profile is reached. Most of the eroded material is deposited offshore forming a bar (sketched in figs. 6 and 7), and a part of it is found out, as indicated later on, in the surf-zone. This does confirm that, despite its selectivity, the breakwater allows onshore transport, under given conditions (Aminti, 1986).

For the unprotected beach, figures 6 and 7 show the formation of two bars; the offshore bar moves in deepwater direction till it reaches a stable position, thus defining the surf-zone width. As the surf-zone width becomes stable, the shoreline reaches a condition close to equilibrium, at about the 7th cycle, as shown in figure 4.

After the 7th cycle of attacks, in the protected beach a sharp deepening of the erosion trough is noticed (fig. 8), as observed in the previous cycles together with the formation of a well-defined bar which causes the breaking of the highest waves and thus a further erosion of the trough until equilibrium is reached.

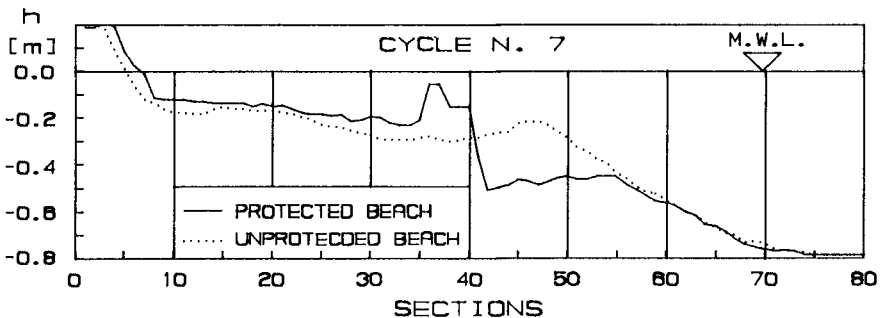


Figure 8. Comparison between protected and unprotected beach profiles.

Starting erosion at the offshore toe of the structure can be mostly related to the back currents coming from the onshore zone. Indeed at the beginning of the experiments only few waves broke before reaching the structure. Therefore, wave breaking cannot be the major active mechanism in the trough formation.

Into the surf-zone of the protected beach a substantial flattening of the profile is observed, with a sharp backing of the shoreline tending to the same position as in the unprotected beach.

In the subsequent cycles (fig. 9) the re-alignment of the shoreline between the unprotected and protected beach, as well as the deepening of the erosion trough and the bar formation in the protected beach are more pronounced until a substantial equilibrium condition is reached.

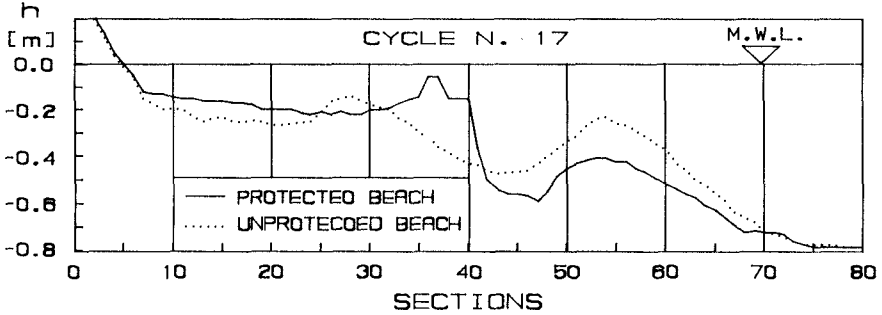


Figure 9. Comparison between protected and unprotected beach profiles.

It was observed that the equilibrium profile of the unprotected beach in the onshore zone before the bars, may be interpreted by Dean's equilibrium profile (Dean, 1977):

$$h = a x^b \tag{1}$$

where  $h$  is the bottom depth in the section considered,  $x$  is the distance from this section to the shoreline and  $a$  is a parameter which, as shown experimentally, mainly depends on the sand beach particle-size (Moore, 1982). Assuming a constant energy dissipation per unit volume in the whole surf-zone, Dean obtained the law (1) theoretically with  $b = 2/3$ . In a beach with a particle-size characterized by  $d_{50} = 0.15\text{mm}$ , the same researcher (Kriebel et al., 1986) found an equilibrium profile which is well interpolated by the law  $h = 0.075 x^{2/3}$ .

Based on many laboratory and field experimental data, relating to beaches of different sand particle-size, Vellinga (1986) found that the law  $h = 0.35 w^{0.44} x^{0.78}$ , where  $w$  is the fall velocity, does well interpolate the onshore equilibrium profile for a wide range of particle-sizes. On the other hand, the same author disproves the constant dissipation assumption made by Dean, stating that coefficient  $b$  can have different values, especially when the sea state is variable and the profile is bar-shaped. Indeed, in the presence of bars, the onshore profile follows the experimental law (1) only in the proximity of the shoreline whereas, approaching the bar, depths tend to be first constant and then to decrease.

Our trials showed that till section 20 the profile is well interpolated by the law  $h = 0.125 x^{0.44}$  which is quite different from the one found by the previous authors on a beach with the same sand mean particle-size.

In figure 10 the unprotected beach profiles, observed in the last storm cycle, and the above indicated interpolation laws are reported; it may be observed that the equilibrium profile shows a greater erosion in the onshore area, near the shoreline.

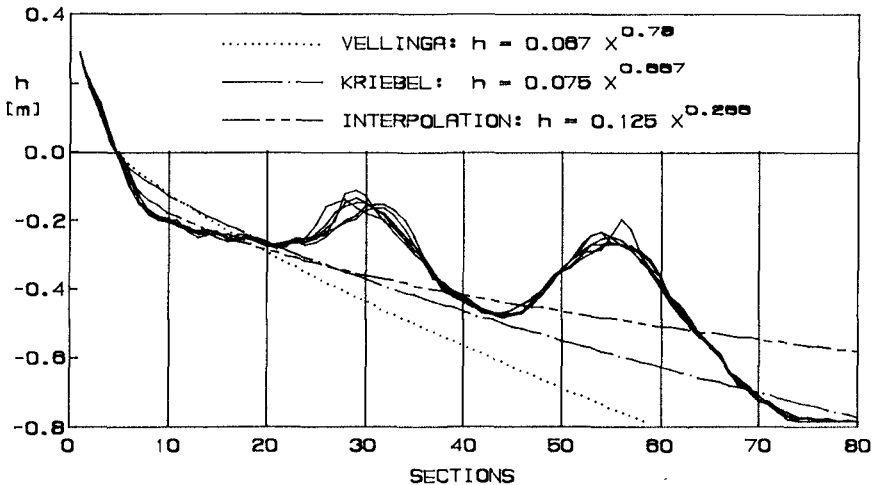


Figure 10. Profiles measured after each wave attack of the last cycle and theoretical and interpolation laws for equilibrium profile.

The behaviour observed in our experimental results is in accordance with those found by other authors (Swart, 1974; Larson 1988), who tested bar-shaped beach profiles. In accordance with Vellinga, it may be stated that this behaviour, which deserves further attention, is to be attributed to the change in the dissipation mechanism in the surf-zone in the presence of a bar on the profile.

In order to evaluate the efficiency of the submerged breakwater under study, for all beach zones, some global parameters of the profile were introduced which enable assessing structure effects on emerged and submerged beaches.

#### 4. ANALYSIS OF BREAKWATER EFFICIENCY

##### 4.1 Shoreline Zone

The parameters selected to describe this area are the swash-zone slope and the shoreline position, both determined after each wave attack. As to the slope, the mean value observed in the first cycle of attacks (about  $8.5^\circ$ ) kept stable with some fluctuations ( $5^\circ \div 14^\circ$ ), due to the different action of single wave attacks; at the end of the trials, however, slope fluctuations in the swash-zone are reduced.

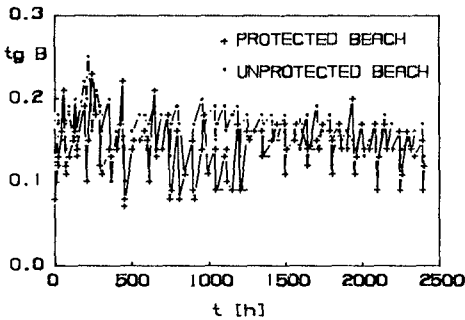


Figure 11. Evolution of swash-zones slope.

Figure 11 shows that, regardless of the type of beach profile considered, the beach slope in the swash-zone is basically affected by the characteristics of the wave attack it is subject to; it is indeed poorly influenced by transformations of waves in their transfer from offshore to the shoreline, although in the case of unprotected beach, slope values are generally a little higher and fluctuations are lower.

Experiments did confirm that the beach slope is inversely proportional to the wave attack energy, and its variations are very rapid; in fact, the slope observed after each storm is reached few minutes after the action of the attack.

The shoreline, at the end of trials, tends to reach more or less the same position both in the presence and in the absence of the breakwater (Fig. 12). Therefore, when the breakwater is used to reduce erosion of the emerged beach, it has no effectiveness in the long period, whereas it proves to be useful in slowing down its backing.

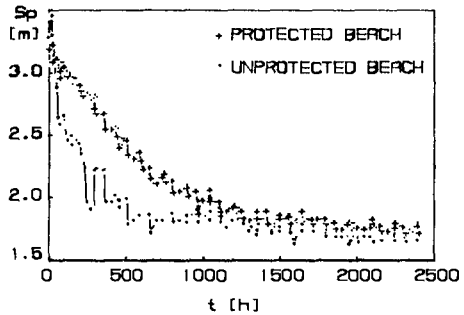


Figure 12. Evolution of shorelines position.

In fact, while in the unprotected beach equilibrium is achieved after about 600 hours, the protected beach needs a double time. The analysis of the action of each wave attack on the shoreline shows that attack 1 is reconstructive, attacks n. 2 and n. 4 are destructive whereas attacks n. 3 and n. 5 are characterized by an intermediate behaviour. These results were observed in both sides of the channel.

#### 4.2 Surf-Zone

Sand transport from the surf-zone to the outer zone of the breakwater was evaluated using the  $B_0$  parameter, i. e. the water volume contained between the breakwater and the first section of the channel, complementary to the sand volume.



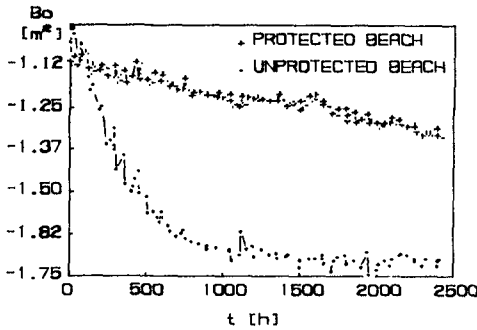


Figure 13. Evolution of water volume contained in the first 40 sections of the channel.

Moreover, under equilibrium condition,  $B_0$  is decreasing in the protected beach, whereas in the unprotected beach, despite some fluctuations,  $B_0$  is constant.

This means that, in the unprotected beach, once the two bars have formed, sand displacements are moderate, because of the action of wave attacks which compensate each other within the cycle.

On the other hand, for the protected beach, although an equilibrium condition is reached in the emerged beach (see Sp and tg  $\beta$ ), a further evolution of the profile is observed in the onshore area. Indeed, due to the sand accumulation at the back of the breakwater, return currents cause an off-shore transport which goes on slowly even when the profile is substantially under equilibrium.

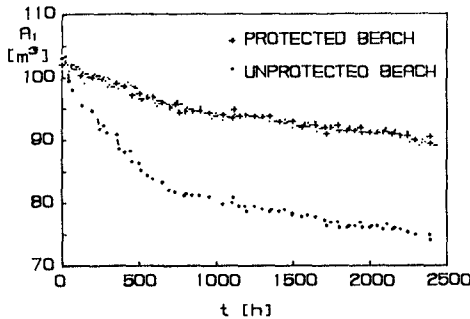


Figure 14. Evolution of integrals of the moments of depths respect to channel central section.

The behaviour of parameter  $A_1$  (integral of the moments of depths observed in each section with respect to the channel central section 40) (fig. 14) shows offshore sand displacement and does confirm the above interpretation of its evolution. Really it can be observed that also in the unprotected beach,  $A_1$  goes on decreasing until the end of tests, denoting a sand displacement inside the

The temporal evolution of  $B_0$ , evaluated assuming a negative depth, is reported in figure 13.

For the unprotected beach,  $B_0$  decreases sharply thus indicating an intensive sand flux offshore, whereas in the presence of the breakwater, sand transport is slower and less marked. The breakwater is clearly shown to be an effective holding structure.

During the trials it was observed that the breakwater under study acts as a filter also to the nourishment action of summer waves, but it allows some onshore transport by the highest waves which suspend the material offshore the breakwater, particularly at the start of experiment.

surf-zone.

An interesting indication is provided by parameter  $B_1$  (integral of moments of depths in the first 40 sections of the channel with respect to section 20). Fig. 15 shows that, for the unprotected beach it first decreases sharply and then it shows a fluctuating evolution (caused by the onshore bar displacements), whereas for the protected beach it decreases and, under equilibrium, tends to a constant value.

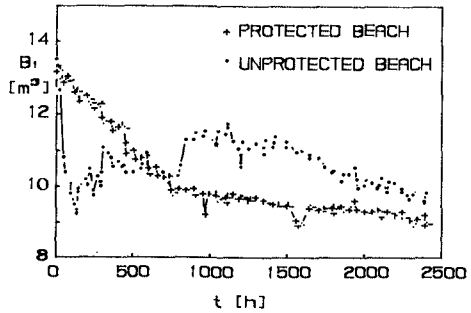


Figure 15. Evolution of integral of the moments of the first 40 section depths with respect to section 20.

This is due to the presence of a well formed deposit area, close to the breakwater, and to the achievement of a stable and flat configuration of the beach profile in the surf-zone.

### 4.3 Offshore Zone

By offshore zone we mean here the zone outside the breakwater which is not necessarily the outer zone of breaking waves; in fact, as previously indicated, under equilibrium conditions, both protected and unprotected beach profiles show a bar around section 53 which causes the breaking of the highest waves, thus dividing the surf-zone from the offshore zone.

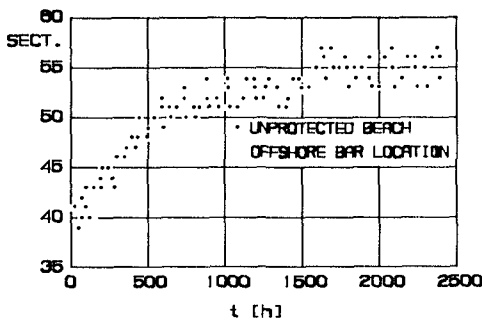


Figure 16. Evolution of offshore bar location in unprotected beach.

The profile of the zone under consideration is indeed characterized by the presence of the bar and by an erosion trough at the toe of the breakwater.

The first difference observed between the protected and unprotected beach concerns the bar position.

Figures 4 and 5 show that, for the unprotected beach, the offshore bar does form initially around section 40 and then migrates offshore and gives a stable length to the surf-zone; on the other hand, the bar on the protected beach does start forming initially in a position close to the final one, without any notable displacement.

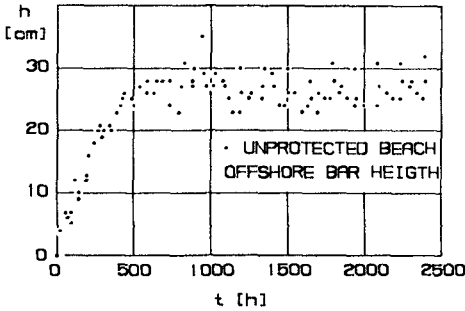


Figure 17. Evolution of offshore bar depth in unprotected beach.

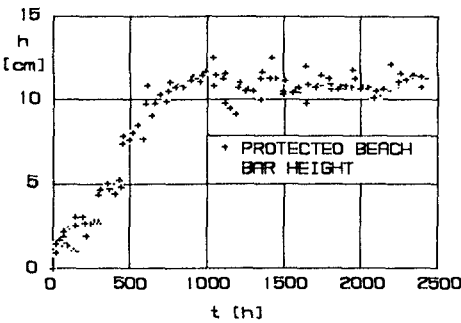


Figure 18. Evolution of bar depth in protected beach.

Fig. 19 shows a good correlation between the pit deepening and the depth reduction on the bar.

This shows that one of the active mechanisms for the trough formation is the presence of the vortex (site of dissipation) produced by the breaking occurring on the bar. This mechanism is the same acting on the unprotected beach.

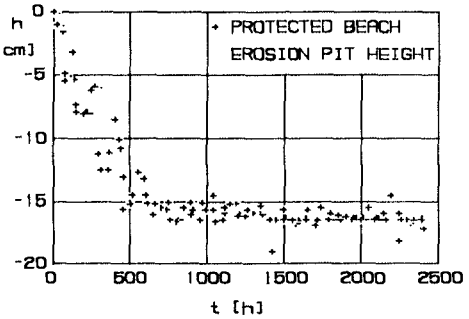


Figure 19. Evolution of depth of eroding trough at the offshore toe of the structure.

Figure 16 shows the offshore bar displacement on the unprotected beach along its evolution, whereas figure 17 reports the depth on the bar, taken as the difference between the initial and actual depth. The end position of the bar is comparable in both sides of the channel, while depth is higher in the case of the protected beach (Fig. 18).

This is due to the fact that the bar in the unprotected beach is formed with all the material eroded in the surf zone, while in the protected beach sand mostly comes from the trough.

Another parameter used to describe the offshore region is, as already mentioned, the erosion trough at the toe of the breakwater, whose genesis needs further studies.

In addition to the previously described mechanism, a contribution to the trough formation in the initial stage of trials is given by return currents as above mentioned.

However, it should be noted that, regardless of the causes which produce

erosion at the toe of the breakwater, the pit depth reaches a maximum equilibrium value so that, to prevent any failure in the foundation, either the bearing surface should go below that depth, or the breakwater should be displaced offshore.

## 5. CONCLUSIONS

Laboratory experimental results enabled assessing the efficiency of the tested submerged breakwater relating to the cross-shore transport action. Breakwater proved to be an excellent holding tool for the sand contained in the surf-zone, although it does not seem selective at all to offshore transport.

On the other hand, the protective action from erosion in the swash-zone is not equally effective; the presence of the breakwater did not reduce the backing of the shoreline which reached almost the same position both in protected and unprotected beach profiles. Nevertheless, it should be pointed out that the breakwater caused a notable slowing down of the wave eroding action on the emerged beach, in fact the time taken for equilibrium to be reached in the protected beach is double as compared to the unprotected one.

In the outer zone of breakwater, the configuration is similar both in the protected and unprotected beach (bar-trough conformation). Some interesting considerations can be drawn from the results relating to the erosion trough. Indeed, although the study on pit formation needs further research, it has been observed that it reaches a constant depth at equilibrium. Such a result can be helpfully used for design, in that the bearing surface of the structure should go below that level to prevent any subsidence which could jeopardize the breakwater stability.

Experimental results need being further processed so as to provide indications on the action of each wave attack and to understand the hydraulic behaviour of the breakwater through the study of the reflection, transmission and dissipation coefficients and the wave set-up in protected and unprotected beach profiles.

## References

- Aminti P., A. Lamberti, G. Libratoro (1983): Experimental Studies on Submerged Barriers as Shore Protection Structure. Int. Conf. on Coastal and Port Eng. in Developing Countries, Colombo (SRILANKA).

- Aminti P. (1986): Indagine Sperimentale sulla Protezione delle Spiagge con Ripascimenti Artificiali.  
Atti del XX Convegno di Idraulica e Costruzioni Idrauliche, Padova (ITALY).
- Chiaia G., L. Damiani, A. Petrillo (1990): Trasformazioni di un Profilo di Spiaggia sottile Sotto l'Azione di un Ciclo di Attacchi Ondosi Casuali di Lunga Durata.  
Atti del XXII Convegno di Idraulica e Costruzioni Idrauliche, Cosenza (ITALY).
- Dean R.G. (1977): Equilibrium Beach Profiles: US Atlantic and Gulf Coasts.  
Univ. of Delaware, Dep. of Civil Eng. Ocean, Eng. Rep. n.12.
- Kriebel D.L., W.R. Dally, R.C. Dean (1986): Undistorted Froude Model for Surf-Zone Sediment Transport.  
Proc. Coastal Eng..
- Lamberti A., U. Tomasicchio (1981): Le Barriere Sommerse, Possibili Strutture a Difesa della Costa.  
Porti Mare Territorio, Anno III n.1.
- Lamberti A., S. Stura, U. Tomasicchio (1984): Il Disegno delle Strutture di Protezione delle Coste.  
CSPP n.18.
- Lamberti A., A. Petrillo, M. Ranieri (1985): A Comparative Analysis of Some Types of Submerged Barriers as Beach Defence Structure.  
Proc. of 21st IAHR Congr., Melbourne (Australia).
- Larson M. (1988): Quantification of beach profile change.  
Lund Sweden.
- Moore B.D. (1982): Beach Profiles Evolution in Response to Changes in Water Level and Wave Height.  
Univ. of Delaware, Newark, DE.
- Swart D.H. (1974): Offshore Sediment Transport and Equilibrium beach Profiles.  
Delft Hydraulics Lab., Comm. n.131.
- Vellinga P. (1986): Beach and Dune Erosion during Storm Surges.  
Delft Hydraulics Lab., Comm. n.372.

## CHAPTER 152

# Equilibrium Beach Profiles with Random Seas

Christopher G. Creed<sup>1</sup>, Robert A. Dalrymple\*  
David L. Kriebel<sup>2</sup>, James M. Kaihatu\*

### Abstract

Three quantitative equilibrium beach profiles models are presented for random wave fields. Two models follow the work of Larson where improvements to the spilling breaker assumption are made with spectral estimations of wave breaking. The third model is established by imposing a no-net sediment transport condition on Bailard's (1982) cross-shore sediment transport formulation. Modelling the flow field as in Roelvink and Stive (1989), an equilibrium solution is achieved which includes a longshore bar.

### Introduction

It has been observed that the beach profile shape is a function of the characteristics of the incident wave field. Dean (1977) examined a number of U.S. East and Gulf Coast beach profiles and found that the majority of the profiles could be described by the following simple equation:

$$h = Ax^m \quad (1)$$

where  $h(x)$  is the water depth and  $x$  is the offshore distance perpendicular to the shoreline. The value of  $m$  which best fit all of the data was 0.667, though  $m$  ranged between 0.1 and 1.4. Dean developed a theoretical justification for a value of  $m$  of  $2/3$ , based on the concept that the rate of energy dissipation per unit volume of fluid,  $\mathcal{D}_*$ , would be constant across the equilibrium beach profile.

$$\frac{d\mathcal{F}}{dx} = -\epsilon_b = -h\mathcal{D}_* \quad (2)$$

---

<sup>1</sup>Center for Applied Coastal Research, Department of Civil Engineering, University of Delaware, Newark, DE 19716

<sup>2</sup>Naval Systems Engineering Department, United States Naval Academy, Annapolis, MD 21402

where  $\mathcal{F}$  is the energy flux, defined as the energy per unit area times the group velocity of the waves,  $C_g (= \sqrt{gh}$  in shallow water), and  $\epsilon_b$  is the dissipation per unit surface area:

$$\mathcal{F} = \frac{1}{8} \rho g H^2 \sqrt{gh} \quad (3)$$

Assuming a spilling breaker ( $H = \kappa h$ , where  $\kappa \sim O(1)$ ), and substituting into Eqn. (2) results in an equation for  $h$ :

$$h(x) = Ax^{2/3} \quad (4)$$

This model, with its concave upwards shape, has proved to be useful in a number of coastal applications (Dean, 1991).

In this paper, several models for equilibrium profiles will be developed using different representations of the wave field. The first, developed by Larson (1988) for monochromatic waves, is extended to a random wave field. The second and third models are based on random breaking models by Thornton and Guza (1983), which were developed from field data taken from California beaches.

**Larson's (1988) Model**—Larson (1988) and Larson and Kraus (1989) replaced Dean's spilling breaker assumption with the breaking model of Dally *et al.* (1985):

$$\frac{d\mathcal{F}}{dx} = -\frac{K}{h} (\mathcal{F} - \mathcal{F}_s) \quad (5)$$

where  $\mathcal{F} = EC_g$ .  $K$  is an empirical constant equal to 0.17, and  $\mathcal{F}_s$  is the stable energy flux the wave field is trying to obtain.  $\mathcal{F}$  is based on a stable breaking wave height,  $H_s = \gamma h$ , where  $\gamma$  is a constant empirically determined to be 0.4. Equating this energy flux relationship to Dean's constant energy dissipation per unit volume yields the following equation for  $H$ :

$$H = \sqrt{\frac{8h^2 D_*}{\rho g \sqrt{gh} K} + \gamma^2 h^2} \quad (6)$$

which provides the wave height across the surf zone as a function of the profile depth,  $h$ . Substituting this into the energy flux equation, (2), leads to

$$2\frac{h}{K} + \frac{5}{24} \rho g^{3/2} \left( \frac{\gamma^2 h^{3/2}}{D_*} \right) = x \quad (7)$$

This equation, which relates the equilibrium water depth to the distance offshore, is best solved for the distance  $x$  in terms of  $h$ . Note the inclusion of a linear term which removes the infinite slope at the shoreline that occurs in Dean's model.

**Application of Random Wave Breaking**—To apply random waves to Larson's model, we first determine the breaker line location via the breaking depth,  $h_*$ .

At this depth, we assume that the breaking index is the correct predictor of breaking wave height.

$$H_b = \kappa h_* = \sqrt{\frac{8h_*^2 D_*}{\rho g \sqrt{g h_*} K} + \gamma^2 h_*^2} \quad (8)$$

from Eqn. 6. Solving for  $h_*$ , we have

$$h_* = \left( \frac{8D_*}{\rho g^{3/2} K (\kappa^2 - \gamma^2)} \right)^2 = \left( \frac{D_*}{\beta} \right)^2, \quad (9)$$

which defines the parameter,  $\beta$  for later use. Rearranging,

$$D_* = \frac{K}{8} \rho g \sqrt{g h_*} (\kappa^2 - \gamma^2) \quad (10)$$

which indicates that the magnitude of the constant energy dissipation/unit volume is dependent on the incident wave height (through  $h_*$ ).

From these expressions we can determine the width of an equilibrium surf zone. Denoting  $W_*$  as this width, we have, from Eqn. 7,

$$W_* = 2 \frac{h_*}{K} + \frac{5}{24} \rho g^{3/2} \left( \frac{\gamma^2 h_*^{3/2}}{D_*} \right) = 2 \frac{h_*}{K} \left[ 1 + \frac{5}{6} \left( \frac{\gamma^2}{\kappa^2 - \gamma^2} \right) \right] \quad (11)$$

By putting in the values of  $\kappa$  and  $\gamma$ , we have  $W_* = 15.0 h_* = 19.3 H_b$  for the equilibrium profile width.

The Larson model shows that the wave height distribution across the surf zone and the beach profile depends on  $\mathcal{D}_*$ , the volumetric dissipation, which in Eqn. 10 is shown to be related to the incident wave height (through the breaking depth). This development was for a single wave train; now we extend it to the case for an random wave field.

Given that the wave height probability distribution is a Rayleigh distribution and that the variables,  $H$ ,  $h_*$  and  $D_*$  are related, the probability density function for  $H$  can be related to those for  $h_*$  and  $D_*$  through a transformation, e.g.,

$$P(h_*) = P(H_*)|_{H_*=\kappa h_*} \frac{dH_*}{dh_*} = \frac{2\kappa^2 h_*}{H_{\text{rms}}^2} e^{-\left(\frac{\kappa^2 h_*^2}{H_{\text{rms}}^2}\right)} \quad (12)$$

Using (9), the probability distribution for  $D_*$  is found by

$$P(D_*) = P(h_*)|_{h_*=D_*^2/\beta^2} \frac{dh_*}{dD_*} = \frac{4\kappa^2 D_*^3}{\beta^4 H_{\text{rms}}^2} e^{-\left(\frac{\kappa^2 D_*^4}{\beta^4 H_{\text{rms}}^2}\right)} \quad (13)$$

with  $\beta$  defined by (9). To find the expected value of  $D_*$ , we integrate:

$$\bar{D}_* = \int_0^\infty D_* P(D_*) dD_* = \sqrt{\frac{\beta^2 H_{\text{rms}}}{\kappa}} \Gamma\left(\frac{5}{4}\right) = \frac{\kappa}{8} \rho g (\kappa^2 - \gamma^2) \sqrt{g h_*} \quad (14)$$



The last expression is similar to (10), except that *expected* values for  $h_*$  are used to find  $\bar{D}_*$ .

**Random Wave Dissipation Models**—A number of random wave breaking models have been developed. For example, Battjes and Janssen (1978) utilized the conservation of energy flux within the surf zone with dissipation determined from a random model of the breaking wave field (based on truncating the Rayleigh probability density function at the local breaking wave height) and a turbulent bore energy dissipation term to predict root-mean-square (or  $H_{rms}$ ) wave heights in the surf zone. This model was modified by Thornton and Guza (1983), who developed two empirical distributions of breaking wave heights within the surf zone: one with a simplified energy dissipation and another with a more accurate dissipation term. Substituting their breaking wave distribution into a bore dissipation model, they determined the expected dissipation of energy within the surf zone. Wave heights predicted from their models agreed with both field and laboratory data very well.

The energy flux wave model for normal wave incidence is given by Eqn. (2). The forms for dissipation term,  $\epsilon_b$ , from Thornton and Guza (1983) are

$$\text{Simple: } \epsilon_b = \frac{3\sqrt{\pi}}{16} \rho g \frac{B^3 \bar{f}}{\gamma^4 h^5} H_{rms}^7 \quad (15)$$

$$\text{Complete: } \epsilon_b = \frac{3\sqrt{\pi}}{16} \rho g \frac{B^3 \bar{f}}{\gamma^2 h^3} H_{rms}^5 \left[ 1 - \frac{1}{(1 + (H_{rms}/\gamma h)^2)^{5/2}} \right] \quad (16)$$

where  $B$  is an empirical constant smaller than unity,  $\bar{f}$  = frequency of the incident wave train, and  $\gamma = 0.42$ , the breaking index based on the assumption that  $H = 0.42 h$  for the inner surf zone.

**Simple EBP Model**—The first step in the simple random EBP model is to use righthand side of the energy equation (2) with the dissipation term (Eqn. 15):  $\epsilon_b = h\mathcal{D}_*$ . This yields a representation for  $H_{rms}$  after some rearranging:

$$H_{rms} = \left( \frac{\gamma^2 \mathcal{D}_*}{A} \right)^{1/7} h^{6/7} \text{ where } A = \frac{3\sqrt{\pi} \rho g B^3 \bar{f}}{16\gamma^2} \quad (17)$$

The equation for  $H_{rms}$  indicates that for equilibrium beaches under random waves the statistical wave height should vary nearly linearly with the water depth.

Substituting this relationship for  $H_{rms}$  into the left hand side of the energy flux relationship (Eqn. 2) allows the calculation of the water depth across the profile, after using the shallow water limit of  $C_g = \sqrt{gh}$ :

$$\frac{\rho g^{3/2}}{8} \left( \frac{\gamma^2 \mathcal{D}_*}{A} \right)^{2/7} \frac{d(h^{12/7} \sqrt{h})}{dx} = h\mathcal{D}_* \quad (18)$$

Simplifying and integrating with respect to the distance offshore,  $x$ , with the initial condition,  $h(x) = 0$ , at  $x = 0$ ,

$$h(x) = \beta x^{14/17} \text{ where } \beta = \left( \frac{136\mathcal{D}_*}{31\rho g^{3/2}} \left\{ \frac{A}{\gamma^2\mathcal{D}_*} \right\}^{2/7} \right)^{14/17} \quad (19)$$

Thus we have arrived at a simple model for the description of the equilibrium beach profile and the associated wave height distribution in closed form for a random sea state.

**Complete EBP Model**—The more inclusive model involves the complete expression for the energy dissipation term within the surf zone, given in Eqn. 16. Equating the dissipation terms, we have

$$h\mathcal{D}_* = \frac{AH_{\text{rms}}^5}{h^3} \left[ 1 - \frac{1}{(1 + (H_{\text{rms}}/\gamma h)^2)^{5/2}} \right] \quad (20)$$

This equation can not be readily solved for  $H_{\text{rms}}$ ; however, it is straightforward to use numerical techniques such as the Newton-Raphson method to obtain solutions. Note that the wave height will depend on parameters such as  $\mathcal{D}_*$  and  $h$ , but not explicitly on the distance offshore.

To find the profile, the energy flux expression (Eqn. 2) is used. It can be rearranged into:

$$\frac{1}{8}\rho g\sqrt{gh}H_{\text{rms}} \left( 2\frac{dH_{\text{rms}}}{dx} + \frac{H_{\text{rms}}}{2h}\frac{dh}{dx} \right) = h\mathcal{D}_* \quad (21)$$

Since  $H_{\text{rms}}$  does not depend explicitly on  $x$ , we use

$$\frac{dH_{\text{rms}}}{dx} = \frac{dH_{\text{rms}}}{dh} \frac{dh}{dx}$$

where the derivative of  $H_{\text{rms}}$  with respect to  $h$  is found from Eqn. 20. We therefore can rewrite the last equation as

$$\frac{dh}{dx} = \frac{8h\mathcal{D}_*}{\rho g\sqrt{gh}H \left( 2\frac{dH_{\text{rms}}}{dh} + \frac{H_{\text{rms}}}{2h} \right)} \quad (22)$$

This equation is integrated numerically to determine the variation of the depth across the equilibrium profile and, given the depth, the wave height is found from Eqn. 20.

**Results**—Figure 1 shows a comparison of the simple and complete equilibrium profile models to data obtained under the National Sediment Transport Study at Torrey Pines Beach, CA (reference). The values of  $B$  and  $\mathcal{D}_*$  are adjusted to

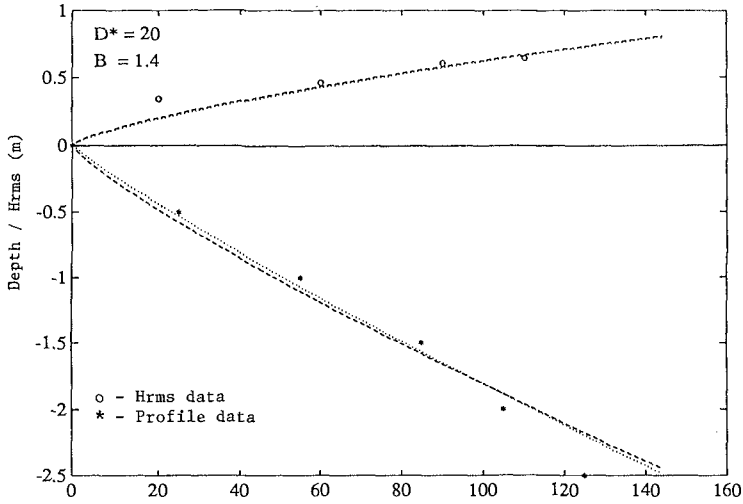


Figure 1: Equilibrium beach profile solutions for *simple* (dashed) and *complete* (dotted) dissipation models compared to wave and profile data. (Torrey Pines CA., November 18, 1978)

achieve the best fit to the wave height and profile data, respectively. As can be seen, both profile models adequately represent the data. The complete model is not a significant improvement over the simple model, suggesting that the analytical model is perhaps sufficient for describing a monotonic equilibrium beach profile under a random wave field.

## Generalized Equilibrium Beach Profile Model

The generalized equilibrium beach profile model (GEBP) is founded on the work of Bowen (1980) which is based on the concept of local time-averaged net sediment transport across the nearshore region. More specifically, the GEBP follows the work of Bailard (1981), who, like Bowen, used Stokes' second order wave theory and Longuet-Higgins' (1953) streaming velocities to model the wave-induced nearshore flow and the mean longshore current, respectively. However, both theories have shortcomings in the nearshore area. Stokes' wave theory is only valid for relatively deep water, and thus inapplicable for most nearshore wave conditions. Longuet-Higgins' streaming velocity solution assumes mean flows in the direction of wave propagation only, which is clearly not the case in the surf zone with undertow present. Thus it is the objective of this work to determine the effects of more accurate representations of the nearshore wave

and current climate to the equilibrium solution of Bailard's sediment transport expression. To do this, the method of Roelvink and Stive (1989), denoted as R&S, is adopted by modelling the asymmetric velocities with a Stream Function representation of the unbroken wave field and the mean current with an undertow model that establishes an offshore directed mean flow inside the surf zone. Here, for simplicity, the turbulent flow induced by wave breaking, which is modelled by R&S to improve the location of the maximum intensity of the undertow, is neglected. Further, only short wave contributions to the total odd moments will be considered and thus group-induced long-wave flows will be excluded.

The GEBP is developed assuming wave energy, mean water surface level and bottom depth are coupled through the energy, momentum and bottom slope equations, respectively. Variations in wave energy across the nearshore region for a random wave field are modelled following the work of Battjes and Stive (1985). The change in energy flux due to random wave breaking is equated to the time-averaged rate of energy dissipation per unit area,  $D$ , as

$$\frac{\partial EC_g}{\partial x} + D = 0, \quad (23)$$

The mean water surface elevation is modelled according to the momentum balance

$$\frac{\partial S_{xx}}{\partial x} + \rho gh \frac{\partial \bar{\eta}}{\partial x} = 0 \quad \text{where } h = d + \bar{\eta}. \quad (24)$$

The bottom slope equation is not as well established. Here we use the total load cross-shore sediment transport equation of Bailard (1982) to describe the interaction of near-bottom water velocities with the sediment in the nearshore region. The time-averaged form of the expression is

$$\langle \vec{i}_x \rangle = c_f \rho \left[ \frac{\varepsilon_b}{\tan \phi} \left[ \langle \vec{u} |\vec{u}|^2 \rangle - \frac{\tan \beta}{\tan \phi} \langle |\vec{u}|^3 \rangle \right] + \frac{\varepsilon_s}{w} \left[ \langle \vec{u} |\vec{u}|^3 \rangle - \frac{\varepsilon_s}{w} \tan \beta \langle |\vec{u}|^5 \rangle \right] \right] \quad (25)$$

where  $\tan \beta = -dd/dx$  is the bottom slope,  $\langle \vec{u} |\vec{u}|^2 \rangle$ ,  $\langle \vec{u} |\vec{u}|^3 \rangle$ ,  $\langle |\vec{u}|^3 \rangle$ ,  $\langle |\vec{u}|^5 \rangle$  are the total velocity moments in the cross-shore direction and the instantaneous, total cross-shore velocity vector is  $\vec{u}_i = (\tilde{u} + \bar{u})\hat{i}$ , where  $\tilde{u}$  is the time-varying velocity component,  $\bar{u}$  is the steady current component, and  $\hat{i}$  is the onshore unit vector.

The equilibrium condition and thus the bottom slope equation is found by applying the time-averaged no-net sediment transport condition ( $\langle \vec{i}_x \rangle = 0$ ) of Bowen (1980) to the sediment transport relationship where the bottom slope is expressed as

$$\tan \beta = \left[ \frac{\varepsilon_b}{\tan \phi} \langle \vec{u} |\vec{u}|^2 \rangle + \frac{\varepsilon_s}{w} \langle \vec{u} |\vec{u}|^3 \rangle \right] \left[ \frac{\varepsilon_b}{\tan^2 \phi} \langle |\vec{u}|^3 \rangle + \left( \frac{\varepsilon_s}{w} \right)^2 \langle |\vec{u}|^5 \rangle \right]^{-1} \quad (26)$$

This form of the bottom slope equation is most general because the total velocity moment terms are expressed in terms of the total bottom velocity,  $u$ . Following R&S, the total velocity moments are expanded and approximated in terms of the steady current,  $\bar{u}$  and a time varying current,  $\tilde{u}$ , where  $\tilde{u} \gg \bar{u}$ . This produces representations of the total velocity moments as combinations of the steady current, and central odd, ( $\langle \tilde{u} |\tilde{u}|^2 \rangle$  and  $\langle \tilde{u} |\tilde{u}|^3 \rangle$ ) and even ( $\langle |\tilde{u}|^3 \rangle$  and  $\langle |\tilde{u}|^5 \rangle$ ) moments as

$$\langle \bar{u} |\bar{u}|^2 \rangle = \langle \tilde{u} |\tilde{u}|^2 \rangle + 3\bar{u} \langle |\tilde{u}|^2 \rangle; \quad \langle \bar{u} |\bar{u}|^3 \rangle = \langle \tilde{u} |\tilde{u}|^3 \rangle + 4\bar{u} \langle |\tilde{u}|^3 \rangle \quad (27)$$

$$\langle |\bar{u}|^3 \rangle = \langle |\tilde{u}|^3 \rangle; \quad \langle |\bar{u}|^5 \rangle = \langle |\tilde{u}|^5 \rangle \quad (28)$$

Only the first terms of the total even moments are retained, assuming that wave asymmetry does not strongly contribute to these terms.

Approximating the odd moments with Stokes second order theory, the even moments with linear theory and the mean current with Longuet-Higgins' streaming velocity solution recovers Bailard's results. Building on these results, the following models for the wave and current fields will be applied to determine the effects of more accurate models to an equilibrium beach profile solution.

**Steady Current Component - Undertow Solution**— Across the nearshore region the mean cross-shore flow is known to move onshore outside the surf zone (where wave breaking is not prevalent) and offshore inside the surf zone. This dominant mean cross-shore flow inside the surf zone is the undertow. To model this transition in mean flow from onshore to offshore we follow Stive and de Vriend (1987), who model the mean flow across the nearshore area as a linear combination of the flow from the unbroken and broken fractions of the wave field across the surf zone. For the unbroken wave field, the Longuet-Higgins streaming velocity solution is applied. For the broken wave field, a three layer approach is adopted. This result provides a continuous solution for the mean current across the nearshore region different than that of a monochromatic breaking wave.

It is of interest to note that a change in the direction of the mean bottom velocity has been hypothesized (Dyhr-Nielsen and Sorensen 1970) to contribute to longshore bar formation. In support of this hypothesis, Dally (1987) observed that the dominant mechanism in the establishment of the longshore bar is the breaking induced mean return flow where, as wave breaking begins, the mean current changes from onshore to offshore. In light of this, the model of Stive and de Vriend seems to be a suitable mean flow model to establish one component of the probable flow conditions required to form a longshore bar in a beach profile.

**Central Odd and Even Velocity Moments**—From the expansion of the total time-averaged flow moments, the terms  $\langle \tilde{u} |\tilde{u}|^2 \rangle$  and  $\langle \tilde{u} |\tilde{u}|^3 \rangle$  are found to contribute to the representation of the total odd moments. As a first approximation,

the group-induced long wave flows are assumed to be negligible and thus we represent the time-averaged central, odd moments with only the short wave flows under nonlinear wave forms as

$$\langle \tilde{u} |\tilde{u}|^2 \rangle = (1 - Q_b) \langle u_s |u_s|^2 \rangle; \quad \langle \tilde{u} |\tilde{u}|^3 \rangle = (1 - Q_b) \langle u_s |u_s|^3 \rangle \quad (29)$$

where  $u_s$  is the bottom-velocity obtained from 6<sup>th</sup> order Stream Function theory. The contributions to the odd moments from the unbroken waves are represented by considering the fraction of waves breaking,  $Q_b$ . These expressions represent the unbroken short wave contributions to the central odd velocity moments. The input monochromatic wave height needed by Stream Function theory is approximated with the  $H_{rms}$  wave height from the breaking model.

The results of Guza and Thornton (1985) are adopted to model the even moments. The even moments  $\langle |\tilde{u}|^n \rangle$  are nonzero for symmetric wave forms and thus do not require the high order nonlinear wave solutions to produce contributions to the mean flows in the surf zone. For the case of a random wave field, Guza and Thornton suggest as a first approximation representing the wave field using a Gaussian description of the wave heights in the surf zone of a linear random sea.

**Model Summary**—The governing equations for the GEBP are the energy, momentum and bottom slope equations. These first order ordinary differential equations are solved numerically as a coupled initial value problem where initial wave height and water depth are given outside the surf zone.

**Results**—The input wave conditions are the deep water incident root-mean-squared wave height,  $H_{rms0}$ , the peak wave period,  $T_p$ . The mean water surface displacement,  $\bar{\eta}$ , is taken to be zero far offshore from the surf zone. The selection of the input depth,  $d$ , is arbitrary as long as wave breaking has not been initiated. Given the deep water incident wave conditions, the effective  $H_{rms}$  wave height,  $H_{rmsc}$ , is determined at the starting depth by linear shoaling theory.

As an example of the use of the GEBP, the 1981 average wave and profile data from the U.S. Army Corps of Engineers Field Research Facility (Miller *et al.* 1981) are used. The  $H_{rms}$  wave height is 1.02 m, the peak wave frequency,  $T_p$  is 10.0 sec and the starting depth is 20 m. The sediment fall velocity is assumed to be 0.04 cm/s and constant across the nearshore region. Bailard's (1981) bedload and suspended load sediment transport efficiency factors of  $\epsilon_b = 0.025$  and  $\epsilon_s = 0.01$ , respectively, are used. The internal angle of friction sand,  $\tan \phi$ , is taken as 0.63, the fluid density,  $\rho$ , is 1000 kg/m<sup>3</sup> and the gravitational acceleration,  $g$ , is 9.81 m/s<sup>2</sup>.

Figure 2a shows the results for the  $H_{rms}$  wave height across the equilibrium beach profile, where  $x$  is positive onshore. As the waves shoal, the  $H_{rms}$  wave height first increases up to a point where the percent of waves breaking is such that energy dissipation is more dominant than wave shoaling. At this point the

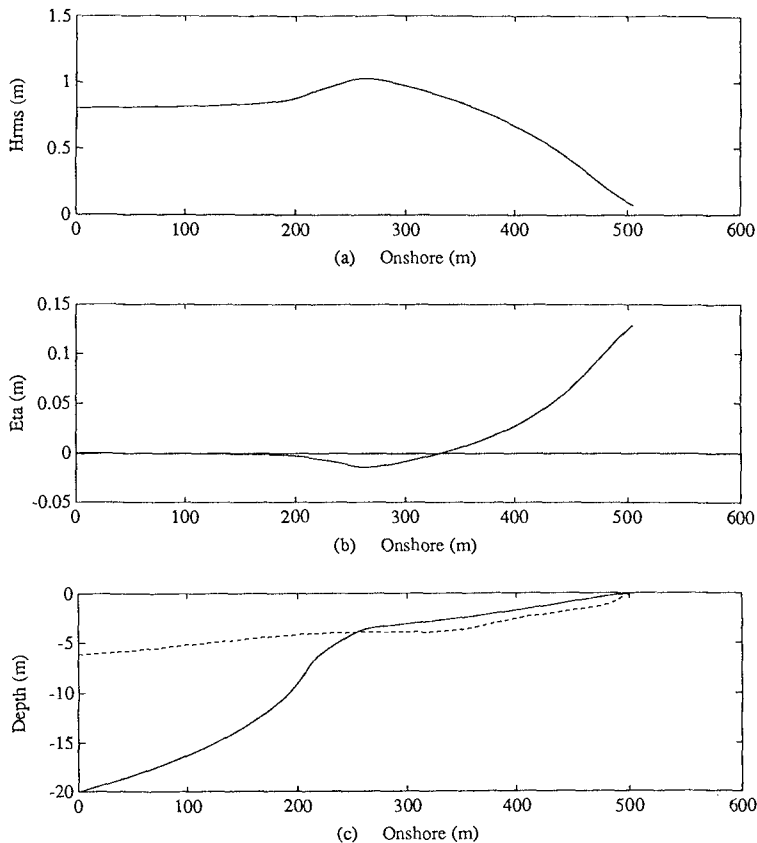


Figure 2: GEBP Solutions; (a)  $H_{rms}$ , (b)  $\bar{\eta}$ , (c)  $d$  (solid) and Mean Profile FRF (1981) (dashed)

$H_{rms}$  wave height will decrease until a stable water depth is reached for all waves or until all energy is dissipated from the waves at the shoreline.

Figure 2b shows the solution for the mean water surface,  $\bar{\eta}$ , across the equilibrium solution. It can be seen that set-down is most pronounced as the waves shoal to their maximum height and set-up increases as wave breaking intensifies.

Figure 2c shows the equilibrium beach profile as a function of onshore distance. The point of interest is the change in slope in the equilibrium solution between  $x = 200$  m and  $x = 250$  m where the slope changes from a steep offshore slope before breaking to a milder foreshore slope after breaking has initiated. This is the result of a change in the direction from onshore to offshore of the steady current,  $\bar{u}$ , as wave breaking dissipation increases with the decrease in depth. In figure 3, the resulting mean flow across the surf zone changes direction at approximately  $x = 200$  m. As seen in Eqn. 26, a change in the steady

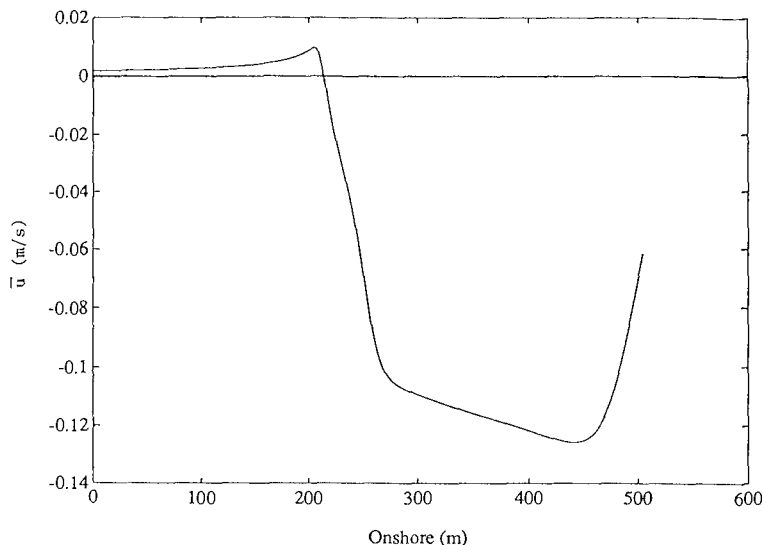


Figure 3: Steady Current,  $\bar{u}$ , Across an Equilibrium Beach Profile.

current,  $\bar{u}$ , is directly related to the bottom slope equation through the total odd velocity moments, and a decrease in magnitude or change in sign of  $\bar{u}$  results in a decrease in bottom slope. In other words, the bottom slope is influenced by a balance of forces between the flow field and gravity. In the offshore region, the flow forcing is entirely in the onshore direction where the mean wave-induced current and asymmetric flows are onshore. The combination of onshore flows works against the effects of gravity and produces a steep bottom slope. This result is equivalent to the findings of Bowen (1980) and Bailard (1981). As wave breaking begins and the mean return flow is established, the onshore flow forcing is reduced as the result of the offshore directed mean current opposing the asymmetric onshore flows and the slope becomes milder. The resulting change in slope due to the change in direction of the steady current is considered to be a longshore bar based on the findings of Dyhr-Neilsen and Sorensen and Dally. The steep slope of the depth solution outside the surf zone is attributed to the inclusion of Longuet-Higgins' streaming velocities for the mean flow in the unbroken wave field. As expected, these slopes are on the same order of magnitude as those found by Bailard.

Figure 4a shows the total odd moments across the equilibrium profile. In the equilibrium state, the magnitude of the total odd moments,  $\langle u|u|^2 \rangle$  and  $\langle u|u|^3 \rangle$  in Eqn. 26, is forced by the relative magnitude of the central moments and the steady current. As seen in figure 4a, the total odd moments are predominately positive across the entire surf zone. This is a result of the net balance of the flow forcing in the onshore direction. The balance is established through the



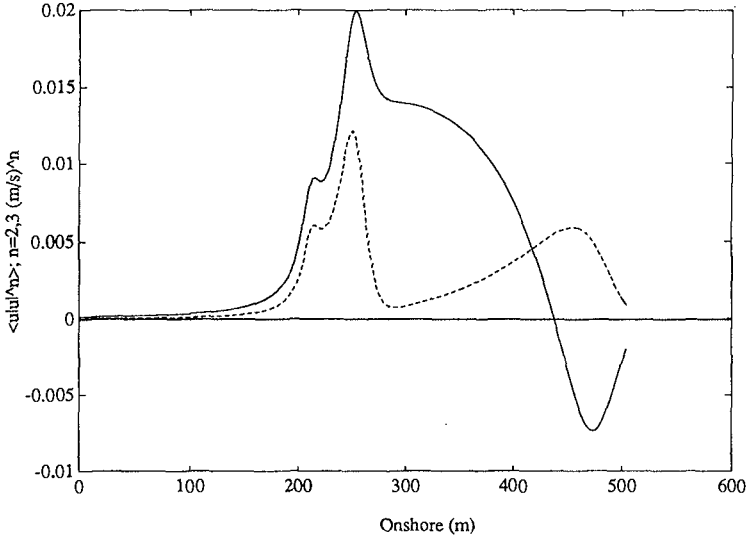


Figure 4: Total Moments Across an Equilibrium Beach Profile (a) Odd:  $\langle u|u|^2$  (solid),  $\langle u|u|^3$  (dashed), (b) Even:  $\langle |u|^3$  (solid),  $\langle |u|^5$  (dashed).

combinations of the central odd and even moments and the steady current where net onshore flows are required to balance the system and maintain a negative sloping bottom, reducing the depth from offshore to onshore.

Figure 5 shows the central odd moments, which are the result of the asymmetric onshore flow of the nonlinear wave form in the nearshore region to maintain positive values across the entire surf zone. The relative magnitudes of these terms in the GEBP model are governed by the balancing of the equilibrium solution between the suspended load and bedload.

For this case, the positive values for the total odd moments across the surf zone exhibit different characteristics as those measured and modelled by R&S. R&S present negative values for the total odd moments across the surf zone. A source of difference possibly lies in the equilibrium or average wave field representation in this example as opposed to the erosive sea state used by R&S. A comprehensive study of the model's response to variations in wave climate and sediment characteristics was conducted by Creed (1992).

## Conclusions

Several approaches to modelling equilibrium beach profiles assuming a random sea state have been addressed. The simple and complete models advance the models of Dean and Larson, but still only offer a monotonic representation

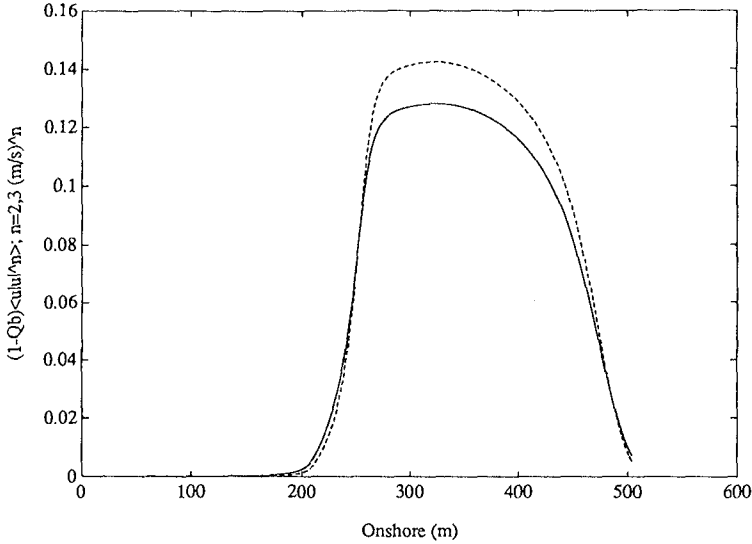


Figure 5: Central Odd Moments Across an Equilibrium Beach Profile:  $\langle \tilde{u}|\tilde{u}|^2 \rangle$  (solid),  $\langle \tilde{u}|\tilde{u}|^3 \rangle$  (dashed).

of the beach profile.

The GEBP can produce non-monotonic equilibrium solutions of a beach profile when a time-averaged no-net sediment transport condition is applied. The formation of a bar in the equilibrium beach profile is attributed to a change in the direction of the near-bottom mean current from onshore to offshore as wave breaking establishes a mean return flow inside the surf zone. The model does not produce realistic bottom slopes outside the surf zone, but inside the surf zone, where the sediment transport characteristics are better quantified, the equilibrium shape of the beach compares favorably with time-averaged field data.

## References

- Bailard, J.A., An energetics total load sediment transport model for a plane sloping beach, *J. Geophys. Res.*, 86, pp. 10,938-10,954, 1981.
- Bailard, J.A., Modelling on-offshore sediment transport in the surf zone, in *Proc. 18<sup>th</sup> Intl. Conf. Coastal Engrg.*, pp. 1419-1438, ASCE, New York, 1982.
- Battjes, J.A. and M. J. F. Stive, Calibration and verification of a dissipation model for random breaking waves, *J. Geophys. Res.*, 90, pp. 9159-9167, 1985.
- Battjes, J.A. and J.P.F.M. Janssen, Energy loss and set-up due to breaking of random wave, in *Proc. 16<sup>th</sup> Intl. Conf. Coastal Engrg.*, pp. 569-588, ASCE, New York, 1978.

- Bowen A.J., Simple models of nearshore sedimentation: beach profiles and longshore bars, in *The Coastline of Canada*, edited by S. B. McCann, pp. 1-11, Geological Survey of Canada, Ottawa, 1980.
- Creed, C.G., Modelling equilibrium beach profiles, M.CE. thesis, Department of Civil Engineering, University of Delaware, Newark, 1992.
- Dally, W.R., Longshore bar formation - Surf beat or undertow?, in *Proc. Specialty Conf. Coastal Sediments*, pp. 71-86, ASCE, New York, 1987.
- Dally, W.R., R.G. Dean, and R.A. Dalrymple, Wave height variation across beaches of arbitrary profile, *J. Geophys. Res.*, 90, No. 6, pp. 2035-2043, 1985.
- Dean, R.G., Equilibrium beach profiles: U.S. Atlantic and Gulf Coasts, *Ocean Engineering Report 12, Department Civil Engineering*, University of Delaware, 1977.
- Dean, R.G., Equilibrium beach profiles: Characteristics and applications, *J. Coastal Research*, 7(1), pp. 53-84, 1991.
- Dyhr-Neilson, M. and T. Sorensen, Sand transport phenomena on coasts and bars, in *Proc. 19<sup>th</sup> Intl. Conf. Coastal Engrg.*, pp. 855-866, ASCE, New York, 1970.
- Guza, R.T. and E.B. Thornton, Velocity moments in nearshore, *J. Waterw., Port, Coastal and Ocean Eng.*, ASCE, Vol. 111, No. 2, pp. 235-256, 1985.
- Larson, M., Quantification of beach profile change, Ph.D. Dissertation, *Report 1008, Department Water Resources Engineering*, University of Lund, Sweden, 1988. This also appears in Larson, M. and Kraus, N.C., SBEACH: Numerical model for simulating storm-induced beach change, *Report 1, U.S. Army Corps of Engineers, CERC, Tech. Rpt.CERC-89-9*, Vicksburg, 1989.
- Longuet-Higgins, M.S., Mass transport in water waves, *Philos. Trans. R. Soc. London, Ser. A*, 245, pp. 535-581, 1953.
- Miller, C.H., W.E. Grogg, Jr., J.R. Rottier, M.W. Leffler and C.R. Townsend, III, Annual data summary for 1981 CERC Field Research Facility, *Technical Report CERC-85-3*, USAE, Vicksburg, Miss., 1985.
- Roelvink, J.A. and M.J.F. Stive, Bar-generating cross-shore flow mechanisms on a beach, *J. Geophys. Res.*, 94, No. C4, pp. 4785-4800, 1989.
- Stive, M.J.F. and H.J. De Vriend, Quasi-3D nearshore current modelling: Wave-induced secondary currents, in *Proc. Specialty Conf. Coastal Hydrodynamics*, pp. 356-370, ASCE, New York, 1987.
- Thornton, E.B. and R.T. Guza, Transformation of wave height distribution, *J. Geophys. Res.*, 88, C10, pp. 5925-5938, 1983.

## CHAPTER 153

### AN OVERVIEW OF THE BRITISH BEACH AND NEARSHORE DYNAMICS (B-BAND) PROGRAMME.

<sup>1</sup>M.A. Davidson, <sup>2</sup>P.E. Russell, <sup>2</sup>D.A. Huntley,  
<sup>3</sup>J. Hardisty and <sup>4</sup>A. Cramp.

#### ABSTRACT

The British Beach And Nearshore Dynamics (B-BAND) programme is a three year collaborative research project aimed at improving understanding of surf zone sediment transport processes. Field studies were carried out on dissipative, intermediate and reflective beaches during both neap and spring tides (tidal range up to 9m), and during storm wave ( $H_b > 3\text{m}$ ) conditions.

The field research system comprises up to 7 pressure transducers (PT's), 11 electromagnetic current meters (EMCM's) and 12 optical backscatter sensors (OBS's). The focal point of the instrument array was a 1600m<sup>2</sup> box which was instrumented at each corner and designed to allow the calculation of alongshore and cross-shore suspended sediment fluxes through the box.

The largest sediment transport rates (up to 0.6 kgm<sup>-2</sup>s<sup>-1</sup>) occurred in the inner surf zone of the dissipative beach during storm conditions and showed strong offshore-directed sand transport at infragravity frequencies. The extent to which infragravity oscillations developed was seen to vary inversely with the degree of beach reflectivity, and directly with the incident breaker height. Sediment transport patterns often exhibited strong tidal asymmetry, attributed to the effects of beach dewatering and to a lag between hydrodynamics and bedform alteration.

---

<sup>1</sup> Dept. of Civ. & Structural Eng., Univ. of Plymouth, UK. <sup>2</sup> Institute of Marine Studies, Univ. of Plymouth. UK. <sup>3</sup> School of Geography, The Univ., Hull, UK. <sup>4</sup> Marine Geosciences Group, Geology Dept., Univ. of Cardiff, UK.

## INTRODUCTION

Many large multi-institutional field studies examining nearshore processes, using dense arrays of fast response sensors, have taken place over the last decade. These include; the Nearshore Sediment Transport Study (NSTS) on the west coast of the USA (Seymour, 1989), the Natural Environmental Research Council (NERC) project in Japan (Horikawa, 1987), the Canadian Coastal Sediment Transport Study (C<sup>2</sup>S<sup>2</sup>, Willis, 1987), and the DUCK experiments (eg. DUCK82, Mason *et al.*, 1984 and SUPERDUCK86, Martens and Thornton, 1987) carried out on the east coast of the USA.

These studies have substantially improved the understanding of surf zone hydrodynamics. However, progress in understanding the sediment response has been disappointing (Battjes, 1988). This is partially due to the fact that many of the field experiments have taken place on microtidal and mesotidal beaches with complex profiles and bedforms. Also our knowledge of the bedload phase is limited, because devices capable of obtaining high frequency bedload measurements on natural beaches are still under development (Hardisty, 1991).

The British Beach And Nearshore Dynamics (B-BAND) programme (1990-93) (Russell *et al.*, 1991) is a UK-based multi-institutional project. Its aim is to improve knowledge of surf zone sediment dynamics and shoreline evolution through the application of dense arrays of fast response sensors and detailed measurements of the associated shoreline change. Data was collected from high energy macrotidal beaches, which typically have a broad tidal and intertidal sand flat of shallow linear slope almost completely devoid of bedforms. A complementary low energy UK field study (Bedform And Suspension EXperiments, BASEX, cf. Osborne and Vincent, this volume) is examining small-scale suspension processes over rippled beds seaward of the surf zone, using acoustic suspension profiling techniques.

This contribution provides an overview of the environments sampled during the B-BAND experiment, the techniques used and some of the results obtained.

## FIELD STUDIES

The field research system comprised up to 7 pressure transducers (measuring depth and surface waves), 11 electromagnetic current meters (measuring bi-directional horizontal near-bed currents) and 12 optical backscatter sensors (measuring suspended sediment concentrations, SSC's). The focal point of the array was a 1600m<sup>2</sup> box which was instrumented at each corner (Figure 1). These corner stations typically consisted of 3 EMCM's at heights of 0.10, 0.25, and 0.63m above the bed, 3 OBS's at heights of 0.04, 0.10, and 0.25m above the bed, and a single PT. This arrangement was designed to allow the calculation of both the alongshore and cross-shore suspended sediment fluxes through the box, whilst standard beach

profiling techniques in conjunction with a dense array of depth of disturbance rods provided estimates of net erosion and accretion within the box over a tidal cycle. Additionally, a cross-shore array of 5 PT's permitted measurements of wave shoaling characteristics across the profile. Self Generated Noise (SGN) and Ultrasonic Current Meter (UCM) sensors were also deployed to estimate bedload sediment transport and 3 dimensional current flow close to the bed, respectively.

The sensors were secured by burying their mountings below the sand surface, and the 200m cables were buried back up to the logging equipment in the mobile laboratory at the head of the beach. The large tidal range on these macrotidal beaches allowed a profile of measurements to be obtained through and beyond the surf zone over a tidal cycle. Care was taken to ensure that the instrument mountings were buried in excess of 10cm below the sediment-water interface so as to prevent self-suspension by the rigs themselves. Depth of disturbance measurements indicated that maximum disturbance depths were less than 10cm over a tidal cycle. The OBS's were mounted to a slender (3mm diameter) stem which protruded out of the sediment-water interface from the subsurface mountings. No signs of scour were observed around these stems.

Signals were low-pass filtered (cut-off frequency = 1Hz) and digitised at a rate of 2Hz on a personal computer. Each data run was 17.07 minutes in duration giving 2048 data points per channel. Data were recorded continuously from just after low water on the flooding tide to just before low water on the ebbing tide. Beach profile and depth of disturbance measurements were obtained during each low water period.

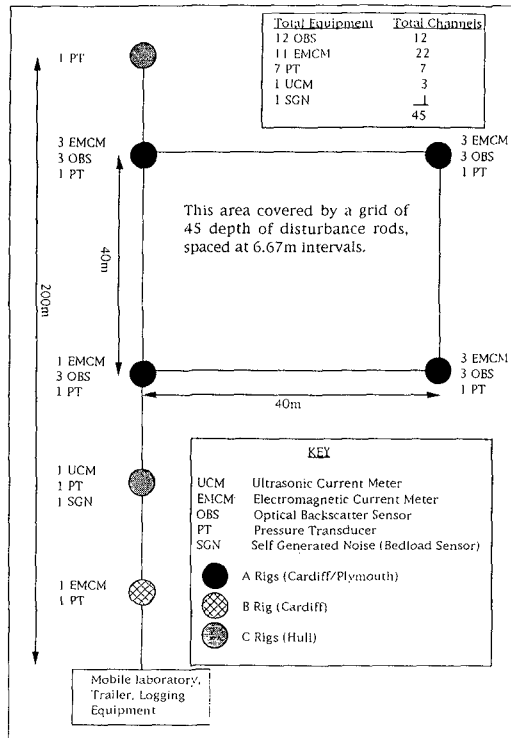


Figure 1: Generalised B-BAND field set-up.

Field investigations were carried out at three macrotidal beach sites: Llangennith, South Wales; Spurn Head, North East England and Teignmouth, South West England (Figure 2). Following Wright and Short's (1984) morphodynamic classification of beaches, these sites will hereafter be referred to as the dissipative, intermediate and reflective beaches respectively.

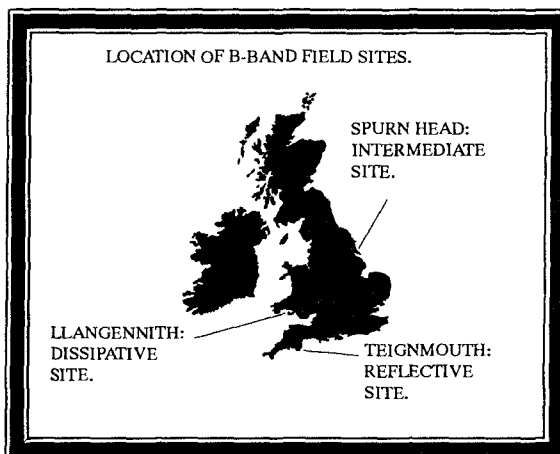


Figure 2: B-BAND field sites.

The dissipative beach is a 10km long, high energy beach with a shallow concave beach profile (gradient = 0.014-0.020) consisting of fine to medium grained quartz sands ( $D_{50} = 0.21\text{mm}$ ). The wave climate on this exposed west facing beach is a mixture of high energy Atlantic swell approaching from the WSW, and locally generated wind waves driven by the prevailing W and SW winds. The low beach gradient, high energy waves and large (up to 9m) tidal range combine to produce both broad surf (up to 350m wide) and intertidal (up to 500m wide) zones.

The intermediate beach site is located near the end of a 5km long spit and faces into the North Sea. The prevailing wave climate is milder than that of the dissipative beach, but the coast is exposed to occasional violent storm waves which approach obliquely from the north-east and can produce plunging breakers with heights in excess of 3m. The beach profile consists of a steep high tide beach (gradient = 0.0975) comprised of fine to medium gravels and a shallow sloping (gradient = 0.023) low tide terrace consisting of a lens of well sorted, medium quartz sands ( $D_{50} = 0.35\text{mm}$ ) overlying boulder clays. Strong (up to 1m/s) rectilinear tidal currents (tidal range = 3 to 6m) run parallel to the coast flowing in a south-westerly direction on the flood and north-easterly direction during the ebb. These currents exert a significant dynamical effect even within the surf zone.

The reflective beach site faces south-east into the English Channel and is consequently sheltered from swell waves generated in the Atlantic Ocean. The local wave climate is dominated by infrequent periods of wind-driven waves from the east. The beach profile is headed at its shoreward extent by a vertical sea wall. The upper profile adjacent to the sea wall is convex and the lower profile seawards of the neap low tide level is slightly concave. The beach is comprised of medium

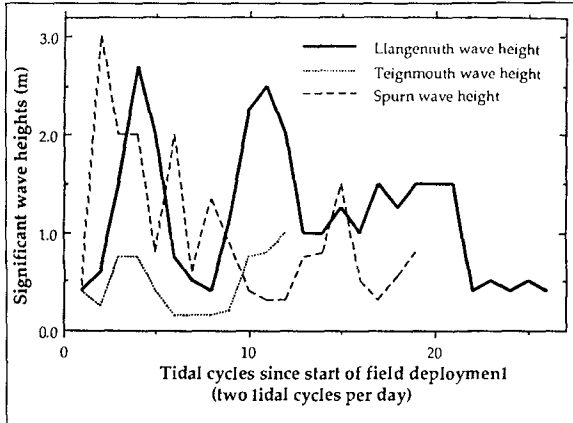


Figure 3: Wave height variation during the B-BAND experiments.

quartz sand ( $D_{50} = 0.24\text{mm}$ ). Due to the steep beach profile (gradient = 0.067 to 0.142) the intertidal zone at the reflective beach is comparatively narrow (<70m) in spite of the large (up to 6m) tidal range in this area.

A wide range in incident wave conditions were experienced during each field deployment (Figure 3). Measurements were obtained during both calm conditions and

through two storm events ( $H_{1/3} = 2$  to  $3\text{m}$ ) at the dissipative beach. The start of the intermediate beach experiment was marked by the largest storm in 3 years ( $H_{1/3} > 3\text{m}$ ) which breached the sand spit leaving it isolated from the mainland at high water. Wave energy levels were much lower during the reflective beach experiment. However, two periods of high wave energy for the locality did occur during the experiment (tides 3-4 and 11-12) when significant wave heights were between 0.5 and 1m.

## RESULTS

The following discussion of the time series data is subdivided into hydrodynamics, sediment suspension, sediment transport and beach response. Further divisions are made where appropriate into oscillatory and steady components.

### Hydrodynamics. a) Oscillatory flows:

The typical cross-shore pattern for the distribution of hydrodynamic variance observed on all the beaches sampled irrespective of the degree of profile reflectivity is shown in Figure 4. This example, recorded at the intermediate beach, shows the variation of the cross-shore current velocity spectrum with offshore distance. The energy distribution with offshore distance of all the principal components (incident, incident harmonics and infragravity components) of the spectrum appears to conform to current theory (cf. Ursell, 1952; Wright *et al.*, 1982). The shorewards decay of incident wave energy and its associated harmonics within the surf zone is accompanied by a simultaneous increase in energy within the infragravity band.

Although this basic pattern for the distribution of hydrodynamic variance is



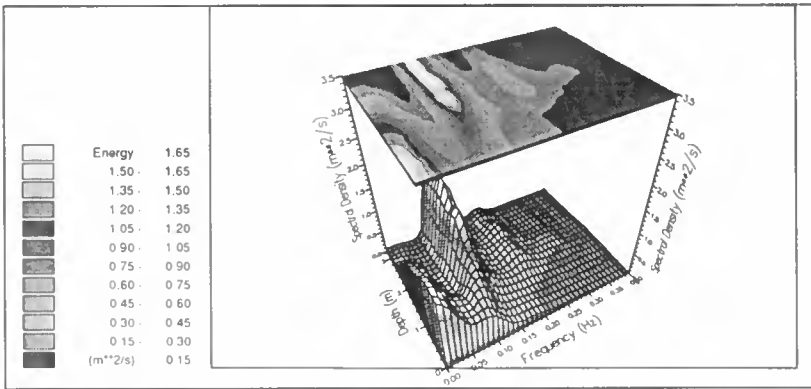


Figure 4: (above) Variation in the cross-shore current spectrum with offshore distance, (intermediate beach).

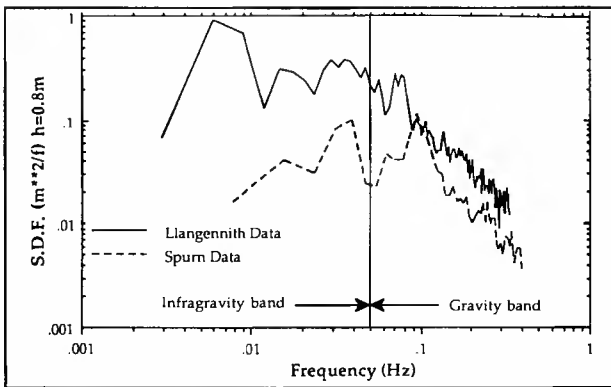
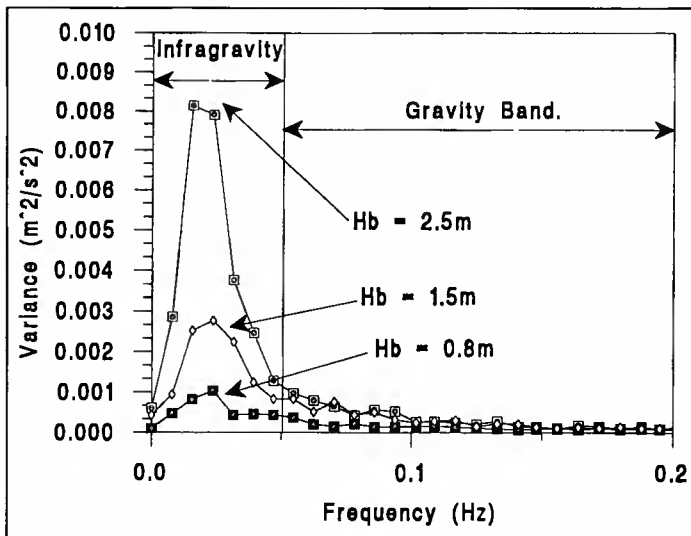


Figure 5: A comparison of cross-shore current spectra from the intermediate and dissipative beaches.

Figure 6: Infragravity response to incident wave forcing. (results from the inner surf zone of the dissipative beach).



common to all the beaches occupied, the relative importance of the principal components of the spectrum varies depending on the reflectivity of the environment. Two cross-shore current velocity spectra from the intermediate and dissipative beaches recorded in equivalent water depths ( $h = 0.8\text{m}$ ) during comparable incident wave conditions ( $H_{1/3} = 2.5\text{m}$ ) are presented in Figure 5. Hydrodynamic spectra recorded at the dissipative beach are strongly dominated by oscillations at infragravity frequencies, whilst at the more reflective environment, incident wave motion dominates the spectrum.

Results obtained in this experiment have supported the findings of other researchers (cf. Holman, 1981) who have demonstrated that, for a given beach, the shoreline infragravity energy levels are linearly related to incident wave height. This proportionate response of the infragravity band with increased incident wave forcing is demonstrated in Figure 6 (and in Huntley *et al.*, 1992). However, observations on beaches of varying reflectivity indicate that levels of long wave energy are not simply a function of the incident wave climate and that beach slope is an important factor which must be considered when predicting infragravity energy within the nearshore zone.

#### b) Mean Flows: Longshore currents.

The typical patterns for the variation in longshore current velocity with offshore distance through and beyond the surf zone at the intermediate and reflective sites are illustrated in Figures 7a and b. These figures show the effect of both the temporal variation in the tidal component and the spatial variation in the wave driven flow. The wave driven longshore flow in both cases is negative (to the south), enhancing tidal flows on the flood tide and opposing tidal flows during the ebb. The variation in the magnitude of the wave driven component conforms qualitatively to the theoretical profile of Longuet-Higgins (1970) which predicts low velocities within the inner/outer surf zone and a mid-surf maximum.

Observations indicated that the net longshore current was the resultant of wave and tidally driven components. The relative importance of these components varied with tidal state, cross-shore location and beach reflectivity.

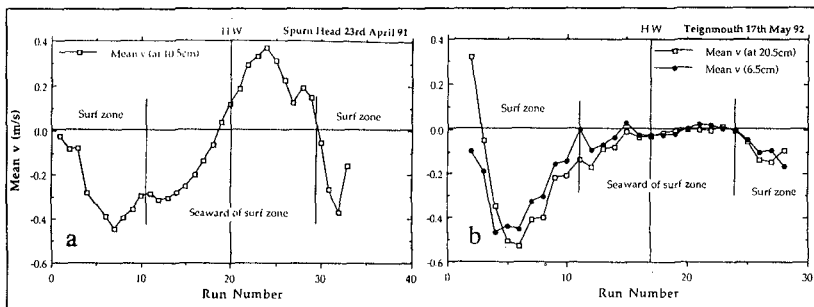


Figure 7a, b: Variations in the mean longshore current with run number (depth) for a) the intermediate beach and b) the reflective beach.

The tidal component was found to be particularly important in coastal regions where dominant tidal flows run parallel to the coast at the intermediate and reflective beach sites. At the dissipative beach, mean longshore flows were found to be weak due to both the low angle of wave attack and the prevalent direction of tidal flow which is perpendicular to the shoreline.

### Mean Flows: Cross-shore currents.

Comparative plots for the cross-shore component of flow are shown in Figure 8a and b. The pattern of flow is very repeatable both temporally within a given environment and at different sites. Within the surf zone, a strong (0.2m/s) near-bed offshore flow (undertow) is evident. On the intermediate beach there is also a weak (0.05m/s) near-bed onshore flow seawards of the surf zone. These results suggest a convergence in the steady near-bed cross-shore flow towards the break point. Similar results have been obtained by other workers, (eg. Bailard, 1987).

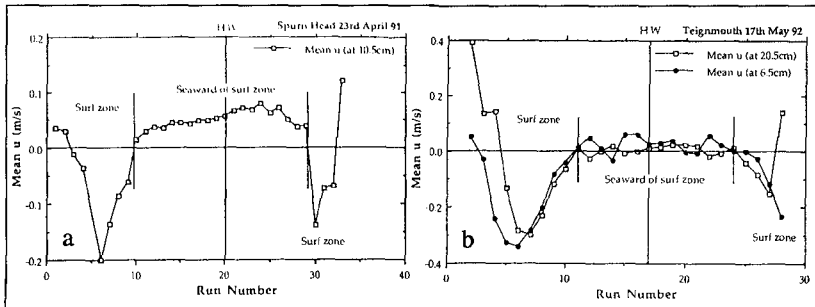


Figure 8a, b: Variation in mean cross-shore current velocity with run number (depth) at a) the intermediate beach and b) the reflective beach.

A second feature of the mean cross-shore flow field commonly observed within the surf zone is an onshore near-surface flow. This is particularly noticeable in the readings obtained from the upper current meters just prior to them coming out of the water. In some cases there is evidence for a vertical flow reversal (see for example runs 2, 3 and 28, Figure 8b) with onshore flow close to the surface and offshore flow at depth. Similar results have been presented by Wright *et al.* (1982) and Bailard (1987).

### Sediment Suspension.

Typical SSC and cross-shore velocity time series measured at the intermediate and dissipative beach are shown in Figures 9a and b respectively. These data were collected in similar water depths ( $h = 0.4-0.45\text{m}$ ) within the inner surf zone during similar (incident) wave conditions. The suspension characteristics shown in Figure 9a are typical of those observed on both the intermediate and reflective beaches, with suspension events generally occurring on each wave cycle at incident

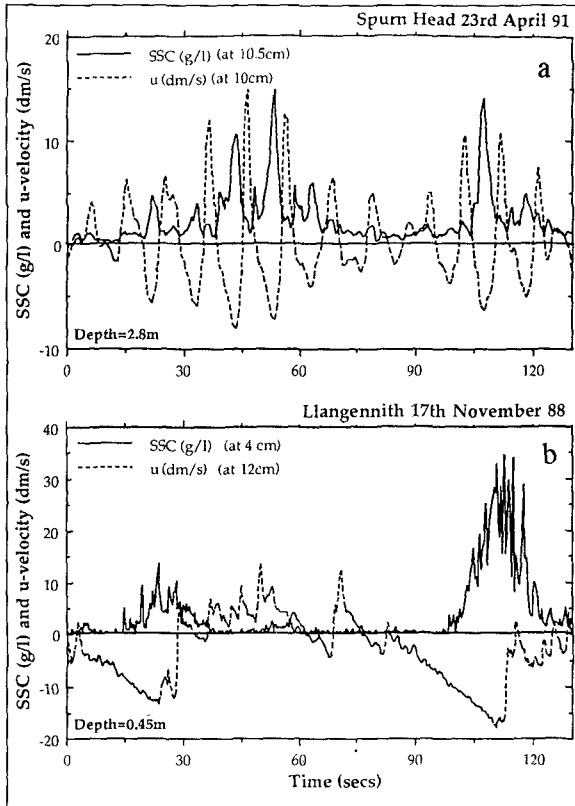


Figure 9a, b: Typical cross-shore current and SSC time series measured in the inner surf zone on a) the intermediate beach and b) the dissipative beach.

wave frequencies and the associated harmonics, with some secondary modulation at infragravity wave frequencies. Conversely, on the dissipative beach, suspension events are long lived (30 to 60s), dense (30 to 50g/l) and closely correlated with prolonged offshore flows at infragravity frequencies.

Several of the B-BAND data sets show a profound tidal asymmetry in both the steady and oscillatory sediment suspension components. Examples of this phenomenon recorded at the intermediate beach during two different tides are shown in Figures 10a to d. These plots illustrate tidal asymmetry in the suspension data at different heights in the water column (top, middle and bottom OBS sensors), and at different spatial locations on the beach (eg rigs A3 and A2) in both the mean (Figures 10a and c) and oscillatory components (Figures 10b and d). The main reasons for the observed tidal asymmetry are thought to be de-watering of the beach during the ebb and a time-lag in bed-form response to changing hydrodynamic conditions (Davidson *et al.*, in press).

## SEDIMENT TRANSPORT.

### 1) Cross-shore

Co-spectral techniques were extensively employed to examine the magnitude and direction of fluctuating sediment fluxes with frequency at different locations.

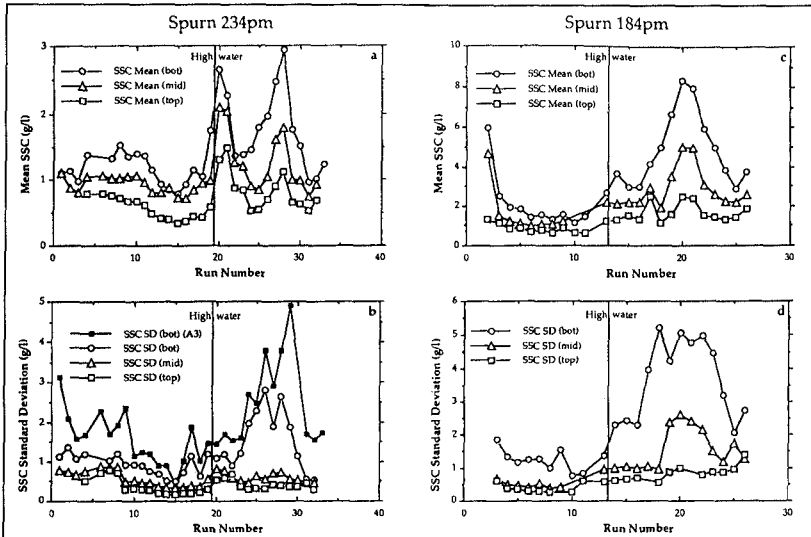


Figure 10a, b, c, d: Variation in steady and oscillatory SSC with run number (offshore distance) and height above the bed (intermediate beach).

These results have supported earlier research carried out on beaches of low tidal range. For example, weak onshore transport at incident wave frequency was found seaward of the surf zone (eg. Huntley and Hanes, 1987, and Figure 11). Conversely, within the surf zone, offshore sediment fluxes at infragravity frequencies were much greater in magnitude than the corresponding onshore transport at incident wave frequencies (eg. Russell, 1990, Figure 12 from the dissipative beach, and Figure 13 from the intermediate beach).

However, other processes can alter this basic pattern. For example, the co-spectrum in Figure 14 illustrates strong offshore transport at incident wave frequencies over a rippled bed seawards of the surf zone at the intermediate site. This reverse transport at

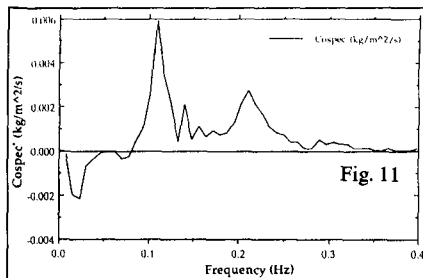


Fig. 11

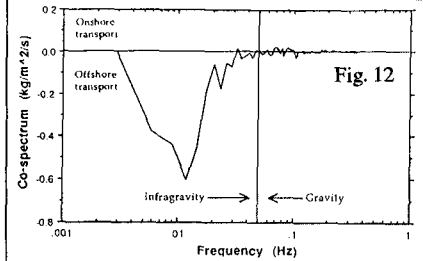


Fig. 12

Figures 11 and 12: Cross-shore current, SSC co-spectra.

incident wave frequencies over rippled beds has been noted by other workers (cf. Dingler and Inman, 1976).

2) Longshore.

In the longshore direction, the oscillatory transport contributions were negligible since the fluctuating component of longshore velocity and SSC were uncorrelated. The steady (both wave-driven and tidally modulated) flows dominated the longshore transport of sediment.

BEACH RESPONSE.

The sequence of beach profiles collected during the dissipative beach deployment are illustrated in Figure 15. This data has been re-plotted in Figure 16 as a 2-dimensional plan to illustrate the change in beach level between consecutive profiles, so that areas of erosion and accretion can be readily observed. The classic pattern of offshore transport from a berm to an offshore bar is observed during the storm wave conditions at the start of the experiment (profile numbers 1-4), followed by a subsequent return of sand from the bar to the berm during small swell wave conditions later in the deployment (profile numbers 8-11).

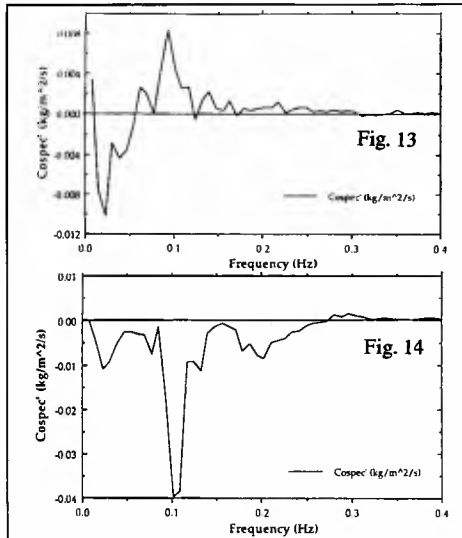


Figure 13 and 14: Cross-shore current, SSC co-spectra. (13) Inner surf zone. (14) Over ripples (14).

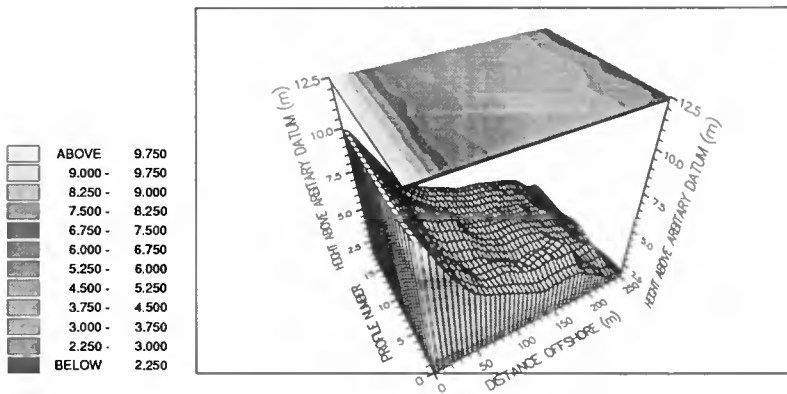


Figure 15: Beach profile evolution (Llangennith).

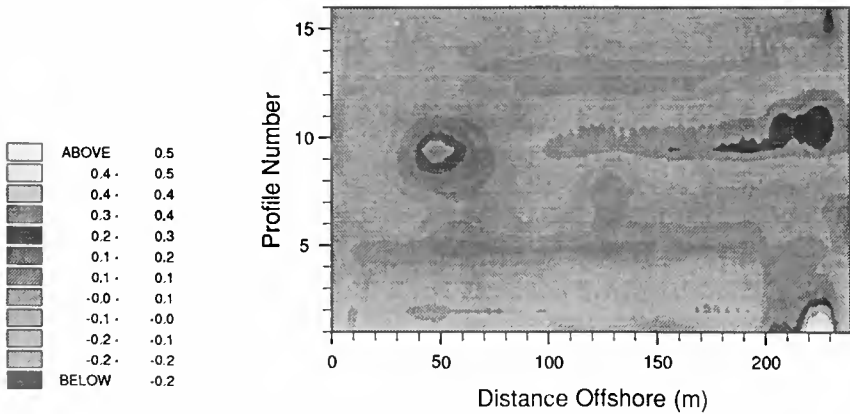


Figure 16: Beach changes during the dissipative beach experiment.

Depth of disturbance (DOD) measurements gave detailed bed level changes inside the box averaged over a tidal cycle. A typical result is illustrated in Figure 17. However, no reliable quantitative comparisons could be made between the measured bed level changes in the box and sediment fluxes measured at fixed heights by the sensors. This is because of the inability of the suspension (OBS) and velocity (EMCM) sensors to measure sediment suspension either within the swash zone or within the bottom boundary layer. Hence, the calculation of accurate time- and depth-integrated sediment fluxes over a tidal cycle was not possible. The accurate measurement of the total load sediment transport rates in the surf zone awaits further development of instruments which are capable of obtaining reliable fast response concentration and velocity profiles which extend well into the bottom boundary layer, and are also capable of measuring within the swash zone.

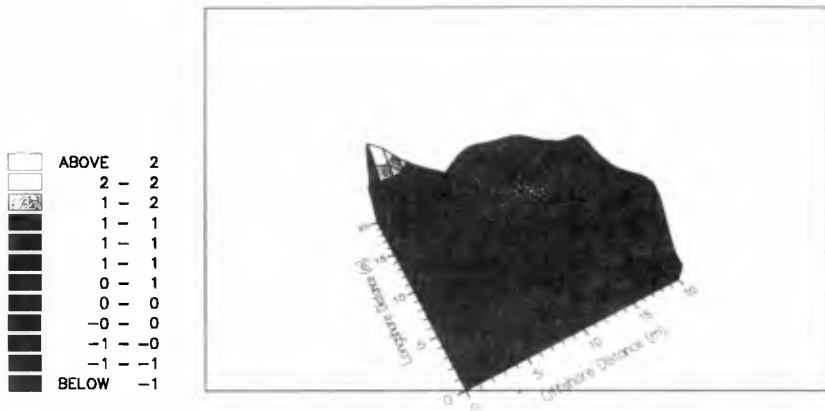


Figure 17: Bed level changes within the box.

## CONCLUSIONS.

Results obtained using dense arrays of PT's, EMCM's and OBS's are invaluable for furthering our understanding of hydrodynamic and sediment transport processes on natural beaches. Results of particular interest so far include:

- i) The tidal asymmetry, affecting sediment transport processes on macrotidal beaches.
- ii) The relative importance of steady flows, long waves (surf beat) and incident waves to the total sediment transport rates in the surf, breaker and offshore zones and on beaches with differing slopes.
- iii) The relationship between infragravity response and incident wave forcing. The magnitude of infragravity perturbations are inversely related to beach reflectivity and directly related to incident breaker height.
- iv) The magnitude and phase relationships between cross-shore flows and sediment suspension with height above the bed.
- v) Assessing the reliability of fast response sensors in the prediction of the divergence of sediment across a given area.

Work is continuing on analysing the vast (325 Mbyte) B-BAND data set, with particular emphasis on the influence of mean flows, reflection from coastal structures, infragravity sediment transport and beach response.

## ACKNOWLEDGEMENTS

The B-BAND experiment is being funded by the Natural Environment Research Council (NERC) (UK) research grant GR3/7128. The post doctoral research associates, Mark Davidson and Paul Russell would like to thank the Welsh Office and the NERC respectively for supporting their work on this project. The authors would also like to extend their thanks to Gareth Lloyd and Steven Jacques for assistance with drafting the figures.

## REFERENCES

- Bailard, J., 1987, Surf zone wave velocity moments, Proc. Coastal Hydrodynamics, ASCE, 328-342.
- Davidson, M.A., P.E. Russell, D.A., Huntley and J. Hardisty, in press, Tidal asymmetry in suspended sand transport on a macrotidal intermediate beach. Mar. Geol.



- Dingler, J.R. and D.L. Inman, 1976, Wave formed ripples in nearshore sands, Proc. 15<sup>th</sup> Coastal Eng. Conf., ASCE, 2109-2126.
- Guza, R.T. and E.B. Thornton, 1982, Swash oscillations on a natural beach, J. Geophys. Res., **87**, 483.
- Hardisty, J., 1991, Bedload transport under low frequency waves, Proc. Coastal Seds. '91, ASCE, 726-733.
- Holman, R.A., 1981, Infragravity energy in the surf zone, J. Geophys. Res., **86(7)**, 6442-6450.
- Horikawa, K., 1987, Nearshore dynamics and coastal processes - theory, measurement and predictive models, Univ. of Tokyo Press, 515pp.
- Huntley, D.A. and Hanes, D.M., 1987, Direct measurement of suspended sand transport, Proc. Coastal Seds., '87, ASCE, 723-737.
- Huntley, D.A., M.A. Davidson, P.E. Russell, Y. Foote and J. Hardisty, in press, Long waves and sediment movement on beaches; recent observations and implications for modelling, J. Coastal Research.
- Longuet-Higgins, M.S., 1970, Longshore currents generated by obliquely incident sea waves, 2, J. Geophys. Res., **75**, no. 33, 6790-6801.
- Martens, D.E. and E.B. Thornton, 1987, Nearshore zone monitoring system. Proc. Coastal Hydrodynamics, ASCE, 579-588.
- Mason, C., A.H. Salenger, R.A. Holman, and W.A. Birkemeier, 1984, DUCK82 - A coastal storm processes experiment, Proc. 19<sup>th</sup> Coastal Eng. Conf., ASCE, 1913-1928.
- Osborne, P.D. and C.E. Vincent, in press, Timescales of bed response in a low energy surf zone. Proc. 23<sup>rd</sup> Coastal Eng. Conf., ASCE.
- Russell, P.E., 1990, Suspended sand transport on a high energy dissipative beach, Unpub. Ph.D. Thesis, Univ. of Wales, 318pp.
- Russell, P.E., M.A. Davidson, D.A. Huntley, A. Cramp, J. Hardisty and G. Lloyd, 1991, The British Beach And Nearshore Dynamics (B-BAND) programme, Proc. Coastal Seds '91, ASCE, 371-384.
- Seymour, R.J., 1989, Nearshore sediment transport, Plenum Press, NY, 450pp.
- Ursell, F., 1952, Edge waves on a sloping beach, Proc. Roy. Soc. London, **214**, 79-97.
- Willis, D.H., 1987, The Canadian Coastal Sediment Transport Study: An overview, Proc. Coastal Sediments '87, ASCE, 682-693.
- Wright, L.D., R.T. Guza and A.D. Short, 1982, Dynamics of a high-energy dissipative surf zone, Mar. Geol., **45**, 41-128.
- Wright, L.D. and Short, A.D., 1984, Morphodynamic variability of surf zones and beaches: a synthesis, Mar. Geol., **56**, 93-11.

## CHAPTER 154

### LONGSHORE BAR GENERATION MECHANISMS

Robert G. Dean<sup>1</sup>, Rajesh Srinivas<sup>1</sup>, and Trimbak M. Parchure<sup>2</sup>

#### ABSTRACT

A laboratory study was conducted to investigate mechanisms of bar formation with particular focus on infragravity wave and break point mechanisms. With one exception, all tests commenced with a planar beach composed of fine sand. Infragravity (IG) waves, the result of a biharmonic primary wave spectrum, were generated and documented. For various frequency differences of the components of the primary spectrum and thus the frequencies of the IG wave, the changes in nodal/antinodal positions were compared with the changes in positions of the bar formed during the experiment. It was found that the bar position experienced relatively small movements whereas the nodal/antinodal positions changed substantially as expected with the difference frequency of the primary waves. The approximately constant bar position was interpreted as due to the relatively constant primary wave height characteristics. The effects of the wave spectrum and wave height distribution on bar formation were investigated. The shape of the wave height probability distribution function was found to exert a noticeable control on the degree of bar relief, with those distributions characterized by a substantial concentration near the maximum wave height causing the more prominent bars. This is interpreted in terms of a transport influence function which, if held stationary, would result in a narrow prominent bar. The distributions with a small concentration near the maximum wave height resulted in a less prominent bar. A conceptual model is proposed which incorporates the transport distribution function and which results in bar characteristics which depend on the initial conditions.

---

<sup>1</sup>Coastal and Oceanographic Engineering Department, University of Florida, Gainesville, Florida 32611 USA.

<sup>2</sup>Hydraulics Laboratory, Waterways Experiment Station, U. S. Army Corps of Engineers, Vicksburg, Mississippi 39801 USA.

## INTRODUCTION

Several mechanisms have been proposed for the formation of offshore bars, which can be described as rather low, generally shore-parallel positive features which rise a substantial fraction of the water depth above the sea floor. Bars occur singly or as a series of such features. In many locations of the world, they are correlated with seasons or episodic events of higher wave activity. In other locations, bars are perennial.

Four mechanisms for the formation of bars are reviewed briefly below: (1) Break point, (2) Standing waves formed by reflection from shore back out to sea, (3) Standing edge waves, and (4) Overtake of harmonic waves.

### Break Point Mechanism

The break point mechanism ascribes bar formation to the convergence of sediment transport due to either or a combination of sand transport seaward and/or landward towards the final bar position. The primary effect is seaward transport by the breaking process due to the vortex formed as the breaking wave transfers a torque to the water column which causes a local seaward bottom velocity. This seaward flow may be considered as undertow compensating for the landward mass transport. However, this undertow is locally reinforced by the aforementioned breaking induced torque. Bars frequently occur in wave tanks under the action of monochromatic waves. Such bars are referred to as "break point" bars in recognition of their causative mechanism.

### Standing Waves Formed by Reflection from Shore Back Out to Sea

A wave propagating toward the shoreline will reflect to some degree from the shoreline forming partial nodes and antinodes. The degree of reflection increases with longer wave periods and steeper beach slopes. The shore parallel nodes and/or antinodes are attractive as an explanation for the bar formation (Sallenger and Howd, 1989). Some proponents of this mechanism suggest that formation can occur under either the nodes or antinodes (Carter et al. 1973). A narrow spectrum will cause the formation of long waves, generally termed as "infragravity" waves with frequency characteristics determined by the spectral width. These long waves reflect efficiently from the beach. It is well-known that bar-like features form in wave tanks under standing wave envelopes.

### Edge Waves

The explanation for this mechanism is somewhat similar to that described in the preceding paragraph. The only difference is that edge waves are trapped by reflection thereby maintaining the energy within the nearshore trapping region

whereas for the preceding mechanism, the waves are "leaky" with the reflected energy propagating offshore.

### Overtake of Harmonic Waves

The basis for this explanation is the alternate reinforcement and cancellation of waves of periods corresponding to the first harmonic of the dominant fundamental wave (e.g., Buhr Hansen and Svendsen, 1974). Two waves of this frequency are required: one bound to the fundamental by nonlinear mechanisms and a second free wave propagating at its own speed. Since the propagational speeds of these two waves are different, they will interfere, alternatively reinforcing and canceling at positions which, for a uniform water depth, are periodically spaced along the direction of wave propagation. Contrary to most field observations in which the bar spacing decreases with decreasing water depth, the overtake mechanism predicts an increasing bar spacing with decreasing water depth.

### EXPERIMENTAL FACILITIES

The experiments described in this study were conducted in the facility shown in Figure 1 which consists of a wave tank with programmable wavemaker. The tank is approximately 37 m long, 2 m wide and 1.3 m deep. A long partition extends from near the wavemaker to the distal end of the tank forming two channels each of 0.9 m width. A beach of initial slope 1:19 was formed of fine sand ( $D_{50\%} \approx 0.21$  mm) in one side of the partitioned tank. The wavemaker is driven by hydraulic actuators at two levels, each of which can be controlled independently.

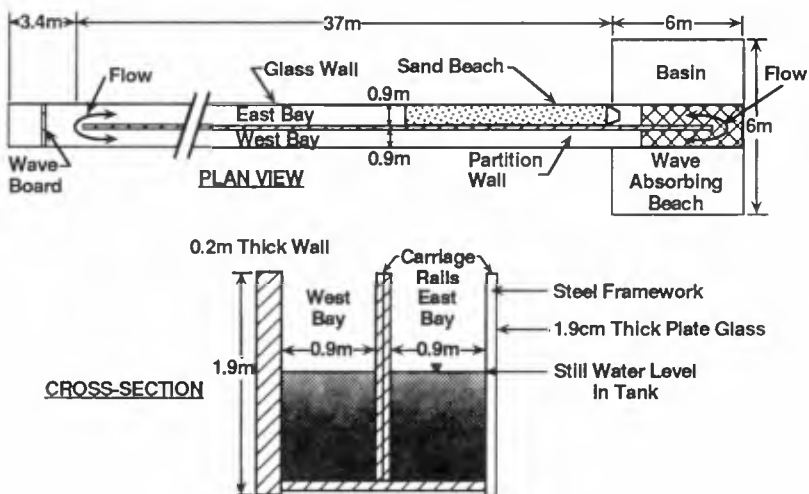


Figure 1. Schematic and Cross-Section of Wave Tank Facility.

## INVESTIGATION CHARACTERISTICS AND RESULTS

The experiments have attempted to address the question of bar formation mechanisms as well as the spectral characteristics that will result in the presence of a bar. All tests were conducted for at least 4.5 hours and the profiles appeared to be near equilibrium. Two study components were carried out and are described below.

### Correlation of Bar Characteristics And Infragravity Waves

This study component is essentially an extension of that conducted by W. R. Dally (1987) in which the incident wave system was biharmonic, i.e. composed of two discrete components, thus resulting in a pronounced infragravity wave component. Reflection of the infragravity component from the wavemaker, an artificiality due to the wave tank, increased its amplitude; the locations of the nodes and antinodes were fixed by the long wave period and the beach profile. The infragravity wave characteristics were measured by a manometer and stilling well apparatus that damped the primary waves. An example of the primary and long wave systems and their associated spectra is presented in Figure 2. The associated wave height probability distribution function and initial and final beach profiles are presented in Figure 3. The method of relating the bar and nodal/antinodal positions to test this hypothesis differed from that of Dally. A total of four experiments of this type was carried out: the analysis and results will be described later.

In addition to documenting the long wave envelope structures generated in the laboratory, they were calculated considering the long wave to be free and represented by the following equation

$$\sigma^2 \eta + g \frac{\partial}{\partial x} \left( h \frac{\partial \eta}{\partial x} \right) = 0$$

which was formulated and solved in finite difference form and found to compare favorably with the analytical solution for a planar beach

$$\eta = J_0 \left( 2\sqrt{\kappa x} \right)$$

where

$$\kappa = \frac{\sigma^2}{g m}$$

and  $J_0$  is the zeroth order Bessel function of the first kind,  $\sigma$  is the long wave angular frequency,  $g$  is gravity and  $m$  is the profile slope. The agreement was found to be good. Figure 4 presents an example of calculated and measured long wave envelopes for Case 3.

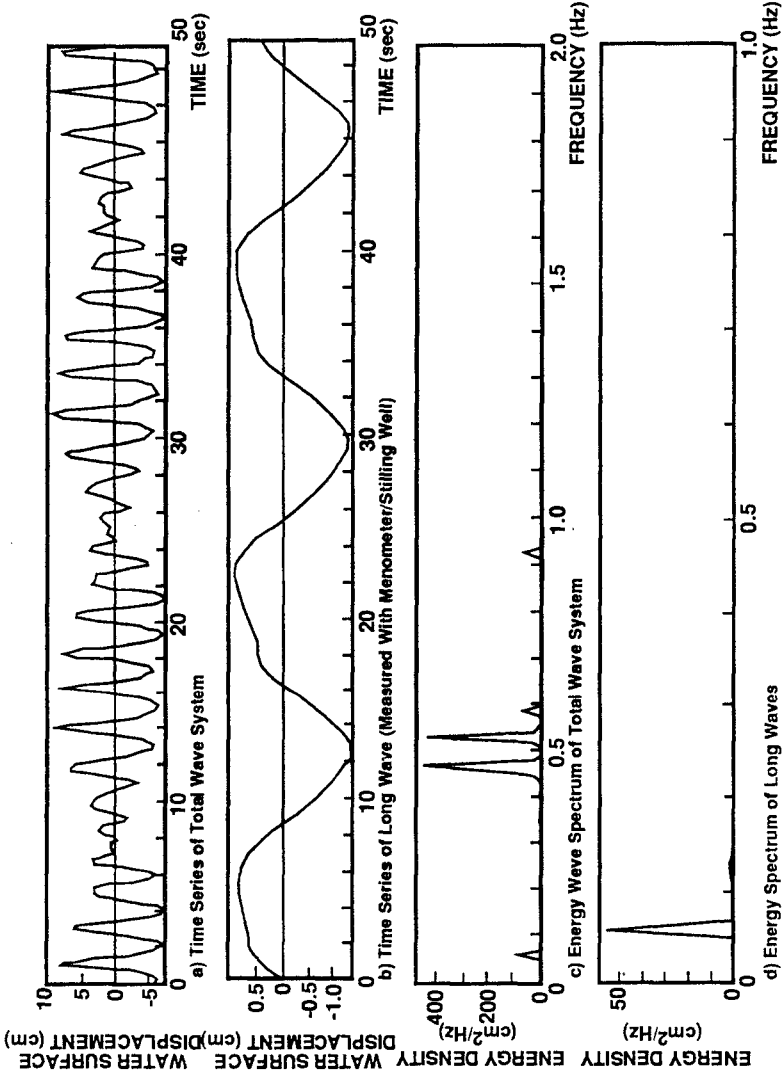
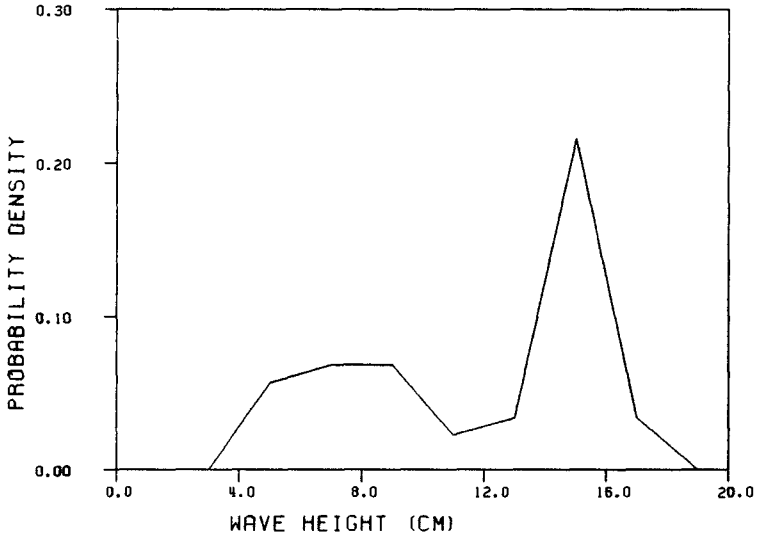
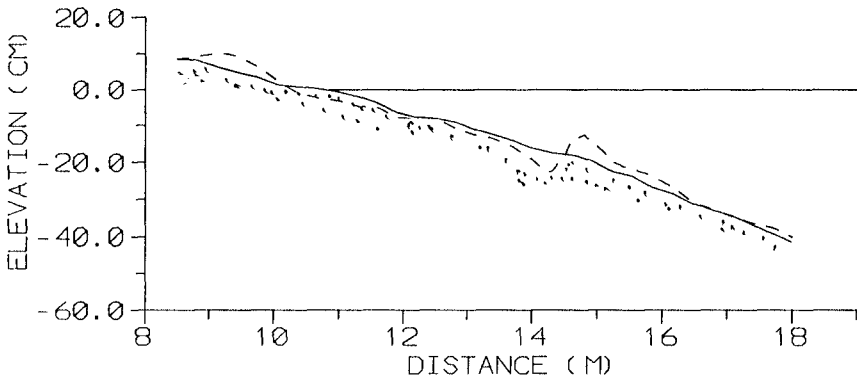


Figure 2. Case 1. Biharmonic Waves. Primary Wave Frequencies = 0.47 and 0.53 Hz.  
 Maximum Primary Wave Height  $\approx$  16 cm.



a) Wave Height Probability Distribution for Case 1.



b) Initial (Solid) and Final (Dashed) Profiles for Case 1.

Figure 3. Wave Height Probability Distribution and Initial and Final Profiles for Case 1.

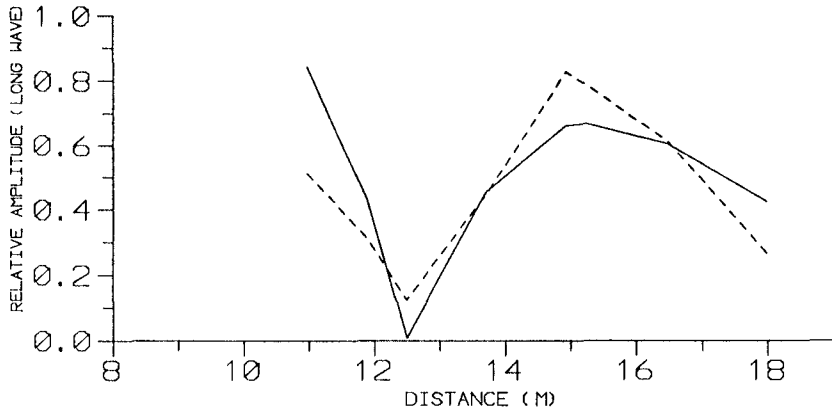


Figure 4. Comparison of Measured (Dashed) and Computed (Solid) Long Wave Envelopes for Case 3.

Table 1 summarizes the positions of the bar and nearest measured IG wave node and antinode. Plotted in Figure 5 is the relationship between the measured changes in bar and measured IG wave nodal/antinodal positions. The changes are relative to the next lower difference frequency (Table 1). If the bar were formed by the infragravity wave system, it is expected that a change in the IG nodal/antinodal position from one frequency to another would correspond to exactly the same change in bar position. Stated differently, the points in Figure 5 should fall along a straight line inclined at  $45^\circ$ , whereas although the positions of the nodes and antinodes changed as expected with IG frequency, the bar location experienced little change. Based on these results, the hypothesis that the bar is caused by the position of envelope of the IG wave is rejected. The nearly unchanging position of the bar position with nearly constant wave height supports the break point hypothesis of bar formation.

#### Effect of Wave Spectra and Wave Height Probability Characteristics on Bar Formation

A series of experiments was conducted to attempt to identify the effects of different incident wave spectral characteristics on bar formation. Table 2 summarizes the characteristics of these tests. Both continuous and discrete spectral shapes were tested. Figures 2 and 3 have presented an example for Case 1 showing primary and long wave records, the associated probability distributions and resulting profiles. Similar results for Case 5 are presented in Figures 6 and 7. Figure 8 documents the wave height probability distribution and initial and final profiles for Case 7 and the profiles for Case 8.



Table 1

Characteristics of Experiments with Biharmonic Primary Waves

Case	Primary Frequencies (Hz)	Difference Frequencies (Hz)	Nodal Position (m)	Antinodal Position (m)	Bar Position (m)
1	0.47, 0.53	0.06	14.3	15.3	14.8
2	0.46, 0.54	0.08	13.5	15.0	14.9
3	0.45, 0.55	0.10	12.5	15.0	14.8
4	0.44, 0.56	0.12	11.6	13.1	14.5

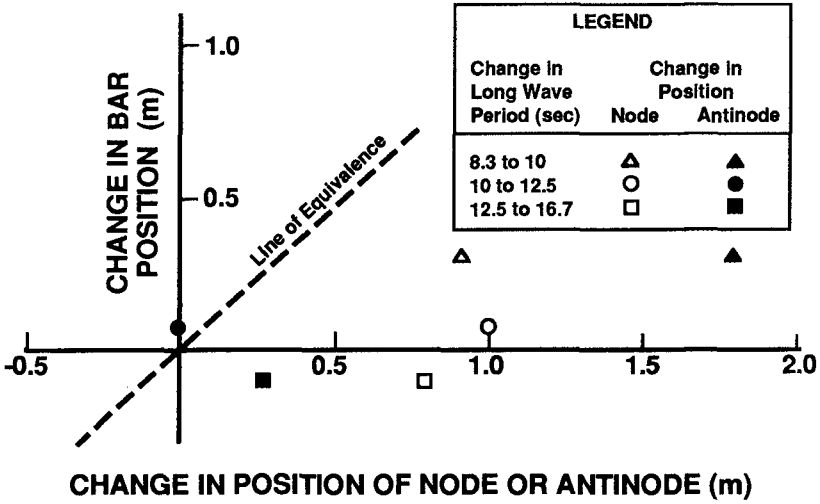


Figure 5. Change in Bar Position vs. Change in Positions of Nodes and Antinodes. Biharmonic Waves.

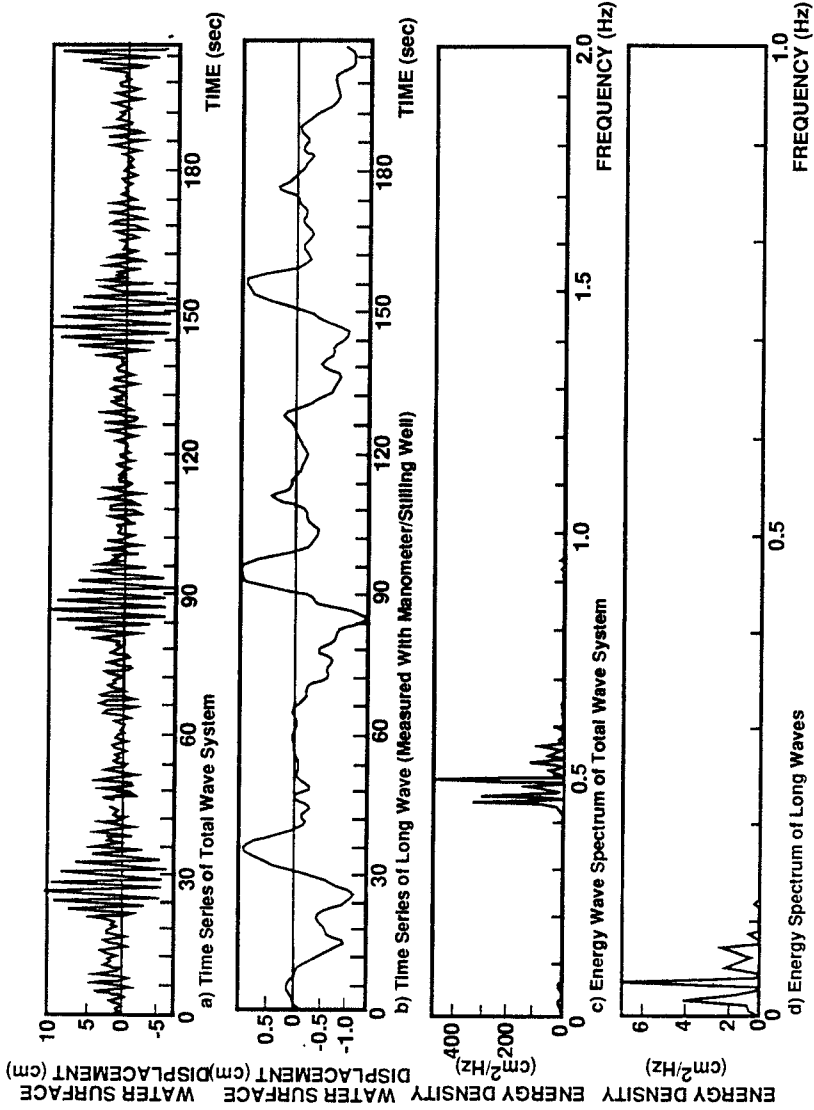
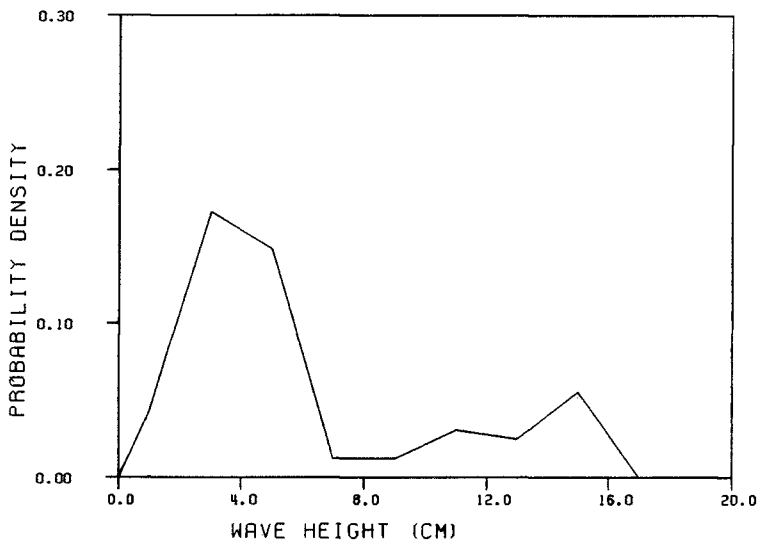
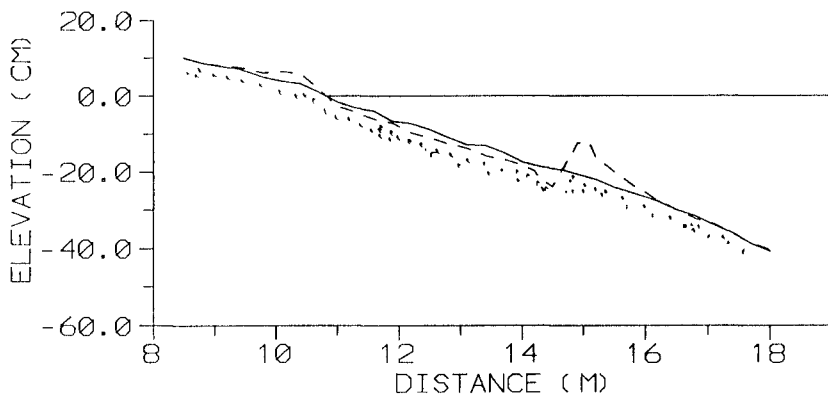


Figure 6. Case 5. Multifrequency Waves. Maximum Primary Wave Height  $\approx 16$  cm.

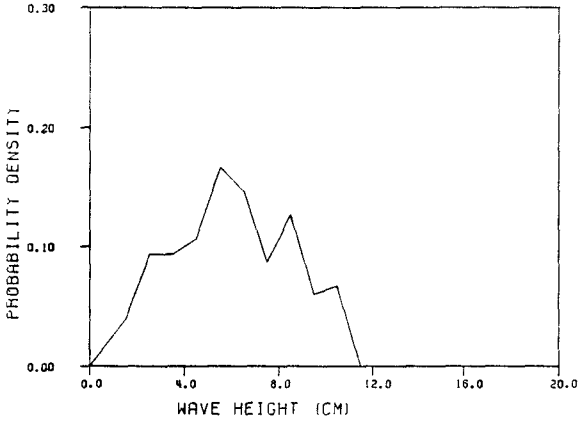


a) Wave Height Probability Density Function

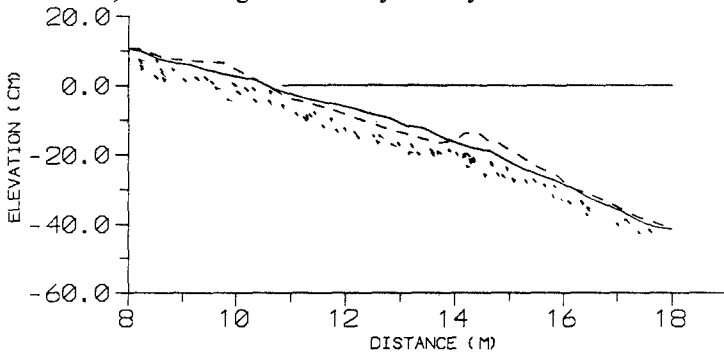


b) Initial (Solid) and Final (Dashed) Profiles

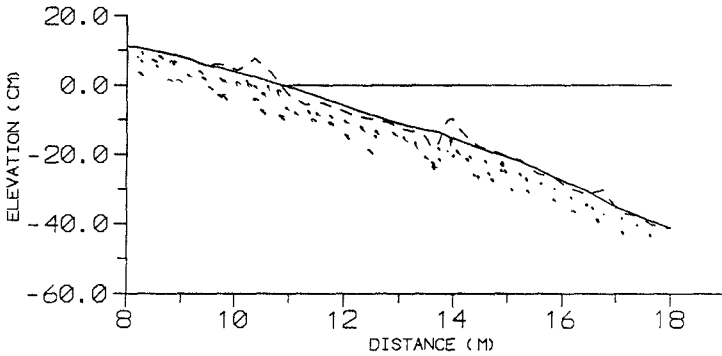
Figure 7. Case 5. Wave Height Probability Density Function and Initial and Final Profiles.



a) Wave Height Probability Density Function. Case 7.



b) Initial (Solid) and Final (Dashed) Profiles. Case 7.



c) Initial (Solid) and Final (Dashed) Profiles. Case 8.

Figure 8. Wave Height Characteristics (Case 7) and Profiles (Cases 7 and 8).

Table 2  
Test Characteristics for Various Spectral Characteristics

Case	Initial Profile	Spectral Character.	Mean Freq. (Hz)	Final Bar Position (m)	Maximum Wave Height (m)
5	Planar	Multifreq.	0.5	15.0	0.16
6	Barred	Multifreq.	0.5	15.0	0.16
7	Planar	Continuous	0.5	14.3	0.11
8	Planar	Monochrom.	0.5	13.9	0.11

The effects of the wave height probability density (WHPD) function are evident by comparing Figures 3, 7 and 8. The WHPD functions for Cases 1 and 5 have either primary or secondary peaks near the maximum wave height, whereas for Case 7, the most probable wave heights occur at a height of approximately one-half the maximum height. For Case 8 (monochromatic), the peak is at the maximum wave height. The final profiles for all cases with primary or secondary peaks near the maximum wave heights have pronounced bars whereas the final profile for the WHPD function with no peak near the maximum wave height is relatively subtle and diffuse (Figures 8a and 8b). Also, it was noticed during the experiments that the rate of evolution towards a fully developed bar was more rapid for those WHPD functions with a primary peak near the maximum wave height.

#### SUGGESTED MECHANISM FOR BAR FORMATION

Based on the results of this and previous studies, the following model is proposed for bar formation. The break point mechanism is responsible for the type of bars investigated here in the laboratory. Moreover, they also apply to bars that we have investigated in the field (Dolan and Dean 1985).

In order for bars to form, the fall velocity parameter  $H_0/(wT)$  ( $H_0$  = deep-water wave height,  $w$  = sediment fall velocity and  $T$  = wave period) must be greater than approximately 3 (Kriebel et al. 1986). Multiple bars require a sufficiently mild slope such that wave reformation and multiple breaking occurs. For conditions that are marginally favorable for bar formation, the probability distribution of breaking wave heights can result in non-formation if the WHPD function does not have a peak near the maximum wave height. Bars tend to be self maintaining by trapping waves to break on the bars. Conditions that are marginally favorable for bar formation can form a prominent bar if a bar feature is initially present.

The mechanism for bar formation can be considered in terms of a transport influence function,  $f(x')$  where  $x'$  is the local coordinate fixed to the time-varying breaking point and the function  $f(x')$  is scaled according to the breaking wave height or wave energy dissipation per unit water volume. Seaward of the breaking point the transport is landward, and landward of the breaking point the transport is directed seaward. When intense breaking wave conditions extend across a wide breaking zone, the net bar generating transport mechanisms are diminished relative to a stable breaking wave position. To reach equilibrium, there must be a negative feedback on the influence function. The failure to date to adequately define this feedback mechanism appears to be one of the major impediments in our attempts to quantify the full mechanisms for bar formation and equilibration.

### SUMMARY AND CONCLUSIONS

A series of wave tank experiments has been conducted to investigate mechanisms of bar formation. Conditions encompassed monochromatic waves and a variety of wave spectra, including cases specifically planned to generate and document the characteristics of the infragravity waves known to accompany a narrow spectrum of primary waves. The conclusions reached from this investigation are presented in the following paragraphs.

The tests conducted with two primary waves which produced a long standing wave were analyzed and the changes in bar position and changes in long wave nodal/antinodal positions compared. It was found that while the long wave nodal/antinodal positions changed as expected with the long wave period, the bar position experienced relatively small displacements. It is concluded that the bar position is governed by the breaking position rather than the long wave envelope structure.

Tests were conducted with a range of spectral shapes and a corresponding range of wave height probability density functions. It was found that for the tests conducted with a density function characterized by a primary or secondary peak near the maximum wave height, intense breaking occurred over a smaller range of positions and the bar was more accentuated and concentrated in position. For conditions with a maximum density near the mid-range of wave heights, breaking occurred over a correspondingly broader range of positions and the bar was somewhat more subdued and less concentrated. These results are interpreted as the result of the dynamic equilibrium in which, as the bar breaks at a particular location, it induces bar formation transport mechanisms; however, due to the aforementioned variation in breaking wave position, the breakpoint transport pattern is not positionally stable for a sufficient duration to cause the bar to form to the degree that would occur under a constant breaking position. On the basis of these findings, a conceptual model for bar formation is proposed, which has as a significant element, a transport influence function with characteristics near the breakpoint that tend to result in bar formation. Depending on the wave height

distribution function and the initial beach profile characteristics, the break point ranges across the active profile and thus results in a dynamic equilibrium.

It is hoped that the results presented herein will stimulate further research on bar formation which will either support the mechanisms presented here or will lead to a more thorough understanding and robust models of bar formation and maintenance.

### ACKNOWLEDGEMENT

The support of the Florida Department of Natural Resources for the work described in this paper is gratefully acknowledged.

### REFERENCES

- Buhr Hansen, J. and I.A. Svendsen (1974) "Laboratory Generation of Waves of Constant Form", Proceedings of the 14<sup>th</sup> Conference on Coastal Engineering, American Society of Civil Engineers, pp. 321-339.
- Carter, T.G., P.L.F. Liu and C.C. Mei (1973) "Mass Transport by Waves and Offshore Sand Bedforms", Journal of Waterways, Harbors and Coastal Engineering Division, American Society of Civil Engineers, Vol. 99, pp. 165-184.
- Dally, W.R. (1987) "Longshore Bar Formation- Surf Beat or Undertow?", Proceedings of the ASCE Specialty Conference on Coastal Sediments '87, pp.71-86.
- Dolan, T.J. and R.G. Dean (1985) "Multiple Longshore Sand Bars in the Upper Chesapeake Bay", Journal of Estuarine, Coastal and Shelf Science, Vol. 21, pp. 727-743.
- Kriebel, D.L., W.R. Dally and R. G. Dean (1986) "Undistorted Froude Model for Surf Zone Sediment Transport", Proceedings of the 20<sup>th</sup> Coastal Engineering Conference, American Society of Civil Engineers, Vol. 2, pp. 1393-1406.
- Sallenger, A.H. and P.A. Howd (1989) "Nearshore Bars and the Break-Point Hypothesis", Journal of Coastal Engineering, Vol.12, pp. 301-313.

## CHAPTER 155

# SHEET FLOW UNDER NONLINEAR WAVES AND CURRENTS

Mohammad Dibajnia <sup>1</sup> and Akira Watanabe <sup>2</sup>

### Abstract

Experiments were conducted on initiation and transport rate of sheet flow under asymmetric oscillations. Values of net sand transport rates under asymmetric oscillations and superimposed currents were also measured. In this paper, based on physical interpretations, a new parameter representing the observed transport mechanism is derived. Using this parameter a general transport formula is then presented and applied to estimating the net transport rate and its direction; fairly good agreement with the experimental results is observed. It is shown that the newly introduced parameter together with the sediment Reynolds number can fairly well express the inception of sheet flow.

### 1. Introduction

This paper is concerned with intense sand transport under high oscillatory shear stress conditions when ripples have been washed out and the bed is flat; the so-called sheet flow transport. As the orbital velocity of fluid over a rippled bed is increased, the oscillatory ripples lose their height and finally will all disappear. Sediment motion then occurs as a sheet of sand within a few centimeters of the bottom, moving with the intense orbital motions. A nearly flat bed with a high sediment transport rate is a condition that can be expected over much of the surf zone during storms (see for example Dingle and Inman, 1976). Therefore,

---

<sup>1</sup>Dr. Eng., Penta-Ocean Construction Co. Ltd., 2-2-8 Koraku, Bunkyo-ku, Tokyo 112, Japan (Post doctoral fellow, Univ. of Tokyo).

<sup>2</sup>Professor, Dept. of Civil Eng., Univ. of Tokyo, Bunkyo-ku, Tokyo 113, Japan.



detail knowledge of sheet flow transport is of decisive importance in a successful modeling of beach topography change.

There have previously been several experimental studies of sheet flow transport from different points of view. Among them Manohar (1955), Chan *et al.* (1972), Komar and Miller (1975), Kaneko (1981), and Horikawa *et al.* (1982) have considered the inception of sheet flow, while Horikawa *et al.* (1982), Sawamoto and Yamashita (1986), and Ahilan and Sleath (1987) have been concerned with the rate of sediment transport. These studies, however, have all considered the sheet flow under purely sinusoidal oscillatory motions. Hence, only transport rates over half a cycle have been obtained, because in a sinusoidal oscillation the net transport over a complete cycle is zero. In reality, however, waves are nonlinear and asymmetry of the near-bottom velocity during the two half cycles of the orbital motion or steady currents superimposed on the waves can produce significant net transport.

The objectives of the present study were to investigate the initiation of sheet flow under asymmetric oscillations, to measure the net sheet sand transport rate under asymmetric oscillations and superimposed steady currents, and, to establish a transport rate formula to be used in modeling of beach topography change.

## 2. Experiments

The present experiments were carried out in a loop-shape oscillatory/steady flow water tunnel at the University of Tokyo. The tunnel is driven by a piston to generate oscillations of any given arbitrary shape and by a pump to superimpose a steady current on the oscillation. It has a horizontal test section of rectangular cross section with glass side walls and removable acrylic ceilings. The test section is of 2.0 m length, 0.22 m height, and 0.24 m width. For the present experiments the width of the test section was reduced to 0.12 m in order to provide large values of velocity. Sand traps made of honeycombs were installed at both ends of the test section in order to trap the sand which would otherwise move out of the test section. Toyo-ura sand with median grain size of 0.2 mm and mean fall velocity,  $W$ , of 2.3 cm/s was used. The depth of the bed of sediment was approximately 7 cm with a length of 1.6 m.

Five oscillation periods ranging from 1 s to 4 s and four nonlinearity indices  $u_{max}/\hat{u} = 0.5, 0.6, 0.7, 0.8$  (see Fig. 1) were selected. Longer oscillation periods could not be used because of the limited length of the test section. Time histories of the water particle displacement were simulated on the base of the first-order cnoidal wave theory which is valid in relatively shallow water. A laser-Doppler velocimeter was used to measure the water particle velocities through the side wall of the tunnel. Velocity profiles corresponding to each case were measured over a fixed bed and were then repeated over the sandy bed.

At first, conditions for disappearance of ripples and inception of sheet flow were investigated and net transport rates due to pure oscillatory motions were

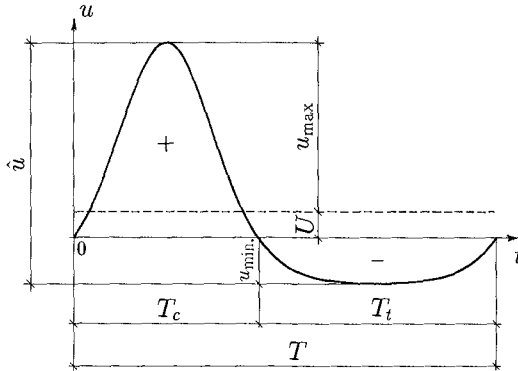


Figure 1: A typical velocity profile.

measured. Then four steady flow velocities ( $U \simeq -20, -10, 10, 20$  cm/s) were superimposed on each of the oscillations and resulting net transport rates were measured.

To investigate the initiation of sheet flow, the normal test procedure was for the tunnel to be set in motion with the required frequency and nonlinearity index, while the bed was flat. At the beginning the amplitude of the oscillation was small in order to let the ripples appear and form. Then the amplitude was gradually increased until the ripples disappear and the bed became flat again. For the measurement of net transport rate the procedure was as follows. First a thin plate was carefully placed at the middle of the test section, to separate its two sides completely, and the sand was weighted and placed in each side in such a way to make a uniform flat bed. Then the plate was removed and the tunnel was set in the required motion for as long as 100 cycles of oscillations provided that the bed remained nearly flat. The test time duration was shorter if the bed started to distort. Finally the thin plate was again placed at the middle of test section and the sand from each side was removed and weighted to give the net transport rate.

### 3. Initiation of Sheet Flow

A total of 18 cases covering periods of 1 to 4 s and nonlinearity indices  $u_{\max}/\hat{u} = 0.5$  to 0.8 were tried. There was no steady current. In order to classify the data by using the conventional parameters, a knowledge of near-bottom orbital velocity amplitude and period is required. Unlike a sinusoidal velocity profile, appropriate definitions for the above mentioned quantities are less clear for an asymmetric velocity profile and they could be different according to the phenomenon under investigation.

Analysis of the current data shows that the maximum velocity for the incep-

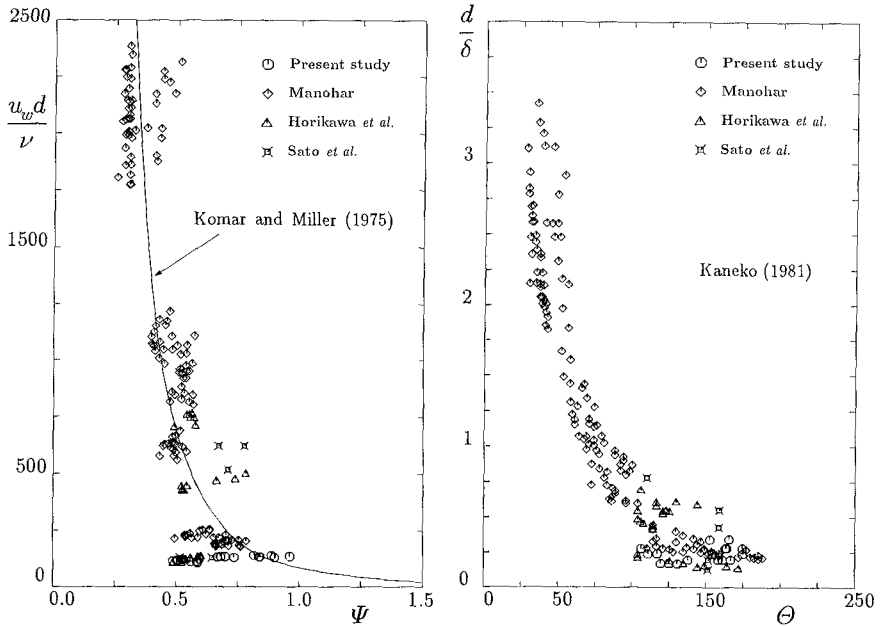


Figure 2: Behavior of two of the available criteria for inception of sheet flow.

tion of sheet flow changes with both the wave period and nonlinearity but the effect of nonlinearity is much more significant; namely, for a given wave period, a more asymmetric velocity profile requires a higher maximum velocity to wash out the ripples and initiate the sheet flow transport. It is concluded that as far as the disappearance of ripples and inception of sheet flow is concerned, it is the energy contained in the near-bottom velocity profile which is the important factor in defining the near-bottom orbital velocity amplitude,  $u_w$ . That is why for a more asymmetric profile, with a slender crest and a wide but small trough, a higher maximum velocity is required. Hence,  $u_w$  is defined as

$$u_w^2 = 2u_{rms}^2 = \frac{2}{T} \int_0^T u^2 dt \tag{1}$$

in which  $u_{rms}$  is the root mean square value of  $u$  and the other definitions are given in Fig. 1. In case of a sinusoidal velocity profile  $u_w$  obtained by (1) is equal to the velocity amplitude. Hence,  $u_w$  defined by (1) is an equivalent sinusoidal velocity amplitude for the asymmetric velocity profile.

Manohar (1955) has reported data on disappearance of ripples for a wide range of sediments and under different flow conditions. His data are reanalyzed and used together with the data of Horikawa *et al.* (1982), Sato *et al.* (1987), and the present data. Several different parameters and their combinations are examined. It is found that the two parameters used by Kaneko (1981),

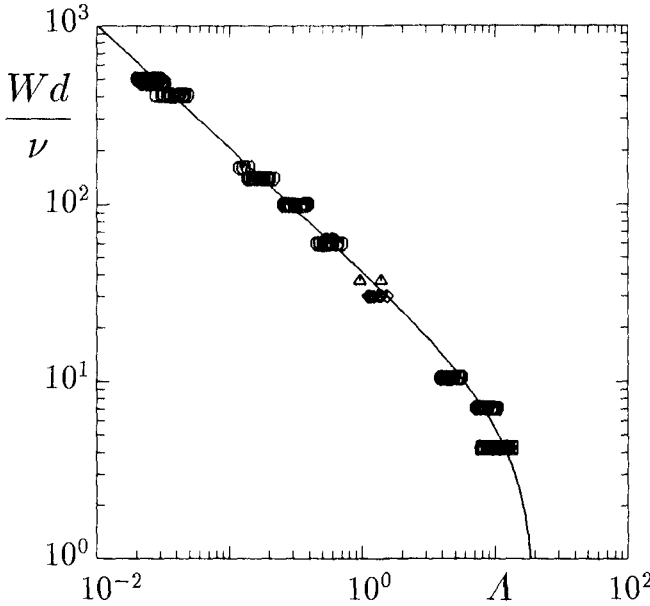


Figure 3: Sheet flow inception criterion of this study.

$$\Theta = \frac{u_w^2}{sgd} \quad \text{and} \quad \frac{d}{\delta} ,$$

give a more continuous and clear trend, shown in Fig. 2, than the other existing criteria including that of Komar and Miller (1975). Here  $d$  is the grain size,  $\delta = \sqrt{2\nu T/\pi}$  the Stokes layer thickness,  $\nu$  the fluid kinematic viscosity,  $g$  the acceleration of gravity, and  $s = (\rho_s - \rho)/\rho$  with  $\rho_s$  and  $\rho$  being the densities of sand and fluid, respectively. One can say that under an intense fluid motion it is the strong turbulence structure near the bottom which destroy the ripples rather than a shear mechanism. Therefore,  $\Theta$  which represents the flow energy or intensity is more appropriate than the relative bottom shear stress,  $\Psi$ , used by Komar and Miller.

In the next section a new parameter,  $\omega$ , is introduced which may be further changed to

$$\Lambda = \frac{u_w^2}{sgWT} \cdot \left(\frac{\delta}{d}\right)^2 . \tag{2}$$

The following relation is then found to give a good inception criterion (Fig. 3).

$$\frac{Wd}{\nu} = 42.5 \left(\frac{1}{\Lambda} - 0.05\right)^{0.69} \tag{3}$$

It should be pointed out again that the present data are for the initiation of sheet flow over a rippled bed. In case of an initially flat bed, however, sheet flow could occur in lower flow velocities. This is because that over a rippled bed an excess amount of energy, comparing with a flat bed, is required to level the bed.

#### 4. Net Transport Rate

More than 100 experiments were carried out and the net transport rates were measured. According to Ahilan and Sleath (1987), the sheet sand transport rate over a half cycle of a sinusoidal oscillation can be well estimated as a function of the Shields stress,  $\Psi$ , by the formula of Shibayama and Horikawa (1980),

$$\phi = 19.0 \Psi^3, \quad (4)$$

which is same as the formula of Madsen and Grant (1976) with a different value of the coefficient. In this relation  $\phi = (1 - \lambda)q/Wd$  is the nondimensional transport rate,  $q$  the volume of transported sand per unit time, and  $\lambda$  the porosity of sand. Madsen and Grant suggested that under an asymmetric oscillation the overall net sediment transport rate,  $\Phi = (1 - \lambda)Q/Wd$ , could be calculated by integrating their formula with respect to time, half cycle by half cycle and taking the difference between the rates during successive half cycles. Denoting this by  $\Phi_{cal.}$ , one may write

$$\Phi_{cal.} = \frac{19.0}{T} (T_c \Psi_c^3 - T_t \Psi_t^3) \quad (5)$$

in which

$$\Psi_c = \frac{1}{2} f_c \frac{u_c^2}{sgd}, \quad \Psi_t = \frac{1}{2} f_t \frac{u_t^2}{sgd}$$

and

$$u_c^2 = \frac{2}{T_c} \int_0^{T_c} u^2 dt, \quad u_t^2 = \frac{2}{T_t} \int_{T_c}^T u^2 dt \quad (6)$$

where  $u_c$  and  $u_t$  are equivalent sinusoidal velocity amplitudes for the positive and negative portions of the velocity profile, respectively, and  $f_c$  and  $f_t$  are their corresponding friction factors. Figure 4 shows the comparison between calculated and measured net transport rates,  $\Phi_{cal.}$  and  $\Phi_{meas.}$ , for all the cases. It is seen that except for few cases the disagreement is generally high and this method fails to predict not only the magnitude of the net transport rate but also its direction. It is clear that such a procedure could be correct only if the sand transports during the two half cycles are completely independent of each other. Then, under such a condition and for a velocity profile similar to the one shown in Fig. 1 (*i.e.*  $|u_{max}| \gg |u_{min}|$  and  $T_c \leq T_t$ ), the net transport rate should usually be in the direction of positive velocity. However, during the present experiments it

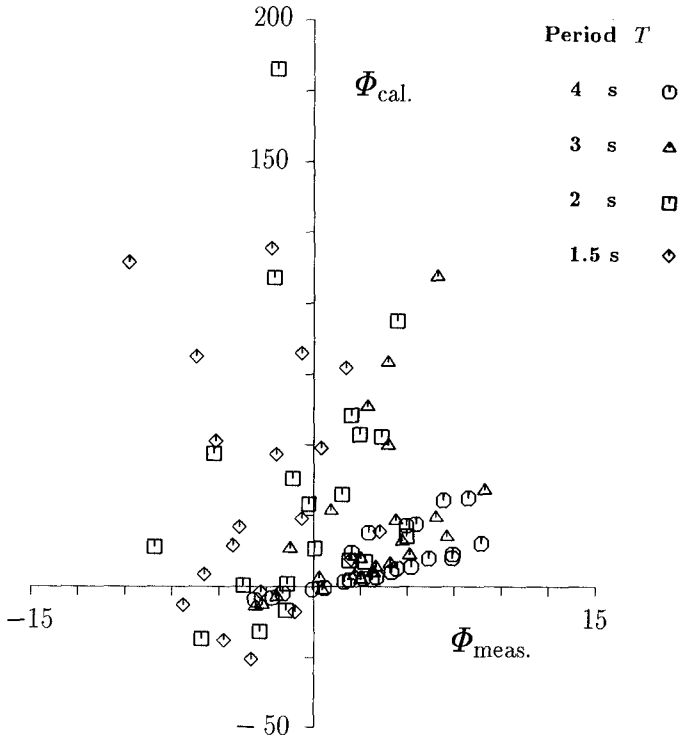


Figure 4: Comparison between  $\Phi_{meas.}$  and  $\Phi_{cal.}$ .

was noticed that especially for highly asymmetric profiles (*i.e.*  $u_{max}/\hat{u} = 0.8$ ) the sand which had been entrained during the positive half cycle, was brought back into the negative direction by the successive negative half cycle; and this mechanism in some cases was strong enough to make the net transport to be in the negative direction. In fact, it was observed that sheet flow is the motion of a condense suspended sand layer which is confined to the region near the bottom and its thickness depends on the magnitude of velocity. Once there was a positive velocity large enough to raise up sand particles to such a level that they could not reach the bottom before the negative velocity occurred, then these particles tended to be carried to the negative direction.

In order to evaluate this mechanism we assume, as a first approximation, that the fluid and sediment should move together with the same velocity, and that the flow kinetic energy is transferred to the required potential energy to raise up sand particles through the strong but confined eddies which exist inside the sand sheet layer. Hence, the kinetic energy,  $E_k$ , of a sand particle with volume  $V$  moving with its ambient fluid, averaged over the time under the positive velocity,  $T_c$ , may be estimated as

$$E_k = \frac{1}{2} \rho V u_c^2 \quad (7)$$

The potential energy,  $E_p$ , required to raise that particle as high as one unit of length is

$$E_p = (\rho_s - \rho) V g \quad (8)$$

Therefore, the distance that a sand particle travels upward, or in other words, the thickness of sand sheet layer,  $\Delta_s$ , can be obtained as

$$\Delta_s = \frac{E_k}{E_p} = \frac{1}{2} \frac{u_c^2}{s g} \quad (9)$$

According to this expression the thickness of sheet layer is proportional to the square of velocity and independent of the grain size. Now let's consider a sand particle which is entrained. It will fall into the bottom by its free fall velocity,  $W$ . The time required for this particle to reach the bed,  $T_{\text{fall}}$ , will be

$$T_{\text{fall}} = \frac{\Delta_s}{W} = \frac{1}{2} \frac{u_c^2}{s g W} \quad (10)$$

Suppose a case in which  $T_{\text{fall}}$  is longer than  $T_c$ . Then what will happen is that before the sand particle reaches the bottom, the negative velocity will occur and will carry it into the negative direction. This means that the ratio of  $T_{\text{fall}}/T_c$  can be an appropriate indication for the phenomenon of our interest. Thus, we define  $\omega_c$  as

$$\omega_c = \frac{1}{2} \frac{u_c^2}{s g W T_c} \quad (11)$$

to represent the intensity of the above suspension mechanism. In Fig. 5 the measured net transport rates,  $\Phi_{\text{meas.}}$ , under pure oscillatory motion are plotted against their corresponding values of  $\omega_c$ . It is seen that  $\Phi_{\text{meas.}}$  increases with increasing  $\omega_c$  until it reaches a maximum at around  $\omega_c = 1$  and, due to the already-mentioned suspension mechanism, starts to decrease thereafter. For values of  $\omega_c$  greater than about 2.5, the mechanism is so strong that makes the net transport to be in the negative direction. From this figure we can see that  $\omega_c$  is an appropriate tool not only for the prediction of transport direction but also for estimating the magnitude of net transport rate. In fact  $\omega_c$  is a time ratio which in turn is an indication of the intensity of suspension, and/or an indication of the sand concentration.

Up to now we have only considered the positive portion of a velocity profile. However the same suspension mechanism could happen during the negative half cycle. Therefore we introduce  $\omega_t$  as

$$\omega_t = \frac{1}{2} \frac{u_t^2}{s g W T_t} \quad (12)$$

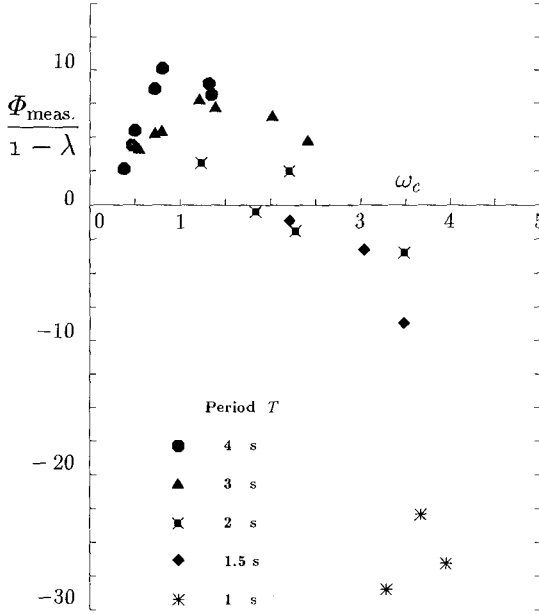


Figure 5: Relation between the measured net transport rates and the parameter  $\omega_c$ .

Now, the net transport rate should be obtained as the difference between the rates during the two half cycles including the effect of suspension during one half cycle on its successive half cycle. It was already described that part of the sand entrained during the positive half cycle of velocity profile may remain in suspension and be carried by the velocity of the successive negative half cycle into the negative direction, and vice versa. Hence, for example, the negative velocity has two groups of sand to carry; one is the sand which is entrained by the negative velocity itself, and the other one is the sand remaining in suspension from the previous positive half cycle. Having this in mind, we define a parameter,  $\Gamma$ , to represent the net transport rate, as

$$\Gamma = \frac{u_c T_c (\Omega_c^3 + \Omega_t'^3) - u_t T_t (\Omega_t^3 + \Omega_c'^3)}{(u_c + u_t) T} \quad (13)$$

In this relation  $\Omega_c'$  represents the amount of suspended sand remaining from the positive half cycle, to be carried by the negative velocity. Similarly  $\Omega_t'$  stands for the amount of sand still in suspension from the negative half cycle which will be transported to the positive direction. On the other hand,  $\Omega_c$  represents that amount of sand which is entrained and carried only by the positive velocity;



and  $\Omega_t$  indicates the amount of sand which is entrained, transported, and settled during the negative half cycle.

It was already discussed that if the values of  $\omega$  ( $\omega_c$  and  $\omega_t$ ) are less than unity there will be no exchange of suspended sand between the two half cycles; both  $\Omega'_c$  and  $\Omega'_t$  will then be equal to zero. It was also mentioned that  $\omega_c$  (or  $\omega_t$ ) is a parameter with two meanings; namely, it represents the time ratio  $T_{fall}/T_c$  (or  $T_{fall}/T_t$ ) and also it indicates the intensity of sand concentration. Now suppose a case in which  $\omega$  ( $\omega_c$  or  $\omega_t$ ) is greater than one. Consider  $\omega$  as representing the sand concentration. It should be divided into two parts; one part corresponding to the sand transported and settled during the current half cycle,  $\omega_m$ , and the second part,  $\omega'$ , corresponding to the sand which will be delivered to the successive half cycle. This time consider  $\omega$  as the time ratio. If this ratio is greater than one the suspension mechanism will be effective. The larger a value of  $\omega$  the more suspended sand to be delivered to the next half cycle. Hence, we may assume that  $\omega'$ , as a first approximation, is equal to the amount that  $\omega$  surpasses unity; namely,

$$\left\{ \begin{array}{l} \text{if } \omega \leq 1 \\ \text{if } \omega > 1 \end{array} \right\} \left\{ \begin{array}{l} \omega_m = \omega \\ \omega' = 0 \\ \omega_m = 1 \\ \omega' = \omega - 1 \end{array} \right. \quad (14)$$

Based on the above interpretation, the following relations are used to estimate values of  $\Omega_c$ ,  $\Omega'_c$ ,  $\Omega_t$ , and  $\Omega'_t$ :

$$\left\{ \begin{array}{l} \text{if } \omega_c \leq 1 \\ \text{if } \omega_c > 1 \\ \text{if } \omega_t \leq 1 \\ \text{if } \omega_t > 1 \end{array} \right\} \left\{ \begin{array}{l} \Omega_c = \omega_c \cdot \frac{WT_c}{d} \\ \Omega'_c = 0 \\ \Omega_c = \frac{WT_c}{d} \\ \Omega'_c = (\omega_c - 1) \cdot \frac{WT_c}{d} \\ \Omega_t = \omega_t \cdot \frac{WT_t}{d} \\ \Omega'_t = 0 \\ \Omega_t = \frac{WT_t}{d} \\ \Omega'_t = (\omega_t - 1) \cdot \frac{WT_t}{d} \end{array} \right. \quad (15)$$

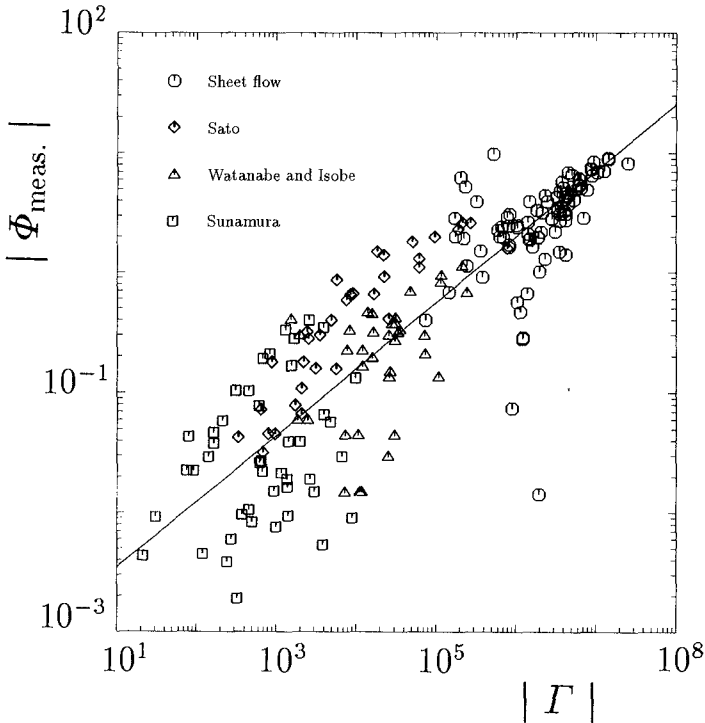


Figure 6: Relation between  $|\Phi_{\text{meas.}}|$  and  $|\Gamma|$ .

Figure 6 shows values of  $|\Gamma|$  plotted versus  $|\Phi_{\text{meas.}}|$  for the present sheet flow data and for the previous data on suspended load above ripples. Fairly good relation is observed for the present data. The solid line which is fitted for the present data reads

$$|\Phi_s| = 0.001 |\Gamma|^{0.55} . \quad (16)$$

Values of  $\Phi_s$  based on this relation are compared with the measured values in Fig. 7;  $\Phi_s$  taking the same sign as  $\Gamma$ . It is seen that both the magnitude and direction of net transport rate under sheet flow condition are very well predicted.

The generality of  $\Gamma$  defined by (13) also permits its application to estimating the net transport rate over ripples. It is well known that suspended load is the predominant transport mode over sand ripples. Although the suspension mechanism above a rippled bed is different from that of sheet flow, but one may expect that the present concepts generally hold, though in a different scale, for suspended transport over ripples. It should be noticed that in the presence

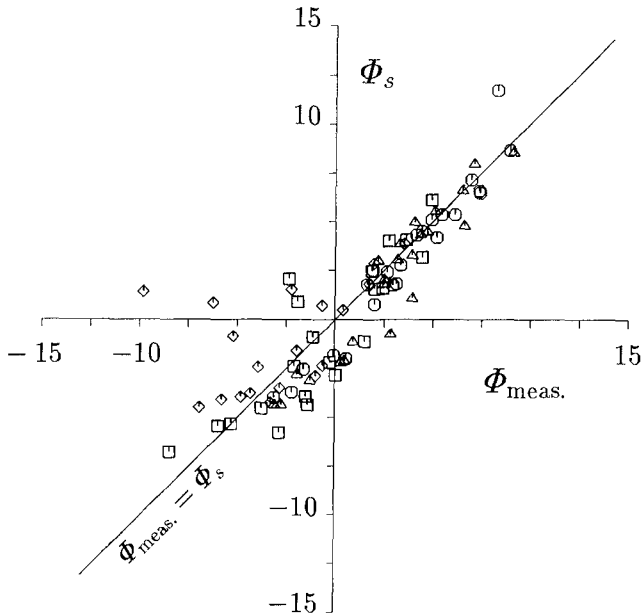


Figure 7: Comparison between  $\Phi_{\text{meas.}}$  and  $\Phi_s$ .

of ripples usually most of the sand suspended during one half cycle is carried by the velocity of the coming successive half cycle. This means that over the ripples values of  $\Omega'$  should be much larger than their corresponding values of  $\Omega$ . Hence, in relations (14), we may change the critical value of  $\omega$  from unity to a value of the order of 0.001 corresponding to bedload condition. This is tried for the experimental data of Sato (1987), Watanabe and Isobe (1990), and Sunamura (1982) and the results are shown in Fig. 7. It should be mentioned that measured velocity profiles for the data of Sato and those of Sunamura were not available; they are calculated by using the Stream Function Method from the reported flow conditions. Also for the data of Watanabe and Isobe, only the maximum and minimum values of velocity and values of  $T_c$  and  $T_t$  were available. Sunamura's data have been obtained in a wave flume, while those of Sato, and Watanabe and Isobe are from the same flow tank as that of the present experiments. Considering these points we can see the reasonable performance of  $\Gamma$  in estimating the transport rate above ripples.

It is instructive to note that the third power of  $\Omega$  which corresponds to the sixth power of velocity is used in relation (13), and then nearly the square root of  $\Gamma$  is taken in (16). This shows the correlation of transport rate with nearly the third power of velocity. However, using a power of 1.5 instead of 3 for  $\Omega$  in (13) gives a slightly weaker correlation than what is seen in Fig. 6.

In a real field, there is a transition region between the rippled bottom of

suspended load and the flat bed of sheet flow. Over this region, the ripple height decreases and the net transport rate changes its direction from the offshoreward suspended load to the shoreward sheet flow. The critical value of  $\omega$ , should then be gradually changed from 0.001 to unity over this transition region. Further study on the critical value of  $\omega$  for suspended load is also required.

## 5. Conclusions

Experiments were conducted on the initiation of sheet flow under asymmetric oscillations, and on the net sand transport rate under asymmetric oscillations and superimposed currents. Concerning the inception of sheet flow it is found that for a velocity profile with an arbitrary shape, it is the energy contained in that velocity profile which is the important factor in defining the near-bottom orbital velocity amplitude. Among the available criteria, it is found that the parameters used by Kaneko (1981) give a more continuous and clear trend than those by the others. A new parameter is also introduced which together with the sediment Reynolds number can fairly well express the inception of sheet flow with a better performance than that of Kaneko.

The validity of the method of Madsen and Grant (1976) in predicting the net transport rate and its direction under sheet flow condition is examined. It is found that except for few cases this method fails to predict not only the magnitude of the net transport rate but also its direction. Their procedure could be correct only if the sand transports during successive half cycles of oscillations are completely independent of each other. In the present study it is found that once there is a positive velocity large enough to raise up sand particles to such a level that they can not reach the bottom before the negative velocity occurs, then these particles tend to be carried to the negative direction. Based on physical interpretations a new parameter representing this phenomenon is derived. Using this parameter a general transport formula is presented in which the above-mentioned mechanism is taken into account. It is shown that both the magnitude and direction of net transport rate under sheet flow condition are very well predicted by the new formula, and that the formula is potentially applicable to estimating the net transport rate of suspended load above ripples.

It should be mentioned that in the present formulation, the steady current velocity is added to the oscillatory velocity profile and the resulting velocity profile is then used and analyzed. This is different from those methods who consider the transports due to waves and currents separately. It is seen that the present method is successful and more realistic, while its application to the horizontal plane problems is also straightforward. Another point is that the Shields parameter is not used in this study for estimating the transport rate. This is because of the uncertainty still involved in estimating values of friction factor under intense flow conditions. Once the shear stress at the bottom could be accurately determined, then it should be used in the formulations.

## 6. References

- Ahilan, R. V. and F. A. Sleath, 1987: Sediment transport in oscillatory flow over flat beds, *J. Hydraul. Eng., ASCE*, Vol. 113, NO. 3, pp. 308-322.
- Chan, K. W., M. H. I. Baird and G. F. Round, 1972: Behaviour of beds of dense particles in a horizontally oscillating liquid, *Proc. R. Soc. Lond.*, A-330, pp. 537-559.
- Dingler, J. R. and D. L. Inman, 1976: Wave-formed ripples in nearshore sands, *Proc. 15th Int. Coastal Eng. Conf., ASCE*, pp. 2109-2126.
- Horikawa, K., A. Watanabe and S. Katori, 1982: Sediment transport under sheet flow condition, *Proc. 18th Int. Coastal Eng. Conf., ASCE*, pp. 1335-1352.
- Kaneko, A., 1981: Oscillation sand ripples in viscous fluids, *Proc. JSCE*, No. 307, pp. 113-124.
- Komar, P. D. and M. C. Miller, 1975: The initiation of oscillatory ripple marks and the development of plane-bed at high shear stresses under waves, *J. Sedimentary Petrology*, Vol. 45, No. 3, pp. 697-703.
- Madsen, O. S. and W. D. Grant, 1976: Quantitative description of sediment transport by waves, *Proc. 15th Int. Coastal Eng. Conf., ASCE*, pp. 1093-1112.
- Manohar, M., 1955: Mechanics of bottom sediment movement due to wave action, *U.S. Army Corps of Engrs., B.E.B. Tech. Memo.*, No. 75, 121 pp.
- Sato, S., 1987: Oscillatory boundary layer flow and sand movement over ripples, *Dr.E. Thesis, Univ. of Tokyo*, 135 pp.
- Sato, S., S. Sugiura and A. Watanabe, 1987: Sand transport mechanism and ripple disappearance in irregular oscillatory flows, *Proc. 34th Japanese Conf. on Coastal Eng., JSCE*, pp. 246-250 (in Japanese).
- Sawamoto, M. and T. Yamashita, 1986: Sediment transport rate due to wave action, *J. Hydrosc. Hydraul. Eng.*, Vol. 4, No. 1, pp. 1-15.
- Shibayama, T. and K. Horikawa, 1980: Bed load measurement and prediction of two-dimensional beach transformation, *Coastal Eng. in Japan*, Vol. 23, pp. 179-190.
- Sunamura, T., 1982: Laboratory study of on-offshore sediment transport rate in shallow water region, *Proc. 29th Japanese Conf. on Coastal Eng., JSCE*, pp. 239-243 (in Japanese).
- Watanabe, A. and M. Isobe, 1990: Sand transport rate under wave-current action, *Proc. 22nd Int. Coastal Eng. Conf., ASCE*, pp. 2495-2507.

## CHAPTER 156

### Assessment of Coastal Processes for the Design and the Construction of the Zeepipe Landfall in Zeebrugge

ir. A. EIDE, Senior Geotechnical Engineer - STATOIL (Norway)  
ir. B. MALHERBE, Project Manager - HAECON N.V. (Belgium)  
ir. M. MERCANTI, Senior Pipeline Engineer - SNAMPROGETTI (Italy)  
ir. E. LAHOUSSE, QA Manager - HAECON N.V. (Belgium)

#### ABSTRACT

Early 1991, Statoil started with the installation of a 40 inch diameter gas pipeline between the Sleipner and later Troll field in the Norwegian sector of the North Sea and the harbour of Zeebrugge on the Belgian coast.

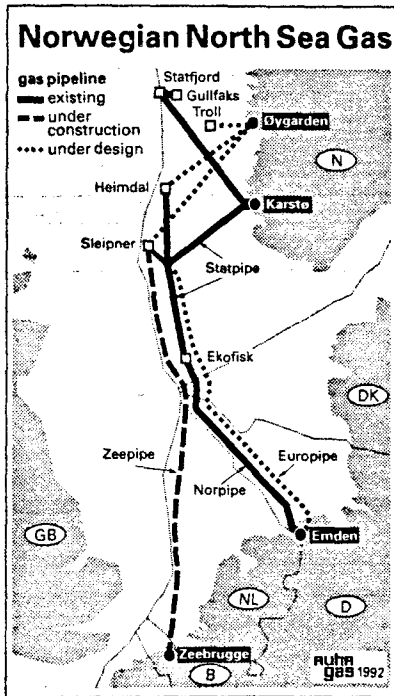
The connection between the offshore and the onshore pipeline was performed in August 1991, in the landfall area of Zeebrugge. The design and the construction of the landfall in the nearshore area required an extensive survey and engineering program taking the environmental parameters and the coastal processes into account.

#### 1. INTRODUCTION

The Zeepipe Gas Pipeline Project for the delivery of natural gas extracted from the Sleipner field was approved by the Norwegian Parliament in December 1986. Den Norske Stats Oljeselskap A.S. (Statoil, Stavanger - Norway) is the operator on behalf of the Zeepipe owners and is responsible for the planning, the construction and the operation of the Zeepipe system.

Zeepipe is the largest offshore pipelaying project undertaken up till 1991. Approximately 810 km of 40", 38 km of 30" and 230 km of 20" pipelines will go through the Norwegian, Danish, German, Dutch and Belgian sectors of the North Sea.

Zeepipe is a pipeline system for the transport of gas from the Norwegian Sleipner field to Zeebrugge on the Belgian Coast.



**Figure 1** : Description of Zeepipe system

In the North Sea (figure 1) the Zeepipe system will also be connected to the existing Statpipe- and Norpipe systems (Stolberg - 1992).

Via the terminal in Zeebrugge Zeepipe will be connected to the European gas distribution system. The gas will be distributed to purchasers from Germany, France, Belgium, the Netherlands and Spain.

The landfall of Zeepipe was planned to be in the Zeebrugge Harbour with the Landfall Valve Station (LVS) on the LNG-peninsula of Zeebrugge.

The design of the landfall had to take all nearshore coastal processes, geotechnical and sedimentological characteristics of the area into account to allow proper pipelaying and pipeline operation.

## 2. THE ZEEBRUGGE LANDFALL AREA

### 2.1. General site description and morphology

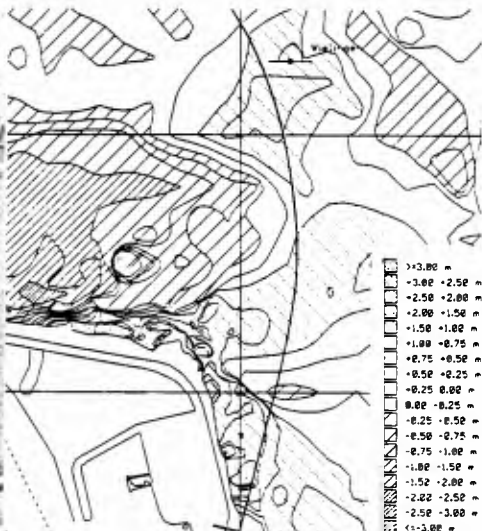
The landfall area on the Belgian Coast is located on the eastside of the Zeebrugge Harbour southeastern dam (rubblemound breakwater). The offshore area in which Zeepipe is installed is a part of the Southern Bight of the North Sea.

The area (figure 2) under concern for Zeepipe and the landfall is part of the fore-delta of the Western Scheldt estuary. Strong hydrodynamic, morphological and sedimentological conditions are characterizing this region of the North Sea where relative "young" quaternary deposits occur on the seabed.

Some kilometers north of the Zeebrugge harbour, two important shipping lanes are draining most of the in- and outgoing traffic to and from the Western Scheldt estuary, i.e. the Scheur and the Wielingen.



**Figure 2 :**  
Nearshore and shore approach  
area for the landfall of  
Zeepipe in Zeebrugge.



**Figure 3 :**  
Differential map (1990-  
1986) of the shore  
approach and beach area  
processed with DTM.

In order to assess the environmental conditions related to the bottom lithology and the soil conditions during the engineering, detailed pre-laying surveys have been executed.

## 2.2. Bathymetric survey

In order to provide recent and detailed data on the seabed topography, bathymetric surveys have been carried out in a corridor, centered along the Zeepipe axis (corridor width : 1000 m).

The bathymetric survey has been executed using the Atlas Fansweep 200 kHz swathe echosounder (sweep angle : 126°) simultaneously with a dual-beam Atlas Deso 20 echosounder (detection of loose mud deposits).

The swathe echosounder Fansweep, used for the first time on operational basis, delivered very detailed bathymetric maps with on average 1 depth value/m<sup>2</sup> (Vessel used : "M.S Pegasus" from Geoconsult A.S). Tide-reduction was achieved by using the official tide-gauges and 1 extra shorebased and 1 extra offshore selfrecording tide gauge.



Bathymetric survey data were processed using advanced DTM-processing (Digital Terrain Model) on HP-9000 CAD-computer to produce the combined survey maps.

Parallel to these bathymetric surveys, all available existing hydrographic data from 1980 to 1990 and in a 5 km wide corridor along Zeepipe were collected (data-base Haecon N.V.) and processed as differential maps to determine natural and man-made recent morphological changes of the seabed (e.g. fig. 3)

### 2.3. Geophysical survey :

Because of the known soil heterogeneity and the local presence of outcropping tertiary geologic layers, shallow seismic survey has been conducted in the surveyed Zeepipe corridor in order to pilot the geotechnical/geologic soil investigation.

A shallow seismic survey was carried out by using alternatively a 50 J EG & G Minisparker and a Thompson Pipeliner (3,5 + 7 kHz) in order to optimize penetration.

The significant seismic reflectors are associated with important layers for the design, i.e. :

- a. the erosion surface of the tertiary layers marking the transition from tertiary to recent quaternary deposits (often associated with gravel) ;
- b. overconsolidated tertiary clay layers

In combination with the shallow seismic tracks, side-scan sonar surveys were executed (apparatus : Klein 531T (100 kHz) + EG & G260 (100 kHz)) in order to identify :

- a. possible obstacles (wrecks, cables, ...) ; 4 significant obstacles were detected ;
- b. morphologic bottom features such as ripples, sand-waves, ... reflecting residual bed-load transport directions ; ripple and sand-wave fields crossing Zeepipe at Bol van Heist Sandbank could clearly be identified.

All geophysical data were digitally transferred to the HP-9000 CAD and Intergraph 6040 workstation for combined map production.

### 2.4. Geotechnical/geologic surveys

Different geotechnical/geologic surveys with corings and piezocone penetration testings (PCPT) were executed along the Zeepipe route in the offshore and onshore part to ascertain/verify geophysical survey and to get

geotechnical information for the design of the pipelaying and landfall works.

Vessels mobilised for the soil investigation include the self-elevating platform "Tijl II" (HSS) and the "M.S. Bucentaur" (Farmand Survey).

Coring was executed by continuous sampling of the soil layers (figure 4). Piezocone penetration testing was done to investigate soil cone resistance, sleeve friction and pore-water pressure ; geotechnical parameters such as friction angle, relative density and undrained shear strength could be deduced.

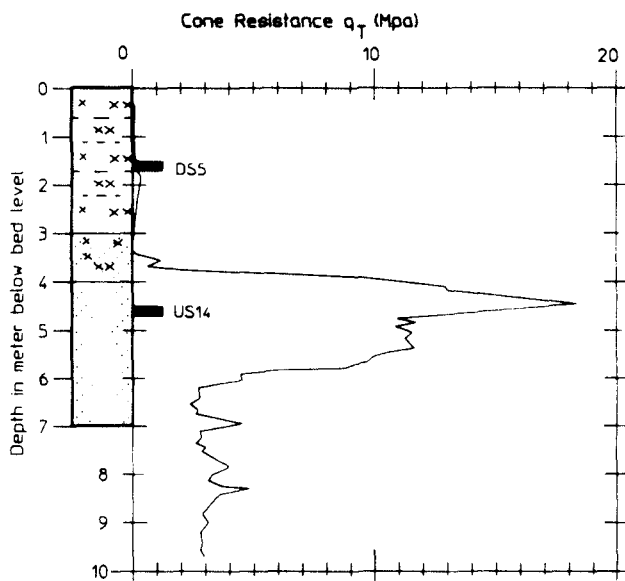


Figure 4 : Example of geotechnical/geologic soil investigation results.  
Coring + PCPT in the landfall area.

All geotechnical data were digitally transferred to the HP-9000 CAD and Intergraph 6040 system for the production of the combined survey maps.

In selected boreholes wireline loggings (density and resistivity logs) were done in order to assess porosity and density of the soil layers. These parameters are important for the assessment of soil compaction degree and liquefaction potential.

### 2.5. Geochemical analysis

During the geotechnical survey, soil samples were frozen and stored in a freezing installation. According to the Convention of Oslo, chemical characteristics of the samples were analysed in order to assess a possible contamination and/or contaminant remobilization during trenching/dredging. Heavy metal and organic compound contents were found to be below base quality reference material contents.

### 2.6. Hydrometeorological conditions

Vertical tides are important in this part of the North Sea. Tides in Zeebrugge range from 3,00 m (Neap Tide) to 5,00 m (Spring Tide).

The tidal currents (SW : ebb ; NE : flood) in relation to the vertical tide are the strongest and highest in the shallow parts of the North Sea such as the Belgian nearshore area. Offshore current roses are either elliptical or circular and nearshore ones are usually bidirectional. This means that offshore water is constantly flowing while nearshore water circulation is similar to that in an estuary.

Storm surges may be particularly dramatic in this part of the North Sea because of wind set-up combined with the relative high tidal ranges. Dominant wind directions are SW with NW for storm conditions. NW, N and NE-winds together with atmospheric depressions are able to cause considerable wind set-ups (up to 2,00 m in extreme conditions).

Wave action is intense in the Southern Bight due to shallow water depths, refraction, reflection and diffraction. Registered wave characteristics show typically short period and steep waves.

## 3. COASTAL PROCESSES

### 3.1. Tidal gulleys

The morphological evolution in the nearshore and landfall area is influenced by the tidal mechanisms in the North Sea, by the discharge of the Scheldt river and also, locally, by the Zeebrugge harbour. Long term seabed variations are due to the continuous development of the ebb - and flood gully system.

Ebb - and flood gulleys are closed in the direction of the residual sediment transport, are typically approx. 4

to 10 km long, approx 1 to 4 km wide and have depths of 0,50 m to 3,50 m w.r.t. original seabed ; they interact closely and form a hydrodynamic and physical equilibrium. Flood gulleys are shallow and more frequent close to shore. Ebb gulleys are deeper and located more offshore.

### 3.2. Sand banks and sand waves

The Zealand banks located in front of the Belgian coast seem to be stable sand bodies. During storms, some of the megaripples and sand waves on top of the banks are crest-cutted but soon afterwards they are built-up again. Sand wave height is approximately 1,5 m to 2,5 m and the wave length ranges between 100 and 200 meters.

### 3.3. Turbidity maximum area (TMA) and sediment transport

The nearshore area is characterized by a much varying bottom lithology with essentially the presence of muddy tidal flats (C. De Meyer, B. Malherbe 1986). Intensive field measurements have been executed in this part of the North Sea since several years. Such measurements allowed to establish a general residual sediment transport pattern. Figure 5 shows the variation of tidal elevation, tidal currents and suspension concentration. They revealed the existence of an encounter zone of residual sediment transports in front of the Belgian Coast which results in a marine Turbidity Maximum Area (T.M.A.).

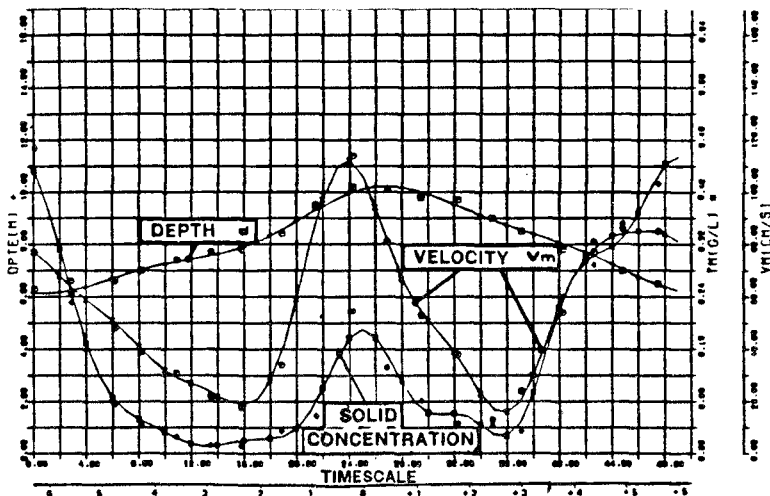


Figure 5 : Simultaneous recordings of tidal elevation, tidal currents and suspension concentration close to the Landfall Area.

The T.M.A. is characterized by a loose mud deposit layer (thickness : 0,50 - 1,00 m) trapped within the T.M.A. The volume of this loose mud is significant and may amount to several millions of tons dry material. The T.M.A. centre of gravity is further moving in function of the residual flow and sediment transport.

#### 3.4. Beach stability

The sandy beach on the landfall area could be subjected to morphological changes due to wave response; these morphological changes are unavoidable modifications in the beach equilibrium profile.

Before the extension works of the Zeebrugge harbour started (1977), the seabottom level was almost equal to MSL -7,00. Afterwards, a progressive accretion / sedimentation has taken place which is due to human activities (disposal of dredged material) and to natural sand accumulation (trapping of longshore transport by eastern dam of Zeebrugge).

#### 4. LANDFALL OF ZEEPIPE : DESIGN ASPECTS

##### 4.1. Design criteria for the landfall

The different criteria used for the design of the Zeepipe Landfall are related to the following parameters :

- a. geotechnical stability of the pipeline
- b. foundation of future marina dams which have to cross the Zeepipe route
- c. depth of the marina access channel and basin
- d. technical requirements for trenching, dredging and pulling equipment
- e. tidal gulley development
- f. allowable stresses in the pipeline
- g. pipelaying/welding requirements
- h. beach erosion
- i. risk analysis of the pipe in relation to navigation
- j. authority requirements

The geotechnical stability is related to the liquefaction potential and the differential settlements.

Liquefaction is likely to occur if no artificial backfill of the trench is done. Natural backfill with sand is very progressive and repeated liquefying effects by short wave action may consequently cause progressive pipeline uplift during trench filling. Natural backfill with loose mud deposits ( $\rho_{sat} = 1,05 - 1,15$ ) will generate more

consolidated mud deposits ( $\rho_{\text{sat}} = 1,40 - 1,50$ ) after ca. 1 or 2 months ; this may as well cause progressive pipeline uplift.

The different marina master plans in this area foresee the building of a sanddune (visual barrier) and a marina dam which will be built as a rubble-mound breakwater with a foundation of soil-replaced sand.

The sanddune (height : ca. 30 m) is likely to cause the most important settlements (up to 0,20 m). Due to the heterogeneity of the quaternary seabed soil layers (mud, sand, peat) differential settlements are to be expected.

The foundation of the marina breakwater dam will need an excavation of the natural quaternary soil layers with poor bearing capacity. Cutter suction excavation works have to be avoided in the close vicinity of Zeepipe. Because there is a limit to the trenching depth of Zeepipe an adapted foundation solution has to be found for this part of the marina breakwater.

The marina access-channel and basin (design depth is greater than TOP : top of pipe) will have to be designed in accordance with the Zeepipe "as-laid" profile.

The equipment for the trenching, dredging and pipe-pulling have given water depth requirements, i.e. ca. MSL - 9,00 m (Castoro II pulling barge ; Vlaanderen XIX CSD). Therefore, the minimal trench depth is fixed to MSL - 9,00 m.

As can be seen on figure 3 a typical flood tidal gully has been developing close to the Zeepipe route since the end of the Zeebrugge Harbour Works. Such tidal gully developments are followed carefully by interpreting differential bathymetric maps.

Regarding the soil-pipeline interaction it can be stated that the pipeline profile will influence the stresses in the pipeline itself. The stresses may be induced by temperature loads, internal pressure settlements (soil deformation), seismic waves, etc ... Thorough stress calculations have been executed, taking the particular soil conditions in this area into account.

To execute the dry tie-in (in a dry cofferdam) of the spool and the landfall-string by welding a maximum working depth within the cofferdam of - 7,25 m MSL was required. This means that the tie-in part of the landfall has been designed at that level.

Beach erosion phenomena may affect the submarine beach up to a depth of ca. - 6,50 m MSL. Beach erosion and equilibrium slope calculations was done to evaluate beach

response to the design storm conditions (water level + wave height with e.g. R.P. of 50 years). Recent beach evolution can also be assessed from differential mapping.

Damaging risks during operation and within life-time (50 years) had to be assessed in order to design the appropriate cover and/or protection. Therefore a risk-analysis was executed taking all external factors such as navigation, maintenance dredging, ship's collision, etc ... into account.

This risk analysis has a major relevance for the crossing of the Scheur and Wielingen navigation channels.

Authority requirements refer essentially to the soil conditions after pipeline-installation and the stability of the existing harbour infrastructure. Furthermore an environmental impact assessment (EIA) had to be done in relation to the planned dredging, trenching and dumping works (LDC/OSCON-convention).

#### 4.2. Landfall design alternatives

The arrival point of the offshore pipeline was fixed, i.e. the Landfall Valve Station on the LNG-peninsula of the Zeebrugge Harbour.

Three major landfall alternatives were identified :

1. by directional drilling and subsequent pipe-pulling from sea to land ;
2. by micro-tunnelling with a pushed tunnel from shore to sea ;
3. with a conventional sheet-piled cofferdam for the shore approach in combination with a cross-breakwater solution.

The original landfall-concepts, by directional drilling or micro-tunneling, were abandoned due to the particular soil conditions and the close vicinity of the rocky rubble-mound breakwater.

The alternative concept basically consists of a conventional landfall, with a sheet-piled cofferdam into which the pipeline, is pulled ashore. The pipeline is tied into a spool piece that goes through and above the breakwater and which connects Zeepipe to the Landfall Valve Station.

#### 4.3. Trenching/dredging of the pipeline

In order to fulfill the design-criteria the pipeline had to be trenched over a wide stretch of the nearshore and shore-approach area.

In the Scheur shipping channel the trench was designed taking into account the risk-analysis, the soil conditions with quaternary sands and tertiary overconsolidated clays and silts, the authority requirements and the plans for deepening the channel. On figure 6 the designed crossing of the Scheur is illustrated. The trenching works were designed to be executed by seagoing cutter suction dredgers. (N. Pille, F. Warnier, B. Lahousse - 1988).

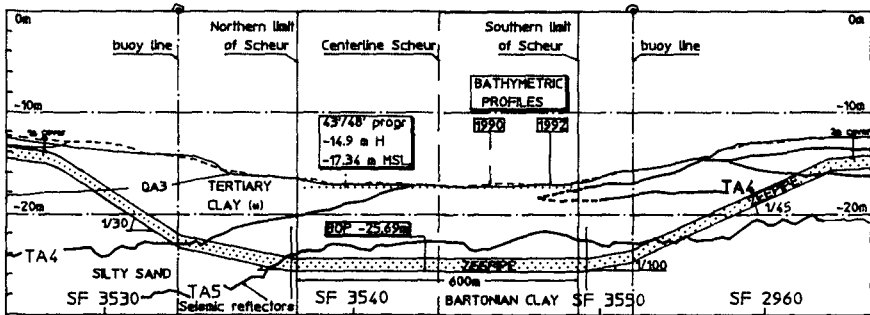


Figure 6 : Design of the crossing of the Scheur shipping lane by Zeepipe.

In the "Wielingen" Shipping Lane the designed pipelaying/trench is less deep than in the Scheur. Therefore a combination of predredging (trailing suction hopper dredgers) and post-trenching (jetting sledge with jet-barge) has been foreseen.

Between the "Wielingen" and the shore a 1750 m shore-approach trench up to - 9 m MSL (bottom width : 50 m) has been designed (initially box-cut and subsequently 1/7 slopes). The shore approach trench connects to the sheet-piled cofferdam (figure 7).

Because of the dry tie-in of the pipeline into a spool piece and the need for extra work space, a temporary artificial island was built along the eastern breakwater. Excavation works were executed within the cofferdam for :

- a. connection between offshore trench and tie-in area ;
- b. soil replacement works (with gravel) because of the presence of muddy soil layers (Cone resistance  $Q_{ct} < 1$  MPa) likely to cause (differential) settlements.



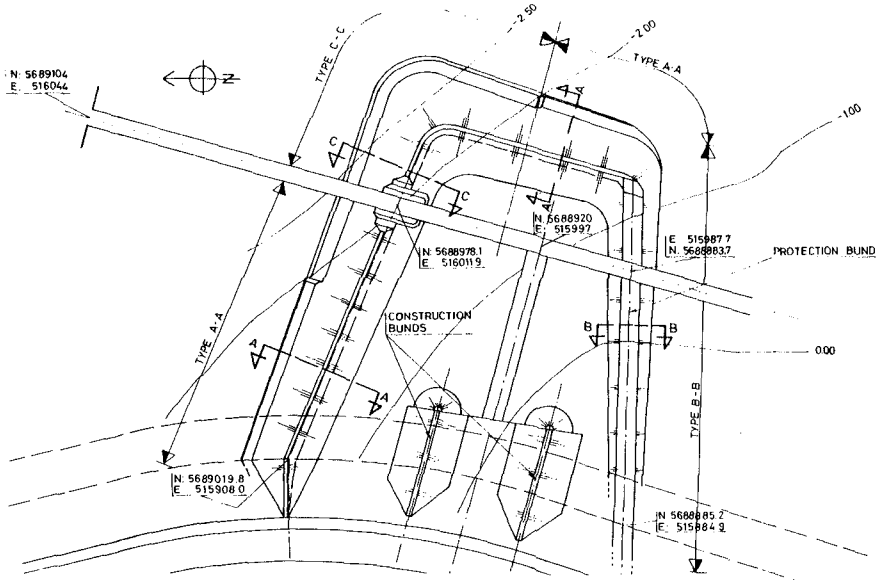


Figure 7 : Shore approach trench in sheet piled cofferdam and artificial landfall island.

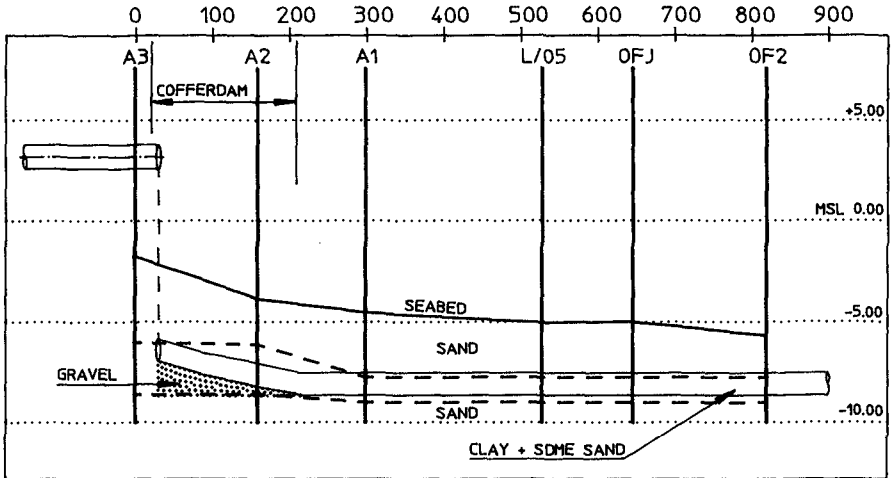


Figure 8 : Pipeline profile in the landfall area

In this way the pipeline would be in a safe operational condition from a stress point of view, i.e. below 70 % of the specified minimum yield strength.

#### 4.4. Backfill of the pipeline trench

To avoid damaging risks of the pipeline due to navigation hazards (trailing anchors, sunken ships, etc ...) and/or maintenance dredging, a continuous gravel cover (gravel diameter : 0,11 m) of the pipeline was designed in the Scheur crossing area.

The design of the backfill of the shore approach trench in the transition zone between pre-trenching and post-trenching does fulfill the criteria, related to, a.o. :

- pipeline stability against liquefaction and flotation
- authority requirements

The backfill was designed by a series of separated gravel berms alternating with sand berms (figure 9) in order to optimize the backfill costs.

The gravel solution was retained because :

- a. it offers a better solution against liquefaction (to ensure vertical stability) ;
- b. it reduces execution problems if the trench is filled with loose mud deposit.

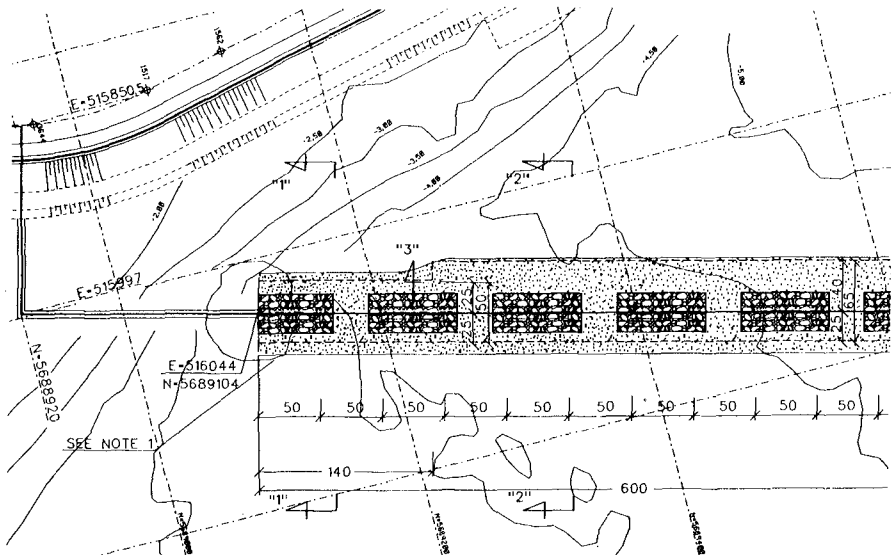


Figure 9 : Scheme of backfill of the shore-approach trench.

The backfill operations were designed to be executed by split hoppers and side-dumping vessels.

#### 4.5. Crossing of the breakwater

For the crossing of the breakwater the upper layers of the rubble-mound structure had to be carefully dismantled, taking into account the as-built drawing and the foundation of the dam (soil replacement, willow-matras, berm). In the berm and breakwater crossing a sandasphalt core in which the spool piece is bedded has been designed (thickness of sandasphalt under and above pipe ca. 1 m).

#### 5. ZEEPIPE LANDFALL CONSTRUCTION

In order to execute the pulling ashore operation in controlled environmental conditions, a sheetpiled cofferdam has been constructed first.

The landward end of the cofferdam has been driven in a temporary artificial island. The purpose of this temporary island was to provide a protection against sea conditions during the opening of the breakwater and the installation of the spoolpiece across the breakwater.

A trench has been excavated within the cofferdam, into which the pipeline has been pulled ashore from a flat bottom laybarge by winches placed on the beach.

The island has than be used as a work platform in front of the trench.

After the pipeline was pulled ashore, the cofferdam has been plugged with clay and dewatered allowing the tie in operation to be done in dry conditions.

The seaward end of the cofferdam has been filled with seagravel and sand.

Finally the pipeline has been tied-into a spoolpiece that has been laid across the breakwater previously.

#### 6. REFERENCES

- Chr. P. De Meyer, B. Malherbe. Terra et aqua nr. 35. "Optimization of maintenance dredging operations in maritime and estuarine areas."
- N. Pille, F. Warnier, B. Lahousse. Antwerp 20-24 June 1988. "The use of dredging equipment for trenching and covering of offshore pipelines." K.VIV 9th International Harbour Congress,
- L. Stolberg. August 1992 "Norway's Zeepipe Project means more gas for Europe" Pipeline & Gas Journal

## CHAPTER 157

# A Field Experiment on a Nourished Beach

A.J. Fernández\*  
G. Gómez Pina \*  
G. Cuenca\*  
J.L. Ramírez\*

### Abstract

The performance of a beach nourishment at "Playa de Castilla" (Huelva, Spain) is evaluated by means of accurate beach profile surveys, visual breaking wave information, buoy-measured wave data and sediment samples. The shoreline recession at the nourished beach due to "profile equilibration" and "spreading out" losses is discussed. The modified equilibrium profile curve proposed by Larson (1991) is shown to accurately describe the profiles with a grain size varying across-shore. The "spreading out" losses measured at "Playa de Castilla" are found to be less than predicted by spreading out formulations. The utilization of borrowed material substantially coarser than the native material is suggested as an explanation.

## 1 INTRODUCTION

Fernández et al. (1990) presented a case study of a sand bypass project at "Playa de Castilla" (Huelva, Spain) and the corresponding monitoring project, that was going to be undertaken. The Beach Nourishment Monitoring Project at the "Playa de Castilla" was begun over two years ago. The project is being

---

\*Dirección General de Costas. M.O.P.T, Madrid (Spain)

carried out to evaluate the performance of a beach fill and to establish effective strategies of coastal management and represents one of the most comprehensive monitoring projects that has been undertaken in Spain. This paper summarizes and discusses the data set for wave climate, beach profiles and sediment samples.

## 2 STUDY SITE & MONITORING PROGRAM

Playa de Castilla, Fig. 1, is a sandy beach located on the South-West coast of Spain between the Guadiana and Gualdalquivir rivers. The beach extends over  $25\text{km}$  between Mazagón and Matalascañas, and has experienced a long-term trend of erosion. The shoreline at Playa de Castilla has been receding at a rate of  $1.5\text{m/year}$  during the last 30 years (Fernández et al., 1990). The main causes of this shoreline recession are the net litoral drift from West to East, that has been evaluated in  $390.000\text{m}^3/\text{year}$  (CEDEX, 1979), and the civil works in the nearby rivers that have reduced the volume of sand carried to the coastline.

In 1989, an artificial nourishment of the beach was carried out. The fill project was conducted by the Ministry of Public Works of Spain and consisted of a sand bypass from the updrift side of the Tinto-Odiel Estuary to Playa de Castilla. The volume of sand moved was  $1.690.000\text{m}^3$ . The sand was dredged by a trailing suction hopper dredger and transported  $2\text{km}$  down drift. The total volume of sand was placed in the updrift extreme of "Playa de Castilla", forming a protruding area about  $2\text{km}$  long and  $115\text{m}$  wide, Fig. 1. The borrowed sand was coarser than the native sand being  $D_{50} = 0.63\text{mm}$  and  $D_{50} = 0.3\text{mm}$  for the borrowed and native sand respectively.

A monitoring program was established to evaluate the performance of the nourishment. The field program includes wave measurements, beach profiles and sand samples (Fig. 2).

The wave climate measurements cover daily visual observations of wave direction in shallow water, surf zone width, wave period and wave height within the surf zone (two measurements per day). In addition, waves are recorded by a buoy gauge located in intermediate depths ( $18\text{m}$ ).

Beach profile data are acquired bimonthly from 42 shore-normal profiles located between Mazagón and Matalascañas. Alongshore spacing of the profiles is approximately  $500\text{m}$ . Each profile is surveyed from the beach dune up to a depth of about  $10\text{m}$ .

Sediment samples are collected from each beach profile during each bi-

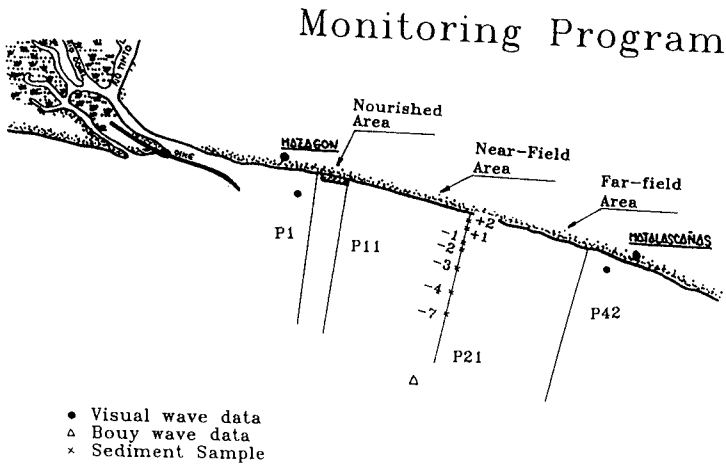
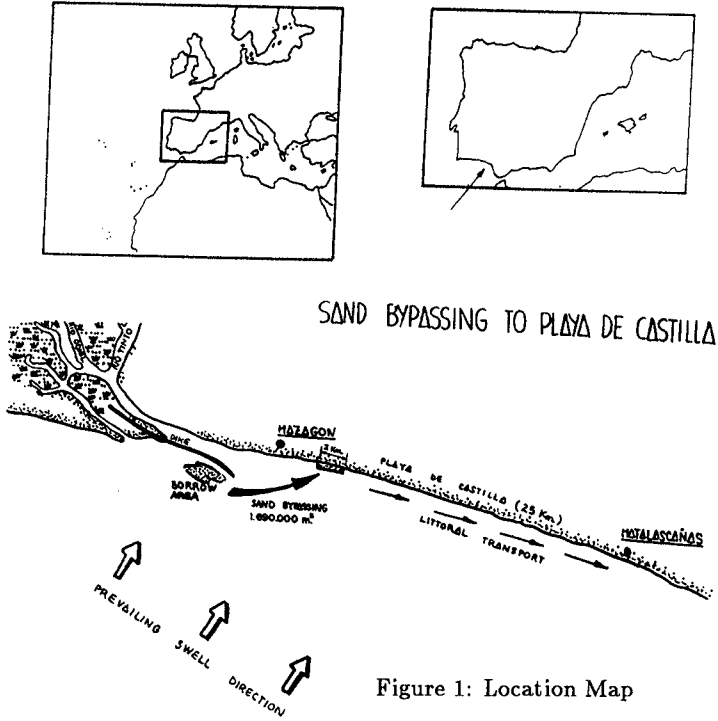


Table 1: Measured Wave Parameters

Variable	Max.	Mean	Min.
$H_s$	3.80 m	0.65 m	-
$H_{max}$	5.90 m	1.00 m	-
$T_z$	9.40 s	4.10 s	2.40 s
$T_s$	15.60 s	5.00 s	2.80 s

monthly survey from the dune to offshore. Samples are collected at the following locations: swash zone, surf zone (-1 m, -2 m), and offshore (-3 m, -4 m, -7 m). Each sample is processed in the laboratory for grain size parameters.

## 3 RESULTS

### 3.1 Wave Climate

Since waves are the primary agent for nearshore changes at Playa Castilla, several wave parameters are collected. Daily, visual observations are taken at Mazagón and at Matalascañas 25km downdrift. Morning and afternoon measurements of the following parameters are recorded: wave direction, breaking width, wave period and breaking wave height.

Average breaking wave height is of the order of 0.4m. Wave heights during the strongest storms are on the order of 2.0m. Most of these storms are locally generated with wave periods in the range of 6 – 8sec. The breaking zone width varies between 5m and 200m with 10m as an average value. The predominant approach direction is from the SW/SSW sector, with more than 60the data corresponds to calm periods.

In order to obtain a more complete description of the wave climate, a permanent station for wave height recording was installed. The station was located in intermediate depths, (18 m) between Mazagón and Matalascañas. The buoy gauge consists of a Data Well Buoy model Waverider 6000, a recording unit and a power source. The data are recorded on cassettes and is computer analyzed to yield significant wave heights and periods. Table I presents the range of values for the different wave parameters.

where  $H_s$  is the significant wave height,  $H_{max}$  is the maximum wave height,  $T_z$  is the upcrossing period and  $T_s$  is the significant period.

### 3.2 Beach Profiles

The beach profile data are acquired bimonthly from 42 shore normal profiles across the nourished beach (profiles 2-6) and adjacent beaches (profile 1 is updrift and profiles 7-12 are downdrift). The transect spacing was designed to monitor the whole beach (nourished and unnourished) and to resolve the long term "spreading out" losses of the nourishment though it might not be adequate to resolve the spacing of rhythmic topography, which can be closely spaced. In the first survey, the alongshore spacing in the nourished beach was 250 meters. These additional profiles were included to determine information about the profile readjustment that occurs from the linear project profile until finally arriving at the natural equilibrium profile.

### 3.3 Unnourished Section, Far Field

The Eastermost profiles are (far apart) from the nourishment and give information from the natural changes of the beach profiles. The storm season profiles (Sep./90 and Jun./91, Fig. 3) show a dissipative profile with a steep beach face, a marked break point bar and a very mild offshore slope beyond the 3 m contour. The bar can be observed in almost all the campaigns with minor changes in its offshore position and seasonal changes in its elevation. During calm periods (Feb./91 and Feb./92), the bar trough is filled and the bar becomes a step which separates the steeper beach face and the milder offshore profile.

The dune erosion process is clearly shown in the measured profiles. During storm conditions, the landward part of the profile retreats and the dune is eroded. The dune material is transported to the offshore part of the profile, beyond the bar (Sep./90 and Jun./91). This excess of sediment in the offshore profile is lost during calm periods (Feb./91 and Feb./92) but the foreshore does not recover the pre-storm position and, consequently, the erosion process is completed.

### 3.4 Unnourished Section, Near Field

The morphology of the profiles which are adjacent to the nourished beach are qualitatively quite similar to those at the far field, with a steep beach face, a marked bar during the storm season and a mild offshore slope beyond the 3 m contour (Fig. 4). However, the magnitude of the bar is not generally as important as in the far field. During calm periods, the bar becomes a step as in the far field. It can be observed from Figure 5, that the foreshore part of



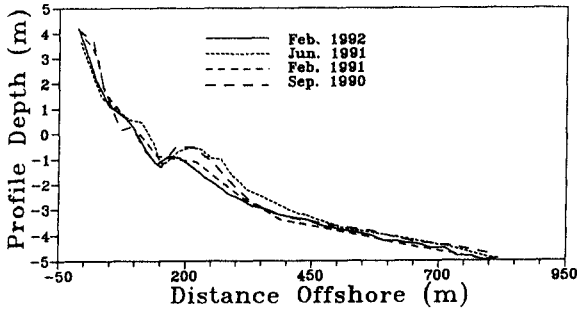


Figure 3: Beach Profile. Far Field

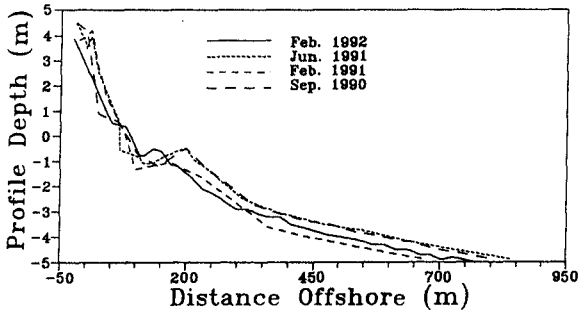


Figure 4: Beach Profile. Near Field

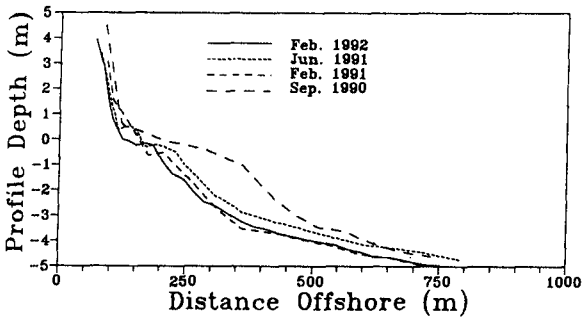


Figure 5: Beach Profile. Nourished Area

the profile benefited from the project, at the beginning, (Sep./90 to Jun./91), with a net accumulation of sediment, mainly above low tide level. However, the offshore part of the profile, retreated afterwards during the period (Feb./91 to Feb./92). This part of the profile, beyond the bar, shows the seasonality above mentioned with a significant accretion during storm conditions and a gradual lowering of the offshore beach during calm periods.

### 3.5 Nourished Section

In the nourished beach there is no bar but a permanent step or a transition between the very steep beach face and the more gently sloping offshore profile (Fig. 5). The offshore changes of the profiles are as important as those encountered at the near field and far field profiles. The foreshore part of most of the profiles displays a loss of material. Nearly all of this loss is located in the swash zone of the intertidal beach.

### 3.6 Sediments

Sediment samples are collected from each beach profile each bimonthly survey. The samples are acquired by hand-operated grab samplers, and represent approximately the upper 10 cm of sediment at each location. The samples are analyzed in the laboratory and grain sizes are computed by sieving according to the ASTM standards. Samples are taken for each profile at the swash zone, surf zone (-1 m, -2 m) and offshore (-3 m, -4 m, - 7 m).

### 3.7 Swash Zone

The grain size at the swash zone (Fig. 6) is the most stable in time of all the locations, with minor changes at the unnourished beach and more important fluctuations at the nourished part. The temporal variations of the mean size exhibit a similar variability in the alongshore direction, being coarser or finer at all the profiles depending on the survey. Spatially, the nourished beach represents a discontinuity in the distribution of grain size.

The unnourished backbeach is characterized by a very uniform grain size in the alongshore direction with an average  $D_{50} = 0.32mm$ , while the nourished beach shows a less uniform alongshore distribution with an average  $D_{50} = 0.51mm$ . There is, however, a slight tendency for decreasing grain size variability both temporally and spatially in the nourished beach throughout the campaigns.

### 3.8 Surf Zone

Grain size temporal variability is much more important in the surf zone than in the backbeach (Fig. 7). The average  $D_{50}$  in the surf zone is  $0.25\text{mm}$  with a range of values from  $0.4\text{mm}$  to  $0.2\text{mm}$ . As in the backbeach, there is a clear trend in the grain size to be coarser or finer in all the profiles depending on the campaign. Unlike the landward location, there is almost no discontinuity in the alongshore direction due to the nourished beach. The nourished beach was coarser during the first campaign but afterwards achieved a grain size similar to the rest of the beach.

### 3.9 Offshore Zone

The offshore part of the beach shows different characteristics depending on the depth. At the  $3\text{m}$  and  $4\text{m}$  contour, the beach shows a fine sand, with slight temporal and spatial variations (Fig. 8). The average  $D_{50}$  is  $0.14\text{mm}$  with values in the range of  $0.2\text{mm}$  and  $0.12\text{mm}$ . No discontinuity is found at the nourished beach. At the  $7\text{m}$  contour, the mean grain size shows great temporal and spatial variation. Samples range from fine sand,  $D_{50} = 0.12\text{mm}$  to coarse sand  $D_{50} = 0.9\text{mm}$ . Most of the coarse samples are obtained at fixed locations throughout the program.

## 4 DISCUSSION

In addition to the seasonal changes that may occur in a natural beach, it is well known that the nourished beaches suffer modifications both in the cross-shore and alongshore directions, due to the profile equilibration and the "spreading out" losses. The performance of a beach nourishment project may be evaluated by the magnitude of these changes compared to the initial configuration of the designed beach fill.

### 4.1 Profile Equilibration

Beach fills are constructed using a broad range of designs, but generally the material is placed using profiles which are steeper than the natural profile for the size of sediment that is used in the beach nourishment project. Thus, the profile will tend to equilibrate to its natural shape. Profile equilibration occurs gradually, depending on the specific project characteristics (sand volume, average grain diameter...) and the wave and water level conditions, and usually

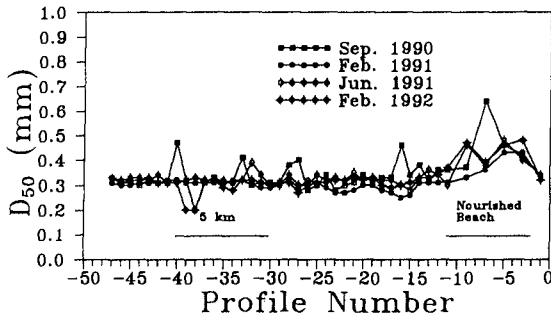


Figure 6: Grain Size. Swash Zone

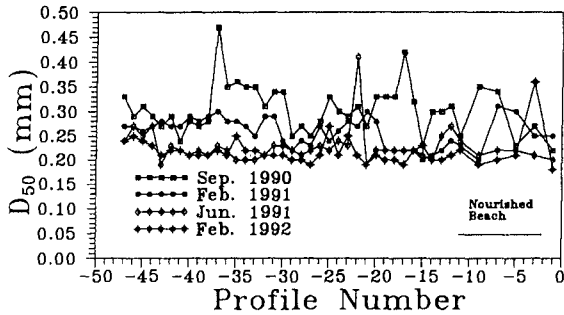


Figure 7: Grain Size. Surf Zone

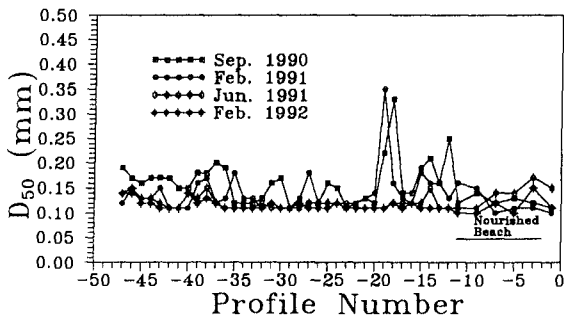


Figure 8 : Grain Size. Offshore Zone (-4)

last for a few years, Dean and Grant (1989). In considering the last profile equilibration, these are the most important questions to be answered: What will be the final equilibrium profile and when will this equilibrium profile be achieved?

Equilibrium beach profiles have been found by Bruun (1954) and Dean (1977) to be reasonably well represented by:

$$h(y) = Ay^{\frac{2}{3}} \quad (4.1)$$

in which  $h$  is the depth at a distance,  $y$  seaward of the shoreline and  $A$  is a scale parameter primarily dependent on sediment size (assumed to be constant along the profile), Moore (1982). If the grain size varies markedly along the profile, as (it occurs) at Playa Castilla, significant deviations may be encountered. Different approaches have been made to take into account the cross-shore distribution of sediment grain sizes.

Larson (1991) modified the equilibrium profile equation to better represent the grain size variation along the profile as:

$$h = A[y + (\frac{D_0}{D_\infty} - 1)(1 - e^{-\lambda y})]^{2/3} \quad (4.2)$$

where  $D_0$  and  $D_\infty$  are the equilibrium energy dissipation for the material at the shoreline and in the offshore respectively ( $D_0 \geq D_\infty$ ) and  $\lambda$  is an empirical coefficient. Eqs. (4.1) and (4.2) are assumed to represent the equilibrium profile up to a "closure depth",  $h_*$ . Usually, Hallermeier (1981), littoral zone limit ( $H_* = 2.28H_{s0.137} - 68.5(H_{s0.137}^2/gT_s^2)$ ) or Birkemeier (1985), ( $H_* = 1.75H_{s0.137} - 57.9(H_{s0.137}^2/gT_s^2)$ ) are adopted.

From the buoy data, the values of the closure depth are found to be 7.74 m and 7.87 m for Hallermeier and Birkemeier formulations, respectively.

Figure 9 displays a comparison between the measured beach profile at Playa Castilla and the least-squared fit of eq. (4.2) and eq.(4.1) for a beach profile located at the nourished beach (Figure 9a) and a beach profile located at the unnourished beach (Figure 9b). As seen from the figures, the agreement between the measured and calculated profile improves considerably if eq. (4.2) is used in comparison to eq.(4.1). The improvement is even more evident at the nourished beach, where there is a strong variation of the sediment size in the cross-shore direction.

From the 378 profiles analyzed, it was found that the best fit, when applying the classical  $2/3 - power$  curve, eq.(4.1), was obtained using a value of the A-

parameter that corresponds roughly with the grain size located at the surf-zone, in accordance with Moore's curve. It is remarkable that the offshore part of the profile beyond the bar (or step), where the sediment size is almost constant, can be well-represented by a simple  $2/3$ -power curve (see Figures 9a and 9b). The modified equilibrium equation provides an improved description of the profiles with decreasing grain size with distance offshore, however, at present, the parameters involved in the equation must be estimated by a best-fit procedure. Additional work is being carried out to establish the dependence of the parameters on the grain and wave characteristics.

From the analysis of the temporal evolution of the constructed profile to the natural equilibrium profile (not shown), it can be concluded, that the equilibrium profile was well achieved in less than one year, as suggested by Kamphuis and Moir (1977).

## 4.2 "Spreading out" Losses

The placement of a beach nourishment project usually results in a planform that interacts with the waves to result in a spreading out of the sediment, with the consequent loss of material from the region in which it was placed. In addition to the erosion due to the anomalous plan form of the nourishment project, there is usually a background erosion which was present prior to the placement of the beach nourishment project (and which made it necessary) that is superposed to the spreading out. The superposition of these two components yields the shoreline recession at the nourished beach.

The equations available to represent the planform evolution are a sediment transport equation and a sand continuity equation.

Using Komar's and Inman (1970) sediment transport equation and combining it with the sand conservation equation, an equation governing the evolution of a beach system can be obtained, Dean and Grant (1989),

$$\frac{\partial y}{\partial t} = G \frac{\partial^2 y}{\partial x^2} \quad (4.3)$$

in which the parameter  $G$  can be interpreted as the alongshore diffusivity, and primarily depends on the wave height and on the sediment transport coefficient,  $K$ , which depends on the sediment size. The wave direction is relatively unimportant on a long uninterrupted shoreline as "Playa de Castilla", Dean and Grant (1989).

The solution of equation (3) can be obtained once an initial condition is established. Using equation (3) with the designed beach nourishment project

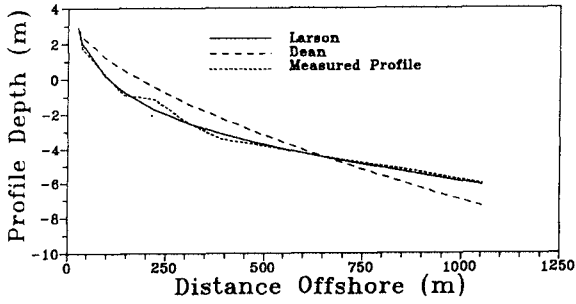


Figure 9a: Measured Profile vs Calculated Profile. Far Field

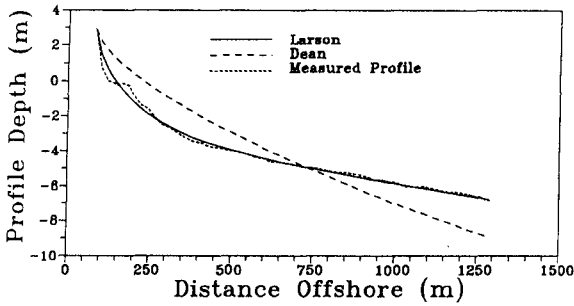


Figure 9b: Measured Profile vs Calculated Profile. Nourished Area

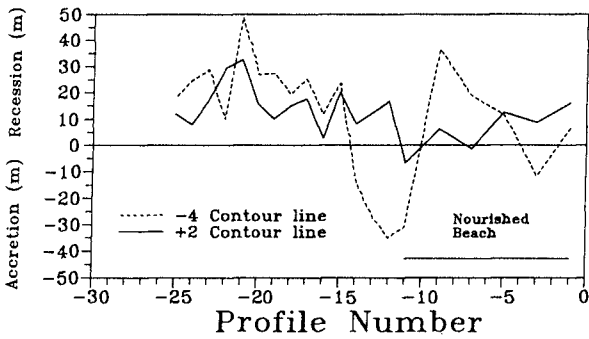


Figure 10: Shoreline Evolution

characteristics at Playa Castilla (borrowed sand diameter  $D_{50} = 0.63$  and background erosion  $1.5m/year$ ), about 20 % of the material should have been spread out in two years; however, except for the initial profile equilibration, no significant loss has been measured at the nourished beach. Furthermore, if we compute the losses with the actual grain size measured during the campaigns and take into account the cross-shore distribution of grain size as in Moutzouris (1988), more than 40 % should have been transported down drift.

It seems that the utilization of a material substantially coarser than the native sand has armor the beach in the nourishment area thereby resulting in less transport from the nourished area. The similarity of the changes of the offshore part of the profiles at the nourished beach and the unnourished beach, and the alongshore uniformity of grain size in the submerged part of the profiles indicate that the natural littoral drift is being re-established and that the nourishment area has been passed, as if it were a jetty.

In Figure 10, the shoreline evolution during the period Feb-91/Feb-92 for the contour lines +2 and -4 is presented. It can be observed from figure 10 that: the shoreline in the unnourished section has retreated with the similar rate of erosion in the far-field and in the near-field. The shoreline in the nourished area shows a tilting motion with recession in the updrift area and accretion in the downdrift area.

## 5 SUMMARY

The "Playa de Castilla" beach nourishment monitoring data set has been presented. The data include beach profiles surveys, wave measurements and sand samples. Availability of accurate levellings and soundings, sea conditions information and sediment distribution has provided the opportunity to evaluate the performance of the beach fill at "Playa de Castilla". The performance has been described in terms of beach "profile equilibrium" and "spreading out" losses. It has been shown that the equilibrium profile was achieved in less than one year, as suggested by Kamphuis and Moir (1977). The classical  $2/3 - power$  curve proposed by Bruun (1954) and Dean (1977) to represent the equilibrium beach profile has been found to be inadequate to describe the strong grain size varying across-shore beach profiles existing at "Playa de Castilla". The modified  $2/3 - power$  curve proposed by Larson (1991) has been shown to accurately represent the profiles with the cross-shore distribution of sediment size of "Playa de Castilla". The "spreading out" losses evaluated by profile measurements were less than those determined by spreading out formulations. It has been suggested that the utilization of a substantially coarser material for the beach fill has armor the beach in the nourished area, resulting in a



decreased transport from the nourished area.

## ACKNOWLEDGEMENTS

The authors are indebted to the Ocean & Coastal Research Group of the University of Cantabria for their valuable comments.

## REFERENCES

- Birkemeier, A.W.**, 1985. "Field Data of Seaward Limit of Profile Change". *Journal of Waterway, Port, Coastal and Ocean Engineering, ASCE*. Vol. 111, No. 3, May.
- Bruun, P.**, 1954. "Coast Erosion and the Development of Beach Profiles". Technical Memorandum No. 44, Beach Erosion Board.
- CEDEX**, 1979. "Informe sobre el transporte litoral en Playa de Castilla". In Spanish.
- Dean, R.G.**, 1977. "Equilibrium Beach Profiles: U.S. Atlantic and Gulf Coasts". Department of Civil Engineering, Ocean Eng. Tech. Rpt. N. 12, University of Delaware, Newark, DE, USA.
- Dean, R.G. and Grant, J.**, 1989. "Development of Methodology for Thirty-Year Shoreline Projections in the Vicinity of Beach Nourishment Projects". Division of Beaches and Shores. Florida Dept. of Natural Resources UFL/COEL-89/026.
- Fernández, J., Gómez-Pina, G. and Muñoz, A.**, 1990. "Sand Bypassing to Playa Castilla, Huelva, Spain". *Proc. 22nd Int. Conf. on Coast. Engrg., ASCE*, pp. 3183-3193.
- Hallermeier, J.R.**, 1981. "A Profile Zonation for Seasonal Sand Beaches from Wave Climate". *Coastal Engineering. ELSEVIER*. No. 4, pp. 253-277.
- Kamphuis, J.W. and Moir, J.R.**, 1977. "Mean Diameter Distribution of Sediment Sizes Before and After Artificial Beach Nourishment". *Proc. Coastal Sediments'77. ASCE*, pp. 197-210.
- Komar, P.D. and Inman, D.L.**, 1970. "Longshore Sand Transport on Beaches". *Jour. of Geophysical Research*, Vol. 75, No. 30, pp. 5914-5927.
- Larson, M.**, 1991. "Equilibrium Profile of a Beach with Varying Grain Size". *Proc. Coastal Sediments'91. ASCE*, pp. 905-919.
- Moore, B.D.**, 1982. "Beach Profile Evolution in Response to Changes in Water Level and Wave Height". Master Thesis, Dept. of Civil Eng., University of Delaware.

## CHAPTER 158

### Thirty Year Erosion Projections in Florida: Project Overview and Status

Emmett R. Foster<sup>1</sup>

#### Abstract

A project to analyze historic shoreline erosion and to predict future erosion in Florida is discussed in this paper. Information is given concerning the data base and the methods of analysis. Some examples are provided illustrating the use of various analysis tools. The utility of numerical modeling as a newly developed analysis tool is discussed in particular. Some of the general results of the study are noted, as well as conclusions and opinions concerning the effectiveness of the program.

#### Introduction

Since 1985, the Florida Department of Natural Resources (DNR), Division of Beaches and Shores, has been required to consider thirty year erosion projections in the regulation of coastal construction. Certain types of major structures are prohibited seaward of the thirty year projection of the "seasonal high water line" (SHWL). This elevation contour is defined by rule to be a function of the mean high water (MHW) elevation and the mean tide range at a site. In many areas of the state the SHWL corresponds well with the vegetation line or the base of the dune escarpment. The SHWL is assumed to move in close correspondence with the MHW line in the longer term.

-----  
<sup>1</sup>Professional Engineer, Florida Department of Natural Resources, Division of Beaches and Shores, 3900 Commonwealth Blvd., Tallahassee, FL 32399-6515.

There are approximately 1250 km (780 miles) of sandy beaches in Florida for which thirty year erosion projections must eventually be made. Due to staffing limitations, first priority is given to analyzing and making erosion projections for areas where there are frequent applications for construction permits. The second priority is completion and updating of the historic data base. The third priority is to perform regional analyses.

The author works for the Division as a coastal engineer assigned to build and maintain the historic shoreline data base, and to analyze the data. In effect, the author acts as a consultant in recommending to the engineering staff and management which erosion rates to apply as thirty year erosion projections. Any of the staff engineers may elect to perform their own analyses. The author's recommendations in a case are subject to acceptance or not, per the judgment of the staff engineers and managers. This allows for useful scientific debate. The party making the final thirty year erosion determination in a case is responsible for its' defense. The following is a description of the DNR historic shoreline data base, and the author's analysis methods and opinions.

#### Data Base

In order to have a reasonable chance of predicting the future, it is helpful to have a reasonably good understanding of the past. Therefore the author's methods of analysis are based on obtaining a high quality, reliable data base, and a working understanding of the coastal processes controlling long term shoreline changes in Florida.

In the initial data acquisition phase, all the U.S. Government historic coastal topographic survey maps of Florida from the 1850's to the 1980's were precision digitized by skilled personnel on state-of-the-art equipment. This was done for the Department at Florida State University, primarily by Dr. S. Demirpolat. The results include an atlas of historic mean high water (MHW) change maps, which are computer-generated map overlays on a common coordinate system. Paper copies on standard scales of 1:24000 and 1:2400 are available. Digital copies which can be used with several computer assisted design (CAD) or geographic information system (GIS) software packages are now becoming available. An example historic shoreline change map is shown as Figure 1.

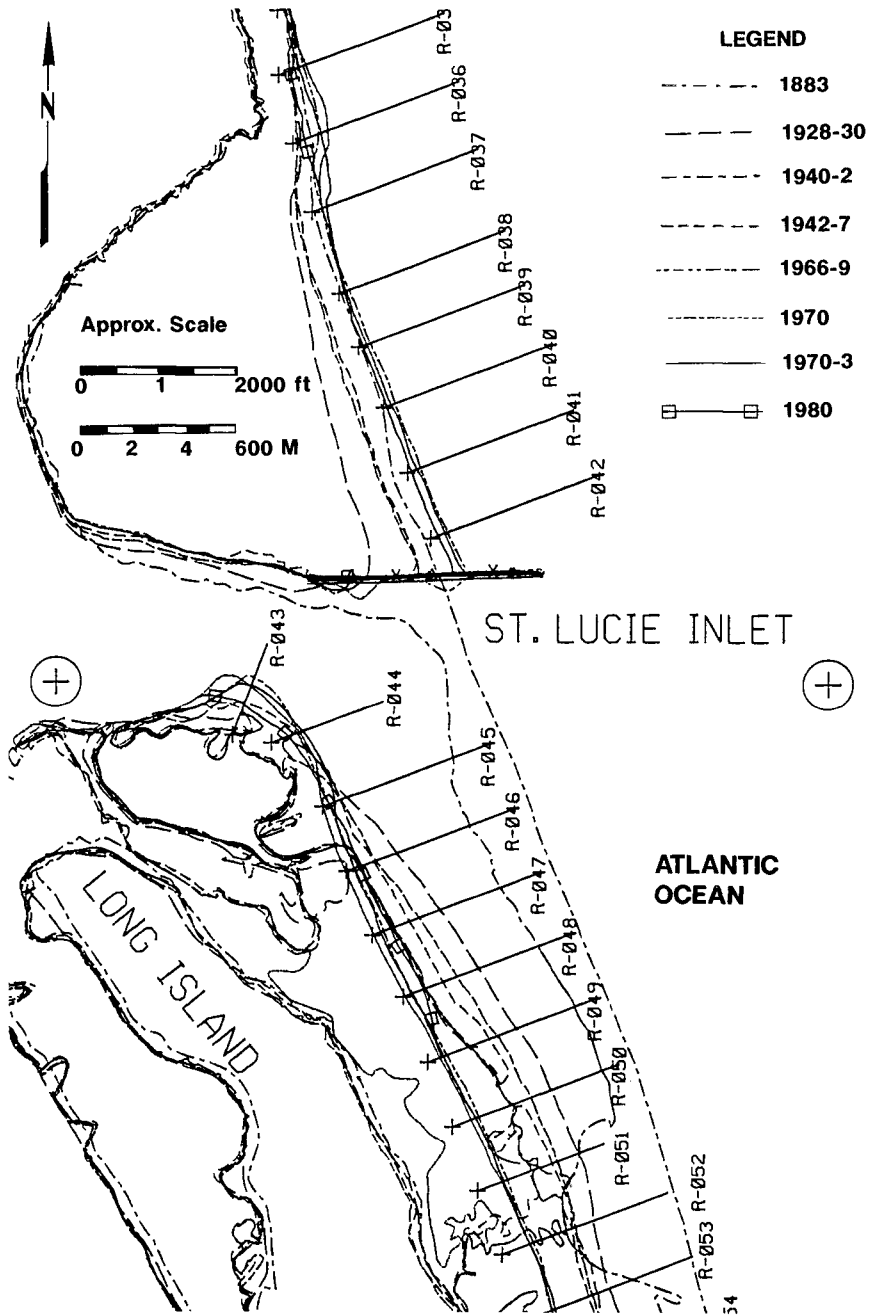


Figure 1. Example, Historic Map

The maps provide the basis for files of tabulated MHW locations referenced to fixed DNR survey points ("R" monuments) at approximate 300 m (1000 ft) intervals along the Florida coast. Beach profiles from these points have been surveyed semi-periodically since the early 1970's. The MHW data from the field surveys is systematically being added to the historic data tables. As new surveys are taken, the data base is continually updated. Strict data quality control is necessary, although this requires a large investment of time and effort. In the past when similar projects have proven unreliable, it was usually because of poor data quality control. The data base is supplemented with sets of controlled and uncontrolled aerial photographs, bathymetric maps, bathymetric profiles, full beach profiles, and access to university and Division libraries.

The accuracy of the historic map data is estimated to be +/- 10-15 meters, or better. The field derived data is +/- 3 meters, and usually better. Not all data are equal. The process of comparing the historic shorelines with physical reality during the analysis helps to determine data of questionable reliability.

### Analysis

A methodology has been developed and tested over several years which works well in analyzing this data set. A useful graphic tool is the distance versus time plot. To illustrate, an example of an enlarged portion of a shoreline change map is shown as Figure 2a. The distances from reference point "R-1" to the various historic shoreline locations, along a fixed, approximately shore-normal direction, are plotted versus time in Figure 2b. A downward sloping line indicates erosion. An upward sloping line indicates accretion. The greater the slope, the more rapid the rate of change. The advantage of the distance versus time plot is simply to give a perspective on the rate of change, which is not readily discernable from the plan view maps. Plots for several adjacent reference points, as shown on the left side of Figure 3, may be combined onto one graph, as shown on the right side of Figure 3. The advantage of the single graph with multiple plots is simply to show that the plots, when viewed in sequence, are related in a pattern.

An example of a non-linear erosion pattern in the historic data is shown in Figures 4a and 4b. The example is the downdrift (south) side of St. Lucie Inlet, in southeast Florida. In a graph such as Figure

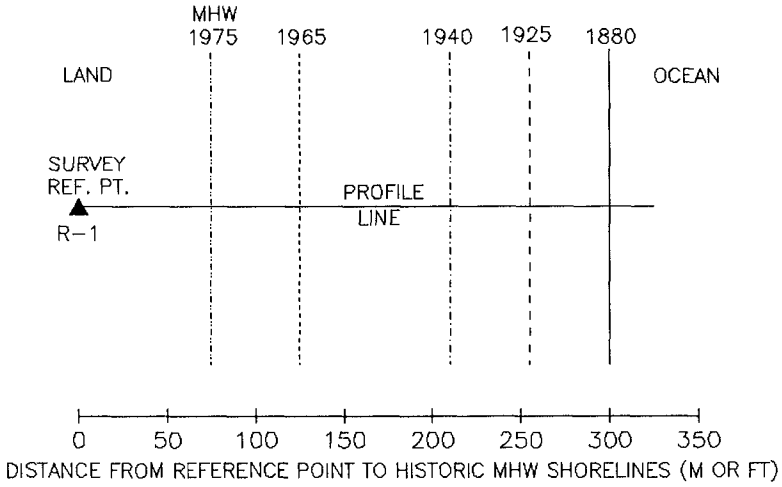


Figure 2a. Example, Enlarged Map Area

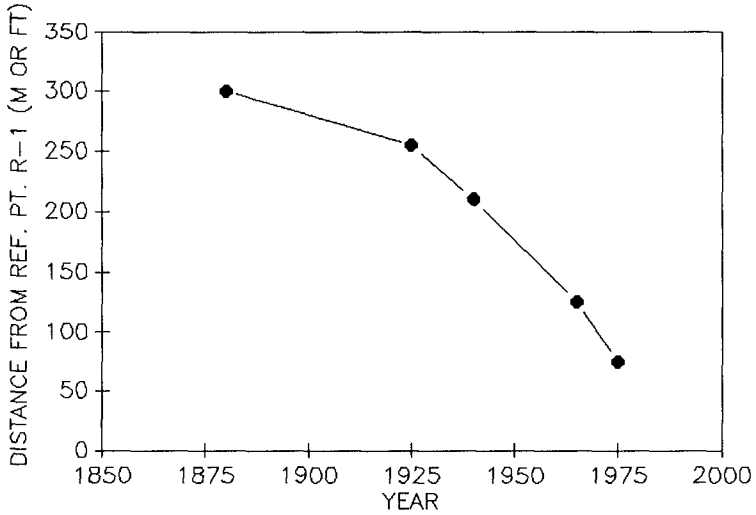


Figure 2b. Example, Distance vs. Time Plot

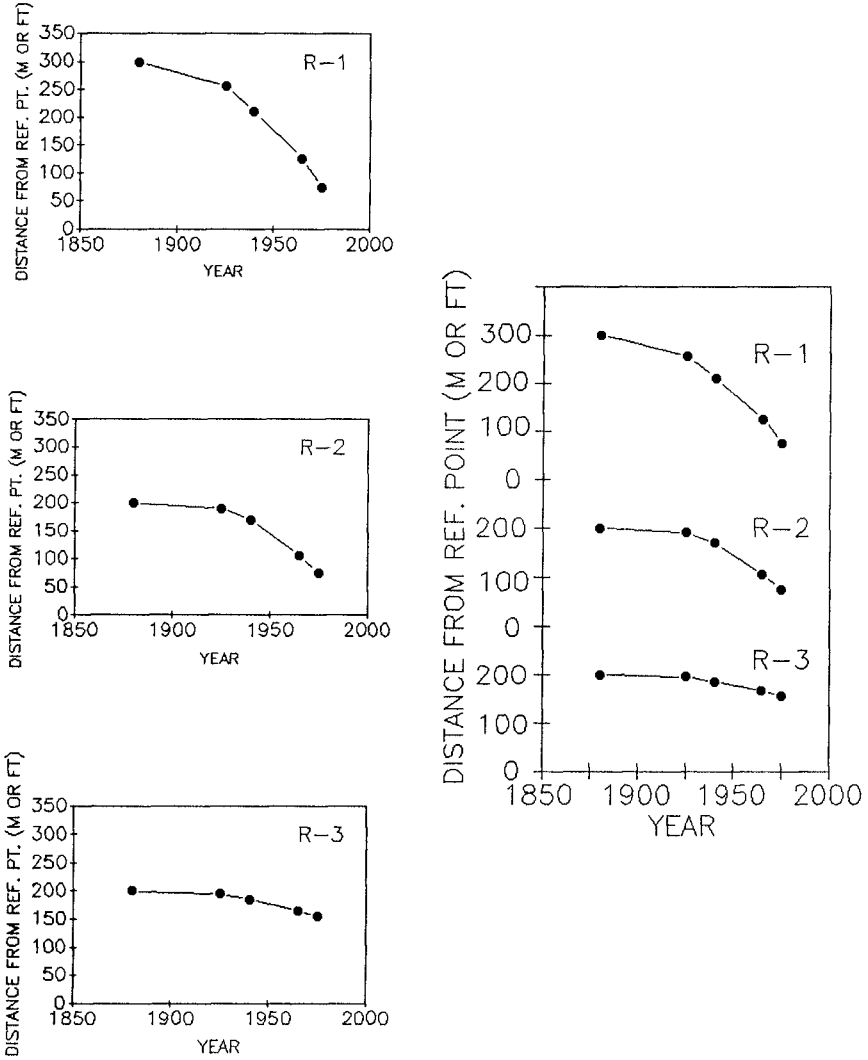


Figure 3. Combining Distance vs. Time Plots

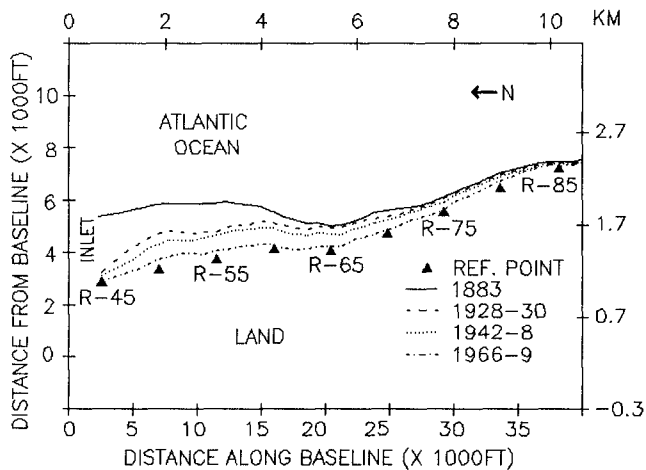


Figure 4a. Plan View, Historic

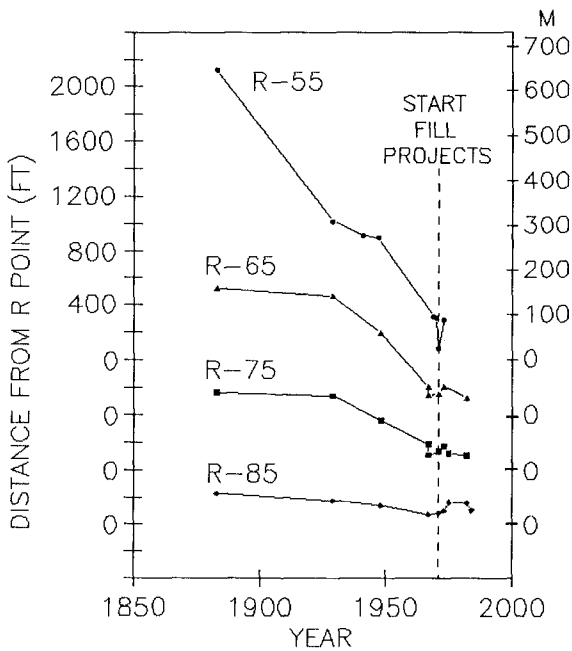


Figure 4b. Time Plot, Historic



4a, the historic shoreline locations at the reference points can be plotted in a connect-the-dot manner, in any coordinate system. The vertical and horizontal scales can be used to exaggerate the longshore features as desired. The time history of shoreline change along a sequence of selected reference points is given in Figure 4b. Note that the erosion pattern was interrupted by renourishment projects in the early 1970's.

The erosion pattern is easily recognized by comparison to a modeled idealized case, shown in Figures 5a and 5b. A one-line, two-season, longshore numerical (finite difference) model was used to illustrate what theoretical erosion pattern to expect downdrift from a jettied inlet. Note the essential similarity of the non-linear erosion curves in Figure 5b to those of Figure 4b, exclusive of the renourishment period.

Once the erosion pattern is recognized, the task is to resolve the pattern into time segments during which the rate of shoreline change is approximately linear. Three rate calculation methods are then applied to each approximately linear time segment to achieve a consensus estimate, thereby avoiding the potential bias of any individual rate calculation method. Rate estimates are generally averaged alongshore with a floating six or seven point averaging technique, unless there is reason not to do so. Longshore averages are usually rounded upward to the nearest  $-0.15$  m/yr ( $-0.5$  ft/yr) as a conservative practice. The data base and analysis methods are described in greater detail by Foster and Savage (1989a).

A case study where the same numerical model as previously mentioned was calibrated with the entire record of historic data is described by Foster (1991a). The location of the case study area and some of the results of that work are shown in Figures 6a and 6b, respectively. Note that the historic data and the model data match reasonably well. There are two physical equations on which the model is based: a version of the longshore transport equation and an equation for volumetric continuity. The primary factors causing shoreline erosion in this case were indicated by the very limited range of parameters in the model which resulted in a match with the historic data. In addition, the model indicated that the erosion process is non-linear and far from completed, both observations that were not necessarily intuitive.

It must be noted that it is not at this time usually practicable to do calibrated modeling for most

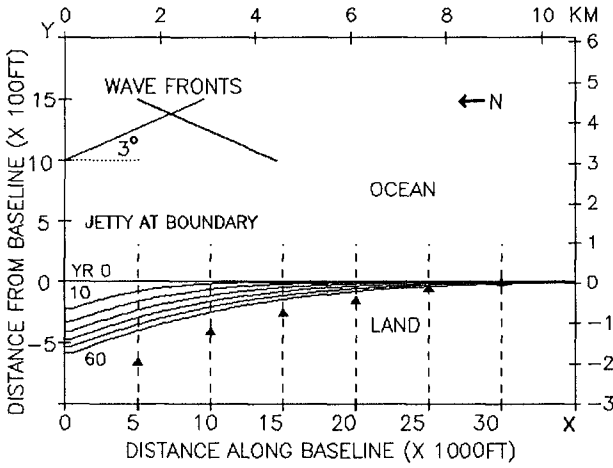


Figure 5a. Plan View, Model

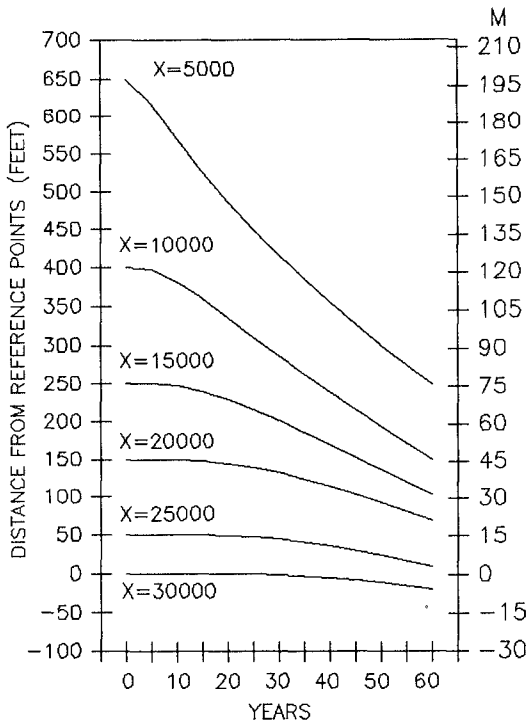


Figure 5b. Time Plot, Model

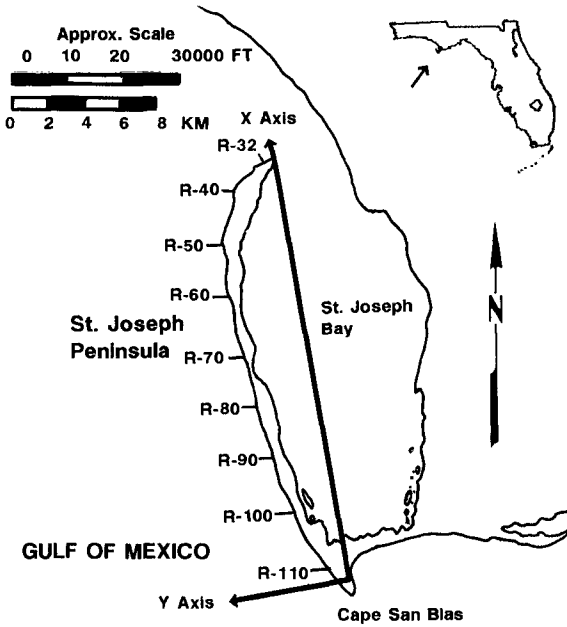


Figure 6a. Location Map

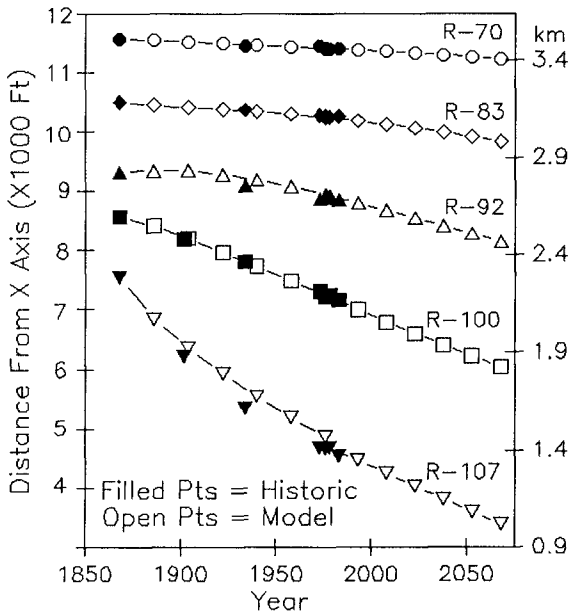


Figure 6b. Comparing Historic Data with Model Results

of the state due to applicability and workload constraints. However, it is becoming increasingly useful to perform general case modeling to help understand and explain to others some of the less obvious erosion patterns. Also, not all areas require an involved analysis for practical results. In some basically stable areas, where inlets are relatively far away, it may not be necessary to know immediately what is occurring as a process throughout the entire region. In such cases, it is usually only necessary to recognize if the historic data are within the range of beach width changes normally observed at the site, and if there is no obvious sand deficit problem. As a conservative practice, a minimum estimate of  $-0.3$  m/yr ( $-1$  ft/yr) is usually forecast for all historically stable areas and even for areas with accretionary trends (exclusive of uncontrolled inlet areas). The use of the minimum estimate allows for some uncertainty about future conditions in general, and about our ability to accurately measure very low levels of shoreline change.

Generally the method of forecasting has been to assume that the most recent major trend will continue linearly forward for the next thirty years. If the case warrants calibrated modeling, such may be used to help project the erosion trend forward for thirty years. However, the use of modeling is a new technique. Typically, the expected rate of change even in a non-linear system is not so rapid as to preclude use of the actual measured data to make projection rates, if the time period for the rate calculation is properly selected.

It is advisable to test the analysis methods and results versus on-site observations and new surveys after several years. If such observations are not consistent with expectations, a review is in order. In our program, preliminary analyses were performed for several regional areas in 1986-89 which are expected to be tested in upcoming years with new regional survey data. Site surveys submitted with permit applications are also used on a daily basis to test previous erosion projections. Another simple test is to ask whether or not the analysis method would have successfully predicted the erosion of the last decade or so, if only data prior to that time were available. If not, the analysis method or the level of understanding about the coastal process is lacking.

The question of the potential effect of sea level rise requires some comment. The historic data necessarily includes the effects of all causes of shoreline change over the last 100+ years, including any

sea level rise and any land subsidence or emergence. Land movement is not believed to have been significant in Florida over the last 100+ year record. The effect of sea level rise appears to be entirely obscured in the data by accuracy limitations, the effects of storms and littoral barriers, and the longshore movement of sand. For the time being, erosion projections will continue to be based on the historic record of change and the observed longshore processes.

## Results

Descriptions of the general findings for some regional areas have been published in various conference proceedings (Foster 1989b, 1991b). However, most of the results exist as in-house reports, pending verification and time to prepare items for publishing.

The historic shoreline maps and data reveal that Florida's sandy beaches have changed in systematic, progressive patterns over the historic record. The shoreline changes appear to be occurring in patterns dictated by the longshore sediment transport equation. The primary factors appear to be the local sand supply situation, the prevailing wave climate, and local geographic features such as rock and peat exposures, nearshore reefs, and man-made littoral barriers. In some areas, the coast is dominated for many kilometers by nearshore rock/reef. It is necessary to account for these features if a thorough understanding of the historic record is to be obtained.

There is certainly randomness in the short term due to seasonal changes, storms, and yearly climatic variations, but these tend to average out over a longer time period. Major storms such as hurricanes also inject an element of randomness by occasionally altering the local conditions, particularly at inlets. In the situation of an uncontrolled inlet, although we may have some understanding of what is occurring, it is not generally a very predictable process.

## Problems

There are several problems which eventually need to be better resolved. At the current staffing level it will necessarily take many years of persistent, careful work to update the data base and to complete the analysis of the state.

One technical issue involves the analysis of areas with existing coastal armoring, including seawalls, revetments, and groinfields. Some of these areas have been armored for most of the historic record, and the condition of the structures varies tremendously. Another technical issue involves setting a thirty year erosion limit in the vicinity of uncontrolled inlets, where large beach width changes are frequent and random. Yet another technical problem involves predicting erosion in the several large areas of the state which have been controlled by repeated beach renourishments over several decades. There is usually insufficient monitoring data for these areas, as well as the complications of varying fill placement volumes, locations, and sand quality. Better monitoring and the use of modeling should help in this situation.

In most areas there is a lack of information regarding nearshore and subsurface geologic features such as rock, peat, and reef formations. The effects on the MHW of dune/bluff recession and overtopping caused by storms are not fully understood at this time. There is also insufficient information to prepare a reliable volumetric budget for many areas.

Beyond the technical issues, there is the human problem of dealing with preconceived, simplistic assumptions about erosion. The data and physics indicate that shorelines are very often not changing at a constant rate, contrary to popular belief and the desire for convenience.

#### Conclusions and Recommendations

A high quality, reliable, updated historical shoreline data base, necessarily including ground truth data, is a worthwhile investment. The data should be related to observed coastal processes in order to reach a basic understanding of cause and effect. The analysis methods and results should include projections of future changes, regardless of whether there is a legal need, and these should be tested over time. In Florida, the shoreline changes are very often non-linear, i.e. not occurring at a constant rate. However, the patterns of shoreline change appear to be very consistent with the physics of the longshore sand transport equation. Longshore models are useful and will probably become necessary in the analysis of many cases.

In the opinion of the author, it is now possible for an analyst to develop a basic understanding of longshore coastal processes for most areas of Florida

based on reliable data and physics, rather than subjective judgments. Many problems remain, but a reasonably good start has been made.

#### References

Foster, E. R. and Savage, R. J. (1989a). "Methods of Historical Shoreline Analysis", Coastal Zone '89, ASCE, Vol. 5, pp. 4434-4448.

Foster, E. R. and Savage, R. J. (1989b). "Historic Shoreline Changes in Southwest Florida", *ibid.*, pp. 4420-4433.

Foster, E. R. (1991a). "Coastal Processes Near Cape San Blas, Florida: A Case Study Using Historic Data and Numerical Modeling", Proceedings of the 4th Annual National Beach Preservation Technology Conference, Florida Shore and Beach Preservation Association, 864 E. Park Ave., Tallahassee, FL 32301, pp. 400-411.

Foster, E. R. (1991b). "Inlet Behavior and the Effects on Beach Erosion in Lee County, Florida", *ibid.*, pp. 178-193.

## CHAPTER 159

### Grain-sorting over ripples induced by sea waves

Enrico Foti<sup>1</sup>, Paolo Blondeaux<sup>2</sup>

#### Abstract

A predictive theory for the formation of ripples under sea waves is presented for a sandy bottom characterized by a large grain-size distribution. The theory is based on a linear stability analysis. The conditions for the amplification or decay of bottom perturbations are determined and the experimentally observed sorting effect due to the presence of the bedforms is modelled. A comparison between the experimental data available in literature and the present results is attempted.

#### Introduction

In the past, the dynamics of sediment in nearshore regions was extensively studied in terms of a uniform material. However, coastal sediment typically has a wide range of grain sizes and the presence of mixtures has a large influence on coastal morphodynamics. Indeed, the grain sorting process which is typical of the transport of mixtures may inhibit or enhance sediment transport in areas characterized by low shear stress. For this reason, the last decade saw a major change in thinking, and important problems involving mixtures were at least formulated correctly and a fair number of them were solved as well, at least for sediment in transport in rivers, (Parker, 1991).

In accordance with this viewpoint, a predictive theory is presented in the present paper for ripple formation under sea waves in the case of a cohesionless bottom made up of a mixture. Following Blondeaux (1990), the theory is based on a linear stability analysis of a flat bottom subject to a viscous oscillatory flow. The aim of the work is twofold: first, to determine the conditions for the decay or the amplification of a bottom perturbation and second to study the grain-sorting

---

<sup>1</sup>Ph.D student, Hydraulic Institute - University of Genoa - Via Montallegro, 1 - 16145 - GENOVA

<sup>2</sup>Associate Professor, Hydraulic Institute - University of Genoa - Via Montallegro, 1 - 16145 - GENOVA



process which leads the coarser fraction to accumulate along the crests of the perturbation while the finer fraction tends to move towards the troughs (Mei, 1989).

The procedure used in the rest of the paper is the following: in the next section, the problem is formulated by focusing our attention on the equation forcing the sediment mass balance and the relationship between sediment transport rate and fluid flow. Indeed, the above equations need particular care when written for a mixture. As discussed more deeply in the following, the continuity equation is written introducing: i) an active layer, scaled on the largest grain sizes and characterized by a vertical uniform size density (Hirano, 1971), which corresponds to the reservoir of material directly available for transport, ii) a bottom layer underneath the active layer, the sediment of which can be entrained by the flow only because of bottom erosion. In the bottom layer, the size density may have a vertical structure. The sediment transport rate is evaluated by means of a formula valid for a uniform sediment times the size density evaluated in the active layer. The sheltering effects exerted by the large grains on small ones are taken into account by introducing a "hiding" factor in the sediment transport rate formula (Parker, 1991).

In §3 an approximate analytical solution for the bed evolution is obtained taking into account that the time scale of the bed time development is much longer than the period of fluid oscillations, i.e. the period of sea waves. Finally in §4 the quantitative results are presented along with a qualitative comparison with the experimental data available in literature.

### Formulation of the problem

As pointed out in the introduction, a significant feature of coastal areas is the wide range of sediment sizes found there. Let us then consider an initially cohesionless sea bottom formed by a sand mixture uniformly distributed in space. To deal with the statistics of the mixture, the logarithmic sedimentological scale  $\phi$  is used, defined by

$$d^*/l^* = 2^{-\phi} \quad (1)$$

where the grain size  $d^*$  is made dimensionless by means of a characteristic length scale of the problem  $l^*$  which will be defined in the following. Hence, the characteristics of the sand mixture are specified in terms of the size distribution  $p_f(\phi)$  or the size density  $p(\phi)$ . The function  $p_f(\phi)$  is defined such that fraction  $p_f(\phi)$  of a sample is finer than size  $\phi$  while  $p(\phi)$  is its derivative, i.e.  $p(\phi) = dp_f(\phi)/d\phi$ .

There are other statistical parameters that summarize the characteristics of the mixture: the geometric mean size  $d_m^*$  and the geometric standard deviation  $\sigma_g$  given by

$$d_m^*/l^* = 2^{-\phi_m} \quad \sigma_g = 2^\sigma \quad (2)$$

where

$$\phi_m = \int_{-\infty}^{+\infty} \phi p(\phi) d\phi \quad \sigma^2 = \int_{-\infty}^{+\infty} (\phi - \phi_m)^2 p(\phi) d\phi \quad (3)$$

A Cartesian orthogonal coordinate system  $(x^*, y^*, z^*)$  is then defined with the  $x^*$  and  $z^*$  axis lying on the sea bottom and the  $y^*$  axis directed upward. Because of the presence of a two-dimensional surface gravity wave, let us assume that the fluid close to the bottom but outside the viscous boundary layer oscillates in time with velocity

$$(u^*, v^*, w^*) = \left(-\frac{1}{2}U_0^* e^{i\omega^* t^*} + c.c., 0, 0\right) \quad (4)$$

where  $t^*$  is time,  $\omega^* = 2\pi/T^*$  the angular frequency of the sea wave,  $U_0^*$  the amplitude of the irrotational velocity oscillations evaluated close to the bottom, c.c. denotes the complex conjugate of a complex number and  $(u^*, v^*, w^*)$  are the velocity components according to the Cartesian coordinate system  $(x^*, y^*, z^*)$ . If the bottom is flat and all the grain sizes in the sand mixture are much smaller than the characteristic thickness of the bottom boundary layer  $\delta^*$ , the fluid motion is described by the well known Stokes' solution and the sediment moves to and fro. The thickness  $\delta^*$ , which can be defined as  $\sqrt{2\nu/\omega^*}$  ( $\nu$  being the kinematic viscosity of sea water), can then be assumed as the length scale of the problem, i.e.  $l^* = \delta^*$ .

The study of the time development of a two-dimensional bottom perturbation in the form

$$y^* = \eta^*(x^*, t^*) = \epsilon^* C_1(t) e^{i\alpha^* x^*} + c.c. \quad (5)$$

is posed by the vorticity equation, the flow and sediment continuity equations plus a relationship between sediment flow rate  $q^*$  and flow properties, along with boundary conditions which force the matching of the flow with the irrotational motion outside the bottom boundary layer and the no-slip condition at  $y^* = \eta^*$ . Because of the presence of the sand mixture, the sediment continuity equation needs to be discussed in detail. Assuming all grains to have the same density, the statement of mass balance for each grain size can be reduced to a similar one for volume balance

$$-\frac{\partial(q^* p_s)}{\partial x^*} = (1-n) \frac{\partial}{\partial t^*} \int_{-\infty}^{\eta^*} p dy^* \quad (6)$$

where it is assumed that the volume transport of bedload per unit time per unit width of grain in the size range  $(\phi, \phi + d\phi)$  is provided by the relationship describing the sediment transport rate for a uniform material ( $q^*(\phi)$ ) times the

size density  $p_s(\phi)$  at the surface. As discussed in Parker (1991), to simplify the problem it is assumed that near the surface there is an active layer characterized by a thickness  $L_a^*$  which corresponds to the reservoir of material directly available for transport and where the grains are well mixed. It follows that the size density  $p_s$  within it has no vertical structure even though it can have a streamwise and time structure. Below the active layer lies the substratum material with size density  $p_b$ . This may vary arbitrarily in  $x^*$  and  $y^*$  but cannot change directly in time because it is not directly subject to movement. Material can be exchanged between the substratum and the active layer through the intermediary of bed aggradation or erosion as outlined below.

By applying Leibnitz's rule, the following result is obtained from (6)

$$-\frac{\partial(p_s q^*)}{\partial x^*} = (1 - n) \left\{ p_i \frac{\partial \eta^*}{\partial t^*} + \frac{\partial}{\partial t^*} (L_a^* p_s) \right\} \tag{7}$$

The value of  $p_i$  can be specified in the case of a degrading bed as  $p_b$ , since substratum is incorporated into the surface layer as the bed elevation drops. In the case of an aggrading bed  $p_i$  can be assumed equal to  $p_s$  since the surface material is transferred directly to the substratum.

$$p_i = \begin{cases} p_s & \text{if } \partial(\eta^* - L_a^*)/\partial t > 0 \\ p_b & \text{if } \partial(\eta^* - L_a^*)/\partial t < 0 \end{cases} \tag{8}$$

Finally, it should be pointed out that  $L_a^*$  can be assumed to scale with some large size, e.g.  $d_{90}^*$ .

Let us then define the following dimensionless variables

$$(x, y) = (x^*, y^*)/\delta^* \quad t = t^*\omega^* \quad \epsilon = \epsilon^*/\delta^* \quad \alpha = \alpha^*\delta^* \quad L_a = L_a^*/\delta^*$$

$$\eta = \eta^*/\delta^* \quad \psi = \psi^*/U_0^*\delta^* \quad q = \frac{q^*}{[(\rho_s - \rho)gd_{m0}^*]^3/2}$$

where  $g$  is the gravity,  $\psi^*$  is the stream function such that  $u^* = \partial\psi^*/\partial y^*$ ,  $v^* = -\partial\psi^*/\partial x^*$  and  $d_{m0}^*$  the mean size of the initial uniform mixture characterized by a size density  $p_o(\phi)$ .

The governing differential problem then reads:

$$\frac{2}{R_\delta} \frac{\partial}{\partial t} (\nabla^2 \psi) + \frac{\partial \psi}{\partial y} \frac{\partial}{\partial x} (\nabla^2 \psi) - \frac{\partial \psi}{\partial x} \frac{\partial}{\partial y} (\nabla^2 \psi) = \frac{1}{R_\delta} (\nabla^4 \psi) \tag{9}$$

$$\frac{\partial \psi}{\partial y} \rightarrow -\frac{1}{2} e^{it} + c.c. \quad \frac{\partial \psi}{\partial x} \rightarrow 0 \quad \text{for } y \rightarrow \infty \tag{10}$$

$$\frac{\partial \psi}{\partial y} = 0 \quad \frac{\partial \psi}{\partial x} = 0 \quad \text{for } y = \eta \tag{11}$$

where the flow Reynolds number  $R_\delta$  is defined as follows:

$$R_\delta = \frac{U_o^* \delta^*}{\nu}$$

As pointed out previously, in order to close the above formulation, we need a relationship between sediment flow rate  $q^*$  and flow properties. Presently, a modified version of the Grass-Ayoub (1982) formula is used. The differences consist in the introduction of the effect of gravity related to the bed elevation and in the introduction of the "hiding" factor  $(\frac{d^*}{d_{mo}^*})^r$ . This formula, even though simple and possibly rough, appears to contain the main physical ingredients controlling the process of transport:

$$q = a \left( \frac{2}{R_{do}} \right)^b \left( \frac{d^*}{d_{mo}^*} \right)^{-0.03-b} \cdot \left| \left( \frac{d^*}{d_{mo}^*} \right)^r v_t - \frac{\beta R_{do}}{2F_{do}^2} \frac{\partial \eta}{\partial x} \right|^{b-1} \cdot \left( \left( \frac{d^*}{d_{mo}^*} \right)^r v_t - \frac{\beta R_{do}}{2F_{do}^2} \frac{\partial \eta}{\partial x} \right) \quad (12)$$

where  $a = 1.23$ ;  $b = 4.28$ ;  $\beta = 0.15$  and  $v_t$  is the fluid velocity evaluated at  $y^* = d^*/2$  parallel to the bed profile. It can be seen that values of  $r$  close to one as discussed by Parker (1991) correspond to the condition for equal-mobility.

The particle Reynolds number  $R_{do}$  and the particle Froude number  $F_{do}$  are defined in terms of the geometric mean size  $d_{mo}^*$  to the initial grain size distribution:

$$R_{do} = \frac{U_o^* d_{mo}^*}{\nu}; \quad F_{do} = \frac{U_o^*}{[(s-1)g d_{mo}^*]^{1/2}}; \quad s = \frac{\rho_s}{\rho};$$

Since the bottom waviness is assumed to be of a small amplitude the quantity  $\epsilon$  can be assumed much smaller than one and the solution to the problem can be expanded in power series of  $\epsilon$  in the form:

$$\psi = \psi_0(y, t) + \epsilon C_1(t) \phi_1(y, t) e^{i\alpha x} + c.c. + 0(\epsilon^2) \quad (13)$$

$$q = q_0(\phi, t) + \epsilon C_1(t) q_1(\phi, t) e^{i\alpha x} + c.c. + 0(\epsilon^2) \quad (14)$$

$$p = p_0(\phi) + \epsilon C_1(t) p_1(\phi, t) e^{i\alpha x} + c.c. + 0(\epsilon^2) \quad (15)$$

By substituting (13)  $\div$  (15) into (9)  $\div$  (12) and equating similar powers of  $\epsilon$ , at order one a problem is found which can easily be solved. As pointed out previously, the flow is described by the well-known Stokes' solution and the sediment moves to and fro. Because the moving material is still considered as belonging to the bottom, the size density  $p_0$  does not change with time. Moreover,  $p_0$  does not depend on  $x$  because of the supposed uniformity of the problem.

At order  $\epsilon$  the problem reads:

$$\begin{aligned} \frac{2}{R_\delta} \frac{\partial}{\partial t} \left( \frac{\partial^2 \phi_1}{\partial y^2} - \alpha^2 \phi_1 \right) + i\alpha \left[ \frac{\partial \psi_0}{\partial y} \left( \frac{\partial^2 \phi_1}{\partial y^2} - \alpha^2 \phi_1 \right) - \frac{\partial^3 \psi_0}{\partial y^3} \phi_1 \right] = \\ = \frac{1}{R_\delta} \left[ \frac{\partial^4 \phi_1}{\partial y^4} - 2\alpha^2 \frac{\partial^2 \phi_1}{\partial y^2} + \alpha^4 \phi_1 \right], \end{aligned} \tag{16}$$

$$\frac{\partial \phi_1}{\partial y} \rightarrow 0, \quad \phi_1 \rightarrow 0, \quad y \rightarrow \infty \tag{17}$$

$$\frac{\partial \phi_1}{\partial y} = -\frac{\partial^2 \psi_0}{\partial y^2}, \quad \phi_1 = 0, \quad y = 0 \tag{18}$$

$$-\frac{2F_{d0}}{R_{d0}}(1-n) \frac{dC_1(t)}{dt} = i\alpha q_1(t) C_1(t), \tag{19}$$

$$\begin{aligned} q_1 = ab \left( \frac{2}{R_{d0}} \right)^b \left( \frac{d^*}{d_{m0}^*} \right)^{-0.03-b} \left| \frac{\partial \psi_0}{\partial y} \left( \frac{d^*}{d_{m0}^*} \right)^r \right|^{b-1} \cdot \\ \cdot \left\{ \left[ \frac{\partial \psi_1}{\partial y} + C(t) e^{i\alpha x} \frac{\partial^2 \psi_0}{\partial y^2} \right]_{y=\frac{d}{2}} \left( \frac{d^*}{d_{m0}^*} \right)^r - \frac{i\alpha \beta R_{d0}}{2F_{d0}^2} C(t) e^{i\alpha x} \left( \frac{d^*}{d_{m0}^*} \right)^2 \right\} \end{aligned} \tag{20}$$

It should be pointed out that at order  $\epsilon$ , the term proportional to the time derivative of  $C_1(t)$  in the vorticity equation has been ignored. From a physical point of view, this corresponds to ignoring the influence of the variation of bottom elevation on fluid motion. From a mathematical point of view, this assumption is justified by the small value usually attained by the dimensionless parameter

$$Q = 0.615((s-1)/s) F_{d0}^{-1.45} (R_{d0}/R_\delta)^{4.28} / (1-n) \sim \frac{dC_1(t)}{dt} / C_1(t). \tag{21}$$

Solution

Because of the assumption  $dC_1/dt \ll C_1(t)$ , flow development has been decoupled from the sediment motion. Equations (16) ÷ (20) and boundary conditions (17) ÷ (18) can then be solved with the same procedure used in Blondeaux (1990) to which the reader should refer for details. Once the stream function is known, the bottom time development can be obtained from the sediment continuity equation and the sediment flow rate formula, which at order  $\epsilon$  provides

$$\begin{aligned} (L_0 p_1 + p_0) \frac{dC_1}{dt} = -L_0 C_1 \frac{\partial p_1}{\partial t} - \\ - \frac{i\alpha R_{d0}}{2F_{d0}(1-n)} [q_0 p_1 + p_0 q_1] C_1 \end{aligned} \tag{22}$$

By integrating (22) over the whole range of  $\phi$  and forcing that

$$\int_{-\infty}^{+\infty} p_0(\phi) d\phi = 1 \quad \int_{-\infty}^{+\infty} p_1(\phi, t) d\phi = 0 \quad (23)$$

an equation for  $C_1(t)$  is obtained which allows the time development of the ripple amplitude to be determined once the function  $p_1(\phi, t)$  is known,

$$\frac{dC_1}{dt} = -\frac{i\alpha R_{d0}}{2F_{d0}(1-n)} \left[ \int_{-\infty}^{+\infty} (q_0 p_1 + p_0 q_1) d\phi \right] C_1 \quad (24)$$

The perturbation of the grain size distribution  $p_1(\phi, t)$ , can be obtained by substituting (22) for (24):

$$\begin{aligned} \frac{\partial p_1}{\partial t} = & -\frac{i\alpha R_{d0}}{2F_{d0}(1-n)L_0} \{ [q_0 p_1 + p_0 q_1] - \\ & - (L_0 p_1 + p_0) \int_{-\infty}^{+\infty} (q_0 p_1 + p_0 q_1) d\phi \} \end{aligned} \quad (25)$$

The solution to the problem posed by equations (24) and (25) cannot be found in closed form. However, an asymptotic solution can be determined by taking advantage of the small values usually attained by the quantity  $Q$ . Indeed, it turns out that:

$$\frac{dC_1}{dt} = -i\alpha Q \left[ \int_{-\infty}^{+\infty} (\tilde{q}_0 p_1 + p_0 \tilde{q}_1) d\phi \right] C_1 \quad (26)$$

$$\frac{\partial p_1}{\partial t} = -\frac{i\alpha Q}{L_0} \left[ \tilde{q}_0 p_1 + p_0 \tilde{q}_1 - (L_0 p_1 + p_0) \int_{-\infty}^{+\infty} (\tilde{q}_0 p_1 + p_0 \tilde{q}_1) d\phi \right] \quad (27)$$

where the quantities  $\tilde{q}_0, \tilde{q}_1$  (defined below) along with  $p_0, p_1, L_0$  are expected to be quantities of order one:

$$(\tilde{q}_0, \tilde{q}_1) = \frac{R_{d0}}{2F_{d0}(1-n)Q} (q_0, q_1) \quad (28)$$

The functions  $C_1(t)$  and  $\phi_1(\phi, t)$  can then be expanded in power series of  $Q$ :

$$C_1(t) = C_{10} + QC_{11}(t) + 0(Q^2); \quad (29)$$

$$p_1(\phi, t) = p_{10}(\phi) + Qp_{11}(\phi, t) + 0(Q^2) \quad (30)$$

The functions  $C_{10}$  and  $p_{10}$  turn out to be time independent. The constant  $C_{10}$  can be fixed equal to one without loss of generality while the function  $p_{10}$  depends on the initial conditions. By substituting (29) and (30) for (26) and (27) it can be seen that

$$\frac{dC_{11}}{dt} = -i\alpha \left[ \int_{-\infty}^{+\infty} \tilde{q}_0 p_{10} + p_0 \tilde{q}_1 d\phi \right] = f(t) \quad (31)$$

$$\frac{\partial p_{11}}{\partial t} = -\frac{i\alpha}{L_0} \{ \tilde{q}_0 p_{10} + p_0 \tilde{q}_1 - (L_0 p_{10} + p_0) \int_{-\infty}^{+\infty} (\tilde{q}_0 p_{10} + p_0 \tilde{q}_1) d\phi \} \quad (32)$$

The right hand side of (31) is a periodic complex function of time denoted  $f(t)$ . The growth or decay of the perturbation amplitude, i.e. ripple formation, is thus controlled by the sign of the real part of the time average of  $f(t)$ . The time average of the imaginary part is related to ripple migration and turns out to vanish because of the symmetry of the problem. The oscillating parts of  $f(t)$  with vanishing time average describe the time variation of the perturbation profile during a wave cycle. More precisely the real part describes oscillations of the amplitude of the bottom perturbation while the imaginary part controls the small longitudinal oscillations of the ripple profile around its average position. The value of the time average of the real part of  $f(t)$  is negative or positive depending on the values attained by the flow and sediment parameters  $\alpha$ ,  $R_\delta$ ,  $R_{do}$ ,  $F_{do}$ ,  $p_o$ .

### Discussion of the results

As in Blondeaux (1990), two contributions to  $\bar{f} = \frac{1}{2\pi} \int_0^{2\pi} f(t) dt$  can be identified. The former is associated with the steady component of the fluid velocity and is usually destabilizing since the steady drift close to the bed tends to carry sediments from the troughs towards the crests of the perturbation, thus causing its growth. The latter contribution is due to the component of the gravity along the bed profile which has a stabilizing effect. In fact, gravity opposes the tendency of the flow to carry sediments from the troughs towards the crests of the perturbation, thus causing the decay of the latter. Assuming that  $p_o(\phi)$  is a normal distribution, so that the standard deviation  $\sigma_o$  identifies the grain size distribution once  $R_{do}$  is fixed, the behaviour of the perturbation is controlled by a balance between the two effects described above which depends on the values of  $\alpha$ ,  $R_\delta$ ,  $R_{do}$ ,  $F_{do}$  and  $\sigma_o$ .

In figure 1 the value of  $\bar{f}$  is plotted versus the wave number of the disturbance  $\alpha$  for fixed values of  $R_\delta$ ,  $R_{do}$  and  $\sigma_o$  and for different values of  $F_{do}$ . It appears that a critical value  $F_{dc}$  of  $F_{do}$  exists such that: for  $F_{do}$  less than  $F_{dc}$  the bottom perturbations characterized by any value of the wave number  $\alpha$  decay; for  $F_{do}$  larger than  $F_{dc}$  disturbances characterized by values of  $\alpha$  falling within a restricted range experience an average amplification during a cycle.

The qualitative behaviour of the results does not change when different values of  $\sigma_o$  are considered. However, in figure 2 it can be seen that the critical value

of  $F_{do}$  increases when increasing values of  $\sigma_o$  are considered: a bottom made up of a mixture is more stable than one composed of well sorted material. Similar results are obtained for different values of  $R_{do}$ .

In figure 3 the critical wave number of the bottom perturbation  $\alpha_c$  is plotted versus  $R_\delta$  for fixed values of  $R_{do}$  and  $\sigma_o$ .

A comparison between the present theoretical findings and experimental data by Blondeaux et al. (1988) is shown in figure 4 where the ratio between the amplitude of fluid displacement  $a^*$  and the critical ripple wavelength  $l^*$  is plotted versus  $R_\delta$ . The theoretical predictions are shown considering sediments characterized by a specific weight  $\rho_s/\rho = 2.65$ ;  $R_{do} = 10$ ;  $\sigma_o = 0.05$ . The experimental data refer to a well sorted silt characterized by a mean diameter equal to 0.124 millimeters, a standard deviation equal to 0.02 millimeters and a specific weight equal to  $2.65t/m^3$ . The experimental conditions are such that  $R_\delta$  ranges between 20 and 85 and the Reynolds number of the sediments falls within the range (5,15). The agreement seems satisfactory even though the lack of experimental data in literature concerning mixtures characterized by large values of the standard deviation  $\sigma_o^*$  does not make a good test for the present theory possible.

The tendency of the process to pile up larger sediments towards the crests is described by means of the integration of equation (32). Also in this case the right hand side of (32) turns out to be a periodic function and the process is thus controlled by the time average of  $\frac{\partial p_{11}}{\partial t}$ . If initial perturbations are absent in the grain size distribution, i.e.  $p_{10}(\phi) = 0$ , the time average of  $\frac{\partial p_{11}}{\partial t}$  shows that smaller grains are shifted towards the troughs and larger grains towards the crests, as experimentally observed (Mei, 1989). Indeed, figure 5 shows that the time average of  $p_{11}$  is real and positive for small values of  $\phi$  and negative for large values of  $\phi$ . It is worthwhile pointing out that values of  $r$  close to one have been used in obtaining the results shown in figure 5. These values of  $r$  are suggested by experimental measurements by Parker (1990) and correspond to equal mobility of all grains, i.e. the bias toward fine material in the bedload relation is almost counteracted by the mean of the hiding function  $(\frac{d^*}{d_{m\phi}})^1$ .

Figure 6 where the time average of  $p_{11}$  is plotted for the same values of the parameters as in figure 5 but for  $r = 0$  shows that the hiding effects exerted by large grains on small ones is essential in describing the sorting process. In fact, when hiding effects are ignored, small grains tend to pile up near the crests and large grains towards the troughs.

The authors would like to thank Professor Parker for his interesting discussions on various issues arising from the work.

This work is part of E.F.'s Ph.D thesis.



References

- Armanini, A., Di Silvio, G. (1988). "A one dimensional model for the transport of a sediment mixture in a non equilibrium condition". *J. Hydr. Res.*, **26**(3), pp. 275-292.
- Blondeaux, P. (1990). "Sand ripples under sea waves. Part 1. Ripple formation". *J. Fluid Mech.* **218**, pp. 1-17.
- Blondeaux, P. Sleath, J.F.A., Vittori, G. (1988). "Experimental data on sand ripples in an oscillatory flow". Rep. 01/88. Inst. Hydraulics, University of Genoa.
- Grass, J.A., Ayoub, N.M. (1982). "Bedload transport of fine sand by laminar and turbulent flow". *Proc. 18<sup>th</sup> Coastal Engineering Conf.*, **2**, pp. 1589-1599.
- Mei, C.C. (1989). "The applied dynamics of ocean surface waves". World Scientific.
- Parker, G. (1990). "Surface-based bedload transport relation for gravel rivers". *J. Hydraulic Res.*, **28**(4), pp. 417-435.
- Parker, G. (1991). "Some random notes on grain sorting". Grain sorting seminar. Ascona, Switzerland, October 21-26.
- Ranga-Raju, K.G. (1985). "Transport of sediment mixtures". Ippen Lecture delivered at the XXI IAHR Congress, Melbourne, Australia.
- Sleath, J.F.A. (1984). "Sea bed mechanics". J. Wiley.

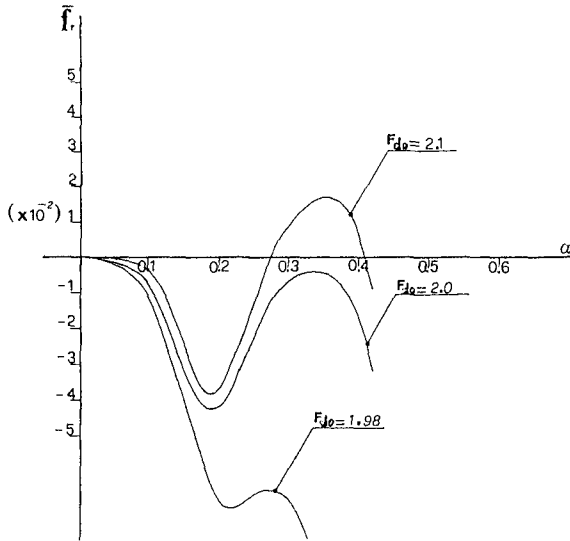


Figure 1. Time averaged amplification factor  $\tilde{f}_r$  versus  $\alpha$  for different values of  $F_{do}$ . ( $R_{do} = 10, \sigma_o = 1, R_\delta = 50$ ).

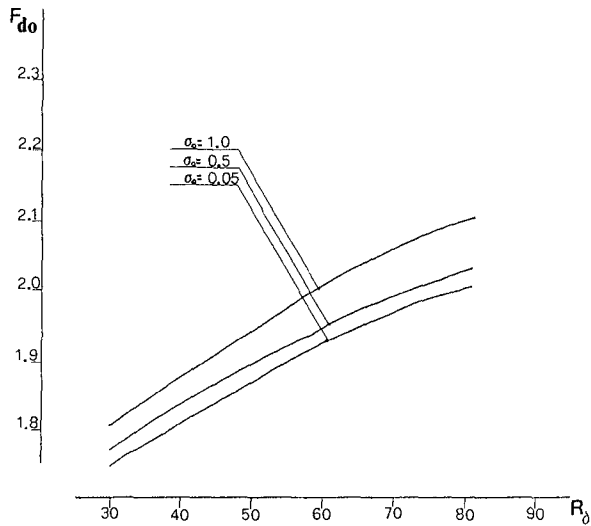


Figure 2. Critical value of the sediment Froude number versus  $R_\delta$  for different values of  $\sigma_o$ . ( $R_{do} = 10$ ).

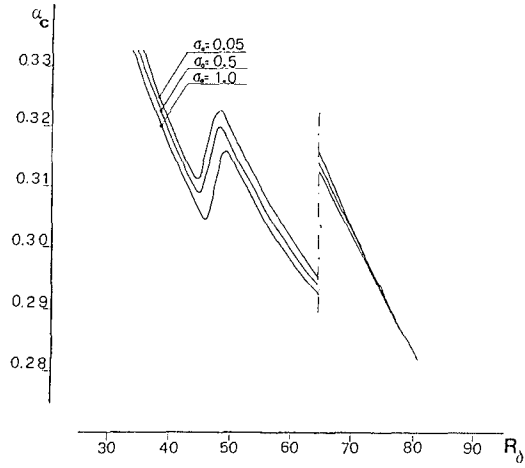


Figure 3. Critical wave number of the bottom perturbation versus  $R_\delta$  for different values of  $\sigma_0$ . ( $R_{d0} = 10$ ).

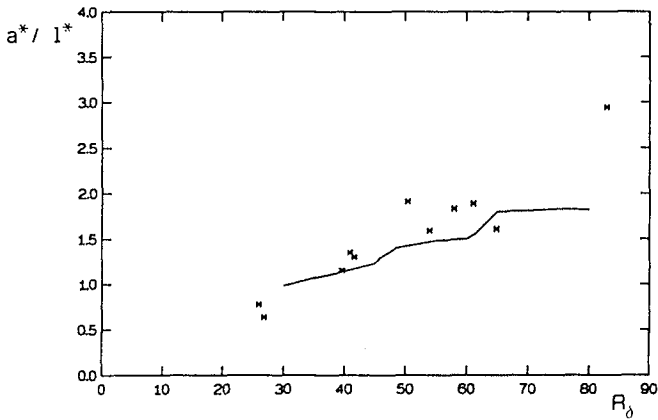


Figure 4. Comparison between experimental and theoretical dimensionless ripple wavelengths.

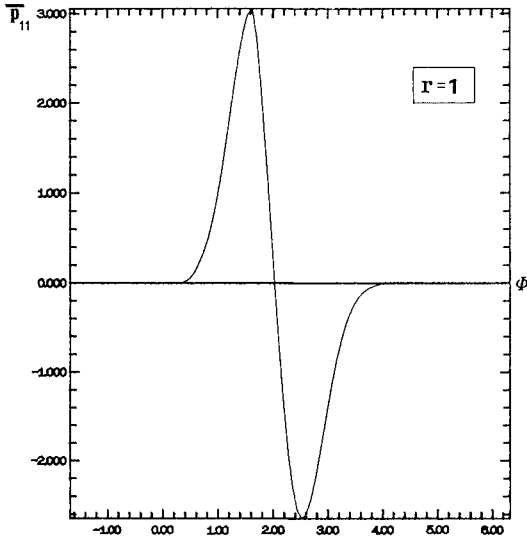


Figure 5. Perturbed density distribution function (averaged over a cycle) versus the  $\phi$ -scale considering the "hiding" factor. ( $F_{do} = 2.3, R_{do} = 10, R_{\delta} = 50, \sigma_o = 0.5$ ).

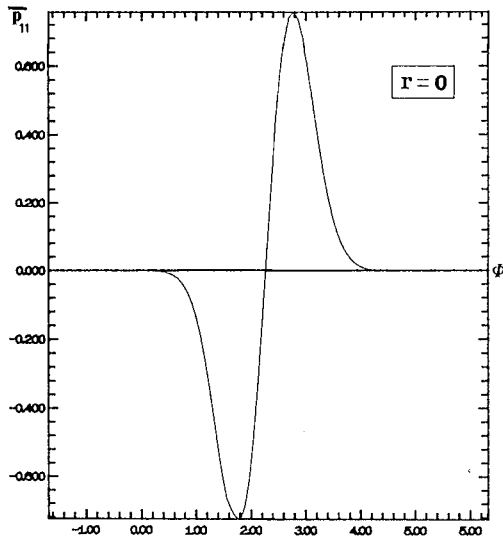


Figure 6. Perturbed density distribution function (averaged over a cycle) versus the  $\phi$ -scale without the "hiding" factor. ( $F_{do} = 2.3, R_{ab} = 10, R_{\delta} = 50, \sigma_o = 0.5$ ).

## CHAPTER 160

### Oscillatory Bedload Transport Studies by Imaging of Tracers

E.L. Gallagher<sup>1</sup> and R.J. Seymour, M. ASCE<sup>2</sup>

#### Abstract

Full scale laboratory flows producing vigorous bed load transport are conducted at varying periods but constant maximum velocities. The time-varying sediment transport in the first half cycle is measured using video imaging of dyed natural sand. The acceleration of the fluid (proportional to the frequency of the oscillation in these experiments) is found to significantly affect the velocity of the sediment response (bedload transport), and the phase and the absolute magnitude of fluid velocity associated with the initiation of sediment motion.

#### Introduction

Bedload has long been recognized as an important element in surfzone sediment transport because, over a great portion of the nearshore, and excepting those areas of greatest near bottom fluid energy, bedload is recognized as the only means for moving sediment. Observing and quantifying bedload is inherently more difficult than for suspended sediment because the density of the carpet flow precludes the conventional acoustical and optical scattering measurements that have been developed for the relatively sparse suspensions above the bed. Further, the assumption that the suspended material moves at the velocity of the adjacent fluid cannot be made for bedload, requiring that both the fluid and the sediment velocities be measured independently to understand the response of the sediment to fluid forcing.

As a result of these difficulties, few observations are available of bedload under oscillatory flows under either field or laboratory conditions and little is known about the character of these important flows. Recognizing this, we began a program of full scale laboratory investigations in an oscillatory tunnel employing traps several years ago (King et al., 1984, King, 1991). More recently, the present authors developed an improved technique for observing bedload remotely in this same tunnel without the problems associated with integrating sediment response over time that is inherent with traps. This method is described in general in the following section and in detail in Gallagher et al. (1991).

---

<sup>1</sup> Graduate Student, <sup>2</sup> Head, Ocean Engineering Research Group, Scripps Institution of Oceanography, University of California San Diego, La Jolla, CA 92093-0222.

As first suggested by King (1991), our work strongly indicated that accelerations played an important role in bedload transport, affecting significantly the magnitude of the sediment velocity with a fixed fluid velocity amplitude, as well as affecting the phase of the response and the initiation of the sediment motion. Given that present predictive models for bedload transport depend only upon the magnitude of the velocity and ignore its time rate of change (see King and Seymour, 1989 for a review of models), we felt that these findings were significant and should be brought to the attention of other researchers concerned with quantifying bedload transport. It should be noted that Hallermeier (1982) discussed the dependence of bedload transport and concluded that fluid accelerations played a "direct role" in sand transport and suggested laboratory work to clarify the effects. The present paper describes our initial work and suggests that these results are of sufficient importance to justify further research in this area, particularly utilizing other means (such as acoustical bedload sensors) to verify and to further quantify these effects.

### Measurement Techniques

The oscillatory flow tunnel (OFT) at the Scripps hydraulic laboratory is a flat U-tube with a long rectangular center section and cylindrical risers on either end (see Figures 1 and 2). It is driven by a hydraulic cylinder powering a ram in one of the risers. The test section is 39.4 cm wide, 40 cm high, and 600 cm in length. The maximum water particle excursion in the test section is 214 cm. There is no free surface and the water is forced in solid body motion of arbitrary waveform by computer control. Additional details are contained in King et al. (1984) and King (1991). As described in Gallagher et al. (1991) and Gallagher and Seymour (1991), a smooth bed of natural sand is prepared in which there is a section of the same sand dyed a contrasting color. The general arrangement is shown in Figure 3. In these experiments, a half cycle of sinusoidal water motion was then commanded with a maximum free stream velocity of 80 cm/s. Holding this maximum velocity constant, the period of the oscillatory motion was varied in each experiment over a range from 3 to 6 seconds. That is, the maximum acceleration varied by a factor of two while the maximum velocity remained constant.

As the fluid accelerates from rest, it reaches a condition at which the sand in the bed begins to move and during the deceleration portion of the half cycle, the sand eventually all comes to rest. The motion is detected in these experiments by video imaging. A video camera with a wide angle lens is mounted just above the transparent top of the OFT and images are recorded at approximately 30 hz. These video records are recorded on super VHS format and can be output as steady single frames from a high quality medical-imaging-type tape player. In the color image, the dyed sand is readily recognizable from the natural sand. Therefore, each image shows the accumulated motion in a single direction, to that time, of the dyed sand, since the flow does not reverse. The single frame images are readily stored in a PC computer using a standard commercial framegrabber board and its related software.

The sediment does not move as a monolithic block. Rather, there is a large dispersion in the response that increases with time and distance downflow, in spite of the well sorted character of the sand (median and mean diameter = 1.1 mm, sorting factor = 0.29, skewness = 0.02, kurtosis = 0.66).. This response dispersion is shown conceptually in Figure 4. Because a particle-by-particle tracking strategy seemed too cumbersome, the method used in Gallagher et al., 1991 was employed. Simply stated, the image in the computer is converted to grey scale and the numbers

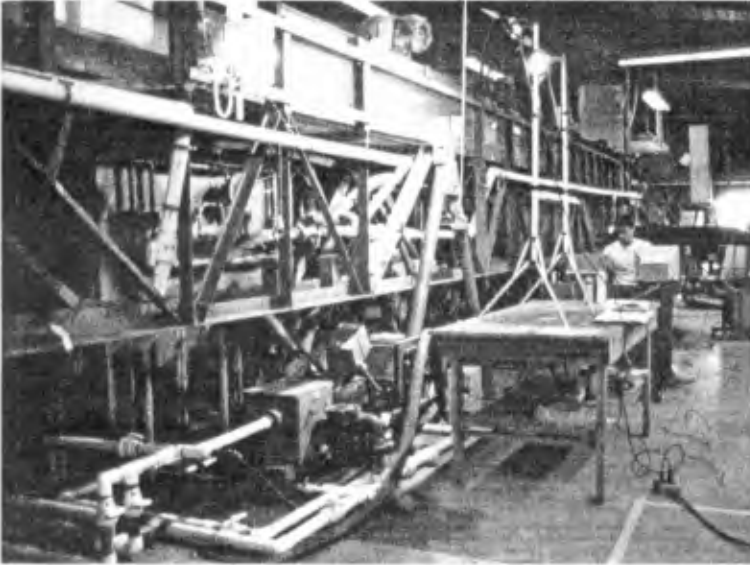


Figure 1. General view of the oscillatory flow tunnel in the SIO hydraulic laboratory.



Figure 2. View of the top of the oscillatory flow tunnel with the lid closed.

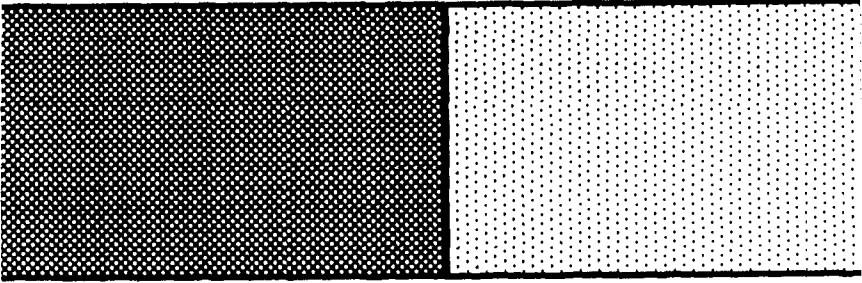


Figure 3. Schematic arrangement of upper surface of the bed prior to the experiment, showing dyed sand section. Motion will be from left to right.

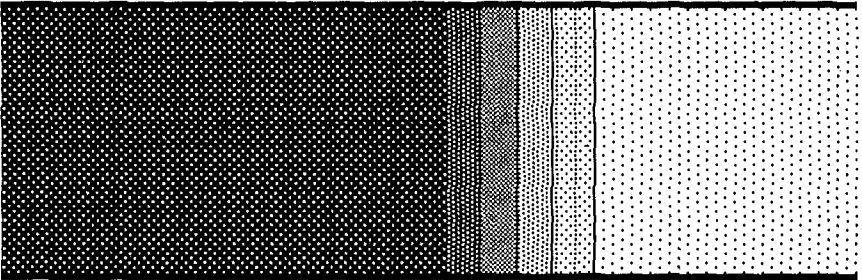


Figure 4. Schematic view of upper surface of the bed following the experiment. Water and sediment motions have been from left to right.



representing the intensity (darkness) of each pixel in the image are averaged over a column extending across the tunnel, orthogonal to the flow. This average color intensity is then a measure of the amount of dyed sand in the upper layer or two that has moved into that column of pixels. In general, this number should increase with time until the sediment motion stops and then remain steady. In practice, that is what is observed. The dyed sand section has sufficient length, relative to the sediment motion, that no undyed sand is imported into the image.

Figure 5 shows a representative plot of these intensities along the flow axis from a single image. Some low level noise of the type shown here is always present, but the data also always show a clear underlying curve representing the distribution of distances travelled by the dyed sand grains. A smooth curve is passed through the data using a high order polynomial fit and this smooth curve then represents the results of a single image from an experiment. To define a representative distance traveled for each of these distributions (images), the intersection of the smooth curve with an arbitrary intensity level was chosen (see dashed line on Figure 5.)

Prior work (King, 1991) had shown that the free stream velocity could be accurately determined from a linear position transducer on the ram and this position was recorded on a PC during the experiment. The computer periodically actuated a light visible in the video image in approximately one out of each 15 images, which allowed time synchronization within about 0.015 seconds. In this manner, the free stream velocity could be obtained by differentiating the ram position and the position of the representative dyed sand intensity contour could be time correlated with it. The sediment velocity and acceleration were obtained by successive differentiation of the positions obtained from the images.

## Results

Experiments were conducted at periods of 3,4,5 and 6 second periods, all with amplitudes resulting in a maximum velocity of 80 cm/s. The response of the sediment is shown in Figure 6. Note that time has been nondimensionalized by the period so that a single curve represents the fluid velocity in each case. It can be clearly seen that the higher accelerations (lower periods) result in an initiation of motion at a later phase than for the lower accelerations. The phases are plotted as angles against peak accelerations in Figure 7. The results are shown in dimensional form in Table I and it is clear that the absolute initiation velocities are higher when the rate of change of fluid velocity is higher, which might be considered counter-intuitive.

The resulting sediment velocities are shown in Figure 8. Smooth curves have been fitted to the calculated velocity values. Note that the maximum sediment velocity increases monotonically with the maximum fluid acceleration and it occurs at a later phase. The shortest period oscillation (3 seconds) results in a maximum sand velocity of almost 60 cm/s - about 75% of the maximum free stream fluid velocity.

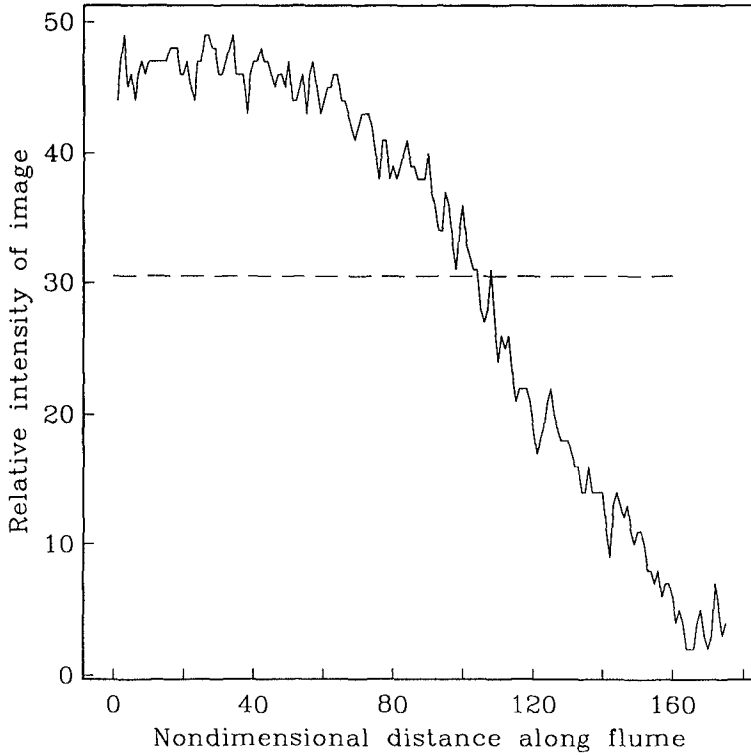


Figure 5. A non-dimensional plot of the intensities of the image (higher intensity signifies greater fraction of dyed versus natural sand) against distance down the flume. The origin of the abscissa is the initial boundary between the dyed and the natural sand.

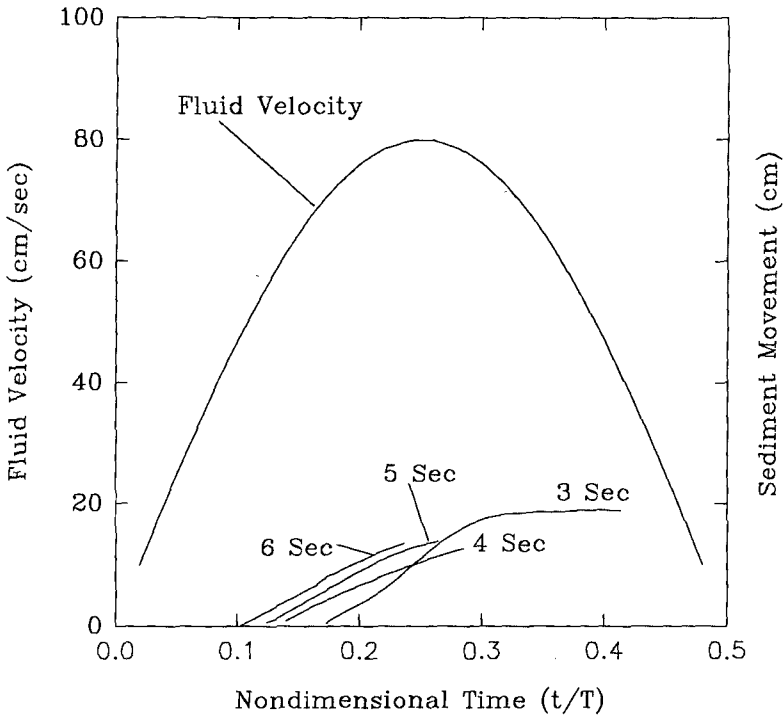


Figure 6. Sediment movement and fluid velocity plotted against nondimensionalized time (fraction of oscillatory period). The periods of the water motions are plotted adjacent to the sediment responses. The effects of acceleration can be clearly recognized.

Exp No.	Period (sec)	Phase (deg)	Velocity (cm/s)	Acceleration (cm/s <sup>2</sup> )
6	3	46.8	58.3	114.7
9	4	41.4	52.9	94.3
12	5	34	44.7	83.3
15	6	31	41.2	71.8

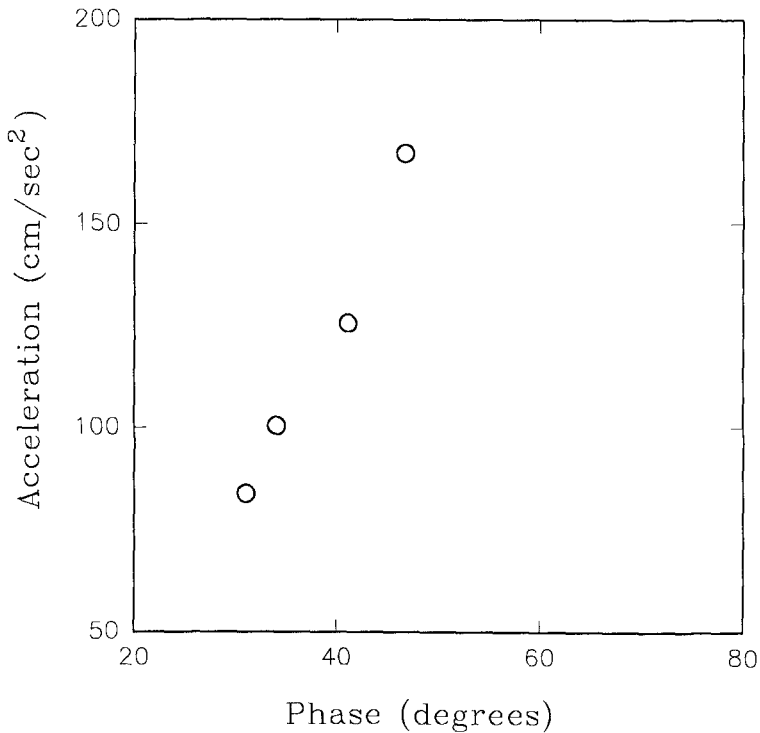


Figure 7. The phase of the initiation of motion (in degrees) plotted against the magnitude of the peak acceleration for each run.

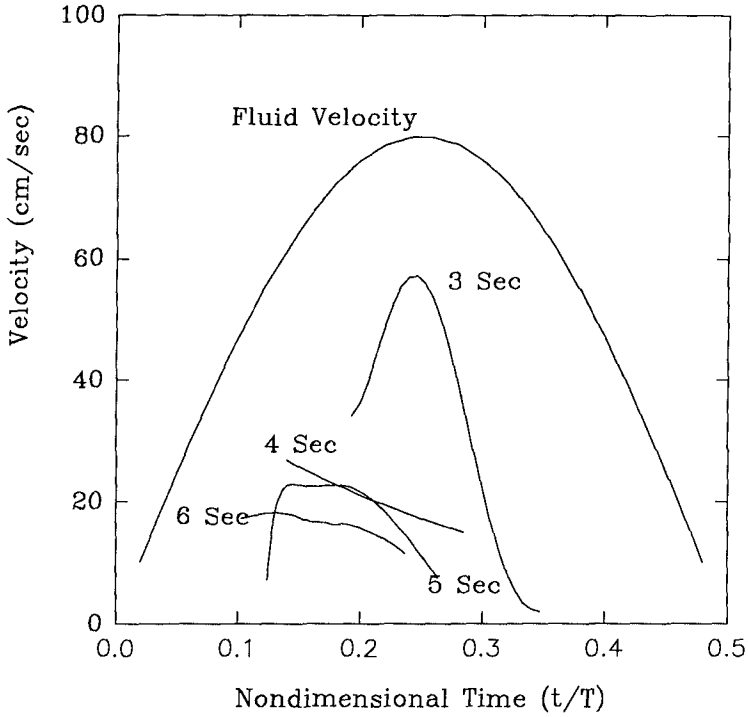


Figure 8. The velocity of the fluid and the resulting velocities of the sediment at various periods of oscillatory flow are plotted against nondimensional time.

### Discussion and Conclusions

These experiments were begun from rest after long stilling periods such that laminar flow conditions existed at least at the initiation of fluid flow. Because the flow was stopped as it decreased to zero (no flow reversal) there was little or no opportunity to develop a boundary layer typical of continuing oscillatory flows - in which the bottom stress is theoretically expected to lead the free stream by  $\pi/4$ . Therefore, there was unlikely to be any substantial phase differences between the free stream and the nearbed flows. In fact, careful observation of suspended particle velocities in King (1991) indicate no discernible phase shift right down to the bed in the half cycle flows.

The significance of this is that any phase shifts between sand and the fluid observed would be a function only of the response of the sediment to the bottom stress. We observed substantial velocity phase leads for the sediment in the longer period experiments, but these reduced to near zero for the shortest period. In fact, in all of the experiments the sediment came to rest either before the maximum free stream velocity had been reached or before it had dropped to 75% of its maximum value. This very surprising result would indicate a response mechanism that is highly sensitive to acceleration - as the positively directed acceleration approaches zero, the bedload ceases, even though the free stream velocity is at or near its maximum value. Sleath (1978) observed a phase lead of the sediment of roughly  $\pi/8$  in continuously oscillating flows and discounted inertial effects because the acceleration leads the velocity by  $\pi/2$ . However, the present evidence - which removes any effects of phase shifts in the boundary layer - seems to indicate that acceleration is indeed a first order factor in bedload transport.

Because the experiments do not replicate the turbulence and the fully developed boundary layer under waves, we do not believe that the absolute numbers measured here for sediment response are useful values. However, we believe we have succeeded in isolating a very important and largely overlooked factor in the forcing of bedload that must be accounted for in realistic predictive models.

### Acknowledgements

This work was supported in part by a grant from the U.S. Army Corps of Engineers Coastal Engineering Research Center under the technical direction of Dr. Thomas E. White. This support is gratefully acknowledged.

### References

- Gallagher, E. L., R. J. Seymour and D. B. King Jr., 1991. Bedload Transport Measurement. Coastal Sediments '91, Symposium on Quantitative Approaches to Coastal Sediment Processes, Seattle, Washington, June 25-27, 1991. Vol. 1, pp. 717-725, American Society of Civil Engineers.
- Gallagher, E. L. and R. J. Seymour, 1991. Preliminary Measurements of Bedload Using Video Imaging Processing. Abstract, American Geophysical Union annual meeting, San Francisco, December 9-13, 1991 (*EOS*, October 29, 1991, 233)

Hallermeier, R.J., 1982. Oscillatory bedload transport: data review and simple formulation. *Continental Shelf Research*, Vol. 1, No. 2, pp 159-190.

1991 King Thesis J. D. Powell, and R. J. Seymour, 1984. A new oscillatory flow tunnel for use in sediment transport experiments. In: *Proc. 19th Int. Conf. on Coastal Engineering*, B. L. Edge, ed., ASCE, Houston, Texas, 3-7 September, 2; 1559-1570.

King, D. B. Jr. and R. J. Seymour, 1989. State of the art in oscillatory sediment transport models. Chap. 16. In: *Nearshore Sediment Transport*. R. J. Seymour, ed. Plenum Press, New York. pp. 371-386

King, D. B. Jr., 1991. Studies in oscillatory flow bedload sediment transport. Ph.D. thesis, University of California San Diego, 184 p.

Sleath, J.F.A., 1978. Measurements of bedload in oscillatory flows. *Journ. Waterway, Port, Coastal and Ocean Div.*, ASCE, Vol. 104, No. WW4. pp 291-307.

## CHAPTER 161

### WAVE-INDUCED POREWATER PRESSURE AND SEABED STABILITY

A. Hattori<sup>1</sup>, T. Sakai<sup>2</sup>, M. ASCE and K. Hatanaka<sup>3</sup>

#### ABSTRACT

The boundary layer approximation solution by Mei and Foda(1981) is applied to and its applicability is confirmed for the porewater pressure variation in a seabed under a breaking wave in a surf zone. Then the approximate solution is modified to take into account effects of the wave-induced bottom shear which is not negligible in the surf zone. This modified solution is applied to estimate the terms in the right hand side of the momentum equations for the solid skeleton under the breaking wave. The instability proposed by Madsen(1974) is discussed based on the estimated results. It is suggested that the instability just after the wave crest passing is more likely to occur than the instability just before the crest passing. Just after the crest passing, the horizontal gradient of the porewater pressure is large, while the vertical effective stress is small.

#### INTRODUCTION

There are two kinds of the porewater pressure response to waves. One is the cyclic excess porewater pressure variation. Another is the mean excess porewater pressure buildup. Earthquake induces the mean excess porewater pressure buildup. Here the cyclic porewater pressure variation is treated.

Under the wave trough, the porewater pressure does not decrease so much as the bottom wave pressure(Fig.1). The porewater pressure bears more load than the vertical effective stress on the solid skeleton

---

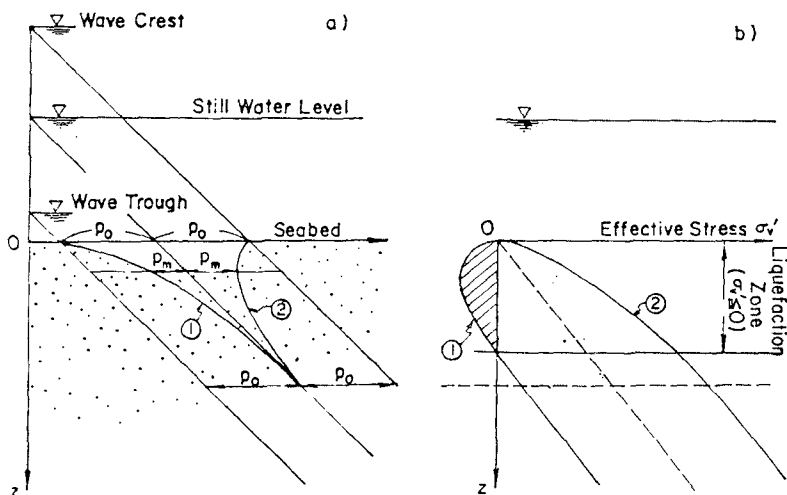
1 Engineer, Engr. & Design Div., Civil Engr. Headquarters, Hazama Corporation, Minato-Ku, Tokyo, 107, Japan.

2 Prof., Dept. of Civil Engr., Kyoto Univ., Sakyo-Ku, Kyoto, 606, Japan.

3 Engineer, Construction Div., West Japan Railway Co., Kita-Ku, Osaka, 530, Japan.



bears. In some cases the vertical effective stress becomes zero near the bed surface. Here we call this "momentary liquefaction".



**Fig.1 Momentary liquefaction of seabed due to waves**  
(Zen et al., 1987)

The depth of this momentary liquefaction can be calculated by using a theory of the transient porewater pressure variation due to waves. Fig.2(Sakai et al., 1992) shows the result by using the boundary layer approximation solution of Mei and Foda(1981). This approximate solution is applicable to a wide range of the wave and soil conditions. The uncoupled analysis proposed by Finn et al.(1983) is applicable only to soft and coarse sand case.

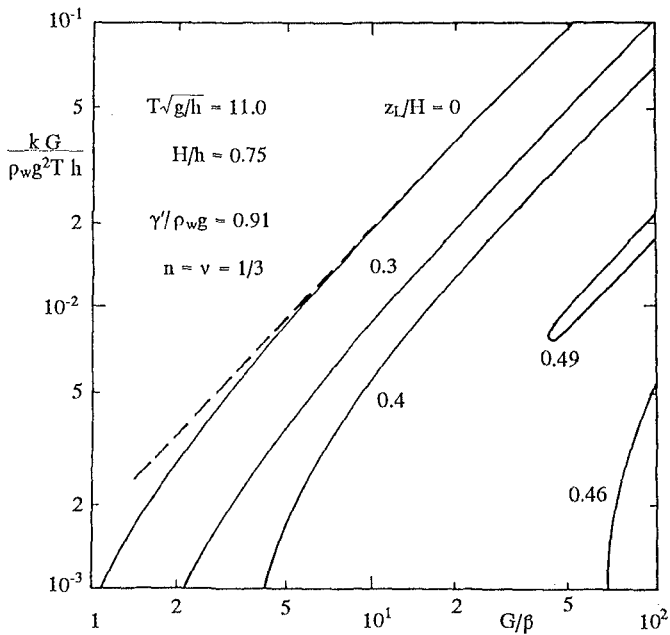
In this figure there are many parameters.  $k$  is the permeability coefficient.  $G$  is the shear modulus of the solid skeleton.  $\beta$  is the effective bulk modulus of the porewater. It is related to the degree of saturation of porewater  $S$ .  $H$  is the wave height.  $z_L$  is the depth of the momentary liquefaction.

$\rho_w$  is the density of the water.  $g$  is the gravity.  $T$  is the wave period.  $h$  is the water depth.  $\gamma'$  is the submerged unit weight of the solid skeleton.  $n$  and  $\nu$  are the porosity and Poisson's ratio of the solid skeleton.

When the bed material becomes fine, the value of  $k$ , so that, the value of the ordinate  $kG/\rho_w g^2 T h$  becomes small. Also, when the porewater becomes soft with increasing amount of gas, the value of  $\beta$

becomes small, so that , the value of the abscissa  $G/\beta$  becomes large. Therefore the finer the bed material and larger the amount of gas in the porewater, the deeper the depth of the momentary liquefaction.

In this analysis, however, the sinusoidal waves were assumed. In surf zone, the wave profile is not sinusoidal but asymmetric. The bottom wave pressure has also an asymmetric time profile.

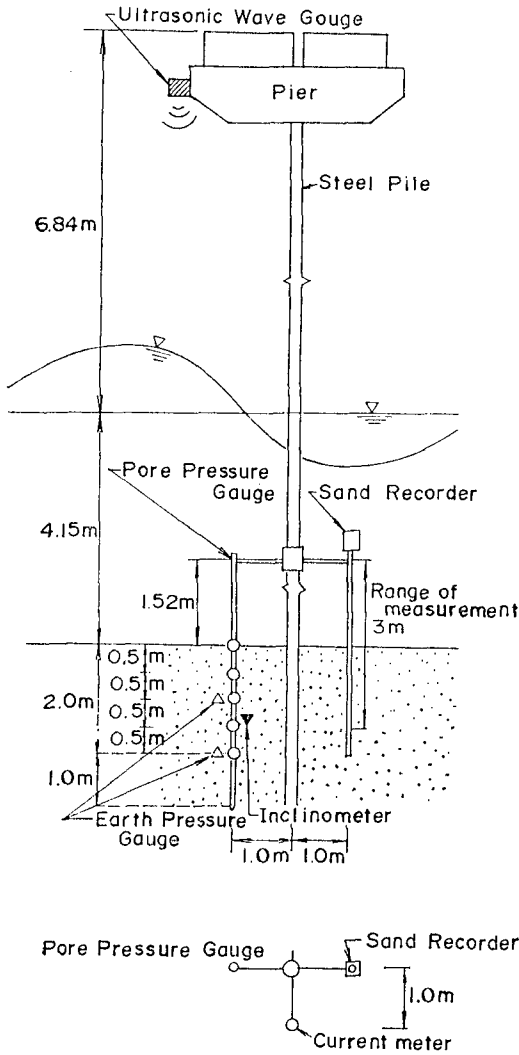


**Fig.2 Momentary liquefaction depth in surf zone (Sakai et al., 1992)**

### **APPLICABILITY OF BOUNDARY LAYER SOLUTION FOR ASYMMETRIC WAVES**

Here the applicability of the boundary layer approximation solution for asymmetric waves in surf zone is examined.

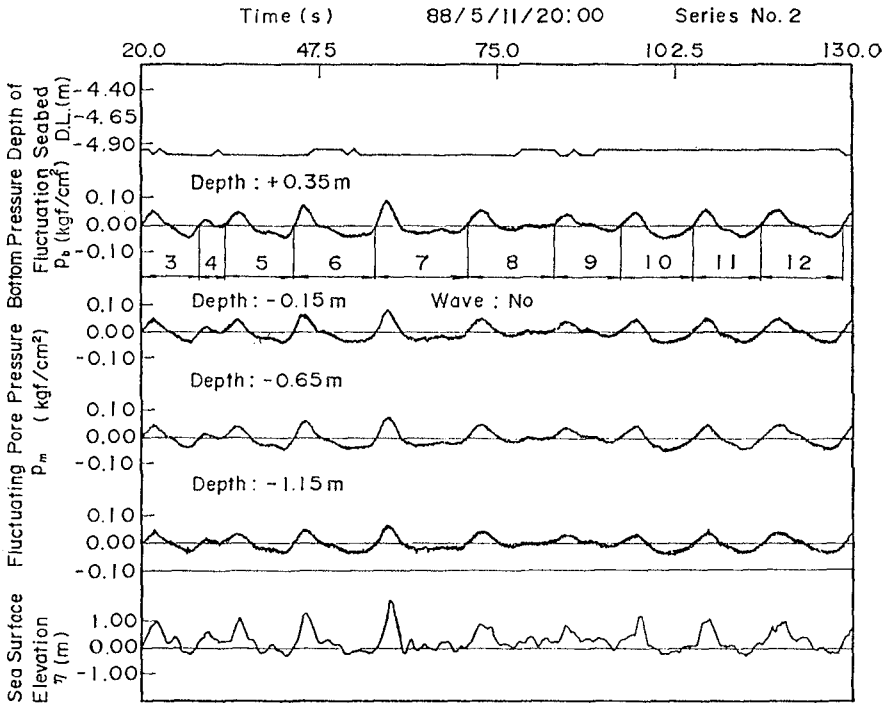
Zen et al.(1989) measured the porewater pressures under waves in a surf zone at a Japanese Pacific Ocean coast. The measurement was done at the head of an observation pier of the Port and Harbour Res. Inst. of Japanese Ministry of Transport. The water depth  $h$  was about 4m(Fig.3). The 50% sand grain size was 0.16mm.



**Fig.3 Measuring apparatus of porewater pressures (Zen et al., 1989)**

Fig. 4 is one of the records(Fig.19(b) in their paper). The second figure shows the bottom wave pressure. The lowest figure shows the water level variation. The three figures from the third to fifth show the porewater pressures at three levels near the bed surface. The wave No.7 was selected as a typical surf zone wave. The wave period  $T$

was 14.7sec, and the wave height  $H$  was 1.9m.



**Fig.4 Example of record of bottom wave pressure and porewater pressures(Zen et al., 1989)**

In the boundary layer approximation solution, when the bottom wave pressure  $p_b$  is given by the small amplitude wave theory as

$$p_b = p_0 \cos(\lambda x - \omega t) = \frac{1}{2} \frac{\rho_w g H}{\cosh(\lambda h)} \cos(\lambda x - \omega t), \quad (1)$$

the porewater pressure variation  $p'$  is given by Eq.(2).

$$p' = p_0 \frac{1}{1+m} \exp\left(\frac{-2\pi z}{L}\right) \cos(\lambda x - \omega t) + p_0 \frac{m}{1+m} \exp\left(\frac{-z}{\sqrt{2}\delta}\right) \cos\left(\lambda x - \omega t + \frac{z}{\sqrt{2}\delta}\right). \quad (2)$$

Eq.(2) includes two parameters  $m$  and  $\delta$ .  $m$  is a non-dimensional parameter proportional to a ratio of  $G$  and  $\beta$ (Eq.(3)).  $\delta$  is the thickness of the boundary layer(Eq.(4)).

$$m = \frac{n}{(1 - 2\nu)} \frac{G}{\beta}, \quad (3)$$

$$\delta = \left( \frac{KG}{\omega} \right)^{\frac{1}{2}} \left( n \frac{G}{\beta} + \frac{1 - 2\nu}{2(1 - \nu)} \right)^{-\frac{1}{2}}. \quad (4)$$

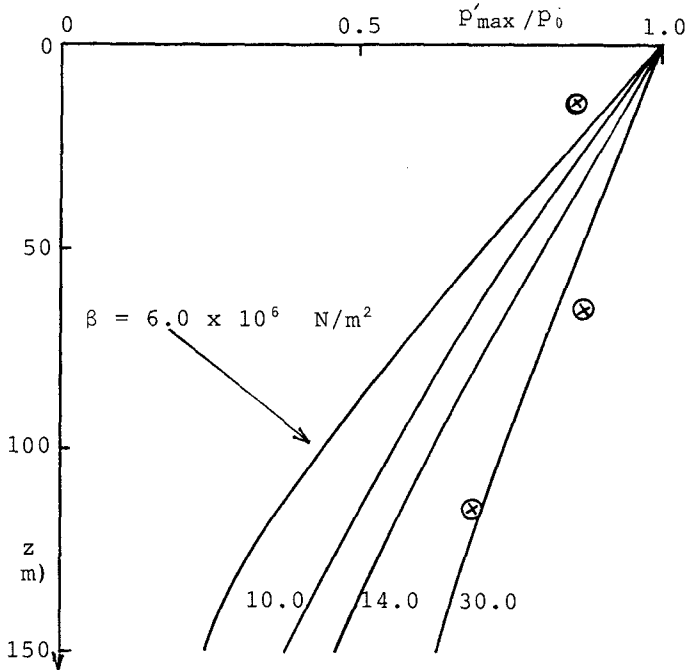
The other parameters are as follows :  $p_0$  is the amplitude of bottom wave pressure,  $\lambda$  ( $= 2\pi/L$ ) is the wave number,  $L$  is the wave length,  $x$  is the horizontal distance in the wave propagation direction,  $\omega$  ( $= 2\pi/T$ ) is the wave angular frequency,  $t$  is the time,  $g$  is the gravity,  $z$  is the depth beneath the seabed surface, and  $K = k/\rho_w g$ .

This solution is linear. The time profile of the bottom wave pressure of the selected wave No.7 was decomposed into its Fourier series components. The porewater pressure variation  $p'$  was calculated for each component by using Eq.(2). The typical values in the sandy bed in the surf zone were used for the parameters ( $n = \nu = 0.33$ ,  $G = 1.0 \times 10^8 \text{N/m}^2$ , and  $k = 2.8 \times 10^{-4} \text{m/sec.}$ ). The porewater pressure variation of wave No.7 was obtained by summing up those of all components.

Fig.5 is a comparison between the calculated and measured results. The comparison was done for the maximum value of the porewater pressure. Four kinds of value were applied to the effective bulk modulus of porewater  $\beta$ . The measured values at lower two levels agree well with the calculated curve of  $\beta = 3 \times 10^7 \text{N/m}^2$ . The measured value at the highest level rather agrees with the calculated curve of  $\beta = 6 \times 10^6 \text{N/m}^2$ . The porewater pressure at the highest level has a different trend from that of other two levels. Nevertheless the boundary layer approximation solution roughly explains the measured porewater pressure even under the asymmetric wave in the surf zone.

#### MODIFIED SOLUTION INCLUDING EFFECTS OF WAVE-INDUCED BOTTOM SHEAR

In surf zone, usually the wave-induced bottom friction is not negligible. The solution by Mei and Foda(1981) neglects this effect. Here a modified solution including the effects of the wave-induced bottom shear is derived.



**Fig.5 Comparison of calculated porewater pressure(-) with measured porewater pressure(x)**

The time profile of the wave-induced bottom shear is not sinusoidal even for sinusoidal waves, because the bottom shear is proportional to the square of the bottom velocity. But here for simplicity, the time profile of wave-induced bottom shear is assumed sinusoidal.

The following boundary conditions are applied:

$$\tau_{xz} = -b \exp\{i(\lambda x - \omega t)\}, \quad \tau_{zz} = -p_0 \exp\{i(\lambda x - \omega t)\}, \quad (5)$$

in which  $\tau_{xz}$  and  $\tau_{zz}$  are the shear stress and vertical total stress on the bed surface,  $b$  is the amplitude of the wave induced bottom shear stress,  $i$  is the imaginary unit. The first equation is added to the condition in Mei and Foda(1981).

The porewater pressure variation  $p'$ , the vertical effective stress variation  $\sigma_{zz}$  and the shear stress  $\sigma_{zx}$  are given as follows :

$$p' = p_0 \frac{1}{1+m} \exp\left(-\frac{2\pi}{L} z\right) \cos \theta + p_0 \frac{m}{1+m} \exp\left(\frac{-z}{\sqrt{2}\delta}\right) \cos\left(\theta + \frac{z}{\sqrt{2}\delta}\right) + b \frac{1}{1+m} \left\{ \exp\left(-\frac{2\pi}{L} z\right) \sin \theta - \exp\left(\frac{-z}{\sqrt{2}\delta}\right) \sin\left(\theta + \frac{z}{\sqrt{2}\delta}\right) \right\}, \quad (6)$$

$$\begin{aligned} \sigma'_{zz} = & p_0 \left( \frac{m}{1+m} + \frac{2\pi}{L} z \right) \exp\left(-\frac{2\pi}{L} z\right) \cos \theta \\ & - p_0 \frac{m}{1+m} \exp\left(\frac{-z}{\sqrt{2}\delta}\right) \cos\left(\theta + \frac{z}{\sqrt{2}\delta}\right) \\ & - b \left( \frac{1}{1+m} - \frac{2\pi}{L} z \right) \exp\left(-\frac{2\pi}{L} z\right) \sin \theta \\ & + b \frac{1}{1+m} \exp\left(\frac{-z}{\sqrt{2}\delta}\right) \sin\left(\theta + \frac{z}{\sqrt{2}\delta}\right), \end{aligned} \quad (7)$$

$$\sigma'_{zx} = p_0 \frac{2\pi}{L} z \exp\left(-\frac{2\pi}{L} z\right) \sin \theta + b \left( 1 - \frac{2\pi}{L} z \right) \exp\left(-\frac{2\pi}{L} z\right). \quad (8)$$

Here  $\theta = \lambda x - \omega t$ . The terms which do not include  $b$  are the solution of Mei and Foda itself.

### SEABED INSTABILITY UNDER BREAKING WAVES

Madsen(1974) proposed a criterion on the stability of sand bed under breaking waves.

$$-\frac{\partial p'}{\partial x} \geq (\rho_t - \rho_w) g \tan \phi, \quad (9)$$

$$-\frac{\partial p'}{\partial z} \geq (\rho_t - \rho_w) g. \quad (10)$$

Eq.(9) is for the horizontal direction, and Eq.(10) is for the vertical direction. Here  $\rho_t$  is the density of the saturated bed material, and  $\phi$  is the angle of internal friction of bed material.

He mentioned in his paper as follows : Under a steep front face of breaking wave, the horizontal gradient of the porewater pressure is larger than the vertical gradient. The angle of internal friction is smaller than 45 degree. The horizontal condition(Eq.(9)) is satisfied before the vertical condition(Eq.(10)) is satisfied.

**Fig.6** is one of the figures of Tsuruya and Korezumi's paper(Fig.7, 1990). This figure shows a part of the record of the measurement of the sediment concentration near the bed( $b$ ) and the porewater pressure( $p_m$  in (e)) near the bed surface and others in an actual surf zone. The figure (d) shows the calculated vertical effective stress( = static stress +  $p_b - p'$  ). The black part indicates 0 effective stress occurrence. They suggested a relation between the high sediment concentration and the momentary liquefaction of the seabed.

The horizontal and vertical gradients of the porewater pressure are included in the right hand side of the horizontal and vertical momentum equations for the solid skeleton,

$$\rho_s \frac{\partial v_{sx}}{\partial t} = \frac{1}{1-n} \left( \frac{\partial \sigma_{xx}}{\partial x} + \frac{\partial \sigma_{zx}}{\partial z} \right) - \frac{\partial p}{\partial x} + \frac{1}{1-n} \frac{n^2}{K} (v_{wx} - v_{sx}), \quad (11)$$

$$\rho_s \frac{\partial v_{sz}}{\partial t} = \frac{1}{1-n} \left( \frac{\partial \sigma_{xz}}{\partial x} + \frac{\partial \sigma_{zz}}{\partial z} \right) - \frac{\partial p}{\partial z} - \rho_s g + \frac{1}{1-n} \frac{n^2}{K} (v_{wz} - v_{sz}). \quad (12)$$

In these equations,  $\rho_s$  is the density of the solid skeleton,  $v_{sx}$ ,  $v_{sz}$ ,  $v_{wx}$  and  $v_{wz}$  are the horizontal and vertical velocities of the solid skeleton and the porewater respectively.  $p$  is the sum of the static pressure and its variation  $p'$ .

To examine Madsen's suggestion, the value of each term in the right hand side of two momentum equations is calculated for the asymmetric wave measured by Zen et al., wave No.7, by using the new solution including the effects of the wave-induced bottom shear, Eq.s (6), (7) and (8).

To emphasize the effects, the wave period is shortened to 7.0sec, and the wave height is multiplied by 1.5. The amplitude of the bottom shear  $b$  is taken to be 1/10 of that of the bottom wave pressure  $p_0$ . The values of the parameters are as follows :  $h = 4.0\text{m}$ ,  $\rho_t = 1,910\text{kg/m}^3$ ,  $n = \nu = 0.33$ ,  $G = 1.0 \times 10^8 \text{N/m}^2$ ,  $\beta = 1.0 \times 10^7 \text{N/m}^2$  and  $k = 2.8 \times 10^{-4} \text{m/sec}$ . The value of  $\beta$  is determined based on the fact that it is  $10^6 \text{N/m}^2$  for the degree of saturation of 99%.

**Fig.7** shows the result at the level of 10cm below the bed surface. The bottom wave pressure is also shown in the top figure. The middle figure shows the phase variation of each term in the right hand side of the horizontal momentum equation for the solid skeleton. The horizontal gradient of the horizontal effective stress  $\partial \sigma_{xx} / \partial x$  and the vertical gradient of the shear stress  $\partial \sigma_{zx} / \partial z$  are as large as the horizontal gradient of the porewater pressure  $\partial p / \partial x$ . The horizontal



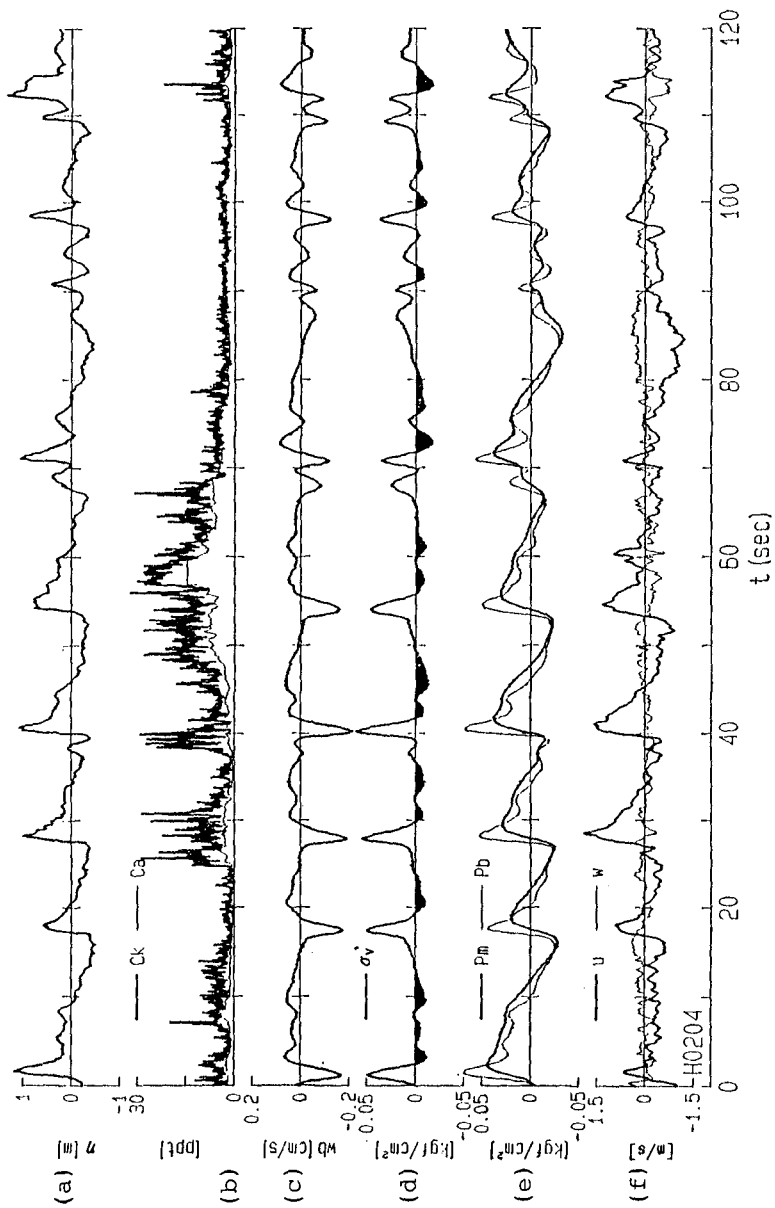
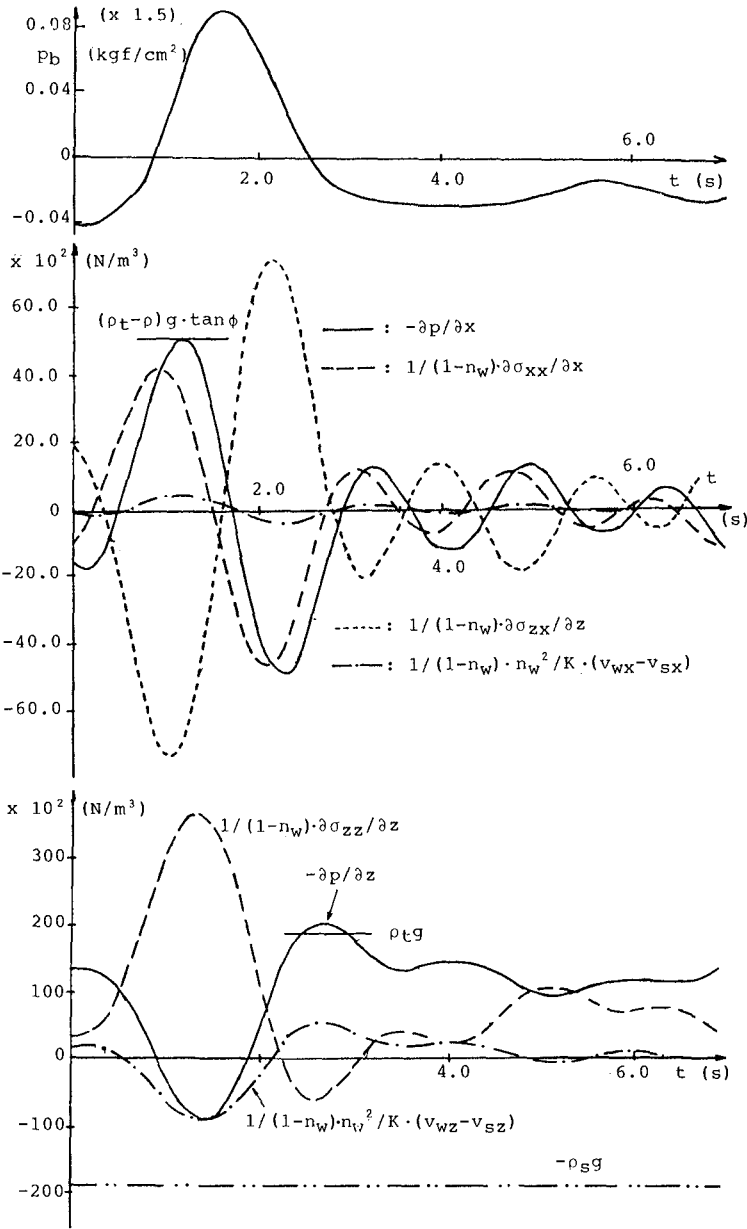


Fig.6 Sediment concentration (b) and vertical effective stress in seabed (d) (Tsuruya and Korezumi, 1990)



**Fig.7 Phase variation of terms in right hand sides of momentum equations of solid skeleton(10cm below bed surface)**

drag force due to the relative velocity of the porewater and solid skeleton  $1/(1-n) \cdot n^2/K \cdot (v_{wx} - v_{sx})$  is negligible.  $-\partial p/\partial x$  becomes maximum at a phase of front of crest ( $t = 1.2\text{sec}$ ), and reaches the critical value of the horizontal momentary failure given by Eq.(9).

The bottom figure shows the phase variation of each terms of the vertical momentum equation for the solid skeleton. The value of term is one order larger than that of terms of the horizontal momentum equation. The vertical gradient of the vertical effective stress  $\partial\sigma_{zz}/\partial z$  and the vertical drag force  $1/(1-n) \cdot n^2/K \cdot (v_{wz} - v_{sz})$  are as large as the vertical gradient of porewater pressure  $\partial p/\partial z$ .  $-\partial p/\partial z$  becomes maximum at a phase of the back of the crest ( $t = 2.6\text{sec}$ ), and is larger than the critical value of the vertical momentary failure given by Eq.(10). It is found also that at this phase the vertical effective stress becomes zero.

From this result we can say as follows : Under a wave having a very steep front face, a momentary failure of the seabed may occur just before the crest passes. Then a momentary liquefaction occurs near the bed surface just after the crest passes. At the same phase, the absolute value of the horizontal porewater pressure gradient becomes large again as seen in the middle figure. The momentary failure of the seabed is therefore more likely to occur just after the crest passing than just before the crest passing.

## CONCLUSIONS

- (1) The boundary layer approximation solution for the wave-induced transient porewater pressure variation in seabed by Mei and Foda(1981) is applicable to an asymmetric wave in a surf zone.
- (2) This solution was modified so as to take into account effects of the wave-induced bottom shear which is not negligible in the surf zone.
- (3) Under a steep breaking wave the momentary failure of the seabed proposed by Madsen(1974) is more likely to occur just after the wave crest passes than just before the crest passes.

## ACKNOWLEDGMENTS

The authors would like to thank Prof. Y.Iwagaki, Meijou Univ. (Emeritus Prof. of Kyoto Univ.) and Prof. Y.Tsuchiya, Disaster Prev. Res. Inst., Kyoto Univ. for their helpful discussions. A part of this investigation was supported by the International Scientific Research Program, Joint Research, No.02044149 of the Japanese Ministry of Education, Science and Culture.

**REFERENCES**

- Finn, W.D., Siddharthan, R. and Martin, G.R.(1983). "Response of seafloor to ocean waves", *Jour. of Geotech. Engr., ASCE*, 109(4), 556-571.
- Madsen, O.S.(1974). "Stability of a sand bed under breaking waves", *Proc. of 14th Conf. on Coastal Engr., ASCE*, 776-794.
- Mei, C.C. and Foda, M.A.(1981). "Wave-induced responses in a fluid-filled poro-elastic solid with a free surface - a boundary layer theory", *Geophys. J.R. astr. Soc.*, 66, 597-631.
- Sakai, T., Hatanaka, K. and Mase, H.(1992). "Wave-induced effective stress in seabed and its momentary liquefaction", *Jour. of Waterway, Port, Coastal, and Ocean Engr., ASCE*, 118(2), 202-206.
- Tsuruya, K. and Korezumi, T.(1990). "Sand liquefaction and resuspension in a surf zone", *Proc. of Coastal Engr., Japan Soc. of Civil Engineers*, 37, 289-293 (in Japanese).
- Zen, K., Yamazaki, H. and Watanabe, A.(1987). "Wave-induced liquefaction and densification in seabed", *Rep. of Port and Harbour Res. Inst., Japanese Ministry of Transport*, 26(4), 125-180 (in Japanese).
- Zen, K., Yamazaki, H. and Sato, Y.(1989). "Wave-induced liquefaction in seabed - Field observation and analysis -", *Rep. of Port and Harbour Res. Inst., Japanese Ministry of Transport*, 28(3), 30-57 (in Japanese).

# CHAPTER 162

## INTERCOMPARISON OF COASTAL PROFILE MODELS

Ida Brøker Hedegaard<sup>1</sup>, J.A. Roelvink<sup>2</sup>, Howard Southgate<sup>3</sup>  
Philippe Pechon<sup>4</sup>, John Nicholson<sup>5</sup>, Luc Hamm<sup>6</sup>

### Abstract

The present paper briefly presents 6 different models for short term coastal profile modelling for direct incoming waves. The models have been tested against measured profile evolutions from a large wave flume. Features such as wave height distribution, cross shore current profiles and sediment transport are compared and discussed.

### Introduction

The described models are all established with the same structure of modules for hydrodynamics, sediment transport and bed level evolution but with different degrees of determinism/empiricism and refinement. The basic structure of the modules and a definition sketch for the coastal profile models are presented in Fig. 1.

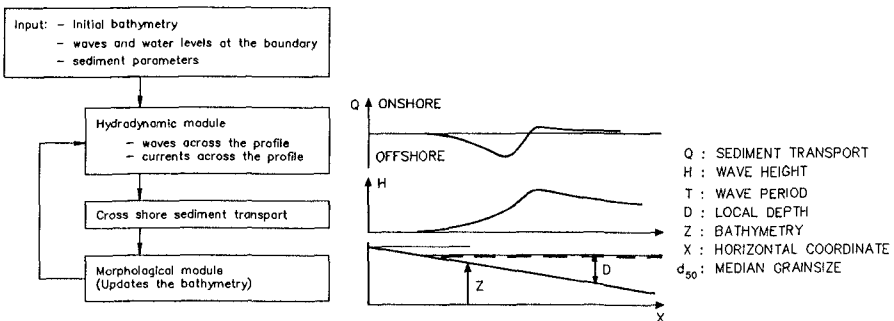


Fig. 1. Basic Structure of the Morphological Models and Definition Sketch.

1) Danish Hydraulic Institute, 2) Delft Hydraulics, 3) HR Wallingford Ltd., 4) Laboratoire National d'Hydraulique, 5) University of Liverpool, 6) Sogreah

### Description of the Models

LITCROSS, Danish Hydraulic Institute.

The variation of the wave heights across the profile is determined from the criteria that the wave has either constant energy flux or wave heights decreases in accordance with an empirical relation first suggested by Andersen and Fredsøe (1983):

$$\frac{H}{D} = 0.5 + 0.3 \exp(-0.11 \frac{\Delta x}{D_B})$$

where  $\Delta x$  is the distance from breaking point and  $D_B$  is the depth at the breaking point. The areas of the surface roller of the breaking waves are assumed to correspond to hydraulic jumps apart from a zone just inside the breaker point where the area is assumed to vary according to measurements by Buhr Hansen (1991). Random waves are treated as individual waves with no interaction.

Hydrodynamic modelling. The vertical distributions of currents and turbulence are assumed to be determined by the local depth, wave conditions and sediment properties. The basis for the model is the combined wave current boundary layer model of Fredsøe (1984). In breaking waves a major contribution to the turbulence comes from the loss of energy in waves and surface rollers. This contribution is calculated by the vertical transport equation for turbulent energy, Deigaard et al. (1986). The vertical distribution of the wave period averaged velocities is derived from the distributions of shear stresses and wave period averaged eddy viscosity. The shear stresses include the contributions from breaking waves, Deigaard and Fredsøe (1989), from streaming, determined as outlined by Longuet Higgins (1953), from the increased density due to suspended sediment in case of sloping bed and from a setup of the water surface which is determined such that the total flux including the wave drift and the water carried in the surface rollers equals zero, Svendsen (1984).

The net sediment transport is calculated as bed and suspended load. The instantaneous bed load and nearbed boundary condition for the vertical distribution of suspended sediment are determined as functions of the instantaneous shear stress, Engelund and Fredsøe (1976). The time varying vertical distribution of suspended concentrations is calculated by the vertical diffusion equation, Deigaard et al. (1986). The total wave period averaged net transport is found from

$$q_s = \frac{1}{T} \int_{\text{period}} \int_{\text{depth}} c \cdot u \, dz \, dt + \int_{\text{depth}} u_1 \cdot \bar{c} \, dz$$

where  $u_1$  is Lagrangian drift. The last term is included to compensate the omission of convective terms in the solution of the concentration field.

The bed level evolutions are determined by the continuity equation for the sediment. The numerical solution is explicit. A modified Lax-Wendroff scheme has been applied to reduce the numerical diffusion and to obtain a stable solution. LITCROSS is described in more detail in Brøker Hedegaard, Deigaard and Fredsøe (1991).

### UNIBEST, Delft Hydraulics.

UNIBEST-TC stands for UNiform BEach Sediment Transport, Time-dependent Cross-shore. It is a direct descendant of the models OSTRAN (Stive and Battjes, 1984) and COSTRAN (Stive, 1986). In Roelvink and Stive (1989), the model has been tested against wave flume measurements and improved on some points. The model aims at predicting long-term development of the profile of beaches that are approximately uniform in along-shore direction, and which are subjected to obliquely incident wave fields, varying water levels and tidal currents. The morphodynamic behaviour due to cross-shore transport only is considered, however, effects of longshore currents on cross-shore transport are accounted for.

For the present study, cross-shore effects only are considered, and the formulations as given in Roelvink and Stive (1989) are used. Mechanisms included here are:

- Wave shoaling and breaking and associated set-up according to Battjes and Janssen (1978);
- Cross-shore current description according to de Vriend and Stive (1987);
- Transition zone effects on the return flow according to Roelvink and Stive (1989); Short wave velocity moments based on Rienecker and Fenton's (1981) Fourier approximation of the stream function method;
- Long wave effects according to the same paper;
- Sediment transport according to Bailard (1981);
- A Fully implicit scheme for the bed evolution.

For the case of regular waves, the wave decay model is adapted simply by setting the fraction of breaking waves to 1 after the wave height exceeds a given fraction of the water depth.

### NPM, Hydraulic Research.

NPM (Nearshore Profile Model) is a model for waves, longshore and cross-shore current and sediment transport on uniform beaches for obliquely or direct incoming waves. A brief summary of the physical processes represented in the NPM is given below.

- Wave transformation by refraction (by depth variations and currents), shoaling, Doppler shifting, bottom friction and wave breaking. For random waves, a Battjes and Janssen (1978) framework is used for determining the distribution of wave height and the fraction of time that waves are breaking at any point.
- Wave setup determined from the gradient of wave radiation stress.
- Driving forces for longshore wave-induced currents, determined directly from the spatial rate of wave energy dissipation.
- Longshore currents from pressure-driven tidal forces and wave-induced forces, and the interaction between the two types of current.
- Cross-shore undertow velocities using a three-layer model of the vertical distribution of cross-shore currents (de Vriend and Stive, 1987).
- Transition zone effects (the transition zone is the distance between where a wave starts to break and where turbulence becomes fully developed).

- Cross-shore and longshore sediment transport rates using an 'energetics' approach (Bailard, 1981; Stive, 1986).
- Seabed level changes due to cross-shore sediment transport using a Lax-Wendroff scheme.

Tests (Southgate, 1991) have shown that the model results are particularly sensitive to the transition zone length and to the height above the seabed at which the undertow velocity is taken for input to the sediment transport calculations. Recent improvements to the NPM therefore include:

- A reanalysis of transition zone data (O'Shea et. al., 1991) to give a more accurate formula for the transition zone length.
- The use of a concentration-weighted average undertow velocity in the sediment transport calculations.

NPM is described in detail in Southgate and Nairn (1993) and Nairn and Southgate (1993).

WATAN 3, University of Liverpool.

The model WATAN3 consists of a wave sub-model and a sediment sub-model. The wave sub-model (Watanabe and Dibajnia, 1988) comprises a set of two equations which are equivalent to a time-dependent version of the mild-slope equation and contain an additional term to allow for energy dissipation in the surf zone. The latter term represents the rate at which energy is dissipated by breaking and is set to zero wherever the broken waves have reformed inside the surf zone, as well as outside the surf zone. An empirical criterion (Watanabe et al, 1984) is used to determine the point of breaking, and setup and setdown are computed by solving the momentum balance equation.

The sediment sub-model (Ohnaka and Watanabe, 1990) is based on the sediment transport rate due to wave action:

$$Q = (A_W (\tau_B - \tau_C) + A_{WB} \tau_T) F_D \hat{u}_B / (\rho g)$$

where  $Q$  is the sediment transport rate,  $A_W$  and  $A_{WB}$  are coefficients,  $\tau_B$  is the maximum nearbed shear stress due to wave action,  $\tau_C$  is the threshold of movement shear stress.  $\tau_T$  is the shear stress generated by breaker turbulence,  $F_D$  is a dimensionless directional function and  $\hat{u}_B$  is the maximum nearbed orbital velocity. Having derived the transport rates throughout the computational domain, the former are then modified to allow for bed slope effects, so that:

$$Q_M = Q - \epsilon |Q| \tan \beta$$

where  $Q_M$  is the modified transport rate,  $\epsilon$  is a coefficient and  $\tan \beta$  is the local bed slope. Finally, the bed level changes are computed using the sediment mass conservation equation.

An additional feature of the present version of the sediment sub-model is the inclusion of a breaker transition length, within which turbulence generated by the post-breaking surface roller is distributed throughout the water column. A re-analysis of work



carried out by Nairn et al (1990) yielded the following expression for the transition length (O'Shea et al, 1991):

$$L_T = L_B (0.56 \xi^{-1.47}) \tan \beta$$

where  $L_T$  is the transition length,  $L_B$  is the wave length at breaking and  $\xi$  is the Iribarren No. The effects of the transition length are incorporated into the sub-model by switching off the breaker turbulence contribution to the transport rate within the transition length.

SEDITEL, Laboratoire National d'Hydraulique.

SEDITEL computes the wave refraction and shoaling, wave height decay in the surf zone, time-averaged three-dimensional currents (2DV currents here) induced by breaking waves, sediment transport rates, bed evolution.

The wave refraction is derived from the classical Snell's law. The wave height is deduced from the equation of the flux of energy where the dissipation is supposed to be similar to the one of a hydraulic jump in the surf zone. In order to have a good estimation of the wave characteristics in shallow water, non-linear effects are considered in the calculation of the flux of energy, see P echon (1987).

The time-averaged currents induced by breaking waves are computed with the three-dimensional model TELEMAC-3D outlined in Lepeintre et al. (1991). In order to establish the equations the instantaneous velocity is separated into three contributions: an unknown mean current, a purely periodic current corresponding to the wave motion, and turbulent fluctuations. In the time-averaged equations some closures are required to express the velocity correlations (see details in P echon, 1992). They are given by previous works of Svendsen (1984), De Vriend and Stive (1987), Deigaard and Freds e (1989).

The sand transport is computed using Bailard's formula, Bailard (1981), but the suspended load efficiency factor is increased in the surf zone to take the breaking effect into account. The proposed expression is:

$$e'_s = \left( 1 + a \frac{|u_b|}{\sqrt{gD}} \right) e_s ;$$

- $e_s$  : efficiency factor, non breaking
- $e'_s$  : efficiency factor, breaking
- $a$  : constant
- $u_b$  : mean velocity at the bottom

The bed evolution is computed by solving the continuity equation for the sediment. To reproduce the process of avalanching of dune in the application presented here, the measured amount of sediment is distributed between the crest of the bar and the shoreline before each hydrodynamic computation. Moreover a maximum stability slope of 15/100 is specified out of the breaking zone.

The wave and current patterns are updated when the bottom evolution becomes significant. However, in order to reduce the number of iterations, an additional treatment is performed during the computation of the bottom evolution: considering the bed evolution

at the breaking point, its location is moved along the coastal profile and the wave and current characteristics are moved the same way.

#### REPLA, SOGREAH.

REPLA is a wave-averaged, finite amplitude, current-depth shoaling and refraction model to simulate regular or random wave propagation from deepwater to the shoreline.

The formulation is detailed in Fornerino et al (1992). A set of four equations is to be solved with an iterative procedure because of the influence of the wave height on the wave celerity.

Stokes third order theory is used for small Ursell numbers. For large Ursell numbers a cnoidal second order theory is used. The model can, however, also be run with Stokes first order waves.

The wave breaking criteria derived by Weggel (1972) is used. In presence of an adverse current, this expression is modified following Sakai et al.(1988). The bore model is used to express the energy dissipation. In order to simulate wave reformation after breaking on a bar, the dissipation rate is put to zero when the wave height is less than half the local maximum wave height.

For random waves, two methods are implemented. The parametric approach of Battjes and Janssen (1978) and the individual wave method Mase and Iwagaki (1982); Mizuguchi (1982) in which each class is propagated independently with the regular wave model.

#### Results from the various Models

The models have been tested against experimental results obtained from the large wave flume in Hannover in 1986 and 1987, Dette and Uliczka (1986) and Dette and Oelerich (1991). The experiment from 1986 was carried out with regular waves. The 1987 experiment was run with irregular waves and included a comprehensive measuring program focusing on waves.

#### Regular Wave Case

The experiment with regular waves constitutes a severe test of the models due to the fact that all waves are breaking nearly at the same position. This first test gives the opportunity to tune the possible model parameters in the various models. Results in the form of calculated and measured profiles from this first test are presented in Fig. 2.

The calculated profile evolution is the integrated result of the modelling of several physical mechanisms. The interpretation of the differences between the modelled evolutions can therefore only be pointed out after comparison of each individual element in the various models. These comparisons are carried out for a similar case, but now the initial profile is a plane beach with an initial slope of 1:20. Below, the initial wave heights, current fields and sediment transport along this plane beach are considered.

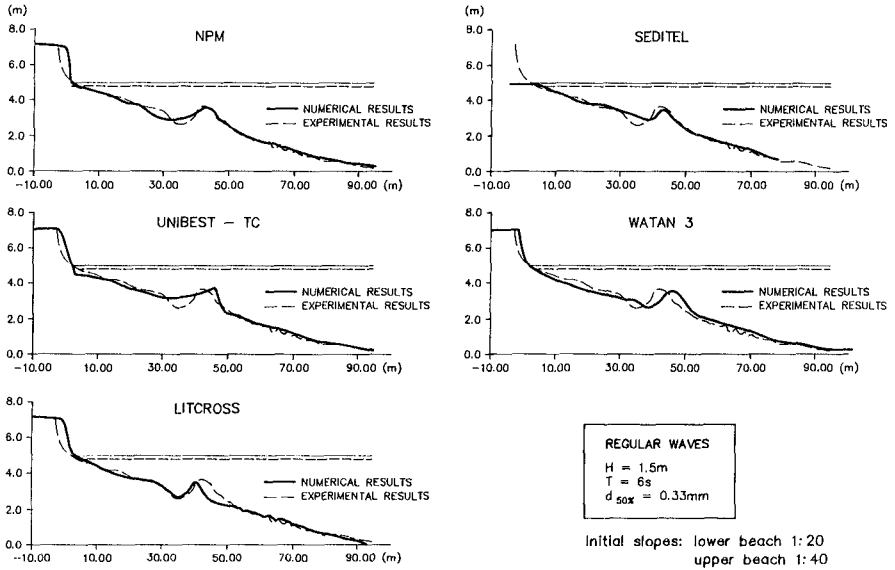


Fig. 2. Comparison of Measured and Calculated Coastal Profiles after 4.3 hours of Exposure.

The figures 3, 4, and 5 show wave heights across the plane profile, vertical distribution of horizontal wave averaged velocities, for Seditel also the vertical velocity component just shoreward of the breaker point and the vertical flow pattern, and the initial cross shore sediment transport. Already the comparison of wave heights show large spreading across the surf zone. This spreading is reflected in deviations in the assumed cross section area of the surface rollers. The differences in the vertical distribution of horizontal velocities exist due to differences in the formulation of the vertical distribution of shear stresses, eddy viscosities and the area of surface rollers.

The above comparisons illustrates differences in the models, but suffer unfortunately from lack of measured data. The calculated initial transport rates highlight the fact that the bar forms at a 'critical' position, seen from a model view point where the onshore transport under the non breaking waves turn into offshore transport inside the surf zone.

Further, although discrepancies exist between the distribution of horizontal velocities calculated by the one DV models and the 2 DV model, Seditel, the 2 DV results indicate that the order of magnitude of vertical velocities shoreward of the breaker point are comparable with the settling velocity of sand. Therefore, in a narrow zone inside the breaker point, the sediment transport models which take into account only velocities parallel to the bottom might underestimate the amount of suspended sediment.

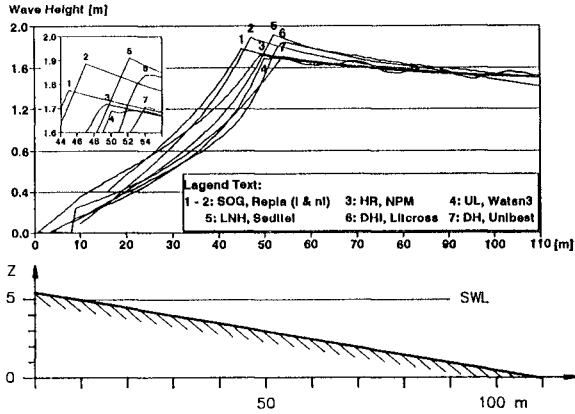


Fig. 3. Wave heights as calculated by 6 different models.

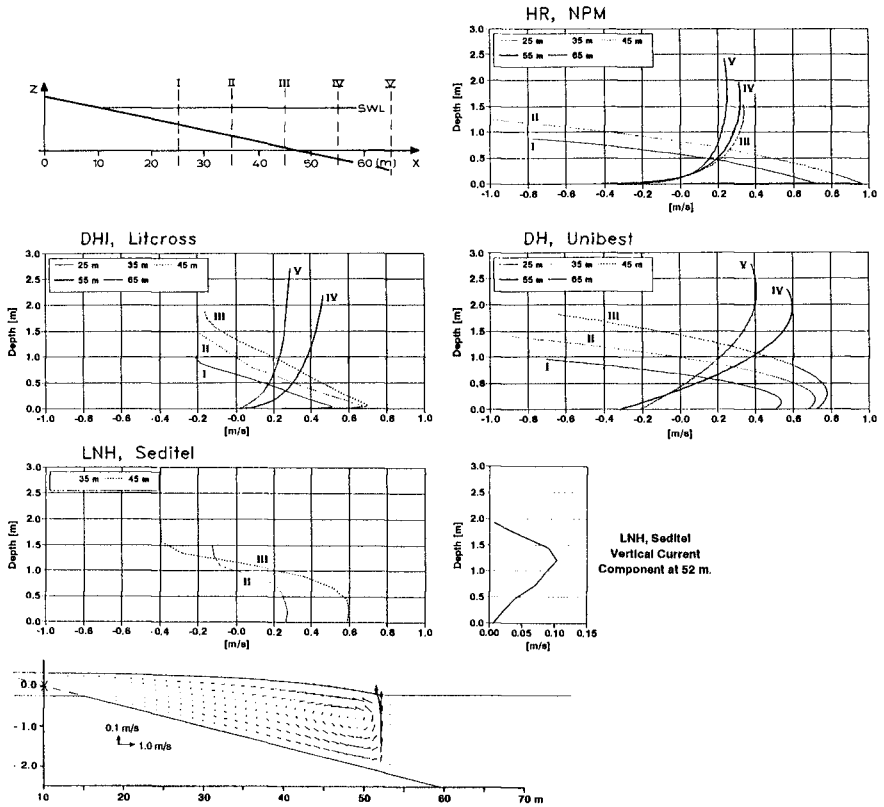


Fig. 4. Velocity components and the 2 DV current field as calculated by Seditel.

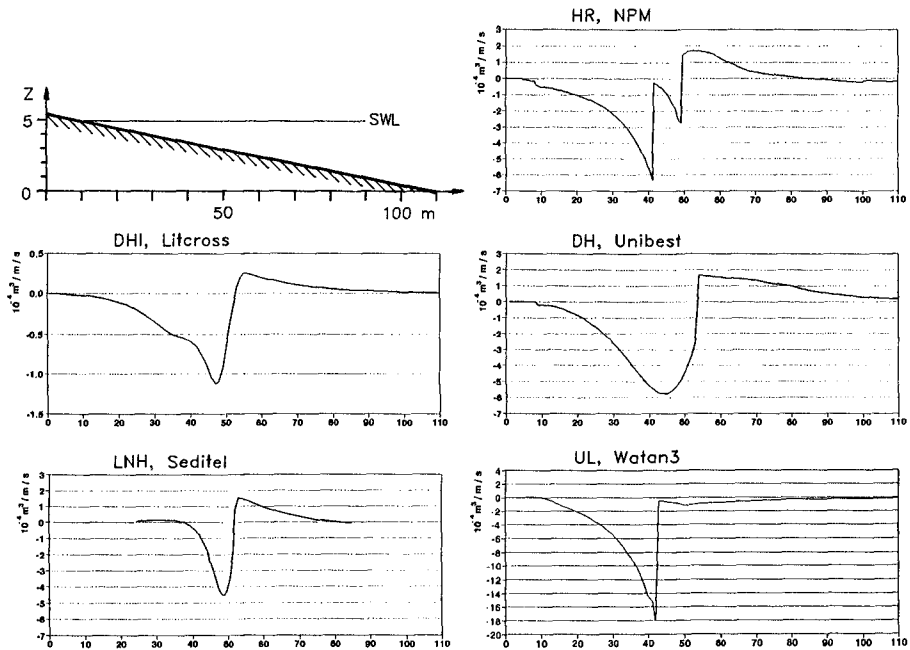


Fig. 5. Cross shore sediment transport calculated by NPM, Unibest, LITCROSS, Seditel and Watan 3.

It appears that the cross shore transport models when applied in a morphological calculation sequence in combination with more or less smoothing, either on the calculated transport or on the bed levels between updates, are able to reproduce to a certain extent the evolution of a breaker bar. In the case of regular waves it seems clear that the mechanisms just shoreward of the breaker point are essential for the bar evolution.

For irregular waves these complex mechanisms are expected to be less important for the profile evolution. In the following the models are compared with measurements in the case of irregular waves.

#### Irregular Waves Case

This test was carried out with irregular waves, Jonswap spectrum, with  $H_s = 1.5\text{m}$  and  $T_p = 6\text{ s}$  at 5 m depth in front of the wavemaker. The profile was built out of natural well sorted sand with a mean diameter of 0.22 mm. The test was subdivided into 45 runs of 780 s each. The wavemaker was stopped after each run. The wave generation was first order with no long waves reflection compensation. The observed bathymetry, the wave heights ( $H_{\text{RMS}}$ ), the sediment transport derived from successive observations of the bed evolution and the wave energy spectrum as measured at three positions are presented in Fig. 6.

In this case a pronounced bar is not formed but the relatively steep profile is flattened out. The wave heights in the surfzone decrease concurrently with the flattening of the profile, i.e. the energy is dissipated further and further offshore. These tendencies are reflected in the cross-shore transport rates which are largest at the beginning of the test. From the spectral analysis of wave energy it appears that the spectra become double-peaked while the waves approach the beach, i.e. in the nearshore area low frequency waves become more important, see figure 6. From analysis of correlations between bound long waves and the observed low frequency waves it seems clear that the major part of the low frequency energy come from reflections in the flume.

In figures 7 and 8 measured and simulated variations of the wave heights across the profile for the observed bathymetries in runs 2, 14 and 32 are compared. These results are produced by REPLA applying both the parametric approach and the individual wave method with both linear and non linear wave theory. With the first approach it appears that when  $\gamma$  is adjusted corresponding to the highest wave heights, the heights inside the surf zone are underestimated for runs 2 and 14. The individual wave method is seen also to underestimate the near shore wave heights. It might be necessary to include mechanisms as the extra variations of the water level and flow due to the long waves and the opposing undertow in the wave modules.

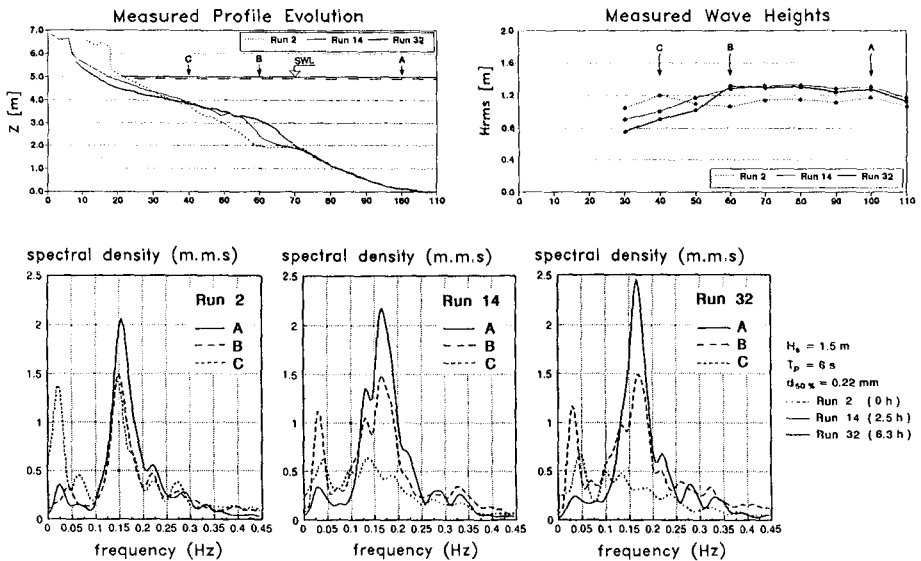


Fig. 6. Observed bathymetries, measured  $H_{RMS}$ , and wave energy spectrum at 3 positions.

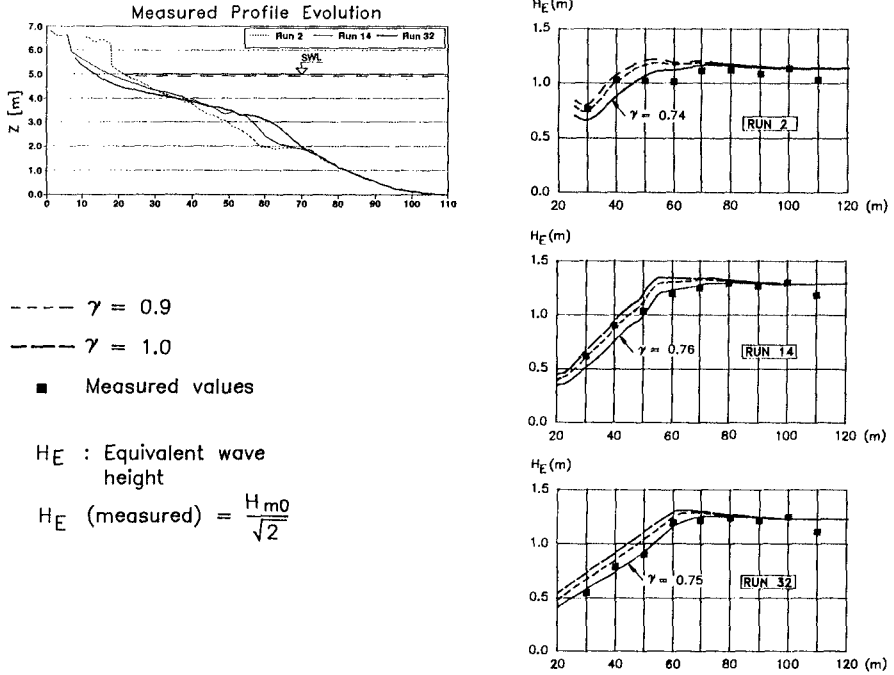


Fig. 7. Measured and calculated equivalent wave heights. Calculations by REPLA applying Battjes and Janssen's parametric approach.

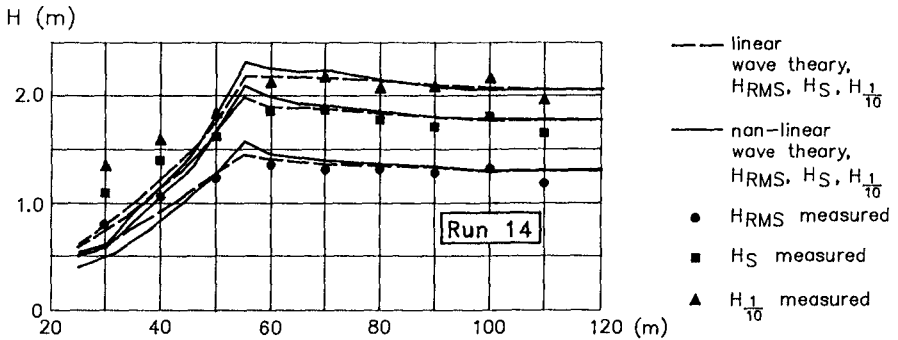


Fig. 8. Measured and calculated  $H_{RMS}$ ,  $H_S$  and  $H_{1/10}$ . Calculations by REPLA applying the individual wave approach with linear and non linear wave theories.

Figure 9 shows the measured and calculated cross-shore transport. It is seen that the models are very sensitive to even small humps in the bed and that the observed relatively

large initial offshore transport is not very well reproduced. The Watan 3 model has been run with 5 wave components only which obviously gives a very scattered transport pattern.

Figure 10 shows results of morphological modelling of the coastal profile. The modelled evolutions obviously suffer from the underestimation of the initial offshore transport and the lack of description of the erosion in the steep dune front.

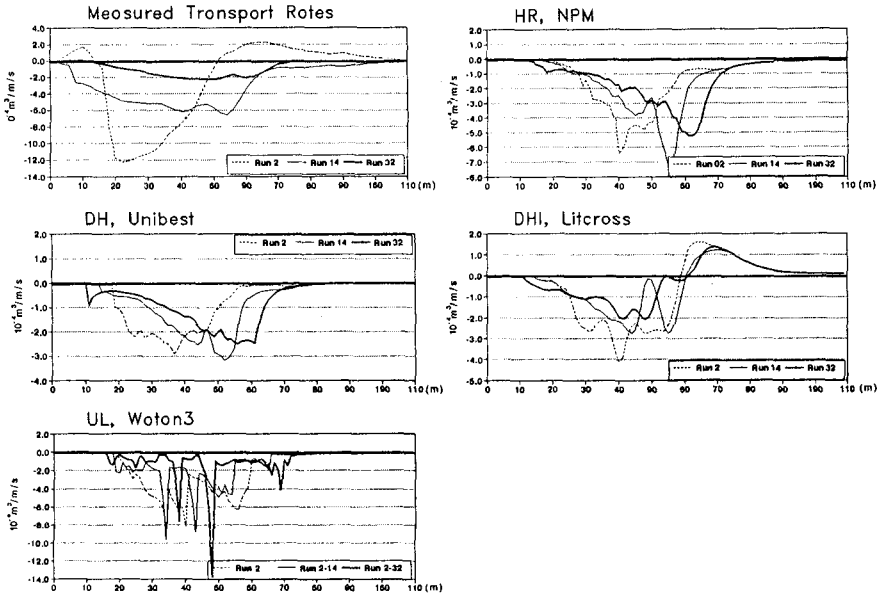


Fig. 9. Measured and calculated cross-shore transport rates. These calculations are carried out with the observed bathymetries.

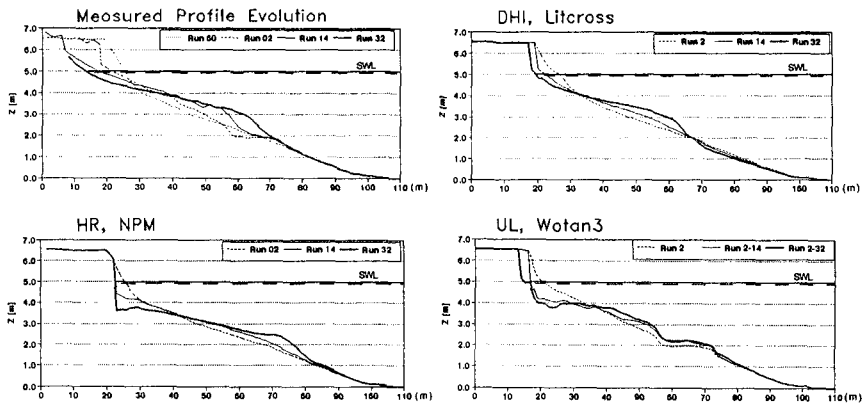


Fig. 10. Measured profile evolution. Simulated evolution. HR, NPM and DHI, LITCROSS from 'initial' to Run 32. UL, WATAN 3 from Run 2 to Run 32.



### Concluding remarks

Large differences exist between the coastal profile models presented above. However, based on the experience gained through the comparisons with experimental data the following general comments are given:

- The models generally underestimate the offshore transport on relatively steep profiles. One reason seems to be related to poor wave description in cases where reflections and long waves, free and bound, exist.
- The swash zone processes and dune erosion are not described in the models. In combination with the above mentioned underestimation of transport on steep slopes the exchange of material from the dune to the bar is too slow in the case of a steep, initial profile.
- The vertical velocities close to the breaker point seem to reach a significant order of magnitude and might influence the bar formation, at least in the case of a closed flume. Generally, the velocity field in the area just before and after the (average) break point is still understood rather poorly.

It is noted that with the outlined concept of a coastal profile model the pronounced breaker bar in regular waves and the flattening of a steep profile in irregular waves can be modelled. In nature the coastal profiles are formed by 3D phenomena. It seems that the understanding of cross-shore processes has now reached a stage where it is relevant to extend the models into 3D to be able to judge where the 'weakest point' appears and where most effort in the future should be spent.

### Acknowledgements

This work has been undertaken as part of the MAST G6 Coastal Morphodynamic Research Programme. It was funded partly by the Commission of European Communities, Directorate General for Science, Research and Development under MAST Contract No. 0035-C and partly by national fundings, among these The Danish Technical Research Council (STVF), Service technique Central des Ports Maritimes et des Voies Navigables (Compiègne, France), The Netherlands 'Coastal Genesis Programme' (Kustgenese).

The authors would like to thank Dr. Dette and Dr. Oelerich, Hannover University, for the delivery of processed data from the experiments in the large wave flume.

### References

- Andersen, O.H. and Fredsøe, J. (1983): Transport of sediment along the coast. Prog. Rep. 59, ISVA, Techn. Univ. of Denmark, pp. 33-46.
- Bailard, J.A. (1981). An Energetics Total Load Sediment Transport Model for Plane Sloping Beach, J. Geophys. Res., Vol. 86, No. C11.
- Battjes, J.A. and Janssen J.P.F.M. (1978) Energy Loss and Set-up due to Breaking of Random Waves, Proc. 16th Int. Conf. on Coastal Eng, ASCE, Hamburg.
- Brøker Hedegaard, I., Deigaard, R., Fredsøe, J. (1991). Onshore/Offshore Sediment Transport and Morphological Modelling of Coastal Profiles. Proc. Coastal Sediments '91, Seattle.
- Buhr Hansen, J. (1991). Air entrainment in surf zone waves, 3rd Int. conf. on Coastal and Port Eng. in Dev. Countries, Mombasa, 1991.

- Deigaard, R., Fredsøe, J. (1989). Shear Stress Distribution in Dissipative Water Waves. *Coastal Eng.* Vol. 13, pp. 357-378.
- Deigaard, R., Fredsøe, J., and Hedegaard, I.B. (1986). Suspended Sediment in the Surf Zone. *J. Waterway, Port, Coastal, and Ocean Eng.*, ASCE, Vol. 112, No. 3.
- Detle, H., Uliczka, K. (1986). Seegangserzeugte Wechselwirkung zwischen Vorland und Vorstrand sowie Küstenschutzbauwerk. Technischer Bericht Nr. 3-SBF 205/TP A6. Universität Hannover.
- Detle, H. and Oelerich (1991): Internal MAST-G6M report.
- De Vriend, H.J. and Stive M.J.F. (1987). Quasi-3D Modelling of Nearshore Currents, *Coastal Engineering*, Vol II, pp. 565-601.
- Engelund, F. and Fredsøe, J. (1976). A Sediment Transport Model for Straight Alluvial Channels. *Nordic Hydrology*, Vol. 7.
- Fornerino, M., P. Sauvagat and L. Hamm (1992). Numerical modelling of finite amplitude wave shoaling in presence of currents in *Hydraulic Engineering Software IV*, Fluid flow modelling, eds. W.R.Blain and E. Cabrera, Computational Mechanics publ., Southampton, pp. 587-598.
- Fredsøe, J. (1984). Turbulent Boundary Layer in Wave and Current Motion, *J. Hydraulic Engineering*, ASCE, Vol. 110, No. 8.
- Lepointre, F., Gest, B., Hervouet, J-M., Péchon, Ph., (1991), 'MITHRIDATE (former name for TELEMAC-3D): a finite element code to solve 3D free surface flow problems'. 2nd International Conference on Computer Modelling in Ocean engineering, Barcelona.
- Longuet-Higgins, M.S. (1953). Mass Transport in Water Waves, *Philos. Trans. R. Soc. London*, Ser. A, 245.
- Mase, H. and Y. Iwagaki (1982). Wave height distributions and wave grouping in surf zone 'Proc. Int. Conf. on Coastal eng., ASCE, 58-76.
- Mizuguchi, M. (1982). Individual wave analysis of irregular wave deformation in the nearshore zone. *Proc. Int. Conf. on Coastal Eng., ASCE*, 485-504.
- Nairn, R.B. and Southgate, H. N. (1993). "Deterministic profile modelling of nearshore processes. Part 2. Sediment transport and beach profile development", *Coastal Engineering* (to appear).
- Nairn, R.B., Roelvink, J.A. and Southgate, H.N. (1990), Transition Zone Width and Implications for Modelling Surfzone Hydrodynamics, *Proc. Twenty-Second Coastal eng. Conf.*, ASCE, pp 68-81.
- O'Shea, K., Nicholson, J. and O'Connor, B.A. (1991). The Transition Zone Length in Cross-Shore Sediment Transport Modelling, Report CE/1/91. Department of Civil Eng., University of Liverpool.
- Ohnaka, S. and Watanabe, A. (1990), 'Modeling of Wave-Current Interaction and Beach Change', *Proc. Twenty-Second Coastal Engineering Conf.*, ASCE, pp. 2443-2456.
- Péchon, P. (1987), 'Modelling of longshore currents with a non-linear wave theory'. ASCE Speciality Conference on Coastal Hydrodynamics, Delaware, 1987.
- Péchon, P., (1992), Numerical modelling of wave-driven currents and sediment transport in the surfzone. Internal report EDF-LNH HF.42/92.15.
- Rienecker, M.M. and J.D. Fenton (1981). A Fourier approximation method for steady water waves. *J. Fluid Mech.*, Vol. 104, pp. 119-137.
- Roelvink, J.A. and Stive M.J.F. (1989). Bar-generating Cross-shore Flow Mechanisms on a Beach, *JGR Vol. 94*, No. C4, pp. 4785-4800.
- Sakai, S., K. Hirayama and H. Saeki (1988). A new parameter for wave breaking with opposing current on sloping bed. *Proc. Int. Conf. on Coastal Eng.*, ASCE, 1035-1044.
- Southgate, H.N. and Nairn, R. B. (1993). "Deterministic profile modelling of nearshore processes. Part 1. Waves and Currents", *Coastal Engineering* (to appear).
- Southgate, H.N. (1991) Beach Profile Modelling: Flume Data Comparisons and Sensitivity Tests, coastal Sediments '91, Seattle, USA.
- Stive, M.J.F. and Battjes, J.A. (1984). 'A Model for Offshore Sediment Transport'. *Proc. 19th Int. Conf. Coastal Eng.*, pp. 1420-1436, ASCE, New York.
- Stive, M.J.F. (1986). A Model for Cross-shore Sediment Transport, *Proc. 20th ICCE*, ASCE, Taiwan.
- Svendsen, L.A. (1984). Mass Flux and Undertow in a Surf Zone. *Coastal Engineering*, Vol.8, No.4.
- Watanabe, A., Hara, T. And Horikawa, K. (1984). Study on Breaking Condition for Compound Wave Trains, *Coastal Engineering in Japan*, vol. 27, pp. 71-82.
- Watanabe, A. and Dibajnia, M. (1988). A Numerical Model of Wave Deformation in Surf zone, *Proc. Twenty-First Coastal Engineering Conf.*, ASCE, pp. 578-587.
- Weggel, J.R. (1972) 'Maximum breaker height for design', *Proc. Int. Conf. on Coastal Eng.*, ASCE, 419-432.

## CHAPTER 163

### OSCILLATORY FLOW BEHAVIOR IN THE VICINITY OF RIPPLE MODELS

Kiyoshi Horikawa<sup>1</sup> F. ASCE  
Suguru Mizutani<sup>2</sup>

#### ABSTRACT

In the previous paper, a fixed ripple model with a sharp crest was used to investigate the characteristics of oscillatory flow in the vicinity of wavy boundary. The above ripple model is useful to proof the adaptability of the analytical treatment presented by Longuet-Higgins (1981) and to extend our knowledge on the present subject. However the stated model is too simple to represent the real shape of sand ripples appeared on the sea bottom. From such a view point, in the present study another fixed ripple model with a round crest was selected. This model has the shape almost similar to the previous one except in the vicinity of the crest.

A two-dimensional LDV was used to measure the flow velocity at preset grid points. By using these velocity data the vorticity at each grid point was calculated and the equivorticity lines were drawn for the sharp crest ripple as well as the round crest ripple at various phases of oscillatory flow. Then the circulation outside the vortex was evaluated. Based on the available data the temporal variation of the circulation was discussed quantitatively. Finally criteria of vortex formation were introduced and the physical meaning of these criteria was discussed.

- 
1. President, Saitama University, 255 Shimo-Okubo, Urawa, Saitama 338, Japan.
  2. Postgraduate, Department of Foundation Engineering, Graduate School of Science and Engineering, Saitama University, 255 Shimo-Okubo, Urawa, Saitama 338, Japan.

## INTRODUCTION

This paper is a continued work to the previous paper on the characteristics of oscillatory flow over a ripple model (Horikawa and Ikeda, 1990). In the foregoing paper were presented the extensive results of laboratory investigations carried out by using an oscillatory flume in which a fixed ripple model with a sharp crest was installed.

Figure 1 shows the shape and size of the stated model which were determined on the basis of the treatment presented by Longuet-Higgins (1981). This ripple model seems to be quite useful to analyze the flow phenomena in the vicinity of a wavy boundary. However the shape with such a sharp crest as this model may be unrealistic as a model of sand ripples appeared on the sea bottom. In order to investigate the actual flow phenomena in the vicinity of sand ripples generated by wave action, a more realistic model was selected.

According to Sleath (1984), the shape of two-dimensional vortex ripples for fine sand can be well expressed by the following equations :

$$\begin{aligned} y &= (Hr/2) \cos kr\xi \\ \xi &= x + (Hr/2) \sin kr\xi \end{aligned} \quad (1)$$

where  $(x,y)$  are the Cartesian coordinates,  $\xi$  is the curvilinear coordinate following the wavy boundary with its origin at  $x=0$  and  $y=Hr/2$ ,  $Hr$  and  $Lr$  are the ripple height and the ripple length respectively, and  $kr=2\pi/Lr$  is the ripple wave number as shown in Figure 2.

In order to keep the continuity and consistency in the series of research work, the ripple length was fixed at 30cm as that of the sharp crest ripple model. The ripple height of the new model was selected to be 4cm instead of 5cm in the previous model to make the height-length ratio 0.133 which is nearly equal to that of natural sand ripples. The shape of the new ripple model thus determined is shown in Figure 3. Figure 4 indicates the difference of both models. That is to say, the overall features of both models are practically similar each other except in the limited region of ripple crests.

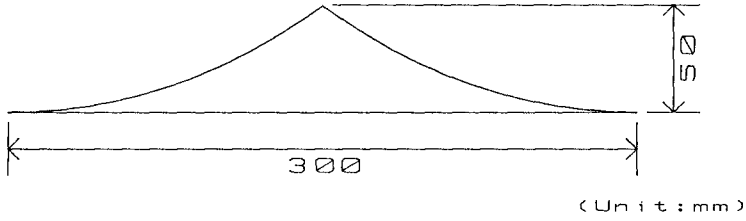


Fig.1 Fixed ripple model with a sharp crest.

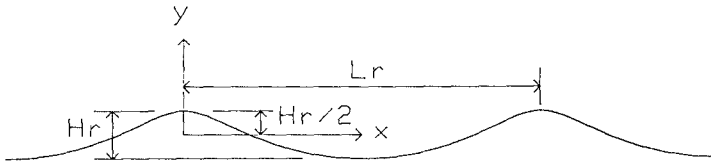


Fig.2 Definition sketch of sand ripple profile.

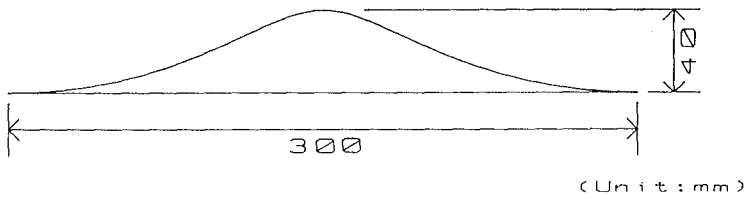


Fig.3 Fixed ripple model with a round crest.

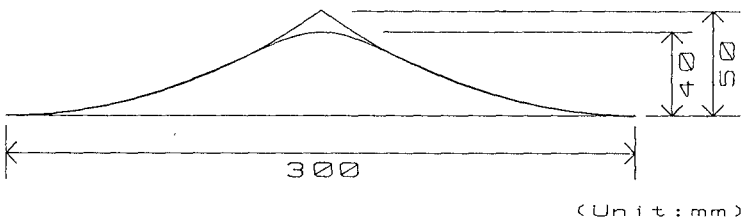


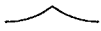

Fig.4 Comparison of both fixed ripple models.

EXPERIMENTAL PROCEDURES

Experimental Conditions

Table 1 gives the experimental conditions adopted so far at the Hydraulic Laboratory, Saitama University by using the fixed ripple model with a sharp crest (Figure 1) as well as that with a round crest (Figure 3) installed inside an oscillatory flow flume with 13m in length and 0.3m x 0.3m in cross-section. Among these, four particular cases namely Cases A, B, C and D in Table 1 will be selected in discussing the characteristic differences of organized vortices formed behind the two kind ripple crests. Particularly in Cases A and B the oscillatory flow conditions are the same, but the shapes of the ripple crest are different each other.

Table 1 Experimental conditions.

Profile	T (s)	3	4	6		9
Sharp 	$d_o$ (cm)	20.0	—	20.0	40.0	40.0
	$U_{max}$ (cm/s)	20.9	—	10.5	20.9	13.9
		(Case C)				(Case A)
Round 	$d_o$ (cm)	—	44.0	—		40.0
	$U_{max}$ (cm/s)	—	34.6	—		13.9
		(Case D)				(Case B)

$d_o$  :orbital total amplitude of fluid just outside the boundary layer at the bed  
 $U_{max}$ :amplitude of free stream horizontal velocity component

Experimental Apparatus and Flow Data Analysis

A 2-D LDV was used to measure horizontal and vertical components of flow velocity at each preset grid point at various phases of oscillatory flow. By using the obtained records various physical quantities such as the temporally averaged fluid velocity, stationary (or residual) velocity, kinematic Reynolds stress, and kinematic eddy viscosity, were calculated and the resulted data were plotted in figures to illustrate the temporal and spatial variations of flow characteristics. The detailed descriptions of the experimental apparatus and data processing were given in the previous paper (Horikawa and Ikeda, 1990).

The main topic in this paper, however, is to investigate the characteristic behavior of an organized vortex formed behind a ripple crest. The discussion on

fine structures of oscillatory flow in the vicinity of ripple crest either with the sharp crest or with the round crest will be made in the forthcoming paper which is now in preparation.

### BEHAVIOR OF AN ORGANIZED VORTEX

#### Overall Pattern of Vorticity

Evaluation of vorticity at each grid point was made by using the temporally averaged velocity components at four grid points surrounding the prescribed point. As a typical example, spatial distribution patterns of vorticity for Cases A and B at the same phase of the oscillatory flow are shown in Figures 5(a) and (b) respectively. The irregularity of distribution patterns is thought to be strongly influenced by the grid spacing of measuring points.

Comparing these two diagrams in Figure 5, it is easily realized that the vorticity formed behind the

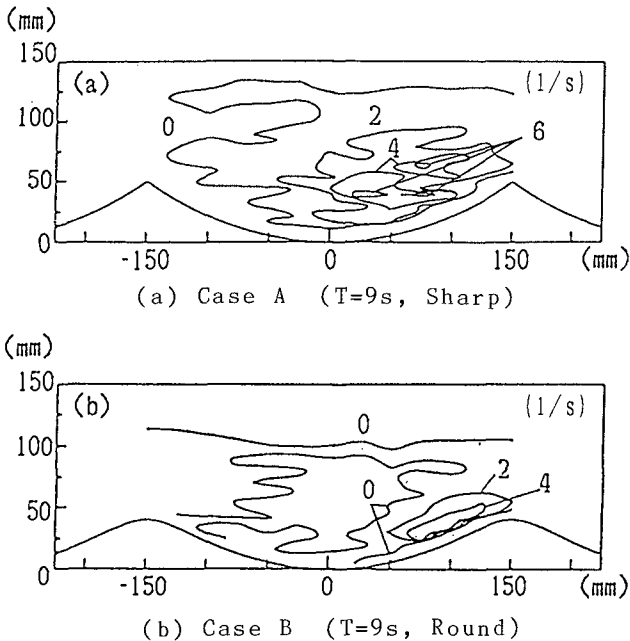


Fig.5 Spatial distribution of vorticity at the phase of  $\omega t = 0$ .  
 [(a) Sharp crest ripple (b) Round crest ripple]

sharp crest (Case A) is stronger than that behind the round crest (Case B) as it is expected. In order to draw more clear pictures, the following treatments were made. The space area enclosed by the equivorticity curve with the prescribed value was calculated at each phase. The obtained values were plotted as indicated in Figures 6(a) and (b) for Cases A and B respectively. From these diagrams the following fact can be easily observed. Here the phases  $-\pi/2$  and  $\pi/2$  correspond to the phases at the maximum free stream velocity.

In case of the sharp crest ripple (Case A) the flow streamline along the ripple bed separates definitely at the crest. The vortex thus formed grows up with the increase of free stream velocity and then diffuses rather rapidly. Finally the overall vorticity decays due to reverse of the free stream direction.

On the other hand, in case of the round crest ripple (Case B) the size of vortex seems to be fairly small in general compared with the previous one. The streamline along the ripple bed separates hardly at the early stage of oscillatory flow phase, but does at a certain phase stage. The vortex area increases up to a certain phase and then decreases gradually.

In both cases, the developing, diffusing and decaying processes of vorticity can be observed clearly in Figures 6 (a) and (b). Even though the magnitude and spacial scale of vortex depend strongly upon the shape of ripple crest and free flow conditions, the processes stated above appears similarly in any case.

In order to investigate the growth and decay of overall vortex strength, the integrated vorticity with respect to the area for Cases A, B, C and D were calculated and the obtained values were plotted in Figure 7. The above integrated vorticity corresponds to the circulation outside the vortex,  $\Gamma$ . From Figure 7 the following can be pointed out :

- (1) In case of the sharp crest ripple (Cases A and C), the flow separation initiates immediately after changing the flow direction. Then the circulation increases very rapidly and reaches its maximum,  $\Gamma_{\max}$ , at the phase of  $-(\pi/4)$ , a little after the maximum velocity of free stream. After that the



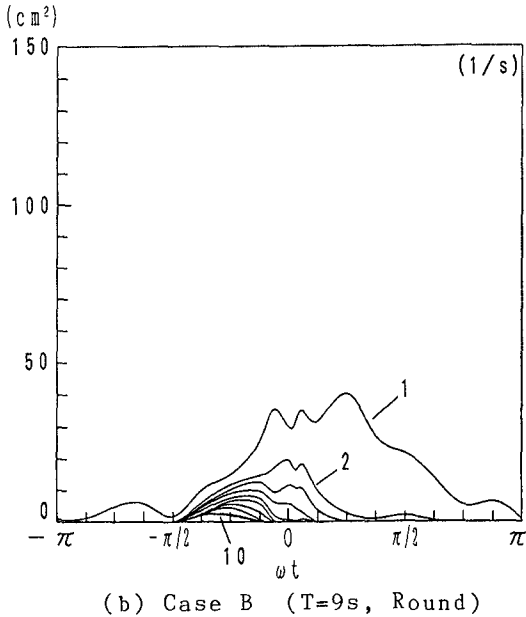
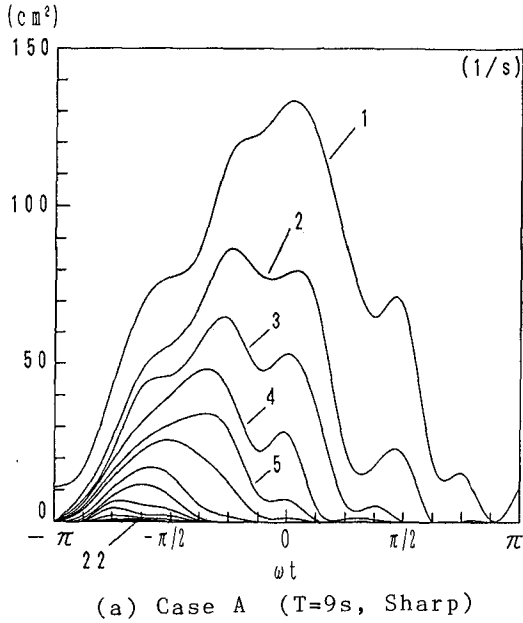


Fig.6 Temporal variation of the area occupied by the vortex with the prescribed vorticity. [Case A : Sharp crest ripple Case B : Round crest ripple]

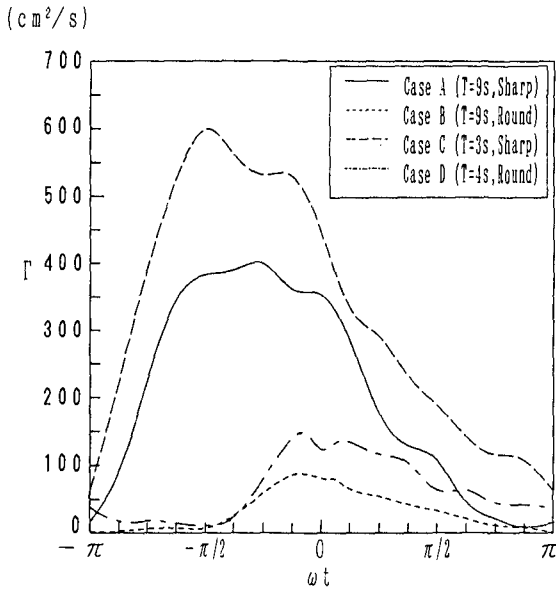


Fig.7 Temporal variation of circulation outside the vortex generated behind a ripple crest.

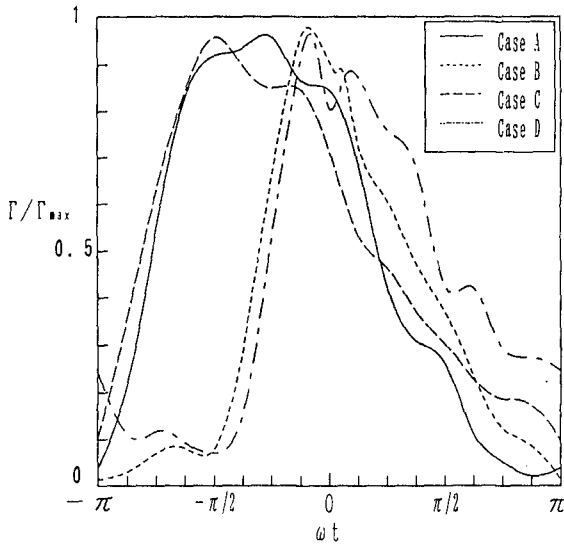


Fig.8 Temporal variation of nondimensional circulation.

circulation decreases gradually to zero at the phase of  $\pi$ .

- (2) In case of the round crest ripple (Cases B and D), the flow separation appears at the phase of  $-(\pi/2)$ . The circulation increases rather rapidly and reaches its maximum at the phase of  $-(\pi/8)$ . Then the circulation decreases gradually to zero.

In order to determine the general form of the temporal variation of the circulation for both the sharp crest ripple and the round ripple crest, the term  $\Gamma/\Gamma_{max}$  is illustrated in Figure 8, where  $\Gamma_{max}$  is the maximum value of  $\Gamma$  for each case. These curves suggest us that the temporal variation of the circulation can be expressed by an appropriate curve for each ripple model. To accomplish the above treatment, the absolute value of  $\Gamma_{max}$  should be determined.

Available data of the maximum value of circulation were summarized in Table 2. The first four data were reported by Ikeda et al. (1988) who used the sharp crest ripple with  $H_r/L_r=0.167$ . The second four data were given by Sawamoto et al. (1980) who used the round crest ripple with  $H_r/L_r=0.100$  installed in an oscillatory air flume. The last four data are those of Cases A, B, C and D in the present investigation, where the values of  $H_r/L_r$  are 0.167 for Cases A and C and 0.133 for Cases B and D.

Table 2 Available data of maximum circulation.

T (s)	$U_{max}$ (cm/s)	$d_o$ (cm)	$L_r$ (cm)	$H_r$ (cm)	$\Gamma_{max}$ ( $cm^2/s$ )	$\frac{H_r}{L_r}$	$\frac{TU_{max}}{H_r}$	$\frac{\Gamma_{max}}{TU_{max}^2}$	$\frac{U_{max}H_r}{\nu}$	
3	43.5	41.5	30	5	1500	0.167	26.1	0.264	$2.18 \times 10^4$	I. S.
6	21.6	41.5	30	5	670	0.167	25.9	0.239	$1.08 \times 10^4$	I. S.
9	14.5	41.5	30	5	555	0.167	26.1	0.293	$7.25 \times 10^3$	I. S.
12	10.9	41.5	30	5	250	0.167	26.2	0.175	$5.45 \times 10^3$	I. S.
6.4	49.0	200	50	5	2100	0.100	62.7	0.137	$1.63 \times 10^5$	S. R.
6.4	29.5	120	50	5	656	0.100	37.8	0.118	$9.89 \times 10^2$	S. R.
6.4	36.8	150	50	5	1172	0.100	47.1	0.135	$9.89 \times 10^2$	S. R.
6.4	61.4	250	50	5	1640	0.100	78.6	0.068	$2.05 \times 10^3$	S. R.
9	13.9	40.0	30	5	417	0.167	25.0	0.240	$6.95 \times 10^3$	H. S.
3	20.9	20.0	30	5	626	0.167	12.5	0.478	$1.05 \times 10^4$	H. S.
9	13.9	40.0	30	4	91	0.133	31.3	0.052	$5.56 \times 10^3$	H. R.
4	34.6	40.0	30	4	154	0.133	34.6	0.032	$1.38 \times 10^4$	H. R.

Ikeda et al. Sharp → I. S.  
 Sawamoto et al. Round → S. R.  
 Horikawa et al. Sharp → H. S.  
 Horikawa et al. Round → H. R.

Two nondimensional terms,  $\Gamma_{max}/(TU_{max}^2)$  and  $U_{max}Hr/\nu$ , were correlated each other in Figure 9, where the effect of ripple model characteristics on the circulation was clearly distinguished. The scattering of data points is fairly large probably due to the fact that the applied evaluation methods for circulation are largely different each other. Therefore tentatively evaluated values are suggested by dotted lines in Figure 9. The ranges of the Reynolds number  $Re=U_{max}Hr/\nu$  and the Keulegan-Carpenter number  $KC=TU_{max}/Hr$  are limited in each group of data (see Table 2). It is needless to say that additional data in a wide range of  $Re$  and  $KC$  are required to make more clear evaluation of the maximum circulation value under the various conditions.

Adaptability of the Present Data

In the previous investigations, the relationship among the grain size, the driving force of fluids, and the resulted sand ripple size was ignored. In order to keep the consistency of laboratory investigations the

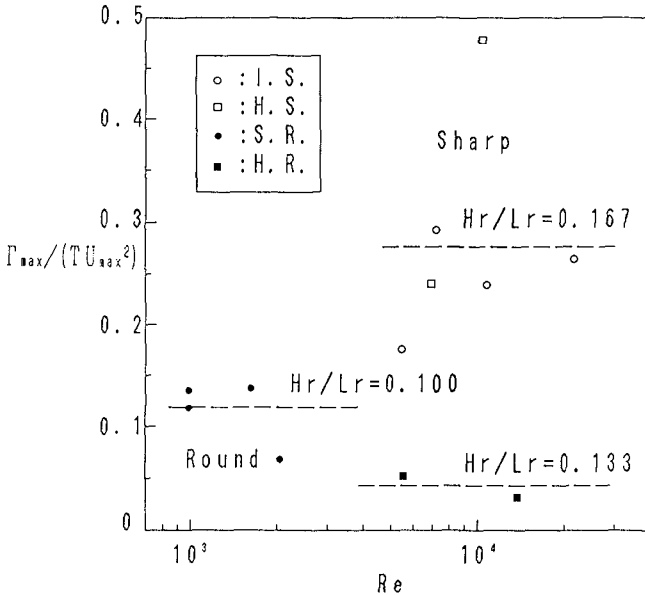


Fig.9 Tentative evaluation of maximum circulation.

oscillatory flow conditions were determined by using two types of empirical diagrams presented by Mogridge and Kamphuis (1972) and Sato (1987) respectively under the conditions of  $H_r=4\text{cm}$ ,  $L_r=30\text{cm}$ , and  $D=0.4\text{mm}$ . Here  $D$  is the grain size of sand. The flow conditions thus obtained are  $T=4\text{s}$  and  $U_{\text{max}}=30\text{cm/s}$  which correspond to the condition of Case D in the present experiments.

Figure 10 gives the cumulative grain size of sand particles adopted to the following experiment. The medium grain size of  $D_{50}=0.43\text{mm}$  is nearly equal to the expected value of  $0.4\text{mm}$ . Figure 11 shows the comparison between the profile of fixed ripple model with the round crest and the measured profile of the sand ripple generated in the oscillatory flow flume. The agreement seems to be extremely good.

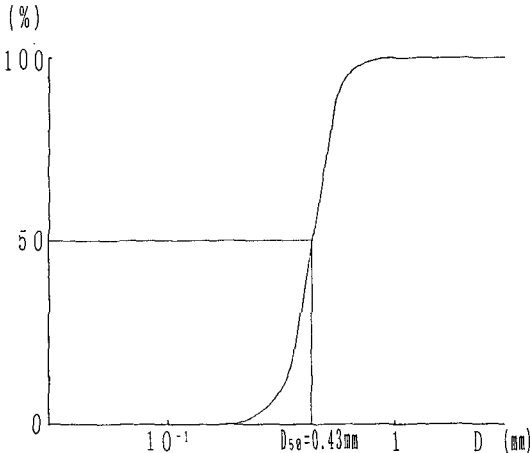


Fig.10 Cumulative grain size curve of sand particles used for the laboratory experiment.

— : Fixed Model  
 ○ : Ripple Measured

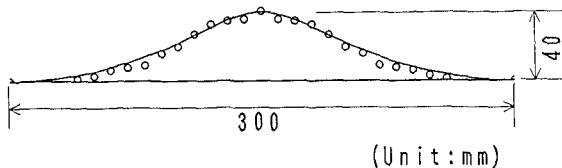


Fig.11 Comparison of measured sand ripple profile with the fixed ripple model.

Criteria of Organized Vortex Formation

Again the fixed model of ripple with the round crest was installed in the oscillatory flume and the maximum horizontal size of organized vortices was measured visually by using a scale under the numerous combinations of period and amplitude of the piston stroke. The measured data were plotted on a diagram with the abscissa of Reynolds number,  $Re$ , and the ordinate of Keulegan-Carpenter number,  $KC$ , as shown in Figure 12. Different symbols were used to indicate roughly the vortex size.

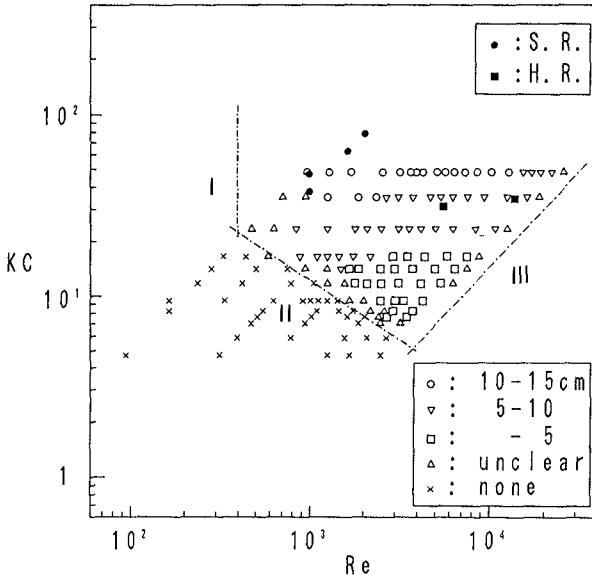


Fig.12 Criterion Curves I, II and III for vortex formation (fixed ripple model with the round crest).

In this figure three different curves denoted by I, II and III were drawn as criteria of vortex formation. The physical meaning of these three curves will be discussed in the following :

- (1) Curve I shows that the Reynolds number should exceed a certain number to generate the organized vortex. The possible minimum value of the Reynolds number might be 400.
- (2) Curve II corresponds to the following condition. It is well known that the Strouhal number of the vortex

shedding induced to a circular cylinder in a steady flow depends upon the Reynolds number. The KC number in the present investigation corresponds to the reciprocal of Strouhal number. Therefore it seems to be natural that the critical KC number for vortex formation depends upon the Reynolds number.

- (3) Sleath (1984) introduced the following relationship for any given sediment to determine the wavelength  $L_r$  of the rolling grain ripples

$$\beta L_r = \alpha = \text{constant} \quad (2)$$

where  $\beta = \sqrt{\omega/2\nu}$ ,  $\omega = 2\pi/T$ , and  $\nu$  is the kinematic viscosity of fluid. Transformation of Equation (2) yields

$$KC = \frac{\pi}{\alpha^2 (H_r/L_r)^2} Re \quad (3)$$

In the present case  $H_r/L_r=0.133$ , hence the KC number is proportional to the Reynolds number. Based on the above discussion, Curve III may be closely related to the criterion of rolling grain ripple formation.

The experimental conditions of the Sawamoto et al. cases, and Cases B and D in the present investigations fall within the region of vortex formation as demonstrated in Figure 12.

### CONCLUSIONS

In this paper the characteristics of the organized vortex formed behind a ripple crest in an oscillatory flow were investigated in detail. Two ripple models were adopted for the present study ; the first is the ripple model with a sharp crest and the second is that with a round crest. The main conclusions are as follows :

- 1) The vorticity of the organized vortex induced by the sharp crest ripple is naturally stronger than that by the round crest ripple.
- 2) The circulation outside the vortex region was evaluated for each phase of oscillatory flow. The nondimensionalized circulation has temporally a specified form for each type of ripple profile. In

order to determine clearly the variational form with the phase of oscillatory flow, additional data are needed.

- 3) Vortex formation due to the round crest ripple was clearly observed in a certain region in the domain of the Reynolds number versus the Keulegan-Carpenter number. The physical meaning of the three criteria was described.

#### REFERENCES

- Horikawa, K. and S. Ikeda : Characteristics of oscillatory flow over ripple models, Proc. 22nd Coastal Engineering Conference, ASCE, pp.661-674, 1990.
- Ikeda, S., S. Kisaki, and S. Kurihara : Modelling of oscillatory flow and vortices in the vicinity of sand ripple, Proc. 35th Japanese Conference on Coastal Engineering, pp.21-24, 1988 (in Japanese).
- Longuet-Higgins, M. S. : Oscillatory flow over steep sand ripples, Journal of Fluid Mechanics, Vol.107, pp.1-35, 1981.
- Mogridge, G. R. and J. W. Kamphuis : Experiments on bed form generation by wave action, Proc. 13th Conf. on Coastal Engineering, ASCE, pp.1123-1142, 1972.
- Sleath, J. F. A. : Sea Bed Mechanics, John Wiley & Sons, p.128, 1984.
- Sato, S. : Oscillatory boundary layer flow and sand movement over ripples, Dr. Eng. Dissertation, University of Tokyo, Japan, 1987.
- Sawamoto, M., T. Yamashita and T. Kurita : Vortex formation over rippled bed under oscillatory flow, Department of Civil Engineering, Tokyo Institute of Technology, Technical Report No.27, pp.75-85, 1980.



## CHAPTER 164

# Berm Formation and Berm Erosion

Kazumasa KATOH<sup>1</sup> and Shin-ichi YANAGISHIMA<sup>2</sup>

### Abstract

To investigate the mechanism of beach erosion in a storm, a daily survey of beach profile and the measurement of infragravity waves near the shoreline have been carried out in a field during two and half years. Analyses of these data reveal that the infragravity waves and the level rising of water table play a important role in the berm erosion in a storm. The infragravity waves run up beyond the berm crest to the backshore. The swashed water permeates into the beach, which contributes to a high water table. The permeated water rises to the surface of foreshore, where the beach is eroded by the backwash of infragravity waves.

### 1. Introduction

In a storm, a beach erodes rapidly within one or two days due to the sand transport from the beach to the offshore. Formerly, wind waves had been considered to be a main external forces of beach erosion in a storm. The wind waves, however, lose their energy when they propagate into the surf zone. Breakers in the surf zone are saturated, that is, the wave height at any point is limited by the local water depth. The larger waves in a storm break further offshore making the surf zone wider but leaving the wave height in the inner surf zone same. Therefore it is basically difficult to attribute the abrupt beach erosion in a storm to the offshore wind waves.

In contrast to the wind waves, the infragravity waves of about 30 seconds to several minutes in a period well develop in a storm (Guza and Thornton, 1982), and do not break in the surf zone, being the largest at the shoreline

---

<sup>1</sup>Chief of the Littoral Drift Laboratory, Port and Harbour Res. Inst., 3-1-1, Nagase, Yokosuka, Kanagawa, JAPAN

<sup>2</sup>Member of the Littoral Drift Laboratory

( eg., Bowen and Huntley, 1984; Holman, 1984). Based on the field data, Katoh and Yanagishima (1990) showed that the berm, or the beach, abruptly erodes in a storm due to not the wind waves but the infragravity waves. Then, in the consideration of the mechanism of beach profile change, it should be very important to take into account the infragravity waves as the external force.

In this study, paying attention to the changes of berm on the shore and the infragravity waves near the shoreline, a field observation has been carried out every day during two and half years. Evidences of berm erosion and berm formation have been abstracted from the data obtained, being 58 cases and 219 cases respectively. By analyzing these data, the differences of physical condition between the berm formation and berm erosion will be examined, by which the mechanism of berm erosion will be discussed.

## 2. Field Observation at Hazaki Oceanographical Research Facility (HORF)

The site of field observation is a entirely natural sandy beach, being exposed to the full wave energy of the Pacific Ocean, and is classified as micro-tidal beach with the tide range of about 1.4 meters ( see Figure 1). On this beach, Port and Harbour Research Institute, Ministry of Transport, constructed the Hazaki Oceanographical Research Facility ( HORF, see Photo.1) in 1986 for carrying out the field observation in the surf zone even under sever sea conditions. The research pier is 427 meters long and supported by concrete-filled steel piles in a single line, at 15 meters interval.

The mean profile during about one year is shown in Figure 2. The foreshore slope is mild, about 1/50 in average, while the mean bottom slope in the surf zone is a little milder, 1/60. The mean diameter of sediments on the

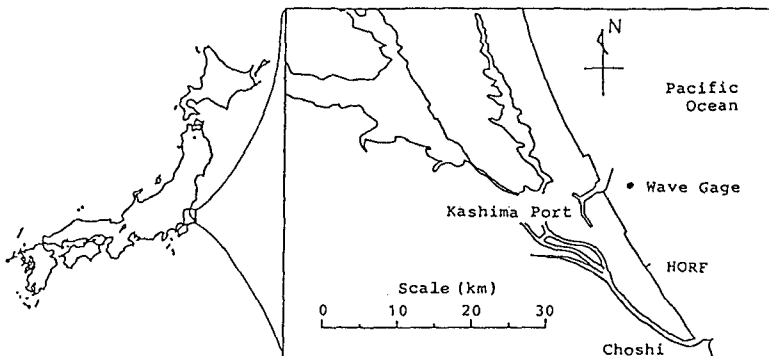


Figure 1 Site of field observation.

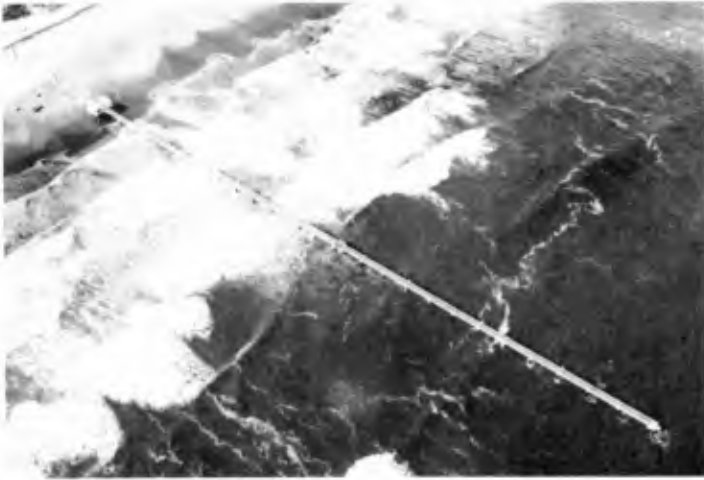


Photo. 1 Hazaki Oceanographical Research Facility.

beach is usually 0.18 mm, which changes occasionally in the narrow range between 0.16 mm and 0.20 mm due to the accumulation and the erosion.

On this beach, the field observations on the berm erosion/formation and the infragravity waves had been carried out for about two and half years from August 1987 to January 1990. The observations conducted in conjunction with this study are as follows;

- (a) survey of the beach profile,
- (b) observation of the infragravity waves near the shoreline,
- (c) wave observation in the offshore,
- (d) observation of the water table under the beach.

The observation methods related to the items from (a) to (c) and the primary analyses of them have been described by Katoh and Yanagishima (1990). To measure the water table, two pipes of 12.5 centimeters in diameter were sunk into

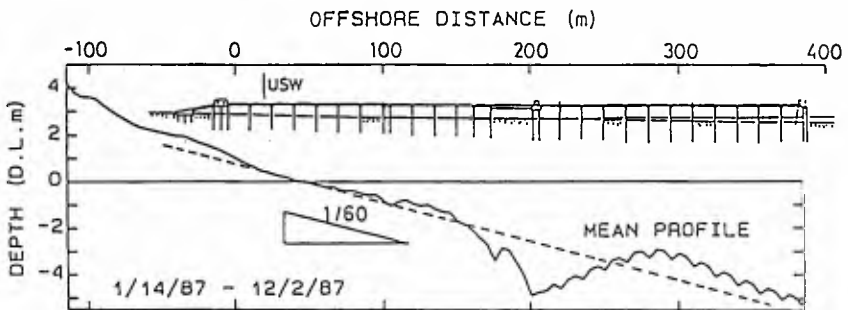


Figure 2 Mean profile of study site.

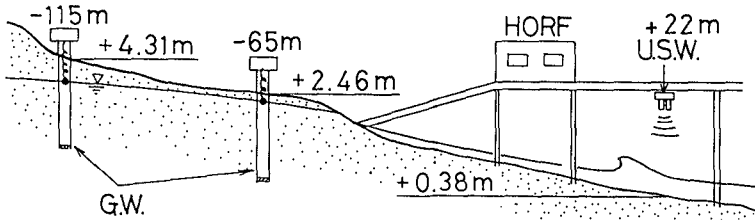


Figure 3 Arrangement of instruments.

the beach at the horizontal reference point of -65m and -115m as shown in Figure 3, and water level meters were installed inside the pipes. The measurement were done during 20 minutes of every hour for about two years from February 1988 to January 1990 including a interruption of about 6 months due to sensor troubles.

3. Level of sand accumulation in the storm

Based on the beach profile data, the evidences of berm erosion have been abstracted. Those are 58 cases in total. Table 1 is the largest ten values of offshore significant wave height in the berm erosions. Two typical examples in the storms have already been reported and discussed by Katoh and Yanagishima (1990) with the data of wind waves and infragravity waves.

Table 1 Large waves in the berm erosions.

Date	$H_{1/3}$ (m)	$T_{1/3}$ (s)
22 Mar. '88	6.51	10.2
17 Sep. '87	5.98	10.9
16 Sep. '88	5.41	11.1
23 May '88	5.00	9.8
23 Jan. '89	4.78	8.7
2 Nov. '89	4.48	12.2
29 Nov. '88	4.29	9.6
12 Oct. '89	4.28	11.2
8 May '88	4.24	8.2
19 Nov. '88	4.02	9.7

Figure 4 shows one of them during the days when the typhoon No.8713 passed near the observation site. The berm had been formed by the 12th of September, but it had eroded within the short term of two days from the 12th to the 14th

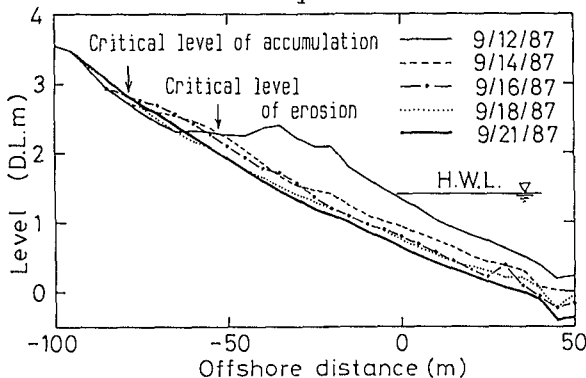


Figure 4 Berm erosion during typhoon No.8713.

of September. One more notice must be given in Figure 4. There was a interesting paradox that the sand deposited on the higher elevation when the berm eroded, as Bascom(1954) had already pointed out. This kind of sand accumulation existed in 48 cases out of 58 evidences of berm erosion.

Katoh and Yanagishima (1990) presented that the critical level of sand accumulation can be predicted by the following equation, which had been empirically obtained with the limited field data,

$$D_L = (\bar{\eta})_0 + 0.96(H_L)_0 + 0.31 \quad (\text{m}). \quad (1)$$

where  $D_L$  is the critical level of sand accumulation in a storm,  $(\bar{\eta})_0$  is the mean sea level at the shoreline,  $(H_L)_0$  is the height of infragravity waves at the shoreline. The third constant term is considered to represent the run-up effect of incident wind waves, because it is independent of the condition of offshore wind waves (Guza and Thornton, 1982).

In Figure 5, the relation between measured values of  $D_L$  and values estimated by Eq.(1) with the data of the mean water level and the height of infragravity waves are plotted for 48 cases of the berm erosion. Since the data are plotted close to the solid line, the validity of Eq.(1) is reconfirmed here.

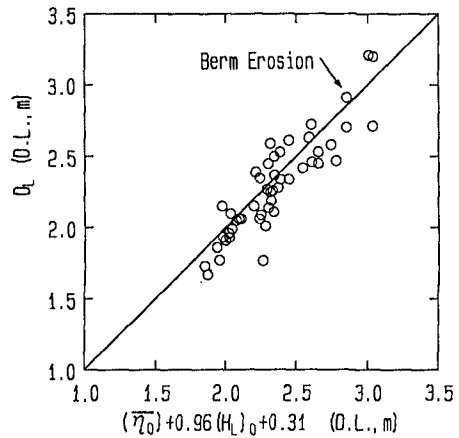


Figure 5 Reconfirmation of Eq.(1).

#### 4. Evidences of the Berm Formation and level of berm crest

Based on the beach profile data, the evidences of successive berm formation for more than several days have been abstracted. Those are 219 cases. Figure 6 shows the typical example of berm formation during the period from the 5th to 15th of August, 1987. The height of offshore wind waves was usually about 1.0 meter with the exception of the short period from the 6th to the 7th when it was 1.8 meters in maximum. The height of infragravity waves at the shoreline was usually smaller than 0.3 meter.

The process of berm formation is characterized as follows;

- (a) The berm was formed with the horizontal berm crest.
- (b) The foreshore slope became gradually steeper.

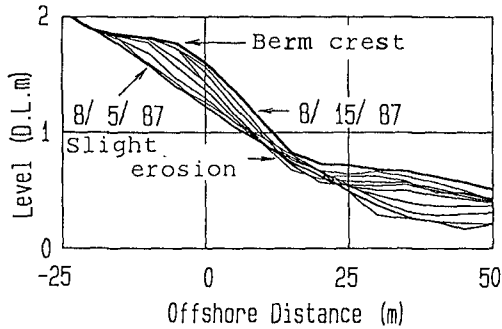


Figure 6 Example of berm formation.

(c) The berm formation was accompanied with a slight erosion at the base of berm.

The features (a) and (b) are recognized in almost all remaining cases. The slight erosions at the base of berm are recognized in 109 cases out of 219 cases. Including the other case that the profile of the base of berm was almost the same as that in the day before, 153 cases are counted in total.

In Figure 7, the relation of the berm crest level,  $A_L$ , which is the upper limit level of sand accumulation in the berm formation, and the value estimated by Eq.(1) is plotted with a symbol of triangle. In this figure, the

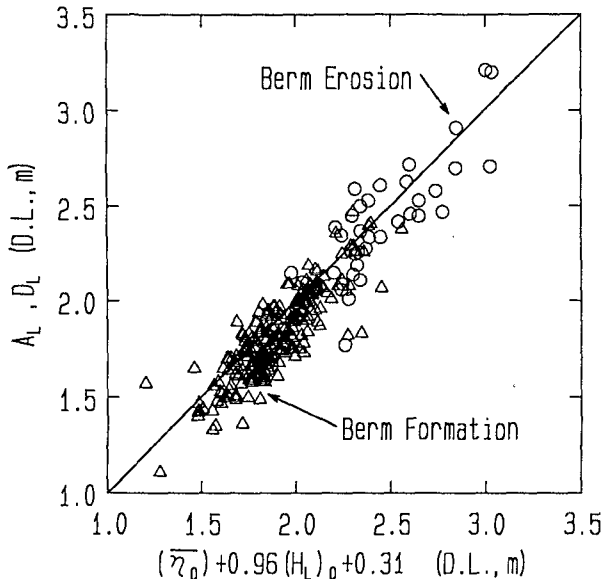


Figure 7 Relation between the berm crest level and the value estimated by Eq.(1).

critical levels of sand accumulation,  $D_L$ , are also plotted with a symbol of circle. As almost all of the data agree well with the straight line, the berm crest level in the process of berm formation can be expressed by the same equation as Eq.(1), that is,

$$A_L = (\bar{\eta})_0 + 0.96(H_L)_0 + 0.31 \quad (m). \quad (2)$$

Although the berm erosion and the formation are the phenomena which are contrary to each other, it has been shown that the critical level of sand accumulation in the berm erosion and the berm crest level in the berm formation can be expressed by the single equation.

**5. Difference of Conditions between the Berm Erosion and the Berm Formation**

Now, the consideration on the correspondence between two kind levels of sand accumulation,  $D_L$  and  $A_L$ , and the wave run-up level,  $R_{MAX}$ , makes us assume

$$R_{MAX} = (\bar{\eta})_0 + 0.96(H_L)_0 + 0.31, \quad (3)$$

with the proviso that this assumption changes the physical meaning of  $R_{MAX}$  from what is called the run-up level of waves to the upper limit level where the waves may make the significant profile change.

The total value of the second term in the right side of Eq.(3) have been calculated for each event of berm erosion and berm formation, respectively. The total value of the third term which is considered to correspond to the run-up height of incident wind waves have been also calculated for each event. Figure 8 shows the rates of resultant values, by normalizing with the total value of the third term in each event. It may be said that the berm eroded when the run-up height of infragravity waves was relatively large, and the berm was formed when the run-up height of incident wind waves was relatively large.

Next, Figure 9 shows the relation between the wave run-up level,  $R_{MAX}$ , and the berm crest level in the previous day, which is denoted by  $(A_L)_{FORMER}$ . A linear quadratic discriminant analysis has been done to

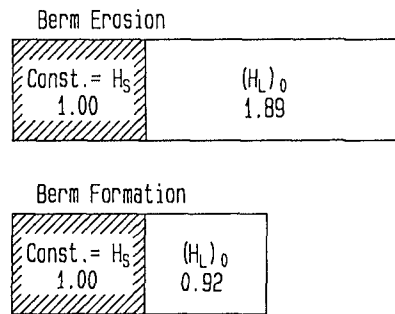


Figure 8 Comparison of run-up heights between the incident wind waves and the infragravity waves in each event.

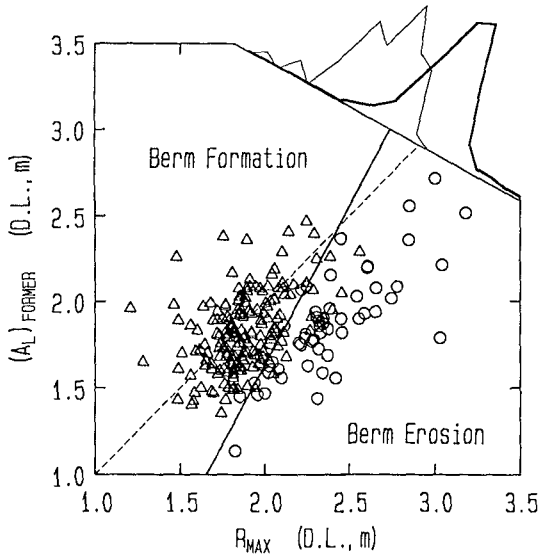


Figure 9 Relation between  $(A_L)_{\text{FORMER}}$  and  $R_{\text{MAX}}$ .

classify these data into two groups. The boundary between two groups is drawn with a straight solid line in Figure 9. The occurrence distribution of data in each group is shown in the upper right corner of Figure 9. From this result, we have

$$R_{\text{MAX}} > 0.54(A_L)_{\text{FORMER}} + 1.11 \quad (\text{m}), \quad (4)$$

as the condition for the berm erosion. In short, the occurrence that the waves run up beyond the existing berm crest to the higher level is a prerequisite for the berm erosion.

Moreover, in Figure 10, the critical level of berm erosion ( see Figure 4 ) and the level of slight erosion in the berm formation (see Figure 6 ) are plotted against the wave run-up levels,  $R_{\text{MAX}}$ . The critical level of berm erosion is 0.39 meter lower than  $R_{\text{MAX}}$ , while the level of slight erosion is about 0.9 meter lower than  $R_{\text{MAX}}$  with some scattering of data. In short, the critical level of berm erosion is relatively higher than the level of slight erosion.

After all, three conditions are known for the berm erosion. When the berm eroded, (a) the height of infragravity waves at the shoreline was large, (b) the waves run up beyond the berm crest to the higher level, and (c) the critical level of erosion was relatively high.



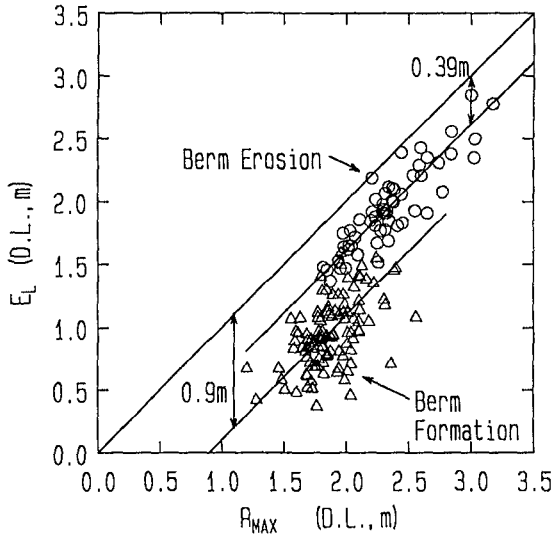


Figure 10 Relation between the erosion level and the wave run-up level.

#### 6. Relation between the Critical Level of Berm Erosion and the Level of Ground Water Table

It has been said for a long time that the position of the water table under the beach has an important bearing on deposition and erosion of the foreshore and backshore. For example, Grant (1948) explained the importance of the wetness or dryness of beach in the changes of beach profile. When the water table under the beach is very high and contiguous with the surface of most of the foreshore, the backwash of the waves is accelerated by addition of water rising to the surface throughout the saturated foreshore. This saturated area is called the effluent zone. The increased volume of backwash by ground water escaping to the surface of the foreshore also dilates the sand and propels the finer grains into the turbulent flow. These enhance the erosion of the foreshore.

The causes of high water table, which have been pointed out up to these days, are;

- (a) The water due to the heavy rain storm in the hinterland flows to the backshore ( Grant, 1948 ),
- (b) As the water table under the beach lags 1 to 3 hours behind the tide, the water table is relatively higher than the tide during the ebb tide ( Emery and Foster, 1948; Duncan, 1964 ),
- (c) Hot springs flow out at some beach in Japan ( Sato et al., 1982 ).

All of these, however, are not the causes which take part



Photo. 2 Maximum wave run-down ( taken from the rooftop of HORF ).

in the berm erosion in a storm. Now, we can add one more cause of high water table which is directly related to the beach erosion in the storm; that is to say, there is a possibility that the water run-up beyond the berm crest penetrates into the beach, which makes the water table high.

In the field observation, it was recognized that the large scale wave run-up beyond the berm crest occurred with a period of 1 to 2 minutes in the storm. Photo. 2 was taken from the rooftop of the laboratory in HORF under the situation of maximum wave run-down. In this picture, the existing berm crest of running in the longshore direction is inspected to be exposed to the air. In the left side, or the land side, the beach was covered with the water which stayed on the backshore for a good while. On the backshore, the authors recognized that air bubbles came out from the ground through the surface of beach, which was due to the replacement with the water penetrated into the ground. As a result, it is not difficult to infer the situation that the level of water table under the beach became higher, and the penetrated water flowed out through the surface of foreshore.

Then, the seepage level, which is the upper limit of the effluent zone, has been determined by the numerical simulation of the finite element method which was developed by Bathe and Khoshgoftaar (1979) for analysis of steady unconfined seepage conditions in two-dimensional case.

The area of simulation is from the reference point of -

115m ( see Figure 3 ) to the offshore in the cross-shore direction, and from the beach surface to the level of -20 meters in the downward direction. The beach profile is approximated by a straight line. In calculation, distorted rectangular elements are made by dividing the area of simulation with the interval of 0.5 meter in the vertical direction, and with the interval of 5 meters, being nearly parallel to the beach slope, in the cross-shore direction. The level of water table measured at the reference point of -115m, which has been confirmed to be usually stable independent of the tide or wave run-up on the beach, is used as the boundary condition at the land side. For the boundary condition at the shoreline, the sum of the mean sea level at the shoreline and the run-up height of incident wind waves, that is  $(\bar{\eta})_0 + 0.31$  (m), is utilized. A reason why the run-up of incident waves is taken into consideration is owing to the fact that the incident waves run up repeatedly with the short period of about 8 seconds, which keeps the beach wet. A coefficient of permeability in the beach is employed as  $1.14 \times 10^{-2}$  cm/s, based on the result of permeability test conducted by Zen et al. (1989) with the sand sampled from the study site.

At first, in order to verify the applicability of simulation model, the water tables have been calculated for the calm wave conditions of 74 cases, in which the significant wave heights and the periods in the offshore were less than 1 meter and 8 seconds, respectively. Figure 11 shows the comparison of the observed levels of water

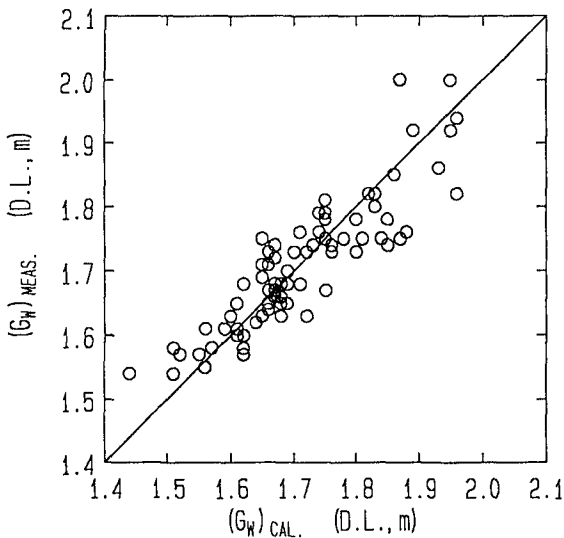


Figure 11 Comparison of observed level of water table with the calculated one.

table,  $(G_w)_{\text{HRS}}$ , at the reference point of  $-65\text{m}$  with the calculated ones,  $(G_w)_{\text{CAL}}$ , at the corresponding point. The calculated water tables agree approximately with the observed ones.

Next, the free surfaces of water table have been calculated for the berm erosions in the storms. The calculated levels of water table at the reference point of  $-65\text{m}$ , however, were lower than measured ones. The difference between them increases with the run-up height of infragravity waves. Therefore, in the calculation of water table in the storm, it is necessary to take into account one more condition that the water on the horizontal portion of the berm penetrates into the beach.

In order to simulate the penetration of water into the beach, the steady discharge of penetration through the beach face has been assumed. The distribution of discharge along the beach surface is set as a triangle, being zero at the wave run-up level,  $R_{\text{MAX}}$ . The value of discharge has been determined by trial and error so as to coincide the calculated water table at the reference point of  $-65\text{m}$  with the measured one in the field. The resultant value of discharge is in a range of  $0.2$  to  $0.5 \text{ m}^3/\text{h}$  per unit longshore length, which has a tendency to increase with the height of infragravity waves.

In this convenient manner, the water table under the

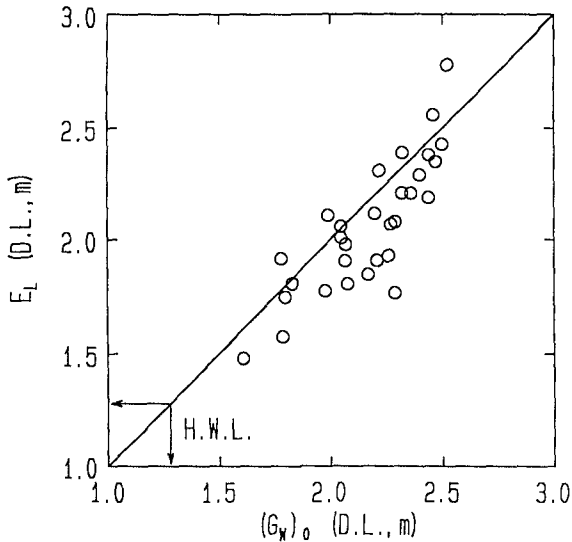


Figure 12 Relation between the critical level of berm erosion and the seepage level of ground water.

beach is calculated for each case of the berm erosion. After that, the seepage level is determined at the intersection of the water table and the foreshore profile, which is denoted by  $(G_w)_0$ . In Figure 12, the seepage levels are plotted against the critical levels of berm erosion in the storms. The plotted data agree approximately with the straight line; that is to say, the critical level of berm erosion corresponds roughly to the seepage level of water.

Based on this result, we can make another consideration. In the process of berm formation, the run-up level is low and the water goes down immediately along the foreshore slope without staying, which is enhanced by the increase of foreshore slope. As a result, the level of slight erosion in the berm formation is relatively lower in comparison with the run-up level ( see Figure 10 ).

## 7. Conclusions

The main conclusions reached in this study are as follows;

- (1) Both the critical level of sand accumulation in the berm erosion and the berm crest level in the berm formation can be expressed by Eq.(3), which contains the effect of run-up of infragravity waves on the beach.
- (2) As the infragravity waves run up beyond the berm crest in the storm, the sea water stays for a good while on the horizontal area of the berm, which accelerates the saturation of water into the beach. As a result, the water table becomes higher, and the water flow out through the surface of foreshore. The seepage level of water corresponds to the critical level of berm erosion.

## Acknowledgement

The authors should like to express our grateful thanks to Dr. Masaki Kobayashi, the Director of the Soil Division of the Port and Harbour Research Institute, for helpful suggestions for using the computer program of seepage flow which has been developed by him.

## References

- 1) Bascom, W.H. (1954): Characteristics of natural beach, Proc. of 4th ICCE, pp.163-180.
- 2) Bathe, K.J. and M.R. Khoshgoftaar (1979): Finite element free surface seepage analysis without mesh iteration, Int. Jour. for Nume. and Analy., Methods in Geomechanics, Vol.3, pp.12-33.
- 3) Bowen, A.J. and D.A. Huntley (1984): Waves, long waves and nearshore morphology, Marine Geology, 60, pp.1-13.
- 4) Duncan, J.R. (1964): The effects of water table and tidal cycle on swash-backwash sediment distribution and beach

- profile development, *Mar. Geol.*, Vol.2, pp.186-197.
- 5) Emery, K.O. and J.F. Foster (1948): Water table in marine beaches, *Jour. of Marine Res.*, Vol.7, No.3, pp.644-654.
  - 6) Grant, U.S. (1948): Influence of the water table on beach aggradation and degradation, *Jour. of Marine Res.*, Vol.7, No.3, pp.655-660.
  - 7) Guza, R.T. and E.B. Thornton (1982): Swash oscillation on a natural beach, *Jour. Geol. Res.*, Vol.87, pp.483-491.
  - 8) Holman, R.A. (1984): Edge waves and the configuration of the shoreline, *CRC Handbook of Coastal Process and Erosion*, CRC Press Inc., pp.21-33.
  - 9) Katoh, K. and S. Yanagishima (1990): Berm erosion due to long period waves, *Proc. of 22nd ICCE*, pp.2073-2086.
  - 10) Sato, M., K. Byoga, M. Kuchinomachi, H. Fukushima and T. Mori (1982): A field observation on mechanism of erosion of Surigahama Beach, *Proc. of 29th Conf. on Coastal Eng. in Japan*, pp.314-318 ( in Japanese ).
  - 11) Zen, K., H. Yamazaki and Y. Sato (1989): Wave-induced liquefaction in seabed, -Field observation and analysis-, *Rep. of PHRI*, Vol.28, No.3, pp.28-57 ( in Japanese ).

## CHAPTER 165

### COUPLING OF A QUASI-3D MODEL FOR THE TRANSPORT WITH A QUASI-3D MODEL FOR THE WAVE INDUCED FLOW

Irene Katopodi<sup>1</sup>, Nikos Kitou<sup>1</sup> and Huib J. de Vriend<sup>2</sup>

#### ABSTRACT

In this paper the coupling of a quasi-3D model for the suspended sediment transport with a quasi-3d model for the wave driven flow is presented. The quasi-3d model for the transport is based on an asymptotic solution of the wave-averaged convection-diffusion equation while the quasi-3D wave driven current model is based on a profile function technique. The resulting model is a low cost but detailed alternative to a full 3D model. An application is presented concerning cross-shore transport. Preliminary conclusions are drawn.

#### 1. INTRODUCTION

The prediction of suspended sediment transport and subsequently of bed evolution in coastal areas is of vital importance for the operation and maintenance of engineering works. Numerical models are expected to play an increasingly significant role as a design and decision tool of the coastal engineer.

A variety of models have been presented in the literature with various degrees of sophistication as far as the constituent models are concerned. The present model involves two basic submodels of the same degree of sophistication: Both wave induced currents and suspended sediment transport are computed using quasi-3D techniques that exhibit the low computational cost of the 2DH models while at the same time provide information about the vertical structure of the flow and the suspended sediment concentration.

Moreover, in cross-shore flows local equilibrium is

---

1 Democritus University of Thrace, Department of Civil Engineering, 67100 Xanthi, Greece.

2 Delft Hydraulics, P.O. Box 152, 8300 AD, Emmeloord, the Netherlands.

assumed for the suspended sediment and as a result suspended sediment transport formulae are widely used for the calculation of the bed-level changes. Herein, in a cross-shore case the full convection-diffusion equation has been used.

## 2. THE QUASI-3D MODEL FOR THE SUSPENDED SEDIMENT TRANSPORT (LOG VELOCITY PROFILE)

The present work is an extension of the suspended sediment transport model presented by Katopodi and Ribberink (1990, 1992). A short description of the model follows:

The model is based on an asymptotic solution of the wave-averaged 3D convection-diffusion equation. The asymptotic solution was developed by Galappatti and Vreugdenhil (1985) for unidirectional flow under certain scale considerations. In the quasi-3D model for currents and waves the wave influence is included through a suitable modification of the vertical mixing coefficient and through the near-bed boundary condition (van Rijn, 1986). Two bed boundary conditions are used: Either the sediment concentration ("concentration" b.c.) or its vertical gradient at the near-bed reference level ("gradient" b.c) is assumed to adapt immediately to equilibrium conditions and are given as functions of local hydraulic and sediment parameters (for expressions see van Rijn, 1986).

Under the assumption that the velocity is described by  $u(x, \zeta, t) = \bar{u}(x, t) p(\zeta)$  and  $v(x, \zeta, t) = \bar{v}(x, t) p(\zeta)$  (one logarithmic component only) and the use of the "concentration" bed boundary condition the depth averaged equation reads:

$$\begin{aligned} \bar{c}_e = \bar{c} + \frac{\gamma_{21}}{\gamma_{11}} \frac{h}{w_s} \frac{\partial \bar{c}}{\partial t} + \frac{\gamma_{22}}{\gamma_{11}} \frac{h \bar{u}}{w_s} \frac{\partial \bar{c}}{\partial x} + \frac{\gamma_{22}}{\gamma_{11}} \frac{h \bar{v}}{w_s} \frac{\partial \bar{c}}{\partial y} - \\ - \frac{\gamma_{21}}{\gamma_{11}} \frac{h}{w_s} \frac{\partial}{\partial x} \left( \epsilon_x \frac{\partial \bar{c}}{\partial x} \right) - \frac{\gamma_{21}}{\gamma_{11}} \frac{h}{w_s} \frac{\partial}{\partial y} \left( \epsilon_y \frac{\partial \bar{c}}{\partial y} \right) \end{aligned} \quad (1)$$

where  $\bar{c}$  and  $\bar{c}_e$  are the depth averaged concentration and equilibrium concentration,  $\bar{u}$  and  $\bar{v}$  depth averaged velocities,  $h$  the water depth, the sediment fall velocity is  $w_s$  and  $\gamma_{ij}$  coefficients that depend only on the explicit knowledge of the vertical mixing coefficient, the fall velocity and the normalized velocity profile  $p(\zeta)$  and can be computed in advance. After equation (1) has been solved for  $c$ , the vertical concentration profile can be constructed in terms of already known profile functions (see Katopodi and Ribberink, 1992).



Equation (1) can be written as:

$$\bar{c}_e = \bar{c} + T_A \frac{\partial \bar{c}}{\partial t} + L_x \frac{\partial \bar{c}}{\partial x} + L_y \frac{\partial \bar{c}}{\partial y} - T_A \left( \frac{\partial}{\partial x} (\epsilon_x \frac{\partial \bar{c}}{\partial x}) + \frac{\partial}{\partial y} (\epsilon_y \frac{\partial \bar{c}}{\partial y}) \right) \quad (2)$$

with

$$T_A = \frac{\gamma_{21}}{\gamma_{11}} \frac{h}{w_s}, \quad L_x = \frac{\gamma_{22}}{\gamma_{11}} \frac{\bar{u}h}{w_s}, \quad L_y = \frac{\gamma_{22}}{\gamma_{11}} \frac{\bar{v}h}{w_s} \quad (3)$$

Equation (2) describes the adjustment of the depth-averaged concentration to its equilibrium value. The parameters  $T_A$ ,  $L_x$  and  $L_y$  represent the characteristic scales in time and space of this adjustment process (adaptation time, adaptation lengths). If the "gradient" bed boundary condition is used, only the expressions for the adaptation time and length change in equation (3), (see Katopodi and Ribberink, 1992).

### 3. THE QUASI-3D MODEL FOR THE WAVE INDUCED FLOW

In (1) the velocity profile was assumed logarithmic which is not realistic in the wave driven nearshore circulation. Instead, the quasi-3D model for nearshore currents presented by de Vriend and Stive (1987) as modified by de Vriend and Ribberink (1988) is employed in this work (DVS in the following). This model is based in a profile function technique combined with a 2DH current formulation. The current is divided into a primary component and a number of secondary components due to the vertical nonuniformities of the various driving forces. The velocity is given as a similarity series:

$$u(x, \zeta, t) = \sum_{i=1}^n \bar{u}_i(x, t) p_i(\zeta) \quad (4a)$$

$$v(x, \zeta, t) = \sum_{i=1}^n \bar{v}_i(x, t) p_i(\zeta) \quad (4b)$$

where  $\bar{u}_1$ ,  $\bar{v}_1$  are depth averaged primary current,  $\bar{u}_i$ ,  $\bar{v}_i$  depth invariant parameters representing secondary current intensity,  $\zeta = z/h$  and  $p_i(\zeta)$  profile functions with:

$$\int_0^1 p_1(\zeta) d\zeta = 1 \quad \text{and} \quad \int_0^1 p_i(\zeta) d\zeta = 0 \quad \text{for } i > 1 \quad (5)$$

Equations (5) imply that the depth averaged flow is entirely determined by the primary current. The model consists of a depth-averaged wave-driven current module

(see application, chapter 5) and the velocity profile extraction part.

In the DVS model complete description of the undertow and the boundary layer streaming is included. The model though is written in a general way so that secondary flows other than those due to waves (like Coriolis induced or wind induced flows) can easily be included.

The wave induced secondary velocity is consisting of a number of components due to various driving forces:

$$\begin{aligned}
 u_s(\zeta) &= u_2(\zeta) + u_3(\zeta) + u_4(\zeta) + u_5(\zeta) \\
 &= \bar{u}_2 p_2(\zeta) + \bar{u}_3 p_3(\zeta) + \bar{u}_3 p_3(\zeta) + \bar{u}_4 p_4(\zeta) \quad (6)
 \end{aligned}$$

where

- $u_2(\zeta)$  secondary current due to the surface shear stress
- $u_3(\zeta)$  secondary current due to secondary bottom shear stress
- $u_4(\zeta)$  near-bottom drift due to spatial variation of the orbital velocity
- $u_5(\zeta)$  near-bottom drift due to the boundary layer.

For expressions for the secondary velocities the reader is referred to Ribberink and de Vriend (1989). In fig.1 the velocity and its components are shown at the cross section of the flume  $x=30$  m (cf.example). Near the bottom the effect of the boundary layer is clear.

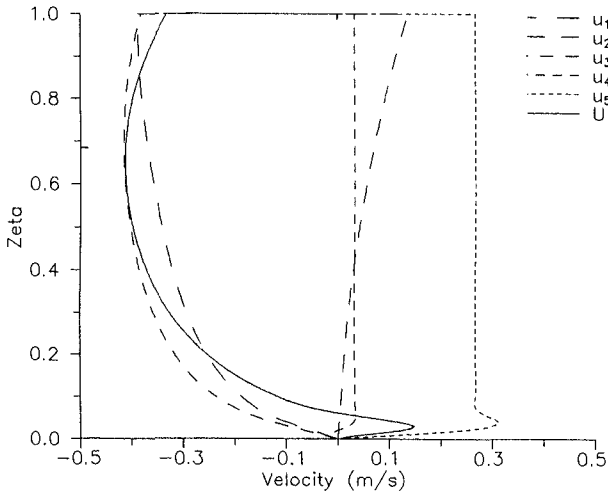


Fig.1 Current velocity and its components (x=30m)

#### 4. COUPLING OF THE TWO QUASI-3D MODELS

In (1) the velocity was consisting of only one component (similarity was assumed). If the velocity is given as a similarity series, eq.(4), then equation (1) becomes:

$$\begin{aligned}
 \bar{c}_e = & \bar{c} + \frac{\gamma_{21}}{\gamma_{11}} \frac{h}{w_s} \frac{\partial \bar{c}}{\partial t} + \\
 & + \left( \sum_{i=1}^n \bar{u}_i \frac{\gamma_{22,i}}{\gamma_{11}} \right) \frac{h}{w_s} \frac{\partial \bar{c}}{\partial x} + \left( \sum_{i=1}^n \bar{v}_i \frac{\gamma_{22,i}}{\gamma_{11}} \right) \frac{h}{w_s} \frac{\partial \bar{c}}{\partial y} \\
 & + \left( \beta \frac{\gamma_{23}}{\gamma_{11}} + \frac{\gamma_{24}}{\gamma_{11}} \right) \frac{1}{1+\beta} \frac{\partial z_s}{\partial t} \frac{1}{w_s} \bar{c} \\
 & + \sum_{i=1}^n \left( \frac{\partial}{\partial x} (\bar{u}_i h) \frac{\gamma_{25,i}}{\gamma_{11}} \right) \frac{1}{w_s} \bar{c} \\
 & + \sum_{i=1}^n \left( \frac{\partial}{\partial y} (\bar{v}_i h) \frac{\gamma_{25,i}}{\gamma_{11}} \right) \frac{1}{w_s} \bar{c} \\
 & - \frac{\gamma_{21}}{\gamma_{11}} \frac{h}{w_s} \left( \frac{\partial}{\partial x} \left( \epsilon_x \frac{\partial \bar{c}}{\partial x} \right) + \frac{\partial}{\partial y} \left( \epsilon_y \frac{\partial \bar{c}}{\partial y} \right) \right) \quad (7)
 \end{aligned}$$

where  $\beta$  is the reference level normalized by the depth.

New terms have been added to the RHS of eq.(7), compared to eq.(1): The third and fourth term are now sums of similar terms due to the separate velocity components. The fifth term arises from the vertical transformation. The sixth and seventh terms are due to the vertical velocities that are computed via the continuity equation.

The above equation can be written in a more convenient form, similar to equation (2):

$$\begin{aligned}
 \bar{c}_e = & (1 + V_T + V_x + V_y) \bar{c} + T_A \frac{\partial \bar{c}}{\partial t} + L_x \frac{\partial \bar{c}}{\partial x} + L_y \frac{\partial \bar{c}}{\partial y} \\
 & - T_A \left( \frac{\partial}{\partial x} \left( \epsilon_x \frac{\partial \bar{c}}{\partial x} \right) + \frac{\partial}{\partial y} \left( \epsilon_y \frac{\partial \bar{c}}{\partial y} \right) \right) \quad (8)
 \end{aligned}$$

with

$$T_A = \frac{\gamma_{21}}{\gamma_{11}} \frac{h}{w_s}$$

$$\begin{aligned}
 L_x &= \left( \sum_{i=1}^n \bar{u}_i \frac{\gamma_{22,i}}{\gamma_{11}} \right) \frac{h}{w_s} & L_y &= \left( \sum_{i=1}^n \bar{v}_i \frac{\gamma_{22,i}}{\gamma_{11}} \right) \frac{h}{w_s} \\
 v_T &= \left( \beta \frac{\gamma_{23}}{\gamma_{11}} + \frac{\gamma_{24}}{\gamma_{11}} \right) \frac{1}{1+\beta} \frac{\partial z_s}{\partial t} \frac{1}{w_s} \\
 v_x &= \sum_{i=1}^n \left( \frac{\partial}{\partial x} (\bar{u}_i h) \frac{\gamma_{25,i}}{\gamma_{11}} \right) \frac{1}{w_s} \\
 v_y &= \sum_{i=1}^n \left( \frac{\partial}{\partial y} (\bar{v}_i h) \frac{\gamma_{25,i}}{\gamma_{11}} \right) \frac{1}{w_s} \tag{9}
 \end{aligned}$$

After (7), or (8), is solved for the depth-averaged concentration, the concentration profile can be constructed in terms of already known profile functions.

If "gradient" bed boundary condition is used only the expressions in (9) are different.

Although the number of coefficients to be computed in equation (7), or (8), has now increased significantly compared to (1), or (2), the time required for their computation keeps the model at operational level.

## 5. APPLICATION

The model described in the previous section was applied for a cross-shore case with field and wave data taken from the experiment conducted in the Hannover Big Wave Flume (Dette and Uliczka, 1986) in order to study the beach profile evolution due to the wave action at prototype scale. This experiment was used for intercomparison of profile models under the MAST-G6 Morphodynamics programme (Hedegaard et al, 1992). The waves were monochromatic ( $H=1.5\text{m}$   $T=6\text{s}$ ) and the wave propagation direction normal to the shore (bed configuration fig.2a).

In the present computation no wave-current interaction was included, the wave field was stationary and the steady-state current was computed. The steps followed are described below:

1. The wave heights (fig.2a) were computed with the use of the energy equation. Dissipation due to breaking was calculated using the bore analogy (see description of UNIBEST in Hedegaard et al, 1992).

2. For depth-averaged current the 1D continuity and momentum equations were solved:

$$\frac{\partial(\bar{u}h)}{\partial x} + \frac{\partial}{\partial x} \left( \frac{M_x}{\rho} \right) = 0 \quad \text{continuity} \tag{10}$$

with

$$M_x = \frac{E}{c} \left( 1 + \frac{7h}{L} Q_b \right) \quad (11)$$

where  $\bar{u}$  is the depth-averaged current velocity,  $M_x$  the wave mass flux,  $E$  the wave energy,  $c$  the wave celerity,  $L$  the wave length,  $h$  the water depth,  $Q_b$  fraction of breaking waves set equal to 1 for breaking waves and to 0 for non-breaking waves and  $\rho$  the water density. The second factor in the parenthesis is the roller contribution.

$$0 = -g \frac{\partial z_s}{\partial x} + \frac{1}{\rho h} \frac{D}{c} - \frac{\tau_{b,p}}{\rho h} \quad \text{momentum} \quad (12)$$

where  $z_s$  is the free surface,  $D$  the total wave energy dissipation (due to breaking and due to bed friction),  $\tau_{b,p}$  primary bed shear stress given by de Vriend and Stive (1987) as function of the depth mean velocity, the eddy viscosity and the bottom roughness amplification factor. In fig.2b and fig.2c the bed configuration and set-up and the depth averaged (primary) velocity are shown along the flume.

3. The secondary velocities were calculated according to Ribberink and de Vriend (1989), and the velocity profiles were constructed (fig.3a). In fig.3b velocity profiles are also shown in more detail (note the vertical axis where the position of the cross-section along the flume is depicted).

4. The adaptation time  $T_\lambda$  and length  $L_x$  (fig.4a and 4b) as well as the factor due to vertical velocities  $V_x$  and the depth-averaged value of  $\bar{c}_e$  (fig.5a) were computed by a separate module before the calculation of  $\bar{c}$ . The term  $V_\tau$  is zero because the steady state is examined.

5. Equation (8), was solved with upstream (shore) condition imposed equilibrium concentration and downstream (offshore) condition zero second derivative of the concentration. For "gradient" bed boundary condition the expressions (9) are different. The value of the horizontal eddy viscosity (fig.4c) was given by:

$$\epsilon_x = M h \left( \frac{D}{\rho} \right)^{1/3} \quad (13)$$

where  $M$  is a coefficient of the order of one. The depth averaged concentration for the two bed boundary conditions is shown in fig.(5a).

6. The concentration profiles (fig.5b and 5c) were then constructed in terms of the depth averaged concentration and profile functions computed before.

7. Finally, the suspended sediment transport rate was

calculated using the following equation:

$$S_x = h \int_0^1 u c \, d\zeta - h \int_0^1 \epsilon_x \frac{\partial c}{\partial x} \, d\zeta \quad (14)$$

In fig.6 the suspended sediment transport rate computed from equation (14) is plotted for "concentration" and for "gradient" boundary condition. In the same plot the suspended sediment transport rate under equilibrium conditions is also shown.

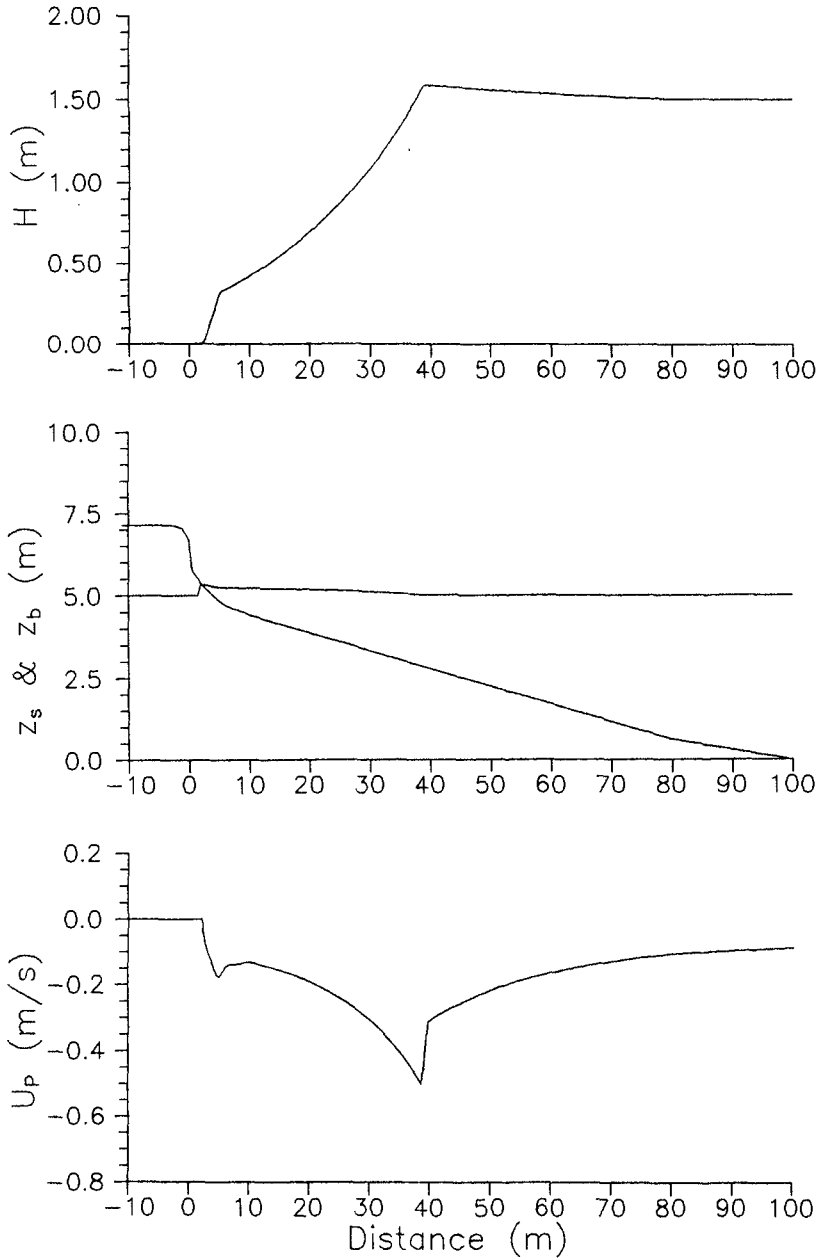
The results of the example are discussed in the following:

Considerable difference exists between the equilibrium concentration and the concentration computed from the convection-diffusion equation. This is shown in fig. (5a) as far as depth-averaged quantities are concerned for both boundary conditions. The difference is more important in cross section at  $x=40m$  where the equilibrium concentration is bigger and at cross section at  $x=50 m$  where the opposite happens. The peak of the concentration is more onshore for equilibrium conditions. In figures 5b, 5c (concentration profiles) the difference between the concentrations computed with the use of the two bed boundary conditions should be noticed, especially in the cross-section at 40m. The gradient bed boundary condition results in somewhat smoother concentration (result of the bigger adaptation length (see fig.4a). No definite conclusion on which boundary condition is appropriate can be drawn until comparison with measurements is made.

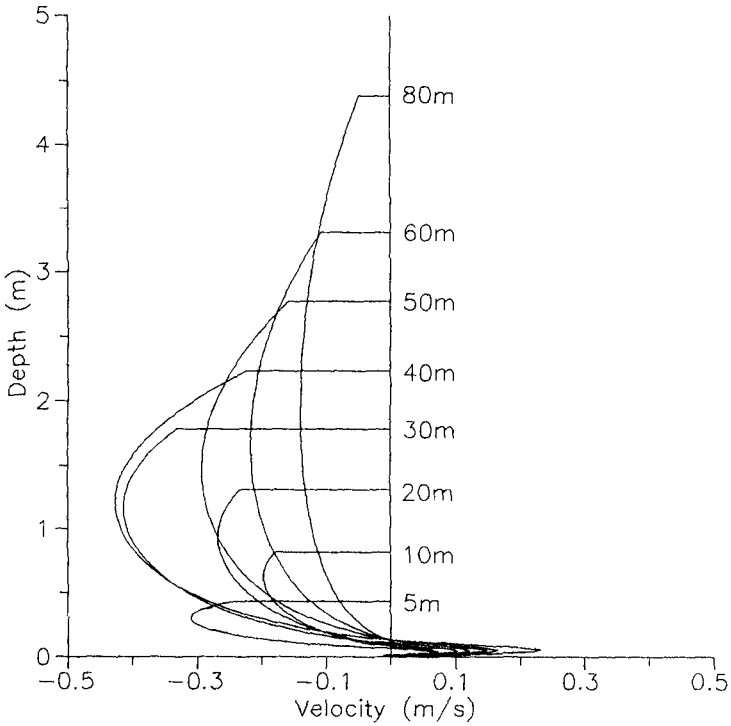
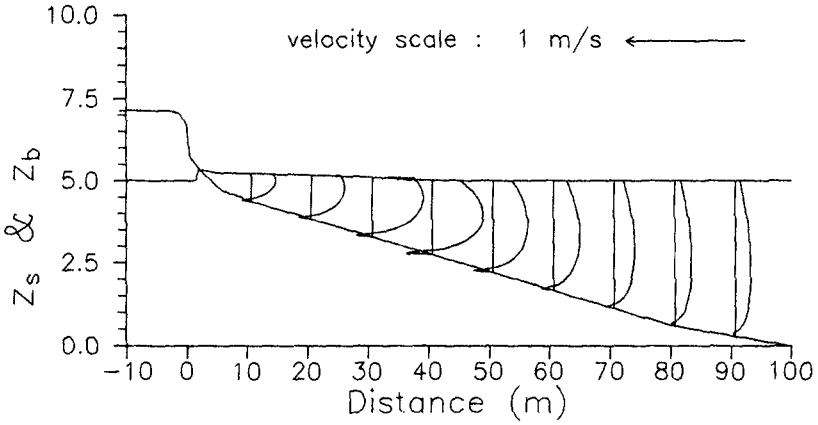
In fig.6 we can see that the non-equilibrium transport presents a discontinuity in cross-section at  $x=40m$ . This is due to the wave formulation we have chosen. In the computation of the wave mass-flux the roller term is added suddenly as soon as the waves start breaking and this causes a discontinuity in the depth averaged velocity. This discontinuity can be removed with an alternative formulation of the roller contribution to the wave mass flux. Inclusion of random waves will make even smoother the quantities involved. The discontinuity occurs in the first term of the RHS of (14) where the concentration is multiplied by the velocity.

Nevertheless, the horizontal gradients of the non-equilibrium transport are smaller than those of the equilibrium one and it is expected that the bar that will be formed will have more damped shape than the one computed if suspended sediment transport is assumed to be in equilibrium (as is implied in transport formulae).

In Katopodi and Ribberink (1990,1992) it was argued that when the space (time) computational grid size is smaller than the adaptation length (time) then the adaptation process (to equilibrium) should be described with the use of a non-equilibrium transport model

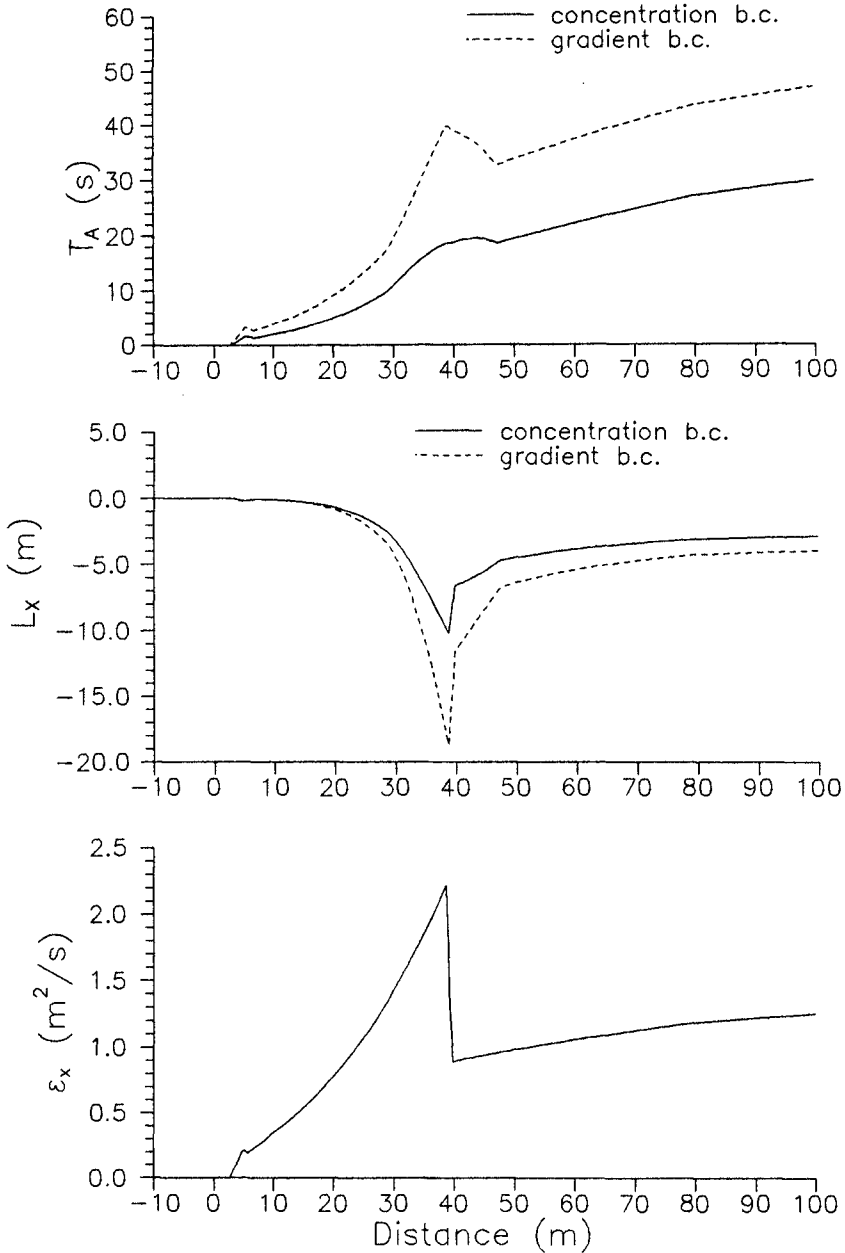


**Fig. 2** a) Wave height, b) Bed configuration and set-up  
c) Depth-averaged (primary) velocity.

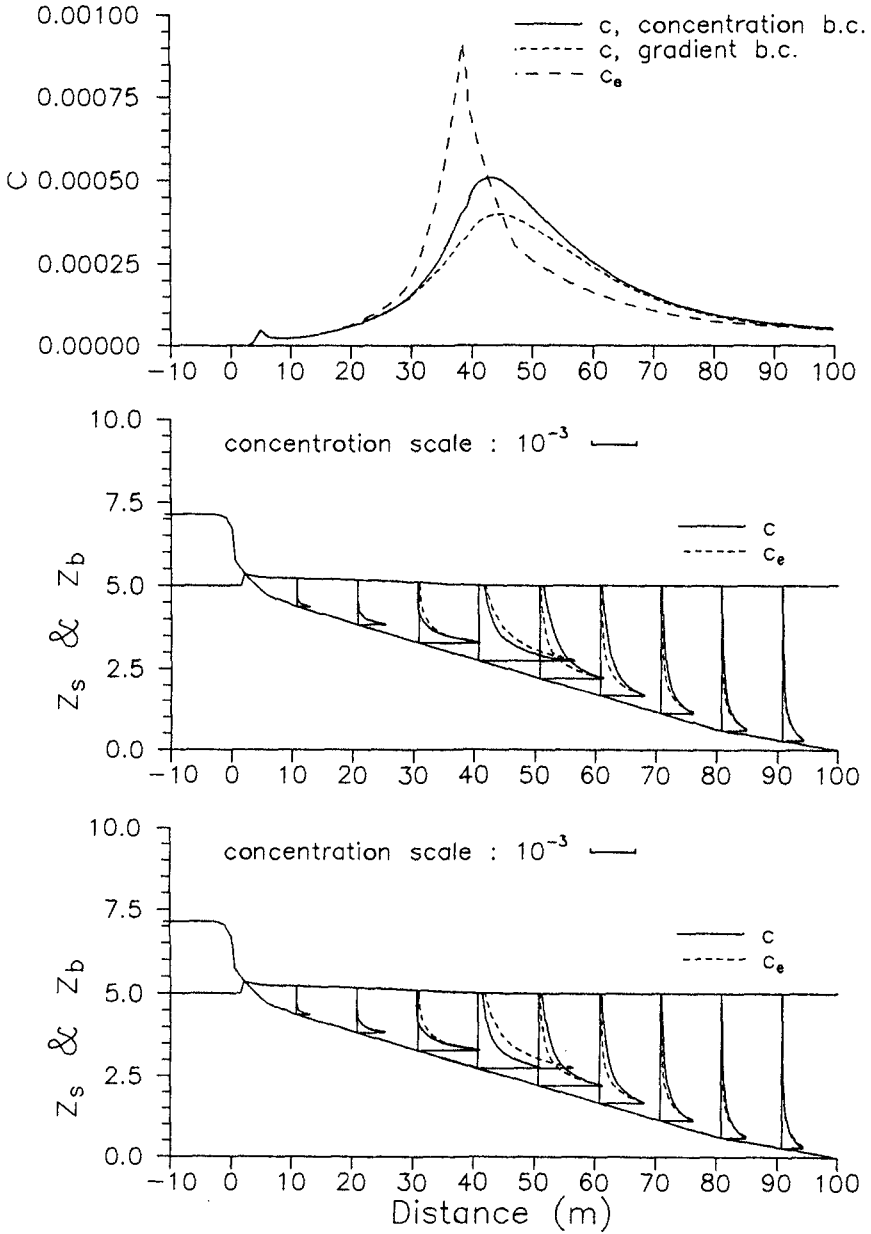


**Fig.3** a) Velocity profiles along the flume,  
 b) Velocity profiles along the flume (detailed)





**Fig. 4** a) Adaptation time, b) Adaptation length  
c) Horizontal eddy viscosity



**Fig.5** a) Depth-averaged concentration,  
 b) Concentration profiles ("concentration" bed bc)  
 c) Concentration profiles ("gradient" bed bc)

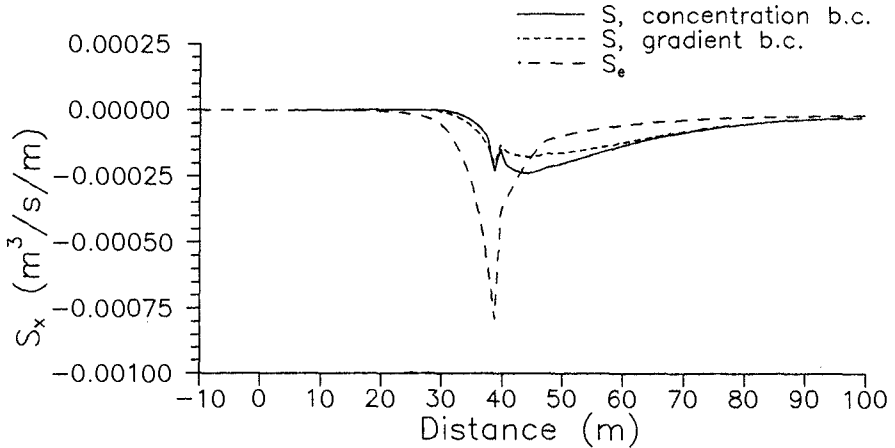


Fig.6 Suspended sediment transport rates

(convection-diffusion equation). Following the above reasoning, the importance of the non-equilibrium effects could be foreseen (before the solution of the convection diffusion equation) by comparison of the adaptation length (fig.4b) with the required computational space grid. In the experiment of Dette and Uliczka (1986) the bar has a width of about 10 m and a grid of about 0.5 m is required to describe it. The grid size is much smaller than the adaptation length in the biggest part of the flume, especially in the surf zone, and this indicates that non equilibrium effects should be taken into account in the transport computation. Of course, their impact on the bed-level changes should be shown quantitatively

## 6. CONCLUSIONS

A model for the suspended sediment transport is presented for wave induced flows. The current velocities are given as a (similarity) series of vertical profiles. The suspended sediment transport is computed with the use of a quasi-3d model of the convection diffusion equation. The effect of the vertical velocity that is computed via the continuity equation is included.

Although the number of coefficients to be computed before the solution of eq. (7) is much larger than when the velocity was consisting of a unique profile, the time required for their computation is very small compared to that of the actual solution of the equation.

Both current and transport modules require gradual changes in hydraulic conditions and are particularly

suitable for large computational areas.

This work is a first attempt to develop a sediment transport model and the effort has been put mostly at the technical part (formulation of the coupling). The Lagrangian and the wave asymmetry transport have not yet been included despite their importance. After the inclusion of the Lagrangian drift correction (as an additional profile), the wave asymmetry transport as well as bed load transport and bed slope effects, we will be able to reach more definite conclusions about the real magnitude and importance of the different phenomena on the sediment transport in the coastal zone.

#### ACKNOWLEDGMENT

This work was undertaken as part of the MAST G6 Coastal Morphodynamics research programme. It was funded by the Commission of the EC, Directorate General for Science, Research and Development, under MAST contract no. 0035-C.

#### APPENDIX I. REFERENCES

- DETTE, H. and ULICZKA, K., 1986.  
Velocity and sediment concentration fields across surf zone. Proc. 20th ICCE, Taipei, Taiwan.
- DE VRIEND, H.J. and STIVE, M.J.F., 1987.  
Quasi-3D modelling of nearshore currents. Coastal Engineering, Vol. 11.
- DE VRIEND, H.J. and RIBBERINK, J., 1988.  
A quasi-3D mathematical model of coastal morphology. Proc. 21st ICCE, Malaga, Spain.
- GALAPPATTI, R. and VREUGDENHIL, C.B., 1985.  
A depth integrated model for suspended sediment transport. J. Hydr. Res. Vol. 23, No. 4.
- HEDEGAARD, I.B., ROELVINK, J.A., PECHON, P., NICKOLSON, J., and HAMM, L., 1992.  
Intercomparison of coastal profile models. Proc., 23rd ICCE, Venice, Italy.
- KATOPODI, I. and RIBBERINK, J.S., 1990.  
A QUASI-3D model for suspended sediment transport by currents and waves. Proc. 22nd ICCE, Delft.
- KATOPODI, I. and RIBBERINK, J.S., 1992.  
Quasi-3D modelling of suspended sediment transport by currents and waves. Coastal Engineering, Vol 18.
- RIBBERINK, J.S. and DE VRIEND, H.J., 1989.  
VOORDELTA morphological study, Report H526, Delft Hydraulics.
- RIJN, L.C. van, 1986.  
Sedimentation of dredged channels by currents and waves. J. of Waterway Port Coastal and Ocean Eng., Vol. 112, No. 5

## CHAPTER 166

### FIELD OBSERVATION ON SAND RIPPLES UNDER ROUGH SEA STATE

Yoshiaki Kawata<sup>1</sup> M. ASCE, Toru Shirai<sup>1</sup> and Yoshito Tsuchiya<sup>2</sup> M. ASCE

#### Abstract

The process of sediment sorting under rough sea state was made clear in the cross-shore direction. Field observation reveals that ripples can be formed under high shear stress in which the Shields number is more than two. The plane bed condition is observed at narrow area of wave breaking. Strong undertow distorts the shape of ripples. The criterion of bed configuration given by Kaneko (1981) is in good agreement with the field data which were rearranged with significant wave characteristics. The criterion of Komar and Miller (1975) is also applicable with mean wave ones.

#### Introduction

In order to develop 3D model of beach processes, it is necessary to get accurate information about sea bottom topography changes, i.e., sediment structure and small scale undulations. The former is the effect of sediment mixture on transport phenomena. In the nearshore environment, sediment sorting is much developed in comparison with that in rivers, but the assumption of uniform sediment in the longshore and cross-shore directions is too rough to predict accurate beach changes. Bottom roughness mainly depends on the formation of wave-formed ripples.

In the field, some observations were conducted at offshore or continental shelf (Forbes et al. 1987, Boyd et al. 1988) and at shallow water environment under moderate wave conditions (Dingler et al. 1976). So far, the measurements were done with the Shields number of less than one. In our observation, simultaneous measurements were also made about waves, currents and sedimentary structures along the T-shaped Observation Pier (TOP) in the surf zone.

---

<sup>1</sup> Associate Professor, Disaster Prevention Research Institute, Kyoto University, Goka-sho, Uji, Kyoto 611, Japan

<sup>2</sup> Professor, ditto

### Observations

The field experiments were conducted in December 5 and 6, 1989. The bottom topography was measured with the comb in which 60 fine stings (each sting is 23cm long and 3cm spacing each other) with grease spread on the sting surface can stick the fine sediment in the bed and trace out of the unevenness of sea bottom of 1.8m long in the cross-shore direction. The compass and VTR were also equipped on the instrument to record the overall bottom surface conditions and confirm their accurate direction. The grease can catch the fine sediment after sticking into the bed. The total weight of the equipment is about 100kg.

At the same position, bottom sediment sampling was done with the Smith-Mackintire sampler with which surface layer sediment in around 10cm deep was picked up. The standard sieve analysis was applied to the sampled sediment. Sediment-size distributions and their moments were calculated.

Fig.1 shows the measuring points and cross-shore changes of mean sediment diameter before and after storms. The maximum significant wave height was 3.34m and its period was 8.64s and the Shields number estimated by small amplitude wave theory was 4.64. The beach profile in the figure was measured in December 5. The formation of shoal was remarkable and in accompany with acceleration of beach erosion due to construction of west breakwater at Naoetsu harbor the beach changed to a wave energy reflected beach. Table 1 shows characteristics of waves, sediment and bottom topography.

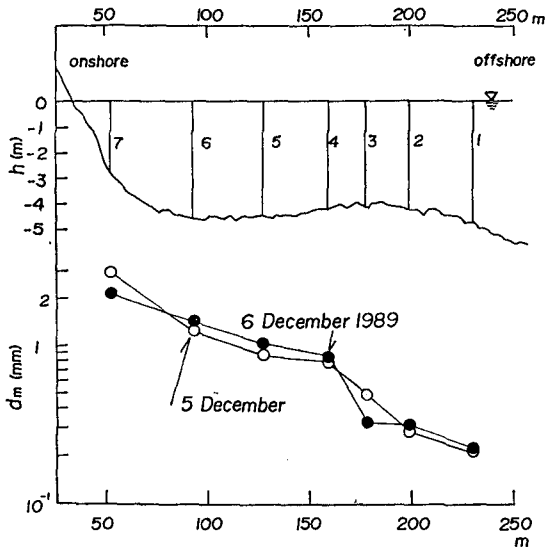


Fig. 1 Measuring points, beach profile and changes of mean sediment diameter in the cross-shore direction

Table 1 Characteristics of waves, sediment and ripples

St.	$H_{1/3}$ (m)	$T_{1/3}$ (s)	$H_m$ (m)	$T_m$ (s)	median diameter $Md\phi$	mean diameter $M\phi$	standard deviation $\sigma\phi$	$\lambda$ (cm)	$\eta$ (cm)
1	3.34	8.6	2.02	6.0	2.32	2.27	0.530	P*	—
2	3.11	7.2	1.88	5.1	1.80	1.87	0.535	P	—
3	3.02	7.2	1.84	5.2	0.90	1.08	0.545	P	—
4	3.02	7.2	1.84	5.2	0.13	0.25	0.460	R	—
5	2.72	5.9	1.66	4.1	-0.02	0.21	0.660	R	—
6	3.04	8.8	1.78	6.2	-0.42	-0.16	0.795	R	—
1	2.50	6.2	1.58	4.8	2.26	2.17	0.565	P	—
2	2.50	6.2	1.58	4.8	1.64	1.62	0.665	47.0	4.5
3	2.58	5.6	1.61	4.4	1.59	1.56	0.605	R	—
4	2.16	5.5	1.36	4.4	0.20	0.31	0.435	121.0	8.1
5	2.16	5.5	1.36	4.4	-0.21	-0.085	0.445	91.5	14.4
6	1.99	4.5	1.27	2.9	-0.50	-0.47	0.455	R	—
7	1.98	4.4	1.12	3.0	-0.68	-0.66	0.430	R	—

\* R : ripple bed, P : plane bed

### Characteristics of sediment

Fig. 2(a) and (b) show the sediment-size distributions with  $\phi$ -scale on a normal probability paper. As already shown in Fig. 1, it was detected that the mean sediment diameter became smaller in the offshore direction and at the end of the TOP the diameter was one tenth of those at the shoreline. Before and after storms, the mean sediment diameter at St. 3 became small and at on and offshore points in the cross-shore direction the sediment changed to rough. This fact shows that relative fine portion of sediment was carried to St. 3 under storm waves. In comparison with Fig. 2(a) and (b), the sediment at St. 3 remarkably became fine after storm. Shirai (1990) has examined annual changes of sediment-size in the cross-shore direction from 1973 to 1979 on the Ogata coast. He pointed out that sediment sorting in a same mother group did not appeared in the field, but eight mother groups of sediment with different mean diameter mixed each other and the four finer sediment groups move in the offshore direction in every storm, even if in summer swell wave conditions. The changes of sediment characteristics in a short-term as shown in Fig. 2 can be regarded as fluctuation of the long-term changes which links to the beach erosion of the Ogata coast.

### Characteristics of bottom topography and its classification

The estimation of bottom roughness depend on the formation of ripples which controls wave transformation and nearshore current system. The field data of bottom roughness were collected with the Shields number of more than four. In our data in Table 1, only three cases include the measurement of height and length of ripples, but in other cases sea bottom conditions were only checked with VTR. With the data, the characteristics of bottom topography could be discussed.

#### (1) Characteristics of bottom topography

Fig. 3(a), (b) and (c) show the bottom topography measured in December 6. The final points of wave breaking were around St. 7, so that it was impossible to measure the bottom topography with the equipment due to rough sediment and washing motion of breaking water. At St. 1, we observed twice. The dominant wave direction was NW, that is parallel to the cross-shore axis of the TOP. VTR recorded as following: St. 1; completely plane bed, Sts. 2 and 3; transition area from ripple bed to plane one. Sts. 4 to 6; irregular (three dimensional) ripples. They were called as irregular ripples or cross ripples (Clifton, 1976). The steep slope crest of ripples were recorded at the vicinity of shoreline. This is due to rapid sorting of sediment by breaking waves, and relatively rough sediment at trough of ripples could not be detected by the measuring stings. After the storms the ripple shape could be clearly measured in December 6, so that the scale was listed in Table 1.



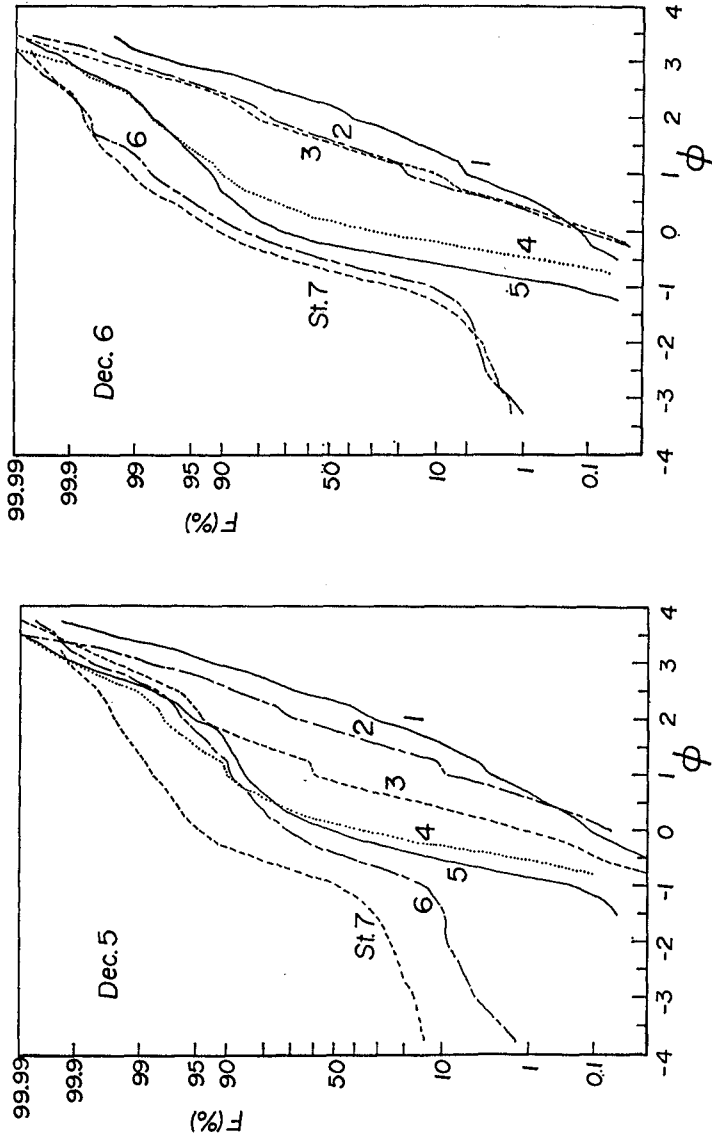
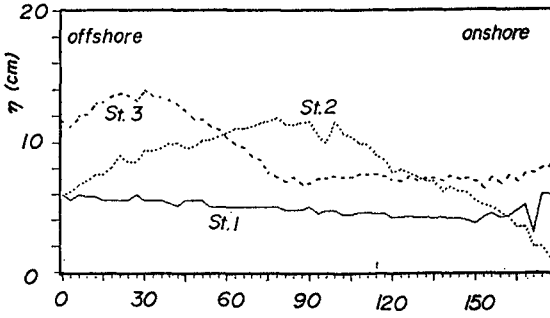
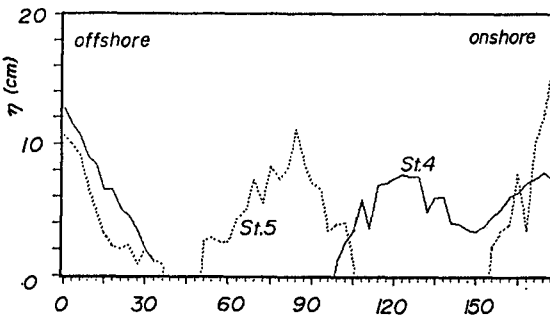


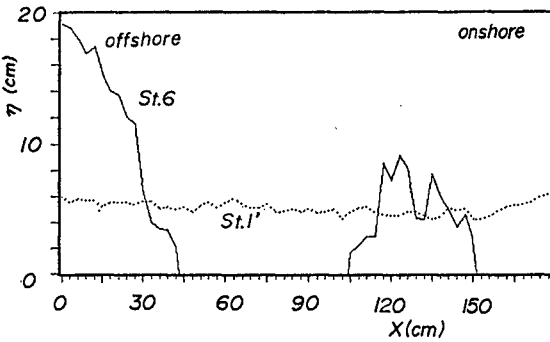
Fig. 2 Sediment-size distributions with  $\phi$ -scale on a normal probability curve



(a) Sts. 1 and 3



(b) Sts. 4 and 5



(c) Sts. 1 and 6

Fig. 3 bottom topography measured

Fig. 4 shows the relationship between  $d_o/D$  and  $\lambda/\sqrt{D}$ , in which  $d_o$ ; trajectory diameter of water particle motion on the bed,  $D$ ; sediment diameter and  $\lambda$ ; ripple length. This relationship was firstly proposed by Clifton (1976). The former ratio shows the effect of acceleration (Abou-Seida, 1964) and the latter ratio was proposed by Bagnold (1946). The data in the figure were collected in the field by Inman (1957) and Dingler et al.(1976). Three open circles shows our data which were calculated with significant wave characteristics. From this figure, it was found that two of them correspond to suborbital ripples whose length is in inverse proportion to  $d_o$  and correlates to  $D$ . Another (the data measured at St. 2 in December 6) exhibits longer length of ripples than usual data. Then, the steepness of ripples was shown in Fig. 5 in which  $u_m$ ; amplitude of water particle velocity on the bed,  $\sigma$  and  $\rho$ ; densities of sediment and water respectively. The semi-empirical curve in the figure was proposed by Dingler et al.(1976). The data measured at St. 2 was plotted far from other data set.

The reason of this discrepancy can be recognized as following: At close to St. 2, we had measured flow velocity at the two points of 1.5m and 2.5m from the bottom with ultra-sonic type current meter. On the Ogata coast, easterly swell waves come after storms and strong undertow at the velocity of 0.5 to 1m/s is generated (Tsuchiya et al., 1989). The wave climate in December 6, 1989 was similar to that at the time when the observation of nearshore currents were carried out. Therefore, the undertow may contribute to the distortion and stretching of the ripple profile.

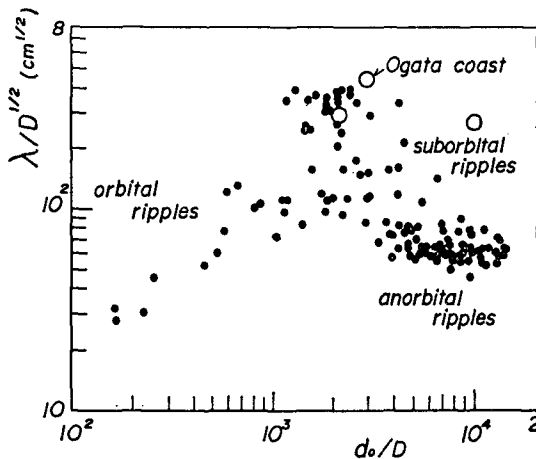


Fig. 4 Relationship between acceleration of wave motion and ripple length (Clifton, 1976)

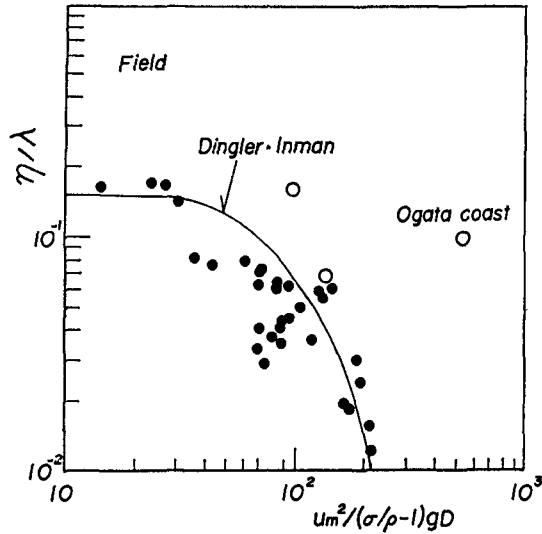


Fig. 5 Relationship between steepness of ripples and dimensionless water particle velocity

## (2) Classification of ripple formation

Fig. 6 shows the classification diagram of wave-ripples formation proposed by Kaneko (1981) in which  $\delta (= \sqrt{2\nu/\omega})$ ; laminar boundary layer thickness,  $\omega$ ; wave frequency and open and black circles show ripple and plane bed conditions respectively. Dimensionless parameters were calculated with small amplitude wave theory using significant wave height and its period. The criterion curves were given by Kaneko (1981). The numbers in the figure show the different kind of ripples such as (1): irregular ripples, (2): two dimensional ripples with steep crest and (3): those with round crest. From this figure it was revealed that the boundary between ripple bed and plane bed can be given by the Kaneko's curve. Moreover, as already shown in Fig. 3, the ripples in a shallow water on the Ogata coast are very irregular so that they belong to ripples in area(1). Therefore, Kaneko's criterion is good for prediction of ripple formation. The arrangement with mean wave height and its period was inadequate.

Fig. 7 shows the relationship between sediment-fluid number  $D_{v*}$  and the Shields number  $\tau_*$ . In the figure, circles with cross bar correspond to significant waves and  $D_{v*} = \{(\sigma/\rho)g/\nu^2\}^{1/3}D$ . The empirical curves in the figure show the boundary between plane bed (black circle) and ripple bed (open circle) and were reduced by Tsuchiya et al.(1987) who used the data of Komar et al.(1975) and Nielsen (1979). The curves slightly changes with the parameter of  $d_o/D$  and in the

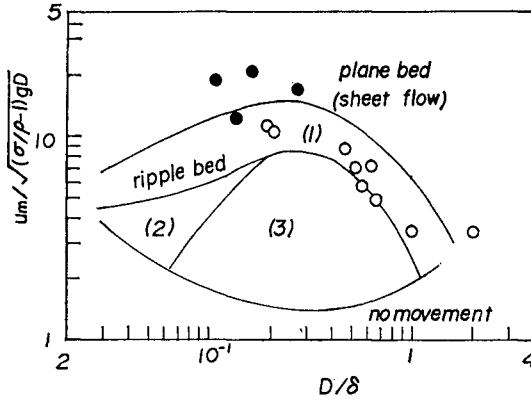


Fig 6 Classification diagram of ripple formation (Kaneko, 1981)

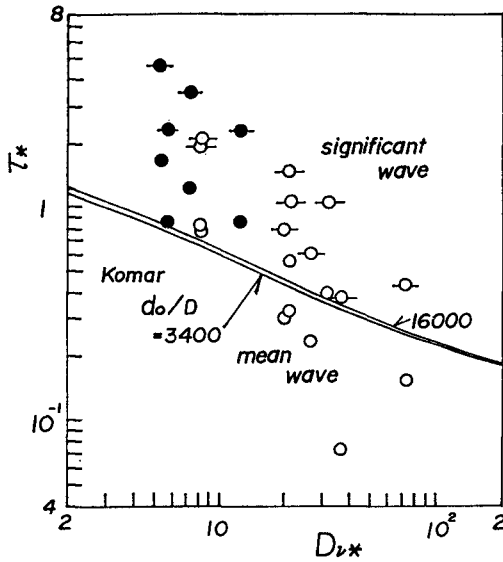


Fig. 7 Classification diagram with sediment-fluid number

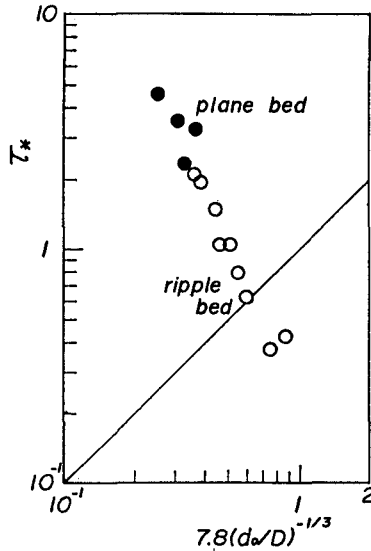


Fig. 8 Classification diagram with wave acceleration

case of calculation with mean wave height and its period, two bed forms can be well divided by the curves.

Fig. 8 shows the criterion of ripple bed and plane bed given by Sato et al.(1987). When we arrange the field data with significant wave characteristics, the criterion can be expressed as,

$$\tau_* = 7.8(d_o/D)^{-1/3} \quad (1)$$

it was found that the curve can not well divide the both bed conditions. The estimation of the Shields number is very difficult in the breaker zone, but Tsuchiya et al.(1987) and Kawata (1989) pointed out that the ratio  $d_o/D$  is not effective to classify such bed conditions.

### Conclusions

The sediment sorting process and classification of ripple formation were analyzed with the field data under storm wave conditions. The major results of this study to date are as following:

1) On the Ogata coast, beach sediment belongs not to single mother group but to eight mother ones. The finer four groups continuously move in the offshore

direction in every storm, therefore beach erosion has been brought in accompany with sediment sorting process.

2) Kaneko's criterion is good for prediction of ripple formation. Relationship between sediment-fluid number and the Shields number is also good to estimate small-scale bottom topography.

### References

- Abou-Seida, M.M. (1964). "sediment transport by waves and currents", Tech. Rep. HEL-2-7, Inst. Eng. Res., Univ. of Cal., 34pp.
- Bagnold, R.A. (1946). "Motion of waves in shallow water, interactions between waves and sand bottoms", Proc. Royal Soc. London, Ser. A, Vol. 187, pp.1-18.
- Boyd, R. et al.(1988). "Time-sequence observations of wave formed sand ripples on an ocean surface", Sedimentology, Vol. 35, pp. 449-464.
- Clifton, H.E. (1976). "Wave-formed sedimentary structures: a conceptual model", Beach and Nearshore Sedimentation, ed. R.A.Davis, Jr. et al., pp.126-148.
- Dingler, J.R. and D.L. Inman (1976). "Wave-formed ripples in nearshore sands", Proc. 15th ICCE, pp. 2109-2126.
- Forbes, D.L. and R. Boyd (1987). "Gravel ripples on the inner Scotian shelf", J. Sedimentary Petrology, Vol. 57, No. 1, pp. 46-54.
- Inman, D.L. (1957). "Wave-generated ripples in nearshore sands", Tech. Memo., No. 100, BEB, pp.66.
- Kaneko, A. (1981). "Oscillation sand ripples in viscous fluid", Proc. JSCE, No. 307, pp. 113-124 (in Japanese).
- Kawata, Y. (1989). "Law of cross-shore sediment transport on a sloping beach", Proc. Coastal Engineering, JSCE, Vol. 36, pp. 289-293 (in Japanese).
- Komar, P.D. and M.C.Miller (1975). "The initiation of oscillatory ripple marks and the development of plane-bed at high shear stresses under waves", J. Sedimentary Petrology, Vol. 45, No. 3, pp. 697-703.
- Nielsen, P. (1979). "Some basic concepts of wave sediment transport", Series Paper No. 20, ISVA, Tech. Univ. of Denmark, 160pp.
- Sato, S. et al.(1987). "Mechanism of sediment transport under irregular oscillating flow and criterion of ripples disappearance", Proc. Coastal Engineering, JSCE, Vol. 34, pp. 246-250 (in Japanese).
- Shirai, T. (1990). "Offshore sediment transport and sediment sorting", unpublished.
- Tsuchiya, Y. and M. Banno (1987). "Patterns of littoral drift and their criterion", Proc. Coastal Engineering, JSCE, Vol. 34, pp. 222-226 (in Japanese).

Tsuchiya, et al.(1989).”Long-term observation of nearshore currents at the breaker zone with a ultra-sonic type current meter”, Proc. Coastal Engineering, JSCE, Vol. 36, pp. 224-228 (in Japanese).



## CHAPTER 167

About Conditions for the Wave Ripple Existence

Ruben D. Kos'yan<sup>1</sup>, Alexander D. Kochergin<sup>2</sup>

### Abstract

For the prognostication of sediment flow during storm period an investigator has to know if there are any microforms at the bottom in a certain place and under certain wave conditions, and what are their characteristics.

On the basis of field and laboratory data we tried to determine the most universal range of conditions for the wave ripple existence.

In the nearshore zone the gradients of near-bottom velocities and shear stress values depend both on wave motion influence upon the erodible bottom and on the bottom form influence upon this motion. To estimate the dependence of hydrodynamical flow structure on the bottom microrelief it is very important to realize in

---

1. Director of the Southern Branch of the P.P.Shirshov Institute of Oceanology, Russian Academy of Sciences. Okeanologiya 353470 Gelendzhik-7 Krasnodar region, Russia.
2. Engineer of the Southern Branch of the P.P.Shirshov Institute of Oceanology, Russian Academy of Sciences. Okeanologiya 353470 Gelendzhik-7 Krasnodar region, Russia

what conditions microforms, usually called ripples, originate, exist and disappear.

The object of this work is to get quantitative estimation of ripple existence on a certain area of the underwater shore slope under the known parameters of surface waves.

It is generally accepted that ripples are formed when near-bottom velocities of water flow slightly exceed those required to set sediment in motion. M. Manohar (1955) estimates the ratio of these velocities as 1, 2 and other authors as 1, 1 (Carstens et al., 1969).

To evaluate the critical velocities for different phases of motion, the relations of the following type are often used:

$$u = K \sqrt{gd} \quad (1)$$

where  $\bar{d}$  is the mean diameter of bed-sediment particles,  $g$  is gravitational acceleration and  $K$  is a constant with some dependence on  $\bar{d}$ . There is a great variety of similar formulae. Beugner (1980) alone gives a selection of 50 equations of this type.

All the criteria for the existence of wave induced ripples differ from similar formulae for progressive flow only in that the maximum value of nearfloor orbital velocity was taken into account rather than the near-floor current velocity. However, some authors (Dingler, 1979; Komar, Miller, 1975; Vongvisessomjai, 1984 and others) indicate that to describe the behaviour of bed particles properly, specific features of the hydrodynamic regimes of various flow types should be considered, the influence of wave period ( $\bar{T}$ ) first of all.

Oscillating water masses affect the erodible floor most visibly when the nearfloor velocity ( $u$ ) becomes maximal. The shorter the surface wave period, the longer the duration of the action of  $u$  during a storm. Moreover, the thickness of the nearfloor boundary layer of

the wave flow is proportional to the square root of the wave period. Thus, waves with shorter periods create favourable conditions for the initiation of sediment motion.

Among the criteria for the initiation of the ripples formation accounting for  $T$  influence, the most common is the empirical equation of P.Komar and M.Miller (1975). It links sediment mobility parameter  $F$  with a ratio of nearbottom orbital diameter  $d_o$  to the sediment particle diameter  $\bar{d}$

$$F_b = b \sqrt{d_o / \bar{d}} \quad (2)$$

where  $F = \frac{\rho u_m}{(\rho_s - \rho) g d}$ ;  $d_o = u_m T / \pi$ ;  $\rho_s$  and  $\rho$  are densities of solid particles and liquid, respectively. To calculate the beginning of ripple formation, the authors propose using a value of the dimensionless coefficient  $b = 0.11$ ; a value of  $b = 0.21$  is used to estimate the initiation of movement of developed ripples.

In some other papers the conditions for the ripple formation are given by the sediment mobility parameter  $F$ :

$$F_b = 3 \quad (\text{Brebner, 1980}) \quad (3)$$

$$F_b = 0.89 (d_o / \bar{d})^{1/3} \quad (\text{Vongvisessomjai, 1984}) \quad (4)$$

$$F_b = 0.033 (d_o / \bar{d})^{2/3} \quad (\text{Kos'yan, 1988}) \quad (5)$$

$$F_b = 0.04 (d_o / \bar{d})^{2/3} \left( \frac{g \bar{d}^3 (\rho_s - \rho)}{\nu^2 \rho} \right) \quad (\text{Dingler, 1979}) \quad (6)$$

where  $\nu$  is a kinematic viscosity coefficient.

The upper limit of ripple existence is controlled by the upper smooth phase of sediment movement when bedforms are obliterated and suspended sediment transport becomes very intensive. According to laboratory tests of Carstens Carstens and others (Carstens et al., 1969), ripples are disappearing when

$$d_o / \bar{d} = 34000 \quad (7)$$

while S.Kennedy and M.Falcon (1965) on the basis of analysis of D.Inman in-situ measurements data (Inman, 1957) got the value:

$$d_o / \bar{d} = 16000 \quad (8)$$

J.Dingler defined the upper limit of ripple existence by mobility factor as:

$$F_c = 240 \tag{9}$$

Having analysed the effect of wave period,

S.Vongvisessomjai (1984) obtained:

$$F_c = 12.7(d_o/\bar{d})^{1/3} \tag{10}$$

In the Kos'yan's paper it was obtained:

$$F_c = 0.54(d_o/\bar{d})^{2/3} \tag{11}$$

The equations (2) - (11) describe the peculiarities of ripple formation more completely than the equation (1) does. But in some cases such limitations may be wrong, as at constant  $U_m$  and  $T$  values, the nature of the bed sediment motion can vary considerably due to artificial damping or increasing of nearbottom turbulence of floor roughness.

The value of the bed tangential stress ( $\tau$ ) takes turbulence and floor roughness into account so it seems logical to use this parameter to characterize the specific interaction between moving water masses and sediment.

The conditions for ripple existence can be determined, for example, by Shield's parameter value ( $\Psi$ ). This parameter expresses the relationship between maximum nearbottom shearing force and the force resisting the wave movement:

$$\Psi = \frac{\tau \bar{d}^2}{(\rho_s - \rho) g \bar{d}^3} = \frac{0.5 f_\tau \rho U_m^2}{(\rho_s - \rho) g \bar{d}} = 0.5 f_\tau F \tag{12}$$

where  $f_\tau$  is a wave friction factor.

According to Nielsen, Shield's parameter, describing the existence of wave ripples varies:

$$\text{from } \Psi_b = 0.04 \quad \text{to} \quad \Psi_c = 1.0 \tag{13}$$

There are another expressions using Shield's parameter for the determination of the upper limit of ripple existence in wave flow:

$$\Psi_c = 4.4 (U_m \bar{d} / \nu)^{-1/3} \quad (\text{Komar, Miller, 1975}) \tag{14}$$

$$\Psi_c = 0.5 - 0.6 \quad (\text{Horikawa et al., 1982}) \tag{15}$$

To verify the criteria for conditions of wave ripple existence and to deduce our own one we used our own laboratory tests and field observations results and those available from literature.

Variation ranges of laboratory test characteristics (Antsyferov et al., 1977; Keremetchiev, private report; Manohar, 1955; Miller, Komar, 1980b; Nielsen, 1979) is given in table 1.

Variation ranges of field observation parameters (Inman, 1957; Kos'yan, 1988; Miller, Komar, 1980a; Nielsen, 1984; Tanner, 1971) are summarized in table 2.

In all the tests the fact of ripple existence under certain parameters of surface waves and of solid particles and liquid characteristics was noted. For all this, the ripple characteristics and forms were not taken into account. In Manohar's experiments (Manohar, 1955) some measurements were made in the moments of ripple disappearance.

V. Tanner (1974) carried out sea works under low waves, when the maximal nearbottom velocities were wittingly less than the shifting ones. In this case only passive ripples were observed, therefore sea data obtained by V. Tanner were not used in this paper. Only his observations in lakes were used. The selection of experimental data obtained by M. Miller and P. Komar (1980a) was made according to their recommendations.

Amplitudes of nearbottom orbital velocities during ripple observations were calculated using the Airy wave theory, when analyzing the data of sea investigations the values of significant (calculated from the height of mean from one third of the largest waves of a group) orbital velocities were taken into account. According to existing estimates (Kos'yan, 1985; Miller, Komar, 1980a; Nielsen, 1981) parameters of these particular waves determine the nature of sediment movement, when waves are irregular. Using these parameters one may

Table 1.

$U_m$ cm/sec	T sec	H m	$\bar{d}$ mm	$d_o$ cm	$h_r$ cm	Number of mea- suring	Author
8.0-42.0	1.0-1.5	0.1-0.5	0.2-0.3	6.5-24.0	1.5-5.5	383	Keremetchiev, private report
20.0-23.0	1.8-2.4	0.6-0.7	0.24	16.0-18.0	4.5-5.0	6	Antsyferov et al., 1977
34.5-69.7	1.9-10.1	-	0.28-1.06	4.6-33.6	0.1-1.9	196	Manohar, 1955
30.1-50.2	3.0-5.0	0.3	0.17	0.13-16.0	-	4	Miller, Komar, 1980
10.3-41.5	1.0-1.7	0.4	0.08-0.55	2.5-16.6	0.41-2.7	89	Nielsen, 1979
14.0-90.0	1.7-13.9	0.12-0.657	0.127-0.646	4.0-139.5	0.1-13.5		Dingler, 1974

Table 2

$U_m$ cm/sec	T sec	H m	$\bar{d}$ mm	$d_o$ cm	$h_r$ cm	Number of mea- suring	Author
16.0-95.0	2.7-6.3	0.7-18	0.08-1.45	5.0-300	0.5-50	89	Kos'yan, 1988
6.1-73.1	0.7-16.0	0.05-33.5	0.081-0.913	2.0-155	0-19.8	89	Inman, 1957
13.3-158.1	0-18.2	3.1-21.3	0.17-0.29	7.6-27.1	-	27	Miller, Komar, 1980
51.0-102.0	5.7-12.9	1.3-1.8	0.11-0.61	35-80	4.3-15	30	Nielsen, 1984
15.9-53.0	0.8-6.2	0.2-0.6	0.13-0.71	3.5-14.6	0.5-3.4	6	Tanner, 1971

compare the results of field works with laboratory tests data, obtained under monochromatical waves.

Equations (1) - (15) limiting the area of wave ripple existence were verified by experimental data. The results of some verifications were published earlier in the works of Kos'yan, 1978; Kos'yan, Pykhov, 1991. Figures 1 - 3 show the typical examples of such verified comparisons of measured and calculated values.

On the basis of accomplished comparisons we can make some conclusions:

1. Various boundary conditions of ripple existence differ greatly from each other, which might result, possibly, from the fact that each author, while deducing his own equation, used a relatively small number of data on ripple observation.

2. The results of verifications show that such criteria as equations (2), (4), (6), (8), (10), (14), (15) are not fulfilled as a great number of test points lie beyond the limits of ripple existence.

3. Almost all of the observation results remain in the range of equations (1), (3), (7), (9), (13). But overwhelming majority of test points lie far from the curves described by these equations. Therefore these criteria may be used only for a rough evaluation of the conditions for ripple formation and flattening.

4. All experimental points, corresponding to the conditions for ripple existence on any coordinate systems occupy the surface contoured on the every side, while the given criteria contour it partially only on one side.

Combining criteria of all authors which give satisfactory results when being compared with field observation data, one can get a range of conditions for ripple existence. In this case this range will be described by the systems of equations which roughly contours the



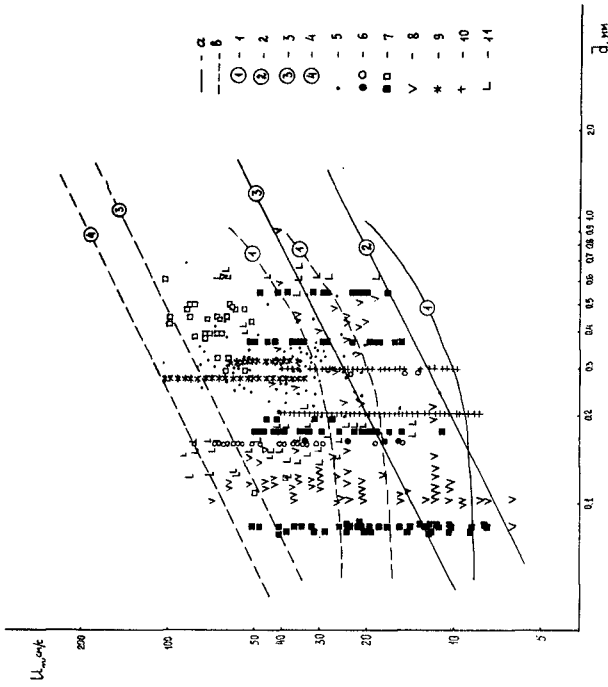


Figure 1. Verified comparison of measured and calculated values  
 a) ripple formation; b) ripple flattening. 1 - Murina, Halpin, 1981;  
 2 - Brebner, 1980; 3 - Vongvissomjai, 1984; 4 - Dingler, 1974;  
 5 - Kos'yan, 1988; 6 - Miller, Komar, 1980; 7 - Nielsen, 1979, 1984;  
 8 - Inman, 1957; 9 - Manohar, 1955; 10 - Keremetchiev, private report;  
 11 - Dingler, 1974.

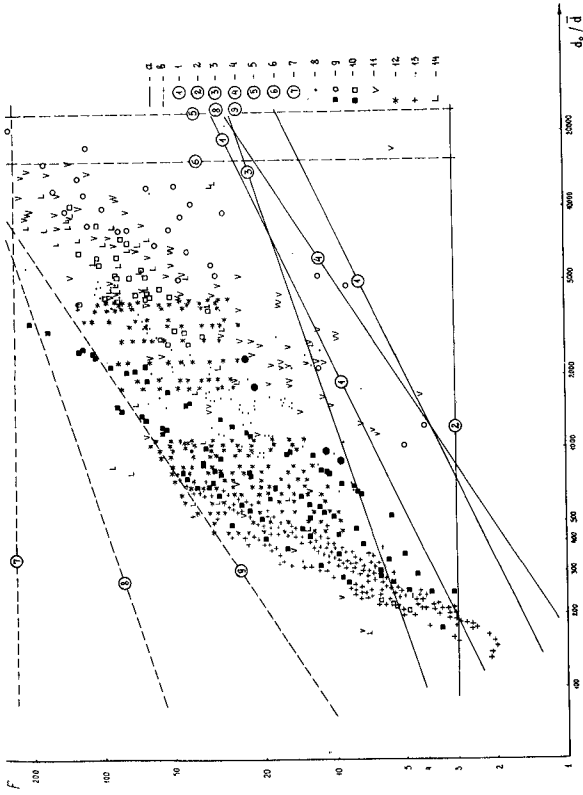


Figure 2. Verified comparison of measured and calculated values  
 a) ripple formation; b) ripple flattening; 1 - Miller, Komar, 1980;  
 2 - Brebner, 1980; 3 - Vongvisessomjai, 1984; 4 - Kos'yan, 1988;  
 5 - Carstens et al., 1969; 6 - Kennedy, Falcon, 1965; 7 - Dingler, 1974;  
 8 - Kos'yan, 1988; 9 - Miller, Komar, 1980; 10 - Nielsen, 1979 and 1984;  
 11 - Inman, 1957; 12 - Manohar, 1955; 13 - Keremetchiev, private report;  
 14 - Dingler, 1974.

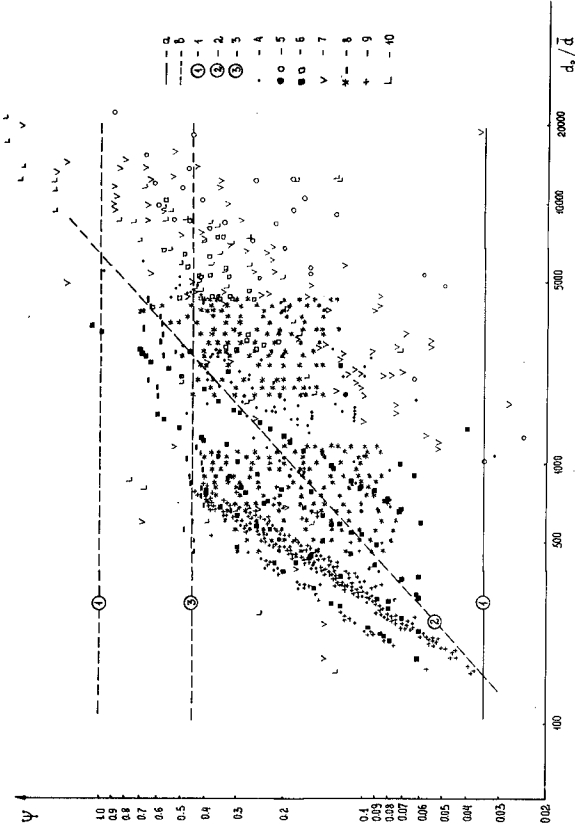


Figure 3. Verified comparison of measured and calculated values

- a) ripple formation; b) ripple flattening
- 1 - Nielsen, 1979; 2 - Kos'yan, 1990; 3 - Horikawa et al., 1982;
- 4 - Kos'yan, 1988; 5 - Miller, Komar, 1980; 6 - Nielsen, 1979 and 1984;
- 7 - Inman, 1957; 8 - Manohar, 1955; 9 - Keremetchiev, private report;
- 10 - Dingler, 1974.

field of points from every side (Kos'yan, Pykhov, 1991).

Let's try to express conditions for ripple existence by the single equation which contours the entire observation field as close as possible.

Universal conditions for bottom form existence accounting for the influence of both the wave period and roughness of bottom may be obtained in the coordinate system of  $\Psi$ ,  $d_0/\bar{d}$ . Best of all the whole field of experimental points is contoured by the ellipsis equation with the following parameters:

$$\frac{(-5.80 + 0.88 \ln d_0/\bar{d} + 0.47 \ln G)^2}{8.41} + \frac{(5 - 0.47 \ln d_0/\bar{d} + 0.88 \ln G)^2}{1.69} = 1 \quad (16)$$

This expression may be simplified and reduced to typical square equation.

In fig. 4 one can see a comparison of experimental data with those calculated by the formula (16). Here the curve (16) contours the absolute majority of test points ( $\sim 98,8\%$ ) very closely from every side. Besides the curve (16) shows a good agreement with results obtained by Manohar for ripple flattening.

Should new results of ripple observations appears, some correction of eqn. (16) parameters determining the dimensions of the ellipsis and its incline to coordinate axes will become possible. But we believe that such a correction will be insignificant.

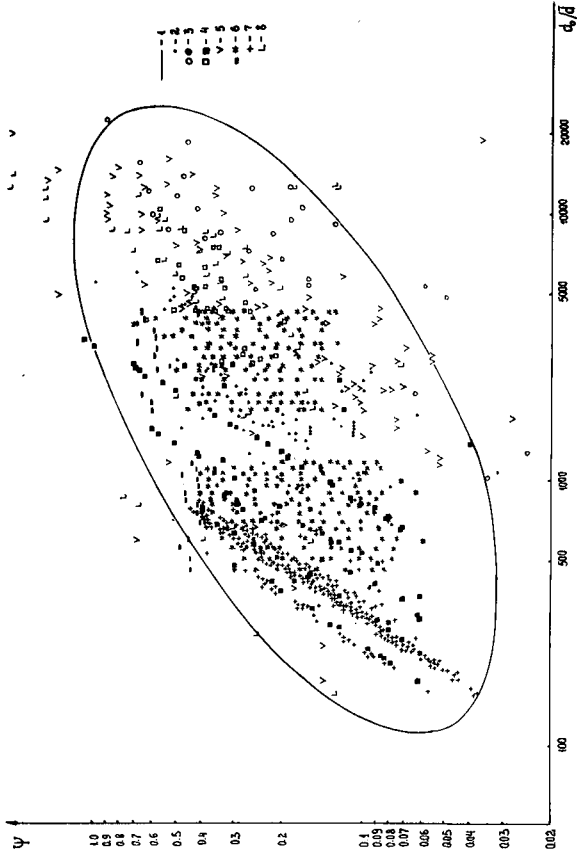


Figure 4. Field of experimental points contoured by the equation (16)  
 1 - equation (16); 2 - Kos'yan, 1988; 3 - Miller, Komar, 1980;  
 4 - Nielsen, 1979 and 1984; 5 - Inman, 1957; 6 - Manohar, 1955;  
 7 - Keremetchiev, private report; 8 - Dingler, 1974.

## References

1. Antsyferov S.M., Kos'yan R.D., Onishenko E.L., Pykhov N.V. About possibility of the suspended sediment concentration measuring in the sea by traps. *Oceanology*, 1977, v.17, N 6, p.1118-1122 (in Russian).
2. Beugner A., 1980. Choice of flow formulae for small plain rivers with non-eroding velocity in GDR. Tr. Tashk.Inst.Iuzh.Irrig. Mekh., 112:76-86 (in Russian).
3. Brebner A., 1980. Sand bed-form length under oscillatory motion. Proc. Coastal Eng. Conf., 17th (Sydney), 2, 1340-1343.
4. Carstens M.R., Nielsen F.M. and Altinbilek H.D., 1969. Bed form generated in the laboratory under an oscillatory flow: analytical and experimental study. U.S. Army Coastal eng. Res. Cent. Tech. Memo, 28:39 pp.
5. Dingler J.R., 1974. Wave-formed ripples in nearshore sands. Ph.D. Thesis, Univ. California, San Diego, 136pp.
6. Dingler J.R., 1979. The threshold of grain motion under oscillatory flow in a laboratory wave channel. *J.Sediment Petrol.*, 49(1): 287-294.
7. Horikawa K., Watanabe A., Katori S. Sediment transport under sheet flow condition // Proc. 18-th coast eng.conf. 1982, p.1335-1352.
8. Inman D.L., 1957. Wave generated ripples nearshore sands. U.S. Army Corps. Eng., Beach Erosion Board Tech. Memo., 100: 67pp.
9. Kennedy I.F., Falcon M. Wave-generated sediment ripples // M&T. Hydrodyn. Lab. Rept. 1965, N 86, 55pp.
10. Komar P.D. and Miller M.C. 1975. The initiation of oscillatory ripple marks and the development of plane beds at high shear stresses under waves. *J.Sediment Petrol.*, 45(3): 697-703.
11. Kos'yan R.D. Vertical distribution of suspended sediment concentrations seawards of the breaking zone // *Coast. Eng.* 1985, vol. 9, p.-171-187.

12. Kos'yan R.D. On the dimensions of passive ripple marks in the nearshore zone // *Mar.Geol.* 1988A, vol.80 p.149-153.
13. Kos'yan R.D. Study of Microforms in the nearshore zone // *Mar.Geol.*, 1988B, vol. 83, p.63-78.
14. Kos'yan R.D., Pykhov N.V. Hydrogenous sediment shift in the coastal zone. Nauka, Moscow, 1991, 280p (in Russian).
15. Manohar M., 1955. Mechanics of bottom sediment movement due to wave action. U.S.Army Corps.Eng. Beach Erosion Board Tech. Memo., 75: 121pp.
16. Miller M.C. and Komar P.D., 1980a. A field investigation of the relationship between oscillation ripple spacing and the near-bottom water orbital motions. *J.Sediment Petrol.* 50: 183-191.
17. Miller M.C., Komar P.D., 1980b. Oscillation sand ripples generated by laboratory apparatus. *J.Sediment Petrol.*, 50: 173-182.
18. Murina E.U. and Halfin I.Sh., 1981. Research on bottom critical velocities during storms. *Vodn.Resus.*, 5: 115-120 (in Russian).
19. Nielsen P., 1979. Some basic concepts of wave sediment transport. *Inst.Hydrodyn.Hydraul.Eng.*, Tech.Univ. Denmark, Ser. Pap. 20, 160 pp.
20. Nielsen P., 1981. Dynamics and geometry of wave generated ripples. *J.Geophys.Res.* 86(7): 6467-6472.
21. Nielsen P. Field measurements of time - averaged suspended sediment concentrations under waves // *Coast. eng.* 1984, vol. 8, p.51-72.
22. Tanner W.H. Numerical estimates of ancient waves, water depth and fetch // *Sedymentology*, 1971, v.103, N 4, p. 439-442.
23. Vongvisessomjai S., 1984. Oscillatory ripple geometry. *J. Hydraul.Eng.* 10(3): 247-266.

## CHAPTER 168

### SUPERTANK LABORATORY DATA COLLECTION PROJECT

Nicholas C. Kraus<sup>1</sup>, Jane McKee Smith<sup>2</sup>, Charles K. Sollitt<sup>3</sup>

**ABSTRACT:** In the summer of 1991, a multi-institutional cooperative laboratory data collection project called SUPERTANK was conducted to investigate cross-shore hydrodynamic and sediment transport processes using the large wave channel located at Oregon State University, Corvallis, Oregon. The channel is 104 m long, 3.7 m wide, and 4.6 m deep, into which a 76-m long sandy beach was emplaced. SUPERTANK is believed to be the most densely and comprehensively instrumented nearshore processes data collection project performed in the laboratory or the field. At the peak of data collection, the channel was instrumented with 16 resistance wave gages, 10 capacitance wave gages, 18 two-component electromagnetic current meters, 34 optical backscatter sensors (OBS), 10 pore-pressure gages, 3 acoustic sediment concentration profilers, 1 acoustic-Doppler current profiler, 1 four-ring acoustic benthic stress gage, 1 laser Doppler velocimeter, 5 video cameras, and 2 underwater video cameras. Broad- and narrow-band random waves and monochromatic waves were run with zero-moment wave heights in the range of 0.2 to 1.0 m and with peak spectral periods in the range of 3 to 10 sec. The wave generator absorbed waves at the peak spectral frequency that were reflected from the beach and structures such as dunes and seawalls. Twenty major data collection runs were made, most defined as starting from a new beach profile, and approximately 350 profile surveys were taken to record beach response during the 129 hr of wave action. This paper gives an overview of the SUPERTANK project and presents example results.

#### INTRODUCTION

The design of beaches to protect against storm erosion, flooding, and wave attack requires quantitative prediction of cross-shore hydrodynamics, sediment transport, and beach profile change. Large wave tanks (LWT) capable of producing waves and beach profile change without scale effects provide an inexpensive means, as compared with field data collection, to obtain data for developing mathematical models of cross-shore processes and to investigate fundamental hydrodynamic and sediment-transport processes under controlled conditions.

---

(1) Senior Scientist, and (2) Research Hydraulic Engineer, USAE Waterways Experiment Station, Coastal Engineering Research Center, 3909 Halls Ferry Road, Vicksburg, MS, 39180-6199, USA; (3) Professor and Director, O. H. Hinsdale Wave Research Laboratory, Department of Civil Engineering, Oregon State University, Corvallis, OR, 97331-2302, USA



A limited number of LWT experiments on beach change have been performed (e.g., Kajima et al. 1982, Vellinga 1986, Dette and Uliczka 1987) since the pioneering study of Saville (1956) and related U.S. Army Corps of Engineers tests (Kraus and Larson 1988), but none has taken advantage of the full range of modern instrumentation to capture the breadth of processes acting across the profile.

In support of numerical model development activities for predicting storm-induced beach erosion (Larson and Kraus 1989), in May 1987 the Coastal Engineering Research Center (CERC) at the U.S. Army Engineer Waterways Experiment Station began planning of a LWT data collection project that was called SUPERTANK. As planning progressed, it was realized that the offshore region would provide an ideal environment for hydrodynamics (waves and currents) and sediment transport measurements by researchers concerned with movement of dredged sediment placed seaward of the surf zone. Thus, one unique characteristic of SUPERTANK was utilization of the entire length of the beach in the LWT channel, extending from near the wave generator through the surf zone to the limit of runup.

This paper presents an overview of the SUPERTANK Laboratory Data Collection Project. Project planning and the major test series are described, and example results are given from the hydrodynamics and beach profile measurements.

## PROJECT PLANNING

SUPERTANK was conducted as a multi-institutional effort similar to cooperative field data collection projects first performed in the 1970s, for example, the Nearshore Sediment Transport Study (NSTS) in the United States (Seymour and Duane 1978), the Nearshore Environment Research Center (NERC) project in Japan (Horikawa and Hattori 1987), and U.S. Army Corps of Engineers-sponsored projects such as DUCK85 (Mason, Birkemeier, and Howd 1987) and SUPERDUCK (Birkemeier et al. 1989). Cooperative efforts that pool expertise, instrumentation, and a wide range of research interests have led to advances unattainable by a single or small group of investigators. The advantages of cooperative research were readily carried over to the LWT environment of SUPERTANK.

Pre-project planning was led by a 6-person steering committee formed of CERC and non-CERC members initially divided in the three basic subject areas of (1) hydrodynamics, (2) sediment transport, and (3) beach profile change, including beach and structure interaction. During the course of periodic planning meetings, steering committee members and principal investigators formed into three operational groups as (1) total-channel hydrodynamics and sediment transport, (2) foreshore and beach profile change, including swash zone hydrodynamics, and (3) instrument tests and measurements made offshore that centered around acoustic instruments and a laser-Doppler velocimeter.

Participants joining CERC at SUPERTANK came from the Florida Institute of Technology, Naval Postgraduate School, North Carolina State University, Ohio State University, Oregon State University, QUEST Integrated, Inc., RD Flow, Inc., Seatech, Inc., U.S. Naval Academy, University of California at Santa Cruz, University of Delaware, University of Florida, and University of Washington. Observers came from the Danish Hydraulics Institute (Denmark), Delft Hydraulics Laboratory (The Netherlands), and one investigator from Nihon University (Japan) actively participated. U.S. Army Corps of Engineers field office personnel and undergraduate and graduate students from various institutions around the U.S. assisted SUPERTANK investigators in data collection.

## PROCEDURE

### Planning

SUPERTANK was conducted using the LWT located at the O.H. Hinsdale Wave Research Laboratory (WRL), Oregon State University. This LWT has the largest wave channel in the United States in which a sandy beach can be emplaced. SUPERTANK subsequently ran for the 8-week period from July 29 to September 19, 1991. With the first and last weeks dedicated to mobilization and demobilization, data were collected over the six weeks from August 5 through September 13. Two 1-week tests of instruments were conducted six months and 1 month before the start of SUPERTANK. These valuable shakedown exercises were one reason that full-scale data collection proceeded without major problems and virtually no instrument down time.

The daily work schedule was 12 hours of wave action and associated activities from Monday through Thursday and 8 hours on Friday, starting from a daily meeting of principal investigators at 7 am. Plans for the day were reviewed and optimized at the morning meetings and in the evenings, for which data taken that day, particularly the beach profile change data, were inspected. Evenings and weekends were spent in major mechanical operations of beach profile reconstruction, emplacement and removal of dunes and seawalls, and inspection and moving of instruments, for which the tank was drained. For example, changes in wave conditions from higher to lower waves required shoreward translation of large numbers of instruments to optimize measurement coverage in the vicinity of the breaker zone and in the surf zone.

Previous LWT projects (and most small-scale laboratory experiments) on beach profile change typically initiated all tests from the same uniform slope in a test series, which required substantial sand transfer and profile regrading with heavy equipment. In the case of SUPERTANK, where a large number of researchers were on site and an even larger number of instruments were mounted in the tank, extensive regrading of the profile, with the associated delays, was not economically feasible or compatible with investigators' schedules. Execution of the pre-planned test series was modified and redirected as necessary through observation of the data (almost all data sets could be inspected during collection or shortly thereafter) and discussion by investigators participating in the particular test.

### Channel, Equipment, and Operating Procedures

The channel of the LWT at the WRL is 104 m long, 3.7 m wide, and 4.6 m deep, into which a 76-m-long beach was constructed for the SUPERTANK project. Fig. 1 shows the interior of the WRL enclosure, and Fig. 2 is a view of the LWT during an instrument change. The beach was composed of approximately 600 cu m of uniform-size quartz sand of 0.22-mm median diameter. The direct, digital controlled servo-hydraulic wave generator was equipped to absorb waves at the peak spectral frequency that were reflected from the beach and structures, such as dunes and seawalls. Broad- and narrow-band random waves and monochromatic waves were run with zero-moment wave heights in the range of 0.2 to 1.0 m and with peak spectral periods in the range of 3 to 10 sec. Waves were run in "bursts" of typically 10, 20, 40, and 70-min duration to enable profile surveys to be made in calm conditions, to adjust instruments and measure elevation changes at the Optical Backscatter (OBS) sensors, and to suppress tank seiching.



Fig. 1. Wide-area view of LWT channel and control room during SUPERTANK

SUPERTANK is believed to be the most densely and comprehensively instrumented nearshore processes data collection project conducted in the laboratory or field. At the peak of data collection activities, the LWT channel was instrumented with 16 resistance wave gages, 10 capacitance wave gages, 18 two-component electromagnetic current meters, 34 OBS sensors, 10 pore-pressure gages, 3 acoustic sediment concentration profilers, 1 acoustic-Doppler current profiler, 1 four-ring acoustic benthic stress gage, 1 laser-Doppler velocimeter, 5 video cameras, and 2 underwater video cameras. The resistance wave gages, capacitance wave gages, and electromagnetic current meters formed the core of SUPERTANK data collection and were maintained throughout the project. Synchronous sampling by separate data acquisitions systems was accomplished by digital input of WWV time code to all computer clocks.

### CORE MEASUREMENTS

Core measurements constitute data collection fundamental to all investigators. The core measurements consist of wave and current data collection and beach profile surveys. CERC investigators were responsible for these measurements.

### Hydrodynamics

Wave transformation was measured with 16 resistance wave gages mounted on the west channel wall (right side of LWT in Fig. 2), spaced 3.7 m apart. The array of resistance gages extended from near the wave generator to a water depth of approximately 0.5 m. An array of 10 capacitance wave gages extended from the most shoreward resistance gage to the maximum runup limit. These gages were also mounted from the west channel wall, but they were mobile with spacing that varied from 0.6 to 1.8 m. In addition to measuring wave



Fig. 2. Close-up view of LWT with SUPERTANK instrumentation

transformation, the capacitance gages also measured runup and the elevation of the sand surface at gages that were intermittently submerged (Fig. 3). Fourteen Marsh-McBirney electromagnetic current meters were mounted on the east channel wall together with arrays of OBS (Fig. 4). The current meters were deployed in vertical arrays of 1 to 4 sensors with vertical spacing of approximately 0.3 m, designed to quantify the undertow profile. Each array was configured to share a timing pulse (close-proximity option) to reduce electronic interference. The meters were deployed in depths of 0.3 to 1.8 m, with selection of sensor position based on the wave conditions, water level, and bottom profile. An additional 4 electromagnetic current meters, 5 OBS, and 1 capacitance wave gage were deployed on a roving carriage (Fig. 5). The current meters were arranged in a vertical array (0.3-m spacing) off an adjustable wing extending beneath the carriage. The carriage was positioned prior to each test to locate the wave gage, current meters, and OBS sensors in the incipient breaking zone, adjacent to a wall-mounted current meter array (for finer vertical resolution), or some other point of interest. Three video cameras, mounted on a scaffold overlooking the surf zone, recorded a continuous image of surf-zone wave transformation, swash, and runup. Ten pressure gages were buried in the sand beach to measure pore pressure.

Portions of the hydrodynamic data were analyzed (spectra and time series) during or immediately after the tests for quality control and planning of subsequent tests. The instrumentation performed extremely well during the project. Instrument noise and cross-talk problems were identified and eliminated prior to the main project in shakedown tests. The wave gages were calibrated once a week during the project by raising and lowering the water level. Wave gage offsets were recorded at the beginning of each test. The current meters were calibrated before and after the project.



Fig. 3. Capacitance bed surface and water surface gages on the foreshore



Fig. 4. Vertical arrays of current meters and optical backscatter sensors



Fig. 5. Roving instrument carriage fully configured at SUPERTANK

The SUPERTANK wave conditions were designed to balance the need for repetition of wave conditions to move the beach profile toward equilibrium and development of a variety of conditions for hydrodynamics studies. The TMA spectral shape, applicable to finite water depths (Bouws et al. 1985), was used to design all random-wave tests, with spectral width parameter  $\gamma$  between 1 (broad-banded) and 100 (narrow-banded). Other parameters that controlled the hydrodynamics, such as water level, bottom profile shape, and shoreward boundary (seawall, dune, and terrace), also varied between tests, changing the nearshore hydrodynamics for the same imposed offshore wave conditions. Low-frequency wave energy (frequencies lying below that of the incident band) did not increase with increasing run length as might be expected due to build-up of channel seiching.

A three-day series of tests conducted during the third week was dedicated to hydrodynamics. These tests included time-varying wave conditions, varying spectral width, and bimodal spectra. The hydrodynamic data will be used to develop and verify advanced hydrodynamic models (vertical current structure, wave breaking, transformation of bimodal spectra, wave setup, and nonlinear wave transformation), as well as support modeling of beach profile change and sediment transport.

### **Beach Profile Change**

Approximately 350 full-length surveys were performed to record the response of the beach profile to wave action and to changes in shoreward boundary conditions, such as emplacement of a seawall. Surveys were made with an auto-tracking infra-red geodimeter, which targeted a prism attached to a survey rod mounted on a carriage that was pushed along the channel by two persons. The survey rod, which could move freely in a sleeve with guide

rollers, made contact with the bed via a pair of wide-tread wheels. Typically, 15 minutes were required to set up equipment and survey the profile with a nominal spacing of 0.3 m, but with much finer resolution over features such as dunes, steps, and bars which had large across-shore gradients in elevation. At the start and end of a major test, the profile was surveyed along the center line of the channel and on lines located 0.9 m from each of the channel walls to assess uniformity of the profile across the channel width. Three-line surveys also were occasionally made when cross-tank flow was observed or suspected. In between wave bursts, surveys were made only along the center line.

Observation of the profile rod wheels indicated a nominal penetration depth of a few millimeters, depending on sediment compaction; this depth would tend to cancel in quantitative comparison of differences between profile surveys. Survey measurements were recorded to the nearest 3 mm in horizontal distance and elevation. Performance of the profiling system was evaluated by conducting 10 consecutive profile surveys in which the four survey crew members rotated in and out of the operation. The 10 unedited profile surveys and the standard deviation in profile elevation are plotted in Fig. 6. The standard deviation is typically less than 0.5 cm. The large deviation in one area offshore was caused by rod operator error in one survey and is easily detected in the data file and corrected.

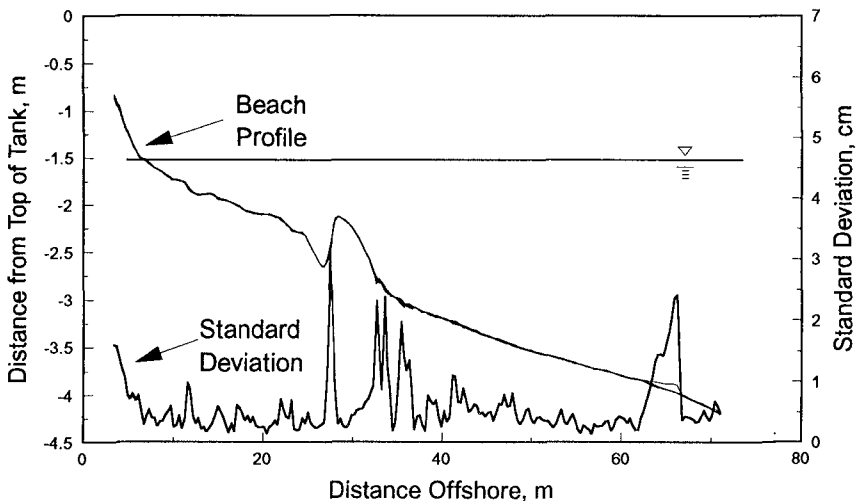


Fig. 6. Plots and standard deviation of ten consecutive beach profile surveys

Although not strictly part of the core measurements, OBS and fluorescent sand tracer measurements were supported by CERC and conducted by Drs. Reginald Beach and Paul Komar of Oregon State University. The fluorescent sand tracer experiments required sampling by SCUBA-equipped divers, and divers also measured and adjusted, as necessary, the bed-referenced elevations of OBS and other sensors at the end of each wave burst. The tracer experiments measured dispersion of sand in the offshore, as a comparison to transport

rates obtained with the OBS, and recorded macro-scale movement and layering of sand in regions of rapid morphologic change, such as in areas of bar formation and dune erosion.

### Test Series

The 20 major data collection tests performed are listed in Table 1. Wave conditions designed to produce erosion or accretion were selected through use of predictive criteria described by Kraus, Larson, and Kriebel (1991). Several tests had objectives separate from monitoring evolution of the beach profile, such as dedicated hydrodynamic, suspended sediment, and instrument tests that examined local fluid and sediment transport conditions. Representative wave conditions are listed in Table 1. For tests involving random waves, the wave height is the significant (zero-moment) height, and the period is the peak spectral period. Sixty-six different wave conditions were run for a total of 129 hr of wave excitation; 70 percent of the wave conditions involved random waves.

Test Number	Description	Date	Representative Significant Wave	
			Height m	Period sec
ST_10	Erosion toward equilibrium, random waves	8/05 – 8/09	0.8	3.0
ST_20	Acoustic profiler tests (random; monochromatic)	8/11 – 8/13	0.2-0.8	8.0-3.0
ST_30	Accretion toward equilibrium, random waves	8/14 – 8/16	0.4	8.0
ST_40	Dedicated hydrodynamics	8/19 – 8/21	0.2-0.8	8.0-3.0
ST_50	Dune erosion, Test 1 of 2	8/22 – 8/22	0.5-0.8	6.0-3.0
ST_60	Dune erosion, Test 2 of 2	8/23 - 8/23	0.5-0.7	6.0-3.0
ST_70	Seawall, Test 1 of 3	8/26 - 8/26	0.7-1.0	4.5
ST_80	Seawall, Test 2 of 3	8/27 – 8/27	0.7	4.5
ST_90	Berm flooding, Test 1 of 2	8/28 am	0.7	3.0
ST_A0	Foredune arosion	8/28 pm	0.7	3.0
ST_B0	Dadicated suspended sediment	8/29 – 8/30	0.3-1.0	10.-3.0
ST_CO	Seawall, Test 3 of 3	9/02	0.4-0.8	8.0-3.0
ST_DO	Berm flooding, Test 2 of 2	9/03 am	0.7	3.0
ST_E0	Lasar Doppler velocimeter, Test 1 of 2	9/03 pm	0.2-0.8	3.0
ST_F0	Laser Doppler velocimeter, Test 2 of 2	9/04 am	0.2-0.7	8.0
ST_GO	Erosion toward equilibrium, mono. waves	9/04 pm	0.8	3.0
ST_H0	Erosion, transition toward accretion, mono. waves	9/05 am	0.5-0.8	4.5-3.0
ST_I0	Accretion toward equilibrium, mono. waves	9/05 – 9/06	0.5	8.0
ST_J0	Narrow-crested offshore mound	9/09 – 9/11	0.5-0.7	8.0-3.0
ST_K0	Broad-crested offshore mound	9/12 – 9/13	0.5-0.7	8.0-3.0



## EXAMPLE RESULTS

In this section we present example results from Test ST\_10 (Table 1), the first and longest test (21 hr of wave action) of SUPERTANK. This test was conducted to observe beach response to erosive random waves together with the associated hydrodynamics and sediment transport. Selected results illustrate beach profile response to random and monochromatic waves, and wave transformation and vertical structure of the mean cross-shore current.

### Profile Change

The beach was configured as a planar foreshore joining to the subaqueous portion formed in a concave shape as  $h = Ax^{2/3}$ , where  $h$  is still-water depth and  $x$  is horizontal distance from the shoreline. Several wave conditions were imposed, starting from an 8-sec, 0.8-m zero-moment wave for the first 400 min of wave action ( $\gamma = 20$  for first 270 min, followed by runs with  $\gamma = 3.3$  or 20), 70 min of monochromatic 3-sec, 0.8-m waves, and 80 min of 3-sec, 0.8-m waves, after which the period was increased to 4.5 sec and water level lowered by 0.15 m to move the bar and to increase runup for promoting change in the foreshore.

Fig. 7 shows beach profile evolution in ST\_10 starting from the initial profile for selected times of 60, 290, 470, and 820 min of wave action. For clarity, the profile was truncated seaward of the bar at a depth of 3 m. After 60 min, the foreshore had already eroded and a break-point bar had formed. By 290 min, the foreshore had eroded considerably, and a gradually sloping terrace formed that led to a trough followed by a substantial bar; this beach configuration did not change appreciably under another 110 min of similar wave action. However, 70 min of monochromatic waves produced a sharply defined and asymmetric larger bar. After that, the longer period (4.5-sec, 8-m) random waves produced a berm while maintaining the terrace that joined with a subdued trough followed by a small bar and more round and symmetric larger bar located farther offshore.

### Hydrodynamics

Beach profile change is driven by such hydrodynamic processes as decay of breaking wave height, vertical profile of the cross-shore current, setup, and long-period swash energy. Figs. 8 and 9 respectively summarize selected hydrodynamic measurements of erosional random waves in the first 20 min and after 550 min of wave action in Test ST\_10 (20-min and 40-min averages, respectively). The decay of the maximum wave height  $H_{\max}$  and statistical significant (average of highest one-third waves) wave height  $H_s$  from the resistance wave gages are shown in the upper half of the figures. The direction and magnitude of the mean cross-shore current measured at various locations is represented with arrows. Wave breaking on the initial profile occurs primarily at the most shoreward resistance gage and further shoreward. The cross-shore current seaward of the surf zone is directed offshore and is weak. After 550 min of wave action, Fig. 9, the wave height envelope shows steep decay over the prominent bar, and the current structure has strong offshore flows in the surf zone and particularly over the bar, with weaker offshore-directed flow seaward of the bar. The bottom half of the figures show the proportioning of wave energy, plotted as wave height, between incident (high pass) and low frequencies. The energy was segregated by using a low-pass filter with a cutoff at half the peak frequency. In both Figs. 8 and 9, the high-pass or incident-band wave height decreases through breaking, whereas the low-pass wave height tends to increase.

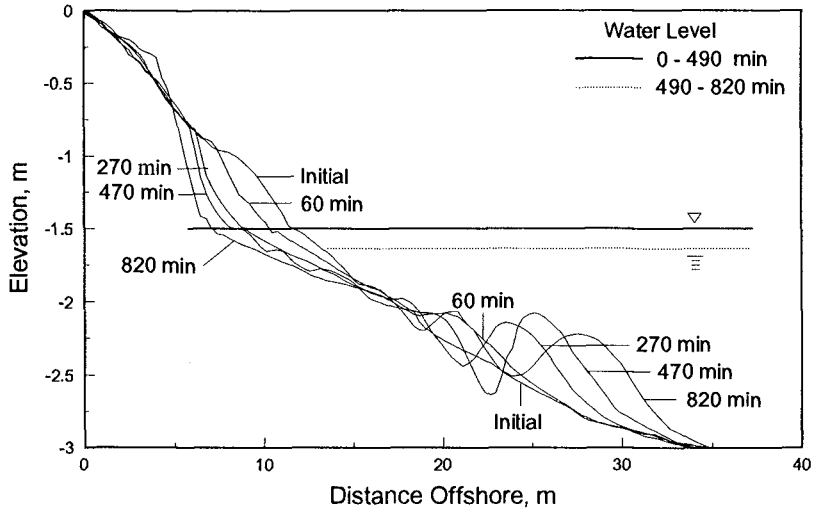


Fig. 7. Selected profile surveys for Test ST\_10

Wave transformation across shore includes not only linear shoaling and wave breaking, but also nonlinear energy transfer to frequencies higher and lower than the peak frequency. Figs. 10 and 11 are measured wave spectra at three cross-shore locations (most seaward gage, a gage in the active surf zone, and the most shoreward gage) for a narrow-band ( $\gamma = 20.0$ ) and a broad-band ( $\gamma = 3.3$ ) incident spectrum, respectively. The narrower spectrum displays clear first and second harmonics of the peak frequency at the shallower measurement locations. The broader spectrum possesses a small peak at the first harmonic and small general increase in energy at higher frequencies. Both cases show an order of magnitude increase in low-frequency energy at shallower depths, similar to what is observed in the field.

## SUMMARY AND FUTURE ACTIVITIES

SUPERTANK succeeded as a cooperative multi-institutional data collection project in which investigators shared resources and expertise toward achieving common goals. Advancements in engineering tools, such as improvement of numerical models of beach change and wave transformation through the surf zone, as well as improved understanding of basic sediment transport and bottom boundary layer processes, are already emerging from the project.

Although data collection has been completed, reduction and analysis of the enormous (multi-gigabyte) data set is still in progress. Significant effort has been dedicated to organize and clean the data sets so that they may be accessed by all researchers, including those who did not participate in SUPERTANK. The first year after SUPERTANK has been devoted to reduction of all major data sets -- converting quantities to engineering units and cleaning and organizing the data. The following two years will include data exchange among SUPERTANK investigators and data analysis. In September, 1994, three years after SUPERTANK was performed, the data will be made available to the public.

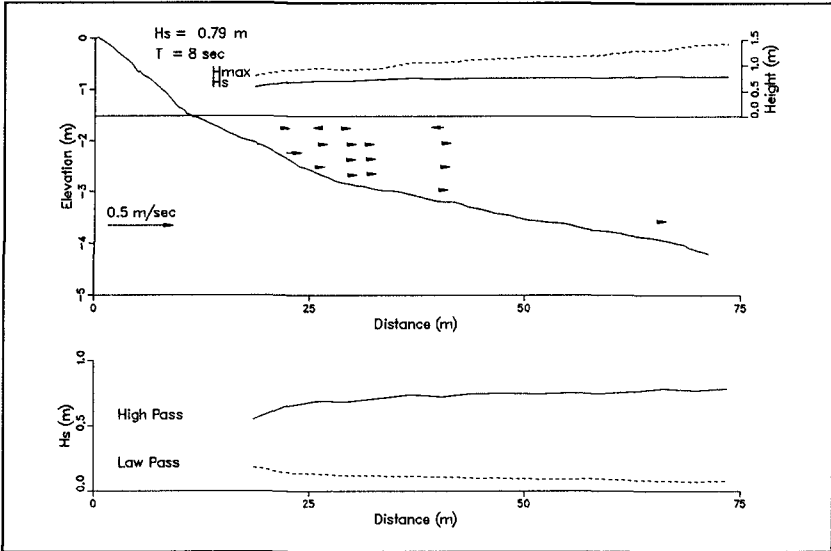


Fig. 8. Wave-height envelope and mean current on the initial beach profile, Test ST\_10, after 20 min (20-min average)

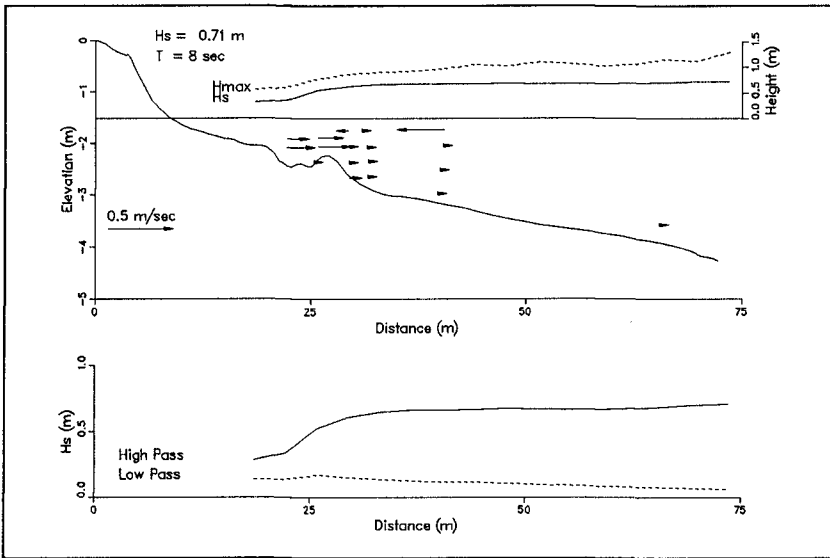


Fig. 9. Wave-height envelope and mean current on a barred beach profile, Test ST\_10, after 290 min (40-min average)

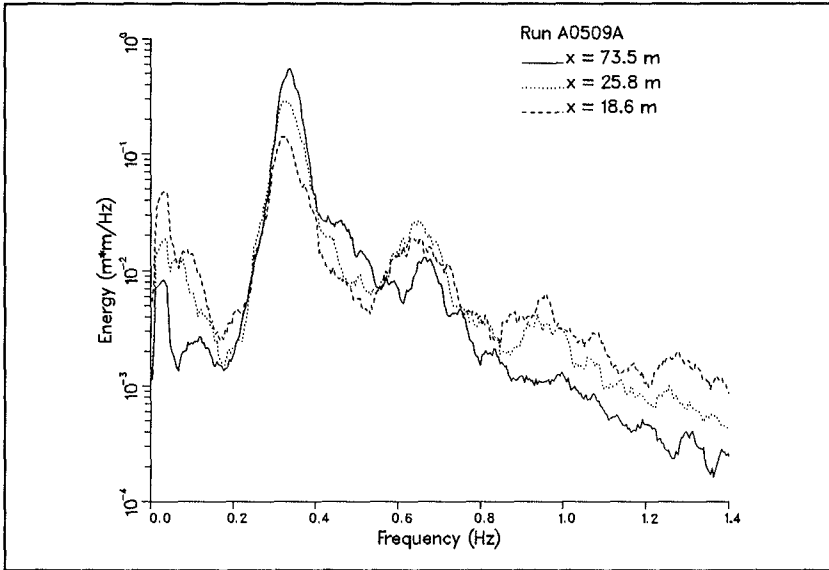


Fig. 10. Transformation of narrow-band wave spectrum across shore, Test ST\_10

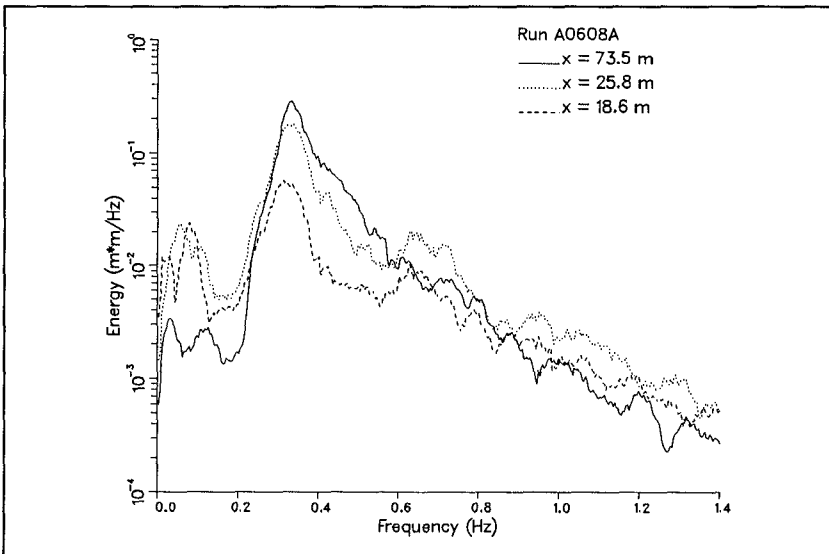


Fig. 11. Transformation of broad-band wave spectrum across shore, Test ST\_10

## ACKNOWLEDGEMENTS

SUPERTANK succeeded through the efforts of numerous individuals who assisted over several years in planning, instrument testing, mobilization, execution of the project, and subsequent demobilization. The tireless efforts and professionalism of the investigators will be forever engraved in the huge, high-quality data set they created for coastal engineering. Drs. William R. Dally, David L. Kriebel, and William G. McDougal were SUPERTANK Steering Committee members together with the authors. We thank Mr. Jesse Pfeiffer, Headquarters, U.S. Army Corps of Engineers, for assisting in the difficult contracting process, and Messrs. Terry Dibble, William Hollings, and David Standley of the Wave Research Laboratory and Mr. William Grogg of the Coastal Engineering Research Center for electronic, mechanical, and computer support. Permission was granted by the Chief of Engineers to publish this information.

## REFERENCES

- Birkemeier, W. A., and others. 1989. SUPERDUCK nearshore processes experiment data summary, CERC Field Research Facility, Misc. Paper CERC-89-16, U.S. Army Engr. Waterways Expt. Stn., Coastal Engrg. Res. Center, Vicksburg, MS.
- Bouws, E., Günther, H., Rosenthal, W., and Vincent, C. L. 1985. Similarity of the Wind Wave Spectrum in Finite Depth Water: 1. Spectral Form, *J. Geophys. Res.*, 90 (C1), 975-986.
- Dette, H. H. and Uliczka, K. 1987. Prototype investigation on Time-Dependent Dune Recession and Beach Erosion, *Proc. Coastal Sediments '87*, ASCE, 1430-1444.
- Horikawa, K. and Hattori, M. 1987. The Nearshore Environment Research Center Project, *Proc. Coastal Sediments '87*, ASCE, 756-771.
- Kajima, R., Shimizu, T., Maruyama, K., and Saito, S. 1982. Experiments on beach profile change with a large wave flume, *Proc. 18th Coastal Engrg. Conf.*, ASCE, 1385-1404.
- Kraus, N. C. and Larson, M. 1988. Beach profile change measured in the tank for large waves, 1956-1957 and 1962, Tech. Rep. CERC-88-6, U.S. Army Engr. Waterways Expt. Stn., Coastal Engrg. Res. Center, Vicksburg, MS.
- Kraus, N. C., Larson, M., and Kriebel, D. L. 1991. Evaluation of beach erosion and accretion predictors, *Proc. Coastal Sediments '91*, ASCE, 572-587.
- Larson, M. and Kraus, N. C. 1989. SBEACH: Numerical Model for Simulating Storm-Induced Beach Change, Report 1, Empirical Foundation and Model Development, Tech. Rep. CERC-89-9, U.S. Army Engr. Waterways Expt. Stn., Coastal Engrg. Res. Center, Vicksburg, MS.
- Mason, C., Birkemeier, W. A., and Howd, P. A. 1987. Overview of DUCK85 Nearshore Processes Experiment, *Proc. Coastal Sediments '87*, ASCE, 818-833.
- Saville, T. 1956. Scale effects in two dimensional beach studies, *Trans. 7th General Meeting*, IAHR, 1, A3.1-A3.10.
- Seymour, R. J. and Duane, D. B. 1978. The Nearshore Sediment Transport Study, *Proc. 16th Coastal Engrg. Conf.*, ASCE, 1555-1562.
- Vellinga, P. 1986. Beach and dune erosion during storm surges, Delft Hydraulics Comm. No. 372, Delft Hydraul. Lab., Delft, The Netherlands.

## CHAPTER 169

# A FIELD EXPERIMENT ON THE FORMATION OF BEACH CUSPS

Michio Sato\*    Keiji Kuroki†    Tomoaki Shinohara‡

### Abstract

This paper describes an attempt at investigating the actual time scale needed to form beach cusps, and the issue whether beach cusps are accretionary features or erosional ones. Data was collected through a field experiment. The experiment was conducted by tracking the process of beach cusp formation on a beach face, which had been flattened in advance by erasing previously formed beach cusps with a bulldozer. New beach cusps gradually developed with every high tide and attained a similar size to the previous ones after three tides.

### INTRODUCTION

Beach cusps have been concerns of many researchers. Main interests seem to have been directed to the aspects on the basic origin and what control their rhythmic spacing. However, in spite of numerous contributions on the subject, contradictory observational results and views in many aspects of beach cusp formation have prevented us from grasping beach cusps in their totality.

It seemed to us that to accumulate measured field data on cusp formation, especially the one which relates the cusp origin to wave conditions, was indispensable. In conducting field measurement, care must be taken to the point whether the waves being measured are the ones which are actually building the cusps or not, as has been pointed out by Johnson (1919). In other words, we should know about the actual time scale needed to form beach cusps.

Smaller cusps are known to be built and eliminated in a relatively short time; in one tide cycle at most (e.g. Longuet-Higgins and Parkin (1962); Komar (1973)). However, the time seemed too short for the formation of beach cusps with spacings of 15 to 20m which the authors sometimes saw. Then, a field experiment was planned to investigate this point.

---

\*Professor, Department of Ocean Civil Engineering, Kagoshima University, 1-21-40 Korimoto, Kagoshima-shi, 890 JAPAN

†ECOH Co., Ltd., Minami-Senju 1-59-7, Arakawaku, Tokyo, 116 JAPAN

‡Sankyū Co., Ltd., Mita 1-4-28, Minatoku, Tokyo, 108 JAPAN

The purpose of this paper is to describe the attempt at investigating the actual time scale needed to form beach cusps, and the issue whether beach cusps are depositional features or erosional ones.

## FIELD EXPERIMENT

**LOCATION OF STUDY** The experiment was carried out from 18 to 21 December, 1980 at Motte Beach, Kagoshima Prefecture, Japan (Figure 1). The beach is a part of sandy beach which extends 8.2km north-north west from the foot of Mt. Kaimon-dake and is exposed to the action of waves from the East China Sea.

Figure 2 shows the cross sectional profile of the center of study area. The beach face had steep slope of over 1/10 and a terrace of 20m wide followed. Beach material was well sorted sand with the median diameter of 0.7mm and the sorting coefficient, introduced by Trask, of 1.29 on average.

**PRELIMINARY SURVEY** The spacing of the beach cusps previously formed was measured over the 500m beach area and was 15.2m on average. The variation of the measured cusp spacing and cusp height along the beach are shown in figure 3. The cusp spacing ranged between 7m to 26m and the histogram is shown as well in the figure.

Though the spacing is widely distributed, the variation of it along the shore seems to have a definite tendency that the spacing increased with the alongshore distance from 100m to 400m, then, decreased abruptly due to the appearance of a small cusp in the middle of pairs of cusps and their growth to the size which determines the spacing. The similar variation seemed to repeat along the beach.

Therefore, our impression was that the broad distribution of cusp spacings in the histogram did not mean the lack of regularity in the spacing of cusps but it was due to the alongshore variation in the cusp spacing controlled by a certain mechanism. Nishi and Sato (1991) pointed out that one unit of the spacing variation corresponded to the spacing of a giant cusp based on the photographs taken from the top of Mt. Kaimon-dake for six years period.

The variation of the height seemed to increase slightly with the increase of cusp spacing.

The experimental site was the center of the measured area.

**FIELD CONDITIONS DURING THE EXPERIMENT** During the experiment, tides were semidiurnal with maximum range of 2.7m, and waves of about 0.5m in significant wave height with periods of 6.5-8.5sec acted on the beach continually (Figure 4). The maximum breaking wave height was about 1m. The change of wave height during the experiment was small though the period changed in the range from 6.5sec to 8.5sec. Wave incidence was almost

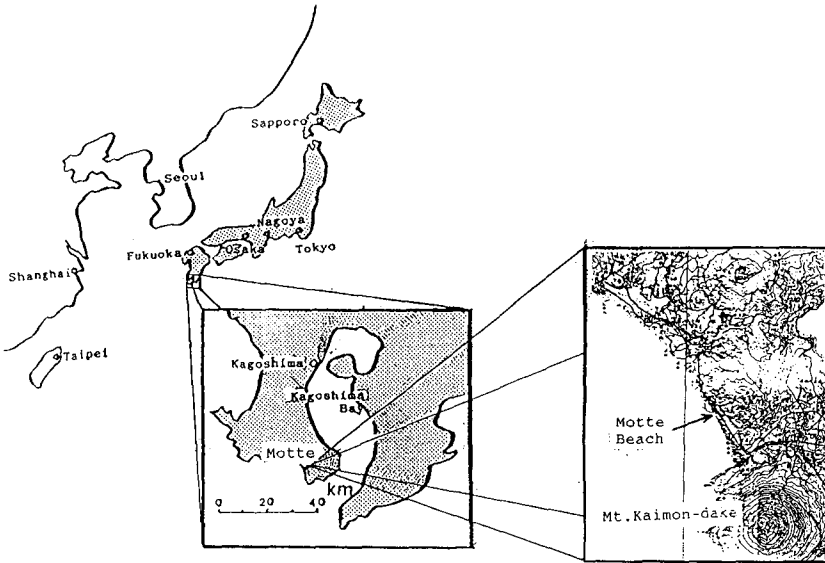


Figure 1: Location of study area

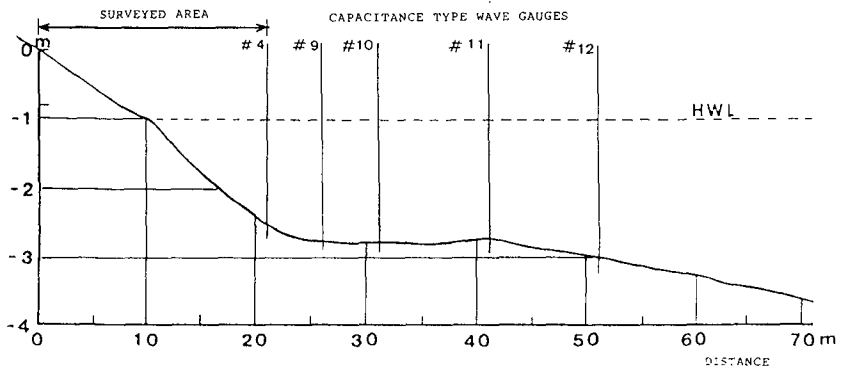
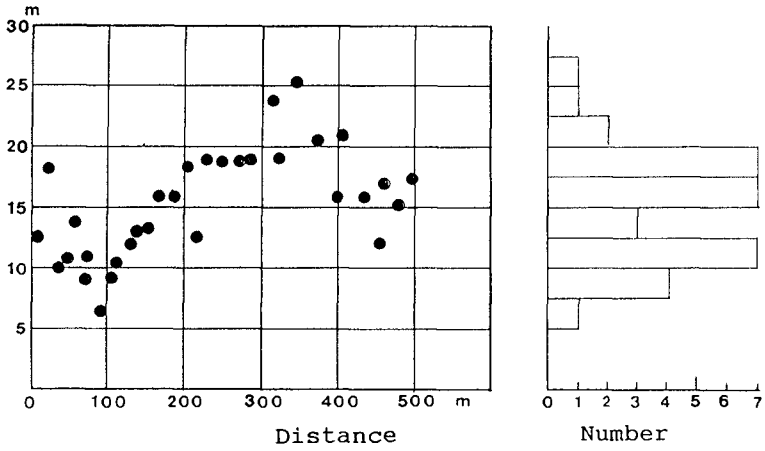
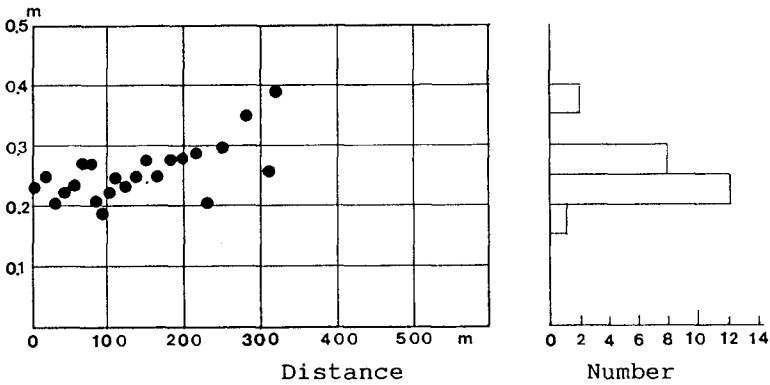


Figure 2: Cross section of the beach



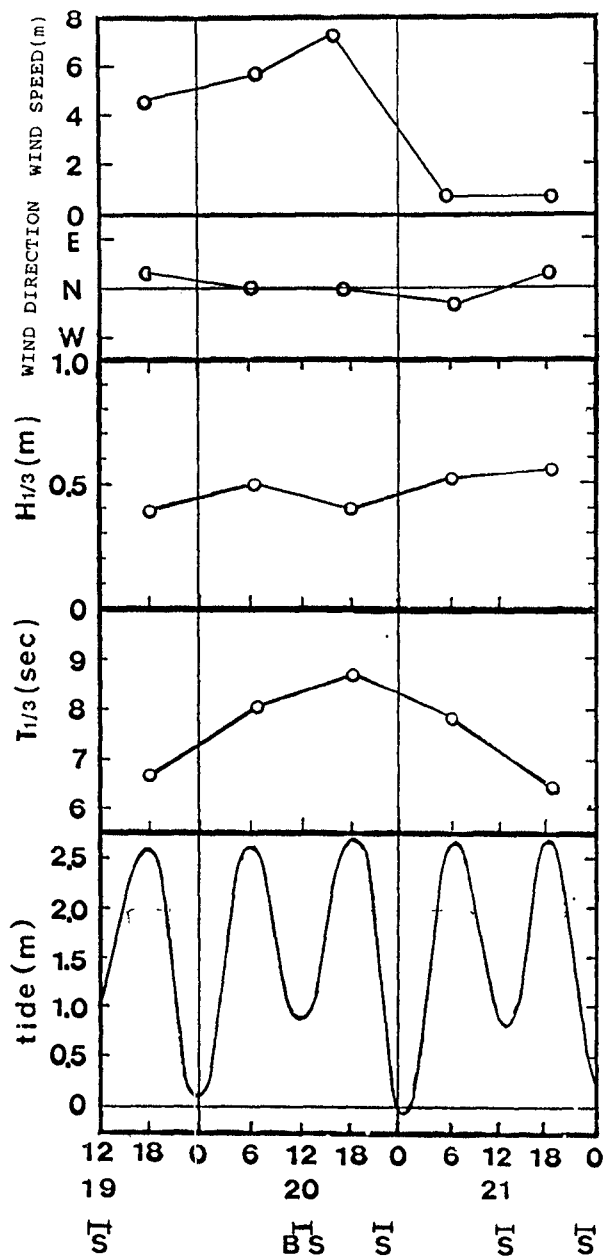


(a) Cusp spacing



(b) Height of cusp

Figure 3: Alongshore variation of cusp spacing and height



S; survey B; bulldozing  
 Figure 4: Field conditions during the experiment

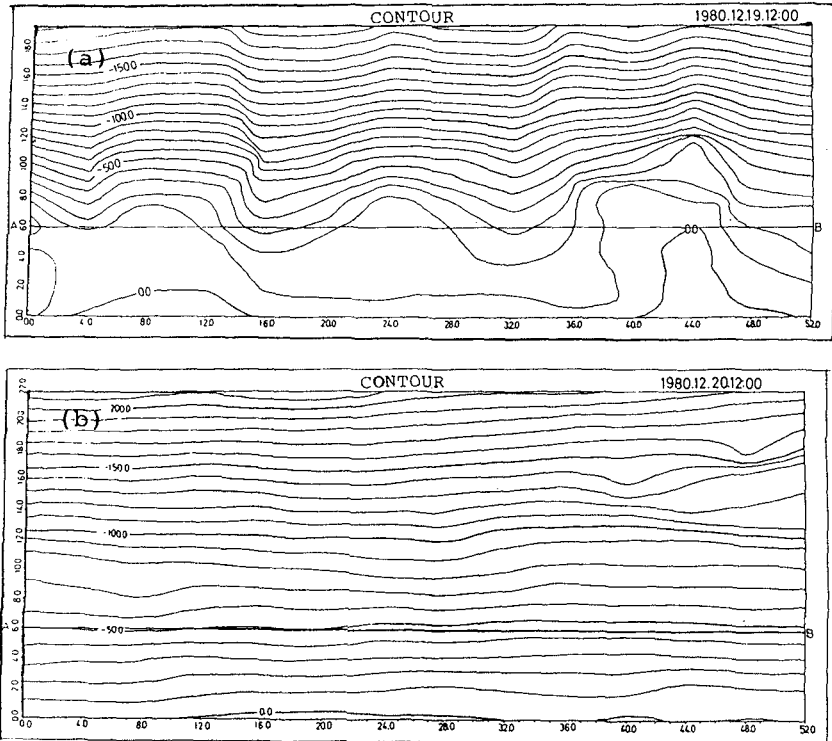


Figure 5: Contour maps of original cusp and topography just after the bulldozing

normal to the beach. North wind of 4 to 7m/sec blew on December 19 and 20, but it almost ceased on the following day.

**ORIGINAL CUSP** Prior to the experiment, the area of both the beach cusp field and the foreshore zone, in a 60m alongshore section, was surveyed at the grid points. The alongshore increment was 4m and the on-offshore one was 1.5m. Elevation of each grid point was accurately measured using a precision level. Figure 5-(a) shows the survey of original beach cusps. Contours were drawn every 0.1m. Cross sectional profile along a line AB parallel to the shoreline is shown in figure 10. We can recognize 3 cusps in this area.

**EXPERIMENTAL METHOD** On the following day, the alongshore area of over 100m including the surveyed part was flattened by a bulldozer during

low tide(Figure 6). Figure 5-(b) is the contour map just after being flattened. Three cusps in figure 5-(a) were completely erased.

After that 168 iron rods, 2m in length, were driven into the beach face at intervals of 4m parallel to the shoreline, and at 2m intervals perpendicular to the shoreline. This made a grid system of 52m  $\times$  22m shown in figure 7.

Repeated levelings of the beach face were carried out every low tide by measuring the amount of the rod exposed. And, in the day time, the subsidence of the iron rods was checked with a level.

Waves were measured with 12 capacitance type wave gauges during every high tide. Eight of the wave gauges were arranged parallel to the shoreline, and the rest were arranged perpendicular to it. The arrangements are shown in figure 7 and figure 2.

In order to track sediment movement, tracer technique was applied by using dyed sand with fluorescent color as the tracer. Two 30 liter buckets of dried sand were dyed red and green, respectively. At 5:30pm December 20, 1980, they were placed on the beachface; red sand at grid point(4,4) and green sand at(9,9) in figure 7. Sampling of about 300 gram of beach materials was done at the grid points at 1:00pm and 10:30pm December 21, 1980. All samples were dried and examined for fluorescent coated particles using ultra-violet lamp. The centroids of the distribution maps of dyed sands were tracked by

$$x = \frac{\sum_{i=1}^n m_i x_i \Delta x \Delta y}{\sum_{i=1}^n m_i \Delta x \Delta y}, \quad y = \frac{\sum_{i=1}^n m_i y_i \Delta x \Delta y}{\sum_{i=1}^n m_i \Delta x \Delta y}$$

where  $(x, y)$  is the position of the centroid,  $\Delta x$  and  $\Delta y$  denote the grid intervals,  $(x_i, y_i)$  is the distance between the origin(i.e. the place where the tracer was deposited initially) and  $i$ -th grid point, and  $m_i$  is the number of fluorescent coated sand particles found per 1,000cm<sup>2</sup>.

## RESULTS

The development of beach cusps after bulldozing can be seen in a series of contour maps(Figures 8). Contours were drawn every 0.1m as well as in figure 5. Figures 9-(a,b,c) show the difference in height between the beach profile just after bulldozing and those after each high tide. Shading in the figures mean eroded part.

In Figure 8-(a), the contour map drawn based on the survey after one high tide from the bulldozing, we can not recognize any cusps. After two high tides, three cusps with a similar spacing to the original ones appeared on almost the same position(figure 8-(b)). And after three high tides they finally attained a similar size to the original cusp formation(figure 8-(c)).

Figures 10-(a,b) are the cross sectional profile along a line A-B parallel to the shoreline of the flattened beach face just after bulldozing and in the course of the development, respectively.



Figure 6: Bulldozing

9 •

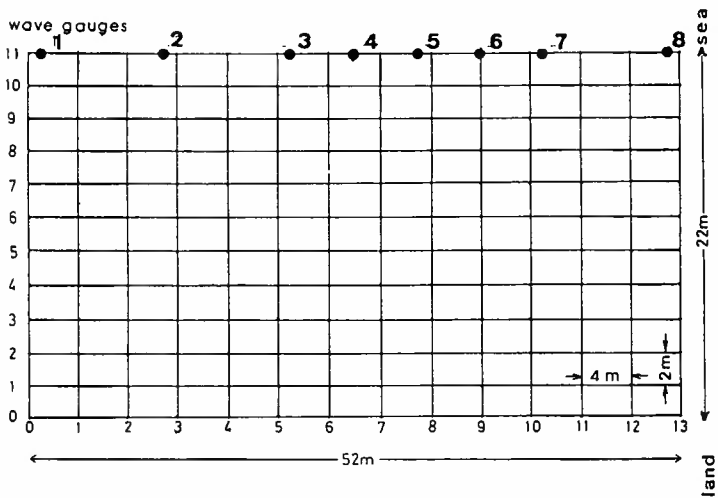


Figure 7: Grid system and arrangement of wave gauges

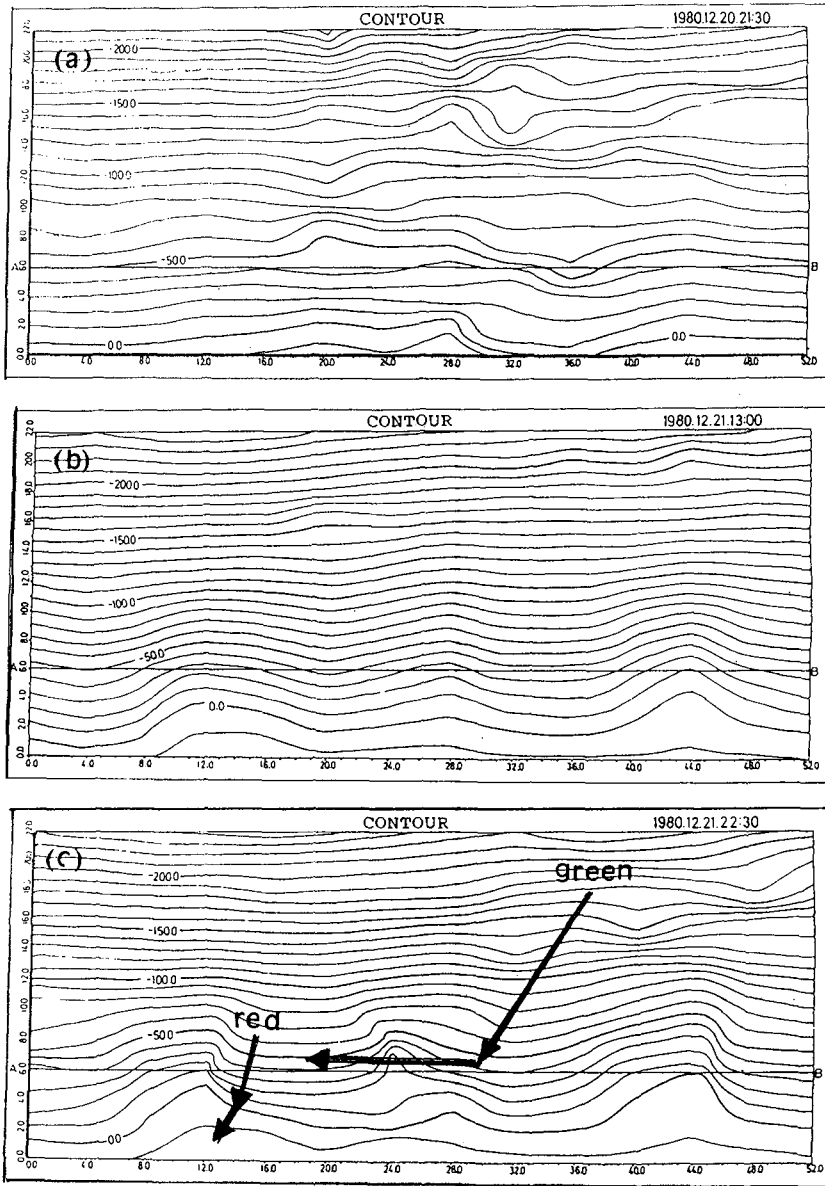


Figure 8: Development of cusps(contour maps)

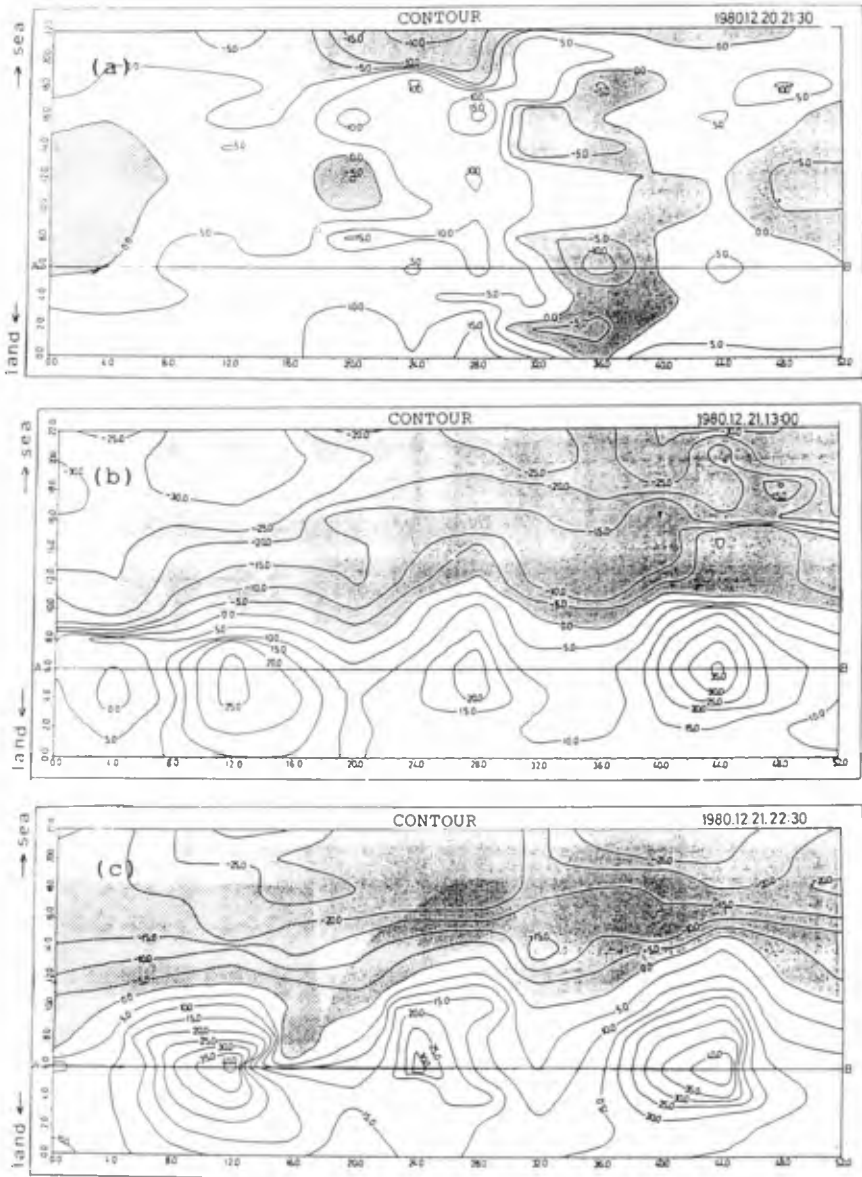


Figure 9: Development of cusps(topographical changes from the flattend contour map)

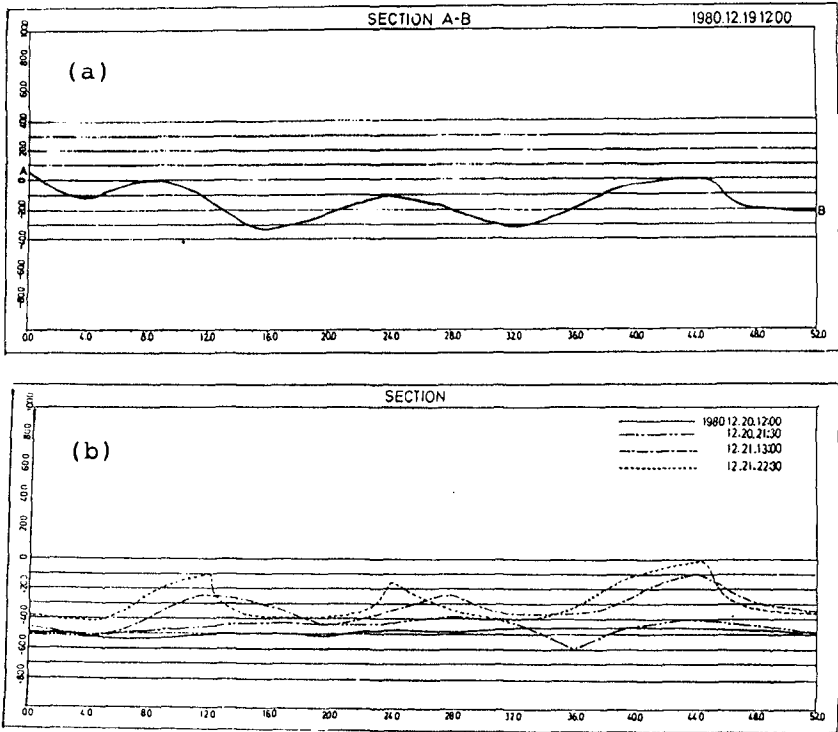


Figure 10: Cross sectional change along the line parallel to the shoreline

It can be seen from these figures that new beach cusps gradually developed. This gradual development was in contrast to the observation of smaller cusp formation (e.g. Longuet-Higgins and Parkin (1962); Komar (1973)). Figures 9-(b) and (c) indicate that sand carried landward from the lower foreshore zone accumulated even in the bay position of the newly formed beach cusps. This is backed up by the trace of dyed sand shown by arrows in figure 8-(c). Thus, beach cusps are purely accretionary features with the horns experiencing more deposition than the bays.

Samples of beach materials were analysed with sieves. Median grain size and sorting coefficient of each sample were obtained. The median diameters ranged from 0.5mm to 1.1mm and the average was 0.7mm as shown in figure 11. In this figure,  $\Delta h$  is the difference in height between the profile just after being flattened and the one after three high tides. Negative  $\Delta h$  corresponds to the lower foreshore part, and larger positive  $\Delta h$  means cusp horns. This figure shows that the sediments of lower foreshore were coarser than cusp area, it also



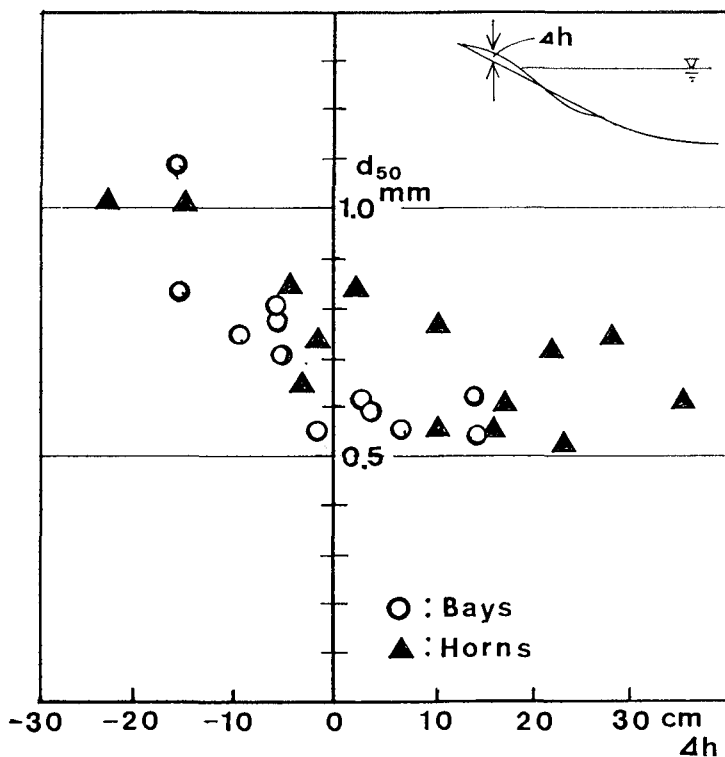


Figure 11: Sediment grain size

shows the median diameters of sediments of cusp horns were slightly larger than the ones of bays.

As to the sorting coefficients, they ranged from 1.14 to 1.8 and the average was 1.29. In lower foreshore area, the sorting coefficients showed larger values; but they were smaller and in cusp and bay field compared to the lower foreshore.

These results add support to the description by King (1972), Williams (1973) and Komar (1973).

Lastly, it may be worth to note about the variation of the density of beach materials in cusp field. When we were pulling out the iron rods from the beach, we found that the rods in cusp area were easily pulled out, but those in bay area were hard to be pulled out and some of them needed two or three persons to be removed. No one realized the difference when we drove the rods into the beach. This seemed to mean that the sediments in bay area became

dense and the ones in cusp area became loose as the cusps developed. The difference of the density of sediments between bay area and cusp area causes the difference of permeability. The difference of permeability has been pointed out by many authors. And the reason has been considered to be the difference in composition of beach materials(Longuet-Higgins and Parkin(1962)). However,even if there is not definite difference in composition of beach materials between cusps and bays,the difference of density,which is due to the difference of compaction,seems to be a reason of the difference in permeability.

## CONCLUSION

A field experiment was conducted by tracking the process of beach cusp formation on a beach face, which had been flattened in advance by erasing previously formed beach cusps with a bulldozer. New beach cusps gradually developed with every high tide and attained a similar size to the previous ones after three tides.

Sand carried landward from the lower foreshore zone accumulated even in the bay position of the newly formed beach cusps. This is backed up by the trace of dyed sand.Thus,beach cusps are purely accretionary features with the horns experiencing more deposition than the bays.

The sediments of lower foreshore were coarser than cusp area,and the median diameters of sediments of cusp horns were slightly larger than the ones of bays.

The sorting coefficients ranged from 1.14 to 1.8 and the average was 1.29. In lower foreshore area,the sorting coefficients showed larger values;but they were smaller in cusp and bay field compared to the lower foreshore.

## REFERENCE

- Dean,R.G. and E.M.Maurmeyer,1981 *Beach cusps at Point Reyes and Drakes Bay Beaches,California*,Proc.17th ICCE,pp.863-884
- Flemming,N.C.,1964 *Tank experiment on the sorting of beach materials during cusp formation*,J.Sed.Petrology,Vol.34,pp.112-122
- King C.A.M.,1972 *Beaches and Coasts(2nd ed., Edward Arnold(Publishers) Ltd.,London,570p*
- Komar P.D.,1973 *Observations of Beach Cusps at Mono Lake,California*,Geol. Soc. Amer. Bull., Vol.84,pp.3593-3600
- Longuet-Higgins M.S. and D.W.Parkin,1962 *Sea waves and beach cusps*, Geogr. Jour., Vol.128, No.2,pp.194-201
- Nishi,R. and M.Sato,1991 *Photographic observation on cusps and wave fields*, Proc.Coastal Eng.,JSCE,Vol.38,pp.296-300

- Otvos, E.G., 1964 *Observations of beach cusps and pebble ridge formation on the Long Island Sound*, J.Sed.Petrology, Vol.34, pp.554-560
- Schwartz, M.L., 1972 *Theoretical approach to the origin of beach cusps*, Geol. Soc. of America Bull., Vol.83, pp.1115-1116
- Seymour, R.J. and Aubrey, D.G., 1985 *Rhythmic beach cusp formation: a conceptual synthesis*, Mar.Geol., Vol.65, pp.289-304
- Sunamura, T., 1989 *Sandy beach geomorphology elucidated by laboratory modelling*, Chapter 6 of "Applications in coastal modeling", V.C.Lakhan and A.S.Trenheile (editors), Elsevier, Amsterdam, 387p.
- Williams A.T., 1973 *The problem of beach cusp development*, J.Sed.Petrology Vol.43, pp.857-866

## CHAPTER 170

### DYNAMICS OF LONGSHORE BARS

Magnus Larson<sup>1</sup> and Nicholas C. Kraus<sup>2</sup>

**ABSTRACT:** This paper presents empirical predictive expressions describing the cross-shore movement of linear nearshore bars, based on intensive analysis of survey data from Duck, North Carolina. The analysis centers on 300 beach profile surveys taken at approximately 2-week intervals for the continuous period from 1981 to 1989, together with accurate measurements of the wave conditions. The geometry and dynamics of bars derived from the surveys are related to wave characteristics, and criteria previously developed by the authors to predict beach erosion and accretion are found to be applicable to bar movement if a multiplicative empirical coefficient in each criterion is modified. The results indicate that onshore movement of bars is more probable than previously estimated. The implication is that linear bars formed of dredged material are more likely to move onshore to nourish the surf zone and beach than previously thought.

#### INTRODUCTION

The beach is a dynamic system that resists inundation and erosion by storage of material on the foreshore and dune complex and by storage of sand in the offshore in longshore bars. Bars also reduce erosive energy entering the surf zone by breaking the higher incident waves. Sediment moves between the shore face and bars according to the wave and water level conditions, grain size of the beach material, and other factors. During storms, characterized by higher waves and water levels, sediment moves from the beach face and, possibly, dunes to form bars, whereas under lower waves bars tend to lose volume and move onshore to resupply the surf zone and beach. Sediment also moves alongshore in a direction mainly controlled by the angle of the incident waves. In the present study, only cross-shore sediment transport processes are considered.

---

1) Assistant Professor, Department of Water Resources Engineering, Institute of Technology, University of Lund, Box 118, S-221 00 Lund, Sweden.

2) Senior Scientist, U.S. Army Engineer Waterways Experiment Station, Coastal Engineering Research Center, 3909 Halls Ferry Road, Vicksburg, MS 39180-6199.

In recognition of the positive effects of bars for promoting beach growth and protecting beaches, nourishment projects have been performed to construct bars or "nearshore berms" from dredged material with the intent of the placed bars to either serve as a wave break and/or to supply or "feed" the beach with material (McLellan 1990, McLellan and Kraus 1991). Engineering motivation for the present study is the need for quantitative criteria for predicting the movement of material placed to serve as an active or feeder berm. In order to derive such criteria, extensive analysis of field data on the characteristics and movement of natural sand bars was carried out, as described further in Larson and Kraus (1992).

In this study, the dynamics of longshore bars were determined from field data and related to the prevailing waves. Depth to bar crest, maximum bar height, bar volume, location of bar center of mass, and time dependencies of these quantities, as well as speed of bar movement, were calculated for a large number of profile surveys made on fixed lines at Duck, North Carolina, at the Field Research Facility (FRF) operated by the Coastal Engineering Research Center (CERC), U.S. Army Engineer Waterways Experiment Station.

The analysis procedures adopted rely on two assumptions; first, the profile change admitted to this study must be dominated by cross-shore transport, meaning that longshore homogeneity exists, and, second, short-period incident waves are the direct and dominant sediment-transport driving mechanism. Engineering studies have long recognized the appearance of three-dimensional patterns in beach morphology in the surf zone (Homma and Sonu 1962). Intensive high-resolution beach profile surveys (Howd and Birkemeier 1987) and inference of morphology through long-term remote sensing (Lippman and Holman 1990) at the FRF indicate that bars tend to become linear (two-dimensional) during storms and rhythmic (three-dimensional) 5 to 16 days following the peaks of storms. Care was taken in the present study to identify potential occurrences of three-dimensionality, mainly through comparison of shapes of the profiles at different survey lines and through censoring of the data by imposing threshold values to consider only larger change. Although incident waves may be one contributing mechanism to the mean flow, other forcing mechanisms such as the tide and wind-generated currents also enter in the total mean flow. Thus, during times of mild wave conditions in particular, correlations between bar movement and incident waves, such as sought in the present study, may be weak and should be viewed with caution.

## DATA EMPLOYED

Beach profile data collected at the FRF were analyzed to provide information on the spatial and temporal properties of natural longshore bars located in the nearshore (depth less than 15 m). The beach profile was surveyed at a nominal 2-week interval along four shore-normal lines from 1981 to 1989, where each survey extended from a base line behind the dune out to a water depth of about 9 m. All depths in this paper are referenced to the National Geodetic Vertical Datum (NGVD), which lies 6.7 cm below mean sea level at the FRF. The locations of the four profile lines, numbered 58, 62, 188, and 190, are given in Howd and Birkemeier (1987). Typically, between 20 to 50 distance-elevation pairs were recorded in each survey, and the total number of surveys during the studied period varied between 250 and 300, depending on the profile line. The surveys were usually carried out to a water depth exceeding the depth of profile closure (Birkemeier 1985). The profiles were surveyed using the Coastal Research Amphibious Buggy (CRAB), which has an accuracy in elevation on the order of 5 cm.

The wave data used in this study were taken by a waverider buoy located in 18-m water depth seaward of the FRF research pier. Wave height was obtained as energy-based significant wave height calculated as four times the standard deviation for a 20-min water level record. The wave period was determined as the period corresponding to the peak in the energy spectrum. Wave height and period were typically recorded every 6 hr but more frequently during the end of the 9-year observation period, for which hourly values are available. The influence of water level was not included in this study, because its period of variation was significantly shorter than the time elapsed between surveys, and the variation in most cases was almost symmetrical about the mean value.

## BASIC PROPERTIES OF PROFILE CHANGE

### Profile Shape

The average profile was computed for each line from all surveys for the period 1981 to 1989. Because individual survey points were taken at varying distances from the baseline, (linear) interpolation was employed between measured points to derive the average profile. Also, maximum and minimum depths recorded at any point were determined across shore together with the standard deviation of elevation. These quantities indicate the profile variability during the measurement period and the areas along the profile where the most active sand transport occurred. Fig. 1 displays the average profile and the aforementioned quantities for Line 62, for which the largest number of surveys exists (in total 300).

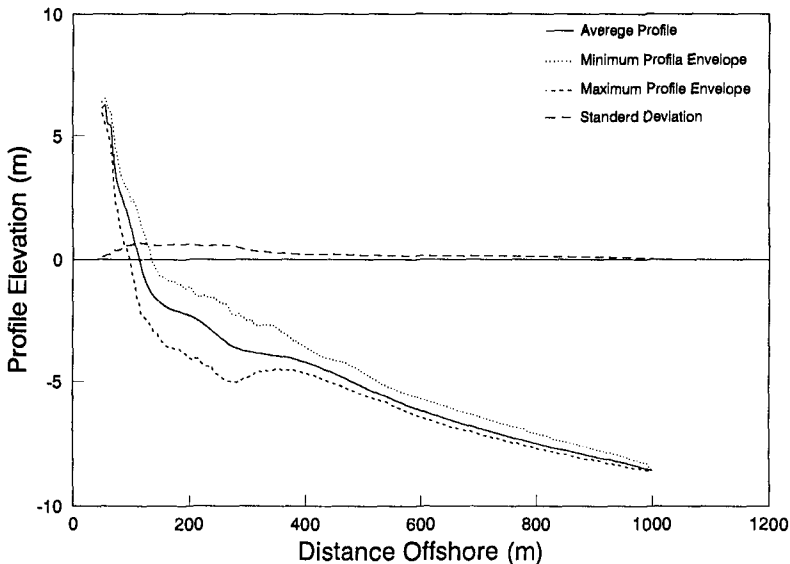


Fig. 1. Average profile and profile variability for Line 62

Average profiles of the four survey lines were similar, having a steep foreshore joining a gently sloping profile at a small distance seaward of the shoreline. Because longshore bars are usually present at the FRF, the average profiles are influenced by these features, and the computed average profiles have two regions where the beach gradient is not monotonically

decreasing, related to the inner and outer bars commonly observed at the FRF. The inner bar in shallower water closer to shore is almost constantly exposed to breaking waves, whereas waves break at distances from the shoreline out to about 400 m (depth between 4 and 5 m) for all survey lines, representing the region of most active sand transport.

The average profile was compared to theoretical equilibrium profile shapes. The modified equilibrium profile equation employed in this study is (Larson 1991),

$$h = A \left[ x - x_s + \frac{1}{\lambda} \left( \frac{D_o}{D_\infty} - 1 \right) \left( 1 - e^{-\lambda[x - x_s]} \right) \right]^{2/3} \quad (1)$$

where  $h$  is depth,  $A$  is a shape parameter,  $x$  is distance from the baseline,  $x_s$  is the location of the shoreline from the baseline,  $D_o$  and  $D_\infty$  are, respectively, the equilibrium wave energy dissipation per unit water volume in the inshore and offshore, and  $\lambda$  is a characteristic (decay) length at which  $D_o$  approaches  $D_\infty$ . The term containing the factor  $1/\lambda$  augments the original equilibrium profile equation  $h = A(x - x_s)^{2/3}$  derived by Dean (1977) and describes a trend of decreasing grain size with distance offshore. The equilibrium profile equation of Dean was least-square fitted to the average profile, determining the optimum value of the shape parameter as  $0.09 \text{ m}^{1/3}$ , with root-mean square error in deviation in depth of  $\Delta h_{\text{rms}} = 0.20 \text{ m}$ . The corresponding median grain size is  $0.20 \text{ mm}$  according to an empirical curve given by Moore (1982).

In the offshore, agreement between the Dean equilibrium profile and average profiles is satisfactory (Fig. 2); however, close to the shoreline the original equilibrium profile equation provided a poor fit, because the average profile is considerably steeper in this region. The larger beach gradient at the shoreline owes to the coarser grain size found near the shoreline. The typical median grain size on the foreshore at the FRF is  $1.0 \text{ mm}$ , whereas the grain size in the offshore region of the profile approaches  $0.1 \text{ mm}$  (Howd and Birkemeier 1987). The trial and error best-fit of eq. 1 used the previous shape parameter and  $D_o/D_\infty = 3.3$  and  $\lambda = 0.039 \text{ m}^{-1}$ , with  $\Delta h_{\text{rms}} = 0.15 \text{ m}$ . The modified equilibrium profile equation well accounted for fining of sediment across the profile and achieved a better overall description of the average or equilibrium shape of the profile.

### Definition of bars

In order to describe and quantify bar formation and movement, a consistent definition of a bar feature is needed. Previous investigations involving laboratory profiles have defined bars with reference to the initial profile (Larson and Kraus 1989). Areas along the subaqueous part of the profile where material accumulates with respect to the initial profile were defined as bars. Crossings between a specific profile and the initial profile defined the beginning and the end of the bar. However, in the field, such a definition is not operational due to the absence of an unambiguous "initial profile," and thus a different method must be employed. In the present study, several methods were tested for defining bars, and, after evaluation, the modified equilibrium profile equation was found to give the most reliable reference profile for definition of a bar and was employed in the following analysis. As an example of how bars were defined, Fig. 3 illustrates a surveyed profile at Line 62 together with the modified equilibrium profile least-square fitted to the 9-year average profile.

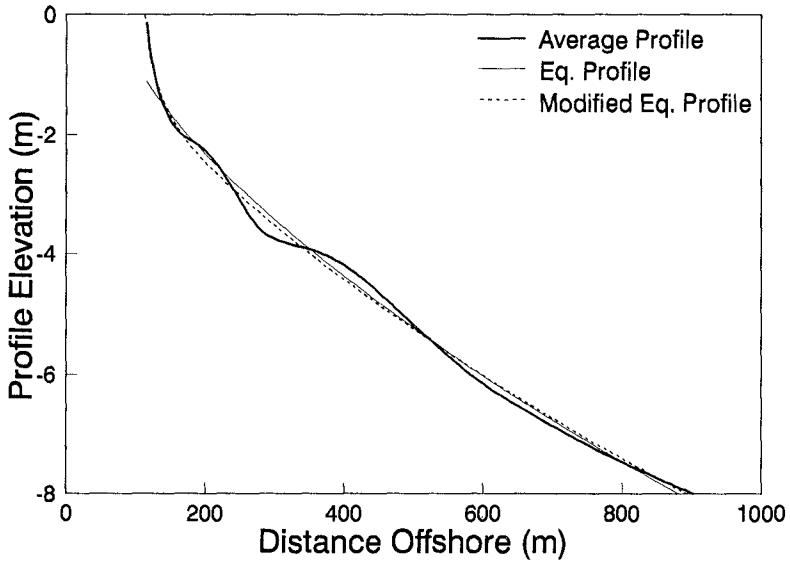


Fig. 2. Average profile at Line 62, equilibrium, and modified equilibrium profiles

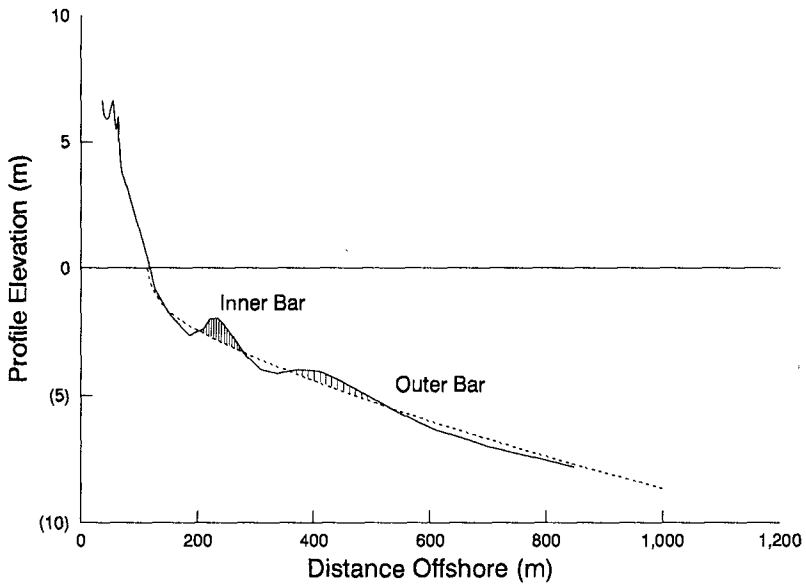


Fig. 3. Definition of longshore bar extent using the modified equilibrium profile equation (hatched areas represent bars)



### Volumetric Profile Change and Contour Movement

To determine and characterize the long-term beach evolution at the FRF, the time-variation in subaerial sand volume above selected elevation contours was calculated. Over the 9-year interval encompassed by the data set, the subaerial portion of the beach at the FRF displayed a slight trend of accretion, especially at Line 62, indicated primarily by a long-term increase in the sand volume above NGVD. Strong seasonal variations, including those attributed to large storms, were superimposed on this trend, with the subaerial sand volume mainly lying below the average value during the first half of the measurement period, and above it during the second half. Fig. 4 displays the variation in the volume of sand above NGVD as a function of time for Line 62. Time is given in consecutive days starting at 810101, and the sand volume is referenced to the average volume,  $104 \text{ m}^3/\text{m}$ , above NGVD from a point located 66 m seaward of the FRF baseline. The 66-m location was the minimal distance seaward common to all profile surveys.

Analysis of volumetric profile change and contour movement showed that the FRF beach accreted somewhat above NGVD for the measurement period, but no long-term change in the subaqueous portion of the beach was detected. Survey lines located north of the FRF research pier (Lines 58 and 62) experienced slightly more accretion than those south of the pier (Lines 188 and 190). The increase in subaerial sand volume is probably due to sand transport by wind. A stable subaqueous beach profile indicates no long-term differential in the longshore sand transport or no significant loss of material to the offshore. Thus, the profile data from the FRF provides a good basis for analysis of natural longshore bar properties because the data set is, on the average, not strongly influenced by a longshore bias. However, short-term longshore variations could still influence profile evolution, and identification of possible times of longshore nonuniformity required tedious visual inspection of the plotted profile surveys.

### BAR PROPERTIES

Because the four profile survey lines displayed similar long-term behavior, analysis of bar properties was focussed on survey Line 62. The largest number of surveys (300) was available for Line 62, and this line was judged to exhibit the most representative bar response. Each profile survey was visually examined for bar features, and shoreward and seaward boundaries of the bar were determined from the crossings between a profile and the modified equilibrium profile. The following properties were calculated for every identified bar from each profile survey:  $V_b$  = bar volume,  $l_b$  = bar length,  $h_c$  = minimum bar depth,  $z_m$  = maximum bar height,  $x_{cg}$  = location of bar center of mass, and  $\Delta x_{cg}/\Delta t$  = speed of bar movement, where  $t$  = time. Fig. 5 schematically illustrates these bar properties for a typical profile survey from the FRF data set (inner bar shown).

#### Inner Bar

Short-term variability in bar properties was considerably greater for the inner bar because it was frequently located in the breaker zone, experiencing significant sand transport and influence of beach change on a shorter time scale than the outer bar. A distinct inner bar was identified in 200 of 300 surveys, and statistical quantities were computed for bar properties (Table 1). Disappearance of the inner bar was primarily due to welding to shore or to offshore movement until the inner bar became or merged with the outer bar. Thus,

minimum and maximum values in Table 1 depend on determination of when the inner bar welded on to the shore or joined with the outer bar as it moved offshore, respectively.

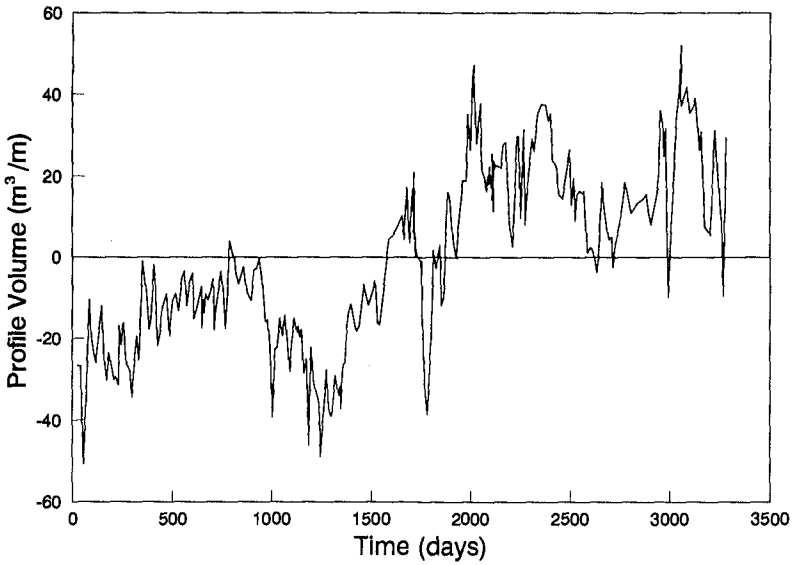


Fig. 4. Temporal variation in subaerial sand volume above NGVD at Line 62

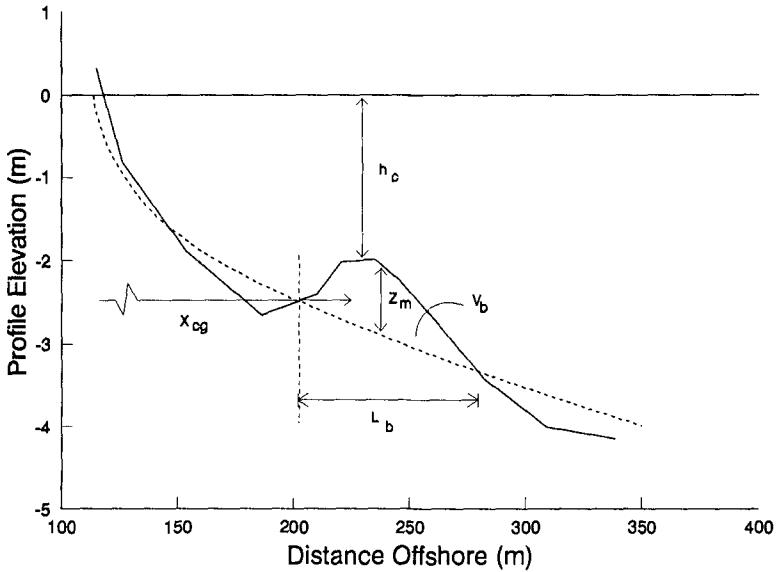


Fig. 5. Definition sketch of bar properties calculated for each survey

Property	Mean	Minimum	Maximum	$Q_{25}^*$	$Q_{75}^*$
Depth to crest, m	1.6	0.6	2.5	1.3	1.9
Bar height, m	0.9	0.2	1.4	0.7	1.0
Bar volume, m <sup>3</sup> /m	42	6	98	27	55
Bar length, m	95	35	280	65	100
Bar mass center, m	215	150	330	195	230

\*  $Q_{25}$  and  $Q_{75}$  denote limits for which 25 % and 75 % of the values are below, respectively.

The average depth to bar crest was 1.6 m, implying a mean breaking wave height of about 2 m, as estimated from an empirical expression given by Larson and Kraus (1989). Bars in large wave tank (LWT) experiments with monochromatic waves (Larson and Kraus 1989) display marked similarities with the inner bar, although bars in the field tend to be smoother due to shifting of forcing under random waves and varying water level. Thus, inner bar volume is similar to that found in LWT experiments, whereas maximum bar height is considerably lower in the field. Fig. 6 illustrates volume of the inner bar with time, in which time periods when no bar existed have been left blank. Change in bar volume was used to derive a time scale for the inner bar by the fractal box-counting method (Larson and Kraus 1992). A break point occurs in the box-counting curve for a box size of about 60 days, which is interpreted as the typical duration between events that move the inner bar offshore.

### Outer Bar

A distinct outer bar was identified for 221 profile surveys, and statistical quantities were computed for the bar properties (Table 2). During extended periods of low waves, the outer bar moved slightly onshore simultaneously with flattening, to finally disappear. The outer bar disappeared as an identifiable morphological feature by flattening before it moved a significant distance onshore. In comparison with the geometric properties of the inner bar, variability of the outer bar is significantly smaller. This is because once the outer bar has formed, it is only exposed to wave breaking and large sand transport during severe storms, and transport induced by non-breaking waves produces less rapid change in bar properties.

Property	Mean	Minimum	Maximum	$Q_{25}^*$	$Q_{75}^*$
Depth to crest, m	3.8	1.3	5.1	3.4	4.1
Bar height, m	0.4	0	1.4	0.27	0.6
Bar volume, m <sup>3</sup> /m	45	0	120	20	67
Bar length, m	170	25	280	150	200
Bar mass center, m	410	200	520	390	440

\*  $Q_{25}$  and  $Q_{75}$  denote limits for which 25 % and 75 % of the values are below, respectively.

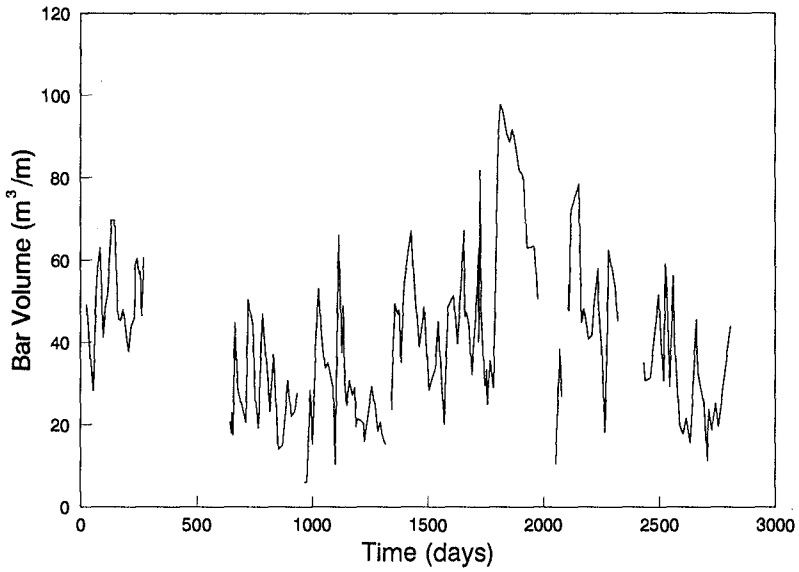


Fig. 6. Volume of inner bar as a function of time

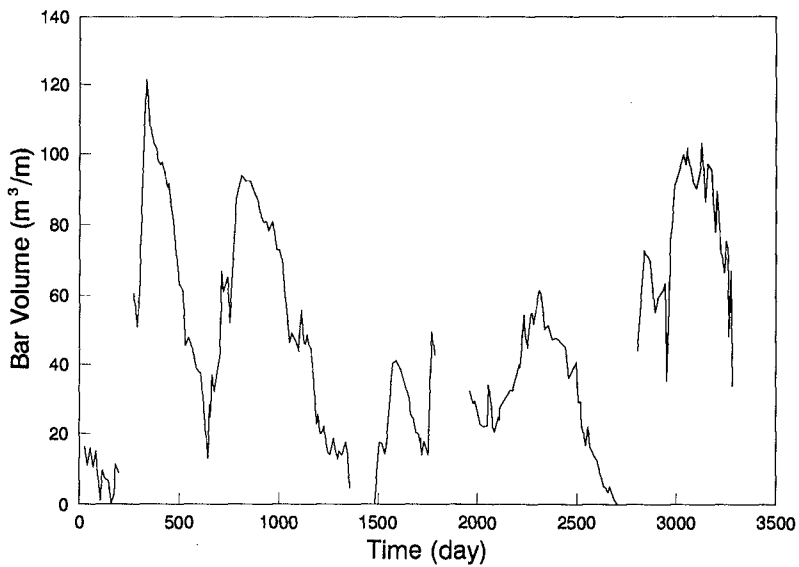


Fig. 7. Volume of outer bar as a function of time

The average depth to bar crest of the outer bar was 3.8 m, which indicates the presence of individual breaking waves with heights on the order of 4 to 5 m associated with modifications of the outer bar. Volume of the outer bar is shown in Fig. 7 as a function of time, displaying regular, long-term variations, where the bar grows rapidly to maximum size after which it decreases in volume at a lower rate until it flattens completely. Comparison of Figs. 6 and 7 illustrates the different time scales in responses of the inner and outer bar to wave forcing in the nearshore. Box-counting analysis of change in outer bar volume produced a break point in the box-counting curve corresponding to 120 days. Thus, the inner bar moves offshore at least every second month, whereas about four months at most separate wave events that move the outer bar seaward.

### Bar Speed

The speed of bar movement was determined for the inner and outer bar as the distance  $\Delta x_{cg}$  the bar center of mass moved between two consecutive surveys divided by the time  $\Delta t$  between the surveys. However, because bar movement may be rapid, particularly during storms (Sallenger, Holman, and Birkemeier 1985, Sunamura and Maruyama 1987, Larson and Kraus 1989), values obtained underestimate bar speed through the assumption that the movement is constant during the time between surveys. A storm with a typical time scale of days that moves a bar offshore would produce rapid bar movement not apparent in the calculation if surveying is done with a longer time interval. If the bar is located outside the region of breaking waves, however, profile change is more gradual under non-breaking waves, and the estimated bar speed should be more accurate.

Onshore and offshore bar movement were analyzed separately, and the inner (outer) bar moved onshore on 99 (122) and offshore on 92 (90) occasions. The average speed of onshore bar movement was 1.5 (0.6) m/day and the maximum onshore bar speed was 8.7 (6.1) m/day for the inner (outer) bar. Corresponding values for offshore bar movement were an average speed of 2.9 (1.1) m/day and a maximum speed of 18.0 (15.2) m/day. The outer bar exhibited considerably lower average speeds than the inner bar, both for onshore and offshore movement, whereas the maximum values were comparable. The average bar speed for the outer bar was approximately one third that of the inner bar. Because the inner bar is more frequently subjected to breaking waves than the outer bar, the average speed of movement is greater for the inner bar. However, if waves broke on the outer bar, the speed of movement was comparable to that of the inner bar, as shown by the similar maximum bar speed for the inner and outer bar.

### RELATIONSHIP BETWEEN BAR AND WAVE PROPERTIES

The average significant wave height for the entire measurement period was 1.1 m, and the average peak spectral wave period was 8.4 sec based on 29,098 individual recordings. Measurements of the incident wave angle were not available for the full 9-year observation period, and in the simultaneous analysis of bar and wave properties the influence of this variable was not quantified. Deep-water wave quantities were calculated from linear-wave theory including shoaling and omitting refraction. Wave quantities were determined from the time period preceding a specific profile survey, and averages were formed for the full record starting from the previous survey.

Larson and Kraus (1992) summarized the results of the correlation analysis between bar and wave properties, covering (1) the correlation between geometric bar properties and wave quantities, (2) the correlation between change in geometric bar properties and wave quantities, and (3) distinguishing between onshore and offshore bar movement. The largest correlation was found between change in the geometric properties of bar volume, maximum bar height, and mass center location, and the fall speed parameter or wave steepness, with correlation coefficients of typically 0.5 to 0.8.

Several criteria were derived to predict onshore and offshore movement of the inner and outer bar. To determine the direction of bar movement, and thus the net direction of the sand transport across the bar, both change in bar volume and change in the location of bar center of mass were examined. Use of bar volume as an indicator of transport direction assumes that bar growth is associated with offshore movement, whereas a decrease in bar volume is caused by onshore movement. In the final analysis for deriving the criteria, a simultaneous increase in bar volume and offshore movement of the center of mass were required as indicators of offshore transport and similarly for onshore transport. A threshold value of 5 m<sup>3</sup>/m on bar volume change was imposed to eliminate events with minor change that were expected to be sensitive to measurement limitations.

The parameters examined to distinguish onshore and offshore bar movement were: wave steepness  $H_o/L_o$ , dimensionless fall speed  $H_o/wT$ , wave height over grain size diameter  $H_o/d_{50}$ , and a Froude number based on grain size  $Fr = w/(gH_o)^{1/2}$ , where  $H$  is wave height,  $L$  is wavelength,  $T$  is wave period,  $w$  is fall speed,  $d_{50}$  is median grain size,  $g$  is acceleration due to gravity, and the subscript  $o$  refers to deep-water conditions. Wave heights and periods associated with the significant wave were taken as the means over the analysis interval. Similar analyses have been performed by Larson and Kraus (1989) primarily for the LWT data sets and limited field data (not examining the Froude number), and by Kraus, Larson, and Kriebel (1991) for the LWT data and an extensive field data set of primarily qualitative observations of beach erosion and accretion (and including the Froude number). The strategy for obtaining the criteria was to plot the data in a diagram encompassing two non-dimensional parameters and subjectively fit a line that best separated onshore and offshore bar movement. In the choice of parameter combinations, at least one parameter contained a variable that characterized the sediment ( $w$  or  $d_{50}$ ).

$$\frac{H_o}{L_o} = 3.92 \cdot 10^{-5} \left[ \frac{H_o}{wT} \right]^3 \quad (2)$$

$$\frac{H_o}{L_o} = 4.5 \cdot 10^9 \left[ \frac{H_o}{D_{50}} \right]^{-3} \quad (3)$$

$$\frac{H_o}{wT} = 2.34 \cdot 10^5 \left[ \frac{w}{\sqrt{gH_o}} \right]^2 \quad (4)$$

Acceptable distinctions between onshore and offshore movement of both the inner and outer bar could be obtained by eqs. 2 to 4. The same exponents are obtained for the non-dimensional quantities as were noted in earlier work, but the constant multipliers have smaller values. This means that application of previous criteria for overall beach response to sand movement in the offshore produces conservative estimates for prediction of onshore sand transport of a bar. The two parameters in eq. 4 may be obtained from the parameters in eq. 2 (Kraus, Larson, and Kriebel 1991); however, the form of eq. 4 is convenient because the wave height appears inversely in the respective parameters, giving a more visually distinct separation of onshore and offshore bar movement. Reasonable predictions are also given by the simple one-parameter criteria:  $H_o/wT = 7.2$ ,  $H_o/D_{s0} = 6,400$ , and  $w/(gH_o)^{1/2} = 0.0055$ . Figs. 8 and 9 show  $H_o/wT$  versus  $w/(gH_o)^{1/2}$  used to distinguish between onshore and offshore bar movement for the inner bar and outer bar, respectively. Criteria developed for the overall response of the beach typically focus on beach evolution in the surf zone, where wave breaking prevails. The tendency for material to be transported onshore is much greater under the action of non-breaking waves in comparison with breaking waves.

## CONCLUDING DISCUSSION

Considerable information on the dynamics of natural longshore bars was obtained from a 9-year record of accurate beach profile surveys made at an average 10-day interval. Availability of data from four survey lines allowed judgement of three-dimensionality which would violate the analysis procedures, and correlations were improved by imposing censoring criteria on combined bar movement and volume. The analysis proceeded by defining bar position from a modified equilibrium profile that accounts for fining of grain size with distance offshore. The analysis covered an inner bar in 2-m depth and an outer bar in 4-m depth, which were tracked through 300 profile surveys.

For the inner bar, average depth to crest was 1.6 m, average maximum bar height 0.9 m, and average bar volume 42 m<sup>3</sup>/m. Average speed of the inner bar was 1.5 m/day for onshore movement and 2.9 m/day for offshore movement, with maximum recorded speeds of 8.7 and 18.0 m/day, respectively. Fractal box-counting analysis showed that the typical maximum duration between wave conditions that moved the inner bar offshore was 2 months.

For the outer bar, average depth to crest was 3.8 m, average maximum bar height was 0.4 m, and average bar volume was 45 m<sup>3</sup>/m. Although the outer bar had, on average, a volume comparable to the inner bar, the maximum height was considerably lower, producing a much more gentle bar shape. Average speed of the outer bar was 0.6 m/day for onshore movement and 1.1 m/day for offshore movement, with maximum recorded speeds of 6.1 and 15.2 m/day, for onshore and offshore movement, respectively. The typical maximum duration between wave conditions that moved the outer bar offshore was about 4 months.

Criteria previously developed by the authors to predict beach erosion and accretion were found to be applicable to bar movement if a multiplicative empirical coefficient in each criterion was modified. The results indicate that onshore movement of bars is more probable than previously estimated. The implication is that linear bars formed of dredged material are more likely to move onshore to nourish the surf zone and beach than previously thought.

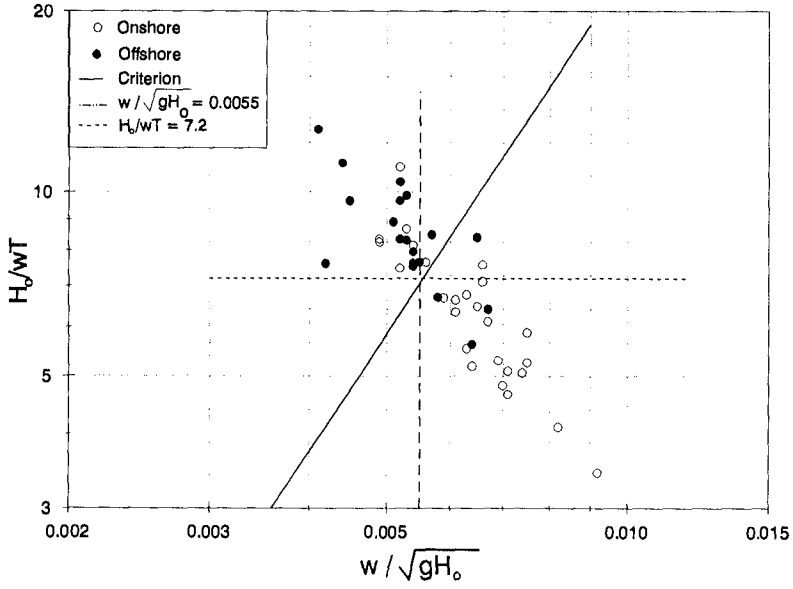


Fig. 8. Cross-shore movement of inner bar predicted using  $w/(gH_o)^{1/2}$  and  $H_o/wT$

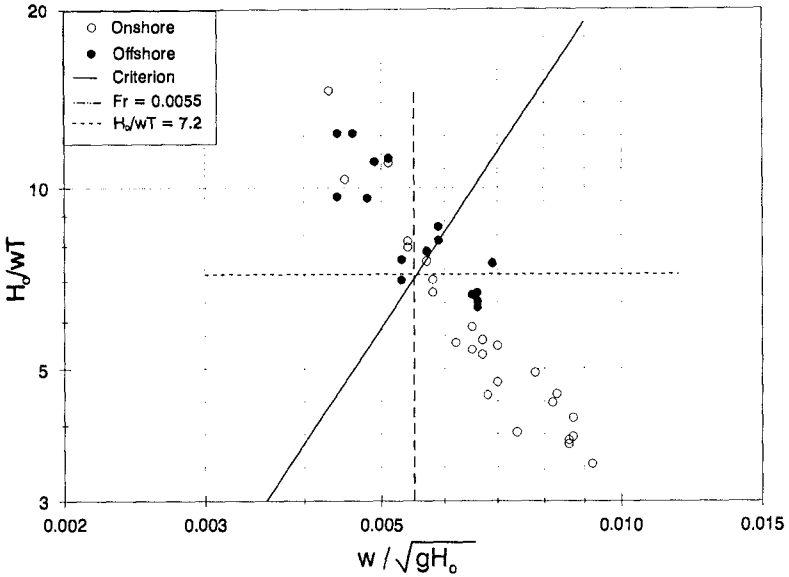


Fig. 9. Cross-shore movement of outer bar predicted using  $w/(gH_o)^{1/2}$  and  $H_o/wT$



Comparison of bar properties from the surveys at a North Carolina beach and results from experiments carried out in large wave tanks indicates similar geometric and dynamic properties (direction of movement and celerity) of bars in the laboratory and in the field. Thus, data sets from large wave tanks are of considerable value for investigating the fundamentals of cross-shore sediment transport and bar movement.

### ACKNOWLEDGEMENTS

This study was conducted as a part of the Dredging Research Program, U.S. Army Corps of Engineers, and performed under the Calculation of Boundary Layer Properties work unit. Contract coordination was provided by the European Research Office of the U.S. Army in London under contract DAJA45-90-C-0020. The beach profile data from Duck, North Carolina, were supplied by Mr. William A. Birkemeier, Chief, Field Research Facility. Permission was granted by the Chief of Engineers to publish this information.

### REFERENCES

- Birkemeier, W. A. 1985. "Field Data on the Seaward Limit of Profile Change," *J. Waterway, Port, Coastal, and Ocean Engrg.*, 111(3), 598-602.
- Dean, R. G. 1977. "Equilibrium Beach Profiles: U.S. Atlantic and the Gulf Coasts," *Ocean Engrg. Rep. No. 12*, Dept. Civil Engrg., U. of Del., Newark, DE.
- Homma, M. and Sonu, C. J. 1962. "Rhythmic Pattern of Longshore Bars Related with Sediment Characteristics," *Proc. 8th Coastal Engrg. Conf.*, ASCE, 248-278.
- Howd, P. A. and Birkemeier, W. A. 1987. "Beach and Nearshore Survey Data: 1981-1984 CERC Field Research Facility," *Tech. Rep. CERC-87-9*, Coastal Engrg. Res. Center, U.S. Army Engr. Waterways Expt. Stn., Vicksburg, MS.
- Kraus, N. C., Larson, M., and Kriebel, D. L. 1991. "Evaluation of Beach Erosion and Accretion Predictors," *Proc. Coastal Sediments '91*, ASCE, 572-587.
- Larson, M. 1991. "Equilibrium Profile of a Beach with Varying Grain Size," *Proc. Coastal Sediments '91*, ASCE, 905-919.
- Larson, M. and Kraus, N. C. 1989. "SBEACH: Numerical Model for Simulating Storm-Induced Beach Change, Report 1: Theory and Model Foundation," *Tech. Rep. CERC-89-9*, Coastal Engrg. Res. Center, U.S. Army Engr. Waterways Expt. Stn., Vicksburg, MS.
- Larson, M. and Kraus, N. C. 1992. "Analysis of Cross-Shore Movement of Natural Longshore Bars and Material Placed to Create Longshore Bars," *Tech. Rep. DRP-92-5*, Coastal Engrg. Res. Center, U.S. Army Engr. Waterways Expt. Stn., Vicksburg, MS.
- Lippman, T. C. and Holman, R. A. 1990. "The Spatial and Temporal Variability of Sand Bar Morphology," *J. Geophys. Res.*, 95(C7), 11,575-11,590.
- McLellan, T. N. 1990. "Nearshore Mound Construction Using Dredged Material," *J. Coastal Res.*, 7, 99-107.
- McLellan, T. N. and Kraus, N. C. 1991. "Design Guidance for Nearshore Berm Construction," *Proc. Coastal Sediments '91*, ASCE, 2000-2011.
- Moore, B. D. 1982. "Beach Profile Evolution in Response to Changes in Water Level and Wave Height," unpub. M.S. thesis, Dept. Civil Engrg., U. of Del., Newark, DE.
- Sallenger, A. S., Holman, R. A., and Birkemeier, W. A. 1985. "Storm-Induced Response of a Nearshore-Bar System," *Mar. Geol.*, 64, 237-257.
- Sunamura, T., and Maruyama, K. 1987. "Wave-Induced Geomorphic Response of Eroding Beaches - with Special Reference to Seaward Migrating Bars," *Proc. Coastal Sediments '87*, ASCE, 788-801.

## CHAPTER 171

# The Punta Umbría (Huelva) Spit

by:

Antonio Lechuga<sup>1</sup> and José María Medina Villaverde<sup>2</sup>

### 1. INTRODUCTION

The Punta Umbría spit is one of the most didactic case studies for spits which can be found along the Spanish coast. The problem the spit presents came to light in the past and has arisen once again causing difficulties for navigation in the channel. The solution adopted for the problem in the past was not totally correct from all points of view, as will be seen later in this study, and, for that reason, the problem has come up once again.

Consequently, the then General Directorate for Ports and Coasts of the Ministry of Public Works and Urban Development<sup>3</sup> commissioned the **Centro de Estudios y Experimentación de Obras Públicas (CEDEX)**, an autonomous organism of the Ministry of Public Works and Transport) to define the problem by making a report on the shore dynamics of the area. This report was undertaken in the facilities which the **Ports and Coasts Research Center** of the CEDEX has in Madrid.

### 2. STUDIES UNDERTAKEN

A report on shore dynamics involves undertaking a number of studies which progressively shed light on the overall problem. In the case of Punta Umbría, the different studies which were done can be outlined as follows:

- ✓ Historical evolution of the coast
- ✓ Geographical and geological study of the coast
- ✓ On site inspection
- ✓ Study of the maritime climate
- ✓ Wave propagation study
- ✓ Hydrodynamic study of the tides

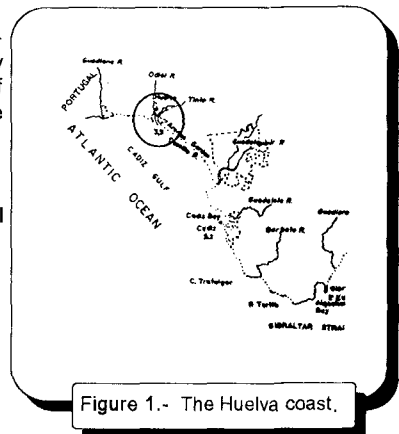


Figure 1.- The Huelva coast.

<sup>1</sup>Ph.D. Civil Engineer. Head of the Coastal Service and Deputy Director of CEPYC-CEDEX.

<sup>2</sup>Ingeniero de Caminos, Canales y Puertos. Director of the Programme of Mathematical Models of CEPYC-CEDEX. (81, Antonio López St. 28026 MADRID, SPAIN)

Once the studies were made, a series of final conclusions were reached from all the information gathered and some precise recommendations were suggested to mitigate the problem

In the following parts of this report, the studies undertaken are commented briefly.

**3. HISTORICAL EVOLUTION OF THE COAST**

The Huelva shoreline can be characterized by the significant movement of sand which takes place, a logical consequence of the huge amounts of sand all along the coast. The proof of this is the fact that the shoreline is made up of only one beach, from Ayamonte on the border with Portugal to Punta del Malandar in the mouth of the Guadalquivir River, the border with the province of Cádiz. This immense sand formation is interrupted only by the mouths of rivers and tidal channels and above all by the Odiel wetlands, located precisely where Punta Umbría and Huelva have access to the sea.

Figure 2 portrays, generally speaking, the evolution of the Huelva coast from ancient times till our days. The present day location of the Punta Umbría spit is indicated by the circle. The arrow indicates the direction of the longshore transport of suspended sediment.

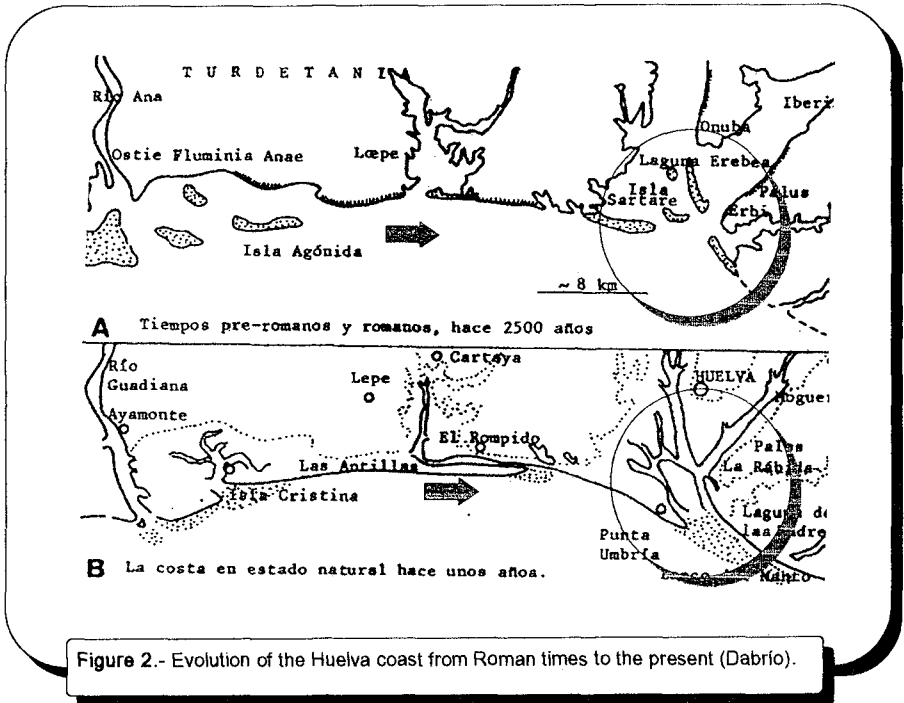


Figure 2.- Evolution of the Huelva coast from Roman times to the present (Dabrio).

As can be seen from the figures, the old rías have slowly undergone a process of sandfill and have been transformed into wetlands, which is what they are today.

<sup>3</sup>Today the General Directorate for Ports of the Ministry of Public Works and Transport.

In antiquity, the coast was made up of estuaries and cliffs and the sea occupied the low lying areas of the river valleys. As a consequence, true rías, like those found in the north-west of Spain (Galicia), were formed in what are now wetlands.

At the same time, the current of net longshore transport, induced by predominant waves from the SW quadrant, among others, and the tide action came together to form two different solid currents. The first current was produced by waves from a W->E<sup>4</sup> direction and the second one by the tide coming from alternating N->S / S->N directions depending on whether the tidal current is flood or ebb.

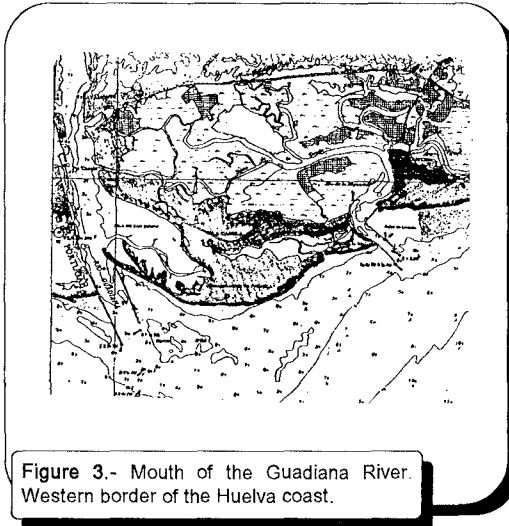


Figure 3.- Mouth of the Guadiana River. Western border of the Huelva coast.

Consequently, sand bars began to appear: the Agónida island (See figure 2A) in the mouth of the Ana river (the present day Guadiana, from the Arabic, "wadi Ana") became the present day Isla Cristina; the ría of the Piedras River became a tidal valley and began to take the shape of the Rompido spit.

Numerous ancient texts exist which date from the VI Century B.C. which confirm the existence of a great estuary in the confluence of the Tinto and Odiel rivers, called "Laguna Erebea" (See figure 2A) by some authors. The growth of the present day Punta Umbria spit in a NW->SE direction aided in the filling of the estuary and the formation of the present

Odiel wetlands, which, in turn, helped to make the spit wider. At the same time, an extensive dune field was formed on the berm.

Barrier islands and the wetlands formed in their shelter existed already in the 19th Century. Straits, narrows or "rompidos" (a local Spanish word that means "little mouth") were formed between the islands.

The net longshore transport current is at present quite significant. The progressive accumulations of sand to the West of the Punta Umbria and Huelva breakwaters, as well as in the Rompido Spit, testify to that fact. In the end of the Rompido Spit (the Punta del Gato), the sand has advanced an average of around 35 m/year. This point has been confirmed by the geological studies consulted<sup>6</sup>, as well as by measurements made on photogrammetric series in the CEPYC.

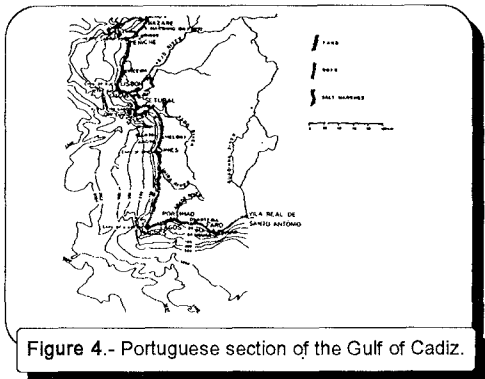


Figure 4.- Portuguese section of the Gulf of Cadiz.

#### 4. MORPHOLOGY OF COASTAL AREA

The Huelva coast extends from the mouths of the Guadiana and Guadalquivir rivers, as was previously mentioned. It is 145 km. long, forms a gentle arc, concave towards SW, and its western end faces a N-80-W direction while its eastern end faces an E-70-S direction. The waters of the Gulf of Cádiz wash its shores.

Owing to historical geological processes, sufficiently treated in the previous part, the coast is made up of coastal formations, typical of the mouths of rivers, and has a gentle equilibrium profile in its last part. The formation of sandbars, points, spits and muddy bogs are also frequent along the coast.

In the area under study, the coastal profile has two features which should be highlighted:

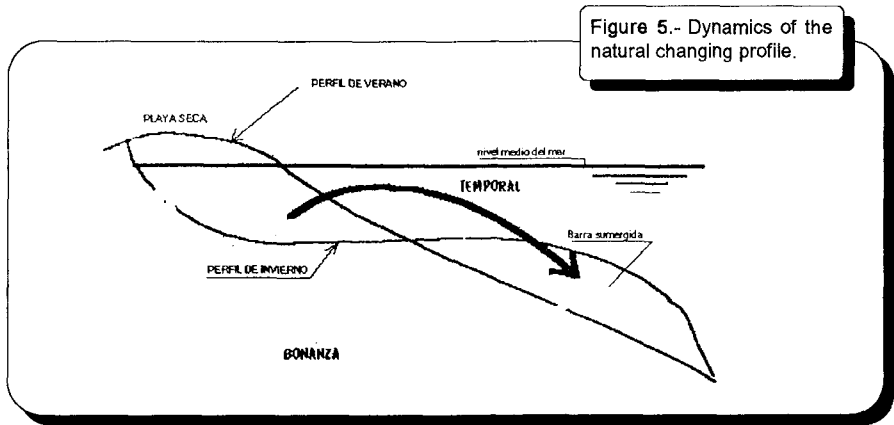


Figure 5.- Dynamics of the natural changing profile.

On the one hand, the mouths of the rivers have considerable extensions of tidal flats which are separated from the sea by sand barriers. These formations are created by the action of the shore current.

On the other hand, a strip of recent sand sediment has been formed between Ayamonte and Punta Umbría. This strip shelters the cliff of siliceous sand, making it inactive and unable to contribute material to the shore dynamics, at least in a direct way, since it is not attacked by the sea.

The city of Punta Umbría was built directly on a spit in the mouth of the Tinto and Odiel rivers occupying the zone of public domain in numerous cases. The design of the numerous streets of the city confirms how the city adapted itself gradually to the growth of the spit. Due to the importance of this type of formations for shore dynamics, it is worth dealing with this point a bit more in detail.

<sup>4</sup>It is interesting to observe at present how an actual river of sand is formed on days when there are storms from the West, even if the storms are not very strong. This river hugs the jetty, which forms the right bank of the Huelva channel, and becomes progressively narrower till it reaches a width of about 30 m.--depending on the intensity of the storm--at the roundhead. Later the river of sand expands throughout the width of the entrance.

<sup>5</sup>C.J. Dabrio, Historia de la Dinámica de Nuestra Costa, Cartaya, 1982.

### Spits, coastal sand formations and their influence on beach profile

Spits are sand bars built up in the direction of the current and are connected to land at one end. They are generally related to the mouths of rivers where sand formations of various types (live dunes, dead dunes, wind-deposited mantles, etc.) are generated. They develop on a small or medium scale anywhere along a coast which combines the topographical conditions and the adequate dynamics. They are more frequent along the Atlantic coast.

Due to their own physical characteristics, coastal sand formations have a very important role in the ecosystem and shoredynamics: they play the role of coastal defence, probably the most effective one that can be found, in contact with the sea and cushion the action of the sea, especially during severe storms. At the same time, they serve as a sand reserve for the beaches.

In addition, the presence of dune fields located on the berm has a determinant effect on the annual cycle of the evolution of the beach which is described in a general fashion in the next section.

### Diagram of the evolution of the beach profile

#### a) Summer profile

As waves approach the coast, they let their effects be felt on the bottom of the sea approximately from the moment where the depth is lower than half a wavelength. From that point on, the sand particles begin to shake back and forth alternatively. The beach profile undergoes modification until the force on the particles is balanced yielding a net result which generally implies a forward movement towards the shore. The finest sand particles are suspended in the area of the surf zone and are thrown along the width of the strand by the waves. Some return to the sea, but the net result still favors deposits on the strand.

#### b) Winter profile

When there is a storm, more waves reach the shore. Thus, more water is transported than in summer and consequently the sand is saturated. This forces the groundwater level to rise. This implies less filtration and eventually produces greater return currents which cause greater erosion. The beach recedes but the sand is deposited on a submerged bar, parallel to the beach and not very far from the shore. This bar acts as a filter for the waves, since it does not allow waves greater than a certain height to pass and obliges them to break due to the effect of the bottom, though this depends on the size of the sandbar.

Figure 5 illustrates this mechanism.

From the previous paragraphs, it becomes clear that if a beach is not wide enough to permit the adopting of a winter profile with a sandbar (for example, if construction was permitted too close to the shoreline), the waves will continue passing through and erode the remaining berm. For that reason, it is **essential** that each beach have a natural deposit of sand (which is usually a dune field) in the back of the beach.

## 5. PUNTA UMBRIA. A CASE STUDY

### Nature

Sand along the Huelva coast is readily available, a fact which will always be a constant problem in many points of the shore due to the resulting lack of depth for navigation. At the same time, however, it provides an efficient defence for the coast in most of its zones, as long as the sand is allowed to evolve as naturally as possible.

### Urban development

Punta Umbria has witnessed the rapid growth of its urban structure, as have the majority of coastal cities whose most important income comes from tourism. The city has grown, like other cities along the Spanish coast, without regard to coastal sand formations, either because of a lack of knowledge concerning their functioning<sup>6</sup>, or because of other reasons which do not take Nature into account.

The growth of the city has always been connected to the growth of the spit, as is reflected in the layout of the streets, which are parallel to the successive alignments of the shoreline.

The problem of the regression of the Punta Umbria beach appears to be provoked artificially by the historical invasion of the sand reserve within the public domain by the sea-front construction. This construction makes it difficult or hinders the formation of the full storm profile of the beach and, consequently, the ulterior regeneration of the summer profile.

### The construction of the jetty

The present day Punta Umbria jetty causes the dominant waves to strike the beach with very little obliqueness. This facilitates the halting of the current, almost completely, which has as its consequence the settling of the material in suspension. This material is at the mercy of the flood and ebb tidal currents which allow it to enter and deposit in the ria by the diffraction of the waves and the tidal current.

The layout of the Punta Umbria jetty has literally cut off the growth of the spit. This has caused the transformation of the part of the spit situated to the east of the jetty into a shoal which is today called Bajo de Nueva Umbria.

The aim pursued initially (to achieve the advance of the beach) has been totally successful. However, the movement of sand was not taken into account, particularly in view of the effect caused to the east of the jetty, in the mouth of the channel. The effect sought after by the construction of the jetty was based on the creation of a partial barrier to the passage of sediments, not only along the bottom but also in suspension, thus facilitating their deposit to the west. Nevertheless, the diffraction provoked on the waves produces a current due to the wave height gradient which leads the sediment into the channel. At the same time, the deficit of longshore transport is compensated by the movement of sand from the shoal, Bajo de Nueva Umbria.

---

<sup>6</sup>It should not be forgotten that Coastal Engineering is still a young and developing science. Some of its fields, such as the understanding of the evolution of the cross-shore profile of a beach, are not sufficiently developed.

The hydrodynamics of the mouth of the channel are not acceptable today, since the ebb tide almost always affects the longshore transport current induced by the obliqueness of the breaking waves, creating a problematic point in the mouth of the ría.

#### Sea level rise

A rise in the sea level brought about by climatic changes would have a greater importance along low lying coasts, as would be the case in Spain along the Gulf of Cádiz and in the Ebro Delta, as well as in other isolated areas in other regions. However, this factor has not been taken into account in this study, since it has a long term effect. A SLR vulnerability assessment for this region is now being carried out at the CEPYC.

## **6. STUDIES UNDERTAKEN**

#### Maritime climate

A study of the maritime climate, based on visual observations of waves, permitted the drawing up of the wave rose, SEA and SWELL type waves. Its aim was to determine the storms which were to be studied.

#### Wave propagation

A study of the wave propagation was accomplished by using a refraction-diffraction parabolic mathematical model<sup>7</sup> based on the resolution of the Berkhoff equations and on the jobs by Kirby and Dalrymple (University of Delaware, U.S.A.). The model permitted the definition of the behavior of the waves as they approached the coast. Various storms of varying directions and periods and in high and low tide were used to achieve this definition.

#### Hydrodynamic behavior of tidal currents

With the help of the MIKE21<sup>8</sup> mathematical model, a simulation of the tide conditions in the wetlands system of the mouth of the Odiel river was undertaken. To accomplish this, the tidal prism, which even included the Huelva ría, was taken into account.

## **7. POSSIBLE SOLUTIONS**

First of all, it is essential to bear in mind that an ideal solution does not exist. Unfortunately, the over abundance of sand along the coast means that dredging can not be avoided.

Notwithstanding this, it is believed that an ideal solution for minimizing the existing problems would involve restoring the primitive channel out to the sea, since it is the natural outlet for the ría. The best way to accomplish this would be to construct an embankment (as shown in figure 6), dredge the former course of the channel and dump what was dredged between the jetty and the embankment, according to the outline indicated in the previous figure. In this way, the spit would be restored and the incident angle between the two currents would be minimized.

---

<sup>7</sup>José María Grassa Garrido, Ports and Coasts Research Center, Madrid, 1990.

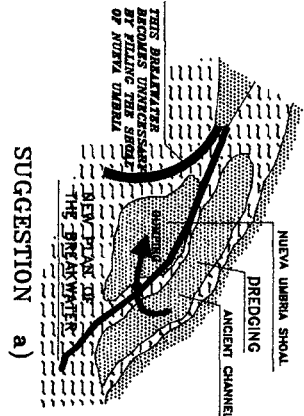
<sup>8</sup>Danish Hydraulic Institute.



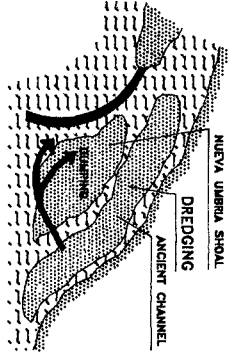
TEMPORAL SE 14 s PLEAMAR - Superficie



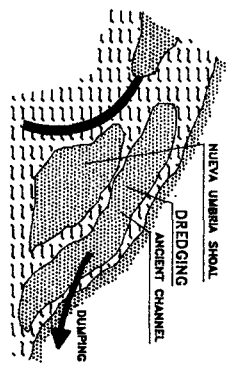
# POSSIBLE SOLUTIONS SUGGESTED



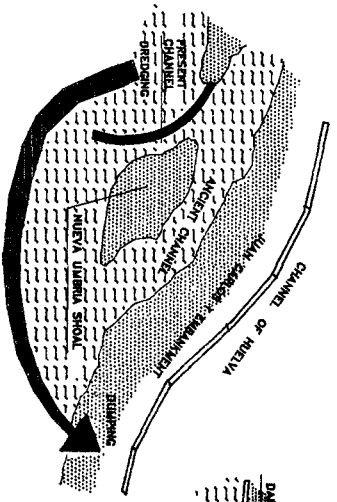
SUGGESTION a)



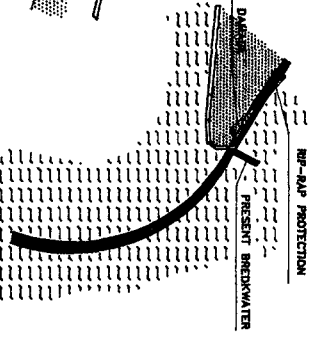
SUGGESTION b)



SUGGESTION c)



SUGGESTION d)



SUGGESTION f)  
( TO AVOID DAMAGES IN RIGHT BANK )

**EFFICIENT PROTECTION OF THE PUBLIC DOMAINE TO AVOID THE DESTRUCTION OF THE DUNES AND OTHER SAND FORMATIONS.**

**ALLOW THE SEA TO PERFORM WITH FREEDOM THE CHANGING OF CROSS-SHORE PROFILE.**

SUGGESTION g)

## CHAPTER 172

### COMPLEX PRINCIPAL COMPONENT ANALYSIS OF SEASONAL VARIATION IN NEARSHORE BATHYMETRY

Guoxiong Liang<sup>1</sup>, Thomas E. White<sup>2</sup>, Member, ASCE  
and Richard J. Seymour<sup>1</sup>, Member, ASCE

**ABSTRACT** Both the conventional Principal Component Analysis (PCA) and the Complex Principal Component Analysis (CPCA) were applied to analyze six nearshore profiles in Siuslaw, Oregon. Results indicated that the first two components derived from CPCA always outperformed those derived from PCA. This suggests that CPCA is a better method of describing the seasonal variation in nearshore bathymetry. The relative performance of CPCA on different profiles depended upon the coherence of the variation within those profiles. Furthermore, the concept of an absolute amount of variance was used in explaining the spatial variation of the predictability of principal components.

#### INTRODUCTION

Complex principal component analysis (CPCA), developed for meteorological application (e.g., Wallace and Dickson, 1972; Barnett, 1983), has been successfully used to describe an event of a fast-moving sand bar (Liang and Seymour, 1991). In comparison with conventional principal component analysis (PCA), also known as the Empirical Orthogonal Function (EOF) technique (e.g. Aubrey *et al.*, 1980; Seymour, 1989), CPCA offers significant advantages. Besides being able to give a more compact description for the variation of the data set (fewer functions required), it can also detect propagating waves.

However, most nearshore bathymetric data sets available consist only of seasonal surveys. One may argue that the seasonal variation in nearshore profiles is more like a standing wave than a propagating feature, and thus it might be unnecessary to apply CPCA to the seasonal bathymetric data. Therefore, a test using

---

<sup>1</sup> Scripps Institution of Oceanography, University of California, San Diego, La Jolla, CA 92093-0222, USA.

<sup>2</sup> USAE Waterways Experiment Station, Coastal Engineering Research Center, 3909 Halls Ferry Road, Vicksburg, MS 39180-6199, USA.

seasonal data appears to be a rigorous method of evaluation. In order to compare the efficiencies of CPCA and PCA in analyzing the seasonal variation in nearshore bathymetry, a set of multiple profile data from Siuslaw, Oregon, was analyzed.

### SEASONAL SURVEY DATA FROM SIUSLAW, OREGON

The bathymetric data were collected from an area that is located in the mouth of Siuslaw River, Oregon (Figure 1). The Helicopter-borne Nearshore Survey System (HBNSS) was applied to measure the seabed elevation (Pollock, in press). The survey helicopter is fitted with a 26-meter weighted cable, graduated like a surveyor's rod. The elevations are read by a shore-based surveyor's level. The horizontal positioning is obtained using a shore-based electronic total distance station (TDS) aiming at a cluster of prisms mounted on the helicopter. The HBNSS surveys were carried out every winter and summer from 1981 to 1990.

Six cross-shore profile sets, which are within an alongshore segment extending 762 m (2500 feet) from the North Jetty, were chosen for analysis. Each of them, with a length of 354 m, includes 30 grid points and 20 time steps. Some profiles show pronounced seasonal cycles (Figure 2).

### ANALYSIS TECHNIQUE AND RESULTS

To apply CPCA, a profile is required to be transformed into a complex data set such as:

$$U_j(t) = u_j(t) + i\hat{u}_j(t)$$

The real part is simply the original scalar field. The imaginary part is the Hilbert transform of the real part. On the basis of the complex data, the complex cross-correlation matrix can be computed, consisting of: the eigenvectors (functional decompositions of the data) and eigenvalues (portions of data's variation represented by each eigenvector). It is customary to evaluate the performance of these analysis tools by the percentage of the variation about the mean, which is represented by each of the principal components. A comparison of PCA and CPCA is shown in Table 1.

Table 1 Percentage of Variation Explained by PCA and CPCA

Profile	1st Component		1st & 2nd Components	
	PC	CPC	PC	CPC
1	86.57	85.65	95.43	95.47
2	77.00	75.28	88.21	89.41
3	60.35	58.65	75.36	78.33
4	56.01	55.50	71.95	73.80
5	38.83	40.71	58.77	64.22
6	36.91	41.63	55.98	64.46

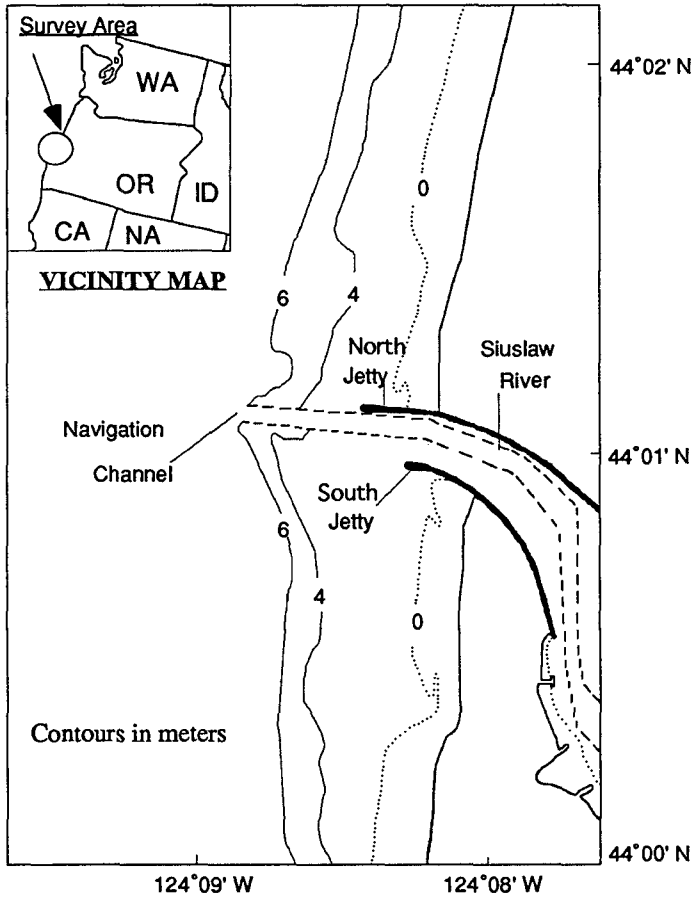


Figure 1. Location map of Siuslaw, Oregon.

The first and second complex components (CPC) can explain more variation than the corresponding conventional components (PC) in every case. In some

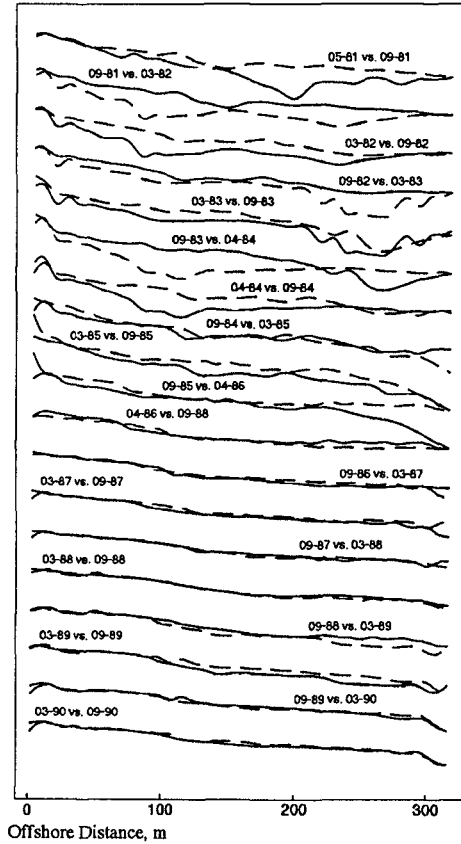


Figure 2. An example of seasonal variation in nearshore profile (Profile 1).

profiles such as profile 6, the CPC is about 8.5% better. The data in Table 1 are shown graphically in Figures 3 and 4.

## DISCUSSION

However, it must be noted that, in some profiles (e.g. Profile 1 and Profile 2), the first conventional component can explain 1% to 2% more variation than the first complex component does. Also, the less variation contained in the first component, the better the performance of the first complex component compared to the conventional one. One possibility is that the complex analysis requires more degrees of freedom, and when artificially constrained to a very low number of functional modes (e.g., only one component), it will not behave reliably statistically. From the data in Table 1, it can be seen that once the number of components exceeds the bare minimum necessary for computation (one), the complex method performs better.

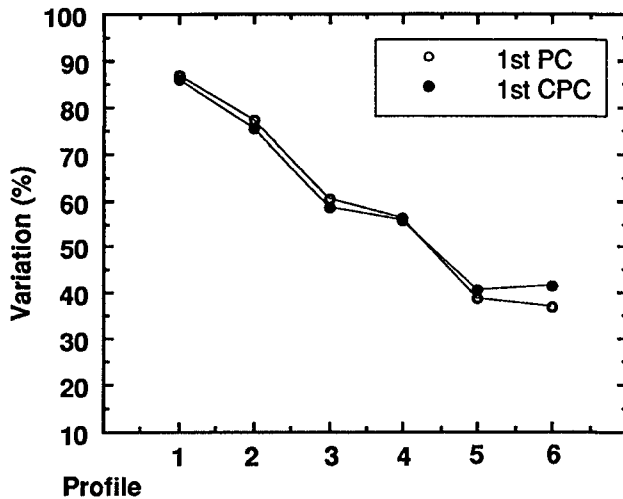


Figure 3. Variation explained by the first component.

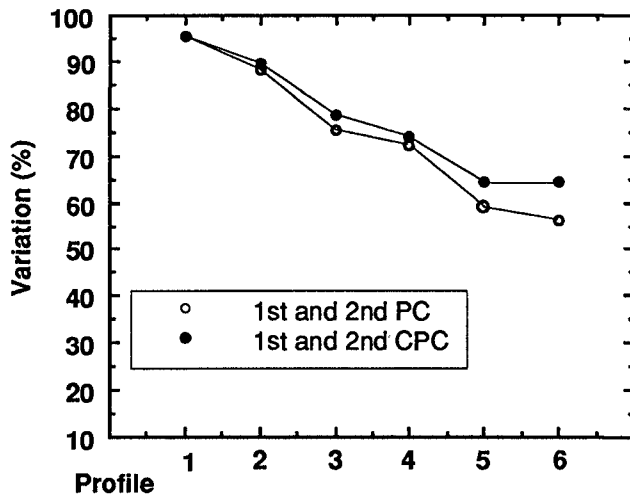


Figure 4. Variation explained by the first and second components

However, for the case of a fast-moving bar, the first component always outperformed the conventional component (Liang and Seymour, 1991).

The data suggest that the relative performance depends upon the coherence of the variation within a profile as described in the following paragraphs. For simple variation (coherent changes), most of the variation can be explained by the first component and the complex method has no particular advantage for a single component. For more complicated variations (non-coherent changes), there is less variation explained by the first component, and CPCA is always more effective.

Figure 5 shows the conventional correlation (left) and complex correlation (right) between each grid point and grid points 5, 10, 15, 20 and 25 in Profile 1.

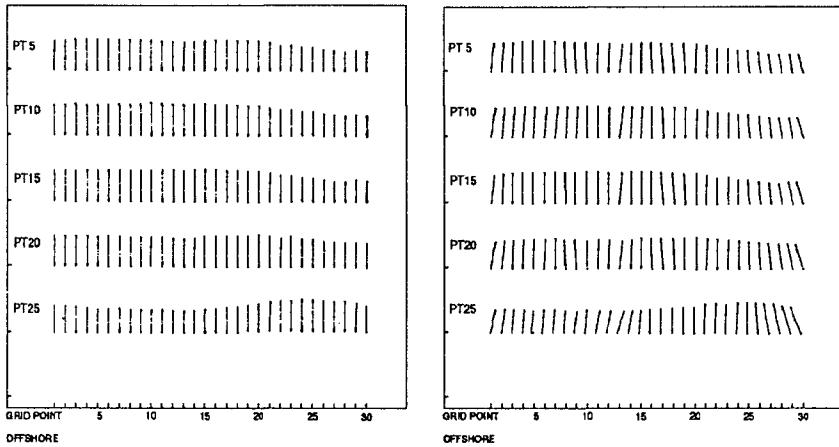


Figure 5. Comparison between conventional correlation (left) and complex correlation (right) in Profile 1.

Each correlation is plotted in a vectorial format where the magnitude is indicated by the length of the vector. Full scale (correlation equals 1.0) is indicated by the correlation between point 5 and itself. For the complex correlation, the phase is arranged like the hour hand of a clock. A vector pointing upwards (downwards) indicates that the two time series are in-phase (out-of-phase); one pointing to the right (left) indicates that the grid point time series lags (leads) the time series indicated in the left margin by  $90^\circ$ , etc. It is obvious that the complex correlation between the grid points within this profile is rather similar to the conventional correlation. Every grid point shows positive correlation with each of the other ones. The entire profile appears to be involved in highly coherent motion. In this case, the results of CPCA and conventional PCA are almost identical.

A different result is revealed in Profile 6 (Figure 6). The difference between complex correlation and conventional correlation is significant. The correlation between grid points are much poorer than those in Profile 1. Also, correlation between certain points show an out-of-phase relationship. It suggests that the motion in this profile is not as coherent as that in Profile 1. In this case, CPCA can explain more variation than conventional PCA does.



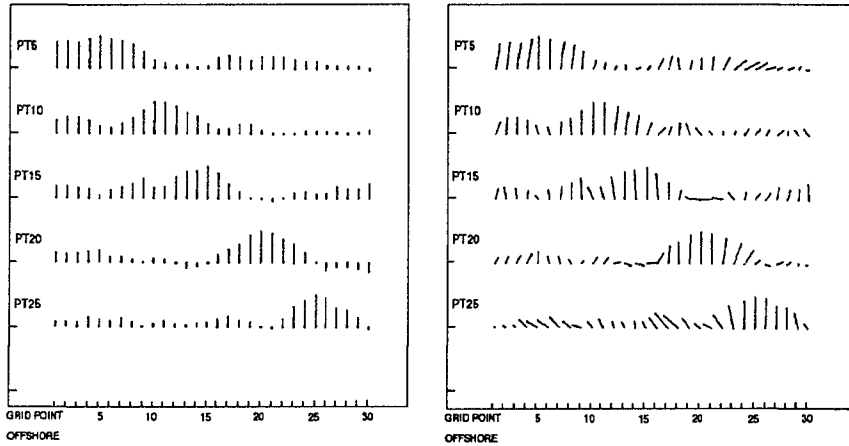


Figure 6. Comparison between conventional correlation (left) and complex correlation (right) in Profile 6.

In many instances, the first CPC may indicate a strong in-phase relationship between the time series at grid points while the second one indicates a weaker, out-of-phase relationship (Horel, 1984). In the conventional PCA, the correlation is simply a scalar. Therefore, it is not possible for it to reveal the phase relationship between different grid points. The data and results described above indicate that, within some standing-wave-like variation in nearshore profiles, both in-phase and out-of-phase correlations can exist. Therefore, since this cannot be determined *a priori*, use of the complex technique appears to be the prudent approach.

One of the other interesting observations is that the percent of the variation explained by either PC or CPC decreases monotonically with distance from the jetty (see Figures 3 and 4), a reduction in predictive capability of about one third. To understand this change better, the absolute value of the variability was calculated. Figure 7 shows the mean value (over time) of the standard deviations (in space) of the six profiles. This shows clearly that there was much greater variability close to the jetty (nearly three times that of the minimum). Figures 8 and 9 show the data of Figures 3 and 4 normalized by the standard deviations shown in Figure 7. These show that, in both PC and CPC, profile 4 is predicted best in terms of the absolute amount of variance, and Figure 7 shows that profile 4 exhibits very close to the minimum amount of absolute variance. Therefore, the performance on profile 4 could be considered to represent the basic capability of the principal component method to extract signals from the noise in the measurements and the physical processes. If this noise is uniform in magnitude, then as the absolute values of the variance increases (toward the jetty) the relative predictability ought to increase – and it does. On the other hand, if noise is somehow proportional to the signal, the relative predictability ought to remain more or less constant – and it does not. The

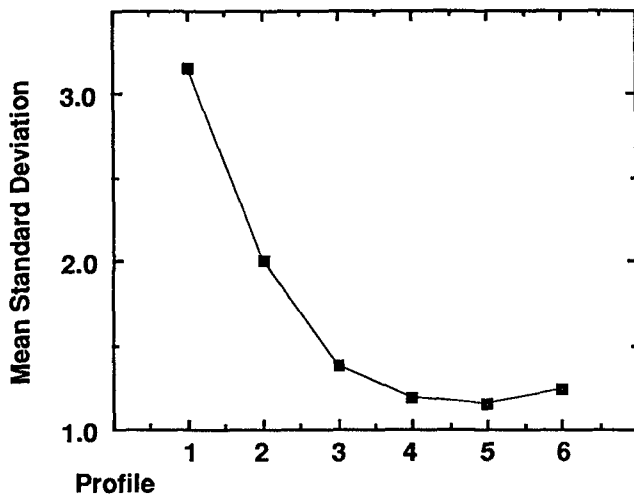


Figure 7. Mean standard deviations of profiles.

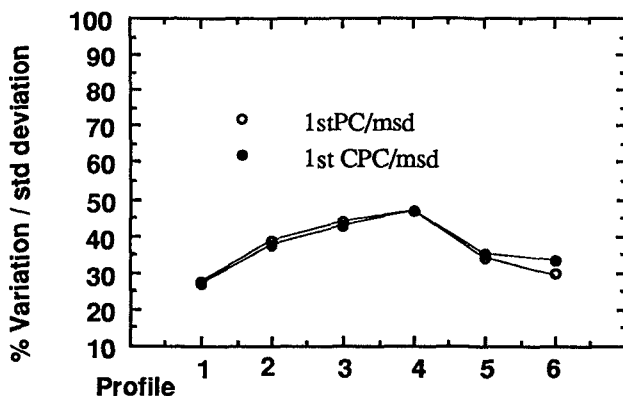


Figure 8. Variation explained by the first component normalized by the standard deviations.

data set is too sparse to make conclusive statements on this hypothesis, but it might be of interest to test this on richer data.

#### ACKNOWLEDGMENTS

This research was supported by US Army Engineer Waterways Experiment Station, contract DACW39-90-K-0007. The CERC MCCP program kindly provided the observed data which made this work possible.

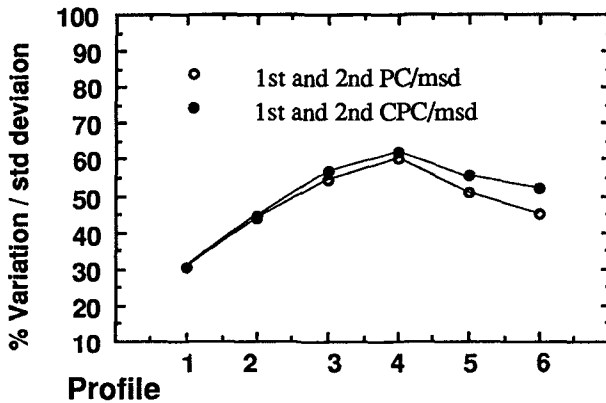


Figure 9. Variation explained by the first and second components normalized by the standard deviations.

#### REFERENCES

- Aubrey, D.G., D.L. Inman and C.D. Winant (1980). The statistical prediction of beach changes in Southern California. *J. Geophys. Res.* 85(C6), 3264-3276.
- Barnett, T.P. (1983). Interaction of the monsoon and Pacific trade wind systems at Interannual time scale. Part I: The equatorial zone. *Mon. Wea. Rev.* 111, 756-773.
- Horel, J.D. (1984). Complex principal analysis: Theory and examples. *J. Climate Appl. Meteor.*, 23, 1660-1673.
- Liang, G. and R.J. Seymour (1991). Complex principal component analysis of wave-like sand motions. In: *Coastal Sediments '91*, N.C. Kraus, K.J. Gingerich and D.L. Kriebel, Eds. ASCE. pp. 2175-2186.
- Pollock, C.E., (1992). Helicopter-borne Nearshore Survey System, a valuable tool in difficult survey area. In press.
- Seymour, R.J. (1989). Cross-shore transport. In R.J. Seymour, Ed., *Nearshore Sediment Transport*, Plenum press, New York. pp. 273-286.
- Wallace, J.M. and R.E. Dickson (1972). Empirical orthogonal representation of time series in the frequency domain, Part I. Theoretical considerations. *J. Appl. Meteor.*, 11, 887-892.

## CHAPTER 173

# TEMPORAL AND SPATIAL CROSS-SHORE DISTRIBUTIONS OF SEDIMENT AT "EL PUNTAL" SPIT, SANTANDER, SPAIN

by

M.A. Losada\*

R. Medina•

C. Vidal•

I.J. Losada•

### ABSTRACT

Sediment samples and beach profile evolution data, collected along one profile line at "El Puntal" Spit, Santander, Spain, are studied by means of Principal Component Analysis (PCA). This analysis technique is used to separate the temporal, spatial and grain size distribution variability of the data. The results show that there is a seasonality in the grain size distribution affecting the fine sand as well as the coarse sand. The variations of the coarse sand percentage, which occur mostly within the bar-berm area, consist of an increase, in the bar zone in winter and in the berm zone in summer. The fine sand presents a different behaviour, changing all along the profile, increasing its percentage offshore the bar in winter, and in the foreshore in summer. Thus, the sediment just relocates in the cross-shore direction.

Further, a "master" grain size distribution, which is constructed by adding all the grain samples, taken from all over the profile, is shown to be

---

\* Ocean & Coastal Research Group. Departamento de Ciencias y Técnicas del Agua y del Medio Ambiente. University of Cantabria. 39005 Santander, Spain.

constant in time. It is suggested that the "master" grain distribution should be used in coastal engineering formulation.

## INTRODUCTION

Investigators have long recognized that there is a relationship between beach profile and sediment size (see Dean, 1977, for a general reference). Though, in almost all relationships proposed, the grain size distribution and grain size related parameters are usually assumed uniform in the cross-shore direction. It is also well known that the sediment characteristics of a beach profile vary both spatial and temporally. A great number of studies have investigated the changes in sediment grain size and the onshore-offshore grain size sorting across the beach profile. Most of the studies involve using statistical granulometric parameter as sample mean, mode and skewness, determined from native sand samples (see recent work by Moutzouris, 1991). Some studies use field data from sand tracers, usually natural sand tagged with fluorescent color or with artificially induced radioactivity (Murray, 1987) and other studies present results from laboratory experiments (Kamphuis and Moir, 1977). However, there is not always agreement on the results described by the different researchers, especially on the trends followed by the degree of sorting across the beach profile.

Attempts have been made to explain and quantify the processes involved in the sorting of grain size across the profile. Two major hypotheses have been proposed in the past: the hypothesis of asymmetrical thresholds under waves (see recent work by Horn, 1991) and the hypothesis of the null-point (e.g. Cornaglia, 1889). Despite the efforts undertaken to understand the processes responsible for the grain size distribution across the profile, the problem remains open and further studies are needed.

Statistical methods, such as Principal Component Analysis (PCA) or Factor Analysis (FA), provide a useful tool to objectively separate the spatial and temporal variability of beach profile data (e.g. Winant et al., 1975; Medina et al., 1991) or of sediment data (Liu and Zarillo, 1989). In all of these works, only two dimensions are considered among offshore-distance, time and grain distribution, resulting in a partial view of the problem. In the present study, sediment data is analyzed by means of the three-way PCA method in which offshore distance, time and grain distribution are used to describe the spatial and temporal structure of the grain size distribution variability.

## ANALYSIS METHOD

Historically, PCA has been carried out for data which depend on two dimensions. If more dimensions were involved, data aggregation or other techniques were used to reduce the problem to a two-dimensional problem. Solutions for three-way data were first proposed by Tucker (1966) and extended by Kroonenberg and De Leeuw (1980).

A detailed discussion of the method can be found in the paper by Kroonenberg and De Leeuw (1980). In brief, one seeks a factorization of a three-way data matrix  $Z$ , such that:

$$Z_{ijk} = \sum_{p=1}^s \sum_{q=1}^t \sum_{r=1}^u [g_{ip} h_{jq} e_{kr} c_{pqr}]$$

where the coefficients  $g_{ip}$ ,  $h_{jq}$  and  $e_{kr}$  are the elements of the columnwise orthonormal matrices  $G$ ,  $H$ ,  $E$ , respectively, and  $c_{pqr}$  are elements of the so-called three-mode core matrix,  $C$ .  $G$ ,  $H$  and  $E$  have similar interpretations as the two-mode eigenvectors and are determined so that the difference between the data and the value obtained from the factorization is minimal according to the mean squared error. In practical applications one is just interested in the first few (two or three) principal components which account for most of the data's variance. The core matrix,  $C$ , however, is no longer a diagonal matrix of eigenvalues. One could conceive of the core matrix as describing the basic relations that exist between the various collection of variables. The solution of the problem is based on the observation that the optimal  $C$  matrix can be expressed uniquely and explicitly in terms of the data modes. The latter components' matrices are optimized by an alternating least squares algorithm.

## STUDY AREA AND FIELD DATA

The study site is located on the Cantabrian Coast of Spain, Gulf of Biscay (Fig. 1). The northern coast of Spain consists of a series of pocket beaches and small inlets separated by pronounced rocky headlands. Santander Bay is one of the largest inlets on the Cantabrian Coast and is located about 200 km West of the French border. The Bay is bounded northward by "El Puntal" Spit, a sandy spit which protrudes well inside the

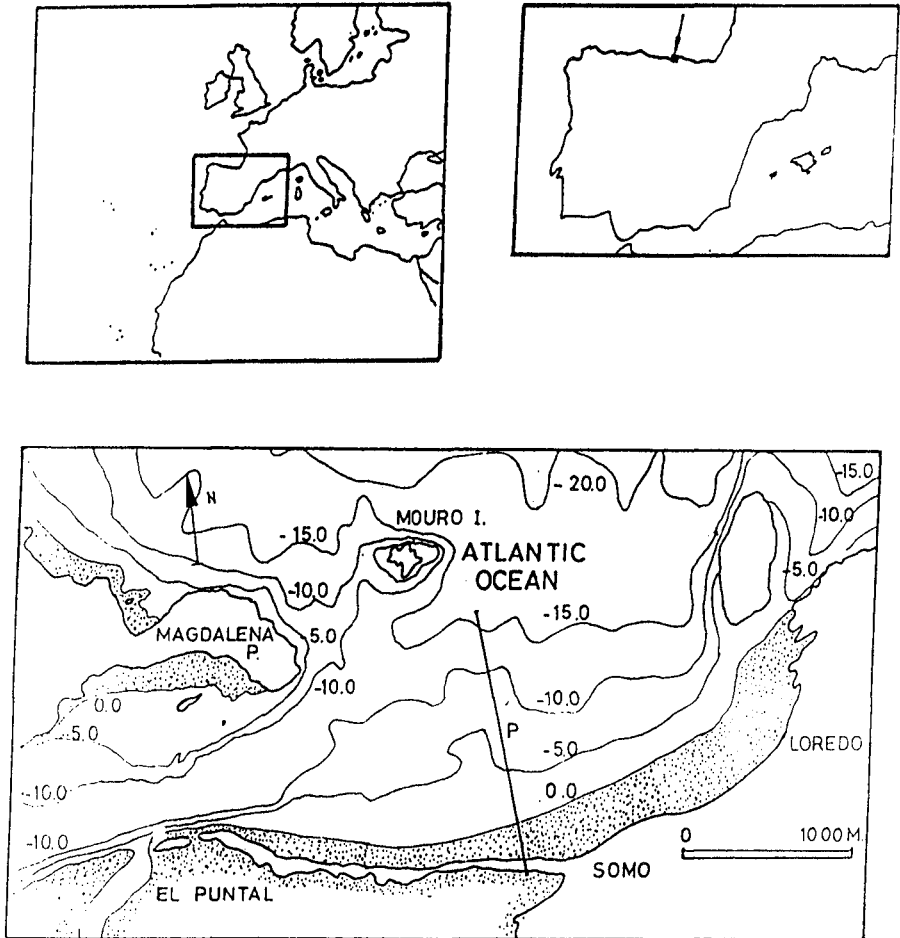


Fig. 1.- Location Map.

bay (see Fig. 1). The predominant wave approach direction is from the N/NW sector and has an annual average significant wave height of  $H_s = 4$  m. Tides along the Cantabrian Coast are semidiurnal. The mean tidal range in Santander Bay is 3 meters and the Spring tidal range is 5 meters.

A monitoring project is being carried out to evaluate the evolution of "El Puntal" Spit. The field program includes wave and current measurements, beach profile and sand samples. A detailed description of the monitoring program can be found in the paper by Losada et al. (1991). We will concentrate our work on the beach profile data and sediment sample data.

Surface sediment grab samples were collected along one profile line at the spit (Fig. 1), over a twenty-month period from May 1990 to January 1992. Profile surveys were taken about once a month, with sediment samples collected during each monthly survey. The beach profile data were collected from permanent monuments landward of the dune seaward to a depth of -15 m, which extended up to 1500 meters. Sediment samples were collected from fifteen positions (see Fig. 2) including the berm and intertidal area, the inner bar and trough area and the nearshore zone. The sediment sampling scheme attempted to locate the sample at the same distance seaward of the base line during each sampling period. Each sample was analyzed in the laboratory and grain sizes were computed by sieving according to ASTM standards using ASTM mesh N<sup>o</sup> 30 (0.59 mm) to N<sup>o</sup> 200 (0.074 mm).

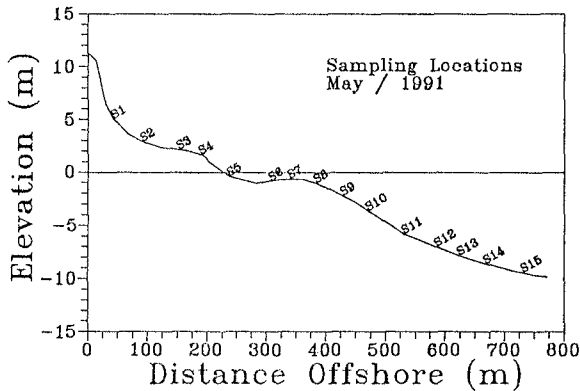


Fig. 2.- Sampling Location.



## RESULTS OF ANALYSIS

### Sediment Data

Since many of the grain size distributions obtained from the samples were not even close to a log-normal distribution, the entire grain size distribution is used instead of the usual statistics such as mean grain size standard deviation, skewness or kurtosis.

Sediment data can be arranged in the form of a matrix  $Z(x,t,d)$ , where  $x$  is offshore distance,  $t$  is time (survey) and  $d$  is grain size distribution. Thus, for each survey and each location we have the complete grain size distribution of the sample. When the three-way PCA method is applied to these data, the internal structure of the data variability is separated into temporal, spatial and grain size distribution variability (eigenvectors  $G$ ,  $H$  and  $E$ ) and the importance of the different modes of variability is given by the core matrix,  $C$ . As previously stated, the method obtains matrices  $G$ ,  $H$  and  $E$  which are columnwise orthonormal, in other words, they have length one. Bartussek (1973) suggested scaling the orthonormal eigenvectors of a three-way PCA analogously to the procedure often encountered in standard PCA. One advantage of this scaling is that the so-determined scales eigenvectors are comparable within a mode and over modes. When scaling the eigenvectors, the core matrix must also be scaled to leave the model invariant.

The corresponding Bartussek core matrix values and the percentage of variation explained by each element of the matrix are given in Table 1. The total variance explained with the first two temporal eigenvectors is, from Table 1, 97.5% with most of the variance explained with the first eigenvectors ( $g_{1i}$ ,  $h_{1i}$ ,  $e_{1i}$ ). This result is not surprising since we are dealing with raw uncentered data and, consequently, the centroid, defined as some mean of the data, can explain most of the data and is the best candidate for the first eigenvector.

In Fig. 3, the first three offshore distance ( $g_{1i}$ ) and grain size distribution ( $h_{1i}$ ) eigenvectors, and the first two temporal ( $e_{1i}$ ) eigenvectors are shown. In order to interpret the results of the 3-way PCA, let us concentrate on the first temporal eigenvector ( $e_1$ ) and the associated offshore distance and grain size distribution eigenvectors.

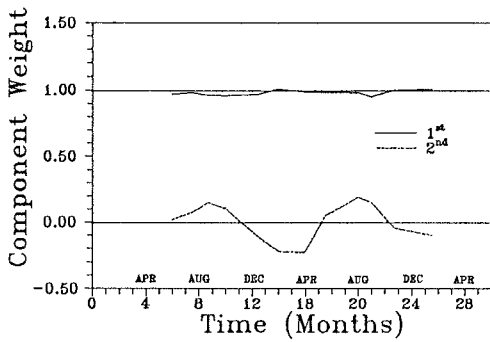
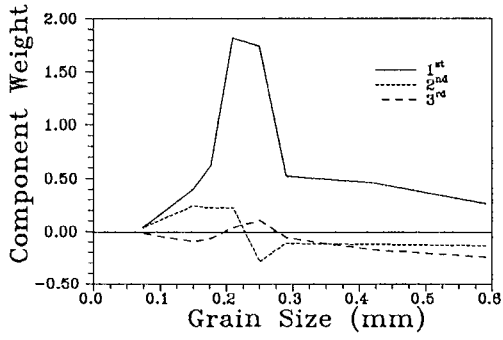
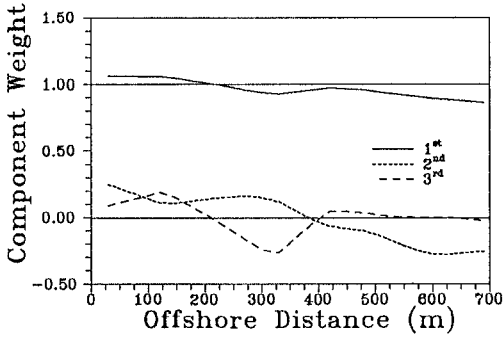


Fig. 3.- Eigenvectors.

Table 1Frontal Planes of Core Matrix

Frontal Plane Time = 1 Down: Offshore Across: Grain size

Explained Variation

Bartussek Scaled

.9240	.0000	.0000	1.060	-.027	-.049
.0000	.0260	.0003	-.027	-4.957	.782
.0000	.0010	.0068	.028	-1.442	5.595

Frontal Plane Time = 2 Down: Offshore Across: Grain size

Explained Variation

Bartussek Scaled

0.002	.0016	.0003	.125	1.745	1.171
.0013	.0036	.0025	1.556	13.875	17.072
.0020	.0006	.0049	-2.874	-8.073	-35.762

The first temporal eigenvector shows an almost constant value in time, thus accounting for the mean (temporal) situation. The first offshore distance eigenvector is also characterized by an almost constant value. Consequently, if we use the first three modes eigenvectors that account for 92.40% of the variance, we obtain a mean grain size distribution in time and space. A better representation of the data can be obtained if we add the combination  $g_2, h_{12}$ , which corresponds to the second offshore distance eigenvector and the second grain size distribution eigenvector, that explains 2.66% of the variance. The second grain size distribution eigenvector accounts primarily for the fine sand and the second offshore distance eigenvectors shows a decreasing trend with a positive value at the beginning of the profile and a negative value at the end of the profile. When multiplying those eigenvectors with the corresponding Bartussek-scaled core-matrix value we get a decrease of fine sand at the beginning of the profile and an increase of

fine sand in the offshore part of the profile. Analogously, more variability of the data can be described using the combination  $g_{13}$ ,  $h_{13}$ . That combination adds 0.68% of explained variance and give information of the coarse sand ( $g_{13}$ ), which has negligible variability in the offshore part of the profile and maximum variability in the berm-bar zone of the profile ( $h_{13}$ ). With these eigenvectors, we add coarse sand at the bar location. The final representation of the mean (temporal) situation is composed of an along-profile constant grain size distribution with finer sand in the offshore part of the profile, some coarse sand at the bar location and a well-sorted material at the beach face area (we subtract fine and coarse sand). See Table 2 for an overall explanation of the sign of each term in the expansion and the action it takes over the first eigenmode.

Table 2

Grain size /Distance	Eigen-mode (1,2,2)				Action over the Eigenmode (1,1,1)
	Time	Offshore distance	Grain size	Core Matrix	
	T	X	G	CM	
>0.30 mm >400 m	+	-	-	-	- Subtracts >0.30 mm
>0.30 mm <400 m	+	+	-	-	+ Adds >0.30 mm
<0.22 mm >400 m	+	-	+	-	+ Adds <0.22 mm
<0.22 mm <400 m	+	+	+	-	- Subtracts <0.22 mm

The second temporal eigenvector (Fig. 3) shows a seasonal dependency with a maximum in the summer season and a minimum in the winter season. The eigenvectors associated with this second temporal eigenvector explain 1.70% of the variance. Among the nine possible combinations of grain size distribution eigenvectors and offshore distance eigenvectors, again the pairs  $g_{23}$   $h_{23}$  and  $g_{22}$   $h_{22}$  are the most important in terms of explained

variance. Notice that the second temporal eigenvector has a different sign depending on the season, thus the effect of the pairs  $g_{23}$ ,  $h_{23}$  and  $g_{22}$ ,  $h_{22}$  changes seasonally. In this way, the pair  $g_{22}$ ,  $h_{22}$  describes a seasonal variation of the fine sand along the profile. If we want to have a better representation of the summer data, we must add fine sand in the landward part of the profile and subtract it in the offshore area. Inversely, in winter, fine sand must be added in the offshore zone and subtracted in the landward part.

The seasonal variability of the coarse sand is controlled by the pair  $g_3$ ,  $h_3$  and bounded in the berm-bar area (see Fig. 3). In winter, more coarse sand is encountered at the bar location while the percentage of coarse sand decreases at the berm position. In summer, however, the bar suffers a decrease of coarse sand that is now located at the berm position.

#### WORKING HYPOTHESIS FOR THE CROSS-SHORE GRAIN SIZE DISTRIBUTION

Besides the information about the grain size distribution and the degree of sorting in the cross-shore direction, the eigenvector expansion suggests new ideas on the sediment transport that occurs in the cross-shore direction. The situation described by the spatial eigenvectors associated with the first temporal eigenvector is a "static" or "no-mobility" situation since it does not change in time. Actually, some sediment transport might exist, but it is balanced so that no temporal variations occur. On the other hand, the situation depicted by the eigenvectors associated with the second temporal eigenvector shows that some sediment transport is taking place since, for example, the percentage of coarse sand is decreasing at the bar location during the summer period. Further, the eigenvector expansion indicates that the coarse sand movement takes place mainly within a zone between the berm and the bar while the fine sand moves all along the profile.

Notice that the second temporal eigenvector shows a seasonal dependency with no net trend. Thus, the sediment transport in the crossshore direction is just a "sediment or grain size relocation": the coarse sand is seasonally redistributed between the bar and the berm and the fine sand between the offshore zone and the landward part of the profile.

For each of the twenty surveys, a "master" grain size sample constructed by adding all the grain samples taken over the profile is obtained. Figure 8 shows the "master distribution" for the winter and summer surveys. Except for minor deviations associated to a discrete sampling technique (only

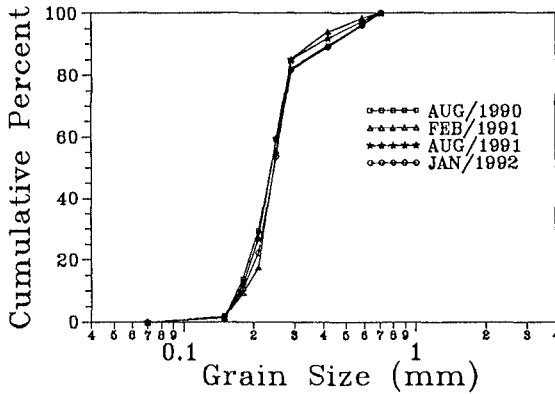


Fig. 4.- "Master sample" grain size distribution.

fifteen samples were taken along the profile for each survey), it can be accepted that a "master grain distribution", which is constant in time, exists. Thus, the following working hypothesis may be anticipated:

*"For a beach profile within a physiographic unit, the "master grain size distribution" obtained by adding all samples taken over the active profile, doesn't depend on time".*

The application of this hypothesis should be useful to select a grain size, representative of the overall behaviour of the sand in the profile. As an example, it is suggested that parameters like "A" of the equilibrium beach profile and "K" of the longshore sediment transport formula should depend on the  $D_{50}$  of the "master" grain size distribution.

Finally, three more remarks: First, the hypothesis simplifies the field work. To know the grain size distribution in a profile, the sample may be collected anytime, since it is invariant. The unique requirement is that the samples have to be taken all over the active profile.

Second, in order to reconstruct a beach profile, the borrowed grain distribution should be as close as possible to the "master" grain distribution of the native sand.

Last, the hypothesis may be extended to 3D cases, extending the idea of "master grain size distribution" to a physiographic unit (like a pocket beach). To check this case, the development of a four-way Principal Component Analysis would be necessary.

## CONCLUSIONS

- \* The Three-way PCA of sediment grain size data is used to separate the temporal, spatial and grain size distribution variability.
- \* For the case of study, it is found that the coarse sand mobility is bounded within the bar-berm area, while the changes in percentage of the fine material take place all along the profile.
- \* A "master" grain size sample is obtained for each of the surveys. This "master" sample is constructed by adding all the grain samples taken along the profile. Comparison between the twenty master samples points out that they are almost equal. Therefore, it can be concluded that there is a "master" grain size distribution for the profile which is constant in time.
- \* Adopting the previous conclusion as a working hypothesis, it is suggested that the "master" grain distribution should be used in coastal engineering formulations to determine the required single grain size value, such as "A" in the equilibrium beach profile or "K" in the longshore sediment transport formula.
- \* One of the main advantages of this conclusion is the remarkable reduction of the field work as one field campaign at any time is enough to obtain the "master" grain size distribution.
- \* Finally, it has to be pointed out that by applying a four-way PCA, a "master" grain size distribution of a physiographic unit may be determined.

## ACKNOWLEDGEMENTS

This work was partially financed by the "Comisión Interministerial de Ciencia y Tecnología", through the research projects PB87-0800 and PB89-0381.

## REFERENCES

- Bartussek, D., 1973. "Zur Interpretation der Kernmatrix in der Driemodalen Faktorenanalyse von L.R. Tucker". *Psychologische Beiträge*, 15, pp. 169-184.
- Cornaglia, P., 1889. "On Beaches". In: Fisher, J.S. and R. Dolan (eds.), 1977. *Beach Processes and Coastal Hydrodynamics*. Stroudsburg, Pennsylvania: Dowden, Hutchinson and Ross, Inc., pp. 11-26.
- Dean, R.G., 1977. "Equilibrium Beach Profiles: U.S. Atlantic and Gulf Coasts". Dept. of Civil Eng., Ocean Eng. Tech. Rpt., No. 12, University of Delaware, Newark, DE, USA.
- Horn, D.P., 1991. "Computer Simulation of Shore-Normal Variations in Sediment Size". *Proc. Coastal Sediments '91*. ASCE. pp. 875-889.
- Kamphuis, J.W. and J.R. Moir, 1977. "Mean Diameter Distribution of Sediment Sizes before and after Artificial Beach Nourishment". *Proc. Coastal Sediments '91*. ASCE. pp. 197-210.
- Kroonenberg, P.M. and J. DeLeeuw, 1980. "Principal Least SqThree-Mode Data by Means of Alternating Squares Algorithms". *Psychometrika*, Vol. 45, pp. 69-97.
- Liu, J.T. and G.A. Zarillo, 1989. "Distribution of Grain Sizes across a Transgressive Shoreface". *Marine Geology*, 87, pp. 121-136.
- Losada, M.A., R. Medina, C. Vidal and A.J. Roldán, 1991. "Historical Evolution and Morphological Analysis of "El Puntal" Spit, Santander (Spain)". *Journal of Coastal Research*, 7(3), pp. 711-722.
- Medina, R., M.A. Losada, R.A. Dalrymple and A.J. Roldán, 1991. "Cross-Shore Sediment Transport Determined by EOF Method". *Proc. Coastal Sediments '91 Conf.* ASCE. pp. 2160-2174.
- Moutzouris, C.I., 1991. "Beach Profiles vs. Cross-Shore Distributions of Sediment Grain Sizes". *Proc. Coastal Sediments '91*. ASCE. pp. 860-874.
- Murray, S.P., 1967. "Control of Grain Dispersion by Particle Size and Wave State". *J. Geol.*, 75, pp. 612-634.



- Tucker, L.R., 1966. "Some Mathematical Notes on Three-Mode Factor Analysis". *Psychometrika*, Vol. 31, pp. 279-311.
- Winant, C.D., C.L. Inman and C.E. Nordstrom, 1975. "Description of Seasonal Beach Changes Using Empirical Eigenfunctions". *Jour. Geophys. Res.* Vol. 80, No. 15, pp. 1979-1986.

## CHAPTER 174

# Three-Mode Principal Component Analysis of Bathymetric Data, applied to "Playa de Castilla" (Huelva, Spain)

Raúl Medina\*  
Cesar Vidal\*  
Miguel A. Losada \*  
Antonio J. Roldan\*

### Abstract

Three-Mode Principal Component Analysis is applied to bathymetric data from a beach nourishment at "Playa de Castilla", Huelva, Spain. This approach is used to separate the temporal and spatial variability of the beach shoreface. The method is shown to describe variations occurring in the cross-shore and in the alongshore direction as well as temporal variations. The results of the analysis show a clear seasonality in the shoreface variations, with bar-berm processes involved in the cross-shore direction and complex sand variations in the alongshore direction. These alongshore variations are induced by the nourished area which avoids the formation of a uniform bar along the beach resulting in a complex sediment redistribution. The results also show an erosion trend in "Playa de Castilla". This erosion, however, is not related to the "spreading out" losses at the nourished beach but with the background erosion.

---

\*Ocean & Coastal Research Group. Departamento de Ciencias y Técnicas del Agua y del Medio Ambiente, Universidad de Cantabria, 39005 Santander, Spain

# 1 INTRODUCTION

The configuration of a sandy coast changes both in time and in space. Processes occurring in the nearshore ocean are extremely dynamic, involving the combined action of waves, currents, tides and sediment transport. Furthermore, their individual characteristics change with various scales in both space and time. Here, day-to-day hydrodynamic processes constantly adjust the beach bathymetry through on-offshore and longshore transport of sand due to the wave field, sediment supply and grain size, tide and wave induced currents and sea level.

The situation described above shows that the morphodynamics of nearshore systems are extremely complex and difficult to treat. One approach is the concept of equilibrium shoreface (equilibrium profile and equilibrium shoreline). This idea is based on the premise that the overall shape and morphology of the shoreface will be maintained with some consistency in response to the typical wave and current regime at a particular location. Once the equilibrium shape is determined, the temporal and spatial variations of the shoreface can be related to the variability of the coastal processes.

Different statistical approaches have been applied to beach profile data. Principal Component Analysis (*PCA*), also known as Empirical Orthogonal Function (*EOF*) technique, is an efficient method of objectively separating the spatial and temporal scales of variability of a beach. *PCA* is a technique of linear statistical predictors which represent a large number of data variables by a few spatial,  $e_n(s)$ , and temporal,  $f_n(t)$ , empirical orthogonal eigenfunctions which describe most of the variance of a data set  $y(s, t)$  by:

$$y(s, t) = \sum_n f_n(t) e_n(s) c_n \quad (1.1)$$

where  $c_n$  is a normalizing factor. The eigenfunctions are ranked according to the percentage of the variance defined as the Mean Square Value (*MSV*) of the data they explain, so that the first eigenfunction explains most of the *MSV* of the data.

This technique has been previously applied to cross-shore beach profile data: Winant et al (1975), Aubrey (1979), Zarillo and Liu (1988), Medina et al. (1991), and to alongshore profiles data: Losada et al. (1990), Liang and Seymour (1991), who showed that the variations in the longshore direction are as complicated as those in the cross-shore direction. In all these works, only one spatial direction is taken into account (cross-shore or alongshore) when analyzing the temporal evolution of a bathymetric data set. The assumption accepted is that the sediment transport occurring in the nearshore region may

be divided into two independent components by direction: cross-shore and longshore. This analysis may be correct in some particular cases, but it is rendered inadequate when two dimensional movements of sand are expected (e.g., response to coastal structures, beach nourishment...).

In the present study, the beach nourishment data set of "Playa de Castilla" (Huelva, Spain) is analyzed by means of the *three-mode PCA* method in which both cross-shore and alongshore variations and interactions are retained as well as time. The method is used to expand the data in the form:

$$y(x, y, t) = \sum_{p=1}^s \sum_{q=1}^t \sum_{r=1}^u [e_p(x) f_q(y) g_r(t) c_{pqr}] \tag{1.2}$$

## 2 THE 3-WAY PCA MODEL

Recently, some techniques have been developed to obtain direct solutions for *three-way* data sets. These dimensions are often referred to as *modes* and the technique is generally referred to as *three-mode* or *three-way PCA*. Procedures of this sort were first proposed by Tucker (1966), and extended by Kroonenberg and DeLeeuw (1980) and TenBerge et al. (1987).

If only some eigenfunctions (e.g.  $k$ ) are used to represent the data, equation 1.1 may be rewritten in matrix form as:

$$Y = ECF' \tag{2.1}$$

where  $Y$  is  $(n \times p)$ ,  $E$  is  $(n \times k)$ ,  $C$  is diagonal  $(k \times k)$ ,  $F$  is  $(p \times k)$  and  $()'$  denotes transpose operator.

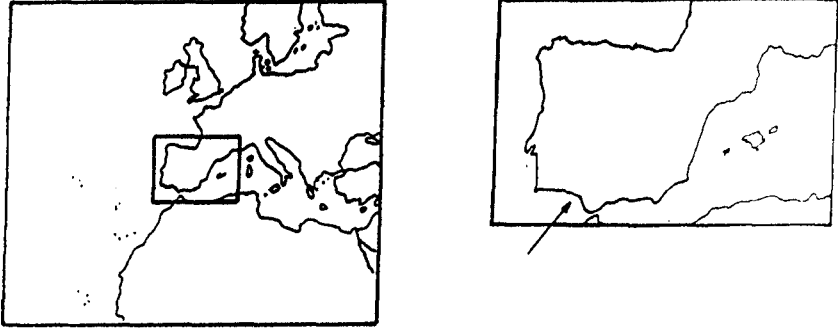
If the data array is augmented to include a third dimension, equation 2.1 will also be augmented by the inclusion of an extra term. In matrix form:

$$Y = EC(F' \otimes G') \tag{2.2}$$

where  $\otimes$  denotes a direct product or Kronecker matrix,  $E$  is  $(n \times k)$ ,  $G$  is  $(p \times k)$ , and  $F$  is  $(r \times k)$ . Since this is a matrix equation, both  $Y$  and  $C$  have to be restated as two-dimensional arrays,  $Y$  being  $(n \times p \times r)$  and  $C$  being  $(k \times k \times k)$ .  $E$ ,  $F$  and  $G$  are columnwise orthonormal matrices and have the same interpretation as the two-mode eigenvectors. However,  $C$ , which is now called the *core* matrix, is no longer a diagonal matrix of eigenvalues. One could conceive of

the *core* matrix as describing the basic relations that exist between the various collections of variables, Kroonenberg and DeLeeuw (1980).

The solution to equation 2.2 is based on the observation that the optimal *C* matrix can be expressed uniquely and explicitly in terms of the data and the component matrices for the three modes. The latter component matrices are optimized by an alternating least squares (ALS). A detailed description of the solution can be found in the paper by Kroonenberg and DeLeeuw (1980).



## Monitoring Program

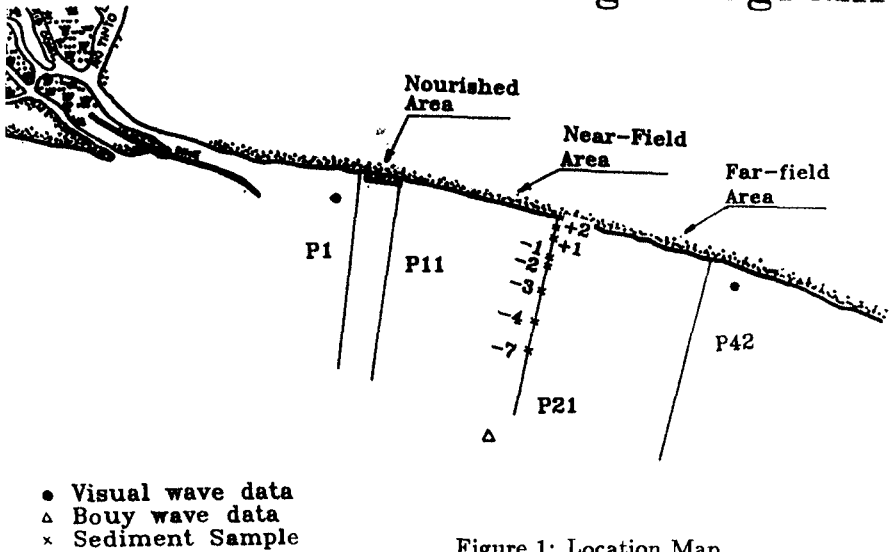


Figure 1: Location Map

### 3 STUDY SITE AND BATHYMETRIC DATA

The study area is located on the Southwest Coast of Spain (province of Huelva), between the Guadiana and Guadalquivir rivers (fig. 1). "Playa de Castilla" is a sandy beach which extends over 25 km between Mazagón and Matalascañas. Landward the beach is bounded by a rock-sand cliff which degrades into fine sand under wave action. The coastline at "Playa de Castilla" has been receding at a rate of 1.5 m/yr during the last 30 years (Fernández et al., 1990). The recession is due to two different reasons: first, the littoral drift from West to East, of about 390,000 m<sup>3</sup>/yr, and second, the reduction in the volume of sand transported by the rivers to the coast mainly caused by human construction.

An artificial nourishment of the beach of more than 1.500.000 m<sup>3</sup> of sand was carried out in 1989. The total volume of sand was pumped to the updrift edge of the beach forming a protruding area about 2 km long and 115 m wide. The borrowed sand was coarser than the native sand, being  $D_{50} = 0.63\text{mm}$  and  $D_{50} = 0.3\text{mm}$  for the borrowed sand and the native material respectively.

In order to study the beach nourishment evolution through time and space, a field measurement program was carried out during the period 1989-1992. The program included wave measurements, sand samples and bathymetry surveys. Bathymetric data were acquired bimonthly from 42 shore-normal profiles located between Mazagón and Matalascañas. Alongshore spacing of the profiles was approximately 500 meters and each profile was surveyed from the beach dune area, seaward to a depth of about 10 metres.

### 4 RESULTS OF ANALYSIS

The "Playa de Castilla" data described above are used for the 3-way PCA analysis. Of the 42 alongshore profiles, only 20 are examined. The profiles include the nourished part of the beach and 7 km down drift. For the cross-shore profiles, only the nearshore zone from the berm crest seaward to a depth of 4.0 m is selected for its variability. Within this area, very pronounced variations can be found both in the cross-shore and longshore direction. Notice that the transect spacing (500 m) was designed to resolve the long-term "spreading out" losses of the nourishment, but is not adequate to resolve the spacing of rhythmic topography, which can be spaced at several hundred meters or less.

The matrices  $E$ ,  $F$  and  $G$  in equation 2.2 are columnwise orthonormal. In other words, the components have length one. In this case, the importance of data is directly reflected by the entries of the core matrix,  $C$ , and not by the eigenvectors. Bartussek (1973) suggested scaling the orthonormal eigenvectors

of a 3-way *PCA* analogously to the procedure often encountered in standard *PCA*. One advantage of this scaling is that the scaled eigenvectors obtained are comparable within a mode and over modes. When scaling the eigenvectors (no longer orthonormals but orthogonal) the *core* matrix must also be scaled to leave the model invariant.

In figures 2a, b, c the first three cross-shore, alongshore and temporal eigenvectors are shown. The corresponding Bartussek *core* matrix values and the percentage of variation explained are given in Table 1. Notice that the first eigenvector of the three modes accounts for the 89.36%. This result is not surprising since we are dealing with raw uncentered data and, consequently, the centroid, defined as the mean of the variables, can explain most of the data. For that reason, the first eigenvectors are often highly correlated with mean vectors. Thus, the combination of the first eigenvectors gives a representation of the mean situation or mean bathymetry. Let us examine the meaning of the combinations of other eigenvectors

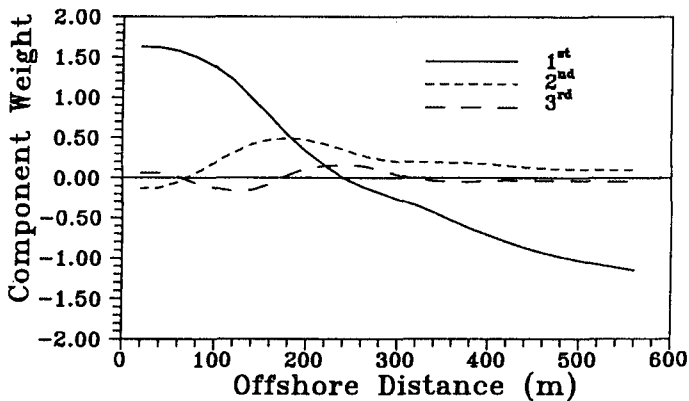


Figure 2a: Cross-shore Eigenvectors

Observing Figure 2a, it is clear that the second cross-shore eigenvector is very important in the upper part of the profile and it will play an important role in determining the upper profile slope. The third cross-shore eigenvector shows the typical S-shape of a berm-bar variability also encountered in standard *PCA* analysis. In Figure 2b, the nourished beach can easily be observed in the second alongshore eigenvector. The third alongshore eigenvector shows a small value with almost zero mean. In Figure 2c, the second temporal

Table 1: Frontal Planes of Core Matrix

Frontal Plane Time = 1 Down: Cross-shore. Across: Alongshore																													
<table border="1" style="width: 100%; border-collapse: collapse;"> <tr><th colspan="3">Core Matrix</th></tr> <tr><td>1.981</td><td>0.007</td><td>0.003</td></tr> <tr><td>-0.006</td><td>3.834</td><td>0.024</td></tr> <tr><td>0.023</td><td>1.017</td><td>6.946</td></tr> </table>			Core Matrix			1.981	0.007	0.003	-0.006	3.834	0.024	0.023	1.017	6.946	<table border="1" style="width: 100%; border-collapse: collapse;"> <tr><th colspan="3">Explained Variation</th></tr> <tr><td>89.36</td><td>0.00</td><td>0.00</td></tr> <tr><td>0.00</td><td>4.09</td><td>0.00</td></tr> <tr><td>0.00</td><td>0.03</td><td>0.26</td></tr> </table>			Explained Variation			89.36	0.00	0.00	0.00	4.09	0.00	0.00	0.03	0.26
Core Matrix																													
1.981	0.007	0.003																											
-0.006	3.834	0.024																											
0.023	1.017	6.946																											
Explained Variation																													
89.36	0.00	0.00																											
0.00	4.09	0.00																											
0.00	0.03	0.26																											
Frontal Plane Time = 2 Down: Cross-shore. Across: Alongshore																													
<table border="1" style="width: 100%; border-collapse: collapse;"> <tr><th colspan="3">Core Matrix</th></tr> <tr><td>0.022</td><td>0.944</td><td>0.559</td></tr> <tr><td>-3.659</td><td>-0.475</td><td>0.837</td></tr> <tr><td>2.112</td><td>-18.364</td><td>-25.445</td></tr> </table>			Core Matrix			0.022	0.944	0.559	-3.659	-0.475	0.837	2.112	-18.364	-25.445	<table border="1" style="width: 100%; border-collapse: collapse;"> <tr><th colspan="3">Explained Variation</th></tr> <tr><td>0.00</td><td>0.08</td><td>0.01</td></tr> <tr><td>1.73</td><td>0.00</td><td>0.00</td></tr> <tr><td>0.06</td><td>0.24</td><td>0.08</td></tr> </table>			Explained Variation			0.00	0.08	0.01	1.73	0.00	0.00	0.06	0.24	0.08
Core Matrix																													
0.022	0.944	0.559																											
-3.659	-0.475	0.837																											
2.112	-18.364	-25.445																											
Explained Variation																													
0.00	0.08	0.01																											
1.73	0.00	0.00																											
0.06	0.24	0.08																											
Frontal Plane Time = 3 Down: Cross-shore. Across: Alongshore																													
<table border="1" style="width: 100%; border-collapse: collapse;"> <tr><th colspan="3">Core Matrix</th></tr> <tr><td>0.130</td><td>-0.474</td><td>2.698</td></tr> <tr><td>0.439</td><td>-9.169</td><td>34.651</td></tr> <tr><td>0.115</td><td>-6.520</td><td>-20.721</td></tr> </table>			Core Matrix			0.130	-0.474	2.698	0.439	-9.169	34.651	0.115	-6.520	-20.721	<table border="1" style="width: 100%; border-collapse: collapse;"> <tr><th colspan="3">Explained Variation</th></tr> <tr><td>0.01</td><td>0.01</td><td>0.03</td></tr> <tr><td>0.01</td><td>0.16</td><td>0.41</td></tr> <tr><td>0.00</td><td>0.01</td><td>0.02</td></tr> </table>			Explained Variation			0.01	0.01	0.03	0.01	0.16	0.41	0.00	0.01	0.02
Core Matrix																													
0.130	-0.474	2.698																											
0.439	-9.169	34.651																											
0.115	-6.520	-20.721																											
Explained Variation																													
0.01	0.01	0.03																											
0.01	0.16	0.41																											
0.00	0.01	0.02																											

eigenvector shows a seasonal dependence. The third eigenvector shows a net trend almost linear from negative values to positive ones. The combination of these eigenvectors explains most of the variability of the evolution of the beach (see Table 1). In order to better interpretate the variability they account for, it is useful to examine the profile or the bathymetry that is obtained by the product of one alongshore eigenvector with one cross-shore eigenvector, and use the corresponding temporal function to determine how the obtained profile or bathymetry evolves in time.

The following pair of eigenvectors is analyzed:  $e_1g_1$  and  $e_2g_2$  for time = 1;  $e_2g_1$  and  $e_3g_2$  for time = 2;  $e_2g_2$  and  $e_2g_3$  for time = 3; where  $e$  denotes cross-shore eigenvector,  $g$  denotes alongshore eigenvector and the subscript denotes the order of the eigenvector. These pairs account for the 96% of the total variance of the data (see Table 1).



- Time = 1, pair  $e_{1g_1}$  (Fig. 3a). As it was previously anticipated, the product of all the first eigenvectors represents a mean bathymetry. This mean bathymetry shows a uniform beach profile with minor changes in the alongshore direction.

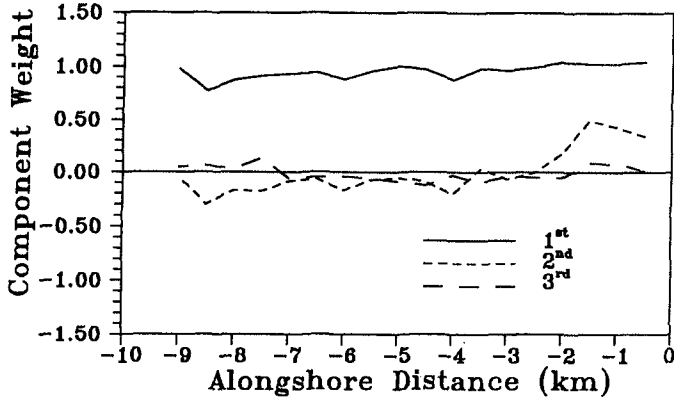


Figure 2b: Alongshore Eigenvectors

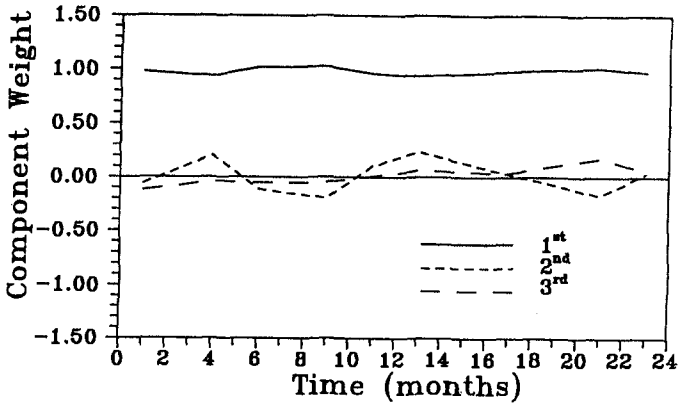


Figure 2c: Temporal Eigenvectors

- Time = 1, pair  $e_{2g_2}$ . This pair is affected by the first temporal eigenfunction (Fig. 2c) which is almost constant in time and, consequently, this pair is

part of the mean bathymetry. The complexity of the bathymetry makes it impossible to achieve a solution just by the product of one cross-shore function and one alongshore function, thus this new pair must be added to the pair  $e_1g_1$  in order to obtain a better representation of the mean situation. Notice that this new pair modifies the upper part of the profile with minor changes in the offshore zone. Further, the modification at the upper shoreface has a different sign at the nourished beach and in the rest of the study area. The final mean bathymetry, achieved by the sumation of the pairs  $e_1g_1$  and  $e_2g_2$  has a much steeper profile at the nourished beach than the native beach (Fig. 3b).

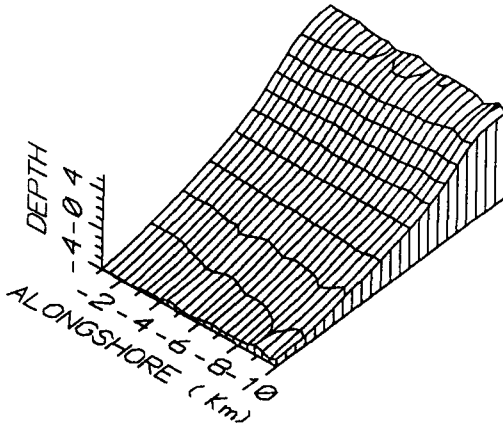


Figure 3a: Mean bathymetry based on  $e_1g_1$

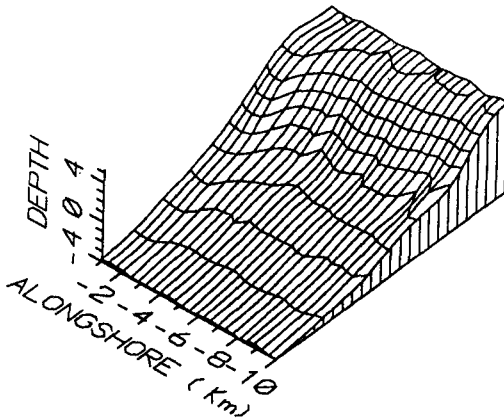


Figure 3b: Mean bathymetry based on  $e_1g_1$  and  $e_2g_2$

- Time = 2, pair  $e_{2g_1}$ . The most important characteristic of the bathymetries associated with the second temporal eigenfunction is the seasonality. The bathymetry achieved by the product of  $e_{2g_1}$ , for instance, must be added or subtracted to the mean bathymetry depending on the season (see Fig. 2c). In particular, pair  $e_{2g_1}$  shows a seasonal variation of the shoreface slope and of the amount of sand in the offshore part of the profile. These changes are almost uniform in the alongshore direction and are related to the erosion of the cliff.

- Time = 2, pair  $e_{3g_2}$ . As previously stated when dealing with the mean bathymetry, the seasonal changes are too complex to be represented by just one product. Consequently, if we want to obtain more information about the seasonal changes, the next pair to be added is  $e_{3g_2}$ . When combining these two eigenvectors, a shift in the location and magnitude of the bar is achieved. The complete picture of the seasonal variability can be found by adding pairs  $e_{2g_1}$  and  $e_{3g_2}$ . When adding those pairs, a clear bar is found in the native beach during the summer period, figure 4a. In the nourished area, however, no bar is formed, as can be observed in figure 4b.

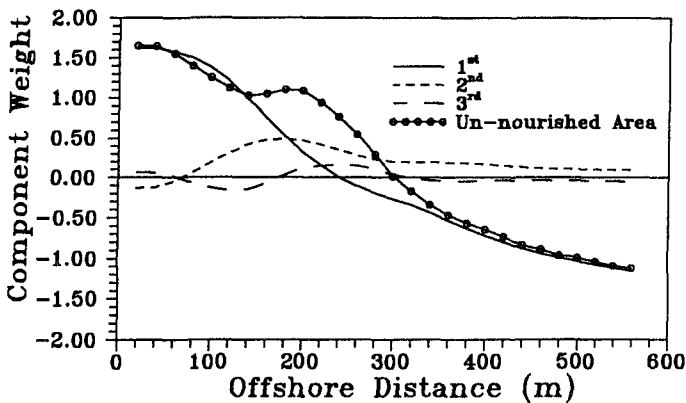


Figure 4a: Seasonal variability. Native area

- Time = 3, pairs  $e_{2g_2}$  and  $e_{3g_2}$ . Only 0.66% of the total variance can be explained by the third temporal eigenvector. However, this variability is very important since it is associated with a net trend in the data. In the native beach the eigenvectors show a net erosion of the whole profile, see figure 5a. In the nourished area almost no changes have occurred during the period of study, see figure 5b.

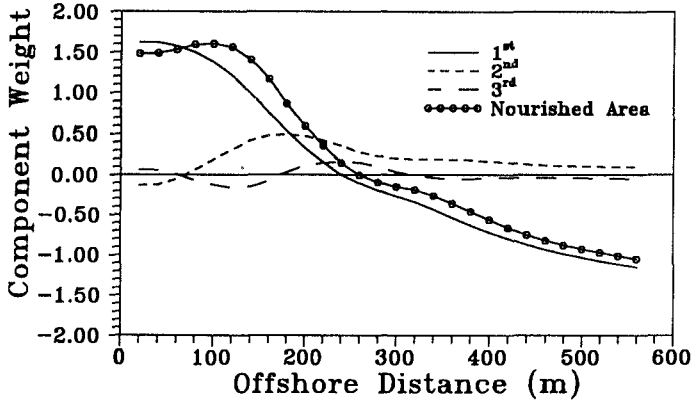


Figure 4b: Seasonal variability. Nourished area

## 5 DISCUSSION

The transect spacing (500 m) and the survey frequency (bimonthly) were designed to resolve the long-term and long scale evolution of the beach nourishment. The results of the analysis show, however, that there is little evolution but significant seasonal variability.

The seasonal changes described by the 3-way PCA method are highly correlated with the seasonal variations of incident wave energy. It is well-known that there is an onshore-offshore movement of nearshore sediments in response to changing wave energy that builds bars and berms in a beach profile. In "Playa de Castilla" there is also a complex sand movement in the longshore direction induced by the protruding nourished area which was built with a coarser grain. The nourished area avoids the formation of a uniform bar along the beach resulting in a complex sediment redistribution. With the alongshore spacing of the transects used in the present study, it is not possible to resolve wave-like sand motions propagating in the longshore direction. This kind of motions have been cited by some authors, but largely ignored in literature. Further studies of these motions should be carried out by means of the 3-way PCA.

The evolution of "Playa de Castilla", described by the third temporal eigenvector and the combinations of pairs  $e_2g_2$  and  $e_3g_2$ , shows a net erosion of the beach as reported by (Fernández et al., 1990). However, there is no evidence of "spreading out" losses in the nourished beach. It seems that the effect of using material which is substantially coarser than the native material armors the beach in the nourishment area thereby resulting in less transport from the nourished area.

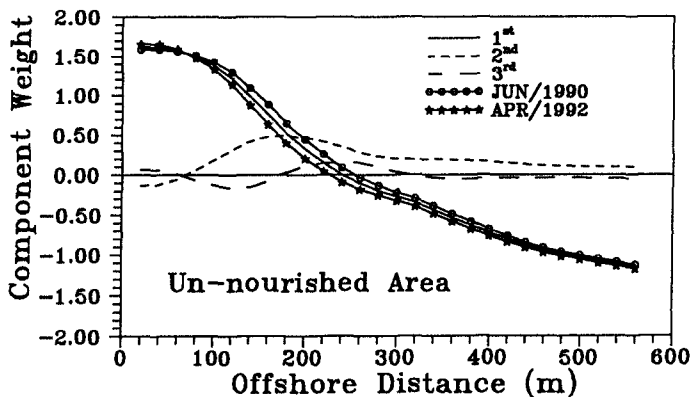


Figure 5a: Net trend. Native area

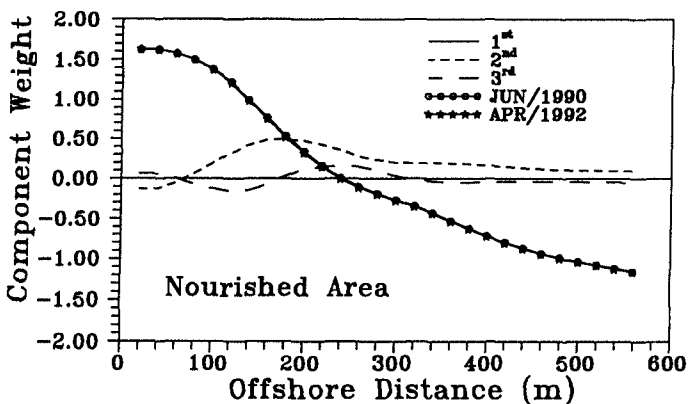


Figure 5b: Net trend. Nourished area

## 6 CONCLUSIONS

Three-Mode Principal Component Analysis has been applied to bathymetric data from a beach nourishment at "Playa de Castilla", Huelva, Spain. The method has been shown to be of great value in analyzing the variations of the shoreface during a two year period. The ability of the method to jointly analyze the cross-shore, alongshore and temporal variations and to separate these variations into orthogonal eigenvectors allow a better understanding of the processes involved. The results of the analysis show that most of the sand movement in "Playa de Castilla" has a seasonal dependency with involved bar-berm processes in the cross-shore direction and a complex sand variability in the alongshore direction induced by the protruding nourished area. The method has also shown an erosion trend in the beach. This erosion, however, is not related to the "spreading out" losses at the nourished beach but background erosion.

## 7 ACKNOWLEDGEMENTS

This work was partially supported by the Comisión Interministerial de Ciencia y Tecnología, through the Research Projects PB87-0800 and PB89-0381. The program TUCKALS 3 for 3 - way PCA analysis was provided by P. Kroonenberg.

## REFERENCES

- Aubrey, D.G., 1979. "Seasonal Patterns of Onshore/Offshore Sediment Movement". *Jour. Geophys. Res.* Vol. 84, C10, pp. 6347-6354.
- Bartussek, D., 1973. "Zur Interpretation der Kernmatrix in der driemodalen Faktorenanalyse von L. T. Tucker". *Psychologische Bie trage*, 15, 169,184.
- Kroonenberg, P. M. and J. DeLeeuw, 1980. "Principal Components Analysis of Three-Modes Data by Means of Alternating Least Squares Algorithms". *Psychometrika*, Vol 45, pp 69-97.
- Liang, G. and J. Seymour, 1991. "Complex Principal Component Analysis of Wave-Like Sand Motions". *Proc. Coastal Sediments' 91 Conf.* A.S.C.E., pp. 2175-2186.
- Losada, M.A., R. Medina, C. Vidal and A.J. Roldán, 1990. "Historical Evolution and Morphological Analysis of El Puntal Spit, Santander (Spain)". *Jour. Coastal Res.*, Vol. 7, No. 3, pp. 711-722.

- Medina, R., M.A. Losada, R.A. Dalrymple and A.J. Roldán, 1991. "Cross-Shore Sediment Transport Determined by EOF Method". *Proc. Coastal Sediments'91. Conf. A.S.C.E.*, pp. 2160-2174.
- Ten Berge, J.M.F., J. DeLeeuw and P.M. Kroonenberg, 1987. "Some additional results on Principal Components Analysis of Three-Mode Data by Means of Alternating Least Squares Algorithms". *Psychometrika*, Vol 52, pp 183-191.
- Tucker, L.R., 1966. "Some Mathematical Notes on Three-Mode Factor Analysis". *Psychometrika*, Vol. 31, pp. 279-311.
- Winant, C.D., C.L. Inman and C.E. Nordstrom, 1975. "Description of Seasonal Beach Changes Using Empirical Eigenfunctions". *Jour. Geophys. Res.* Vol. 80, No. 15, pp. 1979-1986.
- Zarillo, G.A. and J.T. Liu, 1988. "Resolving Bathymetric Components of the Upper Shoreface on a Wave-Dominated Coast". *Marine Geology*, Vol. 82, pp. 169-186.

## CHAPTER 175

### WAVE BREAKER TURBULENCE AS A MECHANISM FOR SEDIMENT SUSPENSION

G P Mocke<sup>1</sup> and G G Smith<sup>1</sup>

#### Abstract

The mechanism whereby sediment particles are suspended under broken waves in the surfzone is investigated through experimental data analysis and computational modelling. The concentration measurements referred to comprise continuous transmissometer and optical backscatter sensor (OBS) values recorded in the field as well as a large database of time-averaged recordings. The measurements analysis, which included a unique set of laboratory observations derived from a specially designed vertical mixing apparatus, clearly highlight the preeminent rôle of wave breaker turbulence in the suspension process. The wave period averaged turbulence structure is found to be well predicted by a two equation ( $k$ ,  $\varepsilon$ ) turbulence model. With the parametrization of the bottom reference concentration using relevant breaker and bottom generated turbulence variables, a scalar extension of the  $k$ ,  $\varepsilon$  model is effective in predicting published time-averaged suspended sediment distributions. Analytical relations founded on the assumption of a predominately diffusive turbulent transport regime furthermore display favourable predictive capabilities.

#### 1. Introduction

Suspended sediment concentrations in the surf zone have been measured to be up to several orders of magnitude higher than is typical for an unbroken wave regime. This is particularly evident at the higher elevations above the bed, with suspended

---

<sup>1</sup>Research Engineers, CSIR, P O Box 320, Stellenbosch, 7600, S Africa



sediment outside the surf-zone often restricted to the limited wave boundary layer.

In assessing the influence of wave breaking on the suspension process, Nielsen (1984) and Shibayama *et al.* (1986) have identified the action of the large scale vortices generated coincident with wave plunging. These essentially two-dimensional vortices are, however, restricted to a limited transition zone, shorewards of which the surf-zone is characterised by an inner bore region.

Experimental measurements through the inner region (Stive, 1980; Nadaoka and Kondoh, 1982) have revealed the presence of a turbulence generating layer in the vicinity of the surface bore from where the turbulence is transported downwards. Nadaoka *et al.* (1989) have furthermore identified an eddy structure whereby the surface bore is dominated by a nearly two-dimensional flow structure, bounded below by strongly three-dimensional obliquely descending eddies bringing highly intermittent turbulence to the bottom.

The dominant action of this turbulence for sediment suspension is verified by means of concentration measurements and visualisation studies made by Nadaoka *et al.* (1988) and Sato *et al.* (1990) in a wave flume. Computations of the turbulence structure using a 1-equation turbulence model have been shown by Deigaard *et al.* (1986) to result in favourable prediction of measured breaker zone suspended sediment concentrations. In the present exercise the suspension process is further investigated with reference to field and laboratory measurements as well as quantitative modelling.

## 2. Concentration Measurements

### Continuous

Particular reference was made to a comprehensive set of continuous measurements of suspended sediment recorded by a vertical array of seven transmissometer units. These units were fixed to a frame together with a pressure transducer and time-averaged concentration suction sampler and deployed at an exposed coastal site (Coppoolse *et al.*, 1992). A limiting factor is that transmissometer signals have a tendency to become saturated at elevated concentrations or if air-bubbles become entrained in the flow. However the analysis of a number of surf-zone time series, which also contain saturated signals, appears to demonstrate the importance of breaker turbulence for sediment suspension.

In a separate exercise, continuous measurements of suspended sediment were made by three optical backscatter sensors (OBS) deployed from a scaffold frame placed in the nearshore. The frame, which also had attached two electromagnetic current meters, a pressure transducer and wave staff, was within the surfzone except for the highest tidal conditions. It was found that elevated concentrations through the depth are not necessarily discreetly correlated with the largest wave heights and

velocities, but rather exhibit a sensitivity to a more intensive, but still intermittent, turbulence coincident with the wave groups.

A rather unique set of measurements were obtained from a laboratory experiment in which turbulence is generated from a vertically oscillating grid within a glass-walled tank. The apparatus is based on similar devices used for experiments on density gradient mixing due to diffused turbulence (E. and Hopfinger, 1986). The suspension of sand from a bed of sand at the base of the tank is recorded at various elevations using an optical backscatter sensor. Figure 1 a) is a typical time series of the measured concentrations recorded at 5 mm above the bottom. Despite a relatively constant time averaged concentration, the occurrence of intermittent suspension events due to the turbulence can be clearly seen. Figure 1 b) is a plot of time-mean concentrations evaluated at various elevations. The distribution exhibiting elevated concentrations throughout the entire depth is typical of suspended sediment measurements taken in the surf zone.

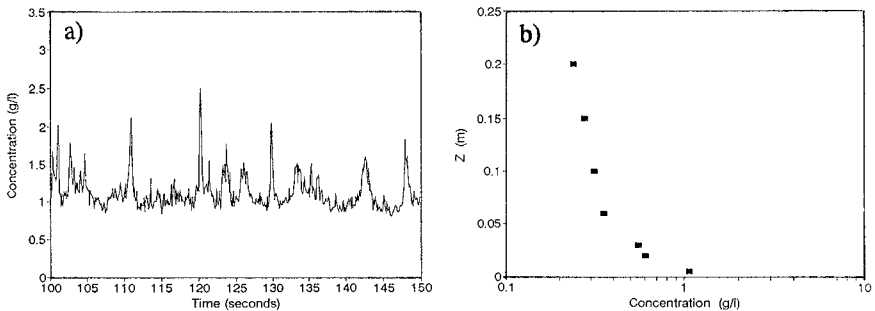


Figure 1 OBS concentrations as a) time series measured 5 mm from the bottom and b) time-averaged at various elevations

### Time averaged measurements

Analyses of experimental turbulence and suspended sediment measurements (Stive, 1980, Nadaoka *et al.*, 1988, Sato *et al.*, 1990) have indicated that phase-averaged quantities display limited variation over time. This underlines the intermittent nature of the turbulence and suspension process and also confirms the validity of using a time-averaged modelling approach.

Time-averaged concentration profiles recorded seawards of the surfzone have been shown to be relatively well described by an exponential distribution over the depth of  $\bar{C}(z) = C_b e^{-z/\ell}$ , where  $\ell$  is an integral length shown by Nielsen (1984) to scale on bed ripple dimensions. Although there is some indication (Hardenberg *et al.*, 1991) that the classical exponential relation describes surf-zone concentrations when averaged over relatively long time periods, it is inappropriate for representing the

strong vertical variability in mixing evident on the time scale of the incident waves. In the analysis of a comprehensive database of field and laboratory measurements of suspended sediment concentration profiles compiled by Van Rijn (1991) it is however assumed that the exponential distribution holds over a limited region near the bed. Hence for some 73 sets of experimental surf-zone measurements an exponential regression curve fitted through the lower three data points is extrapolated for the determination of a reference concentration  $C_b$  at the bottom.

Previous attempts to parametrize this reference value have focused primarily on the rôle of turbulence generated by mean shear near the bottom as reflected in the Shields parameter  $\theta = \tau / (\rho(s-1)gd)$ . Because of the significance of near surface generated wave breaker turbulence, however, it is of fundamental importance to also incorporate this contribution in any parametrization exercise. The energy dissipation in a breaking wave may be modelled as for a periodic bore. Thus the equivalent energy available for sediment suspension is related to this dissipation ( $D \propto H^3/hT$ ).

Complementing this parameter representing the injection of TKE into the flow is the length scale indicating the relative degree of depth penetration. It is proposed that an appropriate scale for this parameter would be the relative wave height ( $H/h$ ). Combining these scales together with the Shields parameter the best fit regression curve against the database measurements is as shown in Fig. 2 and provides the following expression for predicting the bottom reference concentration:

$$C_b = \rho K^{-0.92} (H/h)^{3.32} (H^3/hT)^{-0.92} \theta^{0.37} \quad (1)$$

where  $K = 1.51 \cdot 10^3 \text{ sm}^{-2}$  is a proportionality constant related to the energy dissipation term. In carrying out the exercise the relative importance of component terms such as the wave height was clearly evidenced.

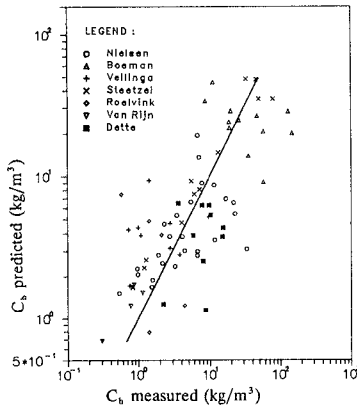


Figure 2 Parametrization of bottom reference concentration  $C_b$  by current and wave variables

The resolution of length scale values (through transformation of the aforementioned exponential relation) for a number of breaker cases included in the Delft database showed interesting tendencies. On the whole magnitudes were relatively small in the immediate vicinity of the bottom, with in most cases a rapid increase to values of between 20 and 40% of the overall water depth at higher elevations. Such magnitudes are in accordance with quantities determined from experimental measurements by Black and Rosenberg (1991) as well as scales determined by George and Flick (private comm.) from field measurements of turbulence .

### 3. Computational Modelling

#### System of equations

The time-mean vertical distribution of suspended sediment is described by the time-independent form of the classical advection-diffusion equation:

$$0 = \frac{\partial}{\partial z} \left[ D_c \frac{\partial C}{\partial z} + w_s C \right] \tag{2}$$

where  $C$  is the sediment concentration,  $w_s$  is the sediment fall velocity and  $D_c$  is the eddy diffusivity which is assumed equivalent to the eddy viscosity  $\nu_t$  defining the turbulent momentum flux. Following the analysis of Prandtl-Kolmogorov the eddy viscosity may be related to the TKE density  $k$  ( $\overline{u_i u_j} = 2k$ ) and its rate of dissipation  $\varepsilon$  such that  $D_c = \nu_t = c_\mu k^2/\varepsilon$ , where  $c_\mu$  is an empirical constant. For a unidimensional flow the dimensionless form of the time-averaged transport equations for  $k$  and  $\varepsilon$  may be expressed in the following manner:

$$0 = \frac{\partial}{\partial z} (D_k \frac{\partial k}{\partial z}) + P_b + P + G - \varepsilon \tag{3}$$

$$0 = \frac{\partial}{\partial z} \left[ D_\varepsilon \frac{\partial \varepsilon}{\partial z} \right] + [c_{1\varepsilon} (P_b + P + G (1 - c_{3\varepsilon})) - c_{2\varepsilon} \varepsilon] \frac{\varepsilon}{k} \tag{4}$$

where the above equations have been made dimensionless by characteristic flow parameters such as the mean water depth  $h$  and the wave celerity  $c(=\sqrt{g\overline{h}})$ . The dimensionless diffusion coefficients are defined as:

$$D_k = 1/Re + \nu_t / \sigma_k , \quad D_\varepsilon = 1/Re + \nu_t / \sigma_\varepsilon \tag{5}$$

where the molecular viscosity term  $Re$ , the flow Reynolds number, is negligible in comparison to the turbulence contribution.

The forcing functions are the production  $P_b$  of TKE due to wave breaker induced turbulence and  $P = \nu_t (\partial u / \partial z)^2$  due to mean shear. The buoyancy term is expressed

as  $G = Ri D_c \partial C / \partial z$ . This term, which includes a reference dimensionless Richardson number  $Ri = g \Delta \rho / \rho h / c^2$ , expresses the effect of turbulence damping due to the gradient in concentration. The choice of empirical constants, discussed in Mocke (1991), are close to classical values (Rodi, 1980) except for  $c_\mu (= 0.3)$ .

### Boundary conditions

The main forcing function for the flow is the production of turbulence in the surface roller. This production is assumed to be imposed at the upper boundary of the flow regime, which is taken at the mean water level. Modelled according to the dissipation in a hydraulic jump the breaker production term may be expressed as:

$$P_b = A_\varepsilon \frac{gH^3}{4h^2T} D' \quad (6)$$

where  $A_\varepsilon$  is a dimensionless dissipation factor expressing the difference between energy dissipation in a wave breaker and hydraulic jump. A series of experimental measurements made by Stive (1984) found this factor to be in the range 1.3 ~ 2.0, and together with other data, suggests a dependence of this factor on the wave breaker type. The dimensionless energy dissipation  $D' = h^2 / h_t h_c$  (Svendsen, 1984), with  $h_t$  and  $h_c$  the depths below the wave trough and crest level respectively.

With the assumption of a zone characterised essentially by local equilibrium between diffusion and dissipation of turbulence, the TKE varies over depth as:

$$k(z) = k_s \exp ((z-h)/\ell_s) \quad (7)$$

where  $k_s$  and  $\ell_s$  are respectively the intensity and length scale of the turbulence at a reference surface level taken at the upper boundary ( $z=h$ ). With the rate of dissipation  $\varepsilon$  related to  $k$  through the turbulent length scale ( $\varepsilon \propto k^{3/2}/\ell$ ), the vertical distribution of  $\varepsilon$  likewise follows an exponential decay:

$$\varepsilon(z) = \varepsilon_s \exp (3/2 (z-h)/\ell_s) \quad (8)$$

Substituting the expressions for  $k$  and  $\varepsilon$  in the purely diffusive formulation of (3), the surface value  $\varepsilon_s$  may be related to  $k_s$  through the length scale  $\ell_s$ :

$$\varepsilon_s = \left( \frac{3}{2} \frac{c_\mu}{\sigma_k} \right)^{1/2} \frac{k_s^{3/2}}{\ell_s} \quad (9)$$

In terms of the previously discussed turbulence generating horizontal vortex in the surface roller and as suggested by Battjes (1975),  $\ell_s$  could be expected to scale on the wave height  $H$  ( $\ell_s = A_t H$ ) where the chosen dimensionless length factor

$A_t = 1/3$  provides a length scale approximately equivalent to the wave trough amplitude ( $h-d$ ). It is also consistent with a dimensionless length scale  $\ell/h \approx 0.2$ , which is in close agreement with estimates made from undertow measurements as well as previously mentioned concentration and turbulence measurements.

At the surface boundary, the vertical turbulent and gravity flux of sediment is assumed to be in equilibrium:

$$D_c \frac{\partial c}{\partial z} + w_s C = 0 \quad (10)$$

The lower boundary condition is not applied at the actual bottom but rather at the outer limit of the viscous boundary layer. As detailed in Rodi (1980), the bottom boundary conditions for  $k$  and  $\varepsilon$  are:

$$k_b = \frac{u_*^2}{\sqrt{c_\mu}} \quad \varepsilon_b = \frac{u_*^3}{\kappa z} \quad (11)$$

where  $u_*$  is the bottom shear velocity,  $\kappa$  the constant of Von Karman ( $\sim 0.4$ ),  $z$  the distance from the bed and  $c_\mu$  the diffusive coefficient where production and dissipation are in local equilibrium ( $=0.09$ ). A constant stress bottom boundary layer is also assumed for the quantification of TKE production due to mean shear. Assuming local equilibrium ( $P/\varepsilon=1$ ); this production may be approximated as:

$$P = \frac{u_*^3}{\kappa z} \quad (12)$$

For the determination of  $u_*$ , reference is made to the bottom roughness and the mean velocity  $\bar{u}$ . Where we do not dispose of measurements the mean velocity is reliably estimated from experimental measurements (Stive, 1980) as  $\bar{u} \approx 0.1c$ . Although the bottom boundary turbulence source is normally greatly outweighed by the surface breaker contribution, it does act as a limiting condition both in the event of low intensity breaker turbulence as well as by implicitly suppressing the turbulence scales due to wall proximity effects.

The bottom boundary condition for the suspended sediment computations relies on the parametrization relation (1), which provides the bottom reference concentration  $C_b$  for the relevant flow condition.

### Resolution procedure

The set of equations are discretized in an implicit scheme using the finite difference method. A central differencing approach is used to construct a tri-diagonal matrix which can be solved analytically by the Thomas algorithm.

#### 4. Computational Results

##### **Wave breaker turbulence**

Initial model simulations were carried out in the absence of the sediment phase in an effort to evaluate the effectiveness of the turbulence model for predicting the observed dynamic as well as measured turbulence parameters. The experimental arrangements and description of measurements are detailed in Stive (1980) and Stive and Wind (1982), Nadaoka and Kondoh (1982) and Hattori and Aono (1985).

In analyzing laser Doppler anemometer (LDA) measurements, Stive (1980) used an ensemble averaging method to separate the time varying wave motions from the purely turbulence contribution. In analogy with the turbulence characteristics of a plane wake, the turbulent kinetic energy under the breakers was computed from the two components of the turbulence fluctuations as  $k=1.33/2(\overline{u'^2}+\overline{w'^2})$ .

The measured wave parameters were exploited for the computation of the TKE breaker production rate using expression (6). This rate was adjusted by the measured dimensionless dissipation factor  $A_s$  to obtain the correct energy dissipation for determining the turbulence production forcing function.

Solving the set of equations (3) and (4), predictions of time-averaged kinetic energy are compared to measurements at different positions after breaking for Stive tests 1 and 2 (Figure 3). In general, comparisons were found to be slightly better with the spilling (test 1) rather than the plunging (test 2) wave case. Although the depth averaged value for the predictions compares favourably with that of the measurements, the simulations were found to display somewhat more variation over the vertical. This characteristic is possibly attributable to a small convective contribution present in the experimental case. However, any such comparisons should be made in consideration of the room for optimization of the model constants, the experimental separation technique employed, and the determination of  $k$  by plane wake analogy.

The significant influence of the technique used for separating wave and purely turbulent fluctuations is evident when considering the measurements of Nadaoka and Kondoh (1982). By confining turbulence to a cut-off frequency of 10 Hz, any components with frequencies lower than this value will be neglected. A consequent underestimation of actual values would appear to be evident from intercomparisons with predictions (Figure 4 a)) and the magnitude of Stive values. As is also shown in a purely numerical exercise a reduction of the breaker height by 50% results in favourable correspondence between predictions and measurements. The separation technique employed by Hattori and Aono (1985) is considered equivalent to that used by Stive (1980). Not surprisingly correspondence between predictions and measurements is favourable (Figure 4 b)).

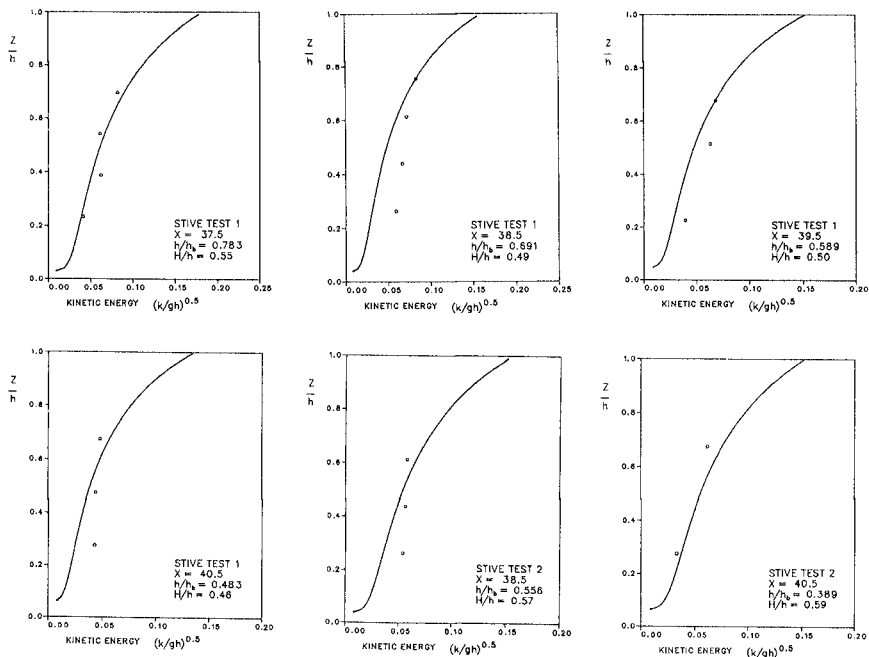


Figure 3 Intercomparison of computed (—) TKE profile and measurements (o) of Stive (1980). Tests 1 and 2.

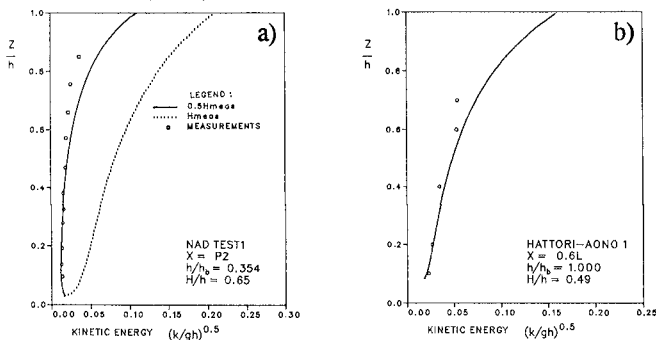


Figure 4 Intercomparison of computed (—) and measured (o) TKE profiles of a) Nadaoka and Kondoh (1982) and b) Hattori and Aono (1985).

The typical dissipation profile computed for the Stive measurements predicts a curve decaying from the surface in much the same manner as for the TKE. Lacking measurements of the dissipation profile, no comparisons with the experimental case may be made. However, the model was found to at least conceptually confirm the observation by Svendsen (1987) that only a relatively



small percentage of the energy lost in the breaker is dissipated below the wave trough level.

Penetrating downwards from the surface production source the computed length scale was found to display a near linear gradient. This is consistent with the integral length scale growth as measured under an oscillating grid by E and Hopfinger (1986). Approaching the bottom boundary the length scale reduces dramatically to attain a value determined by the imposed boundary conditions.

Due to dimensional considerations, the eddy viscosity profile displays similarities to that for  $k$  and  $\epsilon$ , indicating an appreciable variation over depth. Although not a directly measurable quantity, Stive and Wind (1986) estimated the eddy viscosity for test case 1 by considering similarity between the flow fields in breaking waves and wake flows. The resulting eddy viscosity is however considered averaged over the depth. The ensemble of computed profiles predicted depth-averaged values in close agreement with these estimations.

### **suspended sediment**

For the computation of the suspended sediment profiles the turbulence equations (3) and (4) are extended by the scalar diffusion equation (2). Model comparisons are somewhat hindered however, by the fact that presently there exists no simultaneous measurements of suspended sediment and turbulence quantities. Furthermore, there is a lack of suspended sediment measurements that also include an accurate assessment of the cross-shore wave energy loss important for determining local dissipation.

Despite these limitations the model was applied to a number of cases where suspended sediment was measured under breaking waves. In these cases, which include both laboratory and field measurements, the given wave height was exploited for determination of the breaker energy production. For the sake of consistency between cases no adjustment of the bore approximation dissipation term is made (i.e.  $A_\epsilon = 1$ ). Where the sediment fall velocity of the suspended sediment is not provided, it is estimated from the sediment size ( $D_{50}$ ) characteristics.

Although recognized as potentially significant, little attention has been given to incorporating the turbulence damping effect of a concentration gradient in previous attempts at modelling suspended sediment in the surf-zone. With the inclusion of the buoyancy term  $G$  in the equations (3) and (4) however, this contribution can be assessed.

As is in fact shown in Figure 5a) where model simulation with and without the buoyancy term are compared with field measurements of Nielsen (1984), the turbulence damping effect reduces the amount of sediment in suspension. The damping effect on local turbulence is more directly illustrated in the trace of the

mixing length scale shown in Figure 5b), where some reduction in this scale due to the more predominant concentration gradient near the bottom is evident. Superimposed on the predictions are estimates for the relative length scale as estimated from the measurements. The relatively rapid increases in length scale before attaining a magnitude between 20% and 30% of the water depth is evident in both the measured and predicted values.

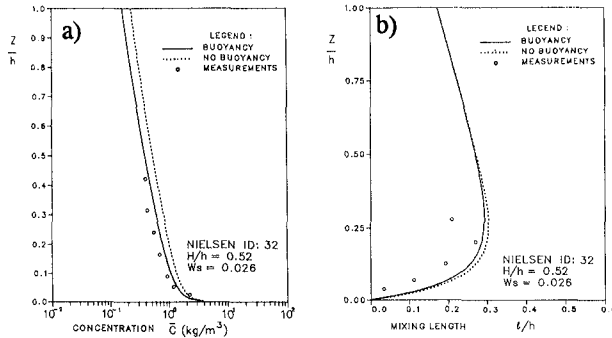


Figure 5 Predicted (a) concentration profile and (b) turbulent length scale with (—) and without (---) buoyancy effects (Van Rijn, 1991)

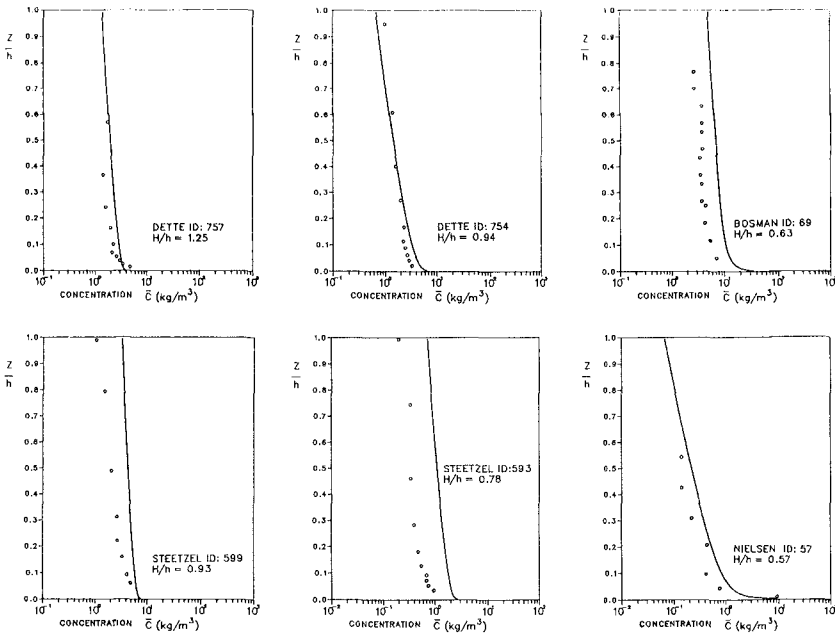


Figure 6 Comparisons between predictions (—) and experimental measurements (o) of suspended sediment as obtained from the Delft database (Van Rijn, 1991).

As may be observed from the examples of field and laboratory concentration measurements presented in Figure 6, predictions are generally in reasonable agreement with measurements. The sensitivity of the model to the wave height and bottom friction velocity and reference concentration was found to be important, with adjustments of less than 10% resulting in improved correlations in many cases.

**Analytical relations**

Assuming an exponential decay it is possible to plot profiles of  $k$  and  $\epsilon$  knowing the surface boundary values of these parameters and the relevant turbulent length scale. Following substitution of expressions (7) and (8) into the Prandtl-Kolmogorov relation the vertical distribution of eddy viscosity may be approximated by the following expression:

$$\nu_t = \nu_{t_s} \exp ( 1/2 (z-h)/\ell_s ) \tag{14}$$

It is clear that an accurate means of evaluating the surface value  $k_s$  would allow reasonable analytical predictions of the vertical profile for all the relevant turbulent parameters. From a joint analysis of  $k_s$  (as determined from the computational model) versus the non-dimensionalised breaker production term  $P_b^+ = P_b hc^{-3}$  for the Stive (1980) measurements the following relation was derived.

$$\sqrt{k_s} = 0.124 u_* \exp (128.2 P_b h.c^{-3}) \tag{15}$$

Although representing only a limited database of measurements, the above relation provides an intuitively correct approximation of the magnitude of breaker induced TKE at the reference surface level. Exploiting the relation (11) and assuming  $A_t = 1/3$ , the approximated eddy viscosity profile may be computed over the depth (Fig 6(a)). As may be seen from Figure 6(b), the resulting eddy viscosity profile predicts a concentration distribution in good comparison with measurements over most of the depth.

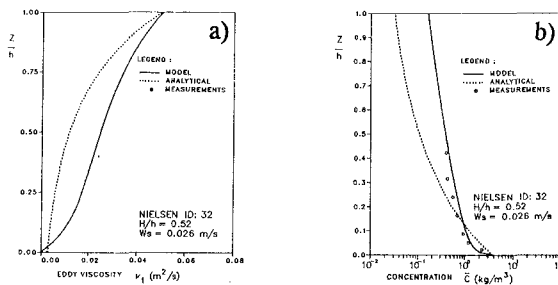


Figure 7 Intercomparison of analytical (—) and modelled (•••) (a)  $\nu_t$  profiles and (b) concentration profiles (Nielsen case 32, Van Rijn, 1991).

## 5. Conclusions

Through qualitative observation and quantitative computation and modelling, the fundamental significance of wave breaker turbulence for sediment suspension is clearly established. Despite the better understanding of surf zone processes through the increased number of flow measurement and visualization studies carried out in recent years there has been limited progress in quantitative predictive modelling of these processes. In adapting a time-independent diffusive turbulence model to the problem of breaker turbulence, a number of significant flow parameters previously measured in wave flume experiments are satisfactorily predicted.

Measurements of suspended sediment have concentrated on the suspended mass with little detail being available concerning the wave and turbulence properties. However in applying the buoyancy extended model with the given wave heights and a parametrized bottom reference concentration measured suspended sediment profiles are well represented. For further model refinement purposes it would however be desirable to have both turbulence and suspended mass measurements for identical conditions.

With the assumption of a diffusive dominated flow, it was possible to develop analytical relations approximating turbulence profiles from their parameter surface value and an appropriate length scale. With a parametrization of the surface scale of TKE using the term for breaker turbulence production, wave bore characteristics may be used for predicting the vertical distribution of suspended sediment.

## Acknowledgements

The authors thank M Stive for providing a comprehensive set of experimental data and L Engelbrecht for technical assistance.

## References

- Battjes, J.A., (1975). Modelling of turbulence in the surf-zone. Proc. Symp. Model. Techniques, ASCE, San Francisco, pp. 1050-61.
- Black, K.P. and Rosenberg, M.A. (1991). Suspended sediment load at three time scales. Proc. Coastal Sediments'91, ASCE, 313-327.
- Coppoolse, R., Schoonees, J., Mocke, G.P., Smith, G. (1992). Hydrodynamics and Sediment Concentrations at Walker Bay. Proc. 23rd ICCE, ASCE.
- Deigaard, R., Fredsoe, J. and Broker-Hedegaard, I. (1986). Suspended sediment in the surf-zone. Jour. of Waterway, Port, Coastal and Ocean. Eng. ASCE.
- E, X. and Hopfinger, E.J. (1986). On mixing across an interface in stably stratified fluid. J. Fluid Mech., vol. 166, pp. 227-244.
- Hardenberg, B. van, Hay, A.E. Sheng, Y, Bowen, A.J. (1991). Field measurements of the vertical structure of suspended sediment. Coastal Sediments'91, ASCE.

- Hattori, M. and Aono, T. (1985). Experimental study on turbulence structures under spilling breakers. *The Ocean Surface*, edited by Y. Toba and H. Mitsuyasu, pp. 419-424, D. Reidel, Hingham, Mass.
- Mocke, G.P. (1991). Turbulence modelling of suspended sediment in the surf zone. *Proc. Coastal Sediments '91*, ASCE, 432-446.
- Nadaoka, K, Ueno, S, Igarashi, T. (1988). Sediment Suspension due to large scale eddies in the surf zone. *Proc. 21st ICCE*, ASCE.
- Nadaoka, K., Hino, M. and Koyano, Y. (1989). Structure of the turbulent flow field under breaking waves in the surf zone. *J. Fluid Mech.* vol. 204, pp 359-387.
- Nadaoka, K. and Kondoh, T. (1982). Laboratory measurements of velocity field structure in the surf zone by LDV. *Coastal Eng. Jpn.*, 25, 125-146.
- Nielsen, P. (1984). Field measurements of time-averaged suspended sediment concentrations under waves. *Coastal Eng.* 8, 51-72.
- Rodi, W. (1980). Turbulence models and their application in hydraulics - a state of the art review. IAHR, Delft.
- Sato, S., Homma, K, Shibayama, T. (1990). Laboratory study on sand suspension due to breaking waves. *Coastal Eng. in Japan*, Vol. 33, No. 2.
- Shibayama, T., Higuchi, A. and Horikawa, K. (1986). Sediment Transport due to breaking waves. *Proc. 20th Coastal Eng. Conf.*, ASCE.
- Stive, M.J.F. (1980). Velocity and pressure field of spilling breakers, *Proc. 17th Coastal Eng. Conf.*
- Svendsen, I.A. (1984). Wave heights and set-up in the surf-zone. *Coastal Eng.* 8: 303-29.
- Svendsen, I.A. (1987). Analysis of Surfzone turbulence. *Jour. Geophys. Res.*, Vol. 92, no. C5.
- Van Rijn, L. (1991). DATA BASE - Sand concentration profiles and sand transport for currents and/or waves. Delft Hydraulics rep. H 1148-04/05.

## CHAPTER 176

### Grain-size Distribution of Suspended Sediments

Ryuichiro Nishi, Michio Sato and Kazuo Nakamura<sup>1</sup>

#### ABSTRACT

Field observations on the grain size distribution of suspended sediment in a surf zone has been carried out at Fukiage beach in 1990 and 1991. In these observations, a suction pump has been used to sample a sufficient amount of suspended sediment for grain size analysis. The instrument designed for the data collection worked well. Vertical distributions of sediment concentration for several grain sizes which compose suspended sediment are obtained. This enable us to do numerical simulations of beach evolution taking the composite character of suspended sediments into consideration. Results are compared with the ones obtained by conventional simulation method which assumes single grain size composition of beach materials, and discussed. The vertical distribution profiles of the concentration of suspended sediments are also compared with existing models and discussed.

#### 1. Preface

The beach is composed of sediment particles of various sizes and shapes. The grain size is one of the parameters that significantly affects the beach shape and evolution, i.e. the movement of bar, formation of berm, etc. Generally, the medium grain size,  $d_{50}$ , used to define suspended sediment concentration.

Regarding grain size distributions of beach material across the shore, Bascom(1970) has conducted extensive grain size analysis of

---

<sup>1</sup>Department of Ocean Civil Engineering, Kagoshima Univ.  
1-21-40 Korimoto, Kagoshima-shi, JAPAN 890

cross-shore material and proposed to use the medium grain size at the shoreline as the representative grain size of the beach. Bowen expressed the equilibrium beach profile as a function of settling velocity of sediment particle. He showed that the larger the grain size, the steeper the equilibrium beach profile. The characteristics and applications of equilibrium beach profiles,  $h=Ay^{2/3}$ , are discussed in detail by Dean(e.g. 1991). In his equilibrium beach profile model, A is a function of sediment diameter and later it is found that A is well predicted by settling velocity of sediment particle. Recently, Kato et al.(1991) has done an extensive analysis of sea bed material at Hazaki Observation Research Facility, HORF, in Chiba prefecture, Japan. However, it seems to be uncertain whether the grain size of the suspended material is the same as the sea bed material, and whether the suspended sediment which composes a wide range of grain sizes in nature can be represented by a single grain size assumption. Also, there is a few sediment transport models which considers the composition of sea bed material. Under river condition, there is evidence that the size of the bed load material is different from original bed material (see Fig.6 Chih Ted yang et al.1991).

Two field observations on grain size distributions of suspended material and sea bed material in a surfzone have been carried out at Fuklage beach in 1990 and 1991 respectively to study the effect of grain size distribution on beach profile changes due to wave action. For grain size distribution analysis of suspended material, it is necessary to obtain sufficient amount of suspended material. Therefore, a suction pump was used. The instrument was designed specifically for this observation and it worked well. This system will be shown in the next section. A similar idea to this suction pump was tested by Irie(1977) and Antsyferov(1983). Vertical distributions of suspended sediment concentration for several grain sizes were obtained.

## 2. Field observations.

Two field observations have been carried out at Fuklage beach one from 18 Oct. to 20 Oct. 1990 and the other from 9 July to 11 July 1991. This sandy beach faces East China Sea and extends 30km in north-south direction along with Satsuma peninsula, Kagoshima prefecture, Japan as shown in Fig.1. The observation base was set at Irikihama beach, however, the base position in 1991 was different from that in 1990.

To sample a sufficient amount of suspended material for sieving analysis from each depth, it is impractical to use instantaneous sand trap such as by Kana(1978) and it is also difficult to record the grain size

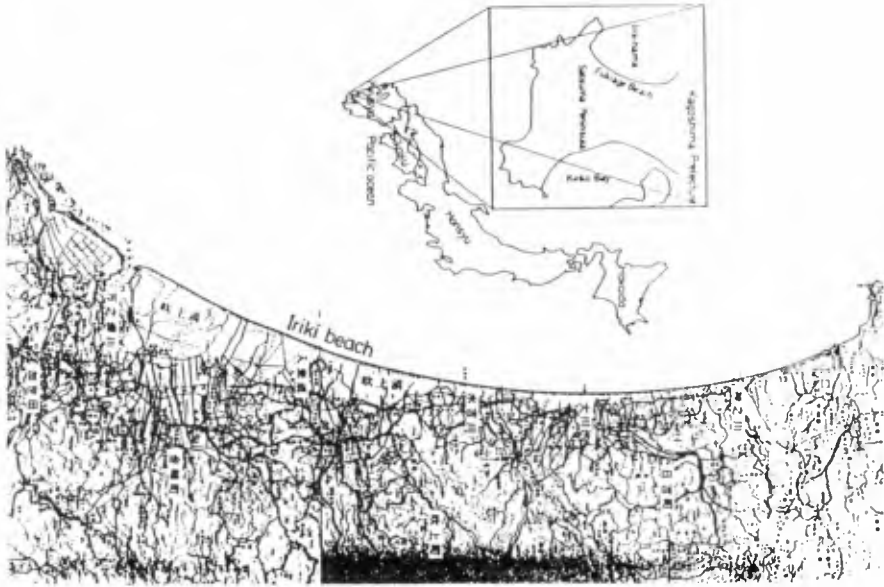


Fig.1 Location of Fukiage Beach



Fig.2 Measuring station (Fukiage beach)





Photo 1. Intake of suction pump



Photo 2. Installation of equipment

distribution by optical and acoustic method. To relate the grain size distribution obtained by such a bamboo trap (Fukushima et al.1955) to local wave condition cannot be achieved, because the water depth and wave condition change during the sampling time in the surfzone. Therefore, a suction pump method was designed to obtain the vertical distribution of grain size of suspended material in short period.

The intake of this suction pump under the water is shown in Photo.1 and design suction speed is faster than settling velocity of the suspended material. The speed is an order of a half meter per second, while the settling velocity of sediment is an order of several centimeters per second. The suction speed was measured before every measurement. The elevation of the intake from the sea bed is adjusted by pulling a rope attached to the suction pipe. In fact, the intake could not be well movable vertically due to the friction of the suction pipe with a sheath and misdesign of a pulley, so that a diver adjusted the elevation of the intake in the first observation. In the second observation, the position of the pulley was adjusted to the upward to avoid being buried into the sea bed and the suction pipe was modified to make less friction with the sheath.

The measuring station is shown in Fig.2. The measuring station was located in the surf zone during high water only. The working area was about 5.4m high from the sea bottom and has a surface dimension of 1.8m by 1.8m. Four capacitance type wave gauges and four pressure type wave gauges were installed between the measuring station and the shoreline. One capacitance type wave gauge is located alongshore the suction pump to relate the local wave conditions to the suspended sediment concentration. The installation of the equipment are shown in Photo.2.

The waves during two observations were relatively low and breakers were of spilling type. The wave condition of the third measurement in the first observation in 1990 is shown in Table 1.

Table 1. Wave conditions

Wave Height		Wave period	
$H_{max}$	33.7 cm	$T_{max}$	6.2 sec
$H_{1/10}$	23.0 cm	$T_{1/10}$	6.3 sec
$H_{1/3}$	18.3 cm	$T_{1/3}$	5.6 sec
$H_{mean}$	11.4 cm	$T_{mean}$	4.0 sec

The beach profiles were measured during low tide just before the measurement. Longshore bar was formed 150m offshore as shown in Fig.3. The cross shore samples of sea bed material were taken at 10m intervals.

The suspended sediment samples were taken at 5cm, 10cm, 15cm, 30cm from the sea bed in the first observation, and at 1cm, 5cm, 10cm, 20cm, 30cm, 50cm in the second observation. It took nearly 1 to 15 minutes to obtain the samples by suction pump depending on the height from the sea bed, generally speaking, the higher the suction point, the longer the suction duration due to reduced suspended sediment concentration. The suction pump was also used in the upper portion of the water column near the water surface, but was unable to collect a sufficient amount of material for the analysis.

The measurements were taken 4 times for the first observation in 1990 and three times for the second observation in 1991. In this paper, the third and the fourth measurements in the first observation are discussed. The third and the fourth measurements were carried out on 19 Oct. 1990. Sieving analyses was carried out to obtain the concentration profiles of several grain sizes of the suspended sediment. In addition, one direct sample used 2000cc polyethylene bottles has been taken by diver during the first observation.

### 3. Data analysis

Data set of grain size distribution of sea bed materials, grain size distribution of suspended materials, the concentration of several grain sizes which compose suspended sediment and total concentration have been taken.

#### 3.1 Grain size distribution

Grain size distributions of suspended material obtained at several depths were sieved, first. In addition, grain size distribution of sea bed material at the measuring station was also obtained to compare with the composition of suspended materials. The grain size distribution from the third measurement is shown in Fig.4(a). The composition of suspended material is smaller than the original sea bed material. As can be seen Fig.4(b), the representative grain size of the bed material does not directly correspond to that of the suspended material in a calm wave condition. Unfortunately, data under severe wave condition is not available.

It is reassured that small waves of short periods do not cause

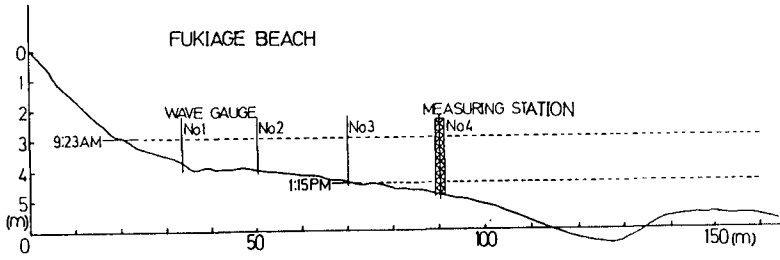


Fig.3 Beach profile

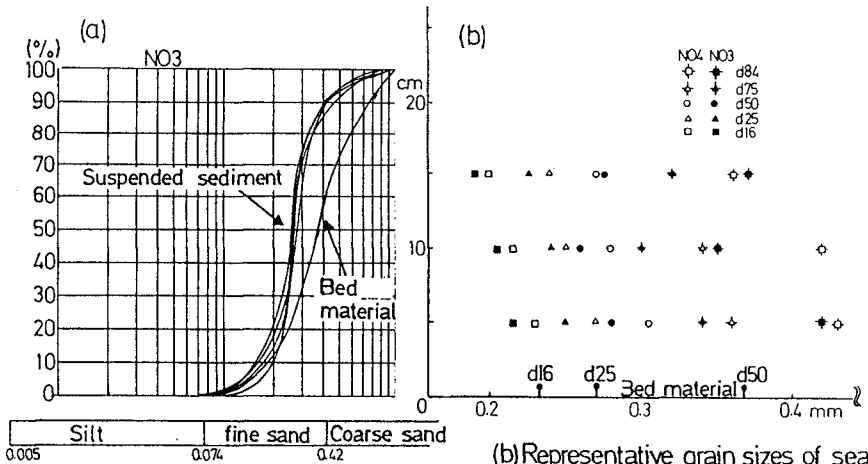


Fig.4 (a) Grain size distribution of sea bed material and suspended sediment

(b) Representative grain sizes of sea bed material and suspended sediment

suspension of the entire original bed material, but only cause suspension of finer sea bed material. Under this condition, the composition of suspended materials are smaller than that of the sea bed material.

### 3.2 Suspended sediment concentration of several grain sizes

The concentrations of several grain sizes are obtained. The results are shown in Fig.5, where, the value of each grain size shown represents the average size of sieve size. The 0.34 mm material which is close to the mean grain size ( $d_{50}$ ) of the sea bed material contributes nearly 50% of the suspended material at 5cm from the sea bed level. The 0.18mm, 0.63mm, 0.09mm material contribute, in respective orders, lesser amount. This order of contributions also holds in the upper layer in the third measurement.

The vertical distribution of concentration at each grain size is assumed to follow an exponential form as shown by eq.(1) (due to Dally et al. 1980).

$$C(z) = C_a \cdot \exp\{F(z-z_a)\} \quad (1)$$

while,

$$F = \frac{-15W}{h} \sqrt{(\tau/\rho)} \quad (2)$$

where,  $C(z)$  is the suspended sediment concentration at depth( $z$ ),  $C_a$  is the concentration at the reference level ( $z_a$ ),  $z$  is a height from the sea bed,  $h$  is a water depth and  $\sqrt{(\tau/\rho)}$  is a shear velocity. The shear velocity  $\sqrt{(\tau/\rho)}$ , is computed by two different methods Noda(1968) and Dally(1980); They are :

$$\sqrt{(\tau/\rho)} = \sqrt{2\pi v/T} \cdot \frac{\pi H}{\tanh(kh)} \quad (3)$$

$$\sqrt{(\tau/\rho)} = (fH^2g/16h)^{0.5} \quad (4)$$

where  $\rho$  is the density of water,  $T$  is the wave period,  $H$  is the wave height and  $v$  is the coefficient of kinematic viscosity set to be equal to 0.01 cm<sup>2</sup>/sec (20 c) in this case.

The concentrations calculated by eq.(4) are also shown in Fig.5. These concentration curves fit quite well to the data in the lower position

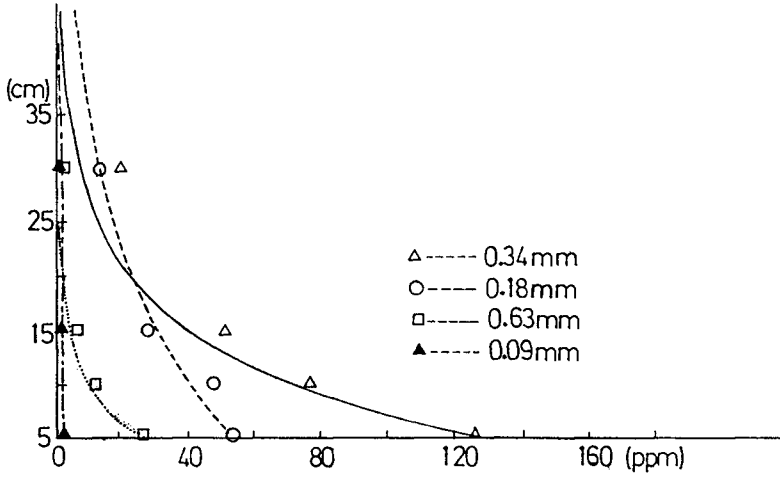


Fig.5 Suspended sediment concentration of individual grain sizes based on Dally's shear velocity eq.(4)

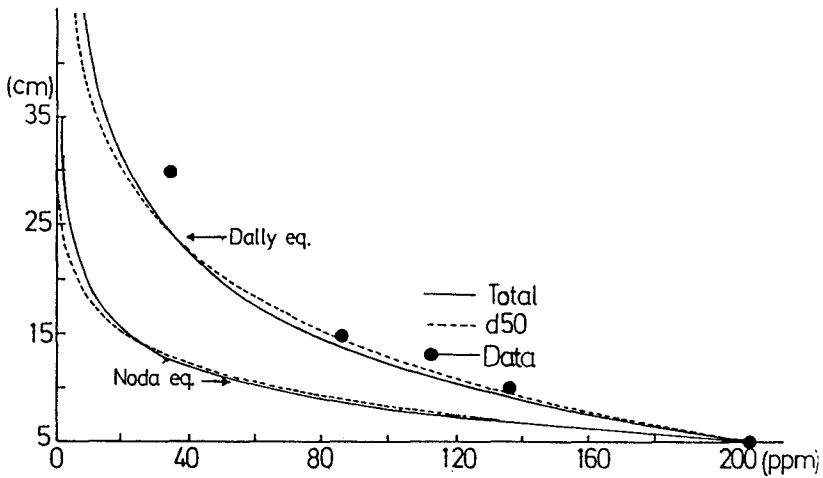


Fig.6 Total concentration of suspended sediment

(i.e., 5cm, 10cm, 15cm), but there is disagreement between the exponential curve and the data in the upper position ( $z=30\text{cm}$ ) for the case of 0.34mm. Combining the calculations of suspended sediment concentrations for several grain sizes, the total concentration of suspended sediment is calculated and is compared to the field data. This total concentration is defined as the sum of concentrations of individual grain sizes, i.e.,

$$C_{\text{total}}(Z) = \sum_{i=1}^N C_{s,i} \cdot \exp\{F_i(Z-Z_a)\} \quad (5)$$

where, the subscript  $i$  refers to the  $i$ th grain size. The total concentration based on

the mean grain size ( $d_{50}$ ) is also calculated, shown as dotted line in Fig.6. The data from the third measurement is also shown in the figure as black circles. It is seen that the concentration calculated by eq.(5) is slightly smaller than that derived from  $d_{50}$  in lower regime, and is higher in the upper regime. However, their difference is small. This might be due to the fact that the waves were small in this measurement, only in the order of 20cm. For large waves, their difference could become larger.

#### 4. Numerical simulation of beach evolution.

In this section, simple numerical simulations of beach evolution were carried out to illustrate the effect of the composite of sea bed materials by comparing the results with the ones obtained by a conventional approach which assume single grain size ( $d_{50}$ ) composition of beach material. Two types of beach profile storm and normal profiles, or bar and berm profiles are used.

The composite characters of sea bed materials used for numerical simulation are shown in Fig.7. Case 1 assumes that the beach is composed of single size grain which is represented by mean grain size ( $d_{50}$ ) set to be 0.2mm. The mean grain sizes of case 2 and 3 are also 0.2mm, but the sorting coefficient of two cases are chosen to be 1.47 and 2.40 respectively; thus the beach is composed of composite sand size. Case 4 assumes a single grain size composition of beach material with mean grain size equal to 0.6mm. The mean grain size of case 5 and 6 are also 0.6mm, but again the sorting coefficients are chosen to be 1.45 and 2.36 respectively.

##### 4.1 Basic equation

The conventional beach evolution model proposed by Dally is applied

to the numerical simulation by taking into consideration the composite characteristics of the bed material. The suspended sediment transport is written as:

$$Q_{ss} = \int_{-h}^0 u(z) \cdot c(z) dz \quad (6)$$

where,  $u(z)$  is a mean horizontal velocity of sediment particles which consists of components; an oscillatory component due to waves, and velocity component due to mean flow,  $c(z)$  is a concentration profile as expressed in eq.(1). To calculate the suspended sediment transport rate, the water column is divided into two layers; one is the inner layer lower than  $DF(=wT)$  and the other is the outer layer higher than  $DF$ , where,  $w$  is the settling velocity. This settling velocity is obtained by Rubey's law.

$$w = \sqrt{\frac{2(\rho_s - \rho)}{3\rho}gd + \frac{36v^2}{d^2}} - \frac{6v}{d} \quad (7)$$

where,  $\rho_s$  is the density of sediment particle,  $g$  is the gravitational acceleration and  $d$  is the diameter of sediment particle.

The calculated total suspended sediment transport rate is applied to the continuity equation given below to obtain the new beach profile.

$$\frac{dh}{dt} = \frac{1}{1-\lambda} \frac{dQ}{dx} \quad (8)$$

This new beach profile is used to revise the input wave condition for the next time step.

The effect of sorting sea bed material due to waves and the silt component of bed material are excluded in the computation.

#### 4.2 Numerical results

The numerical results of beach evolution for 0.2mm mean grain size material and 0.6mm mean grain size material are shown in Fig.8 and Fig.9, respectively.

Based upon a fall velocity criterion proposed by Dean, the wave and sediment condition are expected to produce the storm profiles which are bar formation as shown in Fig.8 and normal profiles which are berm formation as shown in Fig.9. It appears that the size of the bar feature



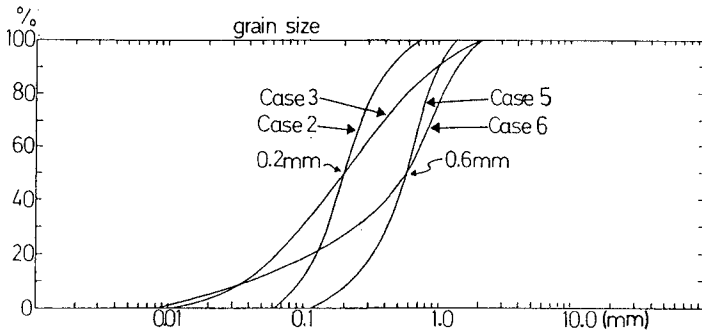


Fig. 7 Composition of bed materials for numerical simulation

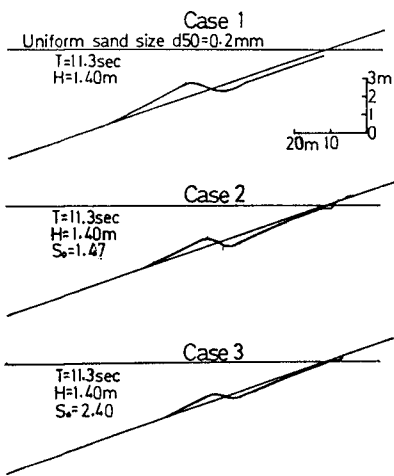


Fig.8 Numerical simulation for bar profile after 200sec

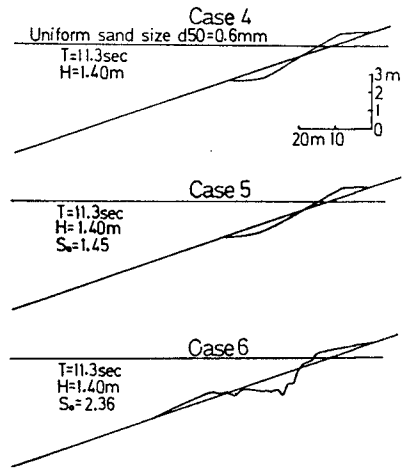


Fig.9 Numerical simulation for berm profile(200sec)

diminish with the increasing of the range of the material size in Fig.8. The position of bar crest is also located slightly shoreward for this wave condition. For the storm profile, the composite beach material appears to have a smoothing effect and the bar formation becomes lower and wider as the range of the sand size increase. For the normal profiles shown in Fig.9, it appears that the closure depth increases with the increasing of the range of the sand size. The cross shore sand transport for case 4 and 5 are onshore sediment transport while that for case 6 is consisted of onshore and offshore sediment transports to cause a different type of beach profile for this wave condition.

Generally, the results for storm and normal profiles based on a single grain size assumption are similar to these profiles produced by a narrow range of beach material, while the profiles are different from the beach profiles produced by a wide range of sea bed material.

## 5. Concluding remarks

The conclusions are ;

(1) The pumping system designed to obtain the suspended materials for grain size analysis worked well in the lower portion of the water column. In the upper portion of the water column, the data could not collect in this measurement, since the reduction of suspended sediment concentration.

(2) The representative grain size of the suspended materials decreases with increasing elevation. The mean grain size of the suspended material is smaller than that of original sea bed material.

(3) Concentration profiles of individual grain size can be represented by the widely accepted exponential equation.

(4) The total concentration defined as the sum of the individual grain size concentrations underestimates in the lower portion of the water column and overestimates in the upper region of the water column with reference to the concentration profile derived from single grain size assumption.

(5) Numerical simulations of beach profile evolution taking into account the composite nature of the suspended material have been carried out for erosional and normal profiles. The results are different from the ones with the conventional approach of using a single grain size. For bar profile, the composite beach material appears to have a smoothing effect. So the bar formation becomes lower and wider as the range of sand size increases. For the berm formation, the profile change of composite beach material becomes also wider as the range of sand size increases.

We hope that the further observations under the severe wave

condition will provide additional information about the effect of the composition of sea bed material on beach profile evolution.

#### Acknowledgements

One of the author is given an opportunity to do research and discuss with Dr.Hsiang Wang at University of Florida. It is very appreciated his kind comments, many suggestions and proofreading. Many thanks go to Ms Rebecca H.Hudson for her kind talk and proofreading, too. The authors really would like to express their special thanks to Dr.Toshiyuki Asano for his comments. The authors also would like to express their thanks to Mr.Kazuya Hamashima, Mr.Hirofumi Kowaki and Mr.Takeshi Uwada for their data collection efforts and to the other member of Coastal Engineering Laboratory, Dept. of Ocean Civil Engineering, Kagoshima University for their kind help in the field experiments.

#### References cited:

- Antsyferov,S.M., Basinssky,T. and Pykhov,N.V.: Measurements of coastal suspended sediment concentrations, Coastal Eng.,7, pp145-166, 1983
- Bascom,W.: Waves and Beaches, Doubleday Anchor Books, 1980
- Bosman,J.J., van der Velden ,E.T.J.M. and Hulsbergen,C.H.: Sediment concentration measurement by transverse suction. Coastal Eng.,2, pp353-370,1987
- Dally,W.R.: A numerical model for beach profile evolution, Thesis for the degree of Civil Engineering, University of Delaware, 1980
- Dean, R.G.: EQUILIBRIUM BEACH PROFILES: CHARACTERISTICS AND APPLICATIONS, Journal of Coastal Research, Vol. 7, No.1,Winter 1991
- Fukushima, H. and H. Mizoguchi: Sediment transport and the measurement, 2nd Japanese Conf. Coastal Eng. pp156-162, 1955
- Irie, T.: In-situ measurements of suspended sediment transport, 22nd Japanese Conf. Coastal Eng. pp313-317,1977
- Kana,T.W.: Surf zone measurement of suspended sediment. Proc. 16th Coastal Eng. Conf., 1978 Kato,K., S.Yanagishima, Y.Kuriyama, T.Isogami, H.Murakami and M.Fujita: Changes of Grain Distribution on Bed Material in the Surf zone -Field Observation at Hazaki Oceanographical Research Facility- REPORT OF THE PORT AND HARBOUR RESEARCH INSTITUTE,Vol.29,No.2, 1980
- Noda, H: Incipient motion of sea bed material due to wave, 13th Japanese Conf. Coastal Eng. pp135-144, 1968
- Shimada,Y. and M.Yoshitaka: Measurement of suspended sediment concentration due to waves, 21st Japanese Conf. Coastal Eng. pp215-218, 1976

## CHAPTER 177

### Bed Boundary Layers

B.A. O'Connor<sup>1</sup>, J.M. Harris<sup>1</sup>, H. Kim<sup>1</sup>,  
Y. K. Wong<sup>1</sup>, H.U. Oebius<sup>2</sup>, and J.J. Williams<sup>3</sup>.

#### ABSTRACT

The paper describes the development and application to laboratory and North Sea field data of a series of random wave and current computer models of bed boundary layer flows and associated suspended sediment concentrations. The EC-funded (MAST 1) work is part of a larger project, which also includes the laboratory testing of a new seabed shear stress meter (SSM) and the field collection of nearbed data using a special boundary layer rig (STABLE). Both two-dimensional (2DV) and one-dimensional (1DV) hydrodynamic models are described based on a mixing length closure but including simulation techniques to enable the inclusion of both long and short-crested random waves and steady currents. A 1DV suspended sediment model is also described with realistic boundary conditions to enable the simulation of vortex entrainment from seabed ripples. Application of the various models to the SSM and STABLE data shows realistic results.

#### 1. INTRODUCTION

The present paper is concerned with the computer simulation of water and sediment movements over rippled seabeds in random wave and current conditions appropriate to the North Sea. It reports on one element of a larger multi-disciplinary research programme involving engineers, oceanographers and geologists, who are studying the formation of nearshore sandbanks and their role in providing protection to adjacent coastlines.

- 
1. Department of Civil Engineering, University of Liverpool, L69 3BX, England.
  2. Versuchsanstalt für Wasserbau und Schiffbau, Berlin, Germany.
  3. Proudman Oceanographic Laboratory, Bidston Observatory, L34 7RA, England.

The research involves the field and laboratory testing of equipment to measure near-bed waves and currents and the associated sediment transport rates. In particular, staff from VWS, Berlin, have tested an improved seabed shear plate (SSM) to enable the direct measurement of seabed shear stress in waves and currents, Oebius (1992). Staff from the NERC's Proudman Oceanographic Laboratory have used a large bed boundary layer rig (STABLE) to provide field information on near-bed turbulence, waves, currents and sediment movements at the Brown Ridge Sandwave Site in the North Sea, Williams (1991). In addition, staff from the Department of Civil Engineering at Liverpool University have developed a series of hydrodynamic and sediment transport computer models to help with the interpretation of the data collected by both the SSM and STABLE rigs.

## 2. MODEL WORK

Four models have been developed: a two-dimensional (x, z) full-depth rough-turbulent hydrodynamic model (2DV) to study advective (mass-transport) effects on vertical mixing; a two-dimensional (x, z) bed boundary layer hydrodynamic model of wave-induced flow over bed ripples to assist with vortex entrainment ideas (2DV); a one-dimensional, rough-turbulent hydrodynamic model (1DV) to simulate wave-current interactions at arbitrary intersection angles in directional random waves; and an associated one-dimensional suspended sediment model (1DV) to study vertical sediment distributions in directional random waves and hence the effect of wave groupiness.

### 2.1. 2DV Hydrodynamic Model

The model solves simplified forms of the horizontal momentum and mass continuity equations for multi-frequency waves using a mixing length closure. The model equations are given as:-

$$\rho \partial u / \partial t + \rho u \partial u / \partial x + \rho w \partial u / \partial z + \partial p / \partial x = \partial \tau_{xz} / \partial z \quad (1a)$$

$$\partial u / \partial x + \partial w / \partial z = 0 \quad (1b)$$

where u and w are the phase-point-average turbulent-mean flow velocities in the horizontal (x) and vertical (z) cartesian co-ordinate directions, respectively; p is pressure;  $\rho$  is the fluid density; and  $\tau_{xz}$  is the horizontal component of the Reynolds stresses.

The wave-induced boundary layer is assumed to be thin and the motion outside it is assumed to be irrotational so that the pressure gradient in equation (1a) can be approximated by the equation:-

$$-\partial p/\partial x = \rho \partial u_w/\partial t + \rho u_w \partial u_w/\partial x \quad (2a)$$

$$\text{with } u_w = \bar{u}_w + \sum_{i=1}^m u_i \cos(\omega t - ikx + \phi_i) \quad (2b)$$

where  $u_w$  is the wave-induced orbital velocity at the sea surface (mean water level);  $\bar{u}_w$  is a wave-period-averaged steady velocity component;  $u_i$  are velocity amplitudes of the  $m$  Fourier frequency components making up the wave signal;  $\omega$  is the wave frequency ( $= 2\pi/T$ ,  $T$  is the wave period); and  $k$  is the wave number ( $= 2\pi/L$ ,  $L$  is the wave length).

The Reynolds stress ( $\tau_{xz}$ ) is approximated by a simple mixing length expression ( $\rho \kappa \partial u/\partial z$ ), where  $\nu_t = \kappa^2 z^2 \partial u/\partial z$  and  $\kappa$  is Von Karman's constant (0.40).

The set of equations is solved using an implicit Crank-Nicolson finite difference technique on a space-staggered grid using zero velocity at the seabed ( $z=z_0$ ), a zero velocity gradient at the water surface and repeating conditions for lateral boundaries, Kim (1993).

## 2.2. 1DV Hydrodynamic Model

The 1DV model also solves simplified flow equations using a mixing length closure. The model works for arbitrary-angled wave and current flows and uses simulation techniques involving surface wave spectra to produce appropriate model boundary conditions. The equations used in the model are given in tensor form as:-

$$\rho \partial u_i/\partial t - \partial p/\partial x_i = \partial \tau_{xz_i}/\partial z \quad (3a)$$

$$\partial p/\partial x_i = \rho \partial u_{\delta i}/\partial t + \rho g \partial H/\partial x_i \quad (3b)$$

$$\tau_{xz_i} = \rho \nu_t \partial u_i/\partial z; \nu_t = \ell^2 \partial V/\partial z; V = \sqrt{(u^2 + v^2)} \quad (3c)$$

$u_i (=u, v)$  are the cartesian velocity components in the horizontal ( $x$ ) and lateral ( $y$ ) co-ordinate directions respectively;  $x_i$  are the co-ordinates  $x$ ,  $y$  respectively;  $g$  is the acceleration due to gravity;  $\partial H/\partial x_i$  is the mean water surface slope;  $\ell$  is a mixing length ( $=\kappa z$ ) and  $u_{\delta i}$  are the  $u$ ,  $v$  components at the top of the wave boundary layer, respectively.

Equation 3 can be solved in terms of a shear velocity ( $p_*$ ,  $\tau_{xz} = \rho p_*^2$ ) - see Bakker (1974), Wong (1984) for the case of co-linear waves and currents. Alternatively, the vertical co-ordinate ( $z$ ) can be transformed by a power law and the transformed equations solved directly for  $u_i$ .

Both approaches have been used in the MAST 1 work. However the transformed co-ordinate approach is simpler to use for directional wave simulations. In this lattermost case the surface boundary conditions for the variation of velocity ( $U_T$ ) with time is obtained from simulation techniques, see for example, Ellis et al (1981).

$$U_T = \sum_{m=1}^M \sum_{n=1}^N \left[ \frac{2\pi f_m}{\sinh(k_m h)} \right] F \quad (4a)$$

$$F = a_{m,n} \cos(2\pi f_m t + \phi_m) \cos \theta_n \quad (4b)$$

where  $f_m$  is the wave frequency ( $=1/T_m$ ,  $T_m$  is the wave period);  $\phi_m$  are random phase angles in the range  $0 - 2\pi$ ;  $k_m$  is the wave number;  $h$  is the water depth;  $t$  is time; and  $a_{m,n}$  is a wave amplitude obtained by integration of the directional wave energy spectrum. Thus:-

$$a_{m,n} = \sqrt{2 S(f_m, \theta_m) \Delta f_m \Delta \theta_n} \quad (5a)$$

$$S(f_m, \theta_m) = S(f_m) \cdot G(f_m, \theta_n) \quad (5b)$$

$$G(f_m, \theta_n) = G_0 \cos^{2s}(\theta_n/2) \quad (5c)$$

$$G_0 = 2^{2s-1} \cdot \Gamma^2(s+1) / (\pi \cdot \Gamma(2s+1)) \quad (5d)$$

where  $G_0$  is a constant dependent upon parameter  $s$ , which varies with peak spectral frequency and has a typical value of 20, Goda (1985);  $\Gamma$  is the Gamma function;  $\theta_n$  is a wave direction in the range  $\pm 90^\circ$  of the dominant wave direction;  $S(f_m, \theta_n)$  is any directional surface wave energy spectrum;  $S(f_m)$  is a surface wave energy frequency spectrum;  $G(f_m, \theta_n)$  is a spectral wave energy spreading function.  $\Delta \theta_n$  is the band width of the  $n$ -th directional wave angle obtained by dividing the range of wave angles ( $\pm 90^\circ$ ) into  $n$  equal intervals and  $\Delta f_m$  is the bandwidth of the  $m$ -th frequency interval obtained from the co-cumulative energy spectrum by using equal energy bands, see Ellis et al (1981).

A zero-velocity bed boundary condition is used ( $u=w=0$ ) at  $z=z_0$ . The value of  $z_0$  can be adjusted in random wave simulations using Madsen's (1990) approach, if desired.

### 2.3. 1DV Sediment model

In order to study the vertical distribution of suspended sediment over a rippled seabed, a one-dimensional sediment model has been used. The model equations used are:-

$$\partial c / \partial t + (\bar{w} - w_f) \partial c / \partial z = \partial (\epsilon_s \partial c / \partial z) / \partial z \quad (6)$$

where  $c$  is the phase-point-averaged turbulent-mean suspended sediment concentration;  $\tilde{w}$  is the vertical wave induced fluid velocity;  $w_f$  is the effective vertical sediment diffusion coefficient.

Previous work has generally ignored the effect of  $\tilde{w}$ , and has determined  $\epsilon_s$  during the wave cycle from the hydrodynamic shear stress determined by a LDV-type model, see for example, Davies (1990). Such an approach does not include all the major processes contributing to vertical mixing, see for example, O'Connor (1991). The inclusion of extra mixing has usually been done in the past by taking a wave-period-average view of vertical sediment distributions and then using the sediment distribution itself to determine effective mixing coefficients see for example, Van Rijn (1989). In the MAST 1 work, a different approach has been used. Sediment is released into the water column at two discrete times during the wave period (at  $t = T/16$  and  $9T/16$  for a mono-wave) at a height of between one and two ripple heights above the mean bed level, as suggested by the 2DV model tests for a rippled bed, see O'Connor et al (1992). Shear-induced entrainment is also allowed during the wave period as dictated by the LDV hydrodynamic bed shear stress, see Figure 1. Additional mixing due to mass-transport is allowed by using the 2DV "flat"-bed hydrodynamic model (see Section 2.1) to provide the  $\epsilon_s$  values.

Solution of equation (6) is achieved by a number of intermediate steps. Firstly, a transformed vertical co-ordinate is used in order to resolve the large near-bed concentration gradients. The same approach was used for the LDV hydrodynamic equations. Secondly, a split operator finite difference approach is used to introduce the vortex entrainment concentrations into the water column at a height of  $1.5 \Delta_r$  above the mean bed level ( $z = 0$ ). Thirdly, the new equations are then solved sequentially using appropriate boundary conditions between the water surface (mean sea level) and the sea bed  $z=z_o$ ; the co-ordinate origin being located half a ripple height above a ripple trough.

The necessary equations are given below:-

$$\partial c / \partial t - w_f \partial c / \partial z = \partial (\epsilon_s \partial c / \partial z) / \partial z \quad (7a)$$

$$\partial c / \partial t + \tilde{w} \partial c / \partial z = S(t) \quad (7b)$$

$$S(t) = M_v / (\Delta_r T_v), \text{ for } \Delta_r \leq z \leq 2\Delta_r, \text{ and} \quad (7c)$$

$$5T/16 \leq t \leq 3T/8, \text{ or } 13T/16 \leq t \leq 7T/8$$

$$M_v = \int_0^{T/2} E_v dt \quad (7d)$$



$$E_v = (1-\alpha)E_t; E_t = A \Phi^{1.5}; T_v = T/16 \quad (7e)$$

$$\Phi = \tau_b(t) / ((\rho_s - \rho) g D_{50}) \quad (7f)$$

Where  $\tau_b(t)$  is the bed ( $z = 0$ ) shear stress from the 1DV model;  $\rho_s$  is the sediment density;  $g$  is the acceleration due to gravity;  $D_{50}$  is the 50% finer grain size of the bed sediment;  $A$ ,  $\alpha$  are model constants determined by field/laboratory tests.

Equation 7a is solved by an implicit finite difference method while equation 7b is solved as a second step using the method of characteristics. The model uses a zero flux condition ( $\epsilon_s \partial c / \partial z = -w_f c$ ) at the water surface and a surface entrainment condition at the seabed ( $\epsilon_s \partial c / \partial z = \alpha E_t$  at  $z = z_o$ ). Values of  $\epsilon_s$  are obtained from the 2DV hydrodynamic model.

### 3. MODEL APPLICATIONS

#### 3.1. 1DV Hydrodynamic Model Tests

The ability of the 1DV model to reproduce conditions in mono-frequency waves was demonstrated using the oscillating tunnel data of Jonsson and Carlsen (1975), see Wong (1984). In addition, data from the VWS flume tests, Oebius (1992) were reproduced using a suitable plate roughness ( $2D_{50}$ ) and scale factor, see Figure 2.

The ability of the Bakker version of the 1DV model to reproduce velocities near the top of the wave boundary layer (10 mm above the bed) with multi-frequency (3 components) waves, and waves and currents was demonstrated by using the small-scale flume data of Savell (1986), see Figures 3,4. Good agreement is apparent for maximum amplitude and phase. The velocity model's ability to reproduce long-crested random waves was tested for conditions approximated to those at the Brown Ridge Site ( $h = 30\text{m}$ ;  $z_o = 0.01\text{ m}$ ). Wave conditions were assumed to be described by a Pierson-Moskowitz (PM) spectrum with significant wave height of  $H_s = 2.5\text{m}$  (wind speed = 11 m/s) and a peak energy period of  $T_m = 8.1\text{ s}$ . The PM spectrum was simulated by 60 frequency components and the velocity time series used to drive the model.

The accuracy of the simulation process can be judged by Figure 5, which shows a comparison between the PM spectrum and the model spectrum obtained by subjecting the model surface elevation time series to a Fast Fourier Transform (FFT) analysis.

Typical bed shear stresses and orbital velocities from the model at the top of the wave boundary layer are shown in Figure 6 for a typical 64s time interval. The random nature of the results is clearly seen as is also the phase shift over the depth of the boundary layer.

Figure 7 shows the root-mean-square (rms) and significant amplitudes of the wave-induced orbital velocities from a direct analysis of model time series for conditions at the Brown Ridge Site. These significant values can be directly compared with the results from the LDV model operated with representative mono-frequency wave heights and wave periods - the 'design-wave' approach. Figure 8 shows the results for the mono-wave simulations using  $H_s$ ,  $T_{max}$  and  $H_s$ ,  $T_z$ . It is clear that the best comparison with the random wave model is obtained with  $H_s$ ,  $T_{max}$  and not with the more traditional  $H_s$ ,  $T_z$  combination.

The LDV model was next used to investigate the effect of short-crested seas. The Brown Ridge model with its PM spectrum was re-run with a Goda spreading function, equation 5,  $s = 20$ . Figure 9 shows the u, v velocity components for a short length of record while Figure 10 shows the corresponding instantaneous wave direction vectors. The groupy nature of the wave signal is clearly seen as is also the lateral scattering effect of the short-crested sea. Such lateral movements will add significantly to the dispersal of both sediment and pollutant within the water volume. Similar results to the LDV model have also been found with the STABLE data, see O'Connor et al (1992).

In order to examine the LDV model's ability to reproduce the correct magnitude and phase of velocities within the boundary layer, use was made of S4 current meter data collected during the STABLE deployment at the Brown Ridge Site, see Williams (1991) Field velocities for a 22 second period at 800mm above the seabed were used as the upper boundary condition in the model. Figure 11 shows the comparison of field results at 800mm and 400mm with model results at 70mm. It is clear that the model reproduces the main features of the field results.

### 3.2. LDV SEDIMENT MODEL APPLICATIONS

The ability of the LDV model to reproduce suspended sediment concentrations during a wave period was tested using laboratory data of Bosman (1982). Figure 12 shows quite a good comparison considering the difficulty in obtaining such laboratory data.

The need for the inclusion of extra mixing in LDV models is illustrated by the wave-period-average results of Figure 14. Both the 2DV and LDV hydrodynamic models were used for conditions appropriate to Bosman's (1984) laboratory studies,

and the wave-period-average mixing coefficient ( $\epsilon_s$ ) determined by period-averaging. The 1DV sediment model was then used with vortex and shear-induced entrainment to reproduce wave-period-average concentrations, Figure 13. It is clear that the extra mixing inherent in the 2DV model is essential for correct simulation of sediment profiles.

Finally, the long-crested 1DV random wave model was used to simulate suspended sediment conditions at the Brown Ridge Site, see Figure 14. The influence of groupiness in the wave and shear records is clearly seen to influence suspended sediment concentrations with the larger groups having the greatest effects. Unfortunately, no comparable field data was obtained from the STABLE deployment and consequently, more field data is needed to test model ideas further.

#### **4. CONCLUSIONS**

A range of 1DV and 2DV bed boundary layer models have been developed to assist with interpretation of field data obtained from the Brown Ridge Sandwave Site in the Southern North Sea. Comparison of model results with mono- and multi-frequency laboratory data for both velocities and shear stresses shows good results. Realistic model simulations were also obtained for both long and short-crested random wave conditions when compared with measured field data. Use of the long-crested 1DV hydrodynamic model also demonstrates the importance of using the correct wave period when using the mono-frequency "design wave" approach to predict seabed velocities and shear stresses.

An 1DV suspended sediment model was also developed with new boundary conditions which attempted to reproduce the influence of both vortex and shear-induced entrainment. Good comparisons were obtained with laboratory data. The importance of including enhanced mixing due to mass-transport currents in 1DV model simulations was also demonstrated as was the influence of wave groupiness on sediment concentrations at the Brown Ridge Field Site.

#### **5. ACKNOWLEDGEMENTS**

The authors are grateful for financial assistance from the Commission of the European Directorate General for Science, Research and Development under Contract No. MAST - 0036(C).

#### **References**

Bakker, W.T., (1974). Sand Concentration in an Oscillatory Flow. Proc. 14th Coastal Eng. Conf. ASCE, pp 1129-1148.

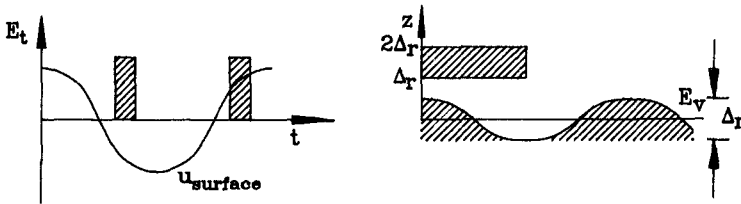
- Bosman, J.J., (1982). Concentration Measurements under Oscillatory Water Motion. Delft Hydraulics Laboratory/TOW Report on Model Investigation M1695 Part II. Delft.
- Bosman, J.J. (1984). Design and Specification of OPCON, on Optical Instrument for Instantaneous Sediment Concentration Measurements. Report on Investigation R716, Part VI, Delft Hydraulics Laboratory.
- Davies, A.C., (1990). Modelling the Vertical Distribution of Suspended Sediment in Combined Wave-Current Flow. Proc. 5th Int. Conf. on the Physics of Estuaries and Coastal Seas. (In Press).
- Ellis, C.P., O'Connor, B.A. and McDowell, D.M., (1981). Generation of Laboratory Waves using a Microcomputer. 2nd Int. Conf. on Engineering Software, Imperial College, London, pp 899-913.
- Coda, Y., (1985). Random Seas and Design of Maritime Structures. University of Tokyo Press, 323 pp.
- Jonsson, I.C. and Carlsen, N.A., (1975). Experimental and Theoretical Investigations in an Oscillatory Turbulent Boundary Layer. J. Hydr. Res., Vol. 14, No. 1, pp 45-60.
- Kim, H., (1993). A Three Dimensional Sediment Transport Model. Ph.D. Thesis, Dept. of Civil Engineering, University of Liverpool (in preparation).
- Madsen, O.S., Mathison, P.P. and Rosengaus, M.M., (1990). Moveable Bed Friction Factors for Spectral Waves. Proc. 22nd Coastal Eng. Conf., ASCE, pp 420-429.
- O'Connor, B.A., (1991). Suspended Sediment Transport in the Coastal Zone, Keynote Lecture, IAHR Symposium, Florence, 2-5 September, 1991, pp 17-63.
- O'Connor, B.A., Williams, J.J., Oebius, H.U. and Sarmento A., (1992). Circulation and Sediment Transport on Sand Banks in European Shelf Seas. Final Report to DCXII, EC MAST Programme. Dept. of Civil Engineering, University of Liverpool.
- Oebius, H.U., (1992). Circulation and Sediment Transport on Sand-Banks in European Shelf Seas. Part: Development of a Shear Stress Meter. Report No. 1208/92, VWS, Berlin, 100pp.
- Savell, I.A., (1986). An Experimental Study of Near-Bed Hydrodynamics of Waves and Steady Current and the Effect of this on Sediment Transport. Ph.D. Thesis. Dept. of Civil Engineering, University of Manchester.

Williams, J.J., (1991). Wave, Current and Sediment Interaction Study. POL Cruise Report No. 13, RRS Challenge 87, 4-20 Dec. 1991, 30pp

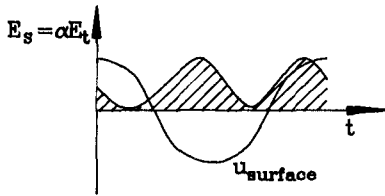
Wong, Y.K., (1984). A Numerical Model for the Interaction of Combined Wave and Current Boundary Layers. M.Sc. Thesis, Dept. of Civil Engineering, University of Manchester.

Van Rijn, L.C., (1989). Handbook Sediment Transport by Currents and Waves. Delft Hydraulics, Report H461.

**Figures**



VORTEX ENTRAINMENT



SHEAR ENTRAINMENT

FIGURE 1

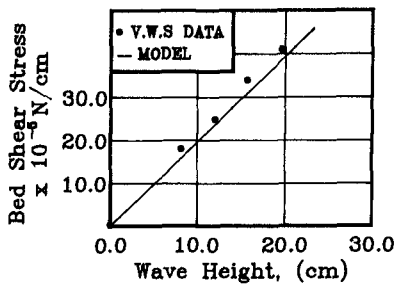


FIGURE 2

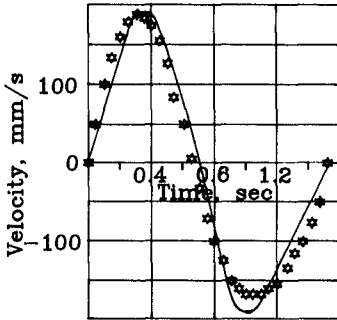


FIGURE 3

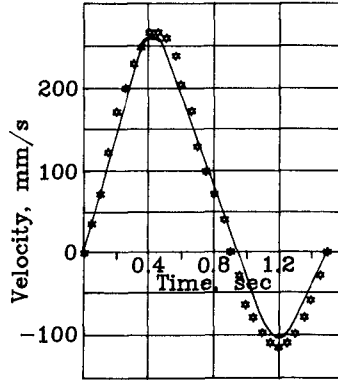


FIGURE 4

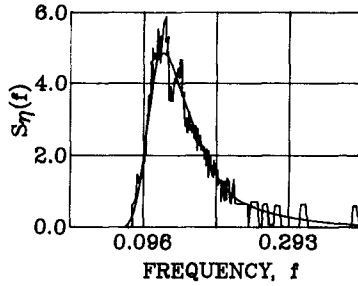


FIGURE 5

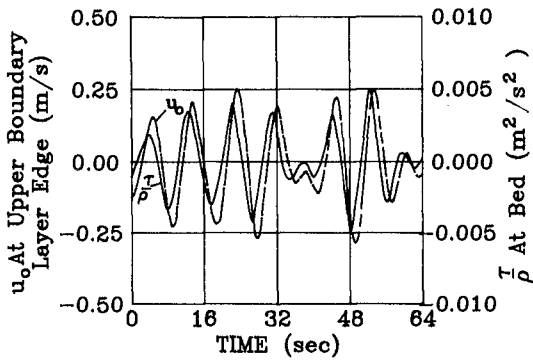


FIGURE 6

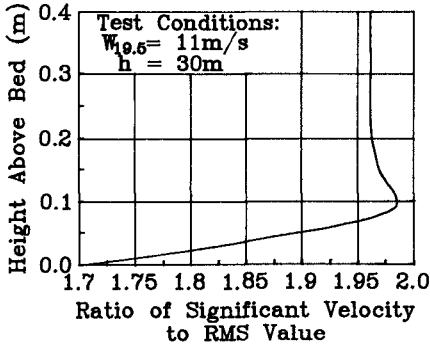


FIGURE 7

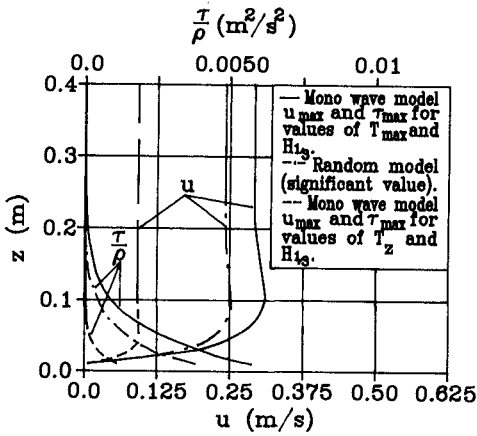


FIGURE 8

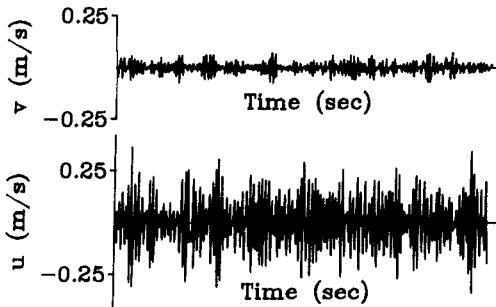


FIGURE 9

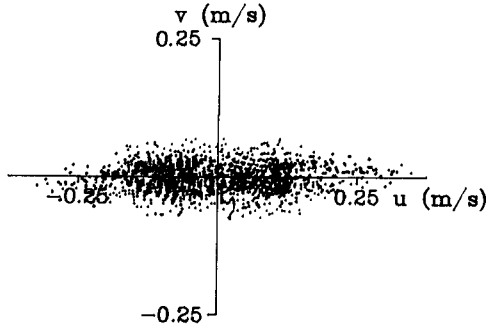


FIGURE 10

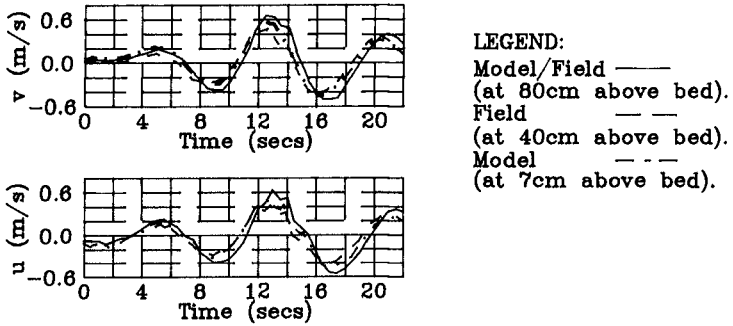


FIGURE 11

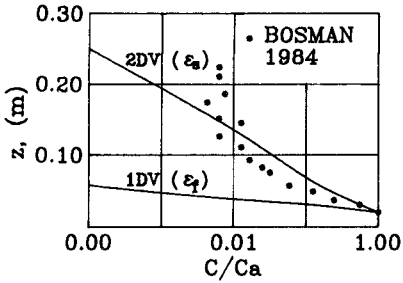


FIGURE 13

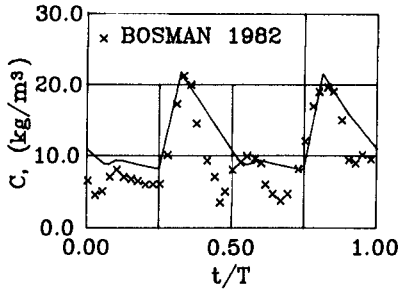


FIGURE 12



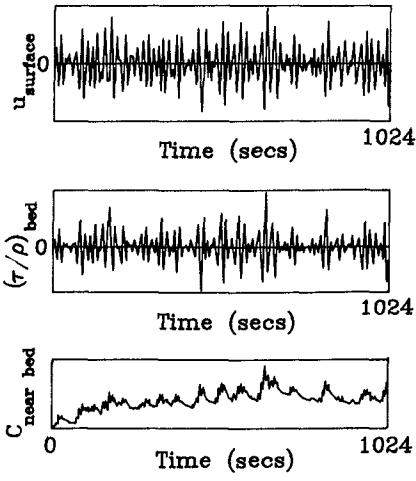


FIGURE 14

## CHAPTER 178

### TIMESCALES OF BED RESPONSE IN A LOW ENERGY SURF ZONE

Philip D. Osborne and Christopher E. Vincent

School of Environmental Sciences, University of East Anglia,  
Norwich, NR4 7TJ, United Kingdom

#### ABSTRACT

Direct and nearly continuous measurements of bed position changes, near-bed velocities and suspended sand concentrations have been made at a single location on a macro tidal beach in the south west of England. The study was conducted in 0.5-2.25 m water depth under low-energy swell conditions with weak currents present. Bed positions and suspended sand concentrations were measured using the 3 transducers of a multi-frequency acoustic backscatter sensor with 5 mm vertical resolution. Large (upto 10 cm) and rapid (upto  $1.0 \text{ cm min}^{-1}$ ) changes in bed elevation were observed in association with local hydrodynamic forcing, bedform development and bedform migration. Large-scale bedforms observed under breaking waves were highly mobile with measured migration rates of upto  $2.2 \text{ cm min}^{-1}$ . Suspended sediment concentrations and transport rates are particularly sensitive to changes in bed position changes and subject to potentially large errors (upto 30 %) without compensation for bed elevation changes relative to sensor position.

#### INTRODUCTION

Bedforms generated by waves and currents on a sandy seabed play an important role in the sand transport process by modifying near bed flows, by enhancing the entrainment and resuspension of sediment, and by influencing the timing and spatial distribution of sand re-suspension. Observations suggest that the time-scales of bed formative processes are quite different from the time-scales of waves or wave groups which also control the suspension process (Vincent et al., 1991; Vincent and Green, 1991). Therefore, knowledge of the ripple history, time-

scales of bed response and accurate positioning of instrumentation is required before the re-suspension and transport processes can be more fully understood.

High-frequency ( $> 1$  MHz) Acoustic Backscatter Sensors (ABS) have been used occasionally for measuring small-scale (both spatial and temporal) changes in sea bed position for nearly two decades (see for example, Dingler, 1974; Dingler et al., 1977; Greenwood et al., 1984; Hanes et al., 1988; Vincent et al., 1991). Despite such efforts, our knowledge of seabed dynamics under natural wave conditions remains limited by a lack of continuous high resolution measurements from a wide variety of conditions. In this paper, we focus on the analysis of measurements of seabed position obtained with a multi-transducer ABS during the Bedforms and Suspension EXperiments (BASEX) field programme. BASEX was designed to investigate the processes controlling sand re-suspension under non-breaking waves and currents, particularly the control exerted by bedforms. Measurements of bedforms, local bed elevation changes, together with suspended sand concentrations, near-bed velocities and water surface elevations, were obtained from a single location near the mid-tide position on a macro-tidal shoreface in the southwest of England. The measurements were taken over a 9 day period in August 1991 during spring tides (range upto 5 m) with mild swell and low energy wind-wave conditions. Time-series of bed positions and reconstructed bed profiles are used to examine the timescales of bed response to changing hydrodynamic conditions and to calculate bedform migration rates.

## LOCATION OF STUDY

Longsands Beach situated on Whitsand Bay, Cornwall (Figure 1) was chosen as a site for BASEX experiments for the following reasons:

- i) The beach is a macrotidal beach with up to 200 m of beach exposed at low tide during spring tides; this feature not only allowed access to the instruments at low tide but provided a range of water depths and wave conditions which could generate a variety of bedforms at a single measurement location even under relatively low energy summer swell.
- ii) The site is exposed to swell from the Atlantic Ocean with no major restrictions on wave approach.
- ii) The shoreface has a relatively simple morphology and sedimentology; the profile is essentially concave upwards with a slope of 1:15 near the mean high water mark and decreasing rather abruptly to a broad uniform slope of 1:70 at approximately 50 m offshore (Figure 2); sand samples from the latter slope were unimodal size distributions with grains ranging in size from 100 to 600 micrometres and a uniform modal size of 212 micrometres (2.25 phi) when dry sieved at 0.25 phi intervals.

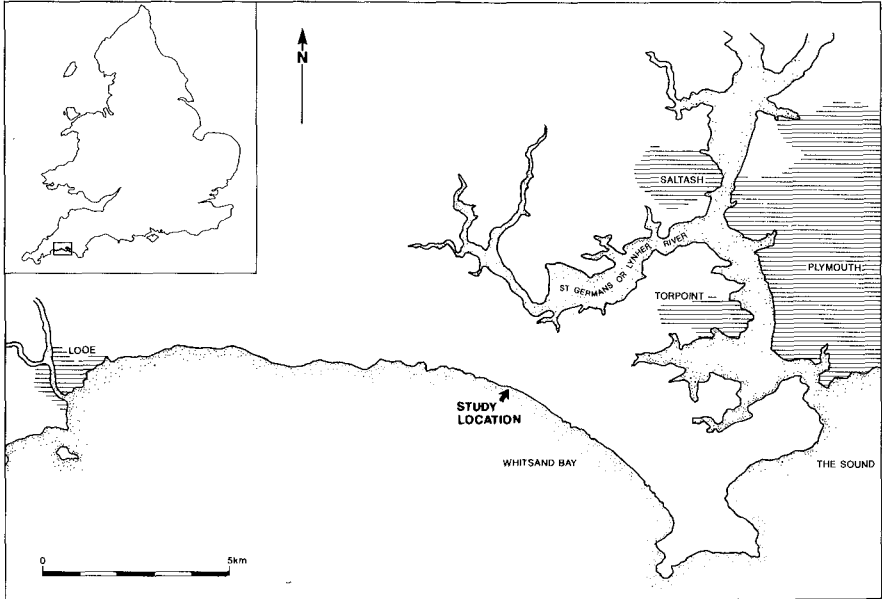


Figure 1. Location of study.

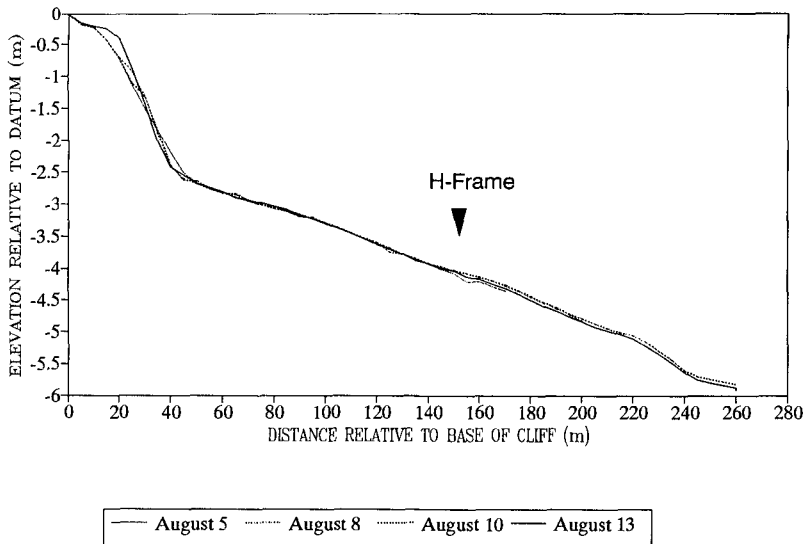


Figure 2. Profiles across Longsands Beach, Whitsand Bay during the experimental period.

## EXPERIMENTAL DESIGN

Instrumentation, consisting of a 3 frequency acoustic backscatter sensor (ABS) (Pearson and Thomas, 1990) and a Valeport 3.2 cm diameter discuss head electromagnetic current meter (EMCM) were mounted on an H-frame at approximately the mid-tide position (Figure 3). Additional instrumentation consisting of electromagnetic current meters, optical backscatterance sensors, pressure sensors and mechanical syringe samplers were also deployed, however, in this paper the analysis has been restricted to the bed position information from the ABS and nearbed current information from the 3.2 cm diameter discuss head EMCM.

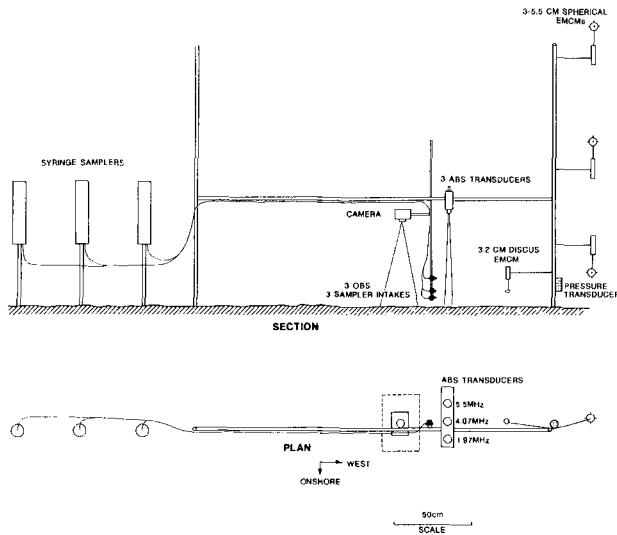


Figure 3. Schematic of the instrumented H-frame.

Local bed elevations were measured with a vertical resolution of 5 mm at 3 horizontal positions approximately 0.10 m apart on a cross-shore transect using the 3 ABS transducers. SCUBA divers also made measurements of the bed profile beneath the ABS transducers by means of a bedform measurement device (Osborne and Vincent, in prep) and took detailed notes on the bedform geometry, bedform migration and suspension characteristics throughout the high-speed data collection runs. Although an underwater camera was mounted adjacent to the ABS, no information on ripple migration could be obtained due to lack of visibility.

The sensors were shore-connected and the data were recorded on a single PC-based data logging system. In order to satisfy the aims and objectives of the BASEX program there was a need for two separate approaches to computerized data collection within the same experimental design. In order to resolve the kinematics of the re-suspension process relative to wave motions and small scale ripple patterns

it was necessary to sample as rapidly as possible to achieve a high spatial and temporal resolution and also to keep runs short enough such that the bed topography did not change significantly relative to the sensors. In order to resolve the effects of different hydrodynamic conditions on bed response it was necessary to collect data over longer periods, more or less continuously, and over a number of tidal cycles. Therefore, two sampling modes were adopted for data collection during this deployment:

1. **Rapid sampling mode** produced short duration data collection runs with relatively high temporal resolution. In this case 12 acoustic profiles initially sampled at 150 kHz were collected from each transducer and averaged to one profile per transducer. The data between 0.10 - 0.65 m range at 0.005 m intervals were stored together with a single digitised value from the EMCM channels. This scheme resulted in an overall collection rate of 4.22 Hz. Available storage space allowed the collection of 1050 profiles for a run duration of 250 s.

2. In **slow sampling mode** run durations were increased to as much as 30 minutes by averaging over a larger number of acoustic profiles (24-48) and storing a smaller vertical range (0.53-0.67 m) of the acoustic data. This scheme resulted in a slower overall collection rate of 1.1-2.1 Hz but enabled continuous observation of bed elevation changes over periods of 30 minutes.

Measurements were made during daylight hours over half tidal cycles from high water down to low water or from low water up to high water.

## ACOUSTIC MEASUREMENTS OF SEA BED POSITION

ABS detect the presence of the bottom boundary due to the change in material density between the fluid and bed which cause a strong acoustic reflection (Hanes et al., 1988). The position of the sea-bed is defined as the position of maximum recorded acoustic pressure. In most acoustic profiles of the water column, the bottom location is clearly identified by a sharp peak in the backscattered pressure. It is therefore relatively simple to produce an algorithm which detects the maximum acoustic return from each profile in order to produce a time-series of bed positions (Figure 4).

Sampling the backscattered acoustic signal at a rate of 150 kHz and range-gating enabled the determination of bed position to  $\pm 0.005$  m under ideal conditions. Clearly, there are random instantaneous variations in the maximum acoustic return above and below the true bed position in Figure 4 which reduce the degree of certainty about the actual bed position at any instant in time. However, these short-term deviations, which may be due to a combination of signal attenuation by suspended sediment and bubbles, and multiple echoes, may be removed relatively easily by a combination of de-spiking and smoothing. More importantly, there are

also significant temporal trends which occur in the data. These variations in the series are interpreted as real changes in the bed position. The series in Figure 4 suggests that 3-4 cm of erosion occurred over a period of 6 minutes followed by 2-3 cm of accretion in the next 6 minutes.

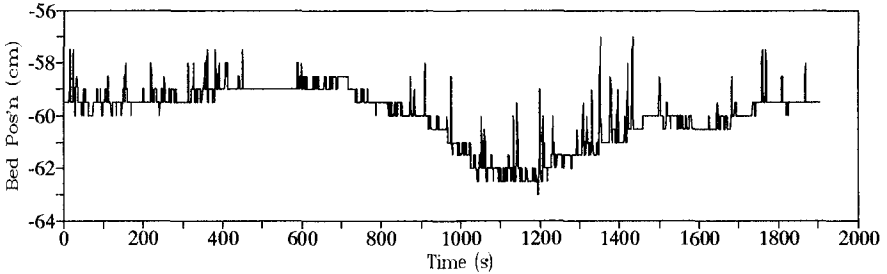


Figure 4. Time-series of the position of maximum backscattered pressure after smoothing by Hanning 3 times. Resolution of the ABS is 5 mm.

### CHANGES IN SEA BED POSITION DURING A TIDAL CYCLE

Time series of bed positions were reduced to one representative value of bed position for each two minute segment of a data run. A series of reduced bed positions from one transducer, representative of a falling portion of a tidal cycle is shown in Figure 5 c. Burst-averaged zero-crossing periods of the cross-shore flow, water depths, cross-shore and shore-parallel velocities, and significant range of cross-shore flows associated with these bed positions are shown in Fig. 5 a and b. The two lines in the bed position series indicate the uncertainty in measured bed position due to sampling resolution ( $\pm 1$  bin) of the ABS. The first 30 minutes of the series shows variations in bed position of no more than 2 cm. Over the next 30 minutes, there is an accretion of 2.5 cm followed by erosion of 6 cm. During the final 15-20 minutes of the series there is a rapid accretion of 8 cm.

In general, the high tide periods (depths 1.5-2.0 m in this experiment) were characterized by near-bed wave-orbital speeds of less than  $0.75 \text{ m s}^{-1}$  and relatively small and gradual changes in vertical bed position (usually  $< 0.5 \text{ cm min}^{-1}$ ) (Figure 6). In contrast, under rapidly rising and falling water levels (depths of 0.5-1.5 m in this experiment), particularly as waves are forced to shoal and break, wave orbital speeds were greater than  $0.75 \text{ m s}^{-1}$  and bed position changes were often substantially larger and more rapid (upto  $1.0 \text{ cm min}^{-1}$ ).

## BED PROFILE RECONSTRUCTION AND BEDFORM MIGRATION

Although the 3 ABS transducers were mounted in fixed positions it is possible to use bed position information together with the detailed diver measurements of the bed beneath the transducers to reconstruct bed profiles and calculate bedform migration rates. A time sequence of bed profiles has been reconstructed (Figure 7) from the ABS bed position measurements (Figure 5) and SCUBA diver observations during the falling tide. The sequence began with small symmetric, two-dimensional vortex ripples (height = 2.5 cm and spacing = 10 cm) and ended with large asymmetric landward lunate megaripples (height = 8 cm and spacing = 40-50 cm). This increase in both height and spacing with time is clearly visible in the profiles. The profiles between 40-65 minutes also indicate shoreward migration of the bedform at a rate of approximately  $2.0 \text{ cm min}^{-1}$ .

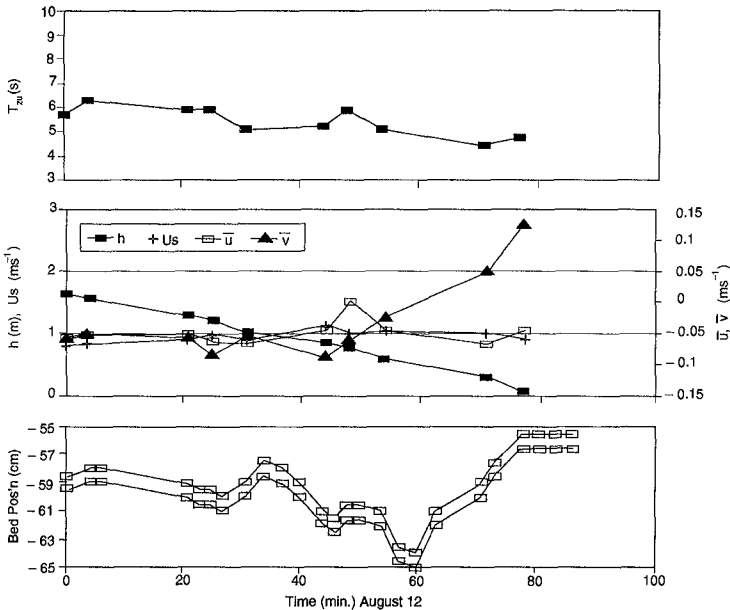


Figure 5. Series of burst-averaged zero crossing periods of the cross-shore flow,  $T_{zu}$ , (a); water depths,  $h$ , cross-shore flows,  $u$ , shore-parallel flows,  $v$ , significant cross-shore velocity ranges,  $U_s$ , (b); and reduced bed positions (c), representative of falling portion of a spring tide.



## DISCUSSION AND CONCLUSIONS

Large and rapid changes in bed elevation were observed during spring tidal cycles under low energy swell conditions with little or no mean currents present. The largest changes in bed elevation are associated with smaller depths when wave induced cross-shore flows are large and waves are either breaking or near breaking. Changes were associated with bedform development resulting from changes in the local hydrodynamic forcing as well as with bedform migration. These processes accounted for local bed elevation changes of upto 10 cm during a series of tidal cycles in which no significant local net erosion or accretion took place.

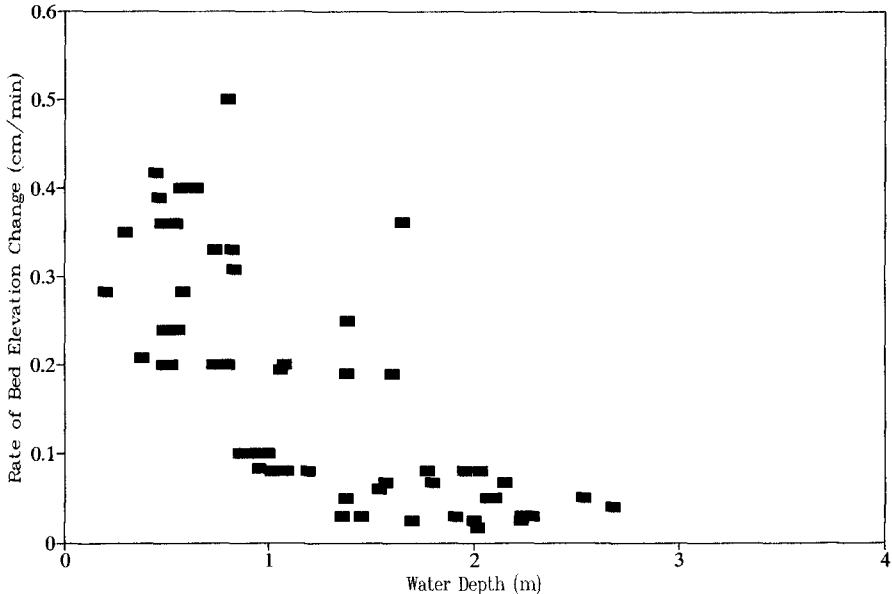


Figure 6. Variations in the time-averaged rate of vertical bed position change as a function of water depth.

Bedform migration rates of upto  $2.2 \text{ cm min}^{-1}$  were associated with well-defined lunate mega-ripples (height = 8 cm; wavelength = 40 cm) under spilling and shoaling waves. Excluding sediment by-passing this represents a total load transport rate of approximately  $0.7 \text{ gm cm}^{-1} \text{ s}^{-1}$ . Evidently, form migration under these conditions represents a significant contribution to the net sediment transport. Bedform migration rates were  $1 \text{ cm min}^{-1}$  and less under the lower energy conditions associated with greater water depths at high tide. The observed bedform migration rates suggest that local bed elevation changes of upto  $1.0 \text{ cm min}^{-1}$  can be expected under large-scale migrating lunate mega-ripples, while rates of bed elevation change upto  $0.6 \text{ cm min}^{-1}$  can be expected under the small-scale three-dimensional and two-dimensional vortex type forms.

These findings have significant implications for measurement and interpretation of sediment transport rates in wave and current environments. As an example, Figure 8 shows time-series of de-spiked and smoothed bed position, suspended sediment concentrations at 2 cm above an arbitrary fixed bed position (indicated by the dashed line in Figure 8 a), suspended sediment concentrations at 2 cm above the measured time-varying bed position, and cross-shore velocity. The uncompensated concentration series (Figure 8 b) is representative of the type of measurements which would be obtained by a fixed point sensor such as an optical backscatterance sensor or transmissometer. There is clearly a non-stationary trend in this series which is coherent with the rising bed position. The trend is absent from the series compensated for bed position change (Figure 8 c). Interpretation of sediment re-suspension processes and computations of sediment transport rates from point measurements of sediment concentration and velocity will be subject to potentially large errors without compensation for bed position changes relative to instrument positions when large and rapid bed elevation changes occur. In the example shown, the time-integrated cross products between velocity and concentration differed by 30 % for the compensated as opposed to uncompensated series. Furthermore, the presence of migrating large-scale bedforms under relatively gentle conditions suggests that spatial variability in sediment concentrations, near-bed velocity structure and sediment transport are likely to be significant.

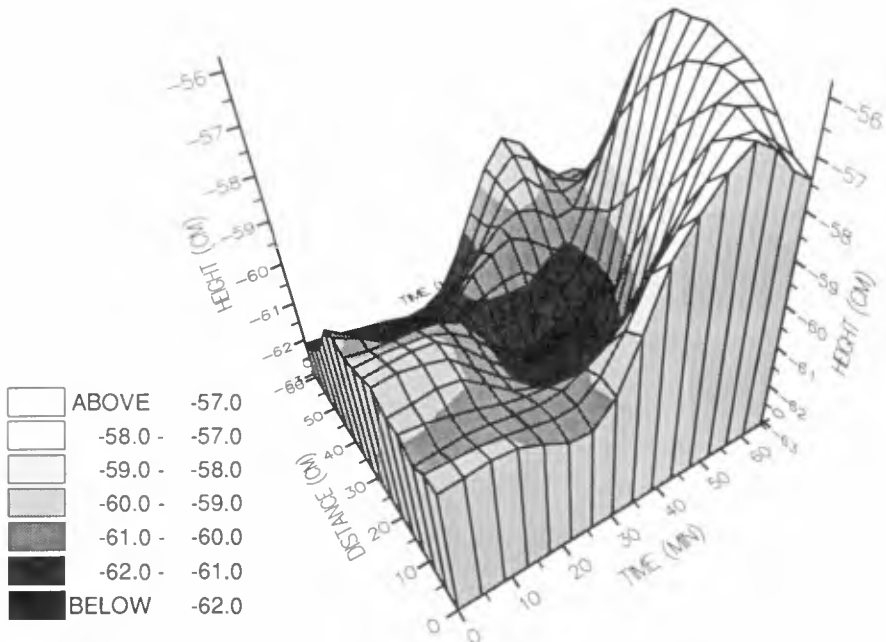


Figure 7. Time-sequence of reconstructed bed profiles during a falling tide.

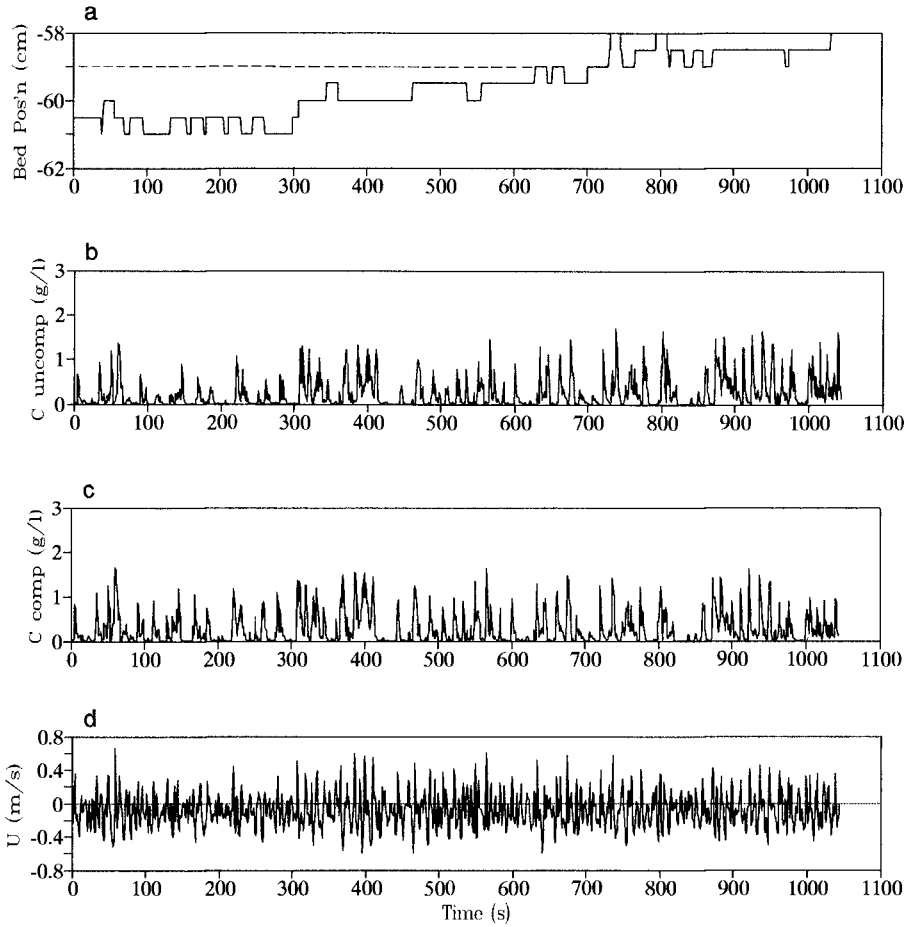


Figure 8. Time-series of: a) smoothed and de-spiked bed position; b) suspended sediment concentration at 2 cm above fixed bed (dashed line in a); c) suspended sediment concentration at 2 cm above true bed position; d) cross-shore velocity.

## ACKNOWLEDGEMENTS

The BASEX programme is a combined project involving the University of East Anglia, Bullard Laboratories, and the University of Plymouth. BASEX is sponsored by the Natural Environment Research Council. PDO also gratefully acknowledges the support of a Natural Sciences and Engineering Research Council of Canada Postdoctoral Fellowship. The authors wish to thank Drs. Malcolm Green, Mark Davidson, Paul Russell and Mr. Gareth Lloyd for their enthusiastic assistance while in the field. Particular thanks to Professor David Huntley for making the B-Band instrumentation available and for arranging access to the beach.

## REFERENCES

- Dingler, J.R. (1974) Wave-formed ripples in nearshore sands. Ph.D. Dissertation, Univ. of California, San Diego, 136 pp.
- Dingler, J.R., Boylls, J.C. and Lowe, R.L (1977) A high-frequency sonar for profiling small-scale subaqueous bedforms. *Marine Geology*, 24: 279-288.
- Greenwood, B., Dingler, J.R., Sherman, D.J., and Anima, R.J. (1984) Bedform dynamics and bedding genesis under waves, Pointe Sapin, New Brunswick: I Design, construction and testing of a high resolution remote tracking sonar (HRRTS). Canadian Coastal Sediment Study C2S2-7, National Research Council of Canada, Associate Committee for Research on Shoreline Erosion and Sedimentation, Ottawa, pp. 75-91.
- Hanes, D.M., Vincent, C.E., Huntley, D.A. and Clarke, T.L. (1988) Acoustic measurements of suspended sand concentration in a wave-dominated nearshore environment. *Continental Shelf Research*, 6 (4): 585-596.
- Osborne, P.D. and Vincent, C.E. (in preparation) Bedform dynamics on a macro tidal beach.
- Pearson, N.D. and Thomas, M.R. (1990) A multi-frequency acoustic backscatter recorder for suspended sediment transport studies. *Proc. Inst. Elec. Eng. Colloquium Monitoring the Sea*, Digest no. 1990/182.
- Vincent, C.E. and Green, M.O. (1990) Field measurements of the suspended sand concentration profiles and fluxes, and of the resuspension coefficient over a rippled bed. *J. Geophys. Res.*, 95: 15591-15601.
- Vincent, C.E., Hanes, D.M. and Bowen, A.J. (1991) Acoustic measurements of suspended sand on the shoreface and the control of concentration by bed roughness. *Marine Geology*. 96: 1-18.

## CHAPTER 179

### SHORELINE CHANGE AT OREGON INLET TERMINAL GROIN

M. F. Overton (M)<sup>1</sup>, J. S. Fisher (M)<sup>2</sup>  
W. A. Dennis (M)<sup>3</sup>, and H. C. Miller (AM)<sup>4</sup>

#### Abstract

The Oregon Inlet Terminal Groin was completed in 1991. The groin was built to provide protection to the bridge crossing the inlet. A detailed monitoring program has analyzed shoreline position with the use of aerial photographs collected every two months. To date, no adverse impacts of the groin have been found on the shoreline within a 6 mile distance downdrift of the groin.

#### Introduction

Oregon Inlet is located between Bodie Island and Pea Island on the North Carolina coast, Figure 1. These islands form a part of the barrier island system generally referred to as the Outer Banks. This inlet formed in 1846 during a major storm, and has remained open to the present. During this 146 year interval the inlet has gone through many changes in width and position, with a net migration to the south of approximately 2 miles. The inlet width has varied from a minimum of about 2,000 ft to a maximum of just over 5,000 ft. While there have been numerous discussions and plans to stabilize it with jetties, Oregon Inlet remains one of the largest unimproved inlets along the east coast of the United States.

The inlet is spanned by the 2.4 mile long Bonner Bridge constructed in 1962, Figure 2. This bridge is located along the

---

<sup>1</sup>Dept. Civil Engineering, NCSU, Raleigh, NC 27695-7908

<sup>2</sup>Dept. Civil Engineering, NCSU, Raleigh, NC 27695-7908

<sup>3</sup>US Army COE, Wilmington District, P.O. Box 1890, Wilmington, NC 28502

<sup>4</sup>US Army COE, FRF, 1261 Duck Rd., Kitty Hawk, NC 27949

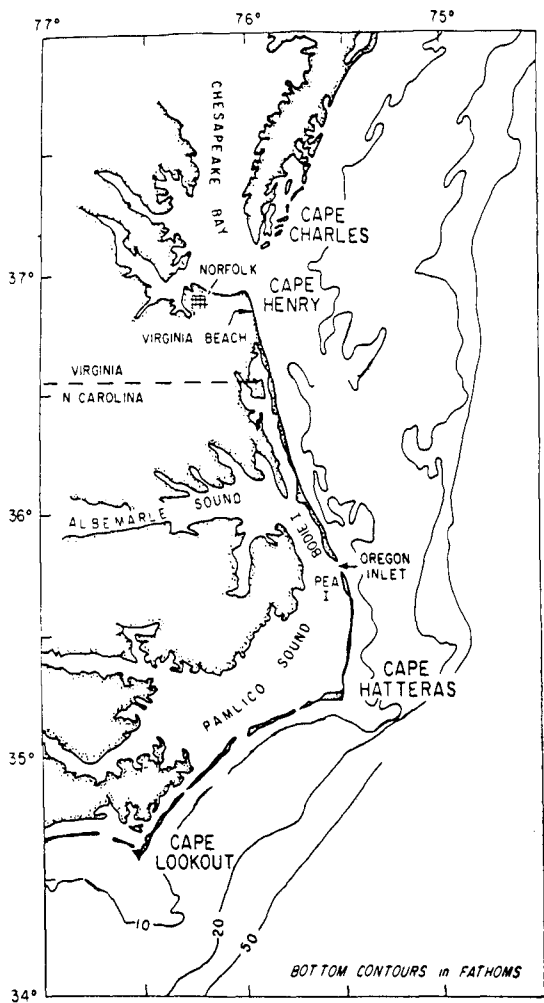


Figure 1. Location of Study Area (from Inman and Dolan, 1989)

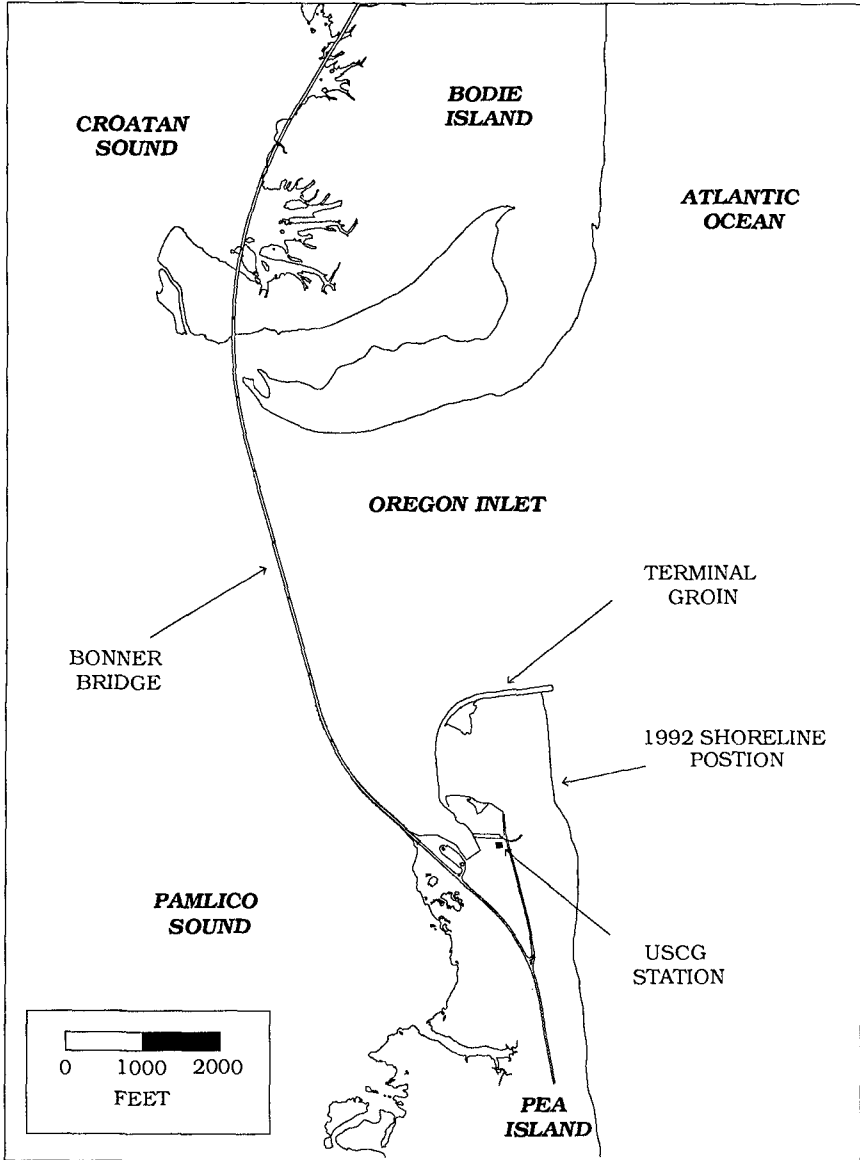


Figure 2. Detail of the Oregon Inlet Area.

principal highway serving the Cape Hatteras National Seashore. Peak summertime traffic is in excess of 10,000 cars per day.

The navigation channel spanned by the Bonner Bridge provides an important marine connection between Croatan and Pamlico Sounds and the Atlantic Ocean. This channel is used by both commercial and sport fishing interests. The channel is maintained by the U. S. Army Corps of Engineers. Maintenance dredging is done annually, with combined dredge volumes for the inner and outer channels in excess of 750,000 yd. The difficulty in dredging this channel has led to the consideration of an inlet stabilization project at this site. Preliminary designs by the Army Corps of Engineers call for a pair of jetties approximately 10,000 ft long.

The persistent migration of the inlet to the south has created an extreme erosion problem on the north end of Pea Island. By 1988 the portion of this island facing the inlet was eroding at an annual rate of about 80 ft/yr (NCDOT, 1988). This high erosion rate created a threat to the future safety of the Bonner Bridge. The North Carolina Department of Transportation (NCDOT) was concerned that the erosion, if left unchecked, would eventually allow storm waves to impact directly on the bridge deck at the southern end where it connects with Pea Island.

Several alternatives were considered to protect the bridge. These alternatives included beach nourishment, a series of short groins, and the selected choice of the single terminal groin (NCDOT, 1988). This latter choice was based upon the assumption that there was substantial local longshore transport to the inlet on the north end of Pea Island for the groin to trap. Thus, the groin would artificially reverse the erosion locally, and the resulting accretion would provide the needed protection to the bridge. The potential for this accretion was documented by a number of sediment budget studies undertaken as part of the evaluation of the proposed jetty project (Inman and Dolan, 1989).

Once NCDOT selected the terminal groin as the preferred solution to protect the bridge, it was necessary to obtain both state and federal permits for construction. The site for the groin is located on a National Wildlife Refuge managed by the U. S. Fish and Wildlife Service. In addition, the inlet is located along the Cape Hatteras National Seashore, managed by the National Park Service. These federal interests, as well as those of the North Carolina Division of Coastal Management necessitated unusual restrictions on the construction permit for the groin. Specifically, NCDOT is required to insure that the groin does not result in an accelerated erosion of the downdrift shoreline. This requirement led to the initiation of a detailed monitoring program to evaluate shoreline change near the groin. The current results of this ongoing monitoring are presented in this paper.



### Description of Groin

The terminal groin was designed for NCDOT by the Wilmington District of the U. S. Army Corps of Engineers. The total length of the groin section is approximately 3,100 ft. At its seaward end the water depth is about 6 ft (mlw). The top width increases from 25 ft at the landward end to 39 ft at the seaward head. Crest elevation is +9.5 ft (msl) at the head. Side slopes are 2 on 1, except at the head where they are 3 on 1. The core material is covered by a layer of rubble ranging in weight from 4 to 2500 lb, with an armor layer of rock with weights from 0.75 to 11 tons. Toe protection on the inlet side of the groin is provided by a 43 ft wide single layer of the armor stone on top of a layer of core material (NCDOT Project 6051020 plans).

### Monitoring

It was expected that a natural sand fillet would begin to form as soon as the groin construction extended beyond the natural shoreline, and that eventually this fillet would extend to the seaward end of the groin. Thus, this accretion caused by the presence of the groin would result in a northern migration of Pea Island and would serve as the needed protection for the bridge.

While the development of the sand fillet adjacent to the groin was the desired outcome of the project, the construction permit required monitoring to insure that this accretion at the groin did not come at the expense of the downdrift shoreline. Specifically, the permit required that the six miles of shoreline just south of the groin be monitored (Overton and Fisher, 1992).

The monitoring program includes the analysis of aerial photographs taken every two months as well as immediately after severe storms, and field surveys collected twice each year. In a separate effort the Corps of Engineers is also collecting data to monitor the performance of the terminal groin. These data include beach and bathymetric surveys in the project area and wave height and direction in the inlet.

The bimonthly aerial photographs are the principal data used to monitor shoreline change. The photographs are made as close to spring high tide as possible, with the shoreline defined as the position of the wet sand line.

The analysis of the shoreline change follows a modification of a procedure developed by Dolan, et al., 1978. For each set of aerial photographs, the position of the shoreline is measured relative to a fixed baseline offshore. The distance from the baseline to the shoreline is determined every 150 ft over the 6 mile length of monitored

shoreline. The shoreline position is digitized from the aerial photographs by NCDOT using an Intergraph Intermap Analytic Stereoplotter Workstation. The distance from the baseline to these digitized shorelines is then determined on a computer.

### Historical Erosion Rates

In order to determine if the terminal groin is causing accelerated shoreline erosion, a comparison is made of the measured shoreline position with the position predicted from historical rates. If the analysis indicates that current rate of erosion exceeds the historical rate, then NCDOT has agreed to correct the excess erosion by beach nourishment. Thresholds for action have been established based upon the assumption that 1 sq ft of erosion determined from the aerial photographs is equivalent to 1 cu yd of volume loss from the beach. Two thresholds are being used; 250,000 cu yd over a 1 mile shoreline segment, and 500,000 cu yd over a 3 mile segment. The threshold must be exceeded for several successive bimonthly survey intervals before remedial action is required (Overton and Fisher, 1992).

The dates selected to establish the project historical erosion rates are September 19, 1984, and October 9, 1988. The 1984 date was chosen because it is the earliest record available after the Corps of Engineers initiated large scale hopper dredging in Oregon Inlet. Since this hopper dredging may have accelerated the erosion of the north end of Pea Island, earlier photographs would potentially bias the calculation to lower erosion rates. The more recent date, October 1988, was chosen because it is the most recent date prior to a severe storm (March 1989) which caused major erosion, and therefore might bias the erosion rates to higher values.

Figure 3 shows the annual historical erosion rate based upon the September 1984 to October 1988 interval. Mile zero in this figure is the location of a United State Coast Guard (USCG) Station, Figure 2. This station is approximately 2,000 ft south of the terminal groin. In general the erosion rate along this portion of Pea Island is relatively high, with a mean value of about 27 ft/yr. The portion of the shoreline nearest the inlet is clearly the area of highest erosion, as one would expect near the inlet. In this area the erosion rate has a maximum value on the order of 100 ft/yr. These relatively high erosion rates near the inlet clearly document the need for the construction of the terminal groin.

The state of North Carolina uses a long term shoreline change rate for shoreline management purposes. This rate is determined from aerial photographs with a method similar to that used to monitor the terminal groin (McCullough, 1988). In this case the long term rate is based upon the interval from 1945 to 1986. This Long Term Rate for the project area is also shown on Figure 3. The higher erosion rates

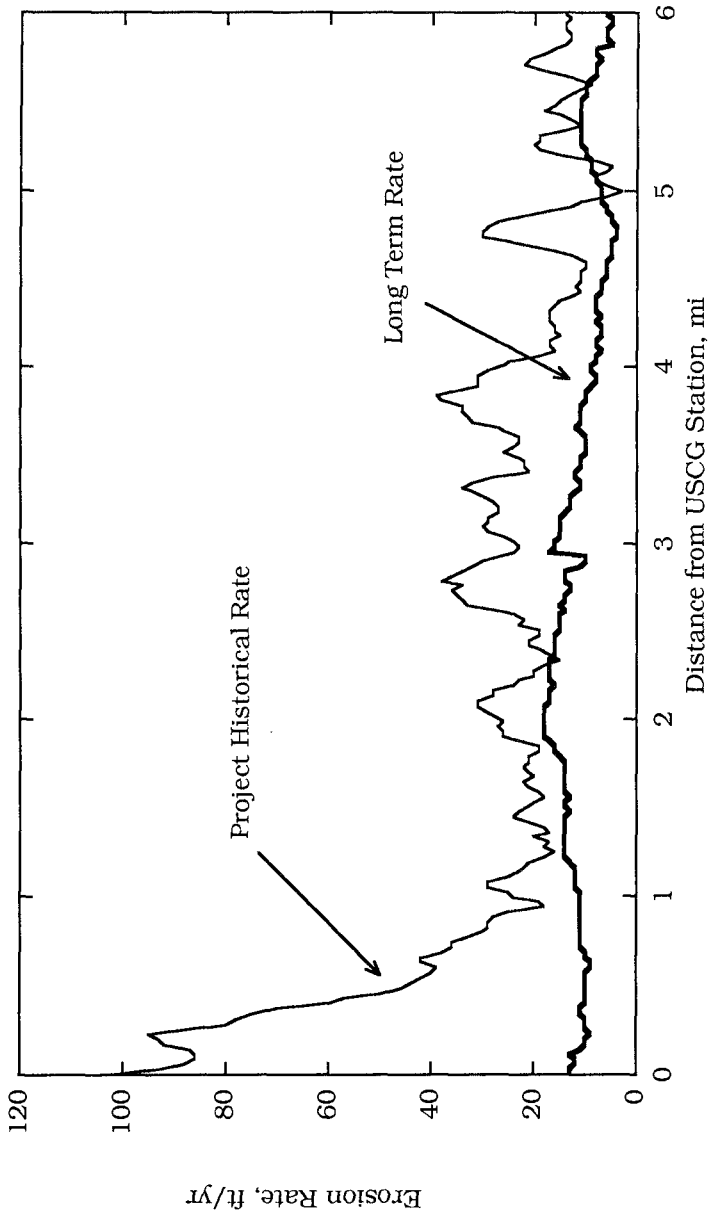


Figure 3. Comparison of the Long Term Rate, based on 1945 - 1986 shoreline position data, and the Project Historical Rate, based on 1984 - 1988 shoreline position data.

near the groin (between mile 0.0 and 1.0) are further indication of the increase in erosion in recent years. Further south the two erosion rates appear to converge. The greater variability in the Project Historical Rate relative to the Long Term Rate is a typical difference between short and long records of shoreline change.

### Beach Nourishment

The initial plans for the terminal groin did not include beach nourishment. However, the project area has benefited from the continued maintenance dredging of Oregon Inlet for navigation purposes. The spoil from this dredging is currently being placed on the beach with the terminal groin project area. Since the groin was completed in March 1991 there have been three separate Corps projects where the beach near the groin was used as a disposal site for the dredging operations. Table 1 summarizes these nourishment events.

Table 1  
Summary of Beach Nourishment Activities

Date	Volume (cu yd)	Location (miles south of USCG)
April 1991	282,600	0.4-1.2
Sept. 1991	157,600	0.2-0.4
Aug. 1992	1,078,000	0.8-1.8

### Severe Storms

In addition to the bimonthly aerial photographs, the monitoring program includes the analysis of any severe storms that might have significant impact along the project. There have been a number of large storms since the construction of the groin. One of these, October 1991 (The Halloween Storm) is estimated to have been larger than the 1962 Ash Wednesday Storm (Dolan and Davis, 1992). The average immediate post-storm erosion along the project was about 75 ft for this storm. In general, the storm history since the construction of the groin has been one of the most severe on record. However, while there is usually considerable erosion caused by the high waves and surge, the beach appears to be able to recover most of the short-term loss during the post-storm periods (Overton and Fisher, 1992).

### Shoreline Change Near the Groin

The shoreline change within the first 3,750 ft south of the groin is shown in Figure 4. October 5, 1989, represents the shoreline position just prior to groin construction. Groin construction began in

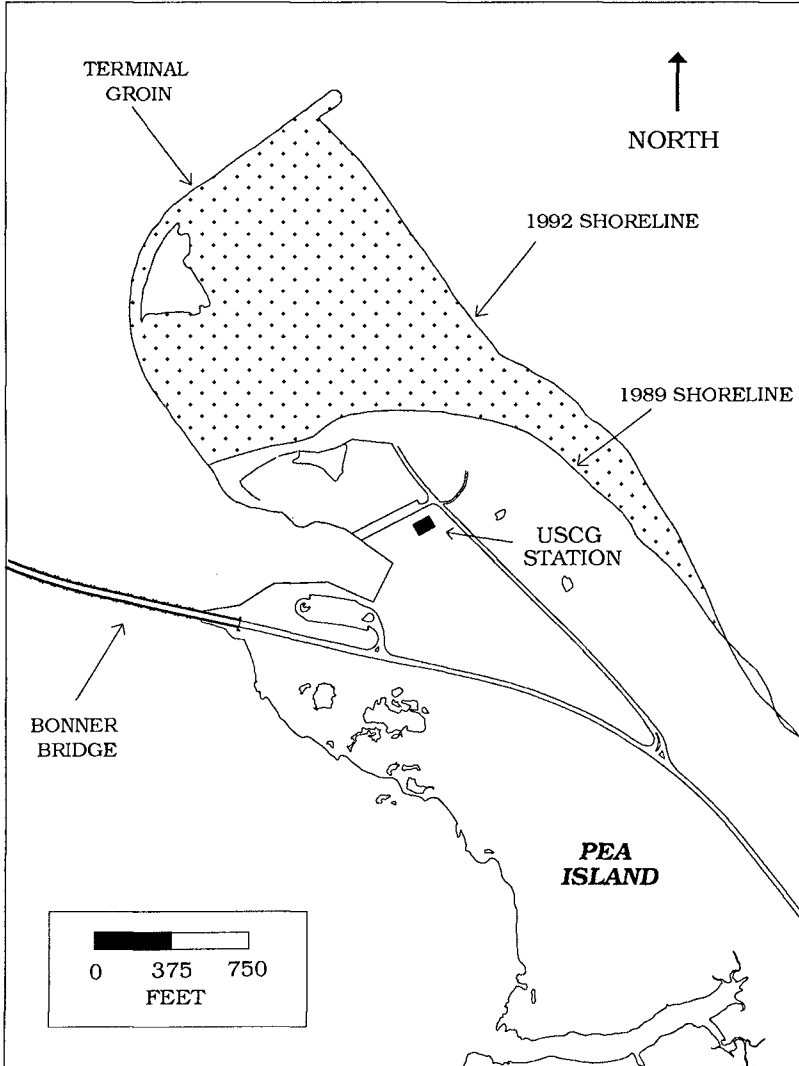


Figure 4. Detail of the groin fillet.

October 1989, and thus the most recent date, October 1992 spans a period of three years. As expected, during this interval there has been substantial accretion at the groin itself. The area of accretion above the mean high water line is estimated to be approximately 2 million sq ft. This figure clearly illustrates the effectiveness of the groin in causing the northern end of Pea Island to accrete to the inlet, thus providing the needed protection for the bridge.

#### Shoreline Change Over the Six Mile Study Area

Figure 5 compares the Project Historical Erosion rate with the Current Project Erosion Rate (defined as the erosion rate computed from October 1989 to the present date) along the six mile study area starting at the Coast Guard Station. For the two miles closest to the groin there has been almost a complete reversal from erosion to accretion. Mile zero on this figure is approximately 2,000 ft of the groin, and thus this accretion is south of the fillet area shown in Figure 4. However, the most recent dredging operation spoiled over 1,000,000 cu yd of sand within the first two mile stretch shown on Figure 5. Therefore, much of the accretion shown in this area can be assumed to be due to this nourishment activity. For the remaining 4 miles of the monitoring area there is essentially no difference between the erosion rates prior to and after groin construction based on the October 1992 shoreline position.

#### Conclusion

On the basis of the record of shoreline change since the construction of the Oregon Inlet terminal groin, there has been no adverse impact of the groin on the downdrift shoreline, Figure 5. The combination of the sand trapping of the groin and the three beach nourishment projects has resulted in substantial accretion near the groin. Further south the erosion rates before and after groin construction are essentially the same. During the three years of monitoring the "excess erosion thresholds" have been reached three times, but the beach has recovered naturally by the date of the succeeding bimonthly surveys. Thus, NCDOT has not had to take any remedial actions to mitigate the impact of the groin.

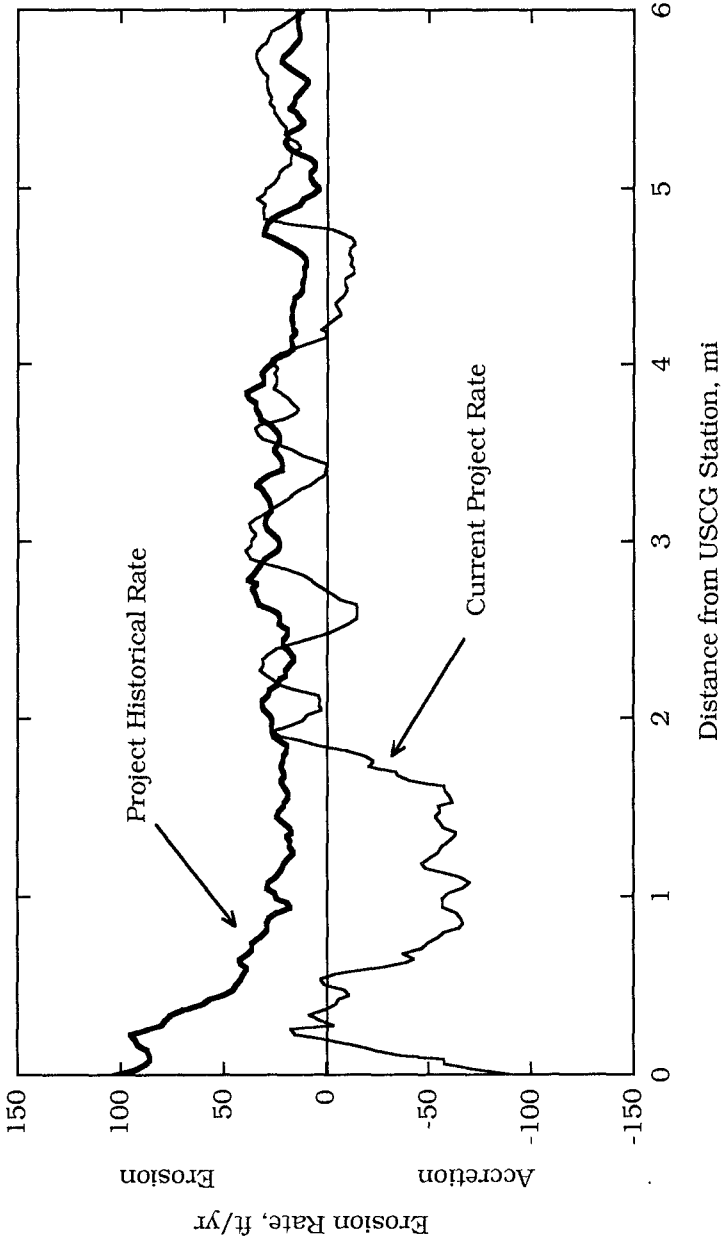


Figure 5. Comparison of the Project Historical Rate and the Current Project Rate which is based on the October 1989 - October 1992 shoreline position data.

### Acknowledgments

The authors want to thank the North Carolina Department of Transportation for their support for this project. In particular, Mr. Archie Hankins and Mr. Cecil Hinnant have provide invaluable aid in the collection of the data used in our analysis.

### References

- Dolan R., and R. E. Davis, "Rating Northeasters", *Mariners Weather Log*, Vol. 36, No. 1, 1992.
- Dolan, R., Hayden, B., and Heywood, J., "A New Photogrammetric Method for Determining Shoreline Erosion", *Journal of Coastal Engineering*, V. 2, 1978.
- Inman, Douglas L., and Robert Dolan, "The Outer Banks of North Carolina: Budget of Sediment and Inlet Dynamics Along a Migrating Barrier System", *Journal of Coastal Research*, 5 No. 2, 1989.
- McCullough, Melissa W., "Average Annual Long Term Erosion Rate Update, Methods Report", Division of Coastal Management, North Carolina Dept. Natural Resources and Community Development, 1988.
- NCDOT, "Oregon Inlet Bridge Task Force Report", 1988.
- Overton, M. F., and John S. Fisher, "Shoreline Monitoring at Oregon Inlet Terminal Groin", Report 5, NCSU Department of Civil Engineering, 1992.



## CHAPTER 180

# Numerical simulation of sand in plunging breakers

C. PEDERSEN<sup>1</sup>, R. DEIGAARD<sup>2</sup>, J. FREDSSØE<sup>3</sup> AND E.A. HANSEN<sup>4</sup>

### ABSTRACT

A discrete vortex model has been applied to describe plunging breakers. The wave breaking is represented by a jet of water impinging on the surface in front of the wave crest. The suspension of sediment has been modelled by a mixed diffusion - convection scheme. Preliminary results in the form of vector plots of the flow field and concentration profiles are presented.

### INTRODUCTION

The surf zone is important for the coastal sediment transport due to the intense production of turbulence and vorticity associated with the wave breaking.

The surf zone is traditionally divided into two regions (Svendsen et al. 1978), the outer surf zone and the inner surf zone. This differentiation is in particular important for the plunging breaking case, where the flow structures in the two regions

---

<sup>1</sup>Ph.D.-student, Institute of Hydrodynamics and Hydraulic Engineering (ISVA), Technical University of Denmark, DK-2800 Lyngby, Denmark.

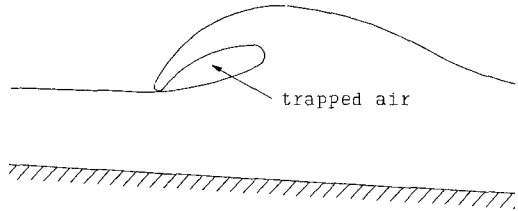
<sup>2</sup>Associate Professor, ISVA.

<sup>3</sup>Professor, ISVA.

<sup>4</sup>Senior research engineer, Danish Hydraulic Institute (DHI), Agern Allé 5, DK-2970 Hørsholm, Denmark

deviate distinctively. In the outer surf zone, the first often violent transformation of the waves takes place. The wave height is reduced rapidly, and the corresponding loss in wave energy is transformed partly into small scale turbulence and partly into kinetic energy in a series of coherent large scale eddy structures, which can stretch over the entire local water depth (see eg. Miller, 1976). In the inner surf zone, the first violent transformation has ceased and the waves migrate towards the shore as turbulent bores. Due to its complex structure, modelling of the flow in the outer surf zone is scarce.

The shoaling process and the transformation of a wave until the initiation of breaking can be described by potential flow theory, and potential flow models are able to represent a plunging breaker until the time when the forward moving jet touches the water surface in front of the wave crest, fig. 1, (Longuet Higgins & Cokelet, 1976).



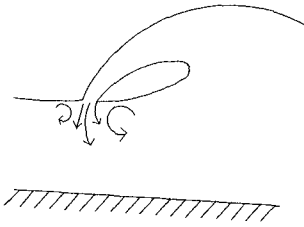
**Fig. 1** Jet impingement in plunging breaking wave.

Outside the surf zone the turbulence is mainly generated in the near-bed boundary layer and the sediment transport can be described by the turbulent diffusion equation in connection with a model for the combined wave-current boundary layer, (Fredsoe et al. 1985).

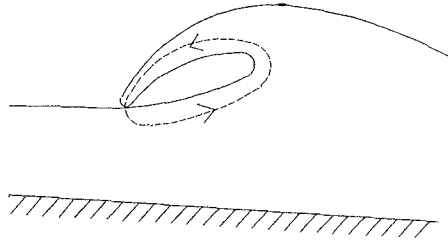
In the inner surf zone, the bore-like broken waves generate turbulence and vortices. The variation in time and space of the turbulence and the suspended sediment can with some accuracy be described by a turbulence model which is coupled with a boundary layer model and the turbulent diffusion equation for the suspended sediment, (Deigaard et al 1986).

The present work is dealing with the situation when the breaking wave plunges, i.e. from the moment when the description by the potential theory breaks down and before the quasi-steady bore approach has become valid. Two mechanisms are dominant for the production of turbulence and vortices.

- The flow pattern generated by the jet impingement on the surface in front of the wave crest, see fig. 2.
- The topologically generated vorticity, see fig. 3. At the instant the jet impinges on the water surface, the domain occupied by the fluid in a vertical section changes from being simply connected to being doubly connected. There is a circulation around the water enclosed core, leading to the formation of a vortex, (Battjes 1988).



**Fig. 2** Vorticity generated by impinging jet.



**Fig. 3** "Topologically generated" vortex.

The mathematical model will concentrate on the first mechanism, describing the effects from the impinging jet.

## THE HYDRODYNAMIC MODEL

### General

Despite a large interest in the plunging breaking process over the recent years, the consequent extensive experimental examinations of the mechanisms involved have not yet provided a generally accepted model for the physical process. There are numerous suggestions to how the flow-field develops from the moment of impingement by the jet on the surface, ranging from complete deflection to total penetration of the jet, (Peregrine 1983). The entrainment in- and subsequent escape of air from the water column is accentuated as a main cause for turbulent mixing by some authors, while it is considered insignificant to the flow structure by others.

The varying opinions may partly be due to the complexity of the flow and the accompanying difficulties in performing experimental investigations, but may also result from the fact, that the regime of breaker types are of a more continuous than discrete character. Plunging breaking ranges from the transition from spilling breaking to the transition to surging breaking, (Galvin 1968), spanning over large differences in the magnitudes of the processes involved.

The present study is based on a "well developed" plunging breaking wave, where the jet is assumed to penetrate the water surface in front of the crest as found by Jansen (1986). Effects from the entrainment of air include variable density, buoyancy and compressibility of the fluid. This might be of considerable importance close to the surface, but towards the bottom, the influence is assumed to be less pronounced, and as a first approach it will be neglected, assuming the density of the fluid to be uniform throughout the domain.

The formation of large-scale vortices - "breaker vortices" is generally emphasized as one of the most important features in connection with the exchange of momentum and turbulence with the lower part of the water column (see e.g. Miller 1976). This makes the breaker vortices prime factors in the agitation and suspension of sediment. Nadaoka (1989) further points to the existence of "obliquely descending" eddy structures. For simplicity it has been chosen to treat the problem two-dimensionally in a vertical plane perpendicular to the incoming wave fronts - neglecting possible three dimensional effects in the long shore direction. The observed flow field in this plane comprises the breaker vortices, which are large scale, coherent, vortical flow structures embedded in a highly turbulent region, and therefore calls for a numerical model capable of providing a fine spatial resolution.

### Discrete vortex model

The discrete vortex model (DVM) directly simulates the distribution of rotation in the fluid by modelling the rotation as "vorticity particles", which for each timestep are assigned convective and diffusive translations in space. This should fulfill the requirement of spatial resolution of the vorticity in the interior of the computational domain. A simple technique based on superposition of a jet on a non-breaking potential-theory wave has been implemented to simulate the free surface. The emphasis is put on the inner flow field composed of the wave orbital motion and the generation of vorticity due to the jet.

The implemented version of the discrete vortex model is largely similar to the one described by Asp Hansen et al. (1992) and will only be described briefly here. An extensive review of vortex methods has been given by Sarpkaya (1988). The boundary conditions at the surface are unique to the present application of the model and will be described in further detail. The governing equations, which are found from the Navier Stokes equations for incompressible flow in two dimensions combined with the continuity equation, are the vorticity transport equation:

$$\frac{d\omega}{dt} = \frac{\partial\omega}{\partial t} + u \frac{\partial\omega}{\partial x} + v \frac{\partial\omega}{\partial y} \quad (1)$$

and the Poisson equation:

$$\nabla^2 \psi = \omega \quad (2)$$

Here  $u$  and  $v$  are the velocities in  $x$ - and  $y$  direction respectively,  $\nu$  is the kinematic viscosity,  $\omega$  is the vorticity given by:

$$\omega = \frac{\partial u}{\partial y} - \frac{\partial v}{\partial x} \quad (3)$$

and  $\psi$  is the stream-function given by:

$$u = \frac{\partial \psi}{\partial y} \quad ; \quad v = -\frac{\partial \psi}{\partial x} \quad (4)$$

The vorticity transport equation consists of a convective and a diffusive part:

$$\frac{\partial \omega_{conv}}{\partial t} = -u \frac{\partial \omega}{\partial x} - v \frac{\partial \omega}{\partial y} \quad (5)$$

$$\frac{\partial \omega_{diff}}{\partial t} = \nu \nabla^2 \omega \quad (6)$$

Numerically, the governing equations are solved by letting discrete vortex particles represent the vorticity. Each particle has a position in the  $(x,y)$  plane and a circulation strength  $\Gamma$ . Further, a finite difference grid is introduced and the calculations performed according to the "cloud in cell" method (Christiansen 1973, Stansby & Dixon 1983). This involves redistribution of the rotation, represented by the discrete vortex particles, to the grid, in which a finite difference version of the Poisson equation is solved. This leads to the stream function  $\psi(x,y)$  and thereby the velocity in the grid points (equations 4). The velocity at the position of each particle is found from interpolation, and the convective movement of the discrete particles is performed. The diffusion is simulated by ascribing each particle a small displacement obtained through a random walk procedure. The displacements satisfy a Gaussian distribution, as required by equation (6).

Advancing the solution of a given problem with certain boundary conditions one timestep basically involves the following steps:

1. Solve Poisson's equation (gives  $\psi(x,y)$ )
2. Determine the velocity field from  $\psi(x,y)$
3. Apply new rotation (discrete vortices) to satisfy boundary conditions
4. Move the vortices convectively - equation (5), and approximate a solution to the diffusive transport, equation (6), by use of a random walk procedure

This is a combination of a Lagrangian and an Eulerian description. The discrete vortices are tracked and moved in a Lagrangian fashion, while the Poisson equation is solved in an Eulerian mesh, making the method numerically effective. The cloud in cell method is especially beneficial for a large number of vortices, which is

essential to satisfy boundary conditions and resolve the flow accurately.

The model is implemented in a curvilinear grid, which is generated by solving the Laplace equation for a specified flow through the computational domain.

**Boundary conditions for stream function**

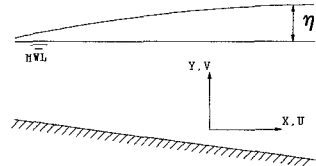
To solve the Poisson equation (2) in a grid, the stream function  $\psi$  needs to be specified along all boundaries of the domain. In the curvilinear grid, the bottom is itself a streamline, implying that  $\psi_{\text{bottom}}$  is constant.

At the surface, the problem of representing a plunging breaking wave in a fixed grid has been approached by splitting the plunger into two parts: An irrotational "basis wave" and a "jet" of water. The two components are calculated separately based on the mean water level and subsequently superimposed in the model, see fig. 5.

The boundary conditions corresponding to the basis wave - a non-breaking progressive wave - are computed by employing an irrotational formulation of the present model, including a linearized free surface, to the domain and then simulate a wave flap at one side. The "free surface" is established on the basis of the kinematic (7) and the dynamic (8) boundary conditions:

$$dy = \frac{\partial \eta}{\partial t} dt + \frac{\partial \eta}{\partial x} dx \tag{7}$$

$$\frac{\partial u}{\partial t} + u \frac{\partial u}{\partial x} + v \frac{\partial u}{\partial y} = -\frac{1}{\rho} \frac{\partial p}{\partial x} \tag{8}$$



**Fig. 4** Definition sketch

Introducing the stream function (4) in the kinematic condition (7) yields:

$$-\frac{\partial \psi}{\partial x} = \frac{\partial \eta}{\partial t} + \frac{\partial \psi}{\partial y} \frac{\partial \eta}{\partial x} \tag{9}$$

Linearizing the dynamic condition (8) eliminates the two convective terms:

$$\frac{\partial u}{\partial t} = -\frac{1}{\rho} \frac{\partial p}{\partial x} \tag{10}$$

Using shallow water theory (hydrostatic pressure distribution) the horizontal pressure gradient is determined by the change in surface elevation:

$$\frac{\partial p}{\partial x} = \rho g \frac{\partial \eta}{\partial x} \quad (11)$$

which introduced in (10) together with the stream function (4) leads to:

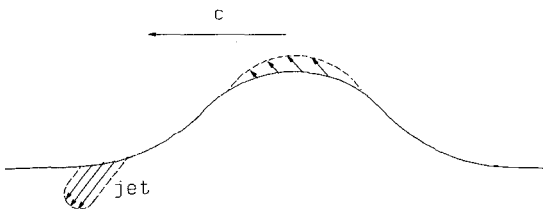
$$\frac{\partial}{\partial t} \left( \frac{\partial \Psi}{\partial y} \right) = -g \frac{\partial \eta}{\partial x} \quad (12)$$

Cross differentiating and combining the kinematic and the dynamic conditions yields:

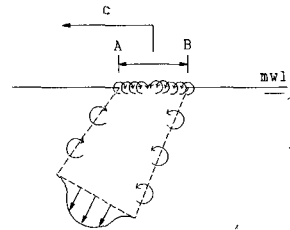
$$\frac{1}{g} \frac{\partial^2}{\partial t^2} \left( \frac{\partial \Psi}{\partial y} \right) = \frac{\partial^2 \Psi}{\partial x^2} \quad (13)$$

which has been integrated over the depth and implemented in a discrete version in the model.

When the boundary conditions ( $\psi$ ) corresponding to a non-breaking wave have been determined, breaking is simulated by decreasing the wave height from the point of breaking and superimposing a jet on the surface in front of the wave crest. The jet (or pulse) is specified as a vertical velocity component and is moved shoreward with the wave celerity (see fig. 5 & 6). The width, velocity and area of impingement of the jet are specified as functions of time. To satisfy the continuity equation at any time, the water flux introduced in the jet is taken at the crest region, see fig. 5.



**Fig. 5** Velocity components introduced to simulate jet and satisfy continuity.



**Fig. 6** Vorticity is introduced between A and B.

The sketched method is obviously quite crude, neglecting effects like the entrainment of air and the formation of a turbulent bore. Since the main interest is not the surface features, but rather the convection/diffusion of vorticity into the flow and the eventual effect on the bottom, the technique can serve as a first approach.

### Generation of vorticity.

The vorticity can only result from shear layers due to forced velocity gradients at the boundaries. At the bottom, the no slip condition has to be satisfied, while at the surface, the jet is introduced as a velocity field forced upon the initial potential flow field arising from the migrating wave. At the surface, the definition of the vorticity:

$$\omega = \frac{\partial u}{\partial y} - \frac{\partial v}{\partial x} \quad (14)$$

is used to specify the circulation. The horizontal gradient in  $v$  has already been specified through  $\psi$ , while the vertical gradient in  $u$  determines the angle of intrusion of the jet. The flux of vorticity during each timestep is calculated through the information about the production of vorticity and the vertical velocity. It is introduced as discrete particles at the position of the jet (from A to B in fig. 6).

At the bottom, the approach by Asp Hansen et al. (1992) has been implemented. Vorticity is introduced based on a calculation of the flux of vorticity in the boundary layer. The production of vorticity only depends on the velocity  $U_0$  at the outer limit of the boundary layer, while the distribution over the depth depends on the velocity profile and boundary layer thickness. Based on simplifying assumptions (a logarithmic velocity profile in the boundary layer; onset and development of a new boundary layer every time the flow reverses; only slight curvature of the boundary), the boundary layer thickness  $\delta$  and the friction velocity  $U_f$  are found from an approach introduced by Fredsøe (1984) to solve the momentum equation for the boundary layer as derived by Von Kármán:

$$\int_0^{\delta} \rho \frac{\partial u}{\partial t} dy + \frac{\partial}{\partial x} \int_0^{\delta} \rho u^2 dy - u_0 \frac{\partial}{\partial x} \int_0^{\delta} \rho u dy = -\delta \frac{\partial p}{\partial x} - \tau_0 \quad (15)$$

The outer velocity  $U_0$  is as a rough approximation taken at a fixed level above the bottom.

### SEDIMENT TRANSPORT

A widely used method to model suspended sediment is by applying a diffusion equation in the vertical direction. This requires knowledge of the vertical distribution of the turbulent quantities of the flow, e.g. represented by the eddy viscosity  $\nu_t$ , which in the present case has a highly non-uniform character. Close to the plunging point, the convection in the vertical direction due to the large scale vortical structures is expected to be dominant, for which reason the diffusion-model is not feasible.



To take full advantage of the spatial resolution of the flow provided by the discrete vortex model, the sediment is represented by a Lagrangian model when it has been brought away from the bottom. Because it is impossible to trace every single grain, the sediment brought into suspension is modelled as "concentration particles", each representing a certain amount of sediment - much like the case for the discrete vortex particles. In the outer flow, the concentration particles are relocated on a pure convective basis with a fall velocity added. The diffusion due to the small-scale turbulence, which is not resolved in the hydrodynamic model, is assumed negligible compared to the convective transport.

In the near-bed boundary layer the small scales of turbulence are important for the vertical transport of sediment through diffusion. This cannot be resolved by the hydrodynamic model, as it would require a grid with mesh-size in the order of the diameter of the sediment grains. Instead, a boundary layer description based on a diffusion process developed by Asp Hansen et al. (1992) has been employed.

The near-bed concentration of sediment  $c_b$  is required as a boundary condition for the diffusion model. The approach by Engelund and Fredsøe (1976), relating the sediment concentration at a distance of twice the grain diameter above the bed to the Shields parameter has been employed. The Shields parameter  $\theta$  is defined as:

$$\theta = \frac{U_f^2}{(s-1)gd} \quad (16)$$

in which  $s$  is the relative density of the sediment,  $g$  is the acceleration of gravity,  $d$  is the grain size and  $U_f$  is the friction velocity obtained from the boundary layer model.

For each timestep the flux of sediment through the level  $2d$  is calculated as function of  $x$  and introduced in the model as "concentration particles". From the time it is introduced till it settles on the bottom, each particle is tracked in a Lagrangian fashion. In the boundary layer a Monte Carlo simulation is used to simulate the diffusion. This is performed in a similar way as for the vortex particles by use of random displacements following a Gaussian distribution.

## RESULTS

The examples of output presented are based on the domain shown in fig. 7. The shoaling waves are propagating from right to left. Breaking is simulated from the point where  $H/D$  reaches 0.8, which occurs

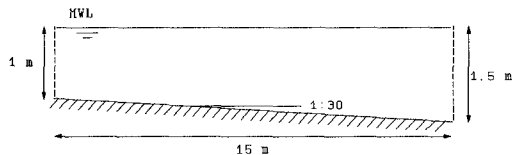
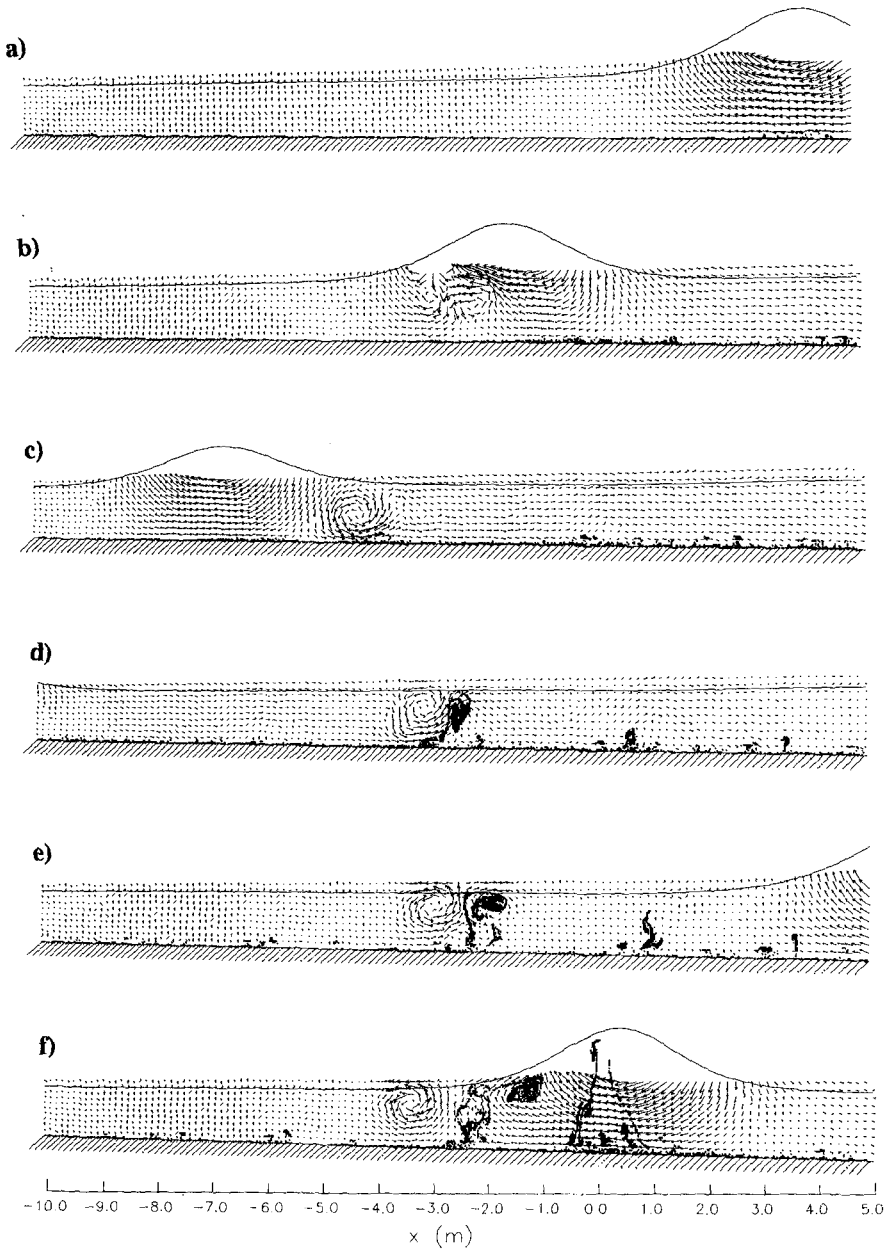


Fig. 7 Model domain

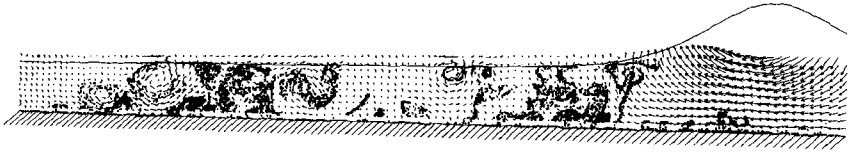


**Fig. 8** Vector plot of velocity field from waves migrating through the model domain. The time between each picture is 1.5 s with a wave-period of 6.55. The black dots superimposed on the vector plot represents suspended sediment.

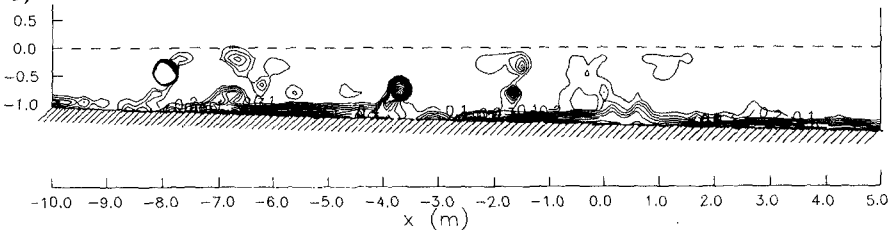
at a water depth of 1.3 m. The wave period is 6.55 sec, the sediment is uniform with a grain size of  $d=0.2$  mm., a relative density of  $s=2.65$  and a settling velocity of  $w_s=0.022$  m/s.

Fig. 8 shows vector plots illustrating the velocity field at various stages. Suspended sediment, represented by concentration particles, is shown as dots. The surface profile represents the wave without the effect from the jet. Picture "a" is a situation before breaking of the first wave, while breaking is occurring in "b". Suspended sediment is still confined to the near-bed region. In "c" one major vortex structure has formed together with weaker disturbances, and in picture "d" these have started convecting sediment into the upper reaches of the flow field. This process develops further in "e" and "f", where the next wave enters the domain.

a)

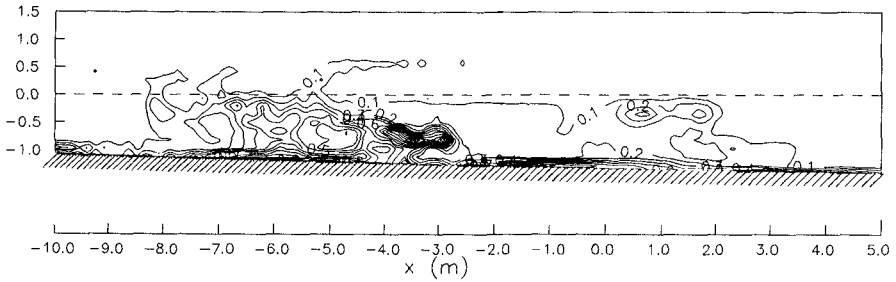


b)



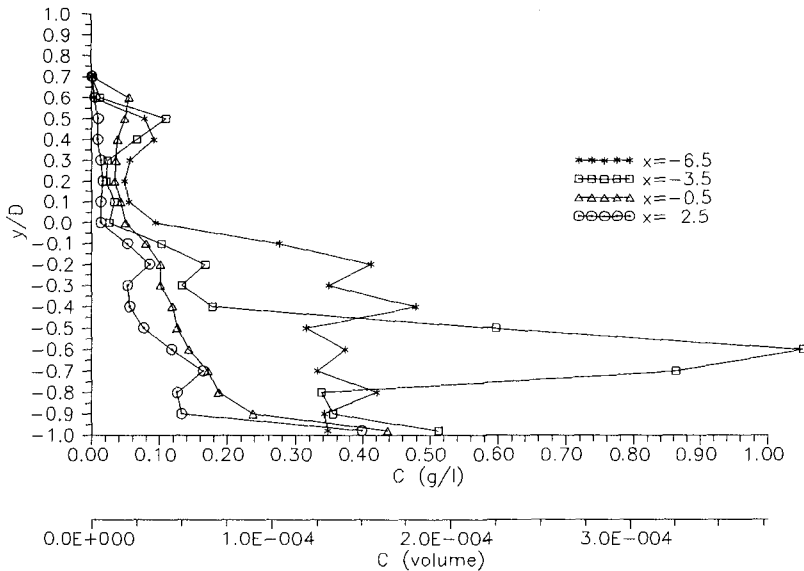
**Fig. 9** "Frozen" picture after 10 waves. a) Velocity vectors and particle positions. b) Contours of concentration in the domain.

Fig. 9.a depicts a situation after several waves have passed the area. The suspension of sediment is clearly associated with the large-scale vortex structures in the flow and occurs as plumes of high concentration. This is also seen in fig. 9.b, which shows a contour plot of the concentration at the same moment as 9.a. The plunge point is situated at  $x=0$ , and the mean water level is at  $y=0$ . The concentration close to the bottom is not resolved accurately in the plot because of the very high concentrations in the thin boundary layer. The concentration in the plumes reaches values of up to  $7$  g/l ( $\approx 2.6 \cdot 10^{-3}$  m<sup>3</sup>/m<sup>3</sup>).



**Fig. 10** Concentration averaged over 5 wave periods

Fig. 10 shows a contour plot of the time averaged concentration. The time averaged concentration is highest between 3m and 4m inshore of the plunge point. This coincides with the position where the major vortex formed at breaking reaches the bottom, as seen from fig. 8. The concentration in fig. 10 has been averaged over 5 wave periods after a "quasi-steady" state has been reached with balance between sediment brought into suspension and sediment settling to the bottom. A more uniform distribution could possibly be obtained by averaging over a higher number of periods. The concentration close to the side boundaries of the domain is underestimated because particles are allowed to be convected out of the domain through the boundaries under the influence of the orbital motion of the fluid, while no sediment is reintroduced through the boundaries when the flow is directed into the domain.



**Fig. 11** Time averaged concentration profiles at selected positions relative to the plunge point.

Fig. 11 shows the concentration plotted as function of the dimensionless position above the bottom ( $y/D$ ) for selected distances relative to the plunge point. The profiles differ distinctively from the "usual" diffusion profile, which can be contributed to the dominating role of convection.

## CONCLUSIONS

The discrete vortex model is capable of resolving the major vortex structures of the flow, which by convection brings sediment from the near-bottom region to the upper reaches of the water column. The small-scale turbulence in the boundary layer cannot be resolved by the discrete vortex model, as this would require too fine discretization in space and time. Instead a diffusion model has been used to simulate the suspension of sediment in the boundary layer.

Under the influence of the wave motion and the vortex structures created by the wave breaking, the sediment is convected through the model domain as unevenly distributed plumes. Preliminary results show, that with waves breaking at a water-depth of 1.3 m and sediment represented by a grain size of 0.2 mm., a relative density to water of 2.65 and a settling velocity of 0.022 m/s, the concentration in the plumes may reach values of 7 g/l ( $\approx 2.6 \cdot 10^{-3} \text{ m}^3/\text{m}^3$ ). The time-averaged concentration away from the bottom reaches a value of 1 g/l at a position approximately 2 times the local water depth in-shore of the plunge point, and decreases towards both sides.

## ACKNOWLEDGEMENT

This work was undertaken as a part of the MAST G6 Coastal Morphodynamics research programme. It was founded jointly by the Danish Technical Research Council (STVF) under the programme "Marin Teknik" and the Commission of the European Communities, Directorate General for Science, Research and Development, under MAST contract no. 0035-C.

## REFERENCES

- Asp Hansen E., J. Fredsøe, R. Deigaard, 1992, "Distribution of suspended sediment over wave-generated ripples", submitted for publication.
- Battjes J.A., 1988, "Surf-zone dynamics", Annual Review of Fluid Mechanics, 1988, Vol. 20, pp. 257-293.
- Christiansen J.P., 1973, "Numerical simulation of hydromechanics by the method of point vortices", Journal of Computer Physics, Vol. 13, pp. 363-379.

Deigaard R., J. Fredsøe, I. Brøker Hedegaard, 1986, "Suspended sediment in the surf zone", *J. of Waterway, Port, Coastal and Ocean Engineering*, ASCE, Vol. 112, No. 1, pp. 115-128.

Engelund F. and J. Fredsøe, 1976, "A sediment transport model for straight alluvial channel", *Nordic Hydrology*, Vol. 7, No. 5, pp. 293-306.

Fredsøe J., 1984, "Turbulent boundary layer in wave and current motion", *J. of Hydraulic Engineering*, ASCE, Vol. 110, No. 8, pp. 1103-1120.

Fredsøe J., O.H. Andersen, S. Silberg, 1985, "Distribution of suspended sediment in large waves", *J. of Waterway, Port, Coastal and Ocean Engineering*, ASCE, Vol. 111, No. 6, pp. 1041-1059.

Galvin C.J., 1968, "Breaker type classification on three laboratory beaches", *Journal of Geophysical Resources*, Vol. 73, pp. 3651-3659.

Jansen P.C.M., 1986, "Laboratory observations of the kinematics in the aerated region of breaking waves", *Coastal Engineering*, Vol. 9, pp. 453-477.

Longuet-Higgins M.S. and E.D. Cokelet, 1976, "The deformation of steep surface waves on water I, a numerical method of computation", *Proc. of the Royal Society, London*, A 350, pp. 1-26.

Miller R.L., 1976, "Role of vortices in surf zone prediction: Sedimentation and wave forces", *Beach and Nearshore Sedimentation*, SEPM Spec. Pub. 23, pp. 92-114.

Nadaoka K., 1989, "Structure of the turbulent flow field under breaking waves in the surf zone", *J. Fluid Mechanics*, Vol. 204, pp. 359-387.

Peregrine D.H., 1983, "Breaking Waves on Beaches", *Annual Review of Fluid Mechanics*, 1983, Vol. 15, pp. 149-178.

Sarpkaya T., 1989, "Computational methods with vortices - the 1988 Freeman Scholar Lecture", *J. of Fluids Engineering*, Vol. 111, pp. 5-52.

Stansby P.K., A.G. Dixon, 1983, "Simulation of flows around cylinders by a Lagrangian vortex scheme", *Appl. Ocean Res.*, Vol. 5, No. 3, pp. 167-178.

Svendsen I.A., P.A. Madsen, J.B. Hansen, 1978, "Wave characteristics in the surf zone", *Proc. 16<sup>th</sup> conf. on coastal eng.* 1978, pp. 520-539.

## CHAPTER 181

### Shingle Beach Profiles and Wave Kinematics

Keith A. Powell,<sup>1</sup> Paul A. Quinn,<sup>2</sup> and Clive A. Greated<sup>3</sup>

#### Abstract

An extensive experimental project has been undertaken, in two parts, to measure both the formation of shingle beach profiles due to wave attack and the wave velocity fields using the technique of Particle Image Velocimetry (PIV). The former was achieved with moveable beach experiments carried out in the wave basin at HR Wallingford, and the latter on models in the 9.75m wave flume in The University of Edinburgh. Waves of several JONSWAP spectra, reflecting storm conditions, were allowed to impinge normally on an initial slope of 1:7, the resulting profiles were found to reach dynamic equilibrium after about 3000 wave periods. These profiles were modelled at The University of Edinburgh for the wave velocity measurements using the relatively new technique of PIV. This technique has the benefit of providing very accurate, full-field, instantaneous velocity data. In these experiments monochromatic waves were measured on smooth, impermeable beaches although the extension to multi-frequency waves on rough, permeable beaches is planned for the near future. The effect of the increased backwash component typical of these steeper beaches is dealt with in some detail.

#### Introduction

The stability of beach profiles, especially under storm conditions, is an important factor in coastal defence and environmental issues. One of the fundamental requirements for a better insight into such coastal processes, is the accurate measurement of the velocity fields of waves breaking on such beaches. In this study the relatively new technique of Particle Image Velocimetry (PIV) has been used to realise the latter. The project has been carried out in two parts. Firstly at HR Wallingford moveable beach experiments were carried out to measure the profile

---

<sup>1</sup>Group Manager, HR Wallingford, Wallingford, Oxon, OX10 8BA, U.K.

<sup>2</sup>Research Associate, Fluid Dynamics Unit, Physics Department, The University of Edinburgh, Edinburgh, EH9 3JZ, U.K.

<sup>3</sup>Director, Fluid Dynamics Unit, Physics Department, The University of Edinburgh, Edinburgh, EH9 3JZ, U.K.

change in the beach from an initial 1:7 plane slope, which is typical of the shingle beaches being modelled. The second part of the experiments, to measure the velocity fields of the breaking waves, was carried out in the 9.75m wave flume at Edinburgh University which has been custom built for PIV measurements. Shingle, or gravel, beaches are common around the U.K. coastline and as the material has a much larger diameter than sand (typically 10-50mm  $D_{50}$ ), it can tolerate steeper beach slopes and provides a good defence material (Powell, 1988).

In general, under storm conditions, the beach profile adopts a formation with a bar at the breaking point, a relatively flat breaking zone and a steep scarp formed by the run-up, just above the Still Water Line (SWL). The length of the relatively flat breaking zone is related to the energy of the incoming wavefield. A typical beach profile is shown in Figure 1.

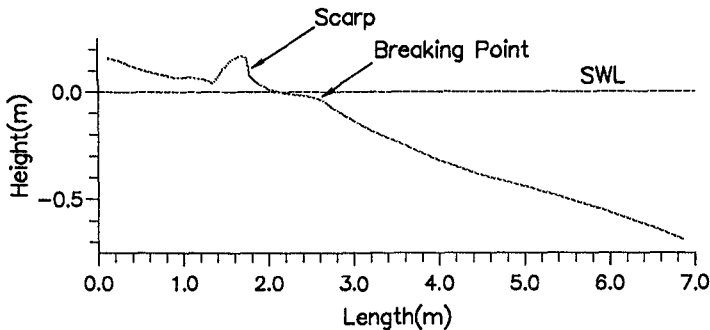


Figure 1: General shingle beach profile formed in a storm

### Beach Profile Experiments

Experiments were carried out in the wave basin at HR Wallingford to measure the beach profile change in response to many wave conditions. The beach consisted of coal particles approximately 3.2mm  $D_{50}$ , chosen to ensure the correct sediment response at the model scale of 1:17. The beach was initially inclined at 1:7 for each experiment, and waves of various JONSWAP spectra were incident normal to the beach. Waves were created by three 5m absorbing wave boards. The beach profile was measured every 500 waves to establish beach stability and evolution. It was found that after 3000 wave periods the beach had reached dynamic equilibrium, and was therefore effectively stable.

The beach profile was measured automatically by a computer driven tactile probe which was mounted on a rig positioned above the wave basin. The rig was stepped in an offshore direction and at each step the probe was lowered until it touched the beach when the height was recorded. It was then retracted and



stepped onto the next position.

Four profiles were selected for the PIV experiments to be carried out in Edinburgh. These correspond to the profiles obtained from the wave spectra shown in Table 1.

<i>Profile</i>	$H_{sig}(m)$	$T_{mean}(s)$	$T_{peak}(s)$	<i>Steepness</i>
1	0.106	1.17	1.35	0.05
2	0.085	1.16	1.33	0.04
3	0.068	1.20	1.38	0.03
4	0.105	1.57	1.81	0.02

Table 1: Wave Parameters for Profiles to be used in PIV tests.

Figure 2 shows three of the four profiles to highlight the effect of the different wave conditions. In particular one should note that the size of the scarp increases with wave energy and tends to move quite significantly in an offshore direction, making the relatively flat breaker zone shorter with increasing wave energy.

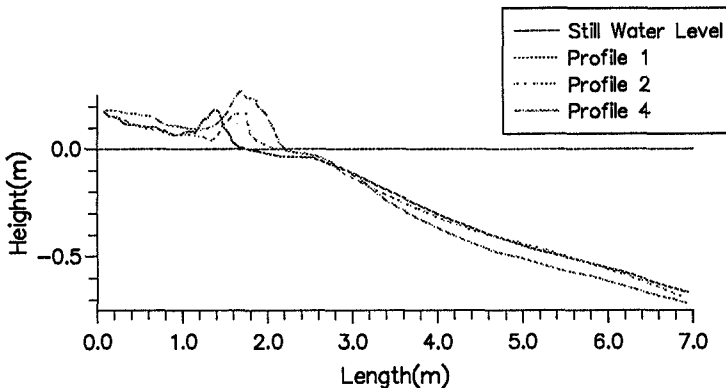


Figure 2: Different profiles formed from the various wave conditions.

### Wave Velocity Measurements

The wave velocity fields were to be measured using the technique of Particle Image Velocimetry (PIV). This method obtains very accurate, instantaneous, full-field velocity data of the flow to be measured. It is an optical method and therefore non-intrusive. It is beyond the scope of this paper to discuss this technique in detail, however Adrian (1988) gives a good introduction and the following papers deal more specifically with hydrodynamic applications, in particular Greated et al (ICCE '92), (Gray & Greated, 1988; Quinn et al, 1991). As this is

a relatively new technique a brief outline of PIV is included.

PIV is a two stage process involving initially photographing the seeded flow which is illuminated stroboscopically. The shutter of the camera is held open for several light pulses so that multiple images of the seeding particles appear on the film. The developed negative is then analysed point-by-point on an automated system to measure the average displacement of the particles at each point. This, coupled with the knowledge of the light pulse period, yields the velocity at each point in the field. The pulsed illumination is provided by a scanning beam system. The beam of a 15W Argon ion laser is scanned by a rotating octagonal mirror along a parabolic mirror which reflects the light in a vertical "*sheet*" up into the tank. This method of illumination has proved to be the best for hydrodynamic flows (Gray et al, 1991).

The analysis method used is the so-called "Young's Fringe" method. The developed negative is probed systematically by a low power He-Ne laser with a beam diameter of about 1mm. The multiple images of the seeding particles cause interference of the laser beam and the light field transmitted by the negative is focussed by a lens forming Young's fringes on the array of a ccd camera. This is transferred to a microcomputer via a frame-grabber and a second mathematical Fourier transform is performed to obtain the autocorrelation plane, the first Fourier transform having been performed optically by the lens in front of the ccd camera. Peaks formed by the autocorrelation of a particle with its nearest image are located using a peak detection program, yielding the average displacement in that small interrogation region. As the illumination scan time is known the velocity at this point is obtained. The computer then steps the translation stage holding the negative onto the next position and the process is repeated.

The inherent accuracy of this technique is one of its main advantages, typical errors range from 1.2% for velocities with small velocity gradients across the interrogation region in the centre of the imaged flow field, to 5.9% for high velocity gradients at the edge of the imaged flow field. It is the velocity gradient across the interrogation region which causes the greatest loss of accuracy, and in extreme cases can cause signal drop-out (Quinn et al, 1991).

One practical requirement for PIV experiments is the large degree of optical access. The wave flume at Edinburgh University was designed specifically for PIV experiments and has glass walls and bottom. It is 9.75m long, 0.4m wide and 1.0m deep with a SWL of 0.75m. The waves are created by a computer driven hinged, absorbing wave maker (Salter, 1982). The laser beam illumination enters through the bottom of the tank and can illuminate a region up to 1m in length. A consequence of this is that the laser beam has to pass through the beach in order to illuminate the wave field. This is achieved by building the beach in two halves, with a 10mm gap running longitudinally down the middle. This gap is

covered by thin transparent plastic to maintain the shape of the beach and the optical access required. A section of the tank with the scanning beam system and measurement zone is shown in Figure 3.

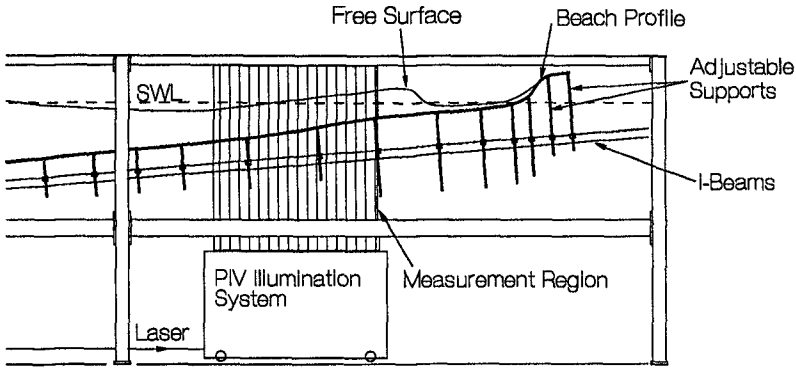


Figure 3: The wave tank, beach and illumination system

As several beach profiles had to be made an elaborate supporting system was designed enabling all the profiles to be made with the same apparatus. Two pairs of fibre-glass "I"-beams provide the main support for the beach, individually adjustable supports are attached to this to hold the beach surface in the correct position. These supports can be located discretely along the length of the "I"-beams and continuously adjusted vertically. The beach surface is made from 10mm thick "Coplast" plastic sheet, except for the breaker region where 3mm thick perspex sheet is required to adopt the more complicated profile. A photograph of the structure of the beach is shown in Figure 4.

### PIV Experiments

As the area of interest of the beach was seaward of the scarp, it was possible to work at a larger scale of 1:10 than the experiments at HR Wallingford. The waves chosen for the present study were monochromatic waves whose frequency matched the mean frequency of the appropriate spectrum and whose height was derived from the significant wave height according to the relations given by:

$$H = \sqrt{2}H_{rms} \qquad H_{rms} = \frac{H_{sig}}{4}$$

The use of monochromatic waves may seem unjustifiable at first, however, this choice was made mainly due to the fact that PIV produces a spatial distribution of the velocity field at an instant, and so measuring a constantly varying wave field as in a JONSWAP spectrum, would provide results of dubious value. One

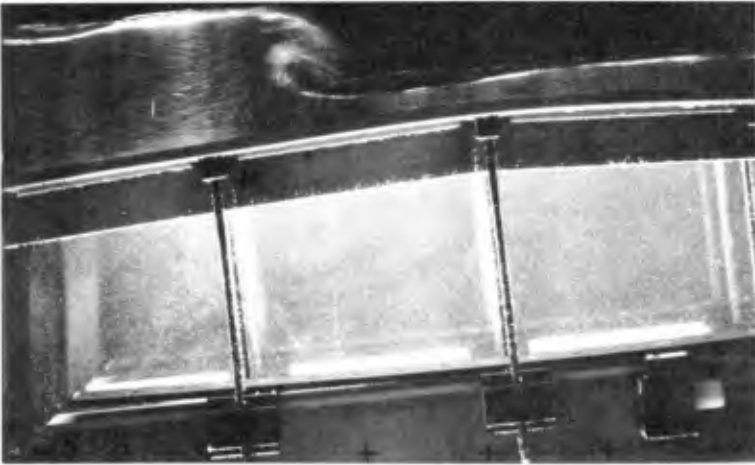


Figure 4: The beach structure

further consideration is that although the beach still reacts to individual waves, the average effect of the spectrum has resulted in a stable profile, hence our use of the mean wave frequency. It is intended, however, to measure bi-chromatic and possibly tri-chromatic waves in the future to represent the original spectra more accurately. This is important as the use of monochromatic waves excludes the significant effects of wave grouping and surf beat.

The wave conditions now Froude scaled in the ratio 1:10 are shown in table 2.

<i>Profile</i>	<i>Frequency(Hz)</i>	<i>Wave Height(mm)</i>
1	0.655	63.72
2	0.660	50.10
3	0.640	40.80
4	0.490	63.10

Table 2: Wave Parameters used in PIV tests.

Measurements were made all along each beach for all of the above wave conditions. At each measurement position four phases of each wave were recorded. In this way a complete flow field all along the beach could be obtained for four phases of all of the waves.

## Results

Some examples of vector plots and PIV photographs of waves measured on the first two profiled beaches are shown. The main points to note are the detail of the PIV measurements and the shape of the breaking waves.

Figures 5, 6 and 7 show vector plots of the three positions near the breaking point on beach profile 2. Figure 7 shows a surging breaker is formed on this beach. Figure 8 shows the same position with the phase changed by  $\pi$  radians. The maximum velocity in Figure 7 is  $0.35\text{ms}^{-1}$  which is considerably less than the maximum velocity in the backwash, shown in Figure 8, which is  $0.74\text{ms}^{-1}$ .

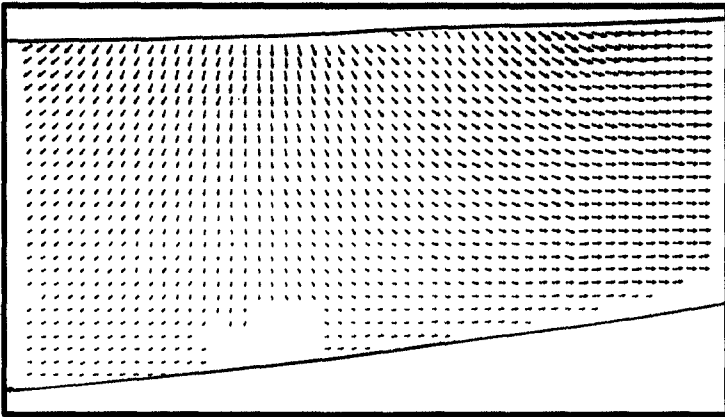


Figure 5: Profiled Beach 2,  $f=0.66\text{Hz}$ ,  $H=50.1\text{mm}$ , Posn.: 3

The photographs in Figures 9 and 11 and the vector plot in Figure 10 show three different frequency waves breaking on beach profile 1. This has a longer breaking zone than profile 2 and a less steep scarp. In all cases plunging breakers are observed.

## Discussion

One of the most significant properties of steep beaches is the increased backwash component, which is further emphasized by the length of the relatively flat breaking zone and the formation of a steep scarp just above the SWL. The effect of this scarp is to rapidly halt the run-up. This, coupled with the fact that for the higher energy waves the length of the breaking zone is shorter (Figure 2), results in the backwash being formed very quickly after the wave has broken. The returning flow can suppress the degree to which a plunging breaker is formed

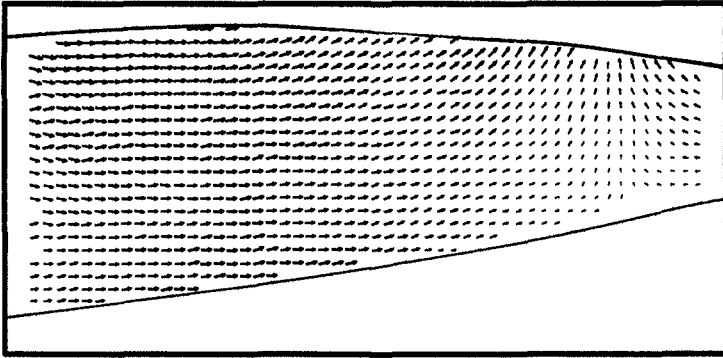


Figure 6: Profiled Beach 2,  $f=0.66\text{Hz}$ ,  $H=50.1\text{mm}$ , Posn.: 2

to the extent that for the case of the second beach profile surging breakers are evident (Figure 7). In the case of a relatively long breaking zone or a plane beach, the increased length of run-up gives time for the incoming wave to break before the backwash is completely formed. This is evident from Figures 9, 10 and 11 on profile 1 where plunging breakers are still formed.

With a wall-like scarp just above the SWL a “standing-wave” is formed in the breaker zone with the almost total reflection being driven by the incoming waves. Obviously this effect is emphasized in these experiments as only monochromatic waves are being measured on an impermeable slope, however, this is perhaps the effect the beach is “trying” to achieve in order to absorb the most energy.

The formation of a “standing wave” in the breaker zone will be affected greatly by multi-frequency waves, not only because they all by definition have different periods, but also because they will break at different positions. In addition to this the permeability of shingle beaches is particularly important due to the large material size. There is significant flow into the beach above the MSL and also within the beach itself. This “draining” of water from the run-up will affect the amount of water returning in backwash.

### Conclusion

Experiments to measure the profiles of shingle beaches formed in simulated storm conditions by waves of various JONSWAP spectra have been carried out. The modelling of these beaches for wave velocity measurements using PIV has also been successful. The detail of the results obtainable from this measurement technique has been shown for the case of monochromatic waves on impermeable beaches. Whilst it is hoped that these results can be used for comparison with numerical models, the extension to measuring multi-frequency waves on imper-

meable slopes would seem the obvious next step.

### Acknowledgement

This collaborative project between HR Wallingford and The University of Edinburgh is funded jointly by the Science and Engineering Research Council (SERC) and by the commission of the European Communities Directorate General for Science, Research and Development under contract N°. MAST 0035C .

### References

- Adrian, R.J., (1988) *Optical Methods for Measuring Vector Velocity Fields. Part II-Techniques*. Proc. von Karman Inst. of Fluid Mechanics. Lecture Series 1988-06.
- Gray, C. and Greated, C.A., (1988) *The Application of Particle Image Velocimetry to the Study of Water Waves*. Optics and Lasers in Engineering, 9.
- Gray, C., Greated, C.A., McCluskey, D.R. and Easson, W.J., (1991) *An Analysis of the Scanning Beam Illumination System*. J. of Measurement Science and Technology, 2, 717-724.
- Greated, C.A., Skyner, D.J. and Bruce, T., (1992) *Particle Image Velocimetry (PIV) in the Coastal Engineering Laboratory*. Proc. 23rd Int. Conf. Coastal Eng.
- Powell, K.A. (1988) *The Dynamic Response of Shingle Beaches to Random Waves*. Proc. 21st Int. Conf. Coastal Eng., 130, 1763-1773.
- Quinn, P.A., Skyner, D.J., Gray, C., Greated, C.A. and Easson (1991) *A Critical Analysis of the Particle Image Velocimetry Technique as Applied to Water Waves*. Proc. Euromech 279 Colloquium, Image Analysis as a Measurement Technique in Flows. (Accepted for Publication)
- Salter, S.H., (1982) *Absorbing Wave Makers and Wide Tanks*. Proc. Conf. Directional Wave Spectra Applications, ASCE, 185-200.

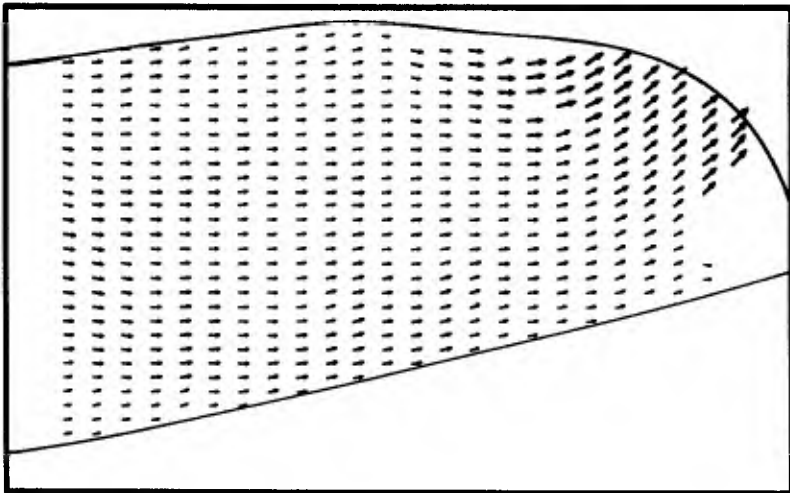
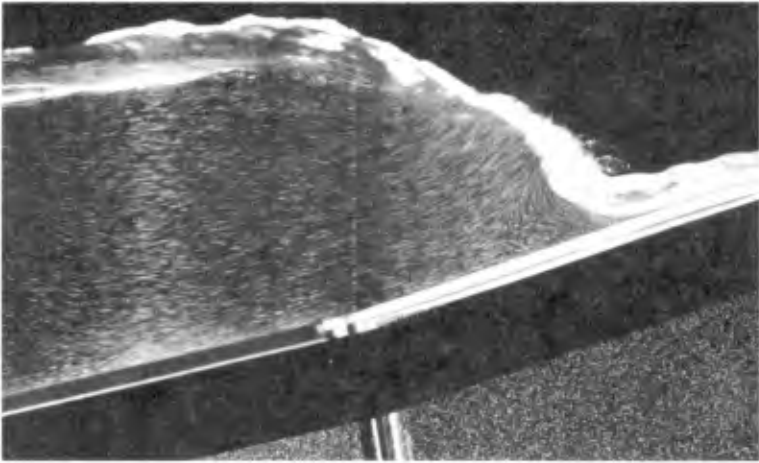


Figure 7: Profiled Beach 2,  $f=0.66\text{Hz}$ ,  $H=50.1\text{mm}$ , Posn.: 1



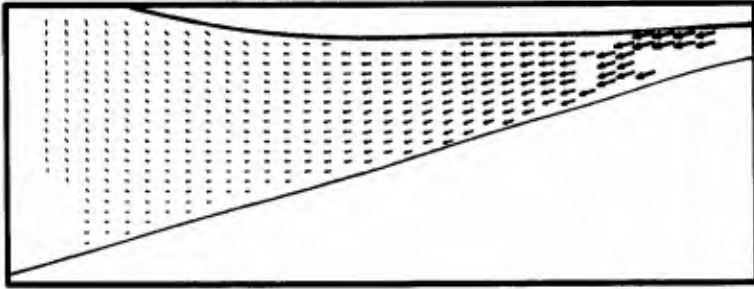


Figure 8: Profiled Beach 2,  $f=0.66\text{Hz}$ ,  $H=50.1\text{mm}$ , Posn.: 1

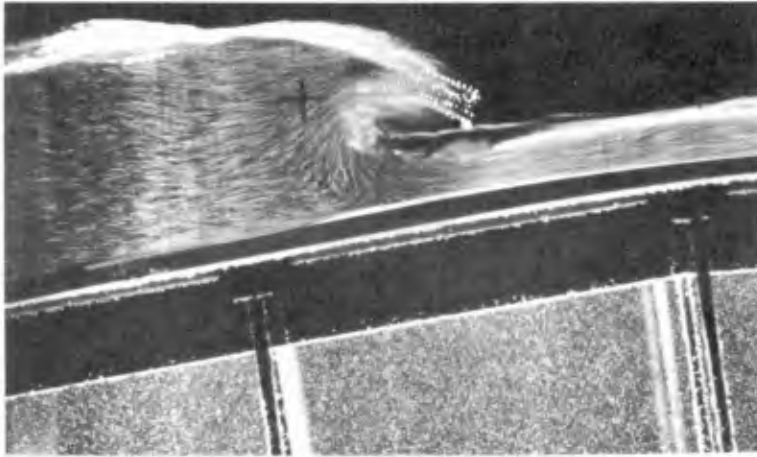


Figure 9: Profiled Beach 1,  $f=0.655\text{Hz}$ ,  $H=63.1\text{mm}$ , Posn.: 1

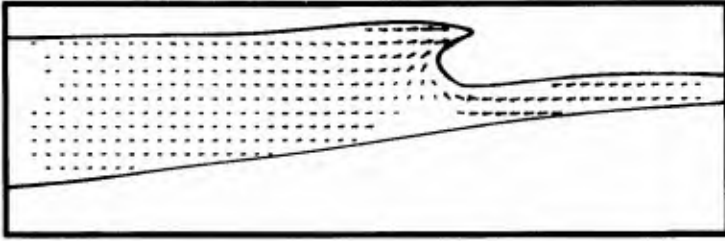


Figure 10: Profiled Beach 1,  $f=0.66\text{Hz}$ ,  $H=50.1\text{mm}$ , Posn.: 1

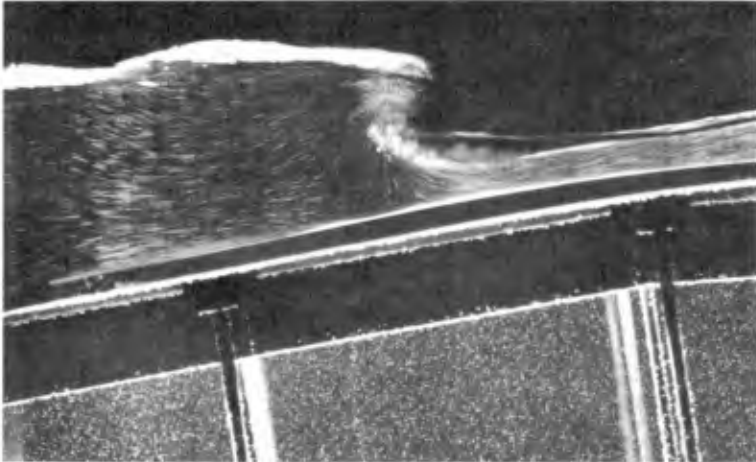


Figure 11: Profiled Beach 1,  $f=0.64\text{Hz}$ ,  $H=40.8\text{mm}$ , Posn.: 1

## CHAPTER 182

### Beach Changes and Sediment Movement in the Surf Zone

Zbigniew Pruszek & Ryszard B. Zeidler <sup>1</sup>

#### Abstract

The South Baltic Sea coastal zone investigated in the years 1983–1989 belongs to multi-bar dissipative ones, with an average slope of 1.5% and sand grain size  $D_{50}=0.22$  mm. EOF have exhibited the most common locations of bars ( $e_{2x}$ ) and the most intensive bed changes ( $e_{3x}$ ). Particularly conspicuous are the bed changes about the inner bar (depths about 3 m). Radioisotopic iridium glass tracers have been employed in three different subzones of the shore profile; 50–60 m from shoreline (depths  $h$  of 0.8–1.2 m), 200–250 m ( $h=2-3$  m), and some 350–450 m ( $h=4-5$  m), respectively.

*During storms* the most intensive sediment motion occurs in the second subzone, where the longshore sediment transport rate  $q$  reaches 40 to 100 kg/(m·h). Closer to shoreline (first subzone), the transport rate ranges from 15 to 40 kg/(m·h), while the smallest rate ( $q \approx 3.5-20$  kg/(m·h)) is encountered in the third subzone. Under conditions of *weak or moderate oblique waves* (e.g. mean wave period and height  $\bar{T} \leq 3-4$  s and  $\bar{H} \leq 0.2$  m in the second subzone), the longshore mode also prevailed but the ratio of longshore to cross-shore rate was lower, about 1.7:1 (13.5 versus 8 kg/(m·h)).

Core samples of tracer sand have provided estimates of the vertical extent and distribution of transport rate in the bed layer. It has been found that the thickness of the bed sublayer in which all grains move in bulk reaches  $\delta \approx 2-5$  cm during storms, versus a few grain diameters to 1.5 cm under weak and moderate waves.

#### 1 Introduction

Most engineering activities take place in coastal areas shallower than 10 m. At the same time, these areas create most practical and scientific problems, and their exploration is still far from complete. Field measurements are usually a

---

<sup>1</sup> Assoc. Prof. & Professor; Polish Academy of Sciences' *Institute of Hydro-Engineering, IBW PAN, 7 Kościarska, 80-953 Gdańsk*

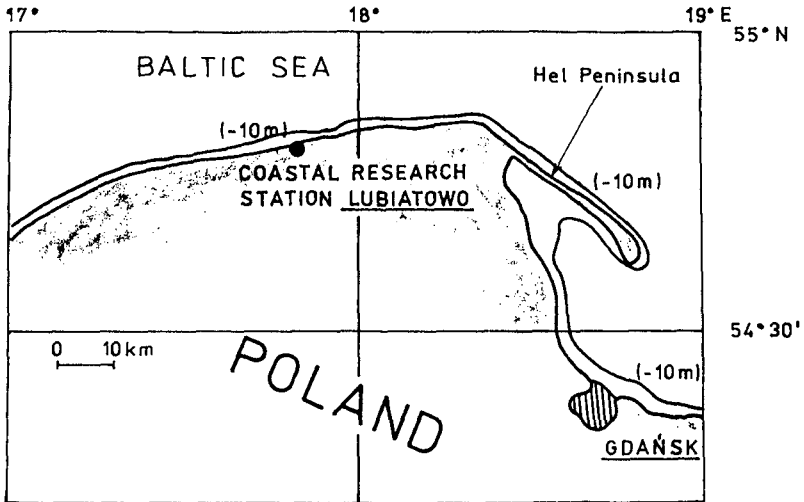


Figure 1. Location Plan of Investigation Site

prerequisite to conduct such activities. To comply with that challenge, at least in some respects, the Authors have initiated an experimental project throwing light on nearshore sediment dynamics. The paper presents results of field studies and analysis of field data relating to sediment movement and beach changes in the South Baltic Sea in the years 1983–1989.

## 2 Site Conditions

The investigations were conducted at *IBW PAN* Coastal Research Station at Lubiatowo, some 75 km NW of Gdańsk (Fig. 1.). The coastal zone belongs to multi-bar dissipative ones, with an average slope of 1–1.5% and sand quartz grain size  $D_{50}=0.22$  mm and density  $\rho_s=2650$  kg/m<sup>3</sup>. Usual maximum storm waves have  $H_s=3.5$ –4.0 m and  $T_s=7$ –8 s at the seaward boundary of the surf zone ( $h \approx 7$  m), primarily from N–NW sector.

Routine measurements of topographic features have been conducted since 1983 on a 2.7-km beach and nearshore zone extending some 800 m from shoreline. The beach profiles have been arranged every 100 m. The systematic measurements have permitted an insight into the variability of coastal features in space and time. By the use of empirical orthogonal functions (EOF) we identified the areas of most intensive dynamics, and tracer studies were carried out in such areas of pronounced bed changes (I, II and III in Figure 2), clearly coupled with underwater bars.

Radioisotopic iridium glass tracers have been employed to track the sediment movement in the three different areas of shore profile. The <sup>192</sup>Ir isotope of 74.4-day half-time had the grain diameter  $D=0.015$ –0.025 mm and density of 2668 kg/m<sup>3</sup>, thanks to its composition (48% SiO<sub>2</sub>, 17% Al<sub>2</sub>O<sub>3</sub>, 6% MgO, 5% SiO<sub>2</sub>, 5% TiO<sub>2</sub>, 5% K<sub>2</sub>O and 0.25% IrO<sub>2</sub>), thus close to natural sand.

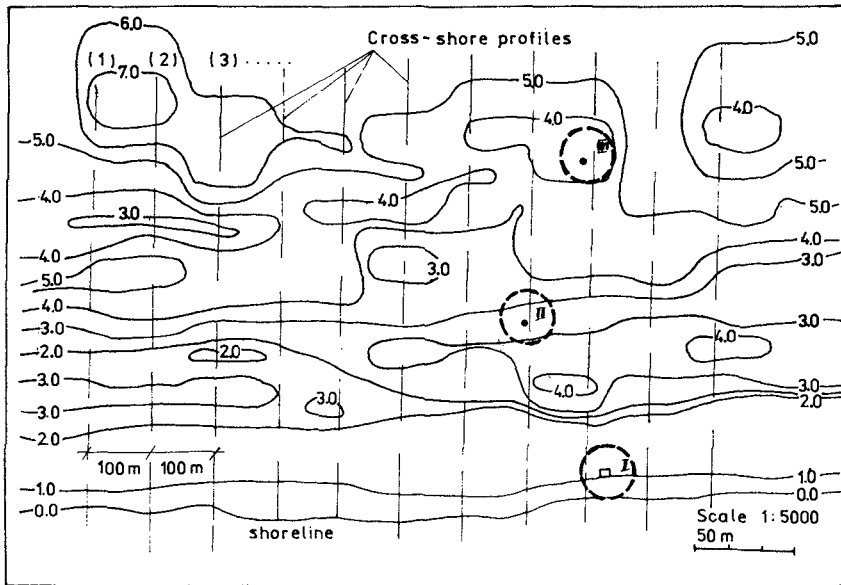


Figure 2. Bed Topography at *IBW PAN* Coastal Research Station at Lubiatowo

The movement of the tracer sand was tracked automatically, if within a special  $10 \times 10$  m steel framework (referred to as 'Spider'), or from boat if far away from shoreline. The quantity of the tracer used was 100 g (area I) up to 1 kg (area II). Calibrated scintillation probes were employed to record the concentration of sand.

Measured simultaneously with changing bed topography and sand concentration were parameters of the controlling dynamics, i.e. wind, waves and currents. At least two series of bed topography measurements (beginning and end of tracer test) were executed. Wind was measured at an altitude of 5 m above MSL. Waves were recorded at a few locations along the shore profile. A wave-riider was deployed on a depth of 7 m, and resistance-type wave probes were installed on shallower measuring posts. Electromagnetic current meters (Interocean and Colbrook) were placed at a few spots, primarily the stationary framework ('Spider'). Examples are shown in Figure 3.

Even a casual glance at the measured hydrometeorologic data shows a considerable nonstationarity of the factors controlling the sediment movement. Periods of intensive dynamics are preceded and followed by 'dormant' or 'stagnant' waves and currents, thus sediment transport as well. Since we have been unable to log sediment and bed characteristics at every single instant, we have focused attention on average hydrodynamical factors for some typical situations labelled 'storms' (case A) and 'medium sea' (case B). An arbitrary definition has been adopted in which 'storm waves' have  $H_s \geq 0.6-0.7$  m on depths  $h \approx 2-3$  m.

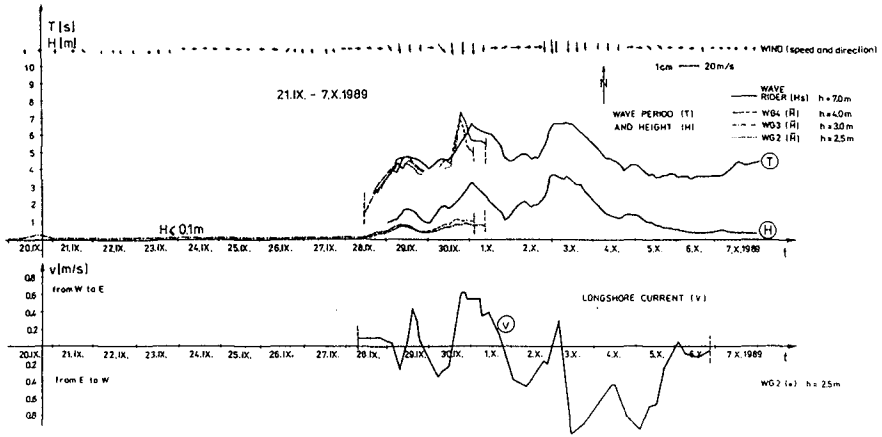


Figure 3. Examples of Measured Time Series of Wind, Waves and Currents

### 3 Results

#### 3.1 Nearshore Bed Changes

Shore profile changes can be employed for reliable description of sediment movement. The profile can be presented as a sum of a certain mean component of Dean type,  $y = Ax^{2/3}$ , and disturbances coupled with bars, shoals, troughs etc (cf. Pruszek 1992). Such a decomposition permits identification of locations with intensive changes in bed and sediment features, judged from the variation of the disturbances (Fig. 4).

Empirical orthogonal functions prove to be an effective tool in analysis of coastal processes. The first three one-dimensional eigenfunctions  $e_1(x)$ ,  $e_2(x)$  and  $e_3(x)$  have exhibited the areas where the bed phenomena were most active. These areas (I, II and III) are tightly correlated with underwater bars — as seen from  $e_2(x)$  — and substantial sediment transport, coupled with conspicuous erosion and accretion, displayed in local extrema of  $e_3(x)$ . Major bed changes in our study area occur on water depths up to 5–6 m, while seasonal changes are encountered on slightly deeper water (6–8 m).

The results depicted in Figure 5 are typical of all distributions obtained within our study. Therefore it has been interesting to examine the locations of high dynamics by other tools. Accordingly, we have harnessed radioisotope sand tracers to shed more light on sediment dynamics.

#### 3.2 Sediment Movement

Radioisotopic iridium glass tracers have been employed to track the sediment movement in three different subzones of the shore profile. The first one (Area I)

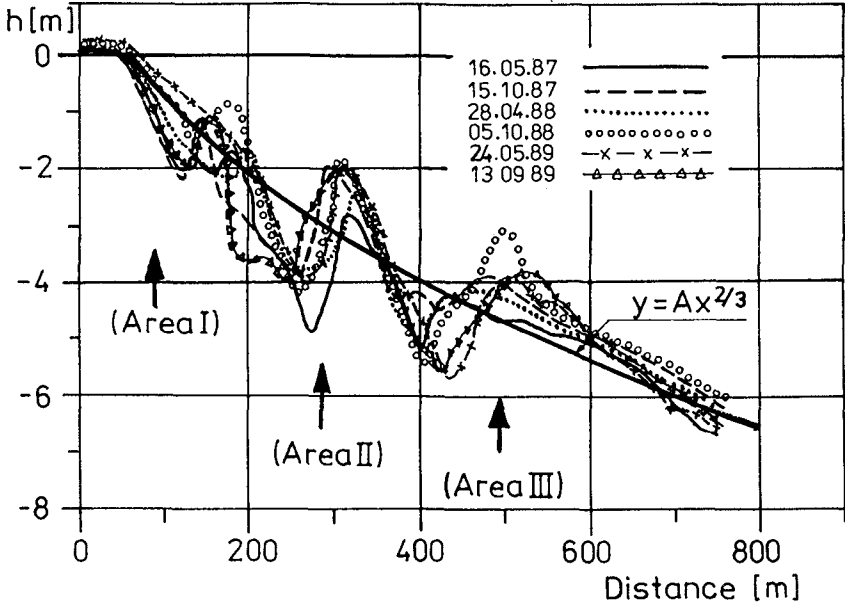


Figure 4. Examples of Measured Shore Profiles

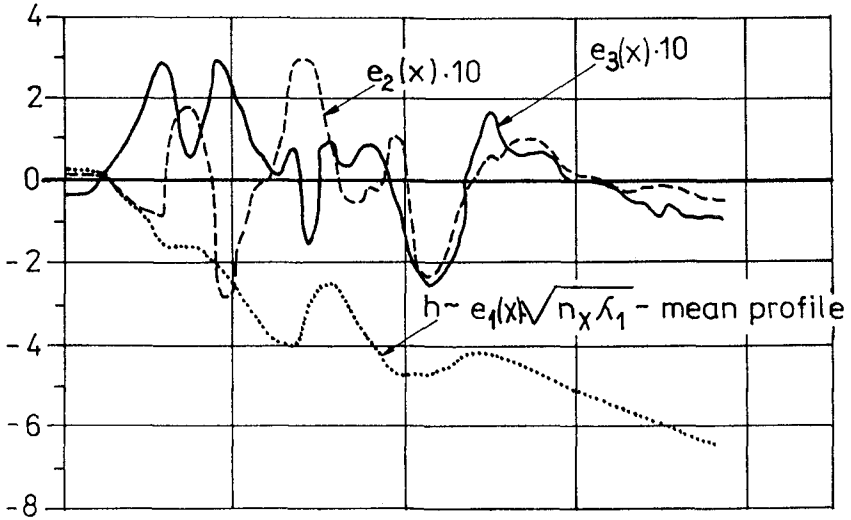


Figure 5. Eigenfunctions Computed for Lubiatowo, 1987-1989

Table 1. Sand and Water Velocities

Wave Conditions	Area (Fig. 2)	Bedload Thickness $\delta$	Surf. Vel. $\bar{v}_s^o$ , cm/h	Bulk Vel. $\bar{v}_s$ , cm/h	Longsh. $\bar{v}$ , cm/s
(A) 'Storm' $\bar{H} > 0.4$ m $h=2-3$ m	I	a few grain	120-150	$\approx 50$	$\approx 40$
	II	dia (surface)	250-300	100-150	$\approx 50$
	III	to 2-5 cm	80	$\approx 15$	-
(B) 'Med. Sea' $\bar{H} \approx 0.2-0.3$ m $h=2-3$ m	I	under storm	90-100	25-30	10-15
	II	conditions	100-120	30-40	$\approx 20$
	III		-	2-10	-

was spaced 50-60 m from shoreline (depths  $h$  of 0.8-1.2 m), between the steady inner bar and the ephemeral bar. Area II occurred 200-250 m from shoreline ( $h=2-3$  m), at the outer bar, most conspicuous and lasting. Area III was most distant (some 350-450 m and  $h=4-5$  m), encompassing the outermost bar, which delimits the seaward boundary of the surf zone.

### 3.2.1 Tracer Advection Velocity

Our measurements have confirmed that sediment transport usually occurs in two layers having different thicknesses and very different speeds. In situations with intensive waves (storms), slower motion some centimetres below static bed line is accompanied by much faster movement on the bed surface, measured in a few grain diameters (Fig. 6). Let alone for their position and weaker interlocking, the surficial grains are much more mobile, and their average speed is two or more times higher than its counterpart in the lower layer. As a result of such a double-layer transport, the tracer plume is smeared, the grains at the surface leading before slower cores some centimetres deeper in bed. An example illustrating this phenomenon in Area II is presented in Figure 7. Under lower waves ('medium sea'), the sediment movement is confined to the surface layer. The chief quantities measured in the three areas, including sand speed, are summarized in Table 1.

The sediment grain speeds have been computed for the effective duration of wave action, i.e. that above the incipient transport threshold. From the computed data one can see that sand speed  $\bar{v}_s$  is 1000 times smaller than the water velocity  $\bar{v}$ , that is one order of magnitude less than postulated by Kraus et al. (1982) and Drapeau et al. (1990) for oceanic coast. It should be noted that our figures have been obtained in numerous experiments executed in various years. The difference can be attributed to dissimilarities in wave and tide conditions (the Baltic Sea is known as nontidal), number of underwater bars, wave breaking etc. First and foremost, however, the duration of effective driving forces was defined differently. The values given in Table 1 characterize mean conditions of a certain category ('storm' or 'medium sea'), averaged over lapses of time with waves above the threshold corresponding to the incipient velocity of water, estimated as 8-10 cm/s by Pruszek & Zeidler (1988).



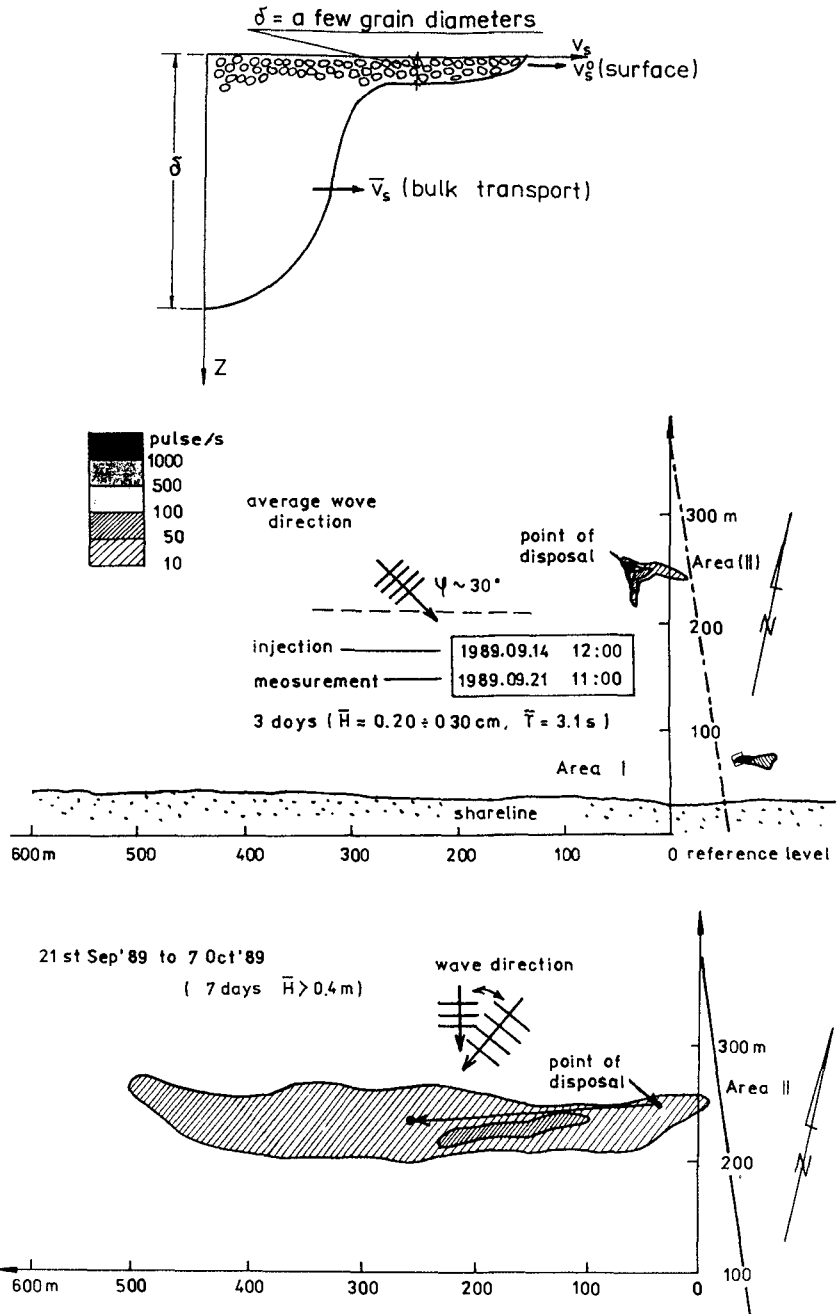


Figure 6. Schematic Sand Advection (top)

Figure 7. Distribution of Radioactive Sand Tracer from 14th to 21st September 1989 (center) and from 21st September to 7th October 1989 (bottom).

### 3.2.2 *Mixing Depth*

The thickness of the bedload layer  $\delta$ , in which all grains are assumed to move, has been found to vary from a few grain diameters to 2 cm under 'medium sea' conditions and 5 cm during storms. Since sand cores were cut out for analysis in layers 2 cm thick, it has appeared impossible to make finer distinctions.

Analysis of the measured data shows that sediment usually moves in a relatively thin layer (below 2 cm) if due to 'medium sea'; that thickness might be even smaller in view of the accuracy of the measurements. On the other hand, the thickness might increase in view of the intersecting paths of grains travelling in different directions and at different speed. This is particularly true for Area I, where meandering of longshore current brings about clear diversification of sediment movement. Further away from shoreline, the thickness  $\delta$  is much greater, from several to a few tens of centimetres, respectively for 'medium sea' and 'storm' (Fig. 8).

Upon comparison with Kraus et al. (1982) and Drapeau et al. (1990), illustrated in Figure 9, the agreement is visible with the former, thus supporting the empirical correlation

$$\delta = 0.027 H_b \quad (1)$$

### 3.2.3 *Sediment Transport Rate*

Most experiments took place upon oblique wave incidence. During storms longshore current prevails, while under case B conditions the longshore and cross-shore modes are equally important. For instance, in case B Area II, the cross-shore to longshore sediment transport rate can be estimated at 1:1.7, in absolute terms roughly 8:13.5 kg/(m·h). Incidentally, the cross-shore transport in case B situations is usually onshore (Fig. 5).

The sediment transport rate is computed from the formula

$$q_i = (\rho_s - \rho) \bar{v}_s \delta \quad (2)$$

in which

$q_i$  = transport rate in Areas I, II and III ( $i=1, 2, 3$ ),

$\delta$  = thickness of sediment motion layer,

$\bar{v}_s$  = mean sediment speed in bed layer.

The ranges of  $\delta$  along the shore profile are illustrated in Figure 6.

As could be expected, the highest transport rate takes place in Area II. During storms, the longshore rate reaches  $q=3.5-20$  kg/(m·h) in Area III, 40-100 kg/(m·h) in Area II and 15-40 kg/(m·h) in Area I. These figures become about five times smaller at 'medium sea', when only two times greater than the cross-shore rate. The gross longshore transport rate across the shore profile stretching from shoreline 700 m off shore is given in Table 2, for various external factors.

Both  $\bar{v}_s$  and  $\delta$  vary in time and space in the two cases A and B.

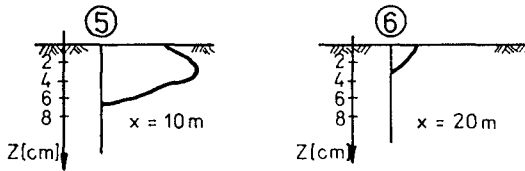
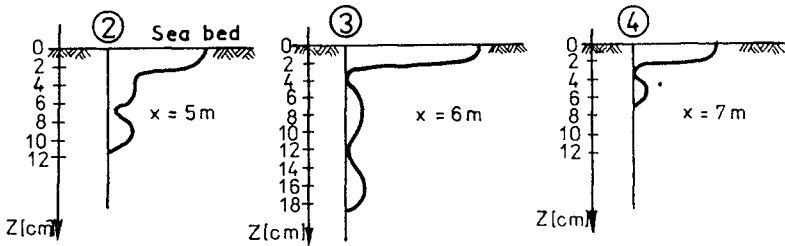
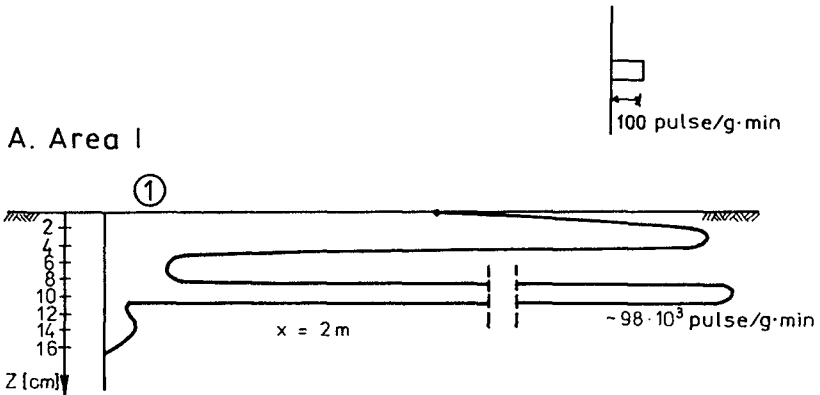
Finally, one can put forth

$$q = q_i \Delta l_i (\Delta \rho)^{-1} \quad (3)$$

in which

$\Delta l_i$  = width of area (I, II or III) measured along shore profile.

The total longshore transport rate in surf zone of width  $l$  varies from 1.95-6.0 m<sup>3</sup>/s in storms to 0.35-1.95 m<sup>3</sup>/s in medium sea.



B. Area II

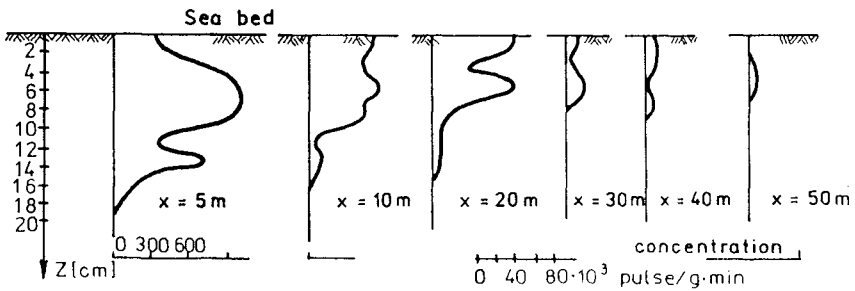


Figure 8. Vertical Distribution of Tracer Concentration

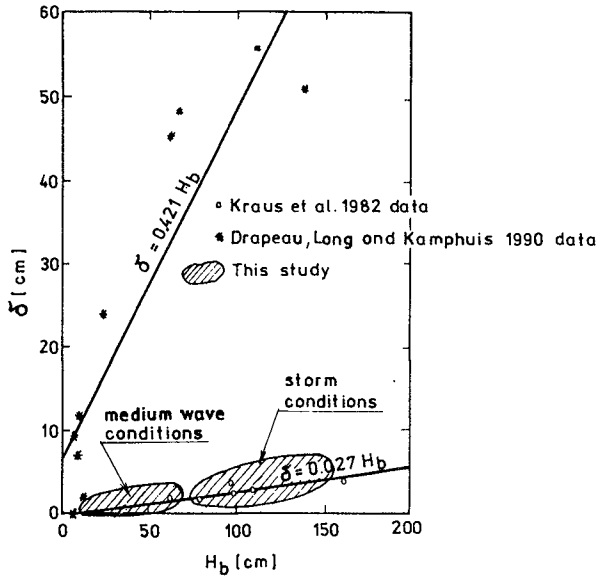


Figure 9. Depth of Mixing

Table 2. Gross Longshore Transport Rate

Case	Area (Fig. 2)	Bulk Vel. $\bar{v}_s$ , cm/h	$\delta$ cm	Computed $10^{-3}q$ , m <sup>3</sup> /s	$\frac{q}{H_b^2 \bar{v}} = K$	Note
(A)	I	50	2-5	1.95-6.0	0.015-0.018	(a)
	II	100-150				
	III	10-15				
(B)	I	25-30	a few	0.35-1.35	0.025-0.026	(b)
	II	30-40	grains			
	III	2-10	to 2 cm			

(a) Gross transport across  $l=700$  m; (b) at 'medium sea' wave breaks close to point I ;  $H_b \approx 0.5$  m. During storms,  $H_b=0.6-1.5$  m in surf zone.

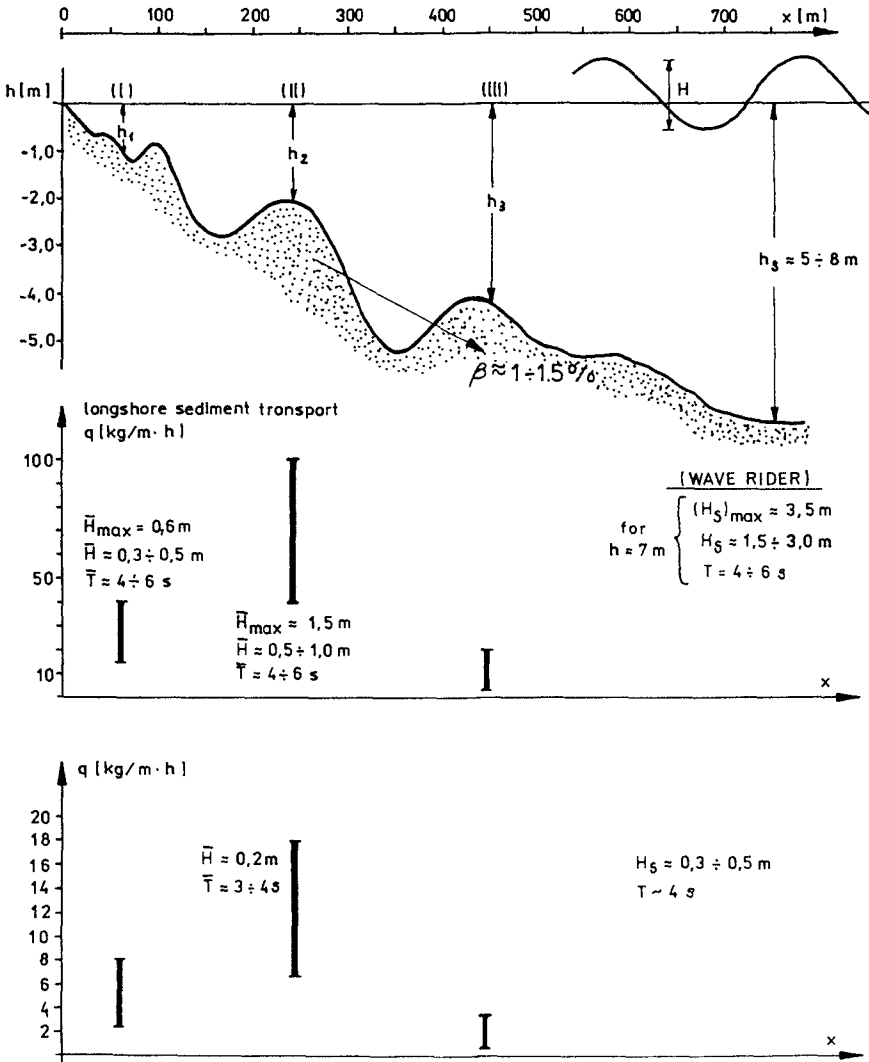


Figure 10. Sediment Transport Rate Estimates

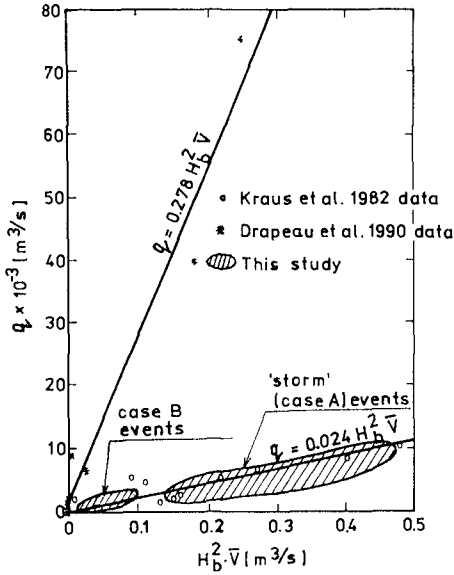


Figure 11. Volumetric Transport Rate; Global Rate,  $q \sim K(H_b^2 \bar{v})$

4 Comparison with Other Studies

Similar investigations have been carried out by Kraus et al. (1982) and Drapeau et al. (1990). Sediment properties ( $D$  and  $\rho_s$ ), bottom slope  $\beta$ , wave breaking index  $H_b/h_b$  etc have been encountered by us and Kraus et al. while those of Drapeau et al. were different in some respects. The difference is thought to bring about the divergence visible in Figure 11.

Major disparity arises in the proportionality factor  $K$  put forth by Kraus et al. :

$$q = \frac{3.8 \cdot 10^{-4}}{\gamma_b \tan \beta} (H_b^2 \bar{v}) = K(H_b^2 \bar{v}) \quad \text{m}^3/\text{s} \quad (4)$$

Kraus et al. give  $K=0.024$  while Drapeau et al. suggest 0.278. We have established that  $K$  depends on the intensity of wave action, and becomes 0.015–0.018 in medium sea and about 0.025–0.026 under storm conditions. The dissimilarities may be attributed to various factors controlling sediment transport phenomena such as deeper penetration of wave motion during storms and the decreasing mobility of sediment grains with depth in sea bed. Energy dissipation mechanisms, different in cases A and B, are also responsible for the scatter of  $K$ .

## 5 Discussion and Concluding Remarks

Aside from the grain speed  $v_s$ , the thickness of bedload layer  $\delta$  is difficult to measure. The magnitude  $\delta \approx 10\text{--}60$  cm given by Drapeau et al. (1982) seems overestimated. If one defines  $\delta$  as the thickness of all  $n$  grain diameters in motion, then  $\delta$  varies from a few  $D_{50}$  to 5 cm, depending on the intensity of wave motion.

Another problem can be seen in the identity of the movements of native sediment and tracer sand. It appears that the identity is complete over short spans of time (minutes or hours at most), whereupon the tracer speed can be deemed equivalent to the instantaneous sand speed. In longer time scales (days and weeks), the average velocities are usually smaller, roughly by one order of magnitude in our experiments. This is due to the random nature of grain motion.

The maximum sediment transport rate occurs in the active zones exhibited by EOF, i.e. usual wave breaking areas. Under storm waves, the longshore sediment transport rate grows locally up to 100 kg/(m·h), about five times more than its 'medium sea' counterpart. The gross transport rate across the entire shore profile, averaged over days, approaches 4 m<sup>3</sup>/s during storms or 0.85 m<sup>3</sup>/s in medium sea. These quantities refer to average conditions of mild slope (1–2%), multiple wave breaking, and medium sand ( $D_{50}=0.22$  mm,  $\rho_s=2650$  kg/m<sup>3</sup>). Since such figures are quite common throughout the world, they can be suggested as general rough estimates for similar environments and time scales of days.

The coefficient of proportionality  $K = \frac{q}{H_s^2 \bar{v}}$  has been found to vary from 0.025–0.026 in case B events to 0.015–0.018 in case A, thus in the range outlined by Kraus et al. (1982). Hence our field findings agree well with the earlier data by Kraus et al. (1982) but are in disagreement with the results published by Drapeau et al. (1990), inter alia their method of computing the total sediment transport rate. It is hoped that our results can modify and improve the engineering estimates of sediment transport.

### Acknowledgements

The research reported on herein has been sponsored by the Polish Academy of Sciences under CPBP 02.12 and other PAN/KBN programmes, which is gratefully acknowledged. The first author expresses his gratitude to the *Stefan Batory Foundation* who granted him the *Soros* scholarship and hereby sponsored his travel to and accomodation in Venice.

### References

- Drapeau G., B.Long & J.W.Kamphuis (1990). Evaluation of radioactive sand tracers to measure longshore sediment transport rates. *Proceed. 22nd ICCE*, Delft, ASCE.
- Krauss N.C., M.Isobe, H.Igarashi, T.O.Sasaki & K.Horikawa (1982). Field experiments on longshore sand transport in the surf zone. *Proceed. 18th ICCE*, Cape Town, ASCE.
- Pruszek Z. (1992). The analysis of beach profile changes using Dean's method and empirical orthogonal functions. *Journal for Coastal, Harbour and Offshore Engineers* (in press).
- Pruszek Z. & R.B.Zeidler (1988). Estimates of cross-shore bedload and bed changes. *Proceed. 21st ICCE*, Malaga, ASCE.

## CHAPTER 183

Velocity measurements close to rippled beds

K.I. Mahesha Ranasoma <sup>1</sup> and J.F.A. Sleath <sup>2</sup>

### Abstract

Velocity measurements have been made with a Laser Doppler Anemometer in oscillatory flow over rippled beds. The ripples were naturally formed in an oscillating tray rig and then stabilised.

Both large-scale mixing, repeatable from cycle to cycle, and turbulence were found to have a significant effect on the velocity profile. Large-scale mixing, which is associated with vortex formulation and ejection, was seen to dominate in the immediate vicinity of the bed but turbulent mixing appeared to be more important at large height. The variation in turbulence intensity with height was found to be qualitatively similar to that previously observed with three-dimensional roughness in oscillatory flow. Time-mean velocities are not well predicted by existing theory. The present measurements show only two re-circulating cells per ripple wavelength.

### Introduction

The sea bed is frequently covered with ripples. Although much progress has been made in recent years there is still relatively little information about the way in which bed geometry changes the velocity distribution. It is the aim of the present investigation to provide more data. The results are relevant to problems such as sediment transport by waves, wave height attenuation and dispersion of pollutants in the sea.

### Experimental apparatus and test conditions

The measurements were made in the apparatus described by Lee-Young and Sleath (1988). This consists of a steady flow flume with a section of bed which can oscillate with simple harmonic motion. In the present experiments

---

<sup>1</sup> Graduate Student, Cambridge University Engineering Department, Trumpington Street, Cambridge CB2 1PZ, England.

<sup>2</sup> Reader, ditto



the steady flow was zero. The oscillating bed is 0.81m wide and 2.13m long. Disturbances generated by the ends of the bed are restricted by vertical baffles which effectively reduce the length of the working section to 1.17m. In the centre of the oscillating bed there is a sunken tray 0.70m wide x 0.70m long x 0.04m deep. Sand of medium diameter 0.41mm was placed in this tray. When the bed was oscillated at the chosen amplitude and period ripples formed on the sand. These ripples were stabilised by sprinkling with a thin coating of cement.

The velocity measurements were carried out with two different rippled beds. Bed 1 was formed by oscillating the tray with amplitude 78mm and period 2.45 secs. The ripples were of length,  $L$ , 100mm and crest-to-trough height,  $h$ , 18.4mm. Bed 2 was formed with amplitude of oscillation 40mm and period 1.25 secs. Ripple length was 50mm and height 9.1mm.

Fluid velocities were measured with a one-component DANTEC fibre-optic Laser Doppler Anemometer operated in backscatter mode. At each position the velocity was sampled 100 times per cycle for 50 cycles. Ensemble-average and root-mean-square velocities were then determined at each phase. At each position, horizontal velocity was measured first and then, by rotating the probe, the vertical velocity. Measurements were made at various vertical heights above the bed and at 11 horizontal positions (equally spaced over one wavelength of the ripple profile). The depth of water was 0.27m throughout.

Table 1 shows the test conditions. In this Table  $U_0$  is the amplitude of the velocity of the bed,  $T$  is the period of oscillation,  $a$  is the amplitude of oscillation,  $\nu$  is kinematic viscosity and  $b$  relates to the turbulence intensity (see below). Further details of the apparatus and test procedure are given by Ranasoma (1992).

### Velocities

Fig 1 shows an example of the ensemble-average velocity vectors at various phases. The velocity of the bed is maximum at  $\omega t = 0^\circ, 180^\circ$  and zero at  $\omega t = 90^\circ, 270^\circ$ . The ripple profiles in this Figure and in Fig 8 are not to scale. They are shown only to indicate position relative to crest and trough.

Measurements were only made above the level of the crests. Even so, the vortex in the ripple lee is clearly shown in Fig 1(a). As the direction of the plate reverses (Fig 1(b)), we see that the lee vortex expands and then is carried back over the crest and into the trough beyond (Figs 1(c) and 1(d)).

As might be expected, the vortex dynamics have a significant effect on the velocity profiles. Fig 2 is an example of the horizontal defect velocity at various values of  $x$  and  $y$  and Fig 3 shows the corresponding curves for the vertical velocity. The broken lines in these Figures represent the theoretical velocity which would be found with this bed profile if the flow were inviscid. In Fig 3 we see that there is an upward surge in velocity, in comparison with the inviscid solution for  $0 < \omega t < 90^\circ$  at  $x/L = 0.4$  (i.e. just to one side of the crest). At the same time and position Fig 2 shows a decrease in horizontal velocity.

These changes are clearly association with the formation and ejection of a vortex on this side of the ripple crest. In comparison, the change in vertical velocity during the other half cycle (for  $180^\circ < \omega t < 270^\circ$ ) is insignificant because the vortex is then on the far side of the crest. Over the crest ( $x/L=0.5$ ) and trough ( $x/L=0$ ) the variations in vertical velocity are more or less the same in the two half cycles because these positions are affected equally by vortices formed on either side of the crest.

Large-scale mixing

Because of the clear influence of vortex formation and ejection on the velocity records it is to be expected that the large-scale exchanges in momentum associated with the vortices would have a dominant effect on the velocity profile. Since vortex formation and ejection repeats from cycle to cycle we will analyse this effect in terms of the ensemble-average components of velocity,  $u$  and  $v$ .

In order to facilitate comparison with the spatial-mean velocity, the spatial-mean value of  $uv$  has been Fourier analysed. Fig 4 shows how the amplitude of the fundamental (i.e. the coefficient of  $\cos \omega t$ ) varies with height. A mean line has been drawn through the experimental points in Fig 4. The equation of this line is

$$\frac{\hat{uv}}{U_0^2} = 0.09e^{-1.76ky} \tag{1}$$

The origin for  $y$  is mid-height between crest and trough and  $k=2\pi/L$ .

There is also a variation in the phase of this fundamental component with height. If we draw a mean line through the experimental points for phase we obtain

$$\overline{uv} = 0.09e^{-1.76ky} \cos(\omega t - 0.46ky - 0.94) \tag{2}$$

If momentum exchange due to large-scale mixing were the only important effect (in other words, if viscosity and turbulence were negligible) we would have

$$\frac{\partial \overline{u}}{\partial t} = -\frac{\partial}{\partial y} (\overline{uv}) \tag{3}$$

Where the overbar indicates the spatial-mean value (averaged in the horizontal direction). Making use of Eqns (2) and (3) we find that the variation with height of the spatial-mean velocity would be

$$\bar{u} = 1.03 \frac{a}{L} e^{-1.76ky} \cos(\omega t - 0.46ky - 2.25) \quad (4)$$

Fig 5 shows how the amplitude of  $\bar{u}$  varies with height. Clearly Eq(4) significantly underestimates the measured values at large heights although the agreement is better as  $ky \rightarrow 0$ . The phase measurements in Fig 6 also show poor agreement with Eq(4).

We conclude that although large-scale mixing produced by the vortices may be the dominant effect at very small values of  $ky$ , other effects are more important further out. Since the flow was fully turbulent, viscous diffusion of momentum is negligible at large  $y$ . We must consequently examine turbulence.

### Turbulence

Fig 7 shows how the root-mean-square components,  $u'$  and  $v'$ , of the horizontal and vertical fluctuations in velocity vary with height. These are the mean values, averaged in the horizontal direction and in time. Sleath (1991) found that for three-dimensional bed roughness the turbulent intensity in oscillatory flow was inversely proportional to height  $y_1$ , above the bed, in the same way as for grid-generated turbulence. In other words, with suitable choice of origin for  $y_1$ ,

$$\frac{1}{v'} = by_1 \quad (5)$$

Where  $b$  is a constant for any given test.

Fig 7 shows that reasonable straight lines can be drawn through the experimental points at values of  $ky$  greater than about 1 or 2. However, there is significant divergence from the straight line closer to the bed. The apparent origin for the straight lines is at  $ky = -0.58$ , which is the level of the troughs. Values of the coefficient  $b$  obtained from the slope of the experimental curves are shown in Table I.

The present tests do not cover a sufficient range of values of  $a$ ,  $T$  and  $k_s$ , where  $k_s$  is the bed roughness length, for it to be possible to investigate whether  $b$  varies in the same way as for three-dimensional roughness. However, if we take  $k_s$  in the present tests equal to  $4h$  the values of  $b$  in Table I are significantly smaller than corresponding values for three-dimensional bed roughness. This is hardly surprising in view of the difference in bed geometry.

In order to assess the effect of this turbulence on the velocity profiles we need to make some simplifying assumptions. Following Sleath (1991), we assume that the eddy viscosity is given by

$$\epsilon_w = v'l \quad (6)$$

where the mixing length  $l$  is given by

$$l = 0.1y_1 \tag{-7}$$

and  $y_1$  has the same origin as in Eq(5). Substituting Eqns (5) and (7) into Eq (6) we see that  $\epsilon_w$  does not vary with height. If momentum exchange due to turbulent mixing is the dominant effect we have

$$\frac{\partial \bar{u}}{\partial t} = \epsilon_w \frac{\partial^2 \bar{u}}{\partial y^2} \tag{-8}$$

consequently

$$\bar{u} = A e^{-\beta_1 y} \cos(\omega t - \beta_1 y - B) \tag{-9}$$

where A and B are constants and

$$\beta_1 = (\omega/2\epsilon_w)^{1/2} = (5\omega b)^{1/2} \tag{-10}$$

Making use of the values of b shown in Table I we obtain:

$$\beta_1/k = 1.37 \text{ for tests 1,2,3,4}$$

$$\beta_1/k = 1.86 \text{ for tests 5,6,7}$$

$$\beta_1/k = 1.11 \text{ for test 8.}$$

The corresponding curves obtained from Eq (9), assuming arbitrary values of the constants A and B, are shown in Figs 5 and 6. It is clear that the slope of the curves for amplitude and phase obtained from Eq (9) is in reasonable agreement with the measurements. Unfortunately we do not have any independent estimate for the values of A and B. Nevertheless, it seems reasonable to conclude that turbulence is the dominant effect on the spatial-mean velocity profile at large  $ky$ .

Time-mean velocity

So far we have been concerned with the oscillatory component of velocity. Fig 8 shows the time-mean Eulerian velocity vectors. As expected from the theoretical studies of Blondeaux and Vittori (1991) and others, we see re-circulating fluid cells associated with each ripple wavelength. However, for the relatively large values of  $\beta L$  in the present experiments the theory predicts four cells per ripple wavelength instead of the two seen in Fig 8. Of course, there might be two cells below the lowest measured level. This is unlikely because these lower cells would be in the wrong direction for ripple formation and both inner and outer cells would be in directions opposite to those predicted by the theory. Equally, there might be re-circulating cells at larger values of  $y$  than shown in Fig 8 but the measurements of Sato et al (1984) and Horikawa and Ikeda (1990) show that this is not the case.

One possible reason for this discrepancy between theory and experiment is that the Reynolds numbers in the present tests are much larger than those for which theoretical mean streamlines have been calculated. Another possible reason is that, because of turbulence, the effective viscosity is much greater than the kinematic viscosity. Consequently, the effective value of  $\beta L$  is much smaller than the calculated value. For small  $\beta L$  the theory does indeed predict only one pair of re-circulating cells with directions of rotation similar to those in Fig 8.

The time-mean velocity is periodic in  $x$ . Fig 9 shows that the fundamental Fourier component (i.e. the term in  $\cos kx$ ) is dominant at all values of  $y$  for both the horizontal velocity  $\bar{u}_e$  and the vertical  $\bar{v}_e$ . The way in which the amplitude of this fundamental component varies with height is shown in Fig 10. Also shown in Fig 10 is the line corresponding to  $\bar{v}_e \propto \exp(-ky)$ . The fact that the experimental points for a given test lie almost parallel to this line at large  $y$  is not surprising since  $L$  is the largest length scale and is consequently dominant far from the bed.

It will be seen from Table I that  $h/L$  is almost the same for all tests and, apart from Test 8, so is  $a/L$ . Consequently, the fact that the points do not lie along a single curve in Fig 10 is an indication that either Reynolds number or  $\beta L$  (or both) have a significant effect on the time-mean velocity.

### Vorticity contours

Fig 11 shows vorticity contours calculated from the velocity measurements in Test n°2. Fig 11(a) shows the lee vortex soon after maximum bed velocity. As the velocity reverses (Fig 11(b)) the vortex is forced out into the flow, carried over the crest (Fig 11(c)) and then on over the trough (Fig 11(d)).

One interesting thing to emerge from these measurements is the relatively short life of the lee vortex once it has been pushed out from the bed by the reversing flow. In Fig 11(a), half way through the new half cycle, it is just possible to detect the old vortex to the right of the ripple crest but it is clear from Fig 11(a) that it is already very weak. This observation appears to contradict Bagnold's (1946) well-known photographs of vortex formation over rippled beds. In reality there is no contradiction. Bagnold's photographs show the trace left by the vortex in the aluminium powder on the water surface. Such a trace can remain long after the vortex which produced it has decayed to zero.

### Conclusions

The velocity measurements close to rippled beds in oscillatory flow show the following results:

- (1) The flow patterns are strongly influenced by vortex formation and ejection. Nevertheless, the measurements show that the exchanges of momentum which are repeatable from cycle to cycle (i.e. not random) are not sufficiently large to explain the observed velocity profile, except in the immediate vicinity of the bed.
- (2) It is concluded that at large distances from the bed the flow is dominated by turbulence. For large  $y$ , turbulence intensity appears to be inversely proportional to height, in the same way as for three-dimensional bed roughness in oscillatory flow. A simple turbulence model shows reasonable agreement with the trend of the velocity measurements at large  $y$ .
- (3) Time-mean velocities are not well predicted by existing theory. The present measurements show only two re-circulating cells per ripple wavelength.
- (4) Patterns of vortex formation and ejection are similar to those described by other investigators. However, once the vortex has been ejected from the lee of the ripple into the flow above it appears to decay much more rapidly than is suggested by Bagnold's (1946) photographs.

### References

Bagnold, R.A. (1946) 'Motion of waves in shallow water. Interaction between waves and sand bottoms'. Proc. Royal Society, London A187, pp1-18.

Blondeaux, P. and G. Vittori (1991): 'Vorticity dynamics in oscillatory flow over a rippled bed'. J. Fluid Mechanics, 226, pp257-289.

Horikawa, K and S. Ikeda (1990): 'Characteristics of oscillatory flow over ripple models'. Proc. 22nd Conf on Coastal Engng. ASCE, New York, pp661-674.

Lee-Young, J.S. and J.F.A. Sleath (1988): 'Initial motion in wave and current flows'. Proc. 21st Conf on Coastal Engng. ASCE, New York, pp1140-1151.

Ranasoma, K.I.M. (1992): 'Measurements in combined oscillatory and steady flow over rippled beds'. Ph.d thesis. University of Cambridge. U.K.

Sato, S, Mimura, N. and A. Watanabe (1984): 'Oscillatory boundary layer flow over rippled beds'. Proc. 19th Conf. on Coastal Engng. ASCE, New York, pp2293-2309.

Sleath, J.F.A. (1991): 'Velocities and shear stresses in wave-current flows'. J. Geophys. Res. 96, NoC8, pp15237-15244.

Test	Ripple Length mm	$h/L$	$a$ mm	$T$ sec	$\frac{U_0 a}{v}$	$b$ sec/m <sup>2</sup>	Symbol
1	100	0.184	78	3.90	9320	935	○
2	100	0.184	78	2.41	14040	578	□
3	100	0.184	78	1.70	19760	408	△
4	100	0.184	78	1.88	20480	451	◇
5	50	0.182	40	1.25	6680	2170	+
6	50	0.182	40	2.47	3380	4290	×
7	50	0.182	40	1.80	4700	3130	*
8	50	0.182	80	2.45	14210	1520	■
9	100	0.184	80	1.53	23900	358	⊕
10	100	0.184	80	2.00	18300	468	⊞
11	100	0.184	80	3.02	12100	706	●

Table 1. Test conditions

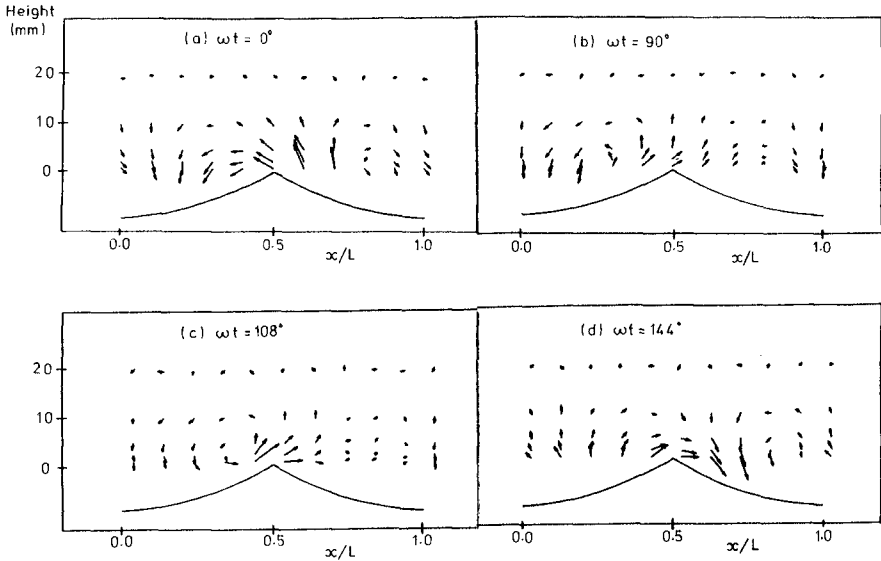


Fig. 1 Defect velocity vectors. Test no.5. (Ripple profile not to scale)

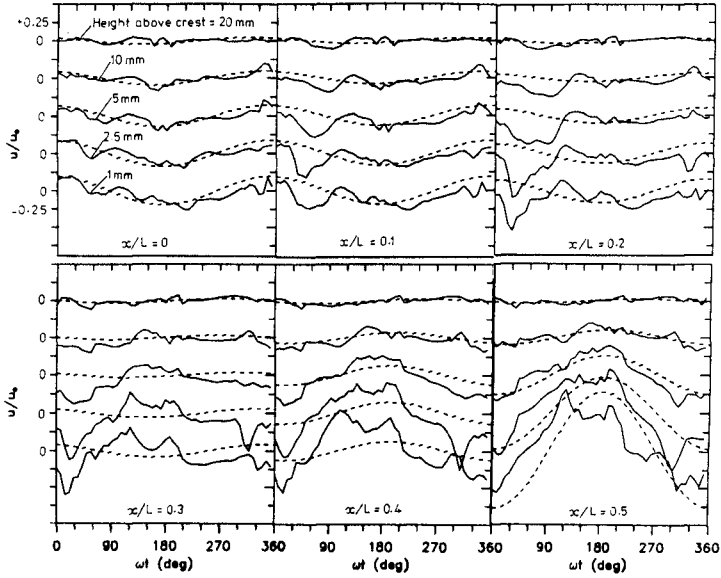


Fig. 2 Horizontal velocity. Test no.5. \_\_\_\_\_ measurements;--- inviscid theory.

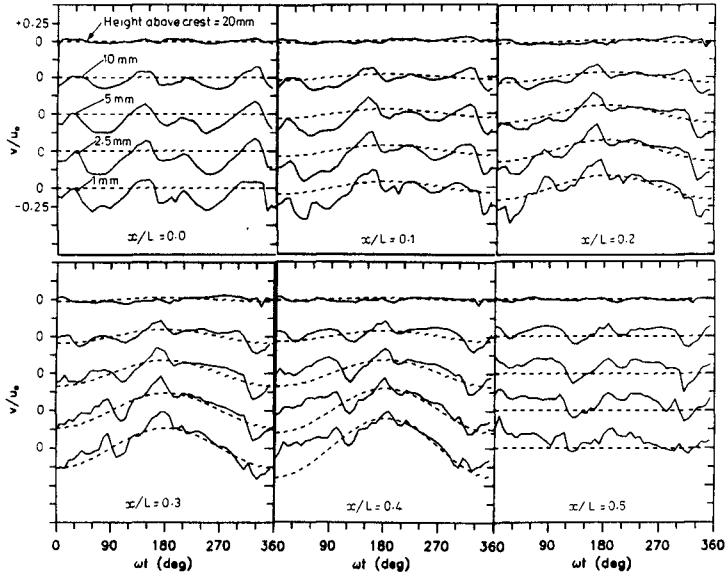


Fig. 3 Vertical velocity. Test no.5. Curves as for Fig. 2



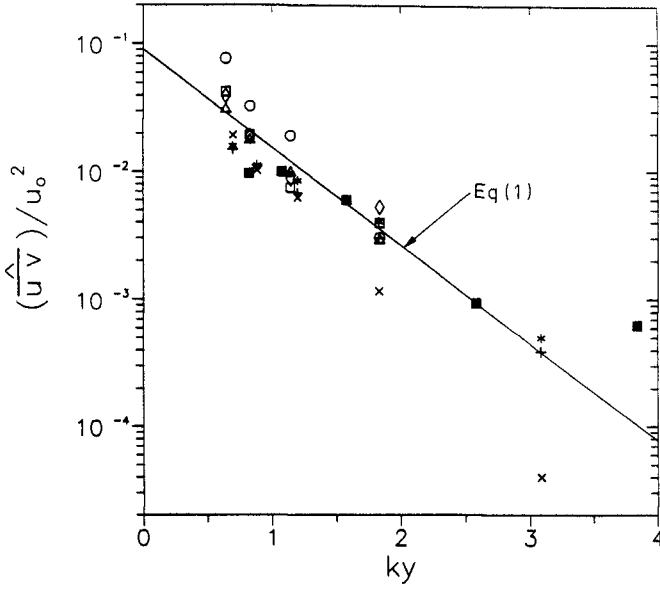


Fig. 4 Variation with height of the amplitude of the fundamental component of  $\hat{uv}$ . Symbols as in Table I

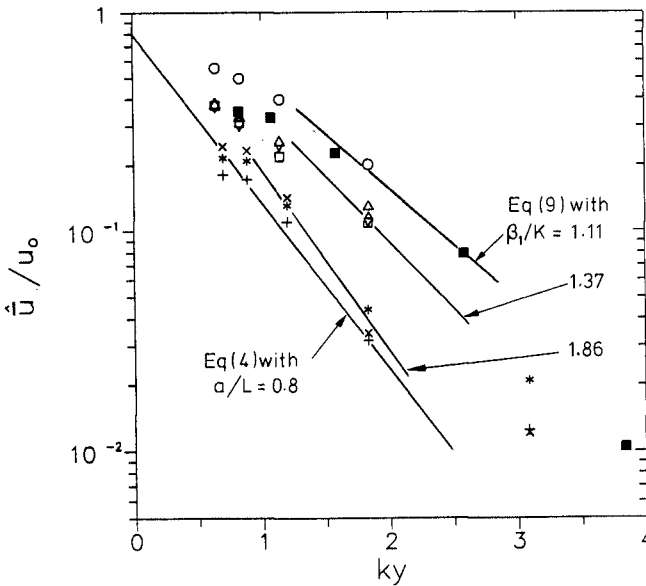


Fig. 5 Variation with height of the amplitude of the fundamental component of the spatial-mean velocity  $\hat{u}$ . Symbols as in Table I

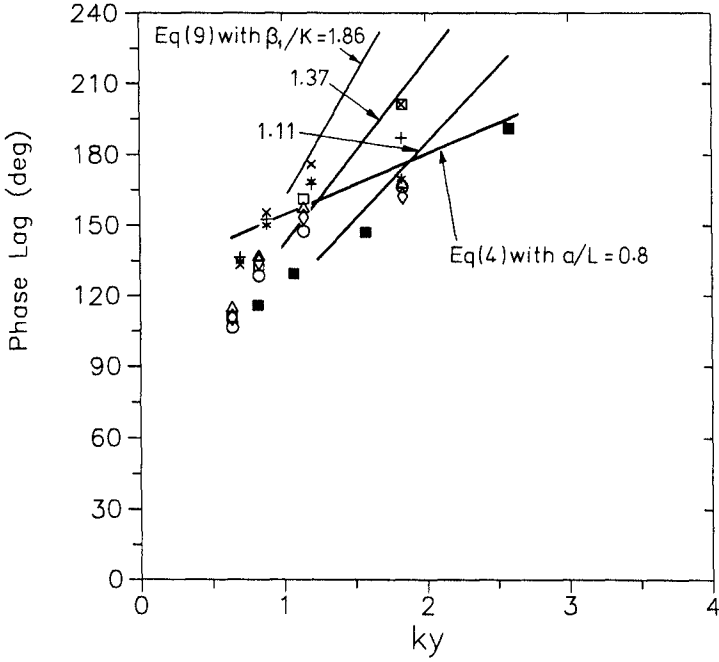


Fig. 6 Variation with height of the phase of the fundamental component of the spatial-mean velocity  $u$ . Symbols as in Table I

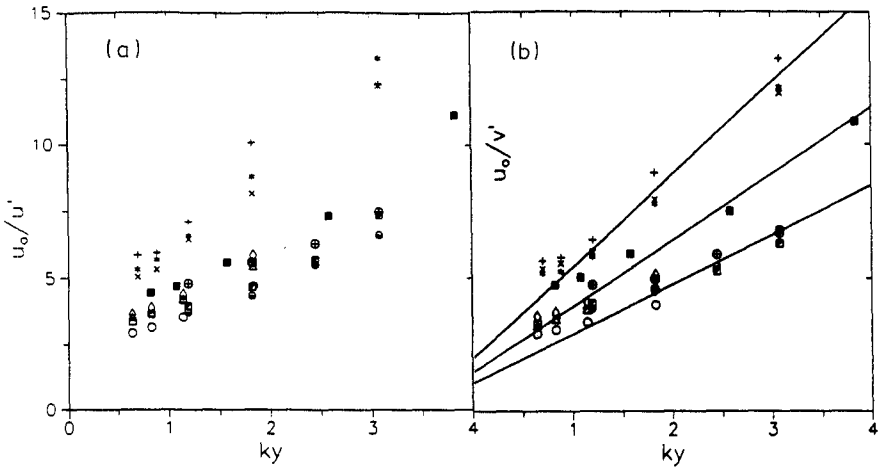


Fig. 7 Variation of turbulence intensity with height; (a) horizontal (b) vertical. Symbols as in Table I

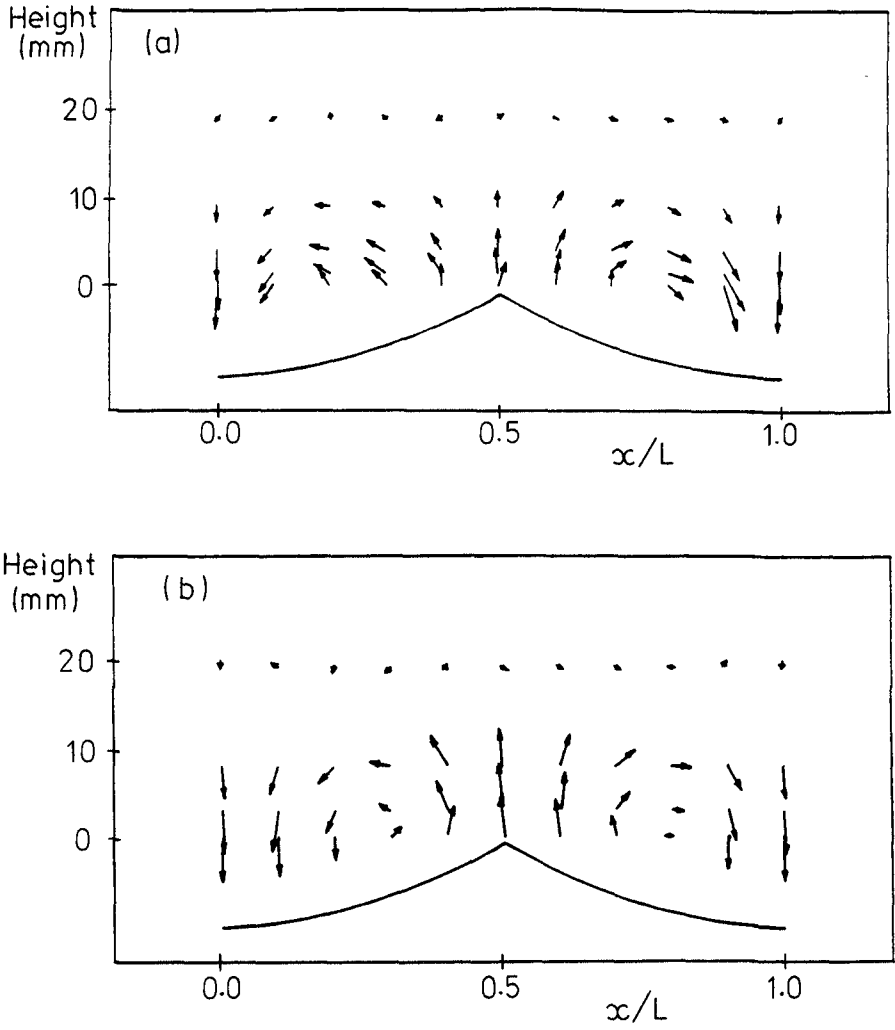


Fig. 8 Time-mean velocity vectors; (a) Test no.5 (b) Test no.2. (Ripple profiles not to scale).

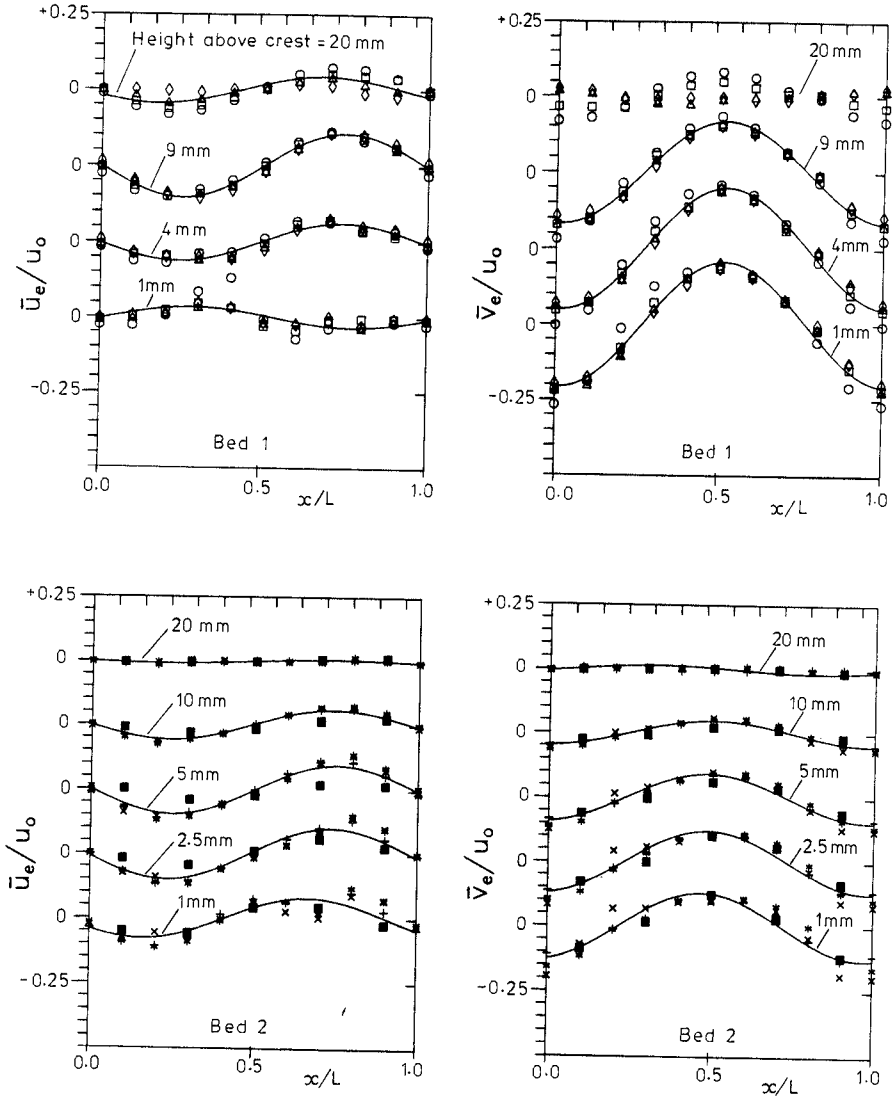


Fig.9 Spatial variation of the time-mean velocity. Symbols as in Table I

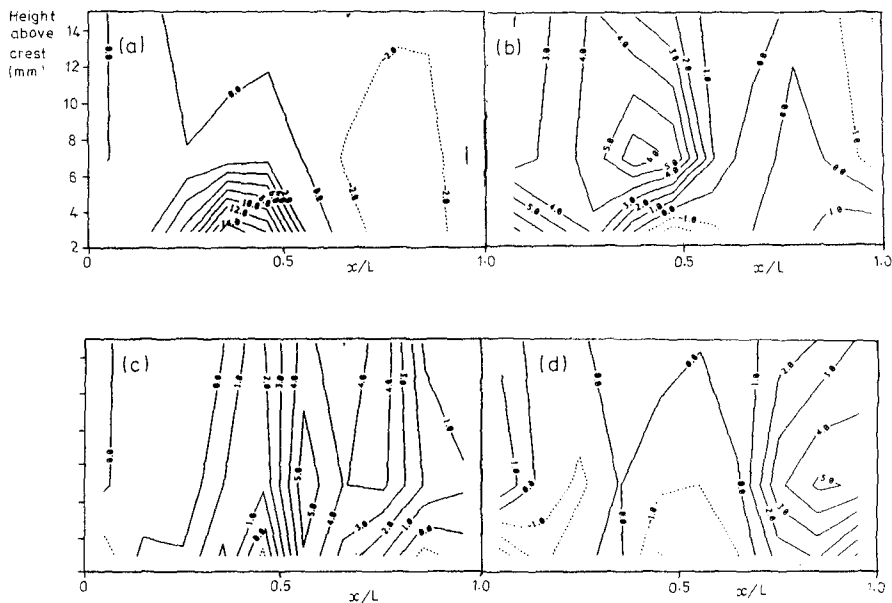


Fig.11 Vorticity contours for Test no.2; (a)  $wt=70$  (b)  $wt=940$  (c)  $wt=1400$  (d)  $wt=1570$

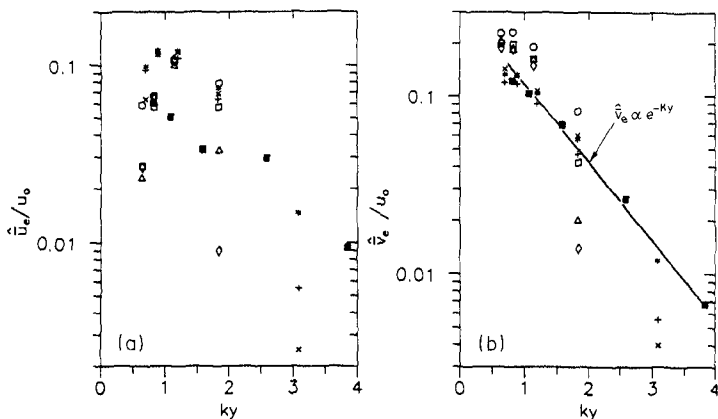


Fig.10 Variation with height of the amplitude of the fundamental component of the time-mean velocity; (a) horizontal velocity (b) vertical velocity. Symbols as in Table I

## CHAPTER 184

### FIELD OBSERVATION OF WAVE-INDUCED POREWATER PRESSURES

T. Sakai<sup>1</sup>, M. ASCE, H. Mase<sup>2</sup>, M. ASCE, D.T. Cox<sup>3</sup> and Y. Ueda<sup>4</sup>

#### ABSTRACT

Wave-induced transient porewater pressures were measured near a seabed surface at a coast facing the Japan Sea. The data are compared with the solution using a boundary layer approximation by Mei and Foda (1981). The effective bulk modulus of porewater,  $\beta$ , is estimated  $1.0 \times 10^8 \text{ N/m}^2$  so that the solution matches the observation. A similar analysis is done for the field data obtained by Zen et al. (1989) at a coast facing the Pacific Ocean. The value of  $\beta$  scatters from  $1.0 \times 10^7 \text{ N/m}^2$  to  $1.0 \times 10^8 \text{ N/m}^2$ .

#### INTRODUCTION

The wave-induced transient porewater pressure is an important quantity for a seabed stability (Sakai et al., 1992). The solution using a boundary layer approximation by Mei and Foda (1981) is simple and useful for the estimation of the wave-induced transient porewater pressures. The uncoupled analysis proposed by Finn et al. (1983) is applicable only to soft and coarse sand.

Mei and Foda (1981) modeled the seabed response to waves as a summation of an elastic response of one-phase medium and a

---

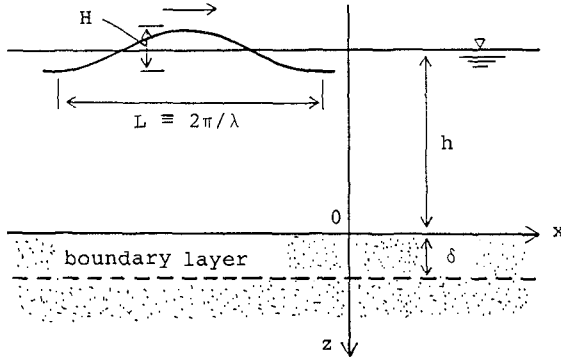
1 Prof., Dept. of Civil Engrg., Kyoto Univ., Sakyo-Ku, Kyoto, 606, Japan.

2 Res. Assoc., Dept. of Civil Engrg., Kyoto Univ., Sakyo-Ku, Kyoto, 606, Japan.

3 Graduate Student, Dept. of Civil Engrg., Univ. of Delaware, Newark, DE 19716, USA.

4 Engineer, Civil Engrg. Design Dept., Maeda Corporation, Chiyoda-Ku, Tokyo, 102, Japan.

seepage flow near the bed surface (Fig.1). The seepage flow is appreciable only in a thin layer near the bed surface. They called this layer "boundary layer".



**Fig.1 Boundary layer approximation of seabed response to waves (Mei and Foda, 1981)**

In the solution using the boundary layer approximation, when the bottom wave pressure,  $p_b$ , is given by the small amplitude wave theory as

$$p_b = p_0 \cos(\lambda x - \omega t) = \frac{1}{2} \frac{\rho_w g H}{\cosh(\lambda h)} \cos(\lambda x - \omega t), \quad (1)$$

the porewater pressure variation,  $p'$ , is given by

$$p' = p_0 \frac{1}{1+m} \exp\left(-\frac{2\pi z}{L}\right) \cos(\lambda x - \omega t) + p_0 \frac{m}{1+m} \exp\left(\frac{-z}{\sqrt{2}\delta}\right) \cos\left(\lambda x - \omega t + \frac{z}{\sqrt{2}\delta}\right), \quad (2)$$

where  $p_0$  is the amplitude of the bottom wave pressure,  $\lambda (= 2\pi/L)$  is the wave number,  $L$  is the wave length,  $x$  is the horizontal distance in the wave propagation direction,  $\omega (= 2\pi/T)$  is the wave angular frequency,  $T$  is the wave period,  $t$  is the time,  $\rho_w$  is the density of the water,  $g$  is the gravity,  $H$  is the wave height,  $h$  is the water depth, and  $z$  is the depth beneath the seabed surface.

The first term in the right hand side of Eq.(2) is the so-called outer solution as the one-phase elastic response. The second term is the boundary layer correction. In the boundary layer correction, a

phase delay  $z/(\sqrt{\Sigma}\delta)$  exists. Eq.(2) includes two parameters  $m$  and  $\delta$ . The  $m$  is a non-dimensional parameter described by Eq.(3), and proportional to a ratio of the shear modulus of the solid skeleton  $G$  and the effective bulk modulus of the porewater  $\beta$ ,

$$m = \frac{n}{(1 - 2\nu)} \frac{G}{\beta} . \quad (3)$$

The  $\delta$  is the thickness of the boundary layer described by Eq.(4):

$$\delta = \left( \frac{KG}{\omega} \right)^{\frac{1}{2}} \left( n \frac{G}{\beta} + \frac{1 - 2\nu}{2(1 - \nu)} \right)^{-\frac{1}{2}} , \quad (4)$$

where  $n$  and  $\nu$  are the porosity and Poisson's ratio of the solid skeleton,  $K = k/\rho_w g$  and  $k$  is the permeability coefficient.

The effective bulk modulus of the porewater  $\beta$  is related to the degree of saturation of porewater,  $S$ , through an empirical equation (Mei and Foda, 1981),

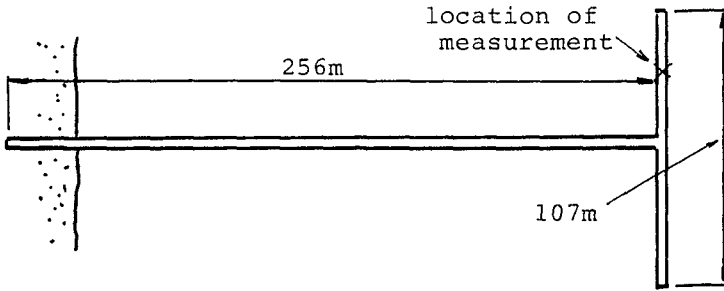
$$\frac{1}{\beta} = \frac{1}{\bar{\beta}} + \frac{1 - S}{\bar{p}} , \quad (5)$$

where  $\bar{\beta}$  is the effective bulk modulus of saturated water, and  $\bar{p}$  is the fluid pressure.  $\beta$  is  $2 \times 10^9$  N/m<sup>2</sup> for saturated porewater, but it decreases rapidly to  $10^6$  N/m<sup>2</sup> due to gas content of 1%. The  $\beta$  is a dominant parameter for a momentary liquefaction (Sakai et al., 1992). In this paper, we try to estimate the value of  $\beta$  from field observation data of the wave-induced transient porewater pressure variation.

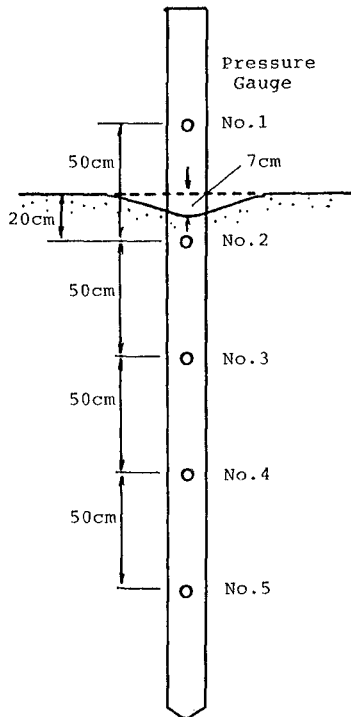
## FIELD OBSERVATION

Field observations were carried out at the Ogata Wave Observatory of Kyoto University. It is facing the Japan Sea. The measurements of the wave-induced porewater pressures were done in a sandy bed under a head of the wave observation pier, shown in Fig.2, in March 1990. The length of the pier is 256 m with a wing of 107 m length at the head. The water depth at the measuring location was about 6 m. The median diameter of the bottom sediment was reported to be from 0.2 mm to 0.5 mm (Akamura, 1989 ; Kawata et al., 1990).





**Fig.2 Pier of Ogata Wave Observatory of Kyoto Univ.**



**Fig.3 Measuring apparatus of porewater pressures**

Five pressure gauges were attached to a side wall of an aluminum pipe of rectangular section as shown in Fig.3. The length of the pipe was 3.0 m. The length between two adjacent gauges was 50 cm. The capacity of the pressure gauges was 1.0 kgf/cm<sup>2</sup>. A brass filter of 40  $\mu$ m was attached to the diaphragm of the gauge.

A part of the pipe of 2.2 m was inserted into the seabed. The highest gauge was located 30 cm above the seabed surface. The second gauge was located 20 cm below the bed surface. The bed surface around the pipe was about 7cm lower than the surrounding bed surface.

Unfortunately the waves were small during the first observation. Two months later after leaving the apparatus in the seabed, the second observation was tried again. But the output was very small compared with that of the first observation. The reason was found, after lifting out the apparatus from the seabed, that the brass filters of the upper three gauges were covered by small marine organic bodies.

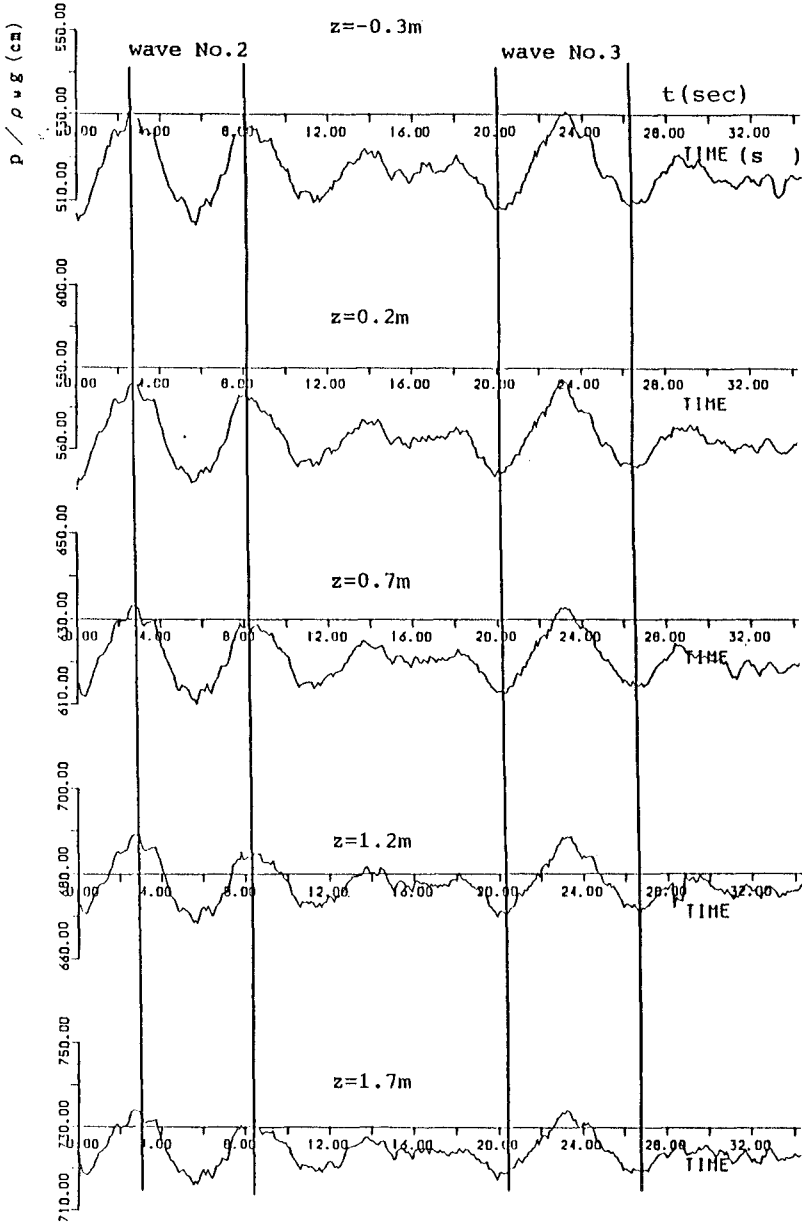
Figure 4 is a part of the record on March 28th, 1990. The unit of the abscissa is second, and that of the ordinate is cm, where the porewater pressure is shown by water head. Several waves, Nos. 2 and 3 of which are shown in the figure, were selected for the following analysis. Figure 5 is a part of the record on March 30th.

Five waves were selected from the record of March 30th. Table 1 shows the wave periods and the total amplitudes of pressure head variation at five pressure gauges for five waves. The amplitude of gauge No.2 of wave No.1 is slightly larger than that of gauge No.1. The same trend was seen in two waves in the record of March 28th. At this moment it is impossible to find the reason. In the following analysis, the level of gauge No.2 is assumed to be the bed surface level.

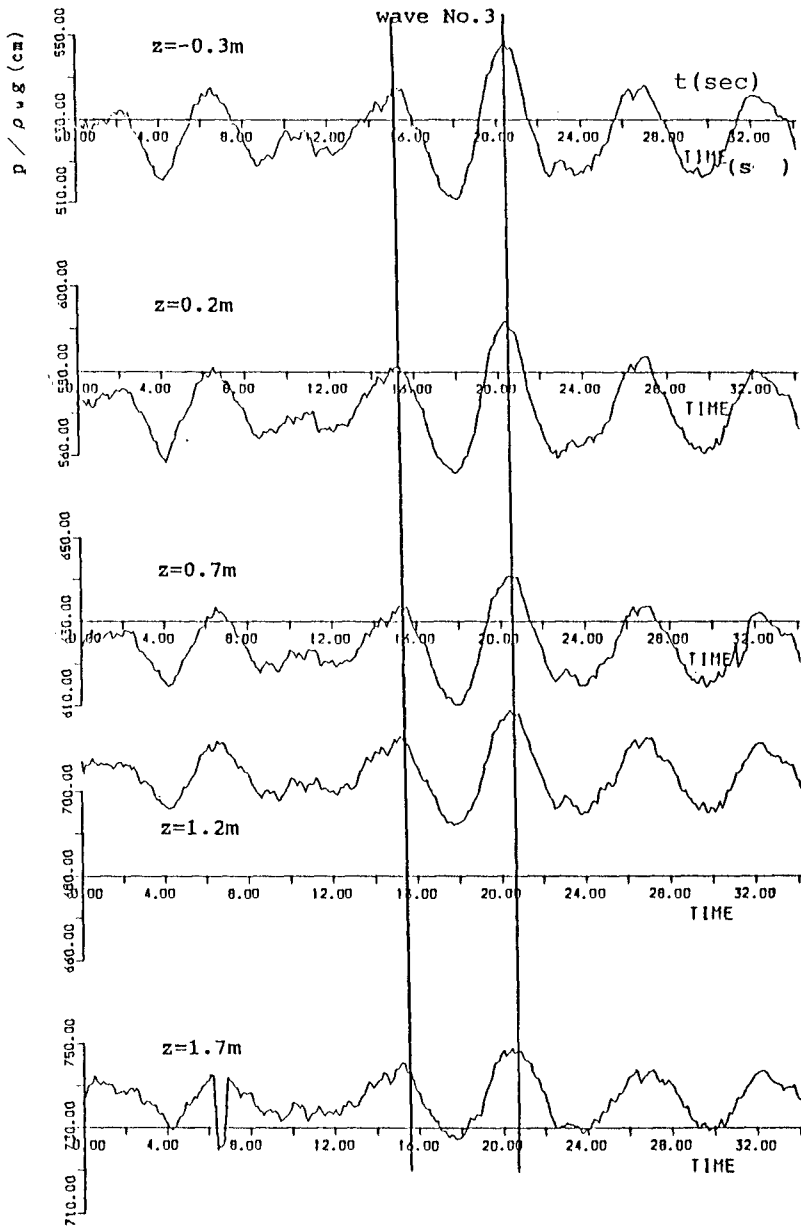
### VALUE OF EFFECTIVE BULK MODULUS OF POREWATER $\beta$

To estimate the value of effective bulk modulus of porewater  $\beta$ , the total amplitude of  $p'$ , given by Eq.(2), was calculated at the lower three levels and compared with the measured amplitude. The value of  $p_0$  in Eq.(2) was taken to be equal to the amplitude of the measured porewater pressure at gauge No.2. The phase lag,  $z/(\sqrt{2}\delta)$ , was neglected.

The values of parameters are as follows:  $n = \nu = 0.33$ ,  $G = 1.0 \times 10^8$  N/m<sup>2</sup>, and  $k = 2.8 \times 10^{-4}$  m/sec. These values are typical



**Fig.4 Example of record of measured porewater pressures (March 28th, 1990)**



**Fig.5 Example of record of measured porewater pressures (March 30th, 1990)**

**Table 1 Total amplitude of porewater pressure head  
(March 30th, 1990)**

wave No.	1	2	3	4	5
wave period(s)	6.0	5.6	5.2	6.4	5.6
pressure gauge	total amplitude (cm)				
No.1	32	25	38	26	27
No.2	33	24	36	25	26
No.3	29	21	31	23	22
No.4	27	19	27	20	20
No.5	23	17	24	18	17

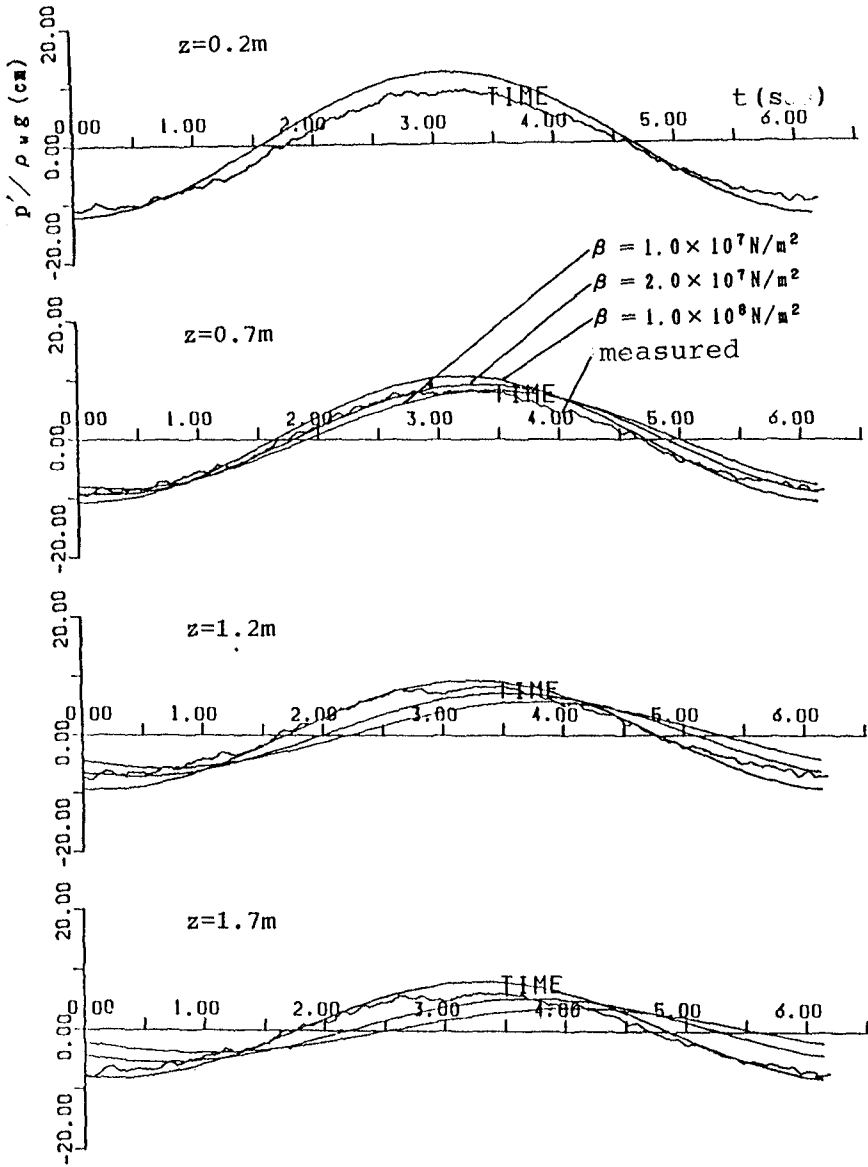
values of sandy bed. As already mentioned, the value of  $\beta$  changes very rapidly due to small content of gas in the porewater. For saturated porewater, the order of  $\beta$  is  $10^9$  N/m<sup>2</sup>. Due to 1% gas content, the order of  $\beta$  decreases to  $10^6$  N/m<sup>2</sup>. Considering this fact, three kinds of value of  $\beta$  are taken,  $\beta = 1.0 \times 10^7$  N/m<sup>2</sup>,  $2.0 \times 10^7$  N/m<sup>2</sup> and  $1.0 \times 10^8$  N/m<sup>2</sup>.  $h = 5.6\text{m} - 5.7\text{m}$ , and  $T = 5.2\text{sec} - 6.4\text{sec}$ .

From the comparison between the measured and calculated total amplitudes of pressures, it was found that the calculated result using  $\beta = 1.0 \times 10^8$  N/m<sup>2</sup> agreed best with the measured results.

As seen from Eqs. (1) and (2), the phase of the porewater pressure variation is not in phase with that of the bottom wave pressure. Then the measured time profile of the porewater pressure variation is compared with the calculated profile. The bottom wave pressure was assumed sinusoidal. **Figure 6** shows one example of the comparison. The given sinusoidal bottom wave pressure does not coincide so well with the measure porewater pressure variation of gauge No.2; However, judging from the phase shift, it is found again that the calculated results using  $\beta = 1.0 \times 10^8$  N/m<sup>2</sup> agrees best with the measured results.

#### **ANALYSIS OF DATA OF ZEN ET AL.(1989)**

Zen et al. (1989) measured the wave-induced porewater pressure in a surf zone at a coast facing the Pacific Ocean. The measurement was done at the head of an observation pier of the Port and Harbour Res. Inst. of Japanese Ministry of Transport. The



**Fig.6 Comparison of measured and calculated time profiles of porewater pressure (March 30th, 1990)**

water depth  $h$  was about 4 m (Hattori et al., 1992). The 50% sand grain size was 0.16 mm.

They showed a part of the records of three observation series. Fig.4 of Hattori et al. (1992) is that of series No.2. The waves had sharp crests as usually seen in surf zone. One wave was selected from each series, including wave No.7 in series No.2.

The time profile of the bottom wave pressure of the selected waves was decomposed into its Fourier series components. The porewater pressure variation  $p'$  was calculated for each component by using Eq.(2). The porewater pressure variation was obtained by summing up those of all components, since the boundary layer approximation solution Eq.(2) is linear. Typical values in sandy bed were used for the parameters:  $n = \nu = 0.33$ ,  $G = 1.0 \times 10^8$  N/m<sup>2</sup>, and  $k = 2.8 \times 10^{-4}$  m/sec. Three kinds of value for the bulk modulus of porewater  $\beta$  were taken,  $1.0 \times 10^7$  N/m<sup>2</sup>,  $3.0 \times 10^7$  N/m<sup>2</sup> and  $1.0 \times 10^8$  N/m<sup>2</sup>.

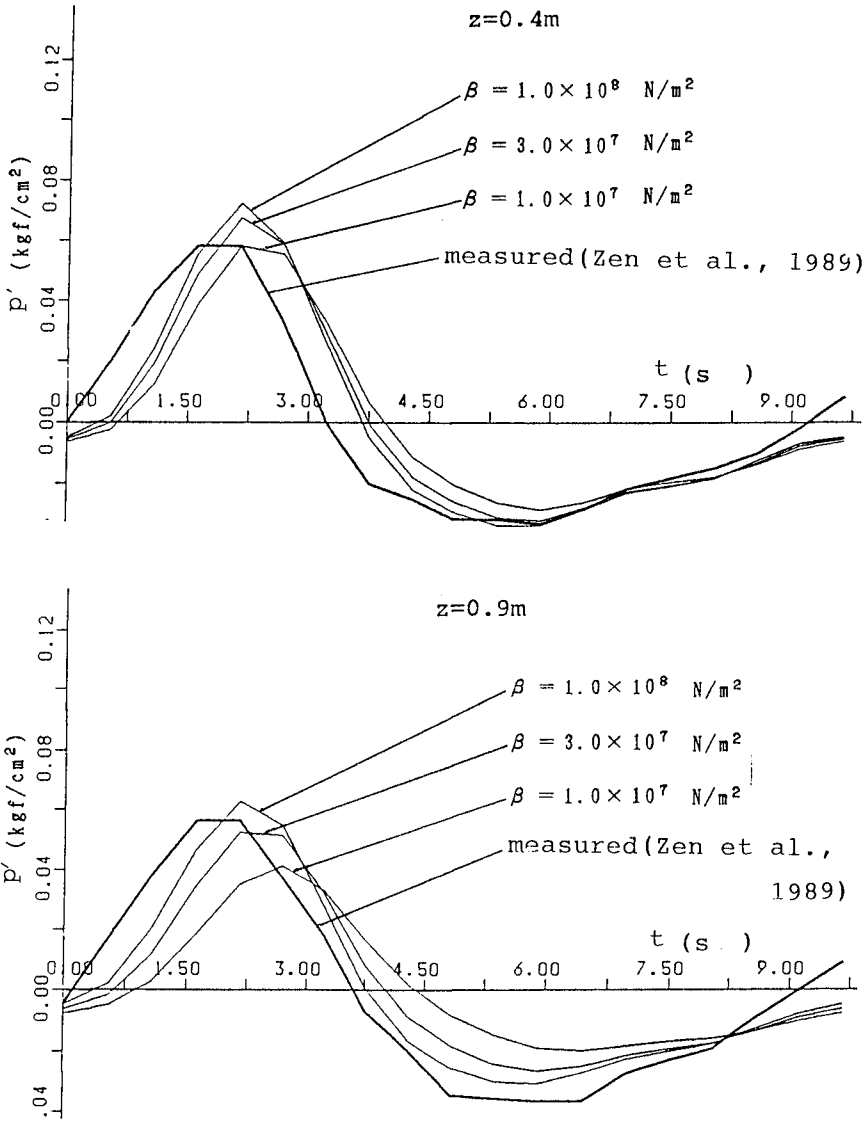
Figure 7 shows the comparison between the calculated and measured results for wave No.7 of series No.1. Since the figures of the time profile of the pressure variation shown in Zen et al.s paper (1989) were small, the time profile could not be read in a small interval. This is the reason why the curves are not smooth.

At the highest level, that is, 40cm below the bed surface, the amplitude of the measured pressure variation is roughly explained by the calculated curve of  $\beta = 1.0 \times 10^7$  N/m<sup>2</sup>. But the phase of the measured profile is not so delayed as the calculated one. At the second level, 90 cm below the bed surface, the value of measured peak is almost the same as the calculated one using  $\beta = 3.0 \times 10^7$  N/m<sup>2</sup> or  $1.0 \times 10^8$  N/m<sup>2</sup>. At the lowest level, 140cm below the bed surface, the tendency is the same as at the second level. The measured peak value is explained by the calculated value using  $\beta = 3.0 \times 10^7$  N/m<sup>2</sup> or  $1.0 \times 10^8$  N/m<sup>2</sup>.

From the similar comparisons for other two waves in series Nos.2 and 3, it is found that the value of  $\beta$  which explains best the measured results varies from  $1.0 \times 10^7$  N/m<sup>2</sup> to  $1.0 \times 10^8$  N/m<sup>2</sup>.

## DISCUSSION

As seen in Eq.(2), the relative importance of the boundary layer correction depends on  $m$  or  $G/\beta$ . In surf zone, a non-dimensional parameter related to the boundary layer thickness  $\delta$  given by Eq.(4) is  $kG/\rho_w g^2 T h$  (Fig.2 in Hattori et al.(1992)). The vertical profile of the non-dimensional porewater pressure variation is determined by



**Fig.7 Comparison between measured and calculated time profiles of porewater pressure ( $z = 40\text{cm}$  and  $90\text{cm}$ , wave No.7, series No.1, Zen et al.(1989))**



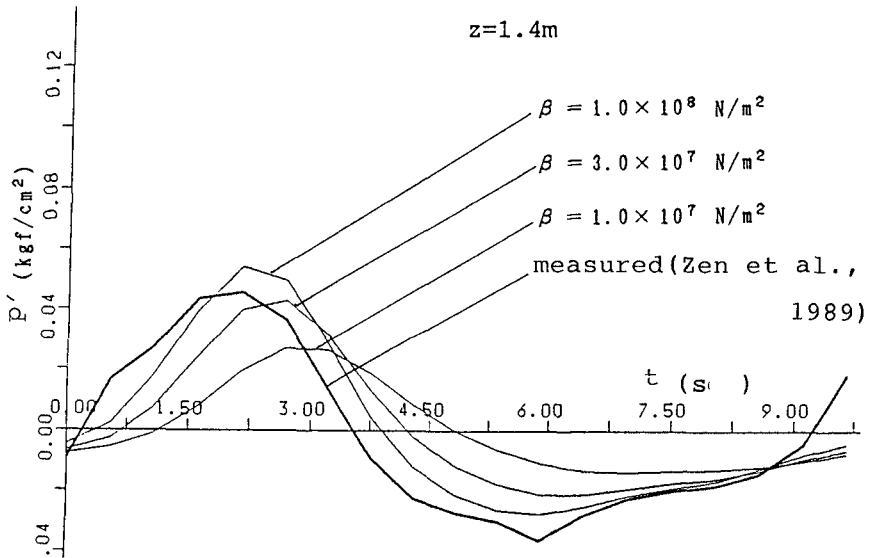
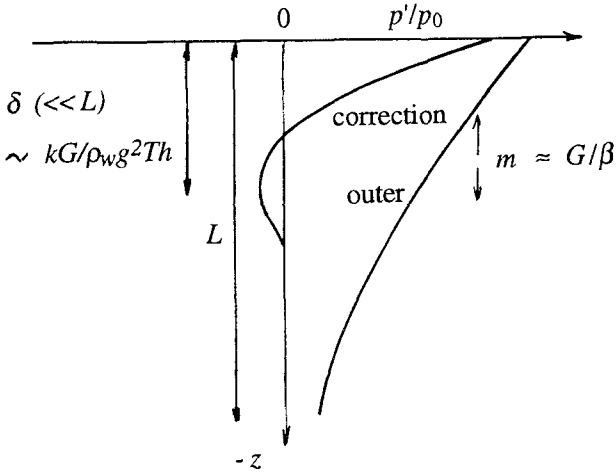


Fig.7 continued ( $z = 140\text{cm}$ )

two non-dimensional parameters  $G/\beta$  and  $kG/\rho_w g^2 T h$ .

When  $G/\beta$  becomes large, the correction becomes large (Fig.8). Then the scale of the vertical profile of porewater pressure variation is dominated by  $\delta$  which is assumed to be smaller than the wave length  $L$ . Also when  $kG/\rho_w g^2 T h$  becomes small, the boundary thickness  $\delta$  becomes small. In both cases, the downward decrease becomes fast.

If the value of  $kG/\rho_w g^2 T h$  is small, a smaller value of  $G/\beta$  explains the vertical profile of measured porewater pressure variation. If the value of  $kG/\rho_w g^2 T h$  is large, a larger value of  $G/\beta$  is necessary to explain the vertical profile. For a given value of  $G$ , if the value of  $k$  is small, a larger value of  $\beta$  explains the vertical profile. If the value of  $k$  is large, a smaller value of  $\beta$  is necessary. The estimation of value of  $\beta$  depends on the assumed value of  $k$ . The result of this investigation should be understood keeping this fact in mind.



**Fig.8 Two non-dimensional parameters  $G/\beta$  and  $kG/\rho_w g^2 T h$  dominating vertical profile of non-dimensional wave-induced transient porewater pressure in surf zone**

**CONCLUSIONS**

A measurement of the wave-induced transient porewater pressures was done near a seabed surface at a coast facing the Japan Sea. The value of the effective bulk modulus of the porewater  $\beta$  was estimated so that the solution using the boundary layer approximation by Mei and Foda(1981) agreed with the measured pressure variation.

- (1) The estimated value of  $\beta$  is  $1.0 \times 10^8$  N/m<sup>2</sup> under the condition of shear modulus of the solid skeleton  $G = 1.0 \times 10^8$  N/m<sup>2</sup> and the permeability coefficient  $k = 2.8 \times 10^{-4}$  m/sec.
- (2) A similar estimation for Zen et al.s data(1989) measured at a coast facing the Pacific Ocean results in from  $\beta = 1.0 \times 10^7$  N/m<sup>2</sup> to  $1.0 \times 10^8$  N/m<sup>2</sup>.
- (3) The estimation of the value of  $\beta$  should be understood keeping in mind that it depends on the assumed value of the permeability coefficient  $k$ .

## ACKNOWLEDGMENTS

The authors would like to thank Prof. Y. Iwagaki, Meijou Univ. (Emeritus Prof. of Kyoto Univ.) and Prof. Y. Tsuchiya, Disaster Prev. Res. Inst., Kyoto Univ. for their helpful discussions. Also the authors wish to thank Assoc. Prof. T. Shirai of Ogata Wave Observatory, Res. Assoc. H. Yoshioka and Engineer S. Fujiki of Disaster Prev. Res. Inst., Kyoto Univ. for their assistance of the observation.

## REFERENCES

- Akamura, S.(1989). "Groundwater effect on beach changes", Master thesis of Graduate School of Civil Engineering, Kyoto Univ..
- Finn, W.D., Siddharthan, R. and Martin, G.R.(1983). "Response of seafloor to ocean waves", *Jour. of Geotech. Engr., ASCE*, 109(4), 556-571.
- Hattori, A., Sakai, T. and Hatanaka, K.(1992). "Wave-induced porewater pressure and seabed stability", *Proc. of 23rd Conf. on Coastal Eng., ASCE*(in printing).
- Kawata, Y., Shirai, T, Yoshioka, H., Itoh, M. and Tsuchiya, Y.(1990). "In-situ measurement of wave-formed ripples", *Proc. of Coastal Eng., JSCE*, 329-333(in Japanese).
- Mei, C.C. and Foda, M.A.(1981). "Wave-induced responses in a fluid-filled poro-elastic solid with a free surface - a boundary layer theory", *Geophys. J. R. astr. Soc.*, 66, 597-631.
- Madsen, O.S.(1974). "Stability of a sand bed under breaking waves", *Proc. of 14th Conf. on Coastal Eng., ASCE*, 776-794.
- Sakai, T., Hatanaka, K. and Mase, H.(1992). "Wave-induced effective stress in seabed and its momentary liquefaction", *Jour. of Waterway, Port, Coastal, and Ocean Eng., ASCE*, 118(2), 202-206.
- Zen, K., Yamazaki, H. and Sato, Y.(1989). "Wave-induced liquefaction in seabed - Field observation and analysis -", *Rep. of Port and Harbour Res. Inst., Japanese Ministry of Transport*, 28(3), 30-57 (in Japanese).

## SUBJECT INDEX

Page number refers to first page of paper

- Absorbers, 281, 726  
Access roads, 2745  
Accretion, 1129, 2205, 2233, 3260, 3357  
Accuracy, 212, 460, 590, 777  
Adaptive systems, 551  
Advection, 2500  
Aeolian sands, 3319  
Aerial photographs, 2332, 2450  
Aggradation, 4  
Air entrainment, 1639  
Air water interactions, 308  
Amplification, 3343  
Amplitude, 804  
Analog models, 1869  
Analysis, 267, 1414  
Analytical techniques, 737, 1341, 2122, 3343  
Application methods, 212  
Approximation methods, 644  
Armor units, 1053, 1091, 1285, 1341, 1400, 1679  
Atmospheric boundary layers, 874  
Attenuation, 563, 2786  
Australia, 240, 1129, 3319
- Backwashing, 2358  
Barges, 3149  
Barrier design, 1851, 2694  
Bars, 51, 2001, 2219, 2370, 2745  
Bathymetry, 391, 2242  
Bayesian analysis, 62, 281  
Beach cusps, 2205  
Beach erosion, 792, 1272, 1400, 1959, 2057, 2136, 2219, 2556, 2772, 3331, 3426  
Beach nourishment, 1129, 2043, 2265, 2464, 2474, 2581, 3305, 3319  
Beaches, 240, 630, 883, 974, 1461, 1924, 1973, 2219, 2358, 3357  
Bed load movement, 2084  
Bed movements, 2321, 2370, 2917  
Bed ripples, 2164, 2383, 2424  
Berms, 1161, 1203, 1448, 1651, 1758, 2136  
Blocks, 1091  
Boston, 3285
- Boulders, 1078  
Boundary conditions, 142, 644, 1030  
Boundary element method, 253, 526, 1189, 1327, 1461, 1599, 1799  
Boundary layer, 350, 2397, 2424, 2629, 2811, 3189  
Boundary shear, 1517  
Boundary value problems, 672  
Brazil, 551  
Breaking, 960, 990, 1461, 2001  
Breaking waves, 42, 89, 103, 156, 240, 253, 419, 488, 576, 698, 918, 1078, 1101, 1357, 1545, 1772, 1785, 1910, 1973, 2043, 2095, 2279, 2321, 2344, 2642, 3012  
Breakwaters, 170, 792, 1006, 1020, 1044, 1053, 1067, 1101, 1115, 1153, 1161, 1189, 1203, 1258, 1299, 1313, 1327, 1357, 1400, 1420, 1489, 1531, 1559, 1613, 1679, 1959, 3343, 3399  
Bubbles, 1639, 1785  
Buoyancy, 1867  
Buoys, 405, 1840
- Caissons, 1475, 1625  
Calibration, 76  
California, 1285  
Canada, 3230  
Channel improvements, 2724  
Channels, waterways, 2786, 2879, 3040  
Characteristics, 253, 281, 295  
Circulation, 2122  
Classification, 1545, 1896  
Closed form solutions, 907  
Cnoidal waves, 737  
Coastal engineering, 1  
Coastal environment, 3496  
Coastal structures, 1758, 1772, 1785, 2599, 2799  
Cohesive sediment, 3107, 3121  
Columbia River, 2893  
Comparative studies, 62, 76, 1651, 2108  
Computation, 89, 1734  
Computer models, 1420, 1448  
Computer programs, 3260  
Concrete blocks, 1573

**Vol. 1 1-1202 Vol. 2 1203-2410 Vol. 3 2411-3516**

- Consolidation, 2962
- Consolidation, soils, 2949
- Construction, 2029, 2599, 2926, 3149, 3285, 3305
- Correlation analysis, 378, 737, 946, 974
- Cost effectiveness, 1503
- Currents, 184, 563, 604, 618, 672, 684, 698, 712, 1938, 2015, 2500, 2528, 2542, 2567, 2613, 2629, 2680, 2724, 2799, 2811, 2839, 2867, 2893, 2937, 3093, 3163, 3246
- Curvature, 184
- Cylinders, 2867
  
- Damage accumulation, 1420
- Damage assessment, 1020, 1679
- Damage prevention, 1006, 1091
- Dams, 2669
- Data analysis, 1067, 1666, 1812, 1840, 1867, 1987, 2057, 2136, 2265, 2397, 2567, 2599, 2745, 2962, 3371
- Data collection, 1910, 2191, 2251
- Decomposition, 51, 526, 777
- Deep water, 184, 322, 364, 630, 658, 1231, 1625
- Depth, 4, 846
- Design, 1503, 1613, 2029, 2474, 2599, 3285
- Design criteria, 1115, 1217, 1385, 1489
- Design data, 1357, 1625
- Design improvements, 1053, 1371
- Design waves, 644, 1851
- Development, 1840
- Diffraction, 129, 1044
- Diffusion, 3202
- Dikes, 526
- Dimensional analysis, 1231
- Dispersion, 42, 2735, 2758, 3189
- Displacements, 1448
- Dissipation, 1613
- Distribution patterns, 103, 308
- Dolos, 1231, 1285, 1385
- Drainage systems, 1129
- Dredging, 2629, 2724
- Dunes, 2669
- Dynamic analysis, 1357, 1475
- Dynamic response, 1475
  
- Earthquake loads, 3343
- Ecosystems, 2710
- Efficiency, 726, 1371, 1613, 1959
- Eigenvectors, 62
  
- Elevation, 240
- Empirical equations, 1559
- Energy conservation, 1245
- Energy dissipation, 103, 308, 336, 502, 540, 563, 1101, 2786
- Energy losses, 1313, 1517, 3040
- Energy transfer, 336, 460, 526
- Entrainment, 308, 336, 2500
- Equations of motion, 76, 391, 474
- Equilibrium profile, 1973, 2556
- Equipment, 295
- Erosion, 4, 1812, 2205, 2265, 2464, 2669, 2937, 2976, 3260, 3273
- Erosion control, 1748, 2581, 3081, 3246, 3331, 3385, 3413
- Estimates, 62, 512
- Estuaries, 2542, 2745, 2879, 2962, 3054, 3121, 3371
- Evaluation, 432, 2043
- Evolution, development, 42
- Examination, 267, 1896, 2370, 3357, 3399
- Experimental data, 308, 378, 405, 447, 540, 604, 974, 1044, 1161, 1258, 1503, 1559, 1613, 1959, 2015, 2279, 2642, 2772, 2917, 3163
- Experimentation, 488, 576, 2358
  
- Failure modes, 1006
- Failures, investigations, 1053, 3343
- Fatigue, 1354
- Feasibility studies, 2581
- Fiber optics, 1327
- Field investigations, 2486, 2694, 2879, 2949
- Field tests, 240, 488, 590, 804, 832, 846, 894, 907, 946, 990, 1175, 1420, 1587, 1625, 1734, 1867, 1879, 1924, 1987, 2043, 2164, 2176, 2205, 2293, 2307, 2397, 2528, 2542, 3026, 3230
- Finite difference method, 860
- Finite element method, 1599, 1706, 2902, 3068
- Flexibility, 1613, 1748
- Flocculants, 3178
- Flood control, 1851
- Flooding, 3496
- Floods, 2917
- Florida, 2057
- Flow, 76, 2150, 2655
- Flow characteristics, 698, 3482

- Flow distribution, 1720  
 Flow patterns, 1938  
 Flow resistance, 1101, 1153  
 Flow simulation, 170, 1030  
 Fluid dynamics, 1938  
 Flumes, 142, 419, 447, 502, 818, 1067, 1142, 2108  
 Force, 1078  
 Forecasting, 116, 1826, 1865, 2057, 2176, 2242, 2293, 2513, 2825, 2902  
 France, 1414  
 Free surfaces, 89  
 Frequency, 364, 391, 832, 918, 1639  
 Frequency analysis, 156, 322, 447, 474, 846  
 Frequency distribution, 894  
 Friction, 350, 960, 1217, 2786  
 Full-scale tests, 1573, 1748, 2084  
  
 Gabions, 1748  
 Gaging stations, 295  
 Gas pipelines, 2029  
 Germany, 1573  
 Grain size, 2071, 2251, 2293  
 Gravity waves, 184  
 Great Britain, 1987  
 Great Lakes, 2976  
 Groins, structures, 2332, 3357  
 Growth projections, 2655  
 Gulf of Mexico, 2629  
 Gulfs, 712  
  
 Harbor engineering, 295  
 Harbors, 804, 832, 1044, 3081, 3216, 3230  
 Headwalls, 3426  
 Hurricanes, 644  
 Hydraulic models, 281, 1217, 1272, 1341, 1475, 1531, 1879  
 Hydraulic pressure, 1217  
 Hydraulic structures, 1693  
 Hydrodynamics, 1869, 2233, 3068, 3454  
  
 Impact forces, 1545, 1785  
 Impact loads, 1475  
 Impact tests, 1067  
 Instrumentation, 405, 1666, 2191  
 Intake structures, 3107  
 Integral equations, 142  
 Interactions, 184, 460, 604, 672, 712, 1924, 2710  
 Islands, 2450  
  
 Israel, 322, 3399  
 Italy, 1826, 1840, 1851, 1865, 1867, 1869, 3305, 3413  
  
 Japan, 2486, 3331, 3426  
 Jetties, 3040  
  
 Kinematics, 618, 644, 1327  
  
 Laboratories, 212, 281, 336, 488  
 Laboratory tests, 630, 658, 792, 883, 960, 1101, 1175, 1313, 1400, 1489, 1734, 1947, 2001, 2176, 2191, 2411, 2438, 2500, 2528, 2976, 3468  
 Lagoons, 4, 1812, 1826, 1851, 1865, 1867, 1869, 1879  
 Landfall, 2029  
 Lasers, 308  
 Least squares method, 777  
 Limiting factors, 551  
 Linear analysis, 184  
 Linear functions, 460  
 Liquefaction, 2937  
 Littoral currents, 2642, 2655, 2758, 2999, 3012  
 Long waves, 447, 792, 804, 832, 860, 883, 960, 974, 2438, 2999  
  
 Maintenance, 1006, 1693, 2745, 2926  
 Mass transport, 3093  
 Mathematical models, 502, 960, 1078, 1639, 1865, 1869, 1879, 2613, 2724, 2839  
 Measurement, 618, 792, 818, 974, 1587, 1651, 1758, 2084, 2279, 2321, 2358, 2383, 2542, 2825, 3026, 3178  
 Measuring instruments, 212, 295  
 Mechanical engineering, 1693  
 Meteorology, 116, 3496  
 Mining, 3331  
 Mixing, 1867, 2642, 2758, 2853, 2999, 3202  
 Model tests, 1020, 1115, 1231, 1245, 1434, 1489, 1545, 2669, 3454  
 Model verification, 2567  
 Modeling, 1947, 2893, 3121, 3202  
 Models, 42, 51, 116, 364, 474, 576, 698, 712, 860, 1203, 1812, 1973, 2108, 2122, 2150, 3012, 3054, 3081  
 Monitoring, 1006, 1285, 1420, 1666, 2332, 3305, 3319, 3385  
 Mooring, 3216

- Morphology, 1812  
 Mud, 2735, 2879, 2937, 2962, 3093  
  
 Nearshore circulation, 226, 364, 860, 2758, 2811, 2825  
 Netherlands, 2474, 2581, 2599  
 Network analysis, 1840  
 New York, State of, 3357  
 Nile River, 3246, 3260, 3273  
 Nonlinear analysis, 350  
 Nonlinear differential equations, 460  
 Nonlinear response, 156  
 North Carolina, 2219  
 North Sea, 874, 2029, 2307  
 Numerical analysis, 142, 322, 712, 1531, 2450  
 Numerical calculations, 540, 737, 946, 1161, 2424  
 Numerical models, 51, 62, 76, 89, 129, 170, 199, 350, 391, 419, 432, 526, 590, 672, 818, 874, 1189, 1299, 1599, 1651, 1772, 1799, 1840, 1938, 2057, 2150, 2344, 2411, 2438, 2513, 2556, 2825, 2879, 2949, 3093, 3107, 3305  
  
 Ocean disposal, 2735  
 Ocean waves, 2893, 3496  
 Offshore structures, 512, 551  
 Oil storage, 2724  
 One dimensional flow, 777  
 Optimization, 1503, 1693  
 Oregon, 2191, 2242, 2332  
 Oscillations, 502, 1639, 1826, 1865, 2655, 2990  
 Oscillatory flow, 604, 1896, 2122, 2424  
 Outfall sewers, 3285  
 Outwash, 2694  
 Overflow, 2669  
 Overtopping, 1758, 2694  
  
 Parameters, 765, 946  
 Particle full velocity, 212, 336, 1651  
 Pendulums, 1475  
 Permeability, 1299, 1517, 1531, 2962  
 Permeability tests, 1587, 1720  
 Perturbation, 684  
 Physical properties, 378, 1587  
 Pipelines, 2839, 2990, 3135  
 Planning, 1693  
 Pollution, 4  
 Pollution control, 3285  
  
 Pore pressure, 1706, 3135  
 Pore pressure measurement, 2962  
 Pore water, 2095  
 Pore water pressure, 2397  
 Porous materials, 170, 726, 1101, 1189, 1434, 1706  
 Porous media flow, 1772  
 Ports, 2926  
 Portugal, 2745  
 Potential flow, 89  
 Power plant location, 3413  
 Predictions, 474, 644, 932, 1189, 1420, 1938, 2219, 2464, 2556, 2724  
 Pressure distribution, 1545, 1599, 1706  
 Pressure measurement, 1573, 1785  
 Pressures, 1078, 1161, 1175, 2095  
 Probabilistic methods, 512  
 Probabilistic models, 540  
 Probability distribution, 103, 378, 932  
 Probability distribution functions, 2001  
 Profile measurement, 1559, 2513, 2694, 3260  
 Profiles, 2108, 2242, 2358, 2474, 3273  
 Progressive waves, 281, 684, 726  
 Prototype tests, 1067  
  
 Quality assurance, 1354  
 Quantitative analysis, 918, 1115, 2464, 2990  
  
 Random waves, 51, 447, 474, 526, 540, 630, 658, 751, 765, 883, 932, 1559, 1910, 1959, 2307, 2411, 2825  
 Rayleigh waves, 894  
 Reflection, 765, 777, 1142, 1625  
 Refraction, 129, 846, 1020, 1044  
 Regression analysis, 253  
 Rehabilitation, 1341  
 Reliability analysis, 1385  
 Research, 1987, 2937  
 Research and development, 1414  
 Resistance, 1091, 1371  
 Resonance, 751, 860  
 Revetments, 1030, 1175, 1299, 1573, 1587  
 Reviews, 2839, 2949  
 Reynolds number, 1720, 2015, 2122  
 Reynolds stress, 2424, 2853  
 Rheology, 3093  
 Risk analysis, 1341  
 Rivers, 240, 2486, 2772  
 Rock strength, 1448

- Roughness, 1758  
 Rubble-mound breakwaters, 1203, 1217,  
     1354, 1371, 1434, 1489, 1503,  
     1531, 1599, 1666, 1706, 1720,  
     1799, 3149  
 Safety analysis, 3216  
 Sand, 2599, 3331, 3426  
 Scattering, 1142, 1258, 3149  
 Scouring, 2799, 2839, 2867, 3482  
 Sea floor, 846, 2095, 2307, 2397, 2990,  
     3135, 3482  
 Sea state, 267, 512, 907  
 Sea walls, 1272, 1734, 1879, 1924  
 Seasonal variations, 2242, 2251, 2265,  
     2450  
 Sediment, 1812, 2205, 2251  
 Sediment concentration, 1910, 1947,  
     2321, 2613, 2680, 2853, 3026, 3202  
 Sediment discharge, 3054, 3202  
 Sediment transport, 832, 1272, 1865,  
     1896, 1910, 1947, 1973, 1987,  
     2015, 2071, 2084, 2108, 2150,  
     2164, 2176, 2191, 2307, 2344,  
     2370, 2411, 2450, 2486, 2500,  
     2513, 2528, 2542, 2567, 2613,  
     2629, 2669, 2680, 2867, 2879,  
     2902, 2917, 3121, 3189, 3273, 3385  
 Sedimentation, 2724, 2949, 3081  
 Sedimentology, 3399  
 Settling velocity, 2853, 3107, 3202  
 Shallow water, 267, 322, 364, 460, 818,  
     1613, 3068  
 Shear, 618, 684, 2642, 2655, 2999, 3189  
 Shear strain, 3163  
 Shear stress, 604, 672, 2164, 2176,  
     2917, 3012, 3093, 3107  
 Shearing, 184  
 Ship motion, 3216  
 Ships, 3216  
 Shoaling, 51, 199, 432, 460  
 Shore protection, 1272, 1414, 1879,  
     2710, 3413  
 Shoreline changes, 2233, 2265, 2332,  
     2772, 2976, 3246, 3273, 3305,  
     3399, 3413  
 Silts, 2879, 2926  
 Simulation, 62, 199, 576, 1101, 1142,  
     1772, 2307, 2902  
 Simulation models, 42, 405, 1531  
 Site selection, 2926  
 Skewness, 974  
 Slopes, 488, 1461  
 Solitary wave, 1161, 1327, 1461  
 South Africa, 3026  
 Spain, 2043, 2233, 2251, 2265, 3385  
 Spectral analysis, 364, 765, 777, 792,  
     1973  
 Spectral density function, 42  
 Speed changes, 199  
 Spits, coastal, 2233, 2694  
 Splitting, 658  
 Stability, 751, 1020, 1030, 1053, 1067,  
     1153, 1217, 1231, 1400, 1559,  
     1625, 1666, 1799, 2095, 2581, 3135  
 Stability analysis, 129, 658, 1573, 1679,  
     2071  
 Stability criteria, 1203, 2799  
 Stabilization, 1129, 2556, 3319, 3426  
 Static stress measurement, 1285  
 Stationary processes, 932  
 Statistical analysis, 512, 1231, 1545,  
     1924, 2474, 3149  
 Stones, 1354  
 Storm surges, 1851  
 Storms, 116, 990, 1748, 2136, 2370,  
     2450  
 Stratification, 2853  
 Stream function, 684  
 Stress, 1053  
 Stress analysis, 874  
 Stress measurement, 1385  
 Structural design, 1285, 1385, 1414  
 Structural failures, 1203  
 Structural materials, 170  
 Structural response, 1371  
 Structural stability, 1115  
 Structures, 765  
 Submerged jets, 1161  
 Submerging, 253, 1142  
 Subsidence, 4  
 Superstructures, 1217, 1489  
 Surf beat, 804, 846, 960  
 Surf zone, 76, 103, 156, 226, 308, 336,  
     576, 590, 698, 818, 832, 883, 918,  
     990, 1987, 2095, 2279, 2293, 2321,  
     2344, 2370, 2438, 2542, 2642,  
     2680, 2811, 2999, 3012, 3026  
 Surface properties, 563  
 Surface roughness, 1720  
 Surface waves, 405, 658, 3135, 3163  
 Surge, 874  
 Surveys, 2043, 2450, 2567, 3026  
 Survays, data collection, 1129, 2029,



- 2136, 2219, 3260
- Suspended load, 1091, 2411
- Suspended sediments, 2150, 2279, 2293, 2438, 2680, 3189
- Testing, 1354
- Tests, 226, 364, 447, 1910, 2383
- Theories, 737, 1258, 1313, 1693, 2071, 2735, 2772, 2867, 3468
- Three-dimensional analysis, 3482
- Three-dimensional flow, 3454
- Three-dimensional models, 1679
- Tidal currents, 3054
- Tidal hydraulics, 1826
- Tides, 4, 3178, 3371
- Tides, astronomical, 1826
- Time dependence, 391, 419, 2464, 2513
- Topography, 129, 860
- Tracers, 2084
- Transformations, 51, 156, 474, 540, 630
- Transient flow, 142
- Transition points, 698
- Transport phenomena, 3068
- Transport rate, 2528
- Trenches, 2902
- Trends, 3371
- Turbidity, 1938, 2735, 3121, 3178
- Turbulence, 2279, 2383, 2424, 2629, 2758, 2853
- Turbulent flow, 1517
- Turkey, 3081
- Undertow, 883, 2164
- United Kingdom, 2694, 3178, 3371
- Uplift pressure, 3135
- Uplift resistance, 1573
- U.S.S.R., 1357
- Validation, 1448, 3468
- Vector analysis, 2344
- Vegetation, 2710
- Velocity, 350, 604, 618, 672, 1078, 1799, 1947, 2084, 2321, 2383, 2486, 2990, 3054
- Velocity distribution, 883, 1153, 2811, 3482
- Venezuela, 2724
- Verification inspection, 2867
- Vertical cylinders, 3482
- Videotape, 918
- Vortex shedding, 3163
- Vortices, 502
- Water circulation, 3068
- Water depth, 726, 832
- Water flow, 502, 1865, 1869
- Water level fluctuations, 1666
- Water pressure, 1666
- Water surface, 576
- Water table, 1129, 2136
- Water tanks, 2191
- Wave action, 1030, 1203, 1420, 1599, 1706, 1799, 1896
- Wave attenuation, 1517
- Wave climatology, 267
- Wave crest, 199, 488
- Wave damping, 3040
- Wave diffraction, 419, 432
- Wave dispersion, 1434
- Wave energy, 336, 502, 1189, 1434, 2528
- Wave forces, 1313, 1357, 1400, 1489, 1639, 3454
- Wave generation, 818, 990, 2893, 3468
- Wave groups, 894, 907, 932, 946, 990, 1503, 2411
- Wave height, 103, 253, 378, 512, 576, 630, 751, 804, 894, 946, 1245, 1734, 2001, 2486, 3230, 3385
- Wave measurement, 226, 322, 551, 2205, 3230
- Wave propagation, 89, 129, 142, 226, 391, 447, 460, 563, 658, 792, 1020, 1044, 1142, 1153, 1461, 2500, 2786, 2893, 3040
- Wave reflection, 630, 1299, 1327
- Wave refraction, 419, 432
- Wave runup, 156, 1245, 1299, 1461, 1734, 1758, 1772
- Wave spectra, 378, 405, 590, 751, 765, 2001
- Wave tanks, 226, 526
- Wave velocity, 2358
- Waves, 1175, 1258, 2015, 2071, 2542, 2567, 2613, 2629, 2710, 2799, 2811, 2839, 2937, 2976, 3093, 3246, 3454, 3468, 3496
- Weather forecasting, 116
- Wind, 907
- Wind forces, 3496
- Wind speed, 1245
- Wind waves, 712
- Working conditions, 3230

## AUTHOR INDEX

Page number refers to first page of paper

- Abecasis, F., 1006  
Adami, Attilio, 1869  
Ahrens, J. P., 1354  
Alexis, Alain, 2949  
Allsop, N. W. H., 1599  
Andersen, O. H., 1020  
Arami, Atsusi, 1785  
Asano, Toshiyuki, 1896, 2710
- Baird, W. F., 1354  
Bakker, W. T., 2599  
Bale, A. J., 3178  
Barbaro, Giuseppe, 907  
Barkaszi, Stephen F., Jr., 1910  
Basco, David R., 103, 1924  
Bassoullet, Philippe, 2949  
Battjes, J. A., 42, 51  
Baumer, Joe, 103  
Bedford, Keith, 2629  
Beji, S., 42, 51  
Bellessort, B., 1414  
Bellomo, Douglas A., 1924  
Benoit, Michel, 62  
Berlamont, Jean, 2962  
Bertotti, Luciana, 116  
Bezuijzen, Adam, 1030, 1587  
Bishop, Craig, 2976  
Blondeaux, Paolo, 2071  
Boccotti, Paolo, 907  
Boer, Sander, 3305  
Booij, N., 1044  
Bowers, E. C., 832  
Bradbury, A. P., 2694  
Breteler, Mark Klein, 1030  
Brocchini, M., 76  
Broekens, R. D., 1772  
Broeze, Jan, 89  
Brooks, P., 3285  
Brørs, Bård, 1938  
Bruce, T., 212, 2990  
Burcharth, H. F., 1354, 1720  
Burcharth, Hans F., 1489  
Burcharth, Hans F., 1053  
Bürger, W. W., 1067
- Cai, Maolong, 103  
Caielli, Alfredo, 1869  
Capobianco, Michele, 2464
- Carrion, Vicente, 3385  
Carson, Fulton C., 3357  
Carvalho, J. L. B., 551  
Castañeda, Ana, 3385  
Cavaleri, L., 1840  
Cavaleri, Luigi, 116  
Ceconi, Giovanni, 1869  
Chae, Jang Won, 129  
Chang, C., 1327  
Chen, Zhiwen, 1947  
Cheung, Kwok Fai, 142  
Chiaia, G., 1959  
Chian, Chimin, 3189  
Chow, K. Ander, 3230  
Chung, Yeong Chyang, 308  
Church, J. C., 2999, 3012  
Chyan, Jih Ming, 308  
Collado, F., 2811  
Converse, H. D., 1354  
Cooker, M. J., 1078, 1639  
Coppoolse, R. C., 3026  
Costa, Fernando Vasco, 1091  
Cox, D. T., 2397  
Cox, Daniel T., 156  
Cramp, A., 974, 1987  
Creed, Christopher G., 1973  
Cruz, Eric C., 1101  
Cuenca, G., 2043
- Dally, William R., 1910  
D'Alpaos, L., 3068  
Dalrymple, R. A., 3468  
Dalrymple, Robert A., 1142, 1973, 3040  
Damiani, L., 1959  
d'Angremond, Kees, 1748  
Davidson, D. D., 1354  
Davidson, M., 974  
Davidson, M. A., 1987  
Davies, B. L., 1115  
Davis, Greg A., 1129  
De Boni, M., 1840  
De Girolamo, Paolo, 1851  
de Groot, M. B., 2599  
de Jager, Jan H., 1748  
de Lange, P. H. M., 1044  
De Rouck, J., 1666  
de Ruig, Joost H. M., 2581  
de Vriend, Huib J., 2150

- De Vriend, Huib J., 2464  
de Waal, J. P., 1758  
de Wit, P. J., 2937  
Dean, R. G., 3260  
Dean, Robert G., 2001  
Debus, Wolf, 1573  
Deguchi, Hiroshi, 2710  
Deguchi, Ichiro, 1517, 2642  
Deigaard, R., 576, 2344  
den Adel, H., 1720  
Dennis, W. A., 2332  
Di Silvio, G., 1865, 1867  
Dibajnia, Mohammad, 2015  
Dodd, Nicholas, 2655  
Drago, M., 76  
Drapeau, G., 3054  
Driscoll, Andrew M., 1142  
Dumais, J. F., 3054  
Dyer, K. R., 3178
- Easson, W. J., 618, 2990  
Edge, B., 1354  
Eide, A., 2029  
Eidsvik, Karl J., 1938  
Eisenberg, Y., 3285  
Elgar, Steve, 846  
Elwany, M. Hany S., 3273  
Elzinga, Th., 3216  
Endoh, Hiroshi, 1625
- Fanos, A. M., 3246, 3260  
Fernández, A. J., 2043  
Ferrante, Andrea, 3305  
Fischer, M., 170  
Fisher, J. S., 2332  
Foote, Y., 974  
Foster, Emmett R., 2057  
Foti, Enrico, 2071  
Fournier, Charles P., 3230  
Franco, Leopoldo, 1879, 3305  
Fredsoe, J., 2344, 2839  
Fujima, Koji, 2450  
Funke, E. R., 3454
- Gallagher, E. L., 2084  
Galland, J. C., 2853  
García, Reinaldo, 2724  
Garzon, A., 3068  
Gerber, Marius, 184  
Goda, Yoshimi, 199  
Gökçe, K. Tunç, 3081  
Golik, A., 322
- Golik, Abraham, 3273  
Gomez-Pina, G., 1679  
Gordon, Angus D., 3319  
Graber, H. C., 405  
Grass, Tony J., 604  
Graw, Kai-Uwe, 1153  
Greated, C. A., 212  
Greated, Clive A., 502, 2358  
Grilli, S. T., 1461  
Grilli, Stéphan T., 1142, 1161  
Grüne, Joachim, 1175  
Gu, George Z., 1189  
Güler, İşikhan, 3081  
Günbak, A. Rıza, 3081  
Guza, R. T., 846
- Habara, Shin, 3426  
Hall, Kevin R., 1203, 1217  
Hamanaka, Ken-ichiro, 2424  
Hamilton, David G., 1217  
Hamm, Luc, 226, 2108  
Hansen, C. P., 551  
Hansen, E. A., 2344  
Hanslow, David J., 240, 1129  
Hara, Masanori, 253  
Hardisty, J., 974, 1987  
Harris, J. M., 2307  
Hashida, M., 3331  
Hatada, Yoshio, 267  
Hatanaka, K., 2095  
Hattori, A., 2095  
Hattori, Masataro, 1785  
Hayashi, Kenjiro, 2450  
Hedegaard, Ida Brøker, 2108  
Herbers, T. H. C., 846  
Hibbert, Kevin, 1129  
Hirakuchi, H., 281  
Holman, R. A., 918  
Holmes, P., 1448  
Holthuijsen, L. H., 1044, 2893  
Holtzhausen, A. H., 1231  
Horikawa, Kiyoshi, 1734, 2122  
Howell, Gary L., 295  
Hughes, S. A., 1354  
Huntley, D., 974  
Huntley, D. A., 1987, 3178  
Hurdle, David, 1851  
Huynh, Trien N., 3093  
Hwung, Hwung Hweng, 308
- Ikeno, M., 281  
Imai, Sumio, 894

- Imberger, J., 1867  
Inman, D. L., 322  
Inman, Douglas L., 3273  
Iosilevskii, Ya. A., 322  
Iovenitti, L., 76  
Iribarren, J. R., 3216  
Irie, Isao, 2879  
Isaacson, Michael, 142  
Isobe, Masahiko, 419, 590, 765, 1101, 3093  
Ito, Kazunori, 751  
Iwata, K., 1400  
Iwata, Koichiro, 336  
  
Jaffe, Bruce, 2680  
Jensen, O. J., 3216  
Jeong, Shin Taek, 129  
Jorissen, R. E., 1693  
Juang, Jea-Tzyy, 1245  
Juhl, J., 170, 1020  
Jui, J., 1272  
  
Kaczmarek, Leszek M., 350  
Kaihatu, James M., 364, 1973  
Kajima, R., 281, 1531  
Kaku, Shuji, 1559  
Kakuno, Shohachi, 1258  
Kamphuis, J. W., 1272  
Kanayama, Susumu, 3107  
Kang, Yoon-Koo, 1503  
Karlikow, Nancy, 3121  
Kashiwagi, Mikio, 2438  
Katayama, Hiroyuki, 883  
Kato, Kazumasa, 990, 2136, 2879  
Kato, Ken, 2735  
Katopodi, Irene, 2150  
Katsui, Hidehiro, 2867  
Kawasaki, Masahiko, 3426  
Kawata, Yoshiaki, 2164, 3426  
Kendall, Thomas R., 1285  
Khafagy, A. A., 3246, 3260  
Khafagy, Ahmed A., 3273  
Kim, H., 2307  
Kim, Jong-Wook, 1503  
Kimura, A., 378  
Kimura, Akira, 3149  
Kirby, James T., 364, 391, 474  
Kitou, Nikos, 2150  
Kiyokawa, Tetsushi, 1613  
Kjeldsen, S. P., 405  
Klammer, P., 1475  
Klatter, H. E., 1693  
  
Klopman, G., 1772  
Kobayashi, Nobuhisa, 156, 1299, 1559, 2710  
Kobayashi, Tomonao, 3482  
Kochergin, Alexander D., 2176  
Kohlhase, S., 1475  
Komar, P. D., 3246  
Komatsu, T., 3331  
Kondo, Kosuke, 804, 894  
Kostense, J. K., 960  
Kos'yan, Ruben D., 2176  
Kotake, Yasuo, 419  
Kranenburg, C., 2937  
Kraus, Nicholas C., 630, 2191, 2219, 3357  
Kriebel, D. L., 1115  
Kriebel, David L., 1313, 1973  
Kroon, Aart, 2613  
Kubo, Yasuhiro, 419, 804  
Kuiper, H., 1693  
Kurata, K., 1400  
Kuroki, Keiji, 2205  
  
Lahousse, B., 2029  
Larson, Magnus, 2219  
Latteux, B., 2500  
Laurence, D., 2853  
Lavallée, D., 3054  
Le Hir, Pierre, 2949, 3121  
Lechuga, Antonio, 2233  
Lee, Changhoon, 391  
Lee, J. J., 1327  
Lee, Jongkook, 2629  
Lee, Jung L., 432  
Liang, Guoxiong, 2242  
Liberatore, Gianfranco, 447  
Ligteringen, H., 1341  
Lima, J. M., 551  
Lin, Li-Hwa, 2513  
Lippmann, T. C., 918  
List, Jeffrey H., 860  
Liu, C. C., 726  
Liu, Philip L.-F., 1258  
Liu, Zhou, 1053  
Losada, I. J., 2251, 2786  
Losada, M. A., 1679, 2251, 2786  
Losada, Miguel A., 1161, 2265  
  
Madsen, P., 576  
Madsen, Per A., 460  
Magda, Waldemar, 3135  
Magoon, O. T., 1354

- Malherbe, B., 2029  
 Mannino, Lucio, 907  
 Mansard, E. P. D., 1679, 3454, 3468  
 Mansard, Etienne, 142  
 Mansour-Tehrani, Mehrdad, 604  
 Marchi, Enrico, 4, 1869  
 Marinski, J. G., 1357  
 Martin, Francisco, 1161  
 Mase, H., 2397  
 Mase, Hajime, 474, 540  
 Mastenbroek, C., 874  
 Matsumi, Yoshiharu, 3149  
 Matsunaga, N., 3331  
 Matsunaga, Nobuhiro, 3163  
 McCabe, J. C., 3178  
 Medina, Josep R., 1371  
 Medina, R., 1679, 2251  
 Medina, Raúl, 2265  
 Medina Villaverde, José María, 2233  
 Mei, Chiang C., 3189  
 Melby, Jeffrey A., 1285, 1385  
 Memos, Constantine D., 3343  
 Mercanti, M., 2029  
 Miao, Gang, 2513  
 Miles, M. D., 3468  
 Miller, H. C., 2332  
 Mizuguchi, M., 488  
 Mizutani, N., 1400  
 Mizutani, Suguru, 2122  
 Mocke, G. P., 2279, 3026  
 Mol, A., 1812  
 Monadier, P., 1414  
 Mori, Nobuhito, 751  
 Morrison, Iain G., 502  
 Mulcahy, Michael W., 3230  
 Muraca, Alessandro, 1420  
 Murakami, Kazuo, 2879  
 Muttray, M., 1434  
  
 Nadaoka, K., 51  
 Nadaoka, Kazuo, 526, 2867  
 Naffaa, M. G., 3260  
 Nairn, Rob, 2976  
 Nakamura, Kazuo, 2293  
 Nakamura, Satoshi, 990  
 Nersesian, Gilbert K., 3357  
 Nicholls, Robert J., 2464  
 Nicholson, John, 2108  
 Nielsen, Peter, 240, 1129, 3202  
 Nishi, Ryuichiro, 2293  
 Nnadi, Fidelia N., 2917  
 Noli, Alberto, 1851  
  
 Norton, P. A., 1448  
  
 Ochi, Michel K., 512  
 O'Connor, B. A., 2307  
 Oda, Kazuki, 1258  
 Oebius, H. U., 2307  
 Ohta, T., 378  
 Ohyama, T., 51  
 Ohyama, Takumi, 526, 1613  
 Okayasu, Akio, 883, 2438  
 Oliveira, I. B. Mota, 2745  
 Oltman-Shay, J., 2999  
 Omata, Atsushi, 1613  
 Ono, Masanobu, 2642  
 O'Reilly, W. C., 846  
 Organizing Committee of the 23rd  
 International Conference on Coastal  
 Engineering, 3496  
 Osborne, Philip D., 2321  
 Ostrowski, Rafal, 350  
 Otta, Ashwini, 1461  
 Oumeraci, H., 1357, 1434, 1475, 1545,  
 1706  
 Overton, M. F., 2332  
  
 Pae, Wi-Gwang, 540  
 Parchure, Trimbak M., 2001  
 Parente, C. E., 551  
 Parle, Patrick, 3371  
 Partenscky, H. W., 1067, 1434, 1475  
 Partenscky, H.-W., 1545  
 Passacantando, Giancarlo, 1851  
 Pechon, Philippe, 2108  
 Pedersen, C., 2344  
 Pedersen, Jan, 1489  
 Peña, Carlos, 3385  
 Peregrine, D. H., 1078, 1639  
 Peregrine, D. Howell, 818  
 Petit, H. A. H., 960, 1772  
 Petrillo, A., 1959  
 Petti, Marco, 447, 792  
 Pina, G. Gómez, 2043  
 Pita, C., 1006  
 Pollock, Cheryl, 1924  
 Powell, K. A., 2694  
 Powell, Keith A., 2358  
 Protonotarios, John N., 3343  
 Pruszek, Zbigniew, 2370  
 Putrevu, Uday, 2758, 2825  
  
 Quinn, Paul A., 2358

- Rakha, K. A., 1272  
 Ramírez, J. L., 2043  
 Ramos, F. Silveira, 1341  
 Ranasoma, K. I. Mahesha, 2383  
 Rasmussen, Chris, 391  
 Rasmussen, E. B., 170  
 Rauw, C. I., 1354  
 Refaat, Hossam El-din A. A., 2772  
 Rigter, Ben, 1587  
 Rodriguez, A., 2811  
 Roelse, Piet, 2581  
 Roelvink, J. A., 960, 2108  
 Roldán, A. J., 2786  
 Roldan, Antonio J., 2265  
 Ropert, F., 1414  
 Rosen, D. S., 322  
 Rosen, Dov S., 3399  
 Rossi, Vito, 1420  
 Ruffin, T. M., Jr., 1400  
 Ruol, Piero, 792  
 Rusconi, A., 1840  
 Russell, P., 974  
 Russell, P. E., 1987  
 Ryu, Cheong-Ro, 1503
- Saito, Eiichi, 2799  
 Sakai, T., 2095, 2397  
 Sakai, Tetsuo, 540  
 Sakakibara, Yukio, 253  
 Sakakiyama, T., 1531  
 Sallenger, Asbury, Jr., 2680  
 Sampaio, R. M., 551  
 Sánchez-Arcilla, A., 2811  
 Sato, Michio, 563, 2205, 2293  
 Sato, Shinji, 2411  
 Sato, Yukio, 2424  
 Sawaragi, Toru, 1517, 2642  
 Sayao, Otavio J., 3230  
 Schäffer, H. A., 576  
 Schäffer, Hemming A., 460  
 Schmidt, R., 1545  
 Schoonees, J. S., 3026  
 Sekimoto, Tsunehiro, 804, 894  
 Seymour, R. J., 2084  
 Seymour, Richard J., 2242  
 Shibano, Teruo, 3426  
 Shibayama, Tomoya, 2438, 2799  
 Shigemura, Toshiyuki, 2450  
 Shimizu, T., 281  
 Shimizu, Takuzo, 590, 804, 894, 3107  
 Shinohara, Tomoaki, 2205  
 Shirai, Toru, 2164
- Shuto, N., 672  
 Shuto, Nobuo, 2486  
 Silva, P., 1812  
 Simonin, O., 2853  
 Simons, Richard R., 604  
 Skafel, Michael, 2976  
 Skjelbreia, James E., 777  
 Skyner, D. J., 212, 618  
 Sleath, J. F. A., 2383  
 Sloth, P., 1020  
 Smidt, H.-J., 1067  
 Smith, A. W. Sam, 1354  
 Smith, Ernest R., 630  
 Smith, G. G., 2279, 3026  
 Smith, Jane McKee, 2191, 2825  
 Smith, W. Gray, 1559  
 Sobey, Rodney J., 644  
 Sollitt, Charles K., 2191  
 Sørensen, Ole R., 460  
 Southgate, Howard, 2108  
 Sparboom, Uwe, 1573  
 Srinivas, Rajesh, 2001  
 Stansberg, C. T., 658  
 Steetzel, Henk J., 2669  
 Stive, Mareel J. F., 2464  
 Stoutjesdijk, Theo, 1587  
 Sulisz, Wojciech, 1799  
 Sumer, B. M., 2839  
 Sun, Z. C., 1599  
 Supharatid, S., 672  
 Svendsen, Ib A., 1461, 2758, 2825  
 Swan, Christopher, 684
- Takahashi, Shigeo, 1625  
 Takehara, Kosei, 3163  
 Tanaka, H., 672  
 Tanaka, Hitoshi, 2486  
 Tanaka, Masahiro, 1613  
 Tanimoto, Katsutoshi, 1625  
 Teatini, P., 1865  
 Teisson, Ch., 2853  
 Teisson, Charles, 2949  
 Thieke, R. J., 698  
 Thornton, E. B., 2999, 3012  
 Thornton, Edward B., 2655  
 Tolman, Hendrik L., 712  
 Tomasicchio, Giuseppe R., 1879, 3413  
 Tomasicchio, Ugo, 1  
 Tomita, Takashi, 336  
 Toorman, Erik, 2962  
 Topliss, M. E., 1639  
 Tørum, Alf, 1651

- Toue, Takao, 2867  
Treadwell, D. D., 1354  
Tsuchiya, Yoshito, 2164, 2556, 2772, 3426  
Tsuruya, Hiroichi, 2879  
Turk, George F., 1385  
Twu, S. W., 726
- Uda, Takaaki, 1613  
Ueda, Y., 2397  
Ueki, Kazuhiro, 3107  
Ukai, Akiyuki, 590  
Uliana, Fiore, 3413
- Valera, Eduardo, 2724  
Van Damme, L., 1666  
van den Berg, Egbert J. F., 1748  
Van den Bosch, Lut, 2962  
van den Bosch, P., 1772  
van der Lem, J. C., 1341  
van der Meer, J. W., 1758, 1772  
van Gent, Marcel, 1651  
van Rijn, Leo C., 2613  
van 't Hoff, J., 2599  
van Vledder, Gerbrant Ph., 946  
Verhagen, Henk Jan, 2474  
Verhagen, L. A., 2893  
Vermeir, D., 1666  
Verwoert, H., 2599  
Vidal, C., 1679, 2251  
Vidal, Cesar, 2265  
Viguier, J., 1414  
Villaret, C., 2500  
Villoria, Carlos, 2724  
Vincent, Christopher E., 2321  
Visser, Paul J., 2669  
Vithana, S. Opatha, 2902
- Vittori, Giovanna, 1826  
Vrijling, J. K., 1693
- Walsh, G., 3054  
Wang, Hsiang, 432, 1189, 2513  
Watanabe, Akira, 419, 765, 1101, 2015, 2528, 3093  
Watson, Gary, 818  
White, Thomas E., 2242  
Whitehouse, Richard J. S., 2542  
Wibbeler, H., 1706  
Williams, A. F., 1599, 1720  
Williams, J. J., 2307  
Wilson, Kenneth C., 2917  
Winterwerp, J. C., 2599  
Won, Y. S., 2893  
Wong, Y. K., 2307  
Wurjanto, Andojo, 156, 1299
- Yamaguchi, Masataka, 267, 737  
Yamamoto, Yoshimichi, 1734  
Yamashita, Takao, 2556, 3426  
Yan, Yixin, 2926  
Yanagishima, Shin-ichi, 2136  
Yasuda, Takashi, 253, 751  
Yauchi, Eiji, 2735  
Yen, Kai, 2926  
Yokoki, Hiromune, 765  
Yu, Ke, 932
- Zeidler, Ryszard B., 2370  
Zelt, J. A., 777  
Zhuang, F., 1327  
Zimmermann, C., 1434  
Zwamborn, J. A., 1231  
Zyserman, Julio A., 2567

## CHAPTER 185

# SAND TRANSPORT UNDER GROUPING WAVES

Shinji Sato<sup>1</sup>

### Abstract

Laboratory experiments as well as numerical modeling were conducted for sand transport under non-breaking grouping waves. Experiments showed that the direction of net transport of fine sand was onshore under grouping waves although it was offshore under monochromatic waves with equivalent wave height. It was also revealed that the long wave bounded to wave group plays an important role in particular for suspended load. A numerical model was developed on the basis of the second-order Stokes wave theory and one-dimensional diffusion equation of sand concentration. The validity of the model was confirmed with experimental data.

## 1. INTRODUCTION

In order to develop a proper model of sediment transport under random waves, we have to understand the mechanism of sand transport under wave groups since waves in nature usually contain various waves groups. Wave grouping may influence the amount and the direction of sand movement through direct action of a series of large waves as well as the interaction of short- and long-wave component involved in the group. For example, Shi and Larson (1984) suggested that the direction of sand transport under grouping waves will be offshore because the bound long wave will induce offshore flow under large waves when more sediment is likely to be suspended. The check of this suggestion by laboratory experiments is one motivation of the present study.

The present study aims at understanding the effect of the grouping of non-breaking waves on local sand movement through extensive laboratory experiments

---

<sup>1</sup> Assoc. Prof., Dept. of Civil Eng., Yokohama National Univ., Hodogaya-Ku, Yokohama 240, Japan



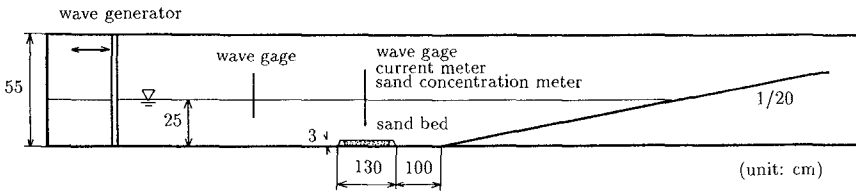


Fig. 1 Experimental setup

and developing a predictive model of sand transport rate under grouping waves. Particular attention will be paid on the effects of long wave and the number of waves in a group on the direction of suspended sediment flux.

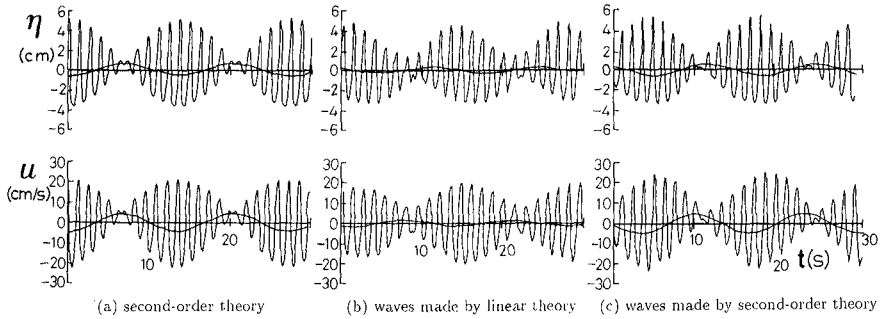
## 2. LABORATORY EXPERIMENTS

A series of experiments were performed in a wave flume in which monochromatic waves and bichromatic grouping waves were generated. Figure 1 shows the layout of experiments. A sand tray was placed at constant depth region where sand was filled to make an initially flat bed. Two kinds of sand with median diameter  $D = 0.02\text{cm}$  and  $0.07\text{cm}$  were used as bed materials. Water surface profile and near-bottom velocity at 5cm above the bottom were measured at the center of the tray by a wave gage and a ultrasonic current meter. In one run of experiments with fine sand ( $H_1 = H_2 = 6\text{cm}$ ,  $T_1 = 1.0\text{s}$ ,  $T_2 = 1.175\text{s}$ ), suspended sand concentration was also measured by an optical concentration meter at various elevations above a ripple crest and a trough. Waves were generated until significant sand transport was observed in the tray. The time duration of wave action in each run of experiments ranged from 20 to 50 minutes. Sand movement due to wave action was recorded by a VTR camera. After each run of experiments, the geometry of sand ripples was measured and a thin plate was inserted at the center of the tray. The sand on the left side and the right side of the tray was collected separately. The net sand transport rate at the center of the tray was estimated from the mass difference of dried sand in both sides of the tray.

The bichromatic waves were simulated by superimposing two sinusoidal wave components with the same heights  $H_1 = H_2$  and slightly different periods  $T_1$  and  $T_2$ . The water surface elevation  $\eta$  of the grouping wave is expressed by the linear theory as

$$\eta = \frac{H_1}{2} \cos(2\pi t/T_1) + \frac{H_2}{2} \cos(2\pi t/T_2 + \varphi) \quad (1)$$

so that the maximum wave height in the group is  $2H_1 (= 2H_2)$ . Since the energy density is proportional to  $\eta^2$ , the energy density of the grouping wave is proportional to  $H_1^2/2$ . The equivalent wave height  $H_e$  of monochromatic wave with the



**Fig. 2** Surface elevation and near-bottom velocity of bichromatic waves

same energy density as the grouping wave is therefore determined by

$$H_e = \sqrt{2}H_1 \quad (2)$$

The period  $T_l$  of the wave group and the mean period  $T_s$  of individual short-wave in the group were given as follows:

$$T_l = \frac{T_1 T_2}{|T_1 - T_2|}, \quad T_s = \frac{2T_1 T_2}{T_1 + T_2} \quad (3)$$

The ratio  $T_l/T_s$  thus indicates the number of waves in a group. These parameters will be used to analyze laboratory data although nonlinear waves were observed in the flume.

Experiments were performed for 30 runs using non-breaking grouping waves. Eleven runs of experiments were also performed by using monochromatic waves with equivalent wave heights  $H_e$ . Experimental conditions as well as measured net sand transport rates were listed in Table 1.

Figure 2 shows an example of water surface elevation  $\eta$  and near-bottom velocity  $u$  under a bichromatic grouping wave. Figure 2 (a) shows theoretical time histories estimated by the second-order Stokes wave theory. It is noticed that long waves are induced in such a way that water level decrease and offshore flow are developed under large waves. Figure 2 (b) shows  $\eta$  and  $u$  measured under bichromatic waves generated by using the linear wave variation expressed by Eq. (1) as the input to the wave generator. It was noticed that the observed waves by the linear wave input did not reproduce the phase correlation between short- and the bound long-waves well. Figure 2 (c) illustrates  $\eta$  and  $u$  where the input signal was simulated by the second-order Stokes wave theory ( *e.g.* Mansard and Barthel, 1984 ). It was found that the desired grouping waves were simulated well as shown in this figure. In the present experiments, the wave generator was controlled by input signals simulated by the second-order Stokes wave theory.

**Table 1** Experimental condition and net sand transport rates

(a) monochromatic waves

$D(\text{cm})$	$T(\text{s})$	$H(\text{cm})$	$Q(\text{cm}^2/\text{s})$
0.02	1.00	7.1	$-0.266 \times 10^{-3}$
0.02	1.00	8.5	$-0.523 \times 10^{-3}$
0.02	1.00	9.9	$-0.678 \times 10^{-3}$
0.02	1.15	7.1	$-0.237 \times 10^{-3}$
0.02	1.15	8.5	$-0.917 \times 10^{-3}$
0.02	1.25	7.1	$-0.026 \times 10^{-3}$
0.02	1.25	8.5	$0.934 \times 10^{-3}$
0.02	1.25	9.9	$3.181 \times 10^{-3}$
0.07	1.25	7.1	0.0
0.07	1.25	8.5	0.0
0.07	1.25	9.9	$0.369 \times 10^{-3}$

(b) bichromatic waves

$D(\text{cm})$	$T_1(\text{s})$	$T_2(\text{s})$	$H_1, H_2(\text{cm})$	$Q(\text{cm}^2/\text{s})$
0.02	1.00	1.100	5.0	$0.176 \times 10^{-3}$
0.02	1.00	1.175	5.0	$1.51 \times 10^{-3}$
0.02	1.00	1.250	5.0	$0.306 \times 10^{-3}$
0.02	1.00	1.100	6.0	$1.59 \times 10^{-3}$
0.02	1.00	1.175	6.0	$3.08 \times 10^{-3}$
0.02	1.00	1.250	6.0	$1.88 \times 10^{-3}$
0.02	1.15	1.265	5.0	$0.359 \times 10^{-3}$
0.02	1.15	1.351	5.0	$0.881 \times 10^{-3}$
0.02	1.15	1.438	5.0	$1.20 \times 10^{-3}$
0.02	1.15	1.265	6.0	$0.584 \times 10^{-3}$
0.02	1.15	1.351	6.0	$2.83 \times 10^{-3}$
0.02	1.15	1.438	6.0	$4.69 \times 10^{-3}$
0.02	1.25	1.375	5.0	$1.71 \times 10^{-3}$
0.02	1.25	1.469	5.0	$0.718 \times 10^{-3}$
0.02	1.25	1.563	5.0	$0.813 \times 10^{-3}$
0.02	1.25	1.375	6.0	$5.12 \times 10^{-3}$
0.02	1.25	1.469	6.0	$3.79 \times 10^{-3}$
0.02	1.25	1.563	6.0	$1.09 \times 10^{-3}$
0.02	1.25	1.375	7.0	$1.67 \times 10^{-3}$
0.02	1.25	1.469	7.0	$3.12 \times 10^{-3}$
0.02	1.25	1.563	7.0	$0.497 \times 10^{-3}$
0.07	1.25	1.375	5.0	$0.111 \times 10^{-3}$
0.07	1.25	1.469	5.0	$0.113 \times 10^{-3}$
0.07	1.25	1.563	5.0	$0.358 \times 10^{-3}$
0.07	1.25	1.375	6.0	$2.87 \times 10^{-3}$
0.07	1.25	1.469	6.0	$2.29 \times 10^{-3}$
0.07	1.25	1.563	6.0	$2.65 \times 10^{-3}$
0.07	1.25	1.375	7.0	$5.11 \times 10^{-3}$
0.07	1.25	1.469	7.0	$3.18 \times 10^{-3}$
0.07	1.25	1.563	7.0	$5.76 \times 10^{-3}$

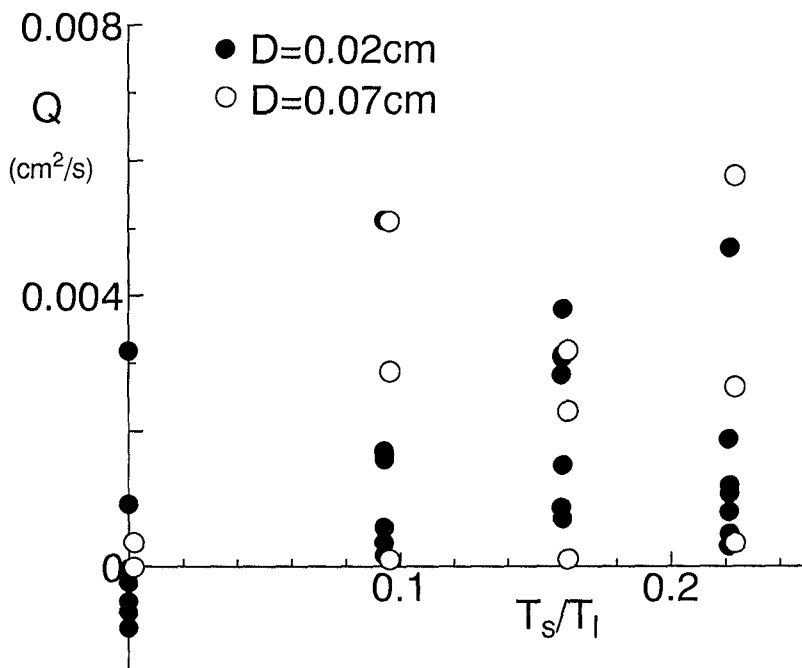


Fig. 3 Measured net sand transport rates

For 0.7mm sand bed, no ripples were developed and sand particles were transported by bed load. Sand particles were observed to be in motion during a few wave period just after the passage of the largest wave in the group. For 0.2mm sand bed, on the other hand, sand ripples were always observed and suspended transport was dominant in all the runs.

Figure 3 shows net sand transport rates measured in all the experimental runs. The positive rates means the onshore transport. The horizontal scale is  $T_s/T_l$ , which is the inverse of the number of waves in a group. Data for monochromatic waves are plotted at  $T_s/T_l = 0$ . The transport direction of coarse sand was always in the onshore direction. Fine sand was also always transported in the onshore direction under grouping waves but the transport direction was offshore in some cases of monochromatic waves. This is because coarse sand was transported by bed load and fine sand was transported primarily by suspended load. Numerical models estimating the net sand transport rate were developed for both bed load and suspended load.

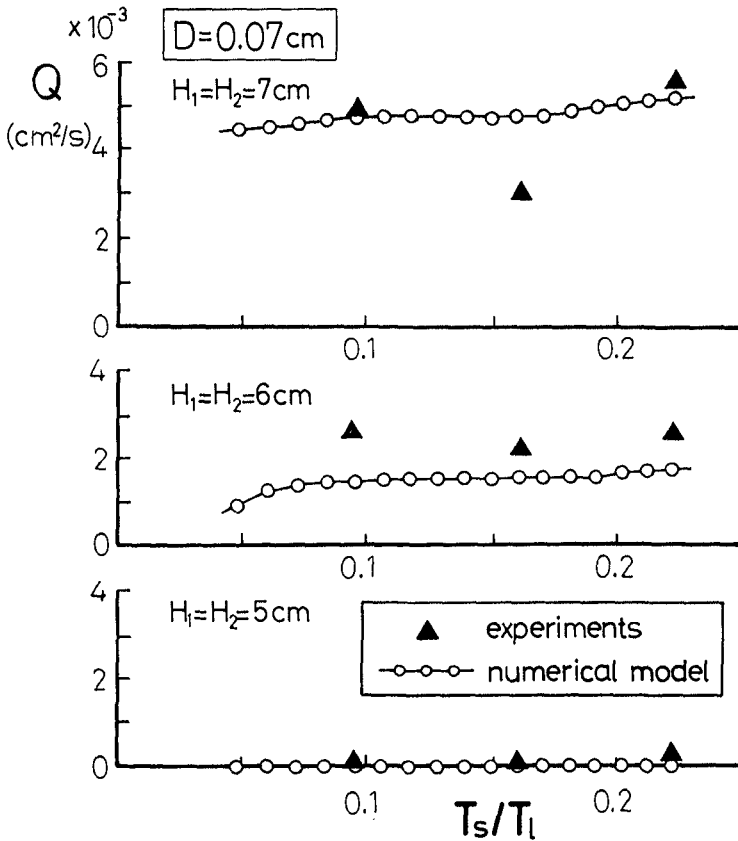


Fig. 4 Net sand transport rates for coarse sand

### 3. NUMERICAL MODEL

#### 3.1 Bed load

Figure 4 shows net sand transport rates  $Q$  for coarse sand. The abscissa  $T_s/T_l$  indicates the inverse of the number of waves in a group. The symbol  $\blacktriangle$  represents measurement and the solid line indicates a numerical computation in which sand transport rate was computed by a power model expressed by

$$Q = \alpha_b w_s D \overline{(\Psi(t) - \Psi_c)u} / \sqrt{sgD} \tag{4}$$

where  $\alpha_b (=1.5)$  was a nondimensional coefficient,  $w_s$  the settling velocity of sand particle,  $\Psi(t)$  the instantaneous Shields parameter,  $\Psi_c$  the critical Shields parameter,  $s$  the specific gravity of sand particle in water and  $g$  the gravity acceleration.

The overbar indicates taking temporal average over the period of wave group.

The Shields parameter was estimated by using the laminar boundary layer theory since turbulence was observed to be weak in all the experiments with coarse sand. The second-order Stokes wave theory was used to compute velocity variation near the bottom. According to the theory, the velocity variation under a bichromatic wave was expressed by the sum of the first-order components and the second-order components as

$$u = u_1 \cos \sigma_1 t + u_2 \cos \sigma_2 t + u_{12} \cos 2\sigma_1 t + u_{22} \cos 2\sigma_2 t + u_{2a} \cos(\sigma_1 + \sigma_2)t + u_{2l} \cos(\sigma_1 - \sigma_2)t \quad (5)$$

where  $\sigma_1 (= 2\pi/T_1)$  and  $\sigma_2 (= 2\pi/T_2)$  are angular frequencies,  $u_1$  and  $u_2$  are velocity amplitudes of the first-order components and  $u_{12}$ ,  $u_{22}$ ,  $u_{2a}$ ,  $u_{2l}$  are velocity amplitudes of the second-order components. Assuming laminar flow in the bottom boundary layer, the bottom shear stress  $\tau$  is expressed by

$$\begin{aligned} \tau(t) = & \rho\sqrt{\sigma_1\nu} u_1 \cos(\sigma_1 t + \pi/4) + \rho\sqrt{\sigma_2\nu} u_2 \cos(\sigma_2 t + \pi/4) \\ & + \rho\sqrt{2\sigma_1\nu} u_{12} \cos(2\sigma_1 t + \pi/4) + \rho\sqrt{2\sigma_2\nu} u_{22} \cos(2\sigma_2 t + \pi/4) \\ & + \rho\sqrt{(\sigma_1 + \sigma_2)\nu} u_{2a} \cos((\sigma_1 + \sigma_2)t + \pi/4) \\ & + \rho\sqrt{|\sigma_1 - \sigma_2|\nu} u_{2l} \cos((\sigma_1 - \sigma_2)t + \pi/4) \end{aligned} \quad (6)$$

where  $\rho$  and  $\nu$  are the density and the kinematic viscosity of water respectively. The instantaneous Shields parameter is related to the bottom shear stress by

$$\Psi(t) = \tau(t)/(\rho sgD) \quad (7)$$

The value of  $\Psi - \Psi_c$  in Eq. (4) was set to be zero when  $\Psi$  was smaller than  $\Psi_c$ . It was confirmed in Fig. 4 that the model predicted the onshore transport of coarse sand in a good accuracy.

### 3.2 Suspended load

For fine sand sand ripples were always observed and suspended sand was dominant above rippled bed. Figure 5 shows the relationship between the ripple wavelength  $\lambda$  and the diameter  $d_o$  of water particle displacement near the bottom. The value of  $d_o$  was estimated by using the linear wave theory. For grouping waves,  $d_o$  was estimated by using energy equivalent wave height  $H_e$  and individual wave period  $T_s$ , where  $H_e$  and  $T_s$  are related to the dimensions of the grouping wave by Eqs. (2) and (3). The ripple wavelength under grouping waves was longer than that under monochromatic waves as long as  $H_e$  was used as the representative wave height.

Figure 6 shows vertical distributions of time-averaged sand concentrations  $\bar{C}$  under a grouping wave and a monochromatic wave with equivalent wave height.

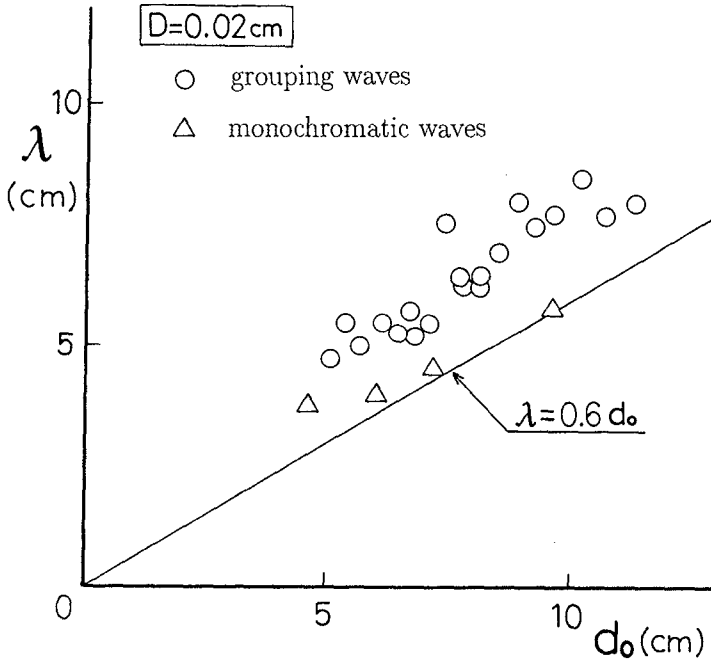


Fig. 5 Wavelength of sand ripples for fine sand

It was found that sand concentration tended to be larger in grouping waves than in monochromatic waves. The eddy diffusivity  $\epsilon$  estimated from Fig. 6 was also larger in grouping waves than in monochromatic waves, which was associated with larger sand ripples observed under grouping waves.

Suspended load was modeled on the basis of the following one-dimensional diffusion equation:

$$\frac{\partial C}{\partial t} = \epsilon \frac{\partial^2 C}{\partial z^2} + w_s \frac{\partial C}{\partial z} \tag{8}$$

The boundary condition at the bed was described by a pick-up function  $p_r(t)$  which simulated intermittent ejection of sand above rippled bed (Nielsen, 1988). The entrainment of sand was assumed to occur at the time of every flow reversal. The time  $t_i$  of the  $i$ -th flow reversal was determined from the velocity variation simulated by the second-order Stokes wave theory. The boundary condition at the bed was then expressed as follows:

$$\epsilon \frac{\partial C}{\partial z} \Big|_{z=0} = -p_r(t) = -\sum_i \rho_s \alpha_s w_s D (\Psi_i - \Psi_c) u_i T_i / (\lambda \sqrt{sgD}) \delta(t - t_i) \tag{9}$$

where  $\alpha_s (=0.2)$  was a coefficient,  $\rho_s$  was the density of sand particle,  $T_i$ ,  $u_i$  and  $\Psi_i$  were the period, the velocity amplitude and the Shields parameter of  $i$ -th wave

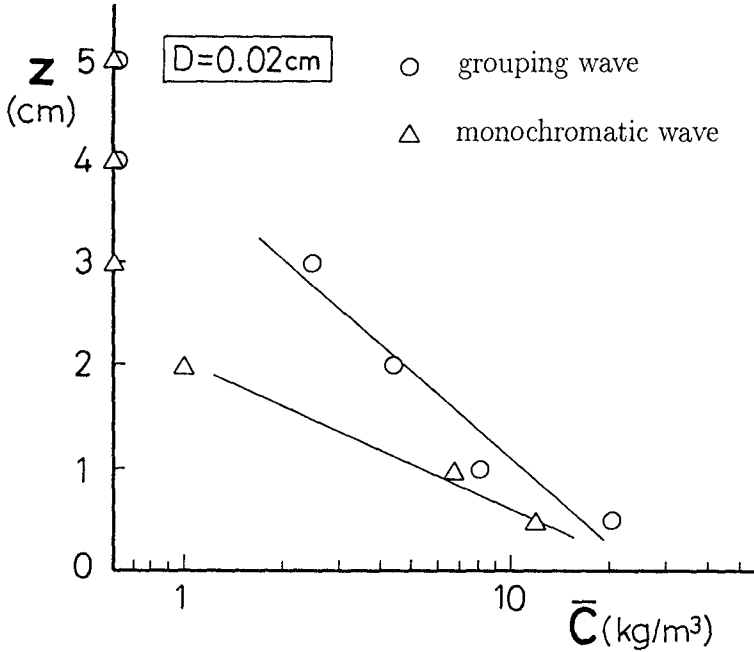


Fig. 6 Vertical distributions of suspended sand concentration

respectively, and  $\delta(t)$  was Dirac's delta function. The Shields parameter  $\Psi_i$  was estimated by

$$\Psi_i = \frac{f_w u_i^2}{2s\bar{g}D} \quad (10)$$

where  $f_w$  was Jonsson's friction factor. For eddy diffusivity, the following relation proposed by Nielsen (1988) was employed:

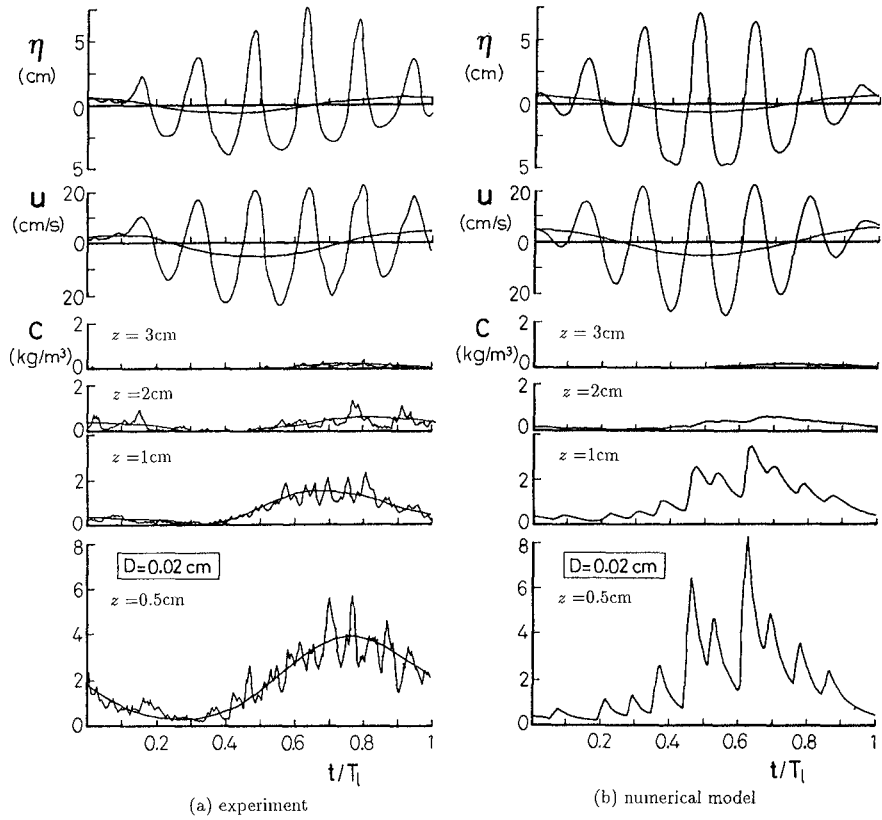
$$\varepsilon = w_s \eta (1.24 \exp[-40(w_s/\hat{u}_{1/3})^2] + 0.2) \quad (11)$$

where  $\eta$  was the wave height of observed sand ripples and  $\hat{u}_{1/3}$  was the significant amplitude of near-bottom velocity variation.

Figure 7 shows an example of temporal variation of water surface elevation  $\eta$ , near-bottom velocity  $u$  and sand concentrations  $C$  measured and simulated by the model. Sand concentrations were compared with measurements at elevations  $z=3\text{ cm}$ ,  $2\text{ cm}$ ,  $1\text{ cm}$ ,  $0.5\text{ cm}$ . The long wave component extracted by a numerical low-pass filter was also shown in the figure. It was reproduced in the model that the sand concentration becomes maximum just after the passage of largest wave in the group.

When we integrate the correlation  $\overline{Cu}$  at various heights, we can estimate suspended sand flux at the section, which can be compared with net sand transport





**Fig. 7** Comparison of numerical computation with measurements

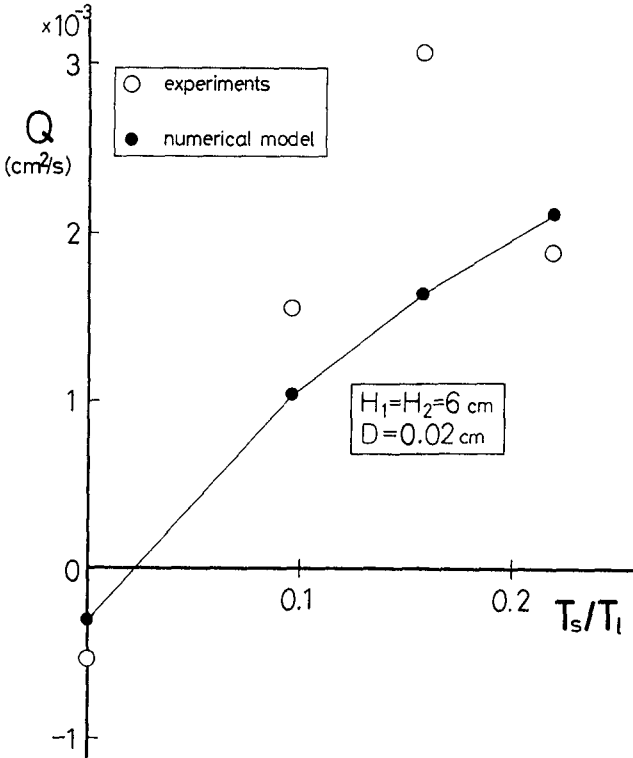


Fig. 8 Comparison of net sand transport rates

rates estimated from the mass difference of sand in sand tray. Figure 8 shows the relationship between the net sand transport rates  $Q$  and  $T_s/T_l$ . Net sand transport rate under monochromatic wave was plotted at  $T_s/T_l=0$ . The numerical model based on the diffusion equation reproduced the experimental results that the direction of net sand transport in grouping waves was opposite to that in monochromatic waves. It is also reproduced in the model that the transport rates increased with the decrease of the number of waves in the wave group.

Figure 9 shows co-spectra between  $C$  and  $u$  for monochromatic wave and grouping wave. The co-spectrum indicates the contribution of each frequency to the total suspended load. There is a sharp peak of offshore transport for monochromatic wave. This is because under shallow water waves propagating over rippled bed, we usually have offshore transport of fine sand since more sand is accumulated in a vortex behind ripple crests during stronger onshore flow and transported offshore after the flow reversal.

Under grouping waves, to the contrary, the contribution at the peak frequency

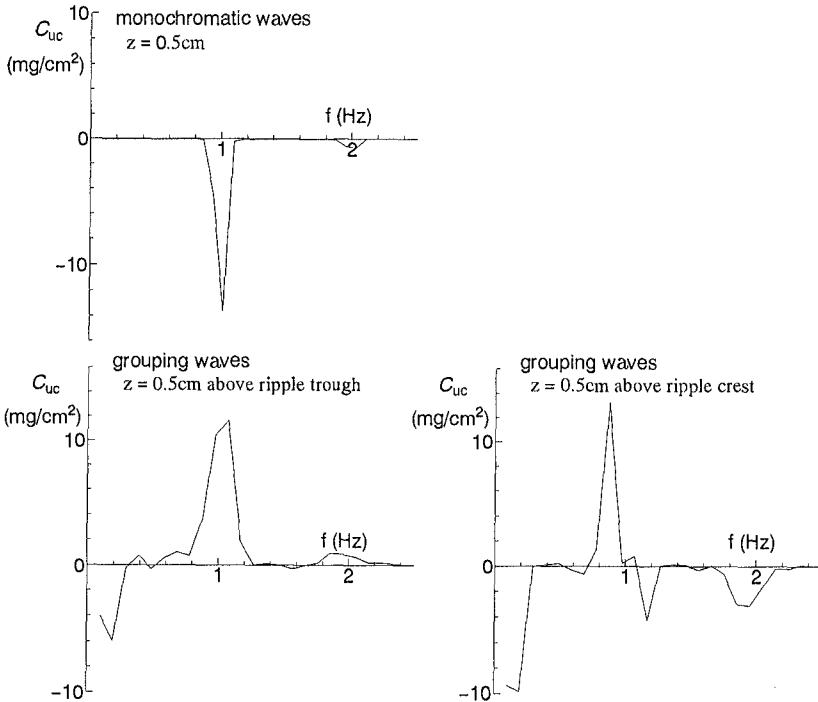


Fig. 9 Co-spectra between  $u$  and  $C$

was reversed to onshore transport. It is also noticed that a large contribution to the offshore was observed by long wave component. The reason for the reversal of the contribution at the peak frequency is explained by the asymmetry in the time history of velocity. Since offshore flow is induced by long wave component under large waves, velocity amplitude of offshore flow becomes larger than that of onshore flow. This makes suspended sand cloud created during offshore flow bigger than that during onshore flow, which results in net onshore transport of suspended sand at the peak frequency. The offshore contribution by the long wave component is explained by the same mechanism suggested by Shi and Larson (1984), that is, more sediment will be suspended under large waves which will be transported by offshore flow induced by the bounded long wave. The direction of the total net sand transport under non-breaking grouping waves will be determined by the balance of these two contributions. Net onshore transport of fine sand observed in the present experiments means that the onshore contribution by the short wave component was always larger than the offshore contribution by the long wave component within the range of experiments.

#### 4. CONCLUSIONS

Laboratory experiments showed that the direction of net transport of fine sand was onshore under non-breaking grouping waves although it was offshore under monochromatic waves with equivalent wave height. Laboratory experiments also proved that wave grouping plays an important role in particular for the case in which suspended load is predominant. A numerical model developed on the basis of diffusion equation of sand concentration was confirmed with experiments.

Extension of the model to random wave conditions will be presented in the next opportunity.

#### REFERENCES

- Mansard, E.P.D. and V. Barthel (1984): Shoaling properties of bounded long waves, *Proc. 19th Conf. on Coastal Engineering*, pp. 798-814.
- Nielsen, P. (1988): Three simple models of wave sediment transport, *Coastal Engineering*, Vol. 12, pp. 43-62.
- Shi, N.C. and L.H. Larson (1984): Reverse sediment transport induced by amplitude-modulated waves, *Mar. Geol.*, 54, pp. 181-200.

## CHAPTER 186

### QUASI-TURBULENT BOUNDARY LAYER OF OSCILLATING FLOW OVER RIPPLES

Yukio Sato<sup>1</sup>  
and  
Ken-ichiro Hamanaka<sup>2</sup>

#### ABSTRACT

When the surface waves propagate in shallow water region, the bottom boundary layer may be turbulent because of sand ripples or other kind of roughness of sea bed. But before the flow becomes fully developed turbulence, there is a state, in a certain range of the Reynolds number, in which the flow is still laminar but has separation and complex structure of vortex. This is termed as quasi-turbulent flow in the present paper. The flow structure of this boundary layer affects the mass transport and sedimentation.

In the present paper, we use a numerical method to solve the boundary layer of oscillatory flow over ripples. When we discuss the overall wave field, the sand ripples can be considered as roughness of the bottom and the flow with the separation and the vortex can be considered as disturbance around mean flow. Therefore, to discuss the averaged flow structure of wave field, the mass transport for example, it is necessary to know some kind of statistical properties of the boundary layer. A particular attention is paid to investigate the mean velocity, the Reynolds stress and turbulent viscosity. It is found that the turbulent viscosity varies along the time during the period of the oscillation. And not only it diversifies as the space derivative of the mean velocity diminishes, but also it has a complex distribution in space and time.

<sup>1</sup> Associate Professor, Dept. of Civil Eng., Kitami Inst. of Tech.,  
Koen-cho 165, Kitami 090, Japan.

<sup>2</sup> Dr. Eng., Research Associate, Dept. of Civil Eng., Hokkaido Univ.,  
N 13, W 8, Sapporo 060, Japan.

## 1. INTRODUCTION

Sand ripples are commonly observed on the sea bed in coastal region, which produce complex flow structures near the bed under the influence of the wave motions. This flow structures strongly affect to the development of ripples, the mass transport inside and outside the boundary layer, and the sedimentation near the bed.

In the case where the flow near the bed is fully developed turbulence, Longuet-Higgins(1958) analyzed the Eulerian mean velocity and the mass transport velocity just outside the boundary layer. He concluded that the Eulerian mean velocity and the mass transport are independent to the distribution of the turbulent viscosity. In his analysis it is assumed that the local turbulent viscosity is constant along with the time during the wave period. But the validity of this assumption seems to be questionable. Furthermore, when we discuss the mass transport inside the boundary layer, we need to know the distribution of the turbulent viscosity even if Longuet-Higgins' assumption is correct.

On the natural sea bed, the wave length of the ripples is very short compared with that of the surface wave. Therefore to investigate the flow structure inside the boundary layer, horizontally oscillating flow can be considered as a first approximation for the ambient flow. Blondeaux and Vittori(1991) investigated this flow structure in a numerical approach. Hamanaka and Sato(1991) also proposed a similar numerical method independently using the spectral method and the finite differential scheme. Both of them confirmed that their methods describe the separations and large vortex structures.

In the present paper, we use the same numerical method of Hamanaka and Sato(1991) and solve the oscillatory boundary layer on ripples under the quasi-turbulence condition. A particular attention is paid to investigate the mean velocity, the Reynolds stress and the turbulent viscosity on the same flow conditions mentioned above. Spatial averaging procedure is taken over the wave length of ripple. The turbulent viscosity is found to be dependent on time during the period of the oscillating flow. Not only it diversifies as the space derivative of the mean velocity diminishes, but also it has a complex pattern of its distribution in space and time. A similar result can be seen in the experimental measurement of Sleath (1987), in the case of fully developed turbulent boundary layer. This fact suggests that

Longuet-Higgins' assumption mentioned above is not correct. A example of this incorrectness is seen in the difference between

Tanaka's model and measurement (Tanaka,1989).

2. FORMULATION OF THE PROBLEM

In the present paper, we follow the same numerical approach of Hamanaka and Sato (1991). We consider two dimensional viscous flow oscillating over a periodic wavy bottom and assume that the wavy bottom vary sinusoidally to the direction of x axis. The vorticity equation and the Poisson equation for the stream function is employed as the governing equation.

$$\omega^* = \phi_{xy} - \phi_{yx} + \nu (\omega_{xx} + \omega_{yy}) \tag{1}$$

$$\phi_{xx} + \phi_{yy} = -\omega \tag{2}$$

where,  $\omega^*$  is vorticity,  $\phi^*$  is stream function and  $\nu^*$  is kinematic viscosity.

The flow outside the boundary layer is given by

$$u^* = \sigma^* A^* \sin(\sigma^* t^*) \quad , \quad v^* = 0 \tag{3}$$

where,  $u^*$  and  $v^*$  are horizontal and vertical velocity components outside the boundary layer. And,  $\sigma^*$  is angular frequency,  $A^*$  is amplitude of velocity.

A new coordinate system is introduced.

$$x^* = \xi^* - a^* \exp(-k^* \eta^*) \sin(k^* \xi^*) \tag{4}$$

$$y^* = \eta^* + a^* \exp(-k^* \eta^*) \cos(k^* \xi^*)$$

where,  $k^*$  and  $a^*$  are wave number and amplitude of the ripple respectively. The ripple profile is mapped into the line  $\eta^* = 0$ .

All variables are nondimensionlized with  $k^*$  and  $\sigma^*$ .

$$\xi = k^* \xi^* \quad , \quad \eta = k^* \eta^* \quad , \quad t = \sigma^* t^* \tag{5}$$

$$\phi = \frac{k^{*2}}{\sigma^*} \phi^* \quad , \quad \omega = \frac{\omega^*}{\sigma^*} \quad , \quad \nu = \frac{k^{*2}}{\sigma^*} \nu^*$$

Then, the governing equations (1) and (2) are represented in ( $\xi, \eta$ ) coordinate system.

$$\omega_t = J^{-1} \{ -\phi_\eta \omega_\xi + \phi_\xi \omega_\eta + \nu (\omega_\xi \xi + \omega_\eta \eta) \} \quad \text{----- (6)}$$

$$\phi_\xi \xi + \phi_\eta \eta = -J \omega \quad \text{----- (7)}$$

where, J is the Jacobian of transformation by Eq.(4) :

$$J = 1 - 2 a \exp(-\eta) \cos(\xi) + a^2 \exp(-\eta) \quad \text{-- (8)}$$

$$J^{-1} = 1 / J$$

The boundary conditions on the bottom are

$$\phi = \phi_\xi = \phi_\eta = 0 \quad \text{on} \quad \eta = 0 \quad \text{----- (9)}$$

and outside the boundary layer,

$$\phi_\xi \rightarrow 0, \quad \phi_\eta \rightarrow A \sin(t), \quad \omega \rightarrow 0 \quad \text{at} \quad \eta \rightarrow \infty \quad \text{-----(10)}$$

where,  $A = k^* a^*$ .

The parameters  $a$ ,  $A$  and  $\nu$  specify this problem.

The parameter  $a$  determines the bottom topography. When  $a$  is constant, the similarity law suggests two dimensionless numbers, Reynolds number (Re) and Strouhal number (S). Let the representative variable of the length scale be the wave length of the ripple profile ( $L^*$ ), the time scale, the period of oscillation ( $T^*$ ), and the velocity, the maximum velocity of oscillation ( $\sigma^* A^*$ ), then, Reynolds number (Re) and Strouhal number (S) are described as follows.

$$Re = \frac{\sigma^* A^* L^*}{\nu^*} = 2\pi \frac{A}{\nu}, \quad S = \frac{\sigma^* A^* T^*}{L^*} = A \quad \text{(11)}$$

Instead of solving this problem directly, we introduce the Fourier series expansion for  $\phi$  and  $\omega$  along the axis  $\xi$ ,

$$\phi = \sum f_m \exp(im\xi), \quad \omega = \sum g_m \exp(im\xi) \quad \text{-----(12)}$$

Substituting (12) into (7), we obtain equation (13).

$$\frac{\partial^2 f_m}{\partial \eta^2} - m^2 f_m = -H_m \quad \text{----- (13)}$$



where,  $J \omega = \sum H_m e^{im}$

In general, there can be considered two way to treat the vorticity equation. When the wave number space (Fourier coefficients) is used, the convolution sum is needed to calculate the nonlinear terms. And when the physical space is used, the inverse Fourier transform is needed in each time step. In the present paper, the latter method is used.

We introduce a new coordinate system in which finer meshes can be defined near the bottom, and coarser ones in the upper region.

$$\eta = \eta_T \frac{\exp(b\zeta) - 1}{\exp(b) - 1} \tag{14}$$

The boundary condition for (12) is on the bottom

$$f_m = 0 \quad \text{on} \quad \zeta = 0 \tag{15}$$

and outside the boundary layer

$$\frac{\partial \zeta}{\partial \eta} \frac{\partial f_m}{\partial \zeta} = \begin{matrix} A \sin(t) & , & m = 0 \\ 0 & , & m \neq 0 \end{matrix} \quad \text{on} \quad \zeta = 1 \tag{16}$$

for the vorticity equation

$$\omega = 0 \quad \text{on} \quad \zeta = 1 \tag{17}$$

The vorticity on the upper boundary is assumed to be zero, and on the bottom it is given by Thom's scheme with the bottom condition of the stream function ( Roache 1972 ).

$$\omega = -J^{-1} \left( \frac{\partial \zeta}{\partial \eta} \right)^2 \frac{2\phi(\Delta\zeta)}{\Delta\zeta} \quad \text{on} \quad \zeta = 0 \tag{18}$$

### 3. NUMERICAL PROCEDURE

The equation (6) and (13) are solved numerically by use of a forward difference scheme for the time derivative, and a central difference scheme for the spatial derivative. The vorticity at new time step is obtained through (6) with three inverse Fourier transform in the right hand side of the equation. The Fourier

coefficient of the stream function is obtained through (13) with Fourier transform of the right hand side. Then, the vorticity on the bottom is obtained through (18). In this procedure, Fourier transform and inverse Fourier transform are needed but FFT algorithm may be available in any computer system.

In this paper, the parameters  $a$  and  $A$  are fixed on 0.5 and 5.0, and several calculations is carried out with the several different value of  $\nu$ . The value of  $A$  is selected as the moving distance of water particles by oscillating flow becomes to a wave length of the ripple. The computation starts from the fluid at rest.

Table 1. gives the computational conditions which are discussed in this paper.  $M$  and  $N$  are the numbers of grids on  $\xi$ -axis and  $\zeta$ -axis respectively.  $NT$  is time step number of one period of the oscillation.

Therefore, the time step  $\Delta t$  becomes

$$\Delta t = 2 \pi / NT$$

RUN	M	N	$\eta \tau$	b	a	A	$\nu$	Re	NT	cycle
4	64	32	5	3	0.5	5	0.05	630	3200	3
23	64	90	7	3	0.5	5	0.03	1050	12000	5
27	64	90	10	3	0.5	5	0.02	1570	12000	6

Table 1. Computational conditions

#### 4. DISCUSSION OF RESULTS

In this problem , three nondimensional parameters  $a$ ,  $A$  and  $\nu$  specify the flow. In the present calculations,  $a$  and  $A$  are fixed while  $\nu$  takes different values as shown in the table 1. This means the Strouhal number remains constant while the Reynolds number varies in the different cases. The flow with these conditions can be confirmed to be stable from the experimental measurements by Du Toit and Sleath (1981).

Fig. 1 shows the contours of vorticity of the flow with the condition of RUN 4 in the table 1, after three cycles from the rest. (a)-(h) in Fig. 1 correspond to the eight successive phases in one cycle. The fluid outside the boundary layer flows from the left to the right during the first half cycle and reverses during the next

half cycle. The bold lines show the positive vorticity ( counter-clockwise ) and the fine lines show the negative one ( clockwise ). The ambient flow is accelerated in (a), takes maximum velocity in (b), is decelerated in (c) and rests in (d).

Fig. 2 shows the contours of stream function of the same flow of Fig. 1. It is found that both the separation on the lee side of the crest and the large vortex shed from the bottom are well described in this numerical method. In Fig. 1 and Fig. 2, corresponding flows in each half cycle ((a)-(e) and (b)-(f) etc.) are almost symmetric. This means that almost stationary oscillating flow is obtained. Furthermore, in the phase of the deceleration larger separation structure is formed than in the acceleration phase. When the ambient flow reverses its direction, a cloud of vorticity is shed from the bottom and drifts with the ambient flow diminishing the intensity of its vorticity.

As mentioned in the section 1, the wave length of the ripples is very short compared with that of the surface wave in normal coastal region. Therefore the ripples can be considered as bottom roughness. In this sense, it would be reasonable to investigate the Reynolds stress and the turbulent viscosity for mean flow. In general, the averaging procedure can be taken in time, in phase or in space. But to investigate Longuet-Higgins' assumption mentioned in section 1, it will be suitable to use the spatial averaging procedure where the mean velocity is calculated from the averaged velocity over a wave length of the ripple. Then, the Reynolds stress  $R_v$  and the turbulent viscosity  $\nu_\tau$  are given by,

$$R_v = -\langle u' v' \rangle \quad \text{-----} \quad (21)$$

$$\nu_\tau = -\langle u' v' \rangle / \frac{dU}{dy} \quad \text{-----} \quad (22)$$

where

$$u = U + u' , \quad U = \langle u \rangle \quad \text{-----} \quad (23)$$

and  $\langle \rangle$  denotes the average over a wave length.

Fig. 3 shows the distribution of the mean horizontal velocity of RUN 4. Fig. 4 and Fig. 5 show the distribution of the Reynolds stress and the turbulent viscosity of the same flow. From Fig. 5, the turbulent viscosity is found to vary its value during the period of oscillation. And not only it has complex distributions but also diverges in different ways ( in positive or negative ) as the space derivative of mean velocity is diminishes. A similar result can

be seen in the experimental measurement in the case of fully developed turbulent boundary layer (Sleath, 1987).

Fig. 6 shows the contours of vorticity in the case of RUN 23. Comparing with Fig. 1, it is found that when the Reynolds number increases the intensity of vorticity becomes higher and its distribution gets much more complexity and the cloud of vortex drifts longer time with the ambient flow.

Fig. 7 and Fig. 8 show the mean velocity and the Reynolds stress of the flow of Fig. 6.

The fundamental characteristics are the same of those of RUN 4. But it can be seen from these figures that the phase shifts in the mean velocity and the Reynolds stress appears at much higher position because of the development of the boundary layer. The turbulent viscosity of this flow also has the same characteristics of RUN 4.

Let us discuss the detail of time dependence of the characteristics of boundary layer. Fig. 9(a) shows the contours of mean velocity of RUN 4 during one cycle. The bold lines denote the positive contours and the fine ones, negative ones. The height at which the mean velocity takes the maximum at each phase rises up lineally with time in each half cycle. A similar result can be seen in the turbulent intensity of fully developed turbulent oscillatory flow from the experimental measurement by Sleath (1987).

Fig. 9(b) shows the contours of the Reynolds stress of RUN 4. The Reynolds stress has two peaks in each half cycle and its intensity at the acceleration phase is higher than that at the deceleration phase.

Fig. 9(c) shows the contours of the turbulent viscosity of RUN 4. The zigzagged line where the positive contour and negative contour are close each other indicates the divergence of the turbulent viscosity. The similar result can be seen in fully developed turbulent flow (Sleath, 1987).

Fig. 10 is for RUN 23 and Fig. 11 is for RUN 27, corresponding to Fig 9 for RUN 4. As expected from the previous discussion, as the Reynolds number increases the distribution of each valuables gets higher complexity. Also it is commonly seen that the turbulent viscosity strongly depends on time and not only it has positive and negative value but also it diversifies positive way and negative way. This result suggests that the Longuet-Higgins' assumption is incorrect. A effect of this incorrectness is seen in the difference between Tanaka's model and measurement (Tanaka, 1989). He proposed a turbulent viscosity model which depends only to the height from the

bottom, and estimated the mean velocity in a fully developed turbulent oscillatory flow. Significant differences can be seen around the peak points of the mean velocity distributions.

## 5. CONCLUSION

The flow structures of oscillatory boundary layer on rippled bottom are investigated in a numerical method. It is confirmed that the turbulent viscosity depends on time and diversifies in positive and negative. This suggests that the Longuet-Higgins' assumption is unreasonable and consequently the Eulerian steady flow and the mass transport under the wave motion should be reinvestigated.

## REFERENCES

- Blondeaux, P. and Vittori, G. (1991) : Vorticity dynamics in an oscillatory flow over a rippled bed, *Jour. of Fluid Mech.* Vol. 226, pp. 257-289
- Du Toit, C.G. and Sleath, J.F.A. (1981) : Velocity measurements close to rippled beds in oscillatory flow, *Jour of Fluid Mech.* Vol. 112, pp. 71-96.
- Hamanaka, K. and Sato, Y. (1991): Separation of oscillating flow over a wavy bed, *Proc. of Int. Meeting on Hydraulic Transients with Water Column Separation*, pp. 156-167
- Longuet-Higgins, M.S. (1958) : An experimental investigation of drift profiles in a closed channel, appendix, in *Proc. of 16 th Int. Conf. on coastal Eng., ASCE*, pp. 184-193.
- Sleath, J.F.A. (1987) : Turbulent oscillatory flow over rough beds, *Jour. Fluid Mech.* Vol. 182, pp. 369-409
- Tanaka, H. (1989) : Bottom boundary layer under non-linear wave motion, *Jour. of Waterway, Port, Coastal, and Ocean Engineering, ASCE*, Vol. 115, No. 1, pp. 40-57

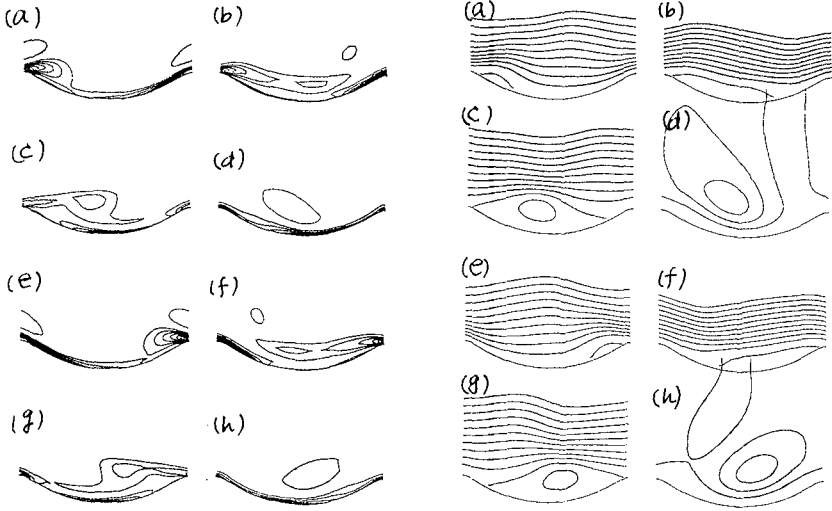


Fig.1 Vorticity contours (Run 4) Fig.2 Stream function contours

$\Delta \omega = 5$

(Run 4) :  $\Delta \phi = 5$

(a):  $2\pi * 1/8$  , (b):  $2\pi * 2/8$  , (c):  $2\pi * 3/8$  , (d):  $2\pi * 4/8$   
 (e):  $2\pi * 5/8$  , (f):  $2\pi * 6/8$  , (g):  $2\pi * 7/8$  , (h):  $2\pi * 8/8$

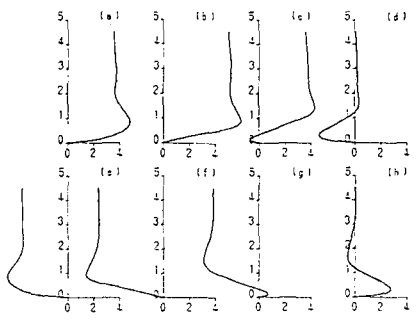


Fig.3 Distributions of mean fluid velocity (U) (Run 4)  
 (a) ~ (h) see Fig.2

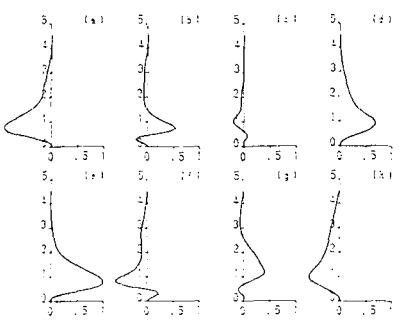


Fig.4 Distributions of Reynolds stress (Ry) (Run 4)  
 (a) ~ (h) see Fig.2

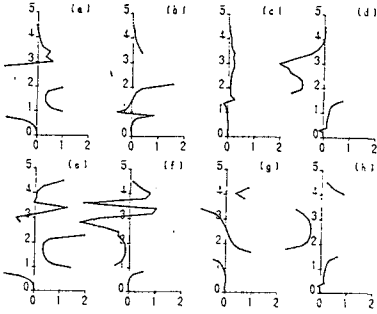


Fig.5 Distributions of turbulent viscosity ( $\nu_T$ ) (Run 4)  
(a) ~ (h) see Fig.2

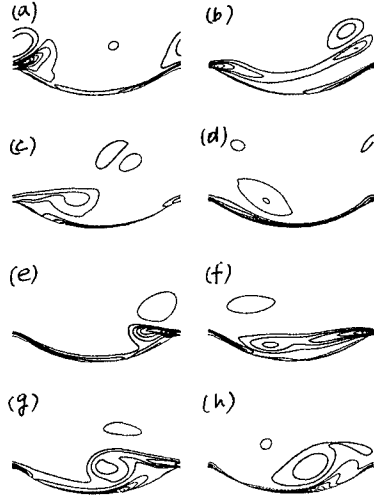


Fig.6 Vorticity contours (Run 23)  
 $\Delta \omega = 5$  : (a) ~ (h) see Fig.2

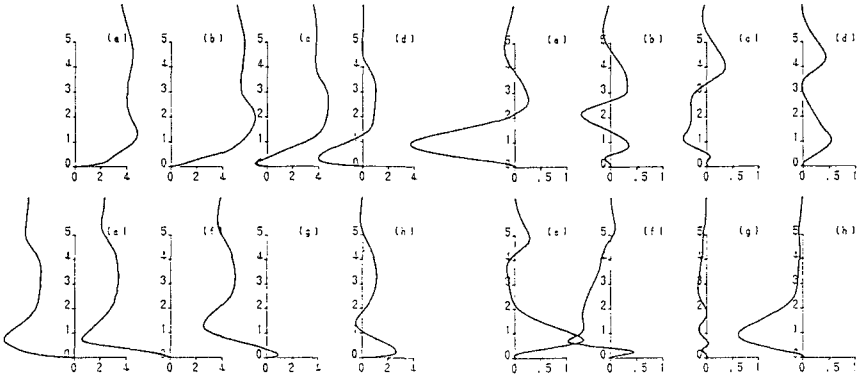


Fig.7 Distributions of mean fluid velocity (U) (Run 23)  
(a) ~ (h) see Fig.2

Fig.8 Distributions of Reynolds stress ( $R_y$ ) (Run 23)  
(a) ~ (h) see Fig.2

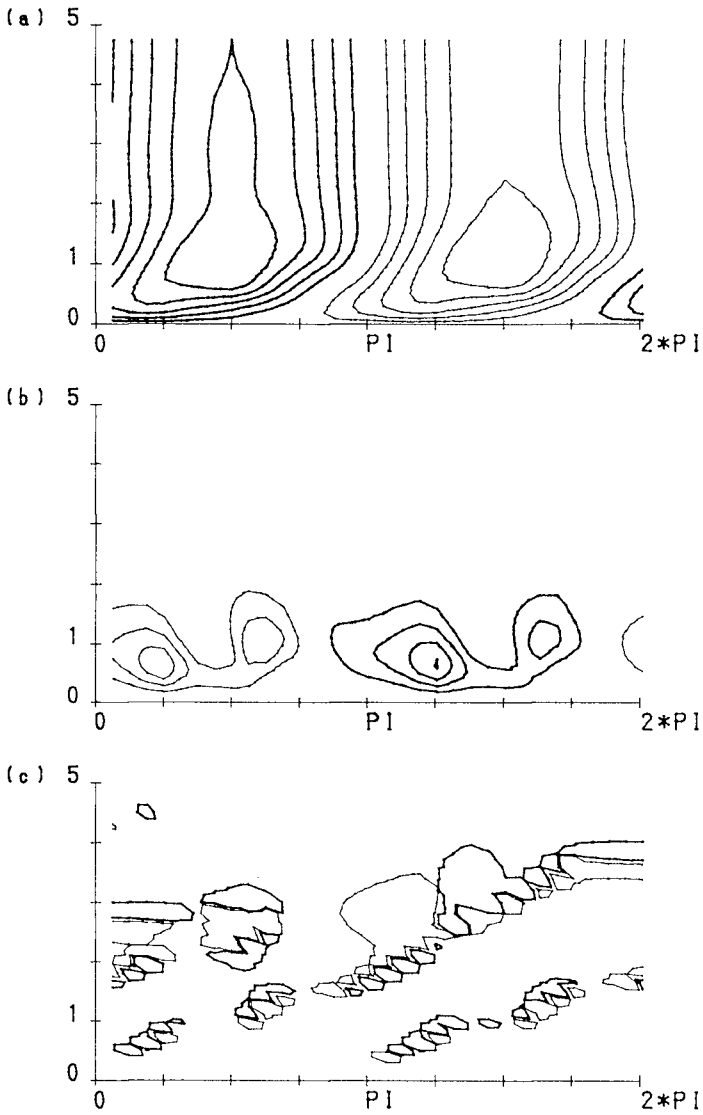


Fig.9 Contours of (a) :mean fluid velocity,(b) :Reynolds stress and (c) :turbulent viscosity (Run 4)



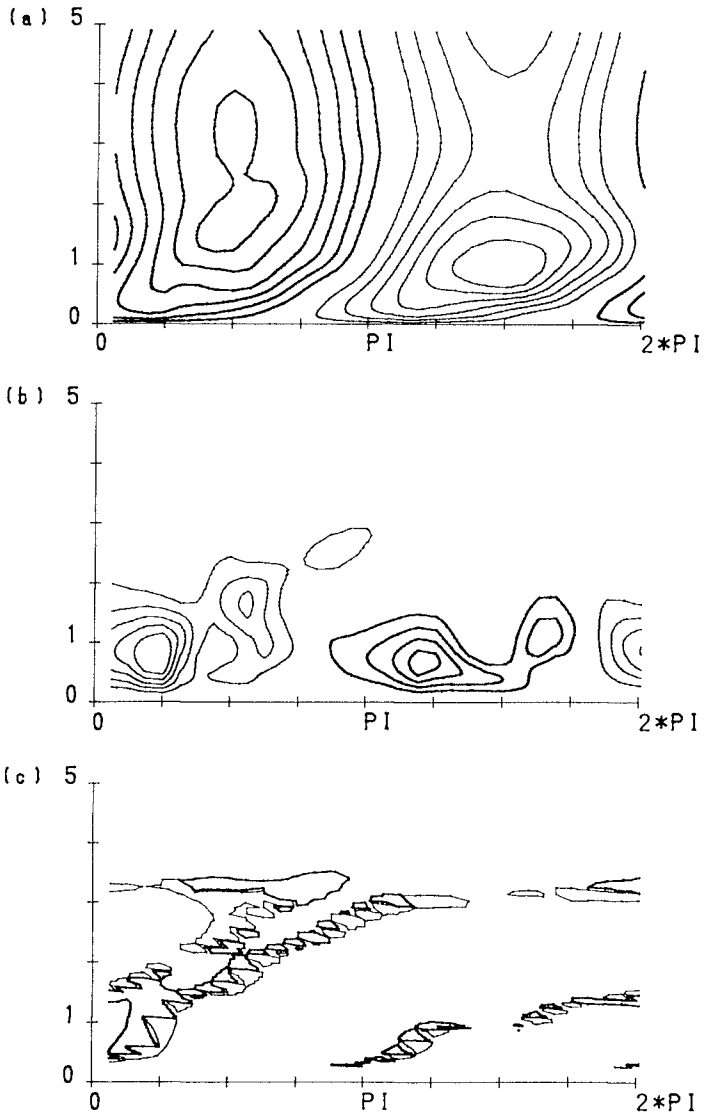


Fig.10 Contours of (a) :mean fluid velocity,(b) :Reynolds stress and (c) :turbulent viscosity (Run 23)

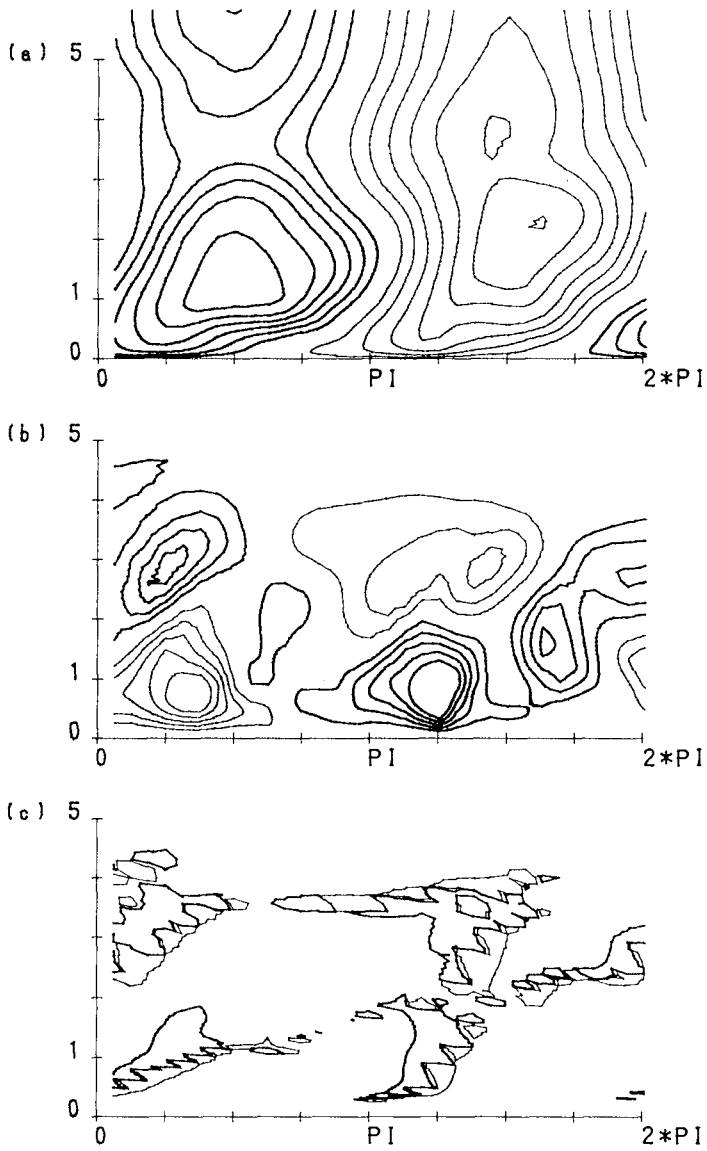


Fig.11 Contours of (a) :mean fluid velocity,(b) :Reynolds stress and (c) :turbulent viscosity (Run 27)

## CHAPTER 187

### LONG PERIOD WAVE AND SUSPENDED SAND TRANSPORT IN THE SURF ZONE

Tomoya Shibayama<sup>1</sup>, Akio Okayasu<sup>2</sup> and Mikio Kashiwagi<sup>2</sup>

#### Abstract

The effect of long period wave to local sand transport rate in the surf zone is analyzed by laboratory and numerical experiments. In the laboratory experiment, surface profile, near-bottom velocity and suspended sand concentration are measured simultaneously and resultant net sand transport rate is measured by mass difference during the experimental runs. It appears that the net sand transport rate is determined by three driving forces which are undertow, long wave and short wave. In mild slope condition, the effect of long wave becomes large. In order to simulate this process, a new numerical model is formulated.

#### 1. Introduction

When irregular waves travel to the shoreline, the long wave component of velocity becomes an important consideration in determining sand transport in the surf zone where sands are transported by both wave motion and turbulence due to wave breaking. For beach deformation process in field, Katoh and Yanagishima (1990) explained the erosion process of berm by the long wave effect. Irregular wave motion consists of a variety of wave periods from long wave to short wave. In this study, the role of long wave to local sediment transport rate is analyzed by laboratory experiments. Investigations are mainly

---

<sup>1</sup> Associate Professor, Department of Civil Engineering, Yokohama National University, Hodogaya-ku, Yokohama 240, Japan

<sup>2</sup> Research Associate, Yokohama National University

<sup>2</sup> Graduate Student, Yokohama National University

focused on sands which are suspended by vortex motion and transported under the influence of long wave velocity. The major difference from the work by Shibayama *et al.* (1991) is that suspended sand flux is considered to be the main factor to control the effect of long wave to total transport rate in this study. In the previous work (Shibayama *et al.*, 1991), near bottom velocity and net sand transport were measured. In their analysis, bed load formula was used to simulate the process and there was no discussion on suspended sand transport because they did not measure the suspended sand concentration.

Shibayama *et al.* (1991) performed numerical simulation to estimate net sand transport rate when near-bottom velocity is given. Their analysis was based on the regular wave analysis of sediment transport rate formula proposed by Shibayama and Horikawa (1985) (also Shibayama and Irie, 1987). In their analysis, it was not possible to include suspended sand movement which is suspended more than one wave cycle. In the present analysis, suspended sand movement will be more directly included in the model.

## 2. Laboratory Experiment

Laboratory experiments were performed with the use of a wave flume which is 17 m long, 0.5 m wide, and 0.55 m deep. Uniform slopes of 1/40 (series A) and 1/20 (series B) were set at the bottom. Figure 1 shows the view of set-up. In the shallow water area, an inspection area of 3 m long and 0.5 m wide was installed where sorted sands of 0.2 mm in diameter were laid. Two inspection sections were set at the inspection area in order to compare the effect of long wave in different depth. An ultra-sonic velocimeter, optical type concentration meter and capacitance wave gage were positioned at the center of the inspection sections. Within the area, a tray was set in order to measure net sand transport rate. The tray was divided into three sections: the onshore, middle and offshore part. By measuring the change of sand mass in each section before and after the experiment, the net sand transport rate in cross-shore direction was obtained for two inspection sections. Table 1 show the conditions of waves which were used in the experiments.

Spectrum analysis was performed from the velocity history measured by the ultra-sonic velocimeter. From the calculated spectra of velocity history, it was determined that long wave component, short wave component and turbulence component had to be separated by frequencies of 0.25 Hz and 5 Hz. The velocity history and concentration time history were then divided into four components: steady flow, long wave, short wave and turbulence with the use of a band passing filter. Fig. 2 shows an example of separation of near-bottom velocity. In the figure, original time history, long wave component, short wave

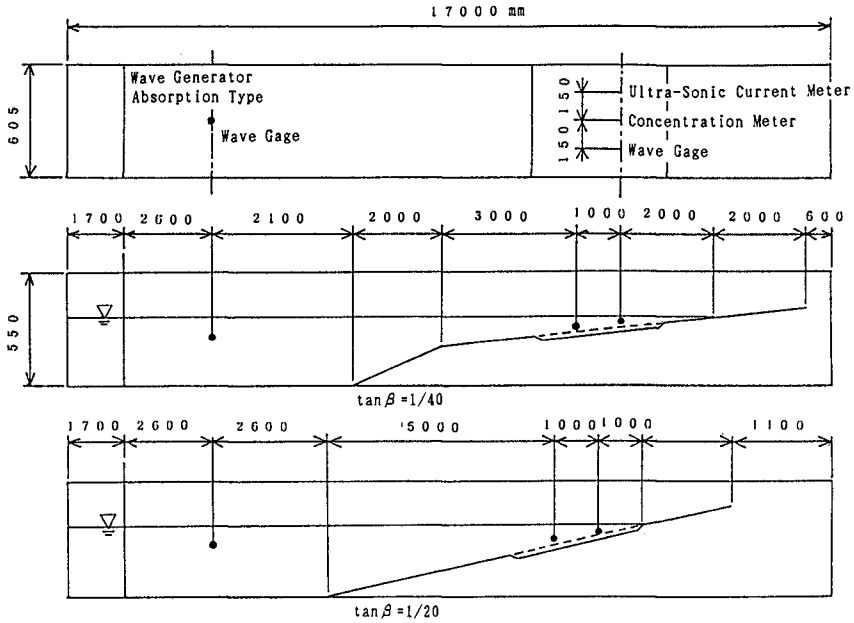


Figure 1: Experimental set-up.

Table 1: Experimental conditions.

Case	Sand Diameter $d_{50}$ (mm)	Constant Depth $h$ (cm)	Slope $\tan\beta$	Significant Wave		Mean Wave	
				$H_{1/3}$ (cm)	$T_{1/3}$ (s)	$\bar{H}$ (cm)	$\bar{T}$ (s)
A - 1	0.18	35.0	1/40	8.2	1.0	5.3	0.9
2				4.9	0.8	3.9	0.7
3				6.9	0.9	4.5	0.8
4				10.0	1.0	6.6	0.9
5				9.5	1.2	6.1	1.0
6				6.6	1.2	4.2	1.0
7				10.7	1.3	7.0	1.2
8				8.9	1.3	5.7	1.1
B - 1	0.18	35.0	1/20	8.1	1.0	5.3	0.9
2				5.2	0.9	3.3	0.8
3				8.1	1.0	5.3	0.9
4				6.6	1.0	4.2	0.9
5				9.5	1.2	6.1	1.0
6				4.8	1.4	2.9	1.0
7				10.6	1.3	6.8	1.1
8				6.8	1.3	4.4	1.2

Bredschneider-Mitsuyasu Type Spectrum

and turbulence are shown. Figure 3 shows an example of the time histories of surface profile, near-bottom velocity and suspended sand concentration. Long wave components are also shown in the figure. Amplitude and period of each wave were also defined for both long wave and short wave by using the zero-down-crossing method.

The effect of long waves to local sediment transport rate were analyzed by comparing the following quantities: steady current, long wave velocity, short wave velocity, long wave concentration of suspended sand concentration, short wave concentration, and the net sand transport rate.

### 3. Results of experiment

From the above experiment, we tried to explain the net sand transport rate by using long wave and short wave component of the near-bottom velocity. This is the same way which was done by Shibayama et al. (1991). Figure 4 shows the result for the cases of which bottom slope was 1/40. From the figure, we can conclude that the larger long wave component causes the larger net sand transport even if the significant values for short wave take almost the same values. For the slope 1/20, the effect of undertow is large and therefore we judged that it is better to analyze the cases for the slope 1/40 to elucidate the effect of long wave.

Figure 5 shows the relationship between the amplitude ratio of long wave velocity to short wave velocity and the net sand transport rate for the slope of 1/40. From the figure, it can be concluded that the ratio has become larger, the net sediment transport rate has increased. In this case, the net transport direction is onshore. During the experiment, when a short wave crest comes over trough of long wave, high concentration area was frequently observed with certain phase lag. This high concentration area is transported to onshore and finally results in net sand transport in onshore direction.

Then we have tried to explain sand transport direction by using the long wave component of velocity and long wave component of suspended sand concentration. Our explanation can further be illustrated in Figure 6. If it is possible to assume that the time history of these two quantities are sinusoidal,  $-\frac{\pi}{2}$  to  $\frac{\pi}{2}$  of the phase shift between results to onshore sand transport. If it is greater than  $\frac{\pi}{2}$ , the flux becomes lesser than zero and results to offshore transport. This relationship is clearly defined in Figure 6 which shows the results of the experiments. There are 32 results in total and in 22 cases, the direction of calculated suspended sand flux and the direction of net sand transport agree. It can therefore be concluded that the transport direction can be explained by the suspended sand flux for these experimental cases.

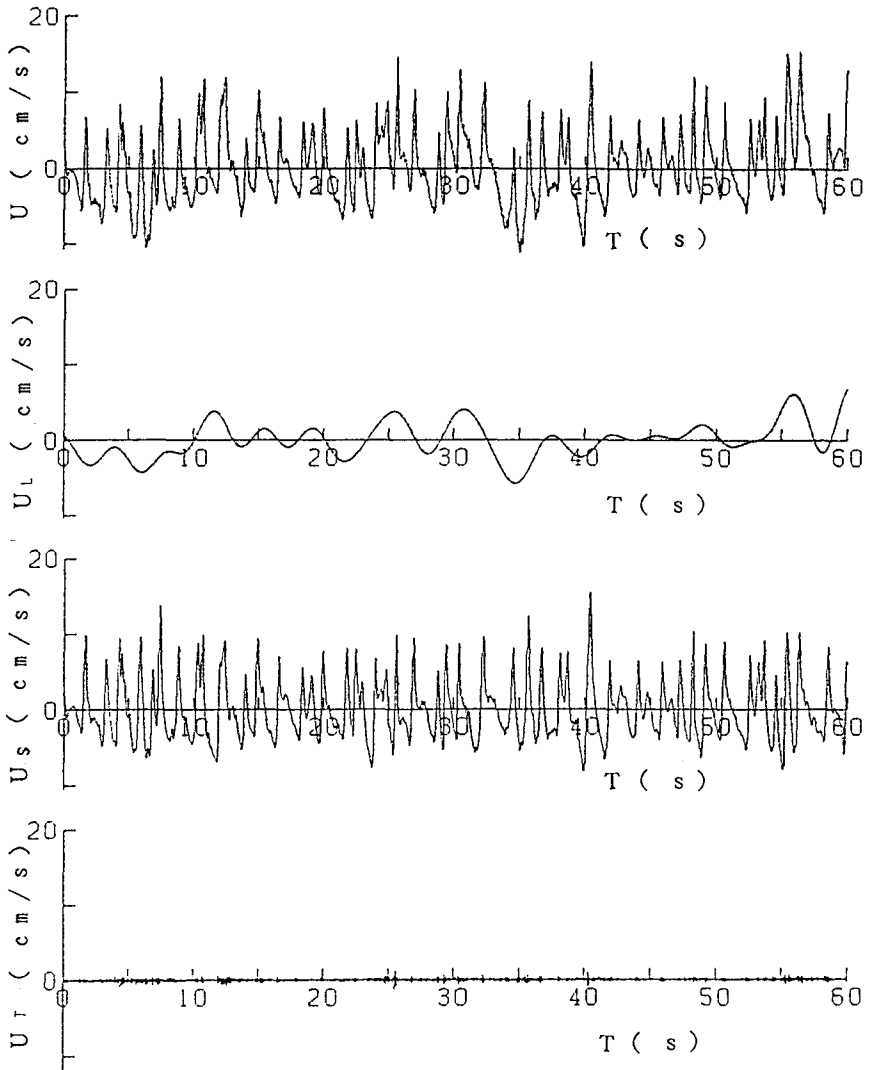


Figure 2: Example of separation.

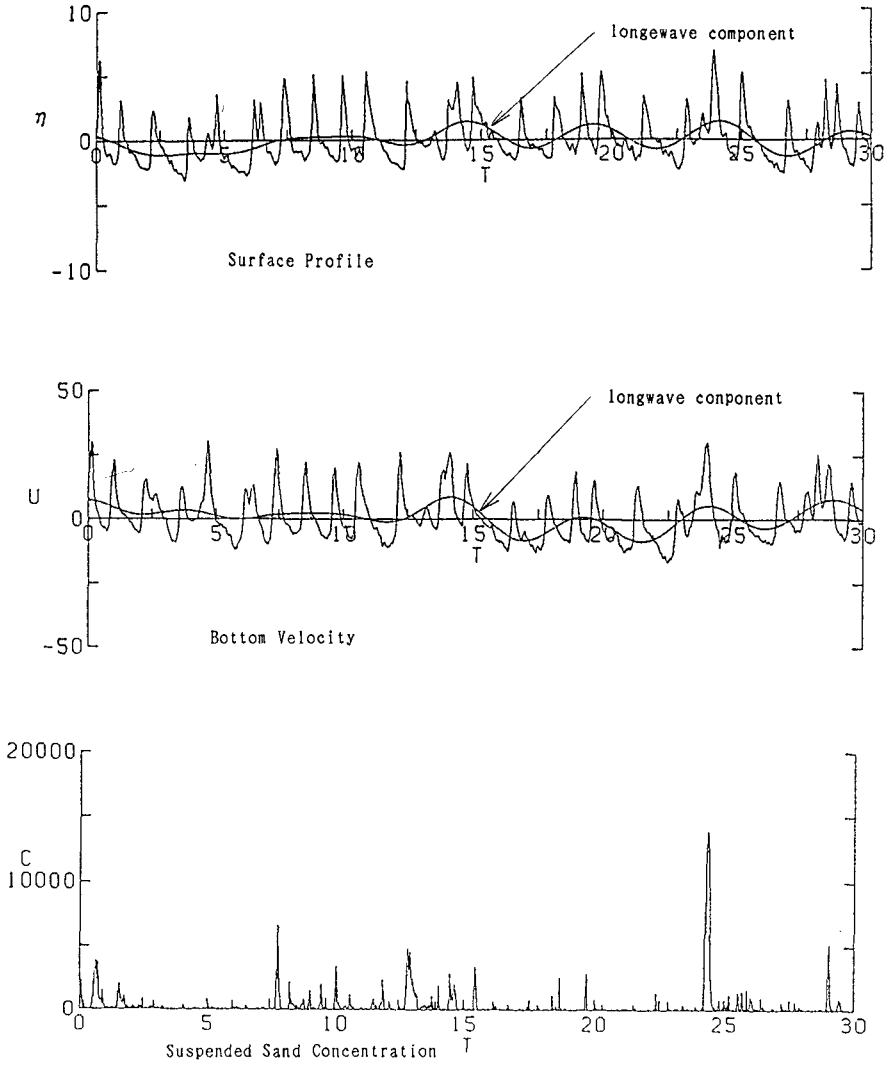


Figure 3: Example of time history.



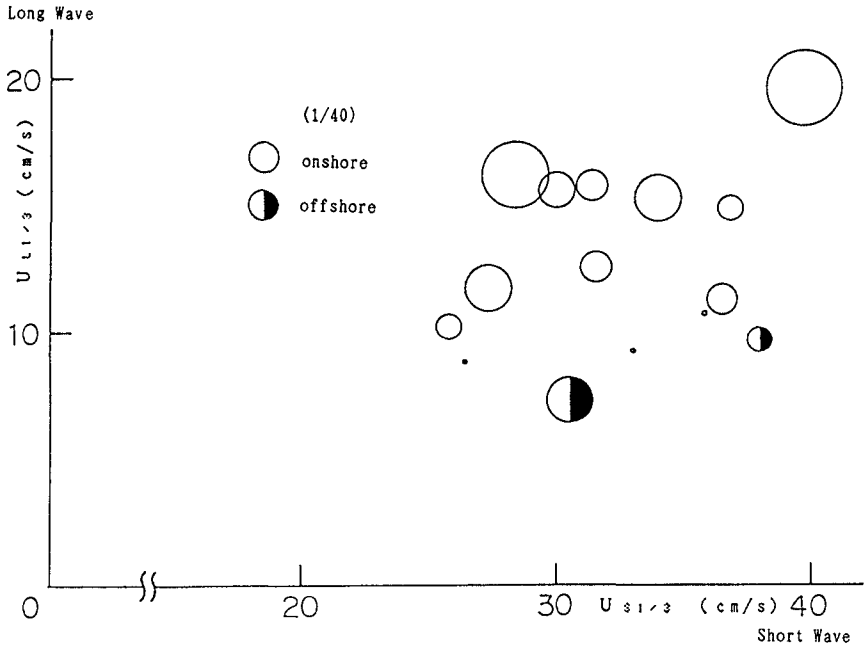


Figure 4: Effect of short wave and long wave to net sand transport rate.

#### 4. Numerical simulation

A numerical model is formulated to examine the movement of suspended sand and the resultant net sand transport rate. From the observation, it is noticed that whether suspended sand in the vicinity of sand ripples are confined in the vortex area or not is a very important point to determine the suspended sand transport direction. Therefore it was tried to distinguish these two processes, confined or not, by using the ratio of the diameter of water particle excursion distance to ripple wave length. This value was used by Shibayama and Horikawa (1985) and the critical value of the ratio was 3. If the ratio is greater than 3, the suspended sand is not confined in vortex and transported to the same direction with flow. If the ration is smaller than 3, the suspended sand is confined in vortex area, and transported after flow direction changes. Figure 7 shows the schematic view of the difference of these two patterns.

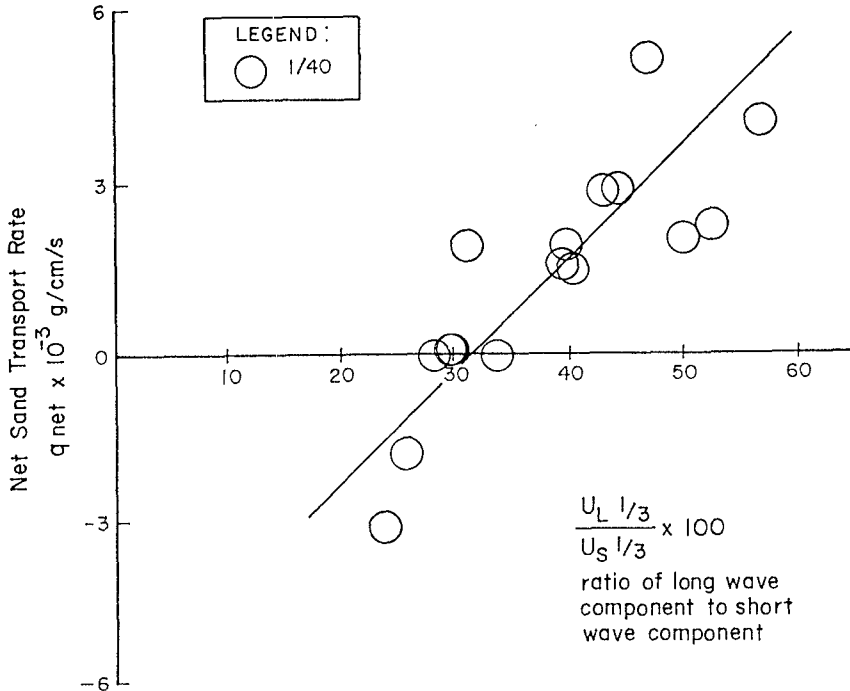


Figure 5: The ratio of long wave component of velocity to short wave component and net sand transport rate.

For the case of suspended sand confined in the vortex area, the model of Nielsen (1988) was used (Sato *et al.*, 1991). The transport rate is given by the following formula,

$$Q = \alpha_b w_s D (\Psi - \Psi_c) u / \sqrt{sgD} \quad (1)$$

where  $\alpha_b$  is 0.2,  $w$  is fall velocity,  $D$  is sand diameter,  $\Psi$  is shields parameter,  $\Psi_c$  is critical value for initiation of the movement,  $u$  is bottom velocity and  $s$  is specific gravity of sand particle. The transport rate is integrated in time for half wave period and will be confined one ripple area and then is transported when flow direction changes. When the ratio is greater than three, suspended sand will not be confined in the vortex and Eq. (1) is directly used for transport process.

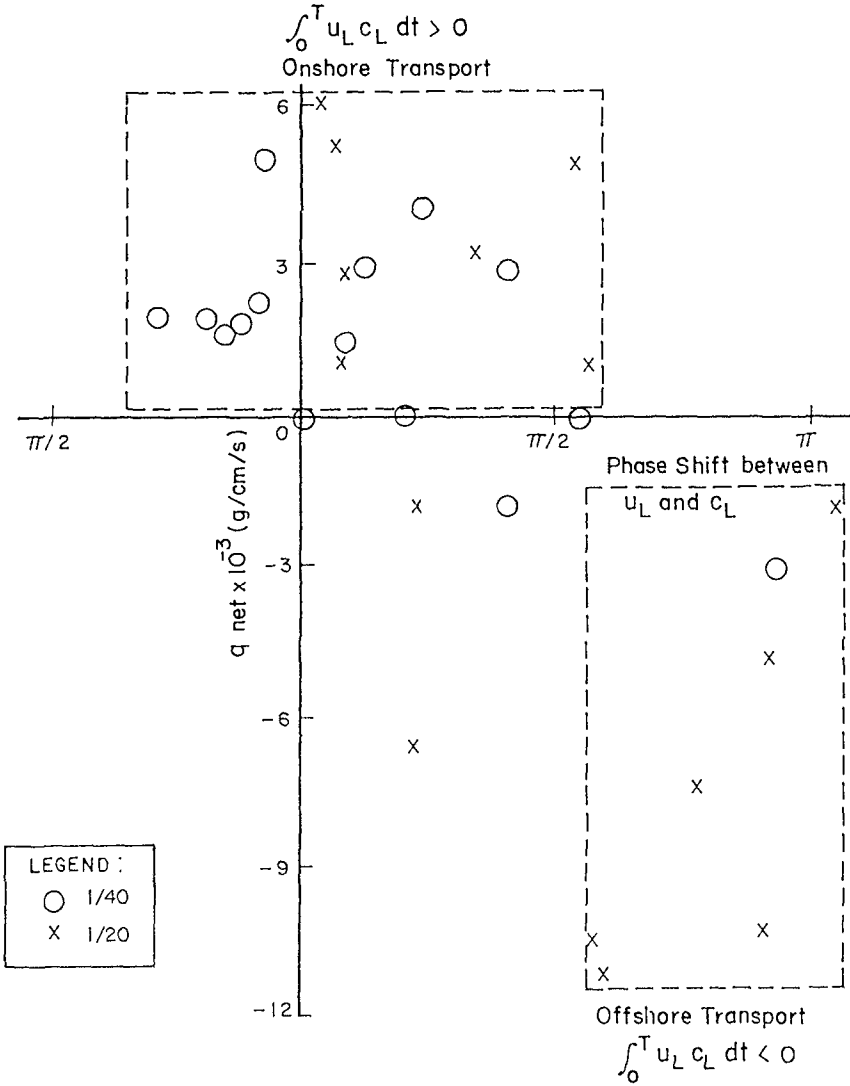


Figure 6: Phase shifts between long wave component of velocity and concentration and their effects to the net transport rate.

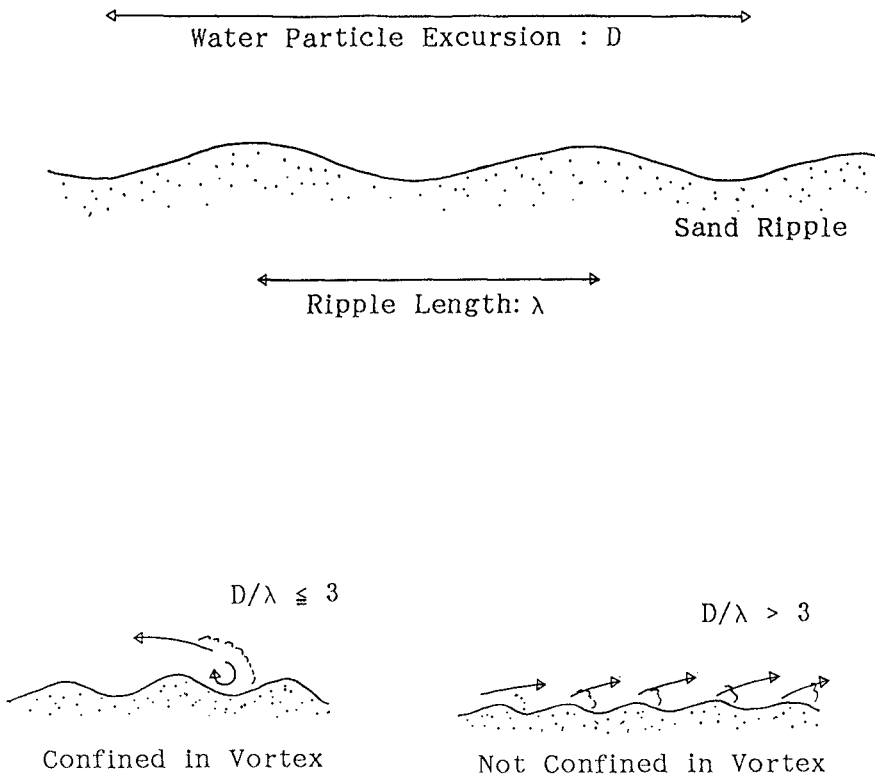


Figure 7: Explanation of sand movement.

Table 2: Results of numerical simulation.

SLOPE 1/40

CASE	DEPTH: 7.5 cm		DEPTH: 5 cm	
	CALCULATION	MEASUREMENT	CALCULATION	MEASUREMENT
A 1			$2.904 \times 10^{-3}$	$9.044 \times 10^{-3}$
A 2	$-3.104 \times 10^{-3}$	$-3.033 \times 10^{-2}$	$-0.042 \times 10^{-3}$	$-2.704 \times 10^{-1}$
A 3	$-0.046 \times 10^{-3}$	$-8.193 \times 10^{-2}$	$1.677 \times 10^{-3}$	$-9.806 \times 10^{-4}$
A 4	$0.039 \times 10^{-3}$	$-1.140 \times 10^{-2}$	$2.040 \times 10^{-3}$	$1.602 \times 10^{-2}$
A 5	$1.902 \times 10^{-3}$	$2.135 \times 10^{-2}$	$2.317 \times 10^{-3}$	$8.135 \times 10^{-4}$
A 6	$-1.821 \times 10^{-3}$	$-3.734 \times 10^{-3}$	$1.940 \times 10^{-3}$	$3.250 \times 10^{-5}$
A 7	$5.132 \times 10^{-3}$	$8.425 \times 10^{-3}$	$4.137 \times 10^{-3}$	$1.421 \times 10^{-3}$
A 8	$1.518 \times 10^{-3}$	$2.130 \times 10^{-3}$	$2.973 \times 10^{-3}$	$1.581 \times 10^{-3}$

UNIT (g/cm/s)

For sand deposition process, one-dimensional diffusion equation is used to evaluate the deposition and diffusion process. It is

$$\frac{\partial c}{\partial t} = \varepsilon \frac{\partial^2 c}{\partial z^2} + w_s \frac{\partial c}{\partial z}. \quad (2)$$

The diffusion coefficient  $\varepsilon$  is given by the following formula (Nielsen, 1988),

$$\varepsilon = w_s \eta \{1.24 \exp[-40(w_s/u_b)^2] + 0.2\} \quad (3)$$

Table 2 shows the comparison between present calculation and measured net sand transport rate. The general tendency of the predictions agrees with the laboratory results but we still have discrepancy. This may be due to the effect of bed load which is not included in the present model.

## 5. Conclusions

By laboratory experiments, it was confirmed that long wave component of velocity and suspended sand concentration has an important effect on local sediment transport rate particularly in the vicinity of shoreline areas where the long wave component is large. In these areas, the relationship between the long wave component and the net sediment transport rate can be empirically obtained. It is possible to explain the direction of net sand transport from the product of long wave component of velocity and long wave component of suspended sand concentration. From numerical experiment, we can say that if movement of suspended sand is correctly estimated, then sand transport rate is correctly evaluated.

## REFERENCES

- Katoh, K. and Yanagishima, S. (1990): Berm erosion due to long period waves, *Proc. 22nd Coastal Eng. Conf.*, ASCE, Vol. 2, pp.2073-2086.
- Nielsen, P. (1988): Three simple models of wave sediment transport, *Coastal Eng.*, Vol. 12, pp.43-62.
- Sato, S., Saito, S. and Kozuki, A. (1991): Effect of wave groupiness to sand transport rate, *Proc. of Coastal Eng.*, JSCE, Vol. 38, pp.246-250, (in Japanese).
- Shibayama, T. and Horikawa, K. (1985): A numerical model for two-dimensional beach transformation, *Proc. JSCE*, No. 357, pp.167-176.
- Shibayama, T. and Irie, Y. (1987): On-offshore sediment transport rate due to irregular waves, *Proc. of 2nd COPEDEC*, pp.1500-1511.
- Shibayama, T., Saito, E. and Okayasu, A. (1991): Effect of long waves to local sediment transport rate, *Proc. of Coastal Sediments*, ASCE, Vol. 1, pp.129-138.

## CHAPTER 188

### OBSERVATION OF FORESHORE VARIATION IN IWO-JIMA

By Toshiyuki Shigemura<sup>1</sup>, Member, ASCE,  
Kenjiro Hayashi<sup>1</sup> and Koji Fujima<sup>1</sup>

#### Abstract

The variation of the foreshore in Iwo-jima is studied by analyzing a series of aerial photographs taken seasonally for the past 4 years since 1987, and data of various surveys obtained for the past 10 years since 1982. These observations are compared with results of numerical analysis of the effects of storm waves on the foreshore. The findings obtained through these analyses are: (1)The island is still rising at a yearly rate of more than 30 cm/year; (2)The foreshore is eroded in summer and fall when typhoons often hit the island, but is restored back in winter and spring of the following year. The seasonal variation of the foreshore area ranges from 300,000 m<sup>2</sup> to 600,000 m<sup>2</sup> depending on the magnitude and frequency of the typhoons hitting the island in a year; (3)The foreshore area is increasing at a rate of 50,000 m<sup>2</sup>/year which is caused by the upheaval of the island; (4)A one-line model can be applicable for the prediction of the short-term variation of the shoreline caused by storm waves.

#### 1. Introduction

Iwo-jima is an isolated volcanic island located in the Pacific Ocean about 1250 km south of Tokyo (24°45' to 24°49'N, 141°17' to 141°21'E). Figure 1 shows the location of the island.

The maximum length of the island is about 8.6 km and its surface area is roughly 23.2 km<sup>2</sup>. The island is relatively flat with a mean altitude of 110 m and its surface is covered with dense vegetation.

The coast is mostly rimmed by a uniform sandy beach approximately 200 m wide, fully exposed to the open sea. Since the island often experiences typhoons in summer and fall, the seasonal variation of the foreshore is quite remarkable. Further, the island has

---

<sup>1</sup> Department of Civil Engineering, National Defense Academy,  
1-10-20 Hashirimizu, Yokosuka, Kanagawa 239 JAPAN

been rising at an unusual rate of more than 30 cm/year in some places, making the variation of the foreshore more complicated. These environmental conditions have prevented us from constructing any operative port facilities in this island.

To investigate the mechanisms by which the foreshore changes, the authors have been conducting various surveys on the shore of the island since 1982, and have been taking aerial photographs since 1987.

This paper intends to clarify the following items through the analysis of these field data:

- (1) The current state of the rate of upheaval of the island.
- (2) The seasonal variation of the foreshore.
- (3) The effect of upheaval on the increase of foreshore area.
- (4) The mechanism by which the foreshore changes due to storm waves.

## 2. Field surveys and Aerial Photographs

### (1) Field surveys on the shore of Iwo-jima

To investigate the variation of the rate of upheaval, the authors have been conducting traverse, level and cross surveys on the shore of Iwo-jima since 1982, with the support of the Topographic Survey Battalion(TSB) of Japan Ground Self Defense Force(JGSDF). Figure 2 shows the location of 53 measuring points provided at an interval of roughly 300 m along the entire backshore of the island.

By using these measuring points, surveys have been carried out at a frequency of at least twice a year. So far, surveys have been conducted 16 times in the period between 1982 and 1991.

In this study, the results of the level and cross surveys will be analyzed to check the current rate of upheaval and the variation of the foreshore slope of the island.

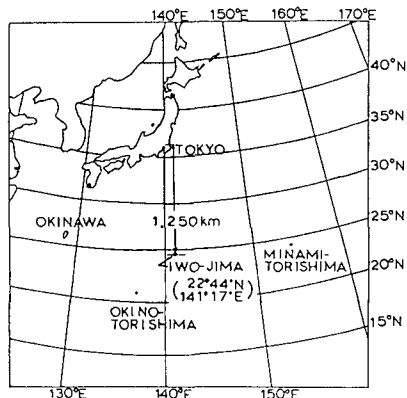


Figure 1 Location of Iwo-jima

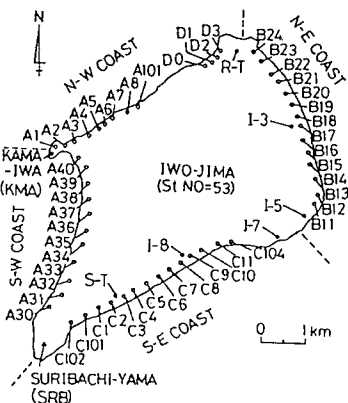


Figure 2 Location of measuring points



## (2) Processing aerial photographs

To investigate the seasonal variation of the foreshore area, the authors have been taking aerial photographs of the island, seasonally since 1987, through the support of the Japan Maritime Self Defense Force (JMSDF). The photographs were taken vertically at an altitude of 3000 m, on three flight courses set in advance over the coast of the island. Photographs were taken at both low and high tides in each photographing operation, setting the overlapping rate to be 60%. Table 1 summarizes the details of the photographing operation.

From these photographs, mosaic maps of the island with a scale of 1/10000 were made with the aid of the TSB. So far, 15 sets of the mosaic maps have been completed. On each one, a common coordinate system was provided as shown in figure 3. Here, the X axis was placed along the runway heading in the ENE direction and the origin was placed at the western end of the runway.

Based on this coordinate system, the shoreline on each mosaic map was digitized at increments of 1 mm by using a special digitizer.

Table 1 Details of the photographing operation

No.	Date	Time	Tide (cm)
1	1987.04.24	1300-1400	60.0 (FLD)
	1987.04.24	1520-1610	81.0 (LHW)
2	1987.07.07	1548-1620	86.0 (HHW)
	1987.07.08	1030-1118	25.0 (LLW)
3	1987.10.28	0855-0912	70.0 (FLD)
	1987.10.28	1142-1150	86.0 (LHW)
4	1988.02.02	0700-0730	86.0 (LHW)
	1988.02.02	1210-1240	51.0 (HLW)
5	1988.04.07	0800-0837	64.0 (FLD)
	1988.04.07	1116-1132	68.0 (EBB)
6	1988.08.22	1531-1644	88.0 (LHW)
	1988.08.23	0853-0948	37.0 (LLW)
7	1988.10.25	0701-0729	106.0 (HHW)
8	1989.01.23	1322-1340	48.0 (HLW)
	1989.01.25	0836-0852	89.0 (HHW)
9	1989.04.20	1212-1313	20.0 (LLW)
	1989.05.15	0900-0940	83.0 (HHW)
10	1989.09.06	1523-1536	64.0 (HLW)
	1989.09.08	1203-1220	82.0 (LHW)
11	1989.11.07	1400-1430	87.0 (LHW)
	1989.11.08	0800-0830	38.0 (LLW)
12	1990.01.16	1608-1657	42.0 (HLW)
	1990.01.17	0941-1254	87.0 (FLD)
13	1990.05.18	1130-1240	76.0 (LHW)
	1990.05.19	0740-0802	53.0 (HLW)
14	1990.07.17	1424-1529	78.0 (EBB)
	1990.07.18	0837-0853	38.0 (LLW)
15	1991.05.23	1531-1610	78.0 (LHW)
	1991.05.24	0915-0936	34.0 (LLW)

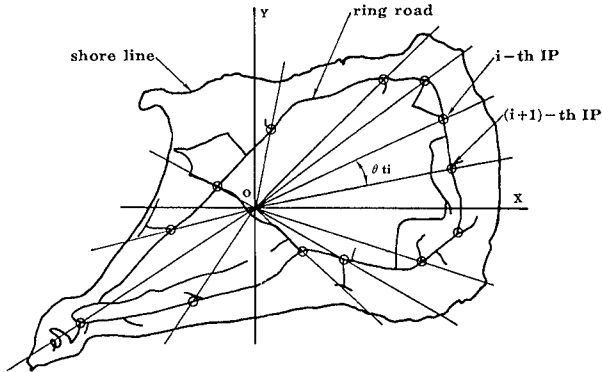


Figure 3 Coordinate system and inspection points provided for the data correction

### (3) Correction of shoreline data

Shoreline data digitized from aerial photographs may include some errors caused either by mishandling of the camera during the photography, or by the incompleteness of the mosaic. Corrections should therefore be made on each set of the shoreline data so that all the measurements should have equivalent reliability.

To carry out this correction, thirteen inspection points were selected along a road that encircled the island (see Figure 3). These points were chosen because they can be distinguished clearly on each mosaic map. They were also identified on a reference map with a scale of 1/10000, made by enlarging the latest topographical map of the island revised in 1982 by the Geographical Survey Institute of the Japanese Ministry of Construction.

The corrections to the shoreline data were performed through the following procedures in each subdivided area defined by two adjacent inspection points and the origin of the coordinate system:

(a) Superpose the origin of the subdivided area on a mosaic map on to the origin of the corresponding area on the reference map, as shown in figure 4(a).

(b) Rotate the shoreline data of the mosaic map so that the bisector of  $\theta_{mi}$  lies on the bisector of  $\theta_{ti}$ , where  $\theta_{mi}$  is an angle determined by the  $i$ -th and the  $(i+1)$ -th inspection points, and the origin of the coordinate on the mosaic map, and  $\theta_{tm}$  is the corresponding angle determined on the reference map (see figure 4(b)).

(c) Make an angle correction on the shoreline data of the mosaic map so that  $\theta_{mi}$  becomes equal to  $\theta_{ti}$ . Divide both  $\theta_{mi}$  and  $\theta_{ti}$  into increments of 1 degree to determine the length of dividing lines,  $l_m$  and  $l_t$ , where  $l_m$  is the length from the origin to the intersection point of a dividing line with the ring road on the mosaic map, and  $l_t$  is the corresponding length on the reference map (see figure 4(c)).

(d) Determine the correction factors  $r_{i,j}$  and  $r_{i,j+1}$  on every dividing line within the  $i$ -th subdivided area, where  $r_{i,j}$  is the

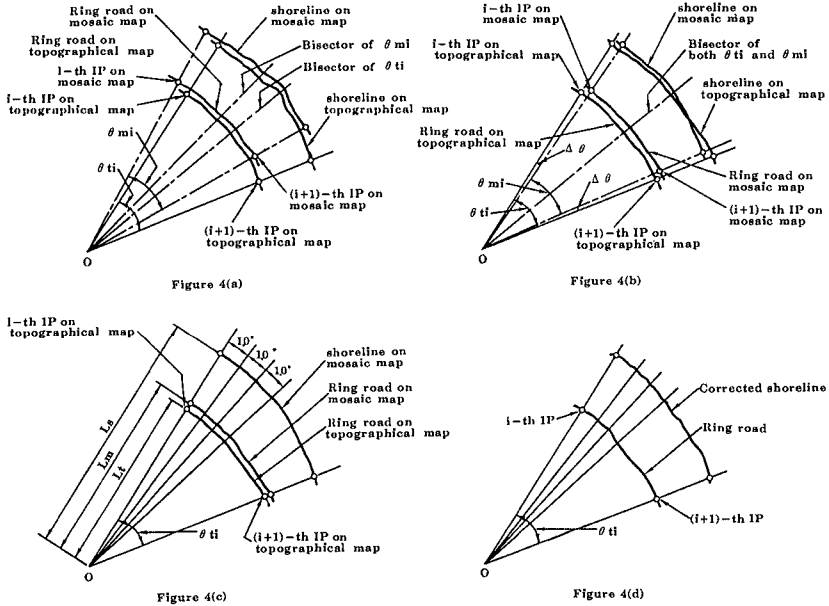


Figure 4 Correction procedures for eliminating the human errors on mosaic map

ratio  $l_t/l_m$  on the  $j$ -th dividing line, and  $r_{i,j+1}$  is ratio  $l_t/l_m$  on the  $(j+1)$ -th dividing line, both in the  $i$ -th subdivided area.

(e) Based on the values of  $r_{i,j}$  and  $r_{i,j+1}$ , determine the correction factor  $r$  for any of the shoreline data in the area surrounded by the  $j$ -th and the  $(j+1)$ -th dividing lines, and multiply each shoreline measurement of the mosaic map by  $r$  to get the corrected shoreline data (see figure 4(d)).

By performing this procedure on the original shoreline data, most of the human errors might possibly be eliminated.

However, these shoreline data, still include some errors caused by differences in tide level at the respective instants when the aerial photographs were taken. In order to eliminate this error, all of the shoreline data have to be adjusted to refer to a common level.

A datum plane (the Indian tide plane) was chosen as the reference level, and it was decided to reduce the shoreline data to this datum plane by using equations derived as follows:

Figure 5 shows a coordinate system used for the derivation of the equations. Suppose that A, B and C in this figure are points on the shoreline whose positions were digitized successively. Further, suppose that the photograph was taken when the tidal level was at an elevation  $\eta_t$  above the datum plane, and that the foreshore slope around these points is  $I_{fs}$ .

Now, we draw two lines at point B, one of them perpendicular to

the line AB and the other perpendicular to the line BC. Points  $B_1'(X_1', Y_1')$  and  $B_2'(X_2', Y_2')$  lie on these normals at the points where the elevation of the foreshore coincides with that of the datum plane. Their coordinates are determined as follows:

$$\begin{aligned}
 L &= \eta_t / I_{fs} & (1) \\
 X_1' &= X + L \sin \theta_1 & (2) \\
 Y_1' &= Y + L \cos \theta_1 & (3) \\
 X_2' &= X + L \sin \theta_2 & (4) \\
 Y_2' &= Y + L \cos \theta_2 & (5)
 \end{aligned}$$

Thus, the position of the point  $B'(X', Y')$ , the midpoint between  $B_1'$  and  $B_2'$ , can be determined by the following equations.

$$\begin{aligned}
 X' &= (X_1' + X_2') / 2 & (6) \\
 Y' &= (Y_1' + Y_2') / 2 & (7)
 \end{aligned}$$

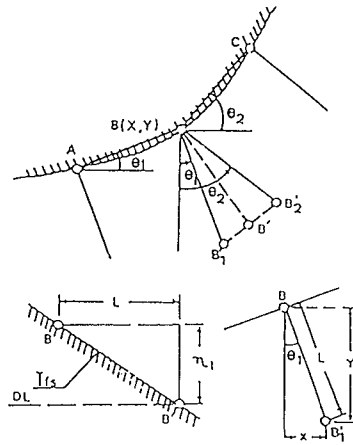


Figure 5 Coordinate system used to determine the shoreline data at the datum plane

By using these equations, errors due to the difference in tide level can also be eliminated from the shoreline data.

### 3. Results of the analyses

#### (1) Seasonal variation of foreshore slope

As stated in the preceding Chapter, the foreshore slope near the swash zone  $I_{fs}$  is needed for converting the shoreline data digitized from a mosaic map into one at the datum plane. To get this information, analyses were made on the results of cross surveys which have been done 16 times in the period between 1982 and 1991.

Figure 6 shows the seasonal variation of mean foreshore slope  $I_{fs}$  on each of the N-W, N-E, S-W and S-E coasts. Each coast was

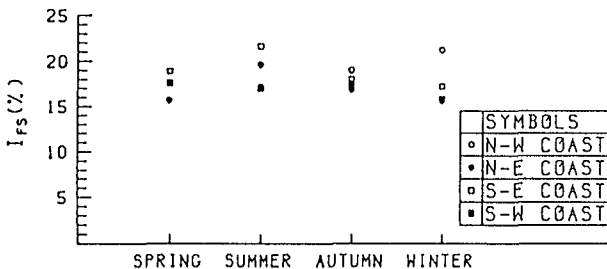


Figure 6 Seasonal variation of mean foreshore slope on each of the subdivided coasts

subdivided to obtain the local trend in the variation of foreshore slope and upheaval (see figure 2). The slopes used in reducing the corresponding shoreline data are the averages of all values of  $I_{fs}$  obtained at the measuring points on each coast.

The following facts were revealed through this analysis:

(a) Local values of  $I_{fs}$  vary in the range from 17 to 20% during summer and fall although they vary in the range from 15 to 19% during winter and spring.

(b) Local trends are not observed clearly in the seasonal variation of  $I_{fs}$ .

By using these values of  $I_{fs}$ , shoreline data were all converted to the datum plane.

## (2) Current state of upheaval

To investigate the current state of upheaval in Iwo-jima, results of level surveys were analyzed intensively. Figure 7 shows the local variation of mean upheaval rate determined at measuring points on each coast. Here, the mean upheaval rate at each point means the rate determined by averaging the upheaval rates observed at the same point 16 times in the period from 1982 to 1991. All rates have been converted into cms per year. Further, the abscissa indicates the distance of each measuring point measured northward from the southernmost measuring point provided on each coast (see figure 2). Through this analysis, the following facts were found:

(a) The mean upheaval rate tends to increase towards the north.

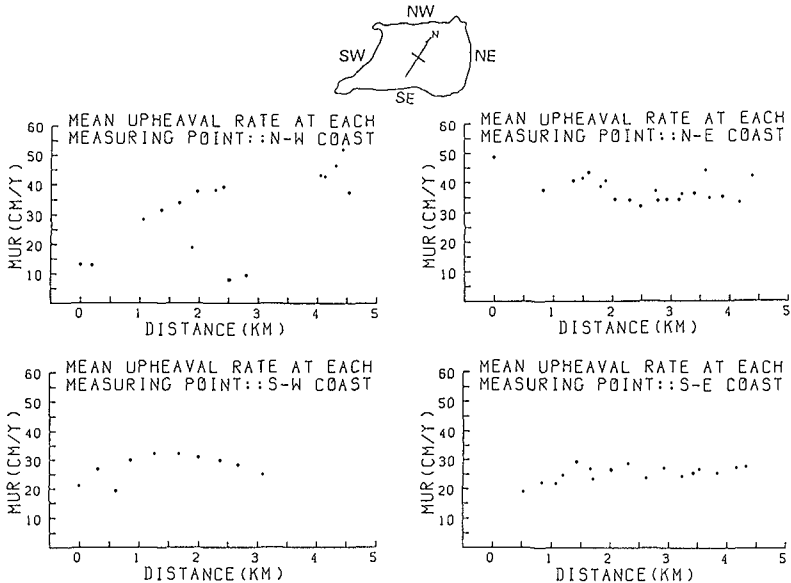


Figure 7 Mean upheaval rate at the measuring points on each of the subdivided coasts

(b) The mean upheaval rate is roughly 20 cm/year around the southern part of the island and 30 to 40 cm/year in the northern part of the island.

Tsuji et al (1969) have investigated the upheaval of Iwo-jima by comparing the elevations shown in a topographical map published by the US Army in 1952 with their surveyed data obtained in 1968. They revealed that the northern part of the island rose roughly 9 m in 16 years after 1952, while the southern part rose roughly 3 m in the same period. Further, Kosaka et al(1979) have analyzed old maps and charts of the island published prior to 1968, together with their own data surveyed in the next decade after 1968, and have reported that the island continued to rise at a rate of roughly 30 cm/year after 1952. Referring to these results, it can be concluded that the island is currently rising in the same way and at a similar rate to those revealed by earlier works.

### (3) Seasonal variation of the foreshore area

Before checking the seasonal variation of the foreshore area in Iwo-jima, we look at the time history of the total surface area, which has increased steadily since 1911.

Figure 8 shows the history of the surface area determined by analyzing old maps, charts published after 1911, and mosaic maps described in the preceding Chapter. Among these data, those prior to 1986 were introduced in the authors' previous work (Shigemura et al, 1986).

Further, data determined from the mosaic maps are shown in the upper right of this figure within a dotted rectangle. From this figure, the following facts were revealed:

(a) Iwo-jima has continued to increase its surface area in the past 8 decades, although the rate of increase has been reduced slightly after 1980.

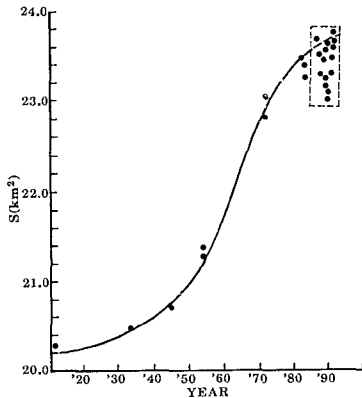


Figure 8 Time-history of the surface area of Iwo-jima after 1911

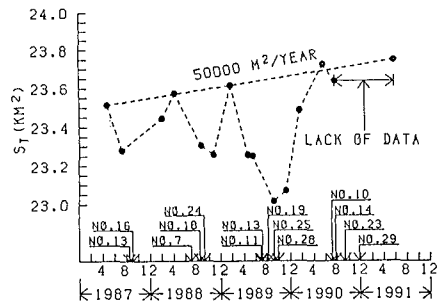


Figure 9 Seasonal variation of the surface area of Iwo-jima after 1987

(b) The envelope for the maximum area determined from the mosaic maps seems to lie on an extension of the curve through observations prior to 1980, although the seasonal variation of surface area is quite remarkable.

Now, we consider the seasonal variation of the foreshore area more closely. Figure 9 shows the seasonal variation of surface area determined by analyzing the mosaic maps. Here it should be noted that the seasonal variation of surface area may indicate that of the foreshore area itself. The numbers shown on the abscissa indicate the typhoons which passed within a range of 500 km from the island. From this figure, the following facts were revealed:

(a) The foreshore area is eroded in the period from summer to fall when typhoons often hit the island, but is restored in the period from winter to spring of the next year in which local waves of roughly 1 m high are predominant.

(b) The seasonal variation of the foreshore area ranges from 300,000 m<sup>2</sup> to 600,000 m<sup>2</sup>, depending on the magnitude and frequency of typhoons which hit the island in a year.

(c) The foreshore area is currently increasing at a rate of roughly 50,000 m<sup>2</sup> per year, which might be caused by the upheaval of the island.

#### (4) Effect of the upheaval on the increase of foreshore area

As stated previously, Iwo-jima is a volcanic island located in the Pacific Ocean. The surface is covered with dense vegetation and there is no river on the island. The source of sediments is therefore quite limited. Nevertheless, the coast of the island is mostly rimmed by a sandy beach roughly 200 m wide. These observations seem to indicate that upheaval is the only possible mechanism for supplying sediments to the shore of the island.

To confirm this, the authors have checked the relationship between the surface area and the cumulative change in elevation that occurred in the period from 1911 to 1978. The change in elevation was determined from the work done by Kosaka et al (1979).

The results was shown in figure 10, where figures in parentheses indicate the dates of observations. Through this analysis, it was ascertained that there was quite a high correlation between the increase of surface area and the cumulative upheaval height, except for the data prior to 1945. Regression analysis on these data after 1952 indicated that the shore area increased by roughly 270,000 m<sup>2</sup> per year in this period for an up-

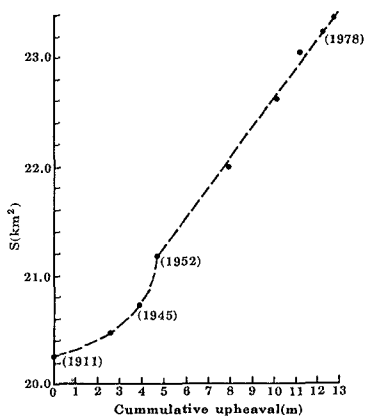


Figure 10 Relationship between the surface area and the cumulative change in elevation

heaval of 1 m. It should be noted that this relationship was found for foreshore areas which had been subject to waves over a certain period.

Next, the increase of the foreshore area due to the upheaval was estimated by applying various upheaval heights and foreshore slopes to the shoreline data of April 24, 1987. The results are shown in figure 11. It should be noted that the increase of foreshore area shown here is the estimated value, without accounting for the effects of waves and currents. If the mean upheaval rate were 30 cm/year, and the mean slope in the surf zone were 1/20, the increase in foreshore area would be roughly 150,000 m<sup>2</sup>/year. This might be a reasonable value considering the fact that the rate at present is roughly 50,000 m<sup>2</sup>/year.

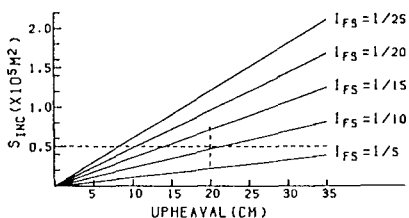


Figure 11 Increase of foreshore area due to the given upheaval height

#### (5) The response of the foreshore to storm waves

The analyses done so far have revealed that the magnitude and frequency of typhoons would be the governing factors in the variation of the foreshore area in Iwo-jima. It was therefore attempted to predict the short term variation of foreshore transformation due to storm waves generated by typhoons, using numerical models.

Two typhoons were selected for the numerical analyses, whose characteristics are summarized in table 2.

Table 2. Characteristics of typhoons at the times when they approached most closely to Iwo-jima.

Typhoons	Date	Time	P(mb)	R-30kt	Location	DIR
#8911	July.26,1989	00:47	940.0	225 km	350km W	SE
#9813	Aug. 4,1989	14:66	950.0	275 km	370km E	WNW

In this table, R-30kt means the semi-diameter of a circle in which wind velocity is greater than 30 kt. The Location column gives the distance and direction of the center of the typhoon from the island, and the DIR column indicates the direction of the typhoon.

These typhoons were chosen because the authors have the mosaic maps produced from the aerial photographs taken just before and after these typhoons hit the island (see table 1), and it is possible to compare the

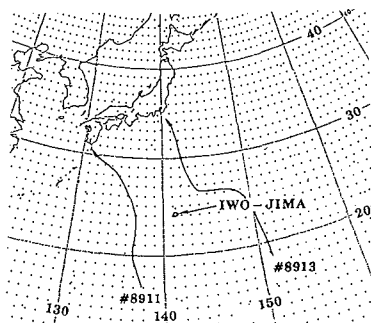


Figure 12 Passage routes of typhoons #8911 and #8913



predicted values with the observed ones.

Figure 12 shows the passage routes of these typhoons. As it is shown in this figure, both typhoons advanced into the NE direction, although typhoon #8911 passed offshore to the west of the island and typhoon #8913 passed to the east.

The numerical analysis consists of a prediction of the offshore waves, calculation of wave transformation and prediction of shoreline variation, as described below.

(a) Prediction of offshore waves generated by typhoons

Prediction of offshore waves was carried out by using the method developed by Goto and Aono (1992) which requires the following steps:

- Determine the typhoon constants at one hour intervals based on the meteorological maps published by Japan Meteorological Agency.
- Compute the wind field around the computational area.
- Select the prediction point of offshore waves at Iwo-jima and calculate the two dimensional energy spectrum  $S(f, \theta)$  which is obtained by composing the energy spectrum of waves approaching the prediction point from 16 directions along the respective wave rays.
- Determine the height and period of significant waves at one hour intervals based on the values of  $S(f, \theta)$ .

(b) Calculation of wave transformation

Wave transformation due to shoaling, refraction and diffraction was calculated as follows using small amplitude wave theory:

- Use a nautical chart published in 1981 by Maritime Safety Agency of Japan for the bathymetry around the island.
- Provide a calculation area around the island in which the depth is less than 100 m. Further, provide a square grid on the calculation area whose length is 50 m.
- Calculate the wave transformation due to shoaling, refraction and diffraction, to determine the magnitude and direction of energy flux at the breaking points. Here, use Goda's breaker formula (1973) as a breaker index.

(c) Prediction of shoreline variation

Shoreline variation was predicted by using a one-line model following the steps shown below:

- Assume the critical water depth for sand movement by waves to be 15 m, and the runup height of waves to be 1 m above mean sea level.
- Compute the longshore sediment transport flux by using the CERC formula, assuming the coefficient of longshore sediment transport rate to be 0.1.
- Assume that the longshore sediment transport flux coming into the computational area through the boundary between adjacent coastal regions to be zero.

Figure 13 shows the time-wise variation of the predicted values of significant wave height, wave period and direction of deep sea

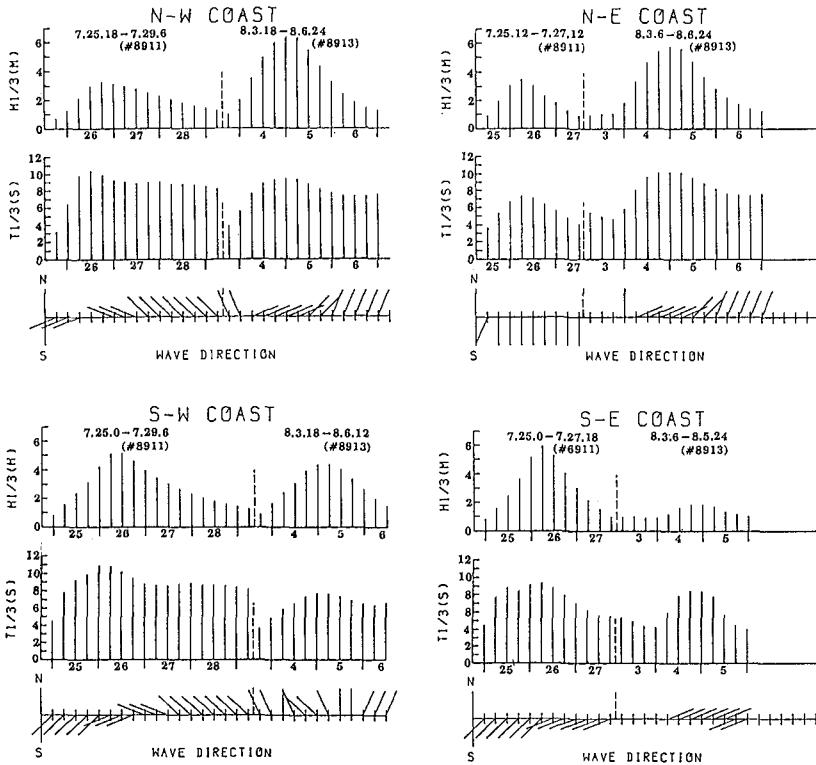


Figure 13 Time-wise variation of the predicted values of significant waves

waves generated by two typhoons. Values after successive intervals of 6 hours are shown in this figure. From this figure, the following facts can be read clearly:

- In the case of typhoon #8911, the direction of generated waves offshore of every subdivided coast at the initial stage is SW. However, it becomes WNW off the west coast, S or WSW off the east coast as the typhoon advances northward. Waves with a peak height of roughly 5.9 m appear off the in S-E coast although wave with peak height of roughly 5.1 m appears in the S-W coast. In the case of typhoon #8913, the wave direction is mainly ENE except for the case of the S-W coast at the initial stage. However, it becomes NNE except for the case of the S-E coast as typhoon advances northward. Waves with a peak height of about 6.4 m appear off the N-W coast, although waves with a peak height of roughly 5.8 m appears off the N-E coast.

Based on these offshore wave predictions, the wave transformation was calculated to determine the breaker characteristics, and

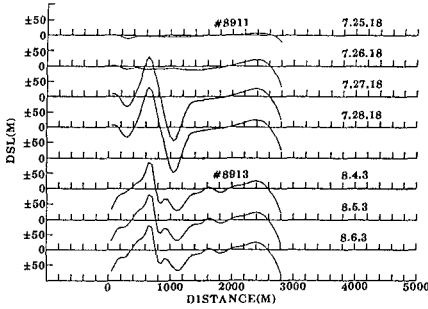


Figure 4(a) Time-wise variation of the shorelines predicted in the S-E coast

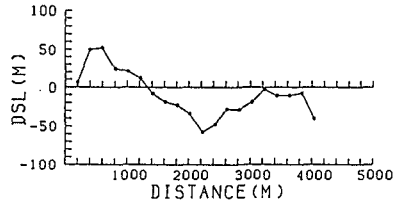


Figure 4(b) Variation of the shoreline observed in the S-E coast in the period between May 15, 1989 and Sep.9, 1989

finally the variation of the shoreline was calculated by the method stated previously. Figure 14(a) shows the time-wise variation of the shorelines predicted for the S-E coast at intervals of 24 hours. On the other hand, figure 14(b) shows the change of the corresponding shoreline determined through the mosaic maps which were made from the aerial photographs taken before and after these typhoons hit the island.

In both figures, the distance shown on the abscissa is that measured southward from the northern boundary on the S-E coast. Here, it should be noted that the predicted variation of the shorelines is based only on the two successive typhoons, although the observed variation of the shoreline is the effect of all waves (including those due to the storm waves during two typhoons) over the period from May 15, 1989 to September 6, 1989. Thus, caution should be exercised in drawing conclusions from a comparison between these two results. However, the numerical analysis clearly indicates that the northern part of the shoreline is considerably eroded by waves with SW direction generated by typhoon #8911 and is restored gradually by waves with NE direction generated by typhoon #8913. Further, the final pattern of the predicted shoreline in figure 14(a) is quite similar to that of the observed shoreline shown in figure 14(b).

Table 3 Comparison of the observed and predicted foreshore areas eroded in summer of 1989

Coasts	S(Observed)	S(Predicted)
N-E	-108,000 m <sup>2</sup>	-38,000 m <sup>2</sup>
N-W	-63,000 m <sup>2</sup>	-54,000 m <sup>2</sup>
S-E	-32,000 m <sup>2</sup>	-29,000 m <sup>2</sup>
S-W	-10,000 m <sup>2</sup>	-11,000 m <sup>2</sup>

Table 3 summarizes both predicted and observed values of foreshore variation in each subdivided coast. In the case of the N-E

coast, the predicted value of the foreshore variation is quite different from the observed value. This might be caused by the fact that both boundaries of this coast are rocky. However, the model used in this study seems to predict the variation of the foreshore area quite satisfactorily.

#### 4. Conclusions

Foreshore variations in Iwo-jima were investigated by analyzing a series of mosaic maps made from the aerial photographs which had been taken seasonally for the past 4 years since 1978. Analysis was also undertaken on the data of level and cross surveys carried out on the entire beach of the island for the past ten years since 1982. Further, numerical analysis was performed to study the short-term variation of the foreshore area due to storm waves generated by two typhoons which had hit the island in July and August, 1989. The predicted variation of the shorelines was compared with that observed in the corresponding period.

As a result, the following facts were revealed:

- (1) The island is still rising at a rate more than 30 cm/year, although the rate of upheaval increases toward the north.
- (2) The foreshore area is eroded in summer and fall when typhoons often hit the island, but is restored in winter and spring of the following year when waves of roughly 1 m high are predominant.
- (3) The seasonal variation of the foreshore area ranges from 300,000 m<sup>2</sup> to 600,000 m<sup>2</sup> per year depending on the magnitude and frequency of the typhoons hitting the island in the year.
- (4) The foreshore area continues to increase currently at a rate of roughly 50,000 m<sup>2</sup>/year, which is undoubtedly caused by the upheaval of the island.
- (5) A one-line model can be applicable for the prediction of short-term variation of the shoreline caused by storm waves.

#### References

- Goda, Y. (1973), "On the breaker index of irregular waves", Proc. of the 20th Japanese Conference on Coastal Engineering, JSCE, 571-573 (in Japanese).
- Goto, C. and Aono, T. (1992), "A Spectral Wave Prediction System For A Single Point", Report of the Port and Harbor Research Institute, Ministry of Transport, Japan, Vol. 31, No. 2, 55-73 (in Japanese).
- Kosaka, J. et al (1979), "Investigation Report of the Volcanic Action Ogasawara-Iwo-jima", Santama Office for isolate islands, Tokyo Metropolitan Government, No. 3, 1-89 (in Japanese).
- Sigemura, T. (1986), "Shore Process along the coast of Iwo-jima", Proc. of the 20th ICCE, Chapter 112, ASCE, 1523-1534.
- Tsuji, S., Kuriyama, M. and Tsurumi, T. (1969), "Investigation Report of Ogasawara Islands", Technical note of Geological Institute, Ministry of Construction, Japan, 1-18 (in Japanese).

## CHAPTER 189

### SHORE NOURISHMENT AND THE ACTIVE ZONE: A TIME SCALE DEPENDENT VIEW

Marcel J.F. Stive<sup>1</sup>, Huib J. De Vriend<sup>2</sup>, Robert J. Nicholls<sup>3</sup> and Michele Capobianco<sup>4</sup>

#### Abstract

First results towards the development of a predictive method of cross-shore spreading of beach and shore nourishments are described. Present interest in nourishment as an appropriate answer to long-term erosion motivates special attention for the time evolution of the cross-shore spreading. Hallermeier's (1981) annual shoreward boundary,  $D_p$ , of the shoal zone is probably the most applied quantitative boundary for the seaward extent of nourishments. The extension of this concept to include time-dependency is a logical and necessary step to improve our understanding of nourishment performance. Moreover, insight into the precise cross-shore variation of the spreading process is lacking.

By application of a detailed process-based, cross-shore morphodynamic model and some inductive assumptions the spreading process is studied as a function of time. The results give qualitative and quantitative indications of the spreading process, in particular concerning the evolution character of the spreading and the relation between the nourishment foot and closure depth.

#### Introduction

The seaward extent and the rate of morphodynamic activity across the active zone are of fundamental importance in designing shore nourishment (Davison et al., 1992). A valuable and useful approach to determine the seaward extent (closure depth) was developed by Hallermeier (1981), who defined it as the

---

<sup>1</sup> Laboratori d'Enginyeria Marítima, Universitat Politècnica de Catalunya, Spain (visiting from Delft Hydraulics, The Netherlands);

<sup>2</sup> Delft Hydraulics, The Netherlands;

<sup>3</sup> Laboratory for Coastal Research, University of Maryland, USA;

<sup>4</sup> Tecnomare S.P.A., Venezia, Italy

annual shoreward boundary of his shoal zone. Obviously, as qualitatively indicated by Hallermeier (1981), the rate of activity varies across the active zone profile. This rate will depend not only on the hydraulic impact, but also on the time scale considered. Similarly, a time scale dependence of the seaward extent of the active zone (the closure depth) can be expected. Taking 20 years of hindcast wave data at Ocean City, Maryland, and considering it on a year-to-year basis, Anders and Hansen (1990) found  $D_1$  had a mean value of about 5 m, but annual values varied from 3.7 to 7.3 m. Suggestions for the time scale dependence were made by Hands (1983) in his analysis of the Great Lakes profile responses to mean lake level variations. Insight into the time scale dependence of the closure depth and the relative activity across the active zone is of importance for more accurate prediction of nourishment behaviour and lifetime. This is particularly true in the light of the likelihood of accelerated global sea-level rise (e.g. Nicholls et al., 1992). Shore nourishment will be required to counteract the resulting shoreline recession in many parts of the world. In this context however, the coastal system is considered on longer time and space scales than has been common practice so far.

Because of the very limited field information about the cross-shore spreading of nourishments, we have chosen to initially rely on a mathematical-physical approach, using the combination of physical inductive concepts and a detailed process-based model. This approach may be termed behaviour oriented modelling. In order to analyse our results and to obtain predictive methods, we also rely on system dynamics related approaches to describe the nourishment behaviour. An example of this is the application of a diffusion-type equations to simulate in the simplest way some aspects of the observed behaviour. The coefficients of such equations are at the moment derived by using a parameter identification method with "experimental" data produced under well defined boundary and initial conditions. We plan further work to generalize our results in order to be able to handle a variation of boundary and initial conditions, and we intend to confront and verify our findings with real world data.

#### Study approach and assumptions

In order to indicate our present scale of interest we distinguish the following scales of profile behaviour (see Table 1).

As can be observed from Table 1 the time and length scales of our topic are larger than years and longer than the surfzone. This implies that we are dealing with what we would define as long term modelling: modelling on a time scale longer than can be handled by existing validated process-based (mathematical-physical) models. This, in turn, implies that we have to fall back on inductive concepts, so that we enter the field of behaviour oriented modelling (Stive et al., 1990). In practice this means that we have to adopt some

assumptions based on our physical intuition and our expectations of the process behaviour.

physical process	cross-shore length scale	approximate time scale
response to relative sea-level rise	total shoreface to inner shelf	decades to a century
spreading of structural shore nourishment	upper to middle shoreface	years to a decade
surfzone bar evolution	surfzone	storms to a year

Table 1 Time and length scales of cross-shore profile behaviour

In fact, we base some of our assumptions on the results due to an interesting application with respect to shore nourishment made by Van Alphen et al. (1990). Based on simulations with the process-based dynamic model of Roelvink and Stive (1989) the efficiency of nourishments, placed at different positions in the active zone, was systematically investigated. The simulations were run over many years with a synthesized, observed wave climate over one full year as hydraulic input. De Vriend and Roelvink (1989) were the first to conclude from the results that the spreading of the nourishments closely resembles the smoothing out of a "disturbance" on an otherwise equilibrium profile. This smoothing process shows a shoreward asymmetry: the smoothing is stronger at the shoreward side. Associated with this asymmetry, the part of these artificial disturbances tending to move onshore exceeds the part tending to move offshore. And finally, the time scale of adjustment after a disturbance increases rapidly with depth.

Stimulated by these conclusions we adopt the following approach to generate results on the spreading behaviour of nourishments. By using a synthesized or schematized wave climate as an input, pairs of profile evolutions are generated by the Roelvink and Stive model: one for an undisturbed, ideal profile (giving the "autonomous" development) and one for a disturbed, ideal profile, which is identical to the former except for the nourishment. Our basic assumption is that -until we know better- the spreading can be derived by comparing a nourished profile development with an autonomous profile development. The reasoning behind this is twofold:

(1) The autonomous profile development on the scale of years to a decade is most probably not well represented by the dynamic model, both because of

deficiencies in this model and because in reality there will be more than just cross-shore processes responsible for the profile development. So, for the time being we assume that in a practical situation, there exists in one form or other an "autonomous" profile development, which is not resolved nor affected by our approach;

(2) Because we may consider the nourishment as a profile disturbance lifting the profile away from "equilibrium" we assume that the dynamic development is more accurately computed by the dynamic model than the "equilibrium" development.

Our present, initial interest is into beach or upper shore nourishments rather than into subaqueous profile nourishments. Although we would promote the application of profile nourishment in general (Stive et al., 1991), common practice is still to feed the beach rather than the subaqueous profile.

The "ideal" profile applied as the initial profile for the calculations, which we term the Dean-Moore-Wiegel profile (DMW-profile), consists of the equilibrium profile with a grain diameter dependence in the proportionality constant (e.g. Dean, 1991). Near the waterline, however, we adopt a constant slope, related to the grain diameter and the exposure of the coast following Wiegel (1964), as follows:

$$D = Ax^{2/3} \quad \text{for } dD/dx \leq \tan\beta$$

$$D = D^* - \tan\beta(x^* - x) \quad \text{for } dD/dx > \tan\beta$$

where  $D$  is the mean still water depth,  $x$  the cross-shore distance from the virtual waterline belonging to the Dean-profile,  $\tan\beta$  the beach slope,  $A$  the proportionality constant and the parameters denoted with an asterisk are evaluated at the location where  $dD/dx = \tan\beta$ .  $D^*$  and  $x^*$  may be easily computed, but since these parameters are imposed by the Dean-profile, it is not possible to directly control the resulting DMW profile value at  $x = 0$ . In the cases presented we have chosen a grain diameter of 200  $\mu\text{m}$  (so that  $A=0.1$ ) and a corresponding beach slope for exposed beaches of 1:75.

On the resulting ideal profile we place a nourishment (i.e.; beach fill) of 100  $\text{m}^3/\text{m}$  which with a triangular shape, maximum height near the waterline and reaching from minus 2.5 m to plus 1 m, bringing the coastline some 57 m seaward. This may be considered as intermediate between a pure dry beach nourishment and a pure subaqueous nourishment. Since, in general, beach fill is spread quickly across the upper part of the profile, the present results can be considered representative for most of the commonly applied beach nourishments.



In compliance with Hallermeier (1981), we have adopted the nearshore wave climate synthesis of Thompson and Harris (1972). They provide a relatively straightforward year distribution for nearshore wave heights as a function of the yearly mean  $H_{sig}$ . Here we have assumed that this distribution may be extrapolated to reach a 10-year climate. We are aware of the fact that this assumption may not be correct. Further efforts into this are foreseen.

## Results

In our analysis of the results, we have so far concentrated on the following three questions:

- (1) How does the nourishment spread (diffusively, advectively) as a function of the process variables?
- (2) Is there a relation between the depth of closure and the "foot" of the nourishment?
- (3) How does the nourishment foot (and the depth-of-closure) evolve in time?

In the present paper we discuss results of the following calculations:

- Run 50 vs run 51, being an undisturbed DMW-profile evolution vs a nourished DMW-profile evolution subject to the same wave climate characterized by a steepness of 3% (see Figure 1);
- Run 60 vs run 61, being an undisturbed DMW-profile evolution vs a nourished DMW-profile evolution subject to the same wave climate characterized by a steepness of 1% (see Figure 2).

The principal variation between these cases is the wave steepness (all cases have a year-mean  $H_{sig}$  of 75 cm). From trial calculations it was concluded that the principal process variable is the wave steepness.

Figures 1 and 2 confirm our earlier thoughts that the beach fill spreads over the profile both diffusively and advectively. To a first approximation, the beach fill spreads like a thinning wedge with its foot going to deeper water, and with the rate of seaward propagation clearly larger for the less steep wave climate. It is interesting to note that the propagation of the nourishment foot more or less follows Hallermeier's closure depth which we have extended for the larger timescale (see Table 2). The extension of Hallermeier is simply realized by assuming that we may replace the important variable  $H_{sx}$ , the significant wave height exceeded 12 hours per year, by  $H_{sx,y}$ , the significant wave height exceeded 12 hours per y year. These results suggest that -to a first order of approximation- we may predict the spreading evolution of a nourishment by applying the suggested extension of Hallermeier for the position of the foot of the nourishment and by assuming that the nourishment volume simply decreases as a thinning wedge.

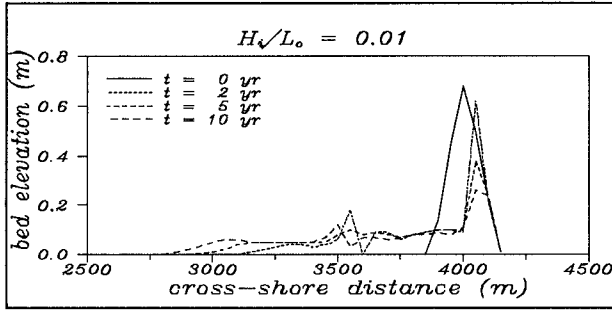


Figure 1 Cross-shore spreading of a triangular beach fill for a low steepness wave climate (SWL at 4000 m)

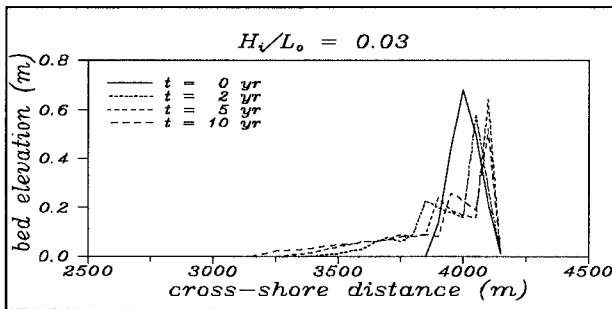


Figure 2 Cross-shore spreading of a triangular beach fill for a high steepness wave climate (SWL at 4000 m)

wave steepness	1/y year storm	$D_{i,Hallermeier}$ ext (m)	$D_{nourishment}$ foot (m)
$H/L_0 = 0.01$	1	7.3	8.1
	2	8.0	8.9
	5	8.9	9.9
	10	9.6	10.9
$H/L_0 = 0.03$	1	6.5	5.6
	2	7.2	6.1
	5	8.0	7.4
	10	8.7	8.6

Table 2 Comparison of the time evolution of the nourishment foot versus an extension of Hallermeier's  $D_i$ .

### Simulation of the observed behaviour

It is one of our objectives to generalize and parameterize the spreading process, both for the purpose of practical applications and scientific understanding. In the context of practical applications it is important to note that the presented computational results require relative high computation times, e.g. a 10 year simulation with a time step of one day on a 33 MHz 386 with coprocessor at 5 MIPS takes 12 hours. Our parameterization method follows the idea to identify space varying parameters in a diffusion-type equation.

In fact, we consider a class of behaviour models, basically proposed by De Vriend and Roelvink (1988) which shows a close similarity to the n-line concept (Perlin and Dean, 1983; De Vroeg et al., 1988). In general terms (e.g. Capobianco, 1992) we consider the following type of diffusion equation for the profile elevation  $z(x,t)$ :

$$\partial z / \partial t = \partial / \partial x [F(x) \partial z / \partial x] + \partial / \partial x [V(x)z] + S(t,x,z)$$

where  $F(x)$  represents partly the diffusion character and partly an advective character,  $V(x)$  the advective character and  $S(t,x,z)$  is a source function. With appropriate initial and boundary conditions the *profile elevation*  $z(x)$  can be described as a function of *cross-shore position*.

The same basic equation may be applied to describe the evolution of the

The same basic equation may be applied to describe the evolution of the *cross-shore position*  $x(z)$  as a function of the *profile elevation*, or the actual cross-shore position  $x(z)-x_e(z)$  referred to an "equilibrium profile position", or the actual cross-shore position  $x(z)-x_a(z)$  referred to an "autonomous profile position".

The vertical variation of the diffusion coefficient allows us to represent a variation of the morphological timescale with the vertical position, and an asymmetry in the longterm residual sand displacement across the profile. The calibration of this parameter is the key element of the model definition: all information, on hydraulic and sediment characteristics as well as on shorter-term dynamics is stored in it. One objective of our study is to assess -in the context of shore nourishment behaviour- whether and to what extent the diffusion model concept stands in practice, and to find simple and manageable parameterized expressions for the diffusion coefficient  $F$  as a function of boundary conditions, geometrical features and environmental parameters.

### Conclusions

The longer term objective of our study is to arrive at a predictive method to establish the cross-shore spreading of beach and shore nourishments. The present interest of coastal authorities in nourishment as an appropriate answer to long-term erosion, particularly in the light of an acceleration of sea-level rise, is our motivation to approach the problem with special interest in the time evolution of the cross-shore spreading. The currently most applied quantitative boundary for the seaward extension of nourishments is probably the annual shoreward boundary,  $D_1$ , of the shoal zone as developed by Hallermeier (1981). The extension of this concept to include time-dependency is a logical and necessary step in improving beach nourishment techniques. Moreover, insight into the more precise cross-shore variation of the spreading process is of great practical importance.

By application of a detailed process-based, cross-shore morphodynamic model and some inductive assumptions the spreading process is studied as a function of time. The results give qualitative and quantitative indications of the spreading process, in particular concerning the evolution character of the spreading and the relation between the nourishment foot and closure depth. We have extended Hallermeier's concept to longer time scales. This extension is simply realized by assuming that we may replace the important variable  $H_{sx}$ , the significant wave height exceeded 12 hours per year, by  $H_{sx,y}$ , the significant wave height exceeded 12 hours per  $y$  year. The propagation of the nourishment foot follows the time-dependent  $D_{1,ext}$  quite closely in both examples. Thus, our results suggest that -to a first order of approximation- we may predict the spreading evolution of a nourishment by applying the suggested extension of Hallermeier

for the position of the foot of the nourishment and by assuming that the nourishment volume simply decreases as a thinning wedge.

### Acknowledgement

This work is partly carried out as part of the European Community MaST G6 Coastal Morphodynamics Project (Directorate General for Science, Research and Development, MaST Contract no. 0035-C) and the Coastal Genesis Research Programme of The Netherlands (Rijkswaterstaat, Tidal Waters Division). MJFS acknowledges the support of the Researchers of Excellence Programme for Catalan Universities of the Generalitat de Catalunya.

### References

- ANDERS, F.J. and HANSEN, M. (1990)  
Beach and borrow site sediment investigation for a beach nourishment at Ocean City, Maryland. U.S. Army Corps of Engineers, Waterways Experiment Station, Coastal Engineering Center, Technical report CERC-90-5, 77 pp
- CAPOBIANCO, M. (1992)  
A class of partial differential equations for modelling and control of medium term evolution of coastal profiles. American Control Conference, Chigaco, Illinois, 24-26 June
- DAVISON, A.T., NICHOLLS, R.J. and LEATHERMAN, S.P. (1992)  
Beach nourishment as a coastal management tool: An annotated bibliography on developments associated with the artificial nourishment of beaches. J Coastal Research, 8, 984-1022
- DEAN, R.G. (1991)  
Equilibrium beach profiles: Characteristics and applications. J Coastal Research, 7, 1, 53-84
- DE VRIEND, H.J. and ROELVINK, J.A. (1989)  
Innovation of coastal defence: interaction with the coastal system. Rijkswaterstaat/Delft Hydraulics, Memorandum "Coastal Defence after 1990", Technical Report no. 19, 39 pp.
- DE VROEG, J.H. SMIT, E.S.P. and BAKKER, W.T. (1988)  
Coastal Genesis. Proceedings 21st Int Conf Coastal Eng, Malaga, Spain, pp 2825-2839

HALLERMEIER, R.J. (1981)

A profile zonation for seasonal sand beaches from wave climate. *Coastal Eng.*, 4: 253-277

HANDS, E.B. (1983)

Erosion of the Great Lakes due to changes in the waterlevel. In: P.D.Komar (Editor), *Handbook of Coastal Processes and Erosion*. CRC Press, Boca Raton, Fl, pp 167-189

NICHOLLS, R.J., DENNIS, K.C., VOLONTE, C.R. and LEATHERMAN, S.P. (1992)

Methods and problems in assessing the impacts of accelerated sea-level rise. Proc. "The World at Risk: Natural Hazards and Climate Change", In press

PERLIN, M. and DEAN, R.G. (1983)

A numerical model to simulate sediment transport in the vicinity of coastal structures. CERC, Vicksburg, Misc. Rept. no. 83-10, 119 pp.

ROELVINK, J.A. and STIVE, M.J.F. (1989)

Bar-generating cross-shore flow mechanisms on a beach. *J. Geophysical Research*, Vol 94, No.C4, pp 4785-4800

STIVE, M.J.F., ROELVINK, J.A. and DE VRIEND, H.J. (1990)

Large-scale coastal evolution concept. Proceedings 22nd Int Conf on Coastal Eng, Delft, The Netherlands, pp 1962-1974

STIVE, M.J.F. , NICHOLLS, R.J. and DE VRIEND, H.J. (1991)

Sea-level rise and shore nourishment: A discussion. *Coastal Eng.*, 16: 147-163

THOMPSON E.F. and HARRIS, D.L. (1972)

A wave climatology for U.S. coastal waters. Proc. Offshore Tech Conf, 4th, Houston, Vol II, pp 675-688

VAN ALPHEN, J.S.L.J., HALLIE, F.P., RIBBERINK, J.S., ROELVINK, J.A. and LOUISSE, C.J. (1990)

Offshore sand extraction and nearshore profile nourishment. Proceedings 22nd Int Conf Coastal Eng, Delft, The Netherlands, pp 1998-2009

WIEGEL, R.L. (1964)

*Oceanographical Engineering*. Prentice-Hall, London

## CHAPTER 190

# METHOD FOR ARTIFICIAL BEACH NOURISHMENT

Henk Jan Verhagen<sup>1</sup>

### Why beach nourishment

For a good design, the purpose of the nourishment has to be clearly defined. In general, there are three reasons for beach nourishment:

1. combatting coastal erosion (chronic erosion)
2. preventing flooding (safety)
3. maintaining a wide recreational beach.

In the Netherlands a political decision has been made to maintain the coastline of 1990. Also, the required funds are available to do so. Thus the main purpose of nourishment in the Netherlands is to combat chronic erosion.

### Available tools

For the design, several tools are available. In general one can distinguish three kinds of tools:

1. mathematical models
2. field observations
3. physical models

Physical models are not recommended for the design of beach nourishment. This is because the process of beach change is caused primarily by irregularities in wave conditions. It is very difficult to accurately model this in a scale model. Mathematical models seem to overcome this problem but in fact they only change the problem. To use these models one needs good input data (waves, etc) and good calibration methods. In order to get them, one needs many years' measurements.

Because of the highly irregular wave climate, the predictive value of mathematical models in the Netherlands is rather low. Mathematical models are therefore used mainly for understanding coastal behaviour and comparing alternatives, and not for the quantitative design of artificial beach nourishment. A more direct design method has proved to be more effective.

When beach data (measured profiles) are used, one does not have the problem of defining a good wave climate or other boundary conditions. They are automatically correct. The main problem is that for a good statistical analysis, one needs much data. Consequently one needs a number of years' measurements. This kind of information is abundant for the Dutch coast.

---

<sup>1</sup> Int. Inst. for Infrastructural, Hydraulic and Environmental Engineering, P.O. Box 3015, 2601 DA Delft, The Netherlands

### The Dutch Design Method

Beach nourishment in the Netherlands is designed in an extremely simple way. Experience has shown that this is a very reliable method. The method is very trustworthy, if applicable.

- step 1: Perform coastal measurements (for at least 10 years).
- step 2: Calculate the "loss of sand" in  $\text{m}^3/\text{year}$  per coastal section.
- step 3: Add 40 % loss.
- step 4: Multiply this quantity with a convenient lifetime (for example five years).
- step 5: Put this quantity somewhere on the beach between the low-water-minus-1-meter line and the dune foot.

This method is simple and straightforward. It does not require mathematical models, but good quality profile measurements are absolutely necessary.

### Problems

Of course, there are also problems with the Dutch Design Method. There is one very important general assumption:

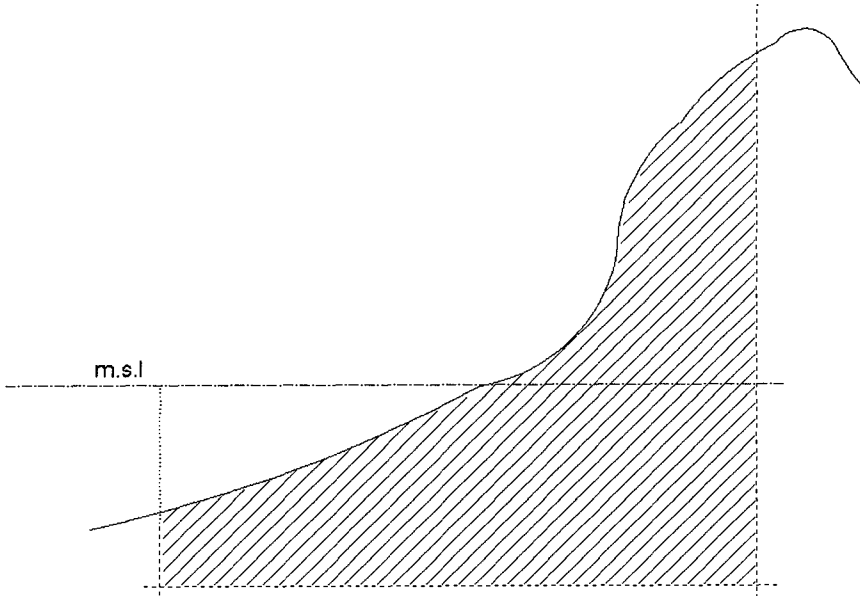
*The beach nourishment has no influence on the long-term natural behaviour of the coast. Or, in other words, the erosion rate before nourishment equals the erosion rate after nourishment.*

This general assumption is true in The Netherlands when beach nourishment is relatively long and the seaward displacement of the water line because of the nourishment is not too great. In The Netherlands the ratio between length of a nourishment (L) and seaward movement of the water line (width of the nourishment, w), L/w, is in the order of 20 - 40. Of course, one should realise that the Dutch coast is a coast with a tidal difference of 2 - 4 meters, a tidal current along the coastline and an almost perpendicular wave attack. Provided the L/w ratio is in the order of 20 or more, this assumption is valid in most areas of the world.

The erosion rate has to be calculated as a volume per unit of time (e.g.  $\text{m}^3/\text{year}$  per m of coastline) In cases where no profile data are available, one may also use the retreat of the high-waterline, but then one implicitly assumes that also the coastal profile is constant in time. That is usually not so. Apart from that the variation in the measured data is also significantly more if one uses coastline retreat instead of volume retreat.

So in fact the first step is to measure the coastal profile for a number of years, and calculate the volume in the profile (see fig. 1). Important is to define good boundaries. The landward boundary has to be placed far enough landward that erosion (also storm-erosion) will "never" pass this boundary. "Never" has to be interpreted as: possible not in the observation period and extrapolation period. The offshore boundary has to be far enough into the sea, that no significant onshore/offshore transports take place over this boundary during normal situations. In any case one should try to place this boundary seaward of possible breaker-bars.





**Figure 1:** control profile

It is usually a problem to match the terrestrial levelling of the beach with the offshore soundings. In case of a big tidal difference this is no problem. The soundings (during H.W.) may overlap the levellings (during L.W.). In case of a smaller tidal difference this might become a problem. In such a situation nearshore sounding with the use of a Hoovercraft may solve the problem.

The next step is plotting the volume data as a function of time (see fig. 2a). Through the data in this figure one may draw a regression line. Usually a linear trend can be assumed, especially when the regression-period is in the order of ten years. This period is recommended for this type of analysis. In very special cases non-linear regression has to be applied. The slope of the regression-line indicates the erosion-rate, e.g.  $Q_m$  ( $m^3/year$ ).

As next step a nice lifetime for a nourishment is selected, for example 5 years. One may select any figure, and optimize this later on. Experience however, has shown that such an optimization usually is completely overrun by non-technical issues, like available budget, available sand, execution schemes, etc. We call this lifetime  $T$ .

The volume to be nourished is thus  $V_N = Q_m * T$  ( $m^3$ ). (see fig. 2b).

However "losses" in longshore direction are not considered. These "losses" occur, because the nourishment has always a limited length. Also there is a wash-out of finer particles (the grain-size distribution of the nourished sand is new equal to the original beach sand).

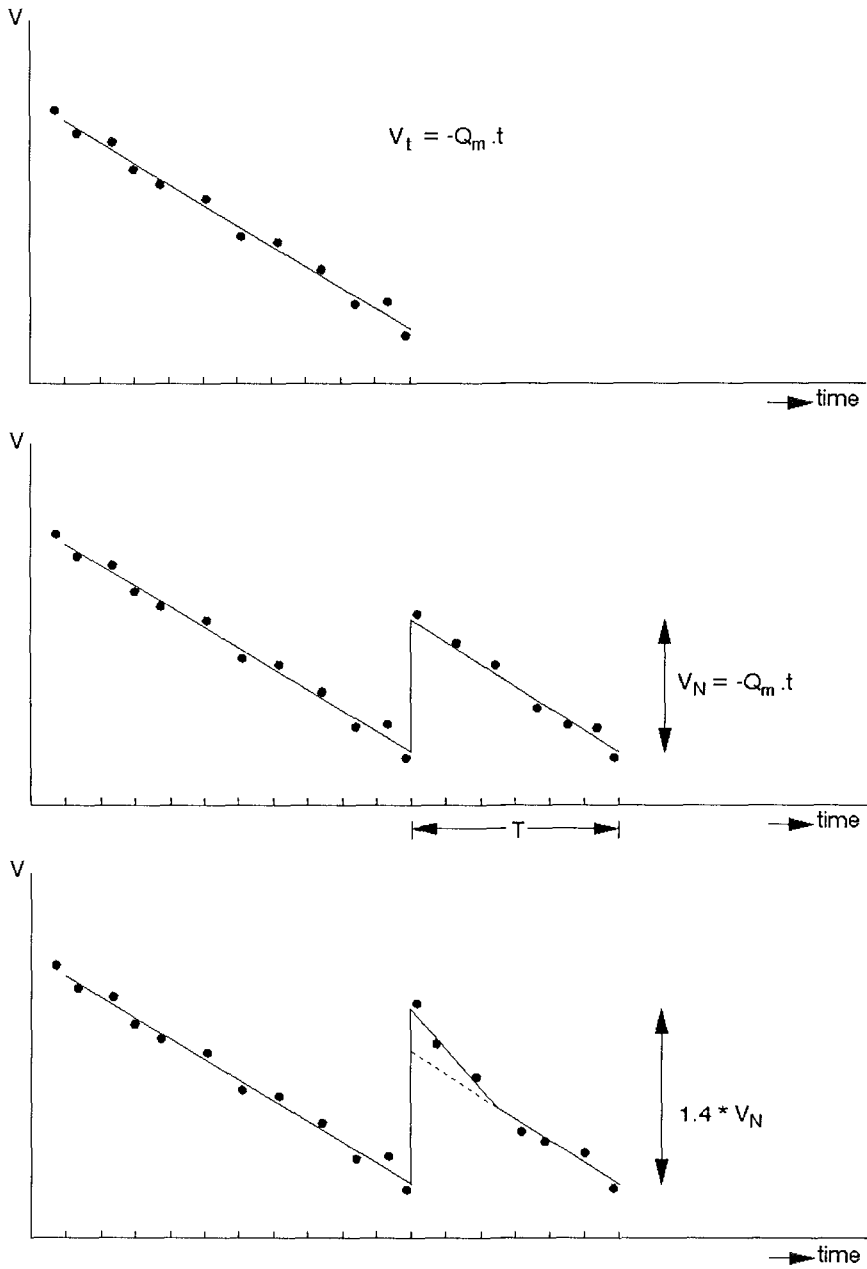
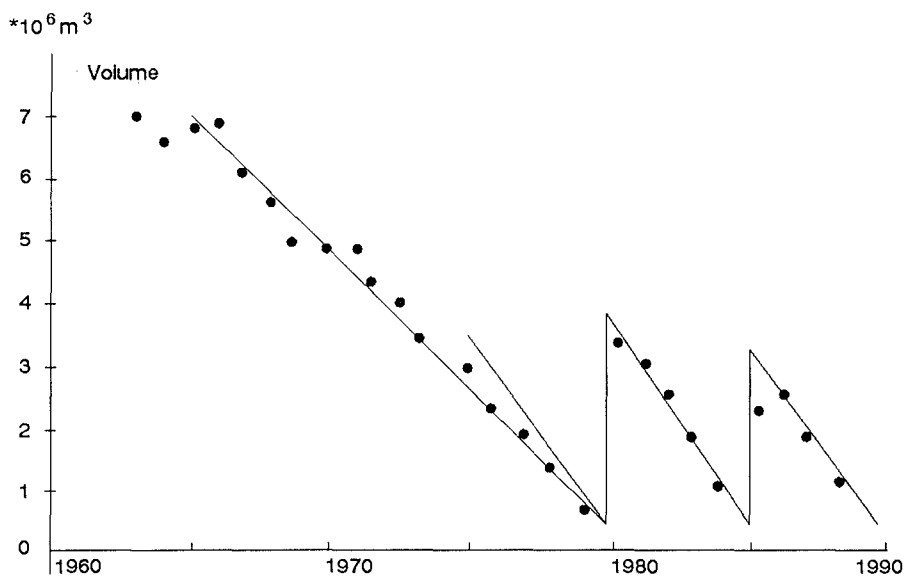


Figure 2: principle of beach nourishment design

Because the beach is somewhat further into the sea, the wave-attack is heavier, and, last-but-not-least their might be a profile adaptation outside our control volume. This last effect becomes less when we place our seaward boundary farther in a seaward direction.

For all these losses we should add something. A first estimate of this surcharge is 40%. This percentage is covering all type of losses (see fig.2c). This percentage can be fine-tuned by using measured data from the evaluation of previous nourishments in the region. We found in the Netherlands that we usually could use a somewhat lower percentage.

As an example the beach nourishment of Texel is presented [Rakhorst, 1989]. The quantity of the nourishments was determined, using linear regression, see fig. 3. As can be seen the yearly erosion-rate increased somewhat after was started with the nourishment schemes. However this change is negligible on the total quantities to be nourished. In this case the surcharge is very small (due to a wide control profile, long nourishment, correct sand).



Texel, km 25-31  
acc. Rakhorst 1989

Figure 3: Coastal volumes at Texel

An other example can be found in the nourishments on Westerland, Sylt (Führböter, 1991, and Führböter & Dette, 1992). See figure 4. One can see clearly that, after a short adaption period, the regression before nourishment. The surcharges, however, vary very much. Also they are quite big. This is mainly caused by the fact that the control volume, is only measured to the MSL-1m line, which is approx, the Low Water Line. This underlines the necessity to make the control volume wide enough.

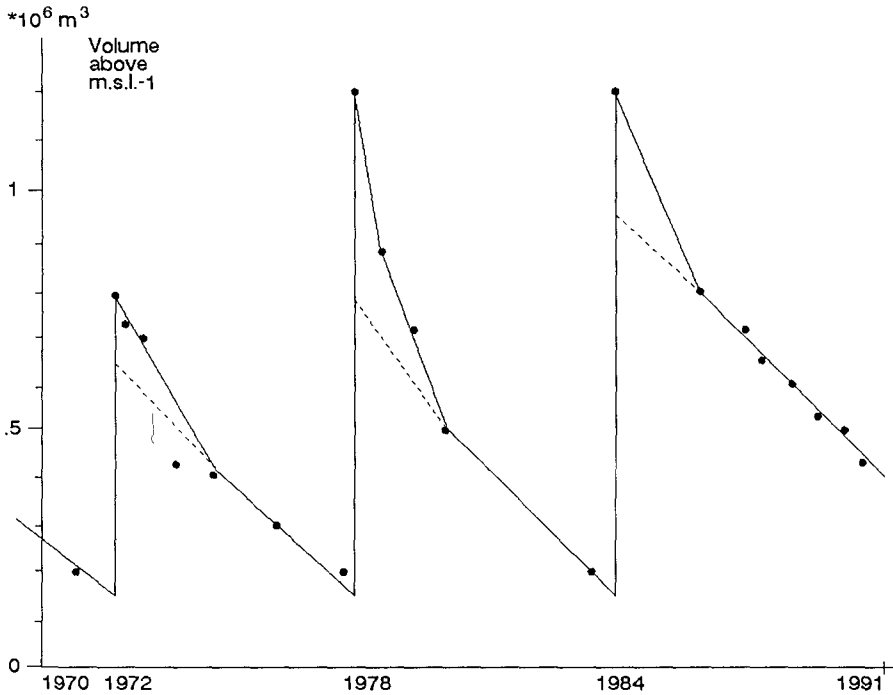


Figure 4: Coastal volumes at Sylt (Westerland)

Westerland [Sylt]  
acc. Führböter 1991

The erosion can be described using :

$$V_t = k_2 e^{k_1 t} + Q_m \cdot t$$

The paper of Dette and Führböter describes a mathematical method to optimize the term  $K_2 \exp(k_1 t)$  in this equation. For practical reasons we do not try to optimize this in the Netherlands, because practice has learned that the effect of other aspects (available budget, time planning, etc.) have a much bigger impact than optimization of this term. Also the fact that using a wider control volume decreases the magnitude of this surcharge is a reason not to focus too much on this point.

The data from Westerland are very interesting when they are plotted in a slightly different way. In fig. 5 the same data are plotted, but now on the vertical axis the deviation from the linear trend is plotted. So in fact only the  $k_2 \exp(k_1 t)$  - part is plotted. The exponential functions can be observed very clear in the 1978 and 1984 nourishments.

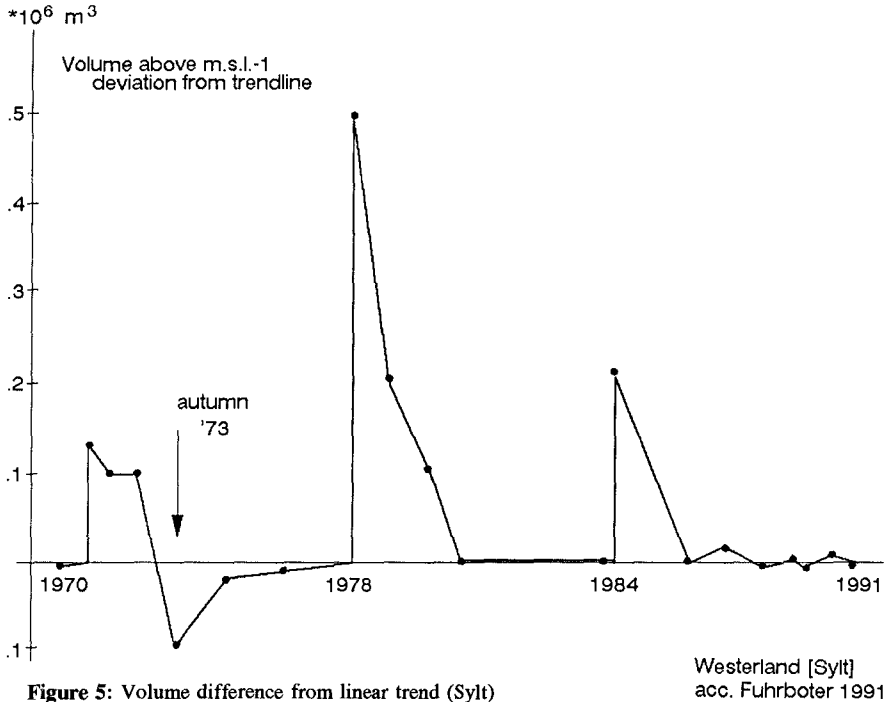


Figure 5: Volume difference from linear trend (Sylt)

Westerland [Sylt]  
acc. Fuhrboter 1991

In autumn 1973 there was a big storm on this coast. Due to this storm much sand eroded from the higher part of the beach and was deposited below the low-water line. Because this deposition was outside the control-volume, it is indicated as a loss. In the calm period after the storm this sand was transported back. The erosion-line comes back to the expected e-power-line. When a wider control volume had been used, one could probably not find this storm in the record. This shows very clear that individual storms like the autumn 1973-storm, not really contribute to the slow and chronic erosion of a beach. Storms do not cause extra erosion to nourished beaches.

Of course, the design-procedure described above is not very exact. One run the risk of making two types of "design errors".

**"design error 1"**

The yearly erosion was not determined correctly, like in the Texel case. See figure 6. Because the real erosion (= slope of regression line) is more than anticipated, the life-time of the nourishment is also shorter than anticipated. So next time one has to nourish somewhat more sand, or define the life-time somewhat shorter (if one wants to use the same nourishment volume)

However one has also to conclude that every grain of the first nourishment has done his job. Only we expected too much. So every dollar invested in the nourishment was invested very well. Therefore one has to conclude that this "design error" does not lead to financial problems.

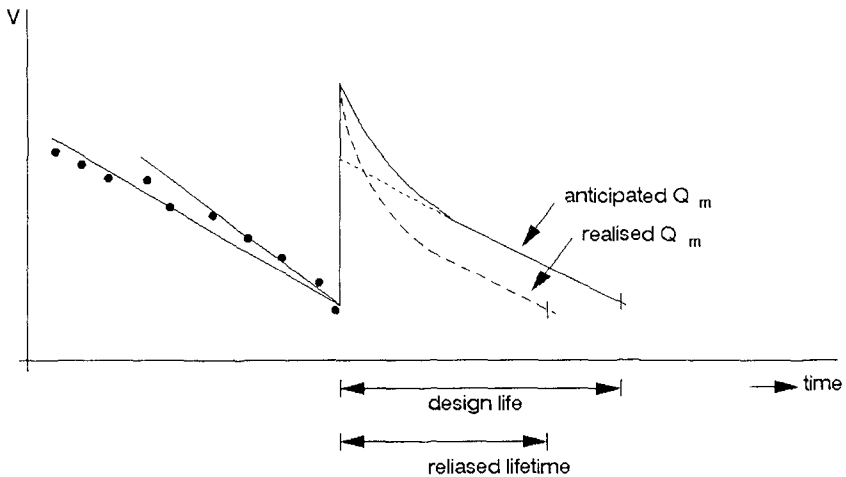


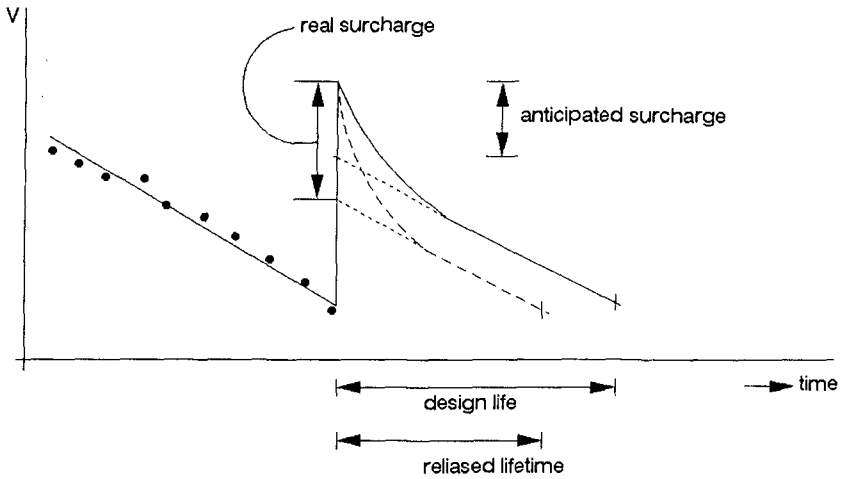
Figure 6: Design error type 1

Design error type 1:  $Q_m$  was not determined correctly

**"design error 2"**

The yearly erosion trend is determined correct, but the surcharge was somewhat too small, see figure 7. This also leads to a shorter lifetime than anticipated, and next time the design can be easily adapted by using the correct surcharge percentage. But also in this case one has to conclude that all nourished sand worked very well, and that one can not speak of a bad investment. This "design error" too does not have considerable financial consequences.

From the above one has to conclude that artificial beach nourishment has, from a financial point of view, a very big advantage. It is in fact an investment on which one has hardly any risk. Every grain of nourished sand is effective. Artificial Beach Nourishment may prove to be somewhat cheaper or more expensive than anticipated,



Design error type 2: surcharge (40%) was not determined correctly

Figure 7: Design error type 2

but what has been invested is not lost.

### Placing the sand

From a morphological point of view there is not much preference where the sand is placed in the beach profile (provided it is between the breakerline and dune-foot or swash-line). Placement outside the breakerzone might be attractive in some cases, but that is outside the scope of this paper.

The first minor storm after the placement of the nourishment will adapt the profile to the natural profile. And nature can do this much better than bulldozers and scrapers.

Experience in the Netherlands has indicated that so-called profile nourishment (i.e. try to make a natural stable profile) does not have any influence on the erosion-rate. It was only found that at very steep, relatively fast eroding beaches, a high placement lasted somewhat longer, because the profile could not adapt quickly enough to the erosion. In fact, because of high nourishment the profile was constantly too steep, and the next nourishment was due before the profile could adapt.

From an economic point of view a placement just above H.W is preferably. Usually dumping from split-barges in the breakerzone can not be realized, and one has to pump the sand ashore. The cheapest way is placing the discharge pipes just

out of the reach of the waves, which implies a nourishment-level just above H.W. The seaward slope is formed by the free flowing sand. No bunds are used.

The consequence of this method is that one has just after the nourishment a beautiful, wide, high and dry beach, but with a seaward slope which is too steep to survive the stormy season. So, the first storm in autumn will rework the profile until it reaches its natural shape, and much sand is transported from the H.W.-line to just below L.W. From a morphological point of view this is absolutely no erosion. In general the public has a different opinion. They see only the dry beach, and they see that it "disappears" after a minor storm. So they regard the nourishment as a failure.

Because of this psychological reason (for funding nourishments one needs public support) it is wise to make the shape of a nourished beach in such a way that the changes in autumn are not too big. In this way one will have more public support for nourishments.

### **The beach profile**

It is very difficult to design the new beach profile. A very good assumption is that the profile after the nourishment will eventually be the same as before the nourishment, provided the same type of sediment has been used.

Nature will form that profile. Therefore it does not matter very much where the sand is placed in the profile. After one or two small storms the complete profile is reworked by nature and the natural (stable) profile is formed. From this one may conclude that one should dump the sand where dumping is the cheapest, as long as it is landward of the breaker line.

In The Netherlands, the cheapest way is placing the sand on the beach, preferably on the higher section. All discharge pipes can be placed out of reach of the waves, and after the nourishment a beautiful, wide beach is formed. However, because the slope just under the low water line is too steep, the first storm in autumn transports sand from the beach towards the underwater shore. From a morphological point of view, this is no problem. From an economical point of view, this is the optimal solution. A number of nourishment projects in the Netherlands have been designed in this way.

However, from a political point of view this is not a good solution. The public has a beautiful beach in the summer, directly after the nourishment. But in autumn, during a minor storm, the public observes that the beach largely disappears. They do not observe that the sand is deposited just below the low water line. The public draws the incorrect conclusion that the nourishment was not successful at all. The wide beach has disappeared.

Because beach nourishment is generally paid for by a public authority, public opinion is important in acquiring sufficient funds. Therefore it is wise to design beach nourishment in such a way that the public sees that the beach is somewhat wider after the nourishment, but that there is no major adaptation in the beach shape during the first storms in autumn. If the purpose of the nourishment is to make a wide recreational beach, this is very important. If the purpose is to prevent flooding,



the best place is as high as possible on the beach. If the purpose is to combat chronic erosion, the best place is in the breaker zone.

### **Sediment size**

The size of the sediment is important. If the sediment is finer than the original material, the equilibrium slope will be more gentle. Some researchers also assume that finer material causes bigger losses. However it is not clear whether these bigger losses are caused by the more gentle beach profile or whether they are a real loss.

In order to get an impression of the effect of the grain size on the beach slope, one may use a general diagram as made by Dalrymple and Thompson [1976]. However, many beaches have slopes of 1:50 or less, and they are not in this diagram. Also the scatter of the data is too wide for practical application.

It is therefore recommended to start from the existing beach slope and use scale relations to derive the change in beach slope. These scale-relations have been developed by Vellinga [1982] and used for calculating the overfill ratio by Pilarczyk, Van Overeem and Bakker [1986]. The formula to be used is  $(l1/l2) = (w1/w2)^{0.56}$ . In this formula  $l$  is a characteristic length and  $w$  is the fall velocity of the beach material.

Suppose the volume to be nourished per meter of coastline is 500 m<sup>3</sup>, and the nourishment height is 5 m. The used sand is 250 micron instead of the original 275 micron. When the original slope was 1:75, the new slope will be 1:80. Because of the more gentle slope an extra volume of  $\frac{1}{2} \times 5 \times 5 \times (80-75) = 60 \text{ m}^3$  is necessary. This is an overfill of 12 %.

If one applies the technique of James, as presented in the US Shore Protection Manual, which is based upon the sorting out of fine particles, in this example one finds a overfill ratio of 20 %. Experience in Holland shows that the SPM method gives relatively high overfill ratios. Also it is expected that the mechanism of sorting out is not the governing mechanism, but only the fact that a more gentle slope will occur.

However, detailed research in this field, based upon a good set of prototype data is not available at this moment.

### **Conclusion**

From the above one can conclude that the presented design method for artificial beach nourishment is simple, straight forward and very reliable. No advanced models are required. The disadvantage is that beach profile data have to be available. Because of this, it is always good to have a good beach monitoring programme (profile measurements to be made once a year, at fixed profiles).

In the Netherlands all nourishment have in fact been designed using this method, except one. That nourishment was for an artificial peninsula, where (of course) no beach data were available. In that case mathematical models were used.

Directly after the nourishment, the shape of the beach is not optimal. Nature will adapt the shape of the nourishment. Also, because the nourishment protrudes into the sea, the current attack will be more. So, some extra loss has to be expected. It is

difficult to calculate this loss exactly. Our experience shows that an extra surcharge of 40 % on the designed quantity covers all losses, also the loss because of the extra current attack. A more mathematical approach to determining this loss is presented by Führböter [1991], although his assumption that an initial loss rate is proportional to the volume of sand available on the beach might not always be true.

### References

- Pilarczyk, K.W., Overeem, J. van, Bakker, W.T., 1986; Design of a beach nourishment scheme; 20th ICCE, Taipei.
- Dalrymple, R.A., Thompson, W.W., 1976; Study of equilibrium beach profiles; 16th ICCE.
- Detle, H.H. and Führböter, A.; A theoretical model for beach nourishment; ICCE 92 (this volume)
- Führböter, A., 1991; Eine theoretische Betrachtung über Sandvorspülungen mit Wiederholungsintervallen; Die Küste, vol 52, pp. 241-254.
- Rakhorst, D., 1989; Veranderingen kustvak Eierland, Rijkwaterstaat, directie Noord-Holland.
- Vellinga, P., 1984; A tentative description of universal erosion profile for sandy beaches and rock beaches; Coastal Engineering, Vol.8, no. 2.

## CHAPTER 191

### FIELD INVESTIGATION AT A MOUTH OF SMALL RIVER

Hitoshi Tanaka<sup>1</sup> and Nobuo Shuto<sup>2</sup>

#### Abstract

Field measurements have been carried out at the mouth of the Nanakita River in Japan. The maximum velocity at the throat section was kept constant, 1 m/sec, although the river mouth topography changed much rapidly in a week. It therefore seems that the equilibrium condition at the river mouth can be expressed in terms of the maximum velocity. The wave set-up height measured in the river mouth was also analyzed and was found to be responsible for the intrusion of sand into the mouth.

#### 1. Introduction

Up to now, a great number of field observation have been carried out at river mouths to understand a dynamic process of sand movement due to combined effect of wave motion, river flow and tidal current. Many of these field measurements are, however, restricted to relatively large rivers ( e.g. Ogawa, Fujita and Shuto (1984), Sawamoto and Shuto (1988) ), since they are of considerable importance from a view point of hydraulic engineering. The process of topography change at a mouth is greatly dependent on the dimensions of the river. It is therefore difficult to generalize the observed results at different river mouths with different dimensions.

---

1 Associate Professor, Water Resources Engineering Division, Asian Institute of Technology, G.P.O. Box 2754, Bangkok 10501, Thailand.

2 Professor, Disaster Control Research Center, Tohoku University, Aoba, Sendai 980, Japan.

We initiated a field study in 1988 at the mouth of the Nanakita River, a typical small river in Japan, to find an appropriate countermeasure against the closure of the mouth. Some interesting features are observed which are distinctly different from those seen at big rivers.

## 2. Study Area

The Nanakita River mouth is located on the Pacific Ocean coast as shown in Fig.1. The catchment area of the river is 229km<sup>2</sup> and the river length is 45km. During rainy season, the tidal discharge and the fresh water discharge are of the same magnitude except for the very short period of big floods induced by typhoon or low pressure. The river discharge during winter season becomes negligibly small as compared with the tidal discharge. Thus, a complete closure of the mouth takes place rather frequently ( Tanaka and Shuto (1991) ).

The Teizan Canal 9km long connects the Nanakita River mouth with another river mouth, the Natori River mouth. The lock gates, located at the joint with the Nanakita River, are kept partially open. Accordingly, a part of discharge of one river might flow to the other if there is a difference in water level between the two rivers.

The planform of the river mouth topography and the shape of the narrowest cross-section have been measured every two weeks since 1988. The water level variation has also been measured by means of automatic water level gauges which are installed at Stations A, B and C in Fig.1. The velocities at the mouth and in the Teizan Canal were continuously measured for 25 hours at the consecutive spring and neap tides on August 20 to 21 and 27 to 28, 1990, using propeller-type currentmeters.

## 3.Results and Discussions

### 3.1 Change of Cross-Sectional Area and Velocity In A Week

Figure 2 shows the change of the planform of the river mouth topography and the narrowest cross-section in a week. The sand spits on both sides intruded into the mouth due to wave action and, subsequently, the narrowest section shifted upstream. Distinct decrease of the cross-sectional area also took place within one week.

The time-variations of the water levels during the first observation are shown in Fig.3(a). It is noted that the water level in the river mouth was almost always

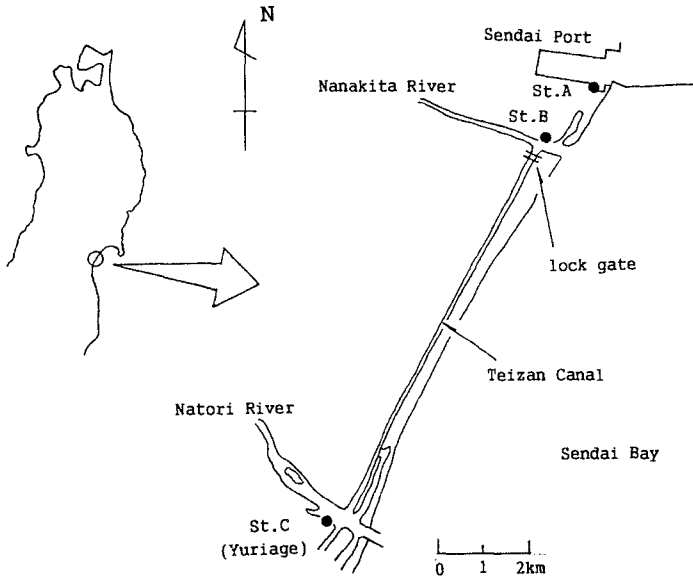


Fig.1 Map of the river mouth.

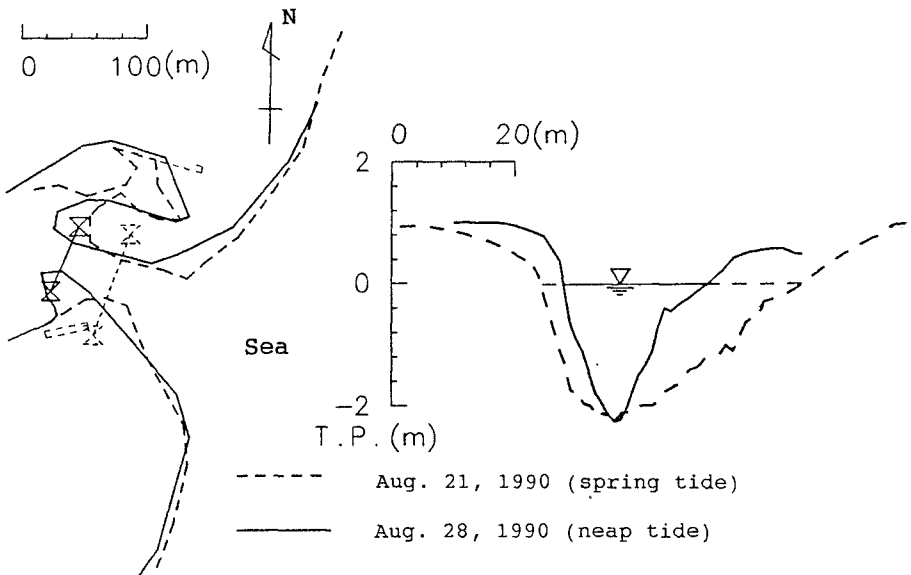


Fig.2 Change of plan topography and cross section in a week.

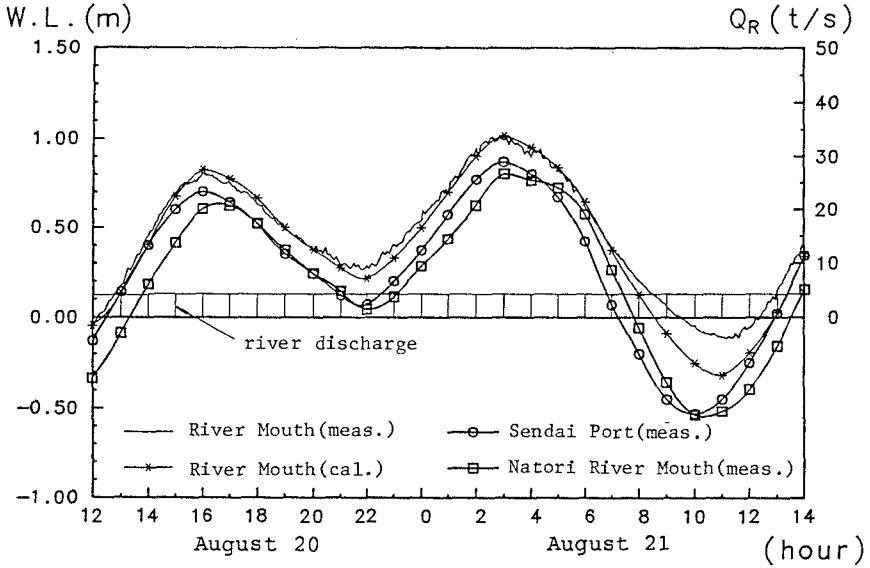


Fig.3(a) Time-variation of water levels.  
(August 20-21, 1990)

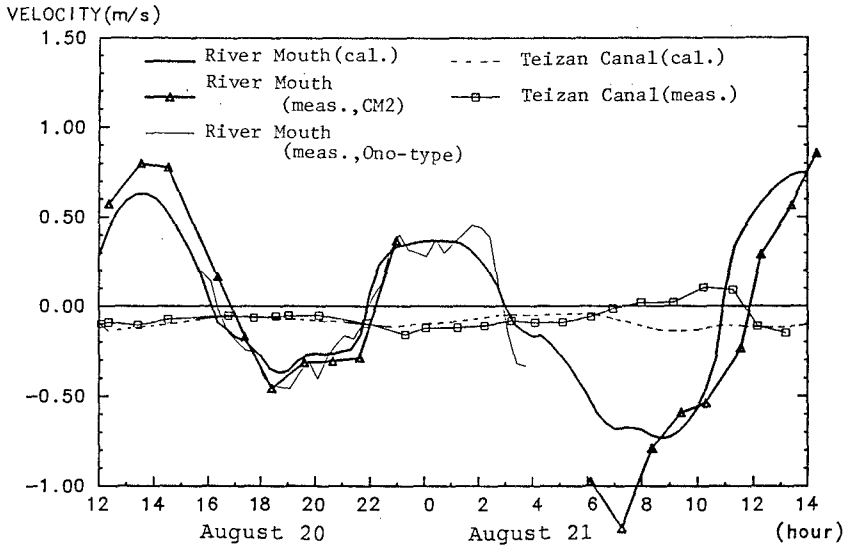


Fig.3(b) Time-variation of velocities.  
(August 20-21, 1990)

higher than that in the sea, while the water elevation measured in the Natori river mouth was almost identical with the sea water level. Such a difference is due to the fact that, at the Natori River mouth, where two jetties have been already constructed, the water depth at the mouth was deep enough to prevent wave motion from breaking, while at the Nanakita River, waves broke in front of the mouth, resulted in the water level rise, that is, the wave set-up.

The corresponding variation of the velocities measured at the Nanakita River mouth and in the Teizan Canal are shown in Fig.3(b). The positive velocities denote the flow into the river from the sea through the mouth or through the Teizan canal. The velocity along the Teizan Canal was always negative, which shows the flow direction in the canal was from the Nanakita to the Natori river due to the difference of water level explained above.

The observed results during the second measurement are shown in Fig.4. The water level rise is smaller than the 1st observation due to the difference of the significant wave height; during the 1st observation, the significant wave height,  $H_{1/3}$ , was 1.4m, while during the second observation,  $H_{1/3}=0.9m$ .

According to Figs.3(b) and 4(b), the maximum current velocity at the mouth was kept 1m/s by tidal and river flows, although the cross-sectional area was rapidly narrowed by waves within one week. This result suggests that the dynamic equilibrium condition of the cross-section at the Nanakita River mouth can be expressed in terms of the maximum velocity. Similar result has already been reported by Bruun (1978).

The solid lines in Figs.3 and 4 show the calculated water levels and velocities obtained using a one-dimensional model which is commonly applied in the analysis of sea-inlet-bay system ( e.g. see Bruun (1978) ). The governing equations are as follows.

Equation of motion:

$$\eta_o - \eta_R = \frac{L_c}{g} \frac{du}{dt} + (K_{en} + K_{ex} + K_{cu} + \frac{2gn^2 L_c}{R^{4/3}}) \frac{|u|u}{2g} \dots\dots\dots(1)$$

Equation of continuity:

$$u = \frac{1}{A_c} ( A_R \frac{d\eta_R}{dt} - Q_R ) \dots\dots\dots(2)$$

where  $\eta_o$  the ocean elevation,  $\eta_R$  the water level in the river mouth,  $L_c$  the length of the channel,  $u$  the velocity at the river mouth,  $K_{en}$ ,  $K_{ex}$ ,  $K_{cu}$  the coefficients of entry loss, exit loss and bend loss, respectively,  $n$  the Manning's friction coefficient,  $R$  the hydraulic radius,  $A_c$  the area of the cross-section at the river mouth,  $A_R$

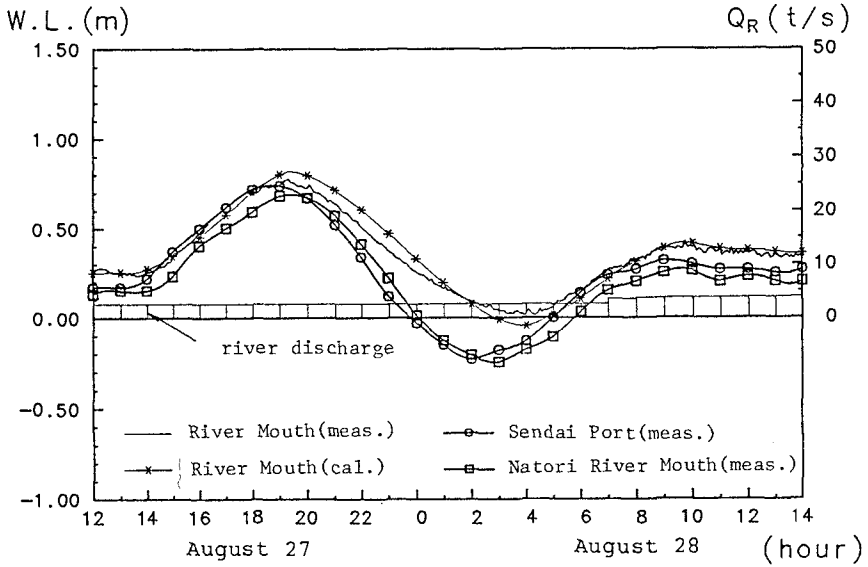


Fig.4(a) Time-variation of water levels.  
(August 27-28, 1990)

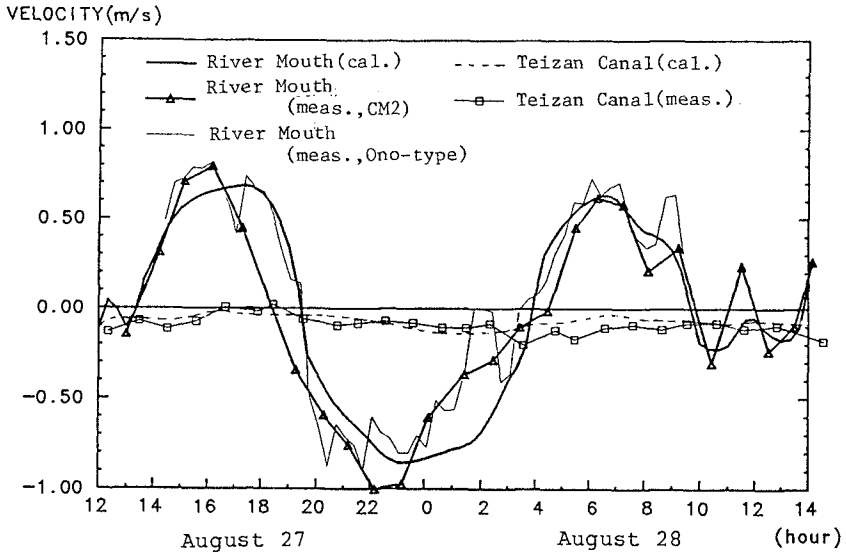


Fig.4(b) Time-variation of velocities.  
(August 27-28, 1990)



the surface area of the river under the influence of tidal variation, and  $Q_R$  the fresh water discharge. The equations for the Nanakita River mouth and those for the Teizan Canal are solved simultaneously using the Runge-Kutter method. In the calculation of the latter, the energy loss due to the lock gates are considered, referring to a diagram proposed by Chow (1959). The effect of the wave set-up height at the Nanakita River mouth is also included in the numerical analysis, assuming that the sea level rise was 10% of the deep water wave height ( see Fig.6 ). The unidirectional current in the Teizan Canal as well as the oscillatory current at the river mouth is predicted very well through the numerical model.

### 3.2 Wave Set-Up in the River Mouth

As seen in the previous section, the wave set-up is remarkable in the Nanakita river mouth. Although the same phenomenon might be observed at a mouth of rivers with similar or smaller dimensions, field studies on the wave set-up at a river mouth have been very few. This is partly due to the fact that most of the field measurement up to the present have been made at big rivers which are of practical importance. At these rivers, the water depth is so large that no wave breaking takes place, consequently, no wave set-up at the river mouth.

At the Nanakita river mouth, wave set-up has great influence on the flow field near the river mouth and must be responsible for the topography change at the mouth. Thus, analysis of wave set-up height is carried out in this section. The set-up height,  $\bar{\eta}$ , can be calculated by taking difference of the water levels at the Nanakita river mouth and the Sendai port, since the water level measured at the latter station was free from the effect of wave breaking as seen in Fig.5. Furthermore, the water level rise induced by other forces such as wind and low pressure must be included equally in both records, because the distance between these stations is only 2km.

Figure 5 shows the water level variations at St.A in the Sendai port, St.B in the Nanakita river mouth and St.C in the Natori river mouth, measured on the day when the maximum set-up height of 66cm was observed at the Nanakita River mouth. As mentioned above, the Natori River mouth is protected by two jetties to keep the cross-section large, while the Sendai port is protected by a breakwater of 2 km long as shown in Fig.1. That is the reason why the water level at St.C was almost identical with the sea level at St.A and was lower than the water elevation measured in the Nanakita River mouth.

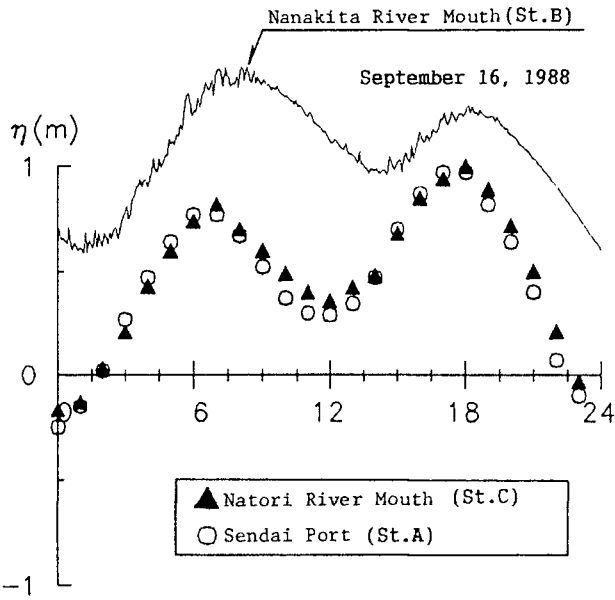


Fig.5 Water level variation (September 16, 1988).

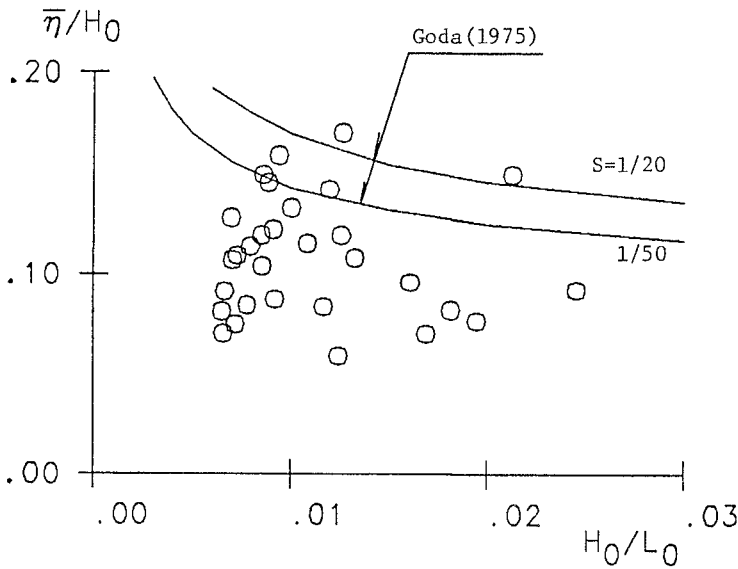


Fig.6 Relationship between wave set-up height and steepness of deep water wave.

Figure 6 shows a correlation between the dimensionless set-up height,  $\bar{\eta}/H_0$ , and the steepness of deep water wave,  $H_0/L_0$ , where  $H_0$  and  $L_0$  are the wave height and the length of deep water waves, respectively. Theoretical curves according to the Goda's theory (1985) are also shown in the figure. Yanagishima and Kato (1990) measured the wave set-up height on the Kajima Coast in Japan and reported that the Goda's theory showed good agreement with their measurement. According to the present measurement, however, the observed data are consistently less than the predicted values by the theory. Possible reasons for this discrepancy are: (i) the wave set-up in front of the river mouth was not two-dimensional phenomenon due to the distorted bottom topography near the river mouth, and (ii) the sea water could intrude into the river mouth when the water elevation in the river mouth was lower than the sea level in the surf zone.

### 3.3 Influence of The Teizan Canal on The River Mouth Topography

At the Nanakita River mouth, the tidal discharge is very important factor to keep the mouth open ( Tanaka and Shuto (1989) ). Generally speaking, the magnitude of the flow induced by flood and ebb tides at a river mouth is of the same order, as the tidal discharge changes sinusoidally. At the Nanakita River mouth, however, the ebb tide flow is of smaller magnitude, because of the southward flow into the Teizan Canal as seen in Figs.3 and 4. This means that the tidal flow is effective to transport sand into the mouth rather than flushing sand out of the mouth.

Photo 1 was taken on February 1st, 1991, when the daily averaged fresh water discharge was  $3.7\text{m}^3/\text{sec}$ , while the tidal discharge was  $7.5\text{m}^3/\text{sec}$ . Sand deposition which is commonly designated "bay shoal" ( Bruun (1978) ) is observed in the river mouth. Dotted lines in the photograph show an upstream edge of the shoals. Such a topography is seemed to be induced by predominant current into the river mouth during the flood tide.

In order to make a quantitative estimation of the effect of the Teizan Canal, the one-dimensional analysis is carried out using Eqs.(1) and (2) under the following three conditions ( see Fig.7 ): (i) assuming that the lock gates at the joint with the Nanakita River are completely open, (ii) the lock gates are kept partially open as the present state, and (iii) the gates are closed completely to prevent the southward flow into the canal. Calculation is carried out for the days in August, 1990,

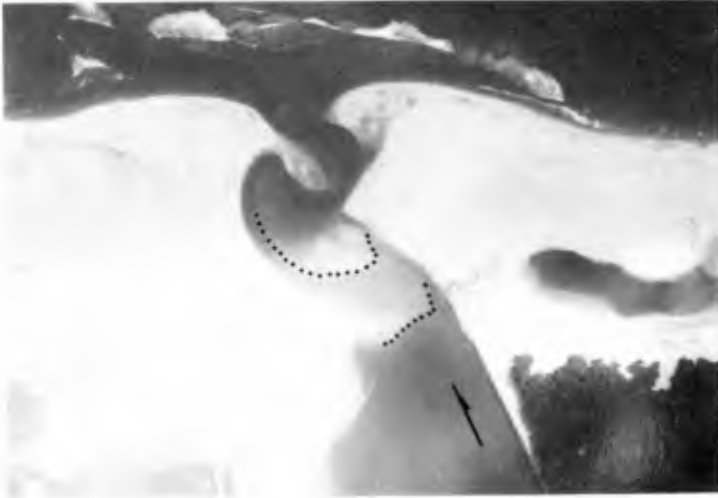


Photo 1 Aerial photograph on January 1, 1991.

when the field observations were continuously made for 25 hours.

The gross volume of water entering or exiting through the mouth and the Teizan Canal is calculated for each flood and ebb tides and is summarized in Table 1, in which the ratio of each volume to the corresponding value in Case 2 is also shown in brackets. The unit of the tabulated value is  $10^3\text{m}^3$  and the positive value shows volume of water entering into the Nanakita river through the mouth or the canal. It is seen that the flow in the Teizan Canal is always negative in Cases 1 and 2 due to the wave set-up effect. In Case 1, the discharge into the Teizan Canal will consistently increase during both flood and ebb tides as compared with Case 2, due to the enlarged cross-sectional area of the Teizan Canal. At the river mouth, the volume during the ebb tide will decrease, while that during the flood tide will increase. Thus, the entering flow into the mouth will become more predominant in Case 1. On the other hand, in Case 3, the reduction rate of the flood tide discharge will attain to 20%, while the ebb tide flow will increase by 16% at its maximum. Therefore, it can be concluded that, by closing the gates, the intrusion of sand into the Nanakita River Mouth during the flood tide will be reduced, resulting in the improvement of the river mouth closure.

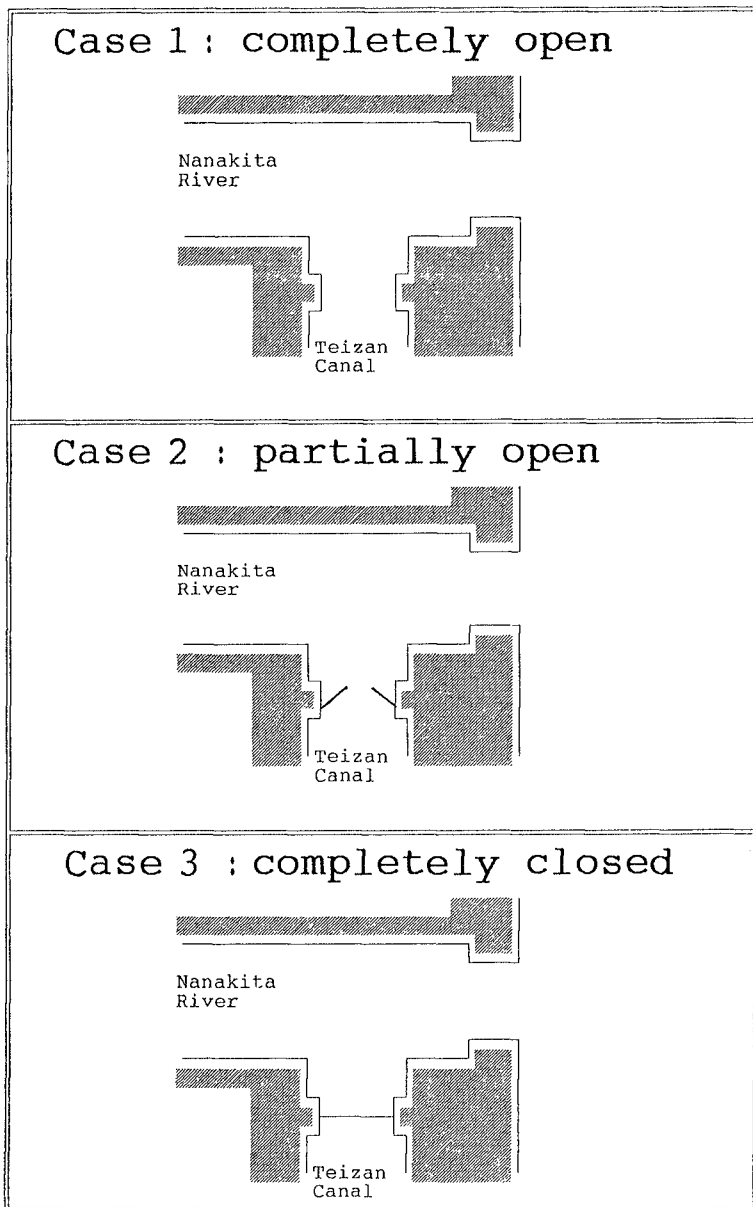


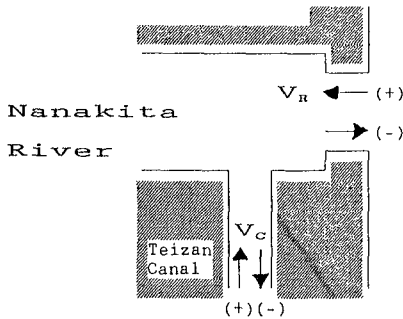
Fig.7 Condition of calculation.

Table 1 Calculated water discharge.

UNIT: 10<sup>3</sup> m<sup>3</sup>

Date		Case 1 (completely open)		Case 2 (partially open)		Case 3 (completely closed)	
		V <sub>C</sub>	V <sub>R</sub>	V <sub>C</sub>	V <sub>R</sub>	V <sub>C</sub>	V <sub>R</sub>
Aug. 20	1st ebb tide	-92 (1.80)	-337 (0.85)	-51 (1.00)	-395 (1.00)	0 (0.00)	-436 (1.10)
	21 1st flood tide	-116 (1.97)	473 (1.13)	-59 (1.00)	419 (1.00)	0 (0.00)	359 (0.86)
	2nd ebb tide	-102 (1.59)	-799 (0.94)	-64 (1.00)	-848 (1.00)	0 (0.00)	-912 (1.08)
Aug. 27	1st flood tide	-77 (1.75)	323 (1.08)	-44 (1.00)	300 (1.00)	0 (0.00)	262 (0.87)
	28 1st ebb tide	-135 (1.44)	-441 (0.91)	-94 (1.00)	-482 (1.00)	0 (0.00)	-560 (1.16)
	2nd flood tide	-57 (1.33)	247 (1.05)	-43 (1.00)	236 (1.00)	0 (0.00)	186 (0.79)

V<sub>C</sub>: discharge through the Teizan Canal  
 V<sub>R</sub>: discharge through the Nanakita River mouth



#### 4. Conclusions

The principal results of the present study are as follows:

- (1) The water level at the Nanakita River mouth was higher than that in the Natori River mouth due to the wave set-up, resulting in a unidirectional flow along the Teizan Canal to the Natori River. This indicates that the tidal flow during the flood tide is effective to transport sand into the river mouth rather than flashing sand out of the mouth. Shoals in the mouth are seemed to be formed due to such a predominant flow into the mouth.
- (2) The cross-sectional area of the narrowest section at the Nanakita river mouth decreased remarkably in a week, while the maximum of the velocity at the throat section was kept constant, 1m/sec. This result suggests that the equilibrium condition at the river mouth can be expressed in terms of the maximum velocity at the narrowest section. The time-variations of water level and the velocity are successfully reproduced by a one-dimensional analysis.
- (3) Wave set-up height measured in the river mouth attained to 10-20% of the deep water wave height, slightly lower than Goga's theory.
- (4) Numerical simulation indicates that, by closing the lock gates at the joint with the Teizan Canal, sand intrusion due to tidal current into the mouth will be reduced. However, further investigation should be made to evaluate the role of the Teizan Canal not only from engineering view point but also from an environmental and ecological view points.

#### 5. Acknowledgements

The authors would like to express their grateful thanks to the members of the River Hydraulic Engineering Laboratory, Tohoku University, for their cooperation during the field observations. The appreciation is extended to the Sendai Office, Ministry of Construction, the Shiogama Office, Ministry of Transport, and the Higashi Sendai Office, Miyagi Prefecture, for their kind supply of the valuable field data. A part of this study was financially supported by a Grant-in-Aid for Scientific Research, Ministry of Education, Science and Culture ( No.01550396 ).

#### 6. References

- Bruun, P (1978): Stability of Tidal Inlets - Theory and Engineering, Elsevier, 510pp.

- Chow, V.T. (1959): *Open Channel Hydraulics*, McGraw-Hill Book Company, 680pp.
- Goda, Y., (1985): *Random Seas and Design of Maritime Structure*, University of Tokyo Press, 323pp.
- Ogawa, Y., Fujita, Y. and Shuto, N. (1984): Change in the cross-sectional area and topography at river mouth, *Coastal Engng. in Japan, J.S.C.E.*, Vol.27, pp.233-247.
- Sawamoto, M. and Shuto, N. (1988): Topography change due to floods and recovery process at the Abukuma river mouth, *Coastal Engng. in Japan, J.S.C.E.*, Vol.30, No.2, pp.99-117.
- Tanaka, H. and Shuto, N. (1989): Field measurement of topography at a river mouth, *Proc. of Int. Symp. on Sediment Transport Modeling, A.S.C.E*, pp.480-485.
- Tanaka, H. and Shuto, N. (1991): Field measurement of the complete closure at the Nanakita River mouth in Japan, *Proc. Int. Symp. on Natural Disaster Reduction and Civil Engng.*, J.S.C.E, pp.67-76.
- Yanagishima, S. and Kato, K. (1990): Field observation on wave set-up near the shore-line, *Proc. 23rd Int. Conf. on Coastal Engng.*, A.S.C.E, pp.95-108.



## CHAPTER 192

### ENTRAINMENT AND TRANSPORT OF FINE SAND BY COMBINED WAVES AND CURRENT: AN EXPERIMENTAL STUDY

by  
C. VILLARET and B. LATTEUX<sup>1</sup>

#### Abstract

Experiments have been performed in a large wave flume in order to measure sediment transport rate of fine sand under combined regular waves and current. Instantaneous velocities and concentrations are measured using ultrasonic velocimeters and optical turbidity probes. Suspended transport rates, as obtained from vertical integration of measured fluxes, are decomposed into a mean current and an oscillatory wave components. Under waves only, the wave contribution is in the direction of wave propagation. Under combined waves and current, the wave contribution is found to systematically oppose the direction of superimposed mean current.

#### 1. Introduction

From previous observations, it is well established that sediment transport is enhanced under combined waves and current, due to the stirring action of waves and advection by mean current. However, the relative contribution of both wave and mean motions to suspended sediment transport is a non-linear process which is still poorly understood (e.g Van Rijn, 1991).

Instantaneous values of velocity  $u$  and concentration  $c$  are classically decomposed into a mean component, time-averaged over the wave period ( $\langle x(t) \rangle = X$ ), and a phase-averaged oscillatory components  $x_w$ :

$$\begin{aligned}u(z,t) &= U(z) + u_w(z,t) + u'(z,t) \\c(z,t) &= C(z) + c_w(z,t) + c'(z,t)\end{aligned}$$

Assuming turbulent fluxes to be small, the time-averaged sediment flux can be written:

$$\langle u(z,t) c(z,t) \rangle = \langle u_w(z,t) c_w(z,t) \rangle + U(z)C(z) \quad (1)$$

Suspended sediment transport rates, as obtained by depth-integration of equation (1), are then decomposed into a mean current and an oscillatory wave contributions.

---

<sup>1</sup>EDF, Laboratoire National d'Hydraulique, 6 quai Watier, 78400 Chatou, FRANCE

The mean current contribution represents advection of mean concentration by the superimposed mean current or by the second-order eulerian drift induced by the wave motion (Longuet-Higgins, 1953). Under combined waves and current, eddy viscosity models have been used successfully to reproduce mean velocity and mean concentration profiles, assuming enhanced turbulence within the wave boundary layer (e.g. Grant and Madsen (1979)).

The contribution of oscillatory wave motion to suspended transport rates is produced by the asymmetry of the phase-averaged velocity forcing and concentration response. Davies (1990) numerical simulations have shown that the time lag between maximum velocities and bottom concentration peaks is an important parameter which determines the wave contribution effect to suspended sediment transport.

The principal objective of the following series of experiments is to obtain direct estimates of sediment fluxes from instantaneous velocity and concentration measurements under combined waves and current. Part 2 is a description of experimental set-up, measuring apparatus and test conditions. Measurements of mean concentration and mean velocity profiles are presented in Part 3. The effect of wave contributions to suspended transport rates is discussed in Part 4. Results of near bottom phase-averaged concentrations and diffusion of concentration peaks away from the bottom are presented in Part 5. Part 6 is a discussion of results and conclusions.

## 2. Experimental Set-Up

Experiments were carried out in a large wave flume (1.50m x 1.50m x 79m) which is equipped with a piston type wave maker. The flow is circulated through a pumping system which can generate a current in both directions. The 20 m long test section is made of a 40 cm high surelevated bottom. A 10 cm thick erodible sand bed is placed above the bottom. Two 10 m long sand traps are located on each side of the test section. The measuring section is situated in the middle of the platform as shown on Figure 1.

An optical turbidity probe (OPCON) is used to measure instantaneous concentrations. Instantaneous velocities are measured at the same elevation using 1-D ultrasonic velocimeter. The two probes are located about 15 cm apart in the same cross section and oriented at 45° from the flow direction in order to minimize disturbances of the flow field. Measurements are repeated at different elevations down to a few mm from ripple crests with at least 8 points in the near bottom 10 cm. Measurements are taken at two different lateral positions in the measuring cross section ( $y=\pm 25$  cm), in order to check the spatial variability of the signal. Instantaneous velocity and concentration measurements are phase-averaged over at least 50 wave periods in order to estimate both mean and periodic components.

Bed elevations are recorded every 4.5 mm using an electromagnetic bed profiler along three longitudinal sections ( $y=0, \pm 25$  cm) above both platform and sand traps. Measurements are made before and after each test, in order to estimate total sand volume per channel width ( $L \Delta z_b$ ) passing through the measuring section. Total transport rates in dry weight,  $Q_t$ , is given by:

$$Q_t = \frac{L \Delta z_b (1-n) \rho_s}{\Delta t} \quad (2)$$

where  $n$  is the sediment bed porosity ( $n=0.4$ ),  $\rho_s$ , the sediment density ( $\rho_s = 2.65 \text{ g/cm}^3$ ) and  $\Delta t$ , the duration of experiment. Mean bed level measurements  $z_b$  need to be corrected for small variations in the reference elevation in order to satisfy mass conservation. Test duration  $\Delta t$  must be less than one hour in order to minimize bed level variation during experiment due to erosion or deposition processes.

The sand bed is made of a well sorted fine sand with mean diameter  $d_{50}=0.09 \text{ mm}$  and mean settling velocity  $w_s = 0.7 \text{ cm/s}$ . The water depth  $h$  above the platform is  $60 \text{ cm}$ . A series of 10 tests have been carried out for wave periods  $T$  of 1.5, 2 and 2.5s and an incident wave height  $H_i$  of about 25 cm. Longitudinal reflected waves,  $H_r$ , are generally less than 10% of incident waves. For each wave condition, a mean current  $U_r$  of about 20 cm/s at a reference level  $z_r=35 \text{ cm}$  is superimposed to the wave field in or against the direction of wave propagation. Hydrodynamic conditions are summarized in Table 1 in which a positive sign means a following current.

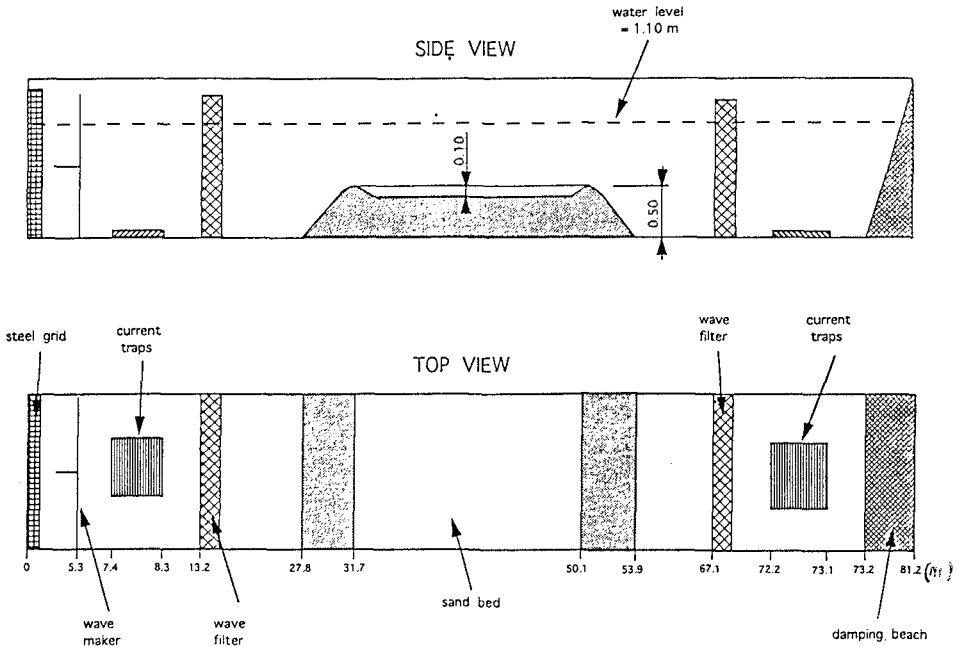


Figure 1: Side and top views of the wave flume

### 3. Experimental Results :

#### Bedforms:

Bedforms are two-dimensional for  $T=1.5$  s and become irregular three-dimensional for  $T=2.5$  s. Bedform dimensions are obtained from statistical analysis of bed profiler data. Typical bedforms heights do not show significant variation with flow parameter ( $\delta_r = 0.65$  cm), while wave length  $\lambda_r$  slightly increases with wave period from 5 to 7 cm. (see Table 1).

Test N°	T (s)	Hi (cm)	Hr (cm)	Ur (cm/s)	$\lambda_r$ (cm)	$\delta_r$ (cm)
35	1.5	23.2	1.0	- 4.6	4.8	0.7
39	2	23.2	1.3	- 5.75	5.5	0.7
42	2.5	25.0	2.15	- 5.9	6.7	0.6
36	1.5	18.8	1.05	17.4	5.0	0.6
40	2	21.0	2.1	17.4	5.0	.65
77	2.5	17.8	2.6	17.0	5.6	.7
38	1.5	17.5	1.25	- 17.0	4.8	0.6
41	2	21.1	1.6	- 18.7	5.5	0.7
54	—	20.1	2.20	-32.75	—	—
45	2.5	21.0	1.6	-17.6	5.8	.6

Table 1: Hydrodynamic test conditions

#### Mean velocity profiles:

In the case of waves only, there is a small eulerian drift which is in the direction of wave propagation near the bottom and against it in the outer flow ( $U_r=-4$  to  $-5$  cm/s) as shown on Figure 2.

Under combined waves and current, mean velocity profiles are fitted to a logarithmic profile in order to estimate both mean friction velocity  $u^*$  and apparent roughness height  $k_a$ , assuming a Karman constant  $K=0.4$  (see Table 2):

$$U = \frac{u^*}{K} \log \left( \frac{33z}{k_a} \right) \quad (3)$$

The main effect of the waves on the mean velocity profiles is to increase the equivalent roughness height  $k_a$  as compared to physical roughness ( $k_s=1.5 \delta_r$ ). This effect is larger for opposing waves and current than for following waves and current. These results are qualitatively in good agreement with expectations from theoretical models (e.g. Grant and Madsen (1979)) and previous observations (e.g. Nap and Van Kampen (1988)).

Mean concentration profiles:

In all our experiments, sediments stay within a thin (<5cm) near bottom layer. An exponential concentration profile gives a reasonably good fit to measurements as indicated by regression coefficients  $r > 0.95$ . Results are interpreted in terms of bottom concentration  $C_0$  and suspended layer thickness  $L_s$ , according to Nielsen's (1979) model (see Table 2):

$$C = C_0 \exp\left(-\frac{z}{L_s}\right) \quad (4)$$

In the case of three dimensional bedforms ( $T=2.5s$ ), there is a lot of scatter in measurements as shown on Figure 3. Under waves only, decrease of mean bottom concentrations with wave period may be due to changes in bedforms geometry from 2D to 3D as period increases.

Under waves only, the suspended layer thickness approximately scales with bedforms height ( $L_s = 2$  to  $3 \delta_r$ ). Significant increase of suspended layer thickness is observed for a following current which is in good agreement with expectations from previous models and observations. In the case of opposing current, this effect can only be observed by increasing opposing current intensity (Test 54). In the other tests with opposing current, the suspended layer thickness is approximately the same as for waves alone. For longer waves with opposing currents ( $T=2.5s$ ),  $L_s$  is actually smaller than for waves alone.

Test N°	$u^*$ (cm/s)	$k_s$ (cm)	r	$L_s$ (cm)	$C_0$ (g/l)	r
35				1.13	35.0	-0.99
39				0.99	30.9	-0.99
42				1.60	15.7	-0.96
36	1.90	8.1	0.95	1.77	9.8	-0.95
40	2.20	12.7	0.98	1.26	16.7	-0.98
77	2.37	14.2	0.95	2.18	8.2	-0.97
38	-1.19	14.1	-0.95	1.05	12.6	-0.95
41	-1.43	15.0	-0.94	1.07	22.6	-0.98
54	-1.96	8.9	0.92	1.90	9.5	-0.99
45	-1.47	14.7	-0.98	0.98	27.8	-0.96

Table 2: Test results

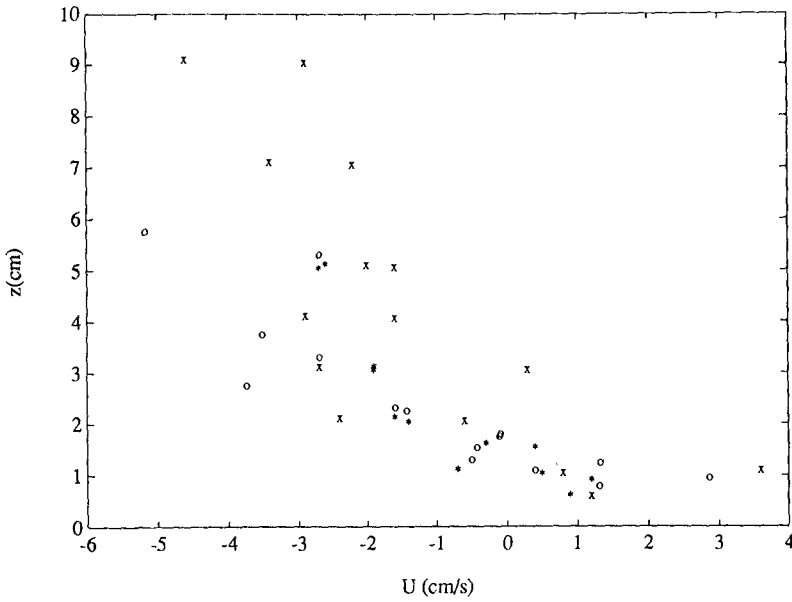


Figure 2: Mean velocity profiles under waves only  
Tests 35 (o: T=1.5 s), 39 (\*: T=2s), 42 (x: T=2.5s).

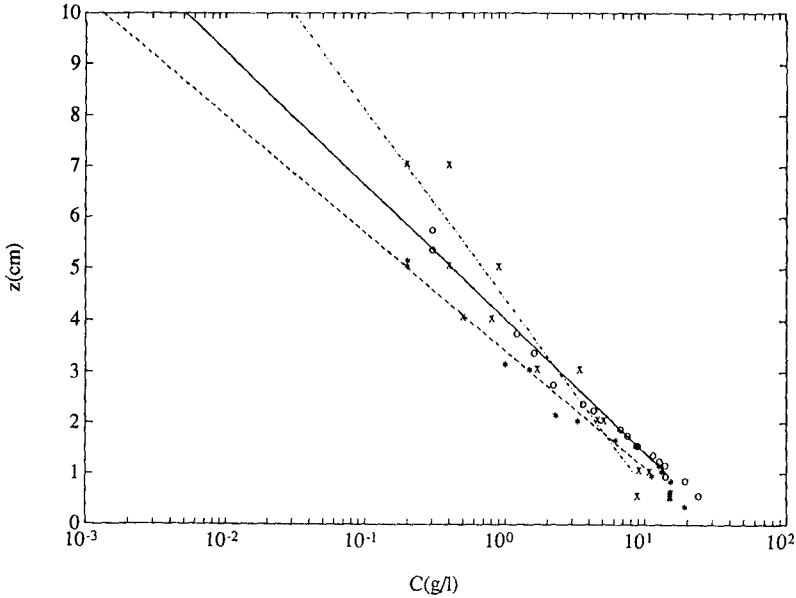


Figure 3: Mean concentration profiles under waves only  
Tests 35 o: T=1.5 s), 39 (\*: T=2s), 42 (x: T=2.5s).

#### 4. Transport rates

Suspended transport rate estimates are decomposed into a wave and a mean current contributions according to equation (1). Measurements are averaged between the two-measuring points at ( $y=\pm 25\text{cm}$ ) across measuring section. Total transport rates  $Q_t$  are estimated from bed profiler data according to equation (2). In most cases, the difference between total transport rates  $Q_t$  and suspended transport rates  $Q_s$  is less than the spatial variability of measurements (30%). This indicates that bed load transport remains relatively small. In the case of opposing currents, net suspended transport rates are also small so that bed load contributions are not negligible anymore; total transport rates are then significantly enhanced in the direction of opposing mean current due to the small bed load contributions (see Table 3).

Under waves only, total transport is in the direction of wave propagation and increases with the wave period. Contribution of the weak eulerian drift to total transport  $Q_c$  remains small. Under combined waves and current, the wave contribution  $Q_w$  to total transport systematically opposes the mean current direction. The direction of total transport depends then on the relative intensity of both contributions. In the case of following current, the wave contribution is opposed to the direction of wave propagation but remains small compared to the mean current contribution  $Q_c$ , so that net transport is in the direction of wave propagation.

Test N°	$Q_c$ $\times 10^{-4}$	$Q_w$ $\times 10^{-4}$	$Q_s$ $\times 10^{-4}$	$Q_t$ $\times 10^{-4}$
35	21	100	121	81
39	2	112	114	137
42	10	160	170	167
36	142	-22	120	126
40	135	-55	80	106
77	166	-38	127	93
38	-29	36	8	-19.5
41	-63	147	84	20
54	-143	133	-10	<del>X</del>
45	-60	95	36	-14

Table 3: Sediment transport rates (Units are in  $\text{kg/m/s}$ )

## 5. Instantaneous concentrations

### Bottom concentration:

Under waves only, the bottom phase-averaged concentration is mainly periodic at half the wave period ( $T=2s$ ) and concentration peaks occur near current reversal ( $u(t)=0$ ), as shown on Figure 4.a. Under combined waves and current, only one maximum concentration peak is observed which systematically occurs slightly after flow reversal when the instantaneous current is opposed to the mean current direction as shown on Figures 4.b and 4.c for  $T=2s$ . Near the bottom, the contribution of the wave motion to total transport is then expected to oppose to the mean flow direction.

### Diffusion of concentration peaks:

Diffusion of concentration at various elevations is shown on Figure 4.a under waves only. The first peak occurring near flow reversal when current starts to oppose direction of wave propagation, cannot be observed away from the bottom. Phase-averaged concentrations show only one maximum peak occurring when current is in the direction of wave propagation ( $u(t)>0$ ). Flux due to oscillatory motion is then expected to be positive at all elevations.

Diffusion of maximum concentration peaks away from the bottom can be observed on Figure 4.b for following current and on Figure 4.c for opposing current. Concentrations are maximum when instantaneous current is negative ( $u(t)<0$ ) in the case of following current and positive ( $u(t)>0$ ) for opposing current. Flux due to oscillatory motion is then expected to oppose the mean current direction at all elevations.

### Flux profiles:

Typical flux profiles, time-averaged over the wave period, obtained for waves only, and combined waves and current are shown on Figures 5.a, b, c ( $T=2s$ ). As expected from near bottom concentration response and diffusion of concentration peaks, sediment transport flux due to oscillatory wave motion is in the direction of wave motion in both cases of waves only and opposing current and waves and in the opposite direction for following current.

## 6. Discussion of results and conclusions:

Results obtained for the mean current and wave contributions to total sediment transport make a qualitatively consistent picture. Under combined waves and current, the wave contribution is found to systematically oppose the mean current direction. In this case, the direction of the wave contribution to total sand transport can be explained by the asymmetrical bottom concentration response. Only one maximum concentration peak is observed which occurs slightly after flow reversal when the instantaneous current starts to oppose the mean flow direction.

It is interesting to note that these results are qualitatively similar with observations by P. Murray and al (1991) in the sheet flow regime. They also found that the total sediment transport rate under combined waves and current is systematically reduced by its wave component; their observations confirm the existence of one maximum peak in the bottom concentration which occurs when the



instantaneous current is opposed to the mean flow direction. These observations suggest that the reduction of total transport by the wave contribution is a fairly general result occurring in both ripples and sheet flow regimes.

Under waves only, the effect of the eulerian drift under waves only as well as second-order Stokes component on mean phase-averaged concentrations still needs to be clarified. A similar dissymetry on the phase-averaged concentration response can be observed under waves only as under opposing current and waves so that transport due to wave motion is in the direction of wave propagation in both cases.

The effect of bedforms dimensions and of measuring technique on concentration profiles is also unclear. In the case of three dimensional bedforms ( $T=2.5s$ ), a spatial averaging technique may become necessary, considering spatial variability of signal.

### Acknowledgments

This study is partly supported by the European Community through the project n° 035 ("G6M-Coastal Morphodynamics") of the MAST program and partly by E.D.F. and by the French Sea State Secretary (S.T.C.).

### References

- Davies, A.(1990): Modelling the vertical distribution of suspended sediment in combined wave-current flow, Proceedings of the 5th International Biennial Conference on the Physics of Estuaries and Coastal Seas, University of Wales.
- Grant, W.D., Madsen, O.S.(1979): Combined Wave and Current Interaction with a Rough Bottom, *Journal of Geophysical Research*, Vol. 84, N°C4, pp. 1797-1808.
- Longuet-Higgins, M.S.(1953): Mass Transport in Water Waves, *Royal Soc. Phil. Trans.*, Vol. 245 A.903, pp.535-581.
- Murray, P.B., Davies, A.G., Soulsby, R.L.(1991): Sediment pick-up in wave and current flows, *Euromech 262, Sand Transport in Rivers, Estuaries and the Sea*, pp. 37-44.
- Nap, E., Van Kampen, A. (1988): Sediment transport in irregular non-breaking waves, Coastal Engineering Department, Delft Univ. of Technology, Delft, The Netherlands.
- Nielsen, P.(1979): Some basic concepts of wave sediment transport, *Instit. of Hydrodynamics and Hydraulic Engineering, Technical University of Denmark, Series Paper N° 20*.
- Van Rijn, L.C. (1991): Sediment transport in combined currents and waves, *Euromech 262, Sand Transport in Rivers, Estuaries and the Sea*, pp.3-16.
- Villaret, C., Menon, J.M.(1992): Sediment transport under combined wave and current, Report on model investigation, E.D.F. report N° 9268.

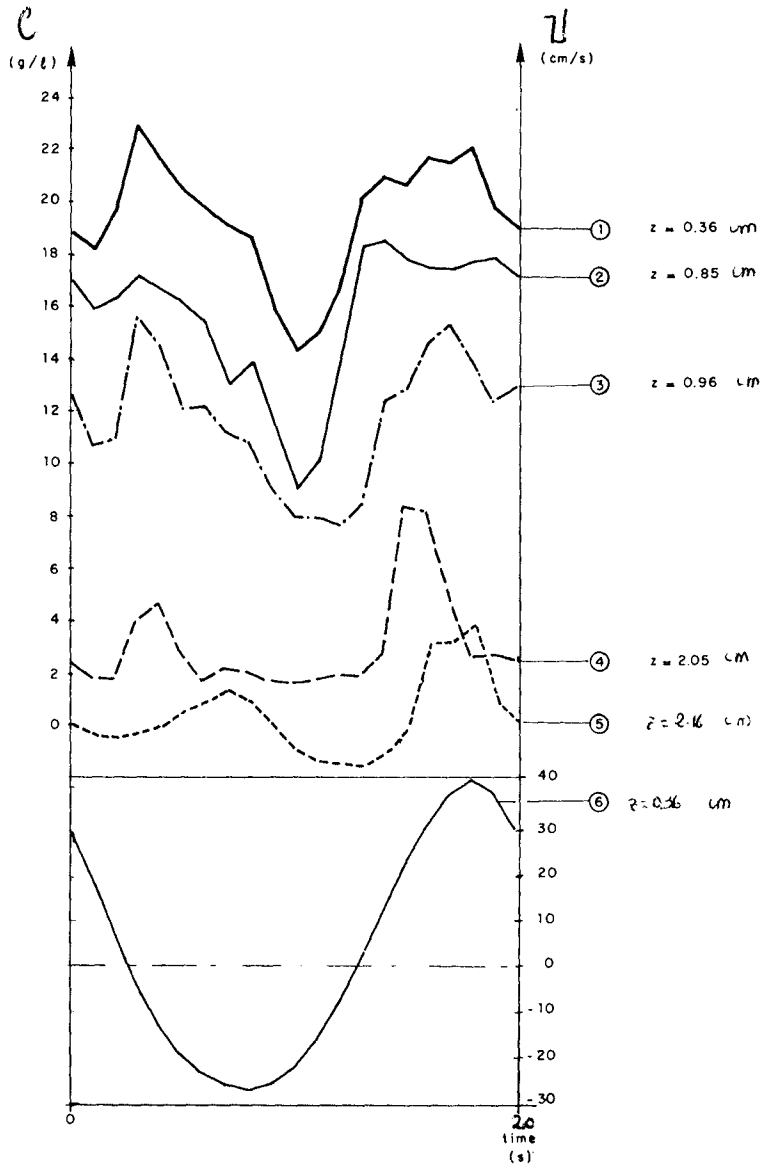


Figure 4.a: Phase-averaged concentrations (1-5) and bottom velocity (6) under wave only for  $T=2$  s (Test 39)

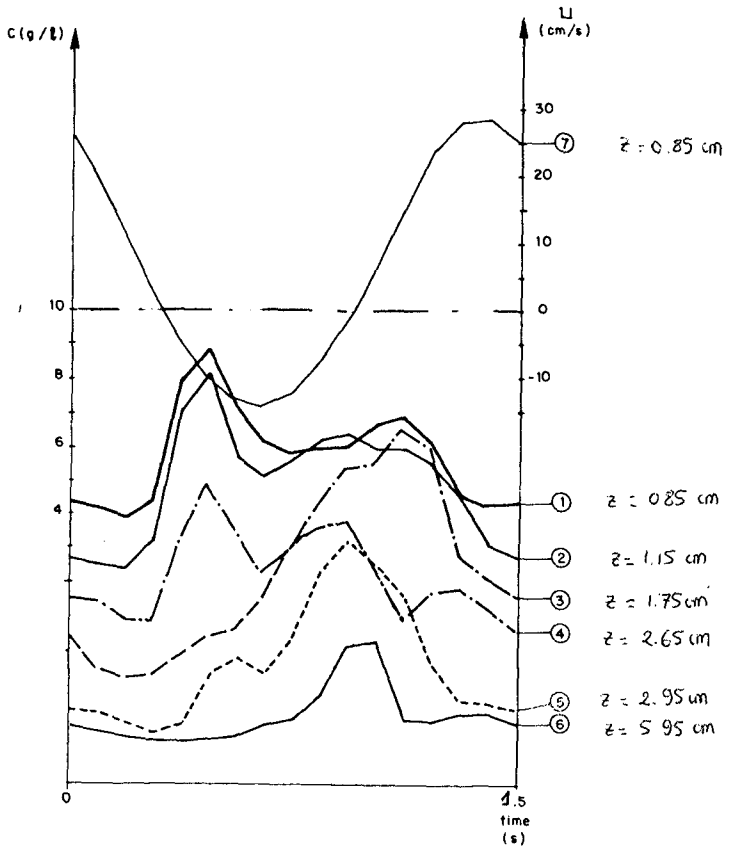


Figure 4.b: Phase-averaged concentration (1-6) and bottom velocity (7) under wave and following current for  $T=1.5$  s (Test 36)

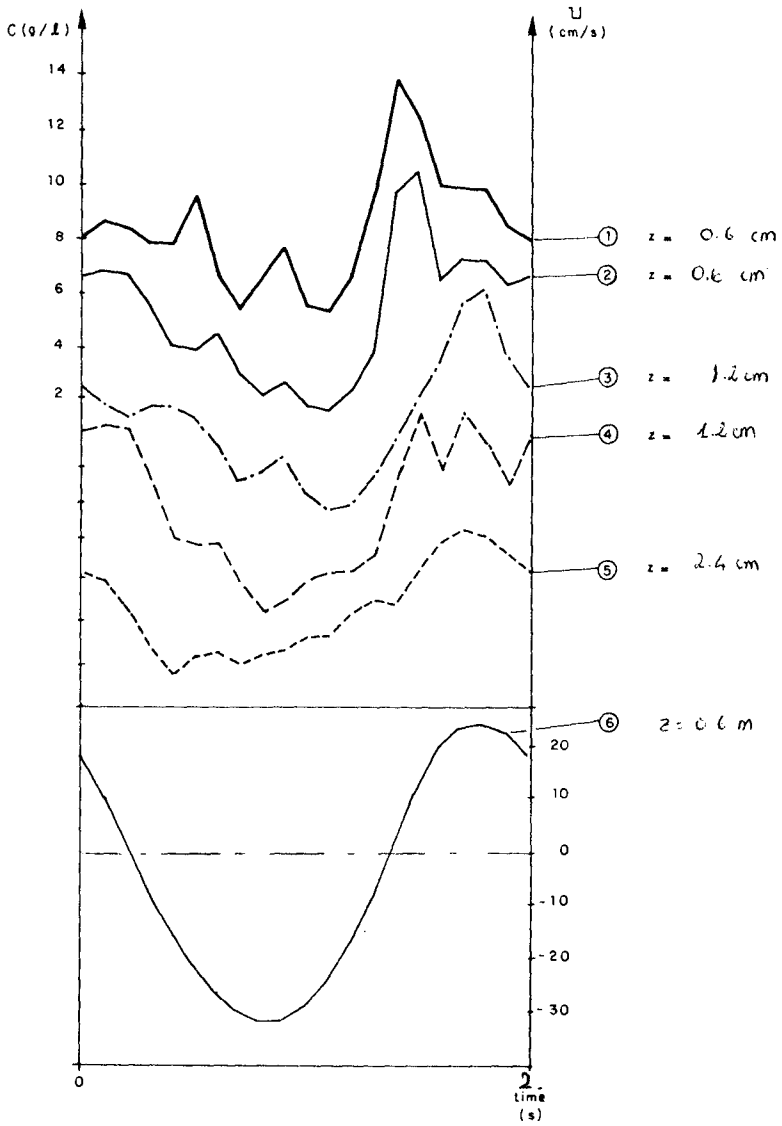


Figure 4.c: Phase-averaged bottom velocity (6) and concentration at various elevations (1 to 5) under wave and opposing current for  $T = 2$  s (Test 54)

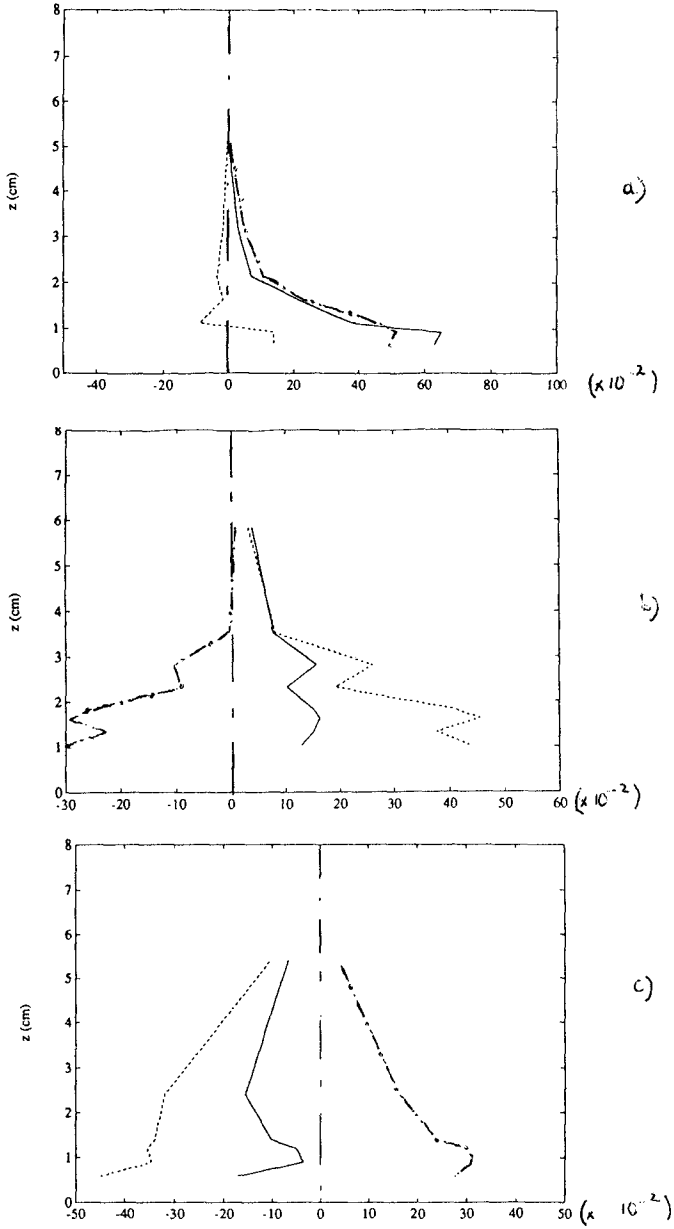


Figure 5: Time-averaged sediment flux profiles at  $T=2s$  ( $\langle u(t) c(t) \rangle$ ): —; UC:- - -;  $u_W(t)c_W(t)$ : - · -. Units are in  $Kg/s/m^2$ .  
 a) Wave only (Test 39); b) following current (Test 40); c) opposing current (Test 54).

## CHAPTER 193

### A TIME—DEPENDENT NEARSHORE MORPHOLOGICAL RESPONSE MODEL

Hsiang Wang<sup>1</sup>, Gang Miao<sup>2</sup> and Li-Hwa Lin<sup>3</sup>

#### Abstract

This paper presents a numerical model for computing time-dependent near-shore hydrographic changes including beach profile responses. The time scale of the model is suitable for storm events to seasonal changes. The model is very stable and is capable of handling complicated topographies including inlets and irregularly-shaped structures such as curved jetties and breakwaters.

The basic approach is similar to many previous investigations utilizing a hydrodynamic model to drive a sediment transport model. The hydrodynamic model computes fully interacted current and wave fields based on coupled mild slope wave equation and depth-averaged circulation equations. The sediment transport model is of energetic type treating the rate of sediment as the summation of two energetic mechanisms one due to the mean current and the other due to the wave induced turbulence.

The model has been successful comparing with the evolution of beach profiles in large wave tank tests as well as other 2-dimensional numerical models of profile evolution. The model is able to predict the bar formation realistically without introducing constraints such as the bar genesis. At present the model consists of four modulars that apply separately for the situation of beach with no subaerial structure but could include non-reflective bottom structure, beach with shore-connected structures, beach with shore-detached structures and beach-inlet system. Test applications are presented here with some comparisons with field data and 3-D movable bed experiments.

#### INTRODUCTION

The nearshore zone is the area where the action of waves and currents on the sea bed is most intense, and where the bed material is almost always in motion. Erosion/accretion of the beach and change in offshore bottom topography occur naturally through the transport of sediment by waves and currents. Perturbations introduced by coastal structures, beach fills and other engineering activities may result in unexpected deformation of beach shapes and nearshore topographies. In the past, the prediction of beach evolution was mainly conducted by relying on experience of similar cases and on the results of hydraulic model tests. In

---

<sup>1</sup>Professor, <sup>2</sup>Post-Doctor, <sup>3</sup>Assistant Scientist, Coastal and Oceanographic Engineering Department, University of Florida, Gainesville, FL 32611, USA

recent years numerical models have gradually been developed and applied for this purpose.

The purpose of three-dimensional models is to predict the change of bottom topography from the spatial distribution of the sediment transport rates, which are evaluated from the nearshore wave and current fields computed point by point in small areas defined by a horizontal grid placed over the region of interest. Models of 3-D beach topography change require much fewer idealizations than do the line models. In this paper, a time-dependent nearshore morphological response model was developed. Test applications are presented together with comparisons of 3-D movable model test results and some field measurements.

### OUTLINE OF THE MODEL

The model consists of three submodels for calculating (1) waves, (2) nearshore currents, and (3) sediment transport and bottom changes. The first two models are fully coupled to provide nearshore hydrodynamic condition. Nearshore waves, through radiation stresses, provide the driving force for the currents which, in turn, modifies the wave field. A compatible current and wave field is obtained through iterative process. This combined sediment transport model is then used as the driving force for the sediment transport model which also calculates bottom changes through sediment conservation equation. The change in topography again modifies the hydrodynamics. therefore, yet another level of current-wave-topographic interaction is required through frequent updating. At the first step, the initial beach topography and the geometry of the structures for the study area are given as input. Next, the wave model determines the spatial distributions of radiation stresses and near-bottom orbital velocities. The circulation model, then, computes the mean water surface level and the depth averaged mean currents using the radiation stresses from the wave model as the forcing terms and includes bottom friction, advective acceleration and the lateral diffusion terms. Finally, the sediment transport rates are computed at the local points from the wave-current conditions calculated in advance, and then the three dimensional bottom topography change is computed by solving the equation of sediment mass conservation. The wave and current fields are updated hourly to incorporate topographic changes and tidal variations.

### Wave Model

Five contemporary numerical wave models were evaluated for their suitability (Lee and Wang, 1992). Two of them originally developed by Winer (1990) and Lee and Wang (1992), respectively were selected and modified for the present purpose. Both models account for current-wave-topography induced shoaling, refraction and diffraction effects. Empirical surf zone mechanics are also incorporated.

Both models are based upon the mild-slope equation given by Kirby (1984). Winer's model is the parabolic approximation version and theoretically is valid only for small incident wave angles. It employs a Crank-Nicholson finite difference scheme to solve the complex wave amplitude,  $A$ , of the following set of equations:

$$\begin{aligned} (C_g \cos \theta + U)A_x + \frac{\sigma}{2} \left( \frac{C_g \cos \theta + U}{\sigma} \right)_x A + VA_y + \frac{\sigma}{2} \left( \frac{V}{\sigma} \right)_y A \\ - \frac{i}{2} k C_g (1 - \cos^2 \theta) A - \frac{i}{2} \left[ CC_g \left( \frac{A}{\sigma} \right)_y \right] + \frac{\kappa}{2} A = 0 \quad (1) \end{aligned}$$

$$\omega = \sigma + \vec{k} \cdot \vec{U} \quad (2)$$

$$\sigma^2 = gk \tanh kh \quad (3)$$

where  $t$  is the time,  $\nabla_h$  is the horizontal gradient operator,  $\vec{U}$  is the depth averaged horizontal velocity vector,  $C$  is the phase velocity,  $C_g$  is the group velocity and  $\sigma$  is the angular frequency. The last term in Eq. 1 is the energy dissipation term, where  $\kappa$  is the energy dissipation coefficient. This term has been added in order to deal with the wave decay and recovery after breaking. Eventually coefficient  $\kappa$  will be related to the energy dissipation due to wave breaking following the work of Dally et al. (1984). This model is exceptionally stable and efficient. It usually only requires very minor adjustment for different applications.

The other model is based upon elliptic wave equation using the Gragg's method to solve for  $\check{\phi}$  which is the wave part of the velocity potential at the mean water level:

$$\begin{aligned} -i\omega[2U \cdot \nabla\check{\phi} + (\nabla \cdot U)\check{\phi}] + (U \cdot \nabla)(U \cdot \nabla\check{\phi}) + (\nabla \cdot U)(U \cdot \nabla\check{\phi}) \quad (4) \\ - \nabla \cdot (CC_g \nabla\check{\phi}) + (\sigma^2 - \omega^2 - k^2 CC_g - i\sigma\kappa)\check{\phi} = 0 \end{aligned}$$

This model has no small wave angle restriction and can accommodate reflective boundary conditions. The model is less stable and sometimes does not converge.

### Circulation Model

The governing equations for the circulation model are the depth integrated time averaged horizontal equations of momentum (Ebersole and Dalrymple, 1979):

$$\frac{\partial U}{\partial t} + U \frac{\partial U}{\partial x} + V \frac{\partial U}{\partial y} + g \frac{\partial \bar{\eta}}{\partial x} + \frac{1}{\rho D} \bar{\pi}_x - \frac{1}{\rho D} \tau_{sx} + \frac{1}{\rho D} \left( \frac{\partial S_{xx}}{\partial x} + \frac{\partial S_{xy}}{\partial y} \right) + \frac{1}{\rho} \frac{\partial \tau_l}{\partial y} = 0 \quad (5)$$

$$\frac{\partial V}{\partial t} + U \frac{\partial V}{\partial x} + V \frac{\partial V}{\partial y} + g \frac{\partial \bar{\eta}}{\partial y} + \frac{1}{\rho D} \bar{\pi}_y - \frac{1}{\rho D} \tau_{sy} + \frac{1}{\rho D} \left( \frac{\partial S_{xy}}{\partial x} + \frac{\partial S_{yy}}{\partial y} \right) + \frac{1}{\rho} \frac{\partial \tau_l}{\partial x} = 0 \quad (6)$$

and the continuity equation

$$\frac{\partial \bar{\eta}}{\partial t} + \frac{\partial}{\partial x}(UD) + \frac{\partial}{\partial y}(VD) = 0 \quad (7)$$

where  $(U, V)$  are the depth-averaged velocity components in the  $x$  and  $y$  directions, respectively,  $D = h + \bar{\eta}$ ,  $h$  is the still water depth, and  $\bar{\eta}$  is the elevation of the mean water level due to wave setup/setdown,  $\tau_l$  is the lateral shear stress due to turbulent mixing,  $(\bar{\pi}_x, \bar{\pi}_y)$  are the bottom shear stresses,  $(\tau_{sx}, \tau_{sy})$  are the surface shear stresses,  $S_{xx}$ ,  $S_{xy}$  and  $S_{yy}$  are the radiation stress components which arise from the excess momentum flux due to waves. The radiation stress terms are forcing terms, whereas the bottom friction terms and the lateral mixing terms represent flow impedances. These equations are obtained by integrating the local  $x$  and  $y$  momentum equations and the continuity equation over the depth of the water column and then time averaging the results. The governing equations in the circulation model are solved by alternating direction implicit (ADI) scheme. In order to treat the wave-current interaction, alternate computations of waves and of currents are necessary.



### Sediment Transport Model

Like the selection of wave model, a number of proven sediment transport models, mainly for 2-D profile modeling, were evaluated. They were compared on their basic transport mechanism. This was accomplished by comparing the transport forcing function expressed in equivalent shear stress term. Table 1 shows the equivalent shear stress terms from various models. The comparison under one specific wave condition is illustrated in Figure 1. It can be seen that they all assume similar shape. The transport model following that developed by Ohnaka and Watanabe (1990) was selected because the formulation is most suitable for 3-D application. The rate of sediment transport is treated as the summation of two energetic mechanisms one due to the mean current and the other due to the wave induced turbulence. The transport due to the mean current is

Table 1: Equivalent Shear Stress from Different Sediment Transport Models

Energy Loss (Dally, Kriebel, Larson and Kraus)
$\tau_e = -\frac{2}{H} \sqrt{\frac{h}{g}} \frac{\partial(EC_d)}{\partial x}$
Time-Averaged Bottom Velocity (Dally)
$\bar{\tau} = \frac{1}{T} \int_0^T \rho \frac{t}{2} u_b^2 dt \quad u_b = \frac{H}{2} \sqrt{\frac{g}{h}} \cos \omega t$
Deficit of Moment of Momentum (Houston and Dean)
$\bar{\tau}_b = -\frac{2}{h} \frac{\partial}{\partial y} \left[ \frac{Eh}{4} \left( 1 + \frac{H^2}{2h^2} \right) \right]$
Combined Bottom Velocity (Watanabe)
$\tau_c = U^2 + V^2 + \hat{u}^2 + 2U\hat{u} \cos \theta + 2V\hat{u} \sin \theta$
$\hat{u} = \frac{\pi H}{T \sinh kh}$

$$\vec{q}_c = \frac{A_c(\tau - \tau_{cr})\vec{U}}{\rho g} \quad (8)$$

where  $A_c$  is a nondimensional coefficient (of the order 0.1 to 1.0), values of which should be empirically determined.  $\tau$  is the maximum value of the bottom shear stress in a wave-current coexistent field.  $\tau_{cr}$  is the critical shear stress for the onset of sediment movement,  $\rho$  is the density of water, and  $g$  is the gravitational acceleration. If  $\tau \leq \tau_{cr}$ ,  $\vec{q}_c$  is zero. The transport due to waves is

$$\Phi = B_w(\Psi_m - \Psi_c)\Psi_m^{1/2} \quad (9)$$

where  $\Phi = (1 - \lambda_v)q_w/w_0d$  is a dimensionless net transport rate,  $d$ ,  $w_0$  and  $\lambda_v$  are the diameter, settling velocity, and void ratio of the sediment, respectively,  $B_w$

is a nondimensional coefficient (of order 2 to 10),  $\Psi_m$  is the Shields parameter and  $\Psi_c$  is the critical value of  $\Psi_m$  for the onset of general movement of sediment. Since  $q_w$  is the absolute value of the net transport rate, a method is needed to determine the direction of the net transport. Criteria for predicting whether a beach will erode or accrete through cross-shore sand transport processes have been suggested by a number of authors. The two most commonly used parameters include one for characterizing the deepwater wave steepness,  $H_0/L_0$ , and the other one related to the relative sediment fall velocity,  $H_0/w_0T$ , also known as the Dean's parameter. A version proposed by Larson et al. (1989) in their SBEACH model was adopted here. The criterion for distinguishing beach erosion and accretion can be expressed by the following equations:

$$\frac{H_0}{L_0} \leq C \left( \frac{H_0}{w_0T} \right)^3, \quad \text{erosion}$$

$$\frac{H_0}{L_0} > C \left( \frac{H_0}{w_0T} \right)^3, \quad \text{accretion}$$

in which  $C = 0.00070$  is an empirical coefficient.

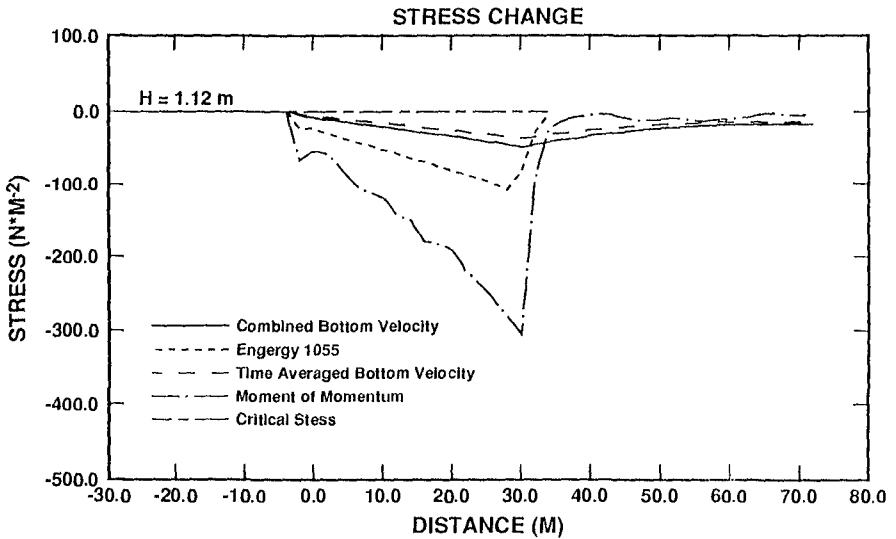


Figure 1: Comparisons of equivalent shear stresses for different transport models.

The change in local bottom elevation,  $z_b$ , or water depth,  $h$ , can readily be computed from the spatial distribution of the sediment transport rates by solving the following equation for the conservation of sediment volume

$$\frac{\partial h}{\partial t} = \frac{\partial q_x}{\partial x} + \frac{\partial q_y}{\partial y} \quad (10)$$

$$\vec{q} = \vec{q}_w + \vec{q}_c = (q_x, q_y) \quad (11)$$

## MODEL VALIDATION AND APPLICATIONS

In order to validate the 3-D morphological response model, several large wave tank results of dune erosion were simulated. These included Saville's (1957) large wave tank tests and the case of a sand beach backed by a sloping dike tested in the BIG WAVE FLUME, Germany (Dette and Uliczka, 1986).

Figure 2 shows a comparison of measured and calculated profiles for CE Case 400, from Saville, for which: initial slope =  $1/15$ ; grain size =  $0.22 \text{ mm}$ ; wave height and period of  $1.62 \text{ m}$  and  $5.6 \text{ sec}$  in the horizontal section of the tank (depth =  $4.42 \text{ m}$ ); and constant water level. The numerical and test results are shown for simulation times of 1, 3, 5, 10, 15, and 20 hours. The numerical model satisfactorily reproduced the observed forshore erosion and main breakpoint bar development. Simulated shoreline retreat and bar growth was initially rapid and gradually slowed as the bar moved offshore to reach a location close to that of the observed bar at the end of the run (20 hr).

A similar comparison is shown in Figure 3 for the case of 'dune with foreshore':  $+2 \text{ m}$  above SWL and  $10 \text{ m}$  wide dune with 1 to 4 seaward slope down to  $1 \text{ m}$  below SWL and following 1 to 20 slope down to channel floor. The BIG WAVE FLUME is  $324 \text{ m}$  long,  $7 \text{ m}$  deep and  $5 \text{ m}$  wide. The test profile was subjected to regular waves ( $H = 1.5 \text{ m}$ ,  $T = 6 \text{ s}$ ,  $h = 5.0 \text{ m}$ ). The predicted profiles are shown at times of 62, 111, 190 and 273 minutes and are compared to the measured profiles. The computed wave height distribution across shore is also shown. The waves cut back the foreshore to produce a vertical scarp, and a bar formed near the break point which grew and moved offshore with continued wave action. The volume of the main breakpoint bar and the amount of erosion on the foreshore are rather well predicted by the numerical model. However, the bar trough is less well reproduced. The model is incapable of simulating micro features such as the bottom undulations inside the breaking zone.

The model is also compared with other 2-D dune erosion models including Kriebel and Dean (1984) and Larson et al. (1989). The comparisons of profile changes in the nearshore zone are all very close; they deviate in bar formations. Figure 4 shows the comparison between the present model and the SBEACH applied to a prototype profile and wave condition. The Kriebel's model (not shown here) almost duplicates the SBEACH in the nearshore zone but produces no bar.

The present numerical model has been applied to a variety of cases including beach nourishment, beach with submerged rocks, offshore detached breakwater, shore-perpendicular structures, inlet-beach system, etc. The model results of waves, currents and topographic changes for a region around Sebastian Inlet are given here as an illustration. Sebastian Inlet is located at the east coast of Florida between the Brevard and Indian River County line approximately 45 miles south of Port Canaveral entrance. The bathymetric map of 1989 is given in Figure 5. It is located in a littoral drift zone predominately from north to south. The inlet has been kept open by means of maintenance dredging and jetty improvements. It suffers from channel shoaling and downdrift beach erosion. Movable bed physical model and field studies were carried out (Wang et al., 1991, 1992) to seek improvement measures.

A few examples are given here to show the comparison between numerical simulation and field or laboratory results. First of all, the wave patterns under

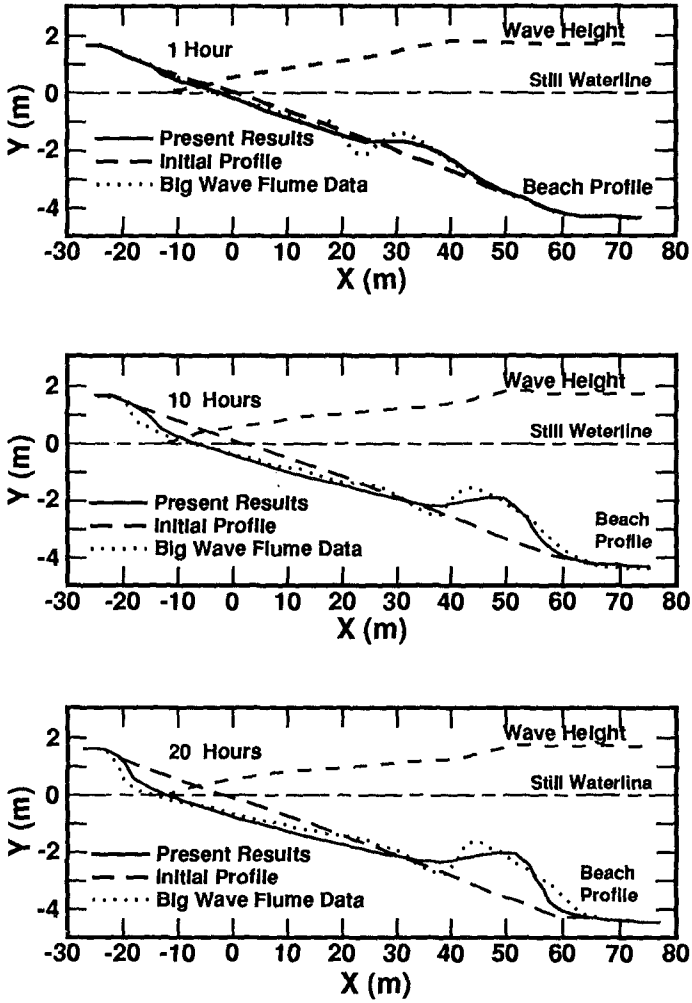


Figure 2: CE case 400, Comparison between simulated and measured beach profiles.  $t = 1, 3, 5, 10, 15, 20$  hours. Data from Saville (1957).

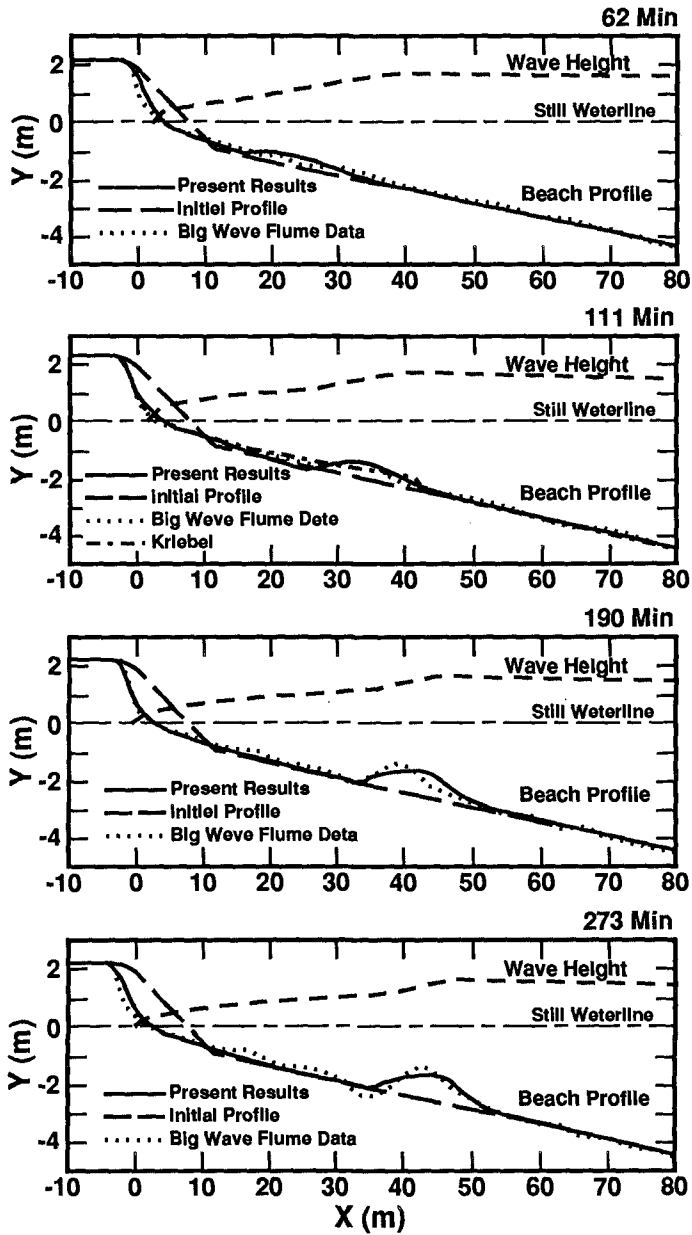


Figure 3: Comparison between simulated and measured beach profiles, measured data from Dr. Dette.  $t = 62, 111, 190, 273 \text{ min}$

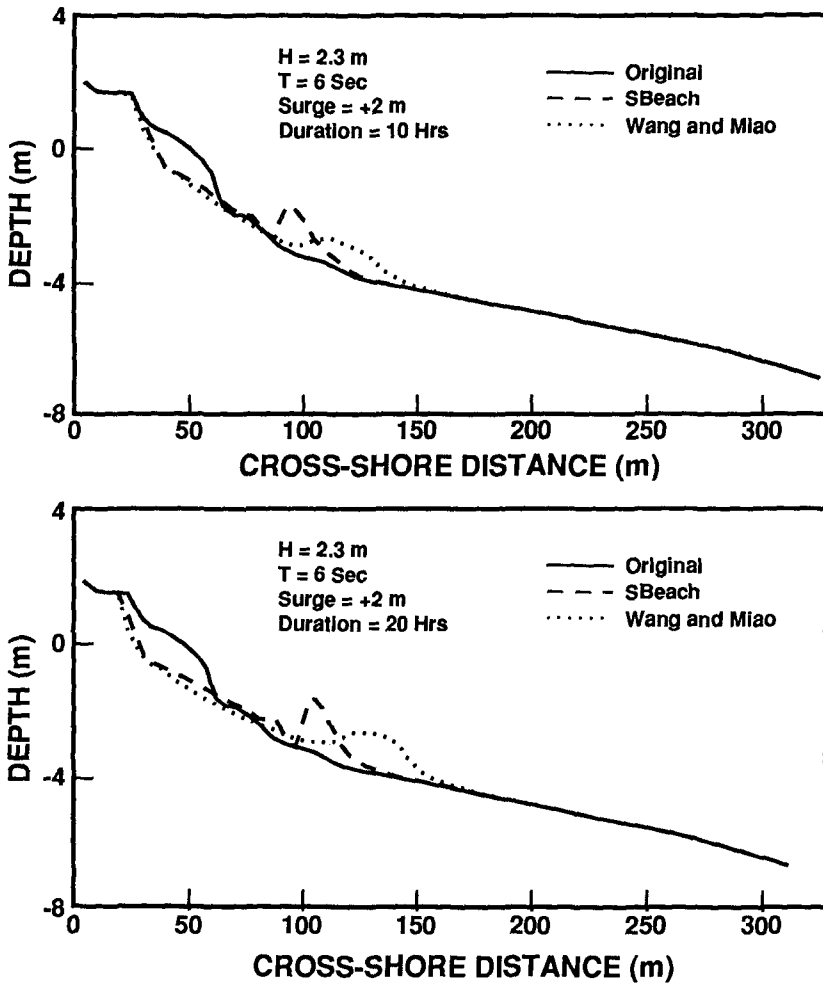


Figure 4: Comparison between present model and SBEACH model

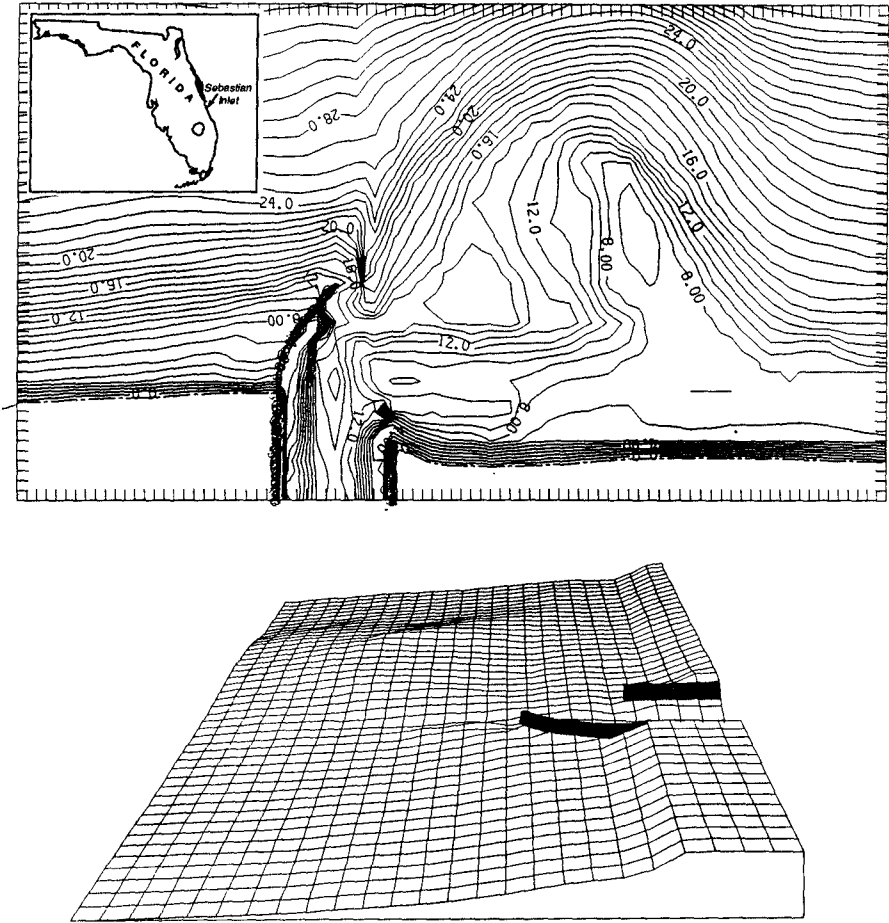


Figure 5: Sebastian Inlet bathymetric map for year 1989.

long crested conditions can be closely simulated by the numerical model. This can be seen in Figure 6 which compares wave pattern recorded by aerial photo with simulation.

The current in the inlet is tidal driven, often reaching to  $2.5\text{ m/s}$  during ebb and flood. In the vicinity and outside the inlet, the current field is very complicated. During ebb cycle, the current behaves like a jet carrying with it a rather concentrated seaward momentum. This jet when deflected by the curved north jetty directs itself towards the southeast, which gradually shaped the main flood-ebb channel. A clockwise vortex is formed on the south side behind the jet stream. During flood cycle, the current converges to the inlet like flow into a funnel. The flow pattern is influenced by both the ebb shoal and the jetties. A very strong current developed near the tip of the south jetty, causing a major scouring hole at its tip. The current patterns simulated by the numerical model are compared with those measured in the field in Figure 7. Again, like wave field simulation, the current pattern appears to be quite reasonably reproduced.

For morphological changes the numerical model is compared with movable bed physical model tests. The model has a horizontal scale of 60 using finer sand than the prototype as bed material (detail see Wang et al., 1992). The actual physical dimensions of the model are approximately alongshore and offshore. Figure 8 compares the numerical and physical model results for a specific case with the following input conditions: the offshore boundary is  $H = 2\text{ m}$ ,  $T = 8\text{ s}$ , and the incident wave angle at the offshore boundary is  $10^\circ$  (from the north-east). The tide is semi-diurnal with a range of  $1.0\text{ m}$ . The plot gives the cumulative bottom changes after a time period equivalent to 6-days in prototype. The solid lines represent accretion and dash lines represent erosion with contour interval of  $0.1\text{ m}$ . The most visible bathymetric changes occur in the nearshore region behind the ebb shoal including the area near the tip of the south jetty. Beach face is eroded by wave action and sand is carried out towards offshore forming offshore bars. Meanwhile, the ebb shoal experienced vigorous sediment motion due to wave breaking and the sediment is also carried into the nearshore region. Although the details are somewhat different the agreement can be considered good macroscopically as most of the prominent topographical changes are correctly predicted.

## CONCLUSIONS

A numerical model has been developed for computing time-dependent nearshore hydrographic changes including beach profile responses. The time scale of the model is suitable for storm events to seasonal changes. The model is very stable and is capable of handling complicated topographies including inlets and irregularly-shaped structures such as curved jetties and breakwaters.

The model has been fairly rigorously calibrated against 2-D large scale beach profile evolution tests carried out in the GWK tank and in the CERC's large tank. The model is also verified with other 2-D numerical models. The model is capable of describing the growth and movement of main breakpoint bars and corresponding berm processes with reasonable reliability. Calibration and verification for 3-D cases are limited. So far, a set of field and laboratory movable bed data concerning one specific inlet configuration has been utilized. The numerical model seems to perform well to predict wave patterns of long crested waves; gives reasonable current patterns. Consequently, the patterns of topographic changes can also be reasonably predicted. Of particular importance is the ability of the model to depict correctly the sediment transport patterns that can add to the



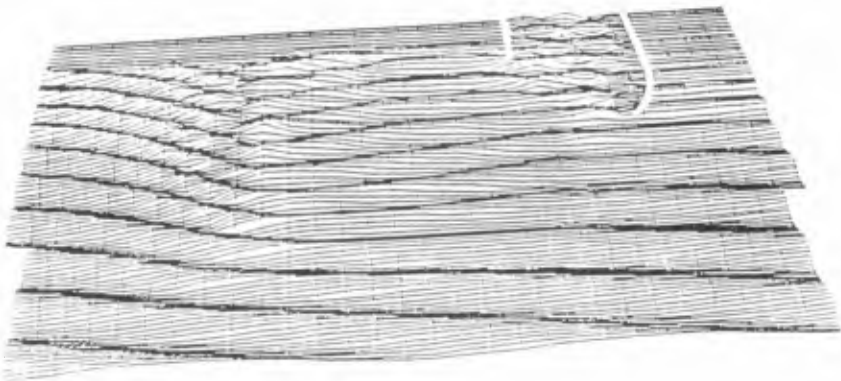


Figure 6: Comparisons of wave patterns from aerial photography and model at Sebastian Inlet.

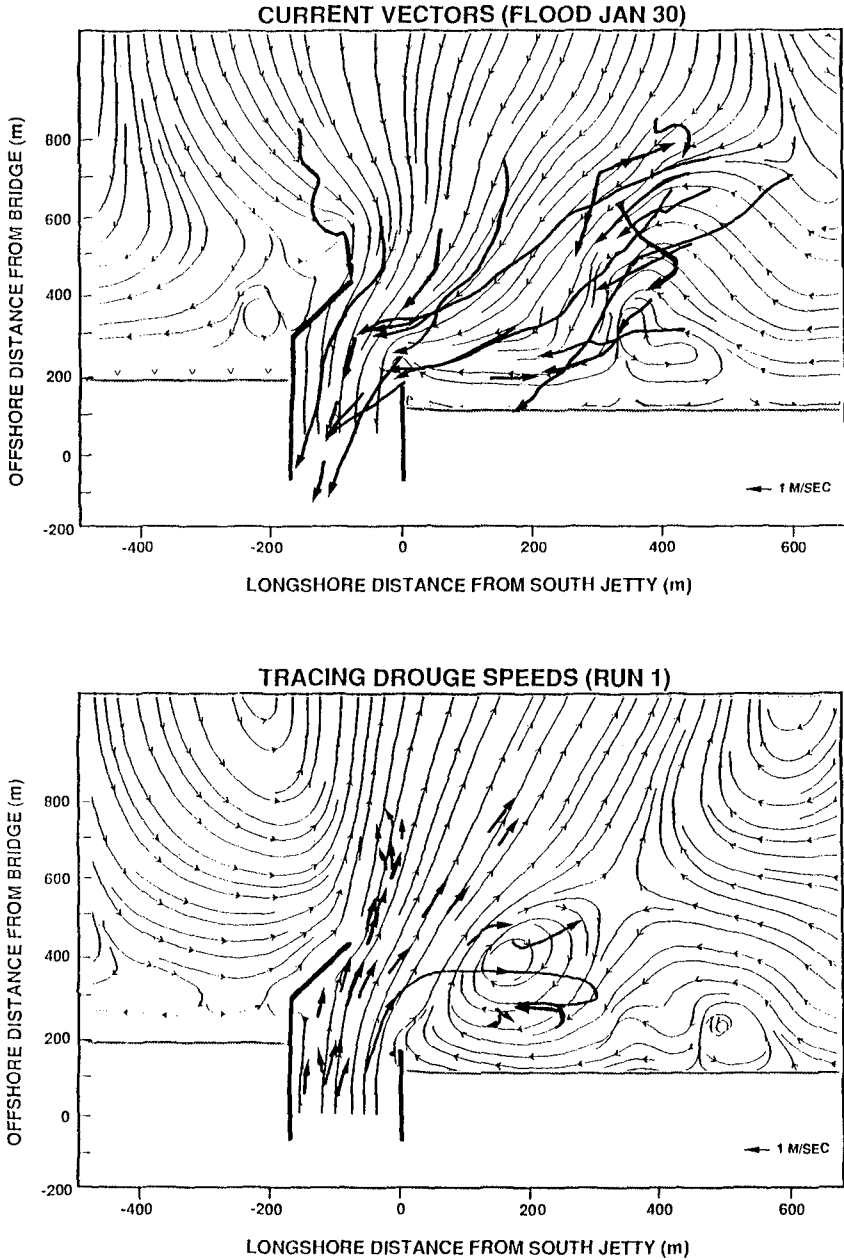


Figure 7: Comparisons of current patterns from the numerical model and field measurements.

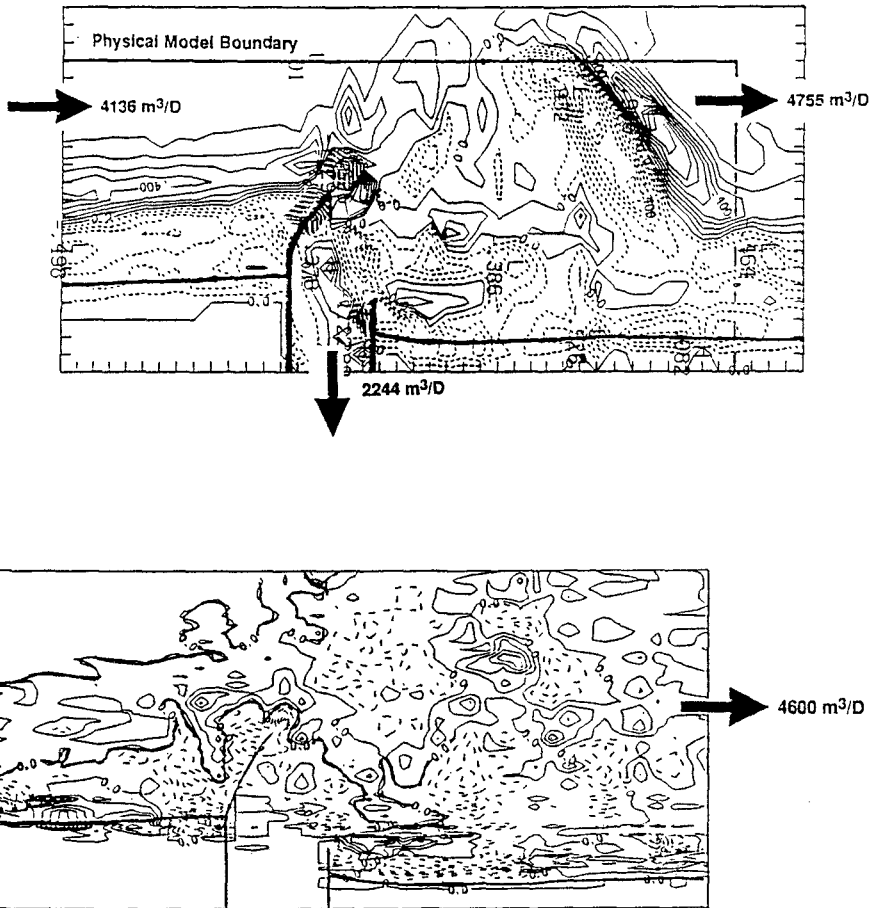


Figure 8: Comparison of bathymetric changes after 6-day NE storm.

insight to the sediment transport process. Of less confidence is the quantity of transport as well as detailed topographic changes. Work is still in progress to improve the reliability of the model as well as expanding the scope of the model.

### ACKNOWLEDGEMENTS

We would like to thank Dr. Hans H. Dette, from Leichtweib-Institut für Wasserbau Technische Universität, for providing the experimental data, and Professor H. Zhong, Mr. J. Lee, Mr. T. Kim, from COE Department of the University of Florida, for their contribution to the movable bed physical model study.

### REFERENCES

- Dally, W. R. , Dean, R. G. and Dalrymple, R. A. (1984). "A Model for Breaker Decay on Beaches" Proc. 19th Inter. Coastal Eng. Conf., ASCE, Houston, Tex., 82-98.
- Dette, H.H. and Uliczka, K. (1986). "Seegangserzeugte Wechselwirkung Zwischen Vorland und Vorstrand und Küstenschutzbauwerk" Technischer Bericht SFB 205/TPA6, University Hannover, Germany.
- Ebersole, B. A., and Dalrymple, R. A. (1979). "A Numerical Model for Near-shore Circulation Including Convective Acceleration and Lateral Mixing" Ocean Engineering Report No. 21, Dept. of Civil Eng., University of Delaware, Newark, Delaware.
- Kirby, J. T. (1984). "A Note on Linear Surface Wave-Current Interaction over Slowly Varying Topography" J. Geophys. Res., Vol. 89, No. C1, pp. 745-747.
- Kriebel, D. L., and Dean R. G. (1984). "Beach and Dune Response to Severe Storm Erosion" Proc. 19th Inter. Coastal Eng. Conf., ASCE, Houston, Tex., 1584-1599.
- Larson, M., Kraus, N. C. and Byrnes, M. R. (1989). "SBEACH: Numerical Model for Simulating Storm-Induced Beach Change" Technical Report CERC-89-9, Coastal Engineering Research Center, US Army Corps of Engineers.
- Lee, J. L. and Wang, H. (1992). "Evaluation of Numerical Models on Wave-Current Interactions" Proc. 23rd Inter. Coastal Eng. Conf., ASCE, Venice, Italy.
- Ohnaka, S. and Watanabe, A. (1990). "Modeling of Wave-Current Interaction and Beach Change" Proc. 22nd Inter. Coastal Eng. Conf., ASCE, Delft, The Netherlands, 2443-2456.
- Saville, T. (1957). "Scale Relationship for Equilibrium Profiles" Int. Assoc. of Hydraulic Research, 1957.
- Wang, H., Lin, L., Zhong, H., and Miao, G. (1991). "Sebastian Inlet Physical Model Studies, Part I — Fixed Bed Model" Coastal and Oceanographic Engineering Department, University of Florida. UFL/COEL-91/001.
- Wang, H., Lin, L., Zhong, H., and Miao, G. (1992). "Sebastian Inlet Physical Model Studies, Part II — Movable Bed Model" Coastal and Oceanographic Engineering Department, University of Florida. UFL/COEL-91/014.
- Winer, H.S. (1988). "Numerical Modeling of Wave-Induced Currents Using a Parabolic Wave Equation" Ph.D. Dissertation, Coastal and Oceanographic Engineering Department, University of Florida. UFL/COEL/TR-080.

## CHAPTER 194

# TOTAL RATE AND DISTRIBUTION OF LONGSHORE SAND TRANSPORT

Akira Watanabe<sup>1</sup>

### Abstract

Longshore sand transport rate has been computed, for 2,520 cases covering field- and laboratory-scale conditions, using a general formula for local transport rate in a coexistent wave-current field proposed by the present author. The computed total transport rate has been well related to the alongshore component of wave power and two other parameters. Cross-shore distributions of the longshore transport rate have also been studied.

### 1. Introduction

Longshore sediment transport plays a very important role particularly in long-term beach evolutions. In the longshore transport, sand grains are set in motion mainly by wave action and then carried by a longshore current. However the total transport rate is usually estimated using the CERC formula or its equivalence, which relates the total rate directly with the so-called longshore component of energy flux (or power) of breakers and does not explicitly involve the longshore current velocity. The CERC-type formulas are based on the power or energetics model concept and field measurements, but their reliability and appropriate values of the coefficients are yet debatable. In addition there have been only few studies on the cross-shore distribution of the local transport rate, which is regarded as important as the total rate for various engineering problems.

Watanabe *et al.* (1986) have proposed a power-model type formula for local sediment transport rate under combined action of waves and currents, whose validity has been confirmed through numerous fundamental studies and practical applications (*e.g.*, Watanabe *et al.*, 1991). This local transport rate formula

---

<sup>1</sup> Professor, Dept. of Civil Eng., Univ. of Tokyo, Bunkyo-ku, Tokyo, 113 Japan.

is applied in the present paper to the evaluation of the total rate and cross-shore distribution of the longshore sand transport under regular waves on straight beaches.

## 2. Computational Procedure for Waves, Currents and Sand Transport

### 2.1 Computational conditions

From the standpoint of such fundamental studies as this, computation of waves, currents and sediment transport should be performed for conditions as simple as possible. It has therefore been assumed in the following computation that the shoreline and depth-contour lines are straight and parallel to each other, that incident waves are regular and uniform in the alongshore direction, and that the sediment grain size is spatially uniform. On the other hand, for the sake of generalization of discussions, the computation has been conducted for a total of 2,520 cases: six values of the sand grain diameter  $d$ , four values of the uniform bottom slope  $\tan \beta$  and a bar-type beach, and three, seven and eight values of the incident wave angle  $\theta_0$ , period  $T$  and height  $H_0$ , respectively, as shown in Table 1, covering field- as well as laboratory-scale conditions.

Table 1 Computational conditions.

$d$ (mm)	$\tan \beta$	$\theta_0$ (deg)	$T$ (s)	$H_0$ (m)
0.2	1/10	15	1.0	0.02
0.5	1/20		1.5	0.04
0.8	1/30	30	2.0	0.16
1.1			6.0	0.3
1.5	1/50	45	10.0	0.6
2.0	bar-type		14.0	1.2
			18.0	2.4

### 2.2 Computation of nearshore waves

A set of time-dependent mild-slope equations, proposed by Watanabe and Maruyama (1986) and improved by Watanabe and Dibajnia (1988), can deal with most of nearshore wave deformation such as shoaling, refraction, reflection, diffraction, breaking and recovery. For the present problem, we can reasonably neglect the wave reflection from the shore and the refraction due to the presence of currents, and then the time-dependent mild-slope equation set reduces to the following simple wave energy equation:

$$\frac{d}{dx}(H^2 C_g \cos \theta) = -n f_D H^2 \quad (1)$$

where  $x$  is the shoreward coordinate,  $H$  is the wave height,  $C_g$  is the group velocity,  $\theta$  is the wave angle, and  $n$  is the shallowness factor. The quantity  $f_D$  is the breaker-induced energy dissipation factor and defined as:

$$f_D = \frac{5}{2} \tan \beta \sqrt{\frac{g}{D}} \sqrt{\frac{(H/D) - \gamma'_r}{\gamma'_s - \gamma'_r}} \quad (2)$$

$$\gamma'_s = 0.8(0.57 + 5.3 \tan \beta), \quad \gamma'_r = 0.4(H/D)_B \quad (3)$$

in which  $D = h + \eta$  is the local mean water depth ( $h$ : the still water depth;  $\eta$ : the mean water surface elevation), and the suffix B indicates the breaking point. Equation (1) has been solved together with Snell's law and Eq. (4) for the wave setup/down to obtain cross-shore distributions of the mean water depth  $D$ , wave height  $H$ , wave angle  $\theta$ , group velocity  $C_g$ , and so on.

$$\frac{d\eta}{dx} = -\frac{1}{\rho g D} \frac{dS_{xx}}{dx} \quad (4)$$

where  $S_{xx}$  is the normal component of the radiation stress, and  $\rho$  is the water density. The location of wave breaking has been determined using a generalized breaker index expressed in terms of the ratio of the horizontal orbital velocity at the wave crest to the wave celerity (Watanabe *et al.*, 1984).

### 2.3 Computation of longshore current

Since the wave field is stationary and uniform in the alongshore direction, the longshore current velocity has been computed by the following equation (Nishimura, 1988):

$$\rho C_t \tilde{W} V_\ell - \frac{d}{dx} \left[ \mu_e D \frac{dV_\ell}{dx} \right] + \frac{dS_{xy}}{dx} = 0 \quad (5)$$

where

$$\left. \begin{aligned} \tilde{W} &= W + (\tilde{u} \cdot \sin \theta)^2 / W, \quad \tilde{u} = (2/\pi) \hat{u}_b \\ W &= \left[ \sqrt{V_\ell^2 + \tilde{u}^2 + 2 V_\ell \tilde{u} \sin \theta} + \sqrt{V_\ell^2 + \tilde{u}^2 - 2 V_\ell \tilde{u} \sin \theta} \right] / 2 \end{aligned} \right\} \quad (6)$$

$$\mu_e = \rho N \xi \sqrt{gD} \quad (7)$$

in which  $V_\ell$  is the longshore current velocity,  $C_t$  is the friction coefficient for the current,  $S_{xy}$  is the tangential radiation stress,  $\hat{u}_b$  is the near-bottom orbital velocity amplitude,  $\mu_e$  is the lateral mixing coefficient, and  $\xi$  is the offshore distance from the mean shoreline. A value of 0.01 has been adopted for  $N$ .

In most of the previous computation of nearshore currents, constant values (on the order of 0.01) have been used for the friction coefficient  $C_t$ . However, since its value significantly affects the magnitude of the longshore current velocity and the resultant sediment transport rate, we should determine  $C_t$  in a more objective and reasonable way. Hence, in the present study, local values of  $C_t$  have been estimated using a frictional law of Tanaka and Shuto (1981) for a wave-current coexistent field and empirical formulas of Sato (1987) for ripple formation due to waves.

For this, first we calculate at each local point the near-bottom orbital diameter  $d_0$  using the small-amplitude wave theory as well as the friction coefficient

$f_{cw}$  using the frictional law, in which the presence of the longshore current is ignored and the equivalent roughness  $k_s$  is set equal to the sand grain diameter  $d$ . The empirical formulas of Sato give the critical conditions for the formation/disappearance of sand ripples and the ripple size as functions of the Shields number and  $d_0/d$ . Then we evaluate the friction coefficient  $C_f$  using the frictional law, in which this time the longshore current is included and the equivalent roughness  $k_s$  is set equal to the local ripple height, if ripples exist, or to the grain diameter  $d$  in case of no ripples. (According to previous studies, the equivalent roughness is about four times as large as the ripple height. However, the ripple height itself has been employed as  $k_s$  in this study, because the ripple crest orientation is rather parallel to the longshore current direction.) Cross-shore distributions of the longshore current velocity  $V_\ell$  have been thus computed by iteratively solving Eq. (5) together with the frictional law for unknowns  $V_\ell$  and  $C_f$ .

## 2.4 Computation of longshore sand transport rate

The sediment transport rate formula proposed by Watanabe *et al.* (1986) gives local transport rate, under general conditions of combined action of waves and currents, as the summation of the transport rate due to mean currents and that due to the direct action of waves. In the present study, by neglecting the latter, the following formula has been used for the computation of local immersed-weight rate  $i_\ell$  of the longshore sand transport.

$$i_\ell(x) = (1 - \varepsilon_v) s \cdot A_c [\hat{\tau}_b(x) - \tau_{cr}] V_\ell(x) \quad (8)$$

in which  $\varepsilon_v$  and  $s (= \rho_s/\rho - 1)$  are the porosity and the immersed specific density of the sediment,  $A_c$  is a dimensionless coefficient,  $\hat{\tau}_b$  is the maximum value of the periodical bottom friction in a coexistent wave-current field, calculated by the frictional law of Tanaka and Shuto (1981) with the equivalent roughness equal to the grain diameter,  $\tau_{cr}$  is the critical shear stress for the onset of general sand movement (Watanabe *et al.*, 1986), and  $V_\ell$  is the longshore current velocity. A value of 2.0 has been adopted for the coefficient  $A_c$  on the basis of recent studies (*e.g.*, Watanabe *et al.*, 1991).

Total immersed-weight rate  $I_\ell$  of the longshore transport has been computed by the cross-shore integration of  $i_\ell(x)$ :

$$I_\ell = \int_{x_0}^{\infty} i_\ell(x) dx \quad (9)$$

where  $x_0$  is the locations of the mean water shoreline. Then total volumetric transport rate  $Q_\ell$  has been calculated by the following equation:

$$Q_\ell = \frac{I_\ell}{(1 - \varepsilon_v)(\rho_s - \rho)g} \quad (10)$$



### 3. Results of Computation and Discussions

#### 3.1 Example of computation results

As one example of the results thus computed, Figure 1 shows cross-shore distributions of the wave height  $H$ , wave angle  $\theta$ , longshore current velocity  $V_L$ , near-bottom orbital velocity amplitude  $\hat{u}_b$ , immersed-weight sand transport rate  $i_L$ , equivalent roughness  $k_s$ , friction coefficient  $C_f$  in the longshore current computation, and friction coefficient  $f_{cw}$  in the transport rate computation, when  $d = 0.2\text{mm}$ ,  $\tan \beta = 1/20$ ,  $\theta_0 = 45^\circ$ ,  $T = 10.0\text{s}$ , and  $H_0 = 1.2\text{m}$ .

The transport rate  $i_L$  becomes maximum between the breaking point and the location of the maximum  $V_L$ , as expected, not only in this case but in all the cases. The range where  $i_L$  takes significant magnitude is narrower than that for  $V_L$  and is comparable to the surf zone width. In the range of about 80m around the breaking point, the equivalent roughness  $k_s$  is equal to the grain size  $d = 0.2\text{mm}$  and hence the friction coefficients  $C_f$  and  $f_{cw}$  take common values. This is because the bottom friction in this range exceeds the critical value for the disappearance of sand ripples or the initiation of the sheet flow.

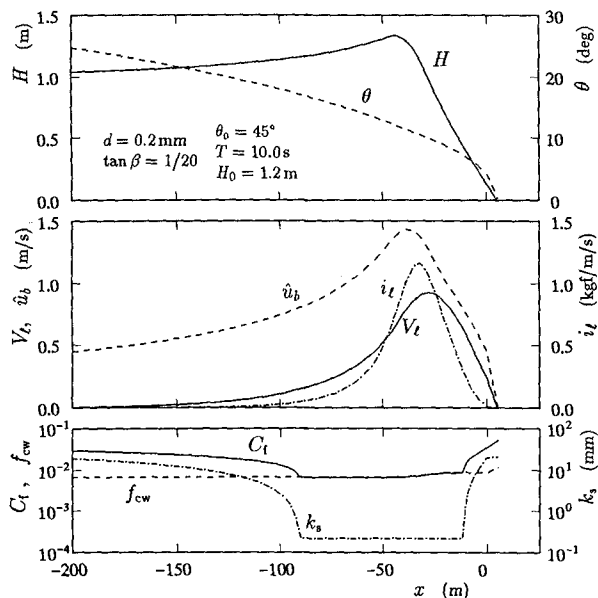


Fig. 1 Example of cross-shore distributions of computed quantities.

**3.2 Total rate of longshore sand transport**

First let us study the relation of the total immersed-weight transport rate  $I_t$  with the longshore component of wave energy flux  $P_l$  at the breaking point:

$$P_l = E_B C_{gB} \cdot \sin \theta_B \cos \theta_B \tag{11}$$

where  $E_B$ ,  $C_{gB}$  and  $\theta_B$  are the energy density, the group velocity and the wave angle of breakers. Komar and Inman (1970) have proposed the following linear relation between  $I_t$  and  $P_l$  on the basis of the energetics concept and field data:

$$I_t = 0.77 P_l \tag{12}$$

in which the proportionality constant 0.77 should be halved if the energy density is calculated from the significant wave height as in the CERC formula.

Figure 2 shows a relation between  $I_t$  and  $P_l$  obtained in the present computation for cases of  $d = 0.2\text{mm}$  and  $\tan \beta = 1/50$ . The relation is remarkably independent of the incident wave period  $T$  and angle  $\theta_0$ . The magnitude of  $I_t$  is nearly proportional to  $P_l$  under field-scale conditions, whereas it rapidly decreases under laboratory conditions, in which the maximum friction  $\hat{\tau}_b$  exceeds the critical shear  $\tau_{cr}$  only slightly in Eq. (8). Such an overall trend is consistent with previous studies (*e.g.*, Komar and Inman, 1970).

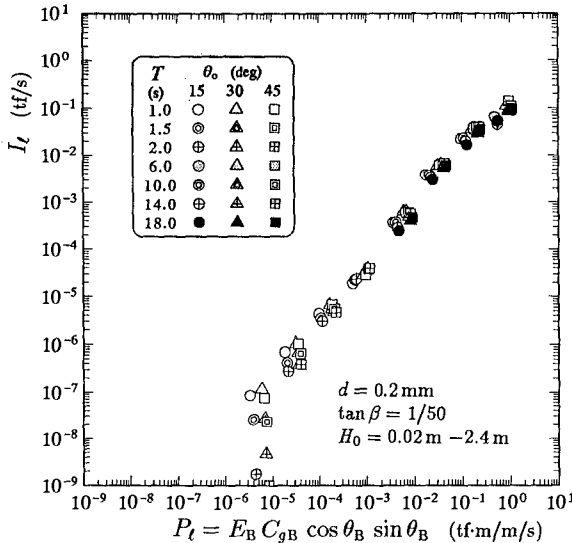


Fig. 2 Example of relation between  $I_t$  and  $P_l$ .

The relation between  $I_t$  and  $P_t$  for all the 2,520 cases is shown in Fig. 3, which indicates a trend similar to that in Fig. 2. In Fig. 3, different symbol marks are used for different grain sizes and beach slopes, but their effect on the  $I_t$ - $P_t$  relation cannot be seen clearly because of the overlapping of many marks.

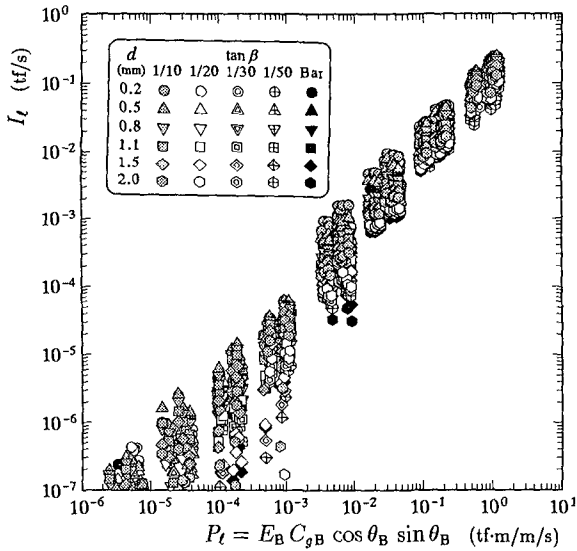


Fig. 3 Relation between  $I_t$  and  $P_t$ .

In order to make this clearer, we assume the linear relation,  $I_t = \alpha_{IP} \cdot P_t$ , for the 1,440 cases under field conditions, and calculate the proportionality coefficient  $\alpha_{IP}$  for each grain size and bottom slope using the least-square method. Figure 4 (a) shows values of  $\alpha_{IP}$  normalized by the mean proportionality coefficient  $\bar{\alpha}_{IP}$  for all the 1,440 cases. It is seen in this figure that  $\alpha_{IP}$  considerably decreases as the grain diameter  $d$  increases, being much less dependent on the bottom slope except for cases of  $\tan \beta = 1/10$ . The values of  $\alpha_{IP}$  range between 0.04 and 0.23 with their average  $\bar{\alpha}_{IP} = 0.078$ , which are very much smaller than 0.77 in Eq. (12) by Komar and Inman (1970) or 0.52 proposed by Kraus *et al.* (1982), being rather close to the value of 0.06-0.12 in an empirical formula presented by Sato and Tanaka (1966). In a summary, according to the present computation, the relation between  $I_t$  and  $P_t$  is approximately expressed as:

$$I_t = (0.04 \sim 0.23) P_t \simeq 0.078 P_t \tag{13}$$

For readers' information, Fig. 5 shows the relation between  $I_t'$ , computed by Eq. (8) with the critical shear  $\tau_{cr} = 0.0$ , and  $P_t$ . They are proportional very well to each other not only for field-scale but also for laboratory-scale conditions.

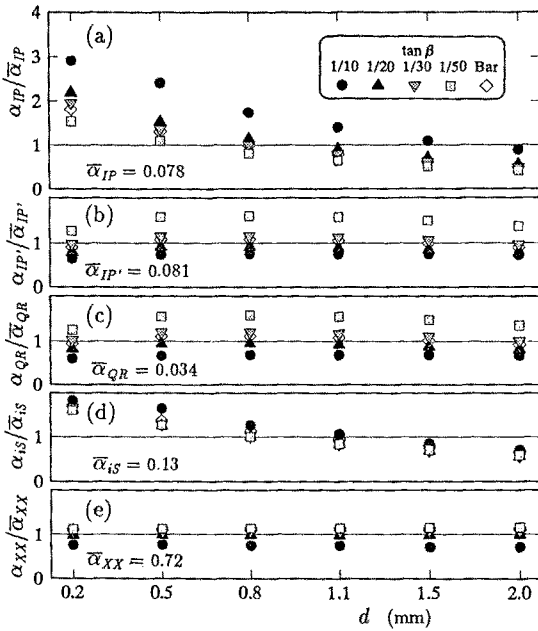


Fig. 4 Dependency of proportionality coefficients on the grain size and the beach slope.

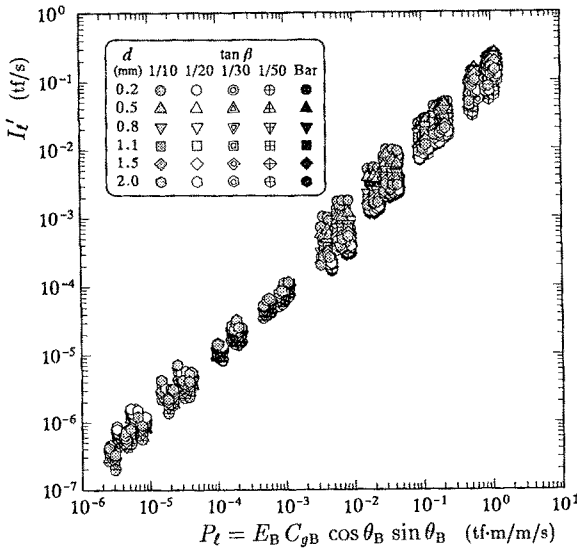


Fig. 5 Relation between  $I_t'$  and  $P_t$ .

Komar and Inman (1970) have reported another empirical formula based on field data as follows:

$$I_t = 0.28 P_t' \tag{14}$$

where

$$P_t' = E_B C_{gB} \cos \theta_B \cdot \bar{V}_t / \hat{u}_{bB} \tag{15}$$

in which  $\bar{V}_t$  is the mean velocity of the longshore current, and  $\hat{u}_{bB}$  is the amplitude of the near-bottom orbital velocity at the breaking point. Figure 6 shows the relation between  $I_t$  and  $P_t'$  in the present computation, in which  $\bar{V}_t$  has been evaluated by simply averaging  $V_t$  over the range from the breaker line to the mean shoreline. Data scattering in Fig. 6 has become small as compared to that in Fig. 3. In addition, as shown in Fig. 4 (b), the dependency of the proportionality coefficient  $\alpha_{IP'}$  on the grain size and on the bottom slope is also weak except for cases of  $\tan \beta = 1/50$ . Values of  $\alpha_{IP'}$  is still much smaller than 0.28 in Eq. (14), and the relation of the two quantities is expressed as:

$$I_t = (0.05 \sim 0.13) P_t' \simeq 0.08 P_t' \tag{16}$$

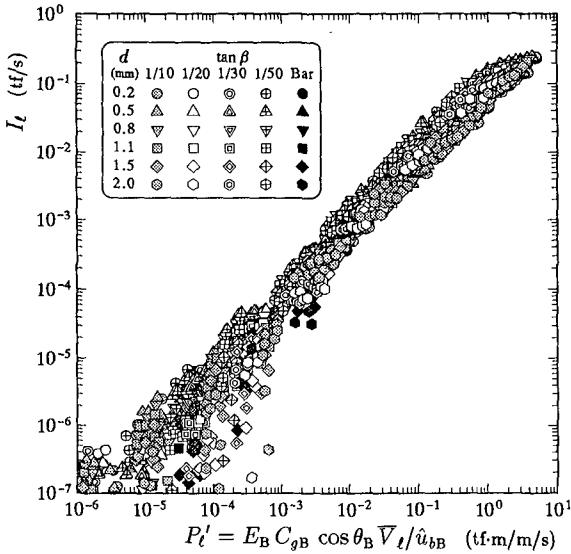


Fig. 6 Relation between  $I_t$  and  $P_t'$ .

In order that the relation  $I_t \propto P_t \propto P_t'$  holds good, the mean longshore current velocity  $\bar{V}_t$  must be proportional to  $\hat{u}_{bB} \cdot \sin \theta_B$ . Their relation is shown in Fig. 7. Although these two quantities approximately satisfy a proportional relation for an individual combination of the grain diameter  $d$  and the bottom slope  $\tan \beta$ , values of the proportionality coefficient change over the range of one-order of magnitude, depending on  $d$  and  $\tan \beta$ .

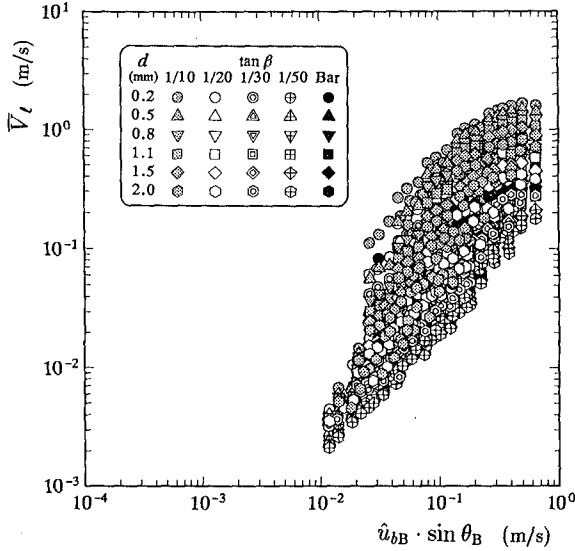


Fig. 7 Relation between  $\bar{V}_l$  and  $\hat{u}_{bB} \cdot \sin \theta_B$ .

Now let us make the following long wave approximation:

$$\left. \begin{aligned} C_{gB} &\simeq \sqrt{gD_B}, \quad \cos \theta_B \simeq 1 \\ \hat{u}_{bB} &\simeq (H_B/2) \sqrt{g/D_B} \simeq (\gamma/2) \sqrt{gD_B} \end{aligned} \right\} \quad (17)$$

for the parameter  $P_l'$  defined by Eq. (15). Then we obtain the relation:

$$P_l' \simeq (\rho g/4\gamma) H_B^2 \bar{V}_l \quad (18)$$

where  $\gamma$  is the ratio of the wave height  $H_B$  to the mean depth  $D_B$ , and is practically constant. Hence we can expect a linear relation between the total volumetric transport rate  $Q_l$  and a new parameter  $R_l$  defined as:

$$R_l = H_B^2 \bar{V}_l \quad (19)$$

which is consistent in the dimension with  $Q_l$ . The relation between  $Q_l$  and  $R_l$  is shown in Fig. 8. As expected, for the field-scale conditions,  $Q_l$  is approximately proportional to  $R_l$  as expressed by the following relation (See Fig. 4 (c)):

$$Q_l = (0.020 \sim 0.053) R_l \simeq 0.034 R_l \quad (20)$$

It is interesting (and strange in a sense) that the value of 0.034 of the mean proportionality coefficient in Eq. (20) is very close to 0.024 in the empirical formula presented by Kraus *et al.* on the basis of field data, because using the same data set they have obtained the value of 0.52 as the proportionality constant in the  $I_l$ - $P_l$  relation, which is very much larger than the value of 0.078 in Eq. (13).

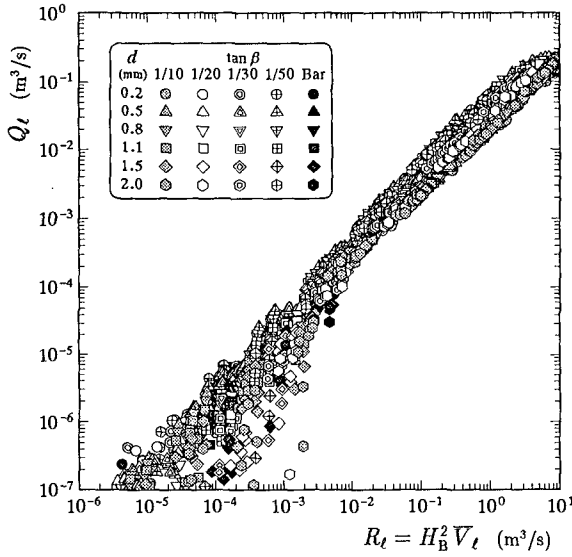


Fig. 8 Relation between  $Q_t$  and  $R_t$ .

### 3.3 Cross-shore distribution of longshore transport rate

As described in 3.1 in reference to Fig. 1, the local rate of the longshore transport  $i_t$  becomes maximum between the breaking point and the location of the maximum longshore current velocity, and takes significant values over a range as wide as the surf zone. However, since the cross-shore distributions of  $i_t$  may not necessarily be similar for various conditions of the grain size, bottom slope and incident waves, it seems difficult to express them in a single normalized form. Hence here we will examine only the magnitude of the maximum local transport rate  $i_{t\max}$  and the offshore distance  $X_{i_{t\max}}$  of the point of  $i_{t\max}$ , which are regarded as the most important representative parameters in the cross-shore distributions of  $i_t$ .

First, concerning the maximum transport rate  $i_{t\max}$ , since the total rate  $I_t$  is approximately proportional to  $P_t$  and the width of the significant longshore transport zone is comparable with the surf zone width  $X_B$  (the distance between the breaking point and the mean shoreline),  $i_{t\max}$  may be related to a parameter  $S_t = P_t/X_B$ . As expected, it is seen in Fig. 9 that a fairly high correlation exists between  $i_{t\max}$  and  $S_t$ . According to Fig. 4 (d), the value of the proportionality coefficient  $\alpha_{iS} = i_{t\max}/S_t$  obtained for the field-scale cases decreases as the grain size increases, being nearly independent of the bottom slope. Under the field-scale conditions, the relation between these two parameters is expressed as:

$$i_{t\max} = (0.075 \sim 0.24) S_t \simeq 0.13 S_t \tag{21}$$

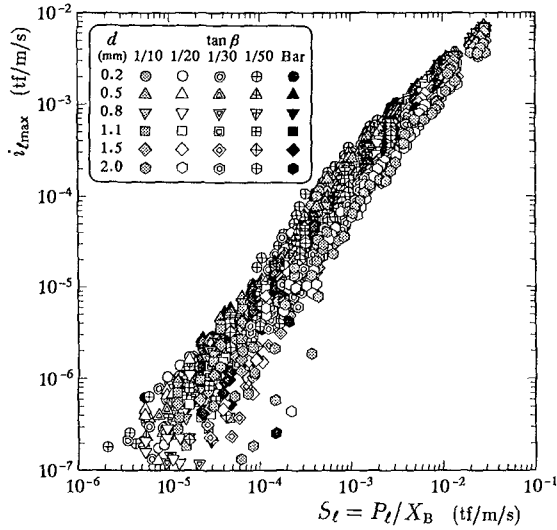


Fig. 9 Relation between  $i_{tmax}$  and  $S_t$ .

Then the relation between  $X_{i_{tmax}}$  (the offshore distance of the point of  $i_{tmax}$  measured from the mean shoreline) and  $X_B$  is shown in Fig. 10, where plotted are points more than 2,300 except for the data with  $i_{tmax} < 10^{-7}$  tf/m/s. The two parameters show such a remarkably highly proportional relation that only a small number of points can be seen because of their overlapping. According to this figure as well as Fig. 4 (e), the proportionality coefficient  $\alpha_{XX} = X_{i_{tmax}}/X_B$  takes nearly constant values depending very weakly on the grain size and the bottom slope. The relation is expressed as:

$$X_{i_{tmax}} = (0.52 \sim 0.83) X_B \simeq 0.72 X_B \tag{22}$$

#### 4. Concluding Remarks

Major conclusions of this study are as follows:

- (1) The validity of the local transport rate formula and that of the conventional total rate formulas for the longshore transport have been reinforced each other at least qualitatively.



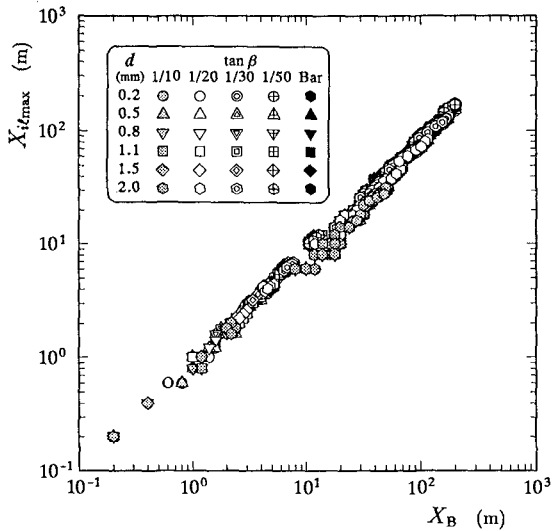


Fig. 10 Relation between  $X_{i_{tmax}}$  and  $X_B$ .

(2) Under the field-scale conditions, the total immersed-weight transport rate  $I_t$  is approximately proportional to the longshore wave power component  $P_t$ . However, the value of the proportionality coefficient obtained in this study is very much smaller than 0.77 in Komar and Inman's formula and is rather close to the value in Sato and Tanaka's formula, decreasing as the grain size increases. It should be noted that in many examples of the actual application of the  $I_t$ - $P_t$  formula to one-line models, values between 0.05 and 0.4 have been adopted for the coefficient on the basis of the calibration using past beach change data.

(3) Under the laboratory-scale conditions, the effect of the critical shear stress  $\tau_{cr}$  cannot be neglected.

(4)  $I_t$  and  $P_t'$  as well as  $Q_t$  and  $R_t$  have also shown a highly proportional relation, respectively, particularly under the field-scale conditions. The proportionality coefficients are weakly dependent on the grain size.

(5) Concerning the cross-shore distributions of the longshore transport rate, it has been found that  $i_{tmax}$  and  $S_t$  as well as  $X_{i_{tmax}}$  and  $X_B$  are also proportional to each other.

Further study should be conducted on the effects of the beach profiles (more realistic profiles, other than uniform slopes, corresponding to given conditions of sediment grain size and incident waves), breaker-induced turbulent stresses, grain size distributions, effective bottom roughness, beach transport in the swash zone, random waves, and so on.

## REFERENCES

- Komar, P.D. and D.L. Inman (1970): Longshore sand transport on beaches, *Jour. Geophys. Res.*, Vol. 75, No. 30, pp. 5914-5927.
- Kraus, N.C., M. Isobe, H. Igarashi, T.O. Sasaki and K. Horikawa (1982): Field experiments on longshore sand transport in the surf zone, *Proc. 18th Coastal Eng. Conf.*, ASCE, pp. 969-988.
- Nishimura, H. (1988): Computation of Nearshore Current, in *Nearshore Dynamics and Coastal Processes* (edited by K. Horikawa), Part. III, Chap. 3, University of Tokyo Press, pp. 272-273.
- Sato, S. and N. Tanaka (1966): Field investigation on sand drift at Port Kashima facing the Pacific Ocean, *Proc. 10th Coastal Eng. Conf.*, ASCE, pp. 595-614.
- Sato, S. (1987): Oscillatory Boundary Layer Flow and Sand Movement over Ripples, *Doctoral Dissertation*, Univ. of Tokyo, 138p.
- Tanaka, H. and N. Shuto (1981): Friction coefficient for a wave-current co-existent system, *Coastal Eng. in Japan*, JSCE, Vol. 24, pp. 105-128.
- Watanabe, A., T. Hara and K. Horikawa (1984): Study on breaking condition for compound wave trains, *Coastal Eng. in Japan*, JSCE, Vol. 27, pp. 71-82.
- Watanabe, A. and K. Maruyama (1986): Numerical modeling of nearshore wave field under combined refraction, diffraction and breaking, *Coastal Eng. in Japan*, JSCE, Vol. 29, pp. 19-39.
- Watanabe, A., K. Maruyama, T. Shimizu and T. Sakakiyama (1986): Numerical prediction model of three-dimensional beach deformation around a structure, *Coastal Eng. in Japan*, JSCE, Vol. 29, pp. 179-194.
- Watanabe, A., T. Shimizu and K. Kondo (1991): Field application of a numerical model of beach topography change, *Proc. Coastal Sediments '91*, ASCE, pp. 1814-1828.
- Watanabe, A. and M. Dibajnia (1988): A numerical model of wave deformation in surf zone, *Proc. 21st Coastal Eng. Conf.*, ASCE, pp. 578-587.

## CHAPTER 195

### COMBINED FLOW SAND TRANSPORT: FIELD MEASUREMENTS

RICHARD J.S. WHITEHOUSE<sup>1</sup>

#### ABSTRACT

This paper compares the results of measurements obtained from two field experiments performed to determine the effect of waves and currents ( $w+c$ ) on the transport of sand in suspension. One set of measurements are from an estuary (Maplin Sands) and the other are from the surf zone (Boscombe Pier). The vertical and temporal variation in and the correlation between some of the hydrodynamic and sediment dynamic parameters are discussed.

#### 1. INTRODUCTION

The ability to predict the transport rate of sandy sediment by combined wave plus current ( $w+c$ ) action is an important aspect of many coastal and estuarine engineering projects. Although the physically based sediment transport formulae are able to be constructed from first principles they often rely upon experimental data to aid in their formulation and for their verification.

In the complex situation of  $w+c$  flow the mean (current) component can be characterised by the depth averaged velocity  $V$  and the periodic component due to wave action by the bottom orbital velocity amplitude  $W$ . Combined flow conditions in the marine environment can be described as current dominated when the ratio  $W/V < 0.2$  or wave dominated when

-----  
<sup>1</sup>Section Manager, Sediments Research Group, HR Wallingford Ltd, Howbery Park, Wallingford, OXON OX10 8BA, UK

$W/V > 0.2$  (Soulsby and Humphery, 1990). Once waves are present they will enhance the entrainment of sand, by the so called stirring process, and hence increase the transport rate of sand over that due to the current alone. Under storm conditions in tidal channels or in the nearshore zone the waves can become the dominant entraining agent. The detailed mechanics of the entrainment process, and the resulting concentration profiles, will depend upon sedimentological factors, whether the waves and currents are small or large, and the value of the ratio  $W/V$ .

This paper presents some results from two field w+c sediment transport experiments that have been performed in two different nearshore environments, at Maplin Sands and at Boscombe in the UK. Previously Owen and Thorn (1978) and Grass (1981) have used a selection of the Maplin data to parameterise functions for the sediment transport rate under w+c. Whitehouse (1991), however, was the first to present profile data from these experiments (Boscombe).

The data provide information with which to examine the physical processes behind the entrainment of sand and the resulting near-bed concentration, the diffusion of sediment into the flow, and subsequently the rate of sand transport.

## 2. MEASUREMENTS

Detailed measurements have been made at two field sites to determine the vertical structure through the water column of hydro and sediment dynamic parameters. Over 350 measured profiles were obtained from the two experiments.

The first series of measurements were made in the Outer Thames Estuary between 1973 and 1975 from a free standing tower sited at the southern edge of Maplin Sands and adjacent to a deep water channel. The site was exposed to wind wave action and experienced strong tidal currents moving in and out of the estuary over a fine sand bed ( $d_{50}=0.141$  mm). These data were collected for the specific purpose of determining the effect of waves in enhancing current dominated sand transport, and also included data for the current alone condition.

The second series of measurements were taken under storm wave conditions in the surf zone at the seaward end of Boscombe Pier (1977-78). At this site, in Poole Bay on the south coast of the UK, the tidal streams are weak but can be enhanced under storm conditions by strong wind induced alongshore currents. The medium diameter sand present at this site was recorded as having a median size of around 0.200mm.

Background information and location maps for both of these experiments have been presented by Owen and Thorn (1978).

In both series of experiments an instrument package was mounted on a trackway to enable the vertical structure measurements to be made starting at 0.05m above the bed. Vertical profiles of the horizontal component of velocity were obtained using a self aligning propeller current meter at Maplin and at Boscombe from a 2 axis electromagnetic current meter (EM), oriented to obtain both the cross shore and alongshore components of velocity. The corresponding suspended sediment concentration profiles were obtained with a pump sampler device. The sand fraction concentrations (sediment larger than 0.04mm) were determined in  $\text{mg l}^{-1}$  as the dry mass of sediment contained in the volume of water that was sampled (20 litres).

Waves at Maplin were measured by a Waverider buoy sited 900m to the east of the tower and at Boscombe by the output from a pressure transducer mounted 1.25m above the bed. The wave velocity  $W$  at Maplin was calculated from the Waverider data and at Boscombe directly from the EM record.

At Maplin only mean velocities were recorded, averaged over 100 seconds, whilst at Boscombe waves and currents were sampled at 4Hz with record lengths of 1 minute or more.

### 3. HYDRODYNAMICS

The results of the flow measurements obtained from both experiments will be discussed further below.

#### 3.1 Maplin data

The velocity measurements taken at this site have allowed the form of the velocity profile through the tidal cycle to be determined at half hourly intervals. An example of the data are plotted in Figure 1a (no waves) in which the numbers at the tops of the profiles indicate the chronological order through the deployment. The negative current velocities, on this and subsequent graphs, represent the measurements made on the flood tide and the positive values correspond to the ebb. The current speed has been assumed to be constant above the height of the topmost measured point and the top of each line has been plotted as to represent the water surface at the time that profile was measured. The locus of points thus formed provides a trace of the water level through the tide, varying by more than 4m, and shows the out of phase relationship between tidal amplitude and tidal currents typical of many estuaries (Dyer, 1973). On the whole the sequence of velocity profiles are well behaved and exhibit the characteristics of a tidal oscillatory

boundary layer, with a mass flow asymmetry in the flood direction.

Similar datasets were obtained on 25 subsequent deployments during which wind waves were present. A detailed analysis of the velocity profiles allows for some influence of the waves on the current structure to be determined but these details will not be discussed any further here.

For practical purposes, however, Soulsby (1990, figure 10 and equation 23) has shown that an empirical current velocity profile appears to provide a reasonable approximation to the vertical structure of the tidal current for a number of estuary and continental shelf sites. The function is a modified version of the 1/7 power law, with constant velocity above mid depth

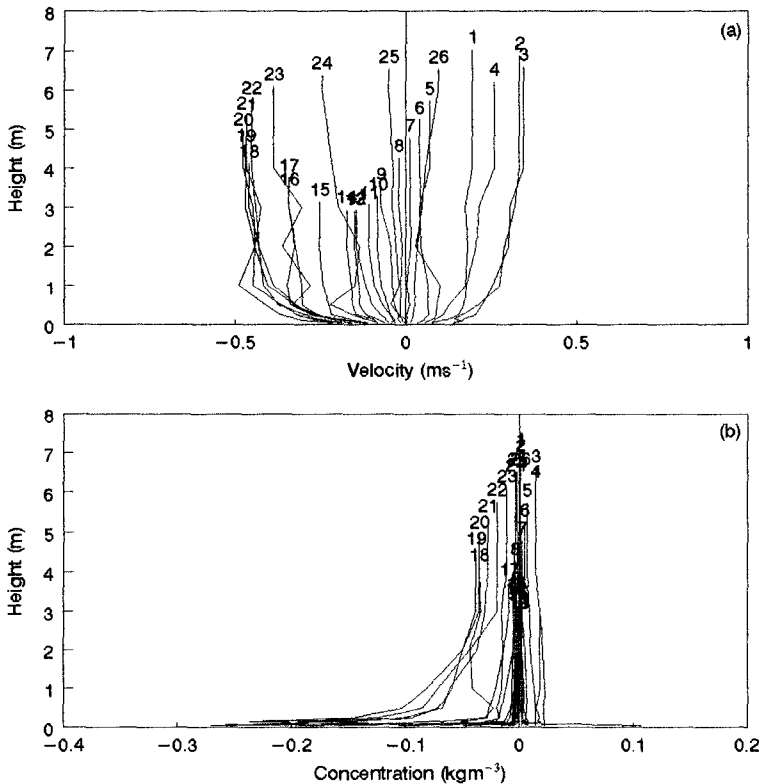


Figure 1. The evolution of (a) the tidal current velocity profile and (b) the sand concentration profile at Maplin Tower through a spring tide with no wave action (1 November 1973). Profiles 1-1 to 1-26

(Equation 1). The height above the bed  $z$  is non dimensionalised with the water depth  $h$  and the current velocity  $V_z$  at height  $z$  with  $V$ .

$$V_z = \left( \frac{z}{0.32h} \right)^{1/7} V \quad 0 \leq z \leq 0.5h \quad (1a)$$

$$V_z = 1.07V \quad 0.5h \leq z \leq h \quad (1b)$$

Five sets of profile data both with and without waves and for flood and ebb tides have been plotted with the empirical function in Figure 2 which confirms the form of Equation 1 on average. The data correspond to measurements made near to the peak excursion of the tidal velocity amplitude (Table 1). Although this profile shape will be unlikely to hold at times around slack water it can be used to approximate the vertical current structure for a large proportion of the tide.

### 3.2 Boscombe data

The EM data provide information both on the vertical structure and on the temporal variation in the velocity field for 26 deployments of the instrument package. An example of the time series data from Boscombe is plotted in Figure 3 showing the variation of the water surface elevation due to the passage of waves in 4.23m of water and the corresponding near bed velocities. The waves in the trace are typical of surf zone conditions producing the characteristic periodicity in the cross shore ( $x$ ) velocity. The record for the  $y$  component of velocity depicts the turbulent alongshore current and that for the resultant velocity is mixed accordingly.

The vertical structure data at this location does not conform to the function employed in Figure 2. Above the bottom 5 or 10% of the water

Table 1. Physical parameters for velocity profiles displayed in Figure 2

Data	Velocity $V$ ( $\text{ms}^{-1}$ )	Wave velocity $W$ ( $\text{ms}^{-1}$ )	Water depth $h$ (m)	Tide
1-3	0.303	0.000	6.59	ebb
2-12	0.251	0.038	7.30	ebb
1-22	0.422	0.000	5.75	flood
4-1	0.440	0.110	7.60	flood
5-7	0.656	0.091	5.03	flood

column the time averaged current velocity becomes approximately equal to the depth averaged value, at least to the height of the measured data which is equivalent to about 70% of the water depth for most cases. The data also indicate a veering of the velocity vector through the water column.

#### 4. SEDIMENT DYNAMICS

The time averaged sediment concentration measurements will be discussed below for both experiments.

##### 4.1 Maplin data

As with the velocity profile measurements the temporal variation in the vertical sand concentration profiles at this site with no wave action can be visualised (Figure 1b). For convenience, the data have been plotted in the same form as the velocity data in Figure 1a. Some interesting features can be observed by following the chronological sequence through the tide from slack water, profile 8.

The concentrations remain low for small flood (negative) velocities but increase markedly as the current velocity exceeds  $0.3\text{ms}^{-1}$  (profile 16), the concentration at  $0.05\text{m}$  increases from  $0.045\text{kgm}^{-3}$  at profile 16 to  $0.196\text{kgm}^{-3}$  at profile 17. Although the magnitude of the velocity has not changed

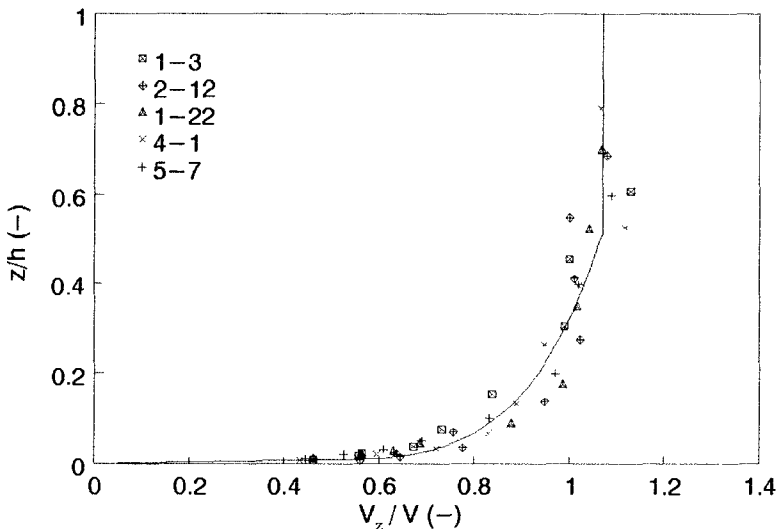


Figure 2. Comparison of selected Maplin Tower velocity profile data with the empirical function presented by Soulsby (1990)



appreciably in the half hour interval between these two observations the magnitude of the near bed sand concentration has increased by a factor of 4. The near bed concentration reaches an equilibrium at profiles 18 to 21, equal to about  $0.270\text{kgm}^{-3}$ .

Thereafter, and for the ensuing ebb tide, the near bed concentrations decrease rapidly due to the downward settling of the sand in suspension until a near vertically uniform distribution is achieved. No significant additional sand entrainment takes place on the ebb tide with the depth averaged velocity not exceeding  $0.3\text{ms}^{-1}$ . The data provide clear evidence to support the use of a threshold velocity for the entrainment of sand into suspension, for the lag in the response of the concentration profiles with increasing flow velocity and for a hysteresis in the velocity concentration correlation.

The influence of waves on the flood tide concentration profiles can

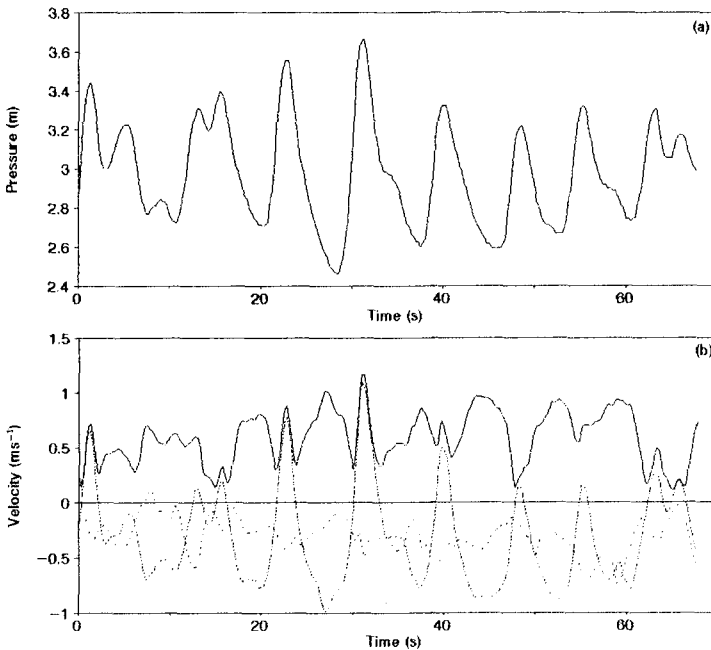


Figure 3. Time series records from the surf zone at Boscombe for: (a) the water surface elevation expressed in m of water and, (b) the x (stippled line) and y (dashes) components of fluid velocity and their resultant (solid line). The velocity measurements were taken at 0.05m above the bed starting at 1523hrs on 15-11-1978. The mean water level on (a) was at 2.98m.

be seen in Figure 4 for similar values of velocity  $V$  and water depth, one for the current alone case and one with wave activity ( $W=0.072\text{ms}^{-1}$ ,  $T_2=2.8\text{s}$ ). Under wave enhanced conditions ( $W/V=0.214$ ) the near bed sand concentration is increased by a factor of 2.7 over the current alone case due to the stirring action of the waves. Additional turbulence diffusing up from the wave boundary layer serves to enhance the sediment load and both factors produce an increase in the depth integrated flux of sand  $q_+$  (see Section 6) by a factor 1.3.

4.2 Boscombe data

The sediment concentration measurements at Boscombe relate only to w+c conditions. Vertical profile data are presented in Figure 5 for two different wave dominated conditions with similar values of the current velocity, water depth and wave period, about 6.5 seconds, but different wave heights  $H_s$ . Under the larger wave conditions the near bed sediment concentration is enhanced by more than a factor of 10 and the magnitude of  $q_+$  by a factor 6.2 above that for the smaller wave case.

Nielsen (1979) has shown in laboratory measurements that the magnitude of the near bed concentration under waves is a function of the bottom boundary layer and independent of breaker type. However, under broken waves in the surf zone there will be two contributions to the turbulence field, one from the wave boundary layer and a second from the downwards dissipation of surface generated turbulence contained within the broken wave as discussed, modelled and verified with experimental data by

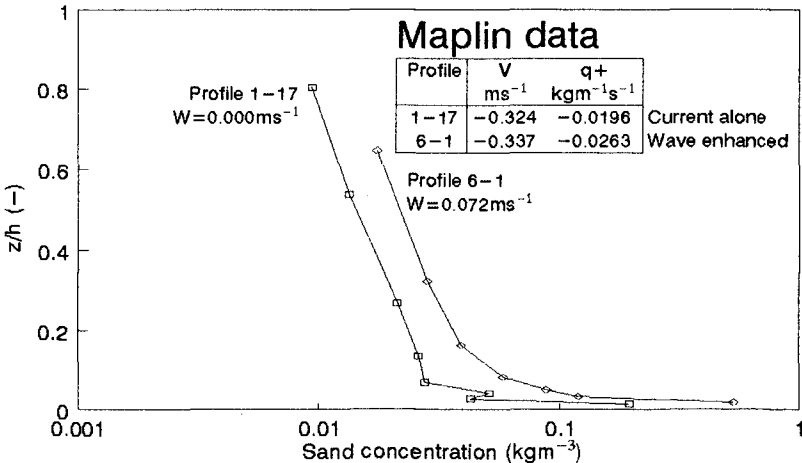


Figure 4. Sand concentration profiles obtained from Maplin under current alone and wave enhanced conditions

Deigaard et al. (1986). At Boscombe the contribution of surface turbulence to supporting the suspension will be appreciable.

For similar values of the current velocity, the data presented in Figure 5 show that an increase in the magnitude of the near bed concentration is produced by the addition of the stronger wave component. The additional contribution to the turbulence energy field from the broken wave, the relative strength of which is symbolised by the ratio  $H_s/h$ , will be important in defining the suspension profiles. This particular case is complicated by the differences between the median grain sizes of the two suspension profiles.

**5. SEDIMENT ENTRAINMENT**

The relationship between the flow conditions and the near bed sediment concentration will now be considered. Sand concentration data measured at a height of 0.1m above the bed has been used for both experiments to enable a comparison to be made, denoted  $C_{0.1}$ .

**5.1 Maplin data**

The data for the variation of  $C_{0.1}$  with the depth averaged current velocity have been plotted in Figure 6. To enable the effect of the waves on the concentration to be viewed the data have been banded in terms of the wave velocity  $W$ . Current alone measurements are plotted as  $W=0$  and are indicated by the thick black line, the other data are plotted for increasing values of  $W$ . The measurements clearly show the effect that waves have in

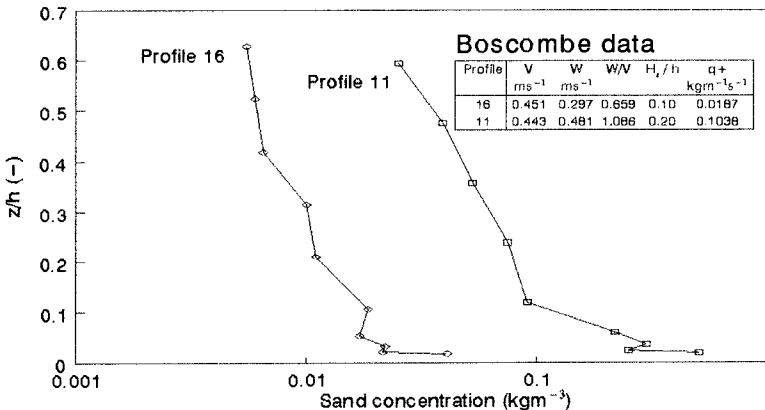


Figure 5. Sand concentration profiles obtained from Boscombe under two different wave dominated conditions

enhancing the near bed sand concentration over a wide range of current velocities.

In some cases, however, the sand concentration is reduced below its current alone value over the range of measured current alone values ( $V < 0.5 \text{ ms}^{-1}$ ). This is not surprising given the potential for scatter in sediment transport measurements. Van Rijn (1984), for example, reports the results of an earlier analysis of well controlled steady flow flume measurements in which he found deviations in the measured total load transport rate by up to a factor of 2 for similar conditions. It is concluded that the overall trend of the data presented in Figure 6 is encouraging.

## 5.2 Boscombe data

Whitehouse (1991) reported that the near bed concentration of sand was correlated more closely with the magnitude of the wave velocity  $W$  than with the current velocity  $V$  which had been found at the Maplin site. Here we have plotted the  $C_{0.1}$  data from Boscombe in Figure 7 on the same axes as the Maplin data in Figure 6 and banded in the same fashion.

Although a direct comparison of the two data sets cannot be made, because we do not have any current alone data from this site with which to

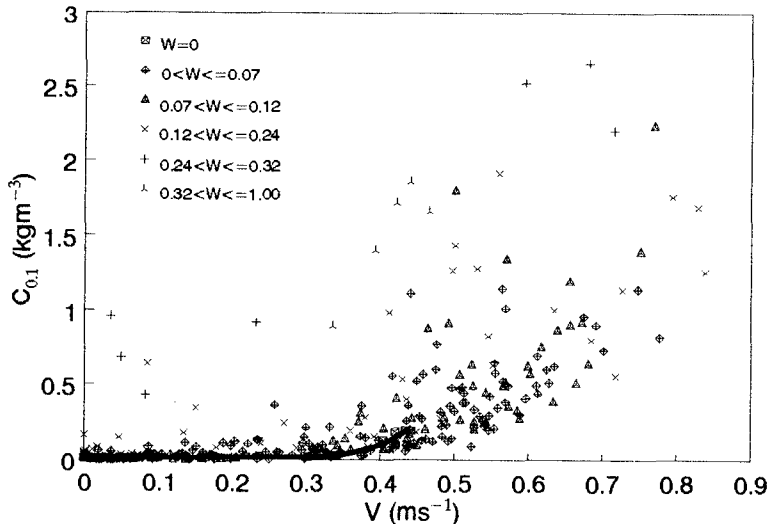


Figure 6. The variation in  $C_{0.1}$  the sand concentration at 0.1m above the bed with current velocity  $V$  at Maplin (all data), banded in terms of the wave velocity amplitude  $W$  ( $\text{ms}^{-1}$ )

assess the grain size difference at the two sites, the larger wave velocities produce higher concentrations of sand near to the bed for a given value of  $V$ . However, the large wave orbital velocities at this site do appear to have a dominant effect in determining the entrainment of sand from the bed.

### 5.3 Vertical mixing

Once the sediment has been entrained from the bed the  $w+c$  concentration profiles for both experiments can be approximated by an exponentially decaying concentration profile over the bottom 10% of the water column, ie constant eddy viscosity.

## 6. SEDIMENT TRANSPORT RATE

The suspended sediment transport rate was determined by integration of the sand flux profiles ( $V_z C_z$  product) through the water depth, assuming that the flux goes to zero both at the bed ( $z=0$ ) and also at the water surface ( $z=h$ ).

### 6.1 Maplin data

The sediment transport rate  $q_s$  has been plotted in Figure 8a to show the variation with the current velocity, the data has been banded in terms of  $W$ . This shows that  $q_s$  increases with increasing  $V$  and in addition that the transport rate is enhanced by the addition of waves, especially obvious for the highest range of  $W$  values. However, the scatter in the data is noticeable at

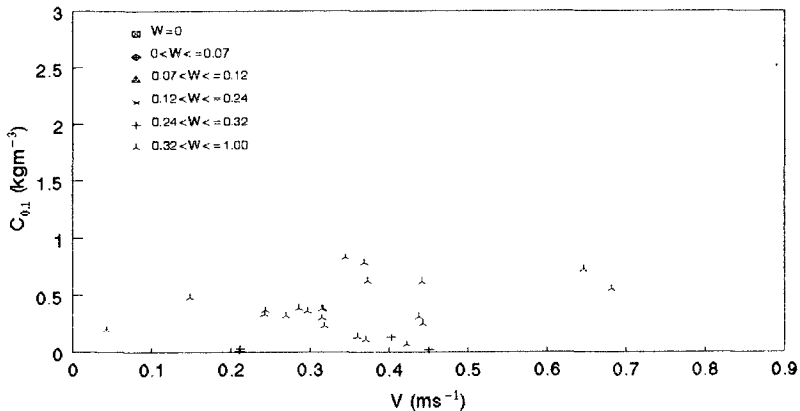


Figure 7. The variation in sand concentration at 0.1m above the bed with current velocity at Boscombe (all data), banded in terms of the wave velocity amplitude  $W$  ( $ms^{-1}$ )

low values of the current velocity ( $V < 1E-1 \text{ms}^{-1}$ ) with the transport rate also appearing to be reduced below the current alone value. Further investigation of the data for those periods with small current velocities is warranted, ie during which non equilibrium conditions prevail.

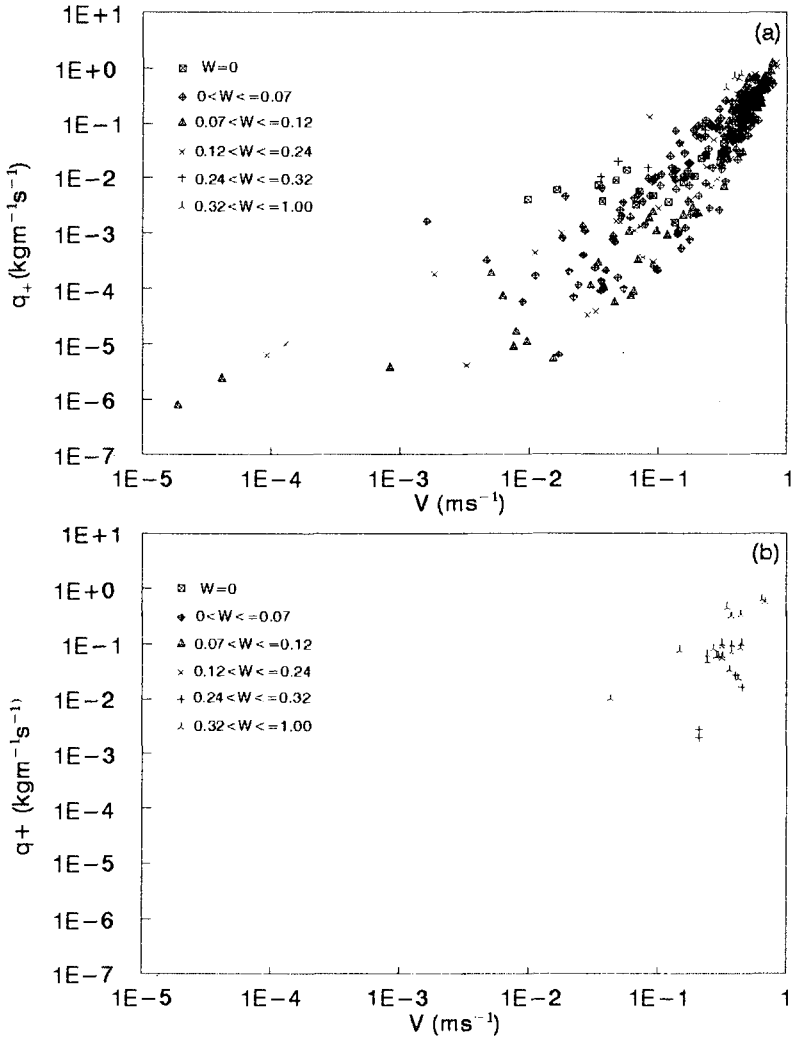


Figure 8. The relationship between the depth integrated suspended sediment transport rate and the current velocity: (a) Maplin data, (b) Boscombe data, banded in terms of the wave velocity amplitude  $W$  ( $\text{ms}^{-1}$ )

Selected data of this form have been collapsed onto a single curve using the concept of an equivalent current velocity (Grass, 1981) or a sand flux multiplier (Owen and Thom, 1978).

## 6.2 Boscombe data

The transport rate data from Boscombe have been plotted in the same axes as for Maplin (Figure 8b). The two ranges of  $W$  banded data show an increasing transport rate with increasing current velocity. However, the limited data set available at Boscombe also indicates a strong positive correlation between the wave velocity and the transport rate (Whitehouse, 1991).

## 7. CONCLUSIONS

This paper has presented the results from two field experiments performed to obtain measurements of suspended sand transport under wave and current action. The data illustrate the potential for waves to increase the near bed suspended sediment concentration above that resulting from the action of a current alone. As a consequence, more sediment is available to be mixed into the water column. This can be accomplished easily with the additional turbulence generated from the wave boundary layer and with the surface contribution to the turbulence levels from broken waves in the surf zone.

The sand transport data obtained from Maplin Sands during equilibrium periods of the tide can be used immediately in further work. The complex situation imposed at non equilibrium times in the tidal cycle, caused by the advection of suspended sand and other processes, requires an analysis in terms of more advanced physical modelling concepts.

The Maplin and Boscombe data taken in combination will be useful in enhancing the value of further analyses of  $w+c$  sediment transport because of the different environments,  $w+c$  conditions and sediment conditions covered.

## 8. ACKNOWLEDGEMENTS

The Maplin Sands measurements were made as a part of the engineering studies for the Third London Airport and the Boscombe Pier experiment was funded by the UK Department of the Environment. The original experiments were conceived and realised by Messrs M.F.C. Thorn and M.W. Owen. This analysis was undertaken as a part of the MAST G6M Coastal Morphodynamics research programme and the author would like to thank Mr P.J. Houghton and Mrs E.C. Stevenson for their contributions in analysing the raw data.

Useful comments were received from Mesrres R.L. Soulsby and M.W. Owen and from the University of Liverpool (Civil Engineering Department) during the analysis. The work was funded in part by the UK Ministry of Agriculture, Fisheries and Food, and in part by the Commission of the European Communities Directorate General for Science, Research and Development under Contract No MAST 0035-C.

## 9. REFERENCES

Deigaard, R., Fredsoe, J. and I.B. Hedegaard. (1986). Suspended sediment in the surf zone. *Journal of Waterway, Port, Coastal and Ocean Engineering*, 112, 1, 115-128.

Dyer, K.R. (1973). Estuaries: A Physical Introduction. John Wiley, London, 140pp.

Grass, A.J. (1981). Sediment transport by waves and currents. Report No FL29, SERC London Centre for Marine Technology, 26pp.

Nielsen, P. (1979). Some basic concepts of wave sediment transport. Institute of Hydraulics and Hydraulic Engineering, Technical University of Denmark, Series Paper 20.

Owen, M.W. and Thorn, M.F.C. (1978). Effect of waves on sand transport by currents. Proceedings 16th Coastal Engineering Conference, ASCE, pp.1675-1687.

Soulsby, R.L. (1990). Tidal-current boundary layers. *In: The Sea, Volume 9, Part A, Ocean Engineering Science*, B. Le Mehaute and D.M. Hanes Eds, Wiley, New York, pp.523-566.

Soulsby, R.L. and Humphery, J.D. (1990). Field observations of wave-current interaction at the sea bed. *In: Water Wave Kinematics*, A. Torum and O.T. Gudmestad Eds, Kluwer Academic Publishers, Netherlands, pp.413-428.

Van Rijn, L.C. (1984). Sediment transport, Part II: Suspended load transport. *Journal of Hydraulic Engineering*, ASCE, 110, 1613-1641.

Whitehouse, R.J.S. (1991). Analysis of field data for suspension transport under waves and currents. HR Published Paper No 55. Originally presented at IAHR International Symposium on the Transport of Suspended Sediments and its Mathematical Modelling, Florence, Italy, September 1991.



## CHAPTER 196

### Numerical Simulation of Pocket Beach Formation

Takao Yamashita<sup>1</sup> and Yoshito Tsuchiya, M.ASCE<sup>2</sup>

#### Abstract

The numerical model for three-dimensional beach change prediction is constructed to simulate a pocket beach formation. The model consists of three modules of waves, currents (include beach change) and sediment transport. Wave transformation module is based on the mild slope equation of hyperbolic type, current module is horizontally two-dimensional with direct interaction with sea bottom change which is evaluated by sediment transport model formulated by Bailard.

Numerical simulation of pocket beach formation was performed under two conditions of an artificial pocket beach formation which is the typical case of beach stabilization by headlands and an empirical pocket beach which is made by combining an equilibrium bay and beach profile.

#### 1. Introduction

Beach erosion control by constructing a series of stable pocket beaches, the headland defense works by Silvester(1972), seems to be one of the effective methods to recover sandy beaches in the area which has been seriously eroded due to both reducing longshore sediment transport and increasing offshore going sediment transported by reflected waves from the sea wall. "Stabilization of Sedimentary Coastlines" is the title of Silvester's paper in Nature(1960) and "Use of Crenulate Shaped Bays to Stabilize Coasts" is the title of paper in the proceedings of 13th ICCE(1972). As can be recognized from these titles, this method is based on the idea of stabilizing beaches with pocket beach formation. Thirty years after Silvester, beach stabilization seems to be a word in vogue and the headland defense works has been recognized as a feasible way to protect sandy beaches in

---

<sup>1</sup>Instructor, Disaster Prevention Research Institute, Kyoto University, Gokasho, Uji, Kyoto 611, Japan

<sup>2</sup>Professor, ditto

place of offshore detached breakwaters which thickly parasite on Japan's eroded beaches.

Following Silvester's frontier works, studies on mechanism of beach stabilization by forming pocket beaches (crenulate-shaped or zeta-shaped bays) have been carried out by several researchers. Hsu et. al.(1987) formulated bay shaped in terms of the 2nd order polynomial. Tsuchiya et. al.(1990) classified a pocket beach into two types of statically and dynamically stable beaches. Theoretical explanation of the existence of statically and dynamically stable pocket beaches has been done by Tsuchiya and Refaat(1990) in terms of the one-line theory with nonuniform longshore sediment transport model.

This study aims to simulate an artificial pocket beach formation by the numerical model for three-dimensional beach change prediction, in which knowledge of wave theory, nearshore dynamics, shoreline change model and sediment transport model are integrated. First numerical model is constructed and then simulation of pocket beach formation is performed under the condition of typical case of stable beach construction by headlands.

## 2. Model Outline

### 2.1 Wave Transformation

The steady state mild slope equation of the elliptic type including terms of uniform currents( $\vec{U}$ ) interaction and wave energy dissipation due to breaking is employed to calculate wave field.

$$\frac{D^2\phi}{Dt^2} + (\nabla \cdot \vec{U}) \frac{D\phi}{Dt} - \nabla \cdot (CC_g \nabla \phi) + (\sigma^2 - k^2 CC_g - i\sigma W)\phi = 0 \quad (1)$$

where  $\phi$  is the velocity potential and the derivative operator is defined as  $D/Dt = \partial/\partial t + U_j \partial/\partial x_j$  (Kirby 1984).

Wave energy dissipation rate  $W$  formulated by Izumiya & Horikawa(1984) is employed here. Using the complex surface elevation  $\zeta$ , the mild slope equation can be written as:

$$\left\{ 1 + \frac{\sigma}{\omega} \left( \frac{C_g}{C} - 1 + \frac{i}{\sigma} W \right) \right\} \frac{\partial^2 \zeta}{\partial t^2} + \frac{\partial}{\partial t} (\nabla \cdot (\vec{U} \zeta)) - \nabla \cdot \left\{ \omega CC_g \nabla \left( \frac{\zeta}{\sigma} \right) \right\} = 0 \quad (2)$$

where  $\omega$  and  $\sigma$  are the absolute and intrinsic angular frequencies, respectively with the following relation

$$\omega = \sigma + \vec{U} \cdot \vec{k}, \quad \sigma = \sqrt{gk \tanh kh} \quad (3)$$

and the wave celerity and group velocity are defined respectively by

$$C = \frac{\sigma}{k}, \quad C_g = \frac{\partial \sigma}{\partial k} \quad (4)$$

For effective numerical calculation, an equivalent hyperbolic system to the elliptic mild slope equation (2) can be derived as : (Warren et. al., 1985; Madsen and Larsen, 1987; Yamashita et. al., 1990).

$$\frac{\partial P}{\partial t} - i\omega P + \omega CC_g \frac{\partial}{\partial x} \left( \frac{S}{\sigma} \right) = 0 \quad (5)$$

$$\frac{\partial Q}{\partial t} - i\omega Q + \omega C C_g \frac{\partial}{\partial y} \left( \frac{S}{\sigma} \right) = 0 \tag{6}$$

$$\frac{\partial P}{\partial x} + \frac{\partial Q}{\partial y} + \frac{1}{\omega} \left\{ 1 + \frac{\sigma}{\omega} \left( \frac{C_g}{C} - 1 + \frac{i}{\sigma} W \right) \right\} \left( \frac{\partial S}{\partial t} - i\omega S \right) + \vec{U} \cdot \nabla S = SS \tag{7}$$

where  $S, P,$  and  $Q$  are the surface elevation and line discharges in the  $x$  and  $y$  direction and  $SS$  is the wave source which is given as

$$SS = \frac{C \Delta s}{\Delta x \Delta y} a_0 e^{i\chi} \tag{8}$$

where  $\chi$  is the phase,  $a_0$  the wave amplitude,  $\theta$  the wave angle and spacial increments are defined  $\Delta x, \Delta y,$  and  $\Delta s = \Delta x / \cos \theta$  respectively.

The sponge layer boundary condition (Larsen and Dancy, 1983) is effective behind the wave source boundary and along the shoreline. An artificial dumping is introduced inside sponge layer of which dumping coefficient  $\mu(x)$  is given by,

$$\mu(x) = \begin{cases} \exp\{ (2^{-x/\Delta x} - 2^{-x_s/\Delta x}) \ln \alpha \} & \text{for } 0 \leq x \leq x_s \\ 1 & \text{for } x_s \leq x \end{cases} \tag{9}$$

where  $x_s$  is the thickness of sponge layer,  $\alpha$  the parameter being dependent on  $x_s$ . This set of equations can be solved numerically by the ADI method.

### 2.2 Sediment Transport Model

The sediment transport rate  $q_i$  can be evaluated by the model of Bailard(1982), which was calibrated by Stive(1986), in which the sediment transport rate  $\vec{q}$  consists of bed-load and suspended-load including the effects of wave asymmetry (suffix  $as$ ), mean currents (suffix  $nc$ ) and bottom slope (suffix  $sl$ ). The total sediment transport vector is calculated by,

$$\vec{q} = \frac{1}{(\rho_s - \rho)g(1 - \lambda)} (\vec{q}_{asb} + \vec{q}_{ass} + \vec{q}_{ncb} + \vec{q}_{ncs} - \vec{q}_{slb} - \vec{q}_{sls}) \tag{10}$$

where

$$\begin{aligned} \vec{q}_{asb} &= \frac{9B_b u_{orb}^4 \cos \phi_2}{C \sinh^2(kD)} \vec{i}, & \vec{q}_{ass} &= \frac{9B_s u_{orb}^5 \cos \phi_2}{5\pi C \sinh^2(kD)} \vec{i} \\ \vec{q}_{ncb} &= \frac{3B_b u_{orb}^2}{2} \vec{U}, & \vec{q}_{ncs} &= 6.4B_s u_{orb}^3 \vec{U} \\ \vec{q}_{slb} &= \frac{1.6B_b u_{orb}^3}{\tan \psi} \frac{\partial D}{\partial x} \vec{i}, & \vec{q}_{sls} &= \frac{8\epsilon_s B_s u_{orb}^5}{w_f} \frac{\partial D}{\partial x} \vec{i} \end{aligned} \tag{11}$$

where  $\vec{i}$  is the unit vector,  $\theta$ : the wave direction,  $u_{orb}$ : the near-bottom orbital velocity of wave motion(linear),  $\vec{U}$ : the near-bottom mean current vector,  $\phi_2$ : the phase lag of second harmonics of the Stokes wave theory,  $\epsilon_s = 0.02, \rho_s, \rho$ : the densities of sea water and sediment,  $g$ : the gravitational acceleration,  $\lambda$ : the sediment porosity,  $w_f$ : the sediment falling velocity and  $k$ : the wave number. Moreover, the parameters for bed-load  $B_b$  and suspended-load  $B_s$  are  $B_b = \rho C_f \epsilon_b / \tan \psi$  and  $B_s = \rho C_f \epsilon_b / w_f$ , respectively. The friction factor  $C_f$  is given by,

$$C_f = \frac{1}{2}f_w = \frac{1}{2} \exp \left\{ 5.2 \left( 2.5 \frac{D_s}{a_w} \right)^2 - 6.0 \right\} \quad (12)$$

where  $D_s$  is the characteristic grain diameter and  $a_w$  the orbital amplitude.

### 2.3 Nearshore Currents and Sea Bottom Change

Momentum equations including terms of interaction with sea bottom changes ( $\partial D/\partial x_i$ ) are derived as:

$$\frac{\partial Q_i}{\partial t} + \beta U_i \frac{\partial Q_j}{\partial x_j} = -gH \left( \frac{\partial H}{\partial x_i} - \frac{\partial D}{\partial x_i} \right) - \frac{1}{\rho} \left( \tau_i^B + \frac{\partial S_{ij}}{\partial x_j} + \frac{\partial T_{ij}}{\partial x_j} \right) \quad (13)$$

where,  $\beta$ : momentum correction coefficient,  $H$ : total depth,  $D$ : still water depth,  $Q_i$  and  $U_i$  are discharges and velocities of nearshore currents,  $\tau_i^B$ : bottom stresses and  $S_{ij}$ : radiation stresses.

$$S_{ij} = \frac{\rho g}{4} \left[ \operatorname{Re} \left( \frac{\partial S}{\partial x_i} \frac{\partial S^*}{\partial x_j} \right) \frac{1}{k^2} \left( 1 + \frac{2kD}{\sinh 2kD} \right) + \delta_{ij} \left\{ |S|^2 \frac{2kD}{\sinh 2kD} + \frac{2kD \coth 2kD - 1}{2k^2} \left( \left| \frac{\partial S}{\partial x} \right|^2 + \left| \frac{\partial S}{\partial y} \right|^2 - k^2 |S|^2 \right) \right\} \right] \quad (14)$$

where  $\delta_{ij}$  is Kroneker's delta and \* indicates complex conjugate. Furthermore, horizontal mixing is formulated as

$$-T_{ji} = \rho H \left( \nu_e \cos \left( \theta + \frac{\pi \delta_{ij}}{2} \right) \left( -\sin \theta \cos \theta \frac{\partial V}{\partial x_j} + \sin \theta \sin \theta \frac{\partial U}{\partial x_j} - \cos \theta \cos \theta \frac{\partial V}{\partial x_i} + \sin \theta \cos \theta \frac{\partial U}{\partial x_i} \right) \right) \quad (15)$$

where  $\nu_e$  is the eddy viscosity estimated by velocity scale [ $u \simeq \sqrt{gH}$ ] and the length scale [ $l$ ] is the distance from the shore.

The continuity equations of water and sediment transport are given respectively by

$$\frac{\partial H}{\partial t} + \frac{\partial Q_i}{\partial x_i} = 0, \quad \frac{\partial D}{\partial t} - \frac{\partial q_i}{\partial x_i} = 0. \quad (16)$$

The sediment transport rate  $q_i$  is evaluated by the model of Bailard(1982). The finite difference ADI method is also employed to solve the nearshore currents and sea bottom changes. The one-line model is employed to predict a long-term shoreline change under the dominant wave field calculated by the wave transformation model shown in 2.1. After determining the shoreline position of a stable beach, the sea bottom topography change is calculated up to getting the equilibrium beach topography. To save CPU time, wave field is renewed several times after calculations of nearshore currents and sea bottom change.

### 3. Pocket Beach Formation

#### 3.1 Artificial Pocket Beach Formation

An initial beach topography is assumed the uniformly sloping bottom ( $s=1/23$ ) constructed by the sand nourishment in the seriously eroded beach together with the construction of two headlands (100 and 50m long each) and groin system (see Figure 1). This beach is called an artificial pocket beach in this paper, of which dimension is typical in the headland defense works (beach stabilization works) under construction or planning in Japan's eroded coasts.

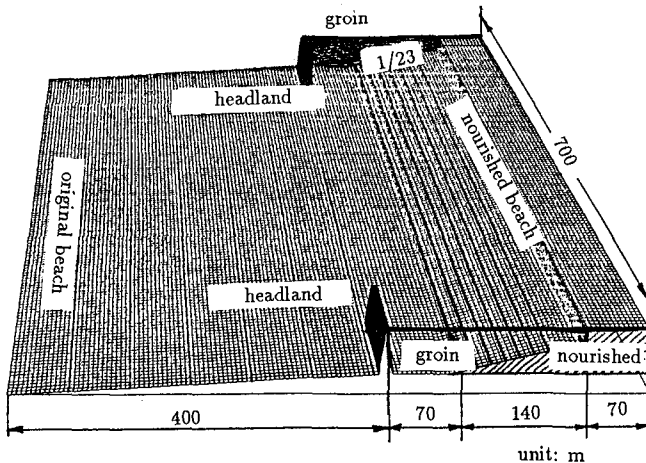


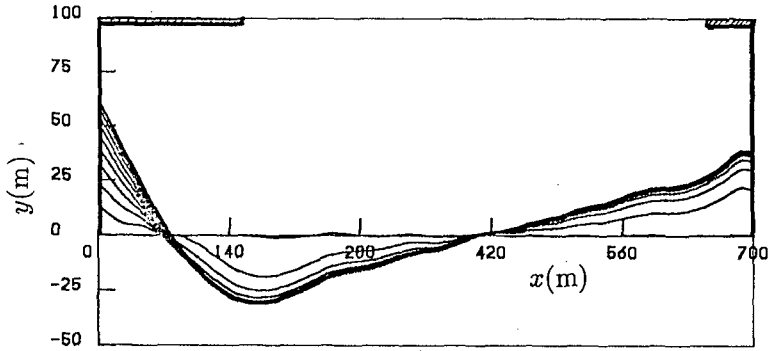
Figure 1. Initial beach topography

Operating the dominant incident waves ( $T=8s$ ,  $H=2m$ ,  $\theta=8^\circ$  are assumed here) and computing the stable shoreline position by the shoreline change model (one-line model including the effect of wave diffraction because the wave field is computed by the wave transformation model mentioned above), computations of nearshore current and sea bottom change start to obtain the statically stable topography of a pocket beach. Figures 2 (a)-(d) show the computed shoreline, beach topography, wave and current fields. It can be observed from these figures that nourished sand may not go out of headlands area to form a zeta-shaped bay in the case of dominant wave operation. Because perfect wave absorption is assumed at the boundaries such as headlands, beaches and side walls, smooth wave and current fields are computed in which wave diffraction and breaking play a main role in forming nearshore circulation.

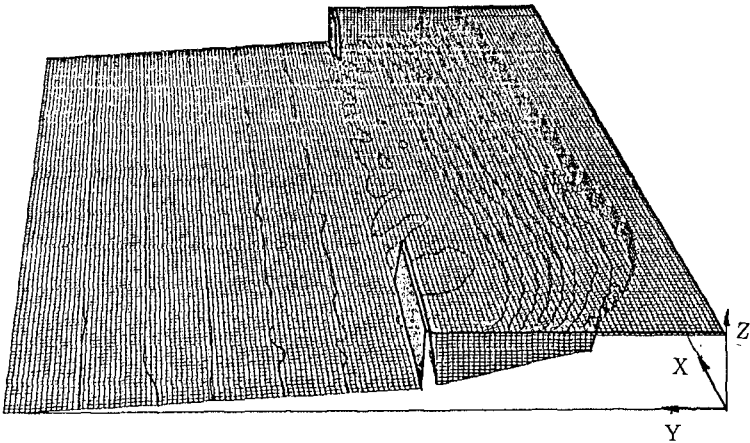
#### 3.2 Changes in Empirical Pocket Beach

In addition to the case of an artificial pocket beach formation, an attempt of an empirical pocket beach formation is conducted. Combining the formulations of

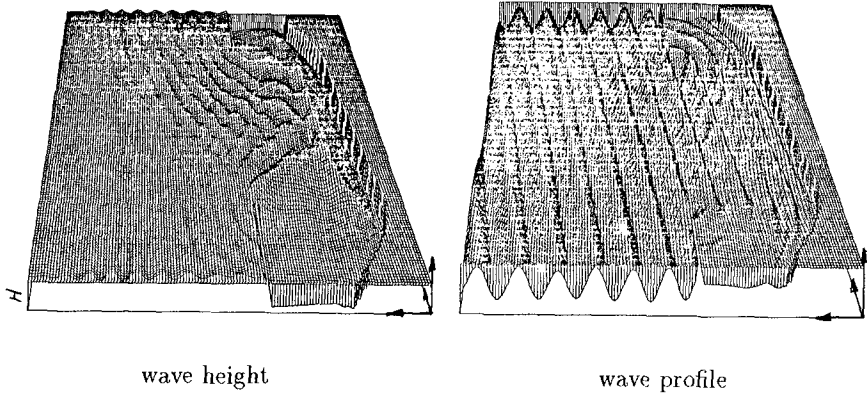
equilibrium bays (Hsu et. al., 1987) and equilibrium beach profiles, we can get the ideal stable beach topography which is called an empirical pocket beach in this paper. The stable shoreline of the pocket beach can be assumed by an equilibrium bay formulated by equation (18) (Hsu et. al.). Fixing the critical depth of beach changes, Dean's (1981) equilibrium beach profile evaluated by equation (17) is assumed along the line between shore and critical depth to determine the topography of stable beach, then we can get the stable beach topography shown in Figure 4.



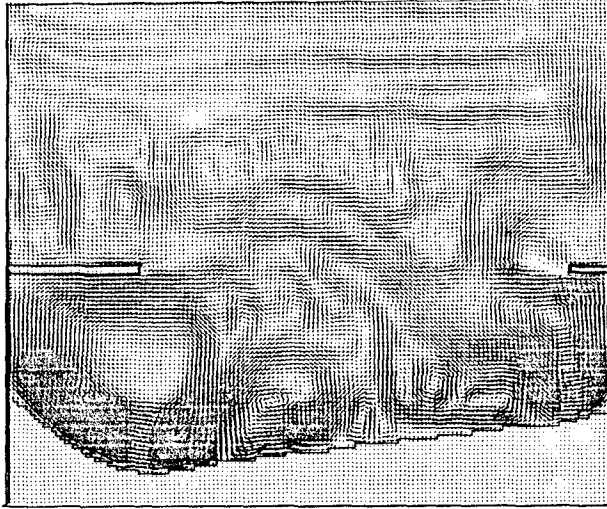
(a) Computed shoreline of the pocket beach



(b) Topography of artificial pocket beach



(c) Wave field



(d) Current field

Figure 2. Artificial Pocket Beach Formation

$$h(x) = A(D_s)x^{2/3} \quad (17)$$

$$\frac{R}{R_0} = C_0 + C_1\left(\frac{\beta}{\theta}\right) + C_2\left(\frac{\beta}{\theta}\right)^2 \quad (18)$$

where the coefficients  $C_0$ ,  $C_1$  and  $C_2$  are dependent on the incident wave angle  $\beta$  and the definition of variables are shown in Figure 3.

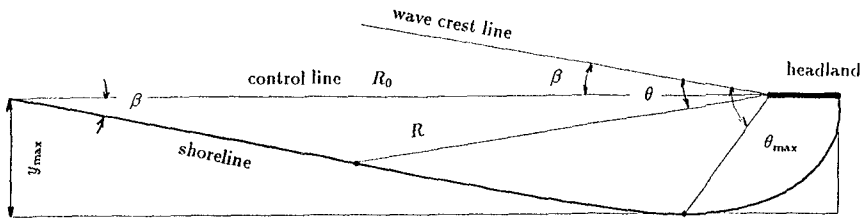


Figure 3. Definition of variables of equilibrium bay (Hsu et. al.)

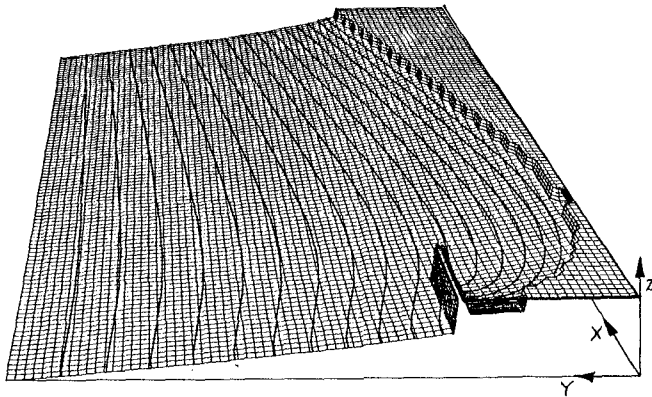


Figure 4. Topography of an empirical pocket beach

Calculations of nearshore currents and sea bottom changes are executed under the same conditions of wave and boundary as those of the case of an artificial pocket beach. Figure 5(a) shows the shoreline position calculated by equation (18) in which the length of headland is 57m. It can be recognized that both the



embayment (about 30m at  $x=140\text{m}$ ) and the salient length of 60m are almost same as artificial bay formation.

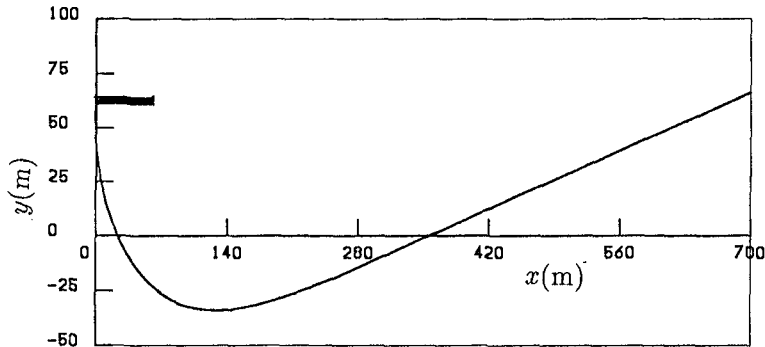
Figures 5(b) and (c) show currents and bottom topography in which no remarkable circulation cells except behind headland is observed and change in topography is also small. This means that pocket beach is stable against dominant waves.

#### 4. Conclusions

A finite difference numerical model for sea bottom topography change was constructed by combining a wave transformation model(steady) and a three dimensional beach change model(unsteady) in which interaction between nearshore currents and bottom change was simultaneously considered. Numerical simulation of an artificial pocket beach formation was performed by the developed model together with the shoreline change model.

Applying the model to the case of artificial pocket beach of which dimension was similar to that of headland defense works (beach stabilization works) under construction in Japan's eroded coast, it was recognized that nourished sand might not go out of headlands area.

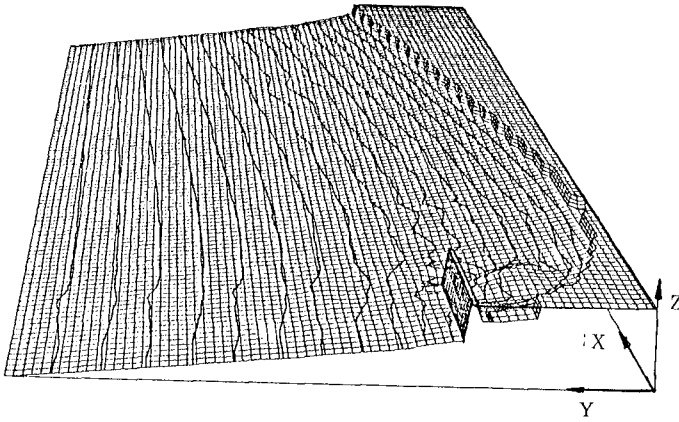
Moreover, combining the formulations of equilibrium bays and equilibrium beach profiles by Dean the initial beach topography was assumed(it was called an empirical pocket beach in this paper). It was shown that no remarkable circulation cells except behind headland are formed and topography change was also small to confirm beach stabilization.



(a) Computed shoreline of the pocket beach



(b) Nearshore currents



(c) Beach topography

Figure 5. Changes in Empirical Pocket Beach

References

- Bailard, J.A.(1982): Modelling on-offshore sediment transport in the surf zone, Proc. 18th ICCE, pp. 1419-1438.
- Dean, R.O.(1981): Equilibrium beach profiles, U.S. Atlantic and Gulf Coasts, Ocean Eng. Rep. No.12, University of Delaware.
- Hsu, J.R.C., R. Silvester and Y.M. Xia(1987): New characteristics of equilibrium bays, Proc. 8th Australian Conf. on Coastal and Ocean Eng., p.140-144.
- Izumiya, T. and K. Horikawa(1984): Wave energy equation applicable in and outside the surf zone, Coastal Eng. in Japan, Vol.27, 1984, pp.119-137.
- Kirby, J.T.(1984): A note on linear surface wave current interaction over slowly varying topography, Jour. Geophys. Res., Vol.89, C1, pp.745-747.
- Madsen P.A. and J. Larsen(1987): An efficient finite difference approach to the mild slope equation, Coastal Engineering, Vol.11, pp.329-351.
- Silvester, R.(1960): Stabilization of Sedimentary Coastlines, Nature, 188, pp.467-469.
- Silvester, R.(1972): Use of Crenulate Shaped Bays to Stabilize Coasts, Proc. 13th ICCE, pp.1347-1365.
- Stive, M.J.F.(1986): A model for cross-shore sediment transport, Proc. 20th ICCE, pp.1551-1564.
- Warren, I.R., J. Larsen and P.A. Madsen(1985): Application of short wave numerical models to harbour design and future development of the model, Int. Conf. on Numerical and Hydraulic Modelling of Ports and Harbours, Birmingham, pp.303-308.
- Yamashita, T., Y. Tsuchiya, M. Matsuyama and T. Suzuki(1990): Numerical calculation of linear wave propagation in the coastal zone, Bull. Disas. Prev. Res. Inst., Kyoto Univ., Vol.40, Part 1, No.345, pp. 15-40.

## CHAPTER 197

### A CRITICAL REVIEW OF AVAILABLE DATA FOR CALIBRATION AND/OR VERIFICATION OF SEDIMENT TRANSPORT MODELS

Julio A. Zyserman<sup>1</sup>

#### Abstract

A survey and a critical review of existing sediment transport data in waves and/or currents has been performed. Special emphasis has been given to the applicability of the data sets for the calibration and/or verification of sediment transport models. Only data sets dealing with non-cohesive sediment have been considered in this review. The eventual need for further experimental research is discussed under the light of the results from the present study.

#### Introduction

The increased understanding achieved in recent years of the phenomena involved in the processes of sediment suspension and transport by streams and by the combined action of waves and currents in the marine environment has led to the formulation of increasingly more detailed (and complex) sediment transport models.

In spite of this improved understanding, the intricacy of the phenomena being described and an incomplete comprehension of all mechanisms involved frequently result in the introduction of crude hypotheses into the models, assumptions that have to be validated against experimental data. Some models are based on calibration factors that can only be determined from experimental results. In other cases, an empirical approach based on measured data is the only feasible way of describing phenomena that are either too complex or poorly understood to allow for a theoretical or semi-empirical description.

The preceding discussion points out the permanent need for sediment transport data of good quality. A critical data review has therefore been performed in order to identify potentially useful data sets for the calibration and/or verification of transport models.

---

<sup>1</sup> Research Engineer, Ph.D., Danish Hydraulic Institute, Agern Allé 5, DK-2970 Hørsholm, Denmark.

### General Requirements to Experimental Data

The flow chart of a generic sediment transport model is shown in figure 1. Most sediment transport models that are provided with adequate input data (hydrodynamic, sediment, bed form and miscellaneous data), will yield the sediment transport rates as output. More advanced models may be constituted by different modules; each module aiming to describe of one or several of the phenomena involved: for example, a module to determine the vertical structure of the flow, another to calculate the turbulence levels along the water column, a third one to determine the concentration profiles of suspended sediment, etc. Output of such advanced models may therefore include information such as velocity profiles (time-mean or instantaneous), concentration profiles (time-mean or instantaneous), etc. Other models may calculate the characteristics of bed forms based on the input data provided, so bed form data can in some cases be found as output from the model.

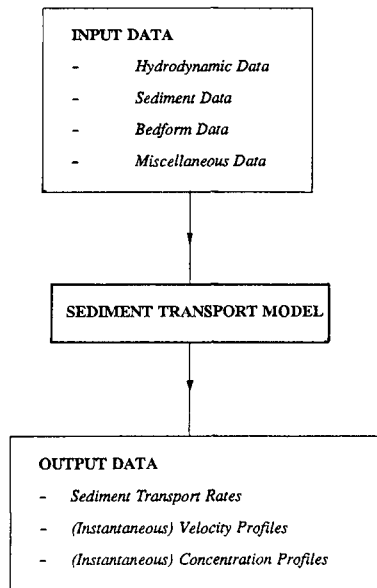


Figure 1. Flow chart of a generic sediment transport model.

It appears from the figure that the model/data interaction takes place at least at two levels, namely at the input and the output levels of the model. In the case of more complex models, the interaction could also occur at the output level of each constituent module. In order to be suitable for the purposes of calibration and/or verification of mathematical models, the data used should fulfill general and specific requirements. The general requirements will be addressed in what follows, whereas the specific ones will be discussed in the next section.

The amount of sediment transported by streams or by the combined action of waves and current in the coastal environment is determined by the complex interaction between the flow

conditions and the bed material. Enough information about all the relevant physical parameters involved should be provided to the transport model in a format suited to its particular formulation, in order to obtain an accurate characterization of the phenomena that the model intends to simulate.

Generally speaking, it can be said that the quantity of the data should be sufficient to ensure that the degree of agreement or discrepancy found between the calculated and the observed transport rates can only be attributed to the assumptions inherent to the model and not to scarce or missing information about the conditions in which the reported transport rates were determined. The data should also be of good quality, obtained under well-defined conditions and using instruments suited for the measurement of the desired magnitudes.

Another general requisite refers to the way in which the measured data is reported. Tabulated form is preferable to graphic form, since it avoids the possible inaccuracies associated with collecting values from a figure, and facilitates the process of handling the data and the supply of information to the transport model. In this connection, data on magnetic media is highly favoured, especially if they have been stored in a database, with the related advantages regarding data retrieval and search for selected ranges of one or several of the physical variables involved.

#### Specific Requirements and Classification of Experimental Data Sets

The amount and degree of detail of the data required for the calibration and/or validation of a given model depends not only on the assumptions and physical principles involved in its derivation but also on the situation the model aims to describe (transport by streams, or under combined current and waves, etc.). More complex models will require in general larger amounts of more detailed input data in order to allow for an adequate description of the phenomena under consideration. More parameters will be required in order to characterize intricate hydrodynamic conditions such as in the case of breaking waves propagating at arbitrary angles with respect to a current than in the relatively simpler situation of a steady current flowing along a laboratory flume.

One out of many possible classifications for the sediment transport data sets consists of separating between those obtained under pure-current situations and those measured in presence of waves or, eventually, in combined waves and current situations. This classification is based not only in the inherent differences between the hydrodynamic conditions but also reflects the trend usually followed when developing sediment transport models. In turn, each case can be split up into data obtained in the laboratory and data acquired in the field. Another item in the classification corresponds to the data collected in oscillating wave tunnels. These laboratory facilities are able to reproduce full-scale flow conditions (although lacking phase-differences along the tunnel and the vertical component of the wave-induced motion) under the controlled conditions of a laboratory.

The number of physical parameters required for a complete characterization of each situation depends not only on the flow condition but also on the particular sediment transport model considered. Instead of addressing a particular model formulation, it was chosen to pose requirements to the experimental data sets that were strict enough so as to ensure their suitability for the calibration and/or validation of the most advanced transport models that

are normally used, namely the deterministic-type model for sediment transport in coastal areas (see for example Zyserman et al. (1991 a) for a classification of models) and models calculating separately bed-load and suspended-load transport in the case of streams.

The requisites regarding the description of the experimental conditions and the measured transport rates vary for the different items in the classification, the major differences being, however, restricted to the characterisation of the hydrodynamic data.

The geometrical properties of the sediment can be appropriately described in any case through its median size  $d_{50}$ , other percentiles  $d_i$ , gradation  $\sigma_g$ , or, conversely, through its grading curve G.C. Another important parameter is the settling velocity  $w$ . If not specified, it can be determined if the sediment density  $\rho_s$  and the kinematic viscosity  $\nu$  or the temperature  $T$  of the water are known. The kinematic viscosity of water has been explicitly included because it is not always a function of the water temperature alone, as in the case when suspended particles of a clay-size fraction are present.

Bed forms are suitably described by means of their type, height  $h$ , length  $l$  and celerity  $a$  under all cases.

The rates of bed-load transport  $q_b$ , suspended-load transport  $q_s$  and total-load transport  $q_t$  are of course of basic interest. Concentration profiles  $c(y)$  are also important, where  $y$  is the elevation about the bottom. For measurements in water tunnels, or under combined waves and currents, the time-mean values of the transport rates  $\bar{q}_b$ ,  $\bar{q}_s$  and  $\bar{q}_t$  are of interest. Vertical profiles of time-mean concentration  $\bar{c}(y)$  and time series of the instantaneous concentration at different elevations (time series of ensemble-average concentration in the case of wave-tunnel data)  $c(y,t)$  are also relevant parameters.

In the case of pure-current flow conditions in the laboratory, the flow is adequately described if information about the dimensions of the flume (length  $L$ , width  $W$  and height  $H$ ), about the water depth  $D$ , discharge  $Q$  and/or mean velocity  $V$  and water surface slope  $I$  is provided. Additionally, vertical profiles of the horizontal velocity component  $u(y)$  could be used to check the hydrodynamic module (if any) of the model considered. The same parameters are valid to describe the flow conditions in the case of currents measured in the field, but information about the orientation  $O$  of the study reach and the cross-section  $A$  of the measuring section should be provided.

Appropriate parameters to describe the flow when considering measurements in water tunnels are the amplitude of the oscillatory motion  $a_0$  or its maximum velocity  $u_0$ , together with the period  $T$ , the discharge of the net current  $Q$  or its mean velocity  $V$ . Useful additional parameters are the vertical profiles of the ensemble-averaged velocity  $\bar{u}(y)$  and time series of the instantaneous velocity recorded at different elevation above the bed  $u(y,t)$ .

Waves plus current conditions in the laboratory can be characterized by means of the water depth  $D$ , the wave height (root-mean-square, significant, etc.)  $H_i$ , the period (peak, zero-up-crossing, etc.)  $T_i$ , the type of breaking wave (if any) and the distance to the point of breaking  $x_b$ . Information about the breaker type and the distance from the measuring position in the surf zone to the breaker line is relevant because the production of turbulence by breaking waves is usually taken equal to that of a bore or hydraulic jump. This assump-

tion may be valid in the case of spilling breakers or of breaking waves of other type in the inner surf zone, but not close to the breaking point in the case of plunging breakers. Important additional parameters are the local bed slope  $S$ , the discharge  $Q$  or the mean velocity  $V$  (when relevant), a time series of the instantaneous elevation of the water surface from which the spectrum can be determined in the case of irregular waves or, conversely, information about the spectral parameters  $\eta(t)$ . Useful additional information for the calibration/validation of the hydrodynamic module of the model (if any) is provided by  $\bar{u}(y)$  and  $u(y,t)$ .

In the case of combined waves and current in the field, the same parameters used to describe the waves and the spectrum in the laboratory can be applied. Due to the two-dimensional (in plan) nature of the problem, it is now necessary to speak about the long-shore and cross-shore components of the bed slope  $S_j$ , of the time- and depth-averaged velocity  $V_j$ , of the time-mean velocity profile  $\bar{u}_j(y)$ , and of the instantaneous velocity  $u_j(y,t)$ . Another important parameter is the angle  $\gamma$  between the current and the direction of wave propagation. Information about the beach profile  $P$  and orientation  $O$  may also be useful.

### Data Sets Reviewed

A list of the 40 data sets reviewed, arranged according to the classification discussed, is listed below. This list is by no means exhaustive, but it has been deemed that the results of their review will provide an overview of the type of data available. A more detailed description of most of the data sets can be found in Zyserman et al. (1991 b).

#### **Pure Current, Laboratory**

Barton and Lin (1955)	Guy et al. (1966)
Laursen (1957)	Lyn (1986)
Meyer-Peter and Müller (1948)	Nomicos (1956)
Stein (1965)	Vanoni and Brooks (1957)
Williams (1970)	Wang and Qian (1992)

#### **Pure Current, Field**

Anderson (1942)	Colby and Hembree (1982)
Culbertson et al. (1972)	Nordin and Dempster (1963)
Scott and Stephens (1966)	

#### **Wave Tunnel**

Hayakawa et al. (1983)	Horikawa et al. (1982)
Murray et al. (1991)	Nakato et al. (1977)
Ribberink and Al Salem (1989)	Sato and Horikawa (1986)
Sawamoto and Yamashita (1986)	Sleath (1982)
Staub et al. (1984)	Steetzel (1984)
Van der Velden (1987)	

#### **Waves (+ Current), Laboratory**

Bosman and Steetzel (1986)	Dette and Uliczka (1986)
Nap and van Kampen (1988)	Nieuwjaar and van der Kaaij (1987)
Skafel and Krishnapan (1984)	Steetzel (1987)
Vellinga (1984)	



**Waves (+ Current), Field**

Downing (1984)

Jaffe et al. (1984)

Kos'yan (1985)

Owen and Thorn (1978)

Fairchild (1977)

Kana and Ward (1980)

Nielsen (1984)

It is important to keep in mind that most of the data sets reviewed were obtained under tests not specifically aimed to the calibration and/or verification of sediment transport models, so the results of the present review must be interpreted under the light of this restriction. On the other hand, the obtention of many of the parameters required to characterize the test conditions from the point of view of sediment transport models could be done without great efforts or additional costs, and would render the data sets useful for more application than those devised when the tests were designed.

Only data sets dealing with non-cohesive sediment of sand-fraction size have been considered in the present review, with the sole exception of the bed-load transport data of Meyer-Peter and Müller, which was obtained using bed materials in the range from coarse sand to gravel.

All data sets reviewed regarding wave-tunnel measurements were obtained under simulated regular wave conditions. Only the tests of Murray et al. included a net current superimposed to the oscillatory motion.

In some cases, the experimental results were not included in the reference reviewed, but a description of the tests, the measuring techniques and the results obtained was included. The review is based on the information provided in the reference, especially in the case of data collected under large field measurement programmes. More detailed information could be possibly found in the original data sets.

**Results of Data Review**

It has been chosen to present the review in tabulated form, in order to allow for a quick interpretation of the results obtained. Tables 1 and 2 include the results for the pure current case in laboratory and the field, respectively. Table 3 refers to wave tunnel data, whereas Tables 4 and 5 deal with the waves plus current cases in laboratory and in the field.

The variables selected for the description of each case have been placed in the columns of the tables and collected in groups for hydrodynamic data, miscellaneous data, sediment data, bed form data and transport data. Information about the format in which the data is presented in the reference (tabulated (T) or graphic (G)) is also provided. Different types of bed material (both with regard to size and/or density) were used in some of the tests performed in the laboratory. This has also been indicated in the corresponding tables.

An open triangle has been used to indicate that the relevant parameter was reported for each data record of the data set, whereas a dot indicates that such information is available only for some data records. A cross means that information about the corresponding variable was not provided in the reference reviewed, but that it can be obtained from other sources,

typically related papers. Finally, an empty circle indicates that no information at all was reported on the parameter.

It can be observed upon examination of the results that, in general, data sets collected in flume experiments in the laboratory are well-documented, with good information about the hydrodynamic conditions (including velocity profiles), and satisfactory details about the sediment and bed form data. Most of those references reporting transport data do so with the total-load transport rates. The Meyer-Peter and Müller data set was intended for the collection of bed-transport data. Laursen (1957) and Guy et al. (1966) also report the suspended transport, although the manner in which it was separated from the bed-load transport differs between both references.

All the data sets reviewed under the classification of pure current in the field except that of Anderson (1942) were collected by the U.S. Geological Survey, and present therefore similar characteristics with regard to the amount and format of the information reported. All five sets provide very good details about the hydrodynamic data, although information about the discharge is missing in Anderson's data set. The bed material is defined mainly through its grading curve, and vertical profiles of velocity and concentration of suspended sediment are reported in all cases, with vertical profiles of the median grain size of suspended sediment indicated in four of them. The information about bed forms is scarce (only the type of the observed bed forms is listed) and no transport rates of any kind are reported at all, probably because of the difficulties related to the effective trapping of the sediment in the field.

The wave-tunnel data reviewed is mainly reported in graphical form. The hydrodynamic conditions of the tests are well described, but measurements of velocity profiles (both ensemble-averaged and instantaneous) are scarce. The water temperature is only reported in two cases, even though its determination is an easy task. The same applies to the grading curve of the bed material, which is mainly defined through its median size  $d_{50}$ . Measurements of the concentration of suspended sediment are also rather scarce. With regard to  $\bar{c}(y)$ , Ribberink and Al Salem, Steetzel and van der Velden measured time-averaged concentration profiles, while the other authors determined ensemble averages. Bed form data may be termed as satisfactory, whereas transport data is very scarce.

The experimental data under combined waves and current considered in the present review were obtained either from profile-evolution tests (Dette and Uliczka, Steetzel, Vellinga) or from experiments with a horizontal or sloping bed. Data is well-documented, in the sense that it is usually presented both in tabulated and in graphic form. The wave conditions and the water depth at the measuring position are well-defined, although the type of breaking waves and the distance to the breaking line are reported only in a few cases. Time-averaged velocity profiles were measured in most data sets. The sediments are described mainly through the median grain size and/or other percentiles. No grading curves are presented. All the data sets reviewed include measured profiles of time-mean concentration of suspended sediment. Neither instantaneous values of concentration nor transport rates were directly determined in any case, although the magnitude of the transport could be estimated from the time sequence of observed profile changes. Bed form data is well defined in all tests with horizontal or uniformly sloping bottom, with exclusion of the rate of migration of bed forms.

When data obtained under waves and current conditions in the field is considered, it appears that the overall quantity of information is scarce. Data are mainly presented in graphical form, with a reasonable amount of details about the local wave conditions, but are rather poor regarding the miscellaneous, sediment and bed form data. Transport data is completely missing. The lack of detailed information can of course be understood if the difficulties related to collecting data in the marine environment are recalled, especially so in the case of measurements within the surf zone.

### Conclusions

The general conclusions presented here are biased by the choice of the transport models selected when describing the particular requirements to be fulfilled by the data. Quite different conclusions may of course be reached if the results of the review are seen under the light of the requirements of transport models based on simpler principles.

It appears that information about sediment transport rates collected in pure current situations in the field is missing. This type of data is important for the verification of models developed using only laboratory data. Similar considerations apply to the characteristics of bed forms.

The total transport rate in combined wave and current motion on a plane or uniformly sloping bottom should also be determined from laboratory tests and compared to the results of similar experiments under pure current situations, in order to evaluate the influence of the waves on the time-mean transport rates.

Vertical profiles of time-mean concentration of suspended sediment were determined in most of the data sets reviewed that were obtained from wave tunnels or under combined current and waves, both in laboratory and in the field. Time-mean transport rates are missing in most cases.

The time-averaged rates of suspended transport can not be accurately evaluated by integration along the vertical of the product of time-mean concentration and velocity, due to the so-called wave-related component of the transport, which is defined as the time-average of the product of the periodic oscillatory components of the velocity and the concentration, see Murray et al (1991) and Zyserman et al. (1991 a) for a discussion. The influence of the wave-related component on the rate of suspended transport becomes more important for wave-dominated or weak-current cases.

Transport data collected from wave tunnels provide a unique possibility of evaluating the vertical structure of the wave-related component of the suspended sediment transport in real-life conditions through the measurement of the ensemble-averaged values of both the velocity and the concentration at the same position at different elevations above the bed under well-controlled test conditions. The influence of this component should therefore be evaluated for different relative magnitudes of the current-related and wave-induced velocities.

Data set	No. of records	No. of mate-rials	Flume dimensions			Data format			Hydrodynamic Data				Misc. Data				Sediment Data					Bed-Form Data			Transport Data										
			L	W	H	T	G	D	I	Q	V	u(y)	T	V	d <sub>50</sub>	d <sub>1</sub>	σ <sub>g</sub>	G.C.C.	W	ρ <sub>s</sub>	d <sub>50</sub> (y)	C(y)	Type	h	l	a	q <sub>b</sub>	q <sub>s</sub>	q <sub>t</sub>						
Barton-Lin	28	1	21.3	1.2	0.6	⊗	⊗	⊗	⊗	⊗	⊗	⊗	⊗	⊗	⊗	⊗	⊗	⊗	⊗	⊗	⊗	⊗	⊗	⊗	⊗	⊗	⊗	⊗	⊗	⊗	⊗	⊗	⊗		
Guy et al.	339	10	45.7 18.3	2.4 0.8	0.8 0.75	⊗	⊗	⊗	⊗	⊗	⊗	⊗	⊗	⊗	⊗	⊗	⊗	⊗	⊗	⊗	⊗	⊗	⊗	⊗	⊗	⊗	⊗	⊗	⊗	⊗	⊗	⊗	⊗		
Laursen	24	2	32.0	0.9	0.45	⊗	⊗	⊗	⊗	⊗	⊗	⊗	⊗	⊗	⊗	⊗	⊗	⊗	⊗	⊗	⊗	⊗	⊗	⊗	⊗	⊗	⊗	⊗	⊗	⊗	⊗	⊗	⊗		
Lyn	4	3	13.0	0.27	0.25	⊗	⊗	⊗	⊗	⊗	⊗	⊗	⊗	⊗	⊗	⊗	⊗	⊗	⊗	⊗	⊗	⊗	⊗	⊗	⊗	⊗	⊗	⊗	⊗	⊗	⊗	⊗	⊗	⊗	
Mayer-Peter	137	11	○	○	○	⊗	⊗	⊗	⊗	⊗	⊗	⊗	⊗	⊗	⊗	⊗	⊗	⊗	⊗	⊗	⊗	⊗	⊗	⊗	⊗	⊗	⊗	⊗	⊗	⊗	⊗	⊗	⊗	⊗	
Nomicos	27	3	13.30	0.27	0.25	⊗	⊗	⊗	⊗	⊗	⊗	⊗	⊗	⊗	⊗	⊗	⊗	⊗	⊗	⊗	⊗	⊗	⊗	⊗	⊗	⊗	⊗	⊗	⊗	⊗	⊗	⊗	⊗	⊗	⊗
Stein	59	1	30.8	1.2	0.6	⊗	⊗	⊗	⊗	⊗	⊗	⊗	⊗	⊗	⊗	⊗	⊗	⊗	⊗	⊗	⊗	⊗	⊗	⊗	⊗	⊗	⊗	⊗	⊗	⊗	⊗	⊗	⊗	⊗	⊗
Vanoni-Brooks	16	1	19.5	0.85	0.3	⊗	⊗	⊗	⊗	⊗	⊗	⊗	⊗	⊗	⊗	⊗	⊗	⊗	⊗	⊗	⊗	⊗	⊗	⊗	⊗	⊗	⊗	⊗	⊗	⊗	⊗	⊗	⊗	⊗	⊗
Williams	177	1	15.8	1.19	⊕	⊗	⊗	⊗	⊗	⊗	⊗	⊗	⊗	⊗	⊗	⊗	⊗	⊗	⊗	⊗	⊗	⊗	⊗	⊗	⊗	⊗	⊗	⊗	⊗	⊗	⊗	⊗	⊗	⊗	⊗
Wang-Qian	23	4	20	0.3	0.4	⊗	⊗	⊗	⊗	⊗	⊗	⊗	⊗	⊗	⊗	⊗	⊗	⊗	⊗	⊗	⊗	⊗	⊗	⊗	⊗	⊗	⊗	⊗	⊗	⊗	⊗	⊗	⊗	⊗	⊗

LEGENDS:

- ⊗ Available
- Not available
- ⊙ Incomplete/some records only
- ⊕ Can be obtained from other sources

Table 1. Pure Current Situation. Laboratory Data.

Data set	No. of records	Info. on Study reach		Data format			Hydrodynamic Data				Misc. Data		Sediment Data					Bed-Form Data			Transport Data																			
		A	0	T	G	D	1	q	v	u(y)	T	1/y	d <sub>50</sub>	d <sub>1</sub>	σ <sub>g</sub>	G.C.C.	W	ρ <sub>s</sub>	C(y)	Type	b	1	a	q <sub>b</sub>	q <sub>t</sub>															
Anderson	6	●		⊗		⊗		⊗		⊗		⊗		⊗		⊗		⊗		⊗		⊗		⊗		⊗		⊗		⊗		⊗		⊗		⊗		⊗		
Colby-Hembree	~160	⊗		⊗		⊗		⊗		⊗		⊗		⊗		⊗		⊗		⊗		⊗		⊗		⊗		⊗		⊗		⊗		⊗		⊗		⊗		
Culbertson et al.	23	⊗		⊗		⊗		⊗		⊗		⊗		⊗		⊗		⊗		⊗		⊗		⊗		⊗		⊗		⊗		⊗		⊗		⊗		⊗		
Nordin-Dempster	26	●		⊗		⊗		⊗		⊗		⊗		⊗		⊗		⊗		⊗		⊗		⊗		⊗		⊗		⊗		⊗		⊗		⊗		⊗		⊗
Scott-Stephens	27	⊗		⊗		⊗		⊗		⊗		⊗		⊗		⊗		⊗		⊗		⊗		⊗		⊗		⊗		⊗		⊗		⊗		⊗		⊗		⊗

Table 2. Pure Current Situation. Field Data.

Data set	No. of records	No. of dimensions		Tunnel		Data format				Hydrodynamic Data				Misc. Data		Sediment Data					Bed-Form Data			Transport Data														
		L	W	H	H	T	G	a.0	U.0	T	q	v	u(y)	T	1/y	d <sub>50</sub>	d <sub>1</sub>	σ <sub>g</sub>	G.C.C.	W	ρ <sub>s</sub>	C(y)	Type	b	1	a	q <sub>b</sub>	q <sub>t</sub>										
Hayakawa et al.	5	1	6.0	0.50	1.10	⊗		⊗		⊗		⊗		⊗		⊗		⊗		⊗		⊗		⊗		⊗		⊗		⊗		⊗		⊗		⊗		⊗
Horikawa et al.	8	6	2.0	0.25	0.25	⊗		⊗		⊗		⊗		⊗		⊗		⊗		⊗		⊗		⊗		⊗		⊗		⊗		⊗		⊗		⊗		⊗
Murray et al.	8	1	9.0	0.50	2.30	⊗		⊗		⊗		⊗		⊗		⊗		⊗		⊗		⊗		⊗		⊗		⊗		⊗		⊗		⊗		⊗		⊗
Nakato et al.	3	1	1.5	0.20	0.25	⊗		⊗		⊗		⊗		⊗		⊗		⊗		⊗		⊗		⊗		⊗		⊗		⊗		⊗		⊗		⊗		⊗
Riberink-Al Saiem	29	1	14.	0.30	0.80	⊗		⊗		⊗		⊗		⊗		⊗		⊗		⊗		⊗		⊗		⊗		⊗		⊗		⊗		⊗		⊗		⊗
Sato-Horikawa	75	1	1.1	0.24	0.24	⊗		⊗		⊗		⊗		⊗		⊗		⊗		⊗		⊗		⊗		⊗		⊗		⊗		⊗		⊗		⊗		⊗
Sawanoto-Yamashita	22	5	1.7	0.15	0.30	⊗		⊗		⊗		⊗		⊗		⊗		⊗		⊗		⊗		⊗		⊗		⊗		⊗		⊗		⊗		⊗		⊗
Sleath	13	2	1.8	0.45	0.45	⊗		⊗		⊗		⊗		⊗		⊗		⊗		⊗		⊗		⊗		⊗		⊗		⊗		⊗		⊗		⊗		⊗
Staub et al.	41	2	10.	0.39	0.36	⊗		⊗		⊗		⊗		⊗		⊗		⊗		⊗		⊗		⊗		⊗		⊗		⊗		⊗		⊗		⊗		⊗
Steetzel	63	1	4.1	0.30	0.40	⊗		⊗		⊗		⊗		⊗		⊗		⊗		⊗		⊗		⊗		⊗		⊗		⊗		⊗		⊗		⊗		⊗
Van Der Velde	91	3	4.1	0.30	0.40	⊗		⊗		⊗		⊗		⊗		⊗		⊗		⊗		⊗		⊗		⊗		⊗		⊗		⊗		⊗		⊗		⊗

Table 3. Wave Tunnel Data.

Data set	No. of records	No. of wave mounds	Flume dimensions			Data format		Hydrodynamic Data					Misc. Data				Sediment Data				Bed-Form Data			Transport Data											
			L	W	H	T	G	D	H <sub>i</sub>	T <sub>i</sub>	Br.	X <sub>B</sub>	S	q	v	η(t)	ū(y,t)	u	d <sub>50</sub>	d <sub>i</sub>	σ <sub>g</sub>	G.C.C.	W	ρ <sub>s</sub>	d <sub>50</sub>	C(y,t)	h	i	a	q <sub>b</sub>	q <sub>s</sub>	q <sub>t</sub>			
Bosman-Steetzel	134	1	50	1	1	⊗	⊗	⊗	⊗	⊗	⊗	⊗	⊗	⊗	⊗	⊗	⊗	⊗	⊗	⊗	⊗	⊗	⊗	⊗	⊗	⊗	⊗	⊗	⊗	⊗	⊗	⊗	⊗	⊗	
Dette-Uliczka	13	1	324	5	7	⊗	⊗	⊗	⊗	⊗	⊗	⊗	⊗	⊗	⊗	⊗	⊗	⊗	⊗	⊗	⊗	⊗	⊗	⊗	⊗	⊗	⊗	⊗	⊗	⊗	⊗	⊗	⊗	⊗	
Nep-van Kampen	29	1	45	0.8	1	⊗	⊗	⊗	⊗	⊗	⊗	⊗	⊗	⊗	⊗	⊗	⊗	⊗	⊗	⊗	⊗	⊗	⊗	⊗	⊗	⊗	⊗	⊗	⊗	⊗	⊗	⊗	⊗	⊗	⊗
Nieuwjaar-van der Kraak	29	1	45	0.8	1	⊗	⊗	⊗	⊗	⊗	⊗	⊗	⊗	⊗	⊗	⊗	⊗	⊗	⊗	⊗	⊗	⊗	⊗	⊗	⊗	⊗	⊗	⊗	⊗	⊗	⊗	⊗	⊗	⊗	⊗
Ssafel-Krishnan	9	1	10	0.3	0.6	⊗	⊗	⊗	⊗	⊗	⊗	⊗	⊗	⊗	⊗	⊗	⊗	⊗	⊗	⊗	⊗	⊗	⊗	⊗	⊗	⊗	⊗	⊗	⊗	⊗	⊗	⊗	⊗	⊗	⊗
Steetzel	61	1	233	0.8	1	⊗	⊗	⊗	⊗	⊗	⊗	⊗	⊗	⊗	⊗	⊗	⊗	⊗	⊗	⊗	⊗	⊗	⊗	⊗	⊗	⊗	⊗	⊗	⊗	⊗	⊗	⊗	⊗	⊗	⊗
Vellinga	41	1	233	0.8	1	⊗	⊗	⊗	⊗	⊗	⊗	⊗	⊗	⊗	⊗	⊗	⊗	⊗	⊗	⊗	⊗	⊗	⊗	⊗	⊗	⊗	⊗	⊗	⊗	⊗	⊗	⊗	⊗	⊗	⊗

Table 4. Waves (+ Current) Situation. Laboratory Data.

Data set	No. of records	Beach Data			Data format		Hydrodynamic Data					Misc. Data				Sediment Data				Bed-Form Data			Transport Data													
		P	O	G	T	G	D	H <sub>i</sub>	T <sub>i</sub>	Br.	X <sub>B</sub>	γ	S <sub>j</sub>	V <sub>j</sub>	η(t)	ū(y,t)	u <sub>j</sub>	d <sub>50</sub>	d <sub>i</sub>	σ <sub>g</sub>	G.C.C.	W	ρ <sub>s</sub>	d <sub>50</sub>	C(y,t)	h	i	a	q <sub>b</sub>	q <sub>s</sub>	q <sub>t</sub>					
Downing	20	⊗	⊗	⊗	⊗	⊗	⊗	⊗	⊗	⊗	⊗	⊗	⊗	⊗	⊗	⊗	⊗	⊗	⊗	⊗	⊗	⊗	⊗	⊗	⊗	⊗	⊗	⊗	⊗	⊗	⊗	⊗	⊗	⊗	⊗	
Fairchild	~700	⊗	⊗	⊗	⊗	⊗	⊗	⊗	⊗	⊗	⊗	⊗	⊗	⊗	⊗	⊗	⊗	⊗	⊗	⊗	⊗	⊗	⊗	⊗	⊗	⊗	⊗	⊗	⊗	⊗	⊗	⊗	⊗	⊗	⊗	⊗
Jaffe et. al.	7	⊕	⊕	⊕	⊕	⊕	⊕	⊕	⊕	⊕	⊕	⊕	⊕	⊕	⊕	⊕	⊕	⊕	⊕	⊕	⊕	⊕	⊕	⊕	⊕	⊕	⊕	⊕	⊕	⊕	⊕	⊕	⊕	⊕	⊕	⊕
Kana-Ward	13	⊗	⊗	⊗	⊗	⊗	⊗	⊗	⊗	⊗	⊗	⊗	⊗	⊗	⊗	⊗	⊗	⊗	⊗	⊗	⊗	⊗	⊗	⊗	⊗	⊗	⊗	⊗	⊗	⊗	⊗	⊗	⊗	⊗	⊗	⊗
Kos'yan	15	⊗	⊗	⊗	⊗	⊗	⊗	⊗	⊗	⊗	⊗	⊗	⊗	⊗	⊗	⊗	⊗	⊗	⊗	⊗	⊗	⊗	⊗	⊗	⊗	⊗	⊗	⊗	⊗	⊗	⊗	⊗	⊗	⊗	⊗	⊗
Nielsen	65	⊗	⊗	⊗	⊗	⊗	⊗	⊗	⊗	⊗	⊗	⊗	⊗	⊗	⊗	⊗	⊗	⊗	⊗	⊗	⊗	⊗	⊗	⊗	⊗	⊗	⊗	⊗	⊗	⊗	⊗	⊗	⊗	⊗	⊗	⊗
Owen-Thorn	360	⊗	⊗	⊗	⊗	⊗	⊗	⊗	⊗	⊗	⊗	⊗	⊗	⊗	⊗	⊗	⊗	⊗	⊗	⊗	⊗	⊗	⊗	⊗	⊗	⊗	⊗	⊗	⊗	⊗	⊗	⊗	⊗	⊗	⊗	⊗

Table 5. Waves (+ Current) Situation. Field Data.

It appears that the obtention of suitable data under the combined action of waves and current in the field will require the careful planning of comprehensive survey campaigns, most probably involving the participation of a large number of researchers with interest in the different aspects related to the phenomena of sediment transport in the marine environment. In this connection, and whenever new experiments aiming to the collection of sediment transport data are being planned, the interaction between researchers and modellers can only be of mutual benefit, and would render the data sets useful for a larger number of potential users.

### Acknowledgement

The present work was undertaken as part of the MAST G6 Coastal Morphodynamics research programme. It was founded jointly by the Danish Technical Research Council (STVF) and by the Commission of the European Communities, Directorate General for Science, Research and Development, under MAST contract no. 0035-C.

### References

- Anderson, A.G.** (1942): "Distribution of suspended sediment in a natural stream". Transaction American Geophysical Union, pp. 678-683.
- Barton, J.R. and Lin P.N.** (1955): "A study of the sediment transport in alluvial channels". Report No. CEF 55 JRB2, Colorado State University, Fort Collins, Colorado, 41 pp.
- Bosman, J.J. and Steetzel, H.J.** (1986): "Time and bed averaged concentrations under waves". Proceedings 20<sup>th</sup> Coastal Engineering Conference, Taipei, Taiwan, pp. 986-1000.
- Colby, B.R. and Hembree, C.H.** (1955): "Computations of total sediment discharge, Niobrara River near Cody, Nebraska". U.S. Geological Survey Water Supply Paper 1357, 187 pp.
- Culbertson, J.K., Scott, C.H. and Bennet, J.P.** (1972): "Summary of alluvial-channel data from Rio Grande conveyance channel, New Mexico, 1965-69". U.S. Geological Survey Professional Paper 562-J, 49 pp.
- Detle, H.H. and Uliczka, K.** (1986): "Wave induced interactions between foreshore and coastal structure" (in German). Technical Reports No. 1-4. SBF 205/TP A6. University of Hannover.
- Downing, J.P.** (1984): "Suspended sand transport on a dissipative beach". Proceedings 19<sup>th</sup> Coastal Engineering Conference, Houston, Texas, U.S.A., pp. 1765-1781.
- Fairchild, J.C.** (1977): "Suspended sediment in the littoral zone at Ventnor, New Jersey, and Nags Head, North Carolina". Technical Paper No. 77-5, CERC.
- Guy, H.P., Simons, D.B. and Richardson, E.V.** (1966): "Summary of alluvial channel data from flume experiments, 1956-61". U.S. Geological Survey Professional Paper 462-I.
- Hayakawa, N., Tsujimoto, G. and Hashimoto, H.** (1983): "Velocity distribution and suspended sediment concentration over large scale ripples". Coastal Engineering in Japan, Vol. 26, pp. 91-100.
- Horikawa, K., Watanabe A. and Katori, S.** (1982): "Sediment transport under sheet flow conditions". Proceedings 18<sup>th</sup> Coastal Engineering Conference, Cape Town, South Africa, pp. 1335-1352.
- Jaffe, B.E., Sternberg, R.W. and Sallenger, A.H.** (1984): "The role of suspended sediment in shore-normal beach profile changes". Proceedings 19<sup>th</sup> Coastal Engineering Conference, Houston, Texas, U.S.A., pp. 1983-1996.

- Kana, T.H. and Ward, L.G.** (1980): "Nearshore suspended sediment load during storm and post-storm conditions". Proceedings 17<sup>th</sup> Coastal Engineering Conference, Sydney, Australia, pp. 1158-1174.
- Kos'yan, R.D.** (1985): "Vertical distribution of suspended sediment concentrations seaward of the breaking zone". Coastal Engineering 9 (2), pp. 171-187.
- Laursen, E.M.** (1957): "An investigation of the total sediment load". Final Report to the Office of Naval Research, Washington. Iowa Institute of Hydraulic Research, State University of Iowa, Iowa.
- Lyn, D.A.** (1986): "Turbulence and turbulent transport in sediment-laden open-channel flows". Report No. KH-R-49, W.M. Keck Laboratory of Hydraulics and Water Resources, CALTECH, Pasadena, California, 244 pp.
- Meyer-Peter, E. and Müller, R.** (1948): "Formulas for bed load transport". Proceedings Second Meeting of the International Association for Hydraulic Structures Research, Stockholm, 26 pp.
- Murray, P.B., Davies, A.G. and Soulsby, R.L.** (1991): "Sediment pick-up in wave and current flows". Proceedings of Euromech 262-Sand Transport in Rivers, Estuaries and the Sea. Soulsby and Bettess Eds. Balkema, Rotterdam.
- Nakato, T., Locher, F.A., Glover, J.R. and Kennedy, J.F.** (1977): "Wave entrainment of sediment from rippled beds". Journal of the Waterway, Port, Coastal and Ocean Div., ASCE, Vol. 103, No. WW1, pp. 83-99.
- Nap, E.M. and van Kampen, H.F.A.** (1988): "Sediment concentrations and sediment transport in case of irregular non-breaking waves with a current". Technical University Delft, Coastal Engineering Department.
- Nielsen, P.** (1984): "Field measurements of time-averaged suspended sediment concentrations under waves". Coastal Engineering 8 (1), pp. 51-72.
- Nieuwjaar, M.W.C. and van der Kaaij, Th.** (1987): "Sediment concentrations and sediment transport in case of irregular non-breaking waves with a current". Technical University Delft, Civil Engineering Department.
- Nomicos, G.N.** (1956): "Effects of sediment load on the velocity field and friction factor of turbulent flow in an open channel". Ph. D. thesis, California Institute of Technology, Pasadena, U.S.A.
- Nordin, C.F. and Dempster, G.R.** (1963): "Vertical distribution of velocity and suspended sediment, Middle Rio Grande, New Mexico". U.S. Geological Survey Professional Paper 462-B, 20 pp.
- Owen, M.W. and Thorn, M.F.C.** (1978): "Effect of waves on sand transport by currents". Proceedings 16<sup>th</sup> Coastal Engineering Conference, Hamburg, Germany, pp. 1675-1687.
- Ribberink, J.S. and Al-Salem, A.** (1989): "Bedforms, near-bed sediment concentrations and sediment transport in simulated regular waves conditions". Report No. H 840 Part III, Delft Hydraulics.
- Sato, S. and Horikawa, K.** (1986): "Laboratory study of sand transport over ripples due to asymmetric oscillatory flows". Proceedings 20<sup>th</sup> Coastal Engineering Conference, Taipei, Taiwan, pp. 1481-1495.
- Sawamoto, S. and Yamashita, T.** (1986): "Sediment transport rate due to wave action". Journal of Hydroscience and Hydraulic Engineering, Vol. 4, No. 1, pp. 1-15.
- Skafel, M.G. and Krishnappan, B.G.** (1984): "Suspended sediment distribution in wave field". Journal of the Waterway, Port, Coastal and Ocean Division, ASCE, Vol. 110, No. 2, pp. 215-230.



- Scott, C.H. and Stephens, H.D.** (1966): "Special sediment investigations, Mississippi River at St. Louis, Missouri, 1961-1963". U.S. Geological Survey Water Supply Paper 1819-J, 35 pp.
- Sleath, J.F.A.** (1982): "The suspension of sand by waves". *Journal of Hydraulic Research*, Vol. 20, No. 5, pp. 439-452.
- Staub, C., Jonsson I.G. and Svendsen I.A.** (1984): "Variation of sediment suspension in oscillatory flow". *Proceedings 19<sup>th</sup> Coastal Engineering Conference*, Houston, Texas, U.S.A., pp. 2310-2321.
- Steetzel, H.** (1984): "Near-bottom sediment suspension under oscillatory water motion" (in Dutch). M.Sc. thesis, Technical University of Delft, Civil Engineering Department, Coastal Division.
- Steetzel, H.** (1987): "Systematic investigation of dune revetments - Large scale tests in the Delta Flume" (in Dutch). Report No. H 298 Part I, Delft Hydraulics.
- Stein, R.A.** (1965): "Laboratory studies of total load and apparent bed load". *Journal of Geophysical Research*, Vol. 70, No. 8, pp. 1831-1842.
- Van der Velden, E.T.J.M.** (1987): "Near-bottom sediment suspension under oscillatory water motion" (in Dutch). M. Sc. thesis, Technical University of Delft, Civil Engineering Department, Coastal Division.
- Vanoni, V.A. and Brooks, N.H.** (1957): "Laboratory studies of the roughness and suspended load of alluvial streams". Report No. E-68, Sedimentation Laboratory, California Institute of Technology, Pasadena, U.S.A.
- Vellinga, P.** (1984): "Large-scale dune erosion tests in the Delta Flume" (in Dutch). Report No. M 1263 Parts III A and III B, Delft Hydraulics.
- Williams, G.P.** (1970): "Flume width and water depth effects in sediment-transport experiments". U.S. Geological Survey Professional Paper 562-H, 37 pp.
- Wang, X. and Qian N.** (1992): "Velocity profiles of sediment-laden flow". *International Journal of Sediment Research*, Vol. 7, No. 1, pp. 27-58.
- Zyserman, J., Fredsøe, J., Deigaard, R. and Hedegaard, I.B.** (1991 a): "Requirements to a sediment transport model for morphological modelling". *Proceeding Second International Conference on Computer Modelling in Ocean Engineering*, Barcelona, Spain. Balkema, Rotterdam, pp. 261-270.
- Zyserman, J., van Rijn L.C., Whitehouse R.J.S. and Latteux B.** (1991 b): "A critical review of suspended sediment transport data in waves and current". Prepared under the MAST G6 Coastal Morphodynamics research programme.

## CHAPTER 198

### A feasibility study of a perched beach concept in the Netherlands

Joost H.M. de Ruig<sup>1</sup>, Piet Roelse<sup>2</sup>

#### **Abstract.**

The present Dutch coastal defence policy is aimed at a full compensation of shoreline retreat, mostly by means of beach nourishment. For some parts of the coast with a small dune ridge attacked by severe erosion, a so-called 'seaward coastal defence strategy' might be more profitable. According to this strategy, measures will be taken to influence the morphological system in such a way that erosion is prevented, which will result in a stable or even progressive coastline.

An analytical policy design was chosen at the onset of the study. A number of seaward coastal defence measures will be tested following a series of selected criteria, such as effects on morphological, financial and construction aspects as well as effects on recreation and ecology. The study works from 'coarse' (entire province of Zeeland, SW-Netherlands; different coastal defence alternatives) to 'fine' (selected location; preferred coastal defence alternative). This has resulted in conclusions and recommendations with regard to the feasibility of a pilot project with a perched beach in the 'Cadzand' area.

#### **1. Introduction.**

##### **1.1 A new coastal defence policy for the Netherlands**

Major parts of the Netherlands are situated below sea level and would be flooded if there was no protection by a coastal defence

---

<sup>1</sup> Rijkswaterstaat, Tidal Waters Division, P.O.Box 20907, 2500 EX The Hague, The Netherlands

<sup>2</sup> Rijkswaterstaat, Tidal Waters Division, P.O.Box 8039, 4330 EA Middelburg, The Netherlands

system. This system consists of dunes and dikes to protect the polders and dams to close off large (former) tidal inlets. The dunes represent about 75% of this line of defence, varying in width from one hundred metres to several kilometres. They give the Netherlands its characteristic landscape and harbour unique natural values for the Northwest of Europe. They also represent an economic value: drinking water supply, recreation, industry and residential.

At present the Dutch coast is 'Delta safe'. It can withstand extreme storms and the associated water levels and waves with a frequency of 1/2000 to 1/10000 per year. This level of safety must be maintained. Constant effort is demanded, as ongoing coastal erosion causes almost half of the coastline to recede, slowly but relentlessly.

Past coastal defence was based on a problem solving policy. For large parts of the coastline, recession was tolerated: dunes underwent 'controlled retreat'. Interests and natural values in the dune area were affected to an increasing extent. Furthermore, sea dikes and other hard barriers came to protrude like bulwarks into the sea.

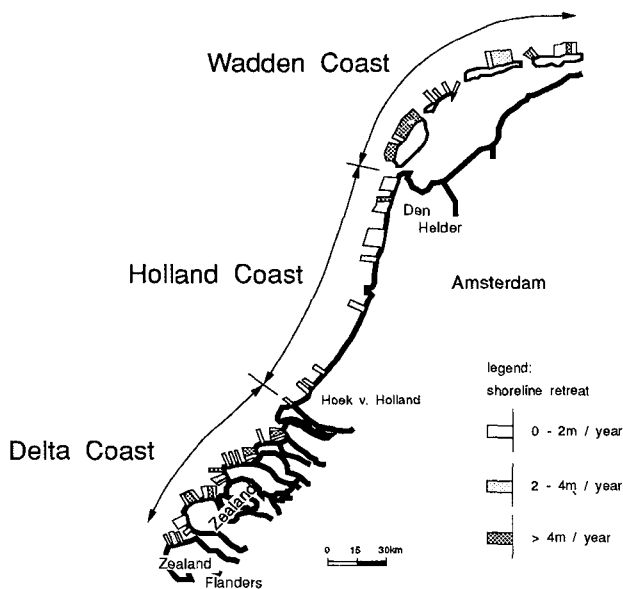


Figure 1. Pattern of erosion along the Dutch coast (Louisse & Kuik, 1990).

Coastal erosion is evident along the entire coastline: more than 50% of the dune coast suffers erosion (figure 1). A more rapid sea level rise will be felt everywhere, resulting in erosion along 80% of the sandy coastline. Not one function of the coast will be left untouched. This problem requires a reconsideration of the coastal policy. The options vary from no protection to full protection of all interests and values:

- Retreat: Coastal erosion is accepted unless polder safety is threatened;
- Selective Preservation: Special values and interests in the dune area are protected;
- Preservation: Coastal erosion is counteracted at all locations;
- Expansion Seaward: Preservation, but at some markedly eroding coastal sections with a relatively weak sea defence the coast will be reinforced by a seaward construction and natural sand sedimentation will be encouraged.

In 1990 the Dutch government made a choice for the 'preservation' alternative, which implies that the coastline will, at the least, be preserved at its 1990 position: all structural erosion will be counteracted (Ministry of Transport, Public Works and Water Management, 1990; Louisse & Kuik, 1990).

## 1.2 Dynamic preservation

By nature, the coastline of a dune coast is not fixed at one single position. Choosing for 'preservation', some allowance should be made for movements of the coastline. At some locations more aeolian dynamics (sand drifts, blow-outs, mobile dunes) will be permitted and so-called 'slufters' (wet dune valleys influenced by the tides) can be formed.

By lending the 'preservation' alternative a certain degree of dynamics, the charm and quality of the natural coasts will be safeguarded: 'preservation' changes into 'dynamic preservation'. The choice for sand nourishments, a 'soft' coastal defence method, as the major means to defend the coast is in line with this philosophy.

## 1.3 Seaward coastal defence strategy

Some parts of the Dutch coast are facing extreme erosion as well as very poor safety reserves. For these locations the application of the 'expansion seaward' alternative can be more profitable or (in time) even necessary, for instance with respect to sea level rise.

This approach is roughly investigated as the 'seaward coastal defence strategy'. According to this strategy, additional measures will be taken to influence the morphological system in such a way that the coastline will not erode any longer, but be kept in

place or even grow in a seaward direction. The effectiveness of this approach has to be compared with maintenance by beach nourishment, as well as the effects it will have elsewhere on the morphological system, nature and other interests (Pluijm, 1990).

#### 1.4 Feasibility study: working from 'coarse' to 'fine'

The difference between the several morphological systems along the Dutch coast makes it impossible to suffice with one seaward solution. In order to gain more insight into these possibilities, plans have been worked out for the most vulnerable locations.

There are two main reasons to realize these plans within the framework of a feasibility study:

- the choice for beach nourishment as the general way to keep the coast-line in its place; along each kilometre of the coast this will be the reference for other coastal defence measures;
- in principle, the effects of seaward constructions on the morphological system, nature and other interests are unknown.

The aim of the feasibility study is to select locations in Zeeland (province in the southwest of the Netherlands) where:

- in practice beach nourishment cannot stop the structural erosion, or:
- (in time) the costs of combating erosion for a seaward approach are less than for beach nourishment, and if so:
- the possible seaward construction will not have any severe negative effect elsewhere.

A stepwise working method is used in this feasibility study. That is, we work from 'coarse' (large scale: entire province of Zeeland; different coastal defence alternatives) to 'fine' (small scale: selected location; preferred seaward construction). This intention is reflected in the headings of the following chapters.

## 2. Possibilities for seaward coastal defence in Zeeland.

### 2.1 The Zeeland coast: an introduction

The Dutch coast is composed of three major units. In the south the Delta coast, consisting of (former) deltas and islands; between Hoek van Holland and Den Helder a stretch of coast not interrupted by tidal inlets (the Holland coast); and in the north the Wadden coast, consisting of series of coastal barrier islands with tidal inlets in between (see figure 1).

The province of Zeeland lies entirely within the Delta area. Its defence system is composed of dunes and dikes, which protect the

polders and dams which close off large estuaries and basins and which have been constructed during the last decades ('the Delta works'). The implementation of these works has induced major changes in hydraulic conditions and the geomorphology of the former ebb tidal deltas (Mulder et al., 1990). Although the shoals in the ebb deltas protect the coast against severe wave attack, the shifting of deep tidal channels causes much erosion. Along these channels very steep shorefaces and small beaches occur, with only little space available for nourishment. Most of the coastal sections with narrow dune ridges are protected with groynes to reduce the coastline withdrawal.

One of the estuaries in the Delta area, the Western Scheldt, is still open, being the shipping entrance to Antwerp. The estuary mouth is an active system of bars and gullies, with important impacts in the form of coastline undulations on the adjacent coastal stretches of Walcheren en Zeeland Flanders (figure 2).

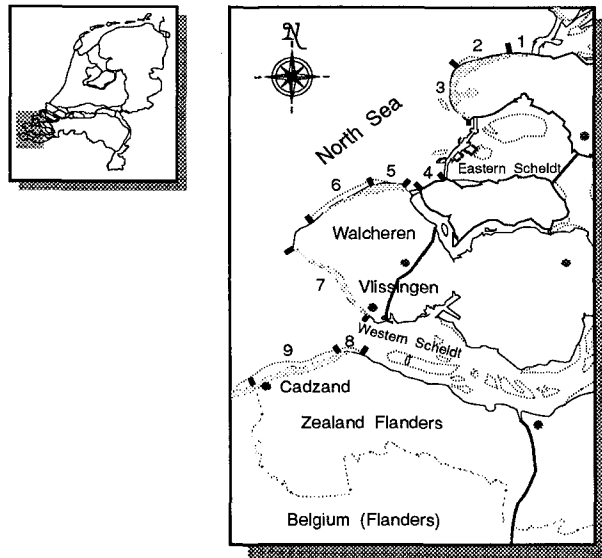


Figure 2. Division of the Zeeland coast used in the feasibility study.

## 2.2 Method

Due to the differences in morphology of the coastal zone and shoreface, the Zeeland coast has been divided into nine sections (figure 2). In this way, the necessity of a seaward defence could be determined for each section.

Ten coastal defence constructions were selected, including large dams perpendicular as well as parallel to the coastline, artifi-

cial channel shifting and perched beaches. Seven of these constructions are illustrated in figure 3.

Coastal erosion is the result of the boundary conditions of waves and tide and the resistance of the coast to these conditions. Some of the selected measures, for instance breakwaters, will act like a screen and diminish the incoming wave height. In the problem area these constructions give rise to good results. Usually, this induces a shortage of sand somewhere else, which will diminish the overall gain. Other measures will raise the resistance temporarily (beach nourishment) or permanently (shoreface protection). A perched beach shows both principles.

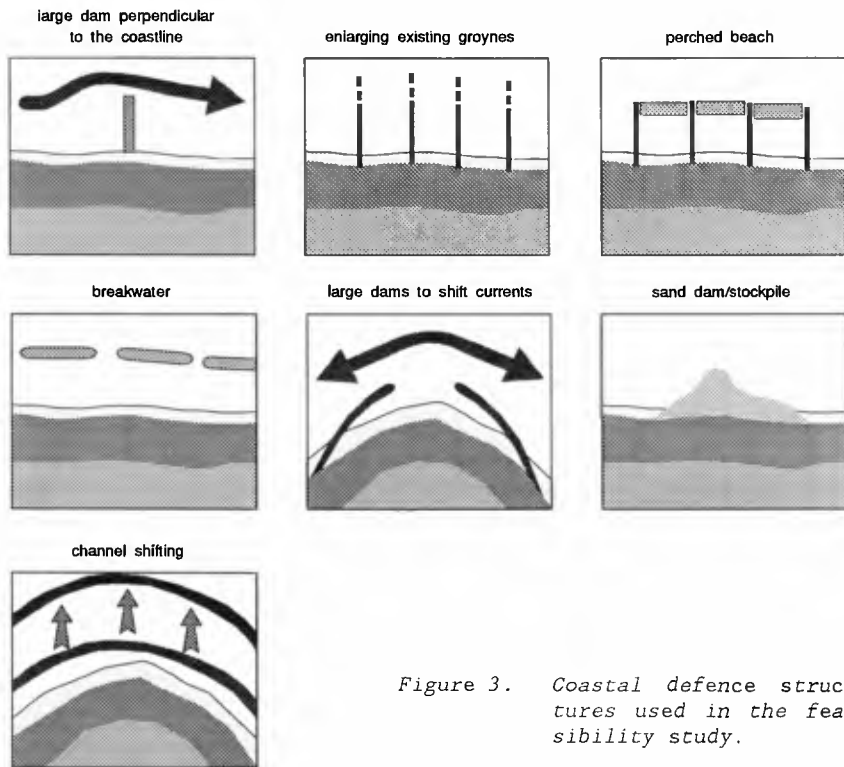


Figure 3. Coastal defence structures used in the feasibility study.

For each coastal section these measures were tested for different criteria and scored within a matrix (Maranus et al., 1990):

- effectiveness;
- effects on other functions and values in the coastal zone;
- costs (initial and maintenance); nullification of capital;
- flexibility and stability;
- consequences for coastal management;
- risk.

Each judgement was based on a rough estimation of the consequences a measure should have for a concerned criterion. For the purpose of the first step in a feasibility study, this seems sufficient.

### 2.3 Results

The method used selects the most promising measures for each coastal section. The necessity to intervene, however, varies and depends on the erosion rate. Both elements combined resulted in three coastal defence measures which could be more effective than beach nourishment. Among them, a perched beach concept for the coasts of SW-Walcheren and Zeeland Flanders was considered for further study.

### 3. A perched beach: theory, effects and experiences.

In general, a perched beach construction consists of a coast parallel dam (breakwater) with a sand nourishment at the landward side of it. Sometimes the nourished beach has been closed off at its extremities by groynes or large dams. In Japan and the U.S.A. it is considered as a new phase in coastal defence systems. It is based on the concept that a 'plane', rather than a 'linear structure', is able to protect the shore effectively (figure 4; Arai & Tamura, 1987; Sawaragi, 1988). The dam and the nourished beach gradually absorb the wave energy, giving the beach a more stable equilibrium profile, resulting in less erosion. The coastal defence system is strengthened and the beach is widened, which gives opportunities for recreation.

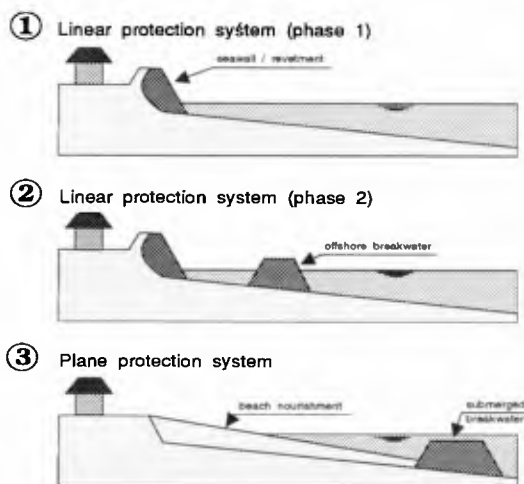


Figure 4. Evolving coastal defence: from 'linear protection system' to 'plane protection system' (after Arai & Tamura, 1987).



During the last decades some experience has been acquired with perched beaches, especially in the United States and Japan. The construction was applied with varying success. Besides the mentioned benefits, some disadvantages became clear:

- development of scour holes on either side of the dam (Sawaragi et al., 1988; Delft Hydraulics, 1990; Franco, 1990);
- blocking of natural beach nourishment during fair weather periods (Douglass & Weggel, 1987);
- possible danger for swimmers and small boats;
- high investments (with respect to beach nourishment).

#### 4. Seaward coastal defence in Zeeland Flanders.

##### 4.1 Defence alternatives

The coast of Zeeland Flanders is bordered by the main tidal channel of the Western Scheldt estuary, the Wielingen (figure 5). During the last centuries, widening and southward displacement of the channel induced a great loss of land.

Today, the 15 km long coastline and adjacent dikes and small dune ridges are defended by 85 groynes, each with a length of about 200 to 300 m. and a spacing of 100 to 300 m.

The shoals in the ebb delta protect the coast against severe wave attack; the maximum yearly significant wave height is about 3 m. The mean tidal difference reaches 3.7 m. Close to the shore, the maximum flood and ebb current amounts to 1.0 - 1.2 m/s.

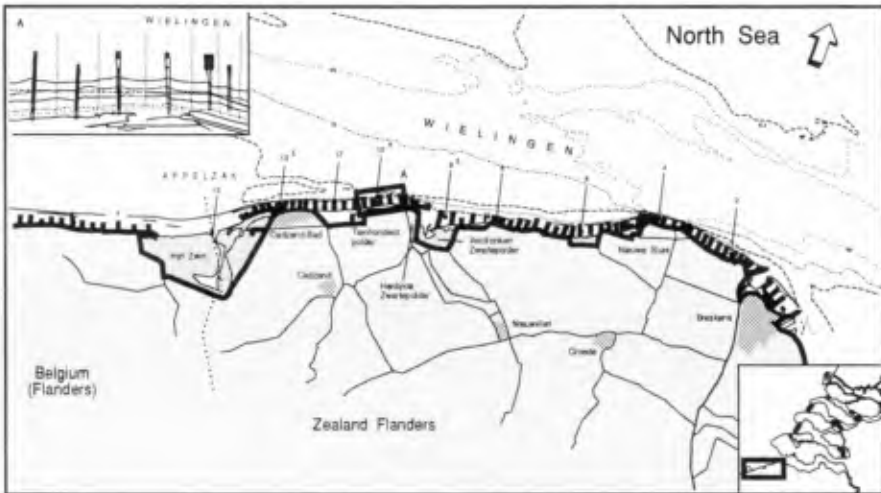


Figure 5. Zeeland Flanders.

The presence of the Wielingen dominates the coastal evolution. Up till now it caused a continuous regression of the coastline, in spite of the intense coastal defence. Superimposed, we find a second order long-term fluctuation caused by so-called 'sand waves' (Verhagen, 1989;), resulting in a pattern of periods with sedimentation and erosion (figure 6).

Nowadays, the most vulnerable section of the coast lies in the neighbourhood of the Tienhonderd Polder (figure 5). The small beach is bounded by a steep shoreface and is influenced by continuous erosion since 1960. The narrow dune ridge shows poor safety reserves. Further study on seaward coastal defence structures is focused on this part of Zeeland Flanders.

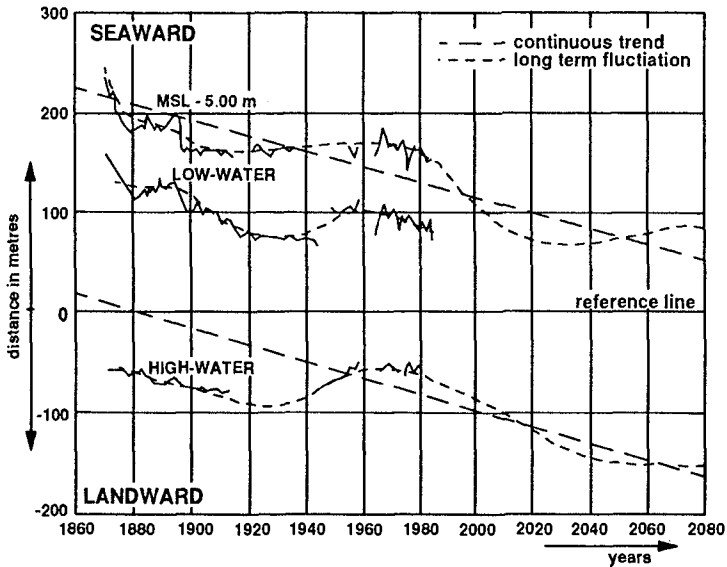


Figure 6. Tienhonderd polder, Zeeland Flanders: Patterns of sedimentation and erosion.

For Zeeland Flanders, the first step in the feasibility approach selected a perched beach concept for further study (2.1). This concept is at the centre of the next step of this strategy. Two perched beach variants are considered. Beach nourishment, as the main coastal defence measure in the present policy, is the reference. For the present, it is assumed that nourishment can indeed counteract the erosion. Other well tried or far reaching possibilities have also been taken into account, which results in the following list of measures (figure 7):

- perched beach (small);
- perched beach (medium);
- large coast parallel dam/breakwater;
- large dam perpendicular to the coast;

- shoreface protection;
- beach nourishment.

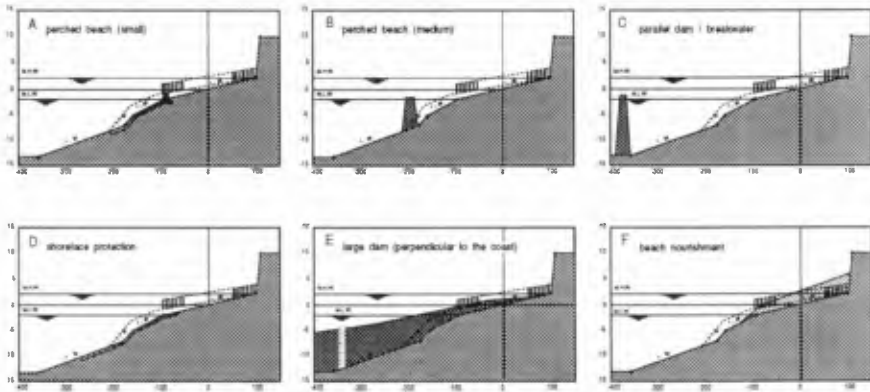


Figure 7. Tienhonderd polder, Zeeland Flanders: Possible coastal defence measures.

#### 4.2 Criteria

As in chapter 2.1, each measure has been tested for several criteria. In fact they are about the same, but testing is done with more detail. Important conditions were the effectiveness of the construction and the future erosion rate. The effectiveness was defined as the percentage of the overall erosion stopped by the construction in question. Every measure except the large dam perpendicular to the coast needs additional sand nourishments to fully counteract the structural erosion.

Indirectly, the initiation of scour holes and lee side erosion also determines the effectiveness to a high degree. Far reaching constructions such as large dams score negatively from this point of view.

The maintenance costs are directly deduced from the future erosion rate. In fact, this rate is unknown. The prediction, consisting of several variants, was based on extrapolation of the first order coastline regression and the superimposed sand waves. In general, it is expected that erosion will continue for another 30 to 40 years (figure 6). Rates of sea level rise higher than the present will lengthen this period.

The resulting costs, including additional nourishments based on the assumed future erosion rate, are brought together in table 1. It can be concluded that a large dam parallel to the coast and a medium sized perched beach cannot compete with the other coastal defence alternatives.

Table 1. Prediction of the total costs for each coastal defence alternative (Tienhonderd Polder, Zealand).

measure	costs (million dutch guilders)
beach nourishment	11 - 16
perched beach (small)	10 - 14
perched beach (medium)	16 - 19
large coast parallel dam / breakwater	48 - 58
shoreface protection	10 - 13
large dam perpendicular to the coast	14 - 15

Especially the greater constructions will influence the recreational and ecological values of the coastal area. Both threats and possibilities will develop. It is not always clear which will dominate.

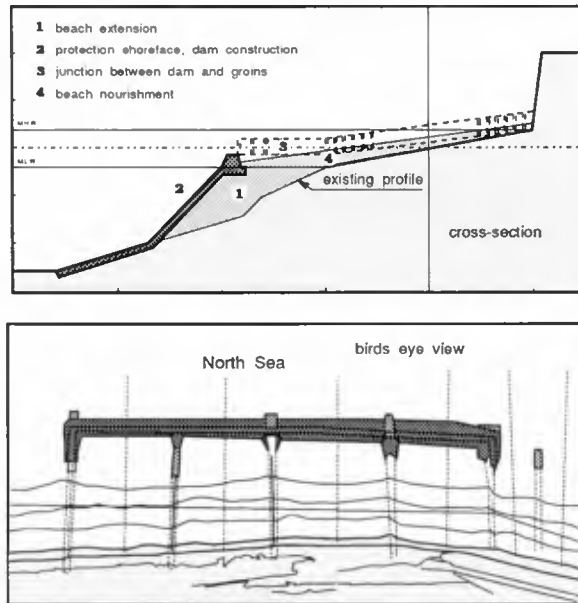


Figure 8. Tienhonderd polder, Zealand Flanders: Preferred perched beach concept.

#### 4.3 Preferred coastal defence construction

Considerations of the different aspects as mentioned above culminated in a preferred perched beach concept as shown in figure 8. In fact, the strong points of a perched beach, sand nourishment and shoreface protection are combined. First, the beach is extended in a seaward direction by means of a nourishment and will approximate his (stable) equilibrium profile. Protection of the shoreface and the construction of a small breakwater connected with the already existing groynes will conserve this situation. Erosion of the shore-face will be prevented and the landward migration of the tidal channel blocked. Finally, a complementary beach nourishment will create a perched beach. Most of this special perched beach construction is made out of sand. This yields profits from the point of view of costs and flexibility.

### 5. Perched beach concept for Zealand Flanders.

#### 5.1 Location and dimensions

The presence of the Wielingen dominates the coastal evolution. Sand losses (about  $20 \text{ m}^3/\text{m.jaar}$ ) from the coastal section of the Tienhonderd Polder are caused by seaward cross shore transport. Rip currents play an important role in this process. The sand drops into the tidal channel and is transported into the the Western Scheldt estuary.

It is expected that the perched beach construction will diminish the cross shore loss of sand and stop the landward migration of the Wielingen. The most suitable location for the breakwater and additional shoreface protection, therefore, seems to be the edge of the tidal channel. A more landward location of the breakwater will have less effect in reducing the erosion rate.

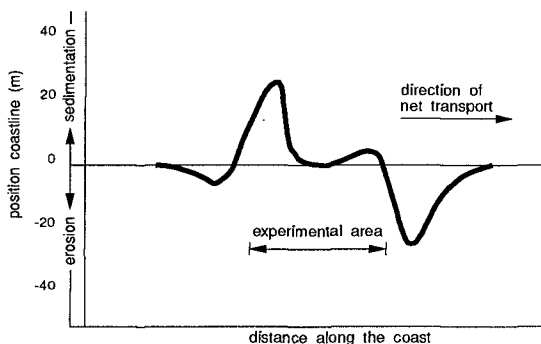


Figure 9. Effect of the perched beach construction (without additional sand nourishment) on the position of the coastline after 3 years (Delft Hydraulics, 1991).

Model computations reveal that the concept will act as an effective coastal defence measure. However, scour holes could develop at the landward side of the dam, which can reduce the effectiveness of the construction. Further study can quantify this problem. The feasibility study shows that after the construction of the perched beach sand nourishment, albeit much less in quantity, will remain necessary until about the year 2030.

The length of the coastal section with severe erosion determines the length of the construction, e.g. almost 900 metres.

As stated, the main purpose of the perched beach is to reduce the sand losses in cross shore direction. This does not mean that the long shore transport of sand remains untouched. Model computations show a distinct lee side erosion at the eastern end of the construction (figure 9; Delft Hydraulics, 1991). In practice the consequences are small. The coastline here consists of a small dike and is therefore rigid. Eastward, the dike is bordered by a nature re-serve (the 'slufter' (chapter 1.2) of the Verdrongen Zwarte polder; figure 5) that is in danger of being buried by sand.

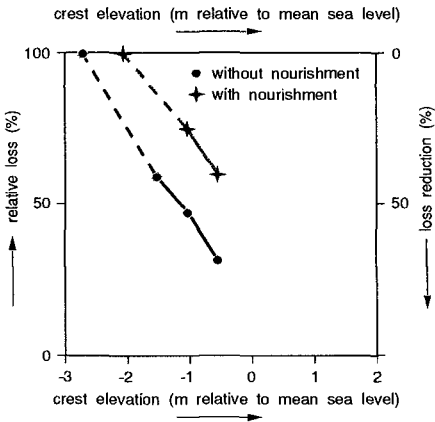


Figure 10. Relation between the crest elevation of the breakwater and the cross shore sand transport losses (Delft Hydraulics, 1991).

The level of the breakwater crest determines the loss of sand from the beach into the Wielingen tidal channel. In general, blocking this transport needs a crest height which is close to the seawater level (Lamberti et al., 1985). The tidal difference (3.7 m) complicates this thesis. Delft Hydraulics (1991) computed a 25% to 50% (with or without additional beach nourishment, respectively) reduced initial sand loss in case of a crest level of about 1 metre below MSL. The long term profits with a raised beach level are uncertain.

Roughly, each metre crest elevation means an extra 15% reduction (figure 10). However, the other side of the picture shows a more pronounced development of scour holes and higher costs and will score negatively from a recreational point of view. A breakwater crest level between 0.5 and 1.0 metre below MSL seems to be a reasonable compromise and offers good opportunities for connection with the already existing groynes.

The width of the breakwater crest is of the utmost importance in reducing the risk of a landward scour holes. Several theories calculate the most effective width under different conditions (Sawaragi, 1988; Delft Hydraulics, 1989). Especially in consideration of costs and recreation, a decision in favour of a limited width seems to be reasonable. After that a wait-and-see policy can be followed.

## 5.2 Estimate of the cost

A comparison of different construction methods showed the cheapest way of execution:

1. extend the shoreface by means of sand fill;
2. defend the exposed new shoreface by a layer of stones;
3. construct the breakwater;
4. fill up the beach and
5. connect the old groynes with the breakwater.

In case of a construction length of about 900 metres, the costs of this operation are estimated at Hfl 7,700,000 (Dutch guilders ( $\pm$  US\$ 4,500,000)). To find out if such an investment can be cost effective, the costs of construction, maintenance and additional sand nourishment are capitalized for a period of 40 years, the expected erosion period. These costs are compared with the capitalized costs of periodical beach nourishment. In fact, the effects on adjacent coastal sections must also be capitalized (policy of dynamic preservation: no structural coastline regression is allowed). However, long term effects are difficult to calculate and are therefore only qualitatively implicated in the comparison. Besides, the effects of lee side erosion within the dike section and neighbouring nature reserve will be small.

In the estimate of costs, the uncertainty of some elements play a major role:

### *future erosion rate:*

Two realistic morphological scenarios are worked out:

- S1 (neutral to pessimistic): coastline withdrawal by continuous regression and long term fluctuations ('sand waves');
- S2 (optimistic): long term coastline fluctuations only.

*effectiveness of the measure:*

The effectiveness of a perched beach in Dutch conditions is part of the feasibility study. In the Netherlands some experience with beach nourishment exists for tide dominated coasts. Based on that experience, in the design practice an effectiveness of 50% to 80% is applied (Roelse, 1990).

*cubic metre price of sand nourishment:*

In the Delta area the sand can be borrowed relatively cheap from shoals near to the shore. Based on projects in the past years prices per  $m^3$  were taken into account varying from Hfl 10 ( $\pm$  US\$ 6) for 0.5 million  $m^3$  to Hfl 14 ( $\pm$  US\$ 8) for 0.02 million  $m^3$ .

The sensitivity of the cost comparison for those variables is illustrated in figure 11. The following example is indicated: Assuming the neutral-pessimistic scenario, a  $m^3$  price of Hfl 10 and an effectiveness of beach nourishment of 80%, a perched beach has to be at least 50% effective (50% reduced erosion rate) to be cheaper than beach nourishment only. In case the coastline development is favourable (optimistic scenario) the perched beach application can only be effective if  $m^3$ -prices rise extremely.

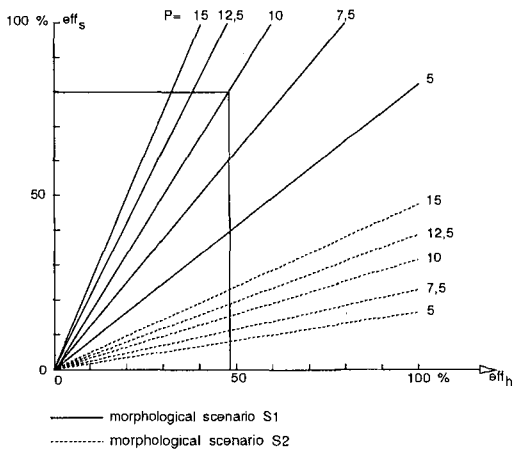


Figure 11. Effectiveness of beach nourishment ( $eff_s$ ) and perched beach ( $eff_h$ ) related to  $m^3$  sand price ( $P$ ).

### 5.3 Effects

The main effects on other interests focus on ecological aspects and recreation.

Recreation is of major importance to the region: Each year about 2 million overnight stays are registered.

The perched beach will initiate a wider beach, which is profita-



ble from a recreational point of view. However, the breakwater itself forms an obstacle for swimmers, surfers and small boats. During some phases of the tidal cycle, dangerous bathing conditions can exist, due to undesirable currents and scour holes.

Avoiding any hindrance results in a far seaward (and hence capital) position of the breakwater.

If there is an overall negative effect on recreation, the project will fit in the provincial planning. In that case, the perched beach is expected to act as a buffer between the crowded seaside resort of Cadzand in the southwest and the nature reserve in the northeast (see 5.1).

The ecological effects are small. In general the application of stonelike materials strengthens the natural diversity. Organisms attach to the stones and others will find shelters.

Biomasses on hard constructions can exceed those of sandy substrates by about 10 to 100 times. On the other hand, the existence of a(nother) stony breakwater within a sandy coast is not in line with preservation of the charm and quality of natural coasts.

#### 5.4 Surplus value and risks.

A decision in favour of a perched beach construction will initiate research results which, in principle, can be translated to other Dutch coasts bounded by tidal channels. Secondly, perched beach experiences are of great use in planning large seaward coastal constructions.

The seaward extension of the perched beach is limited: the main existing hydraulics and sediment transport paths will almost remain the same. Neighbouring coastal sections will hardly be affected.

The dike and the 'slufter' nature reserve downstream of the perched beach confine the risk for neighbouring coasts.

Nevertheless, if the construction produces unacceptable effects, a minor and easy operation can remove the breakwater, after which the material can be added to the shoreface protection.

## 6. Conclusions.

The feasibility study selects a perched beach construction as the most promising seaward coastal defence measure for the vulnerable section of the Tienhonderd Polder in Zeeland, the Netherlands. The construction will act as an effective coastal defence structure. Shoreface and beach protection can be achieved for a reasonable price and without harming the charm of the natural sandy coast. Attention should be focussed on the development of scour holes at the landward side of the dam. Sand nourishment, although

in much reduced quantities, will remain necessary until about the year 2030.

The costs appear to be the most important element and determines the success of the preferred perched beach. The result of a price comparison with beach and shoreface nourishment depends on the future erosion, the costs of sand mining and the effectiveness of both alternatives. Calculations of the total costs (including direct investments and repeated (capitalized) costs for beach nourishments for a period of 30 to 40 years) indicate that a perched beach is roughly as expensive as repeated beach nourishments alone.

The construction method and the location of the proposed perched beach considerably confine the risks of loss of functions and valuable interests within adjacent coastal sections.

In general, the appearance of a 'hard' structure within a sandy coast will score negatively from a recreational point of view because it can give rise to dangerous bathing conditions. On the other hand, the beach is widened and the use of stones will encourage the settlement of several aquatic species.

A final decision on the perched beach alternative is not expected before the summer of 1993. A 'yes' will make a more detailed research (especially of crest width and elevation) necessary.

## **7. Acknowledgements.**

Thanks are extended to Delft Hydraulics, the Waterboard Het Vrije van Sluis, the Province of Zeeland and the Road and Hydraulic Engineering Division of the Rijkswaterstaat for their contributions. Financial support by the Zeeland Directorate of the Rijkswaterstaat is also gratefully acknowledged.

## **8. Literature.**

Arai, Y., Tamura, M. (1987); Erosion control measures and beach restoration plan at the Niigata West coast. Coastal zone, 1987.

Delft Hydraulics (1989); Coastal protection plan Lido di Ostia. Rapport H 891, Delft Hydraulics-De Voorst, Emmeloord, the Netherlands.

Delft Hydraulics (1990); Beach nourishment schemes for the coast of Riccione end Cesanatico. Rapport H 725, Delft Hydraulics-De Voorst, Emmeloord, the Netherlands.

Delft Hydraulics (1991); Field experiment perched beach; preparatory study (in Dutch). Rapport H 1291, Delft Hydraulics-De Voorst, Emmeloord, the Netherlands.

Douglas, S.L., Weggel, J.R. (1987); Performance of a perched beach; Slaughter Beach, Delaware. Coastal Sediments '87, Vol. II, p.1369-1384, ed. N.C. Kraus, American Society of Civil Engineers, New York.

Franco, L. (1990); Effect of constructions on coastal morphology. CEEC course 'Coastal Morphology', Delft, 23-27 april 1990.

Lamberti, A., Petrillo, A., Ranieri, M. (1985); A comparative analysis of some types of submerged barriers as beach defence structure. 21st IAHR congress, Melbourne, Australia, 1985.

Louisse, C.J., Kuik, A.J. (1990); Coastal alternatives in the Netherlands. Coastal Engineering Conference (22nd: 1990: Delft, the Netherlands), pp 1862-1975.

Maranus, J.W., Roelse, P., Ruig, J.H.M. de (1990); Possibilities for seaward coastal defence in Zeeland (in Dutch). Discussie-notitie NXL 89-47, Rijkswaterstaat-Tidal Waters Division & Zeeland Directorate, Middelburg.

Ministry of Transport and Public Works (1990); A new coastal defence policy for the Netherlands. Ministry of Transport, Public Works and Water Management, Rijkswaterstaat, The Hague, The Netherlands.

Mulder, J.P.M., Louters, T., Hallie, F.P., Postma, R., Craeymeersch, J.A., Hamerlynck, O. (1990); Integrated coastal research in the SW Netherlands. Coastal Engineering Conference (22nd: 1990: Delft, the Netherlands), pp 2984-2997.

Pluijm, M. (1990); Seaward coastal defence for the Dutch coast. Coastal Engineering Conference (22nd: 1990: Delft, the Netherlands), pp 2010-2017.

Roelse, P., Maranus, J.W. (1988); Prediction of the coastline development in Zeeland over the period 1990-2090 (in Dutch). Nota CWWS-88.409, Rijkswaterstaat-Tidal Waters Division, Middelburg.

Roelse, P. (1990); Beach and dune nourishment in the Netherlands. Coastal Engineering Conference (22nd: 1990: Delft, the Netherlands), pp 1984-1997.

Sawaragi, T. (1988); Current shore protection works in Japan. J. of Coastal Research 4(4), 531-541. Charlottesville (Virginia).

Sawaragi, T., Deguchi, I., Park, S-K. (1988); Experimental study on the function of submerged breakwater to control cross-shore sediment transport on artificially nourished beaches. Coastal Engineering in Japan, Vol. 31, No.1.

Verhagen, H.J. (1989); Sand waves along the Dutch coast. Coastal Engineering 13, pp. 129-147.

## CHAPTER 199

### ARTIFICIAL SAND FILLS IN WATER

J. van 't Hoff<sup>1</sup>, M.B. de Groot<sup>2</sup>, J.C. Winterwerp<sup>3</sup>  
H. Verwoert<sup>4</sup> and W.T. Bakker<sup>5</sup>

#### 1 Introduction

Experience has been obtained on the construction of sand fills in water as part of several types of structures in the Netherlands. These include the following: (closure) dams, artificial islands or coastal extensions, covering of pipelines, trench back fills and the foundation of submerged tunnels and caissons.

Rijkswaterstaat (Ministry of Transport, Public Works and Watermanagement) Dutch contractors, research institutes and consultancy firms have been involved in the research, design and construction of a large number of projects in the Netherlands and abroad.

In-depth research was carried out especially within the frame work of the preparations of a number of Delta closures constructed with sand.

After the completion of the Deltaworks it seemed important not to leave this knowledge scattered over many study reports and design and evaluation notes, but rather to summarize the data and experience in a manual (Van 't Hoff (ed.) et al, 1992) issued by the Council of the Centre for Civil Engineering Research, Codes and Specifications (CUR).

The theoretical section of this manual provides a description of the process phenomena for the

---

<sup>1</sup> Consulting Engineer, Laan van Vollenhove 814, 3706 AA Zeist, The Netherlands.

<sup>2</sup> Delft Geotechnics, P.O. Box 69, 2600 AB Delft, The Netherlands.

<sup>3</sup> Delft Hydraulics, P.O. Box 177, 2600 MH Delft, The Netherlands.

<sup>4</sup> Rijkswaterstaat, Civil Engineering Division P.O. Box 20.000, 3502 LA Utrecht, The Netherlands.

<sup>5</sup> Rijkswaterstaat, Centre for Coastal Research, P.O. Box 20907, 2500 EX, The Hague

construction with sand in water based on theory development of the physical processes supported by observations of these processes in the field and in the laboratory. In the practical section the design practice is highlighted with thirteen case histories. By means of a detailed elaboration of a practical case the theory is again more extensively verified with project experience. In this paper some results of the theory development are presented followed by an example of calculation results for a practical case.

## 2 Application of study results

The study provides a tool to predict the dimensions of a sand fill constructed in water as a function of the sand characteristics, the sedimentation processes on the fill area and method of sand placement.

## 3 Process phenomena

The processes related to the placement of sand for the construction of sand fills are shown in fig.1. After winning (I) the sand is transported to the fill area (II) by a hopper dredger or via a pipe line. Subject to the means of transport, the sand is either bottom discharged or pipe line placed (III). The sand-water jet makes craters (IV) in the sand body under construction. A sand-water mixture flows across the edge of these craters (V) as well as under water (VI). Under water loss of sand (VII) to the surrounding water can occur. Sand in the mixture flow will settle rapidly to form the slope (VIII).

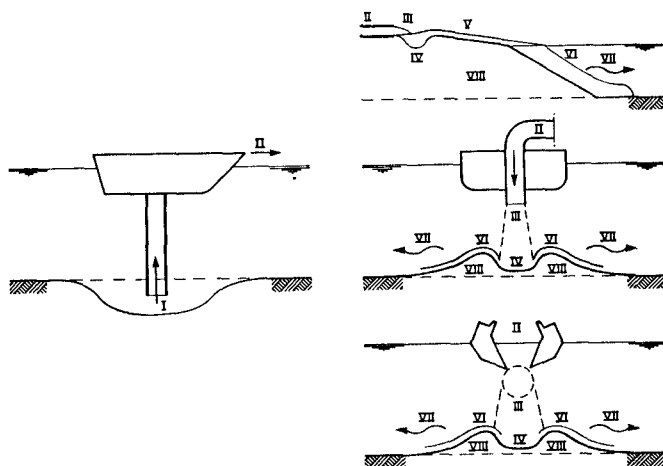


Fig.1 Phases of taking up, transporting and elementary methods of sand placement.

#### 4 Dimensions of a sand fill

The dimensions of a sand fill (fig. 2) placed in water are determined by:

- the behaviour of a sand-water mixture after leaving the discharge pipe or hopper;
- the width of the crater developed during the discharging process as a result of the impact of a sand-water mixture plume or jet
- the sedimentation length
- the initial slope of the above and under water sand fill area directly after placing;
- the occurrence of flow slides;
- the water depth.

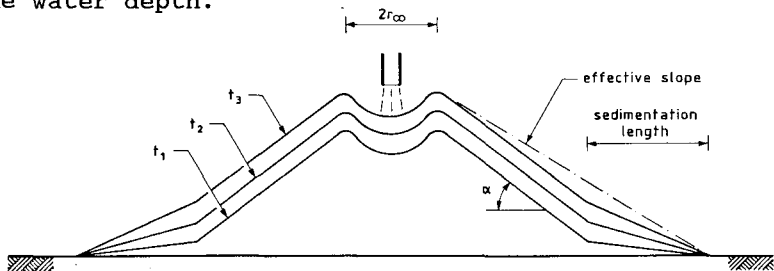


Fig. 2 Parameters determining the shape of a sand fill.

When placing sand in water the sand-water mixture forms a jet or plume with a certain initial flow rate and concentration at the point of discharge of the pipe line or hopper vessel. For a given shape and dimension of discharge opening and for given field conditions, the dimensions, concentrations and velocities along the trajectory of the jet or plume can be predicted as well as the traced path. From these characteristic parameters the dimensions of the crater, which develops when the jet hits the bottom, can be predicted.

#### 5 Crater dimensions

The crater width can be determined using either the theory of Breusers (1991) for conical or round jets and Rajaratnam (1981) for vertical plane shaped jets or the theory of Heezen and Van der Stap (1988). The theory of Breusers and Rajaratnam begins with a description of the erosion under a clear water jet followed by the determination of the influence of sand in the jet on the dimensions of the crater. With the theory of Heezen and Van der Stap the crater dimensions are directly determined from tests and experience with sand-water jets. Because of the limited available space within the context of this paper, only the results of Breusers theory will be presented briefly (fig. 3).

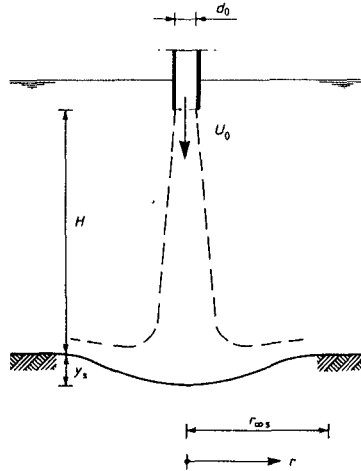


Fig.3. Erosion under a vertical jet.

Based on experiments Breusers recommends the following relations (see also fig. 4):

$$\frac{y_s}{d_0} = 0.075 \frac{U_0}{u_{*cr}} \quad \text{if} \quad \frac{U_0}{u_{*cr}} < 100 \quad (1)$$

$$\frac{y_s}{d_0} = 0.35 \left( \frac{U_0}{u_{*cr}} \right)^{2/3} \quad \text{if} \quad \frac{U_0}{u_{*cr}} > 100$$

In which:

$d_0$  = discharge pipe diameter (m)

$U_0$  = discharge velocity (m/s)

$u_{*cr}$  = critical shear velocity according to Shields (m/s)

$y_s$  = crater depth for clear water (m)

The vertical distance  $H$  to the point of discharge has no influence within the application range of the formula:

$$4 \left\langle \frac{H}{d_0} \right\rangle < 12 @ 20 \quad (2)$$

The effect of the presence of sand in the jet or plume on the dimensions of a crater, can be found by assuming equilibrium between erosion and sedimentation. Because of the presence of sand in the flow, the velocity of the flow on the crater edge must be higher than for clear water in order to prevent sedimentation. As a result of this the crater edge will be closer to the center line of the jet.

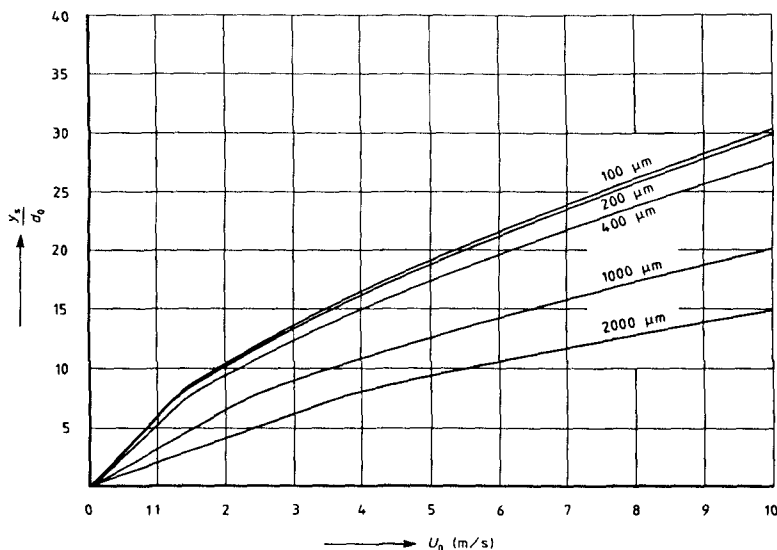


Fig.4. Depth of scour hole for clear water as function of  $U_0$  according to Breusers.

The presence of sand can be accounted for, by reducing the crater dimensions, calculated with formula (1), using a reduction factor which depends on the grain size diameter  $D_{50}$  and on the sand concentration ( $c$ ) in the jet. For jets with coarse sand a reduction of the dimensions of the crater upto a factor 5 is possible.

The ratio between radius and depth does not change, hence the following always applies:

$$\frac{r_{\infty}}{y} = \frac{r_{\infty s}}{y_s} = 2.5 \quad (3)$$

In which:

$r_{\infty}$  = crater radius for sand-water mixture (m)

$r_{\infty s}$  = crater radius for clear water (m)

$y$  = crater depth for sand-water mixture (m)

$y_s$  = crater depth for clear water (m)

## 6 Mixture overflow from crater

Besides the grain diameter, for the determination of the slope gradient, the specific flow rate ( $q$ ) is the most important parameter for the above water fill area and the specific sand production rate ( $s$ ) for the underwater fill area. A large specific flow rate and a large specific sand production rate result in flatter slopes. To be able to determine the values of  $q$  and  $s$  the width ( $B$ ) across which the mixture will spread after passing the crater edge must be assessed.



The specific flow ratio  $q$  and specific sand production rate  $s$  for single point discharging in an under water fill area, follow from the equations:

$$q = U_b \cdot \pi / 4 \cdot d_b^2 / B \quad (4)$$

$$s = \rho_s \cdot q \cdot c_b \quad (5)$$

In which:

$q$  = specific flow rate ( $m^2/s$ )

$U_b$  = mixture velocity in centre of jet just above sea bed ( $m/s$ )

$B$  = spreading width of mixture ( $m$ )

$d_b$  = diameter of round jet just above sea bed ( $m$ )

$s$  = specific sand production rate (solids) ( $kg/ms$ )

$\rho_s$  = density of solids ( $kg/m^3$ )

$c_b$  = volume concentration just above sea bed (-)

The question is, across what width  $B$  the mixture will spread. There is little known about this subject. For that reason the following approach must be regarded as a first attempt to estimate an upper limit  $B_{max}$  and a lower limit  $B_{min}$ . The upper limit is taken equal to the circumference of the crater edge. In principle  $B$  could become even larger after the mixture has passed the crater edge because the size of the crater increases continuously from the discharge point. However it seems very unrealistic that the mixture spreads more than the complete circumference of the crater edge. Hence, for a crater under a round (conical) jet the following applies:

$$B_{max} = 2\pi r_\infty \quad (6)$$

and for a crater under a vertical plane shaped jet with a length equal to the curtain-length or the hopper-length of the vessel from which the sand is discharged, the following applies:

$$B_{max} = 2\pi r_\infty + 2 \times \text{curtain-length} \quad (7)$$

However most likely the mixture will not spread across the complete crater circumference  $B_{max}$ , but will concentrate in a channel.

On the above water fill area the mixture flow can be distributed by means of bulldozers across the full width of the fill area determined by bunds. This is not the case on the under water fill area and hence channel formation cannot be prevented here.

The width  $B$  of this channel determines the specific flow rate  $q$  and the specific sand production rate  $s$  and therefore the under water slopes.

Based on the regime theory, the minimum width of a channel normalized for jet diameter  $d$ , can be derived from (8) (for a round jet, hence for single point discharging in an under water fill area):

$$\frac{B_{\min}}{d} = 0.6 \sqrt{\frac{U}{U_c}} \quad (8)$$

In which:

- $B_{\min}$  = lower limit of spreading width of mixture (m)
- $d$  = jet diameter (m)
- $U$  = mixture flow velocity in centre of jet (m/s)
- $U_c$  = mixture flow velocity for which erosion occurs, (Shields:  $U_c = \sqrt{\Delta g D_{50}}$ ) (m/s)

In fig. 5 this relation is plotted as a function of the flow velocity in the centre of the jet and the grain size diameter.

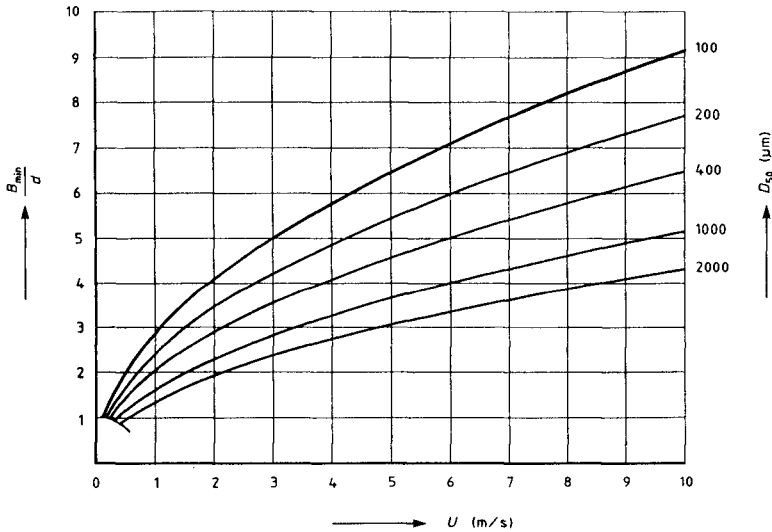


Fig.5. Minimum spreading width of mixture at overflow of crater edge.

## 7 Sedimentation and erosion processes

The extension of a hydraulically placed sand body is the result of sedimentation of sand from a sand-water mixture flow and in some cases the successive replacement of already deposited sand. These sedimentation and erosion processes can be determined in a quantitative way. In principle they are physically independent of each other. The net result can therefore be derived by superimposing the sedimentation- and erosion-velocity.

The sedimentation length is defined as the distance covered by the sand-water mixture flow before the volume

concentration is reduced to 10% of the initial concentration. This sedimentation length can be read from fig. 6 as a function of the specific mixture flow rate, grain size and volume concentration. Because of the hindered settling effect, the sedimentation length is strongly influenced by the concentration.

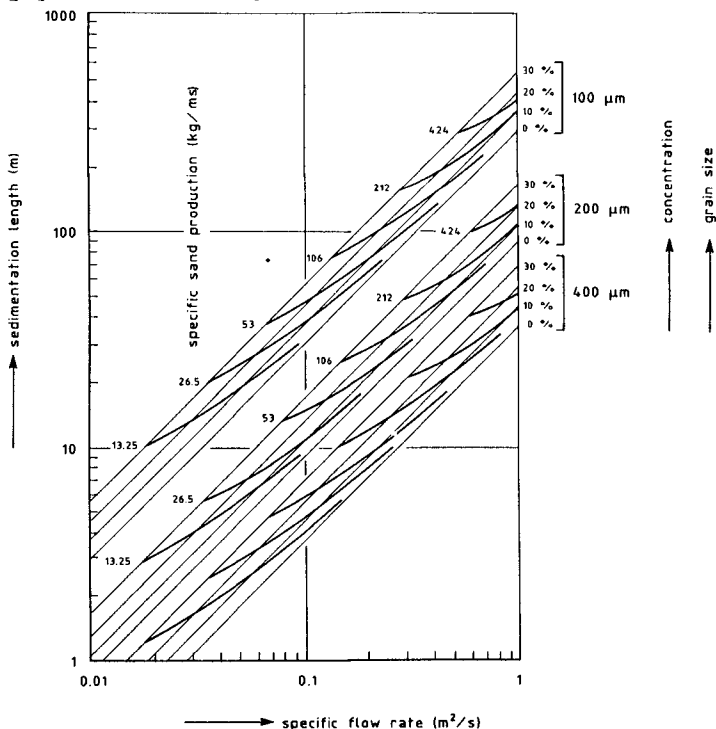


Fig.6. Sedimentation length as a function of specific flow rate, grain size and volume concentration.

## 8 Slope formation above water

The following bed-forms can be observed: terraces, cascades and channel formation.

### Terraces and cascades

Terraces and cascades develop at moderate specific mixture flow rates of the order of 0.01 to 0.3  $\text{m}^2/\text{s}$  (Winterwerp et al, 1992). The anti-dune like bed-form is composed of long, flat sloped terraces where the flow velocity is sub-critical and where sedimentation of sand takes place, see fig. 7. At the end of this terrace a steep cascade is present, where the flow velocity becomes super-critical and where erosion takes place. A hydraulic jump develops between this cascade and the

next terrace at the transition of super-critical flow to sub-critical flow. Because of the erosion of the downstream side and sedimentation at the upstream side, the system of terraces, steps and cascades propagates slowly in upstream direction. A dynamic equilibrium situation can develop between sedimentation on the terraces and erosion on the cascades at a certain average bed slope.

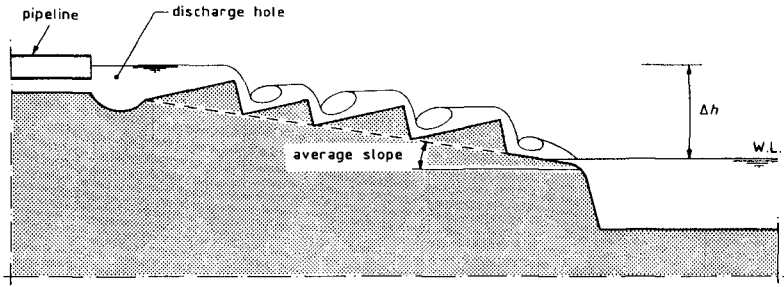


Fig.7. Terrace formation on fill above water level.

### Channels

At high specific mixture flow rates the mixture concentrates in deep channels and the bed-form of terraces and cascades disappears.

### Equilibrium slope above water level

The equilibrium slope is defined by the equilibrium between sedimentation and erosion. This slope is determined with field observations and large scale tilting flume tests as a function of the flow velocity, grain size and concentration (Winterwerp et al 1990). The following empirical formula for this equilibrium slope above water level could be inferred:

$$i = 0.006 \left( \frac{D_{50}}{D_0} - 1 \right) \frac{q^{-0.45}}{q_0} \quad (9)$$

In which:

- $i$  = tangent of the average slope gradient (-)
- $D_{50}$  = medium grain size diameter ( $\mu\text{m}$ )
- $q$  = specific mixture flow rate ( $\text{m}^2/\text{s}$ )
- $D_0$  =  $65 \mu\text{m}$
- $q_0$  =  $1 \text{ m}^2/\text{s}$

This equation was derived for specific mixture flow rates varying from 0.01 and 0.15  $\text{m}^2/\text{s}$  and grain size diameters of respectively 120 and 225  $\mu\text{m}$ . This relation is shown in fig. 8 together with the flume and field surveys. The equilibrium slope showed a strong relation with the specific mixture flow rate and the grain size. The concentration appears to be of minor importance, which can be explained by the effects of hindered settling.

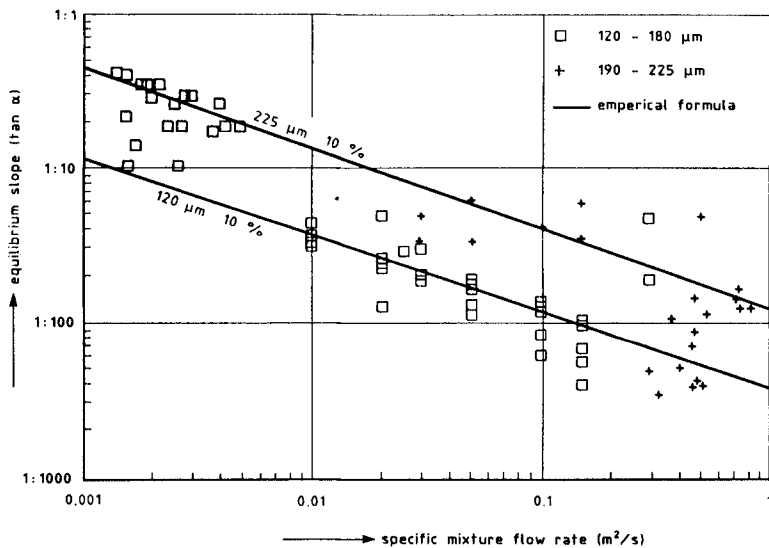


Fig. 8. Equilibrium slopes above water, results of flume tests and field observations and calculations using formula 9.

## 9 Slope formation under water

Compared to the circumstances above water, the soil mechanics properties of the sand body during sand placement under water have a much stronger influence on the development of the slope. Because the deposited sand is always very loosely packed, it is susceptible to liquefaction. Therefore under certain circumstances the slope of the sand body will not be stable and liquefaction may occur followed by a flow slide.

Whether flow slides occur directly after the sand has settled depends on the type of sedimentation. To predict which type can be expected depends on the sedimentation length ( $L$ ), the critical slope height ( $h_{cr}$ ) and the porosity ( $n$ ).

The development of a sand slope under water is illustrated in figures 9a, -b and -c.

During hydraulic placement of sand at low to moderate specific sand production rates and with fine sand in shallow to fairly deep water, the development of the slope takes place in a discontinuous way. This has been observed during field surveys and during experiments in a large flume.

During the hydraulic placement of sand, sedimentation takes place within the first metres of the slope after the sand body has reached the water surface. It then starts to develop in horizontal direction. The slope

increases locally which may result in a critical situation and a flow slide. See fig. 9a. Sedimentation again takes place on the resulting flat slope. The alternating increase and decrease of the slope caused by sedimentation and flow slides, is a continuous process. The flow slides are now the dominating factor for the transportation of sand to the toe of the sand body. For coarser sand and for the same low specific sand production rates and shallow water, however, flow slides will be observed less readily even when the sand is very loose and the porosity of the deposited sand is well beyond the critical value.

It was found that for horizontal slope development a critical slope height exists. Beyond this critical height flow slides occur. For coarse sand this critical slope height is larger than for fine sand. The values for  $h_{cr}$  are based on experience with the construction of sand fills with grain sizes between 100 and 500  $\mu\text{m}$ . The critical slope height can be approximated by:

$$h_{cr} = 0.075D - 8.5 \quad (120 \mu\text{m} < D < 500 \mu\text{m}) \quad (10)$$

In which:

$$h_{cr} = \text{critical slope height (m)}$$

$$D = \text{grain diameter } (\mu\text{m})$$

For  $h < h_{cr}$  the under water sand slope increases up to a certain steep equilibrium angle. The development of the slope takes place in a very regular way and a kind of equilibrium situation establishes, see fig. 9b.

For high specific sand production rates ( $s > 25 \text{ kg/ms}$ ) a turbulent suspension flow will occur, for fine sand as well as for coarse sand, with hydraulic jumps propagating continuously in the upstream direction. This process is very similar to the type of mixture flow above water.

The suspension flow can extend far beyond the toe of the slope resulting in a decreasing under water slope. See fig. 9c. Although flow slides may be present these do not constitute a prevalent sand transport mechanism.

#### **Equilibrium slope below water level**

No unique value can be established for the slope of a hydraulically placed sand body because of the alternating increase and decrease of the slope. Flow slides or breach processes, if present, define the minimum slopes. The average under water sand slope is mainly defined by the grain size and the specific sand production rate.

Average under water slopes observed during the hydraulic placement of sand of various projects are shown in fig. 10 as a function of the specific production rate ( $s$ ) and

grain size. The results of flume tests with fine and medium coarse sand are given for various sand production rates, as well as the results of previously performed small scale flume tests. Since all types of measurements are collected a wide scatter is the result.

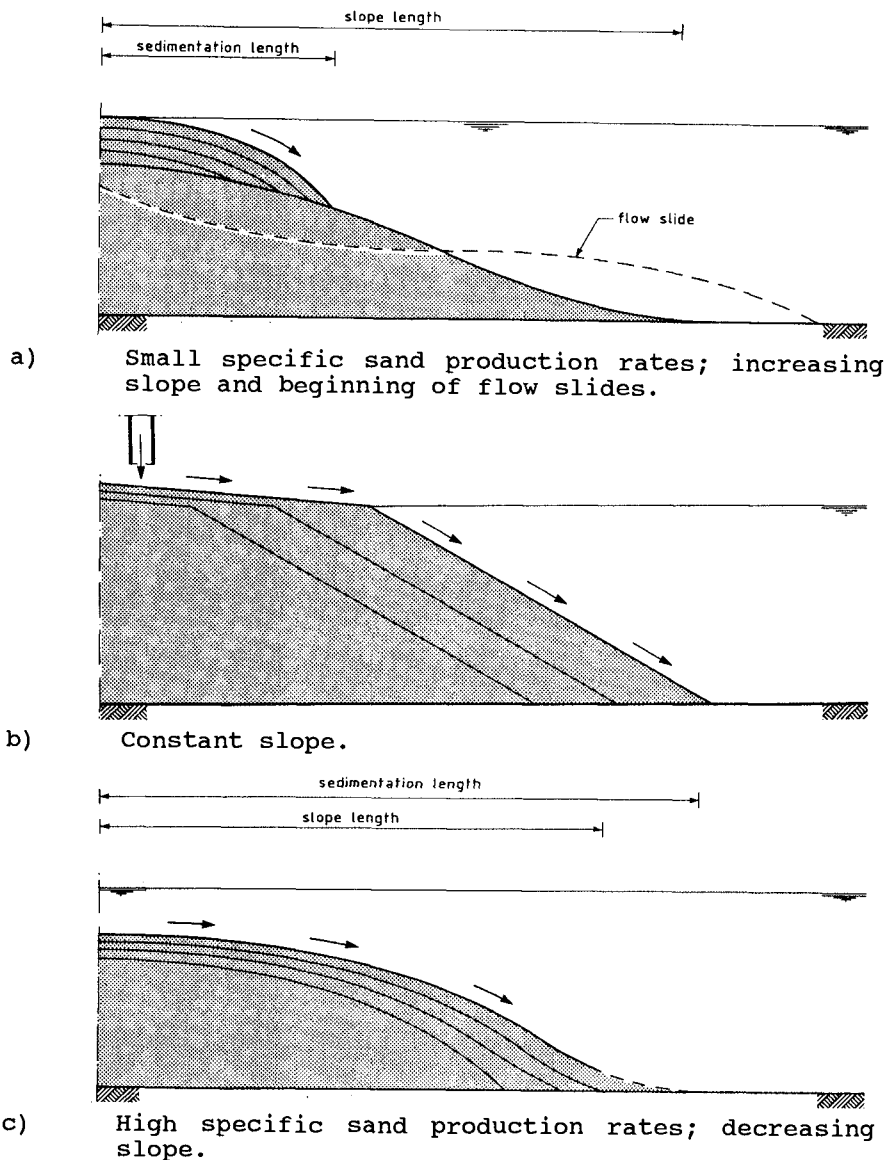


Fig.9 Development of under water sand slopes.

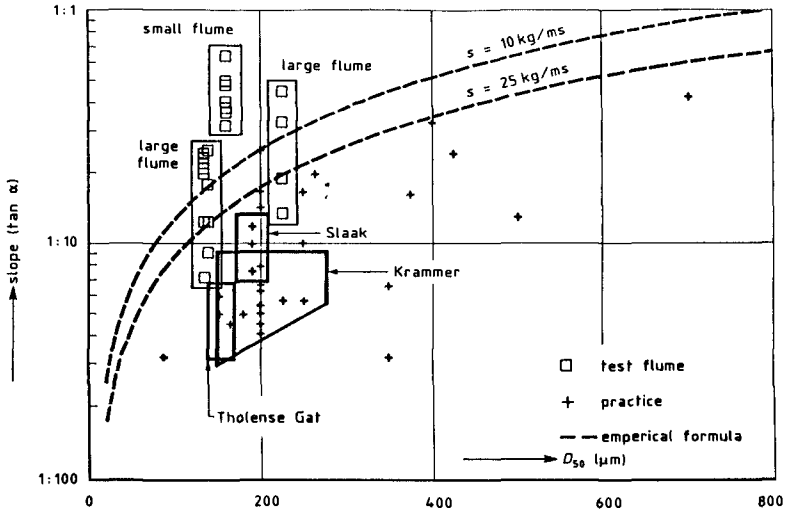


Fig.10. Underwater sand slopes measured in the field and in the laboratory as a function of  $D_{50}$ .

The following empirical formula applies to the average under water slope ( $i$ ) when no flow slides occur:

$$i = 0.0032D \cdot s^{-0.4} \tag{11}$$

In which:

$D$  = grain size ( $\mu\text{m}$ )

$s$  = specific sand production rate (kg/ms)

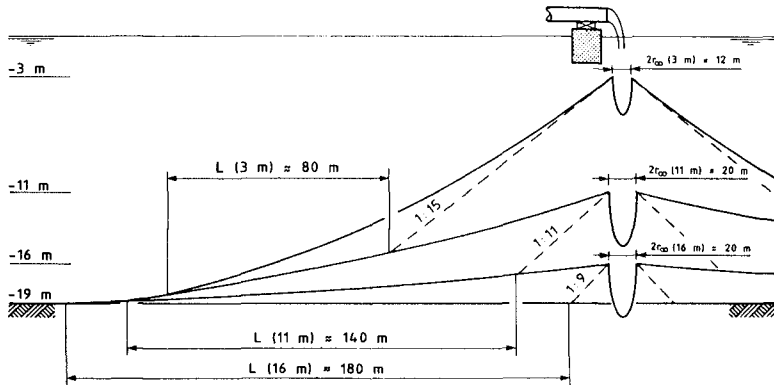


Fig.11 Building up of the artificial island Issungak for hydraulic discharging from the water surface.

It can be read from fig. 10 that in the field often flatter slopes are observed than according to formula (11). These are always practical situations for which



flow slides govern the slope formation. In these cases it is recommended not to use formula (11) but to estimate the slope on the basis of the indicated field observations.

### 10 Prediction of sand fill dimensions

Typical computational results for the building up of an artificial island at varying discharge heights are shown in fig.11 and table 1.

Table 1 Crater dimensions and sedimentation length for discharging from the water surface (Issungak).

magnitude	unit	fall height 19 m	fall height 11 m	fall height 3 m
crater width $2r_c$	m	10-40	8-30	5-20
specific flow rate $q$	$m^2/s$	1.8-2.4	1.4-1.7	0.45-1.1
specific sand production rate $s$	kg/ms	45-200	70-350	170-550
sedimentation length $L$	m	150-250	120-170	50-130
equilibrium slope $\tan \alpha$	(-)	1:7-1:12	1:8-1:14	1:11-1:17

### References

- Breusers, H.N.C. and A.G. Raudkivi (1991). Scouring, *Hydr. Struct. Design Manual*, IAHR, Balkema, Rotterdam.
- Groot de M.B., F.T. Heezen, D.R. Mastbergen and H. Stefess (1988). Slopes and densities of hydraulically placed sands. *Hydraulic fill structures*, ASCE Geot. Div. Spec. Conf., Colorado State University, Fort Collins.
- Heezen, F.T. and A.C.M. van der Stap (1988). An engineering approach to under water dumped sand bodies. *Internat. Symp. on modelling Soil-Water-Structure Interactions*, Delft, Balkema, Rotterdam.
- Rajaratnam, N. (1981). Erosion by plane turbulent jets. *Journal of Hydraulic Research*, nr.4.
- Van 't Hoff (ed.) et al (1992). Artificial Sandfills in Water. *Centre for Civil Engineering Research and Codes*, report no. 152, Balkema, Rotterdam.
- Winterwerp, J.C. W.T. Bakker, D.R. Mastbergen and H. van Rossum (1992). Hyperconcentrated Sand-Water Mixture flows over Erodible Bed. *Journ. of Hydr. Eng.* nr. 11
- Winterwerp, J.C., M.B. de Groot, D.R. Mastbergen and H. Verwoert, (1990). Hyperconcentrated sand-water mixture flow over a flat bed. *Journal of Hydr. Eng.* nr 1.

## CHAPTER 200

### SEDIMENT TRANSPORT BY CURRENTS AND WAVES

Leo C. van Rijn<sup>1)</sup> and Aart Kroon<sup>2)</sup>

#### Abstract

Mathematical and experimental modelling of sediment transport processes in the coastal environment is presented. The convection-diffusion equation for suspended sediment particles has been used to compute the vertical distribution of the time-averaged concentrations. The computed results are compared with measured values of laboratory and field experiments (surf zone Dutch coast).

#### 1. Introduction

Many details of the complicated sediment transport processes in the coastal environment are still unknown. To get a better understanding of the most relevant processes, an integrated research programme has been set up, sponsored by the Coastal Genesis project (Rijkswaterstaat, The Netherlands), the MAST project (EEC research programme) and the Basic Research programme of Delft Hydraulics.

The research programme is focused on theoretical and experimental modelling of the processes involved. The major part of the work is related to experimental work, as follows:

- wave tunnel experiments to study the near-bed phenomena (Ribberink and Al Salem, 1991 and 1992)
- wave-current flume and basin experiments to study the vertical structure of the velocity and sediment concentration (Van Rijn et al, 1993)
- surf zone experiment near the Dutch coast (Kroon and Van Rijn, 1992).

Herein, the mathematical modelling of time-averaged sediment concentrations in the coastal environment is presented. The computed values are compared with measured results from laboratory and field experiments.

- 
- 1) Senior engineer, Delft Hydraulics, P.O. Box 152, 8300 AD Emmeloord, The Netherlands
  - 2) Researcher, Dep. Phys. Geography, Univ. of Utrecht, P.O. Box 80115, Utrecht, The Netherlands

## 2. Mathematical model

### 2.1 Transport processes

The total sediment transport rate ( $q_t$ ) can be computed from the vertical distribution of fluid velocities and sediment concentrations, as follows:

$$q_t = \int_0^{h+\eta} VC \, dz \quad (1)$$

in which:

- V = local instantaneous fluid velocity at height z above bed (m/s)
- C = local instantaneous sediment concentrations at height z above bed (kg/m<sup>3</sup>)
- h = water depth (to mean surface level) (m)
- $\eta$  = water surface elevation (m)

Defining:  $V = v + \tilde{v}$  and  $C = c + \tilde{c}$  (2)

in which:

- v = time and space-averaged fluid velocity at height z (m/s)
- c = time and space-averaged concentration at height z (m/s)
- $\tilde{v}$  = oscillating fluid component (including turbulent component) (m/s)
- $\tilde{c}$  = oscillating concentration component (including turbulent component) (m/s)

Substituting Eq. (2) in Eq. (1) and averaging over time and space, yields:

$$\bar{q}_t = \int_0^h \bar{v}c \, dz + \int_0^h \bar{\tilde{v}\tilde{c}} \, dz = \bar{q}_c + \bar{q}_w \quad (3)$$

in which:

$$\bar{q}_c = \int_0^h \bar{v}c \, dz = \text{time-averaged current-related sediment transport rate (kg/sm)}$$

$$\bar{q}_w = \int_0^h \bar{\tilde{v}\tilde{c}} \, dz = \text{time-averaged wave-related sediment transport rate (kg/sm)}$$

The current-related sediment transport is defined as the transport of sediment particles by the time-averaged (mean) current velocities (longshore currents, rip currents, undertow currents). The current velocities and the sediment concentrations are affected by the wave motion. It is known that the wave motion reduces the current velocities near the bed, but the wave motion strongly increases the near-bed concentrations due to its stirring action. The wave-related sediment transport is defined as the transport of sediment particles by the oscillating fluid components (cross-shore orbital motion).

In this paper the attention is focused on the current-related transport rate.

## 2.2 Time-averaged concentration profile

Usually, the convection-diffusion equation is applied to compute the equilibrium concentration profile in steady flow. This equation reads as:

$$w_{s,m} + \epsilon_{s,cw} \frac{dc}{dz} = 0 \quad (4)$$

in which:

$w_{s,m}$  = fall velocity of suspended sediment in a fluid-sediment mixture (m/s)

$\epsilon_{s,cw}$  = sediment mixing coefficient for combined current and waves (m<sup>2</sup>/s)

$c$  = time-averaged concentration at height  $z$  above the bed (kg/m<sup>3</sup>)

Here, it is assumed that Eq. (4) is also valid for wave-related mixing.

## 2.3 Sediment mixing coefficient

For combined current and wave conditions the sediment mixing coefficient is modeled as:

$$\epsilon_{s,cw} = [(\epsilon_{s,w})^2 + (\epsilon_{s,c})^2]^{0.5} \quad (5)$$

in which:

$\epsilon_{s,w}$  = wave-related mixing coefficient (m<sup>2</sup>/s)

$\epsilon_{s,c}$  = current-related mixing coefficient (m<sup>2</sup>/s)

First, the wave-related mixing is discussed.

Measurements in wave flumes show the presence of suspended sediment particles from the bed up to the water surface (Van Rijn, 1991). The largest concentrations are found close to the bed where the diffusivity is large due to ripple-generated eddies. Further away from the bed the sediment concentrations decrease rapidly because the eddies dissolve rather rapidly travelling upwards.

Various researchers have tried to model the suspension process by introducing an effective wave-related sediment mixing coefficient (see Van Rijn 1989 and 1993).

As the existing relationships do not yield acceptable results, a new approach was presented. Based on analysis of measured concentration profiles, the following characteristics were observed (Van Rijn, 1989, 1993);

- approximately constant mixing coefficient  $\epsilon_{s,w,bed}$  in a layer ( $z \leq \delta_s$ ) near the bed,
- approximately constant mixing coefficient  $\epsilon_{s,w,max}$  in the upper half ( $z \geq 0.5 h$ ) of the water depth,
- approximately linear variation of the mixing coefficient for  $\delta_s < z < 0.5 h$ .

The mathematical formulation reads as (see Figure 1):

$$z \leq \delta_s \quad \epsilon_{s,w} = \epsilon_{s,w,bed} \quad (6a)$$

$$z \geq 0.5 h \quad \epsilon_{s,w} = \epsilon_{s,w,max} \quad (6b)$$

$$\delta_s < z < 0.5 h \quad \epsilon_{s,w} = \epsilon_{s,w,bed} + [\epsilon_{s,w,max} - \epsilon_{s,w,bed}] \left[ \frac{z - \delta_s}{0.5h - \delta_s} \right] \quad (6c)$$

Equation (6) is fully defined when the following three parameters are known:

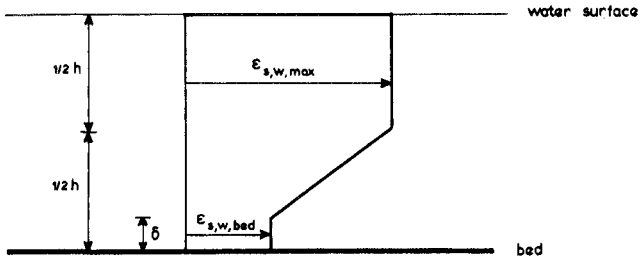
1. Thickness of near-bed sediment mixing layer ( $\delta_s$ ).  
Based on analysis of concentration profiles measured in non-breaking waves, it was found that:

$$\delta_s = 3 \Delta_r \quad (\text{ripple height})$$

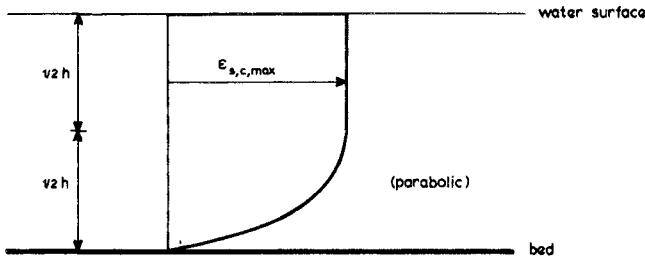
$$\delta_s = 3 \delta_w \quad (\text{sheet flow regime})$$

in which:

- $\Delta_r$  = ripple height (m)
- $\delta_w = 0.072 \hat{\Lambda}_s (\hat{\Lambda}_s / k_{s,w})^{-0.25}$  = wave boundary layer thickness (m)
- $\delta_s$  = thickness of near-bed sediment mixing layer (m)
- $k_{s,w}$  = wave-related bed roughness height (=  $3\Delta_r$  in ripple regime and  $\frac{1}{2} \delta_w$  in sheet flow regime) (m)



A. WAVE-RELATED SEDIMENT MIXING COEFFICIENT



B. CURRENT-RELATED SEDIMENT MIXING COEFFICIENT

Figure 1 Mixing coefficient distribution

2. Mixing coefficient in near-bed layer ( $\epsilon_{s,w,bed}$ )  
 This parameter was found to be:

$$\epsilon_{s,w,bed} = \alpha_b \hat{U}_\delta \delta_s \quad (8)$$

in which:

$\hat{U}_\delta$  = peak value of near-bed orbital velocity (based on significant wave height) (m/s)

$\alpha_b$  = 0.004  $D_*$  = empirical coefficient (-)

$D_*$  =  $d_{50} [(\rho_s - \rho)g / (\rho v^2)]^{1/3}$  = particle size parameter (m)

3. Mixing coefficient in upper layer ( $\epsilon_{s,w,max}$ )  
 This parameter was found to be:

$$\epsilon_{s,w,max} = 0.035 \frac{H_s h}{T_p} \quad (9)$$

in which:

$H_s$  = significant wave height (m)

$T_p$  = peak period of spectrum (s)

$h$  = water depth (m)

Second, the current-related mixing coefficient ( $\epsilon_{s,c}$ ) is presented, which reads as:

$$\begin{aligned} \epsilon_{s,c} &= \kappa \beta u_{*,c} z(1-z/h) && \text{for } z < 0.5 h \\ \epsilon_{s,c} &= 0.25 \beta \kappa u_{*,c} h && \text{for } z \geq 0.5 h \end{aligned} \quad (10)$$

in which:

$u_{*,c}$  =  $(g^{0.5} \bar{v}_R) / C$  = bed-shear velocity (m/s)

$C$  =  $18 \log(12h/k_{s,c})$  = Chézy coefficient ( $m^{0.5}/s$ )

$\bar{v}_R$  = depth-averaged velocity (m/s)

$k_{s,c}$  = current-related bed-roughness height (m)

$h$  = water depth (m)

$\kappa$  = constant of Von Karman (= 0.4)

$\beta$  = coefficient ( $\approx 1$ )

#### 2.4 Reference concentration near the bed

The reference concentration is given by:

$$c_a = 0.015 \frac{d_{50}}{a} \frac{T^{1.5}}{D_*^{0.3}} \quad (11)$$

in which:

$D_*$  = dimensionless particle parameter (-)

$T$  = dimensionless bed-shear stress parameter (-)

$a$  = reference level (m)

The T-parameter is, as follows:

$$T = [\tau'_{b,cw} - \tau'_{b,cr}] / \tau_{b,cr} \quad (12)$$

in which:

$\tau'_{b,cw}$  = time-averaged effective bed-shear stress (N/m<sup>2</sup>)

$\tau'_{b,cr}$  = time-averaged critical bed-shear stress according to Shields (N/m<sup>2</sup>)

The magnitude of the time-averaged bed-shear stress, which is independent of the angle between the wave- and current direction is given by (Van Rijn, 1990):

$$\tau'_{b,cw} = \tau'_{b,c} + \tau'_{b,w} \quad (13)$$

in which:

$\tau'_{b,c} = \mu_c \alpha_{cw} \tau_{b,c}$  = effective current-related bed-shear stress (N/m<sup>2</sup>)

$\tau'_{b,w} = \mu_w \tau_{b,w}$  = effective wave-related bed-shear stress (N/m<sup>2</sup>)

$\tau_{b,c} = \frac{1}{8} \rho f_c (\bar{v}_R)^2$  = current-related bed-shear stress (N/m<sup>2</sup>)

$\tau_{b,w} = \frac{1}{4} \rho f_w (\hat{U}_\delta)^2$  = wave-related bed-shear stress (N/m<sup>2</sup>)

$f_c = 0.24 [\log(12h/k_{s,c})]^{-2}$  = current-related friction factor (-)

$f'_c = 0.24 [\log(12h/3d_{90})]^{-2}$  = grain friction factor (-)

$f_w = \exp[-6+5.2(\hat{\Lambda}_\delta/k_{s,w})^{-0.19}]$  = wave-related friction factor (-)

$\bar{v}_R$  = depth-averaged current-velocity (m/s)

$\hat{U}_\delta$  = peak value of near-bed orbital velocity (m/s)

$\hat{\Lambda}_\delta$  = peak value of near-bed orbital excursion (m)

$h$  = water depth (m)

$k_{s,c}$  = current-related bed-roughness (m)

$k_{s,w}$  = wave-related bed-roughness (m)

$\mu_c = f'_c/f_c$  = current-related efficiency factor (-)

$\mu_w = 0.6/D_*$  = wave-related efficiency factor (-)

$\alpha_{cw}$  = correction factor related wave-current interaction (see next section), (-)

$\rho$  = fluid density (kg/m<sup>3</sup>)

$\rho_s$  = sediment density (kg/m<sup>3</sup>)

## 2.5 Current velocity profile

The current velocity profile (see Fig. 2) is represented as a two-layer system to account for the wave effects in the near-bed layer (Van Rijn, 1993):

$$v(z) = \frac{\bar{v}_x \ln(30z/k_a)}{-1 + \ln(30h/k_a)} \quad \text{for } z \geq 3 \delta_w \quad (14)$$

$$v(z) = \frac{\bar{v}_x \ln(90\delta_w/k_a) \ln(30z/k_{s,c})}{[\ln(90\delta_w/k_{s,c})] [-1 + \ln(30h/k_a)]} \quad \text{for } z < 3 \delta_w$$

in which:

- $k_a = k_{s,c} \exp[\gamma \hat{U}_\delta / \bar{v}_r]$  = apparent roughness related to wave-current interaction ( $k_{a,max} = 10 k_{s,c}$ ) (m)
- $k_{s,c}$  = physical current-related bed roughness (m)
- $\gamma = 0.8 + \phi - 0.3\phi^2$
- $\phi$  = angle between current and wave direction (in radians between 0 and  $\pi$ ;  $90^\circ = \frac{1}{2}\pi$ ,  $180^\circ = \pi$ )
- $\delta_w = 0.072 \hat{A}_\delta (\hat{A}_\delta / k_{s,w})^{-0.25}$  = maximum thickness of wave boundary layer (m)

The  $\alpha_{cw}$ -factor is given by (Van Rijn, 1993):

$$\alpha_{cw} = \left[ \frac{\ln(90 \delta_w / k_a)}{\ln(90 \delta_w / k_{s,c})} \right]^2 \left[ \frac{-1 + \ln(30h / k_{s,c})}{-1 + \ln(30h / k_a)} \right]^2 \tag{15}$$

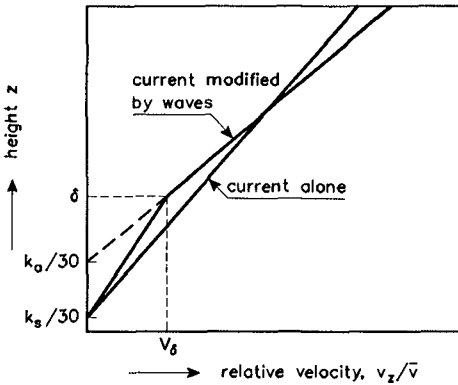


Figure 2 Velocity profile

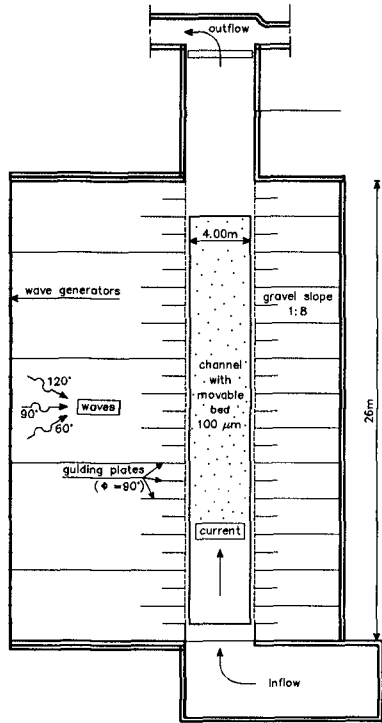


Figure 3 Plan view of wave-current basin



## 2.6 Sediment transport

The suspended load transport is given by:

$$q_{s,c} = \int_a^h vc \, dz \quad (16)$$

The bed-load transport is given by:

$$q_{b,c} = 0.25u'_{*,c} d_{50} T^{1.5} D_*^{-0.3} \quad (17)$$

in which:  $u'_{*,c} = (\tau'_{b,c}/\rho)^{0.5}$

## 3. Laboratory experiments

### 3.1 Experiments

Experiments were carried out in a wave-current basin at Delft Hydraulics to measure the current velocities and sediment concentrations under irregular non-breaking waves combined with a current. The bed material consisted of fine sand with  $d_{10} = 70 \mu\text{m}$ ,  $d_{50} = 100 \mu\text{m}$  and  $d_{90} = 130 \mu\text{m}$ . The water depth was about 0.4 m. Figure 3 shows a plan view of the experimental facility. The current was confined (by guiding plates) in a channel (width = 4 m) with a movable bed consisting of fine sand ( $d_{50} = 100 \mu\text{m}$ ). The guiding plates were placed normal to the wave crests. The (significant) wave heights generated were  $H_s = 0.07$ , 0.1 and 0.14 m. The peak period of the wave spectrum was about 2.3 s. Three current velocities (0.1, 0.2 and 0.3 m/s) were generated by varying the pump discharge. The velocity distribution across the channel was almost uniform. The velocity profiles in the middle of the channel were perfectly logarithmic. The vertical distribution of the turbulence intensity was in good agreement with values reported in the literature. Based on this, it was concluded that the effect of the guiding plates on the current was negligible. The wave propagation direction was set at  $60^\circ$ ,  $90^\circ$  and  $120^\circ$ .

The water entering the channel had no initial sediment load. Consequently, the concentration profiles were generated by erosion of sediment particles from the bed. To provide enough length for establishing equilibrium concentration profiles, the measuring section was situated at a distance of about 30 times the water depth from the channel entrance.

### 3.2 Instruments

Measurements of wave height, velocity and sediment concentration were performed from a carriage moving over rails above the channel. Water level variations were measured by use of a resistance probe near the location where the concentrations and velocities were measured (measuring period = 30 min). Characteristic wave parameters were computed from the data records.

Instantaneous sediment concentrations were measured by use of an acoustic probe; time-averaged sediment concentrations were determined from water-sediment samples using a pump sampler. This latter instrument consisted of an array of ten intake tubes of 3 mm internal diameter connected to the pumps by plastic hoses. The lowest intake tube was placed at about 0.01 m above the crest level of the bed forms. The intake openings were placed in transverse direction to the plane of orbital motion (Bosman et al, 1987). The intake velocity was about 1 m/s satisfying sampling requirements. The 10 liter samples were collected in calibrated buckets.

Instantaneous velocities were measured using an electromagnetic velocity meter (EMS) with a measuring level of about 3 mm below the probe and an acoustical probe (AZTM). The velocities were measured at the same elevations above the mean bed as those of the concentrations starting at the lowest point and working upwards. A time-averaging period of 256 s (approx. 100 waves) was applied.

Space averaging over the bed-form length was performed by moving the sediment concentration and fluid velocity instruments forward and backward over a certain longitudinal distance by use of an oscillating carriage above the channel. The velocity of the moving carriage (approx. 0.01 m/s) was small compared with the fluid velocity and large compared with the bed-form migration velocity. The error in the time-averaged velocity was less than 0.00125 m/s in the present tests. Preliminary tests showed that a space-averaging distance of 0.6 m (approx. 5 ripple lengths) was sufficiently large to give reproducible results.

### 3.3 Time-averaged concentration profiles

Analysis of the time-averaged concentration profiles shows the following results:

- concentrations increase for increasing wave height,
- current velocity does not affect the near-bed concentration; increasing current velocity results in a more uniform concentration profile (larger mixing),
- concentrations are largest when the wave direction is normal to the current direction.

Measured concentration profiles for four tests are shown in Fig. 4. Equation (4) was used to compute the time-averaged concentration profiles based on the following input data:  $d_{50} = 100 \mu\text{m}$ ,  $d_{90} = 130 \mu\text{m}$ ,  $w_s = 0.0065 \text{ m/s}$ ,  $k_{s,w} = k_{s,c} = 3\Delta_r$ ,  $\Delta_r$  = measured ripple height,  $a = 0.5\Delta_r$ ,  $\delta_s = 3\Delta_r$ ,  $\rho = 1000 \text{ kg/m}^3$ ,  $\rho_s = 2650 \text{ kg/m}^3$ .

The Bijker method (1971, 1978) was also used to compute the concentration profiles. The b-coefficient of this method was used as a calibration coefficient. A value of  $b = 1$  gave the best results.

The computed concentration profiles are shown in Fig. 4. Both methods yield reasonable results; the method of Bijker overestimates the measured concentrations at low velocities of 0.1 m/s (T14 10 90).

Computed transport rates showed reasonable agreement with measured values; most computed values are within a factor 2 of measured values.

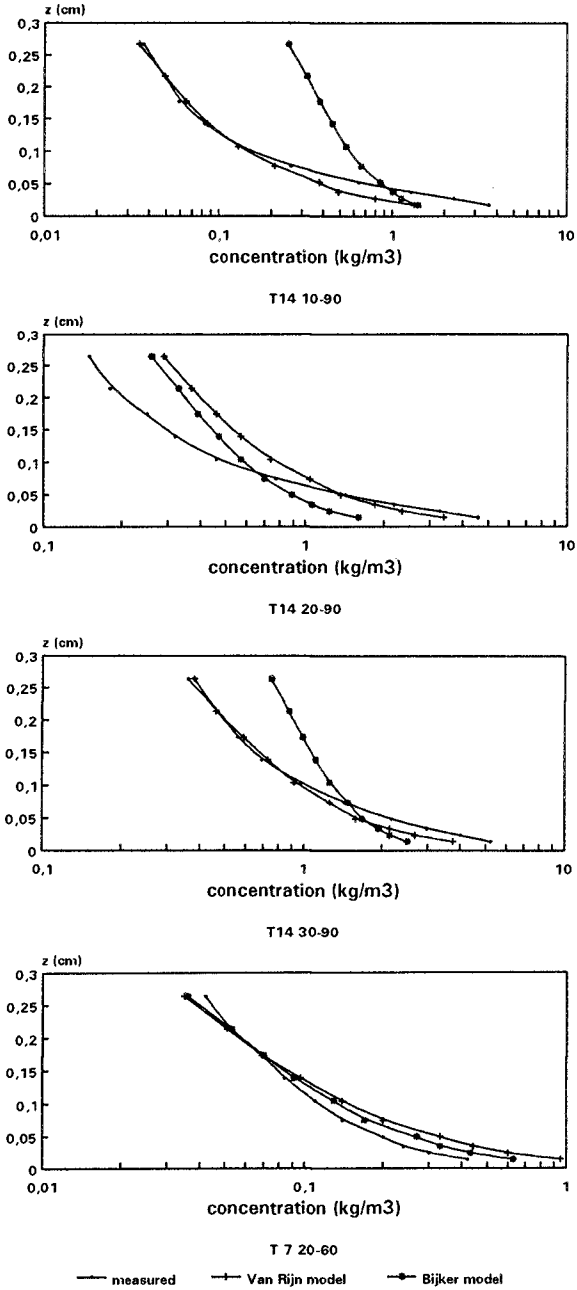


Figure 4 Measured and computed concentration profiles

#### 4. Field experiments

##### 4.1 Site description

The field experiments were performed at the central part of the Dutch coast near Egmond aan Zee. The hydrodynamics near Egmond aan Zee are characteristic for a mixed-energy coast of a semi-enclosed sea. The incoming waves from the North Sea have a mean annual wave height of 1.3 m and come from southwestern to northern directions. The mean semi-diurnal tidal range is 1.65 m, with a maximum range at spring tide of 2.10 m and a minimum range at neap tide of 1.40 m. The tidal curve near Egmond is asymmetrical with a flood period of 4 hours and an ebb period of 8 hours. The morphology of the beach and nearshore zone in this area is characterized by an outer and an inner nearshore bar in the subtidal zone and a swash bar on the beach.

The sediments in the area are well sorted and composed of fine to medium sand. The mean grain size ranges between 250 and 350  $\mu\text{m}$ . Most of the sediments of the bed surface contain shells (especially in the troughs between the bars) or shell fragments (especially in the swash zone, close to the toe of the beach face).

##### 4.2 Measurements

Detailed measurements of the sediment transport processes in the inner nearshore zone were executed with the use of a small platform. The platform is a scaffold construction of 2.5 meter in length and width at 2.5 meter above the bed. During a measurement day the platform is positioned on a location within the inner nearshore zone. The platform is pulled through the water with a tractor and a winch standing on the beach. The platform is equipped with a capacitance wire, three electromagnetic flow devices, two optical backscatterance devices and a pump sampling system. All these instruments are installed on the seaward exposed site of the platform.

The capacitance wire (CAP) measures the free surface elevations of the water column. The three electromagnetic flow devices (EMF) measure the longshore and cross-shore velocity components in the horizontal plane at three heights above the bed.

The cross-shore micro-morphology of the bed over about 2.5 m was determined by use of a mechanical feeler system consisting of a small trolley connected to a rod movable along one side of the platform. The recorded series of the bed morphology have a spatial resolution of 0.05 m.

Herein, the time-averaged sediment concentration profiles and transport rates are discussed.

##### 4.3 Time-averaged concentrations

Time-averaged concentration profiles at different relative wave heights ( $H_s/h$ ) are shown in Figure 5 and 6.

Figure 5 shows measured concentration profiles under various wave conditions in the surf zone with water depths ranging from 0.7 to 1.2 m. The relative wave heights ( $H_s/h$ ) were in the range of 0.4 to 0.7. The near-bed concentrations are in the range of 0.2 to 2 gr/l. The near surface concentrations are in the range of 0.01 to 0.5 gr/l. A clear influence of the relative wave height can be observed. The near-bed concentrations increase for an increasing relative wave height. The concentration profiles also become more uniform for increasing relative wave height.

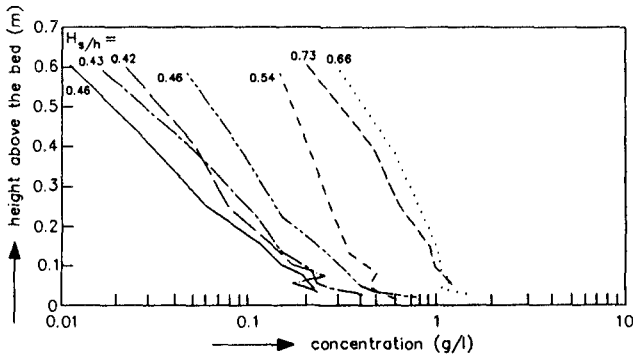


Figure 5 Sand concentration profiles in surf zone

Figure 6 shows concentration profiles in the swash zone with strongly plunging breaking waves. The measured concentrations are a factor 10 larger with near-bed concentrations in the range of 10 to 20 gr/l and a large mixing effect over the depth (more uniform profiles) can be observed.

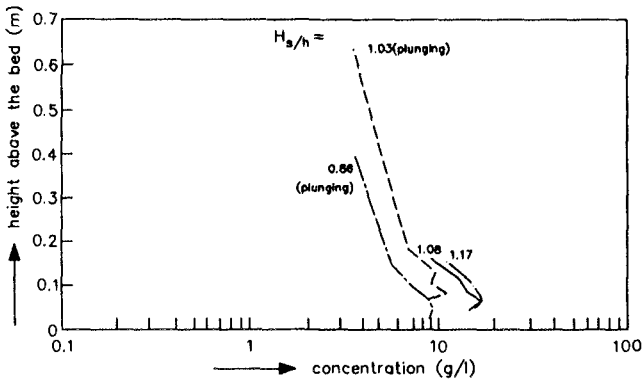


Figure 6 Sand concentration profiles in swash zone

Figure 7 shows the ratio of the concentrations measured at  $z = 0.01$  m and at  $z = 0.1$  m above the bed as a function of relative wave height ( $H_s/h$ ). The ratio sharply decreases for  $H_s/h$  larger than 0.2. A constant value of 2 can be observed for  $H_s/h$  larger than 0.6 which means almost uniform concentration profiles due to the breaking process.

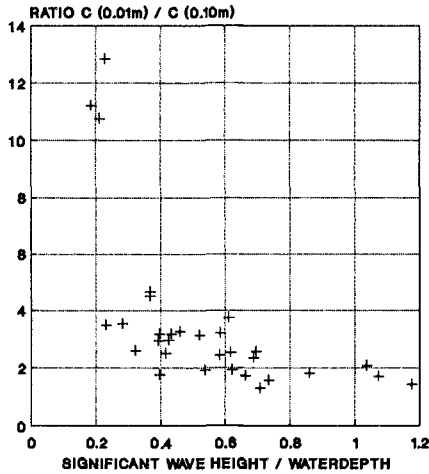


Figure 7 Ratio of concentration at  $z = 0.01$  m and at  $z = 0.1$  m above the bed

Figure 8 shows measured concentrations at  $z = 0.01$  m above the bed as a function of the peak orbital velocity near the bed under the wave crest. Although the scatter is relatively large, the concentrations show an increasing trend for increasing orbital velocities. The experimental results of Ribberink and Al Salem (1991, 1992) measured in wave tunnel conditions are also shown. The relatively large values at low orbital velocities are related to the presence of ripples which are gradually washed out for increasing orbital velocities ( $\hat{U} = 0.8$  m/s).

Equation (4) was used to compute the concentrations at  $z = 0.01$  m above the bed. Reasonable agreement with measured values can be observed. A similar function proposed by Bijker (1971, 1978) was also used (b-factor = 1). As can be observed the Bijker-formula yields almost constant concentrations.

Measured and computed concentration profiles for a range of conditions are shown in Figures 9 and 10. The wave-related bed roughness was taken  $k_{s,w} = 0.05$  m for ripples and  $k_s = 0.01$  m for sheet flow conditions. The significant wave height and the peak period were taken as the characteristic wave parameters. The  $\delta_s$ -parameter expressing the thickness of the near-bed sediment mixing layer in the surfzone, which is an unknown parameter, was used as a calibration parameter. A value of  $\delta_s = 0.2$  m gave good results for all conditions. The ratio of  $\delta_s/h$  shows an increasing trend for increasing values of  $H_s/h$ , see Fig. 11.

Analysis of measured and computed concentration profiles shows reasonably good results for  $H_s/h$ -values upto 0.75 (surf zone), see Figs. 9 and 10. For  $H_s/h$ -values larger than 0.75 (plunging waves in the swash zone) the computed concentrations are systematically smaller than the measured concentrations. Increase of the wave-related bed roughness from  $k_{s,w} = 0.01$  m to  $k_{s,w} = 0.04$  m yields larger concentrations, but the computed values are still a factor of 2 too small. Furthermore, a bed roughness of  $k_{s,w} = 0.04$  m in the swash zone is not realistic. Based on this, it is concluded that the time-averaged concentrations in the swash zone cannot be computed using an equilibrium model concept. The hydrodynamic processes in the swash zone with a relatively steep upsloping bed are strongly non-uniform. Vertical as well as horizontal convective processes are important and should be modeled properly.

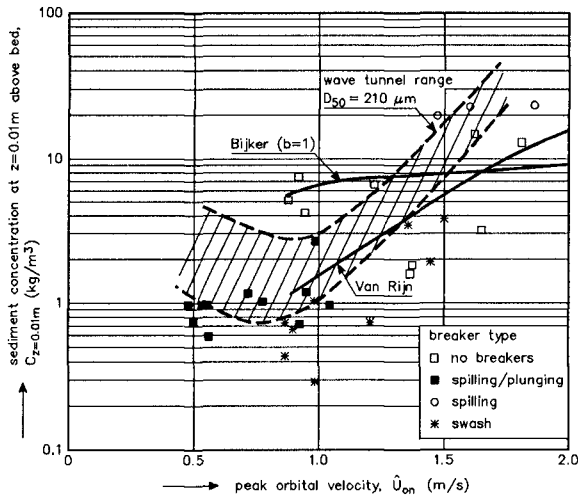


Figure 8 Concentration at  $z = 0.01$  m above the bed

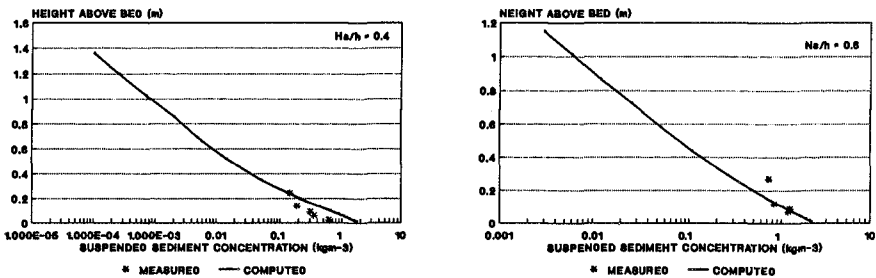


Figure 9 Measured and computed concentration profiles

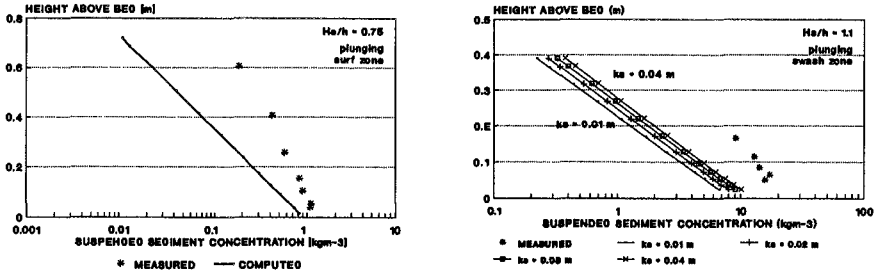


Figure 10 Measured and computed concentration profiles

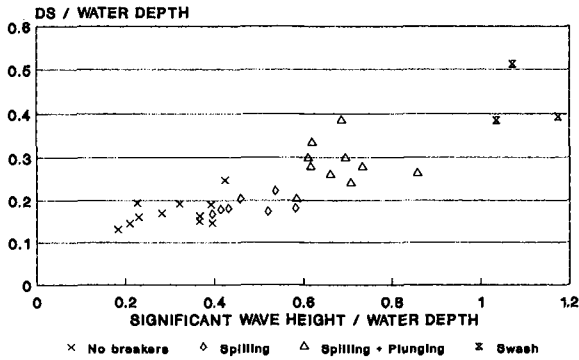


Figure 11 Near-bed sediment mixing layer ( $\delta_s/h$ )

5. Conclusions

The following conclusions are given:

- the current velocity hardly affects the near-bed sediment concentrations; the wave motion is dominant
- the sediment concentrations are maximum when the waves are directed normal to the current (in the ripple regime)
- the sediment concentrations show a large increase under plunging breaking waves, especially in the swash zone
- the concentrations in the swash zone are not locally determined (space lag)
- computed concentration profiles show reasonable agreement with measured values for relative wave heights upto  $H_s/h = 0.7$ .

REFERENCES

Bosman, J.J., Van der Velden, E. and Hulsbergen, C.H., 1987. Sediment Concentration Measurements by Transverse Suction. Coastal Engineering, No. 12.  
 Bijker, E.W., 1971. Longshore Transport Computations. Journal of Waterways, Harbour and Coastal Engineering, Vol. 97, WW4.



- Bijker, E.W., 1978. Lecture Notes Coastal Engineering. Dep. Coastal Engineering, Delft Univ. of Technology, Delft, The Netherlands.
- Kroon, A. and Van Rijn, L.C., 1992. Suspended Sediment Fluxes in the Nearshore Zone at Egmond aan Zee, The Netherlands. Dep. Phys. Geography, Univ. of Utrecht, The Netherlands.
- Ribberink, J.S. and Al Salem, A., 1991. Sediment Transport, Concentrations and Bed Forms in Simulated Asymmetric Wave Conditions. Report H840, Part IV, Delft Hydraulics, Delft, The Netherlands.
- Ribberink, J.S. and Al Salem, A., 1992. Sediment Transport, Concentrations and Bed Forms in Simulated Asymmetric Wave Conditions Report H840, Part V, Delft Hydraulics, Delft, The Netherlands.
- Van Rijn, L.C., 1989. Handbook of Sediment Transport by Current and Waves. Delft Hydraulics, Delft, The Netherlands.
- Van Rijn, L.C., 1990. Principles of Fluid Flow and Surface Waves in Rivers, Estuaries, Seas and Oceans. Aqua Publications, P.O. Box 9896, Amsterdam, The Netherlands.
- Van Rijn, L.C., 1991. Data Base, Sediment Concentration Profiles and Transport for Currents and Waves. Delft Hydraulics, Delft, The Netherlands.
- Van Rijn, L.C., 1993. Principles of Sediment Transport in Rivers, Estuaries, Coastal Seas and Oceans (in Press). Aqua Publications, P.O. Box 9896, Amsterdam, The Netherlands.
- Van Rijn, L.C. et al, 1993. Transport of Fine Sands by Currents and Waves. Journal of Waterways, Port, Coastal and Ocean Engineering, ASCE, March (in Press).

## CHAPTER 201

### A WAVE-CURRENT SEDIMENT BOUNDARY LAYER

Keith Bedford<sup>1</sup> and Jongkook Lee<sup>2</sup>

#### Abstract

A two-hour set of wave-current bottom boundary layer data collected at a dredged material placement site is examined with regard to establishing whether readily measured variables such as turbulent and wave kinetic energy (TWKE) correlate with more difficult to measure near bottom data. The data, collected in Mobile Bay, Gulf of Mexico, consisted of acoustic concentration profile data and velocity measurements at 50 and 114cm above bottom. The Reynolds Stress did not correlate well with any of the near bottom data including vertical flux and total water column mass. TWKE was a much more solid correlate with these variables but still was weak in correlating with near bottom mass. The wave kinetic energy was a solid correlate with near bottom data, particularly the mass in the bottom 5cm.

#### Introduction

Material from dredging operations is often placed in water where both currents (wind driven or tidal generated) and waves exert a pronounced effect on the bottom shear stress and the resulting long term stability of the material. The purpose of this article is to report on aspects of the near-bottom structure of a wave-current bottom boundary layer at a dredged material placement site in Mobile Bay, Gulf of Mexico. The information to be presented here is extracted from a comprehensive report by Bedford *et al.* (1990) which resulted from the authors participation in a comprehensive multi-investigator field experiment performed as part of the US Army Corps Dredging Research Program.

---

<sup>1</sup>Professor, Civil Engineering, Ohio State Univ., 2070 Neil Ave., Columbus, OH 43210

<sup>2</sup>Grad Student, Civil Engineering, Ohio State Univ., 2070 Neil Ave., Columbus, OH 43210

## Field Data Acquisition and Initial Results

### Site Description and Instrumentation

The comprehensive project took place from August 18, 1989 to September 2, 1989 off shore of Mobil Bay, Alabama. The near bottom data presented here were collected by the ARMS (Acoustic Resuspension Measurement System) which was deployed on a Feeder Berm site in 5.75 m of water (low tide datum). The bottom materials were composed of fine grain sands and silts in the 40-60 micron range. While a  $1.45^\circ$  bottom slope existed on the western edge of the Feeder Berm, ARMS was placed in a flat plain almost 300 meters from this slope.

Two fifty-five hour continuously-recording data sets were collected at the site, and the data reported here came from the first deployment collected from 1301 hrs. Central Daylight time (CDT) 22 August '89 to 2033 hrs. CDT 24 August '92.

Table 1 contains a list of the instruments on the bottom sitting tripod and their sampling frequency. The uppermost Marsh McBirney current meter is used to determine wave and current magnitude and direction while vertical flux data are derived from the 50cm Above Bottom (AB) current meter. The acoustic backscatter profiler is interpreted as concentration following Libicki *et al.*, 1989 and the 1.14cm range bins provide an extremely dense profile of 1 Hertz sediment concentration profile data. ARMS wave data were corroborated with additional data supplied from the Shell Well (Shell Oil Company) site and two operational Army Corps PUV gages. The Shell Well data also contained one hour average wind speed, direction, pressure, and air-sea temperature data.

Table 1. Instrumentation and Sampling Summary

VARIABLE MEASURED	SYMBOL	MANUFACTURER	SAMPLING FREQUENCY	SPATIAL LOCATION <sup>2</sup>
Pressure	p	Celesco	2.0 Hz	
Temperature	T	Yellow Springs	1.0 Hz	114 cm
Velocity	u,v	Marsh McBirney	2.0 Hz	114 cm
Velocity	u,w	Marsh McBirney	2.0 Hz	50 cm
Conc. Profile <sup>1</sup>	C(z)	Edo Western 3MHz	1.0 Hz	130 cm

<sup>1</sup>positioned to measure of concentration in a series of 100 range bins, each 1.16cm thick

<sup>2</sup>measured as distance above bottom

In reviewing the fifty-five hour data set, our intention was to focus attention on a wave current period of the record that was suitable for a detailed comparison of the data with proposed theoretical models, particularly the Glenn and Grant (1987) model. The conditions necessary for apply-

ing this model are quite severe (as they are with most theoretically simplified boundary layer models) and include i) constant or equilibrium vertical flux, ii) no horizontal sediment flux gradient, iii) a streamline coordinate system, iv) weak to non-existent vertical tower or instrument tilt, and, for the Glenn and Grant model, v) waves and currents of somewhat equal magnitude. From the fifty-five hour data set, a two-hour period of data was exemplary in meeting all these criteria i.e. 1711 hrs. CDT to 1911 hrs. CDT 22 August '92. One of the notable features of this piece of data is that the total horizontal current vector flows due east for the entire two hours which means that the 50cm AB current vector is sampling the full streamline coordinate average velocity. These two hour data are examined in more detail in the rest of the article and will be referred to as the "data set."

### The Setting

A graphical and analytical review of the average conditions during the data set has appeared in Bedford *et al.*, 1991 and will not be repeated here. In summary, the winds were steady at 5m/sec. coming from 160° having just veered to that direction from 45° during the prior twelve hours. The tide was approaching slack tide at 1700 hrs having reached maximum ebb stage 4 hours earlier. As noted above then the current was directed the east (+x, +u) and uniformly increased over time from 15-22 and 6.5-12cm/sec at the top and bottom current meters, respectively. The significant wave height was approximately 1.0m with a peak period of 5.6 seconds. These data correspond to a wavelength of 37.0m and a bottom orbital velocity of 22cm/sec. The waves progressed to the north west (320°) in contrast to the eastward flowing current.

### Local Averages and Turbulence Definition

The definition of turbulence requires that the local temporal average value be known. This local average must be from a record sufficiently long enough to achieve stationary conditions in the fluctuation statistics. With the short period gravity waves and wave groups being analyzed here, turbulence time scales and wave period fluctuations overlap and lacking any clear theoretical guidance on how to separate wave and turbulent fluctuations the only averaging operation attempted was the traditional Reynolds uniform weight function. The selection of the averaging interval  $T$ , is difficult in time varying flows. Methods suggested by Gross and Nowell (1983) and standard run tests (Bedford *et al.*, 1987) were applied to these data with a ten-minute period selected for averaging. Correspondingly, the data set was subdivided into 12 ten-minute long frames; averages performed for each frame and combined turbulent and wave induced instantaneous fluctuations were defined relative to that local average.

### Average Concentration Field

Figure 1 contains the twelve average near bottom concentration profiles. The extremely sharp vertical gradient 10-20cm AB is a trademark of wave-current bottom boundary layers (WCBL) and separates the current driven region ( $z > 20$ cm AB) from the combined wave-current driven region ( $< 10$ cm AB). Unlike the Glenn and Grant model calculations, there is a smooth (continuous first derivative) transition region ( $10 < z < 25$ cm AB) between the two layers. Explicit comparisons of these profiles with the Glenn and Grant (1987) model are contained in the article by Bedford and Lee (1992). In summary, with no coefficient tuning of any kind, the model reproduced the profiles quite adequately. The near bottom ( $z < 20$ cm) comparison was quite good with the comparisons at or above  $z > 30$ cm being poorer than expected.

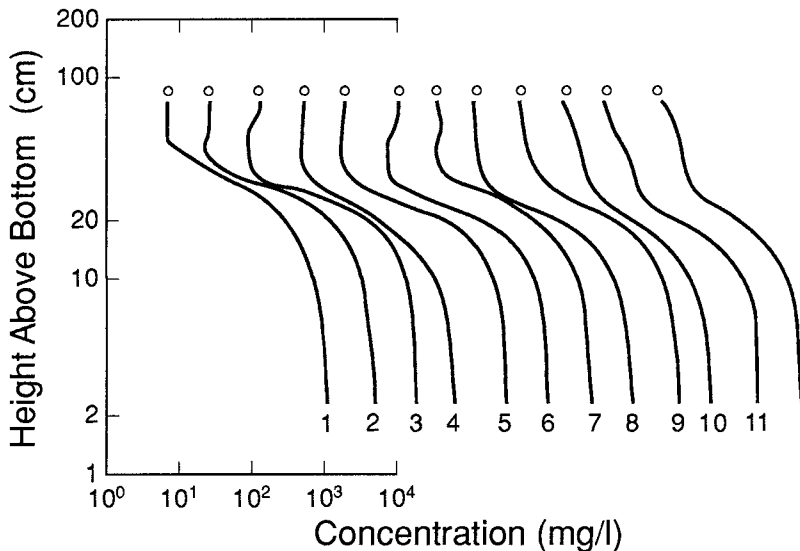


Figure 1. Profiles of the Twelve Ten-Minute Average Concentration Profiles

### Turbulent and Flux Data

#### Turbulent Parameters

With the current meter being 50 cm AB, turbulent data as well as direct flux measurements in the thin WCBL are prohibited. Following are data on the turbulent quantities at 50 cm AB. Figure 2 contains plots of  $\overline{u'w'}$  and the turbulent and wave kinetic energy (TWKE). The "Reynolds stress" varies

between  $-2$  and  $0$  with an average value of  $-1.3 \text{ cm}^2/\text{sec}^2$ . In assessing these values it should be noted that the critical erosion stress for the bottom materials at the site is estimated by the modified Shields diagram (Glenn and Grant 1987) to be  $1.34 \text{ dynes}/\text{cm}^2$  while the Achers and White value was estimated to be  $0.95 \text{ dynes}/\text{cm}^2$ . One can anticipate greater values of measured  $\overline{u'w'}$  near the bottom and therefore assume that erosion is continuous during the period.

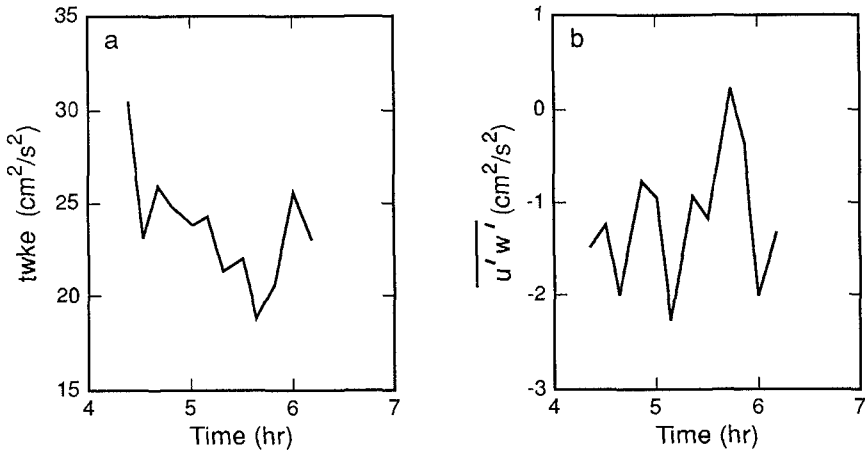


Figure 2. Time Traces of a.) Turbulent and Wave Kinetic Energy (TWKE); and b.) Reynolds Stress  $\overline{u'w'}$

The TWKE average value is  $24 \text{ cm}^2/\text{sec}^2$  varying between  $18\text{--}31 \text{ cm}^2/\text{sec}^2$ . The ratio of the TWKE to total energy is falling continuously during the data set from  $0.45$  to  $0.2$  with the average being  $0.35$ .

#### Flux and Variance Data

The net vertical flux at  $50 \text{ cm AB}$  consists of advective ( $\overline{w\bar{c}}$ ), settling ( $w_s\bar{c}$ ) and turbulent ( $\overline{w'c'}$ ) components. For this data set  $\overline{w\bar{c}}$  is essentially zero; a requirement for boundary layer theories.

Figure 3a contains a time trace of the average concentration at  $50 \text{ cm AB}$  and the normalized root mean square (NRMS) value. As seen, the concentrations are not high being less than  $10\%$  of the average values in the bottom  $10 \text{ cm}$ . Also, the average is comprised of widely varying data achieving NRMS values of  $1.0$  but generally centering on  $0.5$ . By contrast, Fig. 3b contains the same data for  $5 \text{ cm AB}$ . Here again the NRMS is roughly  $0.5$ . The average

concentration is falling a bit more, probably in response to the slightly weakened wave field towards the end of the two hours. Figure 3c contains a plot of the total vertical flux at 50cm AB. It is seen to drop quickly during the first two frames to a value of  $-5(10^{-3})$  mg/cm<sup>2</sup>/sec and then change relatively little.

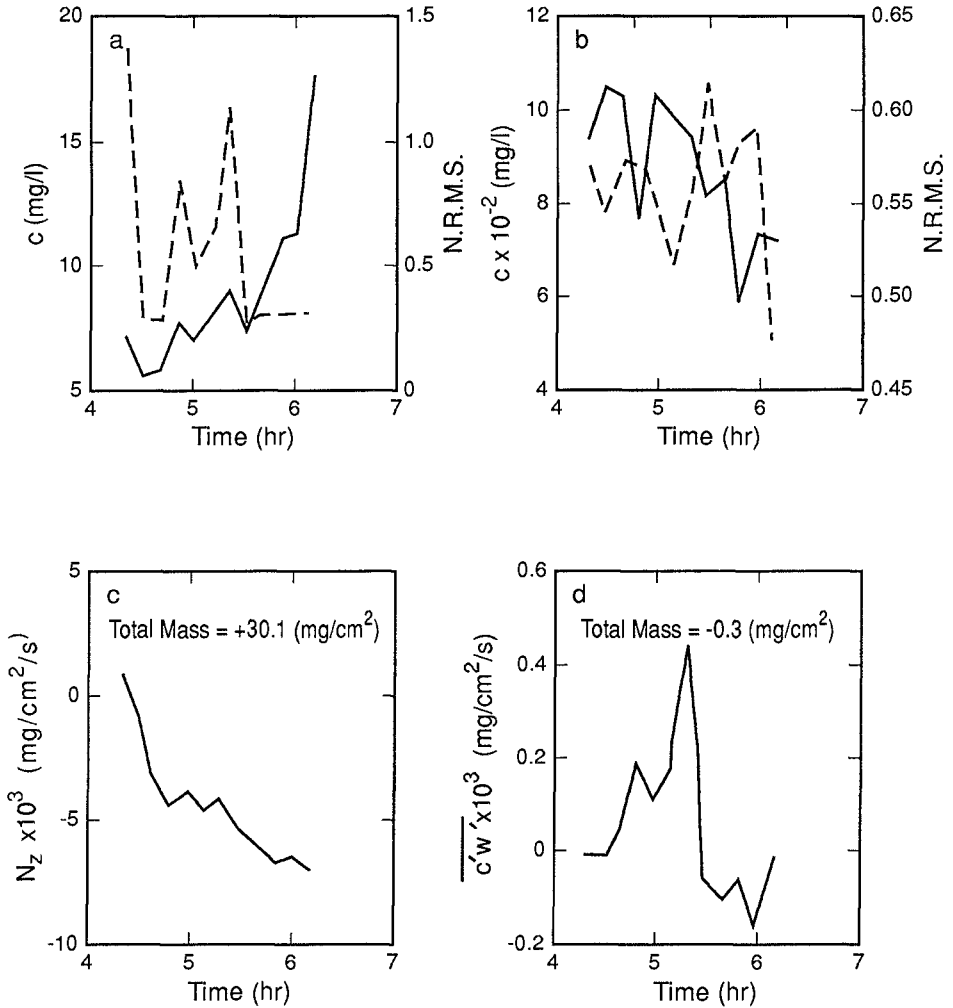


Figure 3. a.) Time Trace of Concentration at 50cm Above Bottom (AB); b.) Time Trace of Concentration at 5cm AB; c.) Time Trace of Vertical Flux,  $N_z$ , at 50cm AB; and d.) Time Trace of Turbulent Flux,  $\overline{c'w'}$ , at 50cm AB.

The net flux then is weakly depositional. Turbulent diffusive flux at 50cm AB (Fig 3d) is quite weak. These calculations assume a settling velocity for the particle size of 0.40 cm/sec. On Figures 4c and 4d the number "total mass" refers to the integrated flux or equivalent mass per square centimeter that would accumulate on (+) or erode from (-) the bottom during the two-hour data set. As easily seen, the net equivalent deposition on the bottom totals 0.1 mm; i.e. a net accumulation of virtually zero.

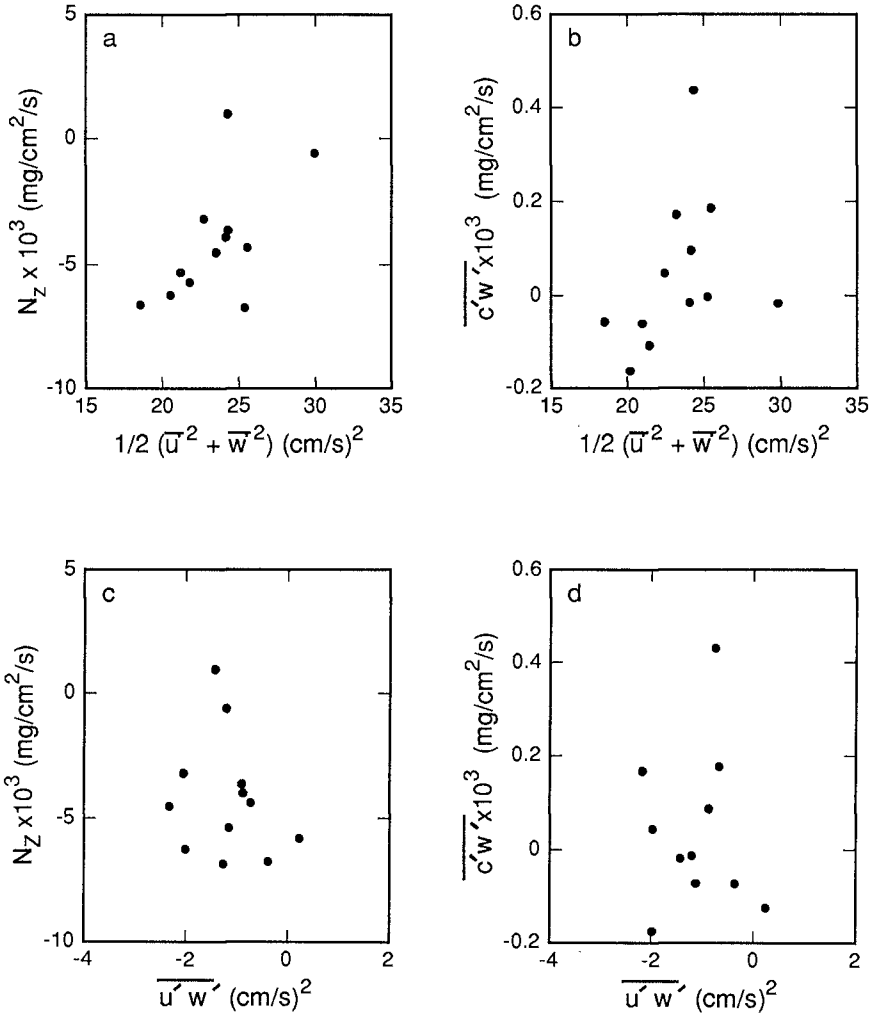


Figure 4. Scatterplots of a.) TWKE vs  $N_z$ ; b.) TWKE vs  $\overline{c'w'}$ ; c.)  $\overline{u'w'}$  vs  $N_z$ ; and d.)  $\overline{u'w'}$  vs  $\overline{c'w'}$



### Flux Correlations

Of management interest to engineers are correlations of near bottom concentration, total mass and flux rates with other measured variables. Figures 4a-d present scatterplots of the TWKE and Reynolds stress with the total flux ( $N_z$ ), and turbulent flux ( $\overline{c'w'}$ ). As can be readily seen the correlations with  $\overline{u'w'}$  or Reynolds stress are poor to nonexistent. The correlations between TWKE and the two fluxes are stronger. That the Reynolds stress is such a poor correlate should be a bit surprising as it is often thought to be strongly representative of the force necessary for erosion at the bottom. That it is such a poor correlate should bring comfort however, as it is very difficult to measure being filled with errors and subject to considerable scatter (Grant and Madsen 1986, Bedford 1992). TWKE, on the other hand, is a much simpler variable to measure and would prove to be an easier correlate to embed in empirical formulations for fluxes, etc. It should be further noted that the correlation between flux  $N_z$  or  $\overline{c'w'}$  and TWKE is at the heart of many phenomenological models of turbulence (e.g. ASCE 1988) and lends field data support to that basic hypothesis.

### Concentration and Total Mass Correlations

Correlations of the average concentrations (at 50 and 5cm AB) with TWKE were inconclusive. This is a bit discouraging, especially at 50cm AB where the nonlinear and confounding effects of ripples, sediment stratification, and vortex shedding, etc., are minimal.

Another type of correlation of a sediment profile measure, the integrated profile mass, was a good deal more successful. Here the instantaneous profiles were integrated from  $z = 0$  to various heights above bottom (e.g. 5 cm, 50 cm) and the resulting integrated mass time averaged. Figures 5a,b contain the integrated mass time variation for  $z = 50$  and 5 cm AB, respectively.  $Q_{50}$  is generally falling in accordance with the gradual decrease of wave energy.  $Q_5$ , even though an integrated and therefore a smoothed measure, is a bit more irregular, an indication of the complexity of the near bottom physics.

Figures 5c,d contain correlations between TWKE and  $Q_{50}$  and  $Q_5$ , respectively. A clear linear relationship between TWKE and  $Q_{50}$  is noted. Again, the lack of clear correlation between TWKE at 50cm AB and local near bottom activity is noted. Clearly, using remote (50cm AB) turbulence data isn't advisable in establishing values of local near bottom concentration and interfacial exchange values.

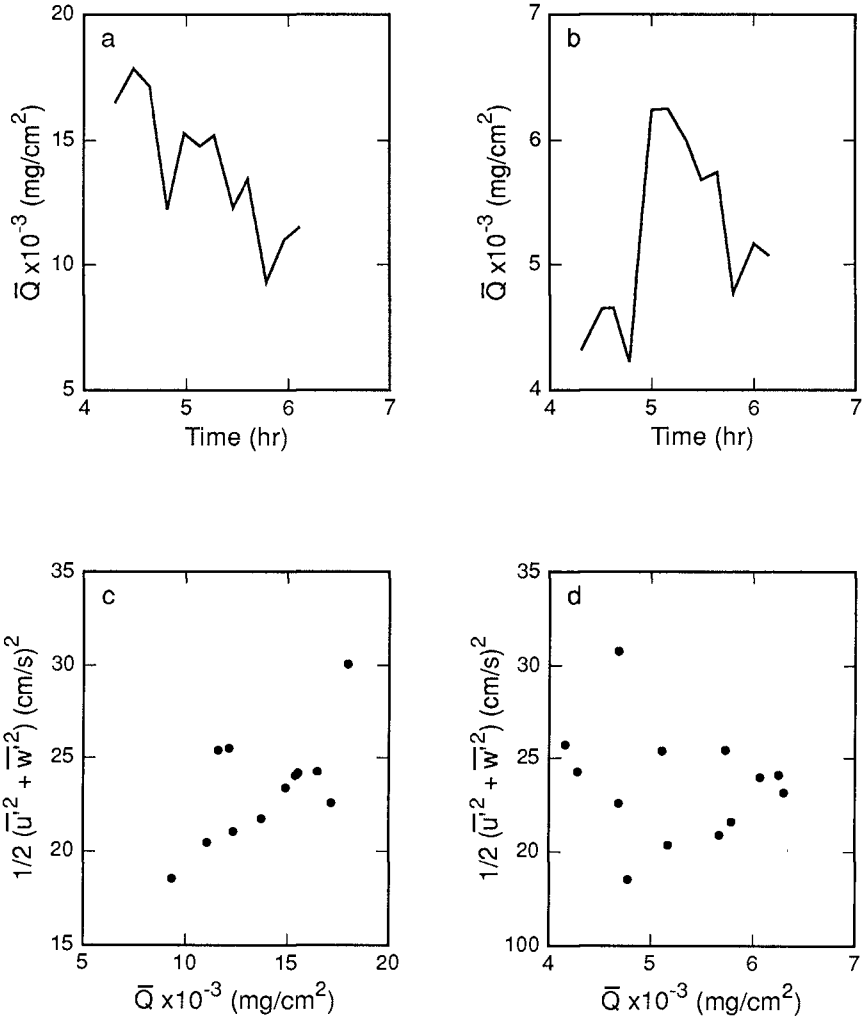


Figure 5. a.) Time Trace of Integrated Mass at 50cm AB,  $Q_{50}$ ;  
 b.) Time Trace of  $Q_5$ ;  
 c.) Scatterplot of TWKE and  $Q_{50}$ ; and  
 d.) Scatterplot of TWKE and  $Q_5$ .

While turbulence measures can be altered dramatically between 50 cm and 5cm AB by for example stratification and therefore provide poor correlation, wave data at 50 cm penetrate relatively unscathed to the near bottom region and thus might be a better correlate under certain conditions. Figures 6a,b contain scatter plots of the wave kinetic energy (as calculated by

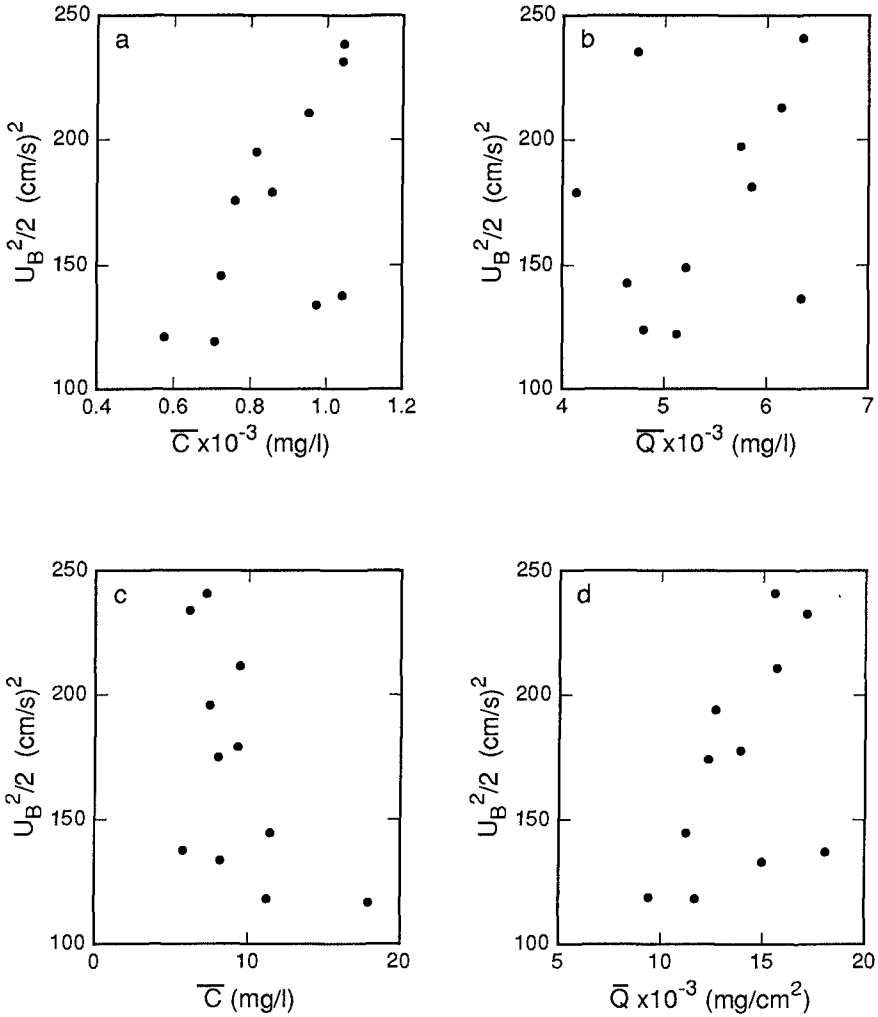


Figure 6. Scatterplots of a.) Bottom Orbital Velocity Energy,  $U_B^2/2$  vs  $C$  at 50cm AB; b.)  $U_B^2/2$  vs  $Q$ ; c.)  $U_B^2/2$  vs  $C$  at 50cm AB; and d.)  $U_B^2/2$  vs  $Q_{50}$

one half the bottom orbital velocity squared), and  $\bar{c}$  and  $Q$  at 5cm AB. Here, a clear linear relationship is at hand; reflecting not only the dominance of the wave in local bottom activity but also a relatively simple procedure for

perhaps constructing empirical relationships for bottom exchange. Figure 6c shows that  $U_b^2/2$  also correlates quite well with the integrated mass measure  $Q_{50}$ . Figure 6d, quite by contrast, shows poor correlation between  $U_b^2/2$  and  $\bar{c}$  at 50cm AB, thus indicating that a more complex suite of physical processes is at work in controlling the values of the two sediment measures.

### Shape Analyses and Correlation

Based upon a geometric shape analysis procedure developed by Velissariou and Bedford (1989) the 12 average profiles were analyzed and four relatively distinct regions separated by three "boundaries" were identified. Figure 7 contains the time series of the heights of the various boundaries. The top of the wave-current boundary layer is seen to be relatively steady at 10-11 cm AB; the transition region occupies the region between 12-24 cm AB and

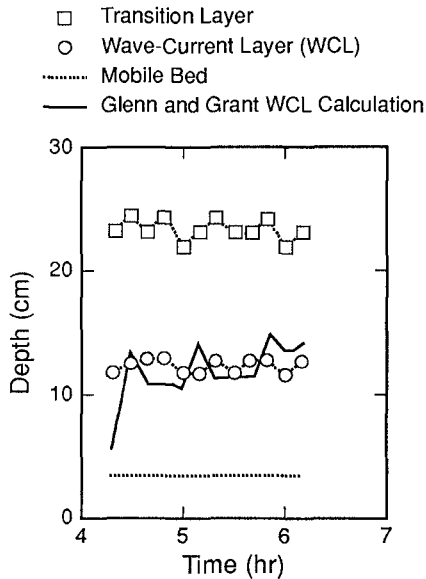


Figure 7. Time Trace of the Heights of the Measured Transition Layer ( $\square$ ), the Measured Wave-Current Boundary Layer ( $\circ$ ), the Measured Mobile Layer (---) and the Calculated Wave-Current Layer (—).

below 3cm we found evidence for a mobile layer. The height of the wave-current boundary layer calculated by Glenn and Grant (1987) is also plotted and is seen to fall squarely on the geometrically determined heights.

Recognizing from the previous correlations how well TWKE and its subsumed but dominant wave kinetic energy correlated with integrated mass measures, it should come as no surprise that it also correlated very well with the total mass in the WCBL ( $Q_{11}$ ) and the total mass just in the transition layer ( $\bar{Q}_{11-24}$ ).

### Summary

The tower by which these data were collected contained an extremely robust and exotic suite of instrumentation. By examining various correlations in these robust data, we can perhaps begin to identify simpler point measurements that can be made with more readily available instruments. Clearly, these results indicate that TWKE, with its subsumed wave kinetic energy component, is a fundamental correlate with a number of important parameters including  $N_z$  ( $z=50$ ),  $\overline{c'w'}$  ( $z = 50$ ),  $Q_{50}$ ,  $Q_{11}$  (the mass in the WCBL) and  $\bar{Q}_{11-24}$  (the mass in the transitional layer). TWKE was a weaker correlate with near bottom  $Q_5$  and provided no correlation with  $C_5$ .

The wave kinetic energy in the form of  $U_B^2 / 2$  was a solid correlate with the bottom activity  $Q_5$ ;  $C_5$ .  $U_B^2 / 2$  didn't correlate well with  $C_{50}$ , nor did TWKE.

The WCBL height predicted by the Glenn and Grant model was identical to that measured by our devices indicating the soundness of that empirical representation as well.

While notable, these simplifications did come from a data set that was selected via some strong restrictions. That there are still many unexplained features and results in these data which suggests we have far to go in achieving understanding when we depart from the benign equilibrium conditions analyzed here.

### Acknowledgements

Funds for this research came from the Army Corps of Engineers Dredging Research Program Contract No. DACW-39-88-K-0040. These funds, and the advice and encouragement of Dr. N. Kraus, the contract monitor, are sincerely appreciated. Additional funds for this research provided by NOAA-Ohio Sea Grant Project RE 11/1 and the College of Engineering, The Ohio State University are also appreciated.

## References

- American Society of Civil Engineers Task Committee on Turbulence Models in Hydraulics Computations, K. Bedford, Chair., 1988. "Turbulence Modeling of Surface Water Flow and Transport," *J. Hydraulic Engineering*, Vol 114, pp 970-1073.
- Bedford, K., 1992. "Sediment Exchange Process Parameterization," in: *Chemical Dynamics in Fresh Water Ecosystems*, ed. F. Gobas and J. McCorquodale, Lewis Pub. Co., pp 53-91.
- Bedford, K. and J. Lee, 1992. "The Near-Bottom Sediment Response to Combined Wave-Current Flows-Mobile Bay, Gulf of Mexico," *J. of Geophysical Research*, submitted.
- Bedford, K., O. Wai, C. Libicki, and R. Van Evra III, 1987. "Sediment Entrainment and Deposition Measurements in Long Island Sound," *J. Hydraulic Engineering*, Vol 113, pp 1325-1342.
- Bedford, K., O. Wai, R. Van Evra III, P. Velissariou, J. Lee and C. Libicki, 1990. "The Local Near Bottom Response of a Dredged Material Placement Site to Wind and Tide Effects," Rept. US Army Corps of Engineers, Coastal Engineering Research Center, Vicksburg, MS.
- Bedford, K., O. Wai, P. Velissariou, R. Van Evra, and J. Lee, 1991. "Fine Material Entrainment and Flux at a Shallow-Water Dredged Mound," in: *Proc. Marine Technology Society*, Nov 10-14, New Orleans, LA, pp 260-264.
- Glenn, S. and W. Grant, 1987. "A Suspended Sediment Stratification Correction for Combined Wave and Current Flows," *J. Geophysical Research*, Vol 92, pp 8244-8264.
- Grant, W. and O. Madsen, 1986. "The Continental Shelf Bottom Boundary Layer," in: *Annual Revi of Fluid Mechanics*, Annual Reviews Inc, pp 265-306.
- Gross, T. and A. Nowell, 1983. "Mean Flow and Turbulence Scalding in a Tidal Boundary Layer," *Continental Shelf Research*, Vol 2, pp 109-126.
- Libicki, C., K. Bedford, and J. Lynch, 1989. "The Interpretation and Evaluation of a 3MHz Acoustic Backscatter Device for Measuring Benthic Boundary Layer Sediment Dynamics," *J. Acous. Soci of America*, Vol 85, pp 1501-1511.
- Velissariou, P. and K. Bedford, 1989. "The Response of Estuarine Concentration Profiles to Weak Swell," in: *Proc. Int. Assn. for Hydraulic Res. Technical Session D. Environmental Hydraulics*, XXIII congress, Ottawa, Canada, National Research Council Canada Publ., pp. D.53-D.60.

## CHAPTER 202

### LONGSHORE CURRENT AND LATERAL MIXING IN THE SURF ZONE

Ichiro Deguchi<sup>1)</sup>, Toru Sawaragi<sup>2)</sup> and Masanobu Ono<sup>3)</sup>

#### **Abstract**

We investigated the occurrence of FIG waves generated by a shear instability of steady longshore current on a uniformly sloping beach so that we can discuss the characteristic of Fig waves with respect to a wave breaking. We also carried out experiment to investigate cross-shore distribution of lateral mixing coefficient that determines the cross-shore profile of longshore current.

It is found that the occurrence and characteristic of FIG waves depend on a cross-shore profile of steady longshore current on the uniformly sloping beach as well as those on a beach of a constant depth analyzed by Bowen et al.(1989). The bottom slope affects FIG waves indirectly through the cross-shore profile of longshore current. The measured lateral mixing coefficient, which also gives influence on longshore currents, becomes maximum within the surf zone and decreases rapidly toward offshore. The locus where the maximum longshore current occurs, that plays an important role in the generation of FIG waves, depends on the surf similarity parameter of the incident wave.

#### **Introduction**

Various research regarding long period waves in a coastal region have been carried out. An object of the most of research is a long period wave corresponding to infragravity band. Wave number  $k_i$  of a long period wave of infragravity band is in a range of  $\sigma^2/g < k_i < \sigma^2/(g \tan \beta)$  and does not become larger than  $\sigma^2/(g \tan \beta)$ , where  $\sigma$  is the angular frequency,  $g$  is the gravitational acceleration and  $\tan \beta$  is the bottom slope.

According to recent field studies, waves of large wave numbers (short wave lengths) were observed in the lower frequency band than the infragravity band. Bowen et al.(1989) named such wave far infragravity wave (FIG wave). They analyzed the occurrence and characteristic of FIG waves and reported that a shear instability of steady longshore current caused FIG waves. However, their analysis was carried out

---

1) Assoc. Prof., 2) Prof. and 3) Research. Assoc., Dept. of Civil Eng.,  
Osaka University, Yamada-oka, Suita-city, Osaka 565, Japan

under the simplified condition where a constant water depth and a linear distribution of longshore current were assumed.

We analyzed the occurrence of FIG wave caused by the shear instability of steady longshore current on a uniformly sloping beach, a more realistic condition. We also examined the characteristic of lateral mixing coefficient that determines the cross-shore distribution of longshore current and accordingly exerts an influence on the occurrence of FIG wave greatly.

### Occurrence condition of FIG wave on a uniformly sloping beach

In this section, we analyze the characteristic of FIG wave under the condition where a steady longshore current develops on a long straight beach with parallel contours. A coordinate system is shown in Fig.1. An  $x$  axis is taken positive in the offshore direction from the still water shoreline and a  $y$  axis in the longshore direction.

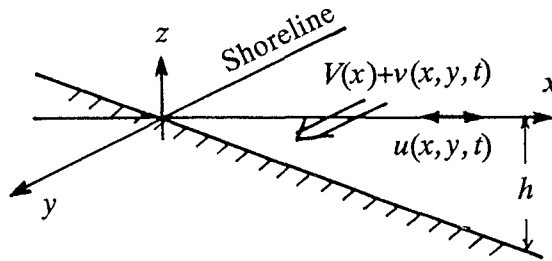


Figure 1 Coordinate system

We assume that a perturbed motion is superimposed on the steady longshore current. Let cross-shore and longshore components of perturbed velocity be  $u(x, y, t)$  and  $v(x, y, t)$  and the depth averaged velocity of steady longshore current be  $V(x)$  where  $V \gg (u \text{ and } v)$ . We also express the surface displacements corresponding to the perturbed motion and a steady component as  $\eta(x, y, t)$  and  $E(x)$ .

The following fundamental equations for the steady component and perturbed component are obtained from a basic equation of a wave-induced current.

$$0 = -\frac{\partial E}{\partial x} - \frac{1}{\rho D} \frac{\partial S_{xx}}{\partial x} \quad (1)$$

$$0 = -\frac{1}{\rho D} \left( \frac{\partial S_{xy}}{\partial x} + \tau_y \right) + K_{xy} \frac{\partial^2 V}{\partial x^2} \quad (2)$$

$$\frac{\partial u}{\partial t} + V \frac{\partial v}{\partial y} = -g \frac{\partial \eta}{\partial x} \quad (3)$$

$$\frac{\partial v}{\partial t} + u \frac{\partial V}{\partial x} + V \frac{\partial v}{\partial y} = -g \frac{\partial \eta}{\partial y} \quad (4)$$

where  $\rho$  is the density of water,  $\tau_y$  is the time averaged bottom shear stress in the longshore direction,  $S_{xx}$  and  $S_{xy}$  are the radiation stresses,  $K_{xy}$  is the lateral mixing coefficient and  $D$  is the total water depth ( $=h+E+\eta$ ).

We also suppose that a temporal variation of  $D$  is sufficiently smaller than spatial gradients of horizontal mass flux ( $uD$  and  $vD$ ) of perturbed motion in cross-shore and



longshore directions. The following equation of continuity for perturbed motion is obtained.

$$\frac{\partial uD}{\partial x} + \frac{\partial vD}{\partial y} = 0 \quad (5)$$

We define a transfer stream function  $\Psi$  by Eq.(6) that has a form of Eq.(7):

$$uD = -\frac{\partial \Psi}{\partial y}, \quad vD = \frac{\partial \Psi}{\partial x} \quad (6)$$

$$\Psi = \text{Re} \{ \phi(x) \exp [i(ky - \sigma t)] \} \quad (7)$$

where  $\text{Re}\{ \}$  expresses a real part of the complex quantity inside  $\{ \}$ ,  $\sigma$  and  $k$  are the angular frequency and the wave length of perturbed motion.

Eliminating  $\eta$  from Eqs.(3) and (4) and replacing  $(u, v)$  with  $\Psi$  by using Eq.(6), the following equation regarding  $\phi(x)$  is obtained.

$$(V - \sigma/k) \{ \phi_{xx} - k^2 \phi - (D_x/D) \phi_x \} - \phi D(V_x/D)_x = 0 \quad (8)$$

where subscript  $x$  indicates a partial differentiation regarding  $x$ . The term  $V_x/D$  indicates the background potential vortex.

Bowen et al.(1989) supposed a triangular distribution of longshore current on a beach of constant water depth. Under such assumption,  $D_x$  in Eq.(8) becomes 0. They solved Eq.(9) and discussed the characteristic of FLG waves based on the solution that is expressed by a hyperbolic function.

$$\phi_{xx} - k^2 \phi = 0 \quad (9)$$

However, there exists a bottom slope actually. Incident waves do break on the sloping bottom and longshore current generates. We examined various bottom profile where an analytical solution to Eq.(10) is obtained under the condition of  $(V_x/D)_x=0$  in Eq.(8).

$$\phi_{xx} - k^2 \phi - (D_x/D) \phi_x = 0 \quad (10)$$

It is found that when the bottom profile is expressed by Eq.(11), Eq.(10) becomes a modified Bessel's differential equation, Eq.(12).

$$D = x \tan \beta \quad (11)$$

$$\phi_{xx} - (1/x) \phi_x - k^2 \phi = 0 \quad (12)$$

A general solution to Eq.(10) is given by the first order modified Bessel functions of 1st and 2nd kind,  $I_1$  and  $K_1$  as follows:

$$\phi = p I_1(kx) + q K_1(kx) \quad (13)$$

where  $p$  and  $q$  are the integral constant. On the other hand, the surface displacement of perturbed motion is calculated by eliminating  $u, v$  from Eq.(4) by using Eqs.(6) and (7) as follows:

$$\eta = -\{ (V - \sigma/k) \phi_x - V_x \phi \} / gD \quad (14)$$

We assume the same profile of  $V_x/D$  as Bowen et al. did. According to this assumption, a distribution of longshore current becomes the full line shown in Fig.2. A notation  $X_0$  is the width of the longshore current whose velocity becomes the maximum ( $V=V_0$ ) at  $x=\delta X_0$  ( $0 < \delta < 1$ ). In the figure, the bottom profile and the distribution of longshore current assumed in the analysis of Bowen et al.(1989) are shown by broken lines.

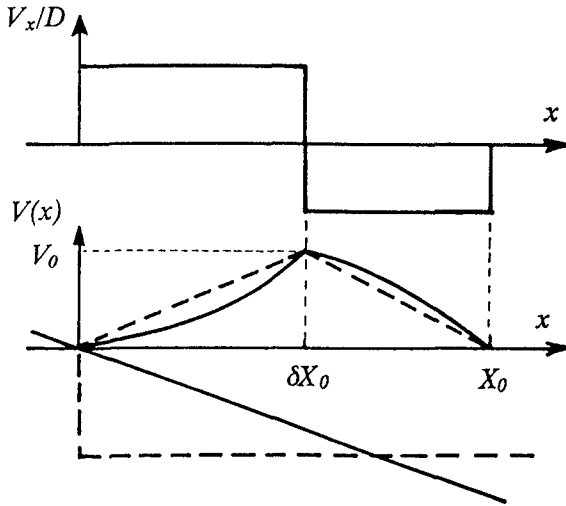


Fig.2 Cross-shore distributions of  $V_x/D$  and  $V(x)$

The boundary conditions that the solutions in the regions of  $0 \leq x \leq \delta X_0$  and  $\delta X_0 \leq x \leq \infty$  have to satisfy are given as follows:

$$\phi(x) = 0 \quad : \quad \text{at } x=0 \text{ and } x=\infty, \text{ and}$$

Continuities of  $\phi$  and  $\eta$  : at  $x=\delta X_0$

When we eliminate integral constants in Eq.(13) by using these boundary conditions, the following dispersion relation for the perturbed motion is obtained:

$$a\sigma'^2 + b\sigma' + c = 0 \tag{15}$$

$$a = F_1 F_d \quad , \quad b = F_d / (1 - \lambda) - F_1 (k' F_d - \lambda)$$

$$c = \{1/(\delta - 1)\} \left[ \lambda \{1 - (I_{1d}/I_{11})(K_{11}/K_{1d})\} - k' F_d \right]$$

$$\lambda = 1/\delta + 1/(1 - \delta) \quad ,$$

$$F_1 = (I_{01} + I_{21}) / (2I_{11}) + (K_{01} + K_{21}) / 2K_{11},$$

$$F_d = (I_{0d} + I_{2d}) / (2I_{1d}) + (K_{0d} + K_{2d}) / 2K_{1d},$$

$$K_{jd} = K_j(k' \delta) \quad , \quad K_{j1} = K_j(k') \quad , \quad I_{jd} = I_j(k' \delta) \quad , \quad I_{j1} = I_j(k') \quad ,$$

where,  $\sigma'$  ( $=\sigma(V_0/X_0)$ ) is the non-dimensional angular frequency,  $k'$  ( $=kX_0$ ) is the non-dimensional wave number,  $I_j$  and  $K_j$  ( $j=0,1,2$ ) are the  $j$ -th order modified Bessel function of 1st and 2nd kinds.

From, Eq.(15), it is found that when  $\sigma'$  becomes a complex ( $\sigma' = \sigma'_r + i\sigma'_i$ ) with the negative imaginary part ( $\sigma'_i < 0$ ), the perturbed motion becomes unstable and the amplitude of perturbed motion increases exponentially with time. FIG waves are generated by this instability and  $\sigma'_r$  becomes a growth rate of FIG wave. This instability occurs under the following condition.

$$b^2 - 4ac < 0 \tag{16}$$

We can also see that the non-dimensional angular frequency is a function of non-dimensional wave number  $k'$  and  $\delta$  that is a parameter indicating the relative location where the maximum longshore current occurs. The bottom slope has nothing to do with the angular frequency explicitly.

Figure 3 shows the relation between  $k'$  and  $\sigma_r'$  calculated from Eq.(15). In the figure, the region where Fig waves can occur is also illustrated. Figure 4 is the relation between  $\sigma_i'$  and  $k'$  when Eq.(15) has complex solutions.

As the value of  $\delta$  increases the region where FIG wave occur spreads to the high waves number. The growth rate of FIG wave also becomes large. According to the results obtained by Bowen et al.(1989) both upper and lower limits in the wave number for the presence of FIG waves exist. However, only the upper limit in the wave number exists on the sloping beach.

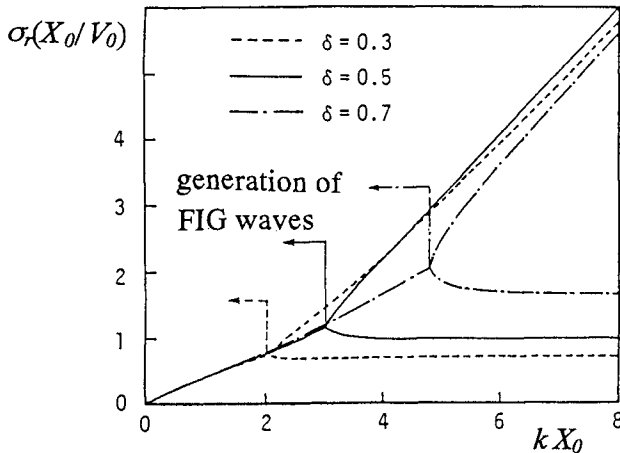


Fig.3 Relation between non-dimensional angular frequency and non-dimensional wave number and occurrence range of FIG waves.

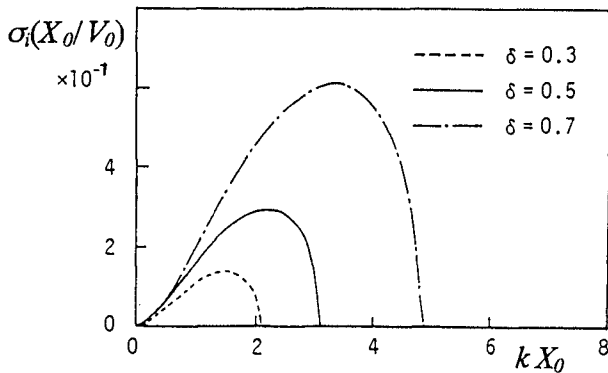


Fig.4 Growth rate of FIG wave

Figure 5 shows a relation between  $\delta$  and the maximum nondimensional wave number  $k'_m$  of FIG wave.

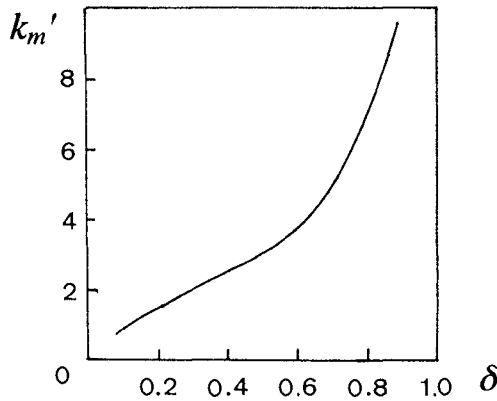


Fig.5 The maximum nondimensional wave number of FIG wave

Figure 6 shows the change of nondimensional celerity  $C_p'$  of FIG wave defined by  $\sigma'/k (= (\sigma/k)/V_0)$  with the non-dimensional wave number  $k'$  in the cases of  $\delta=0.3, 0.5$  and  $0.7$ . The values of  $C_p'$  of different values of  $\delta$  in Fig.6 do not show any significant difference.

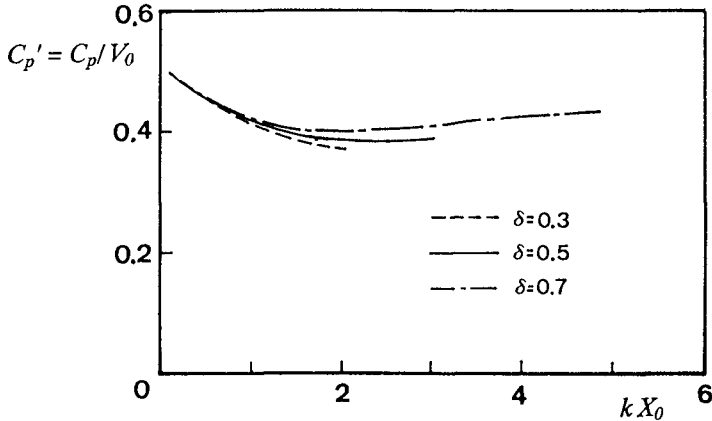


Fig.6 Nondimensional celerity of FIG wave

From these results, it is found that the occurrence of FIG wave depends on only the value of  $\delta$  and the wave number and the angular frequency of FIG wave are determined by the values of  $X_0$ ,  $\delta$  and  $V_0$ . Also, the wave number of FIG wave is sufficiently larger than those of long waves of leaky mode ( $<\sigma^2/g$ ) and of edge

wave( $<\sigma^2/(g\tan\beta)$ ). For instance, when  $V_0=1\text{m/s}$ ,  $X_0=20\text{ m}$ ,  $\tan\beta=0.1$  and  $\delta=0.5$ , FIG wave exists in the region of  $k<0.15$  and  $\sigma<0.058$  from Fig.3. The wave period and the wave length corresponding to the maximum angular frequency are 108s and 41.9 m, respectively.

### Cross-shore distribution of longshore current velocity

As mentioned above, the characteristic of FIG wave deeply depends on a cross-shore distribution of steady longshore current. Many studies have been carried out about the steady longshore current on the long straight beach based on Eqs.(1) and (2). For example, an analytical solution of the velocity of steady longshore current derived by Longuet-Higgins (1970) is expressed as follows:

$$V/V_b = A(x/x_b) + B_1(x/x_b)^r \quad \text{for } x/x_b \leq 1 \quad (17)$$

$$V/V_b = B_2(x/x_b)^s \quad \text{for } x/x_b > 1$$

$$V_b = \frac{5\pi \tan\beta}{16 C_f} \sqrt{gD_b} \sin \theta_b \quad (18)$$

$$p = \pi N \tan\beta / (\gamma C_f) \quad , \quad A = 1/(1 - 5p/2) \quad ,$$

$$r = \left\{ -3/4 + \sqrt{9/16 + 1/p} \right\} \quad , \quad s = \left\{ -3/4 - \sqrt{9/16 + 1/p} \right\} \quad , \quad (19)$$

$$B_1 = A(s-1)/(r-s) \quad , \quad B_2 = A(r-1)/(r-s) \quad ,$$

where  $N$  in the expression of  $p$  is the constant relating to a lateral mixing coefficient,  $\gamma$  is the ratio of wave height to water depth,  $C_f$  is the friction factor and subscript  $b$  indicates the value at the wave breaking point.

As can be seen from Eqs.(17) and (18), the distribution and the absolute value of the longshore current velocity are determined by the values of  $p$  and  $V_b$ . Furthermore,  $V_b$  is decided by the celerity  $C_b$ , the wave direction  $\theta_b$  and  $\gamma_b$  at the wave breaking point if the assumption of  $\tan\beta/C_f = \text{constant}$  (Komar, 1976) is correct. The value of  $p$  also depends on only  $N$  and  $\gamma$ .

The point where the longshore current becomes maximum ( $x=\delta X_0$ ) and the maximum velocity of longshore current ( $V=V_0$ ) are determined by differentiating Eq.(17) with respect to  $x$ . However, we are not able to decide the width  $X_0$  of the longshore current easily. We must newly define the width of the longshore current by some methods, to evaluate the value of  $X_0$ . Here, we approximated the width  $X_0$  by the width of breaker zone  $x_b$ .

Figure 7 shows the relation between the maximum longshore current velocity and the relative location where the velocity of longshore current becomes the maximum to the breaker zone defined by  $\delta' (= \delta X_0/x_b)$ .

When we assume that the orders of  $\tan\beta/C_f$  and  $\gamma$  are 10 and 1, respectively, the value of  $p$  becomes about  $p=30N$  from Eq.(19). At this time, the value of  $p$  changes in a range of  $0.03 < p < 0.9$  with the range of  $N=0.001$  to  $0.03$ . According to these, the value of  $\delta'$  changes between 0.7 and 0.4 from Fig.7. However, the value of  $\tan\beta/C_f$  is not always constant in fact. Even  $\gamma$  changes with the bottom slope and the incident wave characteristic. Therefore, we examine the distribution of longshore current velocity and the value of  $N$  from experimental results.

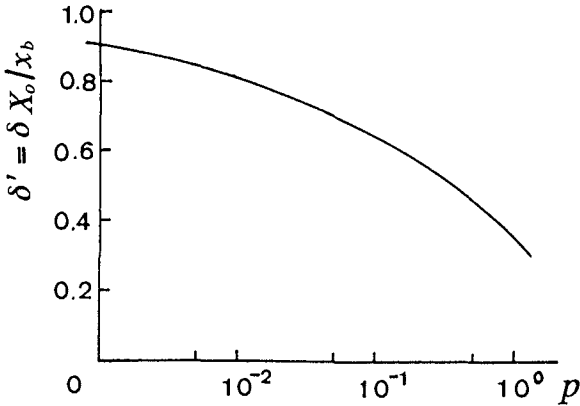


Fig.7 Locus where the maximum velocity of longshore current occurs

### **Experiment on velocity distribution of longshore current and lateral mixing coefficient**

#### (1) Method of experiments and experimental conditions

Some experimental researches have already carried out about the distribution of longshore current. The steady longshore current on a long straight beach of uniform sloping beach is determined from the balance of driving force expressed by the gradient of the radiation stress, the bottom shear stress and the gradient of time and depth averaged Reynolds' stress. This relation is indicated by Eq.(2) and the solution to that is given by, for example, Eq.(17).

Among these, the time and depth averaged Reynolds' stress is usually expressed by the lateral mixing term of diffusion type using lateral mixing coefficient  $K_{xy}$ . However, it is extremely difficult to measure the coefficient, directly. Accordingly, only a few discussions have reported about the lateral mixing coefficient based on the analogy of measured diffusion coefficient  $\epsilon_{xy}$  in the surf zone under limited experimental conditions (for example Kim et al.(1982)). We carried experiments in a wave basin to measure longshore current and diffusion coefficient under a wide range of a surf similarity parameter assuming that the lateral mixing coefficient has similar property to the diffusion coefficient. Based on the measured results, we examine the dependencies of longshore current and the value of  $p$  on the surf similarity parameter and the possibility of the occurrence of FIG waves in the wave basin.

However, the longshore current that occurs in the wave basin with the limited width receives an influence of side walls of the basin. As was already pointed out by Visser(1991), the longshore current in the wave basin is different from that calculated from Eq.(17). We also examine this point based on the experimental results.

The wave basin used in the experiment is 20m long, 10m wide, and 0.6m deep. A mortar coated model uniformly sloping model beach was made at the end of the wave basin. The angle on wave incidence was  $30^\circ$  to the contour of the beach at the depth of 40cm. Two kinds of bottom slopes of 1/10 and 1/20 were examined.

Figure 8 is the illustration of the outline of the experimental set-up and Table-1 shows the experimental condition.

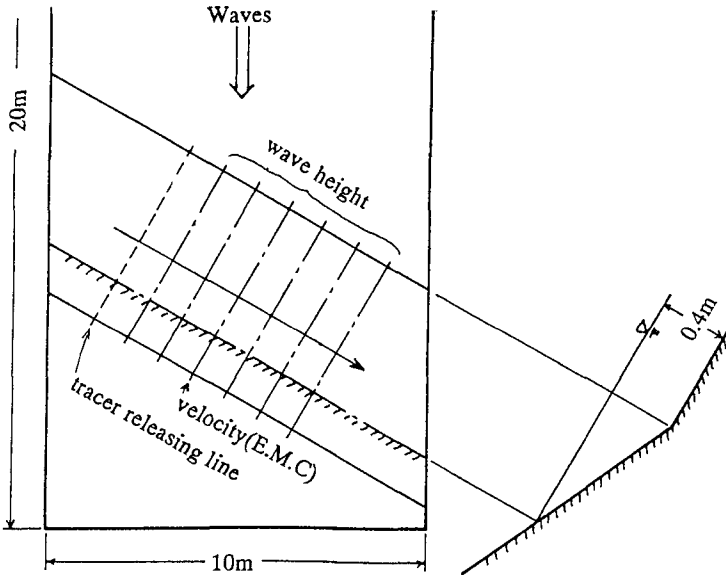


Fig.8 Experimental set-up

Table 1 Experimental condition

Case No.	H (cm)	T (s)	$\xi$	$x_b$ (cm)	$X_0$ (cm)	$V_0$ (cm/s)	$\delta$	$\delta'$
4	10.9	1.0	0.38	170	180	70	0.40	0.42
5	10.3	1.2	0.47	160	170	72	0.47	0.50
6	10.2	1.4	0.55	140	170	75	0.47	0.57
7	7.6	1.0	0.23	210	210	35	0.33	0.33
8	7.0	1.2	0.28	200	220	37	0.38	0.40
9	7.0	1.4	0.33	170	190	40	0.42	0.47
10	10.4	1.0	0.19	270	270	45	0.37	0.37
11	9.5	1.2	0.24	250	260	50	0.38	0.40
12	9.3	1.4	0.29	230	260	44	0.42	0.49

Case 4-6 :  $\tan\beta = 1/10$ , Case 7-12 :  $\tan\beta = 1/20$ ,

In the Table,  $\xi$  is a surf similarity parameter defined by  $\tan\beta\sqrt{H_0/L_0}$ , where  $H_0$  and  $L_0$  are the equivalent wave height and length of incident waves in deep water.

We measured wave height along 5 measuring lines by capacitance type wave gauges at an interval of 10cm in the cross-shore direction. Vertical and cross-shore distributions of water particle velocity along the center measuring line were measured by an electromagnetic current meter. We also measured loci of tracers released at the same point to evaluate longshore current velocity as advection speed and diffusion coefficient by applying a so-called one particle analysis method.

The diffusion coefficient at  $x = X_i$ ,  $\epsilon_{xy}(X_i)$ , was evaluated using the following equation:

$$\epsilon_{xy}(X_i) = \frac{1}{2} \frac{d\sigma_x(X_i, t)^2}{dt} \tag{20}$$

$$\sigma_x(X_i, t)^2 = \sum_{j=1}^{j_e} \{X_i(j, t) - \bar{X}_i\}^2 / j_e \tag{21}$$

where  $j_e$  is a number of tracers,  $\bar{X}_i$  is a mean cross-shore locus of at least 20 tracers whose initial released position is  $X_i$  and  $X_i(j, t)$  ( $j \geq 20$ ) is a position of  $j$ -th tracer after a time  $t$  released at  $X_i$ . The loci of tracers were measured by video analysis at time interval of 0.3s.

**Results and discussion**

(1) Lateral mixing coefficient

Various expressions for the lateral mixing coefficient have already proposed with respect to the steady longshore current on a long straight beach. When we normalize the lateral mixing coefficient by  $x_b \sqrt{gD_b}$  or  $\sqrt{gD_b} D_b / \tan\beta$ , many of them can be expressed by the following form:

$$\epsilon_{xy}' = \epsilon_{xy} / \{ \sqrt{gD_b} D_b / \tan\beta \} = e (D/D_b)^n \tag{22}$$

Some examples of the expression  $e$  in Eq.(22) are shown in Table 2.

Table 2 Examples of expression for lateral mixing coefficient

	$e$	$n$
Longuet-Higgins(1970)	$N (<0.01)$	1.5
James(1974)	$N \quad :D < D_b$ $N(D_b/D)^2 \quad :D_b < D$	1.5
Battjes(1975)	$M(5\gamma^2/16)^{1/3} \tan^{4/3}\beta$	1.5
Author et al.(1986)	$K F^{1/3} \gamma \tan\beta \quad :D < D_b$ $0 \quad :D_b < D$ $F = 5.3 - 3.5\xi - 0.07/\tan\beta$	1.5

According to Longuet-Higgins(1970),  $e$  becomes a constant  $N$ . Battjes' expression implies that  $e$  is a function of  $\tan\beta$  and  $\gamma$ . The author et al.(1982) also proposed that  $e$  is a function of  $\tan\beta$ ,  $\gamma$  and  $\xi$ .

Figure 9 illustrates measured cross-shore distribution of non-dimensional diffusion coefficient  $\epsilon_{xy}' (= \epsilon_{xy} \sqrt{gD_b} D_b / \tan\beta)$ . In the figure, a family of curves corresponds to the values of  $kxy'$  in the cases of  $e=0.00125, 0.0025, .005$  and  $0.008$  in Eq.(22). Numerals in the figure correspond to the case No. in Table 2.

It is found from the figure that measured diffusion coefficient does not show significant dependency on  $\xi$ . However, the values of  $\epsilon_{xy}'$  in the cases of a steep slope beach ( $\tan\beta=1/10$ ) are larger than those in the cases of a gentle slope beach ( $\tan\beta=$



1/20). In the former cases the value of  $\epsilon_{xy}'$  is in the region of 0.005-0.007 and 0.003-0.005 in the latter cases. It is also found that  $\epsilon_{xy}'$  becomes maximum near  $D/D_b=0.7-0.8$  and decreases rapidly toward offshore.

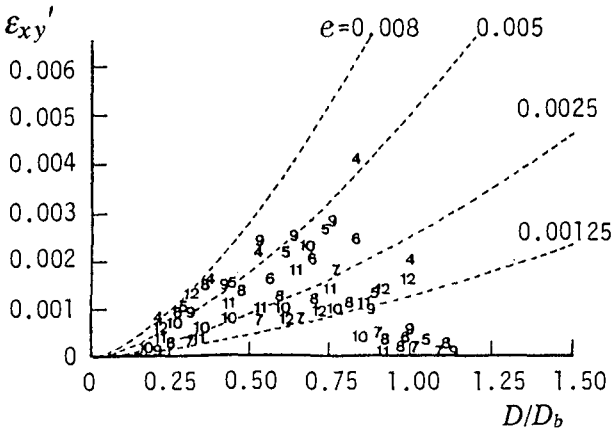


Fig.9 Cross-shore distribution of measured diffusion coefficient

(2) Cross-shore distribution of longshore current

Velocity of longshore current that was measured with an experiment differs from the velocity of longshore current in a seashore on a long straight line that is given with a solution of Eq.(2) due to an influence of a side wall of a reservoir.

Figure 10 show an example of comparison between calculated and measured longshore current velocity (Case-4). A solid line is the calculated result from the analytical solution on the long straight beach (Eq.(17)). Large open circles are the measured velocity by the electro-magnetic current meter and small circles are the advection speed of tracers. In the calculation of the velocity, we used the value of 0.005 for  $N$  in Eq.(17) according to the measured result. The value of friction factor was determined from the laminar boundary layer theory under waves and current.

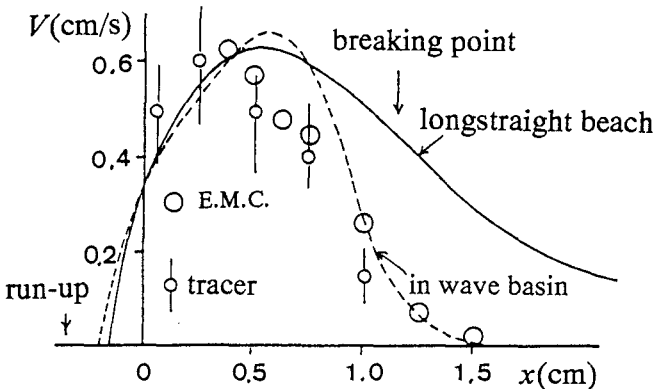


Fig. 10 Cross-shore distribution longshore current (Case-4)

The decrease of the measured velocity near the wave breaking point is faster than the calculated longshore current in the wave basin.

Figure 11 is the wave-induced current pattern obtained from the numerical simulation of wave and current fields in the wave basin.

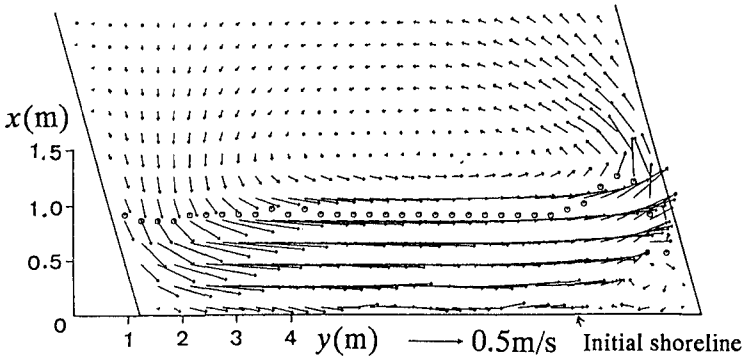


Fig.11 Simulated wave-induced current in the wave basin (Case-4)

It is found that the compensation flow generates outside the breaker zone. The broken line in Fig.10 is the cross-shore profile of longshore current in the center of the wave basin shown in Fig.11. The measure profile of longshore current is reproduced well by the simulated wave-induced current.

Although the measured longshore current in the deeper region around the breaking point is different from that of the analytical result on a long straight beach, the loci where the maximum longshore current occurs in both profiles differ a little. Therefore, we can discuss the relative location of  $\delta X_0$  to the breaker width  $x_b (= \delta')$  based on the experimental results.

Figure 12 shows the relation between  $\delta'$  ( $\delta$ ) and the surf-similarity parameter  $\xi$ . The values of  $\delta$  and  $\delta'$  are shown in Table-1.

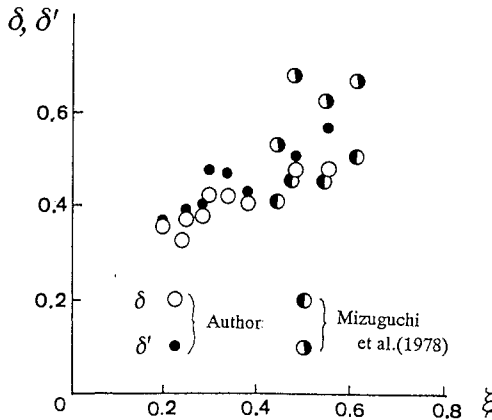


Fig.12 Relation between  $\delta'$  ( $\delta$ ) and  $\xi$

In the figure, experimental results of Mizuguchi et al.(1978) are shown. The value of  $\delta'$  increases from 0.4 to 0.7 with the increase of  $\xi$  from 0.2 to 0.6. As I have already mentioned before, the change in the value of  $N$  corresponding to this change in  $\delta'$  is from 0.001 to 0.03 that is a little larger than the measured change in the value of  $e$ . Therefore, It seems necessary to study the reason for this discrepancy together with the dependency of  $C_f$  and  $\gamma$  on the surf-similarity parameter.

In the experiment, we found the long period fluctuations in water surface displacement and horizontal velocity whose period was about 30s. The corresponding wave length of FIG wave is estimated to be about 6m from the dispersion relation that is about 1/2 of the length of shoreline in the wave basin.

## **Conclusions**

We carried out the analysis of Fig waves on the uniformly sloping beach after the analytical investigation of Fig waves on a beach of constant depth by Bowen et al.. We also conducted experiments to examine the effect of lateral mixing on the cross-shore distribution of longshore current that determines the characteristic of FIG waves.

The main results obtained in this study are summarized as follows:

1. FIG waves on a uniformly sloping beach have upper limits in wave number and frequency.
2. The amplification factor (growth rate) of FIG wave becomes large as the locus where the maximum longshore current occurs becomes deep.
3. Measured diffusion coefficients show a little dependency on the surf-similarity parameter. They become maximum in the surf zone and decrease rapidly toward offshore.
4. The experimental results show that the locus where the maximum longshore current occurs becomes deep according to the increase of the surf-similarity parameter.

## **Reference**

- Battjes J.A., 1975, A note on modeling of turbulence in the surf zone, Proc. Symp. Modeling Technique, pp.1050-1061.
- Bowen, A.J., and Holman, R.A., 1989, Shear instabilities of the mean longshore current (1. Theory), JGR, Vol.94, No.C12, pp.18023-18030.
- James, I.D., 1974, A nonlinear theory of longshore current, Estuarine and Coastal Marine Science, Vol.2, pp.207-234.
- Kim, K.H., Sawaragi, T. and Deguchi, I.,1986, Lateral mixing and wave direction in the surf zone, Proc. 20th ICCE, pp.366-380.
- Komar, P.D., 1976, Beach Processes and Sedimentation, Prentice Hall, pp.192-194.
- Longuet-Higgins, M.S.,1970, Longshore currents generated by obliquely incident sea waves, JGR, Vol.75, No.C33, pp.6778-6789.
- Mizuguchi, S., Ohshima Y. and Horikawa, K., 1978, Vertical distribution of longshore current, Proc. Japanese Conf. on Coastal Engineering, Vol.25, pp.425-429.(in Japanese)
- Visser P.J.,1992, Laboratory measurements of uniform longshore currents, Coastal Engineering, 15, pp.563-593.

## CHAPTER 203

### LONGSHORE CURRENT INSTABILITIES: GROWTH TO FINITE AMPLITUDE.

Nicholas Dodd<sup>1</sup> and Edward B. Thornton<sup>2</sup>

#### Abstract.

The growth of shear instabilities in the longshore current to finite amplitude is studied. It is shown, by considering near-critical conditions and the self-interaction of the fastest growing mode (FGM), that the basic flow is supercritical and that, therefore, the disturbance may be expected to evolve to a finite size, with frequency equal to that predicted by linear stability theory, and final amplitude proportional to the linear growth rate. This is consistent with observation. The mean flow may therefore also be expected to evolve to a new form.

#### 1 Introduction.

The observations of Oltman-Shay *et al.* (1989) (referred to hereinafter as OSHB89), which were made in the presence of a strong longshore current and on a barred beach, show clear evidence of periodic motions at infragravity periods ( $> 50$  s), but with short wavelengths compared to edge waves of similar frequencies. The motions are not attributable to edge or any other form of surface gravity waves. These wave-like disturbances propagate alongshore in the same direction as the longshore current and with a speed proportional to the strength of that current (OSHB89), and, to a first order of approximation, they are non-dispersive (unlike edge waves). Bowen and Holman (1989) (referred to hereinafter as BH89) suggest that the observations are of a shear instability in the longshore current. The observed frequency (for a particular wavenumber  $k$ ) is then considered to be that associated with the fastest growing unstable mode (if more than one such mode is present). A detailed analysis (Dodd *et al.*, 1992—referred to hereinafter

---

<sup>1</sup>Institute for Marine and Atmospheric Research, Utrecht University, Princetonplein 5, 3584 CC, Utrecht, The Netherlands.

<sup>2</sup>Oceanography Department, Naval Postgraduate School, Monterey, CA 93943, U.S.A.

as DOT92) has confirmed that these wave-like motions are indeed shear instabilities. DOT92 also found reasonably good agreement between the shape of the observed variance spectra (especially that for the cross-shore velocity component) and that calculated from the predicted growth rate. They also demonstrated that bottom friction may provide a damping mechanism, which might explain why such instabilities are not seen more often.

So far, only the linear, temporal instability problem has been tackled. However, according to linear theory, unstable modes grow exponentially in time and so that theory may be expected to break down sooner or later, depending on the growth rates of the disturbances, which in turn depend primarily on the longshore current offshore shear and the damping (DOT92 estimate that the fastest growing shear instabilities will grow by a factor  $e$  in 300 to 400 seconds). However, the observations of OSHB89 and DOT92 were over lengths of time far exceeding these comparatively short times: typically one to four hours. This implies that the observed oscillations (instabilities) are fully developed, in some sense, and that finite-amplitude effects are of importance. Nevertheless, using just the linear stability theory, and assuming that only the fastest growing unstable mode is important (for any  $k$ ), DOT92 do notice good agreement between theory and observation (in frequency-wavenumber space). The conclusion seems to be that linearly unstable modes do grow and equilibrate (i.e., evolve to a finite amplitude and a steady form), with their final amplitudes being proportional to their linear growth rate, at least to a "first approximation".

In this paper we consider a weakly nonlinear theory. Unfortunately, this restricts us to so-called near-critical conditions (i.e., the longshore current shear is only just large enough to overcome the bottom friction and allow unstable modes to develop). Therefore, we shall also be restricted to only a small band of wavenumbers, centered on one *critical* value,  $k_c$ , whereas the linear analysis (DOT92) predicts a wider band of unstable wavenumbers whose shape and width correspond to that of the observed spectra. Notwithstanding this, it seems reasonable to expect that the analysis (based on the pioneering work of Stuart (1960) and others) will have physical relevance because it is centred on the wavenumber that will have the largest growth rate, and so and will at least reveal the qualitative long-time behaviour of the disturbances. The aim of this analysis is to confirm that the linear instabilities will evolve to a steady final form and to predict the amplitude of these forms.

In §2 the existing theory of the longshore current and of the shear instabilities of the longshore current are briefly reviewed, and the relation of each to the other is shown. In §3 finite-amplitude effects are introduced, and an evolution equation governing the long-time growth of the instabilities is derived. Results are shown in §4, and some conclusions are presented in §5.

## 2 Linear Theory.

We adopt a right-handed coordinate system in which  $y$  is the alongshore,  $x$  the cross-shore, and  $z$  the vertical coordinate. The water depth,  $z = -h$ , is assumed uniform alongshore: i.e.,  $h = h(x)$ . The total horizontal velocity field is denoted by  $\underline{u} = (u, v)$ , and we write the depth and time averaged horizontal velocity field as  $\underline{U}(x, y, t)$ , and decompose  $\underline{u}$  into

$$\underline{u} = \tilde{\underline{u}}(x, y, z, t) + \underline{U}(x, y, t), \quad (1)$$

where time averaging is performed over one period ( $T_g$ ) of the incident waves.  $\tilde{\underline{u}}$  represents deviations from the averaged velocity field; in particular, it represents the contribution to  $\underline{u}$  from the incoming wind waves, and the definition (1)  $\Rightarrow \langle \int_{-h}^{\eta} \tilde{u}_i dz \rangle = 0$ , where the triangular brackets denote the aforementioned time average.  $\underline{U}$  will only depend on the horizontal coordinates and a long timescale, and will therefore contain both the mean flow (i.e. the longshore current) and any long-time perturbations in that flow (i.e. shear instabilities in the longshore current). Similarly,  $\eta(x, y, t)$  is decomposed into  $\eta = \tilde{\eta} + \langle \eta \rangle = \tilde{\eta}(x, y, t) + \zeta(x, y, t)$ . Shear instabilities in the longshore current possess typical periods of  $O(100-1000 \text{ s})$ , and so their period is an order of magnitude greater than  $T_g$ . These timescales are clearly consistent with the above decomposition.

The shallow water momentum equations may be written as

$$\rho(\zeta + h) \left[ \frac{\partial U_i}{\partial t} + U_j \frac{\partial U_i}{\partial x_j} \right] = -\rho g(\zeta + h) \frac{\partial \zeta}{\partial x_i} - \frac{\partial S_{ij}}{\partial x_j} - \langle \tau_i \rangle, \quad (2)$$

for  $i = 1, 2$  (see Mei, 1989), where  $\langle \tau_i \rangle$  is the  $i$ th component of bottom friction, and  $S_{ij}$  are components of the radiation stress tensor. If, for the moment, we assume that all averaged quantities are time independent—and are therefore dependent on a timescale infinitely, rather than finitely longer than  $T_g$ —and make use of the assumed alongshore uniformity, then continuity  $\Rightarrow \underline{U} = (0, V(x))$  (see Mei, 1989). Therefore, the left side of (2) is identically zero, and the cross-shore momentum equation can be written as

$$0 = -g \frac{\partial \zeta_s}{\partial x} - \frac{1}{\rho(\zeta_s + h)} \frac{\partial S_{11}^{(0)}}{\partial x} \quad (3)$$

and the corresponding alongshore equation as

$$0 = -\frac{\partial S_{12}^{(0)}}{\partial x} - \langle \tau_2^{(0)} \rangle, \quad (4)$$

where  $\zeta = \zeta_s(x)$  is the mean, wave-induced change in the water level (i.e., the set-up/set-down). The superscript '(0)' is used to show that these terms are only included at their leading order (i.e., only the time-independent current  $V(x)$ , and  $\zeta_s(x)$  are included).  $\zeta_s(x)$ , can be found from (3);  $V(x)$ , is found from (4).

In the model of Thornton and Guza (1986)—referred to hereinafter as TG86—which we shall examine in detail, an analytical form is derived, by assuming that the incoming waves are narrow-banded in frequency but Rayleigh distributed in wave height, that the beach is plane with a slope  $s$ , and that the longshore current,  $V \ll \langle |\underline{u}| \rangle$  (the weak current assumption; see Mei, 1989). The alongshore momentum equation (4) then becomes

$$0 = -\frac{\partial}{\partial x} S_{12}^{(1)} - \rho c_f \langle |\underline{u}| \rangle V, \quad (5)$$

and we can write

$$V(x) = -\frac{1}{\rho c_f \langle |\underline{u}| \rangle} \frac{\partial}{\partial x} S_{12}^{(1)} = \mathcal{K}_1 h^{9/10} \{1 + \mathcal{K}_2 h^{23/4}\}^{-6/5}, \quad (6)$$

where  $c_f$  is the bottom friction coefficient, and the constants  $\mathcal{K}_1$  and  $\mathcal{K}_2$  can be found in TG86.  $\zeta_s$  is small compared with the depth for almost all  $x$ . Only very close to the idealised shoreline  $x = 0$  is  $\zeta_s > h$ . This makes virtually no difference to the ensuing analysis, so we shall ignore  $\zeta_s$  in calculations from now on, though we retain it in the derivations for the remainder of this section.

Following BH89, we may examine the linear stability of the mean, laminar, inviscid flow  $\underline{U} = (0, V(x))$  by superimposing a disturbance on that flow. Thus,  $\underline{U}$  is decomposed as

$$\underline{U} = (u'(x, y, t), V(x) + v'(x, y, t)). \quad (7)$$

Here,  $u'$  and  $v'$  represent perturbations in the components of the mean flow  $(0, V(x))$ ;  $\zeta$  is treated similarly:  $\zeta = \zeta_s(x) + \zeta'(x, y, t)$ . Thus,  $\zeta$  now consists of  $\zeta_s$  and an additional contribution due to the perturbations in the mean flow. Substituting (7) back into the momentum equations, we get

$$u'_t + V u'_y + u' u'_x + v' u'_y = -g[\zeta_s + \zeta']_x - \frac{\{S_{11}^{(1)}\}_x + \langle \tau_1^{(1)} \rangle}{\rho(\zeta_s + \zeta' + h)}, \quad (8)$$

$$v'_t + V v'_y + u' v'_x + u' v'_x + v' v'_y = -g\zeta'_y - \frac{\{S_{12}^{(1)}\}_x + \langle \tau_2^{(1)} \rangle}{\rho(\zeta_s + \zeta' + h)}, \quad (9)$$

where the superscript '(1)' denotes the inclusion of the perturbations in these quantities. If we now subtract (3) and (4) from (8) and (9) respectively, we get

$$u'_t + V u'_y + u' u'_x + v' u'_y = -g\zeta'_x - \frac{[\{S_{11}^{(1)}\}_x + \langle \tau_1^{(1)} \rangle]}{\rho(\zeta_s + \zeta' + h)} + \frac{\{S_{11}^{(0)}\}_x}{\rho(\zeta_s + h)} \quad (10)$$

$$v'_t + V v'_y + u' v'_x + u' v'_x + v' v'_y = -g\zeta'_y - \frac{[\{S_{12}^{(1)}\}_x + \langle \tau_2^{(1)} \rangle]}{\rho(\zeta_s + \zeta' + h)} + \frac{\{S_{12}^{(0)}\}_x + \langle \tau_2^{(0)} \rangle}{\rho(\zeta_s + h)} \quad (11)$$

These equations differ from (8) and (9) in that the mean motion has been subtracted out. Thus, (10) and (11) may be regarded as perturbation momentum equations.

Equations (10) and (11) are linearised by assuming that  $u'$  and  $v'$  are much smaller than the longshore current, and that, therefore, products of perturbed quantities are negligible. The quantities are further simplified by assuming that  $S_{ij}^{(1)} \approx S_{ij}^{(0)}$ .  $\zeta_s$  may also be neglected when compared with  $h$ . This gives us

$$u'_t + V u'_y = -g\zeta'_x - \frac{[\langle \tau_1^{(1)} \rangle - \langle \tau_1^{(0)} \rangle]}{\rho h} = -g\zeta'_x - \frac{\tilde{\tau}_1}{h}, \tag{12}$$

$$v'_t + V v'_y + u' V_x = -g\zeta'_y - \frac{[\langle \tau_2^{(1)} \rangle - \langle \tau_2^{(0)} \rangle]}{\rho h} = -g\zeta'_y - \frac{\tilde{\tau}_2}{h}. \tag{13}$$

Finally, a rigid-lid approximation is imposed, which enables us to introduce a stream function  $\Psi$ , where  $u' = -\Psi_y/h$  and  $v' = \Psi_x/h$ , so (12) and (13) can be combined into a single vorticity equation in  $\Psi$ . Assuming a harmonic dependence in  $t$  and  $y$ ,  $\Psi(x, y, t) = \text{Re}\{\phi(x)e^{i(ky-\omega t)}\}$ , then a stability equation analogous to the Rayleigh equation (see Drazin and Reid, 1981) is derived. The form of the stability equation depends on the form of the bottom friction terms on the right of (12) and (13). Here, we use the weak current assumption (for consistency with the TG86 model). In this case,

$$\frac{\tilde{\tau}_1}{h} = \frac{2\mu}{h} u' \text{ and } \frac{\tilde{\tau}_2}{h} = \frac{\mu}{h} v' \text{ where } \mu = c_d \langle |\tilde{u}| \rangle = c_d \frac{2}{\pi} u_0(x), \tag{14}$$

and  $c_d$  is also a bottom friction coefficient, theoretically the same as  $c_f$  and therefore determined empirically, but for our purposes treated as a parameter;  $\frac{2}{\pi} u_0$  is given by equation (16) of TG86. We write the resulting stability equation as

$$(V - i\mu/kh - c)\mathcal{L}\phi = h(V_x/h)_x\phi + (i/k)(\mu/h)_x\phi_x - (i\mu/kh)k^2\phi, \tag{15}$$

where  $\mathcal{L}\phi = \phi_{xx} - (h_x/h)\phi_x - k^2\phi$ , but we shall ignore the last two terms that appear on the right of (15) hereafter. The exclusion of these terms makes only a small difference in results (Dodd, 1992), but the simplified equation is desirable from the point of view of the ensuing weakly nonlinear analysis. Equation (15) is solved subject to the no-normal-flow boundary conditions  $\phi(0) = \phi(\infty) = 0$ . If it is assumed that  $k$  is real, then  $\omega$  and  $c = \omega/k$  are in general complex. If  $\omega$  possesses a positive imaginary part, then the mode grows exponentially (as  $t \rightarrow \infty$ ), and is therefore deemed unstable. Denoting  $\Re(\omega) = \omega_r$  and  $\Im(\omega) = \omega_i$ , then  $\omega_r$  defines the frequency,  $c_r = \omega_r/k$  the phase speed, and  $\omega_i$  the growth rate. If we ignore the bottom friction terms (i.e., put  $c_d = 0$ ), then the stability equation of BH89 is arrived at.

Results of a linear stability analysis of (15) for the  $V$  profile of TG86 are shown in Fig. 1. For  $c_d = 0$ , the fastest growing point on the growth rate curve is situated at  $k \approx .055 \text{ m}^{-1}$  (wavelength  $\lambda = 2\pi/k \approx 114 \text{ m}$ ), and has an associated period (Fig. 1c) of about 360 s. We refer to this disturbance as the fastest growing mode (FGM) (this terminology can be slightly misleading since for the TG86



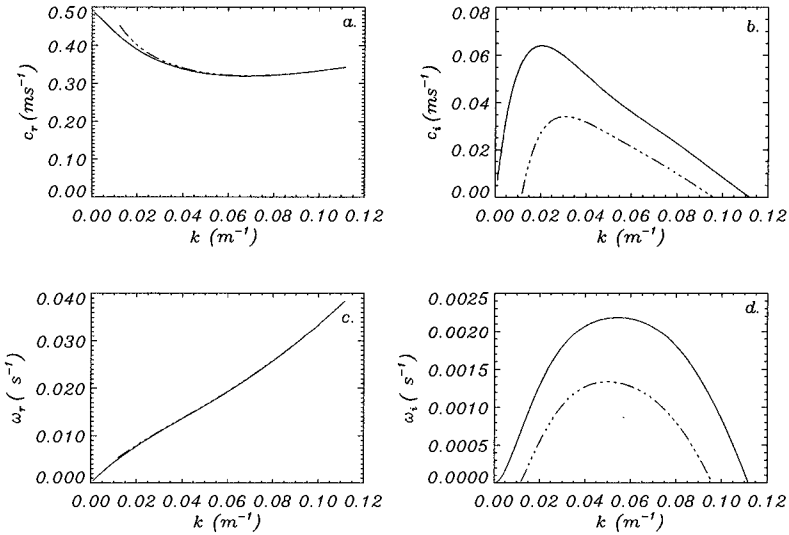


Figure 1: Linear stability for the TG86 model. (a) Real phase velocity, (b) imaginary part of phase velocity, (c) radial frequency, and (d) growth rate. Solid line:  $c_d = 0$ . Chained line:  $c_d = .003$ . ( $c_f = .009$ ).

profile there is only one unstable mode for any  $k$ ; the mode—eigenfunction—is continuously dependent upon  $k$ .

The inclusion of dissipation ( $c_d = .003$ ) reduces growth rates, though not quite uniformly. The position of the FGM is now at  $k \approx .045 m^{-1}$ . Frequencies (or phase velocities) are barely affected by the inclusion of friction. Clearly, at the FGM  $\partial\omega/\partial k = \partial\omega_r/\partial k$ , and in its vicinity,  $\partial\omega/\partial k \approx \partial\omega_r/\partial k$ , and so the group velocity will be the true velocity of displacement. It can also be seen that, to a first approximation, the motions are non-dispersive. Of course, as  $c_d$  is increased the growth rates are reduced still further, and the width of the band of unstable wavenumbers diminishes. The dimensionless parameter  $c_d^{-1}$  plays a similar rôle in this problem to that of the Reynolds number in the viscous stability problem. If  $c_d^{-1}$  is decreased beyond a critical value,  $c_{dc}^{-1}$  (and therefore  $c_d$  increased), then all (small) disturbances will be completely damped and no instability will develop. At  $c_d^{-1} = c_{dc}^{-1}$  all wavelengths are damped except for  $k = k_c$ , which is a neutral disturbance. Therefore,  $k = k_c$  and  $c_d^{-1} = c_{dc}^{-1}$  are referred to as *critical conditions*. In Fig.2, the neutral stability curve for (15) for the TG86 model is shown. If  $c_d^{-1}$  is increased slightly above its critical value, then we have so-called *near-critical conditions*

$$k = k_c \quad \text{and} \quad c_d^{-1} = c_{dc}^{-1} + \Delta c_d^{-1}. \tag{16}$$

Under these conditions, a small set of wavelengths, centred on the critical wavenum-

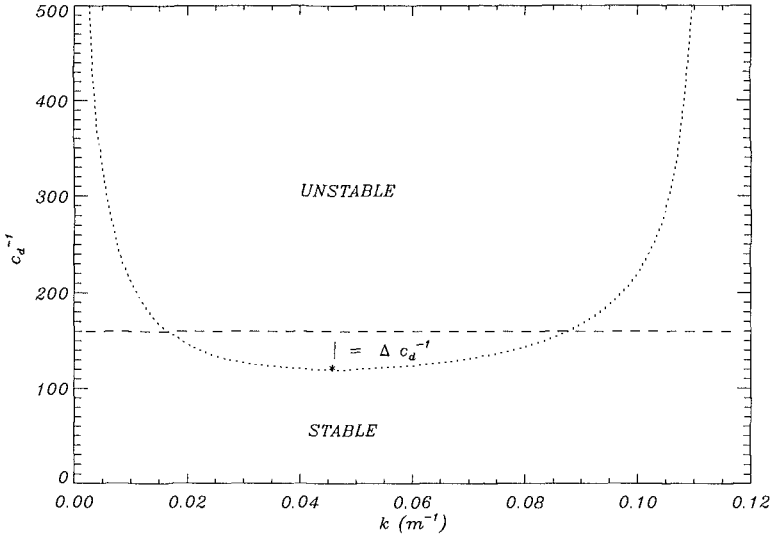


Figure 2: Neutral stability curve for the TG86 model. The asterisk shows the position of critical conditions  $(k_c, c_{dc}^{-1})$

ber  $k = k_c$ , becomes unstable, and propagates in the direction of the current at group velocity  $c_g \approx c_{gr} \approx c_r(k = k_c)$ . It is at these near-critical conditions that the weakly nonlinear analysis of the next section applies.

Finally, it is important to note that  $c_f$  and  $c_d$  are actually one and the same ( $= .009$ , NSTS, Feb. 4th, 1980; see TG86). The value of  $c_d = .003$  was chosen in Fig. 1 so that the effects of bottom friction could be seen without the instabilities being damped entirely (as they are for  $c_d = .009$ ). Thus, it is also important to realise that decreasing (or increasing) the bottom friction coefficient not only reduces (increases) damping of the instabilities, but also increases (reduces) the longshore current shear (cf. (6))—if we were to be consistent and put  $c_d = c_f = .003$  for the stability analysis in Fig. 1, we should expect all quantities to be three times as large. Of course, the case  $c_d = c_f = 0$ , which would predict an infinitely large  $V$ , would be physically meaningless.

From now on, we take  $c_f$  and  $c_d$  to be the same, (called  $c_d$ ) but continue to treat the bottom friction coefficient as a parameter.

### 3 Weakly Nonlinear Theory.

If we dispense with the assumption of small amplitude, then we can define mean momentum equations appropriate for the finite-amplitude disturbance by aver-

aging (8) and (9) over one alongshore wavelength  $\lambda$ :

$$\overline{u'u'_x} + \overline{v'u'_y} = -g \frac{\partial \zeta_s}{\partial x} - \frac{\{S_{11}\}_x + \langle \tau_1^{(1)} \rangle}{\rho(\zeta' + \zeta_s + h')}, \quad (17)$$

$$\overline{u'v'_x} = - \frac{\{S_{12}\}_x + \langle \tau_2^{(1)} \rangle}{\rho(\zeta' + \zeta_s + h')} \quad (18)$$

where the overbar denotes such an average. Amended perturbation equations may also be derived, by subtracting (17) and (18) from the full equations (8) and (9). If we again use the weak current assumption, we get

$$u'_t + V u'_y + u' u'_x + v' u'_y - \overline{u'u'_x} - \overline{v'u'_y} = -g \zeta'_x - 2 \frac{\mu}{h} u', \quad (19)$$

$$v'_t + V v'_y + u' V_x + u' v'_x + v' v'_y - \overline{u'v'_x} = -g \zeta'_y - \frac{\mu}{h} v'. \quad (20)$$

The difference between these equations and those of the preceding section is a different definition of what constitutes a mean.

By cross-differentiating (19) and (20) and then subtracting the second equation from the first, we get

$$\left\{ \frac{\partial}{\partial t} + u' \frac{\partial}{\partial x} + (v' + V) \frac{\partial}{\partial y} \right\} \left( \frac{\Pi + V_x}{h} \right) - \frac{X_x}{h} = \frac{\mu}{h} \left\{ \frac{\partial}{\partial y} \left( \frac{u'}{h} \right) - \frac{\partial}{\partial x} \left( \frac{v'}{h} \right) \right\}, \quad (21)$$

where  $\Pi = v'_x - u'_y$  and  $X = \overline{u'v'_x}$ . Note that all the mean motion has been subtracted out of (21). This motion may straightforwardly be retained in an equation such as (21), but we prefer to keep the equations for mean and fluctuating motions separate. Recall that, for a prescribed longshore current profile ( $V = V(x)$ ), linear theory predicts a stream function  $\Psi$  of the form  $\Psi(x, y, t) = \text{Re}\{\phi(x)e^{i(ky - \omega_r t)}e^{\omega_i t}\}$ . It has been shown (DOT92) that the frequency so predicted ( $\omega_r$ ) is in good agreement with the observed frequency for a given wavenumber,  $k$ . Furthermore, linear theory consistently predicts that  $\omega_r \gg \omega_i$ , even in the absence of bottom friction, so that it may safely be assumed that  $\Psi$  grows appreciably only over times in excess of the linear period,  $2\pi/\omega_r$ . It is, therefore, natural to regard  $e^{\omega_i t}$  as an amplitude modulation function. Clearly, however,  $\Psi$  will not continue growing without bound, and so  $e^{\omega_r t}$  must be considered to be the "short-time" expression of a more general (complex) amplitude modulation function  $a(t)$ . Thus, for the nonlinear problem we have

$$\Psi(x, y, t) = \text{Re}\{a(t)\phi(x)e^{i(ky - \omega_r t)}\}. \quad (22)$$

The initial time  $t = t_0$ , present through the constant  $a_0 = a(t = t_0)$ , provides a measure of how long the linear solution will be valid and the amplitude remain small, and therefore of how long linear theory remains applicable. By hypothesis,  $a(t) \sim e^{\omega_i t}$  as  $t \rightarrow -\infty$ , and  $a_0 \rightarrow 0$ . The long-time asymptote of  $a(t)$ ,  $a_\infty = \lim_{t \rightarrow \infty} a(t)$  (if such a limit exists) is the amplitude to which the initially small disturbances will evolve.

The weakly nonlinear problem can now be formulated by introducing a small parameter  $\epsilon$ , such that at near-critical conditions we have  $c_d^{-1} = c_{dc}^{-1} + \epsilon^2 \kappa$  (cf. equation (16)). We expect  $\omega_i$  and  $\Delta c_d^{-1}$  to be closely related, and expanding  $\omega_i$  in a Taylor series about  $c_{dc}^{-1}$  we find that  $\omega_i(k = k_c, c_d^{-1} = c_{dc}^{-1} + \Delta c_d^{-1}) = \partial \omega_i / \partial c_d^{-1}(k = k_c, c_d^{-1} = c_{dc}^{-1}) \epsilon^2 \kappa + O(\epsilon^4)$ . The amplitude  $a$  is dependent on a "slow" time coordinate  $T = \epsilon^2 t$ . We ignore the small but finite sidebands around  $k = k_c$ , and restrict ourselves to just the one, critical wavenumber; thus the disturbance will grow only by self-interaction.

Physically, we can think of the above conditions as being brought about by waves reaching the coast and building up the longshore current to the extent that the offshore shear in the current just overcomes the critical damping ( $c_{dc}^{-1}$ ), so that instabilities with wavelength  $2\pi/k_c$  develop. It is also implicitly assumed that the mean longshore current from which the instabilities begin to develop is steady.

The ansatz (22) is expanded to allow for self-interaction and for near-critical conditions:

$$\Psi = \sum_{n=1}^{\infty} \frac{1}{2} \{ \psi_n(x, t) e^{ni(k_c y - \omega_r t)} + \hat{\psi}_n(x, t) e^{-ni(k_c y - \omega_r t)} \}, \tag{23}$$

where a circumflex denotes a complex conjugate. Note that (23) still retains the phase velocity  $c_r$ , associated with the linear theory at critical conditions. The functions  $\psi_n$  are expanded as  $\psi_1 = \epsilon a \phi_1(x) + \epsilon^3 a^2 \hat{a} \phi_{11}(x) + \dots$ , and  $\psi_2 = \epsilon^2 a^2 \phi_2(x) + \dots$ , etc., where  $\phi_1(0) = \phi_1(\infty) = \phi_{11}(0) = \phi_{11}(\infty) = \phi_2(0) = \phi_2(\infty) = 0$ , etc.. Thus, the  $O(\epsilon^0)$  mean flow ( $V(x)$ ) becomes unstable, giving rise to  $O(\epsilon)$  fundamental disturbances ( $\psi_1 e^{i(k_c y - \omega_r t)}$  and c.c.). These, in turn, interact with each other, producing either 1st harmonic or mean components at  $O(\epsilon^2)$ . These components interact with components at  $O(\epsilon)$  to produce additional fundamental components and components at 2nd harmonic. This, it turns out, is as far as we need to go, and all terms of  $O(\epsilon^4)$  are ignored; for more details see Stuart (1960). Note that the mean terms are not included in (23), as they have already been subtracted from the momentum equations (see (19) and (20)); all these terms (up to  $O(\epsilon^2)$ ) are present in the mean equations (17) and (18). For the TG86 model, (18) becomes

$$\rho h \overline{u'v'_x} = - \frac{\partial}{\partial x} \overline{S_{12}} - \rho (c_{dc} + \Delta c_d^{-1}) \langle |\underline{u}| \rangle V. \tag{24}$$

More generally, we can write

$$V_2(x, t) = V_1(x) \left( 1 + \frac{\epsilon^2 \kappa}{c_{dc}^{-1}} \right) + \epsilon^2 |a(t)|^2 f(x) \tag{25}$$

where  $V_1$  is the solution at  $O(\epsilon^0)$  (i.e., the TG86 model, (6), at critical conditions).  $\Psi(x, y, t)$  and (23) are substituted into (21), and the various harmonics are collected (see Dodd (1992) for the resulting equation). The mean equation

(up to  $O(\epsilon^2)$ ), is already given by (25). For the fundamental, the equation is (at  $O(\epsilon)$ ) the linear problem of the previous section, (15) (but at *critical* conditions so that  $\mu = \mu_c = c_{dc}|\underline{u}|$  and  $k = k_c$ ). At 1st harmonic ( $O(\epsilon^2)$ ) there is an inhomogeneous equation—inhomogeneous because the fundamentals force the first harmonic by self-interaction. Finally, the fundamental also has a contribution at  $O(\epsilon^3)$ . It is this equation that requires a secularity (or compatibility) condition for its unique solution, and this condition yields the amplitude evolution equation. From this equation, and its c.c., it is easy to derive

$$\frac{d|a|^2}{dt} = 2\sigma|a|^2 - \ell|a|^4, \quad (26)$$

where  $\ell$  is a real constant called the Landau constant, and it can be shown that  $\sigma \approx \omega_i$ . All these equations and expressions are given in Dodd (1992).

The equation (26) is readily integrated to give

$$|a|^2 = \frac{C e^{2\omega_i t}}{\left(1 + \frac{\ell}{2\omega_i} C e^{2\omega_i t}\right)} \quad \text{where} \quad C = \frac{2\omega_i |a_0|^2 e^{-2\omega_i t_0}}{2\omega_i - \ell |a_0|^2}, \quad (27)$$

and where  $\sigma$  has been replaced by  $\omega_i$ . We are only concerned with cases where the longshore current is linearly unstable, i.e.,  $\omega_i > 0$ . In this case, as  $t \rightarrow \infty$ ,  $|a|^2 \rightarrow 2\omega_i/\ell$ , for any  $a_0$ , as long as  $\ell > 0$ . The flow may then be expected to evolve to a new, steady form (i.e., to equilibrate). When  $\ell > 0$  the flow is said to be supercritical. Conversely, if  $\ell < 0$ , then any infinitesimal disturbance will become unbounded after a finite time. In this case, the flow is deemed subcritical, because this breakdown can occur *below* critical conditions, for a *finite* disturbance (see Drazin and Reid, 1981). Physically, we expect the flow to settle down to a new steady form after some time, and that this form will have a period  $2\pi/\omega_r$  (i.e.,  $\ell > 0$ ). For a sufficiently small value of  $t$  the disturbance  $a(t)$  amplifies like  $\exp(\omega_i t)$ , corresponding to linear instability.

## 4 Results.

For the TG86 model,  $k_c \approx .0453 \text{ m}^{-1}$ , and  $c_{dc}^{-1} \approx .0083527$ . Finding the value of  $\ell$  requires a lot of computation: the linear (fundamental) problem must first be solved; then the problem for the first harmonic; and finally the the integrals needed to find  $\ell$  must be calculated. At the above critical conditions, it was found that  $\ell \approx 12300 \text{ s}^{-1}$ . For  $\Delta c_d^{-1} = 40$  (corresponding to a decrease in the bottom friction coefficient of about .0028 from critical conditions),  $a_\infty = \sqrt{2\sigma/\ell} \approx .00052$ . This figure is only meaningful when it multiplies the appropriate quantities. In Fig. 3 the resulting amplitudes of the velocities of with the fundamental and 1st harmonic disturbances are shown. The longshore current maximum is about  $.53 \text{ ms}^{-1}$ , so the fundamental disturbances reach about .066 of this value. The velocities associated with the first harmonic are at  $O(\epsilon^2)$ , and are therefore smaller

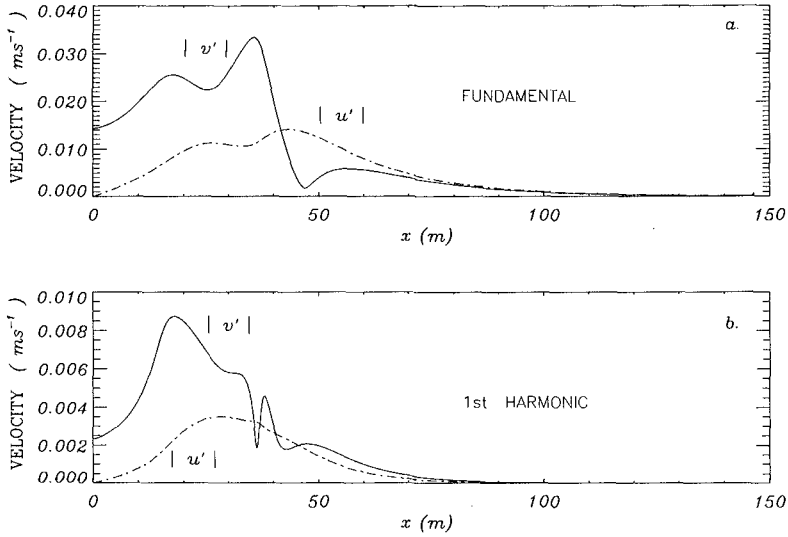


Figure 3: Moduli of complex perturbation velocities:  $\Delta c_d^{-1} = 40$ .

still. Also at this order is the term representing the deformation of the longshore current; it and  $V(x)$  are shown in Fig. 4. The effect of the mean deformation on the TG86 profile can just be discerned in Fig. 4a. For a larger value of  $\Delta c_d^{-1}$  these amplitudes would all be larger ( $|a| \propto \sqrt{\Delta c_d^{-1}}$ ), and vice versa. However, even with  $\Delta c_d^{-1} = 40$ , a large band of unstable wavenumbers is admitted, whose effects on each other are ignored in this analysis. Furthermore, the larger  $\Delta c_d^{-1}$  becomes, the further away from critical conditions we get, and the ordering assumptions behind the analysis breaks down. Nevertheless, for  $\Delta c_d^{-1} = 200$ , the same velocities are shown in Fig. 5. The perturbation velocities reach about  $0.075 \text{ ms}^{-1}$  (about one sixth of the current maximum), which is more typical of the observations of OSHB89, and DOT92.

The analysis of the previous section actually applies for any near-critical conditions; i.e., we can find a Landau constant for any point on the neutral curve shown in Fig. 2. We calculated its value for  $k_c = k_1 = .0209 \text{ m}^{-1}$  and  $k_c = k_2 = .08085 \text{ m}^{-1}$  (both of which share the same critical value of  $c_d = c_{dc} = .00689$ ,  $c_{dc}^{-1} \approx 145$ ). For  $k_1$ ,  $\ell_1 \approx 6900 \text{ s}^{-1}$ , and for  $k_2$ ,  $\ell_2 \approx 200,000 \text{ s}^{-1}$ . Although these values are not absolute indicators of the resulting perturbation amplitudes (because they depend on the normalisation of  $\phi_1$ , which was not uniform for the numerical scheme used herein), they do tell us that (1) for resulting amplitudes for  $k_1$  are bigger than for  $k_2$ , and (2) for all values of  $k$  tried so far,  $\ell > 0$ . Of course, these and all other such points on the neutral stability curve will only

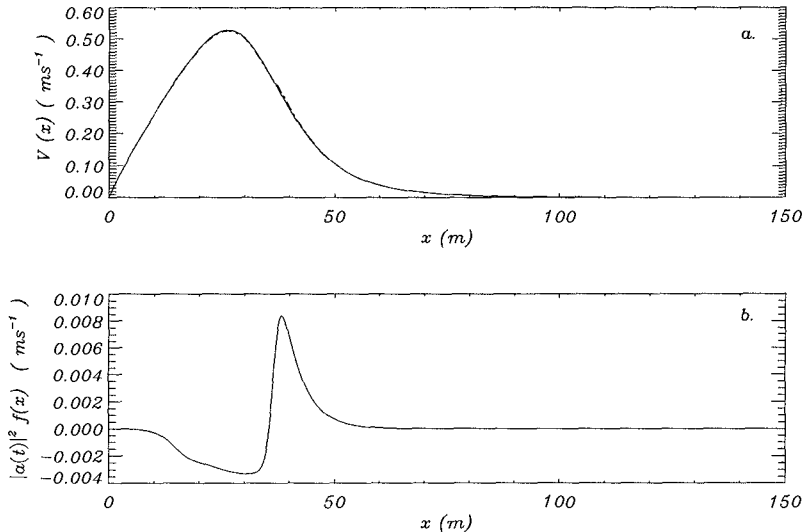


Figure 4: (a)  $V(x)$  for TG86 (solid line), and modified mean current due to instability, (b) mean component due to instability:  $\Delta c_d^{-1} = 40$ .

exhibit instability *after* the overall critical condition (i.e., that at  $k \approx .0453 \text{ m}^{-1}$ ) has been surpassed, and will therefore be of lesser importance.

## 5 Conclusions.

It has been shown that, at least for the TG86  $V$  profile and for the stability equation (15), the longshore current is supercritical and disturbances may be expected to evolve to a finite, steady amplitude ( $\ell > 0$ ). This is in agreement with the observations of OSHB89 and DOT92. Only three positions on the neutral stability curve have been examined, but it seems very likely that  $\ell > 0$  for all  $k$  between  $k_1$  and  $k_2$  at least. Most importantly, this is true for the overall critical condition at  $k = .0453 \text{ m}^{-1}$  (see Fig. 2).

At true near-critical conditions (represented here by  $\Delta c_d^{-1} = 40$ ), the fundamental disturbances evolve to only about 1/15th of the  $V$ -maximum, whereas the observed disturbances were more typically one third of this value. This may be indicative of a number of things: (a) The  $V$  and  $h$  profiles measured at Duck, North Carolina (where the observations of OSHB89 were made) were significantly different from the TG86 model, and the barred beach profile and stronger current shear there may give rise to larger amplitudes (though without doing the weakly nonlinear analysis for these data it is hard to say). If this were so, it might provide

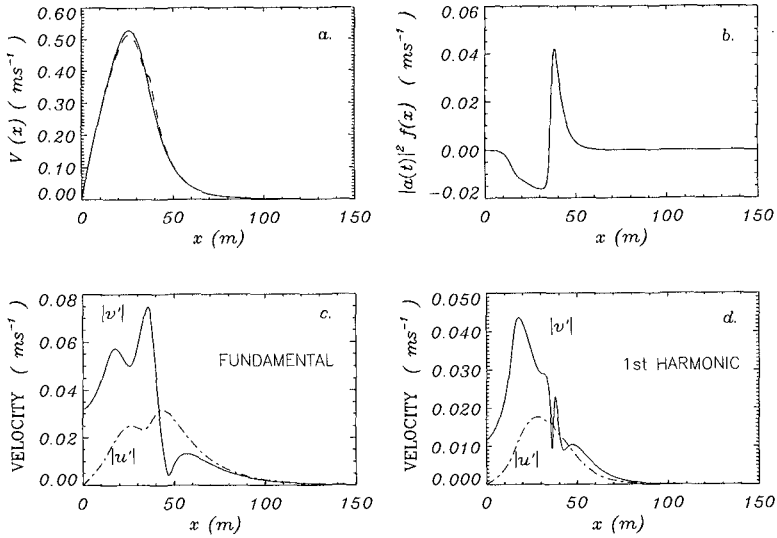


Figure 5: Linear stability for the TG86 model. (a) Original (solid line) and modified mean current, (b) mean component due to instability, (c) and (d) moduli of complex velocities due to instabilities:  $\Delta c_d^{-1} = 200$ .

a further, accompanying (and highly intriguing) mechanism for explaining why longshore currents on a plane beach do not ‘apparently’ become unstable: even if an instability were to develop, it will be restricted by nonlinearity to a small amplitude. Of course, linear growth rates for Duck are much larger than those for the TG86 model (Santa Barbara, California; DOT92), but the weakly nonlinear analysis only applies for near-critical conditions. The problem is then one of whether or not  $V$  continues to increase above critical conditions faster than do the instabilities that would presumably appear as soon as these conditions are first exceeded. In the time series shown by OSHB89 (Fig. 8 of that paper) it appears that the instabilities develop rather faster than  $V$ , as they seem to be established well before the end of the record. Whether this is true in general is not known. If it is not, then the weakly nonlinear approach would not be appropriate.

(b) Though near-critical conditions may be appropriate, the simple model presented here, in which only one wavenumber  $k_c$  is important, may be unrealistic, because  $k_c$  is only a ‘first among equals’ (Drazin and Reid, 1981), wavenumbers immediately to the sides of  $k_c$  having growth rates only infinitesimally smaller than that for the FGM. Thus there will be a group of wavenumbers propagating at group speed  $c_g \approx \partial\omega_r/\partial k$  (see §2). In this case, the appropriate analysis is that of the Ginzburg-Landau equation. The stable solutions given by the theory presented here (stable only to *self-interaction*), may no longer be so for other



wavelengths (there may be a side-band instability), and disturbances may evolve further to a larger amplitude. Work on this topic is now under way.

It is clear that, whatever their eventual amplitude, instabilities will in some measure modify the mean longshore current profile. The appropriate equation for determining this profile would therefore be an equation like (24). However, some confusion seems to have arisen concerning this new, mean profile: the profile produced by the instabilities is only the mean *component* of a fully developed *finite* disturbance; *the flow is stable to disturbances of wavenumber  $k_c$ , and it is no longer laminar, and the methods of linear stability can no longer be applied to it.* Therefore, any new, large shears apparent in the new profile should not be interpreted as leading to new instabilities.

This work provides justification for the growth rate scaling of DOT92. The final amplitude is indeed proportional to the growth rate, and the very large value of  $\ell$  for  $k_2$  indicates that the amplitudes will decrease rapidly with increasing  $k$  ( $\omega_r$ ).

Finally, two points should be mentioned: (1) The rigid-lid assumption does in fact break down in the weakly nonlinear analysis, but only at  $O(\epsilon^3)$ . This produces a small correction to the growth rate; (2) Bottom friction is not the only form of damping of the instabilities; turbulence induced by wave breaking will also have a direct effect, and should be examined in future studies.

## References

- Bowen, A.J. and R.A. Holman, (1989). Shear instabilities of the mean longshore current, 1.Theory. *J. Geophys. Res.*, *94*, 18023–18030.
- Dodd, N., J. Oltman-Shay and E.B. Thornton, (1992). Shear instabilities in the longshore current: a comparison of observations and theory. *J. Phys. Oceanogr.*, *22*, 62–82.
- Dodd, N. (1992). *Weakly-nonlinear stability of shear instabilities in the longshore current*, Institute for Marine and Atmospheric Research Utrecht, report (in preparation).
- Drazin, P.G. and W.H. Reid, (1981). *Hydrodynamic stability*, Cambridge University Press, 527pp.
- Oltman-Shay, J., P.A. Howd and W.A. Birkemeier, (1989). Shear instabilities of the mean longshore current, 2.Field observations. *J. Geophys. Res.*, *94*, 18031–18042.
- Stuart, J.T., (1960). On the non-linear mechanics of wave disturbances in stable and unstable flows. Part 1. The basic behaviour of plane Poiseuille flow. *J. Fluid. Mech.*, *9*, 353–370.
- Thornton, E.B. and R.T. Guza (1986). Surf zone longshore currents and random waves: field data and models. *J. Phys. Oceanogr.*, *16* 1165–1178.

## CHAPTER 204

### PROFILE DEVELOPMENT OF DUNES DUE TO OVERFLOW

by Henk J. Steetzel<sup>1)</sup> and Paul J. Visser<sup>2)</sup>

#### Abstract

The set-up and preliminary results of a series of model investigations on dune breaching is presented. Based on these 2DV-tests the insight into the processes related to the lowering of the crown of a sandy dam during overflow conditions has been enlarged significantly. Although dam erosion is mainly due to transport processes on the inner slope, the angle of the outer upstream slope showed to be very important also. Coarser sand results in larger erosion rates, whereas the effect of packing is only minor.

#### 1. Introduction and background

The Technical Advisory Committee on Water Defences (TAW) in The Netherlands is completing a probabilistic design method for dunes and dikes, which determines its optimal cross section as a function of both construction and expected damage costs (deaths, loss of property, etc.) due to failure of the structure. In order to be able to determine the damage costs, it is necessary to predict the rate of inundation of the polder governed by the discharge rate through a breach.

The effect of a local dike breach in terms of costs, is mainly governed by the final level and speed of inundation. Apart from for example the dimensions of the low-lying polder behind the breach, this level will definitely be related to the flow rate through the breach and thus by its dimensions. These dimensions, e.g. the breach width and depth, will not be constant. Moreover they increase in time, affecting the total discharge rate and thus the expected inundation level and damage costs.

- 
- 1) Senior Research Engineer, Delft Hydraulics, P.O. Box 152, 8300 AD Emmeloord, The Netherlands
  - 2) Scientific Officer, Delft University of Technology, Faculty of Civil Engineering, P.O. Box 5048, 2600 GA Delft, The Netherlands

Detailed knowledge of the process of breach growth to predict the inflow rate is therefore indispensable.

## 2. Approach

### 2.1 Introduction

The process of breaching of dunes and dikes is a very complex phenomenon [Delft Hydraulics, 1988], as clearly confirmed by a field experiment described in [Visser et al., 1990]. As a first result, an useful theoretical model to describe the breaching process is presented by Visser [Visser and Steetzel, 1992].

The final objective of the long-term research program is to enlarge the insight in the obviously rather complicated three-dimensional processes which control the breach growth, this in order to assess the rate of water inflow through an eroding breach into a polder with a mathematical model. This study can be seen as a follow-up on dune erosion studies [Steetzel, 1993], in order to predict the profile development and consequences of a dune failure during a critical storm surge.

### 2.2 Successive research phases

The inflow rate through a breach will mainly be controlled by the decrease of the maximum crown level in the breach (say increase in breach depth) and the increase in the width of the breach along the axis of the defence structure.

Focusing in more detail on a specific cross-section, the development of the breach dimensions, say breach width and breach depth, will depend on:

- the outer hydraulic conditions (water level, intensity of wave attack),
- the dimensions of the structure (crown height, crown length and both the inner and outer slopes) and
- its composition (material present and kind of foundation) as well as
- the inner condition, namely the level of the polder.

Some physical model tests have been carried out to study the breaching process for a sandy structure. The results of these tests are used to develop, calibrate and (afterwards) verify a mathematical model. To study erosion processes in detail, initially a series of two-dimensional model tests were conducted in the Schelde flume of the Delft Hydraulics [Delft Hydraulics, 1991]. Simultaneously, a general applicable mathematical model is being developed in order to compute and predict profile developments and inflow rates for all kinds of hydraulic and geometric conditions.

In a following phase also some tests on three-dimensional breaching have been carried out in a basin, merely to study the processes which control the growth of the breach width.

### 2.3 Outline of present contribution

This paper focuses in more detail on the set-up and results of a series of first model investigations on 2DV-breach growth, which were carried out at the end of 1991. These tests provide the development of the breach along the breach axis. At the end of this paper some concluding remarks are made on both the results of these tests and the next phases of the research program. A related paper on this subject is presented by Visser and Steetzel [1992].

## 3. Model investigations

### 3.1 Model facility

The vertical development of a uniform structure due to overflowing water was investigated in the 50 meter long Schelde flume of the Delft Hydraulics, as shown schematically in Figure 1. The effective width of the flume at the dam location was 0.40 m. A pumping system was installed in the flume to recirculate the overflowing water in order to maintain a more or less constant high outer water level for as long as possible.

### 3.2 Initial cross-section

At about 35 m from the wave board, a sandy dike-like structure was built having a 1.30 m long ( $L_{c,0}$ ) and a 0.70 m high horizontal crown ( $Z_{c,0}$ ). At the top of the crown a temporary defence structure was placed.

In these tests it is assumed that for some reason an initial, small breach is present at the beginning of a test (at  $t = t_0$ ). Consequently, in these 2DV-tests the initial outer water level was chosen to exceed the crown level by 0.05 m. After removal of the sandbag (in fact the start of a test denoted as  $t=t_0$ ), water started flowing down the inner slope and the erosion of the dam occurred.

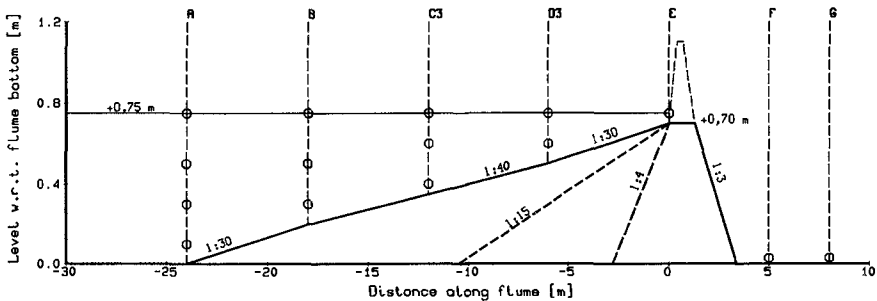


Figure 1 Model set-up, initial profiles (showing three slopes) and measuring positions of water levels and velocities (latter denoted by o-symbols)

In this test set-up three different outer slopes have been tested, ranging from 1 in 4 to 1 in about 35. Furthermore the grain size as well as the bed porosity of the dam have been varied.

### 3.3 Instrumentation

In order to allow a good recording of the erosion process, extensive instrumentation was installed in the flume. In the upstream inflow section, four sets of two electromagnetic velocity meters were placed. Furthermore at 7 positions wave gauges were present to record the development of the local water level.

At the position of the sand dam itself, the glass wall of the flume was utilized with a square (0.10 m) grid. By recording each of the tests with three simultaneously operating video-cameras, the development of the dam profile has been determined by analyzing these recordings with great accuracy.

Model set-up, including initial profiles and position of measuring devices is presented in Figure 1. In this way the profile development due to initial overflow (video-recordings) and a range of seven instantaneous velocity profiles and water depths were monitored during the breaching process.

### 3.4 Test program

The relative, quantitative effect of next parameters has been investigated:

- the seaward bottom slope, ranging from a 1:4 (dike) to 1:15 and a 1:30/40 slope (schematized dune erosion profile);
- the effect of waves on the breaching process, by comparing profile development with and without the presence of wave attack;
- the effect of sediment diameter, by comparing results of  $D_{50} = 105 \mu\text{m}$  and  $D_{50} = 218 \mu\text{m}$ ;
- the effect of porosity, by comparing results of two different porosities (with typical values of 38 and 45 % respectively).

An overview of the tests performed is presented in Table 1.

test number	brief description
T0	Essay experiment
T1, T2 and T3	Set of similar tests with mutually different angles of the outer slope
T4	Repetition of previous test (T3) with additional wave attack
T5 and T6	Repetition of both test T1 and T3 respectively using coarser sand for dam construction
T5A	Repetition of test T5 to check on the reproducibility of a test
T7	Repetition of test T5 for a more loosely packed dam

Table 1 Overview of test program

In total, the development of the sandy dam has been investigated in nine tests. In test T0 - T4 fine sand was utilized, while in the other tests (T5 - T7) coarse dune sand was used to construct the dam.

#### 4. Direct test results

##### 4.1 General

From each of the tests performed, two sets of data were obtained. The direct results, as discussed in this section, consist out of the observed profile development as well as the recordings of water level and water velocities during the erosion process. After analyzing these data, detailed information on the discharge rates and the apparent transport rates have also been obtained. Some examples of latter dataset are presented in the next chapter.

##### 4.2 Profile developments

The schematic development of the cross-section of a dam during the erosion process is shown in Figure 2.

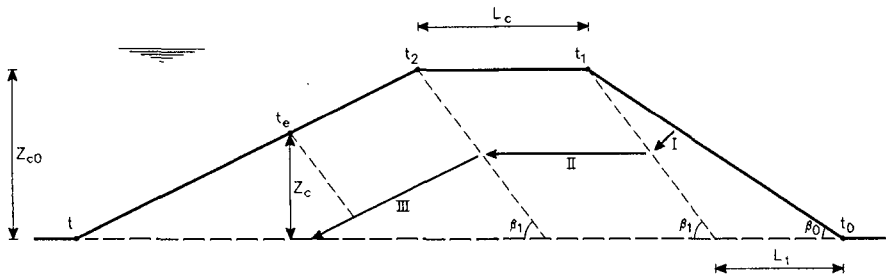


Figure 2 Schematic three-phase development of cross-section:  
I - increasing steepness of inner slope, II - decreasing crown length, III - decreasing crown level

In these tests, three subsequent stages (I, II and III respectively) can be distinguished. Initially the increasing transport rate on the inner slope results in a steepening of this slope up to a critical value. In phase II, the erosion of this slope remains nearly constant in time, resulting in a decrease of the length of the crown ( $L_c$ ). After erosion of the complete crown (at  $t = t_2$ ), the maximum crown level ( $Z_c$ ) starts to reduce. During this third phase, the discharge rate starts to increase strongly.

The grid on the glass wall allowed a direct assessment of both the instantaneous dam profile as well as the water depth contour. Figure 3 shows the observed development of the cross-shore profile (based on the analyses of the video-recordings) in test T5A. The numbers indicate the time in seconds with respect to the actual start of the test. Contours are presented at 20 seconds intervals.

Lowering of the crown started after about 140 s ( $= t_2 - t_0$ ). The average speed of reduction of the crown length amounts about 0.01 m/s. As can be observed, the total duration of such a test lasted only 5 to 6 minutes. At the end the total dam was washed out and, for the most part, in suspension circulating in the flume.

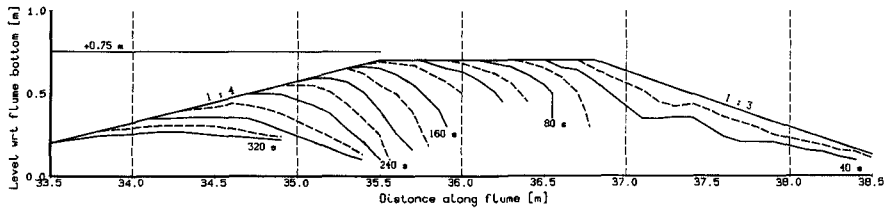


Figure 3 Measured development of cross-section during erosion process (for test T5A)

#### 4.3 Water levels and velocities

The recordings of both water level and flow velocities are very important, since the water motion over the inner slope dominates the process under investigation. The observed velocities on the inner slope range from 0.5 to 3.0 m/s. Moreover the data at the begin of the inflow section will be used as a boundary condition for the mathematical model.

#### 4.4 Additional measurements

During the test program additional measurements were carried out to assess water temperature, grain size distribution and actual volumetric porosity.

### 5. Interpretation of results

#### 5.1 Introduction

A thorough analysis of the results has provided valuable information on the water motion as well as on the sediment transports during the breaching process. The outcomes will also be used in order to check and improve the computational model. As can be seen readily from the former figure, the erosion is taking place at the inner slope of the dam.

#### 5.2 Crown development

The development of the maximum crown elevation for all tests is shown in Figure 4.

In the first stage of decreasing crown length, the crown level remains constant. Next, say from about 140 s, the level decreases. The actual rate of decrease differs for some tests due to the different test conditions. Most clear is the effect of the outer slope,

showing a relative decrease of this rate for the more gentle slopes (as present in tests T2, T3 and T6).

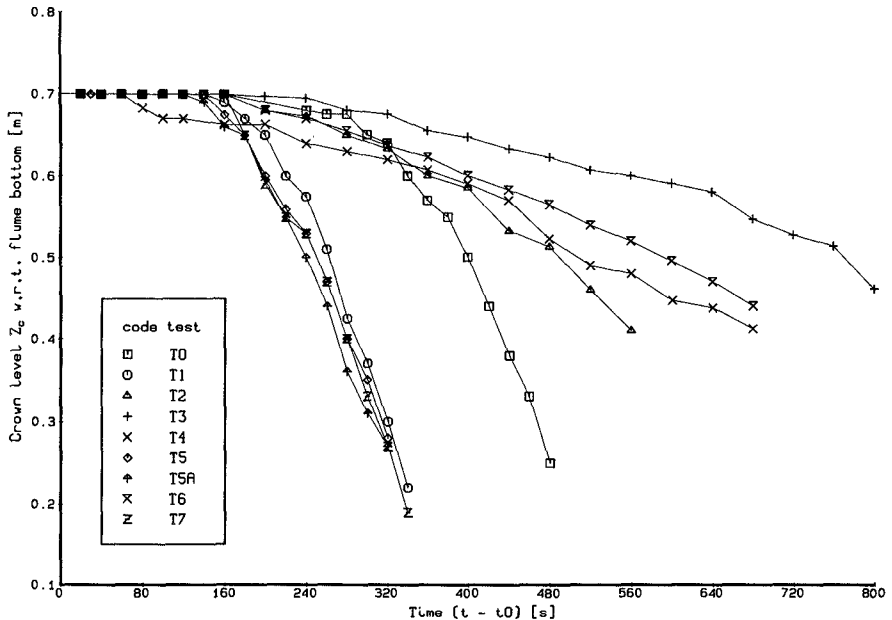


Figure 4 Overview of development of maximum crown level  $Z_c$  for all nine tests performed

### 5.3 Crown discharge rates

From the simultaneously measured velocities and water levels the magnitude of the rate of crown discharge has been estimated. An example of the computed development (for the same test T5A) is shown in Figure 5. In this figure both the instantaneous estimate at a frequency of 25 Hz (denoted by the small dots) as the filtered signal are presented. Furthermore the actual start of the test (denoted by  $t_0$ ) and the start of lowering of the crown level (denoted by  $t_2$ ) can be observed. At  $t = t_2$  the discharge starts to increase dramatically up to a more or less constant magnitude which is related to the installed pump capacity.



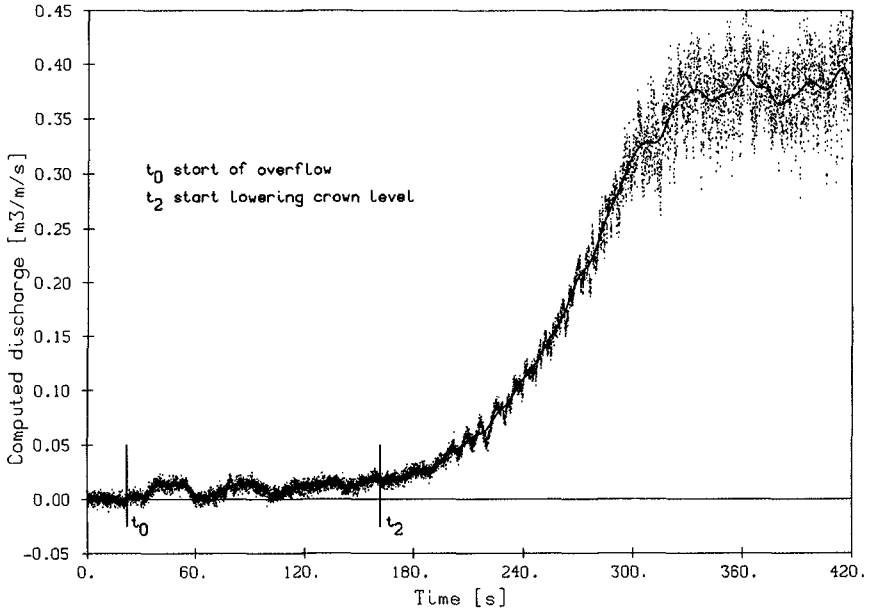


Figure 5 Development of computed (crown) discharge  $Q_c$  (for test T5A); both instantaneous estimate and smoothed signal (denoted by dots and line respectively) are shown

#### 5.4 Transport rates

As a result of the observed and recorded profile development, the apparent transport rate  $S$  was computed from the sediment balance equation at several moments and positions for each test. Figure 6 shows in the down-left corner a detail of the inner slope of the dam in test T5A at  $(t - t_0) = 100$  s.

The calculated transport distribution on a horizontal grid is shown at the top of the figure. The same distribution on a vertical grid is presented on the right, showing a near-linear downward increase of the transport and thus indicating a more or less equilibrium shape of the inner slope for this particular case. From visual observations of the transport process it has been concluded that this increasing transport rate is related to an increase in the thickness of the near-bottom suspension layer (sheetflow layer). The mean concentration within this layer has been estimated to be about 40 to 50% by volume.

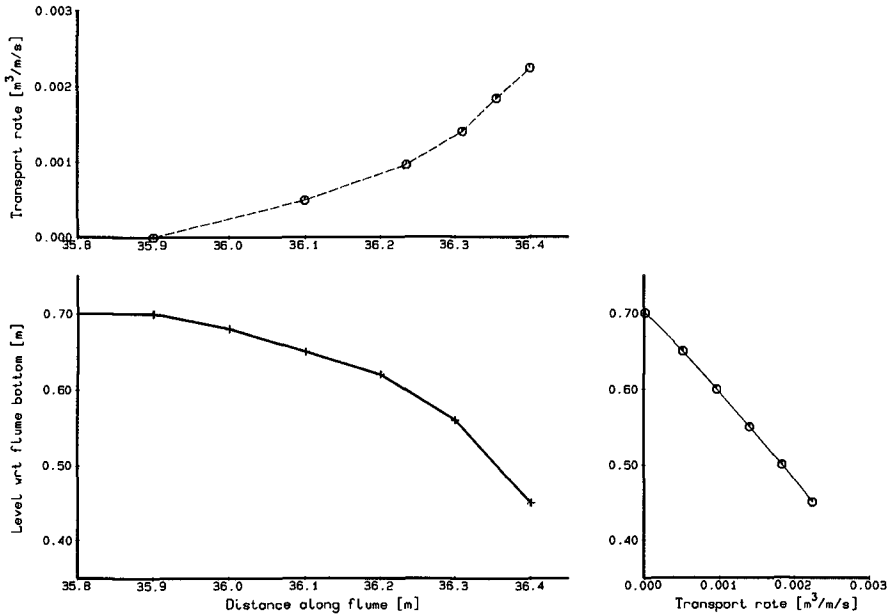


Figure 6 Computed transport distribution ( $S$ ) at inner slope of test T5A after  $(t - t_0) = 100$  s; both  $S = F(x)$  (upper figure) and  $S = F(z)$  (right-hand figure) are presented

## 6. Conclusions

### 6.1 General

Studying breaching processes in a model facility is difficult because of the speed of the processes involved, although in the present tests very accurate data on the breaching process have been obtained. Moreover the repetition of an identical test (test T5 and T5A) showed an almost perfect reproduction of the principal results. Some of the main conclusions are summarized hereafter.

### 6.2 Effect of seaward bottom slope

The influence of the seaward bottom slope is very important and primarily related due to volumetric effects. A relatively steeper outer slope results in a larger erosion rate.

### 6.3 Presence of wave attack

The presence of wave attack leads to accelerated erosion and speeds up the erosion process significantly.

#### 6.4 Sand diameter

Coarser sand increases the erosion rate by 15 to 25 %. This seems mainly due to the effects of hindered erosion present in case of finer material.

#### 6.5 Sand porosity

Effects of sand porosity are relatively small, although a loosely packed dam shows an about 5 % increased transport rate (for coarse sand).

### 7. Next research items

#### 7.1 Introduction

Although very interesting and useful findings have already been obtained, a continuing further analyses of the large amount of available data will enlarge the insight in the processes responsible for the breaching phenomena further.

#### 7.2 Computational model

In the development of the numerical mathematical model, one of the major problems to be dealt with is the formulation of the transport rates.

The sediment transport at high velocities is not yet well understood. Literature review, e.g. [Voogt et al, 1991], indicated that standard formulae tend to overestimate the transport rate. The transport on the inner slope seems to be affected by at least non-local effects and hindered erosion.

The dynamical, computational model will be based on the water motion according to the quasi-steady 'long wave' equations. Crown discharges will be iteratively derived using 'backward fitting', after which the super critical downward flow along the inner slope is computed. The sediment transports will initially be based on an adapted energetics-based Bagnold-formula (see [Visser, 1988]), although ongoing analyses of all the available test results may lead to other formulas.

#### 7.3 Further testing

Some additional tests on three-dimensional breaching in a basin have been carried out also. Next phases of the research program will have to enlarge the insight into the effect of clay and the presence of partial revetments on the breaching process.

Both the results of the computational model as the outcomes of the 2DH/3D-model investigations will be discussed in a forthcoming paper.

## 8. Acknowledgements

The present study is carried out at Delft Hydraulics on behalf of the Technical Advisory Committee on Water Defences of the Ministry of Transport and Public Works (Rijkswaterstaat) in The Netherlands. W.Th.J.N.P. Bakker, J. van de Graaff and A.W. Kraak are acknowledged for their comments and stimulating support during the preparation and elaboration of the tests.

## References

- Delft Hydraulics, 1988. Failure mechanism of dunes; The development of a dune for the ultimate condition, the process of breaching and the consequences. Research report H298, part 7 (in Dutch).
- Delft Hydraulics, 1992. Investigation on breach growth, 2D-model tests. Research report H1242, part 2 (in Dutch).
- Delft Hydraulics, 1993. Investigation on breach growth, 3D-model tests. Research report H1242, part 3 (in Dutch).
- Steetzel, H.J., 1993. Cross-shore transport during storm surges. Ph.D. Thesis, Delft University of Technology (in press).
- Visser, P.J., 1988. A model for breach growth in a dike-burst. Proc. 21st Int. Conf. on Coastal Engineering, Malaga, Spain, pp. 1897-1910.
- Visser, P.J., J.K. Vrijling and H.J. Verhagen, 1990. A field experiment on breach growth in sand-dikes. Proc. 22nd Int. Conf. on Coastal Engineering, Delft, The Netherlands, pp. 2087-2100.
- Visser, P.J. and H.J. Steetzel, 1992. A model for breach growth in sand-dikes. 23rd International Conference on Coastal Engineering, Venice, Italy (in these Proceedings).
- Voogt, L., L.C. van Rijn and J.H. van den Berg, 1991. Sediment transport of fine sands at high velocities. Journal of Hydraulic Engineering, Vol. 117, No. 7, pp. 869-890.

## CHAPTER 205

### THE CONTRIBUTION OF SUSPENSION EVENTS TO SEDIMENT TRANSPORT IN THE SURF ZONE

Bruce Jaffe<sup>1</sup> and Asbury Sallenger, Jr.<sup>2</sup>

#### ABSTRACT

Suspension of sand in the surf zone is intermittent. Especially striking in a time series of concentration are periods of intense suspension, suspension events, when the concentration is an order of magnitude greater than the mean. We used field data collected in the inner half of the surf zone during a large storm (greater than 1.5 m wave heights and 13 second periods) to define and describe suspension events and determine the contribution of events to the sediment transport.

Large suspension events were found throughout the inner half of the surf zone, occurred about once every 1 to 2 minutes, and each had a duration of about 5 seconds. These events tended to occur during onshore flow under the wave crest, resulting in an onshore contribution to the suspended-sediment transport. Even though large events occurred less than 10 percent of the total time, at some locations onshore transport associated with suspension events was greater than the offshore directed transport during non-event periods, causing the net suspended sediment transport to be onshore. Events and longshore velocity were not correlated. However, events did increase the longshore suspended-sediment transport by approximately the amount they increase the mean concentration, ranging from 15 to 55 percent depending on the definition used for events. Because of the lack of correlation, the longshore suspended-sediment transport can be adequately modeled as the vertical integration of the product of the time-averaged longshore velocity and the time-averaged concentration.

---

<sup>1</sup>US Geological Survey, MS 999, 345 Middlefield Rd., Menlo Park, CA 94025 and University of California at Santa Cruz, Dept. of Earth Sciences, Santa Cruz, CA 94064

<sup>2</sup>US Geological Survey, Center for Coastal Geology, 600 4th St. South, St. Petersburg, FL 33701

## INTRODUCTION

Ever since the first surf-zone deployment over 25 years ago of a fast-response instrument that monitored the amount of sediment in suspension (Brenninkmeyer, 1976a,b), researchers have observed short periods of intense suspension when sediment reaches high (order 1 m) into the water column. These intense suspensions were separated by longer quiescent periods when sediment concentrations were an order of magnitude less and suspension was confined to near the bed (order 10 cm). Brenninkmeyer, 1976a, called these intense periods "sand fountains". We will refer to them as "suspension events" following the terminology of Downing (1983).

Models for sediment suspension currently are not able to predict the occurrence of suspension events in the surf zone. In this paper, field data are used to objectively define event periods from a suspended-sediment concentration time series collected in the surf zone during a large storm. The average properties of suspension events are described and the contribution of events to the longshore and cross-shore suspended sediment transport are determined. We show that large suspension events tend to occur during onshore flow under wave crests and result in an onshore transport that can dominate the net suspended transport.

## EXPERIMENT SETTING AND METHODS

A large cooperative field experiment investigating the morphologic response of the nearshore to storms was conducted at the Army Corps of Engineers Field Research Facility (FRF) at Duck, North Carolina in the Fall of 1982 (see Mason and others, 1984, for a description of the experiment). The FRF is located on a long straight beach with bi-modal sand on the foreshore (1.0 mm and 0.3 mm modes), sand and pebbles in the longshore trough, and fine sand (~0.15 mm) offshore.

As part of this experiment the US Geological Survey deployed an underwater sea sled (Sallenger and others, 1983) equipped with instruments to measure waves, currents, sediment suspension, and profile change. Waves were measured using a pressure sensor and horizontal currents were measured at 3 elevations (0.5, 1.0, and 1.75 m above the bed) using 1" Marsh-McBirney electromagnetic current meters. Suspended-sediment concentration was measured at 5 elevations (0.10, 0.13, 0.19, 0.31, and 0.61 m above the bed) using optical backscatter sensors (OBS, Downing, 1981). The nearshore profile was measured using an infrared range-finder sighting on prisms mounted on a 10 m mast as the sled was pulled offshore and onshore by a winch and lines and a system of blocks.

Sled measurements were carried out for a two-week period during which one large extra-tropical cyclone (northeaster) and a smaller storm generated large waves and strong currents at the field site. The standard daily measurement regime was a starting profile extending several hundred meters offshore, processes measurements at up to 8 locations across the surf zone, and an ending profile to determine changes during the processes measurements. The entire procedure took about 6 hours and bracketed the time of high tide to minimize sea-level changes through the measurement period. At each of the measurement locations, 34.1 minutes of data were collected at 2 Hz for each sensor.

The largest profile response occurred during the northeaster of October 10-15. A linear bar formed on October 10th (Sallenger and others, 1985, Mason and others, 1984) and evolved into a crescentic bar by October 15th. The position of the bar crest on the sled transect moved offshore during the 10th, 11th, and 12th at rates as great as 2.2 m/hr and then migrated onshore on October 13th. The data presented in this paper were collected on October 13th.

The waves and currents were influenced by the barred profile of October 13th (Fig. 1). Because of the length of line pulling the sled, it was limited to operating in the inner six-tenths of the surf zone. Measurements were made at 7 locations between 17 and 224 m offshore, in water depths ranging from 2.3 to 4.3 m. The wave period ranged between 13 and 15 seconds. The standard deviation of the horizontal velocity was maximum at the bar crest, lowest in the trough, and fairly uniform at the measurement locations seaward of the bar. The magnitudes of the 34.1-minute-averaged speed and cross-shore velocity at 0.5 m above the bed increased toward the beach and had maximums at the measurement location nearest the deepest part of the longshore trough. The cross-shore mean currents at 0.5 m above the bed were directed offshore at all measurement locations (Fig. 1).

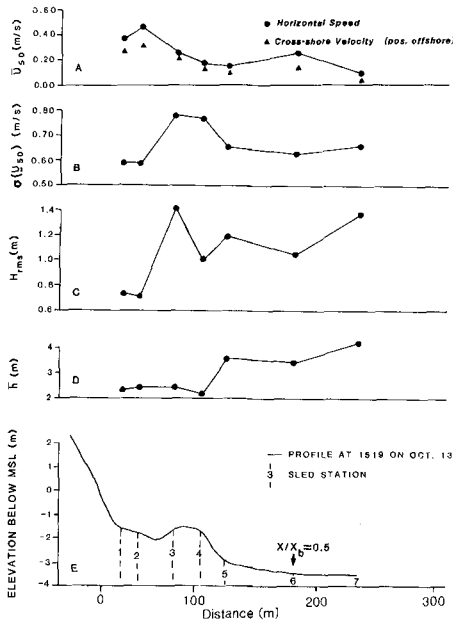


Figure 1- Conditions in the inner half of the surf zone at the Army Corps of Engineers Field Research Facility at Duck, NC during October 13, 1982. Shown from bottom to top are: 1) nearshore profile and measurement locations, 2) depths, 3) RMS wave heights, 4) standard deviation of the horizontal velocity at 50 cm above the bed, 5) mean horizontal speed and cross-shore velocity.

## DEFINITION OF SUSPENSION EVENTS

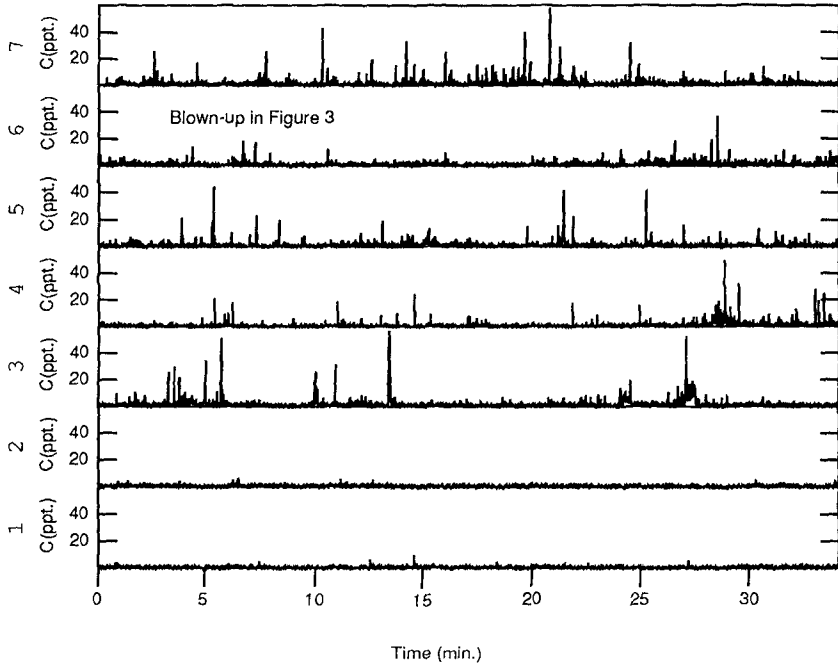


Figure 2- Time series of suspended sediment concentration at 13 cm above the bed for 7 measurement locations.

Suspension of sediment was intermittent at all measurement locations and at all OBS sensor elevations on October 13th. At 13 cm above the bed, concentrations were highest at the bar crest and at the offshore measurement location (Fig. 2, Figure 7 in Jaffe and others, 1984) and lowest in the longshore trough. At the 3 higher sensors (19, 31, and 61 cm) suspension was also intermittent with the intensity of suspension and the rate of occurrence of intense suspension decreasing higher in the water column (for example, see Fig. 3). For the 10-minute period shown in Figure 3 the intense suspension occurred during the passage of wave groups (intense suspension associated with wave groups was also observed by Hanes and Huntley, 1986). Suspension events were not associated with wave groups for other locations in the surf zone. Intense suspension was observed at other measurement locations following a strong offshore flow (also observed by Downing, 1983 at a beach in Washington). Since all of the measurement position were well within the the calculated plane-bed regime (Komar and Miller, 1975, Grant and Madsen, 1982), suspension events were not due to vortices associated with small-scale bedforms. Osborne (this volume) has recently found that larger, irregular bedforms sometimes form under the conditions observed at some of the measurement locations, so we can not rule out flow disturbances from this class of bedform creating suspension events. It is beyond the scope of this paper to



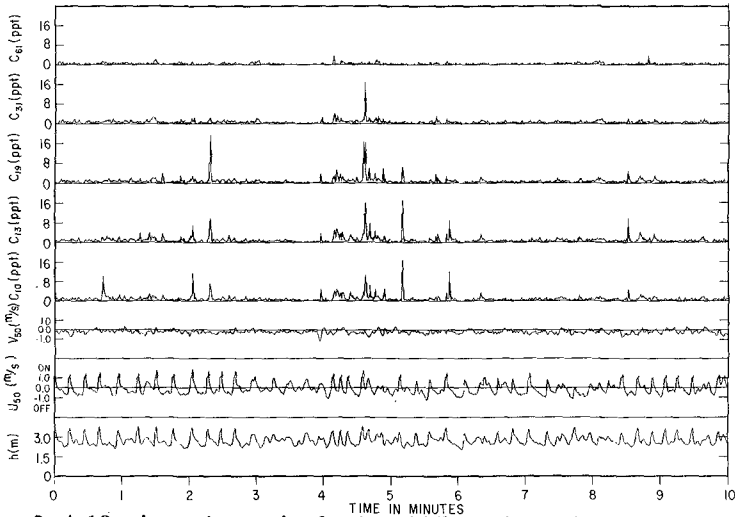


Figure 3- A 10-minute time series for the middle-surf-zone location (6). From the bottom, the hydrostatic approximation to sea level ( $h$ ), cross-shore ( $U$ ) and longshore ( $V$ ) water velocities at 50 cm above the bed, and sediment concentrations (ppt) at 13, 19, 31, and 61 cm above the bed. The time period corresponds to 2 through 12 minutes shown in Figure 2.

determine the processes responsible for producing suspension events. This paper will, however, quantify the characteristics of these periods of intense suspension and their contribution to transport in the surf zone.

Before quantitatively describing the character and transport contribution of the intense suspension periods, an objective criteria must be developed to distinguish these periods from less energetic periods of suspension. One simple definition would be to call periods when the concentration exceeds a threshold value a suspension event. The choice of threshold level will dictate how many events occur and their characteristics. For example, if 20 ppt was chosen as the event threshold there would be no events in the longshore trough ( locations 1 and 2) and some periods where suspension was episodic and intense at other measurement locations would not be considered events (a good example is location 6). To make the choice less arbitrary, event thresholds used in this paper were based on the statistical properties of the concentration distribution. Using the statistics for each location makes the definition of an event scale with the overall intensity of suspension at that location. The distribution of concentrations measured in the surf zone were skewed, with many low values and fewer high values (Fig. 4). Several event thresholds based on the mean and standard deviation of the concentration distribution were tried in order to define events. Two event thresholds are used in this paper to define events. A event was defined to occur when the concentration was greater than the mean plus one standard deviation (Fig. 5). Large events occur when the concentration exceeds the mean plus three standard deviations. In order to include the beginning and end of the event, an event start/end threshold was chosen. In this

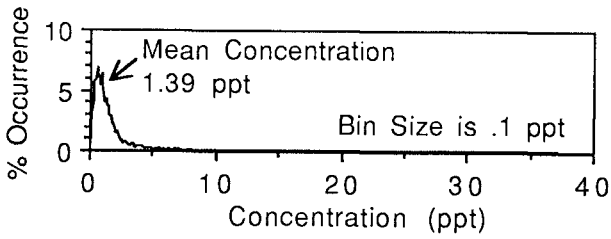


Figure 4- Frequency distribution of sediment concentrations at 13 cm above the bed for the middle-surf-zone location (6).

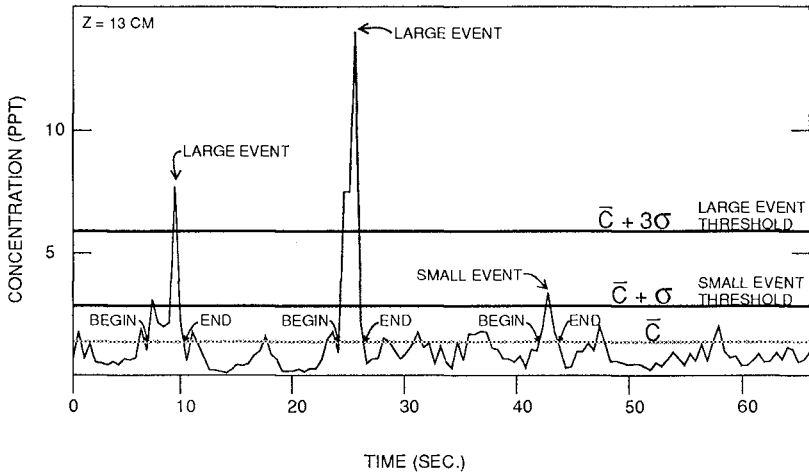


Figure 5- Suspended-sediment time series showing definition of suspension events

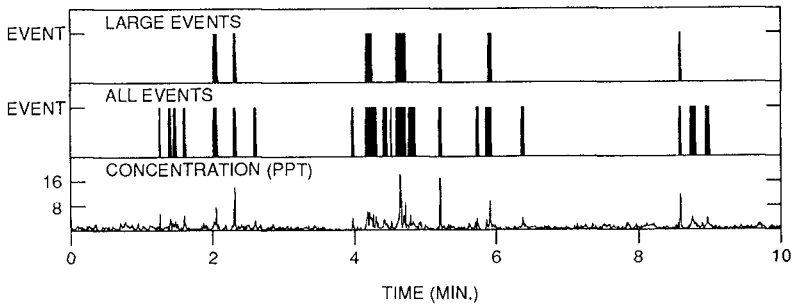


Figure 6- Application of suspension event definitions to the 10-minute series in Figure 3. From bottom to top are: 1) the concentration time series, 2) all events shaded, 3) large events shaded.

paper, the event start/end threshold used was the mean concentration.

Using the above definitions, time series of suspended-sediment concentrations at 13 cm above the bed were transformed to event time series to allow an automated analysis of suspension events (Fig. 6). Characteristics of events, including duration, rate of occurrence, and percent of the total time and concentration, are discussed in the next section.

## PROPERTIES OF SUSPENSION EVENTS IN THE SURF ZONE

Time series of large suspension events are shown for the 7 measurement locations in Figure 7. The measurements were not synoptic, so no information about phasing between events at different cross-shore locations can be extracted from the figure. The number of large events in the 34.1 minute records varies from a low of 15 near the bar crest (location 3) to a high of 37 at the mid-surf-zone location (6). Events tend to occur in packets and there are long intervals of several minutes or more between events at all measurement locations.

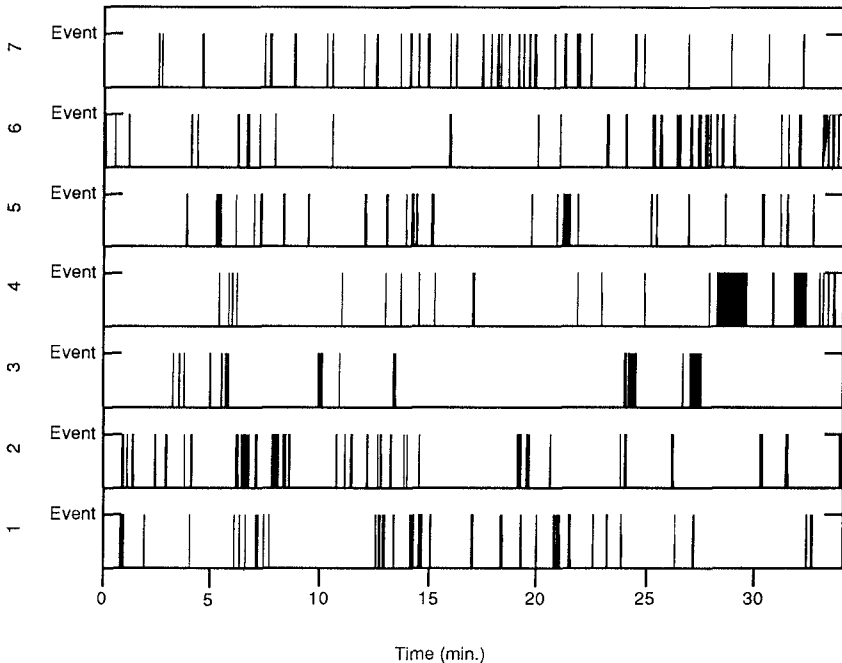


Figure 7- Large event time series for the 7 measurement locations.

The mean behavior of both events and large events are shown in Figure 8. On the average, large events occur about every minute away from the bar crest and every two minutes at the bar crest (Fig. 8a). Events defined with a lower threshold occur more frequently, but the cross-shore structure is similar to the structure for larger events. In the longshore trough these events occur about 5 times a minute (once every 12 seconds) which is less than the wave period, 13 seconds.

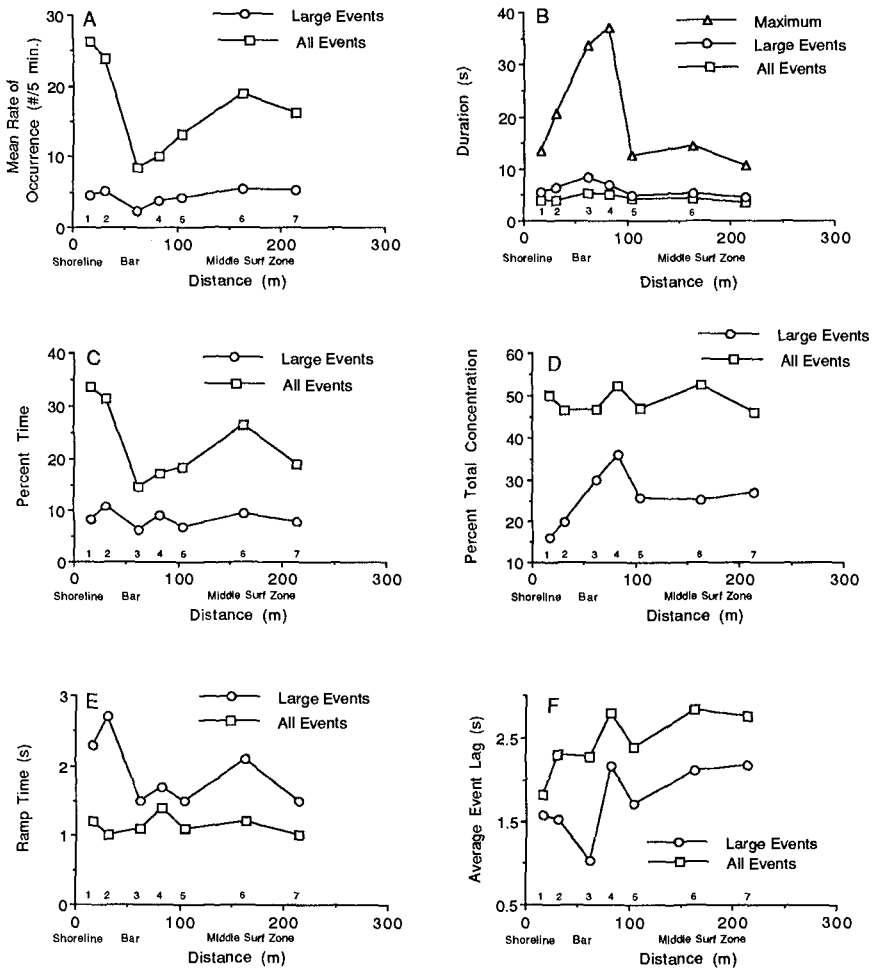


Figure 8- Average event properties for large and all events showing; a) mean rate of occurrence, b) duration, c) percent of the time events occur, d) percent of the total concentration, e) ramp time, and f) average lag of the event relative to the velocity zero up-crossing.

Both large and small events last an average of about 5 seconds, with larger events lasting longer (Fig. 8b). The maximum event duration, about 35 seconds, was near the bar crest where conditions were most energetic. At other locations in the surf zone the longest events lasted 15 or 20 seconds. The quickest events were only 1 or 2 seconds long. Typically, there was a wide distribution of event durations at each measurement location.

Because events occur infrequently and do not last long the percent of time that events occupy is relatively low, about 10 percent for large events and 15 to 35 percent for all events (Fig. 8c). However, the contribution of events to the total concentration is large, about 15 to 35 percent for large events and 45 to 55 percent for all events (Fig. 8d).

Events are typically asymmetric with a rapid increase in concentration and a more gradual decrease. The ramp time, the time from the start of the event until the maximum concentration, averages between 1.5 and 2.7 s for large events and between 1.0 and 1.4 s for all events (Fig. 8e). The ramp time for large events is minimum near the bar crest, one of the most energetic measurement locations. The shortest ramp time combined with the longest average duration makes events near the bar crest the most asymmetrical. Events are the most symmetrical in the trough of the bar.

Events tend to start several seconds after the flow reversal from offshore flow under the wave trough to onshore flow under the crest. On the average, large events start from 1.0 to 2.2 seconds after the velocity zero up crossing (Fig. 8f). The minimum lag time is at measurement location 3, the landward side of the bar crest. Lags are longest at the seaward side of the bar crest (location 4) and the middle-surf-zone locations (6 and 7). When all events are included the average lag time increases, ranging from 1.8 to 2.8 seconds. The distribution of lag times is not symmetrical about the average for large events. For instance, at the middle-surf-zone location (6) the largest number of events was near 0 lag time from the velocity zero up crossing, but the average was several seconds after the crossing because of a few events with long lag times.

## CONTRIBUTION OF SUSPENSION EVENTS TO TRANSPORT

Because suspension events occur infrequently and last for a short time one might think their contribution to the total suspended sediment transport is not very large. On the other hand, because suspension events increase the overall mean concentration by a significant amount, it could be postulated that events are significant to the total transport. To determine the event contribution to transport we made four calculations; 1) transport during large events, 2) transport during all events, 3) transport during non-event periods, and 4) total transport (2 + 3). These transport calculations were for one elevation and used the concentration measured 13 cm above the bed and horizontal velocity measured at 50 cm above the bed. The results, presented below, show that event contributions to longshore and cross-shore transport were very different.

### *Longshore Transport*

Events increase the longshore suspended sediment transport by approximately the amount they increase the mean concentration. For large events, the contribution ranged between 15 and 35 percent at all measurement locations on October 13th. For all events, the contribution was about 50 percent.

There is no preference for events to occur when the longshore velocity is either higher or lower than the mean. The contribution of events to longshore transport,  $\overline{VC}_{event}$ , is approximately equal to the product of the mean longshore velocity,  $\overline{V}$ , the mean concentration during events,  $\overline{C}_{event}$ , and the percentage of time events occurred,  $P_{event}$ . During non-event periods, the concentrations are also not correlated to the longshore velocity so the non-event transport,  $\overline{VC}_{non-event}P_{non-event}$  is approximately  $\overline{V} \overline{C}_{non-event} P_{non-event}$ . The total longshore suspended transport can be adequately calculated by  $\overline{V} (\overline{C}_{event} P_{event} + \overline{C}_{non-event} P_{non-event})$ , or  $\overline{V} \overline{C}_{total}$ . The time variation of the concentration is not needed to accurately predict the longshore suspended sediment transport. However, the vertical structure of the mean velocity and concentration must still be known because suspended-sediment concentration is high near the bed where longshore velocity is low and low higher up in the water column where velocities are higher.

### *Cross-shore Transport*

Suspension events make a significant contribution to the cross-shore suspended-sediment transport. Figure 9 shows the contributions of large events and non-event periods to the total cross-shore transport. The average transport during large events is onshore for all measurement locations seaward of the longshore trough. Transport during non-event periods, moving in the same direction as the near-bottom current, is offshore for all measurement locations. The total suspended-sediment transport is approximately, but not exactly, equal to the sum of large event and non-event periods because transport during small events is slightly offshore. The total transport is offshore for the longshore trough (measurement locations 1 and 2), landward side of the bar crest (3), and middle-surf-zone (6) locations, near zero seaward of the bar at location 5, and onshore on the seaward side of the bar crest (4) and the farthest seaward location (7).

The timing of suspension relative to the wave-induced oscillatory flow results in an average onshore transport during large events. For example, two events at the beginning of the time series in Figure 10 qualitatively show that the most intense suspension occurs during or just after the onshore flow under the wave crest. The average large event starts about 1 to 1.5 seconds after the velocity zero up-crossing (Fig. 8f) when the flow is onshore. Because the maximum

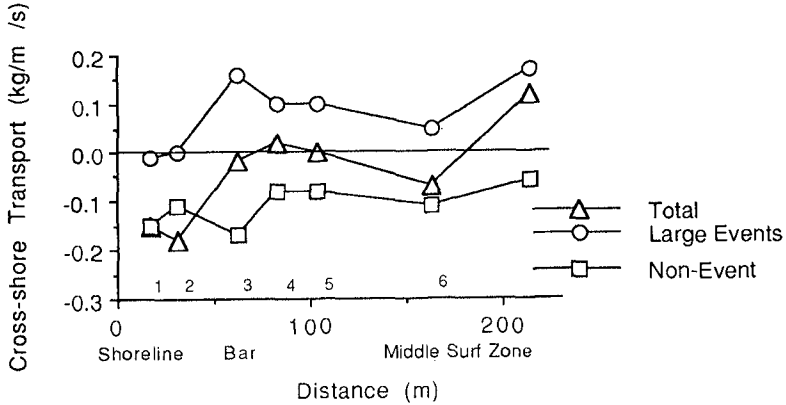


Figure 9- Cross-shore transport 13 cm above the bed for large events, non-event periods, and total. Small event transport is not shown but is small and offshore directed.

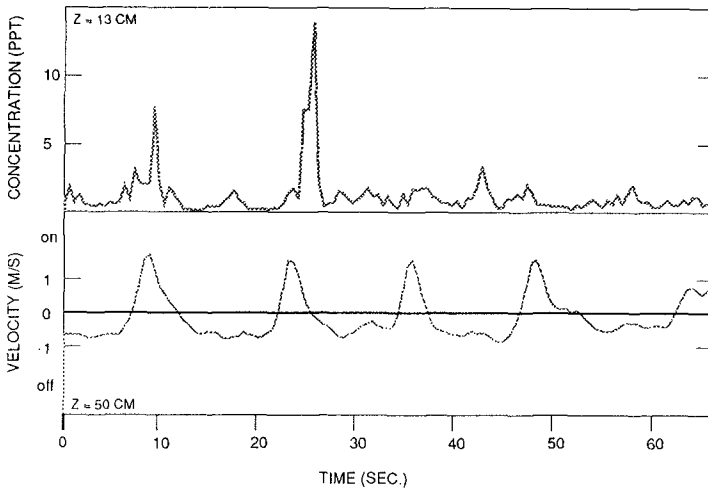


Figure 10- Time series of velocity and concentration showing the tendency for events to occur during onshore flow

concentration is reached quickly, about 1.5 to 2.5 seconds later (Fig. 8e), it too usually occurs during onshore flow.

Ensemble averages for the cross-shore velocity and concentration for three different measurement locations are shown in Figure 11. These averages included all large suspension events and were constructed using the velocity zero up-crossing time for reference for both the velocity and concentration time series. The phase of

events in the longshore trough varied widely resulting in an average large-event concentration with no distinct peak. This lack of phasing between the concentration and velocity resulted in a near zero net transport during large events for longshore trough measurement locations (Fig. 9). Large events at the bar crest and the middle surf zone tended to occur shortly after the velocity zero up-crossing resulting in a peak in the concentration (Fig. 11) and a net onshore transport contribution (Fig. 9).

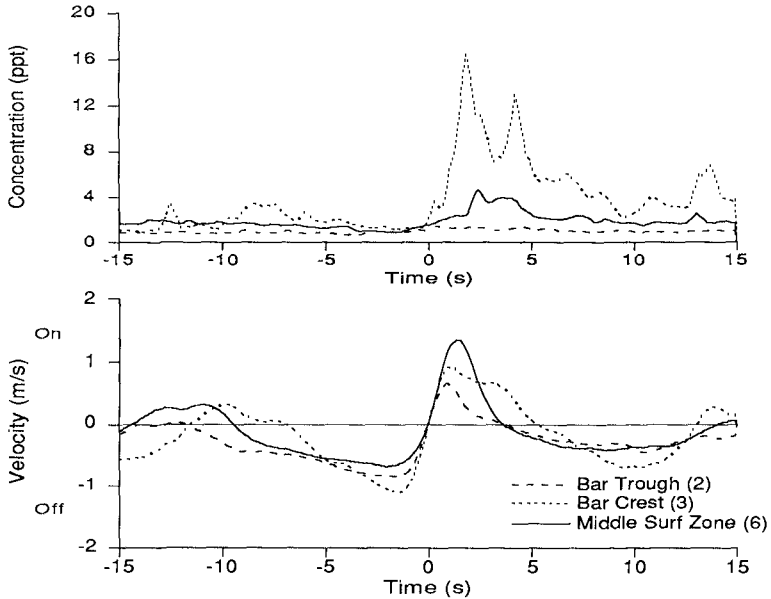


Figure 11- Ensemble averaged velocity and concentration for all events at measurement locations in the bar trough, bar crest, and middle surf zone. The time series are averages of velocities and concentrations for large suspension events with the velocity zero-upcrossing as the common time reference. .

## DISCUSSION

We have found that much of the net cross-shore suspended sediment transport at 13 cm above the bed was contributed by large suspension events. To accurately model the cross-shore transport the event magnitude and phase with velocity must be well predicted. Without modeling the large events, the predicted transport will be more strongly influenced by the mean current velocity (offshore) which would result in a predicted transport in a different direction than the actual transport at some measurement locations.



The results show that events are not as significant to predicting longshore suspended transport because events are not strongly correlated with the longshore velocity. However, inability to model events would result in an underprediction of the magnitude of the longshore transport up to about 50 percent, but unlike the cross-shore transport the direction would be accurately modeled.

Event transport is one part of the "fluctuating flux" addressed in Jaffe and others, 1984. The results in this paper support the conclusion that the time dependency of the flux (transport) is important to the net cross-shore flux, but not to the longshore flux (Jaffe and others Figures 8 and 9). Not addressed in this paper, but still an important property of the cross-shore transport is the tendency for low concentrations (less than the mean) to be correlated with offshore flow.

An improvement to this study would be to assess the vertical variation of events and their contribution to transport. Although we do not expect the conclusions to be significantly altered, the changes in concentration/velocity phasing in the vertical would be helpful information for modeling events.

The definitions for suspension events could possibly be improved. Because the concentration distribution was used to generate the statistics (mean and standard deviation) for the event definitions, it could be argued that instead of defining suspension events we are just looking at a tail of the distribution, which will always exist, so events will always exist. Although it is true there will always be concentration values in the tail, the timing of these high concentration values is not related to the distribution. For example, all the points in the tail could occur in one section of the time series and create one event or they could occur as single points equally spaced in time or a large number of other possibilities. Our definition does a good job of choosing the points that are visually striking when examining a time series of suspension.

## CONCLUSIONS

1) Suspension events, periods of intense suspension, can be defined on the basis of the concentration distribution. Two types of events were defined in this paper: 1) event periods when the concentration exceeded the mean plus one standard deviation, and 2) large events periods when the concentration exceeded the mean plus three standard deviations.

2) Large events were found throughout the inner half of the surf zone, occurred about once every 1 to 2 minutes, and lasted about 5 seconds.

3) Large events tended to occur during onshore flow under the wave crest, resulting in an onshore contribution to the suspended-sediment transport. Even though large events occurred less than 10 percent of the total time, at some locations their onshore transport was greater than the offshore transport during non-event periods. As a consequence, net suspended sediment transport was onshore.

4) Events were not correlated with the longshore flow and increased the longshore suspended sediment transport by approximately the amount they

increased the mean concentration, ranging from 15 to 55 percent depending on the definition used for events. Because concentration and longshore velocity were not strongly correlated, the longshore suspended sediment transport can be adequately predicted as the vertical integration of the product of the time-averaged longshore velocity and the time-averaged concentration.

## ACKNOWLEDGEMENTS

Discussion with David Huntley and Philip Osborne improved this paper. Discussions with Reggie Beach were important in formulating the problem. This manuscript was also improved by the reviews of Guy Gelfenbaum and Jeff List. We wish to thank the personnel at the Army Corps of Engineers Field Research Facility in Duck, North Carolina for their help with the experiment.

## REFERENCES

- Brenninkmeyer, B. M., 1976a, In situ measurements of rapidly fluctuating high sediment concentrations: *Marine Geology*, v. 20, No. 2, p. 117-128.
- Brenninkmeyer, B. M., 1976b, Sand fountains in the surf zone: Beach and Nearshore Sedimentation, *SEPM Spec. Pub.* 24, p. 69-91.
- Downing, J. P., Sternberg, R. W., and Lister, C. R. B., 1981, New instrumentation for the investigation of sedimentary processes in the shallow marine environment: *Marine Geol.*, v. 42, p. 19-34.
- Downing, J. P., 1983, Field studies of suspended sand transport, Twin Harbors Beach, Washington: PhD Thesis, p. 121.
- Grant, W. M. and Madsen, O. S., 1982, Movable bed roughness in unsteady oscillatory flow: *J. Geophys. Res.*, v. 87, no. C1, p. 469-481.
- Hanes, D. M. and Huntley, D. A., 1986, Continuous measurements of suspended sand concentration in a wave dominated nearshore environment: *Continental Shelf Res.*, v. 6, No. 4, p. 585-596.
- Jaffe, B. E., Sternberg, R. W., and Sallenger, A. H., 1984, The role of suspended sediment in shore-normal beach profile changes: *Proc. 19th Coastal Eng. Conf.*, v. 2, p. 1983-1996.
- Komar, P. D. and Miller, M. C., 1975, The initiation of oscillatory ripple marks and the development of plane-bed at high shear stresses under waves: *Journal of Sedimentary Petrology*, v. 45, p. 697-703.
- Mason, C., Sallenger, A. H., Holman, R. A., and Birkemeier, W. A., 1984, Duck82- A coastal storm processes experiment: *Proc. 19th Coastal Eng. Conf.*, v. 2, p. 1913-1927.
- Sallenger, A. H. Jr., Howard, P. C., Fletcher, C. H., and Howard, P. A., 1983, A system for measuring bottom profile, waves and currents in the high-energy nearshore environment: *Marine Geology*, v. 51, p. 63-76.
- Sallenger, A. H. Jr., Holman, R. A., and Birkemeier, W. A., 1985, Storm-induced response of a nearshore-bar system: *Marine Geology*, v. 64, p. 237-257.

## CHAPTER 206

### THE SHORT TERM PROFILE RESPONSE OF SHINGLE SPITS TO STORM WAVE ACTION

Bradbury A P <sup>1</sup> and Powell K A <sup>2</sup>

#### Abstract

The profile performance and the conditions giving rise to overtopping and overwashing of shingle barrier beaches have been examined in an extensive programme of field work and physical model studies. The hydraulic performance of Hurst Spit, on the south coast of the UK, has been examined in detail, and the studies have been used to design a management programme for this barrier beach. This has included the design of a beach replenishment scheme and quantification of overtopping thresholds and alarm conditions, for a range of beach geometries. An extensive series of 3-dimensional physical model tests are discussed and a dimensionless parametric framework is suggested, which provides a method of estimating the conditions that will result in crest accumulation, breaching and crest lowering of shingle barrier beaches, for a wide range of beach geometries.

#### Introduction

Shingle spits often provide the only natural defence from wave attack to the areas of low lying land in their lee. They are hydraulically efficient structures, maximising wave energy dissipation through the high permeability of the shingle. Barrier beaches are particularly important at sites where they protect low lying land, often at the mouths of large tidal inlets. Important sites around the UK include Hurst Spit, Chesil Beach and Orfordness. These beaches are typically less than 100 metres wide above mean water level and may have a crest width of less than 5 metres.

---

<sup>1</sup> Coast Protection Group, New Forest District Council, Lymington, S041 9ZG, UK

<sup>2</sup> Coastal Group, HR, Wallingford, Oxon, OX10 8BA, UK

The natural beach crest is generally formed at a level which is just below the maximum level of wave run-up. This is controlled by a combination of wave conditions, and water levels, and the shingle size and grading. The crest of a shingle barrier beach may be exceeded by wave run-up, resulting in overtopping under extreme conditions. The beach crest is often able to dissipate energy as waves pass over the crest, restricting both water and shingle movement to the seaward side of the beach crest. Under these circumstances any shingle that is pushed or carried to the crest by the wave run-up is deposited at the crest, thus causing the crest level to increase. The high permeability of the beach usually ensures that most wave energy is dissipated before it reaches the lee face of the beach. When the combined effects of freeboard, crest width and wave conditions reach a critical condition however, often during periods of extreme water levels resulting from tidal surges, the beaches become susceptible to overtopping which cannot be confined within the crest. This may result in crest rollback, crest lowering, fan formation and subsequent sudden, and often spectacular failure of the shingle bank. Whilst the leeward position of a shingle beach with a seawall or cliffs on its landward side is fixed, a barrier beach with no retaining wall on its landward side is free to move landwards or "rollback" when waves reach the leeward crest of the beach.

Previous field studies of shingle barrier beach development have discussed various stages of crest evolution (Nicholls, 1985) resulting in:

- a) crest level raising by overtopping;
- b) crest rollback;
- c) crest level lowering by overwashing;
- d) breaching;

Field observations of the performance of barrier beaches have been discussed in some detail by several authors and the sedimentology of the crest features of sand barrier beaches has been studied extensively (Leatherman and Williams, 1977). Whilst the field studies have provided a valuable description of the development of these beaches, they have not quantified the complex interaction of wave and water level conditions, sediment size and the geometry of the beach, which result in the formation of these features. There is a particular dearth of information with respect to shingle barrier beaches, which typically have a  $D_{50}$  grain size in excess of about 5mm.

Recent examples of severe storm activity on Hurst Spit, UK, have demonstrated that catastrophic failure of shingle barrier beaches may occur, resulting in extensive flooding and damage to low lying land in the lee of the beach. The problems of diminishing shingle supply to Hurst Spit present a significant problem to the management of the beach and remedial action was urgently required to maintain the integrity of the beach. This problem presented the opportunity to examine at full scale a barrier beach which was becoming subject to overtopping under storms of increasing frequency.

Recent research on restrained shingle beaches by Powell (1990) and van der Meer (1988) has provided parametric empirical frameworks to predict the profile performance of restrained shingle beaches, but these studies have not examined the evolution of barrier beaches. The processes which result in the dramatic evolution of these beaches are difficult to quantify and as a result coastal managers have little guidance on their management. If natural or renourished shingle barrier beaches are to be used as effective coast protection structures, it is essential that the hydraulic performance of the crest evolution is clearly understood.

### Objectives

The studies were commenced with the intention of providing an understanding of the hydraulic performance of the Hurst Spit shingle bank, and to provide a management strategy to ensure that the spit would continue to provide protection to the land in its lee. This required identification of the conditions that cause crest lowering of the beach, the design of a major beach replenishment scheme and the identification of appropriate alarm conditions for future maintenance of the beach.

In the course of the studies the objectives were extended to investigate the hydraulic performance of shingle barrier beaches of a wide range of geometries, subject to a wide range of wave and water level conditions, thus providing an empirical method to allow the crest processes of these beaches to be quantified.

The study has been divided into three main phases of experimental work.

- a) field studies;
- b) wave climate studies;
- c) 3-dimensional physical model studies.

### Field work

The main focus of the studies has been on the hydraulic performance of Hurst Spit, UK. The spit which is approximately 2.5 kilometres long, protects an extensive area of low lying land, and has a long history of rapid evolution (Nicholls, 1989). Reduced shingle supply to the spit by longshore transport has resulted in a declining beach volume. Consequently, the frequency of overtopping events has increased. The features which result from wave run-up and the overtopping processes discussed in this paper have all been observed, and detailed measurements of beach profile response have been recorded on a regular basis. The field work and wave climate studies were carried out at Hurst Spit, UK, over a five year period between 1987 and 1992.

The beach is surveyed quarterly and also following severe storms along 20 profile lines, at approximately 100m intervals. Wave conditions and tidal conditions have also been monitored at this site, thus allowing the beach response to be quantified with respect to the hydraulic parameters.

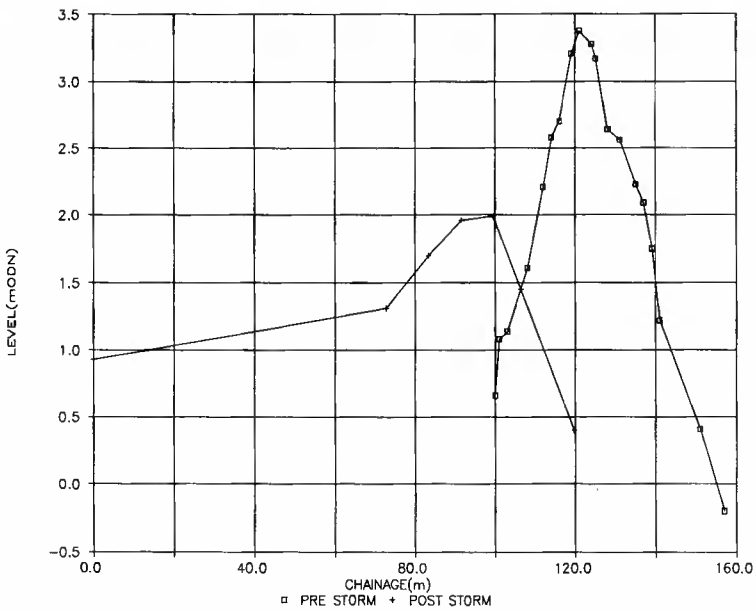
The beach is characterised by a coarse grain size  $D_{50}$  of about 16 mm. The beach crest is generally between 2 - 4 metres above mean high water, with a crest width of 3 - 10 metres. Wave rider records indicate a nearshore wave climate with storms regularly occurring with significant wave heights in excess of 2.5 metres. The complex offshore bathymetry results in different incident wave conditions along the length of the spit. The beach profile response is therefore different at each profile position. The significant wave height of the 1:100 year return period storm varies from 1.8m to 3.5m (in 7 metres of water), from east to west.

The storms of the winter of 1989 have provided data of some considerable interest. Large scale overwashing of the spit occurred in December 1989, resulting in crest lowering along an 800 metre length of the beach. The seaward toe of the beach was rolled back by as much as 60 metres whilst the leeward toe was moved by as much as 80 metres in a single storm event. Crest lowering in the same event resulted in reduction of much of the beach below the level of the peak water level of the storm, a reduction in crest level by as much as 3 metres. Whilst offshore wave conditions were only moderate during this storm, an extreme tidal level resulting from a storm surge at the peak of the storm resulted in a very low freeboard and increased wave conditions at the toe of the beach. This dramatic event provided valuable data about the response of Hurst Spit under extreme conditions and provided excellent data for calibration of the physical model. More severe wave conditions monitored on other occasions at lower water levels also resulted in overtopping and crest rollback, thus providing calibration data for events closer to the threshold of crest roll back.

Further field work is ongoing to provide additional validation of the empirical methods developed in the laboratory and to assess performance of the proposed beach renourishment, which has been designed in conjunction with these studies. The conditions that occurred during the field work programme provided the rare opportunity to carry out concurrent measurements of waves, tides and beach profiles, for a series of severe storms. Whilst the field studies provided a considerable amount of quantitative information about the processes, the restricted number and random nature of the natural storm events provided insufficient data alone to generate a statistically valid method for the prediction of the beach crest evolution. It was therefore necessary to examine the beach response in a more controlled environment to enable threshold conditions to be defined.



Overwashing of Hurst Spit in December 1989



Profile response of Hurst Spit to storm of December 1989

### Physical Model Tests

Recent developments in physical modelling techniques for shingle beaches have provided an appropriate method of study. The use of distorted sediment scaling to produce model beaches with appropriate permeability and sediment movement characteristics to reproduce the correct profile response of the beach has been discussed by Powell (1989). Since detailed physical model studies had not however previously been used to examine the profile response of overtopping shingle barrier beaches, it was necessary to carry out a series of calibration tests to prove the validity of the modelling techniques for this type of beach.

The model tests were conducted in a 3-dimensional wave basin under random wave conditions. The model was constructed at a scale of 1:40, with an active beach frontage of 1000 metres. Model variables included a range of significant wave heights from 1 - 4.5 metres, wave periods of between 6 - 12 seconds and four static water levels. The four water levels provided a variable freeboard between the beach crest and the static water level and also provided the opportunity to examine the effects of varied breaking wave conditions at the toe of the structure. Many of the tests were carried out with normally incident waves, although a large number of tests were also carried out with the beach subject to oblique wave attack, within the range 5-15°. The material used to represent the model beaches was a graded anthracite, scaled to reproduce both the correct beach permeability, threshold and direction of sediment motion and thereby the correct profile response of the beach.

A number of hydraulic variables were kept constant throughout the test programme. These included sediment size and grading, spectral shape (JONSWAP), and storm duration.

The test programme was divided into three phases

- a) validation of the test methodology
- b) evaluation of the hydraulic performance of Hurst Spit
- c) evaluation of the hydraulic performance of an extensive range of barrier beach geometries.

Field data collected from Hurst Spit provided the basis for the design of the first two phases of laboratory tests, ensuring that model beaches, foreshore geometry, sediment size characteristics, wave and water level conditions were all modelled correctly. This provided a typical structure for validation of the test methodology and for examination of the processes identified by field observations.

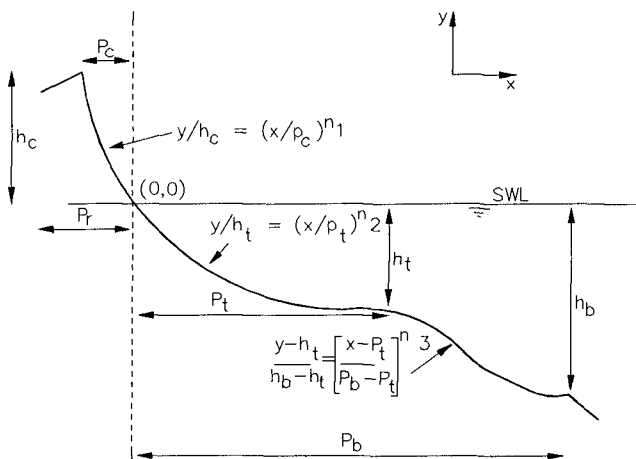
The test conditions were extended to include a wider range of variables as the studies developed. The third phase of testing provided a means of examining



a much wider range of conditions and beach geometries, which might be applicable to sites elsewhere. A wide range of wave conditions, water levels and shingle bank geometries have been examined in a systematic series of tests on the profile response of an extensive range of beach geometries. In excess of 3000 beach profiles were measured in more than 200 physical model tests. Concurrent measurements were also made of wave and water level conditions

The seaward slope geometry has been described by the three stage schematised shingle beach profile proposed by Powell (1990). Additional beach geometry characteristics appropriate to barrier beaches have been defined in terms of beach cross section area, crest level, crest width and beach span at each of a number of beach levels. The primary geometric variables which have been used in the analysis of the beach profile performance are the beach crest level and the crest width. A range of freeboards from 0.5 metres to 6 metres were examined, with beach crest widths ranging from 2 metres to 20 metres.

Pre and post storm profiles were recorded by surveying the beach before and after each test. Profiles were recorded using a computer driven incremental bed profiler, sampling levels at a constant survey interval of 2 metres along each profile line. A number of profiles were recorded along the beach frontage for each test. This provided the basis for the examination of the spatial variation of the beach performance. The tests were generally run for a prototype duration of 3 hours. Video recordings were made of each test from an aerial camera. These recordings were later used in the analysis of the evolution of the crest features.



Schematised shingle beach profile (after Powell, 1990)

## Results

The physical model was validated by reproduction in the model of severe storms that occurred on Hurst Spit in 1989. Field measurements of wave and water level conditions during the storms, and beach profiles monitored before and after the storms have provided the basis for the comparison of the performance of the physical model with Hurst Spit. The results of the physical model provided a remarkably good reproduction of the profile response of Hurst Spit to these storms and demonstrated the validity of the modelling methods for this type of structure.

Observations made during the test programme provided an explanation for many of the features formed during the tests. A number of threshold conditions were identified, both visually and by parametric analysis of the beach profile response to various hydraulic conditions. The first threshold condition occurs when the combination of wave conditions, water level and beach geometry causes crest accumulation. This process is described well by earlier studies (Powell, 1990) which have quantified wave run-up and berm formation. Crest accumulation occurs when waves reach the crest with sufficient energy to spill onto the crest, but with insufficient energy to wash the whole of the way over the crest. The hydraulic conditions giving rise to this process are confined to a very narrow band for any given beach crest width. The validity of the run-up formulae are further restricted by the initial beach crest width which may prevent the predicted beach profile from being reached, if the combination of crest position and crest height require a wider beach to achieve the dynamic equilibrium profile. The formulae do however provide an excellent method of defining the lower boundary conditions for thresholding of damage by overtopping, by reference to both the initial profile and the post storm predicted profile. An appropriate alarm condition for each profile geometry can therefore be derived by reference to the conditions causing crest accumulation. This method has been used to provide an empirical assessment of the alarm conditions for Hurst Spit, thus providing management guidance on the maintenance requirements following beach renourishment. Similarly the threshold geometry for given wave and water level conditions can be calculated to provide the required profile to withstand any event. Accumulations of material at the crest of up to 1.2 metres were measured during the model tests.

A further threshold, resulting in crest lowering, is reached if the combination of wave and water level conditions and beach geometry reach the lee face of the beach. The numeric definition of this threshold is however somewhat more complex, as there is a strong dependency on the crest width as well as the wave conditions. Tests indicated a wide spatial variation in the conditions that resulted in crest lowering and also some scatter in the results of profile response close to this threshold. The spatial variation may be a function of very small localised variations in the initial beach geometry. The beach crest is extremely sensitive to small changes in freeboard and crest width and caution should therefore be exercised when assessing the vulnerability of the beach to crest lowering.

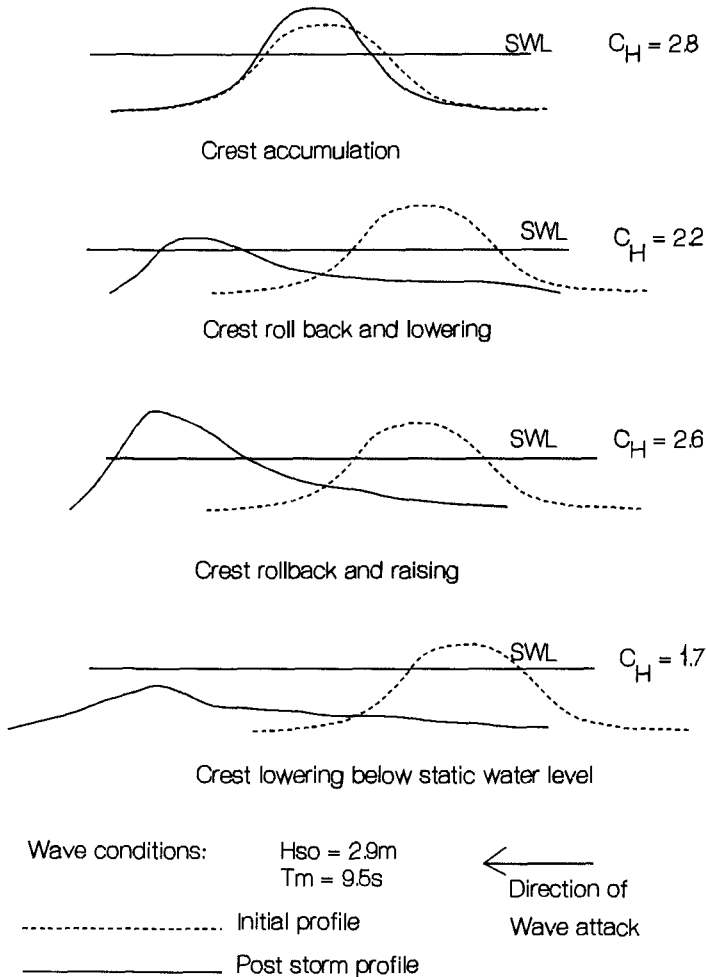
Process development observed in the model helps to explain some of the scattered results measured close to the crest lowering threshold. Small washover fans normally form at first, unless the storm water level is very extreme. These are followed by the formation of more extensive breaches through the bank as the storm progresses, resulting in large scale crest lowering. The size and method of formation of a washover fan is dependent upon the crest width, crest level and wave and water level conditions. If the crest is very narrow a wide breach may form quite rapidly, as waves are able to overtop the bank and lower the crest quickly. If however the crest is rather wider, the rate of formation and size of the overwash fan will be significantly slower and smaller. Once the crest level has been lowered the rate of crest lowering increases rapidly, as the frequency of waves reaching the crest increases. The width of the initial overwash fan ranged in size from approximately 4 metres to 25 metres wide, depending on the shingle bank geometry immediately prior to overtopping. Similarly, the length of the initial fan could extend landwards from approximately 1 metre to 15 metres. The rate of landward progression of the overwash fan is also strongly dependent on the topography of the land in the lee of the beach. Following from the initial formation of an overwash fan the beach plan shape may evolve very rapidly. The fans are quickly widened by outflanking of the upstanding ridges formed on either side of the fan, by overtopping waves. The fan itself provides a preferential flow path for the overtopping waves and a gully forms through the centre of the fan. As the waves flow across the mound the sediment fan is liquified and flows with the wave to the lee side. The fan may then extend landwards very rapidly, moving as much as 10-15 metres in a single wave. As the fan reaches the base of the shingle bank it tends to spread and forms an enlarged head area which accumulates as more material is washed across the crest.

The wave grouping following the initial fan formation is also extremely important. If the waves following the initial fan formation are small, a ridge may form seawards of the crest ridge. This in turn is pushed upwards towards the crest, and can prevent further overtopping. In many instances the wave grouping enables a fan to form, but permits the initial breach to heal. This demonstrates the need to study these processes with random as opposed to regular waves.

As the storm progresses, the width of the shingle bank is reduced, due to the beach attempting to reach a dynamic equilibrium profile for those conditions. Undermining of the beach crest occurs and the crest width is consequently thinned. This may occur even when waves do not reach the crest of the shingle bank, thus demonstrating the importance of both the span and the crest level of the shingle bank. In certain instances the bank can be cut back to such an extent that a breach may form as a result of waves breaking through a narrow ridge as opposed to the more normal failure mechanism occurring by overtopping.

In addition to overtopping, percolation of water occurred through the

permeable model shingle bank, resulting in the formation of streams and washout fans on the lee side of the spit. This process has been noted at a number of locations on Hurst Spit. This condition occurs most commonly where the spit has been cut back by wave action to a small cross section profile, but where waves are too small to reach the crest of the beach. The fact that this process was observed in the model serves as an additional marker that indicates that the physical model is able to reproduce the permeability of the bank correctly.



Profile response of model barrier beaches

### Parametric analysis

Many of the test conditions resulted in the formation of a run-up berm below the level of the beach crest. The measured post storm profiles for these conditions were initially compared with the functional relationships derived by Powell(1990) in earlier studies on restrained shingle beaches. This comparison confirmed the validity of the parametric framework for these conditions, with the results of the studies falling well within the error bands suggested for each of the functional relationships. The coarse grain size resulted in the formation of a steep upper beach slope below the crest berm. The parametric framework maintained validity even as the run-up level increased above the original beach crest, provided that the beach crest width was wide enough to allow deposition of beach material at the crest. The functional parameters to describe crest height ( $h_c$ ) and crest position ( $p_c$ ) given below however, became unstable as the wave and water level conditions became more severe, or as the crest width became narrower.

$$p_c D_{50} / H_s L_m = -0.23 (H_s T_m g^{1/2} / D_{50}^{3/2}) - 0.588$$

$$h_c / H_s = 2.86 - 62.69 (H_s / L_m) + 443.29 (H_s / L_m)^2$$

These equations are corrected for breaking wave conditions by use of the correction factors:

$$p_c = 3.03 (H_s / D_w) + 0.12$$

$$h_c = (H_s / D_w) + 0.41$$

The crest evolution changes from accumulation to crest lowering when the wave and water level conditions in combination with the beach geometry cannot reach a dynamic equilibrium profile within the existing beach cross section. There is therefore a complex relationship between the hydraulic parameters and the beach geometry which defines the threshold of overwashing resulting in crest lowering. This relationship is very sensitive to small changes in freeboard and crest width conditions.

The effects of each of the hydraulic variables are examined in turn. The main influence of the significant wave height is on the crest position ( $p_c$ ). As  $H_s$  increases, the horizontal distance from the beach and the static water level intersection (0,0) is increased. If the dynamic equilibrium position for the wave conditions lies further landward than the width of the unconfined beach crest, the dynamic equilibrium crest position cannot be achieved and the beach crest will be breached, resulting in crest lowering. The situation is further complicated by the other hydraulic variables which in certain combinations may allow the beach crest to reform landwards of its original position.

The effect of increasing the wave period is to raise the crest level of the beach. If there is insufficient beach material available within the crest however, a

raised crest will fail to form and overwashing will occur. The rate of overwashing increases dramatically with increasing period, due to the larger volume of water in longer period waves. Both the wave height and the period variables may reach a threshold condition whereby the beach is overtopped without the crest reforming above the peak run-up level. In this instance crest lowering may occur.

The effects of static water level are twofold. Firstly there is a simple relationship which reduces the exposure of cross sectional area of the beach above static water level, as the water level rises. In this instance the dynamic equilibrium profile moves further landwards as the freeboard is reduced. There clearly comes a point where the freeboard becomes so small that virtually any wave condition may pass over the crest, resulting in rollback and crest lowering. The second relationship is more complex and relates to the breaking wave height at the toe of the beach. This clearly results in larger incident wave conditions at the shoreline as the water depth increases, for the same offshore conditions. Wave run-up is therefore increased. This is reflected by the adjustment factors for wave breaking given in Powell's model.

The test results were very sensitive to small changes in the model test variables and these have resulted in some scatter close to the threshold conditions. The effects of wave grouping appears to have a significant effect on the crest evolution and this appears to contribute to the lack of consistency of certain of the results whilst close to the threshold conditions. Whilst wave grouping was not quantified, it is certainly a feature which must be considered. Observations made during testing identified a number of instances when the beach would be overtopped, causing crest lowering in a period of severe wave activity. Later the same beach section would heal during the same test during periods of less intense wave activity, occasionally resulting in the formation of a higher run-up crest than the initial profile.

Further examination of the data resulted in the formation of a new parametric framework designed to examine the vulnerability of the beach to overtopping and rollback, and to define damage thresholds. Whilst Powell's model of profile response works well within a range of conditions, it becomes more unstable as the freeboard is reduced, the wave period is lengthened or the wave height is increased. The influence of the beach crest width is clearly very important but further work is required before the effects of this variable can be quantified with statistical validity.

The framework proposed for the analysis in this study considers the beach as a simple geometric structure subject to variables defined by freeboard, shallow water breaking wave height and shallow water wave length. A critical freeboard parameter  $C_f$  is proposed. The formula suggests limits for the safe use of Powell's earlier studies and suggests an inundation threshold value beyond which the level of the beach will be reduced below the static water level of the storm peak, for the range of conditions tested in these studies.

The threshold formula is given by:

$$C_f = \frac{C_H}{(H_{sb}^2 L_{ms})^{1/3}}$$

where  $C_f$  is the critical freeboard parameter

$H_{sb}$  is the shallow water breaking wave height calculated from:

$$H_{sb} = 0.12 L_m [1.0 - \exp(-4.712 D_w (1.0 + 15m 1.33) / L_m)]$$

$L_{ms}$  is the shallow water wave length given by

$$L_{ms} = T_m (g D_w)^{1/2}$$

$C_H$  is the freeboard from static water level to the beach crest

When  $C_f > 0.7$  no crest lowering will occur and Powell's parametric framework is valid for profile prediction

and where  $C_f < 0.1$  and  $C_w$  (crest width)  $< 20m$  inundation of the beach will occur, lowering the beach crest below the storm peak static water level.

where  $0.7 < C_f < 0.1$  the beach may respond by crest lowering or crest accretion, depending on the beach crest geometry.

The detailed beach crest evolution is clearly more complex than these simple equations can quantify at this stage. Further crest data analysis is required to refine the findings of these studies which have provided a first step towards quantification of the crest evolution of a barrier beach.

### Conclusions

The processes resulting in crest development of shingle barrier beaches have been examined in field studies and a 3-dimensional physical model, and threshold conditions for each stage of development have been defined. The tests have indicated that the profile response of the crest of shingle banks is very sensitive to small changes in freeboard or wave conditions, when close to the

critical condition which results in either raising or lowering of the crest level. A range of combinations of wave and freeboard conditions have been identified that result in either raising of the unconfined crest level by overwash deposition, or a reduction in the crest level due to wave overtopping. The complex form of the overwash features results in a wide spatial variation. Several types of feature including throat confined overwash fans have been examined in the model. The crest width has been identified as an important parameter in determining the response of the crest geometry to wave action.

The physical model has been used as a design tool for a beach renourishment scheme at Hurst Spit and has provided alarm conditions and damage thresholds for the proposed beach renourishment.

The tests discussed in this study complement the results of an earlier study (Powell, 1990) to predict the profile response of shingle beaches to wave attack. Data has been compared with the parametric empirical model of shingle beach profile response. A critical freeboard parameter has been defined together with suggested limits for the applicability of Powell's parametric model of beach profile response to shingle barrier beaches.

### References

Leatherman S and Williams "Lateral textural grading in overwash sediments" Earth Surface Processes, Vol. 2, 1977

Nicholls R J and Webber N "Characteristics of shingle beaches with reference to Christchurch Bay, S.England" Proc. 21st ICCE, Malaga, Spain, 1989.

Nicholls R J" The stability of the shingle beaches in the eastern half of Christchurch Bay, Ph.D thesis ,University of Southampton ,1985.

Powell K A " The dynamic response of shingle beaches to random waves " Report CP 19, HR Wallingford, 1989.

Powell K A " Predicting the short term profile response for shingle beaches". Hydraulics Research report SR219, Wallingford, Feb 1990

Van der Meer "Rock slopes and gravel beaches under wave attack" Delft Hydraulics communication No 396, 1988.





# PART VI

## Coastal, Estuarine and Environmental Problems



*Porto Cala Galera, Toscana*



*Ventotene Island, Lazio*

## CHAPTER 207

### INTERACTION BETWEEN WATER WAVES AND VEGETATION

by

Toshiyuki Asano <sup>1</sup>

Hiroshi Deguchi <sup>2</sup>

and

Nobuhisa Kobayashi <sup>3</sup>

#### 1. INTRODUCTION

The presence of densely growing vegetation has been observed to result in wave damping and shoreline sediment deposition. Submerged or flooded vegetation, seaweed stands, reed stands and mangrove forests act as a buffer zone against wave attack on the rear beaches. Recently, a new method for shoreline protection by use of artificial seaweed has been attempted (Rogers 1986; Jenkins and Skelly 1987).

Besides the function of shoreline protection, these vegetated areas play an important role in estuarine and nearshore ecosystems. Since the hydrodynamic process is one of the most important governing factors of the ecosystems, the interaction between water waves and vegetation needs to be quantified. Furthermore, the need of improved understanding of this mechanisms may increase since accelerated sea level rise may result in more flooding in vegetated areas (ASCE Task Committee 1992)

One of the authors initiated a study by conducting experiments on wave damping using artificial seaweed (Asano et al. 1988). Recently, an analytical model was developed to describe the vertically two-dimensional problem of small amplitude waves propagating over submerged or subaerial vegetation

---

<sup>1</sup>Dept. of Ocean Civil Engrg., Kagoshima Univ., Korimoto, Kagoshima, 890, JAPAN

<sup>2</sup>Sekisui-House Inc., Kintetsu Dojima Bild., Dojima 2-2-2, Osaka, 530, JAPAN

<sup>3</sup>Dept. of Civil Engrg., Univ. of Delaware, Newark, DE, 19716, U.S.A.

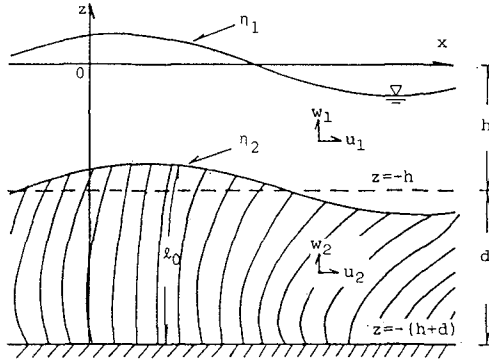


Figure 1: Definition sketch of two layer model

(Kobayashi, Reichle and Asano 1992). This analytical model is referred to as the previous model in this paper.

In the previous model, the effect of vegetation on the flow field was assumed to be expressible in terms of the drag resistance against the fluid motion, whereas the decrease in the drag resistance due to the swaying motion of vegetation was neglected. An analytical solution was obtained for the monochromatic waves whose height decayed exponentially. The comparisons with the artificial seaweed experiments yielded the calibrated drag coefficients  $C_D$  varying in a wide range and affected by the vegetation motion. The calibrated values of  $C_D$  were on the order of 0.1 for the tests with swaying vegetation. A greater value of  $C_D$  would have been resulted if the relative velocity between the fluid and vegetation motion had been used for the drag resistance.

The present paper extends the previous model by including the interaction between the wave and vegetation motion. The present model consists of analyses for the flow field and the swaying motion of an individual vegetation stand. Both solutions are connected by a linearized damping coefficient  $D$  which is determined iteratively. The interaction effects are hence included in the converged solution. The calculated results are compared with the artificial seaweed experiments. The measured wave attenuation is reproduced well by the extended model using a drag coefficient of the order of unity.

## 2. SOLUTION FOR FLOW FIELD

A two-layer model consisting of an upper fluid layer of depth  $h$ , and a lower fluid layer of depth  $d$ , is shown in Fig. 1. The depth  $d$  of the lower layer is the mean height of swaying vegetation and is less than the vegetation length

$l_0$ . In this linearized analysis, small-amplitude monochromatic waves are assumed to propagate in the positive direction of the horizontal coordinate  $x$  and be attenuated by the vegetation. The vertical coordinate  $z$  is taken to be positive upward with  $z = 0$  at the still water level (SWL). Viscous shear stresses acting on the interface and the bottom are neglected because the drag resistance of the vegetation is predominant for most practical applications.

The linearized momentum equations in the upper and lower layers, which are indicated by the subscripts 1 and 2, respectively, may be expressed as

$$\frac{\partial \mathbf{u}_1}{\partial t} = -\frac{1}{\rho} \nabla p_1 \tag{1}$$

$$\frac{\partial \mathbf{u}_2}{\partial t} = -\frac{1}{\rho} \nabla p_2 - \frac{1}{\rho} \mathbf{F} \tag{2}$$

in which,  $t$  = time;  $\mathbf{u} = (\mathbf{u}, \mathbf{w})$  = water particle velocity vector;  $\rho$  = fluid density; and  $p$  = dynamic water pressure due to waves.

The drag force vector per unit volume,  $\mathbf{F}$ , in (2) is assumed to be given by

$$\begin{aligned} F_x &= \frac{1}{2} \rho C_D b N u_r |u_r|, \\ F_z &= 0 \end{aligned} \tag{3}$$

in which  $C_D$  = drag coefficient;  $b$  = area per unit height of each vegetation stand normal to the horizontal velocity;  $N$  = number of vegetation stands per unit horizontal area; and  $u_r = (u_2 - u_v)$  is the relative velocity between the horizontal fluid velocity  $u_2$  and the swaying velocity of vegetation,  $u_v$ . The drag force is assumed to be dominant and the inertia force is neglected in (3).

In order to derive an analytical solution, (3) is linearized as follows:

$$\frac{1}{2} \rho C_D b N u_r |u_r| = \rho D u_2 \tag{4}$$

The damping coefficient  $D$  is determined in such a way that the mean square of the error,  $\overline{E_r^2}$ , of the difference between both sides of (4) is the minimum. The condition of  $\partial \overline{E_r^2} / \partial D = 0$  gives

$$D = \frac{1}{2} C_D b N \frac{\int_{-(h+d)}^{-h} u_r |u_r| u_2 dz}{\int_{-(h+d)}^{-h} u_2^2 dz} \tag{5}$$

The unknown coefficient  $D$  depends on  $u_2$  and  $u_r$  and will be determined by iterations using the solutions for  $u_2$  and  $u_v$  as will be explained later.

Eq.(2) can then be linearized as

$$\begin{aligned} \frac{\partial u_2}{\partial t} &= -\frac{1}{\rho} \frac{\partial p_2}{\partial x} - D u_2, \\ \frac{\partial w_2}{\partial t} &= -\frac{1}{\rho} \frac{\partial p_2}{\partial z} \end{aligned} \tag{6}$$

The momentum equations (1) and (6) as well as the continuity equations for both upper and lower layers are subject to the following linearized boundary conditions at the free surface, interface and bottom boundaries:

$$\begin{aligned} \frac{\partial \eta_1}{\partial t} &= w_1, & p_1 &= \rho g \eta_1 & \text{at } z &= 0, \\ \frac{\partial \eta_2}{\partial t} &= w_1 = w_2, & p_1 &= p_2, & \text{at } z &= -h, \\ w_2 &= 0 & & & \text{at } z &= -(h + d) \end{aligned} \tag{7}$$

where  $\eta_1$  = free surface elevation above SWL;  $\eta_2$  = displacement of the interface; and  $g$  = gravitational acceleration.

In the following,  $\eta_1$  is assumed to be expressible in a sinusoidal form with a complex wave number  $k = (k_r + ik_i)$  as follows:

$$\eta_1 = a_0 \exp\{i(kx - \sigma t)\} \tag{8}$$

in which,  $i^2 = -1$ ;  $a_0$  = wave amplitude at  $x=0$ ; and  $\sigma$  = angular frequency. From the real part of (8), the local wave amplitude is found to decay exponentially

$$a = a_0 \exp(-k_i x) \tag{9}$$

where  $k_i$  = exponential decay coefficient.

The solutions for the horizontal fluid velocities  $u_1$  and  $u_2$  can be shown to be given by

$$u_1 = \frac{gk a_0}{\sigma} \left\{ \cosh(kz) + \frac{\sigma^2}{gk} \sinh(kz) \right\} \exp\{i(kx - \sigma t)\} \tag{10}$$

$$u_2 = \frac{g\alpha^2 a_0}{\sigma k} \left\{ \cosh(kh) - \frac{\sigma^2}{gk} \sinh(kh) \right\} \frac{\cosh[\alpha(z + h + d)]}{\cosh(\alpha d)} \exp\{i(kx - \sigma t)\} \tag{11}$$

with

$$\alpha = k / \sqrt{1 + i(D/\sigma)} \tag{12}$$

Substituting (10) and (11) into (1) and (6) yields the solutions for the pressures  $p_1$  and  $p_2$

$$\begin{aligned} p_1 &= \frac{\rho \sigma}{k} u_1 \\ p_2 &= \frac{\rho(\sigma + iD)}{k} u_2 \end{aligned} \tag{13}$$

The continuity equations together with (10) and (11) yield the solutions for the vertical fluid velocities  $w_1$  and  $w_2$ , which are omitted herein.

Furthermore, the vertical displacement of the interface,  $\eta_2$ , is given by

$$\eta_2 = a_0 \left[ \cosh(kh) - \frac{gk}{\sigma^2} \sinh(kh) \right] \exp\{i(kx - \sigma t)\} \quad (14)$$

Lastly, the dispersion relation is given by

$$\sigma^2 = gk \frac{k \tanh(kh) + \alpha \tanh(\alpha d)}{k + \alpha \tanh(\alpha d) \tanh(kh)} \quad (15)$$

Eq. (15) can be solved to find the unknown complex wave number  $k$  for given  $\sigma$ ,  $h$ ,  $d$ ,  $g$  and  $D$ .

In the case of weak damping  $\sigma \gg D$ , (15) can be expressed more explicitly. Eq.(12) is simplified as

$$\alpha \simeq k \left(1 - i \frac{D}{\sigma}\right)^{1/2} \simeq k \left(1 - i \frac{D}{2\sigma}\right) \quad (16)$$

Since  $\alpha = [k(1 - i\epsilon) + O(\epsilon^2)]$  with  $\epsilon = D/2\sigma$ , (15) becomes

$$\sigma^2 = gk \tanh[k(h+d)] \left[ 1 - i\epsilon \frac{2kd + \sinh(2kd)}{\sinh[2k(h+d)]} \right] \quad (17)$$

The real and imaginary parts of (17) yield the following equations

$$\sigma^2 = gk_r \tanh[k_r(h+d)] \quad (18)$$

$$\frac{k_i}{k_r} = \epsilon \frac{2k_r d + \sinh(2k_r d)}{2k_r(h+d) + \sinh[2k_r(h+d)]} \quad (19)$$

Eq.(18) is the ordinal dispersion relation for small-amplitude water waves, so the presence of vegetation does not change the real wave number  $k_r$  as long as  $\epsilon = (D/2\sigma)$  is much smaller than unity. On the other hand, (19) implies that  $k_i/k_r = O(\epsilon)$

The above analytical solution for the flow field is the same as that obtained by Kobayashi et al. (1992) except that  $D$  was given by (5) with  $u_r = (u_2 - u_v)$  replaced by  $u_2$ .

### 3. SOLUTION FOR VEGETATION MOTION

The behaviour of a vegetation colony under wave action is complex because the vegetation and fluid motions may generate turbulence stresses along the interfacial boundary and among the vegetation stands. However, it is observed that each stand does not move in random but a group of stands sway

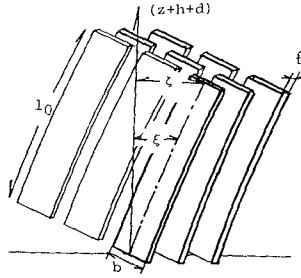


Figure 2: Model of vegetation motion

in an organized manner. As long as the vegetation motion is not so large, it may be treated as a horizontal swaying motion as shown in Fig.2.

As a first attempt, the vegetation motion due to wave action is simply modelled as a forced vibration with one degree of freedom. The buoyancy and stiffness of the vegetation material are considered as the restoring forces of the vibration. The horizontal displacement of a vegetation stand from the vertical  $z$ -axis is denoted by  $\xi$ , while the differentiations with respect to  $t$  and  $z$  are indicated by the over dot and the subscript  $z$ , respectively. The equation of the motion for each stand may be expressed as follows:

$$\begin{aligned} \rho_v b \hat{t} \ddot{\xi} + C_1 \dot{\xi} + EI \xi_{zzzz} &= \frac{1}{2} \rho C_D b |u_2 - \dot{\xi}| (u_2 - \dot{\xi}) \\ &+ \rho (C_M - 1) b \hat{t} (\ddot{u}_2 - \ddot{\xi}) + \rho b \hat{t} \dot{u}_2 - (\rho - \rho_v) g b \hat{t} \xi_z \end{aligned} \tag{20}$$

in which  $\rho_v, b, \hat{t}, EI, C_1$  and  $C_M$  are the density, width, thickness, bending stiffness, attenuation constant, inertia coefficient of the vegetation strip, respectively. It is noted that  $\dot{\xi} = u_v$  and  $u_r = (u_2 - \dot{\xi})$  in (5). The inertia force is included on the right hand side of (20) for completeness, although it is neglected in (3). Assuming that  $C_1 = 0, (\dot{\xi}/u) \ll 1$  and  $\xi$  may be approximated by  $\xi = \{(z + h + d)/d\} \zeta$  with  $\zeta$  being the horizontal displacement at the top of the vegetation strip, (20) may be simplified as follows:

$$\begin{aligned} \frac{1}{2} \{ \rho (C_M - 1) + \rho_v \} V \ddot{\zeta} + \frac{1}{2} \rho C_D |u| A \dot{\zeta} + \left\{ \frac{8EI}{d^3} + (\rho - \rho_v) g \frac{V}{d} \right\} \zeta \\ = \frac{1}{2} \rho C_D A u |u| + \rho C_M V \dot{u} \end{aligned} \tag{21}$$

in which  $A = bd$  and  $V = b \hat{t} d$ . In the derivation of (21), it is assumed

$$\int_{-(h+d)}^{-d} EI \xi_{zzzz} dz = \frac{8EI}{d^3} \zeta \tag{22}$$



which is the relation for the displacement at the top of a cantilever under uniform loading. In addition,  $u$ ,  $\dot{u}$  and  $|u|$  in (21) should be taken as the depth-averaged values of  $u_2$ ,  $\dot{u}_2$  and  $|u_2|$  in the region  $-h \geq z \geq -(h+d)$ .

#### 4. WAVE DAMPING CHARACTERISTICS

##### (1) Interaction Between Fluid and Vegetation Motion

In this analytical model, wave damping due to vegetation is described by the imaginary wave number  $k_i$  as expressed in (9). The linearized damping coefficient  $D$  governs the magnitude of  $k_i$  through the term  $\epsilon$  in (19). On the other hand, the motion of vegetation is determined by (21) if the fluid velocity  $u_2$  of the waves is known. The interaction effect between the wave and vegetation is expressed through the damping coefficient  $D$  which is iteratively calculated by (5) using the relative velocity  $u_r$  between the wave and vegetation motion.

The height of the lower layer,  $d$ , is determined by the following approximate relation based on the length of vegetation,  $l_0$ , and the amplitude of  $\zeta$ , denoted by  $\hat{\zeta}$

$$d = \frac{l_0 + \sqrt{l_0^2 - \hat{\zeta}^2}}{2} \quad (23)$$

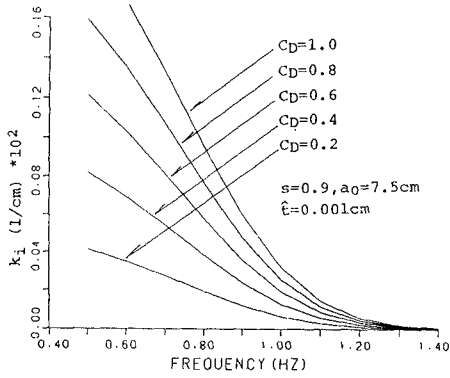
which implies that  $d$  decreases from  $d = l_0$  as  $\hat{\zeta}$  is increased from  $\hat{\zeta} = 0$ .

The calculation proceeds in the following order:

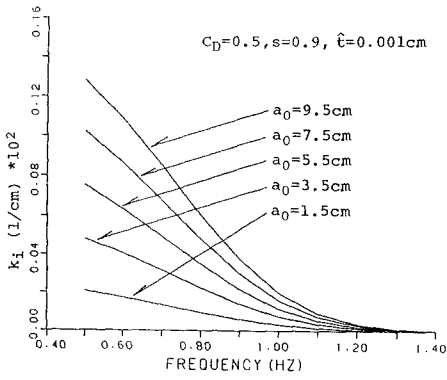
- (i) Starting from the condition of no vegetation motion, for which  $u_v = 0$  and  $d = l_0$ , the fluid velocity and complex wave number are calculated.
- (ii) The motion of vegetation is then computed using (21) where the swaying velocity  $u_v$  is calculated at every vertical point over a whole wave period.
- (iii) The damping coefficient  $D$  is determined by (5) using the relative velocity  $u_r = (u - u_v)$ .
- (iv) The depth of the lower layer is calculated by (23).
- (v) The fluid velocity and complex wave number are re-calculated using the obtained damping coefficient  $D$ .
- (vi) The computation is repeated until the convergence of the solution is achieved.

##### (2) Calculated Results

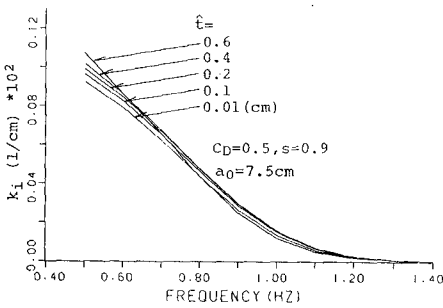
The final expression of the vegetation motion given by (21) has many parameters. Although a sensitivity analysis on the wave decay coefficient  $k_i$  and the wave celerity  $c = \sigma/k_r$  may be made using the non-dimensional parameters, the variations of  $k_i$  and  $c$  are herein illustrated using the dimensional parameters whose ranges are related to the artificial seaweed experiment. In the following computations, use is made of  $h = 27\text{cm}$ ,  $l_0 = 25\text{cm}$ ,  $N = 0.149\text{cm}^{-2}$ ,  $C_M = 2.0$ ,  $b = 5.2\text{cm}$ ,  $E = 9.8 \times 10^7\text{g}/(\text{cm}\cdot\text{sec}^2)$ ,  $I = bl^3/12$ .



(a)



(b)



(c)

Figure 3: Computed wave decay coefficient  $k_i$

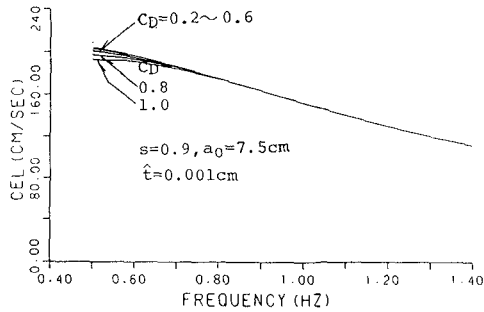


Figure 4: Computed wave celerity  $c$

Fig. 3 (a),(b),(c) shows the variations of  $k_i$  with respect to the frequency ( $\sigma/2\pi$ ) for different values of  $C_D$ ,  $a_0$  and  $\hat{t}$ , respectively. The wave decay coefficient  $k_i$  increases with the drag coefficient  $C_D$  as well as with the wave amplitude  $a_0$ . The dependence of  $k_i$  on the wave amplitude results from the quadratic drag resistance used to estimate  $D$  in (5). Meanwhile, the increase of  $\hat{t}$  results in the increase of the moment of inertia  $I$ , however, the stiffness of the vegetation material changes the wave decay coefficient very little. The change of the specific gravity  $s$  of the vegetation material, which modifies the restoring force by buoyancy, does not affect the decay coefficient much, although the computed results are not presented here.

On the other hand, the wave celerity  $c$  varies very little with the drag coefficient  $C_D$  as shown in Fig. 4. The other parameters  $a_0$ ,  $\hat{t}$ , and  $s$  are also found to have negligible effects on  $c$ .

## 5. COMPARISON WITH EXPERIMENT

### (1) Wave Damping Experiment by Using Artificial Seaweed

The extended model is compared with the artificial seaweed experiment conducted by Asano et al. (1988). The experiment was performed in a wave tank which was 27m long, 0.5m wide and 0.7m high as shown in Fig. 5. The model seaweed was made of polypropylene strips whose specific gravity was 0.9. The length, width and thickness of each strip was  $l_0 = 25\text{cm}$ ,  $b = 5.2\text{cm}$  and  $\hat{t} = 0.03\text{mm}$ , respectively. Each strip was bound to a heavy wire netting such that the strip was normal to the side walls of the tank and could bend with little torsion under the action of monochromatic waves generated in the tank. The number of strips placed uniformly over the area of  $4\text{ m}^2$  was 4400 and 5960. Correspondingly, the number of strips per unit horizontal area was  $N = 0.110$  and  $0.149\text{ cm}^{-2}$ . The water depth above the vertical strips was

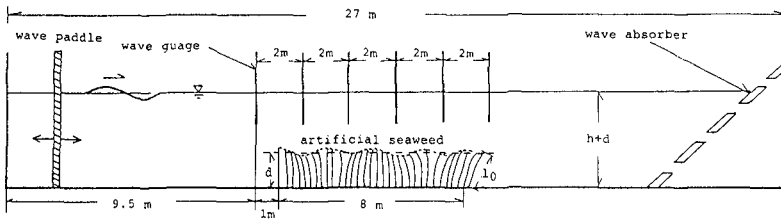


Figure 5: Experimental setup

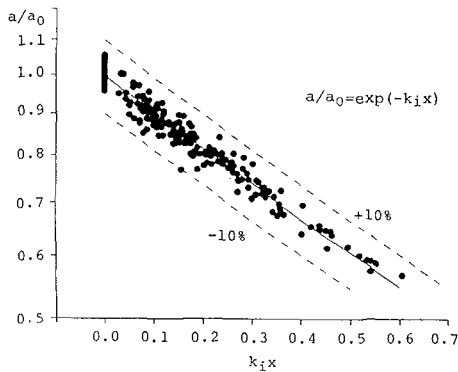


Figure 6: Measured wave amplitudes fitted to exponential decay model

$h = 20$  and  $27\text{cm}$ . In total, sixty test runs were performed.

Six capacitance wave gauges were used to measure the free surface oscillations. Excluding the data from the two gauges at both ends, the data from the remaining four gauges were used in the data analysis because this wave damping model does not account for the presence of lateral boundaries. The location of the second gauge in Fig.5 was taken herein to be the location  $x=0$  and the analysis domain was  $0 \leq x \leq 6$  m.

A regression analysis based on the method of least squares was performed using (9) in which the exponential decay of the local wave amplitude  $a$  is characterized by the initial amplitude  $a_0$  at  $x = 0$  and the exponential decay coefficient  $k_i$ . Fig. 6 shows the measured values of  $a$  at  $x=0, 2, 4$  and  $6$  m for the 60 runs, normalized as  $a/a_0$  as a function of  $k_i x$  where the fitted values of  $a_0$  and  $k_i$  are used for each run.

## (2) RESULTS AND DISCUSSION

The comparisons on the decay coefficient  $k_i$  are shown in Fig. 7, where the circles indicate the measured values. The experimental results are shown separately for the large wave runs ( $a_0 = 4.5 \sim 6.0\text{cm}$ ) and for the small wave runs ( $a_0 = 2.8 \sim 4.2\text{cm}$ ), while the computed results are based on the average wave amplitude;  $a_0=5.25\text{cm}$  for the former and  $a_0=3.50\text{cm}$  for the latter.

The previous model of Kobayashi et al.(1992) reproduced the measured wave decay coefficients only when the drag coefficient  $C_D$  of the order 0.1 was used for the swaying vegetation. The present model including the swaying motion of the vegetation is shown to yield much better agreement with the same data set, using a more realistic value of the drag coefficient of approximately 0.5.

Fig. 8 shows the comparison between the measured and calculated values of the wave celerity  $c$ . Slight overestimation of  $c$  by the present model is apparent for low frequency waves. The agreement with the measured celerity becomes slightly worse when the swaying motion of vegetation is considered.

Besides the wave damping measurements, the horizontal displacements of the top of the vegetation strip under waves were measured. Fig. 9 shows the measured data points in comparison with the computed curves. As the wave frequency  $f$  decreases, the present model tends to overpredict the displacement  $\zeta$ .

Judging from Figs. 8 and 9, the limitations of the present model seems to arise when the swaying motion becomes large. It was observed for low frequency waves that the vegetation swayed considerably and may have generated turbulence along the interface and among the vegetation strips. The present model, however, does not account for the turbulent stress. The modeling of the swaying vegetation is so simple that the complex large swaying motion could not be reproduced very accurately. The drag resistance of the vegetation may no longer be expressible by (3) which neglects the vertical component of the drag resistance.

Although the drag coefficient  $C_D$  is herein taken to be 0.5 as the best value for the measured decay coefficients,  $C_D$  should be a function of Reynolds number defined by the relative velocity and vegetation size. In addition, the proximity effects of surrounding strips on  $C_D$  should be examined because natural vegetation usually grows densely as a colony.

## 6. CONCLUSIONS

The present paper has presented an analytical solution for water waves propagating over submerged vegetation and a mathematical expression for

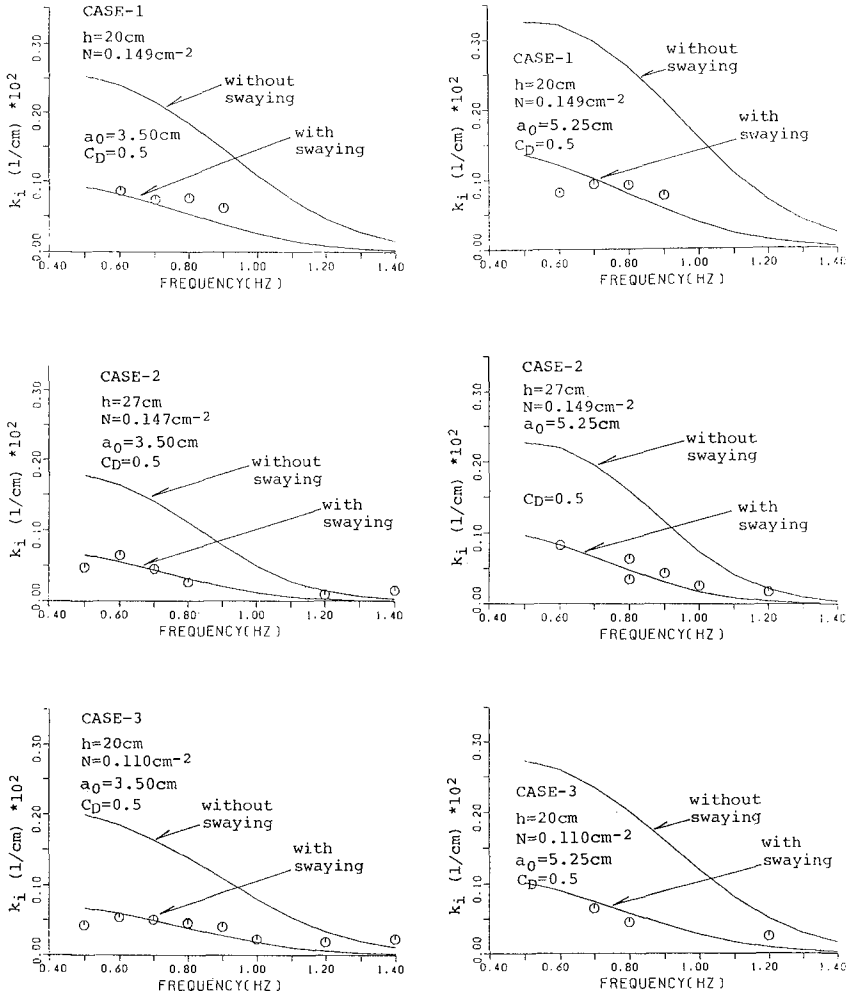


Figure 7: Comparisons between measured and computed decay coefficient  $k_i$

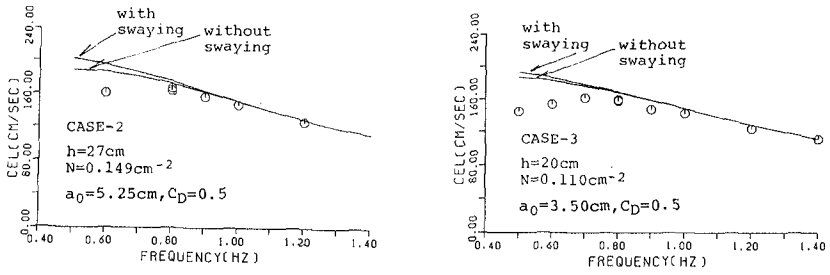


Figure 8: Comparisons between measured and computed wave celerity  $c$

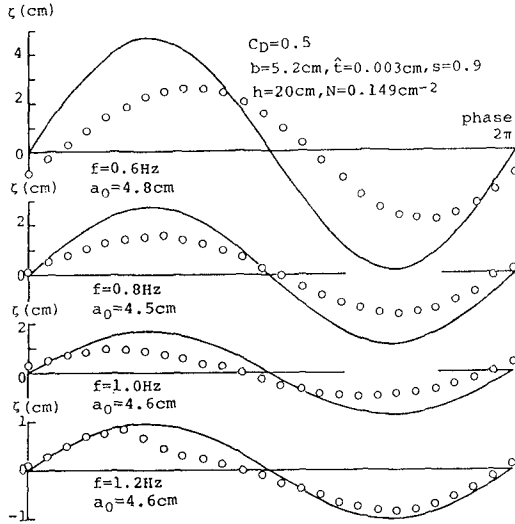


Figure 9: Comparisons between measured and computed horizontal displacement of top of vegetation strip

vegetation motion swayed by the water waves. Both solutions have been linked by the linearized damping coefficient  $D$  through which the interaction effects between the water waves and vegetation motion have been accounted for. The properties of the wave decay coefficient and wave celerity have been examined by performing a sensitivity analysis.

The present model has been compared with the artificial seaweed experiment. The drag coefficient  $C_D$  has been calibrated using the exponential decay coefficient fitted for each run. The calibrated values have been found to be approximately 0.5 which is greater than the values of the order 0.1 obtained by the previous model which neglected the vegetation motion. The drag coefficient of about 0.5 appears to be more realistic. Although the present model is valid only when the swaying motion is not large, the capability for predicting the wave decay has been improved herein by including the vegetation motion in the model.

### REFERENCES

- Asano T., S. Tsutsui and T. Sakai (1988): Wave damping characteristics due to seaweed, Proc. 35th Coast. Engrg. Conf. in Japan, 138-142(in Japanese).
- ASCE Task Committee on sea level rise and its effects on bays and estuaries (1992): Effects of sea level rise on bays and estuaries, J. Hydraulic Engrg., ASCE, 118(1), 1-10.
- Jackson, G.A. (1984): Internal wave attenuation by coastal kelp stands, J. of Physical Oceanography, 14, 1300-1306.
- Jenkins, S. A. and D. W. Skelly(1987): Hydrodynamics of artificial seaweed for shoreline protection, Scripps Inst. Oceano., SIO Ref. Ser., No. 87-16, p.66.
- Kobayashi, N., A. W. Raichle and T. Asano(1992) : Wave attenuation by vegetation, J. of Waterway, Port, Coastal and Ocean Engineering, ASCE, 119(1), (in press).
- Rogers, S. (1986): Artificial seaweed for shoreline erosion control, UNC Sea Grant Pub., UNC-SG-WP-8-6-4, Univ. of North Carolina, p.15.



## CHAPTER 208

### PREDICTION OF CURRENT AND SEDIMENT DEPOSITION PATTERNS IN PUERTO MIRANDA OIL TERMINAL USING 2-D MATHEMATICAL MODELS

Carlos Villoria

INTEVEP, S.A, Gerencia General de Ecología y Ambiente  
Apartado 76343, Caracas 1070-A, Venezuela

Reinaldo García and Eduardo Valera

HydroSoft, c.a. Apartado 47762, Caracas 1041-A, Venezuela

#### ABSTRACT

Puerto Miranda oil terminal, located in the Maracaibo Strait, Venezuela (see figures 1 and 2), is one of the main venezuelan oil industry loading facilities of crude oils. Ships access the terminal from the Gulf of Venezuela by a 40 km long, 300 m wide and 13.7 m depth main channel, which is periodically dredged in order to keep the design depth. A secondary channel leads from the main channel to the terminal itself ( See figure 3). Over the last few years the increase in sedimentation rates in the secondary channel has motivated the need for studies that would determine alternatives to reduce dredging costs.

A previous work [0], based on the circulation and sedimentation patterns in the area under study, proposed the construction of a new access channel with a different orientation regarding the prevailing current direction, that would reduce the sedimentation rate and dredging frequency.

The venezuelan oil industry through its R & D filiate (INTEVEP), has developed a 2-D finite element mathematical model to simulate suspended sediment transport and a 2-D finite difference circulation model for coastal regions.

In this work, these models are applied to determine the evolution of the secondary old and new dredged access channels to Puerto Miranda oil terminal. Both models were calibrated and validated with field data and results are presented for the complex circulation and sedimentation patterns that occur in the area of Puerto Miranda terminal.

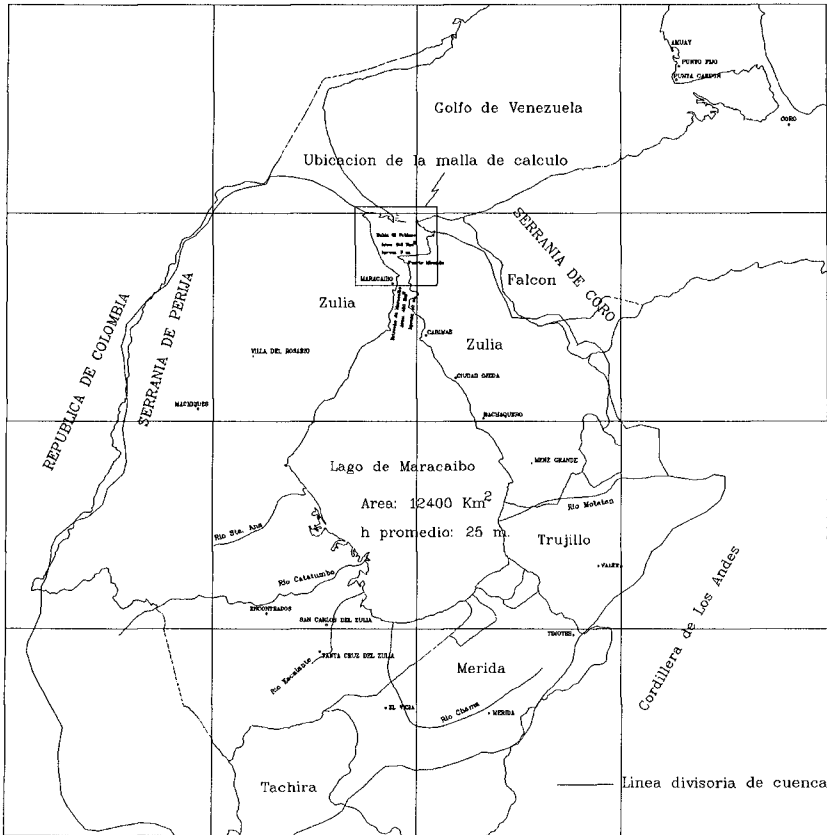


Figure 1.- Map indicating the North-Western Venezuela region. Box indicate study area.

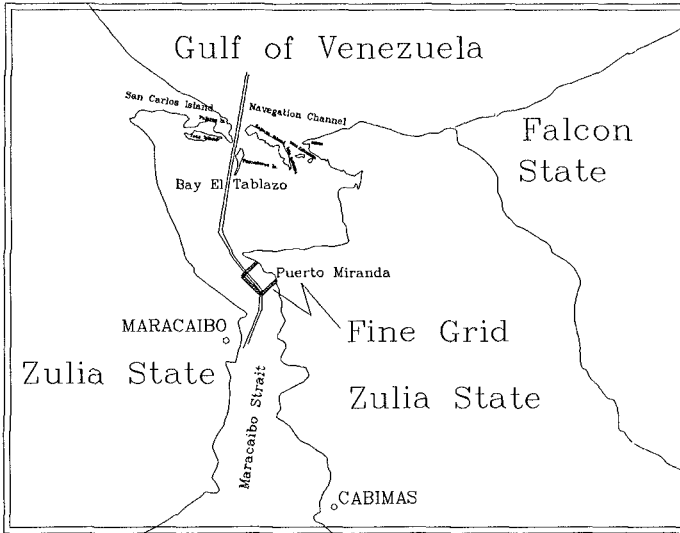


Figure 2.- Detail of study area.

## CIRCULATION MODEL

The circulation model solves the Shallow-Water equations by the MacCormack finite difference scheme as implemented by García and Kahawita [2]. This explicit model has been previously applied to several river and coastal problems, and for this case has been calibrated and validated using field measurements including tidal elevations and velocities at various locations.

In order to resolve the complex circulation patterns that exist in the area, two finite difference grids are used. The first is formed by  $250 \times 250$  m cells and covers a region that includes the El Tablazo bay and the Maracaibo Strait. This grid has 11,480 nodes for a total of 34,440 degrees of freedom, since two velocity components and one tidal elevation is calculated for each node. The tidal elevations and velocities resulting from the simulations on this grid are then transferred to a finer grid composed of  $50 \times 50$  m cells just around the Puerto Miranda area. Results for each time step for several tidal cycles is recorded in a binary file for latter interfacing with the sediment transport model.

Figure 4 shows the comparison between the tidal gage and the model results for the week Apr-01-1989 to Apr-07-1989. These were obtained after adjusting the depth varying Manning coefficient until model results compared favorably with measurements. To investigate how the model performed for a different tidal period, the week of Nov-

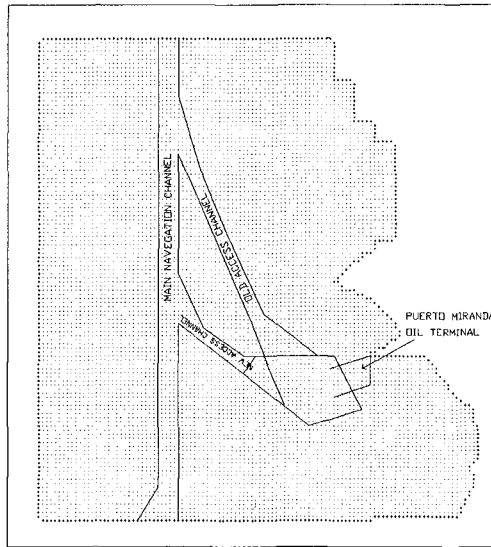


Figure 3.- Puerto Miranda oil terminal area showing the main navigation channel, the old access channel and the proposed or new channel. Points indicate fine grid where velocities are calculated.

08-1989 to Nov-14-1989 was chosen and the model was applied using the same Manning coefficients. As can be seen in figure 5 the model results reproduce correctly the tidal measurements.

Figure 6 and 7 present two flow fields for the fine grid around Miranda terminal. It can be appreciated the occurrence of large scale eddies that have also been observed in the area.

### SEDIMENT TRANSPORT MODELLING

Sediment transport modelling involves the process of advection, erosion and deposition.

For general flow conditions the suspended sediment transport modelling can be formulated in terms of four partial differential equations. Two momentum equations and one conservation of water mass equation that forms the so-called Saint Venant equations, solved by the hydrodynamic model [2], and the two-dimensional (vertically averaged) convection-dispersion sediment mass conservation equation that can be expressed in the following form:

$$\frac{\partial c}{\partial t} + u \frac{\partial c}{\partial x} + v \frac{\partial c}{\partial y} = \frac{\partial}{\partial x} (D_x \frac{\partial c}{\partial x}) + \frac{\partial}{\partial y} (D_y \frac{\partial c}{\partial y}) + \frac{1}{h} S \tag{1}$$

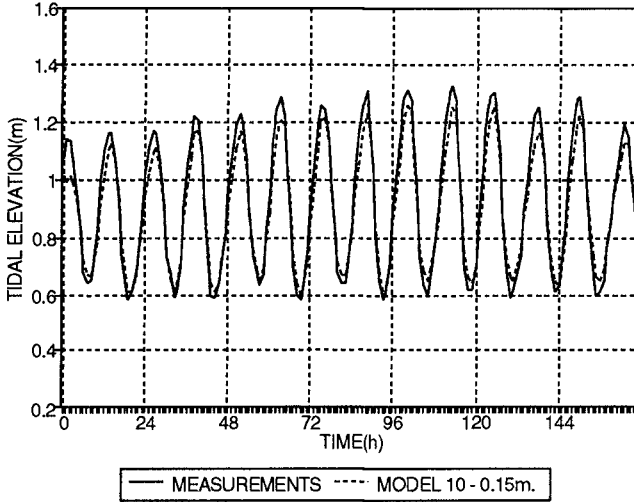


Figure 4.- Comparison of measured tidal elevations with model results (Apr-01-89 to Apr-07-89). Measurements taken from Punta de Palmas tidal gage at the entrance of Maracaibo Strait.

where  $c(x, y, t)$  is the sediment concentration averaged along the vertical direction  $z$ ,  $u(x, y, t)$  is the mean flow velocity in the horizontal  $x$  direction,  $v(x, y, t)$  is the mean flow velocity in the horizontal  $y$  direction,  $h(x, y, t)$  is the flow depth,  $D_x$  and  $D_y$  are the turbulent dispersion coefficients in  $x$  and  $y$  directions respectively, and  $S$  is the source-sink term.

Equation (1) is obtained by integrating the three-dimensional convection-diffusion equation along the vertical direction.

The source-sink term  $S$  takes into account the erosion and deposition processes. The vertical deposition is equal to  $w \partial c / \partial z$ , being  $w$  the sediment settling velocity which for fine particles is given by the Stokes law and  $c$  is the local concentration.

In this study we consider that the sediment concentration is zero at the free surface. In that case, integrating the vertical deposition term gives  $w C_o$  where  $C_o$  is the sediment concentration in the bottom layer that will be taken proportional to the average vertical concentration. In this manner, the source term, corresponding to deposition, is proportional to the local bottom sediment concentration and to the settling velocity  $w$ . (See [1]).

The sink term, also called erosion or resuspension term, determines the remaining boundary condition to satisfy the equilibrium in the bottom layer. There are many for-

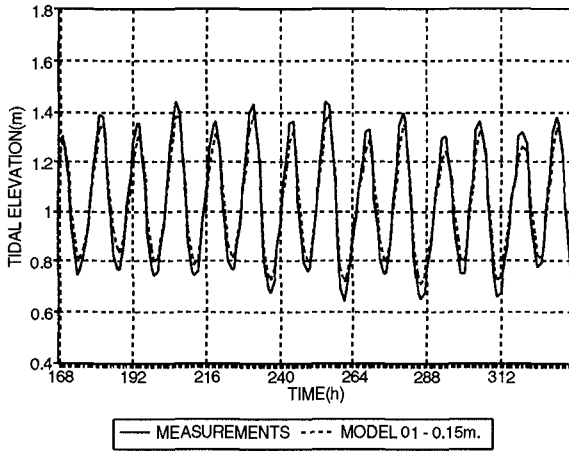


Figure 5.- Comparison of measured tidal elevations with model results (Nov-08-89 to Nov-15-89). Measurements taken from Punta de Palmas tidal gage at the entrance of Maracaibo Strait.

mulae available to represent this term that go from those obtained by semi-analytical methods through integration of the movement equations of the sediment particles to those obtained empirically. The analytical formulae usually come in terms of integrals that complicates the application of the mathematical model and do not give much better results for the extra effort required [4], [5]. On the other hand, the empirical formulations are given in terms of the flow variables and are generally of simple mathematical form giving reasonable results. In this work the formulation for the sink (erosion) term will be based on an empirical formulation proportional to the square of the velocity,  $q^2 = u^2 + v^2$ , and inversally proportional to the local flow depth  $h$ .

Using the source and sink term so defined,  $S$  can be written as:

$$S = \alpha w c - \beta \frac{q^2}{h} H\left(\frac{\tau_b}{\tau_c} - 1\right) \tag{2}$$

where  $\alpha$  and  $\beta$  are proportionality factors,  $\tau_b$  is the bottom surface shear stress,  $\tau_c$  is the bottom surface critical shear stress for the initiation of sediment movement which is determined by the Shields criterion [6].  $H(\tau_b/\tau_c - 1)$  is the Heavieside function defined as  $H = 1$  for  $\tau_b \geq \tau_c$  and  $H = 0$  for  $\tau_b < \tau_c$ ,

The bottom layer equilibrium equation expressed as:

$$(1 - p) \frac{\partial z}{\partial t} = S \tag{3}$$

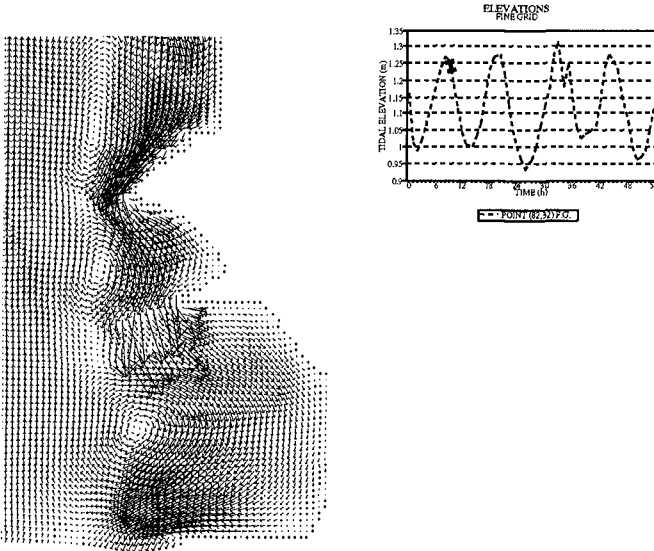


Figure 6.- Flow field in the Puerto Miranda terminal area for the tidal elevation at 9 hours shown in box.

defines the time evolution of the bottom elevation  $z$ , being  $p$  the porosity of the bed sediment.

Lin et al [1], make a mass balance in the bottom layer considering the layer thickness equal to two times the sediment diameter  $d$  and following Einstein sediment transport theory, obtain the following approximate relation for  $\alpha$  and  $\beta$  in equation (2):

$$\alpha \approx \frac{1}{3} \left( \frac{h}{2d} \right)^{w/\psi k u^*} \quad \text{and} \quad \beta \approx \phi \alpha \tag{4}$$

where  $\psi$  and  $\phi$  are empirical coefficients,  $u^* = \sqrt{\tau_b/\rho}$  is the shear velocity in the bottom,  $\rho$  is the water density and  $k = 0.40$  is the Von-Kármán constant in the logarithmic equation for the turbulent vertical velocity distribution.

Finally, the bottom layer equilibrium equation is expressed as:

$$\frac{\partial z}{\partial t} = \frac{1}{3} \left( \frac{h}{2d} \right)^{w/\psi k u^*} \frac{1}{(1-p)} \left[ w c - \phi \frac{q^2}{h} H \left( \frac{\tau_b}{\tau_c} - 1 \right) \right] \tag{5}$$

The parameter  $\phi$  can be determined applying equation (5) in a bottom control point of the region where the erosion and deposition rates are equal (zone of no change in the bottom elevation  $\partial z/\partial t = 0$ ). Applying this condition:

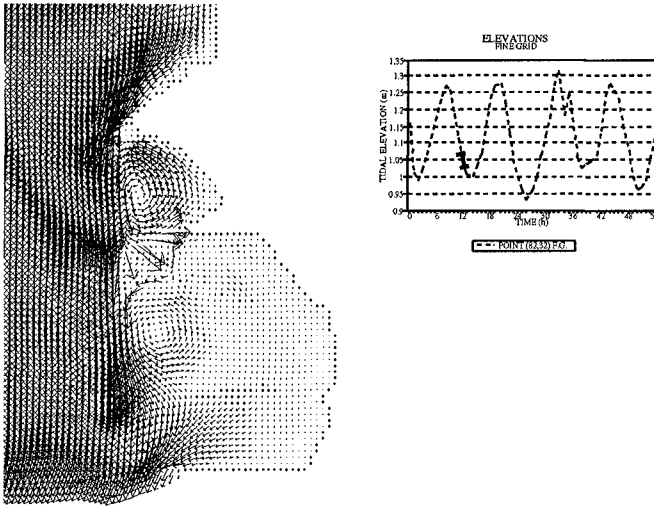


Figure 7.- Flow field in the Puerto Miranda terminal area for the tidal elevation at 12 hours shown in box.

$$\phi = \left( \frac{w c h}{q^2} \right) \tag{6}$$

In the model the bottom shear stress  $\tau_b$  will be calculated by:

$$\tau_b = \frac{\rho g q^2}{C^2} \tag{7}$$

where  $g$  is the gravity acceleration and  $C$  is the Chezy coefficient that for turbulent flow can be expressed in terms of the Manning  $n$  as  $C = h^{1/6}/n$ .

Substituting equations (2, 4, 5, 6 and 7) in equations (1) and (3) we obtain a system of two partial differential equations for  $c(x, y, t)$  and  $z(x, y, t)$  in terms of three parameters:  $D_x, D_y, \psi$ . These parameters have to be determined in the calibration process. The final system is given by:

$$\begin{aligned} \frac{\partial c}{\partial t} + u \frac{\partial c}{\partial x} + v \frac{\partial c}{\partial y} &= \frac{\partial}{\partial x} \left( D_x \frac{\partial c}{\partial x} \right) + \frac{\partial}{\partial y} \left( D_y \frac{\partial c}{\partial y} \right) + \frac{1}{h} \alpha w c - \beta \frac{q^2}{h} H \left( \frac{\tau_b}{\tau_c} - 1 \right) \\ (1 - p) \frac{\partial z}{\partial t} &= \alpha w c - \beta \frac{q^2}{h} H \left( \frac{\tau_b}{\tau_c} - 1 \right) \end{aligned} \tag{8}$$



with the corresponding expressions for the parameters given by equations: (4), (6) and (7).

The model described has three calibration parameters given by the two dispersion coefficients,  $D_x$  and  $D_y$ , and one of the erosion or deposition factors,  $\alpha$  or  $\beta$ . This is possible since, given a fluvial control point where the bottom elevation is constant, then  $\partial z/\partial t = 0$  and from equation (2) we obtain a relation between  $\alpha$  and  $\beta$ .

Starting from a system equivalent to equations (5) and (8) but for one-dimensional problems, Lin et al [1] simulated the sediment transport of the Qiantang river in China. In that reference it is shown that with the preceding approximations, the suspended sediment discharge hydrogram can be accurately predicted for a series of tidal cycles.

In the present work, the two-dimensional system given by equations (5) and (8) that model the sediment transport of fine non-cohesive sediments was solved numerically by the *finite element method*. In any event, for the application of the model, the velocity and depth field is determined by the hydrodynamic model. Then, equation (8) is solved for the sediment concentration given proper initial and boundary conditions and the bottom elevation evolution is obtained applying equation (5).

The finite element mesh is composed of 750 cuadrilateral elements and is superimposed over the  $50 \times 50$  m. finite difference grid in the area of the terminal. Since the nodes of the finite element mesh do not generally have corresponding nodes of the finite difference grid, interpolation of the velocity and tidal elevations is required.

The sediment model was calibrated comparing computed bottom elevations with a series of bathymetries available for the terminal zone. Two calibration parameters were used to reproduce the field measurements. Figure 8 presents the bottom elevation results along a transversal section in the old access channel computed by the model together with the profile obtained from the bathymetries of November 1988 and May 1989. The results in figure 8 show that the model reproduces the evolution of the old access channel with adequate resolution.

Once calibrated, the sediment model was used to predict the bottom evolution of the whole region. The results of this computations, shown in figure 9 indicate that the model correctly reproduces the bottom profile evolution in other areas.

## CONCLUSIONS AND RECOMENDATIONS

In this work, a circulation model and a suspended sediment transport model have been applied to predict the velocity and sediment deposition in the area of Puerto Miranda oil terminal, located in the Maracaibo Strait, Venezuela.

Model results predict the evolution of the dredged access channels to the terminal. Both models were calibrated and validated with field data and results are presented for the complex circulation and sedimentation patterns that occur in the area of Puerto Miranda.

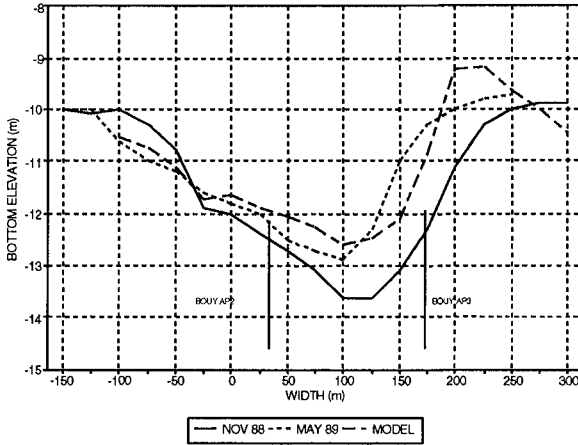


Figure 8.- Bottom elevation results along a cross section of the old access channel. Comparison of computed elevations with measured data.

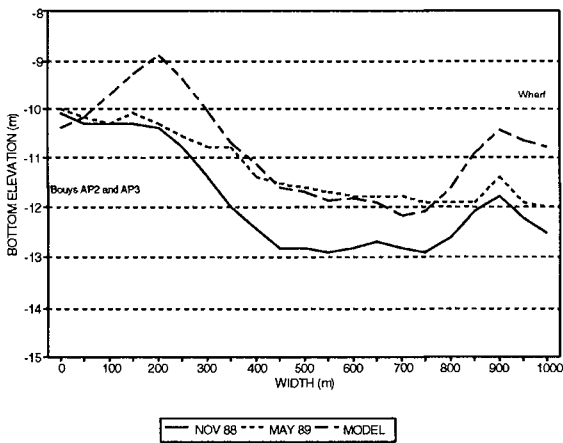


Figure 9.- Bottom elevation results along a cross section of the maneuvering zone. Comparison of computed elevations with measured data.

The proposed models correctly reproduce the measured bottom profile evolution. Field measurements of sediment fall velocity, vertical distribution of suspended

sediment concentrations as well as bed load transport at various locations in the access channel and its surroundings are recommended in order to evaluate the importance of bed load sediment transport (not considered in this model) with respect to suspended sediment transport in the long range sedimentation process acting in Puerto Miranda.

## REFERENCES

- [0] COSA-Incostas **Evaluación del Problema de Sedimentación en la Rada y en Canal de Acceso de Puerto Miranda. Alternativa de Mejoramiento.** Caracas-Maracaibo, March, 1979.
- [1] Lin, Pin-nam, Juqing Huan and Xinquen Li. **Unsteady Transport of Suspended Load at Small Concentrations.** ASCE H109, 1, 1983.
- [2] García R. and Kahawita R. **Numerical Solution of the Saint Venant Equations by the MacCormack Finite-Difference Scheme.** Int. Journal for Num. Meth in Fluids. May, 1986.
- [3] MacCormack, R. W. **The effect of viscosity in hypervelocity impact cratering.** AIAA paper 69-354 (1969)
- [4] Murphy, Peter J. **Equilibrium Boundary Conditions for Suspension.** Journal of Hydraulics, ASCE H111, 1, 1985.
- [5] Tsujimoto, Tetsuro and Tatsuo Yamamoto. **Sediment Suspension Affected by Transition from Bed-Load Motion into Suspension.** J. Hydroscience and Hyd. Eng. Vol. 6, No. 1, 1988.
- [6] Shields, I.A. **Application of Similarity Principles and Turbulence Research to Bed-Load Movement.** U.S. Soil Conserv. Serv. Coop. Lab. California Institute of Technology, Pasadena, California, 1936.
- [7] Zienkiewicz, O.C. **The Finite Element Method in Engineering Science.** MacGraw Hill. London Publication, 1971.

## CHAPTER 209

### Dispersion Process and the Settlement Pattern of Mud Dumped in Oceans

Eiji Yauchi <sup>1</sup> and Ken Katoh <sup>2</sup>

#### Abstract

The settlement of mud lumps dumped in oceans from barges was studied theoretically and the results were compared with data from field and laboratory experiments. The settling pattern and the load of initial turbidity were estimated by a non-dimensional dispersion index and the rate of turbidity load.

## 1 INTRODUCTION

Mud deposited on the bottom of rivers, lakes, or oceans are known to cause many problems. These problems can be classified into two groups. One is the siltation problem within channels, or basins at ports and harbors. As a result of the siltation, the port management body is forced to carry out dredging on a regular basis at a great deal of operational costs. The second problem is a consequence of the dredging, namely the disposal of the dredged mud either in the water or on land. In many instances, land disposal is infeasible because of the high salt content or the fineness of particles in the dredged mud. As a result, disposal of dredged mud in water is increasingly becoming a more frequently used option and therefore requires a more thorough study of its environmental impact.

While the dispersion characteristics of sand dumped in water are mainly affected by the diameter and specific weight of sand, the dispersion and settlement characteristics of dumped mud are affected by water content or cohesion, among other factors. As this field has not been studied sufficiently, the load of initial turbidity, or the falling velocity of dumped mud, has been taken to be the same as for cohesionless sand particles. However, dredged mud with low water content has a lower turbidity than sand and in numerical simulations the turbid area is seen to be larger than observed in the field.

In this paper, the results of a theoretical investigation of the settlement characteristics of mud lumps are presented along with a comparison of theoretical results with data from field and laboratory experiments.

---

<sup>1</sup>TOA CORPORATION, Design Department, 5-Banchi, Yonban-cho, Chiyoda-ku, Tokyo, 102 Japan

<sup>2</sup>ditto, Mechanical Department

## 2 LABORATORY EXPERIMENT

### 2.1 EXPERIMENTAL APPARATUS

Experiments were conducted in the laboratory to investigate the settling characteristics of dumped mud. The tank used in the tests was 0.5 m wide, 2.5 m long and 1.0 m high, as shown in Fig.1.

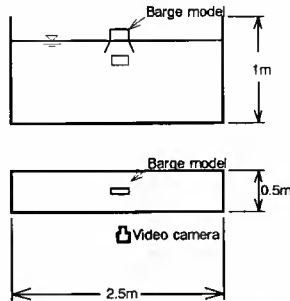


Figure 1: Experimental Apparatus



Figure 2: Shear Meter

The water content of the mud was varied from 170% to 700% and the mud was dumped into the tank from a scaled down model of a 3 cm wide, 4 cm long, and 2 cm high barge. The dispersion process and the settlement pattern were monitored by a video camera. The load of initial turbidity was calculated from the observed dispersion of the mud and diffusion coefficient (Yauchi et. al. :1989).

The shear stress of mud was measured using a vane shear meter shown in Fig.2, specially developed in order to measure the shear strength of soft mud. A stepping motor and a high-sensitivity torque meter were fitted to the axis of the shear meter and its rotation is maintained at a speed of 0.1 deg/s with an accuracy of 0.5%. The range of this shear meter is 1 pa to 10 kpa.

### 2.2 EXPERIMENTAL RESULTS

Fig.3(a) shows the result at a water content of 320% and at this water content the mud reached the bottom as one lump. At a higher value of water content, 429% as

shown in Fig.3(b), the mud lump begins to disintegrate and at a still higher value, 633%, depicted in Fig.3(c), the mud lump disperses.

Based on the experiments, the settlement of mud lumps was classified into three patterns, lump-settling, partial-dispersion and full-dispersion, as shown in Fig.4. Table 1 summarizes the results of the experiments.

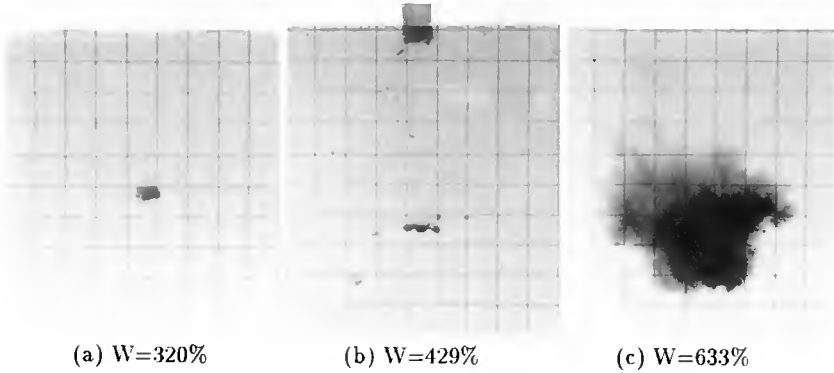


Figure 3: Settling Photo

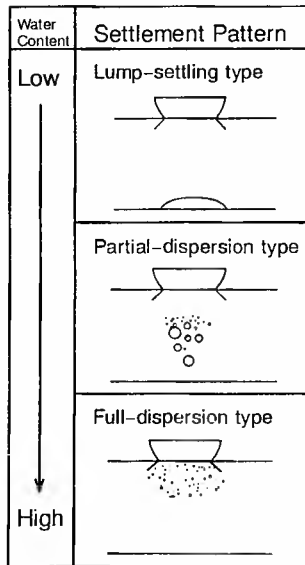


Figure 4: Settling Pattern

Table 1: Experimental Results

Mud	Water Cont. W(%)	Shear Str. $\tau_{mud}$ (Pa)	Diff. Coeff. K(cm <sup>2</sup> /sec)	Turb. Rate. $\phi$	Settl. Vel. $w_{f_s}$ (cm/sec)
A	177	860.4	0	0	26.3
	190	405.7	0	0	
	258	122.5	0	0	
	344	16.8	0.195	0.023	
	394	6.3	1.65	0.199	
	486	2.6	6.04	0.728	
	560	1.2	7.78	0.937	
	633	0.6	8.03	0.967	
	$K_{max}$		8.3	1.0	
B	168	1176.0	0	0	27.0
	194	362.6	0	0	
	320	25.9	0	0	
	375	10.1	0.768	0.179	
	429	5.2	2.53	0.588	
	544	1.4	4.08	0.949	
	681	0.4	4.28	0.995	
	$K_{max}$		4.3	1.0	
C	216	399.8	0	0	27.8
	232	37.7	0	0	
	282	59.1	0	0	
	322	30.9	0	0	
	368	12.0	0	0	
	423	5.6	7.37	0.689	
	482	2.7	8.17	0.764	
	560	1.2	10.04	0.938	
	$K_{max}$		10.7	1.0	

### 3 THEORETICAL ANALYSIS

#### 3.1 SETTLEMENT PATTERN AND MODELING

Two models were considered in the theoretical analysis of the settlement pattern of mud lumps. The models are shown in Fig.5.

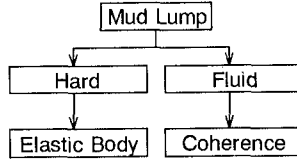


Figure 5: Modeling Type

In the first model, the mud lump is considered to be an elastic solid and in the second the mud lump is treated as a fluid with a high viscosity. If the mud lump is modeled as solid matter, the stress in the mud lump is easily analyzed by structural mechanics. While, if the mud lump is dealt with as a fluid, forces such as van der Waals' forces must be incorporated in the analysis. However, the measurement of van der Waals' forces is not easy and it is probably not very influential in the settling of mud lumps because of the big volumes of mud involved, over  $500m^3$ . Therefore, in this study, the mud lumps are assumed to remain intact and are treated as elastic matter.

#### 3.2 FORCES ON AND RESISTANCE OF MUD LUMPS

The main forces acting on mud lumps during settling are (a) drag force, (b) skin friction, (c) vortex force behind the mud lump and (d) a fluctuating force due to rotation of the mud lump. If the mud lumps are assumed not to rotate and the effect of skin friction is omitted, the governing forces are drag force and vortex force. The vortex force is affected by the shape of the mud lumps and the falling Reynolds number. Thus if, the effect of the vortex force is included in a drag coefficient the only governing force that needs to be considered is the drag force.

The resistance of mud lumps is measured by the shear, compressive and tensile strengths. As these strengths are almost proportional to each other the shear strength was taken as the measure because it could be easily measured in situ.

#### 3.3 NON-DIMENSIONAL DISPERSION INDEX

In laboratory tests the mud lumps begin to break at the center because of the bending moment. In this study the mud lumps were modeled as thin plates, as shown in Fig.6. The mud lump start disintegrating when the shear from the bending exceeds the shear strength of the mud. The equilibrium equation can be expressed as Eq.1,

$$\frac{\partial^4 w}{\partial x^4} + 2\frac{\partial^4 w}{\partial x^2 \partial y^2} + \frac{\partial^4 w}{\partial y^4} = \frac{p}{\gamma} \quad (1)$$



where,  $w$  is the displacement,  $p$  is the force acting on the mud lump, and  $\gamma$  is the stiffness of the mud lump.

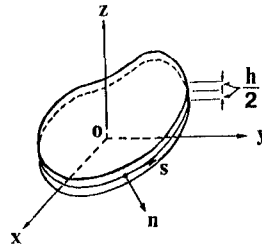


Figure 6: Schematic of a Thin Plate

It is difficult to obtain general solutions because Eq.1 is a non-linear equation. Thus, its solution is carried out analytically by considering the conditions of dumping mud.

The shape of the mud lumps dumped from barges is taken as rectangular parallelepiped. The mud lump starts to disintegrate at the center of mud lump at the region of high bending moment. Therefore, the mud lumps are considered to be simply supported. When the shape of mud lumps is a  $a \times b \times h_{mud}$  rectangular parallelepiped domain, the boundary conditions are as per Eq.2.

$$\begin{aligned} w &= 0 \quad |_{x=0, x=a, y=0, y=b} \\ M_x &= 0 \quad |_{y=0, x=0, x=a, y=0, y=b} \\ M_y &= 0 \quad |_{x=0, x=a, y=0, y=b} \end{aligned} \tag{2}$$

When Eq.2 is used together with Eq.1, Eq.3 known as Navier’s solution is obtained.

$$w = \frac{1}{\pi^4 \gamma} \sum_{m=1}^{\infty} \sum_{n=1}^{\infty} \frac{a_{mn}}{(m^2/a^2 + n^2/b^2)^2} \sin \frac{m\pi x}{a} \sin \frac{n\pi y}{b} \tag{3}$$

The maximum bending moment at the center of the mud lumps is given by Eq.4 and Eq.5.

$$M_x = \frac{16pa^2\lambda_{ab}^2}{\pi^4} \sum_{m=1}^{\infty} \sum_{n=1}^{\infty} \frac{(\lambda_{ab}^2 m^2 + \delta n^2)}{mn(\lambda_{ab}^2 m^2 + n^2)^2} \tag{4}$$

$$M_y = \frac{16pa^2\lambda_{ab}^2}{\pi^4} \sum_{m=1}^{\infty} \sum_{n=1}^{\infty} \frac{(\delta \lambda_{ab}^2 m^2 + n^2)}{mn(\lambda_{ab}^2 m^2 + n^2)^2} \tag{5}$$

Representing the section modulus of the mud lump by  $Z$ , the flexural stress in the mud lump can be expressed by Eq.6.

$$\sigma_x = M_x/Z_x, \quad \sigma_y = M_y/Z_y \tag{6}$$

A new parameter defined by the shear and bending stresses in the mud lumps is introduced for determining the settlement pattern.

$$\Psi = \frac{\sigma_{max}}{\tau_{mud}} \tag{7}$$

$\Psi$  is denoted as the non-dimensional dispersion index.

### 3.4 RATE OF TURBIDITY LOAD

Both the turbidity load and the variation of the non-dimensional dispersion index must be considered in order to be able to estimate the turbidity in numerical simulations. A new factor, the rate of turbidity load,  $\phi$ , is defined to represent the load of initial turbidity. The factor  $\phi$  is based on the rate of the load of initial turbidity,  $q$ , and the maximum turbidity load,  $q_{max}$ , as expressed in Eq.8.

$$\phi = q/q_{max} \tag{8}$$

The rate of turbidity load  $\phi$  increases as the non-dimensional dispersion index increases. The factor  $\phi$  is taken as a measure of the probability of dispersion of dumped mud lumps, as shown in Fig.7.

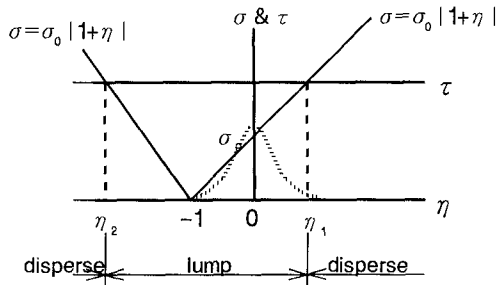


Figure 7: Probability of Disintegration of Mud Lumps

where,  $\eta$  is the fluctuation of  $\Psi$ ,  $\eta_0$  is the standard deviation of  $\eta$ , and  $B$  is a constant.

If the bending stresses in a mud lump,  $\sigma$ , is taken to be distributed randomly, the mud lump shows signs of dispersion when  $\sigma$  is greater than  $\eta_1$  or  $\sigma$  is less than  $\eta_2$ .

Thus,  $\phi$  is equal to one minus the integral between  $\eta_2$  and  $\eta_1$  of the density function of the bending stresses. In this paper the bending stresses were modeled by a Gaussian distribution, as shown in Eq.9.

$$\begin{aligned} \phi &= 1 - \frac{1}{\sqrt{\pi}} \int_{\eta_{*2}}^{\eta_{*1}} e^{-t^2} dt \\ \eta_{*1} &= B_*/\Psi - 1/\eta_0, \\ \eta_{*2} &= -B_*/\Psi - 1/\eta_0, \\ B_* &= B/\eta_0, \end{aligned} \tag{9}$$

where  $\eta_0$  and  $B_*$  are determined by the critical values of the disintegration process.

### 3.5 SETTLING VELOCITY

The settling velocity is an important factor in the evaluation of the the rate of turbidity load. The terminal velocity of a particle settling in a fluid is given by Eq.10.

$$w_f = \sqrt{(4/3)(s-1)gd/C_D} \quad (10)$$

where,  $s$  is the specific weight,  $d$  is a representative diameter, and  $C_D$  is the drag coefficient of the mud lump.

In this study, Wadell's representation equation is used in incorporating the shape factor, defined as  $C_D$ .

### 3.6 CRITICAL VALUES OF THE DISINTEGRATION PROCESS

In this study, the rate of turbidity load is defined by the rate of bending stress and shear strength of mud lump. However, the critical values of the disintegration process are defined in terms of the rate of bending stress and tensile strength. The relationship between tensile strength,  $\sigma_t$ , cohesive force,  $c$ , and shear strength,  $\tau_{mud}$  of clay are given by Eq.11 and Eq.12.

$$\sigma_t = 2c \frac{\cos \theta_0}{1 + \sin \theta_0} \quad (11)$$

$$\tau_{mud} = \sigma_t \tan \theta_0 + c \quad (12)$$

where,  $\theta_0$  is the angle of internal friction.

If the clay is assumed to be ideal,  $\theta_0 = 0$  and  $\sigma_t = 2\tau_{mud}$ , the critical values of the disintegration process of mud lumps can be expressed as follows.

$$\Psi_c = 2.0 \quad (13)$$

In the field, mud usually contains some sand and benthos, etc, and these reduce the tensile strength. Therefore in this study,  $\Psi_c$  is determined from laboratory experiments, as shown by Eq.14.

$$\Psi_c = 1.5 \sim 2.0 \quad (14)$$

Furthermore, we obtain  $\eta_0 = 1.0$  and  $B_* = 4.0$  from Eq.14 and Eq.9, when we take  $\eta_0 = 1.0$  and  $\eta_* = 1.0$ .

### 3.7 COMPARISON WITH EXPERIMENTAL DATA

Fig.8 compares the theoretical results with those from laboratory experiments. Here,  $C_D = 2.01$  and the Poisson rate,  $\delta = 0$ , are assumed.

On the whole, the theoretical predictions were in good agreement with the experimental data. In particular, they were in good agreement at the range of  $\Psi > 20$ , though the assumption of the mud lump being elastic can no longer be applied because at such values the lump is more like a fluid than a solid. The non-dimensional dispersion index is related to the settlement pattern and each pattern was classified using this index, as shown in Eq.15.

$$\begin{aligned} \Psi < \Psi_1 & : \text{Lump - settling type} \\ \Psi_1 \leq \Psi < \Psi_2 & : \text{Partial - dispersion type} \\ \Psi_2 \leq \Psi & : \text{Full - dispersion type} \end{aligned} \quad (15)$$

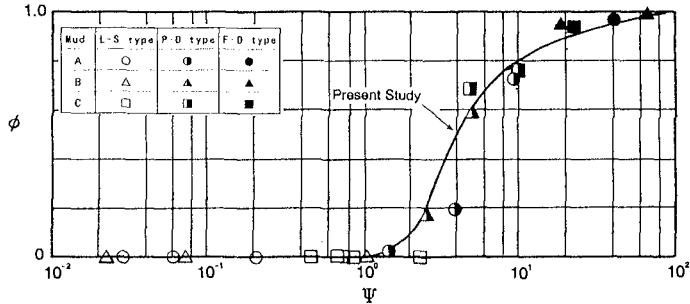


Figure 8: Theoretical Predictions and Laboratory Data

From Fig.8,  $\Psi_1$  and  $\Psi_2$  were determined to be equal to  $1.5 \sim 2.0$  and  $10 \sim 20$ , respectively.

#### 4 FIELD EXPERIMENT

Field experiments were carried out to validate the theoretical predictions. Field measurements were made within a circle of 700 m radius centered around the dumping point at a depth of 41 m. The 50 percentile diameter of the mud used in the tests was  $0.7 \mu\text{m}$  and the mud contained some organic matter. The vertical and horizontal profiles of turbidity, water temperature and salinity, and the falling velocity were measured with the help of six turbidimeters, six salinometers, and three velocimeters. The three dimensional profile of the turbidity was, also, measured by means of an echo-sounding turbidimeter.

Fig.9 shows the vertical turbidity profile. Here, the abscissa is turbidity, and the ordinate is depth.

For small water contents, turbidity could be measured only at the bottom layers. Turbidity measured in the upper layers became larger as the water content of the mud increased. The dispersion indexes are 1.2, 2.6 and 40.1, respectively. The field data are in good agreement with the theoretical predictions.

#### 5 CONCLUSIONS

The settlement pattern of mud lumps dumped in oceans were classified into three patterns. The settlement pattern and the turbidity load can be estimated by the non-dimensional dispersion index,  $\Psi$ , and the rate of turbidity load,  $\phi$ .

#### References

- [1] Timoshenko, S., P. and Woinowsky-Krieger, S. : Theory of plates and shells, 2nd Ed., McGraw-Hill, 580p., 1959.
- [2] Yauchi, E. and Katoh, K. : Diffusion process of dumped mud in oceans., Proc. of Coastal Engineering, JSCE, vol.36, pp.324-328, 1989. (in Japanese)

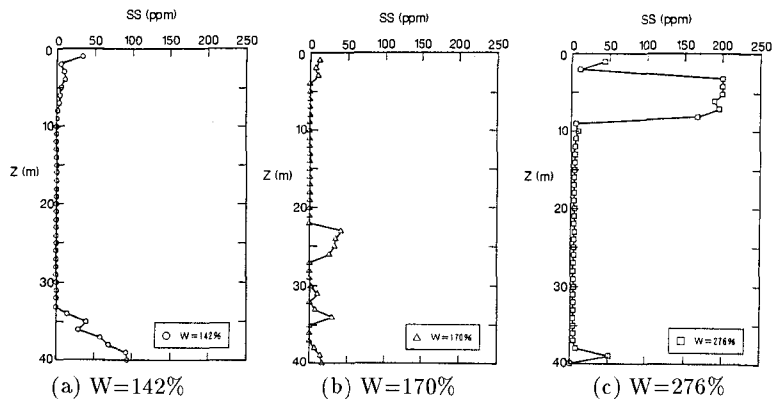


Figure 9: Vertical Turbidity Profile

- [3] Einstein, H., A. : The bed-load function for sediment transport in open channel flows, Technical Bulletin, No.1026, U.S.Dept. of Agric., Washington D.C., pp.1-72, 1950.
- [4] Meakin, P. : Diffusion-controlled flocculation : The effects of attractive and repulsive interactions, Journal of Chemical Physics, vol.79, No.5, pp.2426-2429, 1983.
- [5] Wadell, H. : The coefficient of resistance as a function of Reynolds number for solids of various shapes, Journal of Franklin Institute, vol.217, 1934.

## CHAPTER 210

### PORT OF LISBON IMPROVEMENT OF THE ACCESS CONDITIONS THROUGH THE TAGUS ESTUARY ENTRANCE

I. B. Mota Oliveira<sup>1</sup>

#### ABSTRACT

The Port of Lisbon authority is aiming at the reception of container ships of the fourth generation. For that a deeper and wider artificial channel has to be dredged through the outer bar. The set of studies undertaken (data collection, site investigations, mathematical and physical modelling) put into evidence the importance of the opening of a secondary bar, some 50 years ago, over the general morphological behaviour of the estuary entrance. So a recommendation has been made to close it using an artificial sand dike.

#### 1- INTRODUCTION

The Port of Lisbon takes advantage of the excellent conditions offered by the lower reach of the river Tagus estuary, as a natural harbour.

The port facilities are distributed along the banks of the estuary, mainly along the north bank: 16 km of quays (13 km in the north bank) with depths from 4 up to 17m (CD); 98 ha of reveted embankments; 1100 ha of total dry area under the port authority control (Administração do Porto de Lisboa - APL). In addition the estuary shelters: a major ship repair yard; a navy base; some important industry terminals (steel mill, chemicals, food processing, cement, etc); fishing facilities; small craft (yachting) harbours.

With an annual traffic of 17 million tons (1991), the port of Lisbon is the main portuguese port. General cargo accounts for about 26% of that tonnage, being 39% for liquid bulks and 35% for dry bulks. General cargo is already containerised at a level of 60%, equivalent to about 285 000 TEU.

The Tagus estuary - Figure 1 - affords excellent depths in the lower reach, a "corridor" of some 12 km in length with approximately parallel banks between the entrance and the Praça do Comércio Square in Lisbon. On the contrary, it is very difficult to get here new embankments: on the north side, because of the neighbouring town, namely the historic zone, against which the port is really compressed; on the south side, because of the very steep margins. From Praça do Comércio upstream the situation is reversed: it is easier to get new embankments but natural depths diminish progressively, sedimentation problems in channels and basins worsen and maintenance dredging becomes critical.

<sup>1</sup>Partner, HIDROTÉCNICA PORTUGUESA, Consulting Engineers. Lisboa,  
Professor, INSTITUTO SUPERIOR TÉCNICO, UTL. Lisboa, Portugal

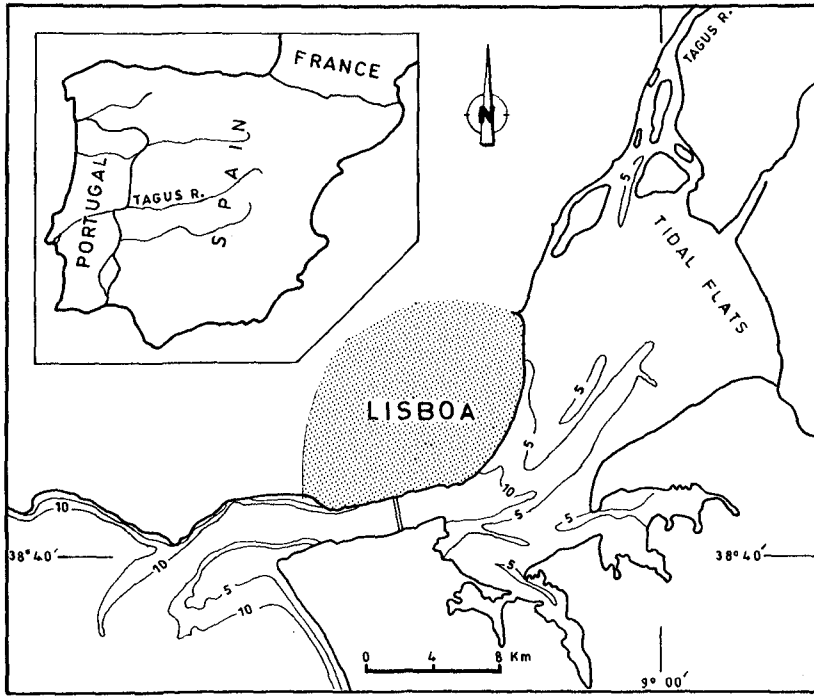


Figure 1 - The River Tagus Estuary

The estuary has a total area of the order of 250 km<sup>2</sup> which, with a spring tide amplitude of almost 4 m, generates a tidal prism around  $1\ 000 \cdot 10^6$  m<sup>3</sup>. The tidal amplitude varies along the estuary and it is worth mentioning that, on account of a small resonance effect, the amplitude inside the estuary is greater than in the outside, growing continuously from the estuary entrance up to the Praça do Comércio Square.

The tidal prism is the main agent in maintaining the excellent depths across the Tagus outer bar: almost 12 m in spring low water and 15 m in mean high water - Figure 2. That explains why only in the last two or three decades the bar began to cause some significant constrains to the navigation of the largest ships calling the port of Lisbon. As a matter of fact, the first dredging works in the outer bar, at a level of (-13.5 m CD), were carried out only in 1969.

It should be mentioned that this bar was crossed by tankers of the 300 000 dwt class (and even 500 000 dwt), mainly empty ships bounded for the repair yard of LISNAVE, within the estuary.

The port authority (APL) is now aiming at the reception of container ships of the so called fourth generation, almost without navigation restrictions in the outer bar (Length: LOA=290 m; Beam: B=32 m; Draft: D=13 m). Several studies were undertaken, including data collection, site investigations, mathematical and physical modelling, improvements in aids to navigation, etc.

The main purpose was to establish the geometry of an artificial channel through the outer bar (alignment, depth, width) and to estimate the corresponding mean annual volume of maintenance dredging. In addition, the evaluation of the

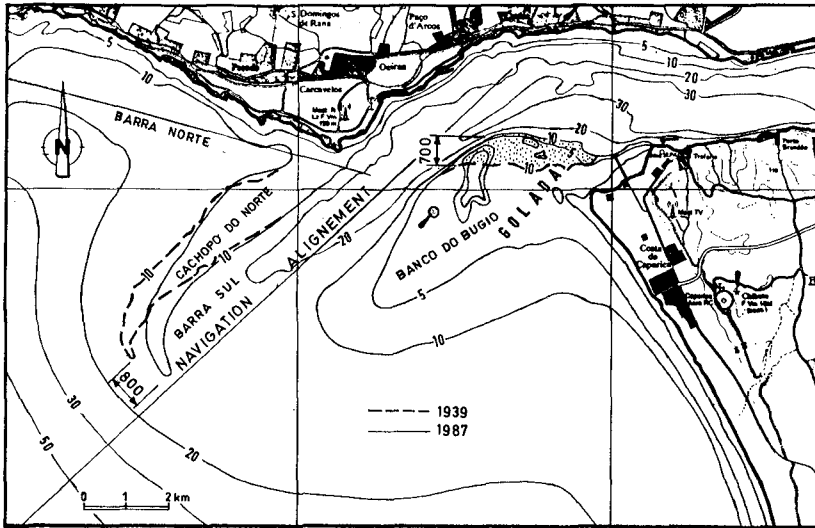


Figure 2 - The Entrance of the Tagus Estuary

general consequences of the closing of the Golada was also considered.

Golada is a secondary bar over the "Banco do Bugio", this latter being a big shoal that defines the southern bank of the main entrance channel - Figure 2. It is a morphologically very unstable area, with very small depths, which in the beginning of this century had yet the nature of a sand spit that, at least in low water, allowed the pedestrian access to the Bugio lighthouse (in effect a fortress of the last years of the 16th century).

During the forties this secondary bar (Golada) "broke" through the Banco do Bugio. So, another question to be answered by the study was: what have been the consequences of that event over the stability of the main outer bar or, what would be the consequences of an artificial closing of the Golada, namely upon the maintenance conditions of the artificial channel to be cut through the main bar?

Only a brief summary of those studies and of their main results can be presented in this paper.

## 2 - ARTIFICIAL CHANNEL THROUGH THE OUTER BAR

### 2.1 - Alignment

It was decided to open the artificial channel according to the "traditional" navigation route, that is to say, the alignment that has been used by pilots for many decades to cross the bar and to navigate along the lower reach of the estuary - Figure 2. In fact, a different alignment would imply:

- a second set of navigation aids ;
- additional steering problems in the transition between the two alignments; the risk of a ship grounding would be particularly high in an outgoing trip during the ebb phase, when ship and tidal velocities add each other; indeed in the area of the channel ebb currents are stronger than flood ones and, in an outgoing manoeuvre, the ship passes from an almost unrestricted



- navigation area, upstream the channel, to a confined path width.
- the change of navigation habits that has been established for a long time (may be, the main reason).

On the other hand, the advantages of the new alignment (mainly, a somehow shorter length of the artificial channel) seems almost irrelevant in relation to those negative points.

## 2.2 - Cross-Section

### 2.2.1 - Depth

In order to obtain the total required depth of the channel the loaded draft of the reference ship must be added to the corresponding "underkeel allowance", that is to say, the clearance between the keel of the standing still ship in calm water and the nominal level of the channel bed. The underkeel allowance faces a number of different ship movements (rolling, pitching, squat), and includes the net clearance which accounts for the minimum allowance under the keel when the ship moves along the channel under the most unfavourable conditions.

In a case like the bar of the Tagus estuary, facing openly the Atlantic Ocean, the most important movements of the ship are by far those resulting from the wave action. In theory, the maximum immersion of the ship due to rolling and pitching could be obtained through the "amplitude response operator" of the ship, relating those movements with the wave period, for a given water depth and angle of wave attack.

Indeed in our case that operator for the "project ship" was not known. Nor physical or mathematical modelling had been foreseen to establish the channel depth.

A bibliographical study was made, taking advantage of the known performance of artificial channels cut in environmentally similar conditions. The main steps of the study were as follows.

Based on data of the "Oceanographic Atlas of the North Atlantic Ocean. Section IV, Sea and Swell" (U. S. Naval Oceanographic Office), the deep water wave climate was defined. By means of regular wave diffraction diagrams, the local wave climate (in the area of the artificial channel) was established in terms of wave heights and angles relative to the channel alignment. In what concerns wave heights, their frequencies have been characterised by height intervals of 0.5 m, from 1.5 m to 4.0 m. In a word, for the mean year it was obtained

Hs < 1.5 m	285	days/year	(78.1 %)
1.5 m < Hs < 4.0 m	77	"	(21.1 %)
Hs > 4.0 m	3	"	( 0.8 %)

After a careful analysis of some case studies ( Richards Bay, South Africa; Ashdod, Israel; Antifer, France; Europort, Netherlands; Inkoo and Tahkoluoto, Finland ) the hypothesis was made that the maximum sinkage (s) of the project ship (rolling and/or pitching) due to a certain wave would be equal to its height (H):  $s=H$ . Taking into account the velocity of the ship and the depth of the channel, a maximum squat of 0.6 m was considered and an underkeel clearance of 0.6 m was accepted. So, the maximum overdraft (underkeel allowance) needed in the presence of a wave height H will be  $Z=H+1.2$  m.

"Distribution" of tide levels in the region of the outer bar was defined by means of a level duration curve. If we think of time intervals while the tide levels remain below a certain value (Tl), we have as an example the following "probabilities"  $pTl = p(\text{tide level} < Tl)$ :

$Tl = 0.7$  m CD,  $pTl = 2\%$ ;  $Tl = 2.7$  m CD,  $pTl = 75\%$ .

Let C be the channel bottom level and D the draft of the project ship (13m).

In order to cross the bar in the presence of a wave height  $H$  a minimum tide level

$$Tl = C + D + Z = C + D + H + 1.2 \text{ m} \quad (1)$$

will be necessary ( $C$  and  $Tl$  are referred to Chart Datum;  $C$  is negative).

If a given wave height  $H$  occurs, the channel will be "inoperative" for any tide level below the value given by expression (1). A measure of the "inoperativeness" ( $Inop$ ) of the channel can be obtained as follows

$$Inop = \sum_i pHi * pTl \quad (2)$$

in which  $pHi$  is the probability associated to the local wave height interval  $(Hi-0.5 \text{ m}) < H < Hi$

Three channel bottom levels were "tested":  $C = -17; -16; -15$  (m CD). The "inoperativeness" can be expressed as a percentage of the total time or, alternatively, it can be thought as the percentage of the number of "project ships" that will suffer some waiting time to cross the artificial channel. In effect the arrivals are random. Taking into account that a ship calling the port crosses the estuary entrance twice, the results obtained were

Channel bottom level (m CD)	Inop (%)	Ships suffering some waiting time to cross the bar
- 15	11.1	1 out of 4 or 5
- 16	3.2	1 out of 16
- 17	0.6	1 out of 85

A nominal bottom level  $C = -16$  m CD was recommended to the port authority. For a tide level of 0.7 m CD (98% exceedence), the project ship ( $D = 13$  m) will afford an overdraft of 28.5% ( $16.7 \text{ m} / 13 \text{ m} = 1.285$ ), which compares with the reference cases: Richards Bay, 35%; Ashdod, 35%; Europort, 32%; Antifer, 10%; Inkoo, 15%.

Of course, the channel has to be built at a somewhat lower level to account for sedimentation between dredging works

### 2.2.2 - Width

Considering the small length of the artificial channel ( $\approx 4$  km) and the relatively small number of ships having to travel within it, a one lane channel was considered suitable in this case. The channel width was assessed preliminarily by means of empirical rules. In a second approach, a mathematical model was elaborated to simulate the ship manoeuvring in the channel.

According to CIERGNA (Commission Internationale pour la Reception des Grands Navires) of PIANC (Buletin n° 35, 1980) the width of a one lane channel should not be smaller than  $5B$ ,  $B$  being the ship beam; in some very severe conditions, for instance strong transverse currents, according to the same commission that width could reach the value of  $10B$ .

In the case of the Lisbon outer bar, ebb and flood currents flow more or less parallel to the navigation channel. On the other hand, strong winds can represent a critical problem on account of the high free-board of the project ship (container ship), in as much as they can occur perpendicularly to the ship path.

The cases mentioned previously (Richards Bay, Ashdod, etc) were carefully analysed, namely the "adimensional" widths ( $n B$ ) when related to their specific environment conditions. Values between  $5 B$  (Tahkoluoto) and  $8.4 B$  (Antifer) were found.

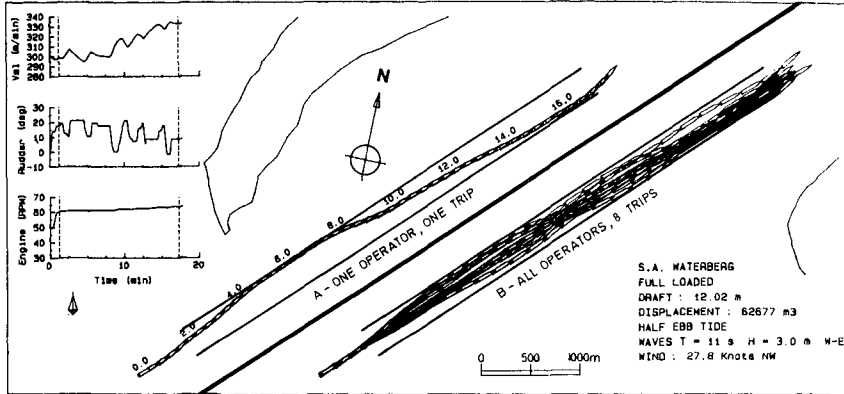


Figure 3 - Ship Motion Controlled by a) One Operator and b) All Operators, for a Given Set of Environmental Conditions

The importance of aids to navigation systems is pointed out by CIERGNA and is put into evidence by the case studies analysed: the poorer the system, the wider the channel has to be.

As a first approximation a width of 300m, corresponding to 9.4 B ( $B=32$  m), was adopted; the capabilities of the present aids to navigation was taken into consideration. It has to be said that pilots claim for an even wider channel (350 m).

A numerical model (SIMNAV) was then elaborated by Laboratório Nacional de Engenharia Civil - LNEC. Its characteristics and capabilities are described by Santos and Rita (1991). It simulates the ship manoeuvring in coastal waters, calculating the time evolution of the ship heading and position, taking into account the motion in the horizontal plane.

The following testing parameters were considered:

- Loading conditions of the ship: fully loaded; in ballast.
- Tide levels: mean tide level; spring low water.
- Currents: tidal currents as obtained from the 2D hydrodynamic model ( see item 3.3).
- Local wind: calm; 50 km/h perpendicular to the ship path.
- Local waves: no waves;  $H=3$  m,  $T=11$  s,  $\alpha=45^\circ$ .

The most unfavourable conditions were obtained combining waves 3 m high with transverse winds of 50 km/h.

Four different operators conducted a reasonable number of manoeuvres in the model for each environment situation. The operator controls the ship by varying the rudder angle and the available torque at the propeller axis. Figure 3 presents a single trip and the superposition of all the trips made by the four operators for the same testing conditions.

The variable considered in the verification of the channel width was the maximum distance per trip between the channel axis and the ship's centre of gravity -  $Y$ . Curves of probability of exceedence of  $|Y|$  were obtained. The conclusion of the model study was: the acceptable channel width will be somewhere between 272 m and 300 m.

### 2. 3 - Maintenance Dredging

The navigation channel through the Lisbon outer bar was firstly dredged in 1969 at a

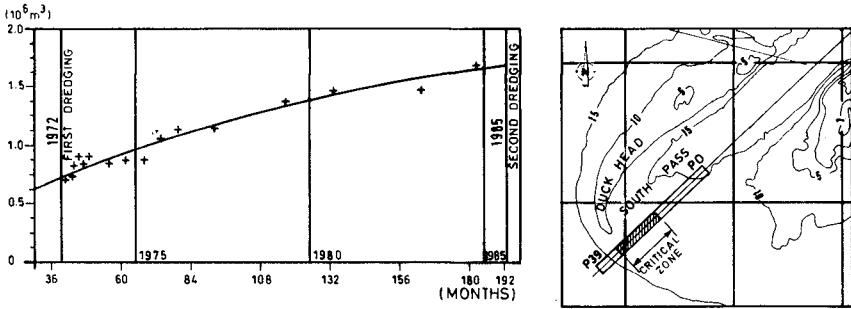


Figure 4 - Infill Process of the Channel Critical Zone

level of (-13.5 m CD); a second and a third dredging took place in 1972 and 1985, at levels of (-15.5) and (-15) respectively.

The subsequent morphological evolution was monitored regularly through a reasonable number of hydrographical surveys. While analysing this evolution we looked into nature as a one to one scale model of itself.

The channel infill process is governed by a complex interaction of tidal currents and a rough and varied wave climate. We have assumed that a exponential law can characterise such a process as a whole, when time scales of several years (at least two or three) are considered. Such a law states that, if a morphological situation is artificially driven away from its natural equilibrium, the difference will diminish exponentially with time. Accordingly we can write

$$V(t) = V_e - (V_e - V_0) \exp(-Ct) \tag{3}$$

where:  $V(t)$  is the channel infill volume at time  $t$ ;  $V_e$  is the volume corresponding to the natural equilibrium situation;  $V_0$  is the volume at  $t=0$ , in principle immediately after the conclusion of the dredging work.

The sand volume at the date of each survey, laying on the volume to be occupied by the artificial channel (bottom: -16 mCD; width: 300 m; side slopes: 1/20), was evaluated. Due to its longer duration (13 years) and to its deeper initial bottom level, only the period between the second and the third dredging was considered in this study.

In theory we would have known  $V_e$  and  $V_0$ , the only unknown to be determined being  $C$ . Indeed, owing to the great scatter of data obtained (reflecting the normal morphological instability of an outer bar controlled by a rough and varied wave climate), we only had first approximations to those values.

The following approach was used: several  $V_e$  values were considered and, for each one of them, several  $V_0$  values were taken; the pair  $V_e, V_0$  determining the best fit of the theoretical curve to the "experimental" points (highest correlation coefficient) was chosen.

The "critical" zone (a 1400 m long reach facing the tip of "Cabeça do Pato" (Duck Head) where the infill rate is the highest), and the whole channel where considered separately. Figure 4 pertains to the critical zone only.

The following values were obtained:

	$V_e$ ( $m^3$ )	$V_0$ ( $m^3$ )	$C$ ( $month^{-1}$ )	Correlation Coefficient
Total channel	3 800 000	790 000	$5.4 \cdot 10^{-3}$	0.924
Critical zone	2 200 000	254 000	$7.0 \cdot 10^{-3}$	0.980

Some comments:

- the "best" value of  $V_e$  for the critical zone compares quite well, and the one of the whole channel compares fairly well, with those measured in the last survey done before the first dredging (1969);
- the higher correlation coefficient obtained for the critical zone is in agreement with its greater physiographical homogeneity when compared with the diversity encountered along the whole channel
- as expected, the  $C$  value is higher in the critical zone than in the whole channel.

After some manipulations over the expression (3), with the corresponding values of  $V_e$ ,  $V_o$  and  $C$ , the following results were obtained

	Over dredging (m)	Initial bottom level (m CD)	Infill volume after 39 months (m <sup>3</sup> )
Critical zone	1.00	-17	680 000
Outside the critical zone	0.5	-16.5	300 000

A final conclusion could be drawn: the artificial channel, with a nominal bottom level of (-16 mCD), will require a maintenance dredging of the order of one million cubic meters every three years.

### 3 - THE TAGUS ESTUARY ENTRANCE. HYDROMORPHOLOGICAL ANALYSIS

#### 3.1 - Past Evolution

The most important event in this century of the Tagus entrance morphological evolution has been the opening, some 50 years ago, of a secondary bar named the Golada over the "Banco do Bugio" - Figure 2. Despite the fact that some people charge the borrow dredgings in the Bugio with being the cause of that event, the analysis of old hydrographic surveys shows that the Golada has passed through narrowing and widening phases in the last 140 years.

If we characterise the amount of closing of this secondary bar looking at the total area over the "Banco do Bugio" above CD level, Figure 5 shows that over the last 140 years the situation has been more of instability than of equilibrium. As a matter of fact, during the last few years an important shoal has been growing in the middle of this secondary bar above low water level.

In the Golada flood currents and waves largely prevail over the ebb currents in what concerns sand transport capacity. As a consequence, a volume of sand of  $36 \cdot 10^6$  m<sup>3</sup> has been accumulating over the northern slope of the "Banco do Bugio" since 1939, forcing it to advance northwardly some 700 m - Figure 6. In the meantime, the estuary main channel was narrowed and its tidal current pattern was changed. Accumulation rates in (m<sup>3</sup>/year) are shown in Figure 6.

The accumulation process has been the result of two opposite actions: the "bringing in" action of flood currents and waves entering through the Golada, and the "flushing out" action of ebb currents in the main entrance channel, more or less parallel to the northern slope of the shoal, "sweeping" the sands downstream in the direction of the main outer bar. So, the sand transport rate through the Golada can be seen as the sum of two parcels: the shoal accreting rate and the ebb flushing rate over the same shoal.

We can assume that the latter equals the rate of erosion of the shoal northern slope registered in the 1929/39 period, when the Golada was almost closed

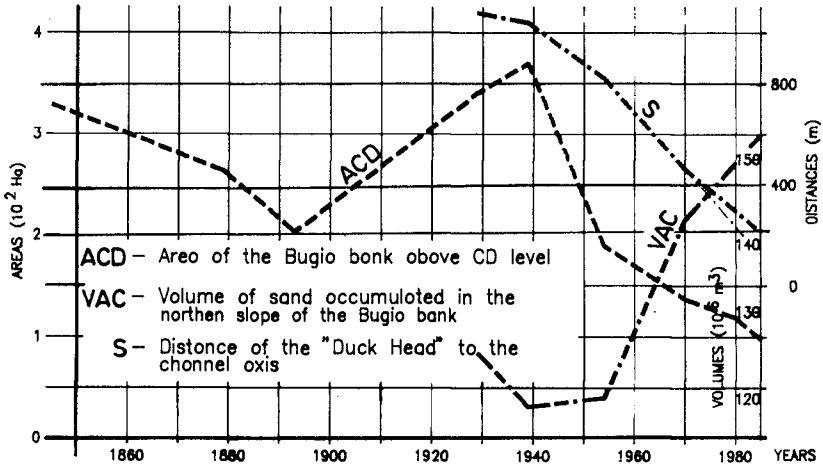
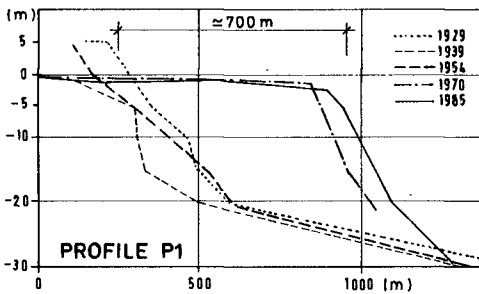
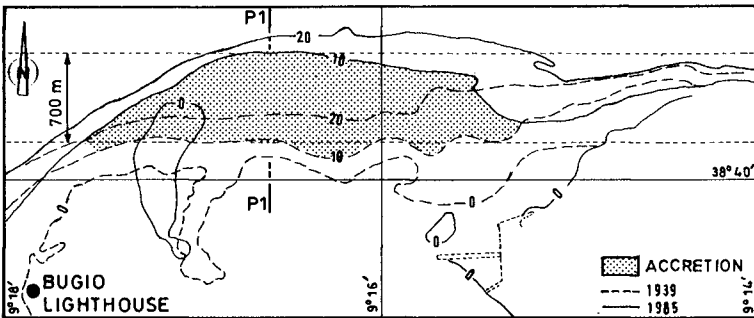


Figure 5 - Morphological Evolution of the Estuary Entrance. Characterization by means of three parameters



DATE	V (10 <sup>6</sup> m <sup>3</sup> )	Δ V (10 <sup>6</sup> m <sup>3</sup> )	r (10 <sup>6</sup> m <sup>3</sup> /Year)
1929	124,5		
1939	117,5	-7,0	-700
1954	118,7	+1,2	+80
1970	142,0	+23,3	+1450
1980	149,5	+7,5	+750
1985	153,3	+3,8	+760

Figure 6 - Northern Slope of the Bugio Bank. Evolution after 1929

(700 000 m<sup>3</sup>/y) - Figure 6 . Some impressive results are then obtained: the sand inward transport rate through the Golada was at least of the order of  $2.2 \cdot 10^6$  m<sup>3</sup>/y in the 1954/70 period and, during the most recent times (1980/85), has been still of the order of  $1.5 \cdot 10^6$  m<sup>3</sup>/y.

Over the same period (1929/1985) the tip of the "Cachopo Norte" (northern shoal of the outer bar - Figure 2) advanced 800 m in a direction almost perpendicular to the navigation channel - Figure 7. It seems that, if there had been no dredgings, the bathimetric (-10), which we considered the best one to characterize the position of that shoal, would have already overpassed the axis of the navigation channel to the south.

In Figure 7 the advancing rates of the "Cachopo Norte" are presented. It is worth mentioning the value of 22.5 m/y during the 1954/70 period. In this period the accreting rate in the "Banco do Bugio" northern slope was the highest.

### 3. 2 - Interpretation

If an entrance outer bar is in a stable morphological condition, this means that a dynamic equilibrium exists everywhere between the opposite actions (transport capacities) of flood currents and waves, on the one hand, and ebb currents, on the other hand.

Assuming that the wave climate has not changed in the last few decades, the advance of the "Cachopo do Norte" is most likely related to the weakening of ebb currents. Indeed, a part of the tidal prism started to flow through the Golada after its opening, and no longer through the main channel. The contribution of the Golada to this flow has been changing with time; according to physical model results, it would have been of the order of 8% and 12% for the ebb and for the flood mean spring tidal prism, respectively, in a morphological situation similar to the one registered in 1985.

Indeed, a fairly good correlation was verified between the opening of the Golada (wet area of the cross section) and the rate of advance of the "Cabeça do Pato" (Duck Head, as it is known the tip of the "Cachopo do Norte"). In Figure 5 the curve ACD (area above CD level) characterizes the degree of closing of the Golada; the smaller ACD, the greater the opening of this secondary bar. If we consider a sudden opening of the Golada, the resulting physiographical desequilibrium over the main outer bar area will determine the shoreward advance of the "Duck Head" at a rate that will be "proportional" to the importance of that desequilibrium, that is to say, to the degree of opening of the Golada. So, in Figure 5 the curve ACD(t) must be compared not with the curve s(t) - s is the distance of the "Duck Head" to the channel axis - but with its derivative.

On the other hand, the critical infill rate zone of the artificial channel is located just in front of the "Duck Head"; as a result of its continuous advancing, the channel infill rate will be aggravating. So, in order to reduce the maintenance dredging effort in the future artificial channel, a decision to close the Golada using a sand dike was made by the port authority (APL). This dike should be built with dredged material from the artificial channel.

It should be stressed that the closing of the Golada would afford some other "secondary" advantages, namely the sheltering of the lower reach of the estuary against the wave energy entering through this secondary bar.

### 3. 3 - Physical and Mathematical Modelling

In order to assess the general "functioning" of the Tagus estuary entrance, a study program was initially set up in which a vertically integrated 2D finite element model of the lower reach of the estuary (including a near-field ocean zone) would be used in connection with a physical model. Mathematical and physical model would be matched at the Lisbon bridge cross-section, that is to say, upstream boundary conditions of the mathematical model would be obtained from the physical model.

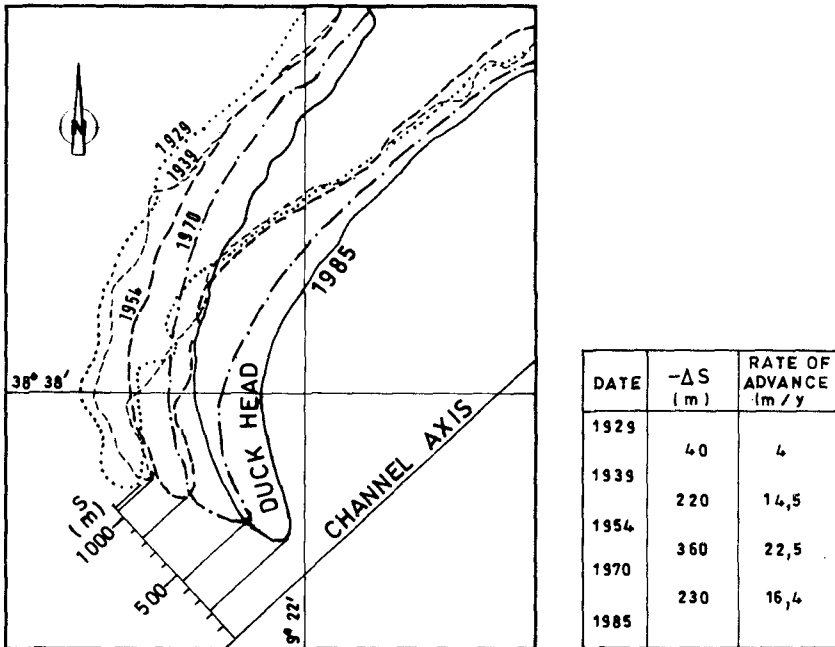


Figure 7 - Advance of the "Duck Head" after 1929

Due to operational reasons the use of the existing physical model had to be abandoned for that purpose, and the initial plan had to be changed: the 2D finite element model was then extended to the whole estuary. However, a strong schematization of the upper estuary region was made. Even so, levels and currents were correctly reproduced in the Lisbon bridge cross-section; velocities and levels were recorded in nature during several tidal cycles.

Three main situations were simulated: the present (reference) situation; the situation immediately after the closing of the Golada; the situation in the long run after the closing. In this third case it was admitted that, after the closing, the northern slope of the "Banco do Bugio" will recede naturally or/and artificially, to its position in the forties, that is to say, some hundred meters to the south. The artificial navigation channel through the outer bar was not considered; in fact, it was assumed that the influence in the hydrodynamics would only be felt locally.

Hourly velocity fields for two tidal periods and tide level curves in some reference stations were obtained, as well as residual currents in some restricted areas. Assuming as a first approximation that the bed load transport capacity depends on  $V^3$  ( $V$  - depth mean velocity), integral values of  $V^3$  were also obtained for the ebb and for the flood tidal periods in some grid points over the outer bar.

Some important results are:

- a - over the outer bar ebb currents significantly prevail over flood currents, as it could be expected;
- b - the predominance of ebb over flood currents will increase as an immediate consequence of the closing of the Golada;
- c - that predominance will increase even more in the long term with the



natural or artificial receding of the shoal accumulated in the northern slope of the Bugio;

d - with the closing of the Golada, the estuary global tidal prism will increase slightly (3%).

The last result is rather unexpected; indeed, how can the parcial closing of the estuary entrance improve its tidal prism?

The most likely explanation lays on the enhancement of the resonant effect within the estuary, which is responsible for a tidal range inside the estuary greater than in the outside. In fact, the estuary can be hydrodynamically interpreted as a great tidal basin connected to the ocean by a relatively straight and narrow channel - Figure 1. The closing sand dike of the Golada will make this channel somewhat longer; as a consequence, the estuary natural period will increase (Baines, 1957), becoming closer to the tidal forcing one (M2) and so intensifying the existing resonant phenomenon.

The results b) and c) mentioned above mean that the tendency of the "Duck Head" to advance in the direction of the artificial channel will be reversed if the Golada is closed. So a decision was taken to close it.

#### 4 - THE "CHANNEL DREDGING AND CLOSING OF THE GOLADA" PROJECT

The dredging of an artificial channel with the geometric characteristics presented in Chap. 2 (length: 4km; width: 300m; bottom level: -16.5 and -17m CD; slopes: 1/ 20) will produce a volume of sand of  $3.5 \cdot 10^6 \text{ m}^3$ . This sand would be used either in the building of a closing sand dike of the Golada or in the nourishment of the Caparica beaches, just to the south of the estuary entrance - Figure 8.

In order to adjust the sand dike to the present morphology of the Bugio bank, it would have a somehow sinuous outline. The total sand volume would amount to  $4.5 \cdot 10^6 \text{ m}^3$  of which approximately  $1.0 \cdot 10^6 \text{ m}^3$  would be deposited around the Bugio lighthouse. The Bugio bank itself would be the borrow area for this building sand or, alternatively, the sand removed from the artificial channel would be used for the same purpose.

The sand volumes resulting from future maintenance dredgings of the artificial channel would be deposited on the seaward (westward) tip of this dike, that is to say, around the Bugio lighthouse in order to compensate for the sand losses due to currents and wave erosion. In the long term the south face of this closing dike would evolve to a continuous sand beach from the Bugio lighthouse to Caparica, resembling the morphological situation of some decades ago when the Golada was almost closed naturally.

#### 5 - ENVIRONMENTAL ASSESSMENT

In the final stage of the studies an Environmental Impact Study was made. Environmental authorities raised a lot of questions. Even the influence of the artificial channel through the outer bar over the estuary hydrodynamics had to be analysed to conclude, as expected, that it will have no practical effect. A lot of additional analysis were performed, namely:

- hourly fields of  $V = V1 - V2$  in all the entrance area (velocity differences after (Af) minus before (Bf), after being in the short term (Af1) and in the long term (Af2); Af1 - immediately after the closing; Af2 - after the receding of the northern slope of the Bugio bank to the 1939 position)
- residual values ( $V_r$ ) of the velocity vector  $V$  (Bf, Af1, Af2)

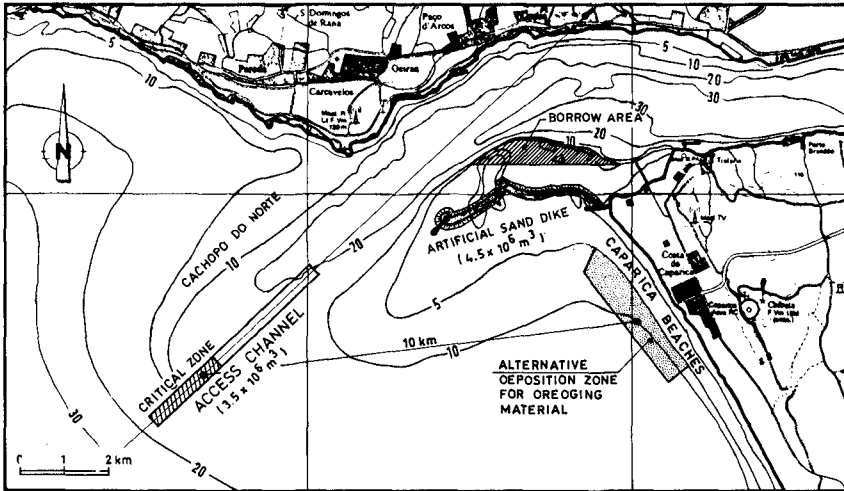


Figure 8 - The "Channel Dredging and Closing of the Golada" Project

- differences of  $V_r$  (Af1 - Bf; Af2 - Bf)
- hourly fields of  $V^3$  (Bf, Af1, Af2)
- residual values ( $V_r3$ ) of  $V^3$  (Bf, Af1, Af2)
- lagrangean simulation of the dispersion of particles emitted every 20 min in three points of the estuary lower reach (Bf, Af1, Af2).

Very recently the dredging of the channel has been approved. On the contrary, the closing dike of the Golada was rejected on the basis that its beneficial effects on the natural maintenance conditions of the artificial channel were not clearly demonstrated.

#### REFERENCES

- SANTOS, J.A. and RITA, M.M. (1991). The Width of the New Artificial Channel of the Port of Lisbon. An Application of the SIMNAV Simulation Model. 7th Symposium on Coastal and Ocean Management - Coastal Zone 91. Long Beach, California, USA.
- BAINES, W.D. (1957). Tidal Currents in Constricted Inlets. Proc. of the 6th Conference on Coastal Engineering, Florida, USA.

#### ACKNOWLEDGMENTS

The author acknowledges the Port of Lisbon Authority (Administração do Porto de Lisboa - APL) for the permission to publish the present results.

## CHAPTER 211

### A MIXING MECHANISM IN THE NEARSHORE REGION

Uday Putrevu, Associate Member, ASCE and Ib A. Svendsen,<sup>1</sup> Member, ASCE.

#### ABSTRACT

A dispersive mixing caused by the interaction of the longshore currents and the undertow is found to exist in the nearshore region. It is found to depend critically on the depth variation of both the cross-shore and the longshore currents. The effect is calculated for the simplest possible current profiles which yield a non-zero contribution. It is demonstrated that the dispersive mixing totally dominates the mixing in the nearshore region, exceeding the effect of turbulence by an order of magnitude even inside the surf-zone. In consequence, accounting for this interaction of the nearshore currents makes it possible to model longshore currents using realistic turbulent mixing levels. The vertical variation of those currents become part of the results provided. The predicted depth variation of the longshore currents is shown to be consistent with the only set of such measurements presently available.

#### 1. INTRODUCTION

Longshore currents on beaches have been analyzed using the concept of radiation stress since the pioneering works of Bowen (1969), Thornton (1970) and Longuet-Higgins (1970). These works clearly demonstrated that a lateral mixing (presumably due to turbulent fluctuations) needs to be included to give predictions of the cross-shore structure of the longshore currents that resemble measured currents in laboratory and field experiments. The works cited above, and the numerous models proposed later, differ primarily in the assumptions related to the lateral mixing due to turbulence.

---

<sup>1</sup>Postdoctoral Fellow and Professor, respectively, Center for Applied Coastal Research, Department of Civil Engineering, University of Delaware, Newark, DE 19716, USA

Models to predict vertical structure of nearshore currents have been proposed by Svendsen (1984), Dally & Dean (1984), Stive & Wind (1986), Svendsen *et al.* (1987) and Svendsen & Hansen (1988) for the cross-shore current (the undertow) and by Svendsen & Lorenz (1989) for the three dimensional current structure.

Svendsen & Putrevu (1990) developed the principles for 3D nearshore circulation modelling using analytical solutions for the 3D current profiles in combination with a numerical solution of the depth integrated 2D horizontal equations. Like Svendsen & Lorenz (1989), however, they neglected the current-current and the wave-current interaction terms. They pointed out that there is an order of magnitude difference between the eddy viscosity required to model accurately the vertical profiles and the eddy viscosity required for lateral mixing to achieve realistic results for the longshore current on a long, straight coast. This contradicts all physical arguments which point to the two being the same order of magnitude.

Svendsen & Putrevu (1992; hereafter referred to as SP92) found that the current-current and wave-current interactions neglected in previous investigations provide the additional lateral mixing. The effect involves the vertical structure of both cross- and longshore currents and turns out to be a generalization of the mechanism for longitudinal dispersion found by Taylor (1954) for pipe flow, Elder (1959) for open channel flow and Fischer (1978) for currents on the continental shelf. It is found to exist even on a long, straight coast with no alongshore variations.

In the present paper we present an analysis of this effect under the simplest possible conditions in order to illustrate the core of the mechanisms involved. It is shown that the dispersion effect is crucially linked to the overall slope of the longshore current profile. It disappears completely for a depth uniform longshore current.

The paper is organized as follows: Section 2 deals with the basic equations and outlines the assumptions involved. Section 3 discusses the dispersion caused under the vertical structure of the currents assumed here. A numerical example is presented in section 4. In section 5 we give a qualitative interpretation of the what we believe to be the essential nature of the dispersion mechanism. The paper concludes with a summary and an discussion of the important results of the paper in section 6.

## 2. BASIC EQUATIONS FOR A LONG STRAIGHT COAST

SP92 derived the basic equations governing the wave averaged nearshore circulation. For a long, straight coast with no alongshore variation these equations are

Depth Integrated continuity

$$\frac{d}{dx} \left[ \int_{-h_0}^{\bar{\zeta}} U dz + Q_w \right] = 0 \quad (1)$$

Depth Integrated Cross-Shore Momentum Equation

$$\frac{1}{\rho} \frac{dS_{xx}}{dx} = -g(h_0 + \bar{\zeta}) \frac{d\bar{\zeta}}{dx} \quad (2)$$

Depth Integrated Alongshore Momentum Equation

$$\frac{1}{\rho} \left[ \frac{d}{dx} (S_{xy} + S'_{xy}) + \tau_{by} \right] + \frac{d}{dx} \left[ \int_{-h_0}^{\bar{\zeta}} UV dz + \overline{\int_{\zeta_t}^{\zeta} (u_w V + v_w U) dz} \right] = 0 \quad (3)$$

In the above  $u_w$  and  $v_w$  are the wave induced velocities in the  $x$  (cross-shore) and  $y$  (alongshore) directions respectively.

These equations differ from the equations found in Phillips (1977) or Mei (1983) in that they allow for the currents to have a vertical variation. Dealing with wave averaged equations, one has to clearly define what is meant by a "current" above wave trough level where there is water only part of the time. When evaluating the terms in these equations, we assume that the mathematical expression defining the currents below trough level is valid above that level also. Such an assumption is implicitly made by Phillips (1977) and Mei (1983). For the case of depth uniform currents, the equations above reduce to the equations found in Phillips and differ slightly from those found in Mei (1983) owing to a difference in the definition of the current velocity.

In (1) - (3) the wave averaged quantities  $Q_w$  (volume flux),  $S_{xx}$  and  $S_{xy}$  (radiation stress components) are defined as

$$Q_w = \overline{\int_{-h_0}^{\zeta} u_w dz} = \overline{\int_{\zeta_t}^{\zeta} u_w dz} \quad (4)$$

$$S_{xx} = \overline{\int_{-h_0}^{\zeta} (\rho u_w^2 + p) dz} - \frac{1}{2} \rho g h^2 \quad (5)$$

$$S_{xy} = \overline{\int_{-h_0}^{\zeta} \rho u_w v_w dz} \quad (6)$$

Figure 1 shows the definitions of the geometrical parameters.  $S'_{xy}$  represents the turbulent radiation stress (depth integrated Reynolds' stress) and is defined by

$$S'_{xy} = \overline{\int_{-h_0}^{\zeta} \tau_{xy} dz} \quad (7)$$

where  $\tau_{xy}$  represents the Reynolds' stress.

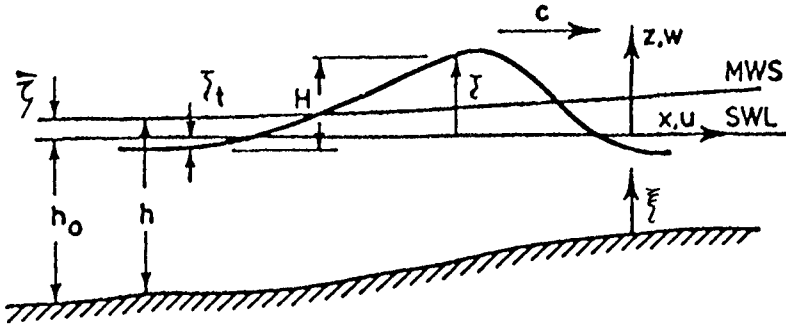


Figure 1: Definition sketch

Using a perturbation expansion based on slowly varying depth SP92 showed that at the lowest order the following equations govern the vertical variation of the cross- and alongshore currents

#### Depth Dependent Cross-Shore Momentum

$$\frac{\partial}{\partial z} \left( \nu_{tz} \frac{\partial U}{\partial z} \right) = g \frac{d\bar{\zeta}}{dx} + \overline{u_w \frac{\partial v_w}{\partial x}} \quad (8)$$

#### Depth Dependent Alongshore Momentum

$$\frac{\partial}{\partial z} \left( \nu_{tz} \frac{\partial V}{\partial z} \right) = \overline{u_w \frac{\partial v_w}{\partial x}} + U \frac{dV_b}{dx} \quad (9)$$

Of particular importance here is the last term in (9) which represents the lowest approximation to the current-current interaction.

SP92 solve these equations for arbitrary  $\nu_{tz}$  and  $u_w, v_w$  distributions.

### 3. SOLUTION FOR DEPTH UNIFORM UNDERTOW

In the present paper we analyze the effect of the interaction terms in (3) for the simple situation where the undertow is constant over depth and the longshore current is quadratic. The longshore current profile corresponds to assuming that  $\nu_{tz}$  and the wave induced velocities are depth uniform (cf. eq. 9). Hence, we assume the following

$$U(\xi) = U_0 = \frac{-Q_w}{h} \quad (10)$$

$$V(\xi) = V_b + b_v \xi + a_v \xi^2 \quad (11)$$

where  $\xi = z + h_0$  is the distance from the bed (see figure 1). While simplifying the analysis, this situation captures the essential nature of the interaction term and the simpler algebra helps exposing the mechanisms involved.

The parameters  $a_v$  and  $b_v$  are then given by

$$a_v = \frac{1}{2\nu_{tz}} \left( u_w \frac{\partial v_w}{\partial x} + U \frac{\partial V_b}{\partial x} \right) \tag{12}$$

as indicated by (9) and

$$b_v = \frac{f_w u_0}{\pi \nu_{tz}} V_b \tag{13}$$

where  $u_0$  is the amplitude of the near bottom wave induced velocity. The equation for  $b_v$  is derived from the bottom boundary condition

$$\rho \nu_{tz} \frac{\partial V}{\partial z} \Big|_{z=-h_0} = \tau_{by} = \frac{\rho f_w u_0 V_b}{\pi} \tag{14}$$

(see Svendsen & Putrevu 1990).

Using (10) and (11) we find that

$$\int_{-h_0}^{\bar{\zeta}} UV dz = -Q_w \left( V_b + \frac{b_v h}{2} + \frac{a_v h^2}{3} \right) \tag{15}$$

and

$$\overline{\int_{\zeta_t}^{\bar{\zeta}} V u_w dz} \approx V(\bar{\zeta}) \overline{\int_{\zeta_t}^{\bar{\zeta}} u_w dz} = Q_w (V_b + b_v h + a_v h^2) \tag{16}$$

The  $Uv_w$  term in (3) is small for small angles of incidence which is the typical situation on long, straight coasts. Hence, this term is neglected in the following.

Equations 15 and 16 clearly show that the terms representing the interaction of the currents oppose one another and for the case of a depth uniform longshore current ( $a_v = b_v = 0$ ) they exactly cancel one another. In total (15) and (16) give

$$\int_{-h_0}^{\bar{\zeta}} UV dz + \overline{\int_{\zeta_t}^{\bar{\zeta}} V u_w dz} = \frac{Q_w h^2 \overline{u_w \partial v_w / \partial x}}{3\nu_{tz}} + \frac{Q_w f_w u_0 h}{2\pi \nu_{tz}} V_b - \frac{Q_w^2 h}{3\nu_{tz}} \frac{dV_b}{dx} \tag{17}$$

Substituting (17) into (3) then leads to

$$\frac{1}{\rho} \frac{d}{dx} (S_{xy} + S'_{xy}) + \frac{\tau_{by}}{\rho} + \frac{d}{dx} \left( \frac{Q_w h^2 \overline{u_w \partial v_w / \partial x}}{3\nu_{tz}} + \frac{Q_w f_w u_0 h}{2\pi \nu_{tz}} V_b - \frac{Q_w^2 h}{3\nu_{tz}} \frac{dV_b}{dx} \right) = 0 \tag{18}$$

The solution of (18) requires the specification of the way in which we parameterize the turbulent radiation stress  $S'_{xy}$  (the bottom stress  $\tau_{by}$  is given by equation 14). For the turbulent radiation stress we use

$$S'_{xy} = \rho h \nu_{tz} \frac{dV_b}{dx} \tag{19}$$

SP92 show that using  $V_b$  in (19) instead of the mean velocity  $V_m$  is consistent to the order of validity of (3). The calculation of  $V_b$  using (18) still requires the specification of  $Q_w$  and  $S_{xy}$ . These are related to the wave motion and are assumed to be known in wave averaged models.

Introducing the definitions

$$D_c = \frac{Q_w^2}{3\nu_{tz}} \quad (20)$$

$$F_1 = \frac{\alpha_y h^2 Q_w}{3\nu_{tz}} \quad (21)$$

$$F_2 = \frac{f_w Q_w u_0 h}{2\pi\nu_{tz}} \quad (22)$$

we may rewrite the equation governing the longshore current in this simplified situation as

$$\frac{d}{dx} \left\{ h (\nu_{tz} + D_c) \frac{dV_b}{dx} \right\} - \frac{d}{dx} (F_2 V_b) - \frac{f_w u_0}{\pi} V_b = \frac{1}{\rho} \frac{dS_{xy}}{dx} + \frac{dF_1}{dx} \quad (23)$$

which clearly demonstrates that the interaction provides mixing - this can be seen from the  $D_c$  term of (23). In addition to the dispersion effect the interaction also produces other effects that are reflected in the  $F_1$  and  $F_2$  terms. The general results for  $D_c$ ,  $F_1$  and  $F_2$  were given by SP92.

#### Discussion of the dispersion effect

Before we proceed any further it is worthwhile to discuss the nature of the dispersion at this stage. We first notice from (20) that the dispersion coefficient  $D_c$  is proportional to the square of the volume flux due to the waves and inversely proportional to the vertical eddy viscosity. This result is analogous to the longitudinal dispersion in pipe flow found by Taylor (1954). The dispersion coefficient  $K$  is given by an expression of the form (see, *e.g.*, Fischer *et al.* 1979, p. 94)

$$K = \frac{d^2 \langle u_d^2 \rangle}{\langle \nu_{tz} \rangle} I \quad (24)$$

where  $d$  is a characteristic length,  $u_d$  is the deviation of the velocity from its cross-sectional average,  $\langle \nu_{tz} \rangle$  is the cross-sectionally averaged mixing coefficient and  $I$  is a dimensionless integral of order 0.1. The angular brackets in (24) represent cross-sectional averaging.

Here  $u_d$ ,  $d$  and  $\langle \nu_{tz} \rangle$  are analogous to our  $U_0$ ,  $h$  and  $\nu_{tz}$  and (20) is analogous to (24). In the present case the contributions to the dispersion also come from the fact that the waves and the fact that the currents are modified by the dispersion which is not the case in simple dispersion of contaminants analyzed by Taylor and others.



We may get a preliminary estimate of the size of the dispersion coefficient relative to  $\nu_{tz}$  by noticing that we typically have (inside the surf-zone)

$$Q_w \sim 0.1 \frac{H^2}{h} \sqrt{gh} \quad (25)$$

$$\frac{H}{h} \sim 0.7 \quad (26)$$

and

$$\nu_{tx} \sim \nu_{tz} \sim 0.01h\sqrt{gh} \quad (27)$$

(see, e.g., Svendsen *et al.* 1987). These estimates imply that

$$D_c \sim 0.08h\sqrt{gh} \quad (28)$$

Comparison of (28) and (27) indicates that with these simplifying assumptions the dispersive effect is about eight times stronger than the lateral mixing. The more detailed calculations of SP92 show that accounting for the actual vertical structure of the undertow enhances this effect approximately by a factor of two. Thus, we see that  $D_c \gg \nu_{tz}$  and we can expect the mixing for the longshore current is dominated by the dispersion.

#### 4. A NUMERICAL EXAMPLE

The numerical example presented below will demonstrate the conclusion of the previous paragraph. In the calculations we have used some simplifying assumptions which do not change the nature of the problem (though they do influence the accuracy of the predictions). These assumptions are:

- Use linear long wave theory to calculate  $S_{xy}$  and  $\alpha_y$ .
- Use  $H \propto h$  inside the surf-zone and  $H \propto h^{-1/4}$  outside the surf-zone.
- Use  $Q_w = 0.1(H^2/h)\sqrt{gh}$ .

The eddy viscosity variation used is given by

$$\nu_{tx} = \nu_{tz} = \begin{cases} 0.01h\sqrt{gh} & \text{inside surf zone} \\ [0.8(h/h_b)^4 + 0.2]\nu_{tb} & \text{outside surf zone} \end{cases} \quad (29)$$

where  $\nu_{tb} = 0.01h_b\sqrt{gh_b}$ . The variation of the eddy viscosity outside the surf-zone represents an estimate based on the assumption that  $\nu_t \propto l\sqrt{k}$  and the measurements of Nadaoka & Kondoh (1982) of the turbulence outside the surf-zone. These measurements show that while the intensity of the turbulence decays seaward of the break point, there is still some residual turbulence even far seaward of the break point (see their figure 9).

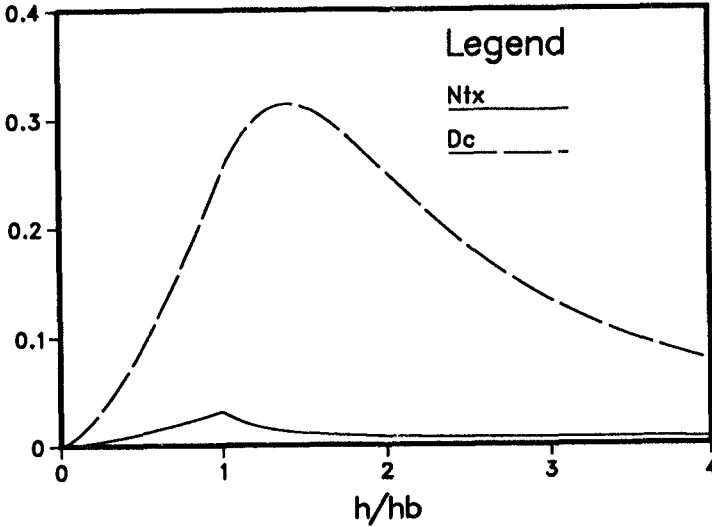


Figure 2: Variation of  $\nu_{tx}$  and  $D_c$

Equation 18 is then solved with boundary conditions  $V_b = 0$  at the shoreline and  $V_b \rightarrow 0$  as  $h/h_b \rightarrow \infty$ . Since the RHS of (18) is discontinuous at the breaker point, the solution has to be matched at that point. The matching conditions used are

$$V_b(x_{b+}) = V_b(x_{b-}) \quad (30)$$

$$\left. \frac{\partial V}{\partial x} \right|_{x_{b+}} = \left. \frac{\partial V}{\partial x} \right|_{x_{b-}} \quad (31)$$

where  $x_b$  represents the breaker location.

Figure 2 shows the variations of the dispersion coefficient and the eddy viscosity with cross-shore location. As mentioned earlier, over the entire nearshore region the dispersion coefficient is significantly larger than the eddy viscosity showing that the dispersion due to current-current interaction totally dominates the nearshore mixing.

The resulting cross-shore distribution of the near bottom longshore current is shown in Figure 3. This figure also shows the solution obtained by neglecting the dispersive mixing. A comparison of the two solutions demonstrates, as expected from the enhanced mixing due to current-current interaction, that the dispersion has significant influence on the cross-shore structure of the longshore current. Specifically, we see that accounting for the current dispersion does bring the

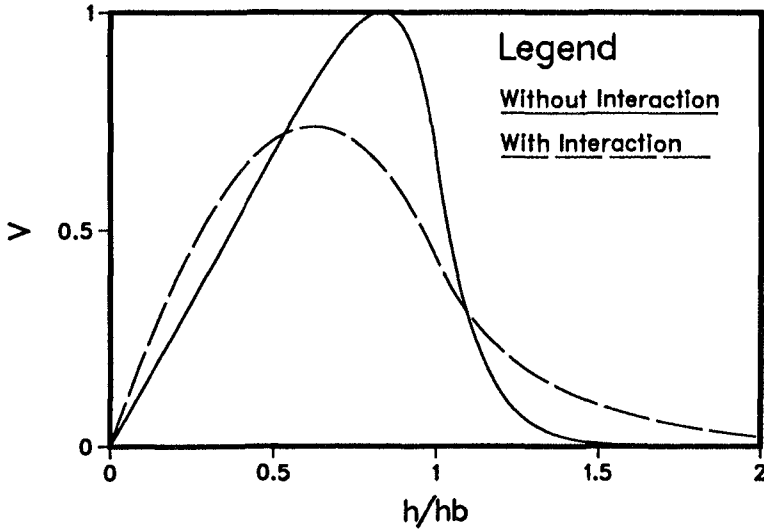


Figure 3: Cross-shore distribution of the near bottom longshore current

cross-shore distribution in line with what the measurements indicate without having to take recourse to a large mixing coefficient (see, *e.g.*, Visser 1984).

Once  $V_b$  is calculated, we may calculate the longshore current profiles using (11) and (13). The profiles so calculated are shown in figure 4. We first notice that the individual longshore current profiles do not show very strong variation with vertical location. This means that the cross-shore distribution of the near bottom longshore current shown in figure 3 is representative of all vertical locations. Second, we notice that the longshore current increases with distance from the bed in the region  $0 < h/h_b < 0.7$  while it decreases with distance from the bed in the region  $h/h_b > 0.7$ . As demonstrated in the next section, this turns out to be the essential feature that is responsible for the dispersion.

The only experimental investigation that reports systematic measurements of the vertical structure of longshore currents is Visser (1984) for a long, straight beach. These measurements consistently confirm the pattern predicted above. As an example, we reproduce in figure 5 one set of Visser's measurements (experiment 2). The measurements clearly show a longshore current increasing with distance from the bed inside the surf-zone (the first four panels) and decreasing with distance from the bed outside (last four panels). Considering the crucial dependence of the dispersion on this trend we believe that the experimental confirmation of the trend predicted by the computations is extremely encouraging.

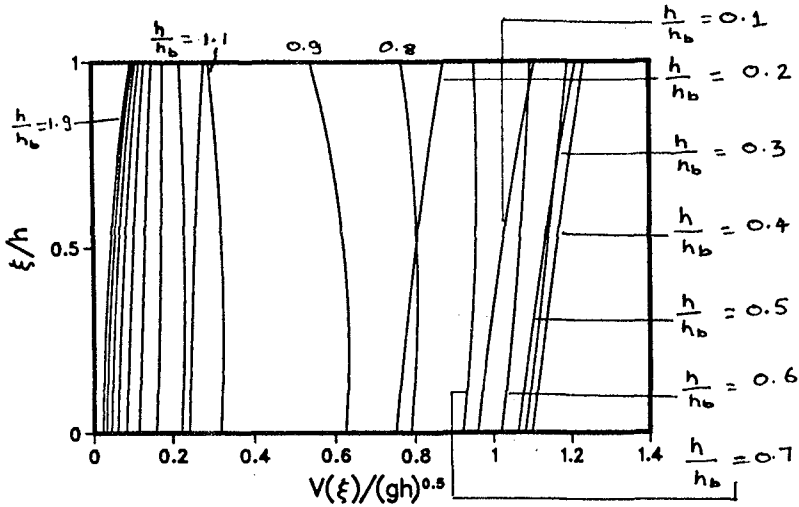


Figure 4: Computed vertical variation of the longshore current

5. QUALITATIVE INTERPRETATION OF THE DISPERSION MECHANISM

Equation 17 shows that the dispersion coefficient,  $D_z$ , originates from the  $U\partial V/\partial x$  term in the forcing for the depth variation for the longshore currents. Since this term contributes to the curvature of the longshore current which, in turn, contributes to the overall slope of the longshore current profile it suggests that it is the overall slope of the longshore current that controls the dispersion. This is discussed further below.

As remarked in the discussion below (16) the contributions from below and above trough levels counteract one another. The overall effect depends on which of the two is stronger. We see that (15) and (16) may be written as

$$\int_{-h_0}^{\bar{\zeta}} UV dz = -Q_w \left( \frac{1}{h} \int_{-h_0}^{\bar{\zeta}} V(z) dz \right) \tag{32}$$

and

$$\int_{\bar{\zeta}}^{\zeta} V u_w dz = Q_w V(\bar{\zeta}) \tag{33}$$

Thus for the undertow variation used here the contribution from above trough level will dominate if

$$V(\bar{\zeta}) > \frac{1}{h} \int_{-h_0}^{\bar{\zeta}} V(z) dz \tag{34}$$

This corresponds to a longshore current that increases with distance from the bottom (figure 6a) which, as figure 4 shows, occurs for  $h/h_b < 0.7$  in the ex-

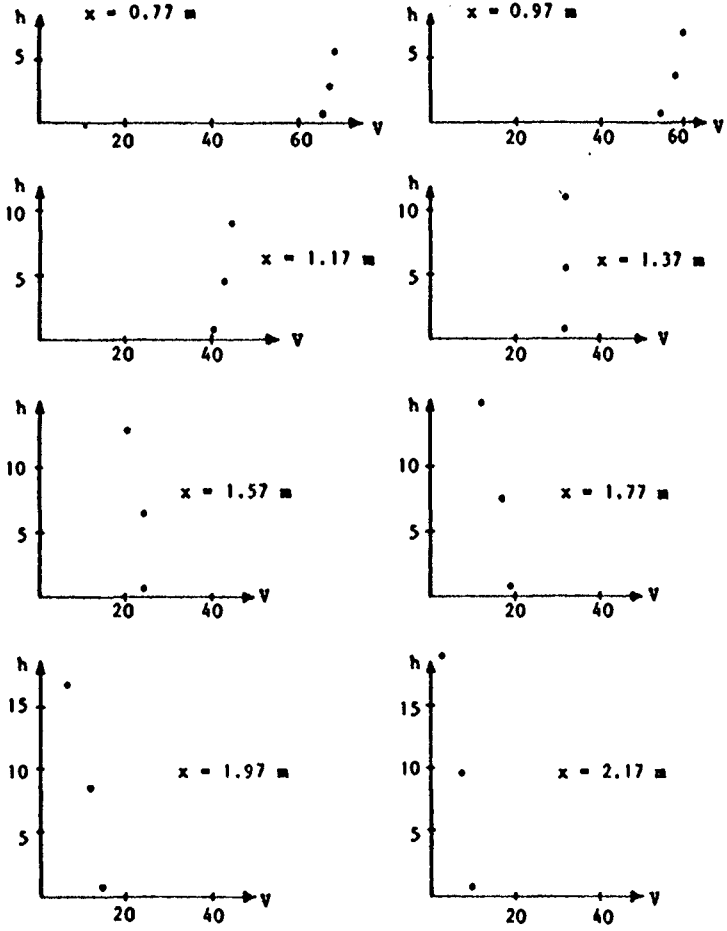


Figure 5: Measured vertical variation of the longshore current (from Visser 1984)

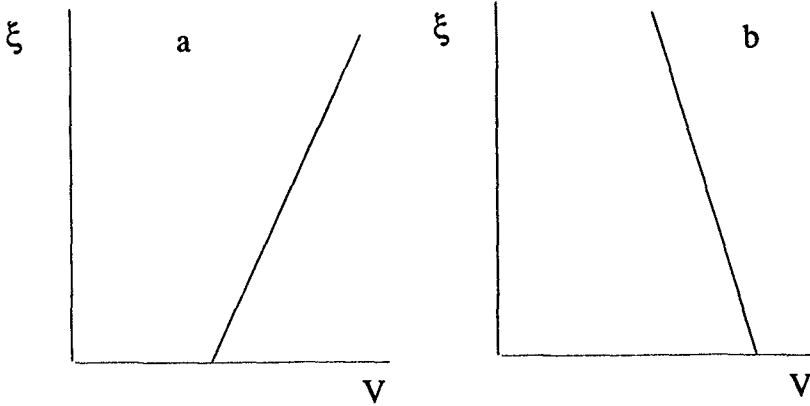


Figure 6: Sketch of the vertical variation of the longshore current  
 a)  $V(\bar{z}) > \frac{1}{h} \int_{-h_0}^{\bar{z}} V(z) dz$       b)  $V(\bar{z}) < \frac{1}{h} \int_{-h_0}^{\bar{z}} V(z) dz$

ample considered. Hence, in this region the net effect of the interaction is to convect the longshore current momentum shorewards and depending on the sign of  $\partial V/\partial x$  this may increase or decrease the local value of  $V$ . Though the shoreward transport of the longshore momentum is at the surface with a smaller seaward transport below, the profile is maintained by the driving force and the vertical mixing. Conversely, in the region  $h/h_b > 0.7$  (in the present example) the situation is reversed. In particular, outside the surf-zone this represents the major source of longshore momentum flux in the seaward direction which is equivalent to mixing.

Hence, although the cross-shore transport of the longshore momentum (equivalent to dispersion or mixing) is provided by cross-shore currents, the net effect depends crucially on the vertical variation of the longshore currents. This is also consistent with the fact that for depth uniform longshore currents we get no dispersion effects.

## 6. SUMMARY AND CONCLUSIONS

It has been demonstrated that the dispersive mixing caused by the interaction of the longshore currents and the undertow totally dominates the mixing in the nearshore region. Even inside the surf-zone it is an order of magnitude stronger than the direct turbulent mixing. In the example given in section 4, the effect was calculated for the simplest possible case which leads to a non-zero value, *viz.*, a depth uniform undertow and a longshore current that varies quadratically with

the vertical coordinate. It turns out that even though the example considered here underestimates the dispersive effect substantially in comparison to the more complete version of the theory given in SP92, it captures the essential nature of the dispersion mechanism and allows us to demonstrate the same in a rather simple manner.

The results show that the nearshore circulation on a beach is essentially a 3D phenomenon with the dispersion caused by the nonlinear interaction of the nearshore currents being a very important contribution. It depends crucially on the vertical profiles of the current, in particular in the longshore direction. While the turbulence contributes very little to the lateral mixing directly it is still very important because the turbulence has a strong influence on the shape of the current profiles.

The existing laboratory measurements support our predictions of the vertical structure of the currents which forms a part of the results. This is very encouraging considering the crucial dependence of the effect on the current profiles. More confirmation of the predictions, both in the laboratory and the field, would be particularly useful.

#### ACKNOWLEDGEMENTS

This work is a result of research sponsored by NOAA Office of Sea Grant, Department of Commerce, under Grant No. NA86AA-D-SG040 (Project No. R/OE-6). The U.S. Government is authorized to produce and distribute reprints for government purposes notwithstanding any copyright notation that may appear herein.

#### REFERENCES

- Bowen, A. J., 1969. The generation of longshore currents on a plane beach. *Journal of Marine Research*, 27, pp. 206-215.
- Dally, W. R. and R. G. Dean, 1984. Suspended sediment transport and beach profile evaluation. *Journal of Waterway, Port, Coastal and Ocean Engineering*, ASCE, 110, pp. 15-33.
- Elder, J. W., 1959. The dispersion of marked fluid in turbulent shear flow. *Journal of Fluid Mechanics*, 5, pp. 544-560.
- Fischer, H. B., 1978. On the tensor form of the bulk dispersion coefficient in a bounded skewed shear flow. *Journal of Geophysical Research*, 83, pp. 2373-2375.
- Fischer, H.B., E. J. List, R. C. Y. Koh, J. Imberger and N. H. Brooks, 1978. *Mixing in Inland and Coastal Waters*. Academic Press Inc., Orlando. 483 pp.
- Longuet-Higgins, M. S., 1970. Longshore currents generated by obliquely incident sea waves. Parts 1 and 2. *Journal of Geophysical Research*, 75, pp. 6778-6789 and pp. 6790-6801.

Liu, P. L.-F. and R. A. Dalrymple, 1978. Bottom frictional stresses and longshore currents due to waves with large angles of incidence. *Journal of Marine Research*, 36, pp. 357-375.

Mei, C. C. 1983. *The applied dynamics of ocean surface waves*. John Wiley and Sons, New York, 740 pp.

Nadaoka, K. and T. Kondoh, 1982, Laboratory measurements of velocity field structure in the surf zone by LDV. *Coastal Engineering in Japan*, 25, pp. 125-145.

Phillips, O. M., 1977. *The dynamics of the upper ocean*. Cambridge University Press, 336 pp.

Stive, M. J. F. and H. G. Wind, 1986. Cross-shore mean flow in the surf-zone. *Coastal Engineering*, 10, pp. 325-340.

Svendsen, I. A., 1984. Mass flux and undertow in a surf-zone. *Coastal Engineering*, 8, pp. 347-365.

Svendsen, I. A. 1987. Analysis of surf zone turbulence. *Journal of Geophysical Research*, 92, pp. 5115-24.

Svendsen, I. A. and J. B. Hansen, 1988. Cross-shore currents in surf-zone modelling. *Coastal Engineering*, 12, pp. 23-42.

Svendsen, I. A. and R. S. Lorenz, 1989. Velocities in combined undertow and longshore currents. *Coastal Engineering*, 13, pp. 55-79.

Svendsen, I. A. and U. Putrevu, 1990. Nearshore circulation with 3-D profiles. *Proceedings of the 22nd Coastal Engineering Conference*. pp. 241-254.

Svendsen, I. A. and U. Putrevu, 1992. *Nearshore Mixing and Dispersion*. Submitted for publication.

Svendsen, I. A., H. A. Schaffer and J. B. Hansen, 1987. The interaction between the undertow and boundary layer flow on a beach. *Journal of Geophysical Research* 92, pp. 845-856.

Taylor, G. I., 1954. The dispersion of matter in a turbulent flow through a pipe. *Proceedings of the Royal Society of London. Series A*, 219, pp. 446-468.

Thornton, E. B., 1970. Variation of longshore current across the surf zone. *Proceedings of the 12th Coastal Engineering Conference*, pp. 291-308.

Visser, P. J., 1984. A mathematical model of uniform longshore currents and comparison with laboratory data. *Communications on Hydraulics. Report 84-2*, Department of Civil Engineering, Delft University of Technology, 151 pp.



## CHAPTER 212

### Formation and Reduction Processes of River Deltas ; Theory and Experiments

Hossam El-din A.A. Refaat<sup>1</sup> and Yoshito Tsuchiya<sup>2</sup>, M.ASCE

#### Abstract

Beach erosion has recently been recognized as accelerating due to change in sediment sources from rivers. This can be considered as reduction processes of river deltas. In this paper, the formation and reduction processes of river deltas are first investigated theoretically by introducing the non-uniformity of longshore sediment transport into the equation of continuity of shoreline changes. Theoretical solutions to shoreline changes in the formation and reduction processes are well explained. Secondly, experiments both on the formation and reduction processes were carried out. The theoretical results of the processes compared favorably with the experimental ones.

#### 1. Introduction

Delta resulted from the relative importance of deposition of river sediments which build the delta seaward, versus the action of waves and currents which transport the sediments and erode the delta. If the rate of sediment deposition from the river is greater than the rate of sediment removal by the longshore currents, the formation process of river delta will take place. On the contrary, if the rate of sediment deposition from the river is less than the rate of sediment removal by the longshore currents, beach erosion occurs resulting in the reduction of river delta. Historically, the term *delta* was first applied by the Greek historian Herodotus, circa 450 B.C., to the triangular alluvial deposit at mouth of the Nile River.

The processes of formation and reduction of river deltas have been investigated through the study of analytical solutions of the so-called one-line theory. The one-line theory was first introduced by Pelnard-Considére (1956), and it has been demonstrated to be adequate in practical applications. Several authors have presented analytical solutions for the one-line theory (e.g. Bakker and Edelman, 1964; Iwagaki, 1966; Tsuchiya, 1973, 1978; Tsuchiya and Yasuda, 1979; Kraus, Hanson and Harikai, 1985; and recently Hanson and Larson, 1987). The fundamental assumption of this theory is that the bottom profile moves in parallel to itself without changing shape. The second major assumption of the theory is that the longshore sediment transport takes place averaging over the beach profile down to a certain offshore limiting depth of the sediment drift zone.

---

<sup>1</sup>Assistant Professor, Faculty of Engineering, Cairo University, Giza, Egypt.

<sup>2</sup>Professor, DPRI, Kyoto University, Gokasho, Uji, Kyoto 611, Japan.

2. Theory of Formation and Reduction Processes of River Deltas

In the formation and reduction processes of river deltas, the non-uniformity of longshore sediment transport along the shoreline must be introduced. Tsuchiya and Refaat (1992) recently developed theoretical approaches to the longshore sediment transport in the non-uniform condition. Introducing this theoretical formulation of the total rate of non-uniform longshore sediment transport, a set of the governing equations of shoreline change is proposed.

2.1 The governing equations and the field equations of delta formation process

The equations governing the formation and reduction processes of river deltas are composed of the equations of continuity of shoreline change and total rate of longshore sediment transport. Taking the coordinate system as shown in Fig. 1, the equation of continuity of shoreline change is expressed as (Tsuchiya ; 1978) :

$$\frac{\partial y_0}{\partial t} + \frac{1}{(1-\lambda)h_k} \frac{\partial Q_x}{\partial x} = \frac{1}{B h_k} Q_R(t) \delta(x-x_0) \tag{1}$$

in which  $y_0$  is the shoreline position from the datum line,  $x$  is the longshore distance from the origin,  $t$  is the time,  $\lambda$  is the porosity of beach sediment,  $h_k$  is the limited water depth of littoral drift,  $B$  is the river width,  $Q_x$  is the total rate of longshore sediment transport, and  $Q_R(t) \delta(x-x_0)$  is the sediment input effective to the shoreline change from a river located at  $x=x_0$  where  $\delta(x-x_0)$  is Dirac's delta function.

The phenomenon of longshore sediment transport around the river deltas are non-uniform owing to the non-uniform characteristics of waves and the effect of the boundary conditions of both longshore currents and beach changes on the longshore sediment transport. The equation of longshore sediment transport in the unsteady, nonuniform condition is given by Tsuchiya and Refaat (1992) as:

$$\frac{\partial Q_x}{\partial t} + \frac{\alpha_2}{\alpha_1 k} \frac{\partial}{\partial x} \left[ \frac{Q_x}{h_b} \right] = k f(x) - \frac{\alpha_3 \sqrt{g} \gamma C_f}{\alpha_1 \sqrt{h_b}} Q_x \tag{2}$$

where

$$f(x) = \frac{\gamma^2}{16} g h_b^2 \left\{ \sin 2\alpha_b - 2 \cos^2 \alpha_b \frac{\partial y_b}{\partial x} - (5\beta_1 - 6\beta_2 + 6\beta_3 \sin^2 \alpha_b) \frac{\partial h_b}{\partial x} - 2\beta_3 h_b \sin 2\alpha_b \frac{\partial \alpha_b}{\partial x} \right\} \tag{3}$$

where  $\alpha_b$  is the breaker angle which is defined as the angle between the wave crest and the shoreline,  $t$  is the time,  $g$  is the acceleration of gravity,  $y_b$  is the offshore distance of the breaking point from the shoreline,  $k$ ,  $\alpha_i$  and  $\beta_i$  ( $i = 1, 2, 3$ ), are the coefficients being nearly constants (Tsuchiya and Refaat, 1992).

In order to express the total rate of longshore sediment transport by a function of the breaker angle and breaker depth, and their derivatives, it can be expressed by Taylor series up to the first order as:

$$Q_x = Q_0 + \frac{\partial Q_x}{\partial \alpha_{b0}} (\alpha_b - \alpha_{b0}) + \frac{\partial Q_x}{\partial h_{b0}} (h_b - h_{b0}) + \dots \tag{4}$$

in which  $Q_0$  denotes the total rate of longshore sediment transport at the initial wave conditions presented by the subscript 0. Reference Fig. 1 the small changes in the breaker angle and depth can be expressed geometrically as:

$$\Delta \alpha_b = \alpha_b - \alpha_{b0} \approx - \frac{\partial y_0}{\partial x} \quad \text{and} \quad \Delta h_b = m \Delta y_0 \tag{5}$$

Substituting Eqs. (4) and (5) to Eq. (1) yields

$$\frac{\partial y_0}{\partial t} + \epsilon_1 \frac{\partial y_0}{\partial x} - \epsilon_2 \frac{\partial^2 y_0}{\partial x^2} = q_R(t) \delta(x - x_0) \tag{6}$$

where

$$\epsilon_1 = \frac{m}{(1 - \lambda) h_k} \left( \frac{\partial Q_x}{\partial h_b} \right)_{h_{b0}}, \quad \epsilon_2 = \frac{1}{(1 - \lambda) h_k} \left( \frac{\partial Q_x}{\partial \alpha_b} \right)_{\alpha_{b0}},$$

$$\text{and } q_R(t) = \frac{1}{B h_k} Q_R(t) \tag{7}$$

The coefficient  $\epsilon_2$  which has the dimensions of length squared over time, is interpreted as a diffusion coefficient. While the coefficient  $\epsilon_1$  having the dimension of length over time, is interpreted as the traveling speed of shoreline towards the longshore direction. In Eq. (7) it is clearly seen that the coefficient  $\epsilon_1$  is proportional to the beach slope. Thus, the coefficient  $\epsilon_1$  can not be ignored when the beach slope changes along the delta. By specifying initial and boundary conditions in the areas which represent conditions prevailing in a specific shoreline evolution, the analytical solutions are directly applicable.

2.2 Solution to shoreline changes in the formation process of river delta by normally incident waves

Since the river delta has an infinite length and waves are approached the shoreline normally, the coefficient  $\epsilon_1$  becomes very small and can be neglected. The general solution of river delta formation can be expressed from Eq. (6) (Carslaw and Jaeger, 1959) as:

$$y_0(x, t) = h_k q_{R0} \sqrt{\frac{t}{\epsilon_2}} \text{jerfc} \left( \frac{x - x_0}{2 \sqrt{\epsilon_2 t}} \right) \quad \text{for } t > 0 \text{ and } -\infty < x < \infty \tag{8}$$

where jerfc denotes the integral of the complementary error function erfc.

In Fig. 2 the solution to Eq. (8) is illustrated. The dimensionless sediment input used to normalize the shoreline position is expressed as:

$$\frac{h_k q_{R0}}{\epsilon_2} = \frac{q_{R0}}{\left( \frac{\partial Q_x}{\partial \alpha_b} \right)_{\alpha_{b0}}} \tag{9}$$

which can be interpreted as a ratio of the sediment input from the river to the derivative of longshore sediment transport rate with respect to the breaker angle.

2.3 Solution to shoreline change in the formation process of river delta by obliquely incident waves

When the waves approach the delta coast obliquely, the expected shape of the delta will be asymmetric. Consider the case where a river mouth has a finite width,  $2a$ , the continuity equation of sediment transport in the full form of Eq. (6) is applied as:

$$\frac{\partial y_{01}}{\partial t} = -\epsilon_1 \frac{\partial y_{01}}{\partial x} + \epsilon_2 \frac{\partial^2 y_{01}}{\partial x^2} + q_{R0} ; -a \leq x \leq a \tag{10}$$

and

$$\frac{\partial y_{02}}{\partial t} = -\epsilon_1 \frac{\partial y_{02}}{\partial x} + \epsilon_2 \frac{\partial^2 y_{02}}{\partial x^2} ; |x| > a \tag{11}$$

The problem consists of two coupled partial differential equations. By specifying the boundary conditions, which are the beach must be continuous at all times over the two zones and the shoreline is unaffected by the sediment input from the river as  $x$  approaches infinity. The solution to Eqs. (10) and (11) are then obtained as:

$$y_0(x, t) = \begin{cases} \exp\left[\frac{3\epsilon_1}{2\epsilon_2}x\right] F_1(x, t) ; & -\infty < x \leq -a \\ \exp\left[\frac{3\epsilon_1}{2\epsilon_2}x\right] F_2(x, t) ; & -a \leq x \leq 0 \\ \exp\left[-\frac{\epsilon_1}{2\epsilon_2}x\right] F_2(x, t) ; & 0 \leq x \leq a \\ \exp\left[-\frac{\epsilon_1}{2\epsilon_2}x\right] F_1(x, t) ; & a \leq x < \infty \end{cases} \tag{12}$$

where

$$F_1(x, t) = 2q_{R0}t \left\{ j^2 \operatorname{erfc}\left(\frac{x-a}{2\sqrt{\epsilon_2 t}}\right) - j^2 \operatorname{erfc}\left(\frac{x+a}{2\sqrt{\epsilon_2 t}}\right) + \frac{\epsilon_1 a}{\epsilon_2} j^3 \operatorname{erfc}\left(\frac{x-a}{2\sqrt{\epsilon_2 t}}\right) - \frac{\epsilon_1 a}{\epsilon_2} j^3 \operatorname{erfc}\left(\frac{x+a}{2\sqrt{\epsilon_2 t}}\right) \exp\left(-\frac{\epsilon_1}{\epsilon_2}a\right) \right\} \tag{13}$$

and

$$F_2(x, t) = q_{R0}t \left\{ 1 - 2j^2 \operatorname{erfc}\left(\frac{a-x}{2\sqrt{\epsilon_2 t}}\right) - 2j^2 \operatorname{erfc}\left(\frac{a+x}{2\sqrt{\epsilon_2 t}}\right) + \frac{2\epsilon_1 a}{\epsilon_2} j^3 \operatorname{erfc}\left(\frac{x-a}{2\sqrt{\epsilon_2 t}}\right) - \frac{2\epsilon_1 a}{\epsilon_2} j^3 \operatorname{erfc}\left(\frac{x+a}{2\sqrt{\epsilon_2 t}}\right) \exp\left(-\frac{\epsilon_1}{\epsilon_2}a\right) \right\} \tag{14}$$

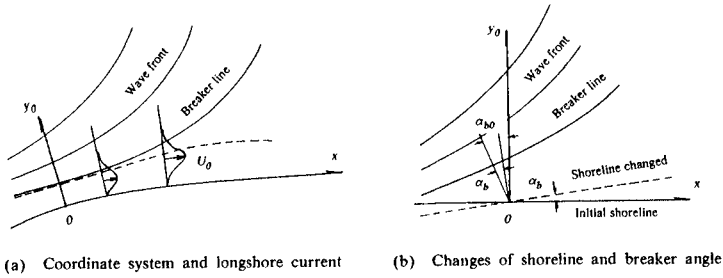


Fig. 1. The coordinate system used in the formation.

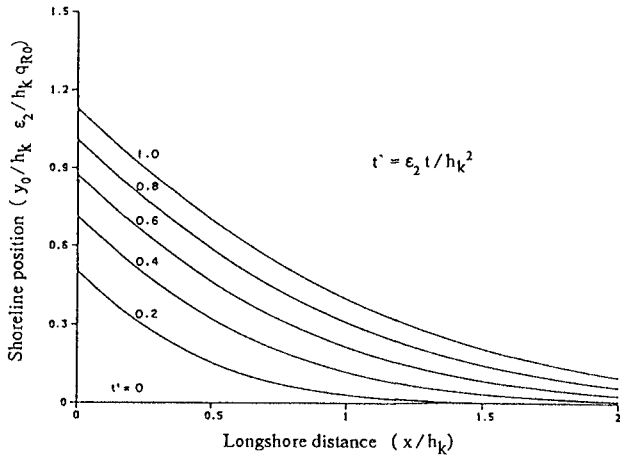


Fig. 2. Shoreline evolution in the formation of river delta of infinite length.

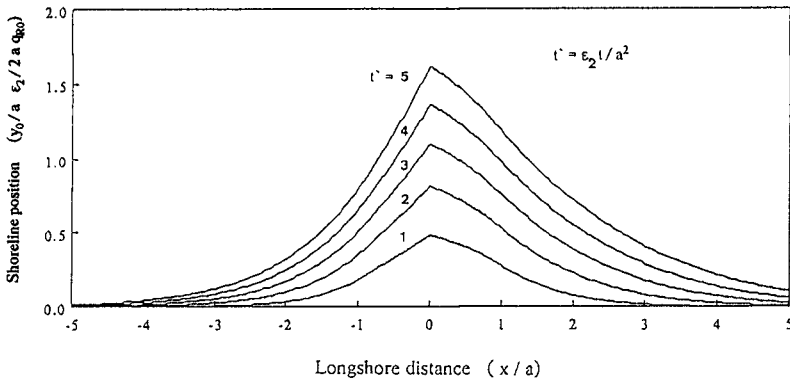


Fig. 3. Shoreline evolution in the formation of river delta by obliquely incident waves

The function  $\text{ierfc}$  is the integral of the complementary error function and  $n$  exponent represents  $n$  time integrations of the complementary error function. The time evolution of river delta by Eq. (12) is illustrated in Fig. 3. It is well understood in this figure that the asymmetric plane shape of the delta is clearly formed by obliquely incident waves.

**2.4 Solution to shoreline changes in the reduction process of river delta**

The reduction process of river delta occurs due to decrease or lack of sediment deposit from the river. Generally, the basic equations describe the shoreline changes in reduction process of river delta are the same equations used to describe the shoreline changes in formation process of river delta except that the river sediment discharge is no longer considered. Therefore, the linear partial differential equation described the shoreline change is given as:

$$\frac{\partial y_0}{\partial t} + \epsilon_1 \frac{\partial y_0}{\partial x} - \epsilon_2 \frac{\partial^2 y_0}{\partial x^2} = 0 \tag{15}$$

By specifying the initial and boundary conditions in the areas which represent conditions prevailing in a specific shoreline evolution, the corresponding analytical solutions are directly applicable. In the following cases of reduction of river delta, the initial shoreline position will be determined with the aid of the formation process of river delta.

**(1) Reduction of river delta of infinite length by normal incident waves**

Since the river delta has an infinite length and waves are assumed to approach the shoreline normally, the coefficient  $\epsilon_1$  becomes very small and can be neglected. Also, the reduction process will take place symmetrically with respect to the center of the river delta. Thus, the solution to shoreline changes is obtained as:

$$y_0(x, t) = \frac{h_k q_R}{2 \epsilon_2 \sqrt{\pi}} \sqrt{\frac{A}{t}} \int_{-\infty}^{\infty} \text{ierfc} \left( \frac{x'}{2 \sqrt{\epsilon_2 A}} \right) \exp \left\{ -\frac{(x-x')^2}{4 \epsilon_2 t} \right\} dx' \tag{16}$$

In Fig. 4 the solution to Eq. (16) is illustrated. In this figure the reduction

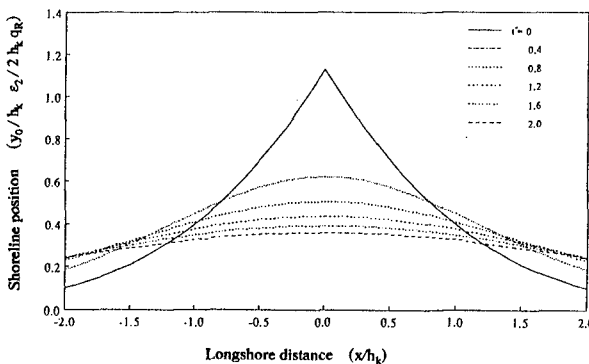


Fig. 4. Time variation of shoreline change in the reduction process of river delta of infinite river length.

process of river delta is taking place symmetrically with respect to the center of the river. The rate of reduction of river delta at the center of the river is diminished with time, while the shoreline at the longshore ends of the river delta is replenished with time. The final stage for the configuration of the delta will become a straight beach.

(2) Asymmetric change of shoreline position of river delta

When the waves approach the coast of river delta obliquely, the shoreline change is expected to occur asymmetrically. Consider the case where the river mouth has a finite width,  $2a$ , the general solution to shoreline change is obtained as:

$$y_0(x, t) = z_0(x, t) \exp\left(\frac{\epsilon_1}{2\epsilon_2} x - \frac{\epsilon_1^2}{4\epsilon_2} t\right) \quad \text{for } t > 0 \text{ and } -\infty < x < \infty \quad (17)$$

where

$$z_0(x, t) = \frac{1}{2\sqrt{\pi\epsilon_2 t}} \left[ \int_{-\infty}^{-a} F_1(x') \exp\left\{-\frac{(x-x')^2}{4\epsilon_2 t} + \frac{\epsilon_1 x'}{\epsilon_2}\right\} dx' + \int_{-a}^0 F_2(x') \exp\left\{-\frac{(x-x')^2}{4\epsilon_2 t} + \frac{\epsilon_1 x'}{\epsilon_2}\right\} dx' + \int_0^a F_2(x') \exp\left\{-\frac{(x-x')^2}{4\epsilon_2 t} - \frac{\epsilon_1 x'}{\epsilon_2}\right\} dx' + \int_a^{\infty} F_1(x') \exp\left\{-\frac{(x-x')^2}{4\epsilon_2 t} - \frac{\epsilon_1 x'}{\epsilon_2}\right\} dx' \right] \quad (18)$$

In Fig. 5 the solution to Eq. (18) is illustrated. The asymmetric shape of the delta is clearly seen in this figure. Since the waves approach the shoreline obliquely, the longshore sediment is predominant. Consequently, most of the sediment moves in the predominant direction of littoral drift. As a result, the

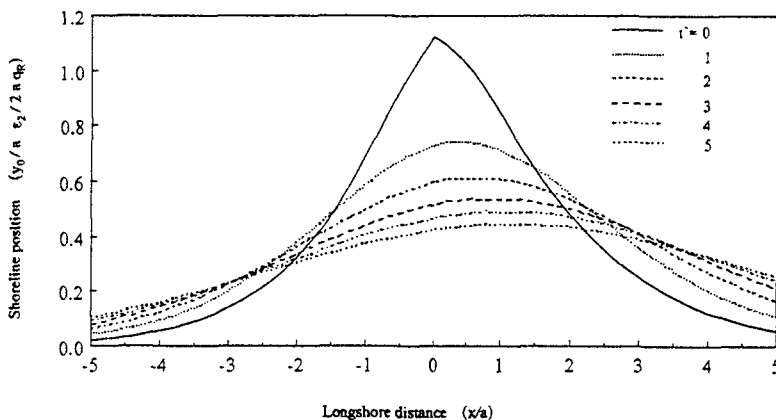


Fig. 5. Time variation in shoreline change in the reduction process of river delta by obliquely incident waves in the case where  $\epsilon_1 a / \epsilon_2 = 0.2$ .

reduction rate of the shoreline on the upcoast side is greater than that on the downcoast. The final stage for the configuration of the delta may become an inclined straight beach which the waves tend to approach normally. Also, the river mouth moves predominantly in the direction of littoral drift, as the reduction process of river delta takes place.

### 3. Experiments on Formation and Reduction Processes of River Deltas

The main objectives of this experimental study are, to demonstrate the process of formation and reduction of river deltas, to determine the changes of beach profile along the shoreline of river delta, and finally to study the effect of oblique wave incident on the symmetrical configuration of the river delta, and on the formation and reduction processes of river deltas.

#### 3.1 Experiments on Formation Process of River Deltas

##### (1) Experimental setup

The experiments were performed in the fan-shaped wave basin (semicircular part :  $r=17.5$  m ; rectangular part :  $35 \times 10$  m) of Ujigawa Hydraulics Laboratory, Disaster Prevention Research Institute, Kyoto University. A smooth concrete beach was constructed with a slope of 1:10. The beach was roughed by bonding light weight aggregate, the same material as the one whose used for modeling river sediment discharge, on to the smooth concrete. The wave guide walls, which are composed of smooth steel plates, were installed in the normal to the wave generator. On the land side, a sediment feeder machine with a controlling speed motor discharging sediment at a constant rate, was set about 1.0 m from the initial shoreline. Two smooth asbestos pipes were connected to the sediment feeder machine at the output opening in order to carry the sediment to the desire position of the point source, (see Fig. 6).

##### (2) Experimental procedure

Measurements of sediment discharge rate were performed: 1) at the beginning of the experiments, and 2) at every 10 min interval time during the experiments, then the rate of sediment discharge was calculated as the average value of the measured sediment ratios. Measurements of shoreline positions were made at 10 min intervals along the delta at 13 stations (50 cm interval distance), see Figure 12. At the end of each experiment, beach profiles as well as shoreline changes were measured every 10 cm interval distance along the delta. The formation process of river delta was observed by taking photographs every 10 minutes interval time.

Measurements of wave heights in the constant depth part were made using capacitance type wave gauges. While on the sloping part, the measurements were made using a wave gauge mounted on a carriage controlled by a personal computer. The angles of incoming wave incidence were measured in the constant depth part by measuring the angles of inclination of the wave generator to the beach. Snell's law and linear wave theory were used to estimate the angles of wave incidence at the breaker line. The longshore currents were visually observed by using colored paper tracers.

##### (3) Experimental results

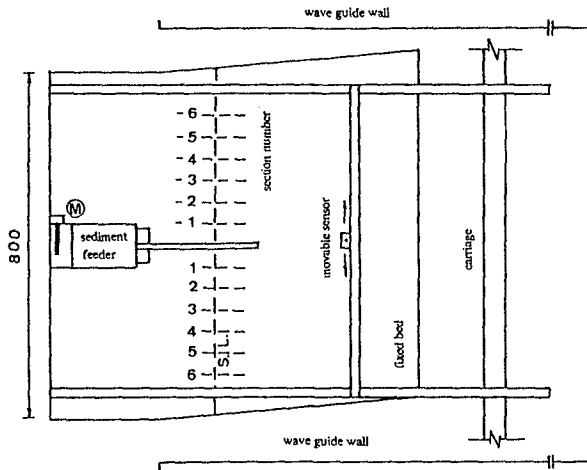
Six experiments were performed, (see Table 1), for a still water depth in the constant depth part of 30 cm, a wave height of 2.0 cm and a wave period of 0.8 sec. The incoming waves were normally incident during the experiments series A and series B, while they were oblique incident during experiments C-1 and D-1, with  $7.5^\circ$  and  $15^\circ$ , respectively. The experimental results are drown as follows :



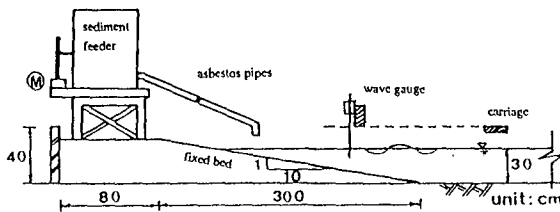
a) **General description of the formation process;** Once the sediment feeder machine supplies sediment to the wave basin, the sediment particles spread along the coast by the effect of the longshore current. Figure 7 shows the behaviors of the growth of river delta in experiments series A. The configuration of the shoreline of river delta in this experiment is nearly symmetric with respect to the center of the river.

Table 1. Experimental conditions of formation process of river delta.

Run	No.	$Q_s$ cm <sup>3</sup> /sec	Run time (min)	$\alpha_0$ (deg.)
Series A	A-1	7.06	50	0
	A-2	7.06	30	0
Series B	B-1	15.08	30	0
	B-2	8.12	30	0
Series C	C-1	11.0	90	7.5
Series D	D-1	11.0	180	15.0



(a) Plane view.



(b) Side view.

Fig. 6. Schematic diagram of experimental arrangement of formation and reduction processes of river deltas.

b) River delta configuration in case of oblique wave incidence; In the case of oblique wave incident, an asymmetrical shape of river delta is expected. Figure 8 illustrates the measured data of shoreline positions in Run C-1 where the angle of wave incident is  $7.5^\circ$ . The black symbols represent the measured data at the upcoast side, whereas the measured data at the downcoast side are represented by the white symbols. It is clear that asymmetrical river deltas are formed in the case of oblique wave incidence. In general, oblique waves generate strong longshore currents, consequently, most of the river sediment discharge is moved in the predominant direction of littoral drift and deposited on the downcoast side. Therefore, the growth rate of the shoreline on the downcoast side is faster than that on the upcoast side.

c) Variation of beach profile and beach slope along a delta coast; The beach profiles measured along the river delta for experimental Run A-2,  $t = 80$  min, for the selected sections are illustrated in Fig. 9. It is seen from this figure that the beach profiles are convex in shape.

Figure 10 demonstrates the variation of beach slope along the river delta for Run B-1,  $t = 30$  min, represented by a white symbol, and Run B-2,  $t = 60$  min, represented by a black symbol, respectively. It is obvious from this figure that; 1) in Run B-1, the beach slope around the river mouth is steeper than the beach slope at the longshore ends of the river delta, where the configuration of river delta was also sharply curved, and 2) when the rate of river sediment input was reduced by half in Run B-2, the configuration of the shoreline of the river delta changed, becoming more gently curved, and therefore the variation of beach profiles along the river delta lessened.

#### (4) Applicability of analytical solutions to experiments

The measurements of shoreline evolution of a river delta for experimental runs A-1 and A-2 are compared with the analytical solution given by Eq. (8), the results are shown in Fig. 11. It is seen from the comparison that the evolution of the shoreline near the river mouth is well predicted. However, near the longshore ends of the river delta less agreement between the measured and computed shoreline position is observed. This may be due to the effect of the roughness of fixed bed in the wave tank, which induced rapid transport of the sediment downcoast, causing the shoreline to rapidly decrease.

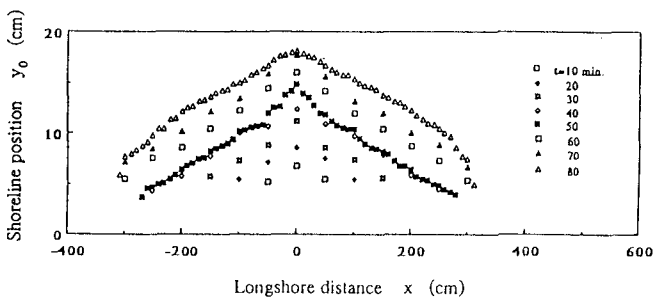


Fig. 7. Accretion process of shoreline in the formation of river delta in the case of Series A.

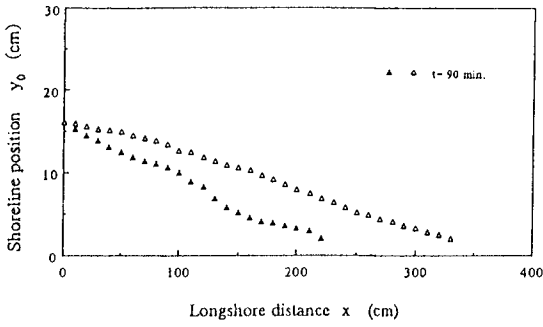


Fig. 8. Asymmetrically of river delta configuration in the case of oblique wave incidence, Run C-1.

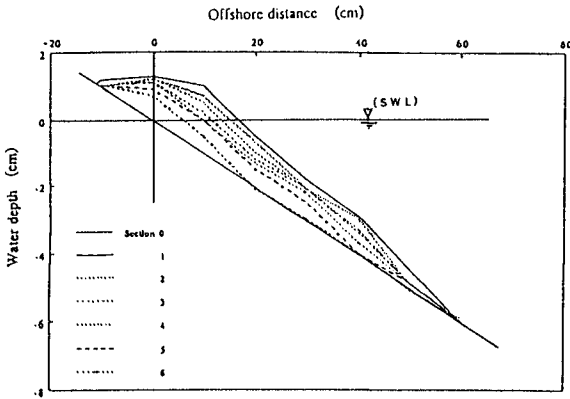


Fig. 9. Variation of beach profiles formed along the shoreline of river delta in the formation process, Run A-2.

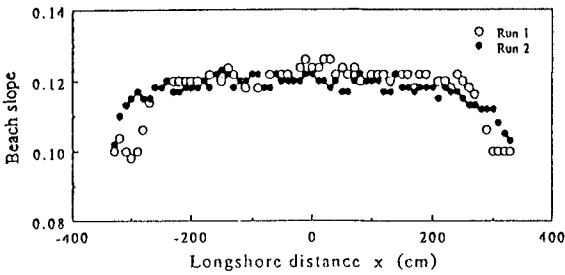


Fig. 10. Longshore changes in beach slope at the shoreline along the river deltas in the case of Series B.

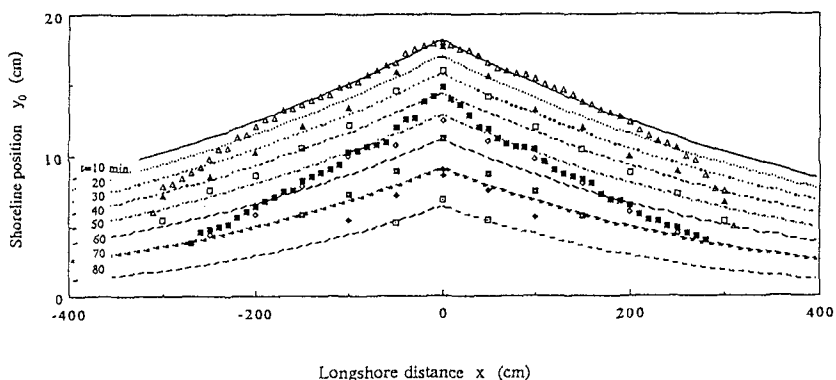


Fig. 11. Comparison between theoretical and experimental shorelines in the formation process of a river delta.

### 3.2 Experiments on Reduction Process of River Deltas

#### (1) Experimental procedure

The initial shoreline and beach profile in this experiment simulated the final ones in the experiment of the formation process of river delta presented in the previous section, (Series A and B). An experiment was halted once no remarkable longshore current existed, with only cross-shore movement. To verify this condition, color tracers were used and the trajectories were observed. Measurements of shoreline changes were made in the same way as in the formation process of river delta.

#### (2) Experimental results

Two experiments were performed, A-3 and B-3, with a still water depth of 30 cm, a wave height of 2.0 cm and a wave period of 0.8 sec. The incoming waves were normally incident during the experiments.

a) General description of river delta reduction process; The reduction process of the river delta is significantly different from the formation process of the river delta. Figure 12 shows the process of river delta reduction for experiment A-3. Due to the lack of sediment input, the shoreline of the delta rapidly becomes to a nearly straight, resulting in erosion near the center of river delta and deposition near the longshore ends of the river delta.

b) Variation of beach profiles; The variation of the beach profiles at selected experiment A-3, is shown in Fig. 13. It is noted that the beach profile changes from a convex type which was in the formation process to a concave one. This phenomenon is completely different from the formation process, and may be due to the rapid erosion in the surf zone to maintain the longshore sediment transport by waves.

### 4. Conclusions

The formation and reduction processes of river deltas were investigated theoretically and experimentally in this paper. The formation and reduction processes are governed by the relation between the rates of sediment input from rivers and longshore sediment transport by waves and currents. From the results of the theoretical solutions, the following conclusions can be drawn:

(1) The solutions of formation process of river deltas of infinite and finite river mouth widths were obtained from linearized equations of shoreline change. It was theoretically found that the configuration of river delta becomes asymmetric when the dimensionless quantity  $\epsilon_1 \rho / \epsilon_2$  is greater than zero.

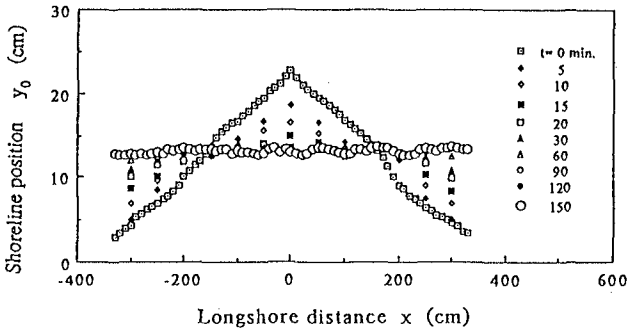


Fig. 12. Time variation of shoreline change in the reduction process of river delta in the case of Series B.

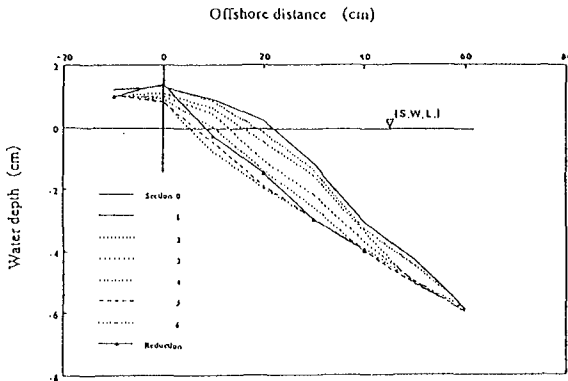


Fig. 13. Variation of beach profiles formed along the shoreline of river delta in the reduction process, Run B-3.

(2) By normal wave incidence, the reduction of the river delta takes place symmetrically with respect to the center of the river. The shoreline at the vicinity of the river mouth is rapidly eroded, while the shorelines at the longshore ends of the river delta retreat slowly. At the final stage, the configuration of the river delta may become a straight beach. By oblique wave incidence, the reduction of the river delta takes place asymmetrically, at a faster rate of reduction on the upcoast side of the delta than on the downcoast side. Also, the river mouth moves predominantly in the direction of littoral drift, as the reduction process of river delta takes place.

In order to understand the physical processes of formation and reduction of river deltas, and to compare the results of the formation process with the theoretical one, experiments on the formation and reduction processes of river deltas were carried out. The following conclusions can be drawn from the experiments:

(1) In the formation process, the shoreline of river delta propagates symmetrically with respect to the center of the river, when the waves is normally incident. On the contrary, by obliquely waves incidence, the shoreline of river delta propagates asymmetrically with respect to the center of the river at faster rate of formation on the downcoast side than that on the upcoast side.

(2) On the contrary of the formation process of river deltas, in the reduction process, the shoreline of river delta is rapidly eroded. It was noted in the reduction process that the beach profile changes from convex type, which was shown in the formation process, to a concave-upward one. This fact is completely different from the formation process, and may be due to the rapid erosion in the surf zone to maintain the longshore sediment transport by waves.

(3) Since the waves approach the shoreline obliquely, the longshore sediment transport is predominant. Consequently, the reduction rate of the shoreline on the upstream coast side is greater than that on the downstream coast side. The final stage for the configuration of the delta may be an inclined straight beach where the waves tend to approach it normally.

(4) In comparison, all experimental parameters in the theoretical solutions must be determined experimentally. It was concluded from the comparison that the evolution of the shoreline near the river mouth is well-predicted.

Finally, further extension of the present study should be directed towards both theoretical investigations of formation and reduction processes of river deltas as one of diffusion processes, which is the task of the near future.

### References

- Bakker, W.T. and Edelman, T., 1964, "The Coastline of River Deltas," Proc. 9th Coastal Eng. Conf., ASCE, pp. 199-218.
- Carslaw, H. and Jaeger, J., 1959, *Conduction of Heat in Solids*, 2nd ed., Clarendon Press, Oxford.
- Hanson, H. and Larson, M., 1987, "Comparison of Analytic and Numerical Solutions of the One-Line Model of Shoreline Change," Proc. of Coastal Sediment '87, ASCE, pp. 500-514.
- Iwagaki, Y., 1966, "A Treatise on Beach Erosion," Summer Seminar on Hydraulics Eng., JSCE, pp. B-17.1-17.17 (in Japanese).
- Kraus, N.C., Hanson, H. and Harikai, S., 1985, "Shoreline Change at Oarai Beach - Past, Present and Future," Proc. 19th Coastal Eng. Conf., ASCE, pp. 2107-2123.
- Pelnaud-Considère, R., 1956, "Essai de l'Evolution des Forms de Rivage en Plage de Sable et de Galets," 4th Journee de l'Hydraulique, des Energies de la Mer, Question III, Rapport No. 1, pp. 289-298.
- Tsuchiya, Y., 1973, "Coastal Sediment Balance and Beach Change," Summer Seminar on Hydraulics Engineering, JSCE, pp. B-3.1-3.19 (in Japanese).
- Tsuchiya, Y., 1978, "Beach Erosion and its Prediction," Annuals, D.P.R.I., Kyoto University, No. 21A, pp. 1-18 (in Japanese).
- Tsuchiya, Y. and Refaat, H., 1992, "Non-uniform Longshore Currents; Theory and Experiments," Jour. Waterway, Port, Coastal and Ocean Engineering, ASCE, 1991 (in review).
- Tsuchiya, Y. and Yasuda, T., 1979, "A Mathematical Model for Beach Change," Proc. 25th Japanese Conf. on Coastal Eng., JSCE, pp. 36-40 (in Japanese).

## CHAPTER 213

# Theoretical Study of the Wave Attenuation in a Channel with Roughened Sides

A.J. Roldán. \*, M.A. Losada\*, I.J. Losada\*

### Abstract

An eigenfunction expansion method is used to analyze the propagation of a plane wave train along a rectangular channel, the side walls which are provided with regularly spaced thin vertical strips. The presence of such strips may produce cross-channel seiching and energy dissipation. The method is extended to take into account the dissipation of energy at each pair of strips. Analytical solutions are obtained for the general case. Theoretical results of wave attenuation along the channel are compared to laboratory experiments, Battjes (1965).

## 1 INTRODUCTION

A harbor is a partially enclosed area connected to the sea by an opening. Sometimes the connection to the sea is through a channel of finite width and length. Entrance channels bounded by rubble-mound jetties are a common way to control wave propagation along the channel and to the harbor. Others, are channels with roughened sides, Battjes (1965) or with corrugated boundaries, Liu (1987). Further references can be found in Liu (1987).

Battjes (1965), did a semiempirical study of the attenuation of water waves in a rectangular channel, the side walls of which had been provided with

---

\*Ocean & Coastal Research Group. Departamento de Ciencias y Técnicas del Agua y del Medio Ambiente. Universidad de Cantabria. 39005 Santander, Spain.

regularly spaced roughness strips. Such strips were found to be highly effective wave dampers. However, the damping effectiveness of the strip sharply decreases when resonance occurs in the space between the strips.

In this paper the eigenfunction expansion method (hereafter called EFEM) is used to analyze the propagation of a plane wave train down a channel provided with thin vertical strips, regularly spaced. The wave solutions are expanded in eigenfunctions over the channel width. Dalrymple and Martin (1991), examined periodically spaced offshore breakwaters, matching eigenfunction expansions at the downwave and upwave side to show that a single incident wave train can generate directional wave trains downwave of the openings. Losada et al. (1992), used a two-dimensional (over the depth and across the channel cross-section) EFEM to analyze the generation and propagation of linear water waves down a wave flume, consisting of a wavemaker, an abrupt expansion, a breakwater and a fully absorbing ending wall. The EFEM method allowed the proper description of the wave motion, including cross-channel seiching as well as the prediction of the reflection and transmission which occurs at the channel junction and the porous structure. In order to evaluate the wave attenuation along the channel under seiching regime, (frictionless case), and energy loss regime, (friction case), an EFEM is used, providing matching conditions at each pair of strips which take into account a loss of kinetic energy.

## 2 FORMULATION OF THE PROBLEM

Figure 1 shows a rectangular channel.

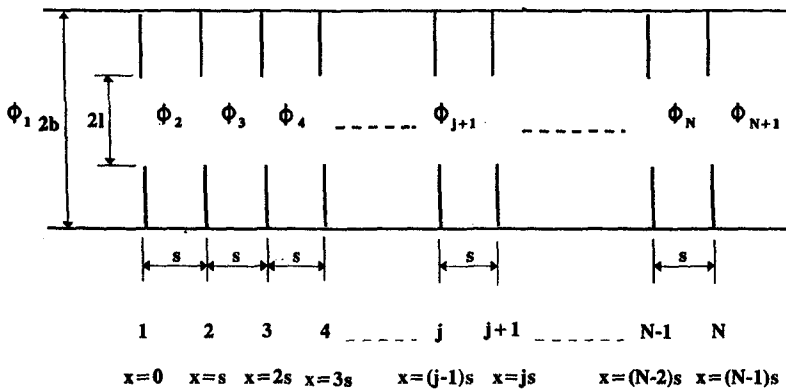


Fig.1.- Definition Sketch



The channel is symmetric about its centerline with constant depth  $h$ , the side walls of which are provided with regularly spaced strips attached vertically to them and extended as flat, thin (theoretically infinitesimal) plates into the channel.

The cross sectional width of the channel is  $2b$ . The gap between aligned pairs of strips is  $2l$  and the distance between two consecutive pairs of strips is denoted by  $s$ . The channel has  $N$  pairs of strips at the centerline of the channel at the still water level, with  $z$  directed upwards and  $x$  pointing downwave. Region 1 is defined by  $x \leq 0$ . Between two consecutive strips a new region is defined. A total of  $N - 1$  regions are defined. Region  $N + 1$  is extended over  $x \geq (N - 1)s$ .

The waves propagate down the channel in the positive direction. Then, as they encounter the first row of strips they get scattered by the roughness elements, partially reflected, and partially transmitted into Region 2. The transmitted waves in Region 2 diffract into the wider channel, dissipating energy through the formation of vortices, jets and eddy zones and reflecting from the side walls. They are then partially reflected and partially transmitted and dissipated after encountering the next row of strips. The transmitted and reflected waves are subsequently scattered and dissipated back and forth between the successive rows of strips until they encounter Region  $N+1$  where they are partially reflected, dissipated and transmitted into the leeward semi-infinite fluid region. As the waves propagate down the channel, they decrease in magnitude.

For an incompressible fluid and irrotational motion, the wave field outside the strip regions can be specified by the velocity potentials:  $\phi_1$  in Region 1 and  $\phi_{N+1}$  in the leeward region. The linear boundary value problem for water of constant depth,  $h$  in a channel of width  $2b$ , is well known. In the regions enclosed by strips it is assumed that the wave field is also describable by a velocity potential,  $\phi_n$ , with  $2 \leq n \leq N$ . Since the solution in the adjacent regions must be continuous at each interface, continuity of mass flux and pressure must be required over the water column and across the channel width. Then, following Mei et al. (1974), it is possible to incorporate to the pressure matching condition a head drop consisting of a loss of kinetic energy due to flow separation and an apparent inertia.

The boundary value problem can be completely solved if the potential,  $\phi_j(x, y, z, t)$ , in the  $j$ th region, is known for  $j = 1, 2, \dots, N+1$ . For each constant depth region, the Laplace's equation and the non-flow boundary conditions at the bottom and at the vertical channel boundaries are assumed to hold. The potentials in each region can be separated as:

$$\Phi_j(x, y, z, t) = \Re[\phi(x, y)I_j(z)e^{i\sigma t}] \quad (2.1)$$

where

$$I_j = \frac{ig \cosh k(z+h)}{\sigma \cosh kh} \quad (2.2)$$

where  $g$  is the gravitational constant,  $T$  is the wave period,  $t$  stands for time and  $\sigma = 2\pi/T$ , is the wave frequency. The wave number in each region,  $k_j$ , satisfies, for any  $j = 1, 2, \dots, N+1$ , the linear dispersion relationship

$$\Gamma_j = \frac{\sigma^2 h}{g} = k_j h \tanh k_j h \quad (2.3)$$

Because of the constant depth in all regions, eq. (2.3) has real roots  $k_{j1}$ , where  $k_{j1} \geq 0$  and has an infinite number of purely imaginary roots,  $k_{jm}$ , with  $m \geq 1$ .

The potentials  $\phi_j$  must solve the following problem

$$\frac{\partial^2 \phi_j}{\partial x^2} + \frac{\partial^2 \phi_j}{\partial y^2} + k_j^2 \phi_j = 0 \quad -h \leq z \leq 0 \quad (2.4)$$

$$\frac{\partial \phi_j}{\partial z} = 0 \quad z = -h \quad (2.5)$$

$$\frac{\partial \phi_j}{\partial z} - \frac{\Gamma_j}{h} \phi_j = 0 \quad z = 0 \quad (2.6)$$

Every potential has to satisfy a non-flow condition across the boundaries given by

$$\frac{\partial \phi_j}{\partial y} = 0 \quad y = \pm b \quad (2.7)$$

Finally, it is assumed that the downwave end of the channel, Region  $N+1$ , is fully absorbent. To take into account this absorbing character, it is enough to specify a radiation condition, requiring that the potential in that region is a downstream progressive wave.

## 2.1 Matching Conditions

Since the solution in adjacent regions must be continuous at each interface, continuity of mass flux and pressure must be required over the water column and across the channel width.

### Frictionless Case

At the strips, the matching conditions for the frictionless case are

$$(\phi_j)_x = (\phi_{j+1})_x = 0 \quad \text{at } x = (j-1)s \quad \text{and } l \leq |y| \leq b \quad (2.8)$$

$$(\phi_j)_x = (\phi_{j+1})_x \quad \text{at } x = (j-1)s \quad \text{and } |y| \leq l \quad (2.9)$$

$$\phi_j - \phi_{j+1} = 0 \quad \text{at } x = (j-1)s \quad \text{and } |y| \leq l \quad (2.10)$$

for  $j = 1, 2, \dots, N + 1$

which guarantee the non-flow condition through the strips and the continuity of mass flux and pressure in the gap.

### Friction Case

Based on a model of quadratic loss and scattering of long waves Mei, Liu and Ippen, (1974), Losada (1991), proposed a similar model to apply for the case of wave scattering by thin vertical barriers. In this model the continuity of pressure at the interface is obtained based on the Bernoulli equation. Thus, the analytical solution satisfies the following matching conditions (2.8) and (2.9), and a new condition given by,

$$\frac{ig}{g}(\phi_j - \phi_{j+1}) = \frac{f}{2g}(\phi_{j+1})_x |(\phi_{j+1})_x| + \frac{L}{g}(\phi_{j+1})_{xt}, x = (j-1)s \quad \text{and } |y| \leq l \quad (2.11)$$

for  $j = 1, 2, \dots, N + 1$

where,  $f$  and  $L$  are two empirical coefficients related to the loss of kinetic energy and apparent inertia respectively at each pair of strips. Following Mei (1974), we will use the following expression for  $f$ :  $f = [(2b/c.2l) - 1]^2$ , with  $c = 0.62 + 0.38(l/b)^3$ .

The good agreement between the analytical and experimental solutions for the case of thin vertical plates, suggests the extension of the model to the multi-strips case. Losada (1991), showed that the proposed approximation gives the

best results for the intermediate and shallow water waves. Furthermore, he showed that for relatively long waves, the apparent inertia term is not too important in comparison to the friction term. In this paper only the friction term will be considered. Moreover, eq. (2.11) will be linearized, therefore

$$\phi_j - \phi_{j+1} = \frac{-ig}{\sigma} C_{ej}(\phi_{j+1})_x \quad (2.12)$$

where  $C_{ej}$  is an equivalent friction term. Following Mei (1974),

$$C_{ej} = \frac{f}{2g} \frac{8}{3\pi} \left| \frac{\partial \phi_j}{\partial x} \right| \quad (2.13)$$

which depends on the potential value at each gap and it is not known before the solution is completed. To solve the problem an iterative procedure has to be used.

### 3 FULL SOLUTION

The potentials  $\phi_j$  for the frictionless and friction cases in each region satisfy the same boundary value problem, and therefore have the same analytical expression. They differ only in the matching conditions, that is, in the numerical value of the coefficients. Because of the constant water depth along the channel the potential  $\phi_j(x, y)$  at each region is

$$\phi_1(x, y) = \sum_{n=0} [A_n^{(1)} e^{-iq_n x} + B_n^{(1)} e^{iq_n x}] \cos(n\lambda y) \quad (3.1)$$

$$\phi_j(x, y) = \sum_{n=0} [A_n^{(j)} e^{-iq_n(x-(j-2)s)} + B_n^{(j)} e^{iq_n(x-(j-1)s)}] \cos(n\lambda y) \quad (3.2)$$

$$\phi_{N+1}(x, y) = \sum_{n=0} [A_n^{(N+1)} e^{-iq_n(x-(N-1)s)}] \cos(n\lambda y) \quad (3.3)$$

where  $q_n = \sqrt{k^2 - (n\lambda)^2}$ ,  $\lambda = \pi/b$ .

The inclusion of the Fourier terms,  $\cos(n\lambda y)$ ,  $n = 1, 2, \dots, \infty$  for all velocity potentials assures no flow through the channel walls. There is an infinite number of eigenvalues,  $\lambda_n = n\lambda$ . The corresponding eigenfunctions form a complete orthogonal set in the domain  $(-b \leq b)$ .

The wave field at each region consists of the incident plane wave train propagating down the channel and the reflected plane wave trains, which are

independent of the  $y$  coordinate ( $n = 0$ ) plus progressive and evanescent standing waves travelling in the negative  $x$  direction. The evanescent modes occur when  $\lambda_n \geq k$ , leading to a dampened motion in the  $x$  direction. The progressive standing wave modes consist of two intersecting wave trains travelling at

$$\theta = \cos^{-1}\left(\frac{\sqrt{k^2 - (n\lambda)^2}}{k}\right) \quad (3.4)$$

to the  $x$  axis.

Note that eqs. (3.1) to (3.3) do not include a family of vertical evanescent modes, which has to be included to satisfy the matching conditions at each interface. However, for intermediate and shallow water waves, the relative error between the plane wave approximation and the full solution is small.

The unknowns of the problem are  $A_m^{(j)}$  and  $B_m^{(j)}$ , with  $m = 0, 1, 2, \dots, n$  and  $j = 1, 2, \dots, N + 1$ . The incident plane wave train is defined by  $A_0^{(1)} = 1$  and  $A_m^{(1)} = 0$ , with  $m \geq 1$ . In order to satisfy the radiation condition in the leeward region,  $B_m^{(N+1)} = 0$ , with  $m \geq 0$ .

Substituting the expression of the potentials into the mass flux condition, eq. (2.9), an expression from  $B_m^{(j)}$  as a function of  $A_m^{(j)}$  can be found.

Next, the two remaining matching conditions are to be prescribed on the velocity eq. (2.8) (non-flow through the strips) and on the pressure eq. (2.10) or on the momentum eq. (2.11). Here, a mixed boundary condition must be prescribed (Dalrymple and Martin, 1991, and Losada et al., 1991).

### 3.1 Dual Series

The two remaining matching conditions to be satisfied at the gap are known as dual series relations, (Sneddon, 1966). They have to be solved for the values of the coefficients  $A_n^{(j)}$ . The two conditions can be combined to make one mixed boundary condition. This condition is

$$G(y) = 0 \quad \text{at } 0 \leq |y| \leq b \quad (3.5)$$

To determine the  $A_n^{(j)}$  several techniques can be used, e.g. least squares method, which requires the value of

$$\int_{-b}^b |G(y)|^2 \cdot dy \quad (3.6)$$

to be a minimum.

Minimizing this integral with respect to each of the  $A_n^{(j)}$  leads to the following system of equations

$$\int_{-l}^l G^{*(2)}(y) \frac{\partial G^{(2)}(y)}{\partial A_n^{(j+1)}} + 2 \int_l^b G^{*(1)}(y) \frac{\partial G^{(1)}(y)}{\partial A_n^{(j+1)}} dy = 0 \quad n = 0, 1, 2, \dots, \infty$$

$$j = 1, 2, 3, \dots, N \quad (3.7)$$

where  $G^*$  is the complex conjugate of  $G$  and  $G^1$  and  $G^2$  are the matching conditions at the gap and at the strip respectively. Truncating eq. (3.7) to  $M$  terms and solving for the  $M * N$  values of  $A_m^{(j)}$  simultaneously, a complex system of  $M * N * N$  matrix equations is obtained which can be solved with the IMSL routine, LEQT1C.

Dual Series for the Frictionless Case

Taking into account the non-flow condition at each pair of strips, eq. (2.8), and matching the pressure using eq. (2.10), we get the mixed matching condition  $G(y) = G_1(y) + G_2(y)$ , which for each  $j = 1, 2, 3, \dots, N$ , is

$$\sum_{n=0}^{\infty} \{-4(e^{-\alpha i q_n s})^* I_{mn} A_n^{*(j)} + \{4I_{mn} + 2[iq_n(\delta e^{-2iq_n s} - 1)]^* [iq_m(\delta e^{-2iq_m s} - 1)] J_{mn}\} A_n^{*(j+1)} + 2 \sum_{p=j+2}^{N_p} \delta(iq_n)^*(e^{-2iq_n s} - 1)^*(e^{-iq_n(p-(j+1)s})^* [iq_m(\delta e^{-2iq_m s} - 1)] J_{mn}\} A_n^{*(p)} - 2\delta(iq_n)^*(e^{-iq_n(N-j)s})^* [iq_m(\delta e^{-2iq_m s} - 1)] J_{mn}\} A_n^{*(N+1)} = 0 \quad (3.8)$$

where  $\delta = 0$ , if  $j = N$  and  $\delta = 1$  otherwise, and  $I_{mn} = \int_{-l}^l \cos(n\lambda y) \cos(m\lambda y) dy$ , and  $J_{mn} = \int_l^b \cos(n\lambda y) \cos(m\lambda y) dy$ .

Dual Series for the Frictional Case

The non-flow condition at each strip is the same as for the frictionless case. The continuity of pressure, eq. (2.10) can now be written as:

$$G^{(2)}(y) \equiv \sum_{n=0}^{\infty} \{2e^{-\alpha i q_n s} A_n^{(j)} - [2 - C'_{ej} i q_n (\delta e^{-2iq_n s} - 1)] A_n^{(j+1)}\}$$

$$\begin{aligned}
 &+ \sum_{p=j+2}^N C'_{ej} i q_n \delta (e^{-2i q_n s} - 1) e^{-i q_n (p-(j+1))s} A_n^{(p)} \\
 &- C'_{ej} i q_n \delta e^{-i q_n (N-j)s} A_n^{(N+1)} \} \cos(n \lambda y) = 0 \quad (3.9)
 \end{aligned}$$

where  $C'_{ej} = -(ig/\sigma)/C_{ej}$

Substituting eqs. (3.9) and the corresponding  $G^{(1)}(y)$  into eq. (3.7) and truncating the series to M terms, we get a set of  $M^*N^*N$  matrix equations that can be easily solved.

### 4 THEORETICAL RESULTS

The reflection coefficient,  $C_r$ , is defined as the absolute value of the most progressive coefficient  $B_0^{(1)}$  of the reflected potential in Region 1. Similarly, the transmission coefficient,  $C_t$ , is defined as the absolute value of the most progressive coefficient,  $A_0^{(N+1)}$ , of the transmitted potential in Region  $N + 1$ .

For the frictionless case, the propagation of a wave train down a channel in two separate cases, one using two pairs of strips and the second using ten pairs of strips, is examined for the following characteristics:  $T = 1.373s$ ,  $h = 0.6m$ ,  $2b = 3.0m$  and  $2l = 2.6m$ .

Figure 2 shows  $C_r$  versus  $ks$  where,  $k$  is the wavenumber. Resonant conditions occur at  $ks = p\pi$ ,  $p = 1, 2, \dots$ . Further results have shown, that increasing the gap to  $2l = 2.8m$ , the amplitude of the resonance is reduced.

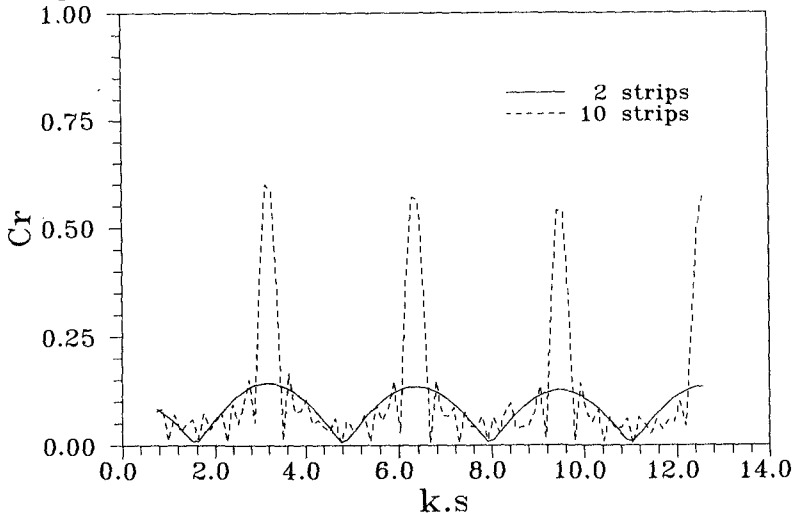


Fig.2.- Reflection Coefficient versus  $k.s$  (without friction)  
 ( $T=1.373 s$ ,  $2.b=3.0 m$ ,  $2.l=2.6 m$ ,  $h=0.6 m$ ,  $M=10$ )

Note, that the resonant conditions are stronger for the channel with a larger number of strips.

Figure 3 shows the dependency on  $C_r$  on the relative gap width  $l/b$ . This time the separation of the strips is  $s = 0.4$ . A sharp increase in  $C_r$  occurs, by decreasing the relative gap from 70% to a 60%.

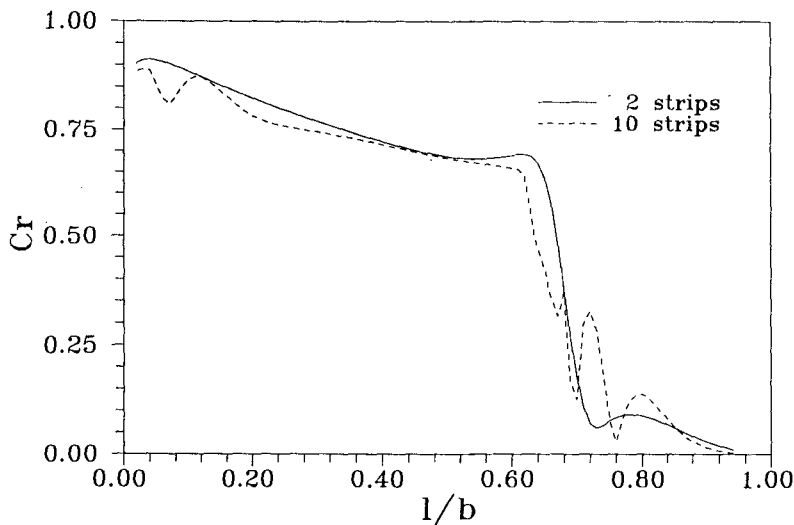


Fig.3.- Reflection Coefficient versus  $l/b$  (without friction)  
 ( $T=1.373$  s,  $2.b=3.0$  m,  $s=0.4$  m,  $h=0.6$  m,  $M=10$ )

Battjes, (1965) reported experimental values of the wave attenuation in a channel with roughened sides. The wave height was measured in eight equidistant points in each cross-section and the average of these heights was taken to represent the wave attenuation at each respective section.

Results without friction have shown that the analytical model underpredicts the wave attenuation measured in the experiments. Further, the amplitude attenuation depends linearly on  $x$ . A similar behavior is obtained if the friction coefficient is kept constant along the channel, as Battjes, (1965) suggested.

Figure 4 shows the evolution of the averaged wave height along a channel, including the friction effect, for the following case:  $h = 0.6$  m,  $T = 1.98$  s,  $2l = 2.9$  m,  $s = .2$  m,  $N = 195$  strips and  $M = 5$ .



This time the overall agreement between analytical and experimental results is good.

Because of time computation, theoretical results were stopped after 195 strips.

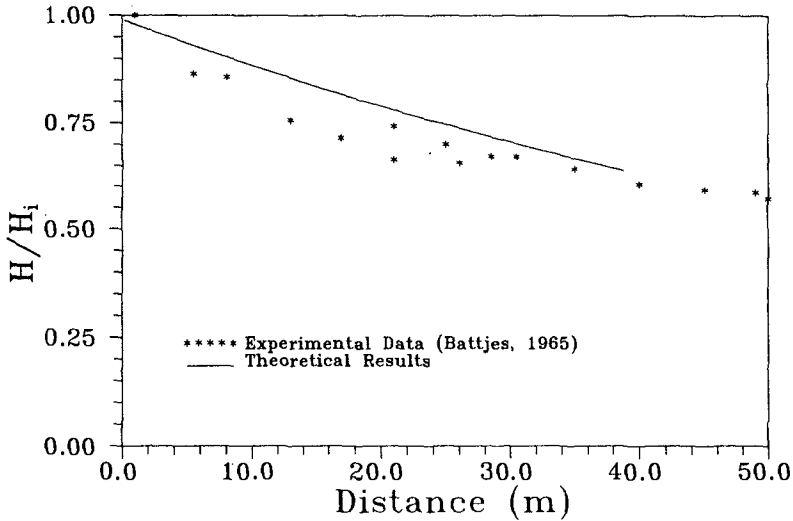


Fig.4.- Wave Height Evolution ( $T=1.98$  s,  $2b=3.0$  m,  $2l=2.9$  m,  $s=0.2$  m,  $h=0.6$  m,  $N=195$ ,  $M=5$ )

The wave height contourlines for,  $h = 0.6m$ ,  $T = 1.373s$ ,  $2l = 2.6m$ ,  $2b = 3.0m$ ,  $s = 0.67m$ ,  $N = 20$  and  $M = 25$  are presented in Figure 5. In this case the wave height varies from the input wave height,  $1m$  to  $0.3m$ .

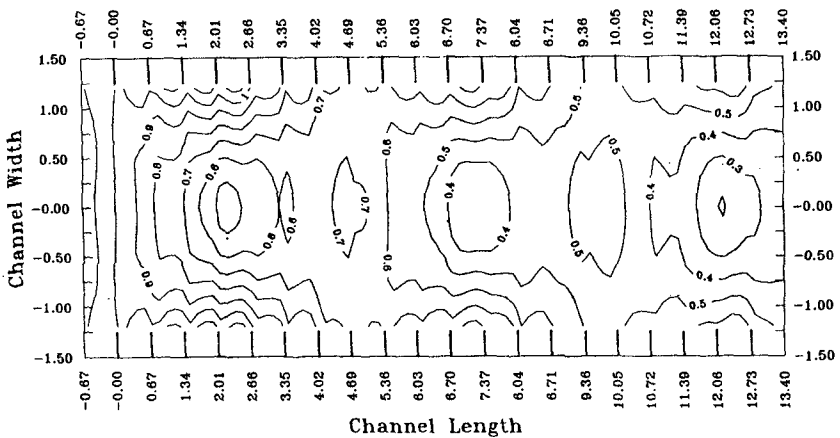


Fig.5.- Wave Height Contourlines

Further analysis has shown, for the same values of the parameters, that the wave height attenuation in a mid-channel section presents an oscillating behavior, due to the resonant conditions caused by the strips.

Finally, it could be also observed that there is also an oscillating behavior present, if we the wave height variations across the channel were analyzed in different sections.

## 5 CONCLUSIONS

Wave propagation in a channel with roughened sides has been studied, using an eigenfunction expansion method (EFEM).

This method is valid to reproduce the wave field in the channel, showing, as the most important characteristic, the wave attenuation with an oscillating behavior.

The model does also reproduce the resonant conditions and the cross-channel variations, due to the presence of the lateral walls and the thin strips.

Frictional effects have been considered using a semi-empirical approach based on Mei et al. (1974). This effect is included in the matching conditions corresponding to the momentum equation at each strip. By applying the EFEM, the local friction effect proposed by Mei et al. is extended to the whole channel width and depth.

Comparison of the analytical results with the experimental data by Battjes (1965), proves the validity of the method.

## ACKNOWLEDGEMENTS

The first and third authors were granted by the Ministerio de Educacion y Ciencia (Spain), Programa de Formacion del Personal Investigador.

The second author thanks the Comision Interministerial de Ciencia y Tecnologia (CICYT) for its support under Grant No PB89-0381.

## References

- Battjes, J.A.**, 1965. Wave attenuation in a channel with roughened sides. *Special Coastal Engineering Conference, ASCE*, Santa Barbara, California, pp. 425-460.
- Dalrymple, R.A. and Martin, P.A.**, 1991. Wave diffraction through offshore breakwaters. *Journal Waterways, Port, Coastal and Ocean Engineering, ASCE*, Vol. 116, No. 6, pp. 727-741.
- Liu, P.L.-F.**, 1987. Resonant reflection of water waves in a long channel with corrugated boundaries. *Journal of Fluid Mechanics*, No. 179, pp. 371-381.
- Losada, I.J.**, 1991. Estudio sobre la propagacion lineal de un tren de ondas sobre un medio discontinuo. (in Spanish) *Ph.D. Dissertation*, University of Cantabria.
- Losada, M.A., Roldan, A.J. and Dalrymple, R.A.**, 1992. Eigenfunction analysis of water waves propagation down a wave flume. (Submitted to Coastal Engineering. Elsevier)
- Mei, C.C., Liu, P.L.-F., and Ippen, A.T.**, 1974. Quadratic loss and scattering of long waves. *Journal Waterways, Harbors and Coastal Engineering Div., ASCE*, Vol. 100, No. WW3, pp. 217-239.
- Sneddon, I.N.**, 1966. Mixed Boundary Value Problems in potential Theory. North Holland Publishing Co.. Amsterdam.

## CHAPTER 214

### LOCAL SCOUR AROUND A LARGE CIRCULAR CYLINDER ON THE UNIFORM BOTTOM SLOPE DUE TO WAVES AND CURRENTS

Eiichi Saito\* and Tomoya Shibayama, M.ASCE\*\*

#### 1. Introduction

In recent years, many kinds of coastal structure, such as man-made island, large-scale piers, marinas and so on, are constructed in the coastal area. Local scour occur around a coastal structure due to waves and currents. The scouring around a structure is important in the estimation of stability of the structures. However, there are no standard of judgement of measures against scour around coastal structures. There are few investigations for mechanism of local scours around a large-scale structures. The dimension of large-scale structure is comparable to the wave length, and the wave field around them is complicated owing to the presence of diffracted waves. The mechanism of sand movement around a large circular cylinder were first investigated experimentally by Toue and Katui(1985). Saito et al.(1990) presented a numerical model for the bottom topography changes around a large circular cylinder. The model consisted of three submodels, that is, wave model, current model and sand transport model. In the model, the wave field was evaluated by using the linear theory derived by McCamy and Fuchs(1954). The current field was evaluated as sum of the depth-integrated current induced by the spatial variation of the radiation stress and the mass transport velocity in the vicinity of the bed. The sand transport rate was calculated in terms of the

---

\*Research Engineer, Tech. Res. Inst., Hazama Corp., Tukuba, Ibaraki 305, Japan

\*\*Assoc. Prof., Dept. of Civil Eng., Yokohama National Univ., Hodogaya-ku, Yokohama 240, Japan

bottom shear stress and near-bottom current velocity. The change of bottom topography was calculated by using the mass conservation equation of the sand. Later, Katsui and Toue(1992) improved the model by using the wave-current friction factor. These investigations, however, were performed under uniform water depth conditions. Since real sea bottom has a slope, wave breaking and additional current appears. The mechanism of sand movement seems to be different. The purpose of the present study is to investigate the mechanism of the local scour around a large circular cylinder installed on the uniform bottom slope due to waves and currents by both laboratory experiment and numerical simulation.

**2.Laboratory Experiment**

Experiments were performed in a 9 times 9m wave basin with a 1/20 slope. About 2.5 times 2.3m test bed was made in the basin. A circular cylinder with a diameter of 52.2cm was installed at the center of the test bed. Two types of test beds, fixed and sand, were used in the experiment. Well-sorted sand with a median diameter of 0.2mm were put in the test section. Experimental equipment is shown in Fig.1, and experimental conditions are listed in Table 1.

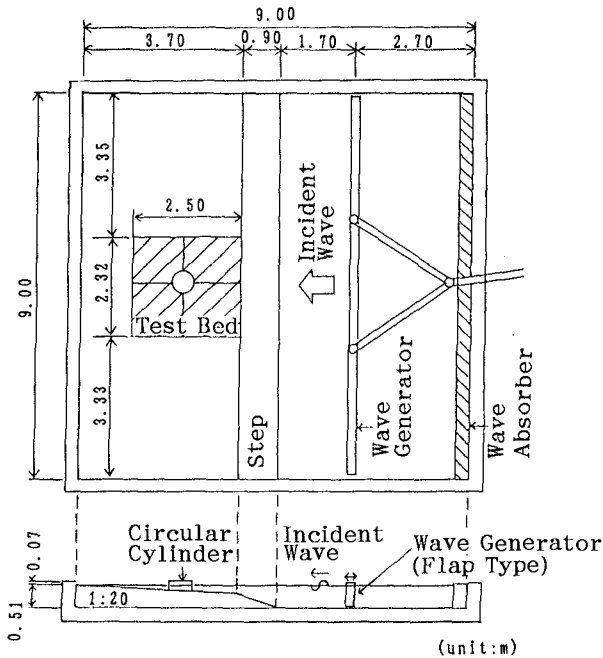


Fig.1 Experimental Set-up(Fixed Bed)

Table 1 Experimental Conditions

Case	1	2
Test Bed	Fixed	Sand
Incident Wave Period $T$ (s)	1.02	
Incident Wave Height $H_0'$ (cm) (at uniform water depth)	9.4	
Deepwater Wave Height $H_0$ (cm)	9.1	
Water Depth at Cylinder $h_c$ (cm)	11.5	
Diameter of Circular Cylinder $D$ (cm)	52.2	
Measured Values	•Wave Height •Steady Current	•Wave Height •Change of Bottom Topography

In the case of fixed bed (case1), the distribution of wave height and the variation of steady current velocities around a cylinder were measured with a horizontal spacing of 10cm. Steady current were measured by using ultra-sonic type current meter or electromagnetic current meter at both upper level and lower level for one measuring point. We set the upper level at 8cm below the mean water level to prevent the current meter from being exposed to the air when the wave trough comes. And we set up the lower level at 1cm above the bottom. In the shallow water area, steady current only at lower level was measured. Measuring points are shown in Fig.2. The whole pattern of current direction was also observed by using dye injection.

In the case of sand bed (case2), the development of sand ripples and change of bottom topography during experimental run were measured by using a bottom profiler. Measuring points are the same with those in Fig.2. The measurements were carried out at 1,2,4 and 6 hours after wave generation. The scouring depth and the depositing height along the cylinder surface were also measured by using scales printed on the cylinder surface. The distribution of wave height were also measured at same point as case 1. The measurements were carried out from 0 ~ 2 hours and from 5 ~ 7 hours upon the initiation of wave action to estimate the influence of the change of bottom topography on the wave height distribution. In this study, the physical meaning of large circular cylinder is considered to be the

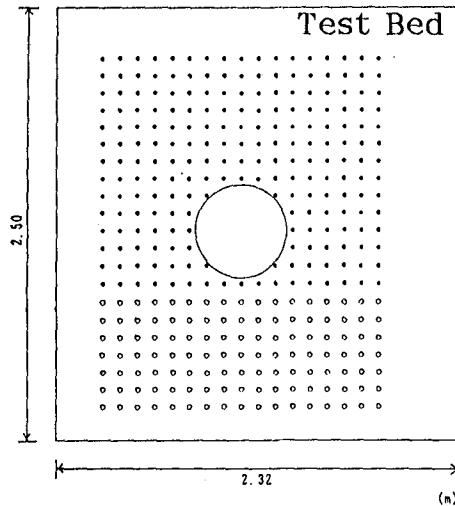


Fig.2 Measuring Points

cylinder which causes obvious diffracted waves. In this experiment, diffracted waves, which passed around behind the cylinder, were observed obviously. Jo(1986) proposed the criteria of large cylinder by using the parameter  $D/L$  and K.C.number( $K.C.=u_b \cdot T/D$ ), where  $D$  is the diameter of the circular cylinder,  $u_b$  the orbital velocity amplitude near the bottom,  $T$  the wave period. The criteria of large cylinder is listed in Table 2. When we calculate these parameters by using the experimental conditions listed in Table 1, we obtained  $D/L=0.52$  and  $K.C.=0.70$ . As a result, the circular cylinder with a diameter of 52cm is considered to be a large circular cylinder in the present experiments.

Table 2 Criteria of Large Cylinder

$D/L$	Small Diameter < 0.2 < Large Diameter
K. C. Number	Small Diameter > 4.0 ~ 5.0 > Large Diameter

The experiments were carried out with the scale of 1/50. Prototype according to the Froude law are listed in Table 3.

Table 3 Prototype Conditions

Case	1	2
Incident Wave Period T(s)	7.21	
Incident Wave Height H <sub>0</sub> ' (m) (at uniform water depth)	4.70	
Deepwater Wave Height H <sub>0</sub> (m)	4.55	
Water Depth at Cylinder h <sub>c</sub> (m)	5.75	
Diameter of Circular Cylinder D(m)	26.1	

**3. Numerical Model**

A numerical model was developed to predict bottom topography changes around structures. The model consists of three sub-models, that is, wave model, current model and sand transport model. The outline of each sub-model is described below.

**3.1 Wave Model**

The wave field was evaluated by using the time dependent mild slope equation derived by Watanabe and Maruyama(1986). It is possible to calculate wave fields around structures on the bottom slope accurately. The equation is as follows:

$$\left. \begin{aligned}
 &\frac{\partial \eta}{\partial t} + \frac{1}{n} \cdot \frac{\partial n Q_x}{\partial x} + \frac{1}{n} \cdot \frac{\partial n Q_y}{\partial y} = 0 \\
 &\frac{\partial Q_x}{\partial t} + C^2 \frac{\partial \eta}{\partial x} + f_D \cdot Q_x = 0 \\
 &\frac{\partial Q_y}{\partial t} + C^2 \frac{\partial \eta}{\partial y} + f_D \cdot Q_y = 0
 \end{aligned} \right\} (1)$$

where

$$Q = \sqrt{Q_x^2 + Q_y^2}, \quad Q_r = 0.25 \sqrt{g h^3}$$

$$f_D = 2.5 \tan \beta \sqrt{(g/h)(Q/Q_r - 1)} \quad (: Q > Q_r)$$



where  $\eta$  : the water elevation,  $Q_x, Q_y$ : the components of the flux in the x-direction and y-direction,  $C$ : wave phase velocity,  $n$ : the ratio wave group velocity to wave phase velocity,  $\tan \beta$  : bottom slope,  $h$ : water depth,  $g$ : acceleration of gravity

### 3.2 Current Model

The steady current, that is, time averaged and depth-integrated current induced by the spatial variation of the radiation stress, was calculated through numerical calculation by using depth-integrated continuity equation and momentum equation expressed as follows:

$$\left. \begin{aligned} \frac{\partial \zeta}{\partial t} + \frac{\partial U (h + \zeta)}{\partial x} + \frac{\partial V (h + \zeta)}{\partial y} &= 0 \\ \frac{\partial U}{\partial t} + U \frac{\partial U}{\partial x} + V \frac{\partial U}{\partial y} + F_x - M_x + R_x + g \frac{\partial \zeta}{\partial x} &= 0 \\ \frac{\partial V}{\partial t} + U \frac{\partial V}{\partial x} + V \frac{\partial V}{\partial y} + F_y - M_y + R_y + g \frac{\partial \zeta}{\partial y} &= 0 \end{aligned} \right\} \quad (2)$$

where  $\zeta$  the mean water level elevation,  $U, V$ : the components of steady current in the x-direction and y-direction,  $F_x, F_y$ : the components of bottom friction term,  $M_x, M_y$ : the components of lateral diffusion term,  $R_x, R_y$ : the components of radiation stress term.

### 3.3 Sand Transport Model

In the experiments, a large quantity of suspended sand movement and obvious steady current were observed near the cylinder. It seemed from experiments that the sand transport direction agreed with the steady current direction in particular near the cylinder. Therefore, the net sand transport rate  $Q$  was calculated by using the following equation under the wave-current field obtained by Shibayama et al. (1989):

$$Q = \frac{\Phi \omega d}{(1 - \lambda)} \quad (3)$$

$$\Phi = 0.9 \Theta^{1.2} \quad (4)$$

$$\Theta = \frac{(\tau_m - \tau_c) u}{\rho (s g d)^{1.5}} \quad (5)$$

where  $\tau_m$  the maximum value of bed shear stress,  $\tau_c$  the critical value of bed shear stress for initial sand movement,  $u$  the steady current velocity,  $\lambda$  the porosity,  $d$  the diameter of sand,  $w$  the fall velocity of sand,  $\rho$  the water density, and  $s$  the specific gravity of sand in water. The change of bottom topography was calculated by using the sand mass conservation equation of sand:

$$\frac{\partial z_b}{\partial t} = - \text{div } Q \quad (6)$$

where  $z_b$  is the bed level.

By using the three sub-models described above, the quantity of local scour and deposition was calculated by using finite difference method with a rectangular calculation grid with a size of 2cm under the same conditions as laboratory experiment.

#### 4. Laboratory Results and Comparison with Numerical Results

##### 4.1 Wave Field

In the experiments, wave breaking was observed at an onshore side of the cylinder. Fig.3 shows the comparison of the distribution of wave height. Fig.3(a) is measured on the fixed bed and Fig.3(b) is measured on the sand from 5 to 7 hours after the wave generation. The numerical results by the time dependent mild slope equation is shown in Fig.3(c). Scour and deposition around 3 to 4cm was observed around a cylinder 6 hours after the wave generation. Therefore, Fig.3(b) shows the distribution of wave height after the bed topography changed in some degree. No significant change exists between Fig.3(a) and Fig.3(b), which means that no great variation in the wave field was developed in this case, even when the bed topography changes with time. Since calculated value, which was shown in Fig.3(c), was a little small compared with two measurements, the overall agreement between the measurements and the calculations is obtained. It is confirmed that the wave field around a large circular cylinder could be evaluated in a good accuracy by the time dependent mild slope equation.

##### 4.2 Current Field

Fig.4 shows comparison of the steady current velocity distribution between experimental results and calculated results. Fig.4(a) shows the distribution of measured steady current at upper level and Fig.4(b) at lower level. The calculated current field is also shown in

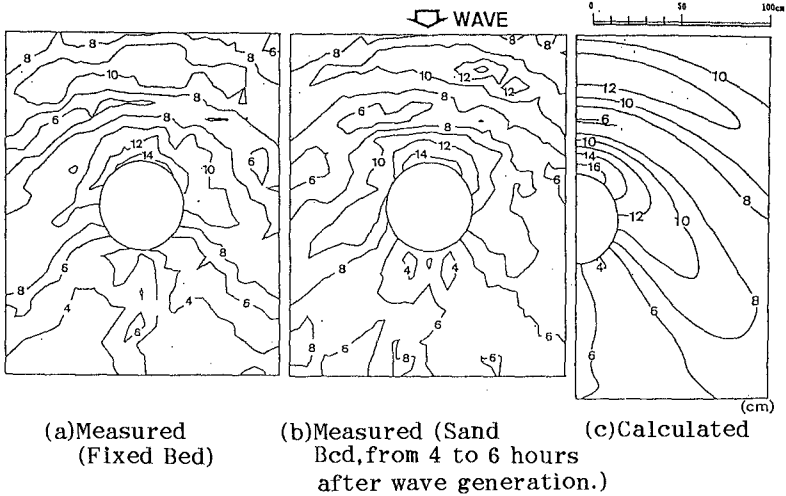


Fig. 3 Distribution of Wave Height ( $H_0=9.4\text{cm}$ ,  $T_0=1.02\text{s}$ )

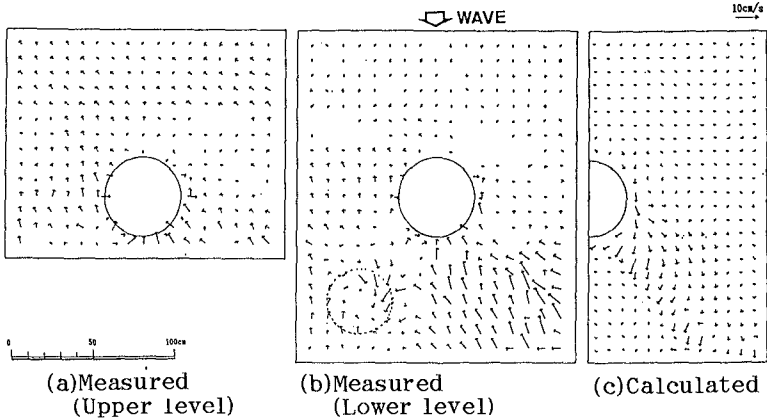


Fig. 4 Steady Current Velocity Field ( $H_0=9.4\text{cm}$ ,  $T_0=1.02\text{s}$ )

Fig.4(c). According to Fig.4(a) and Fig.4(b), the experimental steady currents were generally offshore directed. In particular, strong offshore currents occurred oblique behind the cylinder, where conspicuous wave breaking were observed. On the contrary, however, calculated steady currents have a tendency to be onshore directed on behind the cylinder. The reasons for the discrepancy will be discussed below. In the experiments, it is very difficult to measure

onshore currents perfectly by using current meter. In the surf zone, generally, a mass of water at upper level is transported by breaking, bore-like waves. It causes onshore current at upper level and offshore current at lower level, that is, undertow. Therefore, it is impossible to measure steady currents above the wave trough because the current meter will be exposed to the air at the phase of trough. The steady current in the present numerical model is depth-integrated velocity calculated by assuming that the velocity is uniform over entire water depth. Therefore, undertow was not included in the model.

According to Fig.4(a) and Fig.4(b), steady current vectors direct generally from the right to the left. These longshore currents were generated by wave breaking and energy dispersion. The effect of longshore current is not included in the present model.

A cell of steady current, as shown by the dotted circle line in Fig.4(b), were observed. It indicates the existence of the vortex. In the experiments on sand bed, the bottom topography was considerably scoured in the vortex area. The vortex observed here is the separation vortex induced by the steady currents. In present experiments, however, it was impossible to investigate the vortex mechanism in detail due to the limitation of the measuring device.

#### 4.3 Bottom Topography

Fig.5 shows a comparison of the bottom topography between the laboratory experiment and numerical model. The hatched areas in the figure indicate the eroded area. Since it took approximately 5 to 6 hours for bottom topography to reach equilibrium condition, both measured result and calculated result in Fig.5 are for 6 hours after the wave generation. It can be observed that the calculated results agree qualitatively with experimental results especially near the cylinder. However, some discrepancies exist in the area at a short distance from the surface of the cylinder. The experimental bottom topography shows that the bottom was mainly scoured in the onshore area of the cylinder, conversely, the bottom in the calculation was mainly scoured in the offshore area. Furthermore, the pattern of the experimental bottom topography is not symmetrical. The reasons for the discrepancy will be discussed below.

As was stated previously, undertow and longshore current were observed around a circular cylinder in the experiments. It seems that these currents gave significant effect on the bottom topography. In the experiments, a large quantity of suspended sand, which was transported under the effect of undertow and longshore current, were observed near the cylinder and in the surf zone. For

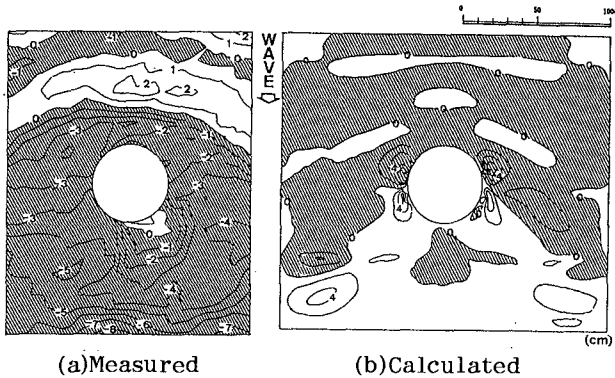


Fig.5 Bottom Topographies  
( 6 hours after wave generation)

this reasons, bottom topography in the surf zone, that is, onshore area of the cylinder, and near the cylinder was scoured and bottom topography in the offshore area was deposited. Furthermore, bottom topography change was asymmetric. According to the experiments carried out by Saito et al.(1990), under the uniform water depth condition, no significant undertow was observed. Saito et al.(1990) concluded that the effects of mass transport velocity and standing waves are important for the sand movement. The mechanism of the sand movement under the uniform water depth condition was different from that of under uniform slope condition. Numano et al.(1989) suggested the importance of the effect of the undertow for the bottom topographical changes by using numerical model. Here also we can conclude that the effect of undertow is important for the case of sloping bottom.

According to the experimental results of the steady current field, the separation vortex due to steady current was observed oblique behind the circular cylinder. Fig.5(a) shows that bottom topography at the vortex generation area shown in Fig.4(b) was considerably scoured. It indicates that in order to estimate the bottom topography change around the cylinder, it is necessary to consider the effect of the separation vortex due to steady currents. Shibayama and Win(1992) indicated the scouring effect of the vortex under steady current field in the surf zone by using a numerical model.

Since effects of undertow, longshore current and vortex are not included in the present numerical model, it is necessary to include these important effects as a next step.

## 5. Conclusions

Investigation for the mechanism of the local scour around a large circular cylinder installed on the uniform bottom slope due to waves and currents were performed experimentally and numerically. Major conclusions are summarized as follows:

- ① Undertow, longshore current and separation vortex due to longshore current were observed in laboratory experiment around a large circular cylinder on an uniform slope in the surf zone. It appeared that these currents and vortex give strong effects on the bottom topography.
- ② A numerical model was proposed for the local scour around a large circular cylinder on an uniform slope. To improve the model prediction, it is necessary to include the effect of undertow and vortex.

## References

- Jo, K. (1986): Laboratory study on local scour around cylinder under wave action, Graduation Thesis, Univ. of Tokyo, 113pp (in Japanese).
- Katsui, H., and T. Toue (1992): Bottom shear stress in coexistent field of superimposed waves and current and scouring around a large scale circular cylinder, Coastal Eng. in Japan, Vol. 35, No. 1, pp. 93-110.
- McCamy, R. C. and R. A. Fuchs (1954): Wave forces on piles, B. E. B. Tech. Memo., No. 69.
- Numano, Y., S. Sato and T. Shibayama (1989): Effects of suspended sand transport and undertow on three dimensional beach deformation, Proc. 36th Japanese Conf. on Coastal Eng., pp. 394-398 (in Japanese).
- Saito, E., S. Sato and T. Shibayama (1990): Local scour around a large circular cylinder due to wave action, Proc. of 22nd Coastal Eng. Conf., pp. 1795-1804.
- Shibayama, T., S. Sato, H. Asada and T. Temmyo (1989): Sediment transport rate in wave-current coexistent field, Coastal Eng. in Japan, Vol. 32, No. 2, pp. 161-171.
- Shibayama, T., and A. Win (1992): A Numerical model for local scour around a cylinder due to waves and currents, Proc. of the 41st Annual Conf., 2, JSCE

Toue, T., and H. Katsui (1985): Scour around a large scale circular cylinder,  
Proc. 32th Japanese Conf. on Coastal Eng., pp. 425-429 (in Japanese).

Watanabe, A., and K. Maruyama (1986): Numerical modeling of nearshore wave field under combined refraction, diffraction and breaking,  
Coastal Eng. in Japan, Vol. 29, pp. 19-39.

## CHAPTER 215

### Vertically Varying Velocity Field in Q-3D Nearshore Circulation

A. Sánchez-Arcilla, F. Collado and A. Rodríguez<sup>1</sup>

#### Abstract

This paper presents an efficient and economic technique to obtain vertical profiles for surf-zone wave-induced currents. The current-wave bottom boundary layer is solved in a parameterized manner, while employing a power series approximation to obtain the solution in the middle layer (extending up to trough level). This "profile extraction technic" has been coupled to a 2DH surf-zone circulation model which is also concisely described. The paper ends with a brief discussion of some obtained results part of the calibration work which is a very much on going task.

#### 1. Introduction

This paper presents a solution for the vertically varying velocity field in a Q-3D modelling context. It is part of an improved version of the Quasi- 3D NEARCIR Model (S.-Arcilla et al., 1990/91) developed during the MAST-I G6M (Currents) Project. The proposed model is able to achieve a detailed simulation of nearshore flows at a reasonable cost (cheaper than a full 3D code). The model works at the current time scale and it is structured into three modules (see fig. 1):

- i) Wave Propagation Module.
- ii) Depth Uniform Current Module.
- iii) Depth Varying Current Module (including Bottom Boundary Layer).

---

<sup>1</sup> Lab. Ing. Marítima , L.I.M., Univ. Politécnic de Cataluña, U.P.C.  
Av. Gran Capitán s/n, 08034 Barcelona, Spain.



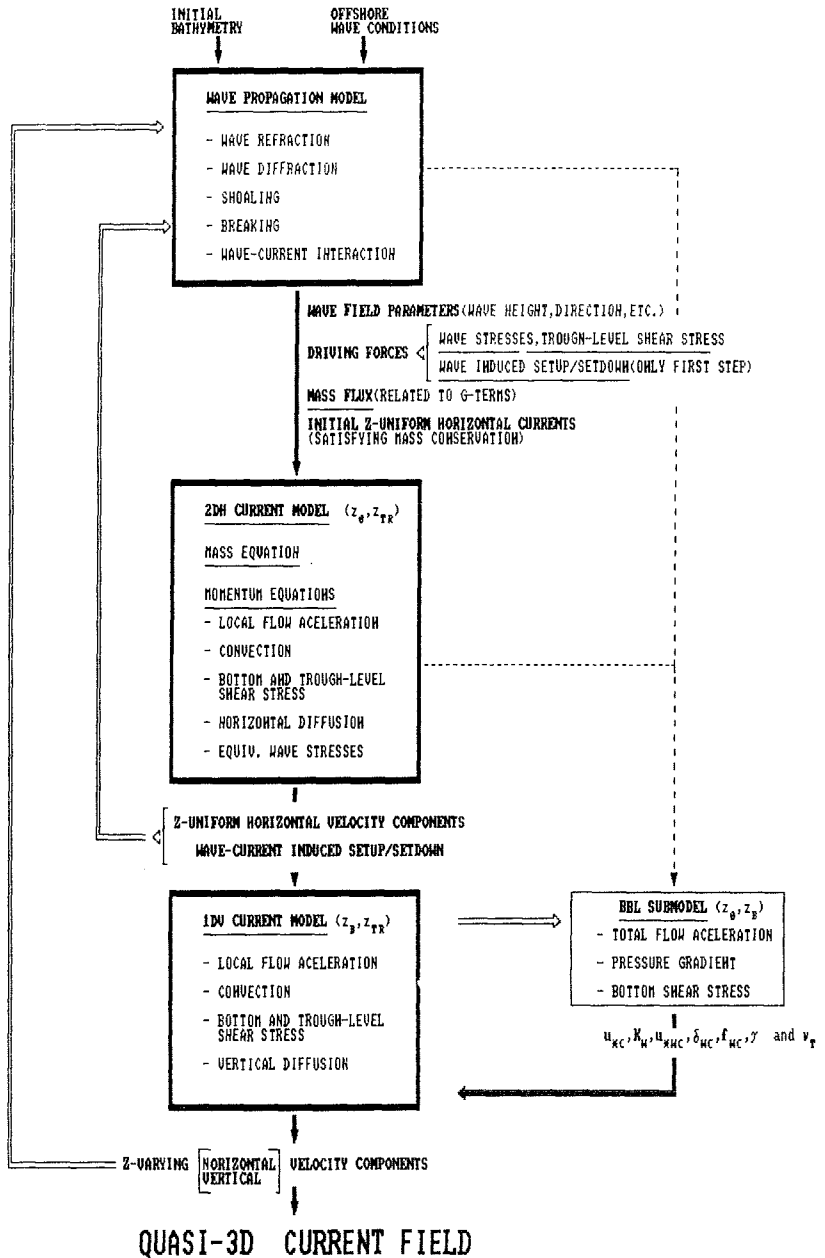


Fig. 1: NEARCIR flow chart.

The three modules operate in a sequential iterative manner (Wave—>Depth Uniform Current—>Depth Varying Current). Iterations are performed until certain prefixed convergence criteria are met. Each module is solved for a stationary solution before going on to the next one.

This paper will concentrate on the depth current module, the main new contribution being the coupling between middle and current-wave boundary layers.

2. Global Model

The model here presented considers a domain vertically splitted into three layers (figure 2). To achieve a Q-3D approach (2DH + 1DV) the total current velocity vector  $\vec{u}$ , is conveniently splitted into depth uniform,  $\vec{u}$ , and depth varying  $\vec{u}$ , components.

$$\vec{u} = \vec{u} + \vec{u} \quad , \quad (1)$$

where :

$$\int_{z_0}^{z_{tr}} \vec{u} dz = 0 \quad \text{and} \quad \int_{z_0}^{z_{tr}} \bar{v} \hat{u} dz = \bar{v} \int_{z_0}^{z_{tr}} \hat{u} dz = 0 \quad \forall \bar{v}, \hat{u} \quad (2)$$

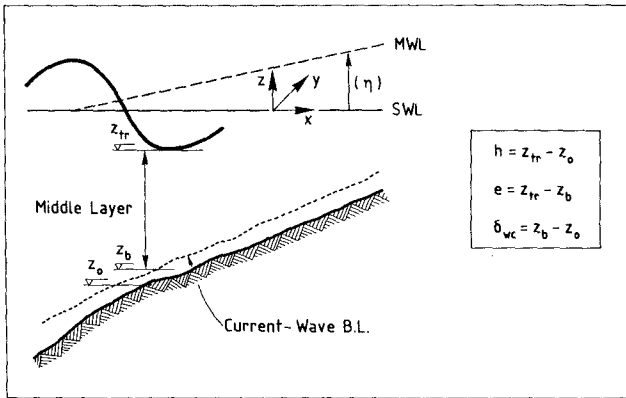


Fig. 2: Physical domain.

The upper layer is not solved. It is considered exclusively through its effects (interaction) with the middle layer via boundary conditions at trough level  $z_{tr}$ . These boundary conditions are related to the mass and momentum fluxes in the upper layer. The formulation obtained in this manner appears to be more consistent from a physical standpoint (identical boundary conditions for  $\bar{u}$  and  $\bar{u}$ , etc...) even though it also appears to be more sensitive to the selected closure submodels.

The depth-uniform Current Module solves a set of 2DH rigid-lid mass and momentum equations in a quite general manner. The equations and solution procedure have been presented elsewhere (S.-Arcilla et al. 1990). The wave driving terms appearing in these 2DH equations are:

$$\tilde{W}_i = -\frac{1}{\rho} \frac{\partial S_{ij}}{\partial x_j} - \langle \tilde{u}_i \tilde{u}_3 \rangle \Big|_{z_o}^{z_{tr}}$$

In expanded notation the  $x$  component (similarly for  $y$ ) is:

$$\tilde{W}_x = -\frac{\partial}{\partial x} \int_{z_o}^{z_{tr}} \langle \tilde{u}^2 - \tilde{w}^2 \rangle dz - \frac{\partial}{\partial y} \int_{z_o}^{z_{tr}} \langle \tilde{u} \tilde{v} \rangle dz - \langle \tilde{u} \tilde{w} \rangle \Big|_{z_o}^{z_{tr}} \quad (3)$$

in which  $\langle \rangle$  denotes time averaging at the scale of the waves and  $(\tilde{u}, \tilde{v}, \tilde{w})$  is the wave velocity vector.

It is important to remark that this term is different from the classical radiation stress tensor due to the integration limits (actual bottom and trough level) and to the inclusion of  $(\tilde{u}, \tilde{w})$  and  $(\tilde{v}, \tilde{w})$  correlations.

The wave velocity field is given by the real part of the gradient of a velocity potential whose expression is:

$$\phi = Z(z) \epsilon(x, y) \exp(-i\omega t) \quad (4)$$

$$\epsilon(x, y) = \frac{-ig}{\sigma} A \exp(iS) \quad (5)$$

in which  $\omega$  is the observed or apparent wave frequency. The wave-number vector  $\vec{K} = (K_1, K_2)$  is given by  $\vec{K} = \vec{\nabla}_H S$  and  $Z$  is the vertical shape function.

Assuming a horizontally varying amplitude field (due to breaking effects and/or diffraction caused by, for instance, a detached breakwater) and a doppler-shifted wave frequency due to the currents, the resulting wave velocity correlations obtained are (for illustration only the correlation product of vertical and horizontal velocities is here presented):

$$\langle \vec{u}_H \vec{w} \rangle = \frac{1}{2} \frac{g^2}{\sigma^2} \frac{\partial Z}{\partial z} Z A \vec{\nabla}_H A \tag{6}$$

in which  $\sigma$  is the intrinsic frequency. Equation (6) could also be considered a generalization for a 2DH context of the expression given by Deigaard and Fredsøe (1989) for normal incidence.

The resulting wave driving terms can then be written as:

$$S_{ij} = \frac{\rho}{2} \left[ \left( \frac{1}{A^2} \frac{\partial A}{\partial x_i} \frac{\partial A}{\partial x_j} + K_i K_j \right) I_1(z_{tr}) + \delta_{ij} I_2(z_{tr}) \right] \frac{g^2}{\sigma^2} A^2 \tag{7}$$

with:

$$I_1(z) = \int_{z_o}^z Z^2 dz \quad ; \quad I_2(z) = \int_{z_o}^z \left( \frac{\partial Z}{\partial z} \right)^2 dz \tag{8}$$

A linear dispersion relation has been used to obtain  $\sigma$  in terms of  $k$  and with  $k$  satisfying a Battjes (1968) type relationship:

$$\vec{K} \cdot \vec{K} = k^2 + \frac{\Delta_H A}{A} \tag{9}$$

These expressions are similar to the classical equations for the radiation stress tensor when the upper limit of integration is equal to mean water level and the correlations of horizontal/vertical wave velocities are taken as 0 (Dingemans et al. 1987). For a more complete derivation where current variations have been considered see Rivero and S.-Arcilla (1992).

The three remaining unknowns are the wave amplitude  $A$  and the wave number vector  $\vec{K}$ , which are obtained by means of a coupled system of equations: the wave action balance equation and the kinematic conservation principle (Yoo and O'Connor 1986/88).

### 3. Depth-varying current module

An alternative treatment to solve coupledly the middle and bottom-boundary layers is here proposed. The Bottom Boundary Layer Model, strongly inspired on Fredsøe (1984), has been parameterized to be compatible with the quasi-3D cost/efficiency philosophy.

#### 3.1 Middle layer

The momentum equations in the middle layer are obtained by subtracting the depth-integrated equations from the general ones. Only a simplified version of these momentum equations for  $\vec{u}$  is presented here:

$$\frac{\partial \vec{u}}{\partial t} + A\vec{u} - \frac{\partial}{\partial z}(\nu_V \frac{\partial \vec{u}}{\partial z}) = \vec{T}(z) \quad (10)$$

With

$$\vec{T}(z) = \frac{\langle \vec{\tau}_o \rangle}{\rho e} - \frac{\langle \vec{\tau}_{tr} \rangle}{\rho e} - 2G\nabla G (P_W^2 - \bar{P}_W^2) \quad (11)$$

$$A = \begin{pmatrix} \frac{\partial \bar{u}}{\partial x} & \frac{\partial \bar{u}}{\partial y} \\ \frac{\partial \bar{v}}{\partial x} & \frac{\partial \bar{v}}{\partial y} \end{pmatrix} \quad (12)$$

$$G = \nabla_H \langle \vec{Q}_s \rangle \quad (13)$$

with  $\vec{Q}_s$  being the wave plus current volume flux in the crest-to-trough layer and  $P_W$  the vertical distribution function of the vertical current velocity,  $W$ . The thickness of the middle layer is given by  $e$  and  $\langle \vec{\tau}_{tr} \rangle$  and  $\langle \vec{\tau}_o \rangle$  are, respectively, the shear stresses at trough and bottom levels.

The main hypotheses required to derive this simplified version of the momentum equation are: i) linearization (in  $\vec{u}$ ) of convective terms, ii) neglect horizontal gradients of  $\vec{u}$ , iii) neglect Coriolis effects and iv) neglect vertical nonuniformities of wave stresses. This is the equation that has been applied in the middle layer ( $z_b, z_{tr}$ ).

#### 3.2 Bottom boundary layer

The model selected for this ( $z_o, z_b$ ) layer is similar to the one proposed by Fredsøe in 1984. It was selected based on a comparison of its numerical results with data and other numerical model results (Simons et al. 1988) and

an extensive intercomparison exercise performed during MAST-I. This model does not consider turbulence from the previous wave and assumes logarithmic velocity profiles for both waves and currents. Two matching boundary conditions are applied at the top of the boundary layer,  $z_b = \delta_m + K_N/30$ , viz. continuity of current velocity and shear-stress (in the current direction). The momentum equation perpendicular to the current velocity is used to obtain an expression of the instantaneous friction velocity,  $u_*$ , as a function of the wave phase. This equation is solved using a classic Runge-Kutta method of sixth order.

### 3.3 Boundary conditions between middle layer and bottom boundary layer

At the top of the current-wave boundary layer,  $z_b$ , the present approach assumes: i) continuity of current velocity  $u$ , ii) continuity of  $\langle \tau \rangle$  (in the current plane), iii) discontinuities of  $u_*$  (from now on shear-stress at the current time-scale),  $\frac{\partial \vec{u}}{\partial z}$ , and  $\nu_V(z_b)$ . For illustration, the current shear velocity jumps from  $u_{*wc}$  (below  $z_b$ ) to  $u_{*c}$  (above  $z_b$ ). The corresponding  $\frac{\partial \vec{u}}{\partial z}$  values are:

$$\left. \frac{\partial \vec{u}}{\partial z} \right|_{z_b}^- = \frac{u_{*wc}}{(\delta_m + K_N/30)\kappa} \tag{14}$$

$$\left. \frac{\partial \vec{u}}{\partial z} \right|_{z_b}^+ = \frac{u_{*c}^2}{\nu_V(z_b)} \tag{15}$$

in which  $\delta_m$  is the mean boundary layer thickness and  $\kappa$  von Karman's constant.

The values of  $\vec{u}$  and  $d\vec{u}/dz$  at the top of the bottom boundary layer (BBL) provided by this model are used as boundary conditions for the middle layer (ML) equations. The third boundary condition is  $d\vec{u}/dz$  at  $z_{tr}$ , obtained through the  $\nu_V$  and  $\langle \vec{\tau}_{tr} \rangle$  closure submodels. The apparent excess of a boundary condition (over stated problem) is solved by considering that the friction (wave plus current) velocity at the top of the BBL is still unknown.  $u_{*c}$  at  $z_b^+$  is in fact due to bottom-induced turbulence but should also be affected by breaking-induced turbulence. This  $u_{*c}$  can be mathematically considered as an extra degree of freedom to obtain a well defined problem that is solved using an iterative process between ML and BBL.

## 4. Numerical solution of Depth Varying Current Module

### 4.1 Numerical solution of $\vec{u}$ equations

The middle layer equations are solved using a power series approximation ( $a_i z^i$ ) to reproduce the vertical variation of the unknown  $\vec{u}$  and the right-hand-side term of the equation. Time is used as a marching variable since only

stationary currents are here considered (to be consistent with the rigid lid approximation of the 2DH equations). The semi-discrete version of equation (10) can be arranged to yield at step  $n+1$  (after discretization of the time derivative):

$$\underbrace{(I + \Delta t A)}_{A_t} \vec{u}^{n+1} - \frac{\partial}{\partial z} \left( \Delta t \nu_V(z) \frac{\partial \vec{u}^{n+1}}{\partial z} \right) = \underbrace{\vec{T}(z) \Delta t + \vec{u}^n}_{\vec{R}(z)} \quad (16)$$

After a change of variable to simplify the vertical domain of variation to the interval  $(0,1)$  and to uncouple the  $(\hat{u}, \hat{v})$  equations, the following power series are introduced into the resulting momentum equation:

$$\left. \begin{aligned} \vec{w}(\xi) &= \sum_0^M \vec{w}_i \xi^i \\ \vec{R}(\xi) &= \sum_0^M \vec{r}_i \xi^i \\ K_t(\xi) &= K_0 + K_1 \xi + K_2 \xi^2 \end{aligned} \right\} \quad (17)$$

in which  $\xi$  is a normalized vertical coordinate,  $\vec{R}$  is the right hand side term of the equation and  $K_t$  is proportional to the eddy viscosity coefficient (for which a parabolic vertical distribution has been assumed). Using equations (16) and (17) a recurrence relation for the  $w_i$  coefficients for each component is obtained:

$$w_{i+1} = \left[ -e^2 r_{i-1} + (\lambda e^2 - K_2 i(i-1) w_{i-1} - i^2 K_1 w_i) \right] \frac{1}{K_0(1+i)i} \quad (18)$$

$i = 1, \dots, M$

in which  $\lambda$  is the corresponding eigen-value coming from the uncoupling of the  $\hat{u} / \hat{v}$  equations.

The solution algorithm starts from  $\frac{d\hat{u}}{dz}(z_b)$  and  $\vec{\hat{u}}(z_b)$  values (given by the BBL model in terms of  $u_{*c}$ ,  $u_{*wc}$ ,  $\delta_m$  and the artificial wave roughness  $K_w$ ) until  $\langle \vec{r}_{tr} \rangle$  is equal to the value given by the external closure submodel. Iterations are performed using  $u_{*c}$  as a degree of freedom until a convergence condition at  $z_{tr}$  is satisfied.

#### 4.2 BBL Parameterization

The main BBL equation to be solved is the momentum equation perpendicular to  $\vec{u}$ , with gives  $u_*(t)$  as a function of  $u_{*c}$ ,  $U_m$  (wave orbital velocity),  $\theta$  (wave phase) and  $\gamma$  (wave-current angle). From the obtained numerical solution the principal BBL variables ( $\delta_m$ ,  $K_w$ ,  $u_{*wc}$  and  $u_{*c}$ ) have been parameterized by means of "simple" algebraic expressions. For illustration purposes only the  $\delta_m$  parameterization is shown here.  $\frac{\delta_m}{K_N}$  is modeled by means of:

$$\frac{\delta_m}{K_N} = \frac{\delta_{90}}{K_N}(\varphi_c, \varphi_a, \gamma = 90^\circ) + \frac{\Delta\delta_\gamma}{K_N}(\varphi_c, \varphi_a, \gamma) \tag{19}$$

$$\varphi_c = \frac{u_m}{u_{*c}}, \varphi_a = \frac{a}{K_N}$$

in which  $a$  is the amplitude of the wave orbital motion and  $K_N$  is the Nikuradse roughness parameter.  $\delta_{90}$  is the boundary layer thickness for waves perpendicular to the current and  $\Delta\delta_\gamma$  is the deviation from the perpendicular case. The resulting  $\delta_m$  is shown in figure 3. As it may be seen,  $\frac{\delta_{90}}{K_N}$  can be modeled by linear expressions at both tails and by an exponential expression in the middle. The deviation,  $\frac{\Delta\delta_\gamma}{K_N}$  is modeled by means of another exponential expression.

The maximum error (with respect to the original numerical results of Fredsøe) of the proposed fit is below 4%. The corresponding error for the parameterization of  $u_{*wc}$  is smaller than 10%.

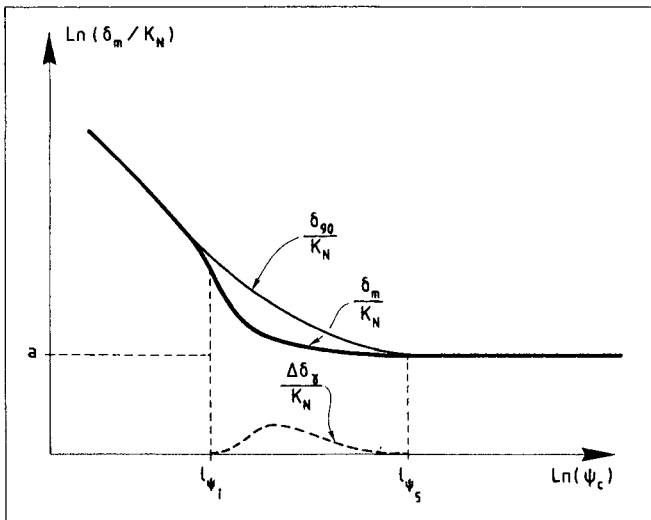


Fig. 3:  $\delta_m$  parameterization.



5. Closure Submodels

Closure submodels have been obtained from state of art formulations, the main emphasis of this paper being on the numerical model for  $\vec{u}$ . The shear stress at  $z_{tr}$  can be modeled following (De Vriend and Stive 1987) and (Svendsen 1984/85), with an equation which includes the effects of the carrying wave, the roller and a possible free surface boundary layer. Alternatively it can also be modeled using the (Deigaard and Fredsøe 1989) and (Deigaard et al. 1991) equations adapted to a 3D case. These equations, including contributions from the wave motion, the roller and the set up, have been assumed to be valid, in the direction of the wave number vector  $\vec{K}$ , for a horizontally varying problem.

The closure submodel for  $\nu_V$  is, at present:

$$\nu_V(z, x) = \frac{\kappa u_{*c}}{z_{tr}} z (z_{tr} - z) + M \left(\frac{D}{\rho}\right)^{1/3} \frac{z^2}{z_{tr}} \tag{20}$$

With  $D$  the mean rate of wave energy dissipation per unit area and  $M$  a parameter of order  $10^{-2}$ . The first term represents the current-induced eddy viscosity and is similar to the one proposed by Coffey and Nielsen (1984). Very near the bottom this term varies approximately in a linear manner with  $z$ , which is consistent with the linear variation assumed by our BBL model.

The second term (after vertical integration) is similar to previous proposals for the breaking induced eddy viscosity (e.g. De Vriend and Stive 1987, Battjes 1983). The total  $\nu_V$  is parabolic with  $z$ , which is in accordance with the latest experimental information (see figure 4).

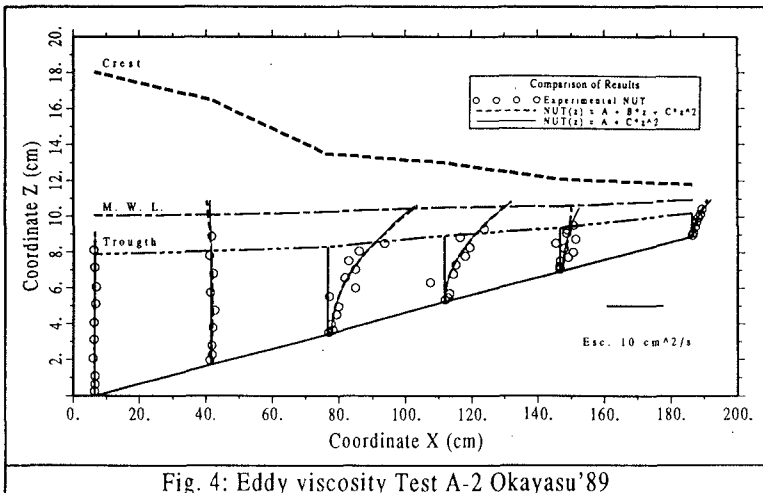


Fig. 4: Eddy viscosity Test A-2 Okayasu '89

The resulting expression may be formally written as:

$$\nu_V(\xi) = a + c\xi^2 \tag{21}$$

in which  $\xi$  is a normalized vertical coordinate ranging from 0 (at the actual bottom) to 1 (at the  $z_{tr}$  level).

6. Calibration

At this stage the model is being calibrated for a 2DV flume case, using a very complete set of data from Okayasu (1989) experiments. Figures 5 and 6 depict preliminary computed undertow profiles (corresponding to case A2 of Okayasu 1989 tests). These results have been obtained using measured data instead of external closure submodels, the main aim being the calibration of the numerical solution technique for  $\tilde{u}$ . The list of measured data used in the simulation is the following: wave height, wave period, water depth, trough level, mean velocity and its horizontal gradient, vertical velocity at  $z_{tr}$ , shear stress at  $z_{tr}$  and eddy viscosity values at  $z_{tr}$  and  $z_b$ . The orbital velocity and amplitude near the bottom have been estimated using linear long wave theory.

The next step of the calibration process corresponds to cases with oblique wave incidence for the following geometries: i) cylindrical beach, ii) semicircular bay and iii) longshore-uniform beach with a river mouth. All these test cases have been proposed within the G8M-MAST II Project.

Finally, it is convenient to remark the importance of continuing theoretical and experimental research to improve and "tune" the different closure submodels. The final solution appears to be strongly dependent on these closure relationships.

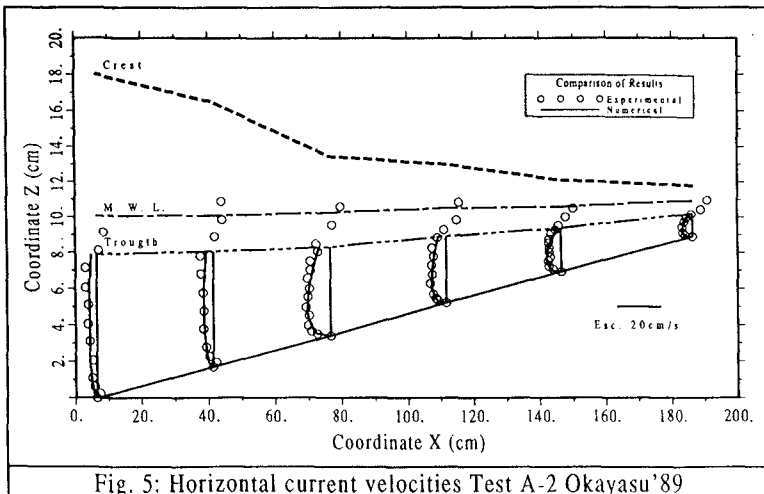


Fig. 5: Horizontal current velocities Test A-2 Okayasu '89

Table 1: Test case A2

The list of measured data used in the simulation of case A2 is:

type of breaking: plunging

wave height (H) : 7.36 cm , wave period (T) : 1.5 s

water depth (h) : 3.66 cm

trough level (  $z_{tr}$  ) : 2.40 cm

mean velocity (  $\bar{u}$  ) : 4.86 cm/s

horizontal gradient of  $\bar{u}$  (  $\frac{\partial \bar{u}}{\partial z}$  ) : 0.014 1/s

vertical velocity at  $z_{tr}$  (  $w(z_{tr})$  ) : 0.1 cm/s

vertical distribution of  $w(z)$

eddy viscosity at  $z_{tr}$  (  $\nu_t(z_{tr})$  ) : 3.0 cm\*\*2/s

eddy viscosity at  $z_b$  (  $\nu_t(z_b)$  ) : 1.0 cm\*\*2/s

bottom roughness (estimated) (  $K_N$  ) : 1.0 mm.

orbital amplitude (a) or max. free stream velocity (  $Um$  ) (estimated by linear long wave theory) : 24.6 cm/s

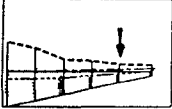
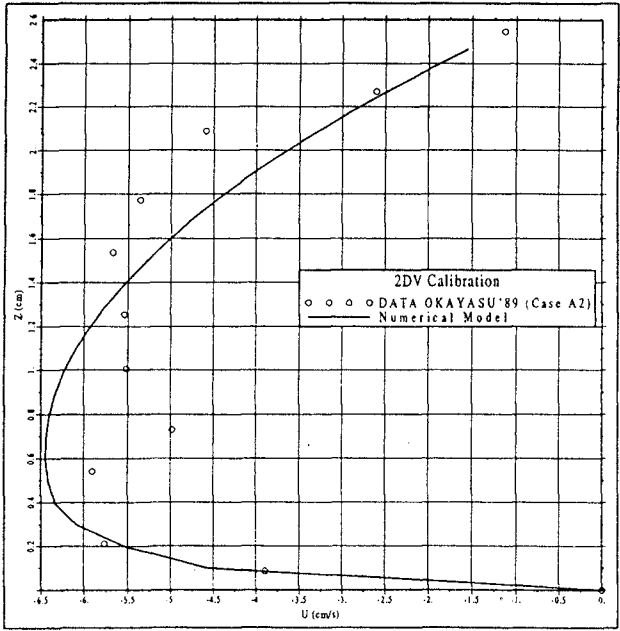



Fig. 6: Measured and computed velocities.

## 7. Discussion and Future Work

**7.1 Discussion:** An economic strategy to combine a 2DH Surf Zone circulation code with a 1DV "profile extraction" model has been established. The use of the current (in the presence of waves) friction velocity,  $u_{*c}$ , as a degree of freedom to solve the apparent over-statement of the problem works well for a  $\nu_V$  corrected by breaking effects at the top of the bottom boundary layer.

The  $\nu_V$  values given by the bottom boundary layer model are well below the experimental values of  $\nu_V$  inside the surf zone. This explains the relatively strong curvature of the  $\hat{u}$  profile right above the bottom boundary layer, which is not very consistent with the experimental data. This means that the  $\nu_V$  increment at  $z_b$  must be larger than the increase given by the bottom boundary layer relationship ( $\nu_V(z_b) = \kappa u_{*c} z_b$ ). This increment is given in the model by the addition the breaking-induced of  $\nu_V$ .

From the standpoint of the numerical solution, the  $\vec{u}$  equation becomes ill-conditioned for very small values of  $\nu_V$ . This is because there is a singularity at  $z_b$  when  $\nu_V(z_b) = 0$ . At this singularity the coefficients of the series expansion become inordinately large. Similar problems also appear with large  $\nu_V$  values near trough level.

The number of terms required in the power series development for  $\hat{u}(z)$ , inside the surf zone, depends on the type of  $z$ -dependence assumed for  $\nu_V$ . The number of terms used is determined by checking that the zero vertical-average condition for  $\vec{u}$  (mass conservation) is accurately satisfied.

The undertow profiles, considered to be more demanding from the standpoint of this model validation, were selected as the first case for calibration. For the  $\hat{v}$  equation (basically the longshore current) the double-logarithm hypothesis at  $z_b$  of the BBL model is expected to hold much more easily (the changes in vertical curvature of  $\hat{v}(z)$  are much smaller).

**7.2 Future work:** With respect to future work there are three main tasks already under way:

- To check the theoretical compatibility between the expressions for  $\langle \vec{\tau}_{ir} \rangle$  and the corresponding equations for the wave-driving terms,  $\vec{W}_i$ .
- To analyze the model sensitivity to the  $\nu_V$  value at  $z_b$  and to obtain  $\nu_V(z)$  closure sub-models which provide a better fit to the observed  $\vec{u}(z)$ .
- To test and improve all external closure sub-models.

The next step is, obviously, to run the model for a true 3D problem, to prove its quasi-3D capabilities. This in spite of the lack of reliable 3D data inside the surf zone.

## 8. Acknowledgements

This work was undertaken as part of the MAST-G6 Coastal Morphodynamics research programme. It was funded jointly by the Programa de Clima Marítimo (PCM-MOPT), Ministerio de E. y C. of Spain and by the Commission of the European Communities D.G.XIII under contract no. MAST-0035-C. Thanks are due to all research staff of LIM-UPC, particularly to Mr. F. Rivero, Mr. M. Coussirat and Mr. J. Flores. The experimental information was kindly facilitated by Dr. A. Okayasu.

## 9. References

- Battjes, J. (1983) "Surf zone turbulence". Proc. 20th IAHR Cong., Moscow.
- Coffey, F.C. and Nielsen, P. (1984) "Aspects of Wave Current Boundary Layer Flows". Proc. I.C.C.E., ASCE, pp 2232-2245.
- Deigaard, R. and Fredsøe, J. (1989) "Shear stress distribution in dissipative water waves". Coastal Engineering, 13, pp. 357-378.
- Deigaard, R.; Justensen, P. and Fredsøe, J. (1991) "Modelling of Undertow by one equation turbulence model", Coastal Engineering, 15, N° 5-6.
- De Vriend, H. and Stive, M.J.F. (1987) "Quasi-3D modelling of nearshore currents". Coastal Engineering, 11, pp 565-601.
- Dingemans, M.; Radder, A. and De Vriend H. (1987) "Computations of the driving forces of wave-induced currents". Coastal Engineering, 11, pp 539-563.
- Fredsøe, J. (1984) "The turbulent boundary layer in Wave-Current Motion", J.H.E, ASCE, Vol 110, N° 8, pp 1103-1120.
- Okayasu, A. (1989) "Characteristics of turbulence structure and undertow in the surf zone", Ph.D. thesis, University of Tokio, Japan.
- Rivero, F. and Sánchez-Arcilla, A. (1992) "Propagation of linear water waves over slowly varying depth and currents". LIM-UPC, Internal report, Universidad Politécnica de Cataluña, Barcelona.
- Sánchez-Arcilla, A.; Collado, F.; Lemos, C. and Rivero, F. (1990) "Another quasi-3D model for surf-zone Flows", ICCE, ASCE, Delft, pp. 316-329.
- Sánchez-Arcilla, A.; Collado, F. and Rodriguez A. (1991) "Nearcir model for Q-3D Nearshore Circulation". Proc. Mid-Term Workshop Coastal Morphodynamics, Edimburg, G6M-MAST, 2.16.
- Simons, R.; Kyriacou, A.; Soulsby, R. and Davies, A. (1988) "Predicting the nearbed turbulent flow in waves and currents". Proc. IAHR Symp., Copenhagen, pp 33-47.
- Svendsen, I.A. (1984) "Mass Flux and Undertow in a Surf-Zone". Coastal Engineering 8, pgs. 299-307.
- Svendsen, I.A. (1985) "On the formulation of the cross shore Wave-current problem". European workshop on Coastal Zones, Athens, pp 1.1-1.9.
- Yoo, D. (1986) "Mathematical modelling of waves-currents interacted flow in shallow waters". Ph.D. Thesis, University of Manchester, U.K.
- Yoo, D. and O'Connor (1988) "Diffraction of waves in caustic". JWW, ASCE, Vol 114, No. 6, pp 715-731.

## CHAPTER 216

### VERTICAL STRUCTURE OF THE NEARSHORE CURRENT AT DELILAH: MEASURED AND MODELED

Jane McKee Smith<sup>1</sup>, Ib A. Svendsen<sup>2</sup>, and Uday Putrevu<sup>3</sup>

**ABSTRACT:** Comprehensive field measurements were made of the vertical current structure on a barred beach profile at the DELILAH project during October of 1990. The current was measured with five electromagnetic current meters mounted on a mobile sled which was stationed at three to eight cross-shore positions. The incident directional wave spectra, bathymetry, tide, wind, and cross-shore wave transformation were also measured. A numerical model was developed to calculate the random wave transformation based on the model of Dally, Dean, and Dalrymple (1985) (Larson and Kraus 1991) and the local vertical current structure (Putrevu and Svendsen 1991). The model predicted the shape of the current profiles well with a root-mean-square error in velocity of 5.9 cm/sec. The model tended to underpredict the velocity over the bar crest.

### INTRODUCTION

Predicting the vertical structure of the cross-shore current is a critical step to advancing the modeling of beach evolution, especially the response of the beach profile to storms, the post-storm profile recovery, and the development and movement of bars. The cross-shore currents have also been shown to be important in describing the mixing for longshore currents (Putrevu and Svendsen 1992, Svendsen and Putrevu 1992b). The lack of high-quality field measurements of the vertical current structure has been a hinderance to the development and validation of cross-shore current models.

In October of 1990, a comprehensive field experiment was performed at the U.S. Army Engineer Waterways Experiment Station, Coastal Engineering Research Center

---

<sup>1</sup>Res. Hyd. Engr., US Army Engr. Waterways Exp. Sta., Coast. Engrg. Res. Center, 3909 Halls Ferry Rd., Vicksburg, MS 39180-6199, USA.

<sup>2</sup>Prof., Dept. of Civil Engrg., Univ. of Delaware, Newark, DE 19716, USA.

<sup>3</sup>Res. Assoc., Dept. of Civil Engrg., Univ. of Delaware, Newark, DE 19716, USA.

(CERC), Field Research Facility (FRF) in Duck, NC, to measure the wind- and wave-forced three-dimensional nearshore hydrodynamics. The DELILAH (Duck Experiment on Low-frequency and Incident-band Longshore and Across-shore Hydrodynamics) experiment was a cooperative project involving researchers from CERC, Naval Postgraduate School, Naval Research Lab, Oregon State University, Quest Integrated, Inc., Scripps Institution of Oceanography, University of California at Santa Cruz, and Washington State University.

The hydrodynamic data collected at DELILAH were used to refine and verify a numerical model developed to calculate the vertical variation of the cross-shore current. The purpose of this paper is to describe the DELILAH field measurements and to describe the application of these data to evaluate the numerical model.

### DELILAH FIELD PROJECT

The core of the DELILAH field project was a fixed array of 19 electromagnetic current meters deployed in one cross-shore array and two longshore arrays to the north of the FRF pier. The cross-shore array consisted of nine sensor positions, extending from the shoreline to 350 m offshore (4-m depth). A pressure gage was deployed along with a current meter at each position in the cross-shore array. The longshore arrays were positioned approximately on the bar crest and in the trough of the beach profile. The longshore arrays were approximately 200 m long.

The bathymetry adjacent to the current meter arrays (340 m by 600 m area) was surveyed daily during the experiment. Accurate surveying was accomplished with a special self-contained vehicle, the CRAB (Coastal Research Amphibious Buggy), that drove along survey transects (Birkemeier and Mason 1984). The position and elevation of the CRAB was determined with a Geodimeter auto-tracking electronic total station. Fig. 1 shows an example of the bathymetry surveyed on 19 October 1990. The bathymetry was generally homogeneous in the longshore direction during the cross-shore current measurements, with a linear bar approximately 100 m offshore. Offshore directional wave spectra were measured with an array of sixteen pressure gages at the 8-m depth contour. Spectra were measured every 3 hours during the experiment and provide offshore boundary conditions for wave forcing of the current model. Fig. 2 shows the two-dimensional spectrum measured on 19 October 1990 at 1300. In Fig. 2, the x-axis is the frequency,  $f$ , the y-axis is the wave direction (measured counter-clockwise from shore normal),  $\theta$ , and the z-axis is the energy density,  $S$ . Over-water winds and tidal elevation were measured at the FRF pier.

### CROSS-SHORE CURRENT MEASUREMENTS

The vertical structure of the current was measured with a vertical array of five electromagnetic current meters mounted on a mobile sled. The meters were mounted at elevations 0.35 m, 0.6 m, 1.0 m, 1.35 m, and 1.75 m above the bed on a vertically sloping beam. The beam was parallel to the shoreline, so the meters were aligned in the cross-shore. The meters were spread over a longshore distance of approximately 3.5 m. The sled was always deployed so that the lower end of the beam was in the updrift direction of the longshore current to reduce interference of the flow. A common timing pulse was used for all the current meters to reduce interference between instruments for this close proximity deployment. The meters measured the longshore and cross-shore components of the

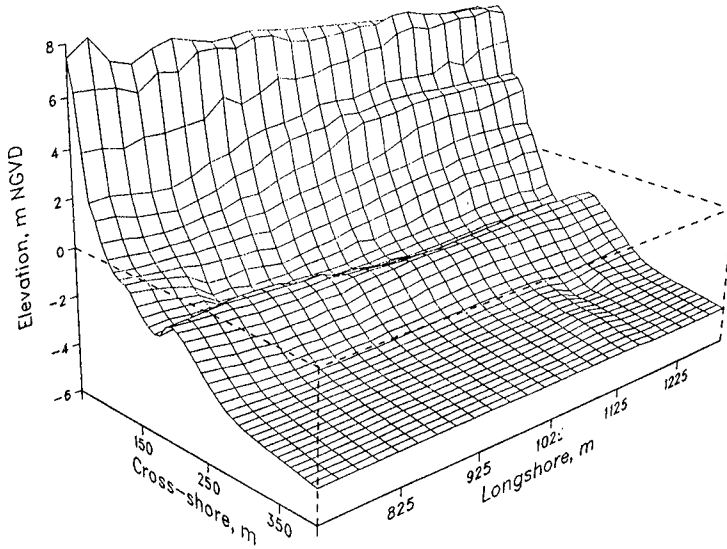


Figure 1. Bathymetry for 19 October 1990.

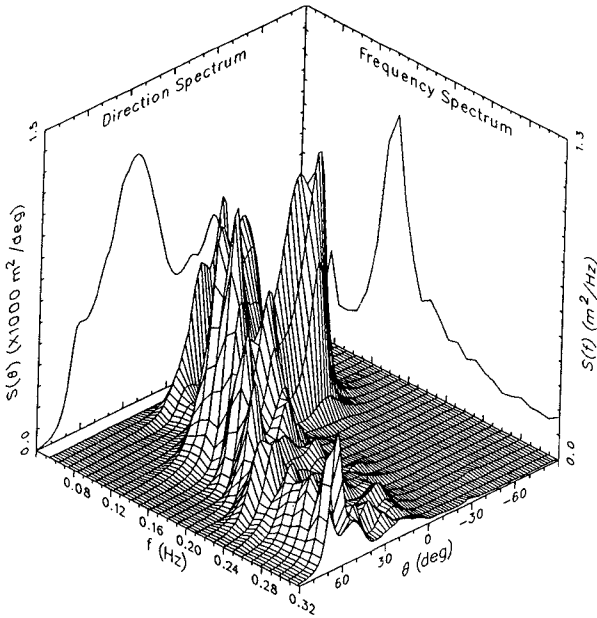


Figure 2. Two-dimensional spectrum for 19 October 1990.



current. The sled was also instrumented with a pressure gage, a resistance wave staff, and an anemometer.

During the experiment, the sled was towed offshore of the breaker zone by the CRAB to a depth of approximately 3 m. The sled was then pulled back to shore with a fork lift in steps of 20 m. At each sled position, data were collected for 34 minutes. The collection period of 34 minutes was selected to balance the competing needs for long time series for stable statistics and short total time for the sled deployment to ensure stationarity of the incident waves. All current data presented are 34 minute averages. The data were telemetered to shore for real-time data quality checking. Three to eight cross-shore positions were occupied during each of eight deployments. The position and orientation of the sled were recorded using an electronic total station which sighted two prisms located on the sled mast.

The sled was deployed near the cross-shore array of current meters and pressure gages. The fixed array gages provided background data on the horizontal structure of the hydrodynamics and on the stationarity of the waves and currents. Fig. 3 shows an example of the vertical structure of the cross-shore current measured during DELILAH. The vectors in Fig. 3 represent cross-shore current magnitude and direction measured at six sled positions on 19 October 1990. The solid lines in Fig. 3 represent the survey datum and bottom profile ( $d$ ). Sled measurements were made during the final six days of the DELILAH experiment. Incident waves during these days provided a variety of conditions with wave heights of 0.5 to 1.5 m, peak spectral periods of 5 to 15 sec, wind speeds of 5 to 15 m/sec, and wave directions both north and south of shorenormal. The maximum time-averaged current velocities exceeded 0.5 m/sec during measurements with the sled.

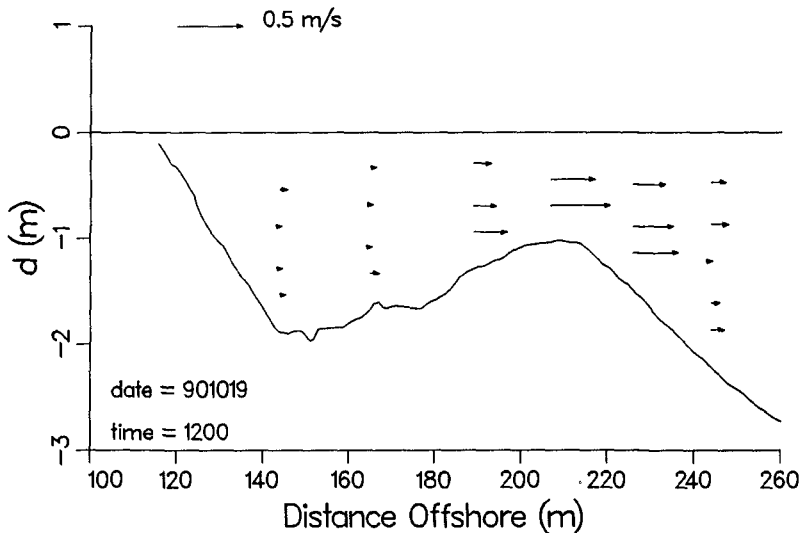


Figure 3. Cross-shore current velocities measured during DELILAH (19 Oct 1990).

## NUMERICAL MODEL

The numerical model consists of two parts, a random wave transformation model and a model of the cross-shore flow. The wave transformation model provides the cross-shore gradient in wave height and the cross-shore variation in the mean water level which are the driving forces of the cross-shore flow. The models assume longshore homogeneity, linear wave theory, and steady-state wave forcing. Wave-current and wave-wave interactions and long wave generation are neglected.

### Wave Transformation

The random wave transformation model is based on the decay and reformation model of Dally, Dean, and Dalrymple (1985) as applied to random waves by Larson and Kraus (1991). The Dally, Dean, and Dalrymple model has been shown to be less accurate than other models for predicting wave setup (Svendsen and Putrevu 1992a), the main driving force for the undertow, but it was chosen because it includes a mechanism for breaking waves to reform in the trough shoreward of the longshore bar. The input wave parameters are the root-mean-square wave height ( $H_{rms}$ ), peak wave period, and peak wave direction measured at the linear array in a depth of 8 m. One hundred wave heights were randomly chosen from a Rayleigh distribution specified by  $H_{rms}$ . Each of the one hundred wave heights was transformed across the beach profile, assuming the same period and incident direction for each wave, according to

$$\frac{d(F \cos \theta)}{dx} = \frac{\kappa}{d} (F - F_s) \quad (1)$$

where

- $F = 0.125 \rho g H^2 C_g$ , energy flux
- $\rho$  = water density
- $g$  = gravitational acceleration
- $H$  = individual wave height
- $C_g$  = group velocity
- $\theta$  = wave direction, relative to shore normal
- $x$  = cross-shore coordinate, positive seaward
- $d$  = total water depth (still-water plus setup)
- $F_s$  = stable energy flux associated with the stable wave height,  $H_s$
- $H_s = \Gamma d$ , with  $\Gamma = 0.4$  (Dally, Dean, and Dalrymple 1985)

The parameter  $\kappa$  is zero seaward of wave breaking, with breaking specified by a height to depth ratio less than 0.78. At incipient wave breaking,  $\kappa$  is set to 0.15. Wave breaking ceases when the broken height is less than  $H_s$ , and  $\kappa$  is reset to zero. The wave directions are determined by Snell's law. The wave parameters were calculated at a 1-m cross-shore spaced grid using an explicit finite difference solution. The  $H_{rms}$  was calculated at each grid point from the 100 individual wave heights.

The wave setup,  $\bar{\eta}$ , is calculated from the time- and depth-averaged cross-shore momentum equation

$$\rho g(h + \bar{\eta}) \frac{d\bar{\eta}}{dx} = -\frac{dS_{xx}}{dx} - \rho_a C_w W W_x \quad (2)$$

where

- $h$  = still-water depth (including the tide)
- $\rho_a$  = air density
- $C_w$  = wind drag coefficient
- $W$  = wind speed
- $W_x$  = cross-shore component of the wind velocity
- $S_{xx}$  = cross-shore component of radiation stress

The two driving forces of the setup are the gradient in radiation stress and the cross-shore wind stress. The radiation stress is calculated using linear wave theory (Longuet-Higgins and Stewart 1964) based on  $H_{rms}$ . Considering the simplifying assumptions used to represent the random wave field, a more sophisticated evaluation of the radiation stress (Svendsen and Putrevu 1992a) is not justified. The wind drag coefficient given by the WAMDI Group (1988) is adopted in the model ( $C_w = .0012875$  for  $W < 7.5$  m/sec;  $C_w = 0.0008 + 0.000065 W$  for  $W > 7.5$  m/sec). The bed shear stress is known to be small and is neglected in Eq. 2. One iteration was required between the calculation of the wave height transformation and the wave setup.

### The Cross-shore Current

The vertical variation of the current is modeled with a three-layer approach (Hansen and Svendsen 1984; Stive and de Vriend 1987; Svendsen and Hansen 1988). The velocity distribution in the central layer is calculated as a local solution of the depth-dependent, cross-shore momentum equation with the surface and lower layers contributing boundary conditions. The central layer extends from the bottom boundary layer to the trough level. The lower layer, the bottom boundary layer, relates the near bottom current velocity to the mean bottom stress (Svendsen and Putrevu 1990). The upper layer contributes the mass flux which is balanced by the undertow in the central layer. In the present application, it is assumed that no net cross-shore flow exists, i.e., the mass flux above the trough balances the undertow. Forcing for the vertical variation includes gradients in radiation stress, mean current, and setup. The horizontal gradient terms in the model are calculated from the depth-integrated, one-dimensional model described above.

The vertical current structure is calculated from a double integration of the depth-dependent, cross-shore momentum equation (Putrevu and Svendsen 1991)

$$U(\zeta) = U_b + \alpha \frac{\zeta^2}{2\nu_{tz}} + \frac{\tau_{bx}\zeta}{\rho\nu_{tz}} \quad (3)$$

where

- $\zeta$  = vertical coordinate, measured positive from the bottom
- $U$  = cross-shore velocity at elevation  $\zeta$

- $\tau_{bx}$  = bottom stress (Eq. 4)
- $U_b$  = bottom velocity (Eq. 5)
- $\alpha$  = driving force for the undertow (Eq. 6)
- $\nu_z$  = eddy viscosity (Eq. 8)

In deriving Eq. 3 both  $\alpha$  and  $\nu_z$  have been assumed constant over depth. The bottom boundary condition includes the bottom stress

$$\tau_{bx} = \rho \frac{2}{\pi} f_w u_0 U_b \tag{4}$$

where

- $f_w$  = bottom friction factor
- $u_0$  = wave orbital velocity at the bottom

and the bottom velocity. The bottom velocity is determined from the depth integration of Eq. 3 with Eq. 4 substituted for the bottom stress

$$U_b = \frac{\bar{U} - \frac{\alpha d_t^2}{6 \nu_{tz}}}{1 + \frac{f_w d_t u_0}{2 \pi \nu_{tz}}} \tag{5}$$

where

- $d_t$  = depth to trough level
- $\bar{U}$  = mean undertow velocity (Eq. 7)

The driving force in Eqs. 3 and 5 is given by

$$\alpha = g \frac{d\bar{\eta}}{dx} + \bar{U} \frac{d\bar{U}}{dx} + u_w \frac{du_w}{dx} + \frac{\rho_a}{\rho} \frac{C_w W W_x}{d_t} \tag{6}$$

where  $u_w$  is the depth-averaged wave velocity and  $\rho_a$  is the density of air. The boundary condition from the upper layer is the mass transport above the trough elevation, which balances the undertow. The mass transport is proportional to  $CH^2/d$ , where  $C$  is the wave celerity, and the constant of proportionality was found to be approximately -0.3 based on the undertow measurements. The mean undertow in Eq. 5 is given by

$$\bar{U} = \frac{0.3 \sqrt{g(h + \bar{\eta})} H^2 \cos \theta}{(h + \bar{\eta})^2} \tag{7}$$

In the numerical computations we have used the same eddy viscosity at all depths, given by

$$v_{rz} = 0.05 \sim 0.01 \sqrt{g(h + \bar{\eta})_b (h + \bar{\eta})_b} \quad (8)$$

where the subscript  $b$  indicates incipient breaking conditions. In laboratory experiments on a plane beach,  $v_z$  has been found to vary as  $h\sqrt{g\bar{h}}$ . The simplification of constant  $v_z$  is chosen because the depth over the region of the DELILAH measurements varies only between 1.2 and 2.2 m, and little information is available about the variation of  $v_z$  under field conditions.

## MODEL RESULTS

The model was applied to the 8 cases of DELILAH sled data. The results from 3 cases are shown in Figs. 4 through 9. These cases were selected because they cover a variety of conditions with the largest number of sled positions. These cases are typical of the conditions and measurements during the final week of DELILAH. Table 1 summarizes the input conditions for the cases shown in Figs. 4 through 9. The wind ( $\phi$ ) and wave directions are measured counter-clockwise from shore normal. The input peak wave direction,  $\theta$ , and peak spectral period,  $T_p$ , were measured at the 8-m array. The peak wave parameters best represent the dominant wave characteristics. Fig. 2 shows considerable spread in the directional distribution of wave energy, which could strongly influence longshore currents, but has less effect on cross-shore currents. The input wave height was taken from the most seaward of the nine nearshore pressure gages (4-m depth), and the height was inversely refracted and shoaled to the 8-m depth to correspond to the wave direction and period inputs. The height measured at the 8-m array caused a 15% overprediction of the wave height at the most seaward pressure gage, which may be attributable to the use of linear refraction and shoaling in the model. The tide and wind measurements were made at the FRF pier and are averaged values over the sled deployment. For these cases, the sled was deployed spanning low tide to minimize the effect of varying tide elevation.

Table 1. Model input conditions for sample results.

Date	Time	$H_{rms}$ (m)	$\theta$ (deg)	$T_p$ (sec)	Tide (m)	$W$ (m/s)	$\phi$ (deg)
10/17	1000	0.54	-15.0	9.7	-0.47	7.8	130.5
10/18	1100	0.57	-43.0	5.6	-0.62	11.9	79.7
10/19	1200	0.65	24.0	7.0	-0.48	9.1	-51.9

The model results are compared to the field measurements in Figs. 4, 6, and 8 for the cases listed in Table 1. The figures show the measured wave height from the cross-shore array (x), calculated wave height (solid line), calculated setup (chain-dot line),

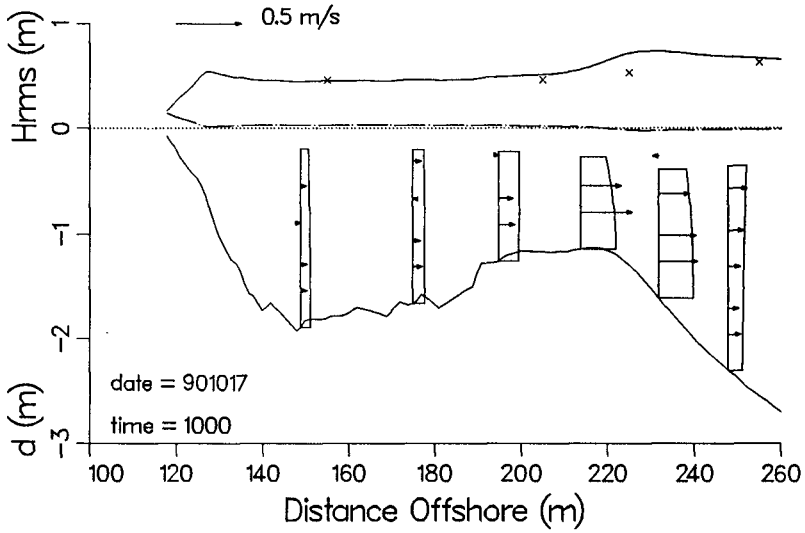


Figure 4. Model results versus measurements (17 October 1990).

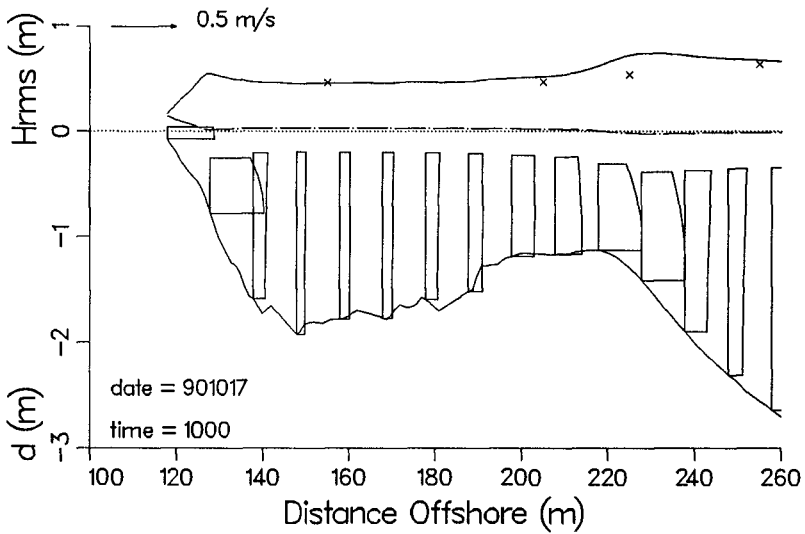


Figure 5. Model results (17 October 1990).

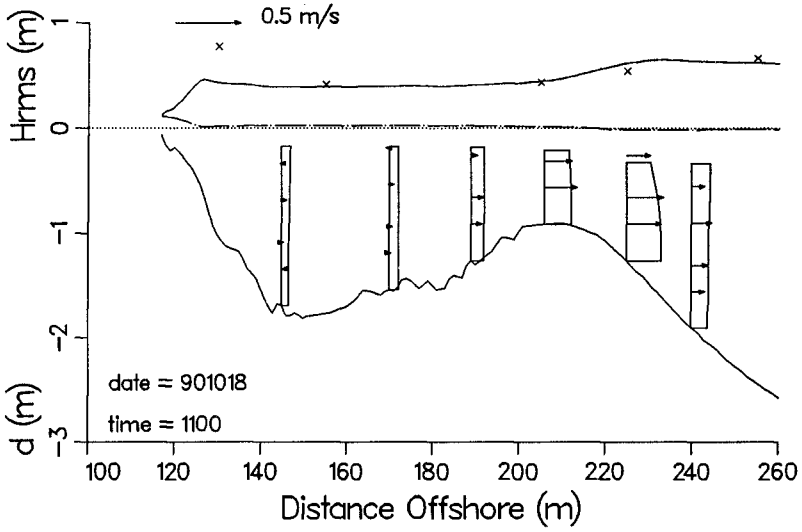


Figure 6. Model results versus measurements (18 October 1990).

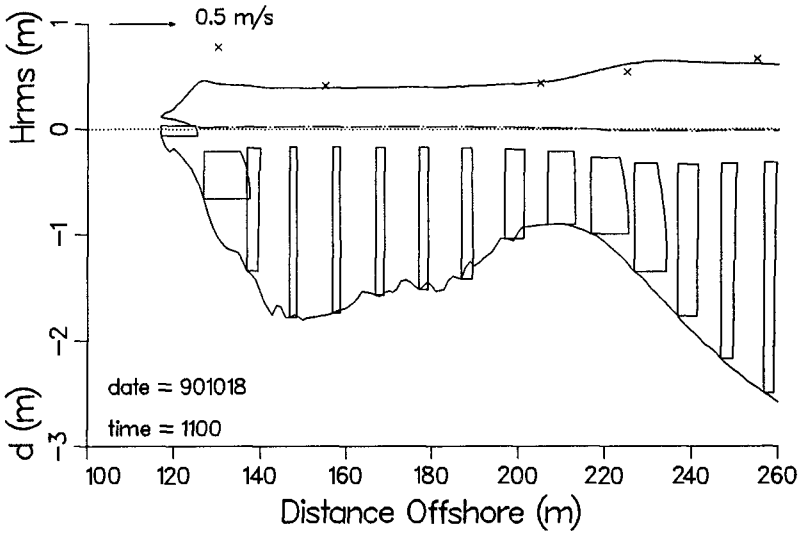


Figure 7. Model results (18 October 1990).

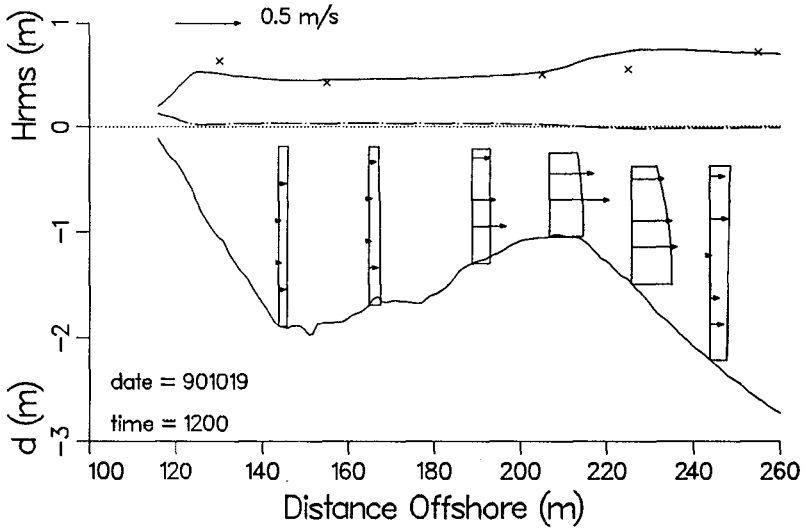


Figure 8. Model results versus measurements (19 October 1990).

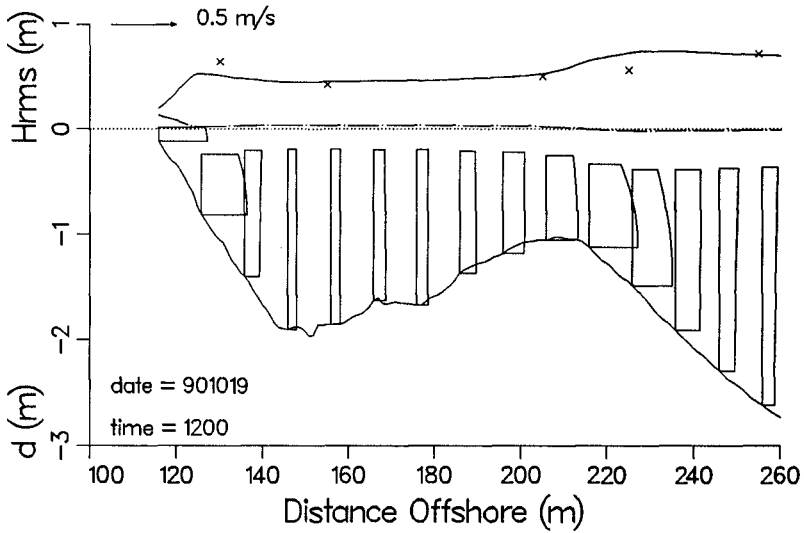


Figure 9. Model results (19 October 1990).



measured cross-shore current from the sled (vectors), and the calculated cross-shore current at the sled positions. Figs. 5, 7, and 9 show the calculated cross-shore current at 10-m intervals to show the cross-shore variation of the undertow profile. Offshore of the breaker zone, the profiles are fairly uniform over depth with a small increase in the offshore velocity near the wave trough level. In the region of rapid wave decay, on the bar crest, the profiles show a characteristic parabolic shape with highest velocities near the bed and smaller velocities at the wave trough. Shoreward of the bar, the waves have reformed and the current profiles are uniform over depth. The cross-shore velocities are low shoreward of the bar. The waves break again on the steep foreshore, and the velocity profiles are similar to those on the bar.

For all cases, the bottom friction factor was set to a constant value of 0.01 and the eddy viscosity to a value of 0.05. The model is relatively insensitive to value of the bottom friction factor, but the shape of the undertow profiles is sensitive to the value of eddy viscosity. Theoretically, the value of the eddy viscosity should be lower in regions of low turbulence (no wave breaking) and higher in regions of intense turbulence (breaker zone), but since the relationship between eddy viscosity and the model parameters is not well known, a constant value was applied. Although the wind speeds were significant during the measurements (8 to 12 m/sec), the wind had very little influence on the results. For the three cases listed in Table 1, the maximum difference in undertow velocity between with- and without-wind simulations was 0.005 m/sec and the root-mean-square (RMS) difference was 0.0012 m/sec.

The RMS error in the cross-shore current results for the 3 cases shown was 5.9 cm/sec. The errors were smallest offshore of the crest of the bar. In the bathymetry trough, the measured velocities were generally 0 to 5 cm/sec, and the RMS error was of the same order. This is not surprising since the low velocities are near the accuracy of the instruments and are susceptible to contamination from the longshore currents which are strong in the trough. The largest RMS errors occurred on the top of the bar (3 to 15 cm/sec), where the model tended to underpredict the measurements, although the model predicted the shape of the undertow profile well. The model results (Figs. 5, 7, and 9) show the maximum undertow velocities just seaward of the crest of the bar, while the measurements show the maximum velocities at the crest of the bar. Errors in the calculation of the wave height may contribute to the underprediction of the undertow at the bar crest (errors in wave height are magnified by squaring the wave height to calculate radiation stress). Also, previous laboratory experiments have shown a shoreward shift in the initiation of setup (the driving force in the model) in the transition region of breaking waves (Svendsen 1984; Roelvink and Stive 1989). This same effect may account for the underprediction of the undertow at the bar crest. Unfortunately, the measurements are not dense enough in the region of the bar crest to resolve this issue.

## CONCLUSIONS

Comprehensive measurements of the vertical current structure and the wave and wind forcing were made during the DELILAH field project in October of 1990 on a barred beach bathymetry. The measurements show strong offshore velocities over the bar (0.5 m/sec), and vertical structure of the current was generally parabolic. In the bathymetry trough, the offshore current was weak (0 to 0.05 m/sec) and the structure was uniform over depth. Offshore of the bar, the current was fairly uniform over depth (0.10 to 0.15 m/sec)

to 0.15 m/sec) with a small increase in velocity near the wave trough.

The numerical model developed to calculate the cross-shore (1-D) random wave transformation and vertical current structure compared well with the measurements. The RMS error in prediction of the current was 5.9 cm/sec. The model represented the shape of the vertical current structure well, but tended to underpredict the current magnitude at the bar crest.

## ACKNOWLEDGMENTS

The authors would like to acknowledge the team that designed and constructed the instrument sled for DELILAH: Messrs. Kent Hathaway, William Grogg, and Eugene Bichner (CERC) and Dr. Edward Thornton and Mr. Robert Wyland (Naval Postgraduate School). Dr. Robert Guza (Scripps Institution of Oceanography) provided useful insight on the field calibration of current meters which was greatly appreciated. The research presented in this paper was conducted under the Nearshore Waves and Currents work unit, Coastal Flooding and Storm Protection Program, by the US Army Engineer Waterways Experiment Station, Coastal Engineering Research Center. Permission to publish this paper was granted by the Office, Chief of Engineers.

## REFERENCES

- Birkemeier, W. A., and Mason, C. (1984). The CRAB: a unique nearshore research vehicle. *J. Surveying Engrg.*, 1-7.
- Dally, W. R., Dean, R. G., and Dalrymple, R. A. (1985). Wave height variation across beaches of arbitrary profile. *J. Geophys. Res.*, 90(C6), 11917-11927.
- Hansen, J. B., and Svendsen, I. A. (1984). A theoretical and experimental study of undertow. *Proc. 19th Coastal Engrg. Conf.*, ASCE, 2246-2262.
- Larson, M., and Kraus, N. C. (1991). Numerical model of longshore current over bar and trough beaches. *J. Waterway, Port, Coast., and Oc. Engrg.*, ASCE, 117(4), 326-347.
- Longuet-Higgins, M. S., and Stewart, R. W. (1964). Radiation stress in water waves; a physical discussion with applications. *Deep Sea Res.*, 11(4), 529-562.
- Putrevu, U., and Svendsen, I. A. (1991). Wave induced nearshore currents: a study of the forcing, mixing and stability characteristics. *Research Report No. CACR-91-11*, Center for Applied Research, University of Delaware.
- Putrevu, U., and Svendsen, I. A. (1992). A mixing mechanism in the nearshore region. *Proc. 23rd Coastal Engrg. Conf.*, ASCE, this volume.
- Roelvink, J. A., and Stive, M. J. F. (1989). Bar-generating cross-shore flow mechanisms on a beach. *J. Geophys. Res.*, 94(C4), 4785-4800.
- Stive, M. J. F., and de Vriend, H. J. (1987). Quasi-3D nearshore current modelling: wave-induced secondary current. *Proc. Coastal Hydrodynamics*, ASCE, 356-370.
- Svendsen, I. A. (1984). Wave heights and set-up in a surf zone. *Coastal Engrg.*, 8, 303-329.
- Svendsen, I. A., and Hansen, J. B. (1988). Cross-shore currents in surf-zone modelling. *Coastal Engrg.*, 12, 23-42.
- Svendsen, I. A., and Putrevu, U. (1990). Nearshore circulation with 3-D profiles. *Proc. 22nd Coastal Engrg. Conf.*, ASCE, 241-254.

- Svendsen, I. A., and Putrevu, U. (1992a). Surf-zone wave parameters from experimental data. *Coastal Engrg.*, in press.
- Svendsen, I. A., and Putrevu, U. (1992b). Nearshore mixing and dispersion. Submitted for publication.
- WAMDI Group (1988). The WAM model: a third generation ocean wave prediction model. *J. Physical Oceanography*, American Meteorological Society, December, 1775-1810.

## CHAPTER 217

### A REVIEW OF WAVE/CURRENT-INDUCED SCOUR AROUND PIPELINES

B.M. Sumer<sup>1</sup> and J. Fredsøe<sup>1</sup>

#### ABSTRACT

A comprehensive review is presented of scour around pipelines in the case of non-cohesive sediment. The review is organized in four main sections, namely the two-dimensional scour, the three-dimensional scour, the effect of scour on forces on and vibrations of pipelines and the mathematical modelling of scour process. Over sixty works were included in the review.

#### 1. INTRODUCTION

Marine pipelines are used for disposal of industrial and municipal wastewater into the sea, for cooling water in nuclear power plants, and for the transportation of gas and crude oil from offshore platforms. Marine cables, on the other hand, are increasingly used for communication.

Design of marine pipelines and marine cables with regard to their stability is a rather complicated problem. One of the factors which needs to be taken into consideration in the design process is the scour around the pipeline.

The scour around the pipeline is caused by the very presence of the pipeline itself. There are numerous aspects of the problem which need to be addressed during the design process, such as the formation of spans (particularly in determining the maximum extent of spans as well as timing of any remedial action), the self-burial of pipelines, the effect of self-burial on the pipeline stability, just to give a few examples.

A large volume of knowledge has been accumulated on the subject during the last decade or so, as a result of intensive research activities in countries such as Holland, Norway, U.K., U.S.A., Denmark and several others. The purpose of the present paper is to review this research work. Only the non-cohesive sediment bed is considered.

---

<sup>1</sup> Institute of Hydrodynamics and Hydraulic Engineering  
Technical University of Denmark

## 2. TWO-DIMENSIONAL SCOUR

### Onset of scour

Consider a pipeline which is laid on an erodible bed. Assume that the bed, soil and flow conditions are the same along the length of the pipe, i.e. the conditions are strictly two-dimensional. If the initial embedment of the pipeline is not very large and if the flow around the pipe is sufficiently strong, scour may break out underneath the pipe. The stage at which the scour breaks out is called the onset of scour.

The onset of scour is directly related to the seepage flow which occurs in the sand beneath the pipe, caused by the pressure difference between the upstream and the downstream of the pipe (Fig. 1c). When the flow velocity is gradually increased, a critical point is approached where the discharge of the seepage flow is increased more rapidly than the driving pressure difference dictates. Simultaneously the surface of the sand at the immediate downstream of the pipe rises and eventually a mixture of sand and water breaks through the space underneath the pipe. This phenomenon is called piping and is well known in soil mechanics in hydraulic structures such as dams, cofferdams etc. (Terzaghi, 1948).

The conditions under which the onset of scour occurs below pipelines have been studied by Mao (1986) and Chiew (1990) in steady currents. Mao described the role of separation vortices that form in front and at the rear of the pipe in the process of the onset of scour. Also, he discussed the seepage flow underneath the pipe in relation to the onset of scour. The latter has been further elaborated by Chiew. Chiew further linked the onset of scour to the phenomenon of piping.

In the case of waves, the piping conditions are created underneath the pipe in the same way as in steady currents. The action is immediate. However, if the conditions are such that the critical condition is not attained immediately, then the action of separation vortices will become important to create scour more early in the wave case. Sumer & Fredsøe (1991) has linked the onset of scour in waves to the latter through the Keulegan-Carpenter number and expressed the critical condition for the onset of scour by the following empirical equation

$$\frac{e_{cr}}{D} = 0.1 \ln(KC) \quad (1)$$

in which  $e_{cr}$  = the critical embedment of the pipe beyond which no scour occurs,  $D$  = the pipe diameter and  $KC$  = the Keulegan-Carpenter number defined by

$$KC = \frac{U_m T_w}{D} \quad (2)$$

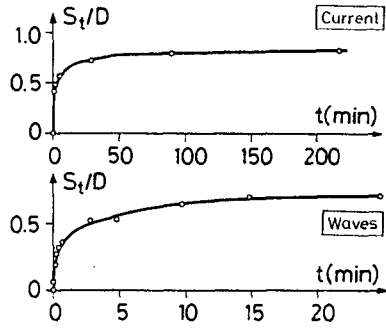
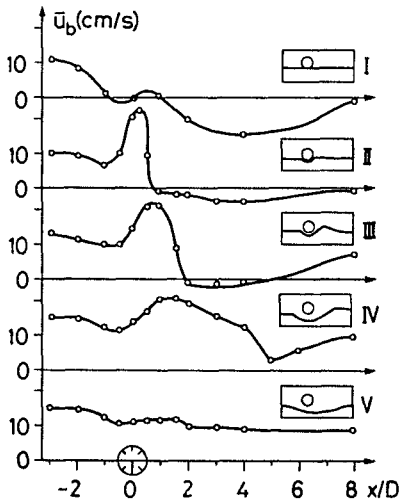
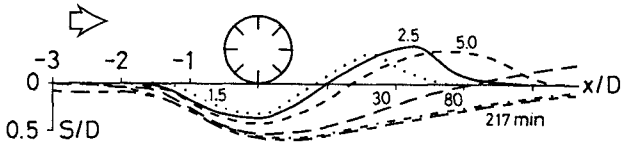
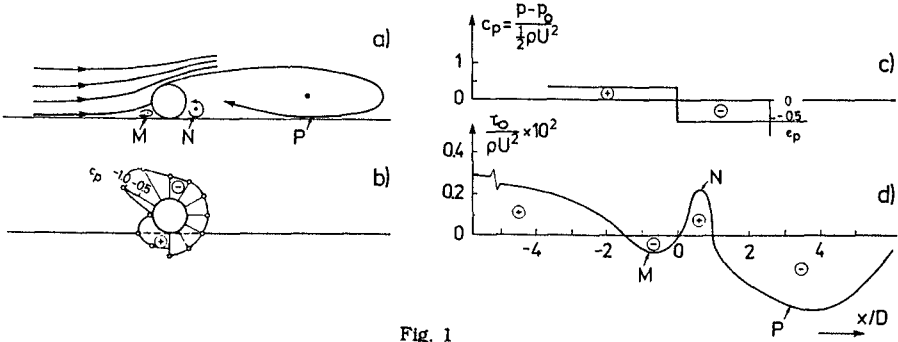
in which  $U_m$  = the maximum value of the orbital velocity of water particles at the bed,  $T_w$  = the wave period. For a sinusoidal motion of water particles  $KC$  will obviously be

$$KC = \frac{2\pi a}{D} \quad (3)$$

in which  $a$  = the amplitude of the orbital motion of water particles at the bed.

### Time development of scour

The onset of scour is followed by the stage of so-called *tunnel erosion* (Leeuwenstein et al., 1985; Hansen et al., 1986). Sumer et al. (1990) present data regarding bed shear stress just under the pipe corresponding to this stage. The data indicate that the bed shear stress is



increased by a factor of 4 with respect to its undisturbed value, resulting in an increase in the sediment transport rate of a factor of 8. This explains why the scour below the pipe occurs so fast and so violently during the tunnel erosion.

The tunnel erosion is followed by the stage called *lee-wake erosion*. In this stage, the scour downstream of the pipe is governed by the lee-wake of the pipe. Sumer et al. (1988b) made an investigation of the effect of lee-wake on scour. This work demonstrates that 1) vortex shedding is present in the lee-wake from rather early stages of the scouring process, and 2) the scour downstream of the pipe is eventually governed by this organized flow.

Fig. 2 shows a typical example where the time development of scour can be seen. The mild slope of the downstream portion of the scour profile is due to the action of the pipe's lee-wake.

As seen from the figure, the scour process attains an equilibrium stage where scouring below the pipe comes to an end. When this stage is reached, the sediment transport will be the same at all sections over the reach of the scour hole, and therefore the amount of sediment which enters the scour hole will obviously be identical to that leaving the scour hole.

Fig. 3 shows the results of Jensen et al.'s (1990) velocity measurements very close to the bed at different stages of the scour process. The figure shows that, while the velocity below the pipe is increased tremendously at the initial stage of the scour process (Profile II), it eventually becomes practically identical to the undisturbed flow velocity, as the scour approaches towards its equilibrium stage (Profile V).

The depth of the scour hole is probably the most significant quantity. Normally, it is taken as the depth of the scour hole just below the pipe.

The scour depth develops towards the fully-developed equilibrium stage through a transitional period, as illustrated in Fig. 4 for a pipe rigidly placed on a bed with initially zero gap. The depth corresponding to the fully-developed stage is called the *equilibrium scour depth*. It is also seen from the figure that a certain period of time must be elapsed for a substantial amount of scour to develop. This time is called the *time scale* of scour process.

The equilibrium scour depth, as well as the time scale of the scour process, constitute two major parameters in scour studies. The remaining part of this section will focus on these two parameters.

### Equilibrium scour depth

Scour depth has been studied extensively in the case of *steady currents* (Chao & Hennessy (1972), Kjeldsen et al. (1973), Littlejohns (1977), Herbich (1981), Bijker & Leeuwenstein (1984), Lucassen (1984), Leeuwenstein et al. (1985), Herbich (1985), Herbich et al. (1984), Bijker (1986), Ibrahim & Nalluri (1986), Mao (1986), Kristiansen (1988) and Kristiansen & Tørum (1989)).

Kjeldsen et al. (1973) was the first to conduct scour experiments under controlled conditions. The experiments were done in live-bed situations. Kjeldsen et al.'s data indicated that the equilibrium scour depth can be expressed by the following relation:

$$S = 0.972 \left( \frac{V^2}{2g} \right)^{0.2} D^{0.8} \quad (4)$$

in which  $V$  = the mean flow velocity. This relation suggests that

$$\frac{S}{D} \propto \theta^{0.2} \quad (5)$$

in which  $\theta$  = the Shields parameter defined by

$$\theta = \frac{U_f^2}{g(s-1)d} \tag{6}$$

in which  $U_f$  = the bed friction velocity, corresponding to the undisturbed flow,  $g$  = the acceleration due to gravity,  $s$  = the specific gravity of sediment grains and  $d$  = the grain size.

Eq. 5 implies that the normalized scour depth  $S/D$  is only a weak function of  $\theta$ . We shall return to this point later in this section.

The exact flow picture created by the presence of the pipe depends on the following quantities: the pipe diameter  $D$ , the flow velocity  $V$ , the kinematic viscosity of the fluid  $\nu$ , the pipe roughness  $k$ , and the grain diameter  $d$  of the bed material. From these quantities, the dimensionless equilibrium scour depth can be found to depend on the following parameters:

$$\frac{S}{D} = \frac{S}{D} (k^*, R, \theta) \tag{7}$$

in which  $k^* = k/D$  is the relative roughness,  $R = VD/\nu$  is the pipe Reynolds number.

Of the three parameters that appear in Eq. 7, the influence of  $k^*$  and the Reynolds number appears through their effect on the downstream flow of the pipe. If the pipe is hydraulically rough, the wake flow is almost unaffected by the Reynolds number, while for a hydraulically smooth pipe some influence of the Reynolds number is expected in the downstream vortex-shedding pattern. Fig. 5 shows a plot of the data by Kjeldsen et al. (1973), Lucassen (1984), Mao (1986) and Kristiansen (1988) on the scour depth below smooth pipes exposed to a current. It is seen in the figure that there is some weak influence of the Reynolds number on the scour depth, because a slight decrease in  $S$  occurs for Reynolds number around  $10^5 - 3 \times 10^5$ . For a free circular cylinder, this coincides with the transition from subcritical to supercritical flow (Schewe (1983), Sumer and Fredsøe (1988)). In this transition region, the vortex shedding becomes less pronounced, which might lead to a smaller lee-wake erosion and hence less scour depth.

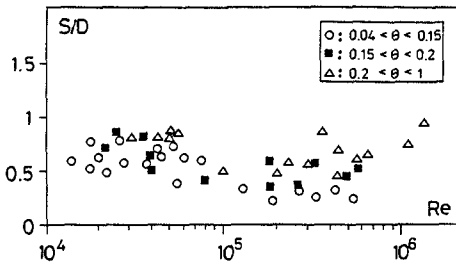


Fig. 5

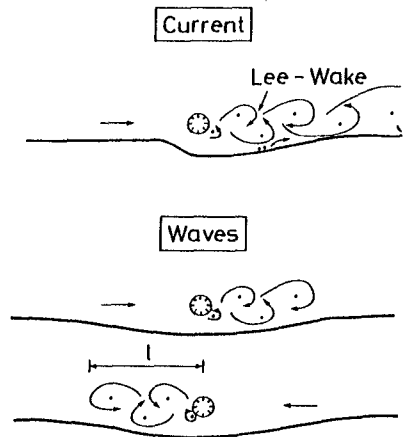


Fig. 6



As far as the influence of  $\theta$  is concerned, this must be examined in two different categories: the clear-water case, where the sediment far from the pipe is not moving ( $\theta < \theta_{cr}$ ), and the live-bed case, where sediment is transported far from the pipe ( $\theta > \theta_{cr}$ ), in which  $\theta_{cr}$  = the threshold value of  $\theta$  for sediment motion. In the clear water case, the variation in scour depth with  $\theta$  is more pronounced: as  $S/D$  increases from 0 at very small  $\theta$ -values up to values of 0.4 - 1.0 when the  $\theta$ -value approaches the live-bed case. However, when the live-bed case is obtained, very small variation in  $S/D$  is observed, as seen from Fig. 5, as has already been pointed out in conjunction with Kjeldsen et al.'s empirical equation (Eqs. 4 and 5). Ignoring this weak variation it may be suggested that, for all practical purposes, the following relation may be used as the design equation, to predict the equilibrium scour depth in steady currents

$$S/D = 0.6 \pm 0.1 \quad (8)$$

in which the first figure on the right hand side of the equation is the mean of the data plotted in Fig. 5, and the second is the standard deviation.

Regarding the scour in *tidal flows and waves*, the main difference between this case and the steady case is that the downstream-formed wake system now occurs on both sides of the pipeline. Here the strong lee-wake erosion, which gives a much more gentle downstream slope, occurs on both sides of the pipe (Fig. 6). The formation and extension of the wake pattern in oscillatory motion is governed by KC number. Therefore it must be expected that there exists a correlation between the equilibrium scour depth and KC number. Sumer & Fredsøe (1990) demonstrated that this is indeed the case. Based on their experimental data and Lucassen's (1984) data (which were recast in terms of KC number), the following empirical equation was established, relating the equilibrium scour depth to KC number for the live-bed situation ( $\theta > \theta_{cr}$ ) and for a pipe initially in contact with the bed:

$$S/D = 0.1\sqrt{KC} \quad (9)$$

The data suggests that this equation is valid in a very broad range of KC, namely from KC = 2 to about 300. This relation has been confirmed later by Gökçe & Günbak's (1991) experiments and Hansen's (1992) numerical-model results.

Sumer & Fredsøe (1990) discussed also the effect of Shields parameter as well as Re-number dependence plus the effect of the presence of ripples in the wave-flume tests.

Generally, the equations given in the preceding, namely Eqs. 4 or 8 and Eq. 9 may be used as design equations. However, there are several other factors which may influence the scour depth. Of these factors, the following may be mentioned: The pipe position in vertical (Leeuwenstein et al. (1985), Mao (1986), Sumer & Fredsøe (1990)), the roughness of pipe surface (Sumer & Fredsøe (1990)), the angle of attack of the flow (Mao (1988), Hansen (1992)), the current in combined waves and current (Hansen (1992)), the case of multiple pipelines (Westerhorstmann et al. (1992)), the armoring of bed sediment (Sidek & Ibrahim (1992)), vibrations of the pipe (Sumer et al. (1988a)) and the Shields parameter in clear-water scour (Mao (1986), Hansen (1992)).

### Time scale

As mentioned previously, the scour depth develops towards its equilibrium stage through a transitional period (Fig. 4), which can be represented by the following relation:

$$S_t = S \left( 1 - \exp\left(-\frac{t}{T}\right) \right) \quad (10)$$

The quantity T is defined as the time scale of the scour process and represents the time period during which a substantial scour develops.

Fredsøe et al. (1992) has made a study of this time scale in both steady currents and waves. They found that the time scale normalized as in the following

$$T^* = \frac{[g(s-1)d^3]^{1/2}}{D^2} T \quad (11)$$

is a function of  $\theta$ , the Shields parameter. Based on their own data as well as the data from Kjeldsen et al. (1973) and Mao (1986), they found that the relation between  $T^*$  and  $\theta$  can be represented by the following simple expression

$$T^* = \frac{1}{50} \theta^{-5/3} \quad (12)$$

for the live bed situation ( $\theta > \theta_{cr}$ ) and for a pipe with an initially zero gap. This equation was found to be valid for both steady currents and waves. Fredsøe et al. (1992) attributed this to the fact that the lee-wake scour -- the key element in the wave induced scour -- is insignificant at the initial stage of the scour process. Therefore the time scale is unable to differentiate whether the flow is a steady-current or a wave-induced flow. In Fredsøe et al. (1992) study, also the effect of change in wave climate has been investigated.

### 3. THREE-DIMENSIONAL SCOUR

#### General description

Two-dimensional scour below pipelines, as observed in two-dimensional flume test with a fixed pipe, must in the field turn to three-dimensional scour picture as sketched in Fig. 7 in order to obtain support for the pipeline. Hereby, a three-dimensional scour pattern arises as sketched in Figs. 7a and 7b: a number of scour holes is interrupted by a stretch, where the pipeline is partially or totally buried.

The scour picture in the free-span areas (Section B-B) is two-dimensional, while at other places, particularly in the neighbourhood of span shoulders (Section A-A), it is three-dimensional. See Fig. 8 for a definition sketch.

At Section A-A, the pipe sinks in the soil. This is due to the combined action of three-dimensional scour and soil failure, as will be explained in the following section.

At Section B-B, on the other hand, the scour, after it breaks out, spreads along the length of the pipeline. When the scour hole becomes sufficiently long, the pipe begins to sag into its naturally created trench hole. This may continue until the pipe comes into the neighbourhood of the bottom, which eventually brings an end to the scouring process. From this moment onwards, the backfilling process starts, and later on, the pipeline may partially or fully become covered by sand (self-burial).

#### Rate of spread of scour along the pipe

The rate of spread of the three-dimensional scour along the pipe is one of the major parameters. Research dealing with this quantity is not extensive. Gravesen & Fredsøe (1983) gave an account of how to deal with the problem when extending the results of model experiments to the nature. Also, various accounts of the spreading process have been given in Leeuwenstein (1985) and Bernetti et al. (1990). Hansen et al. (1991), on the other hand, has presented a semi-empirical model of the process, which can predict the rate of spread of scour along the pipe.

In the case when the current approaches the pipe at an oblique angle, the free span will migrate. This aspect has been investigated by Hansen et al. (1991).

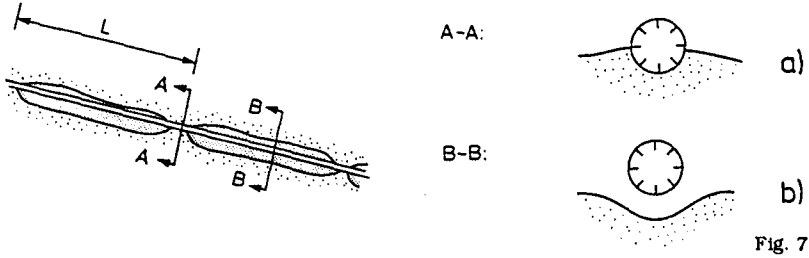


Fig. 7

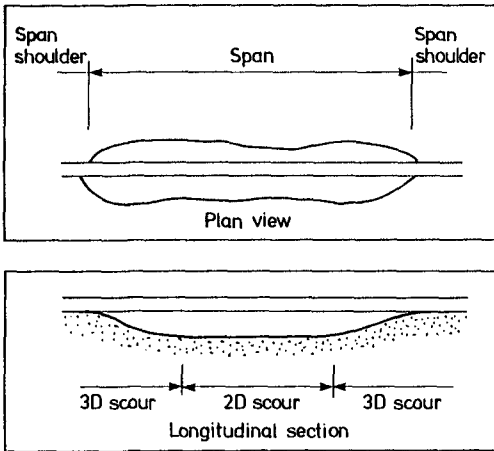


Fig. 8

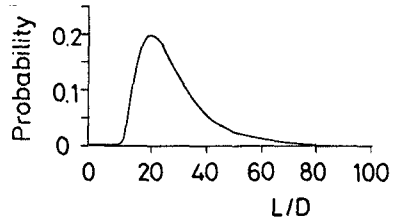


Fig. 9

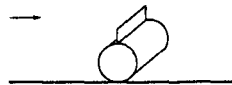


Fig. 10

Effect of pipe sagging on scour

Normally the time scale of span development,  $T_h$ , is large compared with  $T$ , the time scale of the two-dimensional scour described in the preceding section, (Eq. 10). Here  $T_h$  = the time period during which a substantial span length develops to produce some measurable deflection in the middle of the span. The time scales  $T_h$  and  $T$  may be estimated using the relations given in Hansen et al. (1991) and Fredsøe et al. (1992) (Eq. 12), respectively. While  $T_h$  may be in the order of magnitude of days,  $T$  is only in the order of magnitude of hours. This means that the pipe normally begins to sag long after the two-dimensional scour has attained its equilibrium stage. However, the sagging may influence the final scour profile and indeed the final scour depth. Effect of pipe sagging on scour has been investigated by various authors, employing two-dimensional laboratory models (Leeuwenstein et al. (1985), Fredsøe et al. (1988), Gökçe & Günbak (1991)). Backfilling and self-burial in the free-span areas has also been investigated by employing the same two-dimensional models in some of these studies.

Length of free spans

The length of free spans is also of engineering interest. Fig. 9 shows the probability density function of span length obtained by Orgill et al. (1992), based on some limited field data which,

the authors point out, is very site-specific. The figure shows that there is considerable variation in  $L/D$ , ranging from 10 to as much as 100 with the mean value of about 20.

Various authors have considered various factors with regard to the assessment of scour-induced free-span lengths (Fredsoe et al. (1988), Brushi et al. (1986), Eide et al. (1988), Bernetti et al. (1990), Bruschi et al. (1991) and Bijker et al. (1992)). In Fredsoe et al. (1988) work, the free-span length has been related to the so-called stiffness-length of the pipe.

#### Pipe sinking at span shoulders

Pipe sinking is caused by soil failure, as has already been pointed out in the preceding paragraphs. The soil failure itself may be due to a general shear failure or it may be due to liquefaction.

Sumer & Fredsoe (1993) made an investigation of sinking of pipelines at span shoulders employing a rigid pipe in the laboratory in a current flume. Sumer & Fredsoe's investigation was directed towards the understanding of the sinking process of a pipeline in the soil caused by a general shear failure. A simple formula adopted from soil mechanics regarding the bearing capacity of soil was found to give a satisfactory result in relation to the sinking of the pipe at the span shoulder.

The subject liquefaction in relation to pipelines laid on the sea-bed has been investigated by Silvis (1990). Bijker et al. (1991) gives a brief account of the liquefaction potential of seabed with regard to the presence of laid pipelines.

#### Stimulated self-burial

As has been seen in the preceding paragraphs, pipelines laid on the seabed may bury themselves in the seabed by various mechanisms. This may occur in the free-span areas where the pipe sags into its scour hole and is covered by sand upon the termination of the sagging process. It may also occur at the span shoulders where the pipe sinks in the sand.

After the discovery that a few months after a 12" pipeline (laid in 1980 on the North Sea bottom in the Dutch sector) caused the formation of a trench, 3 pipe diameter deep and then it gradually sank in this trench and buried itself with the thickness of the covering sand layer of more than 30 cm (Kroezen et al. (1982)), the Delft Hydraulic Laboratory has launched an extensive series of research to investigate the feasibility of a method, called stimulated self-burial, to exploit the self-burial potential (Hulsbergen (1984), Hulsbergen (1986), Hulsbergen & Bijker (1989)). This is particularly important in the circumstances where pipelines would not bury themselves fast enough or they would not at all bury themselves. The idea is to stimulate a controlled local scour by using fins (called spoiler) attached to the pipeline as sketched in Fig. 10. From the research carried out by the Delft Hydraulics, it was found that, firstly, the spoiler reduces the time necessary to accomplish a given embedment level by a factor of ten with respect to a plain pipe, and secondly, the final depth of burial is larger than in the case of plain pipelines. The same effects have been observed also in waves (Gökçe & Günbak (1991)).

#### 4. EFFECT OF SCOUR ON FORCES AND VIBRATIONS

Obviously forces on and vibrations of a pipe over a scoured bed will be different from those experienced when the pipe sits on a plane bed. Jensen et al. (1990) has investigated forces on a pipe at different stages of scour process in steady current, using frozen scoured-bed models. Stansby & Starr (1991) has measured forces on a pipe gradually sinking in the bed under flow action in both steady current and waves.

Effect of scour on hydroelastic vibrations of pipelines, on the other hand, has been studied

in steady currents (Sumer et al. (1988a), Kristiansen (1988) and Kristiansen & Tørum (1989)) and in waves (Sumer et al. (1989)).

Forces have been measured also on pipeline models with attached spoilers with different embedment ratios (representing different stages of the self-burial process) (Hulsbergen & Bijker (1989)).

## 5. MATHEMATICAL MODELLING

The studies concerning mathematical modelling of scouring process may broadly be divided into three categories: 1) the studies dealing with mathematical models based on potential-flow theory, 2) those dealing with  $k-\epsilon$  models and 3) those dealing with discrete-vortex models.

Regarding the potential-flow models, Chao & Hennessy (1972) was the first to apply the simple potential solution to the flow in the gap between the pipe and the bed. As a matter of fact, the potential flow around a cylinder placed near a wall was described by von Müller in as early as 1929. Müller's potential flow description was modified by Fredsøe & Hansen (1987) by taking into consideration the actual, measured velocity at the top and bottom edges of the cylinder. This modification is significant particularly in the case of very small gaps where the potential theory overpredicts the velocity in the gap. Hansen et al. (1986) later implemented the same line of thought as in Fredsøe & Hansen, and developed a potential theory for the case of a cylinder over a scoured bed. In both models, only the flow upstream of the pipe is described by the potential theory. (Clearly the downstream flow, i.e. the lee-wake, cannot be described by a potential flow model). The results of scour prediction by Hansen et al.'s (1986) potential flow description agreed satisfactorily with the experiments. Recently, Hansen (1992), with a simple representation of the lee wake, extended this model so as to cover waves. His model results give a fairly good agreement with Sumer & Fredsøe's (1990) empirical result (Eq. 9). Using the same model, he also examined the effect of Shields parameter, the effect of current in combined waves and current and the effect of angle of attack. Bernetti et al. (1990) has also developed a mathematical model of scour below pipelines. The model has two main components, namely the two-dimensional scour component and the three-dimensional scour component. The two-dimensional scour component was based on Chao & Hennessy's (1972) potential-flow description. Bernetti et al.'s model is able to predict also the development of the three-dimensional scour, the free-span length and sinking of the pipe at span shoulders. The model has been tested against simple cases where data is available (Mao (1986)). The model performance for these test cases appeared to be quite satisfactory.

The second group of mathematical modelling studies concerns the  $k-\epsilon$  simulation of the flow (Leeuwenstein & Wind (1984) and van Beek & Wind (1990)). As is well known, the  $k-\epsilon$  model is successfully used in various fields of fluid mechanics (Rodi (1984)). Regarding its application in scour below pipelines, Leeuwenstein & Wind has calculated the flow around the pipe over a scoured bed with such a model and made the morphological calculations by use of sediment continuity equation along with a sediment-transport equation. In the follow-up study, van Beek & Wind extended the model so as to cover also the suspended-load transport in the morphological calculations.

The third group of studies in mathematical modelling of scour concerns the discrete-vortex-model simulation of the flow around pipes (Sumer et al. (1988a), Jensen et al. (1990) and Jensen et al. (1989)). The particular model which has been used in these studies is the so-called cloud-in-cell method. The computational details of the method is well documented in the literature (see for example Stansby & Dixon (1983)). The method is able to predict the gross behaviour of the vortices in the lee wake of the pipe. This enabled Sumer et al. (1988b) to study the effect of lee-wake vortices on the bed shear stress downstream of the pipe over both a plane bed and a scoured bed. The method was later used by the same group to simulate flow around a pipe over a scoured bed in steady currents (Jensen et al. (1990) and in waves (Jensen et al. (1989)).

Finally, it may be mentioned that an integrated approach has been adopted recently by

the Danish Hydraulic Institute and the Delft Hydraulics in a joint study, to develop a computer model which would enable the engineer to decide on occurrence and disappearance of scour along a pipeline/cable, pipeline/cable self-burial, trench backfilling, migrating sand waves exposure and undermining of pipelines or cables. A brief account of this study has been reported by Staub & Bijker (1990).

#### ACKNOWLEDGEMENT

The study is partially supported by the research programme "Marine Techniqe" of the Danish Scientific Council (STVF).

#### REFERENCES

- Bearman, P.W. and Zdravkovich, M.M. (1978). Flow around a circular cylinder near a plane boundary. *J. Fluid Mech.*, 89, Part 1, pp. 33-48.
- Bernetti, R., Bruschi, R., Valentini, V. and Venturi, M. (1990). Pipelines placed on erodible seabeds. Proceedings of the 9th Int. Conference on Offshore Mechanics and Arctic Engineering, Houston, Texas, ASME, V., pp. 155-164.
- Bijker, E.W. (1986). Scour around structures. Proc. 20th Coast. Engrg. Conf., Taipei, Taiwan, pp. 1754-1768.
- Bijker, E.W. and Leeuwenstein, N. (1984). Interaction between pipelines and the seabed under the influence of waves and currents. *Seabed Mechanics*, B. Denness, ed., Graham and Trotman, Gettysburg, Md., pp. 235-242.
- Bijker, R., Staub, C., Silvis, S. and Bruschi, R. (1991). Scour-induced free spans. Proceedings of the 23rd Offshore Technology Conference, Houston, Texas, May 6-9, 1991, Paper No. OTC 6762, pp. 583-588.
- Bruschi, R., Cimbali, W., Leopardi, G. and Vincenzi, M. (1986). Scour induced free span analysis. Proceedings of the 5th International Offshore Mechanics and Arctic Engineering Symposium, April 13-18, 1986, III, pp. 656-669.
- Bruschi, R., Curti, G. Tura, F. (1991). Free spanning pipelines: A Review. Presentation at the First International Offshore and Polar Engineering Conference (ISOPE), 11-16 August, 1991, Edinburgh, U.K.
- Chao, J.L. and Hennessy, P.V. (1972). Local scour under ocean outfall pipelines. *Jour. Water Pollution Control Fed.*, 44, No. 7, pp. 1443-1447.
- Chiew, Y-M. (1990). Mechanics of local scour around submarine pipelines. *J. Hydraulic Engineering, ASCE*, 116, No. 4, pp. 515-529.
- Eide, L.O., Leopardi, G. and Bruschi, R. (1988). The experience from the Statpipe system on free span development and analysis. Offshore Pipeline Technology Seminar, Stavanger, Norway.
- Fredsoe, J. and Hansen, E.A. (1987). Lift forces on pipelines in steady flow. *J. Waterway, Port, Coastal and Ocean Engineering, ASCE*, 113, No. 2, pp. 139-155.
- Fredsoe, J., Hansen, E.A., Mao, Y. and Sumer, B.M. (1988). Three-dimensional scour below pipelines. *Trans. ASME, Journal of Offshore Mechanics and Arctic Engineering*, 110, pp. 373-379. Also in: Proceedings of the 6th Int. Symp. on Offshore Mech. and Arctic Engrg., ASME, pp. 29-36, 1987.

- Fredsøe, J., Sumer, B.M. and Arnskov, M.M. (1992). Time scale for wave/current scour below pipelines. *International Jour. Offshore and Polar Engineering*, 2, No. 2, pp. 13-17, 1992. Also in *Proceedings of the First International Offshore and Polar Engng. Conf. (ISOPE 91)*, II, pp. 301-307.
- Gökçe, T. and Günbak, A.R. (1991). Self-burial and stimulated self-burial of pipelines by waves. *Proc. of the First (1991) International Offshore and Polar Engineering Conf., Edinburgh, U.K. 11-16 August, 1991*, II, pp. 308-314.
- Gravesen, H. and Fredsøe, J. (1983). Modelling of liquefaction, scour and natural backfilling process in relation to marine pipelines. *Offshore oil and Gas Pipeline Technology, European Seminar, Feb. 2-3, 1983, Copenhagen*.
- Hansen, E.A. (1992). Scour below pipelines and cables: A simple model. *Proceedings of 11th Offshore Mechanics and Arctic Engineering Conference (OMAE 92), June 7-11, 1992, V-A, Pipeline technology, ASME*, pp. 133-138.
- Hansen, E.A., Fredsøe, J., and Mao, Y. (1986). Two dimensional scour below pipelines. *Fifth Internat. Symp. on Offshore Mech. and Arctic Engrg., ASME*, 3, pp. 670-678.
- Hansen, E.A., Staub, C., Fredsøe, J. and Sumer, B.M. (1991). Time-development of scour induced free spans of pipelines. *Proceedings of the 10th Offshore Mechanics and Arctic Engineering Conference, Stavanger, Norway, V, Pipeline Technology, ASME*, pp. 25-31.
- Herbich, J.B. (1981). Scour around pipelines and other objects. *Offshore pipeline design elements*. Marcell Dekker, Inc., New York, N.Y.
- Herbich, J.B. (1985). Hydromechanics of submarine pipelines: Design problems. *Can. J. Civ. Engrg.*, 12(4), pp. 863-887.
- Herbich, J.B., Schiller, R.E., Jr., Watanabe, R.K. and Dunlap, W.A. (1984). Scour around pipelines. *Sea floor scour-Design guidelines for ocean founded structures (Ocean engineering 4)*, Marcell Dekker, Inc., New York, N.Y., pp. 203-210.
- Hulsbergen, C.H. (1984). Stimulated Self-Burial of Submarine Pipelines. *Proceedings of the 16th Offshore Technology Conference, Houston, Texas, May 7-9, 1984, Paper No. OTC 4667*, pp. 171-177.
- Hulsbergen, C.H. (1986). Spoilers for stimulated self-burial of submarine pipelines. *Proceedings of the 18th Offshore Technology Conference, Houston, Texas, May 5-8, 1986, Paper No. OTC 5339*, pp. 441-444.
- Hulsbergen, C.H. and Bijker, R. (1989). Effect of spoilers on submarine pipeline stability. *Proceedings of the 21st Offshore Technology Conference, Houston, Texas, May 1-4, 1989, Paper No. OTC 6154*, pp. 337-350.
- Ibrahim, A. and Nalluri, C. (1986). Scour prediction around marine pipelines. *Proc. 5th Int. Symp. on Offshore and Arctic Engrg., Tokyo, Japan*, pp. 679-684.
- Jensen, B.L., Sumer, B.M., Jensen, H.R. and Fredsøe, J. (1990). Flow around and forces on a pipeline near a scoured bed in steady current. *Trans. of the ASME, Jour. Offshore Mechanics and Arctic Engineering*, 112, pp. 206-213. Also in: *Proceedings of 7th International Conference on Offshore Mechanics and Arctic Engineering (OMAE), Houston, Texas, Feb. 7-12, 1988, V*, pp. 39-48.
- Jensen, H.R., Jensen, B.L., Sumer, B.M. and Fredsøe, J. (1989). Flow visualization and numerical simulation of the flow around marine pipelines on an erodible bed. *Proc. 8th Int. Conf. on Offshore Mech. and Arctic Engrg., ASME*, 2, 1989, pp. 129-136.

- Kjeldsen, S.P., Gjörsvik, O., Bringaker, K.G. and Jacobsen, J. (1973). Local scour near offshore pipelines. Second Internat. Port and Ocean Engineering under Arctic Conditions, Conf. Iceland, 1973, pp. 308-331.
- Kristiansen, Ø. (1988). Current induced vibrations and scour of pipelines on a sandy bottom. Thesis presented to the University of Trondheim, at Trondheim, Norway, in partial fulfillment of the requirements of the degree of Doctor of Philosophy.
- Kristiansen, Ø. and Tørum, A. (1989). Interaction between current induced vibrations and scour of pipelines on a sandy bottom. Proceedings of the 8th Inter. Conference on Offshore Mechanics and Arctic Engineering, ASME. The Hague, the Netherlands, March 19-23, 1989, V, pp. 167-174.
- Kroezen, M., Vellinga, P., Lindenberg, J. and Burger, A.M. (1982). Geotechnical and hydraulic aspects with regard to seabed and slope stability. Delft Hydraulics Laboratory, Publication No. 272, June, 13 p.
- Leeuwenstein, W. (1985). Natural self-burial of submarine pipelines. MaTS - Stability of pipelines, scour and sedimentation. Coastal Engineering Group, Department of Civil Engineering, Delft University of Technology, Delft, The Netherlands.
- Leeuwenstein, W. and Wind, H.G. (1984). The computation of bed shear in a numerical model. Proceedings of 19th International Conference on Coastal Engineering, Chapter 114, pp. 1685-1702.
- Leeuwenstein, W., Bijker, E.A., Peerbolte, E.B., and Wind, H.G. (1985). The natural self-burial of submarine pipelines. Proc. 4th Int. Conf. on Behaviour of Offshore Structures (BOSS), Elsevier Science Publishers, pp. 717-728.
- Littlejohn, P.S.G. (1977). A study of scour around submarine pipelines. Report No. INT 113, Hydr. Res. Station, Wallingford, England.
- Lucassen, R.J. (1984). Scour underneath submarine pipelines. Report No. PL-4 2A, Netherlands Marine Tech. Res., Netherlands Industrial Council for Oceanology, Delft Univ. of Tech., Delft, the Netherlands, Sep. 1984, 117, Student Thesis supervised by E.W. Bijker and W. Leeuwenstein.
- Mao, Y. (1986). The interaction between a pipeline and an erodible bed. Series Paper 39, Inst. of Hydrodyn. and Hydraulic Engrg., Tech. Univ. Denmark, in partial fulfillment of the requirements for the degree of Doctor of Philosophy.
- Mao, Y. (1988). Seabed scour under pipelines. Proceedings of the 7th International Conference on Offshore Mechanics and Arctic Engineering, Houston, Texas, Feb. 7-12, 1988, V, pp. 33-38.
- Müller, W. von. (1929). System von Doppelquellen in der ebenen Strömung, insbesondere die Strömung um zwei Kreiszyylinder. Zeitschrift f. angew. Math. und Mech. 9, Heft 3, pp. 200-213.
- Orgill, G. Barbas, S.T., Crossley, C.W. and Carter, L.W. (1992). Current practice in determining allowable pipeline free spans. Proceeding of the 11th Offshore Mechanics and Arctic Engineering Conference, June 7-11, 1992, Calgary, Canada, V-A, Pipeline Technology, ASME, pp. 139-145.
- Rodi, W. (1984). Turbulence models and their application in hydraulics. IAHR, Delft, the Netherlands, 104 p.



- Schewe, G. (1983). On the force fluctuations acting on a circular cylinder in cross-flow from subcritical up to transcritical Reynolds numbers. *J. Fluid Mech.*, 113, pp. 265-285.
- Sidek, F.J. and Ibrahim, A.A. (1992). The armouring effects of shell fragments in seabeds beneath pipelines. Proceedings of the 2nd Inter. Offshore and Polar Engineering Conference (ISOPE), San Francisco, U.S.A., 14-19 June, 1992, II, pp. 92-100.
- Silvis, F. (1990). Wave induced liquefaction of seabed below pipelines. 4th Young Geotechnical Engineers' Conference, Delft, the Netherlands, 18-22 June, 1990.
- Stansby, P.K. and Dixon, A.G. (1983). Simulation of flows around cylinders by a Lagrangian vortex scheme. *Applied Ocean Research*, 1983, 5, No. 3, pp. 167-178.
- Stansby, P.K. and Starr, P. (1991). Hydrodynamic forces on a horizontal cylinder resting on a sand bed under waves and currents. Proc. of the First (1991) International Conf., Edinburgh, U.K., 11-16 August, 1991, III, pp. 158-163.
- Staub, C. and Bijker, R. (1990). Dynamic numerical models for sand waves and pipeline self-burial. Proceedings of 22nd International Conference on Coastal Engineering, Delft, the Netherlands, Chapter 190, pp. 2508-2521.
- Sumer, B.M. and Fredsøe, J. (1988). Vibrations of cylinders at high Reynolds numbers. Proc. 7th Int. Offshore Mech. and Arctic Engrg. Symp., ASME, 2, pp. 211-222.
- Sumer, B.M. and Fredsøe, J. (1990). Scour below pipelines in waves. *Journal of Waterway, Port, Coastal and Ocean Engineering*, ASCE, 116, No. 3, May/June 1990, pp. 307-323.
- Sumer, B.M. and Fredsøe, J. (1991). Onset of scour below a pipeline exposed to waves. *International Jour. of Offshore and Polar Engineering*, 1, No. 3, pp. 189-194, 1991. Also in: Proceeding of the First International Offshore and Polar Engrg. Conf. (ISOPE 91), II, pp. 290-295.
- Sumer, B.M. and Fredsøe, J. (1993). Self-burial of pipelines at span shoulders. Paper to be presented at the 3rd ISOPE Conference, Singapore 1993.
- Sumer, B.M., Mao, Y., and Fredsøe, J. (1988a). Interaction between vibrating pipe and erodible bed. *J. Waterway, Port, Coast. and Oc. Engrg.*, ASCE, 114(1), pp. 81-92.
- Sumer, B.M., Jensen, H.R., Mao, Y. and Fredsøe, J. (1988b). The effect of lee-wake on scour below pipelines in current. *J. Waterway, Port, Coastal and Ocean Engineering*, ASCE, 114, No. 5, pp. 599-614.
- Sumer, B.M., Fredsøe, J., Gravesen, H. and Bruschi, R. (1989). Response of marine pipelines in scour trenches. *ASCE Jour. Waterway, Port, Coastal and Ocean Engineering*, 115, No. 4, 1989, pp. 477-496.
- Sumer, B.M., Pedersen, C., Di, Y. and Fredsøe, J. (1990). Bed shear-stress measurements in the vicinity of a pipeline in waves. *Prog. Rep. 71, Inst. Hydrodyn. and Hydraulic Engineering, Techn. Univ. Denmark*, pp. 61-72.
- Sumer, B.M., Jensen, B.L. and Fredsøe, J. (1991). Effect of a plane boundary on oscillatory flow around a circular cylinder. *J. Fluid Mech.*, 225, pp. 271-300.
- Terzaghi, K. (1948). *Theoretical Soil Mechanics*. John Wiley and Sons, Inc., New York.
- van Beck, F.A. and Wind, H.G. (1990). Numerical modelling of erosion and sedimentation around pipelines. *Coastal Engineering*, 14, pp. 107-128.
- Westerhorthmann, J.H., Machemehl, J.L. and Jo, C.H. (1992). Effect of pipe spacing on marine pipeline scour. Proceedings of the 2nd Inter. Offshore and Polar Engineering Conf. (ISOPE), San Francisco, U.S.A., 14-19 June, 1992, II, pp. 101-109.

## CHAPTER 218

### **Turbulence and mud sedimentation: A Reynolds stress model and a two-phase flow model**

**Ch. Teisson, O. Simonin, J.C. Galland and D. Laurence <sup>1</sup>**

#### **Abstract**

Two sophisticated research models, previously used and validated in internal flows, are now applied to sediment laden flows: they give a thorough insight into the vertical distribution of sediment concentration, flow-sediment interaction, stratification and inhibition of vertical mixing. The Reynolds stress model is well adapted to investigate stratification due to density effects: it gives information on turbulent fluxes of momentum and concentration, eddy diffusivity and eddy viscosity profiles, reduction of the bottom shear stress due to the presence of sediment. Results show that suspended sediments affect turbulence even at low concentrations of 1g/l. A dimensional analysis seems to indicate that these stratification effects are not well accounted for in laboratory experiments.

The two-phase flow model enables to describe the vertical profile of sediment in its continuity, from the water surface down to/through the bed, without any definition of the bed water interface. Cohesive sediment processes such as deposition, erosion or consolidation are treated as flow-particles interactions: thus, the model helps in identifying the governing parameters -floc size and density, effective stress- and does not require the classical empirical laws commonly used to describe these processes.

#### **Introduction**

State of the art for simulation of cohesive sediment transport has been considerably enhanced in the past ten years but remained tied to the knowledge of physical processes (Teisson, 1991). The sink and sources terms near the bed (Parker, 1986) and the induced repartition of sediment throughout the water column contribute to the budget of sediment, and consequently to the final output of the models. A better understanding of the complex dynamics of the vertical structure of cohesive sediment suspension (Mehta, 1989a&b) is therefore required to improve the predictability of the models.

---

<sup>1</sup> EDF- Laboratoire National d'Hydraulique, 6 Quai Watier,  
78400 Chatou, France

In that context, it is well known that turbulence is the factor responsible for maintaining in suspension very fine sediment, but is surprisingly still crudely represented in usual cohesive sediment transport models.

Turbulence in sediment laden flows has been most often studied for the case of non cohesive sediment (Lyn, 1986). The marked effects of the presence of sediment upon the flow has been highlighted by numerous laboratory experiments, as reviewed and re-analysed by Mac Lean (1991) or Villaret and Trowbridge (1991). In the experiments, discussion in general focused on the deformation of the vertical profile of velocity, whereas less attention was paid on the concentration profile by itself.

For cohesive sediment, Gust (1976) observed a turbulent drag reduction for flows over cohesive bed, even for a dilute suspension. Krone (1986) outlined the role played by aggregates, which so increase the volume concentration of suspended material that it affects the flow at even modest weight concentrations.

Field observations displayed in numeral situations that stratification effects in coastal and estuarine areas might be unrelated to thermohaline effects, but well due to the presence of sediment, since highly stratified vertical sediment concentration profiles commonly occur in otherwise vertically mixed flow regimes (Mehta, 1989a).

The way that sediment affects turbulence which in turns controls deposition or erosion is of prime importance: large deposition rate at slack waters, generation of fluid mud layers, reduction of the bottom shear stress by the presence of sediment are still unsolved problems.

Two sophisticated research models, previously used and validated in internal flows, have therefore tentatively been applied to sediment laden flows (§ 1 and 2): they give a thorough insight into the vertical distribution of sediment concentration, flow-sediment interaction, stratification and inhibition of vertical mixing.

### **1. A one dimensional second order stress flux model**

Most numerical models rely on the eddy viscosity ( $\nu_t$ ) and diffusivity ( $K_t$ ) concepts for the modelling of the turbulent stress and flux, and the influence of the sediment load on turbulence is then taken into account in various ways : this interaction can affect either only the eddy diffusivity distribution (van Rijn, 1990) or both eddy diffusivity and viscosity profiles through a (gradient) Richardson number dependency following Munk and Anderson (1948). This last approach has led to satisfactory results, most often in reproducing the behaviour of lutoclines (Wolanski et al., 1988 ; Mehta and Ross, 1989; Smith and Kirby, 1989; Costa and Mehta, 1990). Profiles for  $\nu_t$  and  $K_t$  are always derived from an assumed clear-water distribution for  $\nu_t$  (parabolic or parabolic-constant profile).

However, some discrepancies between predictions and experiments or field measurements, some shortcomings (mainly in predicting the bottom friction velocity), let investigators suspect that a stronger interaction between hydrodynamics and sediment exists. This, together with the good results obtained for the atmospheric stratified boundary layer, have pleaded for the use of higher accuracy turbulence models for sediment laden flows. Successfully were applied k- $\epsilon$  model (Celik and Rodi, 1988), algebraic stress model (Hanjalic et al., 1982 ; Sheng and Villaret, 1989) and Reynolds stress model (Teisson et al., 1991 ; Brors, 1991). Hamm et al. (1992), using Sheng and Villaret model, investigated the influence of clear or loaded water on erosion laws in laboratory experiments: they found that stratification effects were most often negligible on bottom shear stress in laboratory experiments. Brors (1991) pointed out that, for the simulation of turbidity currents, only the Reynolds stress model (RSM) appeared to be realistic, k- $\epsilon$  and algebraic stress models giving in particular wrong concentration profiles.

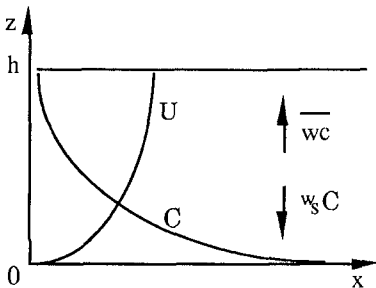
1.1 Scope of this study

The three essential processes involved here are the generation of an upward turbulent flux of particles, the damping of turbulence by gravity and the fluid-particle interaction. If we consider only small particles (mud and not sand), then neglecting the added-mass and other Basset forces, the problem reduces to the stratified turbulence problem. This is the well known thermal hydraulics or atmospheric boundary layer problem, for which Reynolds stress models have been developed and validated at LNH.

What can be expected from the RSM are, of course, mean concentration and velocity profiles, but also turbulent shear stress and sediment flux profiles, eddy diffusivity and viscosity distributions, Richardson numbers profiles and bottom friction velocity. In a more general meaning, the RSM could be helpful in understanding the mechanism of gravity effects and in evaluating the range of availability of the above mentioned turbulence models.

1.2. Mean equations

We consider a long free surface, flat bottom channel loaded with a volumetric concentration of sediments C, the settling velocity of the particles being  $w_s$ . The profile of mean velocity  $U(z)$  and mean concentration  $C(z)$  along the vertical in a channel flow are obtained from the following equations (capital letters represent mean values, small letters fluctuations and  $\bar{\quad}$  a statistical average) :



$$\frac{\partial U}{\partial t} = -\frac{1}{\rho_w} \frac{\partial P^*}{\partial x} - \frac{\partial \overline{uw}}{\partial z} + \nu \frac{\partial^2 U}{\partial z^2}$$

$$\frac{\partial C}{\partial t} + w_s \frac{\partial C}{\partial z} = -\frac{\partial \overline{wc}}{\partial z} + K \frac{\partial^2 C}{\partial z^2} \quad (1)$$

with  $w_s < 0$  (constant)

K : molecular sediment diffusivity

At equilibrium, the total shear stress ( $\tau = \nu \partial U / \partial z - \overline{uw}$ ) is linear so that its gradient is proportional to the pressure gradient  $\partial P^* / \partial x$  ; the settling velocity  $w_s$  induces a downward flux compensated by the gradient of turbulent concentration flux  $\overline{wc}$ .

1.3. Physical processes

When applying a Reynolds stress model, turbulence modelling assumptions are introduced only in the transport equations of the turbulent fluxes and stresses ; so the production and stratification effects, induced on these second moments by velocity and concentration gradients, are accounted for exactly. Although it is apparently complex with the 8 equations added to the mean equations (1), the Reynolds stress model allows a good understanding of the physical processes governing the turbulence-sediment interaction. Let us here concentrate on the three equations driving turbulent phenomena, that are those for the upward turbulent flux of sediments and for

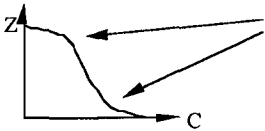
the variances of the vertical and horizontal fluctuating velocities. Developing only the (exact) production terms, while the pressure-strain  $\Phi$ , diffusion  $D$  and dissipation  $\epsilon$  terms respectively are to be modelled, they read :

$$\frac{\partial \overline{wc}}{\partial t} = - \overbrace{\overline{ww} \frac{\partial C}{\partial z}}^A - g\beta \overline{c^2} + \Phi_{i,c} + D_{i,c} \tag{2}$$

$$\frac{\partial \overline{ww}}{\partial t} = \overbrace{-2g\beta \overline{wc}}^B + \Phi_{i,j} + D_{i,j} - \frac{2}{3}\epsilon \quad \text{with } \beta = -\frac{(\rho_s - \rho_w)}{\rho_w} \tag{3}$$

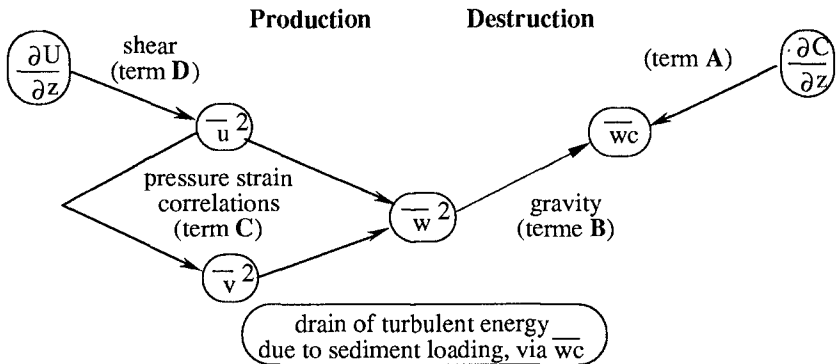
$$\frac{\partial \overline{uu}}{\partial t} = - \overbrace{2\overline{uw} \frac{\partial U}{\partial z}}^D + \overbrace{\Phi_{i,j}}^C + D_{i,j} - \frac{2}{3}\epsilon \tag{4}$$

Considering the concentration profile allows first to understand the mechanism of turbulence destruction due to the sediment load :



The concentration gradient is large, negative here. Then term A has large positive values, and (2) leads to an increase of the turbulent flux of concentration  $\overline{wc}$ . In turn, term B is negative, and (3) implies that the variance  $\overline{ww}$  decreases.

As a consequence, turbulence tends to become two-dimensional and energy is then drained from the two horizontal components  $u$  and  $v$  (eq. (4)), via the pressure-strain correlations, to feed  $w$  (eq. (3)). Finally, this mechanism leads to a decrease of the whole turbulence, which can be summarised by the following scheme :



This sketch naturally yields to the definition of the flux Richardson number  $R_{if}$  (the ratio of terms  $B/D$ ), which is the fraction of the turbulence production that can be diverted from dissipation to act against gravity.

1.4. Reynolds stress model

The second moment closure modelling adopted here is a classical one. A wall echo term is added to take into account the redistribution of energy from the vertical component of the fluctuating velocity  $w$  at the bottom, as at the free surface following the proposition by Gibson and Rodi (1989). Anisotropy affects the dissipation equation through the Launder and Tselepidakis (1991) proposition. The model has first been assessed against clear-water open channel flow data (Nakagawa et al., 1975; Komori et al., 1982).

Results are presented here for the schematic case of a steady, plane open channel flow of depth  $h = 1$  m, bulk velocity  $U_0 = 0.5$  m/s ( $Re = 500\ 000$ ), bulk sediment concentration of 1 g/l (volumetric concentration  $C_0 = 3.75 \cdot 10^{-4}$ ) and particle settling velocity  $w_s = -0.001$  m/s. Initial conditions are a homogeneous sediment concentration over the water depth and a logarithmic velocity profile, boundary condition for the concentration is a zero flux condition at both bottom and free surface.

Figures 1 to 3 show the effect of coupling the gravity (setting  $g = 0$  to  $g = 9.81$  m/s<sup>2</sup>) in the equations for the turbulent stresses on the mean velocity and concentration, and on the shear stress.

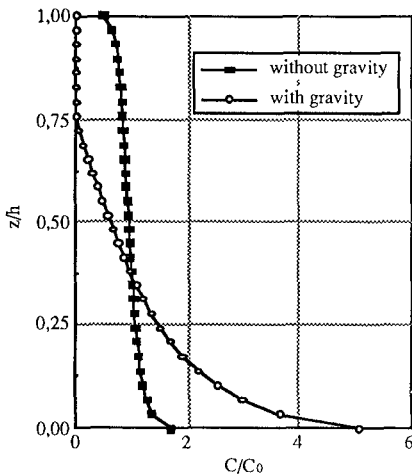


Fig. 1

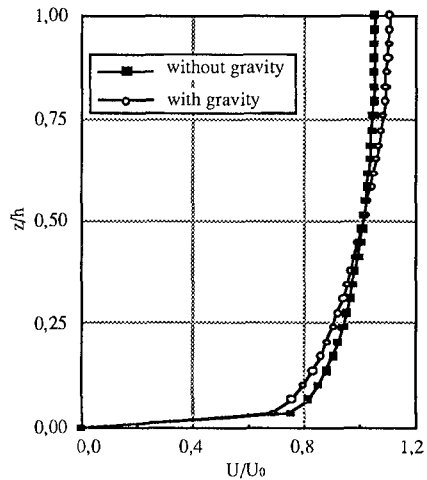


Fig. 2

This effect is seen to be quite strong for the sediment concentration considered here. The concentration dies out to 0 in the 25% upper part of the water column and is multiplied by nearly a factor 3 at the bottom (fig. 1), the velocity profile significantly deviates from the logarithmic one (fig. 2) and the bottom shear stress is reduced by more than 20% at the bottom (fig. 3).

Some experimental and field investigations have already highlighted such deviations from clear-water hydrodynamics. Gust (1976) found, from experiments with cohesive sediment in sea-water, that the bottom friction velocity  $u_*$  was reduced by 20% to 40% and that the thickness of the viscous sub layer was increased by a factor varying between 2 and 5 ; furthermore, the logarithmic profile for the velocity

was shown to be no more valid in the near-wall region. Soulsby and Wainwright (1987) have also pointed out, from field measurements for non-cohesive sediments, that  $u_*$  could be over-estimated by more than 50% when using the logarithmic velocity profile, neglecting thus the suspended sediment effects.

The gradient Richardson number (fig. 4), which is usually used to introduce the influence of sediment on turbulence, is seen to be only weakly correlated to the flux Richardson number, which is the sound parameter to measure buoyancy effect according to the Reynolds stress equations. This suggests that the Reynolds analogy as well as the Munk-Anderson approach could present some shortage for this application.

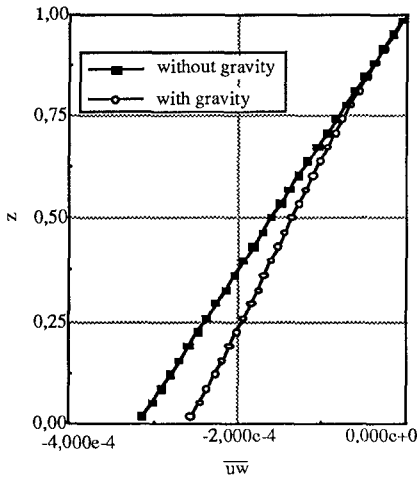


Fig. 3

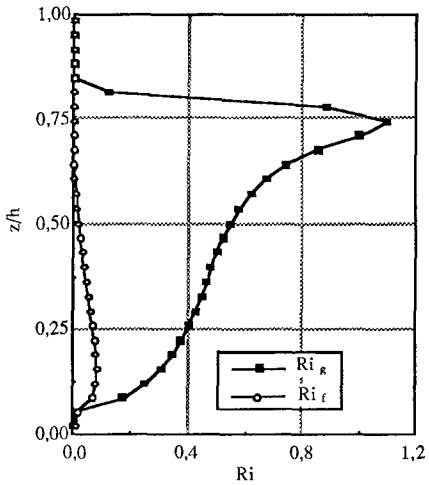


Fig. 4

1.5. Analytical developments

Direct comparison between numerical predictions and measurements is difficult for there are only few data available on cohesive sediment transport, even for the mean variables. Furthermore, as results of the RSM depend entirely on assumptions for modelling the turbulent second moments, validation should concern first turbulence predictions. But there is even less turbulence measurements... In this section we try to make some analytical developments that could help understanding RSM results.

As seen previously, the buoyancy level is defined by the flux Richardson number :

$$Ri_f = \frac{g\beta\overline{wc}}{\overline{uw} \frac{\partial U}{\partial z}} \tag{5}$$

Assuming a logarithmic velocity profile :  $\overline{uw} = -u_*^2(1 - \frac{z}{h})$  and  $\frac{\partial U}{\partial z} = \frac{u_*}{\kappa z}$

and when equilibrium is reached :  $\overline{wc} = -w_s C$

So that, at equilibrium and under the assumption of a logarithmic velocity profile,  $Ri_f$  becomes :

$$Ri_{f\ eq} = g\beta\kappa \frac{w_s z C_{eq}}{u_*^3 (1 - z/h)} \tag{6}$$

The maximum value for  $Ri_f$ , as measured from thermal flow investigations, is 0.25 ; turbulence being totally damped by buoyancy for higher values. We can then derive a formula giving, under the above assumptions, the maximum concentration at each location in the water column that a given flow can hold at equilibrium,  $C_{eq\ max}$  :

$$C_{eq\ max} = \frac{0.25 u_*^3}{g\beta\kappa w_s} \left( \frac{1}{z} - \frac{1}{h} \right) \tag{7}$$

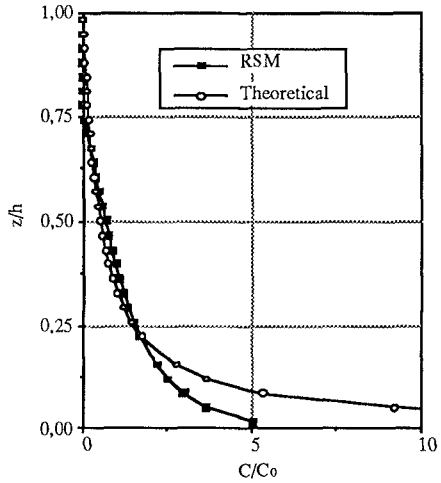


Fig. 5

This analytical expression does not give an equilibrium profile and has no physical meaning, but is an upper boundary for the sediment distribution: concentration profiles should stand below the curve drawn by the formula. According to (7), a reduction of the flow velocity by a factor 2 could reduce the maximum concentration to be carried by a factor 8.

The RSM prediction agrees well with (7) in the bulk of the flow (fig. 5), which means that the drastic reduction in sediment concentration in the upper part of the channel is due to the damping of turbulence by the sediment load. Figure 5 also indicates that the flow could hold much higher concentrations at the bottom, although (5) certainly over-estimates them there because dissipation, which is important at these locations, is neglected.

Let us now make a scale analysis on the flux Richardson number, which can be expressed, under some assumptions as seen previously, by (6). Let suppose a scale model experiment and express by  $\gamma$  the similitude laws ( $\gamma = .lab / .field$ ). Then we get the following expression for the similitude law for  $Ri_f$  :

$$\hat{R}i_f = \frac{\hat{\beta} \hat{w}_s \hat{C} \hat{h}}{\hat{u}_*^3}$$

Consider now a laboratory experiment (deposition or erosion test in a flume or a carousel). Most often, the procedure is:

- to use the same mud as in the field ( $\hat{\beta} = 1$  and  $\hat{w}_s = 1$ ),
- for the same range of concentrations ( $\hat{C} = 1$ ),



- under the same hydrodynamics conditions ( $\hat{u}_* = 1$ )

to derive laws to be introduced in mathematical models for prototype applications.

This procedure leads to a scaling effect on  $Ri_f$  which reduces to the vertical scale  $\hat{h}$ . This result, obtained here from (6) under some assumptions, has also been rigorously derived from a dimensional analysis of the Reynolds stress equations (Laurence et al., 1993). This means that, in a flume with a depth of 0.20 m, stratifications effects will be 50 times less than in the field, with a water depth of 10m, for the same range of concentrations and velocities. This could explain the weak stratification effects found by Hamm et al. (1992) in laboratory, whereas a larger influence is suspected in the field (Gust, 1978). Erosion deposition laws used in modelling high turbid environment in China (Costa and Mehta, 1990) required the use of physical parameters which were significantly different from those determined in laboratory experiments performed with local mud. They concluded that erosion-depositon fluxes can be drastically modified by sediment stratification, and that typical formulations for the bottom fluxes are believed to have limited utility in such environments. The reason could be, as stated above, that, for the same hydrodynamic forcing, in heavily laden flows, stratification effects will be far more important in the field than in the laboratory.

## 2. A separated two-phase flow model

Following Wallis (1969), transport of sediment in suspension can be regarded as a two-phase flow, i.e. mixture of a continuous phase (water) and a dispersed phase (mud flocs) for the case of cohesive sediment transport. And, by writing mass and momentum balance equations separately on each phase, with appropriate momentum transfer rate between phases, the two phase formulation enables to describe how the presence of particles modifies fluid flow characteristics, and reciprocally how the instantaneous fluid flow acts on particles movements.

Mass balance :

$$\frac{\partial}{\partial t} \alpha_k \rho_k + \frac{\partial}{\partial x_i} \alpha_k \rho_k U_{k,i} = \Gamma_k \quad (8)$$

where,  $U_{k,i}$  is the mean velocity i-component for the continuous ( $k=1$ ) and dispersed phases ( $k=2$ ) respectively,  $\alpha_k$  is the volumetric fraction,  $\rho_k$  the mean density and  $\Gamma_k$  the interfacial mass transfer rate between phases. In cohesive sediment transport,  $\Gamma_k$  accounts for water capture by mud flocs during their growth or break-up (transfer of water from the water phase to the mud flocs phase), and therefore for density change of the flocs. For the applications below,  $\Gamma_k$  is set to zero, and the density of the flocs remains constant.

Momentum balance :

$$\alpha_k \rho_k \frac{\partial}{\partial t} U_{k,i} + \alpha_k \rho_k U_{k,j} \frac{\partial}{\partial x_j} U_{k,i} = - \alpha_k \frac{\partial}{\partial x_i} P_1 + \alpha_k \rho_k g_i + I_{k,i} - \Gamma_k U_{k,i} - \frac{\partial}{\partial x_j} [ \alpha_k \langle \rho u''_i u''_j \rangle_k + T_{k,ij} ] \quad (9)$$

where  $u''_i$  is the fluctuating part of the local instantaneous velocity and  $\langle . \rangle_k$  the averaging operator associated to phase k,

$$\alpha_k \rho_k U_{k,i} = \alpha_k \langle \rho u_i \rangle_k \quad \langle \rho u''_i \rangle_k = 0$$

$\langle u''_{k,i} u''_{k,j} \rangle_k$  is the turbulent Reynolds stress tensor of the liquid phase ( $k=1$ ) and the kinetic part of the particulate stress tensor ( $k=2$ ),

$T_{k,ij}$  is the molecular viscous stress tensor ( $k=1$ ) and the collisional part of the particulate stress tensor ( $k=2$ ), set to zero for this application.

$P_1$  is the mean pressure of the continuous phase,

$I_{k,i}$  is the part of the interfacial momentum transfer rate between phases which remains after subtraction of the mean pressure contribution and complies with the mean jump condition derived from the local balance of momentum at the interfaces,

$$\sum_{k=1}^2 I_{k,i} = 0$$

The closure of the averaging equations set is achieved by using :

- practical expressions in terms of the computed variables to approximate the mean interfacial transfer terms and derived from the local description of single particle transfer with the surrounding fluid ;

- second-moment modelling for the continuous phase turbulence and the kinetic (or transport) part of the particulate stress tensor ;

- constitutive relations for the mean transport properties accounting for the molecular viscous stress in the liquid phase and the collisional part of the particulate stress tensor.

Interfacial momentum transfer :

Constitutive relations for the interfacial transfer terms derive by averaging from the particulate expressions, and must be related to the mean computed variables. Neglecting the Basset force, the interfacial momentum transfer term  $I_{k,i}$  induced by the relative motion of dispersed particles, can be written:

$$I_{1,i} = - I_{2,i} = \alpha_2 \rho_1 F_D V_{r,i} - \rho_1 \langle u''_{1,i} u''_{2,j} \rangle_2 \frac{\partial}{\partial x_j} \alpha_2 + \alpha_2 \rho_1 C_A \left[ \frac{\partial V_{r,i}}{\partial t} + U_{2,j} \frac{\partial V_{r,i}}{\partial x_j} \right] + \frac{\partial}{\partial x_j} \alpha_2 \rho_1 C_A \langle u''_{2,j} v''_{r,i} \rangle_2 \tag{10}$$

The first term on the right-hand side represents the drag force, the second the correlation between instantaneous distribution of particles and fluid pressure fluctuations, and the other ones the apparent mass force. The main part of the force induced by the fluid flow is already taken into account by the expression of the pressure gradient term in the momentum equations.

$F_D$ , the average drag coefficient is written in terms of the local mean particle Reynolds number which accounts roughly for the flocs overcrowding and the non-linear dependence on the relative velocity fluctuations :

$$F_D = \frac{3 C_D \langle Re \rangle}{4 \bar{d}} \langle |\vec{v}_r| \rangle \quad \langle |\vec{v}_r| \rangle \approx \sqrt{V_{r,i} V_{r,i} + \langle v''_{r,i} v''_{r,i} \rangle}$$

$$C_D \langle Re \rangle = \frac{24}{\langle Re \rangle} \left[ 1 + 0.15 \langle Re \rangle^{0.687} \right] \alpha_1^{-1.7} \quad \langle Re \rangle = \frac{\alpha_1 \langle |\vec{v}_r| \rangle \bar{d}}{v_1} \tag{11}$$

$V_{r,i}$ , the averaged value of the local relative velocity between each particle and the surrounding fluid, can be expressed in function of the total relative mean velocity  $\Delta U_i = U_{2,i} - U_{1,i}$  and a drifting velocity  $V_{d,i}$  due to the correlation between the

instantaneous distribution of particles and the turbulent fluid motion at large scales with respect to the particle diameter :

$$V_{r,i} = [U_{2,i} - U_{1,i}] - V_{d,i} \quad V_{d,i} = \langle \tilde{u}_{1,i} \rangle_2 - U_{1,i} = \langle u''_{1,i} \rangle_2 \quad (12)$$

The drifting velocity  $V_{d,i}$  takes into account the dispersion effect due to the particles transport by the fluid turbulence and reduces to the single turbulent correlation between the concentration fluctuations and the turbulent fluid velocity when the particle diameter is tending towards zero with respect to the smallest turbulent length scales. According to the theoretical case of particles suspended in homogeneous turbulence (Deutsch and Simonin, 1991) the velocity  $V_{d,i}$  is written as follows :

$$V_{d,i} = -D_{12}^t \left[ \frac{1}{\alpha_2} \frac{\partial \alpha_2}{\partial x_i} - \frac{1}{\alpha_1} \frac{\partial \alpha_1}{\partial x_i} \right] \quad (13)$$

where the fluid-particle turbulent dispersion coefficient  $D_{12}^t$  is given in terms of the covariance between the turbulent velocity fluctuations of both phases and a fluid-particle interaction turbulent characteristic time.

The turbulence model

Turbulence is modelled through the concept of turbulent viscosity  $\nu_k^t$  prescribed by a standard k - ε model, with a different treatment of the continuous and dispersed phase (Bel F'Dhila and Simonin, 1992).

A further balance equation for the particle number :

$$\alpha_2 \rho_2 \frac{\partial}{\partial t} X_p + \alpha_2 \rho_2 U_{2,j} \frac{\partial}{\partial x_j} X_p = \frac{\partial}{\partial x_j} \alpha_2 \rho_2 D_{12}^t \frac{\partial}{\partial x_j} X_p - X_p \Gamma_2 + \Gamma_p \quad (14)$$

where  $\Gamma_p$ , the rate of change in the particle number due to breakup and agglomeration.

$N_p$ , the mean particle number by unit volume of the two-phase mixture can be expressed directly in function of the variable  $X_p$  (the mean particles number by unit of mass of the dispersed phase) :

$$N_p = \alpha_2 \rho_2 X_p$$

and leads to the general definition of the mean diameter :

$$\frac{\pi \bar{d}^3}{6} = \frac{1}{\rho_2 X_p}$$

For cohesive sediment transport, this equation would account for diameter change of the flocs due to break-up or aggregation. For the applications below, this equation is not used , and the diameter of the flocs remains constant.

Applications

The definition of the transition from water body to bed is rather vague (Parker, 1986; Mehta, 1989a) and is one of the motivations to design an approach where this definition is circumvented. In that context, the two-phase flow model appears as the most complete model of the whole process from the water surface to the rigid bed.

Once the diameter and the density of the "inclusions" have been defined as data, the fall velocity  $V_f$  of particles is not prescribed but is an output of the model, as an example of flow-sediment interaction (fig. 6).

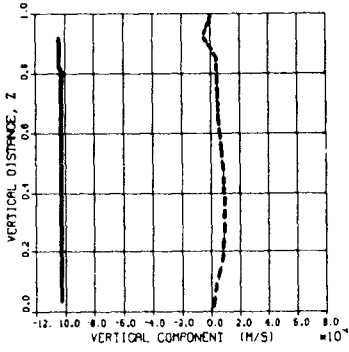


Fig. 6. Mean relative velocity  $V_r$  (solid line) and mean velocity of the dispersed phase  $U_2$  (dash line), at low concentrations. No hindered settling ( $V_r$  constant), equilibrium conditions ( $U_2 \approx 0$ )

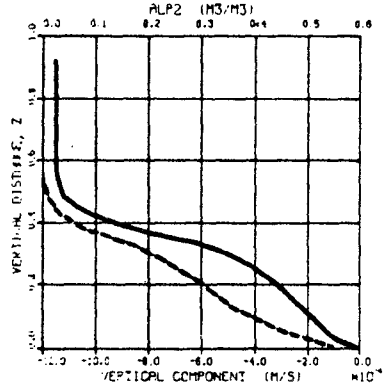


Fig. 7. Vertical profile of  $\alpha_2$ , volumetric fraction of the solid phase (dash line), and vertical relative velocity  $V_r$  (solid line), with strong hindering effect near the bottom for large concentration

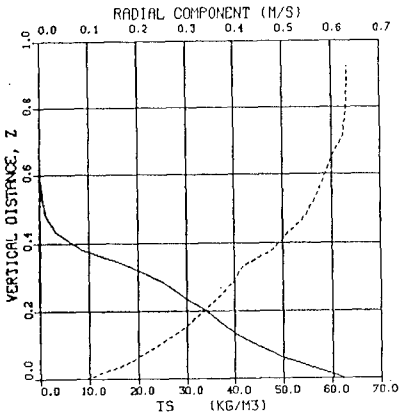


Fig. 8. Vertical profile of concentration (solid line) and velocity (dash line)

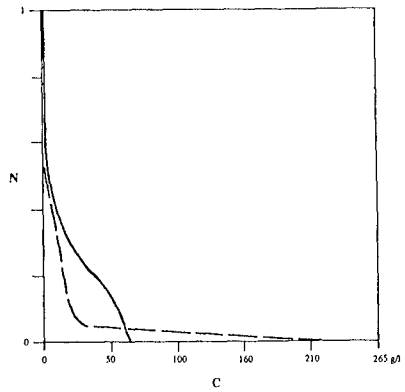


Fig. 9. Vertical profile of concentration for the same settling velocity of 1 mm/s: for flocs of density 1070 kg/m<sup>3</sup> (solid line) and for non cohesive sediment of density 2650 kg/m<sup>3</sup> (dashed line).

Another output of the two-phase flow model is the absolute vertical velocity  $U_2$  of particles in the presence of turbulence: it can be oriented downwards (turbulence too weak to stand deposition), or be zero (equilibrium condition on fig.6) or even be orientated upwards (for instance when mixing in the water column during erosion in accelerating currents). This a fundamental result for sedimentation problem.

The capability of two phase flow approach to analyse hindered settling (fig. 7) has been pointed out by Thacker and Lavelle (1977). The counter flow of the fluid upwards through the falling sediment is included in the model, as a consequence of the mass balance equation (8). The presence of others particles is taken into account in the drag coefficient expression (11).

Results with the two-phase flow model have been obtained for the same schematic case as for the Reynolds stress model (water depth 1 m; mean velocity 0.5 m/s), but for higher concentrations. Vertical profile of flow velocity and concentration have been computed in presence of mud flocs of density  $1070 \text{ kg/m}^3$  and diameter  $160 \mu$  (settling velocity 1 mm/s after the Stokes law), with a bulk initial concentration of 0 (clear water), 4, 8 g/l.

At very low concentration (fig. 6), the profile is in equilibrium ( $U_2 \approx 0$ ) and the relative velocity  $V_r$  given by the model corresponds to the Stokes value (-1 mm/s). For the latter case (8 g/l), classical equilibrium profiles cannot be sustained, and the initial profile completely collapses, with volumetric concentration up to 0.60 near the bottom for the final profile (expressed in massic concentration on fig. 8); hindered settling is very pronounced, at such concentrations (fig. 7). Concerning the liquid phase, the classical logarithmic profile of velocity in clear water is modified by the presence of sediment, with a kink located at the level where the concentration strongly increases downwards (fig. 8). From all the tests performed, the effect of the presence of particles on the turbulence of the flow appears to be noticeable even at "low" concentrations, the order of 1 g/l.

The role of floc size and floc density, which can be taken into account only in such models, is illustrated on fig. 9: this figure presents the vertical profile of concentration, obtained with a flow of 0.5 m/s, for an initial bulk concentration of 8 g/l, for two sediments exhibiting the same settling velocity of 1 mm/s:

- non cohesive sediment (sand) of density  $2650 \text{ kg/m}^3$  and diameter  $31 \mu$ ,
- the same mud flocs as before of density  $1070 \text{ kg/m}^3$  and diameter  $160 \mu$ .

The Stokes law gives, for the two sediments a settling velocity of 1 mm/s. However, they behave completely differently: sand settles rapidly to the bed, whereas mudflocs form a mobile suspension (fig. 9). The volumetric concentration for flocs is of the order of 0.10 to 0.50, against 0.01 to 0.05 for sand, in order to have the same massic concentration: this induces hindered settling for flocs, the water has difficulty to escape between the falling flocs, as nearly half of the volume is occupied by the flocs. Thus, the two-phase flow approach points out that the floc size might play an important role in the generation of fluid mud layers; massic concentration and settling velocity are not sufficient to explain the phenomenon (they are the same for the two sediments). Floc size and density, volumetric concentration seem more appropriate than settling velocity and massic concentration.

In the near future, the two-phase flow model should offer the possibility to study aggregations and break-up of flocs as a function of the level of turbulence, through a further equation (14) on the number of flocs already included in the model, provided information is available on  $\Gamma_p$ .

Last but not least, Wallis (1969) first emphasized the analogy between two-phase flow and classical consolidation equations, by adding in the momentum balance

equation the interparticle stress, the so-called "effective stress" in consolidation theories, which appears as  $T_{k,ij}$  in (9).

Addressing the proper parameters (floc size and density, rate of aggregation and break-up, effective stress) to describe cohesive sediment processes, the two-phase flow approach should help to reduce empiricism in commonly used formulae and encourage further experimental work on these parameters

## Conclusion

Today, a new generation of models, such as Reynolds stress models and two-phase flow models has become available in the industrial domain and we have attempted to apply the most recent ideas and concepts to cohesive sediment laden flow. The philosophy was to represent the hydrodynamics, turbulence and flow sediment interaction in the most accurate way, and, if possible, to get a new understanding of the physical processes in return.

Results provided by the Reynolds stress model show a strong damping of turbulence leading to significant deformation of the mean velocity, concentration and shear stress profiles, when compared with the clear-water ones. According to (6), for a given flow, stratification directly depends on the water depth, the sediment concentration and the settling velocity. The strong effects obtained here for "macroflocs" with  $w_s = 1$  mm/s would then be reduced accordingly for settling velocities 10 or 100 times lower.

In the two-phase flow approach, the physical processes of cohesive sediment are analysed and modelled as flow sediment interaction. This model enables modelling of the vertical profile of concentration from the free surface down into the bed without any definition of the bed water interface, as cohesive sediment processes are treated internally.

Henceforth, the formalism of these turbulence models offers a rigorous framework to study in a unified way the processes of mud transport or sedimentation. Empiricism in the formula commonly used in cohesive sediment transport modelling could be reduced thanks to these better representation of flow-sediment interactions, and predictability of the models consequently increased.

## Acknowledgements

This work has been undertaken as part of the MAST G6 Coastal Morphodynamics Programme. It was funded partly by the Commission of European Communities, Directorate General for Science, Research and Development under MAST Contract n° 0035-C and partly by the French Sea State Secretary (STCPMVN).

## References

- Bel F'Dhila R. and Simonin O., 1992. Eulerian prediction of a turbulent bubbly flow downstream of a sudden pipe expansion. 6th Workshop on Two-Phase Flow Predictions, Erlangen, April 1992.
- Brors, B., 1991. Turbidity current modelling. Dr. Ing. Thesis, Univ. of Trondheim, Trondheim, Norway.
- Celik, I. and Rodi, W., 1988. Modeling suspended sediment transport in nonequilibrium situations. *J. Hydr. Eng.*, vol. 114, n° 10, October.
- Costa, R.G. and Mehta, A.J., 1990. "Flow-fine sediment hysteresis in sediment-stratified coastal waters". Proc. 22nd Int. Conf. on Coastal Eng., Delft, 2047-2060.
- Deutsch E. and Simonin O., 1991. Large eddy simulation applied to the motion of particles in stationary homogeneous fluid turbulence. In "Turbulence Modification in Multiphase Flows, ASME FED, vol 110, pp 35- 42.

- Gibson, N. M., Rodi, W., 1989. Simulation of free surface effects on turbulence with a Reynolds stress model. *J. Hydr. Res.* vol. 27.
- Hamm, L., Huynh-Thanh, S. and Temperville, A., 1992. Simulation of cohesive sediment flume erosion tests by a current with a stratified turbulent transport model. Internal report, MAST G6M- Project 4.(in preparation)
- Gust, G., 1976. Observations on turbulent-drag reduction in a dilute suspension of clay in sea-water. *J. Fluid Mech.*, vol. 75, part 1, pp. 29-47.
- Hanjalic, K., Ivanovic, M., Vujovic, V., Milisic, V., 1982. Buoyancy effects and mutual interaction of suspended particules and velocity field in turbulent shear flows. Proc. of ICMH, Structure of turbulence in H. & M. transf., Hemisphere Eds.
- Komori, S., Ueda, H., Ogino, F., Younis, B., 1982. A. Turbulence structure and transport mechanism at free surface in an open channel flow. *Int. J. Heat and Mass Transfert*, 25, p. 512.
- Krone, R.B., 1986. The significance of aggregate properties to transport processes. Lecture notes on Coastal and Estuarine Studies, vol. 14, ed. A.J. Mehta, pp 66-84.
- Lauder, B. E. and Tselepidakis, 1991. Progress and paradoxes in modelling near-wall turbulence. 8th Symp. Turbulent Shear Flows, Munich, Sept. 1991.
- Laurence, D., Maupu, V., Galland, J.C., Teisson, C., 1993 A sediment laden open channel flow simulation with recent Reynolds stress-flux transport models. 2nd Int. Symp. on Eng. Turbulence Modeling and Measurements. Florence 31 May-2 June 1993 (To be published).
- Lyn, D.A., 1986. Turbulence and turbulent transport in sediment-laden open channel flows. Ph. D. Thesis. Calif. inst. of Technology, Pasadena, report n°KH-R-49.
- Mac Lean S.R., 1991. Stratification effects due to suspended sediments. Preprints of Int. Symp. on Transport of Suspended Sediments, Florence, Sept. 1991.
- Mehta, A.J., 1989a. On estuarine cohesive sediment suspension behavior. *Journ. of Geophysical Research*, vol. 94, n°C10, pp 14303-14314, October 15, 1989.
- Mehta, A.J., 1989b. Fine sediment stratification in coastal waters. Third National Conference on Dock & Harbour Engineering, 6-9 december 1989, Suratkal, 487-491.
- Munk, W. H. and Anderson, E. A., 1948. Notes on a theory of the thermocline. *J. Mar. Res.*, 3(1):276-295.
- Nakagawa, H., Nezu, I., Ueda, H., 1975. Turbulence of open-channel flow over smooth and rough beds. *Proc. JSCE*, 241, pp. 155-168.
- Parker W.R., 1986. On the observation of cohesive sediment behavior for engineering purposes. Lecture notes on Coastal and Estuarine Studies, vol. 14, ed. A.J. Mehta, pp 271- 289.
- Ross, M.A. and Metha, A.J., 1989. On the mechanics of lutoclines and fluid mud. *J. Coastal Res.*, Special Issue n° 5, pp. 51-61.
- Sheng, P. and Villaret, C., 1989. "Modelling the effect of suspended sediment stratification on bottom exchange processes". *J. of Geophysical Res.*, Vol. 94, N°C10, 14,429-14,444.
- Sousby, R. L. and Wainwright, B. L., 1987. A criterion for the effect of suspended sediment on near-bottom velocity profiles. *J. Hydr. Res.*, vol. 25, n° 3.
- Smith T.J. and Kirby R., 1989. Generation, stabilization and dissipation of layered fine sediment suspensions. *J. Coastal Res.*, Special Issue n° 5, pp. 63- 74.
- Teisson, C., Simonin, O., Galland, J.C., Laurence D., Fritsch, D., 1991 Numerical modeling of sediment transport : past experience and new research axes. Preprints of Int. Symp. on Transport of Suspended Sediments, Florence, Sept. 1991.
- Teisson, C., 1991. Cohesive suspended sediment transport: feasibility and limitations of numerical modeling. *J. of Hydr. Res.*, vol. 29, n°6, pp 755-769.
- Thacker, W.C. and Lavelle, J.W., 1977. Two-phase flow analysis of hindered settling. *The Physics of Fluids*, vol. 20, n°9, pp 1577- 1579
- Van Rijn, L. C., 1989. Handbook. Sediment transport by currents and waves. Delft Hydraulics. Report H 461.
- Villaret C. and Trowbridge, J.H., 1991. Effects of stratification by suspended sediments on turbulent shear flows. *Journ. of Geophysical Res.*, vol. 96, n)C6, pp 10 659-10 680.
- Wallis, G.B., 1969 One -dimensional two-phase flow. McGraw-Hill. 409 p.
- Wolanski, E., Chappell, J., Ridd, P. and Vertessy R., 1988. Fluidization of mud in estuaries. *J. of Geoph. Res.*, vol. 93 (C3) pp 2351-2361

## CHAPTER 219

### Mechanism of Sediment Transport around a Large Circular Cylinder

Takao Toue<sup>1</sup>

Hidehiro Katsui<sup>2</sup>

Kazuo Nadaoka<sup>3</sup>

#### ABSTRACT

Mean currents have important roles in sediment transport. The mean currents around a large circular cylinder are carefully measured. The theoretical mass transport rate is verified experimentally, and the movement of sediment on a flat and smooth bed can be numerically simulated well. On the contrary, the currents on sand ripples are quite different with the theoretical value. The currents are caused by the interaction of the return flow and the mass transport on sand ripples.

#### INTRODUCTION

Bathymetric changes and scouring around a large circular cylinder have been studied by Rance (1980), Saito et al (1990), and Katsui and Toue (1988). Fig.-1(a) and (b) are examples of the bathymetric changes around a large circular cylinder presented by Katsui (1992). The wave height is 10cm, and the wave periods are 1.0s and 2.0s and the water depth is 0.3m. In front of the circular cylinder, the feature of bathymetric change is same as that in front of a vertical structure, i.e., the scouring and accretion occur alternatively. The side of the cylinder is always accretion area irrespective to the wave period. According to Katsui et al (1990), this type of changes

---

1 Reserch Engineer, C.E.Structure & Coastal Engineering Reseach Group, Technology Research Center, Taisei Corporation, 344-1 Naze-mach Totsuka-ku, Yokohama, 245, Japan

2 Manager, Senior Reserch Engineer, Ditto

3 Associate Professor, Department of Civil Engineering, Tokyo Institute of Technology 2-12-2, Oookayama, Meguro-ku, Tokyo, 152, Japan



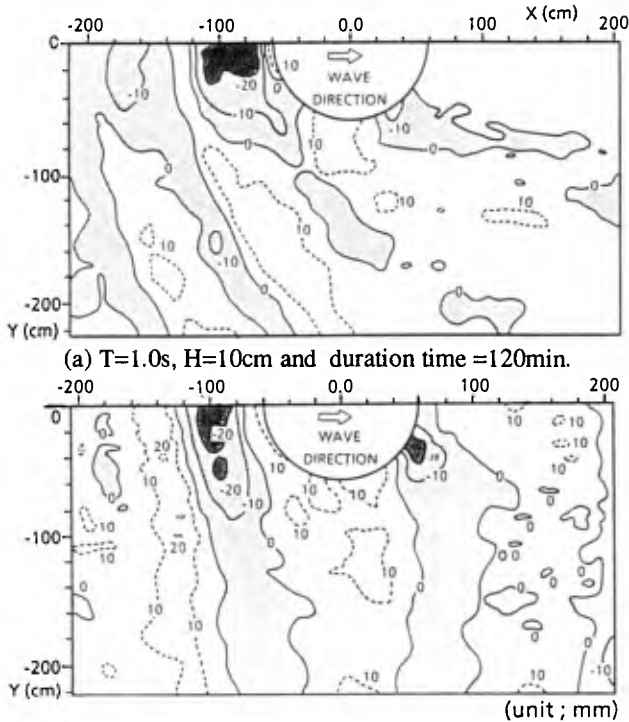


fig.-1 Bathymetric Changes around a Large Circular Cylinder

is called  $N'$  type scouring. In  $N'$  type scouring, the sediment transport rate must be maximum where the gradient of shear stress is maximum. The mechanism of  $N'$  type scouring, however, is not understood well.

Saito et al (1988) simulated these particular changes numerically, but the simulation could not explain the experimental results well probably due to the poor understanding of the mean currents. In their simulation, the mean currents around a cylinder are consist of two different types of currents. One is the mass transport, and the other is the current due to the gradient of radiation stress. The calculated currents, however, are not verified experimentally.

To understand the mechanism of sediment transport around a large circular cylinder, the mean currents should be clarified first. The purposes of this study are to examine the mean current around a large cylinder and its influence on the sediment transport.

## EXPERIMENTAL PROCEDURE

Fig.-2 is the experimental set up. The length of the wave basin is 35.5 m and width is 17m. The water depth,  $h$ , is always 0.3m. The wave height,  $H$ , is 10 cm, and

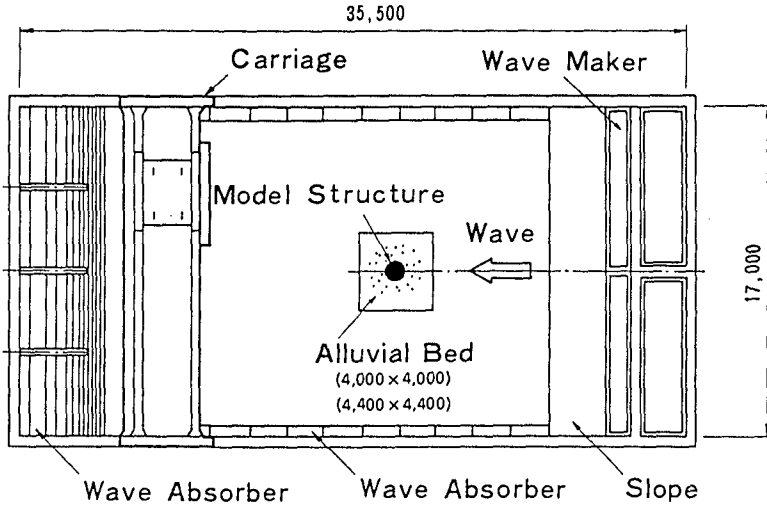


fig.-2 Experiment Set Up

wave periods,  $T$ , are 1.0s and 2.0s. The diameter of the circular cylinder,  $D$ , is 1.17m, thus the ratios of the diameter to wave length are 0.85 and 0.36. Two types of bed conditions are tested. One is a flat smooth bed and the other is the bed with sand ripples (ripple bed). In making the ripple bed, a flat movable sand layer with 5 cm thickness is formed, and then after the ripples form in the all surface by waves, the bed is fixed by cements. To measure the mean currents on the smooth bed in the boundary layer, polyethylene beads are used. Their diameter is 1 mm and the gravity ratio is 1.02. A number of beads are placed on the smooth bed, and the movements of beads are observed by the video and the photograph. The movements of sands are also observed. The sands are fine silica sands and their median diameter,  $d_{50}$ , is 0.15 mm. Mean currents are also measured by the electro-magnetic velocity meter and LASER Doppler velocity meter. The currents are measured at every 30 cm horizontally, and 20,15,10,5,3 cm above the bottom. Table -1 summarized the experiment condition and the experiment cases.

### MEAN CURRENTS ON SMOOTH BED

#### 1) Observation of Movement of Polyethylene Beads

Photo -1(a) shows the movement of polyethylene beads on the smooth beds for case 1. The beads in front of the cylinder gather in semi-circular lines which are coincide to the positions of the standing waves. The beads disappear at the side of the cylinder. All particles, however, are flown to the shore ward finally. Photo -1(b) is for case 2. The beads move more dramatically. Just after the waves reach the experimental area, all beads in front of cylinder move to the direction of waves.

Table -1 Experiment Condition and Cases

case name	wave height H(cm)	wave period T(s)	water depth h(m)	bed condition
case 1	10.0	1.0	0.3	smooth
case 2	10.0	2.0	0.3	smooth
case 3	10.0	1.0	0.3	ripple
case 4	10.0	2.0	0.3	ripple

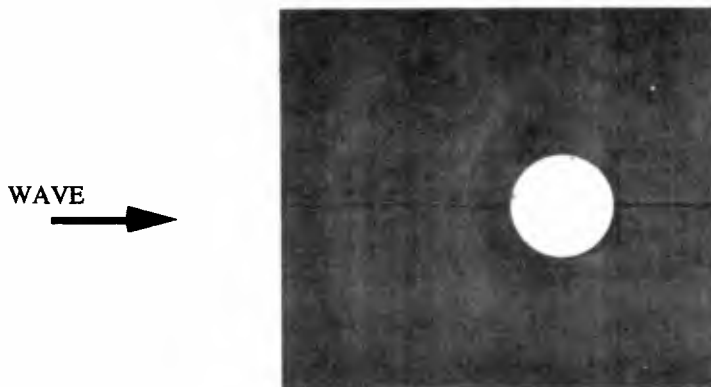
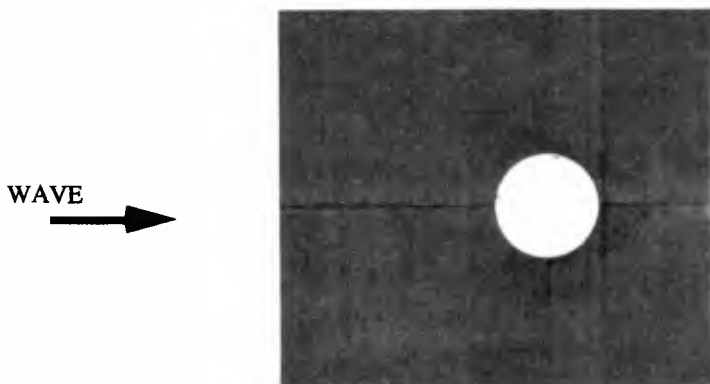
(a)  $T=1.0s$   $H=10cm$   $t=1$  min.(b)  $T=2.0s$   $H=10cm$   $t=1$  min.

Photo-1 Movement of Polyethylene Beads around a Large Circular Cylinder

Simultaneously, the beads at the side of the cylinder also disappear. The shape of the disappearance is heart like. Within 3 or 4 minutes, they disappear completely.

## 2) Mass Transport Rate around a Circular Cylinder on the Smooth Bed

According to Carter et al (1973), the mass transport rate at the outer edge of the boundary layer is given by eq. (1) and (2) in the cylindrical coordinate.

$$U = \frac{1}{4\omega} \text{Re} \left[ F_5 U_w \left( \frac{\partial U_w}{\partial r} \right)^* + F_6 \frac{V_w}{r} \left( \frac{\partial U_w}{\partial \theta} - V_w \right)^* + F_7 \frac{U_w}{r} \left( \frac{\partial V_w}{\partial \theta} + U_w \right)^* \right] \quad (1)$$

$$V = \frac{1}{4\omega} \text{Re} \left[ F_5 \frac{V_w}{r} \left( \frac{\partial V_w}{\partial \theta} + V_w \right)^* + F_6 U_w \left( \frac{\partial V_w}{\partial r} \right)^* + F_7 V_w \left( \frac{\partial U_w}{\partial r} \right)^* \right] \quad (2)$$

where  $U, V$  is the mass transport rate including *Stokes' drift* in the direction of  $r$  and  $\theta$  respectively,  $U_w$  and  $V_w$  are the velocity of wave component at the outer edge of the boundary layer and  $*$  means the complex conjugate.  $F_5, F_6$  and  $F_7$  are the complex

$$F_5 = -3 + 5i, F_6 = -1 + 2i, F_7 = -2 + 3i \quad (3)$$

constants, and given by eq. (3).

## 3) Numerical Simulation of Movements of Polyethylene Beads

If the beads are assumed to be moved by the mass transport rate, the movements of beads are simulated numerically. Fig. -3(a) and (b) are the results of the simulation for case 2. The simulations agree with the experimental results very well. In other words, this is the experimental verification of the theoretical mass transport rate.

## MOVEMENT OF SAND PARTICLES ON SMOOTH BED

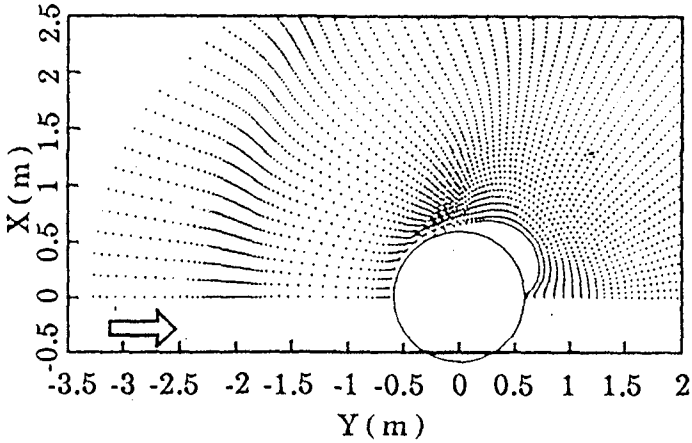
### 1) Observation of Sand Particles on Smooth Bed

The mass transport rate on smooth bed is clear now. Next, the movements of sand particles are examined. The same procedure as that of the experiment for polyethylene beads is used. Photo -2 (a) and (b) is the movement of sands for case 3 and case 4. In the photos, the black part is the place where sands disappear and the white part is the place where sands deposit or do not move. In other part, sand ripples form. The photos were taken after 30 minutes wave duration.

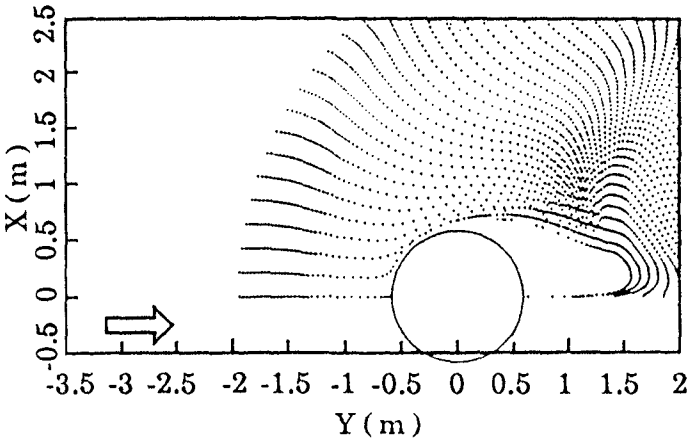
In case 3, sands in front of the cylinder gather at the position of the loop of the standing waves, and disappear at the node of the standing waves. In case 4, however, sands gather at the loop and disappear at the node. The sands at the side of the cylinder disappear for both cases.

### 2) Numerical Simulation of Sand on Smooth Bed

The motion of sands on the smooth bed can be given by eq. (4) and (5).



(a) T=2.0s H=10cm t=10s



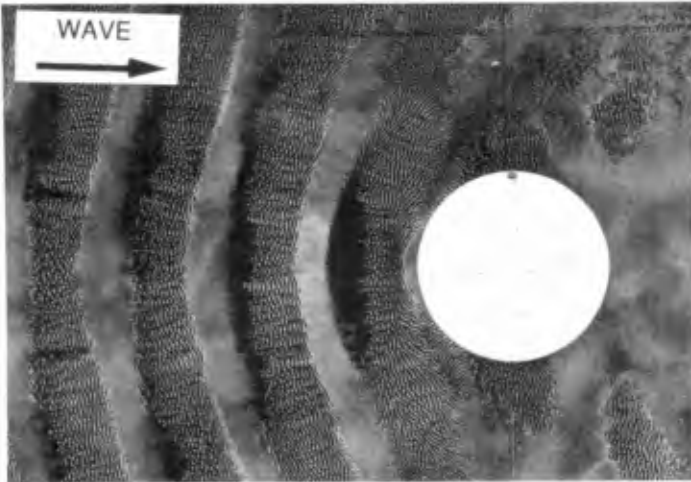
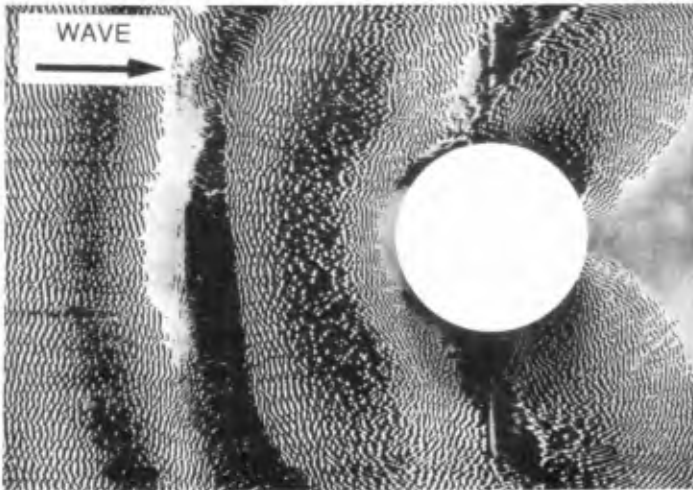
(b) T=2.0s H=10cm t=40s

Fig.-3 Numerical Simulation of Movement of Polyethylene Beads

$$\frac{dx_s}{dt} = u_s \tag{4}$$

$$\frac{du_s}{dt} = \frac{3C_d}{4d(s+C_m)} |u-u_s|(u-u_s) + \frac{1}{s+C_m} \frac{dU_w}{dt} + \frac{C_m}{s+C_m} \frac{du}{dt} - \frac{s-1}{s+C_m} \mu_f \tag{5}$$

where  $u_s$  is the sand particle velocity,  $u$  is the velocity of the fluid and over bar means a vector quantity.  $C_d$  is the drag coefficient,  $C_m$  is the added mass coefficient and  $\mu$  is the friction coefficient.  $C_d$  and  $C_m$  are 0.5. The friction coefficient at rest is 0.6 and

(a)  $T=1.0s$   $H=10cm$   $t=600s$ (a)  $T=1.0s$   $H=10cm$   $t=2220s$ 

#### Photo-2 Movement of Sands on Smooth Bed

changed to 0.1 when sands start to move. The height of the position  $z_0$ , which the fluid acts on the particles is the half of sands diameter, i.e., 0.075mm.  $u$  is given by eq.(6) and (7).

$$u = u_1 + u_2 \quad (6)$$

$$u_1 = \text{Re} \left[ U_w F_1(\xi) \exp(-i\omega t) \right], \xi = z_0/\delta \quad (7)$$

$$F_1(\xi) = 1 - \exp[-(1-i)\xi] \quad (8)$$

where  $u_2$  is the mean current,  $\delta$  is the thickness of the boundary layer.  $F_1$  is given by eq.(8)

Fig.-4 is the trajectory of the sand particles in the simulation. The wave height is 10cm, and wave period is 1.0s. The initial position is  $x=-0.585\text{m}$ ,  $y=0.676\text{m}$ , where the origin of the coordinates is the center of the circular cylinder.  $x$  is the positive toward the direction of the wave propagation. The sands move along the elliptic line changing the mean position toward the center of the cylinder. This movement is the same as the observation. Similar simulation was done by many researchers, such as Hino et al (1982) and Irie et al(1984) for one dimensional sands movement. In one dimensional simulation, sands stop when the velocity is very small. But, since the velocity in the both directions of  $x$  and  $y$  are not small simultaneously in three dimensional case, the sands which start to move do not stop. The simulation for all particles around a cylinder is shown in fig.-5(a) and (b). The results of the simulation agree with the experiment qualitatively. Some differences are due to the sand ripples which is not

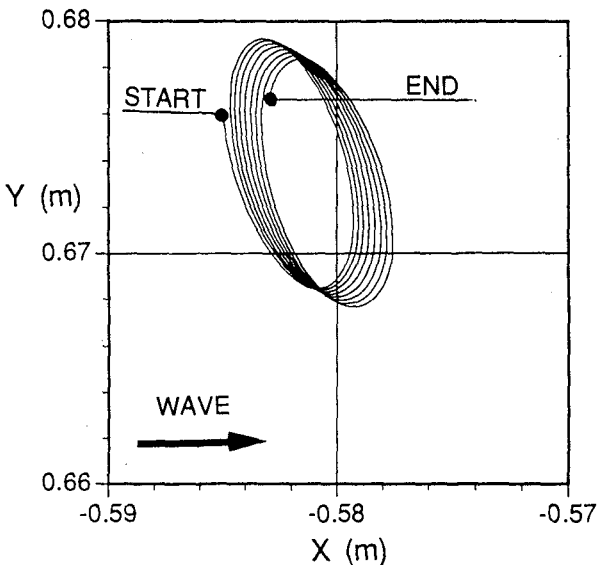


Fig.-4 Trajectory of Sands Movement in Numerical Simulation

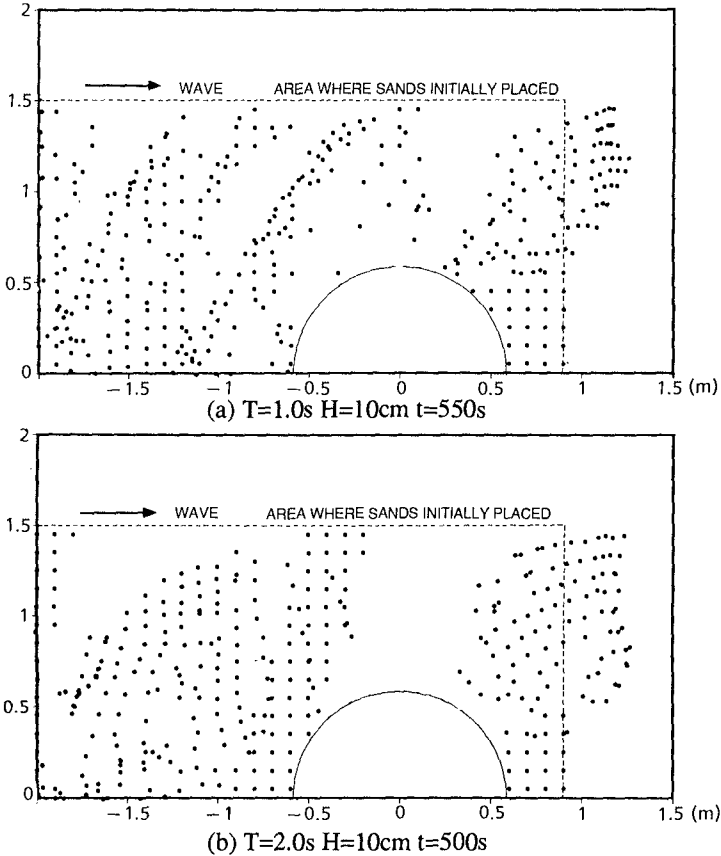


Fig.-5 Numerical Simulation of Sands Movement

included in the simulation. Important findings are the sand particles disappear at the side of the cylinder both in the simulation and the experiment. In other hand, the side of the cylinder is always accretion area in the bathymetric change experiment (see fig.-1(a) and (b)).

#### MEAN CURRENTS ON RIPPLE BED

##### 1) Observation of Movements of Polyethylene Beads

Photo-3 show the movements of polyethylene beads on the ripple bed after 30 minutes wave action. The difference between the movement on the smooth bed and the ripple bed is clear. In the case of the smooth bed, the beads are disappear within 3 or 4 minutes. On the contrary, the beads on the rippled bed remain there for more than 30 minutes. By careful observation, some particular movements of beads are found. The beads at the side of the cylinder move to the down drift side near the bed, but change the direction when the beads go up to the 3 to 5 cm above the bed. This imply the



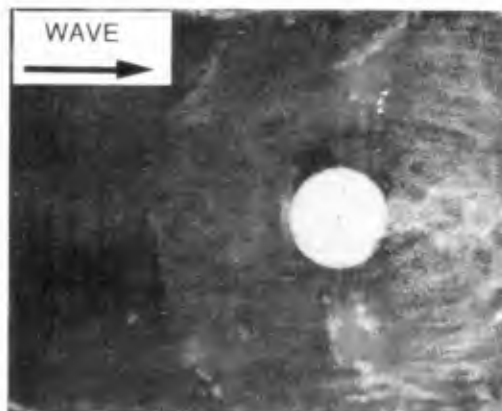


Photo -3 Movement of Polyethylene Beads on Sand Ripple ( $T=2.0s$ ,  $H=10cm$ )

vertical distribution of the mean current might have some important role in this movement.

## 2) Mean Current around a Circular Cylinder

The mean currents measured by the electro-magnetic velocity meter is shown in fig-6. The currents in the upper layer go to the opposite direction of wave propagation. The currents in lower layer go from the rear of the cylinder to the side of the cylinder, therefore the beads would have gathered at the side of the cylinder in Photo 3.

The velocity of the currents is about 5 cm/s. As long as the wave basin is closed in the experiment, there must be a return flow. The order of the return flow is estimated to be about 5cm/s. Thus, the current in the upper layer might be a return flow. The current in the lower layer is more complicate. More detailed measurement by LASER Doppler velocity meter is carried out at the side of the cylinder. The vertical profile is illustrated in fig.-7 with theoretical value. The measured current is quite different with the theoretical current both its value and direction.

Since the theory is for the mass transport in the laminar boundary layer on the smooth flat bed, the differences are not surprising. Furthermore the theory does not consider any significant currents like a return flow outside the boundary layer. This is not so important when the boundary layer is very thin like that on smooth beds. When the boundary layer is considerably thick like that on sand ripples, the effects of the return flow must be considered. Consequently, to know the mean currents around a large circular cylinder, a theory for the mass transport on sand ripples must be developed taking into account of the effects of a return flow .

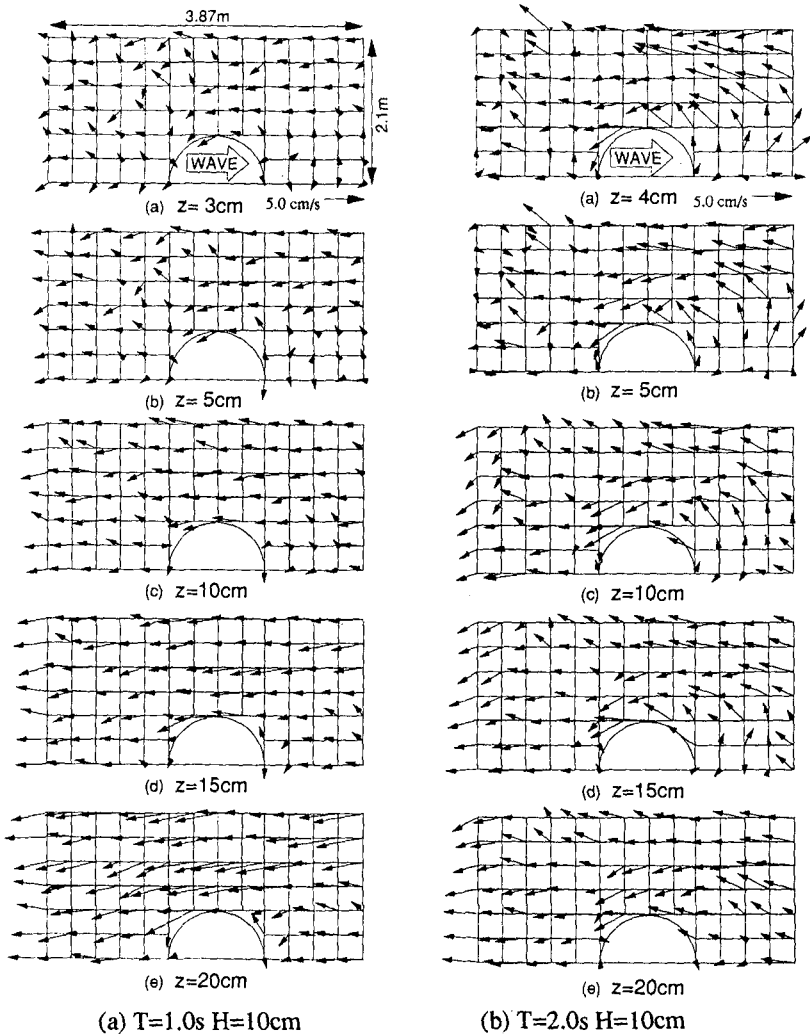


Fig.-6 Mean Currents around a Large Circular Cylinder

CONCLUDING REMARKS

The following conclusions are made;

- 1) The mass transport around a large circular cylinder on the smooth bed are verified experimentally.
- 2) The sand movements around a large circular cylinder on the smooth bed are explained by the numerical simulation well.

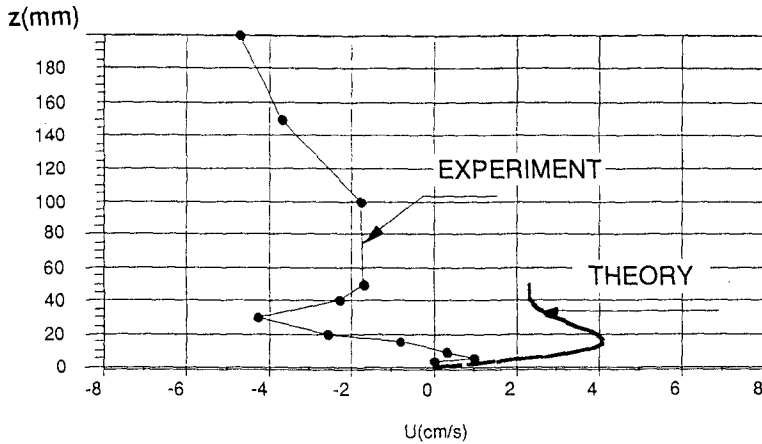


Fig.-7 Vertical Distribution of Mean Current

- 3) The mean current on the sand rippled are clarified by the experiment.
- 4) To know the mean current, theory for the mass transport on sand ripples must be developed taking into account of the effects of a return flow.

#### REFERENCES

- (1) Carter T.G., P.L.E. Liu and C.C.Me(1973): Mass transport by waves and offshore sand bedforms, J. Waterway, Harbour Coastal Eng. Div. ASCE, Vol.99. pp165-184.
- (2) Hino, M, T.Yamashita and S.Yoneyama(1982) : Movement of Sand Particles and Bed Load Transport Rate by Waves, Proc. 29th Japanese Conference on Coastal Engineering, pp.213-217 (in Japanese).
- (3) Irie I., K.Nadaoka, T.Kondo and K.Terasaki(1984): Two Dimensional Seabed Scour in front of Breakwaters by Standing Waves, Report of the Port and Harbour Research Institute, Vol.23, No.1, pp3-52 (in Japanese).
- (4) Katsui, H(1992): Study on Scouring and Scour Protection around Offshore Structures, Doctoral Dissertation, University of Tokyo, p382.(in Japanese).
- (5) Katsui, H. and T. Toue(1988) : Inception of Sand Motion around a Large Obstacle, Proc. 21st International Conference on Coastal Engineering, pp1280-1294.
- (6) Saito, E., S.Sato and T.Shibayama(1990) : Local Scour around a large circular cylinder due to wave action, Proc. of 22nd Coastal Engineering Conference, pp. 1795-1804.
- (7) Rance, P.J.(1980): The potential for scour around large object; Scour Protection Techniques around offshore structure, The Society of Underwater Technology, One-day seminar, pp41-54.

## CHAPTER 220

### Siltation Study in a Long Approach Channel on Large Scale Muddy Tidal Flat

Hiroichi Tsuruya<sup>1</sup>, Kazuo Murakami<sup>1</sup>,  
Isao Irie<sup>2</sup> and Kazumasa Katoh<sup>1</sup>

#### Abstract

Siltation mechanism in a 14km long approach channel on large scale muddy tidal flat is studied based on field investigations and numerical simulation. Natural conditions such as river discharge, waves, tides, tidal currents, and bed materials were measured over one year. The morphological change shows some relations with the grain size distribution of bed materials and current flow patterns. The net movement pattern of bed materials in the muddy tidal flat is given by the analysis of the field data. From the numerical simulation, it is revealed that the resuspended bed materials by waves from the surrounding tidal flat play an important role in the siltation process of the approach channel.

#### 1. Introduction

Many riverine ports in Asian countries have long approach channels which connect the river mouth with offshore through a muddy flat. The study on the transport mechanisms of fine sediments in estuaries is important to develop measures for the reduction of siltation releasing a port management body from high maintenance dredging cost. In the world, there are many estuaries and ports which suffer from siltation, and field investi-

---

<sup>1</sup> Port and Harbour Research Institute, Ministry of Transport, 1-1, Nagase 3 Chome, Yokosuka, 239 Japan

<sup>2</sup> Kyushu University, Dept. of Civil Engineering, 6-10-1, Hako-zaki, Higashi-ku, Fukuoka, 812 Japan

gations have been conducted to understand the mechanism of high concentration mud movement (e.g., *Leussen and Velzen* 1989, *Costa and Mehta* 1990). Typical field investigations have been made for the siltation mechanisms in a monsoon-dominated coasts (*Terwindt et al.* 1987, *Hoekstra et al.* 1988).

In the present study, systematic field investigations were conducted in the port of Banjarmasin in South Kalimantan of the Republic of Indonesia.

The siltation mechanism on a large scale muddy tidal flat is investigated based on the field data. A numerical simulation is used to obtain detailed information on external forces which govern the siltation and the sources of materials deposited in the channel. A practical method to estimate the annual amount of deposition volume is also presented.

### 2. Natural Conditions

Field investigation was conducted from 10th September, 1988 to 10th September, 1989. Figure 1 shows the map of the

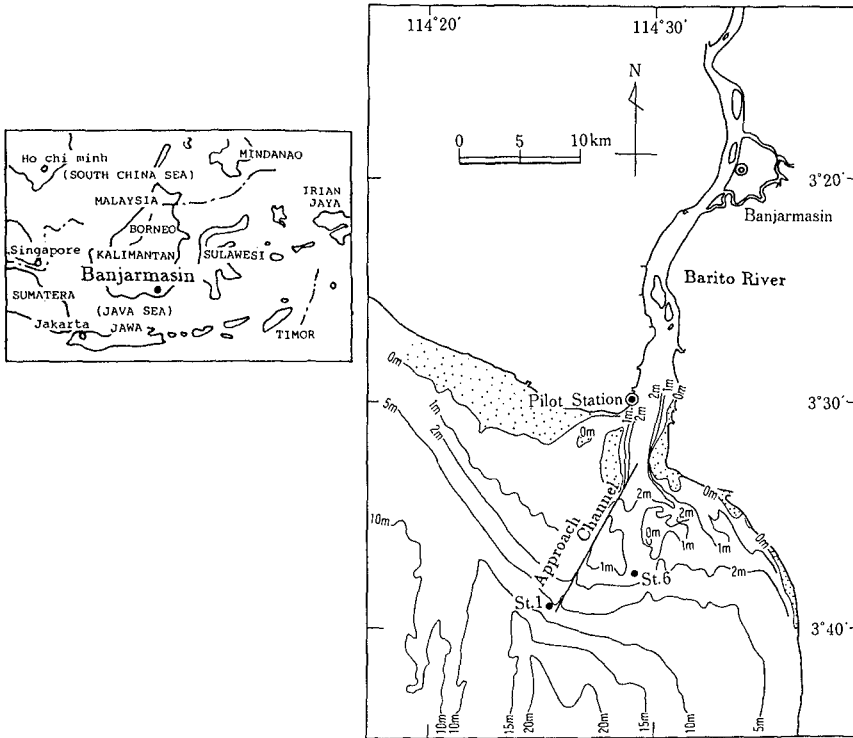


Fig.1 Map of Investigation Site

Table 1 Averaged Wave Conditions

Season	H(m)	T(s)	Direction
Rainy	0.58	4.0	S15° W
Dry	0.43	3.5	S10° W
85days	0.41	3.5	S15° W

investigation site. The port of Banjarmasin locates 26km upstream from the mouth of the Barito River. The size of the approach channel is 14km in length and 60m in width. In spite of the annual dredging (2~3 million  $m^3/y$ ), the planned water depth 6m is scarcely maintained. The river mouth is characterized by the formation of the large fine sand deposits on both sides of the approach channel. Waves, tides and winds were measured for one year. Measurements of tidal currents, saline wedge, turbidity, river discharge, etc. were also conducted.

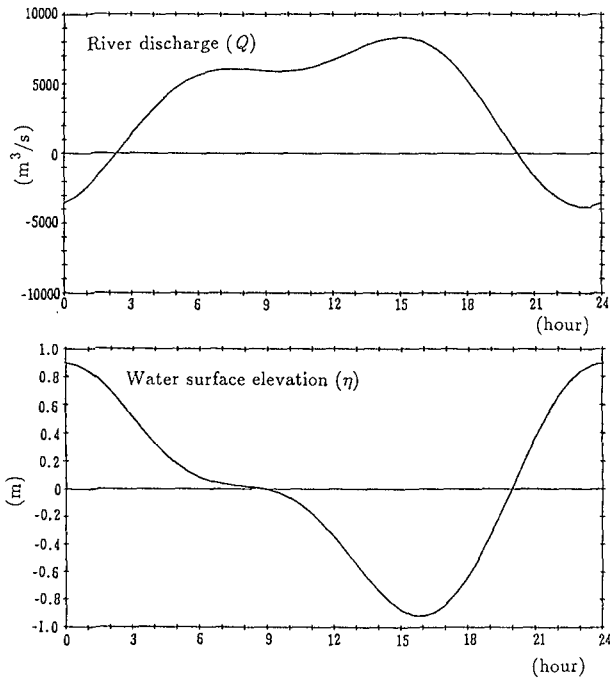


Fig.2 Time Variation of River Discharge and Water Surface Elevation at Pilot Station

From the measurements of river discharge, it can be said that the river discharge in the dry season (from April to September) is less than  $1,000 \text{ m}^3/\text{s}$  and in the wet season (from October to March) is more than  $4,000 \text{ m}^3/\text{s}$ .

Waves were measured at St.1 near the entrance of the approach channel at the water depth of 6m for 1 year continuously at every 2 hours with an ultra-sonic wave gauge. The wave directions were determined by wind directions measured at the pilot station for wave periods less than 3 seconds, and by water particle movement directions for wave periods longer than 3 seconds. The averaged significant wave heights, wave periods and energetically weighted wave directions in each season are summarized in Table 1. In the table, the "85 days" shows the intermission period of dredging during which the actual deposition rate in the channel is estimated for the calibration of the numerical simulation of siltation.

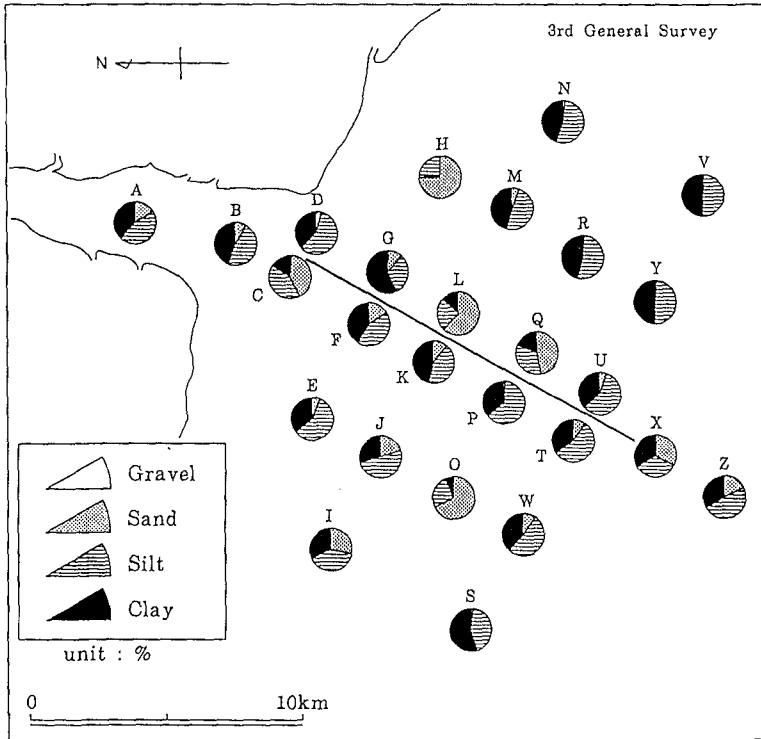
Tide is a basic factor in determining water level changes and currents in an estuary or coastal area. A tide gauge was set at the pier of the Pilot Station. According to the harmonic analysis of tides, the diurnal component  $K_1$  is the largest, and the semi-diurnal component  $M_2$  is the second largest. In the numerical simulation of deposition, the tidal level which is composed of  $K_1$  and  $M_2$  components is taken as the representative value. In the calculation, it is assumed that the periods of  $K_1$  and  $M_2$  components are just 24 hours and 12 hours, respectively. A typical time variations of the river discharge and the water surface elevation in a day is presented in Fig.2.

Tidal current observations were carried out at eleven stations with electro-magnetic current meters. The measuring stations are expressed in Fig.9 which will be shown later.

Another current observations were carried out by tracking the movement of drogues. This method is convenient to grasp the flow pattern briefly. Several drogues were released at the river mouth at high tide, then the observers follow each drogue position from the boat. The measured results will be shown in Fig.11. These current data are used for the calibration of tidal current simulation.

Bed material samplings were carried out in and around the approach channel. The total number of sampling points are 26. An example of the composition of bottom materials is shown in Fig.3. In the figure, bottom materials are classified into gravel ( $d > 2\text{mm}$ ), sand ( $0.074 < d < 2\text{mm}$ ), silt ( $0.005 < d < 0.074\text{mm}$ ), and clay ( $d < 0.005\text{mm}$ ).

At stations C, H, L, O and Q, the bottom sediments mainly



**Fig.3** Composition of Bottom Materials

consist of sand and silt, and the sand content is nearly 50% or more than 50%. At other stations, the bottom sediments mainly consist of clay and silt. From the results of field observations, bottom sediments around the approach channel are generally composed of fine silt materials, except at the tidal flat near the river mouth (Sts. C and H), and other three offshore areas beside the approach channel (Sts. L, O and Q).

### 3. Numerical Simulation

#### 3.1 Grid Arrangement

A three dimensional eight-layered level model with nested grids is used in the calculation (*Tsuruya et al., 1990*). The area for calculation is 40 km×50 km. The width of the approach channel in the present condition is 60 m. The length of it, on



the other hand, is 14 km which is about 230 times greater than the width. For the accurate estimation of the deposition rate in the approach channel, the small grid size is preferable. In the direction of the width, at least two grids must be placed in the approach channel. We can then set the transverse grid size as 30 m. As the square grid is unrealistic because of the requirement of tremendous number of grids, the longitudinal size is set to be ten times greater than the transverse grid size. Moreover, the area for calculation is divided into three areas with respect to grid sizes, that is  $270 \times 2,700\text{m}$ ,  $90 \times 900\text{m}$ , and  $30 \times 300\text{m}$  for each area from the first to the third, respectively. In the calculation the water depth is vertically divided into eight layers.

### 3.2 Tidal Currents

An example of the calculated tidal current distribution for the first layer (from  $-0.5\text{m}$  to  $1.6\text{m}$  measured from the datum level) of the second and the third area is shown in Fig.4. The time is 18 hour from the high tide as shown in Fig.2. The current vector distributions can be understood that the reproduction of current patterns in the numerical model is well in terms of the S-shaped bend of ebb currents (also see Fig.11).

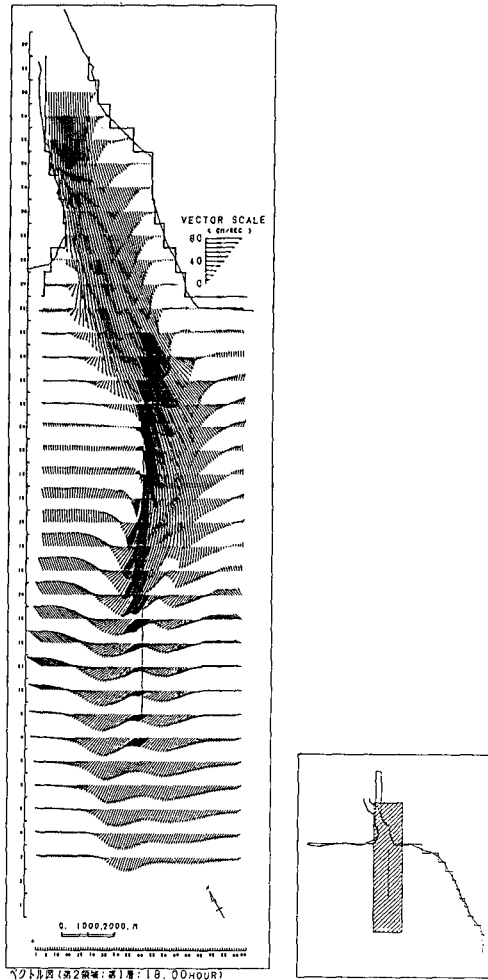
### 3.3 Deposition Rate during Intermission Period of Dredging

The actual deposition rate in the approach channel can be estimated from the siltation volume measured with an echosounder. Dredging works were stopped from February 28th to May 24th 1989 for the measurement of natural mud deposition in the channel. Soundings were performed in the narrow area surrounding the approach channel. The duration of the intermission period of dredging was 85 days.

The measured volume of deposition in the channel within this period is shown in Fig.5 for both frequencies 210 kHz and 33 kHz. The Spot number 0 corresponds to the offshore side of the channel. The volume in the figure are not directly related to the substantial deposition volume to be dredged because the measured depth by echo-sounder varies considerably with the frequency adopted and density of the fluid or mud.

The substantial deposition rate in dry weight of materials per unit area is necessary in comparing the actual and calculated deposition rates. Therefore, the vertical distribution of water content of mud which was estimated by sampling is related to the echo-sounding and lead tests to get the substantial

deposition rate. **Figure 6** shows the measured and assumed vertical distribution of water content. The percentage of water content 110% corresponds to the bulk density about  $1.45\text{g}/\text{cm}^3$ . The water content near the bed which was detected by 33kHz echo-sounder was 110.3% and the level here was almost coincident with that measured by the lead. Around the level measured with the 210kHz echo-sounder, the sample showed high water content at 1,260.4%. At the end of the intermission period of dredging, the level which was detected by 33kHz echo-



**Fig.4** Current Vector Distribution (at 18:00, 1st layer)

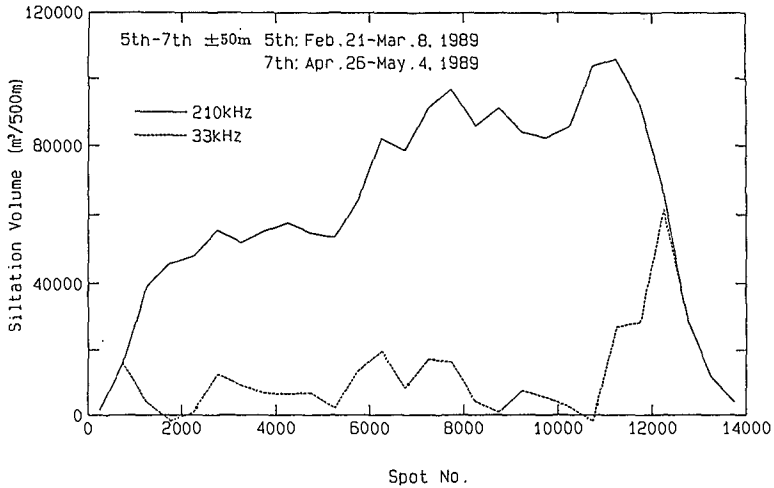


Fig.5 Apparent Siltation Volume along Channel Axis (width ±50m)

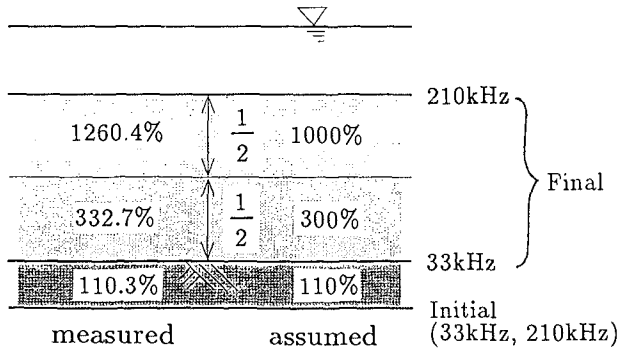


Fig.6 Measured and Assumed Water Content of Mud

sounder increased from the initial level. This means the substantial bed shoaling. Based on the data stated above, we assume the vertical distribution of water content  $W$  (%) in the approach channel as shown in the right hand side of Fig.6. From the assumption we can estimate the substantial deposition rate. The estimated substantial amount of deposition during the intermission period of dredging (85days) is shown in Fig.7 as a histogram. The measured deposition volume is converted to that having the water content of 110%. For this value, the wet bulk density of soil is  $1.45 \text{ t/m}^3$  which is the same as that of the in

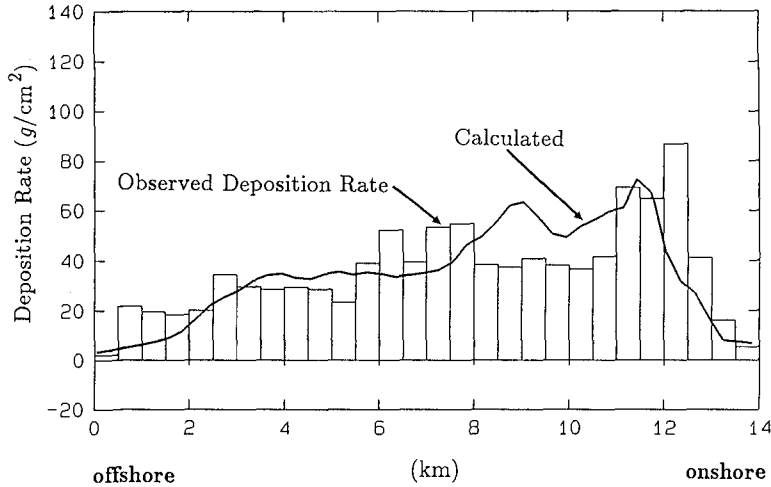


Fig.7 Observed and Calculated Deposition Rate

situ dredged soil. The total amount of deposition in 85 days thus estimated is  $733,000 \text{ m}^3$ .

To calibrate the model, the deposition rate in a day is calculated with a super-computer under the measured natural conditions such as the river discharge ( $3,500 \text{ m}^3/\text{s}$ ), concentration of suspended solids of the river water ( $50 \text{ mg/l}$ ), waves ( $H_{1/3}=41 \text{ cm}$ ,  $T_{1/3}=3.5 \text{ s}$ ), etc. The calculated deposition rate in 85 days is obtained by multiplying 85 by the calculated deposition rate in a day. It can be directly compared with the measured one as shown in Fig.7. Their distribution patterns agree well each other.

#### 4. Results and Discussion

After the calibration of the present model is completed, the deposition rates during the rainy and dry seasons can be estimated with the corresponding natural conditions. Wave direction, significant wave height and period are statistically analyzed for the rainy and dry seasons as already shown in Table 1. The river discharge is given by the field observation as  $5,000 \text{ m}^3/\text{s}$  for the rainy season and  $1,500 \text{ m}^3/\text{s}$  for the dry season. The thick line which is illustrated as "Total" in Fig.8 shows the calculated deposition rate for the rainy season of which duration is 182 days.

To investigate the source of deposited materials in the channel, the direct contribution from the river is estimated by simulation under the assumption of the fixed bed condition in the tidal flat and the approach channel, so that only the sediments from the river are the source of deposited materials. As no erosion in the approach channel is allowed in the calculation of the fixed bed condition, the deposition rate on the onshore side at 13 ~14km is larger than that of the total deposition rate. Although the rate of deposition is not a linear function of the concentration of mud for the free settling region, the difference between two curves in Fig.8 approximately correspond to the settled mud which is resuspended by waves from the surrounding tidal flat. From Fig.8, it can be concluded that the direct contribution from the river is not large except near the river mouth and the resuspended bed materials by waves from the surrounding tidal flat play an important role in the siltation process of the approach channel which is constructed in a large scale muddy tidal flat.

The hodographs of tidal currents in terms of the mean velocity and  $K_1+M_2$  components (50cm above the sea bed) are shown in Fig.9. The numbers of the hodographs correspond to the time from the high tide. The tidal current vector in the west flat (west of the main stream) rotates clockwise and the hodographs show round shapes. In the east flat, on the other hand, they rotate anticlockwise and show long and narrow

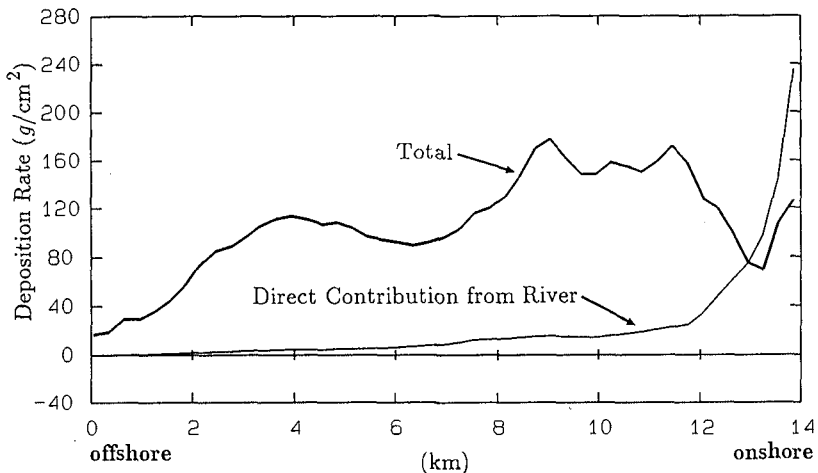


Fig.8 Calculated Deposition Rate for Rainy Season

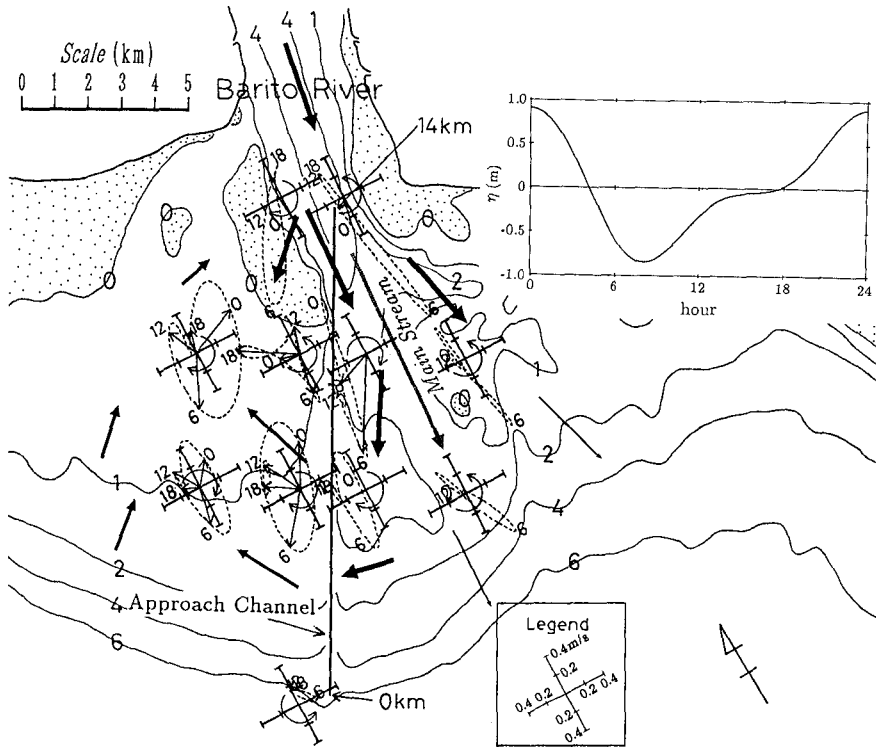


Fig.9 Hodographs of Tidal Currents and Sediment Movements

shapes. As the diurnal constituent  $K_1$  is dominant here, the surface elevation  $\eta$  varies with time as schematically shown in Fig.9. The tidal level given here is somewhat different from that in Fig.2. In general, when  $\eta$  is low or during low tide (5~18hr), the sea bed in the tidal flat is influenced considerably by waves because of the high orbital velocity and the rate of erosion from the bed is larger than that of the high tide. The tidal currents during the low tide in the west flat are dominated by westward currents, whereas during the high tide that are dominated by eastward currents as shown in Fig.9. As a result, the net transport of sediments in the middle part of the west flat is from the south-east to the north-west according to the current direction. The dominant wave direction is south-west and the sediment movement in the west flat is directed to the north-east direction because of the mass transport by waves and asymmetric characteristics of tidal currents. The directions of the net transport of bed materials expected from the above consideration are shown

in Fig.9 as the arrows with the thickness roughly showing the transport quantity.

Morphological change during 84 years is analyzed by comparing the Chart around 1905 with the surveyed sounding data in 1989. In Fig.10, accretion and erosion areas more than 60cm are shown as the thin contour lines. Near the river mouth, typical accretion can be found in the west side of the channel. In the east side near the river mouth, on the other hand, erosion is dominant. At the offshore side of the channel, erosion also can be found in the west side of the channel. In the east side near the river mouth, on the other hand, erosion is dominant. At the offshore side of the channel, erosion also can be found in the west side of the channel. The thick contour lines in the figure show the horizontal distribution of the median diameter of bed materials. There are four distinct peaks for the median diameter contours. In the west bank of the approach channel, there are two peaks and the maximum values are greater than  $1000\mu\text{m}$ . In the east bank, on the other hand, the maximum values ( $940\mu\text{m}$  and  $510\mu\text{m}$ ) are slightly smaller than that of the west bank. Figure 11 shows the loci of drogues which represent the surface current and calculated velocity distribution at the third layer (from 1 to

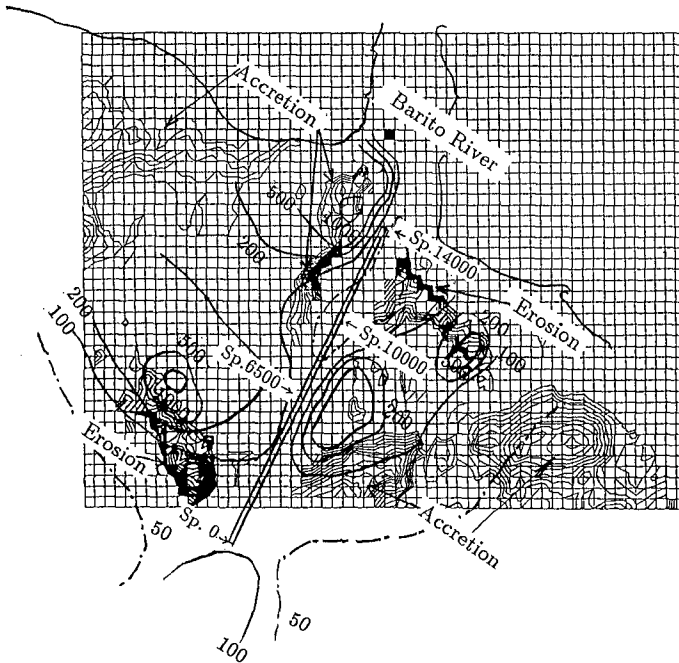
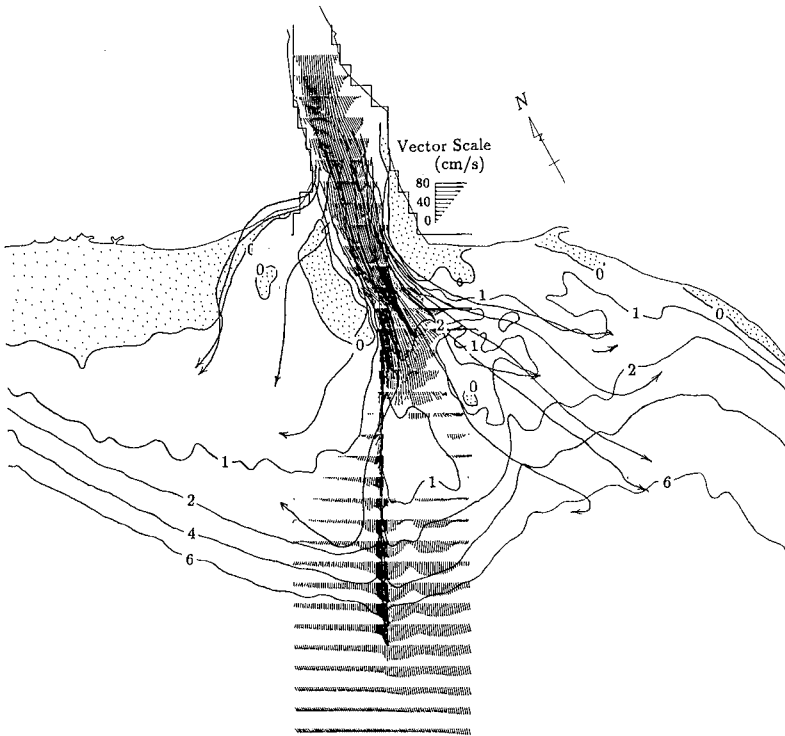


Fig.10 Morphological Change and Grain Size Distribution



**Fig.11** Measured Loci of Drogues and Calculated Flow Pattern

1.5m below the datum level) at an ebb tide. The loci of drogues are shown as thick solid arrows. From **Figs.10** and **11**, it can be thought that the west bank near the river mouth is formed by deposition of coarse sand which is carried from the river because of the sudden decrease of the current speed in this area and of the eastward longshore sand transport due to waves attacking from the dominant SW direction. The eroded area in the east part of the river mouth is formed by the strong current which is directed to the east direction from the river mouth, and only coarse sand which resist the strong tractive force can exist in this area. The accretion areas, therefore, are formed offshore side in the east bank. The erosion area in the west offshore side will be formed by the continuous wave attack.

## 5. Conclusions

The substantial transport direction of fine sediments on the large tidal flat was investigated based on the field data and



numerical simulations. The net transport of sediments is from the south-east to the north-west in the middle part of the west flat. Finally, the sediment movement in the west flat is directed to the north-east direction because of the mass transport by waves and asymmetric characteristics of tidal currents.

From the numerical simulation, it is revealed that the resuspended bed materials by waves from the surrounding tidal flat play an important role in the siltation process of the approach channel.

Current velocity and waves play an important role in the formation of large scale muddy tidal flat.

### Acknowledgements

The authors are greatly indebted to Japan International Cooperation Agency for the support of the present study in connection with "The Study on Maintenance Dredging in the Access Channel of Banjarmasin Port in The Republic of Indonesia".

We also should like to express our grateful thanks to the members of the Directorate General of Sea Communications of the Government of Indonesia and those of the Study Team organized by the Overseas Coastal Area Development Institute of Japan.

### References

Costa, R.G. and A.J. Mehta (1990): Flow-fine sediment hysteresis in sediment-stratified coastal waters, Proc. of 22nd Conf. on Coastal Eng., ASCE, 2047-2060.

Hoekstra, P., P.G.E.F. Augustinus and J.H.J. Terwindt (1988): River outflow and mud deposition in a monsoon-dominated coastal environment, Physical Process in Estuaries, Springer-Verlag, 311-331.

Leussen, W. van and E. van Velzen (1988): High concentration suspensions: their origin and importance in Dutch estuaries and coastal waters, Jour. of Coastal Res. Special Issue No.5, 1-22.

Terwindt, J.H.J., P.G.E.F. Augustinus, J.R. Boersma and P. Hoekstra (1987): Mud discharge, dispersion and deposition in a monsoon-dominated coastal environment, Proc. of Coastal Sediments '87, ASCE, 1796-1988.

Tsuruya, H., K. Murakami and I. Irie (1990): Numerical simulations of mud transport by a multi-layered nested grid model, Proc. of 22nd Conf. on Coastal Eng., ASCE, 2998-3011.

## CHAPTER 221

### MODELLING OCEAN WAVES IN THE COLUMBIA RIVER ENTRANCE

L.A. Verhagen<sup>1,2</sup>, L.H. Holthuijsen<sup>1</sup> and Y.S. Won<sup>1</sup>

#### Abstract

Observations by Gonzalez et al. (1984) and Gonzalez (1984) of swell penetrating the entrance of the Columbia River provide an excellent opportunity to test linear wave theory for wave - current interactions. In the present study a two-dimensional wave model for short-crested waves based on the linear wave theory is used. The model includes the propagation effects of currents and also generation and dissipation of the waves. The results agree fairly well with the wave observations in the river entrance, in spite of an uncertainty in the bathymetry and currents. Numerical experiments show that waves from westerly directions are focused in the entrance by refraction on a bar in front of the entrance and that current induced wave guide effects enhance this focusing in ebb conditions.

#### Introduction

Swell entering the Columbia River (United States west coast) may amplify considerably due to bottom and current effects. Gonzalez et al. (1984) and Gonzalez (1984) acquired observations in the river entrance which provide an excellent opportunity to study wave-current interactions. To compute the wave field, the same authors used a one-dimensional model for monochromatic, long-crested waves. Later, Rao (1990) used a two-dimensional model for random, short-crested waves. However, neither model takes the two-dimensional current structure into account nor generation and dissipation of the waves (except that the wave height or spectrum has an a priori imposed upper limit). In this study we use a model that is based on linear wave theory for short-crested waves with energy sources and sinks (in particular bottom and current induced wave breaking and bottom dissipation). It is a two-dimensional model that computes the two-dimensional wave field so that the two-dimensional structure of the wave field can be related to features in the bottom and current field. The effects of bottom and current induced refraction are addressed explicitly.

<sup>1</sup> Delft University of Technology, Stevinweg 1, 2628 CN, Delft, the Netherlands,  
<sup>2</sup> presently at University College, Australian Defence Force Academy, Campbell, Australia

## Observations

The Columbia River entrance is located on the Pacific east rim at the west coast of the United States of America (see Fig. 1). It is a rather energetic region with high waves (in one of the observed cases the significant wave height of the swell was about 6.5 m) and an average river discharge of 10,000 m<sup>3</sup>/s and peak discharges of more than 40,000 m<sup>3</sup>/s. On the average 850 search and rescue missions are conducted and about 10 lives are lost per year (Gonzalez 1984).

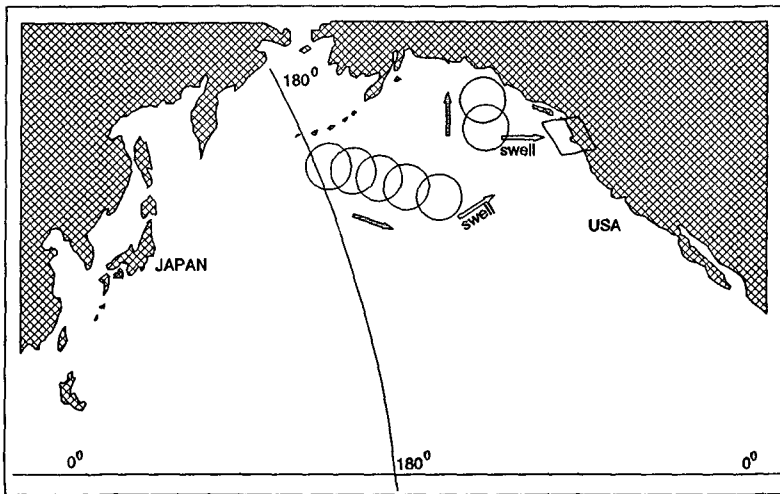


Fig. 1 The tracks of the two swell generating storms of this study. The box indicates the location of the Columbia River entrance.

Gonzalez (1984) and Gonzalez et al. (1984) observed swell that was generated in two severe storms in 1979 and 1981. From local observations at the Columbia River entrance and weather maps Gonzalez (1984) concluded that the first generating storm was a storm moving in a few days across a fair distance in the northern Pacific due west of the Columbia River entrance. The second storm was analyzed by Gonzalez et al. (1984) and they concluded from weather maps that it was a storm relatively nearby, moving from an offshore position to the Canadian coast. The tracks of these storms are schematically indicated in Fig. 1.

The bathymetry of the Columbia River entrance that we used in this study is given in Figs. 2 and 3. It is based on a map from 1983 (US Army Engineer District Portland MC-1-543) for the region seaward from the jetties (outer region) and a map from 1966 (C&GS 6151) for the region up-river from the jetties (inner region). These maps may not properly represent the bathymetry during the observations. In fact, in the outer-region we found considerable differences with the 1966 map (of more than two meters in depth near the south end of the "bar", see Figs. 3a and 3b). The map that we finally used for the outer region (the 1983 map, Fig. 3a) seems to be the closest in time to the observations that were available to us (see acknowledgements). The inner region is regularly dredged and we therefore assume that the bathymetry there has not changed dramatically over the years. To

investigate the effects of this uncertainty in bathymetry we will show results using the map from 1966 for the outer region (Fig. 3b).

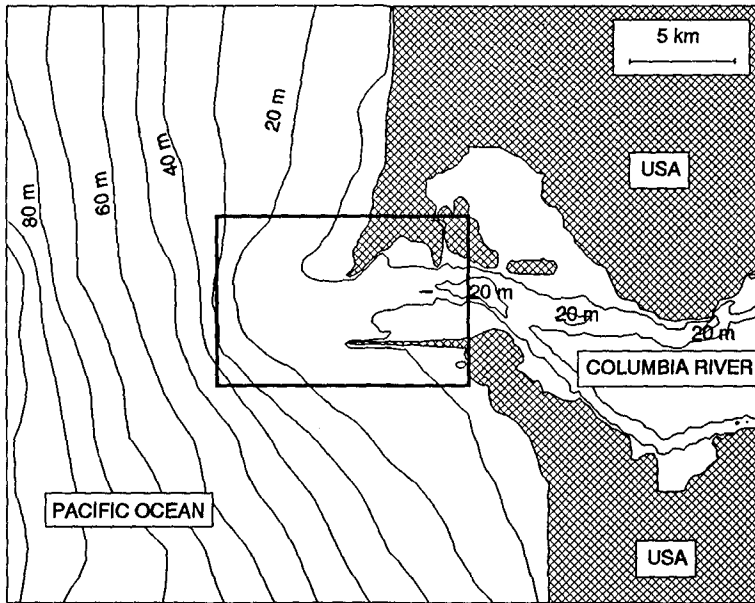


Fig. 2 The large scale bathymetry off the Columbia River entrance. The box indicates the region shown in Figs. 3 and 5.

From the observations we selected a young-swell case and an old-swell case. The young swell arrived on 12 September 1981. It had been generated in a storm moving to Canada a few hundred miles north-west from the Columbia River entrance in the period 8-10 September. The incoming significant wave height and the mean wave period were observed with a wave buoy (NOAA data buoy 46010, located about 10 km offshore) to be 2.8 m and 8.6 s (ebb case, 16:00 PST) and 7.8 s (flood case, 11:00 PST) respectively. We estimate the mean wave direction from the Side-Looking Airborne Radar (SLAR) images in Gonzalez et al. (1984) to be  $290^\circ$  true North. We estimate from the angle of view from the Columbia River entrance to the width of the generating storm area that the directional spreading of the waves was  $13^\circ$  (directional standard deviation of the directional energy distribution). In the river entrance a drifting waverider buoy measured the wave field (tracks shown in Figs. 3c and 3d). The old swell arrived at the location during the period 15 - 20 October 1979. It had been generated 9 days before in a severe storm in the northern Pacific moving from the date line towards the location. On October 19 at 16:00 PST the incoming significant wave height and the mean period were observed with a deployed waverider buoy to be 4 m and 15 s respectively. Gonzalez (1984) estimated the mean wave direction from the time development of the locally observed peak frequency and weather maps to be  $270^\circ$  true North. The directional spreading we estimate with the same technique as above to be  $6^\circ$ . The waves in the entrance were observed near buoy 8 with a waverider buoy (see Figs. 5c and 6).

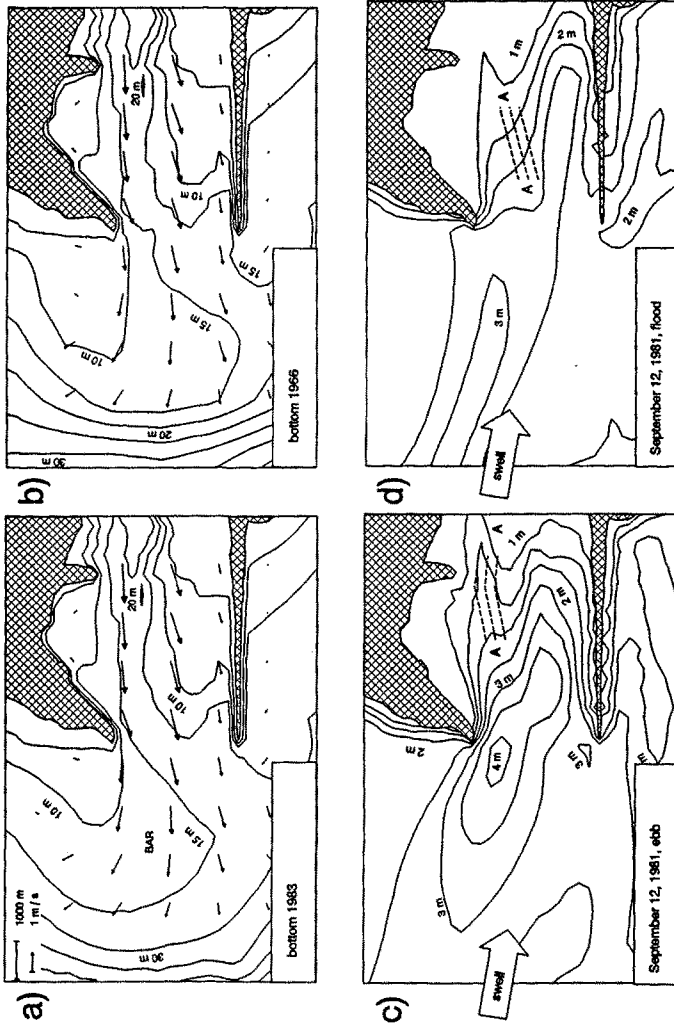


Fig. 3 Panel a) the bathymetry of the Columbia River entrance (1983 information) and the ebb currents for the old swell case. Panel b) same as a) from 1966 information. Panel c) significant wave height young swell case (ebb). Panel d) significant wave height young swell case (flood). Tracks of buoy shown as centre line between A and A (parallel lines at 250 m distance).

### Wave and current models

The wave model that we used (the HISWA model, Holthuijsen et al., 1989) is based on a parameterization of the spectral balance of wave action (defined as wave energy divided by relative frequency). In the absence of a mean current it reduces to a parameterized energy balance. The parameterization is based on the presentation of the waves with a spectrum that is discrete spectral in the directions and parametric in the frequencies. This implies that the spectral representation of short-crestedness of the waves is maintained. All propagation in the model is based on linear wave theory while the sources and sinks are parametric representations of wind growth, wave breaking (whitecapping and surfing), bottom friction and blocking due to counter current. The model computes the spatial variation of this spectrum by integrating the local effects of wind, bottom and currents while propagating with the wave components on a regular grid covering the computational area (identical to the total area of Fig. 2 with 250 m resolution). Refraction is modelled as a continuous directional shifting of wave action in spectral space. For coastal regions the propagation time through the area is small compared to the time scale of wind and current variations. Time has therefore been removed as a variable. In the present study with swell in a coastal region, the only effective sources and sinks in the model are those representing wave breaking and bottom friction.

The tidal model which has been used (the DUCHESS model, Booij, 1989) to simulate the ebb and flood flow in the Columbia River entrance is based on the two-dimensional shallow water equations. It includes hydrostatic and atmospheric pressure gradients, bottom and wind stresses, Coriolis force and horizontal eddy viscosity. The inclusion of nonlinear terms such as advective acceleration, viscosity and stresses makes DUCHESS a nonlinear tidal model.

### Results

To drive the tidal model, the tidal constituents at the open ocean boundary and at Tongue Point (up-river boundary in Fig. 2) were taken from standard tide tables (Admiralty Tide Tables). In spite of choosing a relatively low frictional coefficient, we were not able to reproduce the current observations of Gonzalez et al. (1984) and Gonzalez (1984). We therefore multiplied the magnitude of all computed current vectors with a constant factor to match the observed (corrected to depth-averaged) values (factor 1.08 in the young swell case (ebb), 1.50 in the young swell case (flood) and 1.23 in the old swell case (ebb)). The current pattern for the old swell case is shown in Fig. 3a for the 1983 bathymetry (and in Fig. 3b for the 1966 bathymetry). The ocean wave boundary conditions were taken from the buoy and radar observations.

The young swell case is considered first because the wave observations in this case provide some spatial information of the wave field in the Columbia River entrance and therefore provide a good test of the fidelity of the HISWA model. The wave field is computed with HISWA for one ebb case (12 Sept. 1981, 16:00 PST) and one flood case (12 Sept. 1981, 11:00 PST). The results for the ebb case are shown in Fig. 3c where also the track of the drifting buoy is shown. The maximum significant wave in the area is approximately 4.2 m. The HISWA results along the buoy track (and 250 m north and south of this track) are compared with the drifting buoy observations in Fig. 4. For the two up-river locations, the agreement seems

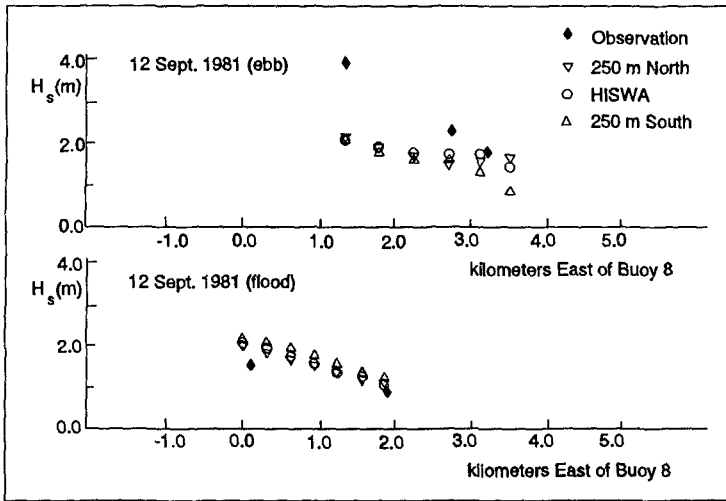


Fig. 4 The computed significant wave height for the young swell case compared with the buoy observations. Upper panel is ebb case, lower panel is flood case. The track of the buoy is shown in Fig. 3.

to be fair, considering the spatial resolution of the model (250 m). For the one down-river location, there is no such agreement (observed 4 m and computed 2 m significant wave height). Considering the spatial distribution of the waves, it seems unlikely that a simple error in the location of the buoy is responsible for this discrepancy. On the other hand, a large error in the model is not very likely either considering the other results (below). The results for the flood case are shown in Fig. 3d and 4 (maximum significant wave height 3.5 m). Again, the results seem to be fair considering the uncertainty in bottom and currents.

The old swell case is rather spectacular with a significant wave height of 4 m amplifying to nearly 6.5 m on the inner bar (near buoy 8). To inspect the physical processes to some extent we first show the HISWA results without currents and without bottom refraction effects (accomplished by de-activating the refraction terms in HISWA). The results are given in Fig. 5a. It is obvious that the remaining processes in the resulting quasi-one-dimensional situation (i.e. rectilinear propagation, bottom induced shoaling and bottom friction) do not affect the wave field considerably (maximum significant wave height of 4.6 m over the bar). When we add bottom induced refraction (still without current), the results are as shown in Fig. 5b. It is obvious that the bar concentrates wave energy in front of and between the jetties, probably by a caustic type refraction pattern. The maximum significant wave height is 5.8 m at the southern edge of the bar. If we finally add ebb currents to the situation we see from Fig. 5c that the current field enhances the waves further, probably by a wave guide effect (trapping of wave components around the centre of a counter current). The maximum significant wave height is now 6.25 m at the southern edge of the bar. There is a second maximum of 6.19 m between the jetties near buoy 8 (Fig. 6). This secondary maximum differs only 4.5 % from the observed 6.48 m of swell "near buoy 8" (quote from Gonzalez, 1984). This is a surprisingly good agreement considering the uncertainty in the bottom and current fields used in the computations. To show the effect of this

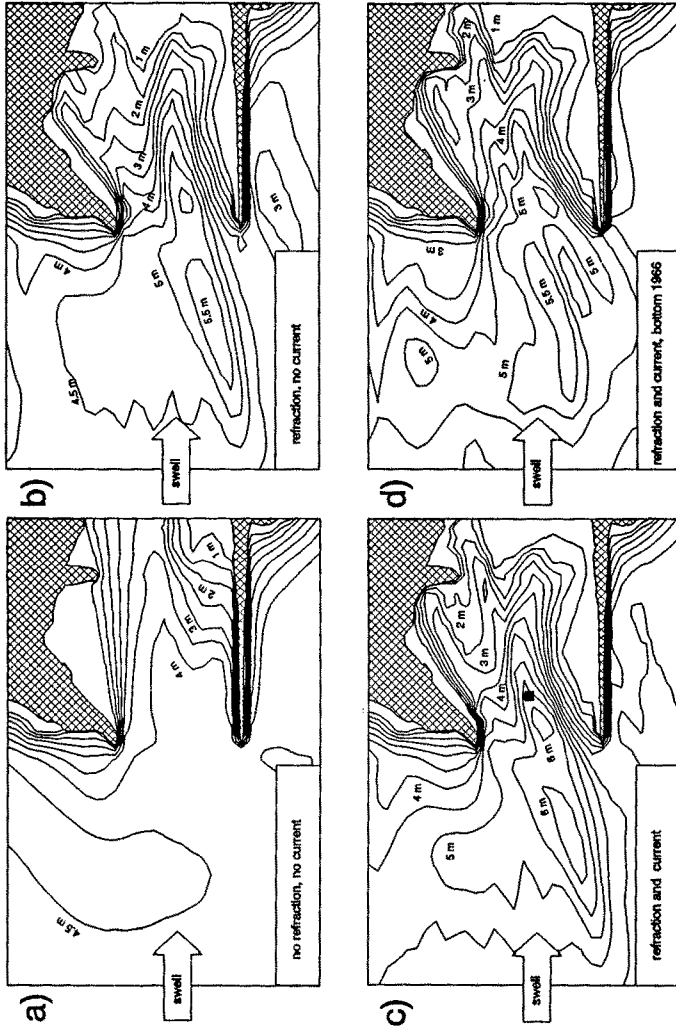


Fig. 5 The computed significant wave height in the old swell case. Panel a) without refraction and without currents (1983 bathymetry). Panel b) with refraction but without currents (1983 bathymetry). Panel c) with refraction and with currents (1983 bathymetry). Panel d) with refraction and with currents but 1966 bathymetry. Location of buoy 8 indicated in panel c) with black square.



uncertainty, we repeat the last computations with the bathymetry from the 1966 map (and corresponding current field). The results are shown in Fig. 5d where the maximum significant wave height is 5.9 m (at the southern edge of the bar).

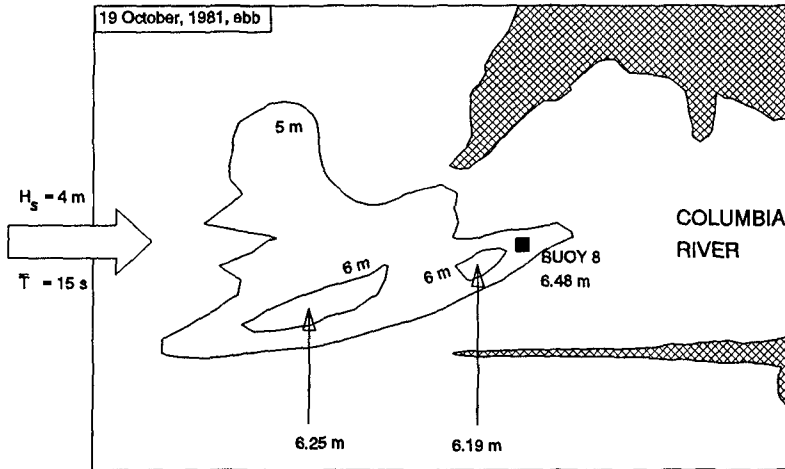


Fig. 6 The computed significant wave height for the old swell case compared with the buoy observation near buoy 8 (copied from Fig. 5c).

## Conclusions

The observations of Gonzalez et al. (1984) and Gonzalez (1984) seem to provide an excellent opportunity to test wave-current interactions within the linear wave theory. This linear wave theory is represented in the HISWA model and we find general agreement between the computational results and the observations. However, this agreement is better than one would expect considering the uncertainty in the bottom and current data used in the computations.

Independent of this uncertainty we can conclude that waves approaching the Columbia River from the west are focused into the river entrance by bottom induced refraction. This focusing is further enhanced in ebb conditions by current induced refraction.

## Acknowledgements

With pleasure we acknowledge that J. List of the U.S. Geological Survey helped us with obtaining the bathymetry in the Columbia River entrance. The work of one of the authors (Y.S.W.) was supported by the European Economic Community under contract MAST-0026-C(MB).

**References**

- Booij, N.** (1989). Delft University Computer program for 2-dimensional Horizontal Estuaries and Sea Surges (DUCHESS), Group of Hydraulic and Geotechnical Engineering, Delft University of Technology.
- Gonzalez, F.I., M.R. Mulhern, E.D. Cokelet, T.C. Kaiser, J.F.R. Gower and J. Wallace** (1984). Wave and current observations at the Columbia River entrance, 10 - 13 September, 1981, NOAA Technical Memorandum ERL PMEL-59, NOAA Environmental Research Laboratories, Pacific Marine Environmental Laboratory, Seattle.
- Gonzalez, F.I.** (1984). A case study of wave-current-bathymetry interaction at the Columbia River entrance, *J. Phys. Oceanogr.*, 14, pp. 1065 - 1078.
- Holthuijsen L.H., N. Booij and T.H.C. Herbers** (1989). A prediction model for stationary, short-crested waves in shallow water with ambient currents, *Coastal Engineering*, pp. 23-54.
- Rao, D.B.** (1990). Local and regional scale wave models, *Proc. Techn. Conf. Ocean Waves*, Paris, 6 - 7 Feb. 1989, Rep. No. 24, World Meteorological Organization, pp. 125 - 138.

## CHAPTER 222

### Sediment Transport in Dredged Trenches

S. Opatha Vithana\*, MICE(Lond.), MIEAust.

#### Abstract

An attempt was made, using a 3-dimensional turbulent model coupled with a comparatively simple depth averaged sand transport model, to assess the computational feasibility of predicting sediment transport in a dredged trench, caused by a steady flow passing across the trench. A sophisticated computer software package was used to simulate 3-dimensional turbulent flow by the finite element method. A Profile Model, which discretized the transport process to enable successive computation of the flow field, was used for morphological evolution of the channel bed. A physical model was built and tested to validate the numerical models.

#### 1.0 Introduction

An attempt to set up a mathematical theory of sedimentation should take into account both the character of the fluid motion and character of the sediment motion. The K-Epsilon model is considered as the best mathematical model available at present to represent turbulent flow. Any mathematical model to represent sediment transport should take into account the movement of sediment by both suspension and bed load. Movement of sediment in suspension is considered to be best described by the diffusion-convection equation. Therefore, if K-Epsilon model is coupled with the diffusion-convection equation together with a bed load formula one can expect a very good mathematical model to represent sediment transport. However, for long term morphological computations implying the successive computation of the flow field, the use of K-Epsilon model or the diffusion-convection equation is still not attractive because of the limitations of available computer resources. To overcome this problem various mathematical models have been proposed by combining the simplified diffusion-convection equation with comparatively simple flow models.

In this paper an attempt made to assess the computational feasibility of solving this complex problem by using a

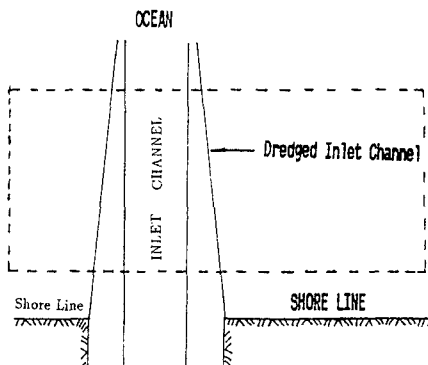
---

\* Superintending Civil Engineer, Sri Lanka Ports Authority, Colombo-1, Sri Lanka.

3-dimensional turbulent model coupled with a comparatively simple sand transport model is presented.

2.0 Physical Model

A physical model of the entry to a dredged navigational channel through a shelving coastline was built to simulate siltation effects. The flow and siltation conditions obtained from the physical model were used to verify the two numerical models which were under assessment.



The plan view of the inlet area considered for study is the area enclosed by broken lines in Fig. 1.0. Dimensions and isometric view of the flow domain are shown in fig.2.0.

Fig. 1.0: Area Considered for Detailed Study.

The slope of the bed in the transverse direction represents the gradient of the sea bed in the shore region.

The bed consisted of fine to medium sand of almost uniform size with the characteristic diameters of:  $d_{10} = 150 \mu\text{m}$ ,  $d_{50} = 240 \mu\text{m}$ , and  $d_{90} = 380 \mu\text{m}$ . A continuous steady flow with a mean flow velocity of about 0.3 m/sec, which was considered to be large enough to initiate movement of the sediment used in the experiment, was maintained into the model during the experiment.

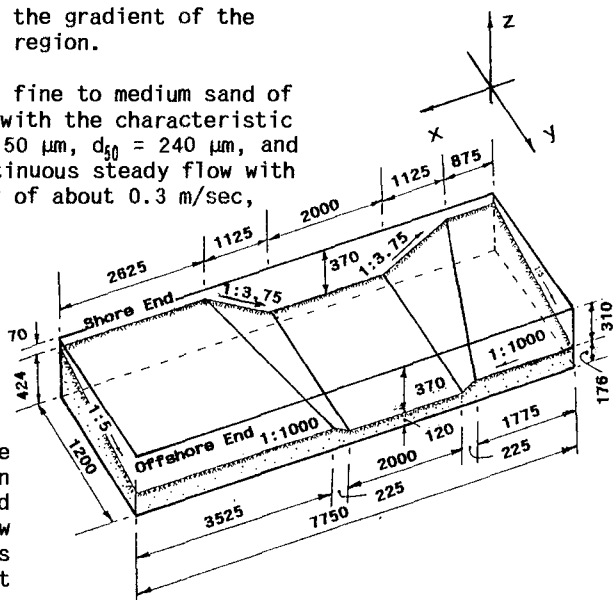


Fig.2.0: Isometric View of the Flow Domain.

For validation of the flow simulation model, inlet and downstream flow velocity measurements should be carried out on a fixed bed model.

Therefore, at the first instance, the entire bed of the physical model was covered with steel sheets to maintain a fixed bed and all flow velocity measurements were carried out using Laser-Doppler velocity measuring equipment. In order to obtain input velocity boundary conditions for the flow simulation model, inlet velocity components in longshore and offshore

directions were measured on all finite element grid lines. For calibration of the flow simulation model, measurement of the longshore velocity components were carried out at four different downstream sections, at  $x = 1.75, 3.0, 4.5$  and  $7.25$  meters.

When calibration of the flow simulation model was completed, the metal sheets used to cover the bed were removed and the flow was restarted to validate the sand transport model. After 6.0 hrs. of continuous steady flow, the flow was discontinued and the bed profiles of the entire area under consideration was measured.

### 3.0 Numerical Models

#### 3.1 Flow Simulation Models

A general purpose computer software package (FIDAP) which uses the finite element method to simulate many classes of incompressible fluid flows was used to simulate turbulent flow across the channel. In FIDAP the three-dimensional, steady, turbulent flow of an incompressible viscous fluid is represented by the following equations:

$$\text{- Mass Conservation; } \frac{\partial u_j}{\partial x_j} = 0$$

$$\text{- Momentum Conservation; } u_j \frac{\partial u_i}{\partial x_j} = - \frac{\partial p}{\partial x_i} + \frac{\partial}{\partial x_j} \left[ \mu \left( \frac{\partial u_i}{\partial x_j} + \frac{\partial u_j}{\partial x_i} \right) \right]$$

where,  $u_j$  = mean fluid velocity component,  $p$  = fluid pressure,  $x_j$  = cartesian coordinates,  $i = 1,2,3$ ,  $j = 1,2,3$ ,  $\mu$  = total viscosity =  $\mu_0 + \mu_t$ ,  $\mu_0$  = laminar viscosity,  $\mu_t$  = turbulent viscosity.

Two possible turbulent models are available in FIDAP to determine the distribution of turbulent viscosity (or eddy viscosity).

##### 3.1.1 K-Epsilon Model

The three-dimensional version of the K-Epsilon model comprises three additional equations as indicated below:

$$\rho u_j \frac{\partial K}{\partial x_j} - \frac{\partial}{\partial x_j} \left( \frac{\mu_t}{\sigma_K} \frac{\partial K}{\partial x_j} \right) - \rho \epsilon$$

$$\rho u_j \frac{\partial \epsilon}{\partial x_j} - \frac{\partial}{\partial x_j} \left( \frac{\mu_t}{\sigma_\epsilon} \frac{\partial \epsilon}{\partial x_j} \right) - \rho C_2 \frac{\epsilon^2}{K}$$

$$\mu_t = \rho C_\mu \frac{K^2}{\epsilon}$$

FIDAP adopts the Galerkin form of the weighted residuals method to solve these differential equations by the finite element method.

##### 3.1.2 Mixing Length Model

In the mixing length model, the turbulent viscosity is represented by the Prandtl mixing length hypothesis.

$$\mu_t = \rho l_m^2 \left[ \left( \frac{\partial u_i}{\partial x_j} + \frac{\partial u_j}{\partial x_i} \right) \frac{\partial u_i}{\partial x_j} \right]^{1/2}$$

In FIDAP the mixing length values are computed based on Nikuradse's (Rodi W., 1980) Formula:

$$\frac{l_m}{R} = 0.14 - 0.08 \left(1 - \frac{y}{R}\right)^2 - 0.06 \left(1 - \frac{y}{R}\right)^4$$

where, R = depth of flow, y = normal distance from the wall.

### 3.1.3 Boundary Conditions for Flow Simulation Models

#### 3.1.3.1 Inlet Boundary

Mean velocities of flow in all three coordinate directions (u,v,w), turbulent kinetic energy (K), and its dissipation rate ( $\epsilon$ ) should be specified at the inlet.

##### (a). Mean Flow Velocities

Inlet velocity components in the longshore and offshore directions measured in the physical model were prescribed as input to the numerical model. Inlet velocity in the vertical direction was assumed to be zero.

##### (b). Turbulent Kinetic Energy

Time-averaged values of the fluctuating components of the fluid velocities  $\bar{u}'$  and  $\bar{v}'$  measured at the inlet by the Laser-Doppler equipment were used in calculating the turbulent kinetic energy (K) at the inlet, using the formula:

$$K = \frac{1}{2} [(\bar{u}')^2 + (\bar{v}')^2 + (\bar{w}')^2]$$

The prescribed initial values of K and  $\epsilon$  at the inlet seems to exert little influence on the predictive accuracy of the flow simulation models (Leschziner M.A., et al. 1979). Therefore, as velocity measurements were not carried out in the vertical direction it was assumed that,  $\bar{w}' = \bar{u}'$ .

##### (c). Dissipation Rate of Turbulent Kinetic Energy

Dissipation rate of turbulent kinetic energy ( $\epsilon$ ) was evaluated from the following formula (Launder B.E., et al. 1974) using the values of measured turbulent kinetic energy (K).

$$\epsilon = \frac{C_\mu^{3/4} K^{3/2}}{l_m} ; \text{ in which } l_m \text{ is a mixing length}$$

It was assumed that the value of mixing length is given by the well-known ramp function for wall boundary layers (Launder B.E., et al. 1972):

$$l_m = \lambda y_G$$

where,  $\lambda$  = a constant in mixing length model,  
 $y_G$  = effective width of shear flow.

The characteristic shear width of flow was calculated using the

measured inlet velocity profiles (Launder B.E., et al. 1972). A value of 0.125 was assumed for  $\lambda$ .

### 3.1.3.2 Wall Boundaries

The variation of the turbulent viscosity within the viscous sublayer in the near-wall region was modelled using van Driest's mixing length model with a transition to the standard high Reynolds number K-Epsilon model in flow region beyond the viscous sublayer where the turbulence is fully developed. In the van Driest mixing length approach, the eddy viscosity is defined as described in Section 3.1.2 and the van Driest mixing length is defined as,

$$l_m = k \delta (1 - e^{-y_{\text{eff}}^*/A})$$

where, A = an empirical constant, k = von Karman constant,  $\delta$  = normal distance from the wall.

In this equation  $y_{\text{eff}}$  is the dimensionless normal distance from the wall defined in terms of the turbulent kinetic energy as,

$$y_{\text{eff}}^* = \rho \delta \frac{(c_\mu^{1/2} K)^{1/2}}{\mu}$$

where,  $c_\mu$  = a turbulent constant,  $\mu$  = dynamic viscosity, K = turbulent kinetic energy.

While the computational domain for the mean flow equations encompasses the flow domain up to the solid boundary, the corresponding computational domain for the K- $\epsilon$  turbulent model only extends to near wall region. As part of near-wall implementation, FIDAP applies the following boundary conditions for K and  $\epsilon$ .

$$\frac{\partial K}{\partial n} = 0 ; \quad \epsilon = \frac{(C_\mu^{1/2} K)^{1.5}}{k \delta}$$

where, n is the direction normal to the boundary.

If no-slip boundary condition is valid at the wall, then all the velocity components assume a zero value at the wall.

### 3.1.3.3 Outlet Boundary

The outlet boundary was located far away from the area of interest so as to allow the redevelopment of fully developed flow downstream. At the outflow no velocity boundary conditions were imposed, resulting in zero normal and tangential stresses at the outflow boundary. Similarly, the turbulent kinetic energy and dissipation were not specified at the outflow boundary.

### 3.1.3.4 Water Surface

The position of the free water surface was assumed to be fixed and at the free water surface the velocity component in the vertical direction was assumed to be zero.

### 3.1.4 Creating Finite Element Mesh

The three-dimensional flow domain was first divided into a set

of 8 node brick elements. All wall boundaries were divided into quadrilaterals with 4 nodes. As the computation time needed to solve the equations is large for a finer mesh, a compromise had to be made between the accuracy and the computation time before selecting the following dimensions.

The longitudinal direction was divided into 31 elements of length 250 mm each and the transverse direction consisted of 8 elements of width 150 mm each. The vertical direction consisted of 8 elements, the dimensions of which were decreased towards the bed to provide a greater resolution in the zone where large velocity gradients exist. The solution domain thus consisted of 1984 brick elements of 8 nodes each and 2592 nodal points.

3.1.5 Fluid Properties

Following data was used as the physical properties in the flow simulation models.

fluid density,  $\gamma = 1000.0 \text{ kg/m}^3$ ; kinematic viscosity,  $\nu = 1 \times 10^{-6} \text{ m}^2/\text{sec}$ ; turbulence constant,  $c_{\mu} = 0.09$ ; empirical constants:  $c_{1E} = 1.44$ ,  $c_{2E} = 1.92$ ,  $\sigma_k = 1.00$ ,  $\sigma_\epsilon = 1.30$ ; von Karman constant,  $k = 0.41$ ; van Driest's constant,  $A = 26.00$ .

3.2 Sand Transport Model

The model considered was basically similar to what was used by Hillier and Jenkins (1976). As shown in Figure 3.0, the model zone was divided into a grid system on the horizontal plane, the longshore and offshore directions being divided into equal number of sections as used in the mesh for flow simulation models.

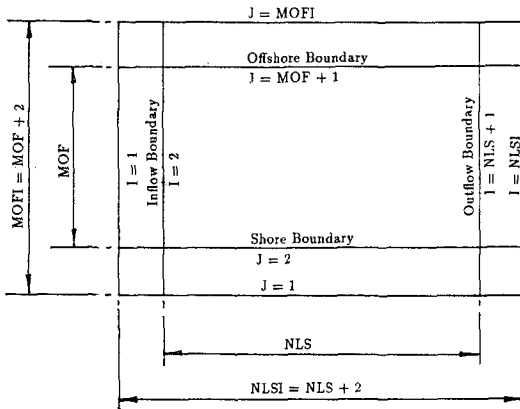


Fig. 3.0: Grid System of the Sand Transport Model

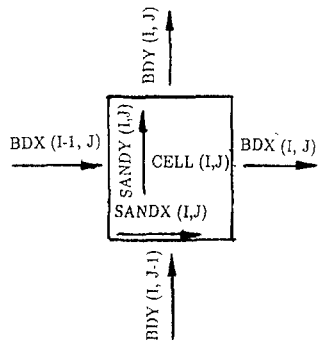


Fig. 4.0: Sediment Transport in a Cell

- MOF = number of cells in the offshore direction = 8
- NLS = number of cells in the longshore direction = 31



For the purpose of comparison, two different formulae were used to calculate the sand transport. In the first method, Shield's (1936) bedload formula and in the second method a new approach to calculate sediment transport by Ackers and White (1973) was used.

### 3.2.1 Shield's Formula

Shield's Bedload Formula for calculation of sand transport can be written as follows:

$$\frac{q_s \gamma_s}{q S \gamma} = 10 \frac{\tau_0 - (\tau_0)_{cr}}{(\gamma_s - \gamma) d}$$

where;  $q_s$ ,  $q$  = rate of bedload and liquid in volume per unit time and unit width respectively,  $S$  = slope of the energy grade line,  $\gamma$  = specific weight of liquid,  $\gamma_s$  = specific weight of sediment,  $\tau_0$  = shear stress,  $(\tau_0)_{cr}$  = critical shear stress at which sediment particles are about to move,  $d = d_{50}$  = mean particle diameter.

The rate of liquid flow can be related to the mean flow velocity as:  $q = V \times H$ ; in which,  $V$  = mean flow velocity,  $H$  = depth of flow.

The bed shear stress can be calculated from (2),  $\tau_0 = \gamma H S$ ; the critical bed shear stress, ( $\text{kg/m}^2$ ), can be related to the mean particle diameter (meters) as (Kalinske A.A.),  $(\tau_0)_{cr} = 192.65 d$ .

The slope of the energy grade line can be expressed in metric units (for manning's  $n = 0.025$ ) as (Graf W.H., 1971),

$$S = \frac{0.0006 \times V^2}{H^{4/3}}$$

Substitution of these values along with  $\gamma_s = 2650.0 \text{ kg/m}^3$  in Shield's Formula will finally yield:

$$q_s = 0.0057 \frac{V^3}{H^{1/3}} [0.59723 \frac{V^2}{H^{1/3}} - 0.04624]$$

Therefore when the values of  $V$  and  $H$  are known, the sediment transport can be calculated using the above equation.

### 3.2.2 Method Proposed by Ackers and White

Ackers and White (1973) has proposed a method to calculate transport of non-cohesive sediment by a steady uniform flow. When the physical properties of the fluid and sediments are substituted, the value of  $S$  is expressed as in Section 3.2.1, and shear velocity is defined as  $v_* = \sqrt{gHS}$ , sediment transport rate can finally be expressed in terms of  $V$  and  $H$  as follows:

$$q_s = 1.2567 \times 10^{-5} \cdot v \cdot H^{0.0936}$$

$$\left[ \frac{7.7019 v}{H^{0.0936} [\log_{10}(4.1667 \times 10^{-4} H)]^{0.4382}} - 1 \right]^{2.9343}$$

Therefore, when the values of the mean velocity ( $V$ ) and the mean

depth of flow (H) are known the sediment transport can be calculated using the above equation.

### 3.2.3 Calculation of Sediment Transport Rate

For calculation of sediment transport rate, depth averaged velocities were used in the sand transport formula. Therefore, the nodal velocities obtained from the flow simulation model were first converted to depth averaged nodal velocities. These depth averaged nodal velocities were then converted to cell velocities in the longitudinal and transverse directions. Using the Sand transport formula, the rate of sediment transport was calculated in longitudinal and transverse directions for each cell.

With reference to Figure 4.0, SANDX(I,J) and SANDY(I,J) are defined as rates of sand transport in Cell (I,J) in x & y directions respectively. If just one cell is considered its sediment transport components can be averaged with those of the surrounding cells to obtain the boundary flow.

$$\begin{aligned} \text{Boundary flow in longitudinal direction} &= \text{BDX}(I,J) \\ &= 1/2.[\text{SANDX}(I,J) + \text{SANDX}(I+1,J)] \\ \text{Boundary flow in transverse direction} &= \text{BDY}(I,J) \\ &= 1/2.[\text{SANDY}(I,J) + \text{SANDY}(I,J+1)] \end{aligned}$$

The sand movement within the cell is then the difference between the transport rates into the cell and the transport rates out of the cell.

$$\begin{aligned} \text{Net longitudinal sand transport in cell}(I,J) &= \text{XMOVE}(I,J) \\ &= \text{BDX}(I-1,J) - \text{BDX}(I,J) \\ \text{Net transverse sand transport in cell}(I,J) &= \text{YMOVE}(I,J) \\ &= \text{BDY}(I,J-1) - \text{BDY}(I,J) \end{aligned}$$

The sediment movement is actually a volume rate per unit time per unit width. Therefore, multiplication by the cell width and an appropriate time interval will yield the volume change of sand. Then simply dividing by the cell area will give the change in depth of the cell.

$$\begin{aligned} \text{The amount of Erosion or Deposition in cell}(I,J) &= \text{RISE} \\ &= [\text{M.XMOVE}(I,J) + \text{N.YMOVE}(I,J)].\text{MTA}/\text{AREA} \end{aligned}$$

where, M,N = width of cell(I,J) in transverse and longitudinal directions respectively, AREA = M x N, MTA = time period for which the sand transport is calculated.

$$\text{New Depth of Cell}(I,J) = H(I,J) - \text{RISE}$$

### 3.2.4 Boundary Conditions for the Sand Transport Model

Following boundary conditions were used in the Sand Transport model.

#### 3.2.4.1 Inflow Boundary

At the inflow boundary it was assumed that the rate of sediment transport in longitudinal direction was equal to the rate of sediment

transport in the first cell in the same direction, figure 3.0.

$SANDX(I,J) = SANDX(2,J)$  and  $H(1,J) = H(2,J)$ ; where,  $J = 2$  to  $MOF+1$

#### 3.2.4.2 Outflow Boundary

At the outflow boundary the rate of sediment transport in longitudinal direction was assumed to be equal to the rate of sediment transport in the last cell in the same direction.

$SANDX(NLSI,J) = SANDX(NLS+1,J)$  ,  $H(NLSI,J) = H(NLS+1,J)$   
where,  $J = 2$  to  $MOF+1$

#### 3.2.4.3 Shore Boundary

At the shore boundary, the rate of sediment transport in the transverse direction was assumed to be zero.

$SANDY(I,1) = 0.0$  and  $H(I,1) = H(I,2)$ ; where,  $I = 2$  to  $NLS+1$

#### 3.2.4.4 Offshore Boundary

Similar to the shore boundary, the rate of sediment transport in the transverse direction was assumed to be zero.

$SANDY(I,MOFI) = 0.0$  and  
 $H(I,MOFI) = H(I,MOF+1)$  where,  
 $I = 2$  to  $NLS+1$

### 3.3 Profile Model

Using a flow simulation model described in Section 3.1 and a sand transport model described in Section 3.2 a Profile Model, as shown in the Flow Chart in Figure 5.0, was developed for morphological evolution of the shore area.

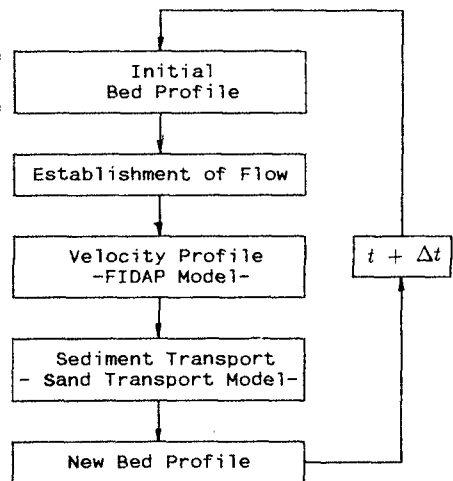


Figure 5.0: Flow Chart of the Profile Model

The constituents of the Profile Model are as follows:

- The initial bed profile of the area under consideration is decided.
- A known flow field is established over the area under consideration.
- The velocity field in the computation domain is numerically simulated using Mixing Length Model.
- Rate of transport of sediment due to known velocity field is calculated using the Sand Transport Model.
- Change of bed profile due to transport of sediment for a time period  $\Delta t$  is calculated and the new bed profile is obtained.

The new bed profile obtained after time  $\Delta t$  was used as the initial profile for the next cycle. This procedure was continued until

sufficient number of cycles are completed over the required time period for which morphological evolution of the shore area is to be determined.

4.0 Results and Discussion

4.1 Flow Simulation Models

Computed velocity profiles using the K-Epsilon and Mixing Length models have been compared against the measured velocities, at four different sections, in Figure 6.0.

It was observed that the K-Epsilon model, in general, predicted velocities closer to the measured values when compared to the Mixing Length Model. Specially, in the flow velocity measuring stations downstream of the dredged channel, ie. at  $x = 4.5$  and  $x = 7.5$  m, the K-Epsilon Model predicted velocities to a fairly good accuracy.

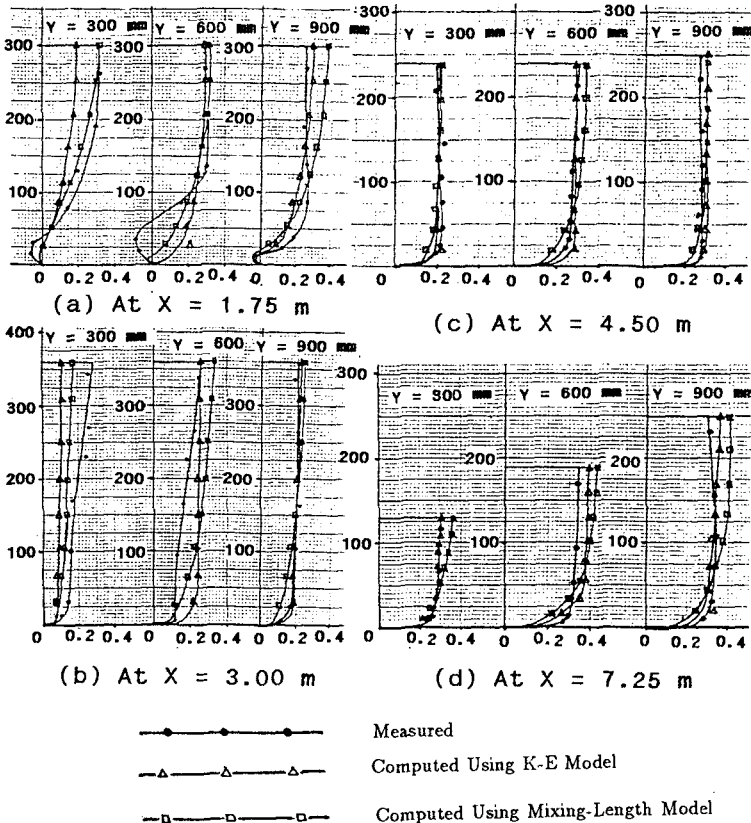


Figure 6.0: Measured and Computed Velocities

However, it was observed that the computed velocities deviated

from the measured velocities in the region from the inlet upto the dredged channel. When the cause for this situation was examined it was observed that selected inlet section was too close to the dredged channel. However, limited space available in the Hydraulic Laboratory did not allow shifting of the inlet section further upstream of the dredged channel.

The following assumptions made in making the numerical models would also have affected the accuracy of the predicted results.

- \* All wall boundaries, including the bed boundary, have been assumed to be fully rough (no-slip boundary condition.)
- \* For specification of normal and tangential boundary condition, the bed boundary has been assumed to be horizontal.

It is also expected that accuracy of computed velocities could be increased by having a finer mesh discretization, specially in the recirculation region.

Therefore, it can be concluded that under assumed conditions flow simulation models gave reasonable to good accuracy except for a few sections in the recirculation and inlet regions which in retrospect would have been expected.

## 4.2 Sand Transport Models

### 4.2.1 Shield's Formula

Shield's formula which is essentially a bed load formula is based on the assumption that shear stress is the main parameter defining sediment transporting power. Transport of sediment by suspension at higher shear velocities has not been taken into account and at all velocities sediment is assumed to be transported as bed load. Further, the resistance to sand movement caused by the bed forms on the deformed bed has not been considered in the formula.

The velocity field existing at the granular surface determines the shear stress on the grains. Therefore, it is more realistic to relate the bed shear velocity to the flow velocity at the bed level. But in this experiment, the bed shear stress, hence the bed shear velocity, in the Shield's formula has been related to the depth averaged mean flow velocity which could be higher than the near bed velocity.

Due to these reasons and also since the sand transport is a function to the fifth power of the mean fluid velocity (Section 3.2.1) exaggerated sand movement can be expected in areas where the velocity is high relative to the depth.

Examination of bed profiles at the inlet region showed that predicted higher velocities have caused exaggerated erosion and deposition of the cells in the region and the model became unstable after few iterations.

As Shield's formula is purely a bed load formula, errors in predicted results can be expected at higher shear velocities relative to the critical shear velocity. Therefore, Shield's formula was not considered as suitable for long term morphological computations.

#### 4.2.2 Ackers and White Method

This method predicts the total load and not the bed-load transport only. In this method average stream velocity has been used in preference to shear stress as the basis of sediment transport function. The grain roughness has been taken into account by relating it to the median sediment diameter. As such this method can be expected to perform better than the Shield's formula.

The following observations can be made when the bed contours, as shown in Fig.8 and bed profiles shown in Fig. 7, are reviewed.

1. A prominent movement of sand in the longshore direction was seen throughout the flow domain; a clear overprediction compared to the Physical Model.

2. In the area downstream of the dredged channel where the computed and measured flow velocities had a better match, measured and computed bed profiles and contours have similar shapes and are almost parallel.

3. The movement of sand in the offshore direction observed in the Physical Model was not seen in the numerical model. This can not be explained in terms of flow velocities as both measured and computed flow velocities in offshore direction were small compared to the longitudinal

velocities. It should be noted here that the effect of gravity has not been taken into consideration in the numerical model. As such it will be interesting to examine whether the gravity has played a role in the movement of sand along the steep gradient in the transverse direction.

4. In the upstream region of the dredged channel where the computed

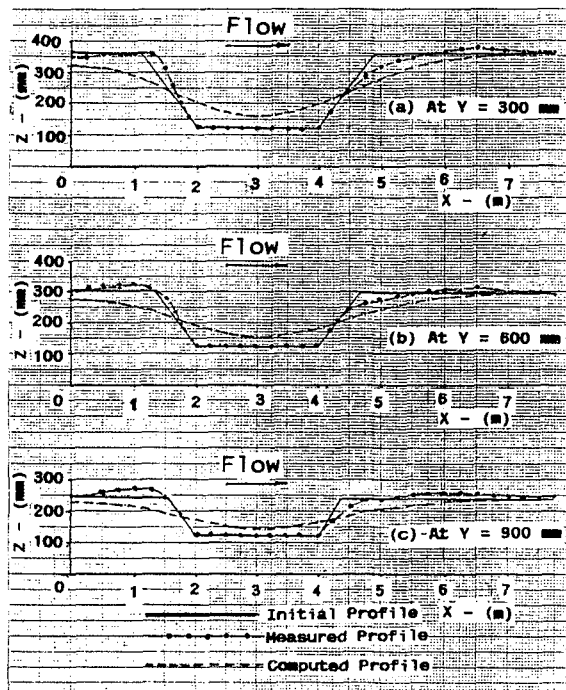


Fig. 7.0: Measured and Computed Bed Profiles

(Mixing Length Model) velocities did not show a good agreement with the measured velocities, the computed bed profiles deviated from the measured profiles as would be expected.

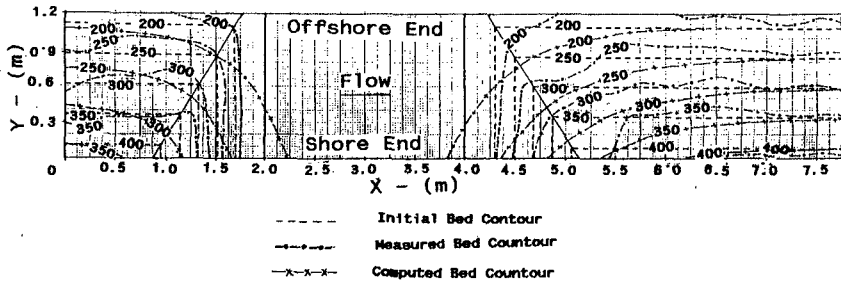


Fig. 8.0: Measured and Computed Bed Contours

An important factor that would have affected the predictions of the sand transport model is the changing bed profile and hence the flow velocities at the inlet which has not been taken into consideration. It was assumed that the prescribed inlet velocities remain unchanged throughout the experiment even though the bed profile was allowed to vary. As the computed flow velocities upstream of the dredged channel were found to be very sensitive specially to the direction and the magnitude of transverse velocities, this would have had a direct effect on the model predictions.

#### 4.3 Conclusions

The sand transport model which used the Ackers and White method performed reasonably well in the areas where the computed velocities were in agreement with the measured velocities. As the sand transport is a function to the fourth power of the mean velocity, (Section 3.2.2), a small error in the predicted flow velocities could accumulate to create a major error in the predictions of the sand transport model when a simulation is carried out over a large number of cycles for long term morphological computations. Thus, the accuracy of predictions of such a long term model will depend critically upon the accuracy of the predicted velocities in the flow simulation model.

It can be concluded that, once calibrated and validated using measured data, an advanced flow simulation model coupled with a simple sand transport model, as used in this experiment, appears feasible at this stage to predict long term morphological computations to a reasonable accuracy.

#### 4.4 Future Work

Since the numerical models performed reasonably well even without improvement, it would be worthwhile to investigate the influence of the factors such as; proximity of the inlet section to the dredged channel, change of cross-section at the inlet, a refined mesh, and influence of gravity, etc. on the performance of the models.

The sand transport model used looks crude compared to the advanced flow models used. However, as this is only the first developmental model better sand transport models can be coupled with the flow model to improve the predictions.

#### 4.5 Acknowledgements

The research project mentioned in this paper was carried out by the author when reading for a degree of Master of Engineering Science at the University of Adelaide, Australia under the supervision of Mr. R.Culver, Hon. Visiting Research Fellow. Thanks are due to the Australian International Development Assistance Bureau for the award of the research scholarship. The financial support for the hire of the commercial computer software package by the Department of Civil Engineering is acknowledged. The author is indebted to the individuals who have helped by various means in this study.

#### References

1. Ackers, Peter, and White, W.R. (1973). "Sediment Transport: New Approach and Analysis". *Journal of the Hydraulics Division*, Vol.99, No.HY11, pp.2041-2060.
2. Graf, W.H. (1971). *Hydraulics of Sediment Transport*. Mc Graw-Hill Book Company.
3. Hiller, M.E., and Jenkin, R.D. (1976). *Digital Coastal Outflow Simulation*. University of Adelaide, Australia.
4. Kalinske, A.A. "Movement of Sediment as Bedload in Rivers". *Transactions of the American Geophysical Union*. Vol.28, No.4, pp.616-620.
5. Launder, B.E., Morse, A., Rodi, W., and Spalding, D.B. (1972). "Prediction of Free Shear Flows - A Comparison of the Performance of Six Turbulence Models". *Proceedings of NASA*. pp.361-414.
6. Launder, B.E., and Spalding, D.B. (1974). "The Numerical Calculation of Turbulent Flows". *Computer Methods in Applied Mechanics and Engineering*. Vol.3, pp.269.
7. Leschziner, M.A., and Rodi, W. (1979). "Calculation of Strongly Curved Open Channel Flow". *Journal of the Hydraulics Division*. ASCE, Vol.105, HY10, pp. 1297-1313.
8. Rodi, W. (1980). "Turbulence Models and Their Application in Hydraulics". *IAHR Section on Fundamentals*. Delft, The Netherlands.
9. Schields, A. (1936). "Anwendung der Aehnlichkeitsmechanik und der Turbulenz-forschung auf die Geschiebebewegunu". *Mitteilungen der reussischen Versuchsanstalt fur Wasserbau und Schiffbau*, Berlin, Germany, Vol.26.



The sand transport model used looks crude compared to the advanced flow models used. However, as this is only the first developmental model better sand transport models can be coupled with the flow model to improve the predictions.

#### 4.5 Acknowledgements

The research project mentioned in this paper was carried out by the author when reading for a degree of Master of Engineering Science at the University of Adelaide, Australia under the supervision of Mr. R.Culver, Hon. Visiting Research Fellow. Thanks are due to the Australian International Development Assistance Bureau for the award of the research scholarship. The financial support for the hire of the commercial computer software package by the Department of Civil Engineering is acknowledged. The author is indebted to the individuals who have helped by various means in this study.

#### References

1. Ackers, Peter, and White, W.R. (1973). "Sediment Transport: New Approach and Analysis". *Journal of the Hydraulics Division*, Vol.99, No.HY11, pp.2041-2060.
2. Graf, W.H. (1971). *Hydraulics of Sediment Transport*. Mc Graw-Hill Book Company.
3. Hiller, M.E., and Jenkin, R.D. (1976). *Digital Coastal Outflow Simulation*. University of Adelaide, Australia.
4. Kalinske, A.A. "Movement of Sediment as Bedload in Rivers". *Transactions of the American Geophysical Union*. Vol.28, No.4, pp.616-620.
5. Launder, B.E., Morse, A., Rodi, W., and Spalding, D.B. (1972). "Prediction of Free Shear Flows - A Comparison of the Performance of Six Turbulence Models". *Proceedings of NASA*. pp.361-414.
6. Launder, B.E., and Spalding, D.B. (1974). "The Numerical Calculation of Turbulent Flows". *Computer Methods in Applied Mechanics and Engineering*. Vol.3, pp.269.
7. Leschziner, M.A., and Rodi, W. (1979). "Calculation of Strongly Curved Open Channel Flow". *Journal of the Hydraulics Division*. ASCE, Vol.105, HY10, pp. 1297-1313.
8. Rodi, W. (1980). "Turbulence Models and Their Application in Hydraulics". *IAHR Section on Fundamentals*. Delft, The Netherlands.
9. Schields, A. (1936). "Anwendung der Aehnlichkeitsmechanik und der Turbulenz-forschung auf die Geschiebepbewegung". *Mitteilungen der reussischen Versuchsanstalt fur Wasserbau und Schiffbau*, Berlin, Germany, Vol.26.

## CHAPTER 223

### MOTION OF MOBILE BEDS AT HIGH SHEAR STRESS

Kenneth C. Wilson<sup>1</sup> and Fidelia N. Nnadi<sup>2</sup>

#### 1. INTRODUCTION

Beds of granular material show various types of behaviour as the dimensionless shear stress or Shields ordinate,  $Y$ , is increased. This quantity is defined as  $\tau/\rho g(S-1)d$ , where  $\tau$  is boundary shear stress,  $\rho$  is fluid density,  $g$  is gravitational acceleration,  $S$  is the ratio of solids density to fluid density and  $d$  is particle diameter. Following the zone of no particle movement at low  $Y$ , there is a range at which sand waves are found, and finally, in the high shear-stress region where  $Y$  exceeds 0.8, the bed tends to become plane.

This high-stress or upper-plane-bed condition may be encountered in rivers in flood, large flows in estuaries, and closures or breaches of cofferdams or dykes. Because of the very high rates of sediment transport associated with this type of flow, it has a disproportionate effect on both natural topographic features and engineering works. The investigation of such behaviour by traditional flume experiments is not easy, but testing in enclosed pressurised conduits can eliminate many of the difficulties (Wilson, 1966; Nnadi and Wilson, 1992).

Nnadi (1992) has described an experimental program carried out recently using a recirculating system located at Queen's University. The test section was a square conduit with side dimension 98 mm, and series of runs were made with three sizes of sand ( $S = 2.67$ ), two sizes

---

<sup>1</sup> Professor, Department of Civil Engineering, Queen's University, Kingston, Ontario, Canada K7L 3N6

<sup>2</sup> Post-Doctoral Fellow, Department of Civil Engineering, McMaster University, Hamilton, Ontario, Canada L8S 4K1

of bakelite ( $S = 1.56$ ) and one size of nylon particles ( $S = 1.14$ ).

## 2. ANALYSIS AND EXPERIMENTAL RESULTS

Analysis based on the experimental findings shows that at high shear stress the bed load moves in a shear layer (the sheet-flow layer) with thickness which is proportional to the shear stress applied by the flow to the mobile boundary. Within this layer, the submerged weight of the grains comprising the bed load (also called the contact load) is counteracted by intergranular contacts, which may be either continuous or sporadic. The thickness of the shear layer,  $\delta_s$ , can be an order of magnitude larger than the particle diameter. For this high-shear-stress configuration, the equivalent roughness of the boundary is not proportional to the size of the individual particles (as had been assumed in the past for the upper-plane-bed regime), but instead varies directly with the shear-layer thickness,  $\delta_s$ , and hence is proportional to the applied shear stress.

The resulting value of the equivalent roughness,  $k$ , is about  $0.5 \delta_s$ . It follows that the value of  $k/d$  is not constant (as for the rough-boundary relation) but increases with  $Y$  in what is essentially a direct proportionality. Wilson and Nnadi (1990) produced a plot of the ratio of equivalent roughness to particle diameter ( $k/d$ ) versus the dimensionless shear stress. This plot is reproduced here as Figure 1. It clearly shows that  $k/d$  is far from constant, but instead increases with  $Y$  in accord with the analytical prediction, which can be approximated (Wilson, 1989) by the simple relation

$$\frac{k}{d} = 5Y \quad [1]$$

More detailed analysis is given by Nnadi and Wilson (1992), but the basic points to be noted is that the effective roughness for sheet flow is no longer proportional to particle diameter, but is strongly affected by increasing shear stress. As seen from the figure, a broad range of the variables is represented, the trend is clear, and the scatter band is less than that usually displayed by moveable-boundary data.

Both the experimental work mentioned above and the associated analysis have been concerned with essentially horizontal flows. It was realized that for certain cases of practical importance, such as wave uprush on beaches or bars, the flow is inclined, and the effect of this

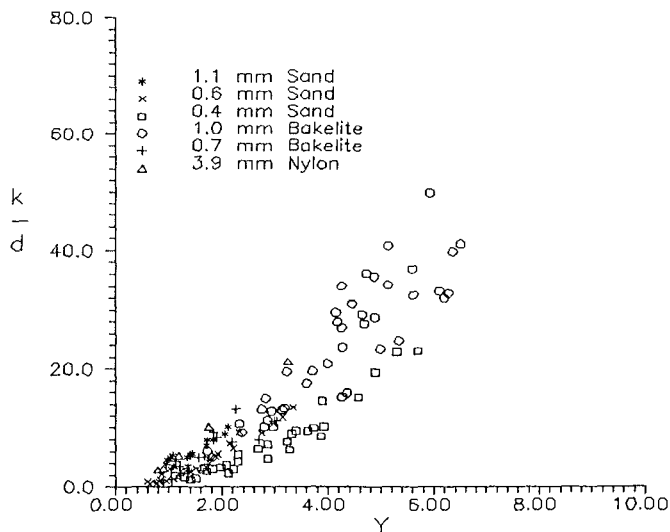


Figure 1 Effective Roughness Ratio for Horizontal Flow

inclination can be important. In order to investigate this effect, it was arranged that the closed-conduit test section could be inclined to the horizontal. Several series of runs in the upper-plane-bed regime were made at inclination angle  $\theta$  (elevation increasing in the direction of flow) of  $10^\circ$ ,  $20^\circ$  and  $30^\circ$ . The values of manometric gradient, mean flow velocity and bed-associated hydraulic radius were obtained for each run, and used to calculate  $k/d$  and  $Y$  in the same fashion employed previously for the horizontal tests. The results for  $10^\circ$ ,  $20^\circ$  and  $30^\circ$  inclination are shown on Figures 2, 3 and 4, respectively. The general trends are very similar to that of the plot for horizontal flows but it is worth noting that for the inclined flows the range of the variables is larger than for the horizontal case, and  $k/d$  has a somewhat larger rate of increase with  $Y$ . The data for the various inclinations indicate that, in the range investigated, the rate of increase of  $k/d$  with  $Y$  is monotonically related to the inclination angle.

Analysis of particle motion in inclined flows showed that a positive inclination introduces a submerged-weight force component which acts opposite to the direction of motion. The resulting behaviour is equivalent to a horizontal flow with a larger effective value of

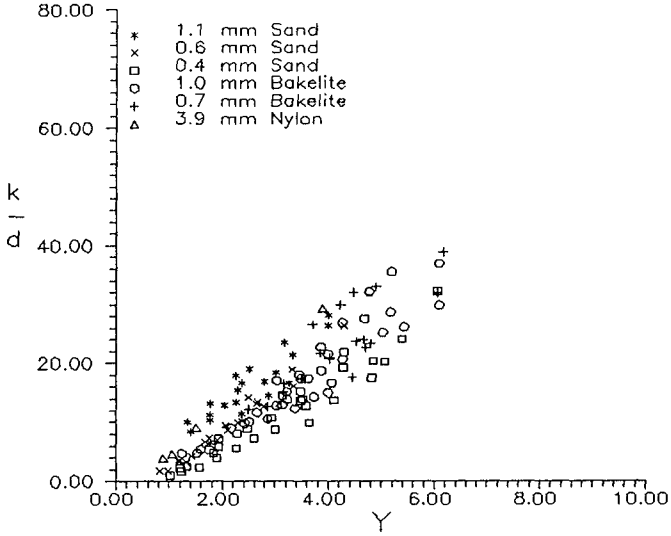


Figure 2 Effective Roughness Ratio for  $\theta = 10^\circ$

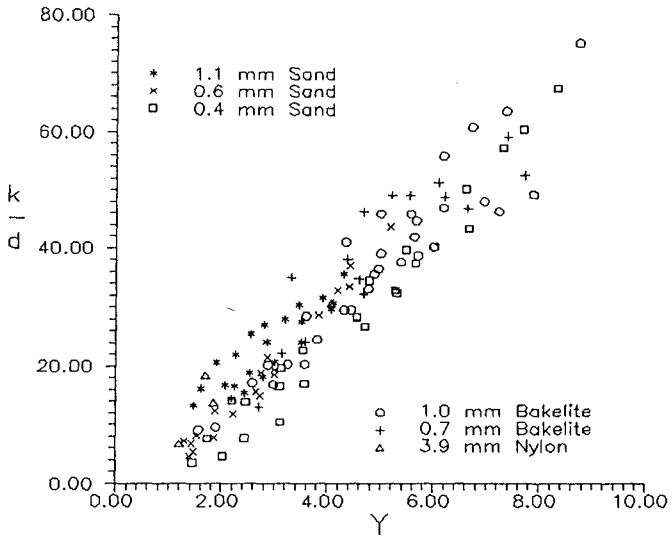


Figure 3 Effective Roughness Ratio for  $\theta = 20^\circ$

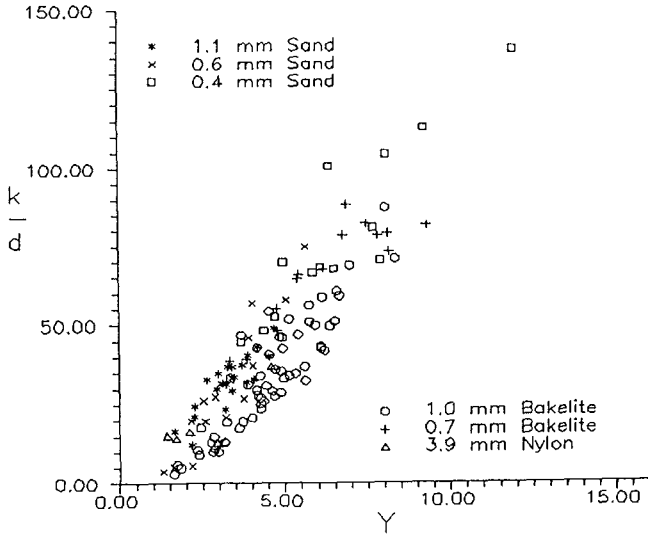


Figure 4 Effective Roughness Ratio for  $\theta = 30^\circ$

submerged relative density, equivalent to multiplying (S-1) by the factor  $\cos\theta(1+\tan\theta/\tan\phi')$ , where  $\phi'$  is the dynamic friction angle of the solids. On this basis it is predicted that the solids transport rate will diminish with increasing inclination  $\theta$  (for given values of hydraulic gradient and bed-associated hydraulic radius).

This effect can be expressed by applying a suitable adjustment to the dimensionless bed-load transport coefficient  $G_s$ , defined by the equation

$$q_s = \frac{G_s}{(S-1)g} \left( \frac{\tau}{\rho} \right)^{1.5} \quad [2]$$

Here  $q_s$  is the volumetric discharge of bed-load solids per unit breadth, and the other symbols have been defined previously. In the high-shear-stress range (where the critical shear stress for the beginning of particle motion is a negligibly small fraction of the applied shear stress) Equation 2 is compatible in form to the equation of Meyer-Peter and Müller. That equation produces a  $G_s$  value of 8.0 for near-horizontal flow. However, as proposed earlier (Wilson, 1966 and 1987),  $G_s \approx 12$  gives a better fit both to sand data at high shear stress and to the theoretical expectations for

horizontal flow in the upper-plane-bed region. The present analysis indicates that  $G_s$  will vary with both  $i/(S-1)$  and the inclination angle  $\theta$ . Figure 5 shows calculated curves for various inclinations up to  $30^\circ$ . Each curve displays an essentially flat initial section, followed by a downturn at higher values of  $i/(S-1)$ . The series of curves shows the expected decrease of  $G_s$  with increasing  $\theta$ .

The experimental data for inclination angles of  $0^\circ$  to  $30^\circ$  were found to be in good accord with the trends shown by the predicted curves. Figures 6, 7, 8 and 9 show the data for  $\theta$  values of  $0^\circ$ ,  $10^\circ$ ,  $20^\circ$  and  $30^\circ$ , respectively.

Although there is a fair degree of scatter in the experimental results for  $G_s$ , each data set clusters about the predicted line. The droop in  $G_s$  at high  $i/(S-1)$ , which is particularly clear from the nylon data, occurs for each of the inclination angles. Comparison of the four data sets clearly shows the downward trend of  $G_s$  with increasing  $\theta$  that follows the general trend of the predicted curves.

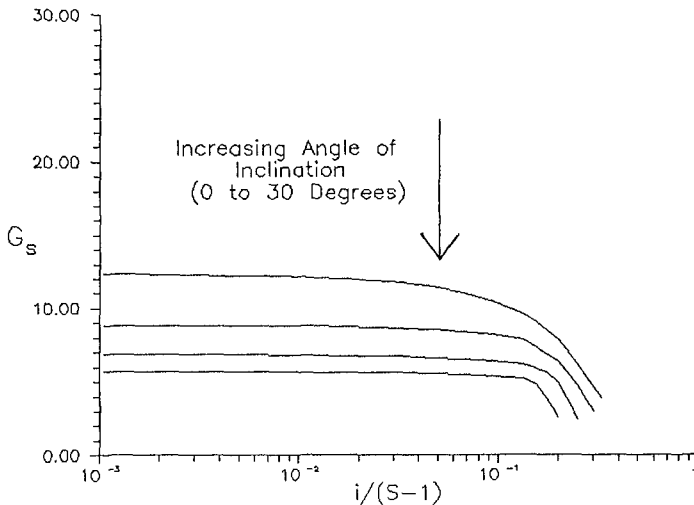


Figure 5 Predicted Transport-Rate Parameter for Various Inclinations

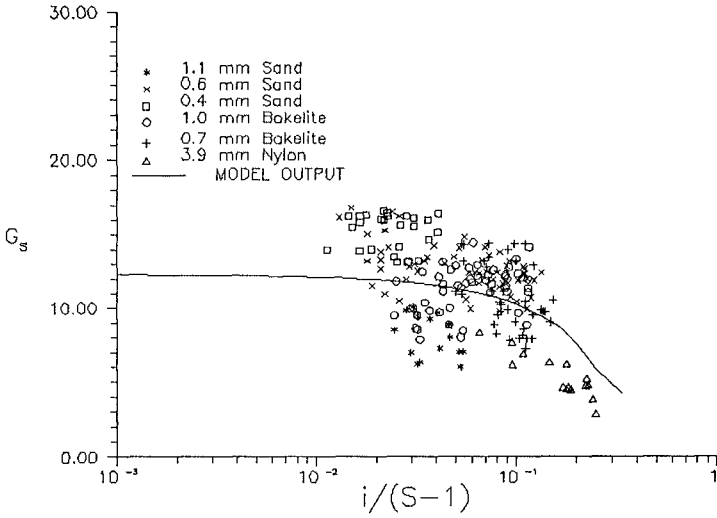


Figure 6 Observed and Predicted Transport-Rate Parameter for Horizontal flow

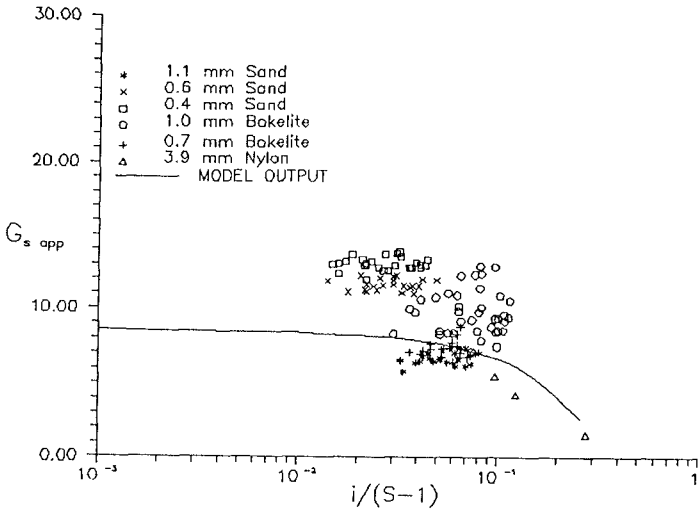


Figure 7 Observed and Predicted Transport-Rate Parameter for  $\theta = 10^\circ$



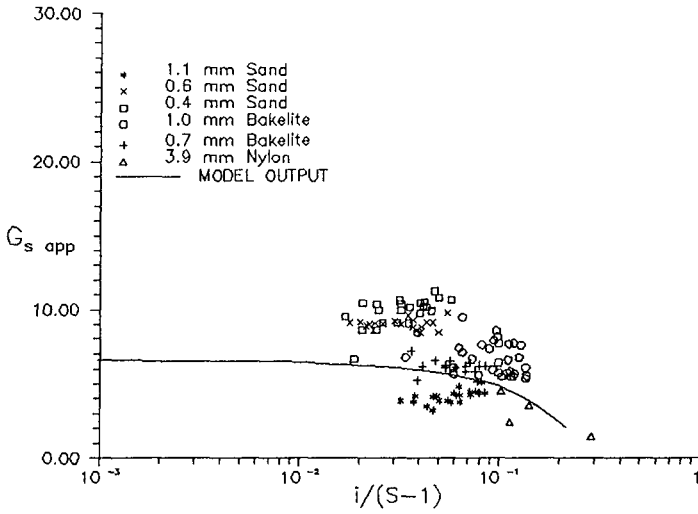


Figure 8 Observed and Predicted Transport-Rate Parameter for  $\theta = 20^\circ$

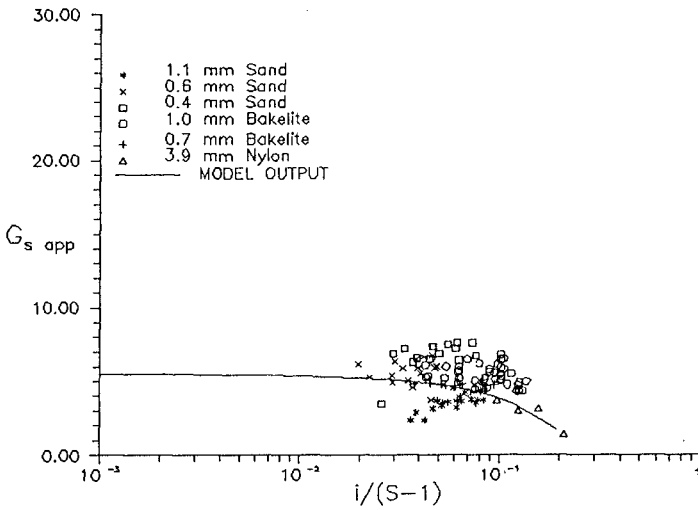


Figure 9 Observed and Predicted Transport-Rate Parameter for  $\theta = 30^\circ$

### 3. CONCLUSION

At high shear stress, beds of granular materials tend to become plane, with bed-load particles forming a sheet-flow layer of thickness proportional to the applied shear stress. Results from both experiments and analysis have shown that this region is characterised by large friction factors and high rates of bed-load transport.

The study of horizontal sheet flow has now been extended to inclined flows, which are significant for beach morphology. The effect of an inclination angle (with bed elevation increasing in the direction of flow) is to increase friction and to diminish bed-load transport rate. Once again, experimental and analytical results are found to be in good accord.

### REFERENCES

- Nnadi, F.N. (1992). Bed-load Transport at High Shear Stress with Application to Rivers and Sand Waves. Ph.D. Thesis, Department of Civil Engineering, Queen's University at Kingston, Ontario.
- Nnadi, F.N. and Wilson, K.C. (1992). Motion of contact-load particles at high shear stress. Scheduled for publication, J. Hydr. Engrg., ASCE 118(12).
- Wilson, K.C. (1966). Bed-load transport at high shear stress. J. Hydr. Div., ASCE 92(6), 49-59.
- Wilson, K.C. (1987). Analysis of bed-load motion at high shear stress. J. Hydr. Engrg., ASCE 113(1), 97-103.
- Wilson, K.C. (1989). Mobile-bed friction at high shear stress. J. Hydr. Engrg., ASCE 115(6) 825-830.
- Wilson, K.C. and Nnadi, F.N. (1990). Behaviour of mobile beds at high shear stress. Proc. 22nd International Conference on Coastal Engineering, Delft, Netherlands, Vol. 3, 2536-2541.

## CHAPTER 224

### Port Site Selection on Coast with Radial Sandbanks

Yixin Yan and Kai Yen

#### Abstract

Along the silty coast of the Jiangsu Province, it was found that on the coast stretch which we call the "Radial Sandbanks" coast stretch, deepwater port sites could be created if suitable tidal inlets were selected and provisions were made to maintain the required deepwater areas for port development.

#### Introduction

The Jiangsu Province, facing the Yellow Sea and the East China Sea, is one of the most developed provinces of China in industrial and agricultural production. China's policy of reform and opening to the outside world has greatly enhanced the economic development of this province. It is therefore urgently needed to build deepwater ports to meet the demand of increasing sea-going traffic. For a long time, the difficulty was to find suitable port sites, because along the entire 1000km coastline of this province, most of the coast stretches are silty coast with very gentle beach slope composed of fine sand and silt, very susceptible to changes under the action of waves and currents. Therefore it was considered impracticable to construct deepwater

- 
- (1) Asso. Professor, Hohai University, Nanjing 210024, China  
(2) Professor, Hohai University, Nanjing 210024, China

ports on such coast. However, during the Nationwide Comprehensive Assessment of Coastal Zone Resources which was carried out from 1980 to 1985 along the entire 18,000 km coastline of China's mainland it was found that there is a coast stretch in the Jiangsu Province where the early and late deposited submarine sediments were disturbed and scoured by waves and currents, sorted, coarsened and redeposited. At last, an extensive area of well sorted fine sand and all kinds of sediments are radially extended towards the sea, thus forming the coast with radial sandbanks. Between the sandbanks are tidal inlets leading to the coastline, and deepwater port sites could be created if suitable tidal inlets were selected and provisions were made to maintain the required water depth for port development.

### Morphological and Hydrological Features of the Radial Sandbanks

The Radial Sandbanks, extending from northwest to southeast along the coast of North Jiangsu, cover an area of the South Yellow Sea from the mouth of Sheyang River to the Yangtze River Estuary and to the east up to 25 m water depth, nearly 20,000 km<sup>2</sup>. About 70 sandbanks lie radially from Jianggang towards the sea, of which 8 are above the Abandoned Yellow River Datum, with total area of 1268 km<sup>2</sup>, the biggest one called Dongsha is 694 km<sup>2</sup> (Fig.1). The rest are underwater sandbanks. Between the sandbanks are tidal channels, the largest one, called Huangsha Yang, is located at the middle of the Radial Sandbanks and extends from the sea westward to the coast near Jianggang. The second large tidal channel, Xi Yang, is located at the west and the third one, Xiaomiao Hong, at the south of the Radial Sandbanks. All these three tidal channels ended in the proximity of the coastline and could therefore be utilized as approach channels for port development.

The Radial Sandbanks were essentially the ancient submarine delta of the Yangtze River. The formation of such typical topography may be attributed to the existence of two tidal systems, one comes from southeast, being a progressive tidal wave from the Pacific, and the other from northwest, being a reflected tidal wave from the Shandong Peninsula. The concurrence of these two tidal systems gives rise to a rotary standing tidal wave with the node point somewhere 80 km beyond the

Abandoned Yellow River Mouth, where the tidal range is nearly zero. Figure 2 shows the  $M_2$  constituent of the tide in harmonic

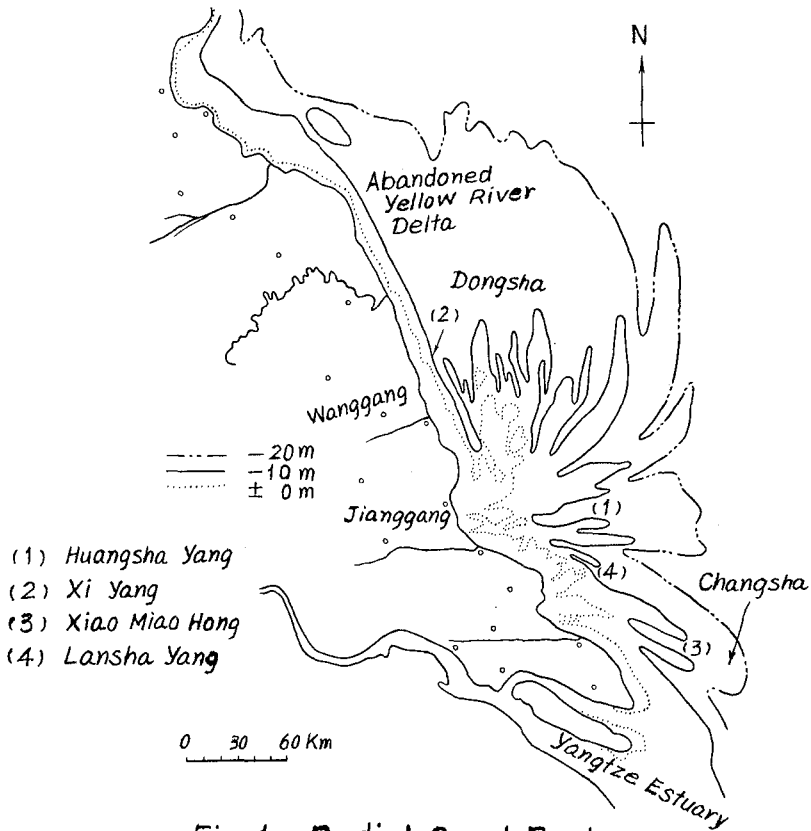


Fig. 1. Radial Sand Banks

analysis. The converging point of the two tidal waves is in the vicinity of Jianggang. Here we find a region of strong tide, the mean tidal range at Jianggang is 3.9 m. It increases to 4.9 m at Yangkou, the end of the main channel of Huangsa Yang, here a max. tidal range of 9.28 m was observed in 1981, which also ranks first along the entire coast of China. The mean tidal ranges in the other two large tidal channels, Xi Yang and Xiaomiao Hong

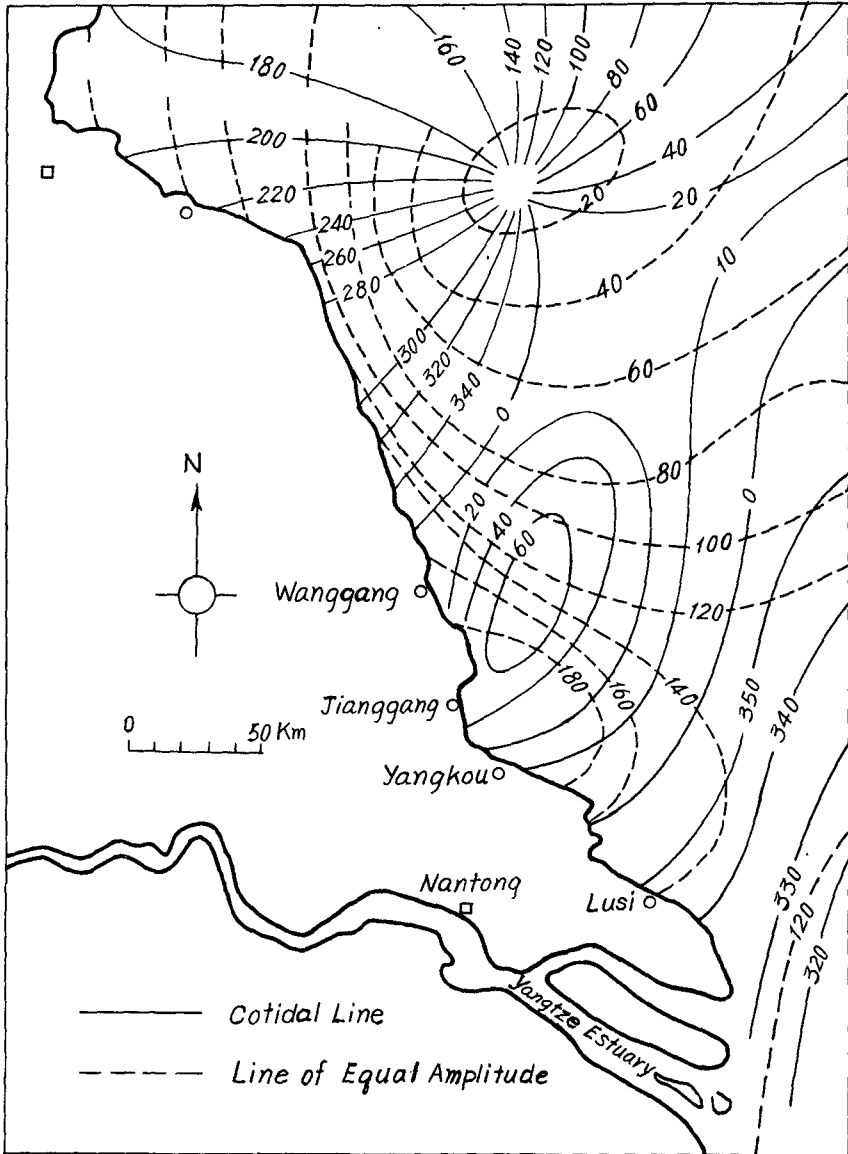


Fig.2.  $M_2$  Constituent in Harmonic Analysis

are respectively **2.64** at Wanggang and **3.68** m at Lusi, with a max. of **5.46** m and **6.87** m respectively (Fig.3). The tidal current in this region is also strong. In Huangsa Yang and Xi Yang, the flood current velocity is higher than that of ebb tide, attaining a max. of **2.5** m/s and **2.0** m/s respectively, while in Xiaomiao Hong the ebb current is stronger, having a max. of over **1.5**m/s.

Waves exercise also significant influence on the Radial Sandbanks. Waves generated by prevailing wind come from NEE and the storm waves come mostly from NW and N. Under the action of waves and currents the Abandoned Yellow River delta is continually under erosion and large amount of the eroded materials are transported to the Radial Sandbanks. The sediments from the Yangtze River, which amounts to ca. **500**×**10<sup>6</sup>**t yearly, are also partly transported to the Radial Sandbanks by flood tides, particularly during the flood season of the Yangtze.

Investigation shows that in the summer the dominant sediment transport is landwards from the sea through the tidal inlets, converging in the vicinity of Jianggang, and in the winter the sediment flow is spreading seawards and to the Yangtze Estuary. It has been found that the littoral drift in the Xi Yang tidal channel is directed southwards, in the Huangsa Yang it is westwards and in the Xiaomiao Hong eastwards. The sediment concentration in the winter is **1.5** to **2** times higher than that in the summer, and it increases from the sea landwards, a max. concentration of **1.2** kg/m<sup>3</sup> has been observed in the vicinity of Jianggang. The sediments are composed mainly of fine sand, sandy silt and silt. The mean sediment diameter of the sediments on the sandbanks ranges from **0.125**~**0.5** mm, in the tidal channels it is **0.07**~**0.18** mm and on tidal flats, **0.03**~**0.09** mm.

As a rough estimate, the yearly sediment transport into the area of Radial Sandbanks is **109**×**10<sup>6</sup>** t from the north, **203**×**10<sup>6</sup>**t from the east and **36**×**10<sup>6</sup>** t from the west, totalling **348**×**10<sup>6</sup>** t, and sediments flowing out of this area is **102**×**10<sup>6</sup>** t. Thus there is a net sediment inflow of **246**×**10<sup>6</sup>** t, and the area of the Radial Sandbanks is continually increasing. Nevertheless, the change is rather slow, as can be also seen by comparing the topographic maps of **1964** and **1979**, as well as from the satellite pictures. It has also been found that the entire Radial Sandbanks including the tidal inlets are relatively stable, and in

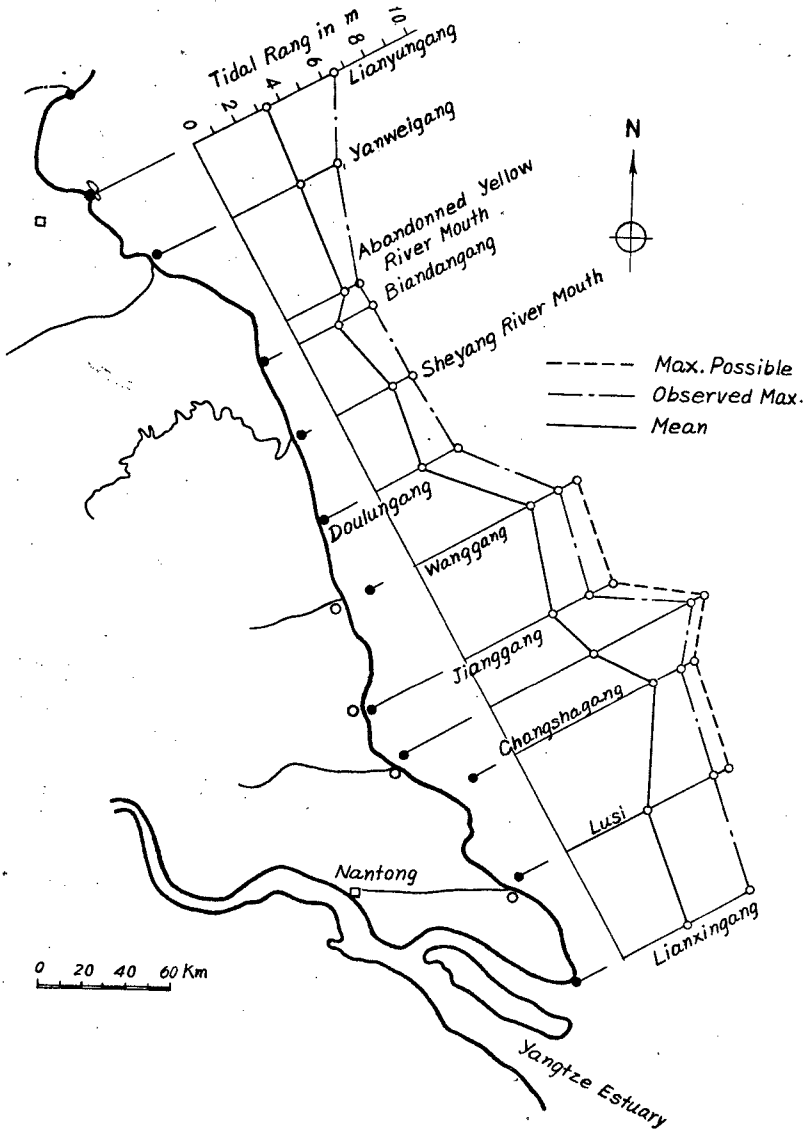


Fig. 3 Tidal Range Along Jiangsu Coast



the above mentioned three tidal inlets deepwater channels underwent little change. Only at the ends of these channels erosion and accretion occurred frequently and this is sometimes aggravated by wanton reclamation of the adjacent tidal flats.

### Selection of Port Sites

A comprehensive investigation had been carried out since early 1980's along the coast of Jiangsu Province, which includes the field survey, laboratory work and theoretical study. One of the main problems to be solved was the stability of the tidal inlets. It has been found that the inlets are relatively stable due to the existence of the strong tidal action. For instance, at Wanggang the depth contours of  $-5$  m and  $-10$  m had been moving seaward at a rate of 100 m and 68 m per year from 1979 to 1990, respectively, but the depth contour of  $-12$  m had been kept basically unchanged. Meanwhile the Xi Yang tidal inlet was enlarged to correspond with the increased tidal discharge, the inlet became deeper and the shore slope turned steeper.

As compared with port on open sea coast or in an estuary, port located inside a tidal inlet has neither the problem of protection against storm waves, which usually needs the building of costly breakwaters, nor the bar forming at the mouth of the estuarine channels, which as a rule gives hindrance to navigation. So the three large tidal inlets of the Radial Sandbanks provide favorable conditions for port development. In these tidal inlets the water areas are well sheltered, the sediment concentration is low and channels are relatively stable. The drawbacks are, however, the large tidal range and wide tidal flat, which bring inconvenience to navigation and difficulties in port layout. Therefore these should be taken into full consideration in the development of ports inside such tidal inlets.

In the selection of deepwater port site along the coast of Jiangsu, we have to bear in mind that the Yangtze River, which flows through the Jiangsu Province and is an important waterway for sea-going traffic, can only allow vessels of under 25,000 t to pass the estuarine channel due to the bar forming at the mouth, and it is a very difficult task to increase its water depth. Hence it is necessary to explore deepwater port sites along the open coast. Moreover, coastal harbours have the

advantage of more direct access to the hinterland of North Jiangsu than ports in the Yangtze Estuary, since for the former there is a network of inland waterways facilitating the connection with the hinterland. In view of the fact that Jiangsu Province is badly short of energy resources, the import of coal and the development of petroleum industry have become of ever increasing importance in the economic construction. For this purpose the creation of deepwater port along the coast with berths of **50,000 to 100,000 t** and over is needed. It has been planned to build deepwater ports in all the above mentioned three large tidal inlets, namely Huangsha Yang, Xi Yang and Xiaomiao Hong, taking due consideration into the rational geographical distribution of ports. We have then in the south a port group with Port Yangkou in the Huangsha Yang tidal inlet, Port Lusi in the Xiaomiao Hong tidal inlet and Port Nantong in the Yangtze Estuary as the major ports; in the middle a port group with Port Wanggang in the Xi Yang tidal inlet as the major port; and in the north a port group with Port Lianyungang as the major port, as shown in Fig.1. The Port Lianyungang is an existing port built in the thirties. It has been rehabilitated, extended and modernized since the founding of the People's Republic, and is now one of the major ports of China, capable of berthing vessels of **50,000 t**.

Except port Nantong and Port Liangyungang all the above mentioned ports are situated in the tidal inlets of the Radial Sandbanks. It is rather unique to built deepwater port under such conditions. In the following a typical example is given for the layout of the Port Yangkou in the Huangsa Yang tidal inlet.

### Preliminary Layout of Port Yangkou

Full use is made of the Huangsa Yang tidal channel in the layout of the Port Yangkou. The water depth of this tidal channel varies from **10 m to 30 m** with channel width of **0.7 km to 2 km**. The channel ends at Yangkou, the selected port site. Here a well sheltered water area is available for port development. The port will mainly serve for oil and coal transportation and to some extent container and general cargo traffic. The layout is shown in Fig.4. As can be seen from the figure, there is **20 m** deepwater area of **2.4 km<sup>2</sup>** at a distance of about **10 km** from the coastline and within this area we find an area **700 m × 2000 m** where the water

depth is 22 m. This can be used to berth the 100,000 t tankers which requires a water depth of 21.5 m. Underwater pipeline will be used to deliver the oil to the oil depot on the bank. It has also been contemplated to provide berths for supertankers of 200,000 t in the future at the location 20 km to the east of Yangkou, called Changsa, where the tidal inlet Lansha Yang joins Huangsha Yang. Here 25 m deepwater area of 4.7 km<sup>2</sup> is available for mooring such supertankers, only that the under water pipeline will be longer, i.e. >16 km.

For coal import, 10,000 t berths will be provided at the -10 m water area and navigation channel should be built for coal transfer. The coal will be transferred by barges of 100 t to 300 t or by highways to the neighboring areas. Container berths will be located at the deepwater area west of the tanker berths, with a connecting trestle leading to the container terminal or transferred by shipment. Trestle for berthing ships of 3,000 t is also provided west of Yangkou for general cargo handling.

Serving as an approach channel to the sea, the Huangsa Yang tidal inlet has a length of 50 km from Port Yangkou to -20m depth in the sea. In order to create a navigable channel for 100,000 t tankers it is estimated that the amount of dredging would be 260,000 m<sup>3</sup>. If the berthing of supertankers of 200,000 t were contemplated, the tidal inlet Lansha Yang - Huangsha Yang should be used as approach channel to the berthing area Changsa, which has a length of about 30 km, and the amount of dredging would be 1,000,000 m<sup>3</sup> to 3,000,000 m<sup>3</sup>.

## 5. Conclusions

Sea port construction is essential to the economic development of the Jiangsu Province and opening to the outside. The aforementioned three port groups along the Jiangsu coast all have good connection with the hinterland. The intercontinental railway connecting Port Lianyungang to Rotterdam, the waterways of the Huai River system and Yangtze River system, together with the Grand Canal and other waterways and highway systems, form a transportation network very convenient to the gathering, distribution and transfer of cargo. The utilization of tidal inlets of the Radial Sandbanks for port construction is technically possible and economically feasible as the preliminary

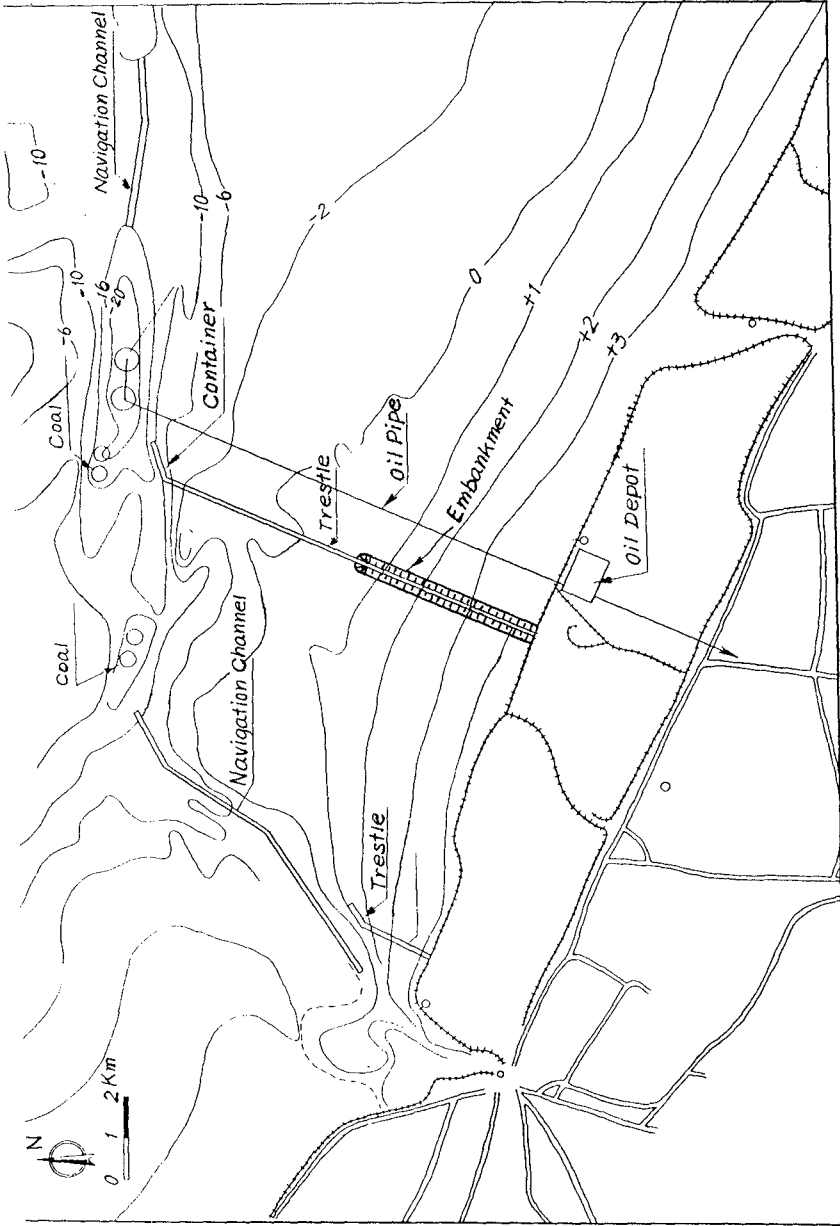


Fig. 4. Layout of Port Yangkou

study of the morphological and hydrological features of this region and the economic assessment have shown. Numerical modelling has been undertaken to study the channel condition of the Huangsha Yang tidal channel. It was found that the channel would be relatively stable and the tidal currents are favorable to maintenance of a stable channel.

## References

Report on the Comprehensive Assessment of Coastal Zone Resources of Jiangsu Province, **1986**, China Ocean Press (in Chinese).

Report on the Feasibility Study of the Yangkou Port Project, **1989**, Hohai University and Nanjing University (in Chinese).

A Study on the Planning of Seaport along the Jiangsu Coast, **1991**, Hohai University (in Chinese)

## CHAPTER 225

### Liquefaction and erosion of China Clay due to waves and current

P.J. de Wit<sup>1</sup> and C. Kranenburg<sup>2</sup>

#### Abstract

A research project was started to study the behaviour of cohesive sediments at the Delft University of Technology in 1989. An existing flume was modified to study the liquefaction and erosion of China Clay due to waves and current. China Clay is an artificial mud, mainly consisting of kaolinite. Among other things, the experimental results showed that fluid mud was generated by wave action if the wave height exceeded a threshold value; the threshold value increases as the consolidation period increases. Waves were significantly damped when a fluid mud layer was present and the damping was only little influenced by a current. Furthermore, the fluid mud is transported very easily by a current and hardly any mud was entrained into the water layer during this process. The pore pressure showed a transient decrease when the mud started to liquefy, succeeded by a gradual build-up of an excess pore pressure to compensate for the vanishing effective stress. Finally, it was found that observations or measurements made at a sidewall during an experiment only give a rough indication of the physical processes away from the sidewall; measurements carried out far from a wall have to be used for a quantitative description of the bulk processes in the bed.

#### Introduction

In several coastal and estuarine areas across the world the bed mainly consists of

---

<sup>1</sup> PhD-student, Delft University of Technology, Department of Civil Engineering, P.O. Box 5048, 2600 GA Delft, The Netherlands.

<sup>2</sup> Senior Research Scientist, same address.

cohesive sediment, often referred to as mud. The influence of these beds on the coastal environment is usually very large due to the specific properties and transport processes of cohesive sediments such as flocculation, settling, deposition, consolidation, liquefaction and erosion.

Two main hydrodynamic forces drive the transport processes of cohesive sediments in these regions: tidal currents and wind waves. Many researchers have studied the erosion or deposition of mud by currents, because of practical reasons as the maintenance of harbours, for instance. Various empirical relationships were derived from experiments and adopted to simulate the transport of mud (Partheniades, 1984).

However, in shallow waters wind waves dominate the hydrodynamic forcing of the cohesive sediment. The erosion of mud due to waves has also been studied experimentally by several researchers (Maa & Mehta, 1987, 1990). In some of the experiments a layer of fluid mud was formed under the influence of waves (Lindenberg et al., 1989). This phenomenon, which has also been observed in coastal areas, is caused by the varying wave loading. The fluid-mud layer may be transported very easily by a tidal current, for instance, yielding in a relatively large transport of sediment material close to the bed.

A striking observation which can be made at a muddy coastline is the marked wave damping as a result of the dissipation of wave energy in the bed. The energy dissipation depends on the rheological properties of the bed. Such damping phenomenon plays an important role in the protection of these coastlines.

The interaction between both waves and currents and a muddy bed has hardly been studied and is not well understood. In particular the liquefaction mechanism, the near-bed turbulence structure and the influence on wave damping require further study. Therefore a research project was started at the Delft University of Technology some three years ago. A set-up was built to study experimentally the influence of waves on the liquefaction process and the influence of both waves and current on the transport and erosion processes of mud. In the present paper only a brief account of the experimental results will be presented. A full description of the experimental results is given by De Wit (1992).

## **Sediment**

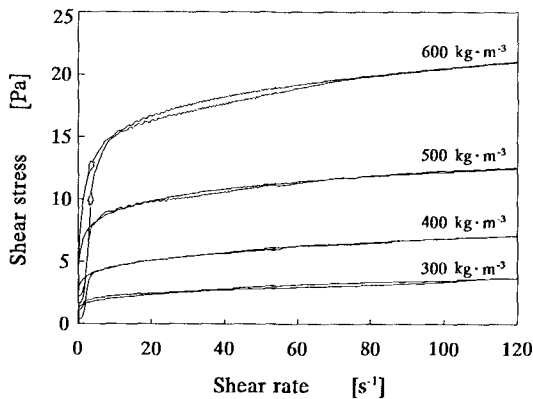
China Clay, an artificial mud mainly consisting of kaolinite, was used as sediment. The main reason for using this artificial mud is to get reproducible measurements. An additional reason is that the small-scale waves in the experiments require a less cohesive mud, which kaolinite is. Furthermore, using natural mud in experiments would involve the use of the natural water. The costs of temperature and light controlled transport and storage of the natural sediment with the accompanying fluid were prohibitive. Several properties characterising this clay were determined and some of them are listed in Table I.

**Table 1** *Properties of China Clay used.*

particle size distribution	> 10 $\mu\text{m}$	14 %
	< 2 $\mu\text{m}$	41 %
C.E.C.		5.0 meq/100g
density		2593 $\text{kg}\cdot\text{m}^{-3}$
specific surface area		29.9 $\text{m}^2\cdot\text{g}^{-1}$
mineralogical composition		mainly kaolinite

There was no free gas in the sediment, and sodium chloride was dissolved in the tap water used (salinity: 5 ‰) to increase the flocculation of kaolinite and to eliminate the possible influence of small quantities of other chemicals on the characteristics of the mud, as for instance the settling velocity. According to Van Leussen (1988) the settling velocity of kaolinite is maximal for chloride concentrations ranging from 2 to 18 ‰.

The rheological behaviour of the China Clay used was determined with a Haake viscometer; model Rotovisco RV100 and measuring system CV100. It is a viscometer capable of testing materials under either steady rotation, or dynamic oscillation with a frequency range from 0.01 to 9.9 cycles per second. The oscillating strain can be superimposed on a steady shear as well. This device is provided with several sample holders, the so-called sensor systems, such as a



**Figure 1** *Rheological behaviour of suspensions of China Clay in saline tap-water (salinity 5 ‰, sensor type: Q30).*



cone-plate and a plate-plate system. Each sensor system is designed to provide a specific range of shear rate, shear stress and viscosity.

Several suspensions of China Clay and saline tap-water were tested with suspended sediment concentrations ranging from 100 to 600 kg·m<sup>-3</sup>. In the tests the shear rate increased from zero to a maximum value of 125 s<sup>-1</sup> in 3 minutes and then decreased in the same period to zero again. Several sensor types were used depending on the concentration. The samples were thoroughly mixed and ultrasonically treated during 5 minutes before they were inserted in the sample holder. The temperature of the samples was 20 ± 0.5°C.

Some results are presented in Figure 1. The dynamic viscosity and the yield strength of a suspension can be estimated using these results. Furthermore, dynamic oscillation experiments were made on various clay samples at different concentrations (De Wit, 1992).

## Experimental set-up

A flume, length about 40 m, width 0.8 m and height 0.8 m, in the Hydro-mechanics Laboratory was modified for the purpose (see Figure 2). A simple mechanical wave maker was mounted at one end of the flume in order to generate regular waves, with a maximum wave amplitude of 0.11 m and a period ranging from 1 to 4 s. At the other end a stainless steel wave damper was mounted in such a way that it reduces wave reflection and would not interfere with generating a current. A recirculation pipe and a centrifugal pump were installed below the flume, which makes it possible to generate a steady current. The maximum flow rate is about 0.05 m<sup>3</sup>·s<sup>-1</sup>. The fluid is withdrawn below the wave damper at the end of the flume and it re-enters the flume via a smooth stainless steel duct installed below the wave maker. Wooden parts were used originally but these were replaced by stainless steel ones, because it was found that after a while fungi, algae and other micro organisms were growing on them. In this way the influence of organic material on the measurements is kept as small as possible.

The test section which holds the sediment is 8.0 m long. The vertical endwalls

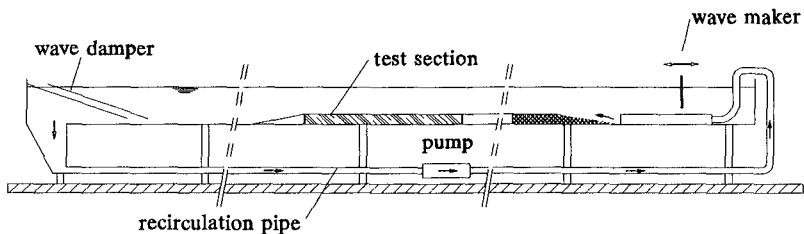


Figure 2 Experimental set-up.

of the test section are 0.2 m high and are formed by stacking four beams of which three can be removed during an experiment. The downstream and upstream endwalls are connected to the bottom and the upstream cement false bottom, respectively, by 2 m long asbestos-cement plates which were made adjustable by means of hinges. In this way the height of the test section can be adjusted during an experiment by removing a beam and lowering the free side of the plate.

## Experimental procedure

Prior to the experiments some tests were carried out to measure the wave decay, the wave reflection and the velocity distribution in the flume without sediment. For this purpose a temporary false bottom, made of cement, was placed over the test section. Measurements were also made in this configuration when both waves and current were present. The results showed that there was no significant wave reflection and no significant wave decay above the closed test section. Furthermore, the velocity distribution for a steady current was almost uniform.

The false bottom over the test section was removed and preparations were made for the experiments with China Clay. The China Clay was thoroughly mixed with saline tap-water (salinity 5‰) in a mixing tank. The tank, in which a continuously revolving grid was installed, contained about 3 m<sup>3</sup> of suspension with a concentration of about 250 kg·m<sup>-3</sup>. The suspension was regularly circulated in the tank; the suspension was withdrawn at the bottom and re-entered the tank at the top. After the suspension had been mixed for at least one week, it was pumped to the test section which was separated from the rest of the flume. Then the suspension was mixed again and finally it was allowed to consolidate. After consolidation the mud layer in the test section was approximately 0.2 m thick.

Prior to the preparation of the mud bed, four miniature pore-pressure transducers (Druck PDCR 81) were fixed in a cross-section in the middle of the test section. The measured accuracy of the devices is  $\pm 5$  Pa. Furthermore, six wave height meters and three electromagnetic velocity meters were installed in the test section. The sensor of the electromagnetic velocity meter has an ellipsoidal shape (11 × 33 mm) and the sensing area is a cylinder just below the sensor with diameter 33 mm and height 5 mm. Concentrations of mud in the supernatant water layer were measured by an optical method and by taking samples. The concentration in the bed was measured using a conductivity probe. The data were recorded on a personal computer and video recordings were made.

Three experiments with China Clay were made. The composition of the China Clay used in experiment III differed very little from the China Clay used in experiments I and II. In all experiments the behaviour and the processes in the mud were studied and measurements were made for different settings of the wave height ( $\leq 0.1$  m) and water velocity ( $\leq 0.2$  m·s<sup>-1</sup>). The wave period was 1.5 s and the depth of the tap-water above the initial bed was 0.30 m. For a detailed

overview of the experimental programmes of the three experiments see De Wit (1992).

During the first, preliminary experiment the configuration was different from the one described above. A description of the configuration used in experiment I is given by De Wit and Kranenburg (1991). In Table 2 the initial heights of the beds and the consolidation periods are listed for the three experiments.

**Table 2** *Consolidation periods and initial heights of the bed.*

Experiment No.	date	initial height of the bed [cm]	consolidation period [days]
I	June 1991	18.5	22
II	December 1991	19.8	9
III	June 1992	18.5	6

## Results

When waves were generated, it was observed that a layer of fluid mud was formed for wave heights exceeding a threshold value. This value increased with the consolidation period. The consolidation periods for the different experiments are listed in Table 2. The mud in experiment I started to liquefy when the wave height was about 7 cm. In experiments II and III liquefaction occurred when the wave height was about 3.0 cm.

Prior to the experiment the concentration profile of the initial mud bed was measured. In Figure 3 concentration profiles are shown measured at two different places in the test section prior to the experiment and when a layer of fluid mud was present. The latter profile was measured at the down-stream end of the test section. The thickness of the mud layer near the downstream endwall did not decrease very much during an experiment, because fluid mud was transported in the downstream direction by the waves. It can be seen that the bed was quite uniform.

Although sometimes overlooked, the shear stresses caused by the streamwise variation in wave-induced pressures seem to play an important role in the liquefaction process of cohesive sediments (Suhayda, 1984). A rough estimation of these pressure-induced shear stresses is made in the appendix assuming an ideal elastic behaviour of the mud. It is shown that the maximum shear stress increases almost linearly with depth. Using the characteristic values of experiment III it was

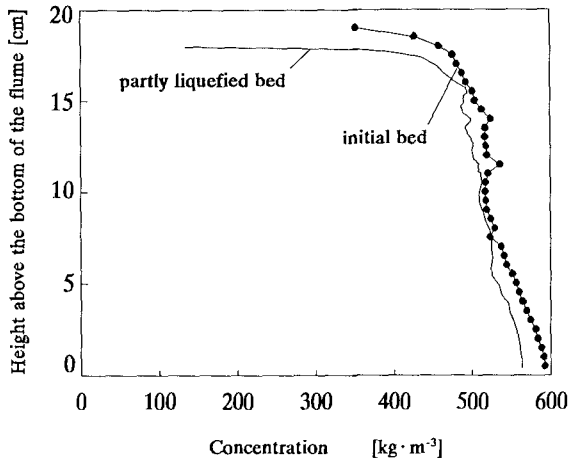


Figure 3 Concentration profiles of the bed at two locations in the test section during experiment III.

found that the maximum shear stress at 1 cm below the water-clay interface, for instance, is approximately 3 Pa for a wave height of 3 cm. The initial concentration of the upper part of the bed was about  $400 \text{ kg}\cdot\text{m}^{-3}$ , see Figure 3. In Figure 1 it is shown that the yield stress of mud with a concentration of  $400 \text{ kg}\cdot\text{m}^{-3}$  is approximately 3.5 Pa, which is of the same order of magnitude as the stress generated by the pressure oscillations. At 15 cm below the water-clay interface, the maximum pressure-induced shear stress is about 30 Pa, which is an order of magnitude greater than the yield stress of the sediment at this level in the bed. Only just below the water-clay interface the pressure-induced shear stress is smaller than the yield stress of the sediment. Consequently, the bed will be liquefied immediately after the generation of waves with a wave height of 3 cm, which corresponds with our observations.

As soon as a layer of fluid mud had been generated, the waves were significantly damped and the damping increased with the thickness of the fluid-mud layer. The damping was only little influenced by a current (see Figure 4).

Visual observations of dye injected near the bed surface seemed to indicate that the turbulence intensities in the overlaying water decreased when fluid mud was present. Furthermore, the fluid mud was easily transported by a current and hardly any mud was entrained into the water during this process.

In a later phase of experiment I erosion prevented the fluid mud to leave the test section, which then was just a trench in the false bottom. Instead a large circulation zone was generated in the fluid mud. This was the main reason for changing the test section into the present configuration. In experiments II and III this problem did not occur.

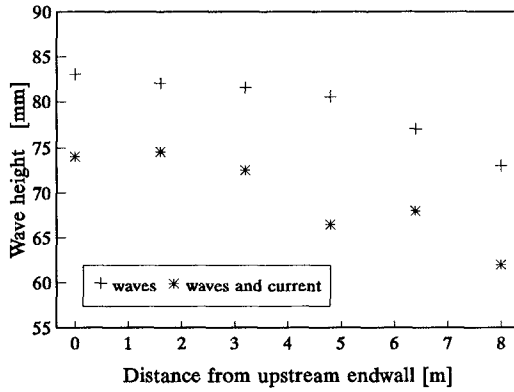


Figure 4 Average wave heights measured above the test section when waves and both waves and current ( $10 \text{ cm}\cdot\text{s}^{-1}$ ) were generated. (Experiment II, fluid-mud layer present)

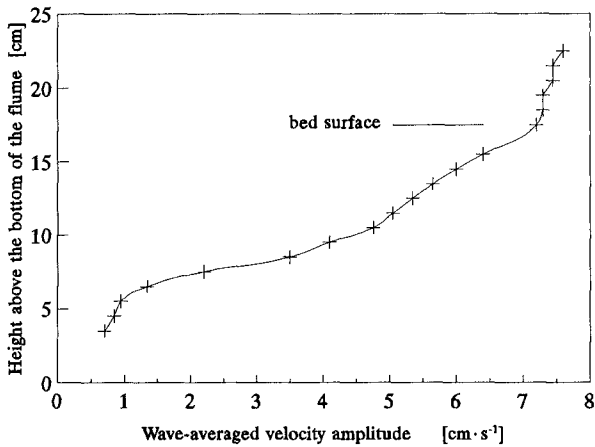


Figure 5 Wave-averaged velocity amplitudes in and above a partly liquefied bed. (standard deviation:  $0.5 \text{ cm}\cdot\text{s}^{-1}$ )

When a significant layer of fluid mud had been generated due to wave action, an electromagnetic velocity meter was used to measure velocity amplitudes just above and in the bed during experiment III. Although the flow of the fluid mud was disturbed significantly by the velocity meter, it was still possible to measure velocities. The calibration of the electromagnetic velocity meter was checked in towing tests prior to the experiment. According to visual observations at that moment, the bed was approximately 17.5 cm thick; the thickness of the fluid mud layer was when judged at the glass sidewall 4 cm. However, the measured wave-averaged velocity amplitudes shown in Figure 5, indicate that in the centre of the flume the whole mud layer had been liquefied.

In experiments II and III, four miniature pore-pressure transducers were installed. Three of them were fixed at several levels in the bed and one was fixed just above the bed as a reference. Wave-averaged water pressure changes measured just above and in the mud layer after the onset of liquefaction are shown in Figure 6. The pressure above the bed hardly changed during liquefaction. The pore pressure, however, showed a transient decrease which was probably caused by the break down of the aggregate structure. Then a gradual build-up of an excess pore

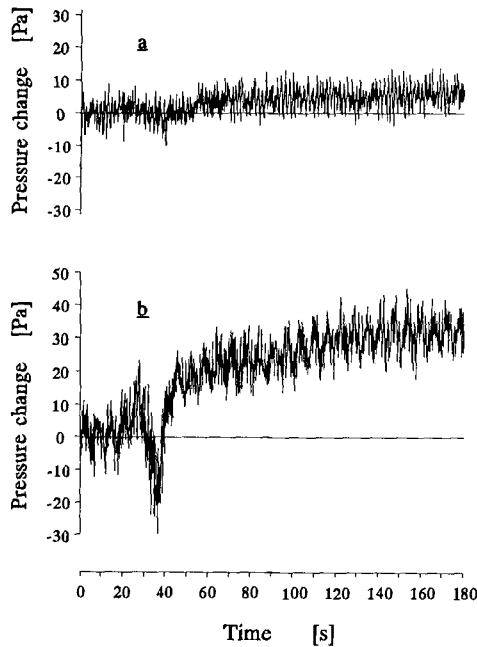


Figure 6 Wave-averaged pressure changes during liquefaction; a pressure at about 23 mm above the bed, b pore pressure 21 mm below the bed surface.

pressure was observed. Due to the low permeability of the mud layer the excess pore pressure did not dissipate, but rose to a final value corresponding with a zero effective stress.

## Discussion and conclusions

In each experiment a layer of fluid mud was generated due to wave action. However, the threshold value of the wave height at which liquefaction occurred depends on the consolidation period of the mud; the threshold value increased as the consolidation period increased.

Although the assumption made in the appendix of cohesive sediment being an elastic material is not quite appropriate, the estimate of the maximum pressure-induced shear stress given shows these stresses play an important role in the liquefaction process of mud.

The wave height was damped significantly as soon as a layer of fluid mud was generated and the damping was only little influenced by a current. Furthermore, dye injections seemed to indicate that the turbulence intensities decreased when a fluid mud was present. However, measurements using laser doppler anemometers or electromagnetic velocity meters are necessary to validate this observation.

The fluid mud was transported very easily by a current and hardly any mud was entrained into the water layer.

Usually visual observations and pressure measurements are made at a transparent wall of a set-up. However, from the measurements made with an electromagnetic velocity meter in the experiments carried out so far it is found that observations or measurements made at a sidewall are not representative of the actual physical processes away from the sidewalls. Only measurements carried out far from a wall give a quantitative description of the bulk processes inside the bed.

Pore-pressure measurements showed a transient decrease possibly caused by the break down of the aggregate structure, succeeded by gradual build up of an excess pore pressure so as to compensate for the vanishing effective stress.

This work will be continued by examining the liquefaction of sediments composed of other clay minerals. Furthermore, mathematical models relating the wave damping to the rheological properties of the bed are being tested.

## Acknowledgements

The authors wish to thank Delft Hydraulics for making available their Haake viscometer. This project was partly funded by the Commission of the European Communities, Directorate General for Science, Research and Development under MAST Contract no. 0035 (G6 Morphodynamics research programme).

## References

- Lindenberg, J., van Rijn, L.C. and Winterwerp, J.C., 1989, "Some experiments on wave-induced liquefaction of soft cohesive soils", *Journal of Coastal Research, Special issue no. 5*, pp. 127 - 137.
- van Leussen, W., 1988, "Aggregation of particles, settling velocity of mud flocs. A review", *Physical Processes in Estuaries*, edited by J. Dronkers and W. van Leusen, Springer-Verlag, pp.347-403.
- Maa, P.-Y. and Mehta, A.J., 1987, "Mud erosion by waves: a laboratory study", *Continental Shelf Research*, Vol. 7, No. 11/12, pp. 1269 - 1284.
- Maa, J. P.-Y. and Mehta, A.J., 1990, "Soft mud response to water waves", *Journal of Waterway, Port, Coastal, and Ocean Engineering*, Vol. 116, no. 5, pp. 634 - 650.
- Partheniades, E., 1984, "A fundamental framework for cohesive sediment dynamics", *Estuarine Cohesive Sediment Dynamics*, edited by A.J. Mehta, Springer-Verlag, Berlin, pp. 217 - 250.
- Suhayda, J.N., 1984, "Interaction between surface waves and muddy bottom sediments", *Estuarine Cohesive Sediment Dynamics*, edited by A.J.Mehta, Springer-Verlag, Berlin, pp. 401 - 428.
- Timoshenko, S., 1951, "*Theory of elasticity*", second edition, McGraw-Hill Book Company, Inc.
- de Wit, P.J. and Kranenburg, C., 1991, "Liquefaction and erosion of mud due to waves and currents", *MAST G6 Coastal Morphodynamics, Book of abstracts of contributions to the Mid-term Workshop*, pp. 4.3.1 - 4.3.4.
- de Wit, P.J., 1992, "*Rheological measurements on artificial muds*", Report no. 9-92, Delft University of Technology.
- de Wit, P.J., 1992, "*Experiments on China Clay*", Report no. 10-92, Delft University of Technology.



### Appendix

#### Wave induced shear stresses in the bed

Waves are capable of generating shear stresses in the bed. The total shear stress is a superposition of the shear stress caused by the oscillating flow and the shear stress caused by the streamwise variation in the pressure on the bed. The shear stress imposed upon the upper bed surface by the oscillating flow can be calculated from viscous flow theory for laminar flow or an empirical equation for turbulent flow. The pressure-induced shear stress is sometimes overlooked, but seems to play an important role in the liquefaction process of cohesive sediments (Suhayda, 1984). This shear stress can be estimated in the following way.

Consider a two-dimensional semi-infinite isotropic linear-elastic solid in the domain  $z \geq 0$ . The  $x$ -axis of the cartesian coordinate system is in the streamwise direction. In the origin of this coordinate system a vertical point force is applied. Boussinesq derived a solution for the resulting stress components at any point in the solid in 1885 (Timoshenko, 1951). Using the principle of superposition the maximum value  $\sigma_{\max}$  of the shear stress  $\sigma_{zx}$  can be calculated for a sinusoidal pressure distribution  $p = \hat{p} \sin(kx)$ , where  $k$  is the wave number. It is thus found that

$$\sigma_{\max} = \hat{p} k z e^{-kz} \quad (1)$$

The maximum shear stress is found for  $kz = 1$ , but liquefaction may start at higher level in the bed because usually the strength of the bed increases with depth. Approximating for small  $kz$ , equation 1 gives  $\sigma_{\max} \approx \hat{p} kz$  which was also found by Maa & Mehta (1990).

The pressure amplitude  $\hat{p}$  at the upper bed surface generated by progressive waves with amplitude  $a$  as calculated using linear short-wave theory is

$$\hat{p} = \frac{\rho g a}{\cosh kD} \quad (2)$$

where  $\rho$  is the density of the fluid,  $g$  the gravitational acceleration and  $D$  the water depth.

## CHAPTER 226

### CONSOLIDATION OF SOFT MARINE SOILS: UNIFYING THEORIES, NUMERICAL MODELLING AND *IN SITU* EXPERIMENTS

Alain Alexis<sup>1</sup>, Philippe Bassoullet<sup>2</sup>, Pierre Le Hir<sup>2</sup>  
and Charles Teisson<sup>3</sup>

#### ABSTRACT

This paper first presents a literature review of consolidation theories. A link between sedimentation and consolidation models is pointed out and a more general formulation is suggested. The constitutive relationships between the void ratio and the effective stress or the permeability are discussed from experimental data available in literature. Then a numerical modelling is used to simulate settling column tests. At last field measurements of mud characteristics are presented.

#### 1 INTRODUCTION

Cohesive sediments are often at the core of coastal problems, either by their undesirable accumulation in estuaries and sheltered areas as harbours, or by their active pollutant role as a carrier of heavy metals or radionuclides. Thus, various numerical models have been developed over the past decade to reproduce cohesive sediment transport, through the well known advection-diffusion equation, with deposition and erosion acting as sink and source terms. But few industrial models do take into account consolidation. Its representation, when it exists, is often empirical and loosely linked with

- 
- (1) IUT de St Nazaire, BP 420, 44606 St Nazaire, FRANCE  
(2) IFREMER, Centre de Brest, BP 70, 29280 Plouzané, FRANCE  
(3) EDF- Laboratoire National d'Hydraulique, 6 quai Watier  
78400 Chatou FRANCE

consolidation theories (HAYTER, 1986; TEISSON and LATTEUX, 1986; LE HIR et al., 1989). Recent approaches try to take into account consolidation by including effective stress as a parameter of the settling velocity (TOORMAN, 1992). However, consolidation is a very important parameter which governs sediment dynamics at a fortnight tidal scale: part of the sediment, which deposits during neap conditions, will have time to consolidate and will not be resuspended during spring conditions, because of its higher critical shear stress. A good prediction of the amount of resuspended sediment and consequently definitive deposit therefore depends on a good simulation of consolidation.

**2 LITERATURE REVIEW**

As soft soils are at the boundary between water and soil, consolidation has been investigated by hydraulicians and geotechnicians, with separate approaches. We use an original tree method, shown in fig.1, to analyse the historical background and study the convergence of the different points of view.

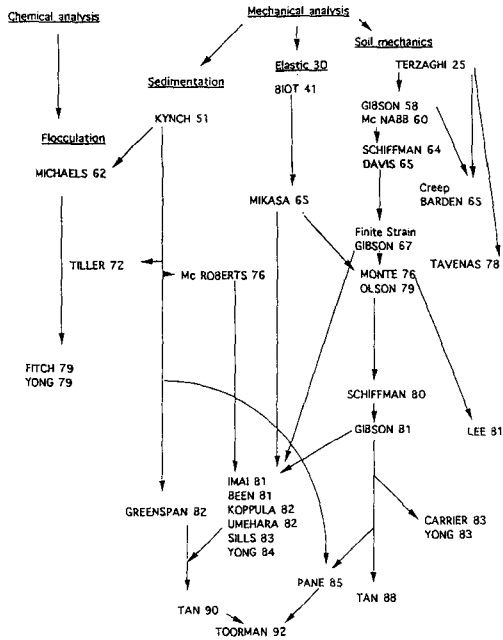


Fig.1: Soft soil consolidation historical tree of theoretical studies.

During the past ten years, some theories have been brought closer, but there is still no real inclusive approach, notably concerning the link between sedimentation and consolidation.

The study of previous theoretical works show that TERZAGHI (1925), KYNCH (1952) and GIBSON et al.. (1967) have been the key papers of this theoretical background. As TERZAGHI's formulation is only valid with small deformations and KYNCH's formulation does not take into account the effective stress, they reveal to be too restrictive. GIBSON's model is more general, but is limited to constitutive relationship only depending on the void ratio, and to incompressible phases.

In order to simulate the behaviour of a very soft marine soil, a relevant model should take into account large deformations, increasing or decreasing effective stresses due to the load history (deposition and erosion), variable or cyclical pore pressure (waves, tide), compressible fluid and grains (unsaturated, organic matter) and long term deformations (creeping).

### 3 TOWARDS A UNIFYING THEORY

As they appear different, models of consolidation have been rewritten using a unique notation system which allows their comparison.

GIBSON's law (1967) appears to be the most general of the previous studies. This formulation needs the use of a Lagrangian coordinate, the material coordinate  $z$ , which is constant for a given slice of sediment and corresponds to the height of solids above the slice. Stresses acting on sediment are studied separately, as effective stress on grains on the one hand, and pore pressure on fluid on the other:

$$\sigma = \sigma' + u_w$$

Mass balance,

$$\frac{\partial v_m}{\partial z} + \frac{\partial e}{\partial t} = 0$$

stresses equilibrium,

$$\frac{\partial \sigma}{\partial z} = \gamma(1+e) \quad \frac{\partial u_0}{\partial z} = \gamma_w(1+e)$$

extended Darcy's law,

$$v_m = -\frac{k_r}{\gamma_w} \frac{\partial u}{\partial z}$$

and constitutive relationships,

$$\sigma' = \sigma'(e) \quad k = k(e)$$

are written to get the Gibson's equation:

$$\frac{\partial e}{\partial t} - \frac{\gamma'_s}{\gamma_w} \frac{dk_r}{de} \frac{\partial e}{\partial z} + \frac{1}{\gamma_w} \frac{\partial}{\partial z} \left( k_r \frac{d\sigma'}{de} \frac{\partial e}{\partial z} \right) = 0 \quad (1)$$

where:  $e$  void ratio,  $k_r$  reduced permeability ( $k/(1+e)$ ),  $\gamma_w$  and  $\gamma'_s$  unit weights of water and of

immersed solids.

When self weight is ignored and small deformations are considered, it follows:

$$\frac{\partial e}{\partial t} = \frac{k E'}{\gamma_w(1+e_0)} \frac{\partial^2 e}{\partial z^2} \quad (2)$$

When effective stress is ignored, it follows:

$$\frac{\partial e}{\partial t} - \frac{\gamma'_s}{\gamma_w} \frac{dk_r}{de} \frac{\partial e}{\partial z} = 0 \quad (3)$$

SCHIFFMAN *et al.* (1985) have shown that the GIBSON'S equation (1) includes TERZAGHI'S equation (1925) (2) used in geotechnics for terrestrial soil and KYNCH'S equation (1952) (3) used in sedimentation as simplified and particular cases, when they are written in the same system of notations.

Moreover, the relation with the two-phase flow approach (TEISSON *et al.*, 1992) can be pointed out.

The usual condition of zero effective stress during the sedimentation phase induces the existence of a boundary void ratio. But a slightly decreasing effective stress down to very small but non zero values, with increasing void ratio, could allow to link sedimentation and consolidation as a continuous process.

We propose a new and extended formulation to take into account the compressibility of fluid and grains and non pure Darcinian flow:

$$\frac{\partial}{\partial z} \left( \gamma_f v_m \left( e, \frac{1}{1+e} \left( \gamma'_s - \frac{\partial \sigma'}{\partial z} \right) \right) \right) = \gamma_s \frac{\partial}{\partial t} \left( e \frac{\gamma_f}{\gamma_s} \right) \quad (4)$$

where the mean relative flow velocity  $v_m$  depends on  $e$  and the excess pore pressure gradient, but not necessarily according to the Darcy's law. It can be easily shown that the simultaneous use of the assumption of incompressibility for solid and fluid phases and of Darcy's law will make Gibson's equation 1 a restrictive case of equation 4.

Let us notice that the grain size distribution remains uniform, because of the use a material coordinate, but that creeping and the history of loading could be taken into account using a relevant effective stress evolution.

#### 4 CONSTITUTIVE RELATIONSHIPS

In order to solve (1) or (4) the representative constitutive laws  $\sigma'(e)$  and  $k(e)$  are definitely needed, which is the most difficult part of the task as these parameters can only be obtained through experimental ways for a given mud. This is all the most difficult as we deal with cohesive sediment and a very large range of concentration (BERLAMONT, 1992).

These two specificities also put the stress upon the necessary link between hydraulics and soil mechanics with a mutual benefit.

We have brought together experimental data issued from a hundred tests available in litterature. Our will was to mix the results of available experiments, in order to point out common trends although the experimental conditions and the soil composition were different in these various tests.

Void ratio was chosen as the main parameter, consistently with geotechnicians' habit. Bibliographic data were harmonized by transforming the other parameters (water content, density, dry density, weight concentration, volumetric concentration). When needed, the average value of 2,65 was taken for the density of solid particules.

For the effective stress, 48 experimental curves from IMAI (1981), UMEHARA and ZEN (1982), PANE et al.(1982), YONG et al.(1983), TAN et al.(1988) have been used.

A random distribution could have been expected, but in spite of the scattered dots, fig.2 shows a trend of the effective stress. This trend is in agreement with the effective stress shape introduced to link sedimentation and consolidation in part 3.

The next stage will consist of separating dots in different families by taking into account their plasticity as the main parameter of their nature.

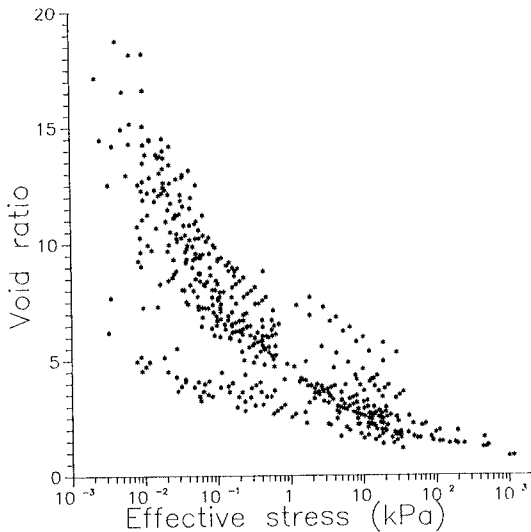


Fig.2: Gathering of effective stress literature experimental data.

A similar diagram has been drawn for the relationship between void ratio and permeability. We have used here 10 experimental curves from PANE et al.(1982), YONG et al.(1983), TAN et al.(1988), TAN et al.(1990) and TOORMAN (1992). Permeability or consolidation tests data are shown in fig.3a, down to a concentration of 300 g/l. In order to represent (fig.3b) very low concentration data, down to 50 g/l, settling velocity data (white squares in fig.3b) were transformed in permeability, using the correspondence:

$$v_s = \frac{k}{\gamma_w} (\gamma' - \frac{\partial \sigma'}{\partial x})$$

with a zero effective stress.

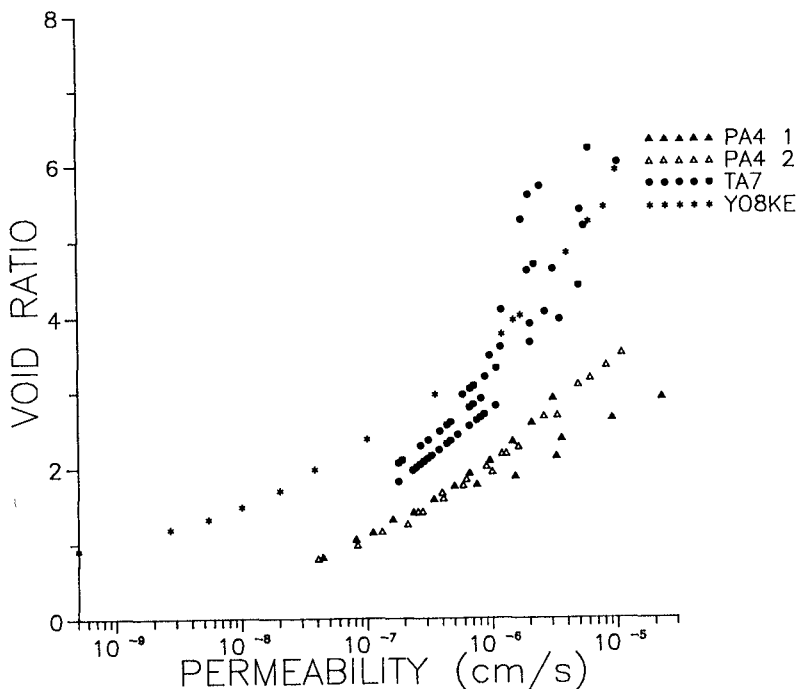


Fig.3a: Gathering of permeability literature experimental data (without settling velocity data).

The trend seems to be of the same nature on these diagrams, except for the fact that higher effect of the

soil composition or structure may lead us to imagine several curves.

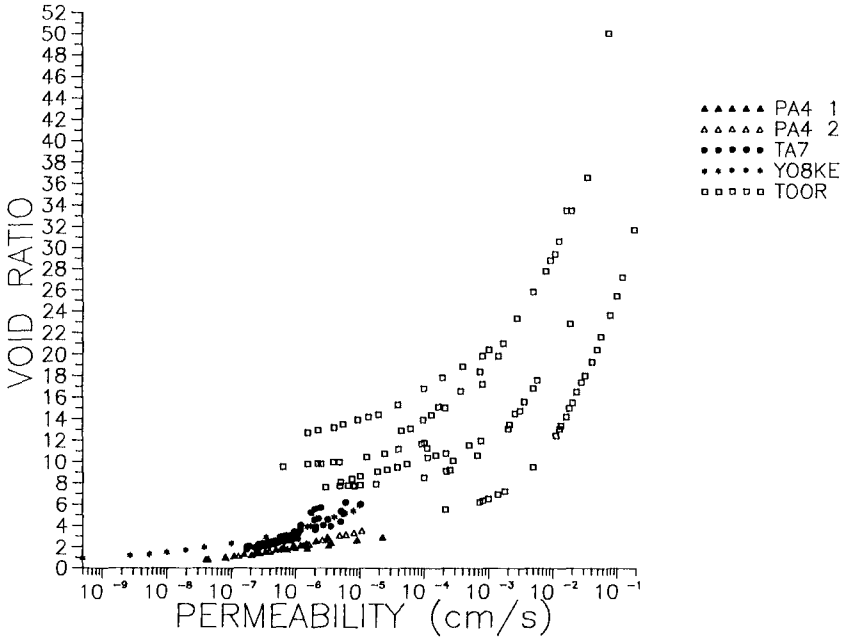


Fig.3b: Gathering of permeability literature experimental data (including settling velocity data).

## 5 NUMERICAL MODELLING

Gibson's equation expresses time and vertical evolution of the void ratio  $e$ , and can be easily modelled as a 1 D vertical advection-diffusion equation, except for the cost of computing due to the required fine vertical discretization. The equation is formulated in finite differences and solved with a semi-implicit numerical scheme. But the main problems lie in the appropriate formulation of the boundary condition at the interface between water and consolidating bed, and in the determination of the constitutive relationships  $k(e)$  and  $\sigma'(e)$ , i.e. permeability and effective stress as a function of the void ratio. Experimental settling tests of BEEN and SILLS (1981) have been satisfactorily reproduced with our model. The simulated height of the sediment column



is in good agreement with the experimental one (fig.4). Density at bottom is well represented but little discrepancies appear in the middle of the column (fig.5). They are probably due to the rather high sensitivity of the model to the constitutive relationships.

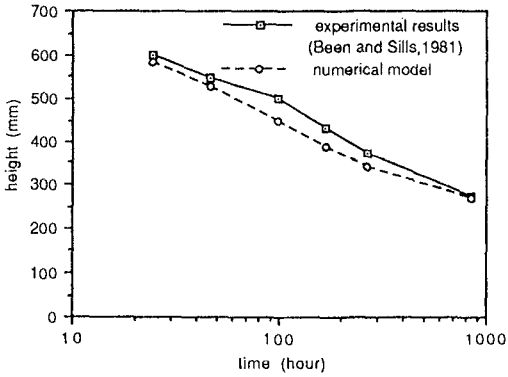


Fig. 4: Time evolution of total height of deposit.

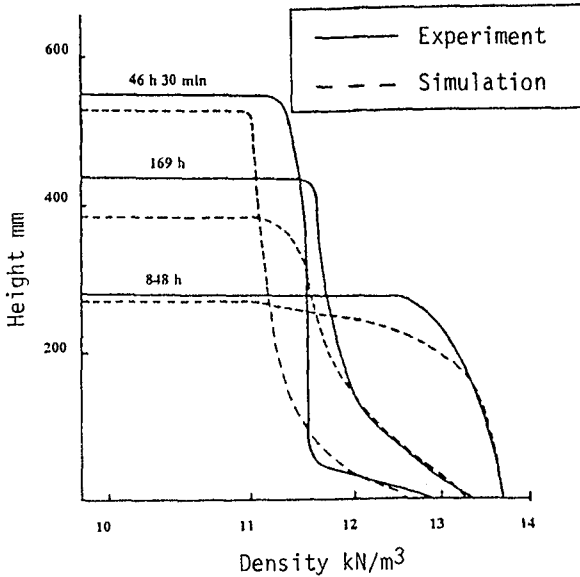


Fig. 5: Comparison of simulation with experiment profiles of BEEN and SILLS (1981).

## 6 IN SITU EXPERIMENTS

Some specific characterization tests are essential to evaluate fine cohesive sediments properties in muddy intertidal environments, in order to determine the relevant parameters for modelling mud erosion and deposition processes and to confront the results of previous theories and simulations with real situations. The involved parameters are naturally the concentration (or dry density) of the surficial sediment but also its shear strength which is assumed to be correlated with the "rigidity" of the mud.

In a same cross-section of the Elorn estuary (Brittany), small cores have been sampled in three locations of the intertidal area, according to three different mud levels, at several moments of the tidal cycle, during spring or neap tides, in winter and summer (december 1990 - june 1991 - january 1992). From these cores, vertical profiles of water content, dry density and yield stress have been measured every two centimeters, just after sampling. Yield stress measurements are made with vane testers which are specifically fitted to soft muds. A short synthesis from some of these cores is presented here. The resulting profiles show classical increases of concentration and shear strength over the first ten centimeters. The gradients can vary according to the tidal amplitude, the season and the location along the cross-section.

### Tidal variations

The effect of the tidal amplitude is more noticeable in the lower part of the mud bank where large irregular variations of dry density appear on spring tides, probably due either to stronger flows or to drainage processes in the cross-section of the mud.

As for the variation during the tidal amplitude, measurements show larger concentrations as well as higher yield stresses before the covering by the flood than just after the uncovering during the ebb, but the differences are only perceptible for the 2-3 upper centimeters. This phenomenon can lead to a variation of mud erodibility within the tidal cycle.

### Seasonal variations

The comparison between winter and summer data, at the same level of the intertidal flat (fig.6 and fig.7), points out more extended gradients in winter, when the surficial mud is less concentrated and less stiff.

These seasonal variations can be attributed to modifications of the deposit rate - due either to erosion elsewhere (L'YAVANC and BASSOULET, 1991) or to temperature effects or more probably to biological processes; several past studies have pointed out the role of biota seasonal variations and, in addition, some positive correlation

between the organic content and the shear strength of the mud (see for example MONTAGUE, 1986).

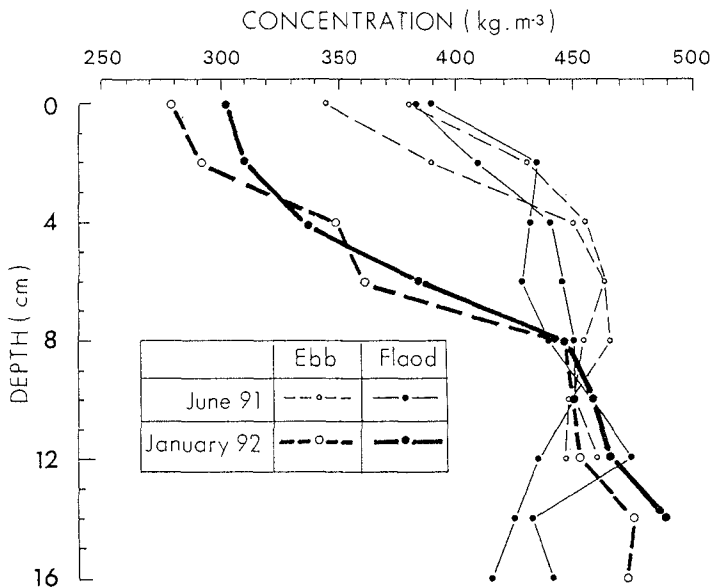


Fig. 6: Concentration profiles at a same location. Winter and summer measurements. Spring tide.

From all these results, it appears that the state of the surficial mud can change according to various processes which are not presently included in theories and models. On the other hand, a rather good correlation between concentrations and yield stress has been obtained and if we assume an additional correlation between yield stress and erosion processes, the previous direct *in situ* measurements can give information on the erodability of natural mud in an intertidal environment.

#### 7 CONCLUSION

The purpose of our survey was first to make a scanning of previous theories with the attempt to bring the light on the implied assumptions and to classify them.

In order to make a skimming of their most representative qualities we have attempted to develop an original formulation with less restrictive assumptions than before.

Gathering experimental literature data has allowed us to distinguish general trends of effective stress and permeability evolution for a large range of void ratios.

In spite of the usual difficulty to obtain relevant constitutive relationships (effective stress and

permeability), we have tried to simulate numerically a sediment settling in a laboratory column with a pair of experimental constitutive laws and have obtained a positive result.

But in situ experiments have shown that our theories still have to be improved, taking into account many other parameters, not considered up to now.

These complementary approaches should lead to a better description, understanding and modelling of consolidation processes, which will benefit to models of cohesive sediment transport.

#### ACKNOWLEDGEMENTS

This work has been undertaken as part of the MAST G6 Coastal Morphodynamics Programme. It was funded partly by the Commission of European Communities, Directorate General for Science, Research and Development under MAST Contract n°0035-C and partly by the French Sea State Secretary (STCPMVN).

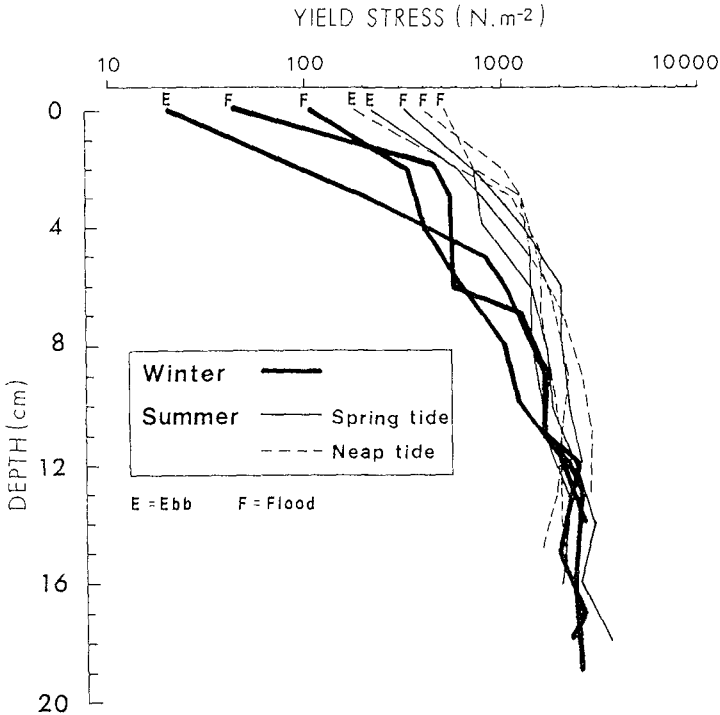


Fig. 7: Yield stress profiles at a same location. Winter and summer measurements.

**Symbols**

$e$  : void ratio  
 $k$  : permeability  
 $k_r$ : reduced permeability  
 $t$  : time  
 $u$  : over pore pressure  
 $u_w$ : pore pressure  
 $u_0$ : hydrostatic pressure  
 $v_m$ : mean relative velocity of water  
 $v_s$ : velocity of solid particules  
 $x$  : Eulerian coordinate  
 $z$  : material coordinate

$\gamma$  : unit weight of soil  
 $\gamma_f$ : unit weight of fluid  
 $\gamma_s$ : unit weight of solid particules  
 $\gamma_w$ : unit weight of water  
 $\gamma'$  : unit weight of submerged soil  
 $\gamma'_s$ : unit weight of submerged solid particules  
 $\sigma$  : total stress  
 $\sigma'$ : effective stress

**REFERENCES**

- BEEN, K., and SILLS G.C., 1981. Self-weight consolidation of soft soils: an experimental and theoretical. *Geotechnique* 31, n°4, pp 519-535.
- BERLAMONT, J., van den BOSCH, L. and TOORMAN, E., 1992. Effective stress and permeability in consolidating mud. *Proceedings of 23rd Int. Conf. on Coastal Engineering, Venice, Oct. 1992.*
- GIBSON, R.E., ENGLUND, G.L. and HUSSEY, M.J.L., 1967. The theory of one-dimensional consolidation of saturated clays. I. *Geotechnique*, 17: p. 261-273.
- HAYTER, E., 1986. Estuarial sediment bed model. In *Estuarine Cohesive Sediment Dynamics*, Ed. Mehta A.J., Springer-Verlag.
- IMAI, G., 1981. Experimental studies on sedimentation mechanism and sediment formation of clay materials. *Soils and Foundations* v21, n°1: p. 7-20
- KYNCH, G.J., 1952. A theory of sedimentation. *Transactions Faraday Society*, 48: p. 166-176.
- LE HIR, P., BASSOULLET, P. and L'YAVANC, J., 1989. New developments about mud transport models. Application to a macrotidal estuary. In "Sediment Transport Modeling", *Proc. Int. Symp. New Orleans*. Ed. Wang S.S.Y., pp.94-99.
- L'YAVANC, J. and BASSOULLET, P., 1991. Nouvelle approche dans l'étude de la dynamique sédimentaire des

estuaires macrotidaux à faible débit fluvial. *Oceanologica Acta*. Sp. Issue n°11. December. p. 129-136

MONTAGUE, C., 1986. Influence of biota on erodibility of sediments. In: Ed. Mehta A.J., *Estuarine cohesive sediment dynamics*. Lect. notes Coastal Est. Stud. n°14, Springer-Verlag, p. 251-269.

PANE, V., CROCE, P., ZNIDARCIC, D., KO, H.Y., OLSEN, H.W., SCHIFFMAN, R.L., 1982. Effects of consolidation on permeability measurements for soft clays. *Geotechnique* v33: p. 67-72

SCHIFFMAN, R.L., PANE, V. and SUNARA, V., 1985. Sedimentation and consolidation. Proc. Engineering Foundation Conf. on Flocculation, Sedimentation and Consolidation. p. 57-121

TAN, S.A., TAN, T.S., TING, L.C, YONG, K.Y., KARUNARATNE, G.P., LEE, S.L., 1988. Determination of consolidation properties for very soft clay. *Geotech. Testing J*, v11 n°14: p. 233-240

TAN, T.S., YONG, K.Y., LEONG, E.C. and LEE, S.L., 1990. Sedimentation of clayey slurry. *Journal of Geotechnical Engineering* vol 116 n°6: p. 885-898

TEISSON, C. and LATTEUX, B., 1986. A depth-intergrated bidimensional model of suspended sediment transport. Proc. of 3rd Int. Symp. on River Sedimentation. Ed. Wang, Shen and Ding. The Univ. of Mississippi, USA, p. 421-429.

TEISSON, C., SIMONIN, O., GALLAND, J.C. and LAURENCE, D., 1992. Turbulence and mud sedimentation: a Reynolds-stress model and a two-phase flow model. Proceedings of 23rd Int. Conf. on Coastal Engineering, Venice, Oct. 1992.

TERZAGHI, K., 1925. *Erbaumechanik auf Bodenphysikalischer Grundlage*. Franz Deuticke, Leipzig und Wein. 399 p.

TOORMAN, E.A., 1992. Modeling of fluid mud flow and consolidation. PhD Thesis. Civil Eng. Dept., K.U. Leuven. 219 p.

UMEHARA, Y., ZEN, K., 1982. Consolidation characteristics of dredged marine bottom sediments with high water content. *Soils and Foundations* vol 22, n°2: p. 40-54

YONG, R.L., SIU, S.K.H. and SHEERAN, D.E. (1983). On the stability and settling of suspended solids in settling ponds. Part I. Piece-wise linear consolidation analysis of sediment layer. *Canadian Geotechnical Journal*. 20: p. 817-826

## CHAPTER 227

### EFFECTIVE STRESSES AND PERMEABILITY IN CONSOLIDATING MUD

Jean Berlamont, Lut Van den Bosch and Erik Toorman<sup>1</sup>

#### Abstract

Measurements of density and pore pressures for consolidation experiments on estuarine mud are analyzed. Results for bulk permeability, local permeability and effective stress are presented and simple relationships between each of these parameters and the density are proposed. The problems associated with the accuracy of the measurements and their consequences on the determination of closure equations for consolidation models are discussed.

#### 1. Introduction

The study of erosion, deposition and transport of sediments is of major importance for the operation of harbours, the planning of maintenance dredging, the spreading of pollutants and the stability of coastal structures. Therefore, many efforts have been devoted during the past few years to develop mathematical models for simulating the movement and deposition of sediments in coastal regions and estuaries. Although various commercially available models are capable of predicting fairly well the behaviour of non-cohesive material (sand), they do hardly better than producing qualitative results when cohesive sediments (mud) are involved. This, unfortunately, is very often the case in harbours and estuaries. The reason is that the basic physical processes involved are not yet fully understood, and thus cannot be modelled adequately.

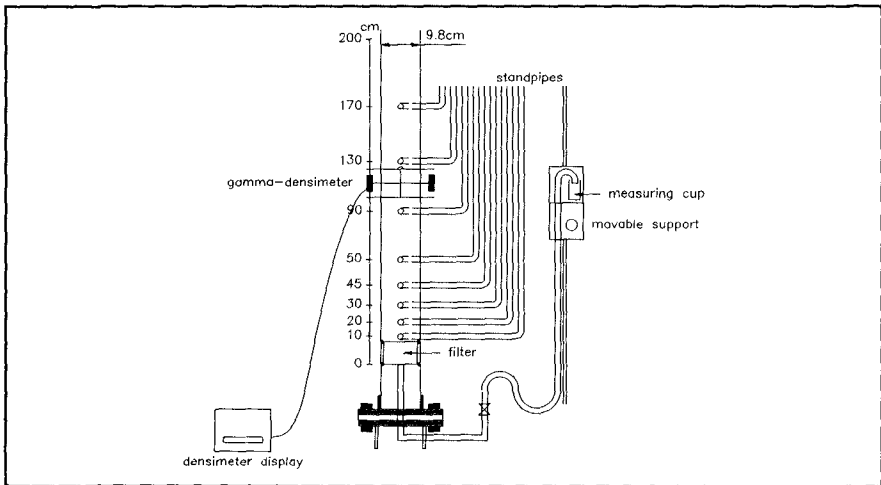
---

<sup>1</sup>Hydraulics Laboratory, Katholieke Universiteit Leuven, De Croylaan 2, B-3001 Heverlee, Belgium

The actual erosion rates and whether or not a muddy bed will be eroded by currents or wave action depend on the degree of consolidation of the bed. Each cohesive sediment transport model should therefore include the modelling of the time history of the bed and its consolidation. A review of consolidation models can be found in (Shiffman *et al.*, 1985) and (Alexis, 1991). More recent approaches, taking into account hindered settling as well, are due to (Tan *et al.*, 1990) and (Toorman, 1992).

The consolidation of a cohesive sediment bed depends on: (1) the expulsion of water through the pores between the solid particles, i.e. on the permeability  $k$  of the mud layer; (2) the deformation of the card-house-like structure of mud flocs, i.e. on the effective stresses  $\sigma' = \sigma - p$ , in which  $\sigma$  is the total stress and  $p$  is the pore water pressure. Therefore, there is a great need for general constitutive equations for the effective stress and for the permeability of a mud layer. Both are still largely unknown.

In the first part of this paper the results of experiments in settling columns will be described and discussed. Experiments were carried out both with drained and undrained mud layers. In the second part an attempt is made to determine permeability and effective stress as a function of bulk density.



**Fig.1:** Settling column: experimental set-up.

## **2. Settling column experiments**

In the Hydraulics Laboratory of the K.U.Leuven several series of consolidation experiments on drained and undrained mud layers were carried out in order to investigate the effect of drainage on the consolidation rate.



### 2.1 Experimental set-up.

Figure 1 shows the experimental set-up of the settling column. The transparent column has a diameter of 0.10 m and is equipped with water pressure gauges. Where the piezometers are connected to the column, a cigarette filter is inserted to prevent mud particles from entering the tubes. The bottom of the column is closed for undrained experiments. In the case of drainage it is replaced by a filter, about 10 cm thick, consisting of a gradation of sand and gravel. The bottom of the filter is connected to a small reservoir of which the level can be changed in order to allow a variation of the imposed head difference over the mud layer. The percolating discharge is measured by regular weighing of the measuring cup. Density profiles can be measured with a nuclear density probe with an accuracy of  $10 \text{ kg/m}^3$  (MAST-G6M Report, 1992).

### 2.2 Experiments

In this paper three sets of experiments are discussed. Table 1 gives an overview of test conditions. In all cases mud from the River Scheldt was used.

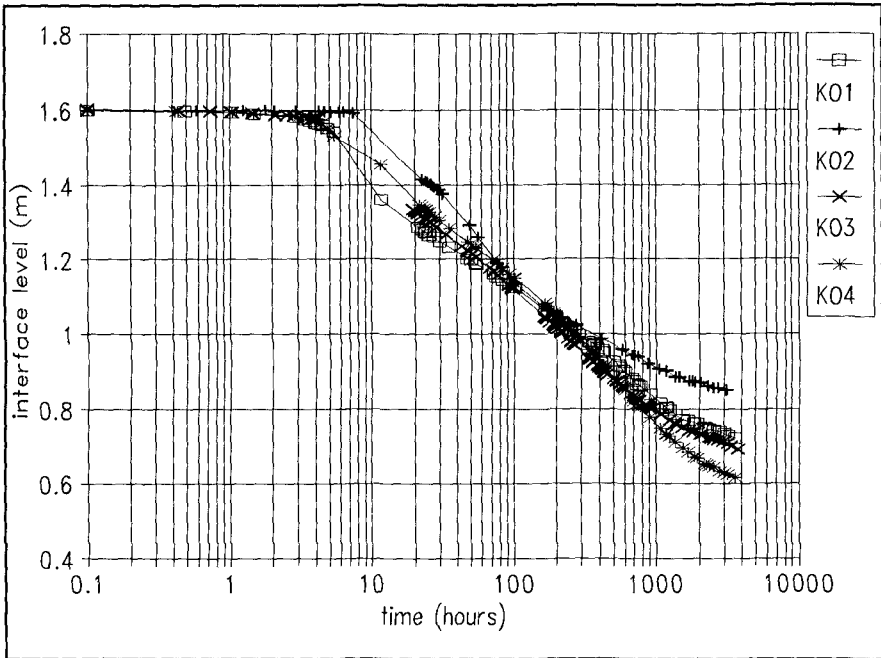
Exper. nr.	$H_0$ (m)	$\rho_0$ ( $\text{kg/m}^3$ )	Drainage	$\Delta h$ (m)	Duration (days)
KO1	1.600	1095	drained	0.0	119
KO2	1.600	1095	undrained	-	97
KO3	1.602	1095	drained	0.8	126
KO4	1.600	1095	drained	1.6	119
KO5	1.604	1095	undrained	-	92
KO6	1.602	1095	drained	variable	92
KO7	1.983	1060	undrained	-	41
KO8	1.993	1095	undrained	-	22
KO9	1.983	1098	undrained	-	26

**Table 1: Experimental conditions**

The first set of experiments (KO1, KO2, KO3, KO4) were ordered by IMDC (International Marine & Dredging Consultants) and fit within the study program for the design and optimization of a mud basin and capture reservoir (Mengé *et al.*, 1991). Afterwards, a second series of experiments (KO5 and KO6) were carried out to investigate optimal compaction through controlled drainage. The initial density in each case was  $1095 \text{ kg/m}^3$ . Interface level, pore pressures, density profiles and percolating discharge were measured. The columns were filled from the top. The columns were cooled at the surface with tap-water to keep them at a constant

temperature ( $\pm 13^{\circ}\text{C}$ ) in order to reduce gas production by organic matter.

In order to evaluate the results of permeability and effective stress values as a function of density, a third set of undrained consolidation experiments has been carried out. The general set-up for the settling columns was the same as for the previous ones except for a larger number of piezometers, which allows better estimation of local permeabilities. Cooling was now obtained by placing the columns in a constant temperature room. Tests are carried out at a temperature of  $8^{\circ}\text{C}$ , which is a more realistic value for in-situ conditions of underwater disposals and almost eliminates gas production. The columns were now filled by sucking up the slurry into the column by creating vacuum, which has the additional advantage of de-airing the mud.



**Fig.2:** Settling curves for experiments KO1-KO4.

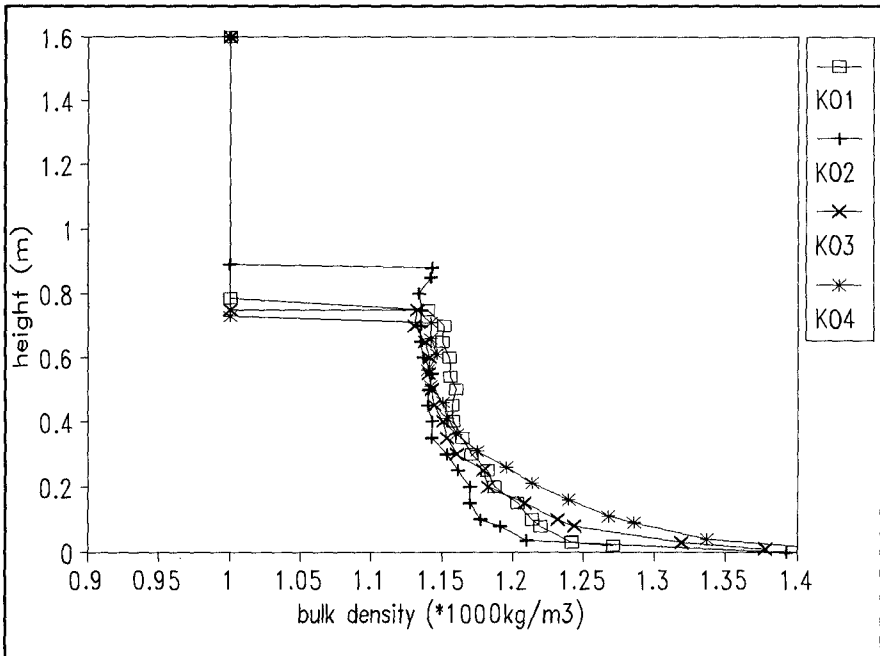
2.3 Discussion of observations

From the settling curves of KO1-KO4 it can be concluded that the descend of the water-mud interface starts earlier when the column is drained. During the first hours the consolidation rate of the undrained column KO2 is much lower than that of the drained column (Fig.2). The consolidation rate of KO1 (head difference  $\Delta h = 0.0$  m) is even larger than that of KO4 ( $\Delta h = 1.6$  m). After 100 hours the mud-water interface of both columns has reached the same level. This means that

consolidation rate of the drained column with head difference 0.0 m has decreased.

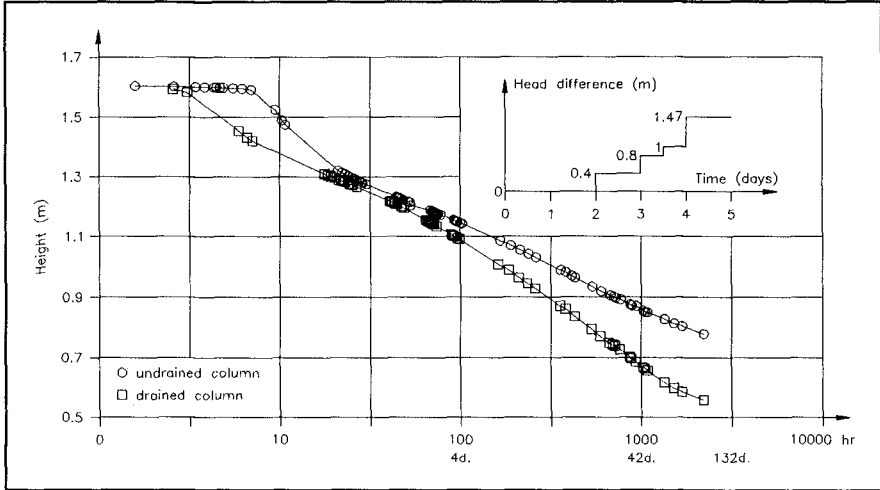
The smaller the head difference during the first hours the higher the consolidation rate at that moment. Afterwards the consolidation rate of the columns with a lower head difference decreases. At the end of the experiments (after 3 months) drainage gives a better compaction. The compaction increases for greater head difference. The compaction of KO1 and KO3 after 3 months is more or less the same. The compaction of KO4 is much higher than the others (i.e. 21 % better than for the undrained column KO2).

Density profiles for drained columns show that there is an upper layer of approximately constant density and a lower zone where the density increases with depth (Fig.3), which is clearly indicated by a distinct inflection point. The zone of constant density is similar to an undrained mud layer. Comparison of the density profiles of KO1-KO4 shows that the height of the zone with high densities increases with the imposed head difference (Fig.3).



**Fig.3:** Density profiles for experiments KO1-KO4 after two months.

In order to combine both effects to maximize compaction, two new experiments (KO5 and KO6) were started. In experiment KO6 the imposed head difference was stepwise varied during the experiment from 0 to nearly the initial column height (Fig.4). The experiment KO5 (undrained) was used as reference.



**Fig.4:** Consolidation curves for columns KO5 (undrained) and KO6 (drained).

As in the first experiments (KO1-KO4), the lowering of the interface starts earlier for the drained column (KO6) than for the undrained column (KO5) (Fig.4). However, although the geometric head difference during the first 2 days was zero, there is a small head difference over the mud sample caused by a difference in density between the fluid mud (initially the mud has no structure) and the water in the tube connecting the filter with the downstream reservoir. Therefore water can migrate downwards through the filter pushed by a small head difference. After a few hours a structure is formed and the head difference disappears. After 2 days the head difference was increased by lowering the reference reservoir level, resulting in an increased consolidation rate. After 4 days the head difference is 1.47 m. After 3 months the compaction in the drained column is 23 % higher than in the reference undrained column KO5. The density profile of KO6 (Fig.5) shows that the bottom zone of high densities is even thicker than in the tests KO1-KO4.

**3. Permeability and effective stress**

**3.1 Mean bulk permeability**

Data of the above discussed experiments have been used to estimate the permeability. For a closed (undrained) column the global permeability of the layer is calculated as a function of the average bulk density  $\rho$  using Darcy's law:

$$\frac{Q}{A} = k \frac{\Delta h}{L} \tag{1}$$

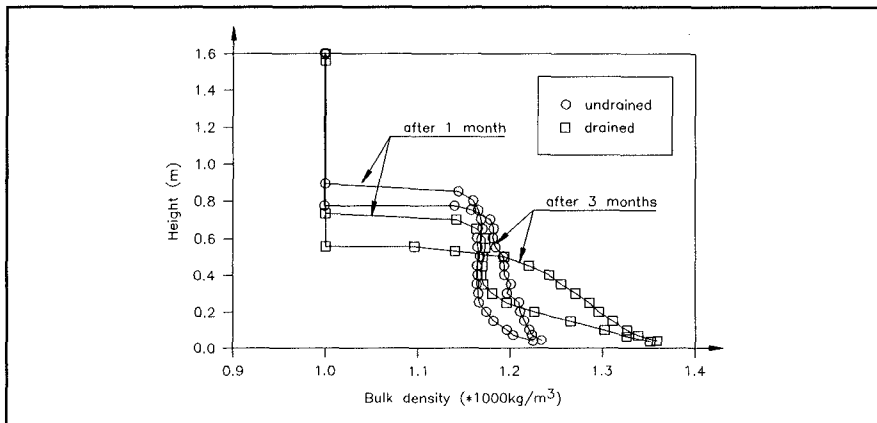


Fig.5: Density profiles for columns KO5 (undrained) and KO6 (drained).

where:  $\Delta h$  = difference over a certain time interval ( $\Delta t = t_{i+1} - t_i$ ) of pressure head above hydrostatic at the bottom of the column;  $L_i$  = mud layer thickness at time  $t_i$ ;  $A$  = cross sectional area of the column;  $Q = A (L_i L_{i+1}) / 2\Delta t$  = average pore water flow rate;  $L = (L_{i+1} + L_i) / 2$  = mean layer thickness.

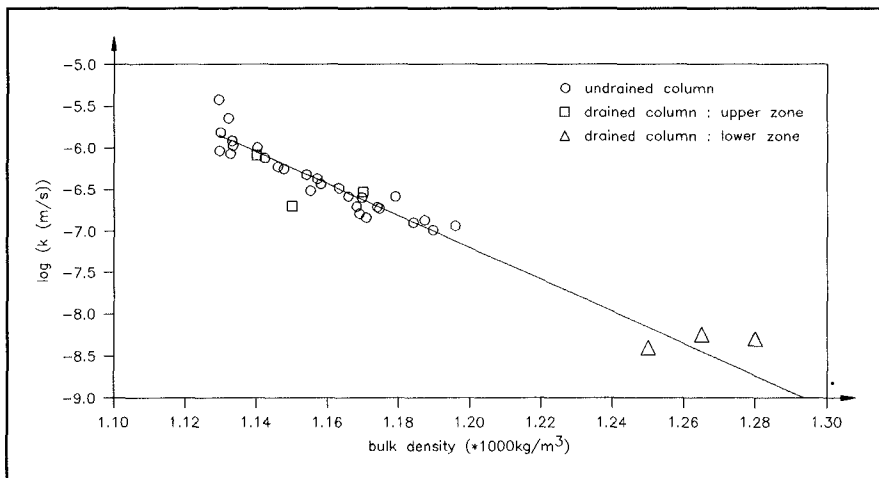


Fig.6: Global permeability as a function of average bulk density for columns KO5 (undrained) and KO6 (drained).

Fig.6 shows the results for columns KO5 and KO6. The relation between  $k$  and  $\rho$  can be approximated (for  $1130 < \rho < 1210 \text{ kg/m}^3$ ) by:

$$\log k = a\rho + b$$

[2]

where:  $a$  and  $b$  are empirical constants.

The inflection point in the density profiles was found to correspond with the level where the water head above hydrostatic reaches its maximum value (Fig.7). Hence, the excess pore water pressure gradient changes sign here, which implies that the pore water flows downward through the filter for the layer under the inflection point and upward for the zone above it. For the drained column the permeability of the upper zone is calculated as above for the undrained columns, whereas for the bottom layer the measured percolated discharge is used in Darcy's law. Hence, in drained columns permeabilities of mud layers of much higher density can be obtained. The obtained values of  $k$  are close to those obtained with Eq.[2] (Fig.6).

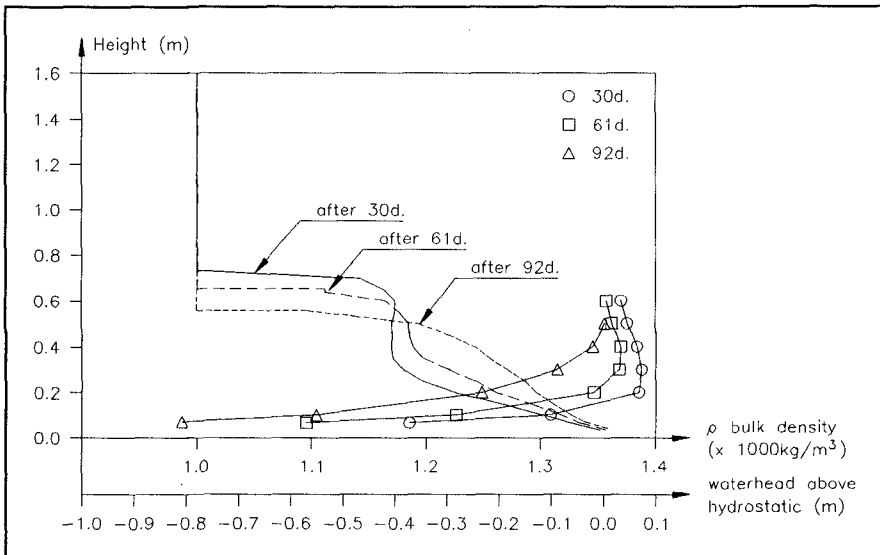


Fig.7: Density profiles and pore pressures above hydrostatic for the drained column KO6.

### 3.2 Effective stress

The total stress  $\sigma$  at a certain level is obtained by integration of the density profile from the surface down to that level. When the pore pressure  $p$  is measured at that point, the local effective stress  $\sigma'$  can be computed as  $\sigma - p$ . Fig.8 shows the total pressure, the pore pressure and the effective stress as a function of the depth for an undrained (KO2) and a drained column (KO4). It can be seen that the effective stresses in the drained mud layer are greater than in the undrained case.

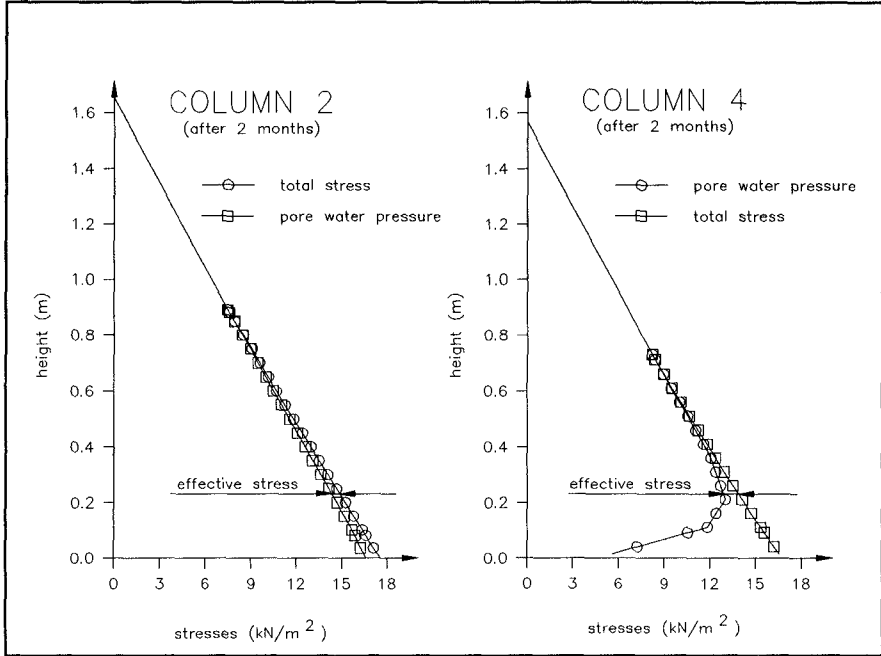


Fig.8: Stresses in the undrained column KO2 and the drained column KO4.

It was found that the dimensionless parameter  $\sigma^* = \sigma'/\rho k^2$  (where  $k$  is calculated with Eq.[2]) gives a rather good linear correlation with  $\rho$  on a semi-logarithmic scale, i.e.:

$$\log \sigma^* = a' \rho + b' \quad [3]$$

Substitution of Eq.[2] in [3] results in:

$$\log(\sigma'/\rho) = a'' \rho + b'' \quad [4]$$

where:  $a'' = a' + 2a$  and  $b'' = b' + 2b$ . Hence a plot of  $\sigma'/\rho$  as a function of  $\rho$  should directly give a linear correlation on a semi-logarithmic scale. The results for an undrained (KO5) and drained (KO6) column can be seen in Fig.9. The large scatter for small  $\sigma'$  values is due to the low accuracy of measuring effective stresses (especially at low  $\rho$ ), because  $\sigma'$  is obtained as the small difference of two parameters ( $\sigma$  and  $p$ ) which are of the same order of magnitude (see *MAST-G6M* Report, 1992).

To check the relationship [4] a new set of consolidation tests (KO7-KO9, Table 1) were carried out. The experimental results for the relationship between

effective stress and local density are shown in Fig.9. The effective stresses during the first two days are not plotted because of the low accuracy of these values. To extend the relationship for low values of effective stress a more accurate measuring method for effective stress is needed. In general it can be concluded that for the range  $1100 < \rho < 1350 \text{ kg/m}^3$  the relationship in a semi-log scale is linear.

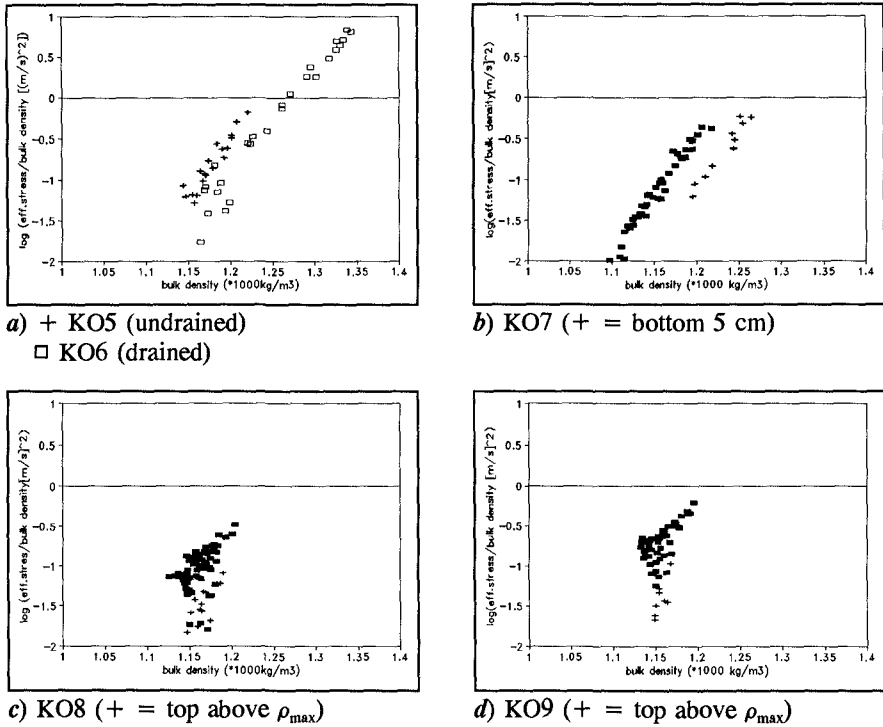


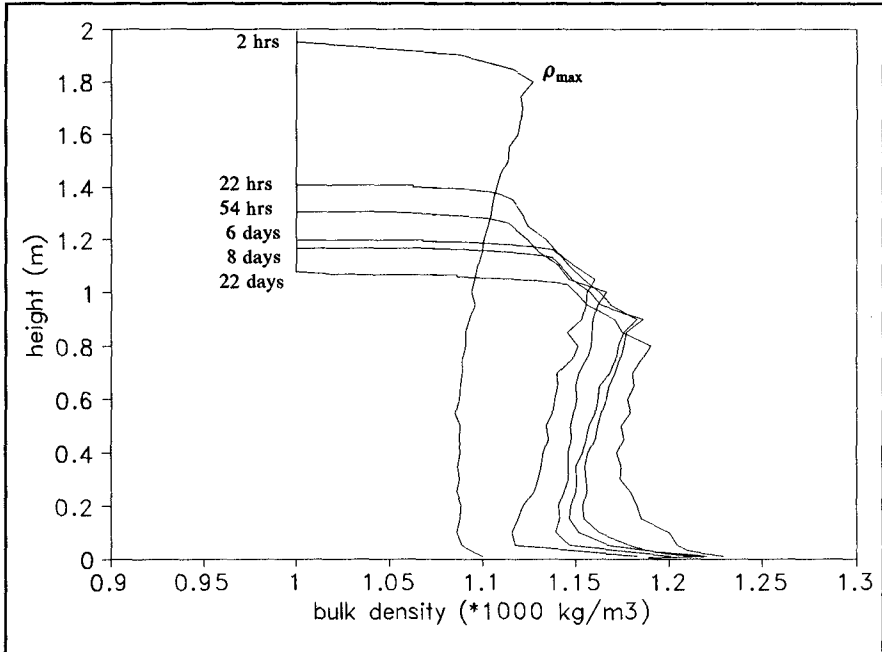
Fig.9: Effective stress as a function of bulk density for columns KO5-KO9.

Looking at the results of the columns KO7-KO9 separately, it can be seen that for KO7 in fact two lines can be distinguished, i.e. for points in the bottom 5 cm of the column and for those above. Possibly, because the initial density ( $1060 \text{ kg/m}^3$ ) of this experiment (KO7) was below the gel-point (the critical concentration for structure formation) of this mud, sand may have migrated to the bottom during the first hours of the experiment, causing a difference in composition of the mud for the points of the two lines. Moreover, the density measurements are biased close to the bottom of the column. A comparison of the results of KO7 with those of KO6 and KO5, shows that the data for the bottom layer of KO7 are comparable to those of the drained column KO6, while the values for the top layer of KO7 are on the same line as for the undrained column KO5, even though the mud in both sets of



experiments originated from different locations in the Scheldt.

The shape of the density profiles of KO8 is not as expected, showing a large zone of decreasing density with depth (Fig.10). Similar density profiles have also been found by *Bowden* (1988). At first sight, the results of effective stress for KO8 do not show a clear linear correlation (Fig.9c). It can be seen that there are two clouds of points. Possibly the relationship depends on the shape of the density profiles. For KO9 similar observations were made as for KO8.



**Fig.10:** Density profiles for column KO8.

### 3.3 Local permeability

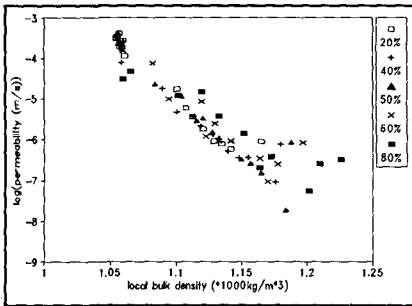
For the experiments KO7-KO9 an attempt was made to determine the local permeability by using the following form of Darcy's law, which is only valid for undrained tests (*Bowden*, 1988):

$$k = \frac{w_s'}{i} \quad [5]$$

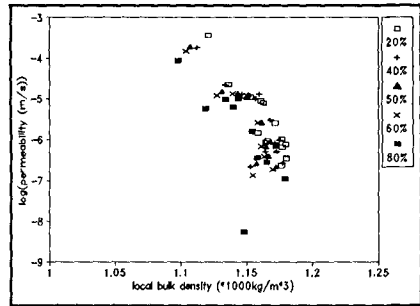
where:  $w_s$  = local settling rate (average solids velocity),  $k$  = permeability,  $i$  = local hydraulic gradient. The settling rate can be estimated from successive density profiles, by following levels in the mud layer below which a certain constant fraction

of the total mass of the sediment is found. The hydraulic gradient can be estimated by the difference in excess hydraulic head between two neighbouring pressure taps divided by the distance between them.

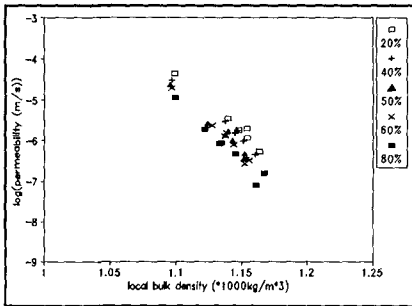
The local permeabilities as a function of local density were calculated for KO7, KO8, KO9 (Fig.11a-c). Again the experimental results can be approximated by a linear relationship between  $\log(k)$  and  $\rho$ . For column KO7 the linear approximation is very good in the range from  $1050 \text{ kg/m}^3 < \rho < 1200 \text{ kg/m}^3$ . For higher densities there is a lot of scatter. For this range the calculation of  $k$  by Eq.[5] is very inaccurate, because the settling rate is determined from two successive density profiles, measured with limited accuracy (§2.1), which hardly change any more at this stage of the consolidation process.



a) KO7



b) KO8



c) KO9

Fig.11: Local permeability as a function of density for columns KO7-KO9.

For KO8 and KO9 a linear relationship between  $\log(k)$  and  $\rho$  is a good approximation. The scatter is larger than for KO7 because the initial density was higher, which reduces the accuracy of the calculation of  $w_s$ . The inaccuracy is largest for the 80% mass level, because the density profiles are integrated all the way from the top down. The values of  $k$  for KO8 and KO9 are a factor 5 to 10 smaller than the permeabilities of KO7. Because the density profiles are used for calculation of

$k$ , a possible explanation can also here be found in the shape of the density profiles, which is influenced by the initial density of the slurry.

### 3.4 A theoretical consideration

Darcy's equation for undrained consolidation, Eq. [5], can more explicitly be written as a relationship between effective stress, permeability and settling rate (Toorman, 1992):

$$\frac{1}{g} \frac{\partial \sigma'}{\partial z} \approx \rho_w \frac{w_s}{k} - \Delta \rho \quad [6]$$

where:  $g$  = gravity constant;  $\Delta \rho = \rho - \rho_{w(\text{atcr})}$ . When the density is below the critical concentration where no structure exists, hindered settling takes place instead of consolidation and thus there is no effective stress. Hence, Eq. [6] reduces to:

$$k = w_s \frac{\rho_w}{\Delta \rho} \quad [7]$$

This was first pointed out by *Been* (1980). Therefore, for low densities Eq. [2] can no longer be valid, because in the limit where  $\Delta \rho$  goes to zero, the permeability becomes infinite since  $w_s$  then equals the (finite) Stokes fall velocity of a sediment particle.

## 4. Conclusions

The settling curves of the drained and the undrained mud layers show that drainage fastens the settling and the consolidation rates. The compaction can be maximized by applying a variable, i.e. increasing, head difference over the mud sample. Higher densities than in undrained conditions are then obtained in a thick layer above the bottom. Hence it is possible to obtain values of permeability and effective stress at higher densities using drained columns.

The presented results suggest linear correlations between  $\log(k)$  and  $\rho$  and between  $\log(\sigma'/\rho)$  and  $\rho$  within the range  $1100 < \rho < 1200 \text{ kg/m}^3$ . Because there is often significant stratification in the mud layer, it is unlikely that the global permeability can be used to calibrate a closure law for  $k$  needed in numerical modelling, since local values are required. Local permeabilities however are harder to measure. Nevertheless, the magnitude of local and bulk permeabilities were found to be comparable. More experimental work is required to get more accurate data for the ranges of low and high densities, as well as to investigate the effect of parameters, such as initial density, structural history, shape of the density profiles, initial height, depth from the interface, etc.

### Acknowledgements

This work has been undertaken as part of the MAST G6 Coastal Morphodynamics Programme. It was funded partly by the Commission of European Communities, Directorate General for Science, Research and Development under MAST Contract No.0035-C and partly by national funding. Part of the settling column experiments (KO1-KO4) were financially supported by IMDC (Int. Marine & Dredging Consultants, Antwerp, Belgium). The last author received a grant from the Belgian National Fund for Scientific Research.

### References

- Alexis, A.** (1991): *Review of consolidation models*. MAST G6-M Project Workshop, Delft.
- Been, K.** (1980): *Stress strain behaviour of a cohesive soil deposited under water*. PhD thesis, Oxford University.
- Bowden, R.K.** (1988): *Compression behaviour and shear strength characteristics of a natural silty clay, sedimented in the laboratory*. PhD Thesis, Oxford University.
- MAST G6M** (1992). *On the methodology and accuracy of measuring physico-chemical properties to characterise cohesive sediments*. Report prepared as part of the EC MAST-1 G6M Coastal Morphodynamics research program.
- Mengé, P., L. Van den Bosch, W. Van Impe and J. Berlamont** (1991). *Mud basin and capture reservoir experimental program. - Laboratory experiments*. Report. Soil Mechanics Laboratory, R.U.Gent and Hydraulics Laboratory, K.U.Leuven (in Dutch).
- Schiffman, R.L., V. Pane and V. Sunara** (1985): *Sedimentation and consolidation*. Proc. Engineering Foundation Conf. on Flocculation, Sedimentation and Consolidation, pp.57-121.
- Tan, T.S., K.Y. Young, E.C. Leong and S.L. Lu** (1990): *Sedimentation of clayey slurry*. ASCE J. Geotechnical Engineering, Vol.116(No.6),885-898.
- Toorman, E.A.**(1992). *Modelling of fluid mud flow and consolidation*. PhD thesis. Civil Eng. Dept., K.U.Leuven.

## CHAPTER 228

### Cohesive Profile Erosion by Waves

Craig Bishop<sup>1</sup>, Michael Skafel<sup>1</sup> and Rob Nairn<sup>2</sup>

#### Abstract

Hydraulic tests of the erosion by waves of a shore profile made from intact samples of till, a cohesive material comprising a large part of the Great Lakes shorelines, have been completed. Over 1000 h of testing in a laboratory flume with random depth-limited breaking waves, varying conditions of sand cover, and varying mean water levels have been run. The vertical erosion rates of the till were measured along the centreline of the 8 m long, 0.35 m wide and 0.25 m thick till profile; its initial shape was the equilibrium form  $y = Ax^{2/3}$  common on sandy beaches. Some of the important findings are that this type of hydraulic test is viable, the role of sand in the erosion process is similar to its role in unidirectional flow model tests but the thickness and volatility of the sand layer are also factors, the main effect of varying water levels is to shift the zone of erosion activity up and down the profile, and that erosion can occur in the absence of sand if the rate of wave energy dissipation is high enough (plunging breakers, steep slopes).

#### Introduction

A large part of the Laurentian Great Lakes shoreline consists of cohesive materials, especially till. Similarly, much of the Black Sea coast, England's North Sea coast and others consist of cohesive materials. These shorelines are typically characterized by an eroding backshore bluff and a small, thin beach; cohesive material underlays the beach of cohesionless (sandy) materials. A shore can be defined as cohesive when a cohesive sediment substratum occupies the dominant role in the change in the shoreline shape (i.e. through erosion). It has been recognized that there are fundamental differences in the erosion process between sandy and cohesive shores. Cohesive shores are often glacial in origin, and they derive their strength from the cohesion of the clay as well as their consolidation from the period of glacia-

-----  
1. National Water Research Institute, Environment Canada, PO Box 5050, Burlington, Ontario, Canada L7R 4A6

2. Coastal Consultant, 316 Maple Ave., Oakville, Ontario, Canada L6J 2H7

tion. Once the material is eroded, it cannot reconstitute itself; it's cohesive nature is lost and the fine particles are advected away from the nearshore zone. Therefore, unlike sandy shores, erosion on cohesive shores is irreversible. The recession of cohesive bluffs is now understood to be controlled by the vertical erosion (downcutting) of the nearshore profile (Kamphuis 1987). Typically, the beach of cohesionless material in front of a cohesive bluff plays a complex role in the erosion process; it can provide some protection or can serve as an abrasion agent depending on its volume and the wave energy. Only when the volume of cohesionless material overlying a cohesive layer is large (of the order  $200 \text{ m}^3/\text{m}$  for the Great Lakes), as can occur at a large obstruction such as a harbour jetty or a headland, does the erosion process return to being the same as that on a sandy shore (Nairn 1992).

The erosion process on a cohesive coast can be demonstrated by a comparison of two cross-sections of a bluff and nearshore profile at a site in Lake Ontario (Nairn 1992). Figure 1 shows the estimate of the underlying cohesive profile and the sand cover in 1952 and again in 1989. The bluff face has receded about 30 m over this 37 year period for an average recession rate of 0.8 m/yr. In order for this to occur, the nearshore lake bed had to be downcut considerably. Furthermore, the profile shape in 1952 is very similar to that in 1989; it has simply shifted shoreward by 30 m. In a review of many field data sets throughout the Great Lakes, profiles were generally found to retain their shape as they receded (Nairn 1992). There appears to be an equilibrium or preferred cohesive profile shape.

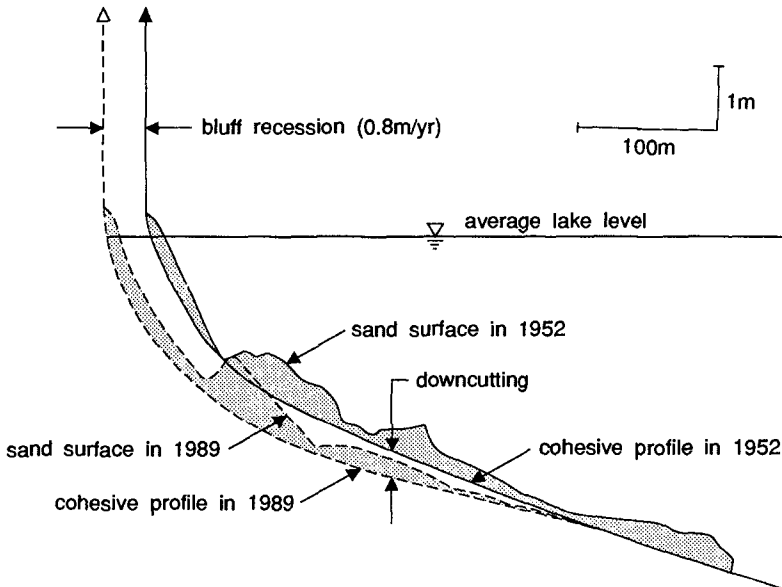


Fig. 1 Lake bottom and till profiles in 1952 and 1989 at Scarborough Bluffs, Lake Ontario (after Nairn, 1992).

In the present work, the processes important in the erosion by waves of a nearshore profile made from intact samples of till are examined by means of hydraulic tests.

### Field Work

A vital component of this study was the collection of intact till samples in the field. Remoulded clays are known to have much reduced resistance to erosion compared with the undisturbed or intact clay (Lefebvre and Rohan 1986). After several field reconnaissance visits to the Lake Erie shoreline, a suitable site located about 200 m from the northshore bluff of Lake Erie was found. The site, Shanks' Gravel Pit #1, is located just west of Port Alma on Highway 3, where, after stripping off the overburden, a sand-gravel layer which overlies Port Stanley till is mined using a dragline. The bluffs and lake bottom over a large part of northwestern Lake Erie consist of Port Stanley till, a relatively homogeneous, cohesive material laid down by glaciers over 10,000 years ago.

Open-ended steel boxes were manufactured using 1/8 inch (3.2 mm) thick steel. The box dimensions are 1.0 m long, 0.35 m wide and 0.45 m high. The front (cutting) end of each box has a bevelled edge and sloped back at an angle of 2, 3 or 7 degrees; these slopes were intended to minimize the surface gaps between blocks when installed in the flume.



2a Backhoe clearing face of till



2b Cutter frame with till sample



2c Till sample in steel box



2d Field site after removing 25 samples

Fig. 2 Photographs of field site

On October 9, 1990 Shanks removed the overburden and sand-gravel layer, prepared a work area and scraped the till surface smooth using a mid-sized bulldozer and a 25-ton crane with a dragline. On October 10, after pumping out accumulated rainwater, the till surface was trimmed by another 30 cm. Then a trencher was used

to cut a smooth vertical face in the till. A backhoe and bulldozer were used to clear the working face of the till (Fig. 2a).

A custom made aluminum cutter frame was positioned and levelled in front of the prepared vertical till face; it was held in place by the trencher and bulldozer. A portable diesel hydraulic unit was used to power a 20-ton hydraulic ram. The ram slowly pushed an empty steel box guided by the cutter frame into the till (Fig. 2b). The end of the box in the till was cut away using a chainsaw with a trenching chain. The box was then lifted (Fig. 2c) and transported to a flatbed truck using the crane. The tops of the samples were covered with cheesecloth, sprayed with water, then the whole till-filled steel box was wrapped in plastic. By repeating this procedure, 25 till blocks were collected on October 10-11 by 8 people (Fig. 2d). When the samples arrived at NWRI, each block was misted again with water, and then put into 2 plastic bags which were then taped shut. Later, on May 23, 1991 all unused till blocks were stored under water until needed.

Size analysis and geotechnical tests on samples of the till gave the following average properties: 21% sand and gravel, 33% silt, 46% clay, mean grain size  $D_{50} = 0.0052$  mm, liquid limit 27, plastic limit 17, plasticity index 10, and vane shear strength 86 kPa.

### Laboratory Flume Setup

Tests were conducted in the 100 m long wind-wave flume at the NWRI Hydraulics Laboratory. An existing smooth plywood beach at a slope of 1:20 was modified to incorporate a 0.37 m wide channel along its centeline. Fig. 3 shows the test setup. A motorized carriage, equipped with a variable speed motor, traversed the working length of the test channel. Its position was monitored using an electronic synchro transmitter with horizontal accuracy of about  $\pm 3$  mm. Profile data were collected at horizontal speeds of the order of 10 mm/s. Vertical profile data were measured with an optical bedplotter device mounted on a bracket attached to the carriage. Light from a light emitting diode is sent through a probe of fibre optic cables; a servo system raises or lowers the probe so as to maintain a preset voltage, corresponding to a vertical gap of about 15 mm, from the light signal reflected from the bed. The accuracy of the system is about  $\pm 1$  mm. A bedplotter reading was taken on a fixed reference plate before and after each profile. Typically, variations between before and after readings were about 0.5 mm.

### Waves

Waves were generated by a piston-type wavemaker using GEDAP (Funke and Mansard 1984) software. One random wave voltage sequence was used to drive the wavemaker for all tests. It was developed for a mean water depth of 100.0 cm, a peak frequency of 0.4 Hertz, a duration of 500 s (200 waves), unspecified groupiness, and a ratio of mean wind speed to wave phase speed ( $U/c_p$ ) of 1.3. Waves were measured by 3 capacitance wave gauges. The spacing between gauges 1 and 2 was 0.706 m, and between 1 and 3 was 1.696 m. Incident and reflected wave spectra were separated using the method of Mansard and Funke (1980). The characteristic wave height ( $H_{m0}$ ) of the incident waves was 0.31 m at a water depth of 1.00 m, 0.29 m at 0.95 m, 0.26 m at 0.85 m, and 0.26 m at 0.75 m. The corresponding values



of peak frequency ( $f_p$ ) varied between 0.33 and 0.39 Hertz.

Since the laboratory tests used intact samples of prototype till and depth-limited breaking waves over most of the profile, these tests can be considered as full scale of the nearshore zone to a water depth of 0.5 to 0.75 m. There may be some model effects due to the peak frequency of the waves being higher than typical storm values of 0.1 to 0.2 Hz in the field.

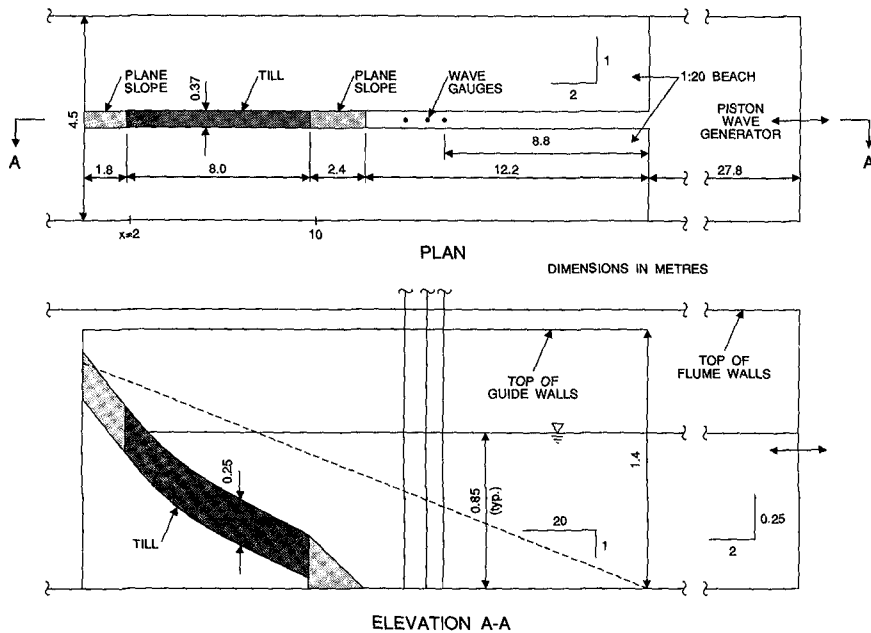


Fig. 3 Test setup in laboratory flume

**Initial Profile**

According to Kamphuis (1987), nearshore profiles on cohesive coasts in wave-dominated environments have a long term, stable shape similar to the so-called "equilibrium" shape of sandy beaches described by Dean (1977). This shape is of the form  $y = Ax^{2/3}$  where  $y$  is the vertical distance measured downward from the mean water level,  $x$  is the horizontal distance measured from the mean water line, and  $A$  is a shape factor. This equation is for the mean profile and inherently ignores sand bars. Moore (1982) relates the shape factor to the mean grain size present on the beach. A medium sand, with  $D_{50} = 0.51$  mm, available in the laboratory, was put in the testing part of the flume and subjected to about 20 h of the test wave spectra. The sand profile reached a stable shape and was measured. Ignoring the bars, the shape corresponds well with the predicted shape using the value of  $A$  given in Moore (1982) for the 0.51 mm sand (Fig. 4).

Based on these preliminary tests with sand, the starting profile for the till was designed to be of the form  $y = 0.18x^{2/3}$ . Eight till blocks, trimmed to a height of 0.25 m, were installed in their steel boxes in the flume; loose till was packed into the seams and then the profile was measured under water. The initial till profile is compared to the design profile in Figure 4. Only a brief summary of results of several different test categories are given here; for a detailed description of tests and results, refer to Bishop and Skafel (1992).

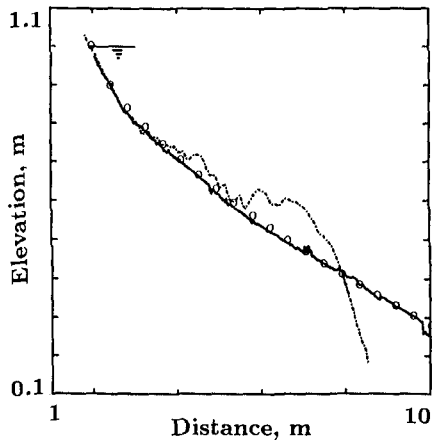


Fig. 4 Equilibrium sand profile (---), design profile (ooo), and initial till profile (—). Water depth = 1 m.

### Scour Hole Formation

The first (exploratory) test series (TS1) was run with a mean water level of 100.0 cm; the most striking observation was the formation of a significant scour hole at the plunge point for a majority of the breaking waves, located in the top till block just below the mean water level. The test began with a large supply (est. 100 L) of 0.51 mm sand on the profile above the top till block. This acted as a sand dune and provided unlimited sand to the till profile for the first few hours of testing. After only 2.08 h of waves, the beginning of the formation of a scour hole from the mean water line to a depth of about 0.18 m was observed. Then, to restrict the sand supply, the sand dune was flattened and then covered with fibrous matting; however, sand was still available by leaking out from under the matting. Sand was being lost from the till surface through gaps at the seams between till blocks; this implies that sand was moving across the till surface. Fig. 5 shows the till profile and rate of change in elevation (erosion rate) at  $t = 8.33$  h at which time only a few sand ripples were left at the bottom of the profile. (In Figures 5 to 13 the solid and dashed lines are the initial and final profiles respectively for the test sequence under discussion; they refer to the left hand vertical axis. The dot-dash line is the erosion rate (right hand vertical axis) and the dotted line is the zero erosion rate.) The scour hole continued to erode rapidly. Over the first 8.33 h the peak erosion rate at the scour hole averaged 13 mm/h; this was the highest rate measured over the entire test program.

The seams were repaired by excavating a narrow trench at each seam, grouting the bottom of the trench, and then backfilling and compacting the seam with remoulded till. A variety of tests were run with and without sand. After 140 h, the till profile is shown in Fig. 6. The scour hole continued to grow in size but the rate of change decreased dramatically.

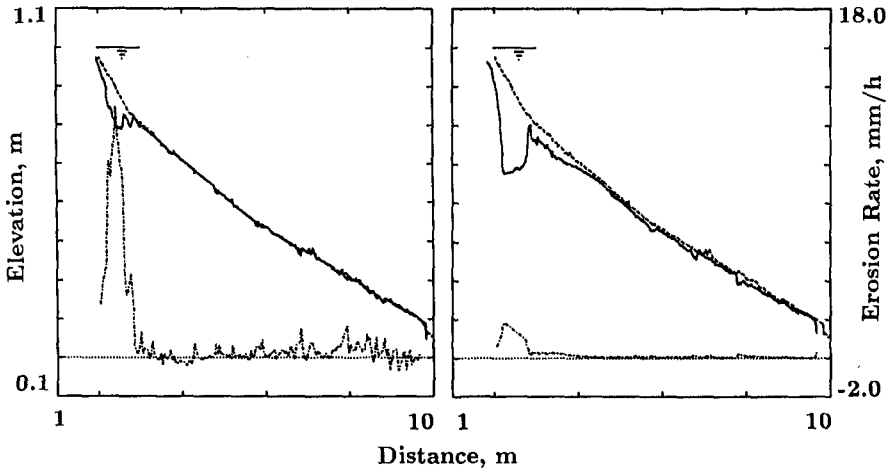


Fig. 5 Till profile and erosion rate after 8.33 h of testing at  $d = 1$  m.

Fig. 6 Till profile and erosion rate after 140 h at  $d = 1$  m.

The second test series (TS2) began with an initial profile that was the eroded profile after 145 h from TS1. In order to avoid effects due to the scour hole, the mean water level was lowered to 85.0 cm. In this and subsequent test series, the test conditions were varied in systematic fashion and the response of the till was measured. At the end of TS1, somewhat less than 8 L sand was left on the profile. This sand moved quickly from  $4 < x < 5$  m to  $5 < x < 6$  m, the latter being the stable sand bar position for the lower water level of TS2. For the first 15 h of TS2, no new sand was added.

The most striking feature of TS2 was that a large scour hole did not form below the MWL as had occurred in TS1. The dominant zone of plunging breakers moved offshore from the scour hole area of TS1 to the region around  $x = 4$  m. In TS1 the scour hole formed where plunging breakers struck an initially steep (1:5.5) till slope. In contrast, for TS2, at the lower water level, the breakers struck a flatter (1:10) initial till slope and were not plunging as intensely.

### No Sand

From the results of unidirectional flow lab tests by Kamphuis (1990), it is known that the erosion rate of till is strongly dependent on the presence of sand in the water. As part of the present study, Kamphuis carried out erosion tests on till samples from Shanks pit in a manner identical to earlier tests of Kamphuis (1988).

When clear water was used to erode the samples, the "critical shear stress" required to begin erosion was about 7 Pa. When sand was introduced into the flow, erosion began at a much lower shear stress of about 0.8 Pa, which corresponds to the threshold for movement of the sand. This indicates that erosion of a cohesive layer subjected to a flow containing some sand begins when the sand becomes mobile as discussed in Kamphuis (1990).

A "no sand" scenario was investigated by draining the flume, washing the till surface, and then running 62.5 h of waves; the only cohesionless material on the profile was that which had been missed in the washing and that which eroded from the till surface during the test. Fig. 7 shows that the erosion rate (note the change in erosion rate scale) is very small (less than 0.2 mm/h); the higher rate around  $x = 4.8$  m is due to some protruding grout having been manually removed. The results agree with the findings of Kamphuis (1990).

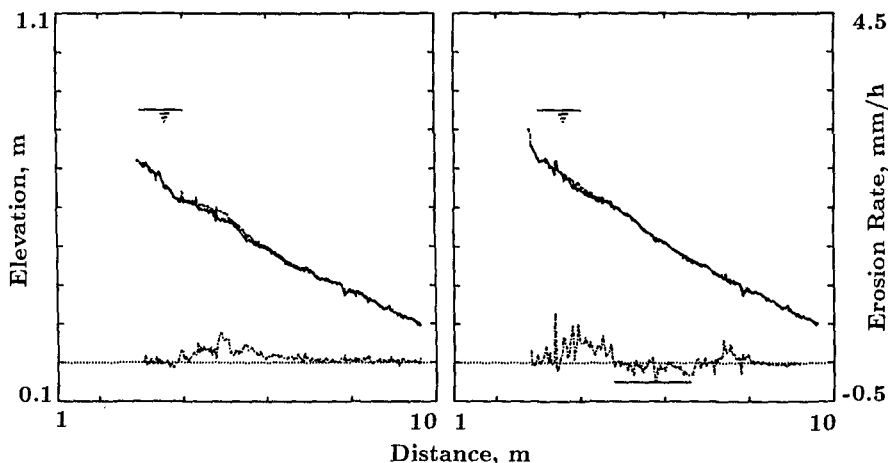


Fig. 7 Till profile and erosion rate after 62.5 h,  $d = 0.85$  m, no sand.

Fig. 8 Till profile and erosion rate after 37.5 h,  $d = 0.85$  m, stationary sand bar.

### Stationary Bar

A stationary bar scenario was investigated by placing 24 L of sand evenly on the profile at  $5 < x < 7$  m; the waves caused a bar to form at the location indicated by the short horizontal line in Fig. 8. Waves were run for 12.5 h, the sand was scraped from the bed and then, after profiling, the sand was placed evenly at  $5 < x < 7$  m again. This sequence was repeated two more times. Over this time Fig. 8 shows virtually no erosion beneath the bar, but some erosion both onshore and offshore; the small accretion rate indicated under the bar is due to some sand being missed when cleaning the till surface. From the results of this and other tests, it has been shown that the presence of a stationary sand layer of 10 mm or more thickness is sufficient to prevent erosion of the underlying till for the wave conditions and grain size characteristics associated with these tests.

### Sparse Sand Cover

A sparse sand cover environment was created by leaving an estimated 2-3 L of sand on the bed after it had been scraped, adding no new sand and running 37.5 h of waves. After this test, the flume was drained, the profile was washed and about 1.5 L of sandy gravel was recovered from the profile and another 0.5 L may have been washed away or missed. Grain size analysis of the recovered material gave  $D_{50} = 1.3$  mm. The profiles and erosion rate for this period are shown in Fig. 9. Clearly, the erosion rate is higher than the case of a stationary bar and the zone of erosion extends across most of the profile, including the former bar location; the null spot around  $x = 4.8$  m is at a hardened seam.

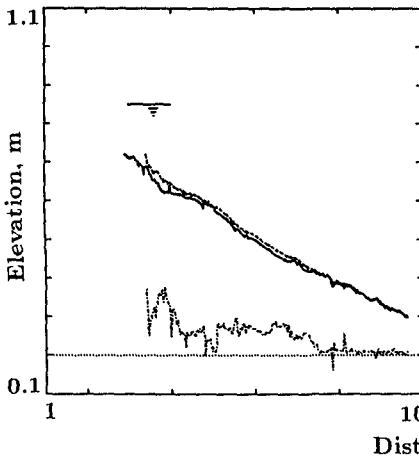


Fig. 9 Till profile and erosion rate after 37.5 h,  $d = 0.85$  m, sparse sand cover.

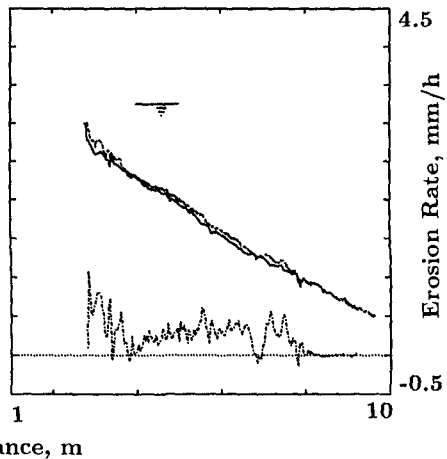


Fig. 10 Till profile and erosion rate after 40 h,  $d = 0.85$  m, recycled bar.

### Recycled Bar

An artificially recycled bar environment was created by adding about 20 L sand at the scour hole, letting it move to the bar location, then scraping it off the bar and placing it in the scour hole again at intervals of 1.25 h. Earlier tests had determined that all the sand moved to its stable bar position within 1.25 h. Fig. 10 shows the erosion rate over this 40 h period. There are null spots around  $x = 3.8$  m and 6.8 m, both at hardened seams, and relatively high erosion rates (up to 0.5 mm/h) out as far as  $x = 8$  m. This scenario is probably fairly representative of three-dimensional conditions in that sand is moving over the profile out to a least  $x = 6$  m and all parts of the profile are fully exposed for some of the time. From the results of this and other tests, the exposure of the till to moving sand, or, expressed another way, the volatility of the sand cover, is an important factor in the erosion process.

**Varying Water Levels**

The objective of this test series (TS4) was to investigate the influence of changing mean water levels on the erosion of the till profile. Tests were conducted at water levels 85, 95, 75 and back to 95 cm. The 8 till blocks used for the first tests were removed and replaced with new till blocks plus an extra one, the ninth, above block 1. The shape of the profile was the same as before, i.e.  $y = 0.18x^{2/3}$ , except that the slope of the top two blocks was reduced to 1:9.4 so as to be the same as the third block, formerly the second block. A sealed wood beach with fibrous matting on top was installed above block 1 at the same 1:9.4 slope.

After 140 h of tests at a mean water level of 85 cm, the mean water level was raised to 95 cm. For the next 60 h waves attacked the profile without any supplementary sand. However, it was observed that quite a lot of gravel eroded from the till and collected over  $3.7 < x < 4.6$  m; gravel filled in any low spots, especially a runnel along the centreline. At 30 h the profile was washed and about 5 L sandy gravel was recovered. For the subsequent 30 h, a recycled bar environment was created again by adding 2 L sand at the mean water level at 3.33 h intervals and scraping the bed underwater at 10 h intervals. After washing the bed, about 5 L sandy gravel was recovered. Fig. 11 shows the profiles at the start and end of the 90 h test with a depth of 95 cm and the corresponding erosion rates. Clearly, the major zone of activity is the upper part of the profile near the mean water line. A distinct scour hole again formed at the upper (steep) part of the profile at the zone of dominant breaking.

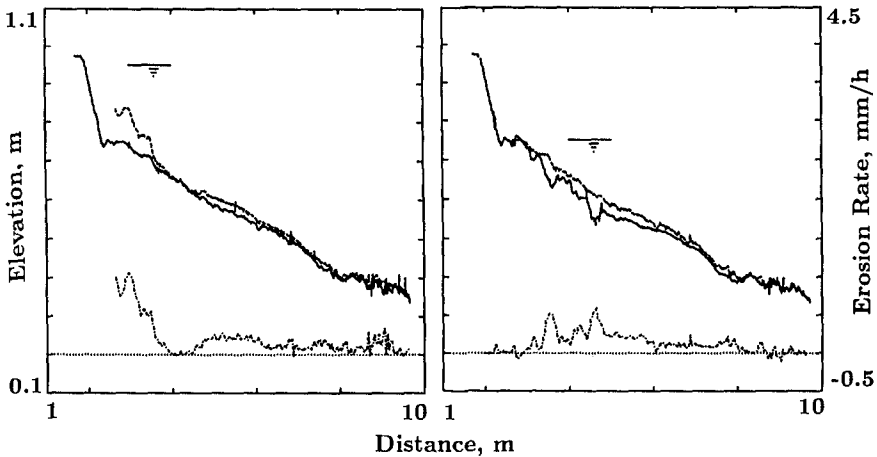


Fig. 11 Till profile and erosion rate after 90 h,  $d = 0.95$  m. Fig. 12 Till profile and erosion rate after 120 h,  $d = 0.75$  m.

After lowering the mean water level to 75 cm, 70 h of waves were run without adding any sand. About 0.5 L of sandy gravel was eroded from the till, and removed by scraping, during each 10 h period. After 70 h the flume was drained and the bed was washed. For the next 50 h, a recycled bar environment was created by

adding 2 L sand just below the mean water line at 3.33 h intervals and scraping the bed underwater at 10 h intervals. Fig. 12 shows the profiles at the start and end of the tests at 75 cm. The major zone of erosion has shifted offshore to the zone of dominant breaking corresponding to the lower water level. The main effect of a change in mean water level is to shift the location on the profile that experiences the breaking waves; for high water, the zone of erosion is further onshore, while for lower water, the zone moves offshore.

The mean water level was raised again to 95 cm and 50 h of waves were run without adding any sand. Fig. 13 shows the beginning and end profiles, and the erosion rate, for TS4 after 400 h (of the series of four water levels). The profile has shifted shoreward and has steepened slightly at its top end. The erosion rate starts near zero around the highest mean water level, quickly reaches a maximum near the dominant plunge point of the breakers at the highest mean water level, then decreases quite uniformly in the offshore direction. These trends agree with the field results depicted in Figure 1.

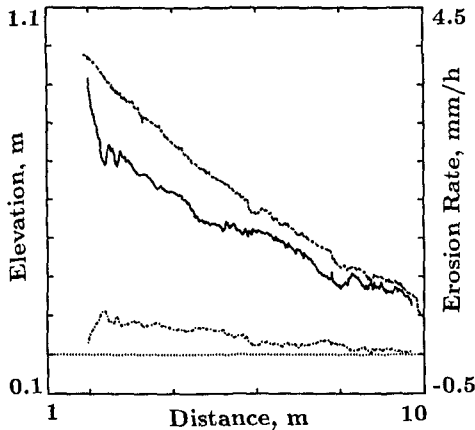


Fig. 13 Till profile and erosion rate after 400 h,  $d = 0.85, 0.95, 0.75$  and  $0.95$  m.

### Numerical Model

A numerical model has been developed to simulate the processes on a cohesive shore profile. The downcutting process of a cohesive profile is more complicated and less well understood than the transport of the overlying sand. The model, first presented by Nairn et al (1986), empirically relates downcutting to two processes: (1) the shear stresses on the bed due to the wave orbital velocities; and (2) the intensity of wave breaking (as indicated by the local gradients in wave energy dissipation across the surf zone) and associated turbulence and jets (due to plunging breakers) impinging on the bottom. The former is dominant outside the surf zone, while the latter is dominant in the surf zone. These concepts are in agreement with the observations that the degree of downcutting increases towards the shore, a result that

cannot be sustained by a model based only on shear due to orbital velocity. Two empirical coefficients are used to relate the downcutting to these processes. The presence of sand overlying the cohesive layer has two distinctly different roles, depending on its thickness. A thin veneer acts as an abrasive agent, increasing the downcutting. A thicker layer, typically greater than 5 to 10 mm in these tests, protects the underlying cohesive material. An updated version of the original model (Nairn 1990) is able to predict the movement of the sand layer over a fixed surface, and so the resultant effects on the cohesive layer can be predicted in the short term. The model upgrade includes the consideration of supply limitation to sediment transport predictions. This type of short term modelling is helpful in developing a better understanding of the erosion processes through an extension of the physical experiments. For long term predictions heavy computational demands of the model and cumulative errors in simulating the sand movement require the use of the model without explicitly accounting for the sand cover, with appropriate coefficients.

Results of the calibration runs for the two types of simulation are shown in Fig. 14 in which the dashed line is the initial profile, the solid line is the experimental erosion rate and the dot-dash line is the numerical model erosion rate. In Fig. 14a, sand cover was explicitly considered in the case of the recycled bar: the relatively high downcutting rates are well represented over most of the surf zone except the very top part. Under the influence of the sparse sand cover the downcutting was reproduced equally well (Fig. 14b) with coefficients that did not take the presence of sand into account. For the sparse sand cover case, the ratio of the values of the coefficients from the two types of simulation indicate that, at any one point, the profile was subjected to downcutting for only 10 to 20% of the time. These numerical model calibration runs provided valuable guidance in extending the numerical work to prediction of the evolution of various cohesive shore types in the Laurentian Great Lakes (Nairn 1992).

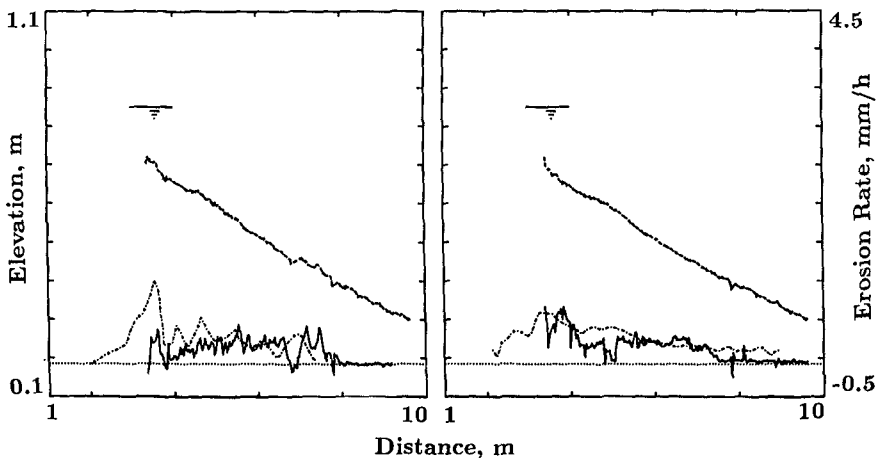


Fig. 14 Till profile (---), lab (—) and numerical model (-.-) erosion rates.  
 (a) After 40 h,  $d = 0.85$  m, recycled bar  
 (b) After 37.5 h,  $d = 0.85$  m, sparse sand cover



## Conclusions

Hydraulic tests of the erosion by waves of a shore profile made of intact till samples have been conducted successfully and have helped to advance our understanding of coastal processes on cohesive shores. The role of sand in the erosion process is very important: in the absence of sand, there is virtually no erosion except where turbulence and/or hydraulic jets reach the cohesive bed; a stationary sand layer of 10 mm thickness or more is sufficient to protect the underlying cohesive material from erosion due to waves tested in this study ( $H_{m0} = 0.3$  m,  $T_p = 0.35$  Hz); and, other factors being equal, the greater the volatility of the sand cover, the greater the erosion rate will be. Long term erosion rates measured inside the surfzone for the wave and water level conditions of this study are of the order of 0.5 mm/h, peaking at the zone of dominant breaking, and decreasing monotonically in the offshore direction. The main effect of varying mean water levels is to shift the zone of dominant breaking up or down the profile: for higher levels, the zone of highest erosion rates shifts onshore, while for lower levels, the zone of highest erosion rates shifts further offshore so that, in the long term, the whole profile tends to maintain an equilibrium shape.

## References

- Bishop, C.T. and Skafel, M.G. 1992. Detailed description of laboratory tests on the erosion by waves of till profiles. NWRI Contribution, National Water Research Institute, Burlington, Ontario.
- Dean, R.G. 1977. Equilibrium beach profiles: U.S. Atlantic and Gulf Coasts. Ocean Eng. Rep. No. 12, Dept. Civil Eng., Univ. of Delaware.
- Funke, E.R. and Mansard, E.P.D. 1984. The NRCC "random" wave generation package. Technical Report HY-002, National Research Council Canada, Ottawa.
- Kamphuis, J.W. 1987. Recession rate of glacial till bluffs. J. Waterway, Port, Coastal and Ocean Engineering, ASCE, 113(1):60-73.
- Kamphuis, J.W. 1988. Competent scour velocity of cohesive soils. Report MAT-88-03, Research and Development Branch, Ontario Ministry of Transportation, Downsview, Ontario. 67 p.
- Kamphuis, J.W. 1990. Influence of sand and gravel on the erosion of cohesive sediment. J. Hydraulic Res., 28(1):43-53.
- Lefebvre, G. and Rohan, K. 1986. On the principal factors controlling erosivity of undisturbed clay. Proc. Symposium on Cohesive Shores, National Research Council Canada, Ottawa, 170-195.
- Mansard, E.P.D. and Funke E.R. 1980. The measurement of incident and reflected spectra using a least squares method. Proc. 17th Int'l. Conf. Coastal Eng., ASCE, 154-172.
- Moore, B. 1982. Beach profile evolution in response to changes in water level and wave height. M.S. Thesis, Univ. of Delaware.

Nairn, R.B., Pinchin, B.M. and Philpott, K.L. 1986. A cohesive coastal development model. Proc. Symposium on Cohesive Shores, National Research Council Canada, 246-261.

Nairn, R.B. 1990. Prediction of cross-shore sediment transport and beach profile evolution. Ph.D. Thesis, Imperial College of Science and Technology, London, England, 391 p.

Nairn, R.B. 1992. Erosion processes evaluation paper. Final Report for the International Joint Commission Great Lakes - St. Lawrence River Levels Reference Study Board. Submitted to Environment Canada, Water Planning & Management Branch, Burlington, Ontario.

## CHAPTER 229

### The Kinematics of Wave Induced Flows Around Near-Bed Pipelines

T.Bruce<sup>1</sup>, W.J.Easson<sup>2</sup>

#### ABSTRACT

Particle Image Velocimetry (PIV) has been applied successfully to give quantitative, full field measurements of instantaneous velocity fields for oscillatory flows past a model of a pipeline above a plane bed. The application of PIV to this problem is discussed, and results for the case of  $KC = 20$  with gap ratios 1.0 and 0.1 are presented in the form of velocity vector maps, and contour plots of vorticity distribution.

#### INTRODUCTION

There is extensive coverage in the literature of research into the fluid loadings experienced by cylindrical structures in a wide variety of flow regimes [eg. Sarpkaya, Isaacson, 1980]. Many studies have focussed on the cyclic variation of drag and lift forces on a horizontal cylinder exposed to wave action. Some of these studies have been extended to investigate the effect of the proximity of a plane bed on cylinder loadings.

Recently, qualitative flow visualisation studies have improved the understanding of loading cycles through wave periods. Williamson [1985] performed simultaneous visualisations and force measurements for a cylinder being oscillated at  $KC$  numbers up to 60, and was able to relate the form of the loading-time curve to the vortex shedding process in a number of distinct shedding regimes. Sumer et al [1991] have extended this work to investigate the influence of a plane boundary close to the cylinder.

The objective of the work reported here was to obtain quantitative, full-field measurements of the kinematics of oscillatory flows past a cylinder near a plane boundary. These flows are unsteady, so building up a quantitative map of the kinematics using a single point measurement technique would be impossible. Attention must therefore be turned to techniques which can measure velocities over

---

<sup>1</sup>Research Associate, Dept. of Mechanical Engineering, The University of Edinburgh, King's Buildings, Edinburgh, EH9 3JL, Scotland. (T.Bruce@ed.ac.uk)

<sup>2</sup>Lecturer, Dept. Mech. Eng (will@mech.ed.ac.uk)

a complete, two-dimensional measurement zone. Established methods such as streak photography which readily give qualitative flow visualisations can be made to yield quantitative data, but the analysis can be laborious and the errors involved are in general large. A technique which suffers none of the above drawback is Particle Image Velocimetry (PIV), and it is this technique's application to oscillatory flows past near-bed cylinders which is described here.

The numerical modelling of unsteady flows past cylinders is becoming increasingly successful. The discrete vortex model has been applied to the flow past a cylinder above a plane boundary [Penoyre and Stansby, 1988] with promising results. However, in order to assess the validity of these models, accurate, full-field quantitative data for the flow kinematics is required. Also, quantitative data of this kind may find use in the modelling of sediment transport and the scour process in the vicinity of a seabed pipeline.

## METHOD

PIV is a relatively new technique which gives a quantitative map of instantaneous flow velocities over a large area. Additionally, the velocities obtained are of high accuracy and high resolution. The basis of PIV is to stroboscopically illuminate a two-dimensional plane through the flow, which has been *seeded* with tiny reflective particles which are assumed to follow the flow accurately. The illuminated plane is then photographed, the shutter being held open long enough to record at least two illuminations. Thus each seeding particle gives rise to at least two particle images. The local flow can then be determined from the separation of these images. A fully automated system is used to *interrogate* the photograph over an array of points to build up a flow velocity map. A detailed description and appraisal of PIV is presented elsewhere in the proceeding of this conference [Greated et al, 1992].

A purpose-built facility has been constructed for these studies, consisting of a rectangular 6m by 1m tank with a water depth of 0.5m, above which runs a computer controlled trolley (figure 1). This trolley tows objects through initially stationary water, and may be programmed to execute complex motion sequences. For the experiments reported here, a horizontal test cylinder (of diameter 50mm) and a false bed were rigidly attached to the trolley and were towed through the tank to give a sinusoidal motion. In general, the flow kinematics resulting from moving an object sinusoidally through initially stationary fluid are identical to those generated by a sinusoidal fluid flow past a fixed object [Garrison, 1980]. However, in the case being studied, it was important that the influence of the bed on the kinematics was correctly included in the tests: In order that the finite length of the false bed did not affect the flows observed, the false bed was more than twice the length of the largest amplitude oscillations.

A two-dimensional plane in the flow is illuminated stroboscopically through the glass bottom of the tank by a 15W Argon Ion continuous wave laser and a *scanning beam* system [Greated et al, 1992, Gray et al, 1991]. The flow is seeded

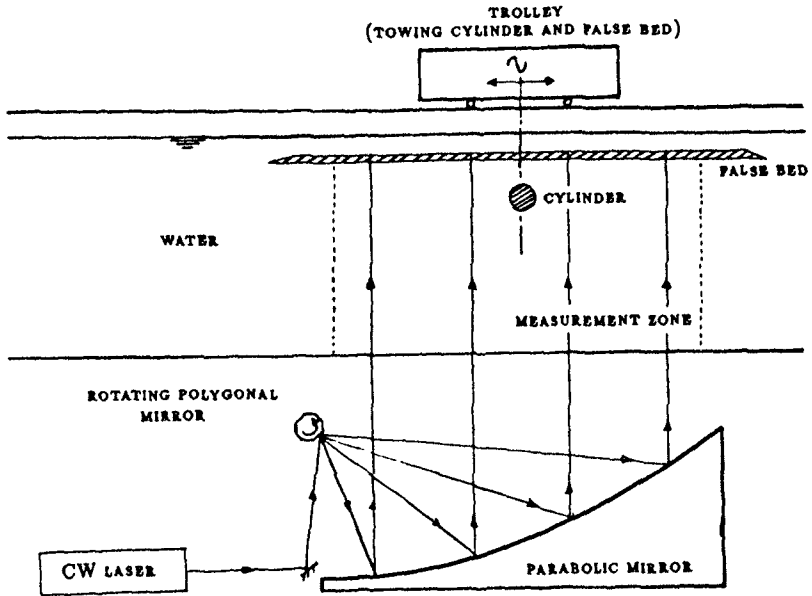


Figure 1: Experimental facility

with conifer pollen and photographed using a Hasselblad *EL/M* medium (55mm) format camera. For these experiments, the camera was triggered electronically from the trolley control system, so that a precise phase of the flow could be selected and captured. Additionally, the camera was panned across the measurement field as the photograph was taken. The reason that it was necessary to pan the camera is as follows:

PIV in its basic form gets velocity information from the separations of double particle images on a photograph. In general there is no way to tell which image is the first, and thus there exists an inherent ambiguity in the sense of the velocity measurement obtained at any given point. In many, indeed most cases, this does not cause a problem; eg in the case of a breaking wave, it is known *a priori* all the motion is in one  $180^\circ$  arc. However, in this application, there are both forward and reverse flows present. Also, PIV in its basic form cannot positively measure a region of zero flow velocity — it relies on measuring the separation of correlated particle images, and if the first and second images overlap, then no correlated separation will be visible and thus no velocity measurable.

Panning the camera as the photograph is taken solves both these problems: As it is being panned, the camera sees the whole flow field as if a large *shift*

velocity had been imposed on the true flow field. The velocities recorded will have this large offset superposed on the true flow. If this *shift* velocity is made sufficiently large, the first particle image will always be to the same side of the second, and particle images which would have been coincident in areas of very low or zero flow velocity are now separated. The shift can be subsequently subtracted from the measured field to give the true flow field. (This *image shifting* technique is analogous to *frequency shifting* in LDA).

## EXPERIMENTAL PARAMETERS

The formation of vortices at the pipeline, and the subsequent motion of these vortices (particularly when they are *swept back* over the pipeline) strongly affect the drag and lift forces on the pipeline. Naturally, the pattern of vortex formation and movement varies a great deal for different flow regimes. The structure of these flows past a smooth pipeline is governed by three dimensionless parameters:

The Keulegan Carpenter number (KC) is defined as

$$KC = \frac{U_m \tau}{D}$$

where  $U_m$  is the magnitude of the maximum velocity of the oscillatory flow,  $\tau$  is the period of the oscillation and  $D$  is the characteristic dimension of the flow; here, the cylinder diameter. Thus the larger KC, the larger the motion of *fluid particles* relative to the size of the cylinder.

The second important parameter is the *gap ratio*,  $e/D$ .

$$e/D = \frac{\text{size of gap between cylinder and bed}}{\text{cylinder diameter}}$$

Finally, the Reynolds number ( $R_e$ )

$$R_e = \frac{U_m D}{\nu}$$

where  $\nu$  is the kinematic viscosity.

The structure of the flow is strongly affected by the combination of KC and  $e/D$ . However, the dependence on  $R_e$  is only weak — all the flows studied here are sub-critical, and the form of the flow is largely independent of  $R_e$  within the sub-critical range of  $R_e$ .

Williamson [1985] studied oscillatory flows past a cylinder in free stream (ie, without a plane boundary) and identified distinct ranges of KC values over which a particular pattern of vortex formation and motion was observed. Sumer et al [1991] reviewed the flow patterns in these regimes for various values of the gap

ratio  $e/D$ . He presents visualisations and loading measurements for  $KC = 4, 10, 20, 30$  and  $e/D$  over the range from 0 to 3.5.

This paper presents results of the first experiments in this study. As such, the work of Sumer et al was considered an excellent starting point. The cases of  $KC = 20$  with  $e/D = 1.0$  and  $e/D = 0.1$  were the first to be studied, and it is these tests that are reported here.

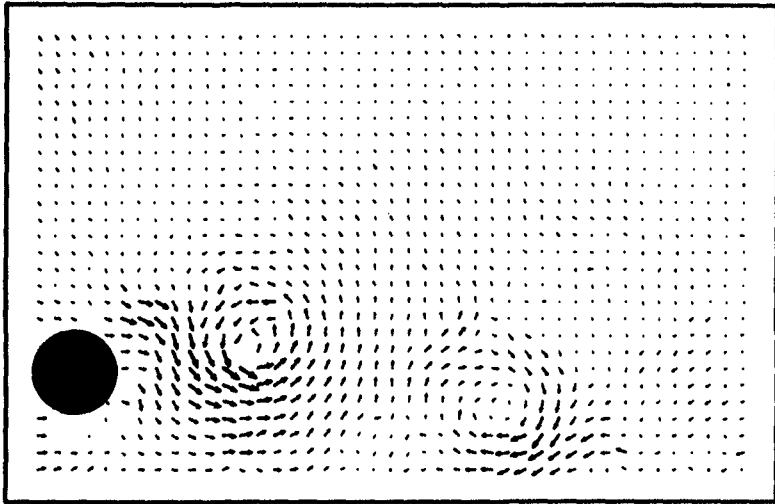


Figure 2: Velocity vectors,  $KC = 20$ ,  $e/D = 1.0$ , phase =  $0^\circ$

## RESULTS

Once the process of obtaining good PIV images has been established for a given application, it is possible to obtain large quantities of data in a short time. Here, there are a large number of flow regimes of interest, each characterised by  $KC$  and  $e/D$  parameters. For each regime, there are a number of interesting events (eg vortex separation) which should be recorded. The results presented here have been chosen to be illustrative of the sort of data obtained. The data is presented in two forms: as velocity vector maps, and as contour plots of the vorticity distribution.

Figure 2 is an example of a velocity vector map. Each of the vectors corresponds to one analysed point on the PIV photograph, so the flow has been measured at around 1000 points from the PIV photograph. No interpolation has been carried out on the data. The map shows the measured flow at the end of one

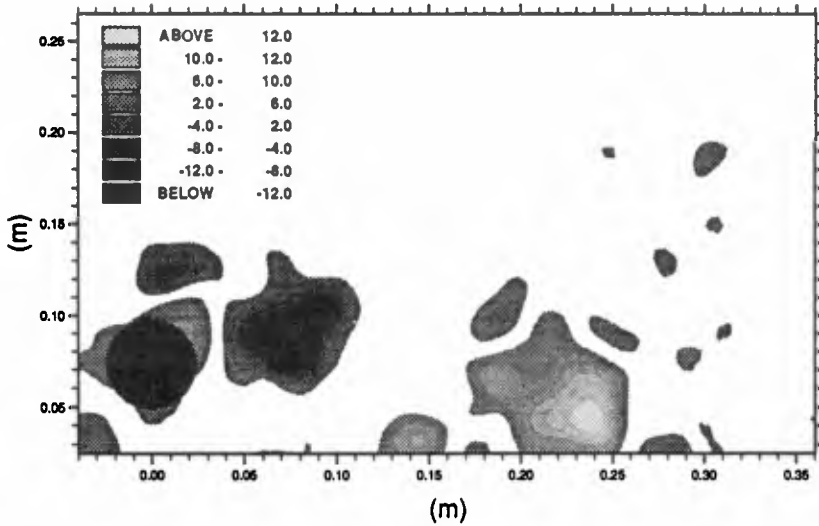


Figure 3: Vorticity,  $KC = 20$ ,  $e/D = 1.0$ , phase =  $0^\circ$

half-cycle for the case  $KC = 20$ ,  $e/D = 1.0$ . The model pipe is instantaneously at rest having moved from right to left over the previous half cycle.

Some interesting features of the flow stand out immediately. There are two vortices clearly visible. The vortex just to the right of the pipe has just been shed. Its rotation is counter-clockwise, so before it was shed, it developed on the side of the pipe adjacent to the wall. In addition to this *wall-side* vortex, there is a second vortex rotating clockwise near the bed whose origin is not clear from this map alone.

An alternative way to present the data is in the form of a map of vorticity distribution. Figure 3 shows the vorticity distribution derived from the same data as shown in figure 2.

The vorticity ( $\Omega$ ) at a point  $(x,y)$  in the field was calculated from

$$\Omega(x, y) = \frac{v_x(x, y + \delta y) - v_x(x, y - \delta y)}{2\delta y} - \frac{v_y(x + \delta x, y) - v_y(x - \delta x, y)}{2\delta x}$$

where the  $v_x(x, y)$  and  $v_y(x, y)$  are the x and y components of the measured velocity at  $(x,y)$ , and  $\delta x$ ,  $\delta y$  is the separation in space between neighbouring ve-



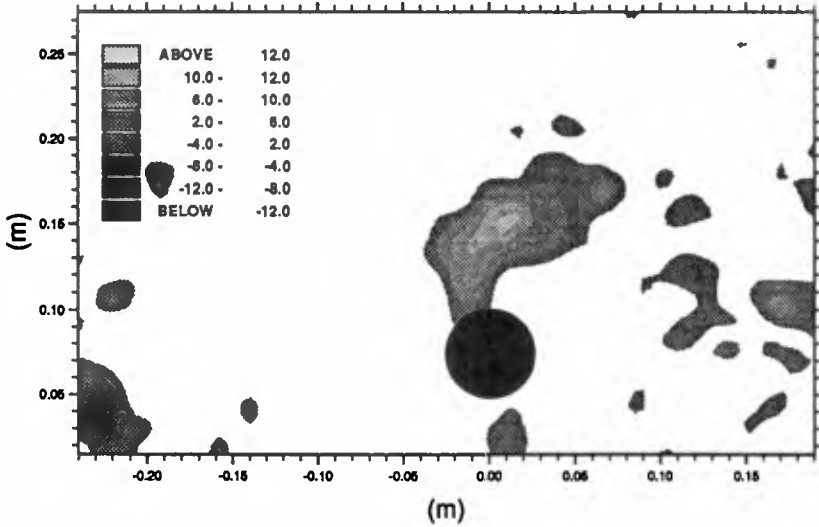


Figure 4: Vorticity,  $KC = 20$ ,  $e/D = 1.0$ , phase =  $270^\circ$

locity points. Such numerical differentiation is very susceptible to errors, but the smoothness of the resulting distribution indicates that these errors are acceptably small.

The white background indicates areas where there is little or no vorticity (or rotation) in the flow. The contoured areas leading to a light centre indicate positive vorticity (clockwise rotation), and the areas leading to a dark centre indicate negative (counter-clockwise rotation). In this case, the structure of the flow is clearly visible on both vector and vorticity maps. However, when there is an area of weak vorticity, this structure often only becomes clearly visible when the vorticity is calculated.

Figure 4 shows the vorticity distribution a quarter cycle ( $90^\circ$ ) before that shown in figure 3, and helps clarify the origin of the large region of positive vorticity visible near the bed in the middle of the previous plots. Here, the pipe is moving from right to left at its maximum velocity of  $200\text{mms}^{-1}$ . It shows clearly a positive vortex being washed over the pipe. It is this vortex which subsequently appears as the rightmost vortex in figure 3. This vortex was the wall-side vortex shed during the previous half-cycle.

When the gap ratio  $e/D$  is reduced from 1.0 to 0.1, the structure of the flow is quite different. Only one vortex (the wall-side vortex) of any size develops

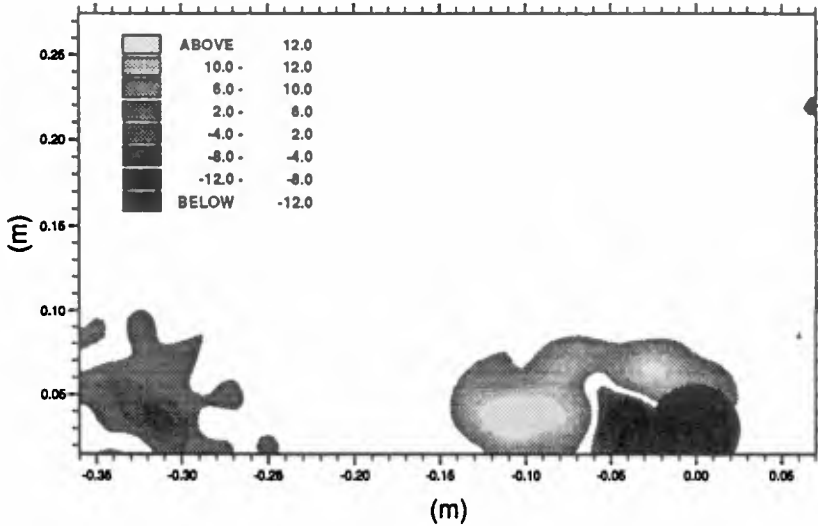


Figure 5: Vorticity,  $KC = 20$ ,  $e/D = 0.1$ , phase =  $165^\circ$

during a half-cycle, and this happens quite near the end of the half-cycle. As the pipe comes to rest and begins to move back on the next half cycle, this vortex is promptly washed back across the pipe. Figure 5 shows the flow as measured at a phase of  $165^\circ$ , just before the end of the left to right half cycle. The wall-side vortex is quite well developed and clearly visible. Also visible is a small area of negative vorticity, lower left of the map. This area is the remnant of the wall-side vortex from the previous half-cycle which was washed over the pipe during the current half-cycle.

## CONCLUDING REMARKS

PIV has been successfully applied to a model of a pipeline above a plane seabed. The quality of the first velocity maps and vorticity contour maps is most encouraging, and detailed comparison with numerically modelled flows should be possible.

In the immediate future, this study will be extended to survey a number of other  $KC$  and  $e/D$  combinations which are representative of the various different flow regimes. It is hoped to place particular emphasis on those flow regimes most relevant to the real coastal environment.

Following the studies of the plane bed, it is intended to move on to investigate

the new kinematics in the case of a scoured bed below the pipeline, and also the case of interaction between cylindrical structures.

## REFERENCES

- Garrison, C.J. (1980).  
*A Review of Drag and Inertia Forces on Circular Cylinders.*  
Proc. 12th Offshore Technology Conference, pp 205-218.
- Gray, C., Greated, C.A., McCluskey, D.R. & Easson, W.J. (1991).  
*An Analysis of the Scanning Beam PIV Illumination System.*  
Journal of Physics (Measurement Science and Technology), 2, pp717-724.
- Penoyre, R.B.S. & Stansby, P.K. (1988).  
*A Computer Program for Simulating Flow Past a Cylinder Above a Plane Boundary.*  
Report of the Simon Engineering Laboratory, University of Manchester.
- Sarpkaya, T. & Isaacson, M. (1981).  
*Mechanics of Wave Forces on Offshore Structures.*  
Van Nostrand Reinhold.
- Skyner, D.J., Gray, C. & Greated, C.A. (1990).  
*A Comparison of Time-Stepping Numerical Predictions with Whole-Field Flow Measurement in Breaking Waves.*  
Water Wave Kinematics, pp491-508, Kluwer Academic Publishers.
- Sumer, B.M., Jenson, B.L. & Fredsøe, J. (1991).  
*Effect of a Plane Boundary on Oscillatory Flow Around a Circular Cylinder.*  
Journal of Fluid Mechanics, 225, pp271-300.
- Williamson, C.H.K. (1985).  
*Sinusoidal Flow Relative to Circular Cylinders.*  
Journal of Fluid Mechanics, 155, pp141-174.

## CHAPTER 230

### MIXING BY SHEAR INSTABILITIES OF THE LONGSHORE CURRENT

J.C. Church<sup>†</sup>, E.B. Thornton<sup>†</sup>, and J. Oltman-Shay<sup>‡</sup>

#### ABSTRACT

Shear instabilities of the longshore current are examined as a possible source of non-zero  $\overline{u'v'}$  values (mixing) within the surfzone. This term is calculated using model generated stream functions whose amplitudes are calibrated with the observed turbulent kinetic energy spectrum. Data from the DELILAH experiment, conducted at the barred beach at Duck, North Carolina is used. Excellent agreement is found between the predicted range of shear instabilities and observations as seen in frequency-wavenumber plots. Maximum predicted values for  $\overline{u'^2}$ ,  $\overline{v'^2}$  and  $\overline{u'v'}$  are .04, .20, and .03 m<sup>2</sup>/s<sup>2</sup>.

#### INTRODUCTION

During 1986 SUPERDUCK, Oltman-Shay *et al.* (1989) observed low frequency oscillations (<0.01 Hz), with wavelengths less than 300m. Free surface gravity waves below 0.05 Hz consist of two classes of waves: edge waves which are trapped by refraction along the beach face, and those which escape seaward as "leaky" waves; these waves have been observed in great detail and are considered "infragravity" waves because of their low frequencies relative to the sea-swell band. The uniqueness of the oscillations observed lies in the fact that the wavelengths observed were an order of magnitude shorter than the shortest infragravity wave under applicable conditions (a function of frequency and beach slope). These oscillations were considered to be kinematically distinct based upon their frequency / wavenumber range.

Energy density distributions represented by gray shading in wavenumber-frequency space for 10 October during the DELILAH experiment are shown in fig. 1. The theoretical dispersion curves for trapped edge waves, modes 0, 1, and 2 are shown for the appropriate beach slope. Significant energy is seen outside of these edge wave curves; this energy is linear in f-K space (where K, cyclic wavenumber, is equal to  $k/2\pi$ ), indicating that these oscillations (considered to be alongshore progressive waves) are non-dispersive. The relationship between the phase speed of these oscillations, given by the wavenumber-frequency slope, and the magnitude

<sup>†</sup> Department of Oceanography, Naval Postgraduate School, Monterey, Ca. 93943

<sup>‡</sup> Quest Integrated, Inc. 21414 - 68th Ave. South, Kent, Washington 98032

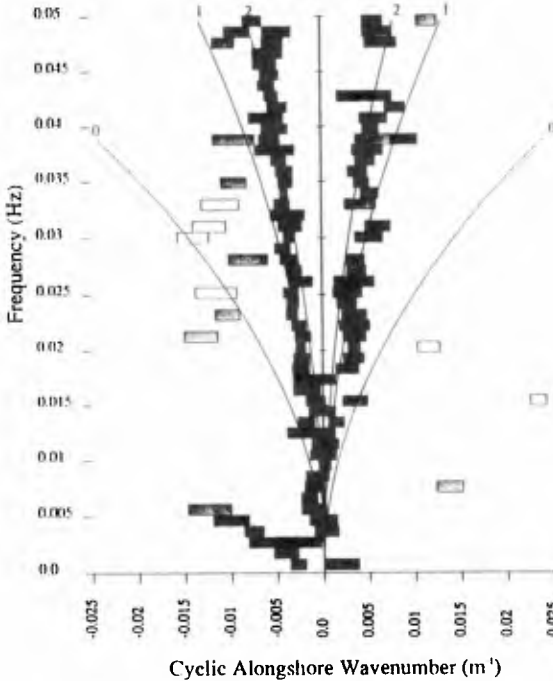


Fig. 1 Frequency-cyclic wavenumber spectrum for 10 Oct. with shading representing log-variance density.  $\Delta f=0.00098$ ,  $\Delta K=0.0005$ . Theoretical edge-wave dispersion curves (modes 0-2) are plotted.

of the mean longshore current, together with the lack of any such oscillations in the absence of mean longshore currents, indicates that the longshore current, and its associated kinetic energy, may be the driving force behind these waves.

Bowan and Holman (1989) formulated a theoretical framework to explain these observations as shear instabilities, deriving a conservation of potential vorticity equation in which the vorticity of the longshore current shear functioned as the restoring force. They also related a phase shift in the stream functions produced by the instabilities to non-zero  $\overline{u'v'}$  values which were suggested as possible sources of significant mixing in the nearshore.

Standard longshore current models (based on an alongshore balance between the radiation stress gradient and bottom shear stress) applied to barred topography predict two current maxima in the form of "jets", the first over the bar, and the second at the beach face. Conversely, observations routinely show a single longshore current maximum, found in the vicinity of the trough. Typically,

longshore current models employ some sort of horizontal mixing term to try to eliminate this disparity. This mixing term is a parameterization of the turbulent radiation stress gradient and is usually described in terms of eddy viscosity. Turbulence is present in the surf zone over a wide range of frequency and spatial scales; in the present work the turbulence (or perturbations) associated with shear instabilities is studied with the specific objective of calculation of the  $\overline{u'v'}$  term, thus avoiding the need for parameterization.

Putrevu and Svendsen (1992) carried out a numerical study of shear instabilities over various topography and using an order of magnitude analysis, concluded that even a weak shear in the longshore current could be capable of producing significant mixing. To quantify this possibility requires calculation of the  $\overline{u'v'}$  associated with the shear instabilities. Unlike non-linear models such as Dodd (1992), which may be used to predict stream function amplitudes, linear models utilize stream functions which are of arbitrary amplitude; thus the predicted velocities, which are based on the gradients of the stream functions, are likewise arbitrary. Calibration of the stream function amplitudes requires one of two approaches. The first, followed in Dodd *et al.* (1992), assumes that the growth rates predicted by the model may be taken as an indication of the ultimate distribution of energy across the wavenumber spectrum. For example, should wavenumber  $k_1$  have a predicted growth rate twice that of wavenumber  $k_2$ , it would be assumed that the steady state energy of  $k_1$  will be twice as great also. Linear theory is then used to relate energy to amplitude squared. This method allows for the inter-comparison of different wavenumbers, but still lacks an absolute reference.

The second method is to measure observed energy at the wavenumbers/frequencies of interest and then scale the stream function amplitudes such that the predicted and observed energies match. This approach does produce an absolute reference and will be used in the current work. The combined  $u$  and  $v$  energies (i.e.  $\overline{u'^2} + \overline{v'^2}$ ) have been used for calibration, being invariant with orientation. Once the stream function amplitudes have been so calibrated, the result is an alongshore averaged profile of  $\overline{u'v'}(x)$  for each wavenumber for which growth is predicted. Integrating these produces a profile which represents the net radiation stress associated with the shear instabilities. Data obtained during the 1990 DELILAH experiment are used to evaluate the magnitude and structure of this term across a barred beach.

## SHEAR INSTABILITY THEORY

### A. Assumptions

Linear wave theory is utilized, with the  $x$ -axis perpendicular to the bathymetry (positive seaward). Both mean and perturbation current velocities are vertically integrated and the mean current is assumed steady state. The longshore current and bathymetry are assumed uniform in the alongshore direction.

### B. Shear Instabilities of the Longshore Current

In the companion paper to Oltman-Shay *et al.* (1989), Bowen and Holman (1989) offered a theoretical basis for shear instabilities. Using conservation of potential vorticity as the restoring force, they were able to relate the mean longshore current shear to observed oscillations.

The momentum equations, with the velocity consisting of perturbations ( $u'$ ,  $v'$ ) and a mean longshore current ( $V$ ) are:

$$1) \quad \frac{\partial u'}{\partial t} + V \frac{\partial u'}{\partial y} = -g \frac{\partial \eta}{\partial x}$$

$$2) \quad \frac{\partial v'}{\partial t} + u' \frac{\partial V}{\partial x} + V \frac{\partial v'}{\partial y} = -g \frac{\partial \eta}{\partial y}$$

where  $\eta$  is surface elevation. These equations are linearized and a non-divergent (rigid lid) approximation is applied allowing the use of a stream function to represent the flow, such that:

$$3) \quad u' = -\frac{1}{h} \frac{\partial \Psi}{\partial y} \quad v' = \frac{1}{h} \frac{\partial \Psi}{\partial x}$$

Cross differentiating to combine equations and eliminate  $\eta$ , the result is:

$$4) \quad \overset{1}{\left(\frac{\partial}{\partial t} + V \frac{\partial}{\partial y}\right)} \overset{2}{\left(\frac{\Psi_{yy}}{h} + \left(\frac{\Psi_x}{h}\right)_x\right)} = \overset{3}{\Psi_y} \overset{4}{\left(\frac{V_x}{h}\right)_x}$$

where the subscripts denote differentiation. Term 1 represents the local rate of change. Term 2 is the advection by the mean longshore current. Term 3 is the relative potential vorticity of the perturbations. Term 4 represents the advection by the perturbations of the potential vorticity of the mean longshore current. This potential vorticity equation is comparable to the barotropic Rossby equation used for planetary scale flow with the exception that the background vorticity of the current shear is substituted in place of the Coriolis parameter.

A solution is then assumed of the form:

$$5) \quad \Psi = \text{Re}\{\phi(x)e^{i(ky - \omega t)}\}$$

where  $\phi$  is the cross-shore structure function. The alongshore wavenumber,  $k$ , is taken to be real, but  $\omega$ , the angular frequency, and  $\phi$  may be complex. The form of the solution which allows growth with time is then:

$$6) \quad \Psi = \exp(\omega_{im} t) \text{Re}\{\phi(x) \exp[i(ky - \omega_{re} t)]\}$$

Inserting this solution in the previous equation yields:

$$7) \quad (V - c)(\phi_{xx} - k^2 \phi - \frac{\phi_x h_x}{h}) - h \phi \left(\frac{V_x}{h}\right)_x = 0$$

where  $c$  is the phase speed of the shear wave, equal to  $\omega/k$ . Dodd *et al.* (1992)

include the dissipative effects of bottom friction through a parameterization,  $\mu=2c_r U_b/\pi$ . The resulting modification of the basic equation produces:

$$8) \quad \left(V - \frac{i\mu}{kh} - c\right) (\phi_{xx} - k^2\phi - \frac{\phi_x h_x}{h}) - h \left(\frac{V_x}{h}\right) \phi + \frac{i\mu}{kh} \left(\frac{\phi_x h_x}{h}\right) = 0$$

The principle result of the inclusion of dissipation is a dampening effect on instabilities as indicated through the model by the reduced range over which growth is predicted. This equation, with  $c_r=0.003$ , is the essence of the shear instability model employed in this study.

After inserting known topography and an *a priori* longshore current profile, this equation takes the form of a quadratic equation in  $\omega$ . This may be written in matrix form as  $[A] \{\phi\} = c [B] \{\phi\}$  which produces the eigenvalues,  $c$ , for each wavenumber. Using  $c=\omega/k$  the real and imaginary parts (should  $\omega$  be complex) may be found. It is the cases when  $\omega_{im}$  is positive that growth is predicted for an instability of that particular wavenumber.

For any instability to grow, (i.e. to have a positive  $\omega_{im}$ ) there must be some source of energy, be it either potential (baroclinic instability) or kinetic (barotropic instability). A mechanism must then exist to transfer this energy from its source, here the longshore current, to the growing perturbation. Dodd and Thornton (1990) derive a set of energy equations to further study this transfer, yielding:

$$9) \quad \frac{\partial}{\partial t} (KE) = - \int_0^\infty \overline{u'v'} V_x dx - g \int_0^\infty \frac{h_x}{h} \overline{u'\eta} dx$$

where KE denotes the kinetic energy of the perturbations and the averaging has been done over the  $y$  direction. The first term on the right hand side represents the role of the Reynolds stresses ( $\overline{u'v'}$ ) in transferring energy and the second term the work done by the surface pressure gradients. This second term can be expected to be small as a result of the ratio of the depth,  $h$ , to the bottom slope in the  $x$  direction. Thus simplified, the required condition for a growing instability is that there must be a negative correlation between  $\overline{u'v'}$  and the shear of the longshore current.

## EXPERIMENT

The 1990 DELILAH experiment, the data from which is the basis of this paper, was conducted at the U.S. Army Corps of Engineers Field Research Facility at Duck, North Carolina, (same site as SUPERDUCK), and was designed specifically to measure shear instabilities. Two alongshore arrays, the first of 5 current meters and located in approximately 1.5 meters of water, monitored conditions in the trough, while the second longshore array, located in approximately 3 meters of water, was positioned on the seaward face of the bar. It is these two arrays which were used in obtaining the normalized, spatially lagged, cross-spectral matrix used with the Iterative Maximum Likelihood Estimator (Pawka 1982) to produce the  $f$ -K spectra. An autonomous Coastal Research Amphibious Buggy (CRAB), which was designed to provide a stable platform for operations within the surf zone, was used for daily bathymetric measurements. A cross-shore array of 9 current meters and wave sensors extending across the surf zone was deployed to define the longshore current. These three principle arrays, shown in figure 2, were



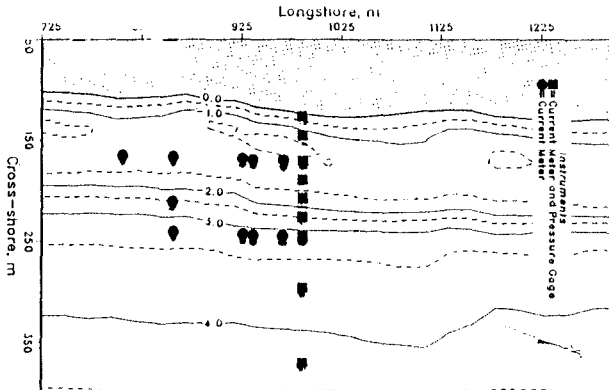


Fig. 2 Meter/gage placement

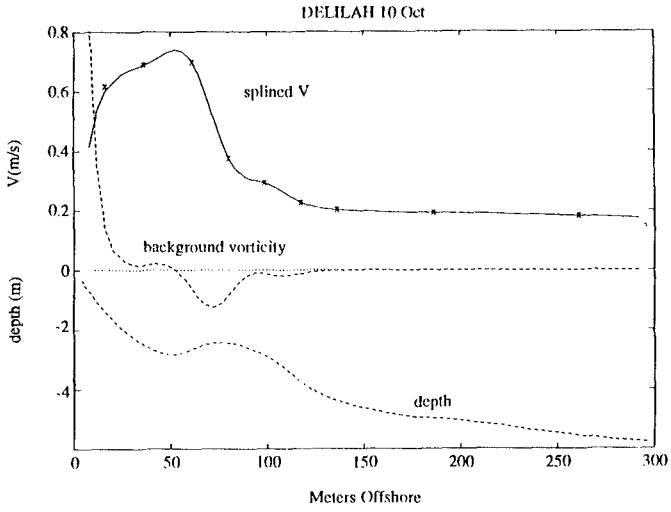
used to acquire data near-continuously throughout the experiment with a sampling rate of 8 Hz. A wide variety of wave conditions occurred during the one month experiment, including a northeaster which drove broad banded waves and a hurricane which generated narrow banded swell, each resulting in strong longshore currents and concomitant shear instabilities.

#### MODEL/DATA COMPARISON

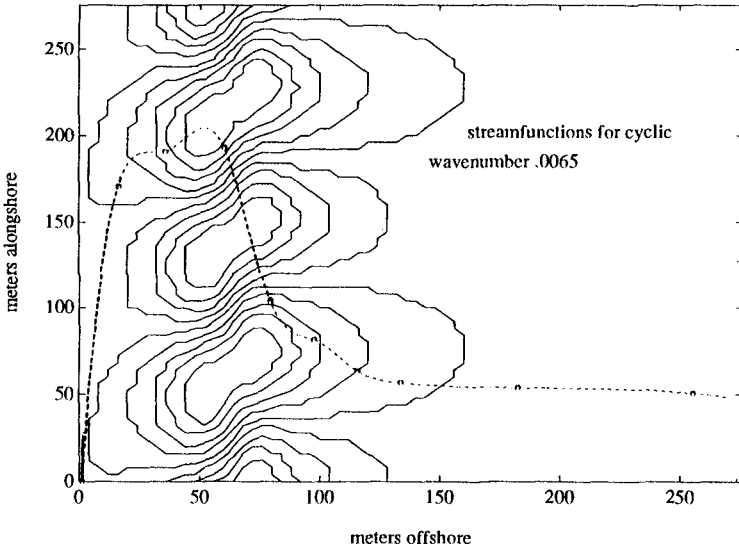
Required as input to the shear instability model is the longshore current profile. In the present work this is obtained through application of a cubic spline to the nine observations. The resulting profile and the measured bathymetry are shown in figure 3 together with the calculated background vorticity (term 4 in eq. (4)). This background vorticity exhibits a relative minima approximately 75 meters offshore. This relative minima corresponds to an elimination of the restoring force and so is the location of the predicted instabilities, an example of which (cyclic wavenumber = .0065) is shown in figure 4. The longshore current profile is overlaid on figure 4 and demonstrates the transfer of energy described by equation (9), (i.e. that the axis of the instabilities are generally opposite to the local current shear).

Predicted growth rate,  $\omega_i$ , and frequency,  $\omega_r$ , (which is linear and therefore non-dispersive) versus cyclic wavenumber are shown in figure 5. Overlaying this predicted dispersion relation on the observed f-K spectra shown in figure 6. demonstrates excellent agreement.

To calibrate the amplitude of the model produced stream functions, the energy density spectra ( $u'^2 + v'^2$ ) were calculated for each of the nine cross-shore current meters. Two hour time series were used with sampling at 8 Hz. The total record length was broken up into 8 sub-records based on the required time interval necessary to produce frequency resolution comparable to that used in the model. An unfortunate result is that the degrees of freedom available remain fairly small and the confidence intervals are therefore excessively large. As an alternative test



**Fig. 3** Splined longshore current velocity profile, measured depth, and calculated background vorticity.



**Fig. 4** Model predicted stream functions and superimposed longshore current profile showing opposing tilt of system as required for energy transfer.

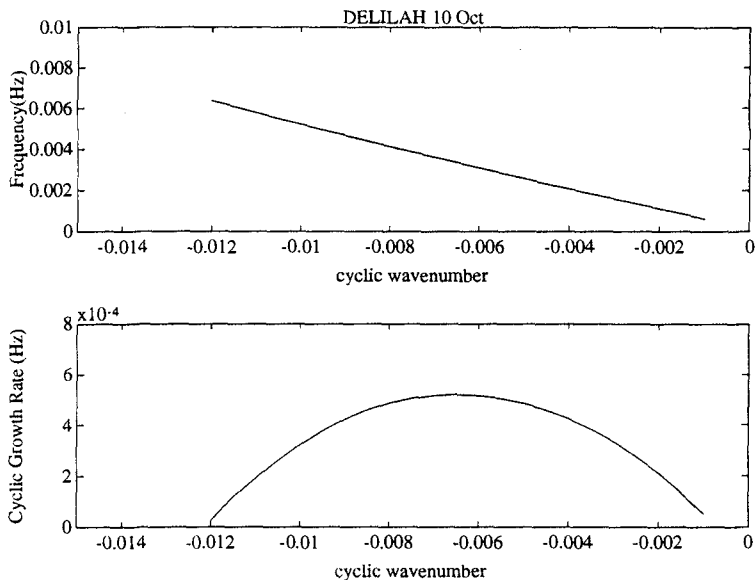


Fig 5. Model predicted frequency ( $\omega_r$ ) and growth rate ( $\omega_m$ ) versus cyclic wavenumber.

of the statistical strength of the data, the consistency over the nine current meters is offered, shown in figure 7. The observed  $u'^2 + v'^2$  as a function of frequency is thus obtained for each of the nine current meters of the cross shore array.

To calculate  $u'^2 + v'^2$  for the model, an analytical solution was obtained by substituting an amplitude variable, A, into eq.(6). The modeled  $u'^2 + v'^2$ , averaged over one wavelength in the alongshore direction can be written then as:

$$10) \quad \overline{u'^2} = \frac{A^2 k^2}{2h^2} (\phi_r^2 + \phi_i^2) \quad \overline{v'^2} = \frac{A^2}{2h^2} \left[ \left( \frac{\partial \phi_r(x)}{\partial x} \right)^2 + \left( \frac{\partial \phi_i(x)}{\partial x} \right)^2 \right]$$

These are combined, providing the modeled  $u'^2 + v'^2$  as a function of cross-shore distance for each of the wavenumbers for which growth was predicted (in this particular case 22). Since the predictions are in wavenumber space, while the observations are in frequency space, the model predicted dispersion relation is used to translate the output into frequency space for comparison.

The observed and predicted  $u'^2 + v'^2$  spectra may each be thought of as an energy surface in two dimensional x-f space. In the case of the observations there are 9 lines of E(f) spread across x, and in the case of the model output, there are 22 lines of E(x) spread across k. The surface given by the model output may be adjusted based upon the values of A(f) and so the two surfaces are matched in a best fit manner. These values of A(f) are then applied to the calculation of  $u'v'$  based on the analytical form (again averaged over the alongshore wavelength) given by:

$$11) \quad \overline{u'v'} = -\frac{A^2 k}{2h^2} \left( \phi_r \frac{\partial \phi_i}{\partial x} - \phi_i \frac{\partial \phi_r}{\partial x} \right)$$

This produces a  $\overline{u'v'}(x)$  profile for each of the modeled wavenumbers. Finally, these are integrated to provide a single  $\overline{u'v'}(x)$  profile representing the net effect of the predicted range of shear instabilities (shown together with  $u'^2$  and  $v'^2$  in figure 8).

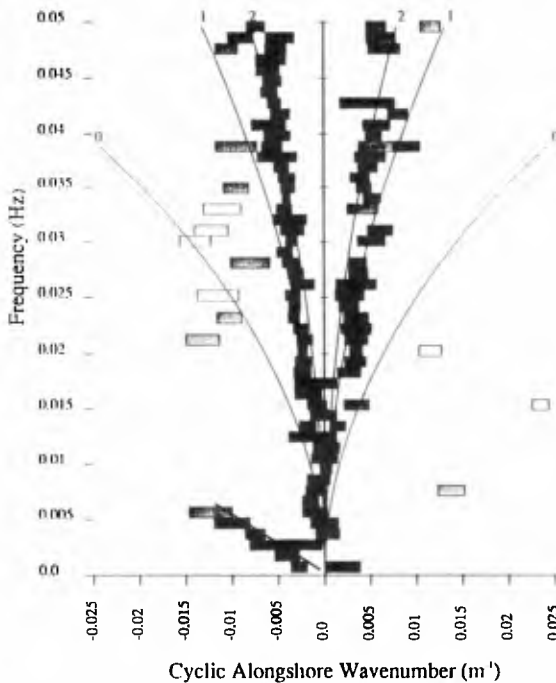


Fig. 6 Same frequency-cyclic wavenumber spectrum as shown in figure 1 with model predicted dispersion relation superimposed.

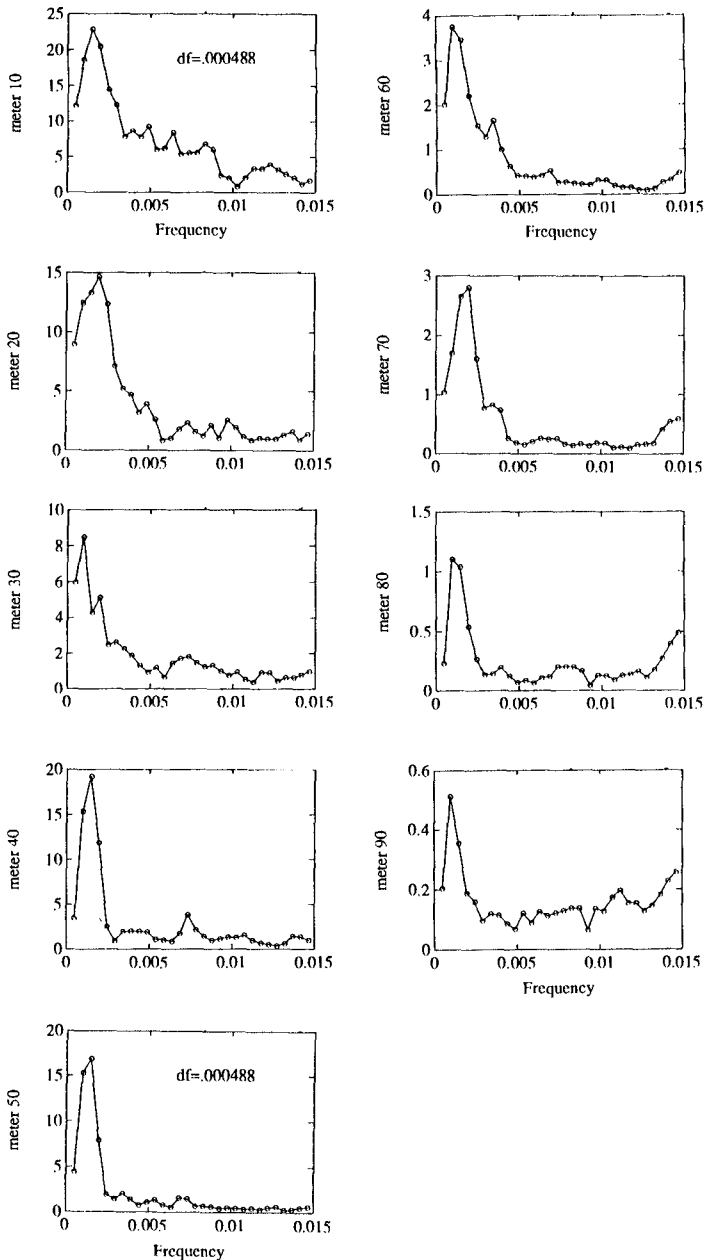


Fig. 7  $(u^2 + v^2)$  energy density spectra over frequency range of interest for each of 9 current meters (cross-shore positioning shown on Figs. 2 and 3).

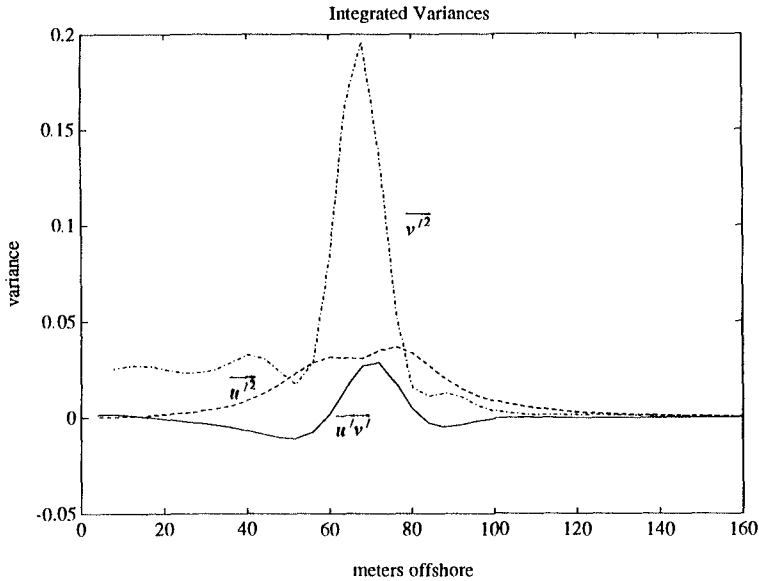


Fig. 8 Integrated  $\overline{u'^2}$ ,  $\overline{v'^2}$  and  $\overline{u'v'}$  profiles based on calibration of model predicted stream functions

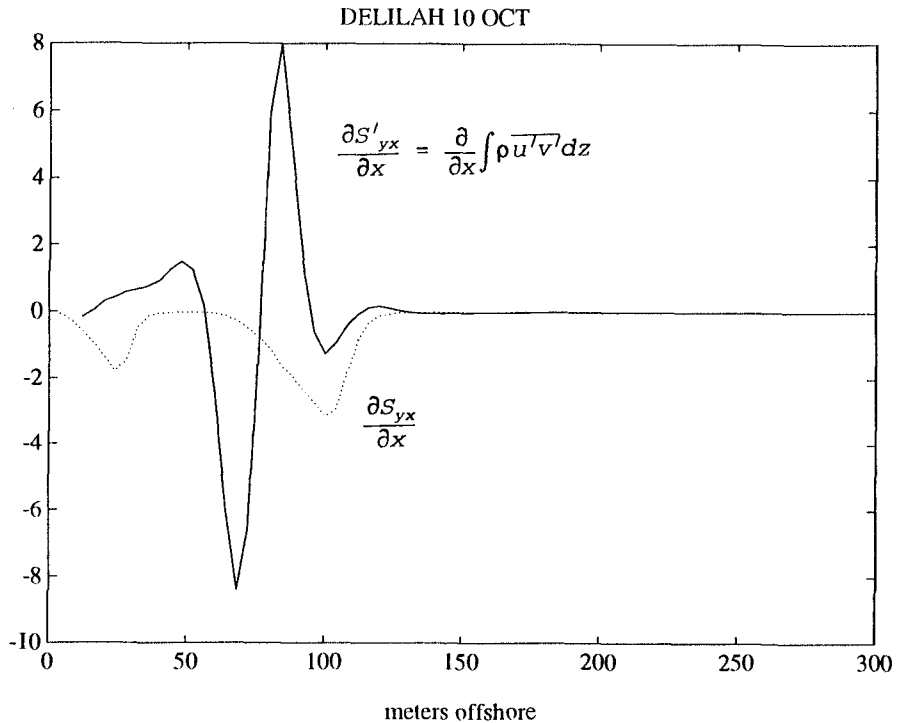
### Summary

The magnitude and cross-shore structure of the turbulent radiation stress associated with shear instabilities of the longshore current has been examined. Through calibration of the model-generated stream function amplitudes, an absolute reference has been incorporated such that dimensional values of  $\overline{u'v'}(x)$  have been obtained. The cross-shore gradients of the radiation stresses due to both waves (calculated through a Thornton and Guza (1983) model) and shear instability turbulence are compared in fig. 9. The model suggests that the turbulence term may well exceed the wave forcing term for this data. Further study will examine additional data from DELILAH and attempt to link the longshore current model predicted "two-jet base state" to the single maximum observed profile, through a series of progressive steps.

### Acknowledgements

The authors wish to express their appreciation to all those who participated in the DELILAH experiment and in particular the staff of the Coastal Engineering Research Center's Field Research Facility, under the direction of Mr. William Birkemeier. Nick Dodd of the Institute for Marine and Atmospheric Research, Utrecht University, is thanked for his initial development of the shear instability model code while formerly associated with the Naval Postgraduate School. In addition, special appreciation is expressed to Rob Wyland, Naval Postgraduate School, and Katie Scott, Univ. of Calif. Santa Cruz, for their roles in acquisition of wave and current data, and to Mary Bristow, Naval Postgraduate School, for

initial processing of the data. EBT was funded by Office of Naval Research Coastal Sciences Grant N00014-92-AF-0002 and JCC is an ONR fellow.



**Fig. 9** Comparison of the model predicted gradients of the shear instability-turbulence radiation stress and the wave radiation stress obtained through a Thornton and Guza (1983) model.

### References

- Bowen, A.J. and R.A. Holman, 1989: Shear instabilities of the longshore current. *J. Geophys. Res.* **94**, 18,023-18,030.
- Dodd, N. and E.B. Thornton, 1990: Growth and energetics of shear waves in the nearshore. *J. Geophys. Res.* **95** (C9), 16,075-16,083.
- Dodd, N., J. Oltman-Shay, and E.B. Thornton, 1992: Shear instabilities in the longshore current: A comparison of observation and theory. *J. Phys. Oceanogr.* **22**, 62-82.
- Dodd, N., 1992: Longshore current instabilities: growth to finite amplitude., *Proc. 23rd Coastal Engr. Conf., ASCE*, (submitted)

Oltman-Shay, J., P.A. Howd, and W. A. Birkemeier, 1989: Shear instabilities of the mean longshore current, 2, Field Observations. *J. Geophys. Res.* **94** (C12), 18,031-18,042.

Thornton, E.B. and R.T. Guza (1983). Transformation of wave height distribution, *J. Geophys. Res.* **88**, 5925-5938.

Thornton, E.B. and R.T. Guza, 1986: Surf zone longshore currents and random waves: Field data and models. *J. Phys. Oceanogr.*, **16**, 1165-1178.

Pawka, S.S., 1982: Wave directional characteristics on a partially sheltered coast. Ph.D. dissertation, Scripps Inst. of Oceanography, UCSD, 246 pp.

Putrevu U. and I.A. Svendsen, 1992: Shear instabilities of longshore currents: a numerical study. *J. Geophys. Res.* **97** (C5), 7283-7303.



## CHAPTER 231

### BOTTOM STRESS MODIFICATION BY BREAKING WAVES WITHIN A LONGSHORE CURRENT MODEL

J.C. Church and E.B. Thornton †

#### Introduction

Early radiation stress models of longshore current generation (Bowen 1969, Longuet-Higgins 1970a, 1970b, Thornton 1970) employing monochromatic wave models produced reasonable cross-shore current distributions over planar beaches, but relied heavily on horizontal mixing for smoothing of the velocity profile. Such mixing is required because the radiation stress associated with the alongshore component of the wave-induced momentum flux,  $S_{yx}$ , is, in theory, conserved outside the surf zone, but at the singular location of breaking predicted for monochromatic waves experiences instantaneous decay, and so an infinite gradient in radiation stress.

Waves observed in nature are seldom monochromatic and so more recent models of wave height transformation employ random wave height descriptions. This randomness is normally invoked through use of a representative statistic, such as  $H_{rms}$ , via either a probabilistic (eg. Thornton and Guza (1983)) or a deterministic/Monte Carlo (eg. Dally *et al.* (1985)) approach. Thornton and Guza (1986) found that for the near-planar beach at Santa Barbara, the distribution of breaker locations produced through such randomness, and the resulting smoothing of the rms-wave height decay, yielded a satisfactory velocity profile without the inclusion of a horizontal mixing term.

The random wave height model is not, however, able to explain longshore currents on barred beaches. The same radiation stress approach which performs well on a planar beach now predicts two maxima in forcing (over the bar and at the shore) and, if mixing is omitted, two maxima in longshore current velocity. This is in direct conflict with observations from the DELILAH experiment, (an acronym for *Duck Experiment on Low-frequency and Incident-band Longshore and Across-shore Hydrodynamics*), which generally show a single maximum in longshore current over the trough, where the radiation stress gradient is near zero.

Most longshore current models assume a spatially constant bottom friction coefficient ( $c_f$ ), which is solved for empirically. Considerable range in the values is found in the literature. Given the extreme variation of fluid flow characteristics across the surf-zone, this assumption of constancy seems perhaps unrealistic. In general, while theories exist relating  $c_f$  to physical parameters such as bottom

---

† Department of Oceanography, Naval Postgraduate School, Monterey, Ca. 93943

roughness and wave steepness (e.g. Jonsson 1967), data suitable to test these theories are extremely sparse.

The present study utilizes non-linear bottom stress in which  $c_f$  is likewise used to relate the free stream velocity to the bottom stress (i.e. the law of the wall), but incorporates the effects of breaking-wave produced turbulence, in that  $c_f = c_{fl} + c_{fr}$ , where  $l$  and  $r$  denote local (bottom boundary layer) and remote (breaking-wave) turbulence effects. In regions of breaking waves, the remotely generated turbulence is hypothesized to be a significant source of vertical mixing of the mean longshore flow and is thus essential to relating the free stream velocity to the bottom stress. Whereas the locally generated (boundary layer) turbulence is limited in magnitude by the restriction of equilibrium between the mixing it induces and the shear which produces it, the mixing potential of the remotely generated turbulence is essentially limitless. The result of this breaking-wave induced mixing is that for a given bottom stress, free stream velocity is decreased (Fig. 1). This modification of the longshore current's vertical profile by the breaking-wave induced turbulence is the essence of the present study. The cross-shore distribution of turbulent kinetic energy (modeled by a simple vertically integrated balance between breaking-wave production and dissipation), combined with a penetration parameter, is proposed to describe the intensity of near bottom breaking-wave induced turbulence, and thereby the modification of the relationship between bottom stress and free stream velocity. Model comparison with data from a barred beach (the DELILAH experiment at Duck, North Carolina) and data from a planar beach (NSTS data from Leadbetter Beach, Santa Barbara, California) yields improved agreement.

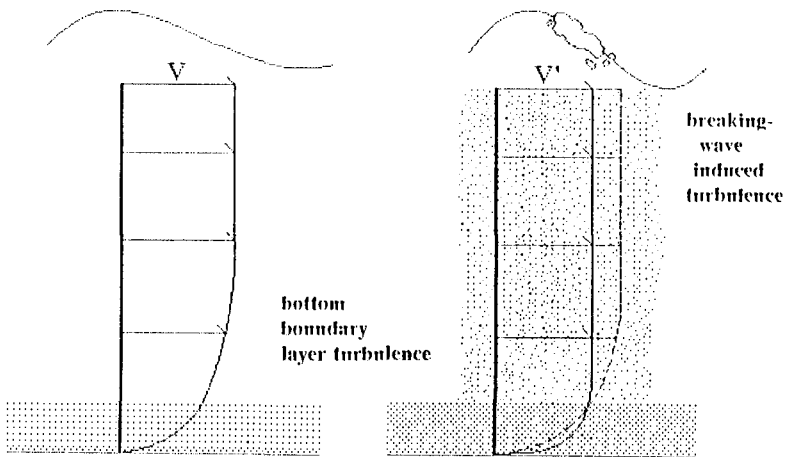


Fig. 1 Schematic of breaking-wave induced turbulence effects on vertical profile of longshore current.

## Longshore Current Formulation

### Assumptions

Linear wave theory is utilized, with x-axis perpendicular to the assumed straight and parallel, but arbitrary, bathymetry. Mean currents are assumed steady state, and are vertically integrated. All quantities are assumed uniform in the alongshore direction. Current shear is assumed sufficiently small that refractive interaction may be neglected. Narrowbandedness is assumed for both direction and frequency of the incident wave field.

### Equations

The time averaged, depth integrated momentum equation in the alongshore direction produces a simple balance between the gradient of the radiation stress and the bottom stress, e.g. Phillips (1966):

$$1) \quad \frac{\partial \overline{S}_{yx}}{\partial x} = \frac{\partial \overline{S}_{yx}}{\partial x} + \frac{\partial S'_{yx}}{\partial x} = \overline{R}_y$$

The radiation stress has been separated into two terms, one associated with the wave motion ( $\overline{S}$ ) and the other due to turbulence ( $S'$ ). It is assumed the wave motion and turbulence are statistically independent of each other. The turbulent radiation stress, typically parameterized as a horizontal mixing term, is neglected. Although mixing is likely to be occurring on numerous scales, driven by numerous mechanisms, the purpose of this study is simply to examine the proposed modification of the bottom stress term. All subsequent references to "radiation stress" will pertain to wave associated radiation stress and the tilde will be omitted.

### *Radiation Stress Forcing*

After applying Snells law for wave refraction based on the assumption of straight and parallel contours, the gradient of the alongshore momentum flux given by linear wave theory may be written as:

$$2) \quad \frac{\partial \overline{S}_{yx}}{\partial x} = \frac{\sin \alpha_0}{c_0} \frac{\partial}{\partial x} (E C_g \cos \alpha)$$

in which energy is given by  $E = \frac{1}{2} \rho g H_{rms}^2$ , with  $H_{rms}$  denoting rms-wave height.  $C_g$  is group velocity and  $\alpha$  is incident wave angle. The subscript o indicates values at some initial point well seaward of breaking. The wave height transformation model of Thornton and Guza (1983) is applied. Two parameters are included in the model;  $\gamma$ , which describes the saturation conditions given by  $\gamma = H_{rms}/h$ , at which all waves are consider to be breaking, and B, a measure of the intensity of breaking as indicated by the portion of the foam region on the breaker face.

### *Bottom Stress*

Neglecting molecular viscosity and surface wind stress, equation (1) becomes a simple balance between the radiation stress gradient and the bottom friction stress.

$$3) \quad \frac{\partial \overline{S}_{yx}}{\partial x} = \tau_y^b$$

The general form of the component of the bottom stress in the alongshore direction is given by:

$$4) \quad \overline{\tau_y^b} = c_f \rho \overline{|\vec{U}|(V+\bar{v})}$$

where the overbar denotes time averaging and  $V$  is the mean longshore current velocity. The magnitude of  $\vec{U}$ , which represents the vector sum of the steady and wave-induced flow is obtained from

$$5) \quad |\vec{U}| = (\bar{u}^2 + 2\bar{u}V\sin\alpha + V^2)^{\frac{1}{2}}$$

where the depth integrated cross-shore mean velocity,  $\bar{U}$ , is assumed equal to zero through conservation of mass. The result is then:

$$6) \quad \overline{\tau_y^b} = \frac{1}{T} \int_T \rho c_f (\bar{u}^2 + 2\bar{u}V\sin\alpha + V^2)^{\frac{1}{2}} (V + \bar{u}\sin\alpha) dt$$

In considering the non-linear form of the bottom stress for the case of random wave heights, specific treatment is required to maintain the ensemble-averaged nature of the radiation stress approach. Specifically,  $\bar{u}$  cannot be solved for based directly on  $H_{rms}$ , but instead the bottom stress for each wave height will be calculated and then ensemble averaged as given by:

$$7) \quad \overline{(\tau_y^b)} = \int_0^\infty \tau_y^b(H) p(H) dH$$

An iterative method described in Thornton and Guza (1986) is used to calculate the longshore current velocity.

Bottom Stress and Free Stream Velocity:

The exact vertical profile of the longshore current within the boundary layer is not required, but it is inherently assumed, in accordance with Prandtl's mixing length hypothesis, that a state of equilibrium exists between the vertical mixing effect of the mechanically generated turbulence and the shear generated through the no-slip condition. In this manner, the friction coefficient,  $c_f$ , not only relates the free stream velocity,  $V$ , to the bottom stress,  $\tau_y^b$ , but also to the characteristic turbulence/friction velocity,  $u_*$ , through:

$$8) \quad \overline{\tau_y^b} = \rho u_*^2 = c_f \rho \overline{|\vec{U}|(V+\bar{v})}$$

In most instances, for homogeneous fluids, the only source of turbulence (as represented by  $u_*$ ) is local mechanical generation linked to the near-bottom current shear. Within the surf-zone, where breaking-wave generated turbulence is present, there are clearly two distinct sources. The intensity of the remotely generated turbulence is not limited by the equilibrium condition and so must be solved for separately. In regions where sufficient remotely produced turbulence is present, its vertical mixing effect may significantly alter the vertical profile of the longshore current. This modification to the relationship between bottom stress and free stream

velocity is included in the proposed model through recognition of distinct components,  $c_n$  and  $c_{fr}$ , producing:

$$9) \quad \overline{\tau_y^b} = (c_n + c_{fr})\rho \overline{|\vec{U}|(V+\vec{v})}$$

Conceptually, for the same free stream longshore velocity, enhanced vertical mixing would increase the velocity near the bed and increase the bottom stress, or conversely, the same bottom stress would be associated with a reduced free stream velocity (see again Fig. 1).

In regions of high breaking-wave induced turbulence penetration,  $c_{fr}$  is expected to dominate, while away from breaking-wave induced turbulence, bottom stress is again governed by the local generation through  $c_n$ . In the present work  $c_n$  will be arbitrarily set to 0.0005.  $c_{fr}$  will be formulated based upon a suggested model of horizontal and vertical distributions of turbulent kinetic energy (tke), a turbulence penetration parameter,  $\chi$ , and a fitting coefficient,  $\Lambda$ .

#### Horizontal Distribution of Turbulent Kinetic Energy:

A one-dimensional turbulent kinetic energy equation (tke- $\epsilon$ ) (see for example Launder and Spalding (1972)) is used to solve for the temporally and vertically averaged breaking-wave induced tke, based on local balance of dissipation and production. Horizontal (cross-shore) advection of the turbulence has been neglected, as in Deigaard *et al.* (1986), based on the small cross-shore net particle velocities considered over the column. Vertical distribution is assumed to be through turbulent vortices injected from the surface, as concluded by Svendsen (1987) in his analysis of experimental data.

The resulting equation is then:

$$10) \quad \frac{\partial(Ec_{gx})}{\partial x} = \rho \int_{-h}^0 c_d \left( \frac{tke}{l_v} \right)^{\frac{3}{2}} dz$$

where the left hand side represents production of tke, and the right hand side, dissipation. Here  $c_d$  is a coefficient taken as 0.08 following Launder and Spalding (1972), and  $l_v$  is the length scale of the vortices estimated as  $0.07h$ , with  $h$  representing depth, following Deigaard *et al.* (1986). Assuming vertically uniform tke and the combining of  $c_d/l_v \approx 1.0/h$ , as done by Roelvink and Stive (1989), integration of (13) yields:

$$11) \quad tke = \left[ \frac{1}{\rho} \frac{\partial Ec_{gx}}{\partial x} \right]^{2/3}$$

#### Vertical Distribution of Turbulent Kinetic Energy:

The vertical distribution of breaking-wave induced turbulence is quite likely non-uniform, but at present is unresolved. Deigaard *et al.* (1991) presents a theoretical model with significant vertical variation, while Svendsen (1987), summarizing a number of field and laboratory studies, found the turbulence to be surprisingly uniform. Different assumptions regarding advection and diffusion are made and the subject appears far from resolved.

The present work reflects this uncertainty in the magnitude of near-bottom breaking-wave induced turbulence through the use of a fitting coefficient,  $\Lambda$ , and a penetration parameter,  $\chi$ , which scales the vertically averaged, wave induced turbulent kinetic energy contribution. This rather crude approach seeks the computational advantage of the assumption of vertically uniform tke, while recognizing that physically there must be some decay in tke close to the bed, ultimately going to zero. Intuitively, one might expect the turbulent penetration to be related to breaker type, with increasing penetration going from spilling, to plunging, to collapsing breakers. A new parameter,

$$12) \quad \chi = \frac{\tan\beta(x)}{gH_{rms0}}$$

is employed. When the product is taken of  $\chi$  and the vertically averaged tke the result is non-dimensional and is proposed to be parameterization of the near bottom mixing effect of the breaking-wave induced turbulence.

The wave height transformation model (Thornton and Guza 1983), which stresses an ensemble view of wave breaking, assumes the wave heights are described by the Rayleigh distribution. Waves may break at any location throughout the surf zone with the likelihood at any given point being some weighted portion of the Rayleigh distribution. Thus, some small portion of the waves might break on the shore side of the bar, a region in which the bottom slope,  $\tan\beta$ , is negative, producing a negative value of  $\chi$ ; use of this parameter in predicting the turbulence penetration would yield non-physical negative values over the shoreward side of the bar. To eliminate this problem with the least disturbance to the relative nature of the parameter  $\chi$ ,  $(\tan\beta+.03)$  was universally inserted in place of  $\tan\beta$ . In all of the cases studied, this was sufficient to ensure positive values throughout the surf zone, (i.e. the shoreward sloping faces do not exceed -0.03). In the planar beach case presented, this is of course unnecessary, but for comparison of the fitting parameter, results with and without this adjustment have been included.

An important point regarding the calculation of either  $\chi$  over barred topography is that near the beach face, where the newly reformed wave rises up to break again, no history of the original wave height is maintained and so the utility of the original  $H_{rms0}$  in such a parameter as  $\chi$  is limited. Instead, it is suggested that a new value of  $H_{rms0}^1$ , i.e. that found over the trough, is used when considering breaking at the beach face. This implies (assumes) that surf characteristics are locally determined and cannot be represented by characteristics measured seaward of some previous breaking region. Values of  $\chi(x)$  at the beach face are significantly increased through inclusion of the trough defined  $H_{rms0}^1$  (175%). Recognition of the relevance of the trough region's  $H_{rms0}^1$  to beach-face breaking is not only significant in the present penetration parameterization, but likewise in any application of a surf parameter on a barred beach. The proposed modification of bottom stress due to the near bottom mixing effect of the breaking-wave produced turbulence is completed by defining:

$$13) \quad c_{fr} = \Lambda \chi(x) tke(x)$$

### Solution Method

A Thornton and Guza (1983) wave height transformation model using bore dissipation theory is used to predict the gradient of cross-shore wave energy flux, used in eq(2) to calculate the radiation stress gradient (which serves as the forcing term in equation eq(3)). Additionally, the penetration parameter (used in eq(13)) is similarly given by the model. The cross-shore distribution of  $tke$  is solved for through eq(11) and is then used in eq(13) to estimate the vertical mixing effect of the breaking-wave induced turbulence. The modification of the bottom stress due to the breaking-wave induced turbulence is then modeled through eq(9). Balancing the radiation stress gradient with the bottom stress in eq(3) allows solution for the longshore current velocity.

### DELILAH Experiment Description

The DELILAH experiment was conducted between October 1 and 21, 1990 at the US Army Corps of Engineers' Field Research Facility (FRF) at Duck, North Carolina, a barred beach which was the site of the previous experiments DUCK 85 and SUPERDUCK. Site selection was based upon the presence of the FRF and its infrastructure, including the permanent directional wave array which the FRF maintains in 8 meters of water, and the relative isolation of the beach. The cross-shore array consisted of 9 current meter/pressure gage stations deployed from the beach face to just beyond the 4 meter contour (Fig. 2). An autonomous Coastal Research Amphibious Buggy (CRAB), was used for daily bathymetric measurements.

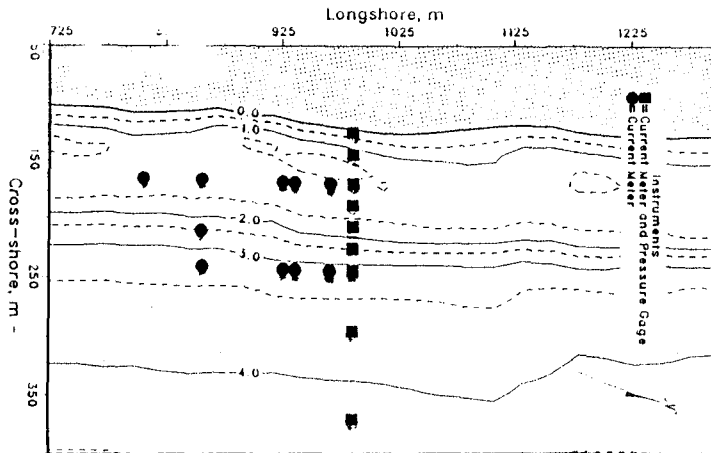
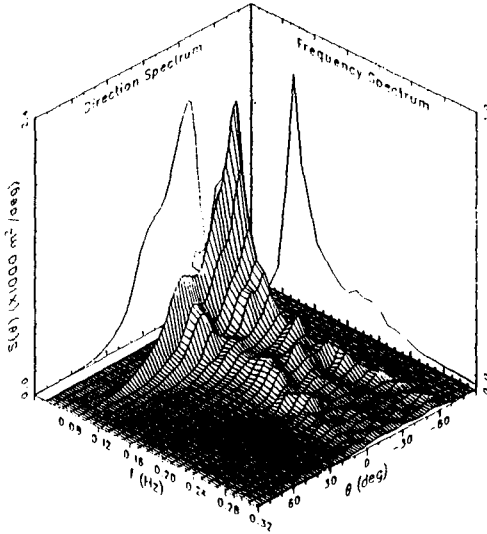


Fig. 2 Meter/gage locations.

Wave conditions on Oct. 10, chosen for model comparisons in the present consisted of an rms wave height of .77m arriving at 16.7 deg. and peak wave frequency of .094. Reasonable narrowbandedness in both frequency and direction can be seen in the two-dimensional energy density spectra (Fig. 3). Measured bathymetry is shown in Fig. 4. Bathymetry for Santa Barbara on 4 Feb is described in Thornton and Guza (1983) and is near planar with a slope of .038.



DELILAH 10 October, 1990

Fig. 3 Frequency/directional energy density spectrum.

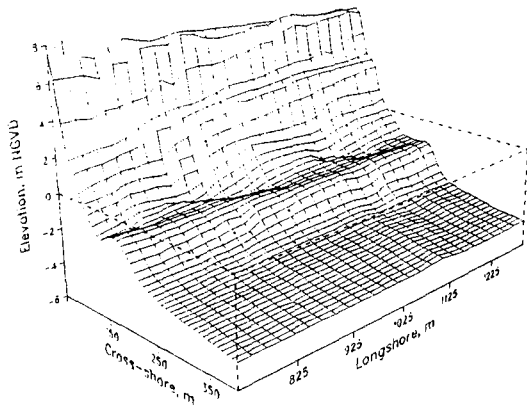


Fig. 4 Measured bathymetry for 10 Oct DELILAH.



## Comparison with Data

Model results are presented in Fig. 5 for Feb. 4 Santa Barbara NSTS data and Fig. 6 for Oct. 10 DELILAH. Each wave height plot contains measured rms-wave height and bathymetry together with predicted rms-wave height and the distributions. Agreement between observed and predicted  $H_{rms}$  is for both days generally good. Values for the two coefficients contained in the wave height transformation model, obtained by fitting the model to the data in a least square sense, are  $\gamma=0.41$  for both days, and  $B=1.28$  for Santa Barbara and 1.30 for DELILAH. Each longshore current plot contains bathymetry and 3 longshore current profiles (one for a linear bottom stress term, one for a non-linear term, and one for the proposed term which is also non-linear, but includes the effects of breaking-wave induced turbulence).

### Longshore Current Modeling

Fitting of the Santa Barbara velocity profiles (Fig. 5), for the two spatially constant  $c_r$  cases, linear and non-linear (without breaking-wave induced turbulence), produces  $c_r$  values of 0.008 and 0.006. The proposed model with  $\Lambda=4.0$  and  $c_n=0.0005$  produces a broader profile with increased velocity on the seaward extreme (where  $c_n$  dominates). The overall result is slightly better agreement with observations. It should be remembered that the adjustment of  $\tan\beta$  necessitated by the bar has been included strictly for comparison and is not physically necessary. Without this adjustment a value of  $\Lambda=7.5$  is found (the resulting velocity profile has been omitted as it is essentially identical to that shown).

In the case of the barred beach (Fig. 6), longshore current profiles for the linear and non-linear (without breaking-wave induced turbulence) cases show maxima at the seaward face of the bar and at the beach face. These are offered for comparison, without fitting, using the values of 0.008 and 0.006 (those found for the Santa Barbara data). Again, none of the velocity profiles include horizontal mixing. For the case of the proposed bottom stress form, fitting of the predicted profiles in the high turbulence regions (the vicinity of the bar and beach face), where  $c_{fr}$  dominates, yields  $\Lambda$  values of 3.0.  $c_n$ , which is important away from the breaking-wave induced turbulence, has been set at 0.0005 arbitrarily in order to demonstrate that significantly lower values may in fact be plausible.

$c_{fr}$  and its two spatially variable components,  $\chi$  and  $k_e$ , are shown in Fig. 7. Sensitivity tests on  $\Lambda$  and  $c_n$  are shown for in Fig. 8. The three profiles of  $V$  shown represent three values of  $\Lambda$  (2.5, 3.0, and 3.5) with  $c_n$  held constant at .0005. It can be seen that the profiles are not overly sensitive to  $\Lambda$  with approximately a 40% change in  $\Lambda$  producing only a 15% change in  $V_{max}$ . The converse situation is also shown where  $\Lambda$  is held constant (3.0) and  $c_n$  is varied. As expected, the changes are found in the trough and seaward of the bar, regions away from the domination of breaking-wave induced turbulence.

## Discussion and Conclusions

The assumption that the relationship between the free stream longshore current velocity and the bottom stress is constant across the surf zone has been brought into question. Field data from DELILAH have been used to demonstrate that inclusion of breaking-wave induced turbulent effects reduces reliance on horizontal mixing for all regions except the trough of a barred beach. In the cases of the two spatially constant  $c_r$ 's (linear and non-linear without wave induced turbulence), current velocities outside the breaking region are greatly under-predicted. Improved agreement with observations is obtained using the proposed form with  $c_n=0.0005$ . Data

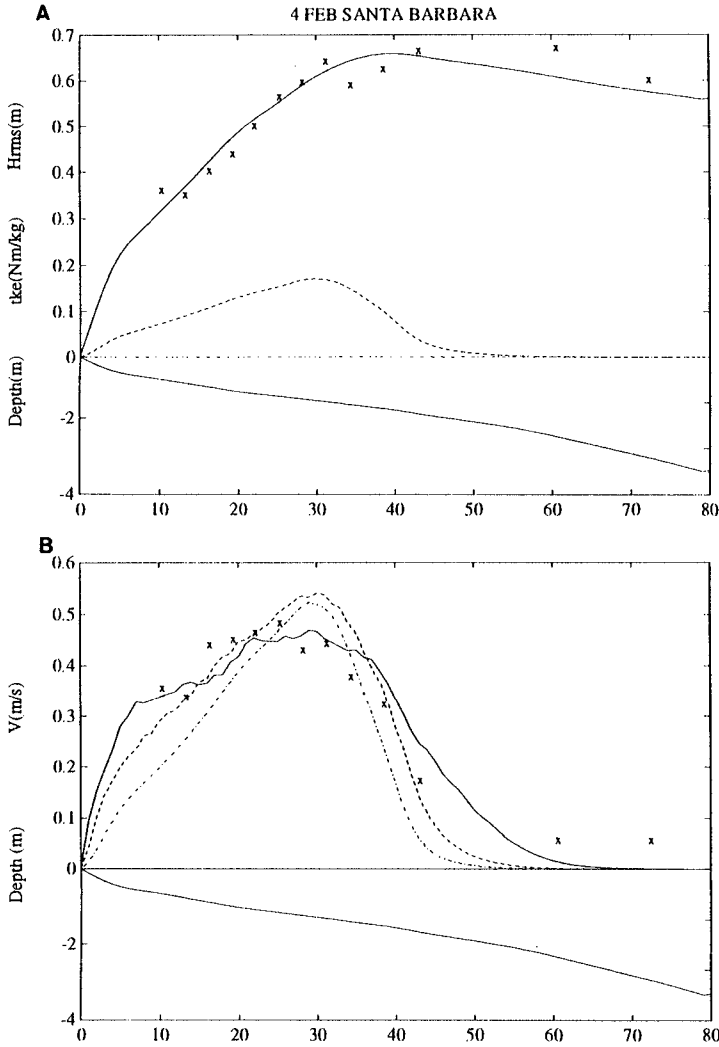


Fig. 5 a) Hrms model prediction (solid), tke (dashed), and measured bathymetry. b) Longshore current model predictions with linear bottom stress (dot-dash,  $C_f=0.008$ ), non-linear (dashed,  $C_f=0.006$ ), and non-linear with wave induced turb. effects (solid,  $\Lambda=4.0$ ,  $C_{fl}=0.0005$ ).

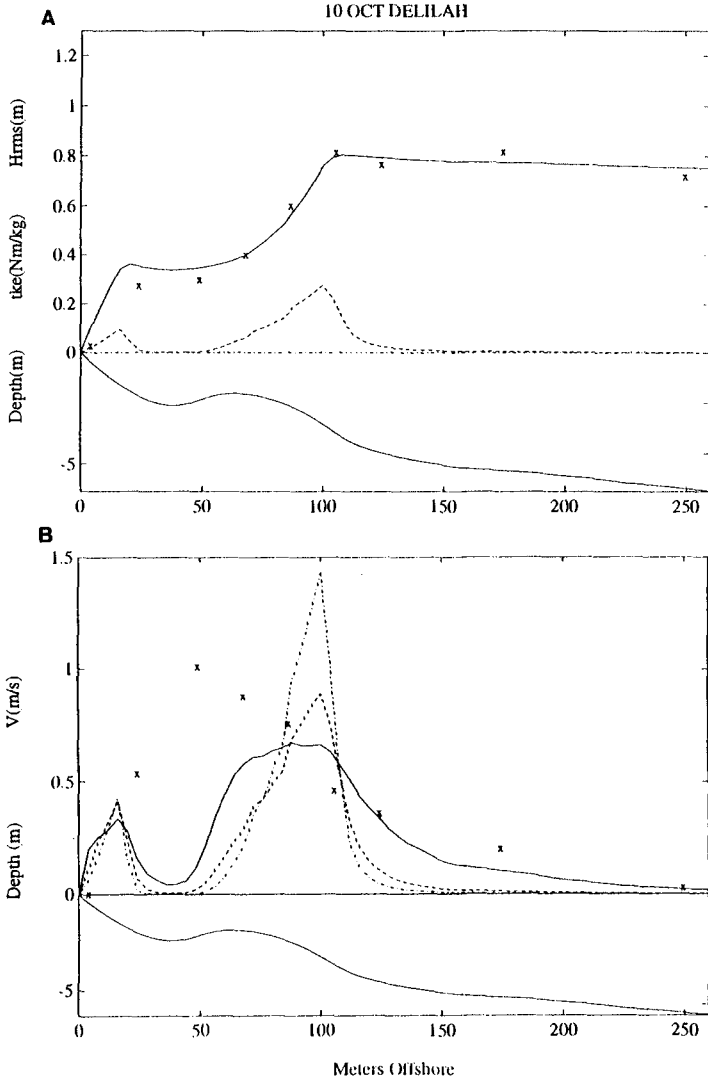


Fig. 6 a) Hrms model prediction (solid), tke (dashed), and measured bathymetry. b) Longshore current model predictions with linear bottom stress (dot-dash,  $C_f=0.008$ ), non-linear (dashed,  $C_f=0.006$ ), and non-linear with wave induced turb. effects (solid,  $\Lambda=3.0$ ,  $C_{fl}=0.0005$ ).

from NSTS Santa Barbara have shown that the proposed model is similarly applicable to planar beaches. Although the calculated value of  $c_n=.0005$ , used throughout this study, is significantly lower than  $c_f$  values used in previous studies, it should be noted that cross-shore mean of  $c_f=c_{fr}+c_n$ , calculated from the shore out to 200m, is .0023 which is more comparable to the spatially constant values found in the literature.

As was noted earlier, horizontal momentum mixing, which has been omitted from the proposed model, does occur to some extent in nature and the contributing roles of mean cross-shore flow and shear instabilities are being explored. Certainly, such mixing would be likely to transfer some longshore momentum into the trough region. It is worthy of note that generation of a velocity maximum between two predicted maxima, via horizontal mixing length theory, requires up-gradient momentum transfer, and therefore does not appear appropriate.

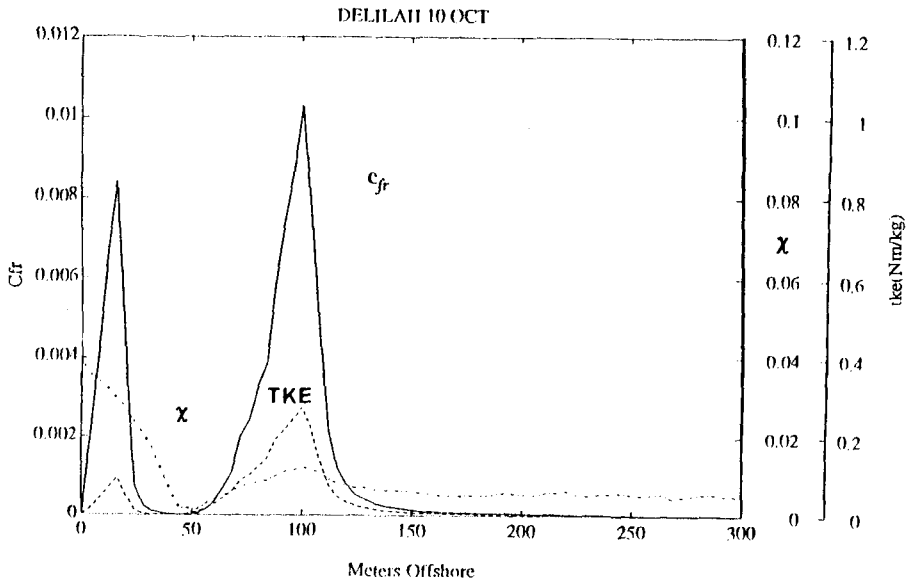


Fig. 7 Bottom friction coefficient associated with breaking-wave turbulence modification ( $C_{fr}$ ) with its principle components  $tke$  and the penetration parameter  $\chi$ .

*Summary:* A spatially variable bottom stress is proposed through the inclusion of the effects of breaking-wave induced turbulence. Employing reasonable assumptions regarding the horizontal and vertical distributions of this turbulence, it is shown that inclusion of breaking-wave induced turbulence effects improves agreement between predicted and observed longshore current velocities for both a planar and barred beach. It is suggested that disparities between predicted and observed velocities over the trough are most likely due to a failure to identify a significant alteration of the forcing mechanism in this particular region.

*Acknowledgements:*

The authors wish to express their appreciation to all those who participated in the DELILAH experiment and in particular the staff of the Coastal Engineering

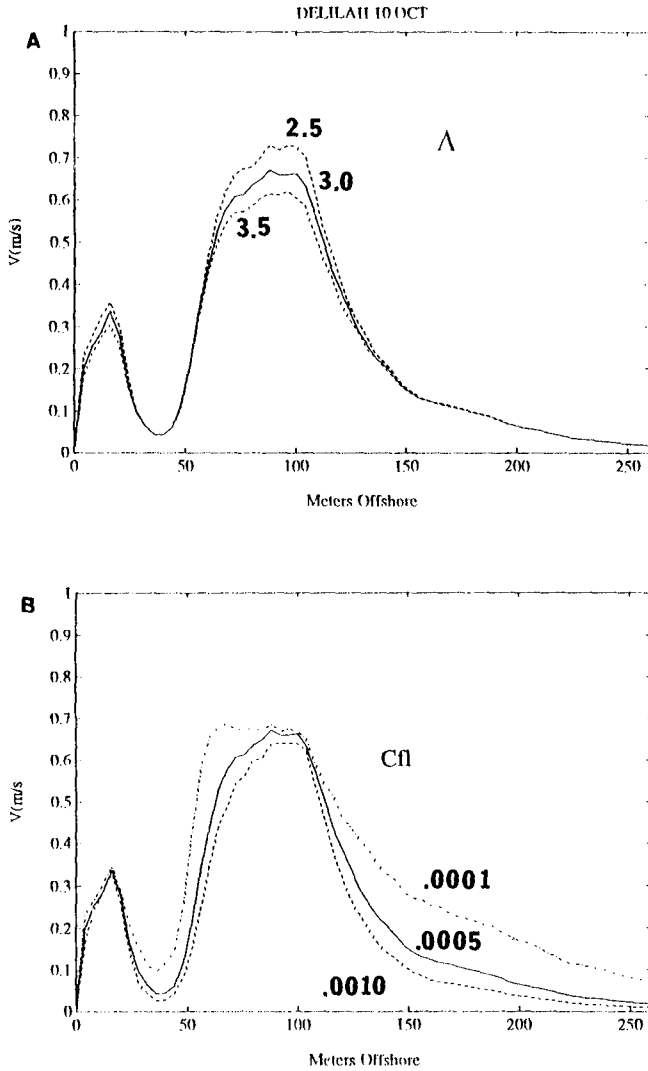


Fig. 8 Sensitivity tests a)  $\Lambda$ ,  $C_{fl}$  held at 0.0005; b)  $C_{fl}$ ,  $\Lambda$  held at 3.0

Research Center's Field Research Facility, under the direction of Mr. William Birkemeier. In addition, special appreciation is expressed to Rob Wyland, Naval Postgraduate School, and Katie Scott, Univ. of Calif. Santa Cruz, for their roles in acquisition of wave and current data, and to Mary Bristow, Naval Postgraduate School, for initial processing of the data. EBT was funded by Office of Naval Research Coastal Sciences Grant N00014-92-AF-0002 and JCC is an ONR fellow.

## REFERENCES

- Bowen, A.J., The generation of longshore currents on a plane beach, *J. Mar. Res.*, 27, 206-215, 1969.
- Dally, W.R., Dean R.G., and R.A. Dalrymple, Wave height variation across beaches of arbitrary profile, *J. Geophysical Res.*, 90(C6), 11,917-11,927, 1985.
- Deigaard, R., Justesen, P, and J. Fredsøe, *Modelling of undertow by a one-equation turbulence model*, Coastal Eng. 15: 431-458, 1991.
- Lauder, B.E., and D.B. Spalding, *Mathematical models of turbulence*, Academic Press, London and New York, 1972.
- Longuet-Higgins, M.S., Longshore currents generated by obliquely incident sea waves, 1. *J. Geophysical Res.*, 75 6778-6789, 1970a.
- Longuet-Higgins, M.S., Longshore currents generated by obliquely incident sea waves, 2. *J. Geophysical Res.*, 75 6790-6801, 1970b.
- Phillips, O.M., *The Dynamics of the Upper Ocean*, University Press, Cambridge, 22-70, 1966.
- Roelvink J.A. and M.J.F. Stive, Bar-generating cross-shore flow mechanisms on a beach, *J. Geophysical Res.* 94(C4) 4785-4800, 1989.
- Svendsen, I.A., Analysis of surf zone turbulence. *J. Geophysical Res.*, 92(C5) 5115-5124, 1987.
- Thornton, E.B. and R.T. Guza, Transformation of wave height distribution, *J. of Geophysical Res.*, 88(C10) 5925-5938, 1983.
- Thornton E.B. and R.T. Guza, Surf zone longshore currents and random waves: Field data and models, *J. Phys. Oceanogr.*, 16, 1165-1178, 1986.
- Thornton, E.B. Variation of longshore current across the surf zone, *Proc. 12th Coastal Engr. Conf., ASCE*, 291-308, 1970.

## CHAPTER 232

### HYDRODYNAMICS AND SEDIMENT CONCENTRATIONS AT WALKER BAY

R C COPPOOLSE, J S SCHOONEES, G G SMITH AND G P MOCKE

#### Abstract

A novel and cost-effective technique for measuring sediment concentrations in high energy surf zones, using a helicopter, was developed and applied at Walker Bay, South Africa. Using this technique, which involved an innovatively operated suspended sediment sampler (TASSS), 280 sediment samples and hours of continuous sediment concentration measurements (with a transmissometer) were acquired at several levels. Currents and waves were also measured at several positions along a cross-shore section. The helicopter was also used to successfully survey the nearshore area using a new method. Spectral analysis of wave and concentration data show responses of the sediment concentration to incident and infragravity waves beyond the surf zone, while suspension is seen to be more intermittent in the surf zone. The concentration profiles beyond the surf zone exhibited typical exponential distributions. Reasonable correlation between the TASSS and the transmissometer was found.

#### Introduction

Knowledge about sediment transport in the nearshore zone is of vital importance for the design of harbours and for the understanding of the processes causing beach erosion and the factors controlling the stability of estuaries. It is against this background that the CSIR undertakes field exercises as part of a research programme. The aims of these exercises (Schoonees, 1990) are to develop low-cost measuring techniques that are capable of measuring in high energy surf zones and to obtain accurate data under South African conditions against which to check the accuracy of predictive techniques.

During a previous exercise in November 1987 (Schoonees, 1990), field measurement techniques were developed to determine suspended sediment concentrations in the inner surf zone. From 12 to 15 and from 19 to 23 February 1990 a fourth field exercise (CAESAR 4) was held at Walker Bay on the Cape South Coast of South Africa (Figure 1) to measure sediment concentrations in the outer surf zone. One of the specific aims of this exercise was to test newly-developed equipment and its deployment procedures, thereby

---

Research Engineers, CSIR, P O Box 320, Stellenbosch, 7599, South Africa

ensuring the capability of measuring sediment concentrations in the outer part of high energy surf zones.

Previous researchers tackled the problem of measuring in the outer surf zone by either deploying instruments from a permanent or temporary pier (e.g. Watts, 1953, Fairchild, 1977, Derks and Stive, 1984 and Antsyferov and Kos'yan, 1990), by using a helicopter (Kilner, 1976) or using a sampler attached to a rope between the shoreline and an offshore anchor (Kilner, 1976). At sites with large tidal variations like in the United Kingdom, it is also possible to deploy instruments in the dry during low tide and then to sample during high tide (Soulsby *et al.* 1990). In South Africa, however, the tidal variations are too small to do this.

It was decided to make use of a helicopter because a pier was not available and would be expensive to construct. In addition, a helicopter is very versatile for other applications during the exercise, (e.g. aerial photographs and survey work) and is useful at remote sites. The helicopter was also used to develop a new technique to measure nearshore profiles.

This paper describes the field exercise, with emphasis on the sediment concentration measurement. Environmental conditions, instrumentation, measuring techniques and finally some results are presented.

### Site Description

Walker Bay, situated about 120 km south-east of Cape Town (Figure 1), is a large sandy bay of about 20 km length, which is completely exposed to the dominant incident southerly to south-westerly deep-sea waves (Schoonees, 1990). The 1 in 1 year and 1 in 100 years deep-sea significant wave heights are 7,6 m and 11,1 m respectively (Rossouw, 1989). Peak wave periods ranged between 5 s and 22 s with a median value of about 12 s. Surf zone widths of up to 500 m are not uncommon.

During the February 1990 exercise, the median grain size of the bed material was 0,30 mm. The slope of the beach face was about 1/16 while the nearshore slope was about 1/90.

Strong longshore currents (often 0,5 m/s) occur regularly. The mean spring tidal range is 1,44 m. The main wind directions are south to east in summer (December to February) and west to north-west in winter (De Decker, 1989).

The layout of the test site is shown in Figure 2. A temporary camp was established just behind the frontal dune where measuring equipment was stored, the helicopter refuelled, water/sediment samples were removed and data from the instrumentation transferred.

### Instrumentation

#### General

Instruments were deployed on a line perpendicular to the shore (Figure 2), in order to measure the cross-shore variation of the wave height, longshore current velocity and the suspended sediment concentration in the



outer surf zone. Outside the surf zone in 20 m of water an Endeco directional wave buoy and a pressure transducer was anchored. A pressure transducer and an array of electro-magnetic current meters (Colbrook meters with discus heads) attached to an H-frame, were jetted into the sandy sea bed by divers at 5 m and 10 m depths .

In the inner surf zone a single current meter was manually installed on a fixed frame. In addition, a helicopter was used to place two frames at different places in the surf zone. One frame contained a pressure transducer and current meter while the second frame contained a "remote controlled" Time Averaged Suspended Sediment Sampler (TASSS), a sub-frame with an array of transmissometers (called Brutus) and a pressure transducer.

Although different sensors have been used to measure instantaneous concentrations (see e.g. Huntley, 1982, Brenninkmeyer, 1974 and Beach and Sternberg, 1988), a transmissometer was chosen for this purposes due to its availability. The Kilner suction sampler (Kilner, 1976) was not used to obtain time-averaged concentrations because it is bulky and as such will disturb the flow and limit the number of samples that could be taken per day.

Because of its reliability and simplicity, it was decided to modify the suction sampler of Nielsen (1984) for deployment with a helicopter.

#### Time-Averaged Suspended Sediment Sampler (TASSS)

The purpose of this sampler was to extract undisturbed water/sand samples at different elevations at a predetermined position so that time-averaged sediment concentrations can be obtained. The actual starting time of sampling was important to correlate the result with the transmissometer at a later stage. The principle of pressure difference between the suction inlet and the air outlet of the sample jars was used to suck in the samples (Nielsen, 1984). The intake velocities (about 1,5 m/s) were checked to give a well-defined relation between measured and real concentrations under field conditions (Bosman, 1982). The sampler was placed landwards of the transmissometer position at the side of the deployment frame in order to minimise the disturbance to the other instrumentation (Figures 3 and 4). In addition, a thin cantilever arm was used from which samples were sucked about a metre away from the main frame (Figure 4). Careful placing of the frame by the helicopter was therefore critical in order to avoid damage to the fragile cantilever arm.

A reliable triggering mechanism was required to initiate sampling as soon as the frame was properly placed on the sea bed and the disturbance to the sediment during placing had subsided. A system of pressurising the sample jars by means of compressed air which is released from a seven litre scuba tank on impact with the water surface was used. Figure 5 shows the pressurising principle in more detail. One common air outlet was used. The triggering mechanism consisted of a float which was attached to a valve on the scuba tank. A lock mechanism was attached to prevent opening and closing of the valve due to wave action after initial triggering. The delay in operation was in the order

of 2 to 3,5 minutes depending on initial pressure in the scuba tank. Considering the relevant settling velocities, this was deemed to be adequate for disturbed bottom sediment to re-settle. The delay in relation to the pressure in the scuba tank was calibrated in the laboratory in 1,3 to 1,5 m tanks and also in a 4,5 m deep pool.

The system was designed so that air bubbles do not disturb the flow regime near the intakes during pressurisation and so that the intake lines are cleared prior to sampling. Special care was also taken in the design to prevent overfilling and subsequent mixing of samples as well as to prevent loss of the samples when retrieving the frame by helicopter.

### Transmissometer

The transmissometer is used to measure sediment concentration continuously, based on the principle of the attenuation of a light beam by suspended sediment. The seven beam transmitter/sensor pairs and the data logger are shown in Figures 3 and 4. These were manufactured at the CSIR. The transmitter housing consists of a PVC tube containing a lens and a light source with its driving circuit. The light shines through a glass window at one end. The receiver housing is similar but slightly longer than that of the transmitter, in order to prevent direct ambient light from reaching a phototransistor and causing erroneous readings. The instrument was operated at a frequency response of 2 Hz.

Since the instrument is sensitive to grain size, it is necessary to calibrate it with the sediment from the site of measurement. The calibration was carried out in a tank in which sand is suspended by the rapid oscillation of a grid. With the use of a pump, the sediment concentrations corresponding to transmissometer readings are obtained, yielding an exponential calibration curve.

The transmissometer is very sensitive to water turbidity due to fine particles. This "background" turbidity had to be removed from the measurements. In addition, the instrument is strongly sensitive to bubbles. Nevertheless, accuracy was sufficient to obtain some useful results.

### Field Procedure

In the inner surf zone a combined pressure transducer and electromagnetic current meter was installed on the sea bed at low tide. Two frames were designed for helicopter deployment. The frames were manufactured from galvanised steel tubing and had overall dimensions of 5 m x 2 m. One frame contained an electromagnetic current meter while the other frame contained the TASSS, transmissometer and a pressure transducer (Figures 3 and 4). Problems that had to be overcome using deployment by helicopter (a small Jet Ranger with a maximum lifting capacity of 450 kg) were:

#### *Placing the frame in a predetermined position*

A series of prisms was connected to the skid of the helicopter and by means of a theodolite and electronic distance meter (EDM) and radio contact

between surveyor and pilot, the pilot could be guided to the correct position. The frame was attached to the quick release hook of the helicopter by means of a rope and swivel connectors. The frame was therefore rotating continuously. The rope was connected to an off-centre arm on the frames (Figures 3 and 4) causing the frame to hang slightly forward (Figures 6 and 7). Before the frame was lowered it was allowed to rotate to the correct position. Thereafter it was dropped on its "back legs" and pushed forward by the waves and the helicopter (Figure 7). Although at this stage the frame was more or less in its correct position, it could still be adjusted by the helicopter. The hoist rope was left in the water with a buoy. This was retrieved with a grip (hook) attached to a thin line by which the rope attached to the frame was pulled up and then reconnected to the helicopter.

### *Stability and strength*

In order to withstand wave impact the frame was given the dimension (in plan) of 5 m x 2 m (5 m perpendicular to the wave crests). The length of five metres was chosen because when lowering the frame in five metres of water (about the maximum placing depth) it was still visible when its "back legs" touched the sea bed. At that stage it could be observed whether the frame was in the correct position and if it would possibly overturn. The 2 m width was chosen as a practical width for stability and for overland transport purposes. The layout of the frame is shown in Figures 3 and 4. To prevent the frame from sinking too deeply into the sand, galvanised steel tubing was used, because this has a relatively large surface area. This also provided the necessary structural strength and caused the least local turbulence. Flat bars were welded on underneath the tubing (Figure 3) to limit the sliding of the frame during deployment. Diving inspections revealed that the frame sank into the sand up to the centre of the bottom tubing.

Weep holes of about 20 mm diameter, were made near the ends of the tubing of the frame. These were covered with permeable cloth preventing sand from entering the tubing but allowing air to escape, thereby improving the stability of the frame. At the same time, these holes allowed the water to run out again when the frame was retrieved so that it was not necessary for the helicopter to have to pick up the added mass of the water.

Five to six deployments were performed over the turn (3 h) of each tide (during which the water level stayed virtually constant). The electromagnetic current meter was first deployed and remained at the same position during the measuring cycle of three hours. The sampler frame was first deployed beyond the surf zone and then subsequently at different positions in the surf zone. Measurements were taken for 20 minutes each time after which the frame was retrieved and sample jars were replaced. The turn around time was about 30 min. Measurements were taken on seven days and 56 helicopter deployments were undertaken in total.

Beach surveys were performed before and after each series of tests. The beach sections were taken by theodolite, EDM and staff with prism. For the nearshore measurements use was made of a 6 m high stand on which three

prisms were attached at the top. This stand was placed in the surf zone by helicopter (Figure 8). Communication between surveyor and pilot was maintained by means of radios. Very accurate surveys were obtained in this way.

## Results

### *Hydrodynamics*

Figure 9 illustrates the prediction of wave height with distance offshore, using the wave transformation model of Battjes and Janssen (1978) and Battjes and Stive (1985) (called the Battjes model hereafter). As can be seen, the model provides a good prediction of the measured values. Furthermore, accurate predictions of wave height and direction, using the refraction model RCPWAVE (Ebersole *et al.*, 1986), were found to compare very well with measurements obtained from the pressure sensors at the 20 m, 10 m and 5 m depths.

### *TASSS*

In total, 280 samples were successfully collected during the 56 deployments. All samples were accurately weighed (to determine the volume) and sediment was separated from the samples. The concentrations were calculated and adapted using the results from calibration tests as presented by Bosman (1982), whereby the measured concentrations were multiplied by a factor of 1,37. The concentrations were subsequently plotted and some typical results are shown in Figure 10.

It can be seen that an exponential distribution exists over the first metre above the sea bed. The samples collected at the highest intake showed relatively high concentrations for that particular day. The reason for this is that the top intakes were sampling only when large waves were passing by, while during lower waves the inlet was exposed to the air. It was often found that the sample jar connected to the top intake was only partly filled.

### *Transmissometer*

Figure 11 illustrates a typical concentration record from the transmissometer in the shoaling region, together with the wave record. Truncation of the concentration record of the lower sensor can be seen; this occurred at high concentrations and in the presence of bubbles. Careful observation shows that the peaks in the sediment concentration record correspond to peaks and troughs in the wave record, indicating a response to wave orbital motion. In addition, an increase in the mean concentration in response to wave groups is evident.

Figure 12a illustrates wave energy spectra and spectra of the sediment concentration in the shoaling region (outside the surf zone) and in the surf zone (measured less than one hour later). In the shoaling region (Figure 12a) a clear peak is evident in the wave energy spectrum at about 0,08 Hz. A second peak can be seen at 0,017 Hz, apparently representing the group-bound infragravity

wave energy. Corresponding to these, clear peaks are evident in the sediment concentration spectrum.

A different situation is, however, evident in the surf zone (Figure 12b). Although an energy peak in the sediment concentration spectrum is evident in response to the incident wave frequency (although somewhat shifted), no clear response occurs at the infragravity wave energy. Rather, an increase in the spectral energy of the concentration with decreasing frequency in the infragravity region towards 0,0 Hz can be seen. Experimentation showed that this type of spectral shape is indicative of intermittent (i.e. non-periodic) sand suspension events.

It is worthwhile to point out that linear spectral analysis of sediment concentrations does have limitations, since the non-linear "spiky" nature of sediment concentration records can cause erroneous energies in the spectrum. This is recognized in the above analysis, which is taken in the context of comparative results between the shoaling region and the surf zone.

Figure 13 illustrates the simultaneously sampled results of the transmissometer and TASSS, averaged over five deployments in the shoaling region under similar wave conditions (depth about 3 m and a significant wave height of about 1 m). The lowest transmissometer result is eliminated from this analysis due to frequent truncation of the record at higher concentrations. As can be seen (excluding the sensor at 1,046 m elevation, which was found to be erratic) the exponential distribution is found from the transmissometer results as is expected beyond the breakers (Nielson, 1984). In the case of the TASSS, an exponential distribution with a similar slope and of the same order of magnitude is found.

Figure 14 illustrates the results of comparisons between concentrations obtained from the TASSS with concentrations measured with the transmissometer. The comparison is limited to cases where the transmissometer record was not truncated due to bubbles or high concentrations. A tendency of the transmissometer to give relatively lower readings at high concentrations is apparent. Over 75 % of the concentrations agree within a factor of four. This type of result is to be expected since the two instruments are approximately 2 m apart, and the timing of their sampling is not perfectly correlated. Huntley (1982) confirms this; he considered that a 50 % agreement between an *in situ* calibration and a laboratory calibration would be a "good match". In a similar comparison, sand flux measured with a streamer trap sampler is compared with measurements from an optical backscatter sensor, OBS (with flow measured with a current meter). Agreement is found within a factor of 3,5 with 68% certainty (Rosati *et al.*, 1991).

#### *Beach and nearshore surveys*

During the exercise seven beach and nearshore surveys were undertaken. The results are shown in Figure 15. It is shown that the largest variation occurred at -0,5 m mean sea level (MSL) to -2 m MSL. A maximum vertical variation of 0,75 m occurred within the seven days. Also clearly shown are the

two offshore bars. These were situated at -3 m MSL and at -1 m MSL. The outer bar was fairly stable while the nearshore bar was highly dynamic.

Reasonable to good correlation was obtained between the helicopter survey and the conventional theodolite and staff method in the regions where the profiles overlapped (Figure 15). It has to be taken into account that the measurements were not done simultaneously nor at exactly the same positions.

### Conclusions

Techniques for measuring in high energy surf zones have been successfully developed. Particularly successful was the use of the helicopter, allowing extreme flexibility and accurate positioning of instrumentation and proving to be cost-effective. In addition, a time-averaged suspended sediment sampler, operating on simple and reliable principles, allowed a large number of samples to be collected in a short time.

Measured wave heights compared favourably with predictions using the Battjes model. Despite some serious limitations, due primarily to truncation of the record and the influence of bubbles, useful recordings were obtained with a transmissometer array, especially with regard to almost instantaneous concentration phenomena. In the shoaling region, sediment suspension due to wave orbital motion and due to wave groups was evident. However, although suspension does occur at the incident wave frequency in the surf zone, it mostly occurs in the form of intermittent events. A further result was the occurrence of exponential distributions of sediment concentrations beyond the breakers. Comparisons of the transmissometer with the TASSS showed that over 75% of the concentrations agree within a factor of four. This type of result is typical of previous, similar studies. Finally a simple yet accurate method was devised to measure the nearshore bathymetry (up to 6 m depth) by means of a helicopter.

### Acknowledgement

The field exercise was a team effort. We would like to thank Messrs J P Möller, F van Dulm, L van der Merwe, A K Theron, C Roux, E Mabile, J de V Serdyn, W Daniels, H J A Davids, Miss J B Crowley and Dr J W Gonsalves for their contribution. A special word of thanks is due to the pilot Mr K Wittle and the flight engineer Mr S Harbottle for excellent flying.

### References

- Antsyferov, S M and Kos'yan, R D (1990). Study of suspended sediment distribution in the coastal zone. *Coastal Engineering* 14: 147-172.
- Battjes, J A and Janssen, J P F M (1978). Energy loss and set-up due to breaking of random waves. *16 International Conf. on Coastal Eng.*, ASCE, Hamburg Vol. 1: 569-587.
- Battjes, J A and Stive, M J F (1985). Calibration and verification of a dissipation model for random breaking waves. *J. of Geophysical Research*, Vol 90(C5) : 9159-9167.
- Beach, R A and Sternberg, R W 1988. Suspended sediment transport in the surf zone: Response to cross-shore infragravity motion. *Marine Geology* 80: 61-79.
- Bosman, J J (1982). Concentration measurements under oscillatory water motion. *Report M1695*, Part II, Delft Hydraulics Laboratory, Delft.

- Brenninkmeyer, B M (1974). Mode and period of sand transport in the surf zone. *14 International Conf. on Coastal Eng.*, ASCE, Copenhagen, Volume 2 : 812-827.
- De Decker, H P (1989). Estuaries of the Cape: Part II: Synopses of available information on individual systems. Report No. 40 Klcin (CSW16). Heydorn, A E F and Morant, P D (eds). *CSIR Research Report 439*, Stellenbosch, South Africa, 89 pp.
- Derks, H and Stive, M J F (1984). Field investigations in the TOW Study Programme for coastal sediment transport in the Netherlands. *19 International Conf. on Coastal Eng.*, ASCE, Houston, Texas, Vol. 2 : 1830-1845.
- Ebersole, B A, Cialone, M A and Prater, M D (1986). Regional coastal processes numerical modelling system; Report 1 : RCPWAVE - A linear wave propagation model for engineering use. *Tech. Rep.* CERC 86-4, U S Army, Corps of Engineers, Washington DC, 155 pp.
- Fairchild, J C (1977). Suspended sediment in the littoral zone at Ventnor, New Jersey and Nags Head, North Carolina. *Report TP 77-5*, U S Army, CERC, Fort Belvoir, 97 pp.
- Huntley, D A (1982). In situ sediment monitoring techniques. A survey of the state of the art in U S A. *Report No C2S2-1*, Canadian Coastal Sediment Study, Dalhousie University, Halifax, N.S., 35 pp.
- Kilner, F A (1976). Measurement of suspended sediment in the surf zone. *15 International Conf. on Coastal Eng.*, ASCE, Honolulu, Hawaii, Vol. 2 : 2045-2059.
- Nielsen, P (1984). Field measurements of time averaged suspended sediment concentrations under waves. *Coastal Engineering*, 8 : 51-72.
- Rosati, J D, Gingerich, K J, Kraus, N C, McKee Smith, J and Beach, R A (1991). Longshore sand transport rate distributions measured in Lake Michigan. *Coastal Sediments '91*, ASCE, Seattle, Washington, Vol. 1 : 156-169.
- Rossouw, J (1989). Design waves for the South African coastline. *Ph.D. Thesis*, University of Stellenbosch, South Africa.
- Schoonees, J S (1990). Field measurements of suspended sediment concentrations in the surf zone at Walker Bay. *Proceedings of Euromech 262 Colloquium on Sand Transport in Rivers, Estuaries and the Sea*, Wallingford: 131 - 138.
- Soulsby, R L, Atkins, R, Waers, C B and Oliver, N (1990). Field measurements of suspended sediments over sand waves. *Proceedings of Eromech 262 Colloquium on Sand Transport in Rivers, Estuaries and the Sea*, Wallingford: 155 - 162.
- Watts, G M (1953). Development and field tests of a sampler for suspended sediment in wave action. *Technical Memorandum No 34*, Beach Erosion Board, Corps of Engineers, U S Army.

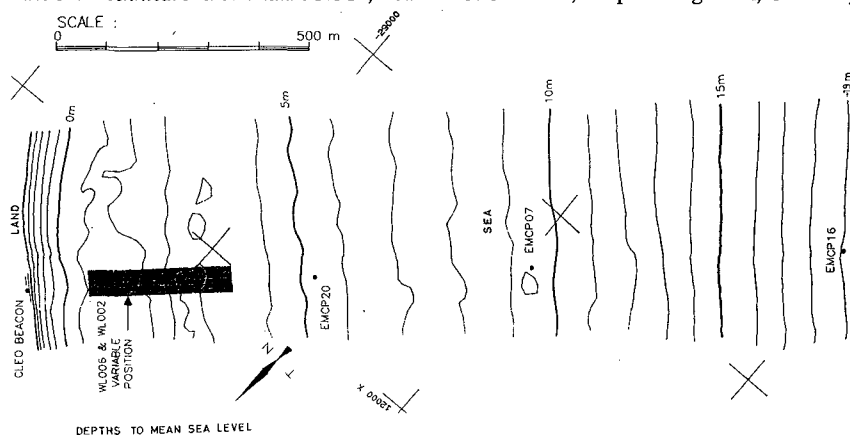


Figure 2. Field experiment layout

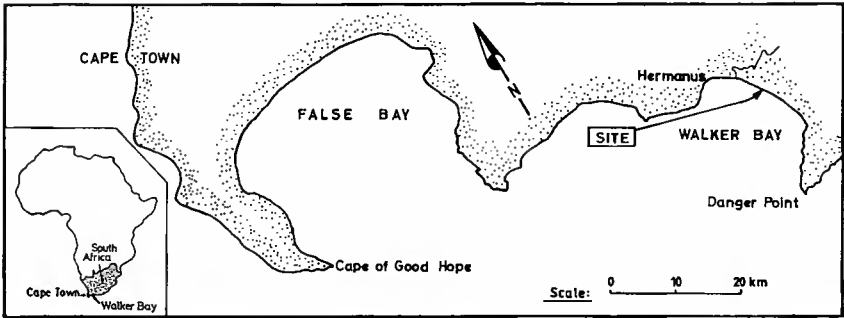


Figure 1. Locality map

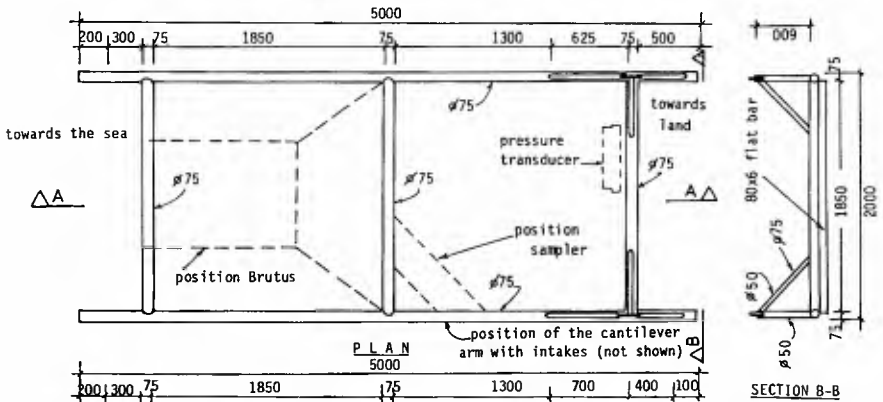


Figure 3. Details of the deployment frame

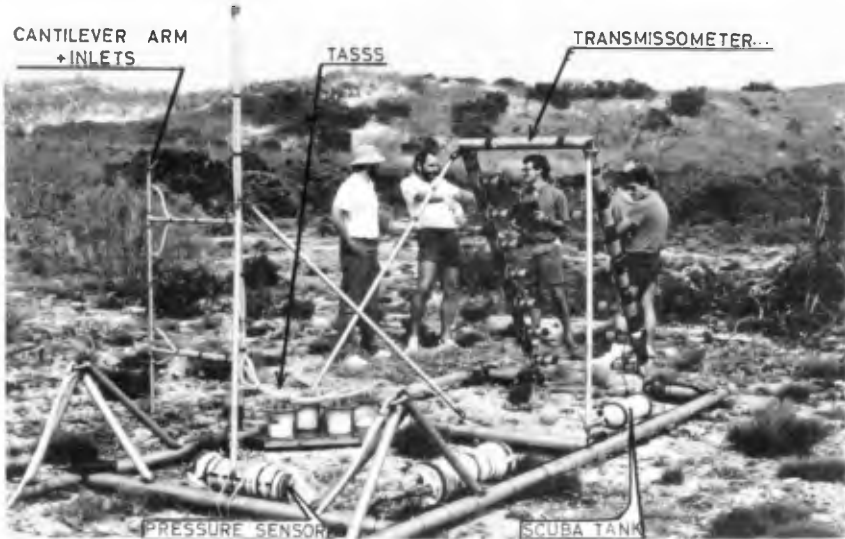


Figure 4. Deployment frame and instrumentation



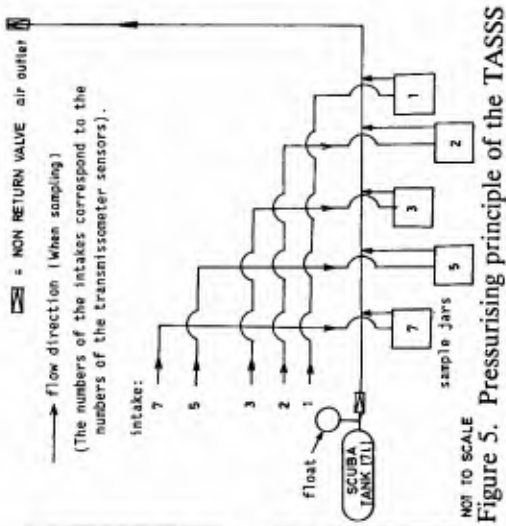


Figure 5. Pressurising principle of the TASS



Figure 7. Placing of the deployment frame



Figure 8. Survey stand deployment

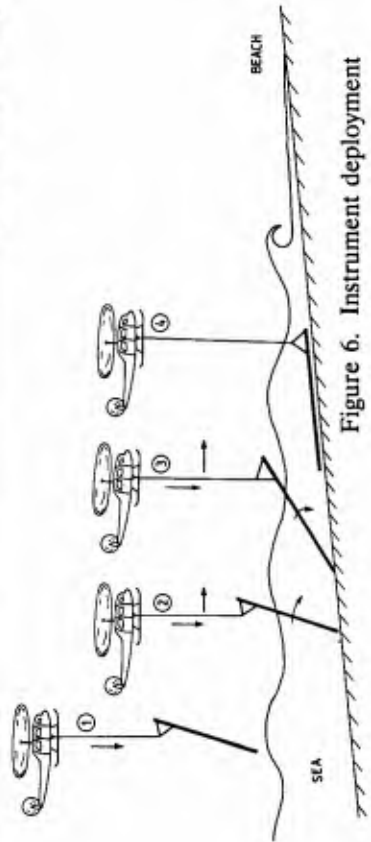


Figure 6. Instrument deployment

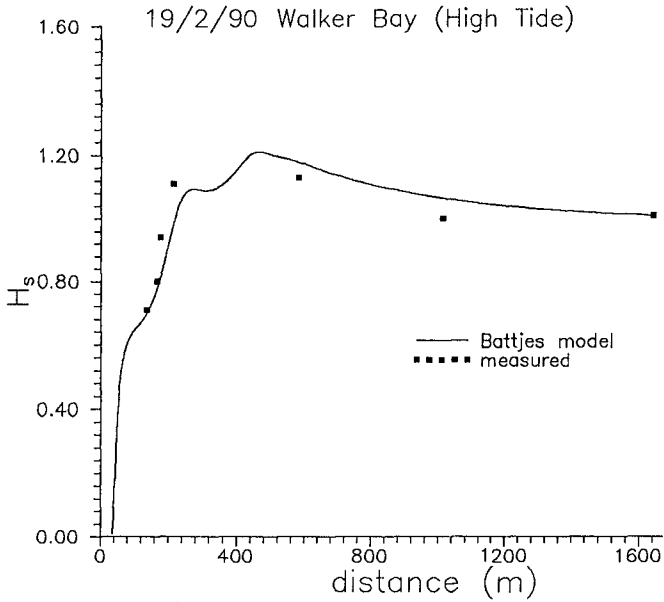


Figure 9. Nearshore wave transformation.

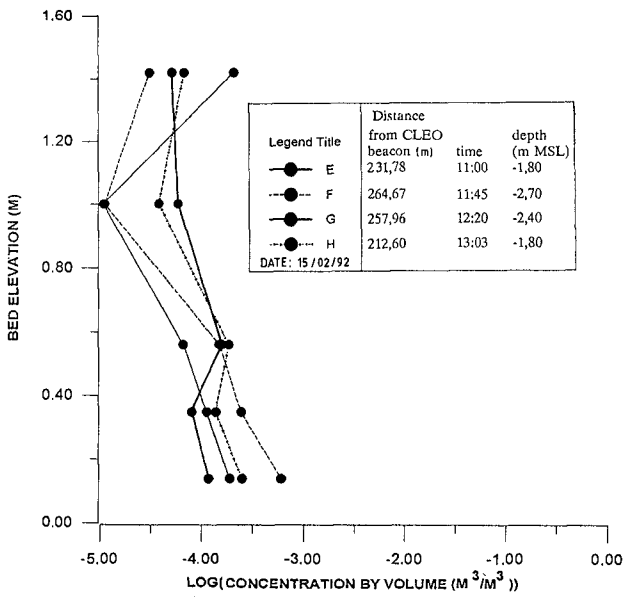


Figure 10. TASSS results

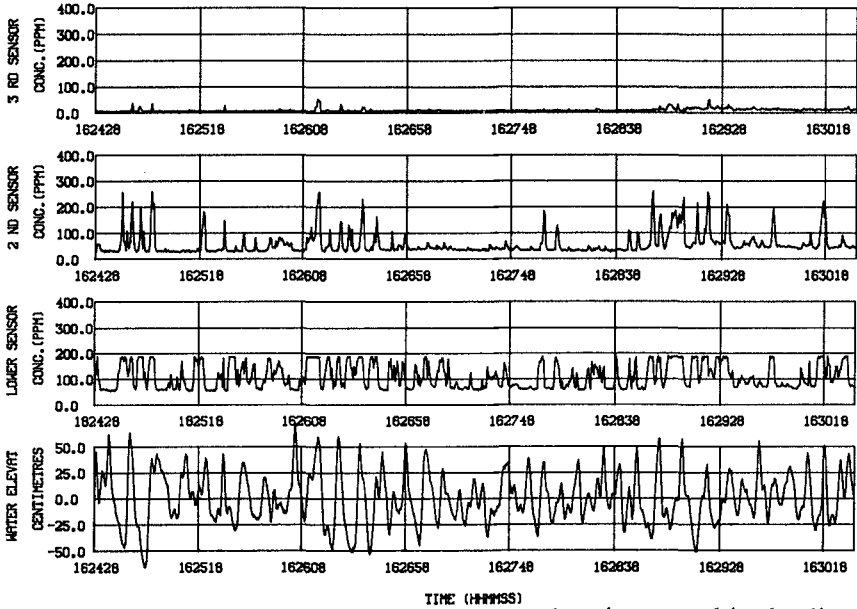


Figure 11. Typical transmissometer and water elevation record in shoaling region (depth = 2,8 m,  $H_{mo}$  1,11 m)

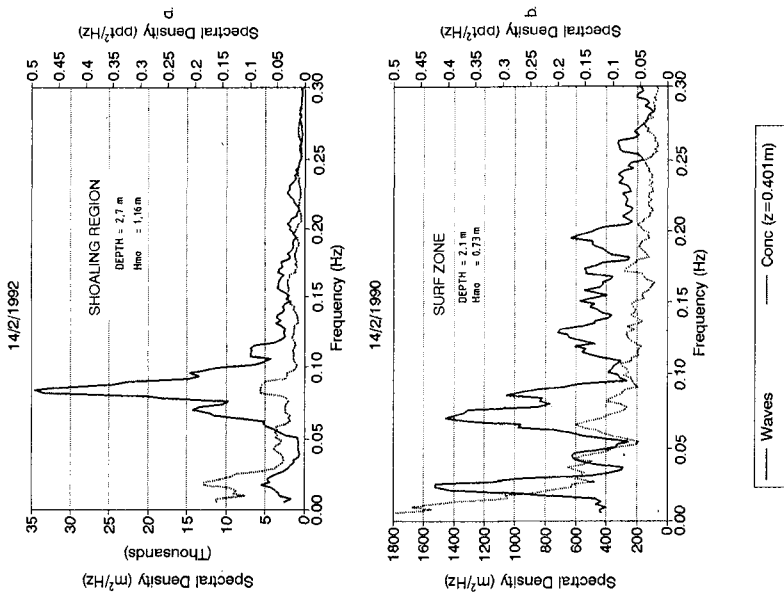


Figure 12. Energy spectra of the wave record and the sediment concentration ( $Z = 0,40$  m)

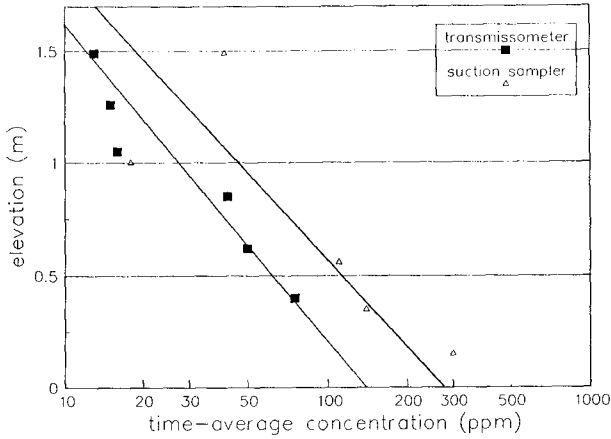


Figure 13. Averaged results of TASSS and transmissometer

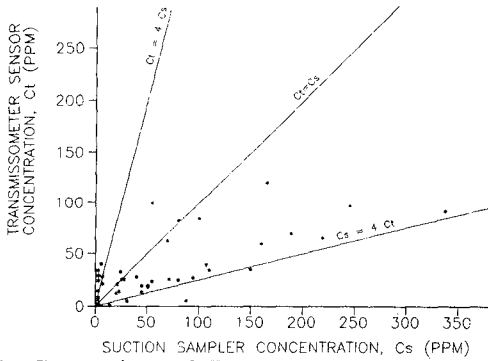


Figure 14. Comparison of TASSS and transmissometer results

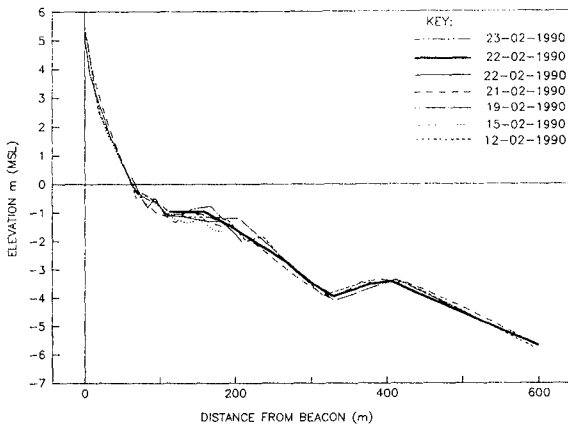


Figure 15. Beach and nearshore survey results

## CHAPTER 233

# Water Wave Propagation in Jettied Channels

Robert A. Dalrymple<sup>1</sup>, F., ASCE

### Abstract

Navigational channels are frequently maintained by the use of jetties. These stabilized channels often form long straight waterways which permit the passage of tidal flows and waves into harbors, lagoons, or rivers. This paper concerns the decay of the waves down the channel due to energy losses within jetties. The analysis involves the use of an impedance boundary conditions at the channel side walls to model the wave dissipation there. The wave motion is described by an eigenfunction expansion for the velocity potential within the channel, with and without tidal currents.

For the case that the water wave length is long with respect to the channel width and no currents are present, the wave height decay down the channel can be described by an exponential decay,  $H = H_0 e^{-\Gamma x}$ , where  $\Gamma = \gamma x / (2kb)$ ,  $\gamma$  is a (real) damping factor,  $k$  is the wave number, and  $2b$  is the width of the channel. For the case of a mean current in the channel, the same expression results, but for a different form of the wave number, (Eq. 24).

### Introduction

Stabilized entrance channels often form long straight waterways which permit the passage of tidal flows and water waves into harbors or lagoons. This paper concerns the interaction of water waves with rubble mound jetties, including the significant energy loss into the jetties, due to turbulent energy dissipation.

The energy decay down a channel may be calculated if the rates of energy loss are known at the bottom and the sides of the channel. The conservation of energy flux down the channel is

$$\frac{d\mathcal{F}}{dx} = -\mathcal{D} \quad (1)$$

---

<sup>1</sup>Professor and Director, Center for Applied Research, Department of Civil Engineering, Univ. Delaware, Newark, DE 19716

where the wave energy flux is  $\mathcal{F} = EC_g(2b) = \frac{1}{4}\rho g H^2 C_g b$ , where  $\rho$  is the fluid density,  $g$  is the acceleration of gravity,  $H$ , the wave height in the channel,  $C_g$  is the group velocity of the waves, and  $b$  is the half-width of the channel.  $\mathcal{D}$  is the energy dissipation per unit length of channel. This expression can be rewritten as

$$\frac{dH}{dx} = -\frac{2\mathcal{D}}{\rho g H C_g b} \quad (2)$$

Hunt (1952) examined the decay of wave height due to laminar boundary layers at the sides and the bottom of a rectangular impermeable channel. In this case,  $\mathcal{D}$  is proportional to  $H^2$ , and therefore Eq. 2 can be written as

$$\frac{dH}{dx} = -\Gamma H \quad (3)$$

which leads to the following expression for wave height down the channel,

$$H(x) = H_o e^{-\Gamma x} \quad (4)$$

where  $\Gamma$  depends on the viscosity of the fluid as well as the other factors.

Battjes (1965) studied the damping of waves in a rectangular wave channel with roughness strips attached to the sidewalls along the length of the channel. The strips were mounted vertically over the depth on the sides of the channel with a fixed spacing. Vortices shed by the wave-induced flow past the strips resulted in a decrease in wave height down the channel. Battjes examined a 'turbulent damping' such that the dissipation as the side walls was assumed to be proportional to  $H^3$ ,

$$\frac{dH}{dx} = -\beta H^2 \quad (5)$$

leading to

$$H = \frac{H_o}{(1 + \beta H_o x)} \quad (6)$$

The experiments were conducted in an approximately 27.5 m long, 3.0 m wide test section of the channel. To get an adequate decay distance, the wave height at the end of the test section after one run, was used as the input to another test. By coupling experiments in this fashion, data on wave height versus distance was generated for an equivalent tank, 6 to 7 times longer. However, since the phenomenon he discusses is nonlinear and cross-tank oscillations occur, it is not likely that this is a valid experimental approach.

Isaacson (1978) applied the same formula as Battjes for the wave height down a prismatic trapezoidal entrance channel laboratory model lined with stone, varying the side slopes. He found that there was a strong dependency of  $\beta$  on wave period, with  $\beta$  increasing with period.

Melo and Guza (1991a,b) in an interesting computational and field study showed that the wave height down the centerline of an entrance channel decreased rapidly, mostly due to the diffraction of the waves into the absorbing jetty structures. They also point out that the diffraction through a breakwater gap of the same width as the entrance channel gives similar damping behavior down the centerline. If the channel is narrow with respect to the wave length of the incident waves, then the diffractive damping is more severe, as discussed by Losada *et al.* (1990). The computational analysis of Melo and Guza consisted of two coupled parabolic models of wave propagation, one in the channel and another within the porous structure, with matching conditions on the jetty face for velocity and pressure.

The intent of this paper is to develop a new methodology for computing the wave field within navigational channels without having to use coupled parabolic wave models (as in Melo and Guza) through the use of the impedance boundary condition.

### Theory

The wave motion will be described within the jetty section, assuming that the wave height is specified across the mouth of the channel. Figure 1 shows the channel and the coordinate system to be used in the analysis. The channel is assumed here to be constant in depth, which simplifies the analysis.

Between the jetties, which are located at  $y = \pm b$ , the wave motion is assumed to be described by linear wave theory which results from the assumption of small amplitude irrotational wave motion within an incompressible fluid. The associated governing equation is the Laplace equation for a velocity potential  $\phi(x, y, z, t)$ ,

$$\nabla^2 \phi = 0 \quad (7)$$

from which the velocities in the fluid can be determined,  $\mathbf{u} = (u, v, w) = -\nabla \phi$ . At the bottom boundary, no flow is permitted,

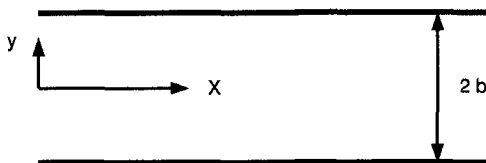


Figure 1: Schematic of Channel

$$-\frac{\partial\phi}{\partial z} = 0 \quad \text{on } z=0. \tag{8}$$

At the jetties, an impedance boundary condition is assumed,

$$\frac{\partial\phi}{\partial y} = i\gamma\phi = ik\beta\phi \quad \text{on } y = |b| \tag{9}$$

where  $\gamma$  is  $k$  (the wave number) times the *specific admittance*,  $\beta$ , of the jetties. This assumption follows from acoustics, where it is used to determine the damping of acoustic waves due to absorbent duct boundaries (e.g. Morse and Ingard, 1968, §6.3). If  $\gamma$  is real, then wave energy is absorbed by the jetties; for  $\gamma$  purely imaginary, this boundary condition leads to 100% reflection with a phase shift. The value of  $\gamma$  (or equivalently the dimensionless  $\beta$ ) will strongly dictate the nature of the solution and its value will be specified later.

The impedance boundary condition on the jetties can be compared to a transmitting condition for plane waves, usually imposed on an open coast model (e.g., Kirby, 1985), which is taken as

$$\frac{\partial\phi}{\partial y} = ik \sin \theta\phi \tag{10}$$

where  $\theta$  is the angle of the wave direction to the  $x$  axis. Comparing to (9), the specific admittance for a transmitting boundary is  $\beta = \sin \theta$ , which varies from 0 to 1. The value of  $\gamma$  then must be less than the wave number,  $k$ , as it implies that waves are normally incident on the jetties and fully transmitting through them.

For the general case, an equivalent admittance will be defined as  $\sin \theta$  when  $\beta$  is real.

Eigenfunction Expansion

The velocity potential in the channel will be similar to that used by Dalrymple (1989), studying ‘designer waves’ for directional wavemakers. In general, the total potential will consist of even and odd eigenfunction components, across the channel, but here we will restrict ourselves to normally incident wave trains, so that only the even modes will be utilized. The potential (in the absence of a mean flow in the channel) is therefore assumed to be

$$\phi(x, y, z, t) = \sum_{n=1}^{\infty} C_n \cos \lambda_n y \frac{\cosh k(h+z)}{\cosh kh} e^{i(\sqrt{k^2-\lambda_n^2}x-\sigma t)} \tag{11}$$

where the set  $\{\cos \lambda_n y\}$  is an anharmonic (orthogonal) Fourier series in  $y$ , and the usual linear wave theory dispersion relationship holds:

$$\sigma^2 = gk \tanh kh, \tag{12}$$



which relates the wave number  $k$  and the water depth and wave angular frequency,  $\sigma = 2\pi/T$ , where  $T$  is the wave period.

The lateral boundary conditions (9) place the following constraints on the  $\lambda_n$  in the Fourier series,

$$-\lambda_n \tan \lambda_n b = i\gamma \quad n = 1, 2, \dots \quad (13)$$

which is a transcendental equation to determine the wave numbers  $\lambda_n$  in the lateral direction. (Note that if  $\gamma$  is zero, then the  $\lambda_n = n\pi/b$ .) This boundary condition leads to the orthogonality of the Fourier series:

$$\int_{-b}^b \cos \lambda_n y \cos \lambda_m y \, dy = \begin{cases} 0, & \text{for } n \neq m, \\ \frac{2\lambda_n b + \sin 2\lambda_n b}{2\lambda_n}, & \text{for } n = m. \end{cases} \quad (14)$$

The velocity potential (11) is composed of an infinite number of wave trains, consisting of wave trains which are 'standing' in the cross-channel direction and either propagating or decaying in the down-channel direction. In fact, only a few terms in  $\phi$  represent propagating wave trains as, for large values of  $n$ , the real part of  $\sqrt{k^2 - \lambda_n^2}$  becomes negative and results in a strongly damped motion in the  $x$  direction. In fact, for incident wave trains with wave lengths larger than  $2b$  (the channel width), or  $kb < \pi$ , then only one wave mode ( $n = 1$ ) propagates down the channel (this is strictly true for  $\gamma = 0$ ; but it serves as a guide).

The values of  $C_n$  are determined by the initial value of  $\phi(0, y, t)$ . By orthogonality of the set  $\{\cos \lambda_n y\}$  over  $-b < y < b$ , we find

$$C_n = \frac{2\lambda_n \int_{-b}^b \phi(0, y, t) \cos \lambda_n y \, dy}{2\lambda_n b + \sin 2\lambda_n b} \quad (15)$$

For a given incident wave train of frequency  $\sigma$ ,  $\phi(0, y, t)$  is taken as unity across the mouth of the channel, and the  $C_n$  can be reduced to

$$C_n = \frac{4 \sin \lambda_n b}{2\lambda_n b + \sin 2\lambda_n b} \quad (16)$$

This initial condition imposes phases on the various wave modes (more on this later).

Examining narrow channels, ( $\gamma b \ll 1$ ) and  $kb < \pi$ , the lateral boundary condition (13) can be approximated for  $\lambda_1$ ,

$$\lambda_1^2 = -i\gamma/b \quad (17)$$

The leading term of  $\phi$  is

$$C_1 \cos \lambda_1 y \frac{\cosh k(h+z)}{\cosh kh} e^{i(\sqrt{k^2 - \lambda_1^2} x - \sigma t)} \quad (18)$$

Introducing the approximation for  $\lambda_1$  yields for the approximate wave decay

$$e^{-\left(\frac{\gamma_r}{2bk}\right)x} = e^{-\left(\frac{\beta_r}{2b}\right)x} \tag{19}$$

as  $C_1$  asymptotically goes to unity. Here, the subscript  $r$  denotes the real part. Comparing with the linear damping formula, (4),  $\Gamma = \gamma_r x / 2bk$ . Therefore, the wave height in a channel decreases exponentially down the channel according to this theory. Further, the damping is inversely proportional to  $b$ , the channel half-width.

Alternatively, since  $\lambda_1^2 \ll k^2$ , the exponential term in  $x$  can be approximated as

$$e^{i\sqrt{k^2 - \lambda_1^2}x} \rightarrow e^{ikx} e^{(\lambda_1)_r(\lambda_1)_i x/k}$$

Thus, given the real and (negative) imaginary parts of  $\lambda_1$ , found from (13), the decay of the first wave mode with  $x$  can be found as

$$e^{(\lambda_1)_r(\lambda_1)_i x/k} \tag{20}$$

Since this expression is based on the lateral boundary condition, rather than an approximation, it is more accurate than that provided in (19).

Effects of Tidal Currents

The previous results were obtained for the case of no currents in the channel. However, it is likely for a majority of the tidal cycle there will be a slowly varying flow in the channel or a current due to a river discharge. Therefore the effects of the currents on the wave field and the damping in the channel must be determined.

To include the current (with uniform speed  $U$ , with  $U \gg |\nabla\phi|$ ), the velocity potential is changed to

$$\phi(x, y, z, t) = \phi_c + \phi_w = -Ux + \sum_{n=1}^{\infty} C_n \cos \lambda_n y \frac{\cosh k_n(h+z)}{\cosh k_n h} e^{i(\sqrt{k_n^2 - \lambda_n^2}x - \sigma t)} \tag{21}$$

where the  $\lambda_n$  satisfy the same impedance relationship (9) as before; however,  $\gamma$  may be different than for the no-current case. Also, the dispersion relationship for the wave number results in a different wave number for each wave mode, due to the wave-current interaction, which depends on the wave direction,

$$\left(\sigma - U\sqrt{k_n^2 - \lambda_n^2}\right)^2 = gk_n \tanh k_n h, \quad n = 1, 2, 3, \dots \tag{22}$$

due to the effects of the current on the linear combined free surface boundary condition (e.g., Dean and Dalrymple, 1991, § 3.4.5)

$$\frac{\partial^2 \phi_w}{\partial t^2} + 2U \frac{\partial^2 \phi_w}{\partial x \partial t} + U^2 \frac{\partial^2 \phi_w}{\partial x^2} + g \frac{\partial \phi_w}{\partial z} = 0 \quad \text{on } z = 0 \tag{23}$$

where  $\phi_w$  is the portion of the velocity potential describing the wave motion. The resulting wave numbers ( $k_n$ ,  $n = 1, 2, 3, \dots, \infty$  from 22) are all complex.

For narrow channels, a similar approximation to (19) can be made for the case of waves on currents. This leads to the following relationship for wave height decay down a channel (for normal wave incidence)

$$e^{-\left(\frac{\gamma_r}{2bk_1}\right)x} \quad (24)$$

where  $k_1$  is given by (22).

### Results and Comparisons to Field and Laboratory Data

Figure 2a shows the instantaneous wave field ( $\eta(x, y) = -(i\sigma/g)\phi(x, y, 0)$ ) and the absolute value of  $\eta$  in a channel with the following characteristics:  $b = 120$  m,  $T = 12$  s,  $h = 8$  m, and specific admittance is 0.156, which is  $\gamma = 0.012$  m<sup>-1</sup>. For this case, the curvature of the wave crests is clear with the waves turning into the jetties by diffraction. For this example, the equivalent transmission angle is 8°.

The absolute value of the water surface is contoured in Fig. 2b, with the contours spaced by 0.1. The initial condition of normally incident waves with unit amplitude leads to a forced phasing of all the modes which comprise the wave field (11), such that as the waves propagate down the channel there is a focussing after two wavelengths, for this wave period (the largest contourline corresponds to 1.1; the smallest, to the far right, is 0.3).

Fig. 3 shows the decay of the absolute magnitude of each of the largest five wave modes down the channel centerline for this example; clearly the higher modes (greater than, say, the third) decay rapidly (note one wavelength corresponds to 102 m) and, after long distances, only the first mode is important.

Melo and Guza (1991b) carried out a field experiment at Mission Bay, CA. The entrance channel is 1200 m long, 250 m wide, with a depth of 8 m. The jetties are sand tight, prohibiting the propagation of waves through the jetties. Pressure sensors were deployed at five locations along the centerline of the jetties as shown in Figure 4. Data was obtained during the period March 2 to April 8, 1985. Using data and parabolic model predictions, Melo and Guza determined that the effects of wave height and bottom friction on the wave height reduction along the channel were small. There was no wave breaking observed in the channel.

The effects of currents were observed to have only a small effect on the damping down the channel. The model given in the section Effects of Tidal Currents can predict the damping factor exactly;  $\Gamma$  is the imaginary part of  $\left(\sqrt{k_1^2 - \lambda_1^2}\right)$ . A variation in  $U$  of  $\pm 1$  m/s had nearly no effect on the value of  $\Gamma$ ; the variation was less than 0.3%.

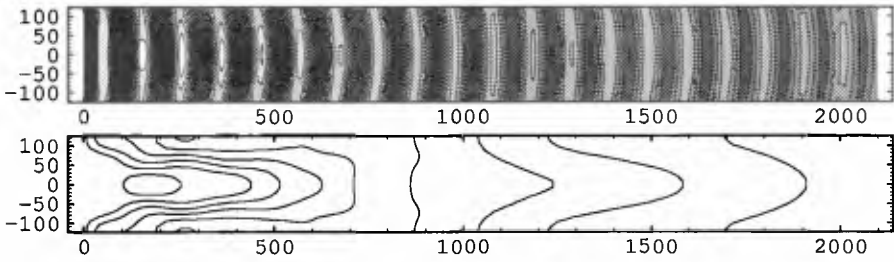


Figure 2: (a) Plane View of Instantaneous Water Surface Elevation in Channel; Ocean at the Left of Figure, Harbor to Right; (b) Absolute Value of Water Surface Elevation, Contours Intervals are 0.1

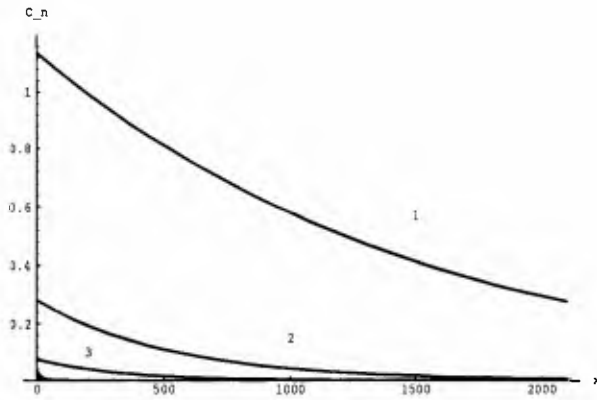


Figure 3: Decay of Each Wave Mode Down Channel (at centerline)

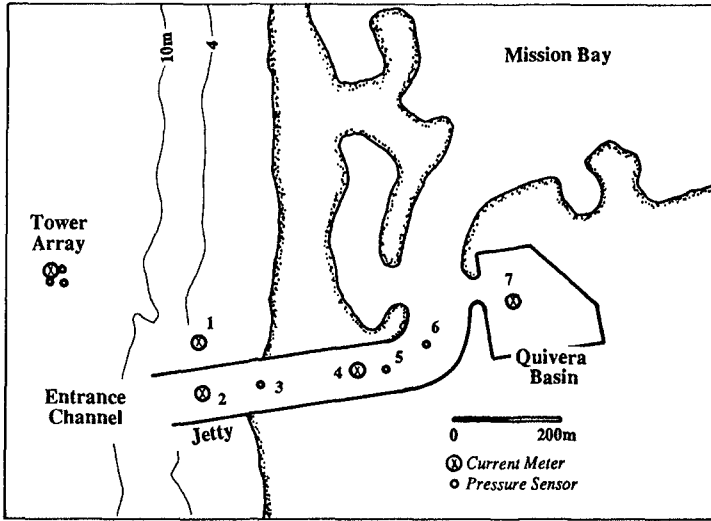


Figure 4: Pressure Sensor Locations for Mission Bay Study (from Melo and Guza, 1991b)

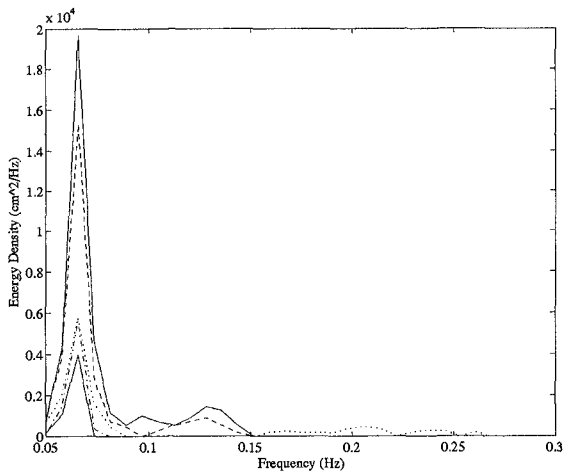


Figure 5: Wave Spectra at the Different Channel Locations (1 April, 1985; adapted from Melo and Guza, 1991b) Legend: Upper Solid Line, P2; Dashed Line, P3; Dotted Line, P4; Dash-Dot, P5; Lower Solid Line, P6.

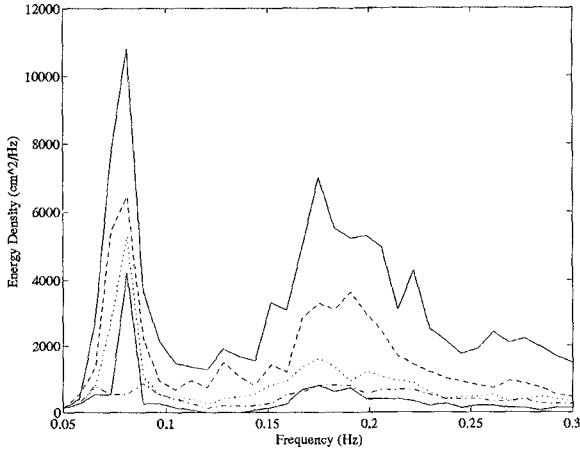


Figure 6: Wave Spectra at the Different Channel Locations (28 March, 1985; adapted from Melo and Guza, 1991b)

The wave spectra observed at the five locations in the channel by Melo and Guza on April 1, 13:31–14:40 hs, 1985 and March 28, 12:24–13:32 hs, 1985 are shown in Figures 5 and 6. Thirty three different frequencies are represented from 0.05 Hz to 0.3 Hz ( $\Delta f = 0.078$  Hz). A comparison of this model to the field data was undertaken by calculating the wave field associated with each of the 33 frequency bands (with unit amplitudes at the channel mouth). The energy densities at the first interior gage, *P2*, were then scaled to match the field data at that location. The wave heights at the other 4 gage locations were then computed from Eq. 11. These heights were then converted into energy densities and plotted. The results for each of the 33 frequency bands are shown in Figure 8 for the 1 April case. By best fit matching of the data, a smoothly varying impedance was chosen, corresponding to an impedance angle linearly varying from  $6.3^\circ$  to  $57.3^\circ$  at the highest frequency (giving  $0.004 \text{ m}^{-1} > \gamma < .04 \text{ m}^{-1}$ , from lowest to the highest frequency). The agreement between model and field data is reasonably good, giving confidence in the model for low frequencies (0.05 to 0.1 Hz; or for a range of dimensionless channel widths,  $4 < kb < 9$ ).

For the spectrum with sea and swell, March 28, the specific admittance was taken the same as for the previous case for the 10 lowest frequencies, but the higher frequencies could not be computed reasonably. The higher frequency wave in the range of 0.15 Hz to 0.30 Hz were predicted to grow down the channel.

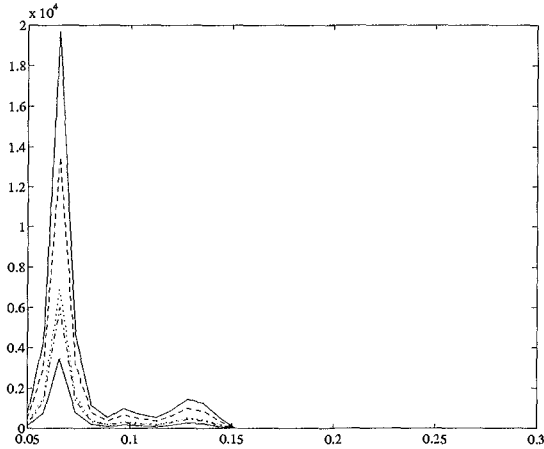


Figure 7: Computed Wave Spectra at the Different Channel Locations, April 1.

The reason for this 'growth' is the location of the focussing region shown in Fig. 2b. For the higher frequencies, this focussing region migrates down the channel, giving an apparent amplification, which is not seen in the field data. These waves (roughly  $14 < kb < 44$ ) are seriously affected by the phases imposed by the initial condition. For the lower frequency waves this was not a problem as the focussing occurred before any of the measurement points. For a realistic case, the phasing of the wave modes will be far different. In Fig. 8,  $\gamma$  was taken somewhat arbitrarily taken as  $0.007(1 - i)$  for the higher frequencies, as it was found by trial and error that the use of a complex value would reduce the amount of focussing.

As an alternative and a simpler approach to this problem, a pure exponential decay (according to Eq. 19) was tried. The wave energy density at P2 was multiplied by

$$e^{-\left(\frac{2\gamma}{2bk}\right)x} = e^{-\frac{\beta}{b}x} \quad (25)$$

where the introduction of the 2 comes about by the energy being proportional to the square of the wave height. Using the specific admittance ( $\beta$ ) of 0.139 (apparent angle of  $8^\circ$  and  $\gamma = k\beta$  ranging from  $0.005 \text{ m}^{-1}$  for the low frequency waves to  $.05 \text{ m}^{-1}$  for the highest frequency) for April 1 and 0.190 (apparent angle of  $11^\circ$ ) for March 28, gives the results in Figs. 9 and 10. For the case of the narrow banded sea state, there is almost no difference between the complete

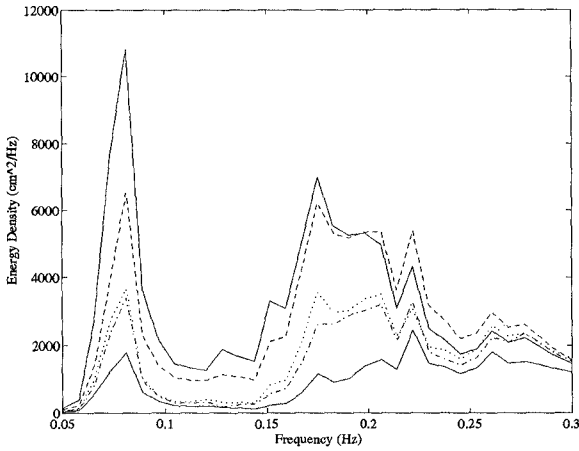


Figure 8: Computed Wave Spectra at the Different Channel Locations, March 28.

model (Fig. 7) and the exponentially decaying model. For the wide-banded seas, the frequency dependency of  $\gamma$  causes the low frequencies to decay too rapidly when compared to the field data. This can of course be improved by varying  $\gamma$  in the model. The exponential model result here is better than the complete model shown in Fig. 8, because only a single wave mode is used and the focussing can not occur.

### Conclusions

The behavior of water waves in straight channels with energy absorbing side walls, such as rubble mound jetties, can be reasonably predicted with a simple eigenfunction expansion model. For the case of Mission Bay, CA, only a very few wave modes are needed to provide an adequate description of the wave field, except for the case of the high frequencies. The absorbing sidewalls are modelled by a simple impedance boundary condition (Eq. 10), where the specific admittance  $\beta$  can be expressed as an equivalent transmission angle,  $\theta$  from  $\beta = \sin \theta$ . The values of  $\theta$  found here are between 8 and 11°.

The complete model predicts the decay of wave spectra at Mission Bay, CA reasonably well for the low frequencies, with problems associated with focussing and the phasing of the initial condition at the higher frequencies. A simple model based on purely exponential decay (Eqs. 19 and 20) provides a useful tool for preliminary estimates of wave decay.



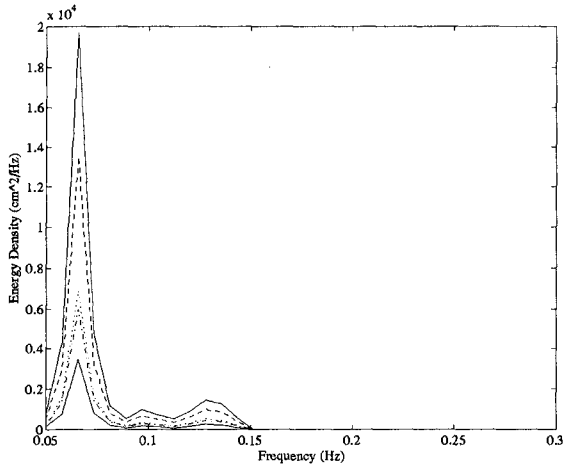


Figure 9: Exponentially Decaying Spectra at the Different Channel Locations; April 1.

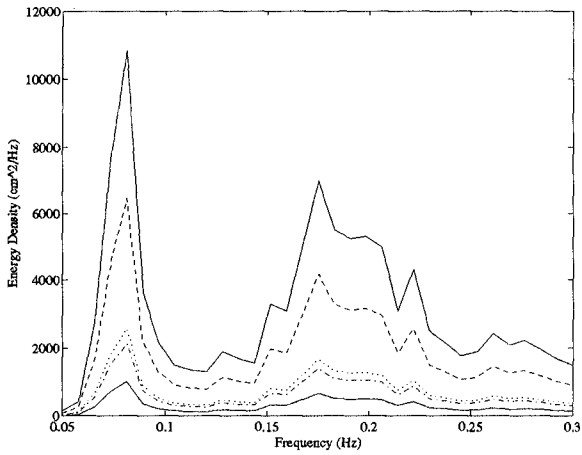


Figure 10: Exponentially Decaying Spectra at the Different Channel Locations; March 28.

### Acknowledgment

This work was partially supported by NOAA Office of Sea Grant, Dept. of Commerce, under Grant No. NA16RG0162-02 (R/OE-7). The U.S. Government is authorized to produce and distribute reprints for government purposes notwithstanding any copyright notation that may appear herein.

### Reference

- Battjes, J.A., "Wave attenuation in a channel with roughened sides," *Proc. Coastal Engineering Specialty Conference*, ASCE, 425-460, 1965.
- Behrendt, L., A finite element model for water wave diffraction including boundary absorption and bottom friction, ISVA, Tech. Univ. Denmark, Series Paper 37, 1985.
- Dalrymple, R.A., "Directional wavemaker theory with sidewall reflection," *Journal of Hydraulic Research*, 27, 1, 23-34, 1989.
- Dalrymple, R.A. and P.A. Martin, "A perfect boundary condition for parabolic water-wave models," *Proc. Royal Soc. of London, A*, 1991.
- Dalrymple, R.A., M.A. Losada and P.A. Martin, "Reflection and transmission from porous structures under oblique wave attack," *J. Fluid Mechanics*, 224, 625-644, 1991.
- Hunt, J.N., "Viscous damping of waves over an inclined bed in a channel of finite width," *Houille Blanche*, 7, 836-842, 1952.
- Isaacson, M. de St.Q, "Wave dampening due to rubblemound breakwaters," *J. Waterways, Port, Coastal and Ocean Engineering*, ASCE, 104, 4, November, 391-405, 1978.
- Losada, M.A., R.A. Dalrymple, and C. Vidal, "Water waves in the vicinity of breakwaters," *J. Coastal Research*, SI #7, 119-137, 1990.
- Melo, E. and R.T. Guza, "Wave propagation in a jettied entrance channels, I: Models" *J. Waterways, Port, Coastal and Ocean Engrg.*, ASCE, 117, 5, 471-492, 1991a.
- Melo, E. and R.T. Guza, "Wave propagation in a jettied entrance channels, II: Observations" *J. Waterways, Port, Coastal and Ocean Engrg.*, ASCE, 117, 5, 493-510, 1991b.
- Morse, P.M. and K.U. Ingard, **Theoretical Acoustics**, Princeton Univ. Press, 927pp., 1968.
- Sollitt, C.K. and R.H. Cross, "Wave transmission through permeable breakwaters," *Proc. 19th Coastal Engng. Conf.*, ASCE, Vancouver, 1827-1846, 1972.
- Sollitt, C.K. and R.H. Cross, Wave reflection and transmission at permeable breakwaters, U.S. Army Coastal Engineering Research Center, Tech. Paper 76-8, 172pp, 1976.
- Sommerfeld, A., "Mathematische Theorie der Diffraction," *Math. Annalen*, 47, 317-374, 1896.

## CHAPTER 234

### DISPERSION MODEL OF DREDGE SPOIL DUMPED IN COASTAL WATERS

G. Drapeau<sup>1</sup>, D. Lavallée<sup>1</sup>, J.F. Dumais<sup>1</sup> and G. Walsh<sup>2</sup>

#### Abstract

This model is specifically conceived to work in estuarine environments characterized by strong tidal currents. It operates on a microcomputer and it is conceived to work with minimal input. The model determines the velocity and radius of the dense sediment cloud, formed by the release of sediments from a scow, during its downfall in the water column. These parameters are used to determine the proportion of sediments settling at the point of impact. Sediments maintained in suspension by the high level of turbulence following impact on the bottom form a density current that spreads out radially. The performance of the model was verified by a series of experiments carried out in the St Lawrence Estuary to monitor the disposal of dredged spoil from a 400 m<sup>3</sup> scow.

#### 1. INTRODUCTION

The present model was initially developed for the Canadian Ministry of Fisheries and Oceans to evaluate the impact of dredged sediments dumped from a scow in different marine biotopes. Prerequisites were that the model works with minimal input and runs on a microcomputer. Another requirement was that the model would be efficient in estuarine environments characterized by strong tidal currents.

---

<sup>1</sup> Centre océanographique de Rimouski, Université du Québec, Rimouski, Québec, Canada, G5L 3A1

<sup>2</sup> Institut Maurice-Lamontagne, Pêches et Océans Canada, Mont-Joli, Québec Canada, G5H 3Z4

The bulk of sediments released from a scow reach the sea floor at the dumping site and only a small percentage remains in the water column. Gordon (1974) estimates that more than 95 per cent of sediments released from a scow reach the sea floor and observations by Tavolaro (1984) lead to similar conclusions. The present model describes the behavior of the dredged sediments that reach the sea floor at the dump site and a companion model is used to determine the fate of sediments dispersed in the water column.

Different mathematical models have been developed to describe the dispersal of dredged sediments. A model was developed by Edge and Dysart (1972), in which the dumped material is assumed to behave as a dense liquid moving in a lighter one. Koh and Chang (1973) used similar concepts to develop a model that deals with each of the three phases of dredged material dispersal and can handle continuous discharge of sediments as well as dumps from a scow. However, this model is not particularly suited for coastal environments and it is much more complex than the model described in this paper. Bokuniewicz et al. (1978) developed a mathematical model that determines potential and kinetic energy of dumped sediments. Based on the energy budget of the dumped sediments, the authors determine the maximum distance reached by the density current that spreads on the sea floor after the dumped sediments impact on the bottom.

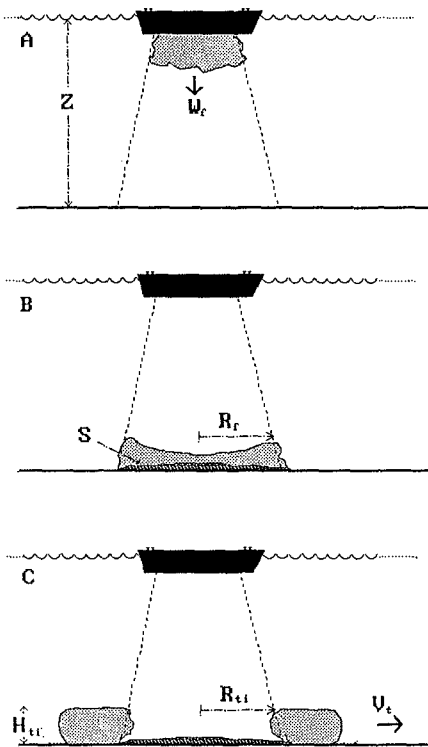
Field measurements to develop this model were carried out in in Canada, in the Lower St. Lawrence Estuary. Measurements took place at Rivière-du-Loup and Rimouski where the tidal range varies between 5 and 6 m. and the dump sites are located in 10 m. and 20 m. water depth respectively.

## **2. MODEL DESCRIPTION**

The dispersal of dredged sediments released from a scow follows three stages (Fig. 1). Upon release, the dredged material descends rapidly through the water column as a well-developed high density jet; subsequently, when the dredged material hits the bottom, part of the sediment load settles at the site of impact; and finally, the high level of turbulence generated by the impact maintains a cloud of sediments in suspension that forms a density current which spreads out radially.

### **2.1 Descent of sediments through the water column**

A series of flume experiments conducted by Krishnappan (1975) have shown that the fall of dumped sediments can be treated in two distinct phases, an entrainment phase when sediments leave the scow followed by a settling phase that develops only when the water depth is sufficient (which is not the case in coastal waters) for the vertical downward velocity to become the same as the settling velocity of sediment particles. During the entrainment phase, the size of the



**Figure 1.** A) The dump load leaves the scow as a massive cloud of sediments that expands during its fall as water is incorporated.

B) At impact on sea floor a portion of the dumped sediments settle on the sea floor and the remainder is maintained in suspension by the high level of turbulence generated by the impact and forms a density current.

C) The density current expands radially taking the shape of a torus. For modeling purposes, the initial radius of the torus is taken to be that of the falling sediment cloud at the moment of impact.

sediment cloud, that forms when the scow opens, grows owing to the incorporation of external fluid while the vertical downward velocity diminishes (Fig. 1a). Flume measurements and dimensional analysis have lead Krishnappan to formulate the downward velocity ( $W_f$ ) as well as the radius ( $R_f$ ) of the sediment cloud as a function of water depth:

$$R_f = \alpha_k Z \quad (1)$$

$$W_f = \beta_k F^{1/2} / Z \quad (2)$$

where  $Z$  is the water depth,  $F$  is the negative buoyancy of sediments and  $\alpha_k$  and  $\beta_k$  are variables whose values are functions of the sediment grain size determined experimentally by Krishnappan.

## 2.2 Settling of sediments at point of impact

No systematic formulation is presently available to determine the exact proportion of the total sediment load that settles on sea floor at the point of impact. The parameters that determine the settling of dumped sediments at the point of

impact are: 1) the sediment grain size and 2) the impact velocity on the sea floor, which is related to water depth. It stands to reason that coarser sediments will have a greater tendency to settle at the point of impact than finer ones. Velocity of the mass of dumped sediments at the moment of impact provides the energy necessary to generate a level of turbulence sufficiently high to bring sediments into suspension. For instance, if the water depth is sufficient to allow sediments to reach their inherent settling velocity, all sediments would settle naturally on the sea floor without further movement, no energy being left to generate turbulence and maintain sediments in suspension.

The proportion of sediments settling directly at the point of impact is defined as follows in the present model:

$$S = 1 - C(W_{fi} - W_s)/W_{fi} \quad (3)$$

where  $W_{fi}$  is the downfall velocity of the mass of dumped sediments at the moment of impact and  $W_s$  is the natural settling velocity of sediment particles (Fig. 1b).  $C$  is a constant; its present value is set at 0.5. This equation determines the "excess energy" available to generate a density current. As explained above, if  $W_{fi}$  diminishes to the point that  $W_{fi} = W_s$ , Then  $S = 1$  and no sediments are left to form a density current.

According to field measurements carried out by Gordon (1974), 80 per cent of the dumped sediment load settles within a 30 m. radius from the point of impact. Other workers (Bokuniewicz et al., 1978; Tavolaro, 1984; Truitt, 1986) observed that a large proportion of dumped sediments settle at the point of impact, but no specific correlation is established with sediment grain size and water depth.

### 2.3 Formation of a density current

Truitt (1988) summarized observations of many workers explaining that dredged sediments form density currents that spread on the sea floor following impact on bottom. Profiles of dredged sediment dispersion, measured by Gordon (1974) and also by Malherbe (1990), on a larger scale, outline this phenomenon.

The principle of conservation of mass is used to determine the transfer from a massive sediment fall before impact on the bottom to the formation of a density current (Fig. 1). The cloud of sediments formed by the content of the scow falling through the water column has a radius  $R_{fm}$  (cf. eq. 1) and a downward velocity  $W_{fm}$  (cf. eq. 2) when it hits the sea floor. The vertical flux is defined as:

$$\text{Flux} = \pi R_{fm}^2 W_{fm} \quad (4)$$

The density current generated by the impact on the sea floor expands radially and it takes the shape of a tore (Bokuniewicz et al., 1978). If  $R_{ti}$  is the initial radius of the tore,  $H_{ti}$  is the initial height, and  $V_{ti}$  is the initial velocity, the initial flux of the density current expanding radially on the sea floor is:

$$\text{Flux} = 2\pi R_{ti} H_{ti} V_{ti} \quad (5)$$

The initial radius  $R_{ti}$  of the density current is that of the sediment cloud when it impacts on the sea floor (Fig. 1b and 1c):

$$R_{ti} = R_{fm} \quad (6)$$

Using the principle of conservation of mass to equate equations 4 and 5, we can write:

$$\pi R_{fm}^2 W_{fm} = 2\pi R_{ti} H_{ti} V_{ti} \quad (7)$$

and:

$$R_{fm} W_{fm} = 2H_{ti} V_{ti} \quad (8)$$

This equation contains two unknowns; the initial height ( $H_{ti}$ ) and the initial velocity ( $V_{ti}$ ) of the density current.

### 2.3.1 Velocity of the density current

Density currents are studied principally to interpret sedimentary facies (Middleton and Southard, 1984). For instance, Keulegan (1957) and Middleton (1966a,b) produced density currents experimentally by releasing brines and suspensions of spherical beads into horizontal channels. Experimental results agree to define the velocity of the density current as follows. The difference density  $D_t$  of the density current is defined as:

$$D_t = p_s/p \quad (9)$$

where  $p_s$  is the excess density of the density current and  $p$  is the density of water; and:

$$V_t = Fr(D_t g H_t)^{1/2} \quad (10)$$

where  $V_t$  is the velocity of the density current,  $Fr$  is the densimetric Froude number,  $D_t$  is the difference density of the density current, and  $H_t$  is the height of the density current. Middleton (1966a) has found experimentally that the densimetric Froude number for density currents generated by sediments into suspension flowing on a horizontal bottom has a constant value of 0.75. The velocity of the density current is then a function of the density difference and the height of the density current. The density difference is determined by the quantity

of sediments brought into suspension following the impact of sediments on the sea floor. This quantity is known from equation 3.

### 2.3.2 Height of the density current

Equation 10 shows that  $V_t$  is a function of  $H_t$  and it is then possible to determine the initial height ( $H_{ti}$ ) of the density current. Equation 10 is introduced in equation 8 and  $H_{ti}$  is defined explicitly as:

$$H_{ti} = [(R_{ti}W_{fi})^2/(4Fr^2gD_{ti})]^{1/3} \quad (11)$$

This algorithm effectively sets the initial height ( $H_{ti}$ ) of the density current in such a way that the conservation of flux is respected, as defined by equations 4 and 5.

### 2.3.3 Evolution of the density current

The following initial conditions are assumed to define the evolution of the density current: 1) the density current forms a torus that expands radially (Bokuniewicz *et al.*, 1978), 2) the volume of the torus is constant, and 3) the width ( $L$ ) of the torus is constant. Consequently, in order to maintain the volume constant, the height of the torus ( $H_t$ ) diminishes as the torus spreads radially. It implies that  $H_t$  is a time dependent variable.

Sediments suspended in the density current are settling on the sea floor according to their nominal settling velocity ( $W_s$ ) and, consequently, the density of the density current diminishes as the settling of sediments on the sea floor progresses. The concentration of sediments in the density current can be defined by the following differential equation:

$$dP_t/dt = -(P_t/M_t)W_sA_t \quad (12)$$

where  $P_t$  is the quantity of sediments in the density current,  $M_t$  is the volume of the density current,  $W_s$  is the settling velocity of sediment particles and  $A_t$  is the surface area of the density current. As:

$$M_t/A_t = H_t \quad (13)$$

where  $H_t$  is the height of the density current. Equation 13 can be rewritten as follows:

$$dP_t/dt = -P_tW_s/H_t \quad (14)$$

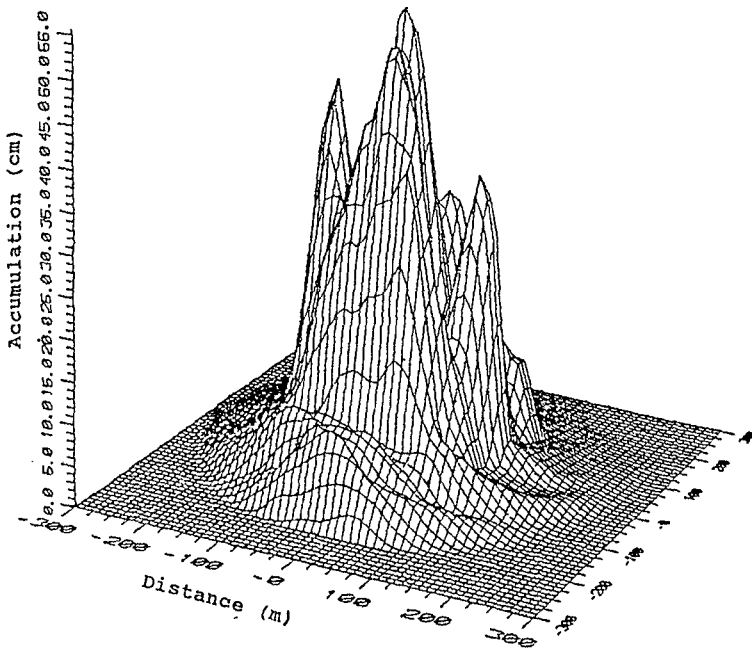
As mentioned above,  $H_t$  is itself time dependent. This equation is solved numerically; initially using a Runge-Kutta algorithm, but it is handled more efficiently by linear iteration.



The rate of deposition on the sea floor of sediments contained in the density current is proportional to the sediment concentration in the density current. That rate of deposition is also inversely proportional to the velocity at which the density current is moving on the the sea floor; for example, when the density current is moving faster, the sediments settling on the sea floor are spread over a larger area.

#### 2.4 Advection by tidal currents

Tidal currents play an important role in estuarine environments. At the present stage of development of the model, tidal currents are simply advecting the density current (Fig. 2). In theory, advection should have an influence on the densimetric Froude number but, in practice, it is not significant within the context of the present model.



**Figure 2.** Three-dimensional mesh of sediment accumulation on the sea floor resulting from the simulation of 125 dumps totaling  $50,000 \text{ m}^3$  of dredged sediments at a water depth of 20 m. and tidal currents reaching  $.4 \text{ ms}^{-1}$ . The bulk of sediments is deposited within a 150 m. radius and the remainder is transported by density currents advected in different directions depending on the phase of the tide.

## **2.5 Sedimentation grid**

The present model is designed to describe the cumulative effect of dredging operations resulting from many dumps at a given site. The cumulative sedimentation resulting from successive dumps is handled by implementing a grid system that works as follows. The spatial and temporal scales to calculate the amount of sedimentation on the sea floor are set to obtain sedimentation measurements spaced approximately 10 m. apart. A 2x2 kilometer grid, using a 10 m. mesh size, is established and each sedimentation calculation is attributed to the corresponding mesh. This procedure permits to record sedimentation from successive dumps even if they do not originate from the same location on the dumpsite (Fig. 2). This feature is important to allow for the possibility to simulate inherent navigation errors and also to take into account that scows are not necessarily completely stopped during dumping operations.

## **2.6 Drifting during dumping**

Most operators prefer not to stop completely during dumping operations. This situation is simulated by spreading sediments settling at the point of impact over a 50x50 m. area instead of a single point. Other dimensions can be chosen at will, depending on the speed of the scow and the time taken to unload.

## **2.7 Positioning error**

The positioning of a scow over a dump site is more or less precise depending on the navigation system used. This inherent error is dealt with by choosing at random a position within a circle corresponding to the positioning uncertainty, typically 150 m. in the St. Lawrence Estuary.

# **3. INPUT / OUTPUT**

## **3.1 Input**

The following parameters are used as input: 1) volume of sediments dumped, 2) number of dumps, 3) water depth, 4) sediment grain size, 5) radius of navigation error, 6) currents (current-meter records or tidal- current ellipses).

Three sediment grain sizes with corresponding percentages are used to describe the texture of dredged sediments. Two options are offered to input current data: current-meter data files or keyboard input of tidal current ellipses. When a current-meter data file is used as input, the data sampling from the file is organized to correspond as closely as possible to the dredging operations. For example, data sampling from the file starts to coincide with the beginning of the dredging operations and sampled data are averaged to correspond to the dumping routine (e.g.

one dump every hour). Furthermore, if dumping operations are not continuous, the idle periods (night time) are not sampled. When current meter data are not available, tidal currents are simulated by the model on the basis of tidal current ellipses. Speeds and directions of tidal current ellipses are input from the keyboard to simulate estuarine conditions prevailing at the studied dump site.

### 3.2 Output

Data produced as output are: a) three files: 1) sedimentation matrix file, 2) N-S cross-section file, 3) W-E cross-section file and b) four graphics: 1) Contours of dredged sediment deposit (Fig. 2 and 5), 2) 3-D mesh of sediment deposit (Fig. 2), 3) N-S sediment deposit cross-sections, and 4) W-E sediment deposit cross-section. Graphics displays are produced by the software package "Surfer" (Golden Software, Boulder, U.S.A.).

## 4. FIELD MEASUREMENTS

### 4.1 Location and dredging equipment

Field experiments were carried out at two locations in the St. Lawrence Estuary to verify the present model. At Rivière-du-Loup the dump site was located in 10 m. water depth and tidal currents reached  $1.5 \text{ ms}^{-1}$ . At Rimouski, the water depth was 20 m. at the dump site and tidal currents reached  $1.0 \text{ ms}^{-1}$ . The dredging equipment operating at both locations was a clamshell dredge loading  $400 \text{ m}^3$  scows.

### 4.2 Sediment types

The operations monitored were maintenance dredging at both sites. The sediments dredged were poorly sorted very fine sands mixed with silty muds, the grain size ranging between 0.015 and 0.250 mm.

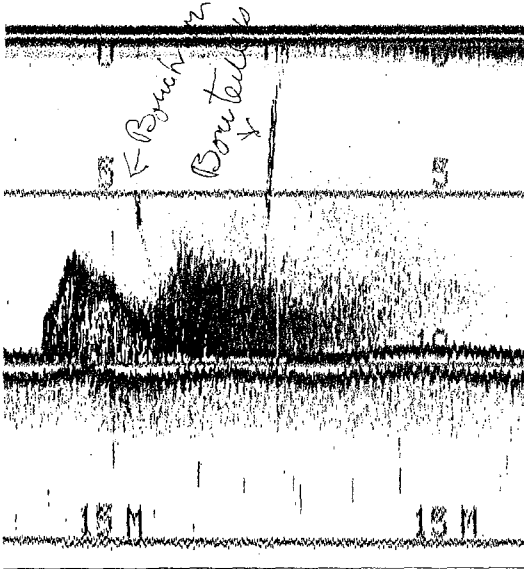
### 4.3 Field measurement equipment

Echosounder: A 200 kHz echosounder was used to track the dispersal of dredged sediments. That frequency is very effective to trace sediment clouds in the water column (Fig. 3).

Transmissometer: Transmissometer measurements could confirm the presence of density currents but more in a qualitative than a quantitative way.

Water samples: Water samples were taken to calibrate transmissometer data.

**Sediment traps:** Sediment traps were very useful to calibrate the model, because they provide factual measurements of sedimentation rates. The traps were made of 30 cm. high by 10 cm. wide plastic cylinders. The cylinders were mounted in lead containers, that were heavy enough to be placed directly on the sea floor.



**Figure 3.** Example of density current observed using a 200 kHz echosounder from a boat anchored in 10 m. water depth. The sharp front of the density current appears on the left side of the recording and the more diffuse tail is recorded in the right portion of the echogram.

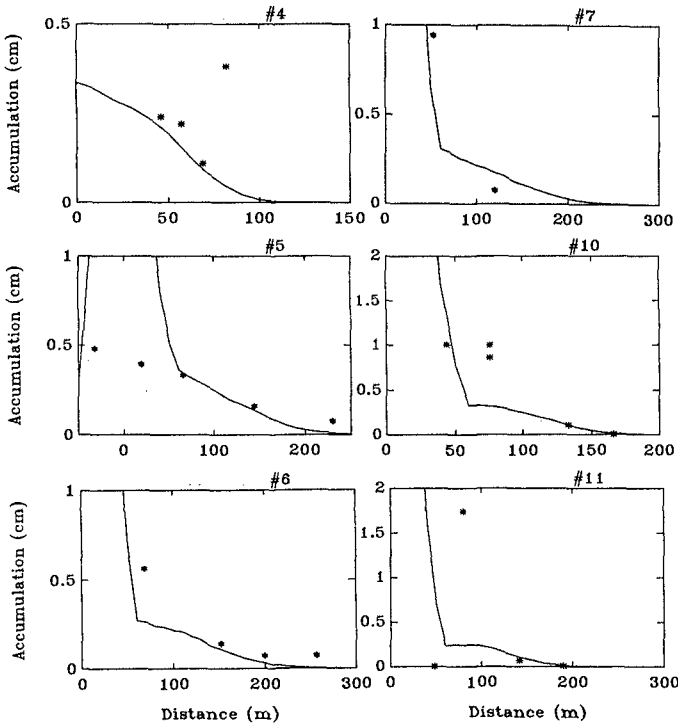
## 5. RESULTS

Model estimates of dredged material accumulation on the sea floor are compared with field measurements obtained from sediment trap deployments. The model is run to simulate the dumps that were monitored with sediment traps and results from the model are compared with sediment trap measurements in figures 4 and 5. The dots on the six diagrams shown in figure 4 are the sediment trap measurements and the full lines show the results of model estimates of sedimentation corresponding to specific dumps monitored at Rivière-du-Loup. The sharp breaks in model estimates result from the fact that sediment accumulation is much higher near the point of impact, where a large proportion of the dumped sediments are settling.

Figure 5 shows the monitoring settings for dumps #4 and #11. Contours of sediment accumulation on the sea floor predicted by the model are plotted on a grid. The location of sediment traps is indicated by dots. Model estimates corresponding to sediment trap measurements are outlined in the upper right corner of each diagram.

### 6. DISCUSSION AND CONCLUSIONS

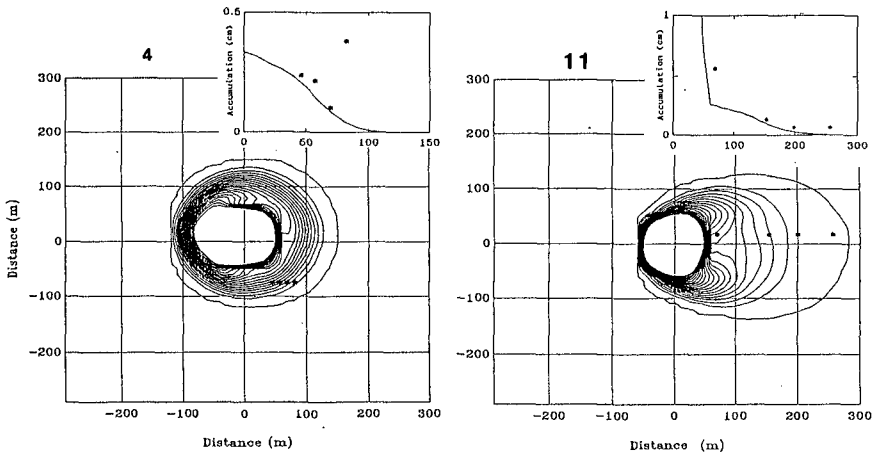
The dumping of dredged sediments from a scow is an operation which is difficult to monitor, particularly when tidal currents are strong. Sediment traps have to be deployed ahead of time before dumping takes place. The success of the operation depends on the ability to foresee the direction and intensity of tidal currents at the very moment the dumping of dredged sediments will take place. Because of tidal currents and winds, dumps do not always take place at the exact location where they had been planned, with the consequence that the alignment of sediment traps is not always optimal. In addition, sediments dredged with a clamshell remain clumsy and scows are equipped with doors that do not open instantly. The result is that dumped sediment loads are not always as uniform as one would like from an experimental point of view.



**Figure 4.** Comparison of model estimates and sediment trap measurements. The full lines on these six diagrams show the model estimates and the dots are the sediment trap measurements. The sharp breaks in model estimates result from the fact that sediment accumulation is much higher near the point of impact, where a large proportion of the dumped sediments settle out.

Despite the problems inherent with the monitoring of dispersal of dredged sediments, the monitoring carried out at Rivière-du-Loup and Rimouski was successful enough to warrant that the concepts used to develop the present model are realistic. As it can be seen in figure 4, dump #4 shows a good agreement between measurements and model except for the fourth sediment trap for which there is no explanation. Dump #5 is one of the most interesting, because it shows that the sedimentation rate as a function of distance from the point of impact is well predicted by the model, although the point of impact of the model (coordinates 0,0) does not coincide with the location where the dump effectively took place. The other diagrams show a relatively good agreement between measurements and estimates. An exact fit between model and field measurements is beyond expectations. However, the overall trends and rates of sedimentation as a function of distance from the point of impact estimated by the model are realistic.

The correlation between model estimates and sediment trap measurements is outlined more explicitly in figure 5. Dump #4 took place when tidal currents were weak,  $.1 \text{ ms}^{-1}$ , and dump #11 was carried out when tidal currents reached  $.7 \text{ ms}^{-1}$ .



**Figure 5.** Examples of sediment distribution for different tidal conditions. Results obtained from the model are compared with accumulation in sediment traps. The quantity of sediments dumped is 400 cubic meters and the water depth is 10 m. Tidal currents are  $.1 \text{ ms}^{-1}$  for the plot on the left and  $.7 \text{ ms}^{-1}$  for the plot on the right. Dots on the plot show the location of the sediment traps. The diagrams on the upper right corner of each plot compare the simulation from the model (the full line) with the measurements from the sediment traps.

In both cases the agreement is good between the model estimates and field measurements. Comparison of these two experiments outlines the importance of tidal currents as well as the capacity of the model to cope with it. The principal effect of tidal currents is to advect dumped sediments. The distance reached by sediments when tidal currents are strong ( $.7 \text{ ms}^{-1}$ , dump #11) is 200 m., which is twice the distance reached under weak tidal currents ( $.1 \text{ ms}^{-1}$ , dump #4).

At the present stage of development, the quantity of sediments settling at the point of impact versus the quantity entrained in a density current is based on approximate qualitative observations. We can only say that the formulation used in the present model seems acceptable because the sediment trap measurements obtained for specific dumps are adequately estimated by the present model configuration. The evaluation of settling of sediments at the point of impact would need to be investigated further. One difficulty is that it is not possible to place sampling instruments directly under the scow, because they would be buried by the sediment load settling at the point of impact. One avenue is to experiment in flume tanks to gain a better understanding of the physics of this phenomenon. An other approach would be to survey the dumping operations with a multi-beam echosounding system. The present experiments were carried out using a single echo-sounder aboard a ship at anchor, which is equivalent to carrying out eulerian measurements at a single point of observation. A stationary multi-beam system would provide a two-dimensional perspective of the phenomenon. Furthermore, if positioning were precise enough and the ship could move rapidly by comparison with the cloud of dumped sediments, a three-dimensional perspective of dumped sediment dispersal could be obtained.

## ACKNOWLEDGMENTS

This publication is a contribution of the Oceanographic Centre of Rimouski - a partnership of INRS (Institut National de la Recherche Scientifique) and UQAR (Université du Québec à Rimouski) operating under the auspices of University of Quebec. The research presented in this paper was sponsored by Fisheries and Oceans Canada, contract No FP707-9-4296/01-XSK. The authors are grateful to Dr. A. Walton for reading the manuscript and they also acknowledge the collaboration of Captain P. Tremblay.

## REFERENCES

- Bokuniewicz, H.J. 1978. Field study of the mechanics of the placement of dredged material at open-water disposal sites. U.S. Army Corps of Engineers, WES-TR-D-78-7, 152 p.

- Edge, B.L. and Dysart, B.C. 1972. Transport mechanisms governing sludges and other materials barged to sea. Civil Engineering and Environmental Systems Engineering, Clemson University.
- Gordon, R.B. 1974. Dispersion of dredge spoil dumped in near-shore waters. *Estuarine and Coastal Marine Science*, 2:349-358.
- Keulegan, G.H. 1957. Thirteenth progress report on model laws for density currents. An experiment study of the motion of saline water from locks into fresh water channels. U.S. Natl. Bur. Standards Rept. 5168.
- Koh, R.C.Y. and Chang, Y.C. 1973. Mathematical Model for Barged Ocean Disposal of Waste. Environmental Protection Technology Series, EPA 660/2-73-029, U.S. Environmental Protection Agency, Washington, D.C.
- Krishnappan, B.G. 1975. Dispersion of granular material dumped in deep water. Canada Centre for Inland Waters, Scientific Ser. no 55, 114 p.
- Malherbe, B. 1990. Case study of dumping in open areas. C. Alzieu and B. Galenne eds. Actes du séminaire international sur les aspects environnementaux liés aux activités de dragages, Nantes, France. p. 227-261.
- Middleton, G.V. 1966a. Experiments on density and turbidity currents (I. Motion of the head). *Canadian Jour. Earth Sci.* 3: 523-546.
- Middleton, G.V. 1966b. Experiments on density and turbidity currents (II. Uniform flow of density currents). *Canadian Jour. Earth Sci.* 3: 627-637.
- Middleton, G.V. and Southard, J.B. 1984. Mechanics of sediment movement. Short Course No. 3 (2nd edition), S.E.P.M. Tulsa, Okla. 401 p.
- Tavolaro, J.F. 1984. A sediment budget study of clamshell dredging and ocean disposal activities in the New Bight. *Environmental Geology and Water Science*, 6 (3): 133-140.
- Truitt, C.L. 1988. Dredged material behavior during open-water disposal. *J. Coastal Res.* 4 (3): 489-497.
- Truitt, C.L. 1986. Long-term effects of dredging operations program - the Duwamish Waterway demonstration project: Engineering analysis and results of physical monitoring. US Army Engineer Waterways Experiment Station. Tech. Rept. D-86-2, 57 p.



## CHAPTER 235

### A modified method of characteristic technique combined with Galerkin finite element method to solve shallow water mass transport problems

A.Garzon (\*), L. D'Alpaos (\*\*)

(\*) Crea s.r.l., Via A.Sacchi 14,37124 Verona, Italy

(\*\*) Institute of Hydraulics "G. Poleni", University of Padova, Padova, Italy

#### Abstract

In order to solve water circulation and solute transport-diffusion problems in two-dimensional hydrodynamical systems a comprehensive simulator, composed by two finite element models, has been developed. In particular the first model, which is of semi-implicit kind, solves hydrodynamical shallow water equations whereas the second, which is an Eulerian-Lagrangian method (ELM), is based on the Modified Method of Characteristics (MMOC) combined with Galerkin finite element method. Semi-implicit procedures for hydrodynamical models are sometimes used with finite differences but are quite rare with finite elements. Nevertheless they have a lot of advantages compared to the others, principally linked to a considerable time saving. This is determined by the fact that the systems of equations in the unknown levels and velocities are uncoupled and the time step is not constrained by Courant-Friedrichs-Levy stability criterion. It can be demonstrated that in the linear case the hydrodynamic model is indefinitely stable and good accuracy can be achieved for velocity field. On the other side, the proposed transport-dispersion model presents interesting features, among which the possibility to obtain good results in mass conservation and minimum numerical oscillations or grid orientation problems even under sharp front conditions. In these papers we shall discuss only the approximation method of transport-dispersion model, showing the theoretical fundamentals and some of its applications.

#### Introduction

The transport-dispersion equation constitutes one of the most difficult problem to solve by numerical methods, since the equation ranges from a parabolic to almost hyperbolic form, depending on the ratio of advection to dispersion, the Peclet number. In particular, when advection terms of the equation are dominant and concentration gradients very steep, using standard finite element many difficulties in the numerical solution arise, such as numerical dispersion, numerical oscillations, grid orientation influences and, even, mass conservation.

To treat this problem many approximations have been developed, but, nevertheless, three broad classes of methods can be identified.

The first group, based on using optimal test functions, is referred to as Optimal Spatial Methods (OMS). Examples of these approximations include the Quadratic Petrov-Galerkin Method (Christie et al., 1976; Bouloutas et al., 1988), the Optimal Test Function Method (OTF) (Celia et al., 1989). The limits of all these schemes consist in the variably upwinded nature of test functions which restrict the range of Peclet numbers allowable without numerical diffusion.

A second broad class is constituted by the Eulerian-Lagrangian methods (ELM), which appear to overcome the problems inherent to advection-dominated transport conditions. The approximations in this class of schemes have, as their common element, a Lagrangian treatment of advection processes. Again there are many examples from literature, including Operator Splitting Method (Baptista, 1987;

Wheeler et al., 1988), Eulerian-Lagrangian Method with the Method of Characteristics (Pinder et al., 1977), Eulerian-Lagrangian Method with the Modified Method of Characteristics (Ewing et al. 1984; Russel, 1985; Chiang et al., 1988). These methods can obtain significant reduction in numerical oscillations and in numerical diffusion even in presence of large Courant numbers. The principal drawbacks of ELM are, in some case, difficulty to conserve mass and to formulate general boundary conditions. However, material balance mass errors can be greatly reduced when an accurate velocity field from the solution of hydrodynamical equations is derived.

The third broad class (ELLAM) combines the ideas of OTF and ELM, by using space-time test functions satisfying a local adjoint condition that introduces a Lagrangian frame of reference (Celia et al., 1989; Zisman, 1988; Russel, 1990). Among other things, ELLAM schemes allow the solution of transport-dispersion equation in the conservative form unlike, for example, ELM methods where the obtained solution concerns the non-conservative form of the same equation. For this reason sometimes ELLAM approximations can achieve a better result in mass conservation than ELM themselves, even if at the expense of a non-irrelevant increase of computational effort.

Taking into account all these considerations, these papers present a comprehensive analysis of a numerical method adopting a Eulerian-Lagrangian Method with the Modified Method of Characteristics (MMOC), with interesting proceedings to evaluate the advection term of diffusion equation. Furthermore two brief reports, regarding a numerical validation and a real case application, are presented.

### Governing equation

The general solute diffusion equation in a non-conservative form has been derived as follows:

$$\frac{\partial c}{\partial t} + \bar{v} \cdot \nabla c - \frac{1}{h} \nabla \cdot (hD \cdot \nabla c) = s \quad (1)$$

where

- c solute concentration, [kg/m<sup>3</sup>];
- D dispersion tensor, [m<sup>2</sup>/s];
- $\bar{v}$  velocity vector, [m/s];
- h water depth, [m] ( $h = Z - Z_f$  where  $Z$ ,  $Z_f$  are surface and bottom levels, relative to a reference plane);
- s solute source or sink, [(kg/m<sup>3</sup>)/s].

The dispersion tensor D in two-dimensional flow fields is defined as (Peaceman, 1966):

$$D = \begin{pmatrix} D_{xx} & D_{xy} \\ D_{yx} & D_{yy} \end{pmatrix} = D_m I + \frac{hg^{1/2}}{C|\bar{v}|} \left\{ \alpha_l \begin{pmatrix} u^2 & uv \\ uv & v^2 \end{pmatrix} + \alpha_t \begin{pmatrix} v^2 & -vu \\ -vu & u^2 \end{pmatrix} \right\} \quad (2)$$

where

- $D_m$  molecular isotropic diffusion coefficient, [m<sup>2</sup>/s];
- I unit tensor, dimensionless;
- $\alpha_l$  longitudinal dispersion coefficient, dimensionless;
- $\alpha_t$  transversal dispersion coefficient, dimensionless;
- u, v velocity components along coordinate axes, [m/s];
- g gravitational constant, [m/s<sup>2</sup>];
- C Chézy coefficient, [m<sup>1/2</sup>/s].

The factors which determine diffusion processes are mainly two: the first, of advection kind, characterized by transport for the fluid base motion; the second, of dispersive nature, linked to whirling motions of turbulent origin internal to fluid masses.

Indeed equation (1) would range from a hyperbolic-type, if the hydrodynamic dispersion were null, to a parabolic-type, if the process were purely dispersive. Numerical proceedings which permit to solve suitably hyperbolic differential equations differ deeply from those applied in case of parabolic-type equations. It is well known that solution for hyperbolic-type equations can be represented from the initial data propagating over well-defined paths, called characteristics, over the surface in direction of flow. The solution of the overall equation (1) can be viewed as spreading or dispersion away from these characteristic curves, along which solute concentration is a smooth function (Douglas and Russel, 1982).

With regard to this, consider a domain  $\Omega$  delimited by a boundary  $\Gamma$  where Dirichlet or null-flux boundary conditions are applied.

Defined the unit vector  $\bar{v}(\bar{x}, t)$  in the characteristic direction, the directional derivative along a characteristic curve in  $\bar{x}$  at time  $t$  can be evaluated through the expression:

$$\frac{\partial}{\partial \tau} = \frac{1}{(|\bar{v}|^2 + 1)^{1/2}} \left( \frac{\partial}{\partial t} + \bar{v} \cdot \nabla \right) \quad (3)$$

where  $\bar{v}$  is the local velocity vector.

If we substitute expression (3) in equation (1), we will obtain:

$$(|\bar{v}|^2 + 1)^{1/2} \frac{\partial c}{\partial \tau} - \frac{1}{h} \nabla \cdot (h D \cdot \nabla c) = s \quad (4)$$

which constitutes the non-divergence form of diffusion equation.

### Time discretization of diffusion equation

Many methods, based on characteristics, fix a point at the current time level and evaluate the final position at the advanced time level. MMOC method takes the opposite view, fixing a point at the advanced time level  $t^{n+1}$  and asking where it came from at the current time level  $t^n$ . Thus the solution grid at the advanced time level is controlled by the method, not the flow, so allowing a fixed finite element mesh to use.

In the mathematical model the derivative along characteristic curves can be approximated by a back-ward finite difference procedure, obtaining in this way:

$$(|\bar{v}|^2 + 1)^{1/2} \frac{\partial c}{\partial \tau} = (|\bar{v}|^2 + 1)^{1/2} \cdot \frac{c(\bar{x}, t^{n+1}) - c(\bar{x}^*, t^n)}{[(\bar{x} - \bar{x}^*)^2 + (t^{n+1} - t^n)^2]^{1/2}} + O(\Delta \tau) \quad (5)$$

If we would assign a precise physical meaning to the problem,  $\bar{x}^*$  might be interpreted as the initial position at time  $t^n$  where a particle, following the flow line, will arrive at time  $t^{n+1}$  from. During the time interval  $\Delta t$  within  $t^n$  and  $t^{n+1}$ , the relation linking  $\bar{x}, \bar{x}^*$  can be achieved, as first approximation, through the following cinematic expression:

$$\bar{x}^* = \bar{x} - \bar{v} \cdot \Delta t + O(\Delta t^2) \tag{6}$$

The backward difference in time makes the procedure implicit in nature and (5) becomes:

$$\left(|\bar{v}|^2 + 1\right)^{1/2} \frac{\partial c}{\partial \tau} = \frac{c(\bar{x}, t^{n+1}) - c(\bar{x}^*, t^n)}{\Delta t} + O(\Delta \tau) \tag{7}$$

The final form of the diffusion equation to solve, by using Galerkin weighted residual method, is thus the following (Neuman, 1981; 1983):

$$\frac{c(\bar{x}, t^{n+1}) - c(\bar{x}^*, t^n)}{\Delta t} - \frac{1}{h} \nabla \cdot (hD \cdot \nabla c^{n+1}) = s' \tag{8}$$

Considering equation (8), it can be noted that, in order to avoid the appearance of an artificial numerical diffusion mainly connected to large time steps often utilized in numerical simulations, the dispersion term is computed at advanced time level  $t^{n+1}$ .

Before proceeding to the mathematical formulation of the finite element method, it is necessary to define some notations. First of all denote the following surface and line integrals:

$$(u, v) = \int_{\Omega} (u \cdot v) d\Omega$$

$$\langle u, v \rangle = \int_{\Gamma} (u \cdot v) d\Gamma$$

where center dot is the inner product. Let  $H^n(\Omega)$  be the Hilbert space of n-order defined in  $\Omega$ . Let also  $H_{\Gamma_1}^n(\Omega)$  be the Hilbert subspace of n-order defined in  $\Omega$  of functions  $u \in H^n(\Omega)$  which vanish on boundary  $\Gamma_1$  where Dirichlet boundary conditions are applied.

The variational problem corresponding to differential equation (8), subject to boundary conditions just pointed out, is then the following:

$$\left( \frac{c(\bar{x}, t^{n+1}) - c(\bar{x}^*, t^n)}{\Delta t} - \frac{1}{h} \nabla \cdot (hD \cdot \nabla c^{n+1}) - s', \psi \right) = 0 \quad (\forall \psi \in H_{\Gamma_1}(\Omega)) \tag{9}$$

Integrating by parts against weight function  $\psi$  with Green formulas, we will obtain the Galerkin form of variational problem:

$$\left( \frac{c(\bar{x}, t^{n+1}) - c(\bar{x}^*, t^n)}{\Delta t}, \psi \right) + \frac{1}{h} (hD \cdot \nabla c^{n+1}, \nabla \psi) - (s', \psi) - \langle D \nabla c \cdot \bar{n}, \psi \rangle = 0 \quad (\forall \psi \in H_{\Gamma_1}(\Omega)) \tag{10}$$

Consider now a base  $\varphi_i$  ( $i = 1, 2, \dots, N$ ) of a subspace  $K_N \subset H_{\Gamma_1}^1(\Omega)$  and suppose unknown concentration  $c$  and weight function  $\psi$  to be approximated by  $C$  and  $\varphi_i$  respectively, belonging to such subspace  $K_N$ ; then equation (10) provides the following  $N$  linear equations in the unknown concentration  $C^{n+1} = C(\bar{x}, t^{n+1})$ :

$$\left( \frac{C^{n+1} - C(\bar{x}^*, t^n)}{\Delta t}, \varphi_i \right) + \frac{1}{h} (hD \cdot \nabla C^{n+1}, \nabla \varphi_i) - (S', \varphi_i) - \langle \frac{q_d^{n+1}}{h}, \varphi_i \rangle = 0 \quad (i=1, 2, \dots, N) \tag{11}$$

where  $q_d$  is the flux on the boundary, for unit length, of only dispersive nature.

Since, for hypothesis, boundary flux is null, developing equation (11) in its full form we will

obtain after all:

$$\begin{aligned} & (C^{n+1}, \varphi_i) + \frac{\Delta t}{h} \left\{ h \left[ D_{xx} \frac{\partial C^{n+1}}{\partial x} + D_{xy} \frac{\partial C^{n+1}}{\partial y} \right] \frac{\partial \varphi_i}{\partial x} \right. \\ & \left. + \left[ h \left[ D_{xy} \frac{\partial C^{n+1}}{\partial x} + D_{yy} \frac{\partial C^{n+1}}{\partial y} \right] \frac{\partial \varphi_i}{\partial y} \right] \right\} = (C(\bar{x}^*, t^n), \varphi_i) + (S', \varphi_i) \Delta t \quad (i=1,2,\dots,N) \end{aligned} \quad (12)$$

Equation (12) completes the procedure which combines the modified method of characteristics with finite element Galerkin method for the simulation of solute transport-dispersion equation. The integral relative to the function  $C(\bar{x}^*, t^n)$  is computed through the well known quadrature formulas in a approximated way, since  $\bar{x}^*$  may belong to several elements as  $\bar{x}$  runs over a single element. Finally note that, being advection term  $C(\bar{x}^*, t^n)$  moved to the right side of (12), the system of linear equations is symmetric and positive definite.

**Backtracking algorithm**

The integrals in (12) are standard in finite element schemes except for the inner product relative to  $C(\bar{x}^*, t^n)$ . The point  $\bar{x}^*$  does not lie, in general, at a precise node of the mesh, since it becomes necessary to utilize some particular procedure for its determination. In particular the integration involving  $C(\bar{x}^*, t^n)$  is calculated by means of Gauss quadrature formulas, with a number of integration points in each element variable from three to twelve, in function of concentration front steepness and relative required solution precision. Consider then a point  $P(\bar{x}_i, t^{n+1})$  within a finite element  $T_S$  at time  $t^{n+1}$  (fig. 1). Actually, even if particle path joining points  $P(\bar{x}_i, t^{n+1})$  and  $P(\bar{x}_i^*, t^n)$  could be determined, as first approximation, from equation (6) using the same time step considered for integration of overall diffusion equation, mainly for increasing method's precision particle path is calculated with a time step  $\Delta t'$  shorter.

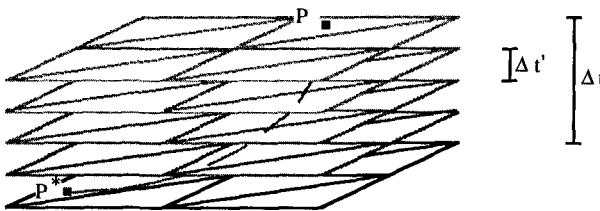


Fig. 1 - Path of a particle along a characteristic curve in the hydrodynamic system during a integration time  $\Delta t$  of dif-fusion equation. Integration time step  $\Delta t'$  of characteristics is often much less than  $\Delta t$ , with the aim to increase method accuracy.

The particular attention reserved to the evaluation of corresponding points  $P(\bar{x}_i, t^{n+1})$ ,  $P(\bar{x}_i^*, t^n)$

resides fundamentally in the aim to evaluate correctly the advection term of transport-dispersion equation, fraction certainly of crucial importance especially in coastal and lagoon problems.

The cinematic differential equations governing particle motion are the following:

$$\frac{dx}{dt}=u(\bar{x},t) \quad , \quad \frac{dy}{dt}=v(\bar{x},t) \quad (13)$$

with initial conditions  $\bar{x}=\bar{x}_i$  at  $t=t^{n+1}$ . The velocities  $u(\bar{x},t)$ ,  $v(\bar{x},t)$  inside a generic  $m$ -node finite element  $T_S$  will be calculated through the expressions:

$$\begin{cases} u(\bar{x},t)=\sum_1^m u_j(t;T_S)\cdot\phi_j(\bar{x};T_S) \\ v(\bar{x},t)=\sum_1^m v_j(t;T_S)\cdot\phi_j(\bar{x};T_S) \end{cases} \quad (14)$$

where  $u_j, v_j$  are  $j$ -th node velocities and  $\phi_j$   $j$ -th node shape function within an element  $T_S$ .

Generally nodal velocities  $u_j, v_j$  from hydrodynamical simulation are stored only at discreet regular intervals, so that it is necessary some type of interpolation to determine velocity values at each time, as required by integration of (13). In this case, to interpolate velocities, linear, quadratic and cubic polynomials are used, depending on number of velocity values available for such node in that particular phase of hydrodynamical simulation.

### Boundary conditions

As we pointed out, one of the principal drawbacks of ELM procedures is the difficulty of formulating them for general boundary conditions. Indeed, during the early development of modified method of characteristics, a no-flow boundary condition was assumed for all boundaries (Neuman, 1981). Actually these schemes are suitable to reproduce both Dirichlet conditions at open boundaries  $\Gamma_1$  ( $I^\circ$  type) and no-flow conditions at closed boundaries  $\Gamma_3$  ( $III^\circ$  type).

For what concerns  $I^\circ$  type conditions, it is necessary to distinguish, first of all, between inflow and outflow at open boundary  $\Gamma_1$ . During inflow boundary conditions are imposed upon the system from the outside, so being sufficient to assign directly the concentration values on boundary nodes. The situation at an outflow boundary is altogether different, since boundary conditions are no longer influenced from the outside. In this case, neglecting dispersion and so making an approximation quite often reasonable in this kind of problems, the concentration value corresponds with that of the particle arriving in a boundary node from inside the system. Therefore it needs only to determine initial position of the particle by the backtracking procedure.

At last in the case of  $III^\circ$  type condition, when  $\bar{x}$  reaches across the boundary, the hydrodynamical velocity field is used to reflect back the particle, implicitly imposing a no-flow boundary condition.

### Model verification

The following presents an analysis of numerical results of the model. It is important to emphasize that, mainly in order to avoid completely the presence of negative concentrations, has been developed a particular procedure able to eliminate negative values and to conserve exactly solute masses without introducing any significant numerical diffusion, as it will be proved later in the numerical tests.

The model has been applied to cases from low to high Peclet numbers, in order to observe model's ability in handling steep concentration gradients. The diffusion equation was solved with a 2-D grid consisting of right isosceles 3-node elements of small legs  $\Delta x$ , where  $\Delta x$  was nodal spacing. Independent parameters include Peclet number  $Pe = u \Delta x / D$ , Courant number  $Cu = u \Delta t / \Delta x$  and the number of elements  $N$  which the source is distributed in flow direction over.

It was analysed the following two sets, whose analytical solutions are known, having assumed in all cases seven integration points for each triangular element, utilized in Gauss quadrature formulas for integration of advection terms.

#### Instantaneous source in a uniform flow

The base one-dimensional equation is the following :

$$\frac{\partial c}{\partial t} + u \frac{\partial c}{\partial x} - D \frac{\partial^2 c}{\partial x^2} = 0$$

with initial condition  $c(x) = C_0 \cdot \exp(-\sigma |x - x_0| / N \Delta x)$  for  $t=0$ .

From numerous tests, mass and phase appear exact for all runs and numerical diffusion, even with a very concentrated source and high  $Pe$ , is quite negligible. In the case of a particularly steep gradient ( $N=2$ ), with parameters  $Cu = 0.48$  and  $Pe = \infty$ , results are shown in Fig.2 for different time steps (0,10,20,30,40 and 50  $\Delta t$ ).

#### Breakthrough distribution in a uniform flow

The same analysis was carried for the case of a breakthrough distribution in a uniform flow.

The graphics in Fig.3 still show the case of a particularly steep gradient ( $N=3$ ),  $Cu = 0.48$  and  $Pe = \infty$  for different time steps (0,10,20,30,40 and 50  $\Delta t$ ). It is possible to note only small oscillations in numerical results, however quickly damped in space, on either edges of the breakthrough curve. However, by numerical experiences, their maximum value and influence tends to decrease with increasing  $N$  and decreasing  $Pe$ .

### Model application to Barbamarco lagoon (Rovigo - ITALY)

Among other things, the model has been set-up and applied to examine diffusion phenomena on Barbamarco lagoon, which is a small coastal lagoon on Delta Po. The hydrodynamical model has been verified on the base of tidal level measurements, caught in four gages all around the lagoon, and contemporary discharges, flowing through the two mouths and a controlled gate dug into Po river.

Because, unfortunately, there were no data measurements relating to diffusion phenomena in the lagoon, to evaluate the effectiveness of the projected canal network to dredge the results of the model were compared with those referring to real situation supposing a instantaneous source release of a conservative solute in different zones of hydrodynamical system, especially where water exchange is

particularly difficult.

The most interesting result is relative to a solute released near West Mouth (fig. 4). In fig. 4a the finite element mesh of Barbamarco lagoon and the Zoom of the zone interested to conservative solute diffusion are represented, while in fig. 4b the initial concentration distribution is shown. The following two pictures (fig. 4c, 4d) illustrate the distribution evolution during the first 12 hours, with 6 hours' time between representations. Finally the last four pictures (fig. 5a, 5b, 5c, 5d), which report the distribution isolines relative to four days from the beginning of hydrodynamical simulation, show the effects of slow plume migration towards East Mouth, so confirming the results obtained with hydrodynamical model where a residual current in the same direction, equal to roughly 10% of total volume exchanged during a tidal cycle, was noted.

## Conclusion

A comprehensive simulator composed by two finite element models, the first solving hydrodynamical shallow water equations whereas the second the diffusion equation, has been developed. However, in this report only the diffusion model, based on the Modified Method of Characteristics (MMOC), is presented.

The important feature of the MMOC procedure is tracking the solution backward in time along the characteristics, in contrast to the forward front tracking or moving point methods. Thus the solution grid at the advanced time is controlled by the method, not the flow, and therefore a fixed grid system can be used for mathematical simulations. Among other advantages algebraic system is symmetric and positive definite.

Since diffusion equation is solved in a non-divergence form, it is required a very accurate velocity field to maintain good numerical material balance. On its hand, the two levels semi-implicit hydrodynamical model seems to furnish a solution accurate enough to assure overall mass conservation.

The accuracy of the model is analyzed through a comparison with analytical solutions. Good agreement between model results and analytical solutions is demonstrated. Furthermore the experiments demonstrate that large time steps can be taken without sacrificing much of MMOC model's solution accuracy. However, the model does require to consider a sufficient number of Gauss points in each finite element to resolve sharp concentration gradients increasing, in this case, computational effort.

## References

- [1] Baptista, A.M., "Solution of advection-dominated transport by Eulerian-Lagrangian methods using the backwards method of characteristics.", Ph. D. Thesis, Massachusetts Institute of Technology, 1987.
- [2] Bouloutas, E.T. and M.A. Celia, "An analysis of a class of Petrov-Galerkin and Optimal Test Functions methods.", Proc. Seventh Int. Conf. Computational Methods in Water Resources (Celia, et al., eds.), 15-20, 1988.
- [3] Brooks, A. and T.J.R. Hughes, "Streamline upwind Petrov-Galerkin formulations for convection dominated flows with particular emphasis on the incompressible Navier-Stokes equations.", CNAME, 32, 199-259, 1982.
- [4] Celia, M.A. and I. Herrera, "Solution of general ordinary differential equations by a unified theory approach.", Numerical Methods for PDE's, 3(2), 117-129, 1987.



- [5] Celia, M.A., I. Herrera, and E.T. Bouloutas, "Adjoint Petrov-Galerkin methods for multi-dimensional flow problems.", *Finite Element Analysis in Fluids*, Chung and Karr, eds., UAH Press, 965-970, 1989.
- [6] Celia, M.A., I. Herrera, E. Bouloutas, and J.S. Kindred, "A new numerical approach for the advective-diffusive transport equation.", *Numerical Methods for PDE's*, 5, 203-226, 1989.
- [7] Celia, M.A., J.S. Kindred, and I. Herrera, "Contaminant transport and biodegradation: I. A numerical model for reactive transport in porous media.", *Water Resources Research*, 25, 1141-1148, 1989.
- [8] Chiang, C.V., Wheeler, M.F. and Bedient, P.B., "A modified method of characteristics technique and mixed finite elements method for simulation of groundwater solute transport.", *Water Resources Research*, 25, 1541-1549, 1989.
- [9] Christie, I., D.F. Griffiths, and A.R. Mitchell, "Finite element methods for second order differential equations with significant first derivatives.", *Int. J. Num. Meth. Engrg.*, 10, 1389-1396, 1976.
- [10] Douglas, J. Jr., and T.F. Russel, "Numerical methods for convection-dominated diffusion problems based on combining the method of characteristics with finite element or finite difference procedures.", *SIAM J. Numer. Anal.*, 19 (1982), 871-885.
- [11] Ewing, R.E., T.F. Russel, and M.F. Wheeler, "Convergence analysis of an approximation of miscible displacement in porous media by mixed finite elements and a modified method of characteristics.", *CNAME*, 47, 73-92, 1984.
- [12] Neuman, S.P., A. "Eulerian-Lagrangian numerical scheme for the dispersion-convection equation using conjugate space-time grids.", *J. Comp. Phys.*, 41, 270-294, 1981.
- [13] Neuman, S.P., "Computer prediction of subsurface radionuclide transport - An adaptive numerical method.", Rep. NURFG CR-3075. U.S. Nucl. Regul. Comm., Washington, D.C., 1983.
- [14] Peaceman, D.W., "Improved treatment of dispersion in numerical calculation of multidimensional miscible displacements.", *Soc. Pet. Eng. J.*, 6, 213-216, 1966.
- [15] Pinder, G.F., and W.G. Gray, "Fin. Element Simulation in Surface and Subsurface Hydrology.", 295 pp., Academic. San Diego, Calif., 1977.
- [16] Russel, T.F., M.F. Wheeler, and C.Y. Chiang, "Large-scale simulation of miscible displacement by mixed and characteristic finite element methods.", *Mathematical and Computational Methods in Seismic Exploration and Reservoir Modeling*, W.E. Fitzgibbon, ed., SIAM, Philadelphia, 1986, pp. 85-107.
- [17] Wheeler, M.F. and C.N. Dawson, "An operator-splitting method for advection-diffusion-reaction problems.", *MAFELAP Proc. VI*, Whiteman, ed., Academic Press, 463-482, 1968.
- [18] Zisman, S., "Simulation of contaminant transport in groundwater systems using Eulerian-Lagrangian localized adjoint methods.", MS Thesis, Dept. Civil Eng., MIT, 1989.

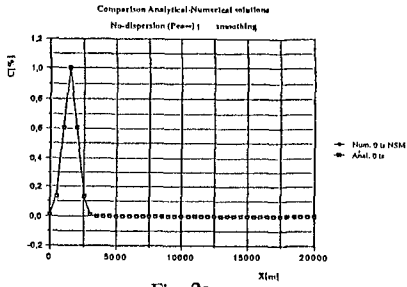


Fig. 2a

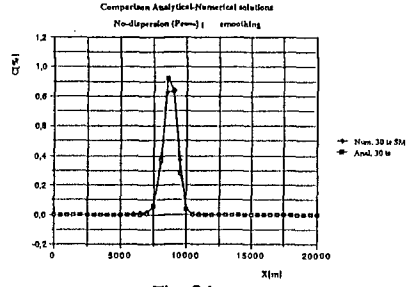


Fig. 2d

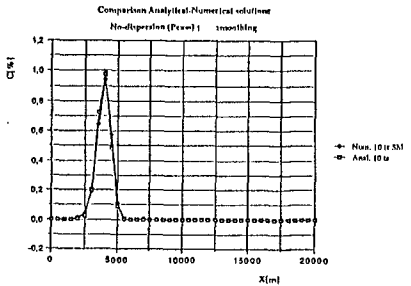


Fig. 2b

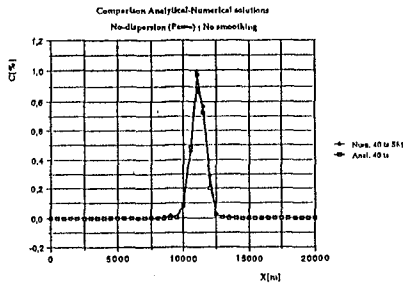


Fig. 2e

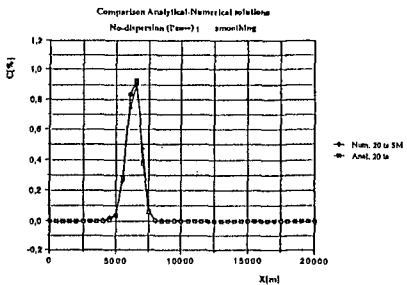


Fig. 2c

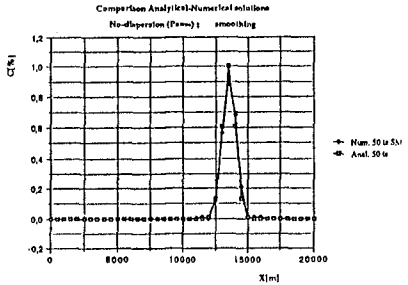


Fig. 2f

FIG. 2 - Instantaneous source in a uniform flow : comparison between analytical and numerical solutions in correspondence to different time steps [ $0 \Delta t$  (fig.2a),  $10 \Delta t$  (fig.2b),  $20 \Delta t$  (fig.2c),  $30 \Delta t$  (fig.2d),  $40 \Delta t$  (fig.2e),  $50 \Delta t$  (fig.2f)] with parameter values  $N=2$ ,  $Cu=0.48$  and  $Pe = \infty$ .

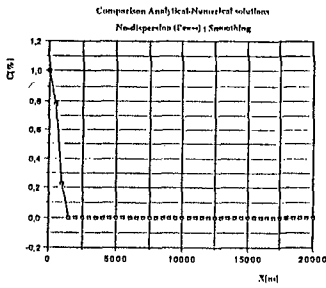


Fig. 3a

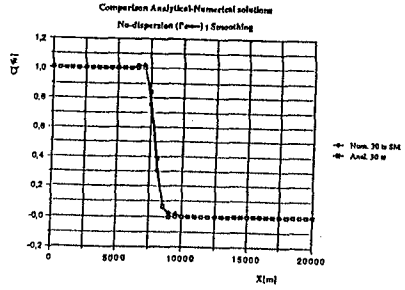


Fig. 3d

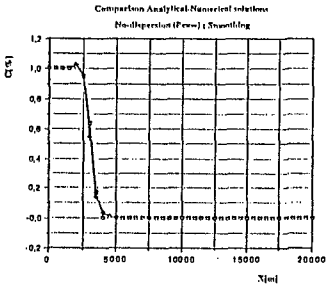


Fig. 3b

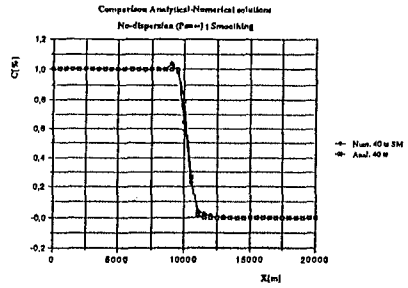


Fig. 3e

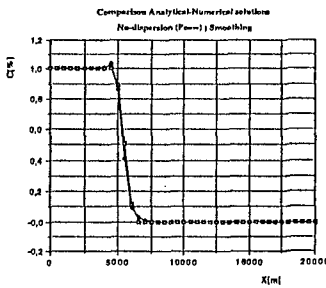


Fig. 3c

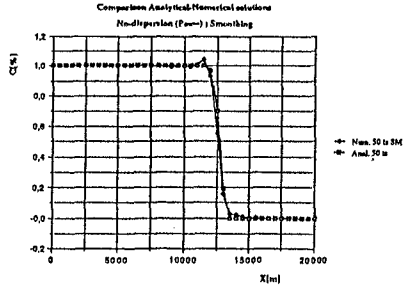


Fig. 3f

FIG. 3 - Breakthrough distribution in a uniform flow : comparison between analytical and numerical solutions in correspondence to different time steps [ $0 \Delta t$  (fig.3a),  $10 \Delta t$  (fig.3b),  $20 \Delta t$  (fig.3c),  $30 \Delta t$  (fig.3d),  $40 \Delta t$  (fig.3e),  $50 \Delta t$  (fig.3f)] with parameter values  $N=2$ ,  $Cu = 0.48$  and  $Pe = \infty$ .

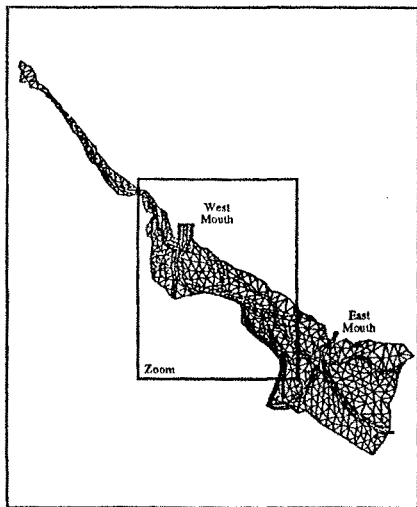


Fig. 4a - Barbamarco lagoon on Delta Po :  
finite element mesh

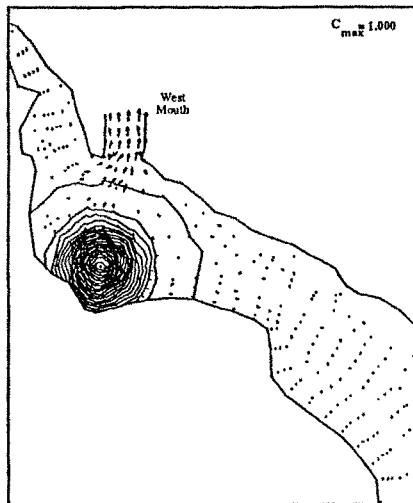


Fig. 4b : Barbamarco Lagoon on Delta Po :  
representation of isoconcentration lines for a  
instantaneous source of solute released near West  
Mouth since 2 [h] from the beginning of simulation

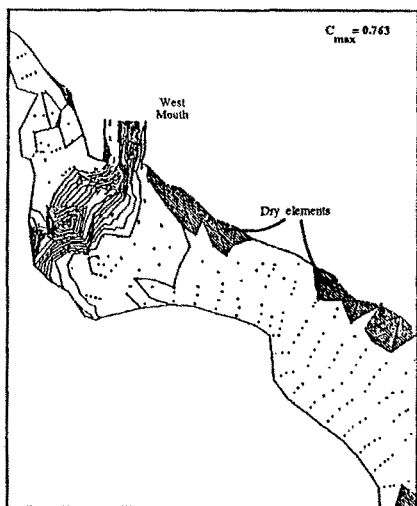


Fig. 4c : Barbamarco Lagoon on Delta Po :  
representation of isoconcentration lines for a  
instantaneous source of solute released near West  
Mouth since 8 [h] from the beginning of simulation

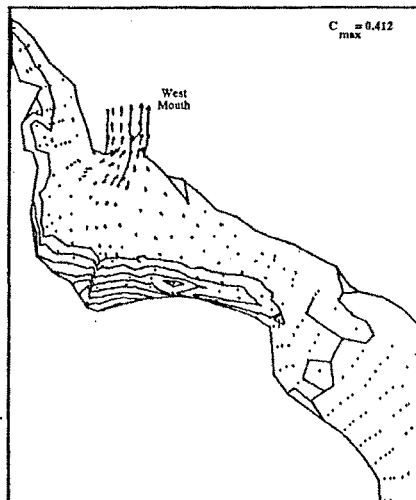


Fig. 4d : Barbamarco Lagoon on Delta Po :  
representation of isoconcentration lines for a  
instantaneous source of solute released near West  
Mouth since 14 [h] from the beginning of simulation

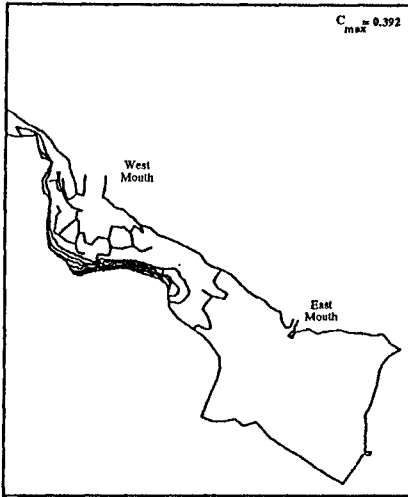


Fig. 5a : Barbamarco Lagoon on Delta Po : representation of isoconcentration lines for a instantaneous source of solute released near West Mouth since 1 [d] from the beginning of simulation

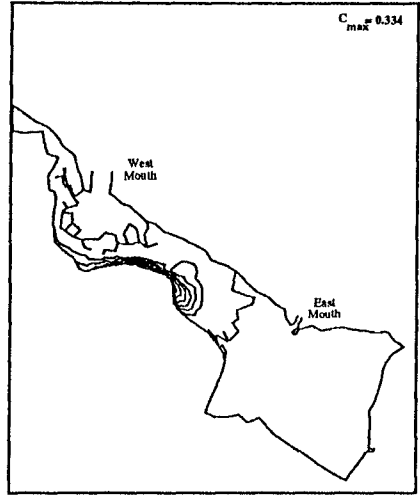


Fig. 5b : Barbamarco Lagoon on Delta Po : representation of isoconcentration lines for a instantaneous source of solute released near West Mouth since 2 [d] from the beginning of simulation

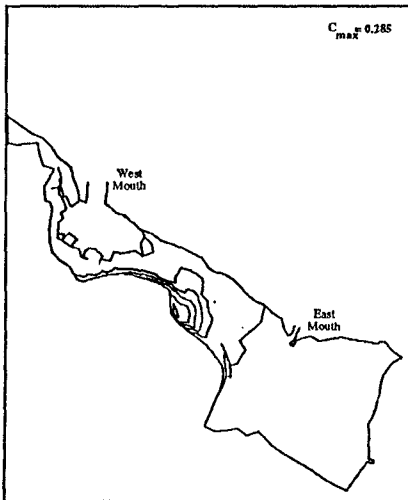


Fig. 5c : Barbamarco Lagoon on Delta Po : representation of isoconcentration lines for a instantaneous source of solute released near West Mouth since 3 [d] from the beginning of simulation

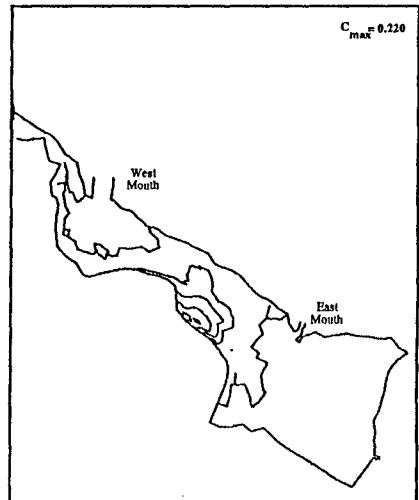


Fig. 5d : Barbamarco Lagoon on Delta Po : representation of isoconcentration lines for a instantaneous source of solute released near West Mouth since 4 [d] from the beginning of simulation

## CHAPTER 236

### SEDIMENTATION AND EROSION PROBLEMS OF YAKAKENT FISHERY HARBOR

A.Rıza GÜNBAK <sup>1</sup>, K. Tunç GÖKÇE <sup>2</sup>, Işıkhan GÜLER <sup>3</sup>

#### **Abstract**

This paper summarises the studies carried out about sedimentation and erosion problems of Yakakent Fishery Harbor. Since the start of the construction of the harbor, accretion in the west coast and erosion in the east coast occurs. Additionally, the entrance of the harbor shoals. As a result of accretion at the west coast shoreline moved towards sea and about 300meters of the breakwater was on land. Erosion at the east coast of the harbor caused collapse of two houses which were about 20meters inside the original shoreline. After identifying the causes, precautions for sedimentation and erosion problems are again studied using one-line model and a series of precautions are recommended.

#### **Introduction**

Yakakent Fishery Harbor is located at the Black Sea coast of Türkiye as shown in figure 1.

Construction of the harbor was started in 1972. Initially the harbor was protected by a 350meters long main breakwater and a secondary breakwater of 230m. length. Then in 1988 the main breakwater was extended to 475m. Figure 2 shows the plan of the harbor after this stage.

---

<sup>1</sup> Prof.Dr., Middle East Tech. Univ. Civ. Engrg. Dept.06531 Ankara,TÜRKIYE

<sup>2</sup> Dr., Middle East Tech. Univ. Civ. Engrg. Dept.06531 Ankara,TÜRKIYE

<sup>3</sup> Civ. Engr., Yüksel Proje Engrg. and Consultant Co.Inc. Ankara, TÜRKIYE

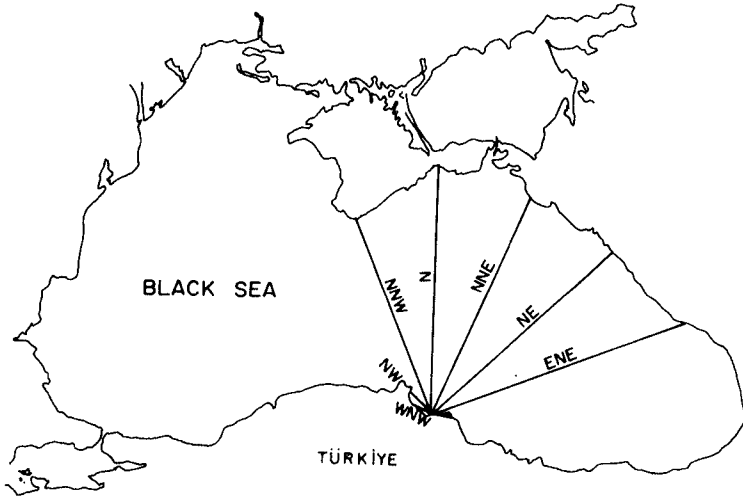


Figure 1 ... Location of Yakakent Fishery Harbor

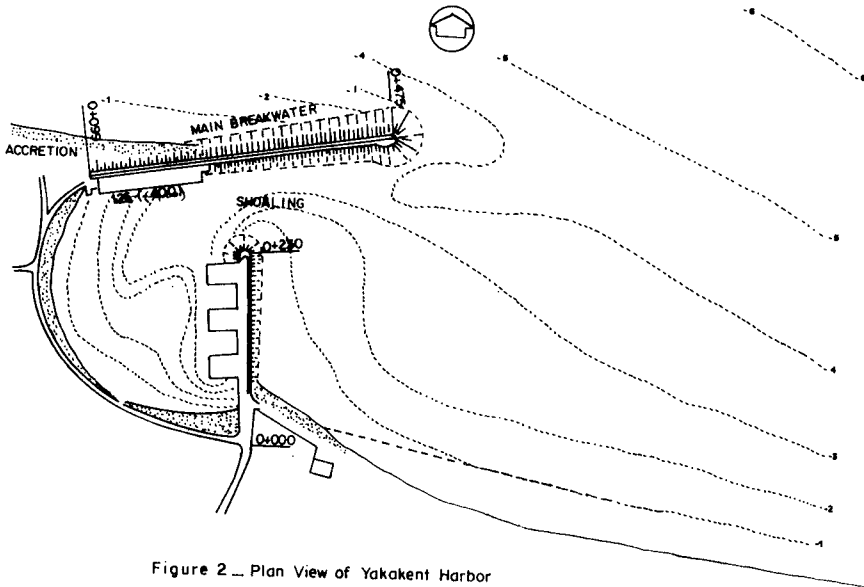


Figure 2 ... Plan View of Yakakent Harbor

Since the start of the construction of the harbor, accretion in the west coast and erosion in the east coasts resulted with considerable change in the shoreline. Additionally the entrance of the harbor which is situated towards east suffered from sedimentation and shoaling. Due to shoaling, depth of entrance of the harbor is about 0.7m. Just after the harbor entrance, depth increases suddenly inside the harbor (~3.0 meter water depth). Consequently continuous dredging was necessary to keep the entrance open even for the small fishing boats. This was tried to overcome by extending the main breakwater to 720m, but problem remained same.

As a result of accretion at the west coast shoreline moved towards the sea and about 300 meters of the breakwater was on land and just behind the secondary breakwater shoreline progressed about 80 meters towards the sea. At the further east coast of the harbor, severe erosion caused collapse of two houses which were about 20 meters inside the original shoreline. Then a seawall having 600 meters length was considered mainly aiming to protect the houses in the vicinity. Although seawall was observed to be functional in this aspect, it also enhanced the erosion down at the east coast. Seawall was further extended, this time to prevent erosion, but the result was same increased erosion at further east.

### Wave Climate

Long term wave analysis were made using hourly average wind records, for a duration of 3 years (Pierson, 1964). Probability distribution of deep water significant wave height,  $(H_{1/3})_0$  are shown on figure 3 and 4. Long term wave statistics showed that dominant wave direction is from NW to NE with 1703 hours per year above 1 meter significant wave height.

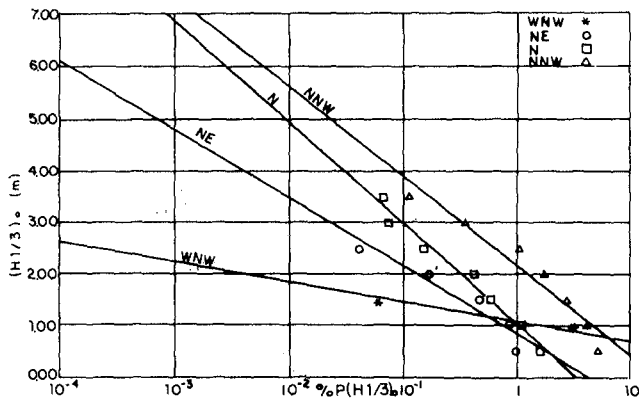


Figure 3 - Longterm Probability Distribution of Deep Water Wave Height



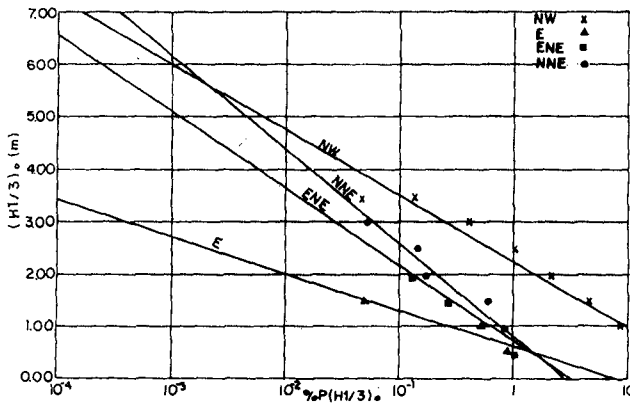


Figure 4 - Longterm Probability Distribution of Deep Water Significant Wave Height

From the long term wave statistics, the mean wave height, period and their occurrence of duration in a year are given in Table 1.

Table 1. For Yakakent Harbor region, mean wave height and their occurrence of duration, t(hr) in a year.

DIRECTION	WAVE HEIGHT(m)	PERIOD	t(hours)
WNW	0.79	3.36	70.1
NW	1.1	4.01	2133.2
NNW	1.32	4.34	794.0
N	1.37	4.44	167.5
NNE	1.33	4.37	127.2
NE	1.14	4.04	154.5
ENE	1.19	4.13	118.7
E	0.88	3.56	129.4

The sea bottom is sand with mean diameter of  $D_{50}=0.16\text{mm}$ . Using Shields Criteria for incipient motion it is found that at the -8 meter water depth, initiation of sediment motion will start with 6 second period and 0.20 meter wave height. Sediment in suspension will occur with 0.52 meter wave height.

### Methodology

Topographic field measurements available through the years were solely not sufficient, but together with the wave hindcast studies and further measurements, they formed guidelines for erosion and sedimentation patterns.

To investigate the variation of shoreline and the bottom topography and their reasons, the harbor region may be divided by six areas. (figure 5)

These are,

1. West Coast of the main breakwater
2. Entrance of the harbor.
- 3-Harbor basin
- 4-East of the secondary breakwater
- 5-Existing seawall at the east coast
- 6-East coast extending after the seawall

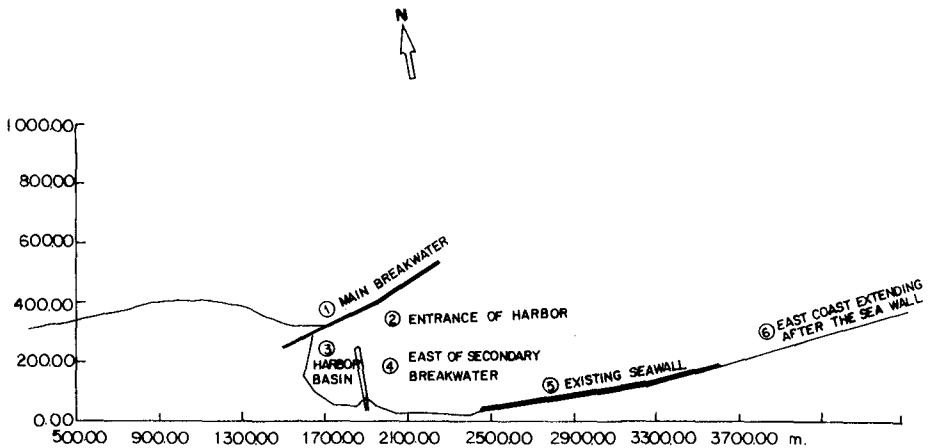


Figure 5 \_ The Regions for Sediment Transport Pattern

Main breakwater protruding from shoreline, presents a littoral barrier and blockage of longshore sediment transport is the main cause of accumulation at the west coast. As normally expected significant erosion is experienced at the east coast. The seawall constructed to prevent erosion was not functional and erosion was enhanced.

Figure 6 gives a schematic explanation of the wave action and current circulation patterns around the breakwater. Based on this figure the sedimentation at the harbor is explained below.

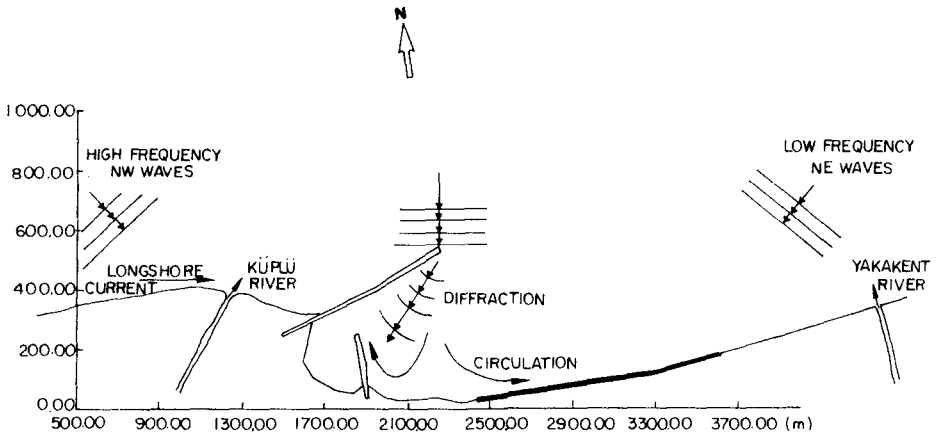


Figure 6 - Mechanism of Sediment Transport

Wave diffraction around the main breakwater resulted in settlement of suspended load as wave diminish in height could not carry suspended sediment any more. This sediment spreads out on a wide area shadowed by the main breakwater which may further be carried towards harbor entrance either by clockwise circulation waves or longshore current created by low frequency NE waves. The suspended sediment is also carried towards the harbor entrance by the diffracted NW waves and settles at the harbor entrance due to sudden drop of wave height in the harbor.

Figure 7 shows the diffractions coefficients ( $K_D$  values) at the various points in the harbor for the NW waves.

The wave height at the head of main breakwater is 2.02 meters as seen from figure 7,  $K_D$  value at the entrance of the harbor is 0.2. At this point, wave height will be 0.40 meters. Just after entrance of the harbor  $K_D$  value drops to 0.09. This means that wave height decreases up to 0.18 meters. Due to this sudden drop of wave height, suspended sediment could not be carried by the waves any more and sediment in suspension will settle. Then entrance of the harbor shoals. Rivers in the adjacent coast discharge huge amounts of the material which considerably increases the suspended sediment.

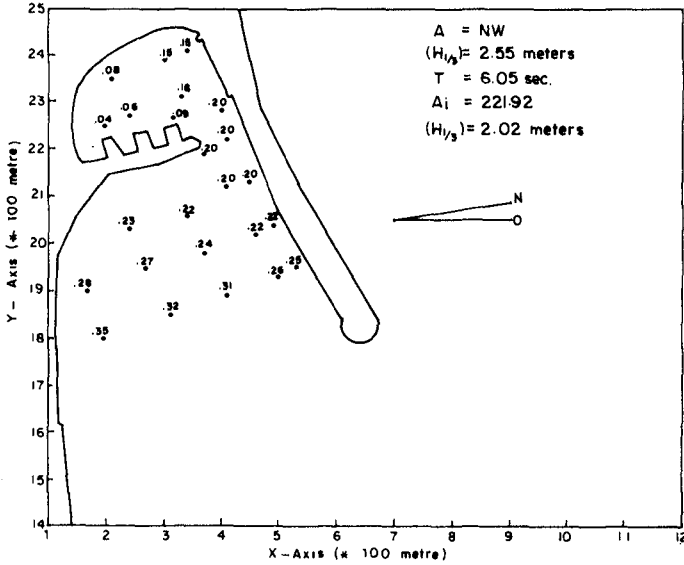


Figure 7 - Diffraction Coefficients for NW waves

**Application of one-line Model**

The hindcasted deep water wave characteristics were transformed up to breaking point by a computer program using Goda's approach (figure 8 and 9). This program calculates breaking wave height distributions and breaking angles along the shore. Breaking wave heights, angles duration of storms, wave period, location of the coastal structures are used in the one-line shore evaluation model (Hanson, 1986). Model is calibrated by existing field measurements.

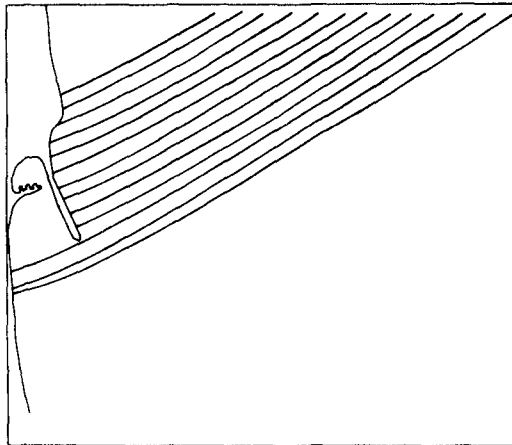


Figure 8 - Wave Refraction Diagram NNW Direction T=6 sec.

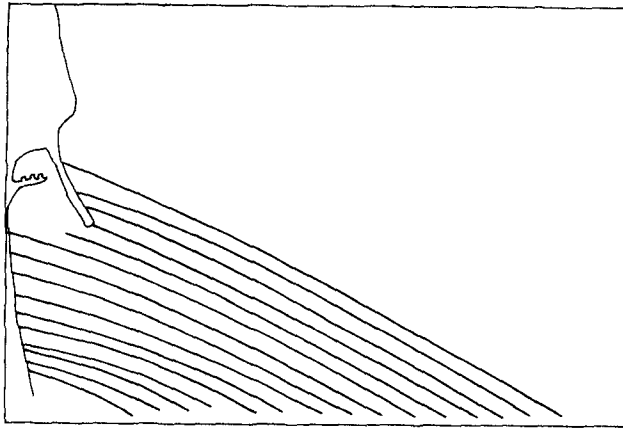


Figure 9 - Wave Refraction Diagram NE Direction  $T = 6$  sec.

For the simulation, a series run were done. Figure 10 shows shoreline variation at the west coast by the effect of NNW waves. For the same waves seawall enhanced the erosion down at the east coast (figure 11) and figure 12 shows the accretion caused by NE waves just behind the secondary breakwater.

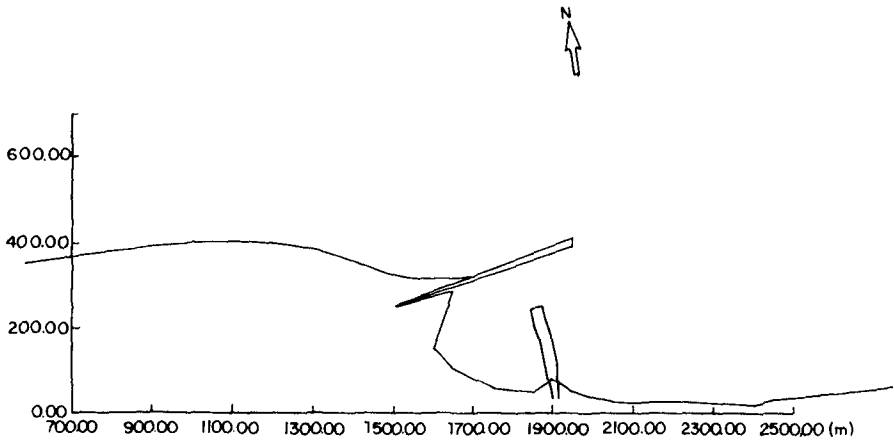


Figure 10 - Shoreline Changes Due To NNW Waves

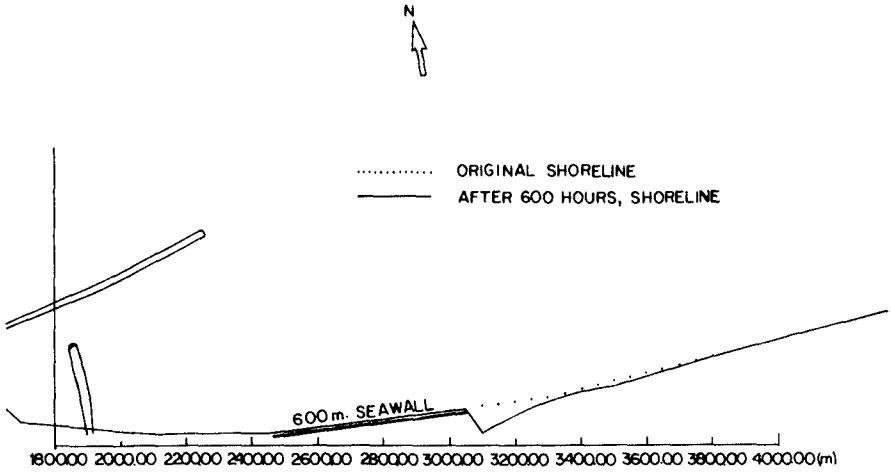


Figure 11 - Effect of Seawall On The Shoreline under NNW Direction waves

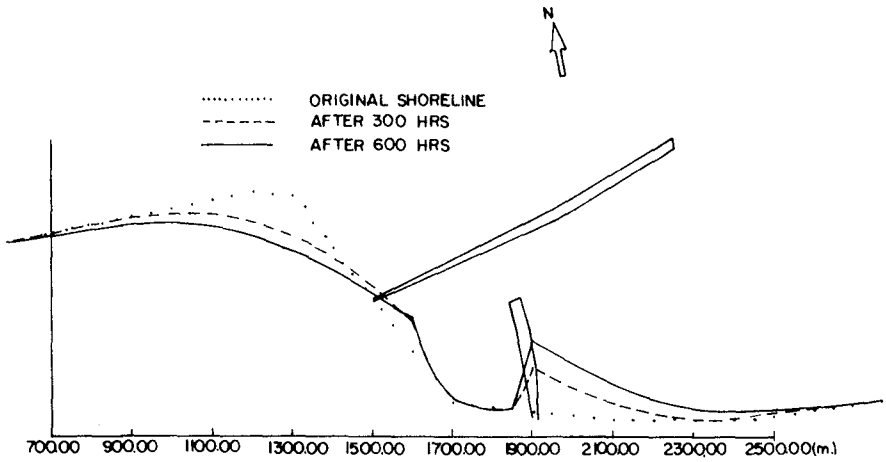


Figure 12 - Accretion The Behind Secondary Breakwater Due To NE Waves

Simulation with the one-line model are found to be satisfactory in the adjacent coast. Since the shoreline cannot reach equilibrium condition at the west coast, it will progress to the breakwater head and depth at the breakwater head will be -3 meter or less (figure 13).

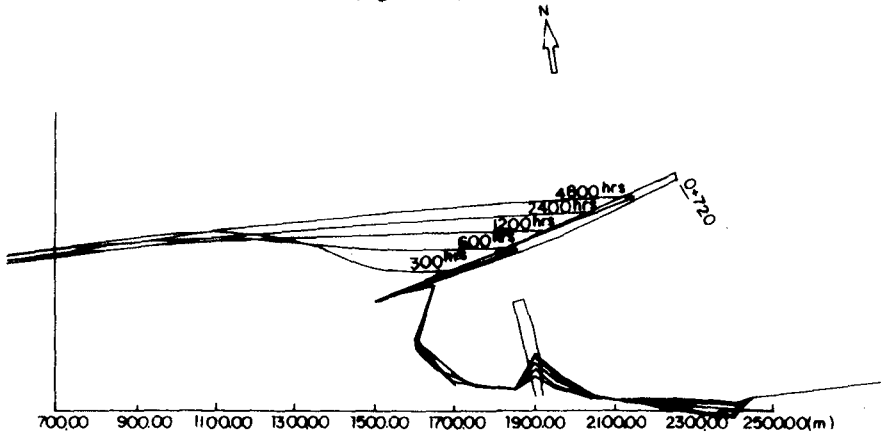


Figure 13. - Shoreline Change by One Line Model Due To NNW Waves

Figure 13 shows the output of the model for the simulation of shoreline change in the close vicinity of the harbor. However, for the entrance as this model is inadequate, sedimentation pattern is studied analytically. Based on these studies the main reason for the siltation at the harbor entrance is found to be due to the settling of suspended sediment as explained above.

**Conclusion and Recommendation**

After identifying the causes, precautions for the sedimentation and erosion problems are again studied using the same one-line model. The effect of one groin on shoreline change at the east coast by the various direction waves is studied and shown in figure 14 and 15.

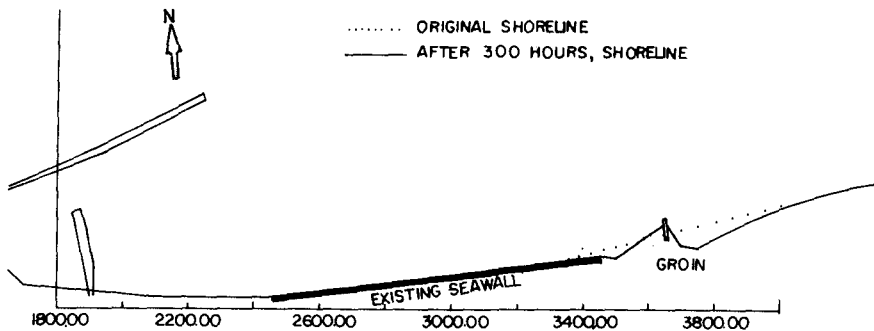


Figure 14. - The Effect of One Groin At The East Coast Due To NW Waves

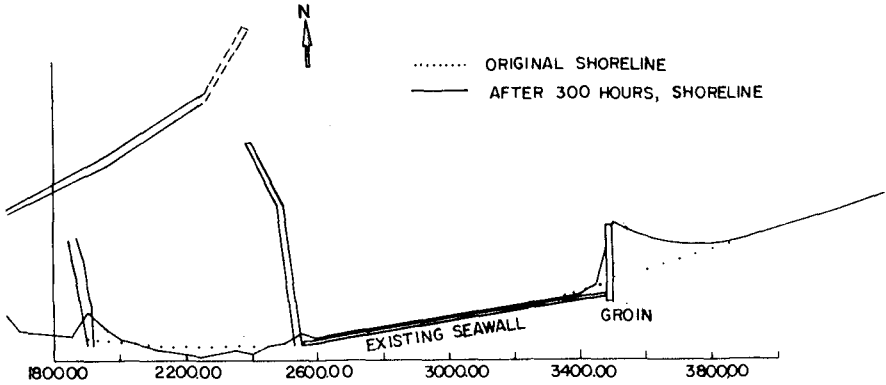


Figure 15 - The Effect of One Groin At The East Coast To NE Waves

A series of precautions shown in figure 16 are recommended which include;

- i. Extension of the main breakwater with a more perpendicular direction to the shore. This aims to cross the west-east directed sediment from sedimentation.
- ii. A new secondary breakwater to provide a relatively more exposed entrance and to reduce circulation area which carries suspended load towards harbor entrance.
- iii. Groin field at the east coast which will start from the existing beach. Sand by passing from west of breakwater to the East and artificial nourishment is recommended for the groinfield.
- iv. Sand by-passing of accreted sediment from west coast to east coast periodically (When necessary)

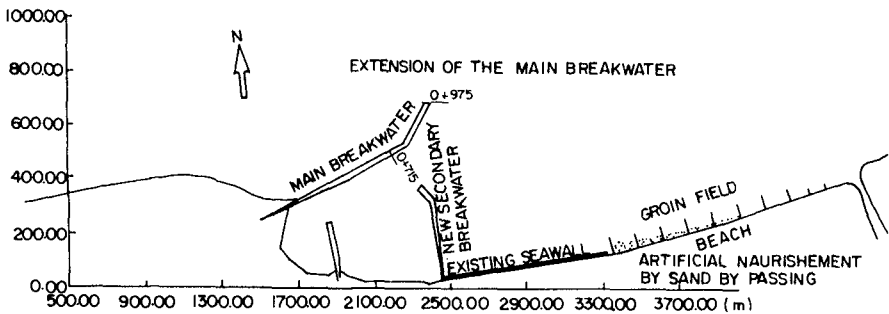


Figure 16 - Recommended System



**APPENDIX I REFERENCES**

Goda, Y. (1985) "Random Seas Design of Maritime Structure," University of Tokyo Press, Japan

Hanson, H., and Kraus, N.C. (1986) " Seawall Boundary Condition in Numerical Models of Shoreline Evaluation", CERC Technical Report No:86-3, US Army Corps of Engineers.

Pierson, W.J. and Moskowitz, L. (1964), "A proposed spectral form for fully developed wind seas based on the similarity theory of Kitaigorodskii", Jour. Geophys. Res., V. 69, no 24.

**APPENDIX II NOTATION**

The following symbols are used in this paper:

$(H_{1/3})_0$  = Deepwater significant wave height;

NW = North-West;

NE = North-East;

NNW = North-North-East;

$D_{50}$  = mean sediment diameter;

$K_d$  = Diffraction coefficients;

## CHAPTER 237

# A Study on Mud Mass Transport under Waves Based on an Empirical Rheology Model

Masahiko Isobe<sup>1</sup> Trien N. Huynh<sup>2</sup> and Akira Watanabe<sup>1</sup>

### Abstract

The rheological properties of mud play an important role in the motion of bed mud due to waves, currents, or combined waves and currents. In this paper, a dynamic rotary shear meter is developed to measure the shear stress in the mud under an arbitrary time history of the shear rate. Kaolinite is tested as an example of bed material and its rheology model is proposed. Another experiment is performed to confirm the predominance of the mud mass transport mode over the suspended mud transport mode in the wave-induced transport. Further experiments examine the role of pressure as an external force of the motion of the bed mud and measure some characteristics of waves on the mud bed. Finally, based on the empirical rheology model, a numerical model is developed to predict the motion of the bed mud, and resulting mud mass transport and wave damping. The calculated mud mass transport velocity and wave height change agree well with measurement.

## 1 Introduction

Muddy coasts represent a type of coastline where the bed material is mainly consists of fine grained, cohesive sediment. Typical muddy coasts are found in China, Vietnam, Indonesia, Bangladesh, Surinam, Brasil, and the United States. Siltation is a problem proper to muddy coasts where the transport mechanism of bed material is quite different from that on sandy coasts. Therefore, it is of great importance to study the transport phenomenon of mud.

The mud transport by waves and currents is separated into two modes: suspended mud transport in the water layer and mud mass transport in the bed. It is expected that the latter mode is quantitatively predominant under a wave action (Shibayama, *et al.*, 1990), but further experimental verification is still needed.

To predict the motion of bed mud and resulting mud mass transport velocity and wave damping, the rheological properties of mud should be given. Rheological models used so far are, for example, elastic, viscous, visco-elastic, visco-plastic, visco-elastic-plastic models (for example, Mei and Liu, 1987; Tsuruya *et al.*, 1987; Sakakiyama and Bijker, 1989; Shibayama *et al.*, 1990). On assuming one of the rheology models, the parameters in the model are determined by using a rotary or oscillatory viscometer, or other similar apparatuses. However, it is necessary to study the relationship between the stress and strain rate under various patterns of motion.

<sup>1</sup>Dept. of Civil Eng., Univ. of Tokyo, Tokyo 113, Japan.

<sup>2</sup>Civil Eng. Div., The Ho Chi Minh Polytechnic Univ., Ho Chi Minh City, Vietnam.

The pressure gradient and bottom friction can be external forces for the motion of bed mud. To develop a numerical model, it is necessary to investigate the dominant external force and to select an appropriate theory to estimate it.

In the following, a series of experiments performed in relation to the above issues are described. Especially in the experiment of the rheological properties of mud, a dynamic rotary shear meter is developed. Based on an empirical rheology model, a one-dimensional numerical model of the motion of bed mud is developed. Calculated mud mass transport velocity and wave height change are compared with measurements.

## 2 Rheological Properties of Mud

In the previous studies, either unidirectional rotary viscometers (Tsuruya *et al.*, 1986; Otsubo and Muraoka, 1988) or oscillatory viscometers (Mehta and Maa, 1986) were used to determine the parameters included in the assumed rheology models. However, it is necessary to examine the general behavior of mud for an arbitrary shear strain or shear rate. For this purpose, a dynamic rotary shear meter is developed in this study.

### 2.1 Dynamic, rotary shear meter

Since muds are tested at mean and high water content ratios, samples cannot stand by themselves. A new apparatus was designed and made as shown in Fig. 1. It consists of two coaxial cylinders of which the outer one is fixed and the inner one can be set in predetermined motions by controlling a stepping motor from a personal computer. The torque which results from the motion of the inner cylinder is measured by strain gages which are attached on an acrylic column supporting the outer cylinder. The gap between two cylinders is made small to ensure a uniform shear stress and the clearance below the inner cylinder is made large to minimize the end effect of the cylinder.

The calibration was performed before each test by static and dynamic loadings. The dynamic loading is performed by a sinusoidal oscillation of a mass and spring system. It was seen that a linear relation is acceptable without a significant error. To check the

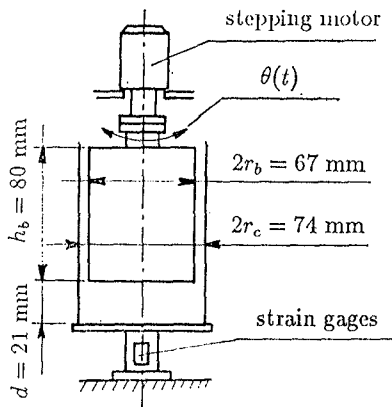


Figure 1: Sketch of the dynamic rotary shear meter.

end effect, a series of tests were done for various depths of mud filled in the gap. By a linear extrapolation of the immersed depth for a null torque, the end effect was found to be equivalent to 1.5 to 2.5 mm which is negligible compared to 70 to 80 mm of the immersed depth.

## 2.2 Experimental condition

### 2.2.1 Patterns of motion

Tests were done for the following patterns of motion.

- 1 ) Pattern S: sinusoidal oscillation which represents wave loading. The amplitude is 0.5 to 8 deg. and the period 1 to 40 s.
- 2 ) Pattern A: linearly varying shear rate in a short duration as shown in Fig. 2. This examines mainly the effect of the shear rate on the shear stress. In the figure,  $T = 10$  to 200 s,  $T_s = 0$  to 20 s, and the rate of change of the shear rate is 0.05 to 1.0 deg./s<sup>2</sup>.
- 3 ) Pattern V: linearly varying shear stress in a long duration. Pattern V is similar to Pattern A but the vertical axis in Fig. 2 is the position in stead of the velocity. The parameter  $T = 100$  to 500 s,  $T_s = 10$  to 200 s, and the rate of change of the position, *i.e.*, the velocity, is 0.01 to 0.2 deg./s.
- 4 ) Pattern SV: combination of constant velocity and oscillation as shown in Fig. 3. This represents the action of combined waves and a current. The velocity is 0.5 to 2 deg./s, the amplitude 1 to 2 deg., and the wave period 1 to 20 s.
- 5 ) Pattern SC: combination of initial shear stress and oscillation as shown in Fig. 4. This examines the effect of creeping.

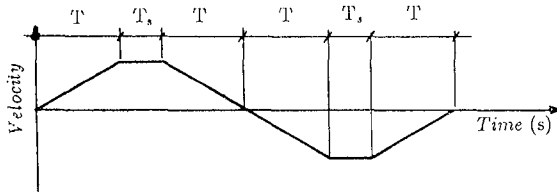


Figure 2: Motion of the inner cylinder (Pattern A).

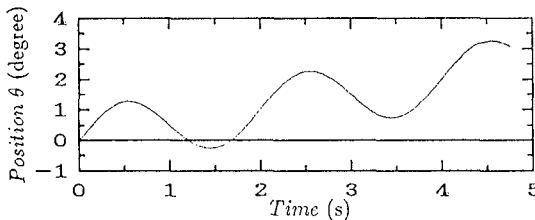


Figure 3: Motion of the inner cylinder (Pattern SV).

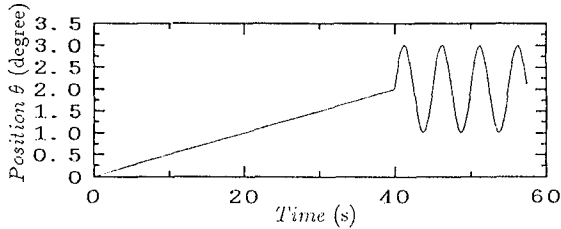


Figure 4: Motion of the inner cylinder (Pattern SC).

### 2.2.2 Mud sample

Commercial kaolinite mixed with tap water was used in the experiments. The water content ratio was 126 to 310 %. By the combination of the motion of the shear meter and the water content ratio, the total number of experiments is more than 100.

## 2.3 Experimental result

### 1) Pattern S

Figure 5 shows the relationship between the shear stress and shear rate for sinusoidal oscillations with various wave periods and a fixed amplitude. Curves are not so smooth because the shear rate is obtained by differentiating the displacement numerically. For long wave periods, the stress increases while the shear rate is positive, which implies that the increase of shear strain results in the increase of the shear stress for small shear rates. On the other hand, for short wave periods and therefore for large shear rates, the stress tends to increase with the shear rate but hysteresis loops are formed.

### 2) Pattern A

Figure 6 shows the results for linearly varying shear rates. A hysteresis loop is formed around the origin and linear relations are found for larger magnitudes of shear rates. The path from the maximum to zero shear rate agrees with that for the Bingham fluid. This result is considered to represent general characteristics, while the results for Patterns S and SV represent parts of this path.

### 3) Pattern V

For Pattern V, after the shear rate changes its direction, the shear stress changes abruptly and then gradually approaches to a constant value.

### 4) Pattern SV

Figures 7(a) to (c) represent the results for Pattern SV in which the constant component of shear rate is smaller than, comparative to, and larger than the oscillatory component, respectively. These results can be understood as parts of Figure 6.

### 5) Pattern SC

For Pattern SC, the average stress in one wave period, which is made positive by the initial shear strain, tends to disappear because of the creeping.

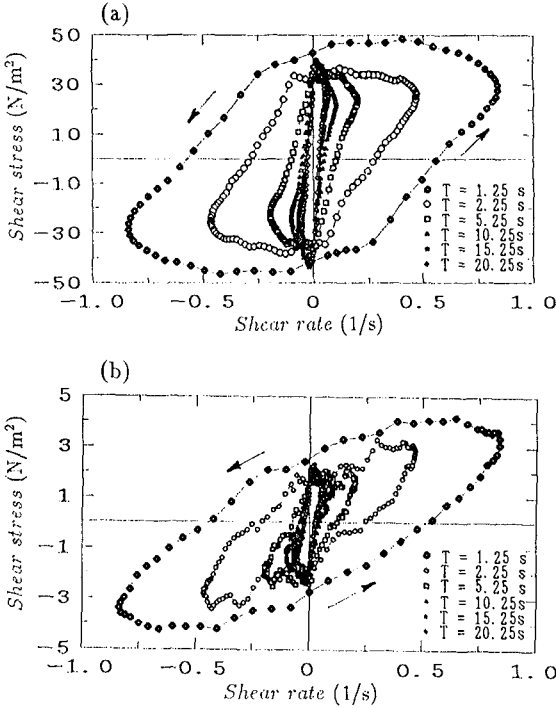


Figure 5: Relationship between shear rate and shear stress (Pattern S).

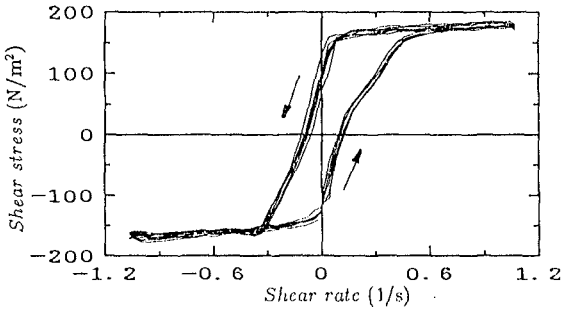


Figure 6: Relationship between shear rate and shear stress (Pattern A).

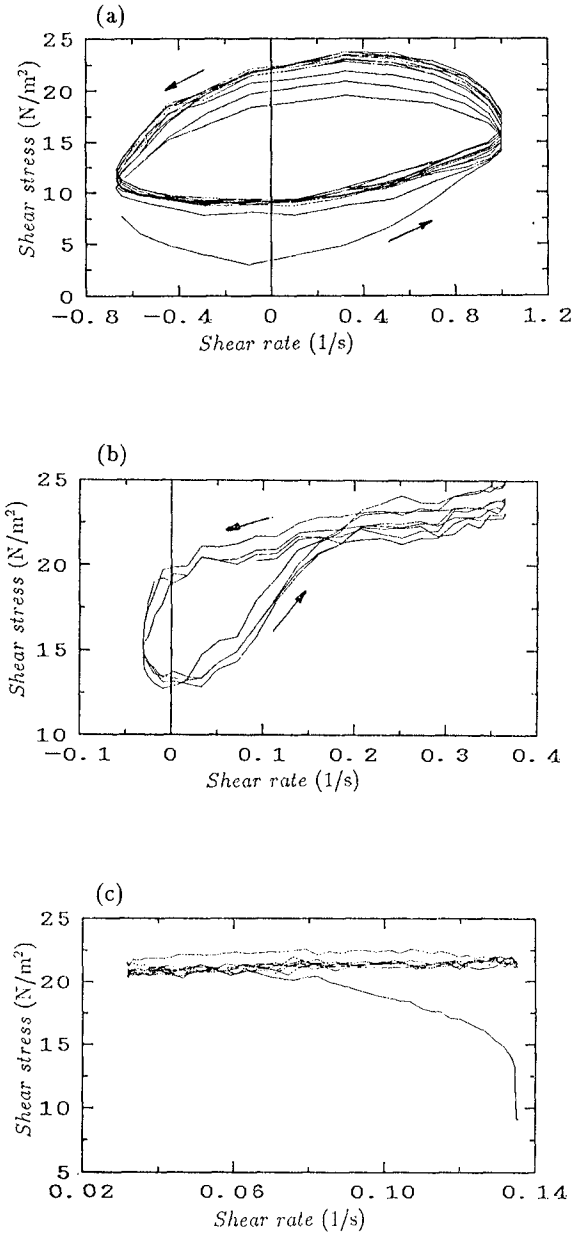


Figure 7: Relationship between shear rate and shear stress (Pattern SV).

2.4 An empirical rheology model

Based on the above experimental results, the following rheology model can be proposed. A backbone curve in Fig. 8 is first introduced:

$$\tau = \begin{cases} \text{sign}(\gamma)\tau_1(|\gamma|/\gamma_c)^n & (|\gamma| \leq \gamma_c) \\ \text{sign}(\gamma)\tau_0 + \mu_1\gamma & (|\gamma| > \gamma_c) \end{cases} \quad (1)$$

When the amplitude of the shear rate is larger than  $\gamma_c$ , the outer path in Fig. 8 is applied:

$$\tau = \begin{cases} \text{sign}(\gamma)\tau_0 + \mu_1\gamma & (|\gamma| \leq \gamma_c, \gamma(d\gamma/dt) \leq 0 \text{ or } |\gamma| > \gamma_c) \\ -\text{sign}(\gamma)\tau_0 + \mu_2\gamma & (|\gamma| \leq \gamma_c, \gamma(d\gamma/dt) > 0) \end{cases} \quad (2)$$

where  $\gamma_c$  is the critical shear rate, and  $\mu_1$  and  $\mu_2$  are viscosities when the magnitude of shear rate is decreasing and increasing, respectively. When the amplitude is smaller than or equal to  $\gamma_c$ , the inner path is applied:

$$\tau = \begin{cases} \text{sign}(\gamma)\tau_{m0} + \mu_1\gamma & (\gamma(d\gamma/dt) \leq 0) \\ -\text{sign}(\gamma)\tau_{m0} + \mu_{m2}\gamma & (\gamma(d\gamma/dt) > 0) \end{cases} \quad (3)$$

where

$$\tau_{m1} = \tau_1(\gamma_{mc}/\gamma_c)^n \quad (4)$$

$$\tau_{m0} = \tau_{m1} - \mu_1\gamma_{mc} \quad (5)$$

$$\mu_{m2} = (\tau_{m1} + \tau_{m0})/\gamma_{mc} \quad (6)$$

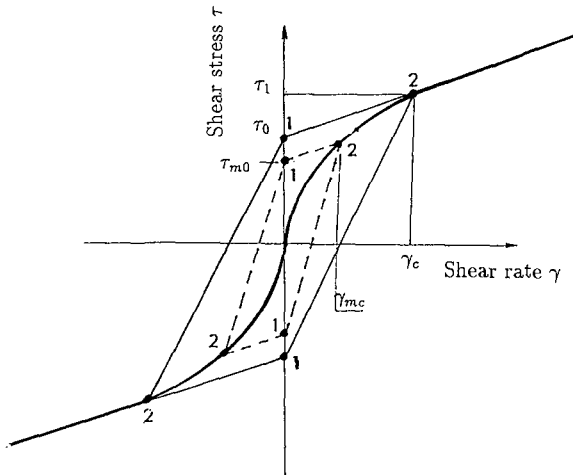


Figure 8: Empirical rheology model.



### 3 Mechanism of Mud Transport

Experiments are done to confirm the predominance of the mud mass transport mode, to measure some properties of waves on mud bed, and to check the importance of the pressure as an external force of the mud mass transport. A wave flume which is 1 m deep, 80 cm wide and 21 m long was used. As shown in Fig. 9, the mud bed was made 12 cm deep and 8 m long.

#### 3.1 Contribution of mud mass transport

A trench of a trapezoidal shape was made at the center of the mud bed and both sides were separated by two walls which prevent the mud mass transport and allow the suspended mud transport. Figure 10 shows the change of bottom configuration due to wave action. As can be seen, the suspended mud transport across the walls is negligible compared to the mud mass transport occurred on seaward and shoreward sides of the walls.

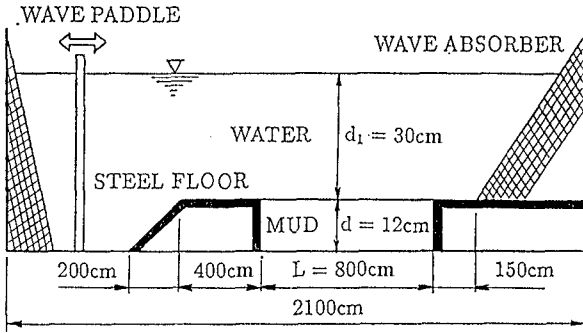


Figure 9: Wave flume and mud bed.

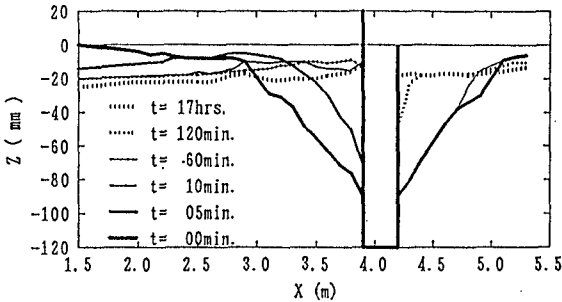


Figure 10: Transformation of trench profile.

### 3.2 Wave properties on the mud bed

#### 3.2.1 wavelength

Figure 11 compares the measured and calculated wavelengths of waves on mud bed. Curves are obtained by the small amplitude wave theory for the depth,  $d_1$ , of the water layer and the total depth,  $d$ , including the depth of mud bed. It is seen that the effect of mud bed on the wavelength is negligible and it is calculated simply from the depth of water.

#### 3.2.2 Pressure in the bed mud

Tsuruya *et al.* (1987) measured the pore pressure in the mud bed. Figure 12 compares the measured and calculated pore pressure. Curves which represent the amplitude of the bottom pressure calculated by the small amplitude wave theory agree well with the measured pore pressure.

### 3.3 Role of pressure as an external force

The gradient of the pressure and shear stress on the bed can be external forces for the bed mud motion. Comparative experiments were done to check the predominance of the pressure. In one experiment, the bed is covered with a nylon sheet which transmits the pressure and at least modifies the shear stress on the bed although it may not cut off completely. The other experiment was done without the cover. Figure 13 compares the wave height decay due to the motion of mud bed with and without the nylon cover. For a wide variety of the incident wave height, the wave height distributions are almost the same, which implies that the pressure gradient due to the wave motion is the dominant external force for the mud motion.

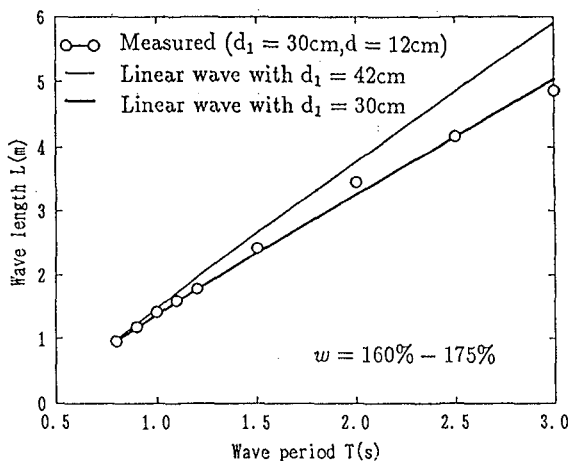


Figure 11: Wavelength of waves on mud bed.

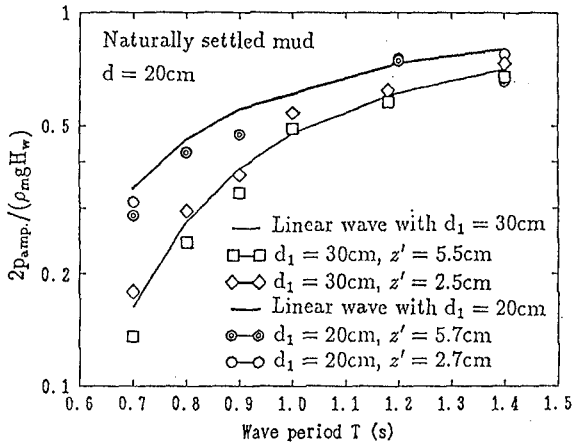


Figure 12: Pore pressure in mud bed.

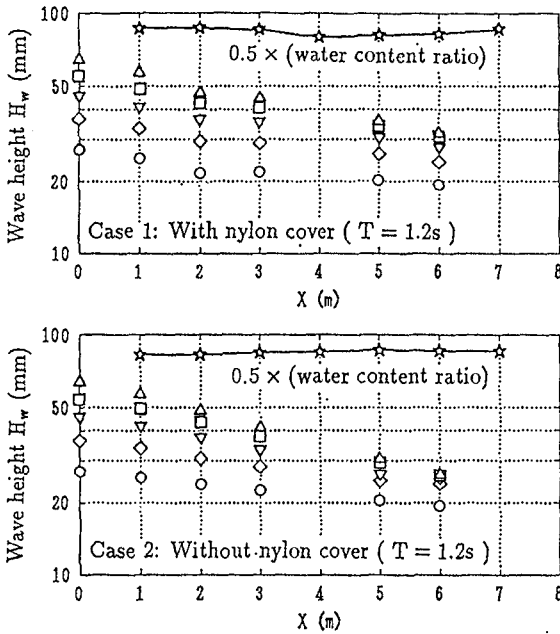


Figure 13: Effect of nylon cover on wave damping.

#### 4 Numerical Model of Mud Mass Transport

##### 4.1 Oscillatory motion of mud

A numerical model was developed based on the rheology model proposed above.

On assuming that the horizontal length scale is much longer than the vertical scale, the horizontal motion of the bed mud is analyzed as a one-dimensional problem in which the gradient of the pressure is given as the external force. The equation of motion for the velocity,  $u = u(z, t)$ , of the mud is

$$\rho_m \frac{\partial u}{\partial t} = -\frac{\partial p}{\partial x} + \frac{\partial \tau}{\partial z} \quad (7)$$

where  $p$  is the pressure,  $\tau$  the shear stress,  $\rho_m$  the density of the mud,  $x$  and  $z$  the horizontal and vertical coordinates, and  $t$  the time. The pressure is given as the bottom pressure predicted by the small amplitude wave theory. By substituting the shear rate,  $\gamma = \partial u / \partial z$ , into the empirical rheology model proposed above, the shear stress is expressed in terms of  $u$ . Thus, the above equation becomes a closed governing equation for  $u$ . The boundary conditions are the non-slip condition at the bottom of the mud bed and zero shear stress on the bed:

$$u(0, t) = 0 \quad (8)$$

$$\tau(d, t) = 0 \quad (9)$$

Considering the above boundary conditions, the mud layer is divided into  $(N+1/2)$  equal-distance sublayers in discretizing the governing equation. The quantity  $u$  is defined at 0 to  $N$  levels, while  $\tau$  at  $1/2$  to  $N+1/2$  levels. The numerical calculation is continued until a periodic solution is obtained.

## 4.2 Wave damping

The wave damping occurs due to the work done through the shear stress in the mud. The equation of the wave energy is

$$\frac{d}{dx}(EC_g) = -D \quad (10)$$

where  $E = \rho g H^2 / 8$  ( $\rho$ : the density of water,  $g$ : the gravitational acceleration,  $H$ : the wave height) is the wave energy density,  $C_g$  the group velocity, and  $D$  the energy dissipation rate which is estimated by

$$D = \int_0^d \tau \frac{\partial u}{\partial z} dz \quad (11)$$

From Eq. (11), the coefficient,  $D_H$ , of the wave height damping is expressed as

$$D_H \equiv -\frac{1}{H} \frac{dH}{dx} = \frac{1}{2} \frac{D}{EC_g} \quad (12)$$

## 4.3 Mud mass transport

The total mud mass transport velocity,  $U$ , is obtained as the sum of the Eulerian mass transport velocity,  $U_E$ , and the Stokes drift,  $U_S$ :

$$U = U_E + U_S \quad (13)$$

By introducing the average viscosity,  $\mu_{ave}$ , in one wave period, the Eulerian mass transport velocity is calculated from the average momentum equation:

$$\mu_{ave} \frac{\partial^2 U_E}{\partial z^2} = \frac{\partial \overline{\rho_m u^2}}{\partial x} = -2D_H \overline{\rho_m u^2} \tag{14}$$

for which the boundary conditions are

$$U_E = 0 \quad (z = 0) \tag{15}$$

$$\frac{\partial U_E}{\partial z} = 0 \quad (z = d) \tag{16}$$

The Stokes drift can be calculated by

$$U_S = \frac{\partial u}{\partial x} \int u dt = \overline{\left( -\frac{1}{C} \frac{\partial u}{\partial t} - u D_H \right) \int u dt} \tag{17}$$

**4.4 Comparison between calculation and experiment**

Four series of experiments were done for the water content ratios of 132, 171, 223 and 379 %. In each series, the mud mass transport velocity was measured for one case and the wave height distribution was measured for various incident wave periods and heights. The mud mass transport was measured by the same procedure as Sakakiyama and Bijker (1989). Figure 14 and 15 show examples of comparison between the calculated and measured wave height distribution and vertical profile of the mud mass transport velocity, respectively. Figure 16 compares the calculated and measured damping coefficients as a function of the wave period (frequency). The agreements are generally good.

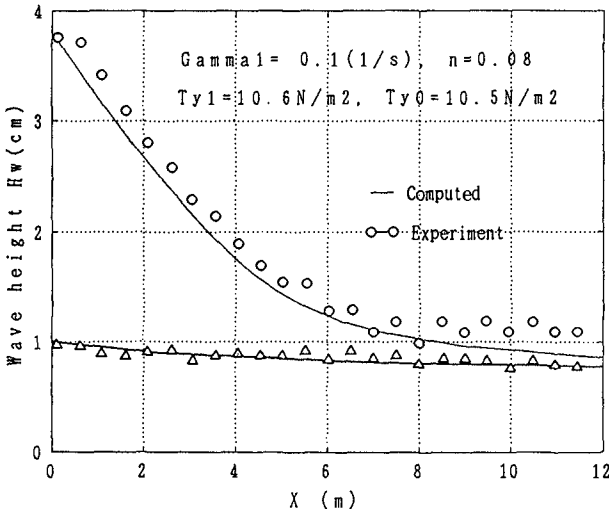


Figure 14: Comparison between calculated and measured wave damping.

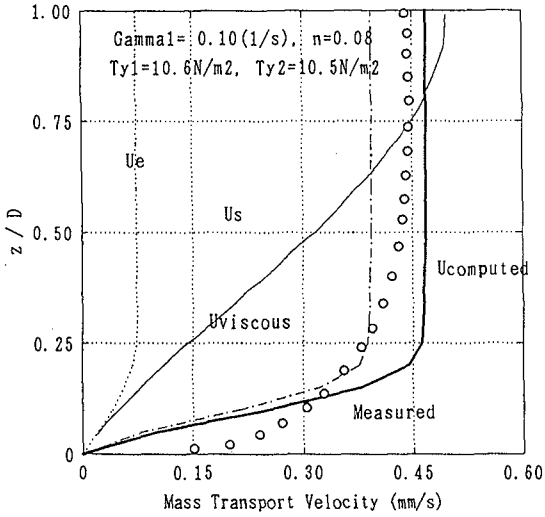


Figure 15: Comparison between calculated and measured vertical profiles of the mud mass transport velocity.

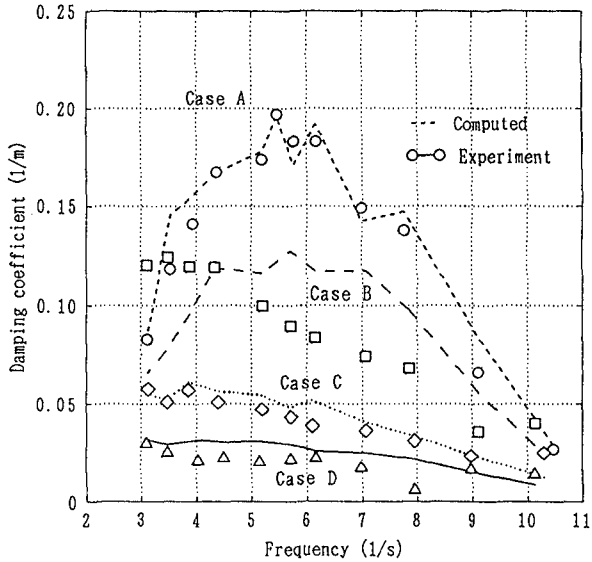


Figure 16: Comparison between calculated and measured damping coefficients.

## 5 Conclusion

The rheological properties of mud are studied by a dynamic rotary shear meter which was designed and made to measure the shear stress under an arbitrary change of shear rate. Experiments are done to confirm the predominance of the mud mass transport mode, the validity of the small amplitude wave theory for predicting wave characteristics and the predominance of the pressure as an external force of the mud motion. Based on the proposed empirical rheology model, a numerical model is developed to simulate the motion of bed mud due to wave action. Comparisons with the measurements show good agreement both for the vertical profile of the mud mass transport velocity and for the wave height damping.

In the future study, the parameters used in the rheology model should be formulated as a function of the water content ratio. In addition, bed materials other than kaolinite should be tested. In the present study, the pressure is assumed to be uniform vertically throughout the bed since its thickness is small enough. However, the vertical motion and consolidation process should be taken into account for analyzing the motion of the bed mud of a large depth.

## References

- [1] Mehta, A. J. and P.-Y. Maa (1986): Waves over mud: Modeling erosion, Proc. 3rd Int. Symp. on River Sedimentation, pp. 588-601.
- [2] Mei, C. C. and P. L.-F. Liu (1987): A Bingham-plastic model for a muddy seabed under long waves, J. of Geophys. Res., Vol. 92, No. C13, pp. 14581-14584.
- [3] Otsubo, K. and K. Muraoka (1988): Critical shear stress of cohesive bottom sediments, J. Hydraulic Eng., Vol. 114, No. 10, pp. 1241-1256.
- [4] Sakakiyama, T. and E. W. Bijker (1989): Mass transport velocity in mud layer due to progressive waves, J. of Waterway, Port, Coastal and Ocean Eng., ASCE, Vol. 115, No. 5, pp. 614-633.
- [5] Shibayama T., M. Okuno and S. Sato (1990): Mud transport rate in mud layer due to wave action, Proc. 22nd Int. Conf. on Coastal Eng., ASCE, pp. 3037-3049.
- [6] Tsuruya, H., S. Nakano and J. Takahama (1987): Interaction between surface waves and a multi-layered mud bed, Rep. Port and Harbour Res. Inst., Ministry of Transport, Japan, Vol. 26, No. 5, pp. 141-173.
- [7] Tsuruya, H., Nakano, S. and J. Takahama (1986): Investigation of rheological properties of soft muds with a rotary visco-meter, Tech. Note Port and Harbour Res. Inst., Ministry of Transport, Japan, No. 566, 29p.

## CHAPTER 238

### SETTLING PROPERTIES OF COHESIVE SEDIMENTS IN A COOLING WATER INTAKE BASIN

Susumu Kanayama <sup>1</sup>, Takuzo Shimizu <sup>1</sup> and Kazuhiro Ueki <sup>2</sup>

#### ABSTRACT

In the present study, with the ultimate objective of developing a numerical model of siltation in a cooling water intake basin of a power plant, the settling velocities of non-uniform sediments are investigated using the settling tube tests. The critical shear stress for deposition of suspended silt and the vertical concentration profile of suspended sediments are investigated on the basis of field data. The deposition rate as well as the grain size distribution of deposited sediments were reproduced satisfactorily by a one-dimensional model.

#### INTRODUCTION

In a power plant basin used for both the intake of cooling water and the navigation channel, siltation usually occurs and a silty area is created inside the harbor, even if the basin is sited in a sandy coast. Cohesive fine sediments are suspended by the wave action outside the harbor under the severe wave conditions and transported by the intake flows through the entrance into the harbor. Most of the inflow fine sediments are settled and deposited on the bottom in a tranquil area inside the harbor.

Figure 1 shows the location map and the layout of the investigation site. The

---

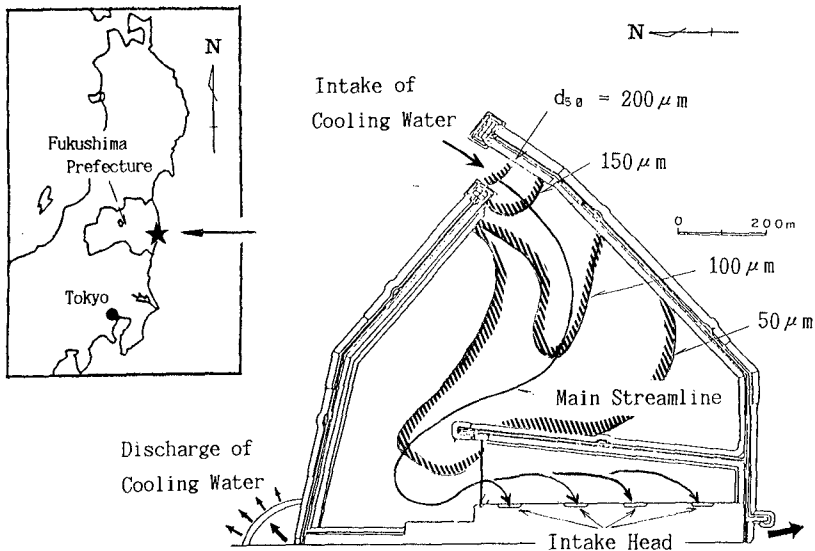
<sup>1</sup>Penta-Ocean Construction Co. Ltd. , 2-2-8 Koraku, Bunkyo-ku, Tokyo, 112 Japan.

<sup>2</sup>Tokyo Electric Power Co. Inc. , 1-1-3 Uchisaiwaicho, Chiyoda-ku, Tokyo, 100 Japan.



investigation site is the harbor basin of Fukushima No.2 Nuclear Power Plant and is located in Fukushima Prefecture, Japan, facing directly the Pacific Ocean. The spatial distribution of the median grain diameters of deposited sediments in the basin is also shown in this figure. A large portion of the basin is occupied by fine sediments with the median diameter below  $100\ \mu\text{m}$ , although the surrounding coast consists of fine sands with the median diameter of approximately  $200\ \mu\text{m}$ . The median grain diameters decrease along the streamline of the intake flow. In the course of transportation and deposition, sediment sorting due to difference of settling velocities occurs because the suspended fine sediments are composed of a wide range of grain sizes approximately from  $1$  to  $100\ \mu\text{m}$ . Consequently, the median grain sizes of deposited sediments show a wide range of spatial distribution from about  $200\ \mu\text{m}$  in the sandy area around the entrance to  $20\ \mu\text{m}$  in the tranquil area near the intake channel.

In developing a numerical model for simulating siltation in such a cooling water intake basin, detail understanding of the depositional properties of non-uniform cohesive sediments is the first subject to be solved. In this study, we aim to discuss about a proper method for estimating the deposition rate by taking into account the effects of flocculation and nonuniformity of the grain size on the basis of the laboratory experimental data and the field measurement data.



## DEPOSITION RATE

One of the well-known expressions for the deposition rate  $D$  is described as follows (e.g. Nicholson and O'Conner, 1987) :

$$D = C_b w_b \left( 1 - \frac{\tau}{\tau_d} \right), \quad \text{for } \tau < \tau_d \quad (1)$$

where  $C_b$  is the near bottom concentration,  $w_b$  the near bottom settling velocity,  $\tau$  the bottom shear stress, and  $\tau_d$  the critical shear stress for deposition. According to this expression, the deposition rate is regarded as the product of three factors; 1)the suspended sediment concentration near the bottom, 2)its settling velocity and 3)the probability of particles sticking to the bed which is described as  $( 1 - \tau/\tau_d )$  in eq. (1).

It is well recognized that the settling velocity of cohesive fine sediments is influenced sensitively by the suspended sediment concentration owing to the effect of flocculation. In the present study, the laboratory experiments in a settling tube were carried out in still water to examine the influence of concentration on the settling velocity of non-uniform sediments.

In depth-integrated models which are widely used for simulating the behavior of suspended particles, the near bottom concentration is to be evaluated from the depth-averaged concentration. Therefore, the vertical concentration profile should be determined for numerical calculation. Also the critical shear stress for deposition  $\tau_d$  is a very important parameter for estimating the depositional rate. In this study, the vertical concentration profiles for different grain sizes and the critical depositional shear stress are evaluated through comparisons between the calculated results and the field data.

## SETTLING VELOCITY

The settling velocities of non-uniform sediments were investigated by the settling tube tests. The sediments used in the tests were sampled from the seabed in the tranquil area of the investigation site. The median grain diameter was 23  $\mu\text{m}$  after passing through a sieve with 106  $\mu\text{m}$  openings. The cation exchange capacity was 27 (meq/100g), and a large portion of absorbed cation was occupied by  $\text{Ca}^{2+}$  and  $\text{Mg}^{2+}$ .

The inner diameter of the settling tube was 27 cm, and the available water depth was 95 cm. Saline water with a temperature of 20°C was used as the settling medium. Sediments were initially stirred to create a state of homogeneous suspended sediment concentration in the tube. The water samplings and the

concentration measurements were conducted six times after 3, 8, 25, 90, 180 and 420 minutes from the start of the test, and the sampling mouth was set at the water depth of 60 cm.

The time series of concentration were transformed to the settling velocity curve. The grain-size distributions were also analyzed by the laser diffraction method after breaking the flocs. Then, the settling velocity curves were obtained for every grain-size class.

Figure 2 shows the relationships between the median settling velocity  $w_{50}$  of each grain-size class and the initial total concentration. It is recognized that in the case of low concentration,  $C < 200$  mg/l, the settling velocity is independent of concentration and can be evaluated by the Stokes law. In the case of  $200 \leq C \leq 2000$  mg/l, the settling velocity increases exponentially with concentration and the following general formula can be used:  $w = kC^m$  ( $k$ : empirical constant,  $m$ : empirical exponent). The settling velocity reaches the equilibrium value of 0.19 (cm/s) for each grain-size class at a concentration of approximately 2000 mg/l.

These tendencies are observed only for the grain-size classes with the median diameter below 48  $\mu\text{m}$ . For the larger grain-size classes, dependence of settling velocities on concentration can not be observed. According to these results, the settling velocity of suspended sediments is formulated as a function of grain size and total concentration as shown in Figure 3. The critical median diameter, 48  $\mu\text{m}$ , above which flocculation is negligible, corresponds to the equilibrium settling velocity of 0.19 cm/s. It should be noticed that these quantities are regarded as local factors which are inherent in the sediment properties of the investigation site. The range of concentration for flocculated settling obtained in this study corresponds to the results of the previous studies (e.g. Ross and Mehta, 1989).

## VERTICAL CONCENTRATION PROFILE AND PROBABILITY OF DEPOSITION

The vertical concentration profile and the probability of deposition were investigated on the basis of field data. The critical shear stress for deposition and the reference level at which the near bottom concentration was defined were evaluated through comparisons between the cumulated depositional fluxes calculated from the measured time histories of concentration and the measured weights of the deposited sediments in the traps.

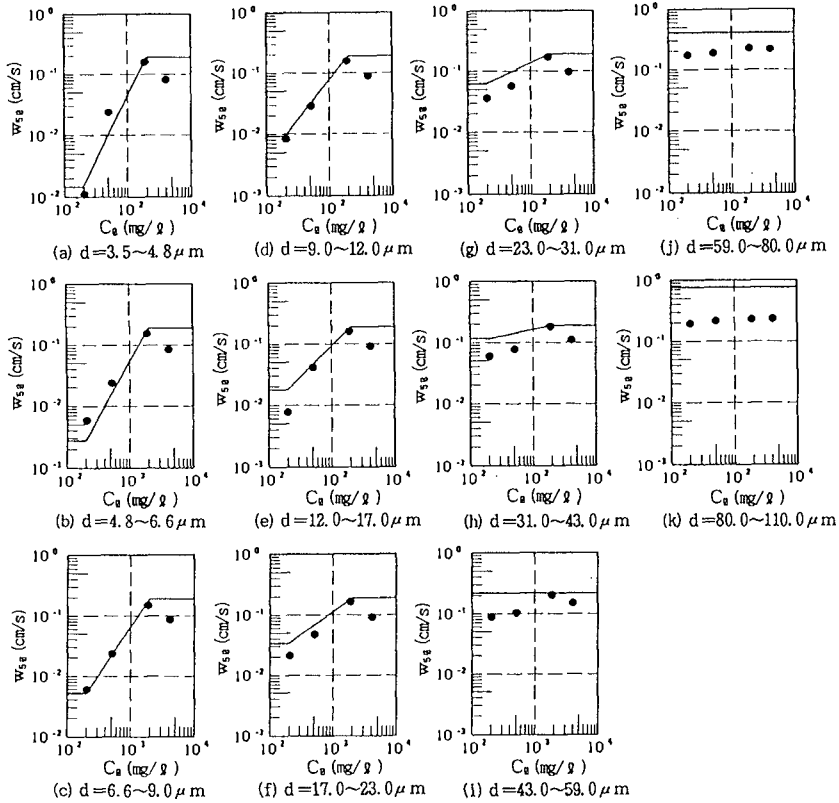
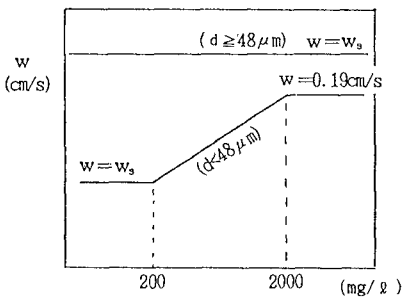


Fig. 2. Relationships between settling velocity of each grain-size class and concentration.



- i)  $d \geq 48 \mu m$   
 $w = w_s$
  - ii)  $d < 48 \mu m$   
    - $w = w_s$  ( $C < 200 \text{ mg/l}$ )
    - $w = \alpha \cdot C^\beta$  ( $200 < C < 2000 \text{ mg/l}$ )
    - $\alpha = \exp((8.8 + 7.6 \cdot \ln(w_s)) / 2.3)$
    - $\beta = -(\ln(w_s) + 1.66) / 2.3$
    - $w = 0.19 \text{ cm/s}$  ( $2000 \text{ mg/l} < C$ )
- d : Grain diameter  
 C : Concentration of suspended silt  
 w : Settling velocity  
 $w_s$  : Settling velocity by Stokes' law

Fig. 3. Formulation of settling velocity as a function of median grain diameter and total concentration.

**Outline of Field Data**

An intensive field investigation was carried out in the harbor basin of Fukushima No.2 Nuclear Power Plant over a period of approximately two months from July to September in 1989 (Shimizu et al., 1990). Figure 4 shows the arrangement of observation points. Among them, three points are concerned in the discussion here. They are point A-2 in the sandy area at the harbor entrance with a median grain diameter of about  $150 \mu\text{m}$ , point A-6 in sand-silt coexisting area with a median grain diameter slightly below  $100 \mu\text{m}$  and point A-8 in the silty area with a median grain diameter of approximately  $50 \mu\text{m}$ .

A synchronized combination of an ultrasonic wave gauge and an electro-magnetic current meter with a pressure gauge and a turbidity meter were placed at each of the above three observation points. Hourly time histories of suspended sediment concentration at 1.5 m above the bottom together with the wave height and near-bottom flow velocity were measured simultaneously. At point A-8, another turbidity meter was set at 3.0 m above the bottom in addition to the one at 1.5 m, so that the ratio of concentrations measured at these two elevations could provide the information about the vertical concentration profile.

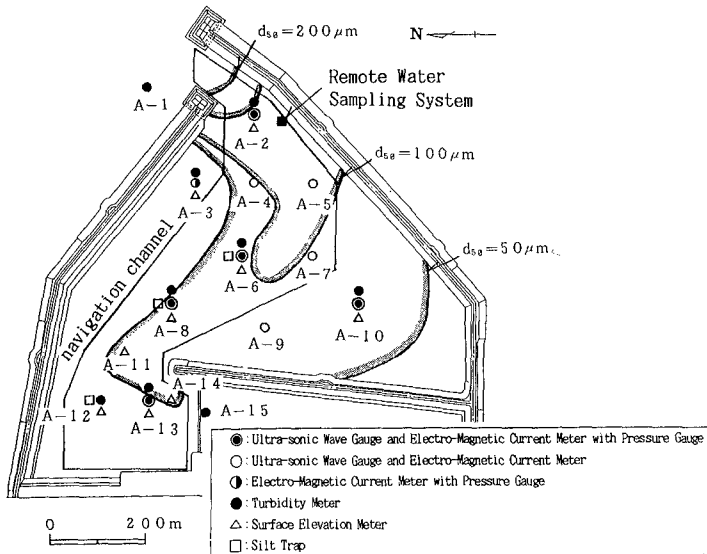


Fig. 4. Location of observation points.

Two types of silt traps were set at points A-6 and A-8, to obtain direct measurements of the weight and the grain-size distribution of newly deposited silt. The photograph of silt traps are shown in Figure 5. Type-A has a trapping mouth at almost the same elevation as the sea bottom, and Type-B has its mouth at 0.3 m above the bottom. The traps were set in pipe lattices so as to trap only the suspended silt falling down into the bed.

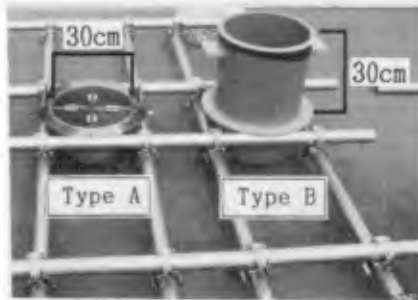


Fig. 5. Photograph of silt traps ( Type A and Type B ).

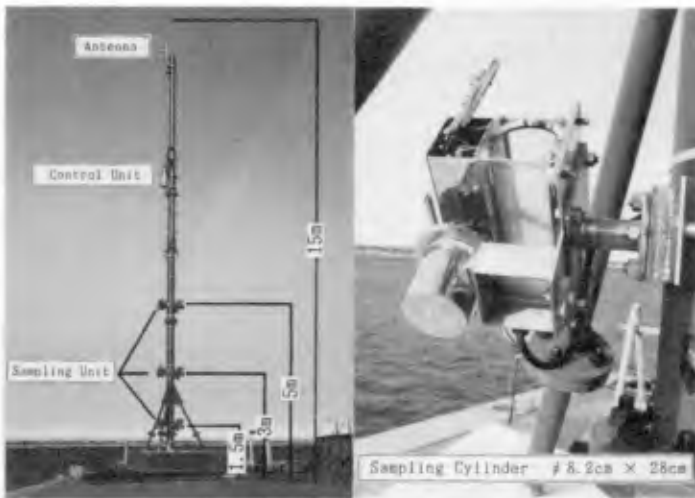


Fig. 6. Photograph of remote water sampling system.

At point A-2, remote water samplings were conducted during severe wave conditions by a newly developed apparatus shown in Figure 6. Figure 7 shows the grain size distribution of suspended silt measured at point A-2 by this apparatus. This will be used as the boundary condition for simulation of grain size sorting, to be discussed later.

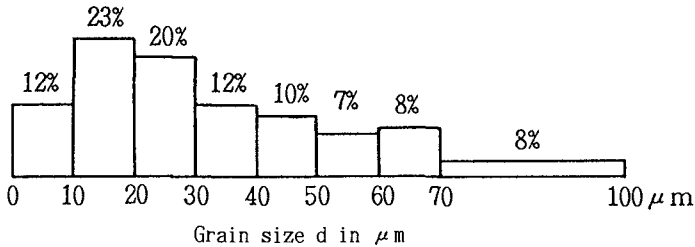


Fig. 7. Grain size distribution of suspended silt at harbor entrance.

### Vertical Concentration Profile

The vertical concentration profile should be determined in order to evaluate the bottom concentration  $C_b$  from the measured concentration at 1.5 m above the bed. In the present study, the vertical concentration profile is assumed to have an exponential form as shown in Figure 8:

$$C(z) = C_\delta \exp\left(-\frac{w}{u_* \kappa \delta}(z - \delta)\right) \quad (2)$$

where  $C(z)$  is the concentration at elevation  $z$  above the bed,  $C_\delta$  is the concentration at the reference level  $\delta$ ,  $w$  the settling velocity of suspended sediment corresponding to the depth averaged concentration, and  $\kappa$  the Karman constant. The bottom concentration is assumed to be equal to  $C_\delta$ . In this expression, the eddy viscosity  $u_* \kappa \delta$  is regarded as vertically constant and proportional to the friction velocity.

By assuming this profile, the concentration related to each grain-size class at 1.5 m above the bed can be estimated using the corresponding settling velocity, and the total concentration at this elevation can be also estimated as the sum of the contributing components. Then,  $C_\delta$  can be determined by comparing the estimated total concentration with the measured one at 1.5 m elevation. However, in estimating the total concentration, the information is needed about the grain size distribution of the suspended sediments at the point of interest.

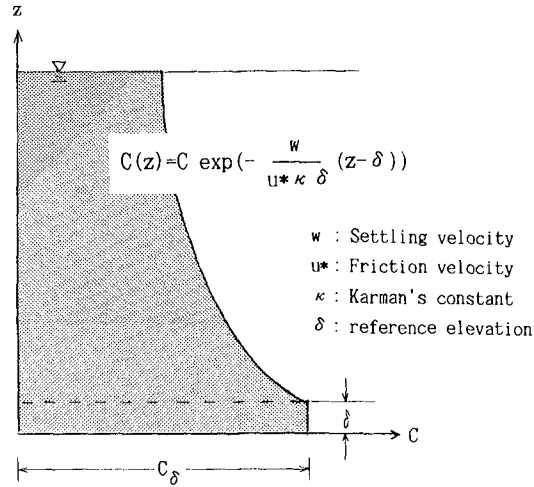


Fig. 8. Assumption of vertical concentration profile.

In the present study, the grain size distributions at points A-6 and A-8 were estimated by a simple numerical model of sediment sorting along the streamline as introduced in the following section. It should be mentioned that in the above calculations, the measured concentration at 1.5 m above the bed has been used as the depth-averaged concentration for estimating the settling velocity in eq.2).

**Sediment Sorting Simulation by One-dimensional Model**

In this study, a one-dimensional depth-integrated model is employed for calculation of sediment sorting. The harbor is regarded as a simple channel along the streamline of intake flow as shown in Figure 9. The channel is divided into 23 grids with an interval of 50 m on the main streamline. Assuming the quasi-equilibrium state and neglecting the diffusion term, the mass conservation of suspended silt for a certain grain-size class is described as follows.

$$u \frac{\partial C}{\partial x} = -\frac{w_b C_{\delta}}{h} \left(1 - \frac{\tau}{\tau_d}\right) \tag{3}$$

where  $C$  is the depth-averaged concentration,  $h$  is the water depth and  $u$  is the current velocity.



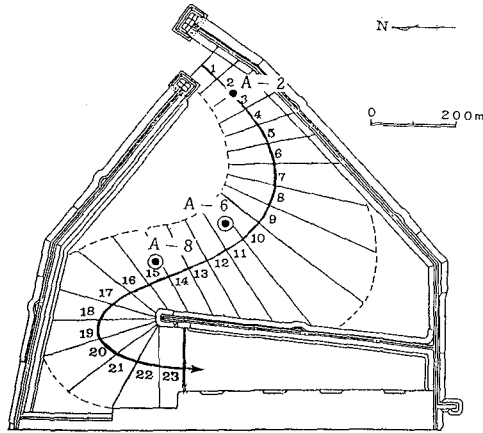


Fig. 9. One-dimnsional modelling of harbor along streamline.

The near bottom concentration  $C_\delta$  is evaluated from the depth-averaged concentration  $C$  by using eq. (2). At each grid, the value of  $C_\delta$  calculated for its preceding grid is used. The settling velocity  $w_b$  on the bottom ( exactly at the elevation  $\delta$  ) is evaluated by the relationship between the diameter of each grain-size class and the total concentration as indicated in Figure 3.

The wave height at each grid is computed by multiplying the diffraction coefficient, calculated in advance, by the measured incident wave height at the harbor entrance. The depth-averaged current velocity is estimated by dividing the intake discharge by the cross-sectional area of each grid. The bottom shear stress at each grid is then evaluated by the friction law for the wave-current coexistent field proposed by Tanaka and Shuto(1981). The measured time history of concentration is given as the boundary condition at the grid No. 3 which corresponds to point A-2. The concentration for each grain-size class at the boundary is given according to its ratio based on the grain size distribution measured at point A-2 during the severe wave conditions as shown in Figure 7.

### Determination of Critical Shear Stress and Reference Level

According to the above procedure, the deposited weights and their grain size distributions at points A-6 and A-8 can be estimated by using the assumed values of  $\tau_c$  and  $\delta$ . The objective here is to find the appropriate values for these parameters which provide the best agreement between calculations and measurements.

However, the effects of these parameters on calculation results are not so simple. The increase of  $\tau_d$  has both effects of increasing the deposition rate owing to the increase in probability of deposition and of decreasing it because of the increase in the deposition rate in the upstream region. The decrease of  $\delta$  has the same effects as those caused by the increase of  $\tau_d$ .

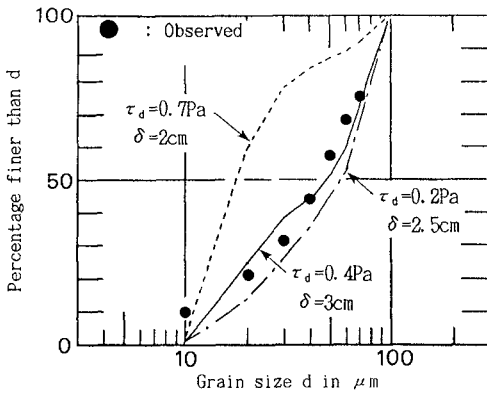
Table 1 shows the measured and the calculated results of deposited weights in the traps at points A-6 and A-8. Three couples of  $\tau_d$  and  $\delta$  listed in the table were selected in order to reproduce the deposited weight at point A-8. By using two of these couples, the deposited weight at point A-6 could also be well reproduced at point A-6.

Figure 10 shows the comparisons between the measured and calculated grain size distributions of trapped silt at points A-6 and A-8. The grain size distribution at point A-6 is reproduced well by setting  $\tau_d$  and  $\delta$  equal 0.4 (Pa) and 3.0 (cm), respectively. At point A-8, on the other hand, the grain size distribution could not be reproduced satisfactorily. In general, judging from these results, it is concluded that the most appropriate values for  $\tau_d$  and  $\delta$  are respectively 0.4 (Pa) and 3.0 (cm).

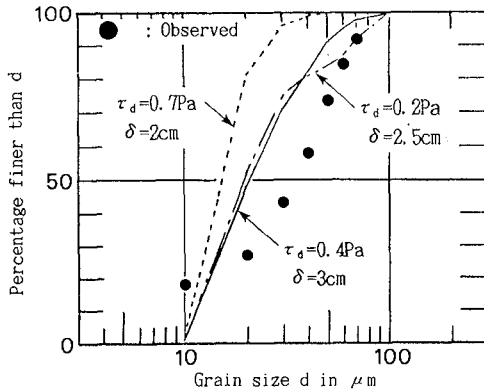
Figure 11 shows the time histories of the measured significant wave height, the estimated bottom shear stress, the measured concentration, the vertical ratio of concentration, the calculated mean grain diameter and the calculated weights of trapped silt at points A-6 and A-8 with  $\tau_d = 0.4$  (Pa) and  $\delta = 3$  (cm). During the observation period, storm waves attacked twice, with the peak significant wave heights of 5.0 m and 3.8 m, respectively. During these stormy periods, considerable deposition occurred. As shown in this figure, the trapped weight of Type-B which has the mouth at 0.3m above the bed could be also reproduced by considering the concentration at 0.3 m above the bottom as the bottom concentration. It is also observed that the calculated time history of the ratio of concentration at 3m above the bottom to that of 1.5 m at point A-8 agrees reasonably well with the measurements.

Table 1. Comparison between measured and calculated weights of trapped silt.

$\tau_d$ (Pa)	$\delta$ (cm)	Trapped Weight (kg)	
		A-6	A-8
0.7	2.0	2.6	4.0
0.4	3.0	3.5	4.3
0.2	2.5	5.4	4.0
Measurement		3.0	4.2



(a) Point A-6



(b) Point A-8

Fig. 10. Comparison between measured and calculated grain size distributions of trapped silt.

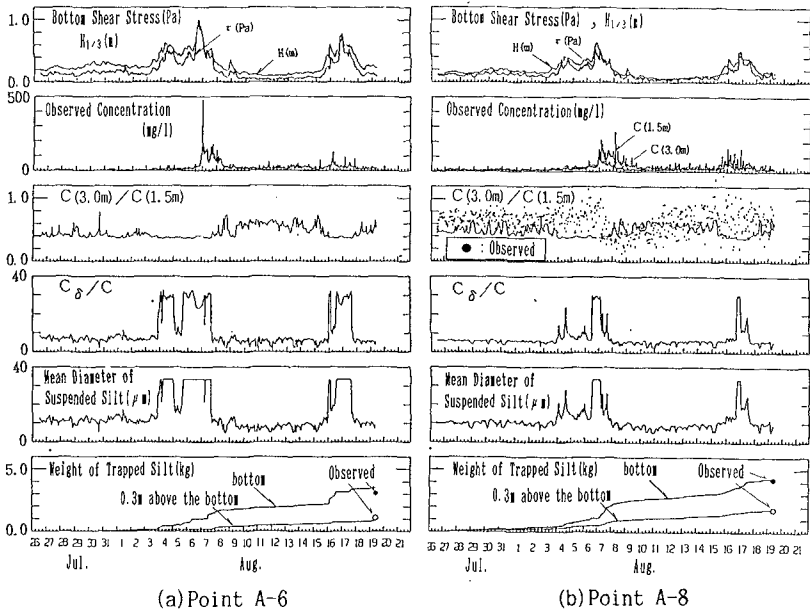


Fig. 11. Time histories of bottom shear stress, significant wave height, observed and calculated concentrations, calculated mean diameter of suspended silt and calculated weight of trapped silt.

CONCLUDING REMARKS

The settling process of nonuniform cohesive sediments in a cooling water intake basin was investigated on the basis of laboratory experiments and field measurements. The settling velocity was formulated empirically as a function of the grain-size and the total concentration by taking into account the effect of flocculation. The critical shear stress for deposition and the vertical concentration profile were also evaluated through comparisons with field measurements. A numerical model was developed to simulate the transportation and deposition of nonuniform sediments in the basin. The deposition rate as well as the grain size distribution of deposited sediments were reproduced satisfactorily by this model.

## ACKNOWLEDGEMENTS

We would like to express our deep appreciation to Prof. Horikawa, president of Saitama Univ. , Prof. Watanabe and Prof. Isobe, Univ. of Tokyo and Associate Prof. Mimura, Ibaragi University. Our thanks are extended to Mr. Kajima and Mr. Sakakiyama of the Central Research Institute of Electric Power Industries for their useful discussions.

## REFERENCES

- Nicolson, J. and B. A. O'Connor, 1986: Cohesive sediment transport model, *Jour. Hydraulic Eng.* , Vol. 112, No. 7, ASCE, pp.621-639.
- Ross, M. A. and A. J. Mehta, 1989: On the mechanics of lutoclines and fluid mud, *Jour. Coastal Res.* , Special Issue, No. 5, pp.51-62.
- Shimizu, T., M. Banno, S. Kanayama, S. Sakauchi, K. Ueki and T. Sakakiyama, 1990: Field investigation of siltation in a cooling water intake basin, *Proc. Coastal Eng.* , Vol. 37, JSCE, pp.424-428 (in Japanese).
- Tanaka, H. and N. Shuto, 1981: Friction coefficient for a wave-current coexistent system, *Coastal Eng. in Japan*, Vol. 24, JSCE, pp.105-128.

## CHAPTER 239

### **Sediment Transport Modelling in a Macrotidal Estuary : do we need to account for Consolidation Processes ?**

Pierre Le Hir and Nancy Karlikow<sup>1</sup>

#### **Abstract**

In order to investigate the role of consolidation processes on the sediment transport in a macrotidal estuary, a simple vertical model of fluid mud consolidation has been coupled to a cross-averaged sediment transport model in the Loire estuary. Simulations show that sediment patterns (turbidity maximum and fluid mud location) are few dependent on consolidation. On the other hand, the consolidation influences the residual deposition after a spring/neap tidal cycle and thus the net transport of sediment through the estuary. It is pointed out that consolidation is in competition with turbulence damping so that both processes have to be considered when predictive simulations are wanted.

#### **Introduction**

The transport of cohesive suspended sediment in a macrotidal estuary is dominated by the occurrence of a turbidity maximum, either due to tidal asymmetry or to density gradients, which partly traps material flowing through the estuary (Allen *et al.*, 1980 ; Nichols and Biggs, 1985).

Besides, many large estuaries are known for their patterns of fluid mud constituted by the deposition of suspended sediment after spring tides, where the turbidity maximum lies. This fluid mud consolidates more or less and then can either be resuspended during the increasing tidal

---

<sup>1</sup> Ifremer, Centre de Brest, B.P. 70, 29280 Plouzané, France.

amplitude or remain as consolidated mud until a larger hydrodynamical forcing occurs. Even if the process is well known, it has rarely been quantified and/or modelled.

The aim of this study is to see how consolidation processes affect the results of suspended sediment transport in order to get tracks of whether and how much one should account for it. More precisely, by means of a mathematical model, we would try to answer the following questions :

- Are the sediment patterns (turbidity maximum and fluid mud) affected by consolidation processes ?
- Is the (long term) sediment transport dependent on consolidation ?
- How accurate should be the consolidation modelling, when computing the transport of cohesive sediment in a macrotidal estuary ?

### **Consolidation modelling**

Many factors can influence the erosive behaviour of a sediment and its consolidation. In particular, the role of biological processes as bioturbation or surficial protection by mucilage have been pointed out (Montague, 1986 ; Paterson *et al.* 1990). Also waves can induce some fluidization of the mud, and thus modify its erodibility without changing its concentration. But in the area of a turbidity maximum within an estuary, these processes are weak : waves are small if compared with the water depth and biota are poor, due to high turbidities. Thus the sediment concentration remains a good parameter to represent the degree of consolidation providing an empirical relationship with the shear strength  $\tau_c$ , the usual parameter for mud erosion (see Mehta *et al.*, 1989).

### **Brief review**

Previous mathematical models for consolidation were mostly empirical when coupled with sediment transport models, for saving computing costs. In first models (Ariathurai and Krone, 1976 ; Onishi, 1982) the soil was discretized in layers of given thicknesses, with

characteristic shear strengths. The exchanges between layers were forced by the deposition rate.

For Teisson and Latteux (1986) the layers were characterized by a given residence time of sediment and naturally a specific shear strength. Hayter (1986) developed a more sophisticated model and considered the time variations of bed density and shear strength according to typical measured profiles. Le Hir *et al.* (1989) introduced a differential law for the bed density variations, allowing any empirical formulation.

All these models could not directly fit the consolidation theories because of the discretization in thick layers. But the performance of new computing facilities allows the required refinement to account for these theories.

### *Consolidation theories*

Two types of conceptual models have been developed (see Alexis *et al.*, 1992).

- The "sedimentation" models express the mass conservation of the solid particles, with vertical exchanges represented by the settling fluxes. A common assumption of this approach is the unique dependence of the settling velocity  $v_s$  on the local suspension density (Kynch, 1952). The usual state variable of these models is the dry density or concentration  $c$ , and the equation can be written :

$$\frac{\partial c}{\partial t} + V(c) \frac{\partial c}{\partial \zeta} = 0 \quad (1)$$

$$\text{where } V(c) = v_s + c \frac{dv_s}{dc}$$

$\zeta$  : vertical coordinate

$t$  : time

- The so-called "consolidation" models account for the mass conservation of pore water and relate its expulsion between particles to the pressure vertical gradient by means of the permeability  $k$ , assuming Darcy's law. From the dynamics point of view, the stress within the soil



can be split into the effective stress ( $\sigma'$ ) on the grains and the pore pressure on the fluid: only the latter forces the water movement. This concept is the basis of geotechnicians' approach for which the void ratio  $e$  is the state variable. When combined with water mass conservation, it leads to Gibson's equation (Gibson *et al.*, 1967), assuming constitutive relationships for permeability and effective stress as a function of the void ratio:

$$\frac{\partial e}{\partial t} - \frac{\gamma'_s}{\gamma_w} \frac{dk_r}{de} \frac{\partial e}{\partial z} + \frac{1}{\gamma_w} \frac{\partial}{\partial z} \left( k_r \frac{d\sigma'}{de} \frac{\partial e}{\partial z} \right) = 0 \quad (2)$$

where  $k_r = k / (1 + e)$  : relative permeability  
 $\gamma'_s$ : immersed unit weight of particles  
 $\gamma_w$ : unit weight of pore water  
 $z$ : material coordinate, representing the thickness of solid particles.

Recently, several authors (Been, 1980, Tan *et al.*, 1990 in Alexis *et al.*, 1992; Toorman and Berlamont, 1991) have pointed out the analogy of these models and proposed unifying theories where the settling velocity can be expressed as a function of the permeability and the effective stress.

The main problem of these theories is the validation of the involved constitutive relationships ( $v_s(c)$ ,  $k(e)$  or  $\sigma'(e)$ ), to which models are very sensitive (see Alexis *et al.*, 1992). Besides, in the present study, the role of effective stresses has a minor importance, as we are mainly dealing with fluid mud and fresh deposit. Thus we choose the sedimentation concept, with the formalism of consolidation models, that is material coordinate  $z$  and void ratio  $e$ . The continuity equation, which can be deduced from (2) with  $\sigma' = 0$ , is written :

$$\frac{\partial e}{\partial t} + \frac{dv_s}{de} \frac{\partial e}{\partial z} = 0 \quad (3)$$

The use of discretized material coordinates prevents the exchanges of material between layers during the consolidation, which is interesting to avoid spurious numerical diffusion, especially when we look for the becoming of marked fractions of sediment.

The fundamental assumption of this simple model is the dependence of the settling velocity on the void ratio, which is equivalent to the Kynch's hypothesis. Nevertheless, such a model can fit rather well many settling tests after appropriate calibrations. In particular it can reproduce steps in density profiles (lutoclines) just by means of strong variations of the derivative  $dv_s/de$ , which are likely to correspond to changes of the soil structure.

### Modelling the Loire estuary

The summer configuration of the Loire estuary, on the Atlantic coast of France has been chosen to test the effects of consolidation. This estuary is about 100 km long (fig. 1), with a tidal range of 5 m on spring tides and a fresh water flow varying from 80 to 5 000  $m^3.s^{-1}$  (average : 800  $m^3.s^{-1}$ ). In the case of low river flow (100-400  $m^3.s^{-1}$ ) a 1-D cross-averaged advection/dispersion model has proved its efficiency in simulating a realistic turbidity maximum, induced by tidal propagation only (Le Hir and Karlikow, 1991). In particular the settling of the turbidity maximum as fluid mud on neap tides and the resuspension of this fluid mud when the tidal range increases was quite well reproduced.

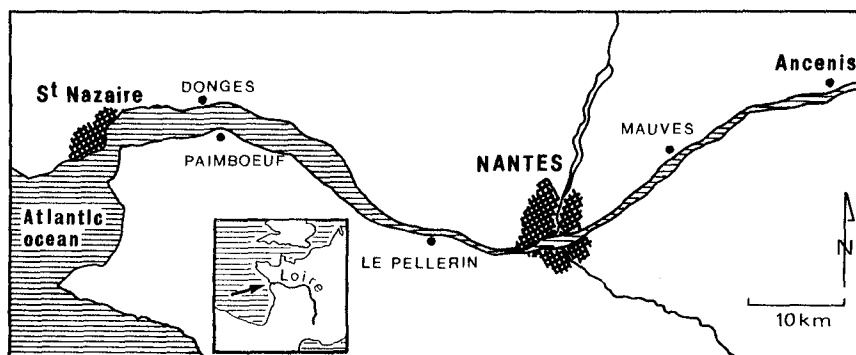


Figure 1: Location of the Loire estuary.

However, consolidation was very crudely accounted for : only two sediment classes (a little concentrated "fluid" mud and a more concentrated mud) were considered, and consolidation was represented as periodic exchanges between these classes.

In the present study, consolidation is computed by means of the previously described sedimentation model, coupled with the horizontal transport model through the deposition and erosion terms. The latter is empirically related to a shear strength which is deduced from the surficial mud concentration according to a power law (Owen in Mehta *et al.*, 1989) :

$$\tau_{ce} = \alpha C_s^\beta \quad (4)$$

$\tau_{ce}$  : critical shear stress for erosion ( $N.m^{-2}$ ).

$C_s$  : surficial sediment concentration, computed by the sedimentation model ( $kg.m^{-3}$ ).

$\alpha, \beta$  : coefficients to be calibrated.

Actually the results are very sensitive to this relationship which is part of the consolidation modelling ; moreover, there can be some compensation between the uncertainty on the computed concentration (however easier to validate) and the lack of knowledge related to the shear strength, especially for fluid mud. Last but not least, the bottom shear stress itself is poorly determined, as the effects of turbulence damping by high suspensions (Teisson *et al.*, 1992) are not accounted for.

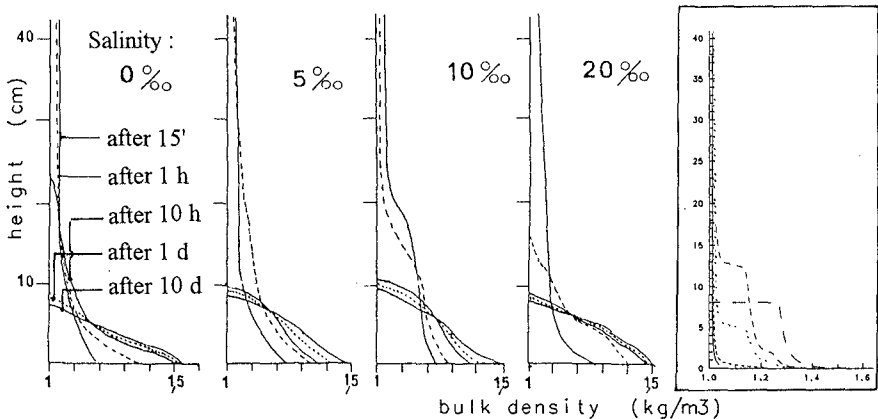


Figure 2: Evolution of sediment density profiles  
(initial height : 2 m ; initial concentration : 20 g/l)  
a) laboratory settling tests with sediment from Loire  
(after Gallenne, 1974).  
b) Simulation with a sedimentation model.

Nevertheless, the sedimentation model has been briefly calibrated with laboratory settling tests made by Gallenne (1974) on the Loire sediment. Although the observations proved the dependence of the sedimentation on the salinity, which is not accounted for by the model, the simulated results are in relative agreement with the experiments (fig. 2). Settling velocities at the beginning of the settling tests have been reduced, in order to maintain low densities (very fluid mud) during the neap tide in the simulations of the Loire system. The resulting relationship  $v_s$  (e or c) is plotted on figure 3 : one can see some continuity with known values of settling velocities for flocculated suspensions (e.g. in Metha *et al.*, 1989).

**settling velocity (m.s<sup>-1</sup>)**

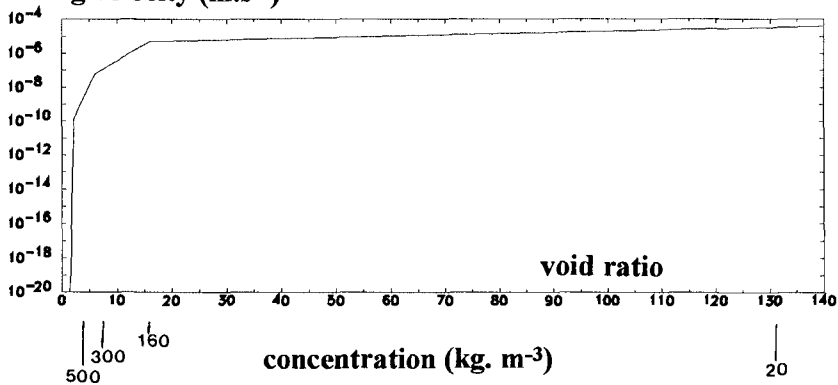


Figure 3 : relationship  $v_s$  (e) used in the sedimentation model of the Loire estuary. The relation between e and c is based on a grain density of 2,65.

In the following, four runs will be compared to show the effect of consolidation on sediment transport in the Loire estuary.

- Run 1 : no consolidation, any deposited sediment has a fixed low shear strength (0,8 N.m<sup>-2</sup>).

- Run 2 : schematic consolidation : two sediment classes with low and high shear strengthes (respectively 0,8 and 1,6 N.m<sup>-2</sup>).

- Run 3 and 4 : full consolidation modelling, as previously described.

The difference between run 3 and run 4 is a change in the relationship

- $\tau_{ce}(C_S)$  : - run 3 :  $\tau_{ce} = 0,14 C_S^{0,4}$  for which resuspension is easy.

- run 4 :  $\tau_{ce} = 0,2 C_S^{0,4}$  leading to hard resuspension .

For each run the tide conditions and river flow are identical, and presented on figure 4.

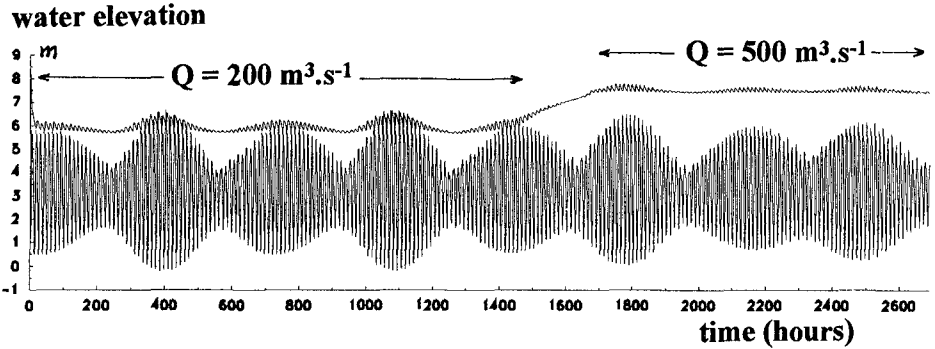


Figure 4 : Tidal forcing and riverflow regime during the simulation of sediment transport in the Loire estuary.

**Note :** a test with no shear strength of the (fluid !) mud has been run. In this case the turbidity patterns are completely unrealistic, with a turbidity maximum at the sea boundary and no stable mud deposit on neap tide. In fact such a result can be induced by the absence of turbulence damping in the model. In reality the latter process could maintain a fluid mud in the estuary. This comment has little impact on the following tests : in fact we are dealing with the consolidation process, that is a change in space and time of sediment characteristics, rather than the rheological behaviour of the mud. Besides, the low value of the exponent in the relation (4) partly accounts for the turbulence damping, as it reduces the large resuspension that would occur for low surficial sediment densities.

### Effects of consolidation processes on the sediment transport in the Loire estuary

On figure 5, the average distribution of suspended sediment during a spring tide for a low river flow is presented for each run. The analogy between the simulated turbidity maxima is obvious. Differences only appear in the extension of the turbidity structure which is more spread when consolidation is badly accounted for, especially in the upper part of the estuary ; this is due to the fact that in such cases, just after deposition, the sediment get instantaneously some shear strength, whereas in a more

realistic scenario, it should not have time to consolidate before the flow is strong enough to resuspend it. The same observation can be made for the total deposited mud (fluid mud and partially consolidated mud) on the following neap tide (fig. 6) : locations are similar but the deposition in the upper estuary is higher for run 4 (consolidation is more effective).

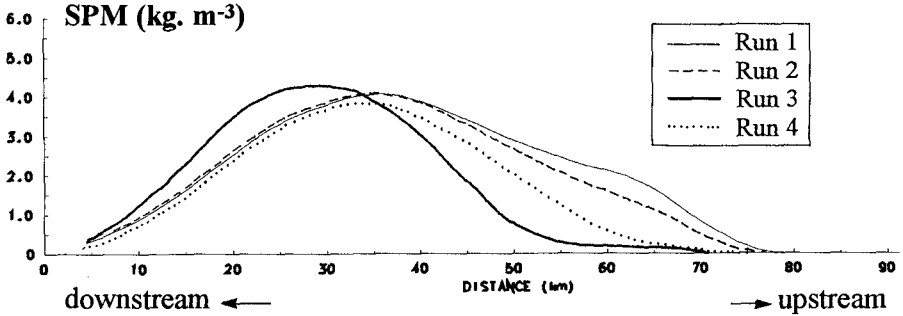


Figure 5 : Computed turbidity maximum (tidally averaged) after 46 days simulation (spring tide ; low river flow =  $200 \text{ m}^3 \cdot \text{s}^{-1}$ ).

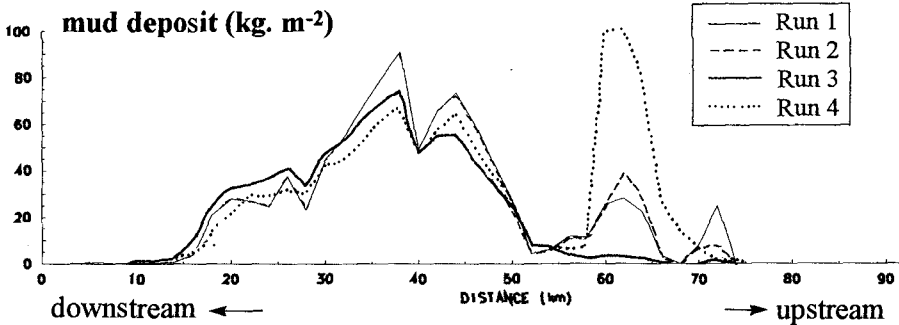


Figure 6 : Computed mud deposits (tidally averaged) after 52 days simulation (neap tide ; low river flow).

Considering the time variation of suspended particulate matter (SPM) and mud deposit in the middle of the estuary during a fortnightly tidal cycle (fig. 7), we still notice a similitude between the four runs, but the phase of resuspension is strongly dependent on the consolidation modelling. In particular, in run 4, consolidation is quick enough to prevent the total resuspension, and a net deposition after the neap/spring tidal cycle is observed. However the range of mud deposition as well as

suspended particulate matter are very similar. It should be noticed that the maximum of SPM does not occur on spring tide but during the mean tides, when exchanges with bottom are maximum. The differences between the minima of SPM at high water during spring tides can be related to the variations of turbidity spreading we mentioned before, as the observation is located on the upstream edge of the turbidity maximum at high water.

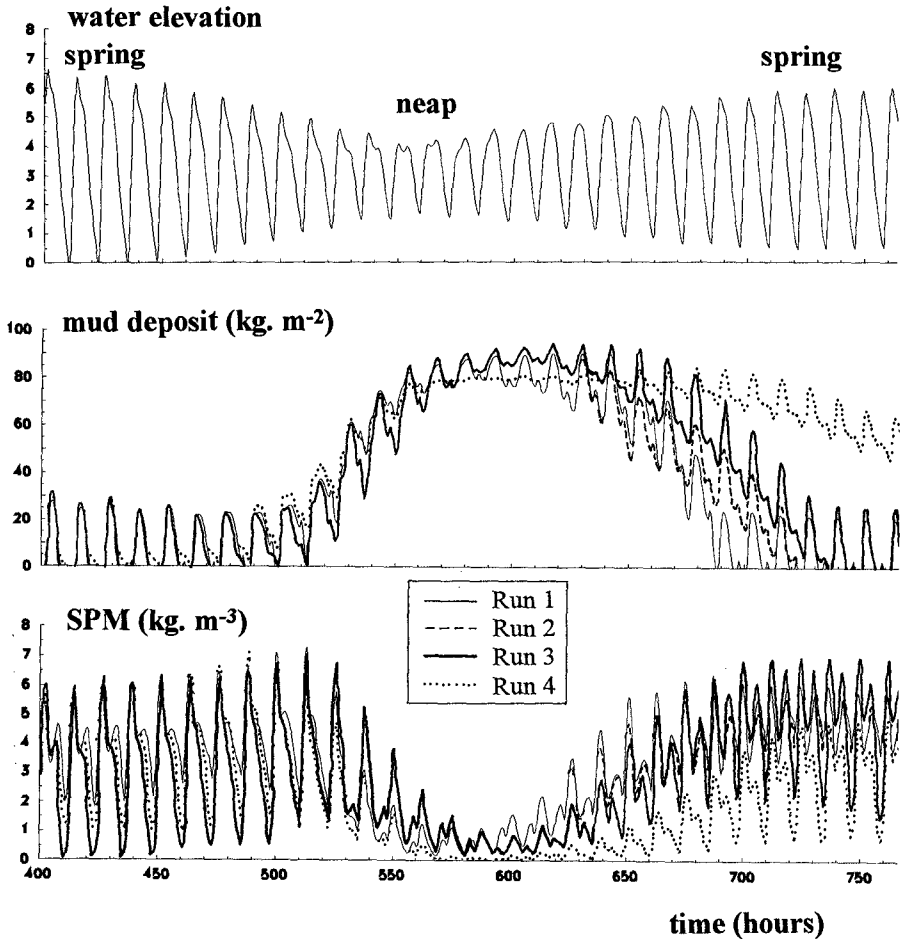


Figure 7 : Time evolution of suspended particulate matter and mud deposit, computed at station "Le Pellerin" (low river flow).

When the river flow is increased, all sediment patterns are shifted downstream (fig. 8 ; Le Hir and Karlikow, 1991). Turbidity maxima still

look like each other, but the ranges can differ, due to possible previous consolidation. This is pointed out on figure 9 : when consolidation effects are more effective (run 4) some sediment previously deposited during the period of low river flow remains in the upper estuary, which notably reduces the seaward transport of material, at least for mean river flow. Thus the consolidation can affect the residual flux of sediment within the estuary during the seasonal changes.

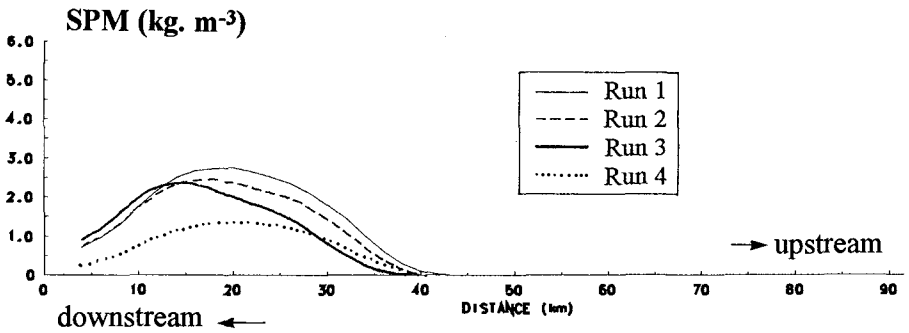


Figure 8 :  
 Computed turbidity maximum (tidally averaged) after 104 days simulation (spring tide ; mean river flow =  $500 \text{ m}^3 \cdot \text{s}^{-1}$ )

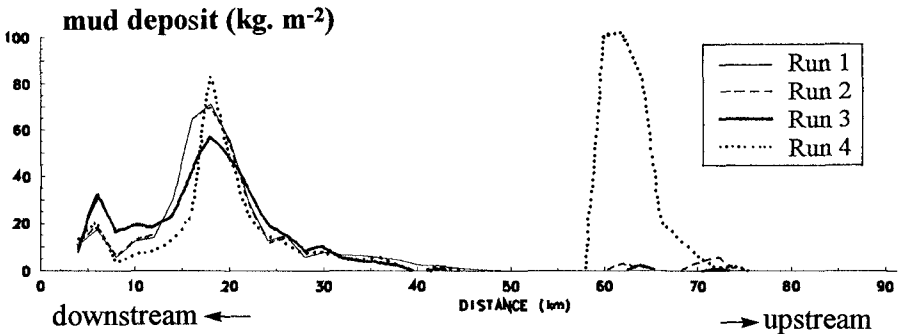


Figure 9 :  
 Computed mud deposits (tidally averaged) after 110 days simulation (neap tide ; mean river flow).



## **Discussion and conclusions**

The simulation of sediment transport in the Loire estuary shows that both turbidity maximum and fluid mud patterns are few dependent on consolidation processes.

However the consolidation influences the time lags between hydrodynamical forcings and sediment processes : for instance within the fortnightly cycle, for the sediment resuspension by tidal currents, or within the seasonal cycle, for the longitudinal transport through the estuary. Thus the consolidation forces the residual deposition or erosion of mud. Naturally these results are specific to a macrotidal estuary and should not be generalized to all cohesive sediment areas.

But this study has also pointed out the sensitivity of simulations to the relationship between the sediment density and its erodibility : our knowledge on this subject is so poor that a sophisticated model for the prediction of mud density would be useless. In addition the required constitutive relationships that any consolidation model involves are still hypothetical. For these reasons we should recommend to use simple consolidation models until the knowledge on soil behaviour progresses substantially.

Lastly, we mentioned the competition between the strengthening of sediment by consolidation and the bottom stress reduction related to the turbulence damping in highly concentrated suspensions. This means that the use of any sophisticated - and presumed realistic - consolidation model should be completed by a bottom stress computation with the same accuracy. Many field validation measurements are required to manage it.

## **Acknowledgements**

The study of the Loire estuary is financed by the "Association pour la Protection des Eaux de l'Estuaire de la Loire" and by IFREMER. The work on consolidation is partly funded by the Commission of European Communities, Directorate General for Science, Research and Development under MAST Contract n° 0035-C. The authors thank Dr. P. Bassoullet for his fruitful comments and D. Guillerm for her help.

## References

- Alexis A., Bassoullet P., Le Hir P., Teisson C. (1992). Consolidation of soft marine soils : unifying theories, numerical modelling and *in situ* experiments. 23rd ICCE, (this volume).
- Allen G.P., Salomon J.C., Bassoullet P., Du Penhoat Y. and De Grandpré C. (1980). Effects of tides on mixing and suspended sediment transport in macrotidal estuaries. *Sedimentary Geology*, 26. pp. 69-90.
- Ariathurai R. and Krone R.B. (1976). Finite element model for cohesive sediment transport. *Journal of the Hydraulics Division ASCE*, vol. 102, n° HY3, March, pp. 323-338.
- Gallenne B. (1974). Les accumulations turbides de l'estuaire de la Loire. Etude de la "crème de vase". Thèse de 3e cycle, Université de Nantes.
- Gibson R.E., Englund G.L., Hussey M.J.L. (1967). The theory of one-dimensional consolidation of saturated clays. I. *Geotechnique*, 17, pp 261-273.
- Hayter E. (1986). Estuarial sediment bed model. In *Estuarine Cohesive Sediment Dynamics*, Ed. A. Mehta, Springer Verlag. pp. 326-359.
- Kynch G.J. (1952). A theory of sedimentation. *Transactions Faraday Society*, 48, pp 166-176.
- Le Hir P., Bassoullet P., L'Yavanc J. (1989). New developments about mud transport models. Application to a macrotidal estuary. In "Sediment Transport Modeling", Proc. Int. Symp. New Orleans. Ed. S.S.Y. Wang, pp. 94-99.
- Le Hir P., Karlikow N. (1991). Balance between turbidity maximum and fluid mud in the Loire estuary. Lessons of a first mathematical modelling. Proceedings of the "Int. Symp. on "the transport of suspended sediments and its mathematical modelling". Florence. Sept., pp. 449-466.

Mehta A.J., Hayter E.J., Parker W.R., Krone R.B. and Teeter A.M. (1989). Cohesive sediment transport. I: Process description. *J. Hydraulic Engineering*, Vol. 115, n° 8, pp. 1076-1093.

Montague C. (1986). Influence of biota on erodibility of sediments. In : Mehta A.J. (ed.), *Estuarine cohesive sediment dynamics*. Lect. notes Coast. Est. Stud., n° 14, Springer Verlag, pp. 251-269.

Nichols M. and Biggs R. (1985). Estuaries. In coastal sedimentary environments. Ed. R. Davis, Springer Verlag, pp. 77-186.

Onishi Y. (1981). Sediment contaminant transport model. *Journal of the Hydraulics Division, ASCE* Vol. 107, n° HY9, Sept., pp. 1089-1105.

Paterson D.M., Crawford R.M., and Little C. (1990). Subaerial exposure and changes in the stability of intertidal estuarine sediments. *Estuarine, coastal and Shelf Sciences*, Vol. 30, pp. 541-556.

Teisson C., Latteux B. (1986). A depth-integrated bidimensional model of suspended sediment transport. *Proc. of 3<sup>rd</sup> Int Symp. on River Sedimentation*. Ed. Wang, Shen and Ding. Univ. of Mississippi, USA, pp. 421-429.

Teisson C., Simonin O, Balland J.C., Laurence D. (1992). Turbulence and mud sedimentation : A Reynolds-stress model and a two phase flow model. *23<sup>rd</sup> ICCE*, (this volume).

Toorman E. and Berlamont (1992). Mathematical modeling of cohesive sediment settling and consolidation. In *Nearshore and Estuarine Cohesive Sediment Transport*, Ed. A. Mehta, Coastal and Estuarine studies series, Vol. 42, (to be published by the AGU).

## CHAPTER 240

### WAVE-INDUCED PORE PRESSURE ACTING ON A BURIED SUBMARINE PIPELINE

Waldemar MAGDA \*

#### ABSTRACT

The response of a sandy seabed to surface water waves, with a special emphasis to wave-induced excess pore water pressure oscillations is studied here in relation to the vertical stability of submarine buried pipelines. The main object of the paper is to present a study of the distribution pattern of the pore water pressure acting around the pipeline, and to calculate the seepage force, the up-lift force particularly, affecting the pipeline stability, under the assumption of compressible both the pore fluid and soil skeleton, for the case of an arbitrary seabed depth as well as for the infinite thickness of the subsoil.

#### INTRODUCTION

Generally, the problem associated with buried submarine pipelines depends, on the water and wave conditions. The wave climate plays a very important role and can influence the interaction between the submarine buried pipeline and the surrounding soil significantly. In practice, pipeline located in water depths up to 60 m are buried, whilst the cover must have a thickness ranging from 0.5 to 1.0 m, depending upon the water depth and the covering material.

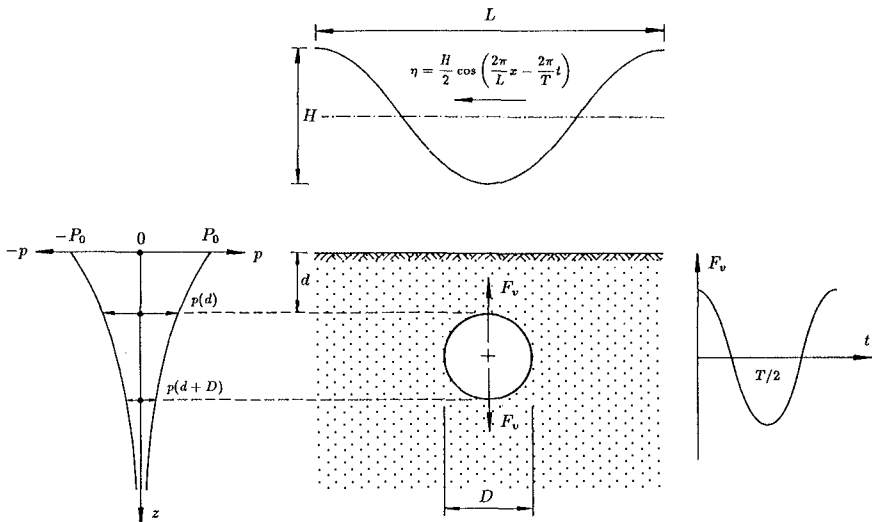
Submarine pipelines buried in a seabed are an engineering means of transport for crude oil and natural gas from "off-shore" oil fields onto a land. When waves pass over a permeable sandy seabed, pore water pressure is continuously

---

\* *Ph.D., Research Engr.*

*University of Hannover, Sonderforschungsbereich 205, Appelstr. 9A, 3000 Hannover 1, Germany (on leave from the Marine Civil Engineering Department, Hydroengineering Faculty, Technical University of Gdańsk, Poland)*

induced within it. Among all environmental loads usually considered in "off-shore" pipelines design, the wave-induced pore water pressure plays one of the most important role. The most critical problem in determining the stability of a pipeline buried in permeable soils under wave loading is the prediction of the pore water pressures in the soil in a vicinity of a pipeline (Dursthoff and Mazurkiewicz, 1985). An excess of the pore water pressure can cause instability of a seabed, liquefaction of the upper sand layer and then floatation which can even lead to a failure of a submarine pipeline. The wave-induced excess pore water pressure developed in a vicinity of a buried pipeline is considered as a one of the main parts in a design procedure. The wave-induced uplift force acting on the pipeline is comparable to the displaced water weight if the pipeline is located in the pore water pressure boundary layer and an inadequate design can cause floatation of pipeline and, subsequently, can lead to costly failures. Therefore, it is essential to improve our knowledge on the interaction among waves, seabed and a submarine pipeline.



**Figure 1** Definition sketch for the uplift force analysis.

It is a very complex and challenging task to define properly the wave-induced excess pore water pressure field around a submarine pipeline buried in a porous seabed. Many researches simplified the problem assuming both the porous medium and pore water incompressible. Under this assumption Lai *et al.* (1974), Liu and O'Donnell (1979) and Lennon (1985) investigated this

problem using a numerical analysis. Liu and O'Donnell (1979) considered two different types of waves acting on the seabed, namely, monochromatic and solitary, and introduced the integral equation method to solve the resulting integral equation. In a numerical solution procedure developed by Lennon (1985) the pressure distribution on the pipeline was calculated using also the boundary integral equation method (BIEM). Employing conformal mapping techniques, MacPherson (1978) and McDougal *et al.* (1988) presented analytical solutions for the case of an infinite depth of the seabed, whereas Monkmeyer *et al.* (1983) developed a solution using so-called 'image pipe' method which, comparing to the former, can be applicable also to a soil layer of a finite thickness.

The common feature in the studies mentioned above is that the effect of compressibility of both the pore water and porous medium was neglected. Moreover, some researchers showed that there is a difference between theoretically computed values of pore water pressure and those observed in experiments. In laboratory studies on the stability of buried pipelines, Philips *et al.* (1979) concluded that potential theory did not generally give an accurate representation of the transmission of wave-induced pressures through the sand, when comparing to the test results.

Reported differences between theoretical and experimental results can have three main reasons, namely:

- the theories are based on the Darcy model and therefore they do not contain all important soil/water parameters (incompressible pore water and nondeformable soil skeleton are assumed),
- boundary conditions applied into computation are not realistic, specially when comparing with laboratory tests environment (seabed layer of a finite thickness),
- values of parameters used in calculations are not exactly the same like these 'in-situ' which accompany laboratory investigations.

The proposed method of calculation is based on:

- the pore water pressure theory where the main soil and pore fluid parameters are considered and a finite sand bed layer system is taken into account,
- the 'image pipe' theory which is able to solve both the upper (at the sea bottom) and the lower (at finite depth of the seabed layer) boundary conditions, and also the boundary condition induced by presence of a pipeline (perturbation or scattering effect).

An implementation of certain soil and pore water parameters, *e.g.* compressibility and permeability, leads not to the Laplace equation, which depends only on a geometry of the problem, but to the storage equation, which is much more complex in form. Using Madsen's (1978) general solution of this equation, an analytical solution for a finite thickness of the seabed layer has been derived and verified qualitatively in numerous large-scale laboratory experiments in a big wave-flume, and quantitatively in small-scale laboratory tests (Magda, 1989,

1991). These tests enabled to study influences of single soil/water parameter changes on the character of the pore water pressure damping within a porous medium. A great attention has been put to modelling and controlling different degrees of saturation which is of a special interest for coastal and tidal areas where, because of a continuous water table movement and wave-breaking zones, the sediment is not and cannot be treated as a saturated medium.

### MATHEMATICAL FORMULATION OF THE PROBLEM

Introducing a pipeline-like structure into a soil body, it is not so easy to derive a solution to the governing equation for flow of a compressible pore fluid in a compressible porous medium (*e.g.* given by: Madsen, 1978; Yamamoto *et al.*, 1978). Therefore, after some mathematical manipulations, and presenting the solution in terms of the pore-water pressure and effective stresses, a new form of the governing equation can be obtained (Okusa, 1985):

$$\nabla^2 \left( \nabla^2 - \frac{1}{c_v} \frac{\partial}{\partial t} \right) p = 0 \quad (1)$$

where  $p$  is the wave-induced excess pore water pressure,  $c_v$  is the coefficient of consolidation,  $t$  is the time, and  $\nabla$  is the Laplacian operator. The coefficient of consolidation,  $c_v$ , can be defined for the unsaturated soil as

$$\frac{1}{c_v} = \frac{\gamma}{k} \left[ \frac{n}{K} + \frac{1 - 2\mu}{2G(1 - \mu)} \right] \quad (2)$$

where  $\gamma$  is the unit weight of the pore fluid,  $k$  is the isotropic coefficient of soil permeability,  $n$  is the porosity of the porous bed,  $\mu$  is the Poisson's ratio,  $K$ , is the bulk modulus of water, and  $G$  is the shear modulus of soil. From this it is easily seen that the solution of Eq. (1) can be formulated as a mixed solution of both the Laplace equation

$$\nabla^2 p = 0 \quad (3)$$

and the consolidation (diffusion) equation

$$\nabla^2 p - \frac{1}{c_v} \frac{\partial p}{\partial t} = 0 \quad (4)$$

in two dimensions. It has to be pointed that sometimes (*e.g.* Qiu and Sun, 1987) the simplification of the solution to the governing flow equation is going too far and, due to the total elimination of the soil displacements, the problem is reduced only to the consolidation equation. However, the correct solution has to be treated as a sum of the general solutions to the last two differential equations of the second order.

SOLUTION METHOD

Assuming that the wave-induced hydrodynamic pressure at the seabed is described by the periodic function

$$p = P_0 \exp[i(ax - \omega t)] \quad (5)$$

where  $a = 2\pi/L$  is the wave number,  $L$  is the wave length,  $\omega = 2\pi/T$  is the angular velocity,  $T$  is the wave period, and  $P_0$  is the pressure amplitude at the seabed, and due to linearity of the above mentioned component equations, all the unknowns in the problem considered (among others: the wave-induced pore pressure) are periodic with  $a$  and  $\omega$ . Then, the wave-induced pore pressure  $p$  is represented by

$$p = f(z) \exp[i(ax - \omega t)] \quad (6)$$

where  $f(z)$  is a function of  $z$  only. Introducing this into Eqs. (3) and (4), the general solution is represented by the sum of the solutions from the two following differential equations

$$\frac{d^2 f}{dz^2} - a^2 f = 0 \quad (7)$$

$$\frac{d^2 f}{dz^2} - \left( a^2 - \frac{\omega}{c_v} i \right) f = 0 \quad (8)$$

Because the governing equations are linear, the wave-induced stresses can be obtained by superposing, as previously indicated by Yamamoto (1981) and Okusa (1985a). The general solutions  $f_1$  of Eq. (7) and  $f_2$  of Eq. (8) are

$$f_1 = C_L \exp(az) + D_L \exp(-az) \quad (9)$$

$$f_2 = C_C \exp(\kappa z) + D_C \exp(-\kappa z) \quad (10)$$

where  $C_L, C_C, D_L, D_C$  are integral constants depending on the boundary conditions and

$$\kappa = \sqrt{a^2 - \frac{\omega}{c_v} i} \quad (11)$$

For the case of infinitely thick homogeneous sediment, the wave-induced pore pressures, stresses, and displacements must tend to zero as  $z \rightarrow \infty$ . Therefore (Okusa, 1985):

$$C_L + C_C = 1 \quad (12)$$



$$C_L = \frac{2(1 + \mu)B}{3 + 2\mu B - B} \quad C_C = \frac{3(1 - B)}{3 + 2\mu B - B} \quad (13)$$

where the Skempton's pore pressure coefficient  $B$  is defined as

$$\frac{1}{B} = 1 + \frac{n\beta}{\alpha} \quad (14)$$

where  $\alpha$  is the volume compressibility of the sediment,  $\beta$  is the volume compressibility of the pore fluid.

Now, using a complementary wave loading method, *i.e.* two waves having the same phase and different amplitudes ( $C_L$  and  $C_C$ ) are assumed for solving the Laplace equation and consolidation equation separately, one can write

$$p = C_L \times \mathbf{L} + C_C \times \mathbf{C} \quad (15)$$

where  $\mathbf{L}$  and  $\mathbf{C}$  denote values obtained from the solutions of Laplace equation and consolidation (diffusion) equation, respectively, assuming for both of them a unit amplitude of the inducing hydrodynamic pressure wave at the seabed.

A contribution of the particular components, supplied by the solutions of Laplace equation and consolidation equation, to the total solution of the problem is illustrated in Tab. 1.

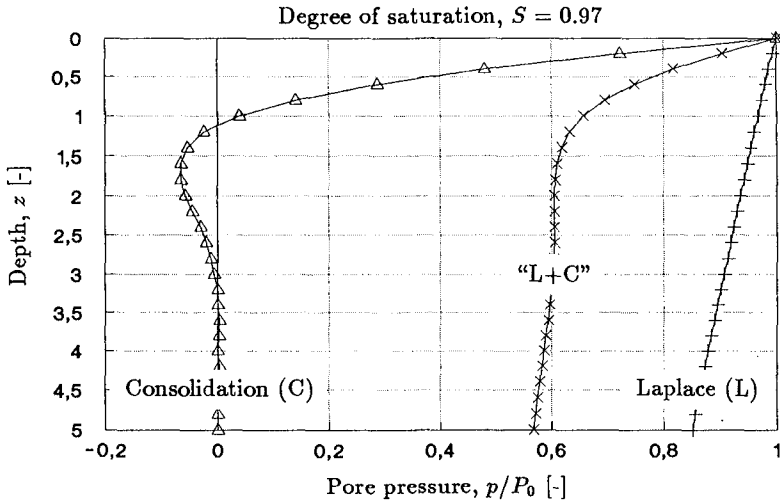
Degree of Saturation	$C_L$	$C_C$
$S = 1.00$	0.998	0.002
$S = 0.99$	0.855	0.145
$S = 0.98$	0.748	0.252
$S = 0.97$	0.665	0.335
$S = 0.96$	0.598	0.402
$S = 0.95$	0.544	0.456

**Table 1** Contribution of single components (from the Laplace equation and consolidation equation) in the total solution, with regard to different saturation conditions.

It has to be stressed once more that the influence of partly saturated seabed conditions is predominant for the investigated case of the uplift force acting on a buried submarine pipeline. Therefore, the both solutions to the Laplace equation and consolidation equation have to be always taken into account simultaneously. To confirm an existence of partly saturated conditions in a natural environment, a measuring campaign was conducted on Norderney Island (Germany). After sampling and statistical analysis of the measured and calculated

results, the mean value of the degree of saturation was found to be 0.975 (Magda and Davidov, 1990).

Fig. 2 shows a set of pore pressure profiles with depth calculated for the singular solutions, *e.g.* the Laplace and consolidation problems, considered separately, comparing them with a solution for the compounded problem of the compressible fluid flow through compressible media.



**Figure 2** Comparison of different solutions for the pore pressure distribution with depth.

A similar analysis can also be performed for the case of a finite thickness of the seabed layer. The formulas describing coefficients  $C_L, C_D, D_L, D_D$  are, however, much more complicated.

The solution to the Laplace equation, Eq. (3), for the boundary conditions problem created by a finite thickness of the seabed layer and a pipe-like structure embedded in the soil sediment, is not trivial but does not bring any troubles. As documented in the introduction, it is possible to obtain this solution using, for example, one of the reported conformal mapping techniques.

It is not an easy task to solve the consolidation partial differential equation, Eq. (4), in the Cartesian coordinate system for the identical to the above mentioned boundary conditions problem. Therefore, to overcome the difficulties, the solution method presented below is based on the cylindrical (circular-cylinder) coordinate system.

The consolidation equation, also known as diffusion or heat conduction equation, is considered. It can be presented in general form as

$$\nabla^2 \varphi = \frac{1}{h^2} \frac{\partial \varphi}{\partial t} \quad (16)$$

The solution of any of the scalar equations like: the Laplace equation, the Poisson equation, the diffusion equation, the wave equation, the damped wave equation, transmission line equation, and the vector wave equation may be reduced to a solution of the scalar Helmholtz equation, or its special case – the Laplace equation (Moon and Spencer, 1971). For the consolidation equation (16), let

$$U(u_i)T(t) \quad (17)$$

where  $U$  is a function of the space coordinates and  $T$  is a function of time only. Substitution into the consolidation equation allows the separation of the time part, giving

$$\nabla^2 U + \kappa U = 0 \quad (18a)$$

$$\frac{dT}{dt} + \kappa^2 h^2 T = 0 \quad (18b)$$

where  $\kappa$  is the separation constant.

The solution of the Helmholtz equation (18a) depends on the space variables and the boundary conditions, and will be different for each problem. The equation in time (18b), however, is independent of the coordinate system. Thus the solution of the consolidation equation is always

$$\varphi = U(u_1, u_2, u_3) e^{-\kappa^2 h^2 t} \quad (19)$$

Geometry of the problem, *i.e.* circular pipe buried in a seabed (see Fig. 1), advises to use the circular-cylinder coordinates

$$\begin{cases} u_1 = r & 0 \leq r < \infty \\ u_2 = \theta & 0 \leq \theta < 2\pi \\ u_3 = z & -\infty < z < +\infty \end{cases} \quad \begin{cases} x = r \cos \theta \\ y = r \sin \theta \\ z = z \end{cases} \quad (20)$$

Rewriting the Helmholtz equation (18a),  $U$  must satisfy, in polar coordinates,

$$\nabla^2 U + \kappa^2 U = \frac{1}{r} \frac{\partial}{\partial r} \left( r \frac{\partial U}{\partial r} \right) + \frac{1}{r^2} \frac{\partial^2 U}{\partial \theta^2} + \kappa^2 U = 0 \quad (21)$$

Separation of the Helmholtz equation (21), in two-dimensional polar coordinate system (in a plane problem  $\theta$  is independent of  $z$  and the circular-cylinder coordinate system is simplified and becomes the polar coordinate system), leads to (Moon and Spencer, 1971):

$$\frac{d^2 R}{dr^2} + \frac{1}{r} \frac{dR}{dr} + \left(\kappa^2 - \frac{\lambda^2}{r^2}\right) R = 0 \quad (22a)$$

$$\frac{d^2 \Theta}{d\theta^2} + \lambda^2 \Theta = 0 \quad (22b)$$

where  $R$ ,  $\theta$  are functions of  $r$ ,  $\theta$ , respectively, and  $\lambda$  and  $c$  are separation constants. These equations are solved for  $R$  and  $\Theta$ , and the solution of the Helmholtz equation has a following form

$$U(r, \theta) = R(r) \Theta(\theta) \quad (23)$$

Differential equation (22b) has a following general solution

$$\Theta(\theta) = \alpha \cos \lambda \theta + \beta \sin \lambda \theta \quad (24)$$

For the governing problem,  $U$  is a harmonic function of  $\theta$  with a period  $2\pi$ , therefore,  $\Theta$  must have the same feature. It is possible only when  $\lambda$  is represented by an integer number. By limiting the range of values of  $\lambda$  only to positive ones ( $\lambda = 0, 1, 2, \dots, n, \dots$ ) both functions  $\Theta(\theta)$  and  $R(r)$  can be written accordingly as

$$\Theta_0(\theta), \Theta_1(\theta), \Theta_2(\theta), \dots, \Theta_n(\theta), \dots \quad ; \quad R_0(r), R_1(r), R_2(r), \dots, R_n(r), \dots \quad (25)$$

In this way, an infinite system of solutions for Eq. (23) is obtained which now can be written as

$$U(r, \theta) = \sum_{n=0}^{\infty} [\alpha_n \cos n\theta + \beta_n \sin n\theta] R_n(r) \quad (26)$$

Eq. (22a) can be considered as the Bessel equation which in general form can be written

$$\frac{d^2 W}{dw^2} + \frac{1}{w} \frac{dW}{dw} + (\mu^2 w^2 + q^2 - s^2/w^2) W = 0 \quad (27)$$

The general series solution of Eq. (27) may be written, for  $s \neq$  integer,

$$W = A \mathcal{J}_s(\mu, q, w) + B \mathcal{J}_{-s}(\mu, q, w) \quad (28)$$

These series are valid everywhere in the finite complex plane. If  $s = n$ , an integer,  $\mathcal{J}_{-s}$  is no longer independent of  $\mathcal{J}_s$  and the general solution of Eq. (27) is

$$W = A \mathcal{J}_n(\mu, q, w) + B \mathcal{Y}_n(\mu, q, w) \quad (29)$$

where  $\mathcal{J}_n$  and  $\mathcal{Y}_n$  are the Bessel wave functions of the first and second kind (also called the Weber function), respectively. If  $\mu = 0$  (this is the case) it can be concluded that the Bessel functions degenerate and Eq. (29) becomes

$$W = A\mathcal{J}_n(qw) + B\mathcal{Y}_n(qw) \quad (30)$$

Introducing the Hankel functions (*i.e.* the Bessel functions of the third kind, which are linear combinations of the Bessel functions of the first and second kinds)

$$\mathcal{H}_n^{(1)}(qw) = \mathcal{J}_n(qw) + i\mathcal{Y}_n(qw) \quad (31)$$

$$\mathcal{H}_n^{(2)}(qw) = \mathcal{J}_n(qw) - i\mathcal{Y}_n(qw) \quad (32)$$

where:  $\mathcal{H}_n^{(1)}$ ,  $\mathcal{H}_n^{(2)}$  are the Hankel functions of the first and second kind, respectively, and of order  $n$ , the general solution of Eq. (27) may be also written (Moon and Spencer, 1971):

$$W = A\mathcal{H}_n^{(1)}(qw) + B\mathcal{H}_n^{(2)}(qw) \quad (33)$$

Comparing now Eq. (22a) and Eq. (27), and replacing  $W$  by  $R$  and  $qw$  by  $\kappa r$ , one has

$$R = A\mathcal{H}_n^{(1)}(\kappa r) + B\mathcal{H}_n^{(2)}(\kappa r) \quad (34)$$

Two-dimensional Helmholtz equation (18a), describing diffraction, after transformation into the polar coordinates system gets a form which is known as the Bessel equation, the solution of which, in two-dimensional scattering by localized objects in a sea of constant depth can be constructed by superposition of the following terms (Mei, 1989):

$$\left\{ \begin{array}{l} \mathcal{H}_n^{(1)}(\kappa r) \\ \mathcal{H}_n^{(2)}(\kappa r) \end{array} \right\} \left\{ \begin{array}{l} \sin n\theta \\ \cos n\theta \end{array} \right\} \quad (35)$$

Because of the asymptotic behaviour of the Hankel functions

$$\left\{ \begin{array}{l} \mathcal{H}_n^{(1)}(\kappa r) \\ \mathcal{H}_n^{(2)}(\kappa r) \end{array} \right\} \simeq \left( \frac{2}{\pi\kappa r} \right)^{1/2} \exp \left[ \pm i \left( \kappa r - \frac{\pi}{4} - \frac{n\pi}{2} \right) \right] \quad (36)$$

$\mathcal{H}_n^{(2)}$  must be discarded when  $\kappa$  is complex with a positive real part (Mei, 1989).

Assuming the hydrodynamic bottom pressure oscillations of a unit amplitude, expressed by harmonic solution

$$p = e^{-i\omega t} \quad (37)$$

where  $i$  denotes the imaginary unit, and comparing it with Eq. (6), the separation constant can be expressed by

$$\kappa = \sqrt{\frac{i\omega}{c_v}} \quad (38)$$

In fact,  $\kappa$  is a complex number and can be presented in a general form as

$$\kappa = \sqrt{a + ib} \quad \text{where} \quad a = 0 \quad \text{and} \quad b \equiv \frac{\omega}{c_v} > 0 \quad (39)$$

This can also be written

$$\kappa = a' + ib' \quad (40)$$

Comparison of the last two expressions shows that

$$a', b' \geq 1 \quad \text{when} \quad b \geq 1 \quad \text{and} \quad 0 \leq a', b' < 1 \quad \text{when} \quad 0 \leq b < 1 \quad (41)$$

So,  $b'$  is always positive without any respect to the positive value of  $b$  ( $b \geq 0$ ).

And thus, the general solution for the scattered (radiated) waves, also pore water pressure waves, may be written as

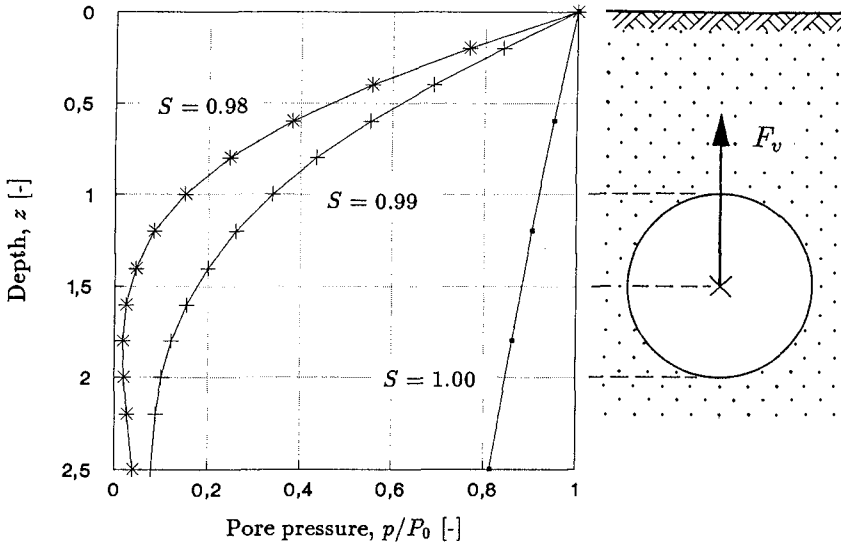
$$U = \sum_{n=0}^{\infty} (\alpha_n \cos n\theta + \beta_n \sin n\theta) H_n^{(1)}(kr) \quad (42)$$

An implementation of the "image pipe" theory (Monkmeyer *et al.*, 1983) allowed to fulfil all requirements concerning the boundary conditions of the problem.

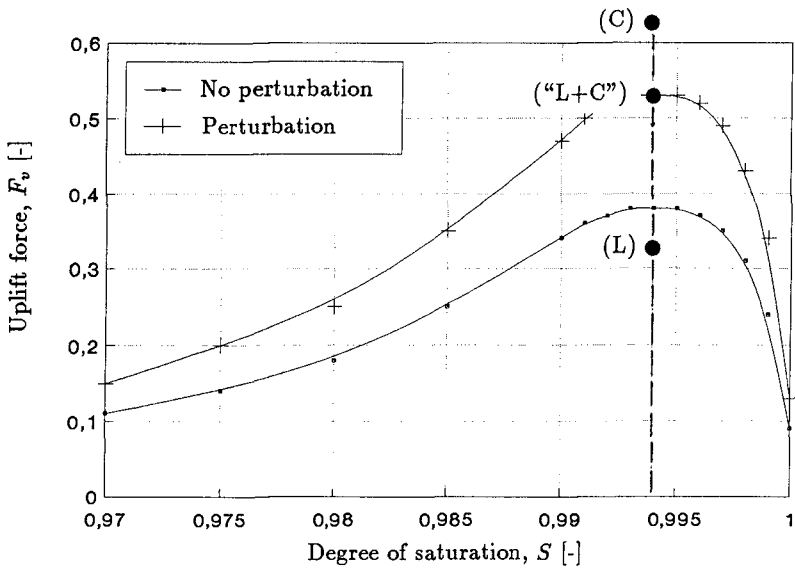
## RESULTS OF CALCULATION

An application of the method is illustrated by some calculation examples where the meaning of the seabed saturation problem is specially emphasized. For a certain geometry (depth of burial, pipeline outside diameter) the pipeline uplift force is computed, taking into account values of the degree of saturation from the range between 0.85 and 1.00, for which the soil can be considered as a saturated soil but with the pore fluid having some degree of compressibility (higher than a pure water) due to the presence of the air bubbles (Esrig and Kirby, 1977).

The solution to Eq. (1) enables to investigate the problem of pore pressure gradient, especially in a vicinity of the seabed surface. Performing series of calculation, the most unfavourable (from the pressure gradient point of view) phase of the pore pressure oscillations can be detected and then, it becomes feasible to calculate the most critical value of the pipeline uplift force. And



**Figure 3** Definition sketch for the uplift force analysis (influence of different saturation conditions).



**Figure 4** Pipeline uplift force versus different saturation conditions of seabed sediments.

thus, Fig. 3 shows the governing problem and Fig. 4 illustrates the results of calculations for a certain set of data where the uplift force is influenced by different values of the degree of saturation.

It can be easily recognized that the pipeline uplift force depends very strongly on the degree of saturation and has a maximum value for the degree of saturation very close to 1.00.

Changing a value of the degree of saturation with a step of 0.01 (*i.e.*, 1%), for example, the most critical situation can be easily omitted. Therefore, looking for an absolute maximum value of the pipeline uplift force, it is required to apply even smaller increment of the degree of saturation when performing a parameter study by means of numerical calculations to obtain a precise picture of possible variations in the pipeline uplift force.

The elaborated method seems to be very useful in a optimization design procedure and gives the result which reflects, among others, the most inconvenient case for the pipeline stability with respect to saturation conditions of the seabed which are, on the other hand, extremely difficult and almost impossible to determine 'in-situ', using engineering methods of testing, with the exactness which is comparable to the necessary step of calculation.

The calculation procedure, presented in the paper and based on the advanced pore water pressure theory, make it feasible to incorporate important soil/water parameters into the pipeline uplift force analysis. Obtained values of the uplift force appear to be greater than these computed from the potential theory; this finding is in accordance with some observations from laboratory tests reported in the literature.

## REFERENCES

- DURSTHOFF, W., MAZURKIEWICZ, B. (1985).  
"Problems related to submarine pipelines," *Mitteilungen des Franzius-Instituts für Wasserbau und Küsteningenieurwesen der Universität Hannover*, Heft 61, pp. 176-238.
- LAI, N.W., DOMINGUEZ, R.F., DUNLAP, W.A. (1974).  
"Numerical solutions for determining wave-induced pressure distributions around buried pipelines," *Texas A & M University, Sea Grant Pub. No. TAMU-SG-75-205*.
- LENNON, G.P. (1985).  
"Wave-induced forces on buried pipelines," *Journal of Waterway, Port, Coastal and Ocean Engineering*, Vol. 111, No. 3, pp. 511-524.
- MACPHERSON, H. (1978).  
"Wave forces on pipeline buried in permeable seabed," *Journal of Waterway, Port, Coastal and Ocean Division*, Vol. 104, No. WW4, pp. 407-419.



- MADSEN, O.S. (1978).  
"Wave-induced pore pressures and effective stresses in a porous bed," *Géotechnique*, Vol. 28, No. 4, pp. 377-393.
- MAGDA, W. (1989).  
"Wave-induced pore water pressure generation in a sand bed," Internal Report No. 1, Sonderforschungsbereich-205 "Küsteningenieurwesen," TP A13, Universität Hannover, June 1989, pp. 1-94.
- MAGDA, W. (1990).  
"Pore water pressure generation in a highly saturated sea bed for shallow water conditions," Proceedings of the 1<sup>st</sup> International Symposium "LITTORAL 1990," Marseille, July 1990, pp. 110-114.
- MAGDA, W., DAVIDOV, N. (1990).  
"On determining of the degree of saturation from 'in-situ' measurements of the seabed performed on Norderney Island," Internal Report No. 2, Sonderforschungsbereich-205 "Küsteningenieurwesen," TP A13, Universität Hannover, July 1989, pp. 1-57.
- MCDUGAL, W.G., DAVIDSON, S.H., MONKMEYER, P.L., SOLLITT, C.K. (1988).  
"Wave-induced forces on buried pipelines," *Journal of Waterway, Port, Coastal, and Ocean Engineering*, Vol. 114, No. 2, pp. 220-236.
- MEI, C.C. (1989).  
"The Applied Dynamics of Ocean Surface Waves," Advanced Series on Ocean Engineering - Vol. I, World Scientific Publishing Co. Pte. Ltd, pp. 1-740.
- MONKMEYER, P.L., MANTOVANI, P., VINCENT, H. (1983).  
"Wave-induced seepage effects on a buried pipeline," Proceedings of the Coastal Structures '83 Conference, pp. 519-531.
- MOON, P., SPENCER, D.E. (1971).  
"Field Theory Handbook; Including Coordinate Systems, Differential Equations and Their Solutions," Springer-Verlag, pp. 1-236.
- OKUSA, S. (1985a).  
"Wave-induced stresses in unsaturated submarine sediments," *Géotechnique*, 35, No. 4, pp. 517-532.
- PHILLIPS, B.A., GHAZZALY, O.I., KALAJIAN, E.H. (1979).  
"Stability of pipeline in sand under wave pressure," Proceedings of the Speciality Conference "Civil Engineering in the Ocean IV," San Francisco, pp. 122-136.
- QIU, H.H., SUN, Z.C. (1987).  
"Wave induced pressures on a buried pipeline," Proceedings of the 6<sup>th</sup> International Symposium on Offshore Mechanics and Arctic Engineering (OMAE), Houston, Texas, March 1-6, 1987.
- YAMAMOTO, T., KONING, H.L., SELLMER, H., HIJUM, E. (1978).  
"On the response of a poro-elastic bed to water waves," *Journal of Fluid Mechanics*, Vol. 87, part 1, pp. 193-206.

## CHAPTER 241

### Hydraulic Approach to Determining Optimum Interval of Discharge Sites of Barge in Constructing Rubble Foundation of Deep Water breakwater

Yoshiharu Matsumi <sup>1</sup> Akira Kimura <sup>2</sup>

#### Abstract

This study aims to establish the effective and economical construction scheme of the rubble mounds which are constructed by discharging a large amount of rubble from hopper barge. Since the plane scatter of the landing rubble on the sea floor directly depends on the random drift force exerted on the settling rubble, the statistical properties for the scattering range of the settling rubble in the still water are fully investigated in experiments. On the basis of the experiments and the discrete block method which equipped to cope with the steeper slope of rubble mound than the angle of repose for rubble, a numerical technique to simulate the spatial geometry of the discharged rubble on the sea floor taking the angle of repose for the rubble into account is developed. An optimum interval of the discharge sites of the barge which makes the uneven property of the mound's surface minimum is discussed in connection with the change in the the design water depth of breakwater and the discharge times.

#### 1 Introduction

Caisson type breakwater is usually placed on a rubble mound foundation. In general the foundations are constructed by discharging a large amount of rubble from hopper barges. An advantage of this construction method exists in its rapid "executability", since barges can carry a large volume of rubble at one time. However the mounds by individual discharge from the barge tend to form uneven surface, since the rubble landing on sea floor distributes widely. This is a drawback of this construction method. Since the design water depth of breakwaters has become deeper and the size of the rubble mound has become greater,

---

<sup>1</sup>Associate Prof. Dept. of Social Systems Engg., Faculty of Engg., Tottori University.  
4-101 Koyama-Minami, Tottori, 680, Japan.

<sup>2</sup>Professor, Dept. of Social Systems Engg., Faculty of Engg., Tottori University.

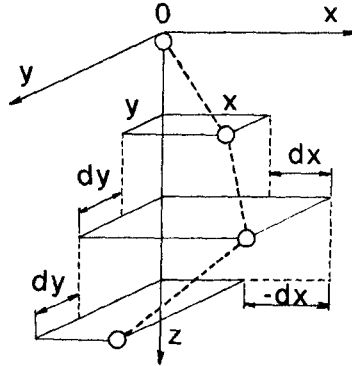


Figure 1: Definition of the fluctuation of the settling rubble.

the portion of the rubble foundation work to the total process of breakwater construction has been increasing. Therefore, the technique to construct a mound for breakwaters effectively and economically has become very important. This study aims to establish the effective construction scheme of the rubble mound by using a hopper barge, firstly the statistical properties of the landing rubble distributions on the sea floor are investigated with the experiments, secondly a numerical technique to simulate the spatial geometry of the discharged rubble mound from hopper barges by taking the angle of repose for the rubble into account is developed. Finally, the effective interval of the discharge points of the barges which minimizes the uneven property of the mound's surface is discussed in connection with the spatial geometry of the rubble mound by multi-discharge and the water depth.

## 2 Stochastic properties for scattering position of settling rubble in still water

In the experiments, the representative sizes of rubble  $d = 2.8 \text{ cm}$ ,  $3.7 \text{ cm}$  and  $4.3 \text{ cm}$  are employed. Experiments have been carried out in a laboratory settling tank with  $2 \text{ m}$  depth and  $1.1 \text{ m} \times 1.1 \text{ m}$  cross-section. Every piece of rubble is dropped from same position on the water surface. The total amount of settled rubbles is 3000 for each rubble diameter. At six different water depths, the  $x$  and  $y$  positions of the settling rubble are measured by two video cameras (Figure 1,  $x$ ,  $y$ ; horizontal axes,  $z$ ; vertical axis).  $O$  is the discharge point of rubble,  $dx$  and  $dy$  are the displacements between specified depths in  $x$  and  $y$  direction. The stochastic properties for  $dx$  and  $dy$  at every water depth are investigated.

Figure 2 shows the distributions for  $dx$  and  $dy$  at six different water depths. These experiments are the case for the average diameter  $d = 2.8 \text{ cm}$ . The shapes of distributions are similar to each other except for the case of  $z/d = 7.1$ . The

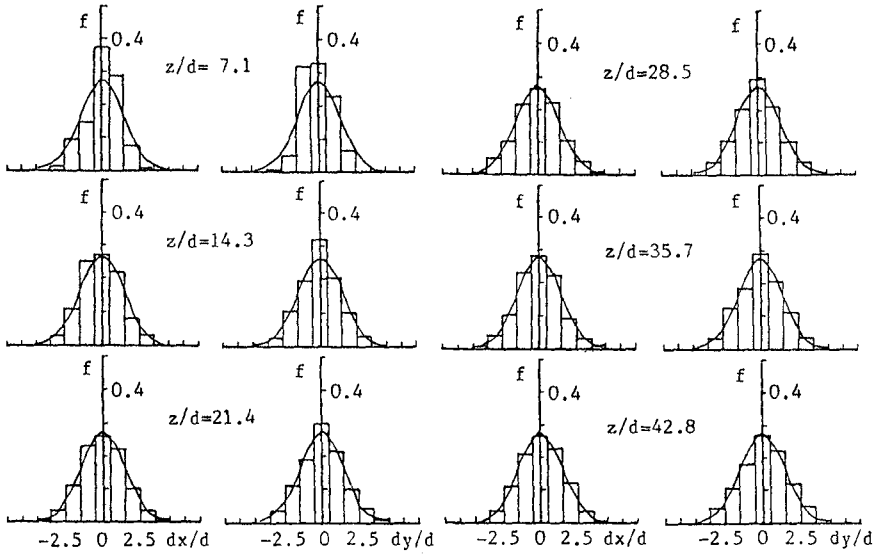


Figure 2: Distributions for  $dx/d$  and  $dy/d$  at six different water depth.

cases for other diameters are the same properties to this case. Therefore, it may be considered that the stochastic property for the displacement of the settling rubble at every section is identical.

Figure 3 shows the change in the mean values ( $dx_m/d, dy_m/d$ ) and the standard deviations ( $\sigma_x, \sigma_y$ ) with respect to the relative water depth from the still water surface. Though the values of  $dx_m/d$  and  $dy_m/d$  at every section show a random fluctuation with changing  $z/d$ , the fluctuation range is less than about 10% of rubble diameter. On the other hand, no practical difference in standard deviations  $\sigma_x$  and  $\sigma_y$  at every section except for  $z/d = 7.1$  is observed. From these investigations, the stochastic properties for the displacement of the settling rubble at every section may be assumed to be identical. In this study, the means for  $dx$  and  $dy$  at every section are assumed to be zero,  $\sigma_x$  and  $\sigma_y$  are assumed to be equal at every section.

### 3 Stochastic simulation technique for spatial geometry of rubble mound discharged from hopper barge

#### 3.1 Probability distribution for settling position of rubble

In this study, the distribution for the displacement of the settling rubble at every section is assumed to be estimated by the Gaussian distribution with zero mean

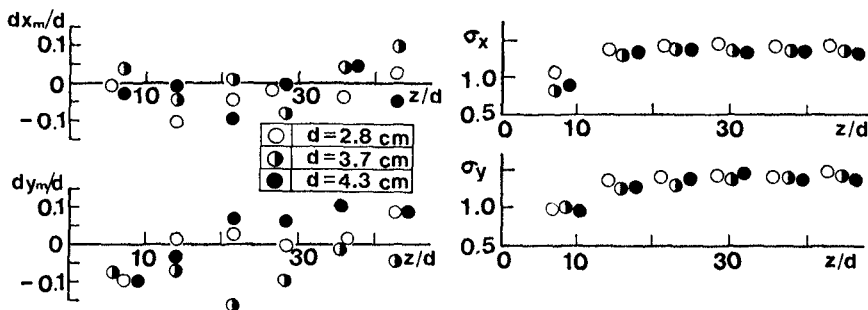


Figure 3: Change in the mean values and the standard deviations for  $dx/d$  and  $dy/d$  with changing water depth.

value as following:

$$f(x^*) = \frac{1}{\sqrt{2\pi}\sigma} \exp\left\{-\frac{1}{2}\left(\frac{x^*}{\sigma}\right)^2\right\} \tag{1}$$

$$f(y^*) = \frac{1}{\sqrt{2\pi}\sigma} \exp\left\{-\frac{1}{2}\left(\frac{y^*}{\sigma}\right)^2\right\} \tag{2}$$

where  $\sigma = (\sigma_x + \sigma_y)/2$ ,  $x^* = x/d$ ,  $y^* = y/d$ . In Figure 2, the solid lines are the calculations of Eq. (1), (2). The calculations and the experiments except for  $z/d = 7.1$  agree reasonably well. The other cases for the rubble diameter were same results also. From these investigations, it may be considered that the stochastic properties for the displacement of the settling rubble at every section are identical and stationary process. Therefore, applying the Markov chain theory to the stochastic process for the displacement of the settling rubble, the stochastic model to estimate the distribution for the settling position of rubble is developed In this study.

The situation space vector  $S$  for the settling position of one piece of rubble in this stochastic model is defined as

$$S = \{-r, -r + 1, \dots, 0, \dots, r - 1, r\} \tag{3}$$

where  $r(= x/d = y/d)$  is the relative longest distance of the plane scatter of the landing rubble on the sea floor in the  $x$  and  $y$  direction, and  $r$  is the positive integral constant. Then, the transition probability matrix  $P$  is given by

$$P = [ p(i, j) ] \quad i = -r \sim r, j = -r \sim r \tag{4}$$

where

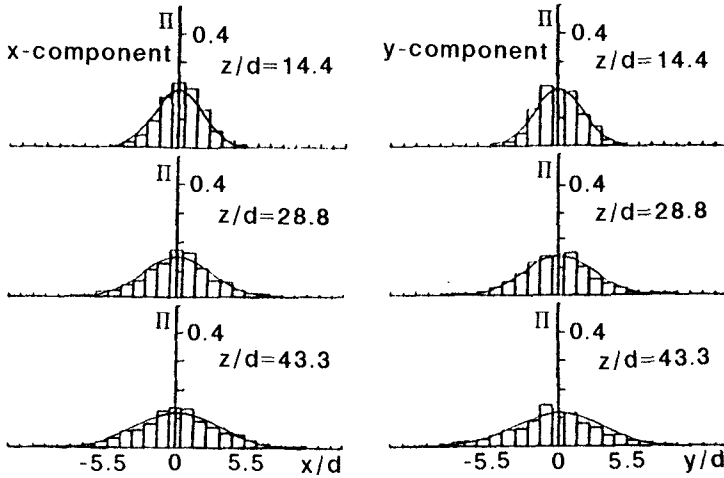


Figure 4: Probability distribution for the settling position of rubble at different water depth.

$$\begin{array}{ll}
 i - j = 0 & p(i, j) = p_0 \\
 i - j = -k & p(i, j) = p_k^+ \\
 i - j = k & p(i, j) = p_k^- \\
 |i - j| > k & p(i, j) = 0 \\
 & (k = 1, 2, \dots, 6)
 \end{array}$$

in which  $p(i, j)$  is a transition probability that the rubble settles from the  $i$ -th position at the  $m$ -th section to the  $j$ -th position at the  $m+1$ -th section,  $p_0$  and  $p_k$  are the probabilities for the cases in which the displacement of the settling rubble at a section is 0 and  $k$  respectively, these values can be calculated from Eq. (1) and (2). Then the probability distribution for the settling position of rubble is given by

$$\begin{aligned}
 \Pi(m) &= \Pi(m - 1) \cdot P \\
 \Pi(0) &= [ \underbrace{0, \dots, 0}_r, 1, \underbrace{0, \dots, 0}_r ]
 \end{aligned}
 \tag{5}$$

where  $\Pi(0)$  is the probability vector for the initial position of rubble at dropping. Figure 4 shows examples of the experimental distributions and the calculated results for the settling position of rubble (solid line). The present stochastic model can simulate the shape of distributions regardless of the relative water depth with sufficient accuracy.

Table 1 shows the correlation coefficient of  $dx/d$  and  $dy/d$  at every sections. The values of correlation coefficient except for  $z/d = 7.1$  may be approximately zero

Table 1: Correlation coefficient between  $dx/d$  and  $dy/d$ .

Section	$d = 2.8 \text{ cm}$	$d = 3.7 \text{ cm}$	$d = 4.3 \text{ cm}$
$z/d = 7.1$	0.176	0.129	0.136
$z/d = 14.3$	0.019	0.006	-0.012
$z/d = 21.4$	-0.002	0.013	-0.021
$z/d = 28.5$	0.017	0.003	-0.047
$z/d = 35.7$	-0.008	0.025	-0.044
$z/d = 42.8$	0.032	0.023	-0.058

regardless of the sections and the case. Therefore, it may be considered that the stochastic properties for the displacements of the settling rubble in the  $x$  and  $y$  direction are independent. Then the probability distribution of the plane scatter for the settling position of rubble is given by

$$p_r(x^*, y^*) = \Pi_x \cdot \Pi_y \quad (6)$$

where  $\Pi_x$  and  $\Pi_y$  can be calculated from Eq. (6).

### 3.2 Spatial geometry of rubble mound discharged from hopper barge

The spatial geometry of individual rubble mound discharged from a hopper barge can be evaluated by combining the volume of rubble at discharge with a probability distribution of the plane scatter for the landing rubble on the sea floor. This probability distribution of can be evaluated as

$$P_r(j) = \left\{ \sum_{i=1}^N p_{ri}(j) \right\} / N \quad (7)$$

where  $N$  is the number of the panels which divid the hopper mouth into the  $d \times d$  plane size in the numerical calculations (Matsumi Y.;1990),  $p_{ri}(j)$  is a probability that the rubble which is fallen from the  $i$ -th discrete portion in the hopper mouth lands to the  $j$ -th discrete portion on the sea floor. The probability  $p_{ri}(j)$  can be calculated from the probability distribution for the settling position of rubble (Eq. (6)). Finally, the spatial geometry of rubble mound which is discharged from a barge can be simulated by

$$H(j) = V \cdot P_r(j) / d^2 \quad (8)$$

where  $H(j)$  is the mound height in the  $j$ -th discrete portion on the sea floor,  $V$  is the volume of rubble at discharge.

Figure 5 shows the comparison of heights of the calculated rubble mounds by the present stochastic simulation technique and experimental data by Okude et al.

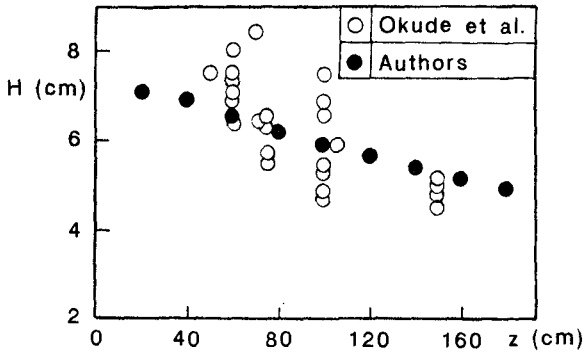


Figure 5: Comparison between height of calculated rubble mounds and experiments.

(1982), in case for the rubble mound which is formed by an single discharge. In the experiments of Okude et al., a 1/20 scale model hopper barge with  $100 \text{ m}^3$  hopper volume was employed. It may be concluded that the spatial geometry of rubble mounds formed by an single discharge can be evaluated with sufficient accuracy by the present stochastic simulation technique.

#### 4 Simulation technique for rubble mound at multi-discharge

In the case for rubble mound formed by multi-times discharge from the same position, the slope of rubble mound approaches the angle of repose for the rubble with increasing discharge times. Then, the rolling rubbles and the sliding those on the slope may occur. The present stochastic simulation technique cannot cope with those phenomena which are recognized in the experiments. Therefore, to cope with the steeper slope of rubble mound than the angle of repose for rubble, the correctional model for the stochastic technique is investigated through the experiments and the numerical calculations.

Experiments have been carried out in a laboratory settling tank with  $1.5 \text{ m}$  depth and  $2 \text{ m} \times 2 \text{ m}$  cross-section. The hopper barge model used was a 1/20 scale model with  $100 \text{ m}^3$  hopper volume. The representative sizes of rubble  $d = 2.8 \text{ cm}$ ,  $3.7 \text{ cm}$  and  $4.3 \text{ cm}$  are employed in the experiments. The height and width of the rubble mound formed by multi-times discharge from the same position were measured by two video cameras which were allocated in the directions of barge width and length. Furthermore, the change in the shape of cross section of the discharged mound with respect to the discharge time was investigated. From the experiments, it has been found that the shape of cross section of the rubble mound formed by multi-times discharge can be classified into three patterns, namely, as the discharge time increases, the sectional shape of rubble mound



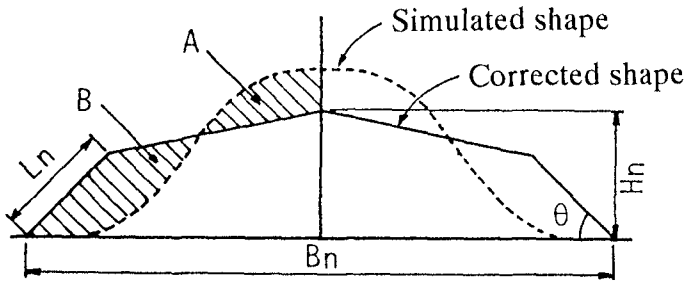


Figure 6: Correctional model for cross section of simulated rubble mound.

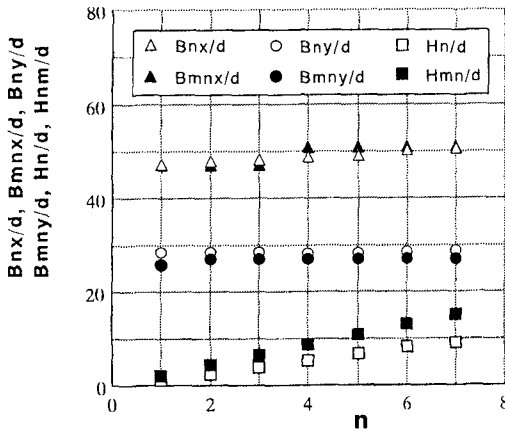


Figure 7: Comparison of calculations for width and height of mound with experiments

transforms from a trapezoidal shape into a pentagonal shape and further into a triangular shape with slope of the angle of repose for the rubble.

From these shape properties of cross section of the rubble mound, a correctional model for the shape of cross section of the simulated mound by the present stochastic technique is devised as shown in Figure 6. In this figure, the dotted line is the cross section of the simulated mound, the solid line is the corrected shape,  $H_n$  and  $B_n$  are the height and width of the corrected mound respectively,  $\theta$  is the angle of repose for rubble. In the case for  $H_n \geq L_n \cdot \sin \theta$ , the shape of cross section of the simulated mound is corrected to the trapezoidal shape or the pentagonal shape such that the areas of shadowed portions A and B become equal. On the other hand, in the case for  $H_n \leq L_n \cdot \sin \theta$ , the shape of cross section of the simulated mound is corrected to the triangular shape with the angle of repose for rubble.

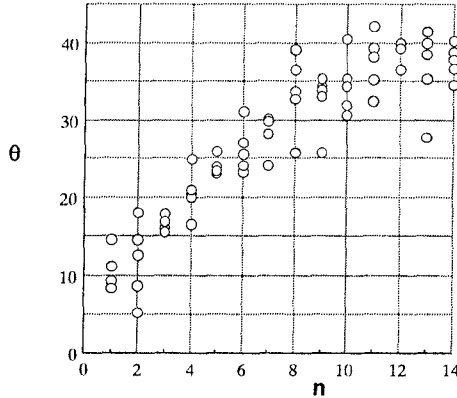


Figure 8: Change in measured  $\theta$  with respect to  $n$ .

The values of  $H_n$  and  $B_n$  in Figure 6 have been given by comparing the calculations for the height and width of the mound at every time discharge with the experiments as shown in Figure 7, in which the abscissa  $n$  is the number of discharge time.  $B_{nx}$  and  $B_{ny}$  are the measured width in the barge length and width directions respectively,  $B_{mnx}$  and  $B_{mny}$  are the calculated those,  $H_n$  and  $H_{mn}$  are the measured height and the calculated that. This Figure is the case for the water depth  $h = 60$  cm. It is found that the calculations for the width of the mound at every time discharge agree with the experiments reasonably well. However, since the present stochastic simulation technique cannot cope with the sliding rubbles and the rolling those on the slope of mound, the calculations for the height and the experiments markedly become to disagree with increasing the discharge time. Then, from the investigation on the relationship between the simulated heights of the mound at every discharge and the measurements, it has been found that a linear relationship between  $H_{mn}$  and  $H_n$  is established and  $H_n$  is given by

$$H_n = 0.6H_{mn} \quad (9)$$

Figure 8 shows the change in the angle of slope of the measured mound with respect to the number of discharge time  $n$ . The values of  $\theta$  show a tendency to approach to about  $40^\circ$  with increasing  $n$ . However, since the measured data vary widely, when reading a value of the angle of repose for the rubble from these results, the error of reading becomes very large. Then, the discrete block method (Cundall P.A., 1971, 1976) are applied to analyze the angle of repose for rubble numerically.

In the discrete block method, the rubble is approximately replaced by a circular element as shown in Figure 9. The elastic and inelastic characteristics of rubble are modeled by an elastic spring (spring coefficient;  $K$ ), a viscous dashpot (vis-

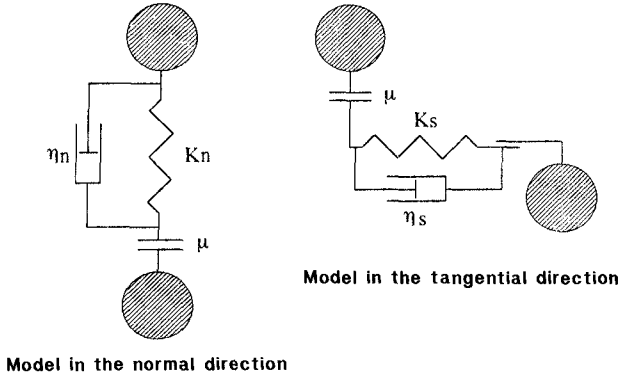


Figure 9: Dynamic system in the discrete block method.

cous coefficient;  $\eta$ ) and a frictional slider (friction coefficient;  $\mu$ ). The behaviours of the rolling and sliding rubbles on the slope of mound can be numerically simulated by solving the simultaneous common differential equations which are set up for the translational and rotational motions for every rubble element. The equations of the translational and rotational motion for every rubble element are given as following difference equations including unknown variables  $u, v$  and  $\phi$  explicitly.

$$\begin{aligned}
 (m + C_M \rho_W V_S) [\ddot{u}]_t &= \\
 & - \eta [\dot{u}]_{t-\Delta t} - K [u]_{t-\Delta t} - 0.5 \rho_W C_D d [|\dot{u}]_{t-\Delta t}| [\dot{u}]_{t-\Delta t} \\
 & + (\rho_S - \rho_W) V g \\
 (m + C_M \rho_W V_S) [\ddot{v}]_t &= \\
 & - \eta [\dot{v}]_{t-\Delta t} - K [v]_{t-\Delta t} - 0.5 \rho_W C_D d [|\dot{v}]_{t-\Delta t}| [\dot{v}]_{t-\Delta t} \\
 I [\ddot{\phi}]_t &= - (\eta [\dot{\phi}]_{t-\Delta t} + K [\phi]_{t-\Delta t}) d^2 / 4
 \end{aligned}
 \tag{10}$$

where  $u$  and  $v$  are the displacements of rubble element in the vertical and horizontal motions,  $\phi$  is the angle of element in the rotational motion,  $m$  and  $V_S$  are the mass and volume of it,  $I$  is the inertia moment of it,  $\rho_S$  and  $\rho_W$  are the density of rubble and fluid,  $C_D$  and  $C_M$  are the drag coefficient ( $= 1.0$ ) and the added-mass coefficient ( $= 2.0$ ) of rubble and  $\Delta t$  is the time interval of numerical calculation. Since the rubble is modeled by a circular element in this study, to prevent the modeled rubble after landing on the sea floor from the rolling motion in the horizontal direction, the sea floor is replaced by the ripples with the diameter of rubble element. In the numerical calculations, the spring coefficients ( $K_n, K_s$ ), the viscous coefficients ( $\eta_n, \eta_s$ ) and the frictional slider coefficient ( $\mu$ ) adopt values listed in Table 2 which contains both cases for the rubble to rubble and the rubble to sea floor respectively. The difference between the values of

Table 2: Values of  $K, \eta, \mu$  and  $\Delta t$ .

Coefficient	Rubble to rubble	Rubble to sea floor
$K_n/\rho_s g$ (cm)	$3.64 \times 10^4$	$(1/5)3.64 \times 10^4$
$K_s/\rho_s g$ (cm)	$9.48 \times 10^3$	$(1/5)9.48 \times 10^3$
$\eta_n/\rho_s g$ (cm/s)	$2.18 \times 10$	$(1/5)2.18 \times 10$
$\eta_s/\rho_s g$ (cm/s)	$2.18 \times 10$	$(1/5)2.18 \times 10$
$\mu$	$\tan 30^\circ$	$\tan 10^\circ$

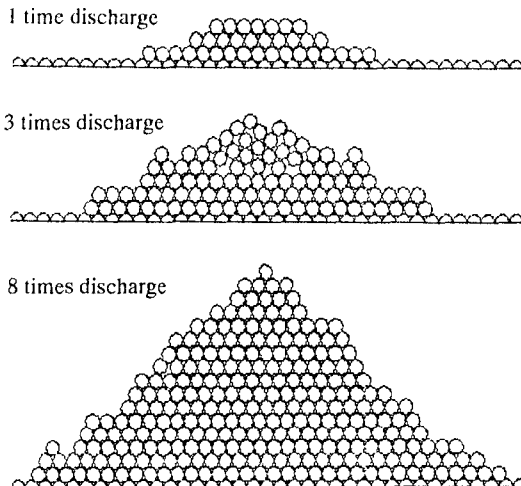


Figure 10: Simulated cross section of rubble mound formed by 1, 3 and 8 times discharge.

coefficients in the case for rubble to rubble and those for rubble to sea floor is to deal successfully with a buffer action effect due to the sand bed in the sea floor. The time interval of the numerical calculation  $\Delta t$  is  $1.0 \times 10^{-4}$ s. The initial positions of rubble elements in the numerical calculations are densely arranged in the simulated cross section by the present stochastic simulation technique. The initial settling velocity of every element in the vertical direction adopts the sinking velocity of rubble (60 cm/s) which has been clarified from the experiments. The calculations in the case for the multi-times discharge were carried out by such method that the rubble elements at the following discharge are fallen on the simulated mound at the previous discharge.

Figure 10 shows the simulated cross section of rubble mound formed by one, three and eight times discharge from the same discharge point. As the number of discharge time increases, the shape of the cross section of rubble mound trans-

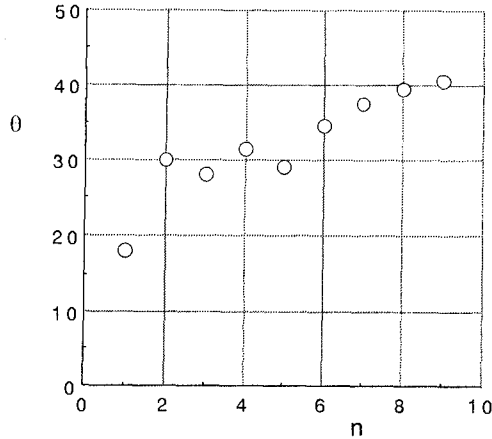


Figure 11: Change in calculated  $\theta$  with respect to  $n$ .

forms from the trapezoidal shape into the pentagonal shape and further into the triangular shape. Therefore, it can be concluded that the present technique simulates the dominant features which are recognized in the experiments with reasonable well. The angles of the slope of mound at every discharge which are read from the cross section of the rubble mound calculated through the discrete block method are shown in Figure 11. It is found that  $\theta$  approaches to about  $40^\circ$  with increasing  $n$ . Therefore, the angle of repose for the rubble is estimated to be  $40^\circ$  in this study, this value is adopted in the present correctional model.

To investigate the application of the present correctional technique, the width and height of the corrected cross section of rubble mound are compared with the experiments in the case for  $h = 120\text{ cm}$  as shown in Figure 12, in which the white and black symbols indicate the experiments and the calculations respectively. Firstly, though the calculated width  $B_{nxc}/d$  of the mound in the barge length direction can evaluate the change in the experiments  $B_{nx}/d$  with respect to  $n$ , the calculations overestimate the experiments. Secondly, in the case for the mound width in the barge width direction,  $B_{ny}/d$  and  $B_{nyc}/d$  agree with sufficient accuracy. Finally, the calculations  $H_{nc}/d$  for the height of the mound agree well with the experiments  $H_n/d$ . Therefore, it may be concluded that the shape of the cross section of rubble mound formed by multi-times discharge from the same point can be evaluated by combining the stochastic simulation technique with the present correctional technique. However, the applicable limitation of this correctional technique for the case of the barge length direction is not sufficiently made clear in this study.

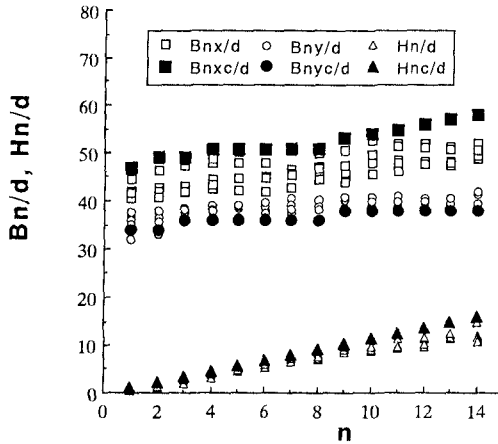


Figure 12: Comparison of calculations for width and height of mound with experiments.

### 5 Optimal Interval of Discharge Sites of Barge

In this study, the optimal interval of discharge sites of barge is defined as a distance between discharge points from barges which minimizes the uneven property of the mound’s surface. Figure 13 shows the change in the size of the gap between mounds with respect to the relative interval of the discharge sites of the barge, in which  $\delta$  is the gap size between individual mounds,  $H$  is the representative height of mound and  $a$  is the distance between the discharge sites of barges. These calculations are the case for 2, 6 and 10 times discharge at two kinds of relative water depths  $h/d = 42.8$  and  $71.4$ . The effective interval of the discharge sites of the barge can be determined by this figure. Comparing the case for  $h/d = 42.8$  with  $h/d = 71.4$ , when the water depth is deeper, the interval of the discharge points of the barge which makes the uneven property of the mound’s surface minimum becomes longer. Therefore, it may be concluded that when deciding the interval of the discharge sites of the barge, the design water depth of breakwater becomes the important parameter.

### 6 Conclusion

Concluding remarks are as follows:

- (1) The stochastic properties for the displacement of the settling rubble at every section are identical and the stationary process. The stochastic simulation technique which is developed by applying the Markov chain model can estimate the distribution for the settling position of rubble regardless of the relative water with sufficient accuracy.

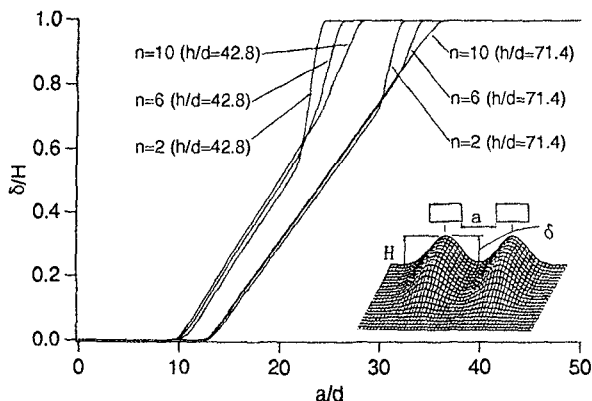


Figure 13: Change in the gap size between mounds with respect to the relative interval of discharge point of barges.

(2) The angle of repose for the rubble can be numerically calculated by applying the discrete block method. The spatial geometry of the multi-times discharged rubble mound from the same point can be successfully simulated by combining the present stochastic technique with the present correctional technique. However, applying this combined simulation technique for the case of the barge length direction, the problem of how to deal with the width of the mound remains still.

(3) The effective interval of the discharge points from barges which makes the uneven property of the mound's surface minimum in the case for the barge width direction is clarified in connection with the design water depth of breakwater and the number of discharge times.

### References

- Cundall P.A.(1971): A computer model for simulating progressive, Large scale movements in blocky rock systems, Symp. ISRM, Nancy, France, Proc. Vol.2, pp.129-136.
- Cundall P.A.(1976): Explicit finite-difference method in geomechanics, Numerical methods in geomechanics (edited by Desai C.S.), Vol.1, pp.132-150.
- Matsumi Y.(1990): A fundamental study on construction scheme for rubble foundation of deep water breakwater from hopper barge, 22nd Inter. Conf. on Coastal Engg.(ASCE), pp.1648-1661.
- Okude T., et al.(1982): Experimental study on construction of rubble mound by split hopper barge, Report of the Port and Harbour Research Institute, Vol.21, No.4, pp.132-171. (in Japanese)

## CHAPTER 242

# Vortex Train in an Offshore Zone

Nobuhiro Matsunaga<sup>1</sup> and Kosei Takehara<sup>2</sup>

### Abstract

A row of vortices forms in an offshore zone when two-dimensional regular surface waves run up on a sloping flat bed. It is called the offshore vortex train. The vortices begin to appear near a breaking point. Moving in the offshore direction, they develop and increase their horizontal length scale through the vortex merging. The vortex train forms due to the shear instability between onshore and offshore drift-currents. After reaching a location of the offshore side, however, they decay rapidly because of the decrease of shear strain rate between the drift-currents. The formation region has been investigated on the basis of visual experiments for three bed slopes. The formation does not depend on the type of wave breaking but is observed when the steepness of deep water waves is smaller than  $4.2 \times 10^{-2}$ . The horizontal length scale of the vortices and the velocity of the vortex movement have also been evaluated empirically.

### Introduction

A coastal region has attracted considerable research attention because of the central role which it plays in the budget of sediment, the generation of nearshore currents, the diffusion of pollutant, etc. This region is usually divided into the

---

- 1 Associate Professor, Department of Earth System Science and Technology, Kyushu University, Kasuga 816, Japan.
- 2 Research Associate, Department of Civil Engineering, Kinki University, Osaka 577, Japan.



nearshore zone and the offshore zone (e. g. Komar 1976). Typical features of the nearshore zone are breaking waves and turbulent fluid motion. Miller (1976) pointed out the formation of breaker vortices from the behavior of air bubbles entrained due to wave breaking. Since his work, the turbulence structure in this zone has been investigated vigorously through field observations and laboratory experiments. Most of these studies, which have been reviewed in detail by Peregrine (1983) and Battjes (1988), are mainly concerned with coherent structures near the free surface. Matsunaga & Honji (1980) and Matsunaga et. al. (1988) showed that the Stokes layer separates periodically near a breaking point when two-dimensional regular waves climb up a sloping flat bed, and that the separated flow forms a vortical pattern and lifts up a large amount of sediment.

On the other hand, the fluid motion is considered usually to be irrotational in the offshore zone. The Lagrangian mass transport of fluid in waves is one of interesting problems in this zone. Bagnold (1947) carried out the experiments in which two-dimensional, regular waves propagated on a horizontal smooth bed. He found a strong, forward drift-current along the bed, and a weak, backward one induced under the water surface. The difference between Bagnold's observation and the well-known 'Stokes drift' created a sensation. Longuet-Higgins (1953) solved it theoretically by taking into account the existence of the Stokes layer. Russell & Osorio (1958) measured the velocities of the forward drift-currents at the outside edge of the Stokes layer for horizontal, up-sloping and down-sloping beds. Their data collapse well on the theoretical curve obtained by Longuet-Higgins. The authors (1988) also carried out laboratory experiments to investigate the drift-currents for the case when two-dimensional regular waves climb up a sloping

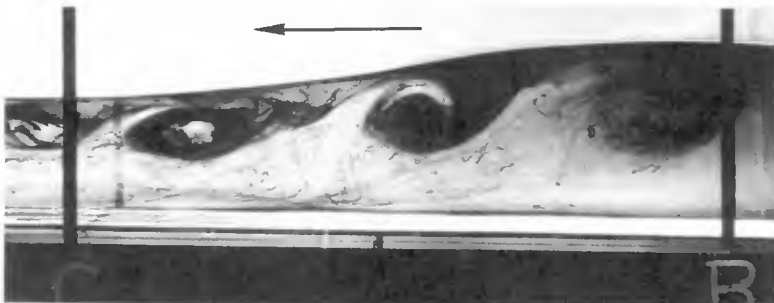


Figure 1. Offshore vortex train.

bed. At that time, they found a row of vortices forming under the waves. As mentioned previously, the fluid motion in the offshore zone has been treated generally as irrotational one. Therefore, this is a fresh phenomenon in the fluid dynamics as well as the coastal engineering. It was called the offshore vortex train. Figure 1 shows one example of the offshore vortices visualized by using dye of aniline blue. The arrow indicates the direction of wave propagation. The interval between B and C was 0.5 m. The mean water depth was 14.0 cm at position B. The bed slope was  $1/23.5$  and the breaking point was 2.68 m shoreward from position C. The vortices with the clockwise rotation are seen obviously. They move slowly in the offshore direction along the water surface and increase their intervals by the vortex merging. After reaching a location of the offshore side, however, they decay rapidly.

In this paper, universal expressions about the formation region of the offshore vortices, the horizontal length scale of the vortices and the velocity of the vortex movement are given through visual experiments for three bed slopes.

### Experimental set-up and procedure

Figure 2 shows schematically an experimental apparatus. The wave tank was 12 m long, 0.4 m deep and 0.15 m wide. It was made of transparent acrylic plates and equipped with a sloping flat bed. The grades of  $\tan \theta = 1/37.0$ ,  $1/23.5$  and  $1/12.3$  were used as a bed slope. Two-dimensional regular waves were made by oscillating a flap. The wave period  $T$  was varied from 0.517 s to 2.59 s. The wavelength in deep water  $L_0$ , being calculated from  $gT^2/2\pi$ , was in the range from 0.417 m to 10.5 m, where  $g$  is the gravitational acceleration. The local wave height  $H$  was measured by using a capacitance-type wave gauge, and the local wave velocity  $C$  by putting a measuring point between two wave gauges. The wave height in deep

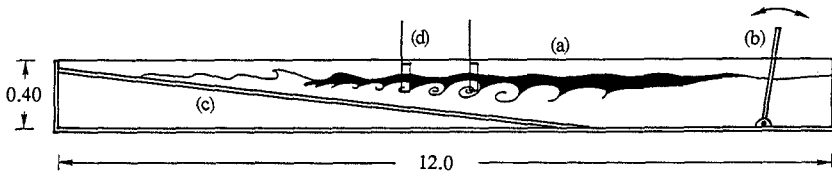


Figure 2. Schematic diagram of experimental set-up (dimensions in m). (a) water tank; (b) wave generator; (c) sloping bed; (d) wave gauges.

water  $H_0$  was evaluated by dividing the shoaling coefficient into  $H$ . The value of  $H_0$  ranged from 0.93 cm to 6.58 cm. The local wavelength  $L$  was calculated from  $L = C T$ .

Drift-currents induced in the offshore side from the breaking point were investigated by means of flow visualization. Dye of water-soluble aniline blue was used as a tracer. Granules of the dye were scattered on the water surface of the offshore zone. Whether the vortex train formed or not was confirmed through visual experiments. The behavior of vortices was videotaped to evaluate their characteristic quantities, i. e., the horizontal length scale of the vortices  $l$  and the velocity of vortex movement  $u$ . The length scale, which is defined by the horizontal distance from center to center, was determined by sampling some dozen of pictures in which the vortices arrange well over a distance of 0.5 m, and by averaging the read vortex intervals over the number of the samples. About ten sampled pictures were used for the evaluation of each value of  $u$ . The value of  $u$  was obtained by dividing a given distance by the time elapsed while a vortex moved through the distance, and by averaging the velocities measured in this way over the sampling number.

### Universal expression for vortex formation

Figure 3 shows a relation between the formation of the offshore vortex train and the types of breaking waves. The open circles and solid ones indicate its formation and non-formation, respectively. The two solid lines arc border lines between three types of breakers, which are given by Gaughan and Komar (1975). It is seen from this figure that the division of the formation region is given by the dash-dot line, i. e.,  $H_0/L_0 = 4.2 \times 10^{-2}$ , and that it is independent of the breaker types.

The formation conditions for the offshore vortices can be determined by using the variables of  $h$ ,  $L$ ,  $H$ ,  $T$ ,  $C$ ,  $g$  and  $\tan\theta$ , where  $h$  is the mean water depth. Two variables can be eliminated by considering into account the dispersion relation of water waves and the relation of  $C = L/T$ . If  $C$  and  $g$  are chosen as the two variables and the dimensional consideration is performed, a non-dimensional expression for the formation region is given by

$$f ( H/L, h/L, \tan\theta ). \quad (1)$$

In figures 4(a) to (c), the regions of the vortex formation and

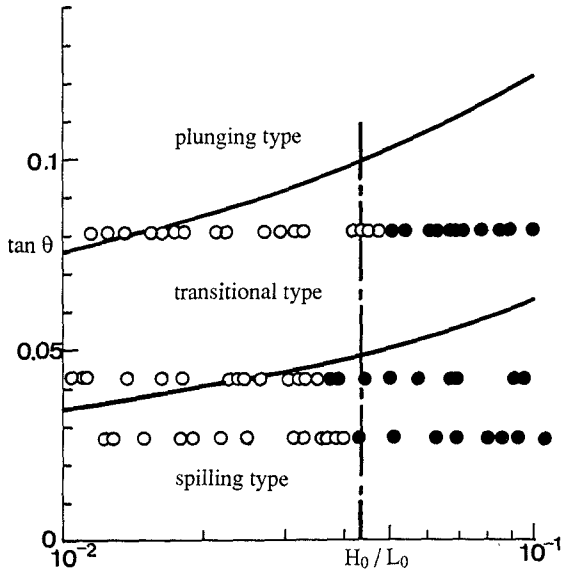


Figure 3. Relation between the formation of offshore vortex train and the types of breaking waves.

non-formation are indicated by the open circles and solid ones, respectively. The solid curves mean the limiting wave steepness. These figures make it clear that the offshore vortices form in a shallow region offshoreward from the breaking point in the case when the wave steepness is relatively small.

Let us try to represent the three formation regions shown in figures 4(a) to (c) universally. For this purpose, at least, a coordinate system should be chosen to give an universal expression for the limiting wave steepness. Various empirical relations between the wavelength  $L_b$ , wave height  $H_b$  and water depth  $h_b$  at the breaking point have been proposed by many researchers (e.g. McCowan 1894 and Miche 1944). Galvin (1972) gives a relation including the bed slope,

$$H_b/L_b = 0.72 (1 + 6.4 \tan\theta) h_b/L_b . \tag{2}$$

In figure 5, the data obtained in this study are plotted to confirm the validity of Galvin's relation. The measured values for  $\tan\theta = 1/10$  are also included in this figure. The linear line shows Galvin's relation and the curved line is obtained by applying the

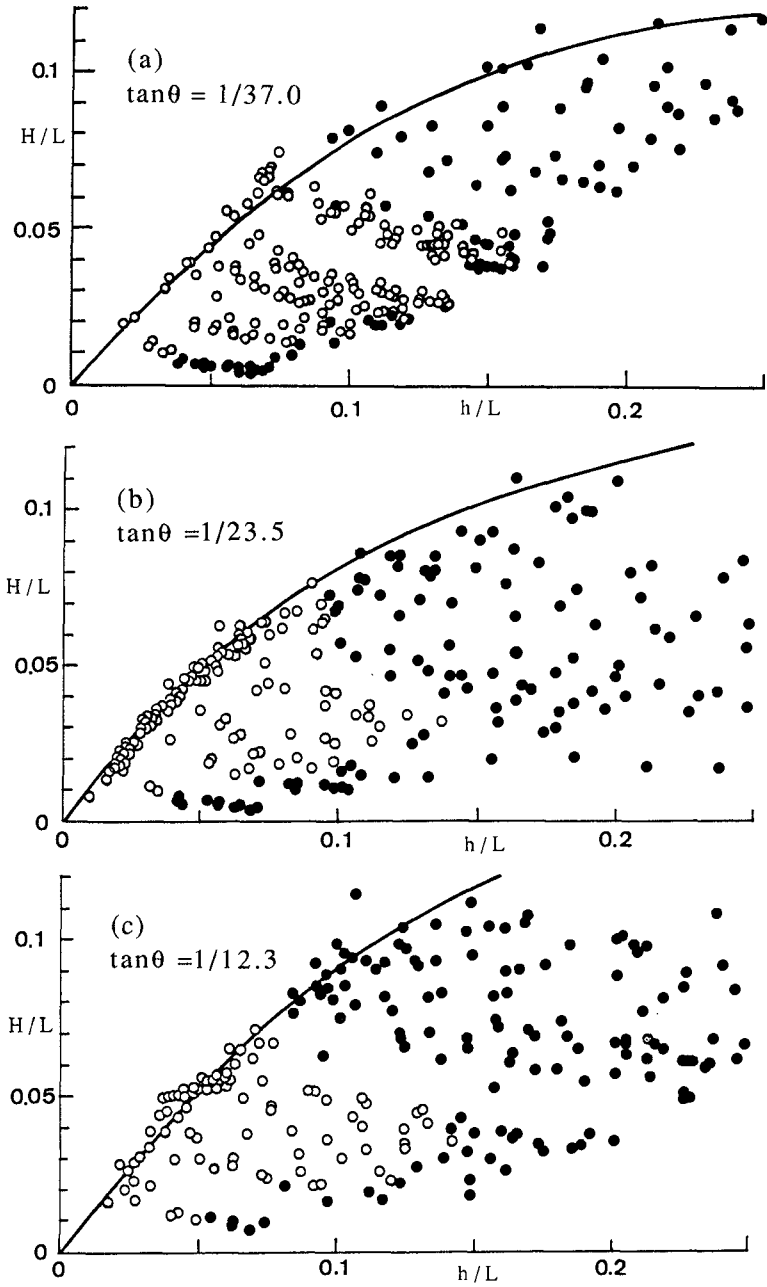


Figure 4. Formation regions of vortices for three bed slopes.

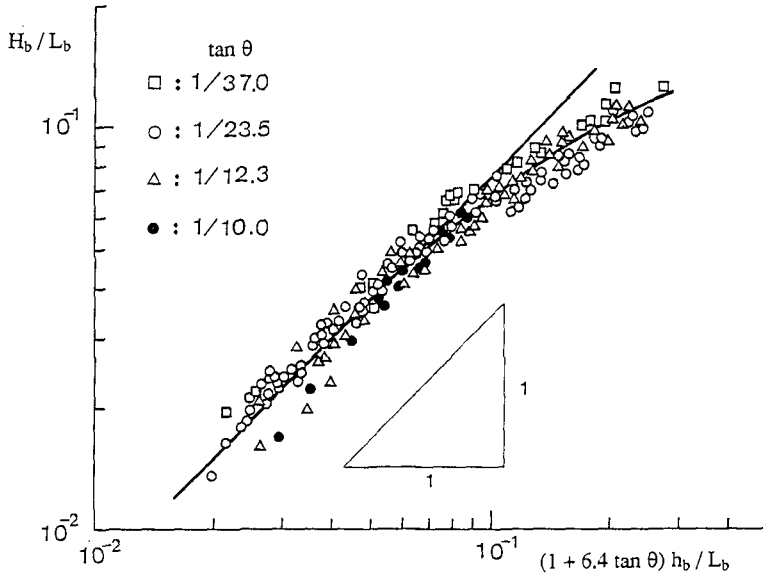


Figure 5. Universal expression for characteristic quantities of breaking waves on various bed slopes.

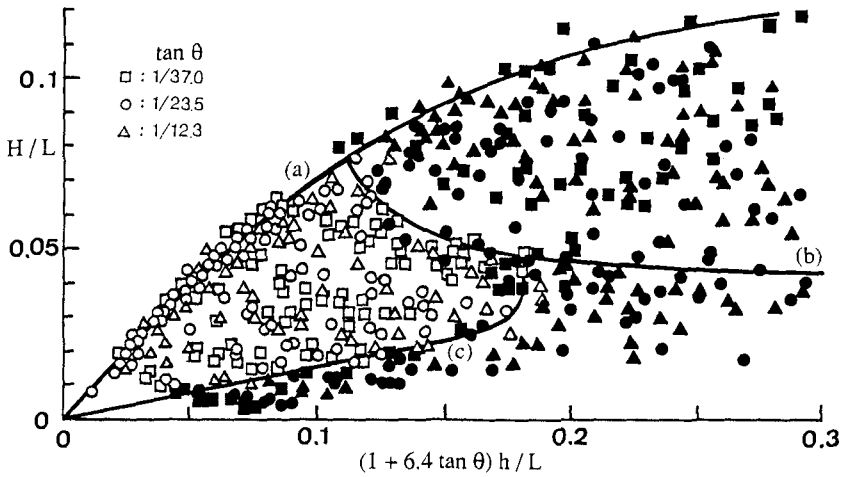


Figure 6. Universal expression for the vortex formation.

least squares method to these data. Though the data agree well with relation (2) at  $H_b/L_b \leq 0.05$ , the disagreement between them becomes remarkable in the range of  $H_b/L_b > 0.05$ . However, it is seen that the use of this coordinate system can express universally the limit of wave steepness over the wide range of  $H_b/L_b$ .

In figure 6, the data shown in figure 4 are rearranged in Galvin's coordinate system. The three formation regions are unified in the region bounded by three solid lines (a), (b) and (c). The offshore vortices form when waves with  $H_0/L_0 \leq 4.2 \times 10^{-2}$  propagate on a sloping bed. The condition is expressed by the region under line (b). The onshore border of the vortex formation is the breaking point, and that of the offshore side is given by line (c).

## Quantitative properties

### 1. Horizontal length scale of offshore vortices

The horizontal interval between offshore vortices  $l$  can be described completely by using the seven characteristic quantities of  $h$ ,  $L$ ,  $H$ ,  $C$ ,  $T$ ,  $g$  and  $\tan\theta$ . As discussed in the previous section, however, two dimensional quantities can be removed from these seven quantities. If  $C$  and  $g$  are eliminated, a dimensionless form of  $l$  is given by

$$l/h = f(H/L, h/L, \tan\theta). \quad (3)$$

Figures 7(a) to (c) show relations between  $l/h$  and  $H/L$  for each value of  $\tan\theta$ . It is seen that  $l/h$  is proportional to  $(H/L)^{-1}$ . Though the value of  $h/L$  was varied from 0.015 to 0.15 in this study, no systematic dependence of  $l/h$  on  $h/L$  was recognized. By approximating these data with the solid lines and plotting the values of  $(l/h) / (H/L)^{-1}$  against  $\tan\theta$ , the relation

$$l/h = 1.2 \times 10^{-2} (\tan\theta)^{-1/3} (H/L)^{-1} \quad (4)$$

is obtained empirically from figure 8. The comparison of the experimental data and equation (4) is shown by figure 9. It gives a good agreement. Another important thing is that  $l/h$  is of order unity. This means that the length scale of the offshore vortices is controlled mainly by the local water depth.

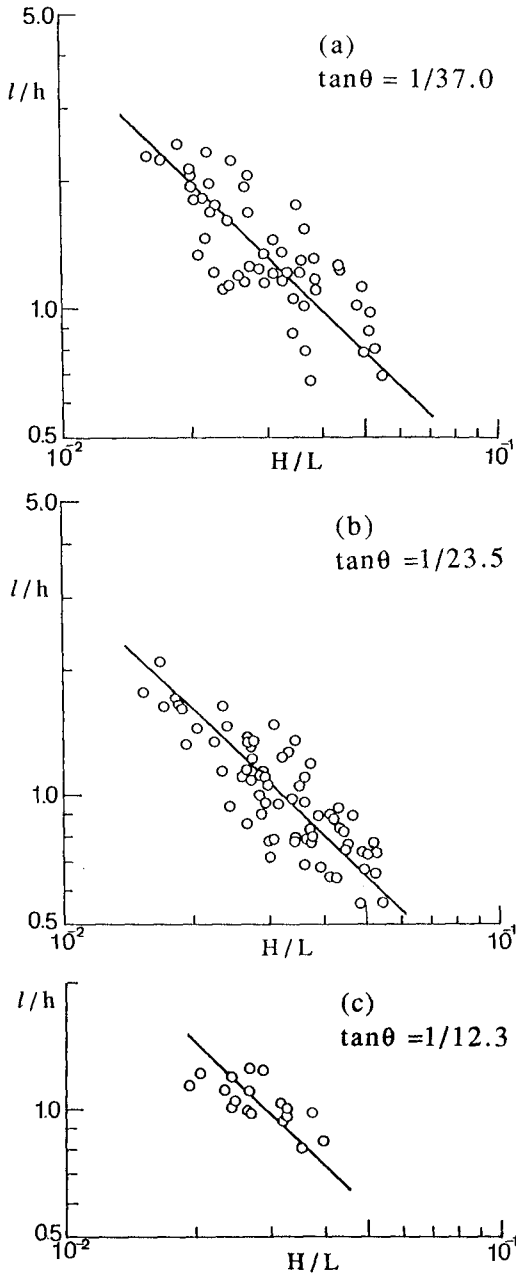


Figure 7. Relations between  $l/h$  and  $H/L$ .



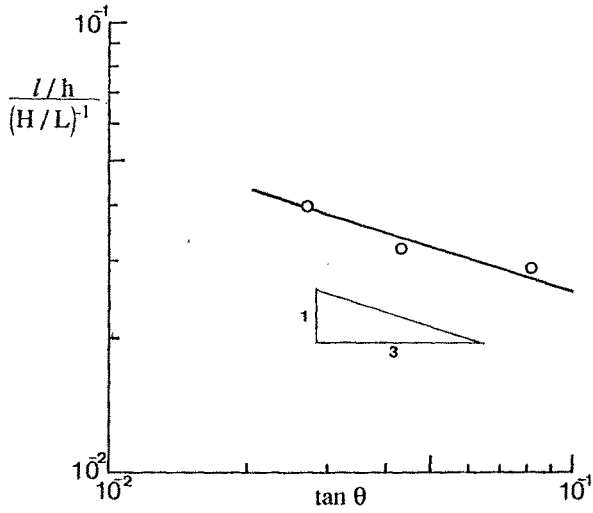


Figure 8. Dependence of  $l/h$  on  $\tan\theta$ .

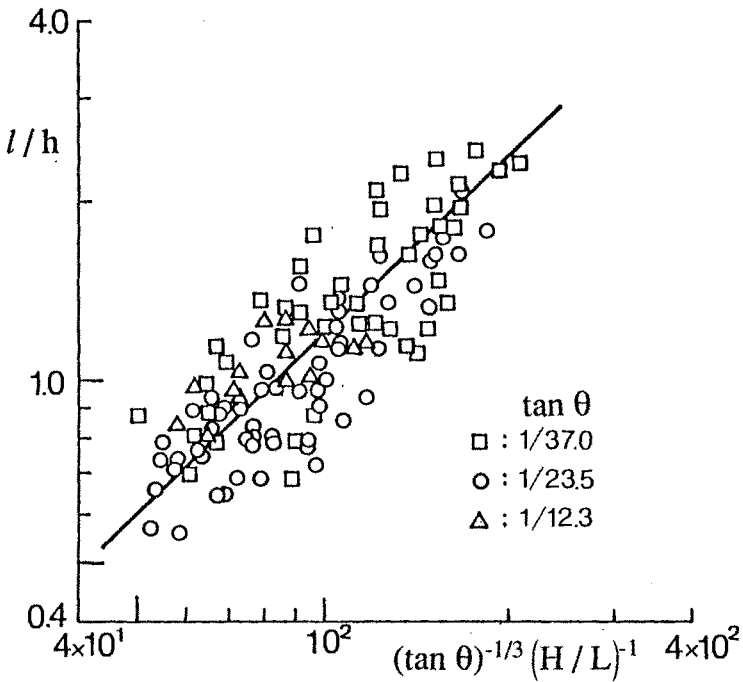


Figure 9. Universal expression for vortex intervals.

2. Velocity of vortex movement

The offshore vortices move slowly in the offshore direction. As discussed above, their velocities  $u$  also depend on  $h$ ,  $L$ ,  $H$ ,  $T$  and  $\tan\theta$ . The dimensional consideration deduces

$$u/(L/T) = f(h/L, H/L, \tan\theta). \tag{5}$$

Since  $u$  and  $L/T$  are of order  $10^{-1}$  cm/s and  $10^2$  cm/s, respectively, the value of  $u/(L/T)$  becomes extremely small. Therefore,  $L/T$  seems to be unsuitable as a quantity to non-dimensionalize  $u$ .

Another representative quantity is the velocity of offshore drift-current in the offshore zone. Longuet-Higgins derived its velocity profile induced by the wave propagation on a horizontal bed, i. e.,

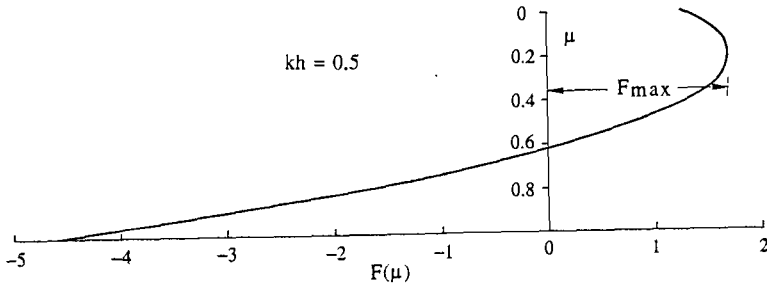


Figure 10. Longuet-Higgins' solution at  $kh = 0.5$

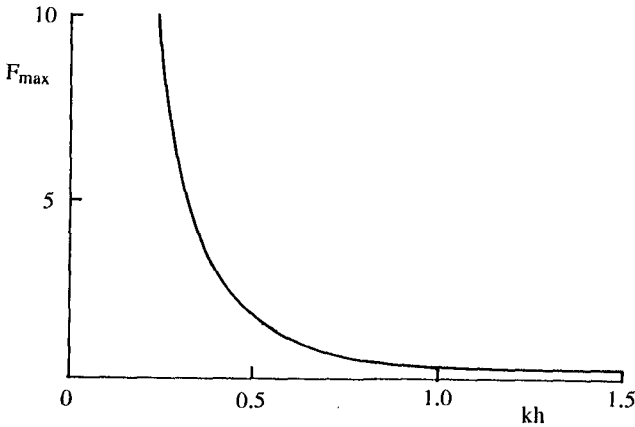


Figure 11. Dependence of  $F_{max}$  on  $kh$ .

$$U(z) = (\pi H/L)^2 C F(z/h), \quad (6)$$

where

$$F(\mu) = \frac{1}{4 \sinh^2 kh} \left[ 2 \cosh \{2 kh(\mu - 1)\} + 3 + kh \sinh \{2 kh (3\mu^2 - 4\mu + 1)\} \right. \\ \left. + 3 \left( \frac{\sinh 2kh}{2 kh} + \frac{3}{2} \right) (\mu^2 - 1) \right], \quad (7)$$

z-axis is taken in the direction downward from the mean water level and  $k$  is the wave number. Figure 10 shows the profile of  $F(\mu)$  at  $kh = 0.5$ . The positive value of  $F(\mu)$  means that  $U(z)$  has the velocity in the offshore direction. The profile given by equation (7) takes a positive maximum value  $F_{\max}$  as shown in figure 10. Figure 11 shows the relation between  $F_{\max}$  and  $kh$  which was obtained numerically. Here, let us use the maximum offshore velocity calculated from

$$U_{\max} = (\pi H/L)^2 C F_{\max} \quad (8)$$

as a characteristic quantity controlling  $u$ , though it is obtained for a horizontal flat bed. In this case, a dimensionless form is given by

$$u/U_{\max} = f(h/L, H/L, \tan\theta). \quad (9)$$

Figures 12 (a) to (c) show the relations between  $u/U_{\max}$  and  $h/L$  for three bed slopes. The tendency that  $u/U_{\max}$  increases in proportion to  $h/L$  is recognized from these figures, but no systematic dependence of  $u/U_{\max}$  on  $H/L$  is seen. The relation between the proportional factors, which are obtained by approximating the data with the solid lines, and  $\tan\theta$  is shown in figure 13. It is seen that the proportional factors depend on  $(\tan\theta)^{2/3}$ . From these results, an empirical relation for the velocity of vortex movement,

$$u/U_{\max} = 3.6 \times 10^1 (\tan\theta)^{2/3} (h/L) \quad (10)$$

is obtained. The comparison of the experimental data and equation (10) is made in figure 14. A good agreement is recognized.

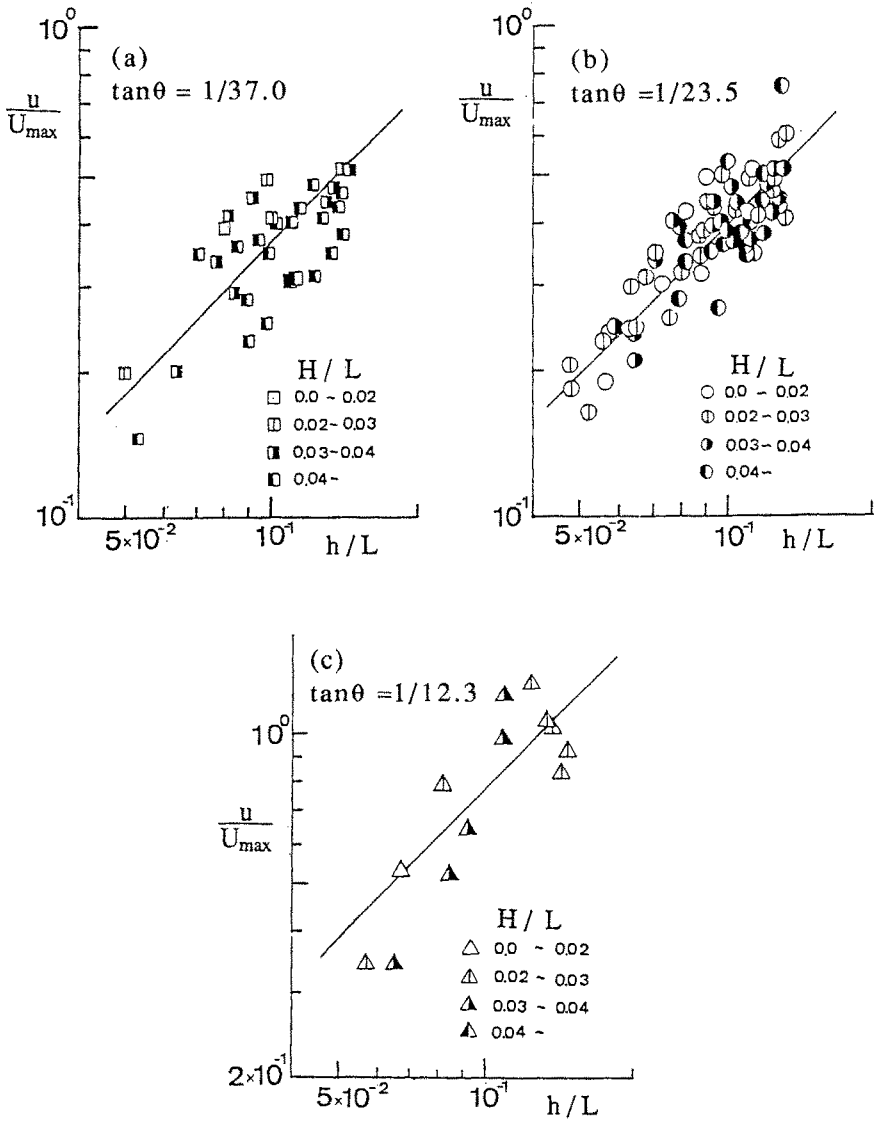


Figure 12. Relations between  $u/U_{max}$  and  $h/L$ .

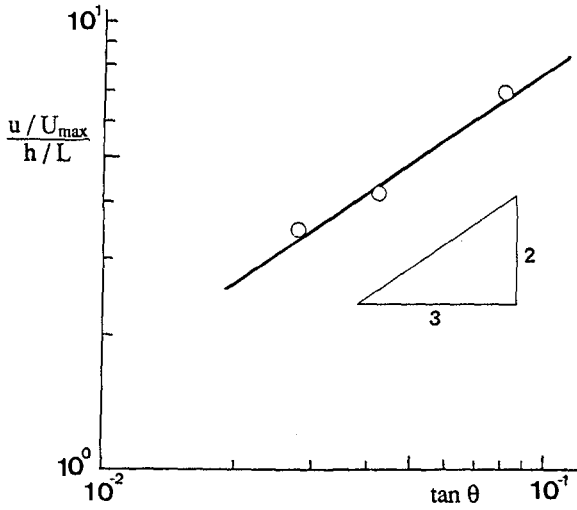


Figure 13. Dependence of  $u/U_{max}$  on  $\tan\theta$ .

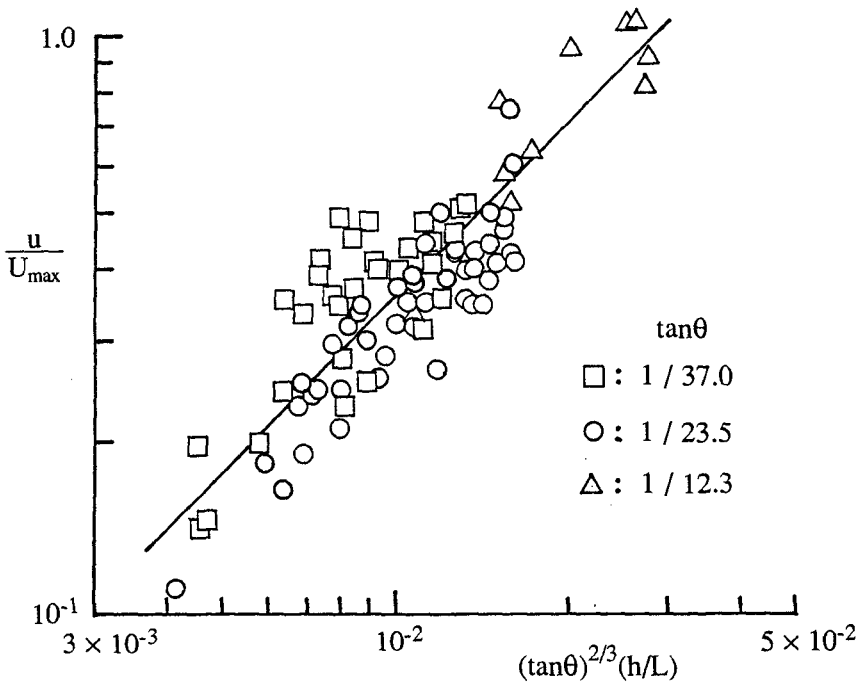


Figure 14. Universal expression for vortex velocities.

## Conclusions

It was found that a row of vortices, which was called the offshore vortex train, forms along the water surface of an offshore zone when two-dimensional regular waves whose steepness in deep water is smaller than  $4.2 \times 10^{-2}$  run up on a sloping bed. It seems to occur owing to the shear instability between the onshore drift-current and the offshore one. The instability starts near the breaking point. Moving in the offshore direction, the vortices merge each other and increase their intervals in the size of water depth. After reaching a location of the offshore side, they begin to decay because of the decrease of the strain rate between the two drift-currents. The universal expressions were also obtained empirically for the formation of the offshore vortices, their horizontal length scales and the velocities of vortex movement.

## REFERENCES

- BAGNOLD, R. A. 1947 Sand movement by waves: some small-scale experiments with sand of very low density. *J. Inst. Civil Engrs.* **27**, 447-469.
- BATTJES, J. A. 1988 Surf-zone dynamics, *Ann. Rev. Fluid Mech.* **20**, 257-293.
- GALVIN, C. J. 1972 Wave breaking in shallow water. In *Waves on Beaches* (ed. R. E. Meyer), Academic Press, pp. 413-456.
- GAUGHAN, M. K. & KOMAR, P. D. 1975 The theory of wave propagation in water of gradually varying depth, and the prediction of breaker type and height. *J. Geophys. Res.* **80**, 2991-2996.
- KOMAR, P. D. 1976 *Beach Processes and Sedimentation*. Prentice-Hall, Inc. pp. 11-13.
- LONGUET-HIGGINS, M. S. 1953 Mass transport in water waves. *Phil. Trans. Roy. Soc. (London) Series A* **245**, 535-581.
- MATSUNAGA, N. & HONJI, H. 1980 The backwash vortex. *J. Fluid Mech.* **99**, 813-815.
- MATSUNAGA, N., TAKEHARA, K. & AWAYA, Y. 1988 Coherent eddies induced by breakers on a sloping bed. *Proc. 21st Conf. on Coastal Engng*, pp. 234-245. ASCE.
- McCOWAN, M. A. 1894 On the highest wave of permanent type. *Phil. Mag. Series 5* **38**, 351-357.
- MICHE, R. 1944 Mouvements ondulatoires de la mers en profondeur constante ou décroissante. *Ann. Ponts Chaussees* **114**, 369-406.
- MILLER, R. L. 1976 Role of vortices in surf zone prediction: sedimentation and wave forces. *Beach and Nearshore Sedimentation, SEPM Spec. Pub.* **23**, pp. 92-114.
- PEREGRINE, D. H. 1983 Breaking waves on beaches. *Ann. Rev. Fluid Mech.* **15**, 149-178.
- RUSSELL, R. C. H. & OSORIO, D. C. 1958 An experimental investigation of drift profiles a closed channel. *Proc. 6th Conf. on Coastal Engng*, pp. 171-183. ASCE.

## CHAPTER 243

The Variation of Floc sizes within a turbidity maximum  
at spring and neap tides

J C McCabe<sup>1</sup>, K R Dyer<sup>2</sup>, D A Huntley<sup>2</sup>, A J Bale<sup>3</sup>

### Abstract

The variation of floc size has been measured during spring and neap tides at a height of 0.5 m above the bed in the turbidity maximum of the Tamar Estuary, UK. Two size populations were present. Small flocs were eroded from the bed during spring flood tides and were transported up estuary. Large flocs were dominant at other times, particularly just after high water when differential settling concentrated large flocs near the tip of the salt intrusion.

### Introduction

Many studies have shown that the size of flocs of cohesive sediment are functions of salinity, temperature, concentration (Owen, 1970), turbulent shearing (Burban et al, 1989) and other factors, such as surface ionic charge (Hunter & Liss, 1982). Most of these studies have been carried out in the laboratory, and the results interpreted in terms of known field situations. However, many of the flocs are fragile and floc sizes and size distributions obtained from samples are not good representations of those present in-situ (Gibbs & Konwar, 1983). There have been few studies where the undisturbed floc sizes have been measured in-situ. Gibbs et al (1989), Eisma et al (1990), Wells (1989), have used an underwater camera; Bale and Morris (1987) a marinized Malvern laser particle sizer, and van Leussen & Cornelisse (1992) an underwater video system.

---

<sup>1</sup> Helston, Cornwall, UK.

<sup>2</sup> Institute of Marine Studies, University of Plymouth,  
UK

<sup>3</sup> Plymouth Marine Laboratory, Plymouth, UK

Despite use of these techniques, it is still not clear what is the spatial and temporal distribution of floc sizes within a turbidity maximum, and what are the controlling processes.

This paper describes an in-situ study of the floc size distribution in the turbidity maximum of a partially mixed estuary carried out over spring and neap tides. The objectives were to consider the question of whether turbulence affects floc sizes in estuaries, but initially a description of the tidal variation of floc size was necessary.

### Methods

A Malvern laser sizer was mounted on a bed frame at a height of 50 cm above the bed. This instrument, described by Bale & Morris (1987), measures the diffraction of a laser beam by suspended particles in a sampling volume of approximately 1 cm<sup>3</sup>. The sizer produces a percentage size distribution in sixteen bands for diameters from 564  $\mu\text{m}$  to less than 5.8  $\mu\text{m}$ . Two distribution samples were recorded every 20 minutes.

Also mounted at a height of 50 cm were two Valeport annular electromagnetic flowmeters. These were mounted orthogonally at 45° to the flow direction so that the longitudinal and lateral components of the flow could be resolved, together with two estimates of the vertical component. Downing Optical Backscatter Gauges (OBS) were mounted at 23 and 50 cm height.

Through depth profiles were carried out every 20 mins to obtain profiles of salinity, temperature, velocity and suspended solids. This paper will concentrate on the results from the vertical profiles and the floc sizer.

Measurements were carried out over two spring tides (4, 5 July 1989) when the tidal range was 4.3 to 4.2 m, and two neap tidal cycles (28, 29 June 1989) with tidal range of 2.9 to 3.0 m at a position near Calstock on the Tamar Estuary (Fig 1). This position, 8 km from the head of the estuary, was within the tidal trajectory of the turbidity maximum and in the area where significant variations of concentration were likely during the tide, together with erosion and settling.

### Results

#### General Structure

During the neap tide (Fig 2) the rig was located within



the river water at low water, with the turbidity maximum to seaward. As the tide flooded, the turbidity maximum was pushed landwards, with concentrations of  $500 \text{ mg l}^{-1}$  being measured near the bed. Maximum velocities at this point coincided with the peak of the concentrations in the turbidity maximum. Once the peak of the turbidity maximum had passed, the saline intrusion appeared as a well mixed water column, rather like a piston pushing up the estuary. At HW there was a period of almost 2 hours of low velocities and salinities of  $>12\text{‰}$  near the bed. The surface outflow started before high water and the almost stationary salt intrusion was gradually eroded down to the bed over a period of about 2 hours with intense shearing at a rate of about  $0.2 \text{ s}^{-1}$  at the interface. Once the salt intrusion had been eroded, and the ebb current penetrated to the bed, the turbidity maximum was carried back on the ebb tide, but with peak concentrations about half and peak velocities about two-thirds those on the flood.

The pattern of change over a spring tidal cycle was remarkably similar, but with somewhat enhanced velocities and concentrations (Figure 3). On the flood tide concentrations in the turbidity maximum reached  $1000 \text{ mg l}^{-1}$  with velocities of  $1 \text{ ms}^{-1}$ . On the ebb tide concentrations were again about half that on the flood, but with velocities the same as that on neaps. The other two tidal cycles gave almost identical information for spring and neap tides.

### Floc Sizes

The size distributions show that there were two predominant modes in the floc distribution, flocs of less than  $5.8 \text{ }\mu\text{m}$  and flocs of  $100 \text{ }\mu\text{m}$  and larger. The relative proportions of these varied consistently through the tide. The smallest particles are thought to be individual grains and microflocs with small settling velocities and with stable structure. The largest flocs are likely to have been prone to break-up during shearing, and to rapid settling at times of low currents. Consequently their relative numbers were related to current speed.

During the first part of the flood tide in the water upstream of the turbidity maximum, the flocs were predominantly in the fine sizes. Within the turbidity maximum on the flood tide, there was a significant difference between spring and neap tides (Fig 4). On neap tides there was a broad peak of large flocs centred at about  $200 \text{ }\mu\text{m}$ , and with very few small flocs. During spring tides, however, there was a predominance

of fine flocs, with no large flocs. There were more flocs in the size range 10-100  $\mu\text{m}$  at spring tides, and these may be the result of turbulent breakup of the larger flocs present at neap tides.

At the seaward end of the turbidity maximum, encountered a little later in the flood tide the proportion of fine flocs diminished rapidly, and large flocs predominated. This period extended over high water and into the beginning of the ebb tide. The peak of the distribution became more and more sharp (better sorted), until during the time when the salt intrusion was being eroded, there were relatively few flocs of less than 100  $\mu\text{m}$  (Figure 5). There is a remarkable similarity between the size distributions at this phase of the tide between neap and spring tides. It is also likely at this time that there were larger flocs still within the water that were beyond the resolution of the instrument.

Within the turbidity maximum on the ebb the proportion of large flocs diminished and the proportion of flocs in the size range 30-200  $\mu\text{m}$  increased (Figure 6). The differences between spring and neap tides in the fraction greater than 10  $\mu\text{m}$  in the ebb turbidity maximum is small in comparison with those in the turbidity maximum on the flood tide. This may reflect the similarity in current velocities and in concentrations on neap and spring ebb tides, and the contrast on the respective flood tides.

Consequently there appears to be a significant variation in floc sizes through the turbidity maximum, with large flocs predominating at the downstream end of the maximum. The fine sizes are present at spring tides and particularly during the maximum flood current.

### Discussion

The most striking feature is that the spring flood turbidity maximum consisted almost entirely of particles less than 6  $\mu\text{m}$  in diameter. The neap flood turbidity maximum consisted mostly of larger particles. The active event seemed to be the spring flood tide when new primary particles were eroded off the bed. These were carried upstream past the rig, but did not all return on the ebb. The distribution of larger particles remained remarkably similar on each ebb and was also similar to that of the neap flood. These observations suggest that there are two populations of particles present, with different characteristics.

It is surprising that the two populations of flocs can be so distinctive especially in the energetic spring

tide situation. The dramatic change in the floc size distribution was associated with the erosion and retreat of the salt intrusion prior to the passage of the main part of the turbidity maximum on the ebb tide. As the salt intrusion was entrained into the upper layer and the interface was eroded down to the height of the instrument, the particle size became steadily larger and better sorted. When the interface was below the level of the sensors, and they were in the upper seaward flowing brackish layer, the sizes abruptly decreased. The size variation during this period may be explained by comparing the rate of entrainment with the particle settling velocity. The entrainment rate of  $\sim 1.5 \text{ m hr}^{-1}$  or the rate of descent of the interface, is comparable with the settling velocity, measured in-situ, of about  $200 \mu\text{m}$  (Fennessy, pers comm). Thus flocs of this size would tend through settling to accumulate at the interface. Larger particles would settle through into the lower layer and reach the bed, though the larger flocs may have an effective density low enough to become neutrally buoyant at the interface. Fine particles would be sheared off downstream in the brackish water layer. Thus, as the thickness of the lower layer reduced, the larger particles became concentrated at the tip of the salt intrusion. This process will enhance the effects of differential settling which will cause larger particles to accumulate near the bed. Differential settling will also take place throughout the turbidity maxima, but redispersion will occur during the maximum currents. In this case some breakup of the flocs is likely to broaden the peak of large flocs and reduce the modal diameter. Thus largest flocs are retained at the downstream end of the turbidity maximum. Gibbs et al (1989) have found in the Gironde Estuary that the maximum of floc size is 30 km seaward of the turbidity maximum, and there are indications of similar floc size distributions within the turbidity maximum of other estuaries (Eisma et al, 1991).

On the flood the maximum is advected upriver picking up any large flocs that settled out during the ebb. On spring tides primary particles are also eroded from the bed to form the bulk of the flocs. The turbidity maximum passes upstream and, since less particulate matter is carried downstream on the ebb, deposition occurs. Differential settling takes place and those settling into the salt intrusion are separated by the velocity shear from the finer flocs. The larger flocs are then re-eroded on the following flood tide.

References

- BALE, A J & MORRIS, A W, 1987. In-situ measurement of particle size in estuarine waters. *Estuar Coastal shelf Science*, 24, 253-263.
- BURBAN, P-Y, LICK, W & LICK, J, 1989. The flocculation of fine grained sediments in estuarine waters. *J Geophy Res*; 94, 8323-8330.
- EISMA, D, SCHUHMACHER, T, BOEKEL, H, van HEERWAARDEN, J, FRANCKEN, H, LAAIN, M, VAARS, A, EIJGENRAAM, F & KALF, J, 1990. A camera and image analysis system for in-situ observation of flocs in natural waters. *Neth Jour Sea Res*, 27, 43-56.
- EISMA, D, BERNARD, P, CADEE, G C, ITTEKKOT, V, KALF, J, LAANE, R, MARTIN, J-M, MOOK, W G, van PUT, A & SCHUHMACHER, T, 1991. Suspended-matter particle size in some West-European estuaries; Part 1; Particle size distribution. *Neth Jour Sea Res*, 28, 193-214.
- GIBBS, R J & KONWAR, L, 1983. Disruption of mineral flocs using Niskin bottles. *Environ Sci Technol*, 17, 374-375.
- GIBBS, R J, TSHUDY, D M, KONWAR, L & MARTIN, J-M, 1989. Coagulation and transport of sediments in the Gironde estuary. *Sedimentology*, 36, 987-999.
- HUNTER, K A & LISS, P S, 1982. Organic matter and the surface charge of suspended particles in estuarine waters. *Limnol Oceanog*. 27, 322-335.
- OWEN, M W, 1970. A detailed study of the settling velocities of an estuary mud. Report NO INT78, Hydraulics Research Station, Wallingford, UK.
- van LEUSSEN, W & CORNELISSE, J, 1992. Direct measurements of sizes and settling velocities of mud flocs in the Ems estuary. *Jour Coastal Res* (in press).
- WELLS, J T, 1989. In-situ measurements of large aggregates over a fluid mud bed. *Jour Coastal Res*, S15 75-86.

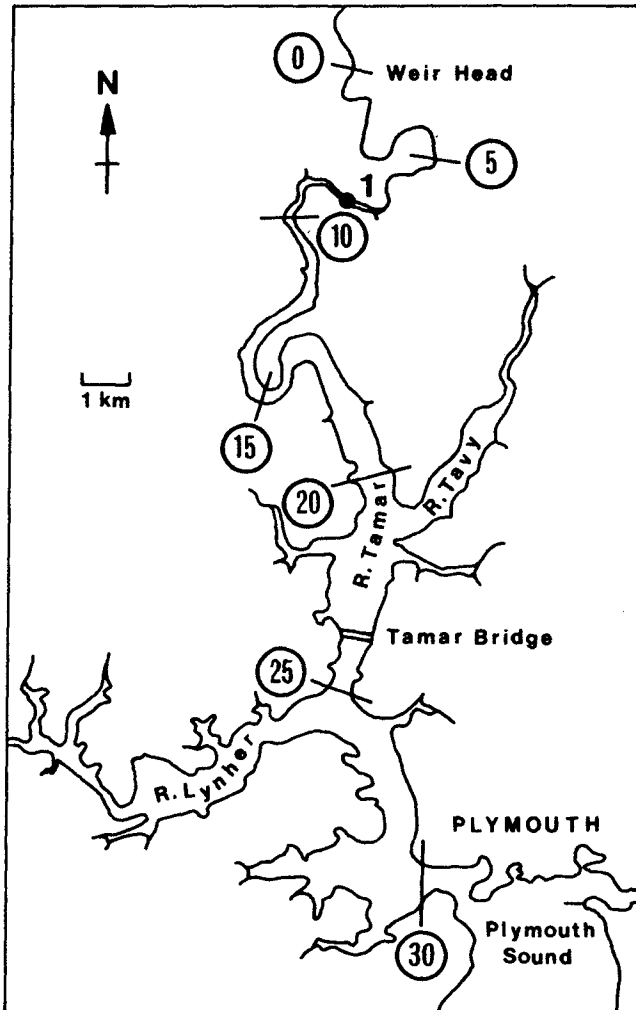


Figure 1. Tamar estuary, Devon, S. England showing location of measurements ( Station 1) and distances in Km from the tidal limit.

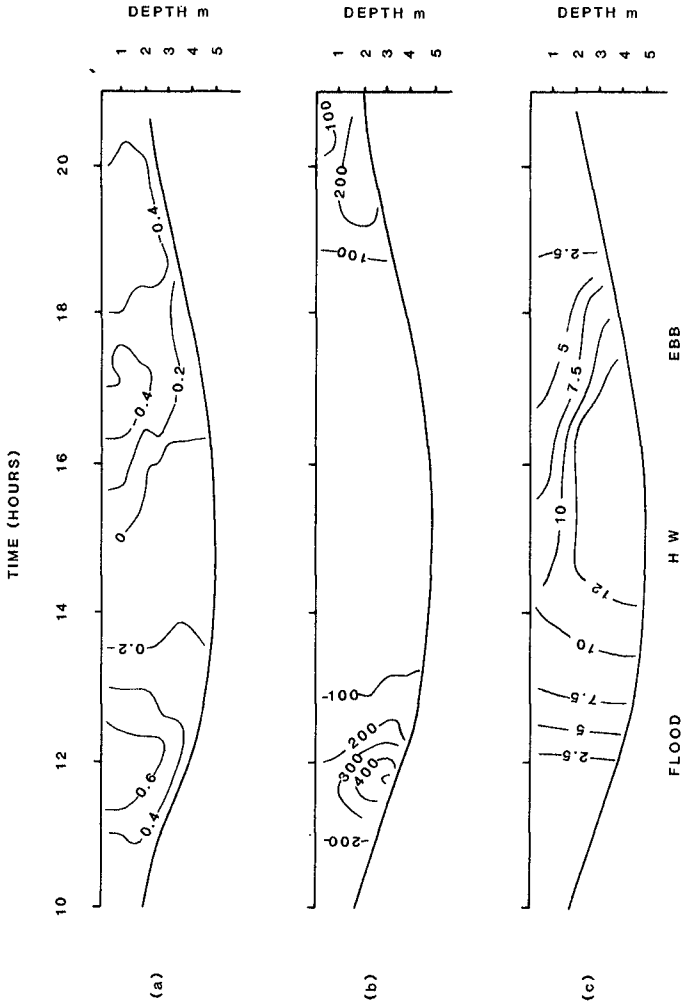


Figure 2. Neap tide variation in: a) current velocity  $\text{ms}^{-1}$ , b) concentration  $\text{mg l}^{-1}$ , c) salinity ppt.

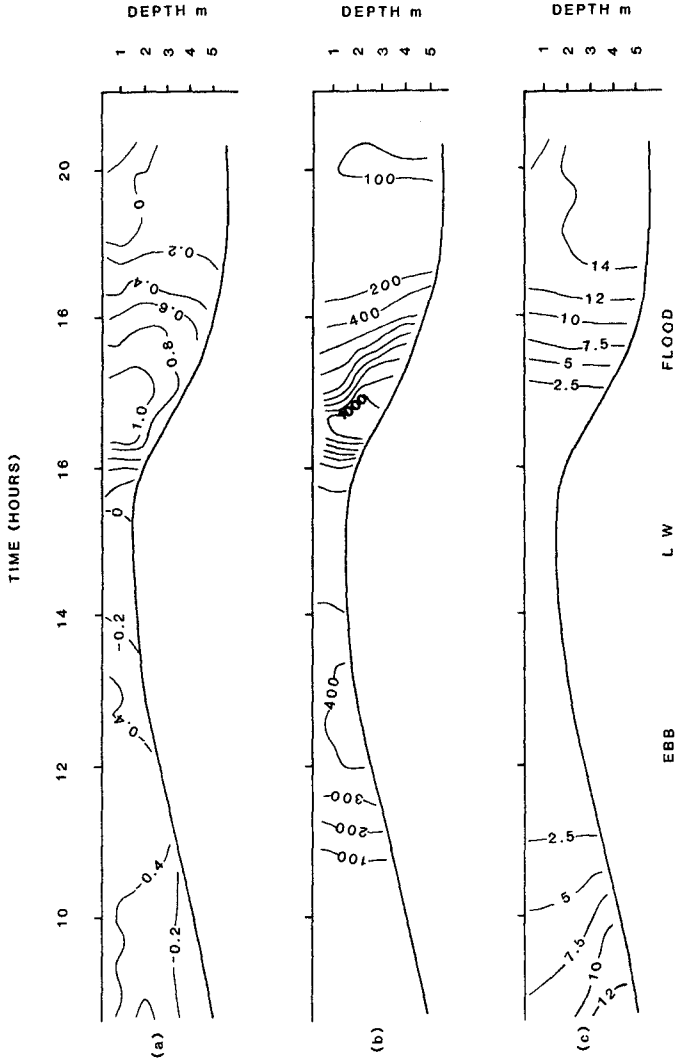


Figure 3. Spring tide variation in: current velocity  $\text{ms}^{-1}$ , b) concentration  $\text{mg l}^{-1}$ , c) salinity ppt.

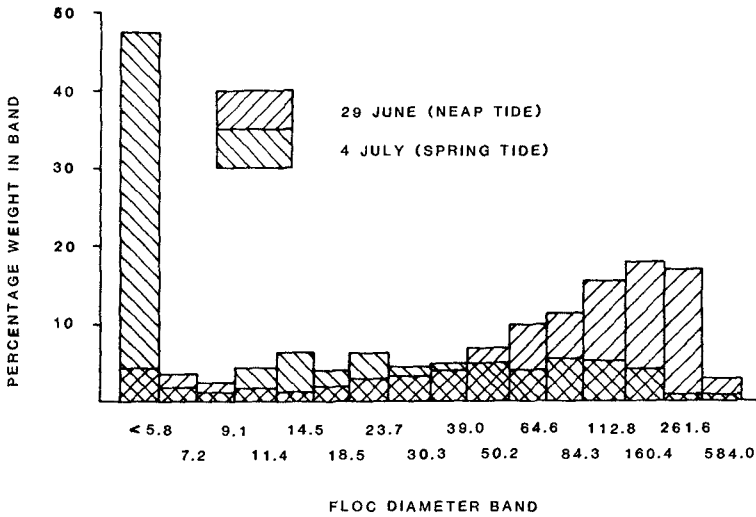


Figure 4. Floc size distribution during the flood turbidity maximum at neap and spring tides.

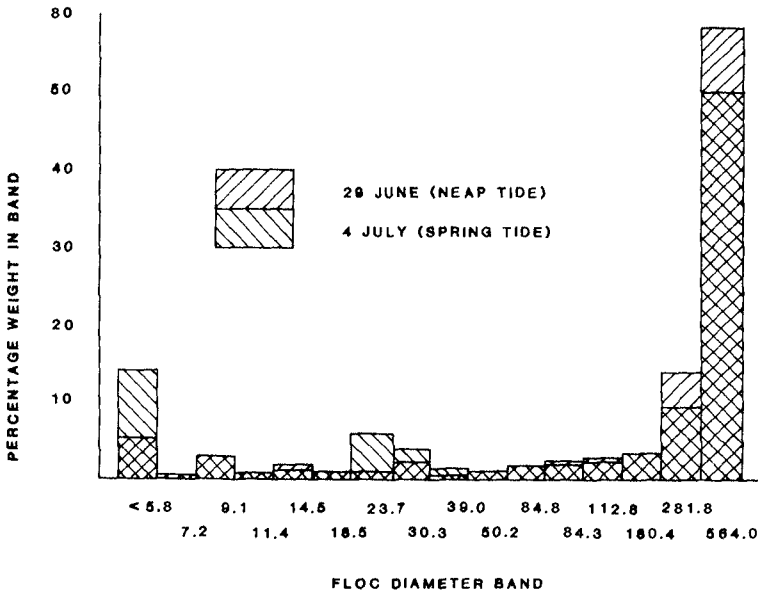


Figure 5. Floc size distribution during the period of salt intrusion erosion at neap and spring tides.



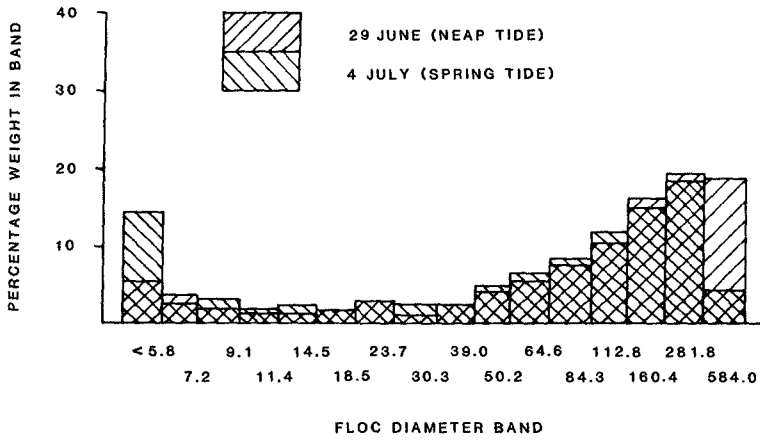


Figure 6. Floc size distribution during the ebb turbidity maximum at neap and spring tides.

## CHAPTER 244

### DISPERSION OF HEAVY SUSPENSIONS IN WAVE BOUNDARY LAYERS

Chiang C. Mei & Chimin Chian  
Department of Civil Engineering  
Massachusetts Institute of Technology

#### 1. Introduction

The transport of suspended particles is of interest to the coastal engineer because it affects the distribution of sediments and the evolution of shorelines. It is also important to pollutant disposal in the sea, and to the transport of nutrients needed for sustaining marine life. Planktonic larvae depend on waves and currents to carry them from offshore to the rock stratum for reproduction and growth. External fertilization of sperms and eggs of marine organisms are further affected by the convection and diffusion processes in the sea.

Taylor's pioneer work in a steady flow through a tube has shown that diffusion, whether molecular or turbulent, is greatly enhanced by transverse shear in the flow. Since in the sea the bottom boundary layer is the zone where shear is the strongest, dispersion must be the most prominent there. For wave-induced boundary layers only the flow field has been studied extensively. For example Stokes laminar boundary layer theory has been extended to turbulent boundary layers by Kajiura(1968), Jonnson & Carlsen(1976), Grant & Madsen(1979) and others. The mean circulation induced in the oscillating boundary layer by Reynolds stresses has been studied under pseudo-laminar model by Longuet-Higgins(1958), Hunt & Johns(1963), Carter, Liu & Mei(1973) etc. Trowbridge & Madsen(1984a,b) further extended it to turbulent flows. So far there has been little theoretical work for predicting dispersion in wave boundary layers.

What is needed is a theory for diffusion of particles in such a transient and nonuniform field of shear. In this paper we outline our recent work obtained by employing the theory of homogenization, which is a systematic technique of taking averages over the period of microscale to obtain the slow variations

over the microscale. The central tool is the method of multiple scales which has been recently applied to dispersion through spatially periodic porous media. The same technique is shown here to be effective for wave problems where there is periodicity in time. Specifically we consider here the dispersion of a cloud of suspension with a prescribed initial distribution in the boundary layer. Attention will be focussed on small amplitude waves without ambient current so that the flow field including the first order oscillations and second order mean can be worked out by a perturbation method, and use will be made of the fact that the boundary layer is much thinner than the horizontal length scale so that the vertical variation can be decoupled from the horizontal problem. Starting with a convective diffusion equation for a heavy suspension for one particle size, we expand the concentration as a perturbation series in powers of the wave steepness. At the leading order the concentration is expected to vary only slowly in time and does not oscillate with the wave because of its weak velocity field. The vertical distribution is due to the balance between vertical diffusion and gravity, but the horizontal distribution is undetermined. The corresponding mathematical problem is a homogeneous boundary value problem in the vertical direction. At the next two orders the fluctuation from the mean is caused by the oscillatory velocity field and consists of both oscillating and slowly varying parts. Their time averages over a wave period are governed by two inhomogeneous boundary value problems in the vertical direction. The solvability condition which imposes constraints on the horizontal and temporal variation of the leading order concentration, leads to the effective diffusion equation. The effective horizontal velocity of convection is shown to be a weighted average of the induced streaming velocity in the boundary layer. For the special model of constant eddy viscosity, the convective velocity and dispersivity tensors are found explicitly in terms of the oscillatory velocity field outside the boundary layer. Specific initial value problems for a prescribed initial concentration cloud will be solved for the following cases, with emphasis on the effects of the initial position of the cloud on its final destiny.

## 2. Perturbation analysis of diffusion in the boundary layer

We assume that the particles are so small that its velocity is nearly equal to the mean velocity of the local fluid, and that the volume concentration is so small that the suspension cloud does not alter the dynamics of the fluid motion.

Let  $C$  denote the volume concentration,  $-w_o$  the fall velocity of the suspended particles, and  $D_H, D_V$  the eddy mass diffusivities. The diffusion equation for the concentration  $C$  of a very dilute sediment cloud can be approximated by

$$\frac{\partial C}{\partial t} + \frac{\partial u_j C}{\partial x_j} + \frac{\partial}{\partial z} [(-w_o + w) C] = \frac{\partial}{\partial x_j} \left( D_H \frac{\partial C}{\partial x_j} \right) + \frac{\partial}{\partial z} \left( D_V \frac{\partial C}{\partial z} \right), \quad (2.4)$$

where  $j = 1, 2$  and  $u_j$  represent the horizontal components of the fluid velocity and  $w$  the vertical component. The crucial boundary condition on the seabed is a matter of considerable uncertainty. For example in steady uniform flows there should not be any net exchange of particles, hence

$$D_V \frac{\partial C}{\partial z} + w_o C = 0, \quad (2.5)$$

This leads to the profile of  $C(z)/C(0)$  but leaves the value of  $C(0)$  undetermined. For spatially nonuniform flows Sayre (1969) proposed the following empirical relation

$$D_v \frac{\partial C}{\partial z} + (1 - \alpha)w_o C + W = 0,$$

where  $\alpha$  is the bed absorbcency coefficient representing the probability that a particle settling to the bed is deposited there,  $W$  the average rate of local entrainment. Direct measurements of  $\alpha$  and  $W$  are obviously difficult and none is known to have been made. To simulate resuspension in wave boundary layers it has been proposed that the rate of concentration flux is an empirical function of time. Others have suggested that the bed concentration is proportional to the excess shear stress over the critical stress to initiate the bed load movement. These empirical consideration are necessary practical measures when local scour is an integral part of the sediment process. However, there are situations where the sediments or contaminants are dumped from ships, or released from a sewage outfall, and not supplied locally from the seabed. Then as long as they can be kept in suspension, the no-flux condition is still appropriate. We shall confine our attention to such cases where the bed is non-erodible bed and particles so small that they are kept in suspension for almost any bed shear. It is reasonable to take  $\alpha = W = 0$  so that

$$D_V \frac{\partial C}{\partial z} + w_o C = 0, \quad z = 0 \quad (2.6)$$

suffices.

At the upper edge of the boundary layer we assume

$$C = 0, \quad z \rightarrow \infty. \quad (2.8)$$

In addition, the initial horizontal distribution of the depth averaged concentration is prescribed in some source area. Thus the physical problem is to seek the long-time diffusion of a sediment cloud from a localized source.

In oceanic flows, momentum eddy diffusivities in horizontal and vertical directions may be quite different (see *e.g.*, Pedlosky, 1979), but the value of the horizontal diffusivity is difficult to estimate reliably. In past theories on dispersion, two assumptions are common. One is the equality of momentum and

mass diffusivities (Reynolds analogy, Taylor, 1953). The second is the equality of the longitudinal and transverse diffusivities (Taylor, 1953; Sayre, 1969 and Sumer, 1974). In wave boundary layers, there is the added complexity that the eddy viscosity may depend on time. However, for coastal applications, most models of eddy viscosity are time-independent (see Sleath 1992 for survey); this simplifying assumption is also adopted here.

In the present problem there are several characteristic length scales in the vertical direction. The first is the thickness of a steady concentration layer due to the balance of downward sedimentation by gravity and vertical diffusion,  $d \sim D_V/w_o$ . Associated with fluid oscillations there are two additional vertical length scales, i.e., the oscillatory boundary layer thicknesses  $\delta \sim \sqrt{2\nu_e/\omega}$  and  $\delta_D \sim \sqrt{2D_V/\omega}$ . For generality, all three scales are assumed to be comparable, i.e., implying that

$$Sc = \frac{\nu_e}{D} \sim \left( \frac{\delta}{\delta_D} \right)^2 = O(1), \quad (2.9)$$

where  $Sc$  is the Schmidt number.

We now consider small amplitude oscillations of high enough frequency so that both the wave steepness,  $kA$ , and the ratio of the oscillatory boundary layer thickness to the wave length,  $k\delta$ , are small, i.e.

$$\epsilon = kA \ll 1, \quad (2.10a)$$

$$\beta = k\delta \sqrt{\frac{D_H}{D_V}} \ll 1. \quad (2.10b)$$

Let us expand the velocity field  $(u_i, w)$  in powers of  $\epsilon$ ,

$$u_i = u_i^{(1)} + u_i^{(2)} + \dots, \quad i = 1, 2; \quad w = w^{(1)} + w^{(2)} + \dots, \quad (2.11)$$

where the superscripts indicate the order in powers of  $\epsilon$ , i.e.,  $u_i^{(n)}, w^{(n)} = O(\epsilon^n)$ . Clearly there are two distinct time scales in the diffusion process, one for the vertical diffusion across the boundary layer,  $O(\delta^2/D_V)$ , and the other for the horizontal diffusion across a wave length,  $O(1/k^2 D_H)$ . The ratio between the two is  $O(k^2 \delta^2 D_H/D_V) = O(\beta^2)$ . It is therefore natural to introduce multiple scale coordinates for time,  $t$  and  $t' = \beta^2 t$ . Assume for generality  $\epsilon = O(\beta)$  so that we may use

$$T = \epsilon^2 t \quad (2.12)$$

instead of  $t'$ , and expand  $C$  as a perturbation series

$$C = C^{(0)} + C^{(1)} + C^{(2)} + \dots, \quad (2.13)$$

where  $C^{(0)}$  is independent of the fast time scale and  $C^{(n)}, n = 1, 2, \dots$  dependent on  $t$  and  $T$ . At the leading order in  $\epsilon$ ,  $C^{(0)}$  satisfies the homogeneous ordinary differential equation

$$-w_o \frac{\partial C^{(0)}}{\partial z} = \frac{\partial}{\partial z} \left( D_V \frac{\partial C^{(0)}}{\partial z} \right), \quad 0 < z < \infty, \tag{2.14}$$

with the homogeneous boundary conditions

$$w_o C^{(0)} + D_V \frac{\partial C^{(0)}}{\partial z} = 0, \quad z = 0; \tag{2.15}$$

$$C^{(0)} = 0, \quad z \rightarrow \infty. \tag{2.16}$$

The nontrivial solution is

$$C^{(0)} = \widehat{C}F, \tag{2.17a}$$

where

$$F = \exp \left( - \int \frac{w_o}{D_V} dz \right) \tag{2.17b}$$

gives the vertical structure and

$$\widehat{C} = \widehat{C}(x_i, T), \quad i = 1, 2 \tag{2.17c}$$

gives the horizontal variation of  $C^{(0)}$ . As in the steady uniform flow  $C^{(0)}$  is so far unknown. At  $O(\epsilon)$ , the period-average of  $C^{(1)}(x, y, t, T)$  can be shown to be zero. Assuming the first order fluid velocity in the boundary layer to be simple harmonic, the time-harmonic part of  $C^{(0)}$  is forced by various products of  $u^{(1)}$  and  $C^{(0)}$  and their derivatives. Therefore  $C^{(1)}$  can be solved in terms of  $C^{(0)}$  and its horizontal gradient. At  $O(\epsilon^2)$ , the period-average of  $C^{(2)}$  satisfies an inhomogeneous differential equation similar to (2.6). Its solution implies that the depth average of the forcing terms must vanish. This leads to

$$\frac{\partial \widehat{C}}{\partial T} \langle F \rangle + \frac{\partial}{\partial x_i} \left[ \langle \bar{u}_i^{(2)} F \rangle \widehat{C} \right] = - \frac{\partial}{\partial x_i} \langle \bar{u}_i^{(1)} C^{(1)} \rangle + \frac{\partial}{\partial x_j} \langle D_H \frac{\partial}{\partial x_j} (\widehat{C}F) \rangle. \tag{2.18}$$

Once a specific choice of  $D_V$  and  $D_H$  is made, the right hand side of (2.18) can be found in terms of  $C^{(0)}$ , hence  $\widehat{C}$ . This then gives the effective convection-diffusion equation for  $\widehat{C}$ . As will be identified later,  $\bar{u}_i^{(2)}$  on the left is Eulerian streaming in the boundary layer. The first term on the right represents the dispersion due to oscillatory shear in the boundary layer and the last term the horizontal turbulent diffusion.

Though the form is entirely expected, every term in (2.18) has been deduced here without *additional* closure hypotheses.

In the rest of the paper the simplifying assumption  $D_H = D_V = D =$  constant will be made to enable explicit analytical results.

**3. The Stokes effective coefficients**

For constant eddy diffusivities the first order velocity is the well known solution of Stokes the second order mean is the Eulerian streaming inferable from Hunt and Johns (see Mei 1983). Details of  $C^{(1)}$  is described elsewhere. After considerable algebra we get the effective diffusion equation for  $\hat{C}$ :

$$\frac{\partial \hat{C}}{\partial T} + \frac{\partial}{\partial x_i} (u_i \hat{C}) = D \frac{\partial^2 \hat{C}}{\partial x_j \partial x_j} + \frac{\partial}{\partial x_i} \left( \mathcal{D}_{ij} \frac{\partial \hat{C}}{\partial x_j} \right), \tag{3.1}$$

where

$$u = \frac{1}{\omega} \Re \left( H_1 U_o \frac{\partial U_o^*}{\partial x} + H_2 V_o \frac{\partial U_o^*}{\partial y} + H_3 U_o \frac{\partial V_o^*}{\partial y} \right), \tag{3.2}$$

$$v = \frac{1}{\omega} \Re \left( H_1 V_o \frac{\partial V_o^*}{\partial y} + H_2 U_o \frac{\partial V_o^*}{\partial x} + H_3 V_o \frac{\partial U_o^*}{\partial x} \right),$$

$$\begin{aligned} \mathcal{D}_{xx} &= \Re \left[ \frac{H_4}{\omega} |U_o|^2 \right], & \mathcal{D}_{xy} &= \Re \left[ \frac{H_4}{\omega} (U_o^* V_o) \right], \\ \mathcal{D}_{yx} &= \Re \left[ \frac{H_4}{\omega} (U_o V_o^*) \right], & \mathcal{D}_{yy} &= \Re \left[ \frac{H_4}{\omega} |V_o|^2 \right]. \end{aligned} \tag{3.3}$$

The coefficients  $H_1, H_2, H_3$  and  $H_4$  are functions of  $M$  and  $Sc$ .

Equation (3.1) may be normalized by defining  $\bar{U}_o$  to be the maximum of the first order velocity  $(U_o^2 + V_o^2)^{1/2}$  and letting

$$U'_{oi} = \frac{U_{oi}}{\bar{U}_o}, \quad x'_i = kx_i, \quad t' = \frac{k^2 \bar{U}_o^2}{\omega} T, \tag{3.4}$$

where primes denote dimensionless quantities. Then

$$\frac{\partial \hat{C}}{\partial t'} + \frac{\partial}{\partial x'_i} (u'_i \hat{C}) = \frac{\partial}{\partial x'_i} \left( K'_{ij} \frac{\partial \hat{C}}{\partial x'_j} \right), \tag{3.5}$$

where

$$u' = \Re \left( H_1 U'_o \frac{\partial U'^*_{o'}}{\partial x'} + H_2 V'_o \frac{\partial U'^*_{o'}}{\partial y'} + H_3 U'_o \frac{\partial V'^*_{o'}}{\partial y'} \right),$$

$$v' = \Re \left( H_1 V'_o \frac{\partial V'^*_{o'}}{\partial y'} + H_2 U'_o \frac{\partial V'^*_{o'}}{\partial x'} + H_3 V'_o \frac{\partial U'^*_{o'}}{\partial x'} \right),$$

$$K'_{xx} = \mathcal{D}'_{xx} + D' = \Re(H_4) |U'_o|^2 + D',$$

$$K'_{xy} = \mathcal{D}'_{xy} = \Re(H_4 U'^*_o V'_o),$$

$$K'_{yx} = \mathcal{D}'_{yx} = \Re(H_4 U'_o V'^*_o),$$

$$K'_{yy} = \mathcal{D}'_{yy} + D' = \Re(H_4) |V'_o|^2 + D',$$

$$D' = D / (\bar{U}_o^2 / \omega),$$

in which  $K'_{ij}$  are components of the total dispersivity tensor.

In steady flows in a channel or a tube the longitudinal dispersion coefficient is usually much greater than diffusivity (molecular or eddy). It can be shown that the shear-enhanced dispersion can be much greater than the eddy diffusivity if the ambient oscillation is sufficiently intense or the frequency sufficiently low. Otherwise the two can be comparable.

We now examine the spatial variations of the dispersion phenomenon by specific examples. For brevity, primes on dimensionless quantities will be dropped for convenience in later discussions. The values of  $H_1, H_2, H_3, H_4$  are for  $M = Sc = 1$ .

**4. Two-dimensional diffusion of a localized cloud in bidirectional waves**

We consider a system of short-crested waves whose inviscid velocity amplitudes near the seabed are described in dimensional variables by

$$\begin{aligned} U_o &= 2i\bar{U}_o \cos \theta \sin(kx \cos \theta) e^{iky \sin \theta}, \\ V_o &= 2\bar{U}_o \sin \theta \cos(kx \cos \theta) e^{iky \sin \theta}. \end{aligned} \tag{4.1}$$

This corresponds to a plane wave incident towards and reflected by a sea wall along the  $y$  axis. The angle of incidence is  $\theta$ . In normalized variables (with primes omitted), we have

$$\begin{aligned} U_o &= 2i \cos \theta \sin(x \cos \theta) e^{iy \sin \theta}, \\ V_o &= 2 \sin \theta \cos(x \cos \theta) e^{iy \sin \theta}. \end{aligned} \tag{4.2}$$

It is easy to calculate the following dimensionless coefficients,

$$\begin{aligned} \mathcal{U} &= [2\Re(H_1) \cos^3 \theta + (\Re(H_3) - \Re(H_2)) \sin \theta \sin 2\theta] \sin(2x \cos \theta), \\ \mathcal{V} &= [2\Im(H_1) \sin^3 \theta + \Im(H_3) \cos \theta \sin 2\theta] 2 \cos^2(x \cos \theta), \\ K_{xx} &= 4\Re(H_4) \cos^2 \theta \sin^2(x \cos \theta) + D, \\ K_{yy} &= 4\Re(H_4) \sin^2 \theta \cos^2(x \cos \theta) + D, \\ K_{xy} &= -K_{yx} = \Im(H_4) \sin 2\theta \sin(2x \cos \theta). \end{aligned} \tag{4.3}$$

Note that the tensor  $\{K_{ij}\}$  is not symmetric.

Let us examine the diffusion due to the impulsive release from a localized Gaussian cloud

$$\hat{C}(x, y, 0) = C_o \exp \left\{ - [(x - x_c)^2 + (y - y_c)^2] / L^2 \right\}. \tag{4.4}$$



The assumption of  $Sc = M = 1$  is still kept, for which  $\Re(H_1) = -0.122$ ,  $\Im(H_1) = \Im(H_3) = 0.659$ ,  $\Re(H_2) = 0.033$ ,  $\Re(H_3) = -0.155$ ,  $\Re(H_4) = 0.024$  and  $\Im(H_4) = 0.234$ . Choosing  $D = 10^{-3}$  and  $L^2 = 0.1$ , the initial value problem is solved numerically by a Peaceman-Rachford ADI (alternating-direction) finite difference method. Three angles of incidence and various positions of the initial source center have been considered.

As a sample we consider oblique incidence  $\theta = \pi/4$ , then

$$\begin{aligned} \mathcal{U} &= \frac{1}{\sqrt{2}} \Re(H_1 + H_3 - H_2) \sin \sqrt{2}x = -0.219 \sin \sqrt{2}x, \\ \mathcal{V} &= \sqrt{2} \Im(H_1 + H_3) \cos^2 \frac{x}{\sqrt{2}} = 1.864 \cos^2 \frac{x}{\sqrt{2}}, \end{aligned} \quad (4.5)$$

and

$$\begin{aligned} K_{xx} &= 2\Re(H_4) \sin^2 \frac{x}{\sqrt{2}} + D = 0.048 \sin^2 \frac{x}{\sqrt{2}} + D, \\ K_{yy} &= 2\Re(H_4) \cos^2 \frac{x}{\sqrt{2}} + D = 0.048 \cos^2 \frac{x}{\sqrt{2}} + D, \\ K_{xy} &= -K_{yx} = \Im(H_4) \sin(\sqrt{2}x) = 0.234 \sin(\sqrt{2}x). \end{aligned} \quad (4.6)$$

Thus for  $x_c = 0$ ,  $\mathcal{V}$  is dominant; the cloud is convected along the line  $x = 0$  and diffused faster in the  $y$  than in  $x$  as shown in figure 1. For  $x_c \cos \theta = x_c/\sqrt{2} = \pi/2$ ,  $K_{xx} > K_{yy}$ , the nonuniform convection velocity causes the cloud to bifurcate towards the lines  $x_c/\sqrt{2} = 0, \pi$  where  $K_{yy} > K_{xx}$ , as in figure 2. For  $x_c \cos \theta = \pi/4$ , most of the pulse is convected to the left, with the front leading the rest in the shape of an eel, as shown in figure 3.

We have also considered a sustained source and solved the inhomogeneous diffusion equation

$$\frac{\partial \hat{C}}{\partial t} + \frac{\partial}{\partial x_i} (u_i \hat{C}) = \frac{\partial}{\partial x_j} \left( K_{ij} \frac{\partial \hat{C}}{\partial x_j} \right) + S(x_i), \quad t > 0. \quad (4.7)$$

The source function  $S$  is chosen to be a cosine-shaped distribution centered around  $(x_c, y_c)$  and maintained at a steady rate after  $t = 0$ . A plume is formed with the front evolving in the same way as the impulsively released cloud, but the plume is always connected back to the steady source. We shall, therefore, omit the results here.

## 5. Concluding remarks

In this paper we have given general formulas for convections and diffusion in a wave boundary layer. As an example we have examined a localized cloud in a bidirectional wave system which may represent an obliquely incident and reflected wave system near a sea wall. The cloud drifts to the nodal line close

to its initial position. When the particle cloud is initially midway between two nodal lines along the  $y$  axis. The cloud then bifurcates towards the two nodal lines on each side while the peaks diminish.

Future improvements must include better models of turbulence, deposition and resuspension. For fine cohesive sediments possible coagulation is worth studying. Finally it is interesting to examine dispersion in the surf zone where breaking waves induce longshore currents.

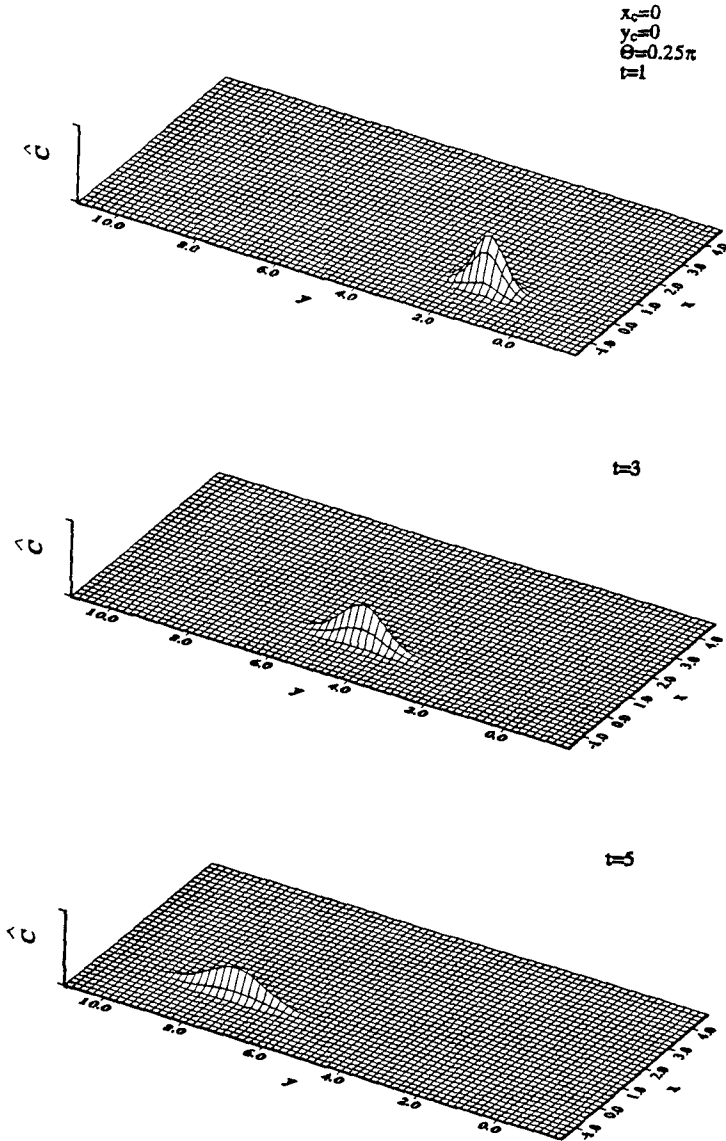
### Acknowledgement

We are grateful for the financial support by the Ocean Engineering Program, U.S. Office of Naval Research Grant, and the Fluid Mechanics/Hydraulics/Particulates Program of the U.S. National Science Foundation.

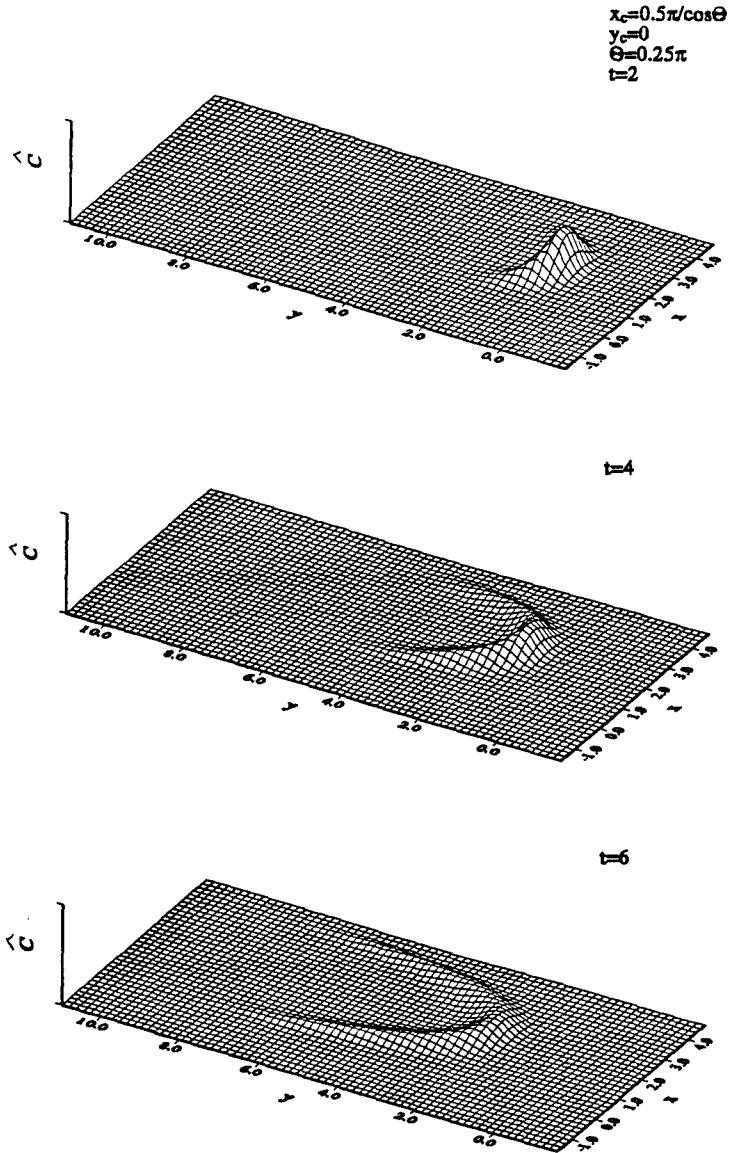
### References

- Carter, T.G., Liu, P.C.F. & Mei, C.C. (1973) "Mass transport by waves and offshore sand bedforms." *J. Waterways Harbors Coastal Engineering Division, ASCE* **99**, 165-184.
- Grant, W.D. & Madsen, O.S. (1979) "Combined waves and current interactions with a rough bottom." *J. Geophys. Res.* **84**(c4), 1797-1808.
- Hunt, J.N. & Johns, B. (1963) "Currents induced by tides and gravity waves." *Tellus* **15**, 4.
- Jonsson, I.G. & Carlsen, N.A. (1976) "Experimental & Theoretical investigation in an oscillatory turbulent boundary layer." *J. Hydraul. Res.* **14**(1), 45.
- Kajiura, K. (1968) "A model of the bottom boundary layer in water waves." *Bull. Earthquake Res. Inst., Univ. Tokyo* **146**, 75-123.
- Lamoure, J. & Mei, C.C. (1976) "Effects of horizontally two dimensional bodies on the mass transport near the sea bottom" *J. Fluid Mech.* **83**, 415-431.
- Longuet-Higgins, M.S. (1953) "Mass transport in water waves." *Phil. Trans. R. Soc. Lond.* **A245**, 535-581.
- Mei, C.C. (1983) *The Applied Dynamics of Ocean Surface Waves*. Wiley-Intersci., New York. 1989, World Scientific.
- Pedlosky, J. (1979) *Geophysical Fluid Dynamics*, Springer
- Rubinstein, J. & Mauri, R. (1986) "Dispersion and convection in periodic porous media." *SIAM J. Applied Math.* **46**, 1018-1023.

- Sayre, W.W. (1968) "Dispersion of mass in open-channel flow." *Colorado State University Hydraul. Paper No. 3*, Feb.
- Sayre, W.W. (1969) "Dispersion of silt particles in open-channel flow. *J. Hydraul. Div, ASCE, HY3*, 6579.
- Sleath, J. F. A. (1990) Seabed boundary layers, in *The Sea, Ocean Engineering Science*, vol 9, edited by B. LeMeute & D. Hanes, Wiley-Interscience.
- Sumer, B.M. (1974) "Mean velocity and longitudinal dispersion of heavy particles in turbulent open-channel flows." *J. Fluid Mech.* **65**, 11-28.
- Taylor, G.I. (1953) "Dispersion of solute matter in solvent flowing slowly through a tube." *Proc. R. Soc. Lond.* **A219**, 186-203.
- Trowbridge, J. & Madsen, O.S. (1984a) Turbulent wave boundary layers, I. Model formulation and first-order solution. *J. Geophys. Res.* **89**, 7989-7997.
- Trowbridge, J. & Madsen, O.S. (1984b) Turbulent wave boundary layers, II. Second-order theory and mass transport. *J. Geophys. Res.* **89**, 7999-8007.

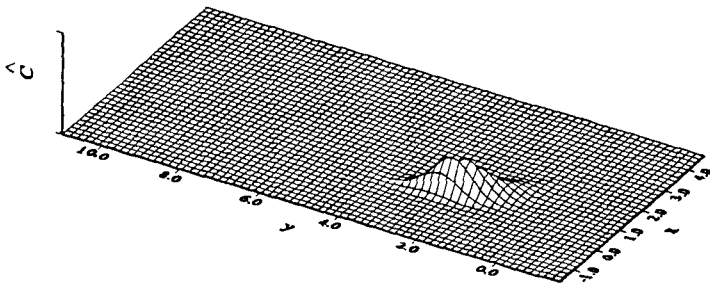


**Figure 1:** Evolution of a concentration released in a bidirectional wave. Initial position at  $x_c = 0$ .

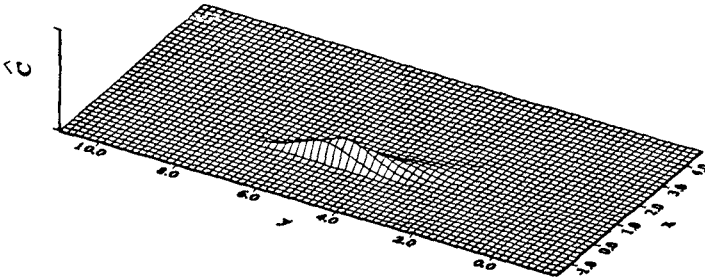


**Figure 2:** Evolution of a concentration released in a bidirectional wave. Initial position at  $x_c/\sqrt{2} = \pi/2$ .

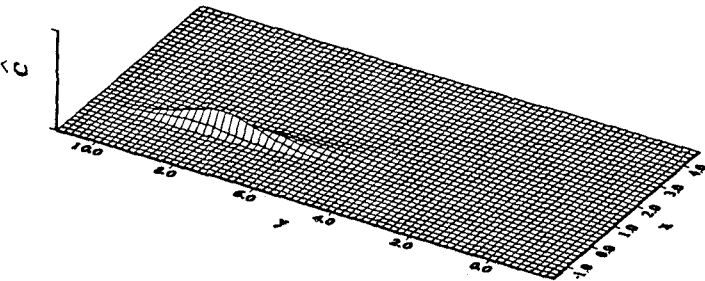
$$\begin{aligned}x_c &= 0.25\pi/\cos\Theta \\ y_c &= 0 \\ \Theta &= 0.25\pi \\ t &= 2\end{aligned}$$



I



II



**Figure 3:** Evolution of a concentration released in a bidirectional wave. Initial position at  $x_c/\sqrt{2} = \pi/4$ .

## CHAPTER 245

### COMBINED CONVECTION-DIFFUSION MODELLING OF SEDIMENT ENTRAINMENT

by

Peter Nielsen

#### Abstract

A new, quantitative framework is presented for the modelling of suspended sediment concentration distributions. It accounts for large scale mixing (convection) as well as small scale mixing. The small scale mixing is modelled in terms of gradient diffusion as usual. It is shown how the new, combined convection-diffusion model can explain the different  $\bar{c}(z)$ -distributions of different sediment sizes in the same flow. Also, the dependence of the  $\bar{c}(z)$ -distribution shape on wave period and sediment settling velocity is explained for oscillatory flow over ripples. It is shown that individual Fourier components of  $c_n(z,t)$  behave differently in diffusion dominated and in convection dominated flows. This makes it possible to determine the dominant entrainment mechanism (convection or diffusion) on the basis of concentration time series taken simultaneously at different levels.

#### 1. Introduction

Experimental data calls for a new description of the distribution of suspended sediment. That is, the traditional gradient diffusion model is inadequate as a description of many natural suspension processes.

Gradient diffusion is suited only as a description for processes where the mixing length  $l_m$  is small compared to the overall scale. It cannot describe details on a scale comparable or smaller than  $l_m$ , see Figure 1.

Some of the natural processes which involve large scale mixing mechanisms are: Entrainment of sand from rippled beds, lifting of sand straight from the bed to the surface behind plunging breakers, entrainment by turbulent bursts in sheet flow, entrainment by the obliquely descending vortices of Nadaoka et al (1988), and from steady streams, entrainment by the vortices which are formed behind dunes and subsequently carry sand to the surface.

-----  
Department of Civil Engineering, The University of Queensland, St Lucia,  
Australia 4072, fax +61 7 365 4599.

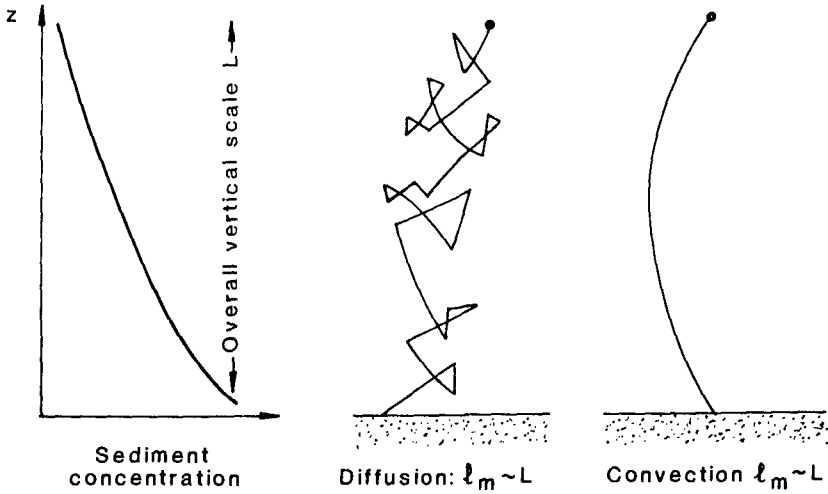


Figure 1: A concentration profile with overall scale  $L$  may be generated by either gradient diffusion ( $l_m < L$ ) or convective entrainment ( $l_m \sim L$ ), but usually it will be due to a mixture of both.

These processes require a different modelling framework than gradient diffusion.

The quantitative framework for the combined convection-diffusion process is briefly derived in Sections 3 and 4. The main new ingredient here is the expression for the convective upward flux proposed by Nielsen (1991).

Section 5 then discusses the shape of the distributions of time-averaged concentrations  $\bar{c}(z)$ . A single shape parameter  $S$  is defined with which variation in shape of the  $\bar{c}(z)$ -profiles with wave period and sediment settling velocity can be explained.

The behaviour of the time dependent (harmonic) components  $c_n(z,t)$  of the concentration is discussed in Section 6. It is shown how the relative importance of convective versus diffusive mixing is indicated by simultaneous concentration time series from different elevations.

### 3. Quantification of the convective entrainment flux

Most natural suspension processes involve mixing on different scales, see Figure 1, and mechanisms with large mixing lengths  $l_m$  compared with the overall scale, require a different mathematical framework than gradient diffusion. A quantitative description for the large scale ( $l_m \sim L$ ) mixing mechanisms is suggested as outlined in Figure 2.



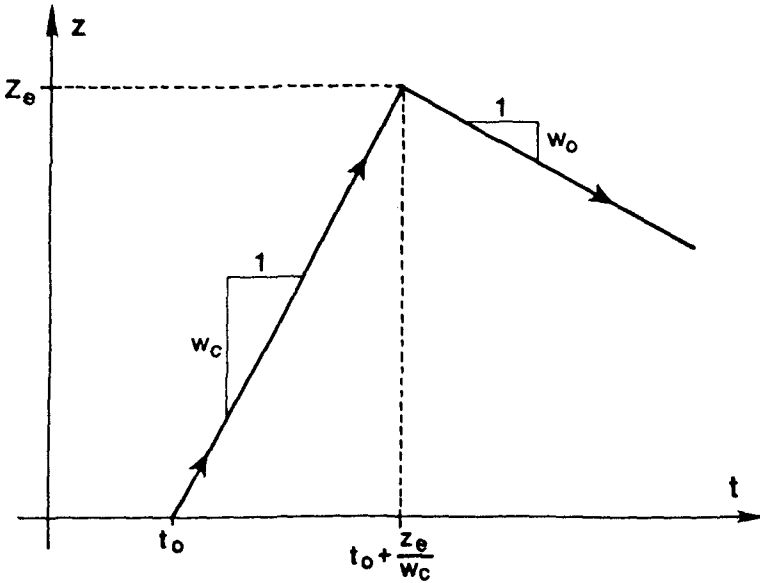


Figure 2: Sand which is entrained from the bed at time  $t_0$  is assumed to travel upwards with speed  $w_c$ . Not all of the sand will reach the same level. The distribution of entrainment levels  $z_e$  is given by  $F(z) = P\{z_e > z\}$ . After reaching its entrainment level  $z_e$  at time  $t_0 + z_e/w_c$ , a sand particle is assumed to settle out with its still water settling velocity  $w_o$ . During the settling process it may be affected by small scale mixing (diffusion).

A quantitative description of the convective, upward sediment flux  $q_c(z,t)$  in accordance with Figure 2, has been derived by Nielsen (1991,1992). He suggested the form

$$q_c(z,t) = p\left(t - \frac{z}{w_c}\right) F(z) \quad (1)$$

where  $p(t)$  is the amount of sand which is picked up from the bed at time  $t$ .

#### 4. Continuity equation for the combined process

The continuity equation for the combined process, i.e., the equation which expresses the conservation of sand in the combined convection diffusion process is

$$\frac{\partial c}{\partial t} = w_o \frac{\partial c}{\partial z} - \frac{\partial q_c}{\partial z} - \frac{\partial q_D}{\partial z} \quad (2)$$

which with the expression (1) inserted for the convective upward flux, and with

the upward diffusive flux  $q_D = -\epsilon_s \frac{\partial c}{\partial z}$  becomes

$$\frac{\partial c}{\partial t} = w_o \frac{\partial c}{\partial z} + \frac{1}{w_c} p'(t - \frac{z}{w_c}) F(z) - p(t - \frac{z}{w_c}) F'(z) + \frac{\partial}{\partial z} (\epsilon_s \frac{\partial c}{\partial z}) \quad (3)$$

or

$$\frac{\partial c}{\partial t} - w_o \frac{\partial c}{\partial z} - \frac{\partial}{\partial z} (\epsilon_s \frac{\partial c}{\partial z}) = \frac{1}{w_c} p'(t - \frac{z}{w_c}) F(z) - p(t - \frac{z}{w_c}) F'(z) \quad (4)$$

from which we see that the homogeneous equation is the usual diffusion equation, while the convective flux enters only through the forcing terms.

#### 4. The shape of the $\bar{c}(z)$ -profiles

The inadequacy of pure gradient diffusion as a universal model for sediment suspension becomes particularly evident when one considers the distributions of different grain sizes in the same flow. An example is shown in Figure 3.

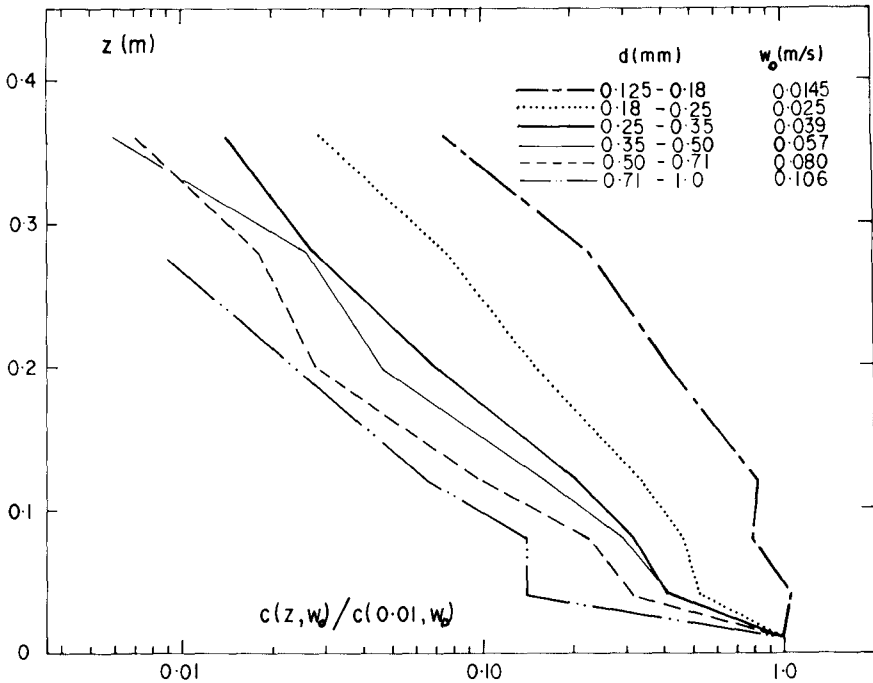


Figure 3: Normalised distributions of different sand sizes in the same flow (oscillatory flow over ripples). The data was obtained by sieving suction samples from each elevation. Data from Nielsen (1983).

The interesting thing about these profiles is that they do not have the same shape. In this case, the fine sand shows typically upward convex profiles while the coarse sand shows upward concave profiles. Such differences between different sand sizes (different settling velocities  $w_o$ ) cannot be explained within the gradient diffusion framework. If the concentration profiles had been a result of pure gradient diffusion with diffusivity  $\epsilon_s(z)$ , they would have had the mathematical form

$$\ln \frac{\bar{c}}{C_o} = -w_o \int_0^z \frac{dz}{\epsilon_s} \quad (5)$$

where  $C_o = \bar{c}(o)$ .

This shows that the profiles for different sand sizes would have similar shapes when plotted as in Figure 3, the role of the settling velocity  $w_o$  would be only to tilt the profiles towards the left.

The same picture as Figure 3 was presented by the natural-ripple-data from a subsequent laboratory study of McFetridge & Nielsen (1985).

Another observation which underlines the need for a new distribution model is that time averaged concentration profiles over rippled beds under waves tend to change shape from upward convex to upward concave with increasing wave period. Examples of this are shown in Figure 4.

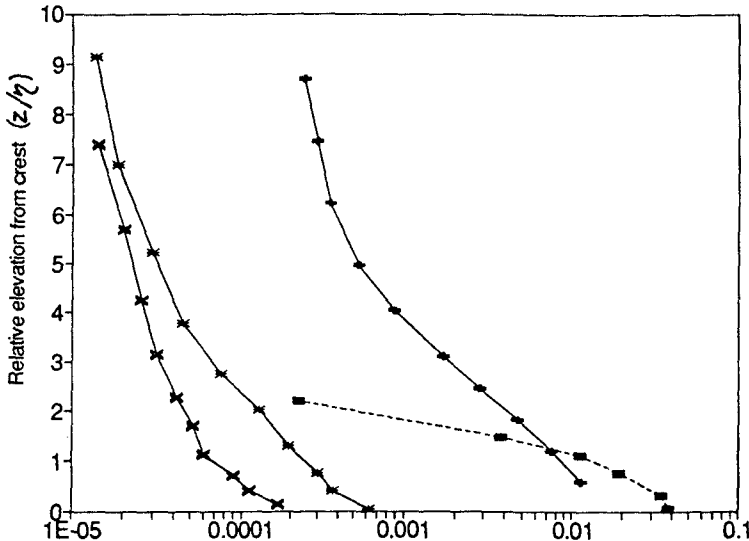


Figure 4: Time averaged concentration profiles over rippled beds in an oscillating water tunnel. For the shortest periods, the  $\bar{c}$ -profiles are upward convex (at least for the first 4 ripple heights). With increasing  $T$ , they become more and more upward concave.  $d_{50}=0.21mm$  in all of the experiments.  $\blacksquare$  :  $T=1s$ ,  $U_{max}=0.5m/s$ ,  $+$  :  $T=2s$ ,  $U_{max}=0.5m/s$ ,  $*$  :  $T=4s$ ,  $U_{max}=0.3m/s$ ,  $\times$  :  $T=10s$ ,  $U_{max}=0.3m/s$ . Data from Bosman (1982) and Ribberink & Al-Salem (1989).

This change of shape of the  $\bar{c}(z)$ -profiles with wave period is difficult to explain within the gradient diffusion framework. The different shapes for  $\bar{c}(z)$  would, in that framework, indicate different distributions of the diffusivity  $\epsilon_s(z)$ . That is however an unlikely explanation, in so far as  $\epsilon_s(z)$  should be closely related to the eddy viscosity and hence similar from experiment to experiment, because the flow conditions were rather similar.

Furthermore, a similar set of concentration profiles measured over flat beds (Horikawa et al 1982) show the same gradual change of shape with increasing period, see Nielsen (1992) p271.

We shall see that both the change from upward convex to upward concave for sediments with increasing settling velocity in the same flow and the analogous change for the same sand in flows with increasing periods can be modelled by the combined convection diffusion model. The shape differences are shown to be consequences of different relative importance of diffusive (small scale) and convective (large scale) mixing, and this is quantified in terms of the shape parameter  $S$ . The shape parameter is found to follow the rough, general rule

$$S \sim \frac{w_o T}{\sqrt{A} r} \tag{6}$$

where  $A$  is the wave induced particle semi excursion just above the boundary layer and  $r$  is the bed roughness.

When  $S$  is small, the  $\bar{c}$ -profiles tend to be upward convex, for large  $S$  they tend to be upward concave.

The derivation of the form of the shape parameter (Nielsen 1992, p 249) is based on the solution to the time-averaged version

$$w_o \bar{c} + \epsilon_s \frac{d\bar{c}}{dz} = \bar{p} F(z) \tag{7}$$

of the continuity equation (3) in the simple case where  $\epsilon_s$  is a constant and  $F(z) = \exp[-z/L]$ . In that case the time averaged concentration is given by

$$\bar{c}(z) = \frac{\bar{p}}{w_o} \left\{ \frac{1}{1 - \epsilon_s/w_o L} e^{-z/L} + \left(1 - \frac{1}{1 - \epsilon_s/w_o L}\right) e^{-w_o z/\epsilon_s} \right\}, \quad \epsilon_s/w_o L \neq 1. \tag{8}$$

This solution shows that the relative importance of the diffusion solution (the last term) and the convection solution (the first term) is measured by the ratio  $\epsilon_s/w_o L$  which may be seen as the ratio between the vertical scale  $\epsilon_s/w_o$  of the pure diffusion solution and that ( $L$ ) of the pure convection solution. The inverse of this ratio is the shape parameter :

$$S = \frac{w_o L}{\epsilon_s} \quad (9)$$

To express the shape parameter in terms of basic flow parameters it is then noted that oscillatory boundary layers over rippled beds usually have a structure which is analogous to that of laminar oscillatory flow over a flat plate. That is, the eddy viscosity is constant, and its value is  $\nu_t = 0.5 \omega z_1^2$  where  $z_1 = 0.09 \sqrt{rA}$ , cf Nielsen (1992) p 40. Hence, assuming that  $\epsilon_s$  is proportional to  $\nu_t$  and that the convective length scale  $L$  is proportional to  $z_1$  we are lead to the formula (6) which agrees with the observations in Figures 3 and 4. That is, in both cases, the transition from upward convex to upward concave profiles happens with increasing values of  $S$ .

It is interesting to note that experiments with suspensions of limited amounts of sand over artificial, fixed ripples give less pronounced  $\bar{c}(z)$ -shape differences between coarse and fine sand fractions. Such experiments were reported by McFetridge & Nielsen (1985) and by van de Graff (1988). In the fixed-ripple-experiments, the  $\bar{c}(z)$ -profiles agree more closely with the gradient diffusion model in the sense of Equation (5). It is believed to be due to the fact that when the sand supply at the bed is limited, the convective entrainment mechanism is less important. Most of the sand stays in suspension rather than being continually picked up and resuspended by the travelling lee vortices. The limiting case in this respect is pure wash load which is hence expected to obey the diffusion equation very closely.

### 5. Time dependent concentrations in pure diffusion

The time dependent diffusion equation

$$\frac{\partial c}{\partial t} - w_o \frac{\partial c}{\partial z} - \frac{\partial}{\partial z} (\epsilon_s \frac{\partial c}{\partial z}) = 0 \quad (10)$$

which emerges from Equation (4) when the convective entrainment flux is zero, with the boundary conditions

$$\begin{aligned} -\epsilon_s \frac{\partial c}{\partial z} &= p(t) \quad \text{for } z = 0 \\ c(z,t) &\rightarrow 0 \quad \text{for } z \rightarrow \infty \end{aligned} \quad (11)$$

was solved by Nielsen et al (1978). The solution is in the form of a Fourier series and based on separation of the variables. Each concentration component  $c_n(z,t)$  which is generated by the corresponding component  $p_n(t) = P_n e^{in\omega t}$  of the pickup function was found to have the form

$$c_n(z,t) = \frac{P_n}{w_o \alpha_n} e^{-\alpha_n \frac{w_o z}{\epsilon_s}} e^{in\omega t} \quad (12)$$

where

$$\alpha_n = \frac{1}{2} + \sqrt{\frac{1}{4} + i \frac{n\omega \epsilon_s}{w_o^2}} \tag{13}$$

Alternatively Equation (12) may be written

$$c_n(z,t) = \frac{P_n}{w_o |\alpha_n|} e^{-Re\{\alpha_n\} \frac{w_o z}{\epsilon_s}} \cos(n\omega t - Arg\{\alpha_n\} - Im\{\alpha_n\} \frac{w_o z}{\epsilon_s}) \tag{14}$$

or with a slight rearrangement of the phase of the cosine function

$$c_n(z,t) = \frac{P_n}{w_o |\alpha_n|} e^{-Re\{\alpha_n\} \frac{w_o z}{\epsilon_s}} \cos [n\omega (t - \frac{Im\{\alpha_n\} w_o}{n \omega \epsilon_s} z) - Arg\{\alpha_n\}]$$

which shows that in a diffusion process with constant diffusivity, a concentration wave with radian frequency  $n\omega$  travels upwards with speed  $w_n = \frac{n \omega \epsilon_s}{w_o Im\{\alpha_n\}}$ . The behaviour of the solution (14) is illustrated in Figure 5 for the case of  $p(t) \sim w_o \cos^6(\omega t/2)$ .

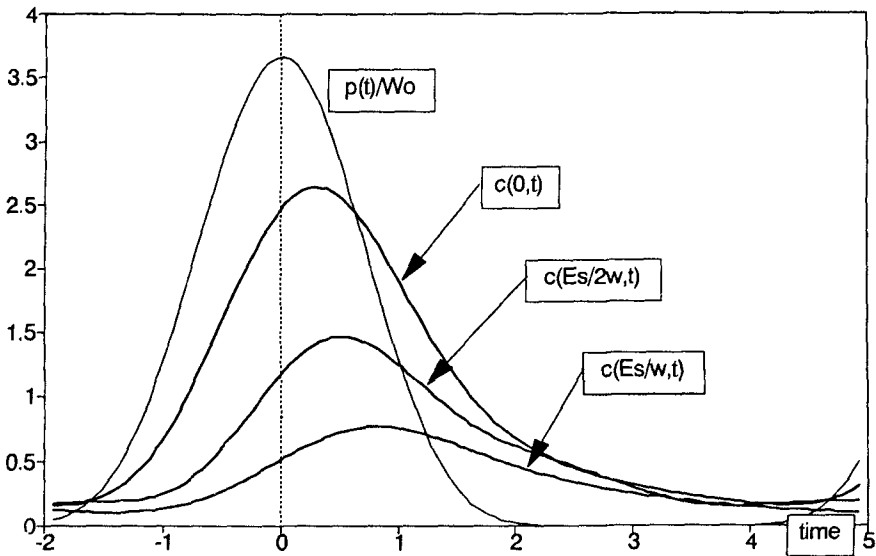


Figure 5: Sediment concentrations at different levels ( $0, \frac{\epsilon_s}{2w_o}$  and  $\frac{\epsilon_s}{w_o}$ ) generated by the shown, periodic pickup function and pure gradient diffusion with constant diffusivity and  $\omega \epsilon_s / w_o^2 = 1$

**6. Time dependent concentrations in pure convection**

For the case of purely convective entrainment we set  $\epsilon_s = 0$  in Equation (4) and get

$$\frac{\partial c}{\partial t} - w_o \frac{\partial c}{\partial z} = \frac{1}{w_c} p'(t - \frac{z}{w_c}) F(z) - p(t - \frac{z}{w_c}) F'(z) \quad (15)$$

For the simple case of  $F(z) = \exp(-z/L)$  this equation has a Fourier series solution, which corresponds to (12), with

$$c_n(z,t) = C_n e^{-\beta_n z/L} e^{in\omega t} \quad (16)$$

where

$$C_n = \frac{P_n}{w_o} \frac{\beta_n}{\beta_n + i \frac{n\omega L}{w_o}} \quad \text{and} \quad \beta_n = 1 + i \frac{n\omega L}{w_c} \quad (17)$$

cf Nielsen (1992) p 240. In analogy with (14) this solution can be written as

$$c_n(z,t) = |C_n| e^{-z/L} \cos[n\omega(t - z/w_c) + \text{Arg}\{C_n\}] \quad (18)$$

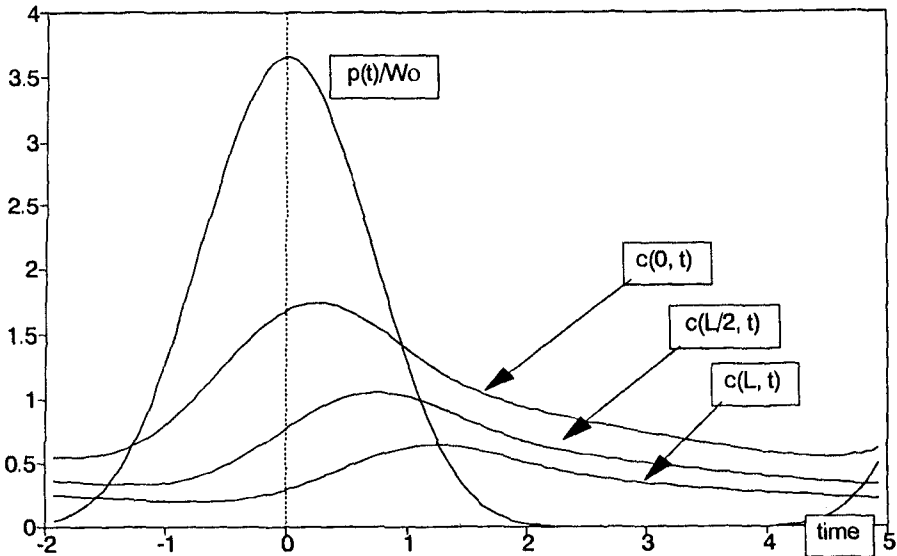


Figure 6: Sediment concentrations at different levels generated by the shown pickup function and purely convective entrainment.  $F(z) = \exp(-z/L)$  and  $\omega L/w_c = 1$ .

This expression illustrates that all the harmonics of the pure convection solution decay at the same rate (as  $F(z)$  in general, and as  $\exp(-z/L)$  in this particular case), and that all time lags grow at the same rate with  $z$ . Compared with the diffusion case, this corresponds to a greater shape similarity between time series at different elevations for the convective case. The nature of the convection solution is illustrated in Figure 6 for the case of  $p(t) \sim w_o \cos^6(\omega t/2)$  (same as for the diffusion solution in Figure 5).

7. Comparison with measured time series

Consider the situation where simultaneous time series  $c(z_i,t)$  have been measured at a number of levels, and one wishes to infer the nature of the sediment entrainment process.

Before such an analysis is undertaken using the framework above one should note, that what has been measured by a point (or line) sensor and what is modelled above as  $c(z_i,t)$  are not conceptually identical. The model assumes horizontal uniformity while the sensor samples from a spotted carpet of concentrations  $c(x,y,z_i,t)$  which move back and forth with the waves. Thus, some of the time variation seen by the sensor is not modelled, and is indeed, not a feature of the horizontally averaged concentration  $c(z_i,t)$ . If the measurements have been taken close to a bed with strong topographical features the difference may be very significant. The problem may be amended (at least in part) by averaging over several sensors in the same horizontal plane or by using line sensors which average over one or more bedform lengths.

Assume now that concentration time series  $c(z_i,t)$  have been measured by such an array of sensors that the abovementioned "spotted carpet effect" is neutralised, and that that the corresponding Fourier series have been obtained

$$\begin{aligned}
 c(z_i,t) &= \sum_0^\infty c_n(z_i,t) = \bar{c}(z_i) + \sum_{n=1}^\infty A_{i,n} \cos n\omega t + B_{i,n} \sin n\omega t \\
 &= \bar{c}(z_i) + \sum_1^\infty R_{i,n} \cos(n\omega t - \varphi_{i,n})
 \end{aligned}
 \tag{19}$$

where  $R_{i,n} = \sqrt{A_{i,n}^2 + B_{i,n}^2}$  and  $\varphi_{i,n} = \tan^{-1} \left( \frac{B_{i,n}}{A_{i,n}} \right)$ .

First consider the possibilities of deriving information about  $\epsilon_s$ ,  $\bar{p}$  and  $F(z)$  from the time averaged concentrations. The time-averaged continuity equation (7) can, if  $\bar{c}(z)$  and  $w_o$  are known, be seen as having two unknowns namely  $\epsilon_s(z)$  and  $\bar{p}F(z)$ . Thus,  $\epsilon_s(z)$  and  $\bar{p}F(z)$  cannot be determined from this equation alone. Additional information is needed. Such information can be sought along different lines.

Firstly, it may be that  $\epsilon_s(z)$  can be inferred from knowledge about the



eddy viscosity  $\nu_t$ . Indeed, one of the benefits of the combined convection diffusion model is that one should be able to assume identity between diffusivity and eddy viscosity.

Alternatively, if concentration profiles  $\bar{c}_1(z)$  and  $\bar{c}_2(z)$  of two different sand sizes with settling velocities  $w_1$  and  $w_2$  are known, we have at each level two equations (two versions of (7)) for finding the two unknowns  $\epsilon_s(z)$  and  $\bar{p}F(z)$ . Unfortunately, such detailed datasets are rare at present.

Thirdly, as pointed out by Nielsen (1992) p 248,  $\bar{p}F(z)$  may be inferred from the shape of  $\bar{c}(z)$  alone for very coarse sand fractions. This is done simply by neglecting the second term in Equation (7).

Most of the available data on suspended sediment concentrations contain too little detail for the analysis outlined above. Usually, the measured concentrations are compounded by a fairly wide distribution of grain sizes and no information is available about the contributions from individual, narrow size fractions. Furthermore, much of the time series data obtained with optical or acoustical instruments suffer from uncertainty about the absolute magnitude of the concentrations.

However, some information can be extracted about the nature of the entrainment process even from such data. Assume that Fourier series of the form (19) have been obtained from at least two different levels and that the settling velocity distribution of the suspended material is narrow. Then the phase shifts and magnitudes of different Fourier components will show quite different developments in the two cases of pure gradient diffusion and purely convective entrainment.

It may be seen from the expressions (12) and (13) that the magnitudes of different Fourier components decay at different rates in a pure diffusion process with constant diffusivity. The decay rates are given by

$$\frac{d \ln|c_n|}{dz} = -\text{Re}\{\alpha_n\} \frac{w_0}{\epsilon_s} \quad (20)$$

which is an increasing function of the frequency  $n\omega$ . In contrast, in the case of purely convective entrainment, all components decay at the same rate, namely as  $F(z)$ . For  $F(z) = \exp(-z/L)$  this means

$$\frac{d \ln|c_n|}{dz} = -1/L \quad \text{for all } n \quad (21)$$

The growth of the phase lags  $\varphi_n(z)$  are also different for the two types of processes. For the gradient diffusion process with constant diffusivity, Equation (14) tells us that

$$\frac{d \varphi_n}{dz} = -\text{Im}\{\alpha_n\} \frac{w_0}{\epsilon_s} \quad (22)$$

while Equation (16) for the convection process with  $F(z) = \exp(-z/L)$  gives

$$\frac{d \varphi_n}{dz} = - \operatorname{Im}\{\beta_n\} \frac{1}{L} = - \frac{n\omega}{w_c} \tag{23}$$

corresponding to the same time lag for all components as was also indicated by Equation (18).

If relative increments

$$Y = \frac{\varphi_n(z_i) - \varphi_n(z_j)}{\ln \bar{c}(z_j) - \ln \bar{c}(z_i)} \tag{24}$$

of the phase shifts  $\varphi_n$  are plotted against the relative increments

$$X = \frac{\ln |c_n(z_j)| - \ln |c_n(z_i)|}{\ln \bar{c}(z_j) - \ln \bar{c}(z_i)} = \frac{\ln R_{j,n} - \ln R_{i,n}}{\ln \bar{c}(z_j) - \ln \bar{c}(z_i)} \tag{25}$$

of  $\ln |c_n|$  as in Figure 7, the result for a pure diffusion process will trace the hyperbola branch  $Y = \sqrt{X^2 - 1}$ ,  $x > 0$  which is the locus for  $\alpha_n$  in the complex plane. For the pure convection case, the points will trace the vertical line  $X = 1$ ,  $Y > 0$ , which is the locus of  $\beta_n$ .

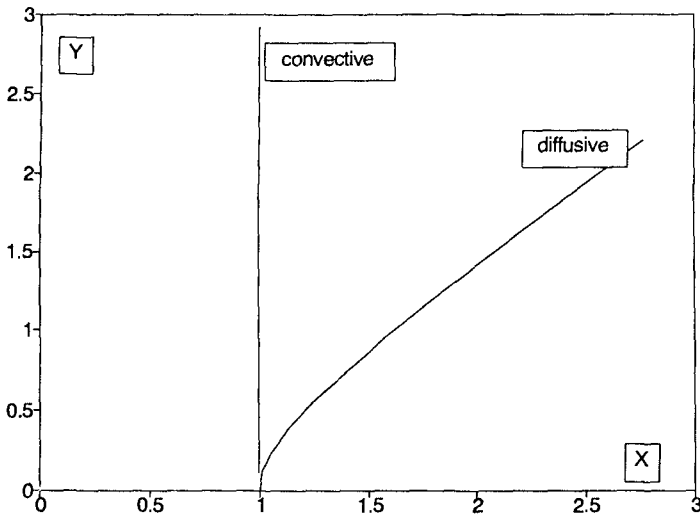


Figure 7: The relative decay rates (X) and phase lag increments (Y) defined by (25) and (24) correspond respectively to the parameters  $\alpha_n$  in pure diffusion with constant  $\varepsilon_s$  and, to  $\beta_n$  for purely convective entrainment with  $F(z) = \exp(-z/L)$ . For details about  $\alpha_n$  see Nielsen (1979), p 131.

Finally, we note that information about the convective entrainment velocity  $w_c$  may be found simply by considering the time difference between the occurrence of identifiable peaks at different levels, cf Equation (18). If a peak arrives at  $z_i$  at time  $t_i$  and at  $z_j$  at time  $t_j$ , the corresponding  $w_c$  in a purely convective entrainment process is given by

$$w_c = \frac{z_j - z_i}{t_j - t_i} \tag{26}$$

In contrast to the convective entrainment process considered above, the upward propagation speed of a concentration wave in a diffusive medium is frequency dependent as mentioned in connection with Equation (14). For constant diffusivity, the speed  $w_n$  of a concentration wave with frequency  $n\omega$  is given by

$$w_n = \frac{n\omega\epsilon_s/w_0}{\text{Im}\{\alpha_n\}} \tag{27}$$

or

$$\frac{w_n}{w_0} = \frac{n\omega\epsilon_s/w_0^2}{\text{Im}\{\alpha_n\}} = \frac{n\omega\epsilon_s/w_0^2}{\text{Im}\left\{\frac{1}{2} + \sqrt{\frac{1}{4} + i\frac{n\omega\epsilon_s}{w_0^2}}\right\}} \tag{28}$$

the behaviour of which is illustrated in Figure 8. In the limit of  $w_0 \rightarrow 0$  i.e. for neutrally buoyant sediments or momentum, the value of  $w_n$  is simply  $\sqrt{2 n \omega \epsilon_s}$ .

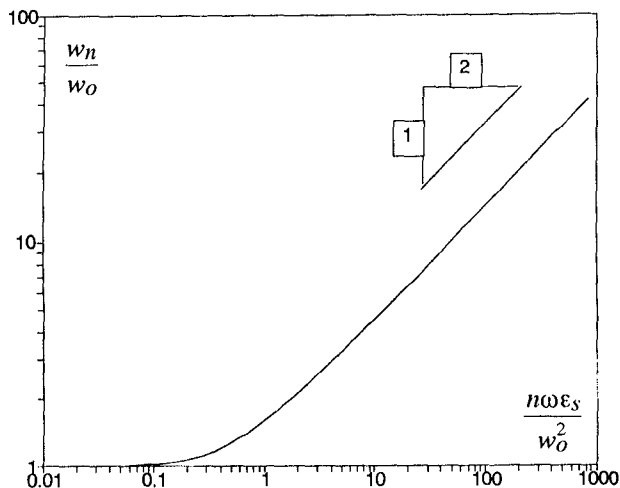


Figure 8: Dependence of  $w_n$  on  $n\omega\epsilon_s/w_0^2$  in a pure gradient diffusion process with constant diffusivity.

## 8. References

- Bosman J J** (1982): Concentration measurements under oscillatory water motion. *Delft Hydraulics rep M1695*, part 2.
- Ribberink, J S & A Al-Salem** (1989): Bedforms, near-bed sediment concentrations and sediment transport in simulated regular wave conditions. *Delft Hydraulics Tech Rep no 840*.
- Horikawa K, A Watanabe & S Katori** (1982): Sediment transport under sheet flow condition. *Proc 18th Int Conf Coastal Eng*, Capetown, pp 1335-1352.
- McFetridge, W F & P Nielsen** (1985): Sediment suspension by non-breaking waves over rippled beds. *Tech Rep COEL- 85/005*, Coastal and Oceanographical Eng Dept, Univ of Florida, 132 pp.
- Nadaoka, K, S Ueno, & T Igarashi** (1988): Sediment suspension due to large eddies in the surf zone. *Proc 22nd Int Conf Coastal Eng*, Malaga, pp 1646-1660.
- Nielsen, P** (1983): *Some basic concepts of wave sediment transport*. Series paper 20, Institute of Hydrodynamics and Hydraulic Engineering (ISVA), Technical Univ Denmark.
- Nielsen, P** (1983): Entrainment and distribution of different sand sizes in the same flow. *J Sedimentary Petrology*, Vol 53, No 2, pp 423-428.
- Nielsen, P** (1991): Combined convection and diffusion: A new framework for suspended sediment modelling, *Proc "Coastal Sediments '91"*, Seattle, pp 418-431.
- Nielsen, P** (1992): *Coastal bottom boundary layers and sediment transport*. World Scientific, Singapore, 324 pp.
- Nielsen, P, I A Svendsen & C Staub** (1978): Onshore-offshore sediment transport on a beach. *Proc 16th Int Conf Coastal Eng*, Hamburg, pp 1475-1492.
- van de Graaff, J** (1988): *Sediment concentration due to wave action*. Dr Eng Thesis, Dept of Civil Engineering, Delft University of Technology.

## CHAPTER 246

### MOVEMENTS OF MOORED SHIPS IN HARBOURS

Th. Elzinga<sup>1</sup>, J.R. Iribarren<sup>2</sup>, O.J. Jensen<sup>3</sup>

#### ABSTRACT

The paper discusses criteria for safe working and safe mooring conditions for various types of seagoing vessels. These criteria are based on acceptable movements for moored ships in harbours and have been established by a working group under the Permanent International Association of Navigation Congresses (PIANC).

#### INTRODUCTION

Modern maritime transport requires minimum time for loading and unloading in ports and at maritime terminals, a requirement often restricted by ship movements at quays. If the ship movements experienced are too large, cargo handling operations will slow down or even cease and ultimately damage to the ship and port installations may occur. In recent years changes in cargo handling methods have resulted in changes of both ship and port installations, changes which may have large economic consequences. Requirements for fast cargo handling operations without delays due to ship motions are increasing.

---

<sup>1</sup> Frederic R. Harris B.V., Badhuisweg 11, 2387 CA The Hague, The Netherlands

<sup>2</sup> Centro de Estudios y Experimentación de Obras Públicas (CEDEX), Alfonso XII, 3-280014, Madrid, Spain

<sup>3</sup> Danish Hydraulic Institute (DHI), Agern Allé, Hørsholm, Denmark.

The Permanent International Association of Navigation Congresses (PIANC) therefore commissioned a special Working Group to study the movements of moored ships in harbours with the aim to establish new criteria for acceptable ship motions in safe working conditions (i.e. when cargo handling operations have to be reduced or even ceased), as well as for safe mooring conditions (i.e. when ships have to leave the berths). Further, it was the aim to assess measures for improving safe working and safe mooring conditions. The main objective in establishing criteria was to provide guidelines for port designers and port operators to minimize downtime for ships in harbours.

The Working Group comprised 14 international members (see Appendix A) and commenced in June 1990. The final report will be published by PIANC in spring 1993. This paper summarises the main findings and conclusions of the Working Group.

### **METHODOLOGY**

The world fleet of ships is divided into the following categories, each category having its own typical characteristics in view of ship motions and cargo handling operations and safe mooring conditions:

- Small craft and pleasure boats.
- Fishing vessels.
- Freighters and coasters.
- Ferries and RO-RO vessels.
- General cargo vessels.
- Container vessels.
- Bulk carriers.
- Oil tankers.
- Gas tankers

For each category the following aspects have been assessed by the Working Group:

- i. Description of the vessels, typical sizes, composition of world fleet, future trends and provisions for mooring outfits on board (positions of winches and fairleads, composition of mooring lines: number, type, diameter).
- ii. Description of typical berths and cargo handling equipment (e.g. types of cranes, ramps, loading arms).

- iii. Description of governing parameters for ship motions, cargo handling operations, efficiency and safety.
- iv. Review and assessment of available literature, including recent test results and prototype measurements.
- v. Recommendations for acceptable ship motions, mooring and fender line forces at berths in safe working and safe mooring conditions, taking into account a reduced efficiency in cargo handling in case of worsening weather.
- vi. Recommendations for improvement of operation and efficiency with respect to berth location and orientation, application of operational criteria for wind and waves, implementation of dedicated berths and modification of mooring arrangements.

## **SHIP MOVEMENTS**

Movements of moored ships can be caused by various external influences such as: winds, currents, waves, seiches, tides, passing ships and cargo handling operations. The report of the Working Group addresses the effects of these parameters on the behaviour of a moored ship. One chapter in particular deals with the physics of ships moored in waves and discusses the use of mathematical and physical models in this respect.

The movements of a moored ship at a berth can be either horizontal (surge, sway and yaw) or vertical (roll, pitch and heave). Vertical ship motions are almost independent of the mooring system, but horizontal motions are typically dependent on the loading conditions of a ship, the mooring arrangements, i.e. geometry and stiffness of mooring lines and fenders, and the type of berth.

When ship movements are too large safe working limits and ultimately safe mooring limits are exceeded. This is illustrated in Figure 1 where the cargo handling efficiency is plotted against the ship motions. When ship motions are between A and B the cargo handling efficiency is 100%. Between B and C cargo handling rates are reduced due to increased ship motions. When the motions exceed level C cargo handling operations are stopped: the safe working limits are reached. Between C and D the vessel can still stay at the berth. Once ship motions exceed level D the vessel has to leave the berth in order to prevent damage to ship and/or quay: safe mooring limits are exceeded.

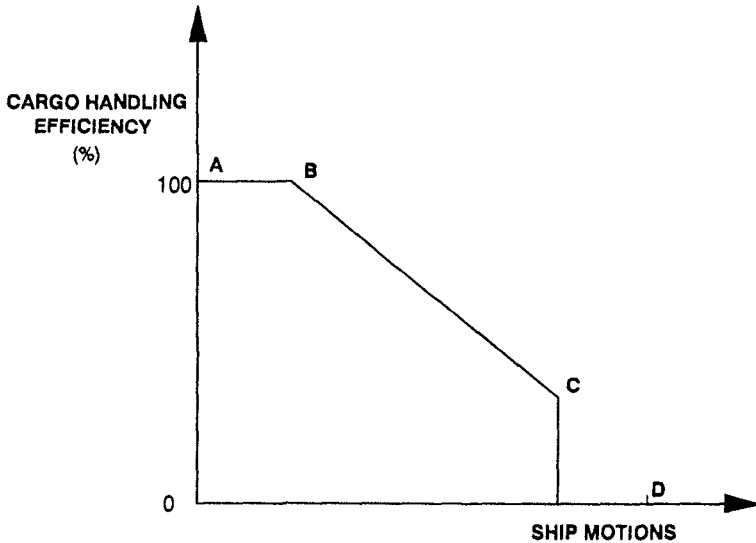


Figure 1. Relation Cargo Handling Efficiency and Ship Motions.

It should be noted that ship motion is one parameter affecting the efficiency of cargo handling operations. Other parameters are, amongst others, cargo handling equipment, skill of crane operators, and operational conditions such as wind, rain, ice, day- and nighttime (light conditions).

### MOORING ARRANGEMENTS

The mooring arrangements for ships moored at berths may comprise the following elements:

- Mooring lines connecting ships to berths
- Bollards and storm bits on shore.
- Mooring hooks or quick release mooring hooks on mooring and breasting dolphins.
- Fenders between ship and berth.
- Mooring winches and bollards on board the ships.



The report of the Working Group contains a brief description of type and characteristics of mooring lines and fenders, mooring arrangement principles and operational considerations for mooring lines. Further, the report discusses the guidelines as issued by various classification societies concerning the number and type of mooring lines to be carried on board. It was felt that an update of these guidelines would be useful. Such new guidelines should reflect that a moored ship is a dynamic system having special requirements with respect to safe working as well as safe mooring conditions.

### **SMALL CRAFT AND PLEASURE BOATS**

Small craft and pleasure boats may be defined as boats with lengths up to 20m. Moored boats are particularly sensitive to short period waves coming from abeam or quartering directions. Their berths require a sheltered location to prevent damage to ships and quays as well as to increase the comfort of passengers on board. In designing harbours for pleasure boats and small craft due attention should be given to the effect of locally generated wind waves having short fetch lengths.

The Working Group has defined acceptable ship motion criteria in terms of wave height and period, because it was felt that these parameters would reflect sufficiently the comfortability criteria for these boats. The criteria are reported in Table 1 and correspond to an acceptable exceedance frequency of once to a few times per year.

### **FISHING VESSELS**

Fishing vessels range from small ships of 10-100 GRT up to large trawlers liners and net boats of 3,000 GRT. These vessels are mainly berthing in their home ports and the berths and mooring arrangements should meet the criteria for safe working as well as safe mooring conditions.

Fishing vessels are typically moored with polypropylene lines against truck tire fenders or rubber fenders. Cranes, elevators and suction pumps are used for unloading the fish. Acceptable ship motion criteria for safe working conditions are determined by sizes of hatches and the dimensions of boxes and tubs handled.

Table 1: Recommended wave criteria small craft and pleasure boats.

Ship Length (m)	Beam/Quartering Seas		Head Seas	
	Period (s)	Height $H_s$ (m)	Period (s)	Height $H_s$ (m)
4 - 10	< 2	0.20	< 2.5	0.20
	2 - 4	0.10	2.5 - 4	0.15
	> 4	0.15	> 4	0.20
10 - 16	< 3	0.25	< 3.5	0.30
	3 - 5	0.15	3.5 - 5.5	0.20
	> 5	0.20	> 5.5	0.30
20 m	< 4	0.30	< 4.5	0.30
	4 - 6	0.15	4.5 - 7.0	0.25
	> 6	0.25	> 7.0	0.30

An extensive research program was carried out by the Nordic countries to establish acceptable criteria of moored fishing vessels. Motions of moored ships were measured at a number of ports for various ships being unloaded by different gear. Acceptable motions were determined based on interviews with ship crews and port operators ( Jensen et al, 1990) and are shown in Table 2.

Requirements for safe mooring conditions for these home port fleets are rather high. In many cases there is no other alternative than to stay in the port once a storm has reached the site. The recommended criteria comprise ship motions as well as velocities and are presented in Table 3 for various ship sizes. Velocities and ship sizes represent the dynamic impact of a moored ship on a berth and are considered adequate parameters regarding safe mooring conditions.

Table 2. Recommended motion criteria<sup>1</sup> for safe working conditions.

Ship Type	Cargo Handling Equipment	Surge (m)	Sway (m)	Heave (m)	Yaw (°)	Pitch (°)	Roll (°)
Fishing vessels	Elevator crane	0.15	0.15				
	Lift-on-Lift-off	1.0	1.0	0.4	3	3	3
	Suction pump	2.0	1.0				
Freighters, coasters	Ship's gear	1.0	1.2	0.6	1	1	2
	Quay Cranes	1.0	1.2	0.8	2	1	3
Ferries, RO-RO	Side ramp <sup>2</sup>	0.6	0.6	0.6	1	1	2
	Bow/stern ramp	0.8	0.6	0.8	1	1	4
	Linkspan	0.4	0.6	0.8	3	2	4
	Rail ramp	0.1	0.1	0.4	-	1	1
General cargo	--	2.0	1.5	1.0	3	2	5
Container vessels	100% efficiency	1.0	0.6	0.8	1	1	3
	50% efficiency	2.0	1.2	1.2	1.5	2	6
Bulk carriers	Cranes	2.0	1.0	1.0	2	2	6
	Elevator/bucket-wheel	1.0	0.5	1.0	2	2	2
	Conveyor belt	5.0	2.5		3		
Oil tankers	Loading arms	3.0 <sup>3</sup>	3.0				
Gas tankers	Loading arms	2.0	2.0		2	2	2

- Remarks:
- <sup>1</sup> Motions refer to peak-peak values (except for sway: zero - peak).
  - <sup>2</sup> Ramps equipped with rollers.
  - <sup>3</sup> For exposed locations 5.0 m (regular loading arms allow large movements).

Table 3. Recommended velocity criteria<sup>1</sup> for safe mooring conditions.

Ship size (DWT)	Surge (m/s)	Sway (m/s)	Heave (m/s)	Yaw (°/s)	Pitch (°/s)	Roll (°/s)
1,000	0.6	0.6	-	2.0	-	2.0
2,000	0.4	0.4	-	1.5	-	1.5
8,000	0.3	0.3	-	1.0	-	1.0

<sup>1</sup> These criteria are applicable for fishing vessels, coasters, freighters, ferries and RO-RO vessels.

A unique system of berth and port classifications has been developed in Iceland, which is based on various exceedance frequencies for critical ship motions as presented in Table 2.

### **COASTERS AND FREIGHTERS**

Coasters and freighters are ships of less than 10,000 DWT sailing on short sea and domestic routes. These vessels are generally moored with polypropylene lines against rubber fenders.

Cargoes can be handled by quay cranes or ship's own gear. Safe working conditions are determined by hatch openings and cargo parcel sizes. The criteria recommended by the Working Group are based on the studies carried out by the Nordic countries as discussed earlier and are shown in Table 2.

### **FERRIES AND RO-RO VESSELS**

Vessel types considered comprise car and rail ferries, and RO-RO vessels. These vessels are characterised by loading and unloading operations taking place horizontally via ramps and walkways. Ramps may be shore ramps, bridge ramps (including link-spans) and ship ramps.

The main function of the mooring arrangements for these ships is to reduce the horizontal ship motions as much as possible, in particular at the position of the ramps or walkways. This can be achieved by tensioning the mooring lines, sometimes up to 40 tonnes.

Recommended criteria for allowable ship motions for safe working conditions are presented in Table 2. In addition, for movable rail ramps and for walkways, the vertical velocity is recommended not to exceed 0.2 m/s and the vertical accelerations should be less than 0.5 m/s<sup>2</sup>.

The governing parameter for safe mooring conditions, defined as the limiting conditions for damage to ship and/or quay, is the kinetic energy, which is characterised by the ship size and velocities. The recommended velocity criteria are presented in Table 3.

### **GENERAL CARGO VESSELS**

General cargo vessels range typically from 5,000 to 10,000 DWT and may carry a wide variety of cargo. Ships are most often moored with polypropylene lines, while large vessels are equipped with nylon ropes and/or steel wires. Generally these vessels are moored with 8 to 10 lines.

The cargo is handled by ship's gear or quay cranes. Acceptable ship motions in safe working conditions are determined by the sizes of the hatches, sizes of boxes and units handled, and by the type of unloading gear. The criteria recommended by the Working Group are based on an extensive Japanese research program (Ueda, 1987; Ueda and Shiraishi, 1988). These criteria have been established based on interviews with port and ship operators in various ports along the Japanese coast. Numerical simulations were applied to correlate identified critical wind speeds and wave heights with acceptable ship motion limits. Provisional limits were then discussed with various operators and authorities to arrive at the final criteria for safe working conditions as presented in Table 2.

In situations where large general cargo ships are exposed to long period waves, it is recommended to use soft mooring systems, i.e. synthetic lines or steel wires with nylon tails and soft fenders. Smaller vessels should preferably be moored in protected port basins (inner harbour) to reduce wave influences on moored ships.

### **CONTAINER VESSELS**

The world fleet of container vessels has increased considerably during the last decades and comprises nowadays small feeders, second and third generation container vessels as well as Post Panamax vessels, which came into operation recently.

Container vessels are generally moored with steel spring lines, to reduce surge motions, and polypropylene mooring lines. All lines are connected to bollards positioned at the front side of the quay wall. Rails for container cranes extend along the whole quay and prevent the use of typical breasting lines.

Containers are handled by shore based gantry cranes and ship motions should be kept to a minimum to provide uninterrupted container handling conditions. Positioning and picking-up of containers for example are hampered and containers can become stuck in their guides in the case of strong roll motions. Maximum container handling rates are an essential requirement for these ships sailing on tight time schedules.

Two levels of safe-working criteria are established by the Working Group for this special category of ships. One level is representing an uninterrupted container handling at an efficiency rate of 90 to 100%, whereas the second level reflects a 50% handling efficiency rate (see Table 2). It should be noted that besides ship motions the skill of the container crane drivers plays an important role for the overall efficiency of handling containers in a port.

### **DRY BULK CARRIERS**

Dry bulk carriers have been developed to transport cargoes such as ore, coal, grain and fertilizer in bulk and mostly in large quantities. Some typical sizes for bulk carriers are the Handy size (30,000-40,000 DWT), Panamax size (70,000-80,000 DWT) and CAPE size (120,000-150,000 DWT).

Bulk carriers are mainly moored with 8 to 10 synthetic lines and 4 steel spring lines. Mooring lines are attached to bollards located at the front side of the quay walls for the same reasons as for the container vessels. Loading operations are generally carried out using conveyors and hoses (grains). For unloading operations cranes, bucket-wheel unloaders, elevators and suction devices are used. A special category of bulk carriers is nowadays the so-called self-unloading bulk carrier. Horizontal ship motions are mainly induced by low frequency waves (and winds). Vertical ship motions are mainly caused by first order wave effects.

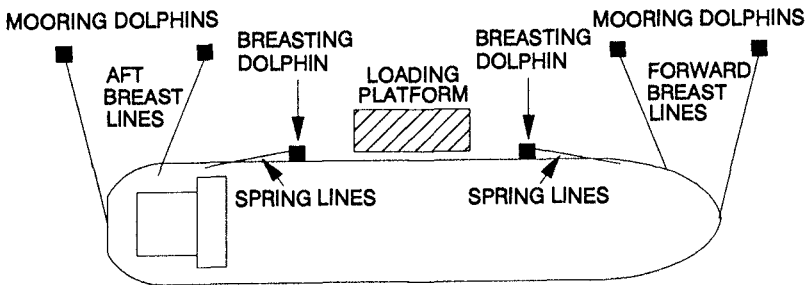
Operational criteria for cargo handling are determined by the risk of cargo handling equipment hitting the hatches or ship's bottom. This is of particular importance for unloading operations. The safe working criteria for bulk carriers recommended by the Working Group are based on practical experiences of port and ship operators (Bruun 1987, Moes 1992), supported by numerical simulations (Ueda and Shiraishi 1988). These criteria are presented in Table 2. Safe mooring conditions are determined by acceptable mooring line and fender forces (BSRA 1969 and OCIMF 1978).

Cargo handling operations may be improved by the application of softer springs and by the use of shore based mooring equipment, particularly when moored ships are exposed to long period wave actions. Further, pretensioning of mooring lines will result in an increase of fender friction and will contribute in reducing surge motions. Particular attention should be paid to the resonance of long waves in harbours (seiches) when designing basins for dry bulk vessels.

**OIL TANKERS**

Oil tankers are used to transport oil and oil products. Oil products are generally transported in tankers under 70,000 DWT, while crude oil is transported in high capacity tankers up to 420,000 DWT. Tankers are loaded and unloaded through the manifold located in the middle and close to the side of the ships. The manifold is connected to the pipelines onshore by loading arms and sometimes by flexible hoses.

A typical berth lay-out for an oil tanker is shown in Figure 2 and comprises breasting and mooring dolphins, and a loading platform. Tankers are moored with spring lines, breast lines and (optionally) head and stern lines. The mooring lines for large tankers are in general steel wires and steel wires with nylon tails. The OCIMF (OCIMF, 1978) has issued guidelines for jetties and mooring arrangements of oil tankers, as well as for the design and operation of loading arms (OCIMF, 1980).



**FIGURE 2. TYPICAL BERTH LAY-OUT FOR TANKERS**

The motions of moored tankers are characterised by low frequency horizontal motions (with typical periods of 1 to 2 minutes) caused by long period wave effects, and relative high frequency vertical motions with periods ranging from 5 to 20 s.

Operational cargo handling criteria are determined by the allowable reach of the loading arms in the surge (longitudinal) and sway (transversal) direction. Other tanker motions are generally well within the design motion envelopes of the loading arms. The criteria recommended for safe working conditions are shown in Table 2.

Berths for large tankers are generally located in deep water and at more exposed locations. Due attention should be given to align a berth with predominant wave and current conditions. Tanker motions may be reduced by pretensioning the breast lines in order to maintain sufficient friction between the ship's hull and fenders.

### **GAS TANKERS**

Gas tankers may range from refrigerated ships of over 100,000 m<sup>3</sup> for the transportation of LNG and LPG to small tankers of up to 5,000 m<sup>3</sup> for the shipment of propane, butane and chemical gases in pressure tankers. The number of gastankers in the world fleet is relatively small; some 780 in 1991.

Berths for LNG and LPG tankers are generally designed for dedicated ships and trades, whereas berths of small gas tankers are multi-functional. The berths and mooring arrangements for gastankers are similar to the ones for oil tankers (Figure 2). Comprehensive guidelines for berths and gas tanker moorings are issued by OCIMF/SIGTTO (1985).

Motions of moored gastankers are in particular induced by currents and low frequency wind and wave effects. Wind effects on gastankers are more important compared to oil tankers because of higher freeboard and the presence of spherical tanks. Acceptable motions are determined by restrictions in the cargo handling systems (i.e. loading arms) and mooring line and fender forces (hull pressure). Recommended values for tanker motions are presented in Table 2.

Particularly for gas and oil tanker berths it is important to establish Operational Manuals including, amongst others, guidelines for mooring arrangements and safety operations as well as checklists to improve the safety of cargo handling operations.

### **ACKNOWLEDGEMENTS**

The authors are very grateful for the permission of the members of the Working Group "Movements of Moored Ships at Berths" as listed in Appendix A to prepare this paper. Without their work and enthusiasm the Working Group would not have completed its task and the data necessary for this paper would not have been collected.



**APPENDIX A. MEMBERS PIANC WORKING GROUP 24****MOVEMENTS OF MOORED SHIPS AT BERTH**

<b>Country</b>	<b>Name</b>	<b>Company</b>
Belgium	H. Smits	Dienst Ontwikkeling Linker Scheldeoever, Antwerp
Denmark	O. J. Jensen (Chairman)	Danish Hydraulic Institute <sup>1</sup> , Hørsholm
	J. M. Thompson	Comar Engineers A/S, Virum
Faroe Islands	S. Heinesen	Landsverkfrødingurin, Torshavn
France	P. Hébert	Port Autonome du Havre, Le Havre
Iceland	G. Viggósson	Icelandic Harbour Authority, Reykjavik
Italy	L. Bolatti Guzzo	Estramed S.P.A., Rome
Japan	S. Ueda	Port and Harbour Research Institute, Min. of Transport
The Netherlands	Th. Elzinga	Frederic R. Harris B.V., The Hague
	S.Th. Schuurmans	Delft Hydraulics, Delft
Norway	S. Bjørdal	Norsk Hydroteknisk Laboratorium, Trondheim
South Africa	H. Moes	Counsel for Scientific and Industrial Research (CSIR), Stellenbosch
Spain	J.R. Iribarren	Centro de Estudios y Experimentación de Obras Públicas (CEDEX), Madrid
United Kingdom	E. Bowers	Hydraulics Research, Wallingford

<sup>1</sup> Danish Hydraulic Institute also provided the secretary Mr. M. Hebsgaard

**APPENDIX B. REFERENCES**

Bruun P. (1987) Marine Terminal Technology, Winch Berthing and Mooring Methods, Recent Developments. Proceedings NATO Advanced Study Institute on Advances in Berthing and Mooring of Ships and Offshore Structures, Trondheim, pp 31 - 61.

BSRA (1969) Research Investigation for the Improvement of Ship Mooring Methods; Second Report, Tankers and Bulk Carriers, Existing Tonnage and New Construction. BSRA Report NS 256.

Jensen O.J. Viggósson G., Thomson J., Bjørdal S., Lundgren J. (1990). Criteria for Ship Movements in Harbours. Proceedings of the International Conference on Coastal Engineering, Venice.

Moes H. (1992) Acceptable Ship Motions for Loading Bulk Carriers In South Africa. Written Contribution to the Working Group 24, Madrid.

OCIMF: Oil Companies International Marine Forum (1978). Guidelines and Recommendations for the safe Mooring of Large Ships at Piers and Sea Islands, London. ISBN 0 900866 33 1.

OCIMF: Oil Companies International Marine Forum (1980). Design and construction Specification for Marine Loading Arms, London.

SIGTTO: Society of Gas Tankers and Terminal Operators (1986). Liquefied Gas Handling Principles on ships and in Terminals, London. ISBN 0 900886 93 5.

Ueda S. (1987). Motions of Moored Ships and their Effect on Wharf Operation Efficiency. Report of the Port and Harbour Research Institute. Vol. 26, No. 5, pp 319-373.

Ueda S. and S. Shiraishi (1988). Allowable Ship Motions for Cargo Handling at Wharves. Report of the Port and Harbour Research Institute. Vol. 27, No. 4, pp 3-61

## CHAPTER 247

### WAVE AGITATION CRITERIA FOR FISHING HARBOURS IN ATLANTIC CANADA

Charles P. Fournier<sup>1</sup>, Michael W. Mulcahy<sup>2</sup>, K. Ander Chow<sup>1</sup>, Otavio J. Sayao<sup>1</sup>, M.ASCE

**ABSTRACT:** The existing criteria for defining allowable levels of wave agitation in Canadian harbours are outlined in the Guidelines of Harbour Accommodation (Fisheries and Oceans). These criteria were developed based on a previous study which concentrated primarily on recreational harbours. However, it was realized that fishing vessels, when berthed or moored, may be able to tolerate a greater degree of wave agitation than pleasure craft because of the different characteristics and functions of the two types of vessels. Furthermore, fishermen tend to have more liberal tolerance limits to wave agitation than pleasure craft owners, and have more rugged craft. To develop new allowable wave agitation criteria for commercial fishing harbours in Atlantic Canada, a field measurement programme was conducted in selected harbours. The objective was to determine the threshold values at which the wave climate at both the service/offloading area and mooring area creates either dangerous, difficult or unacceptable working conditions. This was determined to be the point at which operations must cease or the vessel had to be removed to a more protected area. Wave measurement gauges were installed at two locations within two study harbours, and a wave rider buoy was used to measure nearshore waves for each harbour site. A procedure was also developed whereby daily field observations were taken and recorded by the harbour master. Particular emphasis was given to the wave climate events which rendered the facilities less than adequate, unsafe or unusable. By correlating the harbour masters field observations with the measured wave data, the threshold values for unacceptable wave agitation were determined, and new wave agitation criteria for fishing harbours recommended.

#### INTRODUCTION

The criteria (and practice) for defining allowable levels of wave agitation in Canadian harbours prior to 1991 were developed by the Small Craft Harbours Directorate (SCHD), and are

---

<sup>1</sup> Atria Engineering Hydraulics Inc., 8 Stavebank Rd. N., Suite 301, Mississauga, Ontario, Canada, L5G 2T4.

<sup>2</sup> Fisheries & Oceans Canada, Small Craft Harbours Branch, 200 Kent St., Ottawa, Canada

outlined in the Guidelines of Harbour Accommodation by Fisheries and Oceans (F&O, 1985). These criteria were applicable to harbours which fall under the administration of the SCHD and it was customary to follow these criteria for all work undertaken on behalf of the SCHD.

This study (Atria, 1991) was developed with the objective to revise the acceptable wave agitation criteria that have been used by engineers when engaging in the planning and design of fishing harbours. The criteria (F&O, 1985) which specify the agitation requirements within fishing harbours were developed based on a previous study (NHCL, 1980). The 1980 study to determine acceptable wave climates in small craft harbours concentrated primarily on recreational harbours. It was realized that fishing vessels, when berthed or moored, may accept greater degrees of wave activity than pleasure crafts because of the different characteristics and functions of the two types of vessels. Furthermore, fishermen tend to have more liberal tolerance limits to wave agitation than pleasure craft owners. Also, as a rule fishermen have more rugged craft. A reduction in wave agitation criteria could yield optimized protective structures and hence significant savings in capital costs.

The purpose of the present study was to develop new allowable wave agitation criteria for fishing harbours. The scope of the work consisted of: 1) reviewing existing wave agitation criteria for fishing harbours within Canada and abroad; 2) undertaking a field measurement programme in conjunction with the Marine Environment Data Service (MEDS) at two fishing harbours with the aim of establishing the point at which unacceptable wave conditions occur; and 3) recommending new guidelines of accommodation specifically for allowable wave agitation in fishing harbours.

#### EXISTING WAVE AGITATION CRITERIA

The existing wave agitation criteria were obtained by means of a literature review and a questionnaire survey. The questionnaire was sent to various organizations in Canada and foreign countries such as U.S.A., England, Japan, Denmark, Holland and others. Each organization was asked for information regarding guidelines for fishing harbour design in their country as well as the description of the fishing fleet for which their guidelines apply.

Canada: The Guidelines of Harbour Accommodation, developed by the SCHD (F&O, 1985), outline the criteria (and practice) for defining allowable levels of wave agitation in Canadian harbours. These criteria were based on NHCL (1980). Since this study was restricted to recreational craft, directly applying the results of their findings to fishing harbours likely resulted in conservative allowable agitation levels for fishing harbours. Therefore the criteria that were developed and proposed for all harbours (including fishing harbours) are more stringent when applied to fishing harbours than if the study considered fishing harbours alone. It is customary at Public Works Canada and with consulting engineers when undertaking SCHD projects to design the facility such that the agitation levels within the harbour meet the requirements of the guidelines.

The recommended allowable wave agitation criteria (Tables 1 and 2) were determined by classifying harbours by vessel-metres usage. Class A harbour is defined as over 800 vessel-metres, Class B as between 300 and 900 vessel-metres, and Class C between 0 and 400 vessel-metres. The existing guidelines specify that for Class A, B and C harbours, the hours of significant waves which exceed 0.25 m in height at the service/offloading (i.e. berthing) area cannot be greater than 0.17%, 0.87% and 1.74% of the time respectively. For a 6 month season, these % yield 0.3, 1.6 and 3.2 days (respectively) of wave activity in excess of 0.25 m.

Previous to the NHCL study, the widely accepted rule of practice for the design of wave protection for small craft harbours was that the wave height within the harbour should not exceed 0.3 m (1 ft). Of course, if one waits long enough, a storm will occur and will create waves in excess of this limit. Therefore, wave protection is a function not only of a given acceptable value, but also the probability of occurrence (or exceedance) of the value. The NHCL study examined this "one foot" rule and the many variables affecting wave agitation in marinas, and made recommendations towards an improved set of criteria to define acceptability of wave climates within small craft harbours.

**Table 1 Allowable Maximum Significant Wave Height (from F&O, 1985)**

Location	All Recreational Boats	
	Fishing Boats < 15 m	Fishing Boats > 15 m
Within Harbour Entrance	1.00 m	1.00 m
Mooring Basin	0.50 m	1.00 m
Berthing Area	0.25 m	0.50 m

**Table 2 Classification of Harbours (from F&O, 1985)**

Class of Harbour	Percentage of Time when the Wave Height Criteria May Be Exceeded
A	0.17
B	0.87
C	1.74
D	No Limit

In general, their findings revealed that there has been remarkably little research work performed or reported in the literature with respect to wave agitation criteria for small craft harbours or marinas and on response of moored small craft to waves. However, the available literature related to the general subject of marina design, all made reference to wave criteria which came reasonably close to specifying a 0.3 m significant wave height.

United States of America: The ASCE Task Committee on Small Craft Harbours (1969) published a manual on small craft harbours and they recommended simply "in general, wave heights in the mooring basin should be reduced to a maximum of approximately 0.5 ft (0.15 m) to 1 ft (0.3 m)". These criteria were defined with reference to sport and pleasure craft. They stated that: "harbours for commercial fishing boats may be considered a special type of installation. This is due largely to the type of usage, the characteristics and habits of commercial fishermen, and equipment requirements. Usually utility supersedes appearance, because a fishing boat is a work boat and the operator's work in port is essentially preparation for the next trip".

United Kingdom: In England, guidance for wave agitation in harbours is available in the British Standard Code BS6349 (Part 1, 1984). The acceptable wave conditions for moored boats in fishing harbours are given as follows: "since fishing craft are normally larger and more strongly built than pleasure craft the maximum wave height considered as acceptable for boats

up to 30 m in length is 0.8 m. Typically, this makes the maximum acceptable significant wave height 0.4 m. As in the case of pleasure craft, inner harbours or basins are frequently provided for accommodating fishing boats safely."

**Japan:** Japanese fishery ports are administered by the Ministry of Agriculture and Fishery. This Ministry's report "Guide to Planning of Fishery Ports" outlined the range of wave heights available for mooring and water area facilities (Table 3). The wave heights for mooring and water area facilities varies between 0.3 m to 1.2 m (maximum significant). It also stated that the probability of exceedance of these wave heights was not determined. In general, it recommended that ports should be constructed such that the probability of wave heights less than the permitted level becomes more than 97.5% in a year.

Previous to this criteria, the Overseas Coastal Area Development Institute of Japan (1980) recommended that wave agitation was addressed as basin calmness. It stated that a basin in front of a pier (i.e. service/offloading facility) should be calm to allow mooring for 90 to 95 % or more days per year (or each season, when the seasonal variation of calmness is extreme). Calmness was defined as significant wave heights being less than the defined critical wave height. The critical significant wave height for cargo handling in a basin in front of berthing facilities was defined as  $H_s = 0.3$  m for small craft harbours and  $H_s = 0.5$  m to 0.7 m for other craft. It was noted that these criteria may not apply when the frequency of mooring is low such as would be the case with fishing harbours during the fishing season. However, more work on wave agitation in fishing harbours is presently underway in the National Research Institute of Fisheries Engineering (these new publications are in Japanese).

**Table 3 Maximum Significant Wave Height for Mooring and Water Area Facilities**

Water Depth in Anchorage Area	Less than 3 m	More than 3 m
1. anchoring and mooring in a port is possible	0.60 m	0.70 m
2. water way is available	0.90 m	1.20 m
3. loading and unloading is possible	0.30 m	0.40 m
4. quay for rest is available	0.40 m	0.50 m

Source: "Guide to Planning of Fishery Ports, report by the Ministry of Agriculture and Fishery of Japan.

**Nordic Countries:** The Nordic Council (1986) published a research report which established criteria for acceptable ship movements in harbours. When considering wave agitation, they found that loading / unloading methods, pattern of the vessel, mooring and fender system, and the ability of the vessel to escape the harbour during a storm, were important factors.

For fishing vessels, the type of loading / unloading method used was of concern. When unloading trash fish they considered the elevator crane. With this method problems arise due to the size of the hatch. Small movements can cause damage to both the ship and the crane. Vertical ship movements can also cause damage to the ship bottom and to the crane. Another problem arises when the ship collides with the fenders causing fish to slide within the hold, causing danger to people within the hold.

Safe mooring conditions was another topic considered in the Nordic Council (1986) report.

Acceptable mooring conditions were considered to be where no damage occurred to the ship or to the quay. Also, they outlined for taut mooring of fishing vessels different values than the ones given in Table 4. Thus, criteria for safe mooring conditions at berth are given in Table 5. In determining the final criteria for vessel movement when moored at berth, it was assumed that she was well moored and that the quay was well equipped with fenders.

Other Countries: No official guidelines were available from other countries contacted by questionnaires. Some answers mentioned "empirical, often subjective rules" and most European countries quoted the Nordic Council (1986) study. In Holland, no specific guidance on wave agitation for fishing harbours were obtained. Reference was made to the Nordic Council (1986) study. Vlemmix et al. (1987) set out criteria for bulk carriers and outlined the limiting deep water wave heights. In Spain, the only available document on fishing harbours dates back to the 1960's. Marine Trust Ltd. of Israel follows in house rules as criteria for wave agitation. A significant wave height of 80 cm may not be exceeded for more than two days per year. Their experience comes from harbours for small fishing vessels with few trawlers. Other references related to the design of Small Craft harbours using physical models may be found in literature, for example Rosen and Kit (1984) which report on limiting criteria regarding maximum allowable values of vessel movements and fender forces.

In general it appears that the F&O (1985) guidelines may be considered too stringent. It has the lowest acceptable wave height and the lowest frequency of occurrence. This is understandable since the values were determined from a study for recreational craft and then adapted to fishing vessels.

In the NHCL (1980) study, from which the SCHD guidelines were developed, much emphasis was placed on the one foot (0.3 m) criterion since it is widely accepted by most authorities. Although it provides satisfactory results in marinas, it neglects the fact that fishing vessels unlike recreational craft can tolerate more agitation. They do point out however, that it is important to consider the wave direction, as beam seas are more distressing than head seas. They also point out that boat response depends greatly on the wave period relative to the boat length.

In the Nordic Council (1986) report, they agree with the F&O (1985) guidelines on the wave height criteria for small vessels. They present their conclusions for larger fishing vessels (25 m to 60 m long) with respect to method of loading/unloading, and ship movements. This data are the result of an investigation on 11 harbours. The Nordic report gives extensive information on acceptable movements for large fishing vessels, but does not provide as much information for smaller fishing vessels.

It is difficult to compare wave height criteria since each report bases its findings on different criteria. F&O (1985) presented its guidelines for frequency of occurrence based on vessel-metres usage. The study done by NHCL (1980) referred to significant wave height with respect to direction and period, as did the Vlemmix et al. (1987) study. Japanese criteria was based on the depth of the harbour. In the case of large fishing vessels the criteria were also presented as a function of ship movements.

#### WAVE AGITATION STUDY

To develop new allowable wave agitation criteria for commercial fishing harbour, a field measurement programme, managed by Atria and executed by MEDS, was conducted to

determine (in the field) the threshold values at which the wave climate at the service/offloading area and mooring area created either difficult, dangerous or unacceptable working conditions.

Wave measurement gauges were installed at two locations within two study harbours. Also, a wave rider buoy was used to measure nearshore waves for each harbour site. Wave data were collected during two fishing seasons to ensure that the majority of extreme wave events (events of unacceptable wave agitation) were well defined.

A procedure was developed and established by Atria and the local harbour masters by which daily field observations were taken and recorded by the harbour master. Particular emphasis was given to the wave climate events which rendered the facilities less than adequate, unsafe or unusable. By correlating the harbour masters field observations with the measured wave data inside the harbour, the threshold values for unacceptable wave agitation were determined.

A synthesized wave climate was developed for the study sites using a parametric wave hindcast model (Atria, 1991). First, waves were hindcasted for the wave measurement period and were calibrated with measured wave data obtained from the offshore wave riders. Subsequently, 20 years of hindcast waves were produced at each fishing harbour and analyzed to define a magnitude-duration-frequency relationship, which was assumed to be representative of the wave climate for the study harbours. By correlating the magnitude of unacceptable wave agitation levels determined from the field programme with the 20 year hindcast, the allowable duration and frequency of unacceptable wave agitation levels were obtained.

**Table 4 Criteria for Fishing Vessel Movements during Working Conditions**  
(Nordic Council, 1986)

Type of Vessel	Surge (m)	Sway (m)	Yaw (°)	Heave (m)	Pitch (°)	Roll (°)
Lift on/Lift off	1.0-1.5	1.0-1.5	3.5	0.4-0.6	3	3-5
Elevator crane	0.15	0.15				
Suction pump	2.0-3.0	1.0-2.0				

Note: The movements are maximum peak-peak. Frequency of occurrence of these movements should be less than is 1 week per year (2 % of the time).

**Table 5 Criteria for Fishing Vessel Movements Moored at Berth**  
(Nordic Council, 1986)

Type of Vessel	Surge (m)	Sway (m)	Yaw (°)	Heave (m)	Pitch (°)	Roll (°)
Fishing Vessel (25 m to 60 m length)	1.2-1.5	1.0-2.0	6	0.6-1.0	4	8

Note: The movements are peak-peak values. For the berth to be acceptable, the frequency of the movements should be less than 3 h/year.



Wave Data Acquisition Programme: The field measurement programme was initiated in December 1989 with the installation of the wave gauges and wave riders at their designated locations in Sandford and Stoney Island harbours, in Nova Scotia, Atlantic Canada. The locations of the inner and outer gauges for each harbour (Figure 1), were designed to record wave agitation data at the service/offloading area and at the harbour entrance respectively. The acquisition of data began in January 1990.

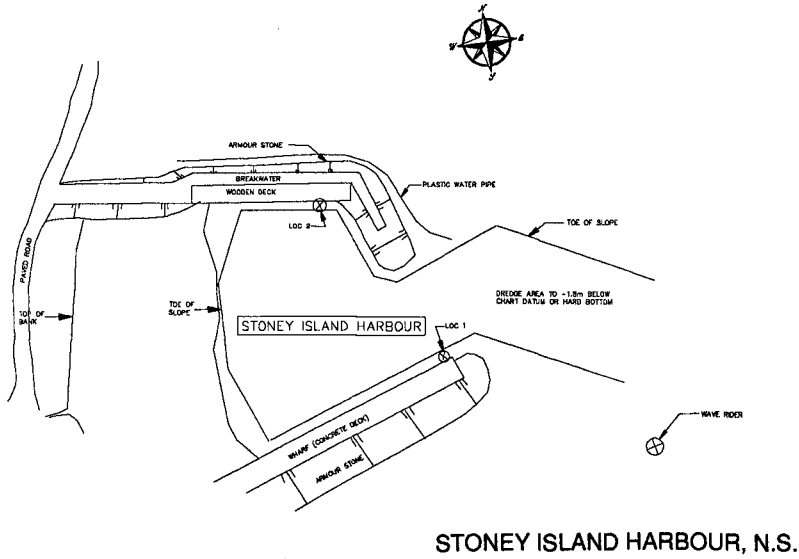
The harbour master field observations covered two field measurement seasons, the first period from December 1989 to end of May 1990 and the second season period from October 1990 to end of January 1990 for both locations. The harbour masters were responsible to visually record wind, wave and harbour conditions on a daily basis. The harbour conditions that were of interest for the present study were those events that could not be tolerated by the fishermen at the service/offloading wharf (i.e. unacceptable harbour conditions) and those events when the wave conditions were severe, but the harbour conditions could be tolerated (i.e. acceptable harbour conditions). The unacceptable conditions provide an indication of the lower bound of wave agitation that is unacceptable, while the acceptable conditions provide the upper bound of wave agitation that is tolerable. Summaries were compiled from the harbour masters field notebooks by condensing the information into categories of weather, waves, and harbour conditions recorded on each day.

The magnitude of the threshold wave height for unacceptable wave agitation at the service/offloading area was determined by simply identifying the measured wave height at the inner wave gauge for each unacceptable event as observed by the harbour master. This process was followed for both harbours. A sample time series plot for Stoney Island was shown in Figure 2 where the occurrences of unacceptable wave conditions were shown as a solid dot at the time of occurrence. Visual inspection of this plot shows a good coherency of measured (by the wave riders) and observed wave data (by the harbour masters) for the unacceptable events.

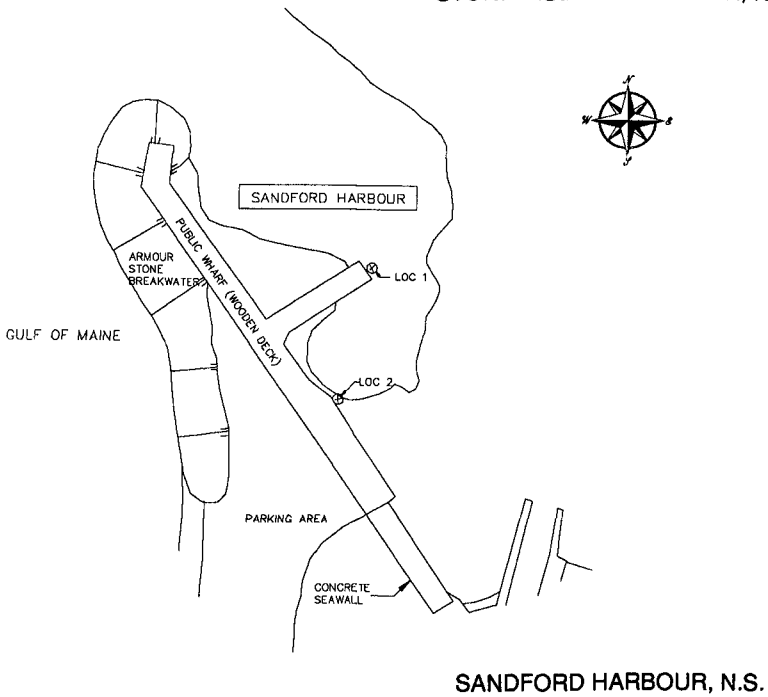
Similarly, acceptable harbour condition occurrences were also indicated on this time series plot as hollow dots. It is interesting to note that for these dates of acceptable (but severe) conditions, the inner gauge at Stoney Island showed a maximum value of 0.39 m and a minimum value of 0.15 m. This indicated that the harbour condition became unacceptable when the significant wave height exceeded 0.4 m.

Wave Hindcast: A 20 year wave hindcast was conducted to simulate the wave climate for each study harbour at the location of the wave riders. A parametric hindcast model based on the SMB equations (Atria, 1991) was used. The hindcast analysis used wind data from Yarmouth, N. S. as primary input to the model. The model was calibrated to the measured wave data at each wave rider, and subsequently, the long term hindcast was conducted for the 20 year data set using the calibration factors determined from the calibration process.

For both harbours, the hindcast model was calibrated by comparing the MEDS wave data measured at the wave riders with the hindcast waves using Yarmouth winds. In the calibration procedure, the original (smoothed) wind data were first used to hindcast waves in 8 and 16 point sectors. The initial hindcast used the original (unfactored) Yarmouth wind data and resulted in the hindcast waves being generally smaller than the measured values. The hindcast waves were then calibrated with the measured MEDS data by adjusting the wind scale factors until a reasonable match was achieved. Procedures to modify the (Yarmouth) wind data using overwater/overland speed ratios were applied and were presented in Atria (1991).



STONEY ISLAND HARBOUR, N.S.



SANFORD HARBOUR, N.S.

FIGURE 1 Location of selected harbours, Nova Scotia, Canada

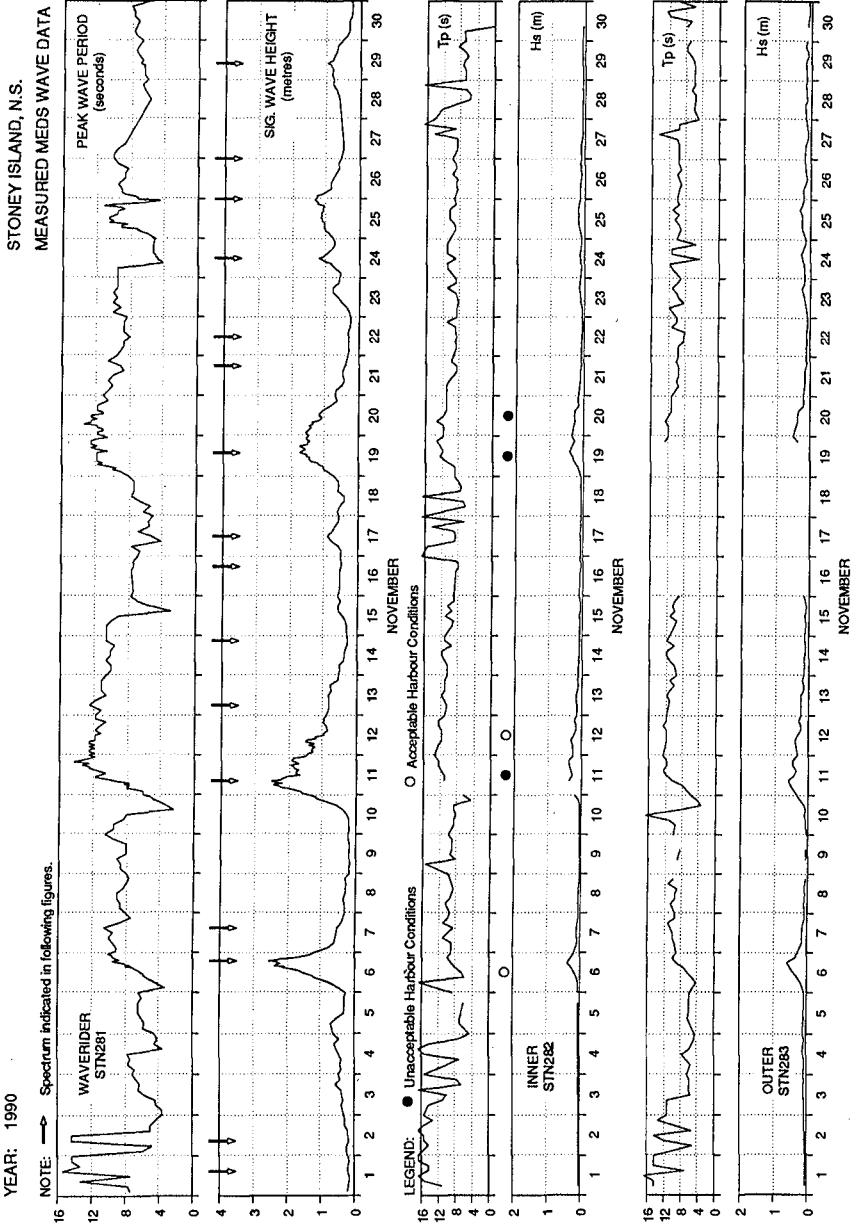


FIGURE 2 Time series plot of wave data for Stoney Island Harbour, November 1990

To establish the directional relationship between the wave conditions inside the harbours and those at the wave riders, the wave heights at inner and outer wave gauges were plotted against those measured at the wave riders for both sites. The fitted equations obtained using linear regression were shown in the plots of Figure 3, for Stoney Island harbour. For this, hindcasted wave directions were used when in concurrence with the wave directions observed by the harbour masters. Otherwise, the observed wave directions were used. Further, a 20 year hindcast representative for the two wave rider locations was performed using the wind data and calibration factors discussed above.

The results of the hindcast were presented in frequency of occurrence tables of the hourly significant wave height and wave period. The 20 year wave climates for both Sandford and Stoney Island, at the harbour wave gauges, were developed using the 20 year wave hindcast and applying the transfer functions given in Figure 3. These transfer functions modify the waves from the wave rider locations to the wave gauge locations. A summary of the wave statistics for all directions for both harbours inner wave gauges was presented in Atria (1991).

Discussion: The threshold value for unacceptable wave agitation (magnitude of wave height which renders the service/offloading area unusable) was determined by linking the harbour master's field observation of harbour agitation conditions to the MEDS measured wave data. The data for Stoney Island is shown in Figure 4. This figure shows a summary plot for all events of unacceptable harbour agitation conditions and the measured wave parameters. Using the Stoney Island inner wave gauge to represent the wave climate at the service/offloading area, the acceptable wave heights range from 0.27 m to 0.43 m and the value of 0.27 m could be considered as the threshold value. Figure 4 also presented a summary plot for the acceptable (but severe) harbour agitation condition. Inspection of the inner wave gauge for Stoney Island indicated that all data for acceptable harbour agitation conditions were under 0.4 m but greater than 0.27 m. This upper bound value could also be considered as the threshold value for unacceptable conditions. These conflicting information may be attributed to measuring errors or other factors such as freezing rain or strong wind conditions, which made the harbour masters feel that the harbour conditions were unacceptable. Closer examination of these two plots indicated that if the data point of 0.27 m wave height is ignored then the unacceptable threshold is about 0.4 m. Considering this, a value of 0.4 m was proposed here as the threshold wave height for unacceptable harbour agitation conditions. Also, this proposed threshold value agrees with the British Standard Code BS6349 that the maximum acceptable significant wave height is 0.4 m for boats up to 30 m. Wave agitation levels greater than this value would induce undesirable vessel motions which could result in vessel damage.

Allowable wave agitation criteria are incomplete without specifications for the frequency of occurrence of the defined threshold value. Determination of the allowable frequency of a specified wave agitation level is basically an economical/policy decision. The scatter diagram for the predicted wave climate for the inner gauge at Stoney Island (Atria, 1991) indicated that the exceedance probability of a wave height greater than 0.4 m is 1.04% and the exceedance probability of a wave height greater than 0.25 m is 4.89%.

According to the SCHD inventory of fishing harbours, both Sandford and Stoney Island harbours are Class B harbours. Under the existing Guidelines of Harbour Accommodation (F&O, 1985), the required allowable maximum wave agitation at the service/offloading area is 0.25 m and its exceedance probability cannot be greater than 0.87%. Based on the existing guideline, Stoney Island harbour would be considered as a problem harbour. However, on average for 15 times per year the fleet at Stoney Island have to abandon the harbour and seek

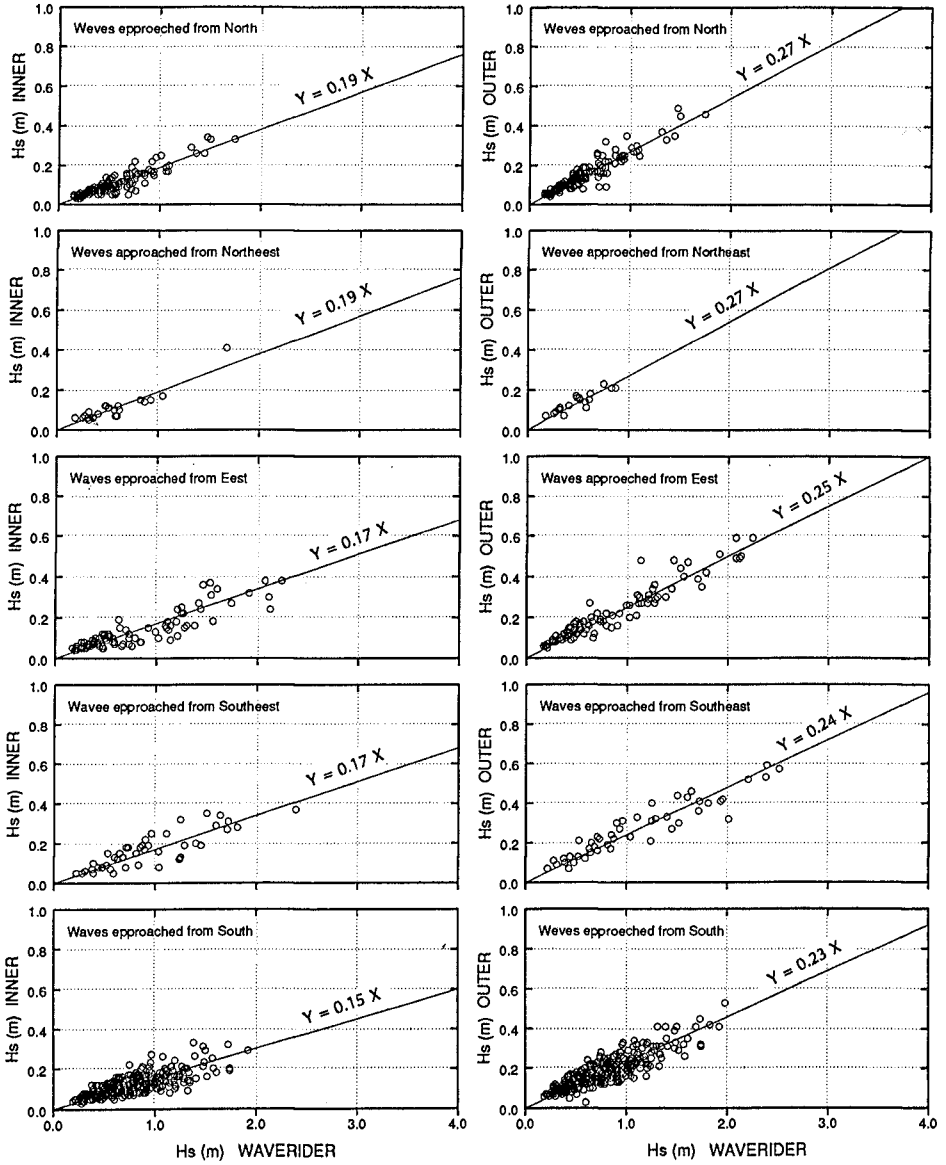


FIGURE 3 Fitted equations for different wave directions, Stoney Island Harbour

refuge at other harbours (J. Ross, SCH, pers. comm., 1991). If this occurrence of refuge seeking is considered acceptable to SCHD, the Stoney Island harbour would be considered as functional and the frequency of wave agitation found in this study could be accepted and applied to other harbours in a generic manner. On the other hand, if SCHD considers this frequency of refuge seeking to be unacceptable, then frequency of 1% may be considered high. When compared to the exceedance probability of 2.5% suggested by the Japanese Ministry of Agriculture and Fisheries for allowable wave heights of 0.4 m, it does not seem unreasonable that the wave height of 0.4 m cannot be exceeded 1% of the time in a year.

The vessels which operate at Sandford and Stoney Island harbours are known as Cape Islanders which fall into the STACAC (Statistical Coordinating Committee for Atlantic Canada) class 2 (35 to 45 ft) category. The wave measurement programme at Sandford and Stoney Island (and resulting recommended allowable levels of wave agitation) applies to STACAC class 2 vessels. The recommended guidelines proposed here towards allowable levels of wave agitation apply to STACAC class 2 and 3 (45 to 60 ft) fishing vessels in Atlantic Canada.

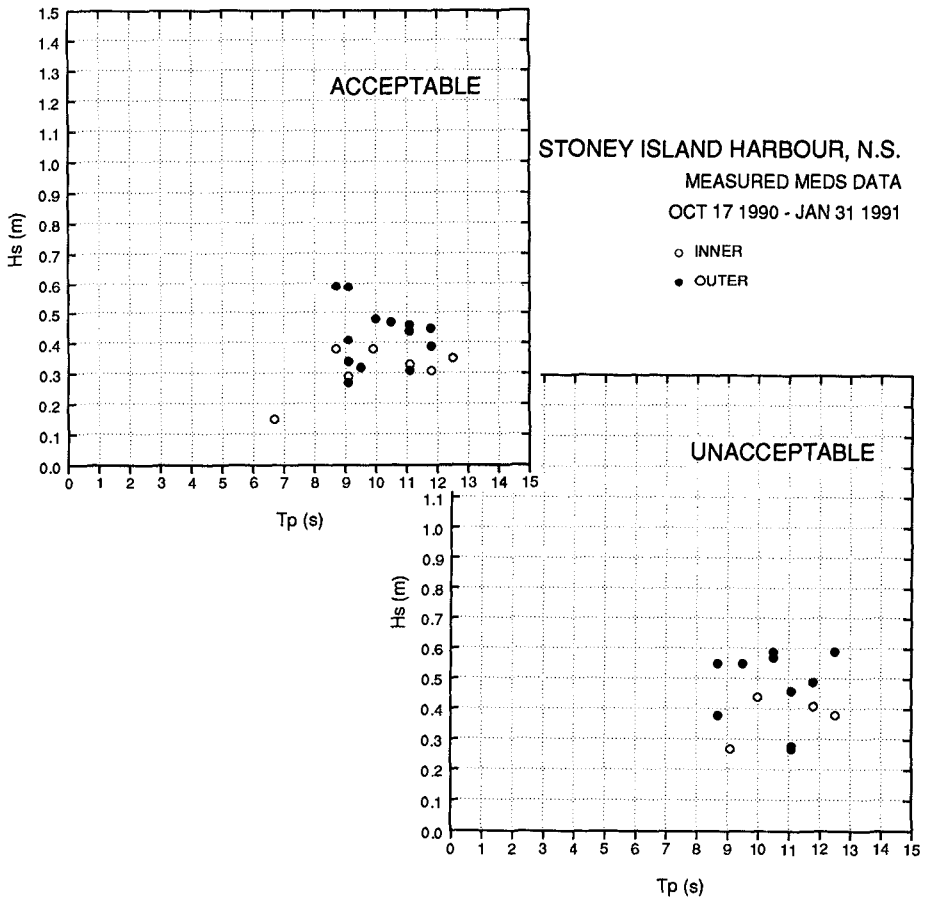


FIGURE 4 Stoney Island Harbour - acceptable and unacceptable harbour conditions

## CONCLUSIONS

It is proposed that harbour classification should not be a parameter governing allowable wave agitation criteria, rather vessel classification should be considered as a governing parameter. The rationale for this can be explained as follows: a given vessel at berth experiencing beam seas, undergoes the same discomfort from the incoming wave attack as ten of the same vessels moored bow to stern under the same wave conditions. On the other hand, fishing vessels of different class will not respond in (exactly) the same manner under the same wave disturbances and therefore experience different levels of discomfort. Therefore the allowable wave agitation level and its frequency of occurrence should depend on the dominant type of vessel in a harbour, rather than the total vessel meters in that harbour.

The associated frequency of occurrences allow for some down time at the service/offloading wharf at which point in time alternate action will have to be sought by the local fishermen. This alternate action may consist of mooring the vessel in a mooring field, removing the vessel from the harbour by a slip or departing from the harbour altogether and seeking refuge in a nearby harbour (which is the case at Stoney Island harbour). Therefore, the alternate action is a function of the facilities available at each site specific harbour.

Measuring waves in a harbour with an organized harbour monitoring programme proved to be an effective means of determining the threshold point of unacceptable wave agitation as applied to fishing vessels on the Canadian east coast. During the planning and design of commercial fishing harbours, the associated frequency of wave agitation recommended in this document apply to wave events which occur during the fishing season alone.

It was concluded that the results of this study, which were based on wave measurements with peak wave periods in the order of 10 to 13 s, may be safely applied to sites with shorter peak wave periods. Inland waters typically have wave climates which have shorter periods than wave climates in Atlantic Canada. Considering this, it is recommended that the above criteria for wave agitation may be safely applied to inland water commercial fishing harbours.

For planning purposes of Canadian east coast commercial fishing harbours which have predominantly STACAC class 2 or class 3 fishing vessels, it is recommended to use the threshold significant wave height with the associated frequency of occurrence listed in Tables 6 and 7 for the service/offloading wharf and for the mooring basin respectively.

**Table 6 Recommended Allowable Wave Agitation Criteria for the Service/Offloading Wharf for STACAC Class 2 and Class 3 Fishing Vessels**

Threshold Significant Wave Height	Frequency of Occurrence
0.40 m	1.0 % - 2.5 %

**Table 7 Recommended Allowable Wave Agitation Criteria for the Mooring Basin for STACAC Class 2 and Class 3 Fishing Vessels**

Threshold Significant Wave Height	Frequency of Occurrence
0.50 m	1.0 % - 2.5 %

Threshold value for unacceptable wave agitation (magnitude of wave height which renders the service/offloading area unusable) for a STACAC class 2 fishing vessel was determined to be 0.4 m. The scatter diagram for the predicted wave climate for the inner gauge at Stoney Island indicated that the exceedance probability of a wave height greater than 0.4 m is 1.04% and the exceedance probability of a wave height greater than 0.25 m is 4.89%. The results of the present study indicated that the frequency of occurrence for wave agitation should be 5 to 6 times greater than the current guidelines values (F&O, 1985).

Allowable wave agitation criteria are incomplete without specifications for the frequency of occurrence of the defined threshold value. Determination of the allowable frequency of a specified wave agitation level is basically an economical/policy decision. A 1% to 2.5% frequency of occurrence of the threshold wave height is recommended.

It is proposed that the results of this study, which apply to STACAC class 2 vessels, may be safely applied to STACAC class 3 vessels. Also, these criteria could possibly be reduced for STACAC class 1 (up to 35 ft) vessels. Atria Engineering Hydraulics Inc. is currently (1992) undertaking a similar field monitoring programme in Newfoundland to determine the threshold values of wave agitation criteria for STACAC class 1 vessels.

#### ACKNOWLEDGEMENTS

The authors would like to express their appreciation to Small Craft Harbours Branch, Fisheries & Oceans Canada, for financial support of the study.

#### REFERENCES

- ATRIA ENGINEERING HYDRAULICS INC., 1991. A Study of Allowable Wave Agitation for Fishing Harbours on the Canadian East Coast. Consultants report submitted to Small Craft Harbours Directorate, Fisheries & Oceans Canada, May 31.
- ASCE TASK COMMITTEE ON SMALL CRAFT HARBOURS, 1969. Report on small craft harbours. ASCE Manuals and Reports on Engineering Practice, No. 50, p. 139.
- FISHERIES AND OCEANS CANADA, 1985. Guidelines of harbour accommodation. Small Craft Harbour Directorate, Ottawa, Canada.
- LE MEHAUTE, B. 1977. Wave agitation criteria for harbours. Proceedings of the 4th Annual Symposium, Waterways, Ports, Coastal and Ocean Division, ASCE, Vol. I, p. 366-372.
- NORDIC COUNCIL, 1986. Ship Movements in Harbours. Results of a joint research project in the nordic countries.
- NORTHWEST HYDRAULIC CONSULTANTS LTD., 1980. Study to determine acceptable wave agitation in small craft harbours. Canadian Manuscript Report of Fisheries and Aquatic Sciences, No. 1581.
- ROSEN, D.S. and KIT, E. 1984. A simulation method for small craft harbour models. Proceedings, 19th International Conference on Coastal Engineering, Houston, Texas, USA, ASCE, p. 2842-2856.
- THE OVERSEAS COASTAL AREA DEVELOPMENT INSTITUTE OF JAPAN, 1980. Technical standards for port and harbour facilities in Japan. Bureau of Ports and Harbours, Ministry of Transport.
- VLEMMIX, W., VAN DER ZANDE, J., BOGAERTS, M.P., VAN DER KAA, E., KASPERS, J., SCHAAP, D.M.A., STRATING, J. VERBEEK, P.R.H., KALFT, F.R., and MOL, A. 1987. Reception and discharge of large coal carriers. PIANC - AIPCN Bulletin 1987, No. 56.





# PART VII

## Case Studies



*Perforated Caisson Breakwater at  
Porto Torres, Sardinia*

## CHAPTER 248

# Erosion of the Damietta Promontory, the Nile Delta

A. M. Fanos\*, A. A. Khafagy\* and P. D. Komar\*\*

### Abstract

The Damietta sediment-formed promontory is located on the eastern half of the Nile Delta, about 40 km west of the Suez Canal breakwaters at Port Said. Following a long period of accretion, the promontory began to erode early this century with shoreline recession rates reaching a maximum of 38 m/yr. This paper documents the shoreline changes, the coastal processes responsible for those changes, and the protective measures that have been erected to control the erosion.

### Introduction

During historical times, the Nile Delta shoreline was built out by sediments delivered to the coast through seven or more distributaries. Since the 9th century, most of the Nile River water and sediment delivered to the coast have passed through the Rosetta and Damietta branches, and these have built out the pronounced promontories apparent in the modern outline of the delta shoreline. The shapes of these promontories reflect the quantities of sediments delivered to the coast versus the effectiveness of the waves and nearshore currents in redistributing the beach sands along the delta shoreline.

About the turn of the century, the general accretion of the Rosetta and Damietta promontories reverted to erosion

---

\*Coastal Research Institute, 15 El Pharaana St., El Shallalat, Alexandria, Egypt

\*\*College of Oceanography, Oregon State University, Corvallis, Oregon 97331

characterized by rapid rates of shoreline retreat. Inducement of this erosion is generally attributed to construction of barrages along the Nile River as part of water-control activities, and in particular to the construction of the Aswan Low Dam in 1902 and the Aswan High Dam in 1964 (Orlova and Zenkovitch, 1974; Inman and Jenkins, 1984; Frihy et al., 1991). Completion of the Aswan High Dam has cut off almost all water discharge from the river and the delivery of sediments to the delta coast.

The focus of this study is on the Damietta promontory which is located about 40 km west of the Suez Canal breakwaters at Port Said. The objectives of this paper are to: (1) illustrate the patterns of shoreline changes from analyses of old maps and recent surveys; (2) to summarize the measurements of waves, longshore currents and beach profiles; (3) to evaluate the longshore sediment transport rates through various techniques; and (4) to highlight the shoreline protective works that have been completed or are being proposed.

### **Patterns of Shoreline Changes**

The shoreline changes, as revealed in old maps and recent surveys, are summarized in Figure 1. There was an overall accretion from the 1800 survey until about the beginning of the 20th century, the maximum seaward growth appearing in the 1912 mapped shoreline. After that date the successive surveys show a rapid retreat of the shoreline to the immediate east of the Damietta river mouth, that long-term maximum erosion averaging 38 m/yr between the 1912 and 1983 shorelines. Development in this erosion area to the east of the river was minimal, with the main impacts being the necessity of moving the coastal highway inland and the recent replacement of the light house which is in danger of being lost.

It is apparent in Figure 1 that the shoreline retreat and the rates of erosion have varied considerably along the length of the promontory shoreline, and actually revert to a zone of accretion to the east of a nodal area, reflected in the progressive seaward advance of the shorelines. Part of this accretion has been the development of a sand spit on the eastern flank of the Damietta promontory, seen in the 1973 and 1983 shorelines (Fig. 1).

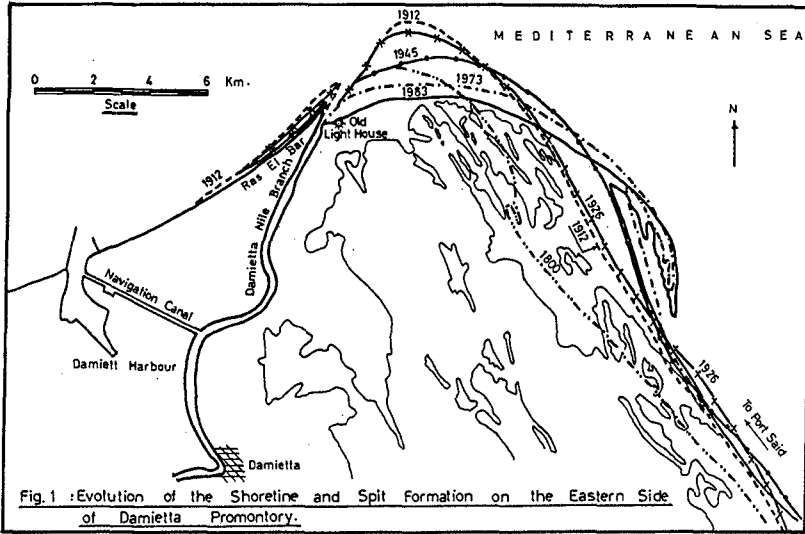


Fig.1 :Evolution of the Shoreline and Spit Formation on the Eastern Side of Damietta Promontory.

The shoreline changes to the west of the river mouth have been particularly critical due to the erosion of the resort community of Ras El Bar. The study of old maps has shown that the Ras El Bar tongue of land grew in length to about 500 meters and widened during the period from 1800 to 1900, corresponding to the time of general growth of the Damietta promontory. Since the turn of the century, the pattern has been primarily one of erosion, during which the Ras El Bar tongue eroded back following the overall shoreline retreat of the promontory. The erosion has been partly stabilized by the placement of a series of groins and a seawall.

It is seen that there have been substantial changes in the shoreline positions along the Damietta promontory since about the turn of the century. The main impact has been one of erosion, with the point of the promontory having retreated by some 3 to 4 km and continuing at a rapid rate. However, beach accretion, partly in the form of a sand spit, has taken place along the eastern flank of the promontory. The inducement of these shoreline changes is undoubtedly a response to the cut-off of sand delivery to the coast through the Damietta branch of

the Nile River. The continued action of waves, longshore currents and sediment transport has acted to displace sediments toward the east, resulting in the observed patterns of shoreline changes.

### **Processes Affecting the Damietta Promontory**

The normal wind regime along the Mediterranean coast of Egypt is controlled by various atmospheric conditions which occur on a seasonal basis. The annual wind rose for the area offshore of Damietta indicates that the winds blow predominantly from the NW and WNW directions. These directions correspond to the maximum fetch distance along the length of the Mediterranean Sea, and account for the observed patterns of wave heights and directions along the Nile Delta coastline.

A program for collecting wave data in the study area began as early as 1964-1966 and has been continuous from 1972 onwards (Fanos et al., 1989; Nafaa et al., 1991). The earliest measurements were collected with pressure gauges termed the Offshore Pressure Operated Suspended System, installed in about 6 meters water depth directly seaward of the point of the Damietta promontory. Its records have been analyzed manually by the zero up-crossing method and/or the Tucker and Drapper method (Tucker, 1963; Drapper, 1966) to obtain significant wave heights and periods, while the wave direction was determined from wind data. In order to obtain a more complete description of the wave climate, a directional wave recording system termed the Cassette Acquisition System has been used since it became fully operational in 1985. It was installed in 7 meters water depth, about 1 km offshore from the Damietta Promontory. Measurements for 34 minutes every 6 hours are recorded on cassettes, and are computer analyzed to yield spectra, significant wave heights, periods, and wave directions (Lowe and Inman, 1984; Elwany et al., 1988; Nafaa et al., 1991).

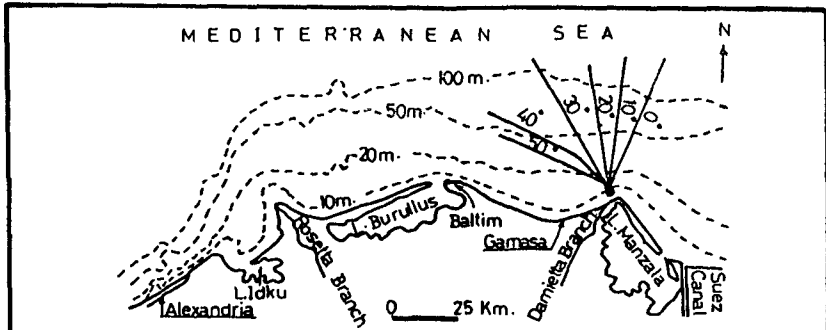
Wave action on the Nile Delta is seasonal, with the intensity and direction following the seasonal patterns of winds. The maximum significant wave height recorded during 1985 to 1990 was 4.3 m. The predominant wave directions are from the WNW, NNW, N and W; a small portion of waves arrived

from the NNE and NE, especially in March through April and possibly in November, due to easterly winds during those months. It is noticeable that wave characteristics vary from season to season and from year to year. These variations cause the changes in wave energy flux which are responsible for the nearshore coastal changes.

All of the wave records are from one point in shallow water, and in order to obtain the deep-water wave characteristics and to determine the wave climate along the length of the promontory shoreline, back and forward refraction calculations have been carried out. Figure 2 shows the back refracted rays of the recorded data (Elwany et al., 1989), and examples of forward refraction of waves from the NNW and WNW (CRI/UNESCO/UNDP, 1978). This figure illustrates the concentration of wave energy on the promontory, and in part explains the severe erosion that has occurred.

Longshore currents have been measured within the surf zone at three stations on each side of the mouth of the Damietta Nile branch. The collected data during 1990 and 1991 have been subjected to monthly, seasonal and yearly statistical analyses to determine the probability distributions of the longshore currents. The predominant current direction on both sides of the river mouth was found to be from west to east, except during the months of March, April, May and November when the current periodically reverses and its direction depends on the daily wind and wave directions.

The shift from erosion to accretion along the eastern flank of the Damietta promontory, Figure 1, reflects the longshore variations in the quantities of sand being transported. As one moves east from the river mouth, the erosion contributes more and more sand to the littoral transport toward the east, so that the total quantity must be progressively increasing. The maximum longshore sediment transport is positioned at the nodal point between the areas of erosion versus accretion. With the change to beach accretion, there is progressively less and less sand being carried as littoral drift. By this interpretation, the longshore sediment transport is everywhere to the east, but its varying quantities account for the shifts from erosion to



A - Backrefraction for Waves Near Damietta Promontory.

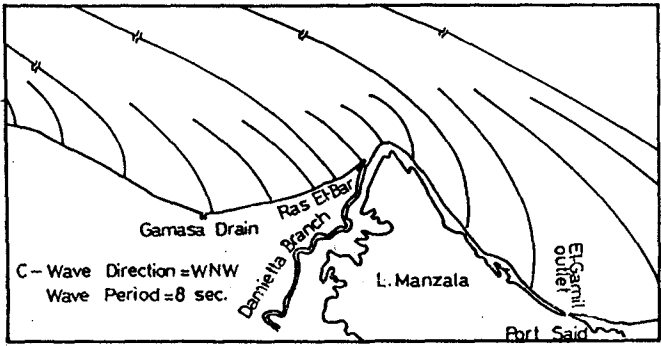
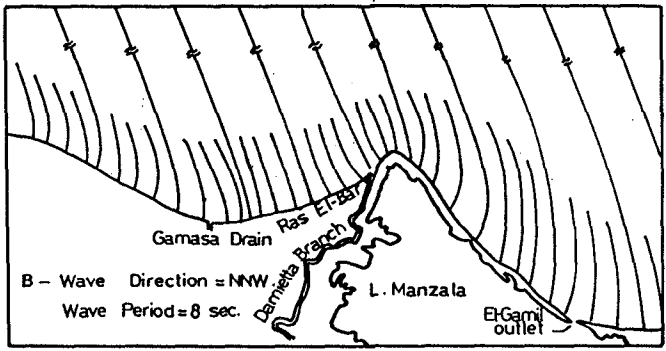


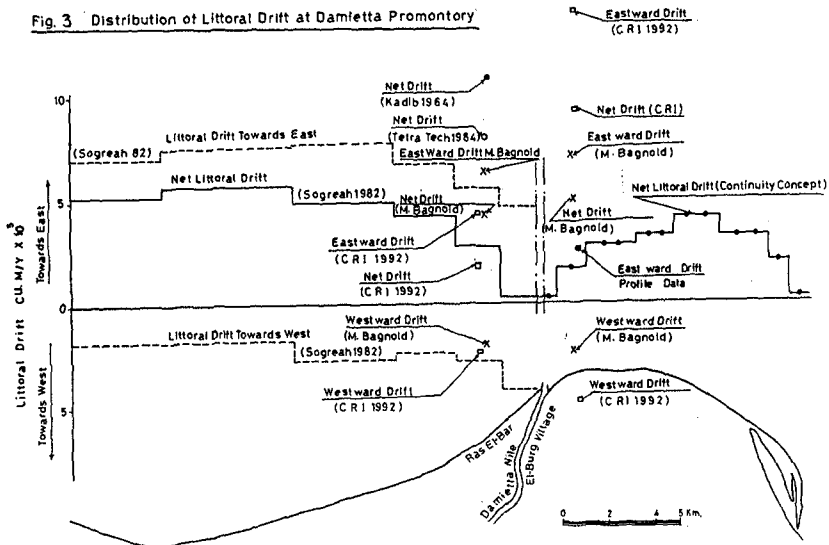
Fig. 2 : Backrefraction and Forward Refraction.



deposition.

This pattern of sediment transport has been quantitatively assessed for the stretch of shoreline east of the Damietta river mouth, similar to the analyses of Frihy et al. (1991) for the Rosetta promontory. The rate of shoreline retreat or advance is related to the longshore gradient of the sand transport rate, rather than to the absolute quantities of that transport. If  $y$  is the shoreline position so that  $dy/dt$  is its time-rate of change ( $dy/dt = -$  signifies erosion,  $dy/dt = +$  represents accretion), then a consideration of sediment continuity yields  $Z(dy/dt) = -dQ_s/dx$  where  $Q_s$  is the local sediment transport rate and  $x$  is in the longshore direction.  $Z$  is an elevation factor that converts the  $dy/dt$  shoreline change into a volume of sand eroded or deposited per unit shoreline length. According to beach profiles from the area, this elevation change is approximately  $Z = 4$  meters. Therefore, there is a simple proportionality between  $dy/dt$  and  $dQ_s/dx$ .

The average rates of shoreline erosion or accretion ( $dy/dt$ ) between the years 1912 and 1983 have been determined from Figure 1. The corresponding  $dQ_s/dx$  local gradients calculated from the continuity equation have been integrated in the longshore direction from west to east, to yield the graph of  $Q_s$  in Figure 3. It has been assumed that  $Q_s = 0$  at the river mouth, that is, there is presently no exchange of sand with the area to the west, either with the river channel or with the western flank of the promontory. If there is in fact some net exchange, then the  $Q_s$  curve of Figure 3 would simply shift up or down by that amount, while retaining its overall shape. It is seen that  $Q_s$  progressively increases with longshore distance from the river, reaches a maximum of approximately  $0.41 \times 10^6 \text{ m}^3/\text{yr}$ , and then decreases. According to the computations of Figure 3, the transport is reduced to essentially zero due to deposition on the sand spit along the eastern flank of the promontory, indicating that there is an approximate balance between the quantities of sand eroded and subsequently deposited. The varying quantities of longshore sediment transport rates found in this analysis are due to systematic changes in breaker angles and wave energies



along this stretch of shore, in turn caused by the refraction of the predominant NW-NNW waves around the shallow offshore of the promontory.

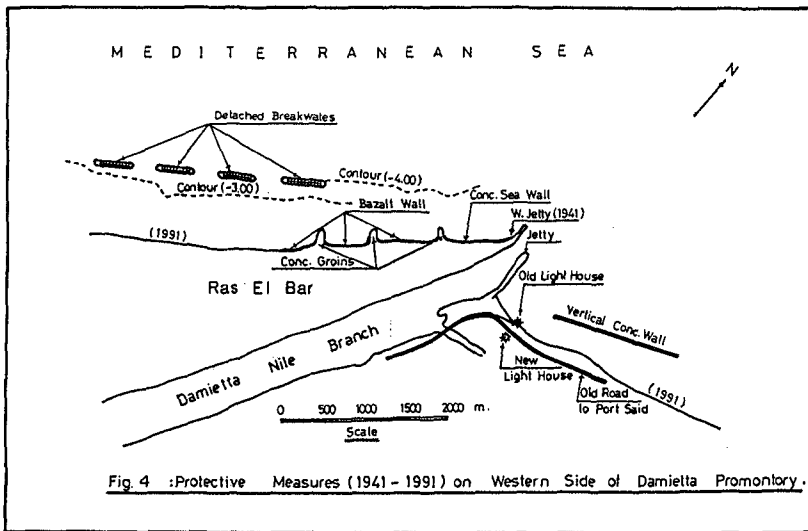
Measurements and/or computations of the littoral drift have been carried out by various investigations along different stretches of the Damietta promontory. Kadib (1969) measured the transport at Ras El Bar using fluorescent tracers, and reported a value of  $1.15 \times 10^6 \text{ m}^3/\text{yr}$  for the net transport toward the east. More recently, experiments by El Fishawi et al. (1992) have been carried out using tracers to determine sand transport rates at two locations, 0.80 km east and 3.0 km west of the Damietta mouth, every month during the period from January to December 1991. The results are graphed in Figure 3, labeled as CRI-1991. To the east of the river the evaluated net littoral drift is  $0.8 \times 10^6 \text{ m}^3/\text{yr}$ , which is substantially greater than determined by the other techniques. To the west of the river along the Ras El Bar shoreline, the net littoral drift is evaluated to be  $0.26 \times 10^6 \text{ m}^3/\text{yr}$  toward the east, a value that is smaller than obtained by the other techniques and studies.

Tetra Tech (1984) estimated the net littoral drift at Ras El Bar to be  $0.8 \times 10^6 \text{ m}^3/\text{yr}$  to the east. Using the CERC equation, Sogreah (1982) evaluated the transport rates along an extended length of shoreline to the west of the river mouth, including the beach along Ras El Bar. The results are graphed in Figure 3. These calculations indicate that the net littoral drift is everywhere toward the east, progressively decreasing from  $0.6 \times 10^6 \text{ m}^3/\text{yr}$  to essentially zero ( $0.03 \times 10^6 \text{ m}^3/\text{yr}$ ) near the Ras El Bar jetty. The calculated values using the CERC equation are very approximate because they depend on the accuracy of measuring the shoreline orientations, the breaker angles, and breaker heights.

Longshore sediment transport rates can be computed from the daily measurements of wave heights ( $H_b$ ) and longshore currents ( $v$ ) with the modified Bagnold equation  $Q_s = 0.026(H_b)^2 v$  as established by Komar (1990). This formula is particularly applicable to analyses of sediment transport rates on the Nile Delta due to the accumulated long-term measurements of waves and longshore currents, and eliminates the requirement of accurate assessments of breaker angles needed in the CERC equation. Applying this relationship with the available wave and current measurements, the average annual eastward and westward littoral drifts on the western side of the river mouth were computed to be  $0.64 \times 10^6 \text{ m}^3/\text{yr}$  and  $0.2 \times 10^6 \text{ m}^3/\text{yr}$  respectively, the net to the east being  $0.4 \times 10^6 \text{ m}^3/\text{yr}$ . These values are graphed in Figure 3 at the position corresponding to the location where the longshore currents were measured to the west of the Ras El Bar jetty. Similar calculations for a position to the east of the river mouth yielded eastward and westward transports of  $0.72 \times 10^6 \text{ m}^3/\text{yr}$  and  $0.23 \times 10^6 \text{ m}^3/\text{yr}$ , with a net  $0.49 \times 10^6 \text{ m}^3/\text{yr}$  toward the east. This is approximately the maximum transport rate as evaluated above from shoreline changes and continuity considerations, but the measurement location is closer to the jetty where the calculated transport from continuity considerations is roughly half that value (Fig. 3). Therefore, the agreement is good only to a factor of 2.

### Shoreline Protection Measures

The protective works on the Damietta promontory began in 1936 in order to defend the Ras El Bar summer resort from the erosion, and also to prevent siltation of the estuary. A 200-m long concrete jetty was constructed during the period 1936-41 at the NE extremity of Ras El Bar (Figure 4). In 1965 a concrete protective sea wall was built along the first 400 m of shoreline to the west of the jetty, fronted by riprap and doloes. Three 150-m long concrete groins were added in 1970 to protect the beach to the southwest of the sea wall, and in 1982 a basalt riprap revetment was constructed between the groins and to the west of the groin field. Presently, four detached breakwaters are under construction to the west of the groins, Figure 4, and the beach behind the breakwaters is being nourished. These combined projects will offer protection to nearly the full length of the Ras El Bar shoreline.



The jetty on the eastern bank of the river mouth was constructed in 1979. However, the earliest shoreline structure to the east of the river mouth was a seawall several kilometers in length, Figure 4, constructed in 1971 to protect the very old

coastal road between Damietta and Port Said. Most of this wall has become submerged in the offshore during the continued retreat of the shoreline. Recent erosion has threatened the lighthouse to the immediate east of the river, and necessitated the placement of a protective riprap wall surrounding the structure and extending to the east. This old lighthouse has become unstable due to the erosion, and has been replaced by a new lighthouse in an inland position. Tetra Tech (1984) has suggested the construction of a revetment having a 6 km length along the coast, using the old road to Port Said as part of the structure. However, erosion would continue at its eastern end as the promontory shoreline continues to retreat. We have suggested that the revetment instead extend for about 1.5 km parallel to the old road, and then turn inland to the south to offer protection from the erosion that will continue further to the east.

### **Summary and Conclusions**

Erosion of the Damietta promontory has been continuous since about the turn of the century, with very high rates of shoreline retreat. This erosion is confined to the central portion of the promontory closest to the river mouth. To the east of the river the rate of shoreline retreat progressively decreases along the flank of the promontory, and beyond a nodal area reverts to accretion and shoreline advance, in part involving the formation of a large sand spit. This reorientation of the shoreline is in response to the continued wave action and longshore sediment transport, while at the same time the sediment delivered to the coast has been cut off due largely to the construction of dams on the Nile River. A program of data collection, including the measurement of waves, beach profiles, longshore currents and sand transport rates, has documented the main processes responsible for the shoreline changes. The measurements of longshore currents and sand transport show a dominant movement toward the east, and this corresponds to the prevailing winds and waves arriving from the NW and WNW directions. Although the net longshore sediment transport is everywhere toward the east, the rates vary due to systematic

longshore variations in wave breaker heights and breaker angles along the length of the promontory shoreline. This variation in rates of eastward transport is responsible for the patterns of shoreline erosion near the river mouth versus accretion at greater distances, the zone of erosion corresponding to the shoreline where the transport is progressively increasing while the accretion is in the zone of decreasing littoral drift.

The promontory erosion has threatened developed areas, in particular the resort community of Ras El Bar to the west of the river. The response to this erosion has been the construction of a jetty, followed by the placement of a seawall and series of groins along the eroding shoreline. Most recent is the placement of four detached breakwaters and nourishment of the sheltered beach. There is less development to the east of the river, but the erosion has destroyed the coastal road to Port Said, requiring its rerouting to a more landward position. The old lighthouse has been undermined by the erosion, necessitating its replacement. Riprap has recently been installed to protect the old lighthouse and extended eastward to offer some protection to the replacement Port Said highway. Plans are being formulated for the construction of a large seawall that will extend for several kilometers to offer additional protection to the eastern shore of the Damietta promontory.

### **Acknowledgements**

This study is part of the Egyptian Water Research Center Project, sponsored by the United States Agency for International Development, under Grant No. 263-0132 to the Consortium of International Development at Colorado State University.

### **References**

- CRI/UNESCO/UNDP (1978) Coastal Protection Studies: Final Technical Report, Volumes I and II, Academy of Scientific Research and Technology.
- Drapper, L. (1966) The analysis and presentation of wave data: A plea for uniformity: Proc. 10th Conf. on Coastal Engineering, Amer. Soc. Civil Engrs.

- El Fishawi, N.M., A.M. Badr and A.A. Khafagy (1992) Fluorescent tracers at the eastern and western beaches of the Damietta mouth: Technical Report, Coastal Research Institute, Alexandria, Egypt.
- Elwany, M.H.S., A.A. Khafagy, D.L. Inman, and A.M. Fanos (1988) Analysis of waves from arrays at Abu Quir and Ras El Bar, Egypt: *Advances in Underwater Technology, Ocean Science and Offshore Engineering*, v. 16: pp. 89-97.
- Elwany, M.H.S., A.A. Khafagy, D.L. Inman, and A.M. Fanos (1989) Prediction of wave climate along the coast of Egypt: International Seminar on Climatic Fluctuations and Water Management, 11-14 December 1989, Cairo, Egypt.
- Fanos, A.M. (1986) Statistical analysis of longshore current data along the Nile Delta coast: *Water Science Journal, Water Res. Center, Cairo*, v. 1, pp. 45-55.
- Fanos, A.M., A.A. Khafagy and S.H. Sharaf El-Din (1989) Coastal changes along the Egyptian Mediterranean coast: International Seminar on Climatic Fluctuations and Water Management, 11-14 December 1989, Cairo, Egypt.
- Frihy, O.E., A.M. Fanos, A.A. Khafagy and P.D. Komar (1991) Patterns of nearshore sediment transport along the Nile Delta, Egypt: *Coastal Engineering*, v. 15, p. 409-429.
- Inman, D.L., and S.A. Jenkins (1984) The Nile littoral cell and man's impact on the coastal zone of the southern Mediterranean: *Proc. Conf. on Coastal Engr.*, pp. 1600-1617.
- Kadib, A. (1969) Rate of littoral drift at Ras El Bar using fluorescent tracers: Suez Canal Research Center, Technical Report No. 42.
- Komar, P.D. (1990) Littoral sediment transport: *Handbook of Coastal and Ocean Engineering*, J.B. Herbich (editor), Vol. 2, Chapter 11, pp. 681-715.
- Lowe, R.L., and D.L. Inman (1984) Wave parameters, Abu Quir array, Egypt: Scripps Institution of Oceanography, Univ. of California, SIO series 84/31.
- Nafaa, M.G., A.M. Fanos and M.A. Elganainy (1991) Characteristics of waves off the Mediterranean coast of Egypt: *Jour. of Coastal Research*, v. 7, p. 665-676.
- Orlova, G., and V. Zenkovitch (1974) Erosion of the shores of the

- Nile Delta: Geoforum, v. 18, p. 68-72.
- Songreah Consulting Eng. (1982) Effects of the construction of the Port of Damietta on the evolution of the littoral, Final report: Report No. 35/1201 R9, August 1982.
- Tetra Tech (1984) Shoreline master plan for the Nile delta coast: Progress Report No. 1.
- Tucker, M.J. (1963) Analysis of sea waves: Proceedings Institute of Civil Engineers, London, v. 26.



## CHAPTER 249

### NEARSHORE COASTAL CHANGES ALONG THE NILE DELTA SHORES

A.A. Khafagy<sup>1</sup>, M.G. Naffaa<sup>1</sup>, A.M. Fanos<sup>1</sup> and R.G. Dean<sup>2</sup>

#### ABSTRACT

The Nile Delta coast is a dynamic system formed by the Nile River sediments discharged into the Mediterranean Sea through the historic seven branches of the Nile. The central headland at Burullus began to erode around the 10th century upon abandonment of the old Nile branch which had been providing sediment to this area. Commencing in the early 20th century the nine barrages along the main river were constructed which initiated a general erosional trend along the Nile Delta with concentrations around the Rosetta and Damietta promontories. This alarming erosion has been aggravated since the erection of the Aswan High Dam in 1964, which trapped essentially all of the flood sediments in its storage basin.

Eighty beach profiles, covering the Delta coast, have been surveyed twice per year since 1976 and surveying is continuing to the present. A computer program was developed to analyze the collected profile data. This program calculates the accretion/erosion quantities and the movement of various contour lines up to 6 meters depth. The results have shown that the changes do not follow a clear pattern except at the Rosetta and Damietta promontories and around the El Burullus area where consistent erosion is evident.

#### INTRODUCTION

The Nile Delta coast consists of sandy beaches approximately 240 km in length (Figure 1). This coastline has two promontories at Rosetta and Damietta and one "bulge" at Burullus with concave shorelines in between. Six outlets exist in this coastal segment, listed from west to east as: Idku Lake Outlet, Rosetta Exit, Burullus Outlet, Gamasa Drain Outlet, Damietta Exit, and El Gamil Outlet. The

---

<sup>1</sup>Coastal Research Institute, 15 El Pharaana St., El Shallalat, Alexandria, Egypt

<sup>2</sup>Coastal and Oceanographic Engineering Department, University of Florida, Gainesville, Florida 32611 USA

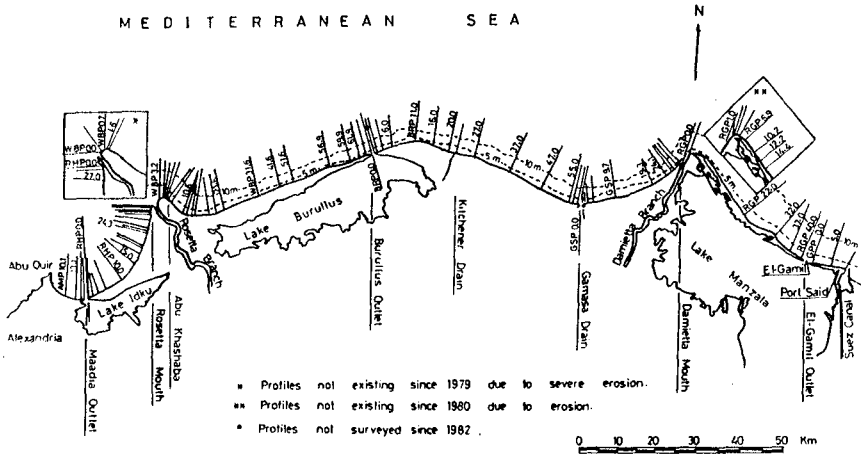


Figure 1. General Layout of Main Profiles along the Nile Delta Coast.

instability of the Nile Delta coastal zone in terms of erosion and accretion has been documented since the beginning of the present century. Local severe erosion has destroyed roads and caused losses of buildings and resort beaches while shoaling due to siltation in lake outlets and estuaries has resulted in navigation hazards and reductions in fish productivity. There has been considerable interest over the last two decades in the marked coastal changes observed along the Nile Delta coast, leading to studies of: coastal geomorphology (Sestini, 1976; Frihy et al., 1988); analysis of beach profiles up to the 6 m depth (Manohar, 1976 a & b); aerial photography analysis (Frihy, 1988); satellite image analysis (Klemas and Abdel Kader, 1982; Smith and Abdel Kader, 1988; Blodge et al., 1991); shoreline changes (Sestini, 1976; Misdorp, 1977); dynamic factors (Khafagy and Manohar, 1979; Manohar, 1981; Fanos, 1986; Elwany et al., 1988; Naffaa et al., 1991) sediment transport (Inman and Jenkins, 1984; Frihy et al., 1991) and sediments (El Askary and Lotfy, 1980).

The erosion and accretion patterns along the Nile Delta coast in general are a result of: 1) a decrease of sediment supply after the construction of the Aswan High Dam and other impoundment structures built on the Nile which have reduced the sediment supply from more than 120 million tons per year to almost zero at present (Orlova and Zenkovitch, 1974; Sharaf El Din, 1974; Smith and Abdel Kader, 1988; Frihy, 1988), 2) rise of sea level in the Mediterranean over the last 40 years at an average rate of about 1.63 mm/yr (Sharaf El Din et al., 1989), 3) subsidence of the land at a rate of 3.5 to 5.0 mm/yr in the northern part of the Delta based on carbon-dated core sections (Stanley, 1988), and 4) dynamic factors including waves and currents which are the principal driving forces for the transport

of sediments and hence the chief agent in beach erosion. Wave action along the Nile Delta coast is seasonal in nature. The energy supplied by severe Winter storms contributes significantly to the total annual energy budget. The maximum wave height recorded is 4.0 m in Winter at Abu Quir Bay. The predominant direction of the waves is WNW-NW with less wave energy from the NNE-NE sector (Naffaa et al., 1991). The predominant littoral current is toward the east with velocities ranging from 20 to 50 cm/sec (Fanos, 1986).

This paper describes the nearshore coastal changes, including the sediment quantities, shoreline changes, bar formation and physiographic nearshore units from the profile data collected during the last ten years, i.e., from 1981 to 1990.

### DATA COLLECTION

The data base for this study has been established from repeated surveys of 80 hydrographic profiles along the Nile Delta coast and simultaneous collection of sediment samples. The most westerly profile is located 6 km west of Maadia Outlet and the most easterly profile 5 km east of El-Gamil Outlet (about 7 km west of Port Said western breakwater). The spacing between adjacent profiles depends on the nature of the coastline and varies from 0.5 km to 10 km with the exception of one 17 km spacing between two profiles west of Rosetta (Figure 1). More detail is provided in Khafagy, Fanos and Naffaa (1992).

The profiles are referred to a permanent baseline which extends, more or less, parallel to the local shoreline. The monument for each profile is a steel angle iron imbedded in a barrel filled with concrete. The hydrographic survey of the coastal profiles extends from the monument to the closer distance of a 6 meter water depth or 1000 m offshore. The surveys have been conducted twice per year since 1976; once during September/October termed "Autumn profiles" which represent the results of the Summer season swell waves and the other during April/May termed "Spring profiles" representing the results of the Winter season storm waves.

The surveys along the profiles are carried out by taking a measurement every 10 meters along the first 250 m from the baseline (surf zone) and then every 50 meters. A surface bottom sediment sample is taken every 100 meters with a grab sampler. The measurements are corrected to the zero Survey Authority datum.

### ANALYSIS OF PROFILE DATA

The profile data have been analyzed in terms of their spatial and temporal variations (Khafagy, Fanos and Naffaa, 1992). Samples are given in Figure 2. Two methods have been used in the analysis of the beach profiles namely: the Eigen-function method (Winant et al., 1975) and the erosion/accretion method (CRI/UNESCO/UNDP, 1978). The first considers the spatial and temporal characteristics of the profiles by computing the first three eigen-functions, representing the mean,

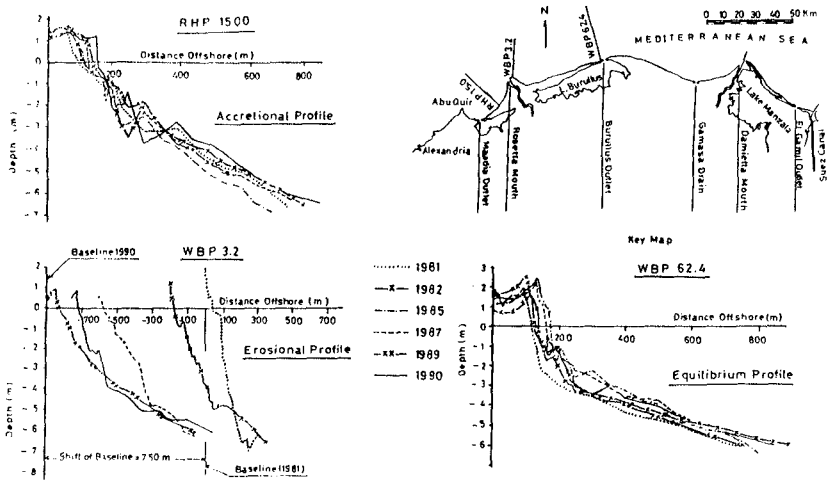


Figure 2. Typical Accretional, Erosional and Equilibrium Profiles.

bar/berm and terrace functions, respectively. The results from this method are beyond the scope of the present paper. Some results for the Burullus area are presented in Khafagy and Fanos (1981). The accretion/erosion method was used to interpret the nearshore changes and the coastal processes of the Nile Delta coast. This method seeks to calculate the nearshore morphology characteristics of the profiles such as the position of the shoreline, depth contours, underwater bars, bed slopes and the volumetric transport rates of the sediments by erosional and/or accretion processes.

A computer program was developed to calculate the accretion/erosion quantities between adjacent profiles. Also computed are the bed slope, bar characteristics and the distances of the 0, 2, 4 and 6 m contours from the original baseline. The surface bottom samples were analyzed mechanically and the mean grain size ( $D_{50}$ ) was computed for each sample.

RESULTS AND DISCUSSIONS

Nearshore Profiles

Based on examination of the 80 profiles along the Egyptian coast, over the period 1981 to 1990, three profile types were identified:

- i. Undernourished profiles characterized by a rapid recession of the beach. These profiles act as sediment sources; the Rosetta Promontory profiles (Figure 2) provide examples.

- ii. Overnourished profiles which are generally accreting and act as sediment sinks, e.g. profiles at Abu Khashaba about 10 km east of Rosetta Branch, and in Abu Quir Bay from Maadia Outlet to 6 km south of Rosetta Exit (Figure 2).
- iii. Dynamically stable profiles which keep their forms at a maximum steepness, and unlike the undernourished profiles which erode continuously, they alter between erosion and accretion. Profiles of this type exist between Kitchener Drain and New Damietta Harbor and west of the Burullus Outlet (Figure 2). Figure 3 gives the seasonal changes for each profile type.

Shoreline and Bed Contour Changes

Measured shoreline and depth contour changes, i.e. 0 m, 2 m, 4 m and 6 m contours during the 10 year period (1981 to 1990) are shown in Figure 4. It is clear that the shoreline is retreating along almost the entire coast except in some short regions between Maadia and west of Rosetta, at Abu-Khasaba, between Kitchener Drain and west of New Damietta Harbor and to the west of Port Said breakwater. Maximum retreat of the shoreline is documented at Rosetta Promontory to be about 70 m/y, while it is about 5 m/y at both of Burullus Headland and Ras El Bar sea resort and about 8 m/y to the east of Damietta branch. There are three regions which are subject to erosion from the shoreline to the 6 m contour. They are Rosetta and Damietta promontories and Baltim Sea resort area which is located about 10 km to the east of Burullus Outlet. This is due to the wave and current action and the absence of the sediment supply from the Nile itself which was balancing some of these losses before the completion of the High Aswan Dam. Also Figure 4 shows that there is accretion for the contours 2, 4 and 6 m along some other areas of the Delta.

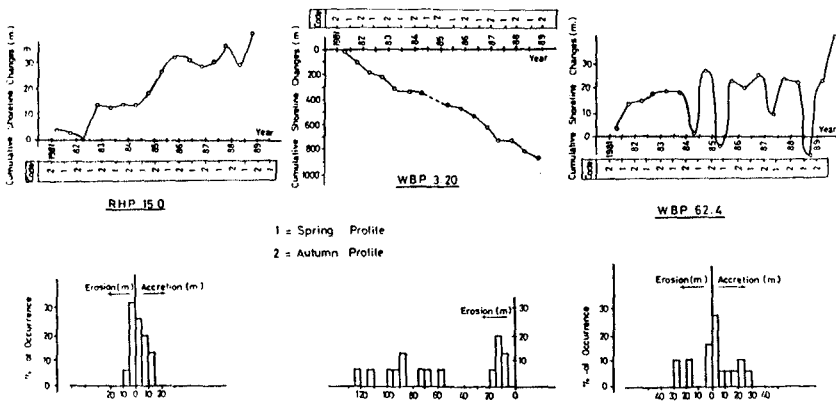


Figure 3. Seasonal Shoreline Variations.

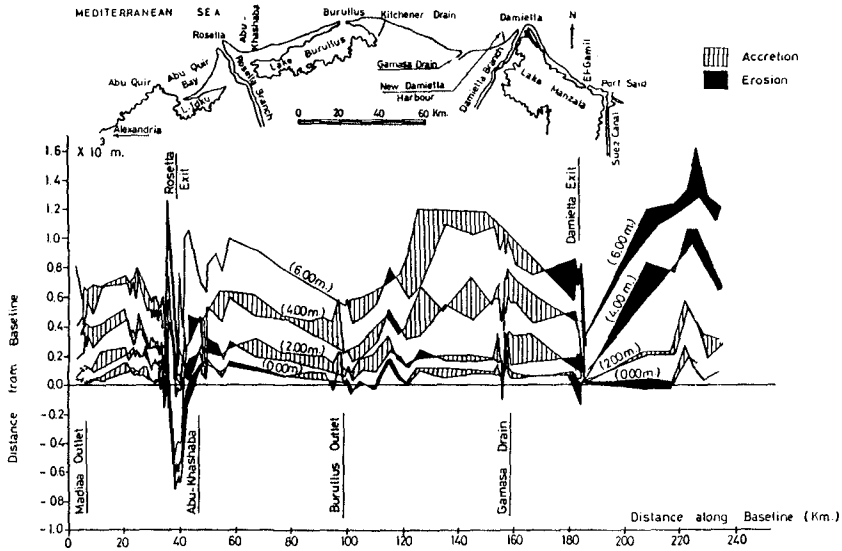


Figure 4. Changes of Contour Lines along the Nile Delta Coast.

### Bed Slope Changes

Based on the profile data it is evident that the Nile coastal beaches have two or three ranges of gradients, with the steeper gradients located in the surf or breaker zone (ranging from 1:76 to 1:140); followed by a seaward transitional milder slope ranging from 1:35 to 1:350 and a still flatter seaward slope ranging from 1:90 to 1:435. The slopes steepen just west of the outlets within and beyond the breaker zone. This is true for all the outlets except those which are provided with protective structures ( Maadia, Burullus and El-Gamil) such as jetties where they are flatter in the breaker zone only due to sedimentation processes. However, for the Damietta Outlet, the slopes are steeper due to the formation of a large eddy west of the jetty which prevents any sediment deposition. East of the outlets, the slopes are steeper than those on the west side, especially in the breaker zone. They gradually flatten for some distance to the east and then steepen again both in and beyond the breaker zone. The very steep slopes (1:5) at the eastern part of the Damietta Promontory are the result of active scour in front of the vertical wall existing in the area and not due to natural causes. The changes in bed slopes during the 1981-1990 period were relatively small.

Grain Size Changes

The size characteristics of the surface bottom samples along the Nile Delta coast during the 1982 to 1989 period show insignificant changes. Some decrease in sediment size was evident from 1982 to 1989, primarily in the zone of maximum wave energy and strong longshore current, namely the breaker zone; from the shoreline to a distance of 300 m offshore. The data showed a clear trend of size reduction in the seaward direction. Coarser sands were also found near Maadia, near Burullus and at Damietta Outlet. These may be a "lag" product resulting from erosion concentrated at the old Nile branches.

Relation between median grain size and bottom slope

It is well known that grain size is an important parameter in determining the profile slopes under water or above water. Figure 5 shows the variation in slope as a function of median grain size  $D_{50}$ , for the beach face and beyond the breaker zone for the entire coast. It is clear that: (i) the slope increases as grain size increases, (ii) the effect of grain size on slopes is greater in the beach zone area than beyond the breaker zone, and (iii) exposure to different wave conditions such as breaking waves modifies the slopes and grain sizes.

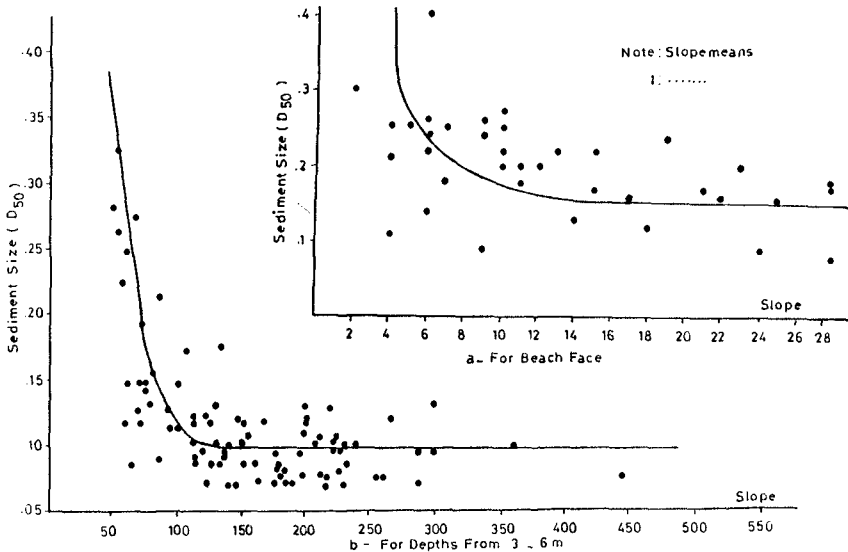


Figure 5. Bottom Slope Versus Medium Grain Size.

### Underwater bars

One characteristic feature of a beach in a relatively enclosed sea with small tidal range such as the Mediterranean Sea is a series of submarine bars (Manohar, 1979). Along most of the Nile Delta coast there are three underwater bars, one in the breaker zone in depths of 0-2 m (summer bar) formed by the short waves and swells, one or two storm bars in water depth ranging from 3-4 m and/or from 5-6 m formed by the largest storm waves. The convex shape of the bars has been interpreted as an index of the existence of more than one predominant wave direction, i.e. waves from NE and NW directions (Khafagy, Fanos, Naffaa, 1992). The bar heights range from 0.30 m to 1.00 m and in some cases are very flat and low in height. Their heights increase in areas of accretion and flatter slopes, whereas in erosional areas their base is large and their heights low. The formation and migration of these bars is a complex phenomenon which is difficult to study in a natural environment.

### Volumetric Changes and Trends in Erosion and Accretion

Coastal processes can be interpreted in terms of changes of profiles and volumes. These types of results were developed from the 1981-1990 profile data and are presented in Figure 6. Figure 6b presents the mass curve (cumulative volume along the baseline). In the mass curve, a steeper upward slope indicates accelerated accretion and a flatter slope means the accretion is less than in the previous zone. A downward slope signifies erosion. Figure 6c presents the total volume of sediments moving on the Nile Delta coast within the zone between the baseline and the 6 meter contour. These figures indicate the following:

1. Volumetric change rates appear to depend on time, for example the volume change during a particular period is not equal to volume change per year multiplied by the number of years.
2. The gross volume change (accretion + erosion) which amounted to  $235 \times 10^6$  cu.m. in the ten year period is by far larger than the net volume change (accretion - erosion) which amounted to  $13 \times 10^6$  cu.m. in the same period.
3. In the breaker zone, erosion predominates over accretion, with a few areas of accretion such as Abu Khashaba east of Rosetta Exit, to the west of Gamasa Drain and near Port Said. The accretion in the Baltim Sea resort area is due in part to the artificial nourishment of the beach.
4. The net volume change over the full length of the coast is sometimes accretion (up to 6 m depth) and sometimes it is erosion. This means that sediments are coming from or lost to depths beyond 6 m. This stresses the importance of extending the profile surveys offshore beyond 6 m to the closure depth.
5. The changes of the profiles do not follow a certain pattern except at Rosetta and Damietta promontories and to the east of Burullus Outlet where they erode progressively.



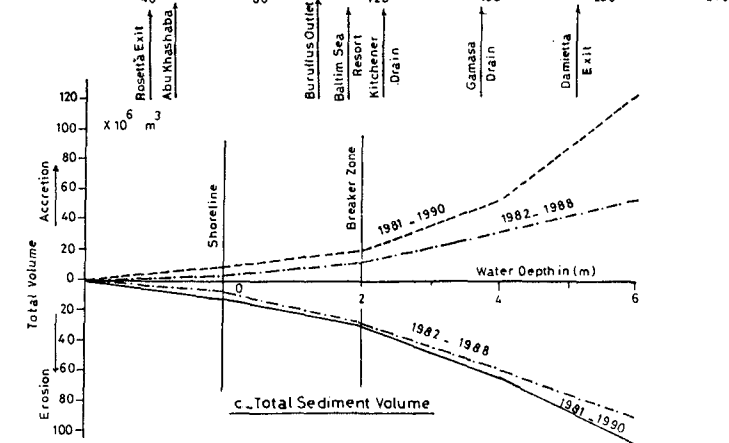
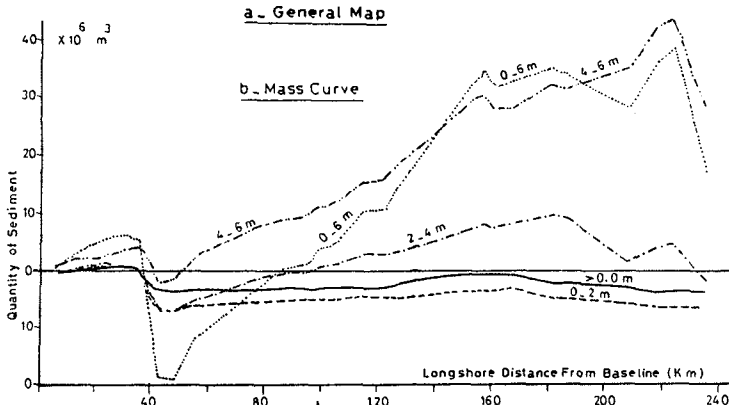
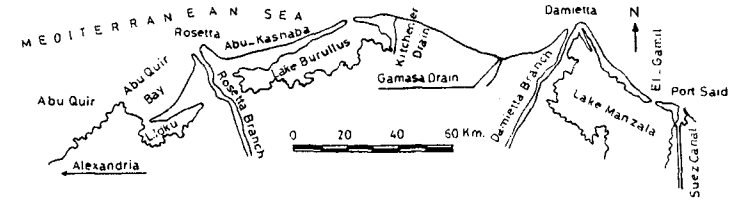


Figure 6. Mass Curve of Total Sediment Volume Determined from Profile Data Along the Nile Delta Coast during the Period from 1981 to 1990.

6. The analysis of the spring profiles shows recession along the coast due to the high waves of the winter season while autumn profiles show redistribution of the sediments and shoreline advancement due to the lower swells of the summer season.

#### Physiographic Nearshore Units

According to the seasonal analysis of the beach profiles many independent physiographic units could be proposed as described below and shown in Figure 7:

1. Abu Quir Bay from Madiaa Outlet to 6 km south of Rosetta Exit is an independent unit although its northern end acts as a sink for the erosional products from the Rosetta Promontory.
2. The Rosetta Promontory, for about 15 km on both sides of the Rosetta Exit behaves as a separate unit acting as sources for adjacent areas.
3. Abu Khashaba zone acts as a sink for erosional material from the Rosetta Promontory.
4. The 40 km east of Abu Khashaba to Burullus Outlet appears to be a unit by itself where the shore is shifting back and forth.
5. The reach from Burullus Outlet to Kitchener Drain is an erosion area with cusp formation at Baltim sea resort.
6. From Kitchener Drain to the western breakwater of New Damietta Harbor is almost stable area with some accretional and erosional pockets.
7. Damietta Promontory on both sides of the Nile estuary is a separate unit similar to the Rosetta unit.
8. The reach from the beginning of the spit and up to 15 km to the east acts as a sink for the promontory erosion and to some extent as a source for the 10 km stretch located immediately eastwards.
9. The remaining stretch appears to be an independent unit and acts as the major source for the Port Said breakwater and its entrance channel.

#### SUMMARY AND CONCLUSIONS

The coastal processes and changes along the Nile Delta shoreline are a result of the dominantly westerly wave incidence, the historic changes in location of the Nile tributaries ( $\approx$  1000 years before present) and the more recent (this century) dramatic reduction in sediment supply due to barrage construction along the Nile River. An effective means of studying the current processes is through analysis of repetitive beach profiles extending a sufficient distance seaward to encompass the active profile.

This study has identified the dominant erosional areas as those characterized by convex outward shorelines as a result of historical sediment supply by the Nile River tributaries. These erosional zones serve as sources of sediment for the accretional areas which are dominantly concave in planform. Consistent with theory

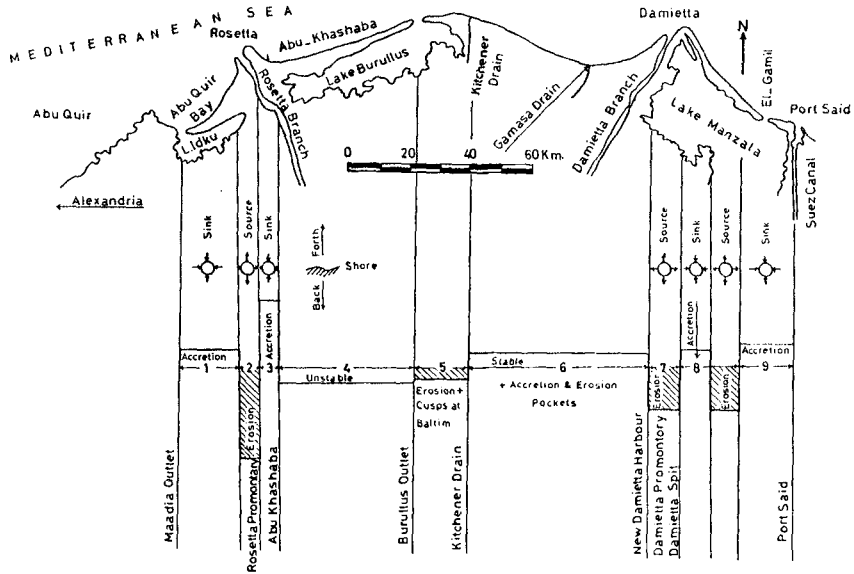


Figure 7. Physiographic Units Identified.

of planform change, it is expected that the erosional zones will broaden with time. The profile and sediment characteristics are qualitatively in agreement with the findings of previous investigators, namely that there is a correlation between local slope and local sediment size. The profile analysis indicates a complex pattern of erosion/accretion both in the longshore and cross-shore directions.

Continued profile measurements will provide a valuable data base which will provide additional understanding of the complex and dynamic coastal processes along the Nile River Delta and will assist in the critical future management decisions relating to this resource.

## REFERENCES

- Blodge, H.W., Taylor, P.T. and Roark, J.H., 1991. Shoreline Changes along the Rosetta, Nile Promontory: Monitoring with Satellite Observations. *Marine Geology*, 99.
- CRI/UNESCO/UNDP, 1978. Coastal Protection Studies. Final Tech. Rep., Paris, France, 155 p.
- El Askary and Lotfy, 1980. Coastal Erosion and Accretion at the East of Damietta, Egypt. *Bulletin of the Faculty of Science, Jeddah*, 4, 257-264.

- Elwany, M.H., Khafagy, A.A., Inman, D.L., and Fanos, A.M., 1988. Analysis of Waves from Arrays at Abu Quir and Ras el Bar, Egypt. *Adv. Underwater Technol., Ocean Sci., Offshore Eng. Soc., Underwater Technol.*, 16: 89-97.
- Fanos, A.M., 1986. Statistical analysis of Longshore Current Data along the Nile Delta Coast. *Water Sci., J., Cairo*, 1:45-55.
- Frihy, O.E., 1988. Nile Delta Shoreline Changes: Aerial Photographic Study of a 28-Year Period. *J. Coastal Research*, 4: 597-606.
- Frihy, O.E., El Fishawi, N.M. and El Askary, M.A., 1988. Geomorphological Features of the Nile Delta Coastal Plain: A Review. *Acta Adriatica (Yugoslavia)*, 29, 51-65.
- Frihy, O.E., Fanos, A.M., Khafagy, A.A. and Komar, P.D., 1991. Patterns of Nearshore Sediment Transport along the Nile Delta, Egypt. *Coastal Engineering*, 15, 405-429.
- Inman, D.L. and Jenkins, S.A., 1984. The Nile Littoral Cell and Man's Impact on the Coastal Zone of the South Eastern Mediterranean. *Scripps Institution of Oceanography Ref. Series 84-31, University of California, La Jolla*, 43 p.
- Khafagy, A.A. and Manohar, M., 1979. Coastal Protection of the Nile Delta. *Nat. Resour.*, 15: 7-13.
- Khafagy, A.A. and Fanos, A.M., 1981. Eigen Function Analysis of Beach Profiles at Burullus Coastal Site. Internal Technical Report, Coastal Research Institute. Alexandria.
- Khafagy, A.A., Fanos, A.M. and Naffaa, M.G., 1992. Beach Profile Analysis During the Period from 1981 to 1990. Internal Technical Report, Coastal Research Institute, Alexandria, Egypt.
- Klemas, V. and Abel Kader, A.M., 1982. Remote Sensing of Coastal Processes with Emphasis on the Nile Delta. In: *International Symposium on Remote Sensing of Environments*. Egypt, 27 p.
- Manohar, M., 1976a. Beach Profiles. *Proceedings of UNESCO Seminar on Nile Delta Sedimentology, Alexandria*, 95-99.
- Manohar, M., 1976b. Dynamic Factors Affecting the Nile Delta Coast. *Proceedings UNESCO Seminar on Nile Delta Sedimentology, Alexandria*, 104-129.
- Manohar, M., 1979. Undulated Bottom Profiles and Onshore-Offshore Transport. *Proceedings of the 16th Conference on Coastal Engineering, N.Y.*, 1454-1474.
- Manohar, M., 1981. Coastal Processes at the Nile Delta Coast. *Shore and Beach*, 49, 8-15.
- Misdorp, R., 1977. The Nile Promontories and the Nile Continental Shelf. *Proceedings UNESCO Seminar on Nile Delta Coastal Processes, Alexandria*, 456-551.
- Naffaa, M.G., Fanos, A.M. and el Ganainy, M.A., 1991. Characteristics of Waves Off the Mediterranean Coast of Egypt. *Journal of Coastal Research*, Vol 7, No. 3.
- Orlova, O. and Zenkovitch, V., 1974. Erosion of the Shores of the Nile Delta. *Geoforum*, 18, 68-72.
- Sestini, G., 1976. Geomorphology of the Nile Delta. *Proceedings UNESCO Seminar on Nile Delta Sedimentology, Alexandria*, 12-24.

- Sharaf El Din, S.H., 1974. Longshore Sand Transport in the Surf Zone Along the Mediterranean Egyptian Coast. *Limnol. Oceanogr.*, 19: 182-189.
- Sharaf El Din, S.H., Ahmed, K.A., Khafagy, A.A., Fanos, A.M. and Ibrahim, A.M., 1989. Extreme Sea Level Values on the Egyptian Mediterranean Coast for the 50 years. *International Seminar on Climatic Fluctuations and Water Management*. Cairo, Egypt.
- Smith, E.S. and Abdel Kader, A., 1988. Coastal Erosion Along the Egyptian Delta, *Journal of Coastal Research*, 2, 245-255.
- Stanley, D.J., 1988. Subsidence in the Northeastern Nile Delta: Rapid Rates, Possible Causes, and Consequences. *Science*, 240, 497-500.
- Winant, C.D., Inman, D.L., and Nordstrom, C.E., 1975. Description of Seasonal Changes Using Empirical Eigenfunctions. *Journal of Geophysical Research*, Vol. 80, No. 15.

## CHAPTER 250

### NILE DELTA PROFILES AND MIGRATING SAND BLANKETS

Douglas L. Inman<sup>1</sup>, M. Hany S. Elwany<sup>2</sup> (M.ASCE),  
Ahmed A. Khafagy<sup>3</sup> and Abraham Golik<sup>4</sup>

#### ABSTRACT

Before construction of the various Nile River dams, the position of the Nile Delta shoreline was in equilibrium between the sediment supplied by the river and the transport of sediment along the coast. Following dam construction sediment yield from the river has virtually ceased. In the absence of sediment from the river, currents, waves and winds are actively eroding the delta. Extensive beach profiling shows that the primary locus of erosion, in excess of  $10 \times 10^6 \text{ m}^3 \text{ yr}$ , is from the Rosetta promontory. This material is carried eastward in part by wave action but predominantly by currents of the east Mediterranean gyre which sweep across the shallow delta shelf with speeds up to 100 cm/sec. Divergence of the current downcoast from Rosetta and Burullus promontories results in formation of accretionary blankets of sand that episodically impinge on the shoreline. Individual blankets of sand form 1.5 m thick covers over the residual profile in depths of 6 to 4 m, and extend for 2 to 4 km along the shore. The sand blankets move progressively downcoast at rates of 0.5 to 1 km/yr, generating series of accretion/erosion waves along the shoreline.

The erosion/accretion/erosion shoreline change is commonly 50 to 100 m and has a periodicity of 3 to 8 years. When the accretionary phase of the wave has passed downcoast, the shoreline returns to its previous form and exhibits a "residual" equilibrium profile. In its residual form, the beach profile goes through characteristic adjustments to seasonal wave climate, exhibiting an equilibrium winter profile with a pronounced bar and a summer profile when the bar tends to migrate onshore. When the nearshore is blanketed with sand during the accretionary part of the cycle, the profile is in disequilibrium with wave forcing and frequently shows several, irregularly spaced bars and troughs. Although the year to year shoreline changes associated with the accretion/erosion waves are large, 0(50 m/yr), the long-term (decadal) changes based on successive residual profiles from the erosion portion of the cycle are relatively moderate, say 0(2 m/yr).

---

<sup>1</sup>Center for Coastal Studies (CCS), Scripps Institution of Oceanography, La Jolla CA 92093-0209

<sup>2</sup>(CCS) and Coastal Research Institute, Alexandria, Egypt 21414

<sup>3</sup>Coastal Research Institute; Alexandria, Egypt 21414

<sup>4</sup>National Institute of Oceanography, IOLR, Haifa 31080, Israel

Findings from this study suggest that the coastal current augmented by waves may transport 10 - 20 million  $m^3/yr$  of sandy sediment, while the longshore sand transport near the shore is about 1 million  $m^3/yr$ . Thus it appears that the blankets of moving sand that episodically impinge on these relatively shallow (6 m deep) profiles are only revealing the "toe of the elephant." Additional study is needed at depths of 20 m or more to resolve this problem.

## INTRODUCTION

The shoreline of the Nile Delta extends along the Mediterranean coast from near Alexandria for 200 km to the east (Figure 1). The Nile River has been the sole source of the sediment for the delta as well as for the entire Nile littoral cell that extends an additional 500 km to Akko, Israel (e.g., Inman and Jenkins 1984; Carmel et al. 1985). The sediment load from the Nile River was deposited along the submerged portion of the delta where it was sorted and transported to the east by the prevailing waves and by currents of the counterclockwise east Mediterranean gyre that commonly flows at about 50 cm/sec over the delta. Prior to 1964, the turbid plume of the flood waters of the Nile River could be traced along the Mediterranean coast for over 700 km to the shores of Lebanon (Orin 1952; Hecht 1964).

Until 1964, the major sediment source of the littoral cell was the Nile River. Construction of the High Aswan Dam, which began filling in 1964, has resulted in a near absence of Nile River flow into the Mediterranean and a corresponding complete loss of the Nile River as a source of nutrients to coastal waters and as an active sediment source for the delta and the coastline of the Nile littoral cell. As a result, the Nile Delta is now subject to severe erosion in a number of localities.

Previous studies have shown that the Nile Delta shoreline is bordered by a ribbon of sand, approximately 10 km-wide, extending from Rosetta promontory to near Damietta promontory (e.g., Fishawi et al. 1976; Misdorp 1977). Curiously, just west of Damietta promontory, this ribbon of sand diverges in a northeasterly direction from the coast, arching seaward from the promontory, leaving a mostly muddy offshore area from Damietta to Port Said (Figure 1). More recent studies by Murray et al. (1980; 1981) show that the Damietta promontory interacts with the east Mediterranean gyre to form a large, stationary eddy that begins at Damietta, extends offshore for up to 35 km and eastward along the coast for about 70 km. The seaward portion of the eddy is a high-speed jet over 5 km wide that forms off the promontory and flows northeasterly and then easterly with measured surface-to-bottom velocities of over 60 cm/sec. The eddy drives a field of actively migrating sand ridges easterly over a smooth mud plain. The sand belt begins in depths of 10 m, flows northeasterly, turns easterly and finally arcs southeasterly towards the coast between Port Said and Bardawil Lagoon (Coleman et al. 1981). This appears to be a major transport path and a partial sink for Nile sand.

The formation of the eddy down-current from Damietta is associated with the abrupt bend to the southeast in coastal orientation at that point. This area, including Manzala Lagoon and its barrier beaches, appears to have subsided at rates up to 0.5 cm/yr during the past 7500 years. Stanley (1988) suggests that the subsidence is associated with the Pelusium Line, a northeast-trending compressional zone bordering the Levant Basin and entering Africa along the axis of the ancient Pelusium Branch of the Nile between Port Said and Bardawil Lagoon (Neev et al. 1976).

## PRESENT STUDY

This report is part of a study of the budget of sediment of the Nile littoral cell sponsored by the U.S. Agency for International Development. It is based on extensive

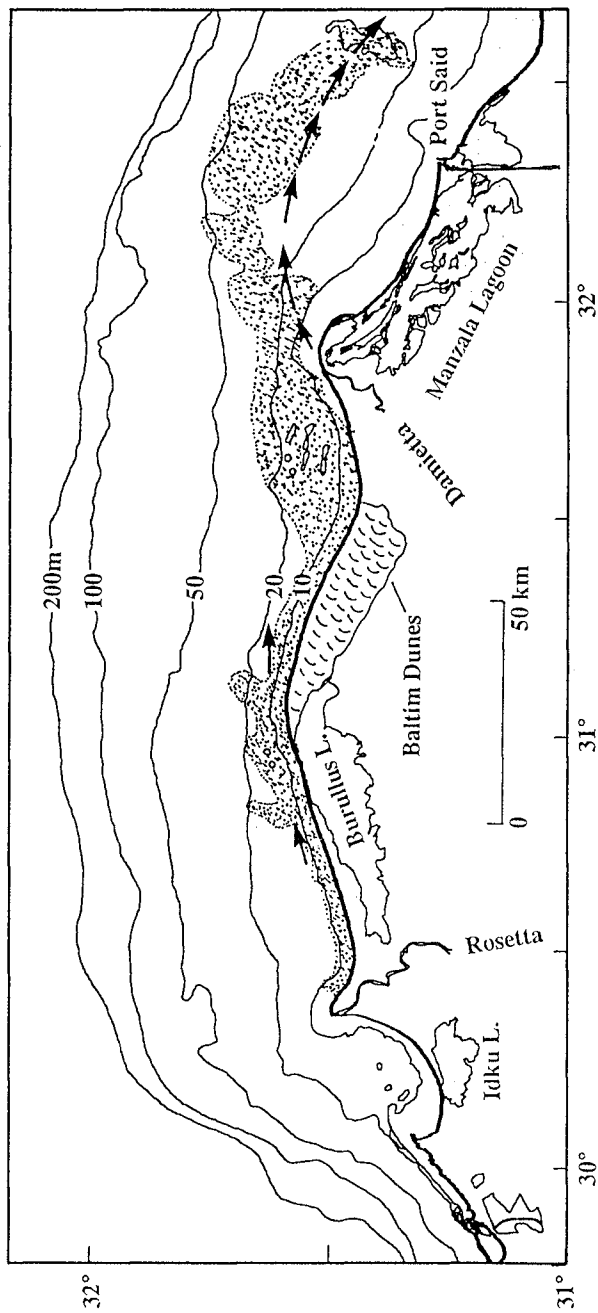


Figure 1. Bathymetry and sediment transport paths on the Nile Delta. Sandy sediment (stippled) after Fishawi et al. (1976), dunes after Sestini (1976) and Stanley et al. (1992), prevailing 25–75 cm/sec currents (central arrows) from hydrographic charts, and 50–75 cm/sec Damietta eddy current (arrows) after Murray et al. (1980).



beach profiling, sediment analysis and wave measurements. The profiling includes 70 ranges extending over the 200 km of Nile Delta shoreline (see Khafagy et al. this proceeding), about 80 % of which were measured twice annually. Measurements during the early winter quarter of the year (October-December) were initiated under a previous UNDP/UNESCO study and, as used in this study, extended over the 18-year period from 1971 to 1988. Measurements during the spring quarter (April - June) extended from 1976 to 1988. These profiles were surveyed to depths of 6 m or distances of 1 km, whichever occurred first.

Sediment sampling accompanied the profile surveying. Samples from the beach face at MSL show a mean grain size of about 250  $\mu\text{m}$  from Rosetta east, coarsening to 340  $\mu\text{m}$  off Burullus and returning to 250  $\mu\text{m}$  in the Baltim segment. Much finer sand, 150  $\mu\text{m}$ , occurs on the Manzala barrier beaches, suggesting that the longshore transport coupling between the Manzala barriers and the Burullus-Baltim area is far from direct.

Wave arrays are located on an oil platform off Abu Quir Bay and in depths of 6 m off Ras el Bar on Damietta promontory. Both are three element arrays that provide wave directional-frequency spectra (Lowe et al. 1972). The Abu Quir array became operational in 1982/83 and the Ras el Bar array in 1985 (Lowe and Inman 1984; Elwany et al. 1988). The arrays show that the predominant waves are from the northwest to west-northwest and the wave climate is characterized by  $1/2 \leq H_s(m) \leq 3$  and  $3 \leq T_p(s) \leq 8$ , where  $H_s$  is the significant wave height and  $T_p$  is the peak spectral period.

## SHORELINE CHANGES

Analysis of the 18 years of profiling along the 70 Nile Delta ranges shows that there are some sections of long-term erosion and accretion while, in other sections, the shoreline exhibits large cyclic changes with periods of 3 - 8 years, but undergoes little net long-term change. An "end-point" analysis of shoreline change over the 18 years is shown in Figure 2 together with the standard deviation of change. The end-point procedure gives

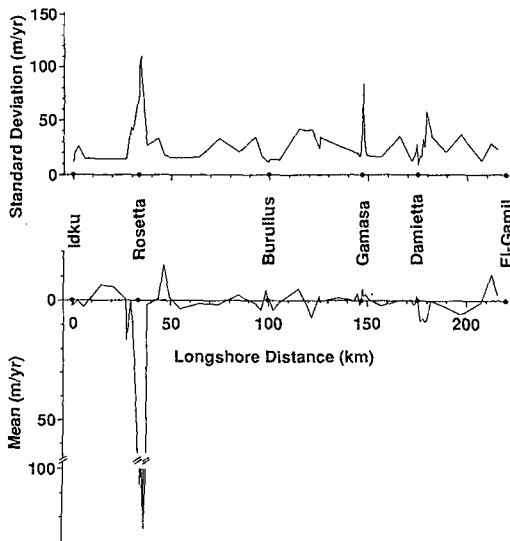


Figure 2. Mean shoreline change rate along the Nile Delta for the survey period 1971-1988 (below) and the standard deviation of the data set (above).

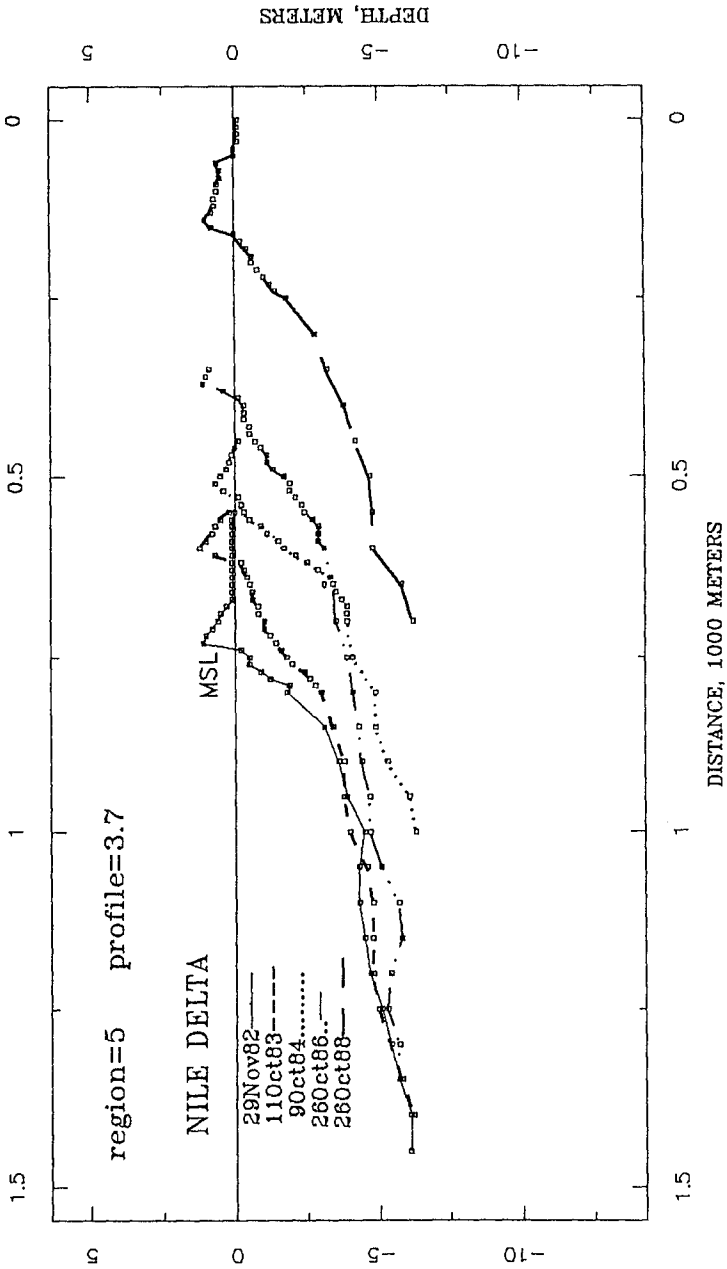


Figure 3. Shoreline retreat of 90 m/yr shown by successive surveys on Rosetta promontory.

valid information where the change in shoreline follows a continuous trend as in Figure 3, but can give biased results when there are cyclic changes in trend, as shown in Figure 4 (e.g., Dolan et al. 1991).

Inspection of Figure 2 shows that the primary locus of erosion is from Rosetta promontory. Volume changes down to the 6 m depths surveyed give the erosion rate as 5 million  $m^3/yr$ . Since the erosion clearly extends to greater depth, and the profile is steepening as it recedes (Figure 3), a conservative estimate is about 10 million  $m^3/yr$ . This material is transported easterly along the delta coast by waves and currents. The strong currents, which may reach their near-bottom velocity maximum in depths of 10 to 30 m, are also likely eroding sediments from these deeper portions of the shelf.

## SAND TRANSPORT

There appear to be two interrelated sand transport mechanisms with somewhat different paths along the Nile Delta coast: a *longshore* and a *coastal current* transport path. The classical longshore sand transport is most intense in and near the surf zone, and is driven by the waves and wave-induced longshore currents. Along the Nile shoreline the longshore sand transport is eastward at rates of about 1 million  $m^3/yr$  (Inman and Jenkins 1984).

A coastal current transport path of sand appears to be primarily driven by the easterly-flowing east Mediterranean gyre that attains velocities of up to 100 cm/sec over the shallow shelf. This transport is undoubtedly enhanced by wave action, particularly during storms when 3-m-high, 8-sec-period waves can move sand in depths of 40 m. However, the sediment distribution and coastal current measurements (e.g., U.S. Hydrographic Chart 56100) suggest that this transport occurs in a band about 5 to 10 km wide centered around depths of 10 to 15 m. Clearly this transport path is carried to much greater depths by the trapped jet off Damietta promontory (Figure 1). Consideration of the overall budget of sediment suggests that the coastal current system may transport sand at rates of 10 to 20 million  $m^3/yr$  along the coast. The coastal transport of sand along the southern California coast, which is largely wave-driven, appears to be about 10% of the longshore transport rate (Inman and Masters 1991). Along the Nile Coast, the coastal current transport is likely an order of magnitude larger than the longshore transport rate.

Pronounced changes in downcoast orientation, as at Damietta promontory, produce large, standing eddies. However, more gradual changes in orientation, as off Burullus, appear to result in a downcoast current divergence or spreading out and a decrease in velocity. This divergence results in a local decrease in the coastal sediment transport rate and the accretion of sand. This may, in part, explain the formation of the Damietta Banks west of Damietta promontory and the formation of the extensive Baltim dune field (Figure 1). This zone of sand accretion also appears to be a contributing factor in the formation of accretion and erosion waves along the shoreline east of Burullus Inlet.

### *Accretion and Erosion Waves*

Divergence of the current downcoast from Rosetta and Burullus promontories results in formation of accretionary blankets of sand that episodically impinge on the shoreline. Downcoast from Burullus promontory, individual blankets of sand from 1 to 2 m thick covers over the residual beach profiles in depths of 4 to 6 m (Figure 5), and extend for 2 to 4 km along the shore. The sand blankets move progressively downcoast at rates of 0.5 to 1 km/yr, generating series of accretion/erosion waves that travel along the shoreline (Inman 1987). These rhythmic features are clearly visible in satellite imagery which shows the turbid plumes in their nearshore circulation pattern (Inman et al. 1976). Their overall shoreline accretion to erosion patterns are shown in Figure 4 and their

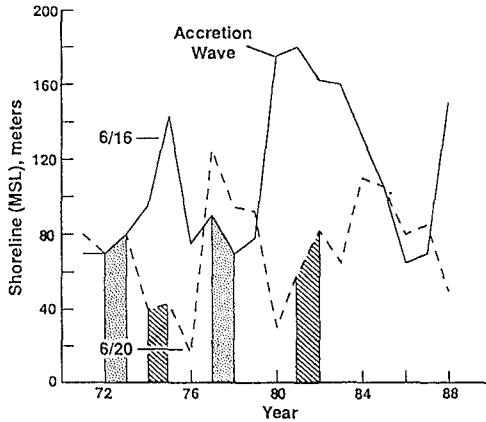


Figure 4. Accretion and erosion waves at ranges 16 and 20 km east of inlet to Burullus Lagoon. Vertical bars show initial impingement of sand blanket on profile. Compare with Figure 5.

temporal and spatial statistics listed in Table 1. The individual sand blankets impinging on the beach profile have volumes of about 2 to 5 million  $m^3$ .

The impingement of the sand blanket on the beach profile is relatively rapid, always appearing in its full thickness ( $\sim 1.5m$ ) between two annual surveys (Figure 5). The initial time of impingement is shown by the vertical bars in Figure 4. Thereafter the blanket gradually thins while the shoreline accretes. After several years the blanket migrates downcoast, and the shoreline erodes back to its former width.

#### *The Residual Equilibrium Profile*

When the accretionary phase of the wave has passed downcoast, the shoreline returns to its previous form and exhibits a "residual" profile. In its residual form, the beach profile goes through characteristic adjustments to seasonal wave climate, exhibiting an equilibrium winter profile with a pronounced bar and a summer profile when the bar tends to migrate onshore (Figure 6a,b). When the nearshore is blanketed with sand during the accretionary part of the cycle, the profile is in disequilibrium with wave forcing and frequently shows several, irregularly spaced bars and troughs. Although the year to year shoreline changes associated with the accretion/erosion waves are large,  $O(50 \text{ m/yr})$ , the long-term (decadal) changes based on successive residual profiles from the erosion portion of the cycle are relatively moderate, say  $O(2 \text{ m/yr})$ .

Table 1. Accretion and Erosion Waves East of Burullus Promontory<sup>a</sup>

Range <sup>b</sup>	6/11	6/16	6/20
Cycle Period <sup>c</sup> , years	6	7	6
Mean Double Amplitude <sup>d</sup> , meters	120	90	95
Number of Surveys <sup>e</sup>	15	15	17
Cycle Phase in 1978	Accretion max	Erosion max	Accretion max

<sup>a</sup> Data source: Cooperative Marine Technology Program for the Middle East, U.S. AID, Coastal Research Institute, Alexandria, Egypt.

<sup>b</sup> Profiles are from region 6 and their range (double digit number) indicates their distance in km east of Burullus Inlet

<sup>c</sup> Crest to crest propagation time

<sup>d</sup> Mean crossshore change from maximum accretion to erosion

<sup>e</sup> Survey period 18 years extending from 1971-1988

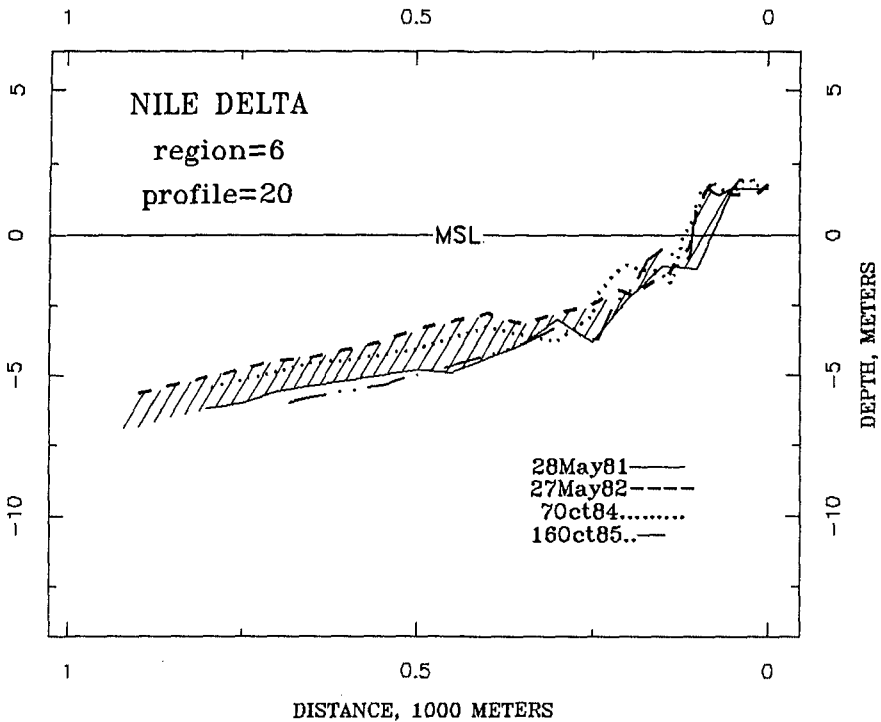


Figure 5. Comparative surveys showing impingement of 1.5 m thick blanket of sand between surveys of 1981/82 on range 20 km east of Burullus Inlet.

The best-fit form for the equilibrium profile follows that suggested by Inman et al. (in press). Their model consists of two contiguous curves, an offshore (shorerise) portion joined at the breakpoint bar with the onshore (bar-berm) portion (Figure 6). Both portions of the profile are well-fitted by parabolic curves of the form  $h = Ax^n$  where  $h$  is positive

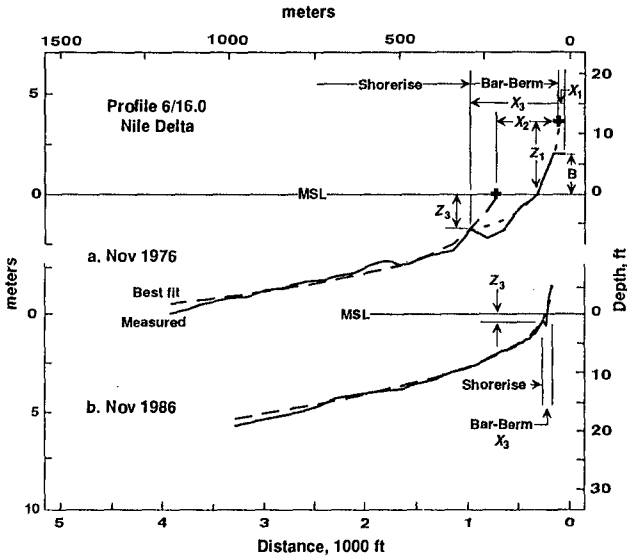


Figure 6. Profiles and definition sketch for compound parabolic curve fitting. Parameters are listed in Table 2.

downward and  $x$  is the positive offshore coordinate (Table 2). It was found that the compound parabolic curves gave the best fit, especially when there was a longshore bar present as in Figure 6a. However, when the bars migrate onshore leaving a reasonably "smooth" profile as in Figure 6b, then a single-fit parabolic curve gives reasonable good fit as shown in Figure 7 and Table 2.

*Acknowledgements*

This report represents results from a trilateral study "Predictive Model for Shoreline Changes Along the Nile Littoral Cell" which is part of the "Cooperative Marine Technology Program for the Middle East" sponsored by the U. S. Agency for International Development.

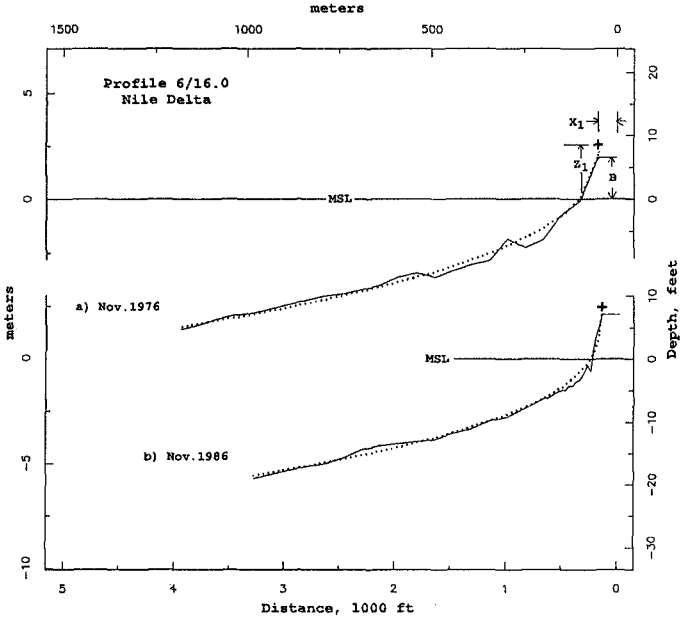


Figure 7. Profiles and single-fitted parabolic curves. Parameters defined in Figure 6 and listed in Table 2.

Table 2. Best-fit Curves of Form  $h = Ax^m$  for Profile Range 6/16

Date	Bar-Berm <sup>a</sup>							Shorerise <sup>a</sup>		
	X <sub>1</sub>	Z <sub>1</sub>	A <sub>1</sub>	m <sub>1</sub>	X <sub>3</sub>	B	Z <sub>3</sub>	X <sub>2</sub>	A <sub>2</sub>	m <sub>2</sub>
<u>Compound-Fitted Curves</u>										
Nov76	37	3.0	0.24	0.32	280	2.0	2.0	234	0.64	0.49
Nov86	50	2.4	0.70	0.40	40	2.0	0.7	32	0.21	0.48
<u>Single-Fitted Curves (Berm and Shorerise)</u>										
Nov76	48	2.7	0.63	0.38		2.0				
Nov86	40	2.4	0.74	0.35		2.0				

<sup>a</sup> Symbols defined in Figure 6; all dimensional units in meters.

## REFERENCES

- Carmel, Z., Inman, D. L., and Golik, A. (1985). "Directional wave measurement at Haifa, Israel, and sediment transport along the Nile littoral cell," *Coastal Engineering*, 9, 21-36.
- Coleman, J. M., Roberts, H. H., Murray, S. P., and Salama, M. (1981). "Morphology and dynamic sedimentology of the eastern Nile delta shelf," p. 301-329 in C. A. Nittrouer (ed.), *Sedimentary Dynamics of Continental Shelves*, Elsevier, Amsterdam and New York, 449 pp.
- Dolan, R., Fenster, M. S. and Holme, J. (1991). "Temporal analysis of shoreline recession and accretion," *Jour. Coastal Research*, 7(3), 723-744.
- Elwany, M. H. S., Khafagy, A. A., Inman, D. L., and Fanos, A. M. (1988). "Analysis of waves from arrays at Abu Quir Ras El-bar, Egypt," p. 89-97 in *Oceanology '88*, Advances in Underwater Technology ... Society for Underwater Technology (Graham & Trotman, London), 16, 304 pp.
- Fishawi, N., Fahmy, M., Sestini, G., and Shawki, A. (1976). "Grain size of the Nile Delta beach sands," p. 79-94 in UNDP/UNESCO, *Proc. Seminar Nile Delta Sedimentology*, Academy Scientific Res. and Technol., Cairo, 257 pp.
- Hecht, A. (1964). "On the turbulent diffusion of the water of the Nile floods in the Mediterranean Sea," *Sea Fisheries Research Station, Haifa, Bull.*, (36), 24 pp.
- Inman, D. L. (1987). "Accretion and erosion waves on beaches," *Shore & Beach*, 55(3/4), 61-66.
- Inman, D. L., Aubrey, D. G., and Pawka, S. S. (1976). "Application of nearshore processes to the Nile Delta," p. 205-255 in UNDP/UNESCO, *Proc. Seminar Nile Delta Sedimentology*, Academy Scientific Res. and Technol., Cairo, 257 pp.
- Inman, D. L., Elwany, M. H. S., and Jenkins, S. A. (submitted). "Shorerise and bar-berm profiles on ocean beaches," *Jour. Geophysical Res.*
- Inman, D. L., and Jenkins, S. A. (1984). "The Nile littoral cell and man's impact on the coastal zone of the southeastern Mediterranean," *Proc. 19th Conf. Coastal Engineering Conf.*, Amer. Soc. Civil Engrs., 2, 1600-1617.
- Inman, D. L., and Masters, P. M. (1991). "Budget of sediment and prediction of the future state of the coast," Chap. 9 (105 pp.) in *State of the Coast Report, San Diego Region, Coast of California Storm and Tidal Waves Study*, U. S. Army Corps of Engineers, Los Angeles District, Chapters 1-10, Appen. A-Q.
- Lowe, R. and Inman, D. L. (1984). "Wave parameters, Abu Quir Array, Egypt," *Univ. of California*, Scripps Inst. Oceanography, SIO Reference Series 84-32, 5 pp., tbl + fig.
- Lowe, R. L., Inman, D. L., and Brush, B. M. (1972). "Simultaneous data system for instrumenting the shelf," *Proc., 13th Conf. Coastal Engineering*, Amer. Soc. Civil Engrs., 1, 95-112.
- Misdorp, R. (1977). "The Nile promontories and the Nile continental shelf," p. 456-551 in UNDP/UNESCO, *Proc. Seminar Nile Delta Coastal Processes*, Academy Scientific Res. and Technol., Cairo, 624 pp.



- Murray, S., Coleman, J. M., Roberts, H. H., and Salama, M. (1980). "Eddy currents and sediment transport off the Damietta Nile," *Proc. 17th Coastal Engineering Conf., Amer. Soc. Civil Engrs.*, 2, 1680-99.
- Murray, S., Coleman, J. M., Roberts, H. H., and Salama, M. (1981). "Accelerated currents and sediment transport of the Damietta Nile promontory," *Nature*, 293(5827), 51-54.
- Neev, D., Almagor, G., Arad, A., Ginzburg, A., and Hall, J. K. (1976). "The geology of the southeastern Mediterranean," *Geological Survey of Israel Bull.*, (68), 51 pp.
- Oren, O. H. (1952). "Some hydrographic features observed off the coast of Israel," *Inst. Oceanography Monaco, Bull.*, (1017), 10 pp.
- Sestini, G. (1976). "Geomorphology of the Nile Delta," p. 12-24 in UNDP/UNESCO, *Proc. Seminar Nile Delta Sedimentology*, Academy Scientific Res. and Technol., Cairo, 257 pp.
- Stanley, D. J. (1988). "Subsidence in the northeastern Nile Delta: rapid rates, possible causes, and consequences," *Science*, 240, 497-500.
- Stanley, D. J., Warne, A. G., Davis, H. R., Bernasconi, M. P., and Chen, Z. (1992). "Nile Delta, the late Quaternary north-central Nile Delta from Manzala to Burullas Lagoons, Egypt," *National Geographic Res. & Explor.*, 8(1), 22-51.

## CHAPTER 251

### DESIGN AND CONSTRUCTION OF THE BOSTON OUTFALL

Y. Eisenberg, F.ASCE  
P. Brooks, MIE (Aust.)

#### ABSTRACT

The Boston Outfall, presently under construction in Massachusetts, U.S.A., is the world's largest tunnel outfall. The outfall represents the latest in tunnel outfall technology and when completed will discharge up to 1300 million gallons per day of secondary treated effluent through a system of seabed diffusers, nine and a half miles off the coast of Boston. Installation of the 55 diffusers and risers are nearing completion, with the construction of the outfall tunnel just commencing. The Outfall is a major component of the Boston Harbor Clean-up Project.

This paper presents a description of the design and construction of the deepwater Boston Outfall.

#### INTRODUCTION

In 1985 the Massachusetts Water Resources Authority (MWRA) was created with an objective to construct a new secondary wastewater treatment plant in order to end the pollution of Boston Harbor. The Boston Harbor Project is an 11 year \$6.1 billion effort, making it the largest wastewater treatment project in the U.S.A. The new facilities, with a capacity to treat more than one billion gallons per day, will replace two antiquated and over-burdened primary sewage treatment plants on Boston's Deer and Nut Islands. In addition to the new treatment plants, the Project also includes a new headworks facility, a five mile hard rock tunnel between the two islands and a nine and a half mile long effluent outfall tunnel from Deer Island. A Site Plan of the Project is shown on Figure 1. Construction on the project began in 1988 and will be completed by 1999. The Boston Harbor Project is being carried out under a "fast track" schedule due to Federal Court mandated milestones.

The outfall construction was bid in July 1990 for a total of \$279 million and is scheduled for completion in April 1995.

## OUTFALL CONFIGURATION

During initial investigations for the Outfall design, concepts were evaluated for both a seabed pipeline and a tunnel for transport of the effluent. Some of the factors that dictated the selection of a tunnel were:

- Preliminary investigations indicated that the dredging of Boston Harbor for the construction of a large diameter pipeline would not be permitted because of environmental reasons.
- The required internal diameter of the Outfall (24.25 feet) would require massive pipe sections and create enormous logistics, handling and connection problems if a seabed pipe was selected.
- Construction of a large diameter pipeline, nine and a half miles out into the Atlantic Ocean presented significant construction risk in terms of both operations and schedule delays.
- Costs for large diameter tunnels become more competitive against pipelines over longer distances.
- Tunnels have reduced operation and maintenance costs, and provide a longer service life in comparison to a pipeline.

Based on the decision to construct a tunnel in preference to a pipeline, an outfall system was developed which consists of the following principal components and features: (Refer to Figure 2.)

- A vertical dropshaft, 30 feet in diameter to a depth of 420 feet below Deer Island. The tunnel depth was dictated by the requirement to have a minimum of four tunnel diameters of competent rock between the tunnel crown and the surface of the rock.
- A submarine outfall tunnel, 24.25 feet in finished diameter, approximately 43,000 feet long to the start of the diffuser zone. The tunnel has an upward grade to allow ground water to drain back to the shaft.
- A tunnel venturi immediately upstream of the diffuser zone to assist in tunnel purging and prevention of seawater intrusion into the tunnel.
- Tapered tunnel in the diffuser zone, 6600 feet long. Tunnel cross section reduces gradually in area to maintain relatively constant effluent velocity.
- 55 riser offtakes connecting the diffuser tunnel to the seabed risers.
- 55 riser pipes, 30 inches in diameter and 250 feet long to carry the effluent from the tunnel up to the seabed diffuser heads.
- 55 diffuser heads, each comprising eight radial ports with conical nozzles attached. The diffusers are spaced 125 feet apart and disperse the effluent in 110 feet of water.

## OUTFALL DESIGN CRITERIA

A prerequisite to the design of the outfall was the establishment of realistic criteria on which to base the design. The key issues influencing the design of any outfall system are:

- Existing and ultimate dry and wet weather flows.
- Internal and external hydraulic performance

- Operational life
- Structural integrity
- Regulatory requirements
- Constructability
- Operations and maintenance (O&M)

Specific quantitative design criteria were developed to meet the site constraints and the regulations of numerous government agencies and local authorities. They reflect multi-disciplinary considerations including oceanography, geology, technical, hydraulics and hydrodynamics, water quality, biology, and empirical observations of existing outfalls.

A summary of the general design criteria assumed by the designers is as follows:

- A design life of 100 years was specified.
- The design water depth took into consideration the greenhouse effect, combined with maximum tide and storm surge.
- The design flows of the system were determined to be 1270 mgd peak to 320 mgd minimum.
- The Outfall was to be designed to allow full seawater purging of the tunnel. Purging flows are 80% of the peak design flows with the specified seawater and effluent densities.
- Minimize sea water intrusion into the tunnel.
- Outfall dewatering. It was a requirement that the outfall be able to withstand being fully dewatered at least 4 times over the 100 year life of the system.
- Maximum surface and seabed currents.
- Design wave height and period typically taken on the 100 year return wave.
- Assessment of accidental impact loads due to anchors, chains or trawling equipment.
- Bedrock and seabed overburden properties.
- Corrosion allowance for steel seabed structures and the elimination of metals as far as possible to reduce the potential for galvanic corrosion.
- Assumed construction guidelines such as installing the riser shafts and diffusers prior to the tunnel construction reaching the diffuser zone.

## **SITE INVESTIGATIONS**

The geotechnical conditions along the outfall alignment presented the design engineers with some challenges. The bedrock is a very competent sedimentary argyllite material of approximately 25,000 psi comprehensive strength, with presence of diabase dikes and fracture zones. Overlying the bedrock, particularly in the diffuser zone are sediments and clays (Boston Blue Clay) in layers up to 100 feet deep. Underlying the clays are bands of glacial till characterized by cobbles and boulders. By any standards, the geology of the area is judged very complex and thus difficult to define precisely.

To assist in the outfall design process, a comprehensive geotechnical and geophysical exploration program was carried out for the Project. In 1988, the

MWRA contracted for the drilling of 25 exploratory borings, geophysical surveys, surface mapping, laboratory tests and other exploratory work in the general vicinity of the alignment. Explorations were also carried out on Deer Island. Based on this information, suitable diffuser sites were selected and a preferred general alignment was established.

In 1989, additional exploration was carried out for the MWRA as part of the outfall design program. These explorations concentrated in a narrower strip along the preferred alignment and included 31 borings, 15 piezocone borings, 96 vibracores, seismic reflection and refraction profiling, a deep digital survey, side scan sonar, and magnetometer profiling, as well as field and laboratory testing. The program represented one of the most intensive geotechnical and marine investigations undertaken for an outfall project.

## **OUTFALL DESIGN**

### **Shaft**

Various methods of ground support were considered for the section of the 30 feet diameter shaft through the glacial till from ground level to -110 feet below Mean Sea Level. These included precast concrete segments, soldier piles and lagging, the New Austrian Tunneling Method (N.A.T.M.) and diaphragm walls. Diaphragm walls were selected by the designers as the most reliable means of support that would meet design criteria and ensure safety during construction operations.

The second section of the shaft, from -110 feet to -365 feet consists of three sections of shaft supported by rock bolts, mesh and a skin of reinforced shotcrete.

The third and lowest portion of the tunnel shaft consists of a back tunnel (Figure 4), a shaft invert and pumping sump and a TBM erection chamber. The final lining for the shaft and the initial length of tunnel up to the point where the main tunnel lining commences is to be unreinforced cast-in-place concrete. This 12 inch thick lining was designed to withstand full external hydrostatic pressure in the temporary condition and full internal hydrostatic pressure in the operational condition. The construction of the shaft commenced in late 1990 and was completed in early 1992.

### **Tunnel**

The 43,000 feet long main outfall tunnel has a 24 feet, 3 inch inside diameter. Approximately 90% of the tunnel was determined to be in competent sedimentary argyllite material, with an approximate compressive strength of 25,000 psi. For the few areas where blocky and seamy rock were encountered, the engineers provided suggested grouting layouts for the Contractor as shown in Figure 5.

Two designs for tunnel lining were provided in the bidding documents:

- 1) Precast segmental liner erected under a shield;
- 2) Cast-in-place liner using a precast invert segment.

Both liners were designed to resist full hydrostatic pressure. The Contractor was permitted in the specifications to offer his own liner design subject to the approval of the engineer. The "as bid" precast liner consisted of six segments per each 5 feet deep ring: an invert segment, four side segments and a "keystone wedge" trapezoidal shaped top segment. The longitudinal joints were "ship-lap" type and the transverse ones were "knuckle" joints. The Contractor submitted his own design for a variation of the precast liner. After passing physical testing and analysis, this liner system was accepted for use. The Contractor's design utilizes equal and interchangeable trapezoidal shaped segments held together longitudinally with pins and held together transversely with guiding rods (see Figures 6 & 7). The precast units are presently being manufactured in Hudson, New Hampshire approximately 50 miles from the outfall site.

### **Diffuser and Riser**

Like all large marine construction projects, the installation method has a major bearing on the design. Because of the high operating spread cost of the equipment involved, the designers sought a configuration that would lend itself to a "production line" installation method. This was especially relevant considering the large number of repetitive tasks involved. Construction issues considered during design included:

- All component makeup was to be performed on shore or on the barge in controlled conditions.
- Critical inspection and QA activities were able to be performed by ROV or by electronic survey instruments.
- Critical path downtime, e.g., such as that typically occurring while waiting on concrete curing, was reduced to a minimum.
- Diver intervention (a major cause of downtime) would be minimized.
- Potential downtime scenarios for several construction methods were analyzed, and allowances made in the design to mitigate their occurrence.
- Installation tolerances were set at achievable levels based on recent historical precedent.

The designers were fortunate in that they had just been involved in the design and construction of the Sydney Ocean Outfalls, which involved the fabrication and installation of 96 diffusers in 250 feet of water off Sydney, Australia, and were then able to take advantage of the experience gained from that project.

Conditions Affecting Design. The combination of site conditions (thick sediment of overlying clay) and loads resulting from external conditions (storm activity, shipping activity) has determined the overall diffuser and riser design from the bedrock to the seabed. Because of the proximity of the diffuser zone to the US Coast Guard Navigation Buoy 'B' and hence the high likelihood of shipping activity in the area, the risk of high impact loads from anchors as well as anchor drag has been taken into account. Another factor that has been considered is the storm activity in the area and the effect of the resulting environmental action (e.g., scour) upon the structure.

The internal and external hydraulic requirements of the outfall have determined the configuration required for the diffuser, while the internal hydraulics (purging and anti-intrusion) have determined the elevation of the diffuser above the seabed.

**Casing.** A steel casing was selected to support the weight of the diffuser and to resist the lateral loads predicted by the anchor risk analysis. The casing also serves various functions during the installation process. These include:

- a) Stabilizes the upper seabed formation and any weathered or fractured bedrock;
- b) Supports the installed riser and diffuser assembly while the riser cement is curing;
- c) Provides vertical restraint against riser buoyancy forces during the riser cementing and cement curing processes;
- d) Provides an installation reference datum to ensure that the diffusers are at the same elevation relative to seabed. Port elevations are fixed with regard to casing height.

Because the casing is a structural component and is required for the full design life, allowances have been included in the form of increased wall thickness and internal and external coatings in the upper section.

**Riser Assembly.** The riser functions as a conduit for the effluent. It has been designed to be strong enough to withstand the external hydrostatic pressures both in the long-term (over 100 years) and in the initial dewatered conditions. The riser was also analyzed for installation loads from wave action, offshore transport and hydrostatic loads from the 250 feet grout column. Fiberglass reinforced plastic (FRP) was chosen for the riser material for its ease of handling, durability, non-corrosive properties and to provide a hydraulically smooth conduit. A riser unit length of 40 feet was selected as a standard length for ease of handling onshore during road transport and offshore on the installation vessels. The riser is to be supported in the drilled hole by a fully grouted annulus of cement.

**Diffuser Head.** The diffuser head has been designed in four components: base, cap, ringwall and protective dome. Concrete has been selected as the main structural element of the base and cap. For durability, the concrete mix is designed for high strength, high density and low permeability. The components are held together by Inconel high nickel alloy rods. These fasteners also double as lifting attachment points for installation purposes.

**Diffuser Base.** The base acts as a foundation for the diffuser cap and transmits all vertical and lateral impact loads to the drilled and grouted casing. To prevent the diffuser head and riser from being "pumped" out of the hole by hydrostatic forces during cementing, the base incorporates a latching mechanism that positively locks and anchors the base to the casing.

**Diffuser Cap.** The cap accommodates the FRP manifold, which is the primary dispersion structure for the effluent. The cap is replaceable in the unlikely event it needs recovery and repair through damage, and it also

incorporates a manhole cover to facilitate future inspection. The manifold consists of eight ports with detachable nozzles and sealing caps to be removed upon commissioning. The material used for the nozzles, cast nylon, has been selected for its high durability and machinable properties, abrasion resistance and low magnitude of roughness.

To assist in installation and commissioning, each diffuser has a pressure gauge to monitor the internal pressure and an internal air bleed-off assembly to equalize pressure prior to removing port caps. The cap and base are locked together with tie rods prior to installation.

Diffuser Dome. The primary concern for the designers with the diffuser structure was the potential for vertical and horizontal impact loads. To accommodate these concerns, the designers developed a durable, flexible, energy-absorbing shell. The principal material requirement of the dome shell is good ductility, corrosion resistance and high impact resistance. Cross-linked high density polyethylene (HDPEX) was selected as the most suitable material for the intended application.

Ringwall. The ringwall provides protection to the nozzles, as well as support for the HDPEX dome. Its design as a separate component allows the manifold and/or dome to be replaced without requiring the removal of the permanently grouted base. The ringwall is made of reinforced concrete. Extra protection to the exterior concrete is provided by a coating of urethane which displays excellent abrasion resistance as well as a low friction coefficient. The diffuser base is similarly coated on all surfaces likely to experience ground tackle or trawl board contact.

The entire diffuser assembly including dome ringwall and base is designed to present as smooth a profile as possible to minimize snagging by anchors, mooring lines or fishing equipment. In the event that anchors or anchor chains do snag or wrap around the diffuser structures, the riser casing and diffuser system has been designed to resist a lateral load of up to 200 tons.

Rock Armor and Filter Layer. The surrounding rock protection is provided to guard against potential scour and undermining of the diffuser cap and dome, and thereby eliminates the possibility of an anchor chain snagging under the diffuser. The rock protection also provides a smooth seabed profile in the vicinity of each diffuser. To prevent migration between the rock armor and the natural sediments, a 1.5/feet minimum sand/gravel filter layer was specified.

Riser Offtake. The riser offtakes provide the link between the pre-installed risers and the outfall tunnel. As this is essentially a horizontal extension of the riser pipe, FRP was the logical choice for material.

Of major importance in the design of any tunnel which is to connect with seabed structures (e.g., power station cooling water intakes, outfalls and ship loading facilities), is the protection of the tunnel worker from accidental flooding through the riser shafts. There are several devices designed to ensure sealing of the risers from the ocean. They are:



- a) Manifold Port Caps - installed with the riser and diffuser. These employ an O-ring fitting to effect a seal. Each port cap and nozzle is individually pressure tested to twice working pressure prior to installation.
- b) Riser Plug and Sealing Mechanism - a secondary sealing mechanism designed to prevent flooding due to loss of a seal at the port caps during initial stages of offtake installation. It is installed with the riser assembly and removed immediately prior to offtake installation.
- c) Offtake Elbow Sealing Plug - this plug fits into a recessed groove in the offtake elbow pipe and guards against flooding in the event of a loss of seal at the port caps after the riser plug is removed.

## **OUTFALL CONSTRUCTION**

### **Contract Package**

The construction contract packages for the tunnel and seabed diffuser work were issued for bid in two ways:

- 1) A contractor could bid for all of the work in both packages.
- 2) A contractor could bid for just one of the packages, diffusers or tunnel.

The reasoning behind this was that it was thought that bidding all the work in one package would reduce the competition among bidders as only very large construction companies would have the resources to undertake all of the work. On the other hand, the designers recognized the potential savings involved if the contractor was to coordinate all of the work, and hence, this option was left open. As expected, the second option (separate contracts) was pursued by the Client upon bid opening. The tunnel contract was awarded to a joint venture of Kiewit Construction Company, Guy F. Atkinson Construction Co., and Kenny Construction Company for \$202 million and the diffuser fabrication and installation contract to a joint venture of J.M. Cashman of Boston and Interbetton of the Netherlands for \$77 million.

### **Tunnel Construction**

The Robbins tunnel boring machine (TBM) purchased for this project is a double shield hard rock rotary machine. The TBM was refurbished by Robbins at their Chicago site and arrived by barge at Deer Island in October 1991. The machine has high thrust capability for hard rock application and a shield to support poor ground while tunnel supports are installed. (For the TBM's Technical Specifications, see Table 1.)

The cutterhead provides basic face stability while cutting. The two piece shield provides full ground support back to the rear of the lining installation area. A forward shield surrounds the cutterhead support structure providing ground support immediately behind the gauge cutters. A large area gripper system provides low unit ground loading for reacting machine thrust, torque

and steering forces. All the major machine structure pieces can be disassembled for removal from a lined tunnel. Included with the TBM is the machine conveyor which terminates approximately 90 feet from the face. The conveyor is supported in the rear on a trailing gantry. Also included is a wheel mounted gantry approximately 30 feet long, a rotary segment erector, segment transport hoist, segment car platform, and the hydraulic and electric power modules for the machine. These modules are mounted on the conveyor structure and trailing gantry.

The TBM has now been fully assembled at the bottom of the shaft and tunneling has begun. The average rate of advance of the TBM including lining is expected to be about 100 feet per day using two 10 hour shifts.

To ensure accurate positional control over the 9 mile length of the drive, the tunneling contractor has elected to use a 3 second gyroscope for tunnel surveying. This instrument is the most accurate available, with a claimed accuracy of 3 seconds of arc. A second system, yet to be determined, will be used to provide an independent parallel check on the gyroscope survey system.

Tunneling in the diffuser zone, which will start at about 43,000 feet east of the shaft, will offer the Contractor special challenges, mainly because of the requirement for the finished tunnel to reduce in cross section. The Contractor has not yet specified what method of construction will be used to form this 6600 feet long tapered section of tunnel. Several options are available including, precast concrete segments, cast in place concrete or concrete pipe segments of reducing diameter. Options for excavation in this zone include continuation of the TBM or use of drill and blast methods to excavate a smaller diameter tunnel. The use of cast in place concrete will require special concrete mixes, including retardants and accelerators because of the long transportation distance. When the tunnel is complete, the off-take adits will be excavated from the main tunnel to the previously drilled and capped risers, the connecting pipes and elbows installed and the off-take adits backfilled. (Figure 8 shows the tunnel and offtake section in the diffuser zone.)

### **Tunnel Offtakes**

The final operation which connects the underground work to offshore work is the installation of the tunnel offtakes.

Probe holes are drilled from the tunnel to ascertain the riser location and to tap and drain the risers of ballast water. (The risers have been installed and filled with fresh water containing green dye - this provides positive proof that the probe drill has intersected the riser and not a ground fault or cement void.) The offtake adits are then excavated horizontally from the tunnel to the pre-installed risers which will be exposed. The risers are then cut and an elbow section installed followed by the offtake pipework linking the riser to the tunnel. The void surrounding the pipework and exposed riser is to be backfilled with concrete (see Figure 8).

### **Diffuser and Riser.**

The contractor chose as his principal construction vessel a 4 leg jackup vessel assisted by a dredge barge, specially equipped grout barge, supply/anchor handling tugs and material barges. The jackup barge is equipped with 2 Wirth pile top shaft drilling rigs, a Manitowoc 4100 ringer crane, a smaller all terrain crane, helideck and construction offices. The grout barge was fitted out with bulk cement and water tanks, mixing equipment and oil field style high pressure cement pumps.

Prior to the jackup commencing installation, the sediment in the immediate vicinity of the riser is excavated by the dredge barge. Typical dredge depths are 6 feet below seabed over a 30 feet radius. Once dredging is complete at a riser site, the dredge continues along the Outfall while the jackup is floated into position using its mooring lines and jacked up over location. To expedite operations, two riser holes are drilled concurrently from the one site. Two sided mounted drilling templates, able to be moved along opposite sides of the barge, are accurately positioned to ensure the risers are within the alignment tolerance and at the correct spacing.

After positioning, a temporary casing is driven into the sediment and restrained laterally at barge level by the drilling templates. The casing is used to support the drilling and stabilize the upper sediments to prevent hole collapse. A 67 inch hole is drilled by reverse circulation air-lift methods and the 61 inch permanent casing is installed. Permanent casing lengths were specified to be a minimum length of 40 feet and 10 feet into solid rock. To date most casings have been 40 feet with several 60 feet and even 100 feet long casings installed to cope with the deeper sediments along the alignment. The casing elevation is checked by lead line, then grouted in stages via four grout lines attached to and lowered with the casing. The first stage forms a neat cement plug at the toe of the casing; this grout is allowed to set up and then the remainder of the annulus is grouted up to the top of the casing. The Designers provided a suggested float shoe design in the bid package, however, the Contractor selected to use a two-stage method.

The next phase comprises the installation of the diffuser and riser. A smaller (53") drill bit is used to drill a hole approximately 250 feet down from the seabed. The hole is surveyed by wire-line tools to ascertain bottom hole coordinates. The Bottom Hole Assembly (BHA) and drill string are now removed from the hole and laid down on the deck of the barge. The pile top rig is removed from the conductor casing, which is now cut off just above the (dredged) seabed and removed. The contractor chose to assemble the FRP riser joints into 120 feet lengths at the onshore staging area to reduce the offshore installation time, hence only two field joints were necessary to make up the 240 feet string. The riser, diffuser base, manifold and ringwall are made up on the drilling template, lowered into the drilled hole and latched into the permanent casing as one unit. Pressure gauges on the diffuser port caps record the internal pressure of the riser, thus detecting any leaks between the sealing caps or between FRP joints. The annulus between the riser and drilled hole is then grouted through two grout lines installed with the riser assembly. A cement slurry of equal parts cement, sand and slag is used to reduce heat of hydration temperatures of the curing cement to less

than 160 degrees Fahrenheit and thus avoid heat induced damage to the FRP. A downhole nuclear density gauge installed in the riser/casing annulus provides real time recording of in situ grout densities, while specially designed overflow ports located in the diffuser base allow for visual observation of cement returns. The entire operation of riser installation is observed using an ROV and recorded on video.

With the riser installed and grouted, the jackup moves onto the next two risers and all that remains is for the installation of the HDPEX protective dome and placement of the sand/gravel and rock armor. These activities are performed from the dredge barge, with divers assisting in dome placement and any topping up of cement levels which have dropped due to slump.

One of the most critical offshore operations is the positioning survey of the seabed diffusers and corresponding riser shafts. The tunnelers will be required to locate the toe of these risers more than nine miles out along the tunnel alignment and 30 feet from the tunnel center line. To minimize the amount of probe drilling that must be performed and to align the tunnel to ensure the correct riser offtake distances can be achieved, it is imperative that the bottom hole coordinates of all risers are within a specified tolerance of one riser diameter, 34 inches.

The offshore surveying is carried out in two stages:

- a) High accuracy survey of the jackup rig position and drilling templates to the baseline coordinates.
- b) Separate downhole surveys providing relative position of the bottom hole coordinates to the drilling platform.

Because the jackup rig was essentially stationary, the contractor was able to employ differential G.P.S. backed up by conventional geodetic survey methods (E.D.M.'s and theodolites) to tie in the rig position to the base line coordinates. As the drilling templates were moved slightly on every riser site, these were surveyed relative to the jackup survey control points on each location.

The bottom hole coordinates of the drilled riser hole were obtained using a two axis wireline deployed gyroscope. Such tools were developed and are commonly used for steering and navigation of directionally drilled oil and gas wells. This survey also had a backup by means of an inverted pendulum shaft survey tool. This method, developed for surveying the verticality of mine ventilation and access shafts, relies on the plumb-bob effect of a suspended mass to move a surface float. The surface float assumes the same horizontal coordinates as the drill bit. Vertical measurements, although not as critical as horizontal accuracy, are obtained by lead line and drill string length.

Because of the number of surveys performed in each loop from the bottom hole survey to positioning the tunnel probe drilling equipment, it is imperative that the same baseline network is used for both tunneling and the diffuser installation. A separate high precision baseline network has been established for use by both contractors.

At the time of writing, the Contractor had installed all 55 of the risers from the jackup barge. The dredge barge will remain on site to finalize dome and rock placement on those sites not completed.

### **Material Fabrication**

There are very few structures built anywhere in the world where the expected service life and environmental conditions are as demanding as for ocean outfalls. With the exception of some parts of the diffuser structure, the riser and diffuser assembly are permanent installations and must remain serviceable for the design life of the system, in this case, 100 years.

Because of this, it is considered essential that a fairly stringent series of quality control tests are specified by the engineer to ensure that the materials selected for the outfall components are of the highest standard and meet specification design requirements. Evaluation of components made from plastics and exotic alloys as opposed to steel and concrete requires specialized testing methods.

For the Boston Outfall Project, specific items in the manufacture of the components were strictly controlled. These include:

- FRP Riser Pipes and Manifolds. Riser bend tests and diffuser cap (External) pressure tests were conducted while specimens were monitored by acoustic emission tests. Barcol Hardness and cube strength tests were performed on the glass and resin samples respectively.
- Cast Nylon Nozzles and Port Caps. Mechanical strength tests on specimens were performed to confirm physical properties with respect to tensile and impact loads.
- HDPEX Dome. Low temperature impact, tensile and density tests were performed on specimens cut from this component.
- Inconel Fasteners. Accelerated corrosion tests were performed to evaluate the resistance of these components to pitting and crevice corrosion.
- Riser Clamps. Tensile and chemical composition tests were performed on samples and radiographic tests were performed on completed cast steel items.

### **CONCLUSION**

The designers of the Boston Outfall sought a configuration that allowed for a rapid installation cycle while exposing the Contractor to as minimum risk as possible. Proof of the success of this approach was borne out by the recent completion of diffuser installation almost a year ahead of schedule, despite the Contractor electing to shut down in the winter months to reduce weather risk to equipment and personnel.

The successful low bid for the offshore construction was \$70 million below the independent engineers estimate; with the construction bids ranging from \$77 to \$173 million dollars. The large spread of bids can be explained by the

uncertainty of method in offshore construction and the wider variety of unknowns for this type of project. Other factors contributing to this effect are:

- increased risk to the Contractor from the marine environment.
- differing construction methods assumed during the bidding process.
- the unique nature of the project, with few contractors having experience and few similar projects for the engineer to base comparisons on.

Tunneling bids, by comparison, were much closer together despite the greater cost magnitude (low bid \$202 million, engineers estimate \$216 million, high bid \$246 million). This reflects a greater familiarity and precedent of this type of work amongst contractors. The tunnel completion date is scheduled for mid-1995, while the entire offshore installation will be complete in September 1992.

Deepwater tunnelled outfalls are proving to be increasingly cost effective when compared to conventional large diameter cut-and-cover pipeline outfalls. Not only is it possible to keep all but a small portion of the system from being exposed to the marine environment and thus achieve the specified longer design life, but per unit costs of recent tunneled outfalls have been lower than an equivalent sized seabed pipeline systems. In this case, the designers ought to achieve a low maintenance system that will still be operational in the year 2100 while keeping costs and construction durations below that of more conventional systems.

#### **ACKNOWLEDGEMENTS**

The owner of the facility is the Massachusetts Water Resources Authority. Parsons Brinckerhoff Quade & Douglas, Inc. was the Project Design Engineer and the senior author was the Design Manager (Project Engineer). Wholohan Grill and Partners, whose USA subsidiary is WGP Engineering, was the sub-consultant to Parsons Brinckerhoff for diffusers and risers and the co-author was the Manager for that effort. Mott Hay Inc. designed the tunnel shaft.

The authors would like to thank the following organizations for their contribution to this paper.

- The Massachusetts Water Resources Authority
- Kiewit, Atkinson, Kenny; The Boston Ocean Outfall Tunneling Contractor.
- Cashman/Interbetton, the Boston Ocean Outfall Diffuser Installation Contractor
- Lead Design Engineer; Metcalf and Eddy.
- Construction Manager; ICF-Kaiser Engineers.

#### **REFERENCES**

Parsons Brinckerhoff, Quade & Douglas, Inc. Boston Effluent Outfall - Conceptual Design Confirmation/Recommendation Report, March 1989.

Parsons Brinckerhoff, Quade & Douglas, Inc. Boston Effluent Outfall - Geotechnical Design Summary Report, March 1990.

R.P. Brooks and Y. Eisenberg. Design and Construction of Deep Water Ocean Outfalls, Ocean Engineering Graduate Seminar, University of California, Berkeley, April 1992.

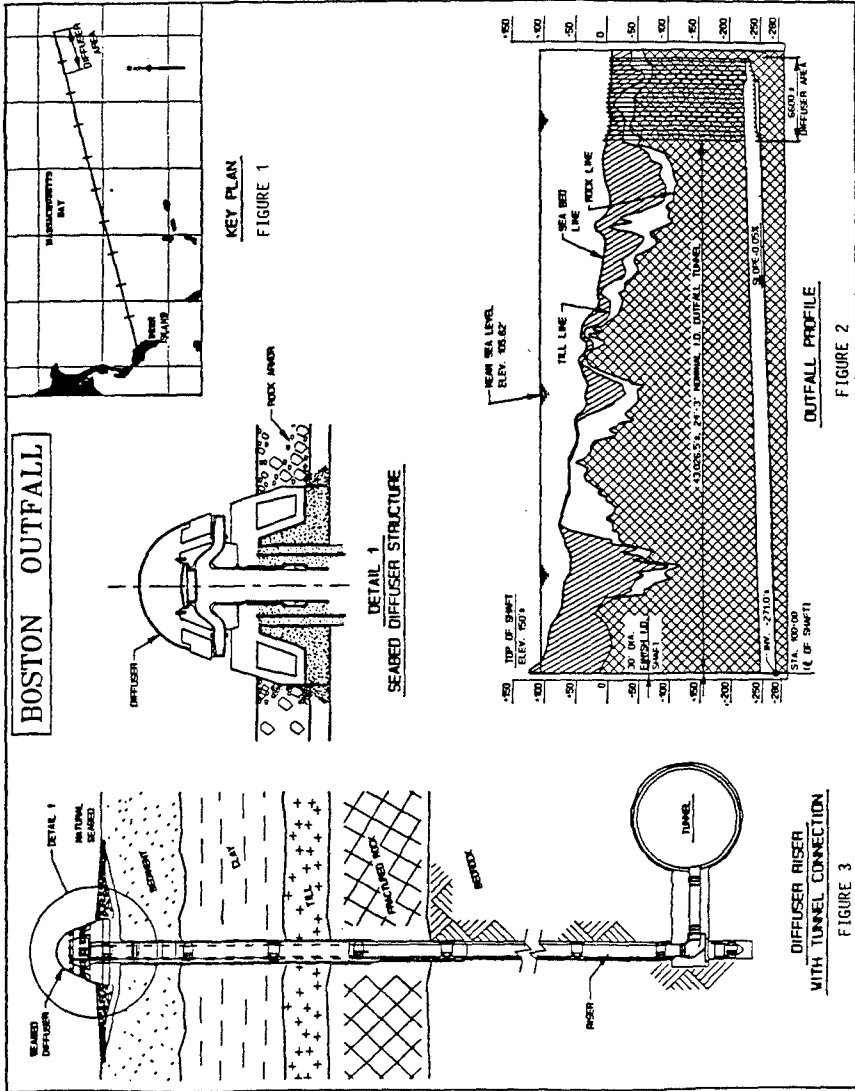
Y. Eisenberg. The Pali Outfall for the City of Taipei, International Conference on Coastal and Port Engineering in Developing Countries, Mombasa, Kenya, September 1991.

R.P. Brooks and J. Perrone, Wholohan, Grill and Partners. Design and Construction Planning of Deepwater Ocean Outfall Riser Shafts and Diffuser Structures, Offshore Technology Conference, May 1990.

Y. Eisenberg, T.C. Gofas, R.A. Fosano and F.S. Hindes. Submarine Siphons for Athens Sewerage System, 21st International Conference on Coastal Engineering, ASCE/Malaga, Spain, June 1988.

G.J. Murphy and Y. Eisenberg. San Francisco Outfall: The Champ?, "Civil Engineering", December 1985.

Y. Eisenberg and D.D. Treadwell. San Francisco's Southwest Ocean Outfall, 18th International Conference on Coastal Engineering, ASCE/Cape Town, South Africa, November 1982.





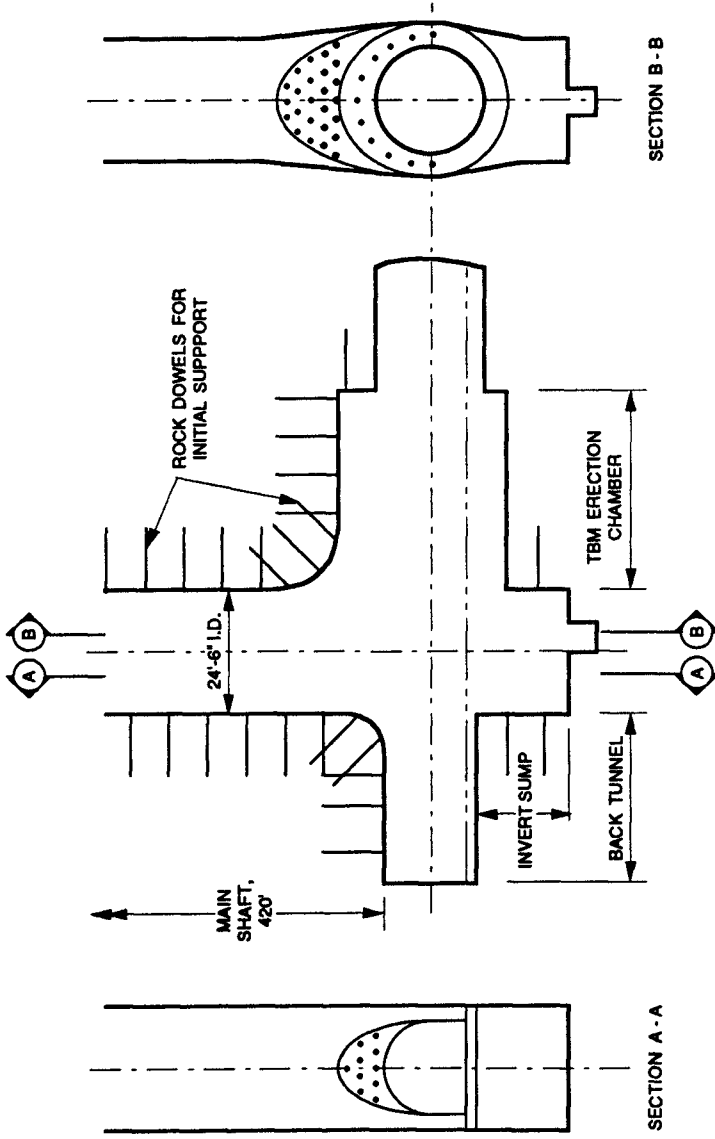
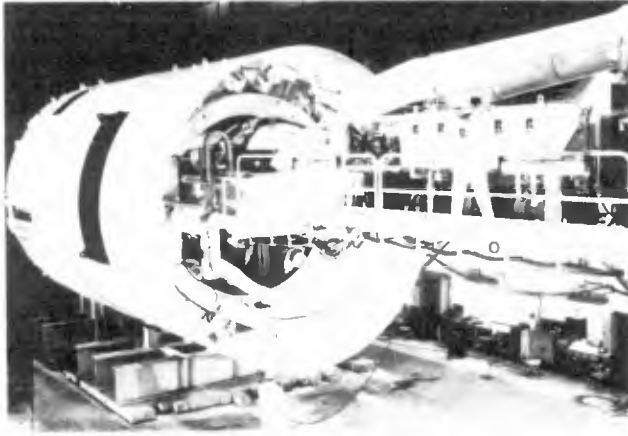


FIGURE 4. ACCESS SHAFT

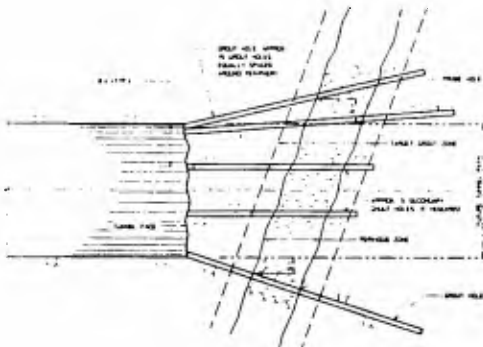


*The Robbins 8.1 m diameter double shield built for the Boston Harbor Sewer Outfall project.*

TABLE 1

TBM TECHNICAL SPECIFICATIONS

Machine Diameter	26 ft. — 6 in.
Cutters	Series 17 Front/Back Loading
Number of disc cutters	50
Maximum recommended Individual cutterload	50,000 lb.
Cutterhead	
Maximum operating Cutterhead thrust	2,500,000 lb.
Maximum shield thrust	6,670,000 lb.
Cutterhead drive	Electric motors with hydraulic clutches
Cutterhead power	3,360 HP (8 @ 420 HP)
Cutterhead speed (approx.)	6.4 RPM
Cutterhead torque (constant power)	2,700,000 lb. — ft.
Conveyor Capacity (nominal)	350 Ft. 3/min
Machine Weight (approx.)	1,540,000 lbs.



**Figure 5**  
SECTIONAL ELEVATION SHOWING  
TYPICAL PROPOSED GROUTING LAYOUT  
AHEAD OF TUNNEL FACE

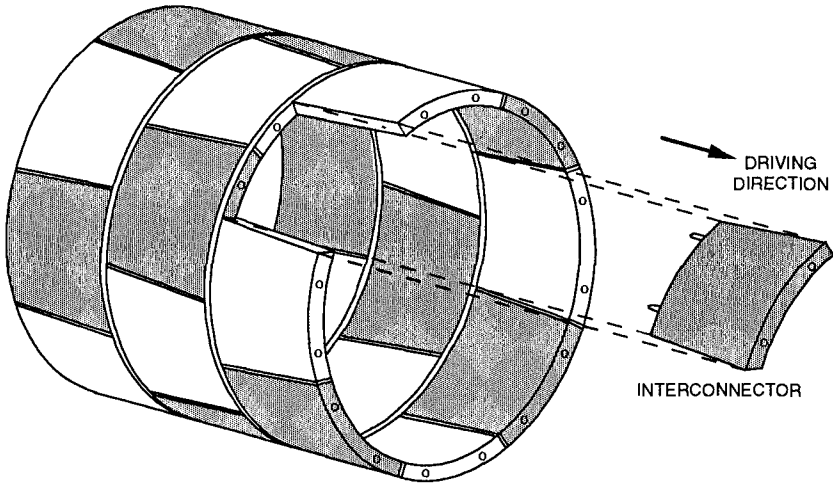


FIGURE 6. PRECAST TUNNEL LINER  
(AS BUILT DESIGN)

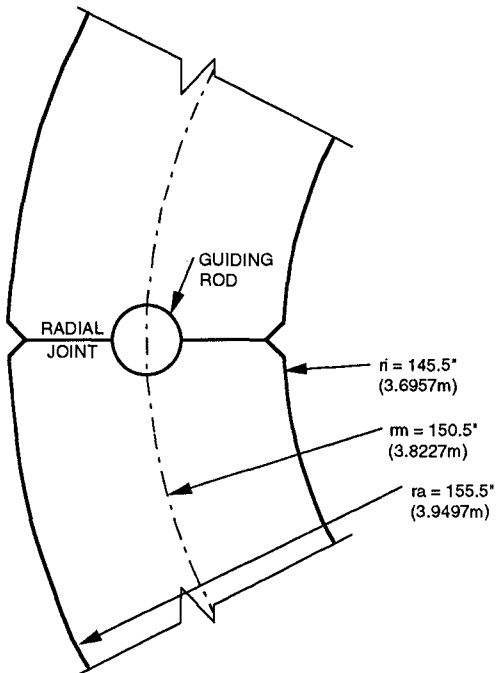


FIGURE 7. PRECAST TUNNEL LINER JOINT DETAIL  
(AS BUILT DESIGN)

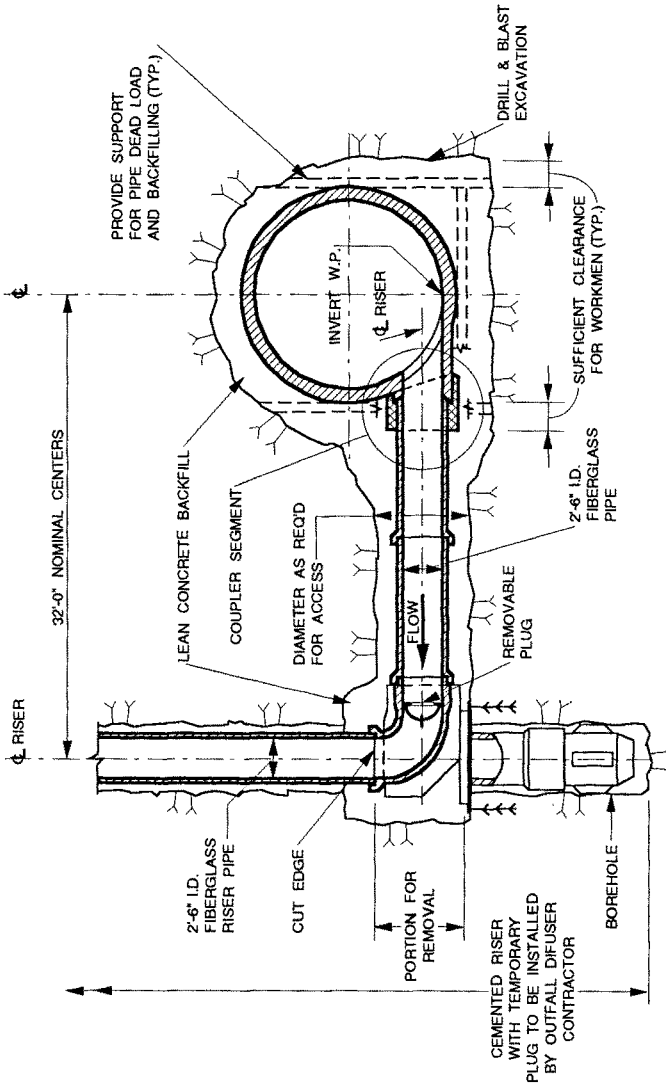


FIGURE & TUNNEL-DIFFUSER CROSS SECTION

JACKUP BARGE  
DRILLING OFFSHORE  
BOSTON

FIGURE 9  
(left)



FRP RISER PIPES  
MADE UP INTO 120'  
STRINGS CAN BE  
SEEN ON THE RIGHT  
SIDE OF THE JACK-  
UP RIG

FIGURE 10  
(below)

DIFFUSER AND DOME  
PRIOR TO TRANSPORT  
OFFSHORE

FIGURE 11  
(bottom left)



## CHAPTER 252

### MODELLING AND MONITORING OF A PERCHED BEACH AT LIDO DI OSTIA (ROME)

Andrea Ferrante<sup>1</sup>, Leopoldo Franco<sup>2</sup>, Sander Boer<sup>3</sup>

#### Abstract

A description is given of a new large project of artificial beach nourishment protected by a submerged sill carried out at Lido di Ostia near Rome in 1989-1991. After a review of the main aspects of the design (supported by model tests) and construction, details are given of the ongoing field monitoring program. Collected data has been used to verify the predictions of numerical models of cross-shore and longshore evolution of the perched beach. Useful preliminary lessons have been drawn from this unconventional experience of coastal protection.

#### Introduction

The sandy beaches of Lido di Ostia stretch along the southern delta cusp of the river Tiber, some 25 km from Rome on the Tyrrhenian Sea, and represent long since a very popular holiday resort for the Roman community (Fig.1). The cusped delta was formed by alluvial sediments carried by the river, producing a progressive coastline advance of more than 4 km from the Roman age until this century (Fig.2). Then, particularly in the last 25 years, a severe erosion process has been taking place reverting the evolution trend to a recession rate of 1.7 m/year. The main cause has been the strong reduction of river sediment supply (due to upstream dams and extraction of building material from the river bed) with a consequent deficit in the coastal sand budget and a trend towards the cusp straightening and smoothing out.

-----  
<sup>1</sup> Designer and supervisor, G.C.OO.MM. Ministry of Public Works, via Monzambano 10, Rome, Italy

<sup>2</sup> Consultant, Professor of Coastal Engineering, Dept. of Hydraulic, Environmental and Surveying Engineering, Politecnico di Milano, P. Leonardo da Vinci 32, Milan, Italy

<sup>3</sup> Project engineer, Delft Hydraulics, Voorsterweg 28, Marknesse, The Netherlands

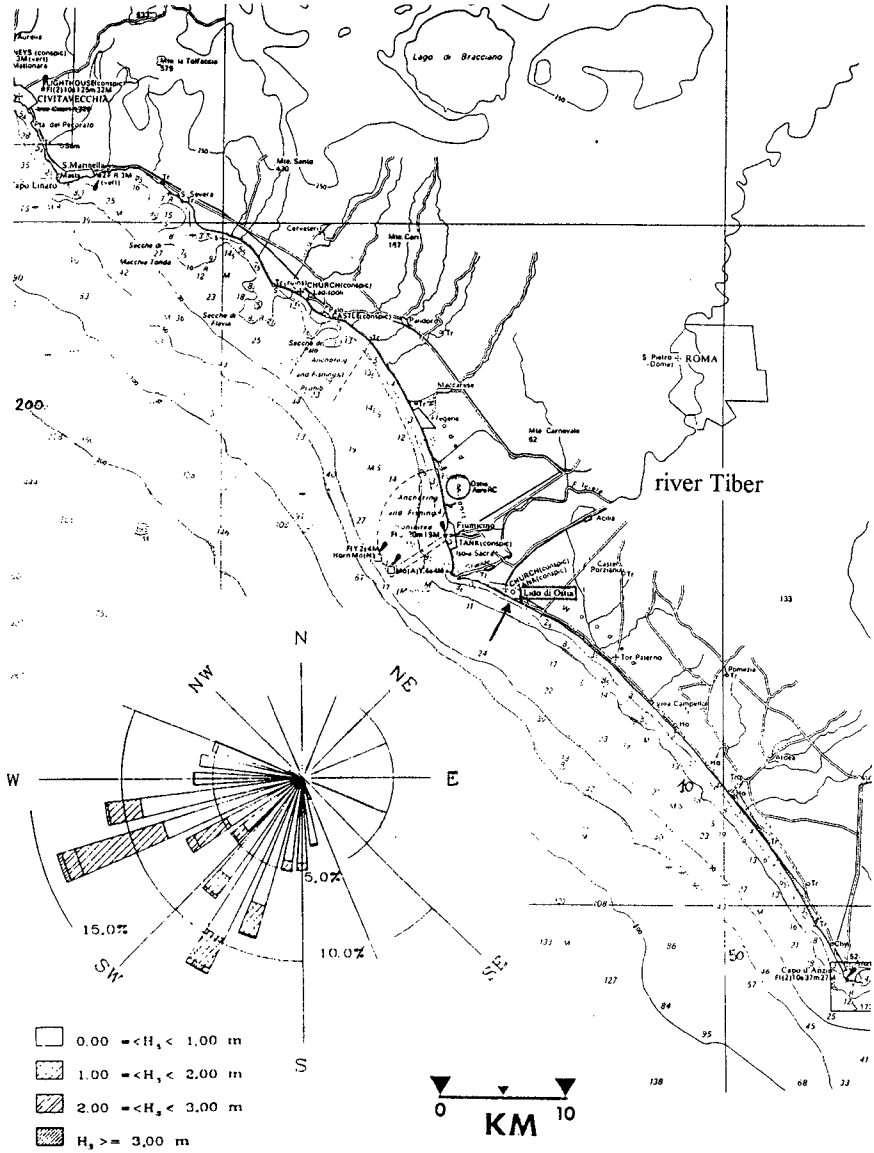


Fig.1. Location map of Ostia Lido and nearshore wave climate recorded in 1990-91

The local tidal range is very small (below 0.5 m), but deepwater waves may exceed a significant height of 5 m and a period of 10 s. Recent coastal protection works have been partially successful, such as the system of detached breakwaters constructed near the river mouth: erosion was shifted downdrift, mainly affecting the southern beach between the Vittoria Pier and the Pescatori Canal, causing damage to the beach clubs and even to the littoral road during storm periods.

An innovative beach nourishment project was then designed in 1988 by the competent Authority, the Office of Civil Engineers ("Genio Civile") for Maritime Works - Rome of the Italian Ministry of Public Works. A preliminary description of the project was given by Toti et al. (1990).

### Project objectives and constraints

The aim of the project was to re-create a wide protective beach with an efficient technical defence solution complying with the economical, managing, political and environmental requirements. In fact the local community rejected any traditional emerging coastal structure to favour tourism, aesthetics and ecology. Indeed the project represents a new approach of the Administration toward a global view in coastal defence, also taking into account the environmental aspects. Financial constraints restricted the project area to the most vulnerable 3 km stretch of coast.

Given the existing high deficit of the littoral sand budget, the proposed beach nourishment needed to be protected by some coastal structure able to dissipate part of the wave energy and reduce the littoral transport, and to retain the new fill material. The most suitable solution then included an offshore underwater rock barrier "fixing" the natural dynamic sandy bar, as a "perched beach" scheme. The submerged bar should hold the artificial beach at a shallower slope, reducing both offshore sand losses and longshore transport, enhancing the development of marine fauna, without endangering bathing and leisure navigation.

Important constraints were also resulting from the scarcity of marine sand for nourishment. The native beach sediments at a depth of MSL-10 m (on a 1% slope) have a too fine grain size with  $D_{50} = 0.1$  mm. Fill material needed to be quarried inland on the alluvial Tiber delta at 20 km distance from the beach: the available material is a poorly sorted mix of well rounded sands and gravels.

### Design scheme and problems to be studied

The protection scheme covers a beach length of 3 km (Figs.3-4) and basically consists of:

a) a sill made with a submerged rubble mound parallel to the shoreline at a distance of some 150 m, with toe level at MSL -4.0/-5.0 m, a 15 m wide crest berm at -1.5 m, seaward slope of 1:5, a multilayer rock mound (maximum stone weight of 1 t) placed above a geotextile and a 5 m wide rock toe protection in a 1 m deep trench;



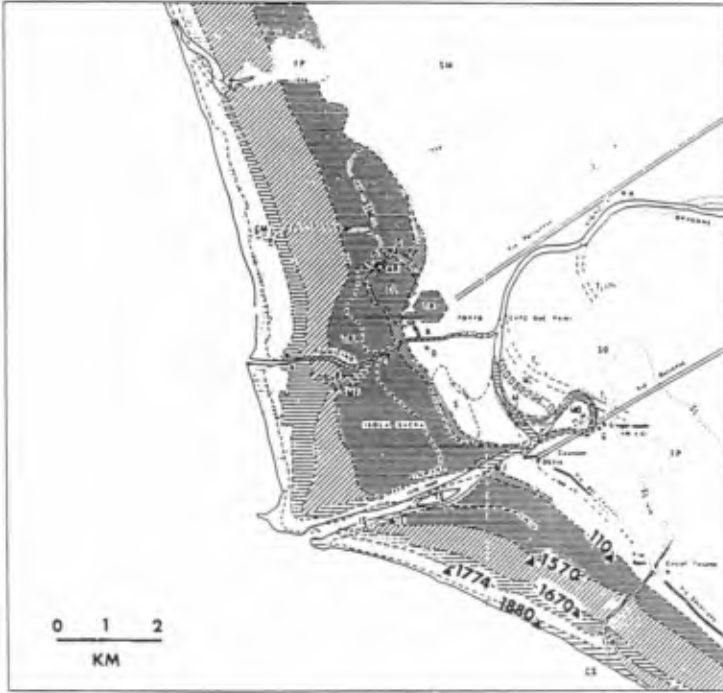


Fig.2. Historical evolution of the river Tiber delta from year 110 a.C. (Segre,1950)

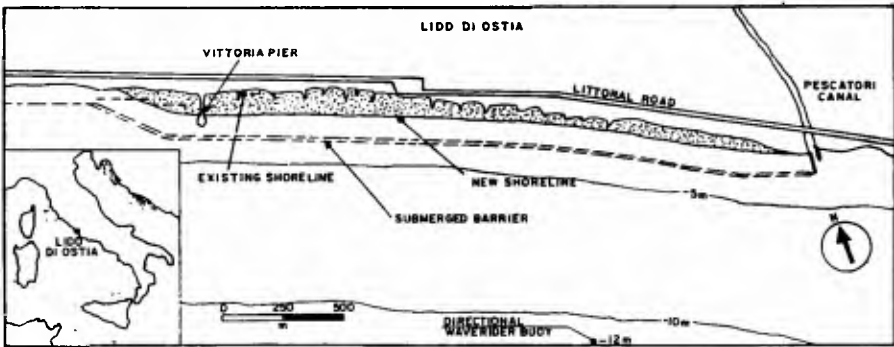


Fig.3. Design plan of the nourishment project

b) a fill with a double layer of quarry material: a lower layer of mixed sandy gravel with a wide grading of 0.08-120 mm, and a 1.0 m thick upper layer of sand with grading 0.3-1.3 mm; the underlayer also acts as a 5 m thick filter between the sand and the rock bar; the beach equilibrium slope is 2.5% and the berm crest located at MSL +1.0 m. The average design shoreline advance is about 60 m.

The main problems to be studied were related to the prediction of: the average losses of beach material due to longshore and cross-shore transport; the effects on the adjacent beaches; and the profile deformation during storms (which should not expose the underlayer). The sill hydraulic stability also needed to be verified.

### Model tests

The above design problems were solved with the support of physical and mathematical model studies carried out by Delft Hydraulics (1989). The one-line mathematical model simulated the long term evolution of the whole shoreline planshape, finding a dynamic equilibrium position just 5 years after construction. A cross-shore numerical model was also used to check the morphological changes of the beach profile. Annual sediment volume losses were estimated in 4-10 m<sup>3</sup>/m for the first year (depending on wave climate severity), reducing by 50% within three years. A minor erosion effect along the initial 700 m of downdrift beach was predicted. A 2-D mobile-bed hydraulic model at a scale 1:15 showed a remarkable stability of both the rock barrier and the artificial beach profile. A maximum 0.3 m vertical erosion was observed, together with an expected steepening of the beach slope at the shoreline and a horizontal recession of 5 m.

### Construction features

The execution of the works was carried out by Condracos, a consortium of specialized Italian contractors. The works started in May 1989 with a 3-month stop in the tourist summer season; in June 1990 a 2150 m beach portion was built, while the final 850 m were completed in the following spring, for a total construction period of only 14 months. The works progressed from the Pescatori Canal to the north against the net littoral drift direction with the following sequence:

- a) construction of longshore and cross-shore causeways to provide access for land-based equipment to build up the offshore barrier (initially emerging);
- b) dumping and shaping of beach granular material with both land-based and marine equipment; some native dark beach sand (iron-rich) was temporarily stockpiled to be mixed with the yellow quarry sand as toplayer .

The construction equipment consisted of one hopper suction dredger, three 600 m<sup>3</sup> capacity barges, one tug, one pontoon, four dumpers, two bulldozers, three excavators and many trucks for material transport from the quarry. The total material quantities were about 1,360,000 m<sup>3</sup> of sand and selected mixed sandy-gravel and about 300,000 m<sup>3</sup> of rock (basalt and limestone from different quarries).

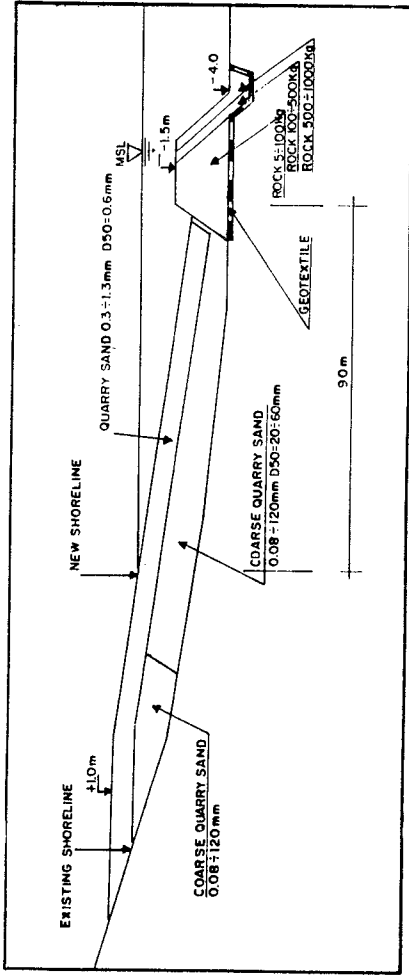


Fig. 4. Design cross section of the perched beach

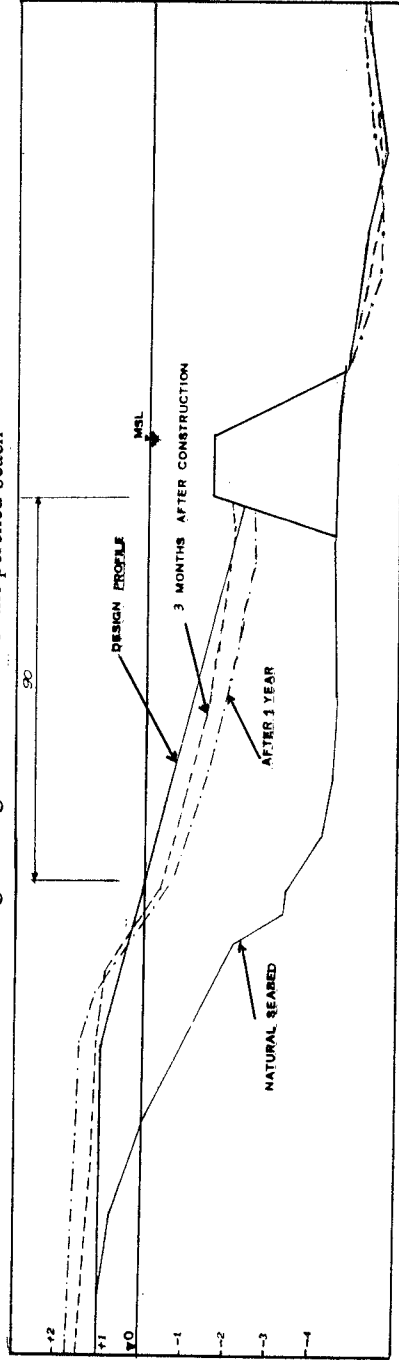


Fig. 5. Measured average perched beach profiles

### Monitoring program and analysis of field observations

Given the innovation of this technical solution and the unusual length of nourished beach without groynes, the Supreme Council of the Ministry of Public Works attributed an experimental character to the works and imposed the setup of a monitoring program since the construction start in mid 1989.

The periodic acquisition of field data includes: aerial photographs (twice a year), beach profile surveys (four per year), sediment sample analysis and directional wave recordings (starting on 3 Jan 1990). Beach profiles are surveyed up to MSL -7.0m at 100 m intervals, while 5 samples are collected across sections spaced 250 m. Local wave activity is recorded by a directional Datawell Waverider buoy moored in a depth of 12 m at 2 km distance from the coast, where a station easily receives the radio signals, supplying wave data in real time. Eight samples of 200 s (26.6 minutes) are processed with FFT and spectral results displayed every half hour. Records are stored every 3 hours unless a threshold of 2.5 m significant wave height is exceeded. Site surveys and underwater inspections were carried out also by the Authors.

The analysis of the topographical surveys has shown a general stability of the new beach with predicted maximum 20-30 m shoreline advance (at southern end) and retreat (at northern end), due to the southbound littoral drift. This sediment transport is reduced by the presence of coarser material and of the fixed bar in the surfzone. Dredging volumes smaller than before were in fact required to open the inlet of Pescatori Canal. No adverse effects have been observed on the adjacent beaches.

Photo 1 shows the original dark beach before the intervention and photos 2,3,4 the new large artificial beach, with gravel ridges typically forming near the cusped shoreline (which also shows an active 3-D inshore circulation).

The elevation of the emerged beach has increased up to MSL+1.5/+2.0 m, while the submerged beach profile generally deepened, as shown in fig. 5. In the first months after construction stagnant water ponds formed on the upper beach due to poor drainage of wave uprush, caused by this shoreline ridge and by the initial impermeability of the mixed surface layers (also compacted by truck transit). However natural wind and wave action later redistributed the sediment avoiding this problem.

Minor scour has been observed at the barrier seaward toe, but some deposition in deeper water may indicate small offshore sand losses. Some fine material has penetrated into the rock sill, thus reducing its permeability, but not the stability.

As far as wave measurements are concerned, the local climate of two years is shown in fig.1. It shows a typical bimodal distribution and the resultant of the wave energy vector is just directed from 225 N, still quite angled to the coastline normal oriented at 210 N, thus confirming the southbound littoral drift. These nearshore wave records have also been correlated with those taken at the deepwater directional station off Ponza island, finding a good correspondance. The main wave direction is typically

refracted inshore with a rotation of 25-30 degrees and the directional spread reduced from 30 to 10 degrees. An annual average of 7 storms with a peak significant wave height  $H_s > 2.5$  m was recorded, with a maximum  $H_s$  of 4.4 m. The corresponding offshore significant wave height of 5.8 m has an estimated return period of 10 years. This was indeed a severe positive test for the just completed perched beach.

#### Post-construction computation of beach deformation

The field data collected during the monitoring program has been used for hindcast computations of beach plan evolution and beach profile deformation, which have been performed with the "Unibest" software suite of Delft Hydraulics.

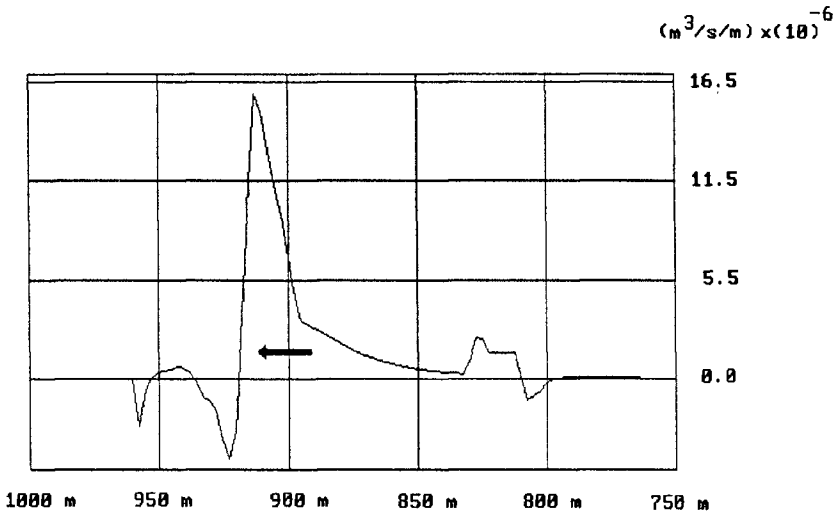
##### a) Profile development

Hindcast computations of the beach profile developments have been performed with "Unibest-TC". In this program the principal processes (wave asymmetry, undertow, gravity) underlying the cross-shore sediment transport are taken into account. The surfzone dynamics are computed by a built-in random wave propagation and decay module (Battjes and Stive, 1984). It includes the wave energy changes due to bottom refraction, shoaling and dissipation due to bottom friction and wave breaking. The secondary currents due to the vertical non-uniformity of the driving forces in the nearshore zone are modelled according to the formulations of Stive and De Vriend (1987). The cross-shore sediment transport along the coastal profile is calculated according to the formulations given by Bailard (1981), which include the transport due to the combined actions of steady current, wave orbital motion and bottom slope effect. The related bottom level changes of the cross-shore profile are computed from the mass balance.

For the computation of the perched beach profile morphodynamics at Ostia the local wave data from the directional Datawell Waverider buoy has been used in chronological sequence. The original wave data has been averaged per day on the basis of wave energy. The computation has been performed for the typical measured cross-shore profile as shown in Fig.5, but only the upper fill layer consisting of 0.3 - 1.3 mm was taken into account. The effect of coarsening of the beach material at the surface due to mixing of the upper and lower fill layer was just considered by increasing the  $D_{50}$  from 0.6 to 0.8 mm. In Figure 6 the computed beach profile developments after 3, 6 and 12 months are shown together with the distribution of the cross-shore transport  $S_y$  at the time step of 3 months. For the computed profile situated below MSL a similar erosion pattern can be observed in comparison with the profile developments which have been measured in nature (see Fig.5), although the calculated erosion seems to be slightly underestimated. Near the waterline the computation also show the formation of a ridge similar to the natural development. However, above MSL, at the emerged beach face, a large difference between calculated and natural development can be observed. In the model the accretion of the upper beach profile does not occur. One explanation for this may be the poor description in "Unibest" of the effect of wave up-rush on ridge formation at the

Cross-shore transport  $S_y$

$t = 90$  days



Profile developments

- $t = 0$  days
- -  $t = 90$  days
- $t = 180$  days
- -  $t = 360$  days

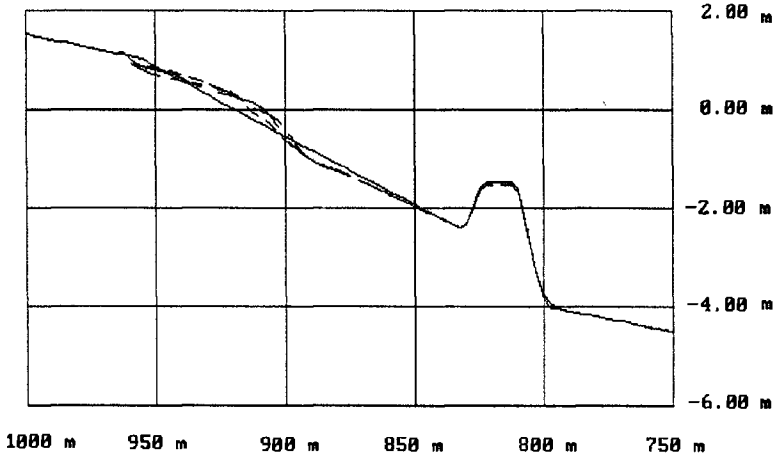


Fig. 6. Cross-shore transport and profile developments computed with UNIBEST-TC (Delft Hydraulics)

waterline. Possibly, aeolic transport along the dry beach face may be another explanation for this difference.

#### b) Beach planshape evolution

Computation of the beach planform shape have been performed with the program "Unibest-CL". This program computes the coastline changes due to longshore sediment transport gradients and cross-shore sediment losses/ gains on the basis of the one-line schematization. The model is based on the well known single line theory, which was first presented by Pelnard-Considère (1956). The profile characterizing the beach is assumed to move horizontally over its entire active height as a result of accretion or erosion. The beach slope therefore does not change. An equation of motion and a continuity equation are used together with specified initial and boundary conditions.

The basic input data for the module "Unibest-CL" is generated with the module "Unibest-LT" which computes tide- and wave-induced longshore currents and sediment transports on a beach of arbitrary profile. The surfzone dynamics are derived from the same built-in random wave propagation and decay model as used in the model "Unibest-TC". The distribution of the longshore current is computed from the momentum equation alongshore taking into account the radiation stress gradient, the bottom friction under combined current and wave action and the tidal surface slope alongshore.

The longshore transport computations have been carried out for the design profile of the beach nourishment with the same grading assumptions. The computations are based on a statistical description of the local directional wave recordings. The longshore transport computation are carried out with the Bijker formula (Bijker, 1971).

For the computation of beach planform development it has been assumed that the active profile extends down to the toe of the submerged rubble mound barrier. At the updrift boundary of the coastline model a zero transport has been imposed; at the downdrift boundary of the model the current transport has been modelled.

Figure 7 shows the results of the coastline computation after approximately 1 year. The initial coastline in January 1991 is also shown. The results display a retreat of the beach in the area south of Pontile della Vittoria due to the southward directed longshore transport and a small accretion in the area north of Canale dei Pescatori. From the computational results it can be noticed that the beach-line fluctuations which are present in the initial situation are slightly smoothed by the model. The reason for this is that longshore transport has been computed in the model for only one typical cross-shore profile. In nature, however, local deviations of the beach profile and nearshore area may cause small differences in beach response. In Figure 7 the corresponding net sediment transport distribution alongshore is shown as well. The sediment transport rate varies between 5,000 and 15,000 m<sup>3</sup>/year.

### Lessons from field experience and conclusions

After nearly three years of monitoring and the occurrence of many severe storms, the behaviour of the new perched beach at Lido di Ostia has been satisfactory. The observed alongshore and cross-shore redistribution of sediments are in good agreement with the design predictions. Volume losses appear to be small and correspond fairly well with the model predictions for a relatively bad wave climate. Negligible effects are observed on the downdrift and offshore beach morphology. Therefore the design choice to avoid groyne construction seems to be correct.

Ecological and aesthetical impacts are also acceptable: the quality of beach sediments and of seawater is satisfactory, as confirmed by the large tourist crowds in summer. The submerged rubble sill is stable and does not affect the beach recreational activities (a part from surfing). It is easily seen as a dark blue strip in the sea, marked with buoys. The rock barrier has favoured the development of marine fauna, being now fully covered with mussels and stimulating leisure fishing.

The experience gained so far from this innovative large-scale project can give some useful technical indications for the design of other perched beaches in similar hydro-morphological conditions.

The rock bar could be composed by a reduced number of gradations and the stone toe protection enlarged and laid directly on the geotextile above the seabed, thus saving the trench dredging. A proper filter layer of small stones should separate the fill toe from the barrier to avoid intrusion of fines into the sill.

The natural beach profile reshaping can be favoured and the construction eased by dumping the fill material on a steeper slope and keeping the cheaper coarse sediments on the submerged profile and the blanket of precious fine sand on the emerged beach face, which can be designed with a higher crest level.

However, final conclusions will be drawn after a longer monitoring period.

Field data has also been used to perform an interesting hindcasting of the beach profile and shoreline development with advanced mathematical models. The models could also be further calibrated to achieve more reliable predictions for the future evolution of the perched beach.

### Acknowledgements

The Authors wish to thank Mr Patrizio Cuccioletta, chief design engineer of the project, and Mr Osvaldo Mazzola, project manager of the consortium of contractors Contracos, for their major efforts in the project finalization and for the supply of useful data. Support and suggestions from prof.A.Noli (University of Rome) are also gratefully acknowledged.



### References

- Bailard, J.A., 1981: An energetics total load sediment transport model for a sloping beach. *Jour. Geophys. Res.*, Vol.86, no. C11, pp. 10,938-10,954.
- Battjes, J.A. and M.J.F. Stive, 1984: Calibration and verification of a dissipation model for random breaking waves, ASCE Proc. 19th ICCE conference, pp. 649-660
- Bijker, E.W., 1971: Longshore transport computations. Proc. ASCE, Journal of the Waterways, Harbors and Coastal Engineering Division, WW4, November 1971.
- Delft Hydraulics, 1989. Coastal protection plan, Lido di Ostia: morphologic study. Report H 891
- Pelnaud-Considère, R., 1956: Essai de théorie de l'évolution des formes de rivages en plages de sable et de galets. IVem Journées de l'hydraulique Question III, Raport 1 (1956) 74-1, 74-10.
- Segre A.G., 1950: Note illustrative della Carta Geologica d'Italia, foglio 149. S.G.I.
- Stive, M.J.F. and H.J. de Vriend, 1987: Quasi-3D current modelling: Wave-induced secondary current. ASCE Specialty conf. "Coastal Hydrodynamics", Delaware.
- Toti, M., P.Cuccioletta and A.Ferrante, 1990. Beach nourishment at Lido di Ostia (Rome). Proc.27th AIPCN Congress, Osaka

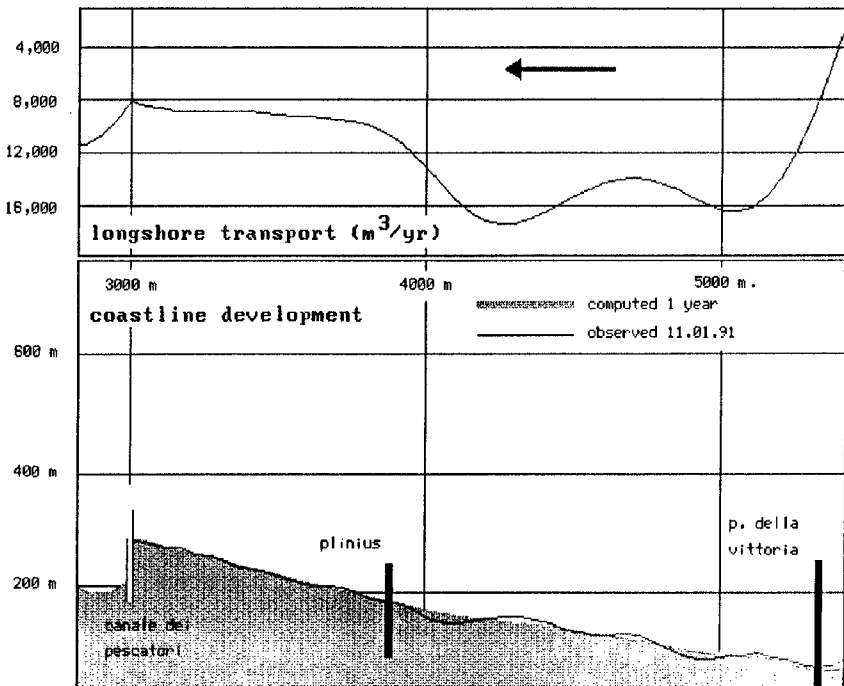


Fig. 7. Longshore sediment transport and shoreline development computed with UNIBEST-LT/CL (Delft Hydraulics)



Photo 1-2. The beach before and after the nourishment  
(Plinius club and jetty seen in the far field)



Photo 3-4. Aerial views of the new beach at Ostia (1991)

## CHAPTER 253

### The Restoration of Bate Bay, Australia - Plugging the Sink

Angus D Gordon<sup>1</sup>

#### Abstract

For more than 200 years aeolian processes have removed sand from the Bate Bay coastal compartment. This ongoing loss resulted in long term recession of the 5.5km beach. By the mid 1970's the recession threatened both public and private assets. A detailed coastal process study was undertaken to develop a management plan aimed at halting the recessional trend. The plan was progressively implemented over a period of 14 years. The result is that the foreshores of Bate Bay are now stable. The management strategy adopted has not only protected the public and private assets but has also enhanced the recreational amenity of the area. Throughout the project monitoring was undertaken of both the coastal process and the management options. These monitoring programs have provided useful information on the pragmatic application of traditional study techniques and on the effectiveness of the selected management options.

#### Introduction

Kurnell Peninsula is located some 25km south of Sydney Heads. The Peninsula is a coast parallel sandy isthmus linking the rock outcrop of Kurnell Headland to the mainland bedrock at Cronulla. It is the sandy barrier which forms the eastern boundary of Botany Bay. On its seaward side, to the east, lies the 5.5km, crescent shaped embayment of Bate Bay. The embayment includes the following beaches (from south to north) South Cronulla, North Cronulla, Elouera, Wanda, Green Hills/Cronulla and Boat Harbour (see Figure 1).

Residential development and formal parkland are the dominant foreshore features along the southern 2km of the Bay. North of Wanda, for a distance of some 1.7km unstable, unvegetated dunes dominated the landscape for at least 200

---

<sup>1</sup>Manager, Manly Hydraulics Laboratory, Public Works Department, 110b King Street, Manly Vale, NSW 2093, Australia

years up until 1975. These dunes bisected the Peninsula, extending inland more than 1.5km, through to Botany Bay. The remaining 1.8km of foreshore consists of foredunes which were initially stabilised in the 1950's by the landholder; the Holt family.

During the period of European settlement, Kurnell Peninsula has undergone many changes of land use. Initially, the areas of natural coastal scrub land were used for grazing purposes. However by early this century South Cronulla had become a weekend recreational retreat. As its popularity grew residential and commercial development took place. Early development was concentrated in the more stable southern region of the Bay but by the 1930's the demand for land pushed the development northward into the unstable dune region at Wanda.

In the early 1950's, Sydney's need for construction and foundry sand focussed attention on commercially viable deposits such as the 30m high transgressive dune field of the Peninsula. In response to this, a major sand extraction industry developed. Over the past 40 years the activities of this industry have resulted in the removal of much of the hind dune region in the centre of the Peninsula.

Severe storms ravaged the Sydney coastline in May-June 1974. These storms resulted in significant erosion of the Bate Bay beaches. The foredune system throughout most of the embayment was destroyed. In response to this damage, coastal process studies were undertaken and a coastal management plan was developed and implemented over a period of 14 years.

The major elements of the plan were:

- nourishment of the embayment by feeding sand into the surf zone at South Cronulla;
- dune reconstruction at North Cronulla;
- seawall construction at Prince Street;
- foredune stabilisation at Elouera and Wanda;
- foredune reconstruction and stabilisation from Wanda to Boat Harbour;
- hinddune stabilisation in the centre of the embayment.

This paper summarises the project from the inception of the coastal process studies to the completion of the management plan and reviews the results.

### **Coastal Process Studies**

Coastal process studies were commenced in 1975 using the methodology outlined by Gordon and Lord (1980). These initial studies provided the basis for the overall management strategy (Foster and Gordon, 1978, and Gordon, unpublished). The coastal processes were then monitored and analysed throughout the 14 years of the project. This enabled on-going "fine tuning" of the management

plan and provided considerable insight as to the effectiveness of the various investigation techniques and the management options employed.

The studies began with extensive bathymetric, seismic and sediment surveys to obtain information on the seabed and subsurface morphology, seabed sediment and reef distribution and the depth of the active profile movement. These studies included side scan sonar, echo sounding and seismic surveys as well as an extensive sediment sampling program. Onshore, a geological survey was carried out to establish the age and mode of formation of the dune features of the Peninsula (Roy and Crawford, 1979).

Longterm shoreline movement trends were examined using both historical ground survey data and photogrammetric analysis of large format vertical aerial photography. The ground survey data was available at a limited number of locations for a period of more than 100 years. The earliest survey (1863) was made available to the study by the Holt family. The photogrammetry focussed on reconstruction of cross sections through the beach and dune region, over time, rather than historical water line movement, as the latter was found to be too unreliable. Thirty five cross sections were established (see Figure 1). These were transferred through the nine sets of photography covering the 35 years prior to implementation of the management plan.

The erosion/accretion rates obtained from this analysis were calculated from both differential volume calculations undertaken for successive cross sections and foredune retreat/advancement measurements taken from comparison of the movement of position of the 3m and 5m contours over time. The average result, reduced as an implied shoreline movement, was then plotted (see Figure 1). Aerial photographs continued to be obtained throughout the implementation phase and the photogrammetry results checked against nine ground survey cross sections established in the embayment to monitor dune and beach movements and to verify the photogrammetric techniques.

Aeolian sand transport was examined by analysing historical survey and photogrammetric data and by developing numerical models of wind born sand transport. The historical information established the rate of landward movement of the transgressive "front" at the rear of the hinddunes, thereby providing the data necessary to calibrate the aeolian sand transport models. Because of the inherent inaccuracies of these models, particularly when applied to a non uniform surface such as a dune field and the need to take into account wetting and drying effects on transport rates, two alternative models were developed. One employed the Bagnold (1974) approach, the other was based on the method of Hsu (1974).

Examination of the longshore surf zone sediment transport processes commenced with a wave refraction/diffraction shoaling analysis for three points in the embayment (see Figure 1, Location A, B and C). The inshore wave height coefficients so obtained were then used in a sediment transport program to calculate

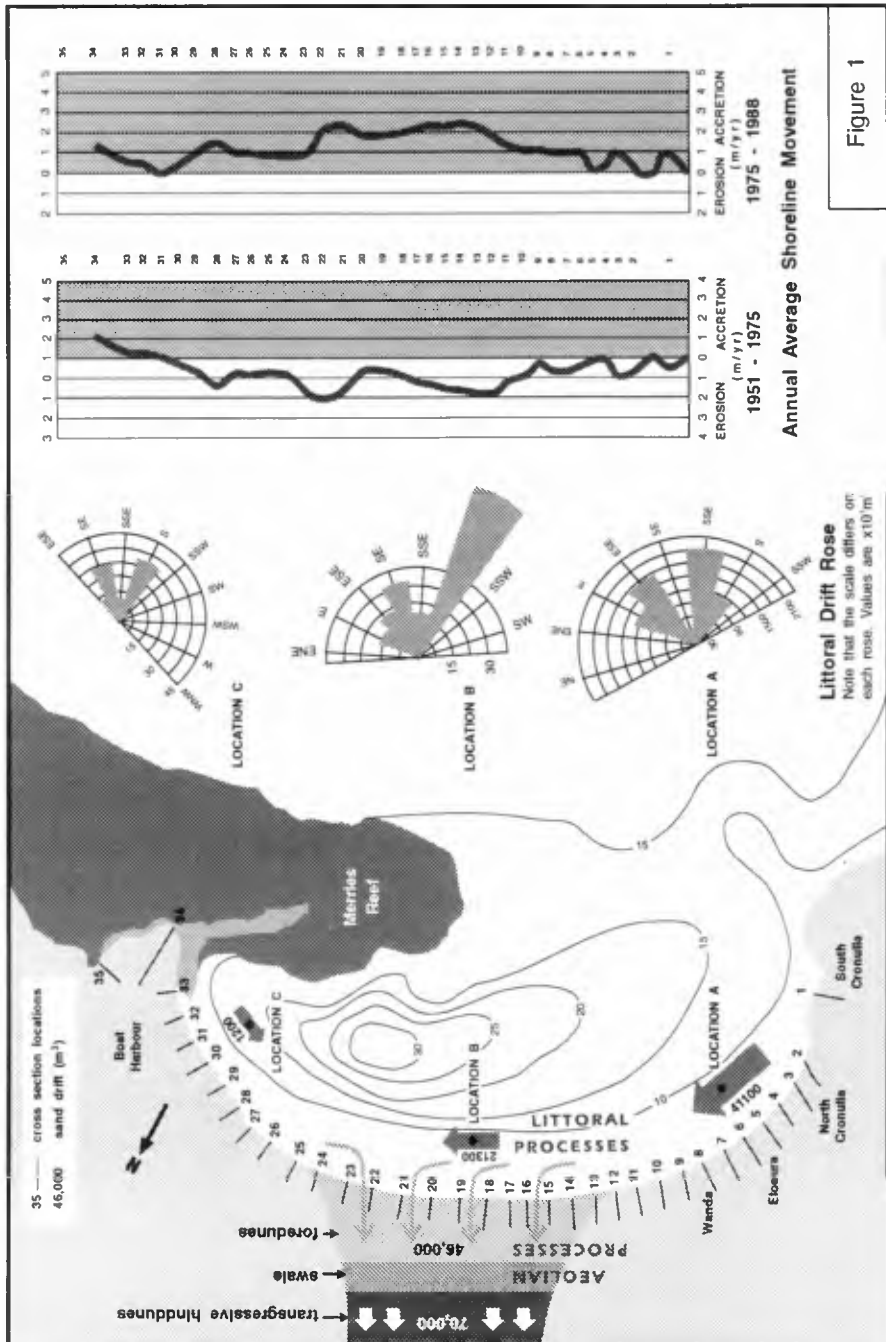


Figure 1

transport roses at each of these points.

The wave refraction analysis was based on a computer program developed from Wilson's method (Wilson, 1966). The results were manually adjusted as outlined in SPM (1973/84) to include diffraction effects. A 46 by 34 numerical grid using a 200 metre grid spacing was adopted and a 10 second deepwater wave period was used for most program runs. The characteristic wave period of 10 seconds was selected after examination of the then available 5 years of data from a Waverider buoy located 3km northeast of Bate Bay in 80m of water. Selected runs were made with 8 and 12 second waves to check sensitivity.

Five offshore wave approach directions were selected to generate a matrix of inshore wave height coefficients. The coherence of the results was checked by plotting the coefficients of refraction/diffraction/shoaling and the wave angle to the contours, along the wave ray, for each deepwater wave approach direction. Discontinuities and/or anomalies were thereby readily identified, examined and numerically smoothed, if appropriate. The inshore wave coefficients given by the refraction/diffraction/shoaling analysis were verified by comparing them to Waverider data from an inshore buoy deployed for two years at Location A, within the bay.

The sediment transport calculations were based on the "SANDGUS" program (published in Gordon and Acikgoz 1984) developed around the CERC equation (SPM 1973/84). This program, which was first developed for this project, uses the annual deepwater wave spectra, shoals, refracts and diffracts that spectra along the rays through the wave coefficient matrices obtained from the refraction/diffraction analysis and then calculates sand transport. The wave coefficient matrices only extended to 10m water depth. Inshore of this depth the model applies the straight parallel contour assumption using Snells Law to calculate refraction. The deepwater wave spectra used was that available from the offshore Waverider site. As the project progressed the data set available from this site increased from 5 years to 20 years and hence some review of earlier calculations was necessary.

For the purposes of this study it was assumed that all longshore transport took place at the break point. This point was calculated for each one metre wave height class. Although an oversimplification, the approach proved quite adequate as no shore normal structures existed or were being considered as management options.

The results of the sediment transport analysis were compared with sand tracer studies. Some 10 tonnes of dyed sand were released into the surf zone at South Cronulla. This material was tracked intensively over a period of 1 month and, to a lesser extent, over a period of 3 months. Initially samples were taken on a 50 metre grid extending 0.5km longshore from the injection point and offshore to 10 metres of water depth. The samples were obtained by divers driving one metre core tubes into the seabed. During the first week the entire grid was covered twice a day. The samples were then sectioned and examined under a microscope. As the grid was



progressively extended the number of grid points rationalised and the sampling rate reduced once the movement pattern of the dyed sand became apparent.

The results of the sand tracer experiment were compared with a data set generated by the "SANDGUS" computer model for the prevailing conditions during the experiment. It was found that for Bate Bay the CERC equation, as presented in SPM 1984, produced results of the same order of magnitude as those obtained from the experiment. This calibration of the CERC constant was seen as critical, as experience elsewhere in NSW had indicated that the constant can vary considerably depending on site conditions.

### **The Sediment Budget of Bate Bay**

Integration of the various studies provided an understanding of the overall coastal process system of the embayment.

The sediment and geological studies showed that Bate Bay is substantially a closed compartment with no significant losses or gains across its longshore boundaries.

Prior to implementation of the management plan, the potential sediment transport rates in the surf zone were calculated to be 41,000m<sup>3</sup>/yr net northward in the southern third of the embayment (Location A), where the gross transport was 700,000m<sup>3</sup>/yr; 21,000m<sup>3</sup>/yr net north transport in the centre of the embayment (Location B) on a gross movement of 165,000m<sup>3</sup>; and 1,200m<sup>3</sup>/yr net southern transport (Location C) on a gross of 86,000m<sup>3</sup> in the northern third of the embayment behind Merries Reef (see Figure 1).

The high values for both gross net drift in the southern end of the embayment were associated with the exposure of this area to a broader range of deepwater wave approach angles and the misalignment of this section of the bay prior to the management plans implementation. The low gross drift in the centre of the embayment was consistent with the relatively high onshore/offshore movements which take place in this area. That is onshore/offshore in the centre of the embayment dominates over the longshore processes. In the northern section of the embayment the low gross and net drift reflect the sheltering of Merries Reef. The net transport rate of 21,000m<sup>3</sup>/yr, northwards, calculated at Location "B" in the centre of the embayment (Figure 1), was consistent with observations that some of the material moving north from the southern end (Location A) had already been lost into the dunes.

The aeolian transport studies were undertaken for both the foredunes and the hinddunes. For the foredunes, the Bagnold approach yielded a net landward potential rate of transport of 24m<sup>3</sup>/m/yr while the Hsu method gave a result of 32m<sup>3</sup>/m/yr (see Figure 2). Based on these results an average rate of 28m<sup>3</sup>/m was adopted as the potential for sand transport in the foredune. This translated into a

net average landward potential for transport of sand in the foredune region of some  $46,000\text{m}^3/\text{m}$ , provided material was available for entrainment.

Applying the same theoretical approach to the hinddunes the calculated annual net landward potential for transport of sand was found to be  $60,000\text{m}^3$ . The analysis of historical survey and photogrammetric data indicated that the average annual movement of the transgressive dune front into the vegetation on the western side of the peninsula was between  $8\text{m}/\text{yr}$  and  $10\text{m}/\text{yr}$  giving a total annual net transport rate westward of  $90,000\text{m}^3$ . Given the assumptions and accuracies of the methods used a figure of  $70,000\text{m}^3/\text{yr}$  was adopted as representing the net westward drift rate in the hinddune.

The difference in availability of sand for entrainment explains the apparent anomaly between the foredune and hinddune transport rates. The beach was an average of  $20\text{m}$  wide whereas the area available to feed the hinddunes was some  $100\text{-}200\text{m}$  wide. This differential in transport was evidenced by the evolving topography of the dunefield. The rate of landward movement of the centroid of mass of the hinddunes had historically been greater than that of the foredunes. This had created an ever widening interdunal swale, the area between the foredunes and hinddunes. The swale was some  $100$  to  $150\text{m}$  wide by 1975.

The photogrammetric analysis supplemented by the historical survey record showed that, prior to implementation of the management plan, longterm coastal retreat was occurring throughout most of the embayment. Figure 1 summarises the recessional trend. Recession rates varied from an average of  $0.5\text{m}/\text{y}$  in the southern end to  $2.0\text{m}/\text{y}$  in the centre of the embayment. The accretion trend shown in Figure 1, from section 30 to 34 in the north of the embayment, was produced by the dune works undertaken in the mid 1950's by the landholder of this portion of the embayment. The high recession rates in the centre of the embayment were associated with the area of unstable foredunes where aeolian processes continuously removed sand from the beach into the transgressive dunefield. The differential recession rates were reflected in the shoreline alignment. The central  $2\text{km}$  of beach became noticeably indented as compared to the overall alignment of the embayment foreshore.

Integration of the recession rates throughout the embayment, for an active profile depth which varied from  $8\text{m}$  at South Cronulla to  $10\text{m}$  in the centre of the embayment and reduced to  $6\text{m}$  in the northern portion behind Marries Reef, indicated that the net loss of was  $51,000\text{m}^3/\text{yr}$ .

Within the accepted accuracies of the methods used to define the coastal processes, this foreshore recession rate of  $51,000\text{m}^3/\text{yr}$  agreed well with the aeolian transport induced loss into the transgressive dune sink of  $46,000\text{m}^3/\text{yr}$  and the net littoral drift feed mechanism of  $42,000\text{m}^3/\text{yr}$ .

In summary, Bate Bay was found to be a closed coastal compartment. The destabilisation of the dunes in the centre of the embayment over 200 years ago allowed an aeolian sink mechanism to develop. The resulting loss of sand from the surf zone, beach and foredunes in the region adjacent to the sink caused the shoreline to retreat. This in turn produced a misalignment of the beach system which propagated to both ends of the bay. The misalignment in turn induced an evolving littoral drift system which increasingly fed sand from both ends of the bay towards the middle. Immediately prior to implementation of the management plan the average annual net quantity involved in this loss was approximately 45,000m<sup>3</sup>.

### **Management Plan - Overview**

The main aim of the management plan was to "plug the sink". Restoration of the beach amenity at the southern end of the embayment and protection of assets threatened in this region were also given high priority. In general, the emphasis was placed on a "soft" management strategy aimed at establishing a well vegetated foredune throughout as much of the embayment as possible. Further, rather than mechanically forcing a new shoreline alignment on the embayment, the technique used involved: the establishment of some initial dunes on the existing alignment; feeding of the surf zone with nourishment sand; allow the natural process to distribute the material throughout the embayment and also allow these processes to adjust the foreshore/dune alignment and the offshore seabed. The final phase of stabilisation included the hinddunes in the centre of the embayment. This work was aimed at retaining sand reserves which may be required in the future for on-going beach nourishment and overcoming the wind blown sand problems associated with these dunes.

The new foredune region was sized to provide a sufficiently large area of stabilised dune to stop the landward loss of beach material by aeolian processes and to provide adequate material to accommodate short term erosion associated with storm events. In the areas where there was insufficient width to establish the necessary foredune because of space constraints, such as at South Cronulla and Prince Street, alternative methods had to be considered. These included the nourishment of South Cronulla Beach and the construction of a seawall at Prince Street where residential buildings were under direct threat from erosion.

The Prince Street seawall option was only selected after an exhaustive series of studies, spanning some 10 years. These studies failed to identify an alternative, acceptable to the community, which would also be more in keeping with the "soft" engineering management philosophy adopted for the remainder of the embayment.

### **Management Plan - Implementation**

The Bate Bay foreshore restoration program commenced in 1975 with the fencing of foredune "paddock" areas along Wanda and Elouera. This was followed by the infilling of blowouts and washthroughs in the foredunes in the centre of the

embayment. Sand catching fences were then erected and well defined beach access tracks constructed.

As the coastal process studies showed that the major sand feed to the aeolian sink in the centre of the embayment was from the south, the decision was taken that, following the initial stabilisation of the foredunes throughout the embayment, sand would be fed into the surf zone process from the south and allowed to distribute by natural means to establish new beach alignments. The nourishment of the embayment was therefore carried out at South Cronulla Beach. The project began during 1977-78. Some 80,000m<sup>3</sup> of sand were trucked from the hinddune region of the centre of the embayment, to South Cronulla. There the sand was spread by bulldozer. Work was halted during the 1977/78 swimming seasons and recommenced in mid 1978 when a further 47,000m<sup>3</sup> were placed. The underwater profile of the surf zone was also allowed to reform by natural processes. A public education program was undertaken in conjunction with the nourishment to overcome community misapprehensions associated with the apparently high initial loss of nourished beach at South Cronulla as sand re-distributed along the beaches to the north and as profile development took place.

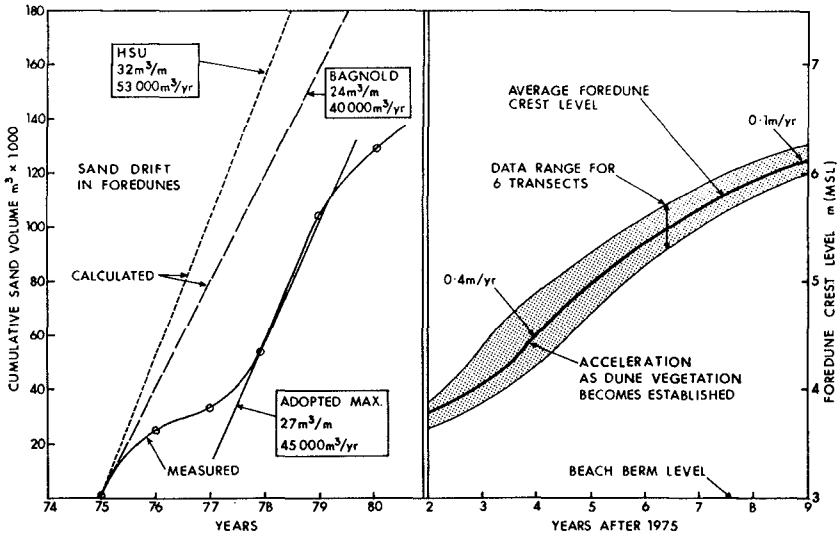
While the South Cronulla nourishment project was underway effort was also concentrated in establishing the primary dune stabilising plants in the Elouera-Wanda foredunes and along the Cronulla/Greenhills foreshore. Thus, as the nourishment sand moved north, the dune fields were ready to trap material. Strengthening and fencing of the vegetated dunes in the northern part of the embayment was also undertaken to produce a similar standard of management throughout the embayment. The overall result was a re-alignment of the embayment foreshore and the natural evolution of a viable foredune system.

Revegetation of the hinddunes in the centre of the embayment (Wanda Reserve) commenced in 1983. The revegetation was completed by 1989.

In 1985 work started on the final link in the plan. A 340m long seawall featuring pre-cast concrete armour units (Seabees) was constructed during 1985/86 along the toe of the Prince Street embankment (Hirst and Foster, 1987). This link joined the dune stabilisation work at North Cronulla to that at Elouera and provided protection to the threatened residential buildings in Prince Street. The ends of the wall were returned into the dunes to allow for the expected storm erosion at these points. Rock filled wire mattresses were placed under the beach in front of the structure to prevent toe erosion. A walkway was incorporated into the seawall crest design thus providing a continuous public foreshore pathway from South Cronulla headland to Elouera.

## Results/Discussion

The Bate Bay foreshore is now fully stabilised, some 5km of vegetated foredunes have been successfully established. In the hinddune dune region the



**Figure 2 Accretion of Sand in the Foredues**

**Figure 3 Buildup of Foredune Crest Level**

transgressive dunes stretching some 1.7km along the foreshores have also been stabilised. The sink has therefore been "plugged", the pre-existing longterm shoreline erosion halted and overall foreshore re-alignment achieved. Recreational beaches now extend from South Cronulla to Boat Harbour. The net shoreline and foredune movement over the 17 years following implementation of the management plan has shown an accretional trend, despite the occurrence of several major storms (Figure 1). The accretion has been greater in the centre of the embayment, as was predicted by the coastal process studies.

The point source feed of nourishment at South Cronulla proved to be the most economic method of achieving a "natural" restructuring of the embayment's beach/dune system.

Dune re-building was monitored throughout the project. Figure 2 shows the cumulative accretion rate and Figure 3 summarises the foredune crest level development at 6 of the survey transects located in the centre of the embayment. These figures show that, following the initial mechanical re-construction, accretion was relatively slow over the first 2 years. This outcome was unexpected at the time as shown by the Bagnold and Hsu based prediction of Figure 2. The delay was due to the difficulties experienced in establishing the pioneer plants in such a harsh environment and on such a large scale. An increase in the rate of accretion began in the 3rd year with maximum rates of accretion achieved in the 4th year when the full potential of the aeolian process were focussed towards dune building. By the

5th year accretion started to taper. Although not shown, by the 12th year it was not possible to discern further buildup. In summary, at Bate Bay the time period required to establish a viable foredune system with a diversity of plant life capable of self sustenance, was found to be some 10 years. Intensive management was necessary for the first 5 years although a lower level of support was required for a further 5 years. This timescale was in part a function of the scale of the project.

The net accretion in the dunes and on the beach of some 180,000m<sup>3</sup> was greater than the 127,000m<sup>3</sup> of the nourishment supplied. It is believed that the additional material was supplied through a subtle steepening of the offshore profile, although survey accuracy makes this difficult to quantify. There remains the possibility however that some material which has moved onshore from deeper water during the beach building conditions and is now trapped in the dunes, will be released during a future extreme storm event.

A key element to the success of the Bate Bay project was the detailed coastal processes studies carried out at inception and the ongoing monitoring of those processes, and the systems response, during implementation of the management plan. Central to this approach was the care taken to calibrate and verify the surf zone and aeolian sand transport models.

The total costs of the initial studies and the ongoing monitoring (adjusted to 1991 values) was A\$700,000. While this is a substantial sum it was only 8% of the overall project costs of A\$8.5M and less than 0.2% of the A\$350M value of the assets protected. Further, the stabilisation of the 5.5km of foreshore has allowed expansion of the public recreation areas and for development to take place in the backdune region. Future development of the embayment is centred on retention and maintenance of the newly established foredunes as a buffer zone.

## **6. Acknowledgments**

The Bate Bay project was funded by the Public Works Department, NSW, through the Beach Improvement Programme, by Sutherland Shire Council and by the Soil Conservation Service of NSW. In addition to the assistance provided by these authorities the writer also wishes to acknowledge the assistance and encouragement over the past 17 years of Prof. Doug Foster, Mr Philip Holt and the late Mr Eric Hirst.

## **Appendix 1. References**

Bagnold, R.A. (1954). *The Physics of Blown Sand and Desert Dunes*, Methuen and Co. Ltd., London, 1954.

Foster, D.N. and Gordon, A.D. (1978). *Beach Protection, Cronulla*. Proceedings 4th Australian Conference on Coastal and Ocean Engineering, Institution of Engineers, Australia, Adelaide, November 1978.

Gordon, A.D. (unpublished report). Coastal Process of Kurnell Peninsula. Public Works Department Report No. 88 047.

Gordon, A.D. and Lord (1980). An Approach for Understanding Coastal Processes. Proceedings 17th International Conference on Coastal Engineering, American Society of Civil Engineering, Sydney March 1980.

Gordon, A.D. and Acikgoz, D.H. (1984). SANDGUS-Surf Zone Sediment Transport Calculation User's Manual. Public Works Department, N.S.W., Coastal Branch, June 1984.

Hirst, E.H.W. and Foster, D.N. (1987). The Design and Construction of Prince Street Seawall, Cronulla. 8th Australian Conference on Coastal and Ocean Engineering, Institution of Engineers, Australia, Launceston, December 1987.

Hsu, S.A. (1974). Computing Aeolian Sand Transport from Routine Weather Data. Proceedings 14th International Conference on Coastal Engineering, American Society of Civil Engineers, Copenhagen, 1974.

Roy, P.S. and Crawford, E.A. (1979). Holocene Geological Evolution of the Botany Bay - Kurnell Region, Central New South Wales Coast. Department of Mineral Resources, New South Wales Geological Survey - Record Volume 20, Part 2, pp 159-250.

SPM (1973/84). Shore Protection Manual. U.S. Army Corps of Engineers, Coastal Engineering Research Center 1973 (Republished most recently 1984).

Wilson, W.S. (1966). A Method for Calculating and Plotting Surface Wave Rays. U.S. Army Corps of Engineers TM-17, Coastal Engineering Research Center, Washington, D.C., Feb. 1966

## CHAPTER 254

# Present Situation of Sea-Sand Mining in Kyushu Island, Japan and Its Influence on Coastal Environment

M. Hashida<sup>1</sup>, N. Matsunaga<sup>2</sup> and T. Komatsu<sup>3</sup>

### Abstract

The sea-sand mining has been carried out in the coast of western part of Japan since the early 1970's. Mined sea-sand is mainly used as fine aggregate of concrete structures. Mining a large amount of sea-sand near the coast induces the possibility of beach erosion and devastation of fishing grounds. In order to evaluate its influence on coastal environment, the present situation of sea-sand mining has been investigated in seven prefectures of Kyushu Island in Japan. The sea-sand mining in Kyushu Island is classified into two types. One is the mining in the sea areas where sea-sand reserves are limited. In these areas, the compatibility between the sea-sand mining and the protection of coastal environment will become very important in future. The other is the type that sea-sand has been supplied constantly from rivers or other sea areas. In this case, it will be the most important to keep the balance between the amount of mined sea-sand and that of supplied one.

- 
- 1 Professor, Department of Civil Engineering, Nippon Bunri University, Oita 870-03, Japan.
  - 2 Associate Professor, Department of Earth System Science and Technology, Kyushu University, Kasuga 816, Japan.
  - 3 Professor, Department of Civil Engineering, Hydraulics and Soil Mechanics, Kyushu University, Fukuoka 812, Japan.



### Introduction

The dependence of fine aggregate of concrete structures on sea sand increases in the western part of Japan. On the other hand, many dams and gates have been constructed across rivers with the object of flood control, water utilization, etc. Both the sea-sand mining and the decrease of sand supply from the rivers may accelerate beach erosion and devastate the coastal



(a)



(b)

Photo 1. Field work of sea-sand mining. These photos were offered by Japan Broadcasting Corporation.

(a) Sea-sand being gathered in cargo space.

(b) Drainage of sea water including mud.

environment. Actually, remarkable beach erosion was observed along the coast of the northern part of Kyushu Island, after the sea-sand mining was approved by prefectural governments. The change of longshore current due to man-made coastal structures, the decrease of sand supply from rivers, the frequent occurrence of storms, the sea-sand mining, etc. have been examined as causes of this erosion. However, what are the most essential causes still has not revealed.

Photos 1(a) and (b) show sea-sand being gathered in the cargo space of a barge ship and the state of drainage of sea water including mud, respectively. The environmental problem that the diffusion and sediment of the mud devastate fishing grounds occurs sometimes.

The purposes of this study are to investigate the present situation of sea-sand mining in seven prefectures of Kyushu Island and to examine its influence on the coastal environment.

### Sea-sand mining in Kyushu Island

Figure 1 shows the control system of sea-sand mining in Japan. The sea-sand mining has been performed under the approval of each prefectural government. The Ministry of International Trade and Industry leads for the control system of each prefectural government. The prefectural government gives the approval for the volume of mined sand to sea-sand mining companies. The companies must report the total volume of sea-sand which they mined actually, to the prefectural government every year. The prefectural government must report the total volume of the mined sea-sand to the Ministry of International Trade and Industry. It also negotiates with Fishermen's Union about compensation for devastation of fishing grounds. The standards of the approval or the compensation for the Fishermen's Unions are different in each prefecture. At the present time, there are even prefectures which do not establish any standards.

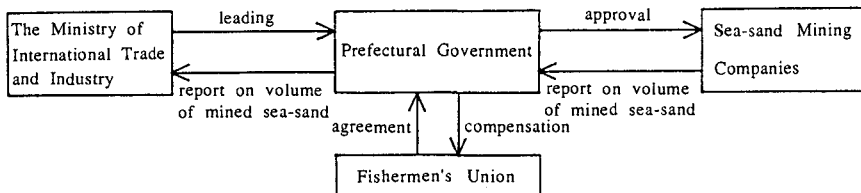


Figure 1. Control system of sea-sand mining in Japan.

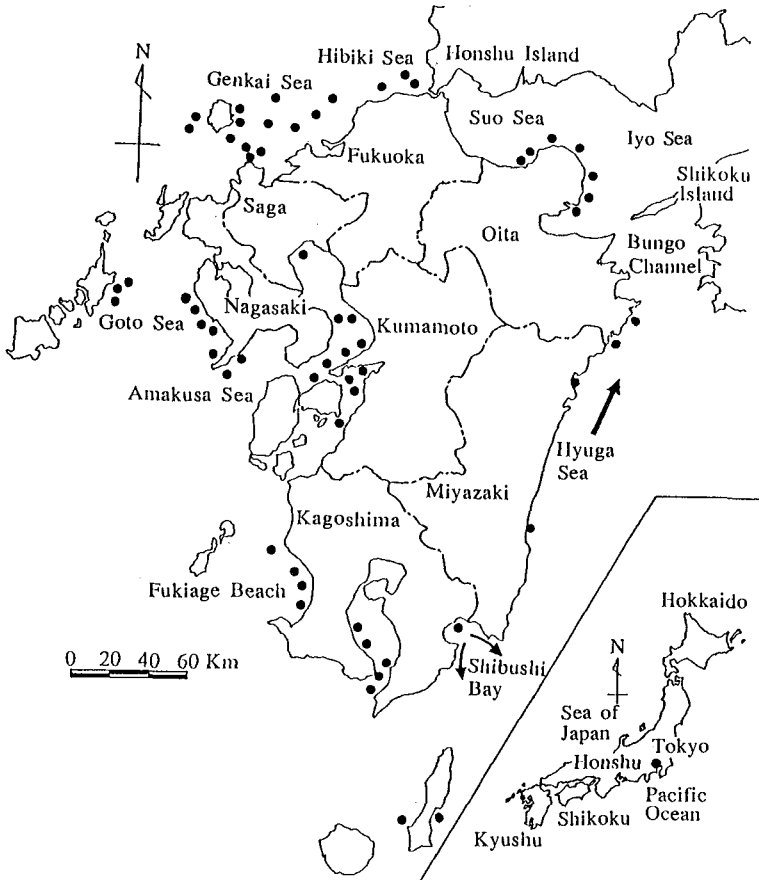


Figure 2. Sites of sea-sand mining in seven prefectures of Kyushu Island.

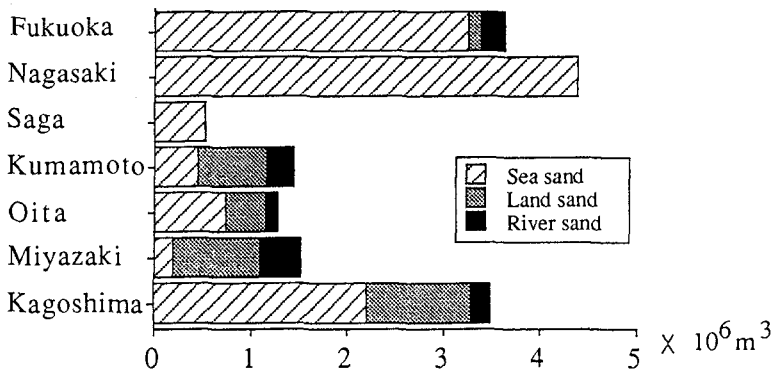


Figure 3. Volume of sand mined in seven prefectures in 1988.

In figure 2, the sites of sea-sand mining in Kyushu Island are shown. Kyushu Island consists of seven prefectures, i. e., Fukuoka, Nagasaki, Saga, Kumamoto, Oita, Miyazaki and Kagoshima Prefectures. The dash-dot lines indicate the border between the seven prefectures. The black circles show the superior direction of sediment transport. It is seen that many sites exist along the coast of Kyushu Island.

Figure 3 shows the volume of sand mined in the seven prefectures in 1988. The mining of both river sand and land sand has been restricted from the standpoint of the prevention of disaster. Therefore, sea-sand above 70 percent of total sand has been mined in Kyushu Island. Sea-sand mined in Fukuoka, Nagasaki and Kagoshima Prefectures is very large in comparison with that in the other four prefectures. The rate of the volume of sea-sand to that of the total sand shows a yearly increase.

### 1. Fukuoka Prefecture

Figure 4 shows the frequency of storm wind, whose mean velocity is larger than 10 m/s, in Fukuoka Prefecture. During 15 years from 1947 to 1961, a remarkable beach erosion was observed along the coast of the Genkai Sea and the Hibiki Sea. The recession of the shoreline averaged 45 m, and 85 m recession was recorded as a maximum value during the 15 years. The Fukuoka Prefectural Government concluded that extraordinary frequent storms induced this erosion (Kojima, H. et al., 1986). Sea-sand mining started in 1972. Though the

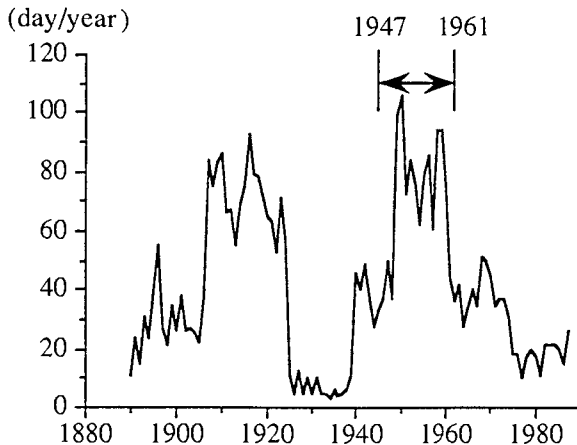


Figure 4. Frequency of storm winds in Fukuoka Prefecture.

frequency of storm decreased after the onset of the sea-sand mining, the progression of beach erosion continued to be seen along some areas of the coast. In Fukuoka Prefecture, a large amount of sea-sand was mined at sea areas shallower than 20 m from 1972 to 1981. When the prefectural government began to investigate the change of shoreline, i. e., in 1981, it also established a restriction on the sea-sand mining. The restriction was that the sea-sand mining has to be performed in principle at sea areas deeper than 40 m after 1981. Generally speaking, a remarkable beach recession has not been observed since 1981's restriction. Therefore, which was the essential cause for this erosion has not still been made clear.

Figure 5 shows the sites of sea-sand mining in the Genkai Sea and the Hibiki Sea of Fukuoka Prefecture. The black triangles indicate the sites shallower than 20 m, and the black circles indicate ones at the water depth over 40 m. Fukuoka Prefectural Government has carried out the level survey along the coast of the Genkai Sea since 1981. The stations are shown by numbered black-rectangles.

Figure 6 shows the correlations between the volume of mined sea-sand and beach elevation at stations 4 and 6 in the Genkai Sea. The open and solid marks indicate the results of level survey and the volume of mined sea-sand, respectively. At the stations, the sea-sand mining was performed at sea areas shallower than 20 m until 1986, but it has been mined only at sea areas deeper than 40 m since 1987. The mining was repeated about twenty times from 1985 to 1986 at Ainoshima and Tsuyazaki. The total volume reached about  $6.0 \times 10^5 \text{ m}^3$ . As shown in this figure, a remarkable erosion was observed at that time. After the sea-sand mining at Ainoshima and Tsuyazaki was stopped in 1987, the beach at station 4 began to recover and reach nearly an equilibrium state. At station 6, the influence of sea-sand mining on the beach elevation did not appear obviously because a small amount of sea-sand was mined at Nogita. The sea-sand mining at Oshima and Nishinoura was continued to 1986. Its influence on beach erosion was not recognized. It may mean that the restriction established by the Fukuoka Prefectural Government was valid. The field investigation on the volume of sea-sand reserved in the Genkai Sea was made by the Ministry of International Trade and Industry. According to its report, sea-sand suitable for the fine aggregate distributes over an area of about  $1.75 \times 10^2 \text{ km}^2$ .

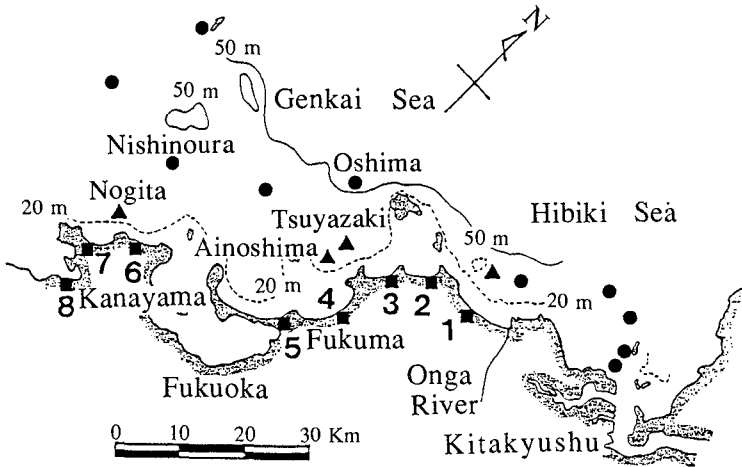


Figure 5. Sites of sea-sand mining ( ● and ▲ ) in the Genkai Sea and the Hibiki Sea, and survey stations ( ■ ).

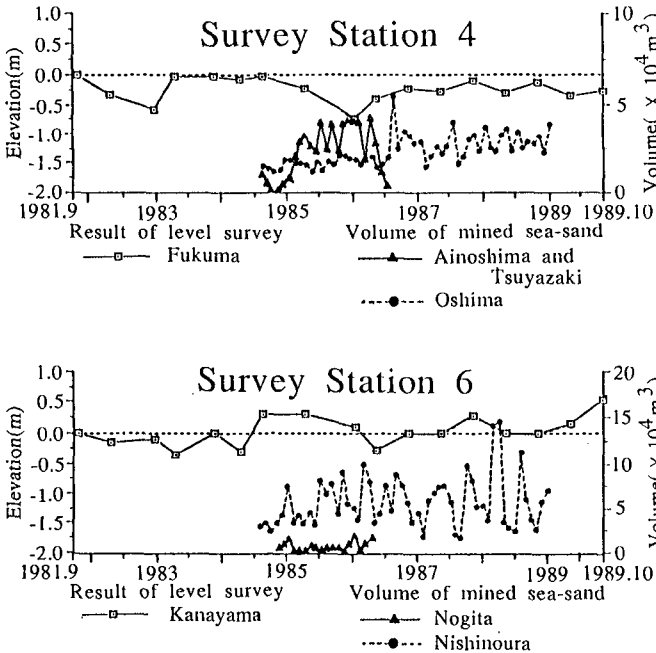


Figure 6. Correlations between volume of mined sea-sand and beach elevation in the Genkai Sea.

## 2. Nagasaki Prefecture

The sites of sea-sand mining in Nagasaki Prefecture are shown in figure 7. The black circles indicate the sites of sea-sand mining. The investigation about the reserves of sea-sand was made in the dotted area by the Ministry of International Trade and Industry. This prefecture is mining the largest amount of sea-sand in Kyushu Island. However, there are few wide, long rivers. Therefore, it seems that the sand supply from river to coast is very little. The Nagasaki Prefectural Government has approved the sea-sand mining in the sea areas where the water depth ranges from 30 m to 70 m. This means that Nagasaki Prefecture is also obliged to seek offshoreward sites. The sea areas have been a good fishing ground for a long time. Surface layer of the region contains a lot of lime composed of shells and dead planktons. Therefore, suitable sea-sand for fine aggregate is very little.

According to this investigation, however, it can be expected that sea-sand of good quality distributes in deeper layer. Its distribution is over about 19.4 km<sup>2</sup>. Recently, a new environmental problem, i. e., the devastation of fishing grounds, is also occurring in this region. The Nagasaki Prefectural Government is looking for countermeasures to realize both sea-sand mining and preservation of nearshore environments.

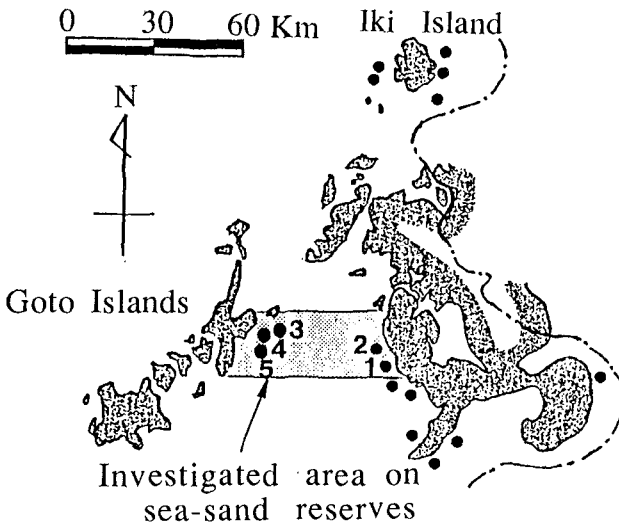


Figure 7. Sites of sea-sand mining in Nagasaki Prefecture.

### 3. Kumamoto Prefecture

Figure 8 shows the sites of sea-sand mining in Kumamoto Prefecture.

The volume of sand mined in this prefecture was  $1.50 \times 10^6 \text{ m}^3$  in 1989.

The volume tends to increase during the last five years. Sea-sand occupies from 30 % to 40 % of the total volume of mined sand.

The sea-sand mining has been carried out at the Ariake Sea, of which the sites are indicated by the black-circles numbered from 1 to 7.

The sites at the Yatsushiro Sea are shown by the black circles numbered from 8 to 11.

Sandy beach remains only along the numbered coast. The other coasts are either tidal flat or gravel coast.

The source of sand supply to the sea area is only inflow from the rivers.

In the case when sea-sand is mined in these seas, therefore, it is necessary to consider the balance between the volume of sea-sand mining and the volume of sand supply from the rivers.

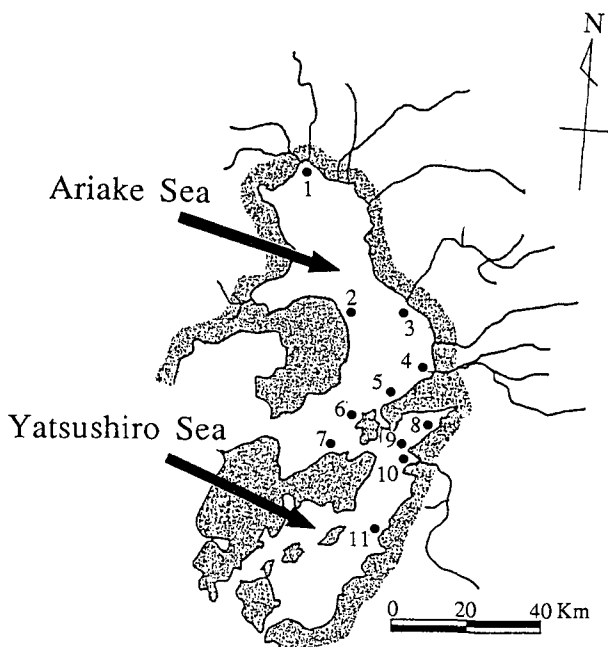


Figure 8. Sites of sea-sand mining in the Ariake Sea and the Yatsushiro Sea.



### 4. Oita Prefecture

Figure 9 shows the sites of sea-sand mining in Oita Prefecture. According to the statistical report on coast, which is presented by the River Office of the Ministry of Construction, the yearly mean expense of public utility enterprise for beach erosion was 40 million yen over the four years from 1984 to 1987. This is very high next to Nagasaki and Miyazaki Prefectures. The ratio of sea-sand to the total sand is from 60 % to 65 %. The sea-sand mining has been carried out mainly at both the northern part and the southern part. Oita Prefecture mined sea-sand of  $6.55 \times 10^6 \text{ m}^3$  during six years from 1984 to 1989. This volume is nearly equivalent to the volume mined over 14 years from 1970 to 1983. It shows the rapid increase of sea-sand demand. During last six years, a large amount of sea-sand has been mined at Jiromaru Coast (number 5), Morie Port (number 7) and Nishinoura Coast (number 8). At Jiromaru Coast, the sea-sand mining has been carried out because of the accumulation of sea-sand. The sand supply from Jiromaru River is very little and erosive coasts have been observed along the northern part of Jiromaru Coast. Therefore, it is necessary to make clear the source of the sand supply to Jiromaru Coast. Morie Port has a tendency to be buried due to sediment from Yasaka and Takayama Rivers. The volume of

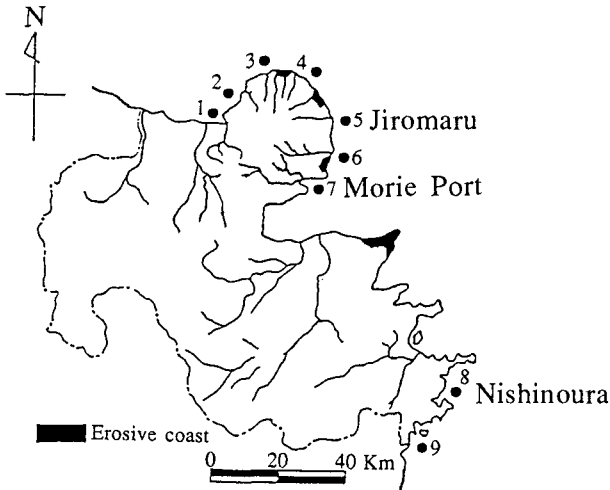


Figure 9. Sites of sea-sand mining in Oita Prefecture.

sea-sand mined in Morie Port is nearly balanced to that of the sediment yield from the rivers. Therefore, the environmental devastation due to the sea-sand mining does not appear in Morie Port. In spite of no rivers along Nishinoura Coast, a large amount of sea-sand has been mined with the object of keeping ship courses and arranging fishing grounds. However, no influence on coastal environment due to the sea-sand mining has been observed for the last 20 years. Therefore, understanding how the sediment transport occurs along Nishinoura Coast is the most important.

### 5. Saga, Miyazaki and Kagoshima Prefectures

Saga Prefecture is mining the smallest amount of sand in Kyushu Island. The total volume of sand is less than about  $8.0 \times 10^5 \text{ m}^3/\text{year}$ , of which most depends on sea-sand. The sea-sand mining has been carried out at four sites. One of them is in the Ariake Sea. The other sites locate in the Genkai Sea. The total volume of mined sea-sand per year is very little. The sea-sand mining in the Genkai Sea has been made at sea areas deeper than 20 m. From these reasons, the influence on coastal environment has not been come to the front.

Miyazaki Prefecture faces the Hyuga Sea. The coast is an erosive large-scale beach. Therefore, the sand mining in sea and river has been prohibited in principle. However, sand and gravel deposited in dams has been dredged to keep up their function. Small volume of sea-sand has been dredged with the object of keeping ship course in Miyazaki Port and Nobeoka Port. It has been used as fine aggregate. The year-mean volume of river sand is about  $4.0 \times 10^5 \text{ m}^3$ , that of sea-sand  $2.5 \times 10^5 \text{ m}^3$ , and that of land sand  $8.5 \times 10^5 \text{ m}^3$ . The total volume is  $1.5 \times 10^6 \text{ m}^3$  per year.

Though Kagoshima Prefecture does not open detailed data about the volume and sites of the sea-sand mining. The year-mean volume of mined sea-sand was about  $2.34 \times 10^6 \text{ m}^3$  during three years from 1987 to 1989. This volume is the third next to Nagasaki and Fukuoka Prefectures.

### Conclusions

In this study, the present situation was investigated about the sea-sand mining in all seven prefectures of Kyushu Island, Japan. Though there are a few prefectures in which the

detailed data on sea-sand mining could not be obtained, we reached the following conclusions.

- (1) Sea-sand reserves of the Genkai, Hibiki and Goto Seas are limited. Therefore, how the sea-sand mining compatible with the protection of coastal environments should be carried out in these seas will become very important in future.
- (2) Sea-sand of the Ariake, Yatsushiro and southern part of Oita Prefecture has been supplied constantly from rivers or seas. In these seas, it is necessary to take into account the balance between the volume of mined sea-sand and the volume of supplied sand .

The authors wish to thank Mr T. Munakata for stimulating discussions and his technical help.

#### REFERENCE

- Kojima, H., T. Ijima and T. Nakamuta (1986). Impact of offshore dredging on beaches along the Genkai Sea, Japan, Proc. 20 th Coastal Eng. Cong., ASCE, 1281-1295.

## CHAPTER 255

### PATRAS BREAKWATER FAILURE DUE TO SEISMIC LOADING

By  
Constantine D. Memos<sup>1</sup> and John N. Protonotarios<sup>1</sup>,  
Members, ASCE

#### Abstract

Investigation of the failure mechanism of the Patras breakwater extension revealed that the seismic loading of the mound was amplified considerably due to the soft foundation soil. This loading induced the overriding of the low safety factors of the structure. Approximate analytical expressions were obtained for the hydrodynamic loading during earthquakes. These were in good agreement with previous results. Recommendations for the completion of the works were given to the harbor authority.

#### INTRODUCTION

Patras is a busy port of western Greece serving as a RoRo gateway to Italy. Its location can be seen in figure 1.

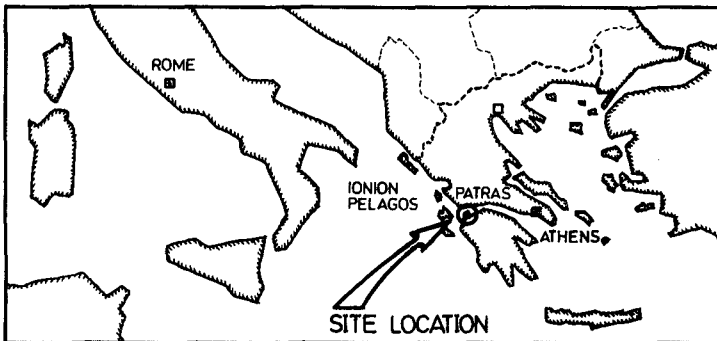


Figure 1. Site location map

<sup>1</sup> Civil Engineering Department, National Technical University of Athens, Greece.

The layout of the harbor is shown in figure 2; it includes a long detached breakwater of rubble mound with concrete capping. During the construction of a southern extension, 120m long, of similar design but without the capping, severe and abrupt settlements of the mound took place leading to a discontinuation of the works.

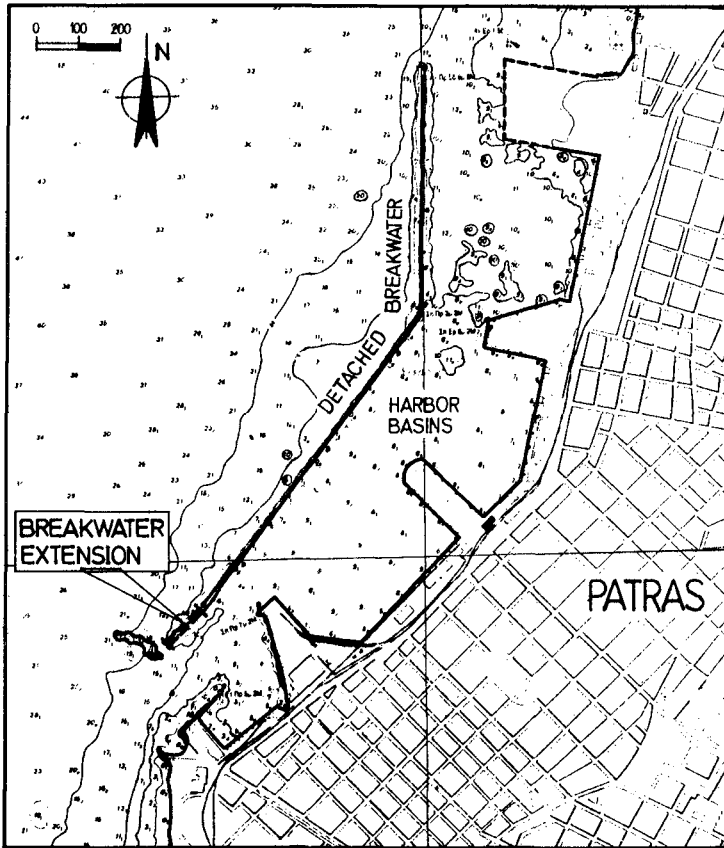


Figure 2. Harbor layout and location of works

A typical cross-section of the new breakwater is contained in figure 3. The primary armor consisted of rock units 4-6t placed at a slope of 1:3 which from -2.0 m downwards steepened to 3:4. The width of the mound at its base, i.e. at -18.0m, reached almost 90 m. It should be noted that the structure was founded on weak soil without any improvement.

Figure 4 shows a characteristic cross-section of the structure as measured before and after the failure. Appreciable settlements of the order of a few metres can be noted.

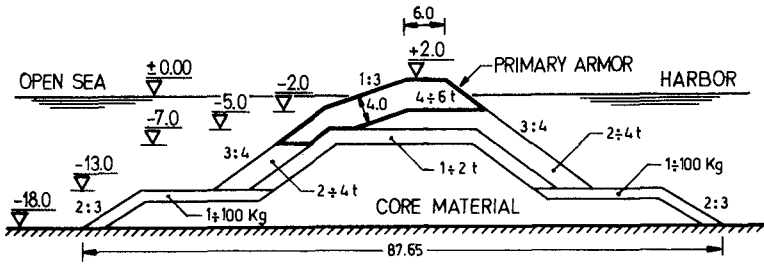


Figure 3. Typical cross-section of the breakwater extension.

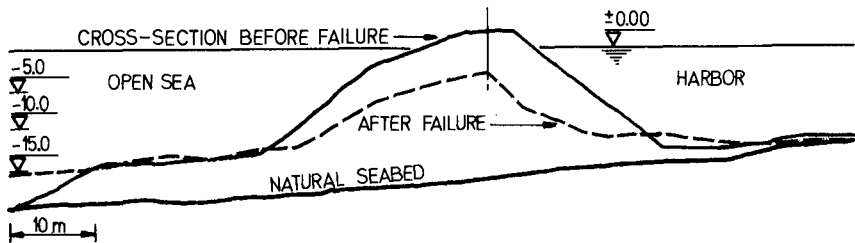


Figure 4. Typical cross-section with outlines before and after the failure

A key element of the present problem was that the failure coincided with moderate seismic activity in the area. Indeed, several earthquakes occurred prior to the major settlement of the structure.

The present research aimed at investigating the dynamic response of the breakwater under construction in order to understand the mechanism that led to its failure. Also, proposals for the completion of the works were to be given to the harbor authority.

The failure mechanism was approached by two complementary points of view, namely hydrodynamic and geotechnical. During the examination of this specific case of failure some more general issues were addressed regarding rubble mounds sitting on soft soils in a seismic area.

In general, the dynamic response of rubble-mound breakwaters has not been so far thoroughly investigated. This can be attributed to the fact that a possible failure of a breakwater entails only a limited reduction of the protection afforded to the harbor. Also, it is usually a matter of routine maintenance to repair such damages by simply adding more stones. For these reasons the current practice of breakwater design is to safeguard stability against wave attack and general soil shear failure, without taking into account the seismic loading. In contrast, the seismic response of similar structures, as earth dams, has been investigated to a far more advanced level, since eventual failure of such structures could well have severe consequences.

An important difference between dams and breakwaters lies in that dams are always designed to sit on firm foundation soils while breakwaters are sometimes

required by other reasons to be constructed on soft soils.

In the following two routes of investigation are presented: the first addresses the hydrodynamic aspects of the problem, i.e. the dynamic loading of the rubble-mound by the surrounding water masses, while the second deals with the seismic analysis of the system "structure-soil".

## HYDRODYNAMIC ANALYSIS AND RESULTS

An investigation of the hydrodynamic characteristics of the problem was undertaken aimed at estimating the hydrodynamic loading on the structure due to the seismic activity and assessing thus its relative importance with respect to the "pure" seismic loading acting directly upon the mound through the underlying soil strata.

A simple estimate of the hydrodynamic pressures can be obtained by taking into account the motion of the virtual mass of water in the vicinity of the structure. There are in general two types of modifications to this estimate referring to the compressibility of the water and the elasticity of the structure. Denoting by  $\omega$  the circular frequency of the horizontal seismic excitation, by  $\omega_1 = \pi c/2h$  the first cutoff frequency of the water body surrounding the structure,  $c$  speed of sound waves in water,  $h$  water depth, and by  $\omega_s$  the natural frequency of the structure, the following remarks can be made.

It has been shown by Chopra (1967) that if  $\omega < \omega_1$ , then in an uncoupled system "breakwater-sea" the compressibility of the water does not play a significant role and can be neglected. In our case we have indeed  $\omega < \omega_1$  by feeding the existing data. In a coupled system "breakwater-sea" the required additional condition for ignoring the water compressibility is  $\omega_1/\omega_s > 2$  (Chopra 1968). This again is applicable in the problem under consideration since the site-specific data give  $\omega_1/\omega_s \approx 7$ .

Regarding the parameter of the elasticity of the structure, recent research has verified that it produces a significant modification on the pressure distribution along the face of a rigid dam with increasing ratio of  $\omega/\omega_1$ . Results by other investigators (Mei et al 1979) show that for  $\omega/\omega_1 < 0.2$  the deviation of the total hydrodynamic force by assuming rigid structure is less than 15%, while for  $\omega/\omega_1 < 0.1$  the difference is negligible, of the order of 1%. In our problem, which represents a typical case of moderate seismic loading, this ratio is about  $\omega/\omega_1 \approx 0.05$ . Such a low value suggests that as a first approximation the elasticity of the structure can be ignored for the calculation of the total hydrodynamic force. However, this is not necessarily the case when one is interested in the detailed structure of the pressure distribution along the face of the breakwater.

Following these qualitative results the investigation proceeded to estimating the major component of the hydrodynamic loading, namely the added mass pressures on a vibrating sloping face in the sea. The nomenclature of the simplified problem can be seen in figure 5. A part of the seawater in contact with the face of the breakwater produces dynamic loading due to the accelerations involved. The corresponding pressures can be calculated analytically by estimating at every level the breadth  $b$  of the water mass that loads dynamically the structure.

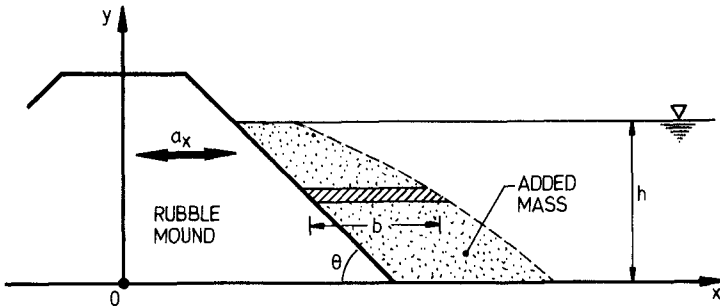


Figure 5. Nomenclature of the simplified problem

An impermeable face was assumed and a no-slip condition was applied at the slope. In figure 6 the external forces acting on a horizontal slice of water mass of height  $dy$  are shown.

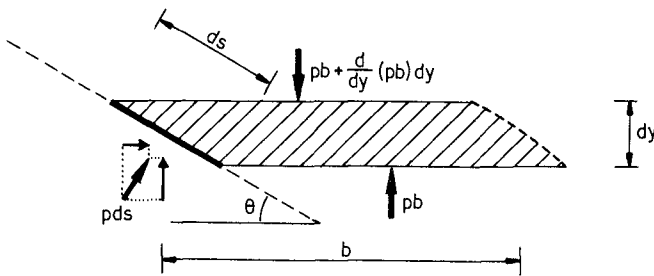


Figure 6. Forces acting on a water element

The equations of motion read,

$$\text{along } y\text{-axis: } p \cot \theta - p \frac{db}{dy} - b \frac{dp}{dy} = \rho b a_{fy} \quad (1)$$

$$\text{along } x\text{-axis } p = \rho b a_{fx} \quad (2)$$

where  $a_{fx}$ ,  $a_{fy}$  the acceleration of the fluid along  $x$ ,  $y$  axis respectively  
 $p$  the pressure

The continuity equation is produced by equating the displaced water volumes due to the motion of the slope during time  $dt$ . This yields

$$a_{fy} = a_x y / b \quad (3)$$

The boundary condition along the rigid slope can be written in general,

$$a_{fx} = a_x - a_{fy} \cot \theta \quad (4)$$



On the free surface the boundary condition, taking  $p=0$  there, is

$$b = h \cot \theta, \quad y=h \quad (5)$$

Equations (1) to (4) give the following differential equation after some algebra

$$\frac{dp}{dy} = \rho \alpha_x \frac{db}{dy} - \rho b \frac{d\alpha_{fy}}{dy} \cot \theta - \rho \alpha_{fy} \frac{db}{dy} \cot \theta \quad (6)$$

From (3) we obtain:

$$\frac{d\alpha_{fy}}{dy} \cdot b + \alpha_x \sin \theta + \alpha_{fy} \frac{db}{dy} = 0 \quad (7)$$

Now, (6) becomes due to (7)

$$\left(\frac{y}{b} \sin \theta \cot \theta - 2\right) \frac{db}{dy} - (\sin \theta + \cot^2 \theta) \frac{y}{b} + (1 - \sin \theta) \cot \theta = 0 \quad (8)$$

Integrating eq.(8) with respect to  $y$  and employing (5) to define the constant of integration we arrive at

$$\log[2b'^2 - b'y' \cot \theta + (1 + \cot^2 \theta)y'^2]^{1/2} = (1/2) \log(1 + 2\cot^2 \theta) + \frac{\cot \theta}{H} \arctan \left( \frac{4b'/y' - \cot \theta}{H} \right) - \frac{\cot \theta}{H} \arctan \frac{3\cot \theta}{H} \quad (9)$$

where the prime denotes non-dimensionalization with respect to  $h$  and  $H = (8 + 7\cot^2 \theta)^{1/2}$ .

If we define a pressure factor  $c_p = p/\alpha_y h$  with  $\alpha = \alpha_x/g$ , then from (2), (3), (4) we obtain

$$c_p = b' - y' \cot \theta \quad (10)$$

The above analytical expression (9) reduces to the following simple formula for the case of a vertical face

$$b' = 0.707 (1 - y'^2)^{1/2} \quad (11)$$

This specific result compares very well with existing experimental data of Wang et al (1978) and Zangar (1952) as shown in the graph of figure 7 drawn in terms of  $c_p$ .

Apart from the detailed pressure distribution the integrated total force  $F = 0.56\rho\alpha_x h^2$  falls quite close to other analytical results, deviating only by 5% from the classical value  $F = 0.58\rho\alpha_x h^2$  given by Westergaard (1933) for the same case of a vertical face.

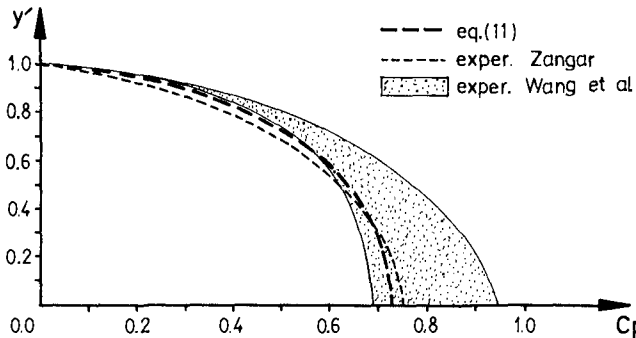


Figure 7. Comparison of analytical expression with experimental results

Application of the general expression to a slope with  $\theta = 30^\circ$  gives results that are comparable with experimental data along a central section of the total water depth, but there are deviations from the experimental results at the upper and lower parts of the water column. Nevertheless, the integrated pressure diagram gives again values of the force in good agreement with experimental data exceeding them by about 15%. The deviations of the pressure distribution especially in the lower part of the sloping face can be attributed mainly to the neglected boundary conditions along the sea bed close to the toe of the breakwater. These conditions induce a redistribution of the hydrodynamic pressures on the slope especially to its lower part.

In order to overcome this difficulty a numerical method has been developed which takes into account the conditions along the whole boundary of the water mass. The technique applied to this problem is the boundary integral element method. Variations of the geometry of the boundary, as e.g. sloping sea bed, as well as of its porosity can be accommodated in the model. Due to space limitations this part of the research is not presented here.

The numerical results for the hydrodynamic force based on the previously presented analytical expressions were found to be rather low when compared to the direct seismic loading on the mound through the foundation soil.

The typical cross-section of the breakwater was also checked against wave attack by using a standard method (CERC, 1984). It was found that although in general terms the cross-section was robust, a few modifications could improve considerably its strength, as e.g. extending downwards the seaward armoring. However, such points contributed only secondarily to the initiation of the failure mechanism.

## GEOTECHNICAL AND SEISMIC ANALYSES AND RESULTS

### Geotechnical Conditions

It was already known from the construction of the older main part of the Patras breakwater and its northern extension that the foundation soil consisted of a rather thick layer of soft compressible clay. Thus prior to the construction of the southern extension, a rather extensive investigation program of its foundation soil was under-

taken. A total number of 21 borings reaching a depth of 50m from the sea level were performed covering a zone 125m long and 100m wide, up to 50m away from the axis of the extension. After the 1984 failure an additional very deep boring was performed to a depth of 104m. Apart from the SPT counts, 1-D consolidation tests as well as drained and undrained triaxial tests were performed on specimens taken from all these borings.

The above in situ and laboratory tests revealed that the foundation subsoil consists of a normally consolidated soft clay layer 30 to 38 meters thick underlain by a thick (>50 meters) moderately overconsolidated medium to stiff clay deposit. Some basic geotechnical parameters of the upper soft clay layer vary as follows:

- Standard Penetration Test Count:  $N = 0 \div 15$
- Initial Unit Density:  $\rho = 1.75 \div 1.92 \text{ Mg/m}^3$
- Initial Void Ratio:  $I = 0.72 \div 1.38$
- Natural Water Content:  $W^p = 25\% \div 30\%$
- Plasticity Index:  $I = 17\% \div 27\%$
- Compressibility Index:  $C^p = 0.20 \div 0.42$
- Undrained Shear Strength:  $C_u^c = 5 \div 40 \text{ kN/m}^2$

The lower stiff soil deposit presented the following values for some important geotechnical parameters

- SPT:  $N = 42 \div >50$
- Unit Density:  $\rho = 1.90 \div 2.00 \text{ Mg/m}^3$
- Void Ratio:  $I = 0.69 \div 0.85$
- Compressibility Index:  $C^c = 0.13 \div 0.18$
- Undrained Shear Strength:  $C_u^c = 120 \div 250 \text{ kN/m}^2$

An idealized soil profile with the selected values of the parameters used in the geotechnical analyses is depicted in figure 8.

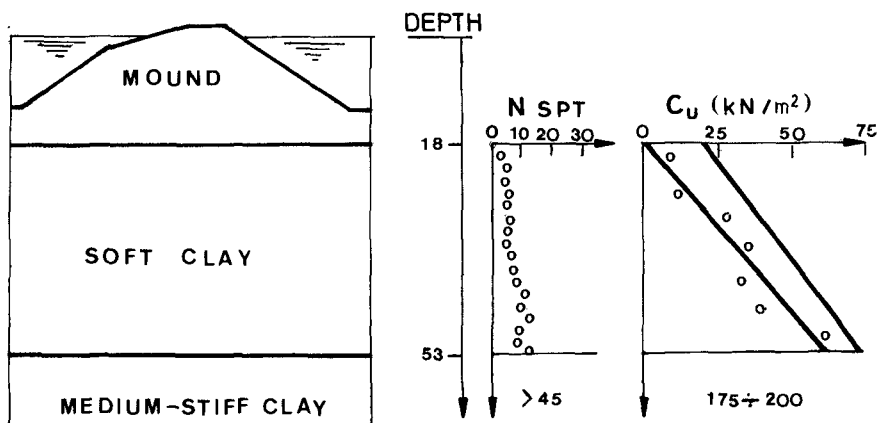


Figure 8. Idealized soil profile and geotechnical parameters

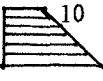
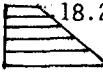
Settlement and Stability Considerations

Settlement and static stability analyses were performed for two stages of construction: one for the phase after the height of the mound had reached the level of 11 meters from its foundation, and a final one for the stage immediately after the completion of construction (height of mound: 18 meters). This was deemed appropriate in order to better simulate the actual history of the construction process, since there was a pause of 6 months after the mound had reached the height of 11 meters, and thus make it possible to account for the changes of the soil parameters caused by the ongoing consolidation process of the upper soft clay layer.

One dimensional settlement analyses yielded as best estimate of the final settlement due to the 11m high rubble mound at its axis approximately 1.5m, whereas the additional settlement due to the rest of the mound was estimated 0.6m, i.e. total settlement 2.1m. The actual settlements was not possible to be measured with accuracy, as they were obscured by the fact that significant amounts of the lower mound material intruded into the soft clay, since no filter zone was provided between the rubble mound and the clay layer. However, the measurements indicated that the total settlement must have been somewhat higher than the above value, approximately 3m; this difference between actual and estimated amount of settlement is mainly due to uncertainties of the clay compressibility parameters estimates, as well as to the limitations of the one-dimensional deformation model considered.

Static stability analyses were performed of the above mentioned two stages of construction. For each stage the undrained shear strength of the upper clay layer was estimated in accordance with the adopted relation  $C_u = 0.20 \cdot \sigma'_v$ , where  $\sigma'_v$  the effective vertical stress, after a suitable degree of consolidation had been assumed. Two suppositions of the distribution of  $C_u$  with depth, uniform and trapezoidal, were considered for each stage. Results produced by the modified Bishop slope stability analysis (Bishop 1955) are presented in table 1.

**TABLE 1**  
**STABILITY SAFETY FACTORS FOR STATIC CONDITIONS**

CONSTRUCTION STAGE (Height of Mound)	UNDRAINED SHEAR STRENGTH DISTRIBUTION IN THE UPPER LAYER $C_u$ (kN/m <sup>2</sup> )	SAFETY FACTOR F
1st Stage (11m)	20 Uniform	1.20
1st Stage (11m)	 10 61.2 Trapezoidal	1.15
2nd Stage (18m)	35 Uniform	1.09
2nd Stage (18m)	 18.2 71.1 Trapezoidal	1.13

It is apparent from these marginal static safety factors that even a moderate dynamic loading might produce failure conditions.

### Seismic Response

In late February 1984 a series of moderate earthquakes of magnitude 3.5 to 4.5 took place in the Patras Gulf near the breakwater site. Immediately after these earthquakes settlements of the order of 3 to 4 meters were measured on the constructed part of the southern extension of the breakwater. In this paragraph we investigate the seismic behavior of the breakwater and its foundation during the strongest of these events, which apparently led to its failure. For this purpose, the bedrock ground motion characteristics were estimated and the seismic response of the "rubble mound-soil foundation" system was calculated, using an appropriate one-dimensional model.

Figure 9 shows a map of the Patras area depicting the epicenters of the two strongest earthquakes with  $M=4.4$  and  $M=4.5$ , corresponding epicentral distances 7 and 8 km, and hypocentral distances 9 and 11 km from the site. According to attenuation relationships suitable for western Greece (Papaioannou 1988), the maximum bedrock ground accelerations were estimated at  $0.015 \div 0.020g$ .

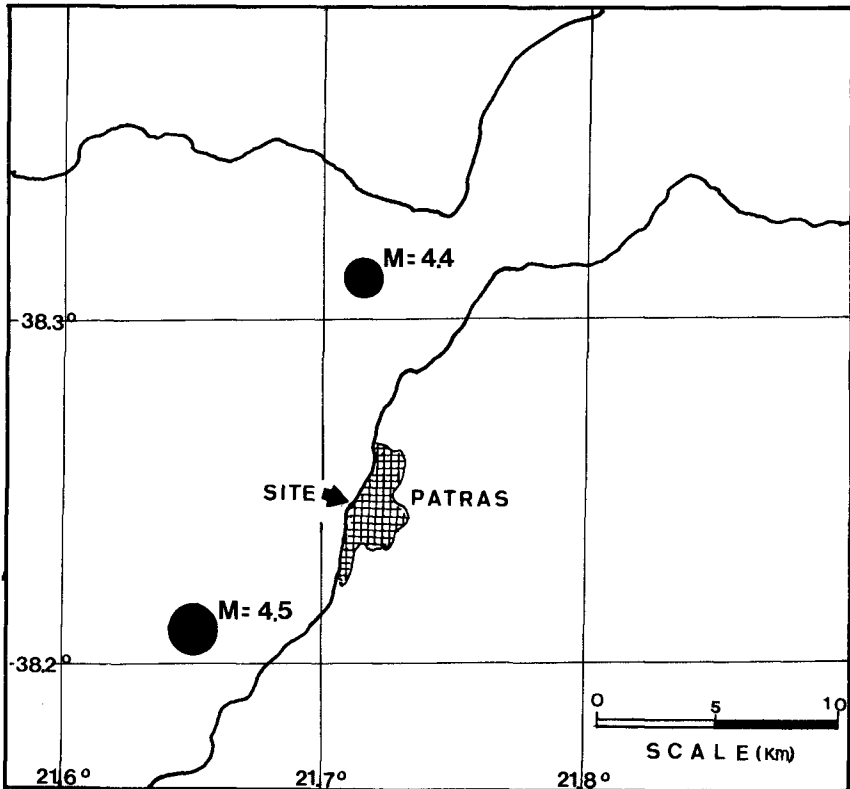


Figure 9. Map showing the location of the epicenters

For the seismic response analysis of the "foundation soil-rubble mound" system as input motions were considered the Kalamata 1986 earthquake record normalized to a peak acceleration of 0.02g (Motion 1) and the Taft earthquake record normalized to a peak acceleration of 0.015g (Motion 2). The first motion was selected because it was recorded at similarly near source site, whereas the second was selected to account for a broader range of fundamental periods.

The seismic response of soil deposit and the rubble mound was calculated by simulating the foundation soils as strata of infinite horizontal extent and the mound as a shear beam (Gazetas 1987). For these analyses the software package SHAKE (Schnabel et al 1972) was used, after a suitable modification. As no dynamic measurements of soil parameters were available, dynamic shear moduli and damping coefficients for the mound and foundation materials were estimated from their density, confining pressure and shear strength characteristics.

Figure 10 shows the variation of initial shear modulus ( $G_0$ ) and shear wave velocity ( $V_{s0}$ ) with the depth of the mound and the soil profile.

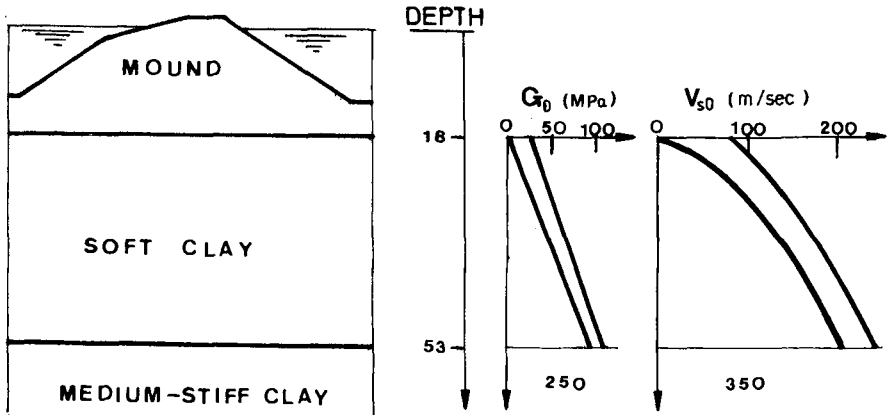


Figure 10. Distribution of dynamic parameters

Results of the analyses as summarized in figure 11 and 12 show that the maximum ground acceleration at the top of the soft stratum was amplified by 2 to 2.5 times. These figures also show that the accelerations were moderately amplified within the mound body.

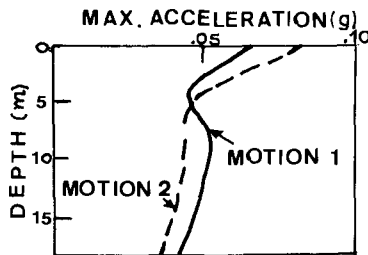


Figure 11. Calculated accelerations along the axis of the mound

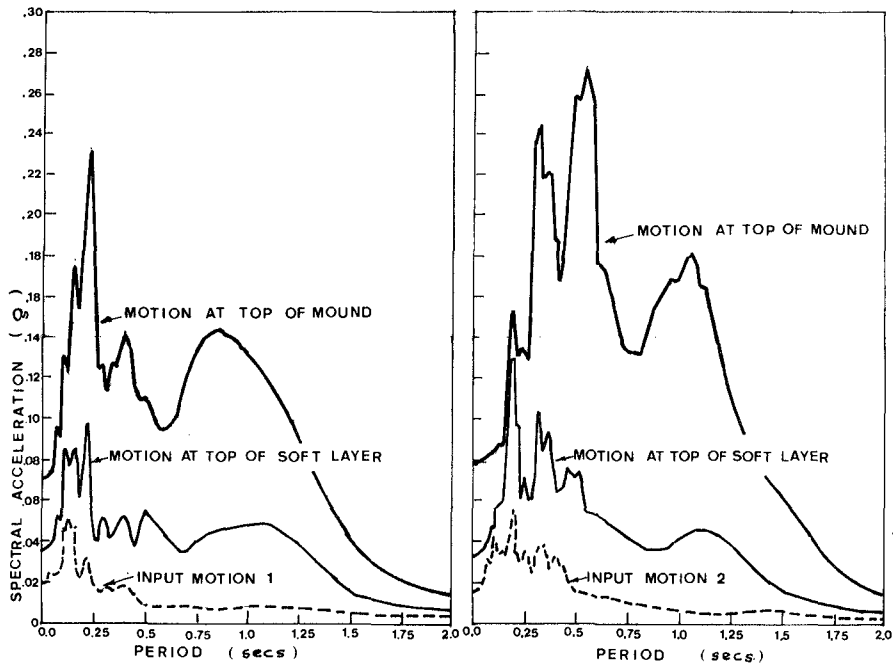

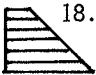


Figure 12. Input and calculated response spectra

Pseudo-dynamic stability analyses were also performed, utilizing the above calculated seismic forces. Results of these analyses are summarized in table 2.

TABLE 2  
STABILITY SAFETY FACTORS FOR SEISMIC CONDITIONS

DISTRIBUTION OF UNDRAINED SHEAR STRENGTH FOR THE SOFT CLAY $C_u$ (kN/m <sup>2</sup> )		SAFETY FACTOR MOTION 1	SAFETY FACTOR MOTION 2
	35 Uniform	0.82	0.75
	18.2 71.1 Trapezoidal	0.88	0.79

The results show clearly that these relatively small earthquakes were sufficient to trigger the failure mechanism of the structure. The main reason for this was the presence of the deep soft clay stratum that amplified considerably the moderate underground seismic motion, overriding the already marginal static safety factor.

## CONCLUSIONS AND RECOMMENDATIONS

Based on the previous analysis of the failure of the Patras breakwater extension the following conclusions can be drawn:

- (1) The failure of the mound was initiated by the seismic activity of February 1984 occurred in the vicinity, which caused the already low safety factors of the structure to fall below an acceptable level. Although the causative earthquakes were rather weak the seismic forces were considerably amplified by the thick soft clay layer on which the mound was founded and caused the shear failure of the low strength foundation.
- (2) The original design needed some improvement to withstand wave attack. However, this played only a secondary role in the failure mechanism.
- (3) The hydrodynamic loading due to the shaking of the mound can be approximated in this particular case by the pressures exerted by the added mass of the water. The structure elasticity as well as the water compressibility can be ignored without affecting appreciably the results.
- (4) The calculated hydrodynamic force due to earthquake activity was small compared to the direct seismic loading on the mound through the foundation soil.
- (5) In general the analytical expression proposed for the hydrodynamic loading on an inclined rigid face is a good first approximation to the total hydrodynamic force and represents an upper bound of the actual load on a porous breakwater face.

The authors believe that this case study represents conditions that can be met in several ports around countries with high seismic activity. Thus a more careful design approach and construction procedure should be followed in such cases. A thorough soil investigation program and a complete seismic analysis included in the design can save unnecessary and costly delays or even failures.

In situations where such adverse conditions are involved, the designer can employ techniques such as: interventions to the geometry of the structure, as e.g. by providing milder slopes or berms; improvement of the foundation soil; use of geotextiles; phasing of progress of works.

Part of the scope of the present research was the proposal of guidelines for the completion of the breakwater extension. In this respect the present geometry of the semi-completed mound, as modified by the wave action over a period of 8 years, has been recorded.

The current layout of the structure as well as standard calculations on armoring against wave attack led us to propose for the trunk section slopes at 1:2 both sides, and for the head of the structure milder slopes at 1:2.5. These new cross-sections were then checked for both static and dynamic stability giving the following factors of safety.

### Trunk section

Static conditions	$F = 1.54$
Dynamic conditions ( $\epsilon=0.06g$ )	$F = 1.18$

### Head section

Static conditions	<i>Short term</i>	<i>Long term</i>
Dynamic conditions ( $\epsilon=0.06g$ )	1.42 1.07	1.76 1.25



The head section was proposed to be completed in phases, since it has been subjected to a smaller degree of preloading and subsequent improvement by consolidation than the trunk section of the breakwater.

Consideration of other methods of foundation soil improvement, such as sand drains, geotextiles, etc, proved uneconomical for this particular case, mainly due to the small size of the project and the fact that a sizeable part of the structure had already been constructed, making thus interventions of the above kind very costly.

Suitable monitoring to record the behavior of the structure with time has been also proposed.

### ACKNOWLEDGEMENTS

This research has been supported by both the General Secretariat for Research & Technology, Greece, and the Patras Harbor Authority, who has kindly supplied us with the relevant data. Nic. Kotta, research assistant at NTUA, performed most of the geotechnical assessment and calculations for static conditions. Our thanks are also extended to the research students M. Symvoulidou, G. Tzivaridou and V. Grosomanides for their help.

### REFERENCES

- Bishop, A.W.: "The Use of the Slip Circle in the Stability Analysis of Slopes", Geotechnique, vol.5, pp. 7-17, 1955.
- CERC: Shore Protection Manual, U.S. Army, 1984.
- Chopra, A.K.: "Hydrodynamic Pressures on Dams during Earthquakes", J. Eng. Mechs Div., ASCE, vol.93, Dec. 1967.
- Chopra, A.K.: "Earthquake Behaviour of Reservoir-Dam Systems", J.Eng.Mechs Div., ASCE, vol.94, Dec. 1968.
- Gazetas, G.: "Seismic Response of Earth Dams: Some Recent Developments" Soil Dynamics and Earthquake Engineering, vol.6, No.1, 1987.
- Mei, C.C., Foda, M.A. and Tong, P.: "Exact and Hybrid-Element Solutions for the Vibration of a Thin Elastic Structure Seated on the Sea Floor", Applied Ocean Research, vol.1, Jan. 1979.
- Papaioannou, K.: "Seismic Risk in Greece" Proceedings of the 1st Symposium on New Developments in Seismology and Geophysics of Greece, Thessaloniki 1988 (in greek).
- Schnabel, P.B., Lysmer, J. & Seed, H.B.: "Shake-a Computer Program for Earthquake Analysis of Horizontal Layered Sites", report No. EER 172-12, December 1972.
- Wang, H., Yang, C.V., Lamison, C. and Chen, S.S.: "Loadings on Rubble-mound Breakwaters due to Earthquake", Proc. Coastal Eng. 1978, vol.III.
- Westergaard, H.M.: "Water Pressures on Dams During Earthquakes", Transactions, ASCE, vol.98, 1933.
- Zangar, C.N.: "Hydrodynamic Pressures on Dams due to Horizontal Earthquake Effects", Eng. Monograph No.11, U.S. Bureau of Reclamation, May, 1952.

## CHAPTER 256

### FUNCTIONING OF GROINS AT WESTHAMPTON BEACH, LONG ISLAND, NEW YORK

Gilbert K. Nersesian<sup>1</sup>, Nicholas C. Kraus<sup>2</sup>, and Fulton C. Carson<sup>3</sup>

**ABSTRACT:** An extended field of 15 long rubble stone groins was constructed in two increments of work at Westhampton Beach, New York, in 1965-66 (11 groins) and in 1969-70 (4 groins), as part of a hurricane storm-protection project. A third increment of work completing the protection to a downdrift point of closure was not undertaken due to political decisions. In addition, the dune and beach fill which was to have been placed in the first 10 groin compartments to complete the protection was not accomplished due to local economic problems. No construction work has been undertaken since 1970. During the 26 years following completion of the original 11 groins, substantial portions of the groin field have been filled naturally by trapping of sediment that moves alongshore with a net rate directed to the west. However, the shore area downdrift of the last westerly groin in the unconstructed increment of work has experienced inordinate recession because of insufficient bypassing of sediment to this area. This paper describes the functioning of the groin field, examining both the extreme downdrift recession and the equally dramatic accretion and beach build up in the groin field, drawing lessons on groin functional design from this historic project.

#### INTRODUCTION

In 1938, the south shore barrier island system along Long Island, New York, was devastated by a hurricane that is the storm of record for this Atlantic coastal area of the United States (Andrews 1938). The barrier islands were greatly eroded and weakened, and erosion was subsequently increased by other extreme hurricanes and extratropical storms that struck the area in 1944, 1950, 1953, 1954, 1958, 1960, and 1962 (USACE 1958, 1963). Since 1962, there have been frequent occurrences of severe extratropical storms, the most

---

(1) Senior Coastal Engineer, U.S. Army Engineer District, New York, 26 Federal Plaza, New York, New York 10278-0090, USA.

(2) Senior Scientist, and (3) Civil Engineer Technician, U.S. Army Engineer Waterways Experiment Station, Coastal Engineering Research Center, 3909 Halls Ferry Road, Vicksburg, Mississippi 39180-6199, USA.

recent being the October 1991 (Halloween) storm and the winter storm of December 10-12, 1992. Many sections of these east-west oriented barrier islands are in danger of breaching and flooding, and property has been lost or jeopardized by erosion. In 1960, storm-protection plans were authorized by the Federal Government for the coastal area between Fire Island Inlet and Montauk Point. One of the reaches included in the project was the barrier island that extends 24.6 km between Moriches Inlet to the west and Shinnecock Inlet to the east (Fig. 1). As part of the plan, groins were constructed initially on the most vulnerable section of the reach, called Westhampton Beach, with the objective of providing a wide beach and dune as a storm-protection measure.

The original plan provided for construction dunes and fronting protective beaches and 23 groins (if needed) in this reach (USACE 1958). Owing to political and economic considerations (Heikoff 1976), only 11 groins were constructed in 1966 in Section 2A without placement of the dune and beach fill along 3.8 km of shore westerly from a point 10.6 km east of Moriches Inlet, as shown on Fig. 2. This work was supplemented in 1970 with completion of four groins in Section 1A along 1.8 km of shore extending west of the existing groins, together with placement of dune and beach fill in the four westerly compartments (USACE 1969). A third increment of work in Section 1B along 2.9 km of shore to the west providing for six additional groins and accompanying fill was not undertaken due to political decisions (Heikoff 1976).

Because construction was halted before implementation of the third increment of work, the downdrift beaches to the west, which would have been spanned by groins, have eroded significantly, as shown in Figs. 3 and 4. In contrast, a huge dune system and wide beach have developed naturally in the 14 groin compartments, fully realizing the original intent of the storm-protection plan for the sections of reach spanned by the groin field. The net potential longshore sand transport rate on these western, fine-to-medium grain size barrier islands is estimated at 300,000 cu m/year to the west (Panuzio 1968).

In the present study, a large, unpublished data set of beach profile surveys and aerial photography was analyzed to quantify the functioning of the groins at Westhampton Beach. These data provide valuable documentation about the site and extensive coastal process information for understanding the general functioning of groins.

## GROIN DESIGN

The project groins, shown in profile in Fig. 5, were designed to reinforce a beach and dune fill intended to provide hurricane and storm protection. The backshore dune had a top width of 7.6 m at elevation +6.1 m National Geodetic Vertical Datum (NGVD), and front and back slopes of 1V:5H. The fronting protective beach had a berm width of 30.5 m at elevation +4.3 m NGVD, with foreshore slopes of 1V:20H from the seaward edge of the berm to elevation -0.6 m, and thence 1V:30H to the existing offshore bottom (USACE 1963).

The groins, which were constructed with quarry stone, have an average spacing of 400 m and are 146.3 m long. The groin design provided a horizontal inshore section 39.6 m long at elevation +4.9 m NGVD, an intermediate section 64.0 m long sloping 1V:15H from the seaward edge of the inshore section to the beginning of a 42.7-m long offshore section at elevation +0.6 m. The groins have side slopes of 1V:2H (USACE 1963). The 15 groins span 5.6 km of shore with the last westerly groin being located 5.0 km east of Moriches Inlet.

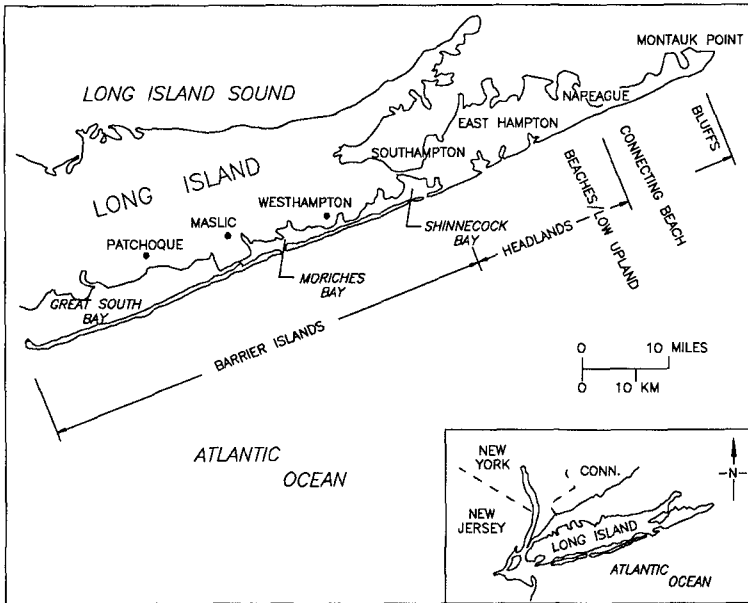


Fig. 1. Site location map for Westhampton Beach, Long Island, New York

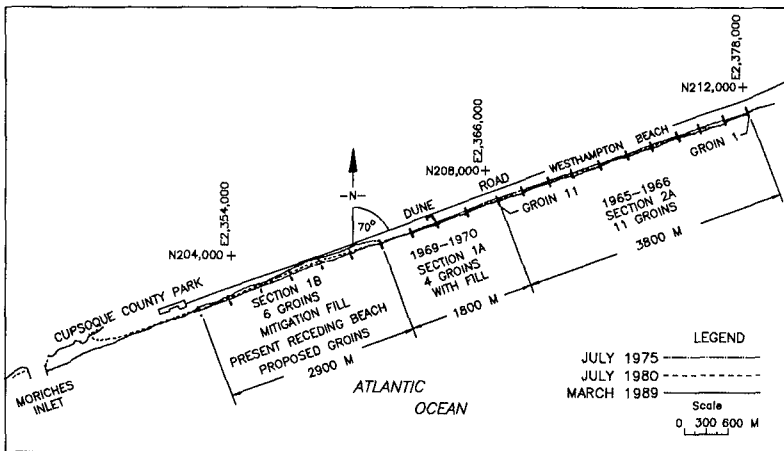


Fig. 2. Construction plan for the Westhampton Beach shore-protection project



Fig. 3. Beach west of Groin 15, Dec. 20, 1983

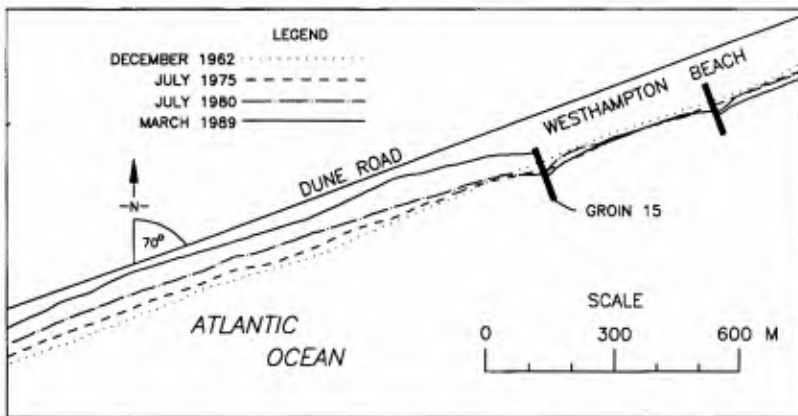


Fig. 4. Shoreline change west of Groin 15, Dec. 1962 - Mar. 1989

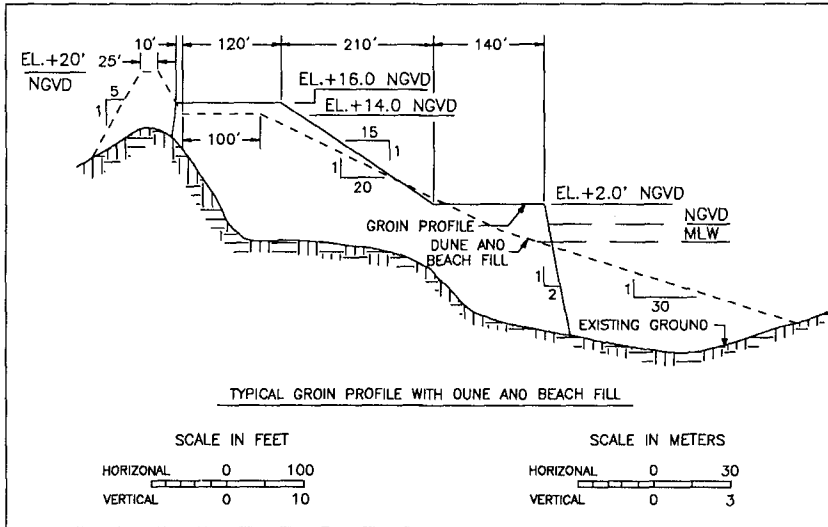


Fig. 5. Cross section view of groin design

## OVERVIEW OF SITE

### Littoral Factors

The origins of the south shore barriers of Long Island are unknown. It is generally believed that the barriers are formed from glacial outwash sediments from the Pleistocene Epoch and have evolved through the Holocene period with rising sea level. The barriers are composed mainly of quartz sand with some garnetiferous and magnetitic sands and shell fragments (Leatherman and Allen 1985).

Tides in the project area are semi-diurnal and have a mean range of 0.9 m and a spring range of 1.1 m. Mean Low Water (MLW) is estimated to be 0.4 m (NOS 1992a) below NGVD. It is estimated that storm tides of +3.0 m NGVD occurred along the project shore during the 1938 hurricane (USACE 1958). Data from observations of the winds in the vicinity of the project area indicate that the prevailing winds are from the southwest with a duration of almost 25 % and secondarily from the northwest of about 20 %. Over 27 % of the winds in excess of 17 m/sec are from the east, 20 % from the northwest and 6 % from the south. Wind speeds as great as 43 m/sec (September 21, 1938) have been recorded at Westhampton Beach. Wind speeds in excess of 22 m/sec have been recorded more frequently during lesser coastal storms (USACE 1958).

Tidal currents at Moriches Inlet and Shinnecock Inlet vary with the tidal stage reversing in direction about every 6 hr. Published values for the maximum average flood and ebb tides at Shinnecock Inlet are 70 and 76 cm/sec, respectively (NOS 1992b). Tidal currents measured during spring tide conditions by the Corps of Engineers in July 1991 (Chu and Nersesian 1992) at Shinnecock Inlet indicated that the maximum average flood and ebb

currents were about 165 cm/sec. For Moriches Inlet the maximum average currents during the same period varied between 243 to 253 cm/sec.

Deep-water heights and return periods in the project area were estimated using a wave climatology study for the South Shore of Long Island, Phase III, Stations 45, 46, 47, and 50. Computed deep-water and breaking wave heights versus return period are shown in Table 1. Breaking wave heights corresponding to the incident wave height were calculated with a refraction coefficient of 1.0 and a flatter post-storm beach slope of 1V:30H. For a 50-year return period, the sea-water level was +3.0 m NGVD, and the wave period was 9 sec. Associated water levels for other wave heights are higher or lower dependent on the return period (USACE 1982, 1986).

Haight	Return Period (years)						
	5	10	20	50	100	200	500
$H'_o$ (m)	4.6	4.9	5.3	5.8	6.2	6.3	6.6
$H_b$ (m)	4.8	5.2	5.4	6.4	6.9	7.4	8.2

$H'_o$  is unrefracted deep-water significant wave height;  $H_b$  is breaking wave height

### Shore History

Examination of prior storm impacts on the shore in the vicinity of the groin field shows that there have been frequent breakthroughs of the barrier beach and dune system as well as creation of new inlets (Andrews 1938, USACE 1963). These impacts, shown in comparative format on Fig. 6, clearly demonstrate that the shore area at Westhampton Beach is susceptible to severe damage by hurricanes and other storms. Of special interest is the shore location about 700 m west of the west bridge at Westhampton Beach where storms created inlets in 1938 and 1962, and a breakthrough in 1958. This location is now bracketed by Groins 5 and 6. Similar repeated impacts can be found in other portions of the project area. The present location of Shinnecock Inlet at the east end of the barrier beach was created by the 1938 hurricane, and later was permanently stabilized by local interests. It was on this basis that the project designers believed there was a definite need to reinforce the dune and beach fill protection with groins.

### ANALYSIS OF DATA

#### Procedure

The data base assembled for this study presently contains 10 beach profile surveys covering the interval 1962-91, seven aerial photographic surveys yielding shoreline positions for the interval 1962-89, and a topometric shoreline mapping survey. The profile surveys typically contain at least three transects per groin compartment and extend from the landward toe of the dune to the 8-m depth. Several aerial surveys extending over the full littoral cell between Moriches Inlet and Shinnecock Inlet enable interpretation of coastal processes through examination of the regional sediment budget, not discussed here. The beach profile and shoreline position data, originally recorded in a variety of formats, were digitized in a controlled georeferenced Geographic Information System for quantitative analysis and visual

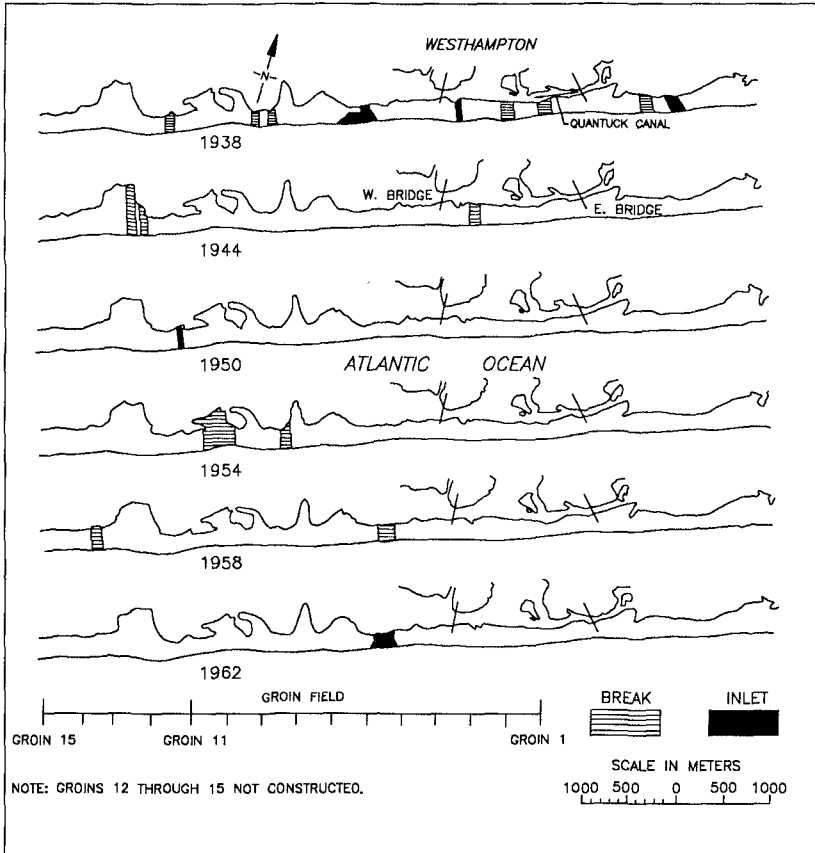


Fig. 6. Locations of historic breaching and inlet creation

interpretation. The first-order analysis included time evolution of shoreline position, volume of the dune and berm complex, and bottom morphology change (not discussed here).

Profile surveys selected for comparison were 12/62, 8/66, 7/75, 12/79, and 12/91. Shoreline position survey data from aerial photography taken in 12/62, 12/79, and 3/89 were integrated in the comparative analyses. The 1962 survey is a base survey which closely approximates the pre-groin construction shore position for the original 11 groins. The 1966 survey approximates the pre-groin construction shore position for the second 4 groins.

#### Shoreline Positions at Westhampton Beach

Comparative plots of shoreline positions at Westhampton Beach for five profile surveys and one shoreline survey between 1962-89 using all survey transects are shown on Fig. 7. The horizontal axis on this figure represents the baseline origin position for the plotted data. To better display the trends, shoreline positions were smoothed by moving average. Inspection of this figure shows that shoreline position advanced from approximately 100 to 70 m or 3.7 to 2.6 m/year, respectively, from east to west, along 3,800 m of shore. The



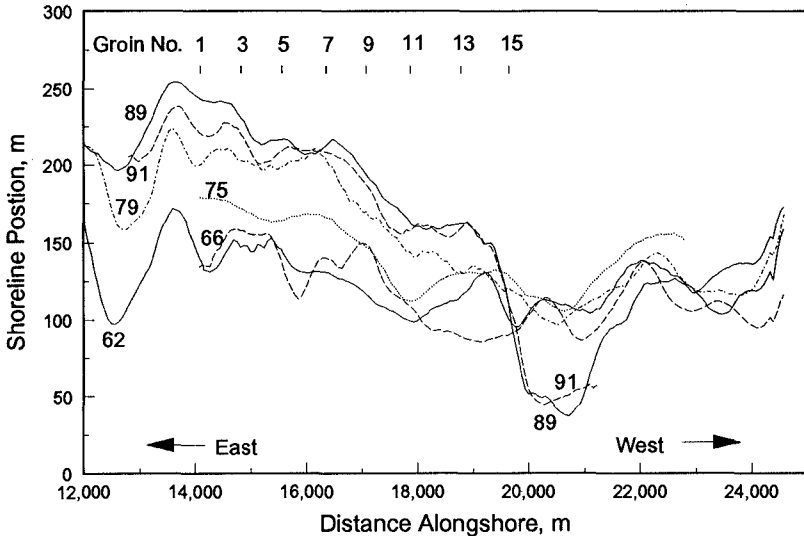


Fig. 7. Smoothed shoreline position in the vicinity of the groin field

general trend of shoreline movement in the first 11 groins during the 1962-89 period was one of continuing advance. From 1989-91 there was minor shoreline recession, which may reflect the impact of the October 1991 storm.

In the shore area encompassed by the second group of 4 groins, shoreline advance over the period 1966-89 was 50 to 55 m, or about 2.3 m/year, and was probably influenced in part by the dune and beach fill that was artificially placed during the second increment of work. In the period 1975-89, there was a shoreline advance of 40 to 20 m or 2.9 to 1.4 m/year, respectively, from east to west, in this area. At a point about 370 m west (downdrift) of Groin 15, the shoreline receded about 6.5 m/year in the period 1975-89. Further westward the rate of recession decreased to about 5.0 m/year. It is noted that the shoreline recession between 1962-75 was 1.9 m/year or less. Accordingly, the rate of recession in the downdrift area tripled following completion of the second increment of work.

#### Shoreline Positions Near Groins

Shoreline position near the groins is more closely examined in Fig. 8. Filling of the groin compartments has resulted in various shoreline alignments through the groin field. Between Groins 1 and 3, the shoreline shows generally straight alignment about 243 m from the baseline origin on Dune Road. Between Groins 3 and 4, the shoreline moved seaward from 243 m to 214 m, respectively, from the origin. This latter shoreline position generally continues westward to Groin 8. Between Groins 8 and 11, the shoreline moved seaward from 214 m to 164 m, respectively, from the origin. Between Groins 11 and 15, shoreline position moved seaward from 164 m to 154 m, respectively, from the origin. The shoreline positions and alignments within the groin demonstrate the natural filling of groin compartments and the bypassing of littoral sediment to downdrift compartments. Between Groins 1

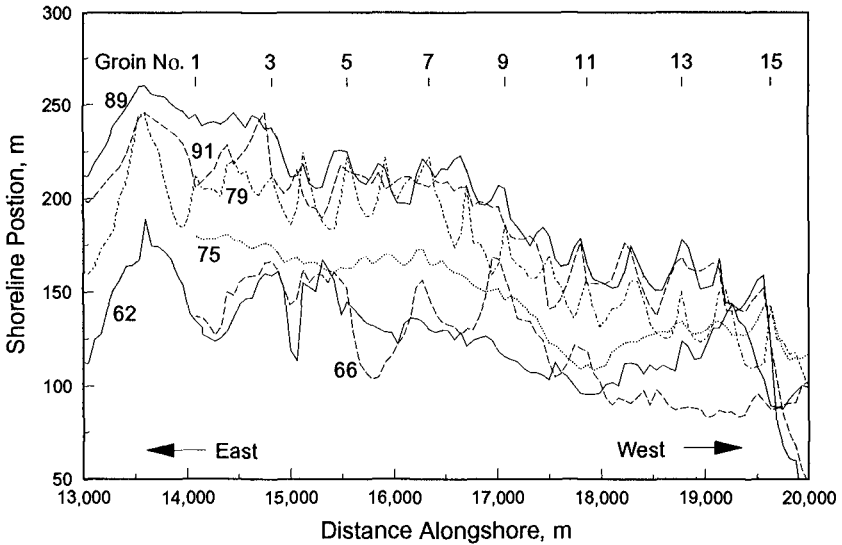


Fig. 8. Shoreline positions in the groin field

and 8, there are two plateaus, indicating that the groin is nearing complete filling in the compartments. It is of interest that the midpoint of the groin field is marked by Groin 8. Comparison of shoreline position between Groins 8 and 11 and between Groins 11 and 15 indicates that filling of the downdrift compartments is proceeding at a much lower rate.

#### Rate of Shoreline Change by Groin Compartment

Mean shoreline change per groin compartment from December 1962 to December 1989 for Compartments 1, 3, 5, 7, 9, 11, 13, and 14 is shown on Fig. 9. The results confirm filling of the groin compartments in the westerly direction. The mean shoreline change for all compartments is shown in Fig. 10, where it is seen that shoreline position in the groin field is approaching equilibrium after 26 years.

#### Comparative Profiles in Center Groin Compartments

Comparative profile plots are shown in Fig. 11 for the centers of Compartments 1, 5, 10, 14, and 15, for surveys taken in December 1962, 1979, and 1991. Compartment 15 is actually the westerly downdrift 400 m of shore area adjacent to Groin 15. The plots clearly show the massive dunes created from trapped sand subsequently moved onshore by wind. These dunes contain vegetation and provide habitat for coastal birds and ground animals.

#### Area and Volume Changes at Westhampton Beach

Computed area extent and volume changes (NGVD intercept to near baseline) in the 14 groin compartments and in the planned, but not constructed downdrift compartments are presented in Figs. 12 and 13. Between 1962-91 the area within the compartments increased by about 75%. Average compartment area in 1991 was about 27,900 sq m, and, based on an average compartment length of 400 m, the average beach width was about 70 m. The

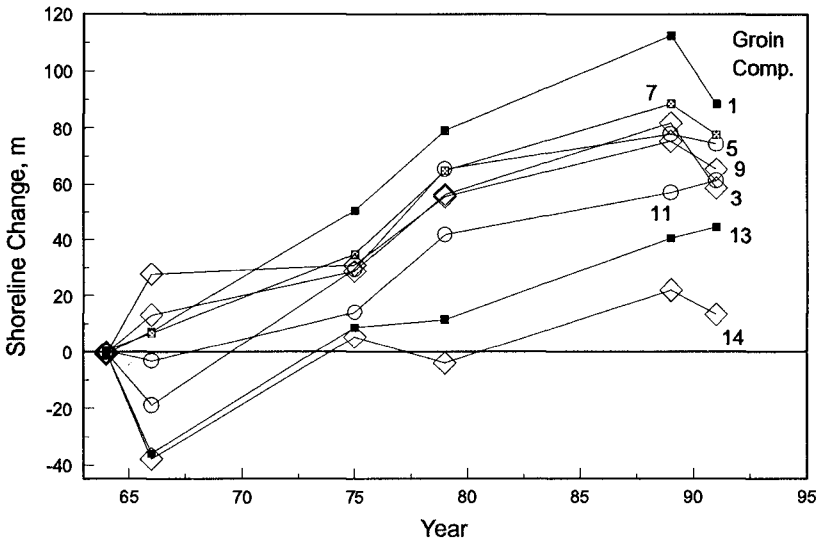


Fig. 9. Mean shoreline change per groin compartment

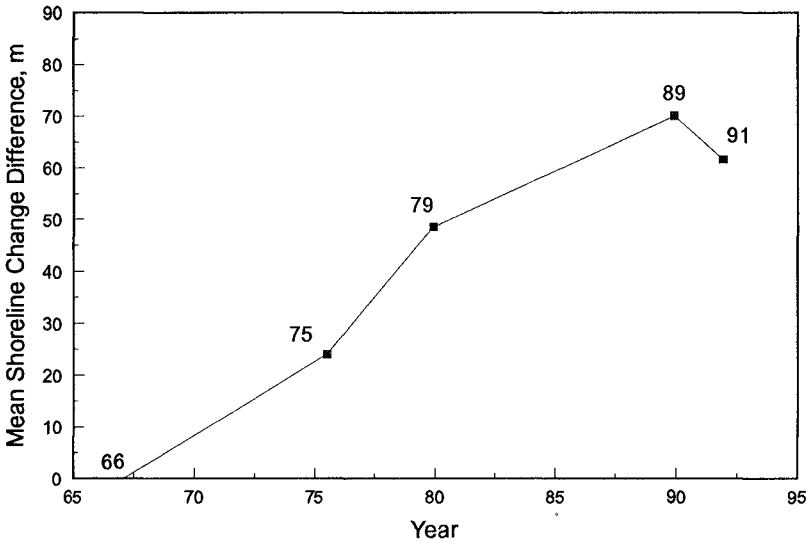


Fig. 10. Mean shoreline change over the groin field

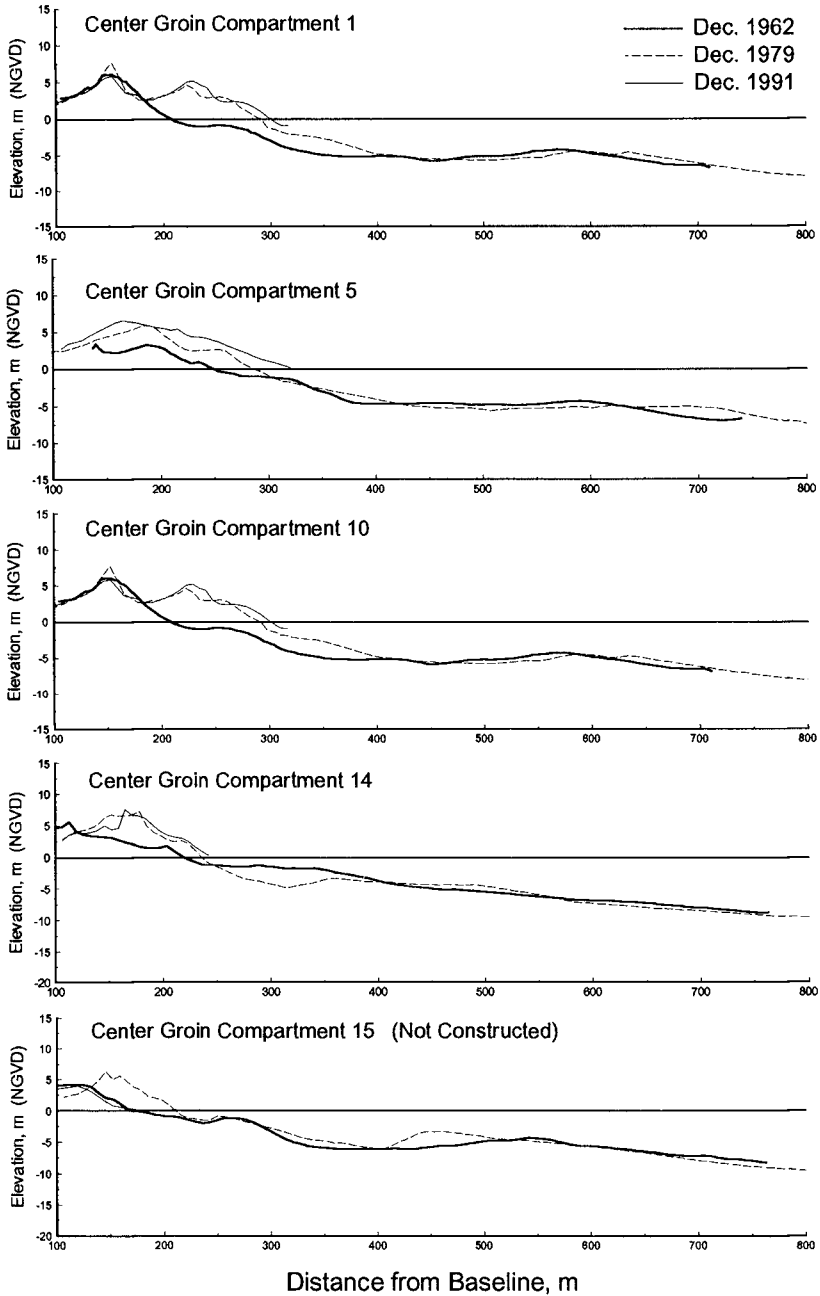


Fig. 11. Selected profile surveys to 800 m from baseline, Dec. 1962 - Dec. 1991

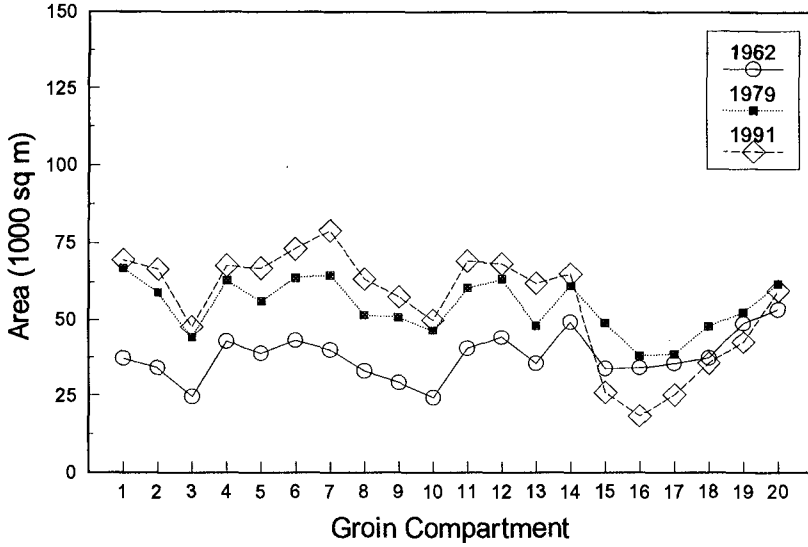


Fig. 12. Area change above NGVD intercept

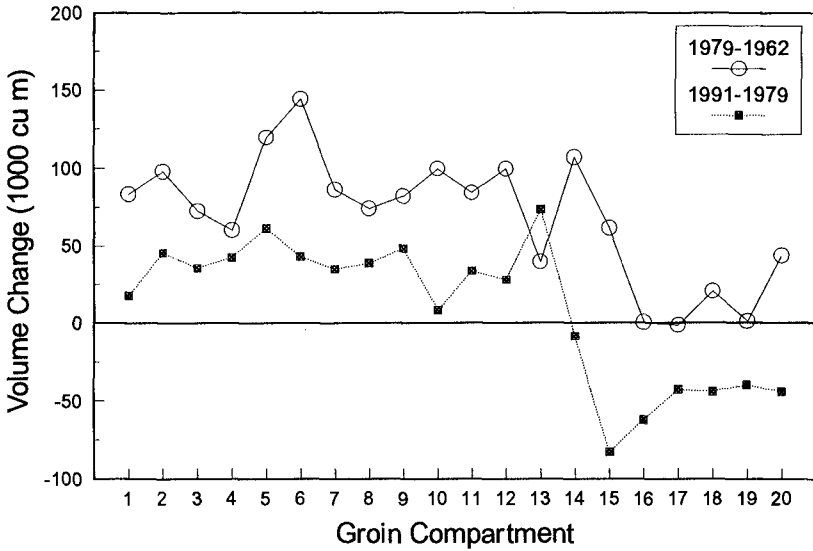


Fig. 13. Volume change above NGVD intercept

greatest increase in area of the groin compartments occurred between 1962-79, and the largest losses occurred downdrift of Groin 15 between 1979-91.

The data for the 14 compartments indicate that, between 1962-91, the average area volume compartment increased on average by 129,000 cu m or by 4,450 cu m/year for a total of 1.8 million cu m trapped by the groin field (above NGVD). The average increase in beach elevation over the period of record was 4.6 m. The greatest increase in volume of the groin compartments occurred between 1962-79, and, as in the case of the area plots, the largest losses, 315,200 cu m, occurred downdrift of Groin 15 between 1979-91. Although not discussed here, the beach profile did not steepen or lose volume seaward of the shoreline.

## **DISCUSSION AND CONCLUSIONS**

Review and analyses of the data strongly demonstrate that introduction of groins at Westhampton Beach has resulted in both adverse and positive impacts. The adverse impact, recession of the shoreline in the area downdrift of the groin field, developed as a result of not completing the project construction as originally intended. The adverse impact, caused by administrative, economic, and political decisions and not engineering miscalculation, has left the barrier island in a weakened condition such that it is still subject to being breached or broken through by storms.

The benefit of the groin field, which typically is not discussed in other analyses of the Westhampton groin field project, is that the groin compartments have been filled naturally or are still being filled from east to west, although taking much longer than the planned method of using artificial fill placement. Compartment filling has been accompanied by formation of high primary backshore dunes and several secondary dunes ridges located seaward of the primary dune. The shore area in the 14 groin compartments has not been significantly affected by storm attack, except for one compartment in 1980. The overall benefit of the groin field bypassing and dune building has been to provide a high level of protection to the barrier island over the area it encompasses.

Significant lessons which can be drawn from experience at Westhampton Beach are:

- a. **COMPLETE PROJECT WITHOUT UNDUE DELAY.** The construction of projects involving groins must be completed without significant delay to permit functioning of the system and to minimize impacts on adjacent shores. If there is a question as to whether the work can be conducted in this fashion, then it should not be initiated.
- b. **PERFORM CASE-BY-CASE EVALUATION.** Groins are not universally bad. Use of groins requires the same type of evaluation as is given in consideration of other protective measures to provide a solution for coastal problems on a case-by-case basis.
- c. **EXAMINE THE NEED FOR SHORE REINFORCEMENT WITH GROINS.** Groins may be needed to reinforce or hold protective beach fills, if their need is demonstrated by shore history and storm attack in the area to be protected. Emplacement of groins without concurrent placement of beach fill is strongly discouraged.
- d. **DEVELOP PROPER DESIGN.** The use of groins requires proper design by qualified professionals to ensure their functioning within a shore system. Designers need to be knowledgeable of the littoral forces affecting the area, the longshore sediment budget, and the sensitivity of adjacent shores to changes that groins can precipitate.

- e. ENSURE BYPASSING OF LONGSHORE SEDIMENT. Where longshore transport is essential to providing nourishment to downdrift shores, the use of groins must provide for bypassing of sediment to adjacent shorelines without interruption. The groin field should be filled, and, at the downdrift terminus of the project, the groin system should be tapered to meet the unimproved shoreline area in a smooth fashion.
- f. PROVIDE LONG-TERM PROTECTION. The 15 groins at Westhampton Beach still continue to function after 26 years to hold and build up the dune and beach in the groin compartments. The life of the groin structure can be extended through proper design, construction, and maintenance. Groins can provide positive and economical long-term protection while blending with the natural surroundings.

### ACKNOWLEDGEMENTS

We thank Coastal Engineering Research Center colleagues Mr. Paul Holt for assistance in developing the Westhampton Beach Geographic Information System, Ms. Holley Messing for typographic support, and Mr. Aram Terchunian, First Coastal Corporation of Westhampton Beach, N.Y., for discussions and assistance in providing reference materials. This study was conducted as part of activities of the Beach Fill Engineering work unit, Shore Protection and Restoration Program, U.S. Army Corps of Engineers. Permission was granted by the Chief of Engineers to publish this information.

### REFERENCES

- Andrews, W. E. 1938. "Restoration and Protection of Fire Island, Suffolk County - Long Island," W. Earl Andrews, Engineer, New York.
- Chu, Y. and Nersesian, G. K. 1992. "Scour Hole Development and Stabilization at Shinnecock and Moriches Inlets, NY," *Proceedings Coastal Engineering Practice '92*, ASCE, 571-582.
- Heikoff, J. M. 1976. *Politics of Shore Erosion: Westhampton Beach*, Ann Arbor Science Publishers, Ann Arbor, MI.
- Leatherman, S. P., and Allen, J. R. 1985. "Geomorphic Analysis, Fire Island Inlet to Montauk Point, Long Island, New York," Final Report to the U.S. Army Engineer District, New York, NY.
- National Ocean Survey. 1992a. "Tide Tables - East Coast of North and South America, Including Greenland," NOAA, Rockville, MD.
- \_\_\_\_\_. 1992b. "Tidal Current Tables at Coast of North America," NOAA, Rockville, MD.
- Panuzio, F. L. 1968. "The Atlantic Coast of Long Island," *Proceedings 11th Coastal Engineering Conference*, ASCE, New York, NY 1222-1241.
- U.S. Army Corps of Engineers. 1958. "Cooperative Beach Erosion Control and Interim Hurricane Study, Atlantic Coast of Long Island, NY, Fire Island Inlet to Montauk Point," U.S. Army Engineer District, New York, NY.
- \_\_\_\_\_. 1963. "General Design Memorandum No. 1, Moriches to Shinnecock Reach, Fire Island Inlet to Montauk Point, NY, Beach Erosion Control and Hurricane Protection Project," September, U.S. Army Engineer District, New York, NY.
- \_\_\_\_\_. 1969. "Supplement No. 1 to General Design Memorandum No. 1, Moriches to Shinnecock Reach, Fire Island Inlet to Montauk Point, NY, Beach Erosion Control and Hurricane Protection Project," February, U.S. Army Engineer District, New York, NY.
- \_\_\_\_\_. 1982. "Wave Climatology Study for the South Shore of Long Island, Phase III, Stations 45, 46, 47, and 50," U.S. Army Engineer Waterways Experiment Station, Coastal Engineering Research Center, Vicksburg, MS.
- \_\_\_\_\_. 1986. "Dune and Beach Design, Fire Island Inlet to Montauk Point, NY, Beach Erosion Control and Hurricane Protection Project," PRC Engineering, New York, NY.

## CHAPTER 257

### SEA LEVEL TRENDS IN THE HUMBER ESTUARY : A CASE STUDY

PATRICK PARLE<sup>1</sup>

#### ABSTRACT

In 1990 Posford Duvivier were commissioned by the National Rivers Authority to collect, audit and place on a database 550 years of tide data from 15 locations on and in the vicinity of the Humber Estuary, UK. As part of this project 373 years of the data, from 10 locations (key stations), were analysed for trends in relative sea level. The areas covered in the trend analysis included: linear trend estimates on yearly average high tide levels from all the key stations; an examination of variations in trends with location and time; and an examination of the correlation between high water trends, mean tide level trends and low water trends. This paper discusses the trend analysis.

#### INTRODUCTION

The National Rivers Authority (Yorkshire, Severn Trent and Anglian Regions) are responsible for extensive tidal defences around the Humber Estuary in the UK. (see Figure 1). Knowledge of extreme water levels and trends in water level is necessary for the design of tidal defences. To enable these NRA regions to produce a consistent and sound strategy for the design of tidal defences in the Humber area, Posford Duvivier were commissioned by NRA Yorkshire Region to collect and analyse tide data from specified tidal stations. This data was to be placed onto a computer database and analysed for trends in water level and extreme water levels.

550 years of tide data from 15 locations (see Figure 2) on and in the vicinity of the Humber were collected, audited, reduced to a common level (mODN) and time (GMT) base and loaded onto the database. 373 years of this data, from 10 locations (key stations) were analysed for trends in relative sea level. These trends were used to establish a coherent trend for the Humber Estuary. This coherent trend was used to adjust high tide data within the database to a common base date, 1990. This adjusted data was then analysed to produce estimates of extreme water levels for use in the

---

<sup>1</sup>Senior Engineer, Posford Duvivier, Consulting Engineers, Peterborough, UK



design of flood defences.

The areas covered in the trend analysis and discussed in this paper are

- Linear trend estimates on yearly average high tide levels from all the key stations
- The correlation between tide station trends
- The variation of trends with time
- The correlation between High Water trends, Mean Tide Level trends and Low Water trends

## **DATABASE**

The layout of the tide data on the database is shown on Table 1. The database holds the date, time and height of both high and low water. Each high water and following low water is held as a pair. Each pair is given a sequence number unique to that tide. This enables a given tide or set of tides to be identified at each location up the estuary. For each tide an adjusted level (as at 1990) has been estimated based on the coherent estuary trend. This adjusted level is held within the database.

Software has been written to enable data that satisfies a set of user defined criteria to be retrieved from the database. This software also allows the user to carry out extreme value analysis and/or trend analysis on a station's full data set or on a specified set of retrieved data.

## **TREND ANALYSIS METHODOLOGY**

Trend analysis was carried out on yearly averaged tide levels. A considerable amount of trend analysis has been carried out, during previous studies, using yearly average tide levels, and following an examination of trends using individual tide levels, monthly and yearly averages, it was considered appropriate that yearly averages be used in this study.

It was initially thought that river flow and surge tides might contaminate the trend estimates. However, at the key stations river flows did not significantly influence high tide level and any influence of these flows on trend estimates was reduced further by the use of yearly averages. Similarly the use of yearly averages effectively removes the effects of individual surge tides.

The use of yearly average tide levels also damps out "noise" in plots of levels against time. Noise may be due to diurnal tide differences, spring/neap tide cycles, monthly variations, random digitising errors, river flow, atmospheric pressure variations and surge tides.

An assessment of the effects of monthly variations in high tide levels at Immingham indicated that if at least ten months tide data was available for a year the average of this data would be a reasonably accurate estimate of the yearly average. Therefore, in auditing data at all stations, a valid yearly average was considered to exist if at least 10 months tide data existed for that year. Table 2 lists the number of valid yearly average high tide levels at each of the key stations.

Accurate assessment of tide level trends requires data uncontaminated by river flow and as long a data record as possible. Because a considerable amount of key station low water data is affected by river flow, (particularly that at Blacktoft and Goole the two stations with the longest data sets) and because high tide data at the key stations is not significantly affected by river flow, the analysis was concentrated on high tide levels. The correlation between trends in high water levels and trends in both low and mean tide levels was obtained from an analysis of Immingham data.

Trend estimates were based on a straight line fit to the tide data using the method of least squares. It was initially intended that the tide data be examined for both linear and curved trends. However, it was found that future water level estimates based on a quadratic fit to the raw data were very sensitive to errors in the curve parameters, and this method was therefore rejected.

#### **ANALYSIS OF HIGH TIDE LEVELS**

Plots of yearly average high tide level against time were examined for each station and are shown in figures 3(a) and 3(b). These plots were found to be consistent with each other and gave no indication that the trend in high tide level changes up the estuary. However, they show that a considerable variation in the trend estimate could occur depending on the data period examined. Therefore, when comparisons of trend estimates for two stations were being made, simultaneous data was used.

Blacktoft had more valid yearly average high tide level data than any other station, except Goole. Since the Blacktoft data was of a more reliable nature, it was decided to compare trends at each station with trends at Blacktoft. Trend estimates were made for each station and compared with the simultaneous trend at Blacktoft.

The results of this comparison are given in table 3. The actual value of the trend estimates are not important as they cover considerably differing data periods for different stations. For the same reason comparisons should only be made across table 3 not vertically. It can be seen that most of the station trend estimates are within one standard deviation of the Blacktoft estimate.

Within statistical error, therefore, table 3 shows no evidence of a change in trend in yearly average high tide levels as one moves up the Humber estuary. The coherent trend, in high tide level, for the estuary should therefore be based upon trend estimates for the station with the longest set of reliable data, which in the case of the Humber

Estuary was Blacktoft.

## NODAL TIDE EFFECTS

### General

Inspection of Figures 3(a) and 3(b) show that the yearly average high tide levels vary with time. The plot of levels for Blacktoft indicate this variation is cyclical with a period close to 20 years. In a study of yearly average water levels in the Thames, Rossiter (1969) refers to oscillations in annual average levels due to the "Nodal tide". The Nodal tide is due to the variation in the plane of orbit of the moon around the earth. This variation has a period 18.61 years. The nodal tide effect causes the tidal ranges to modulate, resulting in tides having a maximum and minimum once every 18.61 years.

### Nodal Tides

In principle, the nodal tide would cause what is known as the  $M_2^*$  tide component to vary by  $\pm 3.7\%$  over 18.61 years, with minima at 1913.4 (approx.)  $\pm N \times 18.61$  years and maxima at 1922.7 (approx.)  $\pm N \times 18.61$  years. The nodal tide could therefore cause the yearly average high water level at Immingham to vary by about 167mm.

However, the nodal oscillations of real tides appear to be less than the theoretical  $\pm 3.7\%$ . The occurrence of minima or maxima are also slightly (+0.5 year for Immingham) out of phase with the theory. Work by P. Woodworth (1991) of POL indicates that the nodal oscillation on high water level at Immingham would cause the yearly average high tide level to vary by 136mm with a minimum at 1951.1. It should be noted that a variation in average water level of 136mm in 9.3 (18.6/2) years gives a short term "trend" of 14.6mm/year.

The nodal tide causes a significant modulation in tidal range but only a small modulation on mean sea level. Woodworth (1987) cites estimates of the amplitude of nodal tidal oscillations on mean sea level of about 9-10mm.

### Effect of Nodal Tide on Estuary Trend

It is therefore important, when estimating a coherent estuary trend, using high tide data, that the period of data used should be an integral number of 18.61 year periods, should be of sufficient length that the effect of the nodal tide is insignificant, or the data should be corrected for nodal tide effects.

---

\* The  $M_2$  component is the lunar tide component, with period 12.42 hours, which dominates tides around the UK coast

It is not yet known how the effect of these nodal oscillations propagate up an estuary. It is thought that they may not vary much. At Immingham the amplitude of the nodal tide is about 3.0% of the  $M_2$  tide. Assuming the nodal tide propagates up the Humber, as 3% of the  $M_2$  component, this will result in a nodal oscillation of 121mm at Blacktoft.

Correcting the yearly average high tide levels at Blacktoft for this assumed nodal tide effect increases the linear trend estimate for the full data set from 3.57 to 3.71mm/year, see table 4. The use of this nodal tide correction causes a reduction in the standard deviation of the trend estimate from, 0.37 to 0.24mm/year. If an accurate estimate of the nodal tide amplitude were known for Blacktoft a more precise trend estimate could therefore be calculated. A plot of this Blacktoft data with nodal tide correction is given in Figure 4.

This increase in precision, though it may be significant in terms of reduction in the standard error of the trend, did not result in a significant change in the trend estimate. It was therefore decided that the estimation of a coherent estuary trend could be based on a trend estimate for the full Blacktoft data set without correction for nodal tide effects.

A coherent estuary trend of 3.57mm/year  $\pm$  0.37mm/year was thus adopted.

## **RELATIONSHIP BETWEEN TRENDS IN HIGH TIDE LEVEL, MEAN TIDE LEVEL AND LOW TIDE LEVEL**

### **General**

The coherent estuary trend of 3.57mm/year  $\pm$  0.37mm/year can be used to adjust past annual maxima data to the 1990 base date. Assuming that these historic trends continue, extreme water level estimates at future dates can be made. These future extreme levels are the extreme estimates based on annual maxima adjusted to 1990, plus a future rise based on historic trends.

Estimates exist for future sea level rise as published by the Intergovernmental Panel on Climate Change (IPCC) (1990). At present there are large uncertainties on these future sea level rise estimates which take account of global warming. In the near future, given a lessening of the uncertainties on sea level rise estimates, one may wish to use these rise estimates in place of historic trends. The greenhouse effect estimates relate to mean sea level, not yearly average high tide level, however, they do not include for local land movements.

To enable use to be made of future sea level used rise estimates it is thus necessary both to know the relationship between trends in high tide levels and trends in mean sea level and to obtain an estimate of land movement for the Humber area.

It should be noted that mean tide level used in this study  $(HW + LW)/2$  is not the same as mean sea level. However, over a period of time mean tide level is a constant amount above or below mean sea level. Therefore a trend in mean tide level is equivalent to a trend in mean sea level.

### **Relationship from other Studies**

Other studies have stated that trends in high tide and mean sea level are not the same. For example, Pugh (1990) cites two studies which indicate that trends in high tide level are higher than trends in mean sea level. One of these studies by J.R. Rossiter (1969) found that at Tower Pier trends on high tide levels were considerably greater than trends on MTL,  $7.74 \pm 1.16\text{mm/year}$  against  $4.33 \pm .82\text{mm/year}$ . During the same study, however, Rossiter found that the trends on high and mean tide levels at Southend were not statistically different. Another study indicated that at Flushing, Holland, the high tide trend was  $3.3\text{mm/year}$ , against  $2.2\text{mm/year}$  for the mean sea level.

Rossiter's study quoted above covers a data period of 30 years. This data period is less than an integral number of nodal tide periods. His study took no account of the nodal variation in tide levels and may therefore be biased.

### **Relationship from Present Study**

To attempt to correlate trends in high, mean and low tide levels in the Humber, Immingham tide data was examined. As discussed earlier, nodal tide effects result in an oscillation of approximately 136mm in high tide levels at Immingham, with a low at 1951.1. Table 5 gives trend estimates and the standard deviation of these trend estimates for yearly average high, mean and low tide level at Immingham, with and without correction for nodal tide effects. Figure 5 gives plots of these yearly average tide levels with and without nodal corrections.

Ignoring nodal tide effects indicate that high tide level is rising slower than both mean tide and low tide level. However, having corrected the high and low water levels for nodal tide effects the difference between the trends for the three levels is not statistically significant. Correcting for nodal tide effects also gives a significant reduction in the standard deviation of the high and low tide trend estimates.

This study indicates, therefore, that an increase in mean sea level will result in a similar increase in high water level.

### **Future Levels**

Based upon the assumption that the difference between relative sea level rise and global mean sea level rise is, in the Humber, due predominantly to land sinkage, and using the  $3.57\text{mm/year}$  rise as the best estimate of relative sea level trend in the Humber, and the IPCC, (1990) estimate of sea level rise of 1 to  $2\text{mm/year}$  over the last 100

years, we estimate the rate of land sinkage in the Humber as 1.57 to 2.57mm/year. It is acknowledged that this is a simplistic approach and that the difference may be due to other factors, not yet fully understood.

At present, therefore, future trend estimates of relative sea level rise based on estimates of absolute sea level rise should consider this estimate of land sinkage as additional.

## CONCLUSIONS

It was found during the study that

- spatial variation in high tide trends for stations within the estuary was found not to be statistically significant
- nodal tide effects must be considered when water level trend estimates are made based on high tide data. The longer the data set the smaller is the effect of nodal tide on trend estimates
- a coherent trend estimate of 3.57mm/year,  $\pm 0.37$ mm/year was found for the Humber estuary. This estimate is based on the Blacktoft data set (70 years)
- this study indicates that, for the Humber estuary, an increase in mean sea level will result in a similar increase in high water level
- in the Humber area, there is an additional 1.57-2.57mm/year increase in relative sea level over global sea level trends. This may be due to land sinkage.

## ACKNOWLEDGEMENT

The author wishes to thank National Rivers Authority, Yorkshire Region, the lead Client, for permission to publish this paper.

## REFERENCES

- Intergovernmental Panel on Climate Change, Working Group 1, 1990, Scientific Assessment of Climate Change : Section 9, Sea Level Rise, Cambridge University Press.
- Pugh, D.T., 1990. Is there a Sea Level Problem. Proceedings of the Institution of Civil Engineers, Part 1, 88, June, 347 - 366.
- Rossiter, J.R., 1969, Tidal Regime of the Thames, Dock Harbour Authority, 49,461.
- Woodworth, P.L., 1987, Trends in UK Mean Sea Level, Mar. Geodsey, 11, 57-87.

Woodworth, P.L., Shaw, S.H. and Blackman, D.L. (1991). Secular Trends in Mean Tidal Range around the British Isles and along the adjacent European Coastline. *Geophys. J.Int.* 104, 593-609.

**TABLE 1**

**Humber Estuary Tidal Defences Database Layout**

Sequence Number	High Date	High Time	High Level	Low Date	Low Time	Low Level	Adj Level
70001	01 Jan 1970	11:20	1.85	01 Jan 1970	16:57	-1.37	1.94
70002	01 Jan 1970	23:20	2.27	02 Jan 1970	05:53	-1.28	2.36
70003	02 Jan 1970	12:08	1.93	02 Jan 1970	17:33	-0.80	2.02
70004	03 Jan 1970	00:31	2.27	03 Jan 1970	06:58	-1.43	2.36
70005	03 Jan 1970	13:29	1.90	03 Jan 1970	19:05	-0.79	1.99
70006	04 Jan 1970	01:41	2.09	04 Jan 1970	08:12	-1.53	2.18
70007	04 Jan 1970	14:29	2.16	04 Jan 1970	20:29	-1.48	2.25
70008	05 Jan 1970	03:00	2.29	05 Jan 1970	09:16	-1.88	2.38
70009	05 Jan 1970	15:34	2.45	05 Jan 1970	21:53	-1.80	2.54
70010	06 Jan 1970	03:47	2.54	06 Jan 1970	10:12	-2.21	2.63
70011	06 Jan 1970	16:40	2.71	06 Jan 1970	22:56	-2.32	2.80
70012	07 Jan 1970	04:53	2.78	07 Jan 1970	11:23	-2.61	2.87
70013	07 Jan 1970	17:24	2.89	07 Jan 1970	23:54	-2.81	2.98
70014	08 Jan 1970	05:46	3.03	08 Jan 1970	12:19	-2.66	3.12
70015	08 Jan 1970	18:17	3.20	09 Jan 1970	00:55	-3.11	3.29
70016	09 Jan 1970	06:53	2.78	09 Jan 1970	13:00	-3.38	2.87
70017	09 Jan 1970	19:04	3.14	10 Jan 1970	01:39	-3.48	3.23
70018	10 Jan 1970	07:40	3.33	10 Jan 1970	13:55	-2.75	3.42
70019	10 Jan 1970	19:48	3.80	11 Jan 1970	02:26	-3.26	3.89

Station	Number of Years
North Shields	20
Scarborough	35
Spurn Point	16
Immingham	29
Hull	11
Brough	36
South Ferriby	10
Blacktoft	66
Goole	69
Keadby	40

TABLE 2

Number of Valid  
Yearly Average High Tide  
Levels each Key Station

TABLE 3

Relationship between Station Trend and Blacktoft Trend \*

Values at Station			Concurrent Values at Blacktoft Station		
	Trend	Std.Dev. of Trend	Trend	Std.Dev.	No. of Years of Concurrent data
Station	mm/yr	mm/yr	mm/yr	mm/yr	
Goole	2.9	0.4	3.5	0.4	65
Keadby	4.5	0.7	4.5	0.9	34
Brough	4.4	0.8	3.9	0.9	36
South Ferriby	11.7	4.9	9.0	3.1	10
Hull	-5.1	2.8	-7.1	2.0	11
Immingham	3.6	0.9	2.6	1.1	29
Spurn Point	0.8	2.5	1.6	2.43	16
Scarborough	3.3	0.6	4.5	0.8	35
North Shields	3.5	0.8	2.9	0.9	20
	Immingham**		North Shields		
	2.26	1.34	3.19	1.00	19

\* Using yearly average high tide levels, concurrent data

\*\* Comparison of Immingham and North Shields



**TABLE 4****Blacktoft Trend Estimate**

	<b>Trend</b>	<b>Std.Dev. of Trend</b>
	mm/yr	mm/yr
Without Nodal Tide Correction	3.57	0.37
With Nodal Tidal Correction	3.71	0.24

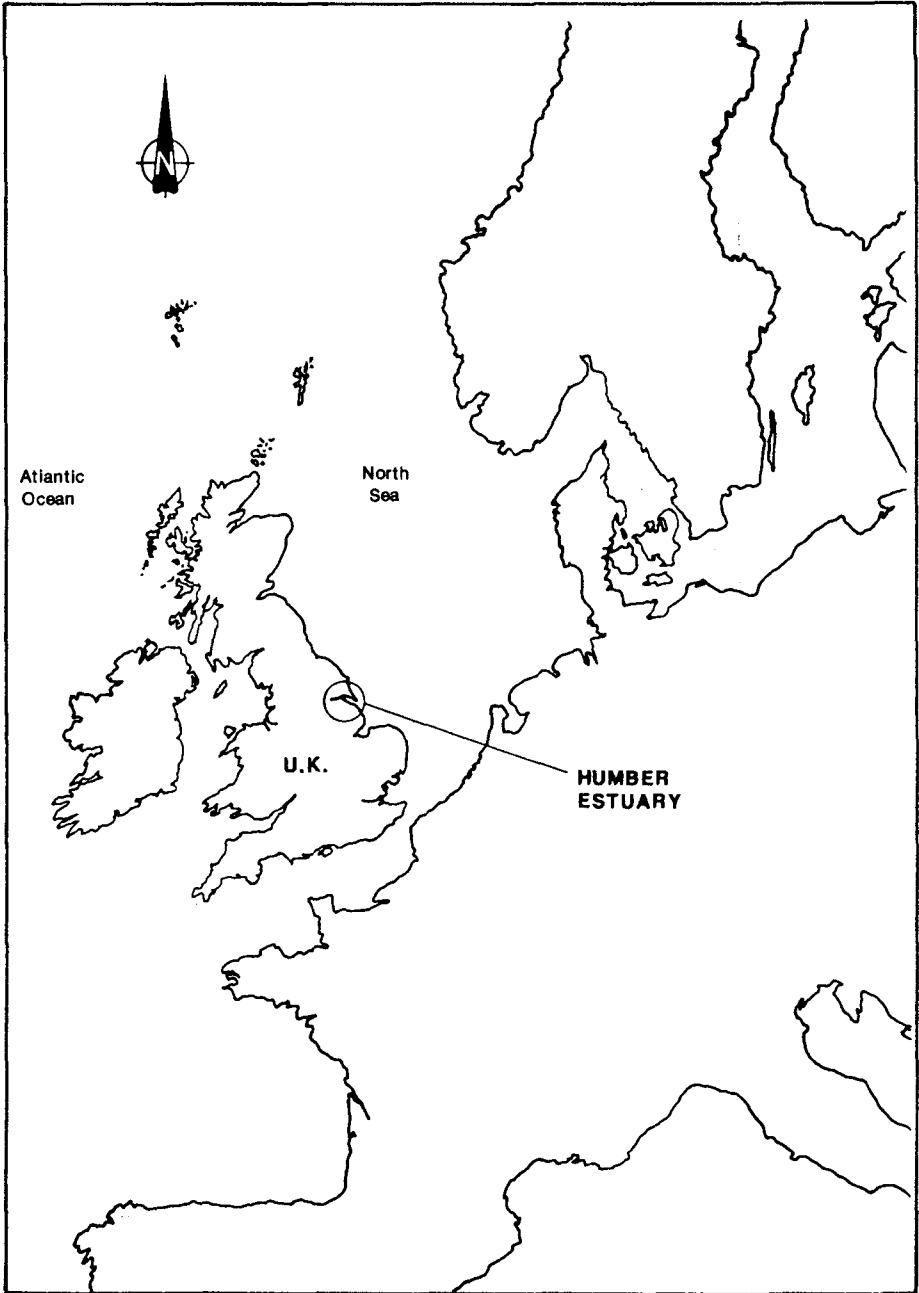
Data set examined 1923 - 1989

**TABLE 5****Immingham: Relationship between Trends in High, Low and Mean Tide Level\***

	<b>With Correction for Nodal Tide</b>		<b>Without Correction for Nodal Tide</b>	
	<b>Trend</b>	<b>Std.Dev. of Trend</b>	<b>Trend</b>	<b>Std.Dev. of Trend</b>
	mm/yr	mm/yr	mm/yr	mm/yr
High Tide	3.43	0.63	2.62	1.07
Mean Tide**	3.40	0.58	3.52	0.57
Low Tide	3.60	0.56	4.41	1.13

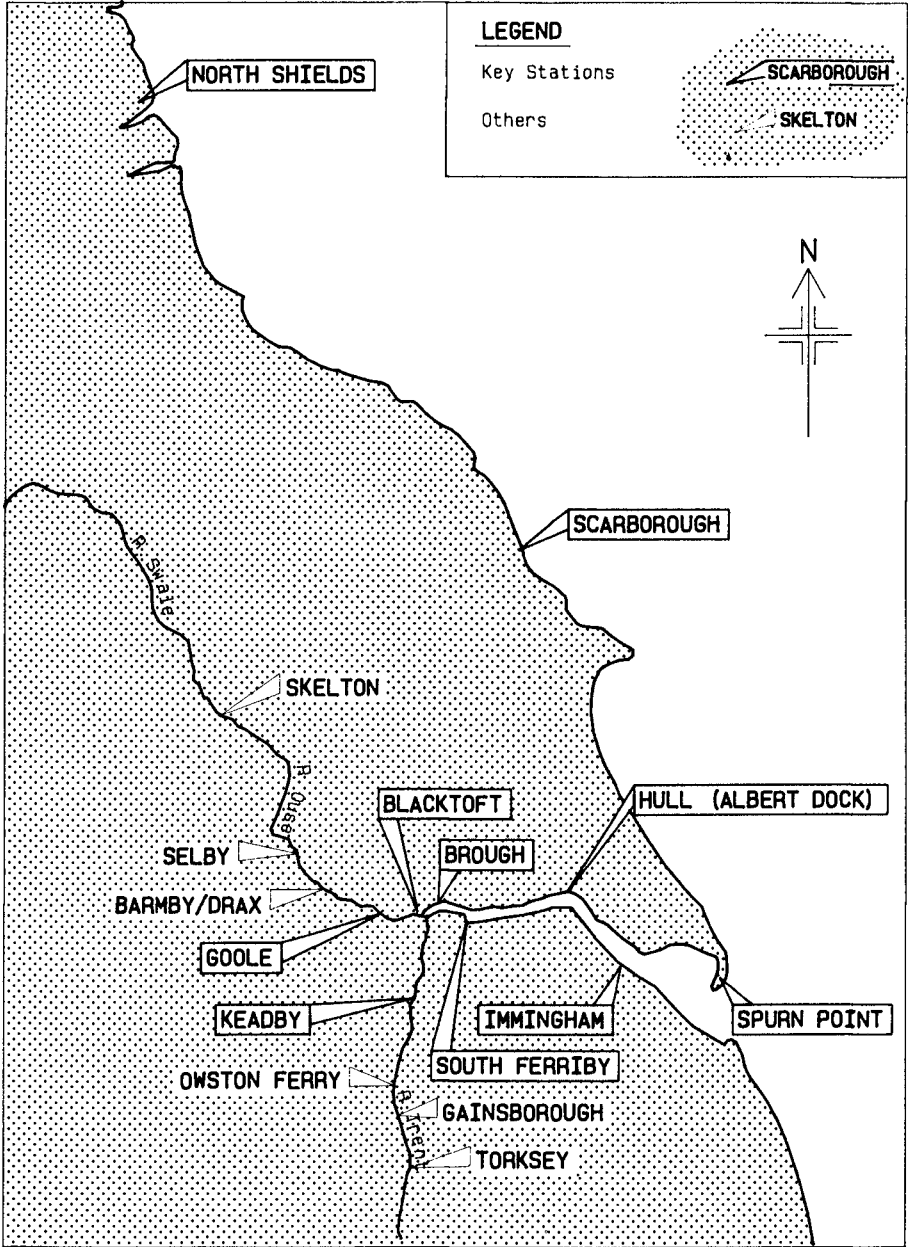
\* levels used are yearly averages

\*\* using a nodal tide amplitude of 10mm



**LOCATION PLAN - HUMBER ESTUARY**

**FIG. 1**



LOCATION OF STATIONS

FIG. 2

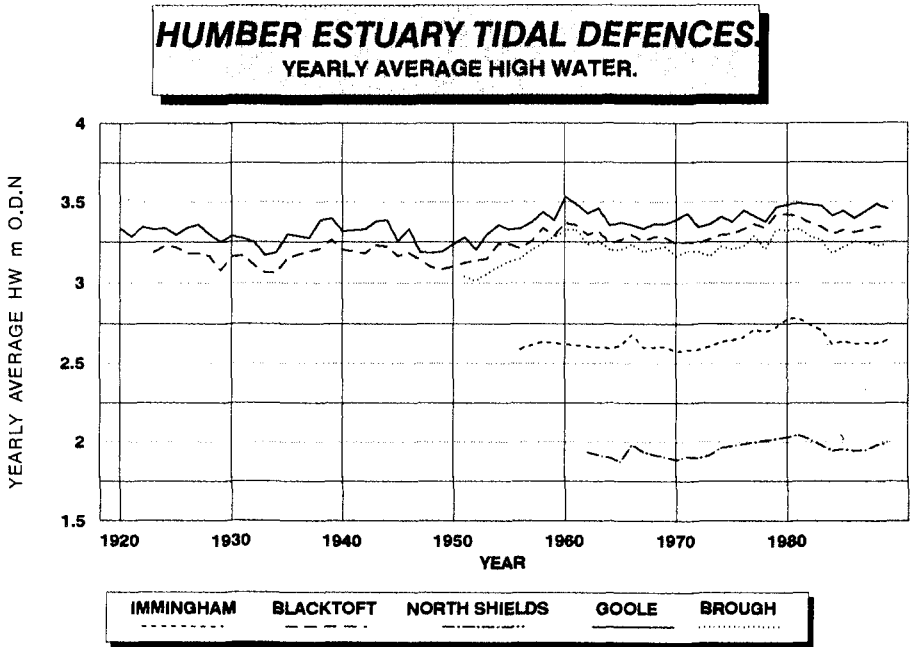


FIG. 3a

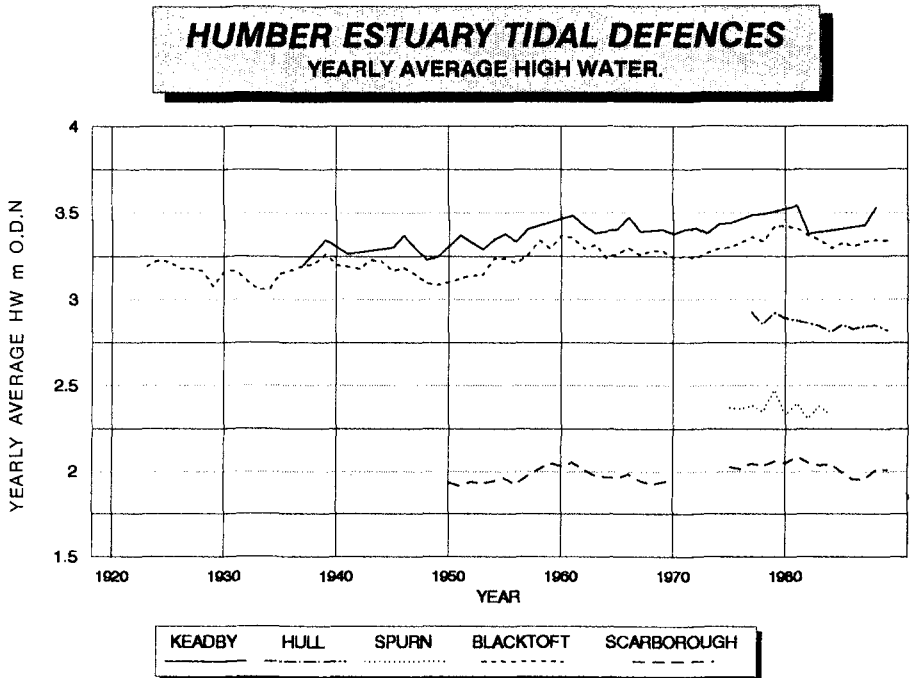


FIG. 3b

**HUMBER ESTUARY TIDAL DEFENCES  
BLACKTOFT: NODAL TIDE EFFECTS.**

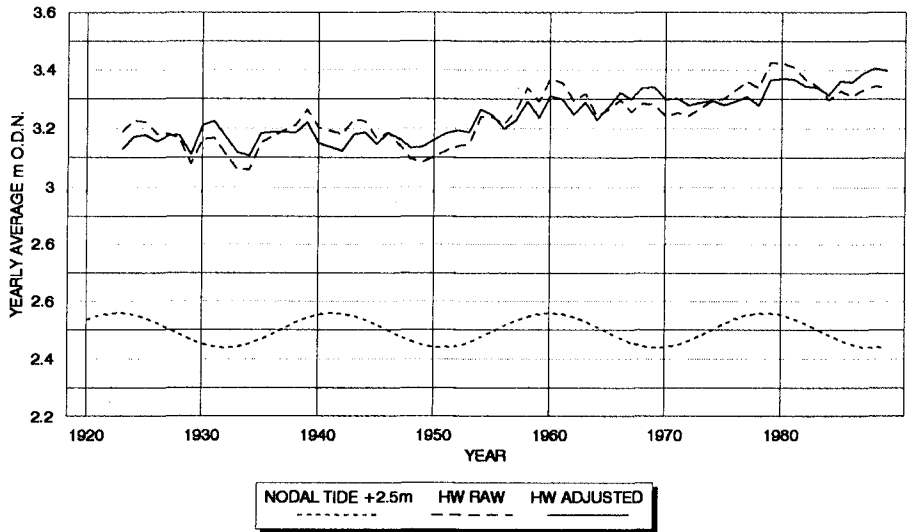


FIG. 4

**HUMBER ESTUARY TIDAL DEFENCES  
IMMINGHAM: NODAL TIDE EFFECTS.**

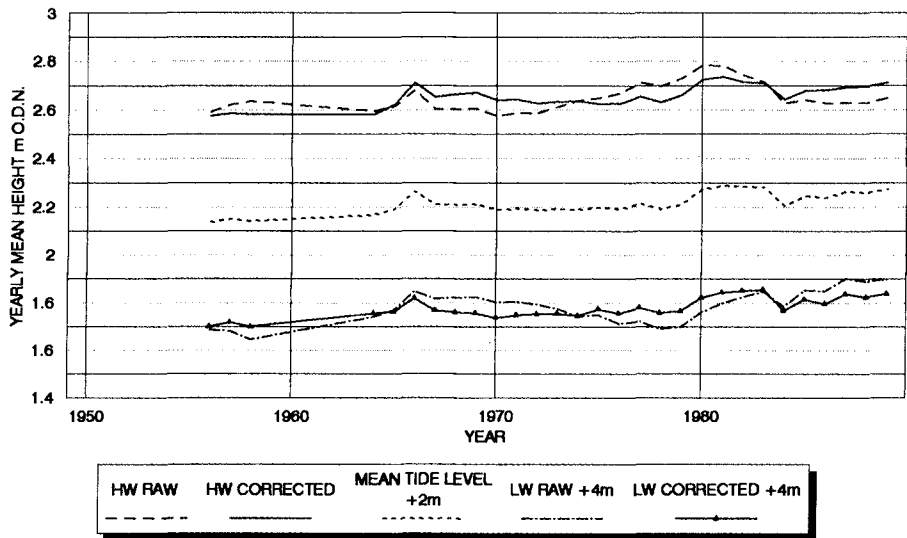


FIG. 5

## CHAPTER 258

### PROJECTS, WORKS AND MONITORING AT BARCELONA COAST

CARLOS PEÑA<sup>1</sup>  
VICENTE CARRION<sup>1</sup>  
ANA CASTAÑEDA<sup>1</sup>

#### 0. INTRODUCCION

Barcelona is the second city in Spain (2.3 million inhabitants) after Madrid (4 million) and is also the city that held the last Olympic Games in July 1992.

Just at the sea-front of the city is the port of Barcelona, the most important in Spain. The coast of the province of Barcelona is divided in two at this point. The northern part of Barcelona's coast runs from this port up to the mouth of the Tordera river, which is the border between the provinces of Barcelona and Girona.

These are 47 kms of the spanish coast which are very heavily degraded in some parts.

In its natural state it was a continuous and broad sandy beach 47 km. long and is some points two or three hundred meters wide, maintained by the sediments transported to the coast by Tordera and other small rivers.

Fig. 1<sup>2</sup> shows the situation of Barcelona in Spain and on the Mediterranean sea.

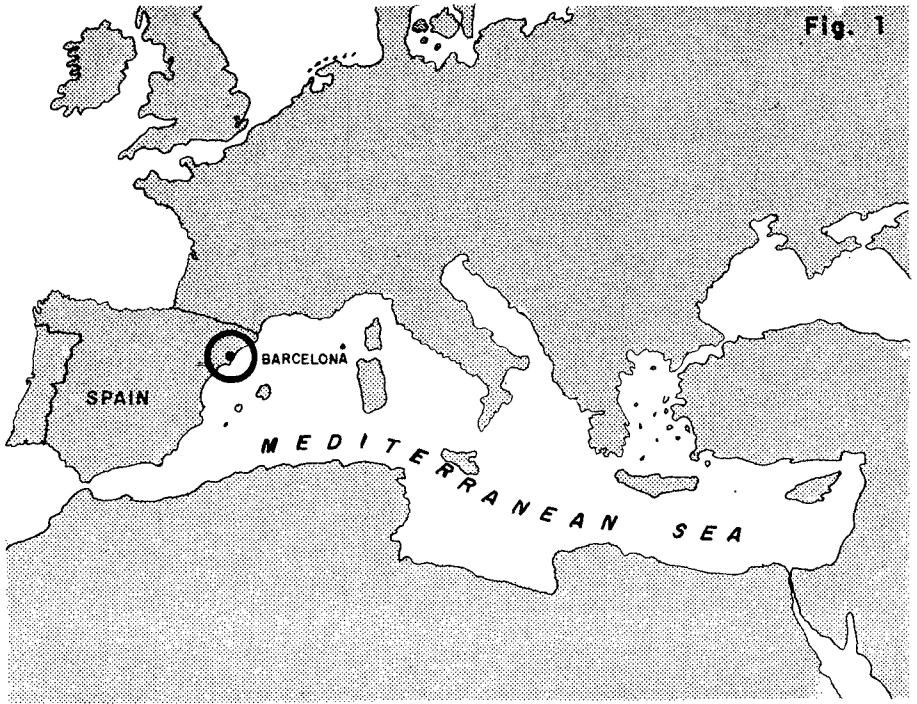
Fig. 2 shows the distribution of wave height all along the different directions focusing on the Barcelona coast. Data of this distribution comes from the well known visual data provided by ships.

Just a look at this fig. 2 shows that there is a potential sand transport capacity from north to south. This sand transport capacity has been evaluated by means of the CERC formula in about 89.000 m<sup>3</sup>/year near Barcelona city.

---

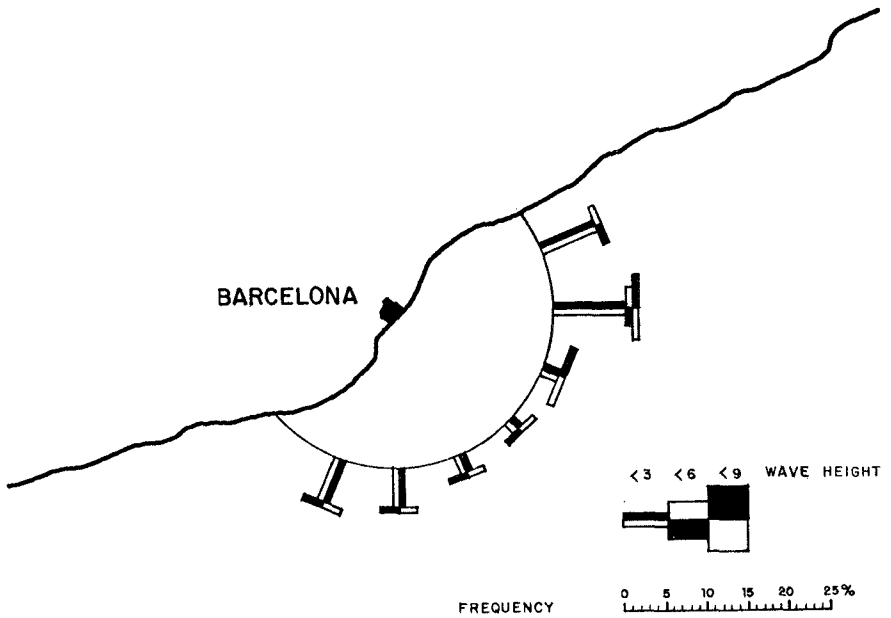
<sup>1</sup> Dirección General de Costas - M.O.P.T.  
Pº de la Castellana, 67 (A-511)  
28046 - MADRID (SPAIN)

<sup>2</sup> All the drawings have been done by M. Miguel



WAVE HEIGHT DISTRIBUTION (1950 - 1983)

Fig. 2



Let's have now a brief description of the whole sector (from Barcelona's port up to the Tordera delta) in its actual state.

In order to do so, the whole sector has been divided in three different segments.(Fig. 3).

## **1. FIRST SEGMENT (Tordera river - Arenys de Mar)**

The first segment goes from the mouth of the Tordera river up to the port of Arenys de Mar. Although the coastal zone has been heavily developed all along these 22,4 kms., the beaches remain in their natural state since the Tordera river delta maintains its enormous capacity to nourish them with coarse sand. Only in a few points some restoring works and nourishments were needed due to small and inadequate artificial works. As a whole we can say that the beach (not the coastal zone) keeps its natural dynamics and its existence is not threatened by a short-fall in sand.

The sand transportation capacity evaluated by the CERC formula is about 66.000 m<sup>3</sup>/year whith the visual wave heights data as input in the formula.

So, the target here is to mantain and improve the natural sediments dynamics, since the Tordera river and its delta are still capable of providing the amount of sediment needed to mantain all the beaches of this segment.

Actual planning is limited to some located sand nourishments, to remove or cut down some small groins and to prevent the beach being occupied.

## **2. SECOND SEGMENT (Arenys de Mar - Besos river)**

The second segment runs from to the port of Arenys de Mar up to the mouth of the Besos river. It is the most heavily degraded.

### **2.1. HISTORY (induced erosion and countermeasures)**

The first outer attack came from the construction in 1850 of the first Spanish railway. It was built in the easiest way and on the flatest land: the beach.

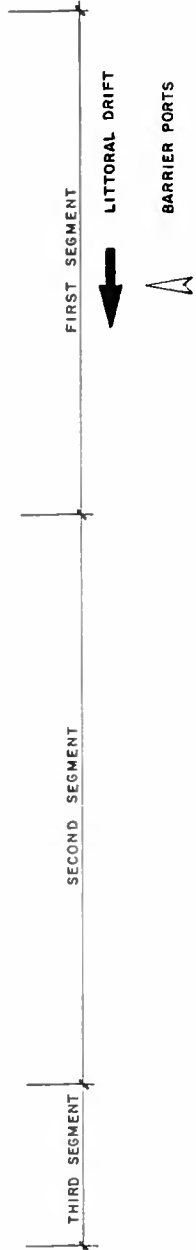
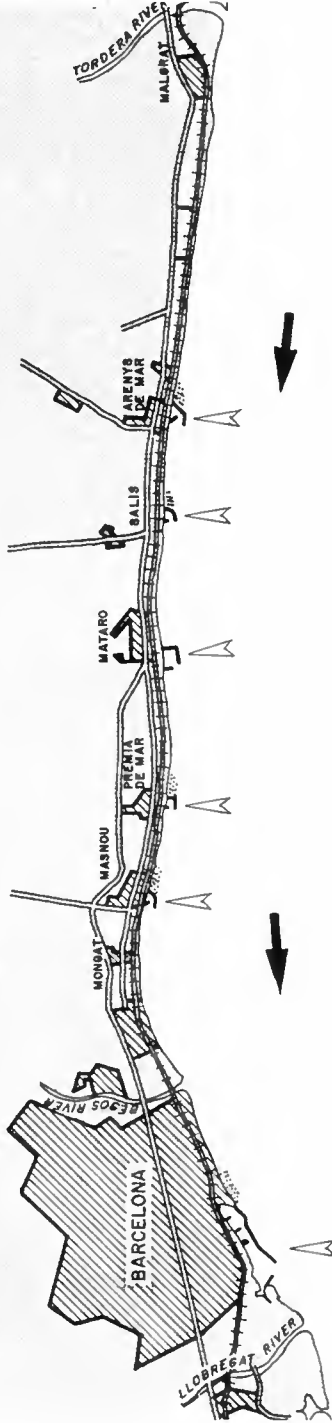
After this, five marinas or leisure ports were built up. The first one was Arenys de Mar in 1907, at the middle of the whole sector and, as a consequence, a very hard and continued erosion began at the southern part of the port for many kilometres. After Arenys de Mar four other ports were constructed: El Balis in 1972, El Masnou in 1972 Premiá de Mar in 1971 and the last one Mataró in 1989 (see fig. 3)

Since all these ports are total barriers to longshore drift of sediments, the immediate consequence was always the same: a small triangular beach at the northern breakwater of the port and a hard erosion at the south up to next port.



FIG. 3

# BARCELONA COAST



The first counter-measure to halt erosion was taken by the railway company. A long line of quarrestones showed up all along many kilometers in order to prevent the railway collapsing. As the beach disappeared quite quickly, some attempts to recover the beach were made. Eleven groins were constructed between the ports of Arenys de Mar and El Balis but they failed in recovering the beach and the only result was a further degradation in the coast landscape. Other small groins were constructed but generally speaking the beach was progressively disappearing; the environment, from the landscape point of view was going from bad to worse, the railway was at the sea-land border and this limit was (and still is) just a long line of quarrestones.

## **2.2. BEACH REPLENISHMENT AND STRATEGY**

The situation from Arenys de Mar up to the south was a few years ago untenable and in 1985, the Spanish Public Works Ministry planned the recovery of all this part of the mediterranean coast. The first step was the replenishment of the beach with 2.228.888 m<sup>3</sup> of coarse sand (0.4 mm) between the groin of Mongat and the port of Premiá de Mar with the port of Masnou at the middle (Fig. 4). There are 4,9 kms. of the coast recovered by means of simple sand replenishment as a first step. The second and necessary step is to by-pass all the ports in order to restore the littoral drift of sediments. The third step will be the replenishment of the remaining parts of the eroded coast and the forth and last step will be the periodical sand nourishment at the beginning of the whole segment: the southern point of the port of Arenys de Mar. So, if the four ports do by-pass the sand from north to south at the rate of sand transport capacity and at the same rate sand is nourished at the beginning of this sector, littoral drift will be restored and the beach all along 22,9 kms. will be recovered.

Theoretically, since sand transport capacity is evaluated by CERC formula in about 90.000 m<sup>3</sup>/year this will be the volume to nourish every year and the same amount must be by-passed by the ports.

## **2.3. MONITORING**

The subsector replenished at the first step (groin of Mongat - Port of Premia) has been monitored by CEPYC (Spanish Official Maritime Research Center<sup>3</sup>) in order to confirm these hypotheses.

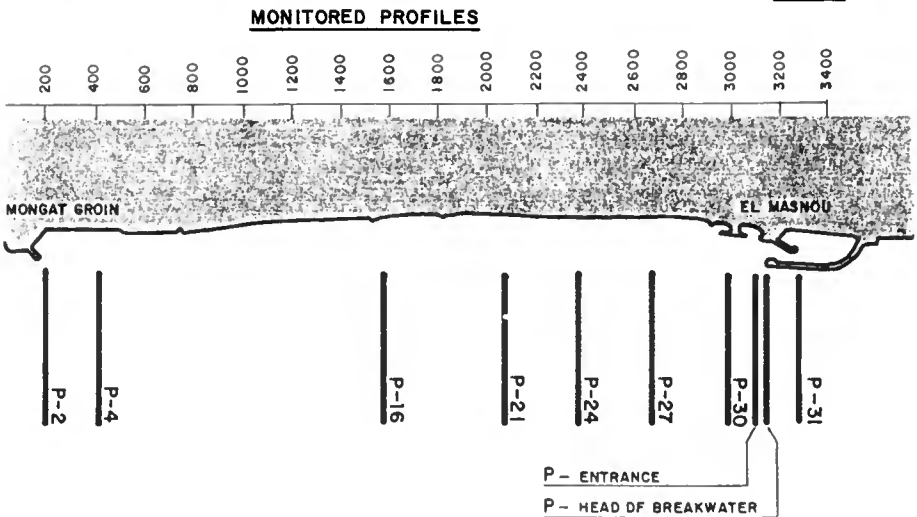
Profiles of the beach have been monitored twice a year in 1987 and 1988 and once a year in 1990 and 1991 (Fig. 5).

---

<sup>3</sup>Centro de Estudios de Puertos y Costas  
C/ Antonio López, 81  
28026-MADRID



FIG. 5



If we focus our attention between the groin of Mongat and the port of Masnou, (see fig. 3) we have 33 profiles of the beach (see fig. 5), each of them taken at May and October 87, May and October 88, May 89, September 90 and November 91. In addition to this, two sand nourishments have been carried out in this period of time. The first one between May 88 and October 88 (the amount was 245.000 m<sup>3</sup>) the second one was between september 90 and November 91 (the amount was 160.000 m<sup>3</sup>).

Figures 6 up to 15 show the result of this monitoring. Let us make a few comments to these profiles.

- Fig. 6 shows the profiles outside the breakwater of the port of Masnou. The sea bottom is growing up because of the sand drifted from the north.
- Fig. 7 shows the profiles at the mouth of the port. Here too, sea bottom is coming up except for the profile measured in 1988 because it was dredged before.
- Fig. 8 shows the profiles about 100 m. from the mouth of the port. We can see that they remain very stable because the port is a total barrier to littoral drift.
- Figs.9 and 10 show the profiles at the points of sand nourishments in 1988 an 1991. These are also the points of most rapid erosion because of the proximity of the port. This is why these profiles move very quickly.
- Fig.11 & 12 show the profiles 20 and 24 at the middle of the stretch.
- Fig.13 and 14 show the profiles near the groin of Mongat. The beach has been quite stabilized.
- Fig.15 shows the profile nº 1 just besides the groing of Mongat where the beach line only retreats under the effect of storms.

The rate at which sand is lost (i.e., drifted to the south) has been measured.

Between May - 87 and May 88..... 110.000 m<sup>3</sup>  
 Between May - 88 and May 89..... 55.000 m<sup>3</sup>

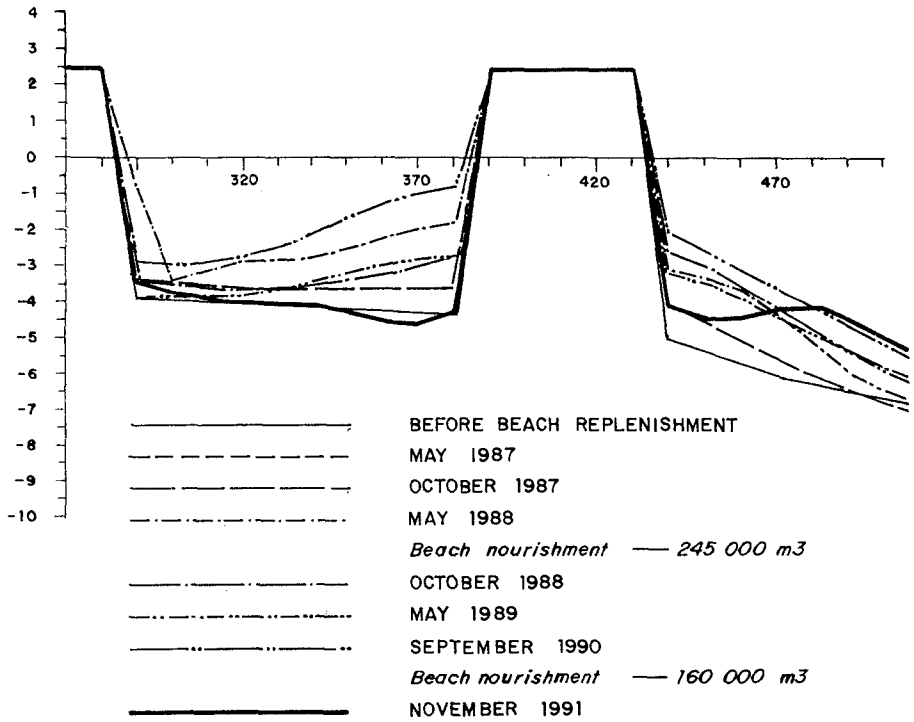
Unfortunately profiles were no longer mesured in the month of May.

Between October 87 and October 88..... 160.000 m<sup>3</sup>  
 Between October 88 and September 90..... 180.000 m<sup>3</sup> (2 years)  
 Between September 90 and November 91.... 120.000 m<sup>3</sup>

-----

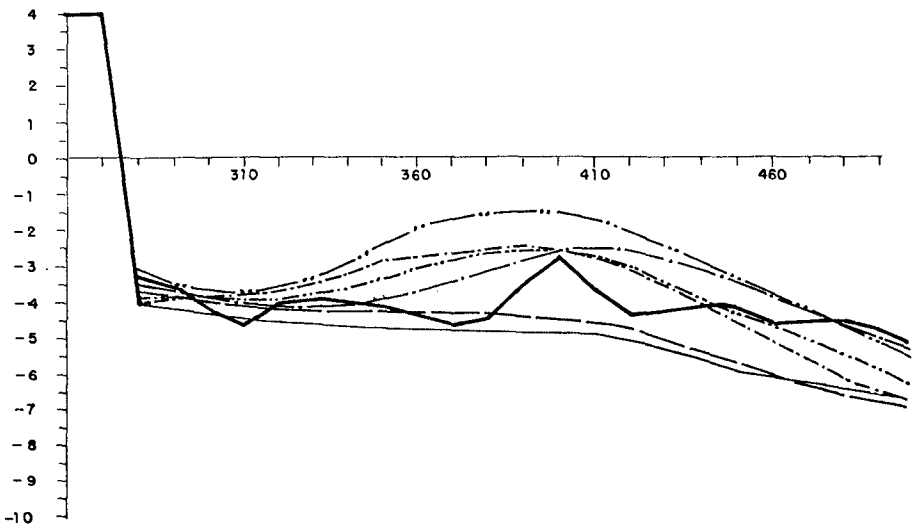
P- HEAD OF BREAKWATER

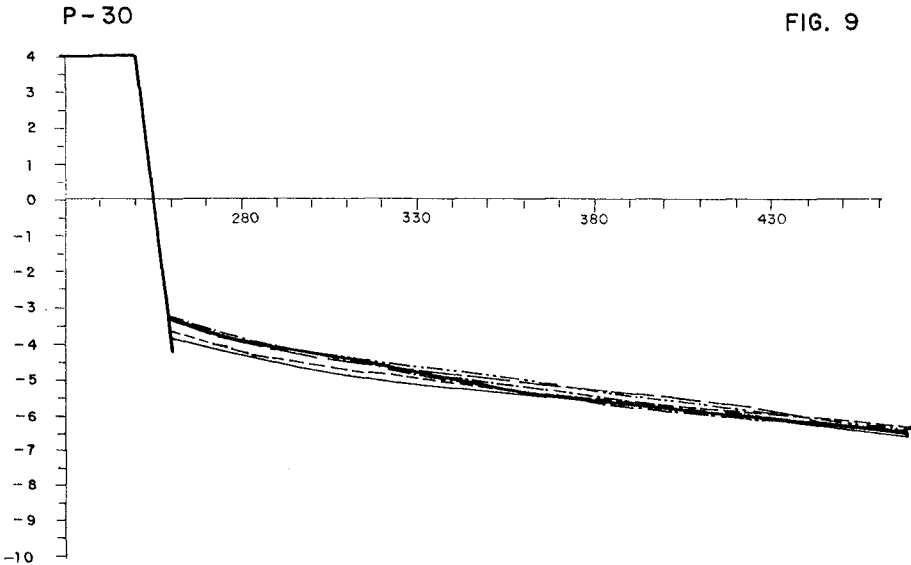
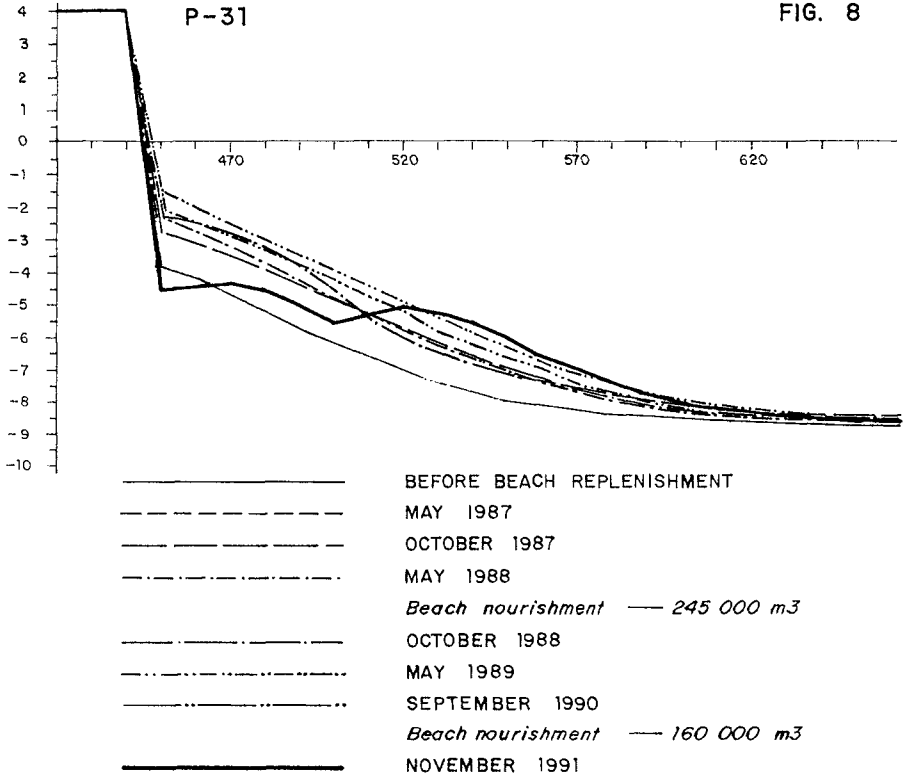
FIG. 6



P- ENTRANCE

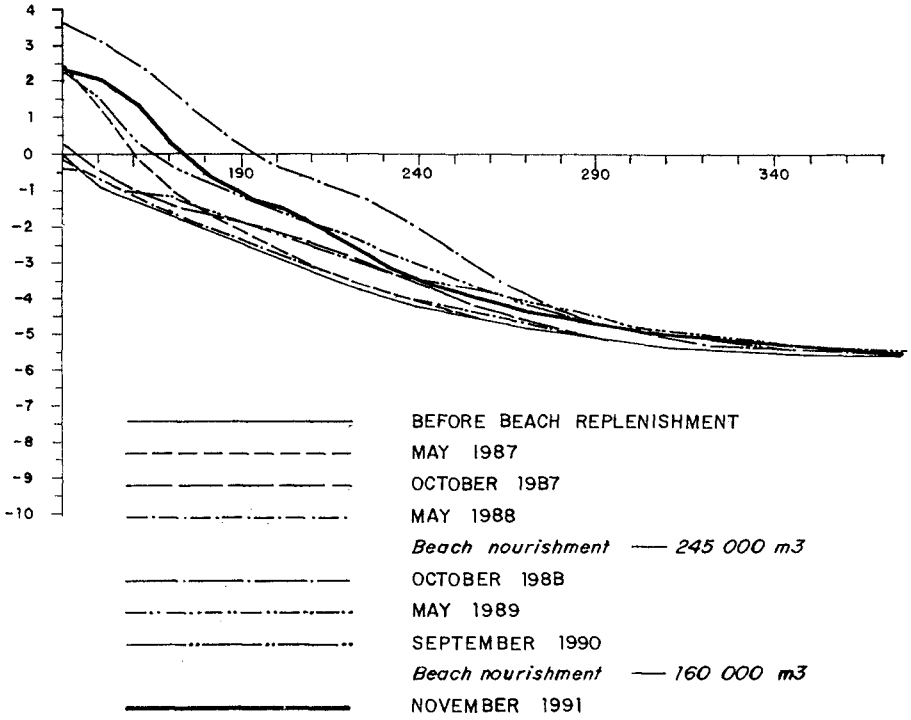
FIG. 7





P - 27

FIG. 10



P - 24

FIG. 11

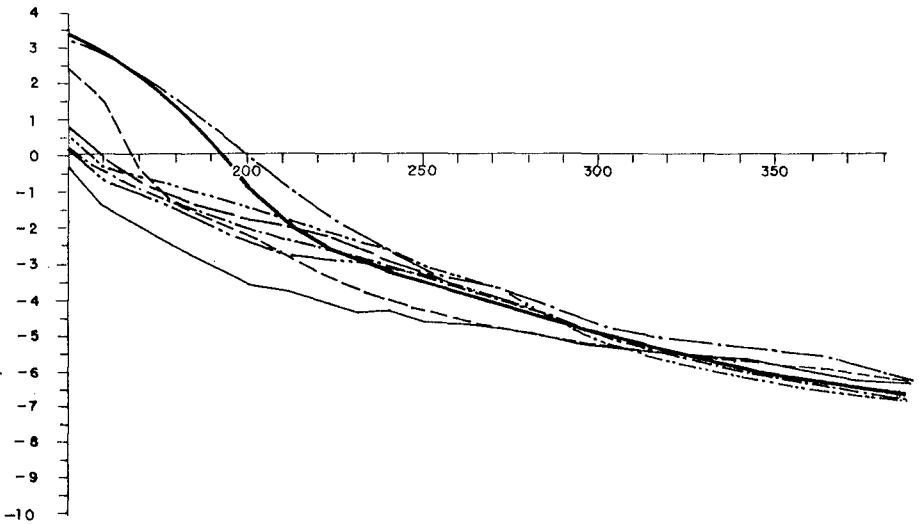


FIG. 12

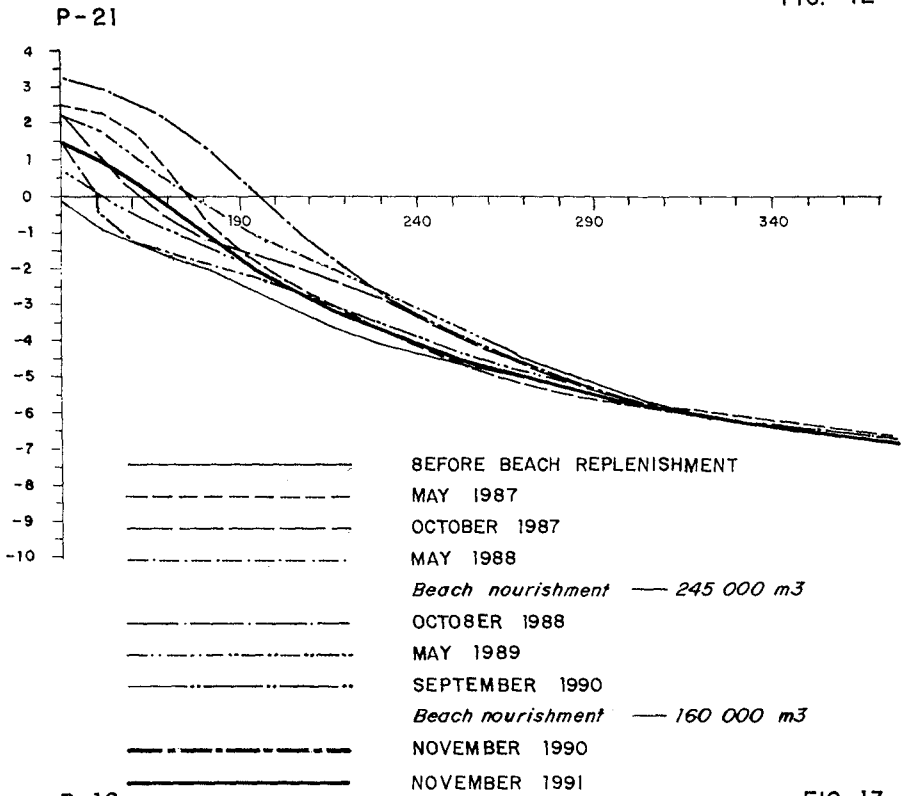


FIG. 13

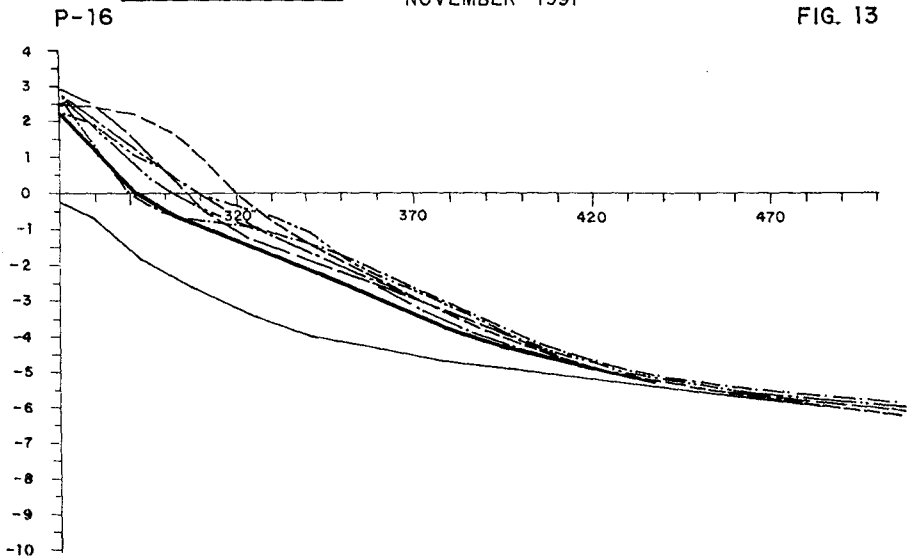




FIG. 14

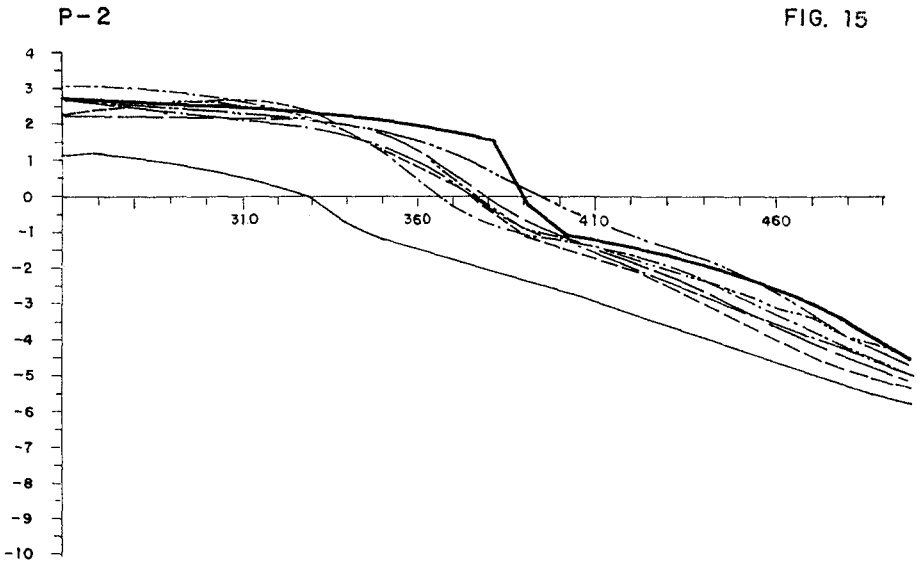
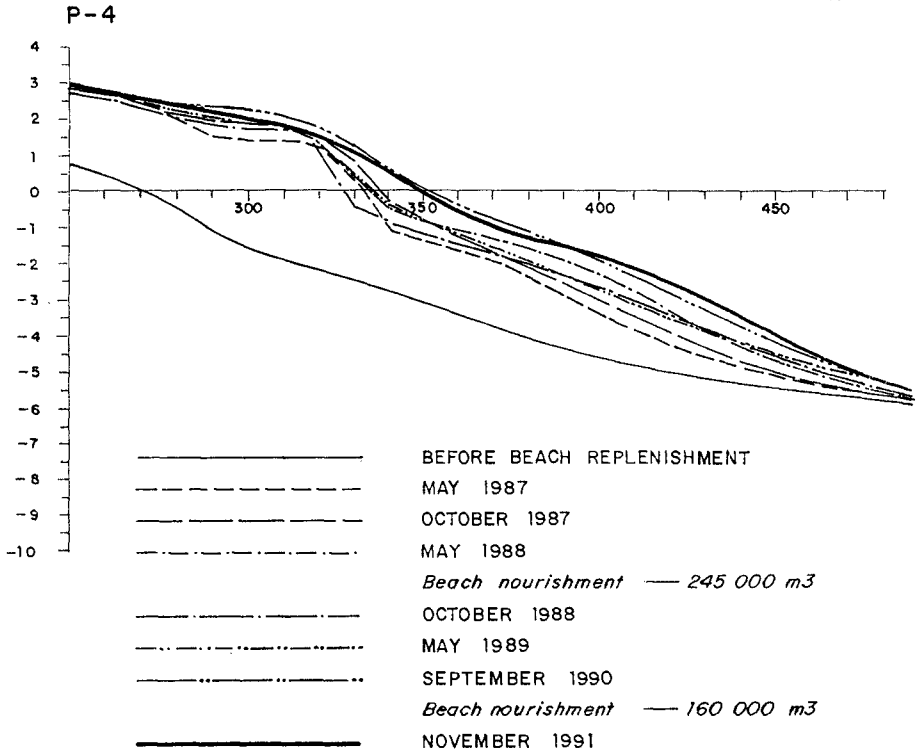


FIG. 15

Between October 87 and November 9..... 460.000 m<sup>3</sup> (4 years)

These results have not yet been checked and compared with the wave-height-visual-data of the same period, but as an average we can provisionally conclude that for this kind of coarse sand (0.5 mm.) CERC formula minimizes longshore transport capacity in about 20%. Differences would probably be greater with finer sand.

### **3. THIRD SEGMENT (Barcelona city sea front)**

This is the third of the three segments of the figure 3. It runs from the mouth of the Besos River up to the port of Barcelona. Works in this segment have been completed just before the Olympic Games, last summer (1992).

A few years ago it was the ugliest and most degraded part of Barcelona's coast. Everybody considered most of the sea-front side of Barcelona as the rubbish dump where everything could be thrown.

In addition to this, there was some groins constructed to assure the discharge of Barcelona sewage draining system (now there are only rain water discharges there).

The landscape has deeply changed; a marina has been constructed as part of the Olympic Games infrastructure, beaches can be found instead of previous rubbish tips, and the groins have been rebuilt in order to assure the stability of the beaches.

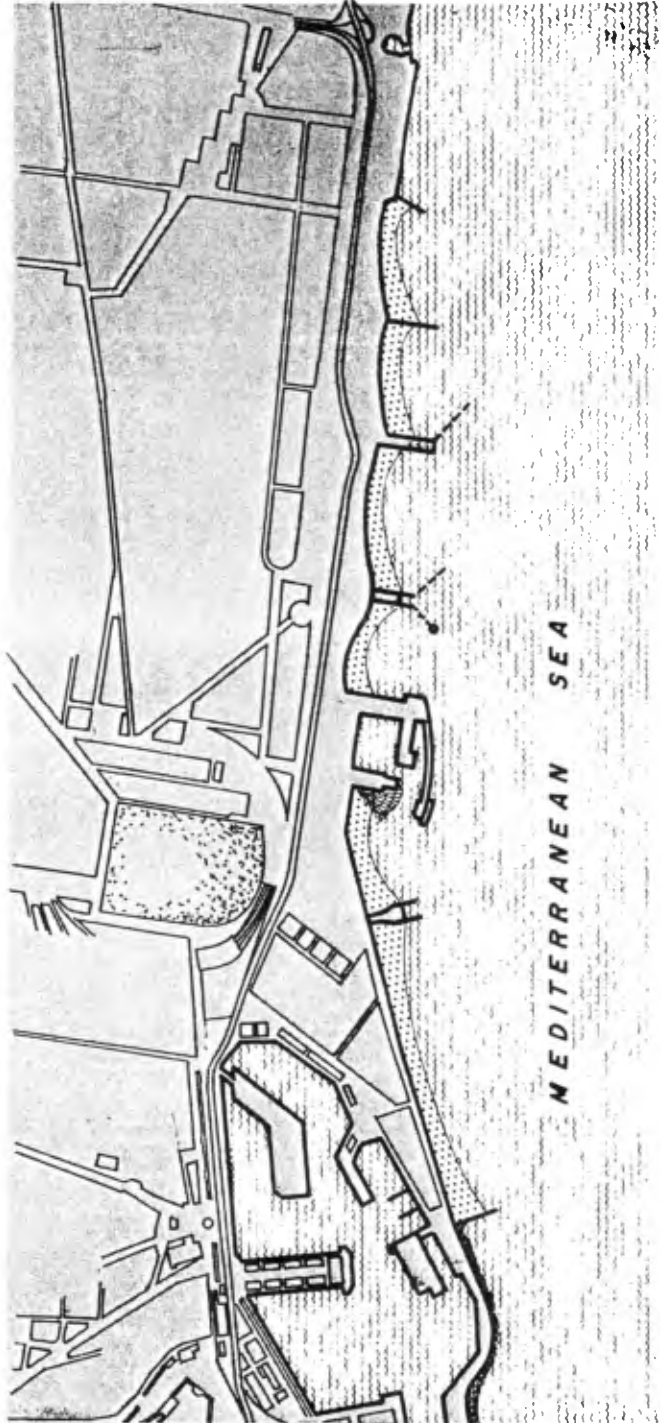
A schematic plan of the whole segment can be seen in fig. 16.

The whole segment is being monitored once or twice a year, but as the works have just been completed a few months ago, only the first bathymetry has been carried out and no conclusions are available.

We hope that in next Coastal Engineering Conference in Kobe more conclusions and results can be discussed.

FIG. 16

BARCELONA CITY SEA-SIDE WORKS



## CHAPTER 259

### STUDY OF 50 YEARS COASTAL CHANGES AT HADERA, ISRAEL

by Dov S. Rosen<sup>1</sup>, MASCE, MIAHR

#### Abstract

An investigation regarding the coastal changes over a period of about 50 years, as depicted from waterline and beach bluff fluctuations was conducted at Hadera-Sdot Yam beach, located at the central sector of the Southeastern Mediterranean coast of Israel. The study was conducted to assess the sedimentological impact of the breakwaters of a neighboring cooling basin, recently built. Processing and analysis methods used, as well as the main findings and conclusions are presented.

#### Introduction

A study of the coastal changes over a period of about 50 years (1937-1989), as depicted from waterline and beach bluff fluctuations measured from bathymetric charts and large scale air photographs was conducted by the author at Hadera-Sdot Yam beach, located at the central sector of the Southeastern Mediterranean coast of Israel (Fig.1). This coast represents a sedimentary unit within the Nile littoral cell extending from the Nile delta to the Haifa Bay. Hence it may serve as a long-term example of the morphodynamics of this littoral cell.

The purpose of the investigation was to assess the sedimentological impact of a cooling basin, built between

---

<sup>1</sup>National Institute of Oceanography, Israel Oceanographic & Limnological Research, POB 8030, Tel Shikmona, HAIFA 31080, ISRAEL, Fax: 972 4511911, Tel: 972 4515205

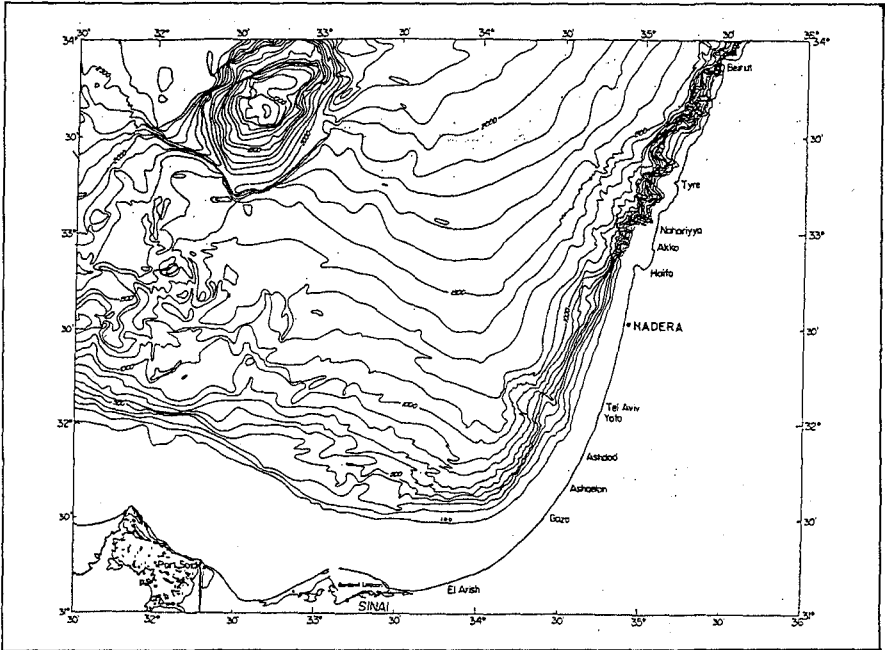


Figure 1. Location Map of Hadera - Sdot-Yam Beach

1977-1980 for a power plant located at Hadera shore, on its northward neighboring beach, downstream of the general net longshore transport .It was initiated due to claims of progressive erosion at the neighboring Sdot-Yam beach, made by local residents. The claims were supported by apparently significant erosion and beach bluff recession at several places along that beach. The erosion was attributed to be due to the recent construction of the cooling basin breakwaters, which were considered to have stopped the longshore sand transport, inducing progressive erosion to the supposedly "starved" neighboring beach some 1800 m to 2500 m away (Fig. 2). The breakwaters creating the cooling basin cover 700 m of coastline, protruding about 600 m into the sea (to -6 m).

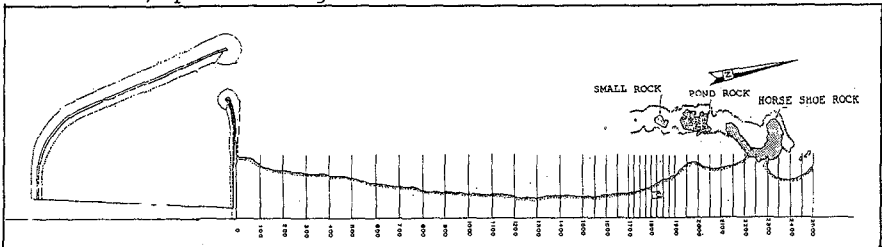


Figure 2. Hadera-Sdot-Yam Coast with Baseline & Sections

### Data Processing and Results

The study was based mainly on the analysis of some 90 aerial photographs of 45 flights and 24 maps and correlation with the wave climate history. The correct determination of the bluff and waterline positions in the various charts and aerial photographs, relative to a fix baseline, parallel to the coastline, represented an important item of the study. In view of the suggestions of other investigators (Lueder-1977, Striem-1965), the prevailing (mean) waterline in the air-photographs at the time they were taken, was marked in the middle of the wet area of beach (dark area - see Fig. 3) and bounded by the visible water line.

The methods employed for the determination of the corrected waterline position (+0.0 m relative to Mean Sea Level - MSL) and of the bluff line position (+2 m above MSL), included:

(a) Analysis of relatively large scale enlargements of the pictures and maps (all at a scale of 1:2500) and marking of the water and bluff lines,

(b) Preparation of a mylar (polyester, i.e. non-shrinking) transparent base map of the area at a scale of 1:2500, on which all present beach features (structures, rocks, etc.) and the baseline and control sections were included ( see Fig. 2)

(c) Measurement of the distances from the base line to the bluff and waterline at each section, by superposing the transparent map on the various maps and air-photographs, using the presence of land marks, or structures and beach rocks.

(d) Assessment of the tide and wave induced super-elevation from wave records and tide records or tide prediction and

(e) Correction of the waterline position line taken from the charts or aerial photograph, due to tide and waves' contributions. Wave set-up correction was based on the Shore Protection Manual (U.S. Army CERC-1984), while for tide correction use was made of the foreshore mean slope at each coastal sector.

The waterline distances measured on the base map were also corrected for varying camera angles and elevations in different air-photographs, by a relatively simple but efficient method. By this method, applicable elsewhere in similar cases, advantage was taken of the presence of beach rocks on the foreshore, near the waterline, with tops at about 0 m to 0.5 m elevation above MSL. By superposing the rocks on the base map with



Figure 3 Example of marking of waterline and bluffline on an aerial photograph (Sdot-Yam 31.07.1970)

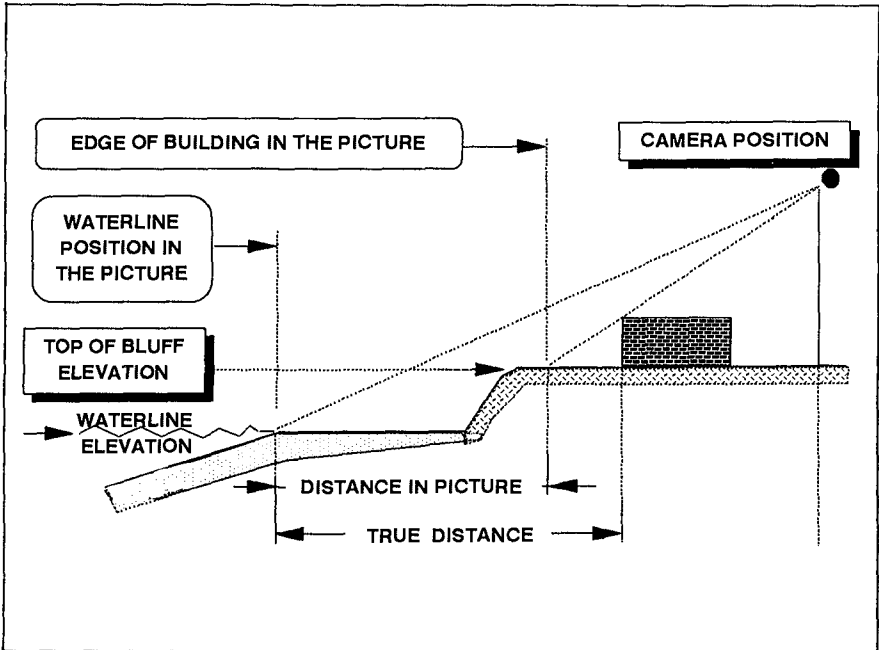


Figure 4 Schematic representation of error source in air photographs due to camera angle and elevation differences

those on the pictures, the distances between the base line and the waterline position at nearby sections could be accurately measured (with very little distortion), since the waterline and rock tops were at about the same elevation (Fig. 4). For correct interpretation of the fluctuating positions of the waterline and bluff with time and along the beach, an evaluation of the errors associated with the values computed for their positions due to various factors like paper shrinkage, drafting accuracy, scaling, positioning, etc., was also performed. The overall errors assessed were 5 m for the maps and 10 m for the air-photographs. Then, the waterline and beach bluff fluctuations prior, during and after the construction of the cooling basin breakwaters were analyzed at constant control sections along the base line (Fig. 2). The distance along the base line between control sections was 100 m, except at certain recently eroded sectors, where the distances were shortened to 25 m. Furthermore, the morphologic features of the coastal sector studied (bars, cusps, rip currents, spits, breakwaters, groins, sea walls and antique coastal structures) were also observed. Time histories of the corrected positions of the bluff and waterlines were



plotted for each control section. Results at representative control sections are presented in Figs. 5 through 16. They were compared to the time histories of the yearly maxima of deep water significant wave heights and of the yearly rain volume (Figs. 17 and 18). The whole waterline and bluffline fluctuations for the whole coastal sector are represented in Figs. 19 and 20 respectively. A isolines map of the waterline fluctuation in time and space was prepared from the data of the waterline position during 50 years along the whole sector of coast studied (Fig.21). This map facilitates to depict the location and duration of erosion or accretion in time along the whole coast. A tri-dimensional view of this fluctuations map in time and space is also presented in Fig. 22.

### Analysis of the Results and Conclusions

The results obtained show that this coastal sector was relatively stable until the beginning of the sixties, when a coastal erosion pattern was observed. The observed erosion seems to have occurred due to extensive quarrying of beach sand for construction purposes, forbidden by law since 1966. By the end of the sixties that erosion ceased, but reappeared for a short period at the beginning of the seventies, after an extreme storm in January 1968 and heavy rain 1969 year, which removed the beach sand, probably to the offshore bar. It disappeared from the mid-seventies, but reappeared in limited locations since 1982 due to local reasons. Beach bluff erosion, which encountered at a location remote 1800 m from the cooling basin was assessed to be due to local land reclamation from the sea without adequate scouring protection. At another sector (2100 m to 2300 m remote from the cooling basin ), a 3 m recesses in bluff position was measured in 1988. The erosion occurred after the cooling basin construction, but was induced by the construction of two groins that stopped longshore sand transport within a local pocket beach. A rather surprising result was that although the ending (northern) sector of that coast suffered from a recent small bluff erosion, it accreted some 15 m within the 1956-1964 period. The outcome indicated that the longshore influence of the cooling basin (accretion) extends for about 1500 m of the neighboring beach and nulls at about 1600 m from the lee breakwater (2.5 times its protrusion into the sea) and that a dynamic sedimentologic equilibrium state was reached after about 8 years from the cooling basin construction. Though some recent

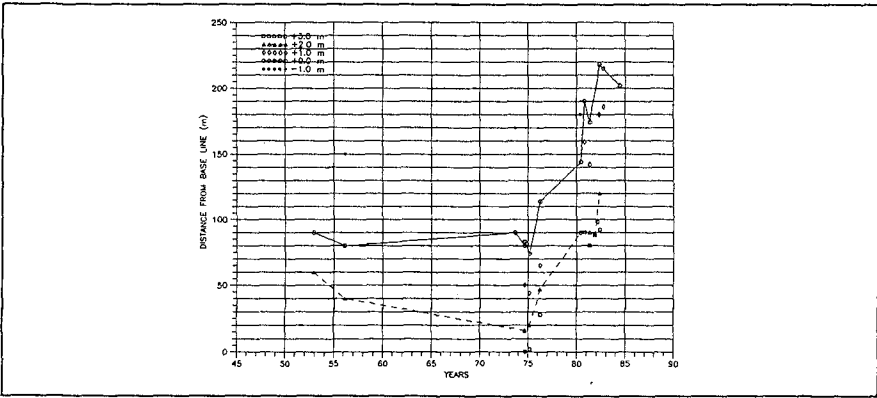


Figure 5. Waterline and Beach Bluff Fluctuations Hadera - Sdot Yam Shore 1945-1990 - Control Section 0m

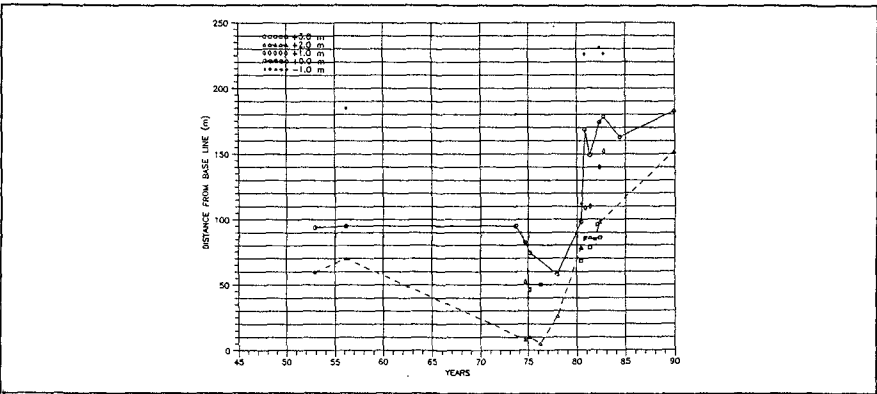


Figure 6. Waterline and Beach Bluff Fluctuations Hadera - Sdot Yam Shore 1945-1990 - Control Section 100m

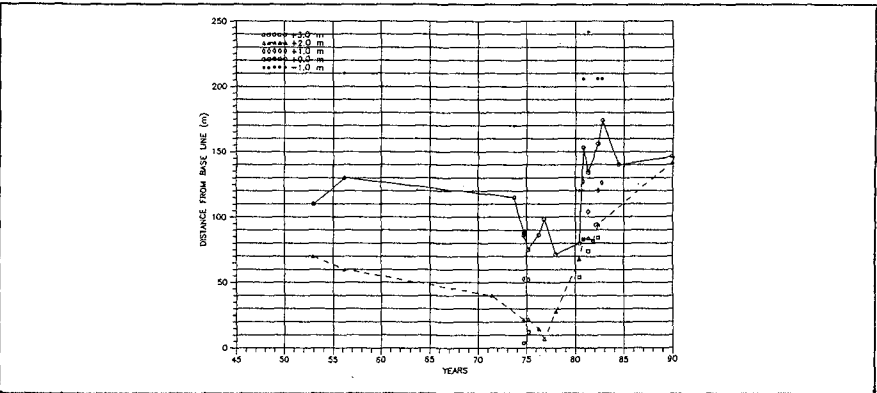


Figure 7. Waterline and Beach Bluff Fluctuations Hadera - Sdot Yam Shore 1945-1990 - Control Section 200m

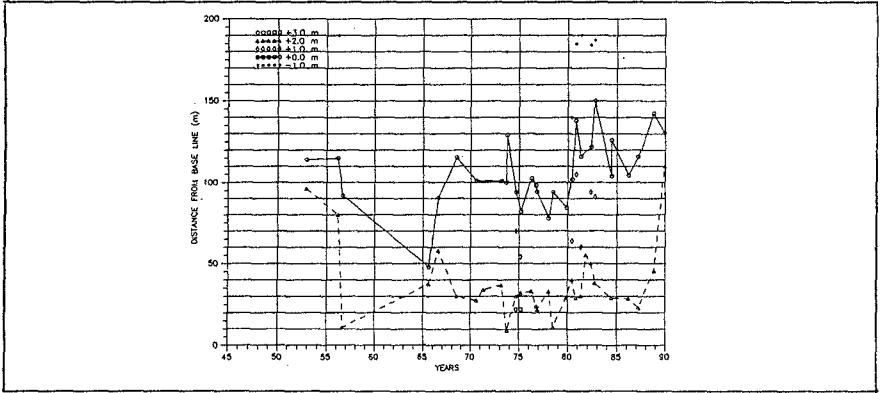


Figure 8. Waterline and Beach Bluff Fluctuations Hadera - Sdot Yam Shore 1945-1990 - Control Section 500m

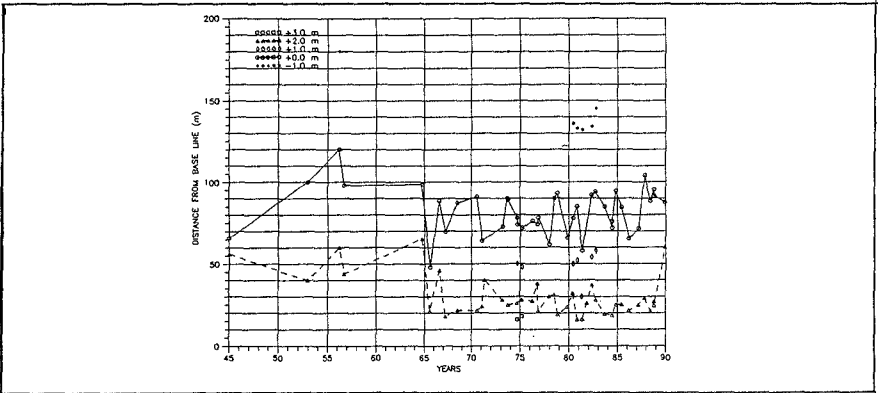


Figure 9. Waterline and Beach Bluff Fluctuations Hadera - Sdot Yam Shore 1945-1990 - Control Section 1000m

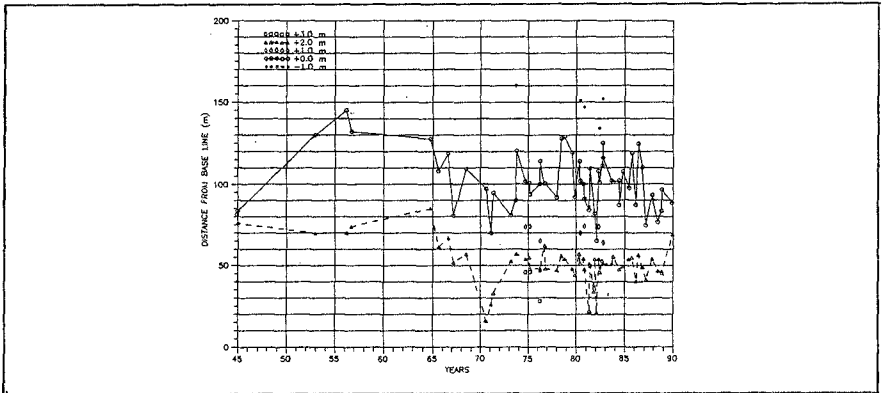


Figure 10. Waterline and Beach Bluff Fluctuations Hadera - Sdot Yam Shore 1945-1990 - Control Section 1500m

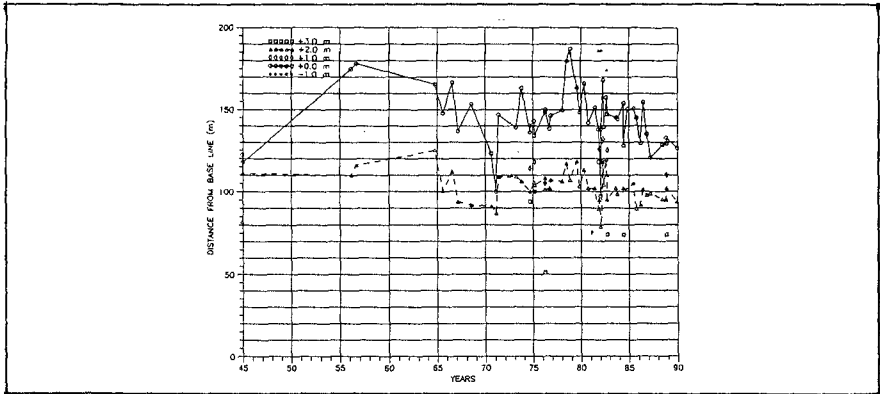


Figure 11. Waterline and Beach Bluff Fluctuations Hadera - Sdot Yam Shore 1945-1990 - Control Section 1750m

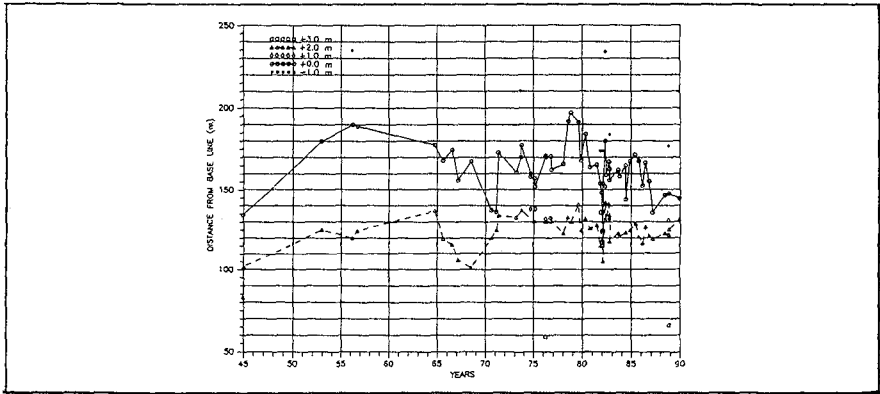


Figure 12. Waterline and Beach Bluff Fluctuations Hadera - Sdot Yam Shore 1945-1990 - Control Section 1800m

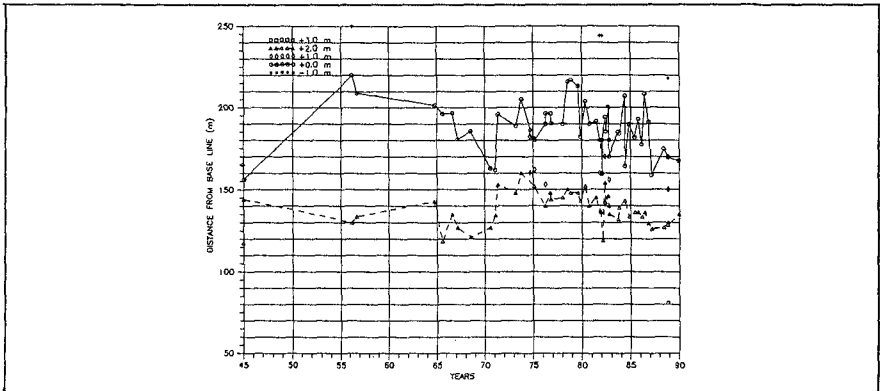


Figure 13. Waterline and Beach Bluff Fluctuations Hadera - Sdot Yam Shore 1945-1990 - Control Section 1850m

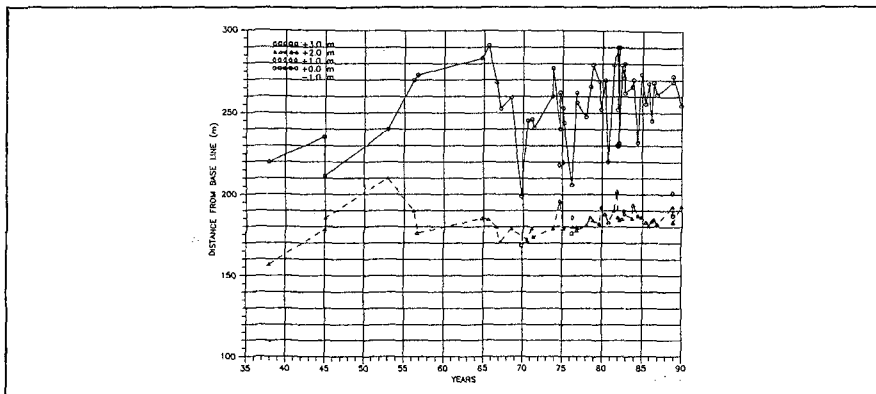


Figure 14. Waterline and Beach Bluff Fluctuations Hadera - Sdot Yam Shore 1937-1990 - Control Section 2200m

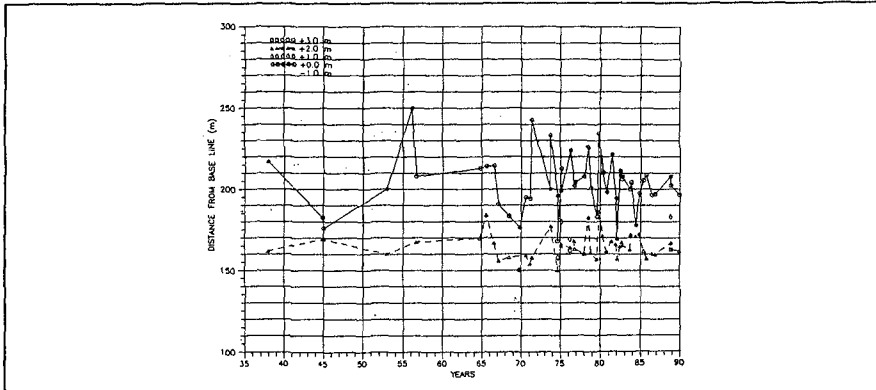


Figure 15. Waterline and Beach Bluff Fluctuations Hadera - Sdot Yam Shore 1937-1990 - Control Section 2300m

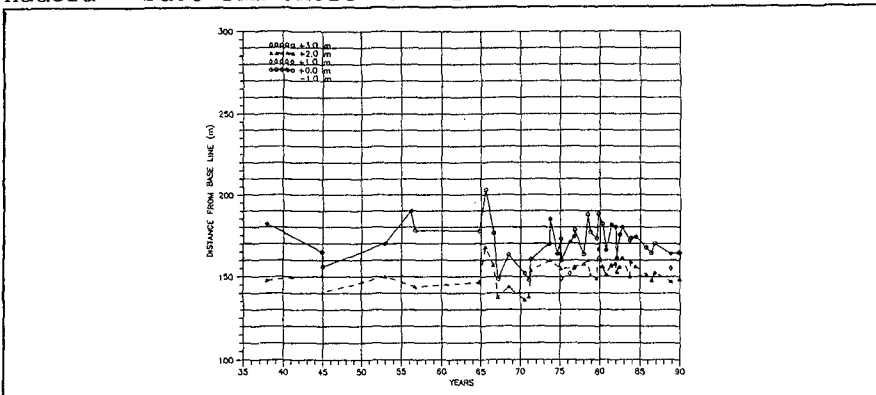


Figure 16. Waterline and Beach Bluff Fluctuations Hadera - Sdot Yam Shore 1937-1990 - Control Section 2400m

erosion was found at a few points as mentioned above, the general waterline and bluff fluctuations remained all within the natural long-term range of fluctuation. No sedimentological impacts were found for the rest of the beach.

### Acknowledgments

This study was financed by the Israel Electric Corporation Ltd., being conducted at the request of the management of Kibbutz Sdot-Yam. The author wishes to express his gratitude to Engrs. E. Berent and P. Porat, of the Israel Electric Co. for their valuable cooperation and assistance and for permission to publish this study. He would also like to thank the Survey of Israel for providing the enlargements of the aerial photographs.

### References

Lueder D. R., (1977), A method for estimating beach trafficability from aerial photographs, in Air Photography & Coastal Problems, Ed. Dowden, Hutchinson and Ross, Inc., USA.

Rosen D. S. and Kit E., (1981), Evaluation of the wave characteristics at the Mediterranean coast of Israel, Israel Journal of Earth Sciences, Vol. 30, 1981, pp. 120-134.

Rosen D. S., Vajda M., (1982), Sedimentological influences of detached breakwaters, Proc. 18th ICCE, Capetown, ASCE Publ., Vol. 2, Ch. 116, November 1982, pp. 1930-1949.

Rosen D. S., (1990), "Engineering consultation regarding long-term sedimentological processes in the Hadera - Sdot-Yam coastal area", P.N. 242/90, Technion, Haifa, March 1990 (in Hebrew).

U.S. Army Corps of Engineers, Coastal Engineering Research Center, (1984), Shore Protection Manual, 2nd ed. Vol.1.

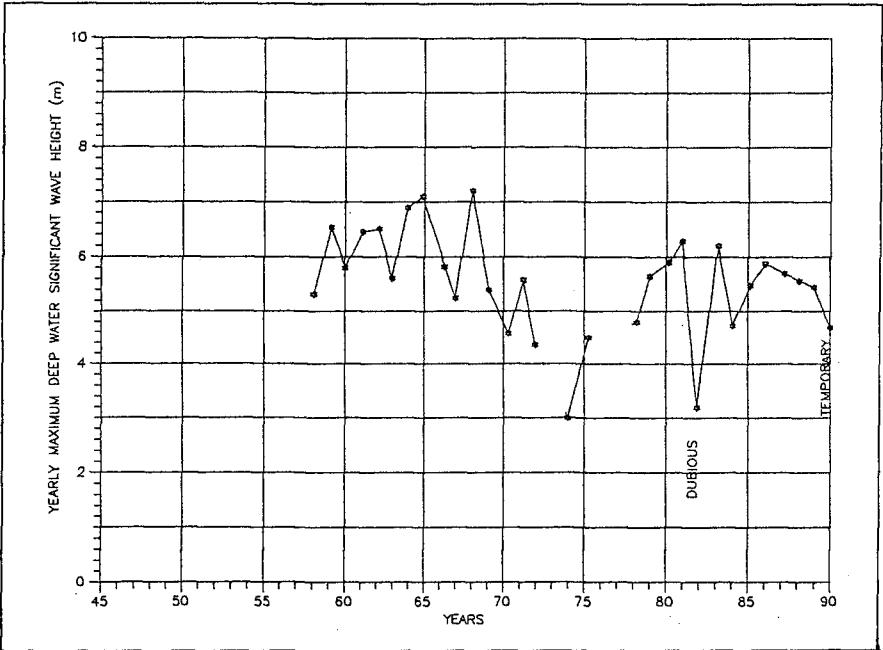


Figure 17 Time History of Yearly Deep Water Hs Maxima

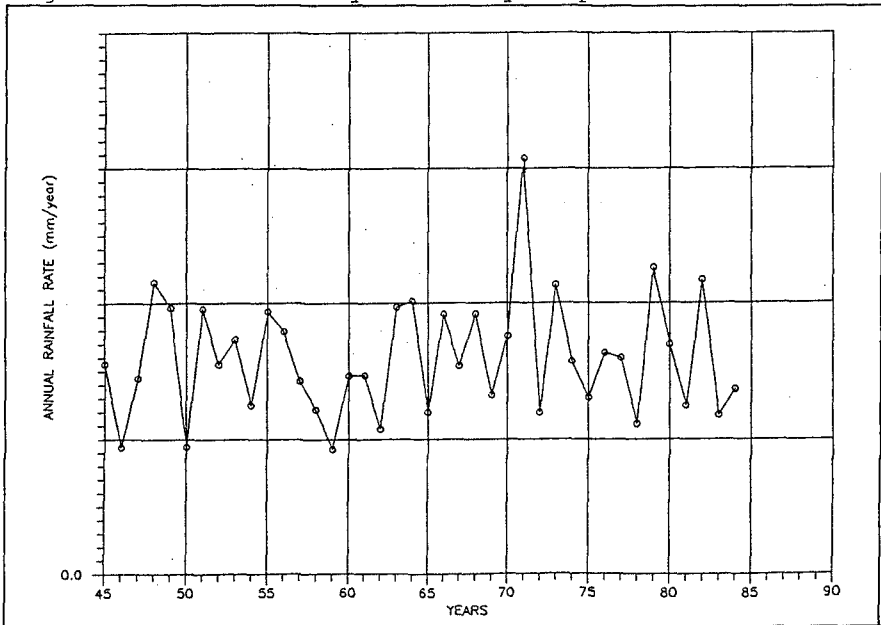


Figure 18 Time History of Yearly Rainfall Volume

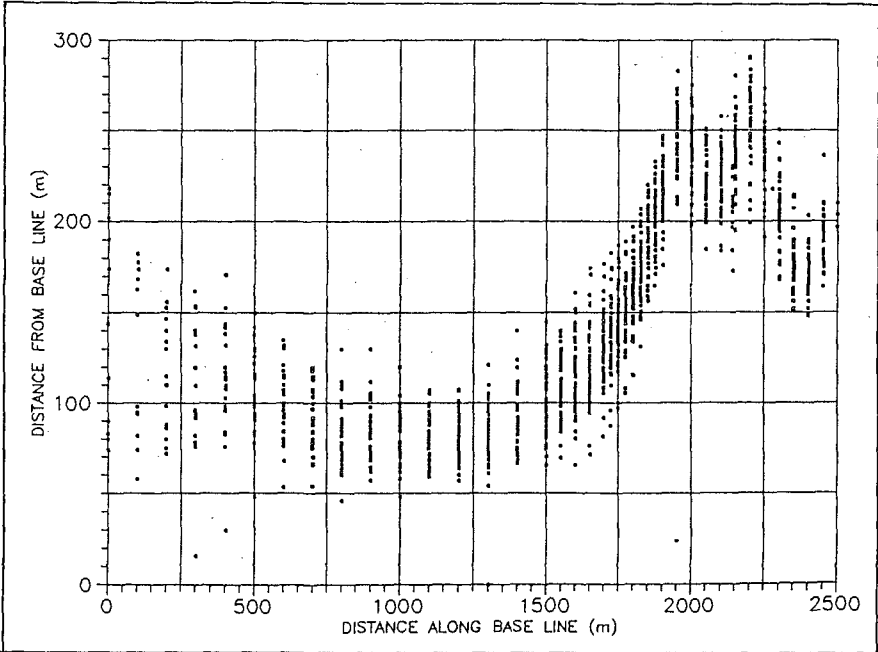


Figure 19 Waterline Fluctuations in the Study Sector

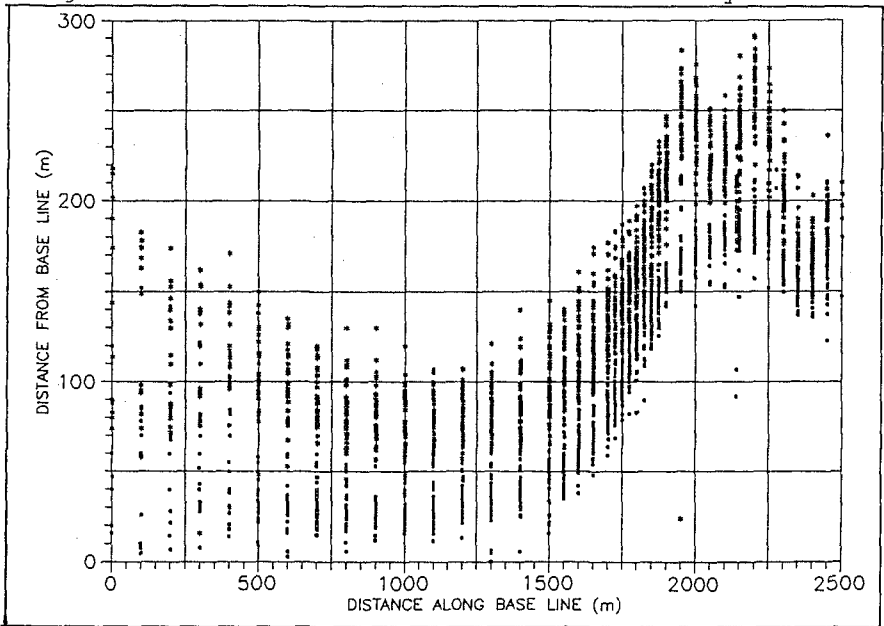


Figure 20 Waterline and Bluffline Fluctuations in the Study Sector (\* -waterline ; O - bluffline)



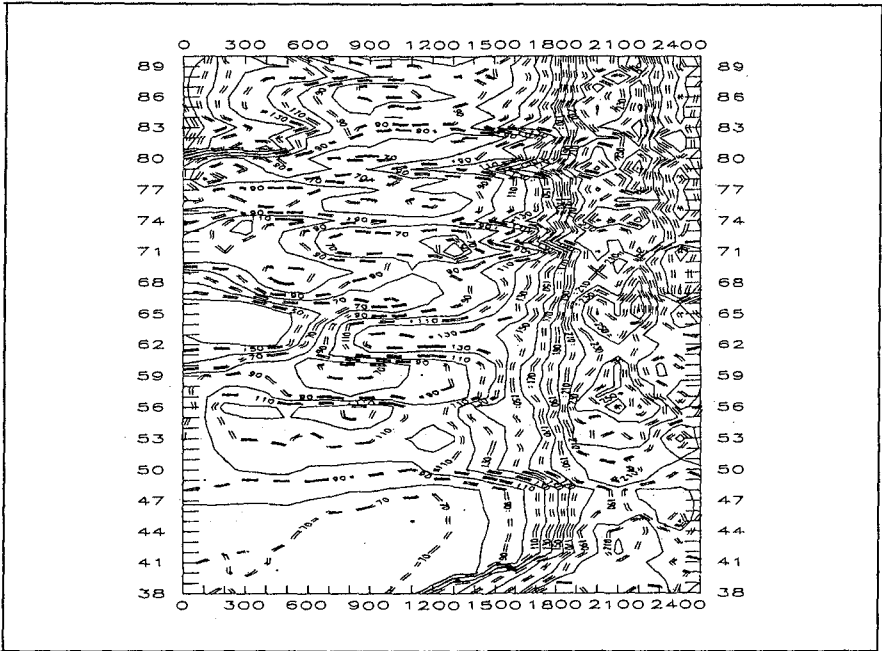


Figure 21. Map of Equidistant Contours from Baseline Hadera Sdot-Yam Coast Waterline (1937-1989)

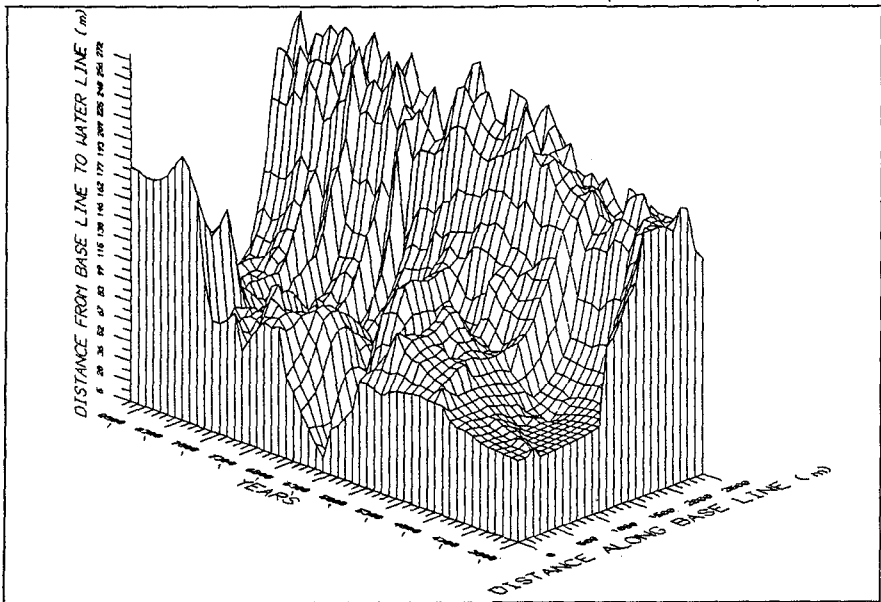


Figure 22 Tri-dimensional View of Hadera Sdot-Yam Coast Waterline Fluctuation in the period 1937-1989

## CHAPTER 260

### INTERVENTIONS ON THE COAST SOUTH OF BRINDISI

Giuseppe R. Tomasicchio<sup>1</sup> & Fiore Uliana<sup>2</sup>

#### Abstract

The coast between Torre Mattarelle and Torre San Gennaro (Italy) is deeply eroded. The recent construction of a thermal-electric power plant changed the natural morphodynamic characteristics and the erosion rate. Interventions on the coast were needed. This paper refers about the phases of design and construction of the maritime defence works and tries to call attention about the need of an extensive study before the construction of a power station along the coast.

#### Introduction

The coast between Torre Mattarelle and Torre San Gennaro, a few kilometers South of Brindisi (Puglia-Italy), consists of a cliff with an overhanging slope subjected to continuous erosion due to the combination of geotechnical instability phenomena, run-off from rain water and the action of the sea waves. ENEL (the Italian national board for electricity) in 1982 started the construction of a thermal power plant (4 units, 440 MW each) in this area. The plant required a system to discharge the cooling water formed by two groynes extending to -7.0 m water depth. The part of coast in front and north of the power plant was protected by a 1.8 Km long seawall system. The maritime works started in 1985.

These interventions effected the natural morphodynamic evolution of the coast; the area to the south no longer received material from the north, therefore, retreat of the coastline and cliff instability increased. A visible effect was the relatively fast disappearance of the swimming beach south of the power plant.

ENEL is involved in the protection works for the portion of coast to the south of the power plant.

---

1 - University of Perugia, Istituto di Idraulica, Perugia - Italy.

2 - ENEL DCO, Via Cardano 10, Milano - Italy.

### The coastline

The planform configuration of the coast represents an independent physiographical unit extending from the prominence at Torre Mattarelle to the headland at Torre San Gennaro, a distance of 6.5 Km. The shoreline develops as a spiral arc from Torre Mattarelle to the swimming beach south of the power plant (fig.1 & 2). After this part an almost straight beach is observed. Afterwards, the coast has a curvilinear trend till Torre San Gennaro (with an orientation from  $40^0$  to  $30^0$  North).

Before any maritime work was started, the sandy emerged beach had an average width of about 5 m for all the coast north and for 1 Km south of the system to discharge the cooling water. Further south, the beach width increased to approximately 15 m.

The cliff has an average height of 13 m above the still water level; next to Torre San Gennaro, the cliff height decreases to about 4 m and then disappears. Only 25 % of the cliff material is sand ( $D_{50}=0.3$  mm), the rest is clay and silt.

Analysis of several samples shown that the submerged beach is composed of material with  $D_{50}=0.3$  mm till water depth -1 m and  $D_{50}=0.075$  mm beyond this limit. The material from the cliff erosion, due to the absence of river estuaries along the coastline, is the only supply for sediment.

To avoid the retreat of the coastline in front of the power plant, a seawall system was built during 1989; the work phases were:

- 1) cliff face adjustment with a slope of 2/3;
- 2) driving of sheet piles in sea bottom along the line representing the external structure of the reef base;
- 3) excavation close to the sheet piles;
- 4) laying on the shore and on the sea bottom of a geotextile cover weighing 300 g/m<sup>2</sup>;
- 5) laying of a "tout venant" bed;
- 6) armour construction consisting of natural rock weighing 500 ÷ 2000 Kg;
- 7) extraction of the sheet piles.

After the construction of the two big groynes to discharge the cooling water and the seawall protecting the coast in front of the power plant, the width of the beach to the south reduced to 1 ÷ 2 m.

### Wave climate and currents

The area is exposed to waves from directions ranging between  $330^0$  and  $120^0$  N. To estimate the offshore wave climate the following informations were used:

- data from KNMI (Royal Dutch Meteorological Institute) for the period 1961-1987 (more than 30000 visual observations of the sea state);
- data for 1983 from the ENEL wave recording system placed out of Brindisi harbour.

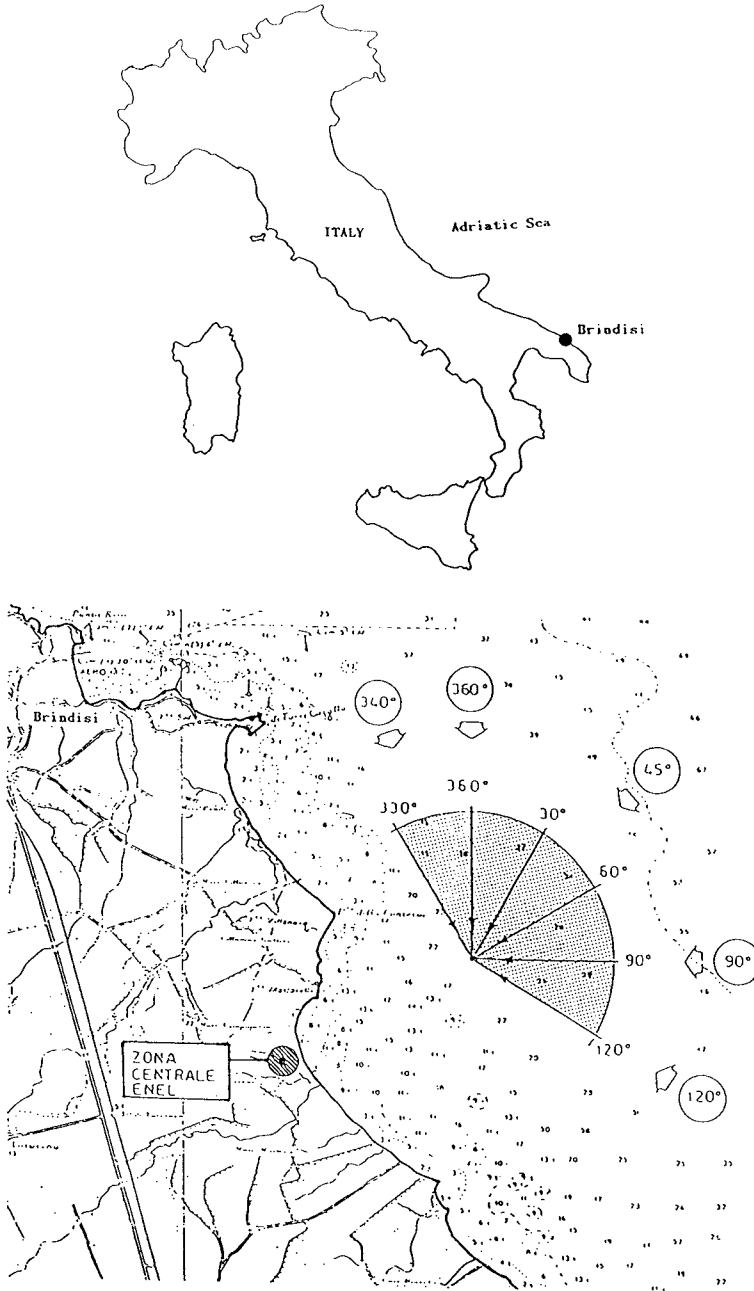


Fig. 1. Location of the power station

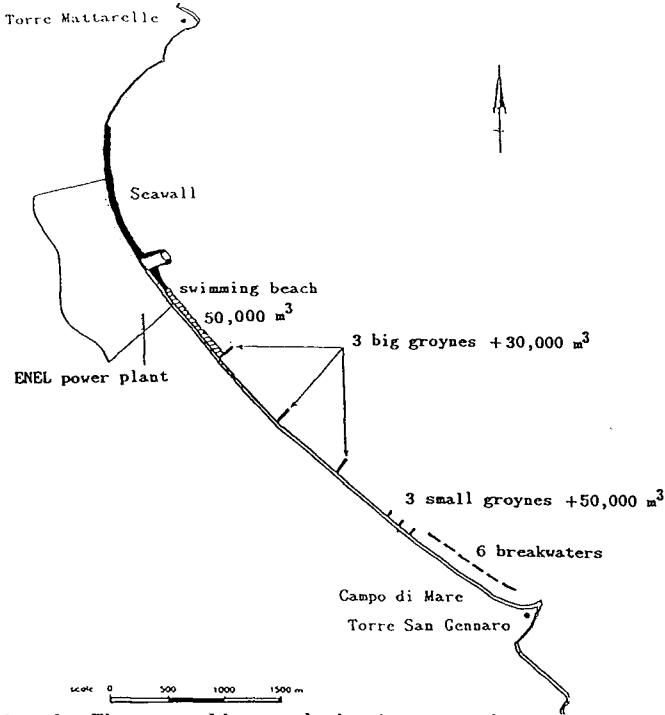


Fig. 2. The coastline and the interventions

years 1961-1980
All directions (330°-120° N)
T = 1 year $H_s = 4.5$ m
T = 10 years $H_s = 6.2$ m
T = 50 years $H_s = 7.5$ m

Direction (°)	$H_s$ for T=1 year	$H_s$ for T=10years
330	3.50 m	5.30 m
0	3.75 m	5.75 m
30	3.50 m	5.30 m
60	3.50 m	5.75 m
90	2.50 m	3.60 m
120	3.00 m	4.30 m

Table 1. Wave climate based on visual observations for different return period T

It was observed (table 1) that the most frequent wave conditions are from the directions  $30^0$  and  $150^0$  N; the last direction is practically out of the sector of exposure of the coast. These characteristics of the wave climate are typical for all the seasons; only during autumn and winter the frequency of waves coming from  $30^0$  and  $60^0$  N is increased.

Five fixed current meters, installed in water  $10 \div 30$  m deep (fig.3), were used to measure currents. The charts from current meter data that ENEL prepared show a large frequency of the currents to S-SE; the currents distribution indicates a net littoral transport to the south. The velocity of the longshore current is rather high (more than 30 cm/s). The observed astronomical tide is small (about 30 cm), consequently the tidal currents are weak.

### Erosion rates and sediment transport calculation

The recent evolution of the shoreline has been assessed using:

- topographical charts by ENEL from years 1982  $\div$  1985;
- aerial photographs series from years 1974, 1981 and 1987.

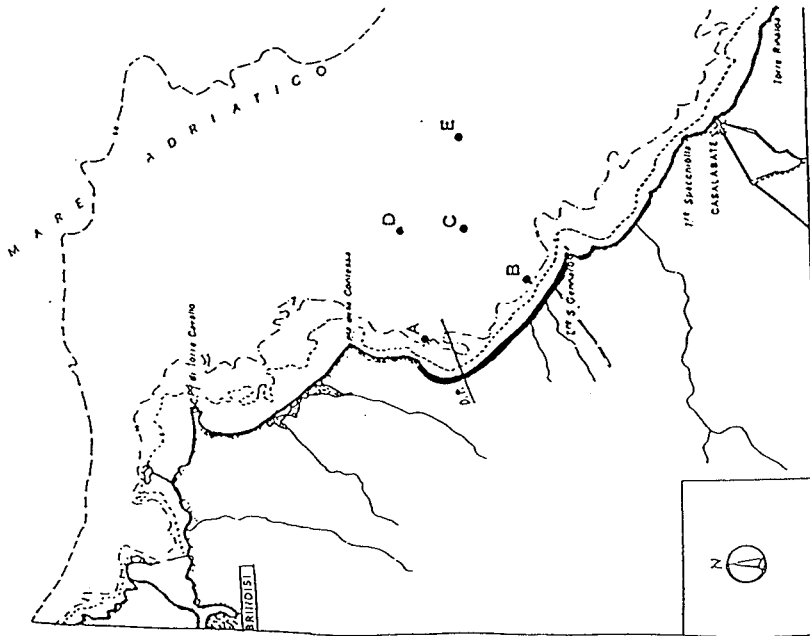
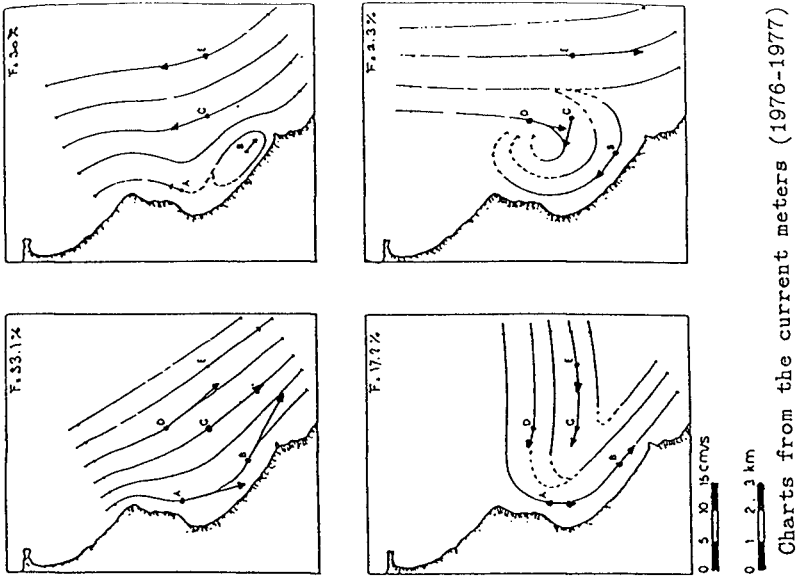
The approximate scale of the photographs was known. The surveys were not perfectly comparable. In the ENEL area the 1987 series were already disturbed because of the works for the sea-water adduction consisting of under water concrete pipe-lines having intake structure about 400 m from the shoreline.

The mean slope of the foreshore along the coast is approximately 1:45.

The observed retreat rate of the cliff (fig.4) before any ENEL intervention was  $1 \div 2$  m/yr for the mid section of the coast and  $0.2 \div 0.5$  m/yr for the remaining part.

The effect of the two groynes forming the system to discharge the cooling water was to subtract for the entire coastline to the south a natural supply of about 20,000 m<sup>3</sup>/yr (assuming that with 1 m coastline retreat a sand volume of 10 m<sup>3</sup>/m is required). This influenced the sediment transport Q distribution, giving an increase in the retreat of the swimming beach coastline from about 1 m/yr of the natural condition to  $4 \div 5$  m/yr (fig. 5).

For the part of coast to the south of the swimming beach, as an average yearly retreat of the coastline, a value of 0.5 m/yr was calculated. The observed yearly erosion of 0.5 m gives consequently a gradient in the longshore transport rate of 5 m<sup>3</sup>/m per year. Basing on almost 4,000 m coastline (south of the power plant), a 20,000 m<sup>3</sup> yearly loss of sand was estimated. An estimated value of the eroded material of the cliff is 50,000 m<sup>3</sup>/yr. Only 25 % of this material (about 13,000 m<sup>3</sup>/yr) consists of sand with a size sufficient to remain stable under the action of the longshore current. Therefore, the erosion of the cliff is not sufficient to increase the dimension of the beach.



Coastal area and position of the current meters  
Fig. 3

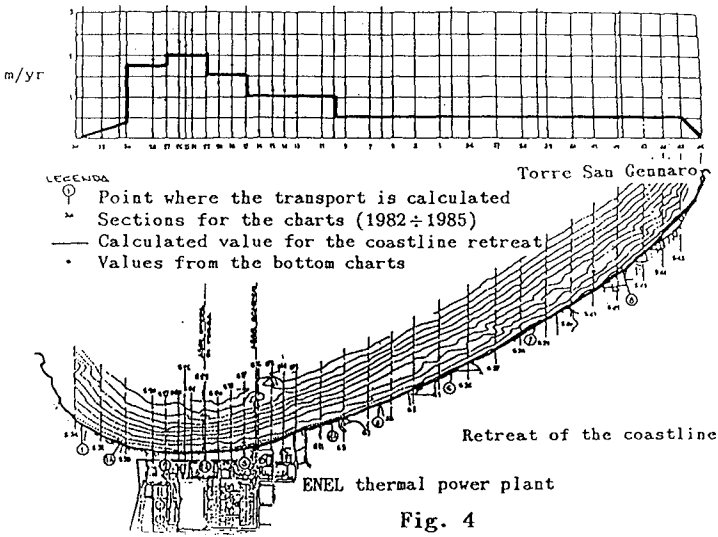
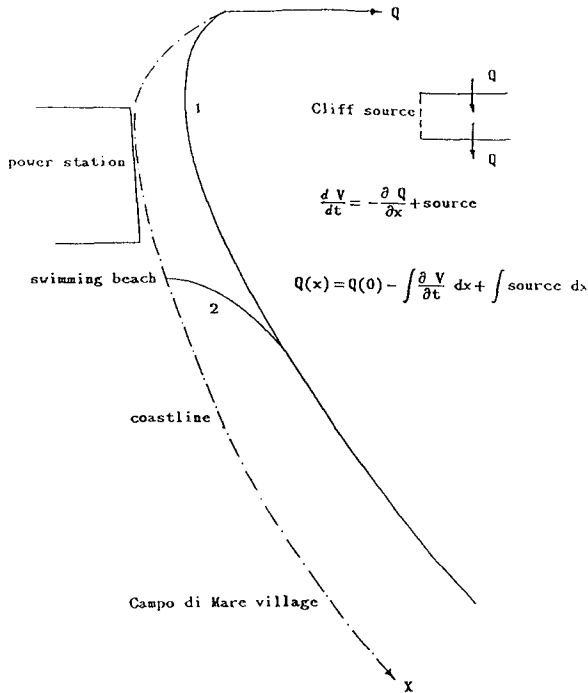


Fig. 4



1-before discharge system and seawall construction  
 2-after discharge system and seawall construction

Fig. 5. Q distribution along the coast



In order to evaluate the direction and the entity of the longshore sediment transport, a study concerning the transformation of the waves from offshore to the limit of the surf zone was carried out. Three refraction models were used for the entire coast taking into account five directions for wave incidence. The longshore transport was evaluated in some positions along the coast.

Calculations were performed using the CERC formula, the Bijker formula and the Engelund-Hansen formula. The results have a range of approximately 3 times the smaller value. The results of the computations (Delft Hydraulics, 1990) with the CERC formula are between the results of the Engelund and the Bijker formulae (giving the smallest value).

Run	Conditions			Total Transport in m <sup>3</sup> /day		
	H <sub>0sig</sub> (m)	T (s)	θ <sub>0</sub> (°)	Engelund	CERC	Bijker
1	1.0	4.5	10	1350	1000	450
2	2.0	6.0	10	11400	5650	3500
3	1.0	4.5	20	2500	1950	800

Conditions: - beach profile slope  $m = 1:45$   
 - particle size  $D_{50} = 200\mu\text{m}$   
 - fall velocity  $w = 0.025 \text{ m/s}$   
 - bottom roughness  $r = 0.05 \text{ m}$

H<sub>0sig</sub> : significant wave height (deep water)

T : wave period

θ<sub>0</sub> : angle of approach (deep water)

Table 2. Comparison sediment transports various formulae

The CERC formula is:

$$S = 0.040 \cdot H_b^2 \cdot n_b \cdot c_b \cdot \sin(\beta_b) \cdot \cos(\beta_b) \quad [\text{m}^3/\text{s}]$$

where:

H<sub>b</sub> = significant wave height;

n<sub>b</sub> = ratio group velocity to wave propagation speed;

c<sub>b</sub> = wave propagation speed;

β<sub>b</sub> = angle of approach of waves with respect to the coastline orientation;

b = index indicating the waves at breaking point.

For some of the selected positions along the coast and for some directions of wave approach the calculation was in good agreement with the field observations. The shadow effect of the headland where the town of Brindisi is located and of Torre Mattarelle gives a large effect that was considered using the transport formulae with weighed coefficients.

### Design and its adjustments

The main purpose of the design was to stop the retreat of the coastline to the south of the power plant. This result had to be reached with a multipurpose series of works: in fact the swimming beach just south of the power plant had to assume again the bathing properties, further south the village Campo di Mare (which promenade was already interrupted) had to be protected from the sea action.

The local Authority, in order to protect effectively the coast, approved the design of six detached breakwaters which were constructed during 1991 in front of Campo di Mare village. They are situated in rather shallow water (about 3 m) and present a crest at + 2.5 m above s.w.l.. The six detached breakwaters were designed to take overtopping only during severe wave conditions. These protection works were chosen to give to inhabitants an impressive idea of safety. Moreover, the local Authority approved the design of three big groynes (which length is about 85 m) that were constructed just south of the swimming beach with an inter-distance between two groynes of about 700 m. The groynes reach -2.0 m water depth and present a crest at +2.5 m above s.w.l..

The design considers a nourishing initial material supply:

- 50,000 m<sup>3</sup> just SE of the ENEL power plant (swimming beach);
- 30,000 m<sup>3</sup> together with the three big groynes south of the swimming beach;
- 50,000 m<sup>3</sup> together with the construction of three small groynes (reaching -1.0 m water depth) just N of Campo di Mare. The three small groynes should have the effect of a hinge between the six detached breakwaters and the big groynes.
- a maintenance sand supply of 20,000 m<sup>3</sup> as an average yearly volume.

Together with the construction of the two last detached breakwaters the nourishment of the swimming beach and the construction of the first one of the three big groynes were started. As nourishing material a mixture has been adopted:

- 40 % material with  $D_{50} = 0.26$  mm;
- 60 % material with  $D_{50} = 5.00$  mm.

The nourishing material is composed of 40 % material having a characteristic diameter even smaller than the natural one ( $D_{50} = 0.3$  mm) from the cliff erosion. The net longshore transport brings a large part of the smaller part of the supplied material to the south together with the natural one.

Nowaday a total of 24,000 m<sup>3</sup> material has been placed to re-create the swimming beach; 6,000 m<sup>3</sup> material has been placed south of each of the 3 big groynes.

### Monitoring programme

To assess how well the project performed the desired function and to optimize the nourishment time schedule, an extensive monitoring programme consisting of bathymetric records normal to the coast and tide level measurements has been initiated. The monitoring consists of 26 bathymetric sections extending to a water depth of 10 m, photographs taken from the sea towards the coast at certain months throughout every year. Informations from the monitoring suggested that a slow supply of sand should be arranged.

The three big groynes do not give a satisfactory defence; in fact, some parts of the coastline are still subjected to retreat. This, probably, is due to the too large interdistance between two groynes. Therefore, the construction of some smaller extra groynes is not excluded; the material for their construction could be get removing stones from the too high crest of the existing groynes.

A massive accumulation of sand behind the six detached breakwaters and an evident tendency toward a tombolo are observed (fig.6 & 7); as expected, the last offshore breakwater (measured from Torre San Gennaro) catches most of the longshore sediment transport. During last winter 6,000 m<sup>3</sup> of naturally stored sand were removed and placed close to the headland Torre San Gennaro. After a few weeks that large amount of sand was lost.

An extra intervention for Torre S. Gennaro headland was necessary in order to protect some private houses; the protection works consisted of a seawall with 1÷2 t rock stones and were carried out during autumn 1992.

The first from the North of the three small groynes was built (completed in November 1992, 56 m long, fig. 8). The proposed construction of the two remaining small groynes (together with 50,000 m<sup>3</sup> material supply) is under discussion: these works will be probably omitted. The common idea is to spend some more time observing the behaviour of the coastline.

### Conclusions

This paper tries to emphasize that the design of a large plant along a sandy coastline requires a very attentive design phase for the maritime works. The design should be verified basing also on physical model tests. Sometime, attention during the design phase helps to save future efforts, which are needed to avoid not expected effects. Even if with large tolerance, nowadays, specialized coastal engineers can successfully foresee the coastline development with or without any human intervention. A monitoring programme assists the designer in defining a nourishing time schedule and in a better understanding of the error for the rates of erosion from the not perfect comparability of the surveys.

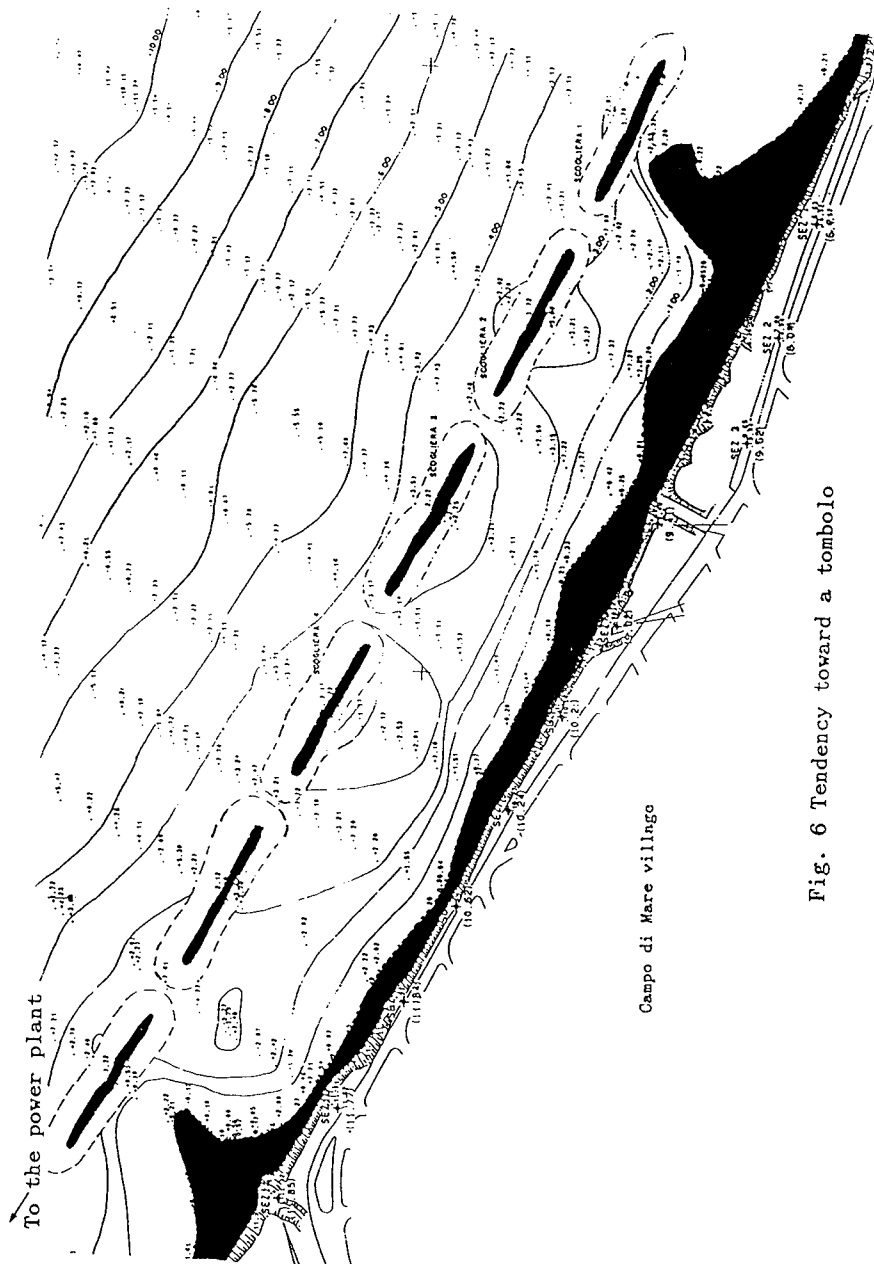


Fig. 6 Tendency toward a tombolo



Fig.7. The first from the south of detached breakwaters and the tombolo



Fig.8. The just built small groyne and the cliff from Campo di Mare village

**Acknowledgements**

We thank very much Prof. Robert G. Dean for the fruitful comments and Mr. Van de Graaf for the useful discussion.

**References**

- CERC, (1984). Shore protection manual.
- Delft Hydraulics, (1990). Some morphodynamic considerations of the Brindisi Sud project. February 1990.
- Polytecna-Harris S.p.A., (1986). Impianto termoelettrico di Brindisi sud, Opere di difesa della centrale ed interventi sul litorale, Progetto esecutivo. Marzo 1986.

## CHAPTER 261

### Sandy Beach Stabilization: Preservation of Shirarahama Beach, Wakayama

Yoshito Tsuchiya, M. ASCE<sup>1</sup>, Yoshiaki Kawata, M. ASCE<sup>2</sup>, Takao Yamashita<sup>3</sup>,  
Teruo Shibano<sup>4</sup>, Masahiko Kawasaki<sup>5</sup>, and Shin Habara<sup>6</sup>

#### Abstract

It is recognized that beach erosion has become a major problem in many countries of the world, but especially in Japan in relation to human activities such as development of coastal areas and river basins. Shirarahama beach in Wakayama facing the Pacific Ocean is a typical pocket beach, but due to preservation of the beach by headlands was proposed. The methodology has shown a very good result in making the beach recovered as preservation of the beach by headlands was proposed. The methodology has shown a very good result in making the beach recovered as a stable sandy beach.

#### Introduction

Recently, beach erosion problems have been remarkable in many countries of the world, but especially in Japan due to development of river basins and coastal areas. Many countermeasures have been attempted for preventing the beaches from severe erosion. It has been learnt from the experiences that no possibility of stabilizing the beaches can be expected, but they have only changed to man-made beaches covered with a great number of concrete units. It is therefore suggested in establishing a methodology for beach erosion control that the long-term characteristics of beach processes in the whole area of the beach must be investigated. Recently, nature-learned ideas have been employed gradually in the preservation and stabilization of such sandy beaches.

---

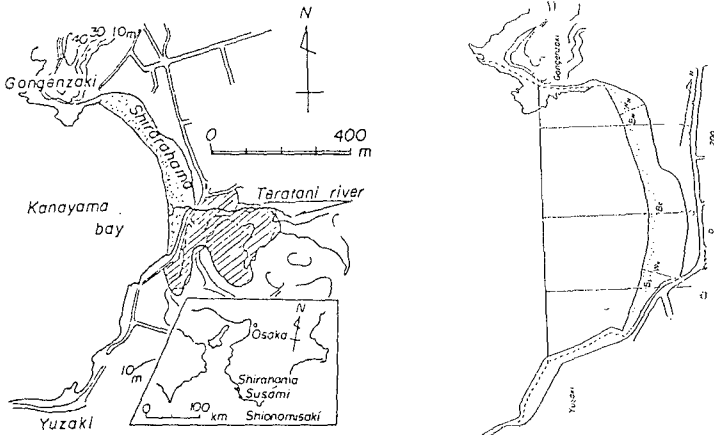
1 Professor, Disaster Prevention Research Institute, Kyoto University, Kyoto 611

2 Associate Professor and 3 Instructor, Ditto

4 Associate Professor, Fukui Institute of Technology, Fukui 910

5 Former Engineer, and 6 Director, River Division, Bureau of Public Works,  
Wakayama Prefecture, Wakayama 640

In this paper, a methodology for beach erosion control by headlands is proposed for stabilizing a pocket sandy beach which has gradually be eroded due to current urbanization of its hinterland. As seen in Figure 1, Shirarahama beach which is located in Kanayama bay facing the Pacific Ocean is a typical pocket beach consisted of white



(a) Location and sediment source area (b) Survey lines of beach width  
Figure 1. Shirarahama beach in Shirahama-cho, Wakayama and its sediment source area

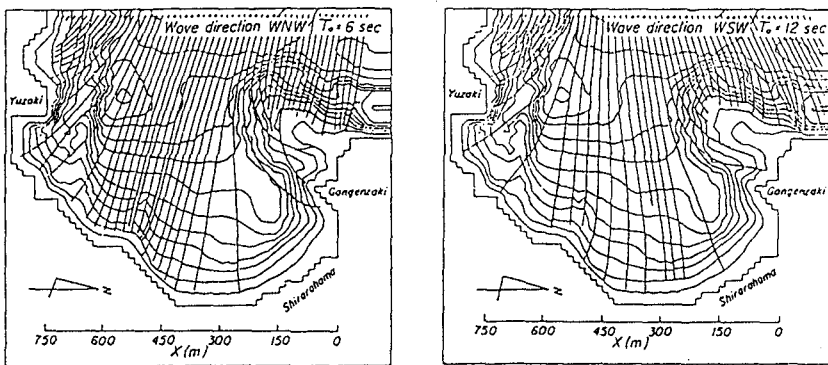
sand, but as sediment input from the hinterland has decreased due to its current urbanization the shoreline has very gradually retreated. Additionally, the area of Shirahama-cho is one of the most famous hot spring resort areas in Japan, so the local government of Wakayama Prefecture has planned to recover the beach by stabilizing and expanding it as possible. Observations of wave, current and shoreline change and field survey of beach and offshore sediment had been carried out since 1976. Numerical predictions of wave transformation, nearshore currents and shoreline change in the beach were also made. It is concluded that the beach has been so well maintained naturally by the sediment source of white sand through the Teratani river, and that it is formed well as a typical sandy pocket beach which had been stable for a long time. Recently, due to lack of the sediment source from the river the shoreline has very gradually retreated, but it is not so severe beach erosion. Based on the characteristics of the pocket beach naturally formed, a methodology for stabilizing the sandy beach by making a stable sandy beach formed by headlands is proposed, and its applicability was examined by physical experiments. After finding the most cooperative condition of two headlands in producing a stable sandy beach by the experiments, the arrangement of the headlands was made. After the construction of headlands, beach nourishment was partly made between the headlands along the original sandy beach, and now being done. It can be concluded at the present stage that a sandy beach is now being formed well and approaching a stable sandy beach between the headlands which was predicted by physical experiments.

Characteristics of Winds and Waves



In the area of Shirarahama beach, there exist two frequent winds which are due to monsoons in winter season and typhoons in summer season, respectively. Monsoon winds are mainly from NW directions from November to February in the next year, and W direction from March to April. Typhoon winds are subjected to typhoon tracks. Therefore there exist two predominant waves; they are monsoon waves from the NNW and NW directions and typhoon waves from the S and WSW directions, respectively. The monsoon waves are 6 to 8 sec in significant wave periods and up to 5 m in significant wave height in deep water, but more frequent than the typhoon waves of which the wave periods are 10 to 14 sec and the significant wave heights are 5 to 6 m frequently and up to about 8 m in deep water.

The wave refraction diagrams for the monsoon and typhoon waves are shown in Figure 2 where the wave periods and directions are assumed as 6 sec and 14 sec, and NW and WSW for the monsoon and typhoon waves respectively. In the figure, the upper and lower figures deal with wider and narrower areas in the wave refraction areas. It was concluded from the wave refraction that both the monsoon and typhoon waves are coming onto the rocky shore which surrounds the beach obliquely, but the shoreline of the sandy beach normally which is located at the end of Kanayama bay. This fact may explain why the sandy beach is formed naturally well as a pocket beach.



(a) In the case of monsoon waves

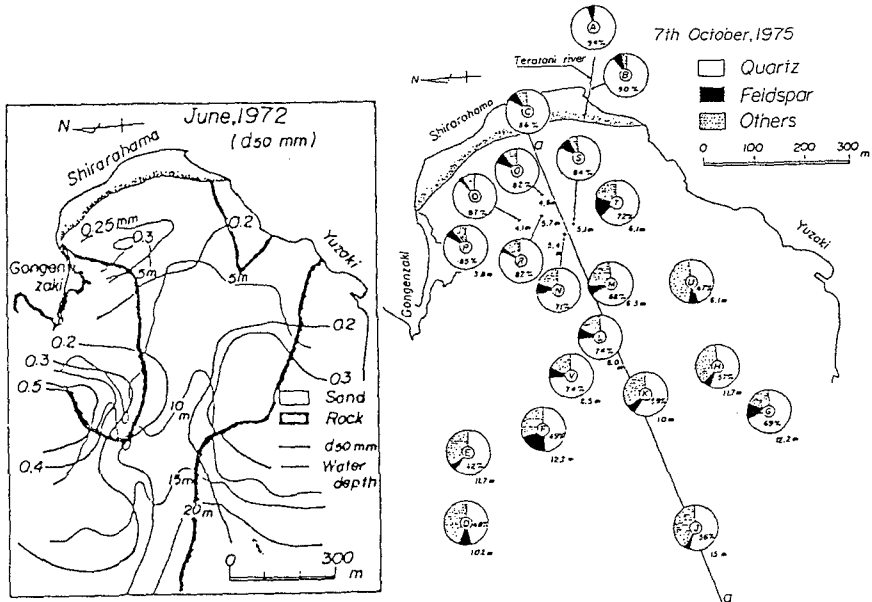
(b) In the case of typhoon waves

Figure 2. Wave refraction diagrams of monsoon and typhoon waves in Kanayama bay

Additionally, the tidal range is about 2.0 m due to semi-diurnal tide. The storm surge was recorded over 1 m in 1961 due to Daini-Muroto typhoon, and the area of sediment sources in the hinterland of the beach has been shown in Figure 1, the main sediment sources

As the area of sediment sources in the hinterland of the beach has been shown in Figure 1, the main sediment sources were due to sediment input from the Teratani river and the area shaded in the figure about twenty years ago. The distribution of mineral composition of sediment on and off Shirarahama beach and Kanayama bay is shown in Figure 3 (a) where the mineral composition is classified by quartz, feldspars and

As the area of sediment sources in the hinterland of the beach has been shown in Figure 1, the main sediment sources were due to sediment input from the Teratani river and the area shaded in the figure about twenty years ago. The distribution of mineral composition of sediment on and off Shirarahama beach and Kanayama bay is shown in Figure 3 (a) where the mineral composition is classified by quartz, feldspars and



(a) Median diameter of sediment (b) Mineral composition of sediment  
 Figure 3. Distribution of median diameter and mineral composition of sediment on and off Shirarahama beach and in Kanayama bay

others which are mainly shell, respectively. The result of mineral composition can explain the sediment sources. The sediment input was a very little from the river, but since then no sediment input can be observed due to development of the hinterland. This fact is only the cause for gradual beach erosion. The distribution of median size of bottom sediment in Kanayama bay is shown in Figure 3 (b) where the depth contours are also shown. It is noted that the sediment of white sand is only on the narrow areas of sea bottom and the beach.

Shoreline Change: Seasonal and Abnormal Changes

Shoreline change in the beach was observed both by direct measurement and aerial photographs to find its seasonal and abnormal changes. Due to monsoon and typhoon waves of which the wave directions are mainly NW and SSW, respectively, the seasonal shoreline change exists as shown in Figure 4 where the beach widths  $w_N$  and  $w_S$ , and  $B_N$  and  $B_S$  are the beach widths defined as shown in Figure 1 (b), the suffixes indicate those near the northern and southern ends, respectively and their ratios are used for seasonal change. The shoreline change for a period of ten years from 1972 is shown in Figure 5. It is recognized that the shoreline has retreated very gradually, and that the abnormal change has taken place sometimes, but the maximum retreat was within 20m and soon recovered. In the case of typhoon the shoreline intends to result in a little accretion near the north end, but retreat near the south end of the beach. Contrarily, in the case of monsoon the shoreline intends to retreat a little near the south

end and to do accretion near the north end. It is however noticed that the sandy beach is nearly in equilibrium even fluctuating a little during the periods of typhoon and monsoon because the incident waves are normally approaching the sandy beach to produce no effective longshore sediment transport in changing the curved beach.

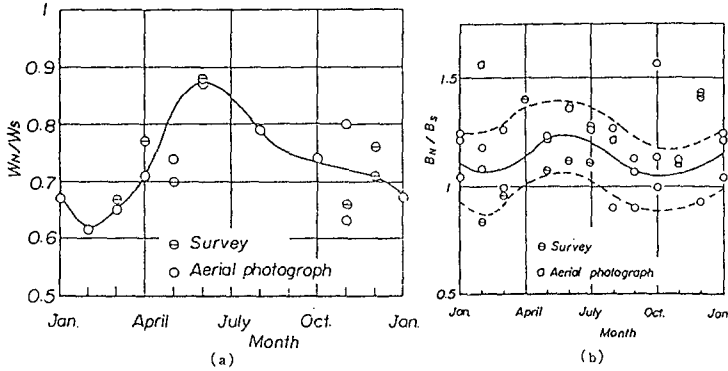


Figure 4. Seasonal change in beach width in terms of beach width ratios on survey lines shown in Figure 1(b)

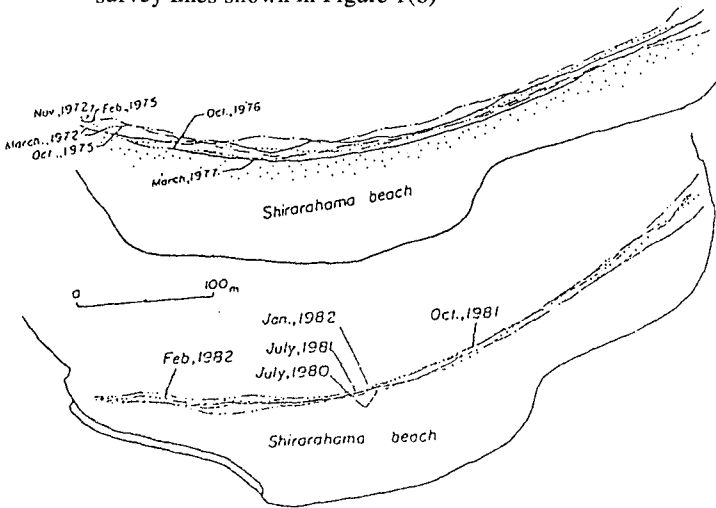


Figure 5. Shoreline changes between 1972 and 1982 in Shirarahama beach

As previously described, beach change in Shirarahama is also due to strong winds resulting in blown sand in spring season. Strong, but dry winds blow from the NW direction and blown sand takes place on the sandy beach to result in beach change as shown in Figure 6 where the erosive and depositional areas are shown in the periods specified. It is recognized from the results that the northern area is eroded, but eroded sediment is deposited in the southern area. The sandy beach intends to be tilted from the northern to southern ends.

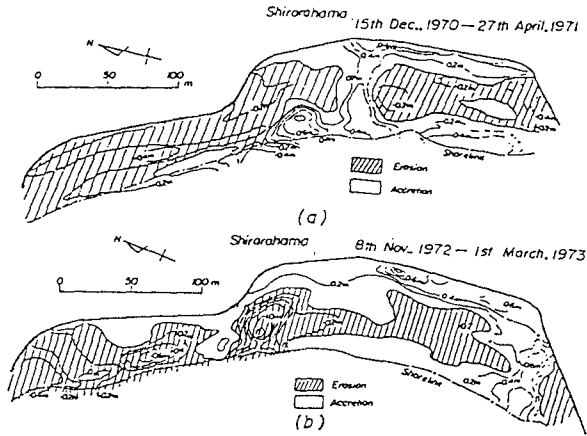


Figure 6. Beach change by blown sand in spring season

#### Longshore Distribution of Wave Power and Prediction of Shoreline Change

In order to investigate the longshore distribution of longshore sediment transport along Shirarahama beach, the wave power which is actually proportional to the rate of longshore sediment transport is employed. By use of wave data for seven years between April in 1970 and March in 1976 at Susami Fishery Harbor which is located about 20 km south from the beach, the longshore distribution of wave power along the beach was calculated. Figure 7 shows the longshore distributions of annual and seasonal wave power along the beach. This figure clearly describes that in the central part of the beach the wave power is nearly vanished, but near the northern end it takes a null point where it increases in the direction of positive wave power north and in the direction of negative wave power south, and near the southern end of the beach it is also vanished, but it takes a null point too where it decreases in the direction of positive wave power south and in the direction of negative wave power north. It is therefore mentioned that at the northern end the beach intends to be eroded, but fortunately no longshore sediment in the northern direction behind Gongenzaki headland which is curved concave may result in no severe retreat of shoreline, and at the southern end the beach intends to accumulate sediment due to both positive and negative wave power in their directions. Due to the positive wave power in the southern area from the null point where the Teratani river is flowing into a little north, white sand as only sediment sources from the river is transported within the beach. In the longshore distributions of seasonal wave power, in summer season (typhoon season) the wave power becomes nearly vanished in almost the beach, but only near the northern end beach change may take place to result in shoreline accretion. This may explain the shoreline change due to typhoon waves. Contrarily, in the winter season (monsoon season) the longshore distribution of wave power is quite similar to the annual one so that the tendency in shoreline change may be similar to the annual change as previously discussed. Near the northern end the wave power may result in to accumulate sediment, but it may tend to retreat shoreline. This tendency may

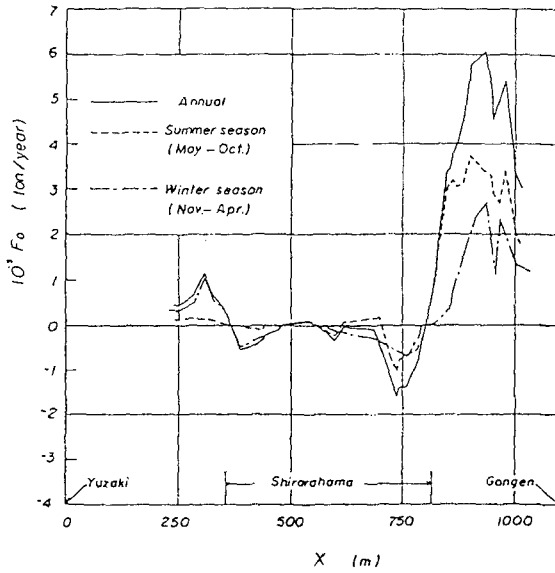
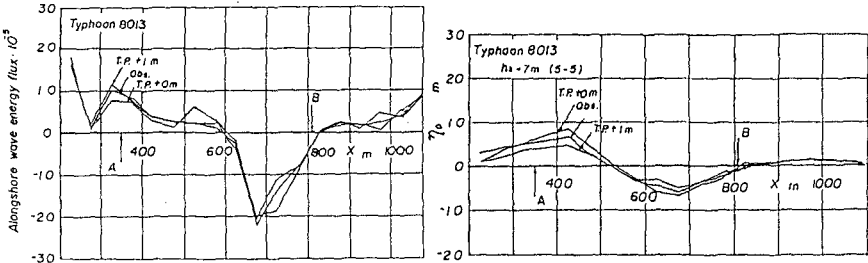


Figure 7. Longshore distribution of annual and seasonal wave power



(a) Wave power distribution (b) Shoreline change predicted

Figure 8. Longshore distributions of wave power generated by Typhoon 8013 along the beach and predicted results of shoreline change

support the shoreline change clearly due to monsoon waves. It can therefore be recognized from these circumstances that the sandy beach is a typical pocket beach naturally well-formed between Yuzaki and Gongenzaki rocky headlands.

Figure 8 (a), as an example, shows the longshore distribution of wave power which is generated by Typhoon 8013 where the tidal levels are shown in T.P. and observed one, and the area of the sandy beach is specified by arrows A and B respectively in the southern and northern ends. Near the northern end it tends to accumulate sediment a little, but near the southern end it shows to result in some rates of longshore sediment transport in the southern direction. The changes in wave power by the typhoons by which the maximum significant wave height of about 7 m in deep water were calculated. By use of the wave power the shoreline changes by the typhoon were

calculated by one line theory of shoreline change prediction as shown in Figure 8 (b) where the threshold water depth in the sand drift zone was assumed as 7 m. The figure shows that only a little shoreline change takes place by typhoons, but the longshore tendency of shoreline change near the southern end is a little different from those in Figure 2, probably due to sediment input from the neighboring rocky shores where no longshore sediment transport exists actually. The duration of the longshore sediment transport in the northern direction was short say about 10 hrs., but no remarkable shoreline change was observed. It is concluded again from the shoreline change that this sandy beach has been in the table condition as a typical pocket beach.

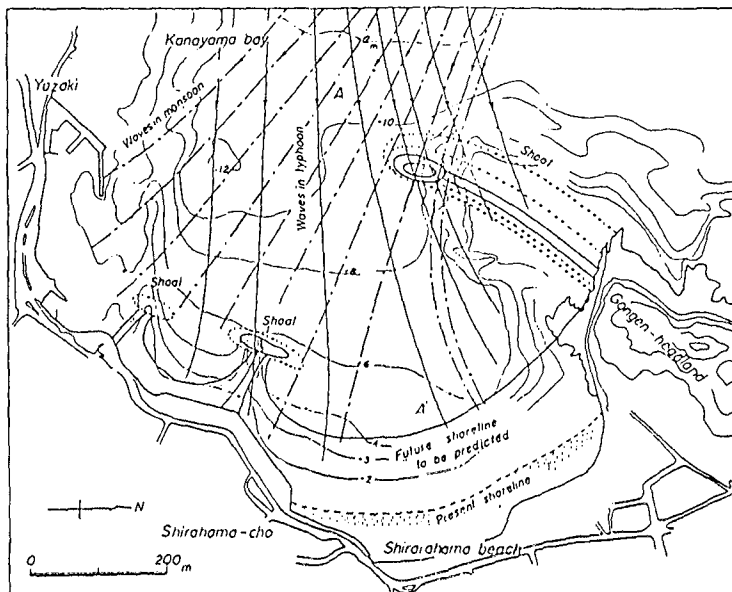


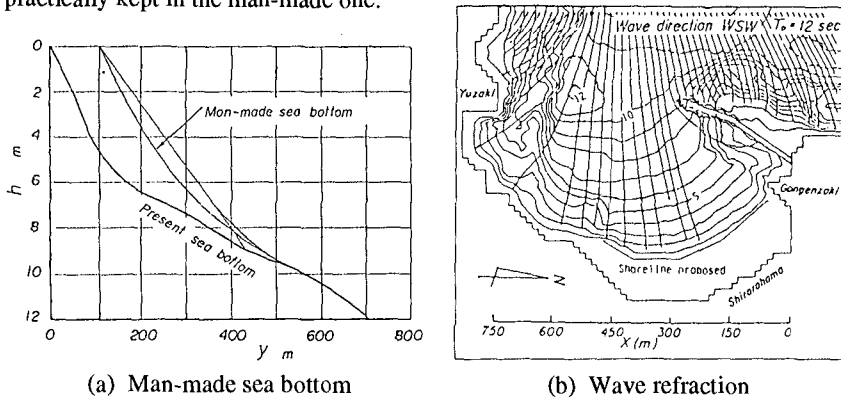
Figure 9. Methodology for preservation of Shirarahama beach by headlands

Additionally, numerical calculations were made to predict nearshore currents by monsoon and typhoon respectively, and drift currents by strong winds during monsoon and typhoon. It was found that a little nearshore circulation exists both in the cases of monsoon and typhoon, but northern drift currents exist by NW wind in monsoon and opposite currents exist by SW wind in typhoon.

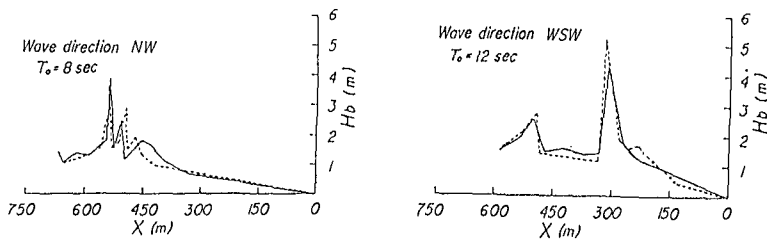
#### Methodology for Beach Preservation by Headlands

Based on the natural circumstances of Shirarahama beach as a well-formed pocket beach and their stability, a methodology for preservation must be proposed. Expanding the beach width about fifty meters offshore for utilization of the beach as marine resort, the sandy beach must be stabilized. The main items in the methodology are 1) a couple of stable sandy beaches are formed as shown in Figure 9. By extending Gongenzaki headland about forty meters in under water, the monsoon and typhoon

waves are controlled to reduce their heights effectively and to make a stable sandy beach formed, and constructing a couple of headlands of T-shaped groins, the waves are also controlled to make sandy beaches formed as tombolos. 2) In order to make stable sandy beaches formed between them, sandy beaches to be formed must be cooperated naturally and dynamically to result in a couple of well-formed stable sandy beaches as pocket beaches. The necessary conditions are verified experimentally. And 3) for marine resort the water mixing in the bay as well as the beach are promoted by tides and incident waves. As previously discussed, the incident waves are approaching the present beach nearly normally. This circumstances of wave incidence must be introduced in the formation of stable sandy beaches. The present beach profiles near Gongenzaki headland are reformed as shown in Figure 10 (a). The incident waves are refracted by the man-made sea bottom to approach the beach nearly normally, as shown in Figure 10 (b). Figure 11 shows changes in breaker height at the present and man-made bottom topography by which the present circumstances of wave refraction is practically kept in the man-made one.



(a) Man-made sea bottom (b) Wave refraction  
 Figure 10. Man-made bottom topography and wave refraction of typhoon waves



(a) In the case of monsoon wave (b) In the case of typhoon wave  
 Figure 11. Comparison between breaker heights on present and man-made bottom topography

Experimental Verification on Formation of Stable Sandy Beaches by Headlands

Physical model experiments of which the experimental setup is shown in Figure 12 were carried out by use of the similitude for beach change by Tsuchiya and Itoh (1981)

in nondistorted model with a horizontal and vertical scale of 1/64 and experimental fine sand with a median size of 0.021 cm and specific gravity of 2.65, respectively. Experimental waves are typhoon and monsoon waves from NW and WSW directions of which the periods are 0.75 and 1.30 sec, respectively. By operating a wave generator of monochromatic waves over 800 hrs in total, fifteen runs were performed in various conditions to find the applicability of the proposed methodology and the most effective lengths of headlands in cooperating sandy beaches to be formed between them as stable sandy beaches. In the experiments, waves and nearshore currents in the beach were also examined experimentally to find characteristics of wave transformation and mixing in nearshore currents. Measured data of waves and currents

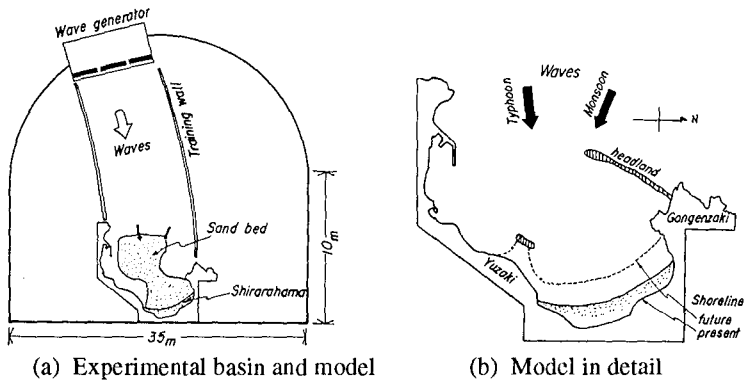


Figure 12. Experimental setup for verification of formation of stable sandy beaches

were compared with their numerical predictions with fairly good agreement. By use of the man-made topography near Gongenzaki headland, wave transformation in the beach were measured to find the efficiency in wave refraction. Additionally, submerged breakwaters for interrupting offshore sediment transport in the beach were examined. The main results of the experiments can be summarized as:

- 1) Reproduction of the formation of present sandy beach was successfully made in the physical model. It was experimentally verified that the beach is really a stable sandy beach as a pocket beach formed well naturally both by Yuzaki and Gongenzaki headlands in relation to the action of monsoon and typhoon waves.
- 2) Shoreline changes in the cases of headlands used were made experimentally. Some of the experimental results in finding the most suitable arrangement of headlands are shown in Figure 13 where the experimental runs are shown, but the detail are omitted. It was concluded that the necessary extending length of Gongenzaki headland by which a stable sandy beach is formed well was determined as about 30 m, and that the other headland should be made as a T-shaped groin being a small island or shoal by which a stable sandy beach is well formed.
- 3) The efficiency of man-made bottom topography for wave refraction and a submerged breakwater as a barrier for interrupting offshore sediment transport were examined experimentally as shown in Figure 14 where the man-made bottom is shown by shaded area in (a) and the barrier is located in the central area of Kanayama bay as shown in (b). It was concluded that the man-made bottom topography is practically



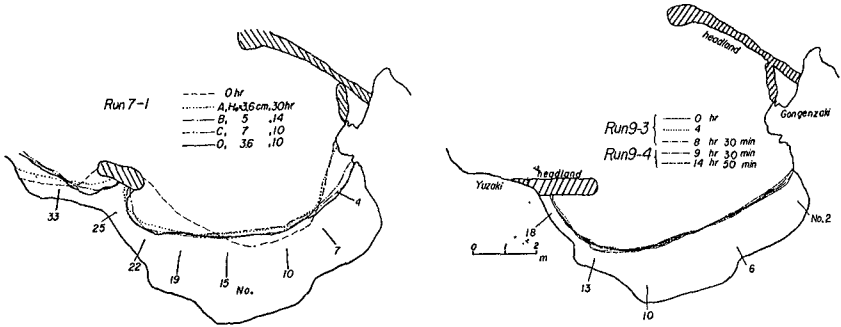
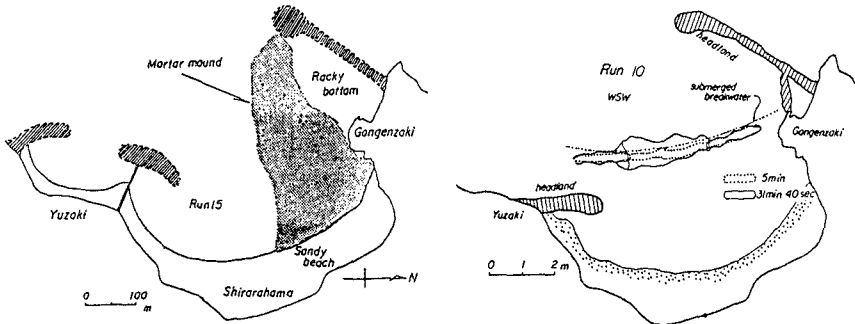


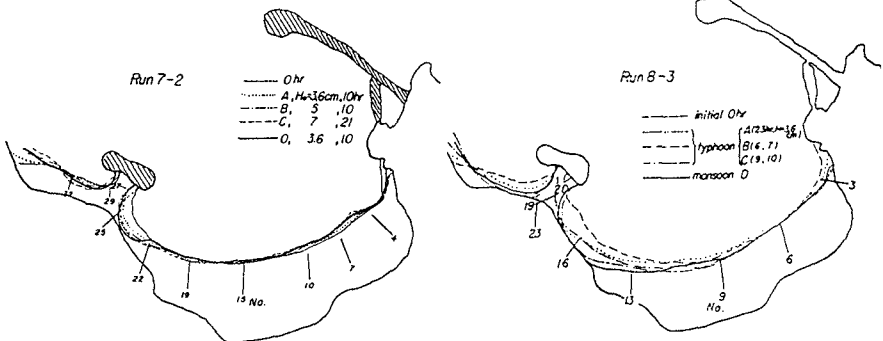
Figure 13. Shoreline changes in the cases of T-shaped groin and inclined groin, and Gogenzaki headland extended about 40 m under water



(a) Bottom topography

(b) Distribution of fluorescent sand

Figure 14. Man-made bottom topography for wave refraction and distribution of fluorescent sand around submerged breakwater as barrier



(a) Impractical beach nourishment (b) Adequate beach nourishment

Figure 15. Shoreline changes in the cases of impractical and adequate beach nourishment in formation of stable sandy beach

effective to make the incident wave refracted to approach normally the beach resulting in a stable sandy beach. It was however noted that the barrier is effective to interrupt

offshore sediment transport, but once sediment has been transported offshore the barrier the sediment can not be transported again onshore through the barrier. It was therefore suggested that such a barrier is not so effective in the formation of stable sandy beaches.

4) The total volume of beach nourishment was experimentally examined in the formation of stable sandy beach by the headlands. As shown in Figure 15 (a), after impractical beach nourishment a stable sandy beach can not be formed well especially near the southern headland of T-shaped groin, and after adequate beach nourishment a stable sandy beach can be well formed as shown in (b). As schematically shown in Figure 16, the formation condition of a stable sandy beach between the headlands can be explained as: By Gongenzaki headland extended, a curved sandy beach is formed

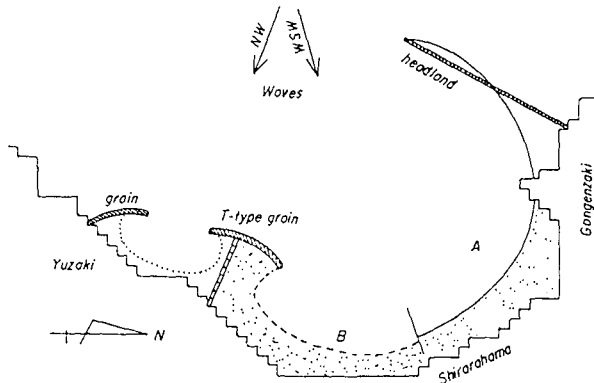
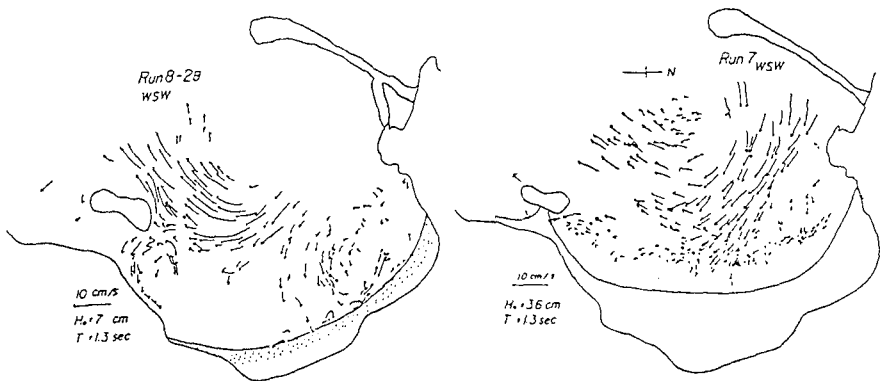


Figure 16. Formation condition of stable sandy beach by headlands



(a) Before beach nourishment (b) After beach nourishment

Figure 17. Examples of nearshore current patterns in stable sandy beach formed by headlands

as A in the figure, but the southern end of the beach extends south. Another sandy beach is formed by the headland of T-shaped groin as shown by B, but the northern

end may extends north. When the two sandy beaches are cooperated by which the southern and northern ends of the beaches must be well-continued smoothly, a stable sandy beach can be well-formed between the headlands.

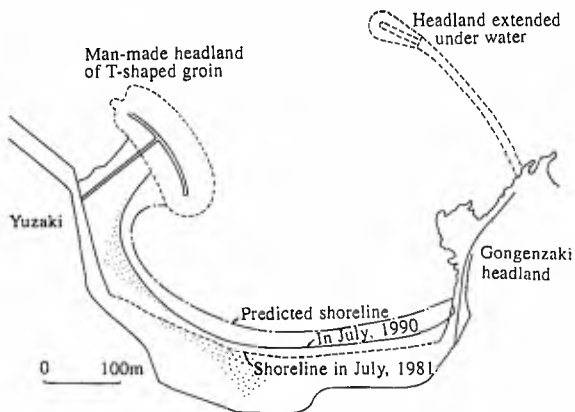


Figure 18. Predicted shoreline of stable sandy beach to be formed by Gongenzaki headland extended and headland of T-shaped groin in Shirarahama beach after adequate beach nourishment and present shorelines after beach nourishment as of 1990

5) Spatial distributions of wave height and current were compared with their numerical results. The comparison was satisfactorily made, and showed that, as shown in Figure 17 for example, mixing phenomena in nearshore current take place due to waves. Based on the experimental verification of the formation of a stable sandy beach, the



Photo. 1. Present aerial view of stable sandy beach being newly formed in Shirarahama beach after beach nourishment as of 1991

shoreline in the formation of stable sandy beach by extending the present shoreline about 50 m offshore is predicted as shown in Figure 18.

#### Construction of Headlands and Beach Nourishment

In 1983 Gongenzaki headland was extended about 40 m, and the headland of T-shaped groin was constructed in 1987. After the construction of the headlands beach nourishment have been made by using nearly same material imported as the original white sand. The total volume of nourished sand is 35,000 m<sup>3</sup> as of 1990. Shorelines along the beach have been measured. In Figure 18, the recent shorelines are shown in comparison with the predicted one. Photo.1 shows the present situation of the newly formed sandy beach between the headlands. The further beach nourishment is needed for the final formation of a stable sandy beach between the headlands, but the shoreline configuration is quite similar to the predicted one.

#### Conclusion

Based on the natural circumstance of Shirarahama beach a methodology of beach preservation by headlands was proposed. The two headlands were constructed and extended, and beach nourishment has being made, but the shoreline configuration has being approaching the predicted final shoreline of a stable sandy beach between the headlands well. It is therefore concluded that the proposed methodology for preservation of Shirarahama beach by headlands could be applied satisfactorily in the formation of a stable sandy beach.

This investigation was partly supported by Grant-in-Aids for Scientific Research, from the Ministry of Education, Science and Culture of Japan, under Grant No. 03452212.

#### References

- Tsuchiya, Y. and M. Ito: 1981, Experimental study on similitude of beach change, Proc. 28th Japanese Conf. on Coastal Eng., JSCE, pp. 315-319 (in Japanese).
- Ito, M. and Y. Tsuchiya: 1984, Scale-model relationship of beach profile, Proc. 19th ICCE, ASCE, Vol. 2, pp. 1386-1402.
- Tsuchiya, Y., Y. Kawata, T. Shibano and T. Yamashita: 1984, Beach processes of Shirarahama beach and its preservation (1), Annuals, DPRI, Kyoto Univ., No. 27B, pp. 513-556 (in Japanese).
- Tsuchiya, Y., Y. Kawata, and R. Silvester: 1985, Beach processes of Shirarahama beach and its preservation (2), Annuals, DPRI, Kyoto Univ., No. 28B, pp. 565-589 (in Japanese).

## CHAPTER 262

### Wave Power Conversion by a Prototype Wave Power Extracting Caisson in Sakata Port

Shigeo TAKAHASHI\*, Hiroaki NAKADA\*\*, Hideaki OHNEDA\*\*\*, and Masazumi SHIKAMORI\*\*\*\*.

#### 1. INTRODUCTION

Ocean wave energy is clean and inexhaustible. Repeated oil crises and the urgent need for environmental preservation on a global scale have made utilization of ocean wave energy increasingly important.

The Japanese Ministry of Transport has been developing a wave power extracting caisson breakwater which can absorb wave power and convert it into electric power. The breakwater shown in Fig.1 is a composite breakwater with a special caisson for absorption and conversion of wave power. The caisson has a so-called air chamber where wave power is converted into air power. The air power activates a turbine-generator in the machine room on the caisson. The use of the breakwater as a wave power converter will effectively cut down the power generation cost. This breakwater also aims at the improvement of the wave resisting stability and performance as a breakwater by absorbing the wave energy.

The research and development work on the wave power converter is being carried out through collaboration by the First District Port Construction Bureau, the Port and Harbour Research Institute and the Coastal Development Institute of Technology under the

- 
- \* Chief of Maritime Structures Laboratory, Port and Harbour Research Institute , MOT, Japan
  - \*\* Head of Niigata Investigation and Design Office, The First District Port Construction Bureau, MOT
  - \*\*\* Head of Sakata Port Construction Office, The First District Port Construction Bureau, MOT
  - \*\*\*\* Director of Research Department, Coastal Development Institute of Technology



Figure 1 Wave Power Extracting Caisson Breakwater in Sakata Port



Photo 1 Wave Action on Wave Power Extracting Caisson

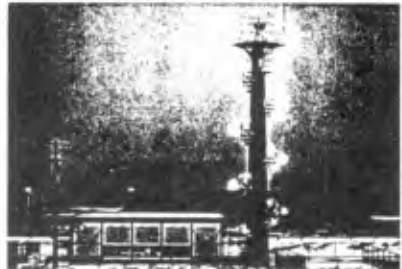


Photo 2 On-land Observation House and Illuminated Tower

guidance of the home office of the Ministry of Transport. The Port and Harbour Research Institute had conducted basic research for five years since 1982<sup>1)2)3)4)</sup>. The 1st District Port Construction Bureau, Ministry of Transport, began a field verification experiment for the breakwater from 1987 in the form of a joint study with the Coastal Development Institute of Technology and twenty private companies. A test breakwater was constructed in the summer of 1989 at Sakata Port in Yamagata Prefecture<sup>5)6)7)</sup>. The breakwater began the power generation in the winter of 1989. Photo 1 shows the wave action on the completed caisson and Photo 2 shows the on-land observation house and a tower illuminated by the converted energy.

The field experiments were conducted for the five years from fiscal 1987 through fiscal 1991 aiming at the following items:

- 1) to confirm the design method of the breakwater caisson including the air chamber against wave forces,
- 2) to verify the design method of the air chamber, turbine and generator as a wave energy converter,
- 3) to study methods of constructing the breakwater
- 4) and also to demonstrate utilization of the power output for various uses.

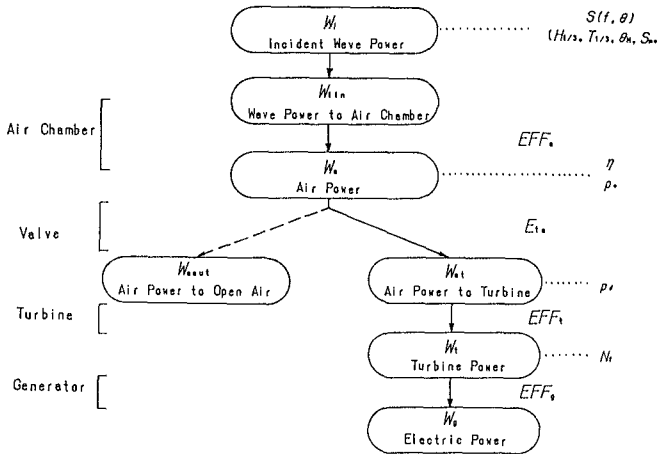


Figure 2 Energy Conversion Process

This paper introduces the system with a wave power extracting caisson in the field experiment and the results of the field experiment, especially on the wave power conversion.

## 2. POWER CONVERSION BY THE CAISSON AND TURBINE GENERATOR

Figure 2 shows the power conversion process by the wave power extracting caisson and its turbine generator. The wave power is converted first into air power in the air chamber, then into turbine power by the turbine and finally into electric power by the generator as follows:

- 1)  $W_i$  denotes the incident wave power which can be obtained from the wave spectrum. The incident wave power is the energy rate which the incident wave transports in an unit time and length.  $W_{iin}$  represents the wave power going into one caisson.
- 2)  $W_a$  denotes the air power converted from wave power in the air chamber, which can be estimated by the vertical speed of water surface movement and the air pressure in the air chamber and the horizontal area of the air chamber. The conversion efficiency  $EFF_a$  from wave power to air power is given by  $W_a/W_{iin}$ . The efficiency depends on the ratio of the air chamber width  $B$  to the wavelength  $L_{1/3}$ , and the turbine diameter  $R_t$  (actually the total area of turbine opening and valve openings, etc.). The conversion efficiency also varies with submerged depth  $d_c$  of the curtain wall of the front wall of the air chamber and the height  $D_0$  of the air chamber<sup>1)2)</sup>. For example, the air chamber width is 13% the wavelength of a wave of 7 s to obtain a high conversion efficiency with a small width as much as possible.
- 3)  $W_{aout}$  represents the wave power released to the atmosphere from control valves and dummy nozzles, while  $W_{at}$  represents the air power into the turbine. The sum of  $W_{aout}$  and  $W_{at}$  equals to the

air power  $W_a$ . The ratio  $W_{at}/W_a$  is defined here as the utilization rate  $E_{ta}$  of air power. The utilization rate of the air power in the system of the experiment is always less than 0.5 because of the existence of the dummy nozzles as will be described in Chapter 3.

- 4)  $W_t$  represents the turbine power which can be obtained from the turbine torque and the rotation speed. The conversion efficiency  $EFF_t$  is given as the ratio  $W_t/W_{at}$ . The fundamental characteristics of the turbine including the turbine efficiency can be obtained from steady wind tests. The turbine efficiency varies with the attacking angle of wind to the turbine blade, and therefore the turbine speed should be controlled to bring a high conversion efficiency <sup>2</sup>.
- 5)  $W_g$  denotes the electric power which can be evaluated by the electric voltage and current. The electric current is determined by the connected electric loads and therefore the electric load should be controlled considering the turbine power. The electric load is controlled using the signal of the speed of turbine in the experiment. The turbine efficiency  $EFF_g$  is given by the ratio  $W_t/W_g$ , which is usually given from a factory test.

The speed of the turbine fluctuates with the frequency of the waves and also that of the wave group. The strength of the fluctuation depends on the inertia moment  $I_{tg}$  of the turbine generator.

- 6) The conversion efficiency  $EFF_{atg}$  from wave to electric power is indicated as the product of  $EFF_a$ ,  $EFF_t$  and  $EFF_g$ . However by the influence of the control valves and dummy nozzles, the actual conversion efficiency  $EFF_{atgo}$  decreases to  $EFF_{atg} \times E_{ta}$ .

### 3. WAVE POWER EXTRACTING CAISSON IN THE EXPERIMENT

#### 3.1 Design of Wave Power Conversion System

A caisson of the Second North breakwater of Sakata Port is used for verification experiments, as shown in Fig. 3. The breakwater is

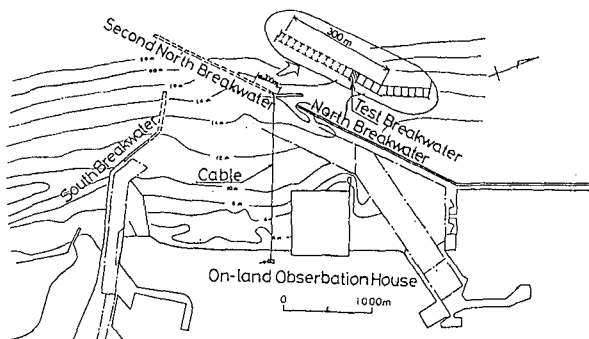


Figure 3 Location Map of Sakata Port



now under construction as a composite breakwater, with a planned length of 1,900 m. The depth of the water is 18 m at the construction site. The sea bottom foundation is mostly sandy with viscous soil in some places. A settlement of the caisson of about 1 m is predicted.

In designing a wave energy converting system, it is necessary to know the wave power available in the designed places and to determine the use of the converted energy. Then the frame plan of the system can be established. The fundamental dimensions of the components of the system such as the diameter of the turbine are determined based on the frame plan. Finally, the components are designed in detail.

Wave data at Sakata Port for about twenty years were analyzed to find the wave conditions there<sup>4</sup>). The system was designed to operate for the waves of 1 to 5 m, and the wave with  $H_{1/3} = 2.2$  m and  $T_{1/3} = 7$  s was selected as a main wave to discuss the conversion efficiencies. However, the design wave for the stability of the air chamber and other devices is  $H_{1/3} = 10.2$  m and  $T_{1/3} = 14.5$  s. Numerical calculations based on the thermodynamics and wave-kinematics theory<sup>123</sup> were conducted to determine the fundamental dimensions of the components of the system.

The wave power extracting caisson has an air chamber of 7 m wide as shown in Fig. 4. The caisson is 20 m long in the direction of the breakwater alignment line. The height is +12.5 m above the datum level level. The horizontal area is 115 m<sup>2</sup>, not including the thickness of the walls.

Figure 5 shows a concept of the machine room. The air flow converts its energy into the kinetic energy by rotating the turbines and the generator shown in Fig. 6, installed at the center of the machine room in the upper portion of the caisson. Two Wells turbines 1,337 m in diameter are employed to get a one-way rotation from the reciprocal flow of the air and sandwich the generator to make a tandem type arrangement canceling the forces

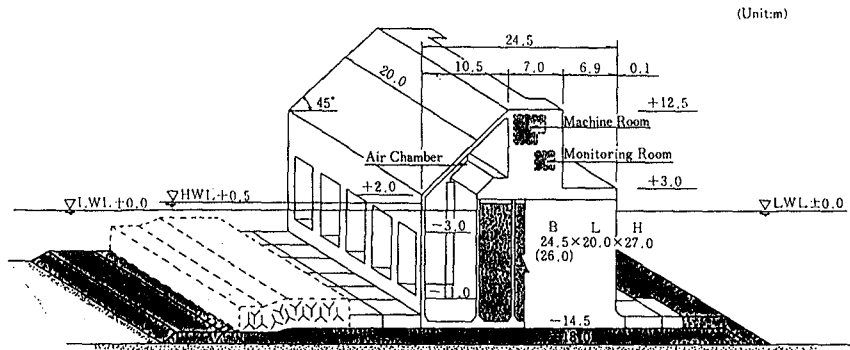


Figure 4 Shape of the Caisson Breakwater

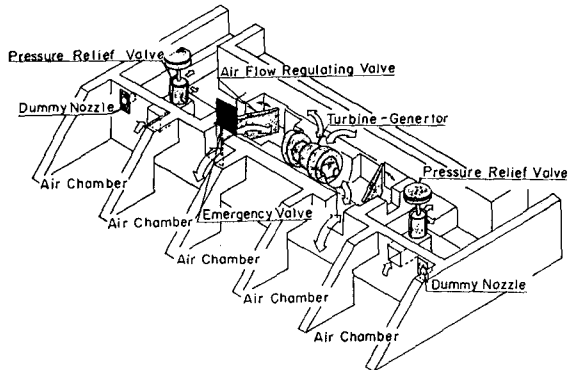


Figure 5 Conceptual View of the Machine Room

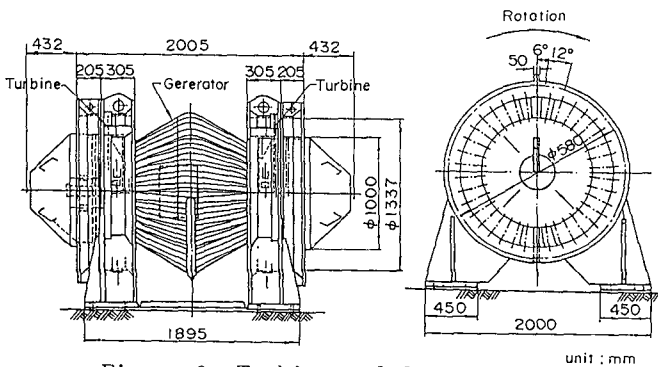


Figure 6 Turbine and Generator

that work in the axial direction of the turbines. The generator is a 200 V synchronous generator with a rated output of 60 kW and a maximum revolution of 3,000 rpm.

The protection devices that control the air flow from the air chamber to the turbine consist of three types of valves: the air-flow regulating valve (bypass valve), the pressure release valve and the emergency cutoff valve. Figure 7 shows the air-flow regulating valve. The valve is of a rectangular box with a butterfly valve inside. The air flow can be controlled by the rotation of the butterfly valve. An electric actuator is equipped to rotate the butterfly valve according to the signal of the turbine speed. The valve closes the opening by 1/4 of the full rotation angle when the turbine speed exceeds a certain limit (simultaneously the valve opens the other opening to release the extra air power. If the turbine speed exceeds again the limit, the valve closes the opening again by one more 1/4 of the full angle. When the turbine speed becomes lower than a certain value the valve opens the opening by every 1/4. Power generation is stopped when waves are extremely

large (when the significant wave height is above 5 m) by terminating the air flow to the turbine and simultaneously fully opening the air flow regulating valve.

It should be noted that the diameter of the turbine in the experiments is set to be much smaller than that of the optimum turbine predicted by the amount of air power from the air chamber. This is because of the limitation of research funds. Two dummy nozzles are installed to release the extra air power, which corresponds to almost half of the total air power.

The power generated is transmitted to the on-land observation station through an underwater cable, where it is consumed by electric resistors. Experiments are also being made to utilize the electric power for various appliances to prepare for the application of the system for actual use.

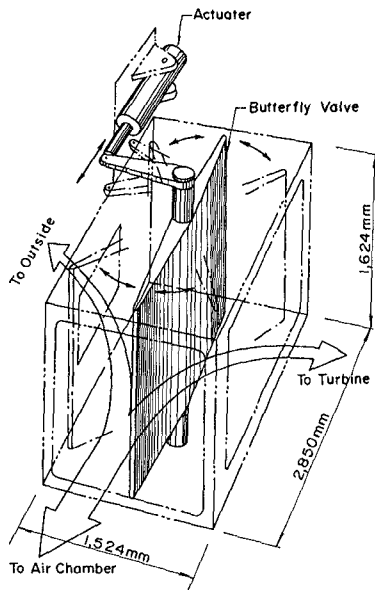


Figure 7 Air-flow Regulating Valve

### 3.2 Operation of the system

The power conversion of the system can be adjusted by changing the setting of the electric load against turbine speed, the threshold pressure of the pressure release valves, and the threshold turbine speed to open/close the air-flow regulating valves.

The system started the power generation from December 1st, 1989. In fiscal 1989, the system was operated rather discreetly under Setting I, while in fiscal 1990, experiments were conducted under Setting III for the optimized control method to generate larger amount of electric power. In the setting III, the electric load is proportional to the 3rd power of the turbine speed and the electric power is 60 kW when the turbine speed is 1800 rpm. The threshold pressures of the two pressure release valves are 1.34 and 1.61  $\text{tf}/\text{m}^2$ , and the air flow regulating valve is controlled to open one step (1/4) at 2000 rpm and to close one step (1/4) at 1700 rpm in the setting III. The results of power conversion with the setting III is described in this report.

Table 1 summarizes the dimensions of the conversion system in the experiment, where  $A_t$ ,  $A_p$ , and  $A_n$  denote the opening area of the turbine, the dummy nozzle, the pressure release valve,

Table 1 Experimental system and Full-size System

	Experiment system	Full-size system
Air Chamber	$B=6.75m$ , $l_B=20m$ $D_0=8m$ , $d_c=3m$ , $A_w=115m^2$	$B=6.75m$ , $l_B=20m$ $D_0=8m$ , $d_c=3m$ , $A_w=115m^2$
Turbine	$2R_t=1.337m$ $A_t=0.6185m^2 \times 2$ $l_{t\phi}=55.0kgm^2 \times 2$	$2R_t=2.40m$ $A_t=1.99m^2 \times 2$ $l_{t\phi}=1650.0kgm^2 \times 2$
Generator	60kW (1800rpm-60kW)	200kW (1000rpm-200kW)
Air-Flow Regulating Valve	close -- Open (1700rpm) (2000rpm) $c_{dv} \varepsilon_v=0.00892$ ( $\approx 1/112$ )	close -- Open (1000rpm) (1300rpm) $c_{dv} \varepsilon_v=0.00892$ ( $\approx 1/112$ )
Dummy Nozzle	$A_n=0.0746m^2 \times 2$ $c_{dv} \varepsilon_n=0.00130$ ( $\approx 1/770$ )	No Dummy Nozzle
Pressure Release Valve	$A_p=0.481m^2 \times 2$ $c_{dv} \varepsilon_p=0.00671$ ( $\approx 1/149$ ) $p_{prv}=1.30, 1.61tf/m^2$	No Pressure Release Valve

respectively,  $C_{dv}$  is contraction coefficient,  $\varepsilon$  is opening ratio of each opening,  $P_{prv}$  is threshold pressure of the pressure release valve. In the table, the dimensions of the full-size system is also listed which will be discussed later.

### 3.3 Measurement

A number of sensors are incorporated in the caisson and the power generating system to make measurements in the following four categories.

- (1) Wave conditions (directional spectrum, heights, periods and directions of incident waves)
- (2) Stability of the breakwater (wave pressure and air pressure)
- (3) Stability of the wall members (stress of the reinforcement)
- (4) Air output and power output (water level and pressure in the air chamber, turbine speed, power output)

Data are amplified and converted into optical signals before they are sent by an opto-electric power combination cable to the observation station on land, where they are analyzed and processed using four personal computers. In addition to the above procedure, detailed data are sampled and stored in a digital recorder, for 20 minutes at one operation, for further analysis of the breakwater stability. However, only the data concerning with the incident waves and the power conversion are discussed in this report.

## 4. OBSERVED WAVES

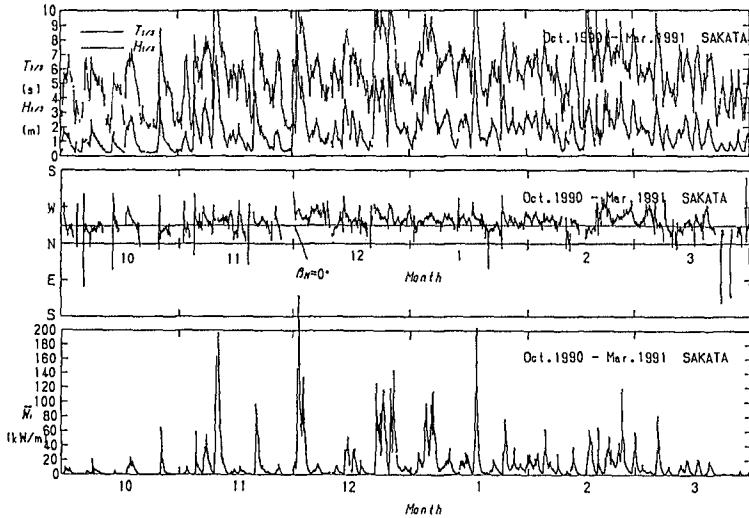


Figure 8 Variation of Significant Wave and Wave Power

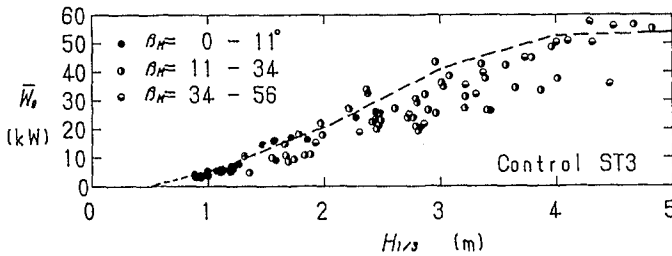


Figure 9 Incident Wave Power

Figure 8 shows the wave data from October 1990 to March 1991. The significant wave height and period, mean wave direction and wave power are shown in the figure. The average significant wave height and period were 1.72 m and 6.2 s, and the average wave power was 13.9 kW/m during this period. The wave height varies very widely and exceeds 5 m several times. The largest value of the significant wave height reached 8.67 m on December 2, 1991. The mean wave direction was usually northwest, which is almost perpendicular to the breakwater alignment. The wave power varies significantly and exceeds even 100 kW/m.

Figure 9 shows the measured and calculated incident wave power. The calculated power is obtained from a standard wave spectrum which was used in the design of the system. For example the calculated incident wave power becomes 18 kW/m at  $H_{1/3} = 2.2$  m and is 67 kW/m at  $H_{1/3} = 4$  m when the mean incident wave angle is 0 degree. The measured values agree well with the calculated ones.

The wave power can be estimated easily by the following formula with significant wave height  $H_{1/3}$  and period  $T_{1/3}$ .

$$W_i = \kappa H_{1/3}^2 T_{1/3} \quad (\text{kW/m}) \tag{1}$$

where,  $\kappa_w$  is 0.4 - 0.5 (kW/m<sup>3</sup>/s) in Sakata. Which is almost equal to the expected value in the preliminary studies<sup>4</sup>). It was also found that the wave power in sakata was reduced to 85 % of that for long crested waves due to directional spreading.

5. WAVE POWER CONVERSION

Figure 10 gives an example of the records of power generation, i.e., the water surface elevation and the air pressure in the air chamber, opening of the air flow regulating valve, pressure difference in the turbine and turbine speed, and power output for 20

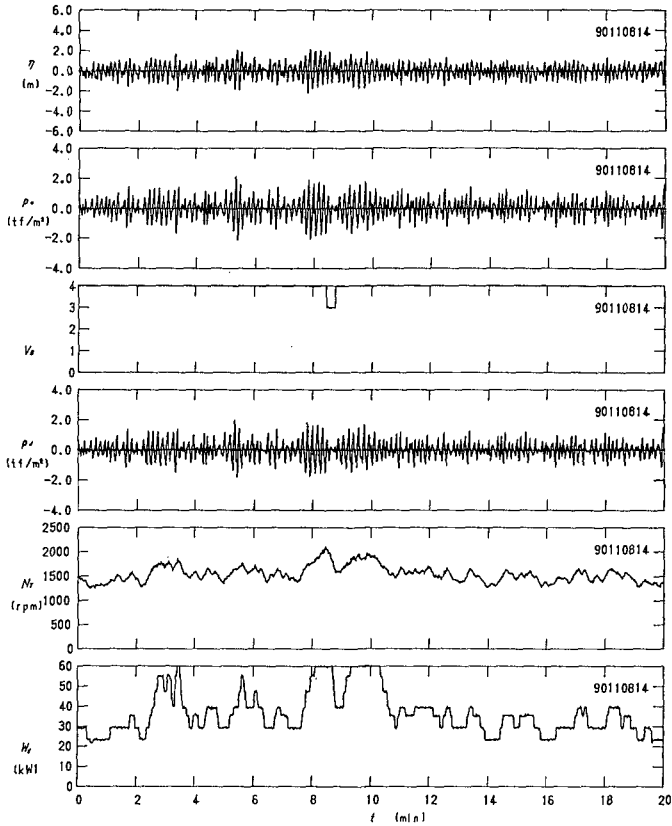


Figure 10 Analogue Data of Wave Power Conversion

minutes, that were recorded at 14:00 on November 8 in 1990, when the significant wave height and period were 3.01 m and 7.9 s, respectively, and the incident wave power was 539 kW/20m. The turbine rotation varies from 1250rpm to 2100 rpm and the electric power varies from 20 kW to 60 kW. As the turbine speed exceeds 2000 rpm the air flow regulating valve opens to reduce the air flow to the turbine as shown in the figure. The average electric power is 36.4 kW, and the conversion efficiencies from wave power to air power, from air power to turbine power and turbine power to electric power are 0.59, 0.37 and 0.91, respectively. However, a large amount of air power is released by the dummy nozzles and valves. Therefore, the utilization rate of air power is very low ( 0.34). If all the power is used, the electric power is about 100 kW.

Table 2 shows the monthly averaged values on power conversion from October 1990 to March 1991. For example, the average incident wave power is 20.3 kW/m and average electric power is 13.25 kW/m in January 1991. The time when the electric power is small and less than 1 kW, occupies only 13 % in the month, while the time occupies 51 % in October 1990.

Figure 11 shows the variation of the electric power to the significant wave height. The electric power increases according to the increase of the wave height. However, the electric power becomes almost constant at about 55 kW where the wave height is above 4 m.

Table 2 Power Generation in Each Month

Year/Month	'90/10	'90/11	'90/12	'91/1	'91/2	'91/3
$(W_i)_{ave}$ (kW/m)	3.3	13.0	23.9	20.3	15.0	6.7
$(W_e)_{ave}$ (kW)	6.03	10.65	13.34	13.25	10.88	9.73
Operation Time	168	172	156	154	155	193
Ratio( $W_e = 0$ kW)	0.39	0.25	0.13	0.02	0.13	0.18
Ratio( $0 \leq W_e < 1$ )	0.51	0.28	0.24	0.13	0.23	0.23

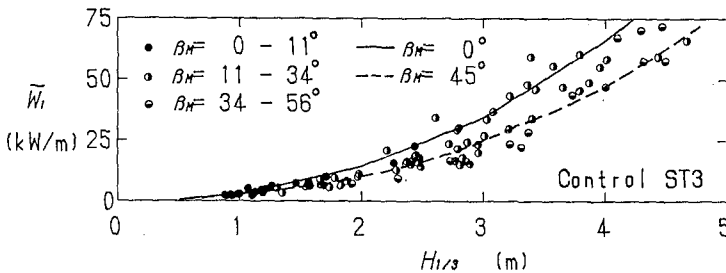


Figure 11 Electric Power

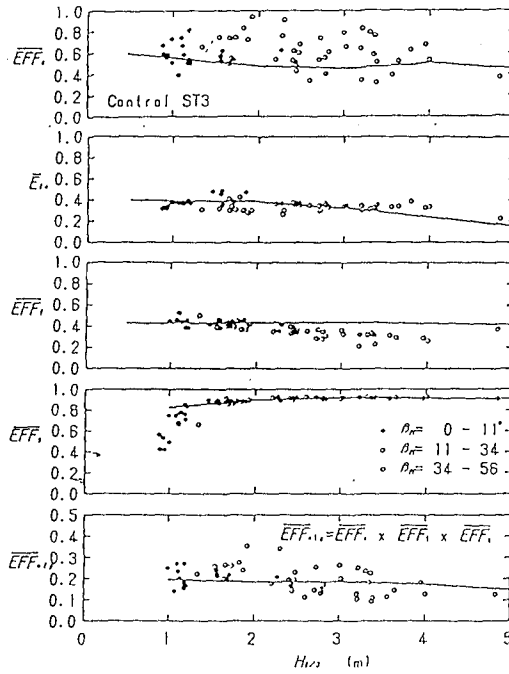


Figure 12 Conversion Efficiencies

This is due to the automatic control of the valves. The system can generate electric power from  $H_{1/3} = 1 \text{ m}$  to  $5 \text{ m}$  as designed. The calculated values for the normal incident waves are shown in the figure by a dotted line. The calculated values, which were used in the design of the present system, agree with the experimental ones for small wave angle. The calculation was based on the thermodynamics and wave-kinematic theory<sup>1)2)3)</sup>.

The conversion efficiencies in the experiment are shown in Fig.12. The conversion efficiency from wave to air power is from 0.4 to 0.8. The turbine efficiency is from 0.2 to 0.5. The generator efficiency is about 0.5 when the wave height is large. The total efficiency which is given by the product of  $EFF_t$ ,  $EFF_g$  and  $EFF_i$  is from 0.1 to 0.3 approximately. However this system includes the control valves and dummy nozzles so that the actual efficiency should be multiplied by the air power utilization rate.

The solid lines indicate the prediction by the thermodynamics and wave-kinematic method. The experimental values of the air power conversion efficiency are larger than the predicted values. This is because only one wave power extracting caisson is installed between the reflective caissons and therefore reflected and refracted waves from neighboring caisson can increase the incident wave power into the caisson with wave power conversion.



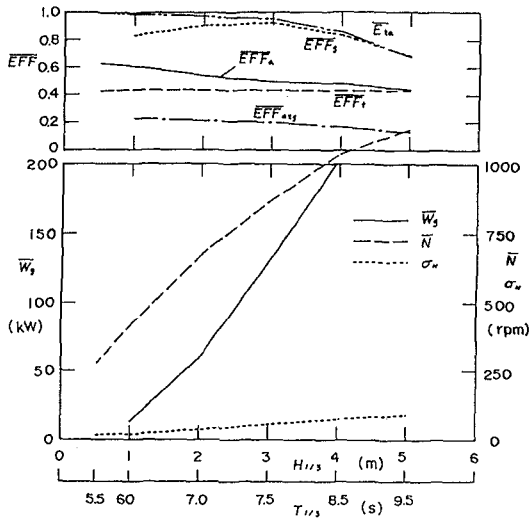


Figure 13 Power Generation by a Full-size System

Table 3 Prediction of Power Generation

	Unit	Sakata (one year)	Sakata (winter)	Wadamari (one year)	Kashima (one year)
Ave. Significant Wave Height	m	1.19	1.79	1.18	1.50
Ave. Significant Wave Period	s	5.64	6.40	7.13	7.88
Ave. Wave Power	kW/m	10.56	19.42	7.60	13.95
Time Rate of Power Generation	%	40.2	65.0	50.0	67.0
Ave. Electric Power	kW/20m	27.3	49.3	23.0	40.9

6. WAVE POWER CONVERSION BY A FULL-SIZE SYSTEM

The turbine-generator is small in the experiment. A full-size system with a larger turbine generator can produce the electricity more. Figure 13 shows the calculated result of the wave power conversion by a full-size system with an optimal turbine generator for the conditions in Sakata Port. The diameter of the turbine is 2.4 m, which is almost twice that in the experiment. The rated power of the generator is 200 kW. The turbine speed is expected to be 700 rpm and the electric power is 75 kW when the significant wave height is 2.2 m. The electric power becomes 200 kW when the significant wave height is 4 m.

Table 3 shows the predicted wave power conversion by a full-size system in Sakata Port, using the conversion efficiencies in Fig. 13 and the observed wave data from 1990 -1991. In the table the predicted results for Wadamari Port in Okino-erabu Island and

Kashima Port in addition to Sakata Port during only winter time are shown for comparison. The annual average electric power in Sakata Port is 27.3 kW and the average value within winter time is 49.3 kW. In Kashima Port the wave power conversion can be made for 67 % of time and the annual average electric power is 40.9 kW.

## 7. CONCLUDING REMARKS

The field experiment was conducted very successfully, although several severe storms attacked the caisson. The characteristics of the wave-activated power generation by the wave power extracting caisson were revealed and the design method of the system was confirmed in this prototype experiments.

Several tests to utilize the output electricity were also made in the experiments. It is important not only to improve the power converter but also to develop the energy utilization systems. The second stage of the field experiment was already started from April 1992, where several utilization systems including a large-scale water pumping system are to be tested and some improvements of the caisson with the turbine generator will be tested.

The field experiments were carried out under the guidance of the advisory committee chaired by professor Y. Goda. The experiments was conducted by the collaboration with many people. The authors wish to express their sincere gratitude to all the people. The authors also wish to thank Dr. Takayama for his crucial review of the manuscript.

## REFERENCES

- 1) OJIMA, R., and Y. GODA: Theory and experiments on extractable wave power by an oscillating water column type breakwater caisson, Coastal Engineering in Japan, Vol. 27, 1984, pp.315-326
- 2) TAKAHASHI, S. et. al.: Turbine Power by wave power extracting system with vertical breakwaters: Proc. of 5th OMAE Conference, April 1986., pp.553-559.
- 3) TAKAHASHI, S.,: Hydrodynamic characteristics of wave power extracting caisson breakwater, 21 ICCE, 1988, pp.2489-2503.
- 4) TAKAHASHI, S., and T. ADACHI: Wave power around Japan from a view point of its utilization, Tech. Note of Port and Harbour Res. Inst. No.654, 1989, 18p.( in Japanese)
- 5) GODA, Y., et. al. : Field verification experiment of a wave power extracting caisson breakwater, - Design and construction of the system and plan for its test operation, International Conference on Ocean Energy Recovery (ICOER), Hawaii, Novem. 1989.
- 6) GODA, Y., et. al. : Construction of a wave power extracting caisson breakwater for field experiments and electric power generation, PACON 90 in Tokyo, June 1990.
- 7) SHIKAMORI, M., et.al.: Field experiment of a wave power extracting caisson breakwater, Coastal Zone 91, July 1991.

## CHAPTER 12

### ON THE TESTING OF MODELS IN MULTIDIRECTIONAL SEAS

E.R. Funke<sup>1</sup> and E.P.D. Mansard<sup>2</sup>

#### Abstract

Although traditional model testing of marine structures in long-crested, uni-directional (2D) waves can lead to conservative results in certain applications, modern multidirectional (3D) wave generators can produce more realistic sea conditions, leading to the design of more accurate, cost-effective and safer structures. This paper justifies the requirements for testing in 3D seas.

#### Introduction

Although wave simulation has been in use for many decades, the first evolutionary step in wave generation technology started approximately 25 years ago with the simulation of long-crested, uni-directional (2D) random waves. These random waves, varying in height and period, were believed to correspond more realistically to sea states encountered in nature.

The next phase in the evolution of wave simulation techniques addressed the control of non-linear waves. These second order waves, which dominate the frequency bands, both below as well as above the first order waves can, under certain circumstances, be of considerable importance to the response of structures.

The present and possibly final phase in the development of wave generation technology is the introduction of directionality to simulation of sea states by means of wave generators whose wave boards are segmented and are able to move with a "serpentine-like" motion. These three-dimensional (3D) seas are made up of

---

<sup>1</sup> Principal Research Officer, <sup>2</sup> Senior Research Officer  
Hydraulics Laboratory, National Research Council of Canada,  
Montreal Road, Ottawa, Canada, K1A 0R6

waves from several directions, and interact to create so-called short-crested seas. Although this concept has been well known for many decades, the ability to individually control, by computer, a large number of contiguous segments has become practical only over the last 15 years. This capability is now expanding very rapidly. It is estimated that there are now 32 institutes throughout the world equipped with this type of wave generator. Nevertheless, most testing of marine structures is still done by two-dimensional irregular regular or wave tests, because many certification authorities still rely on the results obtained from regular wave tests. It is also widely believed that two-dimensional wave simulations of the natural sea state lead to conservative designs, (i.e. results in forces on or motions of structures somewhat greater than in nature).

Therefore, the question arises if it is necessary to provide an expensive multidirectional wave generation capability either when planning new or upgrading existing laboratory facilities. This paper addresses this question.

### Literature Overview

There are now many research publications that compare model tests on marine structures using 2D (unidirectional) or 3D (multidirectional) wave simulation techniques. The results, however, are still somewhat unconvincing, although trends can be identified. Three of the many reasons, which may contribute to a lack of widespread support among design engineers are given below:

- Nearly all laboratories equipped with segmented wave generators for 3D capability, are either totally, or partly, committed to commercial testing work. Consequently, the results of some of the comparative tests are still proprietary to the clients and therefore have not yet been published in the open literature.
- Because multidirectional wave generation technology is relatively recent, there is still disagreement among experts on how best to achieve correct simulations [cf. Sand and Mynett (1987), Miles and Funke 1989 and Miles 1990]. It is difficult and costly to make good quality measurements of the kinematics of three-dimensional waves. In the absence of good measurements, comparisons between multidirectional waves produced in different research institutes are uncertain.
- Many multidirectional sea state simulations have used a spreading index of  $s = 1$  with a  $\cos^2(\theta)$  formulation. This represents only a very limited perspective of the large variety of conditions that may actually prevail.

The Fourier summation technique of wave synthesis is considered to be one of the more satisfactory methods. There are many versions of this method, which would generally lead to similar results if very long wave simulation records were used. However, for scaled physical model studies, the simulations are generally limited to shorter test periods. As a result, several of these currently used synthesis

methods can lead to significant variations in variance and spectral energy distribution, both spatially and temporally. Only the so-called "single summation method", if used over a complete recycling period, will avoid this problem. On the other hand, the single summation method (Miles 1989) also has several variants, some of which may affect the outcome of the test results.

Table 1 summarizes some of the currently available literature on comparative tests between two-dimensional and three-dimensional wave simulations.

### Discussion

The following are a few highlights of the research tabulated in Table 1.

Figure 1a describes the model set-up for the work carried out by Mynett, Bosma and van Vliet (1984). In this study wave loading on a simple, relatively long wave barrier was investigated. The barrier represented a partially submerged gate with 44% immersion and supported by two piers. The barrier was tested to investigate the effect of relative structure-length on wave loading, using both long-crested and short-crested waves.

Figure 1b gives the measured normalized horizontal forces as a function of  $kl$  (*the wave number multiplied by the barrier length*), and compares these to numerical model predictions according to Battjes (1982). When  $s = \infty$ , the spreading function is a spike function, and consequently the sea state is virtually long-crested. On the other hand, for  $s = 1$ , the sea state is short-crested with a broad spreading function [ $\cos^2(\theta)$ ]. As could be expected, a longer barrier is more sensitive to the effects of wave multidirectionality.

As a second example, Figure 2a illustrates a vessel restrained by a single point SALMRA mooring system (Single Anchor Leg Mooring Rigid Arm). The importance of testing such systems in multidirectional seas was first demonstrated by Huntington (1981). His research, which was carried out with an ingenious arrangement of 10 sliding wedge wave generators, placed along a semicircular arch, pointed the way for much of the subsequent development for the testing with realistic sea states.

Figure 2b gives the results that were obtained by Høklie, Stansberg and Werenskiold (1983). These graphs illustrate well how the vessel's motions as well as the forces on the various connecting links differ between short and long-crested wave conditions. All results are presented as a ratio of the standard deviation responses in multidirectional seas to those obtained in long-crested seas. Clearly, roll, yaw and sway are much greater in multidirectional seas. Consequently, the transverse force on the tower and the longitudinal force on the tanker are also much larger.

As a third example the second order long wave phenomenon is considered. As is well known, certain structures, particularly large vessels moored in shallow water, have virtually no response to first order waves, but can experience large motions and mooring forces as a consequence of second order long waves. It is therefore fitting to compare the presence of such second order long waves in either the long-crested wave or the short-crested wave situation. This problem was addressed by Sand (1982).

In two-dimensional (long-crested) waves, all waves with different wave periods propagate in the same direction. The second order long waves are derived from the difference terms derived from pairs of wave frequency components. That is to say, for a component of frequency  $f_1$  and another of frequency  $f_2$ , a second order long wave term of frequency  $(f_1 - f_2)$  is spawned with an amplitude dependent on the water depth and the product of their respective amplitudes,  $a_1 \cdot a_2$ .

In the multidirectional situation, individual frequency components do not travel in the same direction. Although the second order difference frequencies are, as before,  $(f_1 - f_2)$ , their wave lengths are now derived from the vectorial difference given in Figure 3a. The difference wave number vector will be  $k_1 - k_2$ , and will depend on the directional difference,  $\Delta\theta$ , between the two components. The larger the wave number of this difference frequency long wave component, the shorter will be its wave length. Another effect will be that the spreading function of these second order terms will broaden out substantially, as is shown in Figure 3b. It can also be shown that the long wave amplitudes in multidirectional waves are reduced by a factor of 5 to 10, depending on the water depth.

Sand (1982) described this phenomenon, as summarized in Figures 3b and 3c. Figure 3c provides information about the reduction in the wave length of the second order long wave components for bichromatic multidirectional waves. This is presented as a ratio of the resultant wave length difference for the multidirectional case to that for the unidirectional case,  $\Delta L / \Delta L_u$ . The information is given for a normalized frequency, for two frequency ratios  $(f_1 - f_2) / f_2$  and for two angular differences of  $\Delta\theta$ . This result is particularly interesting in connection with natural periods of harbour resonances (i.e. the resonance wave lengths of harbours).

Because the long wave generation process through non-linear wave/wave interaction has been significantly reduced as a result of multidirectionality, it stands to reason that the penetration of this long wave energy into harbours is also reduced significantly. Figure 3d, which was taken from van der Meer (1989) provides an example for two different wave directions relative to the harbour entrance. It also gives the corresponding reductions for a moored vessel's surge motion.

TABLE 1: COMPARISON OF STRUCTURAL RESPONSES IN 2D AND 3D SEAS

TEST STRUCTURE	TYPE OF MODEL	PARAMETERS UNDER STUDY	MAIN CONCLUSIONS FOR TYPICAL CONDITIONS	REFERENCE
Partially submerged barrier supported by two piers	Physical	Horizontal force on the barrier	Reduction in loads up to 50% in 3D seas	Mynett, Bosma and van Vliet (1984)
Haringvliet barrier (Delta project in the Netherlands)	Field study	Fluid dynamic pressures on the barrier	For the highest reliable frequency of the spectrum, the wave load reduction factor due to directional spread could be as small as 0.25.	van Heteren, Botma and Roskam (1989)
Long floating cylinder of arbitrary shape	Theoretical	Wave loads and motions	The 1st order sway and roll force reduction factors could be as low as 0.41 for short-crested seas. Only about 58% of the sway, heave and roll motions obtained under 2D are encountered in 3D situations.	Isaacson and Nwogu (1987)
Forces on a large vertical cylinder	Theoretical and physical	Pressures, forces and moments in 3D seas	The ratio of forces and moments for 3D relative to 2D seas in-line component is: In-line: 0.90 Transverse: 0.45	Huntington and Thompson (1976)
Forces on a pile	Theoretical and physical	In-line and transverse wave forces on a submerged segment	The ratio of RMS values of forces for 3D relative to 2D seas in-line component is: In-line: 0.87 Transverse: 0.50	Isaacson and Nwogu (1988)
Segmented cylinder	Theoretical and physical	In-line and transverse force spectra for a segment above the S.W.L.	The ratio of RMS values of forces for 3D relative to 2D seas is: In-line: 0.83 Transverse: 0.56	Isaacson et al (1988)
Segmented cylinder (submerged segments)	Theoretical and physical	Probability distribution of maxima of resultant forces	Decreasing force maxima with increasing spreading. For instance, the measured values of the ratio of largest force maximum to the standard deviation were 3.98 in long crested and 3.31 in short crested seas.	Nwogu and Isaacson (1989(a))

TABLE 1 (continued 1)

Compliant tower	Physical	In-line, transverse and total response	Directionality has little influence on the total response, but a decrease in in-line response and an increase in transverse response becomes predominant with increasing spreading.	Cornett (1988)
Horizontal accelerations	Theoretical	Spectra of 2 <sup>nd</sup> order horizontal accelerations caused by wave set-down	In shallow water, even for a narrow directional spread, the in-line spectral component of the acceleration could be as low as 10% of the 2D response.	Molin and Fauveau (1984)
Harbour and moored ship	Physical	Low frequency energy within harbour and surge motion	Reduction in 3D seas: up to 30% in low frequency activity and more than 75% in surge motion	van der Meer (1989)
Floating barge, moored	Theoretical and physical	Drift motions and mooring loads	The mean value of the low frequency surge motions was reduced by as much as 50% in 3D seas. The mean, standard deviation and maxima of the mooring line loads were reduced by as much as 37%, 25% and 21% respectively.	Nwogu and Isaacson (1989(b))
Single point mooring	Physical	Motions and yoke / tanker hinge force	In 3D, significant increase in sway, roll and yaw motions and in forces at the hinge points.	Huntington (1981)
Moored vessel in open sea	Physical	Motions and mooring loads	In head seas, mooring loads, sway and yaw motions are larger by a factor of 2 in 3D seas. In beam seas the tendency reverses. In quartering seas, the difference between the results of 2D and 3D are small.	Kirkegaard, Sand, Ottesen-Hansen, and Knudsen (1980)
Large offshore floating structures	Theoretical	Transfer functions of motions and forces	Transverse components of force and motion predicted to be negligible in 2D seas are significant in 3D. Typically, the maximum sway motion represents 59 % of the maximum surge.	Isaacson and Sinha (1986)



TABLE 1 (continued 2)

Coupled, articulated tower/ship system	Theoretical	Wave loading on the yoke and motions of the coupled system	Response in 3D seas: maximum structural response values are about 20-25% lower than those predicted with 2D seas.	Heivacioglu and Incecik (1989)
Bi-articulated mooring column	Physical	Tanker motions and forces on the yoke connections	Head-on conditions: the high frequency motions of sway, roll and yaw are nearly twice as large in 3D as in 2D. The tanker/yoke hinge force is 2 to 2.5 times larger in 3D.	Römeling, Marol and Sand (1984)
Single point moored tanker	Physical	Force on tanker/yoke hinge connection and motions	The longitudinal hinge force is generally increased by a factor of 2.5 in 3D seas while the significant sway and yaw motions are up by a factor of 4.	Høklie, Stansberg and Werenskiold (1983)
Semi-submersible, moored	Physical	Motion and mooring loads	In the low frequency domain, near natural frequencies, heave, pitch and roll motions are reduced by as much as 30% in 3D seas. Similar reduction is also found for the in-line and transverse forces. However, no simple relationship exists between 2D and 3D responses.	Sand, Römeling and Kirkegaard (1987)
Jacket structure on a barge for transportation	Theoretical and physical	Motions of the barge, accelerations at the system's and jacket's centres of gravity and at a mud-mat.	Directional spreading sometimes increases motions, loads and accelerations, and 2D waves may not always provide a conservative approach for design.	Standing, Rowe and Brendling (1986)

### Conclusions

Based on the experience gained with the segmented wave generator system at the Hydraulics Laboratory of the National Research Council of Canada, and on the information available through the published literature or verbal communications, the following statements with regard to the merits of testing in multidirectional waves can be made:

- Whenever significant non-linearities are present in the response of structures to waves, the principle of superposition is not valid. Consequently, it is essential to evaluate such structures through the use of realistic simulations of the natural sea state. Two-dimensional wave simulations are not realistic for this purpose.
- Group-bound long wave activity is significantly lower in three-dimensional than in two-dimensional seas. For the investigation of large floating structures, such as tankers, landing strips, floating plants, which will be subject to wave group-induced drift loads, this will be a significant factor. Three-dimensional waves will lead to smaller drift displacements and mooring loads.
- The excitation of harbour seiches will be smaller with three-dimensional than with two-dimensional waves.
- Structures, which have small torsional resistance, will be subject to larger yaw motions when subjected to three-dimensional seas. Typical examples of such structures are compliant towers or tension leg platforms (TLPs) as well as semi-submersibles.
- Motions of vessels with single point moorings are greater in three-dimensional than in two-dimensional seas, resulting also in larger mooring loads. In particular, "fishtailing" motions will be accentuated.
- Dynamic positioning systems for floating structures will be more difficult to operate in multidirectional than in unidirectional waves.
- Wave loading on fixed, long structures can be assumed to be generally smaller in multidirectional seas.

In summary, the absence of correct three dimensional wave simulations can grossly underestimate design requirements. Although two-dimensional wave simulations can sometimes produce reasonably conservative (i.e. large) results, in many cases it would result in excessive over-design. Therefore, model testing in multidirectional seas is strongly recommended to improve designs of marine structures for cost-effectiveness and safety.

### Acknowledgements

Permission to use illustrations is gratefully acknowledged from: S.E. Sand, C.T. Stansberg, A.E. Mynett, J.W. van der Meer, Elsevier Publishing B.V., and Offshore Technology Conference

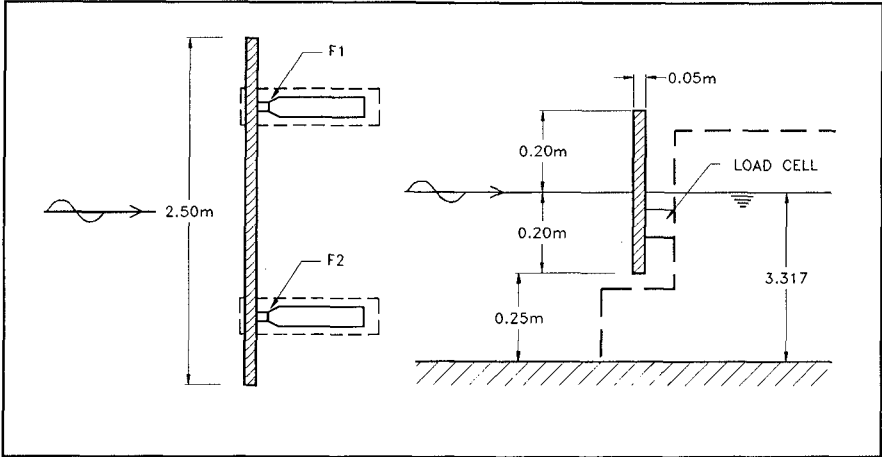


Figure 1a: HYDRAULIC MODEL FOR A STORM SURGE BARRIER

Mynette et al (1984)

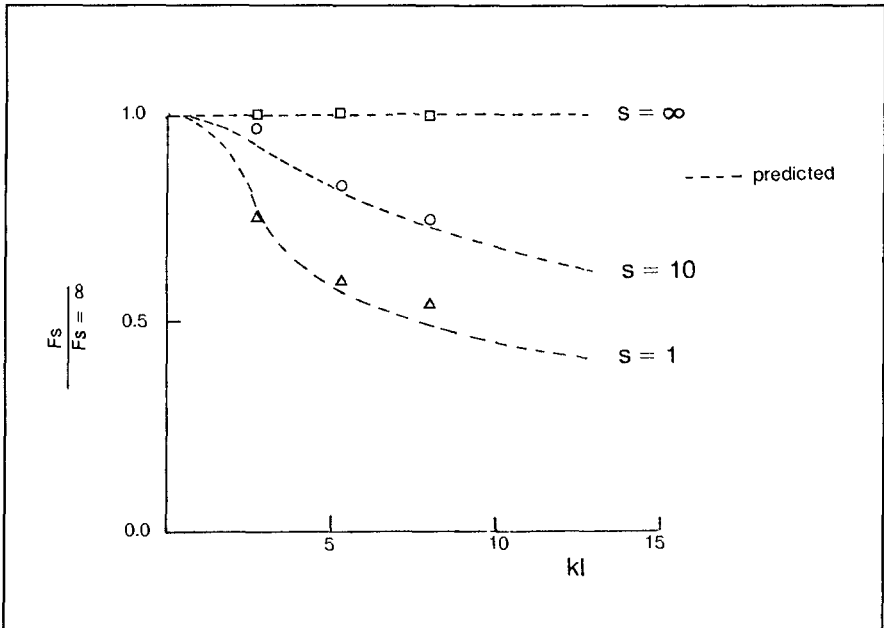


Figure 1b: MEASURED AND COMPUTED FORCE REDUCTION FACTORS

(Mynette et al (1984))

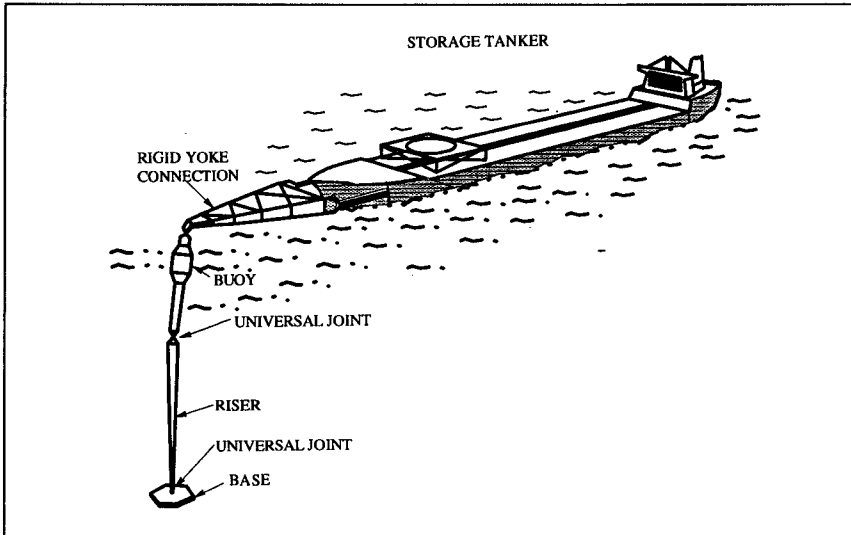


Figure 2a: CONCEPTUAL DESIGN OF SALMRA MOORING SYSTEM

Høkkie et al (1983)

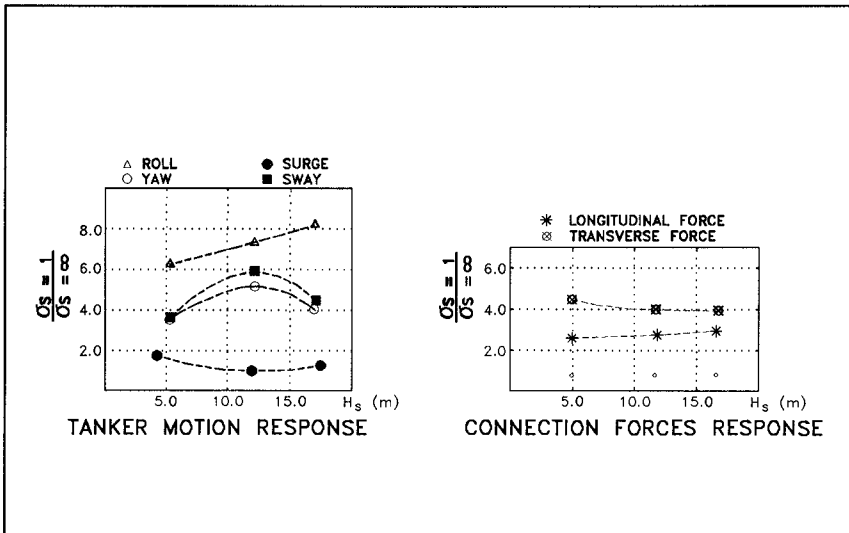
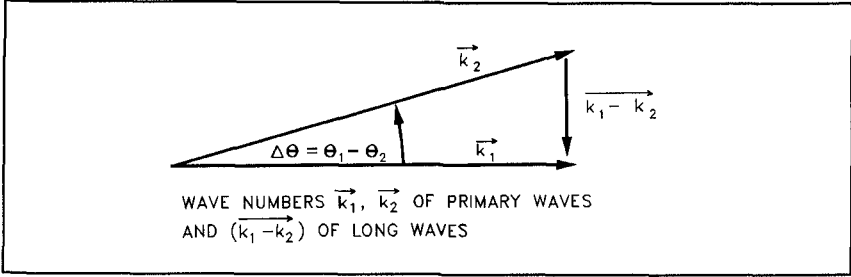
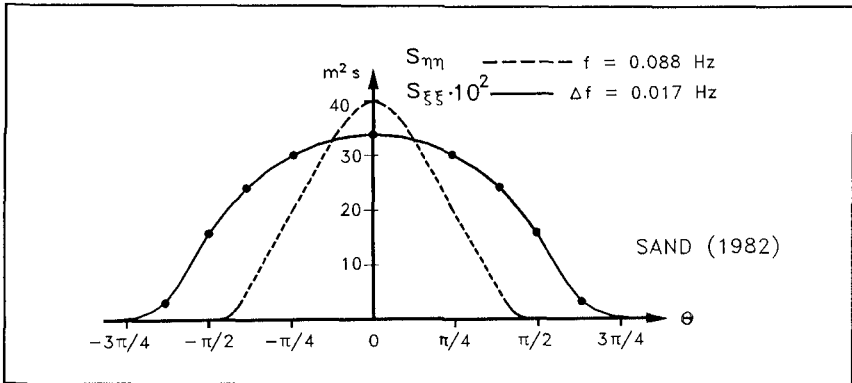


Figure 2b: RESPONSE OF THE MOORING SYSTEM

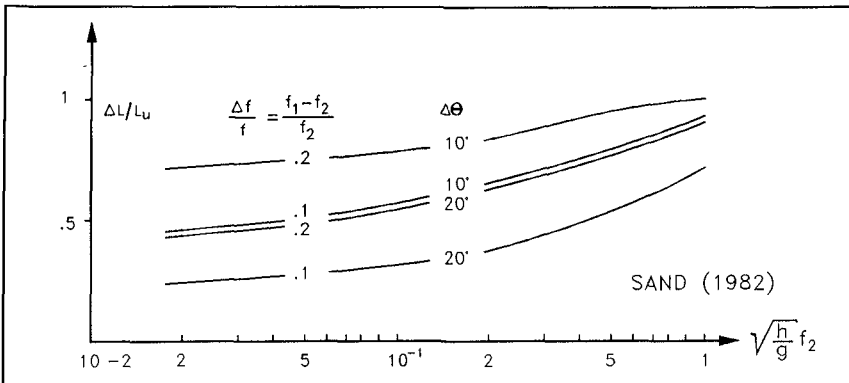
Høkkie et al (1983)



**Figure 3a: WAVE NUMBERS OF SHORT AND LONG WAVES**



**Figure 3b: SPREADING FUNCTIONS OF SHORT AND LONG WAVES**



**Figure 3c: REDUCTION OF WAVE LENGTH OF DIRECTIONAL LONG WAVES**

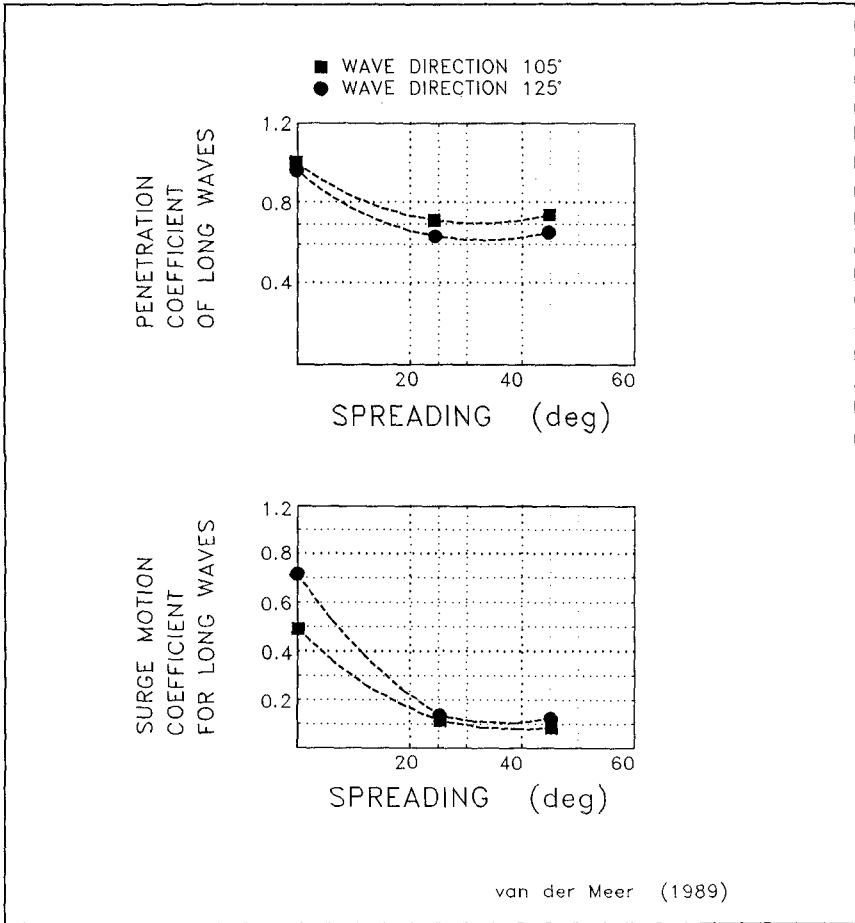


Figure 3d: WAVE DIRECTIONALITY EFFECTS ON LONG WAVE PENETRATION AND SURGE MOTION

### References

1. Battjes, J.A., "Effects of Short-Crestedness on Wave Loads on Long Structures", Applied Ocean Research, Vol. 4, No. 3, pp 165-172.
2. Cornett, A., "Dynamic Response of a Compliant Tower Test Structure in Two- and Three-Dimensional Seas", Proc. Ocean Structural Dynamics Symposium 1988, Oregon, 1988.
3. Helvacioğlu, I.H., and Incecik, A., "Second-Order and Short-Crested Wave Effects in Predicting the Behaviour of a Compliant Structure", Proc. 8th Int. Conf. on Offshore Mechanics and Arctic Engineering, The Hague, The Netherlands, 1989.
4. van Heteren, J., Botma, H.C., and Roskam, A.P., "Field Measurements of Directional Wave Loads on Coastal Structures", Proc. Applied Ocean Research, Vol.11, No.2, 1989.
5. Høklie, M., Stansberg, C.T., and Werenskiold, P., "Model Tests with a Single-Point Mooring System in Short-Crested Waves", paper 4644, 15th Offshore Technology Conference, Texas, 1983.
6. Huntington, S.W. and D.M. Thompson, "Forces on Large Vertical Cylinder in Multidirectional Random Waves", paper 2539, 8th Annual Offshore Technology Conference, Texas, 1976.
7. Huntington, S.W., "Wave Loading in Short Crested Seas", Int. Conf. on Wind and Wave Directionality, Paris 1981.
8. Isaacson, M. and Sinha, S., "Directional Wave Effects on Large Offshore Structures", Journal of Waterway, Port, Coastal and Ocean Engineering, Vol. 112, No. 4, July 1986.
9. Isaacson, M., and Nwogu, O., "Wave Loads and Motions of Long Structures in Directional Seas", Transactions of the ASME, Vol. 109, May 1987.
10. Isaacson, M., Nwogu, O., and Cornett, A., "Short-Crested Wave Forces on a Cylinder", Proc. Ocean Structural Dynamics Symp. 1988, Oregon, 1988.
11. Isaacson, M. and Nwogu, O., "Short-Crested Wave Forces on a Vertical Pile", Proc. 7th Int. Conf. on Offshore Mechanics and Arctic Engineering, Houston, Texas, 1988.
12. Kirkegaard, J., Sand, S.E., Ottesen Hansen, N.-E., and Knudsen, M.H., "Effects of Directional Sea in Model Testing", Proc. Ports 1980, Norfolk, Virginia, 1980.
13. van der Meer, J.W., "Measurement and Analysis of Directional Seas in a Basin", Proc. 23rd IAHR Congress, Ottawa, Ontario 1989.

14. Miles, M.D., "A Note on Directional Random Wave Synthesis by the Single-Summation Method", Proc. 23rd IAHR Congress, Ottawa, Canada, Aug 21-25, 1989.
15. Miles, M.D. and Funke, E.R., "A Comparison of Methods for Synthesis of Directional Seas, A.S.M.E. Journal of Offshore Mechanics and Engineering, Vol. 111, No.1, Feb. 1989, pp 43-48.
16. Miles, M.D., "Numerical Models for Synthesis of Directional Seas", Technical Report, Hydraulics Laboratory, National Research Council of Canada, TR-HY-016, NRC No. 31610, May 1990.
17. Molin, B., and Fauveau, V., "Effect of Wave-Directionality on Second-Order Loads Induced by the Set-Down", Applied Ocean Research, Vol.6, No. 2, 1984.
18. Mynett, A.E., Bosma, J., and van Vliet, P., "Effects of Directional Seas in Coastal Regions", Proc. Symp. on Description and Modelling of Directional Seas, Copenhagen, Denmark, 1984. Also published as Delft report no. S596.
19. Nwogu, O, and Isaacson, M., "Force Distributions Due to Random Short-Crested Waves", Proc. 23rd IAHR Congress, Ottawa, Canada, 1989(a).
20. Nwogu, O, and Isaacson, M., "Drift Motions of a Floating Barge in Regular and Random Multi-Directional Waves", Proc. 8th Int. Conf. on Offshore Mechanics and Arctic Engineering, The Hague, The Netherlands, 1989(b).
21. Römeling, J.U., Marol, P. and Sand, S.E., "Bi-Articulated Mooring Column Tested in Directional Waves", Proc. Symp. on Description and Modelling of Directional Seas", Copenhagen, Denmark, 1984.
22. Sand, S.E., "Long Waves in Directional Seas", Coastal Engineering, Vol. 6, 1982, pp 195-208.
23. Sand, S.E. and Mynett, A.E., "Directional Wave Generation and Analysis", Proc. IAHR Seminar on Wave Analysis and Generation in Laboratory Basins", 22nd IAHR Congress, Lausanne, Switzerland, September 1987.
24. Sand, S.E., Römeling, J., and Kirkegaard, J., "Influence of Wave Directionality on Response of Semisubmersible", Proc. 6th Int. Conference on Offshore Mechanics and Arctic Engineering Symposium, Houston, Texas, 1987.
25. Standing, R.G., Rowe, S.J., and Brendling, W.J., "Jacket Transportation Analysis in Multidirectional Waves", Proc. 18th Offshore Technology Conference, Houston, Texas, 1986.



## CHAPTER 34

### Numerical Validation of Directional Wavemaker Theory with Sidewall Reflections

E.P.D. Mansard,\* M.D. Miles\* and R.A. Dalrymple†

#### ABSTRACT

A directional wavemaker theory has been developed by Dalrymple to produce a desired oblique planar wave train at any cross-section in the basin. This theory, which uses the reflections from the sidewalls of the basin, can also account for slowly varying depths. This paper describes a numerical validation of this theory, for the constant depth situation, by a wave diffraction model that was recently verified through an extensive series of experimental investigations.

#### 1.0 INTRODUCTION

To generate a specified multidirectional wave field in a laboratory basin, the board motions of a segmented wave generator are generally computed on the basis of the snake principle. Although this technique is being used extensively, it has some limitations. For instance, it cannot account for the effects of reflection from sidewalls and the diffraction due to a segmented wave generator of finite length. Also, the size of the optimal testing area inside the model basin that results from this technique can be quite small, particularly if the maximum angle of directional spread is large. In order to overcome some of these limitations, research has been under way in leading hydraulics laboratories around the world into improved techniques for the simulation of multidirectional waves.

Funke & Miles (1987) developed an extension of the snake principle which can be used to obtain a larger useful working area in a multidirectional wave basin. This technique, known as the corner reflection method, makes use of intentional reflections from partial sidewalls about 5m long on both sides of the basin, extending from each end of the wave generator. Like the snake principle itself, however, waves generated by this method are still subject to wave diffraction errors.

---

\*Senior Research Officer, National Research Council of Canada

†Director, Center for Applied Coastal Research, University of Delaware, U.S.A.

Recently, Dalrymple (1989) developed a technique by which an oblique planar wave train of any desired angle of incidence can be generated at any pre-selected cross-section in the basin. This technique was based on a splitting procedure used on the mild slope equation to develop a propagation equation for the wave potential within a wave basin with reflecting sidewalls and a bottom which may have a slope in the direction perpendicular to the wave generator. The resulting equation was solved analytically to determine the wave fields as a function of distance from the generator segments, given their motions.

The major advantage of the Dalrymple theory is that diffraction, refraction and shoaling processes are all properly accounted for, within the realm of linear wave theory. It is also possible to use this technique to calculate the segmented wave generator paddle motions required to produce a pure full-width oblique plane wave train at a specified distance,  $D$ , from the wavemaker. Multidirectional wave fields are typically generated by the linear superposition of many oblique plane wave components. If the Dalrymple theory is used to generate each component, instead of the snake principle, then the area of the basin where the desired multidirectional wave field can be accurately reproduced will be much larger.

The analytic solution used in the Dalrymple method is only applicable to the case of a wave basin with full-length reflecting sidewalls. The desired oblique plane waves are obtained only at the specified distance  $D$  from the wavemaker. As the waves propagate further down the basin, they gradually become contaminated by diffraction and reflection from the sidewalls. The undesired reflection effects can be avoided by using side absorbers at distances greater than  $D$ , although diffraction effects will still occur. In many model testing applications, the use of partial-length sidewalls is also necessary to reduce errors which would otherwise be caused by sidewall reflection of the diffracted wave field produced by the structure being tested.

It was therefore decided to carry out a numerical study to investigate the performance of the Dalrymple method in a typical multidirectional wave basin with partial-length sidewalls. Wave paddle motions were calculated by the Dalrymple method and the resulting wave field in the basin was then computed by using the linear diffraction model developed by Isaacson (1989). This model can calculate the wave field at any position in the basin, whereas the Dalrymple theory can only be used in the region between the reflecting sidewalls. Another reason for choosing the Isaacson model was that it has recently been verified by extensive experiments in a directional wave basin by Hiraishi et al. (1991). The present numerical study was restricted to the case of a constant depth basin because the Isaacson model cannot be used for a basin with a sloping bottom. In addition to investigating partial-length sidewall effects, the Isaacson model also provided an independent verification of the paddle motions predicted by the Dalrymple method.

## 2.0 THEORETICAL BACKGROUND OF DALRYMPLE'S THEORY

A brief description of Dalrymple's theory is outlined here. Dalrymple (1989) contains a more detailed presentation.

The wave basin is rectangular with width  $2b$ . The co-ordinate axes are located at the centre of the wave generator with the  $y$  axis directed along the generator and the  $x$  axis directed perpendicularly into the basin. The sidewalls of the basin at  $y = \pm b$  are impermeable.

The mathematical theory used in this model follows the treatment of Dalrymple and Kirby (1988) for the combined diffraction and refraction of waves on sloping beaches. The assumed linear water wave motion is described by a velocity potential satisfying the mild slope equation. This mild slope equation, which governs the progressive wave mode and neglects the evanescent wave mode, can be written as:

$$\Phi(x, y, z, t) = \phi(x, y) \frac{\cosh k(h+z)}{\cosh kh} \cdot e^{-i\omega t} \quad (1)$$

$$\frac{\partial}{\partial x} \left( CC_g \frac{\partial \phi}{\partial x} \right) + CC_g \frac{\partial^2 \phi}{\partial y^2} + k^2 CC_g \phi = 0 \quad (2)$$

where  $CC_g$  is the product of the wave phase velocity and group velocity. The wave number,  $k$ , is related to the water depth,  $h(x)$ , and the angular wave frequency,  $\omega$ , by the linear dispersion relationship.

The above equations are consistent with small amplitude assumptions and the imposition of a mild bottom slope. At the sidewalls of the basin ( $y = \pm b$ ), there is no flow normal to the walls. Therefore,

$$\frac{\partial \phi}{\partial y} = 0 \quad \text{on} \quad y = \pm b \quad . \quad (3)$$

To satisfy these two lateral boundary conditions,

$$\phi(x, y) = \hat{\phi}(x) \sum_{n=0}^{\infty} (a_n \cos \lambda_n y + b_n \sin \gamma_n y) \quad (4)$$

where  $\lambda_n = (n\pi/b)$  and  $\gamma_n = (n + \frac{1}{2})\pi/b$  for  $n = 0, 1, 2, \dots, \infty$ .

The reduced mild slope equation becomes two equations:

$$\frac{\partial}{\partial x} \left( CC_g \frac{\partial \hat{\phi}}{\partial x} \right) + CC_g (k^2 - \alpha^2) \hat{\phi} = 0 \quad (5)$$

where  $\alpha = \lambda_n$  or  $\gamma_n$  depending on which of the forms of the solution in Equation (4) is used.

The reduced wave potential,  $\hat{\phi}$ , can consist of waves propagating in the positive and negative  $x$  directions, i.e.  $\phi^+$  and  $\phi^-$ . Adopting the splitting procedure,

assuming the reflected waves to be small and, therefore, neglecting the negative potential  $\phi^-$ , the total forward propagating velocity potential can be written as:

$$\Phi(x, y, z, t) = (\phi_e^+ + \phi_o^+) \frac{\cosh k(h+z)}{\cosh kh} e^{-i\omega t} \tag{6}$$

where

$$\phi_e^+ = \sum_{n=0}^{\infty} A_{n0} K_{sr}(x, \lambda_n) e^{i \int_0^x \sqrt{k^2 - \lambda_n^2} dx} \cos \lambda_n y \tag{7}$$

$$\phi_o^+ = \sum_{n=0}^{\infty} B_{n0} K_{sr}(x, \gamma_n) e^{i \int_0^x \sqrt{k^2 - \gamma_n^2} dx} \sin \gamma_n y \tag{8}$$

and  $K_{sr}$  is the product of the shoaling and refraction coefficients. The subscripts  $e$  and  $o$  refer to even and odd solutions about the  $y = 0$  axis. Some of the “progressive” waves are evanescent, those for which  $\lambda_n$  or  $\gamma_n > k(x)$ . In most cases, when only the far wave field is required, the largest value of  $n$  to be retained in the summation is only on the order of 10–20. Although the solution for the velocity potential,  $\phi$ , is analytic, the phase integrals are determined numerically by the Euler integration method.

In the parabolic forms of the equation, the condition at the wave paddles ( $x = 0$ ) is an initial condition that forces the wave-induced water motions (defined by  $\partial\phi/\partial x$ ) to match the motion of each wave paddle.

The wave paddle motion is assumed to have a linear phase shift along the  $y$  axis, leading to the generation of a plane wave train with an angle of incidence,  $\theta$ , with respect to the  $x$  axis. Thus, the paddle motion will be described by the real part of

$$X = S_0 g(z) e^{i(\lambda_0 y - \omega t)} \tag{9}$$

where  $g(z)$  is the vertical dependence of the paddle motion over the water depth,  $\lambda_0 = k \sin \theta$  is the  $y$ -component of the wave number of the desired wave and  $S_0$  is the maximum amplitude of the paddle stroke at the mean free surface.

The linearized initial condition for this wave generator, in terms of the horizontal velocity in the  $x$  direction, is specified by even and odd contributions about the  $y$ -axis. Now matching the even and odd solutions to the horizontal velocity determined from the velocity potential at  $x = 0$ , and exploiting various orthogonal properties of the functions that occur in this problem, the expressions for the coefficients  $A_{n0}$  and  $B_{n0}$  simplify to:

$$A_{n0} = -\frac{2(-1)^n S_0 \omega G \lambda_0 \sin(\lambda_0 b)}{(\lambda_0^2 - \lambda_n^2) \sqrt{k^2 - \lambda_n^2} b} \tag{10}$$

and

$$B_{n0} = -\frac{2i(-1)^n S_0 \omega G \lambda_0 \cos(\lambda_0 b)}{(\lambda_0^2 - \gamma_n^2) \sqrt{k^2 - \gamma_n^2} b} \tag{11}$$

for the case of a wave generator spanning the full width of the basin.

The wave field generated in the basin, for a given set of paddle motions, can be computed with these expressions. Alternatively, if it is required to produce a desired oblique plane wave train extending across the full width of the basin at a given  $x$  location, this can easily be done by determining the initial coefficients  $A_{n0}$  and  $B_{n0}$ , not at  $x = 0$  as before, but at the desired location  $x = x_D$ . This yields new values of the coefficients

$$A'_{n0} = \frac{A_{n0} e^{i \int_0^{x_D} \sqrt{k^2 - \lambda_0^2} dx}}{K_{sr}(x_D, \lambda_n) e^{i \int_0^{x_D} \sqrt{k^2 - \lambda_n^2} dx}} \quad (12)$$

and

$$B'_{n0} = \frac{B_{n0} e^{i \int_0^{x_D} \sqrt{k^2 - \lambda_0^2} dx}}{K_{sr}(x_D, \gamma_n) e^{i \int_0^{x_D} \sqrt{k^2 - \gamma_n^2} dx}} \quad (13)$$

where  $\lambda_0$  is evaluated at  $x_D$ . The wave paddle motion is now obtained from Equations 7 and 8 evaluated at  $x = 0$ , resulting in the summation of various sinusoidal motions.

Although Dalrymple (1989) provides some preliminary validation of this technique using the same theory, a more detailed validation has been carried out in this study using the Isaacson (1989) diffraction model, which has recently been verified by an extensive set of physical experiments. A brief description of the Isaacson model and its experimental verification is given below.

### 3.0 THEORETICAL BACKGROUND OF THE ISAACSON MODEL

This model was developed by Isaacson (1989) to predict the wave field in a multidirectional wave basin. It is based on linear wave diffraction theory and uses a boundary element representation of the segmented wave generator and the reflecting walls of the basin.

Isaacson defines a velocity potential satisfying the Helmholtz equation within the fluid region and the boundary conditions along the generator faces and any specified reflecting walls. A suitable radiation condition is also applied so that the remaining parts of the wave basin boundary are treated as perfect wave absorbers.

The potential  $\phi$  may be expressed as the potential due to a distribution of point wave sources along the generator faces and any reflecting boundaries. Thus,

$$\phi(\mathbf{x}) = \frac{1}{4\pi} \int_S f(\xi) G(\mathbf{x}; \xi) dS \quad (14)$$

where  $S$  denotes the horizontal contour along the generator faces and fixed walls and  $f(\xi)$  represents the source strength distribution function.  $G(\mathbf{x}; \xi)$  is a Green's function for the potential at an arbitrary point  $\mathbf{x}$  due to a point wave source located at the point  $\xi$  on  $S$ , and  $dS$  denotes a differential length along  $S$ .

The boundary condition along  $S$  equates the flow velocity component normal to  $S$  to the wave paddle velocity along a generator face and to zero along a reflecting wall. This gives an integral equation for  $f(\xi)$  which is then solved by using a discrete representation of the horizontal contour,  $S$ , with a finite number of short straight elements and assuming the source strength to be constant over each element. Using this approximation, the integral equation is satisfied at the centre of each boundary element and is thus reduced to a set of linear equations for the source strengths. The velocity potential,  $\phi$ , is obtained from the solution of these equations and a discrete version of Equation 14. Once the potential is known, the height and the phase angle of the waves at any point in the basin can be calculated easily.

The most important parameter in this numerical model is the total number of discrete boundary elements that are required to predict the wave field in the basin. Reducing the boundary element length increases the accuracy of the predicted wave field but eventually leads to excessive computational effort. Hiraishi et al. (1991) undertook a numerical investigation to determine the optimum ratio of boundary element length to wave length required to obtain reliable results. These predictions were subsequently validated by an extensive experimental program.

#### 4.0 EXPERIMENTAL VALIDATION OF THE ISAACSON MODEL

The amplitudes and phases of wave trains predicted by this diffraction model for different combinations of wave periods and angles of incidence, were compared to measurements made at more than 200 locations in a test basin. A brief description of this experimental investigation is given below.

The experiments were carried out in the multidirectional wave basin of the NRC Hydraulics Laboratory, which has a length of nearly 20m and a width of 30m. A segmented wave generator consisting of 60 segments, each with a width of 0.5m is located along one 30m side of the basin.

Perforated sheet metal wave absorbers, developed by the NRC Hydraulics Laboratory to yield less than 5% reflection, were installed along the other three sides of the basin. Removable sidewalls could be used to cover the side absorbers, either totally or partially.

In order to scan the sea states prevailing at different locations in the basin, a steel frame was designed to accommodate nineteen wave gauges. This steel frame, shown in Figure 1, was suspended at a single point from a hoist which was in turn attached to a trolley. This trolley ran, through remote-control, on a track under the ceiling over the centre of the basin aligned in a direction normal to the face of the wave generator. The frame could also be rotated about its suspension point to make simultaneous measurements of wave profiles along a line parallel to the crest of an oblique wave.

Validation of the Isaacson diffraction model was carried out using both long-



Figure 1: Photograph of Steel Frame with Wave Gauges

crested normal and oblique regular waves. Waves with periods ranging from 1.5s to 2.25s were produced by the snake principle and also by the NRC corner reflection method, using short reflecting sidewalls of approximately 5m length.

Since the Isaacson model is based on linear theory, wave heights were kept under 20cm. For each sea state, wave measurements at different cross-sections in the basin were carried out by relocating the 19-probe frame at different target positions. At each position, wave generation and data sampling were exercised for 180s. In order to correlate measurements made at the various cross-sections in the basin, the data acquisition was synchronized with the activation of the wave generator. A large number of tests was carried out to ensure repeatability of the sea states. Sufficient time was allowed for the oscillations in the basin to settle down between successive tests. While a detailed presentation of these investigations can be found in Hiraishi et al. (1991), one example of the comparison between numerical and physical model results is presented here.

The points in Figure 2a show the wave height distribution realized at three different measurement lines, as well as the corresponding numerical predictions, for 2s waves propagating in a line parallel to the wave generator. The distances of these lines, measured from the wave paddles and expressed as  $X_c$ , are indicated in the figure.

Figure 2b illustrates results of oblique waves with  $\theta = 30^\circ$ , measured in a line parallel to the wave generator (i.e.  $\alpha = 0^\circ$ ) and parallel to the crest line ( $\alpha = 30^\circ$ ). For the sake of easier comparison, the measured wave heights,  $H$ , are normalized

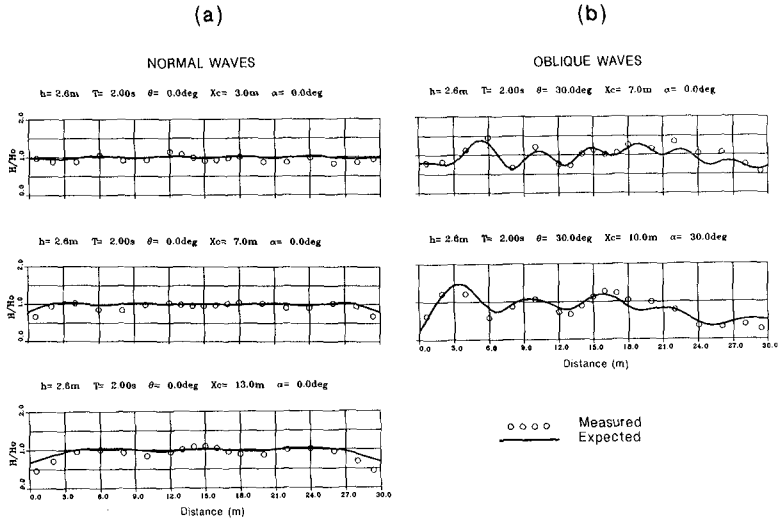


Figure 2: Comparison of Measured and Predicted Waves for Isaacson Model

with respect to the target heights,  $H_0$ . It can be seen from this figure that the measured wave heights agree reasonably well with the predicted ones. Similar cases of good agreement were found for all periods except one that stimulated cross-mode waves in the experimental basin. Interested readers should refer to Hiraishi et al. (1991) for a complete presentation of the results.

Based on these experimental investigations, it was concluded that the Isaacson numerical model can predict the generated wave field quite well for a specified basin layout and a specified set of segmented wave generator paddle motions.

## 5.0 VALIDATION OF DALRYMPLE'S THEORY

### 5.1 Validation Procedure

Since the Isaacson diffraction model has been extensively validated by the experiments described above, it was decided to use it to assess the effectiveness of the Dalrymple method. Although Dalrymple's theory itself can be used to predict the water surface elevation, this can only be done in the region between the reflecting sidewalls. Since the wave field at the wavemaker is rather complex for the Dalrymple method, the accuracy of the oblique plane wave produced may also be limited by the finite width of the wavemaker segments. The Isaacson model allows the wave field to be calculated at all points in a basin of constant depth, and also can model the effects of finite segment width.



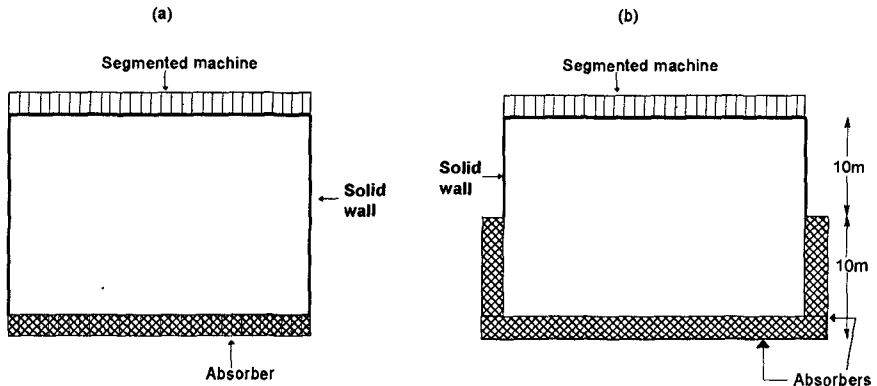


Figure 3: Layout of Basins for Verification of Dalrymple's Theory

In view of these considerations, the following procedure was used to investigate the performance of the Dalrymple method in a typical wave basin:

- Use Dalrymple's theory to estimate the required paddle motions of the segmented wave generator for the reproduction of a given sea state at the desired location.
- Use the computed motions as inputs to the Isaacson diffraction model to predict the wave field inside the test basin and determine how accurately the desired sea state can be realized at various locations.

The layouts of the basin used in this numerical procedure are shown in Figure 3. These layouts correspond to the NRC Hydraulics Laboratory basin described above. Two different cases of sidewall lengths were chosen for this study. Figure 3a represents the situation where the two sides are covered fully with reflecting walls, while Figure 3b corresponds to sidewalls extending only 10m from the paddles; the remaining 10 metres on each side consist of absorbers. In both cases, the wavemaker was assumed to have a segment width of 0.5m.

According to Dalrymple's theory, it is possible to reproduce a desired oblique wave train at any cross-section in the basin up to the limit of the reflecting sidewalls. Consequently, the desired wave train can be produced at any distance from 0 to 20m from the wavemaker in the layout of Figure 3a but only at distances between 0 and 10m for the case of Figure 3b.

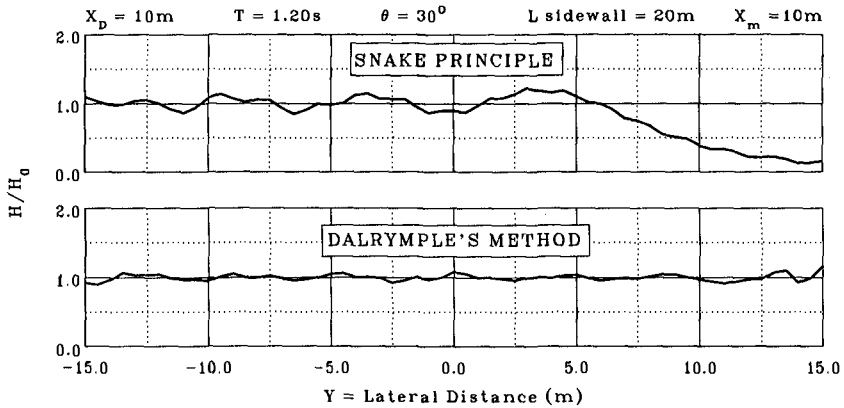


Figure 4: Wave Height Distributions at  $x_D = 10\text{m}$  for Snake Principle and Dalrymple Method

## 5.2 Results of the Validation Procedure

### 5.2.1 Full-length sidewalls

A comparison of the snake principle with no sidewalls and the Dalrymple method with full-length sidewalls is shown in Figure 4 for a wave train with a period of  $T = 1.2\text{s}$  and a propagation angle of  $\theta = 30^\circ$ . The wave height distributions for both methods were calculated by the Isaacson model. It can be seen that wave height uniformity is greatly improved with the Dalrymple method, not only in the main diffraction zone at the right, but in the centre of the basin as well.

Wave height distributions, at various distances from the wavemaker, are shown in Figure 5 for the basin layout shown in Figure 3a. These were predicted by the Isaacson model using the paddle motions computed by Dalrymple's theory. In Figure 5a, the target sea state is a wave train with a period of  $T = 0.75\text{s}$  and a propagation angle of  $\theta = 15^\circ$ . In Figure 5b, the target wave train has a period of  $T = 1.20\text{s}$  and a propagation angle of  $\theta = 30^\circ$ . In both cases, the reproduction distance,  $x_D$ , is  $10\text{m}$ .

These figures demonstrate the capability of Dalrymple's method. It is interesting to note the complexity of the wave field that is required to be produced near the paddles to simulate the desired water surface elevation at the specified locations. Similarly, the influence on the wave field of the reflection from the solid walls extending beyond  $10\text{m}$  can also be appreciated.

### 5.2.2 Partial-length sidewalls

Figure 6 illustrates results similar to those in Figure 5 but for the basin layout depicted in Figure 3b. A target wave train with  $T = 0.75\text{s}$  and  $\theta = 15^\circ$  was used

and wave fields were calculated for two different reproduction distances,  $x_D$ . The results for  $x_D = 5\text{m}$  and  $x_D = 10\text{m}$  are shown in Figures 6a and 6b, respectively. Figure 6b is particularly interesting since it shows the ability to reproduce the desired sea state at the end of the sidewalls. As expected, the absorbers located beyond the 10m limit of the sidewalls help eliminate the reflections, thus ensuring a reasonably good wave field, even beyond the 10m distance.

Once again, these figures illustrate the validity of Dalrymple's theory. It should be noted that, although the water surface elevation realized at the desired locations is very good, a small variability (less than 5%) seems to exist and tends to increase with wave period. Research is continuing to investigate the reasons for this variability. Possible causes include finite segment width effects and the truncation point used for the summations in the Dalrymple theory (e.g. Equations 7 and 8).

## 6.0 SIZE OF AREA WITH HOMOGENEOUS SEA STATES

For model studies of offshore or coastal structures, it is important to ensure that a large area with a homogeneous sea state is available for testing purposes. For this reason, it is of interest to estimate the size of homogeneous area that can be obtained using Dalrymple's theory.

An example of this is shown in Figure 7 which illustrates the boundary inside the wave basin where the wave heights can be expected to be within  $\pm 10\%$  of the target wave height,  $H_0$ . The two basin layouts shown in Figure 3 have been used. The thick line shows the result for full-length reflecting sidewalls, while the dashed line shows the case of partial-length sidewalls. The sea states illustrated in Figure 5b were used in these calculations for the full-length sidewall case.

It can be seen that the homogeneous area extends over the full width of the basin at the reference distance of  $x_D = 10\text{m}$ , where the target wave train was to be reproduced. At larger  $x$  distances, the width of the homogeneous zone gradually decreases. In this case, it is better to use a 10m sidewall on one side to prevent reflection when  $x > x_D$  and a 20m sidewall on the opposite side to reduce diffraction effects. However, in the general multidirectional case, with waves propagating in both positive and negative directions, it would be best to use partial-length sidewalls on both sides. More calculations of this kind are under way in order to determine the optimum sidewall length for various multidirectional wave situations.

## 7.0 CONCLUSIONS

Dalrymple has proposed a theoretical model to reproduce a planar, oblique wave train at any predetermined cross-section in a multidirectional basin. This theory, which uses reflections from sidewalls and the mild slope equation for varying water depth, was validated numerically for a constant depth situation using the Isaacson diffraction model. The results indicate that Dalrymple's method is indeed a

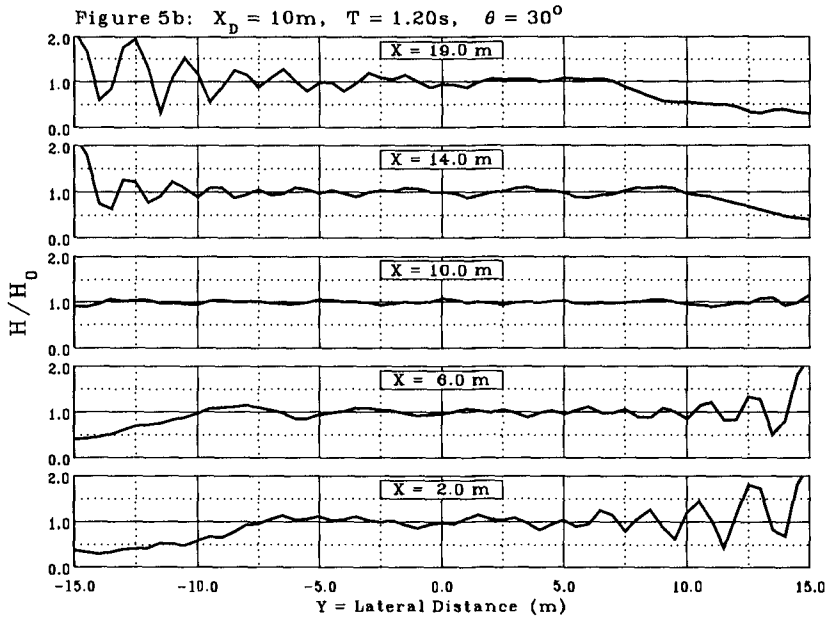
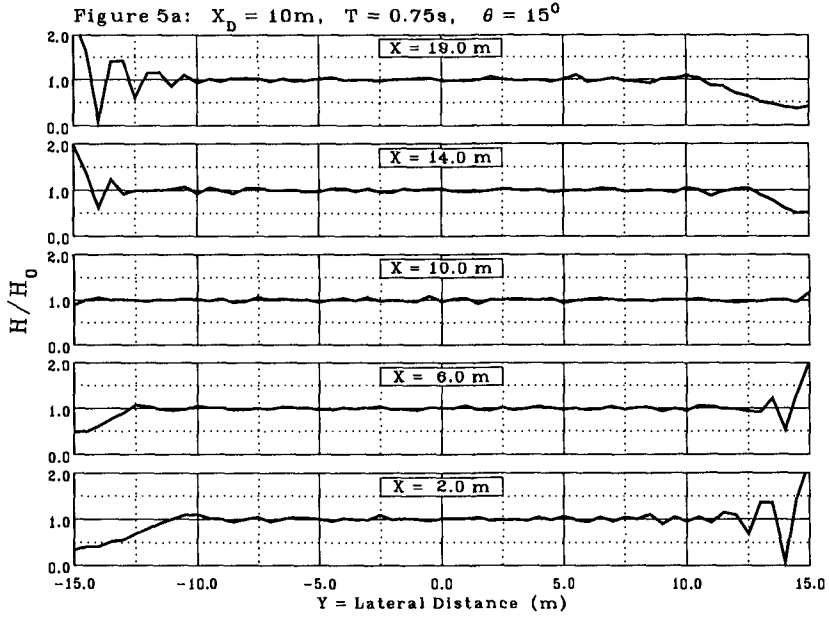


Figure 5: Dalrymple Method Wave Height Distributions for 20m Sidewalls at Various  $X$  Distances from the Wavemaker.

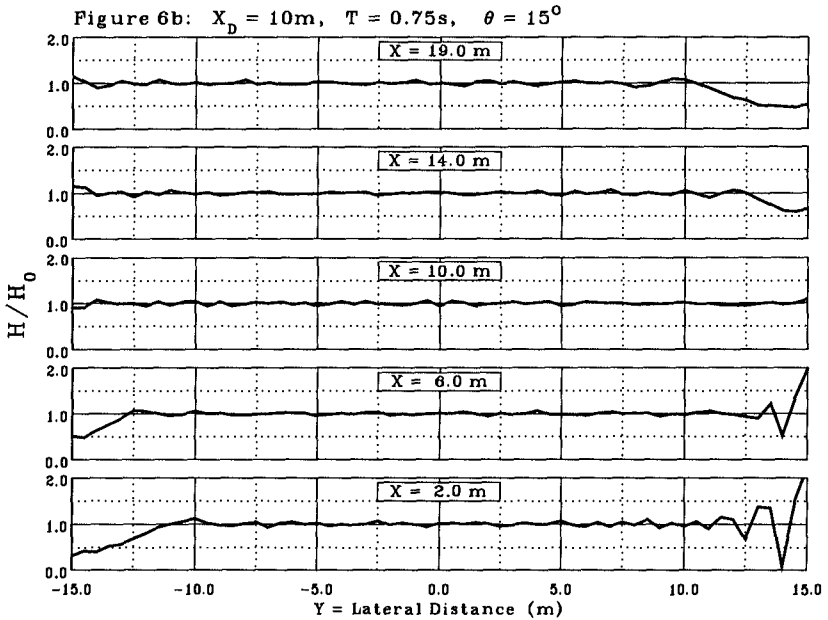
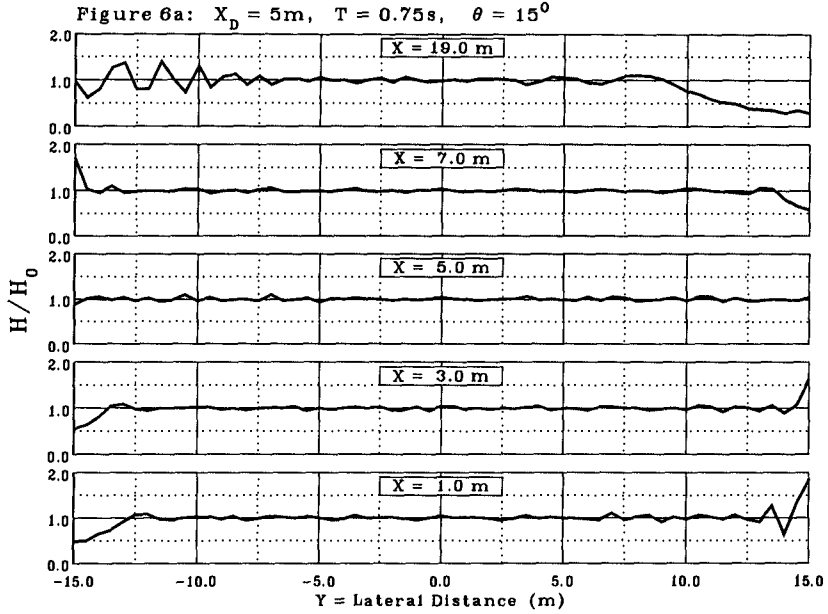


Figure 6: Dalrymple Method Wave Height Distributions for 10m Sidewalls at Various X Distances from the Wavemaker.

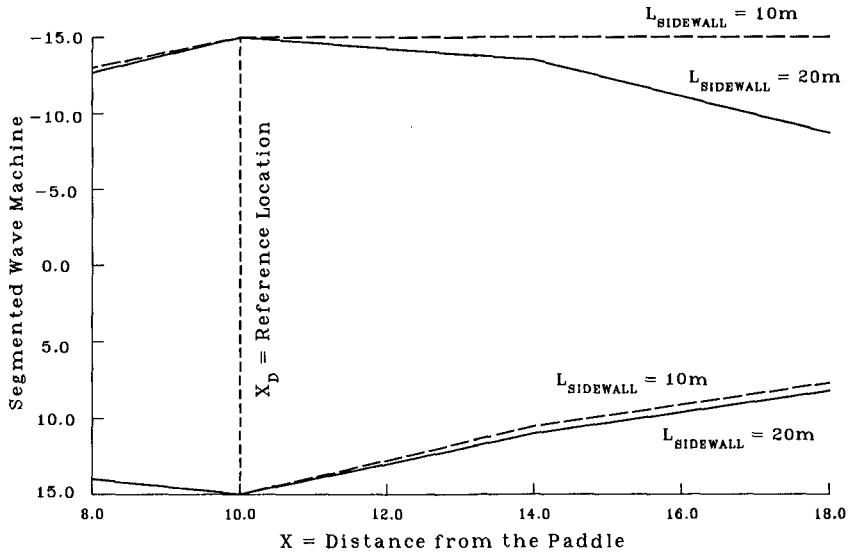


Figure 7: Size of Area with  $\pm 10\%$  Uniformity for  $T = 1.20\text{s}$  and  $\theta = 30^\circ$

powerful tool that can enhance the model testing capability of a multidirectional wave basin. Further work is planned at NRC to evaluate the Dalrymple method experimentally in a basin with a sloping bottom.

## 8.0 REFERENCES

- Dalrymple, R.A. and Kirby, J.T. (1988). *Very Wide Angle Water Wave Models and Wave Diffraction*, Journal of Fluid Mechanics, 192, pp. 33-50.
- Funke, E.R. and Miles, M.D. (1987). *Multidirectional Wave Generation with Corner Reflectors*, Technical Report TR-HY-021, Division of Mechanical Engineering, National Research Council of Canada.
- Isaacson, M. (1989). *Prediction of Directional Waves Due to a Segmented Wave Generator*, Proc. 23rd IAHR Congress, Ottawa, Canada. August 21-25, Vol. C. pp. 435-442.
- Dalrymple, R.A. (1989). *Directional Wavemaker Theory With Sidewall Reflection*, Journal of Hydraulic Research, Vol. 27, No. 1, pp. 23-34.
- Hiraishi, T., Mansard, E.P.D., Miles, M.D., Funke, E.R. and Isaacson, M., (1991). *Validation of a Numerical Diffraction Model for Multidirectional Wave Generation*, Hydraulics Laboratory Technical Report TR-HY-037, National Research Council of Canada.

## CHAPTER 99

### 3-D Analysis of Flow around a Vertical Cylinder on a Scoured Bed

Tomonao Kobayashi<sup>1</sup>

#### ABSTRACT

Velocity distributions around a vertical cylinder on a scoured seabed under waves have been evaluated in three dimensions using a laser Doppler anemometer and the mass-consistent model to explain the mechanism of local scouring in the wave fields. Through their comparisons with the measurements over a flat bottom under the same conditions, effects of the scoured seabed configuration on the vortex behavior around a cylinder and the near-bed flow structures have been clarified. Namely, the scoured seabed topography causes deformation of the vortices and the flow field from a quasi-two-dimensional structure observed above the flat bed into a complex three-dimensional structure. The flow around a cylinder has also been simulated numerically with a three-dimensional vortex segment model. The results have shown a good agreement with those in the experiments.

#### 1. INTRODUCTION

Prediction of local scouring around nearshore and offshore structures is a need for engineers, and many researchers have been challenging to estimate the scour depth and shape. For example, Well and Sorensen (1970) have found the relationships of the ultimate scour depth with the Shields number, Reynolds number, etc. in experiments. Sumer *et al.* (1992) have reported laboratory tests on the scouring and expressed the scour depth as a function of the Keulegan-Carpenter (K.C.) number with continuous sediment motion on beds. However, to develop a reliable prediction model for the local scouring, we need a deeper understanding of the scouring mechanism and the flow features near the bed around structures.

Characteristics of the flow around a vertical cylinder in steady currents have been investigated extensively (*e.g.*, Shen *et al.*, 1969; Breusers *et al.*, 1977). It has been found that a horseshoe vortex above the scoured bed is a dominant factor in the scour process, and that the vortex has a close relationship with the bed profile near the cylinder. The vortex behavior above the scoured bed is thus a very important factor to consider in the estimation of scouring.

---

<sup>1</sup>Research Associate, Department of Civil Engineering, Tokyo Rika University, 2641 Yamazaki, Noda city, Chiba, 278 Japan.

Table 1. Conditions of laboratory experiments.

Water Depth	$h$	100 mm
Water Period	$T$	1.5 s
Wave Height	$H$	38 mm
Ursell Number	$U_r$	83.8
Cylinder Diameter	$D$	48 mm
Maximum Velocity above the Bed	$U_{\max}$	167 mm/s
Keulegan-Carpenter Number	K.C.	5.2

In the wave-related field, relatively few studies have been conducted on this topic. Nishizawa and Sawamoto (1988) and Sumer *et al.* (1992) have studied the flow around a vertical slender cylinder under waves using flow visualization techniques. They have reported relationships between the flow characteristics and the K.C. number based on experimental results for a flat bottom only. In case of a scoured bed, there has been even less literature, probably because the flow near the scoured seabed shows a highly complex three-dimensional pattern owing to the complicated scour shape and the unsteadiness of the main flow itself. It should be emphasized, however, this unsteady three-dimensional near-bed flow with vortices governs the local scouring around the cylinder.

The purpose of this study is to recognize the characteristics of the flow around a vertical cylinder on the scoured bed under waves. First, to show the typical features of the flow and vortices, the measurements of three-dimensional velocity distributions around the cylinder are presented for cases of both the flat bottom and the scoured bed. Then, the results of flow simulation are shown, which have been obtained with a numerical model developed as an initial step to build up a local scouring model.

## 2. EXPERIMENTAL PROCEDURE

### 2.1. Experimental Conditions

Velocity distributions have been measured around a vertical slender cylinder on the flat bottom and on the scoured seabed under the same conditions, which are shown in *Table 1*. The reason why these conditions have been selected is that under them, clear scouring had occurred on a movable bed as described below. *Figure 1* shows the time variation of a water surface elevation in one wave period and the vertical distributions of horizontal velocity near the flat bottom at several phases without disturbances due to the cylinder.

In order to determine the scoured bottom topography around the cylinder, a movable bed test has been conducted using sand with the medium diameter  $d_{50} = 0.6\text{mm}$  and the density  $\rho_s = 2.68\text{g/cm}^3$ , for which the maximum Shields number  $\Psi_m$  is 0.025.

The modified final topography is shown in *Fig. 2*, where the wave direction is from the left to the right. The coordinates  $x$ ,  $y$  and  $z$  are in the streamwise, the lateral and the vertical directions, respectively, and their origin is set on the centerline of the cylinder at the elevation the initial flat bottom. The actual

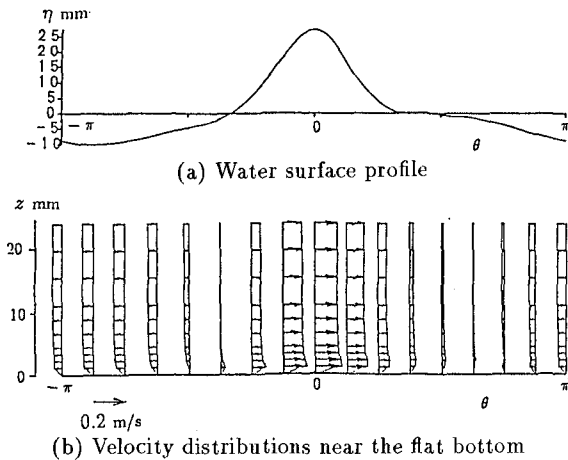


scoured bed topography has been almost symmetric with respect to the vertical  $x$ - $z$  plane. Furthermore, as explained later, the flow pattern has been also satisfactorily symmetric. Hence the bed profile has been modified to be symmetric and employed in the following experiment.

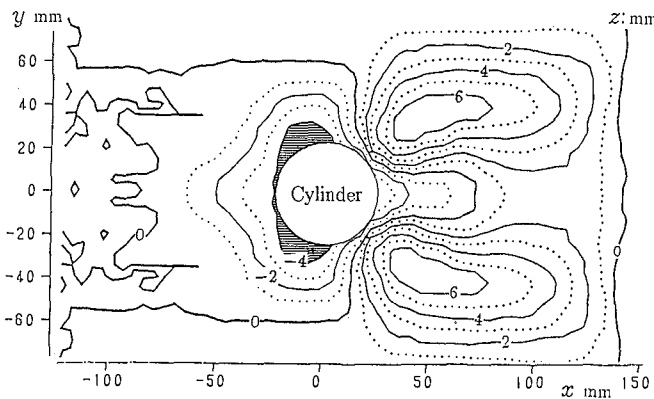
As shown in *Fig. 2*, a pair of deep scour holes are found at the two side edges of the cylinder (the hatched part), and two hills are formed near the down-wave edges.

**2. 2. Experimental Apparatus**

Velocity distributions around the vertical cylinder were measured in full detail using a two-dimensional laser Doppler anemometer, which was set on a movable



*Fig. 1.* Water surface profile and velocity distributions above the flat bottom.



*Fig. 2.* Contour map of the scoured bed around a vertical cylinder.

table. A personal computer was used to control the movable table and a wave maker, and to acquire the output from the anemometer and a wave gage. Thus the velocity distributions around the cylinder near the bottom were automatically recorded by the computer. Nearly 5,000 points of velocity measurement were distributed around the cylinder, and the phase-average velocity data for 100 waves were obtained at each point.

Since the K.C. number is low as shown in *Table 1*, the flow pattern was highly symmetric with respect to the vertical  $x$ - $z$  plane; the symmetry plane is  $y = 0$  mm. Therefore the velocity distributions were measured only in one side ( $y \geq 0$ ). The anemometer directly measured only the two velocity components  $u$  and  $w$ , in the  $x$  and  $z$  directions, respectively. The velocity component  $v$  in the  $y$  direction was not measured but estimated with the following MASCON model.

### 2.3. MASCON Model

The MASCON (mass-consistent) model, developed by Sherman (1978) to adjust field measurement data of wind, is useful to estimate three-dimensional velocity distributions as properly adjusted in a mass-consistent flow field over a complex topography. This model has often been applied to the adjustment of the field velocity data in meteorology. However, its applications to laboratory experiments are very few (*e.g.*, Hino *et al.*, 1989). In the present study, this model is applied to the evaluation of the velocity component  $v$ , which was not measured in the experiments.

The specific function of this model is

$$E(u, v, w, \lambda) = \int_V \left[ \alpha_x^2 (u - u_0)^2 + \alpha_y^2 (v - v_0)^2 + \alpha_z^2 (w - w_0)^2 + \lambda \left( \frac{\partial u}{\partial x} + \frac{\partial v}{\partial y} + \frac{\partial w}{\partial z} \right) \right] dx dy dz \quad (1)$$

where  $u_0$ ,  $v_0$  and  $w_0$  are observed velocity components,  $u$ ,  $v$  and  $w$  are adjusted ones,  $\lambda$  is the Lagrange multiplier, and each  $\alpha$  is a Gauss precision modulus.

The solutions which minimize a value of this function  $E$  satisfy the following relations.

$$u = u_0 + \frac{1}{2\alpha_x^2} \frac{\partial \lambda}{\partial x} \quad (2)$$

$$v = v_0 + \frac{1}{2\alpha_y^2} \frac{\partial \lambda}{\partial y} \quad (3)$$

$$w = w_0 + \frac{1}{2\alpha_z^2} \frac{\partial \lambda}{\partial z} \quad (4)$$

$$\frac{\partial u}{\partial x} + \frac{\partial v}{\partial y} + \frac{\partial w}{\partial z} = 0 \quad (5)$$

$$\frac{1}{\alpha_x^2} \frac{\partial^2 \lambda}{\partial x^2} + \frac{1}{\alpha_y^2} \frac{\partial^2 \lambda}{\partial y^2} + \frac{1}{\alpha_z^2} \frac{\partial^2 \lambda}{\partial z^2} = -2 \left( \frac{\partial u_0}{\partial x} + \frac{\partial v_0}{\partial y} + \frac{\partial w_0}{\partial z} \right) \quad (6)$$

Values of the adjusted velocity component  $u$ ,  $v$  and  $w$  are estimated from *Eqs.* (2) to (6).

Since the purpose of the application of this model to the present study is to evaluate the velocity component  $v$  from the other two measured velocity components  $u_0$  and  $w_0$ , the condition that  $\alpha_y^2$  is larger enough than  $\alpha_x^2$  and  $\alpha_z^2$  must be introduced. Otherwise the adjusted velocity components  $u$  and  $w$  would severely deviate from the measurements of  $u_0$  and  $w_0$  in this model. Hence, values 1.0, 5.0 and 1.0 are employed for  $\alpha_x$ ,  $\alpha_y$  and  $\alpha_z$ , respectively, and  $v_0$  is set to be zero in this study.

### 3. EXPERIMENTAL RESULTS

#### 3.1. Flow Field above the Flat Bottom

First the velocity distributions above the flat bottom were measured under the conditions given in *Table 1*. *Figure 3* shows the phase-average velocity distributions in horizontal planes at  $z = 2\text{mm}$  and  $z = 8\text{mm}$ . The direction of wave propagation is from the left to the right, and the phase  $\theta = 0$  corresponds to the time when the wave crest passes the location of the cylinder. Since *Fig. 3* shows the velocity distributions in horizontal planes, the velocity components  $u$  and  $v$  are indicated by vectors, and the  $w$ -component is shown as contour lines in the figure. Solid and dashed contour lines mean ascending and descending flows, respectively.

A pair of vortices are shed in the wake region after the passing of the wave crest or the trough as shown in *Fig. 3 b, d, g and i*. As the waves are finite amplitude waves, whose Ursell number is 83.8, the main flow under the wave crest is much stronger than that under the wave trough as shown in *Figs. 1 and 3*. However, the weak opposite-directional main flow continues longer than the strong shoreward flow under the wave crest. Hence, the vortices shedding from the cylinder at the up-wave side of the cylinder grow bigger than the ones at the down-wave side of the cylinder as represented in *Fig. 3 b, d, g and i*. These vortices at the up-wave side of the cylinder induce the intense flow on the surface of the cylinder, as shown in *Fig. 3 e and j*. Then, this intense flow supposedly picks up sand and forms a pair of the scour holes at the two side edge of the cylinder in *Fig. 2*. According to the contour maps showing the distributions of  $w$ , concentration of the intense descending flow occurs in the wake, whereas the weak ascending flow regions extend widely around the cylinder to balance the descending flow.

The difference of the velocity distributions between the planes at  $z = 2\text{mm}$  and  $z = 8\text{mm}$  is negligible. The velocity distribution at the plane  $z = 22\text{mm}$  is also similar to them. This indicates that the flow field above the flat bottom is approximately two-dimensional, namely, uniform in the vertical direction.

*Figure 4* shows the distributions of the flow with vorticity vectors at the wave phase  $\theta = \pi/8$ , immediately after the wave crest passing. It is seen in *Fig. 4*, the axis of the vortex shed from the cylinder is nearly vertical. This fact also means that the flow field above the flat bottom is almost two-dimensional or uniform in the vertical direction. The shed vortex is deformed down-wave near the bottom owing to the strong descending flow in the wake.

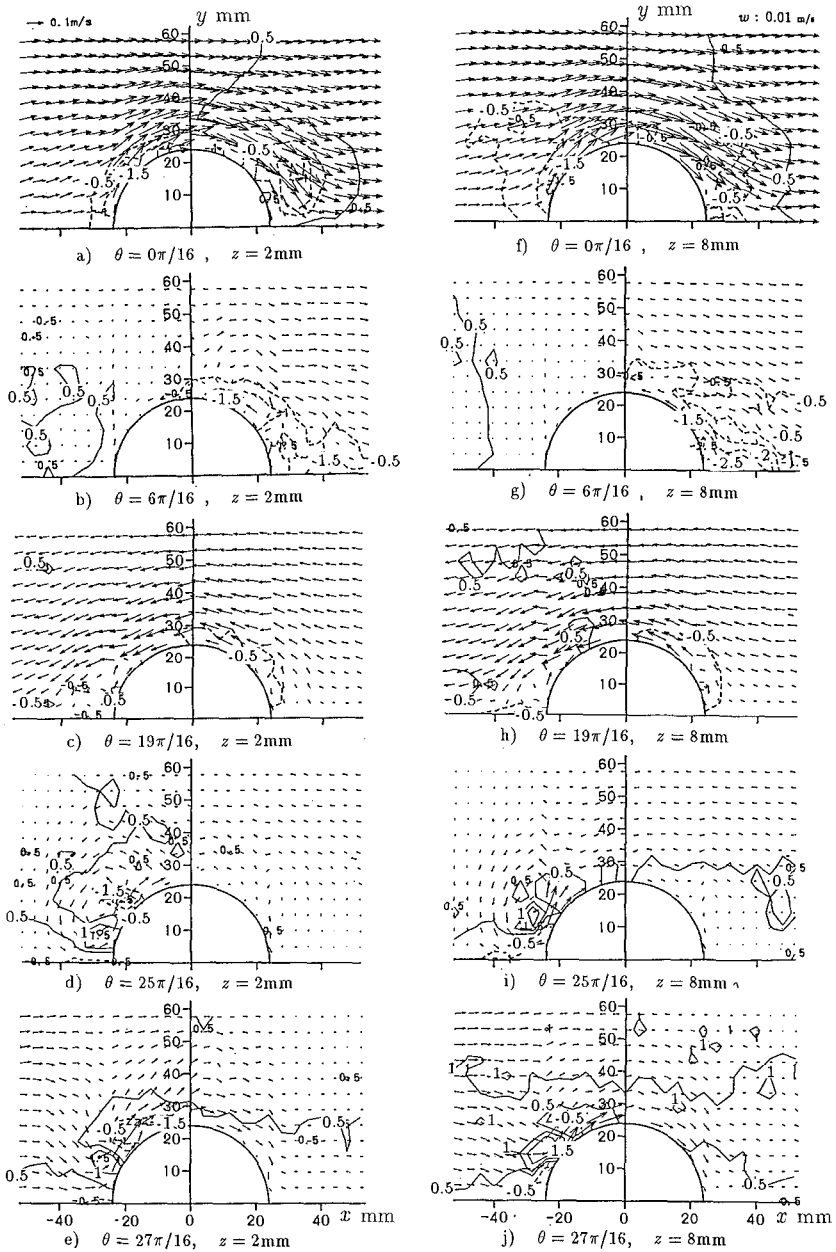


Fig. 3. Phase-average velocity distributions in horizontal planes at  $z = 2\text{mm}$  and  $z = 8\text{mm}$  above the flat bottom. Solid and dashed contour lines show ascending and descending flows ( $w$ -component) respectively.

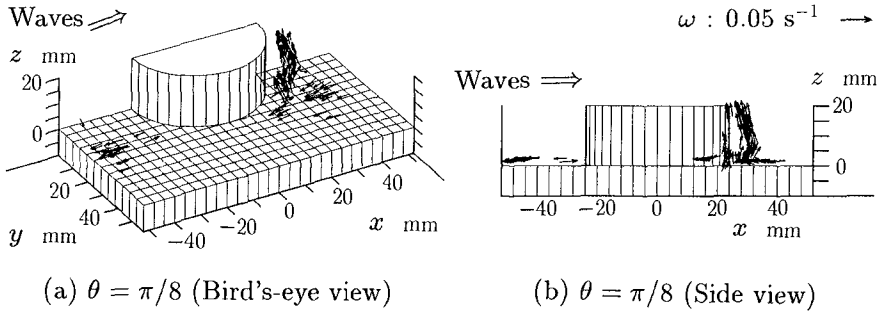


Fig. 4. Vorticity vector distributions above the flat bottom at  $\theta = \pi/8$ .

### 3. 2. Flow Field above the Scoured Seabed

The velocity distributions above the scoured seabed were measured under the same conditions with those for the flat bottom (*Table 1*). To perform the measurement, the scoured bottom topography shown in *Fig. 2* was modeled in wood and surfaced with sand of  $d_{50} = 0.6\text{mm}$ . *Figure 5* shows the velocity distributions in horizontal planes at different heights above the scoured seabed at  $\theta = 0$  and  $\theta = \pi/4$ . The flow structure is very complex because of the scoured bed topography. It is observed that the flow rises over the slope from the scour hole to the hill, and that strong ascending flow occurs at the down-wave side edge of the cylinder. At the phase  $\theta = \pi/4$ , the wake grows in the lee of the cylinder, where the strong flow toward the opposite direction appears at the heights  $z = 6\text{mm}$  and  $z = 10\text{mm}$ . This is not clearly observed at other heights.

*Figure 6* shows the velocity distributions in the vertical  $x$ - $z$  planes at the phase  $\theta = \pi/4$ , in which the cylinder is represented by pairs of the vertical straight lines, the velocity components  $u$  and  $w$  are shown as vectors, and the  $v$ -component is indicated by contour lines. The direction of wave propagation is again from the left to the right. In the symmetry plane ( $y = 0\text{mm}$ ), the descending flow appears in the wake, while in the other planes a vortex with a horizontal axis is clearly seen.

*Figure 7* shows the time evolution of this horizontal vortex. The vortex develops as the wake grows after the wave crest passing, and then it disappears when the main flow decelerates. It is observed from this figure that this vortex induces local intense flow near the bed in a very short period. Under the present conditions, the intensity of this flow was enough to pick up sand. Then, it is seemed that this vortex has a close relationship with the local scouring around the cylinder.

The structure and the time evolution of the vortex are shown in *Figs. 8* and *9*, respectively, with vorticity vectors. The bird's-eye view in *Fig. 8* shows that an arch-shaped vortex with its feet on the hills is formed in the lee of the cylinder, and the side view indicates that the vortex leans down-wave. The vortex concentration is strong at the feet and becomes weak upward or towards the symmetry plane.

According to *Fig. 9*, the arch-shaped vortex does not appear immediately

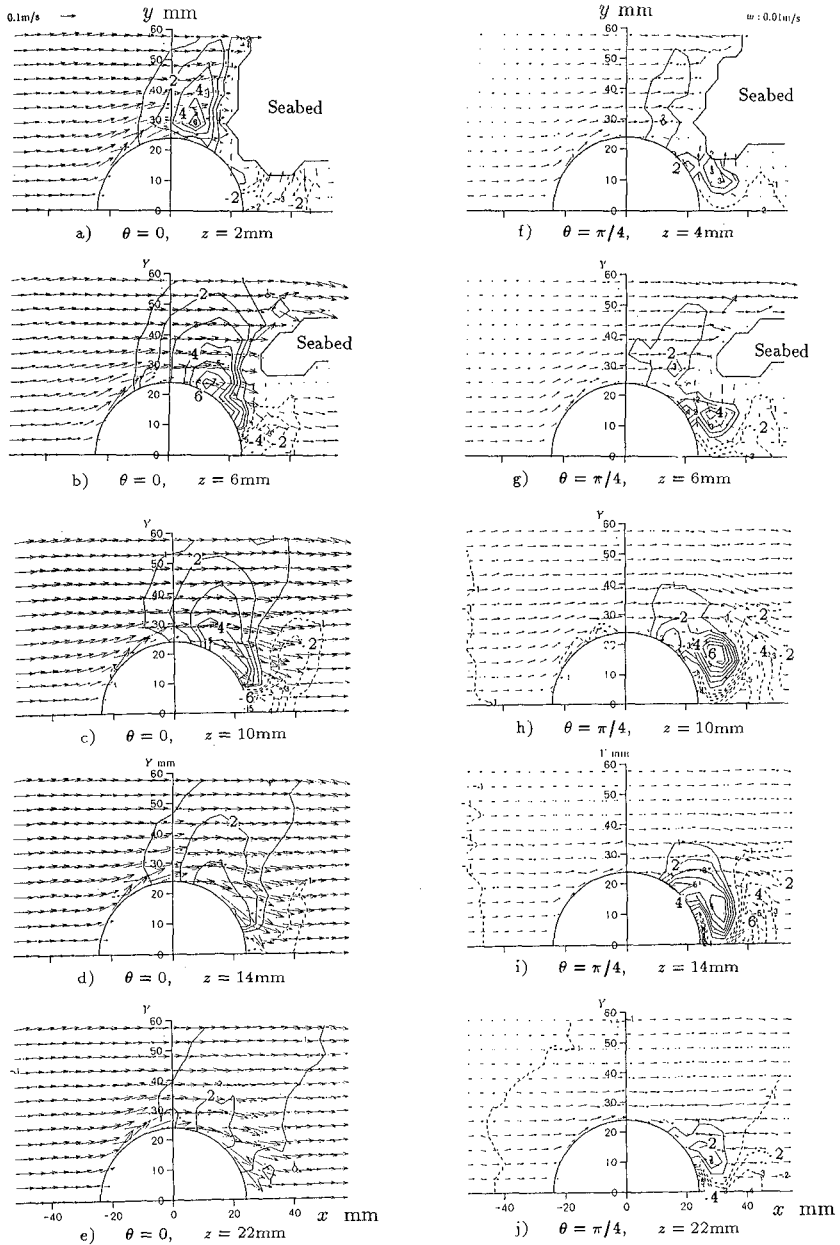
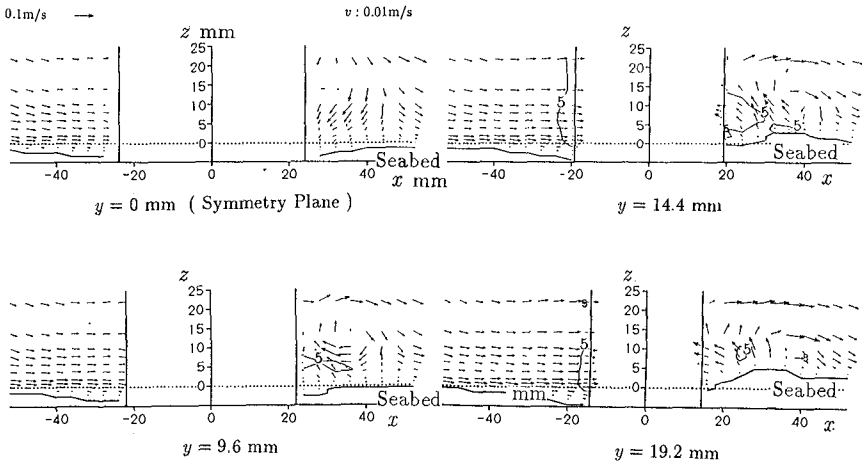
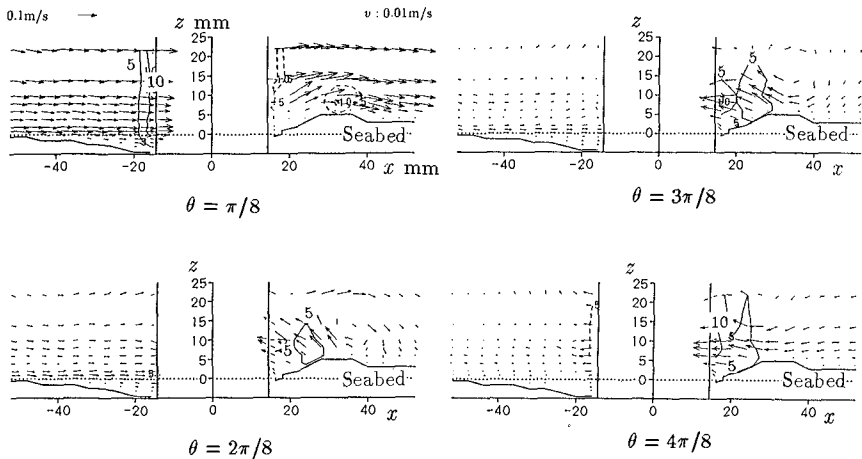


Fig. 5. Velocity distributions in horizontal planes above the scoured seabed.

before and at the phase of wave crest passing ( $\theta = 0$ ); the vortex starts to be produced soon after the crest passing, and then gradually develops and leans down-wave. It is concluded from *Fig. 9* that the interaction of the vortex shed from the cylinder and the separation over the hills induces the arch-shaped vortex above the scoured bed.



*Fig. 6.* Velocity distributions in vertical planes above the scoured seabed at  $\theta = \pi/4$ .

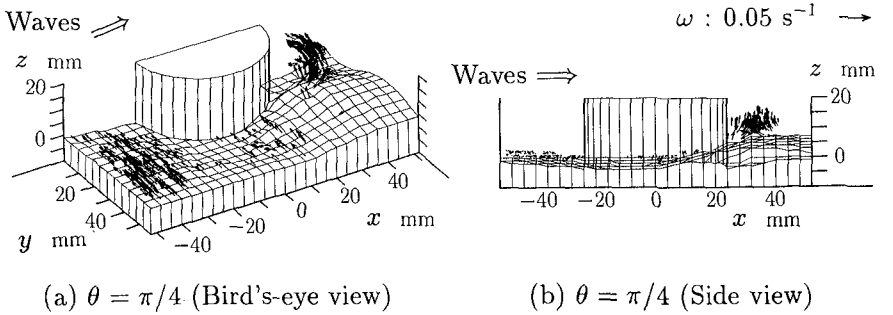


*Fig. 7.* Time evolution of the horizontal vortex ( $y = 19.2\text{mm}$ ).

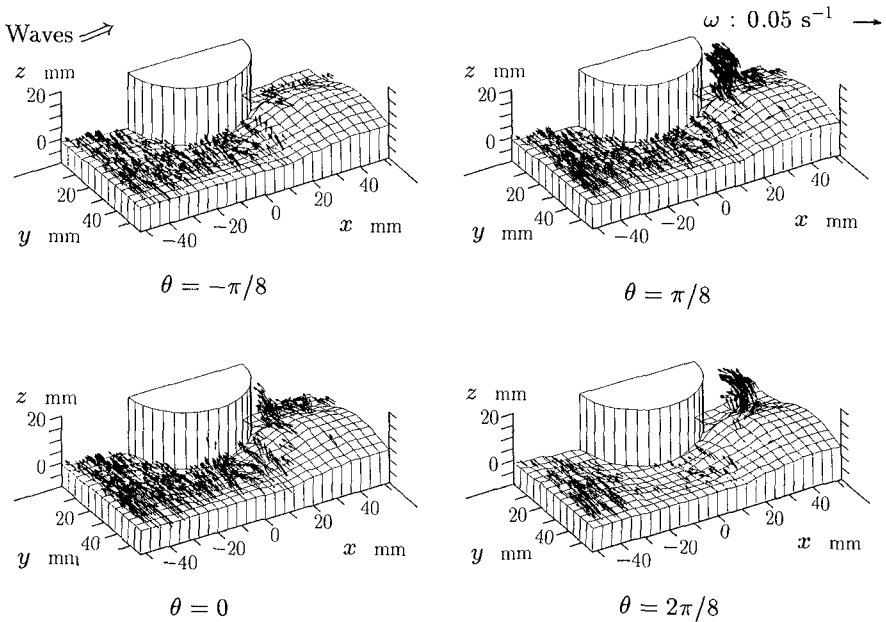
**3.3. Comparison between the Two Flow Fields**

The results of the two experiments are compared to study the effects of the bottom profile on the flow structures.

The vorticity vector distributions in *Fig. 4* indicate that the axis of the vortex shed from the cylinder is almost vertical above the flat bottom. Consequently the flow structure does not change significantly in the vertical direction. On the other hand, as shown in *Figs. 8* and *9*, the velocity distributions over the scoured seabed are very complex and the vortex is deformed into arch-shape. The separation over the hill forces the vortex shed from the cylinder to change to this



*Fig. 8.* Vorticity vector distributions above the scoured seabed at  $\theta = \pi/4$ .



*Fig. 9.* Time evolution of the vortex above the scoured seabed.



arch-shaped one, as explained in the last section. Then this vortex drives local intense reversing flow close to the bed near the down-wave edge of the cylinder as shown in *Fig. 9*. Furthermore the flow produces the scour hole at the down-wave edge of the cylinder between two hills as represented in *Fig. 2*.

From the comparison between the vorticity distributions above the flat bottom and the scoured seabed, it is thus concluded that the deformation of the vortex shed from the cylinder is caused by the effect of the locally scoured seabed configuration. In other words, the rugged seabed topography causes change in the shedding and developing processes of the large vortex from the quasi-two-dimensional to the complex three-dimensional structure.

#### 4. NUMERICAL SIMULATION

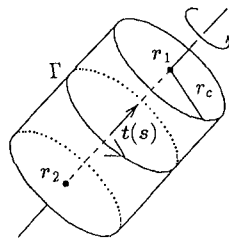
##### 4.1. Vortex-Segment-Model

A three-dimensional Vortex-Segment-Model has been adopted to simulate the flow around a cylinder. This model is one of the Discrete-Vortex-Methods, which deal with a flow field as a vorticity field and are useful to understand the behavior of vortices. Since an element of this model is a vortex segment with finite length, each segment does not satisfy Kelvin's circulation theorem rigidly. However, the model treats a vortex filament as a group of the segments, and hence the theorem is almost fulfilled in this model. Its validity has been reported by Shirayama *et al.* (1984) and others. Differing from the other Discrete-Vortex-Methods, this model can easily express the cut-and-connect processes of vortex filaments and the production of vorticity on the surfaces of solid boundaries due to the non-slip boundary condition. This model is thus useful to simulate the flow fields with the solid boundaries in them.

In this model the structure of a vortex segment is assumed as illustrated in *Fig. 10*, and an induced velocity vector for each vortex segment is given by

$$\mathbf{u}(\mathbf{x}) = -\frac{\Gamma}{4\pi} \int_{r_1}^{r_2} \frac{(\mathbf{x} - \mathbf{s}) \times \mathbf{t}(\mathbf{s})}{|\mathbf{x} - \mathbf{s}|^3} ds, \quad (7)$$

where  $\mathbf{u}(\mathbf{x})$  is the induced velocity vector at a point  $\mathbf{x}$ ,  $\mathbf{s}$  is a position vector along the axis of the vortex segment,  $\mathbf{t}(\mathbf{s})$  is a unit vorticity vector at the position  $\mathbf{s}$ , and  $r_1$  and  $r_2$  are the positions of the two ends of the segment. A finite core radius of the vortex segment is assumed in this model for the stability in numerical



*Fig. 10.* The structure of a vortex segment in the Vortex-Segment-Model.

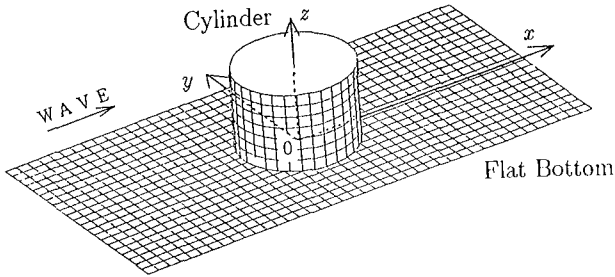


Fig. 11. Computational domain.

computation. To simulate the flow field, a large number of vortex segments are distributed in the computational domain.

#### 4.2. Results of the Simulation

The model has been applied to the numerical simulation of the near-bottom flow field around a vertical slender cylinder under waves. The bottom of the computational domain is flat as shown in Fig. 11. The non-slip condition is imposed on the surfaces both of the cylinder and of the flat bed, and therefore the vorticity is produced on these solid boundaries. The numerical simulation has been conducted under the condition that the Ursell number is 25 and the K.C. number is 5.0, which is close to that of the laboratory experiments.

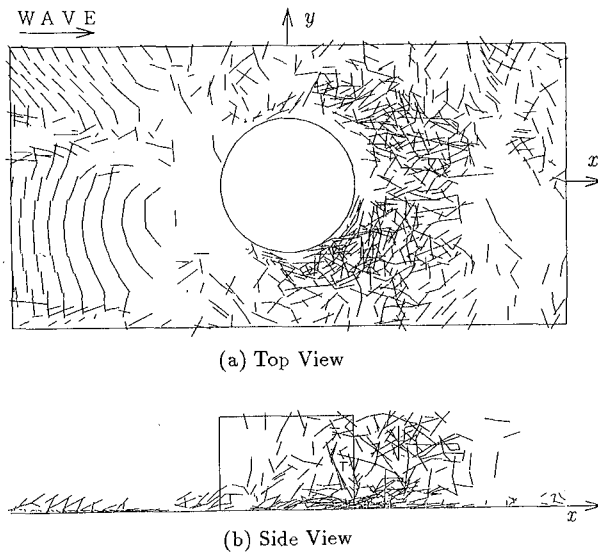


Fig. 12. Vortex segment distributions at  $\theta = \pi/4$ .

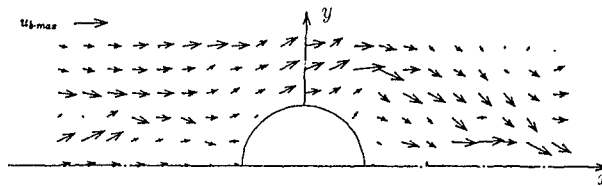
To satisfy the solid boundary conditions mirror-imaged vortex segments are introduced for the flat bottom boundary, and fixed vortex segments are put on the surface of the cylinder. In addition, new vortex segments are generated in close proximity from the solid boundaries to satisfy the non-slip condition in every computational steps.

Figure 12 displays one of the vortex segment distributions obtained by this model. As shown in this figure, flow fields are represented with a number of vortex segments. Under the computational conditions of this study, the distributions of vortex segments are almost symmetric with respect to the vertical  $x$ - $z$  plane, which is consistent with the experimental results.

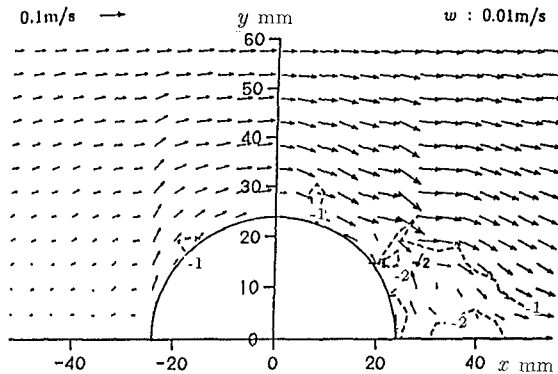
The evaluated velocity distribution in the horizontal plane near the bed and the corresponding experimental result are shown in Fig. 13. It is found that the vortex shedding is well simulated in this case. These figures indicate a fairly good agreement, which implies the validity of this numerical model.

## 5. CONCLUSION

The near-bed velocity distributions around the vertical slender cylinder under waves have been measured and estimated in full detail above both the flat bottom and the scoured seabed. The following characteristics of the flow have been



(a) Result of the Numerical Simulation ( $z = D/20$ )



(b) Experimental Result ( $z = D/8$ )

Fig. 13. Velocity distribution in a horizontal plane at  $\theta = \pi/4$ .

found. Above the flat bottom, the axis of the vortex shed from the cylinder surface is almost straight and vertical. On the other hand, the arch-shaped vortex is formed over the scoured seabed. This arch-shaped vortex drives the local intense reversing flow close the bed near the down-wave edge of the cylinder. It is therefore clear that the rugged seabed shape has a significant influence on the shedding and deforming processes of large vortices to change the flow pattern from the quasi-two-dimensional to the complex three-dimensional structure. Since this three-dimensional vortices cause local intense flow near the bed, the behavior of the vortices is thus very important to study local scouring processes around a vertical cylinder.

In addition the flow around a cylinder over the flat bottom has been simulated numerically with a three-dimensional Vortex-Segment-Model. The results of the simulation have shown a good agreement with those obtained in the laboratory experiments. Hence it is concluded that the numerical model presented here is a promising one for analysis of the scour process and for prediction of the scouring.

#### ACKNOWLEDGEMENTS

I thank Professors A. Watanabe and M. Isobe of the University of Tokyo for their suggestions in this study.

#### REFERENCES

- Breusers, H. N. C., G. Nicollet, and H. W. Shen (1977): Local scour around cylindrical piers, *Journal of Hydraulic Research*, Vol.15, No.3, pp.211-252.
- Hino, M., Y. Meng and M. Murakami (1989): An attempt of estimating a whole instantaneous velocity field from sparse velocity data, Technical Report No.41, Dept. of Civil Eng., Tokyo Institute of Technology, pp.1-8. (in Japanese)
- Nishizawa, M. and M. Sawamoto (1988): Local scour around a vertical cylinder under the wave action, Proc. of the 6th Congress of APD-IAHR, pp.121-128.
- Sharman, C. A. (1978): A mass-consistent model for wind fields over complex terrain, *Journal of Applied Meteorology*, Vol.17, pp.312-319.
- Shen, H. W., V. R. Schneider and S. Karaki (1969): Local scour around bridge piers, *Journal of the Hydraulics Division, ASCE*, Vol.95, HY6, pp.1919-1940.
- Shirayama, S. and K. Kuwahara (1984): Vortex method in three-dimensional flow, Proc. of the 9th Inter. Conf. on Numerical Methods in Fluid Dynamics, Springer, pp.503-507.
- Sumer, B. M., J. Fredsøe, and N. Christiansen (1992): Scour around vertical pile in waves, *Journal of Waterways, Port, Coastal and Ocean Engineering, ASCE*, Vol.118, No.1, pp.15-31.
- Wells, D. R. and R. M. Sorensen (1970): Scour around a circular cylinder due to wave motion, Proc. of the 12th Coastal Eng. Conf., pp.1263-1279.

# A description of the "acqua alta" event on 5th October

the Organizing Committee

## Introduction

""Certainly the "acqua alta" on the first morning of the Conference was a memorable event which every coastal engineer should experience in part because it underscores one of the problems that may face the next generation of coastal engineers. Our colleagues that were unable to attend the Conference will be envious of the *opportunity* to wade to the first session, barefoot and shoes and socks in hand! The sessions and chapters in the Proceedings on the history and plans relating to Venice Lagoon and the protective barrier islands will serve as valuable source documents for the future. The venue in Venezia was both appropriate and unforgettable."" (from a letter of Robert Dean).

What a better introduction than these few words of the new CERC President. Following this stimulation the Organizing Committee has asked some near participants<sup>1</sup> to supply a description of the event in order to fix the experience of those who were present and to give a pale idea to those who could not attend the Conference.

## The meteo- and oceanographic situation

On the first days of October 1992 the meteorological situation over the Mediterranean Sea was characterized by an almost uniform and relatively high atmospheric pressure distribution. Wind speeds and wave heights were very low throughout the basin, due mainly to local actions. This situation changed abruptly on October 3rd (Saturday), when an energetic flow of north-westerly cold air entered the Gulf of Lion from the Carcassonne passage between the Pyrenées and the Massif Central in south-western France (see figure 1.a, relative to 00 UTC 3 October '92).

Interacting with the still warm water of the Western Mediterranean Sea, this led to an intense cyclogenesis. A low centered over Corsica developed (see figure 1.b, relative to 00 UTC 4 October '92) with southerly winds on its eastern side, i.e. over Italy. The flow was intensified by the opposing high pressure zone located over eastern and northern Europe.

The southerly wind produced high wave conditions on the Ionian Sea, particularly on the facing Italian coasts. Over the Adriatic Sea the parallel Appennines ridge on the Italian side and the Dinaric Alps on Yugoslavia

---

<sup>1</sup>Luciana Bertotti, CNR-ISDGM Venice, provided the meteorological description, Manlio De Boni, TEI Milano, the wave records, Giovanni Cecconi, Consorzio Venezia Nuova, and Paolo Canestrelli, Centro Previsioni Maree Venezia, provided the description of the tide, Leopoldo Franco and Ferruccio Egori the photographs.

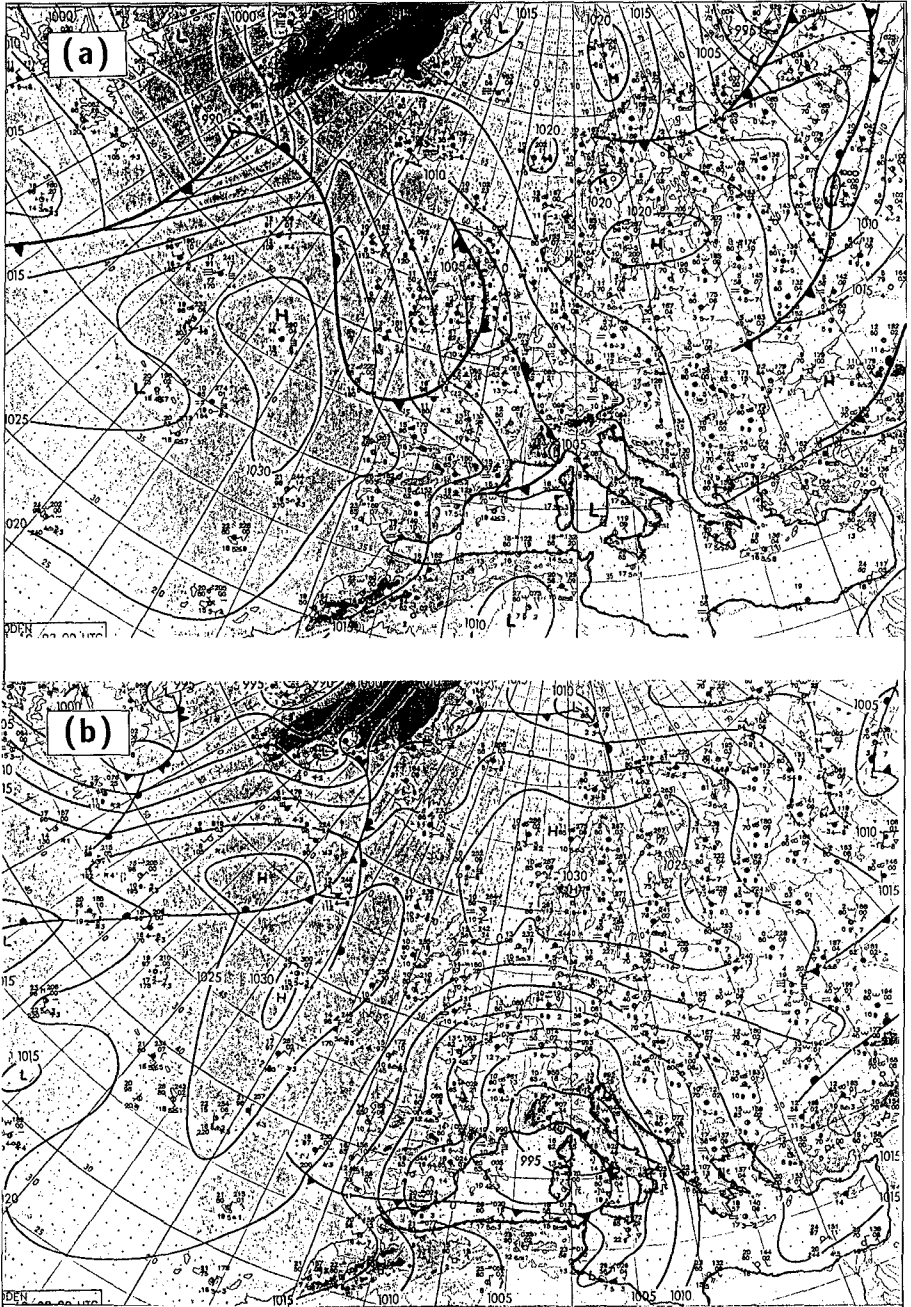
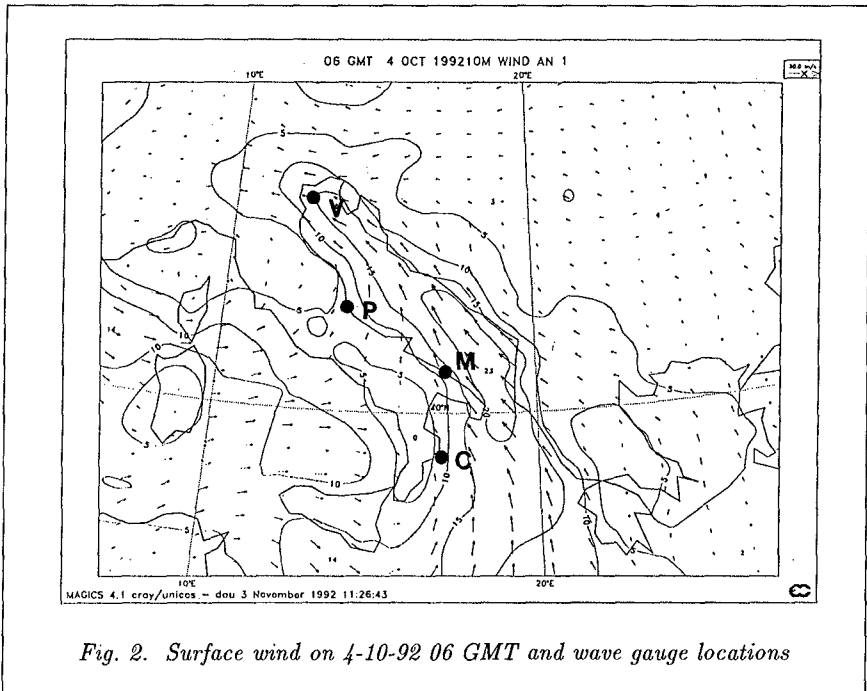


Fig. 1. Weather map at 3-10-92 (a) and 4-10-92 00 UTC (b)

channeled the flow leading to an intense south-easterly wind all along the Adriatic Sea. This is well shown by the distribution of surface wind at 06 UTC 4 October '92 obtained with the meteorological model of the European Center for Medium Range Weather Forecasts, Reading, U.K. (see figure 2).

Wave reacted rapidly. The peak conditions were reached in the first 12 hours of 4 October, with significant wave height  $H_s = 2.0$  m at Pescara, in the mid Adriatic, and  $H_s = 3.4$  m at the oceanic platform of ISDGM, 8 miles off the coast of Venice. The two positions, together with the more southerly Monopoli location in the Adriatic Sea and Crotone in the Ionian coast, are indicated by black dots in figure 2. Figure 3 shows the time series of  $H_s$  at these four locations throughout the storm.



*Fig. 2. Surface wind on 4-10-92 06 GMT and wave gauge locations*

The later decrease of wind speed, following the expansion and filling of the atmospheric low, left in the Adriatic Sea a swell propagating towards North-West, clearly recognizable in the records of figure 3.

### The storm surge in Venice

On Sunday the 4th, at neap tide, without any storm surge, a maximum level of 40 cm due only to the astronomical tide was expected at Punta della Salute, but because of the strong wind along the Adriatic Sea and the local atmospheric low pressure the water level reached 119 cm, with a storm surge component of about 80 cm (see figure 4).

Due to the persistent meteorological conditions, the water level raised on

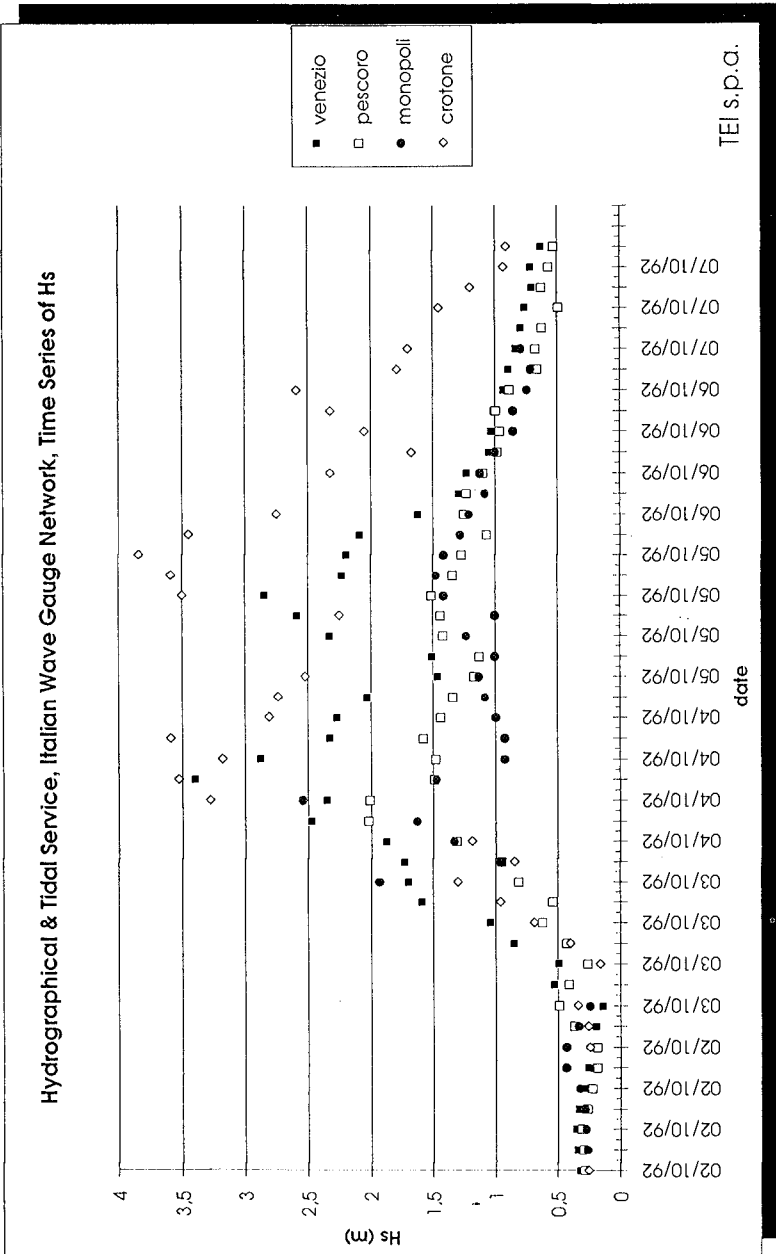


Fig. 3. Time history of recorded wave height in the Adriatic Sea



the following day, the first day of the Conference, flooding the town since 6 am. The flood lasted almost five hours till 11 am reaching the maximum level of 126 cm at 9 am just in time for the opening lecture. During the peak San Marco Square was covered by 46 cm of water and 50 % of the town was flooded.

Should the storm surge have occurred in a spring tide period, when the normal high water level is 75 cm, the water would have been 35 cm higher and the flood would have reached 80% of the town (cf. figure 5).

### The effects

The flood caused more damages and delays than usual due to the peculiar time of occurrence: early on Monday morning, following immediately a holiday. Visitors in particular had difficulties in getting a pair of boots and the 120 cm high walk-ways were not high enough to give a dry passage to the people without boots.

Photo 1 gives you a "look of the quay" near San Marco Square on Monday morning. On the opposite side of the channel participants in the Conference were entering Fondazione Cini with some trouble, cf. photo 2.

Notwithstanding the surprise of participants in the Conference, the flood on Monday October the 5th was not an exceptional one. During the years 1980-'89 this level was exceeded twelve times (cf. figure 5) and its return period is close to one year.

Comparing this flood to historical records, the water depth reached in San Marco Square was just one third of that reached on November 4th 1966, when the most severe recorded flood reached 114 cm water depth in San Marco Square (194 cm recorded water level).

The Conference event was actually much more unexpected than his bare return period tells. Actually most events occurs in late fall and winter and near spring tide and the return period of the "unexpected" storm surge is about 5 years. The storm surge may be decomposed into a quasi static component and in a seiche component, whose main period is ~ 21 hr. During sunday and monday the seiche component was in phase with the astronomical tide; in the following days the seiche amplitude was decreasing and the phase was lost, determining a rapid reduction of high water level.

Subsidence has some influence on the effects of high storm surge events. The reference level above which tide is measured in Venice is the mean sea level in 1897. Nowadays the mean sea level as a consequence mainly of subsidence is about 22 cm above datum and increases at the approximate rate of 0.1 cm/year.

	Normal spring tide	4 Nov. '66	5 Oct. '92	Normal "acqua alta"
Mean sea level	22	20	22	22
Astronomical tide	50	25	20	38
Storm surge	-	150	84	60
quasi static	-	100	40	30
seiche	-	50	44	30

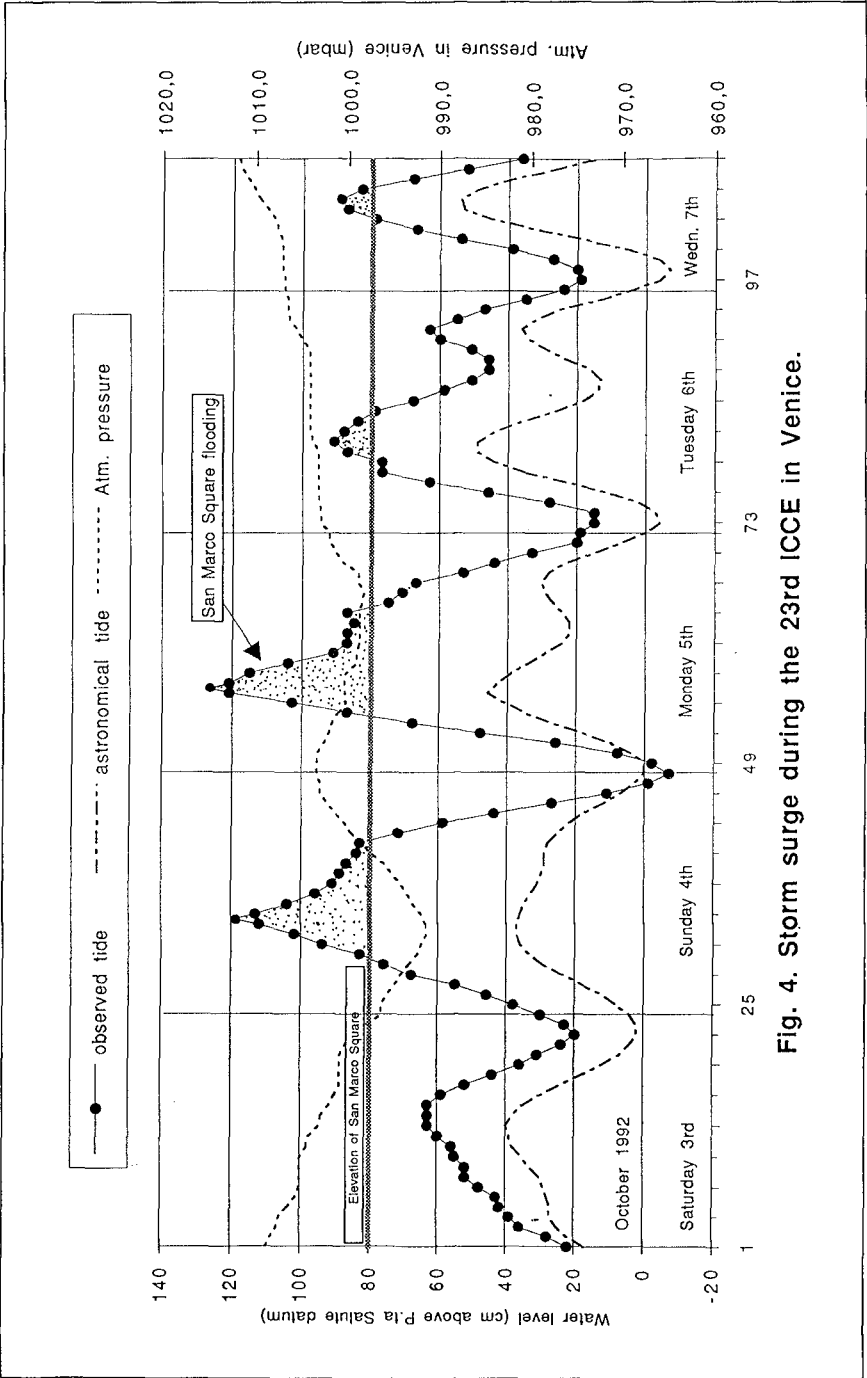


Fig. 4. Storm surge during the 23rd ICCE in Venice.



*Photo 1. San Giorgio Island from San Marco Square on Monday morning*

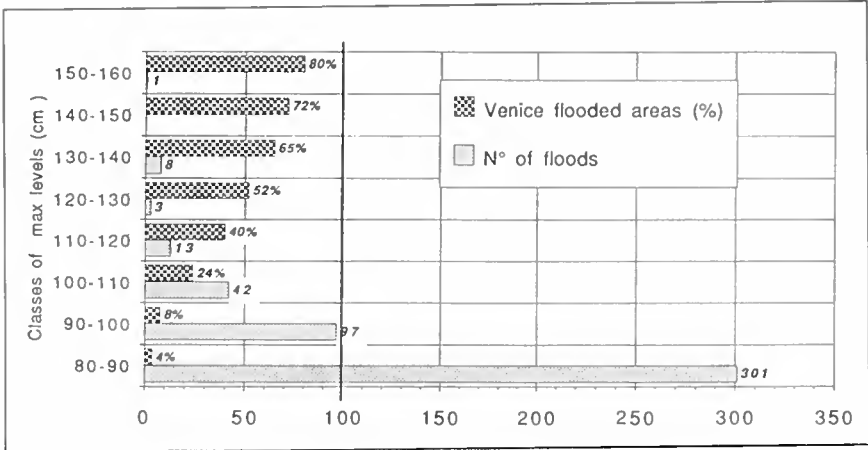


Fig. 5. Number of floods in Venice in the ten years from 1980 to '89



Photo 2. Delegates entering Fondazione Cini on Monday morning



## SUBJECT INDEX

Page number refers to first page of paper

- Absorbers, 281, 726  
Access roads, 2745  
Accretion, 1129, 2205, 2233, 3260, 3357  
Accuracy, 212, 460, 590, 777  
Adaptive systems, 551  
Advection, 2500  
Aeolian sands, 3319  
Aerial photographs, 2332, 2450  
Aggradation, 4  
Air entrainment, 1639  
Air water interactions, 308  
Amplification, 3343  
Amplitude, 804  
Analog models, 1869  
Analysis, 267, 1414  
Analytical techniques, 737, 1341, 2122, 3343  
Application methods, 212  
Approximation methods, 644  
Armor units, 1053, 1091, 1285, 1341, 1400, 1679  
Atmospheric boundary layers, 874  
Attenuation, 563, 2786  
Australia, 240, 1129, 3319
- Backwashing, 2358  
Barges, 3149  
Barrier design, 1851, 2694  
Bars, 51, 2001, 2219, 2370, 2745  
Bathymetry, 391, 2242  
Bayesian analysis, 62, 281  
Beach cusps, 2205  
Beach erosion, 792, 1272, 1400, 1959, 2057, 2136, 2219, 2556, 2772, 3331, 3426  
Beach nourishment, 1129, 2043, 2265, 2464, 2474, 2581, 3305, 3319  
Beaches, 240, 630, 883, 974, 1461, 1924, 1973, 2219, 2358, 3357  
Bed load movement, 2084  
Bed movements, 2321, 2370, 2917  
Bed ripples, 2164, 2383, 2424  
Berms, 1161, 1203, 1448, 1651, 1758, 2136  
Blocks, 1091  
Boston, 3285
- Boulders, 1078  
Boundary conditions, 142, 644, 1030  
Boundary element method, 253, 526, 1189, 1327, 1461, 1599, 1799  
Boundary layer, 350, 2397, 2424, 2629, 2811, 3189  
Boundary shear, 1517  
Boundary value problems, 672  
Brazil, 551  
Breaking, 960, 990, 1461, 2001  
Breaking waves, 42, 89, 103, 156, 240, 253, 419, 488, 576, 698, 918, 1078, 1101, 1357, 1545, 1772, 1785, 1910, 1973, 2043, 2095, 2279, 2321, 2344, 2642, 3012  
Breakwaters, 170, 792, 1006, 1020, 1044, 1053, 1067, 1101, 1115, 1153, 1161, 1189, 1203, 1258, 1299, 1313, 1327, 1357, 1400, 1420, 1489, 1531, 1559, 1613, 1679, 1959, 3343, 3399  
Bubbles, 1639, 1785  
Buoyancy, 1867  
Buoys, 405, 1840
- Caissons, 1475, 1625  
Calibration, 76  
California, 1285  
Canada, 3230  
Channel improvements, 2724  
Channels, waterways, 2786, 2879, 3040  
Characteristics, 253, 281, 295  
Circulation, 2122  
Classification, 1545, 1896  
Closed form solutions, 907  
Cnoidal waves, 737  
Coastal engineering, 1  
Coastal environment, 3496  
Coastal structures, 1758, 1772, 1785, 2599, 2799  
Cohesive sediment, 3107, 3121  
Columbia River, 2893  
Comparative studies, 62, 76, 1651, 2108  
Computation, 89, 1734  
Computer models, 1420, 1448  
Computer programs, 3260  
Concrete blocks, 1573

- Consolidation, 2962  
Consolidation, soils, 2949  
Construction, 2029, 2599, 2926, 3149, 3285, 3305  
Correlation analysis, 378, 737, 946, 974  
Cost effectiveness, 1503  
Currents, 184, 563, 604, 618, 672, 684, 698, 712, 1938, 2015, 2500, 2528, 2542, 2567, 2613, 2629, 2680, 2724, 2799, 2811, 2839, 2867, 2893, 2937, 3093, 3163, 3246  
Curvature, 184  
Cylinders, 2867
- Damage accumulation, 1420  
Damage assessment, 1020, 1679  
Damage prevention, 1006, 1091  
Dams, 2669  
Data analysis, 1067, 1666, 1812, 1840, 1867, 1987, 2057, 2136, 2265, 2397, 2567, 2599, 2745, 2962, 3371  
Data collection, 1910, 2191, 2251  
Decomposition, 51, 526, 777  
Deep water, 184, 322, 364, 630, 658, 1231, 1625  
Depth, 4, 846  
Design, 1503, 1613, 2029, 2474, 2599, 3285  
Design criteria, 1115, 1217, 1385, 1489  
Design data, 1357, 1625  
Design improvements, 1053, 1371  
Design waves, 644, 1851  
Development, 1840  
Diffraction, 129, 1044  
Diffusion, 3202  
Dikes, 526  
Dimensional analysis, 1231  
Dispersion, 42, 2735, 2758, 3189  
Displacements, 1448  
Dissipation, 1613  
Distribution patterns, 103, 308  
Dolos, 1231, 1285, 1385  
Drainage systems, 1129  
Dredging, 2629, 2724  
Dunes, 2669  
Dynamic analysis, 1357, 1475  
Dynamic response, 1475
- Earthquake loads, 3343  
Ecosystems, 2710  
Efficiency, 726, 1371, 1613, 1959  
Eigenvectors, 62  
Elevation, 240  
Empirical equations, 1559  
Energy conservation, 1245  
Energy dissipation, 103, 308, 336, 502, 540, 563, 1101, 2786  
Energy losses, 1313, 1517, 3040  
Energy transfer, 336, 460, 526  
Entrainment, 308, 336, 2500  
Equations of motion, 76, 391, 474  
Equilibrium profile, 1973, 2556  
Equipment, 295  
Erosion, 4, 1812, 2205, 2265, 2464, 2669, 2937, 2976, 3260, 3273  
Erosion control, 1748, 2581, 3081, 3246, 3331, 3385, 3413  
Estimates, 62, 512  
Estuaries, 2542, 2745, 2879, 2962, 3054, 3121, 3371  
Evaluation, 432, 2043  
Evolution, development, 42  
Examination, 267, 1896, 2370, 3357, 3399  
Experimental data, 308, 378, 405, 447, 540, 604, 974, 1044, 1161, 1258, 1503, 1559, 1613, 1959, 2015, 2279, 2642, 2772, 2917, 3163  
Experimentation, 488, 576, 2358
- Failure modes, 1006  
Failures, investigations, 1053, 3343  
Fatigue, 1354  
Feasibility studies, 2581  
Fiber optics, 1327  
Field investigations, 2486, 2694, 2879, 2949  
Field tests, 240, 488, 590, 804, 832, 846, 894, 907, 946, 990, 1175, 1420, 1587, 1625, 1734, 1867, 1879, 1924, 1987, 2043, 2164, 2176, 2205, 2293, 2307, 2397, 2528, 2542, 3026, 3230  
Finite difference method, 860  
Finite element method, 1599, 1706, 2902, 3068  
Flexibility, 1613, 1748  
Flocculants, 3178  
Flood control, 1851  
Flooding, 3496  
Floods, 2917  
Florida, 2057  
Flow, 76, 2150, 2655  
Flow characteristics, 698, 3482

- Flow distribution, 1720  
Flow patterns, 1938  
Flow resistance, 1101, 1153  
Flow simulation, 170, 1030  
Fluid dynamics, 1938  
Flumes, 142, 419, 447, 502, 818, 1067,  
1142, 2108  
Force, 1078  
Forecasting, 116, 1826, 1865, 2057,  
2176, 2242, 2293, 2513, 2825, 2902  
France, 1414  
Free surfaces, 89  
Frequency, 364, 391, 832, 918, 1639  
Frequency analysis, 156, 322, 447, 474,  
846  
Frequency distribution, 894  
Friction, 350, 960, 1217, 2786  
Full-scale tests, 1573, 1748, 2084
- Gabions, 1748  
Gaging stations, 295  
Gas pipelines, 2029  
Germany, 1573  
Grain size, 2071, 2251, 2293  
Gravity waves, 184  
Great Britain, 1987  
Great Lakes, 2976  
Groins, structures, 2332, 3357  
Growth projections, 2655  
Gulf of Mexico, 2629  
Gulfs, 712
- Harbor engineering, 295  
Harbors, 804, 832, 1044, 3081, 3216,  
3230  
Headwalls, 3426  
Hurricanes, 644  
Hydraulic models, 281, 1217, 1272,  
1341, 1475, 1531, 1879  
Hydraulic pressure, 1217  
Hydraulic structures, 1693  
Hydrodynamics, 1869, 2233, 3068, 3454
- Impact forces, 1545, 1785  
Impact loads, 1475  
Impact tests, 1067  
Instrumentation, 405, 1666, 2191  
Intake structures, 3107  
Integral equations, 142  
Interactions, 184, 460, 604, 672, 712,  
1924, 2710  
Islands, 2450
- Israel, 322, 3399  
Italy, 1826, 1840, 1851, 1865, 1867,  
1869, 3305, 3413
- Japan, 2486, 3331, 3426  
Jetties, 3040
- Kinematics, 618, 644, 1327
- Laboratories, 212, 281, 336, 488  
Laboratory tests, 630, 658, 792, 883,  
960, 1101, 1175, 1313, 1400, 1489,  
1734, 1947, 2001, 2176, 2191,  
2411, 2438, 2500, 2528, 2976, 3468  
Lagoons, 4, 1812, 1826, 1851, 1865,  
1867, 1869, 1879  
Landfall, 2029  
Lasers, 308  
Least squares method, 777  
Limiting factors, 551  
Linear analysis, 184  
Linear functions, 460  
Liquefaction, 2937  
Littoral currents, 2642, 2655, 2758,  
2999, 3012  
Long waves, 447, 792, 804, 832, 860,  
883, 960, 974, 2438, 2999
- Maintenance, 1006, 1693, 2745, 2926  
Mass transport, 3093  
Mathematical models, 502, 960, 1078,  
1639, 1865, 1869, 1879, 2613,  
2724, 2839  
Measurement, 618, 792, 818, 974, 1587,  
1651, 1758, 2084, 2279, 2321,  
2358, 2383, 2542, 2825, 3026, 3178  
Measuring instruments, 212, 295  
Mechanical engineering, 1693  
Meteorology, 116, 3496  
Mining, 3331  
Mixing, 1867, 2642, 2758, 2853, 2999,  
3202  
Model tests, 1020, 1115, 1231, 1245,  
1434, 1489, 1545, 2669, 3454  
Model verification, 2567  
Modeling, 1947, 2893, 3121, 3202  
Models, 42, 51, 116, 364, 474, 576, 698,  
712, 860, 1203, 1812, 1973, 2108,  
2122, 2150, 3012, 3054, 3081  
Monitoring, 1006, 1285, 1420, 1666,  
2332, 3305, 3319, 3385  
Mooring, 3216



- Morphology, 1812  
 Mud, 2735, 2879, 2937, 2962, 3093  
  
 Nearshore circulation, 226, 364, 860,  
     2758, 2811, 2825  
 Netherlands, 2474, 2581, 2599  
 Network analysis, 1840  
 New York, State of, 3357  
 Nile River, 3246, 3260, 3273  
 Nonlinear analysis, 350  
 Nonlinear differential equations, 460  
 Nonlinear response, 156  
 North Carolina, 2219  
 North Sea, 874, 2029, 2307  
 Numerical analysis, 142, 322, 712,  
     1531, 2450  
 Numerical calculations, 540, 737, 946,  
     1161, 2424  
 Numerical models, 51, 62, 76, 89, 129,  
     170, 199, 350, 391, 419, 432, 526,  
     590, 672, 818, 874, 1189, 1299,  
     1599, 1651, 1772, 1799, 1840,  
     1938, 2057, 2150, 2344, 2411,  
     2438, 2513, 2556, 2825, 2879,  
     2949, 3093, 3107, 3305  
  
 Ocean disposal, 2735  
 Ocean waves, 2893, 3496  
 Offshore structures, 512, 551  
 Oil storage, 2724  
 One dimensional flow, 777  
 Optimization, 1503, 1693  
 Oregon, 2191, 2242, 2332  
 Oscillations, 502, 1639, 1826, 1865,  
     2655, 2990  
 Oscillatory flow, 604, 1896, 2122, 2424  
 Outfall sewers, 3285  
 Outwash, 2694  
 Overflow, 2669  
 Overtopping, 1758, 2694  
  
 Parameters, 765, 946  
 Particle full velocity, 212, 336, 1651  
 Pendulums, 1475  
 Permeability, 1299, 1517, 1531, 2962  
 Permeability tests, 1587, 1720  
 Perturbation, 684  
 Physical properties, 378, 1587  
 Pipelines, 2839, 2990, 3135  
 Planning, 1693  
 Pollution, 4  
 Pollution control, 3285  
  
 Pore pressure, 1706, 3135  
 Pore pressure measurement, 2962  
 Pore water, 2095  
 Pore water pressure, 2397  
 Porous materials, 170, 726, 1101, 1189,  
     1434, 1706  
 Porous media flow, 1772  
 Ports, 2926  
 Portugal, 2745  
 Potential flow, 89  
 Power plant location, 3413  
 Predictions, 474, 644, 932, 1189, 1420,  
     1938, 2219, 2464, 2556, 2724  
 Pressure distribution, 1545, 1599, 1706  
 Pressure measurement, 1573, 1785  
 Pressures, 1078, 1161, 1175, 2095  
 Probabilistic methods, 512  
 Probabilistic models, 540  
 Probability distribution, 103, 378, 932  
 Probability distribution functions, 2001  
 Profile measurement, 1559, 2513, 2694,  
     3260  
 Profiles, 2108, 2242, 2358, 2474, 3273  
 Progressive waves, 281, 684, 726  
 Prototype tests, 1067  
  
 Quality assurance, 1354  
 Quantitative analysis, 918, 1115, 2464,  
     2990  
  
 Random waves, 51, 447, 474, 526, 540,  
     630, 658, 751, 765, 883, 932, 1559,  
     1910, 1959, 2307, 2411, 2825  
 Rayleigh waves, 894  
 Reflection, 765, 777, 1142, 1625  
 Refraction, 129, 846, 1020, 1044  
 Regression analysis, 253  
 Rehabilitation, 1341  
 Reliability analysis, 1385  
 Research, 1987, 2937  
 Research and development, 1414  
 Resistance, 1091, 1371  
 Resonance, 751, 860  
 Revetments, 1030, 1175, 1299, 1573,  
     1587  
 Reviews, 2839, 2949  
 Reynolds number, 1720, 2015, 2122  
 Reynolds stress, 2424, 2853  
 Rheology, 3093  
 Risk analysis, 1341  
 Rivers, 240, 2486, 2772  
 Rock strength, 1448

- Roughness, 1758  
 Rubble-mound breakwaters, 1203, 1217,  
     1354, 1371, 1434, 1489, 1503,  
     1531, 1599, 1666, 1706, 1720,  
     1799, 3149  
 Safety analysis, 3216  
 Sand, 2599, 3331, 3426  
 Scattering, 1142, 1258, 3149  
 Scouring, 2799, 2839, 2867, 3482  
 Sea floor, 846, 2095, 2307, 2397, 2990,  
     3135, 3482  
 Sea state, 267, 512, 907  
 Sea walls, 1272, 1734, 1879, 1924  
 Seasonal variations, 2242, 2251, 2265,  
     2450  
 Sediment, 1812, 2205, 2251  
 Sediment concentration, 1910, 1947,  
     2321, 2613, 2680, 2853, 3026, 3202  
 Sediment discharge, 3054, 3202  
 Sediment transport, 832, 1272, 1865,  
     1896, 1910, 1947, 1973, 1987,  
     2015, 2071, 2084, 2108, 2150,  
     2164, 2176, 2191, 2307, 2344,  
     2370, 2411, 2450, 2486, 2500,  
     2513, 2528, 2542, 2567, 2613,  
     2629, 2669, 2680, 2867, 2879,  
     2902, 2917, 3121, 3189, 3273, 3385  
 Sedimentation, 2724, 2949, 3081  
 Sedimentology, 3399  
 Settling velocity, 2853, 3107, 3202  
 Shallow water, 267, 322, 364, 460, 818,  
     1613, 3068  
 Shear, 618, 684, 2642, 2655, 2999, 3189  
 Shear strain, 3163  
 Shear stress, 604, 672, 2164, 2176,  
     2917, 3012, 3093, 3107  
 Shearing, 184  
 Ship motion, 3216  
 Ships, 3216  
 Shoaling, 51, 199, 432, 460  
 Shore protection, 1272, 1414, 1879,  
     2710, 3413  
 Shoreline changes, 2233, 2265, 2332,  
     2772, 2976, 3246, 3273, 3305,  
     3399, 3413  
 Silts, 2879, 2926  
 Simulation, 62, 199, 576, 1101, 1142,  
     1772, 2307, 2902  
 Simulation models, 42, 405, 1531  
 Site selection, 2926  
 Skewness, 974  
 Slopes, 488, 1461  
 Solitary wave, 1161, 1327, 1461  
 South Africa, 3026  
 Spain, 2043, 2233, 2251, 2265, 3385  
 Spectral analysis, 364, 765, 777, 792,  
     1973  
 Spectral density function, 42  
 Speed changes, 199  
 Spits, coastal, 2233, 2694  
 Splitting, 658  
 Stability, 751, 1020, 1030, 1053, 1067,  
     1153, 1217, 1231, 1400, 1559,  
     1625, 1666, 1799, 2095, 2581, 3135  
 Stability analysis, 129, 658, 1573, 1679,  
     2071  
 Stability criteria, 1203, 2799  
 Stabilization, 1129, 2556, 3319, 3426  
 Static stress measurement, 1285  
 Stationary processes, 932  
 Statistical analysis, 512, 1231, 1545,  
     1924, 2474, 3149  
 Stones, 1354  
 Storm surges, 1851  
 Storms, 116, 990, 1748, 2136, 2370,  
     2450  
 Stratification, 2853  
 Stream function, 684  
 Stress, 1053  
 Stress analysis, 874  
 Stress measurement, 1385  
 Structural design, 1285, 1385, 1414  
 Structural failures, 1203  
 Structural materials, 170  
 Structural response, 1371  
 Structural stability, 1115  
 Structures, 765  
 Submerged jets, 1161  
 Submerging, 253, 1142  
 Subsidence, 4  
 Superstructures, 1217, 1489  
 Surf beat, 804, 846, 960  
 Surf zone, 76, 103, 156, 226, 308, 336,  
     576, 590, 698, 818, 832, 883, 918,  
     990, 1987, 2095, 2279, 2293, 2321,  
     2344, 2370, 2438, 2542, 2642,  
     2680, 2811, 2999, 3012, 3026  
 Surface properties, 563  
 Surface roughness, 1720  
 Surface waves, 405, 658, 3135, 3163  
 Surge, 874  
 Surveys, 2043, 2450, 2567, 3026  
 Surveys, data collection, 1129, 2029,

- 2136, 2219, 3260  
 Suspended load, 1091, 2411  
 Suspended sediments, 2150, 2279, 2293, 2438, 2680, 3189  
 Testing, 1354  
 Tests, 226, 364, 447, 1910, 2383  
 Theories, 737, 1258, 1313, 1693, 2071, 2735, 2772, 2867, 3468  
 Three-dimensional analysis, 3482  
 Three-dimensional flow, 3454  
 Three-dimensional models, 1679  
 Tidal currents, 3054  
 Tidal hydraulics, 1826  
 Tides, 4, 3178, 3371  
 Tides, astronomical, 1826  
 Time dependence, 391, 419, 2464, 2513  
 Topography, 129, 860  
 Tracers, 2084  
 Transformations, 51, 156, 474, 540, 630  
 Transient flow, 142  
 Transition points, 698  
 Transport phenomena, 3068  
 Transport rate, 2528  
 Trenches, 2902  
 Trends, 3371  
 Turbidity, 1938, 2735, 3121, 3178  
 Turbulence, 2279, 2383, 2424, 2629, 2758, 2853  
 Turbulent flow, 1517  
 Turkey, 3081  
 Undertow, 883, 2164  
 United Kingdom, 2694, 3178, 3371  
 Uplift pressure, 3135  
 Uplift resistance, 1573  
 U.S.S.R., 1357  
 Validation, 1448, 3468  
 Vector analysis, 2344  
 Vegetation, 2710  
 Velocity, 350, 604, 618, 672, 1078, 1799, 1947, 2084, 2321, 2383, 2486, 2990, 3054  
 Velocity distribution, 883, 1153, 2811, 3482  
 Venezuela, 2724  
 Verification inspection, 2867  
 Vertical cylinders, 3482  
 Videotape, 918  
 Vortex shedding, 3163  
 Vortices, 502  
 Water circulation, 3068  
 Water depth, 726, 832  
 Water flow, 502, 1865, 1869  
 Water level fluctuations, 1666  
 Water pressure, 1666  
 Water surface, 576  
 Water table, 1129, 2136  
 Water tanks, 2191  
 Wave action, 1030, 1203, 1420, 1599, 1706, 1799, 1896  
 Wave attenuation, 1517  
 Wave climatology, 267  
 Wave crest, 199, 488  
 Wave damping, 3040  
 Wave diffraction, 419, 432  
 Wave dispersion, 1434  
 Wave energy, 336, 502, 1189, 1434, 2528  
 Wave forces, 1313, 1357, 1400, 1489, 1639, 3454  
 Wave generation, 818, 990, 2893, 3468  
 Wave groups, 894, 907, 932, 946, 990, 1503, 2411  
 Wave height, 103, 253, 378, 512, 576, 630, 751, 804, 894, 946, 1245, 1734, 2001, 2486, 3230, 3385  
 Wave measurement, 226, 322, 551, 2205, 3230  
 Wave propagation, 89, 129, 142, 226, 391, 447, 460, 563, 658, 792, 1020, 1044, 1142, 1153, 1461, 2500, 2786, 2893, 3040  
 Wave reflection, 630, 1299, 1327  
 Wave refraction, 419, 432  
 Wave runup, 156, 1245, 1299, 1461, 1734, 1758, 1772  
 Wave spectra, 378, 405, 590, 751, 765, 2001  
 Wave tanks, 226, 526  
 Wave velocity, 2358  
 Waves, 1175, 1258, 2015, 2071, 2542, 2567, 2613, 2629, 2710, 2799, 2811, 2839, 2937, 2976, 3093, 3246, 3454, 3468, 3496  
 Weather forecasting, 116  
 Wind, 907  
 Wind forces, 3496  
 Wind speed, 1245  
 Wind waves, 712  
 Working conditions, 3230

## AUTHOR INDEX

Page number refers to first page of paper

- Abecasis, F., 1006  
Adami, Attilio, 1869  
Ahrens, J. P., 1354  
Alexis, Alain, 2949  
Allsop, N. W. H., 1599  
Andersen, O. H., 1020  
Arami, Atsusi, 1785  
Asano, Toshiyuki, 1896, 2710
- Baird, W. F., 1354  
Bakker, W. T., 2599  
Bale, A. J., 3178  
Barbaro, Giuseppe, 907  
Barkaszi, Stephen F., Jr., 1910  
Basco, David R., 103, 1924  
Bassoullet, Philippe, 2949  
Battjes, J. A., 42, 51  
Baumer, Joe, 103  
Bedford, Keith, 2629  
Beji, S., 42, 51  
Bellessort, B., 1414  
Bellomo, Douglas A., 1924  
Benoit, Michel, 62  
Berlamont, Jean, 2962  
Bertotti, Luciana, 116  
Bezuijen, Adam, 1030, 1587  
Bishop, Craig, 2976  
Blondeaux, Paolo, 2071  
Boccotti, Paolo, 907  
Boer, Sander, 3305  
Booij, N., 1044  
Bowers, E. C., 832  
Bradbury, A. P., 2694  
Breteler, Mark Klein, 1030  
Brocchini, M., 76  
Broekens, R. D., 1772  
Broeze, Jan, 89  
Brooks, P., 3285  
Brørs, Bård, 1938  
Bruce, T., 212, 2990  
Burcharth, H. F., 1354, 1720  
Burcharth, Hans F., 1489  
Burcharth, Hans. F., 1053  
Bürger, W. W., 1067
- Cai, Maolong, 103  
Caielli, Alfredo, 1869  
Capobianco, Michele, 2464
- Carrion, Vicente, 3385  
Carson, Fulton C., 3357  
Carvalho, J. L. B., 551  
Castañeda, Ana, 3385  
Cavaleri, L., 1840  
Cavaleri, Luigi, 116  
Cecconi, Giovanni, 1869  
Chae, Jang Won, 129  
Chang, C., 1327  
Chen, Zhiwen, 1947  
Cheung, Kwok Fai, 142  
Chiaia, G., 1959  
Chian, Chimin, 3189  
Chow, K. Ander, 3230  
Chung, Yeong Chyang, 308  
Church, J. C., 2999, 3012  
Chyan, Jih Ming, 308  
Collado, F., 2811  
Converse, H. D., 1354  
Cooker, M. J., 1078, 1639  
Coppoolse, R. C., 3026  
Costa, Fernando Vasco, 1091  
Cox, D. T., 2397  
Cox, Daniel T., 156  
Cramp, A., 974, 1987  
Creed, Christopher G., 1973  
Cruz, Eric C., 1101  
Cuenca, G., 2043
- Dally, William R., 1910  
D'Alpaos, L., 3068  
Dalrymple, R. A., 3468  
Dalrymple, Robert A., 1142, 1973, 3040  
Damiani, L., 1959  
d'Angremond, Kees, 1748  
Davidson, D. D., 1354  
Davidson, M., 974  
Davidson, M. A., 1987  
Davies, B. L., 1115  
Davis, Greg A., 1129  
De Boni, M., 1840  
De Girolamo, Paolo, 1851  
de Groot, M. B., 2599  
de Jager, Jan H., 1748  
de Lange, P. H. M., 1044  
De Rouck, J., 1666  
de Ruig, Joost H. M., 2581  
de Vriend, Huib J., 2150

- De Vriend, Huib J., 2464  
 de Waal, J. P., 1758  
 de Wit, P. J., 2937  
 Dean, R. G., 3260  
 Dean, Robert G., 2001  
 Debus, Wolf, 1573  
 Deguchi, Hiroshi, 2710  
 Deguchi, Ichiro, 1517, 2642  
 Deigaard, R., 576, 2344  
 den Adel, H., 1720  
 Dennis, W. A., 2332  
 Di Silvio, G., 1865, 1867  
 Dibajnia, Mohammad, 2015  
 Dodd, Nicholas, 2655  
 Drago, M., 76  
 Drapeau, G., 3054  
 Driscoll, Andrew M., 1142  
 Dumais, J. F., 3054  
 Dyer, K. R., 3178
- Easson, W. J., 618, 2990  
 Edge, B., 1354  
 Eide, A., 2029  
 Eidsvik, Karl J., 1938  
 Eisenberg, Y., 3285  
 Elgar, Steve, 846  
 Elwany, M. Hany S., 3273  
 Elzinga, Th., 3216  
 Endoh, Hiroshi, 1625
- Fanos, A. M., 3246, 3260  
 Fernández, A. J., 2043  
 Ferrante, Andrea, 3305  
 Fischer, M., 170  
 Fisher, J. S., 2332  
 Foote, Y., 974  
 Foster, Emmett R., 2057  
 Foti, Enrico, 2071  
 Fournier, Charles P., 3230  
 Franco, Leopoldo, 1879, 3305  
 Fredsøe, J., 2344, 2839  
 Fujima, Koji, 2450  
 Funke, E. R., 3454
- Gallagher, E. L., 2084  
 Galland, J. C., 2853  
 García, Reinaldo, 2724  
 Garzon, A., 3068  
 Gerber, Marius, 184  
 Goda, Yoshimi, 199  
 Gökçe, K. Tunç, 3081  
 Golik, A., 322
- Golik, Abraham, 3273  
 Gomez-Pina, G., 1679  
 Gordon, Angus D., 3319  
 Graber, H. C., 405  
 Grass, Tony J., 604  
 Graw, Kai-Uwe, 1153  
 Greated, C. A., 212  
 Greated, Clive A., 502, 2358  
 Grilli, S. T., 1461  
 Grilli, Stéphan T., 1142, 1161  
 Grüne, Joachim, 1175  
 Gu, George Z., 1189  
 Güler, İşikhan, 3081  
 Günbak, A. Rıza, 3081  
 Guza, R. T., 846
- Habara, Shin, 3426  
 Hall, Kevin R., 1203, 1217  
 Hamanaka, Ken-ichiro, 2424  
 Hamilton, David G., 1217  
 Hamm, Luc, 226, 2108  
 Hansen, C. P., 551  
 Hansen, E. A., 2344  
 Hanslow, David J., 240, 1129  
 Hara, Masanori, 253  
 Hardisty, J., 974, 1987  
 Harris, J. M., 2307  
 Hashida, M., 3331  
 Hatada, Yoshio, 267  
 Hatanaka, K., 2095  
 Hattori, A., 2095  
 Hattori, Masataro, 1785  
 Hayashi, Kenjiro, 2450  
 Hedegaard, Ida Brøker, 2108  
 Herbers, T. H. C., 846  
 Hibbert, Kevin, 1129  
 Hirakuchi, H., 281  
 Holman, R. A., 918  
 Holmes, P., 1448  
 Holthuijsen, L. H., 1044, 2893  
 Holtzhausen, A. H., 1231  
 Horikawa, Kiyoshi, 1734, 2122  
 Howell, Gary L., 295  
 Hughes, S. A., 1354  
 Huntley, D., 974  
 Huntley, D. A., 1987, 3178  
 Hurdle, David, 1851  
 Huynh, Trien N., 3093  
 Hwung, Hwung Hweng, 308
- Ikeno, M., 281  
 Imai, Sumio, 894

- Imberger, J., 1867  
 Inman, D. L., 322  
 Inman, Douglas L., 3273  
 Iosilevskii, Ya. A., 322  
 Iovenitti, L., 76  
 Iribarren, J. R., 3216  
 Irie, Isao, 2879  
 Isaacson, Michael, 142  
 Isobe, Masahiko, 419, 590, 765, 1101, 3093  
 Ito, Kazunori, 751  
 Iwata, K., 1400  
 Iwata, Koichiro, 336  
  
 Jaffe, Bruce, 2680  
 Jensen, O. J., 3216  
 Jeong, Shin Taek, 129  
 Jorissen, R. E., 1693  
 Juang, Jea-Tzyy, 1245  
 Juhl, J., 170, 1020  
 Jui, J., 1272  
  
 Kaczmarek, Leszek M., 350  
 Kaihatu, James M., 364, 1973  
 Kajima, R., 281, 1531  
 Kaku, Shuji, 1559  
 Kakuno, Shohachi, 1258  
 Kamphuis, J. W., 1272  
 Kanayama, Susumu, 3107  
 Kang, Yoon-Koo, 1503  
 Karlikow, Nancy, 3121  
 Kashiwagi, Mikio, 2438  
 Katayama, Hiroyuki, 883  
 Katoh, Kazumasa, 990, 2136, 2879  
 Katoh, Ken, 2735  
 Katopodi, Irene, 2150  
 Katsui, Hidehiro, 2867  
 Kawasaki, Masahiko, 3426  
 Kawata, Yoshiaki, 2164, 3426  
 Kendall, Thomas R., 1285  
 Khafagy, A. A., 3246, 3260  
 Khafagy, Ahmed A., 3273  
 Kim, H., 2307  
 Kim, Jong-Wook, 1503  
 Kimura, A., 378  
 Kimura, Akira, 3149  
 Kirby, James T., 364, 391, 474  
 Kitou, Nikos, 2150  
 Kiyokawa, Tetsushi, 1613  
 Kjeldsen, S. P., 405  
 Klammer, P., 1475  
 Klatter, H. E., 1693  
  
 Klopman, G., 1772  
 Kobayashi, Nobuhisa, 156, 1299, 1559, 2710  
 Kobayashi, Tomonao, 3482  
 Kochergin, Alexander D., 2176  
 Kohlhase, S., 1475  
 Komar, P. D., 3246  
 Komatsu, T., 3331  
 Kondo, Kosuke, 804, 894  
 Kostense, J. K., 960  
 Kos'yan, Ruben D., 2176  
 Kotake, Yasuo, 419  
 Kranenburg, C., 2937  
 Kraus, Nicholas C., 630, 2191, 2219, 3357  
 Kriebel, D. L., 1115  
 Kriebel, David L., 1313, 1973  
 Kroon, Aart, 2613  
 Kubo, Yasuhiro, 419, 804  
 Kuiper, H., 1693  
 Kurata, K., 1400  
 Kuroki, Keiji, 2205  
  
 Lahousse, B., 2029  
 Larson, Magnus, 2219  
 Latteux, B., 2500  
 Laurence, D., 2853  
 Lavallée, D., 3054  
 Le Hir, Pierre, 2949, 3121  
 Lechuga, Antonio, 2233  
 Lee, Changhoon, 391  
 Lee, J. J., 1327  
 Lee, Jongkook, 2629  
 Lee, Jung L., 432  
 Liang, Guoxiong, 2242  
 Liberatore, Gianfranco, 447  
 Ligteringen, H., 1341  
 Lima, J. M., 551  
 Lin, Li-Hwa, 2513  
 Lippmann, T. C., 918  
 List, Jeffrey H., 860  
 Liu, C. C., 726  
 Liu, Philip L.-F., 1258  
 Liu, Zhou, 1053  
 Losada, I. J., 2251, 2786  
 Losada, M. A., 1679, 2251, 2786  
 Losada, Miguel A., 1161, 2265  
  
 Madsen, P., 576  
 Madsen, Per A., 460  
 Magda, Waldemar, 3135  
 Magoon, O. T., 1354

- Malherbe, B., 2029  
 Mannino, Lucio, 907  
 Mansard, E. P. D., 1679, 3454, 3468  
 Mansard, Etienne, 142  
 Mansour-Tehrani, Mehrdad, 604  
 Marchi, Enrico, 4, 1869  
 Marinski, J. G., 1357  
 Martin, Francisco, 1161  
 Mase, H., 2397  
 Mase, Hajime, 474, 540  
 Mastenbroek, C., 874  
 Matsumi, Yoshiharu, 3149  
 Matsunaga, N., 3331  
 Matsunaga, Nobuhiro, 3163  
 McCabe, J. C., 3178  
 Medina, Josep R., 1371  
 Medina, R., 1679, 2251  
 Medina, Raúl, 2265  
 Medina Villaverde, José María, 2233  
 Mei, Chiang C., 3189  
 Melby, Jeffrey A., 1285, 1385  
 Memos, Constantine D., 3343  
 Mercanti, M., 2029  
 Miao, Gang, 2513  
 Miles, M. D., 3468  
 Miller, H. C., 2332  
 Mizuguchi, M., 488  
 Mizutani, N., 1400  
 Mizutani, Suguru, 2122  
 Mocke, G. P., 2279, 3026  
 Mol, A., 1812  
 Monadier, P., 1414  
 Mori, Nobuhito, 751  
 Morrison, Iain G., 502  
 Mulcahy, Michael W., 3230  
 Muraca, Alessandro, 1420  
 Murakami, Kazuo, 2879  
 Muttray, M., 1434  
  
 Nadaoka, K., 51  
 Nadaoka, Kazuo, 526, 2867  
 Naffaa, M. G., 3260  
 Nairn, Rob, 2976  
 Nakamura, Kazuo, 2293  
 Nakamura, Satoshi, 990  
 Nersesian, Gilbert K., 3357  
 Nicholls, Robert J., 2464  
 Nicholson, John, 2108  
 Nielsen, Peter, 240, 1129, 3202  
 Nishi, Ryuichiro, 2293  
 Nnadi, Fidelia N., 2917  
 Noli, Alberto, 1851  
  
 Norton, P. A., 1448  
  
 Ochi, Michel K., 512  
 O'Connor, B. A., 2307  
 Oda, Kazuki, 1258  
 Oebius, H. U., 2307  
 Ohta, T., 378  
 Ohyama, T., 51  
 Ohyama, Takumi, 526, 1613  
 Okayasu, Akio, 883, 2438  
 Oliveira, I. B. Mota, 2745  
 Oltman-Shay, J., 2999  
 Omata, Atsushi, 1613  
 Ono, Masanobu, 2642  
 O'Reilly, W. C., 846  
 Organizing Committee of the 23rd  
 International Conference on Coastal  
 Engineering, 3496  
 Osborne, Philip D., 2321  
 Ostrowski, Rafal, 350  
 Otta, Ashwini, 1461  
 Oumeraci, H., 1357, 1434, 1475, 1545,  
 1706  
 Overton, M. F., 2332  
  
 Pae, Wi-Gwang, 540  
 Parchure, Trimbak M., 2001  
 Parente, C. E., 551  
 Parle, Patrick, 3371  
 Partensky, H. W., 1067, 1434, 1475  
 Partensky, H.-W., 1545  
 Passacantando, Giancarlo, 1851  
 Pechon, Philippe, 2108  
 Pedersen, C., 2344  
 Pedersen, Jan, 1489  
 Peña, Carlos, 3385  
 Peregrine, D. H., 1078, 1639  
 Peregrine, D. Howell, 818  
 Petit, H. A. H., 960, 1772  
 Petrillo, A., 1959  
 Petti, Marco, 447, 792  
 Pina, G. Gómez, 2043  
 Pita, C., 1006  
 Pollock, Cheryl, 1924  
 Powell, K. A., 2694  
 Powell, Keith A., 2358  
 Protonotarios, John N., 3343  
 Pruszk, Zbigniew, 2370  
 Putrevu, Uday, 2758, 2825  
  
 Quinn, Paul A., 2358

- Rakha, K. A., 1272  
Ramírez, J. L., 2043  
Ramos, F. Silveira, 1341  
Ranasoma, K. I. Mahesha, 2383  
Rasmussen, Chris, 391  
Rasmussen, E. B., 170  
Rauw, C. I., 1354  
Refaat, Hossam El-din A. A., 2772  
Rigter, Ben, 1587  
Rodríguez, A., 2811  
Roelse, Piet, 2581  
Roelvink, J. A., 960, 2108  
Roldán, A. J., 2786  
Roldan, Antonio J., 2265  
Ropert, F., 1414  
Rosen, D. S., 322  
Rosen, Dov S., 3399  
Rossi, Vito, 1420  
Rufin, T. M., Jr., 1400  
Ruol, Piero, 792  
Rusconi, A., 1840  
Russell, P., 974  
Russell, P. E., 1987  
Ryu, Cheong-Ro, 1503
- Saito, Eiichi, 2799  
Sakai, T., 2095, 2397  
Sakai, Tetsuo, 540  
Sakakibara, Yukio, 253  
Sakakiyama, T., 1531  
Sallenger, Asbury, Jr., 2680  
Sampaio, R. M., 551  
Sánchez-Arcilla, A., 2811  
Sato, Michio, 563, 2205, 2293  
Sato, Shinji, 2411  
Sato, Yukio, 2424  
Sawaragi, Toru, 1517, 2642  
Sayao, Otavio J., 3230  
Schäffer, H. A., 576  
Schäffer, Hemming A., 460  
Schmidt, R., 1545  
Schoonees, J. S., 3026  
Sekimoto, Tsunehiro, 804, 894  
Seymour, R. J., 2084  
Seymour, Richard J., 2242  
Shibano, Teruo, 3426  
Shibayama, Tomoya, 2438, 2799  
Shigemura, Toshiyuki, 2450  
Shimizu, T., 281  
Shimizu, Takuzo, 590, 804, 894, 3107  
Shinohara, Tomoaki, 2205  
Shirai, Toru, 2164
- Shuto, N., 672  
Shuto, Nobuo, 2486  
Silva, P., 1812  
Simonin, O., 2853  
Simons, Richard R., 604  
Skafel, Michael, 2976  
Skjelbreia, James E., 777  
Skyner, D. J., 212, 618  
Sleath, J. F. A., 2383  
Sloth, P., 1020  
Smidt, H.-J., 1067  
Smith, A. W. Sam, 1354  
Smith, Ernest R., 630  
Smith, G. G., 2279, 3026  
Smith, Jane McKee, 2191, 2825  
Smith, W. Gray, 1559  
Sobey, Rodney J., 644  
Sollitt, Charles K., 2191  
Sørensen, Ole R., 460  
Southgate, Howard, 2108  
Sparboom, Uwe, 1573  
Srinivas, Rajesh, 2001  
Stansberg, C. T., 658  
Steetzel, Henk J., 2669  
Stive, Marcel J. F., 2464  
Stoutjesdijk, Theo, 1587  
Sulisz, Wojciech, 1799  
Sumer, B. M., 2839  
Sun, Z. C., 1599  
Supharatid, S., 672  
Svendsen, Ib A., 1461, 2758, 2825  
Swan, Christopher, 684
- Takahashi, Shigeo, 1625  
Takehara, Kosci, 3163  
Tanaka, H., 672  
Tanaka, Hitoshi, 2486  
Tanaka, Masahiro, 1613  
Tanimoto, Katsutoshi, 1625  
Teatini, P., 1865  
Teisson, Ch., 2853  
Teisson, Charles, 2949  
Thieke, R. J., 698  
Thornton, E. B., 2999, 3012  
Thornton, Edward B., 2655  
Tolman, Hendrik L., 712  
Tomasicchio, Giuseppe R., 1879, 3413  
Tomasicchio, Ugo, 1  
Tomita, Takashi, 336  
Toorman, Erik, 2962  
Topliss, M. E., 1639  
Tørum, Alf, 1651



- Toue, Takao, 2867  
Treadwell, D. D., 1354  
Tsuchiya, Yoshito, 2164, 2556, 2772, 3426  
Tsuruya, Hiroichi, 2879  
Turk, George F., 1385  
Twu, S. W., 726
- Uda, Takaaki, 1613  
Ueda, Y., 2397  
Ueki, Kazuhiro, 3107  
Ukai, Akiyuki, 590  
Uliana, Fiore, 3413
- Valera, Eduardo, 2724  
Van Damme, L., 1666  
van den Berg, Egbert J. F., 1748  
Van den Bosch, Lut, 2962  
van den Bosch, P., 1772  
van der Lem, J. C., 1341  
van der Meer, J. W., 1758, 1772  
van Gent, Marcel, 1651  
van Rijn, Leo C., 2613  
van 't Hoff, J., 2599  
van Vledder, Gerbrant Ph., 946  
Verhagen, Henk Jan, 2474  
Verhagen, L. A., 2893  
Vermeir, D., 1666  
Verwoert, H., 2599  
Vidal, C., 1679, 2251  
Vidal, Cesar, 2265  
Viguier, J., 1414  
Villaret, C., 2500  
Villoria, Carlos, 2724  
Vincent, Christopher E., 2321  
Visser, Paul J., 2669  
Vithana, S. Opatha, 2902
- Vittori, Giovanna, 1826  
Vrijling, J. K., 1693
- Walsh, G., 3054  
Wang, Hsiang, 432, 1189, 2513  
Watanabe, Akira, 419, 765, 1101, 2015, 2528, 3093  
Watson, Gary, 818  
White, Thomas E., 2242  
Whitehouse, Richard J. S., 2542  
Wibbeler, H., 1706  
Williams, A. F., 1599, 1720  
Williams, J. J., 2307  
Wilson, Kenneth C., 2917  
Winterwerp, J. C., 2599  
Won, Y. S., 2893  
Wong, Y. K., 2307  
Wurjanto, Andojo, 156, 1299
- Yamaguchi, Masataka, 267, 737  
Yamamoto, Yoshimichi, 1734  
Yamashita, Takao, 2556, 3426  
Yan, Yixin, 2926  
Yanagishima, Shin-ichi, 2136  
Yasuda, Takashi, 253, 751  
Yauchi, Eiji, 2735  
Yen, Kai, 2926  
Yokoki, Hiromune, 765  
Yu, Ke, 932
- Zeidler, Ryszard B., 2370  
Zelt, J. A., 777  
Zhuang, F., 1327  
Zimmermann, C., 1434  
Zwamborn, J. A., 1231  
Zyserman, Julio A., 2567